European Community on Computational Methods in Applied Sciences

ECCOMAS Thematic Conference

# COMPDYN 2017

## *6th International Conference on Computational Methods in Structural Dynamics and Earthquake Engineering*

# PROCEEDINGS

## Volume II

M. Papadrakakis, M. Fragiadakis (Eds)

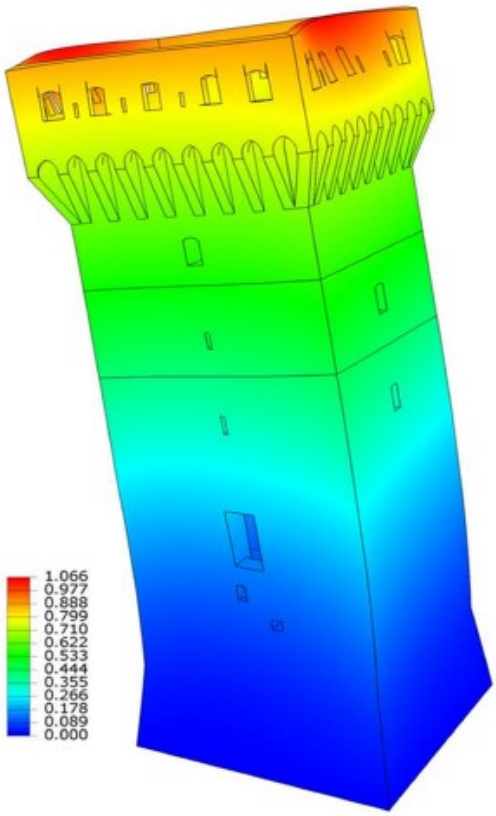


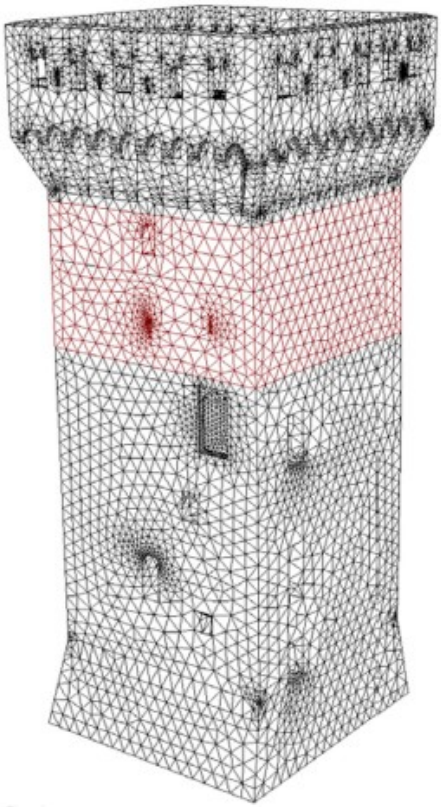

An IACM Special Interest Conference

**COMPDYN 2017**

**Computational Methods in Structural Dynamics and Earthquake Engineering**

Proceedings of the 6th International Conference on Computational
Methods in Structural Dynamics and Earthquake Engineering
Held in Rhodes Island, Greece
15-17 June 2017

Edited by:

**M. Papadrakakis**
National Technical University of Athens, Greece

**M. Fragiadakis**
National Technical University of Athens, Greece

**A publication of:**

Institute of Structural Analysis and Antiseismic Research
School of Civil Engineering
National Technical University of Athens (NTUA)
Greece

**COMPDYN 2017**
**Computational Methods in Structural Dynamics and Earthquake Engineering**
M. Papadrakakis, M. Fragiadakis (Eds)

First Edition, September 2017

© The authors

ISBN (set): **978-618-82844-3-2**
ISBN (vol II): **978-618-82844-2-5**

## PREFACE

This volume contains the full-length papers presented in the 6th International Conference on Computational Methods in Structural Dynamics and Earthquake Engineering (COMPDYN 2017) that was held on June 15-17, 2017 on the Island of Rhodes, Greece.

**COMPDYN 2017**, one of the thematic Conferences of the European Community on Computational Methods in Applied Sciences (ECCOMAS), is a Special Interest Conference of the International Association for Computational Mechanics (IACM) and has been promoted by the European Committee on Computational Solid and Structural Mechanics (ECCSM) of ECCOMAS. The purpose of the Conference is to bring together the scientific communities of Computational Mechanics, Structural Dynamics and Earthquake Engineering in an effort to facilitate the exchange of ideas in topics of mutual interests and to serve as a platform for establishing links between research groups with complementary activities. The communities of Structural Dynamics and Earthquake Engineering will benefit from this interaction, acquainting them with advanced computational methods and software tools which can highly assist in tackling complex problems in dynamic/seismic analysis and design, while also giving the Computational Mechanics community the opportunity to become more familiar with very important application areas of great social interest. The COMPDYN 2017 Conference is supported by the National Technical University of Athens (NTUA), the European Association for Structural Dynamics (EASD), the European Association for Earthquake Engineering (EAEE), the Greek Association for Computational Mechanics (GRACM), the Hellenic Society for Earthquake Engineering (ETAM).

The editors of this volume would like to thank all authors for their contributions. Special thanks go to the colleagues who contributed to the organization of the Minisymposia and to the reviewers who, with their work, contributed to the scientific quality of this e-book.

**M. Papadrakakis**
National Technical University of Athens, Greece

**M. Fragiadakis**
National Technical University of Athens, Greece

**ACKNOWLEDGEMENTS**

The conference organizers acknowledge the support towards the organization of the "6th International Conference on Computational Methods in Structural Dynamics and Earthquake Engineering", to the following organizations:

- European Community on Computational Methods in Applied Sciences (ECCOMAS)
- European Association for Structural Dynamics (EASD)
- European Association for Earthquake Engineering (EAEE)
- Greek Association for Computational Mechanics (GRACM)
- Hellenic Society for Earthquake Engineering (HSEE)
- School of Civil Engineering, National University of Athens (NTUA)
- Research Fund for Coal and Steel (RFCS) for the INNOSEIS Workshop
- Municipality of Rhodes

**Plenary Speakers and Invited Session Organizers**

We would also like to thank the Plenary and Semi-Plenary Speakers and the Minisymposia Organizers for their help in the setting up of a high standard Scientific Programme.

**Plenary Speakers:** Dan M. Frangopol, Hector Jensen, Boris Jeremic, K. C. Park, Alexander Vakakis

**Semi-Plenary Speakers:** Guido De Roeck, Anthony Gravouil, Terje Haukaas, Muneo Hori, Phill-Seung Lee, Roger Ohayon

**MS Organizers:** Sondipon Adhikari, Pedro Alves Costa, Fereydoon Arbabi, António Arêde, Amalia Argyridi, Panagiotis G. Asteris, Rui Carneiro Barros, Anas Batou, Catherine Berge-Thierry, Manuel Braz-Cesar, Bruno Briseghella, Oreste S. Bursi, Donatello Cardone, Giovanni Castellazzi, Serena Cattari, Nicola Cavalagli, Liborio Cavaleri, Gian Paolo Cimellaro, Francesco Clementi, Stefano de Miranda, Guido De Roeck, Ciro Del Vecchio, Pedro Delgado, Raimundo Delgado, Fabio Di Trapani, Elias Dimitrakopoulos, Daniele Ferretti, Michalis Fragiadakis, Fabrice Gatuingt, Yin Gu, Mohammed Hussein, Alexander Idesman, Boris Jeremic, Sakdirat Kaewunruen, Andreas Kappos, Christos Karakostas, Spyros Karamanos, Jin-Gyun Kim, Radek Kolman, Panagiotis Kotronis, Qingming Li, Dimitrios G. Lignos, Kristof Maes, Steve Mahin, Abdollah Malekjafarian, George Manos, Angelo Masi, Konstantinos G. Megalooikonomou, Gabriele Milani, Jiri Naprstek, Camillo Nuti, Roger Ohayon, K.C. Park, Vagelis Plevris, Alex M Remennikov, Edwin Reynders, Emmanouil Rovithis, Evangelos Sapountzakis, Anastatsios Sextos, Castorina Silva Vieira, Sergey Sorokin, Aram Soroushian, Enrico Spacone, Constantine Spyrakos, Anton Tkachuk, Yiannis Tsompanakis, Dimitrios Vamvatsikos, Ivo Vanzi, Humberto Varum, Michalis Vassiliou, Ioannis Vayas, Marco Vona, Yan Xiao, Yeong-Bin Yang

## SUMMARY

**Preface**..... iii

**Acknowledgements**..... iv

**Contents**..... ix

## VOLUME I

**Minisymposia**

**MS 1: ADVANCES IN COMPUTATIONAL STRUCTURAL VIBRATIONS** .....1
*Organized by Evangelos Sapountzakis, Amalia Argyridi*

**MS 2: EXPERIMENTAL MEASUREMENTS AND NUMERICAL SIMULATION ON PROBLEMS IN THE FIELD OF EARTHQUAKE** ..... 78
*Organized by George C. Manos*

**MS 4: VIBRATION ENERGY HARVESTING** .....459
*Organized by Sondipon Adhikari, Anas Batou*

**MS 5: PERIODICITY-INDUCED EFFECTS AND METHODS IN STRUCTURAL DYNAMICS** .....470
*Organized by Sergey Sorokin*

**MS 6: SEISMIC ASSESSMENT OF BRIDGES AND RESILIENCE OF TRANSPORTATION NETWORKS** .....569
*Organized by Andreas Kappos, Anastasios Sextos*

**MS 8: SEISMIC SAFETY ASSESSMENT OF STRUCTURES** .....623
*Organized by Pedro Delgado, António Arêde, Raimundo Delgado*

**MS 9: WORKSHOP OF THE INNOSEIS PROJECT- INNOVATIVE ANTI-SEISMIC DEVICES FOR BUILDINGS** .....790
*Organized by Ioannis Vayas*

**MS 10: ADVANCES IN NUMERICAL METHODS FOR LINEAR AND NON-LINEAR DYNAMICS AND WAVE PROPAGATION** .....946
*Organized by Alexander Idesman*

**MS 11: RECENT ADVANCES AND CHALLENGES IN GEOTECHNICAL EARTHQUAKE ENGINEERING** .....990
*Organized by Castorina Silva Vieira, Yiannis Tsompanakis*

**MS 12: ADVANCES IN MODEL REDUCTION TECHNIQUES IN STRUCTURAL AND MULTI-PHYSICS DYNAMICAL SYSTEMS** .....1107
*Organized by Jin-Gyun Kim, K.C. Park, Roger Ohayon*

**MS 13: EARTHQUAKE SOIL STRUCTURE INTERACTION MODELING AND SIMULATION**.....1155
*Organized by Boris Jeremic*

**MS 15: NON-LINEAR DYNAMICS AND WAVE PROPAGATION** ..... 1240
*Organized by Jiri Naprstek, Radek Kolman, Anton Tkachuk, K .C. Park*

**MS 16: INSTRUMENTATION OF STRUCTURES AND SSI SYSTEMS UNDER DYNAMIC EXCITATIONS** .....1347
*Organized by Emmanouil Rovithis, Christos Karakostas*

**MS 17: COMPUTATIONAL ISSUES IN EARTHQUAKE ENGINEERING** .....1403
*Organized by Aram Soroushian, Fereydoon Arbabi*

**MS 18: MODELING THE NONLINEAR BEHAVIOR OF STRUCTURES** .....1464
*Organized by Enrico Spacone, Humberto Varum*

**MS 19: LOSS, RISK, UNCERTAINTY AND NONLINEAR MODELING FOR PERFORMANCE-BASED EARTHQUAKE ENGINEERING** .....1748
*Organized by Dimitrios G. Lignos, Dimitrios Vamvatsikos*

**MS 20: SEISMIC RESILIENCE OF CRITICAL INFRASTRUCTURE AND LIFELINES** .....1914
*Organized by Ivo Vanzi, Anastastios Sextos, Michalis Fragiadakis, Spyros Karamanos*

**MS 21: GROUND-BORNE NOISE AND VIBRATIONS DUE TO TRAFFIC: PREDICTION AND MITIGATION** .....1950
*Organized by Pedro Alves Costa, Mohammed Hussein*

**MS 22: VIRTUAL CITIES FOR REAL-WORLD CRISIS MANAGEMENT AND RESILIENCE ASSESSMENT OF COMMUNITIES AND INFRASTRUCTURES** ..... 1994
*Organized by Gian Paolo Cimellaro, Steve Mahin*

**MS 23: SINO-EUROPEAN RESEARCH ON EARTHQUAKE ENGINEERING** .....2095
*Organized by Bruno Briseghella, Camillo Nuti, Yan Xiao*

**MS 24: SEISMIC INPUT FOR BRIDGES: FROM SCENARIO EARTHQUAKES TO NONSYNCHRONOUS INPUT** .....2171
*Organized by Camillo Nuti, Yin Gu, Ivo Vanzi, Anastatsios Sextos*

**MS 25: COMPUTATIONAL STRATEGIES FOR THE SEISMIC ASSESSMENT OF CULTURAL HERITAGE MASONRY STRUCTURES** .....2227
*Organized by Giovanni Castellazzi, Serena Cattari, Daniele Ferretti, Stefano de Miranda*

**MS 26: THE SINAPS@ FRENCH RESEARCH PROJECT ON INTEGRATED SEISMIC RISK ASSESSMENT FOR NUCLEAR SAFETY** .....2323
*Organized by Panagiotis Kotronis, Fabrice Gatuingt, Catherine Berge-Thierry*

**MS 27: ADVANCED NUMERICAL METHODS FOR HISTORICAL MASONRY MONUMENTS PRESERVATION IN SEISMIC ZONE** .....2395
*Organized by Nicola Cavalagli, Francesco Clementi, Gabriele Milani, Constantine Spyrakos, Vagelis Plevris*

## VOLUME II

### Minisymposia

**MS 28: NEW EXPERIMENTAL TECHNIQUES FOR STRUCTURAL IDENTIFICATION AND HEALTH MONITORING** ……2695
*Organized by Kristof Maes, Edwin Reynders, Guido De Roeck*

**MS 29: REPAIR AND RETROFIT OF STRUCTURES** ……2739
*Organized by Konstantinos G. Megalooikonomou, Ciro Del Vecchio*

**MS 30: DYNAMICS AND SEISMIC RESPONSE OF ROCKING AND SELF-CENTERING STRUCTURES** ……2852
*Organized by Elias Dimitrakopoulos, Michalis Fragiadakis, Michalis Vassiliou*

**MS 32: EXTREME DYNAMICS** ……3062
*Organized by Sakdirat Kaewunruen, Qingming Li, Alex M Remennikov*

**MS 33: WORKSHOP ON FRAGILITY EVALUATION AND SEISMIC SAFETY ASSESSMENT OF "SPECIAL RISK" INDUSTRIAL PLANTS (INDUSE-2-SAFETY)** ……3102
*Organized by Oreste S. Bursi, Spyros A. Karamanos*

**MS 34: VIBRATIONS, STRUCTURAL ENGINEERING AND CONTROL SYSTEMS** ……3128
*Organized by Rui Carneiro Barros, Manuel Braz-Cesar*

**MS 35: SIMPLIFIED METHODOLOGIES AND NUMERICAL TOOLS FOR THE SEISMIC RISK MITIGATION OF BUILDINGS: RECENT ADVANCES AND OPEN CHALLENGES** ……3163
*Organized by Donatello Cardone, Angelo Masi, Marco Vona*

**MS 36: VEHICLE BRIDGE INTERACTION DYNAMICS AND ITS APPLICATION FOR DRIVE-BY BRIDGE HEALTH MONITORING** ……3235
*Organized by Abdollah Malekjafarian, Yeong-Bin Yang*

**MS 38: COMPUTATIONAL STRATEGIES AND ASSESSMENT OF IN-PLANE AND OUT-OF-PLANE SEISMIC RESPONSE OF INFILLED FRAMES** ……3255
*Organized by Liborio Cavaleri, Fabio Di Trapani, Panagiotis G. Asteris*

### Regular Sessions

**RS 4: DYNAMICS OF CONCRETE STRUCTURES** ……3426

**RS 5: DYNAMICS OF COUPLED PROBLEMS** ……3506

**RS 7: GEOTECHNICAL EARTHQUAKE ENGINEERING** ……3606

**RS 11: NONLINEAR DYNAMICS** ……3682

**RS 12: NUMERICAL SIMULATION METHODS FOR DYNAMIC PROBLEMS** ……3824

**RS 13: OPTIMUM DESIGN AND CONTROL IN STRUCTURAL DYNAMICS AND EARTHQUAKE ENGINEERING** ……3963

**RS 15: PERFORMANCE-BASED EARTHQUAKE ENGINEERING** ..... 4129

**RS 17: REPAIR AND RETROFIT OF STRUCTURES** ..... 4194

**RS 18: SEISMIC ISOLATION** ..... 4288

**RS 19: SEISMIC RISK AND RELIABILITY ANALYSIS** ..... 4426

**RS 21: SOIL DYNAMICS** ..... 4584

**RS 22: SOIL-STRUCTURE INTERACTION** ..... 4634

**RS 26: STOCHASTIC DYNAMICS** ..... 4726

**RS 28: WAVE PROPAGATION** ..... 4752

**RS 30: CONCRETE STRUCTURAL MEMBERS** ..... 4837

**RS 33: STEEL STRUCTURES** ..... 4920

**RS 34: MASONRY STRUCTURES** ..... 5035

# CONTENTS

## VOLUME I

### Minisymposia

**MS 1: ADVANCES IN COMPUTATIONAL STRUCTURAL VIBRATIONS**

SECOND-ORDER TORSIONAL WARPING MODAL ANALYSIS OF THIN-WALLED BEAMS ..... 1
*Justin Murin, Mehdi Aminbaghai, Juraj Hrabovsky, Herbert Mang*

HIGHER ORDER BEAM ELEMENT FOR THE LOCAL BUCKLING ANALYSIS OF BEAMS ..... 20
*Amalia Argyridi, Evangelos Sapountzakis*

PARAMETER OPTIMIZATION OF THE KDAMPER CONCEPT IN SEISMIC ISOLATION OF BRIDGES USING HARMONY SEARCH ALGORITHM ..... 37
*Panagiota Syrimi, Evangelos Sapountzakis, George Tsiatas, Ioannis Antoniadis*

IMPLEMENTATION OF THE KDAMPER CONCEPT TO WIND TURBINE TOWERS ..... 52
*Konstantinos Kapasakalis, Evangelos Sapountzakis, Ioannis Antoniadis*

**MS 2: EXPERIMENTAL MEASUREMENTS AND NUMERICAL SIMULATION ON PROBLEMS IN THE FIELD OF EARTHQUAKE**

SEISMIC PERFORMANCE OF BELL TOWERS IN KEFALONIA, GREECE DURING THE 2014 EARTHQUAKE SEQUENCE ..... 78
*George Manos, Evagelos Kozikopoulos*

CYCLIC EARTHQUAKE-TYPE PERFORMANCE OF ONE-BAY SINGLE-STOREY REINFORCED CONCRETE (R/C) FRAMES RETROFITED WITH AN ENCASED R/C PANEL ..... 101
*George Manos, Vasilios Soulis, Kostas Katakalos, George Koidis, Marios Theofanous*

EXPERIMENTAL MEASUREMENTS AND NUMERICAL SIMUATION OF NOVEL ANCHORING DEVICES FOR OPEN HOOP FIBER REINFORCING POLYMER STRIPS USED IN THE SHEAR UPGRADE OF R/C T-BEAMS ..... 120
*George Manos, Kostas Katakalos, G. Mpalaskas*

EXPERIMENTAL MEASUREMENTS AND NUMERICAL NON-LINEAR SIMULATION OF THE IN-PLANE BEHAVIOUR OF R/C FRAMES WITH MASONRY INFILLS UNDER CYCLIC EARTHQUAKE-TYPE LOADING ..... 142
*George Manos, Vasilios Soulis*

NUMERICAL SIMULATION OF THE SUSPENDED ROOF OF THE NIARCHOS CULTURAL CENTER AT ATHENS – GREECE UTILISING COMPONENT TEST RESULTS ..... 160
*George Manos, V. Kourtides, Kostas Katakalos, Lambros Kotoulas, George Koidis, K. Kyprioti*

EXPERIMENTAL TESTS AND NUMERICAL SIMULATION OF THE PLASTIC CYCLIC BEHAVIOUR OF SIMPLE STEEL COUPONS ..... 178
*George Manos, Alexandra Nalmpantidou, V. Kourtides*

IN-SITU MEASUREMENTS RELATED TO THE PERFORMANCE OF STONE MASONRY BRIDGES IN GREECE ..... 194
*George Manos, Evagelos Kozikopoulos, Lambros Kotoulas, Nick Simos*

NUMERICAL SIMULATION OF THE PERFORMANCE OF A WIND TURBINE TOWER WHEN SUBJECTED TO WIND AND EARTHQUAKE FORCES ..... 220
*George Manos, George Panagiotou, George Manolis*

HIGH DAMPING RUBBER BEARING ISOLATORS: QUASI- LINEAR MECHANICAL MODEL FORMULATIONS ..... 234
*Athanasios Markou, George Manolis*

NUMERICAL SIMULATION OF THE COUPLED TENSION-SHEAR RESPONSE OF AN INNOVATIVE DISSIPATIVE CONNECTION FOR CLT BUILDINGS ..... 247
*Luca Marchi, Davide Trutalli, Roberto Scotta, Luca Pozza*

OBSERVED BEHAVIOUR OF AN INDUSTRIAL COMPLEX WITH PRE-CAST R/C STRUCTURAL MEMBERS SUBJECTED TO THE ATHENS 1999 EARTHQUAKE - NUMERICAL SIMULATION OF ITS RESPONSE ..... 255
*John Mpoufidis, Dimitrios Mpoufidis, George Manos*

EXPERIMENTAL AND ANALYTICAL STUDY ON HOLLOW PRECAST PIERS WITH UNBONDED CONVENTIONAL REINFORCEMENT TO CONTROL SEISMIC AND IN-SERVICE RESPONSE OF ROCKING BRIDGES ..... 282
*Olga Markogiannaki, Nikolaos Orologopoulos, Ioannis Tegos*

NUMERICAL STUDY OF THE BEARING CAPACITY AND MODES OF BUCKLING FAILURE OF A METAL SCAFFOLDING UNIT SUBJECTED TO VERTICAL COMPRESSION ..... 297
*George Manos, Vassilios Soulis, Alexandra Nalmpantidou, V. Kourtides*

ANALYTICAL AND EXPERIMENTAL RESEARCH ON THE POSSIBILITIES OF ATTAINING A MONOLITHIC CONNECTION WITH EARTHQUAKE RESISTANCE, AESTHETIC AND ECONOMIC ADVANTAGES FOR THE PREFABRICATED BRIDGES ..... 315
*Ioannis Papaefthymiou, Ilias Papadopoulos, Dimitrios Pesios, Ioannis Tegos*

EXPERIMENTAL AND NUMERICAL RESPONSE OF CFRP-STRENGTHENED CONCRETE BEAMS WITH LOW OR MEDIUM STEEL CORROSION ..... 343
*Garyfalia Triantafyllou, Theodoros Rousakis, Athanasios Karabinis*

EVALUATION OF AN INNOVATIVE PASSIVE MITIGATION DEVICE THROUGH EXPERIMENTAL AND NUMERICAL INVESTIGATION ..... 353
*Magdalini Titirla, Konstantinos Katakalos*

ANALYTICAL AND EXPERIMENTAL RESEARCH ON IMPROVEMENT OF THE DUCTILITY OF BUILDINGS' R/C SEISMIC WALLS THROUGH SLIP PREVENTION WITH THE USE OF STOPPERS ..... 362
*Theodoros Chrysanidis, Sevasti Tegou, Ioannis Tegos, Sofia Spyridonidou*

INVESTIGATION OF STRENGTHENED MASONRY WALLS MADE OF EARTH BLOCK STRENGTHENED EXTERNALLY WITH GLASS AND STEEL FIBER MESHES UNDER CYCLIC LOADING ..... 379
*Ioanna Papayianni, Christina Batsouka, Konstantinos Katakalos*

EFFECTIVENESS OF THE RBRL ISOLATION SYSTEM: EVIDENCES FROM SEISMIC TESTS AND NUMERICAL SIMULATION ..... 391
*Marco Donà, Alan H. Muhr, Giovanni Tecchio, Simone Salvia, Claudio Modena*

ASSESSMENT OF SPATIALLY VARYING GROUND MOTION COHERENCE BASED ON MICROSEISMIC FIELD MEASUREMENTS AND NUMERICAL ANALYSES ..... 407
*Nick Simos, George Manos,*

ON THE ASSESSMENT OF THE PLAKA BRIDGE COLLAPSE USING NON-LINEAR ANALYSIS PREVENTABLE OR DOOMED? ..... 423
*Nick Simos, George Manos, Evaggelos Kozikopoulos, Lambros Kotoulas*

UNREINFORCED STONE MASONRY UNDER IN-PLANE STATE OF STRESS FROM GRAVITATIONAL AND SEISMIC ACTIONS. MEASURED AND PREDICTED BEHAVIOUR ..... 441
*George Manos, Lambros Kotoulas*

**MS 4: VIBRATION ENERGY HARVESTING**

ENERGY HARVESTING IN A NONLINEAR SYSTEM UNDER HARMONIC AND RANDOM EXCITATIONS ..... 459
*Tiago Pereira, Aline De Paula, Adriano Fabro, Marcelo Savi*

**MS 5: PERIODICITY-INDUCED EFFECTS AND METHODS IN STRUCTURAL DYNAMICS**

APPLICATION OF THE WAVE FINITE ELEMENT APPROACH TO THE STRUCTURAL FREQUENCY RESPONSE OF STIFFENED STRUCTURES ..... 470
*Fabrizio Errico, Mohamed Ichchou, Sergio De Rosa, Olivier Bareille*

A WAVE FINITE ELEMENT STRATEGY TO COMPUTE THE DYNAMIC FLEXIBILITY MODES OF STRUCTURES WITH CYCLIC SYMMETRY AND ITS APPLICATION TO DOMAIN DECOMPOSITION ..... 484
*Jean-Mathieu Mencik*

SENSITIVITY ANALYSIS OF THE FREE WAVE CHARACTERISTICS OF PERIODIC STRUCTURES ..... 500
*Jie Zhang, Guido De Roeck, Edwin Reynders, Geert Lombaert*

CYLINDRICAL WAVES IN STRUCTURES PERIODIC IN POLAR COORDINATES ..... 509
*Alexander Hvatov, Sergey Sorokin*

HARMONIC AND RANDOM VIBRATIONS OF AN ANISOTROPIC BEAM ..... 518
*Petr E. Tovstik, Tatiana M. Tovstik, Natalia V. Naumova*

WAVE PROPAGATION IN PIPES WITH HELICAL PATTERNS ..... 529
*Elisabetta Manconi, Sergey Sorokin, Rinaldo Garziera*

EFFICIENCY OF NEARLY PERIODIC STRUCTURES FOR MITIGATION OF GROUND VIBRATION ..... 537
*Lars Vabbersgaard Andersen, Andrew Peplow, Paulius Bucinskas*

LOW-FREQUENCY VIBRATIONS OF THIN CYLINDRICAL SHELL STIFFENED BY RINGS WITH T-SHAPED CROSS-SECTION ..... 559
*Sergei Filippov*

**MS 6: SEISMIC ASSESSMENT OF BRIDGES AND RESILIENCE OF TRANSPORTATION NETWORKS**

STUDY ON THE RESPONSE OF ELASTOMERIC BEARINGS WITH 3D NUMERICAL SIMULATIONS AND EXPERIMENTAL VALIDATION ..... 569
*Davide Forcellini, Stergios Mitoulis, Kostas Kalfas,*

PERFORMANCE-BASED DESIGN & ASSESSMENT OF SEISMICALLY ISOLATED BRIDGES WITH NON-LINEAR VISCOUS DAMPERS ..... 578
*Konstantinos I. Gkatzogias, Andreas J. Kappos*

SEISMIC CAPACITY AND DEMAND ASSESSMENT IN BRIDGE-SPECIFIC FRAGILITY ANALYSIS ..... 595
*Sotiria Stefanidou, Andreas Kappos*

NONSMOOTH SEISMIC RESPONSE ANALYSIS OF A BENCHMARK STRAIGHT BRIDGE WITH DECK-ABUTMENT IMPACT-INDUCED ROTATION ..... 613
*Zhongqi Shi, Elias Dimitrakopoulos*

**MS 8: SEISMIC SAFETY ASSESSMENT OF STRUCTURES**

MODELLING UNCERTAINTY IN EXISTING ITALIAN RC FRAMES ..... 623
*Gerard O'Reilly, Timothy Sullivan*

A MECHANIC BASED MODEL FOR DEFINITION OF SEISMIC RISK AND REAL TIME DAMAGE SCENARIO OF BUILDINGS ..... 637
*Marta Faravelli, Barbara Borzi, Antonella Di Meo, Diego Polli*

TOWARDS A TAXONOMY FOR PORTUGUESE RC BRIDGES ..... 652
*Claudia Zelaschi, Ricardo Monteiro*

SCALE MODELS FOR THE EXPERIMENTAL ANALYSIS OF THE COLLAPSE MECHANISMS OF MASONRY BAY WINDOWS UNDER HORIZONTAL ACTIONS ..... 663
*Riccardo Barsotti, Stefano Bennati, John A. Ochsendorf, Claudio Tirabasso*

CAPACITY MODELS FOR SHEAR-CRITICAL RC BRIDGE PIERS WITH HOLLOW CROSS-SECTION ..... 675
*Paolino Cassese, Maria Teresa De Risi, Gerardo Mario Verderame*

NON-LINEAR DYNAMIC ANALYSES OF AN RC FRAME BUILDING COLLAPSED DURING L'AQUILA 2009 EARTHQUAKE ..... 689
*Maria Gabriella Mulas, Paolo Martinelli, Susanna Capriotti*

COST OF REPAIR AND RETROFIT OF SEISMIC DAMAGE OF RC HOLLOW-PIERS ..... 703
*Pedro Delgado, Nelson Sá, Mário Marques, António Arêde*

DOWNTIME ESTIMATION FOR RESILIENCE ASSESSMENT ACCOUNTING EXTERNAL FACTORS ..... 720
*Mamak P. Tootkaboni, Danial Mohabat Doost, Gian Paolo Cimellaro, Gordon Warn*

OVERLAPPING LATTICE SIMULATION OF CONCRETE GRAVITY DAM COLLAPSE SCENARIOS ..... 730
*Feyza Soysal Albostan, Beyazit B. Aydin, Kagan Tuncay, Yalin Arici, Baris Binici*

SEISMIC RESPONSE OF RC BRIDGES USING GENERALISED FORCE VECTORS ..... 739
*Camilo Perdomo, Ricardo Monteiro, Haluk Sucuoglu*

PERFORMANCE ASSESSMENT OF INFILLED RC STRUCTURES CONSIDERING THE INFILL MASONRY WALLS OUT-OF-PLANE BEHAVIOUR ..... 754
*André Furtado, Hugo Rodrigues, António Arêde, Humberto Varum, Pedro Delgado*

SEISMIC BEHAVIOUR OF POORLY DETAILED RC BRIDGE PIERS WITH HOLLOW CROSS-SECTION ..... 772
*Paolino Cassese, Maria Teresa De Risi, Gerardo Mario Verderame*

**MS 9: WORKSHOP OF THE INNOSEIS PROJECT- INNOVATIVE ANTI-SEISMIC DEVICES FOR BUILDINGS**

FINITE ELEMENT MODELLING OF DETACHABLE SHORT LINKS ..... 790
*Mariana Zimbru, Mario D'Aniello, Aurel Stratan, Raffaele Landolfo, Dan Dubina*

FINITE ELEMENT ANALYSES ON FREE FROM DAMAGE SEISMIC RESISTING BEAM-TO-COLUMN JOINTS ..... 802
*Mario D'Aniello, Mariana Zimbru, Raffaele Landolfo, Massimo Latour, Gian Vittorio Rizzano, Vincenzo Piluso*

PERFORMANCE ASSESSMENT OF CONCENTRICALLY BRACED FRAMES WITH MODIFIED BRACES DEPENDING ON THE APPLIED BEAM-COLUMN JOINTS ..... 815
*Tzvetan Georgiev, Dimo Zhelev, Lora Raycheva*

DESIGN CRITERIA AND MODELLING OF RE-CENTRING DUAL ECCENTRICALLY BRACED FRAMES ..... 834
*Aurel Stratan, Adriana Chesoan, Dan Dubina*

FUSEIS PIN LINKS: INFORMATION BROCHURES AND DESIGN OF CASE STUDY ..... 849
*Panagiotis Tsarpalis, Ioannis Vayas, Pavlos Thanopoulos*

SEISMIC PROTECTION OF STRUCTURES USING A HYBRID SYSTEM: BUCKLING RESTRAINED BRACE AND MAGNETO RHEOLOGICAL DAMPER ..... 866
*Cristian Vulcu, Dan Dubina*

SEISMIC DESIGN OF STEEL FRAMES WITH FUSEIS BEAM LINK ENERGY DISSIPATION SYSTEMS ..... 878
*Marius Pinkawa, Helen Bartsch, Simon Schaffrath, Benno Hoffmeister, Markus Feldmann*

DUAL STEEL FRAMES WITH RE-CENTERING CAPACITY AND REPLACEABLE STEEL SHEAR PANELS ..... 891
*Calin Neagu, Florea Dinu, Dan Dubina*

SEISMIC BEHAVIOR OF STEEL STRUCTURES EQUIPPED WITH STEEL SELF-CENTERING DEVICES (SSCD) ..... 904
*Francesco Morelli, Andrea Piscini, Walter Salvatore*

Q-FACTOR VERIFICATION OF A 6-STOREY CONCENTRICALLY BRACED FRAME VIA THE INNOSEIS RISK-BASED APPROACH ..... 916
*Dimitrios Vamvatsikos, Konstantinos Bakalis, Stella Pyrza*

A PROCEDURE FOR THE ASSESSMENT OF THE BEHAVIOUR FACTOR FOR STEEL MRF SYSTEMS BASED ON PUSHOVER ANALYSIS ..... 928
*Carlo A. Castiglioni, Amin Alavi, Giovamnni Brambilla, Alper Kanyilmaz*

**MS 10: ADVANCES IN NUMERICAL METHODS FOR LINEAR AND NON-LINEAR DYNAMICS AND WAVE PROPAGATION**

OPTIMAL REDUCTION OF NUMERICAL DISPERSION FOR WAVE PROPAGATION PROBLEMS. APPLICATION TO ISOGEOMETRIC ELEMENTS. ..... 946
*Alexander Idesman*

FLUID-STRUCTURE SIMULATIONS AND BENCHMARKING OF ARTERY ANEURYSMS UNDER PULSATILE BLOOD FLOW ..... 955
*Eugenio Aulisa, Giorgio Bornia, Sara Calandrini*

EFFECT OF GROUND MOTION DIRECTIONALITY ON SEISMIC RESPONSE OF BASE-ISOLATED BUILDINGS CONSIDERING POUNDING TO ADJACENT STRUCTURES ..... 975
*Eftychia Mavronicola, Petros Komodromos*

**MS 11: RECENT ADVANCES AND CHALLENGES IN GEOTECHNICAL EARTHQUAKE ENGINEERING**

NUMERICAL ANALYSIS OF SOIL LIQUEFACTION INDUCED FAILURE OF EMBANKMENTS ..... 990
*Stefania Gobbi, Fernando Lopez Caballero, Davide Forcellini*

ALEATORY VARIABILITY AND SITE EFFECTS: THE PROBLEM OF SOIL CLASSIFICATION ..... 1007
*Stefania Viti, Marco Tanganelli*

OFFSHORE NATURAL GAS PIPELINES SUBJECTED TO KINEMATIC DISTRESS ..... 1018
*Dionysios Chatzidakis, Yiannis Tsompanakis, Prodromos Psarropoulos*

DETAILED SIMULATION OF THE SHAFT INGATE OF A SHIELD TUNNEL UNDER SEISMIC IMPACT ..... 1032
*Jinghua Zhang, Qingqiang Meng, Xinbin Tu, Jian Zhao, Mingqing Xiao, Yong Yuan*

GEOTECHNICAL SEISMIC ISOLATION USING EPS GEOFOAM AROUND PILES ..... 1042
*Xenia Karatzia, George Mylonakis*

REVIEW OF SEISMIC PERFORMANCE OF GEOSYNTHETIC REINFORCED SOIL RETAINING WALLS ..... 1058
*Castorina Silva Vieira*

UNDERSTANDING THE EFFECT OF GEOTECHNICAL PARAMETERS IN SOIL RESPONSE ANALYSIS TO EARTHQUAKE LOADING ..... 1071
*Muhsin Rahhal, Mireille Antabli*

NEW INSIGHTS IN THE LIQUEFACTION POTENTIAL EVALUATION METHODS FOR SOILS ..... 1082
*Muhsin Rahhal, Dona Zakhem*

NUMERICAL MODELLING OF THE DYNAMIC RESPONSE OF LIQUEFIABLE DEPOSITS IN THE PRESENCE OF SMALL SCALE BUILDINGS ..... 1095
*Jovana Borozan, Pedro Alves Costa, Xavier Romão, Julieth Quintero, António Viana da Fonseca*

**MS 12: ADVANCES IN MODEL REDUCTION TECHNIQUES IN STRUCTURAL AND MULTI-PHYSICS DYNAMICAL SYSTEMS**

SEMI-ANALYTICAL REDUCED-ORDER MODELS FOR THE AEROELASTIC BEHAVIOR OF SUBSONIC FLEXIBLE WINGS VIA GENERALISED PLATE AND BEAM FORMULATIONS ..... 1107
*Marco Berci*

TIME INTEGRATION OF DUAL CRAIG-BAMPTON REDUCED SYSTEMS ..... 1135
*Fabian M. Gruber, Max Gille, Daniel J. Rixen*

**MS 13: EARTHQUAKE SOIL STRUCTURE INTERACTION MODELING AND SIMULATION**

3D NUMERICAL SIMULATIONS OF A BASE-ISOLATED RESIDENTIAL BUILDING WITH SOIL STRUCTURE INTERACTION ..... 1155
*Andrea Canini, Davide Forcellini*

TIME-DOMAIN SOIL-STRUCTURE INTERACTION ANALYSIS OF NUCLEAR FACILITIES ..... 1168
*Shaolin Chen, Junquan Wang*

DYNAMIC ANALYSIS OF MODULAR STRUCTURES. CONSIDERING SOIL - PILE - STRUCTURE INTERACTION ..... 1184
*Yingcai Han, N. Gorai, S. Chatterjee, M. Harloff-Bernyk, T. Guo, C. D'Souza*

GEOMETRICALLY NONLINEAR FREE VIBRATIONS OF FUNCTIONALLY GRADED BEAM WITH DISCONTINUITIES RESTING ON NONLINEAR ELASTIC FOUNDATIONS ..... 1194
*Mohcine Chajdi, El bekkaye Merrimi, Khalid El Bikri*

REDUCTION OF SEISMIC LOADING ON STRUCTURES INDUCED BY PILES IN INHOMOGENEOUS SOIL ..... 1203
*Emmanouil Rovithis, Raffaele Di Laora, Maria Iovino, Luca de Sanctis*

EXPANSION OF THE LUMPED PARAMETER METHOD TO NONLINEAR, SOIL-STRUCTURE INTERACTING DYNAMIC SYSTEMS BY MEANS OF A MULTI-OBJECTIVE OPTIMIZATION ALGORITHM ..... 1216
*Nikolaos Lesgidis, Anastasios Sextos, Oh-Sung Kwon*

DYNAMICS OF AN UNDERGROUND PIPELINE WITH SLIPPING CONTACT AT SOIL-PIPILINE INTERFACE UNDER SEISMIC EXCITATION: ANALYTICAL AND NUMERICAL INVESTIGATION OF COUPLED PROBLEMS ..... 1231
*Mukhady Sh. Israilov, Shakhzod M. Takhirov*

**MS 15: NON-LINEAR DYNAMICS AND WAVE PROPAGATION**

NONLINEAR ICE ROD-STRUCTURE VIBRATIONS ..... 1240
*Andrei Abramian, Sergey Vakulenko*

ANALYTICAL APPROACH OF SLENDER STRUCTURE VIBRATION DUE TO RANDOM COMPONENT OF THE WIND VELOCITY ..... 1249
*Jiří Náprstek, Stanislav Hračov*

AN ERROR INDICATOR BASED ON A WAVE DISPERSION ANALYSIS FOR THE IN-PLANE VIBRATION MODES OF ISOTROPIC ELASTIC SOLIDS DISCRETIZED BY ENERGY-ORTHOGONAL FINITE ELEMENTS ..... 1259
*Francisco José Brito Castro*

AN EXPLICIT TIME SCHEME WITH LOCAL TIME STEPPING FOR ONE-DIMENSIONAL WAVE AND IMPACT PROBLEMS IN LAYERED AND FUNCTIONALLY GRADED MATERIALS ..... 1297
*Radek Kolman, Sang Soon Cho, K.C. Park, Jose G. González*

INVERSE MASS MATRIX VIA THE METHOD OF LOCALIZED LAGRANGE MULTIPLIERS ..... 1304
*José A. González, Radek Kolman, Sang Soon Cho, C.A. Felippa, K.C. Park*

ESTIMATION OF STABILITY LIMIT BASED ON GERSHGORIN'S THEOREM FOR EXPLICIT CONTACT-IMPACT ANALYSIS SIGNORINI PROBLEM USING BIPENALTY APPROACH ..... 1312
*Dušan Gabriel, Anton Tkachuk, Ján Kopačka, Radek Kolman, Michal Mracko, Manfred Bischoff, Jiří Plešek*

PROPAGATION OF NON-STATIONARY WAVES IN VISCOELASTIC STRIP COMPOSED OF ORTHOTROPIC LAYERS ..... 1322
*Vitezslav Adamek, Frantisek Vales, Jan Cerv*

MODELLING OF EVANESCENT AND PROPAGATING MODES IN HOMOGENIZED PHONONIC STRUCTURES IN FREQUENCY AND TIME DOMAINS ..... 1330
*Eduard Rohan, Robert Cimrman*

**MS 16: INSTRUMENTATION OF STRUCTURES AND SSI SYSTEMS UNDER DYNAMIC EXCITATIONS**

LARGE SCALE SOIL-FOUNDATION-STRUCTURE MODEL IN GREECE: DYNAMIC TESTS VS FEM SIMULATION …… 1347
*Glenda Abate, Michele Gatto, Maria Rossella Massimino, Dimitris Pitilakis*

QUASI-KINEMATIC RESPONSE OF EMBEDDED FOUNDATIONS: EVIDENCE OF FOUNDATION MASS EFFECT FROM NUMERICAL ANALYSES AND INSTRUMENTED STRUCTURES …… 1360
*Riccardo Conti, Marco Morigi, Giulia Viggiani, Emmanouil Rovithis, Nikos Theodoulidis, Christos Karakostas*

EFFECT OF SOIL-STRUCTURE INTERACTION ON THE SEISMIC RESPONSE OF AN INSTRUMENTED BUILDING DURING THE CEPHALONIA, GREECE EARTHQUAKE OF 26-1-2014 …… 1375
*Christos Karakostas, George Kontogiannis, Konstantinos Morfidis, Emmanouil Rovithis, George Manolis, Nikolaos Theodoulidis*

EQUIVALENT-LINEAR DYNAMIC STIFFNESS OF SURFACE FOOTINGS ON LIQUEFIABLE SOIL …… 1388
*Xenia Karatzia, George Mylonakis, George Bouckovalas*

**MS 17: COMPUTATIONAL ISSUES IN EARTHQUAKE ENGINEERING**

NUMERICAL MODELING OF INFILLS IN ASYMMETRIC STEEL MOMENT FRAMES FOR THEIR DYNAMIC ANALYSIS WITH PROGRESSIVE COLLAPSE APPROACH …… 1403
*Kaveh Nezamisavojbolaghi, Mahmood Hosseini, Abdolmajid Shafiei*

NUMERICAL STUDY ON STIFFENED STEEL PLATE SHEAR WALLS WITH CENTRAL PERFORATION …… 1419
*Kaveh Nezamisavojbolaghi, Akam Gharani*

ON TIME HISTORY ANALYIS WITH STEPS LARGER THAN THE STEPS OF EARTHQUAKE RECORDS INDEPENDENT FROM THE FREQUENCY CONTENTS …… 1432
*Aram Soroushian*

RELATION OF FREQUENCY BANDWIDTH TO CRACK LENGTH IN STRESSED ROCKS …… 1444
*Ziba Ebrahimian*

SEISMIC COLLAPSE RISK ASSESSMENT OF MID-RISE CONCRETE BUILDINGS IN TEHRAN MEGACITY …… 1450
*Mazdak Zahedi, Sassan Eshghi*

**MS 18: MODELING THE NONLINEAR BEHAVIOR OF STRUCTURES**

NUMERICAL INVESTIGATION OF THE IN-PLANE SEISMIC PERFORMANCE OF TIMBER LOG-HAUS WALLS WITH REINFORCED DOVETAILS …… 1464
*C. Bedon, M. Fragiacomo*

RINTC PROJECT: NONLINEAR DYNAMIC ANALYSES OF ITALIAN CODE-CONFORMING REINFORCED CONCRETE BUILDINGS FOR RISK OF COLLAPSE ASSESSMENT ..... 1474
*Guido Camata, Francesca Celano, Maria Teresa De Risi, Paolo Franchin, Gennaro Magliulo, Vincenzo Manfredi, Angelo Masi, Fabrizio Mollaioli, Fabrizio Noto, Paolo Ricci, Enrico Spacone, Marco Terrenzi, Gerardo Verderame*

RINTC PROJECT: NONLINEAR DYNAMIC ANALYSES OF ITALIAN CODE-CONFORMING URM BUILDINGS FOR COLLAPSE RISK ASSESSMENT ..... 1486
*Daniela Camilletti, Serena Cattari, Sergio Lagomarsino, Diego Bonaldo, Giovanni Guidi, Stefano Bracchi, Alessandro Galasco, Guido Magenes, Carlo Filippo Manzini, Andrea Penna, Maria Rota*

RINTC PROJECT: INFLUENCE OF STRUCTURE-RELATED UNCERTAINTIES ON THE RISK OF COLLAPSE OF ITALIAN CODE-CONFORMING REINFORCED CONCRETE BUILDINGS ..... 1503
*Paolo Franchin, Fabrizio Mollaioli, Fabrizio Noto*

PERFORMANCE-BASED COMPARISON OF DIFFERENT RETROFIT METHODS FOR REINFORCED CONCRETE STRUCTURES ..... 1515
*Andrea Miano, Halil Sezen, Fatemeh Jalayer, Andrea Prota*

A NEW DISCRETE MACRO-NODE ELEMENT FOR THE SEISMIC BEHAVIOUR MODELLING OF REINFORCED CONCRETE FRAMES ..... 1536
*Bartolomeo Pantò, Salvatore Caddemi, Ivo Caliò, Enrico Spacone*

RINTC PROJECT - ASSESSING THE (IMPLICIT) SEISMIC RISK OF CODE-CONFORMING STRUCTURES IN ITALY ..... 1545
*Iunio Iervolino, Andrea Spillatura, Paolo Bazzurro*

RINTC PROJECT: NONLINEAR DYNAMIC ANALYSES OF ITALIAN CODE-CONFORMING STEEL SINGLE-STOREY BUILDINGS FOR COLLAPSE RISK ASSESSMENT ..... 1558
*Fabrizio Scozzese, Giusy Terracciano, Alessandro Zona, Gaetano Della Corte, Andrea Dall'Asta, Raffaele Landolfo*

AN EMPIRICAL-BASED APPROACH FOR MODELING AND ASSESSMENT OF RC COLUMNS WITH PLAIN BAR ..... 1574
*Gerardo M. Verderame, Paolo Ricci*

CYCLIC RESPONSE AND NONLINAR MODELING OF EXTERIOR UNREINFORCED RC BEAM-COLUMN JOINTS WITH PLAIN LONGITUDINAL BARS ..... 1590
*Maria Teresa De Risi, Paolo Ricci, Gerardo Mario Verderame*

EMPIRICAL UNREINFORCED MASONRY INFILL MACRO-MODEL ACCOUNTING FOR IN-PLANE/OUT-OF-PLANE INTERACTION ..... 1606
*Mariano Di Domenico, Paolo Ricci, Gerardo M. Verderame*

AXIALLY EQUILIBRATED DISPLACEMENT-BASED BEAM ELEMENT: IMPLEMENTATION IN OPENSEES AND APPLICATION TO DYNAMIC ANALYSIS OF STRUCTURES ..... 1625
*Danilo Tarquini, João Pacheco de Almeida, Katrin Beyer*

RINTC PROJECT: NONLINEAR ANALYSES OF ITALIAN CODE-CONFORMING PRECAST R/C INDUSTRIAL BUILDINGS FOR RISK OF COLLAPSE ASSESSMENT ..... 1636
*Marianna Ercolino, Maddalena Cimmino, Gennaro Magliulo, Davide Bellotti, Roberto Nascimbene*

NONLINEAR SEISMIC ANALYSIS OF GRAVITY-DESIGNED RC STRUCTURES ..... 1645
*Michelangelo Laterza, Michele D'Amato, Rosario Gigliotti*

A MODEL FOR NON-LINEAR DYNAMIC ANALYSIS OF SUB-STANDARD REINFORCED CONCRETE MEMBERS ..... 1656
*Dimitrios Zimos, Panagiotis Mergos, Andreas Kappos*

COMPLETE ANALYTICAL THERMOMECHANICAL MODEL OF DOUBLE FRICTION PENDULUM DEVICES ..... 1667
*Vincenzo Bianco, Giorgio Monti, Nicola Belfiore*

REALISTIC 3D NONLINEAR DYNAMIC ANALYSIS OF EXISTING AND RETROFITTED MULTI-STOREY RC BUILDINGS SUBJECT TO EARTHQUAKE LOADING ..... 1685
*Giuseppe Occhipinti, Bassam Izzuddin, Ivo Calio', Lorenzo Macorini*

EVALUATION OF CODE PROVISIONS FOR SEISMIC PERFORMANCE OF UNACHORED LIQUID STORAGE TANKS ..... 1700
*Bulent Erkmen*

SIMULATION OF MONOTONIC, STATIC AND DYNAMIC RESPONSE OF RC SQUAT WALLS BY MEANS OF PARC_CL 2.0 CRACK MODEL ..... 1711
*Beatrice Belletti, Matteo Scolari, Francesca Vecchi*

RINTC PROJECT: NONLINEAR ANALYSES OF ITALIAN CODE-CONFORMING BASE-ISOLATED BUILDINGS FOR RISK OF COLLAPSE ASSESSMENT ..... 1732
*Dontello Cardone, Nadia Conte, Andrea Dall'Asta, Antonio Di Cesare, Amedeo Flora, Gianmarco Leccese, Antonello Mossucca, Fabio Micozzi, Felice Carlo Ponzo, Laura Ragni*

**MS 19: LOSS, RISK, UNCERTAINTY AND NONLINEAR MODELING FOR PERFORMANCE-BASED EARTHQUAKE ENGINEERING**

FINDING CORRELATIONS BETWEEN ENGINEERING DEMAND PARAMETERS AND INTENSITY MEASURES THROUGH EVOLUTIONARY POLYNOMIAL REGRESSION ..... 1748
*Alessandra Fiore, Fabrizio Mollaioli, Giuseppe Quaranta, Giuseppe Carlo Marano*

SIMPLIFIED PREDICTION OF PEAK FLOOR ACCELERATIONS IN INELASTIC WALL STRUCTURES ..... 1764
*Lukas Moschen, Christoph Adam, Dimitrios Vamvatsikos*

PROBABILISTIC EVALUATION OF SEISMIC PERFORMANCE FOR A STEEL MOMENT FRAME USING DAMAGE INDICES ..... 1779
*Behrouz Asgarian, Behnam Ordoubadi*

PROPOSED METHODOLOGY FOR EARTHQUAKE-INDUCED LOSS ASSESSMENT OF INSTRUMENTED STEEL FRAME BUILDINGS: BUILDING-SPECIFIC AND CITY-SCALE APPROACHES ..... 1797
*Seong-Hoon Hwang, Dimitrios Lignos*

DRIFT-BASED FRAGILITY ASSESSMENT OF MASONRY INFILLS ..... 1816
*Andrea Chiozzi, Eduardo Miranda*

SEISMIC RESILIENCE ASSESSMENT OF THE WESTERN MACEDONIA HIGHWAY NETWORK IN GREECE ..... 1828
*Anastasios Sextos, Ioannis Koilanitis, Andreas Kappos, Magda Pitsiava, Georgios Serdiadis, Basil Margaris, Nikolaos Theodoulidis, Georgios Mylonakis, Panagiotis Panetsos, Kalliopi Kyriakou*

DEVELOPMENT OF FEMA P-58 COMPATIBLE STORY LOSS FUNCTIONS: STEEL OFFICE BUILDINGS IN HIGH SEISMICITY REGIONS ..... 1843
*Athanasios N. Papadopoulos, Dimitrios Vamvatsikos, Athanasia Kazantzi*

CONSIDERING STRUCTURAL MODELLING UNCERATINTIES USING BAYESIAN CLOUD ANALYSIS ..... 1857
*Andrea Miano, Fatemeh Jalayer, Andrea Prota*

UNCERTAINTY IN SEISMIC INTENSITY MEASURES USED FOR FRAGILITY ANALYSIS ..... 1880
*Alin Radu, Mircea Grigoriu*

ANALYSIS OF A NUCLEAR POWER PLANT FAILURE USING TEMPORAL NETWORKS ..... 1890
*Gian Paolo Cimellaro, Alessandro Cardoni, Steve Mahin*

FROM STRUCTURAL PERFORMANCE TO LOSS ESTIMATION FOR (RE)INSURANCE INDUSTRY NEEDS: AN OVERVIEW OF THE VULNERABILITY ESTIMATION APPROACHES WITHIN EARTHQUAKE CATASTROPHE MODELS ..... 1904
*Amaryllis Mouyiannou, Kirsty E. Styles*

**MS 20: SEISMIC RESILIENCE OF CRITICAL INFRASTRUCTURE AND LIFELINES**

RELIABILITY ANALYSIS OF URBAN WATER SYSTEMS UNDER SEISMIC ACTION ..... 1914
*Alessandro Rasulo*

SEISMIC SAFETY EVALUATION OF HISTORICAL CENTRES ..... 1928
*Ivo Vanzi, Samuele Biondi, Alessandra Fiore, Concetta Sulpizio, Nicola Cataldo, Carlo Rago*

NONLINEAR SYSTEMS SUBJECTED TO MULTIPLE SEISMIC EXCITATIONS MATCHED TO THE SAME SPECTRUM: NUMERICAL PREDICTIONS VERSUS SHAKING TABLE TESTS ..... 1938
*Shakhzod M. Takhirov, Eric Fujisaki, Leon Kempner, Michael Riley, Brian Low*

**MS 21: GROUND-BORNE NOISE AND VIBRATIONS DUE TO TRAFFIC: PREDICTION AND MITIGATION**

THE EFFECT OF TRACK UNEVENNESS CORRELATION ON RAILWAY INDUCED GROUND VIBRATION ..... 1950
*Evangelos Ntotsios, David Thompson, Mohammed Hussein*

GROUND VIBRATION GENERATED BY THE PASSING OF A TRUCK ON A SPEED BUMP ..... 1972
*Loïc Ducarne, Daniel Ainalis, Georges Kouroussis*

GROUND-BORNE VIBRATIONS DUE TO RAILWAY TRAFFIC IN URBANIZED AREAS: A NUMERICAL STUDY ABOUT TRAFFIC IN TRENCH CROSS-SECTIONS ..... 1982
*Alexandre Pinto, Pedro Alves Costa, Aires Colaço, Patrícia Lopes, Mohammed Hussein*

**MS 22: VIRTUAL CITIES FOR REAL-WORLD CRISIS MANAGEMENT AND RESILIENCE ASSESSMENT OF COMMUNITIES AND INFRASTRUCTURES**

PROBABILISTIC QUANTIFICATION OF COMMUNITY RESILIENCE USING DISCRETE EVENT SIMULATION ..... 1994
*Hossein Nasrazadani, Mojtaba Mahsuli*

PHYSICS-BASED FIRE FOLLOWING EARTHQUAKE SIMULATION CONSIDERING BUILDING SEISMIC DAMAGE .... 2005
*Xiang Zeng, Xinzheng Lu, Zhen Xu, Qingle Cheng*

A SIMPLIFIED APPROACH FOR THE SEISMIC ASSESSMENT OF HOSPITAL COMPLEX NETWORKS ..... 2016
*Stefania Viti, Marco Tanganelli, Maria Pianigiani, Gian Paolo Cimellaro*

MODELING AIRPORT EVACUATION UNDER EMERGENCY USING AGENT-BASED MODELS ..... 2025
*Gian Paolo Cimellaro, Gerardo Leo, Stephen Mahin*

RESILIENCE ASSESSMENT FOR THE BUILT ENVIRONMENT OF A VIRTUAL CITY ..... 2043
*Sebastiano Marasco, Ali Zamani-Noori, Gian Paolo Cimellaro*

EXPLORING SIMULATION TOOLS FOR URBAN SEISMIC ANALYSIS AND RESILIENCE ASSESSMENT ..... 2056
*Gian Paolo Cimellaro, Marco Domaneschi, Steve Mahin, Gianluca Scutiero*

VIRTUAL CITY FOR WATER DISTRIBUTION RESEARCH IN CRISIS MANAGEMENT ..... 2075
*Marzia Bianco, Gian Paolo Cimellaro, Sean Wilkinson*

VIRTUAL REALITY OF EARTHQUAKE GROUND MOTIONS FOR EMERGENCY RESPONSE ..... 2089
*Ting Lin*

**MS 23: SINO-EUROPEAN RESEARCH ON EARTHQUAKE ENGINEERING**

ACCURACY OF EQUIVALENT LINEAR MODELS FOR BILINEAR OSCILLATORS UNDER PULSE-LIKE GROUND MOTION ..... 2095
*Giuseppe Quaranta, Fabrizio Mollaioli*

SEISMIC RETROFIT OF BUILDINGS WITH BACKBONE DAMPERS ..... 2110
*Nefize Shaban, Seda Ozdemir, Alp Caner, Uğurhan Akyüz*

SEISMIC RESPONSES OF REGULAR HIGHWAY BRIDGES UNDER NEAR-FAULT GROUND MOTIONS ..... 2119
*Hai-Bin Ma, Wei-Dong Zhuo, Gabriele Fiorentino, Davide Lavorato, Camillo Nuti, Ying Sun*

SEISMIC RESPONSE ANALYSIS OF CONTINUOUS HIGHWAY BRIDGES UNDER NEAR-FAULT GROUND MOTIONS …… 2138
*Hai-Bin Ma, Wei-Dong Zhuo, Davide Lavorato, Gabriele Fiorentino, Camillo Nuti, Fabio Sabetta*

ULTRA-HIGH-PERFORMANCE FIBER-REINFORCED CONCRETE JACKET FOR THE REPAIR AND THE SEISMIC RETROFITTING OF ITALIAN AND CHINESE RC BRIDGES …… 2149
*Davide Lavorato, Alessandro Vittorio Bergami, Camillo Nuti, Bruno Briseghella, Junqing Xue, Angelo Marcello Tarantino, Giuseppe Carlo Marano, Silvia Santini*

OPTIMAL DESIGN OF TUNED MASS DAMPERS BY PERFORMANCE–COST ANALYSIS …… 2161
*Rita Greco, Giuseppe Carlo Marano, Alessandra Fiore*

**MS 24: SEISMIC INPUT FOR BRIDGES: FROM SCENARIO EARTHQUAKES TO NONSYNCHRONOUS INPUT**

THE EFFECT OF MULTI-ANGLE, SPATIALLY VARIABLE SEISMIC MOTIONS ON CABLE-STAYED BRIDGES …… 2171
*Eleftheria Efthymiou, Alfredo Camara*

SEISMIC RESPONSE OF A HIGH-PIER BRIDGE SUBJECTED TO OBLIQUE INCIDENCE WAVES …… 2181
*Yin Gu, Hongxiang Guo, Weidong Zhou*

SURFACE GENERATION OF ASYNCHRONOUS SEISMIC SIGNALS FOR THE SEISMIC RESPONSE ANALYSIS OF BRIDGES …… 2203
*Davide Lavorato, Gabriele Fiorentino, Alessandro Vittorio Bergami, Hai-Bin Ma, Camillo Nuti, Bruno Briseghella, Ivo Vanzi, Wei-Dong Zhou*

SEISMIC BEHAVIOUR OF ISOLATED RC BRIDGES SUBJECTED TO ASYNCHRONOUS SEISMIC INPUT …… 2214
*Davide Lavorato, Alessandro Vittorio Bergami, Carlo Rago, Hai-Bin Ma, Camillo Nuti, Ivo Vanzi, Bruno Briseghella, Wei-Dong Zhou*

**MS 25: COMPUTATIONAL STRATEGIES FOR THE SEISMIC ASSESSMENT OF CULTURAL HERITAGE MASONRY STRUCTURES**

THRUST NETWORK ANALYSIS OF MASONRY VAULTS SUBJECT TO VERTICAL AND HORIZONTAL LOADS …… 2227
*Francesco Marmo, Daniele Masi, Salvatore Sessa, Ferdinando Toraldo, Luciano Rosati*

SEISMIC ASSESSMENT OF A MONUMENTAL MASONRY CONSTRUCTION: THE ROCCA ALBORNOZIANA OF SPOLETO …… 2239
*Giulio Castori, Antonio Borri, Marco Corradi, Alessandro De Maria, Romina Sisti*

DYNAMIC BEHAVIOUR OF THE SAN FELICE SUL PANARO FORTRESS: EXPERIMENTAL TESTS AND MODEL UPDATING …… 2253
*Marianna Forghieri, Elisa Bassoli, Loris Vincenzi*

DYNAMIC SIMULATION OF AN IRREGULAR MASONRY BUILDING WITH DIFFERENT REHABILITATION METHODS APPLIED TO TIMBER FLOORS ..... 2269
*Davide Trutalli, Luca Marchi, Roberto Scotta, Luca Pozza*

HOMOGENIZED RIGID BODY AND SPRING MODEL (RBSM) FOR THE NON-LINEAR DYNAMIC ANALYSIS OF HISTORIC MASONRY CHURCH FACADES ..... 2283
*Elisa Bertolesi, Gabriele Milani, Siro Casolo*

SEISMIC ASSESSMENT OF COMPLEX ASSETS THROUGH NONLINEAR STATIC ANALYSES: THE FORTRESS IN SAN FELICE SUL PANARO HIT BY THE 2012 EARTHQUAKE IN ITALY ..... 2291
*Stefania Degli Abbati, Antonio Maria D'Altri, Daria Ottonelli, Giovanni Castellazzi, Serena Cattari, Stefano De Miranda, Sergio Lagomarsino*

NON-LINEAR KINEMATIC ANALYSIS OF MASONRY WALLS OUT-OF-PLANE LOADED. THE COMPARATIVE ROLE OF FRICTION BETWEEN INTERLOCKED WALLS ..... 2301
*Claudia Casapulla, Luca Umberto Argiento*

DETAILED NUMERICAL ANALYSIS OF A HISTORIC BUILDING BASED ON ITS CURRENT CONDITION CAPTURED BY LASER SCANS AND MATERAIL TESTS ..... 2312
*Shakhzod Takhirov, Amir Gilani, Brian Quigley, Liliya Myagkova*

**MS 26: THE SINAPS@ FRENCH RESEARCH PROJECT ON INTEGRATED SEISMIC RISK ASSESSMENT FOR NUCLEAR SAFETY**

ENHANCEMENT OF MULTIFIBER BEAM ELEMENTS IN THE CASE OF REINFORCED CONCRETE STRUCTURES FOR TAKING INTO ACCOUNT THE LATERAL CONFINEMENT OF CONCRETE DUE TO STIRRUP ..... 2323
*Natalia Khoder, Stéphane Grange, Yannick Sieffert*

DYNAMIC SOIL-STRUCTURE INTERACTION MODELING STRATEGIES APPLIED TO KASHIWAZAKI-KARIWA NUCLEAR POWER PLANT CASE-STUDY ..... 2330
*Vinicius Alves Fernandes, Fabien Banci, Georges Devesa, Nicolas Greffet, Matthieu Jacquet, Marc Kham, Alex Nieto-Ferro, François Voldoire, Irmela Zentner*

PHYSICS-BASED SCENARIO OF THE 2007 CHUETSU-OKI EARTHQUAKE ..... 2343
*Filippo Gatti, Fernando Lopez-Caballero, Lucio De Abreu Corrêa, Didier Clouteau, Roberto Paolucci*

HOW ARE THE EQUIVALENT DAMPING RATIOS MODIFIED BY NONLINEAR ENGINEERING DEMAND PARAMETERS? ..... 2362
*Thomas Heitz, Cédric Giry, Benjamin Richard, Frédéric Ragueneau*

STRUCTURE-SOIL-STRUCTURE INTERACTION ANALYSIS OF NUPEC TEST CASES ..... 2381
*Sara Touhami, Vinicius Alves Fernandes, Fernando Lopez Caballero*

**MS 27: ADVANCED NUMERICAL METHODS FOR HISTORICAL MASONRY MONUMENTS PRESERVATION IN SEISMIC ZONE**

A NONLINEAR MACROELEMENT FORMULATION FOR THE SEISMIC ANALYSIS OF MASONRY BUILDINGS ..... 2395
*Domenico Liberatore, Daniela Addessi, Marialuigia Sangirardi*

FAST KINEMATIC LIMIT ANALYSIS OF MASONRY WALLS WITH OUT-OF-PLANE LOADING ..... 2404
*Andrea Chiozzi, Gabriele Milani, Nicola Grillanda, Antonio Tralli*

COMPARATIVE SEISMIC ASSESSMENT OF A MEDIOEVAL MASONRY CHURCH IN SOUTHERN ITALY ..... 2413
*Alfredo Cundari, Gabriele Milani, Giuseppe Failla*

NON LINEAR STATIC AND DYNAMIC ANALYSES OF THE AUGUSTUS BRIDGE IN NARNI, ITALY: AN INSIGHT INTO THE MECHANICAL PROPERTIES OF ROMAN CONCRETE ..... 2423
*Elisa Bertolesi, Gabriele Milani, Maurizio Acito*

TRADITIONAL MASONRY ARCHES AND DOMES WITH FICTILE TUBULES IN MEDITERRANEAN SEISMIC AREAS: ADVANCED NUMERICAL MODELS AND EXPERIMENTATION ..... 2431
*Simone Tiberti, Carmelo Scuro, Rosamaria Codispoti, Renato Sante Olivito, Gabriele Milani*

OUT-OF-PLANE DYNAMIC RESPONSE OF A TUFF MASONRY WALL: SHAKING TABLE TESTING AND NUMERICAL SIMULATION ..... 2449
*Daniela Addessi, Enrico Cappelli, Cristina Gatta, Fabrizio Vestroni*

FINITE ELEMENT MICRO-MODELING FOR THE CHARACTERIZATION OF INCLINED HEAD JOINTS ARCHAEOLOGICAL MASONRY: THE CASE OF VILLA DIOMEDE IN POMPEII ..... 2460
*Matteo Salvalaggio, Pere Roca, Maria Rosa Valluzzi, Filippo Lorenzoni*

ON THE USE OF POINT CONTACT MODELS FOR COLLAPSE MECHANISM AND DYNAMIC ANALYSIS OF MASONRY STRUCTURES ..... 2470
*Francesco Portioli, Lucrezia Cascini, Raffaele Landolfo*

IN-PLANE BEHAVIOUR OF EARTHEN MATERIALS: A NUMERICAL COMPARISON BETWEEN ADOBE MASONRY, RAMMED EARTH AND COB ..... 2478
*Lorenzo Miccoli, Rui A. Silva, Angelo Garofano, Daniel V. Oliveira*

DISCRETE MODEL FOR OUT-OF-PLANE LOADED RANDOM MASONRY ..... 2505
*Daniele Baraldi, Emanuele Reccia, Antonella Cecchi*

SEISMIC VULNERABILITY OF DIFFERENT IN GEOMETRY HISTORIC MASONRY TOWERS ..... 2519
*Vasilis Sarhosis, Francesco Fabbrocino, Antonio Formisano, Gabriele Milani*

SEISMIC ASSESSMENT OF CULTURAL HERITAGE: NONLINEAR 3D ANALYSES OF “SANTA MARIA DELLA CARITÀ” IN ASCOLI PICENO ..... 2533
*Francesco Monni, Francesco Clementi, Enrico Quagliarini, Ersilia Giordano, Stefano Lenci*

DYNAMIC MONITORING AND NONLINEAR ANALYSIS OF THE DOME OF THE BASILICA OF S.MARIA DEGLI ANGELI IN ASSISI ..... 2542
*Nicola Cavalagli, Luca Botticelli, Massimiliano Gioffrè, Vittorio Gusella, Filippo Ubertini*

LIMIT ANALYSIS APPROACH FOR THE SEISMIC VULNERABILITY REDUCTION OF MASONRY TOWERS THROUGH STRENGTHENING WITH TRADITIONAL AND INNOVATIVE MATERIALS ..... 2554
*Gabriele Milani, Rafael Shehu, Marco Valente*

DYNAMIC TESTING AND MONITORING OF HISTORIC TOWERS FOR SEISMIC DAMAGE DETECTION ..... 2564
*Alban Kita, Nicola Cavalagli, Gabriele Comanducci, Filippo Ubertini*

FIBRE-BASED SECTIONAL ANALYSIS OF URM WALLS WITH SINGLE-SIDE FRCM STRENGTHENING ..... 2578
*Costantino Menna, Fulvio Parisi, Andrea Prota*

A RECONSTRUCTION HYPOTHESIS OF COLLAPSED ARCHAEOLOGICAL MASONRY BARREL VAULTS EMPLOYING FRICTIONAL BEARINGS, WITH APPLICATION TO THE CASE STUDY OF THE GALLERIA DELLE VOLTE CROLLATE, IN ROME ..... 2587
*Enrica Di Miceli, Vincenzo Bianco, Giorgio Monti, Maria Grazia Filetici*

EXPERIMENTAL VALIDATION OF IN-PLANE FRICTIONAL RESISTANCES IN DRY BLOCK MASONRY WALLS ..... 2607
*Claudia Casapulla, Luca Umberto Argiento, Carla Ceraldi*

SEISMIC MODELLING AND ANALYSIS OF MASONRY BUILDING IN AGGREGATE: A CASE STUDY ..... 2619
*Siro Casolo, Carlo Alberto Sanjust, Giuseppina Uva, Vito Diana*

FRP-REINFORCED MASONRY STRUCTURES: NUMERICAL MODELING BY MEANS OF A NEW DISCRETE ELEMENT APPROACH ..... 2639
*Salvatore Caddemi, Ivo Caliò, Francesco Cannizzaro, Paulo Lourenco, Bartolomeo Pantò*

HEALTH MONITORING OF A MONUMENT AT ACROPOLIS USING AN EXPERT ACQUISITION SYSTEM AND WIRED OPTICAL SENSORS ..... 2651
*Constantine C. Spyrakos, Cosmas P. Fessas, George A. Andrikopoulos*

A DISCRETE MACRO-MODEL USING HOMOGENIZATION WITH STRAIN-RATE DEPENDENCY FOR THE OUT-OF-PLANE STUDY OF MASONRY PANELS SUBJECTED TO IMPACT LOADING ..... 2659
*Luís C. Silva, Paulo B. Lourenço, Gabriele Milani*

ASSESSMENT AND STRENGTHENING MEASURES OF THE HISTORIC MASONRY COMPLEX: “PROSFYGIKA” IN CENTRAL ATHENS ..... 2670
*Constantine C. Spyrakos, Eleni Panou-Papatheodorou, Dimitrios Kokkinakos*

LITERATURE REVIEW OF MASONRY STRUCTURES UNDER EARTHQUAKE EXCITATION UTILIZING MACHINE LEARNING ALGORITHMS ..... 2685
*Vagelis Plevris, Nikolaos Bakas, Gro Markeset, John Bellos*

## VOLUME II

**MS 28: NEW EXPERIMENTAL TECHNIQUES FOR STRUCTURAL IDENTIFICATION AND HEALTH MONITORING**

3D NUMERICAL SIMULATIONS OF THE SAN MARINO THIRD TOWER (MONTALE) BASED ON 3D MAPPING …… 2695
*GianMarco Guerra, Davide Forcellini, Elona Xhixha, Giacomo Peruzzi, Dario Albarello, Eric Lo, Dominique Mayer, Sabrina Trinh, Emily Zheng, Falko Kuester*

MICROWAVE INTERFEROMETRY MEASUREMENTS FOR RAILWAY-SPECIFIC APPLICATIONS …… 2705
*Andrei Firus, Jens Schneider, Matthias Becker, Jiny Jose Pullamthara, Günther Grunert*

SYNCHRONIZATION OF DATA ACQUISITION SYSTEMS FOR THE PURPOSE OF STRUCTURAL HEALTH MONITORING …… 2719
*Kristof Maes, Edwin Reynders, Ali Rezayat, Guido De Roeck, Geert Lombaert*

INTERPOLATION EVOLUTION METHOD: ANALYSIS OF THE INFLUENCE OF HIGHER MODES RETRIEVED FROM NUMERICAL ANALYSES PERFORMED ON TWO DIFFERENT MODELS OF REINFORCED CONCRETE FRAMED STRUCTURES …… 2729
*Chiara Iacovino, Rocco Ditommaso, Gianluca Auletta, Felice Carlo Ponzo, Maria Giuseppina Limongelli*

**MS 29: REPAIR AND RETROFIT OF STRUCTURES**

A MECHANISTIC APPROACH IN DEFINING INELASTIC ROTATION CAPACITY OF RC COLUMNS …… 2739
*Konstantinos G. Megalooikonomou, Stavroula J. Pantazopoulou, Souzana P. Tastani*

BEHAVIOR OF CFRP CONFINED RC COLUMNS UNDER AXIAL LOAD AND UNIAXIAL CYCLIC LATERAL LOADING …… 2753
*Marta Del Zoppo, Marco Di Ludovico, Alberto Balsamo, Andrea Prota*

EMPIRICAL DAMAGE AND ACTUAL REPAIR COSTS ON MASONRY PRIVATE BUILDINGS AFTER L'AQUILA EARTHQUAKE …… 2765
*Giuseppina De Martino, Marco Di Ludovico, Andrea Prota, Claudio Moroni, Gaetano Manfredi, Mauro Dolce*

ASSESSMENT OF THE EFFECTIVENESS OF CABLING SYSTEM CONFIGURATION IN RETROFITTING STEEL-CONCRETE COMPOSITE BUILDINGS …… 2777
*Georgios S. Papavasileiou*

VALIDATION OF REFINED NUMERICAL MODELING FOR EXISTING RC BUILDINGS: COMPARISON BETWEEN PREDICTED AND OBSERVED EARTHQUAKE DAMAGE …… 2792
*Ciro Del Vecchio, Marco Di Ludovico, Stefano Pampanin, Andrea Prota*

SIMPLIFIED ASSESSMENT OF EXPECTED SEISMIC LOSSES FOR AS BUILT AND RETROFITTED RC BUILDINGS …… 2805
*Marco Gaetani d'Aragona, Maria Polese, Marco Di Ludovico, Andrea Prota*

SEISMIC AMELIORATION OF EXISTING REINFORCED CONCRETE BUILDINGS: STRATEGY TO OPTIMIZE THE AMOUNT OF REINFORCEMENT FOR JOINTS ..... 2823
*Vincenzo Bianco, Giorgio Monti, Alessandro Vari, Gianluigi Palmieri*

NUMERICAL ASSESSMENT OF THE OUT-OF-PLANE RESPONSE OF MASONRY PANELS REINFORCED BY MEANS OF FRCM SYSTEMS ..... 2843
*Bartolomeo Pantò, Marialaura Malena, Gianmarco de Felice*

**MS 30: DYNAMICS AND SEISMIC RESPONSE OF ROCKING AND SELF-CENTERING STRUCTURES**

A CENTRIFUGE INVESTIGATION OF TWO DIFFERENT SOIL-STRUCTURE SYSTEMS WITH ROCKING AND SLIDING ON DENSE SAND ..... 2852
*Iason Pelekis, Gopal Madabhushi, Matthew DeJong*

ROCKING RESONANCE CONDITIONS OF LARGE AND SLENDER RIGID BLOCKS UNDER THE INTENSE PHASE OF AN EARTHQUAKE ..... 2867
*Claudia Casapulla, Alessandra Maione*

ROCKING SPECTRUM INTENSITY MEASURE FOR SEISMIC ASSESSMENT OF ROCKING BLOCKS ..... 2879
*Ioannis Kavvadias, Kosmas Bantilas, Georgios Papachatzakis, Lazaros Vasiliadis, Anaxagoras Elenas*

NUMERICAL STUDY ON THE DYNAMIC RESPONSE OF CLASSICAL COLUMN STANDING FREE ON AN ISOLATED BASE ..... 2893
*Ioannis Kavvadias, Henrik Bibo, Lazaros Vasiliadis*

NON-SMOOTH CONTACT DYNAMICS OF PLANAR MASONRY STRUCTURES USING MATHEMATICAL PROGRAMMING ..... 2902
*Francesco Portioli, Lucrezia Cascini, Raffaele Landolfo*

NONSMOOTH MODELLING OF IMPACTS IN ROCKING STRUCTURES WITH POISSON'S LAW ..... 2910
*Anastasios I. Giouvanidis, Elias G. Dimitrakopoulos*

SEISMIC FRAGILITY OF FREESTANDING BUILDINGS CONTENTS MODELLED AS RIGID BLOCKS ..... 2926
*Luigi Di Sarno, Crescenzo Petrone, Gennaro Magliulo, Edoardo Cosenza*

A NEW COMPUTATIONAL APPROACH FOR THE ROCKING RESPONSE OF DEFORMABLE BODIES CONSIDERING MATERIAL NONLINEARITY ..... 2937
*Evangelos Avgenakis, Ioannis N. Psycharis*

A SIMPLIFIED PREDICTION METHOD FOR SEISMIC RESPONSES OF BUILDING FRAME STRUCTURES ALLOWED TO UPLIFT ..... 2950
*Tatsuya Azuhata, Tadashi Ishihara*

DESIGN STRATEGY FOR THE ROCKING STABILITY OF HORIZONTALLY RESTRAINED MASONRY WALLS ..... 2963
*Linda Giresini*

VULNERABILITY ASSESSMENT OF FLAG-SHAPED HYSTERETIC ROCKING BRIDGE BENTS ..... 2980
*Anastasios I. Giouvanidis, Michalis Fragiadakis, Elias G. Dimitrakopoulos*

ENERGY DISSIPATION INVOLVED IN THE OUT-OF-PLANE RESPONSE OF UNREINFORCED MASONRY WALLS ..... 2996
*Umberto Tomassetti, Francesco Graziotti, Andrea Penna, Guido Magenes*

PROBABILISTIC VALIDATION OF THE HOUSNER ROCKING MODEL ..... 3011
*Jonas Bachmann, Mathias Strand, Michalis Vassiliou, Marco Broccardo, Bozidar Stojadinovic*

SIMPLE MODELS FOR THE SEISMIC RESPONSE OF RIGID OR FLEXIBLE BLOCKS ..... 3027
*Spyros Diamantopoulos, Michalis Fragiadakis*

DYNAMIC RESPONSE OF A RIGID SLAB SUPPORTED BY FOUR RIGID CYLINRICAL ROCKING AND WOBBLING COLUMNS ..... 3045
*Sharveen Rajah, Jonas Bachmann, Michalis Vassiliou, Bozidar Stojadinovic*

**MS 32: EXTREME DYNAMICS**

THE EFFECT OF HIGH IMPACT WHEELS ON RAIL FAILURE ..... 3062
*Harry Tournay, Semih Kalay*

DYNAMIC RESPONSES OF RAILWAY ULTRA-HIGH-STRENGTH CONCRETE SLEEPERS UNDER EXTREME IMPACT LOADING ..... 3074
*Sakdirat Kaewunruen, Alex Remennikov, Shintaro Minoura*

NONLINEAR MODELLING AND ANALYSIS OF MOVING TRAIN LOADS ON INTERSPERSED RAILWAY TRACKS .... 3086
*Sakdirat Kaewunruen, Tomasz Lewandrowski, Kritditorn Chamniprasart*

DYNAMIC AMPLIFICATION FACTORS FOR RAILWAY TURNOUT BEARERS IN SWITCHES AND CROSSINGS ..... 3093
*Sakdirat Kaewunruen, Chayut Ngamkranong, Rims Janeliukstis, Ruilin You*

**MS 33: WORKSHOP ON FRAGILITY EVALUATION AND SEISMIC SAFETY ASSESSMENT OF "SPECIAL RISK" INDUSTRIAL PLANTS (INDUSE-2-SAFETY)**

SEISMIC FRAGILITY OF HORIZONTAL PRESSURE VESSELS - EFFECTS OF STRUCTURAL INTERACTION BETWEEN INDUSTRIAL COMPONENTS ..... 3102
*Jonas Korndörfer, Benno Hoffmeister, Markus Feldmann*

SHAKING TABLE TESTING OF CYLINDRICAL STEEL LIQUID STORAGE TANKS ..... 3112
*Philippe Mongabure, S. Vasic*

**MS 34: VIBRATIONS, STRUCTURAL ENGINEERING AND CONTROL SYSTEMS**

DYNAMIC ANALYSIS AND COMFORT EVALUATION OF A FULL SUSPENSION BICYCLE EQUIPPED WITH A MR DAMPER …… 3128
*Arlindo Pascoal, José Gonçalves, Manuel Braz-César*

DEVELOPMENT OF AN OPTIMAL AND FUZZY SEMI-ACTIVE CONTROL SYSTEM FOR VEHICLE SUSPENSION …… 3134
*Kellie Oliveira, Manuel Braz-César, José Gonçalves*

SEISMIC RESPONSE OF A CANTILEVERED HIGHWAY SIGN SUPPORT WITHOUT AND WITH A TMD DAMPER ….3144
*Fábio Paiva, Rui Barros*

TUBULAR STEEL LATTICE TELECOMMUNICATION TOWERS, SUBJECTED TO WIND LOADING AND VORTEX SHEDDING …… 3154
*Dário Vieira, Rui Barros*

**MS 35: SIMPLIFIED METHODOLOGIES AND NUMERICAL TOOLS FOR THE SEISMIC RISK MITIGATION OF BUILDINGS: RECENT ADVANCES AND OPEN CHALLENGES**

APPROACH TO PREDICTION OF R/C BUILDINGS' SEISMIC DAMAGE AS PATTERN RECOGNITION PROBLEM USING ARTIFICIAL NEURAL NETWORKS …… 3163
*Konstantinos Morfidis, Konstantinos Kostinakis*

FLORENCE: SEISMIC ASSESSMENT OF NOT-HISTORICAL MASONRY BUILDINGS POPULATION …… 3189
*Giulia Metelli, Tommaso Rotunno, Marco Tanganelli, Stefania Viti*

SEISMIC ASSESSMENT OF A RC CASE STUDY BUILDING USING THE SIMPLE LATERAL MECHANISM ANALYSIS, SLAMA, METHOD …… 3201
*Roberto Gentile, Ciro Del Vecchio, Giuseppina Uva, Stefano Pampanin*

NOVEL MODELS AND TOOLS TO EVALUATE THE ECONOMIC FEASIBILITY OF RETROFITTING INTERVENTION …… 3213
*Marco Vona, Monica Mastroberti, Benedetto Manganelli*

NEW SEISMIC RISK INDEX FOR EXISTING BUILDINGS …… 3225
*Monica Mastroberti, Marco Vona*

**MS 36: VEHICLE BRIDGE INTERACTION DYNAMICS AND ITS APPLICATION FOR DRIVE-BY BRIDGE HEALTH MONITORING**

USING AN INSTRUMENTED VEHICLE TO ESTIMATE SURFACE ROUGHNESS OF A BRIDGE …… 3235
*Ying Zhan, Francis T.K. Au*

ON THE ESTIMATION OF BRIDGE MODE SHAPES FROM DRIVE-BY MEASUREMENTS …… 3248
*Abdollah Malekjafarian, Eugene OBrien*

**MS 38: COMPUTATIONAL STRATEGIES AND ASSESSMENT OF IN-PLANE AND OUT-OF-PLANE SEISMIC RESPONSE OF INFILLED FRAMES**

COMPARATIVE ASSESSMENT OF STRUT MODELS FOR THE MODELLING OF IN-PLANE SEISMIC RESPONSE OF INFILL WALLS ..... 3255
*Laura Liberatore, Fabrizio Noto, Fabrizio Mollaioli, Paolo Franchin*

FURTHER DEVELOPMENTS OF A SIMPLIFIED MODELLING OF INFILLED FRAMES FOR REINFORCED CONCRETE BUILDINGS ..... 3269
*Giuseppina Uva, Andrea Fiore, Francesco Porco*

DEFINITION OF A FIBER MACRO-MODEL FOR NONLINEAR ANALYSIS OF INFILLED FRAMES ..... 3281
*Fabio Di Trapani, Liborio Cavaleri, Gabriele Bertagnoli, Giuseppe Mancini, Diego Gino, Marzia Malavisi*

NONLINEAR STATIC ANALYSIS OF INFILLED RC FRAMES: A NOVEL SIMPLIFIED PROCEDURE ..... 3297
*Carmine Lima, Ciro Faella, Enzo Martinelli*

INELASTIC RESPONSE OF MASONRY INFILLED REINFORCED CONCRETE STRUCTURES ..... 3312
*Alkis Fotos, Filippos Foskolos, Athanasios Tsaris, Constantinos Repapis, Panagiotis Asteris*

LATERAL RESPONSE EVALUATION OF STEEL FRAME STRUCTURES WITH MASONRY INFILLS ..... 3323
*Antonios Kritikos, Georgios Ntasis, Dimitrios Zitouniatis, Minas Lemonis, Panagiotis Asteris*

DIRECTIONAL EFFECTS ON COMBINED IN-PLANE AND OUT OF PLANE SEISMIC BEHAVIOR OF MASONRY INFILLS ..... 3332
*Marco Donà, Giovanni Tecchio, Luca Domenicale, Elisa Saler, Massimiliano Minotto, Francesca da Porto*

DEVELOPMENT OF A THREE-DIMENSIONAL COMPUTATIONAL MODEL FOR THE IN-PLANE AND OUT-OF-PLANE ANALYSIS OF MASONRY-INFILLED REINFORCED CONCRETE FRAMES ..... 3352
*Filip Anić, Davorin Penava, Vasilis Sarhosis*

SIMPLIFIED MODELING OF MASONRY INFILL WALLS WITH HORIZONTAL SLIDING JOINTS ..... 3367
*Valentino Bolis, Marco Preti, Andreas Stavridis*

EMPIRICAL-BASED INFILL MODEL ACCOUNTING FOR IN-PLANE/OUT-OF-PLANE INTERACTION APPLIED FOR THE SEISMIC ASSESSMENT OF EC8-DESIGNED RC FRAMES ..... 3380
*Paolo Ricci, Mariano Di Domenico, Gerardo M. Verderame*

INFLUENCE OF IN-PLANE AND OUT-OF-PLANE INTERACTION OF INFILL WALLS ON GLOBAL COLLAPSE RESISTANCE CAPACITY OF INFILLED RC FRAME ..... 3398
*Jianping Han, Zhenlong Zhang, Linjie Huang, Xiaoyun Sun*

IN-PLANE SEISMIC PERFORMANCE OF RC STRUCTURES WITH AN INNOVATIVE MASONRY INFILL WITH SLIDING JOINTS THROUGH NON-LINEAR ANALYSES ..... 3406
*Andrea Rossi, Paolo Morandi, Riccardo Milanesi, Guido Magenes*

## Regular Sessions

### RS 4: DYNAMICS OF CONCRETE STRUCTURES

SEISMIC BEHAVIOR OF PRESTRESSED PRECAST SHEAR WALL BUILDINGS USING MULTIPLE ROCKING JOINTS ..... 3426
*Boya Yang, Xilin Lu*

INFLUENCE OF RIGID FLOOR ASSUMPTION IN SEISMIC ANALYSIS OF RC EXISTING BUILDINGS ..... 3439
*Francesco Porco, Sergio Ruggieri, Domenico Raffaele*

DEVELOPMENT OF A CURVILINEAR HYSTERESIS MODEL FOR REINFORCED CONCRETE STRUCTURES ..... 3450
*Daisuke Kitagawa, Hisashi Umemura*

MRFS DESIGNED ACCORDING TO THE THEORY OF PLASTIC MECHANISM CONTROL VS CODE RULES ..... 3459
*Roberta Muscati*

NONLINEAR FEA OF SOIL-STRUCTURE-INTERACTION EFFECTS ON RC SHEAR WALL STRUCTURES ..... 3476
*Mohammad AlHamaydeh, George Markou, Dina Saadi*

SEISMIC FINITE ELEMENT ANALYSIS OF AN EXISTING OLD CONCRETE STRUCTURE BY USING MULTIFIBER BEAMS: INTRODUCTION OF AN ADAPTIVE PUSHOVER METHOD ..... 3491
*Ahmad Omar, Stéphane Grange, Frédéric Dufour*

### RS 5: DYNAMICS OF COUPLED PROBLEMS

SEISMIC DESIGN OF ABOVEGROUND STORAGE TANKS CONTAINING LIQUID ..... 3506
*Martin Sivy, Milos Musil*

TORSION EFFECT DUE TO ASYMMETRIC SEISMIC POUNDING BETWEEN MULTISTORY RC BUILDINGS ..... 3519
*Christos G. Karayannis, Maria C. Naoum*

DYNAMIC ANALYSIS OF BRIDGE GIRDERS UNDER MOVING LOADS CONSIDERING WARPING EFFECTS: NUMERICAL AND ANALYTICAL BEAM MODELS ..... 3530
*João Serra, Ricardo Vieira, Francisco Virtuoso*

DYNAMICAL BEHAVIOR OF A WIND TURBINE POWER TRAIN CONSIDERING A ROTOR-GEARBOX-GENERATOR COUPLED MODEL ..... 3543
*Rafael Teixeira, Flavia Ohara, Matheus Milhomens, Aline Paula*

INTER-STORY POUNDING AND TORSIONAL EFFECT DUE TO INTERACTION BETWEEN ADJACENT MULTISTORY RC BUILDINGS ..... 3556
*Christos G. Karayannis, Maria C. Naoum*

NUMERICAL SIMULATION OF SOIL-STRUCTURE INTERACTION: A PARAMETRIC STUDY ..... 3568
*Maria Giovanna Durante, Luigi Di Sarno, Armando Lucio Simonelli*

SEISMIC ANALYSIS OF A HISTORIC WATER TOWER: A FLUID-STRUCTURE-SOIL INTERACTION PROBLEM ……..… 3578
*Angeliki Zanni, Michail Spyridis, Dimitris L. Karabalis*

DEVELOPMENT OF AMPLIFIED SEISMIC RESPONSE SPECTRA FOR STRUCTURAL ANALYSIS OF DECOUPLED SMALL BORE PIPES …… 3586
*Anders Blom*

**RS 7: GEOTECHNICAL EARTHQUAKE ENGINEERING**

COMPARISON OF 1D EQUIVALENT-LINEAR AND NONLINEAR SEISMIC SITE RESPONSES IN DEEP SEDIMENT LAYERS …… 3606
*Zhu Jiao, Chen Guoxing, Zhao Kai*

A PLASTICITY MODEL FOR 1D SOIL RESPONSE ANALYSIS …… 3618
*Maria Anthi, Panagiota Tasiopoulou, Nikos Gerolymos*

STEADY-STATE AND TRANSIENT DYNAMIC VISCO-ELASTIC RESPONSE OF CONCRETE AND EARTH DAMS DUE TO DAM-RESERVOIR INTERACTION …… 3630
*Loizos Pelecanos, Stavroula Kontoe, Lidija Zdravkovic*

INVESTIGATING THE EFFECT OF USING SOIL BENTONITE WALL ON DAMAGE MITIGATION OF STEEL BURIED PIPELINES SUBJECTED TO REVERSE FAULT RUPTURE …… 3647
*Farnoud Farzanegan Pour, Meysam Fadaee*

GENERATING ARTIFICIAL TIME HISTORIES USING A NEW COMPUTER-BASED ENVIRONMENTAL PLATFORM: OPENSIGNAL …… 3659
*Marco Baglio, Sebastiano Marasco, Gian Paolo Cimellaro*

NUMERICAL SIMULATIONS WITH CUSHIONING MATERIAL INSTALLED BEHIND THE RETAINING WALL FOR RESILIENT STRUCTURES …… 3671
*Kazuhiro Kaneda, Hiroyuki Yamazaki, Satoru Ohtsuka*

**RS 11: NONLINEAR DYNAMICS**

AN ENERGY-MOMENTUM FORMULATION FOR NONLINEAR DYNAMICS OF PLANAR CO-ROTATING BEAMS … 3682
*Sophy Cchang, Mohammed Hjiaj, Jean-Marc Battini, Carlo Sansour*

NUMERICAL STUDY ON SEISMIC RESPONSE ANALYSIS OF THE PLATE GIRDER BRIDGE DAMAGED BY 2016 KUMAMOTO EARTHQUAKE …… 3697
*Mya Nan Aye, Akira Kasai, Zhipeng Liu*

DISSIPATING EFFECT OF GLAZED CURTAIN WALL STICK SYSTEM INSTALLED ON HIGH-RISE MEGA-BRACED FRAME-CORE BUILDINGS UNDER NONLINEAR SEISMIC EXCITATION …… 3711
*Lorenzo Casagrande, Antonio Bonati, Ferdinando Auricchio, Antonio Occhiuzzi*

A DISCONTINUOUS GALERKIN MATERIAL POINT METHOD (DGMPM) FOR THE SIMULATION OF IMPACT PROBLEMS IN SOLID MECHANICS ..... 3728
*Adrien Renaud, Thomas Heuzé*

THE EFFECT OF INPUT MOTION SELECTION STRATEGIES ON NONLINEAR GROUND RESPONSE PREDICTIONS . 3739
*Yusuf Guzel, Gaetano Elia, Mohamed Rouainia*

STUDY ON IMPACT LOAD RESPONSE OF THE PC SLEEPER FOR RAIL JOINT USING THREE-DIMENSIONAL NUMERICAL ANALYSIS MODEL ..... 3748
*Shintaro Minoura, Tsutomu Watanabe, Kodai Matsuoka, Hiroshi Yamane*

RESONANCE PHENOMENA IN SYSTEMS WITH HYSTERETIC NONLINEARITIES ..... 3756
*Mikhail E. Semenov, Olga O. Reshetova, Olesya I. Kanishcheva, Peter A. Meleshenko, Evgeniya G. Kabulova*

FLUTTER ANALYSIS OF COMPOSITE LAMINATES WITH CURVILINEAR FIBRES ..... 3763
*Hamed Akhavan, Pedro Ribeiro*

ON THE DYNAMIC BEHAVIOR OF A NONLINEAR OSCILLATOR WITH SOFTENING CHARACTERISTICS ATTACHED TO AN ELECTRO-DYNAMIC ACTUATOR ..... 3771
*Alfonso Cutuli, Rosario Aiello, Gianluca Gatti*

MODELLING COCNCRETE MATERIAL BEHAVIOUR UNDER HIGH LOADING RATES ..... 3779
*Alaa Swesi, Ali Abbas, Demetris Cotsovos*

NUMERICAL ANALYSIS OF FLUTTER INSTABILITY IN SIMPLIFIED BLADE CASCADE ..... 3795
*Jan Vimmr, Ondrej Bublik, Ales Pecka, Ludek Pesek*

HYSTERETIC MODEL FOR THE EXPLICIT MATERIAL POINT METHOD ..... 3808
*Christos D. Sofianos, Vlasis K. Koumousis*

THE EVAUATION APPROCH OF SPENT NUCLEAR FUEL INTERGRITY BY USING FINITE ELEEMENT METHOD ..... 3816
*K. H. Kim, Y. I. Yoo, O C. Kwon, J. K. Park, K. B. Eom, S. K. Lee, J. S. Yoo*

**RS 12: NUMERICAL SIMULATION METHODS FOR DYNAMIC PROBLEMS**

NUMERICAL SIMULATION OF IMPACTS ON ELASTIC-VISCOPLASTIC SOLIDS WITH THE FLUX-DIFFERENCE SPLITTING FINITE VOLUME METHOD ..... 3824
*Thomas Heuzé*

AN INTEGRATED PROCEDURE FOR SEISMIC RESPONSE ANALYSIS OF STRUCTURES USING DIFFERENTIAL QUADRATURE METHOD ..... 3835
*Hongjing Li, Xijun Kong, Haojie Xing*

DYNAMICAL PROCESSES ANALYSIS IN THE LOAD BEAMS AFTER PARTIAL DESTRUCTION ..... 3847
*Vladimir Gordon, Olga Pilipenko*

MODAL ANALYSIS PROCEDURE USING COMPLEX LEFT AND RIGHT EIGENVECTORS OF NON-PROPORTIONALLY DAMPED STRUCTURES ..... 3861
*Evgueni Stanoev*

ISOGEOMETRIC METHODS IN DYNAMIC ANALYSIS OF CURVED BEAMS INCLUDING WARPING AND DISTORTIONAL EFFECTS ..... 3892
*Ioannis Tsiptsis, Evangelos Sapountzakis*

ACCURATE NUMERICAL METHODS FOR STUDYING THE NONLINEAR WAVE-DYNAMICS OF TENSEGRITY METAMATERIALS ..... 3911
*Francesco Fabbrocino, Gerardo Carpentieri, Ada Amendola, Rosa Penna, Fernando Fraternali*

ANALYSES OF THE SEISMIC ACTIONS RECORDED DURING THE 2016 CENTRAL ITALY SEISMIC SEQUENCE: OBSERVED VS CODE PROVISION VALUES ..... 3923
*Felice Carlo Ponzo, Rocco Ditommaso, Antonella Nigro, Chiara Iacovino*

ANALYTICAL MODEL OF THE DYNAMICS OF RAILWAY SLEEPER ..... 3937
*Le Hung Tran, Tien Hoang, Gilles Foret, Denis Duhamel, Samir Messad, Arnaud Loaec*

THE USE OF ARTIFICIAL NEURAL NETWORKS (ANN) FOR THE PRELIMINARY DESIGN OF HIGH-RISE BUILDINGS ..... 3949
*Aadhish Man Rajbhandari, Naveed Anwar, Fawad Najam*

**RS 13: OPTIMUM DESIGN AND CONTROL IN STRUCTURAL DYNAMICS AND EARTHQUAKE ENGINEERING**

OPTIMAL FRICTION COEFFICIENTS FOR ISOLATED STRUCTURES DEPENDING ON THE SOIL CONDITION ..... 3963
*Paolo Castaldo, Marianela Ripani*

STUDY ON THE SHEAR WALL STRUCTURE WITH COMBNED FORM OF REPLACEABLE COMPONENTS ..... 3982
*Cong Chen, Xilun Lu, Renjie Xiao*

FINITE ELEMENT ANALYSIS OF EXTERNAL RC WIDE BEAM-COLUMN JOINTS PROVIDED WITH DIFFERENT DETAILING SOLUTIONS ..... 3992
*Giuseppe Santarsiero, Angelo Masi*

INNOVATIVE STRUCTURES FOR DYNAMIC SOLAR FAÇADES ..... 4007
*Raffaele Miranda, Francesco Fabbrocino, Enrico Sicignano, Robert E. Skelton, Fernando Fraternali*

ADAPTIVE NEURO FUZZY CONTROL FOR VIBRATION SUPPRESSION OF A SMART BUILT-IN PLATE WITH ENBEDED PIEZOELECTRIC SENSORS AND ACTUATORS ..... 4017
*Georgios Tairidis, Georgios Stavroulakis*

TORSIONAL BALANCE OF TWO-WAY ASYMMETRIC PLANS WITH OPTIMAL DISTRIBUTION OF VISCOUS DAMPERS ..... 4029
*Amir Shahmohammadian, Mohammad Reza Mansoori, Mir Hamid Hosseini*

A SEMI-ANALYTICAL MODEL FOR DISSIPATIVE SHEAR LINKS: EXPERIMENTAL TESTS AND NUMERICAL ANALYSES ..... 4042
*Silvia Caprili, Nicola Mussini, Walter Salvatore*

DUAL-PHASE STEEL REINFORCING BARS FOR MRFS STRUCTURES IN SEISMIC PRONE AREAS ..... 4053
*Riccardo Aiuti, Cristiano Ascanio, Silvia Caprili, M. Dolšek, Walter Salvatore, Renzo Valentini, J. Žižmond*

COLLAPSE CAPACITY PREDICTION OF SDOF SYSTEMS EQUIPPED WITH FLUID VISCOUS DAMPERS ..... 4066
*Zeynab Gharyanpoor, Benyamin Mohebi, Mansoor Yakhchalian*

ON THE USE OF GENETIC ALGORITHMS TO ASSESS THE SEISMIC RESISTANCE OF PLANAR FRAME STRUCTURES ..... 4076
*Annalisa Greco, Francesco Cannizzaro, Alessandro Pluchino*

SEISMIC PROGRESSIVE COLLAPSE OF MRF-EBF DUAL STEEL SYSTEMS ..... 4088
*Alireza Faroughi, Abdolreza S.Moghadam, Mahmood Hosseini*

REDUCING VIBRATIONS IN A FOOTBRIDGE USING A SEMI-ACTIVE TUNED MASS DAMPER ..... 4099
*Carlos Moutinho, Álvaro Cunha, Elsa Caetano*

AN APPROACH TO THE DYNAMIC CONTROL OF VIBRATIONS IN STRUCTURAL SYSTEMS SUBJECT TO EARTHQUAKES ..... 4115
*Ileana Corbi, Ottavia Corbi, Francesca Tropeano*

DYNAMIC CONTROL OF RIGID-FAILURES MODES IN MASONRY STRUCTURES SUBJECT TO GROUND MOTION ..... 4122
*Ileana Corbi, Ottavia Corbi, Francesca Tropeano*

**RS 15: PERFORMANCE-BASED EARTHQUAKE ENGINEERING**

SEISMIC RELIABILITY-BASED DESIGN OF PERFECTLY ELASTOPLASTIC STRUCTUTRES ISOLATED BY FPS ..... 4129
*Paolo Castaldo, Bruno Palazzo, Tatiana Ferrentino*

SEISMIC RELIABILITY-BASED DESIGN OF INELASTIC STRUCTURES WITH DIFFERENT VALUES OF THE POST-YIELDING STIFFNESS ISOLATED BY FPS ..... 4145
*Paolo Castaldo, Bruno Palazzo, Gaetano Alfano, Mario Francesco Palumbo*

INFLUENCE FACTORS FOR THE ASSESSMENT OF MAXIMUM LATERAL SEISMIC DEFORMATIONS IN ITALIAN MULTISTOREY RC BUILDINGS ..... 4161
*Marco Gaetani d'Aragona, Maria Polese, Andrea Prota*

PROCESSING OF 3D OPTICAL MOTION DATA OF SHAKING TABLE TESTS: FILTERING OPTIMIZATION AND MODAL ANALYSIS ..... 4174
*Ivan Roselli, Daniela Paolini, Marialuisa Mongelli, Gerardo De Canio, Gianmarco de Felice*

PERFORMANCE BASED EARTHQUAKE ASSESSMENT OF AN INDUSTRIAL GAS FILTER STRUCTURE ..... 4184
*Raffaele Laguardia, Andrea Piscini, Marco Faggella, Rosario Gigliotti, Francesco Morelli, Franco Braga, Walter Salvatore*

**RS 17: REPAIR AND RETROFIT OF STRUCTURES**

RATIONAL SEISMIC RETROFITTING OF RC STRUCTURES BASED ON GENETIC ALGORITHMS ..... 4194
*Roberto Falcone, Ciro Faella, Carmine Lima, Enzo Martinelli*

EXPERIMENTAL ASSESSMENT OF CARBON FIBER JACKETING OF STEEL PLATES ..... 4213
*Salvatore Sessa, Ferdinando Toraldo, Francesco Marmo, Daniele Masi, Luciano Rosati*

COMPARING EN1998-3 AND KAN.EPE. MODELS FOR RETROFITTING REINFORCED CONCRETE COLUMNS WITH INADEQUATE DUCTILITY ..... 4224
*Nefeli V. Peponi, Stephanos E. Dritsos, Sotiria N. Athanasopoulou*

PREFABRICATED RESPONSIVE DIAGRIDS FOR HOLISTIC RENOVATION OF EXISTING MID-RISE RC BUILDINGS ..... 4234
*Simone Labò, Chiara Passoni, Alessandra Marini, Andrea Belleri, Guido Camata, Paolo Riva, Enrico Spacone*

REINFORCED CONCRETE FRAMES STRENGTHENED BY TENSION-TIE ELEMENTS UNDER CYCLIC LOADING: A COMPUTATIONAL APPROACH ..... 4245
*Angelos Liolios, Constantin Chalioris*

REINFORCED CONCRETE FRAMES STRENGTHENED BY TENSION-TIE ELEMENTS UNDER CYCLIC LOADING: EXPERIMENTAL INVESTIGATION ..... 4259
*Angelos Liolios, Panagiotis Efthymiopoulos, Theofilos Mergoupis, Vaios Rizavas, Constantin Chalioris*

RESPONSE OF REPAIRED FUSE BEAMS TO DYNAMIC TESTING ..... 4270
*Emmanouil Vougioukas, Stella Avgerinou, Konstantinos Theocharis*

DESIGN OF GROUTS FOR STRENGTHENING THREE OR TWO LEAF MASONRY WITH MUD MORTARS ..... 4277
*Vasiliki Nikolopoulou, Chryssi-Elpida Adami, Elizabeth Vintzileou, Vasiliki Palieraki*

**RS 18: SEISMIC ISOLATION**

NUMERICAL ASSESSMENT OF CONCAVE SLIDING ISOLATOR'S MECHANICAL BEHAVIOR UNDER BI-DIRECTIONAL MOTION ..... 4288
*Dario De Domenico, Giuseppe Ricciardi, Gianmario Benzoni*

CALIBRATION OF CONSTITUTIVE MACRO MODEL FOR A LEAD- CORE BEARING DEVICE: IDENTIFICATION BASED ON RESULTS OBTAINED BY FINITE ELEMENT ANALYSIS ..... 4306
*Todor Zhelyazov, Rajesh Rupakhety, Símon Ólafsson*

EFFECTS OF EQUIVALENT RADIAL ACCELEROGRAMS FOR BIDIRECTIONAL SEISMIC EVENTS ON BASE-ISOLATED STRUCTURES ..... 4315
*Marco Furinghetti, Alberto Pavese, Antonio Foti*

DOWNSIZING OF MEMBERS THROUGH NUMERICAL ANALYSIS OF STEEL MULTI-STORIED FRAME WITH PASSIVE FRICTION DAMPERS AT BASE ..... 4331
*Jingye Liu, Minoru Yamanari*

RESIDUAL LOAD CAPACITY OF FIRE-DAMAGED RUBBER BEARINGS FOR R.C. BASE-ISOLATED BUILDINGS SUBJECTED TO NEAR-FAULT EARTHQUAKES ..... 4342
*Fabio Mazza, Fabio Alesina*

COMPARISON OF FRICTION MODELS FOR THE CURVED SURFACE SLIDING SYSTEM IN THE NONLINEAR SEISMIC ANALYSIS OF BASE-ISOLATED BUILDINGS ..... 4358
*Fabio Mazza, Mattia Loprete*

SEISMIC ASSESSMENT OF AN UNCONVENTIONAL STRUCTURE: THE CRYOSTAT OF "CUORE" EXPERIMENT ..... 4374
*Raffaele Ardito, Oliviero Cremonesi, Federico Perotti*

ON THE DESIGN OF PERFORMANCE-BASED PENTAMODE BEARINGS ..... 4381
*Ada Amendola, Magdalini Titirla, Rosa Penna, Francesco Fabbrocino*

INNOVATIVE DEVICES FOR THE BASE ISOLATION OF EXISTING BUILDINGS ..... 4393
*Francesco Fabbrocino, Magdalini Titirla, Ada Amendola, Gianmario Benzoni, Fernando Fraternali*

FINITE ELEMENT MODELING OF SINGLE AND MULTI-SPHERICAL FRICTION PENDULUM BEARINGS ..... 4408
*Ioannis Kavvadias, Henrick Bibo, Lazaros Vasiliadis*

SENSITIVITY OF THE SEISMIC PERFORMANCE OF LIQUID STORAGE TANKS WITH NONLINEAR ISOLATION SYSTEMS TO DEVIATIONS IN MECHANICAL CHARACTERISTICS OF THE SEISMIC ISOLATORS ..... 4417
*Elif Güler, Hatice Gazi, Cenk Alhan*

**RS 19: SEISMIC RISK AND RELIABILITY ANALYSIS**

EARTHQUAKE DAMAGE ESTIMATION OF FOUR PALACE BUILDINGS AND MEASUREMENTS OF VIBRATION DECREASING FOR CULTURAL RELICS CABINET IN BEIJING FORBIDDEN CITY ..... 4426
*Junwu Dai, Lulu Zhang, Yongqiang Yang*

VULNERABILITY DATA COLLECTION AND DEFINITION OF SEISMIC RISK FOR CITIES IN PALESTINE ..... 4437
*Antonella Di Meo, Barbara Borzi, Marta Faravelli, Diego Polli, Marco Pagano, Alessio Cantoni*

SEISMIC VULNERABILITY MODELS OF PIERS UNDER NEAR-FAULT GROUND MOTIONS ..... 4452
*Li-bo Chen, Hua-he Wang, Yin Gu*

A CLASS-ORIENTED LARGE SCALE COMPARISON WITH POST-EARTHQUAKE DAMAGE FOR ABRUZZI REGION ... 4464
*Carlo Del Gaudio, Paolo Ricci, Gerardo Mario Verderame*

SEISMIC HAZARD ANALYSIS BASED ON FUZZY-PROBABILISTIC APPROACH ..... 4480
*Jelena Andric, Dagang Lu*

PREDICTION OF DUCTILE DAMAGE IN CASE OF SEISMIC ACTION USING INNOVATIVE DAMAGE MECHANICS ... 4496
*Simon Schaffrath, Helen Bartsch, Benno Hoffmeister, Markus Feldmann*

EFFECT OF MAJOR SEISMOLOGICAL PARAMETERS ON DIRECTIVITY DOMINANT SPECTRAL AMPLIFICATION .... 4509
*Saed Moghimi, Sinan Akkar*

SINGLE STATION SIGMA FOR TURKISH STRONG MOTION STATIONS ..... 4527
*Zehra Cagnan, Sinan Akkar*

A NEW DECISION MAKING METHOD TO SELECT PRIORITY INTERVENTIONS AFTER EXTREME EVENTS ..... 4546
*Glen Dervishaj, Gian Paolo Cimellaro, Anil Agrawal*

SIMULATED DESIGN PROCEDURE FOR AN IMPROVED SEISMIC VULNERABILITY ASSESSMENT OF EXISTING RC BRIDGES ..... 4562
*Paola Ceresa, Lorenzo Marziali*

**RS 21: SOIL DYNAMICS**

SMALL-STRAIN STIFFNESS AND DAMPING OF LOESS IN CHINA ..... 4584
*Binghui Song, Angelos Tsinaris, Anastasios Anastasiadis, Kyriazis Pitilakis, Wenwu Chen*

COMPARATIVE STUDY ON THE INFLUENCE OF DIFFERENT DAMPING VALUES IN SEISMIC SITE RESPONSE ANALYSIS ..... 4595
*Haiping Ding, Junling Ma, Jian Liao*

SIMPLIFIED NUMERICAL MODELING STRATEGIES OF DEEP VIBRATORY COMPACTION ..... 4607
*Maximilian Schmitter, Christoph Adam*

DYNAMIC MODULUS AND DAMPING RATIO OF EPS COMPOSITE SOIL UNDER SMALL STRAIN CONDITION ..... 4623
*Hu Ying, Gao Hongmei, Wang Zhihua, Wang Xudong*

**RS 22: SOIL-STRUCTURE INTERACTION**

SENSITIVITY OF STRUCTURES AND GEOLOGICAL DATA ..... 4634
*Valeriy Barvashov, Gennadii Boldyrev*

IMPACT ASSESSMENT OF EPICENTRE DISTANCES AND ENERGIES OF MINING SHOCKS ON THE TRANSMISSION OF FREE-FIELD VIBRATIONS TO THE BUILDING FOUNDATIONS ..... 4645
*Krystyna Kuźniar, Tadeusz Tatara*

IMPEDANCE FUNCTIONS OF ADJACENT STRIP FOUNDATIONS ..... 4654
*Vasiliki Terzi*

LANDSLIDE-PILE-TUNNEL INTERACTION BY 2D AND 3D FINITE ELEMENT MODELLING ..... 4664
*Mayank Mishra, Roberto Vassallo, Giuseppe Santarsiero, Angelo Masi*

STATIC AND DYNAMIC BEHAVIOUR OF PILE FOUNDATIONS IN HOMOGENEOUS AND INHOMOGENEOUS SOILS ..... 4675
*Lutz Auersch, Greta Markfort*

KINEMATIC STRESS RESULTANTS IN INCLINED SINGLE PILES SUBJECTED TO PRAPAGATING SEISMIC WAVES: AN ANALYTICAL FORMULATION ..... 4691
*Sandro Carbonari, Michele Morici, Francesca Dezi, Graziano Leoni*

EXCITATION OF STRUCTURES NEAR RAILWAY TRACKS—ANALYSIS OF THE WAVE PROPAGATION PATH ..... 4702
*Paulius Bucinskas, Lars Vabbersgaard Andersen*

THE INFLUENCE OF IMPERFECTLY KNOWN LOCAL SUBSOIL CONDITIONS ON THE PREDICTION OF GROUND-BORNE VIBRATIONS IN BUILDINGS ..... 4711
*Manthos Papadopoulos, Stijn François, Geert Degrande, Geert Lombaert*

**RS 26: STOCHASTIC DYNAMICS**

STOCHASTIC RESPONSE OF NONLINEAR BASE ISOLATION SYSTEMS ..... 4726
*Athanasios Markou, George Stefanou, George Manolis*

THE EFFECT OF SEISMIC LOADING SIMULATION ON THE RESPONSE VARIABILITY OF STRUCTURES ..... 4740
*Faidon-Apostolos Vagionas, George Stefanou*

**RS 28: WAVE PROPAGATION**

NUMERICAL SIMULATION OF BLAST WAVE PROPAGATION IN LAYERED SOIL FEATURING SOIL-STRUCTURE INTERACTION ..... 4752
*M. Abir, D. Arumugam, B. Dhana Sekaran, T. R. Subash*

QUANTIFICATION OF GUIDED WAVE INTERACTION EFFECTS WITH LOCALISED STRUCTURAL NONLINEARITIES IN COMPLEX, COMPOSITE STRUCTURES ..... 4766
*Victor Thierry, Dimitrios Chronopoulos, I. Ashcroft*

VIBRATION ATTENUATION IN PIPES: DESIGN AND EXPERIMENTAL VALIDATION OF A RESONANT METAMATERIAL SOLUTION ..... 4778
*Alireza Nateghi, Luca Sangiuliano, Claus Claeys, Elke Deckers, Bert Pluymers, Wim Desmet*

EXPERIMENTAL AND NUMERICAL STUDY OF WAVE DYNAMICS IN TENSEGRITY COLUMNS ..... 4796
*Ada Amendola, Francesco Fabbrocino, Antonino Favata, Andrea Micheletti, Fernando Fraternali, Chiara Daraio*

PREDICTION MODELS OF FREE-FIELD VIBRATIONS FROM RAILWAY TRAFFIC ..... 4810
*Jens Malmborg, Kent Persson, Peter Persson, Lars Vabbersgaard Andersen*

THREE-DIMENSIONAL NUMERICAL MODELING OF SEISMIC WAVE PROPAGATION IN WUDU BASIN, CHINA .. 4821
*Xiaolong Zhang, Xiaojun Li, Zhenghua Zhou, Guoxing Chen, Xiaobo Peng, Ming Lu*

**RS 30: CONCRETE STRUCTURAL MEMBERS**

RESONANCE EVALUATION WITH GEOMETRIC STIFFNESS AND CREEP OF SLENDER BEAM OF REINFORCED CONCRETE ..... 4837
*Alexandre de Macêdo Wahrhaftig, Lázaro S. M. S. C. Nascimento, Reyolando M. L. R. F. Brasil*

SIMULATIONS OF CONCRETE FRACTURE AT VARIOUS STRAIN RATES: PARAMETRIC STUDY ..... 4847
*Josef Květoň, Jan Eliáš*

PRELIMINARY COMPARISON BETWEEN DIFFERENT SOFTWARE MODELING OF CONFINED CONCRETE ..... 4857
*Elide Nastri, Maria Ilenia Palese*

NUMERICAL MODELLING AND CALIBRATION OF RC COLUMNS UNDER AXIAL LOADING ..... 4869
*Tuba Tatar, Mário Pimentel, José Miguel Castro, Mário Marques*

TOOL FOR SHEAR ANALYSIS OF PRESTRESSED STEEL FIBER CONCRETE BEAMS ..... 4881
*P. R. Tadepalli, Liang Lu, Y. L. Mo, T.T.C. Hsu*

NONLINEAR ANALYSIS OF SHEAR CRITICAL RC MEMBERS USING CURRENT FE SOFTWARE ..... 4897
*Paola Ceresa, Alonso González Víquez*

SEISMIC PERFORMANCE OF FULL-SCALE RECYCLED AGGREGATE CONCRETE COLUMNS ..... 4914
*Ilyas Saribas, Caglar Goksu, Alper Ilki*

**RS 33: STEEL STRUCTURES**

DETAILED FEM ANALYSIS FOR FULL SCALE STEEL STRUCTURE CONSIDERING FRACTURE OF BEAM ENDS ..... 4920
*Yasunori Mizushima, Yoichi Mukai, Tomoharu Saruwatari*

MASS VARIATION WITH DISSIPATIVE STEEL STRUCTURES UNDER SEISMIC LOADS ..... 4928
*Peter Knoedel, Thomas Ummenhofer*

NUMERICAL STUDY ON ELASTO-PLASTIC BEHAVIOR OF PIPE-SECTIONED PIER-PILE INTEGRAL STEEL STRUCTURE ..... 4943
*Takayuki Omori, Akira Kasai, Rei Kohara*

FINITE ELEMENT ANALYSES ON SEISMIC RESPONSE OF PARTIAL STRENGTH EXTENDED STIFFENED JOINTS ..... 4952
*Roberto Tartaglia, Mario D'Aniello, Raffaele Landolfo, Gian Andrea Rassati, James Swanson*

NUMERICAL STUDY ON COMPARISON BETWEEN DUCTILITY OF UNSTIFFENEE BOX SECTIONED STEEL STUB COLUMNS AND SIMPLY SUPPORTED STEEL PLATES ..... 4965
*Haruna Satomi, Akira Kasai*

ON DYNAMICS OF LIFT BRIDGE ..... 4975
*Peter Rosko, Juraj Kralik*

2D LATTICE STRUCTURES - A PARAMETRIC ANALYSIS ..... 4986
*Agostina Orefice, Ada Amendola, Rosa Penna, Geminiano Mancusi, Luciano Feo*

APPLICATION OF ELASTOMERIC DAMPERS TO STEEL MOMENT RESISTING FRAMES ..... 5000
*Christos Basagiannis, Martin Williams*

THE INFLUENCE OF GEOMETRY, LOADS AND STEEL GRADE FOR THE DEVELOPMENT OF A SPECIFIC COLLAPSE TYPE OF MR-FRAMES ..... 5014
*Elide Nastri*

THE EFFECT OF NUMBER AND LOCATION OF BRACED FRAMES ON COLUMN BEHAVIOR OF THE DUAL STEEL STRUCTURAL SYSTEM (MRF AND EBF) ..... 5026
*Sajjad Mohammadi, Abdolreza S.Moghadam, Alireza Faroughi,*

**RS 34: MASONRY STRUCTURES**

MODELING FLEXURE-SHEAR FAILURES IN MASONRY-INFILLED RC FRAMES WITH INELASTIC FIBER-BASED FRAME ELEMENTS ..... 5035
*Alexander Kagermanov, Paola Ceresa*

A NEW NUMERICAL PROCEDURE FOR ASSESSING THE DYNAMIC BEHAVIOUR OF ANCIENT MASONRY TOWERS ..... 5045
*Daniele Pellegrini, Maria Girardi, Cristina Padovani, Riccardo Maria Azzara*

ADVANCED NUMERICAL MODELS FOR THE ANALYSIS OF UNREINFORCED AND STRENGTHENED MASONRY VAULTS ..... 5056
*Valentino Paolo Berardi, Mariella De Piano, Giuseppe Teodosio, Rosa Penna, Luciano Feo*

SEISMIC BEHAVIOR OF A REINFORCED MASONRY INFILL MADE WITH AN INNOVATIVE NEW BRICK UNIT: RESULTS OF A SHAKING TABLE TEST ..... 5070
*Elizabeth Vintzileou, Chrissy-Elpida Adami, Vasiliki Palieraki, Charalambos Mouzakis, Lucia Karapitta*

DISCUSSION ON THE RESPONSE OF UNREINFORCED MASONRY TO LOW-AMPLITUDE RECURCIVE LOADS: CASE OF GRONINGEN GAS FIELD …… 5084
*Dimitrios Dais, İhsan E. Bal, Eleni Smyrou*

COMPDYN 2017
6th ECCOMAS Thematic Conference on
Computational Methods in Structural Dynamics and Earthquake Engineering
M. Papadrakakis, M. Fragiadakis (eds.)
Rhodes Island, Greece, 15–17 June 2017

# 3D NUMERICAL SIMULATIONS OF THE SAN MARINO THIRD TOWER (MONTALE) BASED ON 3D MAPPING

**G. Guerra[1], D. Forcellini[1], E. Xhixha[2], G. Peruzzi[2], D. Albarello[2], E. Lo[3], D.E. Mayer[3], S. Trinh[3], E. Zheng[3] and F. Kuester[3]**

1 Università di San Marino
Via Salita alla Rocca, 44, 47890, San Marino
davforc@omniway.sm

2 Dipartimento di Scienze Fisiche, della Terra e dell'Ambiente,
Università di Siena, Siena, Italy.
dario.albarello@unisi.it

3 Center of Interdisciplinary Science for Art, Architecture and Archaeology (CISA3)
University of California, San Diego
fkuester@ucsd.edu

**Keywords:** UNESCO, Historical heritage, 3D mapping, numerical simulations

**Abstract.** *San Marino historic centre was included in UNESCO world heritage list in 2008. The site is located in a region characterized by medium seismic hazard levels. Therefore, preventing earthquake damages is an important goal for preserving historical buildings and fundamental in order to sustain tourism, a relevant source for the local incomes. In this regard, the historical center was object of an extended project jointly organized by University of San Marino, University of Siena and the Center of Interdisciplinary Science for Art, Architecture and Archaeology California (CISA 3) at University of California, San Diego. In particular, the three middle-age towers of San Marino can be considered a landmark for the Republic and the world. In this framework, the paper aims at calibrating a 3D numerical finite element (FE) of the third tower, called Montale. This study can be seen as a proposal to assess seismic behaviour of historical towers, as well as an easy-to-use model for engineers and consultants all over the world. The presented outcomes will represent an important basis for risk reduction actions by the San Marino authorities.*

## 1 INTRODUCTION

Cultural heritage is an important asset to the civil, social, cultural and economic life of a country. Its preservation has been improved by adopting various technologies that achieve more effectively the objectives of protection, conservation and valorization of historical and artistic artefacts. The object of this paper is Montale, the third tower among the ones in San Marino and one of its masterpiece (included in UNESCO world heritage list in 2008). The site is located in a region characterized by medium seismic hazard levels. Therefore, preventing earthquake damages is an important goal for conservation of historical buildings and fundamental in order to sustain tourism, a relevant source for the local incomes.

In this regard, the historical center was object of two extended projects jointly organized by University of San Marino, University of Siena and the Center of Interdisciplinary Science for Art, Architecture and Archaeology California (CISA 3) at University of California, San Diego. The first step consisted of the application of ambient vibration technique to the three middle-age towers located in San Marino in order to identifying fundamental (elastic) resonance frequencies, key parameters for assessing seismic behavior of historical buildings. Two campaigns have been carried out on October 2015 and October 2016. The second step was aimed at applying the most credited technologies to register a tridimensional mapping of the historical center. On July 10-17 2016 the mapping campaign was carried out with 3D laser scanners, one cave camera and one drone. The results have been post-processed during the following months at University of California, San Diego. These previous activities gave the possibility to collect many information regarding the dimensions, materials, structural and dynamic characteristics that were fundamental in order to perform a Finite Element Model (FEM) in order to represent the dynamic behavior (the 'response') of the tower under possible seismic motions.

## 2 CASE STUDY

This paper aims at reproducing the seismic response of Montale. tower. It dates back to the end of the XIII century and it is the smallest among the towers. Because of its position for a look-out post, this tower played a strategic role as its defensive purposes. The fortress, with its pentagonal floor plan, has been restored on numerous occasions during the course of the centuries. The last restoration took place in 1935. Inside there is a prison 8 meters deep, called "the bottom of the tower". Montale is surrounded by very large and ancient rocks arranged to form a primitive wall structure.

The tower is 17.68 m tall. The plan section consists of an irregular pentagon with the five sides of different length (see Figure 1). The structure is divided by two floors. The first is made with stones at a high of about 5 m from the ground. The second is built with wood. Since it was impossible to reach the ground floor, it was decided to consider the first floor thickness around 50 cm. The upper slab is a stone arc floor. The arc thickness goes from more than 1 m in the side until about 30 cm for a little stretch in the middle. The roof is made of wood with shingle blocked with some rocks. In correspondence with the highest part of the tower, there are two important medieval components: the shrinkage and the battlements all around the building.

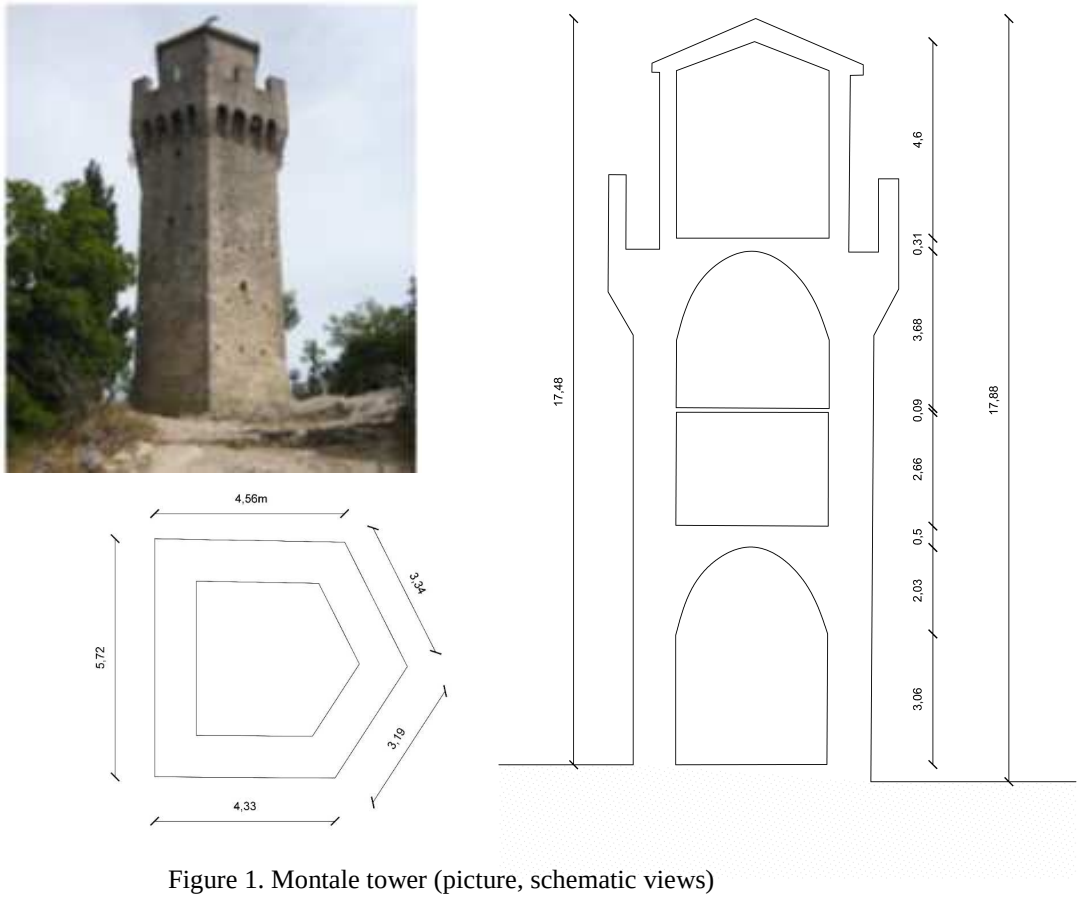


Figure 1. Montale tower (picture, schematic views)

## 3 3D MAPPING

Computer technology has been transferred to artistic and cultural heritage protection and diagnosis [1] and [2]. In this regard, a project joined between University of San Marino and the Center of Interdisciplinary Science for Art, Architecture and Archaeology California (CISA 3) at University of California, San Diego (UCSD) was carried with the aim of realizing a 3D mapping of the historical center, in particular its principal monuments. The project was sponsored by UNESCO national commission in San Marino, the Environmental and the University and Research Ministers of the Repubblic of San Marino.. The aim was the assessment of the actual state of the tower in order to study possible restoration procedures. 3D laser scanner technology was chosen in order to have the complete survey of the building with 2D data (floor plants and section) and 3D data (point cloud of the tower) in the faster and easier way. A difficulty of the project was the total absence of data and reliable plans of many of the historical buildings of the Republic of San Marino and particularly the third tower.

The team from UCSD came to San Marino between July 10$^{th}$ to July 17$^{th}$, 2016. The instruments consisted essentially in the Faro focus, one drone and one cave camera. In order to have a day-by-day preview of the work, at the end of each day, the team sent the acquired files at the computer of California Institute for Telecommunications and Information Technology to post-process the data.

### 3.1 Instrumentations

The laser scanner (3D Faro Focus [3] and [4]) is one of the best instrument for this kind of project and it offers many advantages. It is a non-invasive method to collect data, suitable in cases of detection of historic buildings. The large amount of data obtained in a very short time allows to analyse the current state of the monument. Efficiency is another advantage of such technology, compared to a traditional method of relief. In particular, historical monuments are often characterized by irregular geometries and many imperfections. In this regard, a conventional-way survey would have required more time and human resources. The efficiency consists of high scanning speed and high precision. In particular, Focus3D generates (with millimetre precision) a virtual copy of reality to the speed of 976.000 measurement points per second. After the elaboration of this kind of data it is possible to obtain dense point clouds that can be transformed in geometric elements such as floor plants and section. Faro focus is made of a tripod, with three extensible legs, a screw in the centre of the base to secure the instrument, a toric compass through which you can put the instrument perfectly horizontal. Figure 2 shows the structure of the instrument that essentially consists of a parallelepiped-shaped body with a central rotating mirror that directs the laser beams against the surfaces to be recorded. Faro Focus 3D has a recording range up to a maximum of 305° along the vertical axis and 360° along the horizontal axis.

A complete survey of the tower involved some parts which were difficult to be accessed, like the below part of the roof or some part near the cliff of the mount Titano. For these elements, capturing the data with the Faro Focus 3D was almost impossible. Therefore, one drone (Figure 3(a)) was used for this project. It is a professional drone, named DJI phantom 3 [5] quadcopter with a high resolution camera on the bottom. The camera can register a 4K movie at 30 frame for second and 12-megapixel photo. A 3-axis gimbal was used to stabilize the camera, by the numerous vibrations of the drone. With this data was possible to complete the high external part of the third tower. The use of the drone was essential in order to capture the profile of the entire mount Titano and the city centre of San Marino. It was fundamental to connect the three towers in the 3D point cloud as well.

One cave camera (Figure 3(b)) was used as well. This instrument is composed by a tripod with two cameras fixed at the top of it. Cave camera is able to rotate in the vertical and horizontal axis and take pictures with the two cameras every step for all the 360° for a total of 96 picture for camera. The results consist of two (one per each camera) different single pictures of resolution 32884x16442 pixel and 614 MB of size representing the left and right eyes. The software Agisoft PhotoScan was applied to align the pictures and create a unique one.

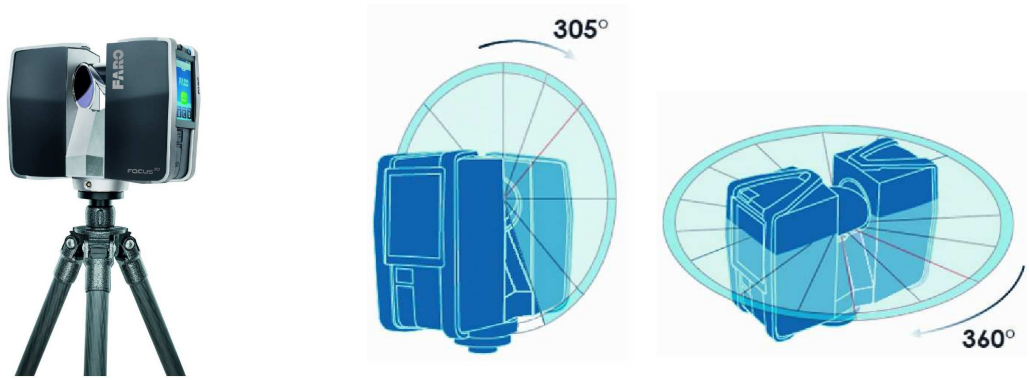


Figure 2. The laser scanner (3D Faro Focus) applied in the study

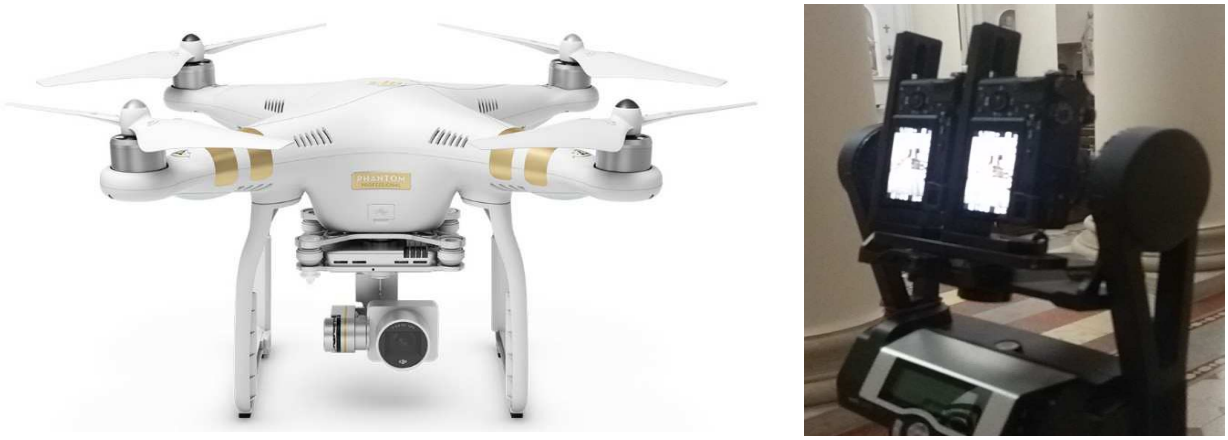

Figure 3. Drone (a) and Cave Camera (b) applied in the study

### 3.2 Post processing

The data were elaborated with Agisoft PhotoScan, a stand-alone software solution for automatic generation of dense point clouds, textured polygonal models, georeferenced true orthomosaics from still images. Agisoft is capable of processing of thousands of high-speed photos and providing at the same time high accurate results (up to 3 cm for aerial and up to 1 mm for close-range photography). After the important operation of alignment of the photos, dense point cloud models can be generated by PhotoScan. Based on the estimated camera positions, the software calculates depth information for each camera to be combined into a single dense point cloud. The photos of input added in the software were 2460. The first step was to align photos and the results is showed in Figure 4(a). Then, it was necessary to reconstruct every shots taken with the drones, to build the dense cloud and to delineate the area around the tower. Figure 4(b) shows the results of this process. The final model was built with triangular meshes that connect the points.



Figure 4 (a): point cloud (first step), (b): final point cloud

## 4 SSR IDENTIFICATION

A preliminary study of identification of the principal dynamic properties of the tower was provided in the frame of a research agreement between University of San Marino and University of Siena [1] and [2]. Resonance frequencies of the tower (in the small strain domain) have been estimated by applying the Standard Spectral Ratios (SSR) approach aiming at evaluating seismic response of old buildings based on ambient vibration monitoring (e.g., [6]). The technique consists in measuring (by velocimetric sensors) average spectral amplitudes of vibrations at any floor or level of the structure induced by ambient ground shaking. These are compared with those obtained (asynchronously) in the free field near the building to be evaluated. Spectral ratios are then computed to identify main natural frequencies of the structure coupled with the soil. In particular, in the presence of a relatively rigid soil (as in the case of San Marino), the contribution of soil-structure interaction can be assumed negligible: in this situation, resonance periods deduced in this way are expected to be close to those of the same structure on a rigid base (at least for the first modes). In principle, this allows for the derivation of the intrinsic properties of the structure from the measurement of displacements. In these conditions, the motion at the base of the structure can be assumed as nearly identical to those of incident ground motion. More details in [1] and [2]. Figure 5 and Table 1 show the results in terms of SSR for the 4 levels of the tower (L0-L4) in the North South (N-S) component and in the East West (E-W) component.

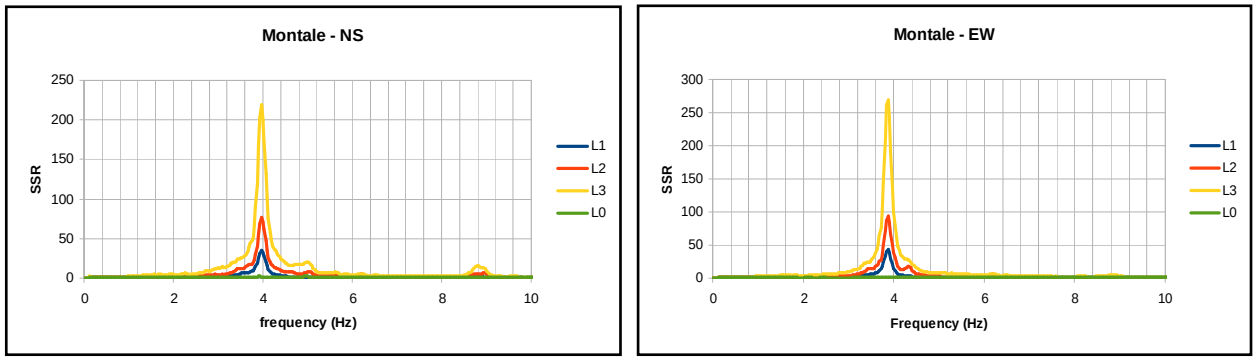


Figure 5 Outcomes of the SSR measurements: (a): N-S component, (b): E-W component

| Frequency | N-S | E-W |
|---|---|---|
| 1st | 4.02 | 3.85 |
| 2nd | 6.19 | 6.18 |
| 3rd | 8.93 | 8.93 |
| 4th | 9.62 | 9.86 |
| 5th | 15.20 | 14.96 |

Table 1: Results from the SSR identification

## 5 FEM MODEL

The finite element model (FEM) of the tower was performed with the software Sap 2000. The model has been calibrated by comparing the resulted fundamental frequencies and shape modes with those from the ambient vibration technique survey. The geometric characteristics have been taken by the database from the 3D mapping. In particular, some simplifications of the geometry were necessary. For example, the intermediate wood slab has been neglected in

the model because it was considered irrelevant in determining the behavior of the tower. The upper arc thickness was considered homogenous and 75 cm thick. The roof was modelled with a 25 cm thickness wood slab. The shrinkage and the battlements were neglected in the model. For this reason, the total mass of the tower was decreased of 300kN, in order to consider the area lost on the wall due to the battlements. In order to take into account the weight, the density of the floor which is at the same level of the battlement has been decreased. Finally, the effects of soil structure interaction have been neglected and the tower was assumed fixed at the ground. This simplification is realistic, since the building is directly founded on a hard rock.

In order to calibrate the model, four models have been performed in terms of overall size and distribution of the finite elements. Since the aim of the study is the reproduction of the frequencies, the fundamental period of the tower was selected as the main parameter to compare the convergence. The performed meshes (Figure 5) have increasing number of joints and elements (Table 2).

Figure 6 shows the first six frequencies of the tower for the four different mesh in the following images. The results show that increasing the number of finite elements, the tower becomes less rigid. There is a good convergence between the four meshes. The most precise mesh is Mesh_04, but computational time was high, that it was decided to use the mesh_03.

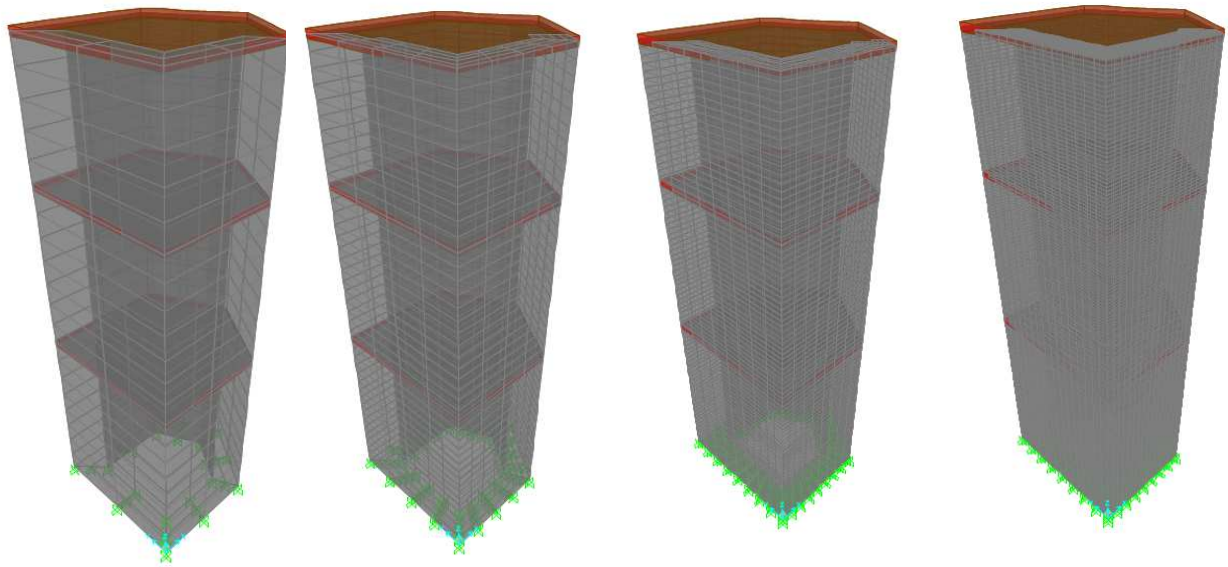

Figure 5: Meshes adopted in the study

| Frequency | joints | 3D elements |
|---|---|---|
| Mesh_01 | 630 | 400 |
| Mesh_02 | 4100 | 3200 |
| Mesh_03 | 29160 | 25600 |
| Mesh_04 | 218960 | 204800 |

Table 2: Meshes adopted in the study

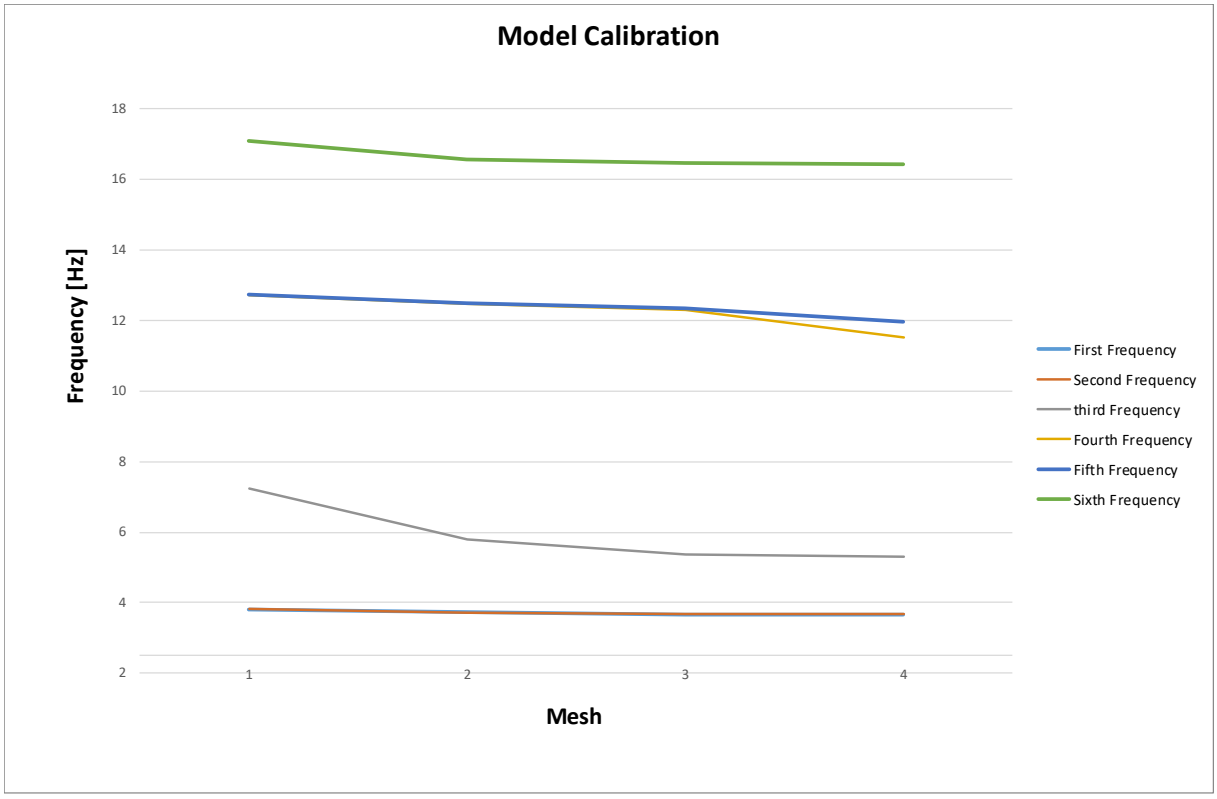


Figure 6: Convergence study

| Frequency | Mesh_01 | Mesh_02 | Mesh_03 | Mesh_04 |
|---|---|---|---|---|
| 1st | 3.805490068 | 3.719211041 | 3.662752134 | 3.669343392 |
| 2nd | 3.823920667 | 3.734800987 | 3.688762513 | 3.685809059 |
| 3rd | 7.217976694 | 5.772516122 | 5.37781980 | 5.298982183 |
| 4th | 12.69843017 | 12.45309568 | 12.29501209 | 11.50587126 |
| 5th | 12.73537497 | 12.48305270 | 12.34966401 | 11.57131375 |
| 6th | 17.07189782 | 16.57264044 | 16.44002199 | 15.52045169 |

Table 3: First six frequency for the 4 meshes adopted in the study

## 6 NUMERICAL MODEL

In order to set up the material parameters, a literature review on several case studies applied to similar structures with the same historical ages was carried out [7], [8] and [9]. In particular, [8] studied the implementation of a finite element model of Chiesa Collegiata, located in Collegiata, Italy. The applied material model was ortotropic material In order to assess the influence of the material parameters, a parametric studies have been performed, by varying several parameters, such as the density, Young modulus and Poisson coefficient. The final characteristics are shown in Table 4 (where 1, 2 and 3 means the directions of the material).

Figure 7 show three shape modes for final mesh adopted in the study. In order to validate the FEM model, these results were compared with the SSR identification shown in paragraph 5. In particular, the first FE model frequency was compared with the NS component of the first modal form, while the second from Sap2000, with the EW component. The superior

modes are compared with both components because the frequency founded with the FEM are combined in both directions. Table 5 shows the results in terms of frequencies. The first and second frequency (translational motions) are close. The mistake in correspondence with the third frequency (the torsional ones) is bigger. The superior frequencies are not so close, but the structure is rigid and the participation masses do not have big influence in the dynamic behavior, since the participation masses on the first frequencies reach the 75% for both NS direction and EW direction, as shown in Table 5.

| Density ($kN/m^3$) | Poisson Coefficient | Coefficient of thermal exp. ($°C^{-1}$) | Modulus of Elasticy (GPa) | | Shear Modulus (GPa) | |
|---|---|---|---|---|---|---|
| 15.5 | 0.15 | $9.90^{-06}$ | $E_1$ | 3.50 | $G_{12}$ | 1.30 |
| | | | $E_2$ | 8.05 | $G_{13}$ | 0.28 |
| | | | $E_3$ | 9.05 | $G_{23}$ | 0.28 |

Table 4: Ortotropic material: characteristics

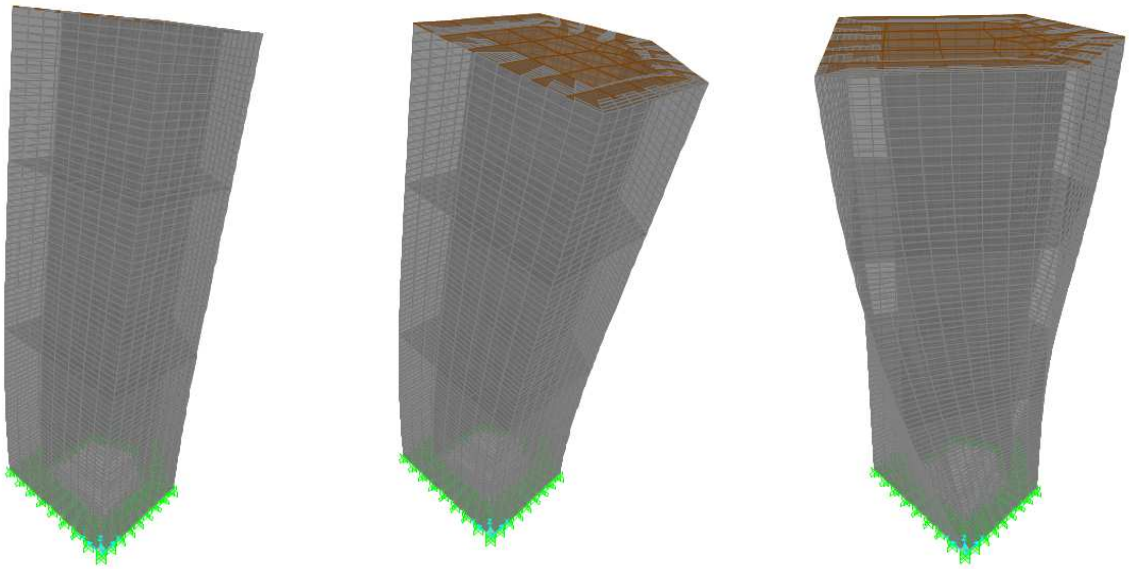

Figure 7: final model performed in the study: first three shape modes

| Freq | SAP2000 | SSR(N/S) | Mx | Error (%) | SSR(E/W) | My | Error (%) |
|---|---|---|---|---|---|---|---|
| 1st | 3.67 | 4.02 | 0.752 | -8.70 | - | 0.017 | |
| 2nd | 3.67 | - | 0.017 | - | 3.85 | 0.753 | -4.68 |
| 3rd | 5.38 | 6.19 | 0.000 | -13.10 | 6.18 | 0.000 | -12.95 |
| 4th | 12.30 | 8.93 | 0.121 | +37.74 | 8.93 | 0.000 | +37.74 |
| 5th | 12.35 | 9.62 | 0.005 | +28.38 | 9.86 | 0.120 | +25.25 |
| 6th | 16.44 | 15.20 | 0.000 | +8.16 | 14.96 | 0.000 | +10.04 |

Table 5: Comparison FEM – SSR frequencies

## 7 CONCLUSIONS

The study presented here is part of a bigger project organized by University of San Marino, University of Siena and the Center of Interdisciplinary Science for Art, Architecture and Archaeology California (CISA 3) at University of California, San Diego. This paper aims at as-

sessing the state of Montale, the third tower in San Marino historical city center. A FEM has been built and performed on the basis of an ambient vibration survey (step 1) and a 3D mapping (step 2). The tower has been performed with SAP2000. The material characteristics have been deduced by a literature review and a parametric study. The frequencies resulted by the numerical simulations have been compared with those resulted by the survey. The presented study can be considered a first attempt to assess seismic behaviors of San Marino historic buildings. The procedure will be extended to other monuments in the historic site. The emerged results can be interesting for San Marino government in order to promote historic heritage conservation actions.

## ACKNOWLEDGEMENTS

The authors want to thank Segreteria di Stato Istruzione e Cultura, Segreteria di Stato per il Territorio e l'Ambiente, Istituti Culturali and Commissione Nazionale Unesco of the Republic of San Marino.

## REFERENCES

[1] G. Peruzzi, D. Forcellini, K. Venturini, D. Albarello, *Ambient vibrations applied to San Marino historical building survey.* Proceedings of the XIV World Conference on Earthquake Engineering, Santiago, Chile, 9-13 January, 2017, Paper N° 985.

[2] G. Peruzzi, D. Forcellini, K. Venturini and D. Albarello, *Seismic Characterization of Historical Buildings in San Marino Republic from Ambient Vibration Monitoring*. International Journal of New Technology and Research, vol. 2, Issue 7, 95-102 ISSN: 2454-4116, 2016.

[3] http://www.faro.com/en-us/products/3d-surveying/faro-focus3d/overview

[4] FARO® Laser Scanner Focus3D Manual October 2011

[5] http://www.dji.com/phantom-3-pro

[6] Lunedei, E., Peruzzi, G. and Albarello, D. (2015). *Ambient vibrations in seismic studying the UNESCO cultural heritage site of San Gimignano (Italy).* Proceedings of the International Conference Georisks in the Mediterrean and their mitigation, Valletta, Malta, 20–21 July 2015, 243-247, ISBN: 978-88-98161-20-1

[7] A. Gregori, H. Salem, T. Harak, K. Fassieh, A. Khalil *collapse analysis of Santo Stefano tower using applied element method* Proceedings of 16th World Conference on Earthquake Engineering, 16WCEE 2017, Santiago Chile, January 9th to 13th 2017, Paper N° 2394

[8] C. Gentile, A. Saisi and A. Cabboi *Structural Identification of a Masonry Tower Based on Operational Modal Analysis*, International Journal of Architectural Heritage: Conservation, analysis and Restoration, 9:2, 98–110, DOI: 10.1080/15583058.2014.951792, 2015

[9] C. Gentile, A. Saisi, *Ambient vibration testing of historic masonry towers for structural identification and damage assessment*, Construction and Building materials 21 (2007) 1311-1321, 2006

COMPDYN 2017
6th ECCOMAS Thematic Conference on
Computational Methods in Structural Dynamics and Earthquake Engineering
M. Papadrakakis, M. Fragiadakis (eds.)
Rhodes Island, Greece, 15–17 June, 2017

# MICROWAVE INTERFEROMETRY MEASUREMENTS FOR RAILWAY-SPECIFIC APPLICATIONS

**Andrei Firus[1], Jens Schneider[1], Matthias Becker[2], Jiny Jose Pullamthara[2], Günther Grunert [3]**

[1]Technische Universität Darmstadt
Institute of Structural Mechanics and Design
Franziska-Braun-Str. 3, 64287 Darmstadt, Germany
e-mail: firus@ismd.tu-darmstadt.de, schneider@ismd.tu-darmstadt.de

[2] Technische Universität Darmstadt
Institute of Geodesy
Franziska-Braun-Str. 7, 64287 Darmstadt, Germany
e-mail: becker@psg.tu-darmstadt.de, pullamthara@psg.tu-darmstadt.de

[3] DB Netz AG
FuE und Regelwerk Brückenbau und Lärmschutzanlagen
Caroline-Michaelis-Strasse 5-11, 10115 Berlin, Germany
e-mail: guenther.grunert@deutschebahn.com

**Keywords:** microwave interferometry, dynamic measurements, railway bridge dynamics

**Abstract.** *The microwave interferometry is a rather new measurement method, whose functioning principle allows the non-contact synchronous acquisition of structural displacements for several points along a structure, with accuracy in sub-millimetre range at a sampling rate of up to 4 kHz. Due to the high sampling rate, the acquisition of dynamic responses is also possible. Hence, main modal structural parameters such as natural frequencies and damping ratios can be straightforwardly identified. Furthermore, the synchronous measurement of several points along the targeted object, achieved due to a range resolution of about 0.75 m, may allow the direct determination of modal shapes. Under consideration of its novel character and a lack of previous experience with respect to railway-specific tasks, the measurement method had to be subjected to a systematic and comprehensive validation process prior to a reliable implementation in everyday practice. The validation process included several parallel measurements and comparisons with conventional measurement techniques. Besides the direct verification of the quality of the results, it was used as well for defining boundary conditions and limitations of the measurement method with respect to railway-specific applications. As a result, an evaluation matrix was created, which illustrates the applicability of the microwave interferometry for different types of structures. This paper gives a brief introduction of the microwave interferometry and presents some aspects and selected results of the validation process, which was performed within a cooperation project between the TU Darmstadt (Germany) and the German Railways (Deutsche Bahn AG).*

## 1 INTRODUCTION

In the actual context of an ageing infrastructure in the railway sector and a rapid development of modern, faster and heavier vehicles with innovative axle arrangements, the reassessment of existing bridges becomes an ever more challenging task for civil engineers. Standard methods for reassessment of existing structures involve in a first instance a numerical analysis, whose level of detail can be varied according to the complexity of the structure and to the required accuracy of the results [1]. However, if the numerical analysis reveals an exceedance of the limit values with respect to the structural capacity or serviceability of the structure, measurements of the real dynamical structural behaviour are required in order to provide a realistic basis for updating the numerical models considered in the structural analysis [1]. This last step is necessary, as the modal parameters obtained through experimental investigations might differ significantly from the parameters resulting from the structural analysis. Such differences occur mostly due to different assumptions, simplifications and uncertainties within the structural model [2, 3]. In that regard, the German Railways (Deutsche Bahn AG) currently carries out a very elaborate reassessment project, which deals with the investigation of the dynamic compatibility of bridges located across the entire German railway network. It was motivated by the introduction of the new high-speed train ICE 4, whose carriage lengths lie outside of the validity range of the high speed load models for dynamic analysis (HSLM) specified in [4, 5]. Besides a significant number of experimental investigations, the reassessment project implies automated numerical analyses of bridge structures as well as comprehensive parametrical studies.

The substantial demand for dynamic measurements over the last decades represented also an optimal condition for technological progress in relation to measurement technologies in civil engineering, which indicates a clear trend towards non-contact, easy-to-use techniques. Among those, the microwave interferometry (MI) represents a rather new measurement method, whose functioning principle allows the non-contact synchronous measurement of structural deflections of several points along a structure, achieving a sub-millimetre accuracy level at a sampling rate of up to 4 kHz. Due to the high sampling rate, dynamic structural responses can also be captured and used for the straightforward identification of structural modal parameters. The non-contact character of the microwave interferometry represents a very important aspect, especially in case of railway bridges, as the conventional methods require high labour efforts, e.g sensors have to be usually mounted on the measured object, whereas several structures cannot be investigated at all due to bad accessibility.

Due to the novel nature of the microwave interferometry, it had to be subjected to a comprehensive validation process, which focused mainly on comparisons with results of synchronous conventional measurements. Section 2 of this paper gives a brief introduction of the microwave interferometry while the main findings of the validation process are presented in Section 3. Conclusions are drawn in Section 4.

## 2 MICROWAVE INTERFEROMETRY

The MI radar device (microwave interferometer) is mounted on a tripod and emits electromagnetic waves, which are reflected by discontinuities of the target objects lying within the antenna beam. The functioning principle of the microwave interferometry is based on the acquisition of amplitude and phase of the backscattered signal [6].

The object displacement $\Delta r$ within a sampling interval can be expressed in dependency of the corresponding phase change $\phi$ and the wavelength $\lambda$ of the emitted microwaves according

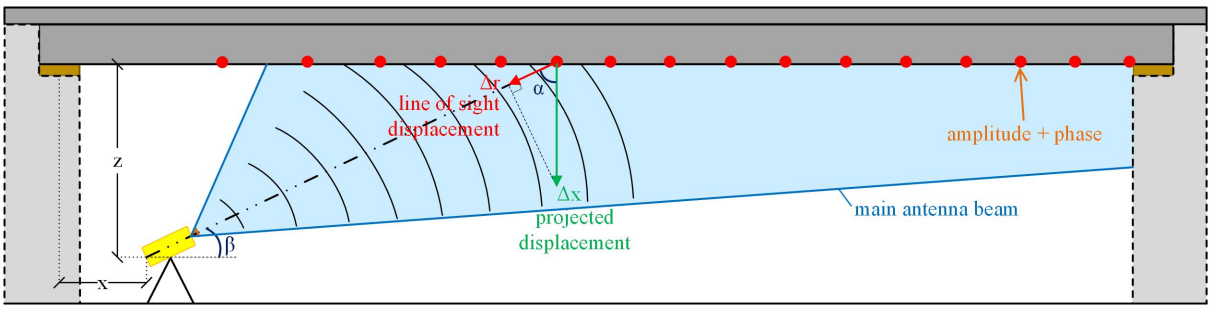


Figure 1: Typical MI measurement situation for bridges (the red dots represent the centres of the resolution cells)

to equation 1.

$$\Delta r = -\frac{\lambda}{4 \cdot \pi} \cdot \phi \tag{1}$$

The interferometric phase $\phi$ can be determined as a function of several influence factors according to equation 2.

$$\phi = \phi_{\text{disp}} + \phi_{\text{atm}} + \phi_{\text{noise}} \pm 2\pi n \tag{2}$$

Here $\phi_{\text{disp}}$ corresponds to the phase difference resulting from movements of the targeted reflecting objects along the line of sight, $\phi_{\text{atm}}$ depicts the phase shift caused by atmospheric effects and $\phi_{\text{noise}}$ represents the measurement noise. However, the short time measurements (typical for investigations in structural dynamics) are usually characterised by insignificant atmospheric changes. The corresponding term $\phi_{\text{atm}}$ in equation 2 can thus be mostly neglected. The term $2\pi n$ indicates the wrapping of the interferometric phase between $-\pi$ and $+\pi$, corresponding to $-\lambda/4$ to $\lambda/4$ due to the double travelled distance, while $n$ represents the phase ambiguity, since only a phase difference can be measured and not the integer number of phase cycles. It can be solved under different assumptions. For example, regarding the displacement of a bridge structure, it can be assumed that it does not exceed a quarter of the wavelength within one sampling interval, i.e. $n = 1$ ($\pm\lambda/4 = \pm 4.4$ mm, $\lambda = 17.4$ mm). Considering an acquisition rate of 200 Hz , a displacement of about 880 mm within one second would still be measurable. This value obviously lies outside the plausible range for regular bridge structures.

Figure 1 shows a typical measurement situation for bridge investigations. It is to be noted, that the microwave interferometers in RAR mode (Real Aperture Radar, suitable for dynamic signal acquisition) can measure only one-dimensional displacements $\Delta r$, i.e. in the line of sight of the device. It is to be subsequently projected with respect to the assumed direction of movement $\Delta x$ according to equation 3 and figure 1. Hence a good understanding of the mechanics of the structure is required in order to make realistic assumptions regarding the real direction of movement, which has to be considered when setting up the device.

$$\Delta x = \frac{\Delta r}{\cos(\alpha)} \tag{3}$$

The amplitude of the backscattered signal is significantly affected by the reflectivity of the targeted objects. In general, a good reflectivity is expected from every discontinuity of the structure, whose dimensions exceed the wavelength $\lambda$ of the transmitted wave. Concerning the reflectivity of bridges, it was observed that steel structures usually present a better reflectivity than reinforced or prestressed concrete, as the bottom surface of concrete bridges, which is

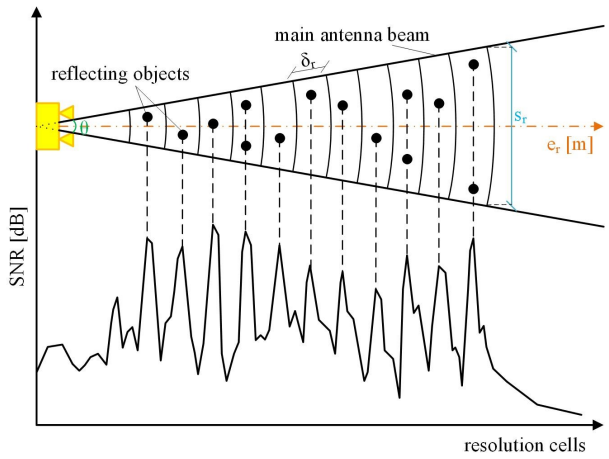


Figure 2: Range resolution cells of a microwave interferometer and corresponding SNR values

illuminated by the antenna beam, is mostly plain. This can lead to a dominant forward reflection of the microwaves and so to a loss of intensity of the backscattered signal [7]. Therefore it is recommended to check the quality of the reflected signal prior to the subsequent analysis. This can be done by means of the signal-to-noise ratio and of the complex representation of signal (polar plot) [8].

Microwave interferometers employ the stepped frequency continuous wave (SFCW) [9] or the frequency modulated continuous wave (FMCW) [10] principle in order ro achieve the range resolution, which can be expressed in dependency of the bandwidth $B$ of the transmitted wave and of the speed of light $c$ according to equation 4. Assuming the maximum bandwidth of $200\ \mathrm{MHz}$ allowed by the German Federal Network Agency, the corresponding range resolution $\delta_\mathrm{r}$ is determined to be $0.75\ \mathrm{m}$.

$$\delta_\mathrm{r} = \frac{c}{2 \cdot B} \tag{4}$$

A possible drawback of the microwave technology is represented by the fact that the microwave interferometers deliver a weighted average of the echoes for every resolution cell. This means that the movements of different reflecting targets situated in the same resolution cell cannot be distinguished (figure 2). However, this effect can be avoided in many situations by choosing a proper position of the MI radar, so that each cell contains only one dominant reflector. An useful mean for this task is the rough estimation of the width $s_\mathrm{r}$ of the antenna beam over the distance $e_\mathrm{r}$, which can be done according to equation 5 (see also figure 2), whereas $\theta$ depicts the horizontal opening angle of the antenna beam.

$$s_\mathrm{r} = 2 \cdot e_\mathrm{r} \cdot \tan\left(\frac{\theta}{2}\right) \tag{5}$$

A more detailed overview of the microwave interferometry is given in [6, 8, 11] while several application examples are presented in [12, 13, 14].

## 3 VALIDATION PROCEDURE

### 3.1 General

The validation process was carried out within the framework of a project initiated by the TU Darmstadt and the German Railways. One of its main aims was to verify the applicability

of the microwave interferometry for regular dynamic measurements of railway bridges. The formulation of boundary conditions and possible limitations of the measurement method was also intended. The procedure included, among others, several simultaneous measurements with conventional systems with the purpose to compare the MI results and the results of the conventional measurements, whereas the latter were considered to be accurate and therefore served as reference for all the comparisons. The primary focus of the investigation was set on the determination of natural frequencies and corresponding damping ratios, as usual dynamic measurements of railway bridges refer to these quantities, which are mostly needed in the model updating process. The verification of the values for the absolute displacements served only as a secondary aim within the actual phase of the project.

Before proceeding to the measurements of railway bridges in operation, several laboratory tests were carried out at the TU Darmstadt. They implied measurements of a simple supported steel beam with span length of 8 meters, installed 6.8 meters above ground level, in order to simulate real measurements situations for bridges. The results were very satisfactory [15].

A total of 18 structures have been investigated by microwave interferometry within the in situ validation process of railway bridges (see table 1). For 13 of them, parallel conventional measurements could be carried out (no. 6 to no. 18 in table 1). The conventional measurements were mostly performed by measurement teams of the German Railways. Therefore the standard

| No. | Bridge | Location | Type | Route no. | km |
|---|---|---|---|---|---|
| 1 | Muhr am See | Muhr am See | filler beam deck | 5321 | 29.39 |
| 2 | Große Sude | Hagenow | prestressed concrete slab | 6100 | 189.49 |
| 3 | Fornbachtal | Coburg | prestressed concrete girder | 5919 | 111.40 |
| 4 | Deutschherrnknai | Frankfurt a. M. | girder grid (steel) | 3660 | 1.58 |
| 5 | Schmutter | Augsburg | box girder (steel) | 5302 | 17.32 |
| 6 | Garather Bach | Düsseldorf | plate girder (steel) | 2650 | 25.17 |
| 7 | Hauptstraße | Laatzen | plate girder (steel) | 1733 | 8.46 |
| 8 | Elbe-Lübeck-Kanal | Büchen | tied arch (steel) | 6100 | 238.26 |
| 9 | Oesterholzstraße | Dortmund | rigid frame (steel) | 2650 | 120.89 |
| 10 | Am Kupferstrange | Hildesheim | prestressed concrete girder | 1770 | 42.62 |
| 11 | Flanitz | Klingenbrunn | plate girder (steel) | 5821 | 15.42 |
| 12 | Scheidestraße | Hannover | rigid frame (reinforced concrete) | 1730 | 3.20 |
| 13 | Kinzig | Offenburg | tied arch (steel) | 4000 | 147.71 |
| 14 | Zusam | Donauwörth | box girder (steel) | 5300 | 39.79 |
| 15 | Siebentischstraße | Augsburg | girder grid (steel) | 5503 | 59.08 |
| 16 | Altmühl | Dietfurt im Mittelfranken | plate girder (steel) | 5501 | 133.29 |
| 17 | Durlacher Allee | Karlsruhe | continuous plate girder (steel) | 4020 | 57.72 |
| 18 | Apfelstädt | Neudietendorf | box girder (steel) | 6298 | 1.29 |

Table 1: Structures investigated by microwave interferometry

evaluation parameters and methods prescribed for their investigations were adopted also for the analysis of the MI measurements, in order to facilitate the comparison process. The analysis method is described in detail in [8, 12].

The conventional measurements were performed employing linear variable displacement transducers (LVDT) and/or conventional acceleration sensors. However, in several situations, the local circumstances (e.g heavy traffic under the bridge or bridges over rivers) did not allow the installation of LVDTs as they require a fixed reference point directly underneath the point of interest. In these cases, the comparisons with regard to the modal parameters were carried out using acceleration data. Direct comparisons of absolute values are then possible only on acceleration level, using the second derivative of the displacement.

### 3.2 Example

The railway bridge *Garather Bach* (figure 3) is situated in Germany, at km 25.17 of the railway route no. 2650 (Köln-Duisburg). From a statical point of view, the bridge consists of two simply suported, uncoupled steel plate girders (denoted as TBW 1 and TBW 2 in figure 4). Figure 4 shows the complete measurement layout of the investigation, which implied both measurements with and without corner reflectors. The corner reflectors were installed only on TBW 1 in the very proximity of the conventional sensors, in order to secure unique dominant signals from the MI resolution cells including the measurement points MP 1 and MP 2. In the following, only results from the first measurement set-up (TBW 1) will be presented, as the results of the comparisons from the second set-up (presented in [13]), which is very similar to set-up 1 (corner reflectors are missing), are very consistent, revealing similar agreement between the different type of sensors as in the first set-up. The following comparisons refer




Figure 3: Railway bridge *Garather Bach* (Düsseldorf, Germany)

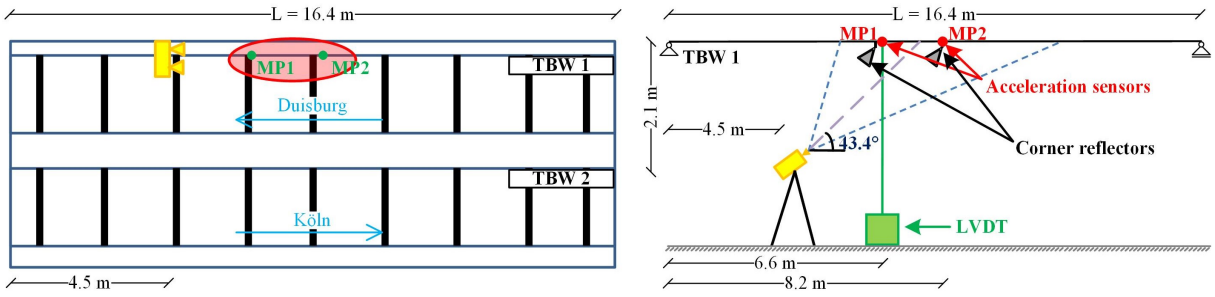


Figure 4: Measurement layout *Garather Bach*: top view (left) and side view (right)

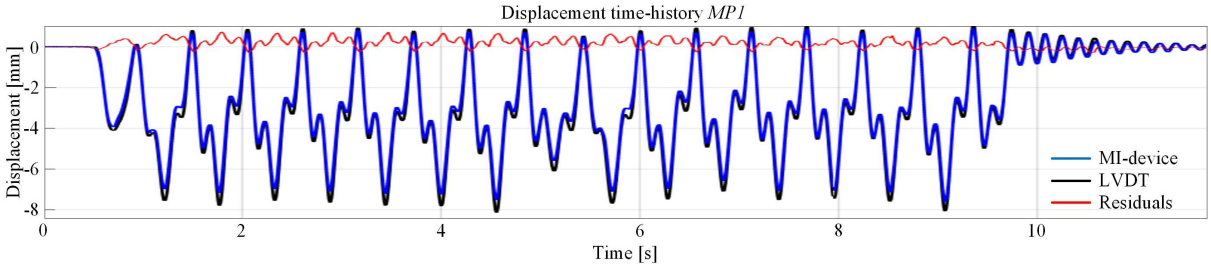


Figure 5: Displacement time series measured with a microwave interferometer and a conventional sensor at MP 1

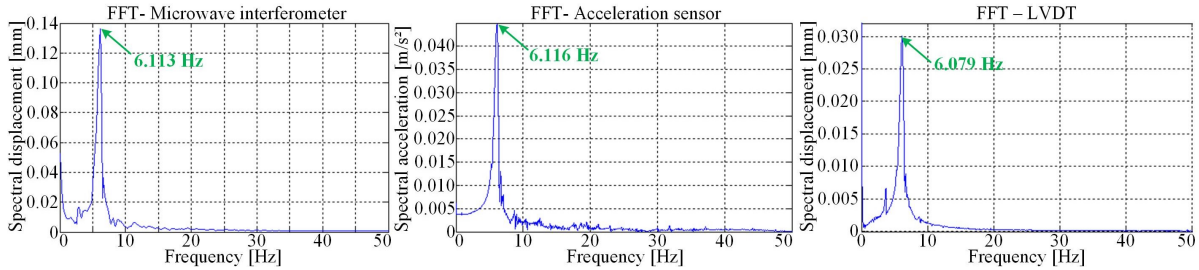


Figure 6: Frequency spectra resulting from the analysis of all employed systems

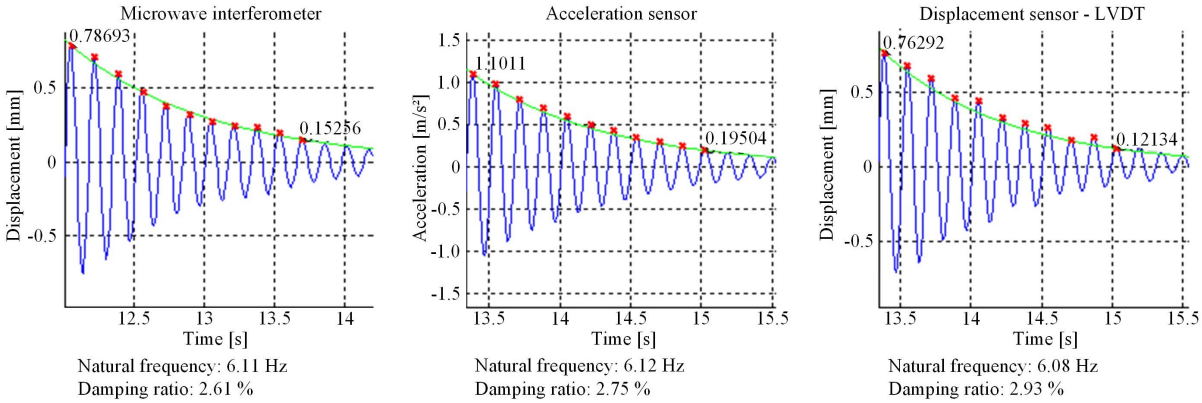


Figure 7: Estimation of the damping ratio with signals from all the measurement sensores used

always to MP 1 and MP 2. However, is to be noted that the results related to the microwave interferometry do not represent the discrete points MP 1 and MP 2, but the resolution cells over a length of $0.75$ m including them.

Figure 5 exemplifies the displacement time history generated by the passage of an ICE 3 train (14:27, see table 2) recorded with the MI radar and with a LVDT. The corresponding residuals are represented as well. Table 2 gives an overview over the maximal displacements of MP 1 for all the five passages recorded as well as the corresponding differences between the values of MI and LVDT. Under consideration of the fact that the displacement delivered by the microwave interferometer represents an integral over all the reflectors in a resolution cell and not of a single discrete point considered in the comparison, the results can be classified as quite satisfactory. However, the intended accuracy of 3% has not been yet achieved.

The comparison of the first natural frequency determined using the data from all the three types of sensors revealed a very good correlation of the results. This can be clearly seen in figure 6, which illustrates the frequency spectra determined from all the sensor data for the train

| Train passage | Time | Maximal displacement [mm] | | |
|---|---|---|---|---|
| | | MI radar | LVDT | Difference MI - LVDT |
| IC | 14:09 | 7.15 | 7.89 | -0.74 |
| ICE 3 | 14:15 | 6.06 | 6.57 | -0.51 |
| RE | 14:18 | 7.12 | 7.85 | -0.73 |
| ICE 3 | 14:27 | 7.61 | 8.14 | -0.53 |
| ICE 3 | 14:31 | 7.47 | 8.13 | -0.66 |
| Average value | | | | -0.63 |
| Standard deviation | | | | 0.10 |

Table 2: Maximal displacements at MP 1

| Train passage | Time | 1st natural frequency [Hz] | | | 1st damping ratio [%] | | |
|---|---|---|---|---|---|---|---|
| | | MI radar | LVDT | acc. sensor | MI radar | LVDT | acc. sensor |
| IC | 14:09 | 6.72 | 6.68 | 6.72 | no clear decay phase | | |
| ICE 3 | 14:15 | 6.36 | 6.46 | 6.46 | 2.50 | 2.39 | 2.04 |
| RE | 14:18 | 6.36 | 6.34 | 6.37 | 2.67 | 2.53 | 2.60 |
| ICE 3 | 14:27 | 6.11 | 6.08 | 6.12 | 2.59 | 2.86 | 2.63 |
| ICE 3 | 14:31 | 6.11 | 6.12 | 6.13 | 2.53 | 3.10 | 2.71 |
| Average value | | 6.33 | 6.34 | 6.36 | 2.57 | 2.72 | 2.49 |
| Standard deviation | | 0.25 | 0.25 | 0.25 | 0.08 | 0.32 | 0.31 |

Table 3: First natural frequencies and the corresponding modal damping ratios (evaluated at MP 1)

passage represented in figure 5. The overview of the corresponding results for all the recorded passages (table 3) confirms the very good accuracy of the MI measurements with respect to the natural frequency estimation.

Figure 7 illustrates the damping estimation for the same train passage displayed in figure 5 using the logarithmic decrement approach [16]. As it can be seen, the estimations using data from the different types of sensors correspond well. The result of this comparison is consistent with the corresponding results for the rest of the passages, which are given in table 3.

### 3.3 Summary of the results and particular findings

#### 3.3.1 General

As already mentioned in the previous section, the investigations focused mainly on the validation of the analysis concerning the natural frequencies and their corresponding modal damping ratios. The overview of the results and some complementary aspects are presented in the following. It is to be mentioned that the following summary of results refer to only 11 out of 13 synchronous measurements, which could be analysed until the time of composing the present paper.

#### 3.3.2 Natural frequencies

Table 4 gives a summary of the results for all of the investigated bridges. As it can be seen, the first natural frequencies obtained through analysis of the MI data are in a good agreement

| No. | Bridge | 1st natural frequency [Hz] | | | 1st damping ratio [%] | | |
|---|---|---|---|---|---|---|---|
| | | MI | Conv. | Diff. [%] | MI | Conv. | Diff. [%] |
| 1 | Garather Bach | 6.33 | 6.36 | -0.47 | 2.57 | 2.49 | +3.11 |
| 2 | Hauptstraße | 3.89 | 3.90 | -0.26 | 1.29 | 1.50 | -16.28 |
| 3 | Elbe-Lübeck-Kanal | 2.73 | 2.73 | 0.00 | - | - | - |
| 4 | Oesterholzstraße | 4.83 | 4.81 | +0.41 | - | - | - |
| 5 | Am Kupferstrange | 4.26 | 4.31 | -1.17 | 1.59 | 1.67 | -5.03 |
| 6 | Scheidestraße | 8.06 | 7.99 | +0.86 | - | 0.94 | - |
| 7 | Kinzig | 1.75 | 1.75 | 0.00 | - | - | - |
| 8 | Zusam | 6.55 | 6.47 | +1.22 | - | 0.95 | - |
| 9 | Siebentischstraße | 4.82 | 4.65 | +3.53 | 1.61 | 1.51 | +6.21 |
| 10 | Altmühl | 6.96 | 6.85 | +1.58 | 1.07 | 0.99 | +7.48 |
| 11 | Durlacher Allee | 5.51 | 5.51 | 0.00 | 0.84 | 0.72 | +14.29 |

Table 4: Results summary of the validation measurements

with the corresponding results from conventional measurements, showing percentage differences of up to 3-4%.

It can be stated that the natural frequencies are the quantities which could be determined robustly and accurately in all the investigated cases. However, in order to allow a computation of the natural frequencies, it is required that they are properly excited. This condition is practically always fulfilled for the first natural frequency of beam-like bridges. In contrast, natural frequencies of higher modes could be determined only in some isolated cases (using MI data) and are therefore not explicitly mentioned in the comparison. The reason for this is that the higher frequencies are usually not adequately excited by normal train passages, since the excitation frequencies at regular travel speeds lie below 10 Hz. This value is by far lower than usual second and third natural frequencies of railway bridges. Furthermore, the authors encountered cases in which higher natural frequencies could be determined from acceleration data but not from MI displacement measurements. This effect, which is not explicitly related to the microwave interferometry principle, occurs due to the proportionality between acceleration and displacement in the free vibration phase with the negative square of the angular frequency as a proportionality constant. This leads to higher, measurable amplitudes in the upper range of the acceleration spectrum.

The MI experience gathered so far shows that concrete bridges present usually lower displacement amplitudes as steel bridges in the free vibration phase due to their higher stiffness and mass distribution. Thus one should expect successful determination of higher natural frequencies of concrete bridges only in exceptional cases.

### 3.3.3 Damping ratios

Regarding the modal damping ratios, the comparisons between the MI and the conventional systems revealed as well differences lying in an acceptable range (0-16%, s. table 4). In general, the determination of modal damping ratios from MI data can succeed independently of the structure type as long as the analysed data series present a clear decay trend in the free vibration phase (after train passage) of the analysed modes. The individual modes can be isolated, for example, by bandpass filtering of the signal used for the determination of natural frequencies. For the damping estimation, it is recommended to consider only displacement amplitudes which

are significantly higher than the device accuracy specified by the manufacturer, e.g. $0.01$ mm (in laboratory conditions) for the microwave interferometer IBIS-S manufactured by IDS - Ingineria del Sistemi S.p.A. [17].

Within the present investigation, the axle arrangement and the travel speed of the trains (i.e. the excitation frequency) could be identified as main influence factors responsible for generating evaluable decay processes. Pronounced dynamic effects and thus considerable displacement amplitudes in the decay phase are expected in case the excitation frequency lies close to one of the natural frequencies of the structure. The structure type only plays a subordinate role. However, the previous experience showed that concrete bridges present suitable decay amplitudes only in sporadic cases due to their higher stiffness, mass and damping ratios.

Furthermore, damping ratios of higher modes could be determined only in some isolated cases. The reason for this is usually, as mentioned above, the discrepancy between the excitation frequencies and the higher natural frequencies of the structure, which does not facilitate the occurrence of significant dynamic effects (i.e. proper displacement amplitudes) in the higher modes.

### 3.3.4 Absolute displacements

Although the accuracy of the displacements achieved within the few measurements of railway bridges in operation performed with parallel LVDTs lies in a satisfactory sub-millimetre range, the validation of the absolute displacements requires further investigations since the accuracy level of 3% intended by the authors has not been reached yet.

One of the main issues the MI users have to consider is the exact identification of the dominant reflector in each resolution cell, as the elevation angle $\beta$ of the MI radar and the vertical distance $z$ from the zero reference point of the MI device to the reflecting point of the structure (s. figure 1) are the quantities used in the projection of the line of sight movement to the vertical displacement. Slight errors in the input of vertical distances lead to erroneous projection of the displacement. This effect should be paid attention to, especially in case steel bridges presenting visible cross beams at the bottom side. This is clearly illustrated in figure 8 on the example of a tied arch bridge. As it can be seen, the difference between the vertical displacements obtained by projecting the line of sight displacement with respect to the upper edge of the cross beam (distance $z_1$) and to the lower edge of the cross beam (distance $z_2$) can be considerable. In comparison with the conventionally measured vertical displacement, the consideration of $z_1$ as

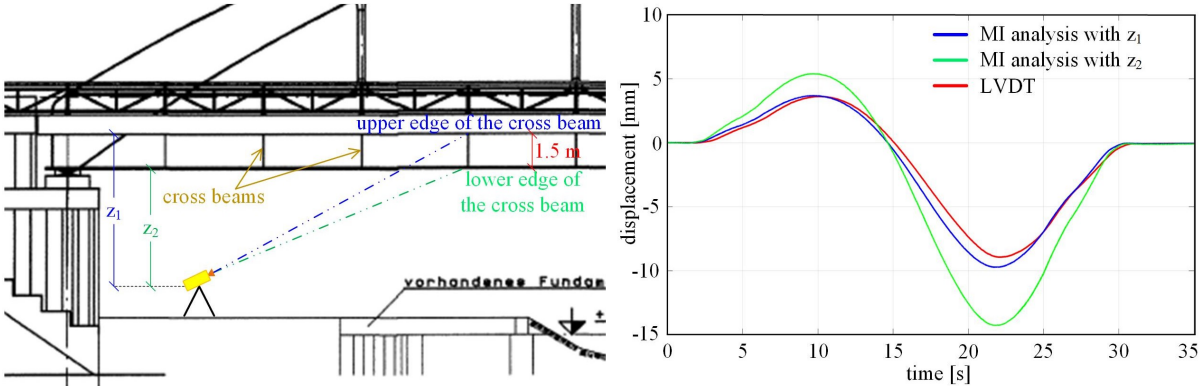


Figure 8: Sketch of a measurement set-up for a tied arch bridge (left) and analysis of vertical displacement considering two different reference points with the heights $z_1$ and $z_2$ respectively for the vertical coordinate of the MI device (right)

distance to the reference reflecting point delivers appropriate results. The reason for this is the reflectivity of the joint cross beam-bridge deck (at the upper flange of the cross beam), which is significantly higher than the reflectivity at the lower flange.

Another problem which has to be considered within the analysis of vertical displacements refers to the broadening of the antenna beam. Due to the increasing width of the beam over the distance, the distant resolution cells might contain several reflectors with different movement behaviour (s. figure 2). The resulting displacement in this case represents an integral over the movements of all the reflectors lying in the specific resolution cell, whereas the weighting factor of the different reflectors can not be determined. Therefore it is recommended to install the MI devices as close as possible to the points of interest, so that they fall in closer resolution cells with reasonable widths.

Furthermore it is to be noted that the analysis of MI measurements assumes pure vertical (e.g. in case of bridges) or pure horizontal (e.g. noise insulation walls) displacements of the measured object with respect to the vertical plane which includes the line of sight of the device. In both cases, the angle which has to be considered in the projection of the line of sight displacement is the angle between the line of sight and the assumed movement direction. Measurement set-ups with expected movements in both directions are to be avoided, as the individual components can not be separated.

### 3.3.5 Mode shapes

The fulfilment of the quality criteria (signal-to-noise ratio and polar plot) for several resolution cells along the structure is a necessary condition for the determination of modal shapes using MI data. Furthermore, suitable displacement amplitudes in the investigated mode are required. On that account, an analysis of mode shapes is rather possible in case of steel structures which mostly present several constructive elements with good reflectivity at the bottom side (e.g. cross beams). In addition, the displacement in the free vibrations phase are expected to be higher in case of steel bridges than for concrete structures due to the different mass, stiffness and damping parameters. Within the previous investigations only few structures (exclusively steel) allowed a clear determination of the mode shapes.

Figure 9 exemplary shows the first two mode shapes of a continuous beam bridge (no. 7 in table 1, two spans à 21.13 m) obtained using MI data. It is to be noted that the mode shapes determined from MI measurements possess only a qualitative character, especially in case of structures with multiple tracks. This is due to the fact that the width of the antenna beam is

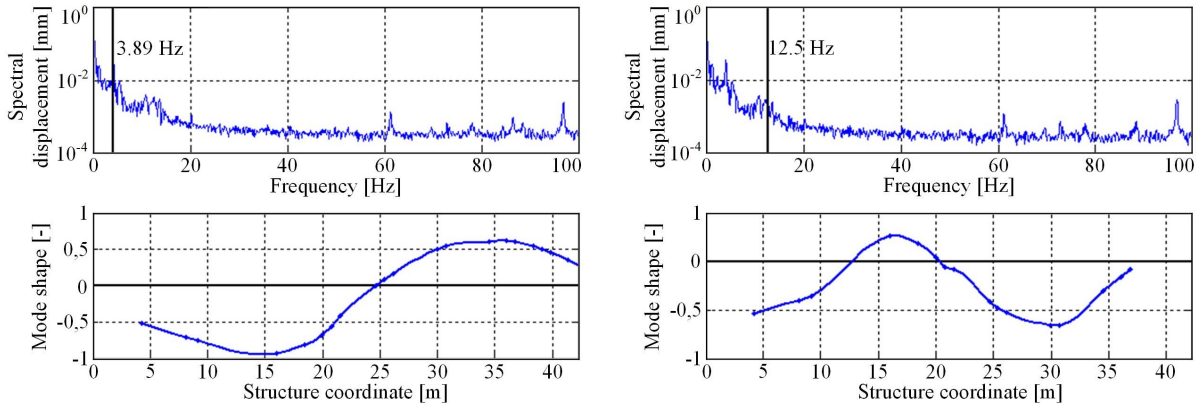


Figure 9: First two mode shapes of a continuous beam bridge from a MI measurement

wider in the distant resolution cells (s. figure 2), which are likely to include additional, unwanted reflecting elements of the structure. Nevertheless, the qualitative determination of mode shapes is very helpful for the correlation of the measured to the computed natural frequencies and mode shapes. It represents a proper tool for the plausibility check of the measurement.

### 3.4 Evaluation matrix

As a result of the comprehensive investigation, an evaluation matrix was created (s. table 5). It should illustrate the applicability of the microwave interferometry for different types of structures and measurements tasks. For the sake of completeness, the matrix also contains informations about noise insulating walls, which were not addressed explicitly in this paper. However, the cooperation project between the TU Darmstadt and the German Railways included as well experimental investigations on this topic.

| Task / Structure type | abs. disp. | natural frequency 1st | natural frequency higher | damping ratios 1st mode | damping ratios higher modes | mode shapes |
|---|---|---|---|---|---|---|
| Girder grid (steel) | +++ | +++ | ++ | +++ | + | ++ |
| Plate girder (steel) | +++ | +++ | ++ | +++ | + | ++ |
| Tied arch (steel) | +++ | +++ | ++ | +++ | + | ++ |
| Rigid frame (steel) | +++ | +++ | ++ | +++ | + | ++ |
| Box girder (steel) | ++ | ++ | ++ | +++ | + | + |
| Concrete bridges | ++ | ++ | + | ++ | - | + |
| Filler beam deck | ++ | ++ | + | ++ | + | + |
| Noise insulation walls | +++ | +++ | ++ | +++ | + | ++ |

Legend: +++ highly suitable, ++ partially suitable, dependent on different influence factors, + suitable only in isolated cases, under certain circumstances, - not suitable

Table 5: Evaluation matrix for judging the applicability of MI for various types of bridges

It should be noted that several factors which are not related to the MI measurement technique underlie the specifications for the natural frequencies and damping ratios of higher modes, such as the previously mentioned lower displacement amplitudes in the higher modes. Furthermore, it is to be mentioned that the evaluation of tied arch bridges refer to the bottom chord (bridge deck girder) and not to the arch itself and that the category of concrete bridges comprises both prestressed and reinforced structures, due to the transferability of the relevant properties.

## 4 CONCLUSIONS

- A systematic and comprehensive process for the validation of microwave interferometry measurements was conducted within a joint project of the TU Darmstadt and the German Railways.
- The results achieved so far concerning the natural frequencies and damping ratios are generally in a good agreement with reference results of conventional sensors.
- Some complementary aspects which should be considered within the measurement and the subsequent analysis were presented, e.g. possible projection errors occurring due to incorrect identification of the main reflecting points or erroneous results which might occur due to multiple reflectors with different movement behaviours lying in the same resolution cell.

- The comparison of the absolute displacements was only a secondary focus of the investigations. Under consideration of the fact that discrete points are compared to integral displacements over whole resolution cells, the results can be seen as satisfactory (accuracy in sub-millimetre range). However further investigations on this topic are envisaged, in order to achieve an accuracy of 3% (intended by the authors).
- As a result of the comprehensive investigations, an evaluation matrix was created, which illustrates the applicability of microwave interferometry for different structure types and various railway-specific measurement tasks.
- The microwave interferometry can be regarded as a promising technology which can be reliably implemented within the experimental investigations required in the updating process for numerical models of railway bridges.

## REFERENCES

[1] Ril 805, *Richtlinie 805 - Tragsicherheit bestehender Eisenbahnbrücken*. DB Netz AG, September 2010.

[2] T. Rauert, *Zum Einfluss baulicher Randbedingungen auf das dynamische Verhalten von WIB-Eisenbahnbrücken*. PhD Thesis, RWTH Aachen, Institut und Lehrstuhl für Stahlbau und Leichtmetallbau, Aachen, 2011.

[3] V. Zabel, M. Brehm, Das dynamische Verhalten von Eisenbahnbrücken mit kurzer Spannweite - numerische und experimentelle Untersuchungen. *Bauningenieur, D-A-CH Mitteilungsblatt*, **83**, 9-14, 2008.

[4] EN 1991-2, *Eurocode 1: Action on structures - Part 2: Traffic loads on bridges*. German version EN 1991-2:2003 + AC:2010.

[5] Ril 804, *Richtlinie 804 - Eisenbahnbrücken (und sonstige Ingenieurbauwerke) planen bauen und instand halten*. DB Netz AG, January 2013.

[6] G. Bernardini, G. De-Pasquale, A. Bicci, A. Mara, F. Coppi, P. Ricci, M. Pieraccini, Microwave interferometer for ambient vibration measurement on civil engineering structures: 1. Principles of the radar technique and laboratory tests. *Proceedings of EVACES '07 - Experimental Vibration Analysis for Civil Engineering Structures*, Porto, Portugal, October 24-26, 2007.

[7] M. Becker, J. Schneider, A. Firus, S. Leinen, J.J. Pullamthara, Research Report: *Strukturanalyse mit Mikrowelleninterferometrie (STRAMIK) – Stufe 2, Teil A, Forschungsanteil*, TU Darmstadt, February 2017, unpublished.

[8] A. Firus, J. Schneider, M. Becker, G. Grunert, J.J. Pullamthara, Dynamische Verformungsmessungen an Eisenbahnbrücken mittels Mikrowelleninterferometrie. Teil 1: Messverfahren. *Bautechnik*, **93**, 700-711, 2016.

[9] J.D. Tayor, *Ultra-widebamd radar technology*. CRC Press, 2001.

[10] R. Iglesias, A. Aguasca, X. Fabregas, J.J. Mollorqui, D. Monells, C. López Martínez, L. Pipia, Ground-Based Polarimetric SAR Interferometry for the Monitoring of Terrain Displacement Phenomena - Part I: Theoretical Description. *IEEE Journal of Selected Topics in Apllied Earth Observations and Remote Sensing*, **8**, 980-933, 2015.

[11] S. Rödelsperger, G. Läufer, C. Gerstenecker, M. Becker, Terrestrische Mikrowelleninterferometrie - Prinzip und Anwendungen. *Allgemeine Vermessungsnachrichten (AVN)*, **10**, 324-333, 2010.

[12] A. Firus, J. Schneider, M. Becker, G. Grunert, J.J. Pullamthara, Validation of microwave interferometry measurements for applications in railway bridge dynamics. *German-Japanese Bridge Symposium GJBS 2016*, Osaka, Japan, August 30-31, 2016.

[13] J. Schneider, M. Becker, A. Firus, J.J. Pullamthara, M. Drass, Identifikation dynamischer Strukturparameter von Eisenbahnbrücken mittels terrestrischer Mikrowelleninterferometrie. M. Curbach, H. Opitz, S. Scheerer eds. *9. Symposium Experimentelle Untersuchungen von Baukonstruktionen*, Dresden, Germany, September 24, 2015.

[14] J. Schneider, M. Becker, G. Läufer, J. Hilcken, Monitoring of Dynamic Properties of Bridges by Terrestrial Microwave Interferometry. *German-Japanese Bridge Symposium GJBS 2012*, Kyoto, Japan, September 10-11, 2012.

[15] A. Firus, J.J. Pullamthara, J. Schneider, M. Becker, W. Francke, Applicability of displacement measurements by microwave interferometry in bridge dynamics. *International Scientific Conference CIBv 2015*, Brasov, Romania, October 30-31, 2015.

[16] C. Petersen, *Dynamik der Baukonstruktionen*. Friedr. Vieweg & Sohn Verlagsgesellschaft mbH, 1996.

[17] IDS-Ingineria del Sistemi S.p.A., *IBIS Surveyor v. 01.01 - User Manual*. Pisa, Italy, November, 2015.

COMPDYN 2017
6th ECCOMAS Thematic Conference on
Computational Methods in Structural Dynamics and Earthquake Engineering
M. Papadrakakis, M. Fragiadakis (eds.)
Rhodes Island, Greece, 15–17 June, 2017

# SYNCHRONIZATION OF DATA ACQUISITION SYSTEMS FOR THE PURPOSE OF STRUCTURAL HEALTH MONITORING

**K. Maes[1], E. Reynders[1], A. Rezayat[2], G. De Roeck[1], and G. Lombaert[1]**

[1]KU Leuven, Department of Civil Engineering
Kasteelpark Arenberg 40, 3001 Leuven, Belgium
e-mail: kristof.maes@kuleuven.be

[2] Vrije Universiteit Brussel, Department of Mechanical Engineering
Pleinlaan 2, 1050 Brussels, Belgium
e-mail: arezayat@vub.ac.be

**Keywords:** Time synchronization, data acquisition, system identification, output-only, structural health monitoring

**Abstract.** *This paper presents a technique for offline time synchronization of data acquisition systems for linear structures with proportional damping. The technique can be applied when direct synchronization of data acquisition systems is impossible or not sufficiently accurate, for example when multiple measurement nodes with different clock signals are embedded in a health monitoring network. The synchronization is based on the acquired dynamic response of the structure only, and does not require the acquisition of a shared sensor signal or a trigger signal. The time delay is identified from the spurious phase shift of the mode shape components that are obtained from system identification. A demonstration for a laboratory experiment on a cantilever steel beam shows that the proposed methodology can be used for accurate time synchronization, resulting in a significant improvement of the accuracy of the identified mode shapes.*

## 1 INTRODUCTION

Structural health monitoring often requires the use of multiple data acquisition systems, due to the large number of measurement channels, the large distance between sensors, or the need for heterogeneous sensor data. This creates the need for synchronization of data acquisition systems. Currently, monitoring systems consisting of multiple wireless nodes are being developed [2, 10]. Each of the nodes has its own data acquisition, and–to date–synchronization of the nodes remains a challenge. Several techniques for (online) synchronization of measurement systems have been proposed so far, amongst which time stamping through GPS [5], and synchronization through fiber optical cables or radio communication.

When direct time synchronization of data acquisition systems is impossible or insufficiently accurate, offline synchronization of recorded vibration data is needed. When a sensor signal is shared by multiple data acquisition systems, offline synchronization can be easily performed by applying correlation techniques or by calculating the transfer function that relates both measured signals [1]. This is not always possible, for example when a network of independent wireless sensors at different locations on the structure is used. This paper presents a technique that enables for offline time synchronization of data acquisition systems. The technique assumes linear time-invariant dynamic behavior of the structure and proportional damping of the structural modes. The synchronization time delay is identified from the spurious phase shift of the mode shape components, that are obtained from system identification.

The paper is outlined as follows. Section 2 shows that a synchronization time lag results in a phase shift of the identified mode shapes, whereas the identified natural frequencies and modal damping ratios are unchanged. Next, section 3 demonstrates using data obtained from a laboratory experiment on a cantilever beam how the findings in section 2 can be applied for offline synchronization of data acquisition systems. Finally, in section 4, the work is concluded.

## 2 MATHEMATICAL BACKGROUND

Consider two response signals $d_1(t)$ and $d_2(t)$ obtained from sensors installed at arbitrary locations on the structure. The signals may correspond to different response quantities, e.g. acceleration or strain. Under the assumption of linear system behavior, the Laplace transform of the response signals, $d_1(s) \in \mathbb{C}$ and $d_2(s) \in \mathbb{C}$, are related through the transmissibility function $T(s) \in \mathbb{C}$ as follows [11]:

$$d_1(s) = T(s)d_2(s) \tag{1}$$

where $s \in \mathbb{C}$ is the Laplace variable [12]. Furthermore, the Laplace transform of the response signals $d_1(s)$ and $d_2(s)$ is related to the Laplace transform of the load vector $\mathbf{p}(s) \in \mathbb{C}^{n_\mathrm{p}}$ through the transfer function matrices $\mathbf{H}_1(s) \in \mathbb{C}^{1\times n_\mathrm{p}}$ and $\mathbf{H}_2(s) \in \mathbb{C}^{1\times n_\mathrm{p}}$, respectively, as given by the following equation:

$$d_1(s) = \mathbf{H}_1(s)\mathbf{p}(s) \tag{2}$$

$$d_2(s) = \mathbf{H}_2(s)\mathbf{p}(s) \tag{3}$$

It assumed here that $n_\mathrm{p}$ loads are acting on the structure. The number of loads and their location is not important for the derivation following next, however. Under the assumption that the response of the structure within a certain frequency range of interest is well approximated by a limited number of structural modes ($n_\mathrm{m}$ modes), and assuming in addition proportional

damping, the transfer function matrices $\mathbf{H}_1(s)$ and $\mathbf{H}_2(s)$ are given by:

$$\mathbf{H}_1(s) = \sum_{m=1}^{n_\mathrm{m}} \frac{s^{q_1}\phi_{\mathrm{d}_1 m}}{s^2 + 2\xi_m\omega_m s + \omega_m^2}\boldsymbol{\phi}_{\mathrm{p}m} = \sum_{m=1}^{n_\mathrm{m}} s^{q_1}\phi_{\mathrm{d}_1 m}\mathbf{H}'_m(s) \tag{4}$$

$$\mathbf{H}_2(s) = \sum_{m=1}^{n_\mathrm{m}} \frac{s^{q_2}\phi_{\mathrm{d}_2 m}}{s^2 + 2\xi_m\omega_m s + \omega_m^2}\boldsymbol{\phi}_{\mathrm{p}m} = \sum_{m=1}^{n_\mathrm{m}} s^{q_2}\phi_{\mathrm{d}_2 m}\mathbf{H}'_m(s) \tag{5}$$

where $\mathbf{H}'_m(s) = \boldsymbol{\phi}_{\mathrm{p}m}/(s^2 + 2\xi_m\omega_m s + \omega_m^2)$, with $\boldsymbol{\phi}_{\mathrm{p}m} \in \mathbb{R}^{1\times n_\mathrm{p}}$ the vector of mode shape components corresponding to mode $m$ at the $n_\mathrm{p}$ force locations. $\omega_m$ and $\xi_m$ are the undamped natural frequency and the modal damping ratio of mode $m$, respectively. $\phi_{\mathrm{d}_1 m}$ and $\phi_{\mathrm{d}_2 m}$ are obtained by selecting the component of the mode shape vector corresponding to mode $m$ at the sensor locations of $d_1$ and $d_2$, respectively. The integers $q_1$ and $q_2$ equal 0 for displacement or strain measurements, 1 for velocity measurements, and 2 for acceleration measurements.

The system has $2n_\mathrm{m}$ poles, occurring in complex conjugate pairs, $\lambda_{m1}$ and $\lambda_{m2}$ ($m = 1, \ldots, n_\mathrm{m}$), given by the following expression [6]:

$$\lambda_{m1,2} = -\omega_m\xi_m \pm i\omega_m\sqrt{1-\xi_m^2} \tag{6}$$

where $i = \sqrt{-1}$. The poles $\lambda_{m1}$ and $\lambda_{m2}$ correspond to the natural frequency $\omega_m$ and modal damping ratio $\xi_m$ of mode $m$. When the transfer function matrices in Eqs. (4) and (5) are evaluated at a system pole, i.e. $s = \lambda_{m1}$, only the corresponding mode $m$ contributes to the system response [4], and the following expressions are obtained:

$$\mathbf{H}_1(\lambda_{m1}) = \lambda_{m1}^{q_1}\phi_{\mathrm{d}_1 m}\mathbf{H}'_m(\lambda_{m1}) \tag{7}$$

$$\mathbf{H}_2(\lambda_{m1}) = \lambda_{m1}^{q_2}\phi_{\mathrm{d}_2 m}\mathbf{H}'_m(\lambda_{m1}) \tag{8}$$

Combination of Eqs. (7) and (8) directly yields:

$$\mathbf{H}_1(\lambda_{m1}) = \frac{\lambda_{m1}^{q_1}\phi_{\mathrm{d}_1 m}}{\lambda_{m1}^{q_2}\phi_{\mathrm{d}_2 m}}\mathbf{H}_2(\lambda_{m1}) \tag{9}$$

Evaluation of Eqs. (2) and (3) at the system pole $s = \lambda_{m1}$, and taking into account Eq. (9) yields:

$$d_1(\lambda_{m1}) = \frac{\lambda_{m1}^{q_1}\phi_{\mathrm{d}_1 m}}{\lambda_{m1}^{q_2}\phi_{\mathrm{d}_2 m}}d_2(\lambda_{m1}) \tag{10}$$

such that

$$T(\lambda_{m1}) = \frac{\lambda_{m1}^{q_1}\phi_{\mathrm{d}_1 m}}{\lambda_{m1}^{q_2}\phi_{\mathrm{d}_2 m}} \tag{11}$$

Next, consider the response signal $d'_2(t)$, that is obtained by applying a time delay $\delta t$ to the response signal $d_2(t)$, i.e. $d'_2(t) = d_2(t-\delta t)$. The Laplace transforms of the response signals $d_1(t)$ and $d'_2(t)$ are related through the transmissibility function $T'(s)$, i.e. $d_1(s) = T'(s)d'_2(s)$. The transmissibility function $T'(s)$ is related to the transmissibility function $T(s)$ as follows [12]:

$$T'(s) = T(s)e^{s\delta t} \tag{12}$$

Evaluation of the transmissibility function $T'(s)$ at the system pole $s = \lambda_{m1}$ yields:

$$T'(\lambda_{m1}) = \frac{\lambda_{m1}^{q_1}\phi_{\mathrm{d}_1 m}}{\lambda_{m1}^{q_2}\phi'_{\mathrm{d}_2 m}} = \frac{\lambda_{m1}^{q_1}\phi_{\mathrm{d}_1 m}}{\lambda_{m1}^{q_2}\phi_{\mathrm{d}_2 m}e^{-\lambda_{m1}\delta t}} \tag{13}$$

Comparison of Eqs. (11) and (13) shows that processing the time delayed data $d_2'(t)$ together with other non-delayed data results in a (complex) mode shape component $\phi'_{\mathrm{d}_2 m}$, that is obtained from the mode shape component $\phi_{\mathrm{d}_2 m}$ by multiplication with $e^{-\lambda_{m1}\delta t}$. This corresponds to a phase shift $\theta_m$ (in radians) and a rescaling of the mode shape by the factor $A_m$, defined as

$$\theta_m = -\delta t\, \omega_m \sqrt{1-\xi_m^2} \tag{14}$$

$$A_m = e^{\omega_m \xi_m \delta t} \tag{15}$$

The poles of the system and, therefore, the natural frequencies and modal damping ratios, are not affected by the time delay.

For linear structures with proportional damping, the (complex) mode shape vectors $\boldsymbol{\phi}_m \in \mathbb{C}^{n_\mathrm{d}}$, containing the components $\phi_{\mathrm{d}_j m}$, can be rescaled such that real vectors are obtained. This is illustrated in Fig. 1, where a mode shape vector $\boldsymbol{\phi}_m$ is schematically represented in the complex plane, after rescaling such that the largest mode shape component becomes 1 (a.k.a. rescaling to unit modal displacement). The figure also shows the mode shape component $\phi'_{\mathrm{d}_2 m}$ as obtained from the time delayed response signal $d_2'(t)$ and using the same scaling factor. The phase angle between the mode shape components $\phi_{\mathrm{d}_2 m}$ and $\phi'_{\mathrm{d}_2 m}$ is $\theta_m$, and is introduced by the multiplication of $\phi_{\mathrm{d}_2 m}$ with $e^{-\lambda_{m1}\delta t}$. The rescaling of the mode shape amplitude by $A_m$ is also shown in the figure.

The phase shift of the mode shape components, introduced by the time delay $\delta t$, can be used for offline synchronization of data acquisition systems, as illustrated in Section 3.

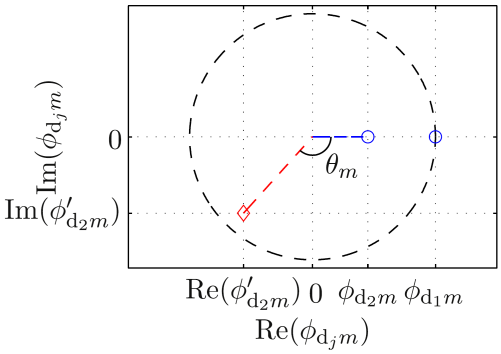


Figure 1: Representation of the mode shape components $\phi_{\mathrm{d}_1 m}$ and $\phi_{\mathrm{d}_2 m}$ (blue circles), and $\phi'_{\mathrm{d}_2 m}$ (red diamond) in the complex plane. The mode shape vector is normalized to unit modal displacement.

## 3 SYNCHRONIZATION APPROACH

It is demonstrated in this section how system identification techniques can be used for offline synchronization of data acquisition systems, based on the findings of Section 2. The test setup considered in the demonstration consists of a cantilever steel beam (Fig. 2a), that has been equipped with 2 uniaxial accelerometers and 22 optical fiber strain gauges (Fig. 2b). The beam has a free length of 855 mm and a rectangular cross section of 30 mm by 10 mm. The beam is clamped between two metallic plates of 200 mm by 300 mm by 20 mm each, that are bolted to a concrete support by five bolts (see Fig. 2a). The beam is clamped over a length of 120 mm. The structure is excited vertically by an inertial shaker, that has been installed underneath the beam (Fig. 2c). A load cell has been installed between the shaker and the beam to measure the applied (external) force. In addition, a small instrumented impact hammer is used for excitation. The sensor configuration is shown in Fig. 3.

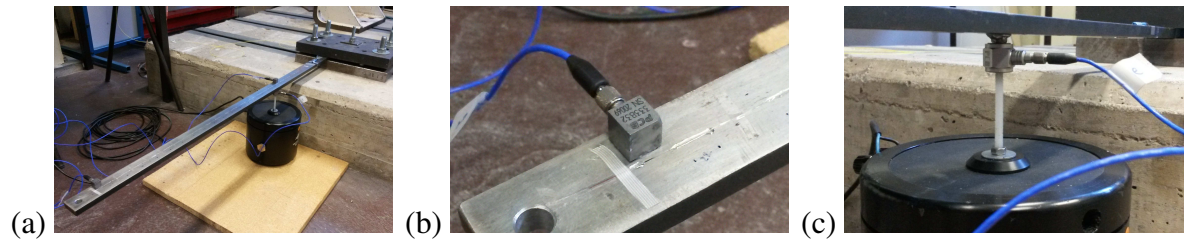

Figure 2: Overview (a) cantilever beam, (b) uniaxial accelerometer and optical fiber strain gauges, and (c) shaker and load cell.

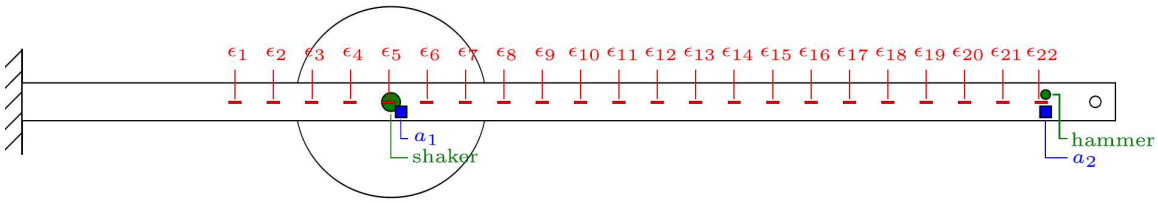


Figure 3: Sensor configuration of the laboratory experiment ($a_i$: accelerometer $i$, $\epsilon_i$: strain gauge $i$).

Two data acquisition systems are used in the setup. A National Instruments (NI) data acquisition system (NI USB-6229) is used to record the data from the uniaxial accelerometers (PCB 333B32), the impact hammer (PCB 302A07) and the load cell (PCB 208B02). An FBG-Scan 700 measurement device (FBGS) has been used to record the data from the optical fiber strain gauges. A sampling frequency $f_\mathrm{s}$ of 1000 Hz has been used for both systems. The synchronization of the data acquisition systems is performed as follows: a trigger pulse is sent by the NI system to the FBGS system at every sampling time step. The FBGS system records a sample of the strain signals on receipt of this pulse. During the data processing, a lack of synchronization between both systems was observed. The synchronization time lag, which is in this case due to processing within the FBGS system, is determined in the following.

### 3.1 System identification

The modal parameters of the cantilever beam have been experimentally identified by means of an input-output system identification. The measurements for system identification were performed with vertical swept sine excitation, applied by the inertial shaker. The excitation frequency varies from 0 Hz to 500 Hz in 10 s. Fifteen sweep cycles of 10 s are considered, yielding a total measurement duration of 150 s.

The output signals used in the system identification consist of the two acceleration signals (units: $\mathrm{m/s^2}$), obtained from the NI system, and the 22 strain signals (units: $\mu\mathrm{m/m}$), obtained from the FBGS system. For all acceleration signals, the (physically meaningless) DC component is removed. The input signal consists of the shaker force signal, obtained from the NI system. The output and input signals are processed using the reference-based data-driven combined deterministic-stochastic subspace identification (CSI-data/ref) algorithm [7]. The entire record of 150 s is processed at once. No averaging or windowing is applied. The input-output modal test allows to obtain the natural frequencies, modal damping ratios, and mode shapes corresponding to the first four vertical bending modes of the cantilever beam. Table 1 presents for each of the identified modes the undamped natural frequency, the modal damping ratio, and the mode type. Fig. 4 represents the identified mode shapes in the complex plane. The amplitude of the strain mode shape components has been modified for plotting, in order to obtain

displacement and strain mode shapes with similar amplitude. After rescaling, both the displacement and strain mode shapes have a maximum amplitude of 1. The displacement mode shapes, as obtained from the acceleration data, are out of phase with the strain mode shapes. This is emphasized by plotting a line fit for the displacement and strain mode shapes separately. The angle between the fitted line and the real axis is also known as the mean phase (MP) of the mode shape, and is calculated by solving the following total least squares problem [8, 9]:

$$\mathrm{MP}(\boldsymbol{\phi}_m) = \arg\min_{\boldsymbol{\alpha}\in\mathbb{R}} \frac{||\mathrm{Im}(\boldsymbol{\phi}_m) - \tan(\alpha)\mathrm{Re}(\boldsymbol{\phi}_m)||_2^2}{1+\tan(\alpha)} \tag{16}$$

The solution is obtained as [3]:

$$\mathrm{MP}(\boldsymbol{\phi}_m) = \arctan\left(\frac{-V_{12}}{V_{22}}\right) \tag{17}$$

where $V_{12}$ and $V_{22}$ are the elements (1,2) and (2,2) of the matrix of right singular vectors $\mathbf{V} \in \mathbb{R}^{2\times 2}$, obtained from the singular value decomposition $\mathbf{USV}^{\mathrm{T}} = [\mathrm{Re}(\boldsymbol{\phi}_m)\ \mathrm{Im}(\boldsymbol{\phi}_m)]$, with $\mathbf{U} \in \mathbb{R}^{n_\mathrm{d}\times 2}$ and $\mathbf{S} \in \mathbb{R}^{2\times 2}$. Note that the calculation of the MP in Eq. (17) is more accurate than the classical expression for the MP provided in [4]. The latter fails when the mode shape components have an imaginary part that becomes large compared to the real part (see also [8]).

In this case, a distinction is made between the MP of the displacement mode shapes $\boldsymbol{\phi}_{am}$ and of the strain mode shapes $\boldsymbol{\phi}'_{\epsilon m}$, in order to distinguish between both measurement systems. Given that the displacement and strain mode shapes are both collinear (Fig. 4), it can be assumed that the studied system is proportionally damped, and that the difference in MP between the displacement and strain mode shapes mainly originates from the synchronization error. The time delay $\delta t$ between both data acquisition systems is determined in the following section.

| No. | $f_\mathrm{id}$ [Hz] | $\xi_\mathrm{id}$ [%] | Type |
|---|---|---|---|
| 1 | 10.86 | 2.39 | 1st vertical bending mode |
| 2 | 67.67 | 0.29 | 2nd vertical bending mode |
| 3 | 189.37 | 0.28 | 3rd vertical bending mode |
| 4 | 375.45 | 0.11 | 4th vertical bending mode |

Table 1: Identified modal characteristics ($f_\mathrm{id}$: undamped natural frequency, $\xi_\mathrm{id}$: modal damping ratio).

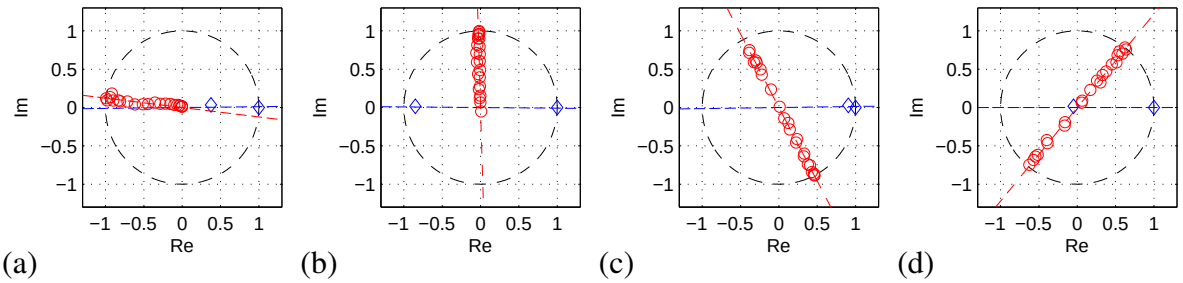


Figure 4: Representation of (a) mode 1, (b) mode 2, (c) mode 3, and (d) mode 4, in the complex plane. The displacement mode shape components obtained from the acceleration measurements are indicated by blue diamonds. The strain mode shape components are indicated by red circles. A line fit for the displacement and strain mode shape is shown by a blue and red dashed line, respectively.

### 3.2 Synchronization

The time delay $\delta t$ is estimated by minimization of the objective function $f(\delta t)$, that gives the average difference between the MP of the displacement and the strain mode shapes over all modes. In the calculation of the objective function, the strain mode shapes $\boldsymbol{\phi}'_{\epsilon m}$ are rescaled, in order to account for a time delay $\delta t$. The displacement mode shapes $\boldsymbol{\phi}_{\mathrm{a}m}$ are not rescaled.

$$\delta t^\star = \arg\min_{\delta t \in \mathbb{R}} f(\delta t) = \arg\min_{\delta t \in \mathbb{R}} \frac{1}{n_\mathrm{m}} \sum_{m=1}^{n_\mathrm{m}} \left| \mathrm{MP}(\boldsymbol{\phi}'_{\epsilon m} e^{\lambda_{m1}\delta t}) - \mathrm{MP}(\boldsymbol{\phi}_{\mathrm{a}m}) \right| \tag{18}$$

Equal weight is given to the contribution of all modes in the objective function. For modes with a higher natural frequency, however, the phase shift $\theta_m$ introduced by a time delay $\delta t$ becomes larger than for modes with a low natural frequency, as seen from Eq. (14). Modes with a higher natural frequency are therefore more sensitive to a time delay.

Figure 5 shows the objective function $f(\delta t)$ as a function the time delay $\delta t$. The objective function is not smooth and shows multiple local minima. The non smooth problem is solved by applying a sweep over all possible values of $\delta t$. The global minimum is in this case obtained for $\delta t = 3.6$ ms $(= \delta t^\star)$. The use of multiple modes is essential when estimating the time delay. If a single mode is used in the estimation, the objective function in Eq. (18) shows multiple (local) minima at $\delta t^\star \pm \pi/(\omega_m \sqrt{1-\xi_m^2})$. By including more modes, the number of minima is reduced. Since the presence of multiple optima cannot be avoided, an initial guess of the time delay is required in any case, however. This initial guess can for example be obtained by applying conventional correlation techniques. Note that the initial guess obtained from correlation techniques equals an integer number of time steps $\Delta t$ $(= 1$ ms$)$ used in the data acquisition, whereas the time delay $\delta t$ obtained by applying synchronization based on system identification can take any real number. This generally allows for more accurate synchronization.

Figure 6 shows the representation of the displacement and strain mode shapes obtained after compensation for the time delay $\delta t^\star$ in the complex plane. After minimization, some differences in MP remain $(f(3.6 \text{ ms}) \neq 0)$. This is also seen from table 2, which summarizes the results of the optimization. For modes 2, 3, and 4, the difference in MP value between the displacement and strain mode shape is significantly reduced. However, for mode 1, the difference in MP is not significantly reduced after the optimization. The remaining differences result from identification inaccuracies and violation of the assumptions in the proposed method. In the next section, it is shown that the estimated time delay $\delta t^\star$ is accurate, however, resulting in reliable estimates of the displacement and strain mode shapes.

When synchronization of more than two $(n_\mathrm{acq})$ acquisition systems is needed, a reference system is chosen and the optimization procedure outlined in this section is repeated $n_\mathrm{acq} - 1$ times.

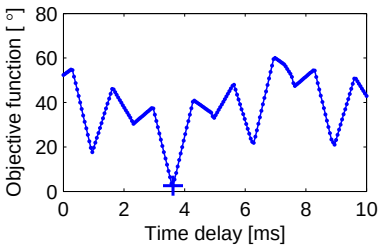


Figure 5: Variation of the objective function $f(\delta t)$ with the time delay $\delta t$. The marker (+) indicates the optimum.

Table 2: Summary of the optimization applied for the estimation of the time delay $\delta t$.

| | mode 1 | mode 2 | mode 3 | mode 4 |
|---|---|---|---|---|
| $\mathrm{MP}(\boldsymbol{\phi}'_{\epsilon m}) - \mathrm{MP}(\boldsymbol{\phi}_{am})$ | $-7.64$ | $-87.80$ | $-63.29$ | $50.70$ |
| $\mathrm{MP}(\boldsymbol{\phi}'_{\epsilon m} e^{\lambda_{m1}\delta t^\star}) - \mathrm{MP}(\boldsymbol{\phi}_{am})$ | $6.51$ | $0.38$ | $3.50$ | $-0.01$ |
| $\theta^\star_m$ | $-14.15$ | $-88.18$ | $-246.79$ | $-489.29$ |
| | | | $(= -66.79 - 180)$ | $(= 50.71 - 540)$ |
| $A^\star_m$ | 0.99 | 1.00 | 0.99 | 0.99 |

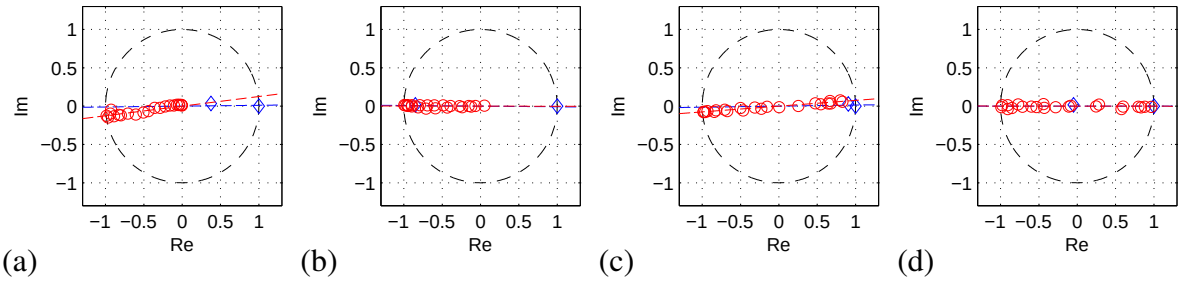


(a) (b) (c) (d)

Figure 6: Displacement (blue diamonds) and strain (red circles) mode shape components obtained after compensation for the time delay $\delta t^\star$ for (a) mode 1, (b) mode 2, (c) mode 3, and (d) mode 4, in the complex plane. A line fit for the displacement and strain mode shape is shown by a blue and red dashed line, respectively.

### 3.3 Verification

A verification experiment was performed. A vertical impact force was applied at the tip of the beam using the instrumented hammer (Fig. 3). The response of the beam was measured in all sensors. Fig. 7 shows a detail of the force time history, and the time history of the response obtained from accelerometer $a_1$ and strain gauge $\epsilon_5$, that physically coincide. The force and acceleration signal have been acquired by the NI system, the strain signal by the FBGS system. A significant increase of the acceleration level is observed right after the impact is applied (Fig. 7b). The strain signal remains very small the first 4 ms after the impact, thereafter showing a significant decrease. The observed delay of $4\ \mathrm{ms} \pm 0.5\ \mathrm{ms}$ is in line with the delay $\delta t$ of 3.62 ms that has been identified in Section 3.2.

Fig. 8 finally shows the displacement and strain mode shapes along the beam after accounting for the phase shift and amplitude modification introduced by the synchronization error. Only the real part of the mode shapes is retained. Due to the limited number of accelerometers, a proper distinction between the displacement mode shapes for different modes cannot be made. The strain mode shapes have a regular shape. The apparent deviation of the mode shape at sensor $\epsilon_3$ is due to the presence of a bolt that is welded at the lower side of the beam to connect the shaker (see Fig. 2c). This results in (locally) lower strain levels.

## 4 CONCLUSIONS

It is shown in this paper that for linear structures with proportional damping a time lag between measured response signals results in a spurious phase shift of the corresponding mode shape components, whereas the natural frequencies and damping characteristics are unchanged. This observation can be used for (offline) synchronization of data acquisition systems, using the modal characteristics obtained from a system identification. The time lag is estimated from the solution of an optimization problem. A demonstration for a laboratory experiment on a cantilever steel beam has shown that the proposed methodology can be used for accurate time synchronization, with significant improvement of the accuracy of the identified mode shapes.

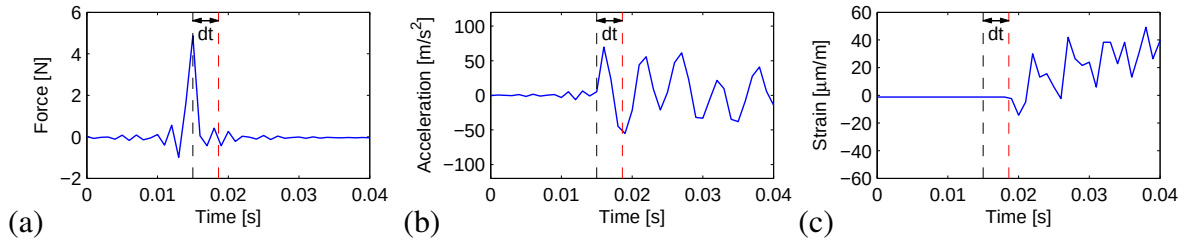


Figure 7: Time history of (a) the hammer impact and time history of the corresponding acceleration $a_1$ (b) and strain $\epsilon_1$ (c). The time step corresponding to the peak force is indicated by a dashed black line. The time delay $\delta t$ (=3.6 ms) is found as the horizontal distance between the dashed black line and the dashed red line.

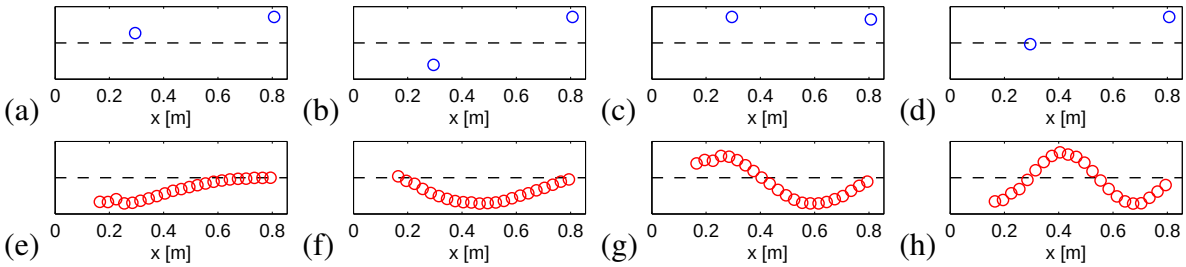


Figure 8: Displacement mode shapes (top, a – d) and strain mode shapes (bottom, e – h) along the axis of the beam, for mode 1 (a and e), mode 2 (b and f), mode 3 (c and g), and mode 4 (d and h).

## ACKNOWLEDGEMENTS

The research presented in this paper has been performed within the framework of the project G.0738.11 “Inverse identification of wind loads on structures”, funded by the Research Foundation Flanders (FWO), Belgium. Kristof Maes is a Postdoctoral Fellow of KU Leuven. The financial support of FWO and KU Leuven is gratefully acknowledged. The authors affiliated to KU Leuven are all members of the KU Leuven - BOF PFV/10/002 OPTEC - Optimization in Engineering Center.

## REFERENCES

[1] S. Amador, F. Magalhães, N. Martins, E. Caetano, and Á. Cunha. High spatial resolution operational modal analysis of a football stadium suspension roof. In Á. Cunha, L.F. Ramos, E. Caetano, and P. Lourenço, editors, *Proceedings of the 5th International Operational Modal Analysis Conference, IOMAC 2013*, Guimarães, Portugal, May 2013.

[2] A. Araujo, J. Garcia-Palacios, J. Blesa, F. Tirado, E. Romero, A. Samartin, and O. Nieto-Taladriz. Wireless measurement system for structural health monitoring with high time-synchronization accuracy. *IEEE Transactions on Instrumentation and Measurement*, 61(3):801–810, 2012.

[3] G.H. Golub and C.F. Van Loan. *Matrix computations*. John Hopkins University Press, Baltimore, MD, 3rd edition, 1996.

[4] W. Heylen, S. Lammens, and P. Sas. *Modal analysis theory and testing*. Department of Mechanical Engineering, Katholieke Universiteit Leuven, Leuven, Belgium, 1997.

[5] R. Kim, T. Nagayama, H. Jo, and B.F. Spencer Jr. Preliminary study of low-cost GPS receivers for time synchronization of wireless sensor networks. In *Proceedings of SPIE,*

*Sensors and Smart Structures Technologies for Civil, Mechanical, and Aerospace Systems 2012*, volume 8345, pages 83451A–1, 2012.

[6] E. Reynders. System identification methods for (operational) modal analysis: review and comparison. *Archives of Computational Methods in Engineering*, 19(1):51–124, 2012.

[7] E. Reynders and G. De Roeck. Reference-based combined deterministic-stochastic subspace identification for experimental and operational modal analysis. *Mechanical Systems and Signal Processing*, 22(3):617–637, 2008.

[8] E. Reynders, J. Houbrechts, and G. De Roeck. Fully automated (operational) modal analysis. *Mechanical Systems and Signal Processing*, 29:228–250, 2012.

[9] S. Van Huffel and J. Vandewalle. *The total least squares problem*. SIAM, Philadelphia, PA, 1991.

[10] M.L. Wang, J.P. Lynch, and H. Sohn, editors. *Sensor Technologies for Civil Infrastructures: Sensing Hardware and Data Collection Methods for Performance Assessment.*, volume 1. Elsevier, 2014.

[11] W. Weijtjens, G. De Sitter, C. Devriendt, and P. Guillaume. Operational modal parameter estimation of MIMO systems using transmissibility functions. *Automatica*, 50(2):559 – 564, 2014.

[12] D.V. Widder. *The Laplace Transform*. Princeton University Press, Princeton, 1946.

COMPDYN 2017
6th ECCOMAS Thematic Conference on
Computational Methods in Structural Dynamics and Earthquake Engineering
M. Papadrakakis, M. Fragiadakis (eds.)
Rhodes Island, Greece, 15–17 June 2017

# INTERPOLATION EVOLUTION METHOD: ANALYSIS OF THE INFLUENCE OF HIGHER MODES RETRIEVED FROM NONLINEAR NUMERICAL ANALYSES PERFORMED ON TWO DIFFERENT MODELS OF REINFORCED CONCRETE FRAMED STRUCTURES

**C. Iacovino[1], R. Ditommaso[1], G. Auletta[1], F.C. Ponzo[1], M.P. Limongelli[2]**

[1] School of Engineering, University of Basilicata, Italy
chiara.iacovino@unibas.it
r.ditommaso@unibas.it
gianluca.auletta@tiscali.it
felice.ponzo@unibas.it

[2]Department of Architecture, Built Environment and Construction Engineering, Milano, Italy
mariagiuseppina.limongelli@polimi.it

**Keywords:** Structural Health Monitoring; Structural Damage Localization; Higher modes; Curvature Evolution Method, Interpolation Method, Band-Variable Filter

**Abstract.** *Continuous monitoring based on vibrational identification methods is increasingly employed in order to evaluate the state of health of existing structures and infrastructures in operative conditions and after relevant earthquakes. Most of the damage identification methods are based on the variations of damage indices defined in terms modal and/or non-modal parameters. Most of simplified methods for structural health monitoring and damage detection are based on the observation of the evolution of the dynamic characteristics associated to the fundamental mode of vibration of a monitored structure. The contribution of higher modes to the dynamic response of multi degree-of-freedom systems is an issue of relevant importance affecting both the design of new structures and the assessment of existing ones. The contribution of higher modes could be effective also in the inverse procedures for structural damage detection. In this paper the Interpolation Evolution Method, previously applied considering only the contribution of the fundamental mode of vibration, has been applied taking into account the contribution of the higher modes. Preliminary results retrieved from a numerical campaign based on nonlinear finite element models excited by several strong motion earthquakes are presented.*

## 1 INTRODUCTION

Systems for structural health monitoring could be a relevant tool in seismic regions after a strong motion earthquake performing an objective estimation of possible structural damage. Vibration based damage identification techniques have been widely applied for the assessment of the health state of buildings. Researchers have worked to set-up new methodologies for SHM based on the detection of variations, after a strong seismic event, of the structural dynamic characteristics, namely the modal parameter (frequencies, mode shapes, damping) or non-modal parameters like the operational deflection shapes (ODS) [1]. Damage identification is generally carried out through a comparison between the original (undamaged) state and the (possibly damaged) current state [2]-[4]. Methods based on frequency changes can be reliably applied to detect damage, but they are hardly able to give information about the location of damage. To this aim are more effective methods based on the time-evolution analyses ([5]-[8]) able to detect changes of modal or operational mode shapes and/or of their derivatives such as slopes, curvatures or strain energy [9]-[13].

Most of simplified methods for structural health monitoring and damage detection are based on the analysis of the evolutive dynamic characteristics associated to the fundamental mode of vibration of a monitored structure. The contribution of higher modes to the dynamic response of multi degree-of-freedom systems is a topic of relevance for the design of new structures and the assessment of existing ones, and it could be effective also in the inverse procedures for structural damage detection.

In this paper the Interpolation Evolution Method (IEM), a combination of two existing methods, named Curvature Evolution Method (CEM) and Interpolation Method (IM), has been applied taking into account the contribution of higher modes in the procedure for damage localization. The Interpolation Method [9] is based on a damage feature defined in terms of the loss of smoothness (that is local increases of curvature) of the operational mode shapes, induced by a local reduction of stiffness. The damage feature is defined in terms of the variation of the interpolation error between a reference and a (potentially) damaged configuration. The interpolation error is computed for each configuration by interpolating with a smooth function (namely a cubic spline for a beam-like structure) the operational (or the modal) shapes computed from responses recorded on the structure during vibrations. In the Curvature Evolution Method [10] the damage feature is defined in terms of the mode curvature. This parameter is evaluated overtime from the responses recorded during the earthquake and the comparison of its values at different times allows the detection of its possible variations. In this method it is possible to analyse the nonlinear response of each mode of vibration of the monitored structure through the Band-Variable Filter [14].

The combined approach has been applied to nonlinear numerical models of reinforced concrete framed structures excited by several strong motion earthquakes.

## 2 INTERPOLATION EVOLUTION METHOD (IEM)

The main idea at the base of the combined IEM approach is to jointly exploit the performance of the Curvature Evolution Method with the stability of the Interpolation Method. The interpolation is applied to the fundamental mode shape continuously extracted at each time instant before, during and after a strong motion event. A further advantage connected to the proposed procedure consist in the possibility of computing a set of values of the damage feature (variation of the interpolation error) allowing to recover its statistics thus taking into account its variability due to uncertainties induced by noise in recorded data.

The Curvature Evolution Method [10] for damage localization is based on the use of the Band-Variable Filter [14] able to extract the nonlinear response of each mode of vibration, acting simultaneously in both time and frequency domain. The detection of possible changes occurred during a single earthquake is carried out in terms of a damage feature defined in terms of the mode curvature. The Band-Variable Filter gives the possibility to extract from a non-stationary and/or nonlinear signal just the energy content related to a single mode of vibration, preserving both amplitude and phase over time [15]. The Band-Variable Filter allows to evaluate both frequency and mode shape variations during an earthquake. The basic idea is to isolate, by mean the Band-Variable Filter, the fundamental mode over time and evaluate its changes in terms of both shape and related curvature [16].

The Interpolation Method [9] is based on the observation that the comparison of the operational mode shapes related to the undamaged and damaged phases points out a sharp reduction of smoothness of the deformed shape at the damaged story. The damage feature is thus defined as the variation of the error related to the use of a (smooth) cubic spline function in interpolating the operational or the modal shapes of the monitored structure. A variation of the interpolation error between a reference and a possible damaged configuration indicates the onset of damage. In order to remove the influence of the amplitude of displacements on the evaluation of the interpolation error and to remove the numerical errors related to the estimation of displacements from recorded accelerations, the interpolation error is defined in terms of the difference between the transfer functions of the recorded and interpolated accelerations with respect to the input acceleration [17]. The value of the damage feature at each location equipped with a sensor is computed as the positive difference between the values of the interpolation error in the inspection $E_i$ and in the reference $E_0$ phases.

The combination of the two methods CEM and IM is performed herein using the Band-Variable Filter to extract the non-linear response of the structure and assuming as a damage feature the variation of the interpolation error computed at different times during the strong motion.

In this paper, the Band-Variable Filter has been used in order to extract both the first and the second mode of vibration (in the same direction) of the structure. The structural mode shapes have been evaluated over time and have been interpolated through a spline shape function at each location $x$ and time $t$. After the computation of the interpolation error, the variation of the interpolation error with respect to the initial value have been computed at each location $x$ and time $t$. finally has been selected the damaged location as that corresponding to the highest frequency of detection over the duration of the strong motion.

## 3 NUMERICAL CASE STUDIES

The Interpolation Evolution Method has been applied to nonlinear numerical models of two reinforced concrete framed structures of respectively 5 and 8 floors with regular geometric configuration (Figure 1) and designed only for gravity loads. The height of each story is 3 m, for a total height of the buildings equal to 15 m for the 5 story building and of 24m for the 8 story building (Figure 2).

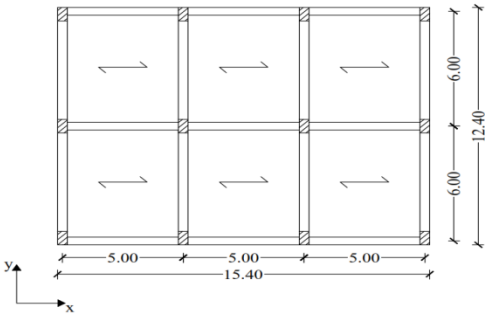


Figure 1: Geometric plan.

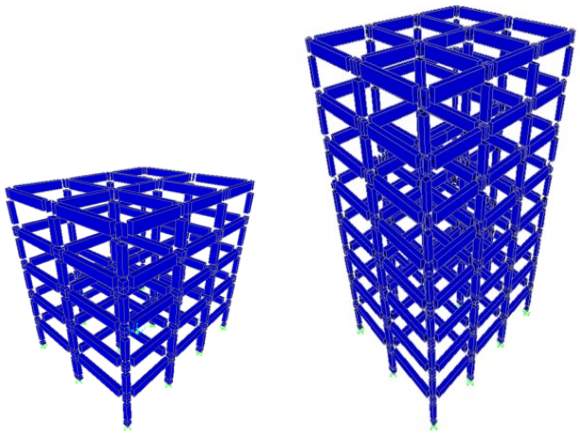

Figure 2: Nonlinear FEM models: (a) 5 story, (b) 8 story.

Nonlinear dynamic analyses have been carried out using a nonlinear 3D model built in SAP2000 non-linear [18]. In order to simulate a structural nonlinear behaviour during a strong ground motion, link elements and plastic hinges were modelled at the ends of both beam and column elements. Link elements have a Pivot hysteretic behaviour, while plastic hinges have an axial load-dependent one. Table 1 shows the Peak Ground Acceleration (PGA) values of the natural accelerograms selected for the numerical simulations.

| | **A1** | **A2** | **A3** | **A4** | **A5** | **A6** | **A7** |
|---|---|---|---|---|---|---|---|
| **PGA (g)** | 0.34 | 0.34 | 0.13 | 0.15 | 0.22 | 0.48 | 0.35 |

Table 1: PGA related to the natural accelerograms used for the numerical simulations.

İn order to identify the reference fundamental frequency before the earthquake and the final fundamental frequency after the earthquake, 20 seconds of pink noise have been added at the beginning and at the end of each time-history used as input. Figure 3 shows the response spectra of the seven accelerograms compatible with the Italian Seismic Code for a soil type B [19].

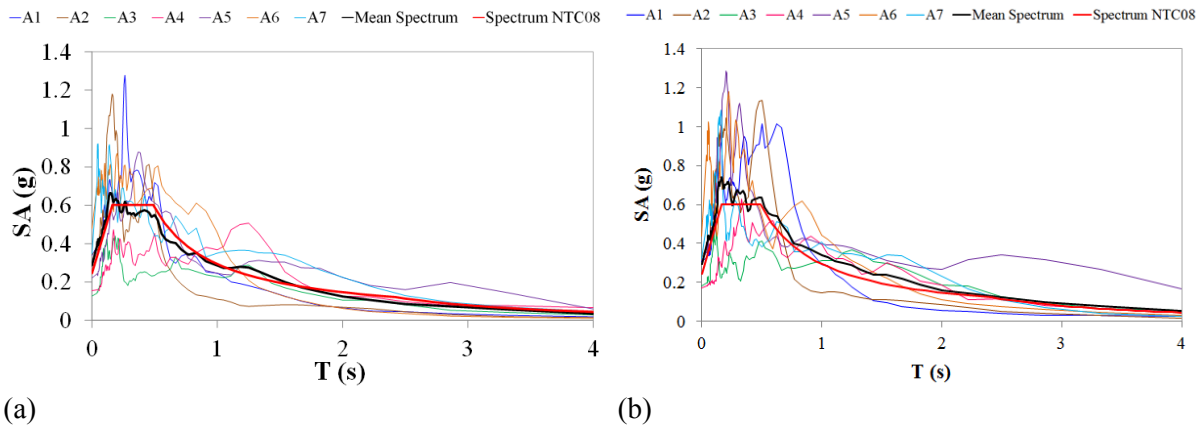


Figure 3: Response spectra of the natural accelerograms: (a) NS component; (b) WE component.

## 4 DISCUSSION OF RESULTS

This section shows the preliminary results obtained by applying the Interpolation Evolution Method to the case data simulated using the 5 and 8 storey nonlinear models. In order to test the robustness of the IEM approach and to perform realistic simulations, each nonlinear numerical analysis has been performed using both NS and WE component of each selected earthquake. After each simulation, as described in section 2, the first step was the identification of the first and the second mode of vibration along the same direction and the computation of the corresponding operational mode shape (evaluated considering just the contribution of the first two modes along a single direction). Then, the interpolation through the cubic spline function has been applied and the time history of the damage feature (variation of the interpolation error) has been evaluated at each instrumented location. At each time instant, the location where the maximum value of the damage feature (among all the instrumented locations) was attained, has been chosen as the damaged one. For each event and for each storey, the frequency of detection (number of times the location was detected as the damaged one over the total duration of the event) was assumed as representative of the probability of detection at the storey. Table 2 shows the initial modal characteristics of the used numerical models and the considered modes (1° and 2° modes along the same direction corresponds to the 1° and 4° modes highlighted in Table 2).

| | 5 story building | | | 8 story building | | |
|---|---|---|---|---|---|---|
| **mode** | **f (Hz)** | **mass particip. (dir. x)** | **mass particip. (dir. y)** | **f (Hz)** | **mass particip. (dir. x)** | **mass particip. (dir. y)** |
| **1** | **0.84** | **78.00%** | **0.00%** | **0.66** | **0.00%** | **66.24%** |
| 2 | 0.59 | 0.00% | 77.00% | 0.80 | 61.23% | 0.01% |
| 3 | 0.58 | 0.00% | 0.76% | 0.86 | 2.16% | 0.15% |
| **4** | **0.27** | **10.00%** | **0.00%** | **1.99** | **0.00%** | **8.57%** |
| 5 | 0.19 | 0.00% | 0.00% | 2.41 | 8.21% | 0.00% |
| 6 | 0.19 | 0.00% | 10.00% | 2.58 | 0.34% | 0.02% |

Table 2: Values of frequency and mass participation of the mode of vibration considered for the analysis.

From Figure 4 to Figure 7, the results obtained by applying the IEM selecting only the first fundamental mode of vibration are compared with the results obtained by considering both the first and the second mode of vibration.

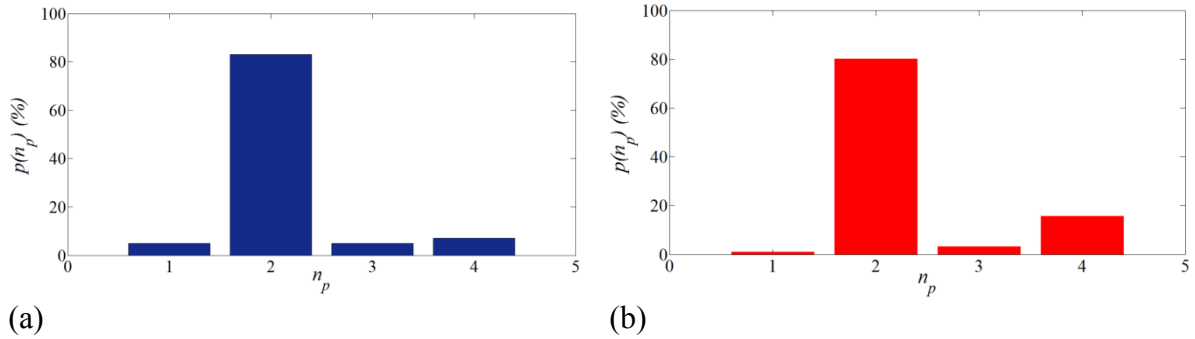


Figure 4. Histograms of probability to detect damage at each floor of the 5 story building - accelerogram A1: (a) only first fundamental mode; (b) first and second fundamental mode.

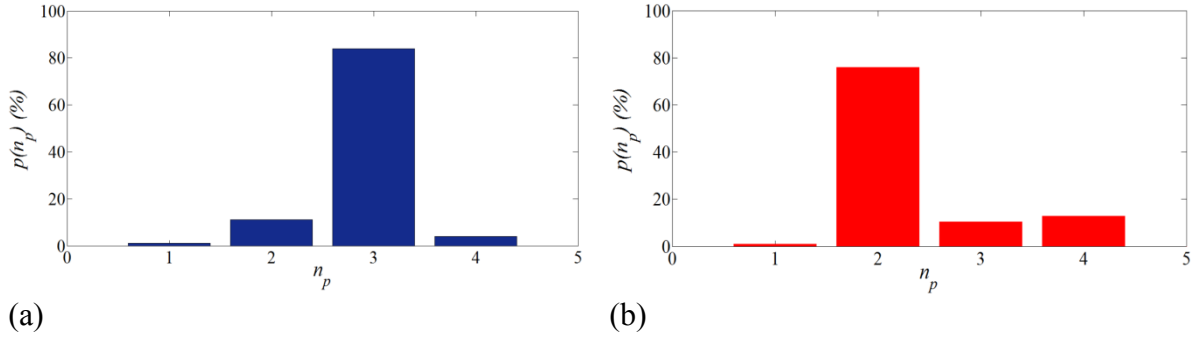


Figure 5. Histograms of probability to detect damage at each floor of the 5 story building - accelerogram A5: (a) only first fundamental mode; (b) first and second fundamental mode.

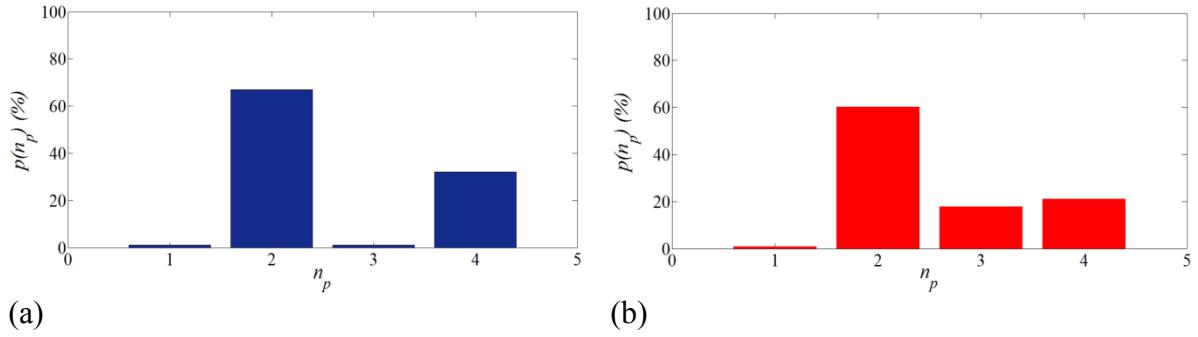


Figure 6. Histograms of probability to detect damage at each floor of the 5 story building - accelerogram A6: (a) only first fundamental mode; (b) first and second fundamental mode.

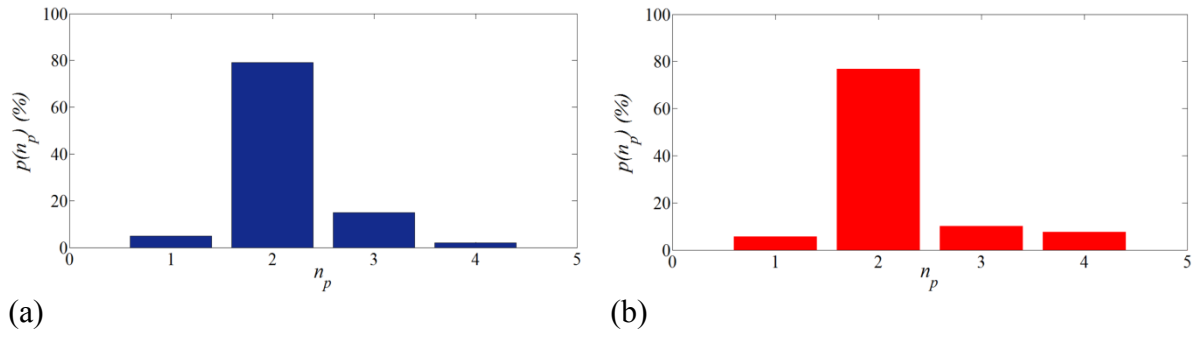


Figure 7. Histograms of probability to detect damage at each floor of the 5 story building - accelerogram A6: (a) only first fundamental mode; (b) first and second fundamental mode.

The nonlinear dynamic analysis carried out on the two multi-storey frames show that the different earthquakes caused the formation of plastic hinges at the ends of all columns between the second and third floors for the 5 storey model and between the first and second floors for the 8 storey model. The maximum variation of the interpolation error occurs at the second and the third floor (only for the accelerogram A5) considering the first fundamental mode. By applying the procedure through the selection of both the first and the second mode of vibration, the maximum values are at the second floor of the structure. The highest value of the damage feature is attained at the damaged locations allowing the correct localization of damage.

Table 3 summarizes the probability to detect damage at each floor obtained from data of the 5 story building excited by the selected ground motions.

| | **A1** | | **A5** | | **A6** | | **A7** | |
|---|---|---|---|---|---|---|---|---|
| | **1st mode** | **1st + 2nd mode** | **1st mode** | **1st + 2nd mode** | **1st mode** | **1st + 2nd mode** | **1st mode** | **1st + 2nd mode** |
| $n_p$ | $p(n_p)$ (%) | $p(n_p)$ (%) | $p(n_p)$ (%) | $p(n_p)$ (%) | $p(n_p)$ (%) | $p(n_p)$ (%) | $p(n_p)$ (%) | $p(n_p)$ (%) |
| 0 | 0.00 | 0.00 | 0.00 | 0.00 | 0.00 | 0.00 | 0.00 | 0.00 |
| 1 | 5.08 | 1.04 | 0.63 | 0.86 | 0.59 | 0.85 | 4.66 | 5.64 |
| 2 | **83.05** | **80.21** | 10.63 | **75.97** | **67.06** | **60.17** | **76.27** | **76.69** |
| 3 | 5.08 | 3.13 | **84.38** | 10.30 | 0.59 | 17.80 | 14.41 | 10.15 |
| 4 | 6.78 | 15.63 | 4.38 | 12.88 | 31.76 | 21.19 | 1.69 | 7.52 |
| 5 | 0.00 | 0.00 | 0.00 | 0.00 | 0.00 | 0.00 | 0.00 | 0.00 |
| Max Drift | 2° floor | | 2° floor | | 2° floor | | 2° floor | |

Table 3: Comparison of probability to detect damage at each floor of the 5 story building considering only the first fundamental mode, the first and second modes and the floor where the maximum drift occurred.

The maximum values of the frequency of detection are similar in all the analysed cases and occur at the most damaged floor. The following figures show the comparison between the frequency if detection obtained considering only the first fundamental mode and or both the first and the second modes of vibration of the 8 story building.

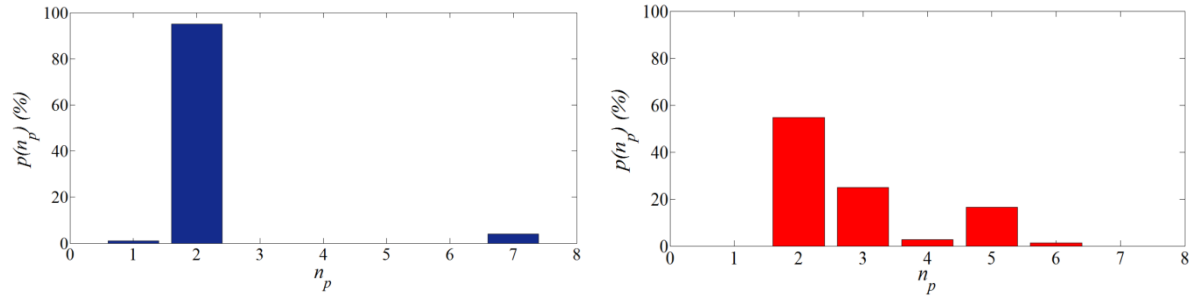


Figure 8. Histograms of probability to detect damage at each floor of the 8 story building - accelerogram A1: (a) only first fundamental mode; (b) first and second fundamental mode.

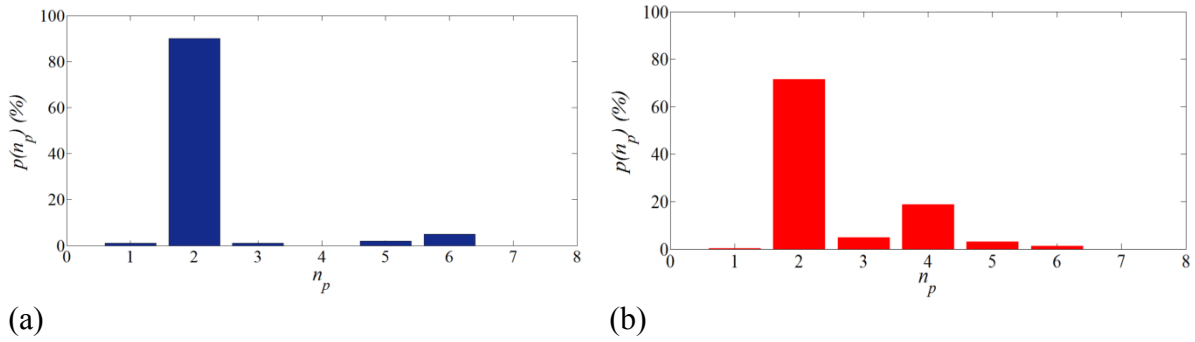


Figure 9. Histograms of probability to detect damage at each floor of the 8 story building - accelerogram A5: (a) only first fundamental mode; (b) first and second fundamental mode.

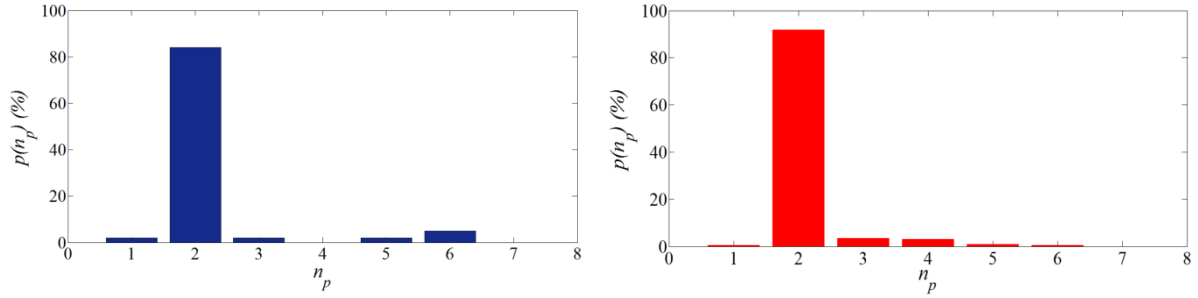


Figure 10. Histograms of probability to detect damage at each floor of the 8 story building - accelerogram A6: (a) only first fundamental mode; (b) first and second fundamental mode.

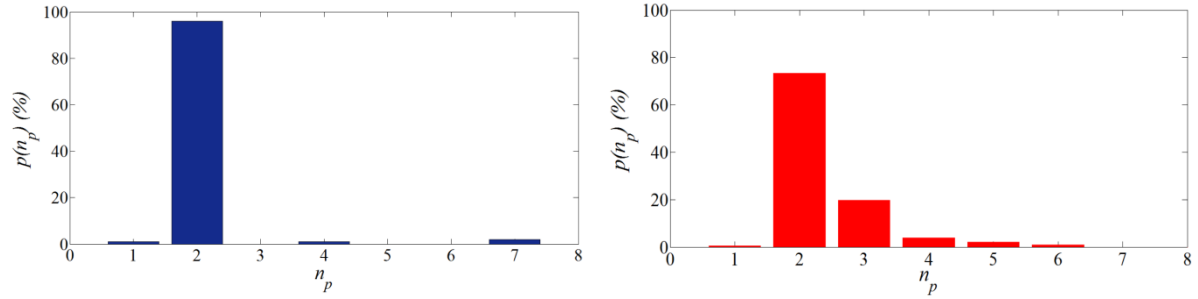


Figure 11. Histograms of probability to detect damage at each floor of the 8 story building - accelerogram A7: (a) only first fundamental mode; (b) first and second fundamental mode.

Table 4 summarizes the probability to detect damage at each floor obtained from data of the 8 story building excited by the selected ground motions.

| | **A1** | | **A5** | | **A6** | | **A7** | |
|---|---|---|---|---|---|---|---|---|
| | **1st mode** | **1st + 2nd mode** | **1st mode** | **1st + 2nd mode** | **1st mode** | **1st + 2nd mode** | **1st mode** | **1st + 2nd mode** |
| $n_p$ | $p(n_p)$ (%) | $p(n_p)$ (%) | $p(n_p)$ (%) | $p(n_p)$ (%) | $p(n_p)$ (%) | $p(n_p)$ (%) | $p(n_p)$ (%) | $p(n_p)$ (%) |
| 0 | 0.00 | 0.00 | 0.00 | 0.00 | 0.00 | 0.00 | 0.00 | 0.00 |
| 1 | 1.05 | 0.00 | 1.01 | 0.35 | 2.11 | 0.43 | 0.82 | 0.42 |
| 2 | **94.74** | **54.61** | **90.91** | **71.53** | **88.42** | **91.88** | **95.90** | **73.22** |
| 3 | 0.00 | 25.00 | 1.01 | 4.86 | 2.11 | 3.42 | 0.00 | 19.67 |
| 4 | 0.00 | 2.63 | 0.00 | 18.75 | 0.00 | 2.99 | 0.82 | 3.77 |
| 5 | 0.00 | 16.45 | 2.02 | 3.13 | 2.11 | 0.85 | 0.00 | 2.09 |
| 6 | 0.00 | 1.32 | 5.05 | 1.39 | 5.26 | 0.43 | 0.00 | 0.84 |
| 7 | 4.21 | 0.00 | 0.00 | 0.00 | 0.00 | 0.00 | 2.46 | 0.00 |
| 8 | 0.00 | 0.00 | 0.00 | 0.00 | 0.00 | 0.00 | 0.00 | 0.00 |
| Max Drift | 2° floor | | 2° floor | | 2° floor | | 2° floor | |

Table 4: Comparison of probability to detect damage at each floor of the 8 story building considering only first fundamental mode, the first and second modes and the floor where the maximum drift occurred.

The results are in agreement with those presented above. The maximum values of the damage indices occur at the damaged locations leading to a correct localization of damage. However, for the 8-story structure, the probability values obtained considering only the first fundamental mode of vibration are higher than the values obtained in the second case (1st + 2nd mode of vibration) except for accelerogram A6.

The last circumstance is probably due to the lower reliability of the time evolution of the second mode with respect to the first which is the one that exhibits the higher contribution to the frame response as shown by the values of the modal participation factors.

## 5 CONCLUSIONS

In this work the Interpolation Evolution Method for damage localization has been applied using responses obtained using nonlinear finite element models excited by several real strong motion earthquakes. The novelty of the paper consists in taking into account the effects of higher modes of vibration on the damage localization procedure. The method was applied to two case studies comparing results obtained considering only the first fundamental mode of vibration with those retrieved considering also the second mode of vibration.

Results show that for both the cases, the combined method is able to successfully detect the correct location of structural damage. Particularly, the maximum values of the damage feature occur at the most damaged floor. For the 5 story building, higher modes do not increase the reliability of the procedure but confirm the results obtained by considering only the first mode of vibration. Whereas the maximum probability to detect damage at each floor of the 8 story building decrease if higher modes are considered, therefore the procedure for damage detection is more reliable based only on the first fundamental mode.

## ACKNOWLEDGEMENTS

This study was partially funded by the Italian Department of Civil Protection within the project DPC-RELUIS 2016 - RS4 ‘‘Seismic observatory of structures and health monitoring’’.

## REFERENCES

[1] P.F. Pai, L.G. Young, Damage detection of beams using operational deflection shapes. *International journal of Solids and Structures*, **38**, 3161-3192, 2001.

[2] J.P. Amezquita-Sanchez, H. Adeli, Signal Processing Techniques for Vibration-Based Health Monitoring of Smart Structures. *Archives of Computational Methods in Engineering*, **23**, 1-15, 2016.

[3] W. Fan, P. Qiao, Vibration-based damage identification methods: a review and comparative study. *Structural Health Monitoring*, **10**, 83–29, 2011.

[4] L. A. S. Kouris, A. Penna, G. Magenes, Seismic damage diagnosis of a masonry building using short-term damping measurements. *Journal of Sound and Vibration*, **394**, 366-391, 2017.

[5] R. Ditommaso, F.C. Ponzo, Automatic evaluation of the fundamental frequency variations and related damping factor of reinforced concrete framed structures using the short time impulse response function (STIRF). *Engineering Structures*, **82**, 104–112, 2015.

[6] C. Iacovino, R. Ditommaso, M.P. Limongelli, F.C. Ponzo, Experimental damage localization in a full-scale 7 storey benchmark building under seismic excitation. *SPIE-Smart Structures/NDE*, Portland, Oregon, United States, 2017.

[7] G. Fan, L.-M. Zhang, J.-J. Zhang, C.-W. Yang, Time-frequency analysis of instantaneous seismic safety of bedding rock slopes. *Soil Dynamics and Earthquake Engineering*, **94**, 92-101, 2017.

[8] M. Picozzi, S. Parolai, M. Mucciarelli, C. Milkereit, D. Bindi, R. Ditommaso, M. Vona, M.R. Gallipoli, J. Zschau, Interferometric analysis of strong ground motion for structural health monitoring: The example of the L'Aquila, Italy, seismic sequence of 2009. *Bulletin of the Seismological Society of America*, **101-2**, 635-651, 2011.

[9] M.P. Limongelli, The interpolation damage detection method for frames under seismic excitation. *Journal of Sound and Vibration*, **330**, 5474–5489, 2011.

[10] R. Ditommaso, F.C. Ponzo, G. Auletta, Damage detection on framed structures: modal curvature evaluation using Stockwell Transform under seismic excitation. *Earthquake Engineering and Engineering Vibration,***14**, 265-274, 2015.

[11] M.P. Limongelli, Structural damage localization using the modal interpolation method. *Proc. 8EWSHM*. Bilbao, Spain, July 2016.

[12] R.P.C. Sampaio, N.M.M. Maia, J.M.M. Silva, Damage detection using the frequency response function curvature method. *Journal of Sound and Vibration*, **226**, 1029-1042, 1999.

[13] C.P. Ratcliffe, Damage Detection Using A Modified Laplacian Operator On Mode Shape Data. *Journal of Sound and Vibration*, **204,** 505-517, 1997.

[14] R. Ditommaso, M. Mucciarelli, F.C. Ponzo, Analysis of non-stationary structural systems by using a band-variable filter. *Bulletin of Earthquake Engineering,* **10**, 895-911, 2012.

[15] R. Ditommaso, M. Mucciarelli, F.C. Ponzo, S-Transform: A Band-Variable Filter to Extract the Nonlinear Dynamic Behaviour of Soil and Structures. *EACS 2012 – 5th European Conference on Structural Control,* Genoa, Italy – June 18-20, 2012.

[16] Ditommaso R, Ponzo FC, Auletta G, Iacovino C. Testing a new procedure for damage detection on framed structures subjected to strong motion earthquakes. *Second European conference on Earthquake Engineering and Seismology*, Istanbul, August 25-29, 2014.

[17] M.P. Limongelli, Frequency response function interpolation for damage detection under changing environment. MSSP doi:10.1016/j.ymssp.2010.03.004, 2010.

[18] SAP2000. Computers & Structures. https://www.csiamerica.com/products/sap2000

[19] Nuove norme tecniche per le costruzioni. D.M. Infrastrutture 14 Gennaio 2008.

COMPDYN 2017
6th ECCOMAS Thematic Conference on
Computational Methods in Structural Dynamics and Earthquake Engineering
M. Papadrakakis, M. Fragiadakis (eds.)
Rhodes Island, Greece, 15–17 June 2017

# A MECHANISTIC APPROACH IN DEFINING INELASTIC ROTATION CAPACITY OF RC COLUMNS

**Konstantinos G. Megalooikonomou[1], Stavroula J. Pantazopoulou[2], and Souzana P. Tastani[3]**

[1] Department of Civil and Environmental Engineering, University of Cyprus, P.O. Box 20537, 1687 Nicosia, Cyprus, kmegal01@ucy.ac.cy

[2]The Lassonde Faculty of Engrg., York University, 4700 Keele St, Toronto ON. M3J 1P3, Canada
pantazo@yorku.ca

[3]Democritus University of Thrace, Kimmeria Campus, Building B, Xanthi 67100, Greece
stastani@civil.duth.gr

**Keywords:** Shear Span, Bond, Yield-Penetration, Plastic Hinge Length, Inelastic Rotation.

**Abstract.** *When a reinforced concrete (RC) column is subjected to lateral sway as a result of earthquake action, the large strain demand in the end sections is supported by development of strains in the anchorage. This causes the bars to displace (or slip) relative to the anchoring concrete at the column fixed end(s). The lumped slip causes rigid-body rotation of the column, thereby alleviating partially the column deformation. This reinforcement slip is assumed to occur in the tension bars only and cause the rotation about the neutral axis. Development of flexural yielding and large rotation ductilities in the plastic hinge zones of frame members is synonymous with the spread of bar reinforcement yielding. Yield penetration in the anchored reinforcing bar inside the shear span of the column where it occurs, destroys interfacial bond between bar and concrete and reduces the strain development capacity of the reinforcement. This affects the plastic rotation of the member by increasing the contribution of bar slippage. In order to establish the plastic rotation in a manner consistent with the above definition, this paper uses the explicit solution of the field equations of bond over the shear span of a column. Through this approach, the bar strain distributions and the extent of yield penetration from the yielding cross section towards the shear span are resolved and calculated analytically. By obtaining this solution the aim is to illustrate the true parametric sensitivities of plastic hinge length as a design variable for practical use in seismic assessment of existing structures. Results obtained from the analytical procedures are compared with experimental evidence from tests conducted on reinforced concrete columns under seismic loading reported in the literature.*

## 1. INTRODUCTION

Pullout rotation accounts for a significant fraction of the deformation capacity of reinforced concrete (RC) columns. It occurs in the critical sections near the end supports as a result of the penetration of strains both inside the support of the member (*e.g.* footing) but also inside the shear span. In columns that do not fail by web crushing, strains spread further into the anchorage gradually with increasing applied chord rotation, claiming a predominant share of the members' deformation capacity near the ultimate limit state. This aspect of the response is evaluated from estimation of reinforcement slip; slip may be estimated approximately or it may be evaluated from solution of the field equations of bond along the principal reinforcement of the column as it sways laterally. Slip of the bars occurs where large inelastic strains may develop – i.e. in the yield penetration length over the anchorage and in the plastic hinge zone in the shear span. The kinematics of the pullout slip are accompanied by, (a) vertical displacement which is reported to occur at the tip of the cantilever column during cycling under lateral loading (b) acceleration of crushing of the concrete cover in the compression zone due to the local increase in compression strains [1].

Degradation of bond - beyond a critical slip value that marks the initiation of the descending branch in the local bond-slip law causes spreading of strains away from the critical section so that a larger fraction of the bar is eventually exposed to large strains. Analytical models representing the state of bond along the lateral surface of an embedded reinforcing bar are intended for interpretation and simulation/prediction of the behavior of structural concrete in a manner consistent with first principles. Previous studies have illustrated how detailed bond models may be used in the study of stress states arising in the assessment of the rotation capacity of RC members [2]. Through evaluation of the strain distribution it is possible to estimate the localization of excessive strain magnitudes in the critical zones, thereby enabling a novel approach for evaluation of the plastic hinge length in flexure-shear members. Additionally, the reinforcement stress and strain response and its displacement with respect to the surrounding concrete can be explicitly described through the solution of the equations of bond in the shear span of the member; this enables a detailed study of the tension stiffening phenomena, and how these affect the behavior of cracked concrete.

In this paper, a unidirectional model of bond is considered as a basis for the evaluation of the longitudinal strain distribution of the primary reinforcement of the column. Although several solutions that refer to the problem of force development along the anchorage have been proposed, yet the problem of strain penetration in the anchorage has received limited attention from researchers [3, 4]. Related studies have been conducted for lap splices developed in a region of constant moment (no shear) [5]. On the other hand, the problem of strain penetration in the shear span of the member has not been addressed explicitly yet.

## 2. CONSTITUTIVE RELATIONSHIPS FOR BAR TO CONCRETE BOND

The basic equations that describe force transfer lengthwise from a bar to the surrounding concrete through bond are derived from force equilibrium applied to an elementary bar segment of length $dx$ and from compatibility between bar translation (slip), axial bar strain $\varepsilon$, and concrete strain $\varepsilon_c$ over $dx$, namely [6,7]:

$$df/dx = -(4/D_b)f_b\ ,\ ds/dx = -(\varepsilon - \varepsilon_c) \cong -\varepsilon \tag{1}$$

where $f$ is the axial stress of the bar; $D_b$ is the bar diameter ; $f_b$ is the local bond stress and $s$ is the relative slip of the bar with respect to the surrounding concrete. The terms in Eq. (1) are related through the bond-slip law, $f_b = f_b(s)$ and the bar material stress-strain relationship,

$f=f(\varepsilon)$. The concrete contribution to relative slip is $\varepsilon_c dx$; this term is neglected when dealing with normal-weight concrete, considering that the average concrete strain is an order of magnitude smaller than the average bar strain. Solution of Eq. (1) is possible though exact integration, resulting in closed-form solutions for the state of stress and strain along the anchorage, through pertinent selection of simple models for the material laws (*e.g.* piecewise linear relations). This approach has a clear advantage over the numerical solution alternative in that it enables transparent insight into the role of the various design parameters on the behavior of bar anchorages.

Solution of Eq. (1) requires that the general form of the constitutive relationships of the bar and the local bond-slip law are known (Fig. 1). Here the reinforcing bar stress-strain relationship is considered elastoplastic with hardening (representing conventional steel reinforcement) (Fig. 1a). Without loss of generality, and to facilitate derivation of closed-form solutions, a linear elastic, perfectly plastic local bond-slip relationship with residual bond is assumed. The last branch represents the residual friction between the concrete cover and the steel bar after failure of the rib interlocking mechanism (Fig. 1b). The plateau in the local bond-slip law implies sustained bond strength. This feature is not always manifested in the test data; to be measured it requires redundancy in the anchorage (i.e., availability of longer anchorages to enable force redistribution before failure). In the assumed law the end of the plateau is marked by abrupt loss of bond strength to a residual value $f_b^{res}$. (Note that $f_b^{res}$ is taken nonzero only in the case of ribbed steel bars, but not for smooth steel bars.)

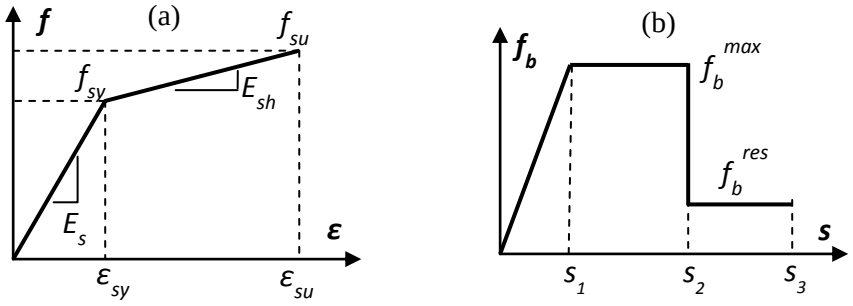


Figure 1: (a) Stress-strain law of steel bar and (b) local bond law

## 3. TENSION-STIFFENING MODEL

It was mentioned earlier that spread of inelastic strains occurs on both sides of a critical section (*e.g.* at the base of a column). The process of inelastic strain penetration in the anchorage of a reinforcing bar has already been demonstrated in [8]. This section is dedicated to solving the same problem in the other side of the critical section, that is, along the shear span of a column. Here the problem is different from that of the anchorage only in the type of boundary conditions that may be enforced (in other words, the governing differential equation is the same); with regards to the bond-slip law, although the general form of the multilinear envelope may be taken the same, the bond strength value, $f_b^{max}$, may be less in the shear span as compared to the anchorage due to the reduced confinement available. Considering the column under lateral sway, the moment-shear relationship in the span of a cantilever RC column under horizontal loading is identical to that occurring over the length of the actual frame member extending from the inflection point at midheight (this is the point of zero moment, zero curvature) to the fixed end support.

Before any kind of cracking takes place along the length of the flexural member, the bar strain is estimated from the flexural analysis of the uncracked column cross section *(i.e.* the

moment-curvature analysis) as per the Eq. (2) where $M(x)$ is the moment at distance $x$ from the support, $E$ is the elastic modulus of concrete, $I_g$ is the moment of inertia of the uncracked section with area $A$ (referred to as gross section), $N$ is the axial load, $h$ is the section height and $c$ is the cover (Fig. 2a):

$$\varepsilon(x) = \left(M(x) \cdot y_{s.na} / \left(E \cdot I_g\right)\right) - N/(E \cdot A)\ ,\ y_{s.na} = (h/2) - c - 0.5D_b \tag{2}$$

$$\text{or more generally: } \varepsilon(x) = \varphi(x) \cdot y_{s.na} \tag{3}$$

with $y_{s.na}$ the distance from the neutral axis to the centroid of tension reinforcement (Fig. 2a), and $\varphi(x)$ the curvature on the cross section at distance $x$ from the support. The distance to the neutral axis changes significantly from the initial linear elastic state $y_{s.na}^{gr}$, to the cracked state of a cross section $y_{s.na}^{cr}$. If the concrete tension zone of the member is uncracked, the position of the neutral axis may be estimated from equilibrium requirements; same holds in locations where distinct cracks have formed if it may be assumed that "plane sections remain plane". Based on classical flexural analysis concepts, a RC member may be considered "cracked" in regions where the flexural moment exceeds the cracking moment. Although a large region may satisfy this definition, however, cracks occur at discrete locations $x_{icr}$. Thus, if an analysis of the cracked cross section is available, the reinforcement strains $\varepsilon(x_{icr})$ that occur in the crack locations may be calculated from Eq. (3). However, it is clear that in the segment between cracks, where moment may exceed the cracking value, bar strains cannot be estimated from flexural analysis as prescribed by Eq. (3). The reason is that due to reinforcement slip, the degree of strain compatibility between steel and concrete in these locations is not well understood, as would be required by the "plane-sections remain plane" assumption, nor can the concrete be considered inert as would happen in a fully cracked tension zone. Because it takes some distance from a crack location before the reinforcement may fully engage its concrete cover in tension so as to satisfy the conditions of strain compatibility, it is clear that Eq. (3) may be invalid even in regions adjacent to a flexural crack, even if the moment in these regions falls below the cracking limit. The bar strain in these regions may be estimated from solution of the differential equation of bond. To address all the possible exceptions to the validity of the flexural requirement stated by Eqs. (2,3), here the term "undisturbed" is used as a qualifier to "uncracked" in order to refer to sections that satisfy the plane sections remain plane compatibility requirement, where concrete and reinforcement strains at the same

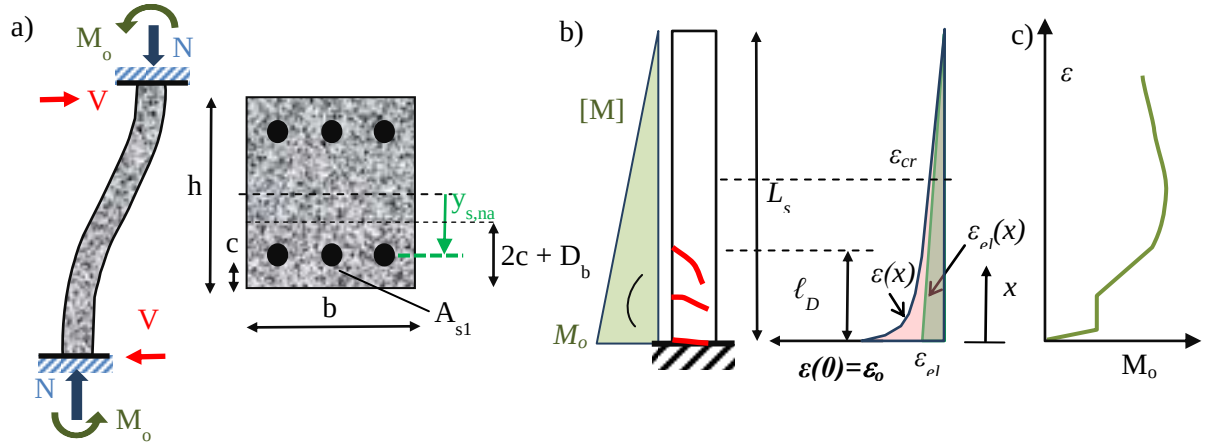


Figure 2: a) Definition of terms for lateral sway. b) Moment distribution along the shear span $L_s$ and definition of disturbed region, $l_D$. c) The bar strain at the critical section experiences a significant jump upon cracking even though the moment from the uncracked to the cracked stage may be imperceptible.

distance from the neutral axis may be assumed equal. Thus, in regions where strains are ob-

tained from solution of the bond equation, this requirement is not valid – therefore even if apparently uncracked, the region may be "disturbed" according with this definition.

The length of shear span is referred to henceforth as $L_s$. The flexural moment in any cross section $x$ (Fig. 2b), where $x$ is measured from the face of the support, may be obtained from equilibrium with reference to the flexural moment occurring at the support, $M_o$ ($\varepsilon_o$ is the corresponding steel strain), according with:

$$\mathrm{M(x)} = \mathrm{M_0} \cdot (1 - \mathrm{x/L_s}) \tag{4}$$

As the sequence of crack formation is critical for the occurrence of disturbed regions and for the problem of strain penetration that will be subsequently addressed, in the present discussion the static problem represented by Eq. (4) will be solved for a gradually increasing moment at the support. As a starting point in the following derivation, it is assumed that the characteristic flexural resistance curve of any cross section along the shear span (*i.e.* the moment – curvature and moment – bar strain diagram) are available from classical flexural analysis over the entire range of the response.

For a member with uniform primary reinforcement over its length, the moment distribution that follows Eq. (4) will cause first cracking at the face of the support. According with the preceding discussion, the bar strain at the base of a cantilever column with shear span $L_s$ experiences a significant jump upon cracking of the tension zone to maintain equilibrium. For example, if the cracked section stiffness is about 1/3 of the uncracked value, the bar strain at the critical section is expected to increase threefold by the mere occurrence of the crack even though the moment change from the uncracked to the cracked stage may be imperceptible (Fig. 2c). Thus suddenly the whole region adjacent to the cracked location becomes "*disturbed*". Over the length of the disturbed region, the reinforcement strain is described by the solution of the bond equation [4] *i.e.*:

$$\varepsilon(\mathrm{x}) = \mathrm{C_1} \cdot \mathrm{e}^{-\omega \mathrm{x}} + \mathrm{C_2} \cdot \mathrm{e}^{\omega \mathrm{x}}, \quad \omega = [4 \mathrm{f_b^{max}}/(\mathrm{E_s} \cdot \mathrm{D_b} \cdot \mathrm{s_1})]^{0.5} \tag{5}$$

The solution of Eq. (5) is valid provided bond is in the elastic range (ascending branch in the bond slip law). Before the creation of any other crack, the disturbed region extends over a distance $\ell_D$ from the critical section. What characterizes the end of the disturbed region is that a) at that point the gradient of the bar strain distribution, $\psi = d\varepsilon(x)/dx$, obtained from Eq. (5), matches the slope of the strain diagram as would be obtained from the flexural analysis of the member, whereas b) the bar strain $\varepsilon(x)$ at that location satisfies simultaneously Eqs. (2,3,5). Therefore, from Eq. (4) it follows that the slope of the strain gradient owing to flexural moments at uncracked location $\ell_D$ is (Fig. 3):

$$\psi = \mathrm{d}\varepsilon(\mathrm{x})/\mathrm{dx} = -\left[\underbrace{\left(\mathrm{M_0} \cdot \mathrm{y_{s.na}^{gr}}\right)/\mathrm{EI_{gr}}}_{\varepsilon_{\mathrm{el}}}\right] \cdot 1/\mathrm{L_s} = \omega \cdot \left(-\mathrm{C_1} \cdot \mathrm{e}^{-\omega \ell_\mathrm{D}} + \mathrm{C_2} \cdot \mathrm{e}^{\omega \ell_\mathrm{D}}\right) \tag{6}$$

$$\varepsilon(\ell_\mathrm{D}) = \mathrm{C_1} \cdot \mathrm{e}^{-\omega \ell_\mathrm{D}} + \mathrm{C_2} \cdot \mathrm{e}^{\omega \ell_\mathrm{D}} = \varepsilon_{\mathrm{el}} \cdot (1 - \ell_\mathrm{D}/\mathrm{L_s}) - \mathrm{N}/(\mathrm{E} \cdot \mathrm{A}) \tag{7}$$

From the system of Eqs. (6, 7) the length of disturbed region adjacent to the crack may be determined if the moment at the support $M_o$ is known. The solution given by Eq. (5) is also subject to the following boundary condition (Fig. 2b):

$$\varepsilon(0) = \mathrm{C_1} + \mathrm{C_2} = \varepsilon_\mathrm{o} \tag{8}$$

In an algorithm developed to solve Eq. (6,7,8) numerically, the controlling parameter is $\varepsilon_o$; therefore, at each incremental step which begins by selecting the value of $\varepsilon_o$, the corresponding moment $M_o$ is uniquely determined from the moment- bar strain diagram of the member

cross section under study. Equations (6,7,8) are a system of three equations having three unknowns – given the value of $\varepsilon_o$ and $\omega$ the unknowns are $C_1$, $C_2$ and $\ell_D$. At this point it is relevant to determine the location of the next crack formation. Whether the next crack will form within the undisturbed or the disturbed region depends on the magnitude of tensile stress transferred through bond to concrete:

a) A check is performed regarding whether next cracking will occur in the disturbed region. The least value of coordinate $x< \ell_D$ should be determined that also satisfies the requirement:

$$[(E_s \cdot A_{s1})/(f_{ct} \cdot A_{c.eff})] \cdot [\varepsilon_o - \varepsilon(x)] = 1, \quad A_{c.eff} = b \cdot (2c + D_b) - A_{s1} \tag{9}$$

In Eq. (9) $A_{s1}$ is the area of the tensile reinforcement, $A_{c.eff}$ is the area of concrete effectively engaged in tension, $f_{ct}$ is the tensile concrete strength, $b$ is the width of the section of the column (Fig. 2a). For a crack to be formed into $\ell_D$ the force undertaken by bond mechanism (i.e. $E_s A_{s1}[\varepsilon_o - \varepsilon(x)]$) should exceed the force of the effectively engaged in tension concrete (i.e. $f_{ct} A_{eff}$); in this case the left-hand expression of Eq. (9) should be >1 else no further cracking is possible in the disturbed zone as long as the reinforcement remains elastic.

b) A check is performed regarding whether next cracking will occur in the undisturbed region. Therefore the coordinate $x \geq \ell_D$ should be determined that satisfies the following requirement ($\varepsilon_{c.cr}$ is the cracking concrete strain) based on Eqs. (2,4):

$$\varepsilon(x) = \varepsilon_{el}(1 - x/L_s) - N/(E \cdot A) = \varepsilon_{c.cr} \Rightarrow x = L_s \cdot [1 - \varepsilon_{c.cr}/\varepsilon_{el} - N/(EA\,\varepsilon_{el})] \tag{10}$$

This process is repeated as the value of the strain $\varepsilon_o$ in the support is increased. If the criterion (b) controls, *i.e.* the next crack forms in the undisturbed region, then from there on this becomes the controlling strain value and the next disturbed region that begins from that point and extends away from the support is calculated. The new disturbed region is defined for this crack, $\ell_{D2}$; the total disturbed region of the cantilever extends from the support to the end of $\ell_{D2}$ beyond the second crack. This is denoted henceforth as $\ell_D$ (Fig. 3a). As the support strain increases this process is continued with more cracks forming towards the tip of the cantilever, with the disturbed region spreading further over the shear span. Its significance is that *over the total disturbed zone $\ell_D$, bar strains are calculated from the solution of the bond equation, as in this region the assumption of plane-sections remaining plane is no longer valid.*

After stabilization of cracking (no more primary cracks develop) and beyond elasticity of the steel bar the yielded segment of the disturbed region undergoes simultaneous degradation of bond. Thus, of the total length $\ell_D$, there is a segment $l_r$ where yielding has penetrated (Fig. 3b). For that portion of the disturbed zone, bar strains increase without a commensurate increase of stress: this means that bond must have degraded to zero as a consequence of Eq. (1), since $df_s/dx=0$ and thus $f_b$=0. Even if the yield-plateau is neglected, and the bar stress-strain diagram is considered bilinear with hardening, it is clear that the small hardening slope may only be supported by the residual bond strength – in other words in order for a bar to yield, it must have slipped beyond the limit $s_2$ in the bond - slip law (Fig. 1). Note that limit $s_2$ is not an intrinsic property of the bar – concrete interface as several Codes define, rather it depends on the available bonded length [9].

Similar to the derivation of strain, slip and bond plastification for the yield penetration length of an elastoplastic bar in the anchorage [8], the following equations are defined for a yielded bar in a shear span. Since hardening is included in the steel's constitutive law a residual bond strength is obtained through the application of Eq. (1). Again the solution of Eq. (1)

consists of the yield penetration length $l_r$, the bond plastification length $l_p$ and the elastic bar length:

$For\ 0 \le x \le l_r$

$$\varepsilon(x) = \varepsilon(0) - \frac{4f_b^{res}}{E_{sh}D_b}x \tag{11}$$

$$s(x) = s_2 + 0.5(l_r - x)\left[\varepsilon(x) + \varepsilon_{sy}\right] \tag{12}$$

$$f_b(x) = f_b^{res} \tag{13}$$

$For\ l_r \le x \le l_r + l_p:$

$$\varepsilon(x) = \varepsilon_{sy} - \frac{4f_b^{max}}{ED_b}(x - l_r) \tag{14}$$

$$s(x) = s_1 + 0.5\left(l_r + l_p - x\right)\left[\varepsilon(x) + \varepsilon_{el}^3\right] \tag{15}$$

$$f_b(x) = f_b^{max} \tag{16}$$

$$\varepsilon_{el}^3 = \varepsilon_{sy} - \frac{4f_b^{max}}{ED_b}l_p \tag{17}$$

For $l_r + l_p \le x \le \ell_D$:

$$\varepsilon(x) = C_1 \cdot e^{-\omega\left(x - l_p - l_r\right)} + C_2 \cdot e^{\omega\left(x - l_p - l_r\right)} \tag{18}$$

$$C_1 = \frac{\varepsilon(\ell_D) - \varepsilon_{el}^3 \cdot e^{\omega(\ell_D - l_p - l_r)}}{e^{-\omega(\ell_D - l_p - l_r)} - e^{\omega(\ell_D - l_p - l_r)}} \quad \text{and } C_2 = \varepsilon_{el}^3 - C_1 \tag{19}$$

$$s(x) = \frac{1}{\omega}\left(C_1 \cdot e^{-\omega\left(x - l_p - l_r\right)} - C_2 \cdot e^{\omega\left(x - l_p - l_r\right)}\right) \tag{20}$$

$$f_b(x) = \frac{f_b^{max}}{s_1} \cdot s(x) \tag{21}$$

The length of yield penetration $l_r$ may be estimated if continuity of strain is considered at $x = l_r$, as

$$l_r = \left(\varepsilon(0) - \varepsilon_{sy}\right) \cdot \frac{E_{sh}D_b}{4f_b^{res}} \tag{22}$$

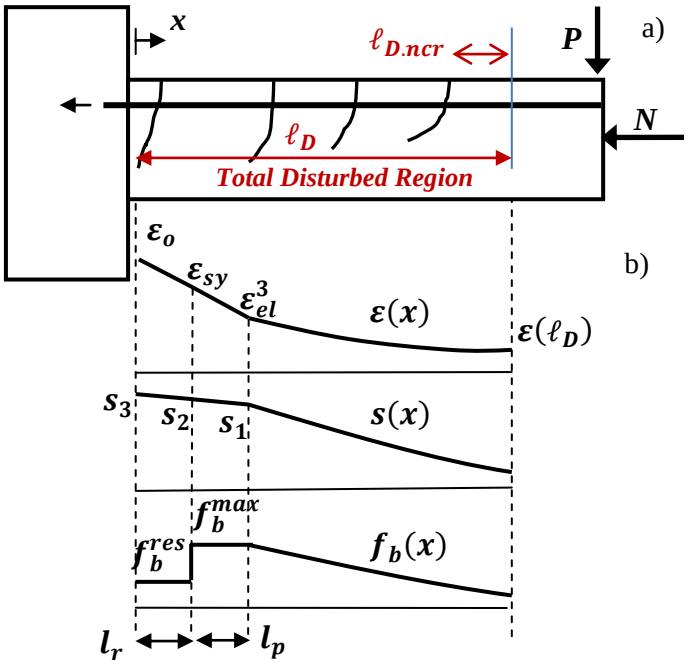


Figure 3: a) Definition of the ongoing development of the disturbed region. b) Plastic tensile bar response in the shear span of a cantilever RC column.

Equation (22) for the yield penetration length, common for the anchorage and the disturbed region, defines the plastic hinge having two interesting implications: first, it is a strain-based criterion for the spread of yielding in the shear span, as opposed to the stress-based definition given by Eq. (1a); there the coefficient *a* refers to the flexural overstrength normalized by the yielding moment.

A second more subtle point is the observation that the plastic hinge length is influenced by several parameters indirectly, through the determining effect that these have on $f_b^{res}$. For example the presence of axial load on a member that undergoes cyclic displacement reversals weakens the cover over a larger portion of the shear span length leading to cover delamination due to excessive compressive strains; upon reversal of load, the crushed cover cannot support significant bond action for the reinforcement when it is stressed in tension, leading to a reduced value of $f_b^{res}$, which in turn causes increased penetration depth for columns carrying a higher axial load; this is consistent with experimental reports.

### 3.1 Empirical relationships for plastic hinge length

The plastic hinge length $\ell_{pl}$ is defined in the literature as the length over which the flexural moments exceed the yielding capacity: $\ell_{pl} = (M_u - M_y) \cdot L_s / M_u$ ($M_u$ is the ultimate moment and $M_y$ is the yielding moment). However this theoretical definition does not comply with the experimental evidence; it is inconsistent too, since it would lead to a zero plastic hinge length region in the absence of hardening (when $M_y = M_u$). The plastic hinge length measured from the critical section towards the shear span signifies the region where intense inelasticity occurs during the earthquake. Despite the shortcomings associated with the mathematical definition of $\ell_{pl}$, it was considered as a convenient artifact in earthquake engineering, necessary in order to conduct calculations of plastic rotation capacity due to flexure (according with $\theta_{pl} = (\varphi_u - \varphi_y) \cdot \ell_{pl}$ [10], $\theta_{pl}$ is the plastic rotation and $\varphi_u$, $\varphi_y$ is the ultimate and yielding curvature). To avoid the inaccuracies associated with the mathematical expressions above, $\ell_{pl}$ is determined in design code procedures through calibrated empirical relationships that account primarily for the length of the shear span and the diameter of primary reinforcing bars (Eq. (23) [11], Eq. (24) [10], *h* = depth of the member):

$$\ell_{pl} = 0.08 \cdot L_s + 0.022 \cdot D_b \cdot f_y \tag{23}$$

$$\ell_{pl} = 0.1 \cdot L_s + 0.17 \cdot h + 0.24 \cdot D_b \cdot f_y / \sqrt{f_c} \tag{24}$$

In the context of the present paper, the length of plastic hinge is by definition the length of yield penetration (thus $\ell_{pl} = l_r$, $l_r$ from Eq. (22)), occurring from the critical section towards the shear span; physically it refers to the extent of the nonlinear region and it may be used to calculate the inelastic rotation capacity of the column in the critical section. Contrary to the fixed design values adopted by codes of assessment, the former is actually the only consistent definition of the notion of the plastic hinge length.

## 4. MODEL VERIFICATION AND PARAMETRIC SENSITIVITY

The solution algorithm developed is applied in this section in order to establish the parametric sensitivities of the estimated plastic hinge to the important design parameters. As a reference point of the parametric analysis, which follows is the column experiment U3 [14]. The column specimen was tested as cantilever, simulating half a clear column length under lateral sway such as would occur during an earthquake with cross section detailing as shown in Fig. 4a. The specimen had a 350 mm square cross section reinforced with eight evenly distributed longitudinal reinforcing bars of $D_b$=25mm and stirrups of $D_{b,st}$=10mm spaced at 75mm o.c.

(on centers) and clear cover $C_{cov}$=32.5mm (*i.e.*, $d$=350-45=305mm). Concrete strength was $f_c'$=34.8MPa. Longitudinal steel yielding strength was 430MPa with a 5% hardening. Stirrup yield strength was 470MPa. Column shear span was $L_s$=1.0m and the axial load ratio [$\nu=N/(f_c' bd)$] was 0.16. Figure 4b plots the unified $M$-$\phi$-$\varepsilon$ relationship obtained for this axial load using fiber section analysis with the modified Kent & Park model for confined concrete [15]; a Hognestad-type parabola was used to model the compression stress-strain response of unconfined concrete [16]. Bond strength was taken equal to $f_b^{max}=1.25\sqrt{f_c'}$ (7.4MPa) for the anchorage (anchorage with a hook having an equivalent straight length of $L_b$=800mm). For the shear span the bond strength was calculated using a frictional model [32] that accounts for separate contributions of the cover concrete and stirrups as $f_b^{max}$ =7.2MPa which drops to 2.75MPa after cover delamination. Due to the reversed cyclic nature of the displacement history, cover on the tension reinforcement is assumed to have delaminated or split if during the opposite direction of loading the compressive strain has attained the limit value of 0.004. The residual bond strength $f_b^{res}$ is defined as 20% of the maximum bond strength and parameter $s_1$ = 0.2mm; $s_2$ mainly depends on the anchorage length which is equal to the shear span if the latter is transmitted to total disturbed region. For the present problem, $s_2$ is found equal to 0.5mm at the ultimate state of reinforcement (see Fig. 6a).

After evaluation of the process of crack formation according with the proposed algorithm, the resulting distribution of strains is illustrated in Fig. 5. Note that stabilization of cracking occurred before yielding of the tensile bars (just after formation of the 4$^{th}$ crack). Ultimate strain corresponded to a disturbed region extending over the entire length of the column shear span including an equivalent additional length equal to 12.5$D_b$ (313 mm) – thus $\ell_{Do}^{max}=L_s+12.5D_b$– in order to account for the end detail of reinforcement at the tip of the column being welded on a steel plate (this additional length is the anchorage length equivalent of a T-headed anchorage– here this is a conservative estimate).

From Figure 5d it is seen that the yield penetration length over the shear span at the last step of the calculation was 319mm (0.91$h$ or 0.32$L_s$) whereas the corresponding pullout slip was $s_u^{span}(x=0)$=2.36mm. When including the yield penetration in the footing as is intended in the formal definition of $\ell_{pl}$ (Eq. 22) - the total plastic hinge length is 632mm. (Note that the

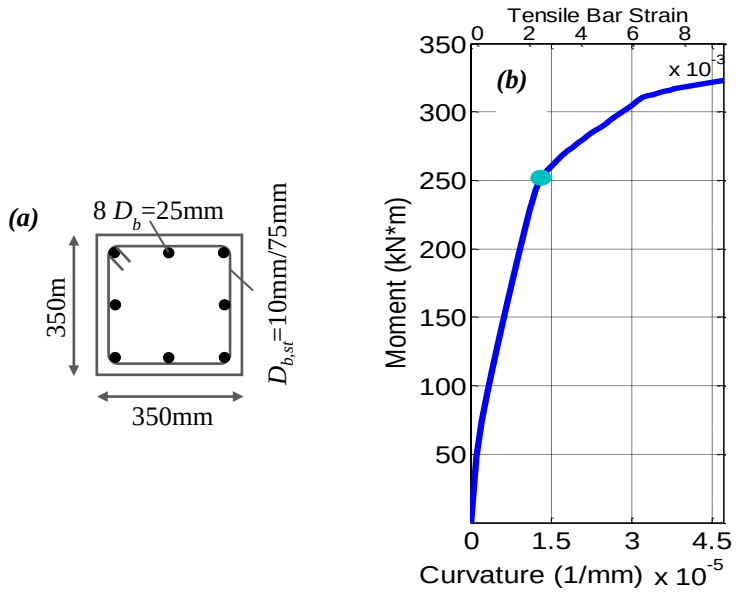


Figure 4: Specimen U3 a) cross section details, b) moment - curvature - tensile bar strain diagrams.

yield penetration length inside the footing is 313mm or $0.029D_b f_y$ and the corresponding slip is $s_u^{anch}(x=0)$=2.33mm.) Figure 6b compares this value with the empirical estimates of Eq. (24); the easy estimate of *0.5d* is also noted. Also included is the result of the classical definition of plastic hinge length $(1-M_y/M_u)L_s$. For comparison it is noted (red dashed line in Fig. 6b) that cover delamination extended over 520mm measured from the face of the support, according with the experimental report of specimen U3 [14].

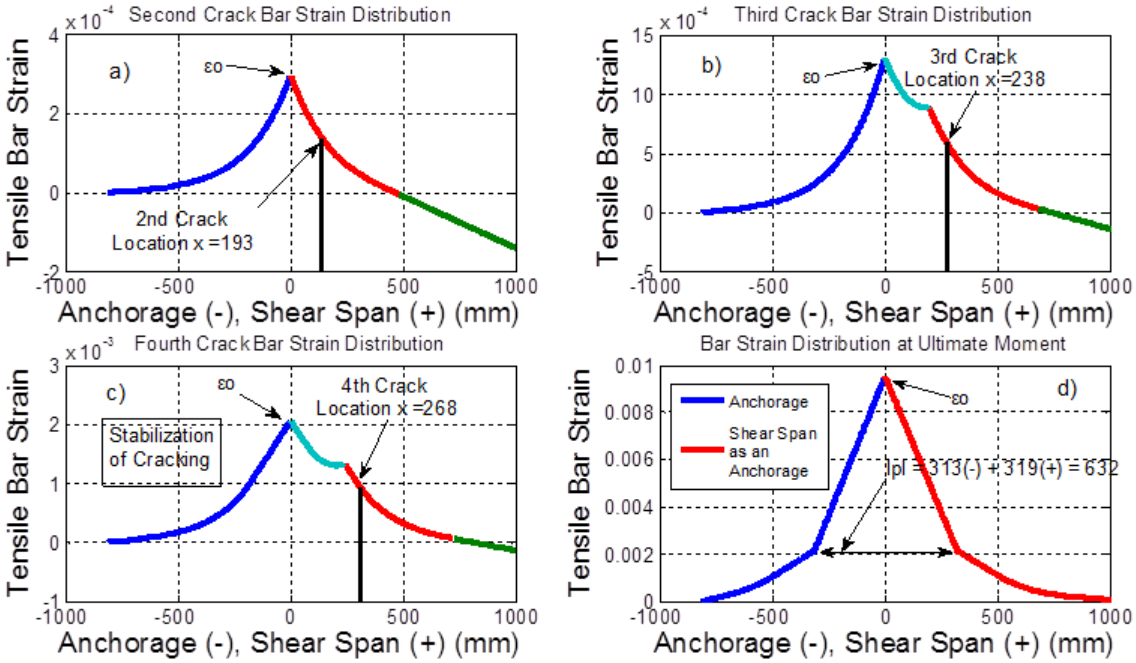


Figure 5: Column U3 (a), (b) (c) tensile bar strain distributions along the anchorage (blue curves) and the shear span (cyan-red-green curves). Location of estimated successive cracks is indicated until crack stabilization. d) Strain state of reinforcement at ultimate, where $\ell_{pl}$ is calculated.

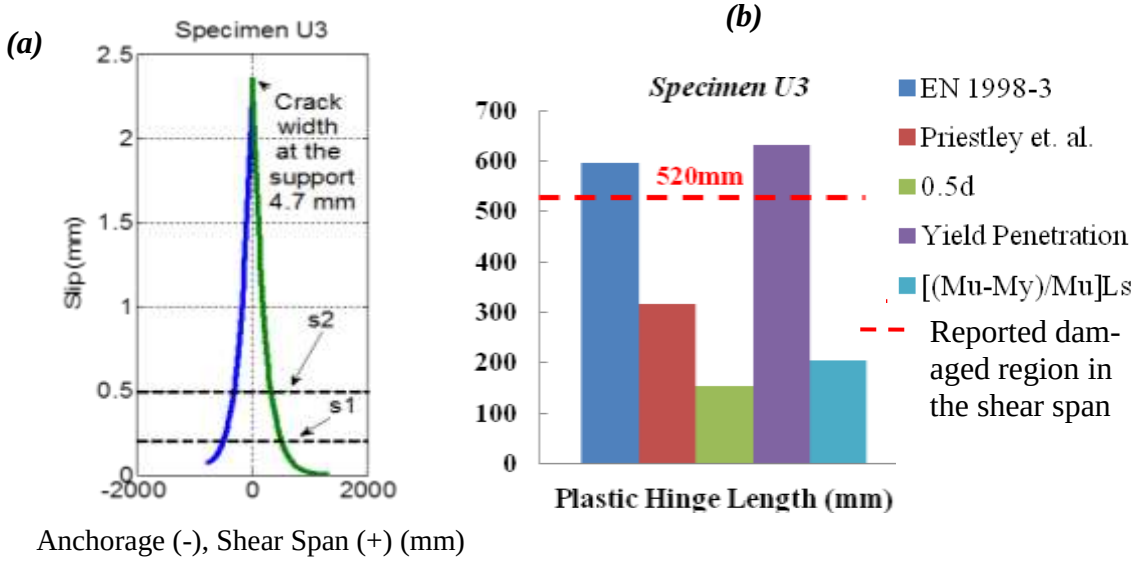


Figure 6: For specimen U3 a) slip distributions along the bar length at ultimate strain (where $\ell_{pl}$ is calculated) and b) analytical calculation of the plastic hinge length $\ell_{pl}$ (purple bar) and its correlation with the design equations.

Next a sensitivity analysis of the model is illustrated, using the column analyzed in the preceding as a reference case: the parameters studied were the applied axial load $v$ (0.15, 0.3 and 0.5), the bond strength (3, 5, 7 MPa), the residual bond strength $f_b^{res}$ (1, 2, 3MPa), the hardening modulus $E_{sh}$ (1, 2.5 and 5% of $E_s$), the shear span length $L_s$ (2, 3 and 4 times the section height $h$) and the bar size $D_b$ (25 and 18mm), all included in Table 1. In each case one parameter is varied at a time keeping the reference values for all other variables constant (so the possible interaction effects between variables have not been considered in conducting the sensitivity analysis).

| **Parameter** | **values** | | |
|---|---|---|---|
| Axial load: $\nu=N/(f_c' bd)$ | 0.15 | 0.3 | 0.5 |
| Bond strength, $f_b^{max}$ | 3 | 5 | 7 |
| Residual bond strength, $f_b^{res}$ | 1 | 2 | 3 |
| Hardening modulus, $E_{sh}$ | 1% | 2.5% | 5% |
| Shear span, $L_s$ | 2h | 3h | 4h |
| Bas size, $D_b$ | 25 | | 18 |

Table 1: Parametric Investigation – Properties similar to specimen U3 (units: mm, MPa)

Figure 7a portrays the influence of the variables on the plastic hinge length of the reference specimen, as well as on the associated reinforcement tensile strain capacity of the critical cross section. Each curve in these diagrams is read as follows:

- Reducing the bond strength $f_b^{max}$ (the associated residual value is $f_b^{res}=20\%f_b^{max}$) gradually from 7 to 3MPa (red arrow next to the brown curve pointing down) results in the increase of the plastic hinge length attained at lower bar strain,
- Increasing the axial normalized load $v$ (red arrow next to light blue curve pointing up) lowers the strain capacity and the associated hinge length,
- Increasing the hardening modulus $E_{sh}$ (red arrow next to green curve pointing up) increases the plastic hinge length and reduces the strain (as is implied by Eq. (22)),
- Increasing the bar size $D_b$ (red arrow next to dark blue curve pointing up) increases the hinge length and reduces the strain (as is implied by Eq. (22)).
- The hinge length is relatively insensitive to $L_s/h$ at low axial loads (all points coincide with the reference point (intersection of all curves; i.e. for $L_s/h$= 2, 3 and 4 the $\ell_{pl}/h$ is 1.8 and the associated strain is 0.017).

As was noted previously, the presence of axial load on a member that undergoes cyclic displacement reversals weakens the cover over a larger portion of the shear span length speeding up cover delamination due to excessive compressive strains; upon reversal of load, the crushed cover cannot support significant bond action for the reinforcement when it is stressed in tension, leading to a reduced value of $f_b^{res}$, which in turn causes increased penetration depth for columns carrying a higher axial load; this is consistent with experimental reports. Based on this experimental response, Fig. 7b depicts the effect of the studied variables on the hinge length when the axial load is relatively high ($v$=0.5) (in the reference case term $f_b^{max}$ was reduced from 7.2MPa to 2.75 after cover loss):

- Reducing bond strength $f_b^{max}$ from 7 to 3MPa (blue curve in Fig. 7b) results in increased plastic hinge length, attained at a higher bar strain,

- Reducing the residual bond strength $f_b^{res}$ (orange curve in Fig. 7b) increases the hinge length and lowers the associated strain capacity.
- higher hardening modulus $E_{sh}$ (green curve in Fig. 7b) increases the hinge length and also the strain.

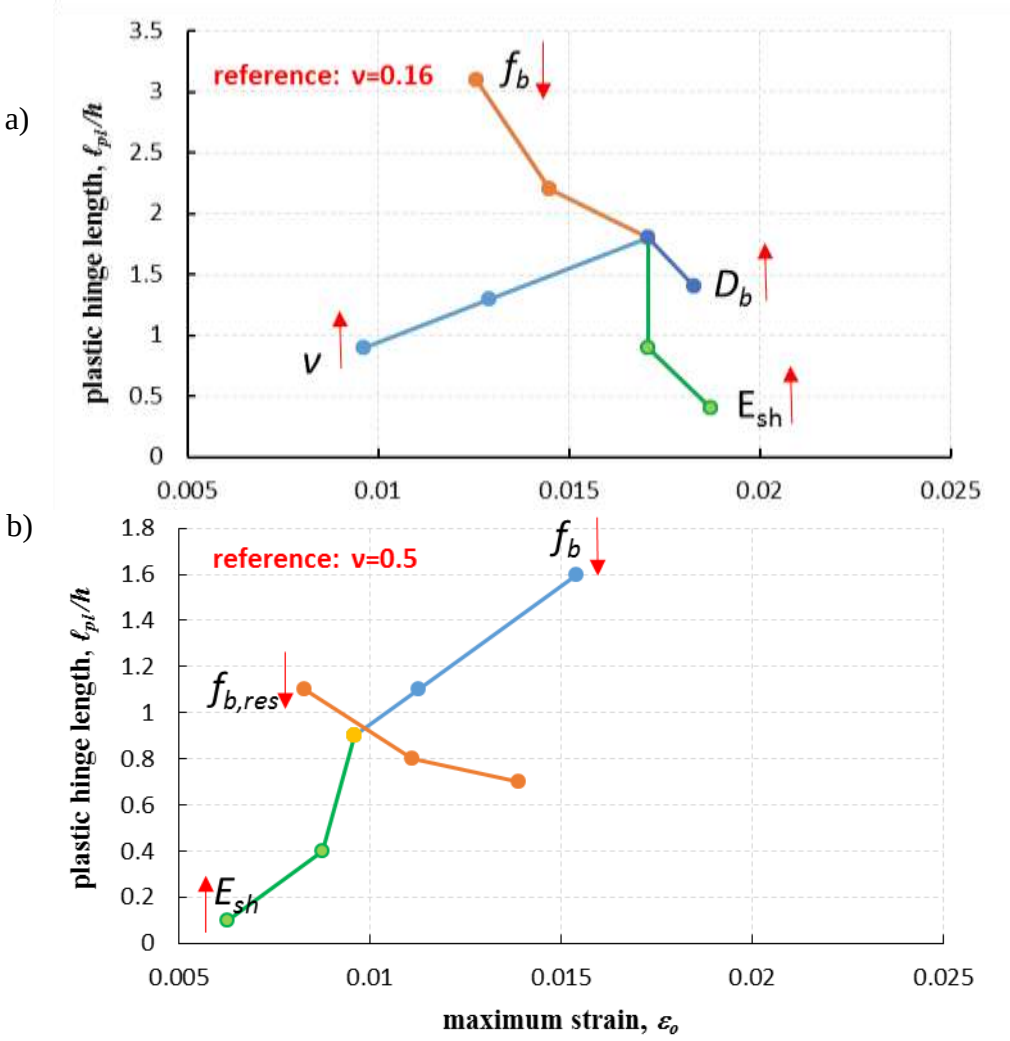


Figure 7: Sensitivity analysis (neglecting interactions): diagrams of normalized plastic hinge length to the cross section height versus the associated reinforcement maximum tensile strain for a) low ($v$=0.16) and b) high ($v$=0.5) axial load.

## CONCLUSIONS

- Yield penetration occurs from the critical section towards both the shear span and the support of columns; physically it refers to the extent of the nonlinear region and determines the pullout slip measured at the critical section.
- Contrary to the fixed design values adopted by codes of assessment, the yield penetration length is actually the only consistent definition of the notion of the plastic hinge length, whereas the latter determines the contribution of pullout rotation to column drift and column stiffness.

- In order to establish the plastic hinge length in a manner consistent to the above definition, this paper pursued the explicit solution of the field equations of bond over the shear span of a column.
- Through this approach, the bar strain distributions and the extent of yield penetration from the yielding cross section towards the shear span were resolved and calculated analytically.
- By obtaining this solution a consistent definition of plastic hinge length is established, by reference to the state of reinforcement strain (replacing the stress based definition used previously).
- The true parametric sensitivities of this design variable for practical use in seismic assessment of existing structures are illustrated.
- The numerical results show good agreement with the experimental evidence and are consistent with the experimental trends supported by test databases, confirming that the plastic hinge length is controlled by the residual bond that may be mobilized along the yielded reinforcement.

**ACKNOWLEDGEMENTS**

The first author would like to thank the Alexander S. Onassis Public Benefit Foundation whose financial support is greatly appreciated.

## 7. References

[1] Syntzirma D. V., Pantazopoulou S. J. and Aschheim M. (2010), Load history effects on deformation capacity of flexural members limited by bar buckling. ASCE, Journal of Structural Engineering,136 (1),1−11.

[2] Bigaj A.J. (1999). Structural Dependence of Rotation Capacity of Plastic Hinges in RC Beams and Slabs PhD Thesis, Faculty of Civil Engineering, Delft University of Technology, Delft, The Netherlands.

[3] Bonacci, J., Marquez, J. (1994). Tests of Yielding Anchorages under Monotonic Loadings. ASCE, Journal of Structural Engineering, 120(3), 987-997.

[4] Tastani, S. P., and Pantazopoulou, S. J. (2013). Reinforcement and concrete bond: State determination along the development length. ASCE, Journal of Structural Engineering, 139(9), 1567−1581.

[5] Tastani, S. P., Brokalaki E., Pantazopoulou, S. J. (2015). State of Bond along Lap Splices. ASCE, Journal of Structural Engineering, 141(10), 04015007.

[6] Filippou, F., Popov, E., and Bertero, V. (1983). Modeling of R/C joints under cyclic excitations. ASCE, Journal of Structural Engineering, 109(11), 2666–2684.

[7] Tassios, T. P., and Yannopoulos, P. J. (1981). Analytical studies onreinforced concrete members under cyclic loading based on bond-sliprelationships. ACI Materials Journal, 78(3), 206-216.

[8] Tastani S.P., Pantazopoulou S.J. (2013). Yield penetration in seismically loaded anchorages: effects on member deformation capacity. Techno press Earthquake and Structures, 5(5):527-552.

[9] Tastani S.P, Thermou G.E., Pantazopoulou S.J. (2012). Deformation analysis of reinforced concrete columns after repair with FRP jacketing. 15th World Conference on Earthquake Engineering, September 24-28, Lisbon, Portugal (paper no. 3164).

[10] Eurocode 8, (2005). Design of structures for earthquake resistance − Part 3: Assessment and retrofitting of buildings , European Committee for Standardisation.

[11] Priestley, M.J.N., Seible F., and Calvi M. (1996). Seismic Design and Retrofit of Bridges. J. Wiley & Sons Inc., N. York.

[12] Scott, B.D., Park, R., and Priestley, M.J.N. (1982). Stress-strain behavior of concrete confined by overlapping hoops at low and high strain rates. J. American Concrete Institute, 79, 13-27.

[13] Fib Model Code (2010), Chapter 6:Interface Characteristics, Ernst & Sohn Publications, Berlin, Germany, pp.434.

[14] Saatcioglu M., and Ozcebe G. (1989). Response of Reinforced Concrete Columns to Simulated Seismic Loading. ACI Structural Journal, 86(1), 3-12.

[15] Scott, B.D., Park, R., and Priestley, M.J.N. (1982). Stress-strain behavior of concrete confined by overlapping hoops at low and high strain rates. J. *American Concrete Institute*, **79**, 13-27.

[16] Hognestad, E. (1951). *A Study of Combined Bending and Axial Load in Reinforced Concrete Members*. Bulletin No. 399, Engineering Experimental Station, University of Illinois.

COMPDYN 2017
6th ECCOMAS Thematic Conference on
Computational Methods in Structural Dynamics and Earthquake Engineering
M. Papadrakakis, M. Fragiadakis (eds.)
Rhodes Island, Greece, 15–17 June 2017

# BEHAVIOR OF CFRP CONFINED RC COLUMNS UNDER AXIAL LOAD AND UNIAXIAL CYCLIC LATERAL LOADING

**Marta Del Zoppo[1], Marco Di Ludovico[2], Alberto Balsamo[2] and Andrea Prota[2]**

[1] Department of Engineering, University of Naples "Parthenope"
Centro Direzionale, Isola C4, Naples (Italy)
e-mail: marta.delzoppo@uniparthenope.it

[2] Department of Structures for Engineering and Architecture, University of Naples "Federico II"
Via Claudio 21, Naples (Italy)
{diludovi, abalsamo, aprota}@unina.it

**Keywords:** confinement, CFRP, RC columns, ductility, deformation capacity.

**Abstract.** *In recent years, the use of FRP wrapping of reinforced concrete (RC) members has been recognized as a reliable method for seismic retrofit of existing structures. The external confinement of existing RC columns with FRPs is a sound technique for increasing the columns ductility, by preventing brittle mechanisms such as bars buckling or post-yielding shear failures and by improving the mechanical properties of concrete due to the lateral confining effect. Several models have been developed for predicting the ultimate displacement capacity and the ductility of FRP confined RC columns, however the accuracy of predictions has not been well established yet. In this study, the experimental behavior of a RC column confined at the plastic hinge region with one ply of carbon fibers (CFRP) is firstly analyzed and compared with the response of the unstrengthened control column. The specimens are cantilevers loaded with a low compressive axial load and subjected to uniaxial cyclic horizontal displacements. The responses of the columns have been analyzed and compared in terms of failure modes and strength and deformation capacity. Particular attention has been focused on the strain distribution recorded on the CFRP strips used to confine the RC column end; the strain profiles along the cross-section perimeter in case of axial load and bending moment interaction are presented and discussed at different load levels. In the second part of the study, the deformation capacity of FRP confined RC column is analytically obtained, by using models for FRP confined square columns available in literature. The comparison between analytical and experimental results showed that currently available models give conservative predictions of ultimate deformation capacity of confined columns.*

# 1 INTRODUCTION

Recent earthquakes confirmed the high vulnerability of existing reinforced concrete (i.e. RC) structures to seismic event, due to the lack of proper seismic detailing. To overcome the common deficiencies of RC members derived from the use of non-seismic design criteria, the use of fiber reinforce polymers (i.e. FRP) has been recognized as a reliable method for increasing members capacity [1-4]. In case of RC columns, mainly subjected to axial load and horizontal cyclic displacements, the ultimate deformation capacity can be increased by using an external confinement at the member's end, where the plastic hinge region is located, with unidirectional fibers orthogonal to the member longitudinal axis [5-10]. Indeed, the external confinement prevents mechanisms that can limit the ductility, such as longitudinal bars buckling, bond failure of lap-spliced reinforcement, and increases the ultimate strain of compressed concrete, enhancing the ductility of the member.

Several analytical models for the stress-strain relationship of FRP confined concrete subjected to axial compression have been developed in literature [11-16]. Two stress-strain models for FRP confined concrete [17, 18] were also implemented in the open-source platform OpenSees [19]. Nevertheless, most of them are developed for circular members and only a few models are available for square and rectangular sections. Moreover, differently from the case of pure compression, in presence of combined axial load and bending moment a gradient of concrete lateral dilatation occurs, because a part of the cross-section is in tension. Only few authors investigated on the effectiveness of confinement and on the mechanical properties of confined concrete in case of eccentric axial load [20-23].

Stress-strain models for FRP confined concrete can be used for predicting the ultimate deformation capacity of strengthened columns and for supporting the design of the retrofit intervention. However, few comparisons have been found in literature between analytical predictions and experimental results that validate the reliability of such models [16, 24].

In the first part of this study the experimental behavior of a square RC column confined at the plastic hinge region with one layer of carbon fibers (CFRP) is presented and discussed in comparison with a control column, which achieved a shear failure after the flexural yielding. The specimens were cantilevers loaded with a low compressive axial load and subjected to cyclic horizontal displacements. The responses of the columns have been analyzed in terms of failure modes and increased deformation capacity in case of external CFRP confinement. Particular attention has been focused on the increased deformation capacity (i.e. ultimate drift and ductility) due to the external wrapping with respect to the control column. Moreover, in order to investigate on the effectiveness of CFRP confinement in case of axial load and bending moment interaction, a detailed analysis related to the axial strains distribution along the fibers is reported.

The second part of the study presents the analytical predictions about the behavior of FRP confined column, obtained making use of the analytical stress-strain relationships found in literature and the plastic hinge concept. The comparison between analytical predictions and experimental results showed a conservative trend of analytical predictions of ultimate deformation capacity of retrofitted columns.

# 2 EXPERIMENTAL STUDY

## 2.1 Specimens geometry and material properties

Two square RC columns were designed in order to attain a brittle behavior after the flexural yielding, due to the reduction of shear capacity caused by the increasing ductility demand (i.e. flexure-shear failure mode).

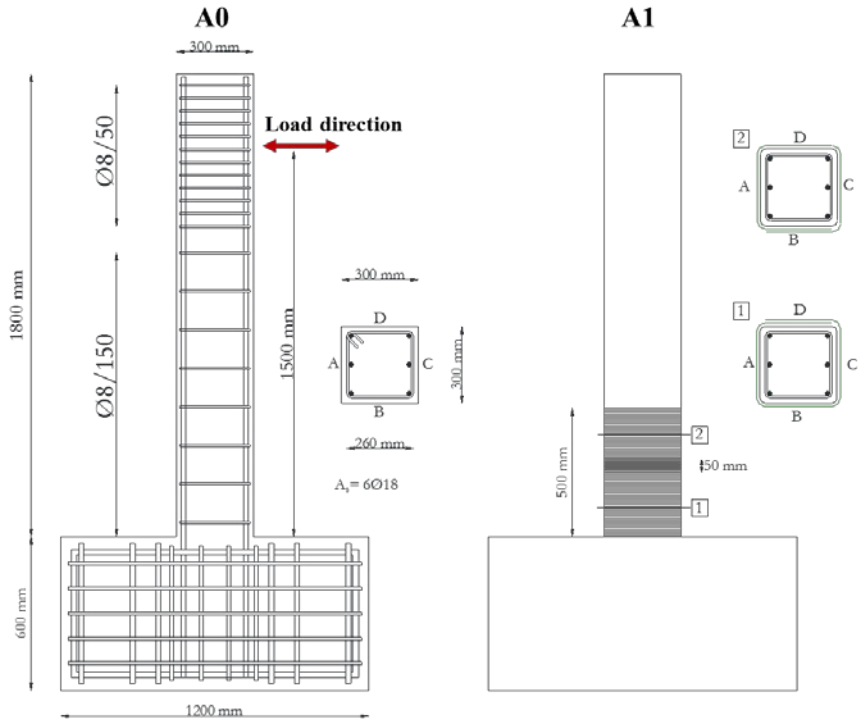


Figure 1: Geometry of specimens: control specimen (a) and CFRP confined specimen (b).

Each specimen had a square cross-section 300 x 300 mm reinforced with six 18 mm diameter deformed rebars along the column principal direction (longitudinal geometrical reinforcement ratio, $\rho_l = A_s/bh$ = 1.7% with $A_s$ total area of longitudinal steel reinforcement and *b,h,* cross section dimensions). No additional longitudinal reinforcement, which could help in shear resisting mechanism, was provided in the column secondary directions as typically found in existing structures. Transverse reinforcement was made of 8 mm diameter ties, spaced at 150 mm apart (transverse geometrical reinforcement ratio, $\rho_w = A_w/bs$ = 0.22% with $A_w$ total area of transverse steel reinforcement and *s* the spacing). A reduced spacing has been adopted in the zone of load application to avoid localized damages. The geometrical properties and reinforcement detailing reported for the two specimens in Figure 1.

The specimens were cantilevers made by a column and a foundation block: the column height was 1,800 mm, the foundation block was 1,200 x 1,200 x 600 mm. The foundation block and the columns of each specimen were cast in two phases to reproduce the discontinuity of concrete at the column-foundation interface, as common practice in concrete casting procedures. The lateral load was applied at a distance of 1,500 mm from the foundation block, in order to simulate the behavior of a typical 3,000 mm height column, assuming that shear length $L_s$ was the column mid-eight (i.e $L_s$ = 1,500 mm).

One of the two specimens (named **A0**) was used as a control specimen whereas the other (named **A1**) was confined at the column base with uniaxial CFRP sheets with fibers perpendicular with respect to the column longitudinal axis. The confinement was extended for 500 mm from the column-foundation interface, where the plastic hinge usually is developed. The radius of rounded corners is $R$ = 20 mm. The column **A1** was confined with one layer of CFRP, with a thickness of dry fibers $t_f$ = 0.33 mm. Since the CFRP sheets width was 300 mm, two sheets have been used for the confinement, with a 50 mm vertical overlap region located at the mid height of the confined zone. Further details of CFRP jacketing are reported in Figure 1b.

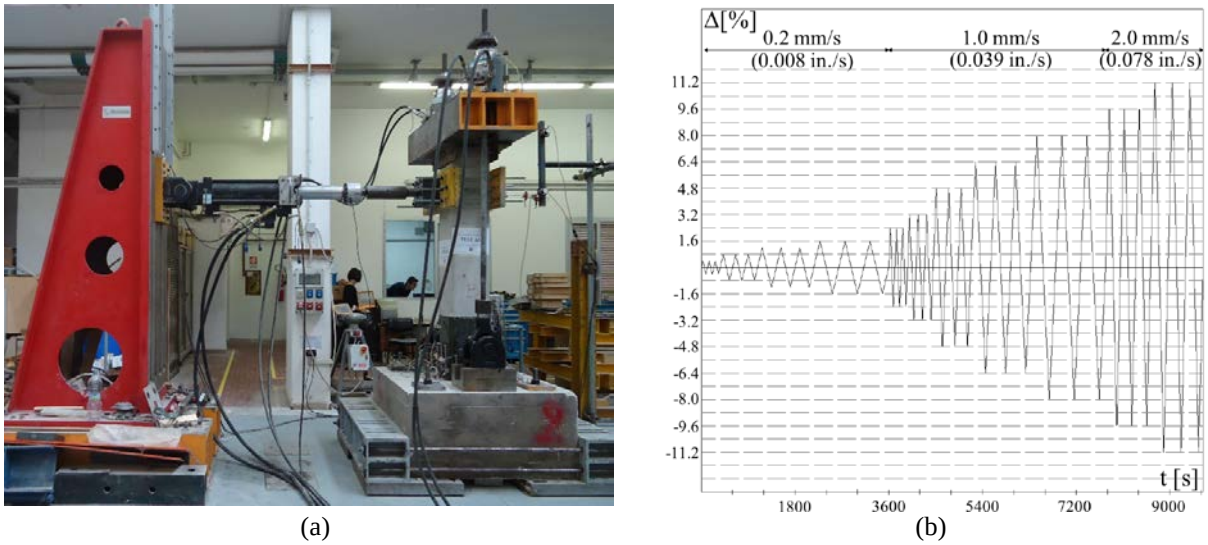


(a) (b)

Figure 2: Test setup (a) and displacement protocol (b).

The average concrete compressive strengths, derived from compression tests on four concrete cylinders for each specimen, were $f_c$ = 16.3 MPa and $f_c$ = 14.9 MPa for columns **A0** and **A1**, respectively. The same class of steel has been used for longitudinal and transverse reinforcement, characterized by an average yielding strength $f_y$ = 531 MPa. The average tensile modulus and minimum ultimate strain of carbon fibers given by the manufacturer are $E_f$ = 230 GPa and $\varepsilon_{fu}$ = 1.3%, respectively. The CFRP sheets unit weight was 600 g/m$^2$.

### 2.2 Test setup and instrumentation

The columns were subjected to constant axial load and horizontal cyclic loads. The test setup and instrumentation are described in detail in [25] and shown in Figure 2a. All the specimens were subjected to a constant axial load ratio ($\nu = N / A_c f_c$, where $N$ is the axial load, $A_c$ is the concrete gross area and $f_c$ is the mean cylindrical concrete strength) equal to 0.1 and a lateral cyclic loading under displacements control, see Figure 2b. A displacement rate of 0.2 mm/s was used for initial four cycles, then a higher rate 1.0 mm/s was adopted for the next five cycles and a rate 2.0 mm/s was used for the last cycles. In each cycle, the target displacement was achieved three times, see Figure 2b.

## 3 DISCUSSION OF EXPERIMENTAL RESULTS

The experimental force-drift relationships recorded for the two tests are reported in Figure 3. The control specimen **A0** achieved a peak force $F_{max}$ = +86.1 kN and $F_{max}$ = -85.4 kN in the positive and negative direction, respectively (see Figure 3a). The drift ratio ($\Delta = d / L_s$ with $d$ equal to the top column horizontal displacement and $L_s$ the shear length) at the peak load was $\Delta_{Fmax}$ = 4.8% both in the positive and negative load action directions. During the cycle at $\Delta$ = 6.4%, a sudden decrease of strength and stiffness has been observed among the three consecutive repetitions and the loading branch of the next cycle, so that the test was stopped. Thus, the ultimate drift ratio has been assumed equal to the one of last cycle, $\Delta_{0.8Fmax}$ = ± 6.4%, cause a strength degradation of 20% of the peak force (i.e. a lateral force lower than 80% of the maximum one) has not been achieved. At a drift ratio of 1.6%, diagonal cracks appeared along the sides B-D parallel to the load action direction especially in the plastic hinge region. During the cycles at imposed drift of 4.8%, the first concrete spalling has been observed along

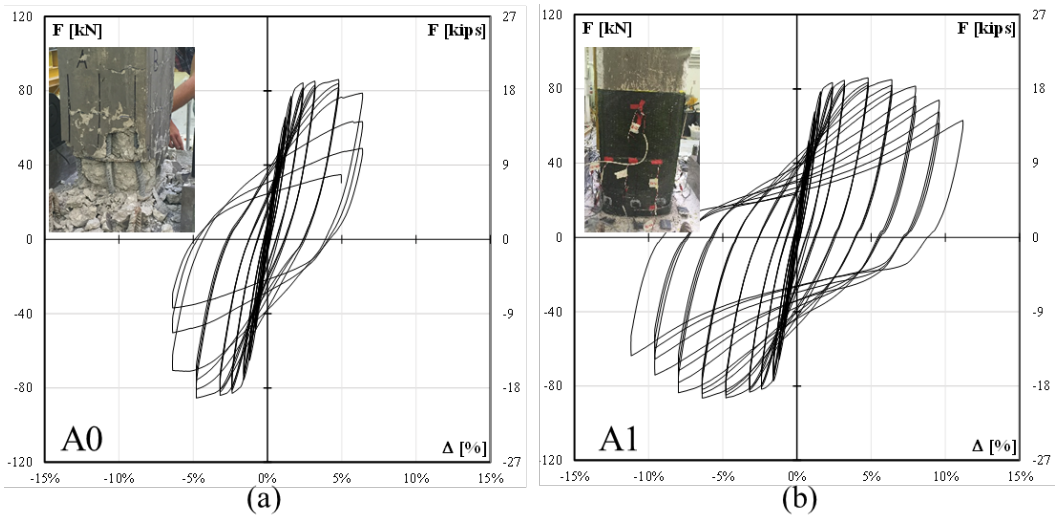


Figure 3: Force-Drift curves for control column A0 (a) and column A1 confined with one ply of CFRP (b).

the side A of the specimen. At this stage, the buckling of longitudinal bars was also detected. At failure, the concrete cover was completely spalled off; the spalling of concrete involved a region with a height of about 470 mm from the fixed end. As expected, the failure mode of specimen **A0** was "quasi-ductile", since plastic deformations were attained before a premature failure due to the reduced shear capacity in the plastic hinge region.

A similar response in terms of peak forces has been recorded on specimen **A1** confined with one ply of CFRP, so no increase of global strength has been recorded. However, the global deformation and energy dissipation capacity was strongly improved by means of the CFRP wrapping, see Figure 3b. In particular, the experimental peak forces were $F_{max}$ = +86 kN and $F_{max}$ = -86.5 kN in the positive and negative direction, respectively. Also in this case, the drift corresponding at the peak loads was $\Delta_{Fmax}$ = 4.8% both in the positive and negative load action directions. By contrast, the ultimate conventional drift ratio, corresponding to a strength degradation of 20% of the peak force, was significantly greater than in the case of **A0** test and equal to $\Delta_{0.8Fmax}$ = ± 10.4%. Thus, the brittle mechanism observed in the control specimen was prevented by the external confinement and a pure flexural behavior has been attained. However, at a drift ratio of 6.4%, some diagonal cracks were detected in the unconfined region along the B-D sides of the specimen. At failure, the confined concrete was totally cracked. No CFRP tensile failure or debonding have been observed, but a premature failure given by horizontal cracks between fibres was detected. In particular, longitudinal cracks along the fibres direction developed at about 50 mm from the fixed-end, due to a concentration of stresses provided by the lateral dilatation of damaged concrete in the direction orthogonal to the fibres.

Thus, the CFRP confinement of the specimen increased the ultimate deformation capacity of +62.4% with respect to the control specimen.

## 4 PREDICTION OF ULTIMATE DRIFT

### 4.1 Analytical approach

Analytical models and predictive equations for defining a simplified force-drift curve of FRP confined RC columns are herein investigated. The envelope curve of cyclic response of the confined RC columns can be approximated with a bilinear curve, which consists of a three

data points: the origin, the point corresponding to the first yielding of internal steel reinforcement and the point corresponding to the ultimate deformation capacity at flexural failure.

The elastic drift corresponding to the first yielding of internal steel rebars, $\Delta_y$, can be calculated according to the formulation suggested in [16], which account for the flexural and shear deformations and for the fix-end rotation before the yielding:

$$\Delta_y = \frac{1}{3}\phi_y\left(Ls + 0.5z\right) + 0.0014\left(1 + 1.5\frac{h}{Ls}\right) + 0.125\phi_y\frac{d_b f_y}{\sqrt{f_c}} \quad (1)$$

where $\phi_y = 2\varepsilon_y/h$ the simplified yielding curvature, $z$ the internal lever arm and $d_b$ the longitudinal steel bars diameter.

The ultimate deformation capacity is calculated as the sum of the elastic drift ratio, $\Delta_y$, and the plastic one, $\Delta_{pl}$. Two different approaches reported Biskinis and Fardis (2013) [16] can be followed for evaluating the plastic drift ratio: (*i*) by using an empirical formulation calibrated on 219 experimental tests on FRP confined members and reported in Eq. (2) or (*ii*) by using a mechanical formulation based on the plastic hinge concept and reported in Eq. (3).

$$\Delta_{pl,emp.} = 0.0088\left(1 + \frac{1}{1.6}\right)\left(0.25\right)^{\nu}\left(\frac{\max\left(0.01;\omega'\right)}{\max\left(0.01;\omega\right)}\right)^{0.3} f_c^{\,0.2}\left(\frac{Ls}{h}\right)^{0.35} 25^{\left[\frac{\alpha_w\rho_w f_y}{fc} + \left(\frac{\alpha_f\rho_f E_f\varepsilon_{f,eff}}{fc}\right)_{eff}\right]} 1.275^{100\rho_l} \quad (2)$$

$$\Delta_{pl,\text{mech.}} = \left(\phi_u - \phi_y\right)L_p\left(1 - 0.5\frac{L_p}{Ls}\right) + 5d_b\left(\phi_u + \phi_y\right) \quad (3)$$

where $\alpha_w$ and $\alpha_f$ are factors accounting for the effectiveness of confinement for steel and FRP reinforcement, respectively, $\phi_u$ is the ultimate curvature and $L_p$ is the plastic hinge length. The last term of Eq. (3) represents the post-elastic fixed-end rotation, empirically obtained as best fitting of experimental results on unconfined members. A further description of the aforementioned formulations can be found in [16].

The plastic hinge length is herein calculated as reported in [16] in case of cyclic loading for unconfined members:

$$L_p = 0.2h\left[1 + \frac{1}{3}\min\left(9;\frac{Ls}{h}\right)\right] \quad (4)$$

The lateral force corresponding to the elastic curvature and the ultimate curvature, corresponding to the achievement of an ultimate concrete compressive strain, are calculated performing a moment-curvature analysis for the column critical cross-section by using a fiber model [26]. For the non-circular FRP confined concrete, six stress-strain models were selected from the international codes provisions and recent literature: *fib* Bulletin 14 – Spoelstra and Monti (2001) [27], ACI 440 (2008) [28], CNR DT-200 (2013) [29], Biskinis and Fardis (2013) [16], Pantazopoulou et al. (2016) [30] and Ghatte et al. (2017) [24]. The main expressions for ultimate strength, $f_{cu}$, and strain, $\varepsilon_{cu}$, of FRP confined concrete according to selected models are reported in Table 1 as a function of the unconfined concrete peak strength and corresponding strain, $f_{c0}$ and $\varepsilon_{c0}$. The effective lateral confinement pressure, $f_l$', exerted by the FRP confinement is calculated as:

$$f_l' = \alpha_f\rho_f E_f\varepsilon_{f,eff} \quad (5)$$

where $\alpha_f$ is the FRP effectiveness of confinement factor, $\rho_f$ is geometrical ratio of FRP external reinforcement and $\varepsilon_{f,eff} = k_{eff}\,\varepsilon_{fu}$ is the FRP effective strain.

Since the main purpose of the analysis is the evaluation of the ultimate curvature under combined axial load and bending moment, the concrete stress-strain relationships were considered as follows: the first part is parabolic up to the peak strength of unconfined concrete (strength equal to the experimental $f_{c0} = f_c$ and conventional strain at peak strength $\varepsilon_{c0} = 0.002$); the second part is linear up to the ultimate strength and strain calculated as reported in Table 1. For steel internal reinforcement, an elasto-plastic model has been selected.

In order to compare the different stress-strain models for FRP confined concrete, the ultimate strength and deformations calculated according to the expressions in Table 1 are summarized in Table 2, along with the limitation adopted in each model for the FRP effective strain $\varepsilon_{f,eff}$ and $k_{eff}$. The stress-strain relationships for the FRP confined concrete are also plotted in Fig. 7.

| **Model** | $f_{cu}/f_{c0}$ | $\varepsilon_{cu}/\varepsilon_{c0}$ |
|---|---|---|
| *fib* Bulletin 14 (2001) | $0.2+3\left(f_l'/f_{c0}\right)^{0.5}$ | $2+1.25\varepsilon_{f,eff}\left(E_c/f_{c0}\right)\left(f_l'/f_{c0}\right)^{0.5}$ |
| ACI 440.2R (2008) | $1+3.3f_l'/f_{c0}$ | $1.5+12\left(f_l'/f_{c0}\right)\left(\varepsilon_{f,eff}/\varepsilon_{c0}\right)^{0.45}$ |
| CNR DT-200 (2013) | 1 | $\left(0.0035+0.015\left(f_l'/f_{c0}\right)^{0.5}\right)/\varepsilon_{c0}$ |
| Biskinis and Fardis (2013) | $1+3.3f_l'/f_{c0}$ | $\left(0.0035+\left(10/h\right)^2+0.4f_l'/f_{cu}\right)/\varepsilon_{c0}$ |
| Pantazopoulou et al. (2016) | 0.85 | $\left(0.0035+0.075\left(\alpha_w\rho_w f_y+f_l'\right)/f_{c0}\right)/\varepsilon_{c0}$ |
| Ghatte et al. (2017) | $1+2.54f_l'/f_{c0}$ | $1+\left(h/b\right)19.27\left(f_l'/f_{c0}\right)^{0.53}$ |

Table 1: Expressions for FRP confined concrete ultimate strength and strain ($f_{c0}$ and $\varepsilon_{c0}$ are the peak strength and strain of unconfined concrete).

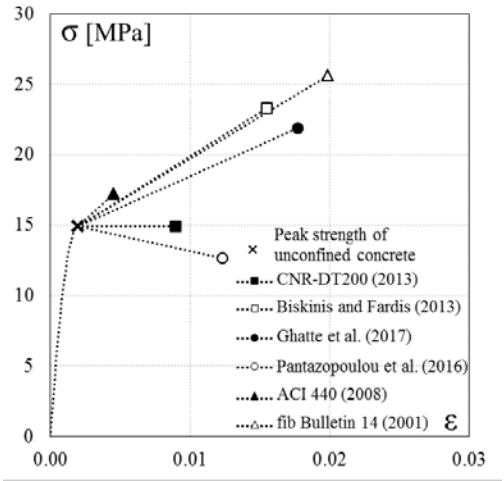


Figure 7: Stress-strain models for FRP confined concrete.

| | ***fib* Bulletin 14 (2001)** | **ACI 440 (2008)** | **CNR 200 (2013)** | **Biskinis and Fardis (2013)** | **Pantazopoulou et al. (2016)** | **Ghatte et al. (2017)** | **Empiric form Eq. (2)** |
|---|---|---|---|---|---|---|---|
| $\varepsilon_{cu}$ | 0.0199 | 0.0045 | 0.0090 | 0.0155 | 0.0123 | 0.0177 | - |
| $f_{cu}$ **[MPa]** | 25.6 | 17.2 | 14.9 | - | 12.7 | 21.9 | - |
| $k_{eff}$ | 0.58 | 0.31 | 0.60 | 0.58 | 0.70 | 0.85 | 1 |
| $\varepsilon_{f,eff}$ | 0.008 | 0.004 | 0.008 | 0.008 | 0.009 | 0.011 | 0.013 |

Table 2: Main parameters calculated for selected models.

From the comparison among different axial stress-strain models for FRP confined concrete, see Figure 7, it is observed that most of them assume a hardening behavior up to the failure, due to the elastic behavior of FRP material [i.e. *fib* Bulletin 14 – Spoelstra and Monti (2001), ACI 440 (2008), Biskinis and Fardis (2013), Ghatte et al. (2017)]. The model proposed by CNR DT-200 (2013) for evaluating the ultimate drift or chord rotation is a parabolic-rectangular model, with ultimate strain increased by the FRP confining effect. On the contrary, the model proposed by Pantazopoulou et al. (2016) for FRP confined concrete is similar to that of concrete confined by steel hoops, with a descending branch after the peak. Moreover, the model proposed by Pantazopoulou et al. (2016) takes into account also the confinement provided by internal transverse steel reinforcement.

### 4.2 Comparison between experimental, analytical and numerical results

Firstly, the experimental behavior of control column **A0** has been compared with the analytical predictions given by Eq. (2) and Eq. (3) in case of steel confinement only, in order to evaluate the reliability of the approaches. For the unconfined concrete, a Mander [31] model has been used with a concrete ultimate compressive strain of 0.004. The experimental force-drift curve is reported in Figure 8 along with the experimental envelope curve, the analytical bilinear curve obtained within Eq. (2) and the analytical bilinear curve obtained by using Eq. (3). In particular, Figure 8a reports the analytical curve obtained by using Eq. (2), whereas Figure 8b shows the analytical curve obtained by using Eq. (3).

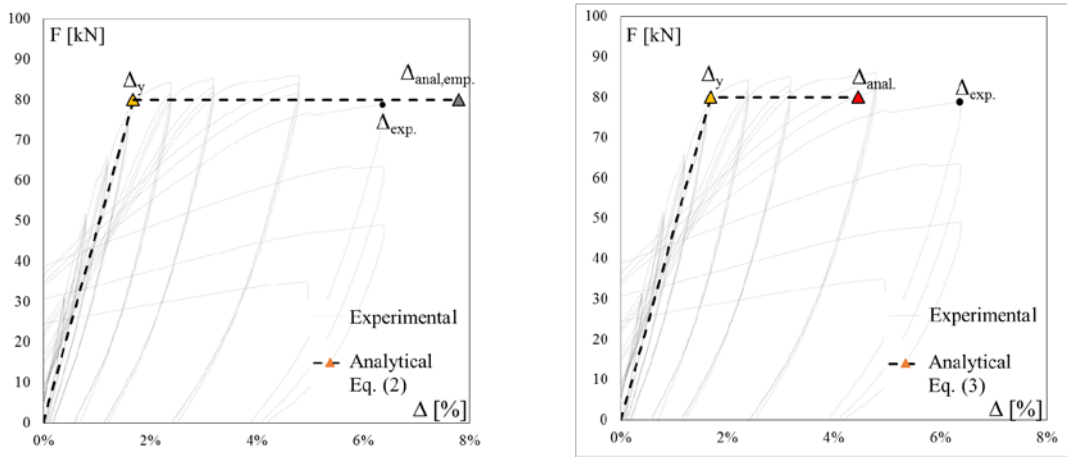


(a) (b)

Figure 8: Comparison of experimental, analytical (Eq. (2) and Eq. (3)) results for control specimen A0.

For the control specimen **A0**, the limitation of concrete ultimate strain to 0.004 leads to conservative predictions (i.e. -30%) of ultimate deformation capacity for the analytical approach based on curvatures. Conversely, the analytical approach based on empirical formulation in Eq. (2) overestimated the deformation capacity of the member of +22%. The main results in terms of ultimate deformation capacity obtained for specimen **A0** are summarized in Table 3 ($\Delta_{exp.}$ experimental ultimate drift, $\Delta_{anal.}$ analytical drift according to Eq. (3), $\Delta_{anal,emp.}$ ultimate drift according to empiric formulation in Eq. (2)).

| $\Delta_{exp.}$ | $\Delta_{anal,emp.}$ (Eq. (2)) | *Error* | $\Delta_{anal.}$ (Eq. (3)) | *Error* |
|---|---|---|---|---|
| 6.4% | 7.8% | *+22%* | 4.5% | *-30%* |

Table 3: Predictions of ultimate drift ratio for control specimen A0.

However, it should be noted that the ultimate flexural drift ratio of control specimen has not been achieved during the test, due to the premature brittle failure that is not taken into account in these analytical approaches.

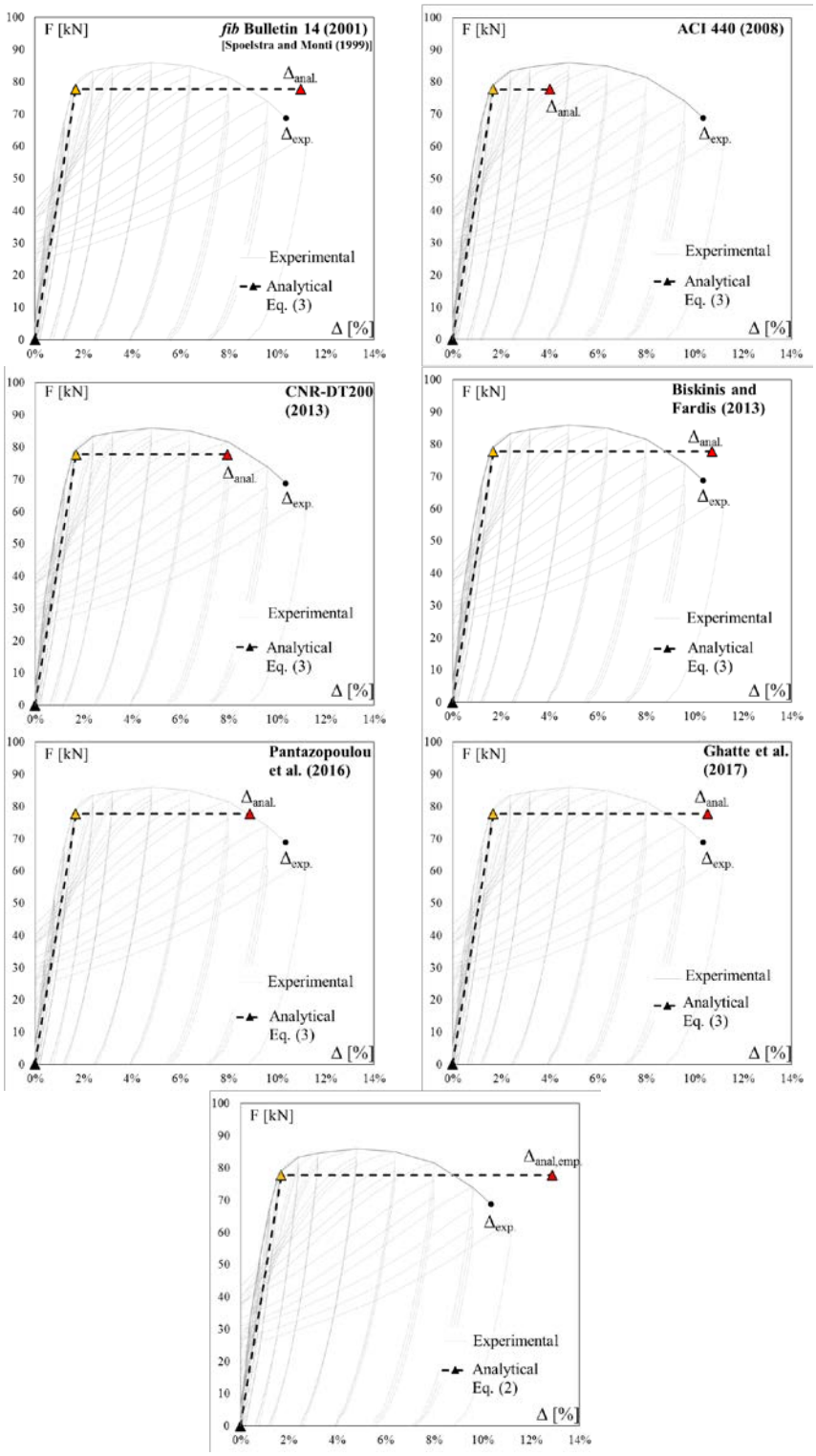


Figure 9: Comparison of experimental and analytical force-drift curves for specimen A1 according to different stress-strain FRP confined concrete models.

| Model | $\Delta_{exp}$ | $\Delta_{anal}$ | *Error* | $\Delta_{anal,emp.}$ | *Error* |
|---|---|---|---|---|---|
| *fib* Bulletin 14 (2001) | 10.4% | 11.0% | *+6%* | 12.9% | *+25%* |
| ACI 400 (2008) | | 4.0% | *-61%* | | |
| CNR-DT200 (2013) | | 7.9% | *-23%* | | |
| Biskinis et al. (2013) | | 10.7% | *+3%* | | |
| Pantazopoulou et al. (2016) | | 8.9% | *-14%* | | |
| Ghatte et al. (2017) | | 10.5% | *+2%* | | |

Table 4: Prediction of ultimate drift for control specimen A1.

The main results in terms of ultimate deformation capacity for FRP confined specimen **A1** are summarized in Table 4 for selected models.

The comparison between experimental and analytical results based on plastic hinge concept (i.e. derived from Eq. (3)) shows that the adoption of stress-strain models proposed by ACI 440 (2008), CNR DT-200 (2013) and Pantazopoulou et al. (2016) for calculating the ultimate drift ratio of the confined column under cyclic loading give results sensitively lower than the experimental one (i.e. errors of -61%, -23% and -14% respectively). Conversely, models proposed by Ghatte et al. (2017), Biskinis and Fardis (2013) and *fib* Bulletin 14 (2001) give results more close to the experimental ultimate drift ratio (i.e. errors of +2%, +3% and +6%, respectively). On the other hand, the empirical approach based on regression of experimental results (i.e. derived from Eq. (2)) gives a non-conservative result and overestimates the ultimate capacity of the confined member of +25%. This result is consistent with the *CoV* declared by the authors in [16] for the empirical formulation in Eq. (2) equal to ± 30.6%.

## 5 CONCLUSIONS

The experimental behavior of a RC column subjected to combined axial load and cyclic uniaxial bending and confined at the plastic hinge region with CFRP uniaxial sheets has been presented and discussed in comparison with an unconfined control specimen. The confinement of the potential plastic hinge region did not changed the member strength capacity but prevented the brittle failure observed in the control specimen and significantly increased its deformation capacity (+60.4%), due to the external lateral compression exerted by the fibers.

Then, analytical approaches provided by international codes and recent literature for predicting the ultimate drift ratio of confined members have been analyzed and applied for the specimen experimentally tested. The comparison between the experimental result of the column confined with FRP and the analytical results, according to plastic hinge concept, shows that the stress-strain models for confined concrete proposed by ACI 440 (2008) strongly underestimate the ultimate deformation capacity (-61%) whereas the models proposed by *fib* Bulletin 14 (2001), Biskinis and Fardis (2013), Ghatte et al. (2017) give a good prediction of ultimate drift ratio, with errors lower than +6%. On the other hand, the empirical approach based on regression of experimental results overestimated the ultimate drift ratio of confined specimen of 25%. All the results are based on a single experimental tests and can not be generalized for CFRP confined RC members.

## ACKNOWLEDGEMENTS

This study was performed in the Framework of PE 2014-2016; joint program DPC-Reluis Task 1.2: Seismic capacity of RC structural members: beams, columns, beam-column joints and shear walls.

## REFERENCES


[1] H. Katsumata, Y. Kobatake, T. Takeda, A study on strengthening with carbon fiber for earthquake-resistant capacity of existing reinforced concrete columns. *Ninth World Conference on Earthquake Engineering*, 1988.

[2] H. Saadatmanesh, M.R. Ehsani, M.W. Li, Strength and Ductility of Concrete Columns Externally Reinforced with Fiber Composite Straps. *ACI Structural Journal*, **91**, 434-447, 1994.

[3] A. Nanni, M. Norris, FRP jacketed concrete under flexure and combined flexure-compression. *Construction and Building Materials*, **9**(5), 273-281, 1995.

[4] F. Seible, M.J.N. Priestley, G.A. Hegermier, D. Innamorato, Seismic retrofit of rc columns with continuous carbon fiber jackets. *Journal for Composites for Construction*, **1**(2), 52-62, 1997.

[5] R.D. Iacobucci, S.A. Sheikh, O. Bayrak, Retrofit of square concrete columns with carbon fiber-reinforced polymer for seismic resistance. *ACI Structural Journal*, **100**(6), 785-794, 2003.

[6] M.H. Harajli, Z. Khalil, Seismic FRP retrofit of bond-critical regions in circular RC columns: validation of proposed design methods. *ACI Structural Journal*, **105**(6), 760, 2008.

[7] M. Di Ludovico, G. Manfredi, E. Mola, P. Negro, A. Prota, Seismic Behavior of a Full-Scale RC Structure Retrofitted Using GFRP Laminates. *ASCE – Journal of Structural Engineering*, **134**(5), 810-821, 2008.

[8] M. Di Ludovico, A. Balsamo, A. Prota, G. Manfredi, Comparative Assessment of Seismic Rehabilitation Techniques on a Full-Scale 3-Story RC Moment Frame Structure. *Structural Engineering and Mechanics*, **28**(6), 727-747, 2008.

[9] O. Ozcan, B. Binici, G. Ozcebe, Seismic strengthening of rectangular reinforced concrete columns using fiber reinforced polymers. *Engineering Structures*, **32**(4), 964-973, 2010.

[10] H.F. Ghatte, M. Comert, C. Demir, A. Ilki, Seismic performance of full-Scale FRP Retrofitted substandard RC Columns Loaded In The Weak Direction. *Applied Mechanics & Materials*, **847**, 2016.

[11] M. Samaan, A. Mirmiran, M. Shahawy, Model of concrete confined by fiber composites. *ASCE – Journal of Structural Engineering*, **124**, 1025–1031, 1998.

[12] L. Lam, J.G. Teng, Design-oriented stress-strain model for FRP-confined concrete in rectangular columns. *J. Reinf. Plast. Compos*, **22**, 1149–1186, 2003.

[13] M.H. Harajli, Axial stress-strain relationship for FRP-confined circular and rectangular concrete columns. *Cem. Concr. Compos*, **28**, 938–948, 2006.

[14] G.P. Lignola, A. Prota, G. Manfredi, E. Cosenza, Unified theory for confinement of RC solid and hollow circular columns. *Compos. Part B*, **39**, 1151–1160, 2008.

[15] M. Di Ludovico, A. Prota, G. Manfredi, Structural upgrade using basalt fibers for concrete confinement. *Journal of composites for construction*, **14**(5), 541-552, 2010.

[16] D. Biskinis, M.N. Fardis, Models for FRP-wrapped rectangular RC columns with continuous or lap-spliced bars under cyclic lateral loading. *Eng. Struct*., **57**, 199–212, 2013.

[17] F. Braga, R. Gigliotti, M. Laterza, Analytical stress–strain relationship for concrete confined by steel stirrups and/or FRP jackets. *Journal of structural engineering*, **132**(9), 1402-1416, 2006.

[18] K.G. Megalooikonomou, G. Monti, S. Santini, Constitutive model for fiber-reinforced polymer-and tie-confined concrete. *ACI Structural Journal*, **109**(4), 569, 2012.

[19] S. Mazzoni, F. McKenna, M.H. Scott, G.L. Fenves, OpenSees command language manual. *Pacific Earthquake Engineering Research (PEER) Center*, 2006.

[20] A. Parvin, W. Wang, Behavior of FRP jacketed concrete columns under eccentric loading. *Journal of Composites for Construction*, **5**(3), 146-152, 2001.

[21] M.N.S. Hadi, Behaviour of FRP wrapped normal strength concrete columns under eccentric loading. *Composite Structures*, **72**, 503-511, 2006.

[22] J.Y. Park, Y.H. Lee, A. Scanlon, Confined concrete model for columns under combined axial load and bending. *Mag. Concr. Res.*, **64**, 827–836, 2012.

[23] Y.F. Wu, C. Jiang, Effect of load eccentricity on the stress–strain relationship of FRP-confined concrete columns. *Compos. Struct.*, **98**, 228–241, 2013.

[24] H. Ghatte, M. Comert, C. Demir, A. Ilki, Evaluation of FRP Confinement Models for Substandard Rectangular RC Columns Based on Full-Scale Reversed Cyclic Lateral Loading Tests in Strong and Weak Directions. *Polymers*, **8**(9), 323, 2017.

[25] M. Di Ludovico, G. Verderame, A. Prota, G. Manfredi, E. Cosenza, Cyclic Behavior of Nonconforming Full-Scale RC Columns. *Journal of Structural Engineering*, 2013.

[26] M. Del Zoppo, M. Di Ludovico, A. Ghersi, Behaviour of non-conforming rc members under compressive axial load and biaxial bending. *5th ECCOMAS thematic conference on computational methods in structural dynamics and earthquake (COMPDYN 2015)*, Crete, Greece, 2015.

[27] *fib* Bulletin 14. Externally bonded FRP reinforcement for RC structures. CH-1015, Lausanne, 2001.

[28] Guide for Design and Construction of Externally Bonded FRP Systems for Strengthening Concrete Structures, ACI 440.2R-08, ACI: Farmington Hills, MI, USA, 2008.

[29] Consiglio Nazionale Delle Ricerche (CNR). Instructions for design, execution and control of strengthening interventions through fiber-reinforced composites. CNR-DT 200-13, Consiglio Nazionale delle Ricerche, Rome, Italy; 2013.

[30] S.J. Pantazopoulou, S.P. Tastani, G.E. Thermou, T. Triantafillou, G. Monti, D. Bournas, M. Guadagnini, Background to the European seismic design provisions for retrofitting RC elements using FRP materials. *Structural Concrete*, **17**(2), 194-219, 2016.

[31] J.B. Mander, M.J. Priestley, R. Park, Theoretical stress-strain model for confined concrete. *Journal of structural engineering*, **114**(8), 1804-1826, 1988.

COMPDYN 2017
6th ECCOMAS Thematic Conference on
Computational Methods in Structural Dynamics and Earthquake Engineering
M. Papadrakakis, M. Fragiadakis (eds.)
Rhodes Island, Greece, 15–17 June 2017

# EMPIRICAL DAMAGE AND ACTUAL REPAIR COSTS ON MASONRY PRIVATE BUILDINGS AFTER L'AQUILA EARTHQUAKE

**G. De Martino [(1)], M. Di Ludovico[(2)], A. Prota [(3)], C. Moroni[(4)], G. Manfredi[(5)], M. Dolce[(6)]**

[(1)] University of Naples Federico II, giuseppina.demartino2@unina.it
[(2)] University of Naples Federico II, diludovi@unina.it
[(3)] University of Naples Federico II, aprota@unina.it
[(4)]Department of Civil Protection, Presidency of Council of Ministers, Claudio.Moroni@protezionecivile.it
[(5)] University of Naples Federico II, gamanfre@unina.it
[(6)]Department of Civil Protection, Presidency of Council of Ministers, Mauro.Dolce@protezionecivile.it

**Keywords:** empirical damage, repair costs, loss estimation

***Abstract.*** *In the first phase of the emergency management after the April 6, 2009, L'Aquila earthquake, field inspections were carried out through the AeDES form, a first level survey form for post-earthquake damage and usability assessment, to evaluate the usability conditions of buildings. Once the damage and usability assessment was completed, the reconstruction process of residential buildings outside the historical centre of L'Aquila and surrounding municipalities was regulated by several Ordinances of the Prime Minister. The public grant was released according to funding requests made by practitioners and checked by a proper commission entrusted by the Government. The data collected on a set of about 1,000 residential masonry buildings in terms of vulnerability class, construction age, number of storyes, empirical damage, as well as of Actual Repair Costs (ARCs) are herein discussed and presented. Building Damage Factor, DF has been computed based on the damage data of structural and non-structural component collected with the AeDES forms. A calibration of different parameters, as the damage extent and severity on each structural and non-structural component and the weight of the damage on a single component on the total repair costs of the building, was carried out. The calibration allow us to determine the best correlation between the empirical damage and ARC. The proposed relationship between empirical damage and ARC may drive decision makers, in the immediate post-earthquake, to make preliminary estimates of the repair costs, only based on quick surveys on residential buildings. The relationship may also be used as a tool to figure out repair costs based on damage scenarios.*

## 1 INTRODUCTION

The frequent occurrence of strong earthquakes and their devastating effects have drawn the attention to the importance rule played by the usability and damage assessment in the emergency phase. The concept of usability assessment, although with different procedures, is common to all earthquake prone countries and it is a worldwide task in the emergency phase [1,2,3,4,5]. Instead, the damage assessment, aimed at quantifying the direct economic losses caused by the earthquake, is carried out only in few earthquake prone countries. After 2009 L'Aquila earthquake the damage assessment was carried out together with the usability assessment by means of the AeDES form [5], the first level survey form adopted by government to assess the safety conditions of the buildings. This form has been filled during in situ inspections effectuated by team of experts. The damage data collected are related to the four damage level and relevant extent both for structural components (i.e. Vertical Structure, VS, Floor, F, Roof, R, Stairs, S) and not structural components (i.e. Infill-Partition, IP). The genesis of definition of damage to different structural components has been defined according to the European Macroseismic Scale EMS- 98 [6]; however, EMS-98 reports six damage states and they are related to the buildings and not to the single components. In literature, several methodologies have been applied to convert the damage to structural and non-structural components in a global damage of the building. In [7] a procedure is outlined to determine the global damage of a building as the sum of the damages detected on structural and non-structural members weighted by coefficients calibrated based on average repair costs. The damage for each member is computed as the sum of damage levels, Di, multiplied by their extension, ei. Then six levels, from 0 to 5, can be determined to represent the global damage index. In [8,9] starting from the procedure reported in [7] only the damages detected on the vertical structures to find a global damage index has been taken into account. In [10] the same approach has been assumed, but the damage extension on the structural components has not been taken into account. By contrast, the damage grades D2-D3 and D4-D5 were split into the corresponding EMS-98 damage state depending only on the mean damage detected on VS for the building class in the selected location: the higher the mean damage, the higher the probability of being in the heaviest DS. A correlation between empirical damage derived by AeDES form and the six damage grades as defined by EMS-98 was provided also by [11] and [12]. According to [11] the maximum damage detected on structural components VS, F, and R is accounted for the correlation between empirical damage and the building DS. In [12], the damage on IP is taken into account as a key parameter to define the building damage state attained due to the earthquake; the maximum damage detected on VS or IP is accounted for the correlation between empirical damage and the building DS. In spite of the numerous studies revised carried out to analyze the empirical damage, a study to correlate the empirical damage to the cost computed by practitioners to repair the damage suffered by each structural and non-structural component, namely Actual Repair Costs, ARC, is still lacking. To fill this gap, a study to evaluate the relationship between damage detected by in-situ inspections and repair costs determined according to repair interventions designed and computed by practitioners engaged by owners in the L'Aquila post-earthquake reconstruction process is herein presented. The management of L'Aquila post-earthquake reconstruction process is briefly presented herein along with the data collected on 1,000 masonry residential buildings in terms of vulnerability classes, buildings characteristics and damage levels. Finally, a further suitable index, named Damage Factor (DF), specifically calibrated to take into account the weight and extent of damage to each structural component on repair costs, is presented. Furthermore, a correlation between DF and ARC is presented. The proposed relationship may allow making a preliminary estimate of the repair costs, based on a quick inspection on the damaged residential

building. The same relationship has been carried out also for 1,500 RC residential buildings damaged by L'Aquila earthquake and reported in [13].

## 2 RECONSTRUCTION POLICY FOR RESIDENTIAL BUILDINGS

The reconstruction process of residential buildings outside the historical centers damaged by the L'Aquila earthquake was calibrated based on usability assessment of each private building. Depending on the severity of structural damage detected, the team of experts provided six possible outcomes of usability conditions of the building, named with a letter from A to F. The reconstruction process was supported by the Italian Government using public resources and the technical and financial review provided by a commission, called "Filiera" (i.e. an Italian word to indicate a supply chain mechanism) properly set up to oversee the projects and relevant funding applications related to residential buildings with B or C and E usability rating. Details about the reconstruction process are reported in [14;15] According to the ordinances specifically issued for the reconstruction of damaged buildings [16,17,18,19,20], the repair costs to restore original condition of damaged structural or nonstructural components were fully covered by the public grant. In addition, according to the "building back better" principle, strengthening costs were also covered by the government in order to reduce the vulnerability of repaired buildings. The maximum grant for strengthening works was established as a function of the usability rating of buildings. Technical and economic information on 5,775 buildings outside the historical centers of Abruzzi Region municipalities has been collected in a database thanks to the Filiera activity; in the next sections, the data related to 1,000 masonry buildings derived both by the AeDES forms and the applications for funding, checked and approved by the Filiera are presented and discussed.

## 3 BUILDING DATASET

The usability assessment of buildings and the technical approval process of application for funding of damaged buildings allowed to collect in a database both technical, economic and damage data related to 1,000 masonry residential buildings outside the historical centers of Abruzzi Region municipalities. The data related to these buildings are presented and discussed in this section in terms of: vulnerability classes; construction age and number of storeys, severity and extent of damage detected by in situ inspections on building structural and nonstructural components, and repair costs. The building features contained in the AeDES survey forms, as type of vertical and horizontal structures, allow us to divided the dataset in three vulnerability classes, A, B and C, as a function of the building seismic behavior according to criteria adopted in [7,10]. The most vulnerable class, A, consists of 405 (about 40%) buildings while the other vulnerable classes, B and C, consist of 216 and 379 buildings (about 22% and 38%), respectively. The percentage ratio of buildings belonging to A, B and C vulnerability classes as a function of buildings' construction age or number of storeys is reported in Figure 1a,b, respectively. The construction age is grouped in eight different periods in the AeDES form according to the census data collections made by National Statistics Institute, ISTAT (i.e. before 1919, 1919- 1945, 1946-1961, 1962-1971, 1972-1981, 1982-1991, 1992-2001, >2001). The buildings built after 1981 were grouped in classes after 1981 in Figure 1a because few buildings are found in these classes in the dataset. Figure 1a also reports the number of buildings belonging to each construction age period. Except for after 1981 period, Figure 1a shows that the percentage of buildings belonging to A and B vulnerability classes has a clearly decreasing trend for more recent construction age periods, while an opposite trend can be observed for C vulnerability class. In terms of number of storeys, the buildings are distributed between one and six storeys, with a peak for two or three storeys classes,

which account about 75% (756 buildings, 286 with 2 storeys and 470 buildings with 3 storeys) of the whole dataset. By contrast, the number of buildings with 1 story or 6 storeys is almost negligible (they represent about 3% of the dataset). Figure 1b shows that the higher the number of storeys better is the quality of masonry and more rigid are the horizontal structures. By contrast, the percentage ratio of B vulnerability class buildings is almost constant by varying the number of storeys.

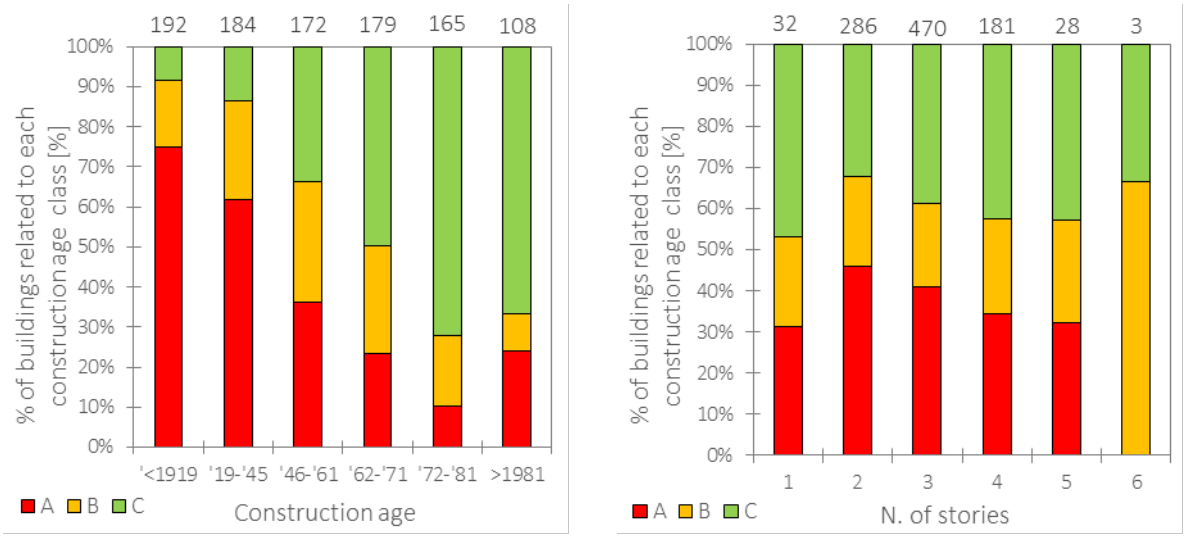


(a) (b)

Figure 1 – Funding classes of RC buildings measured against construction age (a) or number of storeys (b)

In Figure 2 the distribution of the empirical damage detected on Vertical Structures (VS), Floors (F), Stairs (S), Roofs (R) and Infills-Partitions (IP) of 1,000 masonry buildings is reported. In particular, Figures 2a depicts the number of buildings with null damage, D0, to each component; in the other graphs of Figure 2 the number of buildings with damage level defined according to Section 4 - Damage to the structural components"of the AeDES (D1, slight damage; D2-D3 medium-severe damage; D4-D5 very heavy damage or collapse) and relevant extent (i.e. lower than 1/3, between 1/3 and 2/3, and greater than 2/3 of the storey components) are reported for each structural component. Figures 2a shows that only 142 buildings, corresponding to about 14% of the dataset of masonry buildings, had null damage on VS while on S and R components the null damage was found in for more than 700 buildings, that is more than 70% of the dataset. In particular, the less damaged component resulted the stairs, S, D0 on 792 buildings while the most damaged one, except for VS, was the infill-partitions, IP, D0 on 273 buildings. Furthermore, Figures 2b,c,d,e show that for F, S, R and IP the most frequent damage was D1, with an extent lower than 1/3 of the story components, while on VS the most frequent damage was D2-D3 with an extent between 1/3 and 2/3. The very heavy damage level, D4-D5, was detected in 162 buildings on VS, 30 buildings on F, 27 buildings on S, 31 buildings on R, 80 buildings on IP.

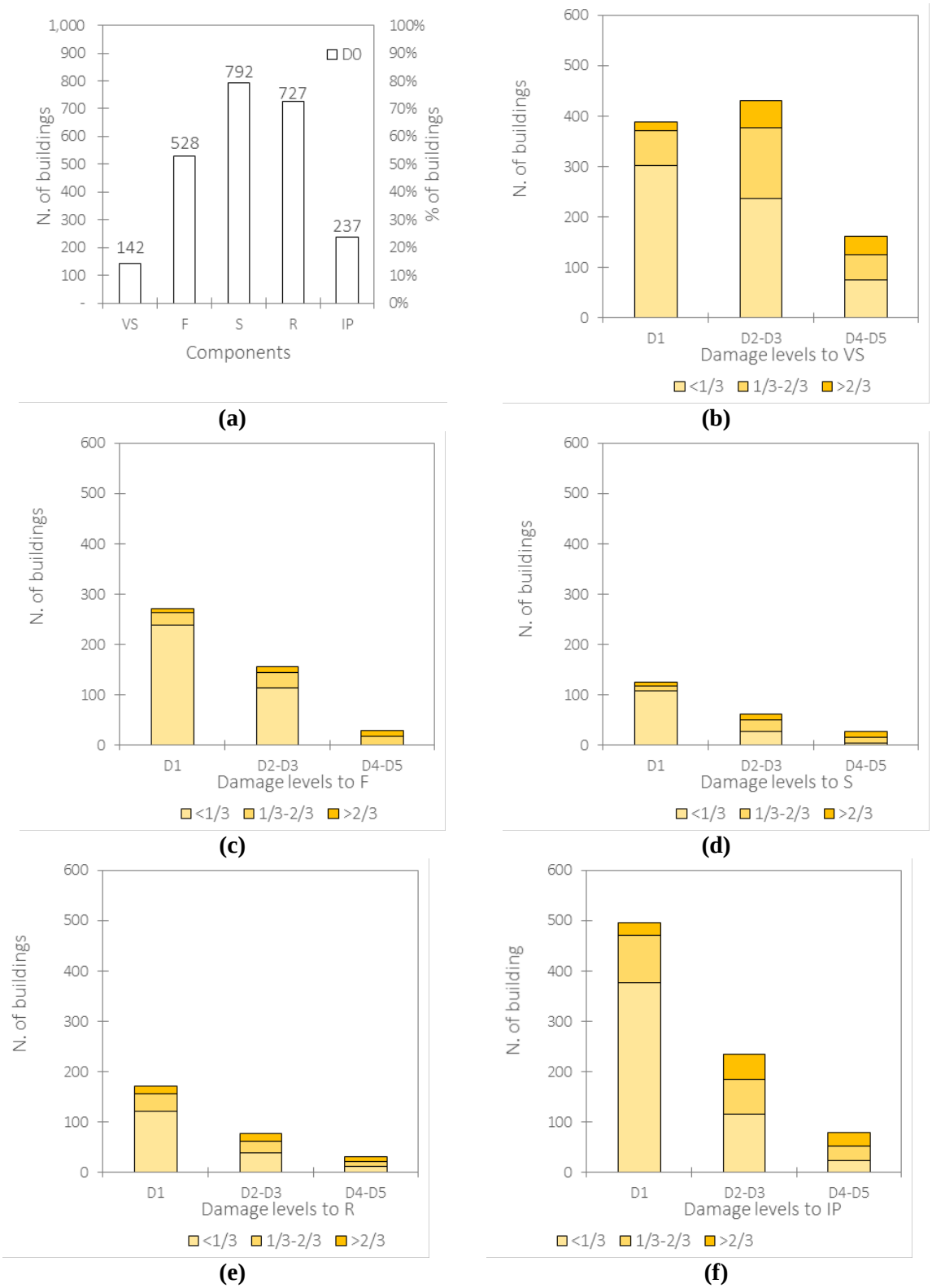


Figure 2. Distribution of null damage D0 for each component (a), distribution of damage levels D1, D2-D3, D4-D5, and relevant extent related to VS (b), F (c), S (d), R (e), and IP (f).

The building damage has been defined according to [7]. To this end, the following expression has been assumed:

$$DF = \sum_j D_j \cdot \gamma_j \tag{1}$$

where

- $D_j$ is the damage level and extent related to the $j^{th}$ structural component (i.e. j=*VS*, *F*, *S*, *R* and *IP*)
- $\gamma_j$ is a coefficient, ranging between 0 and 1, which takes into account the weight of the damage on the $j^{th}$ structural component on the building repair costs.

The damage level and extent related to the $j^{th}$ structural component, $D_j$, can be computed according to the following expression:

$$D_j = \frac{\sum_{D=D0}^{D5} D \cdot e_{k,D}}{5} \tag{2}$$

where:

- $D$ is the damage level (D0 = 0; D1 = 1; D2-D3 = 2.5; D4-D5 = 4.5),
- $e_{k,D}$ is a coefficient, ranging between 0 and 1,which takes into account the damage level extent k less than 1/3, between 1/3 and 2/3, and greater than 2/3 ($e_{k,D1} = e_{k,D2\text{-}D3} = e_{k,D4\text{-}D5} = 0.17$ for k<1/3, $e_{k,D1} = e_{k,D2\text{-}D3} = e_{k,D4\text{-}D5} = 0.5$ for 1/3<k<2/3, and $e_{k,D1} = e_{k,D2\text{-}D3} = e_{k,D4\text{-}D5} = 0.83$ for k>2/3).

The DF assessed according to (1) and (2) varies between 0 and 0.75 and it is on average equal to 0.08. Over the 90% of building dataset has a damage factor in the range 0-0.2. The DF has been also computed with reference to the building vulnerability classes. The DF resulted on average equal to 0.1, 0.08 and 0.06, respectively for A, B and C vulnerability classes. Figure 3 confirms the relationship between DF and vulnerability classes. Indeed the percentage of A buildings increases from the 0-0.2 DF class to 0.6-0.8 DF class (i.e. 38% of the sub-dataset of building pertaining to the initial DF interval up to 67% of the sub-dataset of buildings pertaining to last one).

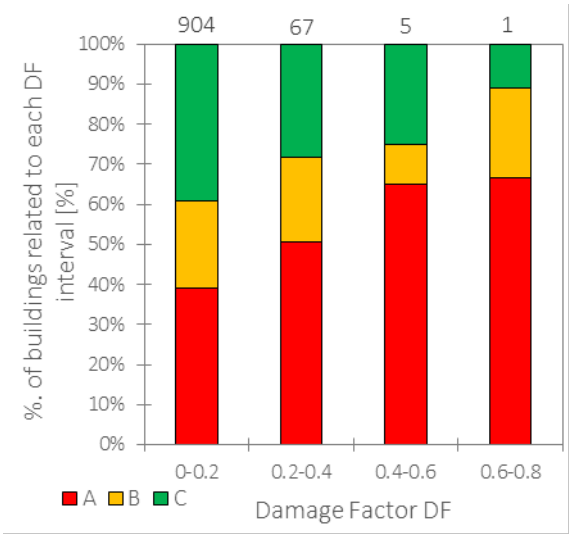


| Vulnerability class | 0-0.2 | 0.2-0.4 | 0.4-0.6 | 0.6-0.8 | Total |
|---|---|---|---|---|---|
| **A** | 352 | 34 | 13 | 6 | 405 |
| **B** | 198 | 14 | 2 | 2 | 216 |
| **C** | 354 | 19 | 5 | 1 | 379 |
| **Total** | 904 | 67 | 20 | 9 | 1000 |

Figure 3. Vulnerability classes of masonry buildings measured against damage factor, DF

## 4 DF - ARC REGRESSION FUNCTIONS

The relationship between the empirical damage and ARC is investigated in this section.

In order to determine the best correlation between the empirical damage and Actual Repair Costs, ARC granted after the Filiera checks, a proper Damage Factor has been assessed by varying the value of the damage extent, $e_{k,D}$ on each structural and non-structural component and the weight of the damage on a single component on the total repair costs of the building, $\gamma_j$ in the equations (1, 2).
The ARC are related to repair interventions of damaged non-structural parts and relevant finishing works; local repair of damaged structural components; demolition and reconstruction of fully damaged or unsafe non-structural or secondary structural elements (i.e. interior or exterior infills, outdoor curtains, heavy plasters, fireplaces and chimney-pots, porches, eaves, repair of damaged facilities, etc.). The ARCs are not inclusive of VAT (equal to 10% of costs for repair and local strengthening interventions and 20% for other costs). The ARC are computed with reference to the overall building gross surface area, that is the area of the building footprint.
In order to define a proper DF, first of all it was necessary to define the constraints for the value of $\gamma_j$ and $e_{k,D}$. In particular, it was assumed:

- $\sum \gamma_j = 1$.
- for a given damage extent *k*, $e_{k,D1} \leq e_{k,D2\text{-}D3} \leq e_{k,D4\text{-}D5}$;
- for a given damage level *D*, $e_{k<1/3,D} < e_{1/3<k<2/3,D} < e_{k>2/3,D}$;
- $\sum_{D=D0}^{D5} D \cdot e_{k,D} \leq 5$

Defined the constrains, the calibration of $\gamma_j$ and $e_{k,D}$. values started in order to obtain the best correlation (i.e. maximum value of coefficient of determination, $R^2$ ) between DF and ARC. The calibration is based on iterative procedure as shown in Figure 4. It consists of the following steps: i) assume $\gamma_j$ and $e_{k,D}$. values of first tentative; ii) compute DF according to expression (1) and (2) for each building of the dataset and the relevant actual repair cost, ARC, is associated to each building; iii) find the regression function which provides the correlation between DF and ARC; iv) steps i) to iii) are repeated by varying $\gamma_j$ and $e_{k,D}$ values according to constraints until the coefficient of determination $R^2$ of regression function attains its maximum value.

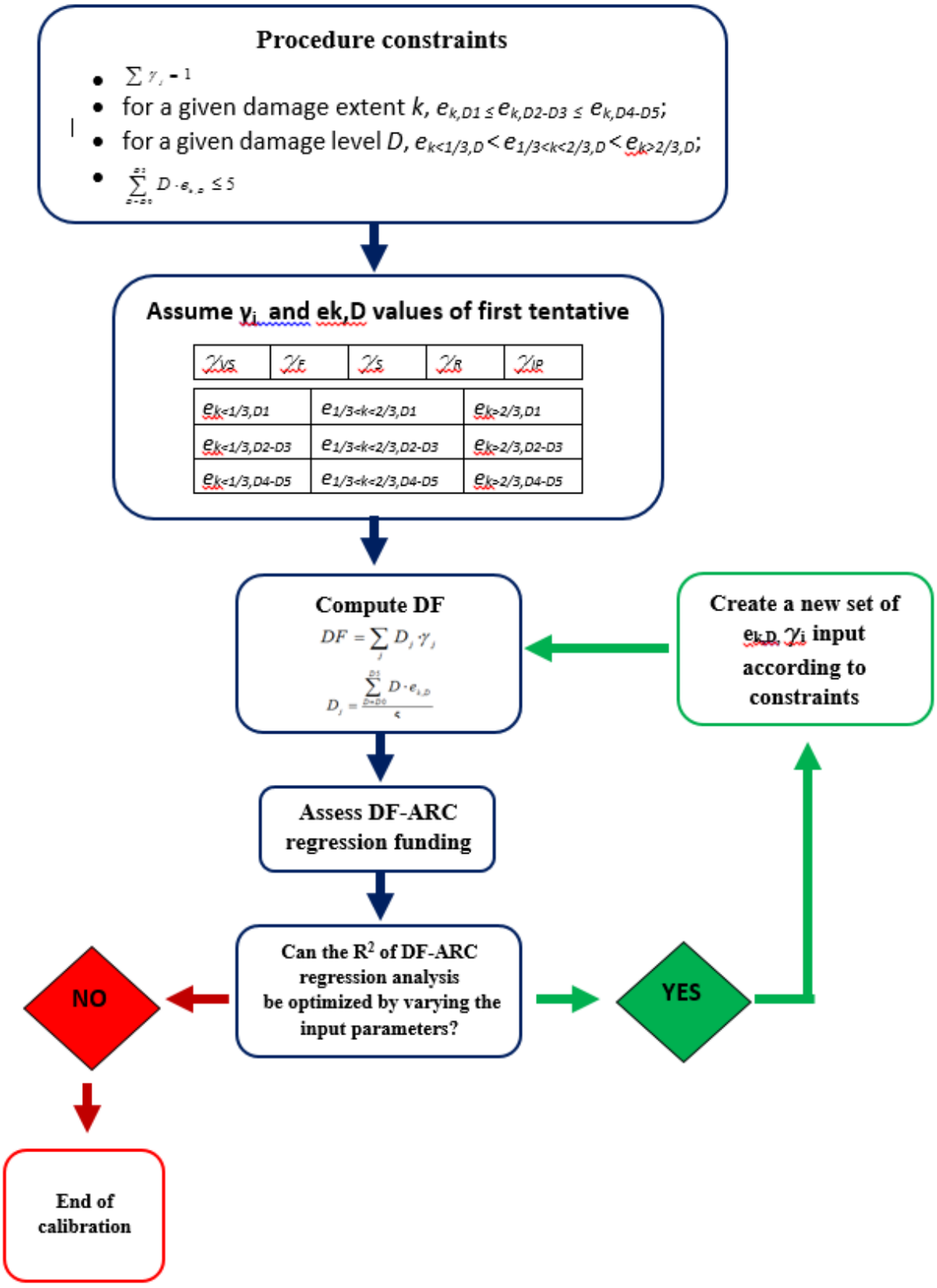


Figure 4. Flowchart related to the iterative procedure

The $\gamma_j$, $e_{k,D}$, and $D \cdot e_{k,D}$ values calibrated according to such procedure are summarized in Table 1, Table 2, Table 3.

**Table 1. Coefficient $\gamma_f$**

| | |
|---|---|
| $\gamma_{VS}$ | 0.40 |
| $\gamma_F$ | 0.12 |
| $\gamma_S$ | 0.00 |
| $\gamma_R$ | 0.30 |
| $\gamma_{IP}$ | 0.18 |

**Table 2. Coefficient $e_{k,D}$**

| | k<1/3 | 1/3<k<2/3 | k>2/3 |
|---|---|---|---|
| $e_{k,D1}$ | 0.40 | 0.60 | 0.80 |
| $e_{k,D2\text{-}D3}$ | 0.40 | 0.70 | 0.89 |
| $e_{k,D4\text{-}D5}$ | 0.50 | 0.80 | 0.89 |

**Table 3. $D \cdot e_{k,D}$.**

| | k<1/3 | 1/3<k<2/3 | k>2/3 |
|---|---|---|---|
| $D1 \cdot e_{k,D1}$ | 0.40 | 0.60 | 0.80 |
| $D2\text{-}D3 \cdot e_{k,D2\text{-}D3}$ | 1.00 | 1.75 | 2.23 |
| $D4\text{-}D5 \cdot e_{k,D4\text{-}D5}$ | 2.25 | 3.60 | 4.00 |

The (DFb, ARCb) points related to each building and the regression functions are reported in Figures 4. Each point represents one building and the vulnerability class is also reported. In Figure 5, it is possible to note that the most vulnerable building classes are mainly represented by points located in the upper-right zone of the graph which is representative of significant level of damage and amount of ARC. By contrast, the C vulnerability class is represented mainly by points located in the lower-right zone of the graph. Furthermore, the relationship between DF and ARC is also reported in terms of an a-dimensional cost ratio obtained as a ratio between the actual repair costs related to the building and the average building demolition and reconstruction cost, Building Repair Cost Ratio (Cr). The unit costs for demolition and reconstruction of private residential buildings damaged by L'Aquila earthquake resulted 1,192.00 €/m$^2$, [12,13]. Based on the regression analyses the following function has been determined:

$$C_r = 0.12+0.71 \cdot DF-0.23DF^2 \qquad [ARC = 143+849DF-277DF^2] \tag{3}$$

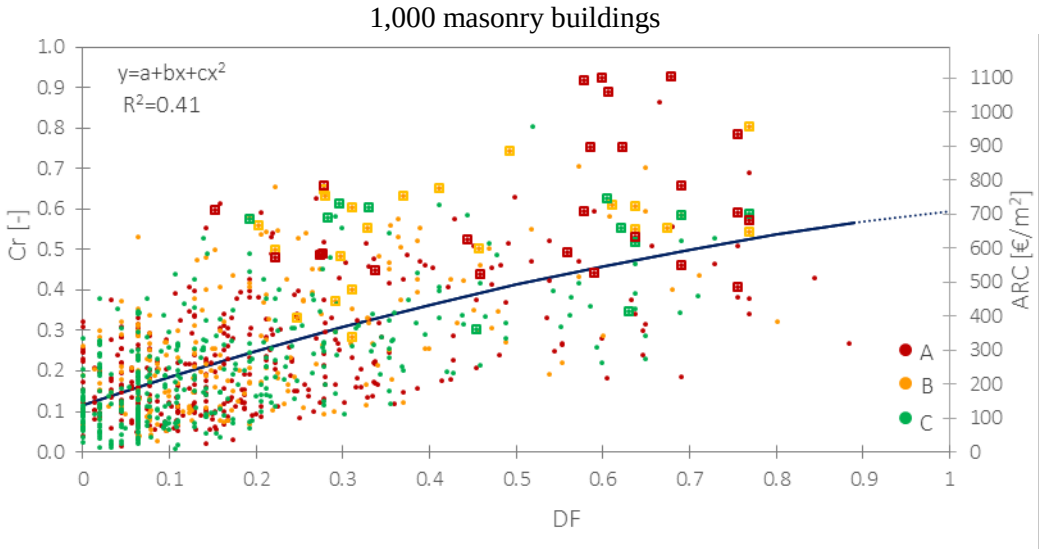


Figure 5. DF – ARC regression function

Figure 5 shows that the regression functions gives Cr = 0.12 in case of DF = 0. This is because even on buildings with DF = 0 damage to non-structural components (i.e. false ceiling, chimneys, parapets, services, etc.) was detected.
The point marked in Figures 4 with a square are related to 56 masonry buildings out of 1,000 of the dataset, for which the demolition and reconstruction resulted economically more viable than repair and strengthening works. This means that the ARC (or Cr) computed for these buildings and depicted in Figures 4 are related to the design of repair interventions although they actually were not realized. On these buildings, the DF and ARC expressed in terms of Cr vary as follows: Cr = 0.28-0.93 with a median of 0.57. It is pointed out that the class of demolished buildings is represented in Figures 10 by points mainly located in the upper-right zone of the graph.
Finally, the regression functions in the range of *DF* greater than those attained for the buildings of the database (i.e. *DF*>0.89) is represented with a dashed line in Figure 5.

## 5 CONCLUSIONS

The data collected by field inspections in the aftermath of a damaging earthquake aim to establish the building usability in view of aftershocks. To this goal, the main characteristics of the buildings and the level and extent of damage on components are commonly detected and reported in suitable damage and vulnerability assessment forms. The data collected with ref-erence to 1,000 masonry buildings outside the historical centres after the 2009 L'Aquila earthquake have been presented and discussed in the paper along with the actual repair costs derived from funding requests on private residential buildings damaged by the 2009 L'Aquila earthquake. The data presented in this study have shown that:

- the most damaged component have come out to be the vertical structures
- three classes for masonry buildings based on the type of vertical and horizontal structures have been defined according to building in situ inspection. A good correlation was found between the proposed vulnerability classes and the empirical damage detected on each building component.
- a proper damage factor *DF* is necessary to determine a correlation between empirical damage and actual repair costs, *ARC*; the damage factor should take into account not only the damage level on each building component but also the damage extent and the weight of the damage on a single component on the total repair costs of the building.

A calibration of extent of damage and of the coefficient, ranging between 0 and 1, which takes into account the weight of the damage on the $j^{th}$ structural component on the building repair costs have been carried out in order to determine an optimised the relationship between *DF* and *ARC*. The proposed relationships may represent a useful tool to predict costs of repair for residential buildings outside historical centres when subjected to earthquakes.

## REFERENCES

[1] Building Research Institute, 2002; Building Research Institute, Guideline for Damage Survey Methods of Earthquake Disaster Related with Buildings and Houses, 2002

[2] ATC 20, Procedures for post-earthquake safety evaluation of buildings, 1989

[3] ATC 20-2, Addendum to ATC 20 Procedures for post-earthquake safety evaluation of buildings, 1995.

[4] Dandoulaki M., Panoutsosopoulou M., Ioannides K, An Overwie of Post-earthquake Building Inspection Practice in Grece and the Introducttion of a Rapid Building Usability Evaluation Procedure after the Konitsa Earthquake, Proceedings XI European Conference on Earthquake Engineering, Balkema, Rotterdam, 1998.

[5] Baggio C, Bernardini A, Colozza R, Di Pasquale G, Dolce M, Goretti A, Martinelli A, Orsini G, Papa F, Zuccaro G, Pinto AV and Taucer F, Field Manual for post-earthquake damage and safety assessment and short term countermeasures (AeDES). EUR 22868 EN, Joint Research Center, Ispra, Italy, 2007.

[6] Grünthal G. (1998). Cahiers du Centre Européen de Géodynamique et de Séismologie: Volume 15 – European Macroseismic Scale 1998. *European Center for Geodynamics and Seismology, Luxembourg.*

[7] Dolce M., Moroni C., Samela, C., Marino, M., Masi, A., Vona, M., Una Procedura di Normalizzazione del Danno per la Valutazione degli Effetti di Amplificazione Locale, Proceedings of the X National con-ference of seismic engineering in Italy, Potenza-Matera, 9–13 September 2001 (in Italian).

[8] Di Pasquale G., Goretti A. Functional and economic vulnerability of residential buildings affected by recent Italian earthquakes. Proceedings X National conference of seismic engineering in Italy, Potenza- Matera, 9–13 September 2001 (in Italian)

[9] Goretti A., Di Pasquale G.,Building inspection and damage data for the 2002 Molise, Italy, earthquake. Earthq Spectra 20 (special Issue I), 2004, pp. 167–190

[10] Dolce M. and Goretti A. 2015. "Building damage assessment after the 2009 Abruzzi earthquake." Bulletin of Earthquake Engineering, 1-24.

[11] Rota M., Penna A., and Strobbia C.L. (2008). Processing Italian damage data to derive typological fragility curves. Soil Dynamics and Earthquake Engineering, 28.10: 933-947.

[12] Del Gaudio C., De Martino G., Di Ludovico M., Ricci P., Verderame G.M. Empirical fragility curves from damage data on RC buildings after the 2009 L'Aquila earthquake, submitted to Bulletin of Earthquake Engineering, 2016.

[13] De Martino, G., Di Ludovico, M., Prota, A., Moroni, C., Manfredi, G., & Dolce, M. Estimation of repair costs for RC and masonry residential buildings based on damage data collected by post-earthquake visual inspection. Bulletin of Earthquake Engineering, 1-26.

[14] Di Ludovico M., Prota A., Moroni C., Manfredi G., Dolce M., "Reconstruction process of damaged residential buildings outside historical centres after the L'Aquila earthquake - Part I: "Light Damage" Reconstruction, Bull Earthquake Eng (2017) 15: 667. doi:10.1007/s10518-016-9877-8

[15] Di Ludovico M., Prota A., Moroni C., Manfredi G., Dolce M., " Reconstruction process of damaged residential buildings outside historical centres after the L'Aquila earthquake - Part II: "Heavy Damage" Reconstruction", Di Ludovico, M., Prota, A., Moroni, C. et al. Bull Earthquake Eng (2017) 15: 693. doi:10.1007/s10518-016-9979-3

[16] Ordinance of the President of the Council of Ministers, O.P.C.M. n. 3779, June 6, 2009 - "Urgent interventions to deal with seismic events occurred in the Abruzzi region on April 6, 2009 and other urgent civil protection provisions". (In Italian), O.P.C.M. n. 3779 del 6 giugno 2009 - "Ulteriori interventi urgenti diretti a fronteggiare gli eventi si-

smici verificatisi nella regione Abruzzo il giorno 6 aprile 2009 e altre disposizioni urgenti di protezione civile", Pubblicata nella Gazzetta Ufficiale n. 132 del 10 giugno 2009".

[17] Annex to O.P.C.M. n. 3790 - "Guidelines for the implementation of the measures referred to the Ordinance of the President of the Council of Ministers n. 3790 July 9, 2009". (In Italian), "Indirizzi per l'esecuzione degli interventi di cui all'Ordinanza del Presidente del Consiglio dei Ministri n. 3790 del 9 luglio 2009".

[18] Ordinance of the President of the Council of Ministers, O.P.C.M. n. 3790, July 9, 2009 - "Urgent interventions to deal with seismic events occurred in the Abruzzo region on April 6, 2009 and other urgent civil protection provisions" (In Italian), O.P.C.M. n. 3790 del 9 luglio - " Ulteriori interventi urgenti diretti a fronteggiare gli eventi sismici verificatisi nella regione Abruzzo il giorno 6 aprile 2009 e altre disposizioni urgenti di protezione civile", Pubblicata nella Gazzetta Ufficiale n. 166 del 20 luglio 2009.

[19] Annex to O.P.C.M. n. 3779 - "Guidelines for the implementation of the measures referred to the Ordinance of the President of the Council of Ministers n. 3779 June 6, 2009". (In Italian), "Indirizzi per l'esecuzione degli interventi di cui all'Ordinanza del Presidente del Consiglio dei Ministri n. 3779 del 6 giugno 2009".

[20] Ordinance of the President of the Council of Ministers, O.P.C.M. n. 3881, June 11, 2010 -"Urgent interventions to deal with seismic events occurred in the Abruzzo region on April 6, 2009 and other urgent civil protection provisions" (In Italian), O.P.C.M. n. 3881 del 11 giugno 2010 - "Ulteriori interventi urgenti diretti a fronteggiare gli eventi sismici verificatisi nella regione Abruzzo il giorno 6 aprile 2009 e altre disposizioni urgenti di protezione civile", Pubblicata nella Gazzetta Ufficiale n. 166.

COMPDYN 2017
6th ECCOMAS Thematic Conference on
Computational Methods in Structural Dynamics and Earthquake Engineering
M. Papadrakakis, M. Fragiadakis (eds.)
Rhodes Island, Greece, 15–17 June 2017

# ASSESSMENT OF THE EFFECTIVENESS OF CABLING SYSTEM CONFIGURATION IN RETROFITTING STEEL-CONCRETE COMPOSITE BUILDINGS

**Georgios S. Papavasileiou**[1]

[1] Department of Mechanical Engineering, School of Technological Applications
University of Applied Sciences of Thessaly
Larissa 41110, Greece
gpapav@teilar.gr, george.papav@gmail.com

**Keywords:** Progressive Collapse, Retrofit, Steel Cables, Post-Tensioned, Steel-Concrete Composite Buildings

**Abstract.** *Steel cables have been extensively used in structural design. Even though their most prominent use is in the design of large span cable stayed or prestressed bridges, a variety of applications in buildings has also been realized. In structural design, cables are mainly used as components of (a) prestressed concrete or post-tensioned steel beams, in order to increase their resistance in bending moment, (b) self-centering systems as a means to restore the connected element to its initial position, or (c) bracing systems as an alternative to the typical steel sections. In the past decade, the use of cables has been proposed as a means of creating ties within a structure, in order to increase its collapse resistance.*

*The mechanical behavior of steel cables and its numerical modeling has been extensively investigated experimentally and numerically [1-16]. However, a concise numerical investigation of their effectiveness in retrofitting steel-concrete composite buildings using three-dimensional models has not been performed. In this work, various cable system configurations are assessed with respect to their effectiveness in retrofitting steel-concrete composite buildings. The selected buildings have been found to be deficient regarding their progressive collapse resistance. Cables are installed (a) in various bays of the building, (b) parallel to its structural elements and (c) under the composite slab in order to improve their performance. The effect of post-tensioning on the efficiency of the steel cables is also evaluated. The results yielded illustrate the effectiveness of each configuration.*

## 1 INTRODUCTION

In structural design against seismic loads, apart from the required ductility, structural elements need to have an adequate stiffness so that the overall fundamental period of the structure is sufficiently limited. In steel and composite buildings, this is either achieved entirely by their columns (moment resisting frames) or using bracings (braced frames). Typical bracing sections used in practice are angular sections (L-shaped) or hollow circular or rectangular sections. L-shaped sections are easier to assemble as they are bolted directly to the connection plates, but are susceptible to buckling under compression or torsion when the horizontal loads on the structure are not parallel to the bracing's longitudinal axis. The buckling resistance of hollow sections is particularly larger, but damage has often been found to concentrate on their connections increasing significantly the cost of repair. This has led researchers to propose and test novel connections that remain damage-free, as specific components yield before all others, so the damage is limited in them [17-21]. Despite their undoubted efficiency, engineers often do not take into consideration their application in conventional buildings mainly due to lack of knowledge. Steel cables are a suitable alternative, as they receive only tension, while they deform in compression or torsion without losing their properties. Hence, they do not transfer strong compressive loads to their connections which would damage them. Therefore, they are a conventional solution with simple application that could be more attractive to engineers in practice, provided that there are guidelines to support the design procedure indicating the appropriate positioning and selection of characteristics.

Progressive collapse is a topic of increased scientific interest [22-52], as it is large scale structural failure caused as a chain reaction by small scale initial damage. It is an unacceptable failure type, not only due to the disproportionate propagation of structural damage, but also because it usually takes place extremely fast, or practically instantly. Available guidelines such as UFC 4-023-03 [53-54] or the GSA guidelines [55] provide the general framework to enhance the robustness of a building in order to increase its progressive collapse resistance. Design of structures against such scenarios is not compulsory in the existing design codes, mainly because of the lack of adequate scientific literature, even though such documents are currently in preparation. Hence, buildings designed according to the latest design codes but without taking into consideration damage scenarios that might cause progressive collapse need to be retrofitted in order to minimize their progressive collapse potential.

Retrofitting a building, whether it is achieved by strengthening individual existing members, such as columns or beams, or by installing additional ones, such as bracings or cables, should be as less invasive as possible. This is required in order to reduce the total cost of the operation as well as its effect on the buildings typical use. Hence, the locations where the operations take place need to be strategically defined in order to maximize the beneficial effect of the retrofit. The selection can performed either manually using specific guidelines that describe the approach with the maximum efficiency, or by automatic optimization algorithms that use a probabilistic approach to select and evaluate different solutions, until an optimum is defined [43-44,56].

## 2 STRUCTURAL MODELING & ANALYSIS

For the purposes of this work, all buildings are simulated using the OpenSEES software [57]. The steel-concrete composite columns are designed as fully encased I-shaped sections. The longitudinal and transversal reinforcement are considered to be the same for all designs: 10mm bars for longitudinal reinforcement and 8mm stirrups spaced 10cm from center to center. The concrete cover is taken 3 cm from the centroid of the longitudinal reinforcement, while an additional 2cm space is considered from the edges of the steel core. Cover concrete

is distinguished from the confined concrete with reduced capacity and ductility. The beams are modeled as purely steel elements and the effect of the composite slab is taken into account indirectly by defining rigid diaphragms on each floor. The cables are modeled using section-defined truss elements. Fiber sections are used for all structural elements, as illustrated in Figure 1, while 10 integration points are defined along their longitudinal axis (local x- axis). The column bases are modeled as moment-restrained.

The 'Concrete01' material is used for both the cover and the confined concrete. The steel beams and the core sections of the composite columns are modeled using the 'Steel01' material, while the 'ReinforcingSteel' material is employed for the longitudinal and transversal bars. The cables installed are modeled using the "ElasticPP" (Elastic – Perfectly Plastic) material with zero capacity in compression. Post-tensioning in the cables is simulated by calculating the initial strain required to shift the stress-strain curve properly. The applicable limit values ensure that the material models employed do not exceed the ultimate strain of the simulated material, as it would affect the accuracy of the modelling.

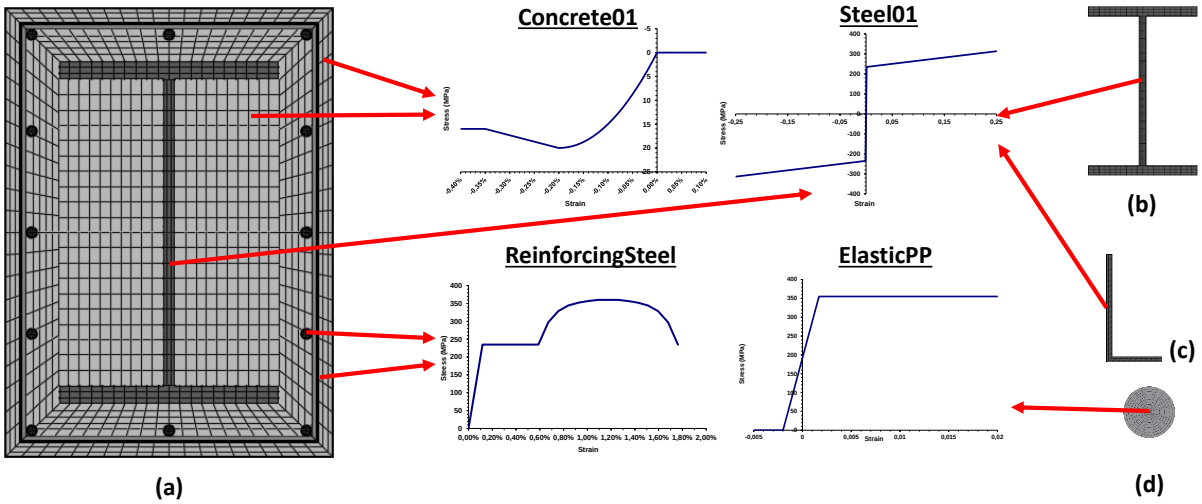


Figure 1: Structural element modeling and discretization into fibers (a) composite column, (b) steel beam, (c) bracing, (d) steel cable

## 3 RETROFIT AGAINST PROGRESSIVE COLLAPSE

### 3.1 Damage scenarios

Loss of load-bearing elements is typically the result of extreme events taking place on the structure, such as strong earthquakes, accidents occurring outside or inside the building, or even malevolent human actions. The effect of extreme natural phenomena such as earthquakes on the structure is difficult to be simulated, as their precise characteristics cannot be accurately determined. However, the prediction of the result of accidents or human actions is more straightforward. In this work, two extreme actions are considered: (a) the collision of a heavy loaded truck that causes the loss of a corner column (DS1), another peripheral column (DS2) or multiple neighboring columns (DS3) and (b) an explosion at the base of the building which results in loss of multiple structural elements on two storeys (DS4). The damaged elements are considered to be unable to provide further support to the building and are removed from the model as illustrated in Figures 2 and 3 In DS4 not only columns are damaged, but beams as well, since the blast has a spherical range of effect. The event is assumed to take

place instantly and the loads from the failing members are transferred to the neighboring elements which are currently undamaged.

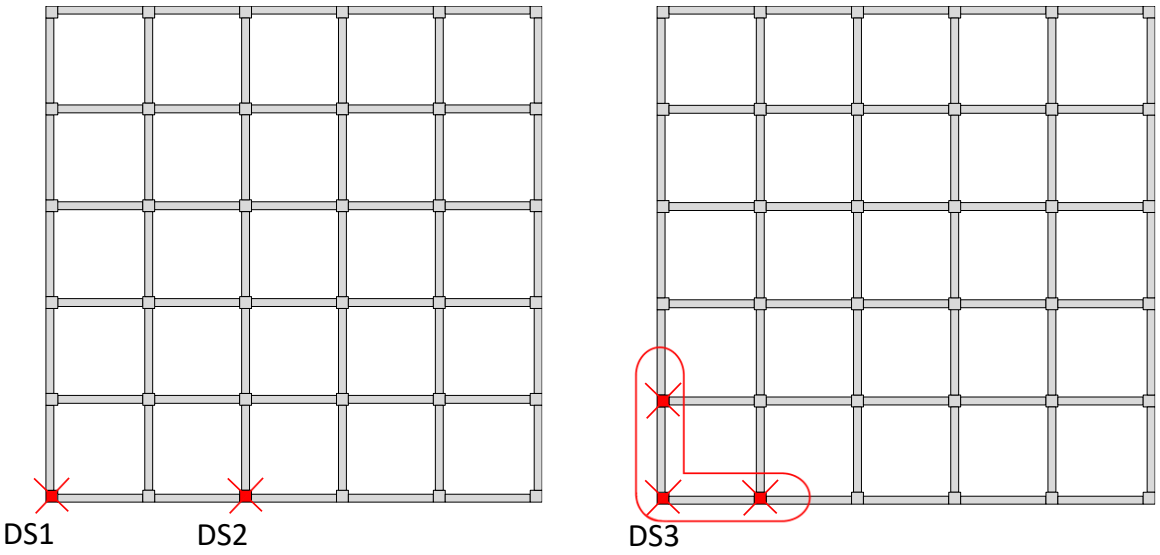


Figure 2: Simulated damage scenarios (a) single-column, (b) multi-column.

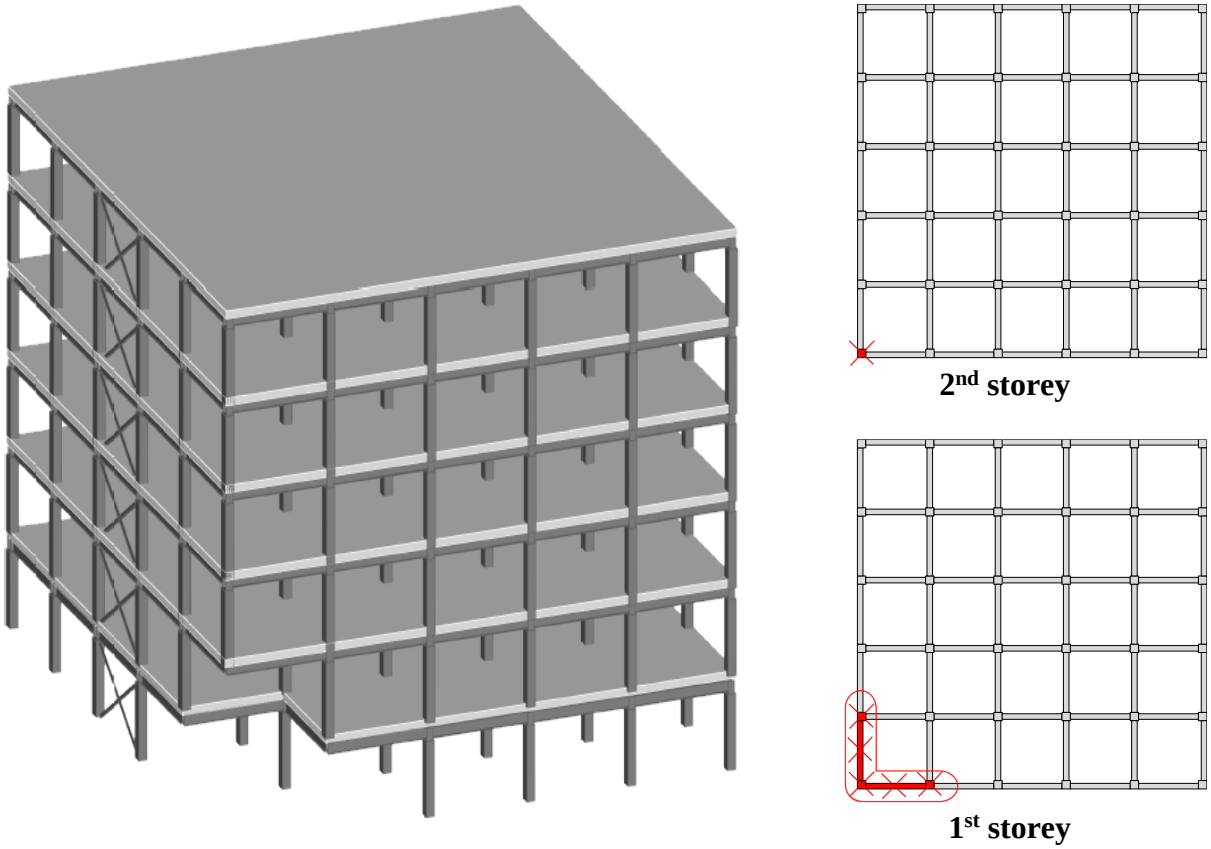


Figure 3: Simulated three-dimensional damage scenario (DS4)

### 3.2 Design against earthquake and assessment of progressive collapse resistance

The buildings considered in this work need to possess particular characteristics appropriately selected:

(a) they should not be oversimplified or particularly complex, as this might affect the final results,

(b) they should not contain extremely large number of elements, as it would delay the analyses performed without additional benefit to the investigation,

(c) the investigation of various parameters which might affect the efficiency of the retrofit scheme should be possible in each building.

The selected buildings are designed against earthquake according to the provisions of EN 1998 [58]. Steel and composite members are designed according to EN 1993-1-1 [59] and EN1994-1-1 [60] respectively. All buildings have six storeys and consist of five by five bays. The beam span from column center to column center is the same in both horizontal directions. All columns have the same orientation: their major axis is parallel to the global y-axis, so that their flanges are vertical to the global x-direction. Beam-column joints in x-direction are considered to be fixed, forming this way moment resisting frames. Beams on y-direction are simply supported. The required stiffness is provided by bracings installed in the middle bays of both external faces parallel to the y-direction. Five beam spans are considered from 5m to 9m with an increment of 1m. The designs defined are presented in Table 1.

The performance of each building under the considered damage scenarios is assessed according to the provisions of UFC 4-023-03 [53-54]. The maximum plastic rotation at the end of the undamaged beams is used as an indicator for the progressive collapse resistance of the buildings. The results are presented in Table 1.

| Beam span (m) | Columns | | | Beams | Maximum ratio of deflection over span | | | |
|---|---|---|---|---|---|---|---|---|
| | 1st-2nd | 3rd-4th | 5th-6th | All storeys | DS1 | DS2 | DS3 | DS4 |
| 5m | HE280B | HE260B | HE180B | IPE270 | 12,35% | > 50% | > 50% | > 50% |
| 6m | HE300B | HE280B | HE220B | IPE330 | > 50% | > 50% | > 50% | > 50% |
| 7m | HE360B | HE280B | HE240B | IPE400 | > 50% | > 50% | > 50% | > 50% |
| 8m | HE550B | HE320B | HE260B | IPE450 | > 50% | > 50% | > 50% | > 50% |
| 9m | HE600B | HE320B | HE280B | IPE550 | > 50% | > 50% | > 50% | > 50% |

Table 1: Buildings designed only against earthquake

A recorded ratio of deflection over beam span (vertical drift) larger than 20% indicates high potential for collapse under the simulated damage scenario. Even though the modeling applied in this work is suitable for capturing large deformations, values larger than 50% are particularly large and are considered as strong indication for collapse.

### 3.3 Retrofit of the deficient buildings

Cables are installed as a means to retrofit the deficient buildings over the bay where the damage occurs. In order to exclude ineffective topologies, one end of the cable needs to be over the top node of a removed column. This end does not necessarily need to be the particular node, but should be indirectly connected, e.g. through the undamaged columns, so that a proportion of the failed column's load can be received by the cable. The location of the second end of the cable may vary within a single bay depending on the intended function:

- In x- and y-direction parallel to the undamaged beams.

- In z-direction parallel to existing columns.
- In x-z and y-z planes installed as bracings.
- In x-y plane installed as horizontal bracings below the slab.

In DS3 and DS4 where more than one bay are affected, all relative locations are taken into consideration. All cables can also be post-tensioned. PT cables in x- and y-direction act as tendons which compress the steel beams so that their deflection is reduced. Selected results are illustrated in Figures 4 to 7. In order to enable the comparison between values referring to different buildings, the deflection ratio (*i.e.* deflection with retrofit over deflection without retrofit) is used in Figures 4 to 6 and the vertical drift (*i.e.* deflection over beam span) in Figure 7. It should be noted that Figures 4 and 5 allow the visualization the effect of the cable system configuration to the modeled buildings. Comparison between the deflection ratios for two buildings in the same figure is not possible.

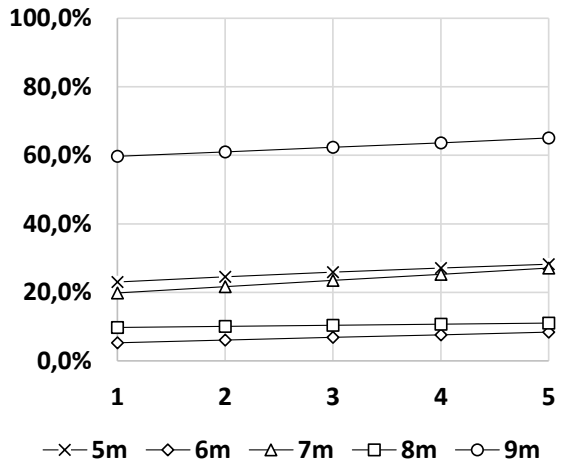


Figure 4: Deflection ratio vs. location of cables in y-z plane (DS1)

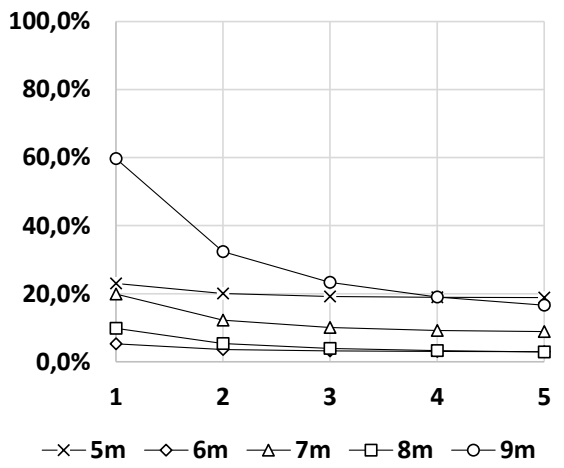


Figure 5: Deflection ratio vs. number of retrofitted bays/storeys – cables in y-z plane (DS1)

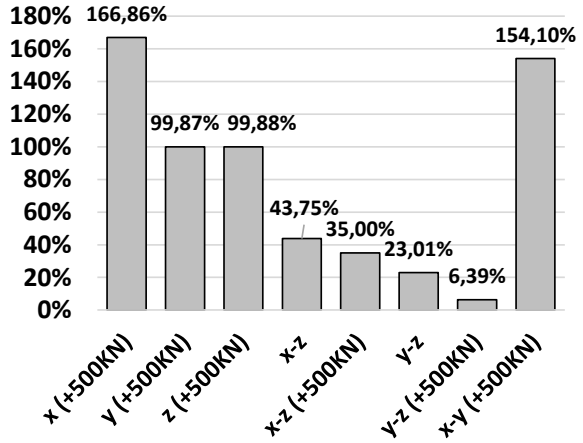


Figure 6: Deflection ratio vs. cable direction (value in parenthesis: post-tensioning applied)

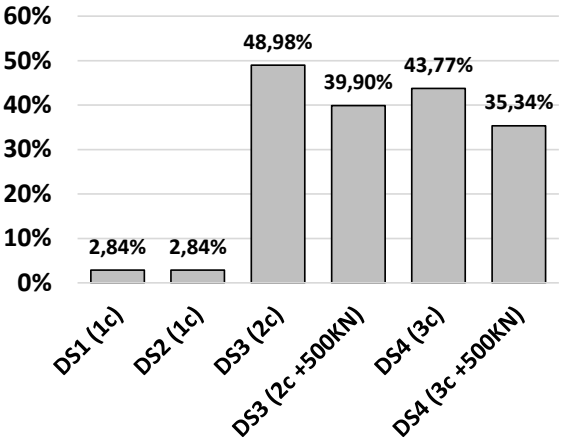


Figure 7: Vertical drift for beam span 5m (values in parenthesis: number of cables + post-tensioning)

The effectiveness of a configuration is related to the damage scenario modeled. Damage scenarios that affect more structural elements require increased number of cables. Post-tensioning has a beneficial effect in all simulated damage scenarios when cables are installed in x-z and y-z planes which is proportional to the applied force. It is also remarkable that the

vertical drift recorded for DS1 and DS2 (illustrated in Figure 7) when one cable is installed is the same. The load applied on the top of the failed node is twice as much as the one in DS1. However, there are twice as many beams connected to the column, while the cable is installed in the y-z plane, so all contributing elements are symmetrically placed.

Installation of cable in the y-z plane is more advantageous than in the x-z plane. This is due to the beam-column connections modeled. In x-z plane the elements form a MRF which possesses adequate resistance in order to redistribute the loads from the failed column to the neighboring beams on all storeys above it and so limit the deformations. In the y-z plane this does not apply, because all connections are modeled as hinges. The frames on this plane have no collapse resistance, as their stability relies entirely on the columns, with the exception of the middle bay where bracings are installed. Failure of a column results in free movement of the bays above and which would results in partial collapse of the frame if there was no contribution of the beams in the x direction. Installation of a diagonal element in tension (*i.e.* the cables in this work) forms a truss-type structure which substitutes the missing column and restores the stability of the frame. Moreover, when a single damage scenario is considered, solutions with cables of increased yielding stress are favored, while for multiple damage scenarios this is a disadvantage, as the solution depends mainly on the overall distribution of the cables.

Cables installed in x and y directions and the x-y plane seem to offer no additional assistance in the limitation of the vertical deflections, as the end of the beam over the damaged column also moves towards the neighboring columns, so the distance between the two ends of the cable reduces. Moreover, when post-tensioning force is applied its effect is either minor or negative. It is because of the additional moment applied on the beams due to the large deflection and the post-tensioning force, which causes extra deformation to the beam.

Of particular interest is the effect of cables installed in z direction. The purpose of such an addition is be to aid the columns in receiving the load and transferring it to the beams. When cables are not post-tensioned, the deflection recorded is not altered. This is a strong indicator that the column capacity in tension is particularly larger than it is required, so an additional steel area as small as that of a cable makes no substantial difference. When post-tensioning is applied, the force is mainly received by the column which is in compression. Thanks to the change in its internal forces, the concrete contributes as well to its stiffness, which would be advantageous when designing against earthquake, but its contribution to the building's progressive collapse resistance is negligible. It is evident that in the damage scenarios typically anticipated, the capacity of the columns suffices for the role they play in the alternate path, so the retrofit scheme selected should focus on enhancing the capacity of the beams or receiving a proportion of the extra loads.

The location of the cable seems to affect the deflection of the beams connected to the top of the failed column as well, regardless of the plane they are installed in (x-z or y-z). This is related to the alternate load path developed. When cables are connected directly to the top of the damaged column, a large proportion of the loads is transferred through them to the structural elements of the undamaged bays. If cables are installed one storey above, they are still included in the load path, but at the same time, as the loads are transferred through the column, an increased proportion is received by the additional beams below the location of the cable. Hence, as the distance of the cables from the top of the damaged column increases, their contribution in the alternate load path is reduced. Nevertheless, the reduction in the effectiveness is minor compared to their beneficial effect, so a retrofit scheme based on suspension of the loads on the damaged bay through the columns to the cables could be particularly advantageous when multiple scenarios are taken into account.

An increased number of cables results in a reduction to the deflection recorded. However, the reduction is not proportional as the contribution of the additional cables is related to their

location compared to the damaged column, as indicated before. Nevertheless, cables installed in multiple storeys can capture potential damage which occurs on storeys above the one considered (e.g. a gas explosion such as the one that caused the collapse of the Ronan Point building [61]).

## 4 APPLICATION ON STRUCTURAL OPTIMIZATION

An application that can take advantage of the results of this work is the determination of suitable penalty functions in structural optimization. Structural design optimization is a topic of particular interest, as it allows engineers to define solutions with minimum cost in problems with particularly large number of variables, where manual seek of the solution is impractical. Such problems include the sizing of individual members (sizing optimization problems), the selection of the most efficient placing of structural members (topology optimization) or a combination of both in order to achieve a single or multiple goals at the same time (multi-objective optimization). The existing literature is rich of papers proposing and applying optimization algorithms in structural problems [62-78].

In this section, a mixed sizing-topology discrete optimization problem is defined. A building of those presented in Table 1 (*i.e.* the 5m building) needs to be retrofitted in order to be able to sustain the aforementioned damage scenarios DS1 and DS3 without its beams exceeding the deflection limit defined for low requirements in UFC 4-023-03 [53-54], *i.e.* 20% of the total beam span. Cables can be installed in all bays of the building, but they may not change its internal plan configuration (they cannot be installed in planes x-z and y-z internally). Should each cable be designed independently, this would result in 1230 variables with various characteristics. In order to limit this number to a more manageable one, (a) a maximum number of 20 cables can be installed anywhere in the building, (b) their total area may differ using standard sizes and (c) cables should be installed symmetrically. Taking all aforementioned into consideration, the number of independent variables reduces to 10.

Two optimizations were performed: one allowing the free selection of each alternative and one where solutions with configurations that were found in the previous section to be less effective than their counterparts would be properly penalized. They can be summarized as follows:

- Cables on higher bays are favored by reducing the cable's cost in the objective function. The purpose of this function is to take into account that they create an alternate path that is effective against damage scenarios not considered in the optimization, which is a desirable property, even though it is not required in the particular problem.
- Cables installed in bays that were found to be ineffective in the previous section, such as the middle bays on each side are penalized by increasing the cable's cost in the objective function.
- Cables connecting to at least one common node are penalized by increasing the cost of the cable with the smaller cross-sectional area, in order to avoid solutions that are fit only for the investigated damage scenarios. In case of cables with the same size, one of them is randomly selected. If two cables are installed in the same location, *i.e.* both their ends coincide, the penalty function receives its maximum value which is 20 times the weight of a cable designed using the largest size available.
- Cables installed in a direction that is expected to create compression to the cable are penalized by multiplying their cost by a large value (here it is 10). These solutions are not totally discarded, as they might be effective against damage scenarios not considered or form an alternate path not anticipated, so that they are finally in tension.

- Cables installed in a direction that occupies an internal bay are replaced by random selection of another configuration. This is a problem-specified restriction.

The optimization procedure described in [70] was modified appropriately for the purposes of this work. The results are illustrated in Figure 8.

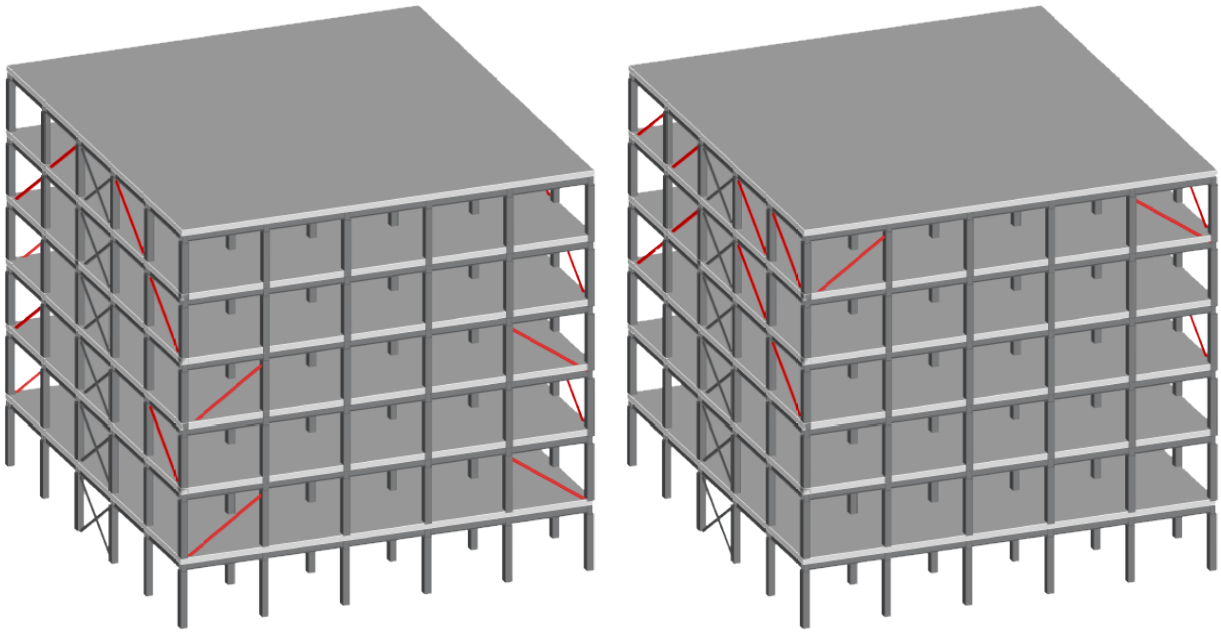

**(a)** **(b)**

Figure 8: Optimized retrofit (a) without penalty functions (OPT1) and (b) using penalty functions (OPT2). The installed cables are illustrated with thick red lines.

Maximum recorded vertical drift for the optimized designs is 19.46% for OPT1 and 19.80% for OPT2. Both values are indicative of an optimum reached, as they are close to the constraint applied (20%) and further reduction of the total cost could potentially lead to exceeding vertical drifts.

In both solutions, no cables are installed in the middle bays. Their contribution to the collapse resistance of the buildings is negligible for the considered damage scenarios, so this penalty function can be omitted, as the solution is expected to have increased cost compared to others evaluated by the optimization algorithm. However, it has been noticed that, due to the probabilistic selection of candidate solutions, unless it taken into consideration there is always a possibility that this might lead to the selection of a local minimum.

Cables in OPT1 are installed in various storeys. Cables are installed in the lower storeys where their effectiveness against the simulated damage scenarios is increased. Two out of five cables available for each quarter of the building are installed in the x-z plane that is not as effective as the y-z plane. There is one cable installed in each storey above the location of the damage. The advantage of this configuration is that it could be effective for simultaneous loss of two columns, e.g. in the 1$^{st}$ and 3$^{rd}$ storey, while in OPT2 there is no cable to offer additional collapse resistance.

In OPT2 there is a concentration of cables on the top storeys, as intended. One out of five cables is installed in the x-z plane, even though this is not preferred. Further investigation indicates that the particular cable's contribution is not related with DS1, but with DS3. It can be observed that in the top storey is formed a truss-type mechanism. The remaining two cables are in the same direction and connect at one end; a similar configuration is formed in OPT1 as

well. This creates a tie from the corner of the building to the middle bay on this side that has increased stiffness due to the bracings installed.

Comparison between the two designs illustrates the effect of the penalty functions used in the definition of the final design. It is remarkable that, while for OPT1 the configuration seems to have an inherit randomness, in OPT2 a pattern starts to develop: a truss belt is constructed on the top storey and a diagonal tie which reaches up to the enhanced zone created at the top of the building. Nevertheless, it should be noted that further investigation is required in order to propose an optimization framework for the retrofit of composite buildings against progressive collapse.

## 5 CONCLUDING REMARKS

- The consequences of damage scenarios involving a single element or neighboring elements can be mitigated by retrofit schemes that are focused on the area above the affected bay. However, when multiple scenarios are considered, a more generalized solution needs to be sought.
- The number of bays affected by the retrofit operation can be limited using cables of increased load bearing capacity. Still, when the overall robustness of the building needs to be enhanced, this might not be feasible.
- Installation of cables on the top storeys of the buildings renders them less efficient than installation directly above the damaged columns, but it can also capture damage on the columns above the bay where the failure is expected to occur. So, considering its overall effect, creating an alternate load path that utilizes the existing structural elements is more advantageous than focusing on the most expected damage scenarios.
- In problems with a large number of variables, use of an automatic optimization algorithm can provide solutions with reduced total cost than manual techniques. A suitable use of the applied penalty functions reduces the possibility of yielding configurations that are local minima. The calibration of the penalty functions should be performed for each problem independently based on the intended outcome.

## REFERENCES

[1] Jiang, W. G. (2012). A concise finite element model for pure bending analysis of simple wire strand. *International Journal of Mechanical Sciences*,*54*(1), 69-73.

[2] Jiang, W. G., Henshall, J. L., & Walton, J. M. (2000). A concise finite element model for three-layered straight wire rope strand. *International Journal of Mechanical Sciences*, *42*(1), 63-86.

[3] Nawrocki, A., & Labrosse, M. (2000). A finite element model for simple straight wire rope strands. *Computers & Structures*, *77*(4), 345-359.

[4] Serra, M., Shahbazian, A., da Silva, L. S., Marques, L., Rebelo, C., & da Silva Vellasco, P. C. G. (2015). A full scale experimental study of prestressed stayed columns. *Engineering Structures*, *100*, 490-510.

[5] Foti, F., & Martinelli, L. (2016). An analytical approach to model the hysteretic bending behavior of spiral strands. *Applied Mathematical Modelling*, *40*(13), 6451-6467.

[6] Usabiaga, H., & Pagalday, J. M. (2008). Analytical procedure for modelling recursively and wire by wire stranded ropes subjected to traction and torsion loads. *International Journal of Solids and Structures*, *45*(21), 5503-5520.

[7] Stanova, E., Fedorko, G., Fabian, M., & Kmet, S. (2011). Computer modelling of wire strands and ropes Part I: Theory and computer implementation. *Advances in Engineering Software*, *42*(6), 305-315.

[8] Jun, M. A., Ge, S. R., & Zhang, D. K. (2008). Distribution of wire deformation within strands of wire ropes. *Journal of China University of Mining and Technology*, *18*(3), 475-478.

[9] Kmet, S., Stanova, E., Fedorko, G., Fabian, M., & Brodniansky, J. (2013). Experimental investigation and finite element analysis of a four-layered spiral strand bent over a curved support. *Engineering Structures*, *57*, 475-483.

[10] Suh, J. I., & Chang, S. P. (2000). Experimental study on fatigue behaviour of wire ropes. *International Journal of Fatigue*, *22*(4), 339-347.

[11] Giglio, M., & Manes, A. (2005). Life prediction of a wire rope subjected to axial and bending loads. *Engineering Failure Analysis*, *12*(4), 549-568.

[12] Forni, D., Chiaia, B., & Cadoni, E. (2016). Strain rate behaviour in tension of S355 steel: Base for progressive collapse analysis. *Engineering Structures*,*119*, 164-173.

[13] Martins, J. P., Shahbazian, A., da Silva, L. S., Rebelo, C., & Simões, R. (2016). Structural behaviour of prestressed stayed columns with single and double cross-arms using normal and high strength steel. *Archives of Civil and Mechanical Engineering*, *16*(4), 618-633.

[14] Astaneh-Asl, A., Madsen, E. A., Noble, C., Jung, R., McCallen, D. B., Hoehler, M. S., ... & Hwa, R. (2001). Use of catenary cables to prevent progressive collapse of buildings. *Report No.: UCB/CEE-STEEL-2001/02*.

[15] Ghoreishi, S. R., Messager, T., Cartraud, P., & Davies, P. (2007). Validity and limitations of linear analytical models for steel wire strands under axial loading, using a 3D FE model. *International Journal of Mechanical Sciences*,*49*(11), 1251-1261.

[16] Foti, F., & Martinelli, L. (2016). Mechanical modeling of metallic strands subjected to tension, torsion and bending. *International Journal of Solids and Structures*, *91*, 1-17.

[17] Wolski, M., Ricles, J. M., & Sause, R. (2009). Experimental study of a self-centering beam–column connection with bottom flange friction device. *Journal of Structural Engineering*, *135*(5), 479-488.

[18] Speicher, M. S., DesRoches, R., & Leon, R. T. (2011). Experimental results of a NiTi shape memory alloy (SMA)-based recentering beam-column connection. *Engineering structures*, *33*(9), 2448-2457.

[19] Latour, M., Piluso, V., & Rizzano, G. (2015). Free from damage beam-to-column joints: testing and design of DST connections with friction pads. *Engineering Structures*, *85*, 219-233.

[20] Roke, D., Sause, R., Ricles, J. M., & Gonner, N. (2009). Design concepts for damage-free seismic-resistant self-centering steel concentrically braced frames. In *Structures Congress 2009: Don't Mess with Structural Engineers: Expanding Our Role* (pp. 1-10).

[21] Piluso, V., Montuori, R., & Troisi, M. (2014). Innovative structural details in MR-frames for free from damage structures. *Mechanics Research Communications, 58*, 146-156.

[22] Crawford, J. E. (2002). Retrofit methods to mitigate progressive collapse. In *The Multi-hazard Mitigation Council of the National Institute of Building Sciences, Report on the July 2002 National Workshop and Recommendations for Future Effort*.

[23] Galai K., El-Sawy T., "Effect of retrofit strategies on mitigating progressive collapse of steel frame structures", *Journal of Constructional Steel Research*, 2010

[24] Kwasniewski, L. (2010). Nonlinear dynamic simulations of progressive collapse for a multistory building. *Engineering Structures*, *32*(5), 1223-1235.

[25] Astaneh-Asl, A. (2003). Progressive collapse prevention in new and existing buildings. In *Proc., 9th Arab Structural Engineering Conf., Abu Dhabi, UAE, Nov*.

[26] Ellingwood, B. (2006). Mitigating risk from abnormal loads and progressive collapse. *Journal of Performance of Constructed Facilities*, *20* (4), 315-323.

[27] Ellingwood, B., & Dusenberry, D. (2005). Building design for abnormal loads and progressive collapse. *Computer-Aided Civil and Infrustructure Engineering*, *20*, 194-205.

[28] Faber, M. (2011). Robustness of structures – Final report of COST action TU0601. *COST (European Cooperation in Science and Technology)* .

[29] Izzuddin, B., Vlassis, A., Elghazouli, A., & Nethercot, D. (2008). Progressive collapse of multi-storey buildings due to sudden column loss - Part I: Simpified assessment framework. *Engineering Structures*, *30*, 1308-1318.

[30] Jahromi, H. Z., Vlassis, A. G., & Izzuddin, B. A. (2013). Modelling approaches for robustness assessment of multi-storey steel-composite buildings. *Engineering Structures, 51*, 278-294.

[31] Khandelwal, K., & El-Tawil, S. (2011). Pushdown resistance as a measure of robustness in progressive collapse analysis. *Engineering Structures*, *33* (9), 2653-2661.

[32] Khandelwal, K., El-Tawil, S., & Sadek, F. (2008). Progressive collapse analysis of seismically designed steel braced frames. *Journal of Constructional Steel Research, 65* (3), 699-708.

[33] Khandelwal, K., El-Tawil, S., & Sadek, F. (2008). Progressive collapse analysis of seismically designed steel braced frames. *Journal of Constructional Steel Research, 65* (3), 699-708.

[34] Kim, T., & Kim, J. P. (2009). Investigation of progressive collapse-resisting capability of steel moment frames using push-down analysis. *ASCE Journal of Performance of Constructed Facilities, 23* (5), 327-335.

[35] Kim, T., Kim, U., & Kim, J. (2010). Collapse Resistance of Unreinforced Steel Moment Connections. *The Structural Design of Tall and SpecialBuildings*, *21* (10), 724-735.

[36] Li, G.-q., Wang, K.-q., Liu, Y.-s., & Chen, S.-w. (2012). Catenary action of restrained steel beam against progressive collapse of. *J. Cent. SouthUniv., 19*, 537-546.

[37] Liu, M. (2013). A new dynamic increase factor for nonlinear static alternate path analysis of building frames against progressive collapse. *48*, 666-673.

[38] Liu, M. (2011). Progressive Collapse Design of Seismic Steel Frames Using Structural Optimization. *Journal of Constructional Steel Research*, 322-332.

[39] Liu, M. (2013). A new dynamic increase factor for nonlinear static alternate path analysis of building frames against progressive collapse. *48*, 666-673.

[40] Liu, M. (2011). Progressive Collapse Design of Seismic Steel Frames Using Structural Optimization. *Journal of Constructional Steel Research*, 322-332.

[41] Naji, A., & Irani, F. (2012). Progressive collapse analysis of steel frames: Simplified procedure and explicit expression for dynamic increase factor. *International Journal of Steel Structures, 12* (4), 537-549.

[42] Papavasileiou, G.S. and Charmpis, D.C. (2012). Design optimization of steel-concrete composite structures with requirements on progressive collapse resistance – In *Proceedings of the 15th World Conference on Earthquake Engineering.*

[43] Papavasileiou, G.S. and Charmpis, D.C. (2014). Enhancing the Progressive Collapse Resistance of Seismically Designed Steel-Concrete Composite Buildings, In *Proceedings of the 8th Hellenic National Conference on Steel Structures.*

[44] Papavasileiou G.S. and Charmpis D.C. (2015). Optimized retrofit of seismically designed buildings to withstand progressive collapse – In *Proceedings of the 5th International Conference on Computational Methods in Structural Dynamics and Earthquake Engineering.*

[45] Quiel, S. E., & Marjanishvili, S. M. (2012). Fire resistance of a damaged steel building frame designed to resist progressive collapse. *Journal of Performance of Constructed Facilities, 26*, 402-409.

[46] Song, B. I., & Sezen, H. (2013). Experimental and analytical progressive collapse assessment of a steel frame building. *Engineering Structures, 56*, 664-672.

[47] Stoddart, E. P., Byfield, M. P., Davison, J. B., & Tyas, A. (2012). Strain rate dependet component based connection modelling for use in non-linear dynamic progressive collapse analysis. *Journal of Engineering Structures*.

[48] Szyniszewski, S., & Krauthhammer, T. (2012). Energy flow in progressive collapse of steel framed buildings. *Engineering Structures, 42*, 142-153.

[49] Valipour, H. R., & Bradford, M. (2012). An efficient compound-element for potential progressive collapse analysis of steel frames with semi-rigid connections. *Finite Elements in Analysis and Desgin, 60*, 35-48.

[50] Vlassis, A. G., Izzuddin, B. A., Elghazouli, A. Y., & Nethercot, D. A. (2009). Progressive collapse of multi-storey buildings due to failed floor impact. *Engineering Structures, 31*, 1522-1534.

[51] Vlassis, A. G., Izzuddin, B. A., Elghazouli, A. Y., & Nethercot, D. A. (2008). Progressive collapse of multi-storey buildings due to sudden column loss - Part II: Application. *Journal of Engineeirng Structures, 30*, 1424-1438.

[52] Wang, T. C., Li, Z. P., & Zhao, H. L. (2013). Progressive Collapse Resistance of RC Structures with Tension Cables. In *Applied Mechanics and Materials* (Vol. 405, pp. 835-840). Trans Tech Publications.

[53] DoD, U. F. C. (2005). UFC 4-023-03. *Design of Building to Resist Progressive Collapse," Unified Facility Criteria, United States Department of Defense, Washington, DC.*

[54] DoD, U. F. C. (2010). UFC 4-023-03. *Design of Building to Resist Progressive Collapse," Unified Facility Criteria, United States Department of Defense, Washington, DC.*

[55] G.S.A. (2004). '*Progressive Collapse Design Guidelines Applied to Concrete Moment-Resisting Frame Buildings',* General Services Administration, Nashville, Tennessee.

[56] Papavasileiou, G. S., Charmpis, D. C., & Lagaros, N. D. (2011). Optimized seismic retrofit of steelconcrete composite frames. In *Proceedings of the 3rd ECCOMAS Thematic Conference on Computational Methods in Structural Dynamics and Earthquake Engineering* (pp. 4573-4586).

[57] Mazzoni, S., McKenna, F., Scott, M. H., & Fenves, G. L. (2006). OpenSees command language manual. *Pacific Earthquake Engineering Research (PEER) Center*.

[58] Comité Européen de Normalisation (CEN), "Eurocode 8: Design provisions for earthquake resistance of structures (ENV 1998)' Part 1-1/1994 General rules - Seismic action and general requirements for structures.", *CEN Publications*, Brussels, Belgium, 2003

[59] Comité Européen de Normalisation (CEN), "Eurocode 3: Design of steel structures (ENV 1993)' Part 1-1/1992 General rules and rules for buildings", *CEN Publications*, Brussels, Belgium, 2003

[60] Comité Européen de Normalisation (CEN), "Eurocode 4: Design of composite structures (ENV 1994)' Part 1-1/1992 General rules and rules for buildings", *CEN Publications*, Brussels, Belgium, 2003

[61] Pearson, C., & Delatte, N. (2005). Ronan point apartment tower collapse and its effect on building codes. *Journal of Performance of Constructed Facilities*, *19*(2), 172-177.

[62] Liu M, Burns SA, Wen YK. Optimal seismic design of steel frame buildings based on life cycle cost considerations. Earthquake Engng Struct Dyn 2003; 32:1313–1332.

[63] Fragiadakis M, Lagaros ND, Papadrakakis M. Performance-based multiobjective optimum design of steel structures considering life-cycle cost. Struct Multidisc Optim 2006; 32: 1–11.

[64] Greco R, Marano GC. Optimal constrained design of steel structures by differential evolutionary algorithms. Int J Optim Civil Eng 2011; 3:449-474.

[65] Choi SW, Park HS. Multi-objective seismic design method for ensuring beam-hinging mechanism in steel frames. J Constr Steel Res 2012; 74: 17–25.

[66] Li G, Jiang Y, Yang D. Modified-modal-pushover-based seismic optimum design for steel structures considering life-cycle cost. Struct Multidisc Optim 2012; 45: 861–874.

[67] Gong Y, Xue Y, Xu L. Optimal capacity design of eccentrically braced steel frameworks using nonlinear response history analysis. Eng Struct 2013; 48: 28–36.

[68] Maheri MR, Narimani MM. An enhanced harmony search algorithm for optimum design of side sway steel frames. Comput Struct 2014; 136: 78–89.

[69] Kim H, Adeli H. Discrete cost optimization of composite floors using a floating-point genetic algorithm. Eng Opt 2001; 33: 485-501.

[70] Papavasileiou, G. S., & Charmpis, D. C. (2016). Seismic design optimization of multi–storey steel–concrete composite buildings. *Computers & Structures, 170*, 49-61.

[71] Kaveh A, Abadi ASM. Cost optimization of a composite floor system using an improved harmony search algorithm. J Constr Steel Res 2010; 66: 664-669.

[72] Poitras G, Lefrancois G, Cormier G. Optimization of steel floor systems using particle swarm optimization. J Constr Steel Res 2011; 67: 1225-1231.

[73] Musa YI, Diaz MA. Design optimization of composite steel box girder in flexure. ASCE Pract Periodical Struct Des Constr 2007; 12(3): 146-152.

[74] Senouci AB, Al-Ansari MS. Cost optimization of composite beams using genetic algorithms. Adv Eng Softw 2009; 40: 1112-1118.

[75] Luo Y, Li A, Kang Z. Reliability-based design optimization of adhesive bonded steel–concrete composite beams with probabilistic and non-probabilistic uncertainties. Eng Struct 2011; 33: 2110-2119.

[76] Luo Y, Wang MY, Zhou M, Deng Z. Optimal topology design of steel-concrete composite structures under stiffness and strength constraints. Comput Struct 2012; 112-113: 433–444.

[77] Chan CM. Optimal lateral stiffness design of tall buildings of mixed steel and concrete construction. J Struct Design Tall Build 2001; 10: 155-177.

[78] Cheng L, Chan CM. Optimal lateral stiffness design of composite steel and concrete tall frameworks. Eng Struct 2009; 31: 523-533.

COMPDYN 2017
6th ECCOMAS Thematic Conference on
Computational Methods in Structural Dynamics and Earthquake Engineering
M. Papadrakakis, M. Fragiadakis (eds.)
Rhodes Island, Greece, 15–17 June 2017

# VALIDATION OF REFINED NUMERICAL MODELING FOR EXISTING RC BUILDINGS: COMPARISON BETWEEN PREDICTED AND OBSERVED EARTHQUAKE DAMAGE

**C. Del Vecchio[1], M. Di Ludovico[2], S. Pampanin[3] and A. Prota[2]**

[1] University of Napoli "Federico II"
Department of Structures for Engineering and Architecture, via Claudio 21, 80125 Napoli, Italy
e-mail: ciro.delvecchio@unina.it

[2] University of Napoli "Federico II"
Department of Structures for Engineering and Architecture, via Claudio 21, 80125 Napoli, Italy
e-mail: diludovi@unina.it, aprota@unina.it

[3] University of Rome "La Sapienza"
Department of Structural and Geotechnical Engineering, Via Eudossiana, 18, 00184 Roma, Italy
e-mail: stefano.pampanin@uniroma1.it
University of Canterbury
Department of Civil and Natural Resources Engineering, Christchurch, New Zealand
e-mail: stefano.pampanin@canterbury.ac.nz

**Keywords:** Numerical modeling, earthquake damage, non-linear behavior, RC structures, infill wall, beam-column joints.

**Abstract.** *A reliable estimation of the seismic performances of existing reinforced concrete building is of paramount importance to design proper retrofit solutions. Number of refined numerical models are nowadays available, nevertheless predicting the seismic performance and the earthquake damage at component level is still a challenging task. Marked nonlinear phenomena, strength and stiffness degradation and pinching affect the cyclic behavior of structural members designed with reinforcement details non-conforming with current seismic codes. This, along with the interaction between the bare frame and the stiff infills, makes complex the reproduction of the global structural behavior. This study focuses on a refined modeling procedure properly developed for existing RC frames. The modeling assumptions, the hysteresis assigned to the different building components and the modeling strategy accounting for the infill contribution are presented and discussed. The model validation at component and building level related to case-study buildings damaged by the L'Aquila (2009) earthquake is presented. A component-by-component comparison between predicted and observed damage is shown. The proposed numerical model and the in-depth discussion on the earthquake damage are useful to identify the building weaknesses, estimate the repair costs and design proper retrofit solutions.*

## 1 INTRODUCTION

Recent seismic events showed the significant damage to existing RC buildings and the amount of economic and social resources involved in the reconstruction process [1–3]. Scientific studies and damage observations in the aftermath of the L'Aquila 2009 earthquake [4,5] outlined that infill wall and partitions are the most damaged nonstructural components (see Figure 1a). This is because of the interaction with the surrounding RC frames and to the high stiffness of hollow clay brick systems typical of the Mediterranean. The repair costs concerning the repair/substitution of damaged infill, finishes and services (i.e. plumbing and electrical system, commonly incorporated in the infill or partitions) represent the majority of the total building repair cost. Thus, reliable earthquake loss assessment procedures necessarily have to account for the contribution and the damage of infill/partition walls [6,7]. Furthermore, the presence of infill walls significantly increase the building stiffness increasing the seismic demand transmitted to the structural members and the occurrence of shear failures (see Figure 1b,c). This makes the modeling of such components of paramount importance to have reliable estimation of the earthquake damage, of the seismic capacity and to design proper retrofit solutions.



(a) (b) (c)

Figure 1: L'Aquila 2009 earthquake damage: severe damage to exterior infill (a); cracking of a corner beam-column joint (b); damage to stairs and short columns (c).

The advanced numerical models proposed in the recent years improved accuracy in reproducing the nonlinear behavior of RC structural systems [8,9] and the contribution of infill walls. New mechanical models and solution algorithms have been developed, and a great effort has been made to combine them with the state-of-the-art knowledge in refined tools (e.g., [10,11]) suitable for the use in the practical applications. However, they requires continuous calibrations and validations both at subassembly and at system level. Recently, several lumped plasticity models have been proposed to reproduce the nonlinear behavior of poorly detailed beam-column joints [12] and infill walls [13]. They were widely validated on experimental tests on subassemblies or entire structural systems [14,15].

This paper deals with the application of a refined modeling strategy in a nonlinear FEM environment to case study RC buildings experiencing significant damage to non-structural components. The building characteristic, the modeling procedures and the earthquake damage are described in detail. Particular attention is reserved to the damage quantification and modeling of infills and RC joints. A component-by-component comparison between predicted and observed damage is shown. A useful correspondence between engineering demand parameters (EDPs), available damage states classifications and damage scale commonly adopted in the inspections in the immediate aftermath of the earthquakes is proposed.

## 2 CASE STUDY BUILDINGS

The reconstruction process after L'Aquila earthquake (2009) has been a unique occasion to collect reconstruction costs data at large scale. A detailed description of the reconstruction policy, the regulation and an overview of the data related to the reconstruction of 5,775 residential buildings damaged by the L'Aquila earthquake is reported in Di Ludovico et al. [2,3]. To obtain the public founding for the reconstruction of the damaged buildings, documentation was required to illustrate the damage and the design of repair and strengthening interventions. A team was set up to oversee these projects and establish the technical and economic feasibility of the intervention. All the documents were collected in a big database containing detailed information on the buildings geometry, material properties, reinforcement details, earthquake damage and technical and economic documents submitted for funding application. The existing buildings described in this database are of particular interest because they have material properties and reinforcement details typical of Mediterranean building stock and very difficult to reproduce. Furthermore, the damage detected in the aftermath of the L'Aquila earthquake (2009) reflects the building weaknesses typical of the existing buildings. The buildings were classified using the AeDES [16] classification which directly reflect the damage severity.

In this study, two case study buildings were selected from the L'Aquila database and analyzed in detail. RC buildings with moment resisting frames and stiff infills (i.e. hollow brick wall) have been investigated as representative of residential buildings in the Mediterranean area. In order to reduce the uncertainty in the input motion, which may strongly affect the structural response and, in turn, the resulting damage, the case-study buildings were selected in the L'Aquila municipality and very close to the epicenter. The two buildings are located close to the accelerometric stations AQU and AQK (maximum distance about 2.5 km, see Figure 2).

Building 1 (B1) is a four storey building (plus basement), built in the 1972-1981 period and rated in the B-C class due to non-structural damage only and low repair cost. Building 2 (B2) is a three storey building, built in the 1982-1991 period and rated in the E-B class.
The case study buildings experienced different levels of non-structural damage and only limited damage to structural components (beam-column joints). **Error! Reference source not found.-Error! Reference source not found.** show the building elevation views and the main damage detected on structural and non-structural components due to the 2009 L'Aquila earthquake. The location of the damage is also reported. The building B1 (class B-C) experienced in general slight damage (with the exception of very heavy damage for a few panels) to infill, partitions and to the floor finishes (see **Error! Reference source not found.**). The building B2 (class E-B) experienced significant damage to non-structural components such as infill, partitions and floor finishes (see **Error! Reference source not found.**).

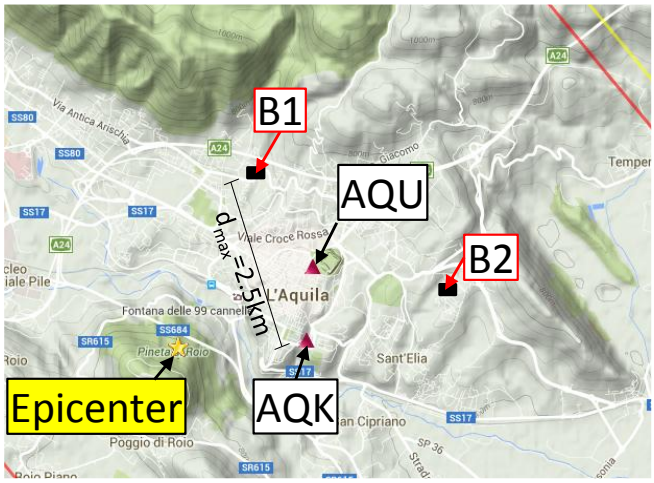

Figure 2: Building location and accelerometric stations of the L'Aquila earthquake (2009).

All the selected buildings rely on RC moment resisting frames as primary structural system and have in plan and elevation structural regularity (see Figure 6a,c and Figure 7a,c), in order to avoid particular cases where the reconstruction costs could have been strongly affected by irregularity in the structural response. The reinforcement details of beams and columns are summarized in Table 1.

| | | | | Direction X | | | | | | Direction Y | | | | | |
|---|---|---|---|---|---|---|---|---|---|---|---|---|---|---|---|
| | | | | Columns | | | Beams | | | Columns | | | Beams | | |
| ID | $f_{cm}$ [MPa] | $f_{ym}$ [MPa] | Storey | h (b) [mm] | $A_{s,t}$ =$A_{s,b}$ | Stirr. d (sp.) [mm] | h (b) [mm] | $A_{s,t}$ ($A_{s,b}$) | Stirr. d (sp.) [mm]] | h (b) [mm] | $A_{s,t}$ =$A_{s,b}$ | Stirr. d (sp.) [mm] | h (b) [mm] | $A_{s,t}$ ($A_{s,b}$) | Stirr. d (sp.) [mm] |
| B1 | 20 | 380 | All | 300 (500) | 3ϕ16 | ϕ8 (200) | 500 (300) | 5ϕ16 (3ϕ16) | ϕ8 (200) | 500 (300) | 2ϕ16 | ϕ8 (200) | 500 (300) | 5ϕ16 (3ϕ16) | ϕ8 (200) |
| B2 | 29 | 516 | All | 300 (500) | 3ϕ16 | ϕ6 (100) | 500 (300) | 5ϕ16 (4ϕ16) | ϕ6 (60) | 500 (300) | 2ϕ16 | ϕ6 (100) | 500 (300) | 5ϕ16 (4ϕ16) | ϕ6 (60) |

Table 1: Material properties and reinforcement details of the case study buildings.

## 3 NUMERICAL MODELING

A two dimensional refined numerical model developed in the finite element method (FEM) software Ruaumoko [11] has been adopted to assess the seismic performances of case study buildings. In order to reproduce the building performances by using a single 2D frame model, a proper distribution of the floor masses, considering the number of frames in each direction and the different stiffness, is needed. A lumped plasticity approach, concentrating RC member nonlinearities in critical members such as portion ends of beam and column, beam-column joints and stiff infill walls has been adopted. Number of literature studies [17,18] and inspections in the aftermath of recent seismic events demonstrated the high vulnerability of poorly detailed beam-column joints. Numerical studies [9,17] pointed out that modeling the nonlinear behavior of beam-column joints is of paramount importance to properly assess the building seismic performances. Stiff infill walls and partition have been found to significantly affect the building global and local response [14,15]. To account for these criticism in the seismic performance of existing RC frames typical of the Mediterranean

area, proper capacity models and refined hysteretic rules have been proposed for beam-column joints [12], non-conforming RC members (modified Takeda, [19] and clay brick infills [13]. For this purpose the influence of joint response on rotational capacity of faming members (with not negligible effects on the interstory drift and frame deformability) has been considered including rotational springs (see Figure 3a). Plastic hinges and lumped springs have been characterized basing on member geometries, reinforcement details and material properties available in structural drawings and material properties characterization tests performed by the practitioners engaged for funding applications. The material properties, the member cross-sections and the reinforcement details used for the plastic hinge characterization are summarized in Table 1. Beams and columns were modelled by mono-dimensional elastic elements with inelastic behavior concentrated at the edges in plastic hinge regions (Giberson model, Figure 3a) and defined by appropriate stiffness degrading moment-curvature hysteresis rules available in the library of Ruaumoko to account for shear strength degradation and poor transverse confinement.

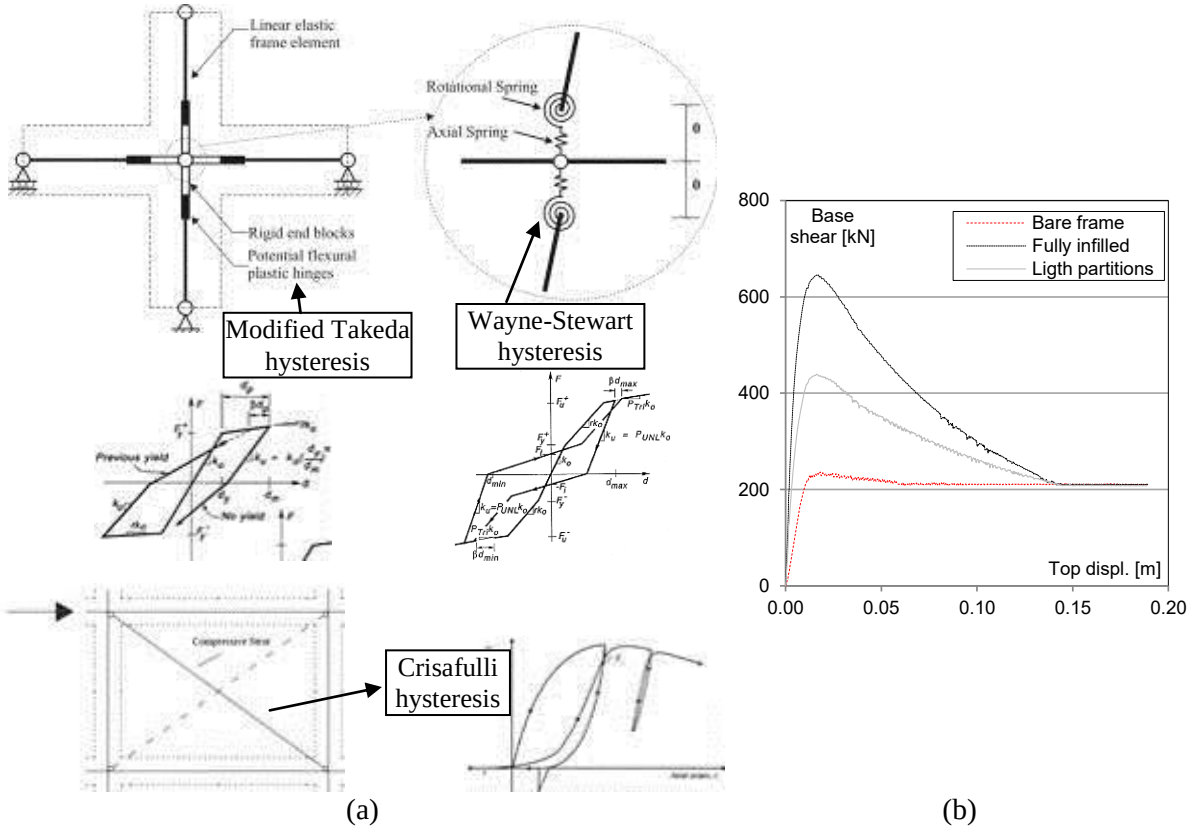


Figure 3: Adopted numerical model after Galli [15] (a); and typical capacity curve of building frames (b);

The modified-Takeda hysteresis model [19] was adopted for beam and column elements. To account for the axial load variation in the column members the yield surface was defined based on the moment-axial load strength domain. The cyclic behavior of the joint rotational spring has been modeled using the Wayne-Stewart [11] hysteresis model (Figure 3a) able to describe the stiffness degrading characteristics of a beam-column joint with the peculiar expected pinching effects typical of cracked joints [12]. The cyclic behavior of the infill panel was been modelled adopting the hysteresis rule proposed by Crisafulli [13] to simulate the axial response. Infill mechanical properties have been quantified according to available literature formulations [20] calibrated on experimental tests on infill wall typical of the Italian con-

structions. Diagonal strut connects beam and column ends in correspondence of the plastic hinges by means of stiff elements able to transmit only compression actions. This in order to account for the infill action on RC member deformability. The proposed numerical models have been widely validate at both at subassembly and frame levels [15,20] under static and dynamic actions.

Pushover analyses were carried out to investigate the damage and collapse mechanism and the differences in terms of initial stiffness between bare-frame, fully infilled frame and interior frame with partitions (see Figure 3b). Capacity curves typical of the case study buildings show a collapse mechanism characterized by joint shear failure involving the first storey members. The infill wall and interior partition significantly affect the frame response in terms of strength, stiffness and collapse mechanism. This need to be properly accounted in the mass distribution on each frame to be representative of the overall building response.

The numerical model of the exterior frame was then used for NLTH analyses. The gravity loads assigned to the reference frame was computed considering the frame tributary area. However, the seismic mass assigned at each floor was computed to reproduce the overall building response in the reference direction. In particular, the mass was distributed between bare frame, infilled frame and interior frame with light partitions as a function of the frame lateral stiffness (see Figure 3b) and number of frames in each direction [7]. This procedure allows to account for the higher stiffness of the fully infilled exterior RC frame, resulting in higher lateral forces transmitted to the structural member and the foundation. The adequacy of the developed numerical model is investigated by comparing the predicted damage with that observed in the aftermath of the earthquake for the reference case studies, as discussed in the further section.

The gravity loads assigned to the reference frame has been computed considering the frame tributary area. The numerical model of the exterior frame has been used for NLTH analysis. However, the seismic mass assigned at each floor has been computed to reproduce the overall building response in the reference direction. In particular, the mass has been distributed between bare frame, infilled frame and interior frame with light partitions as function of the frame lateral stiffness. The number of frames available in the structural system is known from structural and architectural drawings and confirmed by in-situ inspection carried by engaged practitioners for funding applications. With these assumptions the numerical model is able to reproduce with reasonable accuracy the building lateral response in each of the two directions. A further validation, comparing the predicted and observed damage is reported below.

L'Aquila 2009 earthquake's mainshock, Magnitude (Mw) of 6.3 was characterized by a normal fault mechanism 8.8km depth and epicenter about 6 km far from the city of L'Aquila. Earthquake ground shaking was considered in the form of acceleration histories recorded at AQU and AQK stations acquired on firm soil, i.e. soil class B according to Eurocode classification [21]. The accelerometric signals have a PGA ranging between 0.25-0.35g and were extracted from the Italian Accelerometric Archive [22]. Horizontal components of the chosen records were rotated in the orientation in plan of lateral resisting frames of the buildings. Geometrical formulations commonly adopted to identify the two components in near fault ground motions [23] were adopted. This allow to account for the pulse effects of the ground shaking at specific sites (AQK, as outlined by [24].

## 4 PREDICTED VS. OBSERVED DAMAGE

The simulations pointed out that none of the buildings reached the collapse, but they experienced significant structural and non-structural damage. The largest drift are concentrated at the first floors and significant non-structural damage to infill and partitions were detected.

A direct comparison between observed and predicted damage is proposed in order to assess the accuracy of the adopted numerical model to reproduce the earthquake response. The actual earthquake damage were classified using the AeDES [16] classification. It reports the damage grade (Slight, Medium-Severe, Very Heavy) and the damage extent on the entire building (<1/3, 1/3-2/3, >2/3) of structural and non-structural components (i.e. Vertical structures, Floors, Stairs, Roof, Infill-Partitions). The detected damage are reported on the building front view in both the X and Y direction, based on the results of the AeDES form and the damage observation available in the damage report and pictures.

To compare the observed earthquake damage and the damage predicted by means of the numerical model, a correspondence between Engineering Demand Parameters (EDPs), resulting from NLTH analysis, and damage states (DS) needs to be adopted. In the following paragraphs, the correspondence between EDPs and damage states for infill walls and beam-column joints is reported basing on available literature studies and the observations used to develop the AeDES damage classification.

The detected damage, the EDPs estimations and the nonlinear response of the structural and non-structural components for the two case study buildings are reported in Figure 6, Figure 7 and Figure 8.

## 4.1 Correspondence between damage levels and EDPs for infill walls

The AeDES damage classification [16] is based on the EMS98 scale [25] and it identifies the damage to infill and partitions with three damage grades: D1, Small diagonal cracks ($\leqslant$ 1 mm), small separation of the masonry panels from the structure; D2-D3, diagonal cracks or displacements of few mm, visible crushing at the infills corners; D4-D5, total collapse of infill panels. An example of the different damage grades is reported in top of Figure 5.

Even though different capacity models and experimental tests are available in literature, few works proposed a correspondence of the damage states and the EDPs. With reference to infill walls, a first correspondence between the damages and EDP expressed as function of the axial strain in the diagonal compressive strut, was proposed by Magnes and Pampanin [14] as function of the axial deformation in the equivalent strut, $\varepsilon'_{w,}$ commonly used to model the infill action. In particular, no damage or minor cracking (DS1) $\varepsilon'_w$ <0.002; extensive damage (DS2) 0.002≤$\varepsilon'_w$ <0.005; severe damage/incipient collapse (DS3) 0.005≤$\varepsilon'_w$.

| Sassun et al. (2016)-All type of Infill | | | | | | | | | | Corresponding AeDES Damage level |
|---|---|---|---|---|---|---|---|---|---|---|
| DS | Description | IDR (%) | | | | $\varepsilon_{strut}$ (%) | | | | |
| [-] | [-] | median | β | 16$^{th}$ perc. | 84$^{th}$ perc. | median | β | 16$^{th}$ perc. | 84° perc. | [-] |
| DS1 | Ligth cracking (w<1mm) | 0.18 | 0.52 | <u>0.11</u> | 0.30 | 0.08 | 0.51 | <u>0.05</u> | 0.13 | D1 |
| DS2 | Extensive diagonal cracking (1<w<2mm) | 0.46 | 0.54 | <u>0.27</u> | 0.79 | 0.22 | 0.52 | <u>0.13</u> | 0.37 | D2-D3 |
| DS3 | Brick unit crushing or spalling, sliding joints, local collapse | 1.05 | 0.40 | <u>0.70</u> | 1.57 | 0.51 | 0.40 | <u>0.34</u> | 0.76 | D4-D5 |
| DS4 | Near collapse | 1.88 | 0.38 | 1.29 | <u>2.75</u> | 0.89 | 0.37 | 0.61 | <u>1.29</u> | |

Note: the percentile underlined represent the limits assigned to the AeDES damage levels

Table 2: Correspondence between available damage states, the relevant EDPs and the AeDES damage levels

Furthermore they introduced a simple relationship which allows to estimate the interstorey drift knowing the strut axial deformation and the panel geometric aspect ratio (L/H).

$$\delta = \frac{L}{H} - \sqrt{(1-\varepsilon_w)^2\left(1+\left(\frac{L}{H}\right)^2\right)} - 1$$

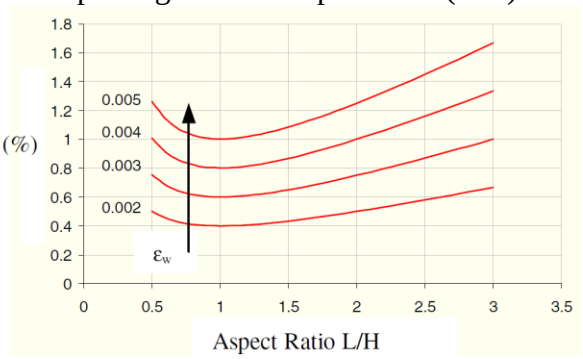


Figure 4: Relationship between strut axial strain, interstorey drift and aspect ratio L/H [14].

Recently, Cardone et al. [26] and Sassun et al. [27], proposed fragility functions for the infill and partitions based on a wide database of experimental tests for four the damage states. They correlate the probability of achieving a specific damage with the experimental interstorey drift or the the axial deformation in the equivalent strut, $\varepsilon'_w$, estimated with a numerical model.
The results are summarized in Table 2 which also report the correspondence between the DS assumed by Cardone et al. [26] and Sassun et al. [27] and the damage grades of the AeDES form. This correspondence is proposed based on the damage description of the damage grades or damage states as summarized in Figure 5.

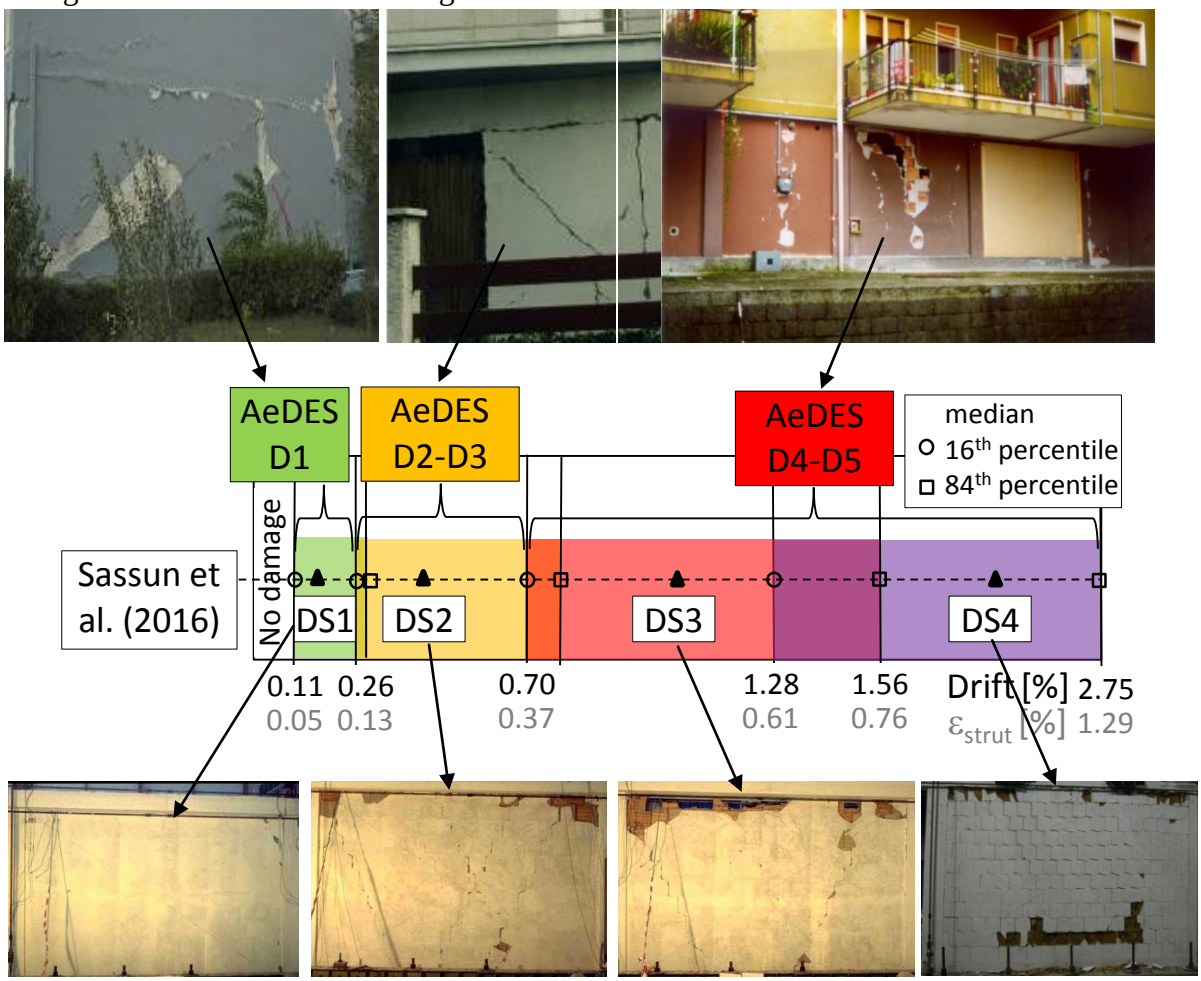


Figure 5: Correspondence between available damage classifications for clay brick infill (after [16,27]).

The interstorey drift predicted using the formulation proposed by Magnes and Pampanin [14] at the axial strain limits proposed by Sassun et al. (2016) well matches the intersotrey drift limits proposed by Sassun at al. (2016) and based on experimental observations. This confirm the accuracy of the formulation proposed by Magnes and Pampanin [14] which also account for the geometry of the infill.

It is worth mentioning that the damage grades proposed by the AeDES form include also the effects of the out-of-plane actions on the infill and the corresponding damage. By contrast, reliable and accurate damage descriptions and the corresponding EDPs due to the out-of-plane actions are currently not available due to the lack an adequate number of experimental tests. Thus, the damage predicted by using numerical models or available literature damage classification could underestimate the actual earthquake damage.

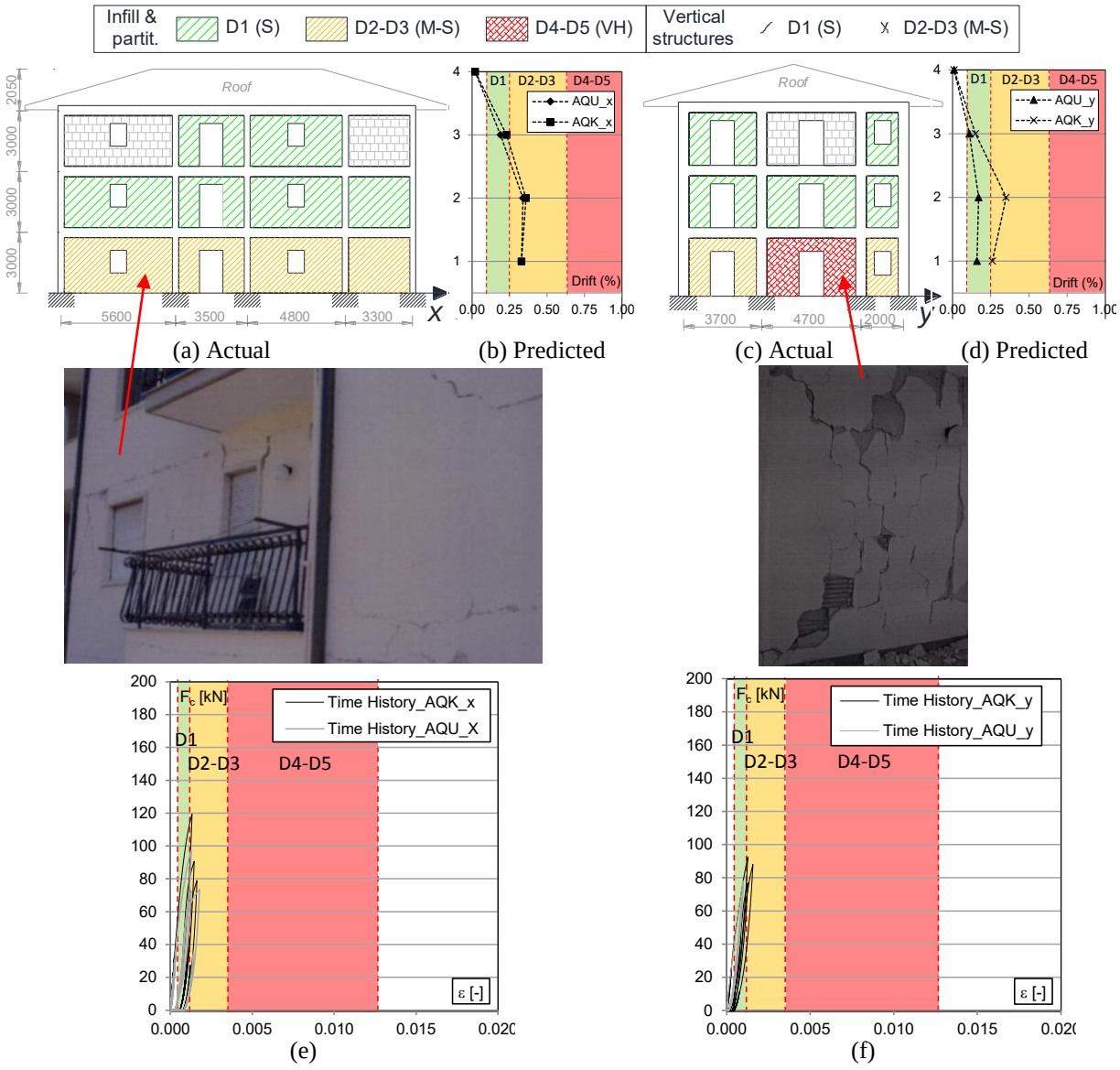


Figure 6: Building B1 (B-C) comparison between observed and predicted earthquake damage: actual damage in the X direction (a); predicted drift in the X direction (b); actual damage in the Y direction (c); predicted drift in the Y direction (d); predicted damage to exterior infill in the X and Y direction (e) and (f), respectively;

The detected earthquake damage on B1 in the X direction, see Figure 6a, were medium-severe (D2-D3) on the ground floor infill and slight (D1) on the upper floors. This well

matches with the damage associated to the drift response, estimated by means of refined NLTHs, see Figure 6b, and the local damage achieved by the equivalent strut representative of the infill action, see Figure 6e.

In the Y direction, the building B1 exhibited medium-severe damage at the ground floor infills, see Figure 6c, matching with the predicted damage in terms of interstorey drift, see Figure 6d. It is worth mentioning that in-situ inspection reported a very high damage (D4-D5) to one of the ground floor infill (see Figure 6c) due to out of plane actions. Actually, this cannot be considered with available capacity models which predicted a D2-D3, medium-severe damage, see Figure 6d,f.

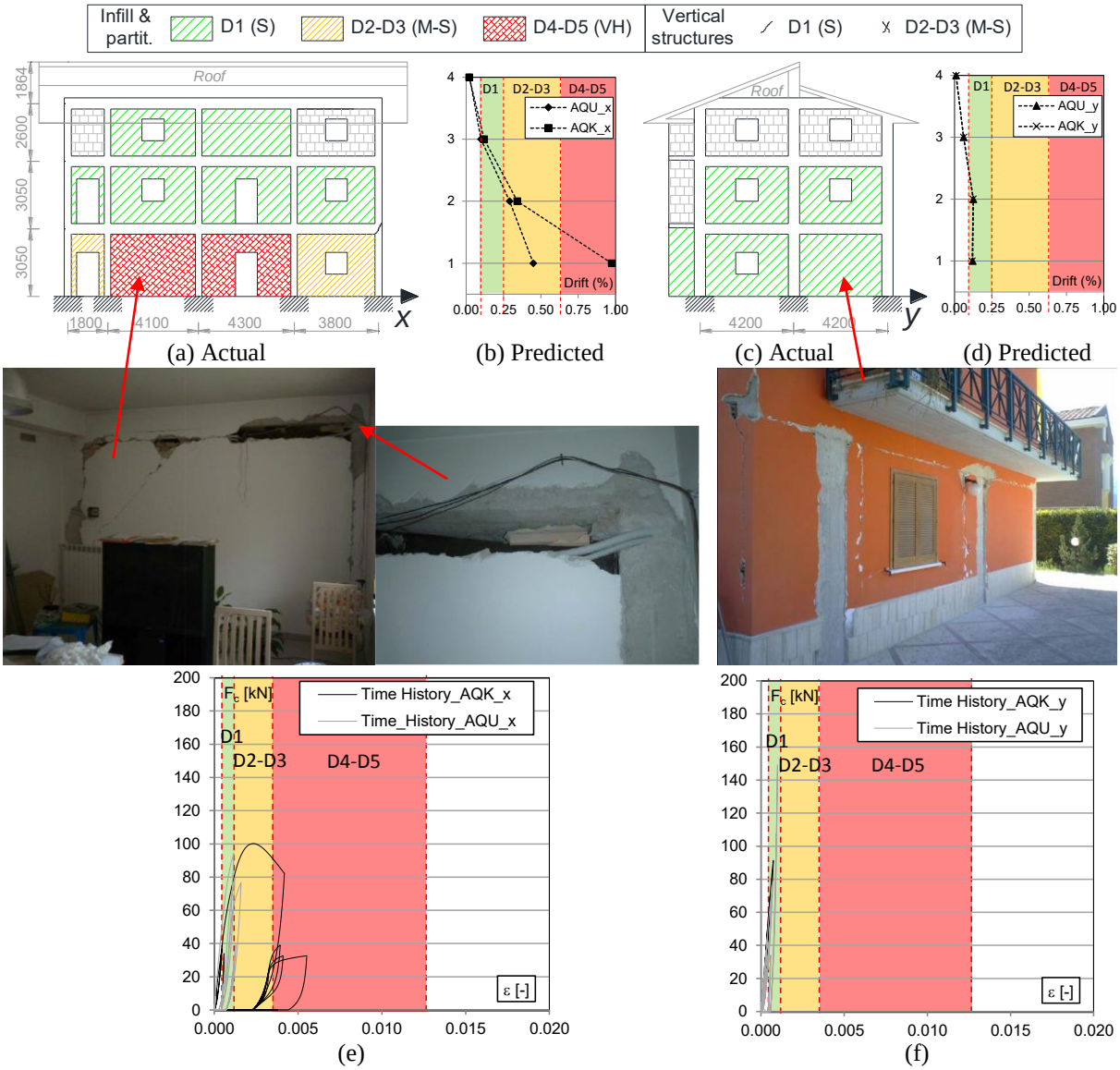


Figure 7: Building B2 (E-B) comparison between observed and predicted earthquake damage: actual damage in the X direction (a); predicted drift in the X direction (b); actual damage in the Y direction (c); predicted drift in the Y direction (d); predicted damage to exterior infill in the X and Y direction (e) and (f), respectively.

Figure 7a shows the extensive damage to ground floor infill. Medium-Severe (D2-D3) and very high (D4-D5) damage were detected on the B2 in the direction X. This is well predicted both by means of the proposed intertorey drift-damage correlation (Figure 7b) and in terms of

stress-strain response on the single infill panels, see Figure 7e. Figure 7c shows the slight damage (D1) on ground and first floor infill of the B2 in the direction Y. Also in this case the predicted earthquake response match with the observed damage (see Figure 7d, f).

### 4.2 Correspondence between damage levels and EDPs for beam-column joints

A proposal to correlate the earthquake damage and the EDPs for poorly detailed beam-column joints was proposed by Magenes and Pampanin [14]. In particular, damage to poorly detailed beam-column joints can be expressed as function of the joint shear distortion, $\gamma$ : first diagonal cracking (DS1) $0.0002 \leq \gamma < 0.005$; extensive damage (DS2) $0.005 \leq \gamma < 0.01$; severe damage/incipient collapse (DS3) $0.01 \leq \gamma$. The comparison between the proposed damage states and the nonlinear response of the corner joint at the first floor of the Building B2 that experienced slight shear cracking is reported in Figure 8.

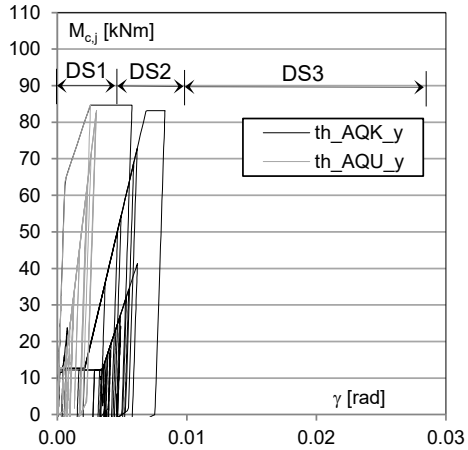


Figure 8: Building B2 (E-B) comparison between predicted nonlinear time-history response and damage states: for the corner joint at the first level in the X direction.

The comparison outlined a significant difference between the response due to the AQU and AQK record. This is because of the pulse effects related to the AQK record [24], which may lead to increase the earthquake demand on the structural system. On average, a slight to medium damage (DS1-DS2) to the joint panel is predicted, which matches with the in-situ observation.

## 5 CONCLUSIONS

The paper presents a refined numerical model developed in a FEM environment able to reproduce the nonlinear behavior of existing RC buildings both at global and component level. This allow the use of the proposed model in refined loss-assessment methodologies. The comparison between observed and predicted damage at global and component level of two case study buildings outlines a reasonable accuracy of the numerical models. In particular:

- The proposed numerical model is a reliable tool to reproduce the nonlinear dynamic response of existing RC buildings subjected to recorded acceleration histories. The capabilities of the model to reproduce the nonlinear behavior of infill wall with significant strength and stiffness degradation allow to reproduce severe damage states and the interaction with the RC frame.

- Two case study buildings with different damage levels on the infills and beam-column joints were used for the model validation. The comparison shows the good match between observed and predicted damage to infill walls at different levels experiencing slight, severe and very heavy earthquake damage.

- The proposed correspondence between AeDES damage grades and the EDPs allows to predict the damage to infill and partition using a floor-by-floor estimation of the interstorey drift with reasonable accuracy.

- A significant gap between actual and predicted damage can be observed for the infill panel experiencing out-of-plane damage due to the bidirectional effect of the ground shaking. This phenomena significantly affects the damage to drift-sensitive non-structural components and a further research effort is needed to develop detailed relationships between damage states and EDPs.

## ACKNOWLEDGMENTS

This study was performed in the framework of PE 2014–2018 joint program DPC-ReLUIS, Task RS-4: "Post-earthquake analysis: usability, damages, seismic design of repair and strengthening interventions" and in the "SAFER Concrete" project, funded by the New Zealand Natural Hazard Research Platform (NHRP).

## REFERENCES

[1] Pampanin S, Kam WY, Akguzel U, Tasligedik AS, Quintana Gallo PI. Seismic Performance of Reinforced Concrete Buildings in the Christchurch CBD in 22 February 2011 Earthquake Part II : Damage Observation. Christchurch, New Zealand: 2012.

[2] Di Ludovico M, Prota A, Moroni C, Manfredi G, Dolce M. Reconstruction process of damaged residential buildings outside the historical centres after L'Aquila earthquake - Part I: Light Reconstruction. Bull Earthq Eng 2017;15:667–92. doi:10.1007/s10518-016-9877-8.

[3] Di Ludovico M, Prota A, Moroni C, Manfredi G, Dolce M. Reconstruction process of damaged residential buildings outside the historical centres after L'Aquila earthquake - Part II: Heavy Reconstruction. Bull Earthq Eng 2017;15:693–729. doi:10.1007/s10518-016-9979-3.

[4] Del Vecchio C, Di Ludovico M, Pampanin S, Prota A. Repair costs analysis for case study buildings damaged in the 2009 L ' Aquila earthquake. NZSEE Conf., Christchurch, New Zealand: 2016.

[5] De Martino G, Di Ludovico M, Prota A, Moroni C, Manfredi G, Dolce M. Estimation of repair costs for RC and masonry residential buildings based on damage data collected by post-earthquake visual inspection. Bull Earthq Eng 2016;doi:10.1007/s10518-016-0039-9.

[6] Cardone D, Perrone G. Damage and Loss Assessment of Pre-70 RC Frame Buildings with FEMA P-58. J Earthq Eng 2016;00:1–39. doi:10.1080/13632469.2016.1149893.

[7] Del Vecchio C, Di Ludovico M, Pampanin S, Prota A. Actual versus predicted repair costs: case studies on RC buildings damaged by L'Aquila earthquake. 16th World Conf. Earthq. Eng., Santiago, Chile: 2017, p. Paper N° 2754.

[8] Del Vecchio C, Kwon O, Di Sarno L, Prota A. Accuracy of nonlinear static procedures for the seismic assessment of shear critical structures. Earthq Eng Struct Dyn 2015;44. doi:10.1002/eqe.2540.

[9] Del Vecchio C, Di Ludovico M, Prota A, Manfredi G. Modelling beam-column joints and FRP strengthening in the seismic performance assessment of RC existing frames.

Compos Struct 2016;142:107–16. doi:10.1016/j.compstruct.2016.01.077.
[10] OpenSees: Open system for earthquake engineering simulation 2006. http://opensees.berkeley.edu.
[11] Carr A. Ruaumoko 2D, Nonlinear FEM Computer Program 2009.
[12] Pampanin S, Magenes G, Carr A. Modelling of Shear Hinge Mechanism in Poorly Detailed RC Beam-Column Joints. fib 2003 Symp. "Concrete Str. Seism. Reg.", May 2003. Pap. n. 171, 2003.
[13] Crisafulli FJ. Seismic Behaviour of Reinforced Concrete Structures with Masonry Infills. University of Canterbury, New Zealand, 1997.
[14] Magenes G, Pampanin S. Seismic response of gravity-load design frames with masonry infills. 13th World Conf Earthq Eng 2004.
[15] Galli M. Evaluation of the seismic response of existing r.c. frame buildings with masonry infills. IUSS, Pavia, 2005.
[16] Baggio C, Bernardini A, Colozza R, Corazza L, Bella M, Di Pasquale G, et al. Field Manual for post-earthquake damage and safety assessment and short term countermeasures ( AeDES ). ISPRA, Italy: 2007.
[17] Calvi GM, Magenes G, Pampanin S. Relevance of beam-column joint damage and collapse in RC frame assessment. J Earthq Eng 2002;6:75–100. doi:10.1080/13632460209350433.
[18] Del Vecchio C, Di Ludovico M, Balsamo A, Prota A, Manfredi G, Dolce M. Experimental investigation of exterior RC beam-column joints retrofitted with FRP systems. ASCE J Compos Constr 2014;18:1–13. doi:ASCE, ISSN 1090-0268/04014002(13)/$25.00.
[19] Otani S. SAKE: A Computer Program for Inelastic Response of R/C Frames to Earthquakes. Urbana, Illinois: 1974.
[20] Magenes G, Pampanin S. Seismic Response of Gravity-Load Design Frame with Masonry Infills. 13 th World Conf. Earthq. Eng., Vancuver, Canada: 2004.
[21] CEN. "Design of structures for earthquake resistance, part 1: General rules, seismic actions and rules for buildings." EN 1998-1, Eurocode 8. vol. 3. Brussels: European Committee for Standardization; 2004.
[22] ITACA working group. ITalian ACcelerometric Archive, version 2.1. 2016. doi:10.13127/ITACA/2.1.
[23] Somerville P. Characterizing Near Fault Ground Motion For The Design And Evaluation Of Bridges. Proc. Third Natl. Seism. Conf. Work. Bridg. Highw. 01/2002, 2002.
[24] Chioccarelli E, Iervolino I. Near-source seismic demand and pulse-like records: A discussion for L'Aquila earthquake. Earthq Eng Struct Dyn 2010;39:1039–62. doi:10.1002/eqe.987.
[25] Grünthal G. European Macroseismic Scale 1998. vol. 15. European S. Luxembourg: Centre Europèen de Géodynamique et de Séismologie; 1998.
[26] Cardone D, Perrone G. Developing fragility curves and loss functions for masonry infill walls.Earthquakes Struct 2015;9:257–79. doi:http://dx.doi.org/10.12989/eas.2015.9.1.257.
[27] Sassun K, Sullivan TJ, Morandi P, Cardone D. Characterising the in-plane seismic performance of infill masonry. Bull New Zeal Soc Earthq Eng, March 2016;49:100–17.

COMPDYN 2017
6th ECCOMAS Thematic Conference on
Computational Methods in Structural Dynamics and Earthquake Engineering
M. Papadrakakis, M. Fragiadakis (eds.)
Rhodes Island, Greece, 15–17 June 2017

# SIMPLIFIED ASSESSMENT OF EXPECTED SEISMIC LOSSES FOR AS BUILT AND RETROFITTED RC BUILDINGS

**Marco Gaetani d'Aragona**[1], **Maria Polese**[1], **Marco Di Ludovico**[1] **and Andrea Prota**[1]

[1] Department of Structures for Engineering and Architecture, University of Naples Federico II
via Claudio 21, 80125 Naples, Italy
{marco.gaetanidaragona, maria.polese, diludovi, andrea.prota}@unina.it

**Keywords:** seismic losses, retrofit, pushover, Non-linear Response History.

**Abstract.** *Seismic risk is a key factor influencing several important decision-making processes from performance-based design of new structures, to investments for rehabilitation of existing buildings and even to seismic mitigation campaigns of large building stocks. In order to evaluate the economic convenience of alternative mitigation strategies the expected seismic losses for different solutions (including the "do nothing") in a given timeframe should be compared. The PEER performance-based earthquake engineering framework is normally adopted in order to compute losses. However, its application with a number of Non-linear Response History analyses as a basis for assessment of expected Engineering Demand Parameters and associated losses is an elaborate and time-consuming task, hardly employable for the assessment of earthquake losses for large building portfolios. This paper tests the applicability of a simplified pushover based approach for computation of earthquake losses. Referring to a case study building the results of application of classical PEER approach, i.e. based on Non-linear Response History analyses, are compared with the losses computed with pushover-based assessment, showing encouraging results. In addition, the simplified approach is used to investigate the effect of alternative retrofit strategies on the variation of expected seismic losses.*

## 1 INTRODUCTION

Seismic risk is a key factor influencing several important decision-making processes from performance-based design of new structures, to investments for rehabilitation of existing buildings and even to seismic mitigation campaigns of large building stocks. Within the PEER performance-based earthquake engineering (PBEE) framework [1] the economic losses are adopted as a one of the metrics for measuring seismic risk. In the framework, direct economic losses, that include costs for repairing or replacing damaged buildings, are strongly influenced by the probability of replacement of building (i.e. probability of collapse). Further, if a mitigation action is implemented, the earthquake economic losses are generally reduced, while the costs of building retrofit should be included in the evaluation process [2-5] along with additional metrics in order to account for post-earthquake residual capacity [6,7].
In FEMA P-58 [8], the implementation of the PEER framework is described considering either Non-linear Response History (NLRH) based analyses, either a quicker approach relying on simplified modeling and analysis of the building response that involves the adoption of the SPO2IDA [9] for computation of building fragility.
Starting from the idea of simplifying the computational effort normally required for implementation of the PEER framework, the present paper tests the applicability of standard pushover analysis in combination to the capacity spectrum method, CSM [10] as a basis for the assessment of engineering demand parameters (EDPs) and related damage and losses. The results of detailed evaluation with standard PEER PBEE approach, entailing the execution of a number of Nonlinear Response History (NLRH) analyses and evaluation of EDPs, are compared with results obtained through pushover based assessment of EDPs for a case study non-ductile reinforced concrete (RC) building. In addition, the effect of alternative retrofit strategies is investigated and the variation of expected losses estimated, showing encouraging results on the possibility to adopt pushover-based analyses for estimation of expected costs.
The following section briefly describe the different methods for computation of economic losses. Next, section 3 introduces the reference building, its analytical model, and the design of possible retrofit schemes. Section 4 presents an application of the detailed and simplified assessment for the original building, comparing the results. Finally, the seismic vulnerability reduction as well as the variation of losses are evaluated for adopted retrofit schemes with the simplified approach.

## 2 EVALUATION OF SEISMIC LOSSES

The PEER PBEE framework, that is probably the most refined procedure currently available, allows quantifying different seismic performance measures such as expected number of injuries or Deaths, economic losses (e.g. expressed in terms of Dollars) and time to recovery or Downtime (the 3Ds). The general approach to loss estimation relies on structural analysis to calculate engineering demand parameters (EDPs) such as deformations and accelerations throughout the structure during an earthquake, which are used to predict the damage in structural, non-structural components, and building contents. Damages are the base for computation of expected losses in terms of one or more of the established metrics (e.g., economic losses in dollars or casualties). The framework operates with four analysis stages: hazard analysis, structural analysis, damage analysis and loss analysis, as synthetically shown in Figure 1.

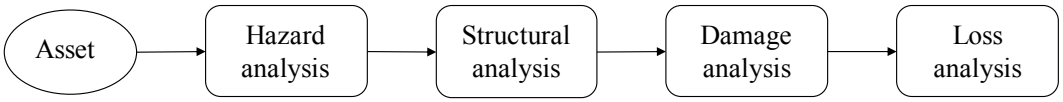


Figure 1. PEER framework [1]

The outcome of each analysis is then integrated using the Total Probability Theorem, allowing to take into account combined numerical integration of all the conditional probabilities and to propagate the uncertainties from one level of analysis to the next, resulting in probabilistic prediction of performance. As noted in [11] the PEER framework is very flexible, since no restrictions are imposed on the approach used to quantify hazard, to perform structural analysis and to relate EDPs to losses and other performance measures. Of course, the results will depend on the assumptions made in applying the procedure and the risk parameters of interest. Different applications of the PEER framework, implementing component-based (e.g. [12,13]) or storey-based damage assessment (e.g. [14]), are available. In this study, a component-based approach is adopted.
In section 2.1 the implementation of the PEER framework proposed by [15] is synthetized, while section 2.2 describes the main differences in the application when pushover based structural analyses for evaluation of EDPs are employed.

## 2.1 Implementation of the Performance-Assessment Framework for Repair Cost Evaluation

The performance assessment procedure implemented in [15] starts from the identification within the considered facility of the relevant performance groups (PGs), i.e. groups of structural or nonstructural components whose performance is similarly affected by a particular EDP, e.g. acceleration at a given story or $IDR_{max}$ at another story.

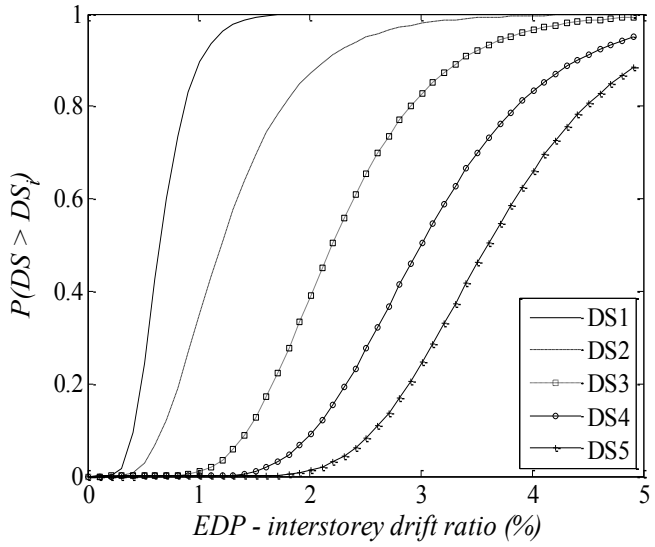


Figure 2. Example of adopted fragility curve

For each PG significant damage states that have a clear correlation with repair actions (and related costs) shall be identified and suitable damage model defined; the latter are expressed in terms of component-level fragility curves, relating EDP (e.g. maximum interstorey drift

ratio, $IDR_{max}$) to the probability of attaining different damage states for the assigned component type (e.g., Figure 2). In order to allow for quantitative evaluation of the needed repair actions, the number of components or their measurable extension within each PG of the considered facility is estimated.

After selection, e.g. with conventional seismic hazard analysis, of suites of ground motion records, the response of the building is evaluated using NLRH analysis. To allow statistical characterization of EDP at various intensity levels the authors suggest the execution of a number of NLRH analyses with suites of ground motions and for increasing level of hazard. The peak EDP values obtained with NLRH analyses for each record are summarized in an EDP matrix (one matrix for each intensity level); the latter has one column for each considered EDP and one row for each record. Starting from EDP matrices evaluated with structural analysis, additional EDPs are estimated with a simulation-based method that, assuming a joint lognormal distribution among the parameters, enables the generation of large numbers of artificial EDP vectors that have the same statistical distribution as the data that were derived with NRH analyses. This way, large sample of realizations necessary to perform loss evaluations are obtained, and additional sources of uncertainties can be accounted for [8]. The generic EDP realization corresponds to a state of damage. In order to select among possible DSs, given the EDP, a Montecarlo simulation is performed, extracting a random number from the uniform distribution over the interval [0,1]. For example, if the uniform random number generator produces a number of 0.6 and the EDP value shown in Figure 2 is 2.5%, the PG is in DS3.

In this study, 1000 realizations were performed for each intensity level to obtain stable cost estimates. For each realization and PG, a unique damage state was determined. Once the damage state for a performance group is identified, the repair action and the associate repair cost for that performance group is obtained by multiplying cost of new elements by corresponding normalized repair costs by the number of elements in the considered PG. If collapse has not occurred, losses are calculated for each realization based on the damage sustained by each component and the consequence functions assigned to each performance group and by summing repair costs of each PG. If structural collapse was detected, the total repair cost is calculated using the replacement value of the building plus additional costs related to demolition and debris removal. When retrofit strategy is applied, the additional cost due to retrofit intervention is accounted as a repair cost determining a shift to the right of the normalized cost curve.

Finally, considering the repair quantities for each item in the PG, multiplying by a unit repair cost (for each DS) and summing over all items, the total repair cost for the building is computed. To account for possible collapse cases occurred, for each realization an additional Montecarlo simulation is performed based on the collapse fragility curve for the building. For further information about adopted component fragilities and repair costs, refer to [5].

### 2.2 Simplified assessment employing pushover analysis

A key aspect in the procedure described in 2.1 is the execution of a number of structural analyses performing NLRH with a suite of ground motion records and for different levels of hazard, i.e. for increasing intensity levels. On the other hand, a simpler approach for practitioners is desirable.

Static nonlinear pushover PO, under its applicability hypotheses, allows to investigate a building's nonlinear behavior, assessing damage progression and related variation of displacement profile for increasing levels of seismic demand. Moreover, SPO allows investiga-

tion of damage distribution within the structural system, hence representing a useful tool in the assessment of post-earthquake condition. SPO may be employed for simplified response calculation; by applying the CSM to the capacity curve resulting from pushover analysis [10], the building response to earthquakes of assigned spectral shapes may be found. Scaling the demand spectrum, median expected drift profiles for increasing levels of earthquake intensity can be obtained, hence EDPs in terms of $IDR_{max}$ are determined. Median peak floor acceleration (PFA), can be derived using existing proposals in literature [16-18, 8]. According to FEMA P-58 [8], PFA at floor *i* can be calculated as a function of peak ground acceleration (*PGA)* and an acceleration correction factor $H_{ai}$ (see Equation 1) depending on the strength ratio S, the elastic period of the building T, total building height H and the height above the effective base of the building to floor level *i,* $h_i$.

$$a_i^* = H_{ai}(S, T, h_i, H) \cdot PGA \qquad \mathrm{i} = 2 \text{ to } \mathrm{N}+1 \tag{1}$$

Statistical distributions of the relevant EDPs (e.g. $IDR_{max}$ of PFA at the different floors) can be derived hypothesizing they have a lognormal distribution and considering the obtained median values (one for each considered intensity level) and suitable dispersions β. By introducing values of dispersion due to modeling uncertainties $\beta_m$ and inherent randomness associated to earthquake variability, $\beta_{a\Delta}$ or $\beta_{aa}$ for drift or acceleration respectively, a global value of β may be calculated and EDP probabilistic distribution obtained for each considered intensity level (see e.g. Eq. (2) – valid to assess drift dispersion - and (3)). In Eq. (3) $d_{IM}$ is the median value of drift demand obtained from application of CSM using the demand spectrum scaled at the generic intensity level IM.

$$\beta_{SD} = \sqrt{\beta_{a\Delta}^2 + \beta_m^2} \tag{2}$$

$$P[drift > d \mid IM] = \Phi\left[\frac{1}{\beta} \cdot \ln\left(\frac{d}{\hat{d}_{IM}}\right)\right] \tag{3}$$

Suitable values of $\beta_m$ and of $\beta_{a\Delta}$ or $\beta_{aa}$ are suggested in FEMA P-58 as a function of available information for modeling (for $\beta_m$) or period and strength ratio S (for $\beta_{a\Delta}$ and $\beta_{aa}$).

Once the probabilistic distribution of EDP (e.g. $IDR_{max}$) at each level of considered intensity are obtained, they can be used similarly to the approach described in 2.1 for computation of expected losses.

## 3 BUILDING MODEL

The building selected for this study is a seven-story five-bay frame representative of mid-rise non-ductile reinforced concrete building, see Figure 3, "extracted" from the perimeter moment resisting frame of the Van Nuys Holiday Inn located in Los Angeles, California. The concrete nominal strength is $f'_c$=5 ksi for the first story columns, 4 ksi for the second story columns and second floor beams, and 3 ksi for columns from third story to the seventh and for beams from the third floor to the roof. Column sections is constant along the height and equal to 14"x 20". For further details, refer to [19].

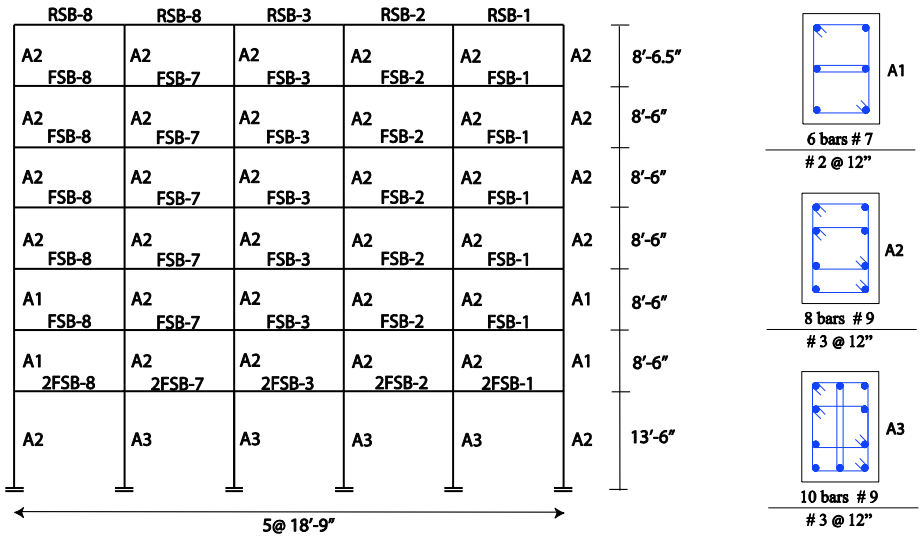


Figure 3. Schematic view of the frame with element number and column rebar arrangement

Similarly, shear and axial failure are expected to occur in non-ductile detailed columns, and consequently shear and axial failure in the columns are explicitly modeled using the Limit State material [20]. P-Δ effects are not included. A schematic view of the building model is shown in Figure 4.

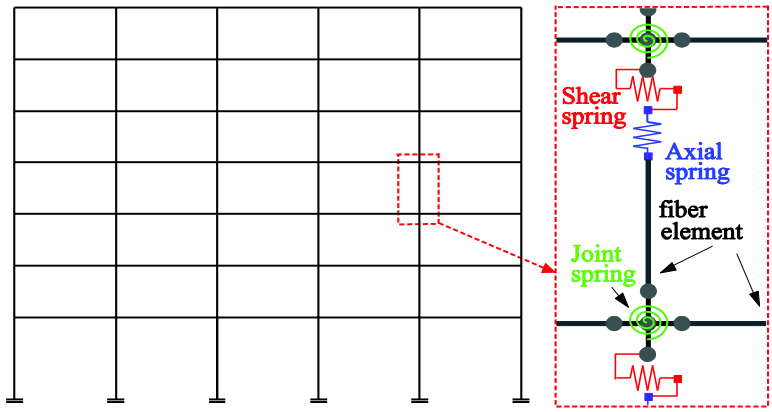


Figure 4. Schematic view of the analytical model

A two-dimensional finite element multi-degree of freedom model developed using [21] is adopted to simulate the seismic response of the building. Beams and columns are modelled using the nonlinear beam-column element [22]. Due to non-ductile details that characterize the structure, is expected that the joints may influence the failure mechanism, consequently the joints are modeled adopting the "scissor model" by [23], including a pinching hysteric behavior [24] to account for the nonlinear shear deformation of the joint.

The eigenvalue analysis of the original structure provides a fundamental vibration period of 1.05 sec. A damping of 2% is assigned to the first and third modes using Rayleigh damping.

To capture the actual capacity for the original non-ductile frame, this study considers two possible system-level collapse mechanisms: Side-sway collapse (SSC) and Gravity load collapse (GLC). The SSC occurs when a single storey has reached its capacity to withstand lat-

eral loads (i.e., when every column in a given floor has reached its residual shear capacity at the same time). GLC occurs when vertical load demand exceeds the total vertical load capacity at a given storey. Collapse is detected based on a comparison of storey-level gravity load demands and capacities (adjusted at each time step to account for member damage and load redistribution). An internal algorithm monitors the dynamically varying capacity of each element and checks the GLC and SSC criteria throughout each nonlinear time history analysis to detect the collapse (with a precision of 0.05g). The collapse is considered as the first between GLC, SSC.

### 3.1 Retrofit solution with FRP wrapping of selected columns

The first retrofit strategies consist in the application of CFRP layers to enhance the structural performance of RC columns. The wrapping is applied to all columns of selected stories and columns are fully wrapped for their entire height to provide an efficient confinement effect. Column wrapping is designed in order to prevent columns shear failure after yielding.

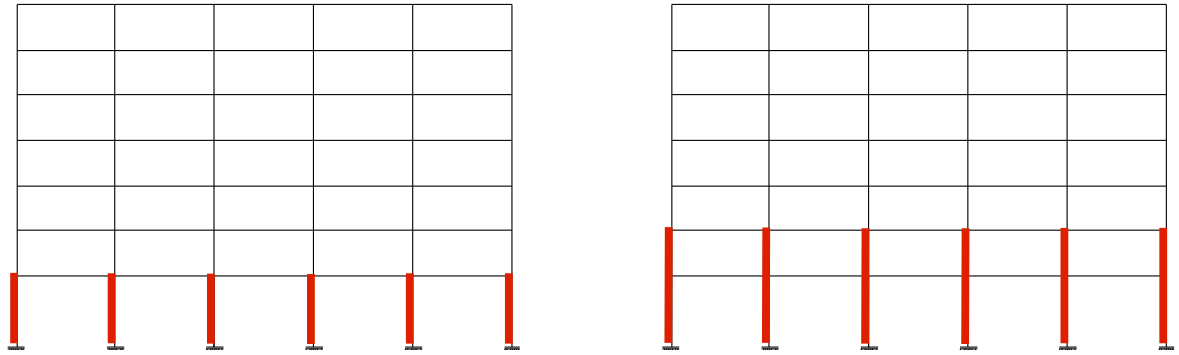

(a) (b)

Figure 5. Schematic view of wrapping configuration adopted: (a) wrap1 and (b) wrap12

In particular, the [25] is adopted in the design process in order to provide a shear resistance such that flexural failure is ensured [26]. Two different wrapping configurations are adopted: in the first configuration (*wrap1*) columns at 1st story are fully wrapped (see Fig. 5(a)), while in the second (*wrap12*) columns at 1st and from 2nd story are fully wrapped (see Fig. 5(b)), allowing a higher increment of displacement capacity. For both models, when the wrapping is applied to columns, brittle failure is avoided for all storey columns and their behavior is modeled considering only flexural behavior. The modified behavior of columns materials, due to confining action applied by the CFRP wrapping, is accounted for implementing stress-strain relationship proposed in [27]. When CFRP wrapping is applied, an additional collapse criterion is considered: when in that storey a small increase in ground-shaking intensity causes a large increase in lateral drift response, or when $IDR_{max}$ exceeds the 10% threshold.

### 3.2 Retrofit solution with insertion of RC wall

The third retrofit strategy consists into adding a RC wall to increase the stiffness and strength of the system. This strategy would have the benefit of reducing the displacement demands but would have the negative effect of increasing acceleration demands.

In particular, the frame is retrofitted by converting the exterior bay to a shear wall composed of a cast-in-place RC panel and boundary columns. The RC panel geometry and reinforcements were designed according to minimum design requirements provided in NIST GCR 11-917-11REV-1 [28].
Analytical model of a coupled wall-frame building system was generated by substituting the right exterior bay with a structural wall modeled adopting the Multiple Vertical Line Element Model (MVLEM) proposed in [29]. The remaining RC frame was connected to the MVLEM implementing rigid diaphragms within each story level. In order to account for the finite size of the shear wall, a rigid beam-column element was adopted within each story level to connect the centerline of the shear wall element with the boundary column at the interface between the frame and the wall.

When the coupled wall-frame strategy is adopted, a substitute collapse criterion is adopted: the system-level collapse is considered attained when the system lateral capacity drops to the 80% of its maximum value.

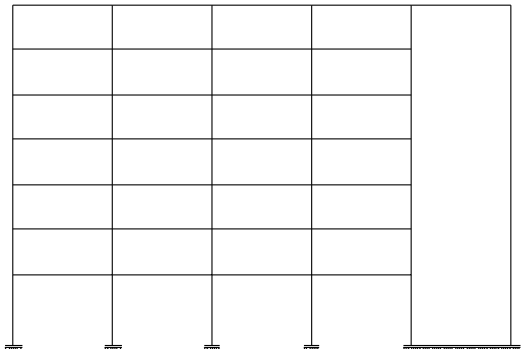

Figure 6. Schematic view of retrofit scheme with shear wall

## 4 EVALUATION OF EXPECTED LOSSES

### 4.1 NLRA and cost assessment

*Original building*

In this section, NLRH analyses are initially adopted to estimate building's collapse capacity through successive scaling until collapse [30] and to estimate building response in terms of EDPs. NLRH analyses are performed for increasing intensities of the seismic action appropriately scaling each record to cover the entire range of structural response, from elastic to ultimate response.

In order to perform NLRH analyses, the set of 30 ground motions adopted in [31] is adopted.

Applying the procedure outlined in 2.1, and considering a total of 1000 realizations for each intensity level to obtain stable cost estimates, total repair costs are obtained.

Figure 7 shows the complementary cumulative distribution function (CCDF) of the total repair cost of the building normalized by building replacement cost (including expected demolition costs), $c_r$, obtained through the dynamic approach; seven different intensity levels ranging from 0.1g to 0.7g are considered.

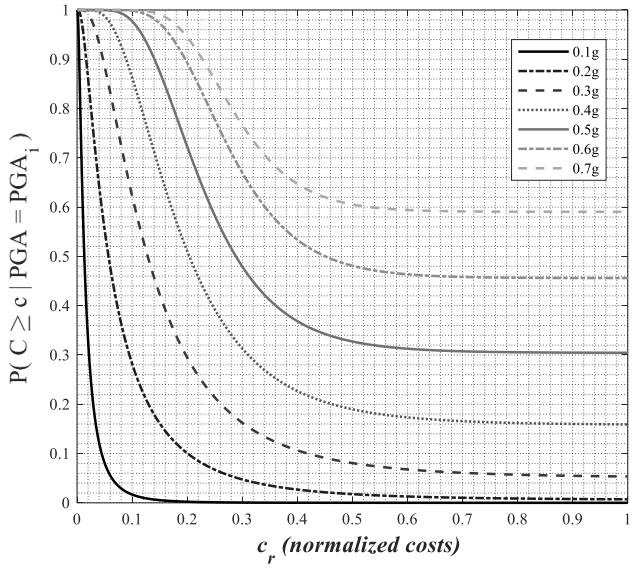


Figure 7. CCDFs of total normalized repair costs ($c_r$) for different PGAs obtained through NLRH procedure for the original building.

Note that the probability of exceeding a certain level of total normalized repair cost accounting for both the collapse and non-collapse cases is calculated as:

$$P(C_r \geq x) = P(C_r \geq x \mid IM, NC)[1 - P(C \mid IM)] + P(C_r \geq x \mid IM, C)P(C \mid IM) \quad (4)$$

where $P(C_r \geq x \mid IM, NC)$ is the probability conditioned on IM when the structure do not collapses that the normalized repair cost exceeds x; $P(C_r \geq x \mid IM, C)$ is the probability of exceeding the normalized repair cost x given the collapse, that is actually independent from IM and equal to the replacement value of the building; $P(C \mid IM)$ is the probability of collapse conditioned on IM.

Figure 7 shows that with the increase of the damaging action the repair cost inflates making the curve translate rightward, while dispersion of results increases. It is worth to note that the $c_r$ is strongly influenced by the number of collapse cases occurred during the simulation process; consequently, its influence increases as PGA increases (i.e., the probability of collapse increases) making the curve translate upward.

### 4.2 Simplified assessment via pushover

*Original building*

In this section, Mass proportional and 1st mode proportional SPO are performed for the original building. Both analyses indicate the activation of a 1st story collapse mechanism, with attainment of gravity load collapse at a roof displacement $\Delta_{Top}$ of 0.26 and 0.28 m respectively, corresponding to drifts of 6.24 and 6.84 %.

Figure 8 shows the two pushover curves along with the results of the NLRH analysis, expressed in terms of roof displacement vs base shear, for record Imperial Valley scaled at an

intensity of PGA=0.5g. First story collapse mechanism is attained for 93% of the considered records.

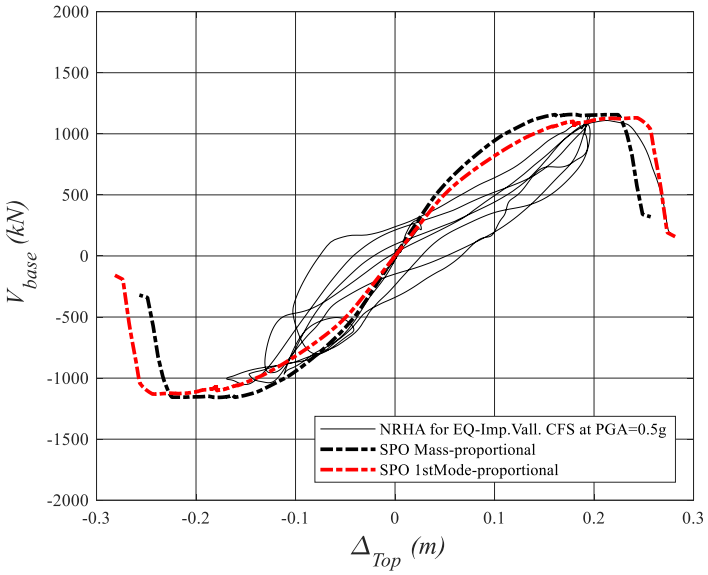


Figure 8. Comparison between Mass and 1st Mode-proportional SPO and NRHA for Imperial Valley 1979 record scaled at PGA=0.5g.

The capacity curves obtained from SPO analyses are transformed in multi-linear curves representing the backbone curve of equivalent SDOF system and IN2 method [32] is applied to compute building capacity and to obtain seismic demand for earthquakes of varying intensity level. The spectrum utilized to apply IN2 method is the mean spectrum of the 30 records utilized for NLRH analyses. Seismic capacity is expressed in terms of peak ground acceleration and indicated as $PGA_c$(g).

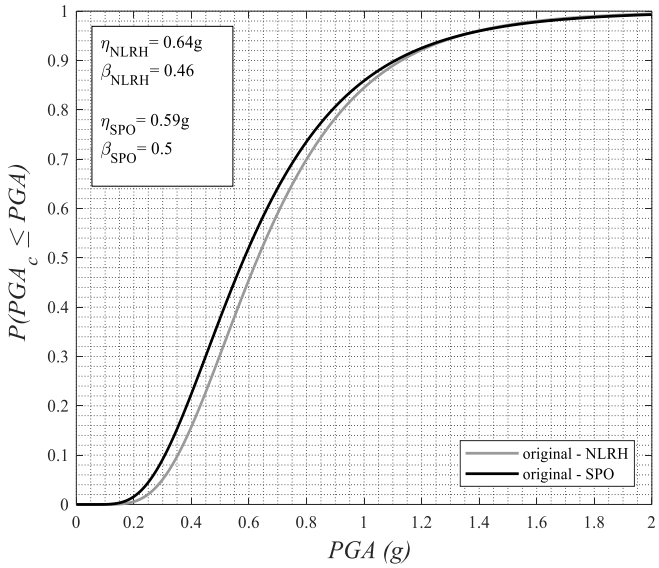


Figure 9. Collapse fragilities for the original building obtained through NLRH and SPO approach.

In particular, the mean result from both SPO analyses is considered, obtaining $PGA_{c,PO}$=0.59g. Median capacity from NLRH analyses is $PGA_{c,NLRH}$=0.64g.

Figure 10 shows the collapse fragility curves obtained from NLRH analyses and with SPO based approach. The latter curve is built considering $PGA_{c,PO}$ as median capacity and the logarithmic dispersion β=0.5, as indicated in [33] for mid-rise old RC frame buildings. It can be noted that the fragility curve representation obtained starting from SPO analyses allows a fair approximation of NLRH-based curve.

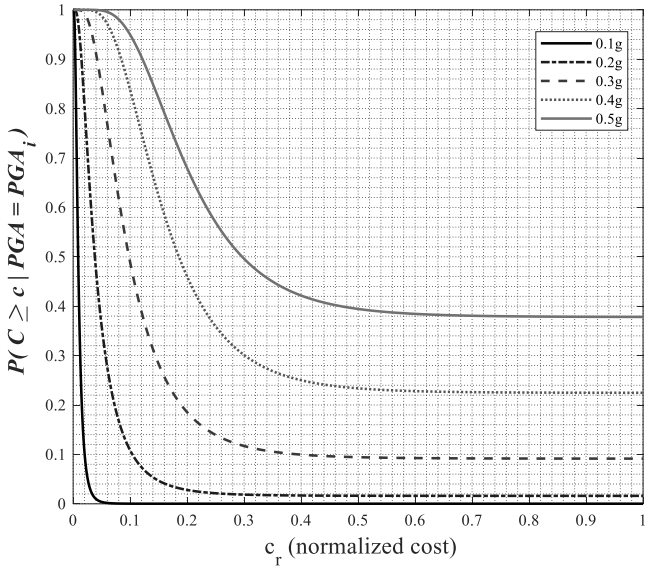


Figure 10. CCDFs of total normalized repair costs ($c_r$) for different PGAs obtained through SPO procedure for the original building.

In Figure 10, the CCDF of the total normalized repair cost obtained with the SPO approach are depicted. Note that the maximum considered IM corresponds to $a_g$=0.5 since for higher IMs the SPO considers the structure collapsed. Curves obtained adopting SPO approach show a very similar trend to curves obtained with NLRH. In particular, the SPO-based curves generally underestimate total repair costs for lower intensities, while lead to an overestimation of costs for higher intensities. However, the scatter between detailed and simplified approach is very low. In fact, the higher error between two calculations is attained for PGA=0.1g, where the ratio between the static and the dynamic median $c_r$, obtained by applying Eq. (4), is about 13%, while the difference between two computations decreases to 5% for 0.3g leading to a slight overestimation when the SPO approach is adopted.

*Retrofitted building*

Figures 11 and 12 show the SPO curves obtained with Mass-proportional and 1st Mode-proportional load patterns for the three building configurations. As it can be seen, in any cases the retrofit intervention allows an increase of building capacity. In particular, the application of CFRP wrapping increases system ductility not significantly influencing strength, and this effect more sensible in the case of wrap12; while the retrofit scheme that adopts shear wall reduces system ductility while increases system strength. Coherently, the collapse fragility curves obtained using the IN2, shown in Figure 13, evidence a higher shift of the curve of

wrap12 with respect to original building if compared to the shift of wrap1, while the collapse fragility for wall is situated between the two wrap schemes.

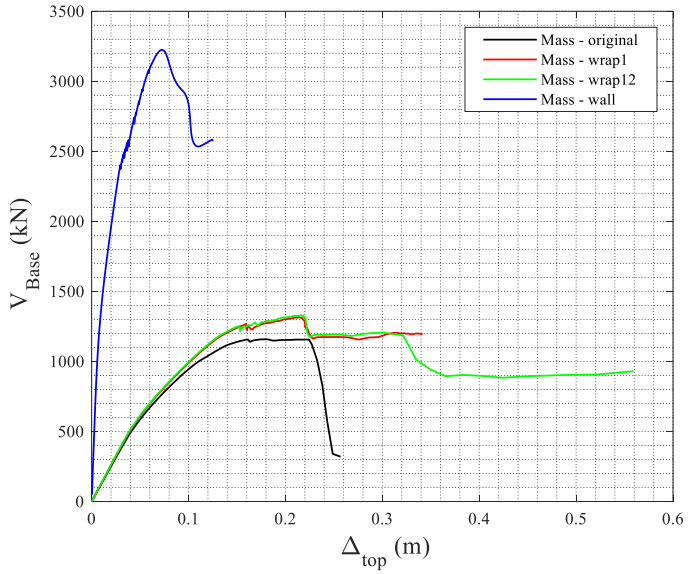


Figure 11. SPO curves obtained with Mass-proportional load pattern for original building and for the three retrofit configurations (wrap1, wrap12, wall)

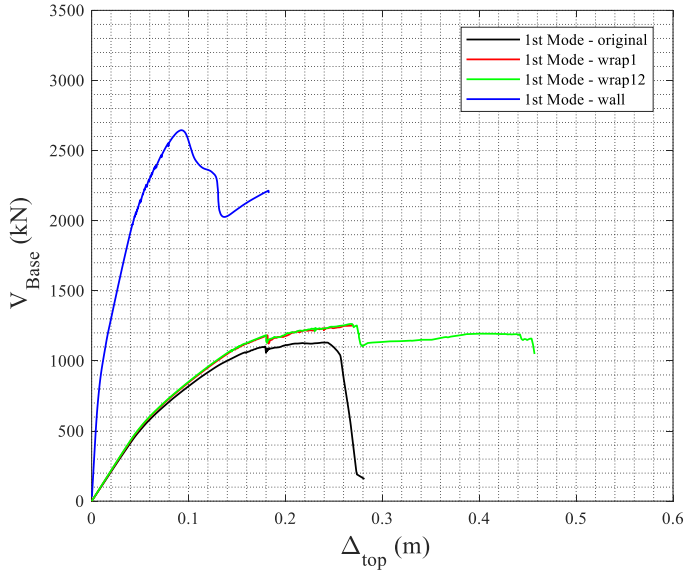


Figure 12. SPO curves obtained with 1st Mode-proportional load pattern for original building and for the three retrofit configurations (wrap1, wrap12, wall)

In fact, as depicted in Figure 13, the median capacity for wrap1 increases from the original value of $PGA_{c,PO}$ =0.58g to $PGA_{c,PO,wrap1}$=0.72g while for the wrap12 and wall configuration it increases up to $PGA_{c,PO,wrap12}$=1.06g and $PGA_{c,PO,wall}$=0.81g. Note that for the retrofit wall that adopts shear wall a logarithmic dispersion β=0.63, as indicated in [33] for mid-rise coupled wall-frame buildings is adopted.

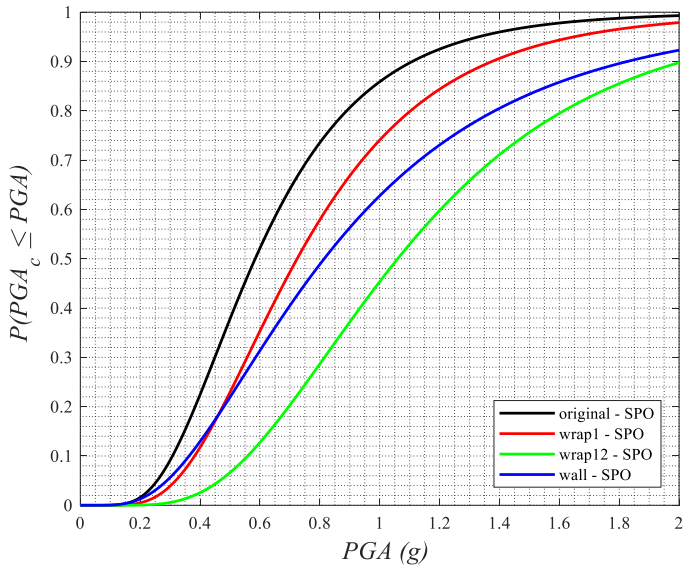


Figure 13. Collapse fragilities for the original building obtained through NLRH and SPO approach and for the three retrofit configurations (wrap1, wrap12, wall) through SPO

Total repair costs are calculated for three building configurations and different earthquake intensities adopting the SPO approach and the procedure outlined in 2.2. For each simulation, the cost of retrofit is added to total repair costs.

Figure 10 shows the CCDFs of the $c_r$ obtained through the SPO approach for three different PGAs and three considered building configurations.

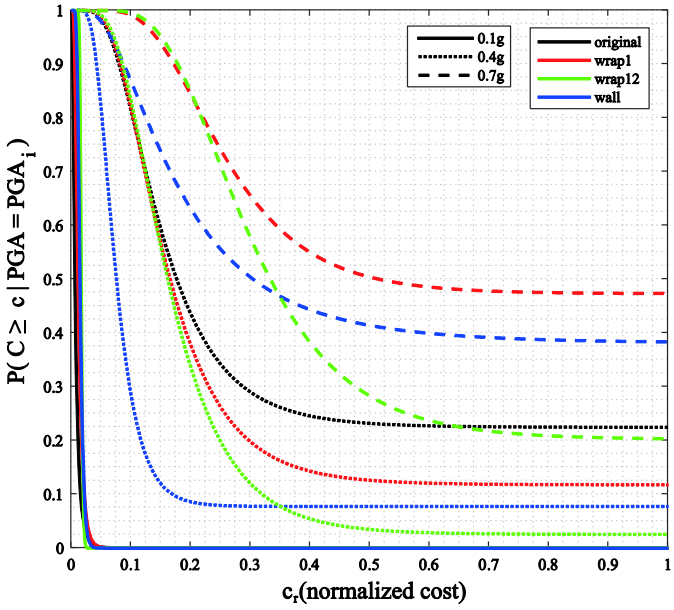


Figure 14. CCDFs of total normalized repair costs ($c_r$) for different PGAs obtained through SPO procedure

Figure 14 shows that the effectiveness of the retrofit strategy varies depending on the earthquake intensity. In particular, retrofit results to be ineffective for lower intensities where repair costs are mainly ascribable to damage in acceleration-sensitive components while the

influence of collapse probability is negligible. The applied strategies do not significantly modify the peak floor acceleration response of the building, and similar repair costs for four building configurations are expected. As the intensity of ground motion increases, the influence of drift-sensitive components and collapse cases on total repair cost becomes more noticeable. In fact, for $a_g$=0.4g and for wrap1 and wrap12 the median repair cost decreases of about 6% and 9%, respectively, while for the retrofit scheme introducing shear wall a decrease in repair costs of about 130% is attained due to reduction of drift demand. Further, for higher PGAs, the effectiveness of retrofit in reducing repair costs increases as the collapse capacity increases due to retrofit. For instance, for PGA=0.7g the median value of normalized repair cost drops from 100% (given that structure collapses for $PGA_{c,PO}$=0.59g) for the original building, to 51% for wrap1, 33% for wrap12 and to 30% for wall. Thus, due to the different collapse probabilities when adopting wrap12 and wall schemes, the beneficial effect of the two retrofit strategies becomes similar for higher seismic intensities, when the collapse capacity has the highest influence on repair costs.

## 5 CONCLUSIONS AND FUTURE STUDIES

The study presented in this paper aims at contributing in the evaluation of the usability of a simplified static pushover (SPO) based approach for the computation of total repair costs.

The efficiency of the SPO approach is demonstrated through an application to a case-study building representative of an existing non-ductile reinforced concrete frame. The response of the frame is simulated using a refined 2D finite element model that properly accounts for possible brittle failures of structural members and captures typical non-ductile RC frames failure modes.

The first comparison in terms of collapse fragility shows that the SPO, coupled to the IN2 method [32], fairly captures the median capacity of the building. In fact, due to the ability of the SPO to capture the most likely collapse mechanism, median capacity evidenced from NLRH is captured by SPO approach with an error of 8%.

Then, the results in terms of total repair costs obtained starting from the classical NLRH approach are compared to those obtained through a SPO-based approach. For both cases, total repair costs are calculated adopting the PEER PBEE framework [1] using a Montecarlo simulation. Additional EDPs are generated using a simulation-based method [15].

In the static approach the IN2 method for increasing earthquake intensities is applied and the EDPs in terms of interstorey drift are calculated. Peak floor accelerations are obtained by simplified formulas [8]. Suitable dispersions are adopted to account for uncertainties not accounted for in SPO.

The results show $c_r$ is strongly influenced by the number of collapse cases occurred during the simulation process; consequently, the incidence of collapse increases as the PGA increases.

The simplified SPO approach shows encouraging results leading to very similar losses obtained through more refined methods when the structure experiences nonlinear deformations, while some improvements are required when the linear range is investigated. In fact, the higher error is attained for PGA=0.1g, where the ratio between the SPO and the NLRH median $c_r$ is of about 13%, while the difference between two methods is lower than 10% for higher PGAs, where the SPO approach leading to a slight overestimation.

These results suggest that, although the results SPO-based procedure will be inevitably affected by a certain degree of approximation with respect to NLRH analyses, the approximated results are justified in the view of a significant reduction of computational burden.

Finally, the SPO approach is implemented considering three possible retrofit schemes adopting complete full-height CFRP wrapping to avoid brittle failures in first (wrap1) and first two storeys (wrap12), and the strengthening of the system through the adoption of a shear wall (wall). In any cases the retrofit intervention allows an increase of median building capacity, that is particularly noticeable for wrap12 (about 80%).

The results of cost analysis show that, the effectiveness of the retrofit schemes vary depending on the earthquake scenario.

In particular, retrofit results to be ineffective for lower intensities where repair costs are mainly ascribable to damage to acceleration-sensitive components while the influence of collapse probability is negligible. The applied strategies do not significantly modify the peak floor acceleration response of the building, and similar repair costs for four building configurations are expected. As the intensity of ground motion increases, the influence of drift-sensitive components and collapse cases on total repair cost becomes noticeable. In fact, for ag=0.4g and for wrap1 and wrap12 the median repair cost decreases of about 6% and 9%, respectively, while for the retrofit scheme introducing shear wall a decrease in repair costs of about 130% is attained due to reduction of drift demand. Further, for higher PGAs, the effectiveness of retrofit in reducing repair costs increases as the collapse capacity increases due to retrofit. For instance, for PGA=0.7g the median value of normalized repair cost drops from 100% for the original building, to 51% for wrap1, 33% for wrap12 and to 30% for wall. Thus, due to the different collapse probabilities when adopting wrap12 and wall schemes, the beneficial effect of the two retrofit strategies becomes similar for higher seismic intensities, when the collapse capacity significantly influences repair costs.

The present study shows that, as expected, the adoption of retrofit strategies increasing ductility capacity does not significantly vary repair costs, except the portion depending on costs related to collapse. Further, it evidences that the adoption of retrofit strategies increasing strength has a slight influence for lower seismic intensities while it significantly reduces repair costs for mid intensities leading to similar effects to those produced by retrofit strategies increasing ductility for higher intensities.

The study does not pretend to be exhaustive, having compared the results of SPO with NLRH for only one case-study frame building.

Additional studies are required to assess the advantages of other alternative strategies in terms of seismic performances, to improve repair cost prediction for low seismic demand and to further simplify the computation of repair costs for an easier application to large building inventories.

## ACKNOWLEDGEMENTS

This study was performed within the framework of the PON METROPOLIS "Metodologie e tecnologie integrate e sostenibili per l'adattamento e la sicurezza di sistemi urbani" grant n. PON03PE_00093_4 and the joint program DPC-Reluis 2014-2016 Task 3.3: Reparability limit state and damage cumulated effects. The S.Co.P.E. computing infrastructure at the University of Naples Federico II was used for the parallel computing.

## REFERENCES

[1] K.A. Porter. An overview of PEER's performance-based earthquake engineering methodology. In Proceedings of 9th International Conference on Applications of Statistics and Probability in Civil Engineering, 2003.

[2] A.B. Liel, & G.G. Deierlein. Cost-benefit evaluation of seismic risk mitigation alternatives for older concrete frame buildings. Earthquake Spectra, 29(4), 1391-1411, 2013.

[3] M. Polese, M. Marcolini, M. Gaetani d'Aragona, & E. Cosenza. Reconstruction policies: explicitating the link of decisions thresholds to safety level and costs for RC buildings. Bulletin of Earthquake Engineering, 15(2), 759-785, 2017 DOI: 10.1007/s10518-015-9824-0.

[4] M. Gaetani d'Aragona, M.Polese, M. Di Ludovico. Building retrofit prior to damaging earthquakes: reduction of residual capacity and repair costs, paper ID 2490, 16th World conference on Earthquake Engineering, Santiago Chile, January 9th to 13th 2017.

[5] M. Gaetani d'Aragona, M. Polese, A. & Prota. Relationship between the variation of seismic capacity after damaging earthquakes, collapse probability and repair costs: detailed evaluation for a non-ductile building. In 5th ECCOMAS Thematic Conference on Computational Methods in Structural Dynamics and Earthquake Engineering, Crete Island, Greece, 25–27 May 2015 (pp. 1478-1495).

[6] M. Polese, M. Gaetani d'Aragona, A. Prota, & G. Manfredi. Seismic behavior of damaged buildings: a comparison of static and dynamic nonlinear approach, paper #1134, In 4th ECCOMAS Thematic Conference on Computational Methods in Structural Dynamics and Earthquake Engineering, 2013 (pp. 608-625).

[7] M. Gaetani d'Aragona, M. Polese, K.J. Elwood, M. Baradaran Shoraka, & A. Prota. Aftershock collapse fragility curves for non-ductile RC buildings: a scenario ‐ based assessment. Earthquake Engng Struct. Dyn., 2017. doi: 10.1002/eqe.2894.

[8] ATC. 2012. FEMA P-58-1: Seismic Performance Assessment of Buildings. Volume 1– Methodology, 2012.

[9] D. Vamvatsikos, A. Cornell. Direct Estimation of the Seismic Demand and Capacity of Oscillators with Multi-Linear Static Pushovers through IDA. Earthquake Engineering and Structural Dynamics; 35:1097–1117, 2006.

[10] P. Fajfar. Capacity spectrum method based on inelastic demand spectra. Earthquake Engineering and Structural Dynamics; 28:979–93, 1999.

[11] G.M. Calvi, T.J. Sullivan, & D.P. Welch. A seismic performance classification framework to provide increased seismic resilience. In Perspectives on European Earthquake Engineering and Seismology; pp. 361-400, 2014.

[12] H. Aslani, & E. Miranda. Probabilistic Earthquake Loss Estimation and Loss Disaggregation in Buildings, Report No. 157. Stanford, CA: John A. Blume Earthquake Engineering Center, Stanford University, Stanford, 2009.

[13] C.M. Ramirez, A.B. Liel, J. Mitrani-Reiser, C.B. Haselton, A.D. Spear, J. Steiner, ... & E. Miranda. Expected earthquake damage and repair costs in reinforced concrete frame buildings. Earthquake Engineering & Structural Dynamics, 41(11), 1455-1475, 2012.

[14] C.M. Ramirez, E. Miranda. Building-Specific Loss Estimation Methods & Tools for Simplified Performance-Based Earthquake Engineering Report No 171, John A. Blume Eartquake Engineering Research Center, Standford University, Stanford, 2009.

[15] T.Y. Yang, J Moehle, B. Stojadinovic, & A. Der Kiureghian. Seismic performance evaluation of facilities: methodology and implementation. Journal of Structural Engineering, 135(10), 1146-1154, 2009.

[16] C. Petrone, G. Magliulo, & G. Manfredi. Seismic demand on light acceleration‐sensitive nonstructural components in European reinforced concrete buildings. Earthquake Engineering & Structural Dynamics, 44(8), 1203-1217, 2015.

[17] V. Vukobratović, & P. Fajfar. A method for the direct estimation of floor acceleration spectra for elastic and inelastic MDOF structures. Earthquake Engineering & Structural Dynamics, 2016.

[18] T.J Sullivan, P.M. Calvi, & R. Nascimbene. Towards improved floor spectra estimates for seismic design. Earthquakes and Structures, 4(1), 109-132, 2013.

[19] H. Krawinkler. Van Nuys Hotel Building Testbed Report: Exercising Seismic Performance Assessment, PEER 2005/11, University of California, Berkeley, Oct. 2005.

[20] K.J. Elwood. Modelling Failures in Existing Reinforced Concrete Columns. Canadian Journal of Civil Engineering: 846-859, 2004.

[21] OpenSees. Open system for earthquake engineering simulation OpenSees framework-Version 2.5.0. Pacific Earthquake Engineering Research Center, Univ. of California, Berkeley, 2016.

[22] E. Spacone, V. Ciampi, F.C. Filippou. A Beam Element for Seismic Damage Analysis. Report No. UCB/EERC-92/07. Earthquake Engineering Research Center, College of Engineering, University of California, Berkeley, 1992.

[23] S. Alath, S.K. Kunnath. Modeling inelastic shear deformation in RC beam-column joints. Engineering Mechanics Proceedings of 10th Conference, May 21-24, ASCE, Boulder, CO, USA; 822–825, 1995.

[24] W.M. Hassan, J.P. & Moehle. A Cyclic Nonlinear Mac-ro Model for Numerical Simulation of Beam-Column Joints in Existing Concrete Buildings. In Proceedings of the 15th World Conference of Earthquake Engineering, 2012.

[25] ACI 369R-11. Guide for Seismic Rehabilitation of Exist-ing Concrete Frame Buildings and Commentary. Report by ACI committee 369, American Concrete Institute, 2011. ISBN: 978-0-87031-419-3.

[26] ACI 440.2R-08. Guide for the design and construction of externally bonded FRP systems for strengthening concrete structures. Report by ACI Committee 440.2R-08. Farmington Hills, MI, USA: American Concrete Institute, 2008.

[27] M.R. Spoelstra, & G. Monti. FRP-confined concrete model. *Journal of composites for construction*, 3(3), 143-150, 1999.

[28] J.P. Moehle, T. Ghodsi, J.D. Hooper, D.C. Fields, & R. Gedhada. Seismic design of cast-in-place concrete special structural walls and coupling beams: A guide for practicing engineers, NEHRP Seismic Design Technical Brief No. 6, NIST GCR 11-917-11REV-1, Gaithersburg, MD, 2011.

[29] L.M. Massone, K. Orakcal, & Wallace, J.W. Shear-Flexure Interaction for Structural Walls. SP-236, ACI Special Publication – Deformation Capacity and Shear Strength of Reinforced Concrete Members Under Cyclic Loading, editors: Adolfo Matamoros & Kenneth Elwood, 127-150, 2006.

[30] D. Vamvatsikos, A. Cornel.l Incremental dynamic analysis. Earthquake Engng Struct. Dyn. 31 (3), 491-514, 2002.

[31] D. Vamvatsikos, A. Cornell. Seismic Performance, Capacity and Reliability of Structures as Seen Through Incre-mental Dynamic Analysis. Report No 151, John A. Blume Earthquake Engineering Research Center, Stanford University, 2005.

[32] M. Dolsek, & P. Fajfar. Simplified non-linear seismic analysis of infilled reinforced concrete frames. Earthquake engineering & structural dynamics, 34(1), 49-66, 2005.

[33] M. Kosič, P. Fajfar, & M. Dolšek. Approximate seismic risk assessment of building structures with explicit consideration of uncertainties. Earthquake Engineering & Structural Dynamics, 43(10), 1483-1502, 2014.

COMPDYN 2017
6th ECCOMAS Thematic Conference on
Computational Methods in Structural Dynamics and Earthquake Engineering
M. Papadrakakis, M. Fragiadakis (eds.)
Rhodes Island, Greece, 15–17 June 2017

# SEISMIC AMELIORATION OF EXISTING REINFORCED CONCRETE BUILDINGS: STRATEGY TO OPTIMIZE THE AMOUNT OF REINFORCEMENT FOR JOINTS

**Vincenzo Bianco[1], Giorgio Monti[1], Alessandro Vari[2] and Gianluigi Palmieri[2]**

[1] Department of Structural Engineering and Geotechnics – Sapienza University of Rome, Italy
via Antonio Gramsci n°53 00197 - Rome
{vincenzo.bianco, giorgio.monti}@uniroma1.it

[2] Research and Development Department – Edil CAM Sistemi s.r.l.
via dei Genieri n°39 00143 - Rome
{a.vari, g.palmieri}@edilcamsistemi.com

**Keywords:** Reinforced Concrete, Existing Buildings, Seismic Amelioration, Design, Beam-Column Joints.

**Abstract.** *Most of the existing Reinforced Concrete (RC) buildings in Italy were built according to obsolete regulations that were not enough aware of issues related to seismic design so that they need to be upgraded by pursuing either amelioration or full seismic rehabilitation. In doing that, the first step is to figure out what is, based on the results of the initial analysis of the structure in its ante-operam version, the best overall dissipative mechanism that could be obtained by a number of suitable and economically convenient local interventions. The choice of the overall dissipative mechanism strongly affects the amount of reinforcement to be adopted for the beam-column joints. For new buildings, the current adopted capacity design philosophy pursues an overall beam-sway mechanism in which plastic hinges first form in beams and at last at the base of the columns. On the contrary, for existing ones, often very irregular and gravity-load-dominated, pursuing such overall mechanism may result either uneconomic or even extremely difficult to implement due to the amount of reinforcement to be inserted in the joints. In such cases, an overall dissipative mechanism allowing, at some extent, columns flexural plasticization should be accepted and clearly identified in advance. Anyway, such approach needs to be addressed properly in order to avoid the formation of column-sways at one story only that would result very dangerous due to the excessive demand of plastic rotations on the resulting hinges. This paper presents two simple models that may help the designer in dealing with the operations above. The former is a model that allows to understand if, given the existing RC building case-study, either the beam-sway or a hybrid beam-column-sway mechanism should be conveniently pursued during the design of the retrofitting intervention. The latter is a model that allows to design a hybrid beam-column-sway overall mechanism involving a suitable number of stories such as to guarantee a uniform and reasonable demand of plastic rotations in the involved columns.*

## 1 INTRODUCTION

A large amount of the built heritage in most of the European earthquake-prone countries is composed of existing Reinforced Concrete (RC) buildings around a century old. These buildings were certainly built in compliance with very obsolete Building Codes (*e.g.* [1]) showing no or little awareness of the seismic-behavior-related issues so that they are certainly inadequate to sustain the design earthquake specified by current regulations (*e.g.* [2,4]). Such buildings require either amelioration or full-rehabilitation interventions. The former means making the building capable to sustain, for a given Ultimate Limit State (ULS), a larger percentage (less than 100 %) of the Code-specified earthquake while the latter means intervening to such an extent to make the building capable to withstand one hundred percent of the seismic action.

Following the recent seismic events that have struck the Italian territory, *i.e.* the city of L'Aquila (2009), the region of Emilia Romagna (2012) and the city of Amatrice (2016), professional engineers have undertaken many of such retrofitting intervention designs. Independently of the aim of the intervention, either amelioration or full rehabilitation, there has been a widespread tendency to use innovative techniques for the local strengthening of deficient RC members, either beams, columns, or joints. Among these techniques in particular, either 1) the use of Fiber Reinforced Polymer (FRP) wrappings, or 2) the so-called CAM®, which is the acronym of the Italian name *Cucitura Attiva dei Manufatti* (literally: *Artefacts Active Sewing*), have been attracting the attention of the technical community and also applied, in many case-studies (Fig. 1). According to the latter, existing RC elements are wrapped by high strength steel strips that are slightly pretensioned in order to confine the retrofitted element thus providing a readily available source of extra-strength that, differently from the FRPs, does not need the element deformation in order to be activated. The CAM® has also the advantage to allow the RC element be literally sewed whatever the geometrical boundary conditions characterizing the specific case study might be. The FRPs on the contrary, even if not active, offer the advantage to be lighter and easier to apply. Anyway, those techniques are still more expensive with respect to the more traditional ones contemplating the jacketing of existing RC elements by either 1) plain steel cold formed elements joined *in situ* by fillet welds or 2) reinforced concrete coatings. For this reason, since very conservative interventions may result excessively expensive thus discouraging both the application and the further spread of those innovative techniques, there is a growing attention towards the way to optimize the amount of the reinforcement.

The intense post-earthquake retrofitting design activity that has taken place in Italy has shown that the necessity to optimize the amount of reinforcement is particularly important for the case of RC joints. The Italian Building Code offers two alternative strategies to evaluate the amount of stirrups to strengthen the joint panel that are: 1) the formulation presented in the main cogent document [2], which are transposed from the European Codes [3,4], and 2) the formulation reported in the explanatory (not cogent) document [5]. The former is a formulation that seems to be derived from the pioneering works on the *capacity design philosophy* [6] and that is essentially based on the resisting mechanisms that characterize the joint behavior at its ultimate state when, due to the presence of thoroughly smeared cracks, it is far from being constituted of an homogenous and isotropic continuum material. While the latter, implicitly proposed for the case of existing buildings, is based on the application of the Mohr circle to a joint assumed composed of an homogeneous and isotropic elastic material. The former formulation seems to be well contextualized in the ambit of the performance-based design philosophy, which is already adopted by the Euro Codes, and is based on the conception of an overall dis-

sipative mechanism according to which the new building is expected to behave during an earthquake attack. On the contrary, the latter one seems to be an inheritance of the former prescriptive design philosophy according to which, in the case of existing buildings, we can just strengthen the joints, regardless of the overall dissipative mechanism induced. Such approach indeed is justified by the difficulty to intervene on existing buildings that can be very irregular, either in plan or in elevation, and that, due to the gravity-loads-based original design, are often characterized by the presence of strong beams and weak columns. On the contrary, for the conception of new buildings, the formation of an overall dissipative mechanism that envisages the formation of plastic hinges in the beams extremities first and then at the lowermost extremity of the columns, is favored by the adoption of a weak-beam-strong column regular conception. In the case of existing buildings, the design of interventions capable to induce a proper overall dissipative mechanism is relatively more cumbersome.

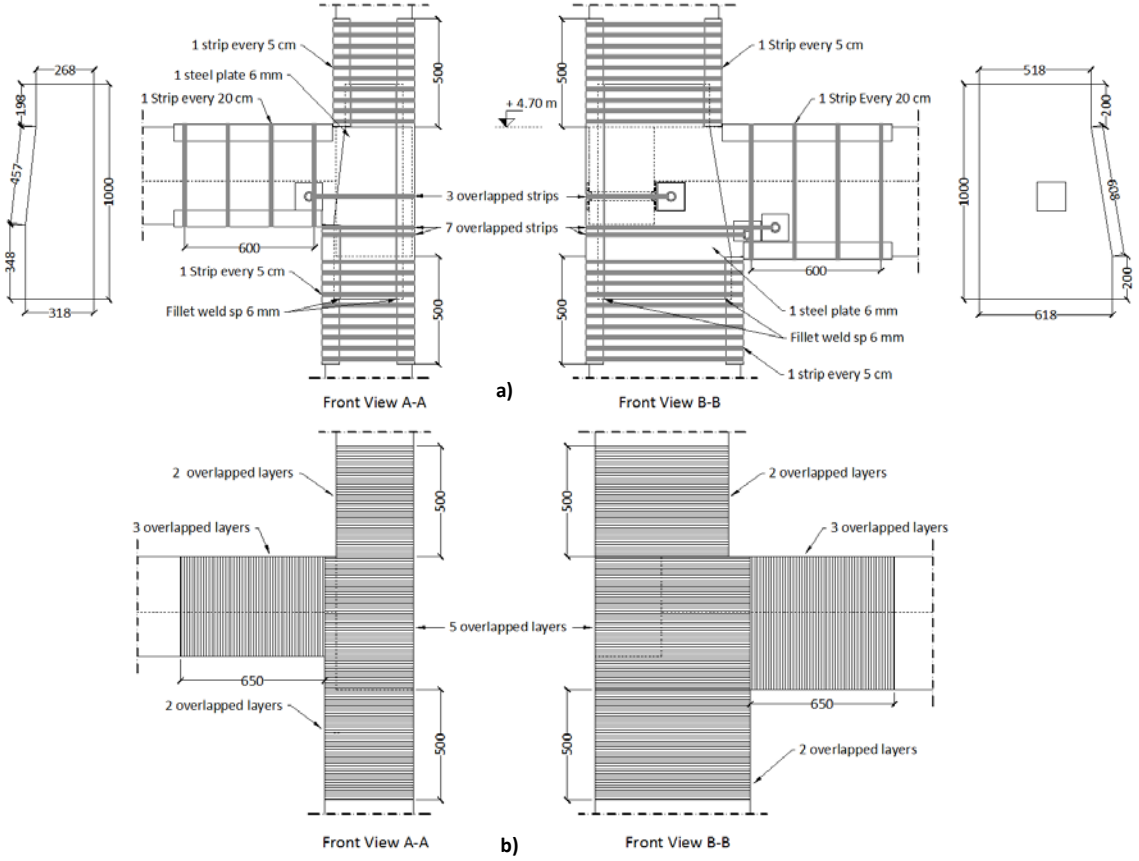


Figure 1 Most common innovative techniques recently adopted in Italy to strengthen RC joints: a) CAM® wrapping by high strength steel strips and b) FRP layers.

In this scenario, even though design is carried out at the Life Safety ULS, in which the use of the first formulation would be more appropriate, practitioners have diffusely implemented the second one that has brought to more reasonable amounts of reinforcements, even though in a complete unawareness of the overall dissipative mechanism thus induced.

With the aim to contribute to a more rational design of the seismic retrofitting interventions on existing RC buildings, the present work proposes a strategy to optimize the amount of reinforcement for joints by taking also into consideration the overall dissipative mechanism to be pursued by means of local interventions.

## 2 OVERALL DISSIPATIVE MECHANISM

### 2.1 New RC buildings

When it comes to new RC buildings, the widely accepted tendency is to design ductile Moment Resisting Framed (MRF) structures, by means of the so-called *Capacity Design*, which was early introduced by Paulay and Priestly [6]. The objective is to design MRF structures that are capable to withstand acceptable excursions in the plastic range, during the earthquake-induced oscillations, thus dissipating the input energy.

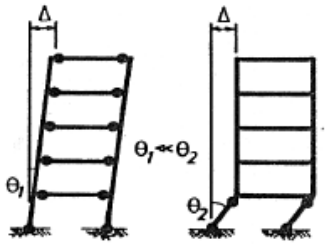


Figure 2 Energy-dissipating mechanisms: a) mechanism with smeared formation of plastic hinges, in all beams and at the base of the columns, b) soft story mechanism.

The overall energy dissipating mechanism is selected in advance. The most favorable mechanism is the one in which flexural plastic hinges form at the extremities of all the beams first, and then at the lowermost extremity of all the columns. This mechanism (Fig. 2a) is the most suitable one since it guarantees a uniform distribution of plastic hinges throughout the development of the building, both in plan and elevation, thus fulfilling the overall displacement ductility requiring the smallest inelastic rotational demands in the plastic hinges. On the contrary, the so-called *soft-story* mechanisms (Fig. 2b), in which plastic hinges form at both the extremities of all the columns of a story, should be avoided since they imply that, for the same overall displacement ductility requirement, the local rotational demand in the plastic hinges is much larger. Such plastic hinges rotational demands may be too large so that, even with good detailing of the affected regions, would be difficult to accommodate. Another aspect that would further complicate the management of a soft-story mechanism is the $P-\Delta$ effect associated with the corresponding large horizontal displacement. Contextually to the selection of the overall dissipative mechanism, the location of the plastic hinges has to be determined with a relatively high degree of precision. Parts of the structure that are intended to remain elastic are designed so that under maximum feasible actions corresponding to the development of overstrength in the plastic hinges, no inelastic deformations should occur in those regions. Therefore, it is immaterial whether the failure of regions, intended to remain elastic, would be ductile or brittle. The actions originating from plastic hinges are those associated with the overstrength of these regions. The required strength of all other regions is then in excess of the strength demand corresponding to the overstrength of relevant plastic hinges. The care in the detailing of the plastic hinge regions is larger than that dedicated to the regions that are to remain elastic.

To guarantee the dissipative mechanism above, the formation of plastic hinges, in all the beams and columns, should occur almost simultaneously, which means for the same value of the overall displacement ductility demand. In this scenario, what are the operational instruments that designers have to induce such overall behavior? At this early stage of design, they can 1) manipulate the building geometry, and 2) redistribute the design actions. The former means trying to have a very regular structure where the concept of *regularity* also implies, beyond the even distribution of mass and stiffness [2-5], both in plan and elevation, that beams and columns be of practically the same length. This is necessary in order to have almost the same value of

rotational demand in all the beams plastic hinges, for a given value of the overall displacement demand. The *redistribution* means that, relying on the elasto-plastic behavior of the plastic hinge zones, bending moments can be transferred, on a given story, from one joint to another, thus reducing the capacity required to a beam extremity that will yield earlier and plastically rotate thus transferring the bending moment in another point. The moment redistribution is also useful to achieve a more efficient structural design of the steel reinforcement [6].

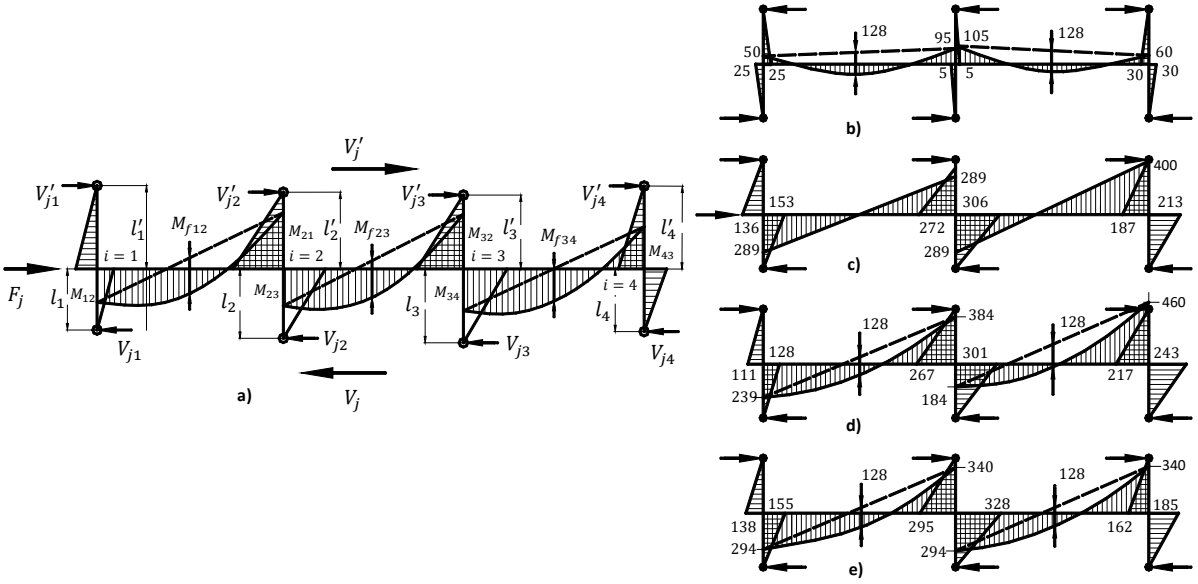


Figure 3 Features of moments redistribution: a) equilibrium of a subframe, b) gravity moments, c) earthquake moments, d) combined gravity and earthquake moments, e) redistributed gravity and earthquake moments.

The essential requirement of the moment redistribution process is that equilibrium under the applied seismic forces and gravity loads must be maintained. Fig. 3a represents a typical subframe of a multistory frame isolated by cutting columns above and beneath the beams at column contraflexure points. The moment pattern shown resulted from an elastic analysis for the simultaneous action of gravity loads and earthquake loads, duly factored. The total shear forces transmitted by the columns below and above the floor are $V_j$ and $V_j'$, respectively, for the rightward direction of the earthquake forces considered. In considering equilibrium criteria, the simplifying assumption is made that the distance between the two column points of contraflexure, above and below the beam centerline, is the same for each column of the frame, and this distance does not change while beam moments are redistributed. This means that $l_i' + l_i = l_c$ is a constant length. During moment redistribution, the moment applied to the ends of the beams may be changed, but the total moment input to the columns must remain unchanged, and equal to the sum of the moments input by the column to the beam at joint $i$, that is:

$$\sum_i \left(M_{i,i-1} + M_{i,i+1}\right) = \sum_i M_{bi} = \sum_i M_{ci} \tag{1}$$

where: $M_{bi}$ is the bending moment introduced to a column by the beams that are joined to the column at node point $i$, and $M_{ci}$ is the moment input to the continuous beam at joint $i$.

There are two characteristic situations for moment redistribution along continuous beams: a) the first involves beam moments redistribution across a joint, and b) the second type of moment redistribution in the beam involves redistribution of actions between columns. The former implies that, if a beam moment at a joint is changed, the other at the same joint, must change

accordingly but, since the total beam moment input to the joint remains unaltered, the moments and shear forces for the relevant column remain the same as before. The latter means that, when a beam moment change (*e.g.* a reduction) at a given joint $i$ is compensated by a beam moment change in other joints (an increase), even though Eq. (1) is satisfied, since the moment input to these latter columns has changed, the shear forces in these latter will also change. Thus, redistribution of both moments and shear forces between columns will take place.

In an attempt to achieve a desirable solution, the designer manipulates end moments of beams. Gravity load equilibrium will be maintained provided that the part of the bending moment that originates from gravity load only, and is applicable to a simply supported beam (i.e. the moment superimposed on a straight baseline which extends between the beam end moments), is not changed. A change of beam end moments in any span will change the beam reactions and hence the forces introduced to individual columns below the beam under consideration.

An example of moment redistribution for a regular earthquake dominated frame is shown in Fig. 3b-e. The moment pattern (Fig. 3d) due to the superimposition of the patterns due to gravity loads (Fig. 3b) and to the earthquake equivalent lateral force (Fig. 3c) is redistributed (Fig. 3e) in order to have almost equal values of positive and negative bending moments, thus yielding a more uniformly distributed steel reinforcement along the beam length.

The application of the Capacity Design, intended to induce the formation of the desired overall dissipative mechanism, encompasses the following steps, to be undertaken in sequence: 1) beam flexural design, 2) beam shear design, 3) column flexural design, 4) column shear design, 5) beam-column joint design. Beam flexural design is carried out in such a way that, at the selected plastic hinge locations, flexural strength is as close as possible to the moment requirement resulting from the redistribution process while elsewhere, flexural strength is selected so as not to allow plastic hinges to form. Shear strength at all sections of the beam is designed to be higher than the shear corresponding to the flexural overstrength, due to the steel strain hardening, at the beam plastic hinges. Consideration of joint moment equilibrium and possible higher mode amplification are used to determine the maximum feasible column moment corresponding to beam flexural overstrength. Ideal column moment capacity is matched to these required strengths to ensure that the weak beam-strong column hierarchy is achieved. The determination of the necessary amount of transverse reinforcement is based on the more stringent of the requirements for shear strength, which are: confinement of compressed concrete, stability of compression reinforcement, and lapped bar splices. An estimate of the maximum feasible shear force in the column is made based on equilibrium considerations at beam flexural overstrength. Because beam-column joints are poor sources of energy dissipation, inelastic deformations due to joint shear forces or bond deterioration must be minimized. The ideal strength of joints is matched to the input from adjacent beams when these develop flexural overstrength at the critical sections of plastic hinges.

How can the Capacity Design philosophy described hereinabove be interpreted in energetic terms [7-9]? Referring to an elasto-plastic Single Degree Of Freedom System (SDOF), subject to a seismic action, the energy balance can be written as follows [9]:

$$E_I(t) = E_S(t) + E_K(t) + E_D(t) + E_H(t) \tag{2}$$

where: at a generic time instant $t$, $E_S(t)$ and $E_K(t)$ are the instantaneous values of a) strain energy stored by the structure and b) the kinetic energy of the moving mass, respectively; $E_I(t)$, $E_D(t)$, and $E_H(t)$ are the value of energy, cumulated since the time instant $t_0$, and respectively c) input in the structure, d) dissipated by viscous damping and e) dissipated by hysteresis. The hysteretic and viscous components of the energy, are increasing functions of time since they represent forms of energy that cannot be recovered while, on the contrary, both kinetic an strain

energy can be recovered. After the end of the earthquake, at time $t_f$, the structure undergoes free oscillations with decreasing amplitude with time, which vanish at the time instant $t_q > t_f$, when all kinetic and elastic deformation energy has been dissipated. The cumulative equation of the energy balance in the instant in which stillness has been restored, can be written as follows:

$$E_I(t_q) = E_D(t_q) + E_H(t_q) \tag{3}$$

that shows the overall input energy has been dissipated by both viscous and hysteretic energy. In particular, if the structure has remained in the elastic range throughout the earthquake duration, it is $E_H(t_q) = 0$ and all the input energy has been dissipated by viscous damping $E_I(t_q) = E_D(t_q)$. On the contrary, if the structure has undergone excursions in the plastic range, it is $E_D(t_q) \ll E_I(t_q)$ and the structure has dissipated most of the input energy by hysteresis, which means $E_H(t_q) \cong E_I(t_q)$.

Thus, since $E_S(t)$ and $E_K(t)$ are instantaneous values of strain and kinetic energy, and since there is an instantaneous transfer of energy from the former to the latter form of energy, their instantaneous sum is constant. In this way, the objective to induce the formation of the desired dissipative mechanism in the structure by flexural yielding in predefined points, is equivalent to imposing that the potential elastic energy associated to the desired dissipative mechanism be the minimum of all possible mechanisms. Moreover, such potential elastic energy has to be slightly smaller than the kinetic energy corresponding to the Damage Limit State (DLS), that is:

$$E_{Sey} = min(E_{Sey,j}) \leq E_{K,DLS} = \frac{1}{2} \cdot M \cdot S_{V,DLS}^2 \tag{4}$$

where: $E_{Sey,j}$ is the elastic strain energy at yielding for the generic $j$-th dissipative mechanism, $M$ is the mass of the structure, and $S_{V,DLS}$ is the value of the velocity spectrum.

## 2.2 Existing RC buildings

When it comes to existing RC buildings, since they were built in compliance with obsolete Building Codes [1], unaware of seismic behavior, they are often neither regular nor designed to dissipate energy according to a well-defined dissipative mechanism. Moreover, since they were most probably built to resist gravity loads only, they typically present a strong beam-weak column typology. In cases in which there are beams longer than the others, they are most probably gravity-load-dominated which means that, at the beam-column joints, the negative bending moment is much larger than the seismic positive bending moment and their combination yields a negative moment. In this case, after the formation of the first (negative) hinge at one of the beam extremities, the formation of the second one would require a large increase of lateral force or displacement. Even though a skillful application of the either moment redistribution or relocation of plastic hinges away from column faces to zones where both gravity loads and lateral forces generate positive moments may help, in many situations the most meticulous allocation of beam hinge strength will not offset the excess potential lateral force resistance.

In such cases, insisting on pursuing the dissipative mechanism described in the previous section may result extremely difficult if not impossible. The design of the retrofitting intervention would be particularly difficult for joints. Thus, the possibility to intervene inducing other dissipative mechanisms would be preferable.

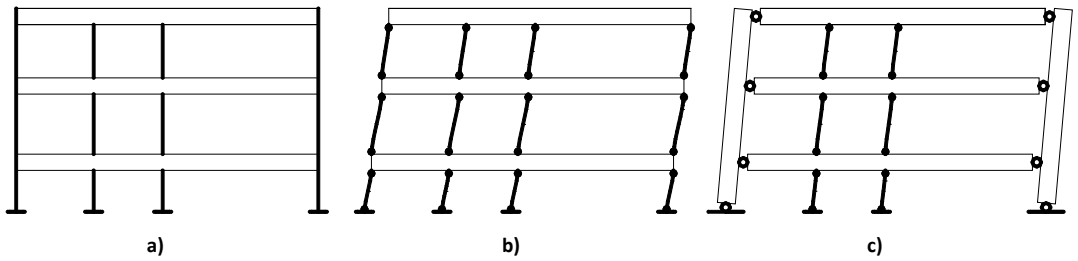


Figure 4 Existing strong-beam-weak-column RC buildings: a) typical example frame, b) shear-type (column-sway) dissipative mechanism, and c) hybrid column and beam sway dissipative mechanism.

Alternative solutions may be the following:

1) A shear-type mechanism (Fig. 4b), in which hinges are allowed to form in the columns extremities even though the right expedient has to be found in order to both a) force the formation of plastic hinges at the extremities of the columns of several stories, if not all, and b) ensure that, even after the formation of plastic hinges, the post-elastic oscillations do not concentrate on one story only. In fact, in this latter case, a soft story mechanism would take place.
2) A hybrid column and beam sway mechanism (Fig. 4c) in which at least a partial beam sway mechanism should develop to ensure that no column sway mechanism (soft story) can form. This can be achieved if plastic hinges are made to develop in the outer spans of beams close to exterior columns, which in turn may need to be strengthened in order to have adequate flexural strength to absorb without yielding the moment input from these outer beam spans. Column hinges above level one will thus not develop in the two outer columns of the frame. At the inner beam-column joints, column hinges below and above each floor will need to form to complete the frame mechanism. Since such mechanism has to rely on the flexural ductility capacity of the columns, which may not be desirable, the overall ductility demand may be restricted by increasing the lateral resistance of the frame to lateral forces.

Each of these alternative overall dissipative mechanisms will yield the beneficial effect to reduce the horizontal strengthening in most of the joints since the beam cross section at the column face does not yield. This aspect will be clarified in next sections.

## 3 CHOICE OF THE OVERALL DISSIPATIVE MECHANISM

In this paragraph a simple model is proposed that may help the designer figure out if, for the given case-study, it is convenient to orient the retrofitting intervention towards the reproduction of a beam-sway mechanism or instead it is more rational to purse one of the alternative overall dissipative mechanisms. A typical existing RC building characterized by beams and columns of different length and by the Strong-Beam-Weak-Column features is represented in Fig. 5.

The idea is to evaluate if, given the geometrical and mechanical characteristics of the various elements, once shear failures have been excluded [10,11], plastic hinge formation occurs in the columns earlier than in the beams, which means if:

$$u_{c,yc} \ll u_{c,yb} \tag{5}$$

where: $u_{c,yc}$ and $u_{c,yb}$ are the values of displacement of the control point $u_c$ corresponding to the yielding of columns (the first one to yield, actually) and beams, respectively. If that is the case, trying to induce a classical beam sway mechanism is worthless.

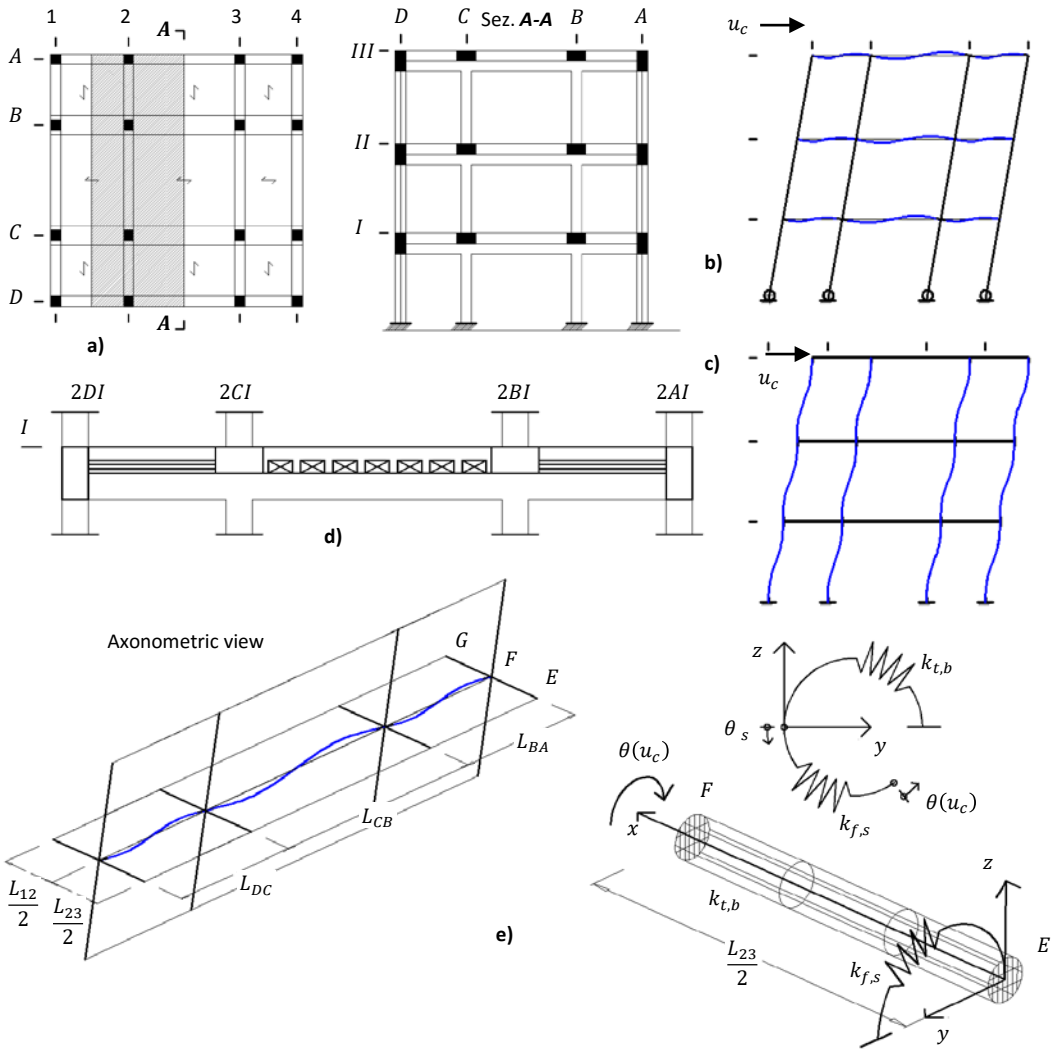


Figure 5 Typical existing Strong-Beam-Weak-Column RC building: a) plan and elevation, b) simplified frame model to study beams, c) simplified model to study columns, d) details of the RC slab (topping) along with the supporting beams, and e) details of the model for beams taking into account the torsional retainer offered by beams orthogonal to the earthquake direction.

The values of $u_{c,yc}$ and $u_{c,yb}$ can be calculated by simplified plane frame and conservative models [10,11] that contemplate the concentration of deformations on columns or beams only, respectively (Fig. 5bc). As general assumptions, it is assumed that: (1) all frame elements are inextensible, and (2) floors are infinitely rigid in their plane. In this way: (1) all joints just move horizontally, and (2) both their horizontal and vertical mutual distances remain unchanged. In particular for beams (Fig. 5b), since the model herein presented has to be as simple as possible, the conservative model is adopted in which the whole seismic-induced deformation is concentrated on beams. This means adopting a model in which columns are hinged at the base and just rigidly rotate around their lowermost extremity during the imposition of increasing horizontal displacements. For the generic horizontal beam, due to the assumption of inextensibility of columns, vertical displacements in their extremities are null, while end rotations are assumed to be equal to each other. When the earthquake strikes, it imposes, through the resulting inertia forces, a rotation at the beam extremity, and the bending moment due to such rotation is given by [12]:

$$M_{Sd} = \frac{8 \cdot E_b \cdot I_b}{L_b} \cdot \theta = \frac{6 \cdot E_b \cdot I_b}{L_b \cdot H_{tot}} \cdot u_c \tag{6}$$

where: $E_b$ is the beam cross section Young's modulus, $I_b$ the beam cross sectional inertia, $L_b$ the beam length, and $H_{tot}$ the total height of the building.

If there are also edge beams, due to the flexural stiffness of the deck framing on them, these constitute a torsional restraint that ends up limiting the rotation of the beam extremity. So that, when such restraints cannot be neglected (Fig. 5), the counter-moment applied by the assembly of edge beam and deck has to be subtracted from Eq. (6). Such torsional restraint-induced bending moment can be evaluated by considering the very simple model (Fig. 5e) composed by two torsional springs, arranged in series to each other, and one with the torsional stiffness of the half edge beam $k_{t,b}$ and the other with the flexural stiffness (in the direction parallel to the earthquake) of the slab $k_{f,b}$. This latter can be, in first instance, concentrated in the internal extremity of half beam length (point E in Fig. 5e), and is given by:

$$k_{f,s} = \frac{4 \cdot E_s \cdot I_s}{L_s} \tag{7}$$

where: $L_s$ is the length of the slab framing into the edge beam, and $E_s$, $I_s$ are the slab cross section Young's Modulus and sectional inertia, respectively.

While the edge beam torsional stiffness is given by:

$$k_{t,b} = \frac{I_t \cdot G_t}{L_t} \tag{8}$$

where: $L_t$ is the edge beam length, and $I_t$, $G_t$ are the beam cross section inertia and transversal stiffness modulus, respectively.

Due to the combination in series of the two springs above, the kinematic compatibility yields that the overall earthquake-imposed end rotation is equal to the sum of a) the torsional rotation undergone by the edge beam $\theta_b$ and b) the flexural end rotation undergone by the portion of slab insisting on the edge beam $\theta_s$, which means:

$$\theta(u_c) = \theta_b + \theta_s \tag{9}$$

Moreover, for the equilibrium to be fulfilled, the torsional moment $M_{t,b}$ in the edge beam has to be equal to the bending moment in the slab $M_{f,s}$, which means:

$$M_{t,b} = M_{f,s} \tag{10}$$

Thus, by combining Eq. (9) and Eq. (10), we obtain:

$$\theta(u_c) = \theta_b + \theta_s = \frac{M_{t,b}}{k_{t,b}} + \frac{M_{f,s}}{k_{f,s}} \tag{11}$$

from which the value of the counter-moment can be evaluated as follows:

$$M_{t,b} = M_{f,s} = \theta(u_c) \cdot \left(k_{f,s} \cdot k_{t,b}\right) / \left(k_{f,s} + k_{t,b}\right) = \frac{u_c \cdot \left(k_{f,s} \cdot k_{t,b}\right)}{H_{tot} \cdot \left(k_{f,s} + k_{t,b}\right)} \tag{12}$$

In conclusion, the end bending moment will be given, combining Eq. (6) and Eq. (12), by the following expression:

$$M_{Sd} = \left[\frac{6 \cdot E_b \cdot I_b}{L_b \cdot H_{tot}} - \frac{\left(k_{f,s} + k_{t,b}\right)}{H_{tot} \cdot \left(k_{f,s} \cdot k_{t,b}\right)}\right] \cdot u_c \tag{13}$$

Introducing the beam yield strength $M_{bRyd}$ in Eq. (13) and making it explicit with respect to the control point displacement, the $u_{c,yb}$ value can be obtained.

For the case of the column, given the column yield strength $M_{cRyd}$, the corresponding value of the control point displacement can be obtained by:

$$u_{c,yc} = u_c\left(M_{cRyd}\right) = \frac{L_c^2 \cdot M_{cRyd}}{6 \cdot E_c \cdot I_c} \cdot \frac{H_{tot}}{H_i} \tag{14}$$

where: $L_c$ is the length of the column, $E_c$, $I_c$ are the column cross section Young's Modulus and sectional inertia, respectively, and $H_i$ is the $i$-th story height.

## 4 CAPACITY MODEL FOR THE JOINT

Joints of RC buildings can be typically classified according to either one of two criteria: 1) one based on the geometry of the boundary conditions, or 2) one based on the possibility that inelastic deformations occurred in the beam longitudinal bars may or not spread within the joint core. Based on the former criterion, joints can be either 1) *exterior*, in case one beam only frames into the relevant column, or 2) *interior*, in case two beams frame into the relevant column. According to the latter criterion, a joint can be either *elastic* or *inelastic* if plastic hinges are allowed to form in the beam cross sections far from the column or adjacent to the column, respectively.

### 4.1 Original model

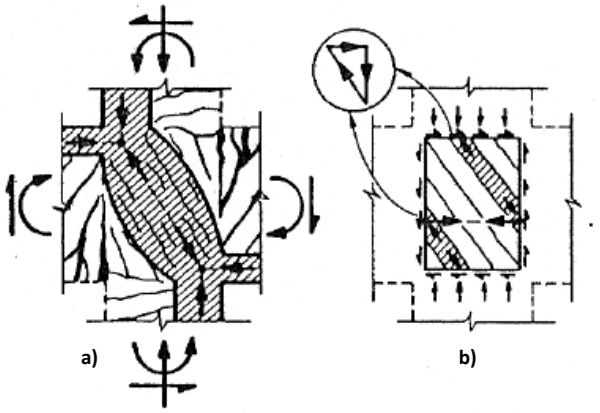


Figure 6 Mechanisms of shear transfer at an interior joint: a) concrete strut and b) diagonal compression field.

In general, two resisting mechanisms can be singled out in a joint, which are (Fig. 6): 1) concrete diagonal compression strut and 2) diagonal compression field. The latter is based on the assumption that concrete joint core is thoroughly cracked so that no (diagonal) tensile stress can be transmitted by the concrete. When beams with very small amounts of flexural reinforcement are used, or when column sections relative to beam sizes are large, joint shear stresses may be rather small and no or very few diagonal cracks may develop. As the concrete core in such cases will resist shear by means of diagonal tensile stresses, the truss mechanism in Fig. 6 will be hardly mobilized. The strut mechanism does not rely on steel contributions, but the truss

mechanism may require considerable amounts of reinforcement, particularly in the horizontal direction.

In the two limit situations of a) absence of axial compression (even axial tension) or b) large value of axial compression, the compression strut inclination will be less and more steep, respectively. In the latter case, due to the beneficial effect of normal stresses on bond strength, the relative importance of the transfer mechanism of the *diagonal compression field* will be larger.

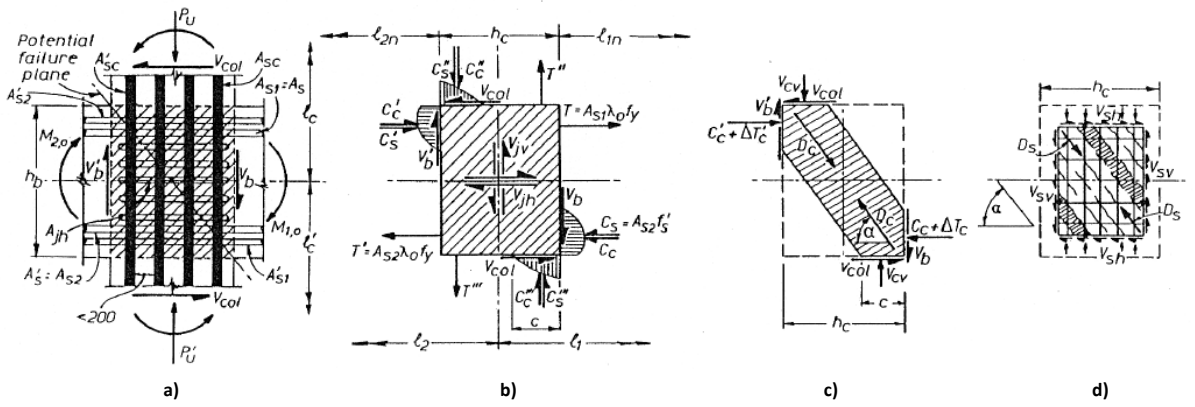


Figure 7 External actions and internal stress resultants at an interior joint.

With reference to the interior joint (Fig. 7), horizontal shear force will be given by:

$$V_{jSh} = T_s + C'_c + C'_s - V_{col} \tag{15}$$

in which: $T_s$ is the internal horizontal tension introduced in the joint by the beam upper longitudinal reinforcement, $C'_c$ is the compression force in the concrete, $C'_s$ is the axial compression in the beam upper longitudinal reinforcement (on the left-hand side of the figure), and $V_{col}$ is the average of column shears above and below the joint. Even though the sum of terms $T_s + C'_s$ is transferred to the concrete of the joint core by means of bond stresses, a fraction $\Delta T'_c$ will be transmitted to the diagonal strut in correspondence of the flexural compression zone of the column above (stress-block). Thus the value of the horizontal shear force transmitted to the diagonal strut mechanism, is given by:

$$V_{ch} = C'_c + \Delta T'_c - V_{col} \tag{16}$$

while the fraction carried by the truss mechanism is:

$$V_{sh} = T_s + C'_s - \Delta T'_c \tag{17}$$

After making reasonable assumptions about the likely distribution of tangential bond stresses inside the joint core and along the beam upper longitudinal reinforcement, Paulay and Priestley [6] suggested the following expression:

$$V_{ch} = \left(1.55 \cdot \frac{c}{h_c} + \beta - 0.55\right) \cdot T_s - V_{col} \tag{18}$$

in which: $\beta = A'_s/A_s$ is the ratio of the beam compressed longitudinal reinforcement to the tensile steel cross section, $c$ is the depth of the flexural compression zone of the elastic column above, which can be approximated by:

$$c = \left(0.25 + 0.85 \cdot \frac{P_u}{f_c' \cdot A_g}\right) \cdot h_c \tag{19}$$

where: $P_u$ is the minimum compression force acting on the column $P_u = 0.25 \cdot f_c' \cdot A_g$, $f_c'$ is the concrete cylindrical compressive strength, $A_g$ the gross cross section area of the column. From the expressions above, it yields:

$$V_{sh} = V_{jSh} - V_{ch} \cong \left(1.15 - 1.3 \cdot \frac{P_u}{f_c' \cdot A_g}\right) \cdot T_s \tag{20}$$

The term $V_{ch}$ is to be carried by the concrete compression strut while the term $V_{sh}$ will be carried by the horizontal reinforcement within the joint core.

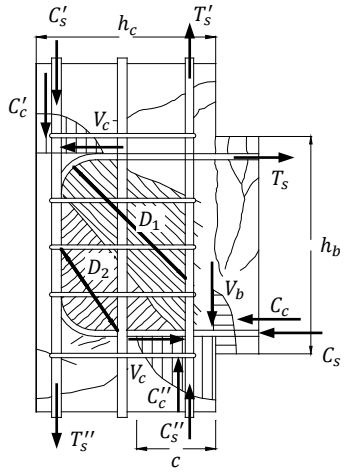


Figure 8 Exterior Joint: external actions and internal stress resultants. The compression strut is included between the two boundary lines $D_1$ and $D_2$.

Likewise, for an exterior joint, the horizontal shear force is given by:

$$V_{jSh} = T_s - V_{col} \tag{21}$$

where the value of the tension force $T_s$ is either $f_s \cdot A_s$ or $\lambda_0 \cdot f_y \cdot A_s$, depending on whether an elastic beam section or the critical section of a beam plastic hinge at the face of the column is being considered. Even in this case, a diagonal strut similar to that shown in Fig. 8 will develop between the bend of the hooked top tension beam bars and the lower right-hand corner of the joint, where compression forces in both the horizontal and vertical directions are introduced. Similarly to what already introduced for the case of the interior joints, the horizontal component of the compression strut mechanism is given by:

$$V_{ch} = C_c \ + \Delta T_c \ - V_{col} \tag{22}$$

where: $\Delta T_c$ is the fraction of the steel compression force $C_s$ developed in the bottom beam reinforcement, introduced to the strut by means of bond over the length of bar subjected to transverse compression from the lower column.

Even in this case, based on reasonable assumptions about the likely distribution of the shear tangential stresses along the longitudinal reinforcement within the joint core, Paulay and Priestley [6] proposed the following expression to evaluate the fraction of shear force that has to be carried by the horizontal reinforcement in the joint:

$$V_{sh} = V_{jSh} - V_{ch} \cong \frac{\beta}{\lambda_0} \cdot \left(0.7 - \frac{P_u}{f_c' \cdot A_g}\right) \cdot T_s \tag{23}$$

and the complement to $V_{jSh}$ will flow in the compression strut mechanism.

### 4.2 Code-suggested model

As already outlined, the Italian Code [2,5] (implicitly) distinguishes between the case of new and existing buildings. For the former [2] distinction in made between joints that are 1) *fully confined* or 2) *not fully confined*. The fully confined joints are those in which beams frame into all four sides and their width is at least three quarters of the parallel cross-sectional dimension of the column and on both pairs of opposite faces of the joint, beam cross sections cover each other for at least $3/4$ of their depth. Not fully confined joints are all those not belonging to the previous category.

The horizontal shear acting on the core of a joint shall be determined taking into account the most adverse conditions under seismic actions. In absence of more accurate evaluations, shear force acting on the concrete core of the joint can be calculated, for each direction of the seismic action, by the following expressions:

$$\begin{aligned} V_{jbd} &= \gamma_{Rd} \cdot A_{s1} \cdot f_{yd} - V_c \text{ for exterior joints} \\ V_{jbd} &= \gamma_{Rd} \cdot (A_{s1} + A_{s2}) \cdot f_{yd} - V_c \text{ for interior joints} \end{aligned} \tag{24}$$

where: $\gamma_{Rd} = 1.2$ is the factor to account for overstrength due to steel strain-hardening, $A_{s1}$ and $A_{s2}$ are the beam cross section top and bottom steel reinforcement, respectively; $f_{yd}$ is the steel design value of yield strength; and $V_c$ is the shear force in the column above the joint. Strength verification should be carried out only for joints of high ductility buildings.

Joint shear strength associated to the concrete strut crushing $V_{jRd1}$ can be evaluated by:

$$V_{jRd1} = \eta \cdot f_{cd} \cdot b_j \cdot h_{jc} \cdot \sqrt{1 - \frac{\nu_d}{\eta}} \tag{25}$$

in which:

$$\eta = \alpha_j \cdot \left(1 - \frac{f_{ck}}{250}\right) \text{ with } f_{ck} \text{ in } MPa \tag{26}$$

$$\alpha_j = \begin{cases} 0.6 \text{ for interior joints} \\ 0.48 \text{ for exterior joints} \end{cases} \tag{27}$$

$f_{ck}, f_{cd}$ are concrete cylindrical strength's characteristic and design value, respectively; $\nu_d = N_{Sd}/(A_c \cdot f_{cd})$ is the axial force in the column above the joint normalized with respect to the compressive strength of the concrete section; $h_{jc}$ is the distance between the outermost longitudinal steel bars alignments; and $b_j$ is the joint effective width, assumed as the minimum between 1) the larger between column and beam section width and 2) the smaller between column and beam section width, both increased by half of the column cross section depth.

Adequate confinement of the joint, both horizontal and vertical, should be provided, to limit the maximum diagonal tensile stress of concrete to the concrete design tensile strength $f_{ctd}$. In the absence of a more precise model, this requirement may be satisfied by providing horizontal hoops with a diameter of not less than 6 $mm$ within the joint, such that:

$$\frac{A_{sh} \cdot f_{ywd}}{b_j \cdot h_{jw}} \geq \frac{V_{jbd}^2}{\left(b_j \cdot h_{jc}\right)^2 \cdot \left(f_{ctd} + \nu_d \cdot f_{cd}\right)} - f_{ctd} \tag{28}$$

where: $A_{sh}$ is the total area of horizontal hoops, $V_{jbd}$ is given by Eq. (24), $h_{jw}$ is the distance between the top and the bottom reinforcement of the beam, $h_{jc}$ is the distance between extreme layers of column reinforcement, $b_j$ is the joint effective width.

It must be stressed that some perplexity arises when Eq. (28) is analyzed in depth since it seems to be based on a contradiction. In fact, while it is purposely meant to design steel hoops in order to keep the joint concrete un-cracked, it relies on the steel yield strength $f_{yd}$ that can only be attained if the steel has actually yielded, which means that the steel bars elongation has reached $\varepsilon_{yd} \cong 20‰$. However, such strain value can only be attained if the steel bars have undergone large elongation, across the formed cracks. Provided that further research is desirable in order to overcome such contradictions, it must also be stressed that the CAM® technique, due to the inherent pre-tension, applies a confinement without need of deformations thus resulting much more effective, in keeping the joint concrete un-cracked, than any other passive available technique, including the use of FRPs.

As an alternative, the integrity of the joint after diagonal cracking may be ensured by horizontal hoop reinforcement. To this end the following total area of horizontal hoops should be provided in the joint:

$$\begin{aligned} A_{sh} \cdot f_{ywd} &\geq \gamma_{Rd} \cdot (A_{s1} + A_{s2}) \cdot f_{yd} \cdot (1 - 0.8 \cdot \nu_d) \text{ for interior joints} \\ A_{sh} \cdot f_{ywd} &\geq \gamma_{Rd} \cdot A_{s2} \cdot f_{yd} \cdot (1 - 0.8 \cdot \nu_d) \text{ for exterior joints} \end{aligned} \tag{29}$$

### 4.3 Confinement-modified model

In the present section, a first proposal is made about a possible way to evaluate the amount of reinforcement to strengthen the joints. Even though we highly support the adoption of active techniques, such as the CAM® [13], the formulation herein proposed is actually applicable also to the case of passive confinements such as the FRPs jacketing. The preference for active methods is due to the fact that confinement does not need any structure deformation to be activated but, on the contrary, it is readily available.

Conservatively, and contrarily to what suggested by Paulay and Priestley [6], we do not distinguish the amount of the overall joint shear force $V_{jbd}$ that is carried by the concrete strut $V_{ch}$ and the truss $V_{sh}$. In fact, we assume that the truss does not form due to the reason that, in order for it to be actually mobilized, horizontal reinforcement should be diffuse while, for an existing building, such reinforcement is always rather discrete, due to the complex geometrical boundary conditions. Given that, the joint verification is carried out by comparing the shear force $V_{jbd}$ with the shear strength that can be evaluated as follows:

$$V_{jRd} = min\left(V_{jRd1}; V_{jRd2}; V_{jRd3}\right) \tag{30}$$

in which: $V_{jRd1}$ is the joint shear strength associated to concrete strut crushing; $V_{jRd2}$ is the joint shear strength associated to concrete diagonal cracking and $V_{jRd3}$ is the joint shear strength associated to the steel stirrups failure, in case they are actually present. Even though the NTC2008 considers the term associated to concrete diagonal cracking, it may not be considered since it is too conservative for a calculation carried out at the ultimate limit states, in which joints are definitely cracked. In fact, joints are supposed to be cracked since the serviceability limit state,

through which the structure has already gone for values of $u_c$ much smaller than those corresponding to the ultimate state.

The joint shear force can be evaluated, as function of the control point displacement, as follows:

$$V_{jSd} = \frac{M_{sd}^{l}(u_c)}{d^{l}} + \frac{M_{sd}^{r}(u_c)}{d^{r}} - V_c(u_c) \text{ for interior joints} \tag{31}$$

$$V_{jSd} = \frac{M_{Sd}(u_c)}{d} - V_c(u_c) \text{ for exterior joints} \tag{32}$$

in which $M_{sd}^{l}(u_c)$ and $M_{sd}^{r}(u_c)$ are the bending moments applied by the two beams framing into the joint, left and rightwards respectively.

The term $V_{jRd2}$, which is herein reported for sake of completeness, can be evaluated as follows:

$$V_{jRd2} = b_j \cdot h_{jc} \cdot \sqrt{f_{ctd} \cdot (f_{ctd} + \nu_d \cdot f_{cd})} \tag{33}$$

in which $f_{ctd}$ is concrete design tensile strength.

The term $V_{jRd3}$ can be evaluated as follows:

$$V_{jRd3} = A_{sh} \cdot f_{ywd} \tag{34}$$

The term $V_{jRd1}$ can be evaluated by Eq. (25) in which $f_{cd}$ has to be substituted by the design cylindrical strength of the confined concrete $f_{ccd}$. The cylindrical strength $f_{cc}$ of the confined concrete may be evaluated by the method proposed by Braga *et al.* in [14]. This model allows the whole stress strain $\sigma_z - \varepsilon_z$ constitutive law of the confined concrete to be evaluated, as increment with respect to the constitutive law of the unconfined concrete, as follows:

$$\sigma_z(\varepsilon_z) = \sigma_{z0}(\varepsilon_z) + \Delta\sigma_z(\varepsilon_z) \tag{35}$$

where: $\sigma_z$ and $\sigma_{z0}$ are the stresses of the confined and unconfined concrete respectively and $\varepsilon_z$ is the related strain. The term $\Delta\sigma_z$ represents the stress increment related to the triaxial state. The curve $\sigma_{z0}(\varepsilon_z)$ can be assumed as the classical parabola-rectangle diagram (Fig. 9) adopted by [2]. The model is based on the assumptions of 1) elastic material, 2) plain strain condition and 3) passive confinement.

Even though we are taking into consideration the case of existing RC buildings, in which case the joint does not contain any steel stirrups, the model contemplates the possibility to have complex confinement systems, with multiple horizontal hoops (Fig. 9). For each $i$-th hoop, the radial confining pressure $f_{ri}$ can be evaluated, for each value of $\varepsilon_z$, and assuming null bending inertia for each confining strip, be it made of either FRP or high strength steel as in the case of CAM®. For a square section column the following expression is provided [14]:

$$f_{ri}(\varepsilon_z) = \frac{36 \cdot E_c \cdot E_m \cdot t_m \cdot (b_m/S) \cdot \nu}{25 \cdot E_c \cdot d + 24 \cdot E_m \cdot t_m \cdot (b_m/S) \cdot (2 \cdot \nu + 5)} \cdot \varepsilon_z \tag{36}$$

where: $d$ is the square cross-section dimension; $E_c$ and $E_m$ are the Young's modulus of the concrete and the confining material, respectively; $t_m$ and $b_m$ are the wrapping depth and width, respectively; $S$ is the wrapping spacing and $\nu$ is the concrete Poisson's ratio. Whereas, for circular section columns with external radius $R_{ce}$, the confining pressure is expressed by the following equation:

$$f_{ri}(\varepsilon_z) = \frac{E_c \cdot E_m \cdot t_m \cdot (b_m/S) \cdot \nu}{E_c \cdot R_{ce} + E_m \cdot t_m \cdot (b_m/S) \cdot (1 - \nu) \cdot (\varepsilon_z \cdot \nu + 1)} \cdot \varepsilon_z \tag{37}$$

and in case continuous wrapping is used, the ratio $b_m/S = 1$.

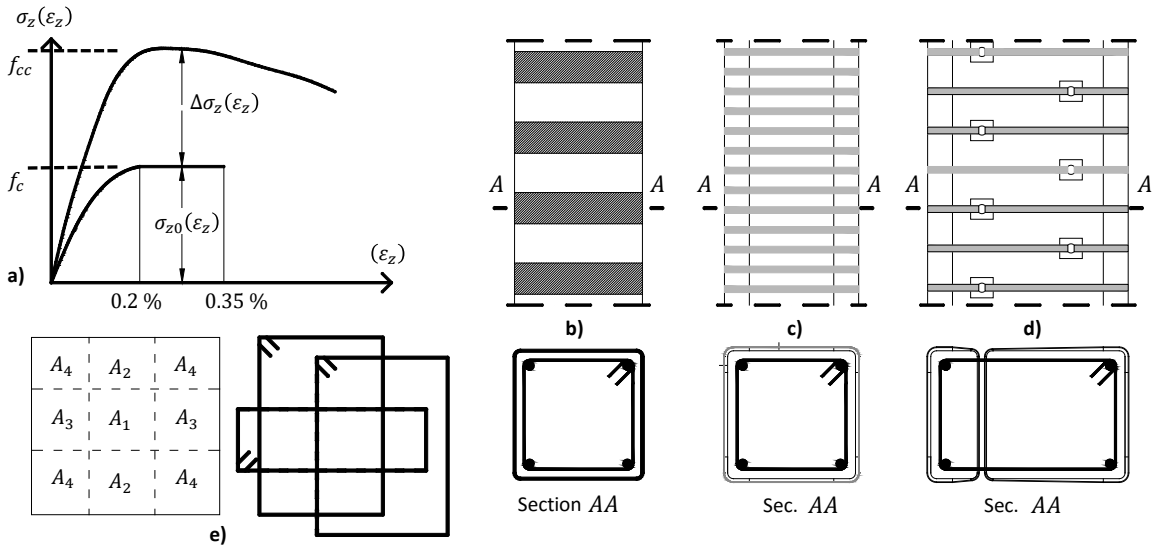


Figure 9 Confined concrete stress-strain relationship by means of the model by Braga *et al.* [14]: a) increment over the unconfined concrete constitutive law; details of a square RC cross section column strengthened by either b) FRP or c) CAM® wrappings, respectively; d) rectangular cross section strengthened by CAM®, and e) case of complex confinement system (very general).

In the most general case of existing internal stirrups and external wrapping, the average radial confining pressure can be evaluated as follows:

$$f_{rm}(\varepsilon_z) = \frac{A_{int}}{A_{ext}} f_{r,int} + f_{r,ext} \tag{38}$$

where: $f_{r,int}$ and $f_{r,ext}$ are the radial confining pressures induced by the internal stirrups and by the external wrapping, respectively; $A_{int}$ is the amount of area of the cross section within the internal stirrup and $A_{ext}$ is the area contained within the external wrapping. In the most general configuration of confinement reinforcement (Fig. 9e), the superposition method is applied to evaluate the average radial confining pressure, as follows:

$$f_{rm}(\varepsilon_z) = \frac{1}{A_e} \cdot (f_{rA1} \cdot A_1 + 2 \cdot f_{rA2} \cdot A_2 + 2 \cdot f_{rA3} \cdot A_3 + 4 \cdot f_{rA4} \cdot A_4) \tag{39}$$

where:

$$f_{rA1} = f_{r2} + 2 \cdot f_{r1};\ f_{rA2} = 2 \cdot f_{r1};\ f_{rA3} = f_{r2} + f_{r1};\ f_{rA4} = f_{r1} \tag{40}$$

The pressures applied by the stirrups are actually spread in the concrete along the longitudinal development of the RC element, by means of two mechanisms that are: 1) the arch effect, which develops between two adjacent stirrups, thus reducing the real confined concrete volume, and 2) the mechanism due to the bending stiffness of the longitudinal bars. As a result, the confining pressure varies along the element with maximum value at the tie level and minimum values midway between two stirrups. Therefore, the concrete is entirely subject to a lateral confining pressure lower than the mean value calculated at tie level when assuming a homogeneous distribution. Two reduction coefficients can be evaluated, separately, for each of the mechanisms above. For the concrete mechanism, the coefficient can be evaluated by the following equation:

$$k_c = \left(1 - \frac{s}{4 \cdot l_{st}}\right)^2 \tag{41}$$

where: $l_{st}$ is the length of the stirrup. For the reductive coefficient associated to the bending stiffness of the longitudinal bars, the following expression is provided:

$$k_{sl} = \frac{45 \cdot \xi_l^3}{45 \cdot \xi_l^3 + \beta \cdot \xi_{st}} \tag{42}$$

where:

$$\xi_l = \frac{\phi_{long}}{s};\ \beta = \frac{\phi_{st}}{\phi_{long}};\ \xi_{st} = \frac{\phi_{st}}{l} \tag{43}$$

in which: $\phi_{st}$ and $\phi_{long}$ are the diameters of the stirrup and longitudinal bar, respectively; $l$ is the element length. When the bending stiffness of the longitudinal bars becomes negligible, only the arching effect between two stirrups spreads the confining pressures along the column and it can be assumed that $k_{sl} \gg k_c$. However, in the most general case, the effective confining pressure to which the column (*i.e.* the joint panel) confined by either square or circular hoops is subject, is given by the following expression:

$$f_r = k_c \cdot k_{sl} \cdot f_{rm} \tag{44}$$

and the corresponding value of the stress increment is given by:

$$\Delta\sigma_z(\varepsilon_z) = \Delta\sigma_z(f_{rm}) = -2 \cdot \nu \cdot f_{rm} \tag{45}$$

The strength of the confined concrete is thus given by:

$$f_{cc} = max\left(\sigma_z(\varepsilon_z)\right) \tag{46}$$

and this value has to be implemented into the Eq. (25) in order to obtain the value of $V_{jRd1}$.

The weak points of this model are that 1) the whole constitutive law of the confined concrete has to be evaluated first, in order to obtain the relevant strength $f_{cc}$, and 2) the confinement contemplated is the passive one. Further research is, in this respect, desirable and already being carried out.

## 5 OVERALL DISSIPATIVE MECHANISM

In this context, the retrofitting design strategy may be based on the following steps, to be undertaken in sequence:

Evaluate, by means of the simple models described in previous paragraph §. 3, the ratio between $u_{c,yb}$ and $u_{c,yc}$ ;

If it happens that:

$$u_{c,yb} < u_{c,yc} \tag{47}$$

the classical overall dissipative mechanism can be adopted and the strengthening of the joints can be calculated by means of the model described in the paragraph §. 4.3;

If it happens that:

$$u_{c,yc} < u_{c,yb} \tag{48}$$

the classical overall dissipative mechanism can be tentatively pursued by adopting either one of the following strategies: 1) moments redistribution or 2) repositioning of the plastic hinges;

If it happens that:

$$u_{c,yc} \ll u_{c,yb} \tag{49}$$

an hybrid beam-column-sway mechanism should be accepted and identified by means of an energy-based approach.

Further research is already being carried out in order to formalize this procedure.

## 6 CONCLUSIONS

This work addressed the problem of the optimization of the amount of strengthening to be implemented for joints of existing RC buildings in a seismic retrofitting intervention. In fact the retrofitting design activity that has characterized the aftermath of the recent Italian earthquakes has shown that the application of the cogent Italian Building Code may lead to excessively conservative interventions that would result both difficult to realize and detrimental to the diffusion of innovative and promising strengthening techniques.

The first step to be undertaken during the design of a retrofitting intervention is the selection of a suitable overall dissipative mechanism. While a beam-sway overall dissipative mechanism can be pursued with relative ease for new buildings by means of the Capacity Design Philosophy, it may lead to unnecessarily conservative solutions for existing buildings. In fact, since these latter were most probably designed for gravity loads only, they are characterized by the Strong-Beam-Weak-Column typology. Thus, for these buildings, an alternative overall mechanism, characterized by plasticization on both beams and columns, may be selected.

A simple model was developed to help the designers figure out which overall dissipative mechanism is more suitable to pursue for the specific case study they are dealing with. Such model is based on the evaluation and comparison of the value of the displacement of the control point of the single Moment Resisting frame corresponding to the flexural yielding of beams and columns. In cases in which, due to the presence of strong beams and weak columns, these latter yield much earlier than beams, the hybrid column-beam-sway mechanism should be selected.

After reviewing the model for shear strengthening of joints implemented by the cogent Italian Building Code and the one from which it was derived, a way to improve it was suggested, in absence of a newly developed model. The beneficial effect of confinement on the concrete strut resisting mechanism may be accounted for by evaluating the confined concrete strength by means of the model by Braga *et al.*, which has been briefly described.

Ultimately, the energy-based strategy to design the hybrid overall dissipative mechanism was described. Anyway, in this respect, further research is necessary.

This work implicitly addressed the Moment Resisting Framed typology of RC buildings, adopting simplified models. As further developments, the case of dual systems, characterized by the presence of frames and walls in parallel to each other will be also addressed. Moreover, the way in which to deal with the presence of stairs, with either cantilever steps or a climbing slab, will be also analyzed.

## REFERENCES

[1] Royal Decree Law n°22291, (1939), “Norme per l’esecuzione delle opere in congolmerato cementizio semplice od armato”, published on *Gazzetta Ufficiale della Repubblica Italiana*, n°92, 18 April 1940.

[2] NTC 2008 – DM 14 Gennaio 2008. Nuove norme tecniche per le costruzioni. *Gazzetta Ufficiale della Repubblica Italiana*, 4 febbraio 2008, n. 29.

[3] UNI EN 1998-1, Eurocode 8 - Design of structures for earthquake resistance - Part 1: General rules, seismic actions and rules for buildings. CEN European Committee for Standardization.

[4] UNI EN 1992-1-1, Eurocode 2: Design of concrete structures – Part 1-1: General rules and rules for buildings. CEN European Committee for Standardization.

[5] Circolare dei Lavori Pubblici n°617. Istruzioni per l'applicazione delle nuove Norme tecniche per le Costruzioni di cui al Decreto Ministeriale 2008. Italian Ministry of Public Works, April 2009; 2009.

[6] T. Paulay, M.J.N. Priestley, *Seismic design of reinforced concrete and masonry buildings*, John Wiley & Sons, Inc., 1992.

[7] H. Akiyama, *Earthquake Resistant Limit-State Design for Buildings*, University of Tokyo Press, 1985.

[8] C.H. Uang, V.V. Bertero, Evaluation of seismic energy in structures, *Earthquake Engineering and Structural Dynamics*, **19**, 77-90, 1990.

[9] M.D. Symans, F.A. Charney, A.S. Whittaker, M.C. Constantinou, C.A. Kircher, M.W. Johnson, R.J. McNamara, Energy Dissipation Systems for Seismic Applications: Current Practice and Recent Developments, *Journal of Structural Engineering*, ASCE, January 2008.

[10] V. Bianco, S. Granati, Exploring the possibility to carry out an expeditious non linear static assessment of an existing RC building, *XV Convegno ANIDIS, Associazione Nazionale Italiana Di Ingegneria Sismica*, Padova, Italy, 30 Giugno-4Luglio, 2013.

[11] V. Bianco, S. Granati, Expeditious seismic assessment of existing moment-resisting frame reinforced concrete buildings: proposal of a calculation method, *Engineering Structures*, **101**, 715-732, 2015.

[12] R.W. Clough, J. Penzien, *Dynamics of Structures*, Computers and Structures, Inc., Berkley, CA, 1995.

[13] M. Dolce, R. Gigliotti, M. Laterza, D. Nigro, R. Marnetto, Il rafforzamento di pilastri in c.a. mediante il sistema CAM, *10th International Conference L'ingegneria Sismica in Italia*, Potenza-Matera, Italy, September 9-13, 2001.

[14] F. Braga, R. Gigliotti, M. Laterza, Analytical Stress-Strain Relationship for Concrete Confined by Steel Stirrups and/or FRP Jackets, Journal of Structural Engineering, ASCE, 132(9), 1402-1416, 2006.

COMPDYN 2017
6th ECCOMAS Thematic Conference on
Computational Methods in Structural Dynamics and Earthquake Engineering
M. Papadrakakis, M. Fragiadakis (eds.)
Rhodes Island, Greece, 15–17 June 2017

# NUMERICAL ASSESSMENT OF THE OUT-OF-PLANE RESPONSE OF MASONRY PANELS REINFORCED BY MEANS OF FRCM SYSTEMS

**B. Pantò[1], M. Malena[1] and G. de Felice[1]**

[1] Department of Civil Engineering of Roma Tre University
Via Vito Volterra 62, 00146 Roma
e-mail: {marialaura.malena, bartolomeo.panto, gianmarco.defelice}@uniroma3.it

**Keywords:** Out-of-plane behaviour of masonry walls, Composite materials, FRCM reinforcing systems, bond-slip, Non-linear modeling, Macro-model approach.

**Abstract.** *The use of Fibre Reinforced Cementitious Matrix (FRCM) materials, is becoming a very common technique of retrofitting for historical and monumental masonry buildings. This technique, if compared to the use of fiber polymeric materials (FRP), is more compatible with the mechanical property of the masonry and more appropriate with the preservation needs of cultural heritage, associated to the historical constructions. The effectiveness of such a type of reinforcement for improving the out-of-plane seismic capacity of masonry walls, in comparison with traditional reinforcements with steel tie-bars, was investigated in a previous experimental campaign. In the present work, a macro-modeling approach, already available in the literature for modeling masonry structures with plane and curved geometry, was used to predicting the out-of-plane response of masonry structures reinforced by means of FRCM. The model was validated by mean of the simulation of the previous cited experimental tests.*

# 1 INTRODUCTION

The recent seismic events, such as the Emilia (2012) and the L'Aquila (2009) earthquake, have shown the great vulnerability of existing masonry buildings, not designed to withstand seismic loads. During the seismic event, the building, being characterized by weak connections between the walls at the corners and between walls and diaphragms, does not have a box behavior. Each wall shows an independent response, characterized by a complex non-linear interaction between its in-plane and out-of-plane behavior, that usually end with collapse by overturning. Aiming at reducing seismic vulnerability of existing masonry buildings, several strengthening techniques that make use of composite materials have been developed and investigated by means of experimental tests and numerical simulations. The use of Fabric Reinforced system, applied through Cementitious Matrix (FRCM), has become a common technique for retrofitting existing masonry buildings.

In this paper a macro-modeling approach, already developed for modeling masonry structures [1,2], is used to predict the out-of-plane response of a masonry prototype reinforced by means of FRCM, experimentally investigated through shaking table tests [3,4].

Masonry is considered as made of macro-elements interacting though non-linear interfaces. The reinforcement is modeled by a rigid plate, while the interaction between the reinforcement and the masonry substrate is governed by a discrete zero-thickness interface, able to take into account both the tensile (mode I) and shear (mode II) failure modes [5]. A refined bond-slip constitutive law, suitable for FRCM materials and experimentally validated by means of debonding tests [5], is employed. The capability of the model to predict the effective behavior of masonry repaired with FRCM is evaluated through comparison with experimental tests: the out-of-plane capacity curve of the specimen with and without FRCM reinforcement are obtained and compared with shaking table tests, in terms of ultimate strength and collapse mode.

# 2 THE DISCRETE MACRO MODELLING APPROACH

The discrete macro modelling approach represents an innovative tool for simulating the non-linear behaviour of masonry structures that requires a limited computational effort when compared to non-linear finite element method. Originally restricted to a 2D-kinematic for simulating the in-plane response of masonry [1,2], the model was extended to simulate the out-of-plane response of masonry panels, while also simulating the response of monumental structures [6,7]. In the present paper, a recent formulation that allows to model the interaction between masonry and the FRCM reinforcement [8] is applied.

## 2.1 The spatial macro-model for simulating the masonry

The kinematics of the macro-element is governed by 7 degrees of freedom: six DOF associated to the rigid body motions and one associated to the in-plane shear deformability of the element. This latter is described by a diagonal link, while the interactions between two contiguous panels are simulated by means of zero thickness 3D-interfaces. The flexural response is governed by a layer of transversal links, the shear in-plane sliding is controlled by a non linear spring while the out-of-plane sliding and the torsional behaviour of the panel are controlled by two further sliding links (Figure 1). The calibration procedure of the non linear links is based on energy equivalence, as are reported in [1,6].

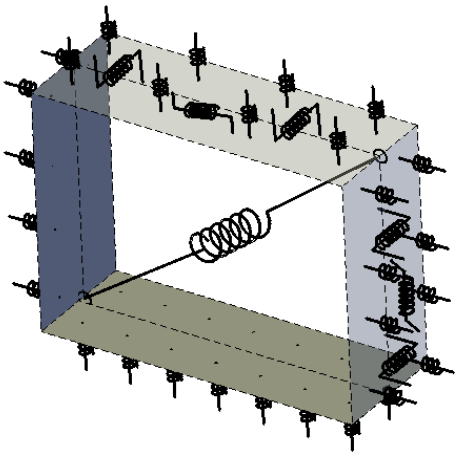

Figure 1. geometric representation of the spatial macro-model.

## 2.2 The macro-model for simulating the reinforcing

Following [8], the presence of composite reinforcing, applied by unidirectional strips, 2D webs or grids, is simulated by introducing plate elements bonded to masonry with non-linear transversal and longitudinal links. A further set of springs represents the membrane behavior of the reinforcement (Figure 2).

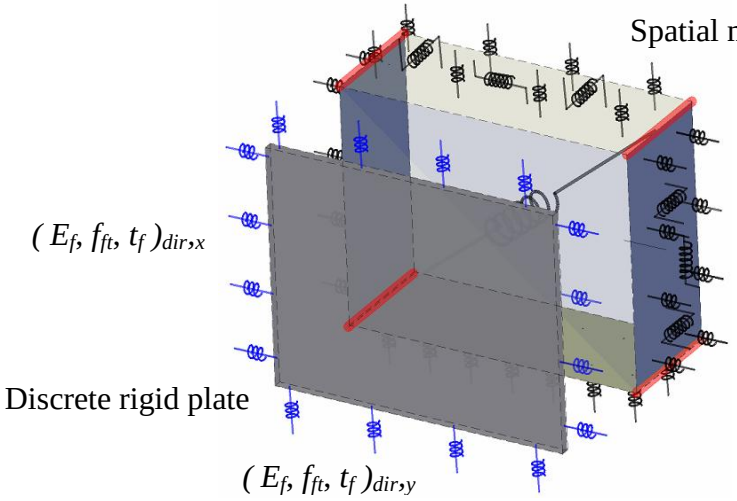


Figure 2. modeling of reinforcing by discrete rigid plate [8].

The macroscopic tensile behaviour of the reinforcement, comprehensive of the fabric and the matrix, is assumed as elastic-perfectly brittle, with equivalent elastic modulus $E_f$, and ultimate tensile strength $f_{ft}$. These properties are referred to the net area of the reinforcement that is defined by the equivalent thickness $t_f$. The model accounts for the anisotropic behaviour of the reinforcement when the reinforcement amount is different along the two directions. The non-linear links that connect two plates are calibrated through a simple elastic equivalence between the continuous elastic solid and the discrete equivalent model. The normal and tangential interaction between the reinforcement and the masonry substrate are modeled by means of a zero-thickness discrete interface, composed by transversal N-links for simulating the normal interaction and two N-links for simulating the bond-slip constitutive law. The transversal N-links are assumed as elastic, while the longitudinal links are modeled through a refined elasto-plastic bond-slip constitutive law with a post-peak softening branch as proposed in [5], to take into account the cracking process within the cementitious matrix.

## 3 CALIBRATION OF THE BOND-SLIP CONSTITUTIVE LAW

In the case of FRCM systems made of steel cords, failure usually occurs within the mortar matrix at the interface with the reinforcement [5,9]. Aiming at describing the debonding process, the key element is the adoption of a reliable bond shear stress-slip law [10,11,12].

In the present work, the bond law in the tangential direction, expressed in terms of slip displacement ($d_t$) and tangential stress ($p_t$), is described by an ascending elastic branch ending at the point ($d_{tm}$; $p_{tm}$), a linear softening branch ending at the tangential debonding displacement $d_{td}$ and a plane frictional branch, with constant stress $p_{t0}$. This latter branch describes the interlocking phenomenon between the fibers and the surrounding matrix (see Fig. 3), typical of such a type of reinforcement.

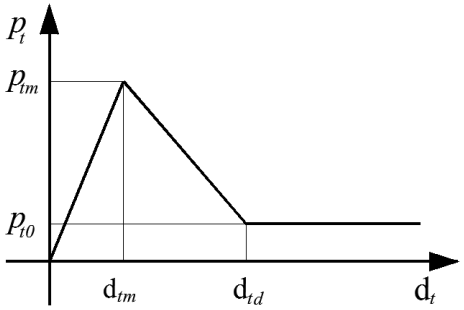


Figure 3. Trilinear shear stress-slip interface law.

## 4 SIMULATIONS

Aiming at showing the capability of the macro-modeling approach, to reproduce the out-of-plane response of masonry structures reinforced by means of FRCM, the results of the experimental campaign described in [3,4], were numerically simulated.

### 4.1 The prototype

The structural prototype modelled in the present work consists of a façade wall and two transverse walls, with an overall U-shaped configuration. The façade is 3.30m long, while the transverse walls are 2.3m long. All the walls are 3.44m high and 0.25m thick (Fig.4). The façade is connected to the transverse walls by a vertical mortar bed joint in order to simulate a weak connection in view of the out-of-plane overturning of the façade.

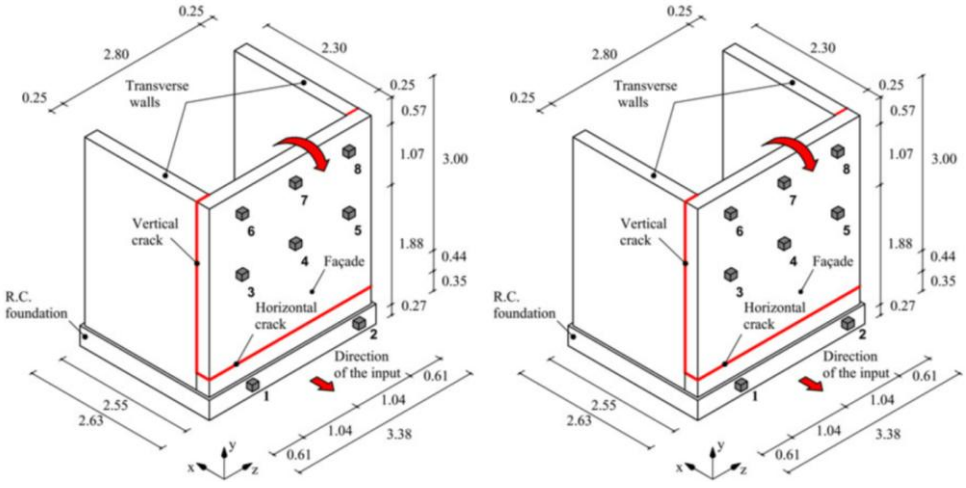


Figure 4. Geometry of the prototype [3].

The walls are made of tuff units (250x370x110mm) and hydraulic lime mortar. The mean mechanical properties of the masonry components are: unit weight 12.06 kN/m3, cubic compressive strength 5.98 MPa, Young Modulus 1575 MPa for the blocks; cubic compressive strength 4.08 MPa, Young Modulus 2038 MPa, tensile strength 0.84 MPa for the mortar.

The specimen was initially subjected to a shake table test series without reinforcement [3], which caused the detachment of the façade from the transverse walls and its out-of-plane overturning (Fig. 5(a)).

In order to investigate the effectiveness of traditional retrofitting devices, a further test series was carried out on the specimen retrofitted with two Ø20-mm steel tie-bars installed at a distance of 0.85m from the top of the wall and 0.30m from the corner. The height of the rods (about 75% of the whole height of the façade) maximized the stabilizing effect and, at the same time, prevented failure by overturning. A vertical crack developed in the middle section of the façade, induced by the out-of-plane horizontal bending (Fig. 5(b)) and some diagonal cracks formed at the top and mid-height of the front wall, probably related to the impact and the punching effect of the end-plates (Fig. 5(c)).

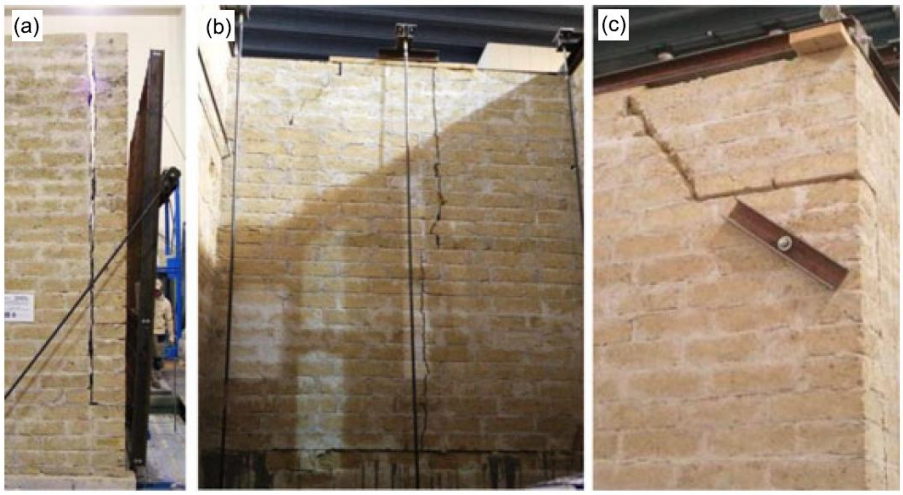


Figure 5. Damage pattern before the installation of SRG reinforcement [3]: lateral view (a), back view of the façade (b), detail of the anchorage of the reinforcing tie rod (c).

A last test series was carried out on the specimen retrofitted with FRCM made of unidirectional Ultra High Tensile Strength Steel (UHTSS) cords [3] that currently are referred as Steel Reinforced Grout (SRG). The strengthened system is made of 12 steel connectors retaining the out-of-plane overturning of the façade, four horizontal SRG strips applied to the side walls to transfer the load from the connectors to the masonry, two horizontal SRG strips applied to the front wall to transfer the retaining effect of the connectors to the façade. These strips are installed to provide also an increase of the seismic capacity of the wall with respect to horizontal bending. The textile has density of 4 cords/in, a design thickness equal to 0.084 mm and a mass density equal to 640 g/m$^2$. A mineral-NHL mortar was used as a matrix having compressive strength, Elastic Modulus, tensile strength and grain size range, equal to 20.6 N/mm$^2$, 11.42 KN/mm$^2$, 5.42 N/mm$^2$ and 0-1.4 mm, respectively.

### 4.2 Numerical modeling of the structural prototype

Three different models, representative of the unreinforced, tie rods reinforced and SRG reinforced prototypes, were developed and implemented in the code Histra [13]. The First step was the calibration of the model in term of mechanical characteristics of masonry.

The compression of masonry was fixed equal to the compressive strength of the tuff units, while the tensile strength and the tensile fracture energy, along the direction orthogonal to the bed mortar joints ($f_{tv}$, $G_{tv}$), were determined by fitting the experimental results relative to the unreinforced prototype. With this aim, Figure 6 shows the influence of the tensile strength on the prototype response, keeping constant the fractural tensile energy equal to 0,06 N/mm according to the mechanical properties of the mortar [2]. From such a parametric analysis, the value of the tensile strength that allows to the numerical model to best fit the experimental results was 0,015Mpa. The corresponding collapse mechanism was reported in Figure 7 in which a representation of the flexural damage was included by using a gray-scale proportional to the cumulate plastic energy [6]. The sliding is governed by a Mohr-Coulomb yielding surface with cohesion ($c$) equal to 0,15Mpa, friction factor μ=0,57 and fracture energy in sliding $G_s = 0.3N/mm$. The tensile strength along the direction parallel to the horizontal bed joints ($f_{th}$) was evaluated by the expression $f_{th} = f_{tv} + \frac{b}{2h}c$, where $b$ and $h$ are respectively the base and height of the brick units. Analogously, the fracture energy along that direction was determined by the expression $G_{th} = G_{tv} + \frac{b}{2h}G_s$. The masonry parameters of the masonry, adopted in the analyses, are reported in Table 1.

| Direction | E [N/mm$^2$] | G [N/mm$^2$] | $f_c$ [N/mm$^2$] | $f_t$ [N/mm$^2$] | $G_c$ [N/mm] | $G_t$ [N/mm] | c [Mpa] | μ [-] | $G_s$ [N/mm] |
|---|---|---|---|---|---|---|---|---|---|
| Vertical ($v$) | 1614 | 645 | 5,98 | 0,40 | 0,50 | 0,50 | 0.15 | 0,57 | 0,30 |
| Horizontal ($h$) | 1606 | | | 0,15 | | 0,06 | | | |

Table 1: Mechanical parameters of the masonry used in the simulations.

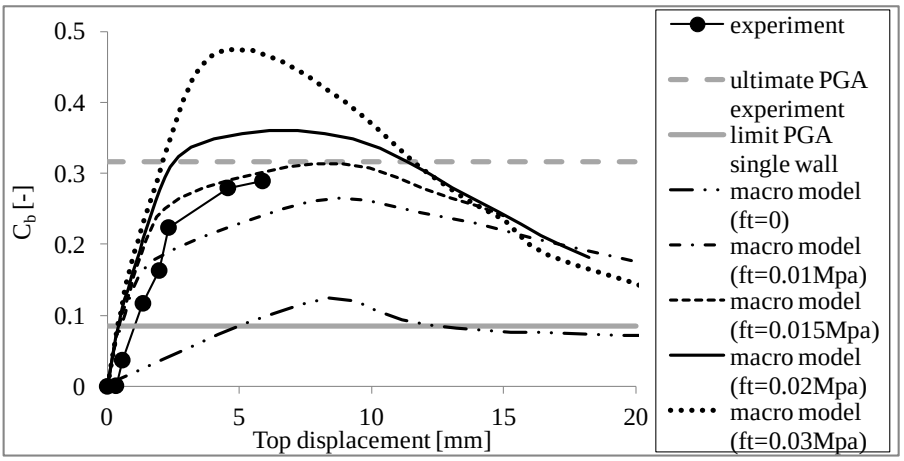


Figure 6. Unreinforced model – Load versus displacement curve.

In Fig. 6 the gray continuous line represents the theoretical limit strength corresponding to the out-of-plane overturning of the façade considered isolated, and considering a no-tension material, while the dashed gray line represents the ultimate lateral strength registered during the experiment. The push-over capacity curve is represented in terms of the maximum out-of-plane displacement of the façade as function of the base shear coefficient ($C_b$), corresponding to the base shear of the structure dimensionless by the total weight ($W$=108 kN). The results of the dynamic analyses, expressed in terms of maximum displacement versus PGA, are included in the graph and superposed to the capacity curve.

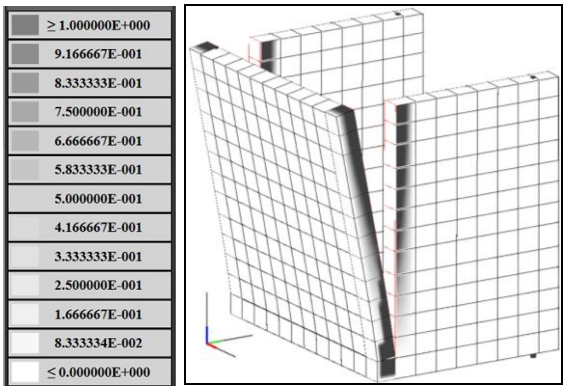


Figure 7. Numerical collapse mechanism obtained for the unreinforced prototype.

The results of the numerical analyses performed on the prototype reinforced by means of the two horizontal tie rods, are reported in Figure 8, both in terms of collapse mechanism and capacity curve. It can be observed a good agreement with the experimental analyses.

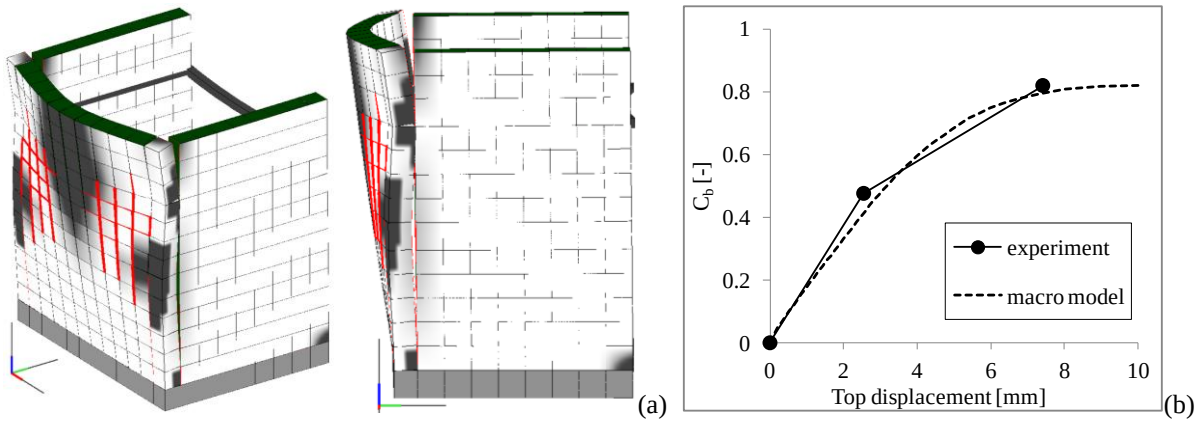


Figure 8. Prototype reinforced by tie rods: deformed mesh at the failure (a) and capacity curve (b).

It is worth noting that the model was able to represent the variation of the collapse mechanism from the unreinforced prototype to the reinforced one. In the latter case the numerical damage was concentrated mainly at the central part of the façade (Figure 8) according to the experimental observations [3,4].

Afterwards, aiming at reproducing the results of the last series of tests, the behaviour of the prototype reinforced by two horizontal SRG composite strips, was numerically analyzed. The trilinear bond slip law, defined in the previous section, was derived by mean of the procedure proposed in [11] ($p_{tm}$=1.267 N/mm, $d_{tm}$=0.005 mm, $d_{td}$=1.1 mm, $p_{t0}$=10%$p_{tm}$). In Figure 9, the numerical results related to such a simulation are represented in terms of plastic strain concentration and global load-displacement curve.

The ultimate experimental PGA of the reinforced system was about 1,4g against the ultimate value of 0,3g observed for the unreinforced prototype. The model is able to reproduce the increasing of the global strength, as shown in Figure 9c. The numerical failure mechanism is characterized by the damage of the façade, mainly concentrated in the central zone between the two reinforcing strips (Figure 9a). Also, the transversal walls were damaged at the corners and at the base section (Figure 9b).

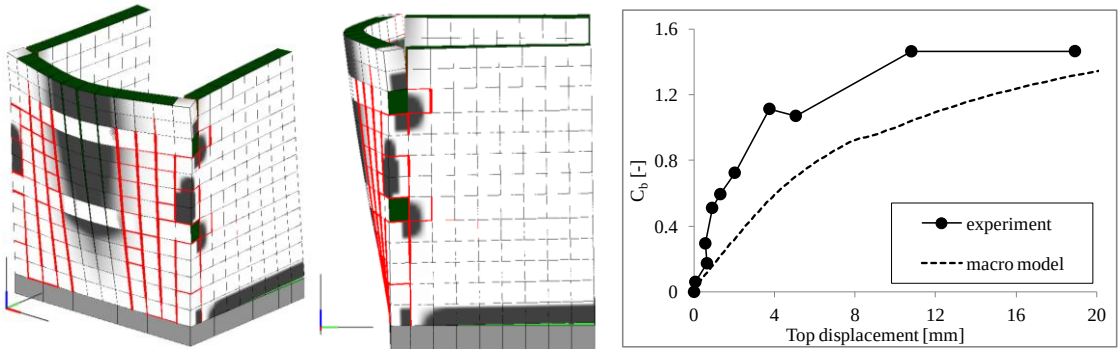


(a) (b) (c)

Figure 9. Failure mechanism of the SRG reinforced prototype: plastic damage at the façade (a) and at the transversal wall (b); capacity curve compared to the experimental results (c).

## 5 CONCLUSIONS

In this paper the out-of-plane behaviour of masonry structures strengthened with FRCM is numerically investigated. A discrete macro-modeling approach, able to simulate the non-linear behaviour of the masonry and its bond-slip interaction with the composite reinforcing is employed. A refined bond-slip interaction between the composite reinforcement and the mortar matrix is considered. The model is used to simulate the response of a three-dimensional masonry prototype composed by a façade wall and two transversal walls experimentally investigated in the literature by means of dynamic tests. Three different configurations were numerically reproduced: the unreinforced prototype, the prototype reinforced by tie rods and the prototype reinforced by SRG composite strips. The experimental behaviour of the prototype was strongly characterized by the presence of the reinforcing system: the simple out-of-plane overturning of the façade, observed in the unreinforced configuration, moved to a global mechanism after the addition of the reinforcement. The numerical simulations presented in the paper are based on static push-over analysis, carried out on a three-dimensional model in the three tested configurations. The numerical results are in a good agreement with the experimental ones, both in terms of capacity curves and failure mechanisms, demonstrating the capability of the model in predicting the efficacy of SRG reinforcement against out-of-plain failure of masonry structures.

## REFERENCES

[1] I. Caliò, M. Marletta, B. Pantò (2012), “A new discrete element model for the evaluation of the seismic behaviour of unreinforced masonry buildings”, Engineering Structures, 40, 2012, pp 327-338.

[2] I. Caliò, B. Pantò, "A macro-element modelling approach of Infilled Frame Structures", Computers & Structures, 143, pp 91-107, 2014.

[3] S. De Santis, P.B. Casadei, G. De Canio, G. de Felice, M. Malena, M. Mongelli, I. Roselli. Seismic performance of masonry walls retrofitted with steel reinforced grout. Earthquake Engineering and Structural Dynamics 45(2): 229-251, 2016.

[4] O. Alshawa, G. de Felice, A. Mauro, L. Sorrentino. Out-of-plane seismic behaviour of rocking masonry walls. Earthquake Engineering and Structural Dynamics 41(5):949-968, 2012.

[5] M. Malena, De Santis, B. Pantò, G. de Felice: A Closed-Form Analytical Solution to the Debonding of SRG on Curved Masonry Substrate, 5th International Conference on Mechanics of Masonry Structures Strengthened with Composite Materials, Bologna, Italy, 2017.

[6] B. Pantò, F.Cannizzaro, S. Caddemi, I. Caliò, "3D macro-element modelling approach for seismic assessment of historical masonry churches", Advances in Engineering Software 97, 40-59, 2016.

[7] B. Pantò, L. Giresini, M. Sassu, I. Caliò, "Non-linear modeling of masonry churches through a discrete macro-element approach", Earthquakes and Structures (2017) 12(2), 223-236.

[8] S. Caddemi, I. Caliò, F. Cannizzaro, P.B. Lourenço, B. Pantò: FRP-reinforced masonry structures: numerical modeling by means of a new discrete element approach. 6th Int. Conf. on Comp. Meth.in Structural Dynamics and Earthquake Engineering, Rhodes Island, Greece, 2017.

[9] B. Pantò, M. Malena, G. de Felice: Non-linear modeling of masonry arches strengthened with FRCM, 5th International Conference on Mechanics of Masonry Structures Strengthened with Composite Materials, Bologna, June 28th - 30th, 2017.

[10] M. Malena, F. Focacci, C. Carloni, G. de Felice. The effect of the shape of the cohesive material law on the stress transfer at the FRP-masonry interface. Composites Part B: Engineering 110: 368-380, 2017.

[11] F. Ceroni, G. de Felice, E. Grande, M. Malena, C. Mazzotti, F. Murgo, E. Sacco, M.R. Valluzzi, M.R. Analytical and numerical modeling of composite-to-brick bond. Materials and Structures/Materiaux et Constructions 47(12):1987-2003, 2014.

[12] M. Malena, G. de Felice. Debonding of composites on a curved masonry substrate: Experimental results and analytical formulation. Composite Structures 112:194-206, 2014.

[13] HiStrA (Historical Structure Analysis). HISTRA s.r.l, (Italy). Rel. 17.4.02, <http://www.histra.it>.

COMPDYN 2017
6th ECCOMAS Thematic Conference on
Computational Methods in Structural Dynamics and Earthquake Engineering
M. Papadrakakis, M. Fragiadakis (eds.)
Rhodes Island, Greece, 15–17 June 2017

# A CENTRIFUGE INVESTIGATION OF TWO DIFFERENT SOIL-STRUCTURE SYSTEMS WITH ROCKING AND SLIDING ON DENSE SAND

**Iason Pelekis**[1], **Gopal S. P. Madabhushi**[2], **and Matthew J. DeJong**[1]

[1] University of Cambridge, Department of Engineering
Trumpington Street, Cambridge, CB2 1PZ
e-mail: {ip312, mjd97}@cam.ac.uk

[2] University of Cambridge, Department of Engineering
Schofield Centre, High Cross, Madingley Road, Cambridge, CB3 0EL
mspg1@cam.ac.uk

**Keywords:** Earthquake, Centrifuge Testing, Soil-Structure Interaction, Structural Rocking, Foundation Rocking.

**Abstract.** *Seismic protection of structures by means of rocking isolation is becoming increasingly popular, because allowing uplift is an inexpensive way to reduce structural demand. However, understanding the role of soil–structure interaction in the response of rocking systems is important to define what type of rocking system might be most effective. To address this challenge, a campaign based on centrifuge modelling and testing is currently ongoing. The primary objective is to assess the force demand that rocking systems experience during their motion. Flexible structures that rock while stepping on discrete footings (structural rocking) and flexible structures with discrete footings rocking on soil (foundation rocking) are both considered. Following this distinction, two building models were designed with the only difference being the connectivity of the columns to the footings. For structural rocking, columns were designed to detach and step on their footings, while for foundation rocking the footing-column connection was designed to be rigid. The two building models were tested side-by-side in a centrifuge. A second test was also conducted, where thin steel "fuses" were installed in the interface of structural rocking, to further study the allocation of energy dissipation between structural elements and fuses, and soil medium. The building models were placed on the surface of dense sand and then tested using sinusoidal ground motions which caused a combination of sliding and rocking. The global response of the models in terms of overturning moment and storey shear was investigated and back validated by obtaining directly the internal loads, which were found capped regardless of the extent of rotation. Moreover, the base isolation effect was evident during large amplitude resonant excitations, whereas during a low frequency low amplitude excitation there was no clear benefit of rocking. Finally, no significant effect was observed in limiting the base shear demand by using the steel fuses.*

## 1 INTRODUCTION

In areas prone to earthquakes of catastrophic magnitude, the current design approach of damage tolerance may result in poor structural performance regarding repair costs, downtime and business disruption. For example, the Christchurch earthquake in New Zealand has led building stakeholders to ask for improved seismic performance and damage mitigation technologies, to avoid disruption, economic loses and dependence on insurance in future earthquakes [1]. Similarly, in the aftermath of Chile's 2010 earthquake, it was concluded that "*efforts still need be made for better construction practices*", while the economic loses reached a third of the country's gross domestic product [2]. Consequently, design objectives are now becoming more stringent, incorporating economic and social implications of earthquake damage.

Seismic protection by means of rocking isolation is becoming increasingly popular, since allowing uplift is an inexpensive way to reduce structural damage demand. Structures idealized as rigid rocking blocks were studied by Housner [3] back in the 1960s. Since then, the overturning tendency and self-centering nature of rocking [4, 5], the implementation of rocking with dampers to suppress swaying motion [6–15], the coupling of flexibility and rocking, [16–19] and the role of the higher modes [17, 18, 20, 21] have been studied both from an experimental and analytical point of view, with a clear focus on the structural performance (structural rocking). In practice, while the base shear reduces due to structural rocking, excitation due to impacts at the interface of the stepping mechanism might amplify internal loads significantly. Parallel to these studies, there has been extensive research on the response of rocking foundations which utilize soil as an energy dissipater and are combined with an admissible failure mechanism of their superstructure (foundation rocking). The uplifting and earthquake response [22–26], the achieved damping [15, 27] and the parameters of soil and superstructure regarding structures with rocking foundations [28] lead to the conclusion that the more a foundation is allowed to rock, the lesser can be the damage in the superstructure, but this will come at the expense of larger displacements and residual differential settlements.

The objective of this paper is to examine the force demand of two small scale flexible building models that can rock above (model RA, structural rocking) or below their foundation level (model RB, foundation rocking), including soil-structure interaction effects, based on observations from centrifuge testing (Figure 1). The design of the two rocking models are first presented, including the design of an energy dissipation element (fuse) used in structural rocking. The models were first tested side-by-side and on a separate test two yielding plates were installed to act as energy dissipating fuses in the RA model. Having subjected the models to multi-frequency ground excitations, the internal loadings from structural components were examined and the potential base isolation effect against typical fixed base oscillators were quantified.

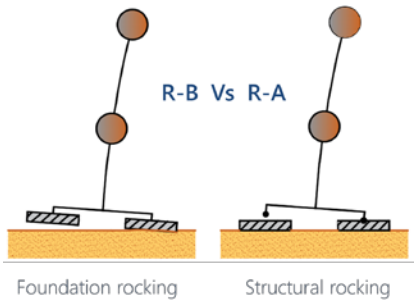


Figure 1: Two models of flexible structures (2DOF) rocking on discretized footings and soil, below the foundation level (left) and above that (right).

## 2 DESIGN OF ROCKING MODELS

Two linear elastic building models were designed as identical, with their only difference being the connectivity of their columns to the footings (Figure 2). For the model rocking above the foundation (RA), columns were designed to detach and step on their footings, while for the model rocking below the foundation (RB) the footing-column connection was designed to be rigid. While not in rocking action and assuming the soil-footing interface as a fixed boundary, the RA and RB models correspond to a hinged base frame and a fixed base frame, respectively.

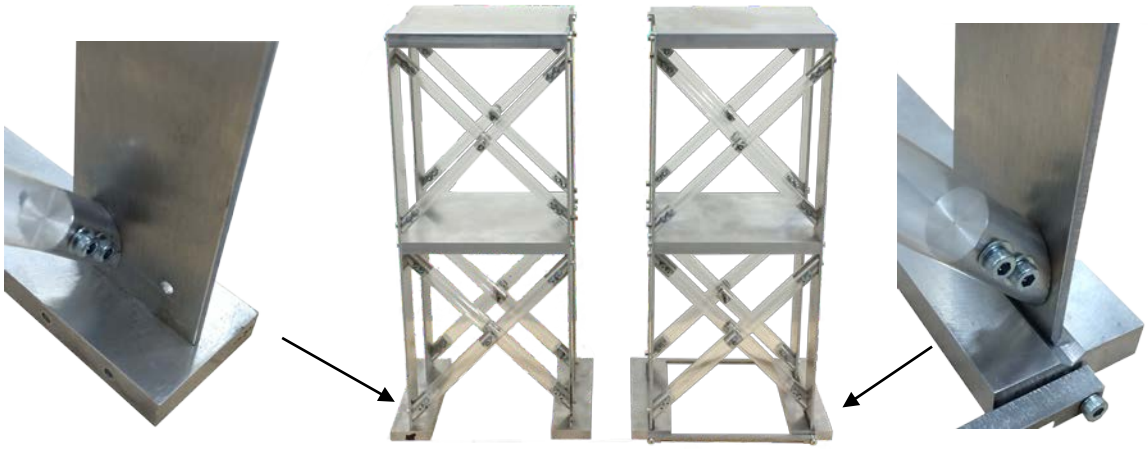

Figure 2: Column fixed to column for foundation rocking (far left), rocking below the foundation model (RB, left), rocking above the foundation (RA, right), connection for hinged support and structural rocking (far right).

The overall dimensions, the sizing of the members and the dynamic response properties are governed by a combination of factors covering the experimental needs and relating the models to a prototype building (Table 1, Figure 3). Therefore, in prototype scale, the models represent 3-4 storey buildings with a natural period of 0.70s (1.4Hz). Such buildings are represented well by their first two lateral modes in unidirectional ground shaking and therefore, the centrifuge models were designed as 2DOF oscillators for shaking and rocking in one direction. Moreover, the distance between the discrete footings is larger than two times a footing's width to avoid generating a mat foundation response. This also applies to the side-by-side testing for adjacent footings to minimize structure-soil-structure interaction of the models in the centrifuge box (Figure 3).

| Properties | | Fixed base (RB) | Hinged base (RA) |
|---|---|---|---|
| First mode period (prototype) | | 0.66s | 0.70s |
| Experimental first mode frequency (model) | | 53Hz | 46Hz |
| Experimental second mode frequency (model) | | 147Hz | 136Hz |
| Design stiffness (prototype) | Top storey | 7.9MN/m | 7.9MN/m |
| | Bottom storey | 16.5MN/m | 15.9MN/m |
| Design stiffness (model) | Top storey | 0.24MN/m | 0.24MN/m |
| | Bottom storey | 0.50MN/m | 0.48MN/m |
| Total superstructure mass (prototype) | | 60 metric tonnes | |
| Dynamic storey mass (model) | | 0.83kg | |
| Slenderness ratio | | 0.25 | |
| Bearing pressure | | 80kPa/footing, FoS=2.3 (DA1/2 [29]) | |
| Experimental centrifuge scale | | 33 | |

Table 1: Basic properties of the buildings models subjected to centrifuge testing

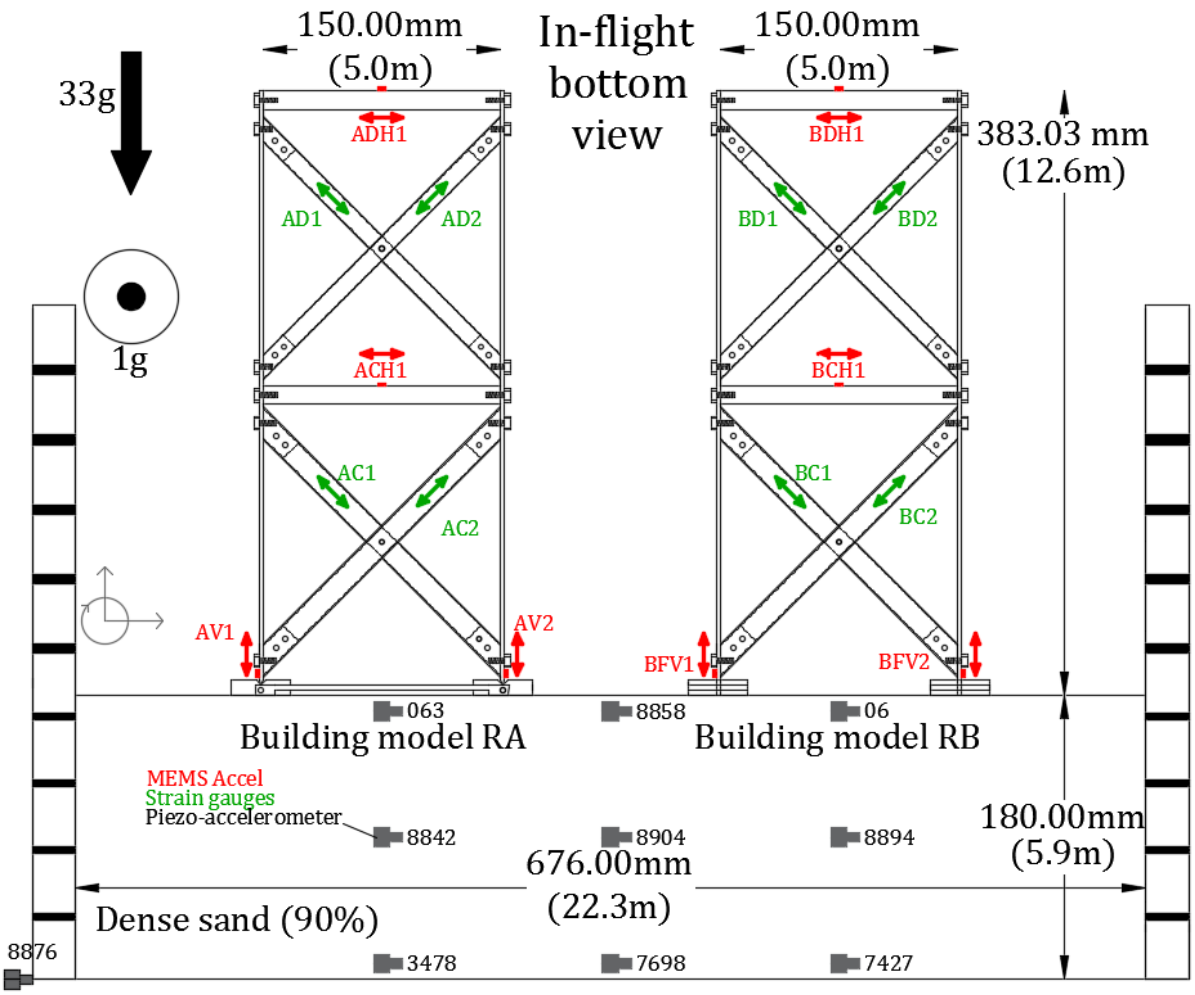


Figure 3: Side-by-side centrifuge testing and overall dimensions of the models RA and RB

To design the members two load cases were considered. Those consisted of the case at which the models are at the onset of uplift and the case at which the maximum rocking angle is achieved before toppling, that is the slenderness angle. For the first load case, a linear elastic response was assumed and a spectral acceleration was identified iteratively, so that a zero-tension load in the uplifting columns was achieved. The design base shear was identified for this spectral acceleration, as this shear is capped by rocking; the maximum base shear should not be larger than the value at the onset of uplift. For the second load case, when rocking develops the weight of the structure is transferred to the soil through the columns of the one side of the structure. These columns were designed for the increased compressional forces due to this redistribution of loading.

All columns (6082-T6) and bracing elements (plastic PETG tube sections) were designed as linear elastic to avoid masking the rocking action with local failures (e. g. material failure) or other out of interest nonlinear events (e. g. buckling). The key in the similarity of the natural frequencies stems from the bracing configurations which form the primary lateral load resistance mechanism prior uplift. By minimizing the columns' width, the lateral stiffness prior uplift is governed by the bracings, regardless of the boundary conditions at the column base (fixed base or hinged base). This allows for a direct comparison between the two models, with only the parameter of the type of rocking mechanism to be the governing factor causing any potential differences in the earthquake response. The linear elastic performance of the PETG bracing elements and their connections in axial cyclic loading were tested and verified experimentally.

An energy dissipation element was also designed to be installed into the RA model, for a separate side-by-side testing with the RB model. This is a steel tapered plate (S275, Figure 4) which deforms in bending. Its root is bolted to the footing while its free end is linked to the column tip. When the column tip uplifts once rocking initiates, the fuse deforms in bending and dissipates energy due to hysteresis. The performance of this element was predicted computationally and was verified experimentally prior its installation into the RA model (Figure 4).

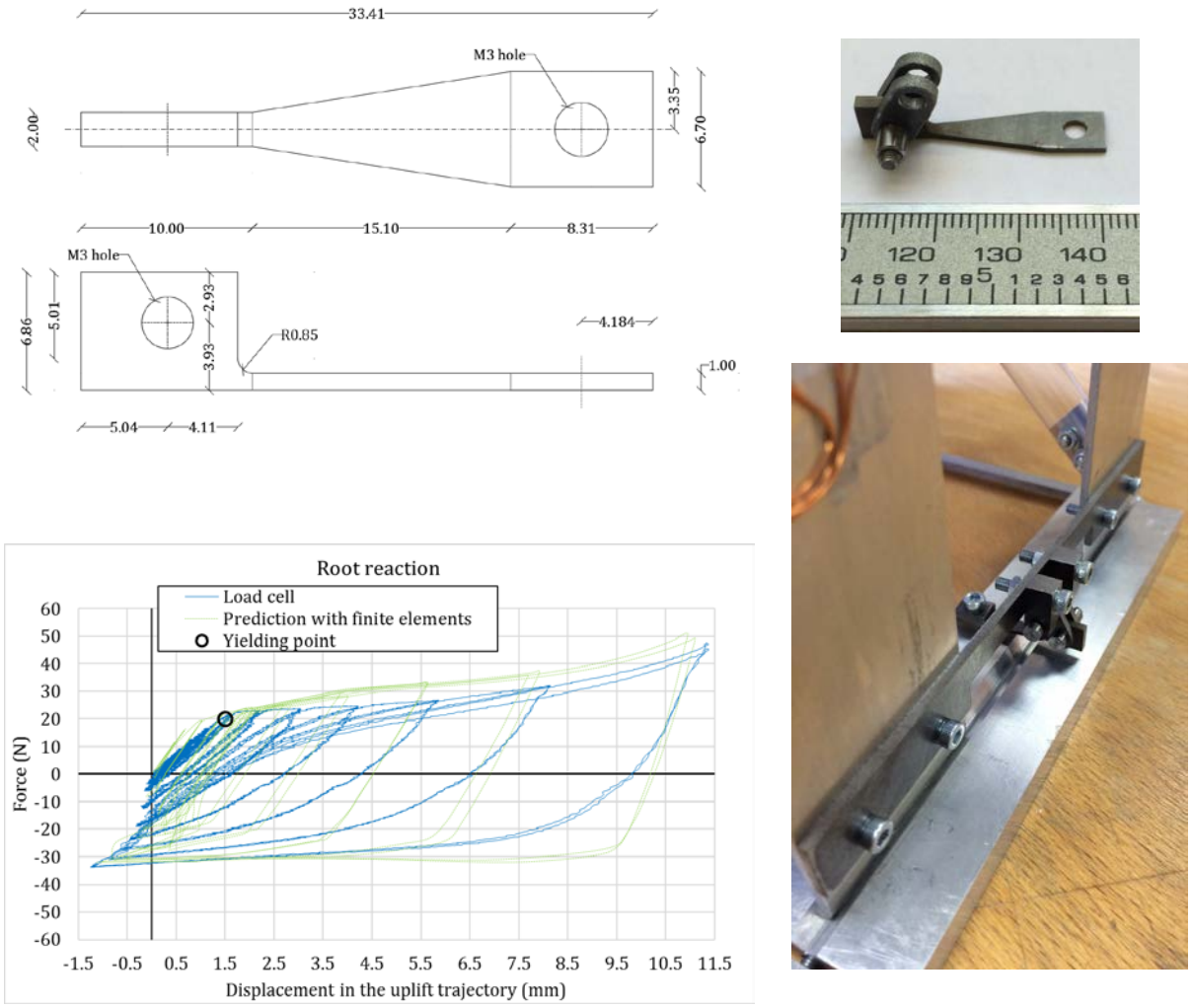


Figure 4: Detailing of the energy dissipation steel plate (top left), steel plate with additional linkage rod (top right), cyclic performance of plate-rod assembly (bottom left), plate installed into model RA (bottom right)

## 3 EXPERIMENTAL PROGRAM FOR CENTRIFUGE TESTING

The testing of the rocking performance involved two separate centrifuge flights. The setup (Figure 3) of the first flight (Test 1) involved the models RA and RB simply resting (with no embedment) on dense sand ($D_r$=90%) and allowing them to slide and rock upon the earthquake excitation. The setup of the second flight (Test 2) was the same, with the only difference being that a fuse was installed at each footing of the model RA.

The earthquake response of the models was monitored in terms of accelerations and internal loadings. Micro-Electro-Mechanical System (MEMS) accelerometers were used to monitor the storey lateral accelerations and the vertical acceleration due to impact on the interface of rocking. The PETG bracing elements were essentially converted to load cells, by calibrat-

ing strain gauges that clearly registered the axial strain due to the axial tension or compression of their tube sections. In addition, a series of piezo-electric accelerometers were used to monitor the centrifuge box input excitation and the ground excitation below the foundation level of each model.

The input excitations, measured near the sand surface and between the models, consisted of weak and large amplitude multi-frequency motions (Table 2, Figure 5). In Test 1, a weak ground motion was used first, followed by a strong motion with the target excitation frequency equal to 50Hz to induce resonance. In Test 2, the same input motions were specified, followed by a third motion with a lower frequency content. In both tests, higher harmonics of the centrifuge beam-actuator-package system developed, which were at similar frequencies of the models. The weak motions (EQ-1) were specified to induce a linear elastic response and hence produce a control dataset. The strong motions (EQ-2) and the low frequency motion (EQ-3) were used to induce the uplift of the models.

| TEST | EQ | CODE | PGA Model (Prototype) | TARGET FREQUENCY | TESTING |
|---|---|---|---|---|---|
| 1 | 1 | TEST-1 EQ-1 | 1.9g (0.06g) | 50Hz low amplitude | RA w/o fuse VS RB |
| 1 | 2 | TEST-1 EQ-2 | 23g. (0.70g) | 50Hz large amplitude | RA w/o fuse VS RB |
| 2 | 1 | TEST-2 EQ-1 | 2.1g (0.06g) | 50Hz low amplitude | RA w fuse VS RB |
| 2 | 2 | TEST-2 EQ-2 | 20.3g (0.61g) | 50Hz large amplitude | RA w fuse VS RB |
| 2 | 3 | TEST-2 EQ-3 | 11.0g (0.33g) | 35Hz low amplitude | RA w fuse VS RB |

Table 2: Input motion details and model's testing configuration

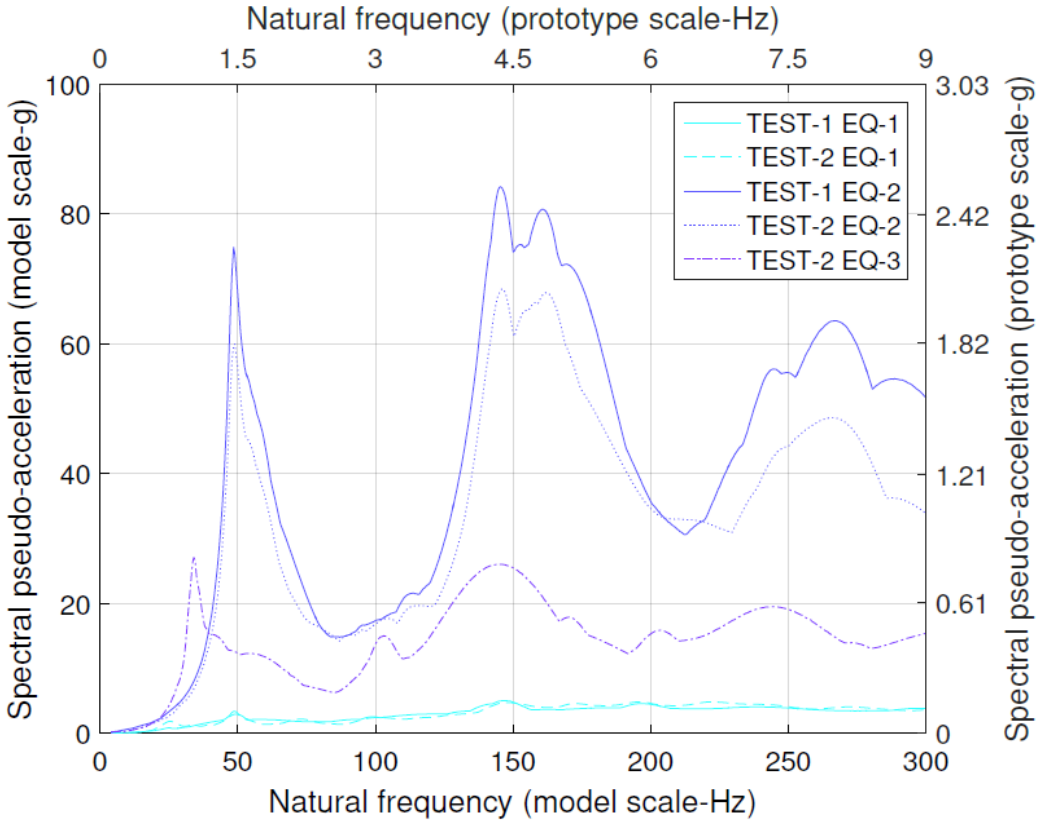


Figure 5: Spectral pseudo acceleration of each ground motion measured on the sand surface, between the models (damping ratio, $\zeta$=5%)

# 4 RESULTS

## 4.1 Verification of uplift and observed response

A sequence of strong impacts was detected by the accelerometers monitoring the vertical movement of the column tips near the footings. Those sequences appeared with a close to zero magnitude in the weak earthquakes, whereas they were very strong during the larger magnitude earthquakes suggesting that uplift and consequently rocking action developed (Figure 6). Analyzing the frequency content of the vertical accelerations and of the lateral acceleration below the soil surface, reveals that the excitation frequencies drove the rocking motion in both models.

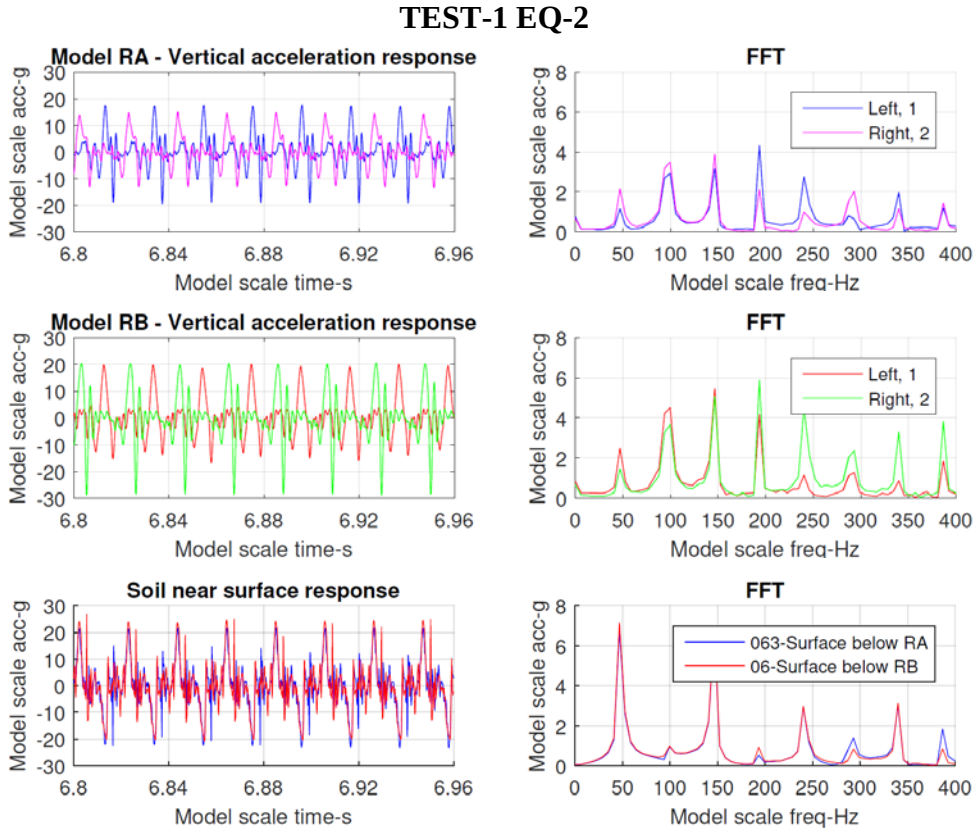


Figure 6: Vertical acceleration response at the column tips as measured from the accelerometers during the steady state in TEST-1 EQ-2 (model scale, 33g)

In other words, as expected, during the small amplitude earthquakes, the response of both models was linear elastic. During the large amplitude earthquakes and the low frequency earthquake, the models rocked and impacts occurred. Model RB was observed to slide during the shaking on the sand surface with a mixed motion of rocking and sliding, with this combination being more evident in the low frequency excitation, and leading to small acceleration demands (Figure 7). On the contrary, the footings of the model RA stayed in position and therefore rocking was developed by that model with partial lateral sliding of the column tips into the grooves of the footings. During the large amplitude earthquakes and low frequency earthquake, the time-historey accelerations suggest an out of phase storey profile, which if combined with the existence of the impacts, it further suggests the development of an uplifted mode of vibration [18, 30], driven by the input motion frequencies.

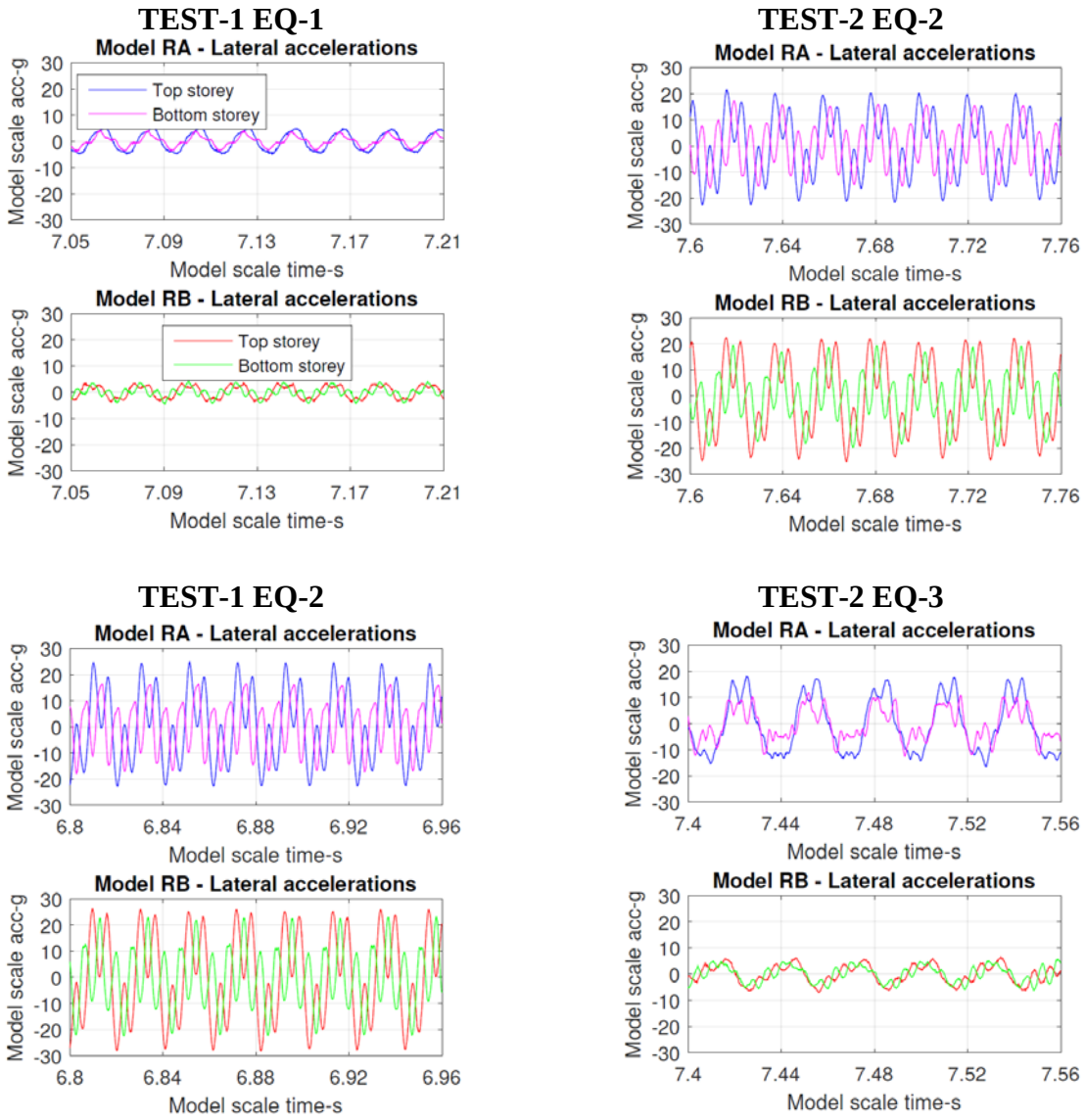


Figure 7: Steady state storey lateral acceleration response (model scale, 33g)

## 4.2 Moment – rocking angle response

By integrating twice the acceleration trace of the vertical accelerometers at the base of the models, an approximation of the rocking angle was obtained, informative of the extent of rocking that developed. The restraining moment was calculated as the difference of the overturning moment and the rotational acceleration component of the storey slabs which was calculated directly by using the storey horizontal acceleration records.

During the small magnitude earthquakes, both models developed a restraining moment smaller than the required one to cause uplift (Figures 8, 9). During earthquakes EQ-2, the responses of model RA were very similar, indicating that the uplift during rocking was too small to push the fuse to its yielding point (Figure 8). However, after inspection at the end of Test 2, a residual deflection of 0.1mm was measured at the free end of the fuses, which is smaller than the deflection at the yielding point (Figure 4). Considering that during EQ-3 model RA experienced larger rotations than in EQ-2 (Figure 8), it is indicated that EQ-3 was the excitation which activated the fuse noticeably, but still not to the extent a long plastic plateau could develop regarding the local response of the fuses (Figure 4).

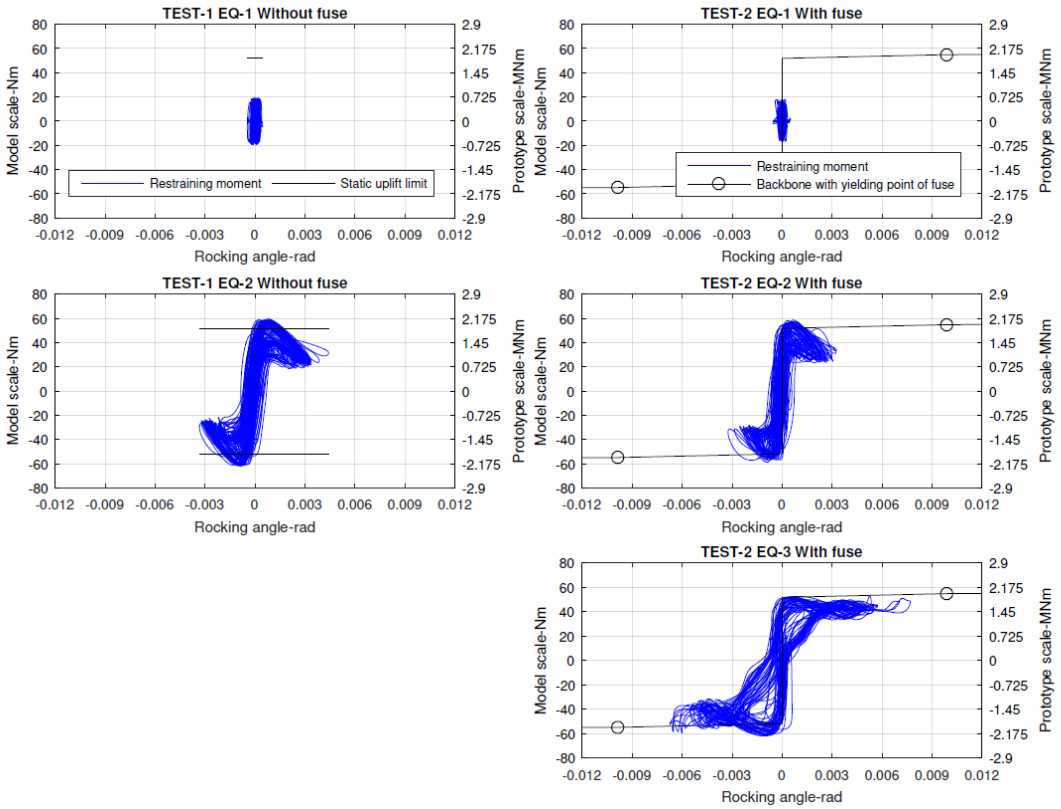


Figure 8: Restraining moment versus rocking angle. Response of model RA during the first test without the fuse (left column) and during the second test with the fuse (right column)

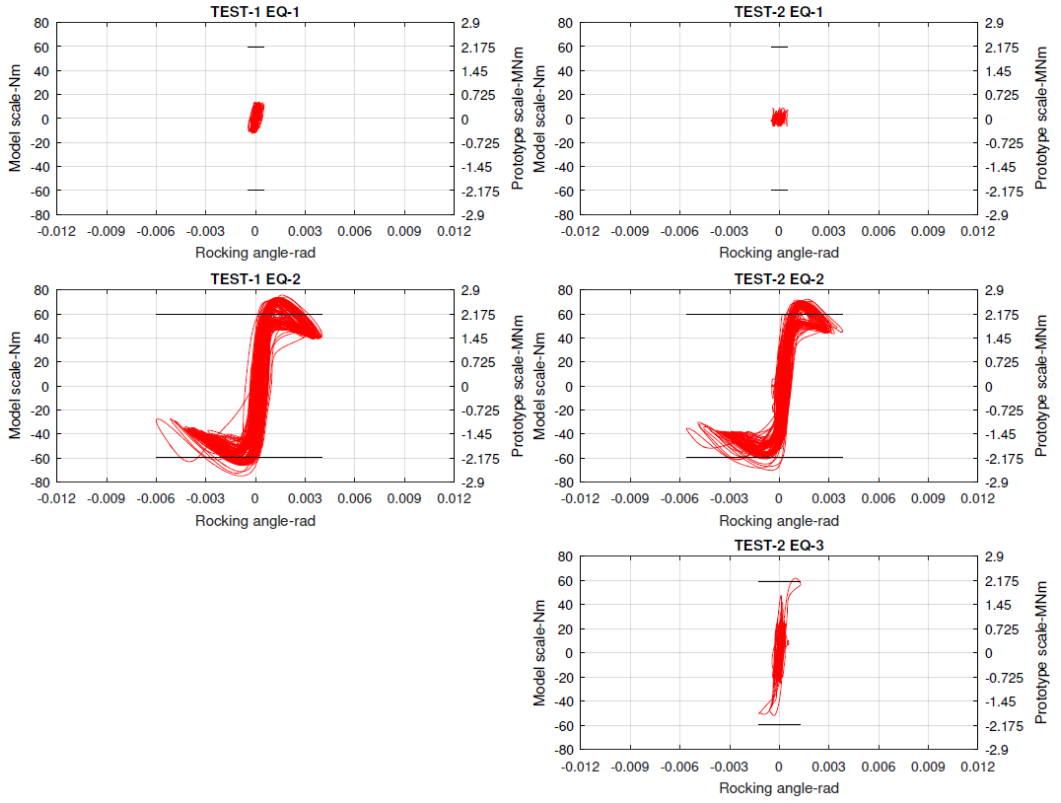


Figure 9: Restraining moment versus rocking angle. Response of the model RB during the first test (left column) and during the second test (right column).

Both models developed transient responses which extended the amount of rotation of the rocking angle initially, whereas the steady state response, represented by the dense loops in Figures 8 and 9 led to smaller rotations. The amount of rotation was similar for both models during the large amplitude earthquakes during both tests. However, during the low frequency earthquake model RB experienced significantly smaller rotations than model RA, although extensive sliding occurred at the same time.

### 4.3 Storey and bracing response

The load demand on the structure was estimated by utilizing the storey accelerometers and was validated with the strain gauges on the bracing members. From the measurements obtained from the accelerometers (Figures 10, 11), it was observed during the larger magnitude earthquakes, the top storey shear was capped and was found to reduce to zero at the extreme angle of rocking that was experienced by both models. Regarding the RA model during the low frequency excitation, the top storey shear was bound between a maximum and a non-zero minimum value. For the RB model, only the initial transient terms reached the extreme rocking angle during the low frequency earthquake, again due to the subsequent sliding that occurred. The base shear plots were also found to reflect the trend obtained from the restraining moment.

The shear force trends were reflected in the load response of the bracing elements generated by the strain gauges on them. Figures 10 and 11 show that, while the axial force of the top storey bracings was fairly symmetric about the zero-force axis, the bottom storey bracings followed an asymmetric response in the force axis of the plots. In particular, at the extreme angle the models were supported on only one side, with the axial members coinciding at the point of rotation experiencing increased compressional forces. The superstructure weight redistributes due to contact loss on the uplifting side, where the tensional force of the bracing element there dropped to zero. Moreover, the force values that bound the performance of the bracings were constant and the same for both models, indicating that the extent of the rocking angle is of little importance when assessing the load demand once the uplift and rocking begins.

### 4.4 Base isolation effect

The quantification of the base isolation effect was carried out in terms of base shear values. By using the recorded acceleration on the sand surface, the SDOF response spectra were created. Then, by using the SRSS method with the range of damping ratios obtained from the free vibration traces of the storey accelerations and bracings, the base shear maxima were estimated for similar (hypothetical) fixed base 2DOF models. The estimations were then compared with the base shear maxima directly obtained from the response accelerations (Figure 12). It was found that the base isolation effect was clear during the large amplitude earthquakes, while it was minimal during the low frequency earthquake for both models (Table 3). Finally, the installation of the fuses in model RA did not contribute in any apparent reduction in the base shear demand as observed from the results of Table 3 between the first and second tests for the earthquakes EQ-2.

## 5 CONCLUSIONS

The dynamic soil-structure interaction of twin small scale buildings with foundation rocking and structural rocking was investigated in a proof of concept pilot centrifuge experiment. The following conclusions were drawn:

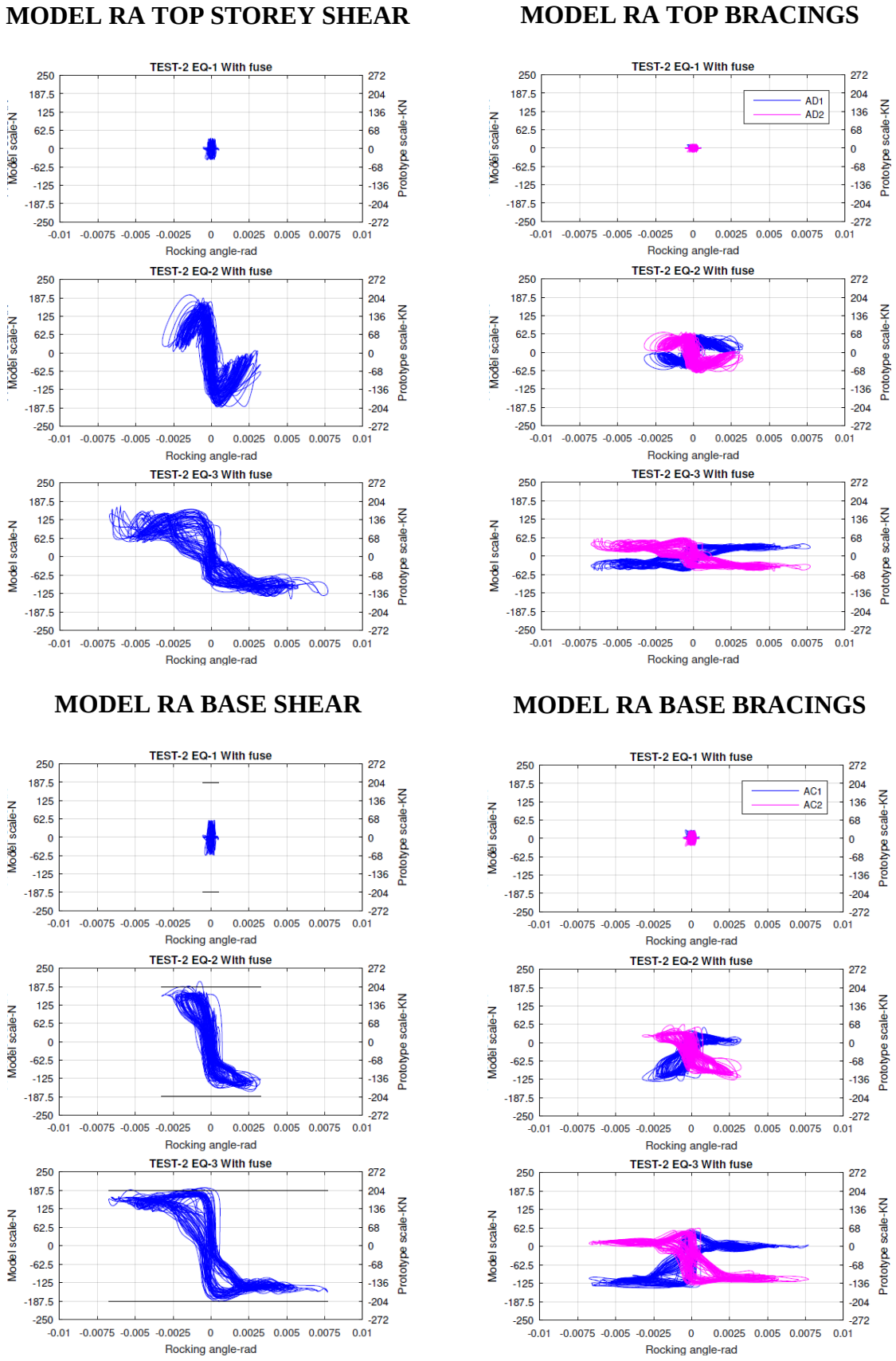


Figure 10: Model RA, top storey shear response (left top) and corresponding bracing axial response (right top), bottom storey shear response (left bottom) and corresponding bracing axial response (right bottom)

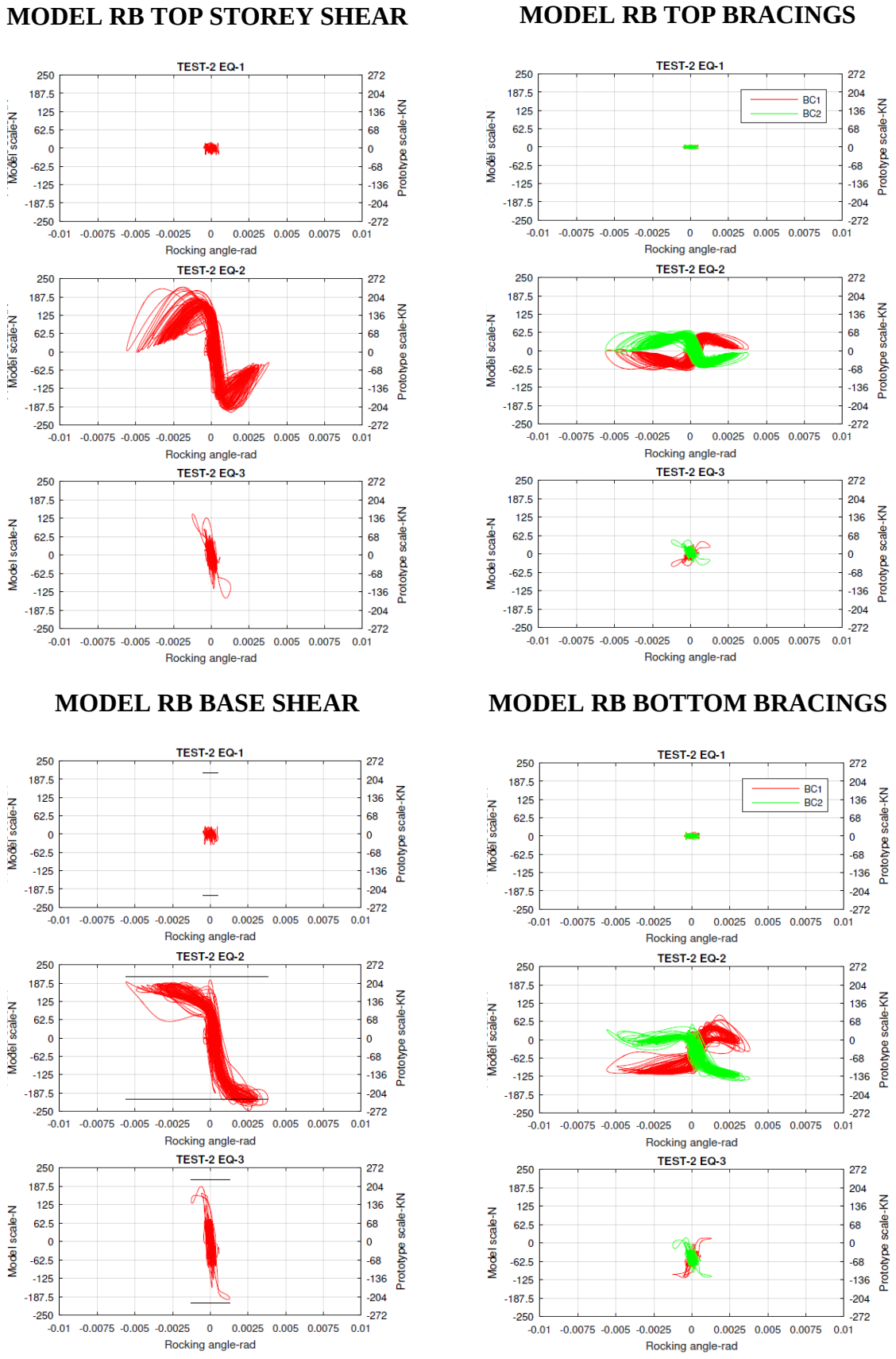


Figure 11: Model RB, top storey shear response (left top) and corresponding bracing axial response (right top), bottom storey shear response (left bottom) and corresponding bracing axial response (right bottom)

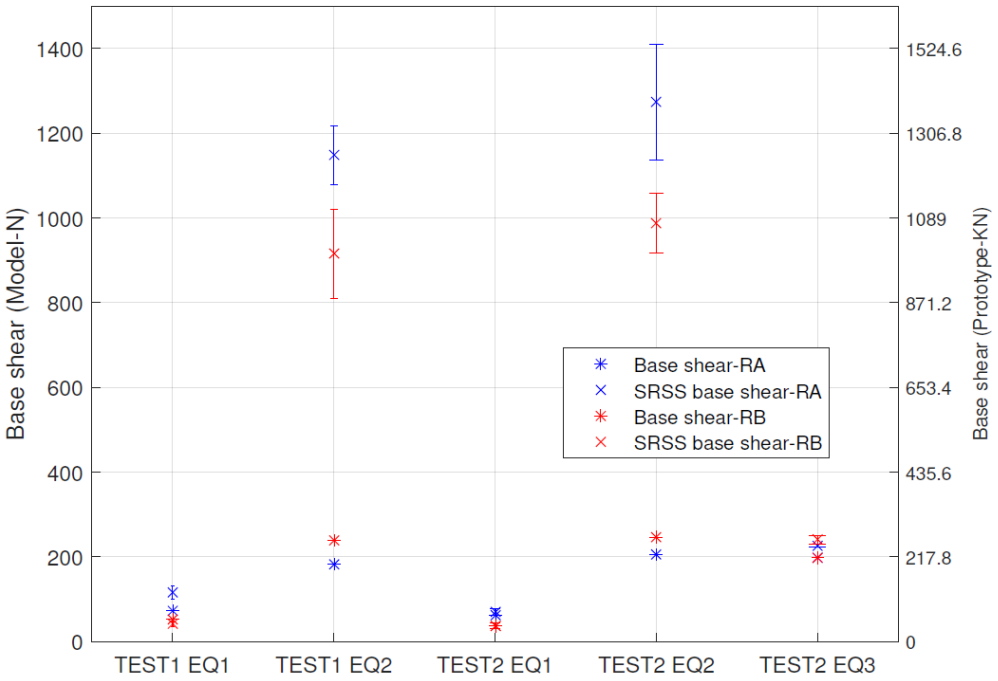


Figure 12: Base shear maxima from fixed base SRSS solution and as obtained from the centrifuge testing

| BASE SHEAR DIFFERENCE (%) | TEST-1 EQ-1 | TEST-1 EQ-2 | TEST-2 EQ-1 | TEST-2 EQ-2 | TEST-2 EQ-3 |
|---|---|---|---|---|---|
| RA | -38 | -84 | -13 | -83 | -13 |
| RB | +23 | -74 | -2 | -75 | -18 |

Table 3: Percentage difference of the experimental base shear with respect to the average SRSS solution

- The manifestation of rocking was detected by observing large amplitude spike accelerations close to the pivot points, driven by the excitation frequency content.
- Internal loadings of the twin models reflected the global response in terms of storey shear and overturning moment and were bound between the same extrema, regardless of the extent of rotation during rocking. This indicates that, for the two models considered, structural rocking and foundation rocking produced very similar beneficial effect of reducing the superstructure force demand.
- The base isolation effect was evident during large amplitude excitations with a target excitation frequency matching the natural frequency of the models and during these, rocking with minor sliding was observed for both models. During a low frequency excitation, the response varied significantly between the two models due to different levels of sliding. However, more tests which cause larger amplitude rocking are needed to investigate further the role of rocking and the relative effects of any additional structural or soil energy dissipation.

## REFERENCES

[1] Marquis, F., Kim, J.J., Elwood, K.J., Chang, S.E., Understanding post-earthquake

decisions on multi-storey concrete buildings in Christchurch, New Zealand. *Bulletin of Earthquake Engineering*, **15**, 731–758, 2017.

[2] Franco, G., Siembieda, W., Chile's 2010 M8.8 earthquake and tsunami: Initial observations on resilience. *Journal of Disaster Research*, **5**, 577–590, 2010.

[3] Housner, G.W., The behaviour of inverted pendulum structures during earthquakes. *Bulletin of Seismological Society of America*, **53**, 403–417, 1963.

[4] Plaut, R.H., Fielder, W.T., Virgin, L.N., Fractal behavior of an asymmetric rigid block overturning due to harmonic motion of a tilted foundation. *Chaos, Solitons & Fractals*, **7**, 177–196, 1996.

[5] Makris, N., A half-century of rocking isolation. *Earthquakes and Structures*, **7**, 1187–1221, 2014.

[6] Ajrab, J.J., Pekcan, G., Mander, J.B., Rocking wall-frame structures with supplemental tendon systems. *Journal of Structural Engineering*, **130**, 895–903, 2004.

[7] Ma, X., Deierlein, G., Eatherton, M., Krawinkler, H., et al., Large-scale shaking table tests of steel braced frame with controlled rocking and energy dissipating fuses. *Proceedings of the 9th U.S. National and 10th Canadian Conference on Earthquake Engineering*, 2010.

[8] Hajjar, J.F., Sesen, H.A., Jampole, E., Wetherbee, A., *A synopsis of sustainable structural systems with rocking, self centering, and articulated energy-dissipating fuses*, Boston 2013.

[9] Kelly, J.M., Skinner, R.I., Heine, A.J., Mechanisms of energy absorption in special devices for use in earthquake resistant structures. *Bulletin of the New Zealand Society for Earthquake Engineering*, **5**, 63–73, 1972.

[10] Sharpe, R.D., Skinner, R.I., The seismic design of an industrial chimney with rocking base. *Bulletin of the New Zealand National Society for Earthquake Engineering*, **16**, 98–106, 1983.

[11] Tyler, R.G., Tapered steel energy dissipators for earthquake resistant structures. *Bulletin of the New Zealand National Society for Earthquake Engineering*, **11**, 1978.

[12] Acikgoz, S., Argyle, A., DeJong, M.J., The role of supplemental damping in limiting forces and displacements in a rocking structure. *Proceedings of the 2nd European Conference on Earthquake Engineering and Seismology*, 1–12, 2014.

[13] Pollino, M., Bruneau, M., Seismic retrofit of bridge steel truss piers using a controlled rocking approach. *Journal of Bridge Engineering*, **12**, 600–610, 2007.

[14] Tremblay, R., Poirier, L., Bouaanani, N., Leclerc, M., et al., Innovative Viscously Damped Rocking Braced Steel Frames. *The 14th World Conference on Earthquake Engineering (14 WCEE), October 12-17*, 2008.

[15] Gajan, S., Saravanathiiban, D.S., Modeling of energy dissipation in structural devices and foundation soil during seismic loading. *Soil Dynamics and Earthquake Engineering*, **31**, 1106–1122, 2011.

[16] Acikgoz, S., DeJong, M.J., The rocking response of large flexible structures to earthquakes. *Bulletin of Earthquake Engineering*, **12**, 875–908, 2013.

[17] Acikgoz, S., Ma, Q., Palermo, A., DeJong, M.J., Experimental Identification of the

Dynamic Characteristics of a Flexible Rocking Structure. *Journal of Earthquake Engineering*, **20**, 1199–1221, 2016.

[18] Acikgoz, S., DeJong, M.J., Analytical modelling of multi-mass flexible rocking structures. *Earthquake Engineering & Structural Dynamics*, **45**, 2103–2122, 2016.

[19] Vassiliou, M.F., Mackie, K.R., Stojadinović, B., Dynamic response analysis of solitary flexible rocking bodies: modeling and behavior under pulse-like ground excitation. *Earthquake Engineering & Structural Dynamics*, **43**, 1463–1481, 2014.

[20] Wiebe, L., Christopoulos, C., Tremblay, R., Leclerc, M., Mechanisms to limit higher mode effects in a controlled rocking steel frame. 1: Concept, modelling, and low-amplitude shake table testing. *Earthquake Engineering & Structural Dynamics*, **42**, 1053–1068, 2013.

[21] Wiebe, L., Christopoulos, C., A cantilever beam analogy for quantifying higher mode effects in multistorey buildings. *Earthquake Engineering & Structural Dynamics*, **44**, 1697–1716, 2015.

[22] Gazetas, G., Apostolou, M., Nonlinear soil – structure interaction: Foundation uplifting and soil yielding. *Proceedings Third UJNR Workshop on Soil-Structure Interaction*, 1–16, 2004.

[23] Loli, M., Knappett, J.A., Brown, M.J., Anastasopoulos, I., Gazetas, G., Centrifuge modeling of rocking-isolated inelastic RC bridge piers. *Earthquake Engineering & Structural Dynamics*, **43**, 2341–2359, 2014.

[24] Deng, L., Kutter, B.L., Kunnath, S.K., Centrifuge modeling of bridge systems designed for rocking foundations. *Journal of Geotechnical and Geoenvironmental Engineering*, **138**, 335–344, 2012.

[25] Gelagoti, F., Kourkoulis, R., Anastasopoulos, I., Gazetas, G., Rocking-isolated frame structures: Margins of safety against toppling collapse and simplified design approach. *Soil Dynamics and Earthquake Engineering*, **32**, 87–102, 2012.

[26] Liu, W., Hutchinson, T.C., Gavras, A.G., Kutter, B.L., Hakhamaneshi, M., Seismic Behaviour of Frame-Wall-Rocking Foundation Systems. I: Test Program and Slow Cyclic Results. *Journal of Structural Engineering*, **141**, 4015059, 2015.

[27] Gajan, S., Kutter, B.L., Capacity, settlement, and energy dissipation of shallow footings subjected to rocking. *Journal of Geotechnical and Geoenvironmental Engineering*, **134**, 1129–1141, 2008.

[28] Heron, C.M., The Dynamic Soil Structure Interaction of Shallow Foundations on Dry Sand Beds. 2013.

[29] CEN, Eurocode 7: Geotechnical design - Part 1: General rules 2004.

[30] Acikgoz, S., DeJong, M.J., The interaction of elasticity and rocking in flexible structures allowed to uplift. *Earthquake Engineering & Structural Dynamics*, **41**, 2177–2194, 2012.

COMPDYN 2017
6th ECCOMAS Thematic Conference on
Computational Methods in Structural Dynamics and Earthquake Engineering
M. Papadrakakis, M. Fragiadakis (eds.)
Rhodes Island, Greece, 15–17 June 2017

# ROCKING RESONANCE CONDITIONS OF LARGE AND SLENDER RIGID BLOCKS UNDER THE INTENSE PHASE OF AN EARTHQUAKE

**Claudia Casapulla**[1], **Alessandra Maione**[2]

[1] University of Napoli "Federico II"
Department of Structures for Engineering and Architecture, Napoli, Italy
casacla@unina.it

[2] University of Napoli "Federico II"
Department of Structures for Engineering and Architecture, Napoli, Italy
arch.maione@gmail.com

**Keywords:** Multiple impulses, rigid block dynamics, rocking amplification, size effect, resonance effects.

**Abstract.** *A simplified approach is proposed in this paper for assessing the safety levels of the seismic response of large and slender rigid masonry blocks. The dynamic behavior of rigid free-standing blocks subjected to earthquake ground motions is highly non-linear and sensitive to small perturbations of various parameters. Many difficulties arise in defining reliable response spectra for such systems and these are well known in the literature. An artificial limit accelerogram is herein proposed to represent the most unfavorable effects of the intense phase of an earthquake. This consists of a sequence of instantaneous impulses, all applied right after the impact of the blocks on the ground. The resonance conditions also aim at highlighting to what extent the ground motion details and the system parameters can influence the rocking response. A secondary sequence of intermediate impulses is then introduced to reduce the resonance effects and to cover a broad range of conditions. Approximate equations of motion of the rocking blocks are also proposed and numerical analyses are performed to highlight the most significant aspects of the proposed approach.*

## 1 INTRODUCTION

Ancient masonry structures are generally regarded as sets of macro-elements under earthquake actions. The seismic vulnerability of these elements can be assessed throughout rocking analyses or energy-based approaches [1]. Rocking motion is frequently observed when the morphology of the wall sections allows a monolithic behavior. In this case, in absence of proper connections between orthogonal walls and between walls and floors, out-of-plane mechanisms may occur with discretization of the walls in few rigid macro-blocks articulated by hinges. Here rocking and sliding motions may take place. The analysis of the local failure modes is also provided by the multi-level approach of the Italian Guidelines on Cultural Heritage [2].

In order to evaluate the static load factor causing the onset of this kind of mechanisms, non-standard limit analysis procedures can be applied [3-9]. A dynamic approach, however, is useful to investigate the time-history evolution of the rocking response and the sensitivity to the features of the seismic action. Moreover, the response of a rocking block is extremely sensitive to boundary conditions, very relevant for masonry panels. In that sense, some methods were recently proposed to consider the interaction with transverse walls [10], roofs [11], or vertical restrainers [12].

From this perspective, the reference model for the rocking motion without sliding of a rigid block resting on a rigid foundation was first developed by Housner [13]. He proposed a linear model to describe the rocking motion of slender blocks, highlighting, with the definition of "inverted pendulum", how the frequency parameter of the blocks depends on their size and on the gravitational acceleration but not on their mass. His pioneering work, moreover, provided a simple expression of the coefficient of restitution only depending on the slenderness; it represents an upper bound of the loss of energy due to the impact of the block on the ground. Housner defined the overturning conditions under horizontal actions schematized as single rectangular or half-sine impulse of acceleration; however, his analysis highlighted the difficulty to identify a stable relation between the geometric features of the block (size and slenderness) and the characteristics of the seismic input, so that the problem could only be treated through probabilistic approaches. This difficulty was also confirmed by the works of many other authors [14-17] who have examined the response of the block using both real or simulated accelerograms and harmonic loadings, highlighting the great sensitivity of the response to small variations in both system parameters and ground motion details. On the other hand, also other approaches ([18], [19]) based on response spectra have concluded that rocking block cannot be treated as an "equivalent" elastic SDOF because substantial differences are recognizable in its dynamic behavior.

Over the last years, increasing attention has been focused on the identification of the worst input scenario corresponding to the resonant response of the blocks and of single-degree-of-freedom (SDOF) inelastic structures [20-24]. In particular, the pioneering works by Casapulla et al. [20] and Casapulla [24] proposed a simplified representation of the seismic input as a sequence of instantaneous impulses of acceleration and identified the resonant condition with a time interval between these impulses coincident with the amplitude-dependent durations of the half-cycles of the motion. This approach allows describing the response of the block within the generic half-cycle as a natural motion. A powerful simplification of the equation of the motion was also proposed by the authors and a simply criterion of minimization of the error was validated through a comparison with the Housner model [25], [26].

More recently Kojima et al. [27] and Kojima and Takewaki [28] have proposed to schematize the impulsive component of a near-fault earthquake as a double impulse. Such a kind of input has been first used to identify the resonant condition of elastic-plastic systems and then

extended by Nabeshima et al. [29] to obtain closed-form overturning limit for rigid blocks. This simplification has also been used to represent long duration earthquakes as a multiple impulse input [30]. Many other implications can be derived by simulating the near-field ground motions, which contain long-period directivity pulses [31, 32].

In this paper the analysis of rocking motion of large and slender rigid blocks is developed with reference to the intense phase of the seismic action described through an artificial accelerogram. In particular, this artificial accelerogram is described in Section 2 as resulting from the superposition of two sequences of instantaneous impulses: a main sequence, acting when the block impacts on the ground, defines the resonant condition; a secondary sequence of intermediate impulses, acting within the half-cycles, is then introduced in order to obtain a more realistic input condition. The closed-form equations governing the response of the block to the resonant sequence and a step-by-step procedure to obtain the response in the presence of intermediate impulses are presented in Section 3. Lastly, in Section 4 numerical results are presented, which take into account the effect of the amplitude of the intermediate impulses on the maximum response of the block and on the duration of the half-cycles, together with the influence of the restitution coefficient. Further developments of this study are contained in more extended works [33, 34].

## 2 ARTIFICIAL ACCELEROGRAMS AS SEQUENCES OF ISTANTANEOUS IMPULSES

The definition of the resonance condition for the rocking motion of rigid masonry blocks represents a basic reference in the analysis of their seismic response. Taking into account that the rocking motion is characterized by the oscillation of the blocks around the two vertex of the base with amplitude-dependent period, the maximization of the resonant effects has been obtained through an artificial accelerogram made up of sequences of instantaneous Dirac impulses; these impulses act at the beginning of each half-cycle of the rocking motion, right after the impact of the block on the ground. As a consequence the critical timing of impulses is not constant, but it increases with the duration of the half-cycle of the block oscillation, as schematically shown in Figure 1 [20]. The amplitude $I$ of the single impulse of this accelerogram is defined through the integral of a half-wave of the ground horizontal acceleration assuming that the impulse is applied at the centroid of such a half-wave.

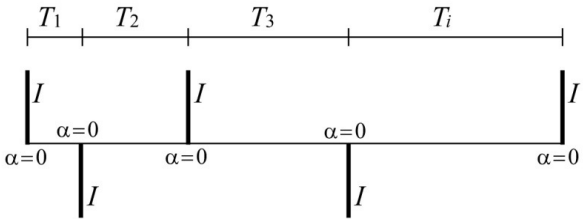


Figure 1: Limit artificial accelerogram as resonance sequence of instantaneous impulses.

This resonance sequence represents a theoretical input that allows investigating the rocking response to the worst input scenario, but it is quite unrealistic because, in particular, the critical timing of the impulses can be too long. Thereafter a secondary sequence of intermediate impulses acting during the half-cycle of motion of the block is introduced; this secondary sequence is also characterized by instantaneous impulses, all with the same amplitude $\underline{I}_s$, applied with alternate signs at equal time intervals $\underline{\Delta T}$ (the parameters and results referred to the secondary sequence are herein denoted by an underscore). The number of intermediate impulses between two subsequent impulses $I$ of the limit accelerogram (main impulses), is an even

number, so that their sum is zero (a typical property of all real accelerograms). Hence the secondary sequence is characterized by only two variable parameters, the amplitude and the frequency of the impulses, and it fulfills two specific requirements: to reduce the resonance effects of the limit accelerogram and to represent, with appropriate calibration of a few parameters, a large range of effects caused by the intense phases of recorded accelerograms. The corresponding scheme is shown in Figure 2.

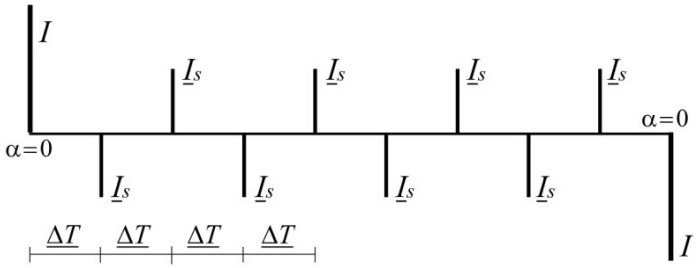


Figure 2: Secondary sequence of instantaneous intermediate impulses.

## 3 THE MODEL FOR THE ANALYSIS OF THE ROCKING MOTION OF THE BLOCKS

The hypothesis of instantaneous application of the impulses characterizing the seismic input described in the previous section allows treating the response of the block as a natural motion between two subsequent impulses. As well known, the natural motion of rigid free standing blocks, with slenderness $\lambda \geq 3$ ($\lambda = a/b$ in Figure 3), can be expressed by the linearized equation introduced by Housner [13]. Hence with the positive signs of forces and angles indicated in Figure 3, it is:

$$I_O \ddot{\alpha} + Mg(\alpha_c - \alpha) = 0 \qquad \Leftrightarrow \qquad \ddot{\alpha} + p^2(\alpha_c - \alpha) = 0 \tag{1}$$

in which $M$ is the mass, $I_O = 4\,M(a^2+b^2)/3$ is the corresponding moment of inertia (with respect to O), $\alpha_c = \tan^{-1}(1/\lambda)$ is the maximum rotational angle of the block and $p = \sqrt{3g/(4R)}$ is the frequency parameter, being $g$ the acceleration of gravity and $R$ the half-diameter of the block.

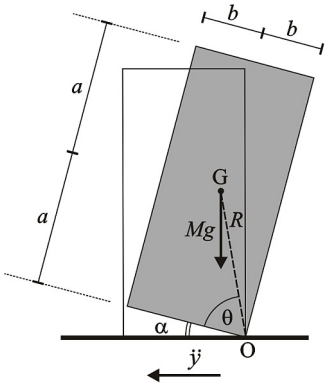


Figure 3: Rocking rigid block.

With the initial conditions $\alpha = \alpha_0$ and $\dot{\alpha} = \dot{\alpha}_0$, the solution of Eq. (1), in terms of rotational angle and velocity, is given by the following closed form expressions:

$$\begin{aligned} \alpha &= \alpha_c + (A_1 - \alpha_c)\cosh pt + A_2 \sinh pt \\ \dot{\alpha} &= (A_1 - \alpha_c)p \sinh pt + A_2 p \cosh pt \end{aligned} \tag{2}$$

with the constants $A_1$ and $A_2$ depending on the initial conditions.

In the analysis it is assumed that the coefficient of friction is sufficiently large as to prevent sliding between the block and the supporting base, while the dissipation of the energy due to impact of the block on the ground is represented by the coefficient of restitution. This coefficient is assumed to be a variable of the problem to account also for other damping effects (e.g. local plastic deformations).

### 3.1 The response to the artificial resonance input

Each impulse $I$ of the resonance sequence is applied immediately after the impact of the block on the ground ($\alpha = 0$) and causes an increment $\dot{\alpha}_1$ of the rotational velocity which is defined by the law of conservation of the angular momentum [20], [29]:

$$\dot{\alpha}_1 = \frac{M\, I\, a}{I_O} = \frac{\lambda\, \ddot{\alpha}_g\, I}{g} \tag{3}$$

where $\ddot{\alpha}_g$ is given by:

$$\ddot{\alpha}_g = \frac{3}{4}\frac{b}{a^2 + b^2} g \tag{4}$$

Let $C$ denote the coefficient of restitution. The rotational velocity at the beginning of the generic half-cycle of the motion between two subsequent impacts is:

$$\dot{\alpha}_i = \dot{\alpha}_{i-1} C + \dot{\alpha}_1 = \dot{\alpha}_1 \left[ \left( 1 + \sum_{j=1}^{i-1} C^j \right) - C^{i-1} \right] \tag{5}$$

Assuming $\alpha(0) = 0$ and $\dot{\alpha}(0) = \dot{\alpha}_i$ as initial conditions for the half-cycle $i$, the constants in Eqs. (2) take the values $A_{1i} = 0$ and $A_{2i} = \dot{\alpha}_i/p$.

The maximum rotational angle, reached when $\dot{\alpha} = 0$, is:

$$\alpha_{i\max} = \alpha_c \left[ 1 - \cosh\left( \tanh^{-1} \frac{\dot{\alpha}_i}{\alpha_c p} \right) \right] + \frac{\dot{\alpha}_i}{p} \sinh\left( \tanh^{-1} \frac{\dot{\alpha}_i}{\alpha_c p} \right) \tag{6}$$

while the duration of the half-cycle $i$ is:

$$\frac{T_i}{2} = \frac{2}{p} \tanh^{-1} \frac{\dot{\alpha}_i}{\alpha_c p} \tag{7}$$

Eq. (7) is similar to the formulation proposed by Housner [13] for the duration of the half-cycle, but it is expressed in terms of initial rotational velocity rather than in terms of initial rotational angle. Being $\tanh(x) < 1$, the validity of Eqs. (6) and (7) is restricted to the condition:

$$\frac{\dot{\alpha}_i}{\alpha_c p} = \frac{\dot{\alpha}_i}{\dot{\alpha}_c} < 1 \tag{8}$$

which also represents the safe region for $\dot{\alpha}_i$ to prevent overturning, as it can easily been verified by equating Eq. (6) to $\alpha_c$. This limiting initial velocity, say $\dot{\alpha}_c = \alpha_c p$, also depends on the

slenderness and the base dimension, consistently with the frequency parameter as showed in [25], [26].

By equating Eq. (5) to the critical velocity $\dot{\alpha}_c$, it is possible to define from Eq. (3) the critical value $I_{ic}$ of the impulse causing overturning at the half-cycle $i$. It is:

$$I_{ic} = \frac{g\dot{\alpha}_c}{\lambda \ddot{\alpha}_g}\left[\left(1+\sum_{j=1}^{i-1} C^j\right) - C^{i-1}\right]^{-1} \tag{9}$$

It results that the impulse causing overturning at a fixed half-cycle $i$ increases with decreasing slenderness and coefficient of restitution and with increasing size of the block. The increasing of $I_{ic}$ implies of course that the block is less vulnerable to overturning.

It is worth highlighting that assuming $i = 2$ in Eq. (9), the value of the critical impulse $I_{2c}$ is comparable with the velocity $V_c$ of the critical double impulse defined by Nabeshima et al. [29] used to describe the impulsive component of the near-fault earthquakes.

At last, iterating Eq. (5) for $i \to \infty$, it is obtained that the rotational velocity does not increase indefinitely but converges to the limit value $\dot{\alpha}^*$ given by:

$$\dot{\alpha}^* = \lim_{i\to\infty} \dot{\alpha}_i = \frac{\dot{\alpha}_1}{1-C} \tag{10}$$

This case implies that, when overturning does not occur before, also the duration of the half-cycles tends to stabilize so that the motion of the block becomes of periodic type. An extensive parametric analysis of the influence of slenderness, size and coefficient of restitution of the block on the attainment of this stabilized phase was developed in [24].

### 3.2 The response to the secondary sequence of intermediate impulses

When a secondary sequence of intermediate impulses is taken into account, a step-by-step procedure is required to describe the motion of the block between two subsequent impacts. This motion, however, is still treated as a natural motion according to Eqs. (2), but the constants $A_1$ and $A_2$ have to be up dated at the application of each intermediate impulse $\underline{I}_s$. The increment of rotational velocity $\underline{\dot{\alpha}}_s$ caused by a single intermediate impulse is approximately evaluated as:

$$\underline{\dot{\alpha}}_s = \frac{\underline{I}_s}{I}\dot{\alpha}_1 \tag{11}$$

The procedure required to describe the rocking motion in the presence of intermediate impulses between two subsequent impacts is herein presented with reference to the first half-cycle, but it is also suitable for the generic half-cycle with assigned initial rotational velocity. This procedure implies the following steps:

1. Assign the main impulse $I$ and compute the initial velocity $\dot{\alpha}_1$ by Eq. (3).
2. Compute the duration $T_1/2$ of the half-cycle by Eq. (7).
3. Select a trial value $\underline{\Delta T}$ of the time interval between two intermediate impulses ($\underline{\Delta T} < T_1/2$).
4. Compute step-by-step the rotational angle and velocity at each application of the intermediate impulses $\underline{I}_s$ by using Eqs. (2). Find approximated $\underline{T}_1 = \underline{n}\ \underline{\Delta T}$ at $\alpha$ close to zero ($\underline{n}$ is the number of $\underline{I}_s$ within the half-cycle).
5. Correct $\underline{\Delta T}$, and therefore $\underline{T}_1$, such that $\alpha(\underline{T}_1) = 0$ by strictly imposing the condition to have an even number $\underline{n}$ of intermediate impulses.

6. Compute step-by-step, with the corrected $\underline{\Delta T}$, the rotational angle and the velocity at each application of the intermediate impulses $\underline{I_s}$ by using Eqs. (2) and obtain the maximum angle of rotation $\underline{\alpha}_{1\max}$ and the rotational velocity at the end of the half-cycle $\underline{\dot{\alpha}}_{1r}$. Compute the initial velocity $\dot{\alpha}_{i=2}$ of the subsequent half-cycle by Eq. (5), using $\underline{\dot{\alpha}}_{i-1r}$ instead of $\underline{\dot{\alpha}}_{i-1}$.

## 4 PARAMETRIC ANALYSIS AND DISCUSSION OF THE RESULTS

The response of the block to the resonance input corrected with the secondary sequence of impulses has been investigated assuming that the so defined input represents the intense phase of an earthquake with duration limited to 20 s. Figure 4 shows the role of the main parameters characterizing the seismic input and of the coefficient of restitution on the maximum angle of rotation obtained within the limited time of 20 s; in fact, the $\underline{\alpha}_{\max}/\alpha_c$ ratio is plotted vs. different values of the intermediate impulses measured by the $\underline{I_s} / I$ ratio, for different values of the main impulses, expressed by the $I / I_{1c}$ ratio, being $I_{1c}$ the critical impulse for the first half-cycle (Eq. (9) with $i = 1$). Only values comprised between 0.3 and 0.7 are considered for $\underline{I_s} / I$ since values of $\underline{I_s} / I < 0.3$ are unrealistic, while large $\underline{I_s} / I$ ratios ($\underline{I_s} / I > 0.7$) imply less resonance effects, as will be shown. These non-dimensional parameters allow obtaining results independent of the geometric features of the blocks (block dimension and slenderness) and only dependent on the amplitude of the impulses and on the coefficient of restitution.

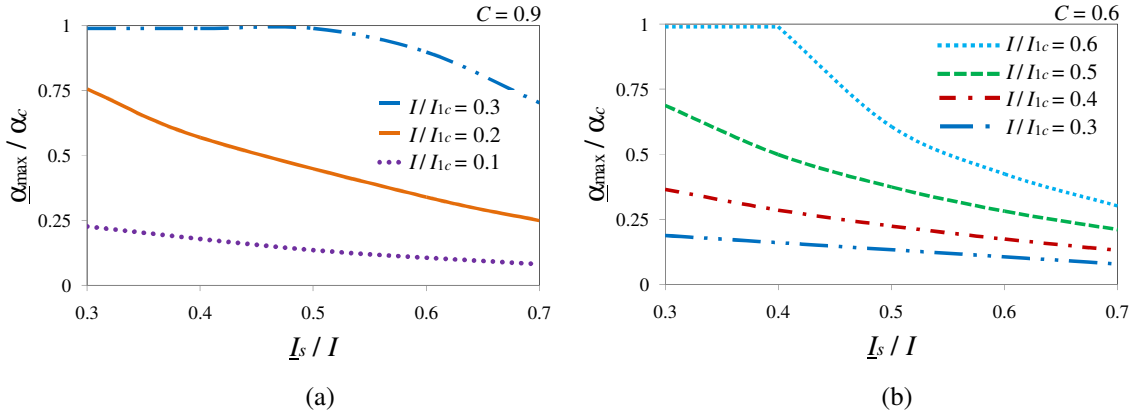


Figure 4: Values of $\underline{\alpha}_{\max}/\alpha_c$ related to a limited duration of the seismic input (20 s) vs. $\underline{I_s} / I$ ratio for different values of the $I / I_{1c}$ ratio, with (a) $C = 0.9$ and (b) $C = 0.6$.

The curves in Figure 4 show that the secondary impulses $\underline{I_s}$ play an opposite role with respect to the impulses $I$ of the limit accelerogram. In fact, for a fixed value of the $I / I_{1c}$ ratio, the maximum angle of rotation is decreasing with increasing $\underline{I_s} / I$ ratio. The intermediate impulses have therefore a stabilizing effect, increasing with their amplitude. This trend can be explained by the consideration that large $\underline{I_s} / I$ ratios imply large variations of the rotational velocity with alternate sign at each application of the intermediate impulses, causing the angle of rotation to decrease. Conversely, if the $\underline{I_s} / I$ ratio is fixed, the increase in the amplitude of the impulses $I$ implies the increase of $\underline{\alpha}_{\max}/\alpha_c$, as easily predictable.

The influence of the coefficient of restitution is evaluated by comparing Figs. 4(a) and 4(b), related to the results obtained for $C = 0.9$ and $C = 0.6$, respectively. Obviously larger values of $C$, with the other parameters kept constant, imply the increase of the destabilizing effects.

To investigate the influence of the geometric features of the blocks on the time evolution of their rocking response, two blocks with the same size ($2b = 1$ m) and different slenderness

($\lambda \approx 4$ when $R = 2$ m and $\lambda \approx 8$ when $R = 4$ m) are compared (Figure 5), taking into account the reference values of the restitution coefficient previously introduced ($C = 0.6$ and $C = 0.9$). The amplitude of the main impulses is assumed coincident with that of the critical impulse $I_{2c}$ (Eq. (9) with $i = 2$) causing overturning at the second half-cycle if the secondary sequence is not taken into account ($\underline{I}_s / I = 0$). As already pointed out, the amplitude of this impulse is lower for the more slender block and also depends on the restitution coefficient. The reference to $I_{2c}$ for the main impulses allows to compare the results related to $\underline{I}_s / I = 0$ with the results obtained by Nabeshima et al. [29] by considering the critical double impulses $V_c$. However, it must be remarked that in the present analysis the restitution coefficient $C$ is a constant value independent of the slenderness of the blocks, while Nabeshima et al. [29] use the formulation proposed by Housner to define this parameter. Despite this, for $C = 0.9$ a very good agreement can be observed between the two formulations in terms both of the amplitudes of the main impulses and of the critical timings $t_0$ of application of the second impulse.

In Figure 5 the time-history responses of the two chosen blocks are reported in terms of the $\underline{\alpha}(t) / \alpha_c$ ratio, for different values of $\underline{I}_s / I$ and $C$.

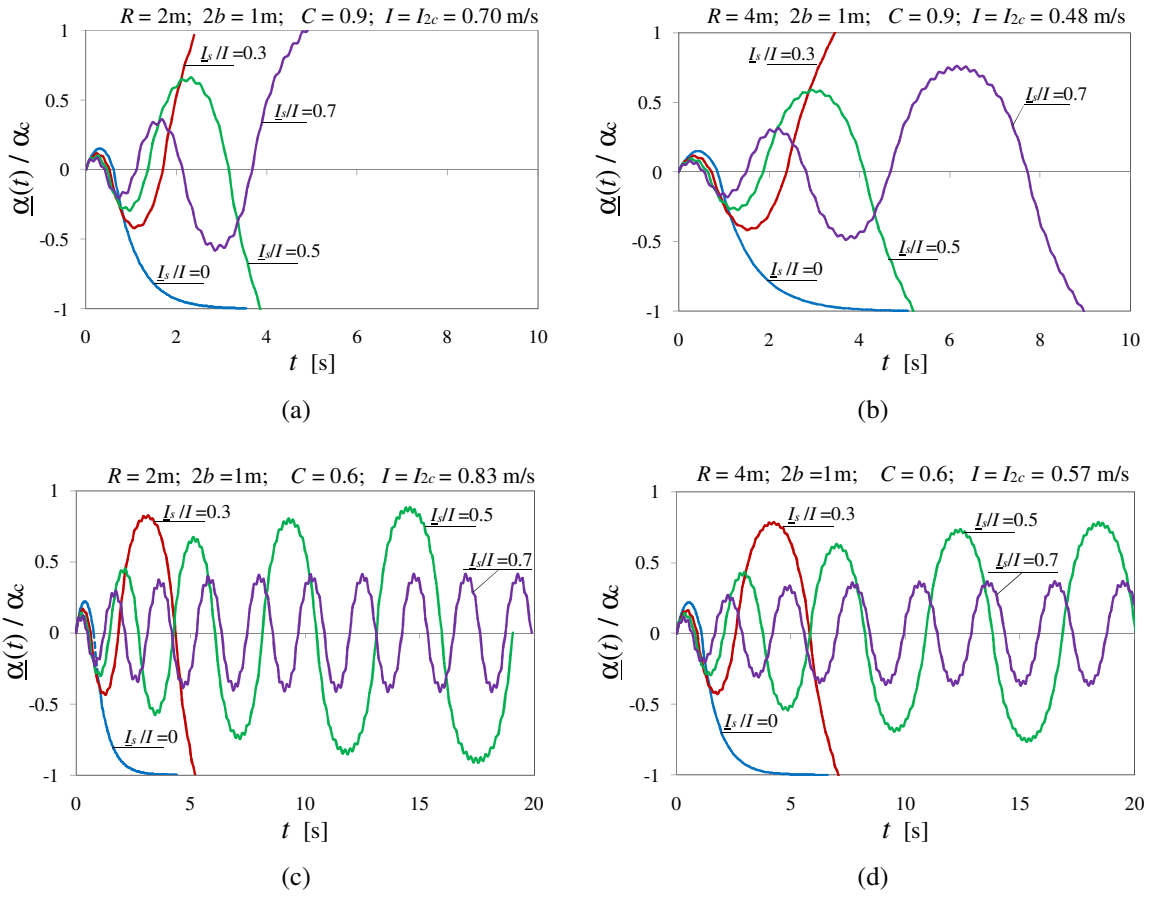


Figure 5: Time-history responses in terms of $\underline{\alpha}(t)/\alpha_c$ of two blocks with $2b = 1$ m and $R = 2$ m ((a), (c)) and $R = 4$ m ((b), (d)), related to the critical impulse $I_{2c}$, for different values of $\underline{I}_s / I$ and $C$.

First of all, these curves show that for each block the action of the intermediate impulses not only implies the reduction of the maximum rotation angle at each half-cycle, but also the reduction of the duration of the same half-cycles. These effects are increasing with increasing $\underline{I}_s / I$ ratios. In fact, when $\underline{I}_s / I \neq 0$, both blocks do not overturn at the second half-cycle but

perform a number of half-cycles increasing with $\underline{I}_s / I$ . For a fixed value of this ratio and of the restitution coefficient, the influence of the different slenderness of the two blocks - only due to the different values of $R$, being the size $2b$ constant - is manly expressed in the reduction of the duration of the half-cycles, so that the more slender block ($R = 4$ m) achieves the overturning in a longer time than the other ($R = 2$ m), although performing the same number of half-cycles (Figs. 5(a) and 5(b)). The case of $\underline{I}_s / I = 0.7$ implies a slight increment also of the number of half-cycles for the more slender block. The higher stability of the more slender block is justified in this case by the lower amplitude of the main impulse.

Lastly, the effect of the lower value of the restitution coefficient on the obtained results, keeping constant the other parameters, is confirmed in terms of reduction of the maximum angle of rotation and of the duration of the half-cycles, while their number increases in the limit duration of 20 s of the input. Moreover, when $C = 0.6$, with increasing values of $\underline{I}_s / I$, both the blocks tend to reach a stabilized phase characterized by a periodic motion with constant values of the maximum rotational angle at each half-cycle and of the duration of these half-cycles.

## 5 CONCLUSIONS

The great sensitivity of the rocking response of rigid blocks to small variations of the seismic action makes very difficult to define a stable relation to their geometric features and the parameters characterizing the seismic input. Starting from this consideration, widely confirmed by the scientific literature on this subject, the approach proposed in this paper consists in the definition of simplified artificial accelerograms characterized by few parameters, both capable of representing the most unfavorable effects of the intense phase of an earthquake and of covering the widest range of real accelerograms.

First, the resonant conditions for the rocking motion were investigated by means of a main sequence of instantaneous impulses applied just after the impact of the block on the ground; then a secondary sequence of intermediate impulses acting within the half-cycle of the block motion was introduced. The intent was to obtain a parametric model of accelerogram that can reproduce the same effects of any registered accelerogram, trough a proper calibration of the characteristic parameters, i.e the amplitudes of the impulses of both the main and the secondary sequence and the time interval of the secondary impulses.

The critical response of the block to the proposed accelerogram, represented by the achievement of the overturning, has resulted to be mainly affected by the following issues: the size and slenderness of the rigid block; the amplitudes of the main and of the intermediate impulses, the restitution coefficient. The analysis enables, in particular, to distinguish the actions which cause overturning from those that cause the stabilization of the motion in relation with the influencing parameters. It was also shown that the increasing amplitude of the intermediate impulses implies not only the reduction of the maximum response of the block, but also the duration of the half-cycles of the motion. The opposite trend was reported for increasing values of the coefficient of restitution; with the other parameters kept constant, in fact, the maximum response of the block and the duration of the half-cycles are increasing with this coefficient.

Clearly, the specification of the parameters that characterize the artificial accelerogram should be depending on the specific characteristics of the sites. This aspect could be the further developed in order to apply the proposed procedure to real accelerograms. On the other hand, the synthesis of the various aspects can allow translating clear specific indications in final sufficiently reliable evaluations.

## ACKNOWLEDGEMENTS

The authors acknowledge the sponsorship of the Italian Civil Protection, through the RELUIS Project - Line: Masonry Structures (2017).

## REFERENCES

[1] L. Giresini, Energy-based method for identifying vulnerable macro-elements in historic masonry churches. *Bulletin of Earthquake Engineering*, **44**(13), 919-942, 2015.

[2] C. Casapulla, A. Maione, L.U. Argiento, Seismic analysis of an existing masonry building according to the multi-level approach of the Italian Guidelines on Cultural Heritage. *Ingegneria Sismica*, **1**, 2017, 1-21.

[3] C. Casapulla, Dry rigid block masonry: Safe solutions in presence of Coulomb friction. *Advances in Architecture Series*, **7**, 251-261, 2001.

[4] C. Casapulla, L. Cascini, F. Portioli, R. Landolfo, 3D macro and micro-block models for limit analysis of out-of-plane loaded masonry walls with non-associative Coulomb friction. *Meccanica*, **49**(7), 1653-1678, 2014.

[5] C. Casapulla, F. Portioli, Experimental and analytical investigation on the frictional contact behavior of 3D masonry block assemblages. *Construction and Building Materials*, **78**, 126-143, 2015.

[6] C, Casapulla, A. Maione, Formulating the torsion strength of dry-stacked stone blocks by comparing convex and concave contact formulations and experimental results. *Indian Journal of Science and Technology*, 9(46), 107346, 2016.

[7] C. Casapulla, L.U. Argiento, The comparative role of friction in local out-of-plane mechanisms of masonry buildings. Pushover analysis and experimental investigation. *Engineering Structures,* **126**, 158-173, 2016.

[8] C. Casapulla, L.U. Argiento, Non-linear kinematic analysis of masonry walls out-of-plane loaded. the comparative role of friction between interlocked walls. *6th International Conference on Computational Methods in Structural Dynamics and Earthquake Engineering*, Rhodes Island, Greece, June 15-17, 2017.

[9] C. Casapulla, L.U. Argiento, C. Ceraldi, Experimental validation of in-plane frictional resistances in dry block masonry walls. *6th International Conference on Computational Methods in Structural Dynamics and Earthquake Engineering*, Rhodes Island, Greece, June 15-17, 2017.

[10] L. Giresini, M. Sassu, Horizontally restrained rocking blocks: evaluation of the role of boundary conditions with static and dynamic approaches. *Bulletin of Earthquake Engineering*, **15**(1), 385-410, 2016.

[11] L. Giresini, M. Fragiacomo, M. Sassu, Rocking analysis of masonry walls interacting with roofs. *Engineering Structures*, **116**, 107-120, 2016.

[12] N. Makris, M.F. Vassiliou, Dynamics of the rocking frame with vertical restrainers. *Journal of Structural Engineering* (ASCE), **141**(10), 1-13,2015.

[13] G.W. Housner, The behaviour of inverted pendulum structures during earthquakes. *Bulletin of the Seismological Society of America,* **53**(2), 403-417, 1963.

[14] C.K. Yim, A.K. Chopra, J. Penzien, Rocking response of rigid blocks to earthquakes. *Earthquake Engineering and Structural Dynamics*, **8**(6), 565-587, 1980.

[15] M. Aslam, W.G. Godden, D.T. Scalise, Earthquake rocking response of rigid bodies. *Journal of Engineering Mechanics ASCE*, **106**(2), 377-392, 1980.

[16] P.D. Spanos, A.S. Koh, Rocking of rigid blocks due to harmonic shaking. *Journal of Engineering Mechanics ASCE*, **110**(11), 1627-1642, 1984.

[17] S.J. Hogan, On the dynamics of rigid-block motion under harmonic forcing. *Proceedings of Royal Society A,* **425**(1869), 441–476, 1989.

[18] N. Makris, D. Konstantinidis, The rocking spectrum and the limitations of practical design methodologies. *Earthquake Engineering and Structural Dynamics*, **32**(2), 265-289, 2003.

[19] S. Lagomarsino, Seismic assessment of rocking masonry structures. *Bulletin of Earthquake Engineering*, **13**(1), 97-128, 2015.

[20] C. Casapulla, P. Jossa, A. Maione, Rocking motion of a masonry rigid block under seismic actions: a new strategy based on the progressive correction of the resonance response. *Ingegneria Sismica*, **27**(4), 35-48, 2010.

[21] A. Moustafa, K. Ueno, I. Takewaki, Critical earthquake loads for SDOF inelastic structures considering evolution of seismic waves. *Earthquake and Structures*, **1**(2), 147-162, 2010.

[22] I. Takewaki, *Critical Excitation Methods in Earthquake Engineering, 2nd Edition*. Elsevier, 2013.

[23] I. Takewaki, A. Moustafa, K. Fujita, *Improving the Earthquake Resilience of Buildings: The Worst Case Approach*. Springer-Verlag, London, 2013.

[24] C. Casapulla, On the resonance conditions of rigid rocking blocks. *International Journal of Engineering and Technology*, **7**(2), 760-771, 2015.

[25] C. Casapulla, A. Maione, Free damped vibrations of rocking rigid blocks as uniformly accelerated motions. *International Journal of Structural Stability and Dynamics* [online], September 2016, http://dx.doi.org/10.1142/S0219455417500584.

[26] C. Casapulla, A. Maione, A simplified equation of motion for free rocking rigid blocks. *Insights and Innovations in Structural Engineering, Mechanics and Computation*, 120-126, Cape Town, South Africa, September 2016.

[27] K. Kojima, K. Fujita, I. Takewaki, Critical double impulse input and bound of earthquake input energy to building structure. *Frontiers in Built Environment*, **1**(5), 1-8, 2015.

[28] K. Kojima, I. Takewaki, Critical earthquake response of elastic-plastic structures under near-fault ground motions (part 1: fling-step input). *Frontiers in Built Environment*, **1**(12), 1-11, 2015.

[29] K. Nabeshima, R. Taniguchi, K. Kojima, I. Takewaki, Closed-form overturning limit of rigid block under critical near-fault ground motions. *Frontiers in Built Environment*, **2**(9), 1-11, 2016.

[30] K. Kojima, I. Takewaki, Critical input and response of elastic-plastic structures under long-duration earthquake ground motions. *Frontiers in Built Environment*, **1**(15), 1-13, 2015.

[31] I.N. Psycharis, M. Fragiadakis, I. Stefanou, Seismic reliability assessment of classical columns subjected to near-fault ground motions. *Earthquake Engineering and Structural Dynamics*, **42**(14), 2061-2079.

[32] E.G. Dimitrakopoulos, T.S. Paraskeva, Seismic reliability assessment of rocking behaviour under near-fault excitations. *5th ECCOMAS Thematic Conference on Computational Methods in Structural Dynamics and Earthquake Engineering*, Crete Island, Greece, May 25-27, 2015.

[33] C. Casapulla, A. Maione, Critical response of free-standing rocking blocks to the intense phase of an earthquake. *International Review of Civil Engineering*, **8**(1), 1-10, 2017.

[34] C. Casapulla, P. Jossa, A. Maione, A simplified procedure for the seismic safety of large and slender rigid masonry blocks. *International Journal of Earthquake and Impact Engineering*, **1**(4), 333-359, 2016.

COMPDYN 2017
6th ECCOMAS Thematic Conference on
Computational Methods in Structural Dynamics and Earthquake Engineering
M. Papadrakakis, M. Fragiadakis (eds.)
Rhodes Island, Greece, 15–17 June 2017

# ROCKING SPECTRUM INTENSITY MEASURE FOR SEISMIC ASSESSMENT OF ROCKING BLOCKS

**Ioannis E. Kavvadias[1], Kosmas E. Bantilas[1], George A. Papachatzakis[1], Lazaros K. Vasiliadis[1] and Anaxagoras Elenas[1]**

[1] Democritus University of Thrace, Department of Civil Engineering
Campus of Kimmeria, 67100 Xanthi, Greece
e-mail: {ikavvadi, kbantila, gpapacha, lvasila, elenas}@civil.duth.gr

**Keywords:** Intensity Measure, Rocking Response, Rocking Spectrum, Probabilistic Analysis, Earthquake Engineering.

**Abstract.** *In this study a spectral ground motion intensity measure (IM) is presented. The proposed IM is calculated throughout the rocking spectrum which is illustrated as a 3D surface diagram, with the slenderness α and the period T, the two horizontal axes. Thus, the IM is defined as the volume under the rocking spectrum, evaluated throughout integration. The suggested IM is intended to have strong correlation with the rocking response of free standing blocks. Several rocking rigid blocks subjected to multiple ground motion records are assumed in order to identify the capability of the IM to predict the rocking response concerning the variability of the block dimensions. The selection of the dimensions was made in order to correspond to slender rocking structures such as electric equipment, ancient monolithic columns and bridges piers. The evaluation of the IM was also made by examining characteristics such as efficiency and proficiency. Further, the performance of the proposed IM is contrasted with the performance of others well-known ground motion parameters, to highlight the adequacy of the former in predicting the rocking seismic response.*

## 1 INTRODUCTION

Probabilistic seismic assessment has emerged in recent years as a useful tool for both the design of new structures and the assessment of existing ones. Vulnerability assessment, are based on the probabilistic seismic demand model (PSDM) that the links the structural response with the intensity of the ground motion. Consequently, these two parameters are described in literature as Engineering Demand Parameter (EDP) and Intensity Measure (IM). The demand uncertainties introduced in the model depends on the IM used. Thus, the selection of the IM that describe with better accuracy the response of the examined structural system is of significant importance. Several criteria has been proposed in the literature in order to suggest an IM as an optimal one [1-4].

Over the years several researchers have developed ground motion parameters to represent the seismic excitation intensity. These IMs can be classified into time history, energy, spectral, and frequency content parameters [5]. Among the others, the spectral parameters are the only that contain structural information, therefore they are aimed to have strong correlation with the structural damage [6]. Nevertheless, response spectra of SDOF oscillators are not adequate to describe the rocking response [7]. Thus, defining spectral intensity measures that could enclose information about the rocking structures, is expected to be a better descriptor of the rocking response.

The seismic response of structural systems that exhibit pure rocking behavior are very sensitive to even minus alteration on the excitation characteristics or on the blocks dimensions [8]. Spanos and Koh [9] taking that fact into account, have been studied the rocking response under a probabilistic framework. Recently, Acikgoz and DeJong [10], examined large flexible rocking structures subjected to pulse type excitations in order to conduct to a predictive framework. Seismic vulnerability assessment of rocking structural systems are presented in the literature. Psycharis et al. [11] have been assessed the seismic reliability of ancient multi-drum columns, while Dimitrakopoulos and Paraskeva [12] have been evaluated the efficiency of dimensionless IMs in predicting rocking response. Kavvadias et al. [13] have been examined several IMs in order to conclude to these that describe with better accuracy the rocking response of rigid blocks.

Taking all the above under consideration, a scalar IM, intended to have strong correlation with the seismic rocking performance is proposed in the present study. This IM, based on rocking rotation spectrum, form an attempt to quantify the information provided by the rocking response of rigid blocks. The ground motion parameter named as Rocking Rotation Spectral Intensity (RRSI), is defined by the volume under the normalized rocking spectrum, as though, is evaluated by integration of the rocking rotation spectrum. The integration limits of the period T and the slenderness $\alpha$, was adopted in order to construct an IM that could take into account structural response information for the majority of the slender rocking blocks. Using this IM, a reduction of the uncertainty associated with the median demand of rocking response is sought.

To assess the adequacy of the IM, 12 rigid blocks subjected to a set of 35 ground motion record were examined. Correlation coefficients between the proposed ground motion parameter and the developed damage, as well as criteria such as efficiency and proficiency, are adopted in order to evaluate the IM. Moreover, velocity based and frequency content IMs are also examined. These IMs are known that have strong correlation with the rocking response [12, 13], thus the comparison of those performance with the performance of the proposed IM could assure their suitability for usage to vulnerability analysis of rocking structures.

## 2 SEISMIC ROCKING RESPONSE OF RIGID BLOCK

A rigid block standing free on a rigid base, with slenderness a, semi-diagonal R and frequency parameter p, oscillates about the centers of rotation O and O' when rocking motion initiates (Figure 1). The minimum acceleration of a ground excitation that enables rocking can be computed from static analysis, and yields to $\ddot{u}/g \geq \tan(\alpha)$. The problem of a rigid rocking block motion under a seismic excitation can be described by the following equation [14]:

$$\ddot{\theta} = -p^2 \cdot \left\{ \sin[\alpha \cdot sgn(\theta) - \theta] + \frac{\ddot{u}_g}{g} \cdot \cos[\alpha \cdot sgn(\theta) - \theta] \right\} \tag{1}$$

where sgn() is the sign function, $p = \sqrt{3g/4R}$ is the frequency parameter of the rigid block and R is the semi-diagonal.

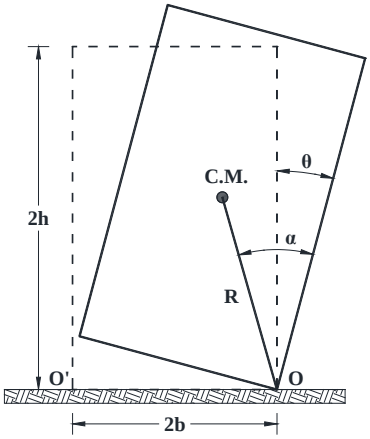


Figure 1: Characteristics of a rigid rocking block.

During the rocking motion, energy is lost only during impact (when the rotation changes sign at θ =0) which causes a reduction of the rotational velocity after it:

$$\dot{\theta}_{n+1}{}^2 = r \cdot \dot{\theta}_n{}^2 \tag{2}$$

where r is the restitution coefficient, $\dot{\theta}_n$ is the velocity before the impact and $\dot{\theta}_{n+1}$ is the velocity after the impact.

Considering that the angular momentum remains constant about point O exactly before the impact and right after it, the coefficient of restitution for a rigid rectangular block is given by the following equation [15]:

$$r = [1 - \frac{3}{2}(\sin\alpha)^2]^2 \tag{3}$$

The restitution coefficient depends only on the slenderness and expresses the energy dissipation during rocking motion considering inelastic impact. Since the actual restitution coefficient is material dependent, several experiments were performed in order to determine it accurately [16, 17], and improved formulas has been proposed [18]. In the current study the restitution coefficient of Eq. (3) is used for the analyses. The seismic rocking response is calculated, by solving the equations listed above, in Matlab R2016 [19], using the Runge - Kutta integration technic named ode45.

## 3 ROCKING SPECTRA

In correspondence with response spectra for single-degree-of-freedom (SDOF) models, rotation and velocity rocking spectra are firstly presented by Makris and Konstantinidis [7]. Despite the fact that the SDOF can be characterized only by the period T, the rocking block has two representative parameters, the frequency parameter p and slenderness α. Thus, the rocking spectra usually are depicted with diagrams which correspond to blocks of individual slenderness.

In this study rocking spectra are pictured as 3D surface diagrams in which the two horizontal axes are the period T and the slenderness α. In such way, the outcome of the ground motions to the rocking response is easily observed. The surface diagram compared with the classic 2D one, provide more clearly the rocking response of blocks with a wide range of geometric characteristics. Moreover, features of the ground motion excitations can be conducted by rocking spectra. The values of the rotational rocking spectra are normalized to the slenderness of the blocks α. It is known that in rare cases, a rocking block could develop rotation higher than its slenderness without overturning, while when it overturns the EDP takes infinite value. Nonetheless, the limit of the normalized rotation when collapse occurs is considered $\theta_{max}/\alpha = 1$. The rocking spectra is created for a range of slenderness α = 0.1-0.3 rad and T = 1-8 rad/s.

Rocking spectra obtained by two ground motions are presented in Figures 2. In the above figure the surface spectra are depicted among with the acceleration time histories. The excitations have PGA values adequate to uplift the total range of the blocks. However, due to their frequency content, difference at the spectra are observed. As seen in spectrum created from Imperial Valley, rocking is initiated for the most blocks, but due to its low mean period $T_m$, it can barely induce uplift to a block with slenderness higher than α = 0.2 rad. On the contrary, the Northridge excitation, which has the same PGA but higher $T_m$, proves to have more detrimental effect on rocking.

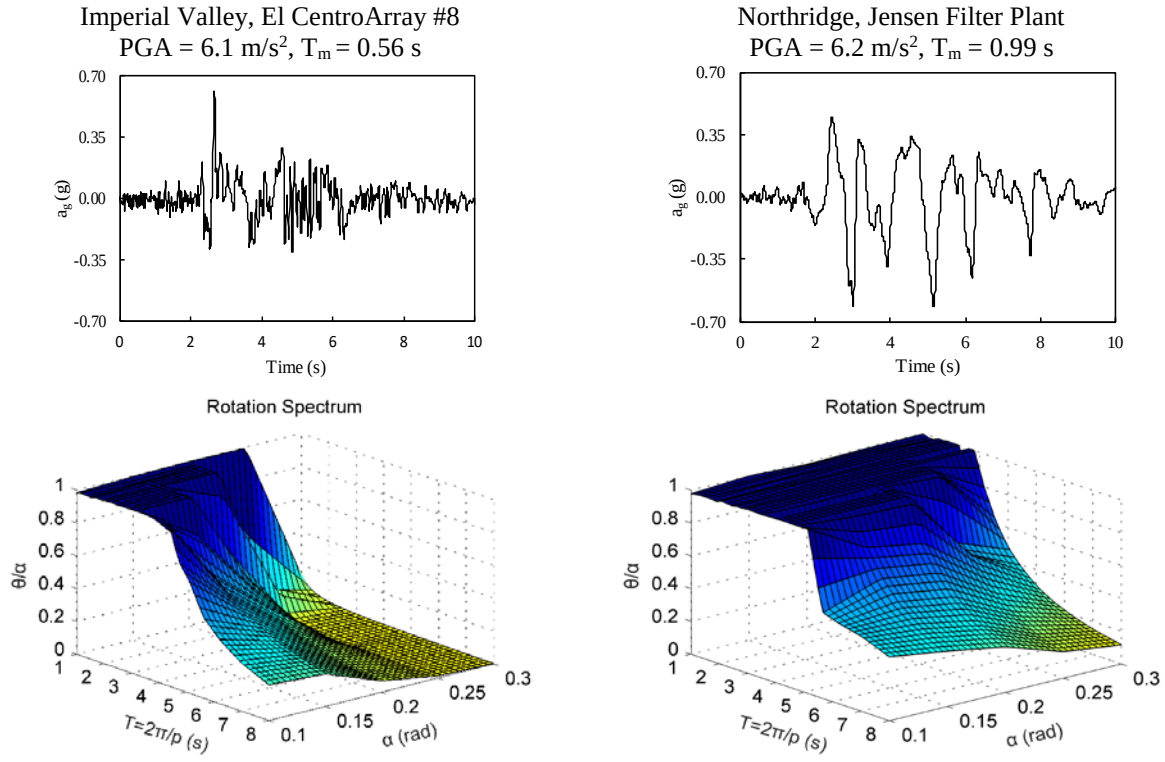


Figure 2: Acceleration time histories and the corresponding normalized rocking spectra.

## 4 PROPOSED INTENSITY MEASURES

A proper selection of IMs is crucial in order to exhibit high correlation with the structural damage. By representing ground motion intensity through appropriate IMs, it is possible to obtain an optimized response prediction. It is known that rocking response is affected by the frequency content of the excitation [15]. The strong dependence of the velocity characteristics of the ground motion with rocking response is verified in recent studies [12]. Also, Intensity Measures such as Housner's Spectral Intensity ($SI_H$), containing information of the elastic response of SDOF, affects significantly the response of free standing rigid blocks [13].

Intensity measures that contain apart from ground motion information, information about the structural response is expected to be a more efficient IM regarding the engineering demand prediction. Spectral parameters constitute IMs that counts information about the structural features. Thought, there are numerous IMs calculated by the SDOF response spectra, none is proposed based on the rocking one. Thus, a rational approach is to select IMs defined by the rocking spectra, which could form a strong correlated parameter with the rocking response.

In the present study, the proposed IM are determined in order to contain information about the earthquake record, as well as information about the structural response of free standing rigid blocks, aiming for a better description of the rocking performance. The proposed parameters named Rocking Rotation Spectral Intensity (RRSI), is defined as the volume under the spectrum calculated via integration of the rocking rotation spectrum. Thus, it forms an attempt to quantify the information provided rocking spectra. The definition of the IMs are the followings:

$$RRSI = \int_{a_{\min}}^{a_{\max}} \int_{T_{\min}}^{T_{\max}} S_r(T,a)\, dT da \tag{3}$$

where $S_r$ is the rocking rotation spectrum surface.

The integration limits of period T and slenderness α are chosen in order to reflect to a wide variety of slender rocking structures. For the evaluation of the frequency parameter p examples from previous studies are considered ranged from $p \approx 3.5$ rad/s for a typical tombstone to $p < 1$ rad/s for relatively tall building frame structures [10]. As a result, the integration limits for the period T are adopted from 1-8 s. Concerning slenderness, the adopted limits are $\alpha =$ 0.1-0.3 rad moving from slender structure to firm ones. In these values rocking structures from Electrical transformers ($\alpha \approx 0.30$ rad) and ancient columns ($\alpha \approx 0.15$ rad) to bridge piers ($\alpha \approx 0.10$ rad) are included.

## 5 OPTIMAL SELECTION OF INTENSITY MEASURE USED FOR VULNERABILITY ANALYSIS

In recent years, probabilistic analysis became widely used for structural engineering purposes and Probabilistic Seismic Demand Models (PSDM) were developed aiming to predict the response of a structure under earthquakes of certain intensities. Specifically, the fragility analysis expresses the probability (P) that the capacity (C) of a specific measured engineer parameter (EDP) of a structure will exceed a certain level of demand (D), for a specific ground motion intensity measure (IM), as defined by the following equation [1]:

$$P = P[D \geq C \,|\, IM] \tag{5}$$

Regarding the rocking response, the results of the time history analyses have to be treated with two different methods. In order to calculate the probability of exceeding a certain capacity value, using only the non-collapse data, the following expression is used [4]:

$$P[D \geq C \mid IM] = \Phi\left(\frac{\ln(S_d / S_c)}{\sqrt{\beta_{D|IM}{}^2}}\right) \tag{6}$$

where $\Phi$ is the standard normal cumulative distribution function, $S_c$ is the median value of the capacity which is estimated through the adopted limit states and $\beta_{D|IM}$ is the dispersion or logarithmic standard deviation for the demand conditioned the IM.

The median seismic demand $S_D$, is related with an examined IM with the following expression:

$$S_d = a\,(IM)^b \tag{7}$$

where a and b are the linear regression coefficients for the logarithmic expression of the assumed scale law.

The linear regression analysis is performed between the engineering demand parameter calculated via the time history analyses, and the corresponding IM values. The logarithmic standard deviation (Eq.(8)) of the linear regression analysis indicates the dispersion of the median demand. This parameter consist the demand uncertainty introduced in the probabilistic model.

$$\beta_{D|IM} \cong \sqrt{\frac{\sum (\ln(d_i) - \ln(a\,(IM)^b))^2}{N-2}} \tag{8}$$

The above methodology (Eqs. (6)-(8)) corresponds when rocking occurs excluding the rocking collapse cases. To calculate the fragility of the structural system by taking into account the rocking overturn data the Eq. (6) is altered to:

$$P[D \geq C \mid IM] = P_o + (1 - P_o) \cdot \Phi\left(\frac{\ln(S_d / S_c)}{\sqrt{\beta_{D|IM}{}^2}}\right) \tag{9}$$

where $P_o$ is the probability of rocking collapse.

When rocking overturn occurs the rotation values rich infinite values. Assuming that fact, the problem should be considered as a categorical one, by grouping the data into non-collapse and collapse ones in order to estimate the probability of overturning. So, to estimate the parameters of the fragility function (mean $\mu$ and standard deviation $\beta$) that provides the probability of collapse, the maximum likelihood approach is adopted [20-21]. The maximum likelihood function L is defined as follows:

$$L = \prod_{j=1}^{m} \binom{n_j}{z_j} p_j{}^{z_j} \left(1 - p_j\right)^{n_j - z_j} \tag{10}$$

where the probability of $z_j$ collapses out of $n_j$ ground motions of a certain value of IM is given by the binomial distribution, $p_j$ is the probability that a ground motion of a particular IM value, will cause the collapse of the structure, m is the number of IM levels and $\Pi$ denotes a product over all IM levels.

Assuming lognormal cumulative distribution for the overturning probability, Eq. (7) converts to the following:

$$L = \prod_{j=1}^{m} \binom{n_j}{z_j} \Phi\left(\frac{\ln x_j - \mu}{\beta}\right)^{z_j} \left(1 - \Phi\left(\frac{\ln x_j - \mu}{\beta}\right)\right)^{n_j - z_j} \tag{11}$$

The maximization of L gives the statistical moments $\hat{\mu}_{MLE}$ and $\hat{\beta}_{MLE}$ via an optimization process.

$$\left\{\hat{\mu}_{MLE}, \hat{\beta}_{MLE}\right\} = \max_{\mu,\beta} \prod_{j=1}^{m} \binom{n_j}{z_j} \Phi\left(\frac{\ln x_j - \mu}{\beta}\right)^{z_j} \left(1 - \Phi\left(\frac{\ln x_j - \mu}{\beta}\right)\right)^{n_j - z_j} \tag{12}$$

The appropriate selection of an IM plays an important role of the in the accuracy of a probabilistic seismic demand analysis (PSDA) for structures. As though, the choice must be made based on criteria, presented in the literature, that help to distinguish the accuracy of the seismic assessment. An optimal IM is defined by primary factors such as efficiency, practicality, proficiency and sufficiency [1-4] Efficient IMs are the ones that eliminates the dispersion of the results about the median, which means decrease of the uncertainties introduced to the PSDM, resulting in superior fragility curves during the vulnerability assessment. A distinguished IM according to it efficiency is represented is by a lower logarithmic standard deviation $\beta_{D|IM}$ (Eq. (8)).

Proficiency is a complex measure, assessing the effect of both practicality and efficiency. Practicality refers to whether or not there is any direct correlation between an IM and the demand placed on the structure and is measured by the regression parameter b in the PSDM. Thus, the proficiency consists of parameters that combine the logarithmic standard deviation and the slope of the regression analysis and defined as:

$$\zeta = \frac{\beta_{D|IM}}{b} \tag{13}$$

From the aforementioned characteristics, efficiency and proficiency are most commonly used to distinguish whether an IM is optimal regarding the appropriateness of predicting the structural damage.

Another measure in order to evaluate the grade of interdependency between the examined IMs and the EDP is the correlation coefficient by Pearson' (Eq. (16)) which shows how well the data fit a linear relationship, and is derived from the regression analysis of each PSDM (Eq. (1)).

$$r_{Pearson} = \frac{\sum_{i=1}^{N}(X_i - \bar{X})(Y_i - \bar{Y})}{\sqrt{\sum_{i=1}^{N}(X_i - \bar{X})^2 \sum_{i=1}^{N}(Y_i - \bar{Y})^2}} \tag{15}$$

where:

$X_i$ is the value of the seismic intensity parameter of the i-th accelerogram, $Y_i$ is the value of the seismic response parameter to the i-th accelerogram and finally $\bar{X}$, $\bar{Y}$ are the mean values of $X_i$ and $Y_i$.

## 6 IMS EVALUATION PROCEDURE

The adequacy of the proposed IMs in describing the rocking behavior of slender rigid blocks is examining thoroughly. In order to investigate the robustness of the IMs regarding the structural characteristics, 12 different rigid blocks are considered. The blocks have slenderness of 0.10, 0.15 and 0.20 rad and frequency parameter p equal to 2.73, 2.00, 1.35 and 0.86 (rad/s). The selection of the blocks dimensions and slenderness was made to be in accordance with typical rocking structures such as bridge piers, ancient columns, electrical transformers and laboratory or home equipment. The procedure could be extended also to rocking frames [22], or rocking flexible oscillators [23].

A cloud analysis is conducted using a set of 35 ground motion time histories as input base acceleration for the analyses. Excitations generated from different types of fault types, with earthquake magnitudes (Ms) between 5.3 and 7.6, including both near-fault and far-fault records, are employed in order to present a wide range of intensities and frequency contents. A further aspect which has been taken into consideration is the expected damage potential of the seismic excitation on the rocking structures. Seismic excitations which provide a wide spectrum of structural damage, from negligible to severe, are taken into account. Based on the above assumption, a rigorous selection of ground motions carried out from the Pacific Earthquake Engineering Research Centre (PEER) [24] and the European strong motion [25] databases has been carried out, using non-scaled records. The complete list of the natural ground motions used for the analyses is shown in Table 1.

The engineering demand parameter (EDP) chosen in the present study provides an estimate of the structural damage state and collapse potential. Due to the nature of the rocking behavior, the most representative parameter to assess structural capacity has to be based on the rocking rotation. As a result, the absolute peak rocking rotation $|\theta_{max}|$ scaled with respect to the slenderness $\alpha$ is adopted:

$$EDP = \frac{|\theta_{max}|}{\alpha} \tag{16}$$

The correlation coefficients by Spearman are demonstrated, as the metric of evaluating the interdependency of the IMs with the EDP. Moreover, to highlight the efficiency of the proposed parameters the dispersion estimators $\beta$ and $\zeta$, calculated by Eq. (8) and Eq. (13) respectively are presented. Assuming the maximum likelihood estimator, to calculate the overturning fragility, $\beta_{MLE}$ values are presented (Eq. (12)), due to the fact that it could considered as an additional efficiency parameter.

Further, the performance of the PGV, $SI_H$, $I_{FVF}$, $T_m$ and $L_m$ [5, 26] in assessing the vulnerability of the examined structural systems is also presented. These ground motion characteristics are strongly correlated with the rocking response of slender rigid blocks [13]. Thus, the comparison of their results with those obtained by the proposed spectral IMs, will deduce the superiority of the latter.

## 7 RESULTS

In Figure 3 the linear regression between the developing rocking rotation and the RRSI are depicted. It can be seen that the linear regression is capable to describe the relationship between the IM and the EDP. Moreover, in a first glans the RRSI it seems to be suitable in describing the safe rocking response for the total of the rocking blocks.

| Earthquake | Station | Date | $M_s$ | R (km) | RRSI (rad·s) |
|---|---|---|---|---|---|
| Aigion | AIGA | 25/06/1995 | 6.40 | 21.50 | 0.31 |
| Athens | ATH4 | 07/09/1999 | 5.90 | 16.62 | 0.09 |
| Bucharest | Bucharest | 04/03/1977 | 7.50 | 115.0 | 0.41 |
| Chi-Chi | CHY035 | 20/09/1999 | 7.62 | 12.56 | 0.28 |
| Chi-Chi | CHY101 | 20/09/1999 | 7.62 | 9.94 | 0.89 |
| Chi-Chi | TCU88 | 20/09/1999 | 7.62 | 18.16 | 0.19 |
| Chuetsuoki | Nakanoshima Nagaoka | 16/07/2007 | 6.80 | 19.89 | 0.39 |
| Coalinga | Fault Zone 14 | 02/05/1983 | 6.36 | 29.48 | 0.58 |
| Corinth | Corinth | 24/02/1981 | 6.60 | 10.28 | 0.20 |
| Darfield | Papanui High School | 04/09/2010 | 7.00 | 26.76 | 0.42 |
| Denali | TAPS Pump Station #10 | 03/11/2002 | 7.90 | 2.74 | 0.53 |
| Duzce | Lamont 531 | 12/11/1999 | 7.14 | 8.03 | 0.04 |
| Erzincan | Erzincan | 19/03/1992 | 6.69 | 4.38 | 0.96 |
| Friuli | Tolmezo | 06/05/1976 | 6.50 | 15.82 | 0.32 |
| Gazli | Karakyr | 17/05/1976 | 6.80 | 5.46 | 0.72 |
| Imperial Valley | El Centro Array #9 | 19/05/1940 | 6.95 | 6.09 | 0.43 |
| Imperial Valley | El Centro Array #7 | 15/02/1979 | 6.53 | 0.56 | 0.52 |
| Imperial Valley | El Centro Array #8 | 15/02/1979 | 6.53 | 3.86 | 0.48 |
| Irpinia | Sturno | 23/11/1980 | 6.90 | 10.84 | 0.52 |
| Iwake | Ichinoseki Maikawa | 14/07/2008 | 6.90 | 23.02 | 0.02 |
| Kalamata | Kalamata | 13/09/1986 | 6.20 | 10.00 | 0.24 |
| Kobe | Nishi -Akashi | 16/01/1995 | 6.90 | 7.08 | 0.42 |
| Kobe | Port Island | 16/01/1995 | 6.90 | 3.31 | 0.74 |
| Landers | Joshua Tree | 28/06/1992 | 7.28 | 11.03 | 0.37 |
| Loma Prietta | Los Gatos - Lexington Dam | 17/11/1986 | 6.93 | 5.02 | 0.72 |
| El Mayor Cucapah | Chihuahua | 04/04/2010 | 7.20 | 19.47 | 0.85 |
| Northridge | Jensen Filter Plant | 17/01/1994 | 6.69 | 5.92 | 0.99 |
| Northridge | Newhall – Fire Station | 17/01/1994 | 6.69 | 5.43 | 0.56 |
| Northridge | Paicoma Dam | 17/01/1994 | 6.69 | 7.01 | 0.36 |
| Parkfield | Cholame #2 | 28/06/1966 | 6.20 | 17.64 | 0.64 |
| San Fernando | Paicoma Dam | 09/02/1970 | 6.61 | 1.81 | 0.12 |
| SMART1Taiwan (40) | Smart1 M02 | 15/111986 | 6.32 | 60.89 | 0.14 |
| Superstition Hill | Mtn Camera | 24/11/1987 | 6.54 | 5.61 | 0.35 |
| Tabas | Dayhook | 16/09/1978 | 7.35 | 13.94 | 0.19 |
| Whittier | LA - Obregon Park | 01/10/1987 | 5.27 | 13.62 | 0.06 |

Table 1: List of the used ground motions and RRSI values

In Figure 4 the correlation coefficients between the proposed and the other examined IMs with the EDP are presented. The RRSI displays on average the highest correlation with the rocking response in contrast with the other IMs. In more detail, it affect significantly the blocks with slenderness lesser than 0.15 rad regardless of their size. It performance tend decreasing only according less slender blocks of small size. Regarding the other examined IMs those that constitutes velocity based ones, demonstrate similar performance with the RRSI, while the $T_m$ is the IM that picture the lowest grade of interdependency with the rocking.

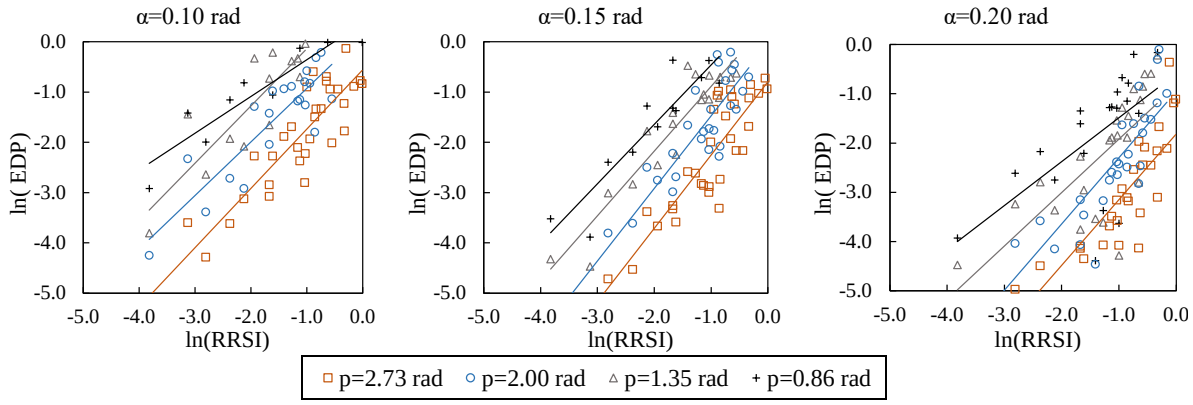


Figure 3: Linear regression analysis between ln(RRSI) and ln(EDP).

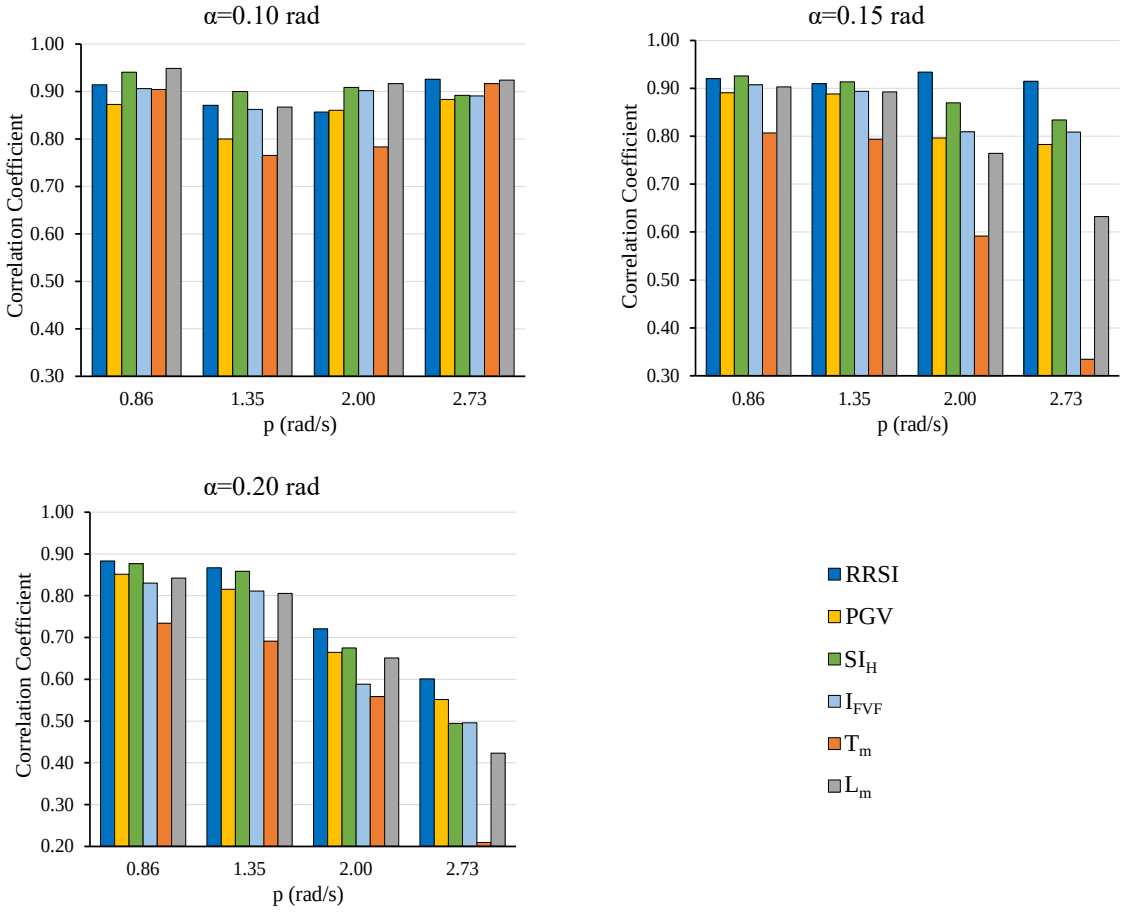


Figure 4: Correlation coefficients between the IMs and the EDP.

The logarithmic standard deviations β, which are calculated via the linear regression analysis, are depicted in Figure 5. The RRSI present considerable low values of β regardless the rigid block examined. Regarding the other IMs examined, the $SI_H$ and the $I_{FVF}$ decreases notably the dispersion of the PSDM. Moreover, $T_m$ and $L_m$ performs well especially for more slender blocks. Between the proposed IM and the other 5 examined, the RRSI present the lowest logarithmic standard deviation on average with value of β=0.62.

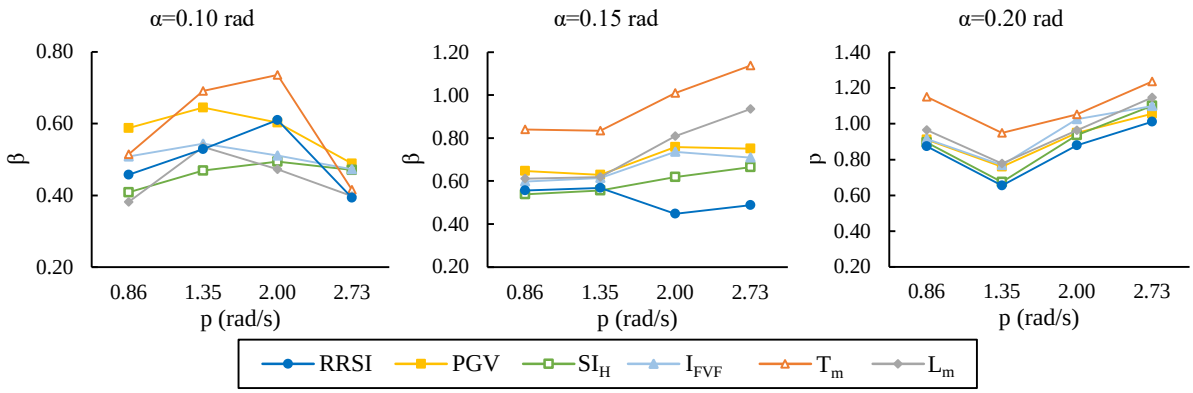


Figure 5: Logarithmic standard deviation (β) of the examined IMs for the examined rigid blocks.

Except of the logarithmic standard deviations β, another more complex dispersion metric, the proficiency ζ, is calculated. Figure 6 displayed the ζ parameter per block, for each one of the IMs. According to these results, the $I_{FVF}$ displays the better performance in average. The lowest proficiency is presented by $T_m$ and $L_m$, while the other parameters performs as well as regarding the efficiency parameter β with the RRSI being one of the best parameters.

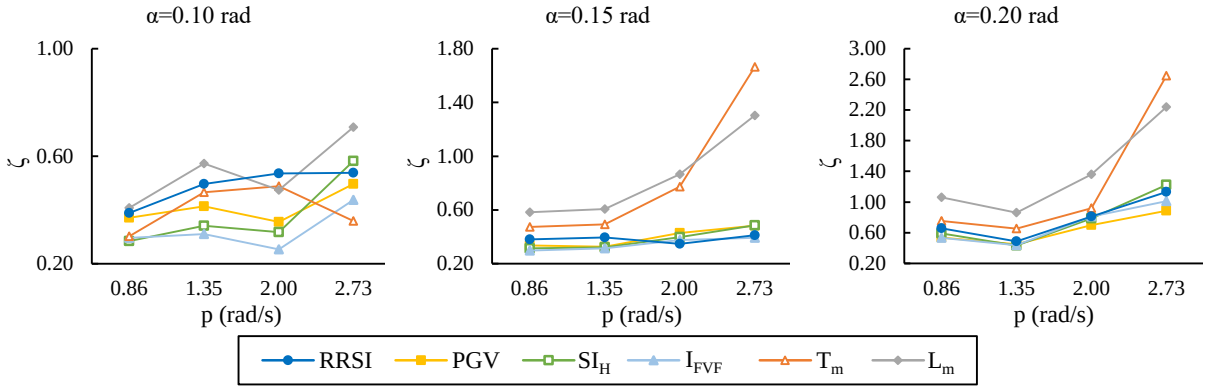


Figure 6: Proficiency measure (ζ) of the examined IMs for the examined rigid blocks.

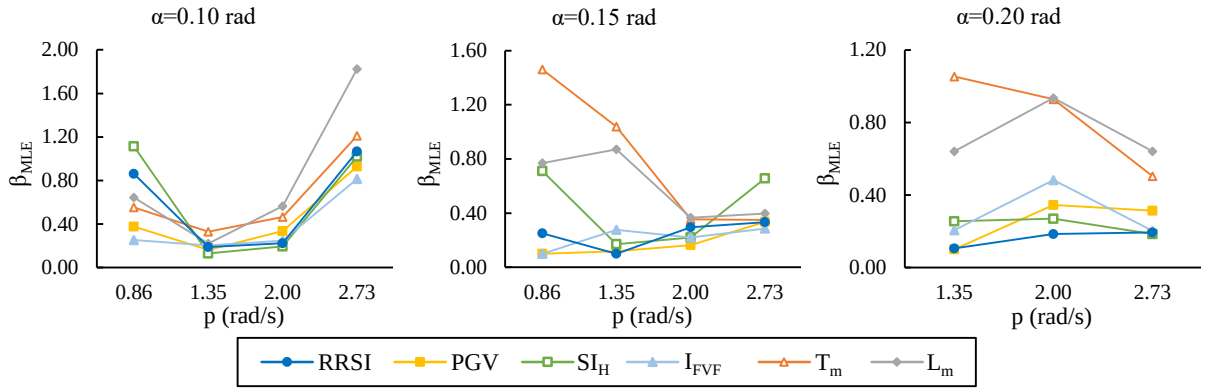


Figure 7: Standard deviation ($\beta_{MLE}$) of overturning fragility curves for the examined rigid blocks.

The standard deviation $\beta_{MLE}$ obtained by the maximum likelihood estimator approach could also form an efficiency parameter. Therefore these values are presented in Figure 7. The block with slenderness α=0.20 rad and frequency parameter p=0.86 rad/s did not collapse subjected under any of the 35 ground motions. Thus, at the third subfigure in the row there are

depicted results from only three blocks. The $T_m$ and the $L_m$ consist the parameters that could predict the overturning of the blocks with the larger values of dispersion compared with the other IMs. Except of the RRSI, the PGV and the $I_{FVF}$ lead to minimum values of dispersion.

## 8 CONCLUSIONS

A scalar IM named as Rocking Rotation Spectral Intensity (RRSI) is proposed in the present study. The proposed parameter is defined by the volume under the rocking spectrum, which is pictured as a surface diagram. The spectral volumes that consist the RRSI is evaluated by integration of the rocking rotation spectrum. The integration limits of the period T and the slenderness α, was adopted in order to construct IM which take into account structural response information for the majority of the slender rocking blocks. The proposed IM are determined with the intention of having strong correlation with the seismic rocking performance.

To assess the adequacy of the IM, 12 rigid blocks subjected to a set of 35 ground motion record were examined. Using only the non-collapse data, linear regression analyses are performed between the proposed IM and the developed rocking rotation, from which the correlation coefficients are extracted. Further, criteria such as efficiency, proficiency and practicality are adopted in order to evaluate the IM. Moreover, the standard deviations calculated by the maximum likelihood method are presented, as an efficiency parameter. In order to highlight the superiority of the IMs, their results are compared with those obtained by 5 well known IMs which affects the rocking response.

- Regarding the correlation coefficients, the RRSI developed the higher values on average (r=0.86), while it ranged from 0.6 to 0.94.
- The RRSI proved to be the more efficient IM on average (β=0.62) having similar performance with the $SI_H$ and the $I_{FVF}$.
- Based on the proficiency criteria, the $I_{FVF}$ presents the better performance. However, RRSI demonstrate low values of the parameters ζ too.
- Similar outcomes are arise from the standard deviation which is calculated throughout the maximum likelihood estimator process. With the RRSI being the parameter that decrease the variation of predicting the rocking overturn collapse.

## REFERENCES

[1] P. Giovenale, A.C. Cornell, L. Esteva, Comparing the adequacy of alternative ground motion intensity measures for the estimation of structural responses. *Earthquake Engineering and Structural Dynamics*, **33,** 951-979, 2004.

[2] N. Luco, and C. A.Cornell, Structure-specific scalar intensity measures for near-source and ordinary earthquake motions. *Earthquake Spectra*, **23**, 357–392, 2007.

[3] K.R. Mackie, B. Stojadinovi¢, Fragility basis for California highway overpass bridge seismic decision making, PEER Report, University of California, Berkeley, CA, 2005.

[4] J.E. Padgett, B.G Nielson, R. DesRoches, Selection of optimal intensity measures in probabilistic seismic demand models of highway bridge portfolios. *Earthquake Engineering & Structural Dynamics*, **37**, 711-725, 2008.

[5] A. Elenas Seismic-Parameter-Based Statistical Procedures for the Approximate Assessment of Structural Damage. *Mathematical Problems in Engineering*, Article ID 916820, 22 pages, doi:10.1155/2014/916820, 2014.

[6] K. Kostinakis, I.K. Fontara, A.M. Athanatopoulou, Scalar Structure-Specific Ground Motion Intensity Measures for Assessing the Seismic Performance of Structures: A Review. *Journal of Earthquake Engineering*, 2016.

[7] N. Makris, D. Konstantinidis, The rocking spectrum and the limitations of practical design methodologies. *Earthquake Engineering & Structural Dynamics*, **32**, 265–289, 2003.

[8] C.S. Yim, A.K. Chopra, J. Penzien, Rocking response of rigid blocks to earthquakes. *Earthquake Engineering & Structural Dynamics*, **8**, 565-587, 1980.

[9] P.D. Spanos, A.S. Koh, Analysis of block random rocking. *Soil Dynamics and Earthquake Engineering*, **5**, 178-183, 1986.

[10] M.S. Acikgoz M.J. DeJong, The rocking response of large flexible structures to earthquakes, Bulletin of Earthquake Engineering, **12**, 875-908, 2014.

[11] I.N. Psycharis, M. Fragiadakis, I. Stefanou, Seismic reliability assessment of classical columns subjected to near-fault ground motions. *Earthquake Engineering & Structural Dynamics*, **42**, 2061-2079, 2013.

[12] E.G. Dimitrakopoulos, T.S. Paraskeva, Dimensionless fragility curves for rocking response to near-fault excitations. *Earthquake Engineering & Structural Dynamics*, **44**, 2015-2033, 2015.

[13] I.E. Kavvadias, L.K. Vasiliadis, E. Elenas, Seismic response parametric study of ancient rocking columns. International Journal of Architectural Heritage, doi: 10.1080/15583058.2017.1298009, 2017.

[14] J. Zhang, N. Makris, 2001. Rocking response of free-standing blocks under cycloidal pulses. *Journal of Engineering Mechanics ASCE*, **127**, 473-483, 2001.

[15] G.W. Housner, The behavior of inverted pendulum structures during earthquakes. *Bulletin of the Seismological Society of America*, **53**, 403-417, 1963.

[16] F. Peña, P.B. Lourenço, A Campos Costa, Experimental dynamic behavior of freestanding multi-block structures under seismic loadings. *Journal of Earthquake Engineering*, **12**, 953-979, 2008.

[17] M.A. El Gawady, Q. Ma, J.W. Butterworth, J. Ingham, Effects of interface material on the performance of free rocking blocks. *Earthquake Engineering and Structural Dynamics*, **40**, 375–392, 2010.

[18] Kalliontzis, D., Sritharan, S., Schultz, A, Improved coefficient of restitution estimation for free rocking members. *Journal of Structural Engineering*, **142**, 06016002, 2016.

[19] Natick MA. MATLAB, Mathworks, 2016.

[20] J.W. Baker, Efficient analytical fragility function fitting using dynamic structural analysis. *Earthquake Spectra*, **31**, 579–599, 2015.

[21] M.Shinozuka, M.Q. Feng, J. Lee, T. Naganuma, Statistical analysis of fragility curves. *Journal of Engineering Mechanics ASCE*, **126**, 1224–1231, 2000.

[22] N. Makris, M.F. Vassiliou, 2013. Planar rocking response and stability analysis of an array of free-standing columns capped with a freely supported rigid beam. *Earthquake Engineering & Structural Dynamics*, **42**,431-449, 2013.

[23] M.F. Vassiliou, K.R. Mackie, B. Stojadinović, Dynamic response analysis of solitary flexible rocking bodies: modeling and behavior under pulse ‐ like ground excitation. *Earthquake Engineering & Structural Dynamics*, **43**, 1463-1481, 2014.

[24] Pacific Earthquake Engineering Research Centre (PEER). Strong motion database, http://ngawest2.berkeley.edu/; 2016.

[25] European Strong-Motion Database, http://www.isesd.hi.is/ESD_Local/frameset.htm; 2016.

[26] E. Dimitrakopoulos, A.J. Kappos, N. Makris, Dimensional analysis of yielding and pounding structures for records without distinct pulses. *Soil Dynamics and Earthquake Engineering*, **29**, 1170-1180, 2009.

COMPDYN 2017
6th ECCOMAS Thematic Conference on
Computational Methods in Structural Dynamics and Earthquake Engineering
M. Papadrakakis, M. Fragiadakis (eds.)
Rhodes Island, Greece, 15–17 June 2017

# NUMERICAL STUDY ON THE DYNAMIC RESPONSE OF CLASSICAL COLUMN STANDING FREE ON AN ISOLATED BASE

**Ioannis E. Kavvadias**[1], **Henrik F. Bibo**[1], **and Lazaros K. Vasiliadis**[1]

[1] Democritus University of Thrace, Department of Civil Engineering
Campus of Kimmeria, 67100 Xanthi, Greece
{ikavvadi, ebimpo, lvasilia}@civil.duth.gr

**Keywords:** Rocking Response, Base Isolation, Friction Pendulum Bearings, Classical Monuments, Earthquake Engineering.

**Abstract.** *A numerical study of the seismic response of base isolated free standing monolithic ancient column is presented in this paper. These rocking structural systems are analyzed standing free on an isolated base supported on friction pendulum (FP) bearings. Specifically, the implementation of multi-spherical friction bearings is examined. The rocking columns as well as the friction pendulum bearings were simulated using finite element method. Of particular importance is the detailed modeling of the isolators, which seismic behavior are validated. It is known that subjected to lower predominant period excitations, free standing rocking blocks exhibits increased stability. While, they are vulnerable to long period excitations. That opposes to the main characteristic of the base isolation technic which is to elongate the oscillation period. Thus, a thorough investigation of the influence of the FP bearings radius on the seismic response of free standing columns is caring out, to result in optimal design of the isolation devices in order to avoid rocking overturning.*

## 1 INTRODUCTION

The seismic response of ancient structural systems receive an increased attention the last years. As they constitute cultural heritage assets and as such they are irreplaceable, their seismic protection is of utmost importance for the international community. Due to the fact that their form must remain intact, contemporary intervention methods should be preferred that traditional ones.

Monument structures such as Classical columns displays rocking seismic response as they standing free on the base, thus they are analyzed as rocking rigid blocks. Seismic response of rocking blocks present very complex behavior. In this way a plethora of researchers investigated the seismic response of rigid blocks and specifically ancient column in order to unveil the hidden aspects of their behavior. Seismic behavior of monolithic and multidrum columns have been thoroughly investigated both numerically and analytically [1-9]. Moreover, the influence of the epistyle mass on the rocking response of the colonnade has been examined by Makris and Vasiliou[10]. The influence of the IMs in the rocking response has been also examined [11, 12]

The seismic risk mitigation of museum artifact and ancient structural systems form a challenging task to researchers. The intervention method has to be not-intrusive to the form of the monument. Hence, the base isolation seem to be the only method that fulfill this restriction. The implementation of base isolation has been studied as a technique of protecting art objects and statues in museums [13-18]. The response of rocking blocks standing free on isolated base has been investigated extensively by Vassiliou and Makris [19]. They suggested that base isolation is not efficient when it is applied to large blocks or when it is subjected to high frequency excitations.

The isolation devices are divided into two general categories, the rubber and the friction bearings. Based on the friction pendulum bearings principles [20], more sophisticated systems have been proposed such as double pendulum bearings and triple pendulum bearings [21-24]. These isolation devices, among their beneficial performance in seismic mitigation, demonstrate adaptive seismic behavior, although they consist passive protection systems.

In the present study, the seismic response of an ancient column standing free on an isolated base is examined. Multi-spherical friction pendulum bearing are applied as isolation devices. A parametric investigation focusing on the effect of the friction pendulum radius on the seismic response of the rocking column is presented. Both, double pendulum friction bearing and a triple friction bearing are utilized. For the purpose of this study validated finite element models are adopted, for the simulation of both the rocking column as well as the friction pendulum bearings.

## 2 NUMERICAL MODELING

For the purpose of this study, finite element models are utilized for simulation of the examined structural systems. Despite the fact that the structural members being modeled as 3D members, planar analyses are performed. Explicit dynamic analyses were employed as it is computationally efficient for discontinuous events like impact problems, using the central difference algorithm.

The response of the rocking column is validated with results obtained from the numerical solution of the rocking motion equation [25]. The analyses results of the friction pendulum isolators models are also verified with those obtained by analyses in other commercial software which encapsulate link models appropriate for the simulation of friction pendulum bearing. The validation procedure is presented by Kavvadias et al. [26].

In the current study a column with 8m height and slenderness α=0.165rad is studied. The dimensions of the column are representative of a classical column. Specifically, the columns of the Temple of Olympic Zeus and the Temple of Apollo in Syracuse are 8 m high whereas, the Parthenon Pronaos columns have a slenderness of 0.16 rad.

Regarding the friction pendulum bearings, two double friction pendulum bearings (DFP), and one triple friction pendulum bearing (TFP) are considered. The double friction pendulum isolators have the same radius and coefficient of friction in both concave surfaces. Particularly, the friction coefficient in both isolators are consider equal to μ=0.1. Moreover, the radius of the bearing are selected as R=1.18 m and 0.65 m, which correspond to an isolation period $T_{is}$= 3 s and 2 s respectively. Concerning the triple friction pendulum bearing, the friction coefficients are μ=0.03 for the two inner surfaces and μ=0.1 for the two outer. Further, the radius are R=0.53 m and 2.05 m for the inner and the outer concave surfaces. According to these characteristics, the isolation period is equal to $T_{is}$= 2 s or 4.5 s, which is depending on the magnitude of the ground motion. In Figure 1 is depicted the examined rocking column, the friction pendulum bearings considered in the study and finally, the implementation of those.

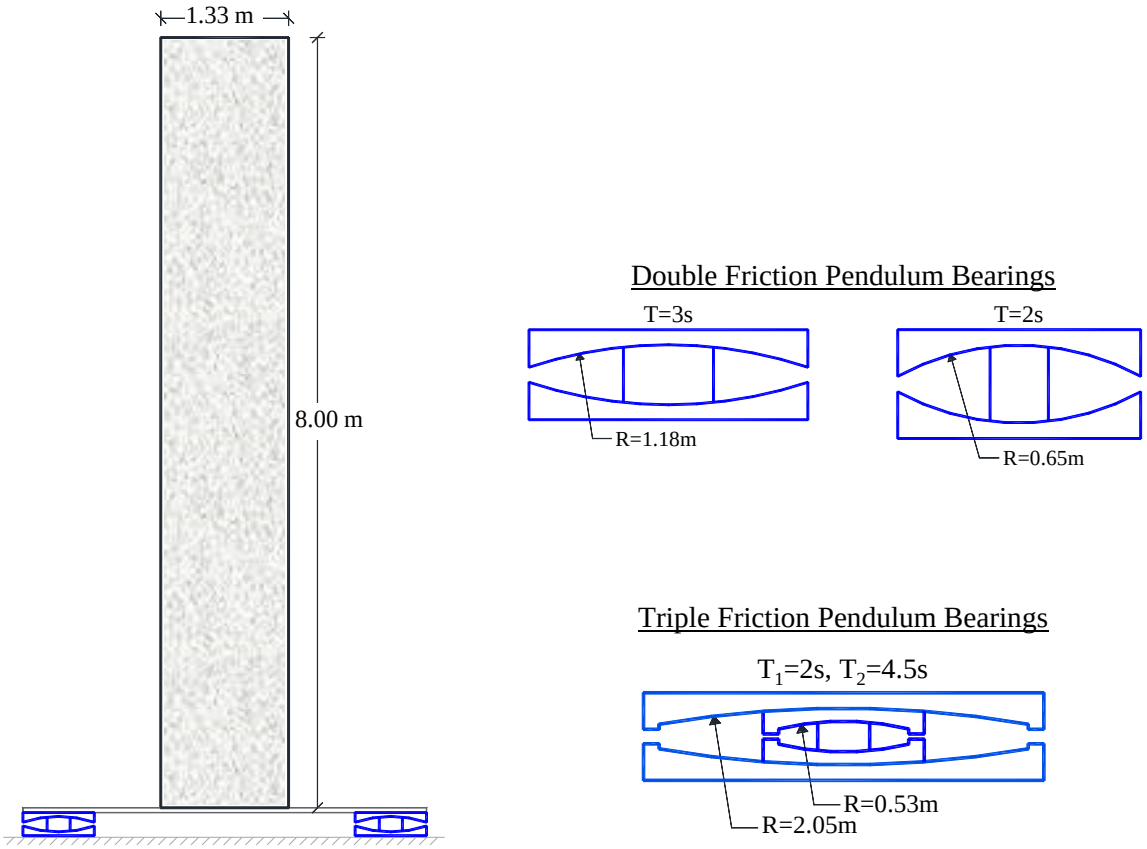


Figure 1. Examined column and friction pendulum bearings.

In order to investigate the performance of the isolation systems to mitigate the seismic risk of monumental rocking structures such as the examined column, a set of 35 ground motion records is used. Excitations with earthquake magnitudes (Ms) between 5.3 and 7.6, including both near-fault and far-fault records are employed, in order to present a wide range of intensities and frequency contents. Regarding their frequency content, the main period $T_m$ [27] is ranged $T_m$ = 0.10 - 1.68 s. In Table 1 the ground motion considered in this study are listed shorted by increasing values of $T_m$ [28, 29].

| Earthquake | Station | Date | $M_s$ | R (km) | $T_m$ (s) |
|---|---|---|---|---|---|
| Iwake | Ichinoseki Maikawa | 14/7/2008 | 6.9 | 23.02 | 0.10 |
| Chi-Chi | TCU88 | 20/9/1999 | 7.62 | 18.16 | 0.16 |
| Whittier | LA - Obregon Park | 1/10/1987 | 5.27 | 13.62 | 0.24 |
| Athens | ATH4 | 7/9/1999 | 5.9 | 16.62 | 0.26 |
| Tabas | Dayhook | 16/9/1978 | 7.35 | 13.94 | 0.33 |
| Superstition Hill | Mtn Camera | 24/11/1987 | 6.54 | 5.61 | 0.33 |
| Duzce | Lamont 531 | 12/11/1999 | 7.14 | 8.03 | 0.35 |
| San Fernando | Paicoma Dam | 9/2/1970 | 6.61 | 1.81 | 0.35 |
| Gazli | Karakyr | 17/5/1976 | 6.8 | 5.46 | 0.40 |
| Northridge | Paicoma Dam | 17/1/1994 | 6.69 | 7.01 | 0.46 |
| Aigion | AIGA | 25/6/1995 | 6.4 | 21.5 | 0.48 |
| Kobe | Nishi -Akashi | 16/1/1995 | 6.9 | 7.08 | 0.49 |
| Friuli | Tolmezo | 6/5/1976 | 6.5 | 15.82 | 0.50 |
| Imperial Valley | El Centro Array #9 | 19/5/1940 | 6.95 | 6.09 | 0.53 |
| Coalinga | Fault Zone 14 | 2/5/1983 | 6.36 | 29.48 | 0.55 |
| Corinth | Corinth | 24/2/1981 | 6.6 | 10.28 | 0.56 |
| Kalamata | Kalamata | 13/9/1986 | 6.2 | 10 | 0.58 |
| Imperial Valley | El Centro Array #8 | 15/2/1979 | 6.53 | 3.86 | 0.60 |
| Chi-Chi | CHY035 | 20/9/1999 | 7.62 | 12.56 | 0.72 |
| El Mayor Cucapah | Chihuahua | 4/4/2010 | 7.2 | 19.47 | 0.74 |
| Landers | Joshua Tree | 28/6/1992 | 7.28 | 11.03 | 0.78 |
| Parkfield | Cholame #2 | 28/6/1966 | 6.2 | 17.64 | 0.83 |
| Taiwan SMART1(40) | Smart1 M02 | 15/111986 | 6.32 | 60.89 | 0.83 |
| Chuetsuoki | Nakanoshima Nagaoka | 16/7/2007 | 6.8 | 19.89 | 0.86 |
| Irpinia | Sturno | 23/11/1980 | 6.9 | 10.84 | 0.87 |
| Loma Prietta | Los Gatos - Lexington Dam | 17/11/1986 | 6.93 | 5.02 | 0.89 |
| Chi-Chi | CHY101 | 20/9/1999 | 7.62 | 9.94 | 0.89 |
| Imperial Valley | El Centro Array #7 | 15/2/1979 | 6.53 | 0.56 | 0.96 |
| Northridge | Jensen Filter Plant | 17/1/1994 | 6.69 | 5.92 | 0.99 |
| Darfield | Papanui High School | 4/9/2010 | 7 | 26.76 | 1.19 |
| Northridge | Newhall – Fire Station | 17/1/1994 | 6.69 | 5.43 | 1.19 |
| Denali | TAPS Pump Station #10 | 3/11/2002 | 7.9 | 2.74 | 1.31 |
| Erzincan | Erzincan | 19/3/1992 | 6.69 | 4.38 | 1.38 |
| Kobe | Port Island | 16/1/1995 | 6.9 | 3.31 | 1.47 |
| Bucharest | Bucharest | 4/3/1977 | 7.5 | 115 | 1.68 |

Table 1. Ground motion records sorted by increasing values of $T_m$.

## 3 RESULTS

### 3.1 Transmissibility of the isolation systems

The first results in order to evaluate the efficiency of the multi-spherical friction pendulum systems implementation, should be their affection in the ground motion excitation. The main feature of the base isolation technique is that it decrease the acceleration values of the seismic signal. However, due to the fact that it elongates the period of the excitation wave it could be harmful for implementation to rocking structures [19]. Moreover, it is known that the rocking

response of slender blocks is affected mainly by the velocity characteristics of the excitation [11, 12].

Based on the above facts, the peak acceleration and the velocities that are transmitted from the isolator to the rocking classical column are depicted. In Figure 2 the peak acceleration of the initial excitations are compared with those developed on the isolated base for all the isolation cases. Among with these values, the marginal acceleration $a_{min}$ [30] that initiates the rocking is depicted. The base isolation seems to be more effective for high frequency excitations as it reduces the acceleration to values even lower to the critical acceleration for the rocking block. As the frequency of the excitation tends lower, the accelerations did not reduces in such grade. It is obvious also that as the isolation period is increased, the accelerations are decreased. Comparing the different types of friction pendulum systems, the TFP bearings are notably more effective than the DFP ones, except of the case when it is subjected under the CHY101 (No 27) excitation. Initially it is marked an extremely high value of acceleration (a = 1.60 g) which is observed due to the fact that the displacement capacity of the isolator is reached. After redefining the displacement capacities of the TFP bearing, a favorable response is displayed.

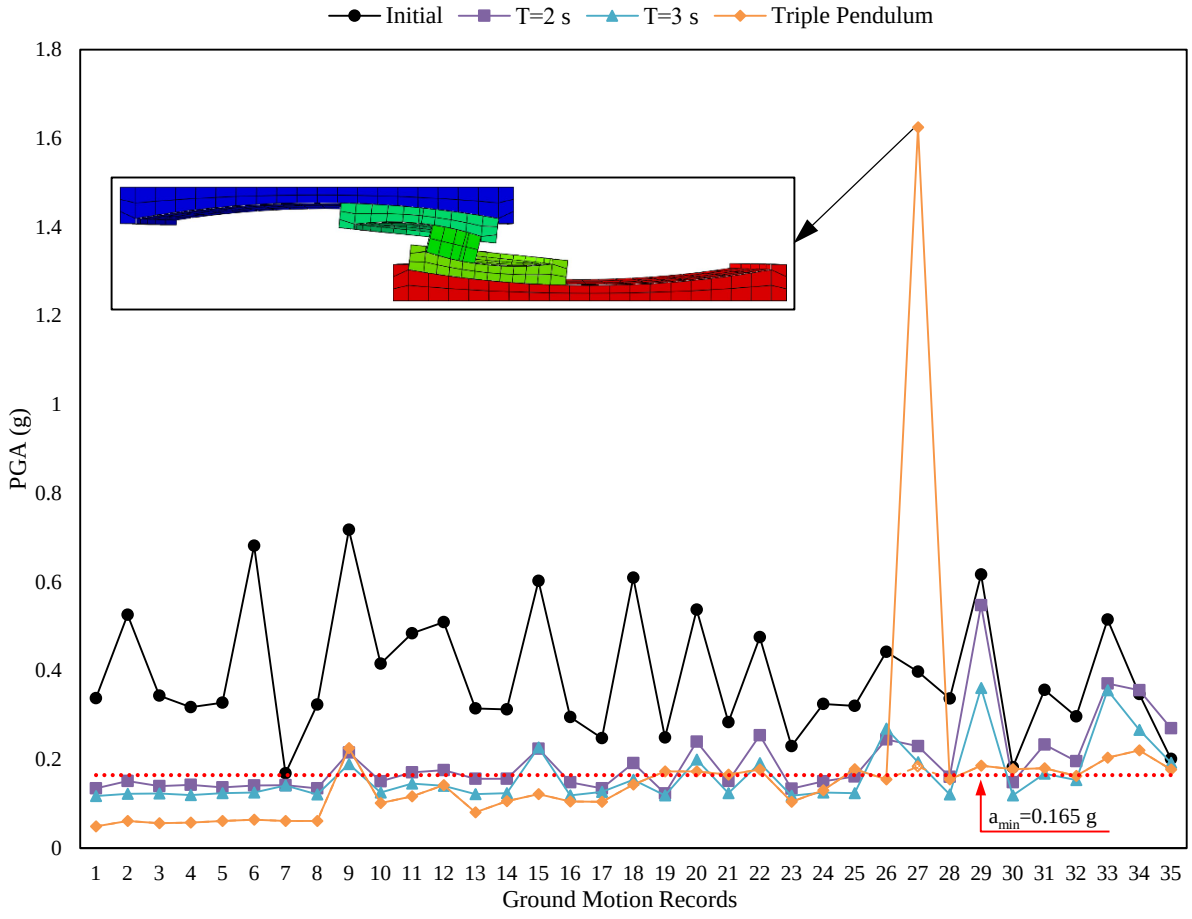


Figure 2. Peak acceleration values of the initial excitation and the signal at the isolated base.

The acceleration of the isolated base is reduced as expected. An important ground motion characteristic is the velocity of the base. Velocity is dependent of both the acceleration amplitude and the frequency content of the excitation. Due to the fact that the acceleration values are reduced due to the base isolation but simultaneously it period is elongated, it is difficult to estimate the expected results of the velocities. In Figure 3 the peak velocities of the fixed base

as well as the velocities of the isolated bases are presented. It could be seen that the velocities are not altered as the acceleration values. On average, there is not a notable influence of the base isolation in the peak velocities of the transmitted signal. There is depicted both increasing and decreasing of the velocities values. The velocity of an excitation consist a ground motion parameter that affects importantly the rocking response.

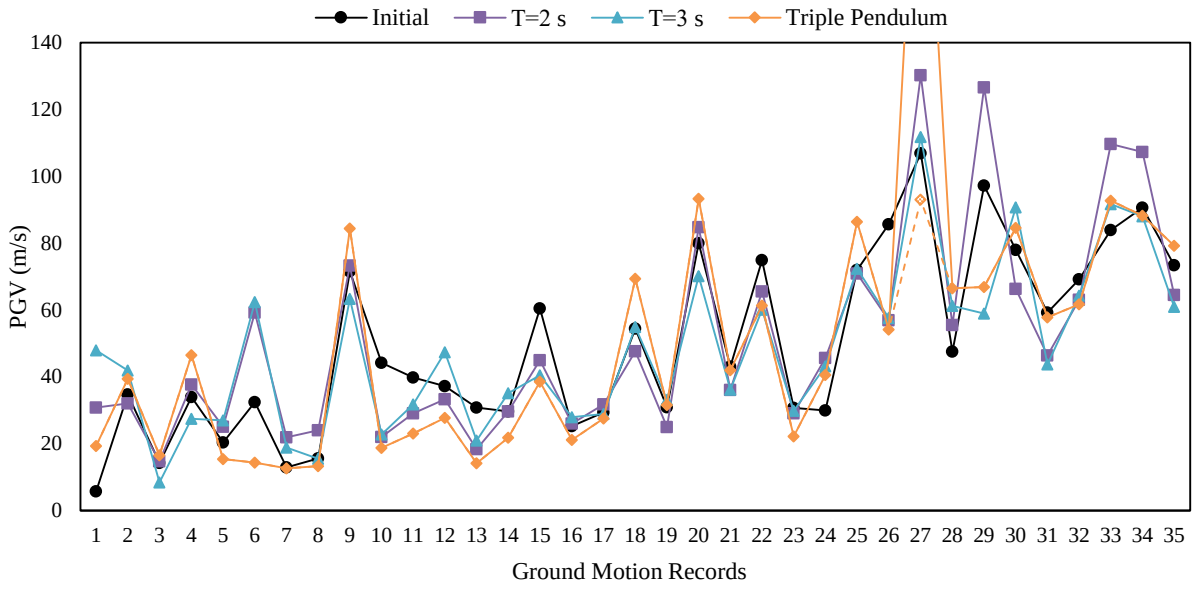


Figure 3. Peak velocity values of the initial excitation and the signal at the isolated base.

## 3.2 Seismic response of the rocking classical column

The velocity of an excitation consist a ground motion parameter that affects importantly the rocking response. Thus any increase of the velocity values combined with acceleration values that exceed the minimum acceleration that activates uplift should be devastating for the rocking blocks. In Figure 4 the maximum developed rocking rotations normalized to the slenderness of the block is pictured.

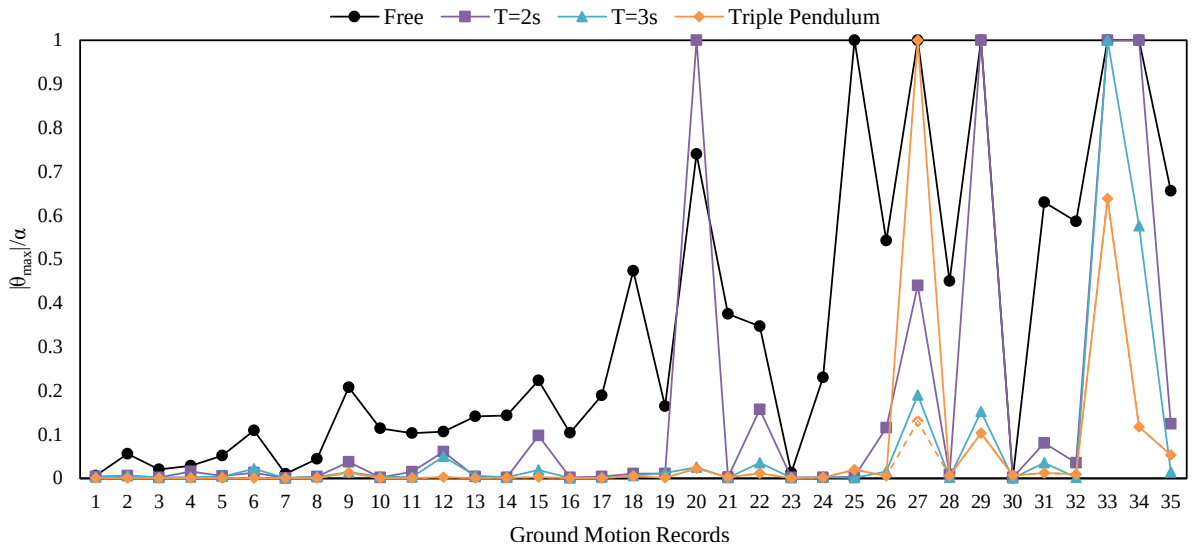


Figure 4. Peak normalized rotation values of the rocking block standing free on a fixed and isolated bases.

For the cases that the acceleration values (Figure 3) did not overcome the $a_{min}$, the developed rocking rotations are equal to zero. When rocking initiates, the velocity of the seismic excitation constitutes an accurate indicator of it destructiveness. That fact is confirmed by the developed rocking rotation in Figure 4. The rocking block standing free on an isolated base with period $T_{is}$=2 s, overturns when is subjected 4 ground motions. In these cases the acceleration values exceed the minimum acceleration that initiates rocking, while the velocities are increased compared with the initial signal. Standing on an isolated base with period $T_{is}$=3 s, it overturns only subjected under one seismic excitation. The implementation of DFP bearings to isolate free standing blocks has been thoroughly instigated by Vassiliou and Makris [19], showing their detrimental effect for large blocks or when it is subjected to high frequency pulses.

Examining the rocking block standing free on a rigid base which is isolated with the use of TFP bearings, interesting remarks are arose. The implementation of TFP result in the most reduced acceleration values of the high frequency content ground motions. Subjected to the excitation with the longer main period their performance are in general the best comparing with the DFP bearings. The most important fact is that the rocking block did not overturn under any ground motion excitation. Only when the displacement capacity of the TFP is restricted, collapse occurred.

## 4 CONCLUSIONS

In the present study base isolation technique is examined as a protection system of free standing ancient columns. These structural systems consist irreplaceable cultural heritage elements, and as though have to be preserved throughout the years. The effectiveness of three different isolation bearings in the seismic risk mitigation of a slender rocking column is investigated. Two double friction pendulum bearings (DFP) and one triple friction pendulum bearings (TFP) are considered.

For the ground motions set considered in this study the seismic isolation with the use of TFP appear to be beneficial for the seismic protection of the examined free standing column. Despite the fact that in general the seismic signal period is elongated due to the base isolation, when TFP bearing is implemented, the accelerations are reduced in such grade that lead to restricted rocking rotation. The results indicated that the usage of TFP bearings, with a carefully selection of it displacement capacity, can form an intervention solution that results in enhanced seismic performance of structures such as free standing classical columns.

## REFERENCES

[1] I.N. Psycharis, D.Y. Papastamatiou, A.P. Alexandris, Parametric investigation of the stability of classical columns under harmonic and earthquake excitations. *Earthquake Engineering and Structural Dynamics*, **29**, 1093-1109, 2000.

[2] D. Konstantinidis, N. Makris, Seismic response analysis of multidrum classical columns. *Earthquake Engineering and Structural Dynamics*, **34**, 1243-1270. 2005.

[3] C. Papantonopoulos, I.N. Psycharis, D.Y. Papastamatiou, J.V. Lemos, H. Mouzakis, Numerical prediction of the earthquake response of classical columns using the distinct element method. *Earthquake Engineering and Structural Dynamics*, **31**, 1699-1717, 2002.

[4] I.N. Psycharis, J.V. Lemos, D.Y. Papastamatiou, C. Zambas, Numerical study of the seismic behaviour of a part of the Parthenon Pronaos. *Earthquake Engineering and Structural Dynamics*, **32**, 2063-2084, 2003.

[5] L. Papaloizou, P. Komodromos, Planar investigation of the seismic response of ancient columns and colonnades with epistyles using a custom-made software. *Soil Dynamics and Earthquake Engineering*, **29**, 1437-1454, 2009.

[6] P. Komodromos, L. Papaloizou, P. Polycarpou, Simulation of the response of ancient columns under harmonic and earthquake excitations. *Engineering Structures*, **30**, 2154-2164, 2008.

[7] I.N. Psycharis, Dynamic behaviour of rocking two-block assemblies. *Earthquake Engineering and Structural Dynamics*, **19**, 555-575, 1990.

[8] P.D. Spanos, P.C. Roussis, N.P. Politis, Dynamic analysis of stacked rigid blocks. *Soil Dynamics and Earthquake Engineering*, **21**, 559-578, 2001.

[9] A.N. Kounadis, G.J. Papadopoulos, On the rocking instability of a three-rigid block system under ground excitation. *Archive of Applied Mechanics*, **86**, 957-977, 2016.

[10] N. Makris, M.F. Vassiliou, Planar rocking response and stability analysis of an array of free - standing columns capped with a freely supported rigid beam. *Earthquake Engineering and Structural Dynamics*, **42**(3), 431-449, 2013.

[11] E.G. Dimitrakopoulos, T.S. Paraskeva, Dimensionless fragility curves for rocking response to near‐fault excitations. *Earthquake Engineering and Structural Dynamics*, **44**, 2015-2033, 2015.

[12] I.E. Kavvadias, L.K. Vasiliadis, E. Elenas, Seismic response parametric study of ancient rocking columns. International Journal of Architectural Heritage, **doi: 10.1080/15583058.2017.1298009**, 2017.

[13] G. Augusti, M. Ciampoli, L. Airoldi Mitigation of seismic risk for museum contents. *Proceedings of the 10th World Conference in Earthquake Engineering*, Madrid, 1992.

[14] F. Vestroni, S. Di Cinto, Base isolation for seismic protection of statues. *Twelfth World Conference on Earthquake Engineering*, New Zealand, 2000.

[15] I. Calio, M. Marletta, Passive control of the seismic response of art objects. *Engineering Structures*, **25**, 1009–1018, 2003.

[16] Roussis PC, Pavlou EA, Pisiara EC. Base-isolation technology for earthquake protection of art objects. *The 14th World Conference on Earthquake Engineering: Innovation Practice Safety*, Beijing, China, October 2008.

[17] A. Contento, A. Di Egidio, Investigations into benefits of base isolation for non-symmetric rigid blocks. *Earthquake Engineering and Structural Dynamics*, **38,** 849–866, 2009.

[18] C.Z. Chrysostomou, N. Kyriakides, P.C. Roussis, P.G Asteris, Emerging Technologies and Materials for the Seismic Protection of Cultural Heritage. *In Handbook of Research on Seismic Assessment and Rehabilitation of Historic Structures* Editing by P. Asteris and V. Plevris. IGI Global, 2015

[19] M.F. Vassiliou, N. Makris, Analysis of the rocking response of rigid blocks standing free on a seismically isolated base. *Earthquake Engineering and Structural Dynamics*, **41**, 177–196, 2012.

[20] Zayas V, Low SS, Mahin SA. A simple pendulum technique for achieving seismic isolation. *Earthquake Spectra*, **6**, 317–333, 1990

[21] Fenz DM, Constantinou MC. Behavior of the double concave Friction Pendulum bearing. *Earthquake Engineering and Structural Dynamics*, **35**, 1403–1424., 2006.

[22] Fenz DM, Constantinou MC. Spherical sliding isolation bearings with adaptive behavior: theory. *Earthquake Engineering and Structural Dynamics*, **37**, 163–183, 2008.

[23] T.A. Morgan, S.A. Mahin, Achieving reliable seismic performance enhancement usingmulti-stage friction pendulum isolators. *Earthquake Engineering and Structural Dynamic*, **39**,1443–1461, 2010

[24] A.A Sarlis, M.C. Constantinou, A model of triple friction pendulum bearing for general geometric and frictional parameters. *Earthquake Engineering and Structural Dynamic*, **45**, 1837–1853, 2016.

[25] N. Makris, Y. Roussos, Rocking response of rigid blocks under near-source ground motions. *Geotechnique*, **50**, 243–262, 2000.

[26] I.E. Kavvadias, H.E. Bibo, L.K. Vasiliadis, Finite element modeling of single and multispherical friction pendulum bearings. *6th International Conference on Computational Methods in Structural Dynamics and Earthquake Engineering*, Rhode Island, Greece, 2016.

[27] E.M. Rathje, N.A. Abrahamson, J.D. Bray, Simplified frequency content estimates of earthquake ground motions. *Journal of Geotechnical and Geoenviromental Engineering*, **124**, 150-159, 1998.

[28] Pacific Earthquake Engineering Research Centre (PEER). Strong motion database http://ngawest2.berkeley.edu/; 2015.

[29] European Strong-Motion Database. http://www.isesd.hi.is/ESD_Local/frameset.htm;, 2015.

[30] G.W. Housner, The behavior of inverted pendulum structures during earthquakes. *Bulletin of the Seismological Society of America*, **53**, 403-417, 1963.

COMPDYN 2017
6th ECCOMAS Thematic Conference on
Computational Methods in Structural Dynamics and Earthquake Engineering
M. Papadrakakis, M. Fragiadakis (eds.)
Rhodes Island, Greece, 15–17 June 2017

# NON-SMOOTH CONTACT DYNAMICS OF PLANAR MASONRY STRUCTURES USING MATHEMATICAL PROGRAMMING

**Francesco Portioli[1], Lucrezia Cascini[2], and Raffaele Landolfo[2]**

[1] University of Naples Federico II, Department of Structures for Engineering and Architecture, Via Forno Vecchio 36, 80134 Naples
e-mail: fportiol@unina.it

[2] University of Naples Federico II, Department of Structures for Engineering and Architecture, Via Forno Vecchio 36, 80134 Naples
{lucrezia.cascini, landolfo}@unina.it

**Keywords:** Masonry block structures; Rigid blocks; Non-smooth contact dynamics; Mathematical programming.

**Abstract.** *In this paper an incremental formulation for contact dynamic analysis of masonry block structures is presented. The model is composed of rigid bodies interacting at potential contact points located at the vertexes of the block interfaces. A no-tension behavior with finite friction and infinite compressive strength is assumed at contact interfaces. The contact dynamic problem is governed by equilibrium equations, which relate external, inertial and contact forces, and by kinematic equations, which ensure compatibility between contact displacement rates and block degrees of freedom. Quadratic programming is used to solve the optimization problem arising from the formulation of the variational problem associated to dynamics of the block assemblages. To evaluate the accuracy and computational efficiency of the implemented formulation, applications to case studies from the literature are presented.*

## 1 INTRODUCTION

In recent years, there has been a growing interest in the use of non-smooth contact analysis to dynamics and rocking behavior of masonry block structures [1-5].

This is mainly because this modelling approach allows to take into account contact interactions directly by setting up a system of proper inequalities and complementarity conditions rather than introducing additional elements in the models such in the case of distinct element models, where penalty methods are generally used.

In this perspective, starting from previous studies in the field of granular materials [6, 7], a non-smooth contact dynamic formulation for the analysis of masonry structures has been recently developed [8, 9] and herein applied to a numerical case study taken from the literature [10] to show potentialities of the adopted modelling approach.

As such, the paper is organized as follows. Sections 2 presents and overview of the adopted rigid block dynamic model. The static and kinematic variables as well as the relationships governing the behavior of the rigid block model are introduced. The quadratic programming formulation which is used to carry out the dynamic analysis of planar masonry assemblages is discussed in Section 3. In Section 4 an application of the proposed formulation to an in-plane wall panel is illustrated to show the ability of the implemented formulation to capture rocking behavior of multi-block assemblages.

## 2 THE RIGID BLOCK DYNAMIC MODEL

The masonry texture is discretized into a multi-body assemblage made of rectangular rigid blocks *i* interacting at potential contact points *k* located at the vertexes of the interface *j* (Fig. 1).

A no-tension and associative frictional behavior with infinite compressive strength is assumed at contact interfaces.

The dynamic model is formulated following the approach proposed in [6,7] for granular materials, though now detailed for two-dimensional assemblages of rectangular blocks.

The contact variables are the internal forces acting at each contact point *k*, which are located at a vertex of interface *j* of block *i* (Fig. 1a). These variables are collected in vector $\boldsymbol{c}$ and include the shear force component $t_k$ and the normal force $n_k$ along the local coordinate axes.

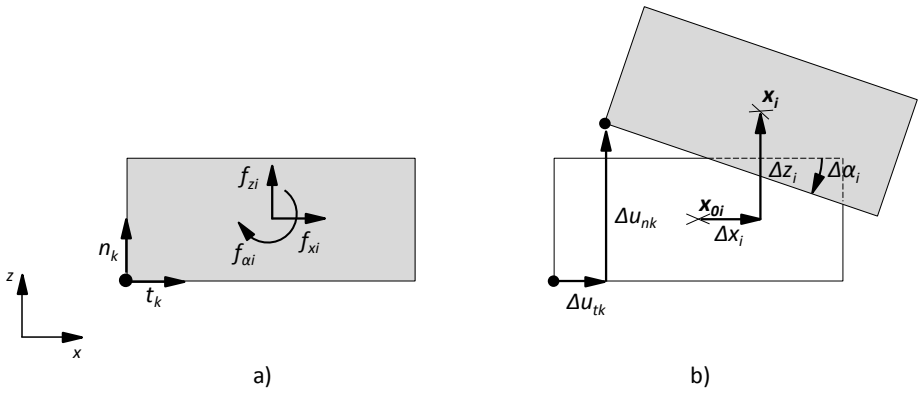


Figure 1: a) Contact forces and b) kinematic variables at block centroid *i*, and contact point *k*.

The kinematic variables associated in a virtual work sense to the contact forces are the relative displacement rates at the contact points, namely the tangential and normal displacement rates $\Delta u_{tk}$ and $\Delta u_{nk}$ (Fig. 1b), which are collected in the vector $\boldsymbol{\Delta u}$. The positions $x_i$, $y_i$ and $\alpha_i$ related to the degrees of freedom of each block $i$ are collected in the vector $\boldsymbol{x}$.

External loads applied to the centroid of rigid block $i$ are collected in vector of external forces $\boldsymbol{f_{ext}}$ (Fig. 1a).

The equations of motions are discretized with respect to time using the $\theta$-method and assuming:

$$\dot{\boldsymbol{x}}(t) = \frac{1}{\theta}\left[\frac{\boldsymbol{\Delta x}}{\Delta t} - (1-\theta)\dot{\boldsymbol{x}}_{\boldsymbol{0}}\right] \tag{1}$$

where $\boldsymbol{\Delta x} = \boldsymbol{x} - \boldsymbol{x_0}$ is the displacement vector, $\boldsymbol{x_0}$ and $\dot{\boldsymbol{x}}_{\boldsymbol{0}}$ are the known position and velocity at time $t_0$ and $\theta \geq 0.5$.

On the basis of the incremental expression (1), the equations of motion of the rigid block assemblage interacting at potential contact points can be posed as follows:

$$\bar{\boldsymbol{M}}\boldsymbol{\Delta x} + \boldsymbol{A_0 c} = \bar{\boldsymbol{f}}_{\boldsymbol{0}} \tag{2}$$

where:
$\boldsymbol{A_0}$ is the equilibrium matrix corresponding to contact forces; (3)

$\bar{\boldsymbol{M}} = \frac{1}{\theta \Delta t^2}\boldsymbol{M}$, being $\boldsymbol{M}$ the mass matrix collecting the mass $m_i$ and the mass moment of inertia $J_i$ of each block; (4)

$$\bar{\boldsymbol{f}}_{\boldsymbol{0}} = \boldsymbol{f_{ext}} + \bar{\boldsymbol{M}}\dot{\boldsymbol{x}}_0 \Delta t, \tag{5}$$

Contact conditions are expressed imposing that the normal component of the relative displacement at contact point $k$ has not to be greater than the initial gap, as follows:

$$\hat{\boldsymbol{n}}_{\boldsymbol{0k}}^{\mathrm{T}}\,\boldsymbol{\Delta u_k} \leq \mathrm{g}_{0k} \tag{6}$$

where $\hat{\boldsymbol{n}}_{\boldsymbol{0k}}$ is the initial normal associated with the surface $j$ and $g_{0k}$ is the initial gap.

For contact interactions, a complementarity condition is included as follows:

$$n_k\left[\hat{\boldsymbol{n}}_{\boldsymbol{0k}}^{\mathrm{T}}\,\boldsymbol{\Delta u_k} - \mathrm{g}_{0k}\right] = 0 \tag{7}$$

Considering that $n_k \geq 0$, this condition ensures that contact forces occur only if the gap is closed otherwise are zero.

Eqs. (6), (7) express in matrix form the so-called Signorini unilateral contact conditions at a contact point $k$ in terms of displacement rates.

The behaviour at contact interfaces undergoing sliding failure is governed by failure conditions which are expressed according to the Coulomb friction law.

In vector notation, the limit conditions for sliding failure can be written as:

$$\pm \boldsymbol{t} \leq \mu \boldsymbol{n} \tag{8}$$

where μ is the friction coefficient.

## 3 FORMULATION OF THE QP PROBLEM AND IMPLEMENTATION

Under the assumption of associative flow rule for displacement increments, the equilibrium equations (2), kinematic conditions (6-7) and sliding friction conditions (8) are equivalent to the following force–based problem [6-9]:

$$\begin{aligned} \max \quad & -\tfrac{1}{2}\boldsymbol{r}^{\mathrm{T}}\,\bar{\boldsymbol{M}}^{-1}\boldsymbol{r} - \boldsymbol{g}_{\boldsymbol{0}}^{\mathrm{T}}\boldsymbol{c} \\ \text{s.t.} \quad & \boldsymbol{r} + \boldsymbol{A}_{\boldsymbol{0}}\boldsymbol{c} = \overline{\boldsymbol{f}}_{\boldsymbol{0}} \\ & \pm \boldsymbol{t} - \mu \boldsymbol{n} \leq \boldsymbol{0}, \;\; \boldsymbol{n} \geq \boldsymbol{0} \end{aligned} \tag{9}$$

where $\boldsymbol{r}$ is the vector of dynamic forces associated with the degrees of freedom of the blocks.

The optimization problem (9) was the problem which was actually implemented and solved in the present formulation, with kinematic variables derived as Lagrange multipliers associated with the various constraints, according to the solution procedure detailed in the following section.

To calculate and update positions of the blocks and contact gaps, a simple incremental procedure was implemented [8, 9].

The procedure was implemented in a computer code, *DynoBlock_2D*, which provides as outputs the time histories of contact forces and kinematic variables as well as the plots of the failure mechanisms at different time steps.

The quadratic programming problem associated to (9) were solved using the primal–dual interior-point solver in MOSEK [11].

The analyses were carried out using a PC containing a 3.3GHz Intel Xeon E3-1245 processor with 8 GB of RAM.

## 4 DYNAMIC ANALYSIS OF A BLOCK MASONRY PANEL UNDER GROUND ACCELERATION TIME HISTORY

An application of the adopted formulation to the case of a block masonry wall tested by Restrepo-Vélez et al. [10] is reported in this section.

The experimental wall panel comprises a front panel and three side walls. The panel was built adopting a scaling factor of 1:5 and using marble blocks with nominal dimensions of 80×40×30 mm which were dry-jointed. The masonry wall panel was tested on a tilting table to investigate the failure mechanism and the collapse load under constant and uniformly distributed horizontal acceleration.

For numerical analysis, a 2D rigid block model of the side wall was generated (Fig. 2). The average value of the unit weight of the blocks was 26.8 kN/m$^3$ and the friction coefficient used in the computations was 0.7, in accordance with values measured experimentally. The mass of the half blocks along the sides of the wall was increased to take into account the effects of the

orthogonal walls on the failure mechanism considering an effective length of 3.5 bricks. A time increment of 0.001 sec. was used and the θ value was set equal to 0.7.

The numerical model was first validated against experimental test on the tilting table of the small scale specimen using a quasi-static analysis [8].

Afterwards, in order to evaluate the computational cost of the adopted formulation in the case of a real scale structure subjected to earthquake ground motion, a full scale numerical model was implemented to perform dynamic time history analysis. The full scale numerical model was generated from the small-scale model, using a scaling factor of 5 so to comply with geometric dimensions of a real structure.

The failure mechanism predicted by the quasi-static analysis is shown in Figure 2b and the corresponding acceleration magnitude is 0.199g (Table 1). A good agreement with experimental outcomes was observed. The crack pattern in the numerical model mainly develops on the left pier and involves the spandrel as well. The stepped diagonal cracks in the spandrel follow the crack pattern observed after experimental investigation.

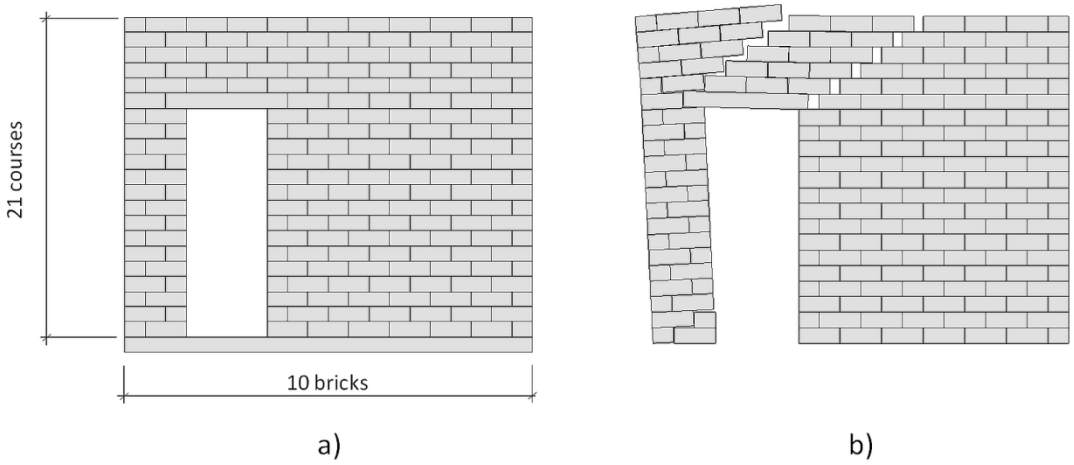


Figure 2: S22 wall panel [Restrepo Vélez et al., 2014]: a) rigid block model used for contact dynamic analysis; b) Failure mode obtained for quasi-static analysis under constant and uniformly distributed horizontal acceleration.

| Case study | Model size ($b \times c$) | Exp. (Restrepo Vélez et al. 2014) | Full scale model | | | |
|---|---|---|---|---|---|---|
| | | | Quasi-static analysis | | Acceleration time history | |
| | | λ | $a_g$ (g) | CPU Time (s) | $a_g$ (g) | CPU Time (s) |
| S22 | 196 × 1072 | 0.197 | 0.199 | 940 | 1.06 | 4210 |

TABLE 1: Block masonry wall S22: ground acceleration at failure and CPU time.

For seismic analysis on the full scale model, the acceleration time series AQA.HNN recorded by the Italian Civil Protection Department seismic network (IT) at L'Aquila, N-S component, occurred on 06.04.2009, was considered [12]. The peak amplitude of the ground acceleration is 0.44g.

A set of dynamic time history analysis was carried out with increasing level of excitation, considering for the record the time interval from 15 to 22 s. For values of the scaling factor greater than 240% AQA, the sliding displacement computed for the lintel was larger than the size of block staggering (half a block), thus involving collapse of the spandrel on the top and overturning of the left pier.

The results of the seismic analysis for AQA earthquake with acceleration amplitudes scaled by the factor of 2.4 (240% AQA) are shown in Figs. 3-4.

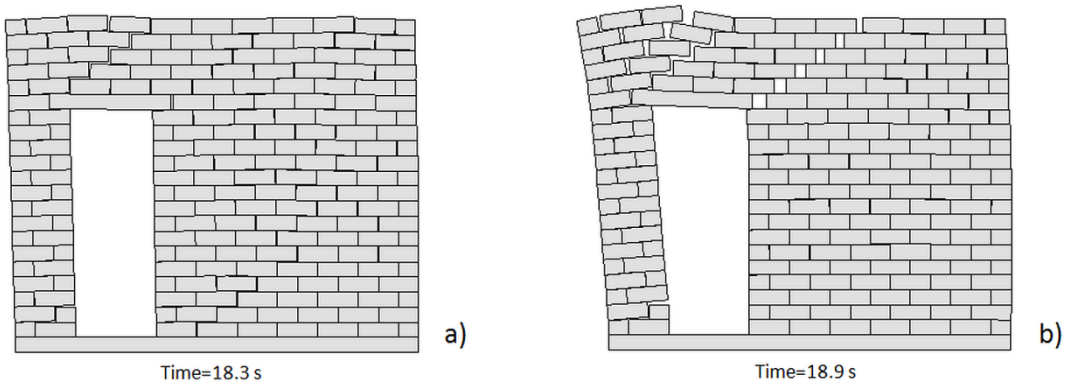


Figure 3: Time history response to the 240% AQA earthquake.

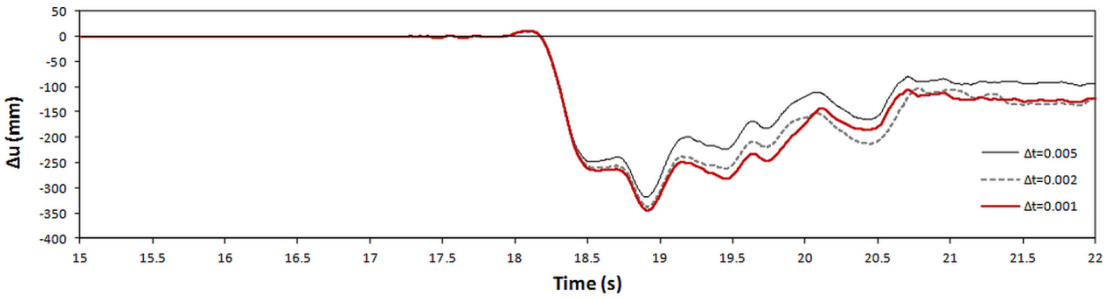


Figure 4: Time history of top relative displacement and sensitivity analysis to time increment.

The results show that in the case of AQA earthquake the seismic resistance of the structure computed from dynamic analysis is up to 5 times the value computed for quasi-static overturning under uniform and constant distribution of acceleration. The difference with quasi-static results should be ascribed to the combined effect of impulsive actions associated to the earthquake motion and to the displacement capacity related to the regular staggering of blocks and their aspect ratio. However, considering that the results of the numerical dynamic analysis are not directly supported by experimental tests and that simple assumptions were adopted for contact point specification, those should be intended as indicative of the differences with quasi-static results.

Sensitivity analyses to time increment were also carried out. Figure 4 shows the time history response computed for the relative horizontal displacement calculated between the top and base blocks. It can be seen that although a remarkable difference of predicted residual displacement is observed using a step of 0.005 s, the peak response is slightly affected by time increment in the considered range.

## 5 CONCLUSIONS

- A variational formulation for dynamic analysis of masonry block structures was presented in this paper. The formulation assumes a no-tension, frictional behavior at contact joints and uses quadratic programming to solve the contact dynamic problem.
- A quasi-static analysis of a dry-jointed masonry block panel from the literature was carried out using the formulation adopted and a good agreement in terms of failure mechanism and collapse load was observed.
- Dynamic time history analysis under ground acceleration motion was carried out to compare numerical results and to evaluate the computational efficiency and the convergence stability of the implemented procedure. Those were found to be encouraging, also considering the small number of mechanical and algorithm parameters associated to the adopted formulation.

## ACKNOWLEDGEMENTS

The financial support of PRIN 2015 Programme by the Ministry of Education, University and Research (MIUR) is gratefully acknowledged for funding the research project "Protecting the Cultural Heritage from water-soil interaction related threats", which is the main framework of the study presented in this article.

## REFERENCES

[1] B. Chetouane, F. Dubois, M. Vinches, C. Bohatier, NSCD discrete element method for modeling masonry structures, *Int. Journal for Numerical Methods in Engineering*, **64**, pp.65-94, 2005.

[2] G. Lancioni, S. Lenci, Q. Piattoni, E. Quagliarini, Dynamics and failure mechanisms of ancient masonry churches subjected to seismic actions by using the NSCD method: The case of the medieval church of S. Maria in Portuno, *Engineering Structures*, **56**, pp. 1527-1546, 2013.

[3] A. Rafiee, M. Vinches, C. Bohatier, Modelling and analysis of the Nîmes arena and the Arles aqueduct subjected to a seismic loading, using the Non-Smooth Contact Dynamics method, *Engineering Structures*, **30** (12), pp. 3457-3467, 2008.

[4] A. Rafiee, M. Vinches, C. Bohatier, Application of the NSCD method to analyse the dynamic behaviour of stone arched structures, *Int J Solids Struct* **45**, pp. 6269–83, 2008.

[5] A.I. Giouvanidis, E.G. Dimitrakopoulos, Nonsmooth dynamic analysis of sticking impacts in rocking structures, *Bulletin of Earthquake Engineering*, pp. 1-32, 2016, Article in press.

[6] K. Krabbenhoft, A.V. Lyamin, J. Huang, M. Vicente da Silva, Granular contact dynamics using mathematical programming methods," *Computers and Geotechnics*, **43**, pp. 165-176, 2012.

[7] J. Huang, M.V. da Silva, K. Krabbenhoft, Three-dimensional granular contact dynamics with rolling resistance," *Computers and Geotechnics*, 49, pp. 289-298, 2013.

[8] F. Portioli, L. Cascini, Contact Dynamics of Masonry Block Structures Using Mathematical Programming Journal of Earthquake Engineering, pp. 1-32, 2016, Article in Press.

[9] F. Portioli, L. Cascini, R. Landolfo, Rocking response of masonry block structures using mathematical programming, *ECCOMAS Congress 2016 - Proceedings of the 7th European Congress on Computational Methods in Applied Sciences and Engineering*, 3, pp. 4959-4968, 2016.

[10] Restrepo Vélez, L.F., Magenes, G., Griffith, M.C., Dry stone masonry walls in bending-Part I: Static tests, *International Journal of Architectural Heritage*, **8** (1), pp. 1-28, 2014.

[11] The MOSEK optimization tools manual (2011). Version 8.0. MOSEK ApS, Denmark 2011. http://www.mosek.com

[12] ESM Working Group [2015] Engineering Strong-Motion database, version 1.0, DOI:10.13127/ESM.

COMPDYN 2017
6th ECCOMAS Thematic Conference on
Computational Methods in Structural Dynamics and Earthquake Engineering
M. Papadrakakis, M. Fragiadakis (eds.)
Rhodes Island, Greece, 15–17 June, 2017

# NONSMOOTH MODELLING OF IMPACTS IN ROCKING STRUCTURES WITH POISSON'S LAW

**Anastasios I. Giouvanidis**[1] **and Elias G. Dimitrakopoulos**[1]

[1]Department of Civil and Environmental Engineering, The Hong Kong University of Science and Technology
Kowloon Bay, Hong Kong
e-mail: agiouvanidis@connect.ust.hk
e-mail: ilias@ust.hk

**Keywords:** rocking, nonsmooth dynamics, linear complementarity problem, impact, flexible rocking structures, Poisson's contact law.

**Abstract.** *Rocking action offers a favorable seismic isolation effect that relieves the structure from deformation and damage during strong earthquakes. A complete description of the dynamics of a rocking structure requires, apart from the equation of motion, an appropriate treatment of the contact phenomenon. During rocking, when rotation reverses, the smooth motion of the structure is interrupted by nonsmooth impacts. To date, most analytical and numerical investigations on the rocking behavior treat impacts adopting the 'classical' model of the angular coefficient of restitution or with ad-hoc assumptions. This paper revisits the contact process encountered in two archetypal rocking structures: the rigid rocking block and the flexible rocking oscillator from a nonsmooth dynamics perspective. It considers impact as an instantaneous event and treats it through a system of inequalities known as the linear complementarity problem (LCP). This study models contact behavior with a set-valued Poisson's law in the normal direction and assumes sticking behavior in the tangential direction. The analysis demonstrates the ability of the proposed methodology to capture the impact behavior of different structures rocking on a rigid base. The results show that the proposed LCPs verify corresponding analytical results of other methodologies. Specifically, regarding the rocking block, comparisons of the nonsmooth model with the 'classical' impact model reveal perfect agreement. This study further unveils the substantial role of the Poisson's coefficient of restitution in capturing the experimental response of the flexible rocking oscillator in cases where other analytical models fail. Most importantly, the nonsmooth dynamics approach captures all physically feasible post-impact states, which can be solved both analytically and numerically. Finally, the proposed approach offers a more concise description of the impact problem in rocking structures and it contributes to a more realistic treatment and better understanding of the contact phenomenon during rocking.*

## 1 INTRODUCTION

Rocking action isolates the structure during strong earthquakes (e.g., [27]) and relieves it from deformation and damage. Therefore, rocking motion attracts the attention of many researchers who examine the dynamic behavior of rocking structures either experimentally ([30] and references therein) or analytically ([37, 16, 17, 36, 12, 13, 22, 20, 21, 24, 43] among others). So far, most analytical studies assume rigid planar rocking behavior. Chopra and Yim [9] and Psycharis [35] first examined the dynamics of flexible (deforming) rocking structures. Those studies compared flexible base-fixed structures with structures allowed to uplift, and showed that in most cases base-fixed structures exhibit larger deformations than rocking structures. Recently, studies such as [32, 1, 2, 40, 41, 39, 3, 42, 23, 4, 6] revisited the stability of flexible rocking structures liberating from the small rotations/deformations assumption and considering overturning of the structure.

In general, a complete description of the rocking dynamics requires, apart from the equation of motion, an appropriate treatment of the impact. To date, most analytical studies on the rocking behavior treat impact adopting the 'classical' impact model introduced by Housner [27]. The 'classical' impact model hinges on the conservation of angular momentum and results in a coefficient of restitution which connects the angular velocities before and after the impact (see e.g., [31, 19, 25] among others). However, considering flexible rocking behavior the contact phenomenon becomes more challenging and flexible rocking structures might exhibit a variety of post-impact states [23]. Therefore, more systematic approaches have been proposed in the context of nonsmooth dynamics ([7, 26, 28, 33] and references therein). Such methods rely on either a rigid multibody approach [8, 23], or assume deformable contact points [5], or utilize compliant elements between the contacting bodies [44].

The present study extends [23] and examines the contact behavior of rocking structures from a nonsmooth dynamics perspective adopting Poisson's law. Specifically, it (i) presents the nonsmooth approach to treat sticking (i.e., non-sliding) impacts and (ii) evaluates its implementation to various rocking structures (i.e., rigid block and flexible oscillator).

## 2 PROPOSED NONSMOOTH APPROACH

### 2.1 Nonsmooth dynamics

The proposed event-based nonsmooth dynamics approach decomposes the rocking behavior into *smooth motion* and *nonsmooth impacts* [7, 26, 14, 15, 18, 38]. The present study focuses on the impact phenomenon in two archetypal rocking structures (Fig. 2): (i) the rigid block, and (ii) the flexible oscillator. Throughout the study, impact occurs between rigid bodies which cannot overlap (impenetrability constraint) and is considered instantaneous. The analysis assumes that all non-impulsive forces are considered negligible and wave effects within the body are neglected. Further, the deformation the bodies undergoes at the contact points is considered negligible in the body's scale [5]. The focus of the present study is on structures designed to exhibit planar rocking behavior. Hence, sticking (i.e., non-sliding) between contacting bodies is allowed.

### 2.2 Linear complementarity problem for impact

A linear complementarity problem (LCP) is a set of linear equations in the form of $\mathbf{y} = \mathbf{A}\mathbf{x} + \mathbf{b}$, with matrices $\mathbf{A}$ and $\mathbf{b}$ known, and (to be determined) unknowns non-negative vectors $\mathbf{x} \geq 0$ and $\mathbf{y} \geq 0$ which satisfy the complementarity condition: $\mathbf{y}^T\mathbf{x} = 0$. The LCP

has a wide range of applications in many scientific fields and several algorithmic schemes can solve it numerically (e.g., Lemke's algorithm [29, 11] among others).

The equation of motion for a multibody system with unilateral contacts can be written as:

$$\mathbf{M}\ddot{\mathbf{q}} - \mathbf{h}(\mathbf{C}, \mathbf{K}, \ddot{u}_g(t)) - \mathbf{W}_N\boldsymbol{\lambda}_N - \mathbf{W}_T\boldsymbol{\lambda}_T = \mathbf{0} \tag{1}$$

where $\mathbf{q}$ is the generalized coordinates vector. $\mathbf{M}$, $\mathbf{C}$ and $\mathbf{K}$ are the mass, the damping and the stiffness matrices respectively, and $\mathbf{h}$ is the vector containing all non-impulsive forces e.g., external excitation $\ddot{u}_g(t)$, dissipating and elastic forces. $\mathbf{W}$ are the direction matrices of the contact forces in the normal (subscript '*N*') and the tangential (subscript '*T*') direction of contact. $\boldsymbol{\lambda}$ are the pertinent contact force vectors which are considered positive when they are compressive/repulsive.

**Poisson's contact law** : Poisson's law divides the impact into two phases, (i) compression and (ii) expansion. The compression phase starts with the initiation of contact at time instant $t^-$ and ends at $t^0$ when the approaching process of the bodies has been completed. The expansion phase follows, starting at $t^0$ and finishing at $t^+$ with the separation of the contacting bodies. Further, Poisson's law defines a coefficient of restitution $\overline{\overline{\varepsilon}}_p$ equal to the ratio of the impulses stored during these two phases: $\boldsymbol{\Lambda}_N^+ = \overline{\overline{\varepsilon}}_p\boldsymbol{\Lambda}_N^0$, where $\overline{\overline{\varepsilon}}_p$ is the diagonal matrix of the Poisson's coefficient of restitution $\varepsilon_P$. To derive the LCPs for the two phases of impact, we integrate the equation of motion (Eq. (1)) once over the time interval of the compression phase (i.e., from $t^-$ to $t^0$) and once over the time interval of the expansion phase (i.e., from $t^0$ to $t^+$) [28].

**LCP of the compression phase of impact** : Integrating over the time interval of the compression phase Eq. (1) becomes:

$$\dot{\mathbf{q}}^{\mathbf{0}} + \dot{\mathbf{q}}^- = \mathbf{M}^{-1}\mathbf{W}_N\boldsymbol{\Lambda}_N^0 + \mathbf{M}^{-1}\mathbf{W}_T\boldsymbol{\Lambda}_T^0 \tag{2}$$

where vector $\dot{\mathbf{q}}$ denotes the generalized velocities. Pre-multiplying Eq. (2) by $\mathbf{W}_N^T$ (and $\mathbf{W}_T^T$) returns the vectors of the relative contact velocities in the normal $\dot{\mathbf{g}}_N = \mathbf{W}_N^T\dot{\mathbf{q}}$ (and in the tangential $\dot{\mathbf{g}}_T = \mathbf{W}_T^T\dot{\mathbf{q}}$) direction accordingly:

$$\begin{aligned} \dot{\mathbf{g}}_N^0 - \dot{\mathbf{g}}_N^- &= \mathbf{G}_{NN}\boldsymbol{\Lambda}_N^0 + \mathbf{G}_{NT}\boldsymbol{\Lambda}_T^0 \\ \dot{\mathbf{g}}_T^0 - \dot{\mathbf{g}}_T^- &= \mathbf{G}_{TN}\boldsymbol{\Lambda}_N^0 + \mathbf{G}_{TT}\boldsymbol{\Lambda}_T^0 \end{aligned} \tag{3}$$

where the $\mathbf{G}$ matrices are:

$$\begin{aligned} \mathbf{G}_{NN} &= \mathbf{W}_N^T\mathbf{M}^{-1}\mathbf{W}_N, \quad \mathbf{G}_{NT} = \mathbf{W}_N^T\mathbf{M}^{-1}\mathbf{W}_T \\ \mathbf{G}_{TN} &= \mathbf{W}_T^T\mathbf{M}^{-1}\mathbf{W}_N, \quad \mathbf{G}_{TT} = \mathbf{W}_T^T\mathbf{M}^{-1}\mathbf{W}_T \end{aligned} \tag{4}$$

$\boldsymbol{\Lambda}_N^0$, $\boldsymbol{\Lambda}_T^0$ are the impulses in the normal and tangential direction respectively transferred to the body during the compression phase of impact. This study assumes that sliding is prevented. Therefore, the tangential relative (contact) velocity is zero $\dot{\mathbf{g}}_T^0 = \dot{\mathbf{g}}_T^- = \mathbf{0}$ and Eq. (3) gives:

$$\boldsymbol{\Lambda}_T^0 = -\mathbf{G}_{TT}^{-1}\mathbf{G}_{TN}\boldsymbol{\Lambda}_N^0 \tag{5}$$

With the aid of Eq. (5), Eq. (3) yields the LCP for the compression phase of impact

$$\dot{\mathbf{g}}_N^0 = \left(\mathbf{G}_{NN} - \mathbf{G}_{NT}\mathbf{G}_{TT}^{-1}\mathbf{G}_{TN}\right)\boldsymbol{\Lambda}_N^0 + \dot{\mathbf{g}}_N^- \tag{6}$$

with complementarity conditions

$$\dot{\mathbf{g}}_N^0 \geq \mathbf{0}, \;\; \boldsymbol{\Lambda}_N^0 \geq \mathbf{0}, \;\; {\dot{\mathbf{g}}_N^0}^T\boldsymbol{\Lambda}_N^0 = 0 \tag{7}$$

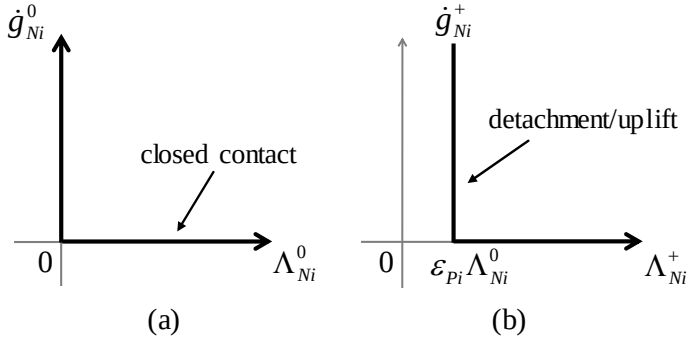


Figure 1: The (unilateral) inequality character of contact. Contact law for (a) the compression and (b) the expansion phase of impact [34].

**LCP of the expansion phase of impact** : Similarly, integrating Eq. (1) over the time interval of the expansion phase:

$$\dot{\mathbf{q}}^+ + \dot{\mathbf{q}}^0 = \mathbf{M}^{-1}\mathbf{W}_N\boldsymbol{\Lambda}_{NP} + \mathbf{M}^{-1}\mathbf{W}_N\bar{\bar{\varepsilon}}_p\boldsymbol{\Lambda}^0_N + \mathbf{M}^{-1}\mathbf{W}_T\boldsymbol{\Lambda}^+_T \tag{8}$$

and pre-multiplying by $\mathbf{W}^T_N$ and $\mathbf{W}^T_T$:

$$\begin{aligned}\dot{\mathbf{g}}^+_N - \dot{\mathbf{g}}^0_N &= \mathbf{G}_{NN}\boldsymbol{\Lambda}_{NP} + \mathbf{G}_{NN}\bar{\bar{\varepsilon}}_p\boldsymbol{\Lambda}^0_N + \mathbf{G}_{NT}\boldsymbol{\Lambda}^+_T \\ \dot{\mathbf{g}}^+_T - \dot{\mathbf{g}}^0_T &= \mathbf{G}_{TN}\boldsymbol{\Lambda}_{NP} + \mathbf{G}_{TN}\bar{\bar{\varepsilon}}_p\boldsymbol{\Lambda}^0_N + \mathbf{G}_{TT}\boldsymbol{\Lambda}^+_T\end{aligned} \tag{9}$$

Impulse $\boldsymbol{\Lambda}_{NP} = \boldsymbol{\Lambda}^+_N - \bar{\bar{\varepsilon}}_p\boldsymbol{\Lambda}^0_N$ is a modification of the original Poisson's impulse ($\boldsymbol{\Lambda}^+_N$) which ensures the satisfaction of the impenetrability constraint for multi-point impact problems [28]. Again, assuming zero tangential relative velocity, Eq. (9) gives:

$$\boldsymbol{\Lambda}^+_T = -\mathbf{G}^{-1}_{TT}\mathbf{G}_{TN}\boldsymbol{\Lambda}_{NP} - \mathbf{G}^{-1}_{TT}\mathbf{G}_{TN}\bar{\bar{\varepsilon}}_p\boldsymbol{\Lambda}^0_N \tag{10}$$

and Eq. (9) with the aid of Eq. (10) yields the LCP for the expansion phase of impact

$$\dot{\mathbf{g}}^+_N = \left(\mathbf{G}_{NN} - \mathbf{G}_{NT}\mathbf{G}^{-1}_{TT}\mathbf{G}_{TN}\right)\boldsymbol{\Lambda}_{NP} + \left(\mathbf{G}_{NN} - \mathbf{G}_{NT}\mathbf{G}^{-1}_{TT}\mathbf{G}_{TN}\right)\bar{\bar{\varepsilon}}_p\boldsymbol{\Lambda}^0_N + \dot{\mathbf{g}}^0_N \tag{11}$$

with complementarity conditions

$$\dot{\mathbf{g}}^+_N \geq \mathbf{0},\ \ \boldsymbol{\Lambda}_{NP} \geq \mathbf{0},\ \ \dot{\mathbf{g}}^{+T}_N\boldsymbol{\Lambda}_{NP} = 0 \tag{12}$$

## 3 RIGID ROCKING BLOCK USING THE PROPOSED NONSMOOTH APPROACH

The present section revisits the impact behavior of the rigid rocking block of Fig. 2(a) adopting the proposed nonsmooth dynamics approach. Firstly, this study offers closed-form expressions for all the feasible post-impact states solving analytically the proposed LCPs (Eqs (6), (11)). Consider the rigid block of Fig. 2(a) with base-width $2b$ and height $2H$. The generalized coordinates vector for the planar rocking motion of the block is: $\mathbf{q} = \left[\begin{array}{ccc} x & y & \phi \end{array}\right]^T$, where $x$ and $y$ are the translations along the pertinent axes, and $\phi$ is the planar rocking rotation. Following [14, 15, 18], the two closed contact points (i.e., pivot points '1' and '2') produce two forces/impulses in the normal direction of contact (one force per contact point), but only one force in the tangential direction of contact; the resultant of the two tangential forces at the two pivot points as in Fig. 3. Thus, the mass matrix and the direction matrices in the normal and tangential direction of contact become respectively [23]:

$$\mathbf{M} = \left[\begin{array}{ccc} m & 0 & 0 \\ 0 & m & 0 \\ 0 & 0 & I_G \end{array}\right],\ \mathbf{W}_N = \left[\begin{array}{cc} 0 & 0 \\ 1 & 1 \\ -b & b \end{array}\right],\ \mathbf{W}_T = \left[\begin{array}{c} 1 \\ 0 \\ H \end{array}\right] \tag{13}$$

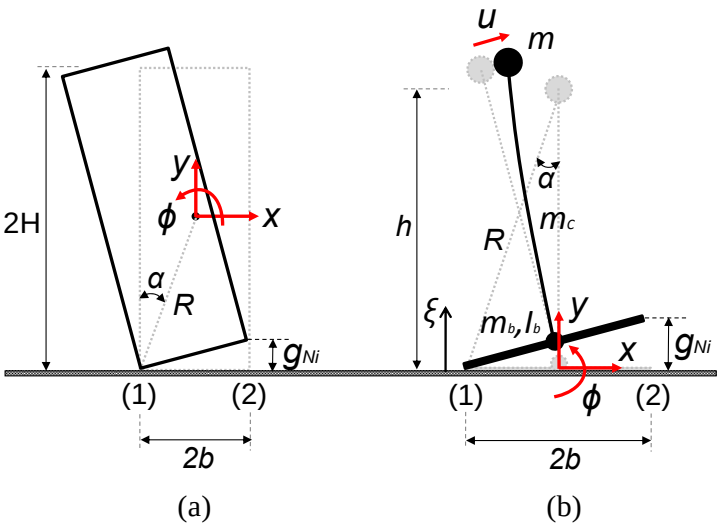


Figure 2: The examined rocking structures: (a) rigid block, (b) flexible oscillator.

where $I_G$ is the mass moment of inertia with respect to the center of mass of the block. For a rectangular block $I_G = (1/3)\, mR^2$, where $m$ is the total mass of the block and $R$ is the half-diagonal distance (Fig. 2(a)).

### 3.1 Analysis of all physically feasible post-impact states

With reference to Fig. 3, consider a rigid block performing pure rotation (i.e., non-sliding) about pivot point '1' ($g_{N1}^- = \dot{g}_{N1}^- = 0$). Impact takes place at pivot point '2' at the moment $g_{N2}^- = 0$ and with pre-impact contact velocity $\dot{g}_{N2}^- = 2b\dot{\phi}^- < 0$. Note that, negative velocity $\dot{g}_{Ni}$ indicates approach. Fig. 3 illustrates all the physically feasible states during the compression and the expansion phase of impact according to Poisson's law.

#### 3.1.1 Poisson's law - Compression phase

Fig. 3($C$) illustrates the potential impact states during the compression phase. The grey color in Fig. 3 indicates the unfeasible impact states.

**Bouncing ($A \rightarrow C_1$) (Fig. 3)** : The analysis shows that bouncing is not a feasible state during the compression phase of impact according to Poisson's law, since it results to violation of the impenetrability constraint.

**Full contact ($A \rightarrow C_2$) (Fig. 3)** : Assume that both contact points of the block remain in full contact with the ground during the compression phase of impact. Hence, the normal relative velocities at both contact points are $\dot{g}_{N1}^0 = \dot{g}_{N2}^0 = 0$, and hence known. Therefore, the remaining two unknowns, the two impulses $\Lambda_{N1}^0$, $\Lambda_{N2}^0$, are both positive because of the complementarity behavior of Eq. (7). The solution of the LCP of Eq. (6) yields:

$$\frac{\Lambda_{N1}^0}{m\dot{g}_{N2}^-} = \frac{1}{3\sin^2\alpha} - \frac{1}{2}, \quad \frac{\Lambda_{N2}^0}{m\dot{g}_{N2}^-} = -\frac{1}{3\sin^2\alpha} \tag{14}$$

with the help of which, Eq. (5) provides the (dimensionless) tangential impulse:

$$\frac{\Lambda_T^0}{m\dot{g}_{N2}^-} = \frac{\cot\alpha}{2} \tag{15}$$

The inequality character of contact determines the (existential) conditions under which each state occurs. Specifically, the $\Lambda_{N1}^0 > 0$ condition of Eq. (7) and Eq. (14) show that the block remains in full contact with the ground when:

$$\frac{H}{b} < \frac{1}{\sqrt{2}} \tag{16}$$

in agreement with [27, 8] using different impact models.

**Rocking ($A \rightarrow C_3$) (Fig. 3)** : Assume that the block changes pivot point and rocks during the compression phase of impact as Fig. 3($C_3$) shows. Hence, contact at point '1' is lost $\dot{g}_{N1}^0 > 0$, while the new contact at point '2' is maintained $\dot{g}_{N2}^0 = 0$. The complementarity conditions (Eq. (7)) return $\Lambda_{N1}^0 = 0$ and $\Lambda_{N2}^0 > 0$. The solution of the LCP of Eq. (6) yields the remaining two unknowns, the normal contact velocity $\dot{g}_{N1}^0$ of point '1' and the normal impulse $\Lambda_{N2}^0$ at point '2':

$$\frac{\dot{g}_{N1}^0}{\dot{g}_{N2}^-} = \frac{3\sin^2\alpha}{2} - 1, \quad \frac{\Lambda_{N2}^0}{m\dot{g}_{N2}^-} = \frac{3\sin^2\alpha}{4} - 1 \tag{17}$$

and from Eq. (5), the tangential impulse becomes:

$$\frac{\Lambda_T^0}{m\dot{g}_{N2}^-} = \frac{3}{4}\sin\alpha\cos\alpha \tag{18}$$

Similarly, the inequality character of contact dictates the (existential) conditions of each state. Specifically, the complementary behavior (Eq. 7) requires $\dot{g}_{N1}^0 > 0$. Hence Eq. (17) implies [27, 8]:

$$\frac{H}{b} > \frac{1}{\sqrt{2}} \tag{19}$$

### 3.1.2 Poisson's law - Expansion phase

Fig. 3($E$) illustrates the physically feasible states during the expansion phase of impact. Note that, the expansion phase is a continuation of the compression phase, hence only the valid compression phase states (i.e., full contact $C_2$ and rocking $C_3$) are considered. Again, the grey color in Fig. 3 indicates the unfeasible states.

**Rocking ($A \rightarrow C_2 \rightarrow E_2$) (Fig. 3)** : The analysis shows that rocking during the expansion phase after full contact in the compression phase is not a feasible state, since the results contradict the impenetrability constraint.

**Bouncing ($A \rightarrow C_2 \rightarrow E_1$) (Fig. 3)** : After the full contact state during the compression phase of impact, point '1' remains in contact with the ground ($\dot{g}_{N1}^+ = 0$), while contact at point

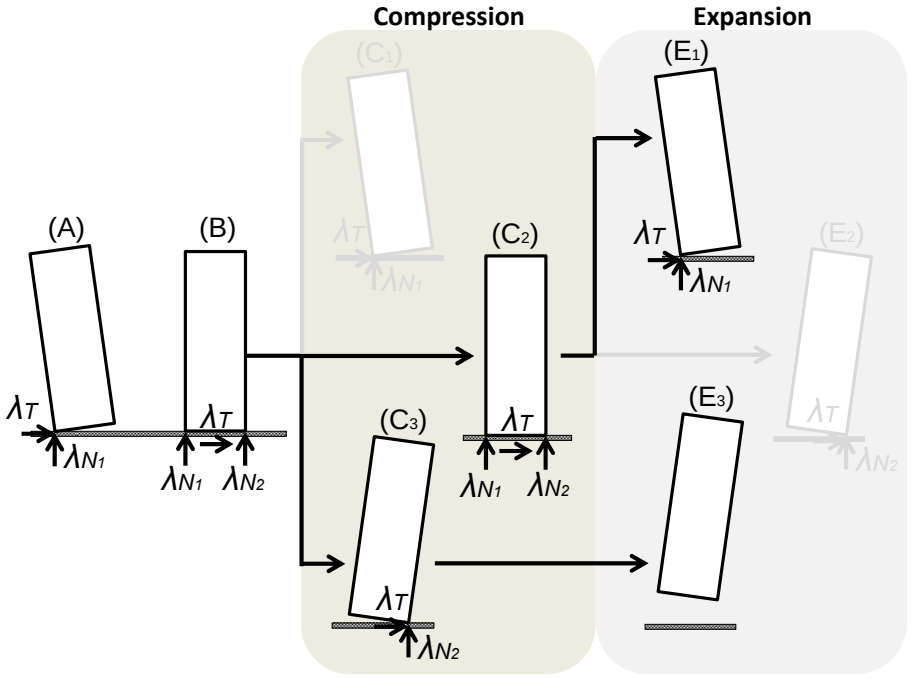


Figure 3: Impact states during the compression ($C$) and the expansion phase ($E$) of the rocking block according to Poisson's law.

'2' is lost ($\dot{g}_{N2}^{+} > 0$). Hence, the complementarity conditions of Eq. (12) imply $\Lambda_{NP1} > 0$ and $\Lambda_{NP2} = 0 \Leftrightarrow \Lambda_{N2}^{+} = \varepsilon_p \Lambda_{N2}^{0}$, where $\Lambda_{N2}^{0}$ is given by Eq. (14). The solution of Eq. (11) gives:

$$\frac{\dot{g}_{N2}^{+}}{\dot{g}_{N2}^{-}} = -\varepsilon_p, \quad \frac{\Lambda_{N1}^{+}}{m\dot{g}_{N2}^{-}} = \varepsilon_p \left( \frac{1}{3\sin^2\alpha} - \frac{1}{2} \right) \tag{20}$$

Therefore, the tangential impulse becomes (Eq. (10)):

$$\frac{\Lambda_{T}^{+}}{m\dot{g}_{N2}^{-}} = \varepsilon_P \frac{\cot\alpha}{2} \tag{21}$$

The (unilateral) inequality character of contact returns the existential conditions for this state to occur. In particular, the complementarity behavior of Eq. (12) and Eq. (20) imply that bouncing becomes feasible when $H/b < 1/\sqrt{2}$; in accordance with Eq. 16.

**Flight ($A \rightarrow C_3 \rightarrow E_3$) (Fig. 3)** : Point '1' has already lost contact with the ground during the compression phase of impact ($\dot{g}_{N1}^{+} > 0$). Assume that contact at point '2' is also lost at the expansion phase of impact ($\dot{g}_{N2}^{+} > 0$). The complementarity behavior of Eq. (12) yields: $\Lambda_{NP1} = 0 \Leftrightarrow \Lambda_{N1}^{+} = \varepsilon_p \Lambda_{N1}^{0} = 0$ (where $\Lambda_{N1}^{0} = 0$ during the compression phase of impact) and $\Lambda_{NP2} = 0 \Leftrightarrow \Lambda_{N2}^{+} = \varepsilon_p \Lambda_{N2}^{0}$, where Eq. (17) gives $\Lambda_{N2}^{0}$. The solution of the LCP of Eq. (11) returns the two unknown relative contact velocities $\dot{g}_{N1}^{+}, \dot{g}_{N2}^{+}$.

$$\frac{\dot{g}_{N2}^{+}}{\dot{g}_{N2}^{-}} = -\varepsilon_p, \quad \frac{\dot{g}_{N1}^{+}}{\dot{g}_{N2}^{-}} = (1+\varepsilon_p) \left( \frac{3\sin^2\alpha}{2} - 1 \right) \tag{22}$$

Eq.(10) yields:

$$\frac{\Lambda_{T}^{+}}{m\dot{g}_{N2}^{-}} = \frac{3}{4}\varepsilon_p \sin\alpha\cos\alpha \tag{23}$$

Similarly, the complementarity behavior of Eq. (12) provides the existential conditions of this state. Specifically, 'flight' becomes a feasible state during the expansion phase of impact only after the rocking state during the compression phase and when $H/b > 1/\sqrt{2}$; in total agreement with Eq. (19).

### 3.2 Comparison with different impact models/approaches

Eqs (14) to (23) describe completely all possible impact states for the rigid rocking block according to Poisson's contact law. Eqs (14) to (23) prove that the proposed methodology verifies corresponding results from other methodologies, while, at the same time, it encapsulates all physically feasible post-impact states. Specifically, the geometric slenderness criterion derived by [27, 8] is in agreement with Eqs (16), (19). For non-sliding (sticking) impacts, a rocking block is considered 'stocky' when Eq. (16) is satisfied, whereas when Eq. (19) holds the block is regarded as 'slender'.

In many studies, (see e.g., [16, 13, 19, 25] among others), the ratio $\eta = \dot{\phi}^+/\dot{\phi}^-$ defines a coefficient of restitution with respect to the angular velocities before and after the impact. When a (slender) block rocks and 'flights' from the ground during the compression and the expansion phase of impact respectively (Fig. 3($C_3$/$E_3$)), Eqs (2), (8) with the aid of Eqs (17), (18), (22) and (23) yield the relationship between pre- and post-impact angular velocities:

$$\eta = \frac{\dot{\phi}^+}{\dot{\phi}^-} = 1 - \frac{3}{2}\sin^2\alpha - \frac{3}{2}\varepsilon_P \sin^2\alpha \tag{24}$$

Assuming impact is perfectly inelastic (plastic) ($\varepsilon_P = 0$), the impact process terminates at the end of the compression phase and the block exhibits pure rocking behavior (Fig. 3($C_3$)). In that case, Eq. (24) agrees with the Housner's angular coefficient of restitution [27].

Eqs (14), (15), 20) and (21) treat the full contact and the bouncing behavior of the block (Fig. 3($C_2$/$E_1$)), with the help of which Eqs (2), (8) give:

$$\eta = \frac{\dot{\phi}^+}{\dot{\phi}^-} = -\varepsilon_p \tag{25}$$

Eq. (25) shows that for $\varepsilon_P = 0$ the block remains in full contact with the ground ($\dot{\phi}^+/\dot{\phi}^- = 0$) and the impact terminates at the end of the compression phase (Fig. 3($C_2$)). For perfectly elastic impacts though ($\varepsilon_P = 1$), impulse is transferred to the structure from the compression phase and the block bounces during the expansion phase without any loss of kinetic energy (Fig. 3($E_1$)).

### 3.3 Numerical evaluation of the proposed approach for the rocking block

This section illustrates the versatility of the proposed approach by numerically investigating the response of the rigid rocking block of Fig. 2(a). Following [23], consider (i) a stocky block with $2b$ = 1 m base-width and $H/b = 0.7$ and (ii) a slender block with the same base but $H/b = 7$ (Fig. 2(a)). Fig. 4 illustrates the free rocking response of both structures. Both blocks have the same initial rotation $\phi_0/\alpha = 1/3$, where $\alpha$ is the slenderness of the block. Fig. 4(left) plots the response of the stocky block for three different values of the Poisson's coefficient of restitution and unveils their influence on the response. In particular, the values of the Poisson's coefficient $\varepsilon_P$ in Fig. 4(left) simulate different impact conditions. When the impact is considered perfectly inelastic ($\varepsilon_P = 0$), a stocky block stays in full contact with the ground and the impact terminates at the end of the compression phase. However, for perfectly

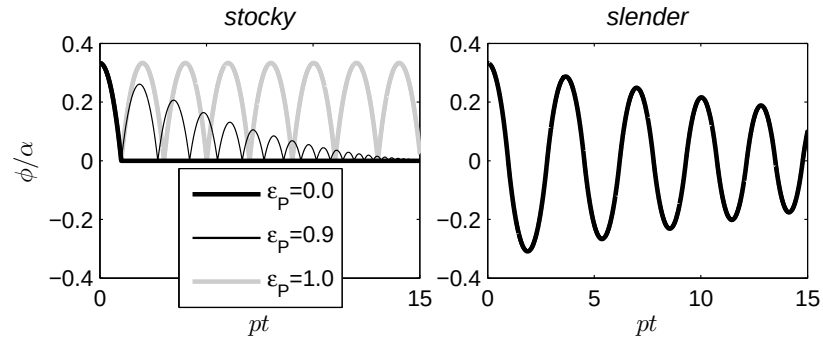


Figure 4: Free rocking response of a stocky ($H/b = 0.7$) and a slender block ($H/b = 7$) starting from the same initial rotation $\phi_0/\alpha = 1/3$ using the proposed nonsmooth approach.

elastic impacts ($\varepsilon_P = 1$) a stocky block bounces without any loss of kinetic energy at every impact; in accordance with the findings of Section 3.2. On the contrary, a slender block, starting from the same initial conditions, changes pivot point and exhibits pure rocking motion for $\varepsilon_P = 0$ (Fig. 4(right)). Note that, all feasible states i.e., full contact, bouncing and pure rocking are captured and solved analytically with the aid of the proposed LCPs of Eqs (6), (11) (Section 3.1).

Fig. 5 assumes that the rocking block starts from rest position under the presence of a ground excitation. Fig. 5 compares the response of the slender rocking block using the proposed nonsmooth approach ($\varepsilon_P = 0$) with the pertinent response using the 'classical' Housner's impact model [27]. The two (identical) blocks exhibit pure rocking motion when subjected to the same sinusoidal pulse with $\alpha_g/g = 0.45$ and $\omega_g/p = 5.75$, where $p = \sqrt{3g/4R}$ is the frequency parameter of the block. $g$ is the gravitational acceleration and $R$ is the half-diagonal length (Fig. 2(a)). Fig. 5 shows that the response of the proposed methodology is in total agreement with the pertinent response of the 'classical' impact model. However, note that, the nonsmooth approach encapsulates all physically feasible post-impact states (i.e., bouncing, flight); something that is not feasible with the 'classical' model.

## 4 FLEXIBLE ROCKING OSCILLATOR USING THE PROPOSED NONSMOOTH APPROACH

This section investigates the impact phenomenon during the rocking motion of the flexible oscillator of Fig. 2(b) when adopting the proposed nonsmooth dynamics approach. Consider the flexible rocking oscillator of Fig. 2(b) with a lumped mass $m$ at height $h$, a deformable column with total mass $m_c$ uniformly distributed along its length and a rigid base with mass $m_b$ and width $2b$. Note that, the height of the base is considered negligible compared to its width. The slenderness $\alpha$ of the structure is defined as $\alpha = \operatorname{atan}(b/h)$ (Fig. 2(b)). Assume the concentrated lumped mass $m$ has zero moment of inertia, while the base mass $m_b$ gives moment of inertia $I_b = (1/3)\, m_b b^2$ with respect to its center of mass. The generalized coordinates vector for the planar rocking motion of the flexible rocking oscillator is: $\mathbf{q} = \begin{bmatrix} u & x & y & \phi \end{bmatrix}^T$, where $x$ and $y$ are the translations of the base mass along the pertinent axes, $u$ is the horizontal flexural translation of the lumped mass and $\phi$ is the planar rocking rotation (Fig. 2(b)). With reference to Fig. 2(b), assume the polynomial shape function of

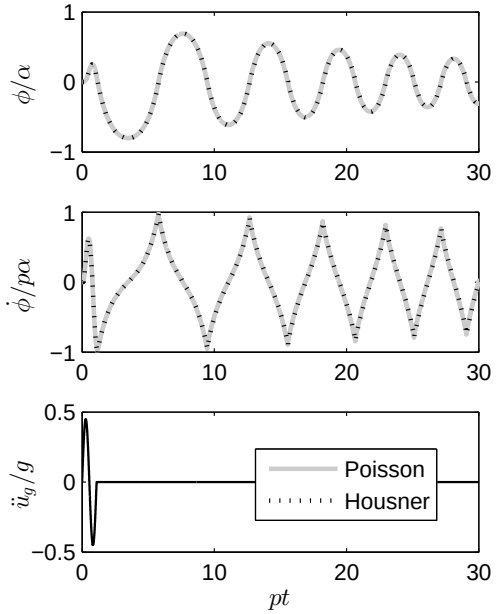


Figure 5: Comparison between the proposed nonsmooth dynamics approach (Poisson's contact law with $\varepsilon_P = 0$) and the 'classical' Housner's impact model [27] for a (slender) rocking block subjected to a sinusoidal pulse with $\alpha_g/g = 0.45$ and $\omega_g/p = 5.75$.

Eq. (26) to describe the deformation of the column [10].

$$\psi(\xi) = \alpha_3 \frac{\xi^3}{h^3} + \alpha_2 \frac{\xi^2}{h^2} + \alpha_1 \frac{\xi}{h} + \alpha_0 \tag{26}$$

where $\xi$ is the distance measured from the base of the column (Fig. 2(b)) and $\alpha_0$, $\alpha_1$, $\alpha_2$, $\alpha_3$ are constant coefficients. Therefore, the deformation of the column at any arbitrary point is defined as: $u_\xi(\xi, t) = u(t)\,\psi(\xi)$, where $u(t)$ is the generalized coordinate which stands for the flexural translation of the lumped mass.

Before rocking initiates, the oscillator behaves as a single degree of freedom system with generalized mass and stiffness respectively [23]:

$$\begin{aligned} \tilde{m} &= m + \int_0^h \frac{m_c}{h}(\psi(\xi))^2 d\xi = m + \left( \begin{array}{l} \frac{\alpha_3^2}{7} + \frac{\alpha_3\alpha_2}{3} + \frac{2\alpha_3\alpha_1}{5} + \frac{\alpha_3\alpha_0}{2} + \frac{\alpha_2^2}{5} \\ + \frac{\alpha_2\alpha_1}{2} + \frac{2\alpha_2\alpha_0}{3} + \frac{\alpha_1^2}{3} + \alpha_1\alpha_0 + \alpha_0^2 \end{array} \right) m_c \\ \tilde{k} &= \int_0^h EI(\psi''(\xi))^2 d\xi = \tfrac{4EI}{h^3}\left(3\alpha_3^2 + \alpha_2^2 + 3\alpha_3\alpha_2\right) \end{aligned} \tag{27}$$

Following [23], rocking initiates when:

$$\left( \begin{array}{l} \frac{h}{b}\frac{\left(1+\frac{11}{40}\gamma_{m_c}\right)}{\left(1+\frac{33}{140}\gamma_{m_c}\right)} \left( \frac{2\zeta\sqrt{\tilde{m}\tilde{k}}}{mg}\dot{u} + \frac{\tilde{k}}{mg}u + \left(1+\frac{3}{8}\gamma_{m_c}\right)\frac{\ddot{u}_g(t)}{g} \right) \\ -\left(1+\gamma_{m_b}+\gamma_{m_c}\right) - \frac{h}{b}\left(1+\frac{1}{2}\gamma_{m_c}\right)\frac{\ddot{u}_g(t)}{g} + \left(1+\frac{3}{8}\gamma_{m_c}\right)\frac{u}{b} \end{array} \right) \geq 0 \tag{28}$$

where $\gamma_{m_c} = m_c/m$ and $\gamma_{m_b} = m_b/m$. $\zeta$ is the damping ratio responsible for the energy dissipation while the structure vibrates. Assuming $\zeta = 0$, $\omega_n = \sqrt{\tilde{k}/\tilde{m}}$ and quasi-static

conditions, Eq. (28) yields the 'critical' (horizontal) flexural translation ($u_{cr}$) of the lumped mass $m$ necessary to initiate rocking [23].

$$u_{cr} = \frac{\left(1+\gamma_{m_b}+\gamma_{m_c}\right) bg}{\left(1+\frac{11}{40}\gamma_{m_c}\right) h\omega_n^2 + \left(1+\frac{3}{8}\gamma_{m_c}\right) g} \tag{29}$$

After the initiation of rocking, the equations which describe the motion of the flexible rocking oscillator can be derived using the general form of the Lagrange's equation:

$$\frac{d}{dt}\left(\frac{\partial L}{\partial \dot{\phi}}\right) - \frac{\partial L}{\partial \phi} = Q \tag{30}$$

$L = T - V$, where $T$ is the kinetic energy, $V$ is the potential energy and $Q$ is the generalized force. Hence, the equations of motion of the flexible rocking oscillator become [23]:

$$\begin{cases}
\tilde{m}\ddot{u} + \left(m + \left(\frac{\alpha_3}{4}+\frac{\alpha_2}{3}+\frac{\alpha_1}{2}+\alpha_0\right) m_c\right)\cos\phi\ddot{x} + \left(m + \left(\frac{\alpha_3}{4}+\frac{\alpha_2}{3}+\frac{\alpha_1}{2}+\alpha_0\right) m_c\right)\sin\phi\ddot{y} \\
- \left(m + \left(\frac{\alpha_3}{5}+\frac{\alpha_2}{4}+\frac{\alpha_1}{3}+\frac{\alpha_0}{2}\right) m_c\right) h\ddot{\phi} = \\
-2\zeta\sqrt{\tilde{m}\tilde{k}}\dot{u} - \tilde{k}u + \tilde{m}u\dot{\phi}^2 - \left(m + \left(\frac{\alpha_3}{4}+\frac{\alpha_2}{3}+\frac{\alpha_1}{2}+\alpha_0\right) m_c\right)\cos\phi\ddot{u}_g \\
- \left(m + \left(\frac{\alpha_3}{4}+\frac{\alpha_2}{3}+\frac{\alpha_1}{2}+\alpha_0\right) m_c\right)\sin\phi g \\
\\
\left(m + \left(\frac{\alpha_3}{4}+\frac{\alpha_2}{3}+\frac{\alpha_1}{2}+\alpha_0\right) m_c\right)\cos\phi\ddot{u} + \left(m + m_b + m_c\right)\ddot{x} \\
- \left(mh\cos\phi + mu\sin\phi + \frac{1}{2}m_c h\cos\phi + \left(\frac{\alpha_3}{4}+\frac{\alpha_2}{3}+\frac{\alpha_1}{2}+\alpha_0\right) m_c u\sin\phi\right)\ddot{\phi} = \\
- \left(mh\sin\phi - mu\cos\phi + \frac{1}{2}m_c h\sin\phi - \left(\frac{\alpha_3}{4}+\frac{\alpha_2}{3}+\frac{\alpha_1}{2}+\alpha_0\right) m_c u\cos\phi\right)\dot{\phi}^2 \\
+2\left(m + \left(\frac{\alpha_3}{4}+\frac{\alpha_2}{3}+\frac{\alpha_1}{2}+\alpha_0\right) m_c\right)\sin\phi\dot{u}\dot{\phi} - \left(m + m_b + m_c\right)\ddot{u}_g \\
\\
\left(m + \left(\frac{\alpha_3}{4}+\frac{\alpha_2}{3}+\frac{\alpha_1}{2}+\alpha_0\right) m_c\right)\sin\phi\ddot{u} + \left(m + m_b + m_c\right)\ddot{y} \\
+ \left(-mh\sin\phi + mu\cos\phi - \frac{1}{2}m_c h\sin\phi + \left(\frac{\alpha_3}{4}+\frac{\alpha_2}{3}+\frac{\alpha_1}{2}+\alpha_0\right) m_c u\cos\phi\right)\ddot{\phi} = \\
\left(mh\cos\phi + mu\sin\phi + \frac{1}{2}m_c h\cos\phi + \left(\frac{\alpha_3}{4}+\frac{\alpha_2}{3}+\frac{\alpha_1}{2}+\alpha_0\right) m_c u\sin\phi\right)\dot{\phi}^2 \\
-2\left(m + \left(\frac{\alpha_3}{4}+\frac{\alpha_2}{3}+\frac{\alpha_1}{2}+\alpha_0\right) m_c\right)\cos\phi\dot{u}\dot{\phi} - \left(m + m_b + m_c\right) g \\
\\
- \left(m + \left(\frac{\alpha_3}{5}+\frac{\alpha_2}{4}+\frac{\alpha_1}{3}+\frac{\alpha_0}{2}\right) m_c\right) h\ddot{u} - \left(\begin{array}{l} mh\cos\phi + mu\sin\phi + \frac{1}{2}m_c h\cos\phi \\ + \left(\frac{\alpha_3}{4}+\frac{\alpha_2}{3}+\frac{\alpha_1}{2}+\alpha_0\right) m_c u\sin\phi \end{array}\right)\ddot{x} \\
+ \left(-mh\sin\phi + mu\cos\phi - \frac{1}{2}m_c h\sin\phi + \left(\frac{\alpha_3}{4}+\frac{\alpha_2}{3}+\frac{\alpha_1}{2}+\alpha_0\right) m_c u\cos\phi\right)\ddot{y} \\
+ \left(I_{m_b} + mh^2 + \frac{1}{3}m_c h^2 + \tilde{m}u^2\right)\ddot{\phi} = \\
-2\tilde{m}u\dot{u}\dot{\phi} + \left(mh\cos\phi + mu\sin\phi + \frac{1}{2}m_c h\cos\phi + \left(\frac{\alpha_3}{4}+\frac{\alpha_2}{3}+\frac{\alpha_1}{2}+\alpha_0\right) m_c u\sin\phi\right)\ddot{u}_g \\
- \left(-mh\sin\phi + mu\cos\phi - \frac{1}{2}m_c h\sin\phi + \left(\frac{\alpha_3}{4}+\frac{\alpha_2}{3}+\frac{\alpha_1}{2}+\alpha_0\right) m_c u\cos\phi\right) g
\end{cases} \tag{31}$$

For simplicity, the remaining part of the present section adopts $\alpha_0 = \alpha_1 = 0$, $\alpha_2 = 3/2$ and $\alpha_3 = -1/2$ [10]. Further, all the properties of the oscillator and the adopted ground excitations are summarized in [23].

### 4.1 Numerical evaluation of the proposed approach for the rocking oscillator

This section focuses on the response-history evaluation of the flexible rocking oscillator of Fig. 2(b). Specifically, Fig. 6 compares the response of the oscillator using the proposed nonsmooth approach with the pertinent analytical response (abbreviated as 'VVEL') from [41] and the experimental response from [39] when subjected to the same Ricker pulses. Fig. 6 shows that the proposed nonsmooth model captures very well the experimental response. Further, Fig. 6 unveils the effect of the column elasticity on the response; the stiffer the column, the

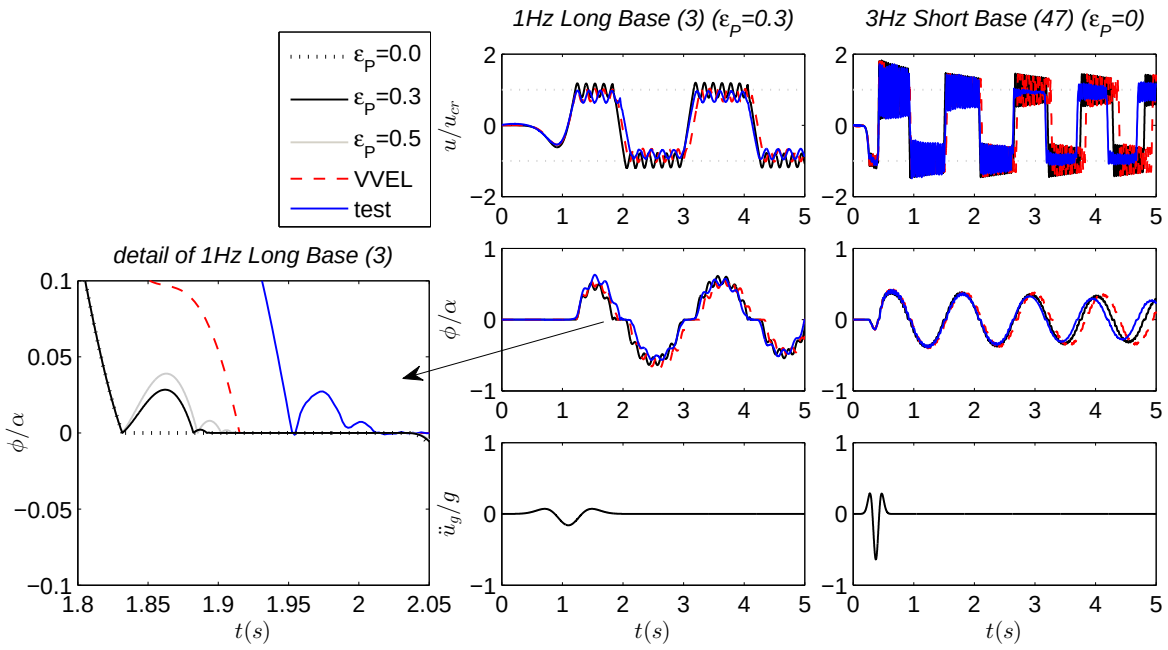


Figure 6: Response-history comparison of the nonsmooth approach with analytical ('VVEL') [41] and experimental results ('test') [39] of the rocking oscillator of Fig. 2(b) when subjected to different Ricker pulses reported in [23] with $\alpha_g/g = 0.16$, $\omega_g/p = 1.95$ (middle) and $\alpha_g/g = 0.64$, $\omega_g/p = 7.73$ (right) accordingly. The nonsmooth response is plotted with an opposite sense to match the assumed positive clockwise rotation in [39, 41].

smoother the rocking motion. A distinct advantage of the proposed nonsmooth model is that it encapsulates all physically feasible post-impact states, with the same mathematical formulation (i.e., the LCPs of Eqs (6), (11)). Fig. 6 reveals that for $\varepsilon_P > 0$ the proposed model predicts bouncing behavior; in agreement with the experimentally observed response. The insert of Fig. 6 illustrates the influence of the Poisson's coefficient of restitution on the response. Note that, the bouncing behavior is more pronounced the more flexible the structure is (i.e., the '1Hz Long Base' compared to the '3Hz Short Base' specimen). Therefore, the stiffer the structure, the smaller the value of the Poisson's coefficient of restitution required to capture the experimental response of the oscillator (Fig. 6).

Fig. 7 compares the response-histories of the rocking oscillator when subjected to historic earthquake records. For consistency, Fig. 7 uses the same values of the Poisson's coefficient of restitution as in Fig. 6. Fig. 7 shows that both analytical models (nonsmooth and 'VVEL') capture well the maximum response of the '1Hz Long Base' specimen. However, after the first rotation cycle the nonsmooth model underestimates the response while the 'VVEL' overestimates it. This underestimation of the response might be caused because of the adopted value of the damping constant $\zeta$ presented in [41, 23], or the value of the Poisson's coefficient of restitution $\varepsilon_P$. Recall that, depending on the value of the Poisson's coefficient different amount of energy is dissipated at each impact. The appropriate value is hard to define and merits further investigation. However, this is beyond the scope of the present study. Note that, this is not the case for the '3Hz Short Base' specimen, which the nonsmooth model satisfactorily captures the experimental response.

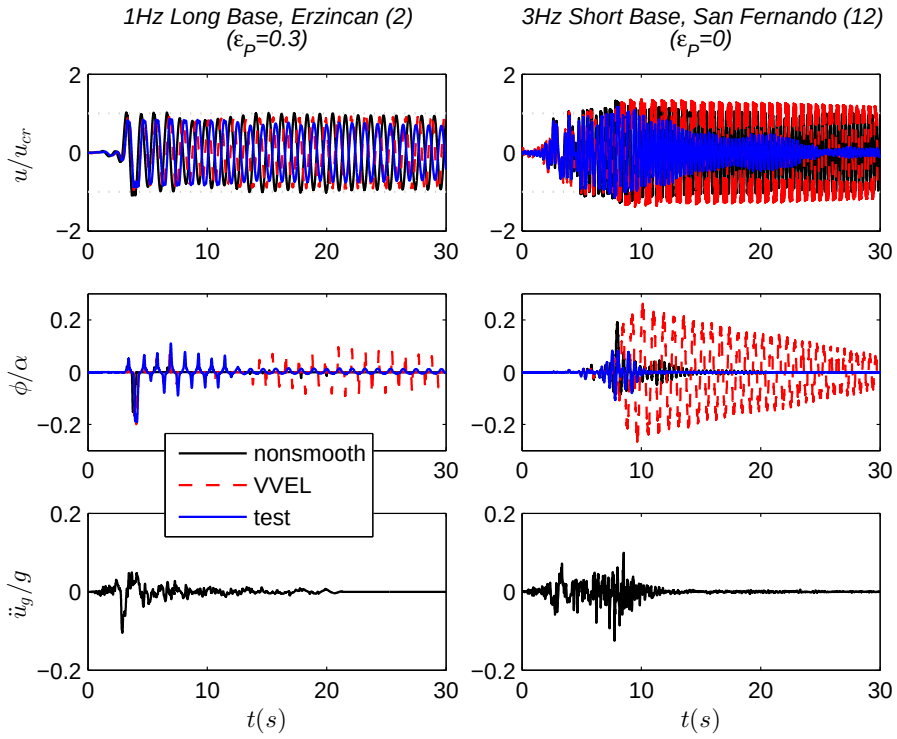


Figure 7: Response-history comparison of the nonsmooth approach with analytical ('VVEL') [41] and experimental results ('test') [39] of the rocking oscillator of Fig. 2(b) when subjected to historic earthquake records reported in [23]. The nonsmooth response is plotted with an opposite sense to match the assumed positive clockwise rotation in [39, 41].

## 5 CONCLUSIONS

The present study revisits the contact phenomenon encountered in rocking structures adopting a nonsmooth dynamics approach. Two archetypal rocking structures are considered: the rigid rocking block and the flexible rocking oscillator. Throughout the study, impact is considered to be instantaneous. Poisson's law models the behavior in the normal direction of the unilateral contact and sticking behavior is assumed in the tangential direction. This study formulates the impact problem as a system of inequalities, known as the linear complementarity problem (LCP). The proposed LCPs encapsulate all physically feasible post-impact states and liberate from the need for additional ad-hoc assumptions. The analysis shows that, for the case of the rocking block, the closed-form solutions are in total agreement with the pertinent analytical results of other methodologies. Further, the proposed response-history analysis of the flexible rocking oscillator is also validated with numerical and experimental results from literature. Specifically, the analysis shows that with the aid of the Poisson's coefficient of restitution the nonsmooth model captures the complex post-impact experimental response in a way that other analytical models fail. Overall, this work demonstrates the ability of the proposed nonsmooth dynamics approach to capture all physically feasible post-impact states and paves the way for further systematic treatment of the contact phenomenon during rocking.

## REFERENCES


[1] Acikgoz, S., DeJong, M. J., The interaction of elasticity and rocking in flexible structures allowed to uplift. *Earthquake Engineering & Structural Dynamics*, **41**(15), 2177–2194, 2012.

[2] Acikgoz, S., DeJong, M. J., The rocking response of large flexible structures to earthquakes. *Bulletin of Earthquake Engineering*, **12**(2), 875–908, 2014.

[3] Acikgoz, S., DeJong, M. J., Analytical modelling of multi-mass flexible rocking structures. *Earthquake Engineering & Structural Dynamics*, **45**(13), 2103-2122, 2016.

[4] Acikgoz, S., DeJong, M. J., Vibration modes and equivalent models for flexible rocking structures. *Bulletin of Earthquake Engineering*, **doi:10.1007/s10518-017-0128-4**, 2017.

[5] Andreaus, U., Casini, P., Dynamics of three-block assemblies with unilateral deformable contacts. Part 1: contact modelling. *Earthquake Engineering & Structural Dynamics*, **28**(12), 1621–1636, 1999.

[6] Avgenakis, E., Psycharis, I. N., Modeling of rocking elastic flexible bodies under static loading considering the nonlinear stress distribution at their base. *Journal of Structural Engineering*, **doi:10.1061/(ASCE)ST.1943-541X.0001783**, 2017.

[7] Brogliato, B., *Nonsmooth mechanics: models, dynamics and control*. Springer, 1999.

[8] Brogliato, B., Zhang, H., Liu, C., Analysis of a generalized kinematic impact law for multibody-multicontact systems, with application to the planar rocking block and chains of balls. *Multibody System Dynamics*, **27**(3), 351–382, 2012.

[9] Chopra, A. K., Yim, S. C. S., Simplified earthquake analysis of structures with foundation uplift. *Journal of Structural Engineering*, **111**(4), 906–930, 1985.

[10] Chopra, A. K., *Dynamics of structures, vol. 4*. Prentice Hall, 1995.

[11] Cottle, R. W., Dantzig, G. B., Complementary pivot theory of mathematical programming. *Linear algebra and its applications*, **1**(1), 103–125, 1968.

[12] DeJong, M. J., Amplification of rocking due to horizontal ground motion. *Earthquake Spectra*, **28**(4), 1405–1421, 2012.

[13] DeJong, M. J., Dimitrakopoulos, E. G., Dynamically equivalent rocking structures. *Earthquake Engineering & Structural Dynamics*, **43**(10), 1543–1563, 2014.

[14] Dimitrakopoulos, E. G., Analysis of a frictional oblique impact observed in skew bridges. *Nonlinear Dynamics*, **60**(4), 575–595, 2010.

[15] Dimitrakopoulos, E. G., Seismic response analysis of skew bridges with pounding deck-abutment joints. *Engineering Structures*, **33**(3), 813–826, 2011.

[16] Dimitrakopoulos, E. G., DeJong, M. J., Revisiting the rocking block: closed-form solutions and similarity laws. *Proceedings of the Royal Society A: Mathematical, Physical and Engineering Science*, **468**(2144), 2294–2318, 2012.

[17] Dimitrakopoulos, E. G., DeJong, M. J., Overturning of retrofitted rocking structures under pulse-type excitations. *Journal of Engineering Mechanics*, **138**(8), 963–972, 2012.

[18] Dimitrakopoulos, E. G., Nonsmooth analysis of the impact between successive skew bridge-segments. *Nonlinear Dynamics*, **74**(4), 911–928, 2013.

[19] Dimitrakopoulos, E. G., Giouvanidis, A. I., Seismic response analysis of the planar rocking frame. *Journal of Engineering Mechanics*, **141**(7), 04015003, 2015.

[20] Dimitrakopoulos, E. G., Paraskeva, T. S., Dimensionless fragility curves for rocking response to near-fault excitations. *Earthquake Engineering & Structural Dynamics*, **44**(12), 2015-2033, 2015.

[21] Dimitrakopoulos, E. G., Fung, E. D. W., Closed-form rocking overturning conditions for a family of pulse ground motions. *Proceedings of the Royal Society A: Mathematical, Physical and Engineering Science*, **472**(2196), 20160662, 2016.

[22] Giouvanidis, A. I., Dimitrakopoulos, E. G., Seismic analysis of hybrid rocking bridge bents. *Proceedings of the 2nd European Conference on Earthquake Engineering and Seismology*, Paper No 2251, Istanbul, Turkey, 2014.

[23] Giouvanidis, A. I., Dimitrakopoulos, E. G., Nonsmooth dynamic analysis of sticking impacts in rocking structures. *Bulletin of Earthquake Engineering*, **15**(3), 2273-2304, 2017.

[24] Giouvanidis, A. I., Dimitrakopoulos, E. G., Seismic reliability assessment of rocking bridge bents with flag-shaped hysteretic behavior. *Proceedings of the 16th World Conference on Earthquake Engineering*, Paper No 1259, Santiago, Chile, 2017.

[25] Giouvanidis, A. I., Dimitrakopoulos, E. G., Seismic performance of rocking frames with flag-shaped hysteretic behavior. *Journal of Engineering Mechanics*, **143**(5), 04017008, 2017.

[26] Glocker, C., *Set-valued force laws: dynamics of non-smooth systems*. Springer, 2001.

[27] Housner, G. W., The behavior of inverted pendulum structures during earthquakes. *Bulletin of the Seismological Society of America*, **53**(2), 403–417, 1963.

[28] Leine, R. I., Van Campen, D. H., Glocker, C. H., Nonlinear dynamics and modeling of various wooden toys with impact and friction. *Journal of Vibration and Control*, **9**(1-2), 25–78, 2003.

[29] Lemke, C. E., Bimatrix equilibrium points and mathematical programming. *Management Science*, **11**(7), 681–689, 1965.

[30] Lipscombe, P. R., Pellegrino, S., Free rocking of prismatic blocks. *Journal of Engineering Mechanics*, **119**(7), 1387–1410, 1993.

[31] Makris, N., Vassiliou, M. F., Planar rocking response and stability analysis of an array of free-standing columns capped with a freely supported rigid beam. *Earthquake Engineering & Structural Dynamics*, **42**(3), 431–449, 2012.

[32] Oliveto, G., Calio, I., Greco, A., Large displacement behaviour of a structural model with foundation uplift under impulsive and earthquake excitations. *Earthquake Engineering & Structural Dynamics*, **32**(3), 369–393, 2003.

[33] Payr, M., Glocker, C., Oblique frictional impact of a bar: analysis and comparison of different impact laws. *Nonlinear Dynamics*, **41**(4), 361–383, 2005.

[34] Pfeiffer, F., Glocker, C., *Multibody dynamics with unilateral contacts*. Springer Science & Business Media, 2000.

[35] Psycharis, I. N., Effect of base uplift on dynamic response of SDOF structures. *Journal of Structural Engineering*, **117**(3), 733–754, 1991.

[36] Psycharis, I. N., Fragiadakis, M., Stefanou, I., Seismic reliability assessment of classical columns subjected to near-fault ground motions. *Earthquake Engineering & Structural Dynamics*, **42**(14), 2061–2079, 2013.

[37] Shenton III, H. W., Jones, N., P., Base excitation of rigid bodies. I: Formulation. *Journal of Engineering Mechanics*, **117**(10), 2286–2306, 1991.

[38] Shi, Z., Dimitrakopoulos, E. G., Nonsmooth dynamics prediction of measured bridge response involving deck-abutment pounding. *Earthquake Engineering & Structural Dynamics*, **doi:10.1002/eqe.2863**, 2017.

[39] Truniger, R., Vassiliou, M. F., Stojadinovic B., An analytical model of a deformable cantilever structure rocking on a rigid surface: experimental validation. *Earthquake Engineering & Structural Dynamics*, **44**(15), 2795–2815, 2015.

[40] Vassiliou, M. F., Mackie, K. R., Stojadinovic B., Dynamic response analysis of solitary flexible rocking bodies: modeling and behavior under pulse-like ground excitation. *Earthquake Engineering & Structural Dynamics*, **43**(10), 1463–1481, 2014.

[41] Vassiliou, M. F., Truniger, R., Stojadinovic B., An analytical model of a deformable cantilever structure rocking on a rigid surface: development and verification. *Earthquake Engineering & Structural Dynamics*, **44**(15), 2775–2794, 2015.

[42] Vassiliou, M. F., Mackie, K. R., Stojadinovic B., A finite element model for seismic response analysis of deformable rocking frames. *Earthquake Engineering & Structural Dynamics*, **46**(3), 447-466, 2016.

[43] Vassiliou, M. F., Burger, S., Egger, M., Bachmann, J. A., Broccardo, M., Stojadinović, B., The three-dimensional behavior of inverted pendulum cylindrical structures during earthquakes. *Earthquake Engineering & Structural Dynamics*, **doi:10.1002/eqe.2903**, 2017.

[44] Yilmaz, C., Gharib, M., Hurmuzlu, Y., Solving frictionless rocking block problem with multiple impacts. *Proceedings of the Royal Society A: Mathematical, Physical and Engineering Science*, **doi:10.1098/rspa.2009.0273**, 2009.

COMPDYN 2017
6th ECCOMAS Thematic Conference on
Computational Methods in Structural Dynamics and Earthquake Engineering
M. Papadrakakis, M. Fragiadakis (eds.)
Rhodes Island, Greece, 15–17 June 2017

# SEISMIC FRAGILITY OF FREESTANDING BUILDINGS CONTENTS MODELLED AS RIGID BLOCKS

**L. Di Sarno[1], C. Petrone[2], G. Magliulo[3, 4] and E. Cosenza[3, 4]**

[1] University of Sannio, Department of Engineering, Piazza Roma 21, 82100 Benevento, Italy, email: ldisarno@unisannio.it

[2] University College London, Department of Civil, Environmental & Geomatic Engineering, Chadwick Building, Gower Street, WC1E 6BT London, UK, email: c.petrone@ucl.ac.uk

[3] University of Naples Federico II, Department of Structures for Engineering and Architecture, via Claudio 21, 80125 Naples, Italy, email: gmagliul@unina.it; cosenza@unina.it

[4] Construction Technologies Institute ITC-CNR, Via Claudio 21, 80125 Naples, Italy

**Keywords:** Rigid blocks, fragility analysis, hospital buildings, intensity measure, .

**Abstract.** *The loss of functionality of health care facilities, which should be guaranteed particularly in the aftermath of moderate-to-severe earthquake ground motions, is typically caused by damage to nonstructural elements, such as freestanding cabinets. The assessment of the seismic fragility of such components assumes a key role in the evaluation of the performance of a healthcare facility.*

*The present work is aimed to assess the adequacy of the rigid block modeling approach in predicting the seismic response of freestanding nonstructural components with rocking-dominated response. The outcomes of the numerical analyses show that the considered modeling technique can provide a reliable prediction of the occurrence of rocking mechanism and predict the occurrence of the overturning. In particular, the overturning PFA is slightly underestimated in case a 1.0 coefficient of restitution is considered. But the question then arises as to which intensity measure (IM) is well correlated to the seismic performance of rigid blocks. A fragility study on a number of rigid blocks is therefore conducted in the present paper. Comprehensive incremental dynamic analyses on different rigid blocks highlight that the dimensionless intensity measure PGA/(g tanα) is an efficient intensity measures to predict rocking occurrence in a generic rigid block. The intensity measure pPGV/ (g tanα) is the most efficient one only for large, say R larger than 2.0 m, rigid blocks. Very small, say R<1.0 m, rigid blocks tend to overturn as soon as they start rocking and are therefore ''PGA-dominated''. PGA/(g tanα) is therefore more efficient for such blocks. The use of these intensity measures allows assessing a unique fragility curve for rigid blocks characterized by different geometries, which may serve as a simple tool for the estimation of the damage occurred in rigid blocks after earthquakes.*

## 1 INTRODUCTION

Post-earthquake surveys carried out world-wide in building structures have shown (e.g. [1; 2], among others) that widespread damage affects non-structural components, especially building contents, mechanical and electrical services. Overturning of slender cabinets, e.g. containing medical files with patient details or allocating drug boxes, the failure of electronic units, such control panels, rooters and monitors, have been typically observed in hospitals and medical facilities, especially at intermediate and top floors in multistory structures. The failure of such components generates tremendous losses, which, in turn, impose high economical and societal pressure on the affected communities. Furthermore, they may endanger the functionality of critical facilities which should be designed to remain fully operational in the aftermath of major earthquakes.

To date, the seismic design and performance assessment of building contents in referral medical facilities is poorly addressed (e.g. [3], among others). The existing codes of practice for new (e.g. [4; 5]) and existing structures (e.g. [6; 7] ) provide scarce provisions primarily for unanchored components. Consequently, there has been extensive experimental and theoretical research ([3; 8; 9; 10]) focusing on the seismic performance of a variety of medical appliances and service utilities of typical hospital buildings and pharmacies. The seismic behavior of such components is not straightforward because of the complexity and variety of connections and functioning, thus requiring the use of experimental methods. However, the use of testing facilities is often time-consuming and costly. Conversely, numerical models may be an efficient means to simulate the dynamic response of building contents, as proved especially by studies focusing on sliding-dominated components [11; 12; 13]; their use should be promoted also for routine design office applications.

The aim of the present analytical work is three-fold: (i) use of rigid block analysis for free-standing medical components, (ii) identification of the most efficient seismic intensity measure for rigid blocks and (iii) the influence of the geometric properties of rigid blocks on their dynamic performance. The results of the comprehensive numerical study are presented in terms of fragility analysis.

## 2 DESCRIPTION OF CASE STUDIES

Two rigid block models are considered herein to assess the most efficient IM. Rigid block no. 1 is the block representative of a single-window cabinet, with $R = 0.717m$ and $h/b = 3.9$ (Fig. 1); rigid block no. 2 is taken from Yim et al. [14] and is characterized by a 3.05 m (10 feet) $R$ and an aspect ratio $h/b$ equal to 5 (Fig. 1). The two blocks are respectively representative of a typical cabinet and a large rigid block, in order to investigate the influence of the geometry of the block on the seismic response. The blocks are subjected to incremental dynamic analyses, using the set of earthquake strong motions included in ATC 63 [15]. Two different datasets are considered herein: (a) a far field and (b) a near field dataset. Far field and near field record sets are used to study the rigid block dynamic behavior. The amplitude of vibration decreases with increasing distance from the epicenter in far field input, and the strong motion record moves to lower frequencies for the effects of selective absorption. The decay of the amplitude does not occur with regularity and the characteristics of the shaking are governed mainly by the focal mechanisms in near fault conditions.

In the comprehensive parametric analysis, additional four rigid blocks have also been considered for each of the two rigid blocks by modifying alternatively their slenderness $h/b$ and dimension $R$. The four rigid blocks obtained from the single window cabinet are characterized

by (a) R=1.43m and h/b=3.91; (b) R=0.359m and h/b=3.91; (c) R=0.717m and h/b=7.83; (d) R=0.717m and h/b=1.96. The four rigid blocks corresponding to the block by Yim et al. [14] are characterized by (a) R=1.52m (5 feet) and h/b=5.0; (b) R=4.57m (15 feet) and h/b=5.0; (c) R=3.05m (10 feet) and h/b=2.5; (d) R=3.05m (10 feet) and h/b=7.5.

## 3 RIGID BLOCK ANALYSIS

Medical components, such as the metallic slender cabinets tested with shaking table in [3], typically exhibit a rocking behavior as the seismic intensity increases. Thus, rigid block model becomes a good candidate to model the dynamic response of these components.

In the present analytical study, tested cabinets are modeled as equivalent rigid blocks and subjected to the experimental base accelerations; the ability to predict the occurrence of both rocking mechanism and overturning is verified. Given the adequate model fidelity, the research outcomes presented hereafter are aimed at the identification of the most efficient seismic intensity measure (IM) for rigid blocks and the influence of the geometric properties of rigid blocks on their dynamic performance.

### 3.1 Numerical modelling

As previously discussed, tested cabinets may be also modeled as rigid blocks, whose dynamic behavior was extensively investigated in past decades (e.g. [16-21], among many others). A rigid block may be set into rocking or move rigidly with the ground, depending on its geometric features; if it sets into rocking, it will oscillate about two centers of rotation at its base corners. In this study it is assumed that the block and base surfaces in contact are perfectly smooth so that the block will rock around the edges and no intermediate location. Moreover, the coefficient of friction is assumed to be sufficiently large so that there will be no sliding between the block and the base. This assumption is typically valid for the tested cabinets, given their slenderness and interface material with the floor. It is assumed that the mass is uniformly distributed within the cabinet.

The equation of motion is developed and adopted in several existing studies (e.g. [3], among others). In this study it is solved through Runge-Kutta Ordinary Differential Equations (ODE) solver, available in Matlab [22].

Rocking mechanism occurs alternatively around O and O' (Fig. 1). It is assumed that the rotation continues smoothly from point O to O', when the angle of rotation reverses [18]. A reduction of the angular velocity is imposed when the rotation reverses, to account for the energy loss at every impact [21]. Such a reduction is evaluated by equating angular momentum about *O* just before and immediately after the impact.

The coefficient of restitution, i.e. the ratio between angular velocities after and before the impact, is evaluated as $1 - 1.5 \sin^2\alpha$. The sample single-window cabinet is modeled as a rigid block characterized by 0.36 m base ($2b$ in Fig. 1) and 1.39 m height ($2h$ in Fig. 1); the critical angle is 0.250 rad.

### 3.2 Fragility analysis

The experimental-to-numerical comparison described in [23] demonstrates that hospital building cabinets overturning can be modeled by means of rigid blocks. The question arises as to which IM is well correlated to the seismic demand on rigid blocks.

From a performance-based earthquake engineering perspective, the identification of an efficient IM which is valid for a generic rigid block assumes a key role, as well as the assessment of fragility curves for loss assessment [24]. A fragility study of rigid blocks is therefore con-

ducted aimed at two different objectives: (a) assessment of the most efficient IM; (b) influence of geometric properties of the rigid block on its performance. The assessment of the most efficient IM is conducted on the two sample rigid blocks, as discussed earlier, considering both near- and far-field earthquake records.

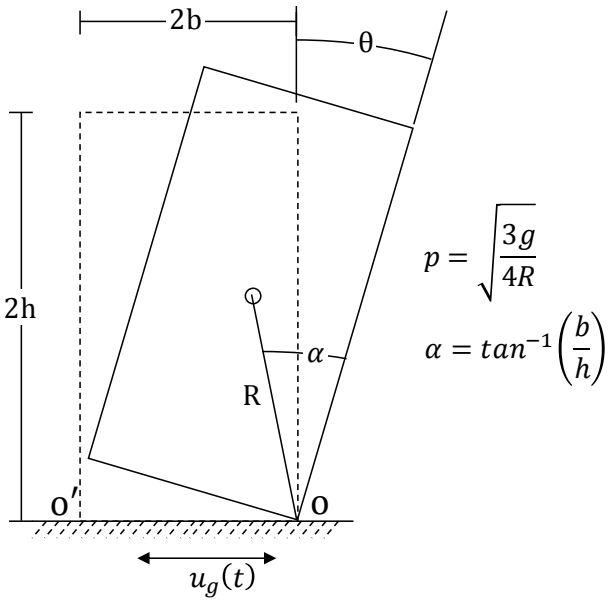


**Fig. 1. Rigid block geometry and parameters.**

Two Damage States (DSs) are defined to study the rigid block fragility during the numerical simulation: a rocking damage state and a collapse damage state.
The rigid block reaches the rocking damage state when the rotation is larger than a conventionally small value, say $0.01\alpha$, whereas it attains the collapse damage state when the rotation is larger than the critical angle $\alpha$ (Fig. 1).
Porter method "A" [25] is employed to create the lognormal fragility curves according to the different intensity measures. Different IMs are adopted to plot the fragility curves [23] among the ones typically adopted in literature studies [26]. Several typical IMs are considered among the most commonly adopted in earthquake engineering. Three IMs are taken from literature: they are defined as dimensionless slenderness IMs.
Fragility curves in terms of peak ground acceleration (PGA) and velocity (PGV) are shown in Fig. 2 for both the damage states and the suite of sample accelerograms. Input type may influence the fragility curve: it is shown that median IM values required to reach a given damage state may significantly vary from far field to near field input motions. The influence of the set of accelerograms on the fragility curve could be more/less evident depending on the damage state, as shown in Fig. 2 for both PGA and PGV.
An IM is efficient when it induces a small variability of a damage measure given IM [27]; an efficient IM would allow reducing the number of nonlinear dynamic analyses required to assess the fragility curve with adequate precision [28].
The efficiency of an IM is typically assessed from the dispersion of the engineering demand parameter (EDP) at a given IM level (e.g. [29] among many others).
For rigid blocks, it should be considered that the occurrence of rocking or overturning is far more important than the attainment of a given engineering demand parameter, e.g. rigid block rotation $\theta$. The behavior of (and the consequences on) the rigid block is not significantly influenced by the amplitude of the rigid block motion, provided it is smaller than the critical

angle $\alpha$. Thus, IM efficiency can be directly measured from the standard deviation $\beta$ of the fragility curves: the lower the standard deviation the more efficient the IM.

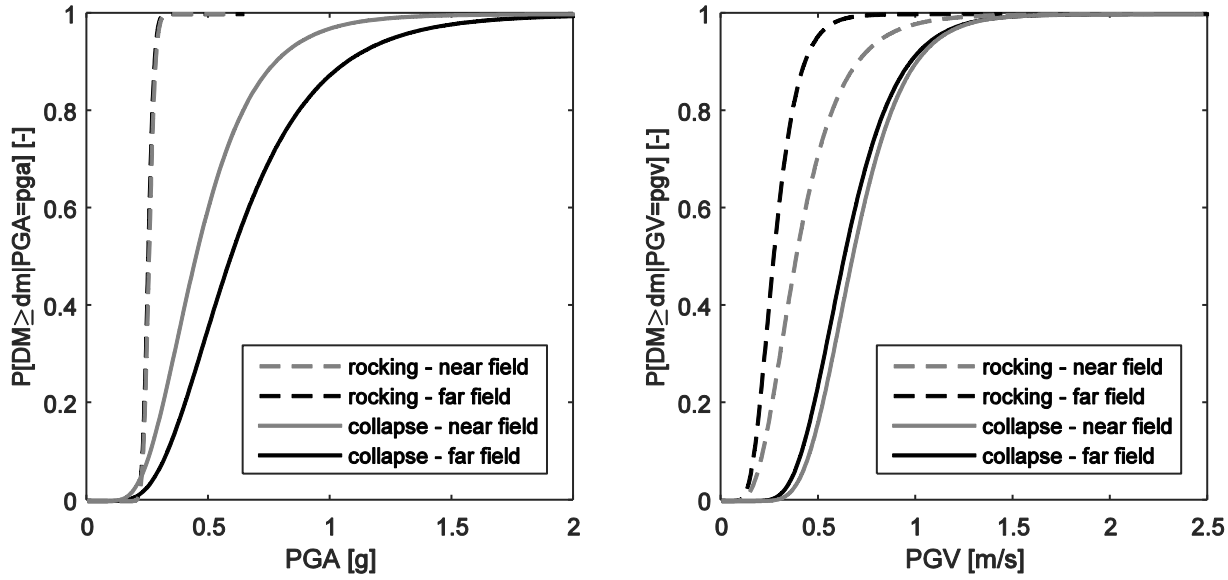


**(A)** **(B)**

**Fig. 2. Rigid block fragility curves for far-field and near-field inputs considering both (a) PGA and (b) PGV as IM for rigid block no. 2.**

Table 1 includes the logarithmic standard deviation $\beta$ of the different fragility curves, assessed for the different IMs and sets of accelerograms. The values listed in the table show that $PGA$ and $IM_4$, which is derived from $PGA$, are well correlated to the occurrence of the rocking mechanism. Such response is due to the rocking mechanism which is observed when overturning moment exceeds stabilizing moment due to gravity loads; simple equilibrium calculations yield that the minimum acceleration required to let the block rock is $b/h \cdot g$, which is consistent with the observed median values of the fragility curves for the rigid blocks.
Median $PGA_IM_4$ values are about 20% larger than expected from rotational equilibrium, due to (a) the dynamic nature of the motion and (b) the finite threshold value associated to the occurrence of rocking.
Collapse/overturning damage state is better correlated to $PGV_IM_5$ than $PGA_IM_4$ for the rigid block no. 2, as highlighted by the smaller dispersion of the fragility curve in terms of $PGV$-$IM_5$. The standard deviations of the dimensionless intensity measures $IM_4 = \frac{PGA}{g\,tan\alpha}$ and $IM_5 = \frac{p\,PGV}{g\,tan\alpha}$ are equal to the corresponding deviations for $PGA$ and $PGV$, respectively, since the dimensionless IMs are directly estimated from $PGA$ and $PGV$ through some geometric parameters of the investigated block. $IM_{Fajfar}$ intensity measure, which is based on PGV, also provides a good efficiency in predicting overturning of rigid block no. 2. For rigid block no.1, it is noted that PGA is the most efficient IM. The outcomes of the analysis on these two blocks do not allow a unique identification of the efficient IM for overturning.
The dispersion values for the most efficient IMs are not sensitive to the seismic input type, i.e. near-field and far-field motions produce similar dispersion values for the sample rigid blocks.

| IM | Rocking | | | | Overturning | | | |
|---|---|---|---|---|---|---|---|---|
| | Far field | | Near field | | Far field | | Near field | |
| | Block no. 1 | Block no. 2 | Block no. 1 | Block no. 2 | Block no. 1 | Block no. 2 | Block no. 1 | Block no. 2 |
| $PGA\ [g]$ | **0.063** | **0.078** | **0.066** | **0.080** | **0.230** | 0.459 | **0.208** | 0.428 |
| $PGV\ [m/s]$ | 0.360 | 0.367 | 0.470 | 0.468 | 0.338 | **0.335** | 0.398 | **0.309** |
| $I_A\ [m/s]$ | 0.583 | 0.561 | 0.853 | 0.883 | 0.644 | 0.880 | 0.920 | 0.881 |
| $IM_4$ | **0.063** | **0.078** | **0.066** | **0.080** | **0.230** | 0.459 | **0.208** | 0.428 |
| $IM_5$ | 0.360 | 0.367 | 0.470 | 0.468 | 0.338 | **0.335** | 0.398 | **0.309** |
| $IM_6$ | 0.245 | 0.244 | 0.312 | 0.296 | 0.312 | 0.445 | 0.400 | 0.522 |
| $IM_{Fajfar}$ | 0.385 | 0.392 | 0.509 | 0.513 | 0.357 | **0.310** | 0.452 | **0.358** |
| $CAV\ [m/s]$ | 0.578 | 0.567 | 0.816 | 0.832 | 0.584 | 0.588 | 0.816 | 0.766 |
| $ASI\ [m/s]$ | 0.173 | 0.156 | 0.265 | 0.251 | 0.248 | 0.486 | 0.271 | 0.427 |
| $S_a(T_p)\ [g]$ | 0.576 | 0.770 | 0.600 | 0.721 | 0.510 | 0.481 | 0.494 | 0.519 |
| $S_v(T_p)\ [m/s]$ | 0.576 | 0.770 | 0.600 | 0.721 | 0.510 | 0.481 | 0.494 | 0.519 |
| $HI\ [m]$ | 0.173 | 0.156 | 0.265 | 0.251 | 0.248 | 0.486 | 0.271 | 0.427 |

**Table 1. Fragility curve logarithmic standard deviation for different intensity measures; lowest standard deviation values for rocking and overturning are in bold.**

Since there was no agreement between the two selected rigid blocks, other four rigid blocks are considered for each of the two rigid blocks by modifying alternatively their slenderness $h/b$ and dimension $R$, as mentioned earlier. Incremental dynamic analysis with the two above mentioned sets of accelerograms are performed and lognormal fragility curves are estimated for each block subjected to each input motion set, as detailed above.

It is confirmed that $PGA$ and $IM_4$ are the most efficient IMs for rocking, while the most efficient IM for overturning is influenced by the dimension $R$ of the block (Fig. 3a). The dispersion of $PGV - IM_5$ overturning fragility curves is not influenced by $R$; it is included in the range between 0.3 and 0.4 for the different blocks and input considered. The logarithmic standard deviation of $PGA - IM_4$ overturning fragility curves is influenced by the dimension of the block; an increase in $R$ corresponds to an increase in $\beta$. It is concluded that $PGA - IM_4$ are the most efficient IMs for small rigid blocks, say R smaller than 1.0m, whereas $PGV - IM_5$ are more efficient for large rigid blocks, say R larger than 2.0m.

Housner [21] also suggested that the overturning of blocks was well correlated to the energy required to uplift and rotate the block by an $\alpha$ angle, which can be inferred by the peak velocity. For intermediate $R$ values the efficiency of $PGA - IM_4$ and $PGV - IM_5$ is similar.

It is worth mentioning that overturning fragility increases as dimension $R$ decreases, as also discussed in [21, 30]. Very small rigid blocks tend to overturn as soon as they start rocking, as highlighted by the discrepancy between median rocking PGA and median overturning PGA (Fig. 3b) for the ten different rigid blocks considered herein.

Additionally, the ratio in Fig. 3b tends to zero as the dimension $R$ tends to 0. At such small $R$ values, the dispersion of the overturning fragility curve (Fig. 3a) tends to be the same as the rocking fragility curves, which is in the range 0.05-0.08 for the different rigid blocks. Very small rigid blocks, say $R < 1.0m$, are therefore "PGA-dominated", with the overturning fragility curve that approaches the rocking one, both in terms of median value and dispersion.

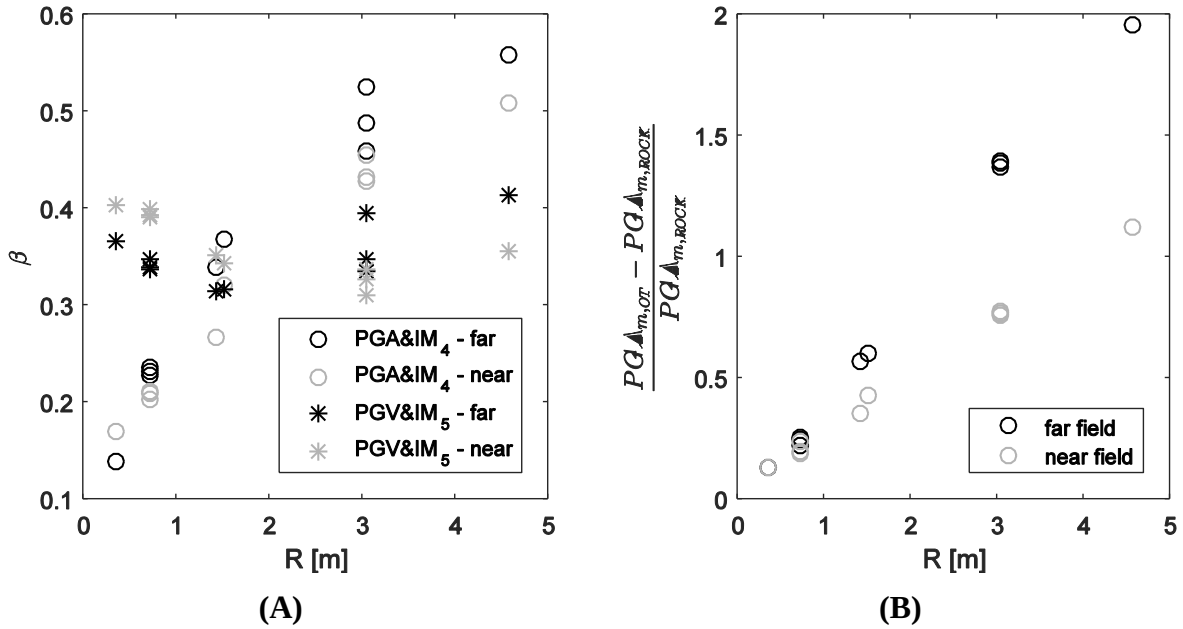


**Fig. 3. (a) Logarithmic standard deviation of overturning fragility curves for different rigid blocks and (b) discrepancy among overturning median PGA and rocking PGA.**

The influence of block dimensions on its behavior is also highlighted in the trend of median fragility curve values for the dimensionless IMs used by Dimitrakopoulos and Paraskeva [20] (Fig. 4). Median $IM_5$ values tend to be constantly around 0.5 and there is negligible discrepancy among near and far field input motion for large $R$ values, which confirms that $IM_5$ may be a good generalized intensity measure for overturning in large rigid blocks.
At small $R$ values, instead, median $IM_5 = \frac{p\ PGV}{g\ tan\alpha}$ deviates from 0.5 and there is a significant discrepancy among far field and near field, since the failure is "PGA-dominated". Interestingly, $IM_4 = \frac{PGA}{g\ tan\alpha}$ median values are not influenced by the nature of the input motion at small R values, which confirms that the PGA governs the overturning of small rigid blocks. $IM_4$ median values tend to assume value close to the ideal value of 1.0 as R becomes close to zero.
It can be also demonstrated that $IM_5$ median value scales with $1/\sqrt{R}$ for very small $R$ values if it is assumed that overturning occurs as soon as the block starts rocking, i.e. $IM_{4,overt} = IM_{4,rock} \cong 1.23$ (Fig. 5a). Under such an assumption the overturning $IM_5$ can be estimated as $IM_{5,overt} \cong \frac{1.23p\ PGV}{PGA}$. Considering that $\frac{PGV}{PGA}$ is a feature of the selected accelerogram and it is not influenced by the block, it can be concluded that $IM_{5,overt} \propto p$ or, alternatively, $IM_{5,overt} \propto \sqrt{\frac{1}{R}}$. Moreover, $IM_5$ median value is proportional to $PGV/PGA$, justifying the discrepancies of the $IM_5$ median values for near- and far-field input motions at low $R$ values. It should be finally highlighted that the influence of block slenderness on overturning and rocking is not significant when dimensionless IMs are adopted.
The twenty fragility curves, i.e. for each rigid block subjected to one of the two input motion typologies, tend to overlap on a unique curve (Fig. 5) if expressed in terms of $IM_4 = \frac{PGA}{g\ tan\alpha}$ for rocking and $IM_5 = \frac{p\ PGV}{g\ tan\alpha}$ for overturning, respectively. The overlapping fragility curves for rocking with $IM_4$ suggest that the adopted dimensionless IM is an adequate candidate for generalized IM. The overturning fragility curves tend to overlap only for $R > 1.0m$, as antici-

pated above. A generalized IM is intended as an intensity measure which induces a unique fragility curve for all the rigid blocks regardless of their geometric properties. The definition of a generalized IM would be a powerful means in simplifying the assessment of seismic fragility of components behaving as rigid blocks.

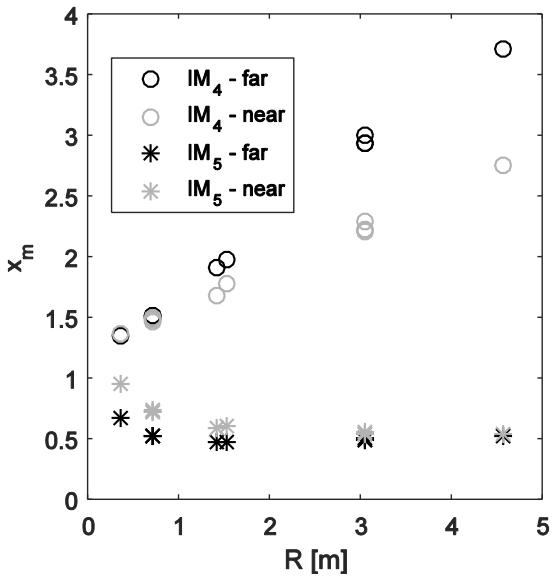


**Fig. 4. Median values of the overturning fragility curves for different dimensionless intensity measures.**

A unique fragility curve can be therefore assessed, considering the numerical data of the ten considered rigid blocks subjected to both far field and near field input motions for rocking and only the blocks with $R > 1.0m$ for overturning. A generalization cannot be made for small rigid blocks. However, median overturning $PGA$ is not much larger than rocking $PGA$ for such blocks, i.e. less than 30% (Fig. 3b). As such, future investigations might be focused on the definition of a generalized fragility curve for overturning of small rigid blocks by considering a PGA-based intensity measure.

It is therefore concluded that the curves in Fig. 5 can serve as a simple tool for the estimation of the damage occurred in rigid blocks after earthquakes. Moreover, they can be also included in performance-based design software for the estimation of the expected loss due to earthquake, for a rapid assessment of the damage occurred in non-structural components which behave as rigid blocks.

The above results apply to a rigid block placed at a given story of a structure. They suggest that structural engineers should also control peak floor velocities in addition to peak floor accelerations, in order to assess the performance of freestanding rigid nonstructural components. This preliminary analysis can be rigorously applied only to rigid blocks placed at the ground floor of buildings, due to the assumed set of accelerograms.

Future studies will deal with the investigation of rigid blocks subjected to typical floor motions, whose frequency content may be significantly different than base motion content. Moreover, more refined modelling techniques, which take into account the interaction between elasticity and rigid block behavior [22], will also be considered.

## 4 CONCLUSIONS AND FURTHER WORK

The present analytical study has assessed the reliability of using rigid block analysis to predict the earthquake response of freestanding medical cabinets. The outcomes of the parametric

analysis demonstrate that, when a 1.0 coefficient of restitution is considered, a slightly safe-sided estimation of the overturning PFA threshold can be achieved. The rocking initiation is well predicted. Thus rigid block models can be employed in assessing reliably the performance of hospital cabinets, especially for routine applications in design offices.

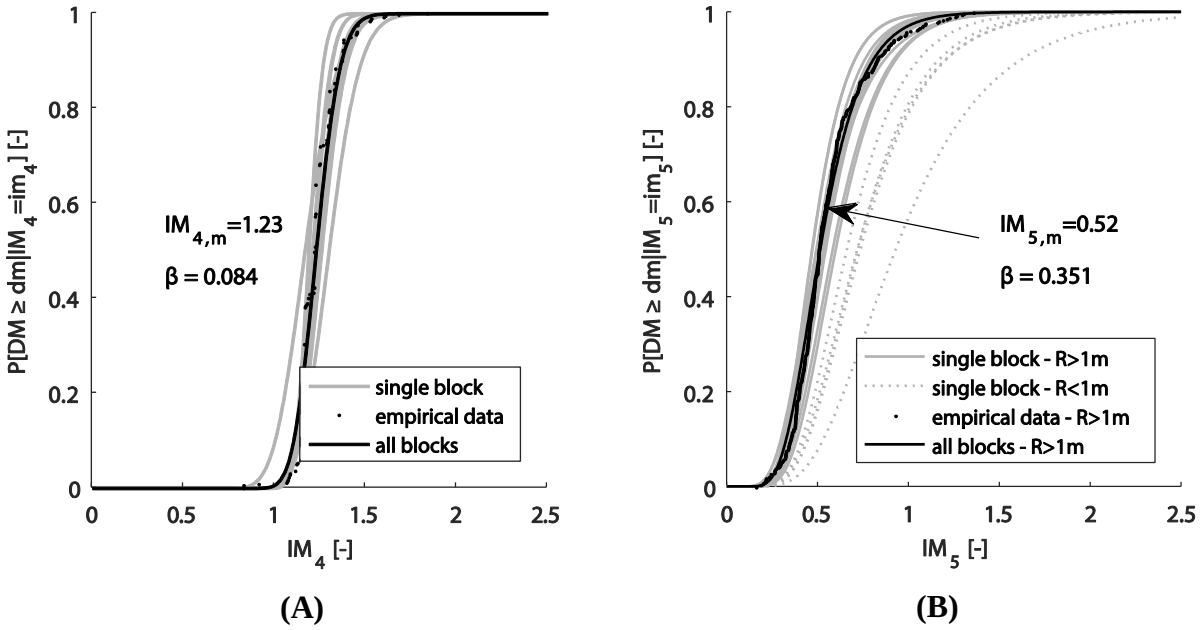


**Fig. 5. Fragility curves considering ten different rigid blocks and both far and near input motions, for (a) rocking and (b) overturning, with dimensionless intensity measures.**

The comprehensive incremental dynamic analyses carried out on different rigid blocks have shown that the dimensionless intensity measure PGA/(g tanα) is an efficient intensity measures to predict rocking occurrence in a generic rigid block.
The intensity measure pPGV/ (g tanα) is the most efficient one only for large, say R larger than 2.0 m, rigid blocks. Very small, say R<1.0 m, rigid blocks tend to overturn as soon as they start rocking and are therefore ‘‘PGA-dominated’’. PGA/(g tanα) is therefore more efficient for such blocks. The use of these intensity measures allows assessing a unique fragility curve for rigid blocks characterized by different geometries, which may serve as a simple tool for the estimation of the damage occurred in rigid blocks after earthquakes. Additionally, the use of the peak velocity is also of paramount importance for the performance assessment of slender cabinets, especially to control the overturning. Thus, structural engineers should also control peak floor velocities in addition to peak floor accelerations, in order to accurately assess the performance of freestanding rigid nonstructural components.
It is suggested that future numerical simulations should focus on the analysis of rigid blocks subjected to typical floor motions, whose frequency content may be significantly different than base motion content. The effects of the elastic response of the typical freestanding components should also be further assessed, both numerically and with experimental testing.

## ACKNOWLEDGEMENTS

The research study presented in the present paper has been funded by the Italian Department of Civil Protection in the framework of the national project DPC-ReLUIS 2015-2016, RS9

"*Health Care Facilities*". The financial support of the funding agency is gratefully acknowledged.

## REFERENCES

[1] Masi A, Santarsiero G, Gallipoli M, Mucciarelli M, Manfredi V, Dusi A and Stabile T. Performance of the health facilities during the 2012 Emilia (Italy) earthquake and analysis of the Mirandola hospital case study, Bulletin of Earthquake Engineering, 2013: 1-25.

[2] Jacques CC, McIntosh J, Giovinazzi S, Kirsch TD, Wilson T and Mitrani-Reiser J. Resilience of the Canterbury Hospital System to the 2011 Christchurch Earthquake, Earthquake Spectra, 2014, 30(1): 533-554.

[3] Cosenza E, Di Sarno L, Maddaloni G, Magliulo G, Petrone C and Prota A. Shake table tests for the seismic fragility evaluation of hospital rooms, Earthquake Engineering and Structural Dynamics, 2014, 44(1): 23-40

[4] American Society of Civil Engineers (2010) ASCE/SEI 7-10: Minimum Design Loads for Buildings and Other Structures. Reston, Virginia, US

[5] CEN (2006) Eurocode 8: Design of structures for earthquake resistance - Part 1: General rules, seismic actions and rules for buildings. EN 1998-1. Brussels, Belgium.

[6] American Society of Civil Engineers (2010) ASCE/SEI 41-6: Seismic Rehabilitation of Existing Buildings. Reston, Virginia, US.

[7] CEN (2006) Eurocode 8: design of structures for earthquake resistance - Part 1: Assessment and Retrofitting of Builidngs. EN 1998-1. Brussels, Belgium.

[8] Kuo K-C, Suzuki Y, Katsuragi S and Yao GC. Shake table tests on clutter levels of typical medicine shelves and contents subjected to earthquakes, Earthquake Engineering & Structural Dynamics, 2011, 40(12): 1367-1386.

[9] Furukawa S, Sato E, Shi Y, Becker T and Nakashima M. Full-scale shaking table test of a base-isolated medical facility subjected to vertical motions, Earthquake Engineering & Structural Dynamics, 2013, 42(13): 1931-1949.

[10] Shi Y, Kurata M and Nakashima M. Disorder and damage of base-isolated medical facilities when subjected to near-fault and long-period ground motions, Earthquake Engineering & Structural Dynamics, 2014: 43(11): 1683-1701.

[11] Konstantinidis D and Makris N. Experimental and analytical studies on the response of freestanding laboratory equipment to earthquake shaking, Earthquake Engineering & Structural Dynamics, 2009, 38(6): 827-848.

[12] Konstantinidis D and Nikfar F. Seismic response of sliding equipment and contents in base-isolated buildings subjected to broadband ground motions, Earthquake Engineering & Structural Dynamics, 2015, 44(6): 865-887.

[13] Lin S-L, MacRae GA, Dhakal RP and Yeow TZ. Building contents sliding demands in elastically responding structures, Engineering Structures, 2015, 86: 182-191.

[14] C.-S. Yim, A.K. Chopra, J. Penzien, Rocking response of rigid blocks to earthquakes. *Earthquake Engineering & Structural Dynamics*, **8**, 565-587, 1980.

[15] Applied Technology Council, Quantification of building seismic performance factors. ATC 63. Redwood city, California, 2008.

[16] Y. Ishiyama, Motions of rigid bodies and criteria for overturning by earthquake excitations. *Earthquake Engineering & Structural Dynamics*, **10**, 635-650, 1982.

[17] J. Zhang, N. Makris, Rocking Response of Free-Standing Blocks under Cycloidal Pulses. *Journal of Engineering Mechanics*, **127**, 473-483, 2001.

[18] N. Makris, D. Konstantinidis, The rocking spectrum and the limitations of practical design methodologies. *Earthquake Engineering & Structural Dynamics*, **32**, 265-289, 2003.
[19] E. Dimitrakopoulos, M. DeJong, Overturning of Retrofitted Rocking Structures under Pulse-Type Excitations. *Journal of Engineering Mechanics*, **138**, 963-972, 2012.
[20] E.G. Dimitrakopoulos, T.S. Paraskeva, Dimensionless fragility curves for rocking response to near-fault excitations. *Earthquake Engineering & Structural Dynamics*, **44**, 2015-2033, 2015.
[21] G.W. Housner, The behavior of inverted pendulum structures during earthquakes. *Bulletin of the Seismological Society of America*, **53**, 403-417, 1963.
[22] The MathWorks Inc., MATLAB 8.5 Natick, MA, 2015.
[23] C. Petrone, L. Di Sarno, G. Magliulo, E. Cosenza, Numerical modelling and fragility assessment of typical freestanding building contents. *Bulletin of Earthquake Engineering*, **15**, 1609-1633, 2017.
[24] M. De Biasio, S. Grange, F. Dufour, F. Allain, I. Petre-Lazar, Intensity measures for probabilistic assessment of non-structural components acceleration demand. *Earthquake Engineering & Structural Dynamics*, **44**, 2261-2280, 2015.
[25] K. Porter, R. Kennedy, R. Bachman, Creating Fragility Functions for Performance-Based Earthquake Engineering. *Earthquake Spectra*, **23**, 471-489, 2007.
[26] E. Cosenza, G. Manfredi, Damage indices and damage measures. *Progress in Structural Engineering and Materials*, **2**, 50-59, 2000.
[27] N. Luco, C.A. Cornell, Structure-Specific Scalar Intensity Measures for Near-Source and Ordinary Earthquake Ground Motions. *Earthquake Spectra*, **23**, 357-392, 2007.
[28] N. Shome, C.A. Cornell, Probabilistic seismic demand analysis of nonlinear structures, Reliability of Marine Structures Program Report No. RMS-35. Department of Civil and Environmental Engineering, Stanford University, California, 1999.
[29] J. Donaire-Ávila, F. Mollaioli, A. Lucchini, A. Benavent-Climent, Intensity measures for the seismic response prediction of mid-rise buildings with hysteretic dampers. *Engineering Structures*, **102**, 278-295, 2015.
[30] N. Makris, M. Vassiliou, Are Some Top-Heavy Structures More Stable? *Journal of Structural Engineering*, **140**, 06014001, 2014.

COMPDYN 2017
6th ECCOMAS Thematic Conference on
Computational Methods in Structural Dynamics and Earthquake Engineering
M. Papadrakakis, M. Fragiadakis (eds.)
Rhodes Island, Greece, 15–17 June, 2017

# A NEW COMPUTATIONAL APPROACH FOR THE ROCKING RESPONSE OF DEFORMABLE BODIES CONSIDERING MATERIAL NONLINEARITY

**Evangelos Avgenakis and Ioannis N. Psycharis**

School of Civil Engineering
National Technical University of Athens, Greece
Polytechnic Campus, Heroon Polytechniou 9, 15780 Zografou
e-mail: vavgen@outlook.com, ipsych@central.ntua.gr

**Keywords:** Rocking, Macroelement, Nonlinear analysis, Inelastic response, Resilient structures.

**Abstract.** *An increasing interest in the use of rocking members in earthquake resistant structural systems has been observed in recent years. The benefits of such members include the limitation of the damage, re-centering capabilities and reduction of seismic forces transmitted to the rest of the structure due to a yield-like response.*

*Despite the importance of such members, few models able to describe the response of flexible rocking members in structural systems realistically can be found in literature, since most of the research focuses on the response of rigid bodies or ignores the stress nonlinearity near the contact area, which is considered crucial to the accurate determination of the rocking response of deformable rocking bodies. A new macro-element formulation for elastic rocking members has been proposed by the authors in previous papers which is able to take into account this stress nonlinearity, producing results which are very close to the ones produced by conventional finite element programs.*

*Rocking members in structural systems are expected to behave inelastically for large seismic excitations. In this paper, the macroelement presented previously by the authors, which considered the element material to be elastic, is extended to also take material nonlinearity into account. The effect of the nonlinear stress distribution across the rocking interface on the member displacements is determined and approximate formulas for their determination are included in the macro-element formulation. The results produced by the macro-element with the inelastic material are finally compared to the ones of conventional finite element codes, showing very good agreement between the results of the two methods.*

## 1 INTRODUCTION

The rocking motion of rigid bodies and structural members has recently gained an increased attention from the scientific community. Unlike members considered in classical mechanics, which can transmit tensile stresses through their base, members unrestrained or partially restrained at their base can develop only compressive stresses, while uplift occurs, altering significantly their response. When large enough horizontal forces are imposed on the member, its base partially detaches from the ground and the body rotates about one of its corners. The vertical force acts as the restoring force that tends to bring the body back to its original equilibrium position.

The inclusion of rocking members in real structures is considered a promising solution to the design of resilient structures. During a seismic event, conventional structural elements are designed to gradually yield and develop damage and residual deformations, requiring repairs afterwards. In contrast, rocking members exhibit a yield-like response, able to limit the forces transmitted to the structure during an earthquake, developing however little damage and residual deformations.

Up to date, rocking members have been applied in case of bridge piers (e.g. the Rangitikei Railway Bridge [1]), while extensive analytical and experimental work has been performed on rocking shear walls in precast structures (e.g. [2], [3], [4]). Furthermore, guidelines addressing this alternative seismic design have been published by several organizations.

Various analytic solutions exist regarding the motion of the rigid rocking block (e.g. [5], [6], [7], [8]), as well as approximate formulas for the design of controlled rocking systems. However, few computational models exist for modeling the response of deformable rocking bodies (e.g. [9], [10], [11], [12], [13], [14], [15], [16], [17]). Most of these studies, though, consider the rocking base to be rigid, take into account the stress nonlinearity only across the rocking interface or make simplifications regarding the stress distribution near the contact area.

A new macroelement formulation has been recently proposed by the authors ([18]), which is able to take into account both the deformability of the rocking member along its height, as well as the stress nonlinearity near the contact area, which is crucial in many applications, especially regarding members with constrained rocking motion. The material in this macroelement was assumed to be elastic. However, rocking members in structural systems are expected to behave inelastically for large seismic excitations. So, in this paper, the previous formulation is extended to also take material nonlinearity into account for monotonic loading.

## 2 ELASTIC MATERIAL FORMULATION

The basic steps of the elastic material formulation found in [18] are summarized here, since this also serves as the basis of the material nonlinearity formulation.

First of all, the member is examined in a natural coordinate system without rigid body modes. This coordinate system corresponds to a coordinate system of a simply supported beam along the deformed position of the member and has three independent degrees of freedom, $\bar{\boldsymbol{q}}$. For space reasons, the conversion between the local and the natural coordinate system is not repeated here, but can be found in the original paper.

Given the natural system displacements and the corresponding displacement increments, a vector of natural system nodal forces, $\bar{\boldsymbol{Q}}$, is estimated using the existing stiffness matrix. From these forces, a vector of displacements according to the techical theory of bending can be calculated, as in conventional finite elements.

However, since these forces do not act on the whole rocking interface, as only compressive

stresses are allowed to develop, the stress distributions at the contact surface differ from those of the technical theory of bending and produce nonlinear stress distributions near the contact area. In order to account for the difference between the stresses assumed by the technical theory and the real ones, self-equilibrating stresses at the rocking interface are considered, which influence the local deformations and give rise to additional displacements. The influence of these self-equilibrating stresses is examined by considering the equivalent problem of a semi-infinite strip loaded with self-equilibrating stresses on its free side [19].

For a given natural system force vector, $\bar{\boldsymbol{Q}}$, the forces at the rocking end, $\bar{\boldsymbol{Q}}_{\mathrm{r}} = [N_{\mathrm{r}}, M_{\mathrm{r}}, Q_{\mathrm{r}}]^{\mathrm{T}}$, for a member with length $L$, normalized with respect to the member thickness, $W$, are given by

$$\bar{\boldsymbol{Q}}_{\mathrm{r}} = \boldsymbol{S}_1 \, \bar{\boldsymbol{Q}} \tag{1}$$

where

$$\boldsymbol{S}_1 = \frac{1}{W} \begin{bmatrix} 1 & 0 & 0 \\ 0 & 1 & 0 \\ 0 & -\dfrac{1}{L} & -\dfrac{1}{L} \end{bmatrix} \tag{2}$$

Assuming a triangular normal and a parabolic shear stress distribution at the rocking interface, the normalized stress distribution parameter vector, $\boldsymbol{r} = [c, \widetilde{\sigma}_{\mathrm{m}}, \widetilde{\tau}_{\mathrm{m}}]^T$, correspoding to the normalized contact length, the maximum normal and the maximum shear stress of a member with semiwidth $b = 1$, is calculated:

$$\boldsymbol{r} = \begin{Bmatrix} 3\left(1 + \dfrac{\rho M_{\mathrm{r}}}{b N_{\mathrm{r}}}\right) \\ \dfrac{2}{3} \dfrac{N_{\mathrm{r}}}{b + \frac{\rho M_{\mathrm{r}}}{N_{\mathrm{r}}}} \\ \dfrac{1}{2} \dfrac{\rho Q_{\mathrm{r}}}{b + \frac{\rho M_{\mathrm{r}}}{N_{\mathrm{r}}}} \end{Bmatrix} \tag{3}$$

where $\rho$ is the signum function of $M_{\mathrm{r}}$ and $b$ is the semiwidth of the original member.

The additional displacements due to the self-equilibrating stresses can be evaluated by approximating the fiber elongation profile across the loaded area of the rocking interface using a linear distribution, whose parameters correspond to the axial elongation at the center of the section and the rotation of the rocking end. Using the load parameter vector, $\boldsymbol{r}$, these additional displacements can be estimated from

$$\boldsymbol{u} = \frac{1}{E} \begin{Bmatrix} \left(\widetilde{\sigma}_{\mathrm{m}} \, \boldsymbol{V}_{\sigma}^{\mathrm{T}} + \widetilde{\tau}_{\mathrm{m}} \, \boldsymbol{V}_{\tau}^{\mathrm{T}}\right) \boldsymbol{P}_c \\ \left(\widetilde{\sigma}_{\mathrm{m}} \, \boldsymbol{R}_{\sigma}^{\mathrm{T}} + \widetilde{\tau}_{\mathrm{m}} \, \boldsymbol{R}_{\tau}^{\mathrm{T}}\right) \boldsymbol{P}_c \end{Bmatrix} \tag{4}$$

in which

$$\boldsymbol{P}_c = \begin{bmatrix} c^6 & c^5 & c^4 & c^3 & c^2 & c & 1 \end{bmatrix}^T \tag{5}$$

$$\begin{aligned} \boldsymbol{V}_{\tau} &= \boldsymbol{V}_{\tau 0} + \nu \boldsymbol{V}_{\tau \nu} \\ \boldsymbol{R}_{\tau} &= \boldsymbol{R}_{\tau 0} + \nu \boldsymbol{R}_{\tau \nu} \end{aligned} \tag{6}$$

and the polynomial constant term $\boldsymbol{V}_{\sigma}$ and $\boldsymbol{R}_{\sigma}$ (for the normal stress contribution) and $\boldsymbol{V}_{\tau 0}$, $\boldsymbol{V}_{\tau \nu}$, $\boldsymbol{R}_{\tau 0}$, $\boldsymbol{R}_{\tau \nu}$ (for the shear stress contribution) vectors given in [18].

Thus, the displacements due to the self-equilibrating stresses in the original member natural coordinate system are:

$$\bar{\boldsymbol{q}}_{\text{se}} = \boldsymbol{S}_3\, \boldsymbol{u} \tag{7}$$

where

$$\boldsymbol{S}_3 = \begin{bmatrix} b & 0 \\ 0 & \rho \\ 0 & 0 \end{bmatrix} \tag{8}$$

The corresponding flexibility matrix of the self-equilibrating stresses contribution is

$$\bar{\boldsymbol{F}}_{\text{se}} = \frac{\partial \bar{\boldsymbol{q}}_{\text{se}}}{\partial \bar{\boldsymbol{Q}}} = \boldsymbol{S}_3\, \bar{\boldsymbol{F}}_n\, \boldsymbol{S}_2\, \boldsymbol{S}_1 \tag{9}$$

where

$$\boldsymbol{S}_2 = \frac{\partial \boldsymbol{r}}{\partial \bar{\boldsymbol{Q}}_{\text{r}}} = \begin{bmatrix} \dfrac{6-2c}{bc\widetilde{\sigma}_{\text{m}}} & \dfrac{6\rho}{b^2 c\widetilde{\sigma}_{\text{m}}} & 0 \\ \dfrac{4c-6}{bc^2} & -\dfrac{6\rho}{b^2c^2} & 0 \\ \dfrac{2\widetilde{\tau}_{\text{m}}(c-3)}{bc^2\widetilde{\sigma}_{\text{m}}} & -\dfrac{6\rho\widetilde{\tau}_{\text{m}}}{b^2c^2\widetilde{\sigma}_{\text{m}}} & \dfrac{3\rho}{2bc} \end{bmatrix} \tag{10}$$

and

$$\bar{\boldsymbol{F}}_n = \frac{1}{E} \begin{bmatrix} \left(\widetilde{\sigma}_{\text{m}}\, \boldsymbol{V}_\sigma^{\text{T}} + \widetilde{\tau}_{\text{m}}\, \boldsymbol{V}_\tau^{\text{T}}\right) \boldsymbol{P}_c' & \boldsymbol{V}_\sigma^{\text{T}}\, \boldsymbol{P}_c & \boldsymbol{V}_\tau^{\text{T}}\, \boldsymbol{P}_c \\ \left(\widetilde{\sigma}_{\text{m}}\, \boldsymbol{R}_\sigma^{\text{T}} + \widetilde{\tau}_{\text{m}}\, \boldsymbol{R}_\tau^{\text{T}}\right) \boldsymbol{P}_c' & \boldsymbol{R}_\sigma^{\text{T}}\, \boldsymbol{P}_c & \boldsymbol{R}_\tau^{\text{T}}\, \boldsymbol{P}_c \end{bmatrix} \tag{11}$$

with

$$\boldsymbol{P}_c' = \begin{bmatrix} 6c^5 & 5c^4 & 4c^3 & 3c^2 & 2c & 1 & 0 \end{bmatrix}^T \tag{12}$$

The displacements and the flexibility matrix of the self-equilibrating stresses contribution are finally added to those of the technical theory of bending. Since these natural system displacements generally differ from the ones assumed in the beginning, their difference is multiplied with the total flexibility matrix and this additional term is added to the nodal forces assumed. If this term is large enough, an iteration of the procedure is performed.

## 3 EXTENSION TO THE INELASTIC MATERIAL CASE

For the solution of the inelastic material case, new stress distributions acting on the rocking interface have to be assumed. As a simplification, the area inside the element is considered to behave elastically, so that the existing solution of the semi-infinite strip stress problem, based on the theory of elasticity, as well as the principle of superposition hold. However, as discussed in the ensuing, this assumption does not lead to results far from the reality, since only the elongations of the elastic portion of the section are taken into account.

For the normal stresses, a trapezoidal stress distribution is assumed to act on the rocking interface, after yielding occurs (Fig. 1). In order to examine the response of the member under the trapezoidal loading, a new parameter $\mu$ can be defined:

$$\mu = \frac{c_y}{c} \tag{13}$$

where $c_y$ is the length of the contact area which has yielded.

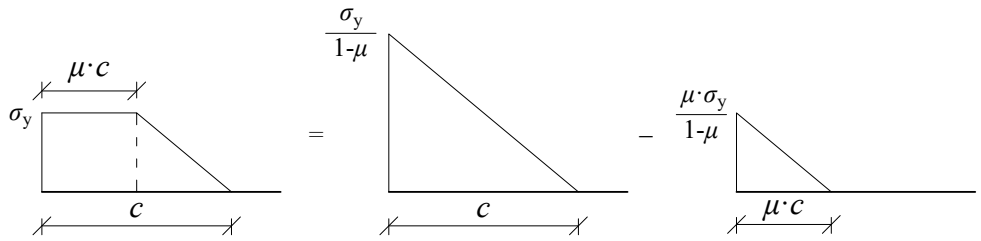


Figure 1: Normal stress distribution acting on the rocking interface after yielding and decomposition into triangular distributions.

The resultant axial force and moment can be expressed as:

$$N_{\mathrm{r}} = \frac{1}{2}(1+\mu)bc\sigma_y \tag{14}$$

$$M_{\mathrm{r}} = \rho\left[\frac{1}{2}(1+\mu)b^2c\left(\frac{c}{3}-1\right)\sigma_y + \frac{1}{6}\mu^2b^2c^2\sigma_y\right] \tag{15}$$

where $\rho$ is the signum function of $M$.

The trapezoidal distribution can be expressed as the difference of the two triangular distributions with parameters ($\sigma_y/(1-\mu)$,$c$) and ($\mu\sigma_y/(1-\mu)$,$\mu c$) shown in Fig. 1. Assuming that the shear stress distribution results from the difference of two parabolic distributions corresponding to the aforementioned triangular normal stress distributions and that the ratio of the maximum shear stress values is the same as the maximum normal stresses ratio, the resultant shear force is

$$Q_{\mathrm{r}} = \rho\frac{2}{3}(1-\mu^2)bct \tag{16}$$

where $t$ is the maximum shear stress corresponding to the distribution of contact length $c$.

Given a vector of resultant forces acting on the rocking interface, $\bar{\boldsymbol{Q}}_{\mathrm{r}}$, the load distribution parameter vector, $\boldsymbol{r}_{\mathrm{y}} = [c, \mu, t]^T$, can be calculated from:

$$\boldsymbol{r}_{\mathrm{y}} = \begin{Bmatrix} c \\ \mu \\ t \end{Bmatrix} = \begin{Bmatrix} \dfrac{N_{\mathrm{r}}\omega}{\sigma_{\mathrm{y}}b} \\ \dfrac{2}{\omega} - 1 \\ \dfrac{3\rho\omega^2 Q_{\mathrm{r}}}{8(\omega-1)bc} \end{Bmatrix} \tag{17}$$

where

$$\omega = \sqrt{3\left(\frac{2b\sigma_{\mathrm{y}}}{N_{\mathrm{r}}} + \frac{2\rho M_{\mathrm{r}}\sigma_{\mathrm{y}}}{N_{\mathrm{r}}^2} - 1\right)} + 1 \tag{18}$$

The corresponding derivative matrix of the load parameters to the rocking end forces is

$$\boldsymbol{S}_{2\mathrm{y}} = \frac{\partial \boldsymbol{r}_{\mathrm{y}}}{\partial \bar{\boldsymbol{Q}}_{\mathrm{r}}} = \begin{bmatrix} \dfrac{2(c+2\mu c-3)}{(\mu-1)bc\sigma_{\mathrm{y}}} & -\dfrac{6\rho}{(\mu-1)b^2c\sigma_{\mathrm{y}}} & 0 \\ \dfrac{6(\mu+1)-4(1+\mu+\mu^2)c}{(\mu-1)bc^2\sigma_{\mathrm{y}}} & \dfrac{6\rho(\mu+1)}{(\mu-1)b^2c^2\sigma_{\mathrm{y}}} & 0 \\ \dfrac{2ct(2\mu^3+3\mu^2+6\mu+1)-6t(1+\mu)^2}{(\mu-1)^2(\mu+1)bc^2\sigma_{\mathrm{y}}} & -\dfrac{6\rho t(\mu+1)}{(\mu-1)^2b^2c^2\sigma_{\mathrm{y}}} & \dfrac{3\rho}{2bc(1-\mu^2)} \end{bmatrix} \tag{19}$$

It is noted that the material yields when

$$\sigma_{\mathrm{y}} > \frac{2N_{\mathrm{r}}}{3\left(b + \frac{\rho M_{\mathrm{r}}}{N_{\mathrm{r}}}\right)} \tag{20}$$

## 4 ADDITIONAL DISPLACEMENTS DUE TO THE SELF-EQUILIBRATING STRESSES

As for the elastic material case, the self-equilibrating stress distributions originating from the aforementioned ones are examined using the semi-infinite strip problem solution. However, the additional displacements due to these self equilibrating stresses are not calculated by approximation of the whole contact area fiber elongation profile with a linear distribution, but only of the portion of the section that remains elastic, that is in the interval $[-1+\mu c, -1+c]$. This can be applied, since the fibers under this area are assumed to remain elastic, in contrast to the fibers under the yielded contact zone.

Using the aforementioned procedure, the self-equilibrating stresses normalized displacement approximation formula presented next is produced, giving very good results for $c \leq 2/(\mu+1)$, which includes most of the usual cases:

$$\boldsymbol{u}_y = \frac{1}{E}\begin{Bmatrix}\sigma_{\mathrm{y}}\delta_\sigma(c,\mu) + t\delta_\tau(c,\mu)\\ \sigma_{\mathrm{y}}\theta_\sigma(c,\mu) + t\theta_\tau(c,\mu)\end{Bmatrix} \tag{21}$$

where the functions $\delta_\sigma(c,\mu), \theta_\sigma(c,\mu), \delta_t(c,\mu), \theta_t(c,\mu)$ are presented in the following.

**Normal stresses** Introducing a normalized contact length $c_{\mathrm{n}} = c(\mu+1)$, functions $\delta_\sigma(c,\mu)$ and $\theta_\sigma(c,\mu)$ are given by:

$$\delta_\sigma = \delta_A(c_{\mathrm{n}}) + \delta_B(\mu)(c_{\mathrm{n}} - 2) \tag{22}$$
$$\theta_\sigma = \theta_A(c_{\mathrm{n}}) + \theta_B(\mu) + \theta_C(\mu)\theta_D(c_{\mathrm{n}}) \tag{23}$$

where the various functions appearing in these equations have the forms:

$$\delta_A(c_{\mathrm{n}}) = a_1\left[1 - (c_{\mathrm{n}}/2)^{a_2}\right]^{a_3} \tag{24}$$
$$\delta_B(\mu) = a_1\tan(a_2\mu) + a_3\mu + a_4\mu^2 + a_5\mu^3 \tag{25}$$
$$\theta_A(c_{\mathrm{n}}) = a_1\left[1 - (c_{\mathrm{n}}/2)^{a_2}\right]^{a_3}(1 - c_{\mathrm{n}}/2)^2 \tag{26}$$
$$\theta_B(\mu) = a_1\tan(a_2\mu) + a_3\mu + a_4\mu^2 + a_5\mu^3 \tag{27}$$
$$\delta_C(\mu) = a_1\mu^4 + a_2\mu^3 + a_3\mu^2 + (-4a_1 - 3a_2 - 2a_3)\mu \tag{28}$$
$$\delta_D(c_{\mathrm{n}}) = a_1 c_{\mathrm{n}}^6 + a_2 c_{\mathrm{n}}^5 + a_3 c_{\mathrm{n}}^4 + a_4 c_{\mathrm{n}}^3 + (-16a_1 - 8a_2 - 4a_3 - 2a_4 + 0.25)c_{\mathrm{n}}^2 \tag{29}$$

The constant parameters appearing in these equations are given in Table 1.

Furthermore, the following derivatives are calculated, which are needed in the following:

$$\frac{\partial\delta_\sigma}{\partial c} = (\mu+1)\left(\frac{d\delta_A}{dc_{\mathrm{n}}} + \delta_B\right) \tag{30}$$
$$\frac{\partial\delta_\sigma}{\partial \mu} = c\left(\frac{d\delta_A}{dc_{\mathrm{n}}} + \delta_B\right) + \frac{d\delta_B}{d\mu}(c_{\mathrm{n}} - 2) \tag{31}$$
$$\frac{\partial\theta_\sigma}{\partial c} = (\mu+1)\left(\frac{d\theta_A}{dc_{\mathrm{n}}} + \theta_C\frac{d\theta_D}{dc_{\mathrm{n}}}\right) \tag{32}$$
$$\frac{\partial\theta_\sigma}{\partial \mu} = c\left(\frac{d\theta_A}{dc_{\mathrm{n}}} + \theta_C\frac{d\theta_D}{dc_{\mathrm{n}}}\right) + \frac{d\theta_B}{d\mu} + \theta_D\frac{d\theta_C}{d\mu} \tag{33}$$

Table 1: Approximation functions constant term vectors

| Function | $a_1$ | $a_2$ | $a_3$ | $a_4$ |
|---|---|---|---|---|
| $\delta_A$ | -1.61868182 | 0.74341712 | 2.38990044 | |
| $\delta_B$ | 0.02707282 | 0.71805567 | -0.42532673 | 0.64748945 |
| $\theta_A$ | -1.60601045 | 2.71616773 | 0.52133449 | |
| $\theta_B$ | -0.05393963 | -1.54431579 | 0.98577157 | -1.35812515 |
| $\theta_C$ | -0.4009598 | 1.46727493 | -2.19487061 | |
| $\theta_D$ | -0.03040586 | 0.15378978 | -0.33644138 | 0.38440043 |
| $\delta_1$ | 2.48001601 | 0.68431159 | 1.80867566 | |
| $\delta_2$ | -0.43362038 | | | |
| $\theta_1$ | 2.35842517 | 0.98635297 | 1.52894546 | |
| $\theta_2$ | -0.45228844 | | | |

It is noted that for $c > 2/(\mu+1)$, due to the symmetry of the self-equilibrating normal stresses, the following equations hold:

$$\delta_\sigma(c,\mu) = -\delta_\sigma(2-\mu c,(2-c)/(2-\mu c)) \tag{34}$$
$$\theta_\sigma(c,\mu) = \theta_\sigma(2-\mu c,(2-c)/(2-\mu c)) \tag{35}$$

A comparison between the semi-infinite strip problem results and the ones predicted from the aforementioned equations can be seen in Fig. 2.

**Shear stresses**

$$\delta_\tau = \delta_1(c)\delta_2(\mu) \tag{36}$$
$$\theta_\tau = \theta_1(c)\theta_2(\mu) \tag{37}$$

where the functions appearing in these equations have the forms:

$$\delta_1(c) = a_1\left[1-(c/2)^{a_2}\right]^{a_3} \tag{38}$$
$$\delta_2(\mu) = (a_1\mu-1)(\mu-1) \tag{39}$$
$$\theta_1(c) = a_1\left[1-(c/2)^{a_2}\right]^{a_3} \tag{40}$$
$$\theta_2(\mu) = (a_1\mu-1)(\mu-1) \tag{41}$$

The constant parameters appearing in these equations are given in Table 1.

A comparison between the semi-infinite strip problem results and the ones predicted from the aforementioned equations can be seen in Fig. 3.

**Derivative matrix** The derivative matrix, $\bar{\boldsymbol{F}}_{ny}$ of the normalized displacements due to the self equilibrating stresses, $\boldsymbol{u}_y$ with respect to the normalized load parameters, $\boldsymbol{r}_\mathrm{y}$ is:

$$\bar{\boldsymbol{F}}_{ny} = \frac{\partial \boldsymbol{u}_y}{\partial \boldsymbol{r}_\mathrm{y}} = \frac{1}{E}\begin{bmatrix} \sigma_y\dfrac{\partial\delta_\sigma}{\partial c}+t\dfrac{\partial\delta_\tau}{\partial c} & \sigma_y\dfrac{\partial\delta_\sigma}{\partial\mu}+t\dfrac{\partial\delta_\tau}{\partial\mu} & \delta_\tau \\ \sigma_y\dfrac{\partial\theta_\sigma}{\partial c}+t\dfrac{\partial\theta_\tau}{\partial c} & \sigma_y\dfrac{\partial\theta_\sigma}{\partial\mu}+t\dfrac{\partial\theta_\tau}{\partial\mu} & \theta_\tau \end{bmatrix} \tag{42}$$

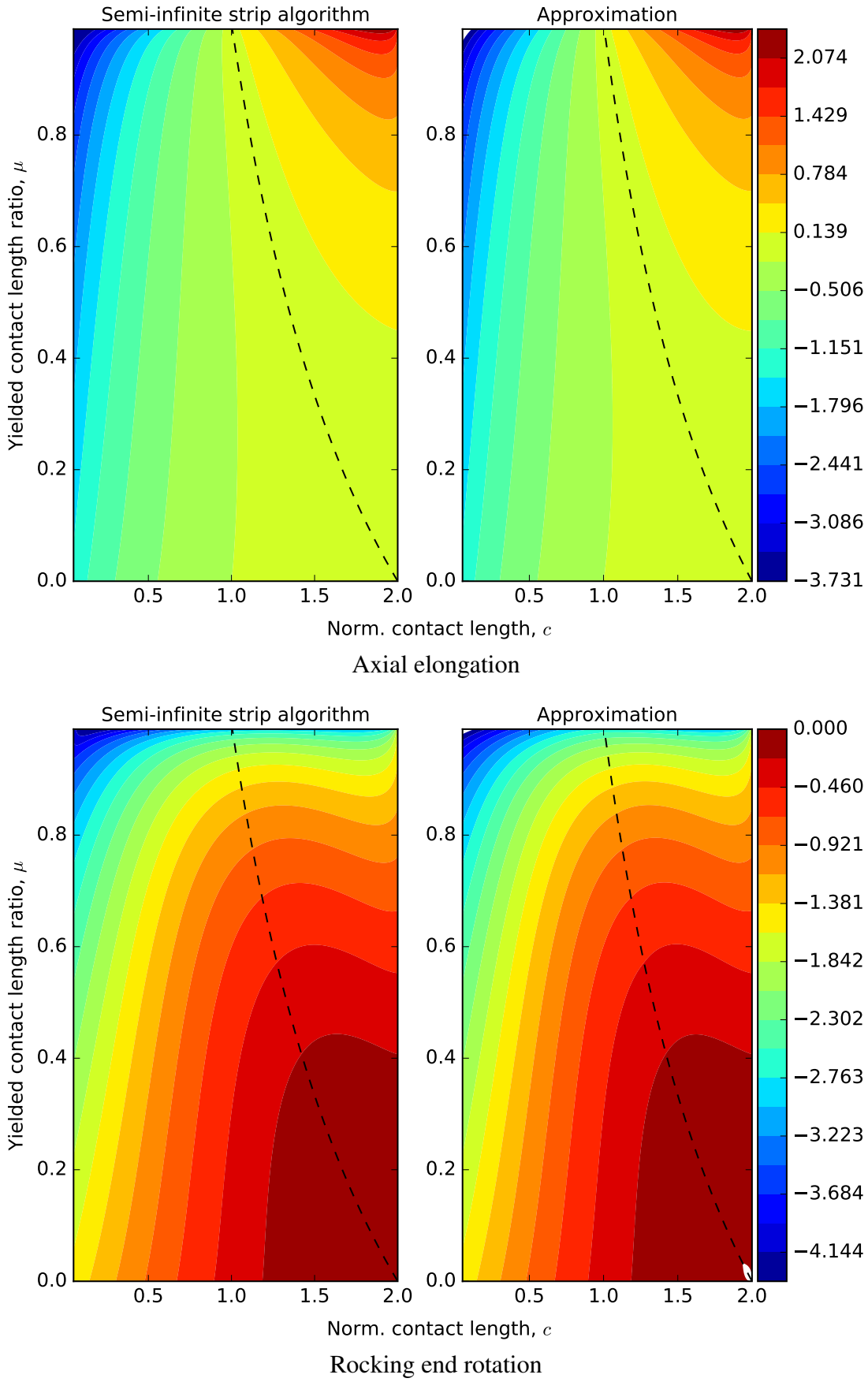


Figure 2: Normalized axial elongation and rocking end rotation for $\sigma_y = 1$.

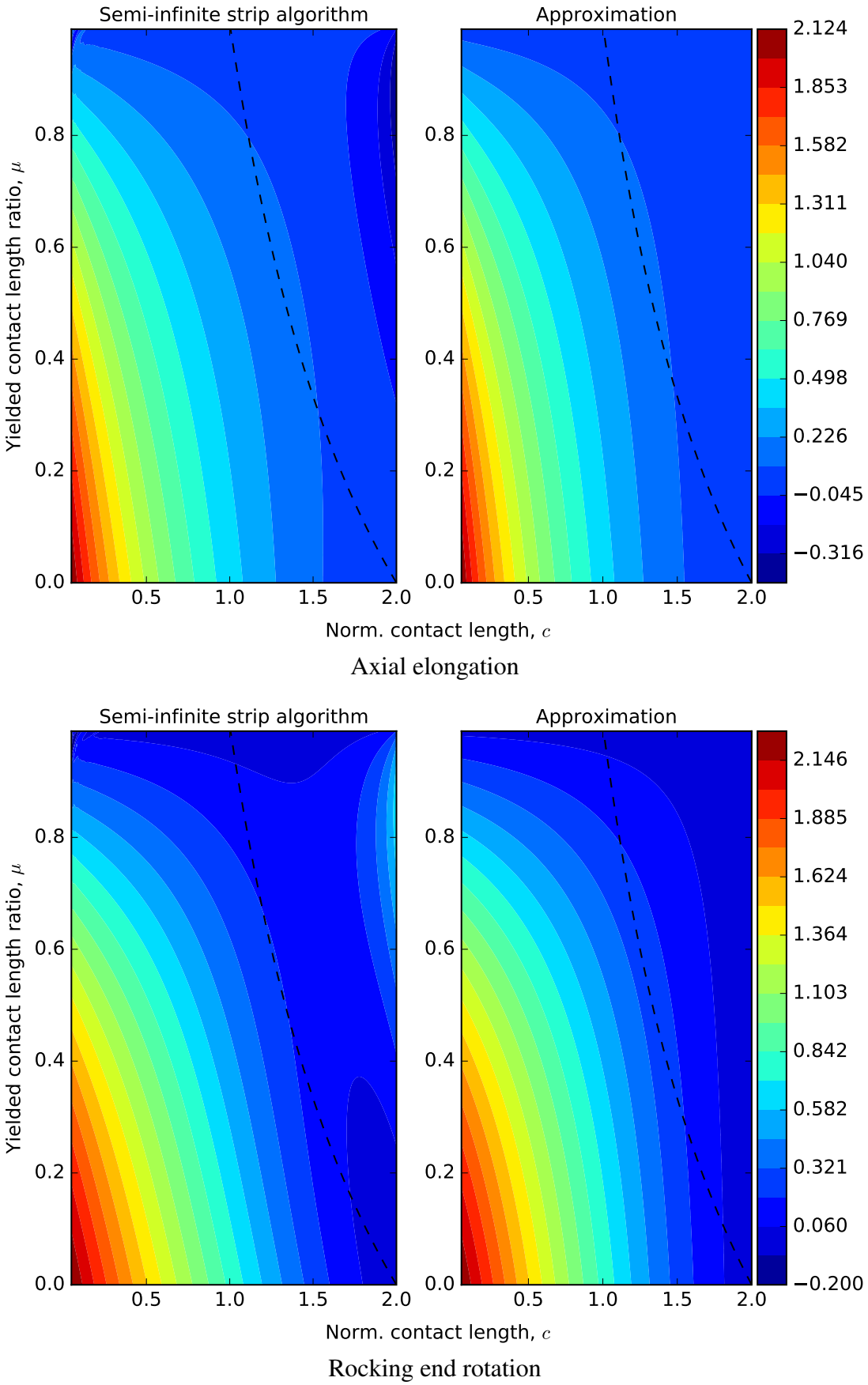


Figure 3: Normalized axial elongation and rocking end rotation for $t = 1$. The approximation is accurate enough for $c \leq 2/(\mu + 1)$.

**Changes in the macroelement algorithm due to yielding** After the calculation of the rocking interface forces, $\bar{\boldsymbol{Q}}_{\mathrm{r}}$, the yielding condition of Eq. 20 is checked. If the material has yielded, then the following changes are performed in the original algorithm:

- The load parameter vector, $\boldsymbol{r}$ of Eq. 3 is substituted with $\boldsymbol{r}_y$ of Eq. 17
- The corresponding derivative matrix, $\boldsymbol{S}_2$ of Eq. 10 is substituted with $\boldsymbol{S}_{2y}$ of Eq. 19
- The normalized displacement vector due to the self-equilibrating stresses, $\boldsymbol{u}$, (Eq. 4) is substituted with $\boldsymbol{u}_y$ of Eq. 21
- The corresponding derivative matrix, $\bar{\boldsymbol{F}}_n$ of Eq. 11 is substituted with $\bar{\boldsymbol{F}}_{ny}$ of Eq. 42

The rest of the algorithm steps remain the same as in the original elastic material algorithm.

## 5 EXAMPLES

### 5.1 Rocking body with constant vertical force with varying yield stress

In this example, a simple rocking body is examined, with height $H = 4$ m, width $B = 1$ m and depth $W = 1$ m and Young's modulus $E = 30$ GPa. The body is loaded on its top central node with a constant vertical force, $N = -2500$ kN (Fig. 4a).

Fig. 4b shows the pushover capacity curves (horizontal force versus horizontal displacement) of this body for varying yield stress values. It can be seen that the maximum strength and the ultimate displacement decrease for decreasing yield stress values.

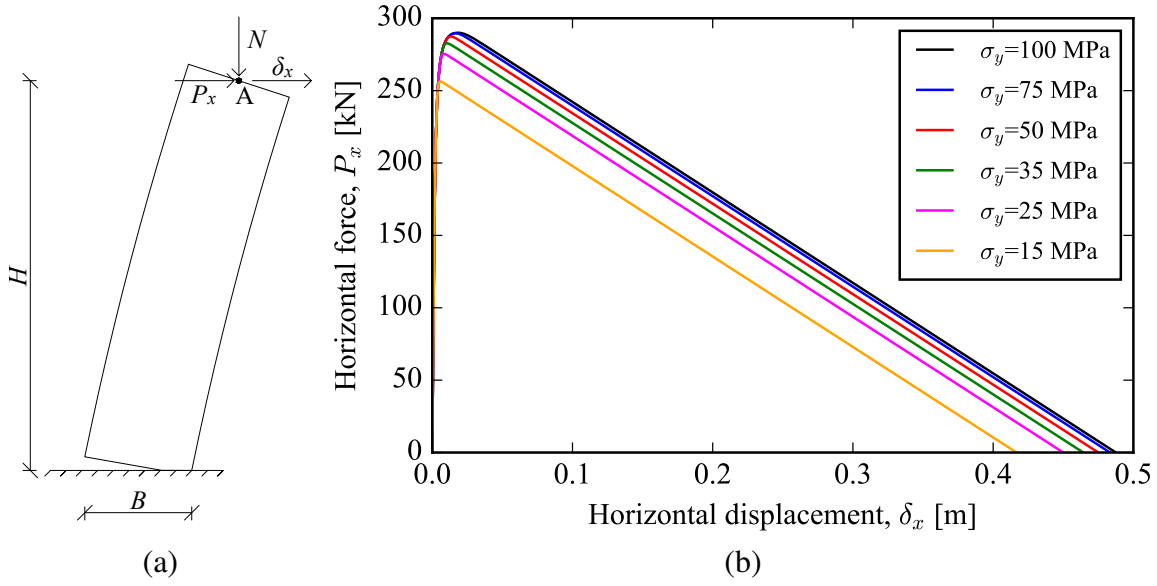


(a) (b)

Figure 4: Rocking body with constant vertical force model and pushover capacity curves for varying stress yield values.

### 5.2 Comparison of results with Abaqus

In this example, the results produced with the macroelement are compared to those of the commercial software Abaqus [20]. Unfortunately, pushover capacity curves for rocking bodies are very difficult to obtain with Abaqus for a yielding material due to convergence problems.

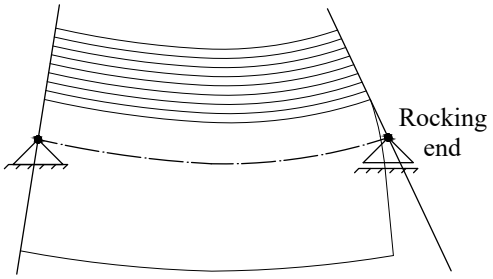


Figure 5: Simply supported beam with rocking end.

For this reason, comparisons are performed for a simply supported beam with a rocking end, which corresponds to the macroelement natural coordinate system (Fig. 5).

The simply supported beam examined has length $L = 8$ m, width $B = 2$ m, depth $W = 1$ m, Young's modulus $E = 30$ GPa, yield stress $\sigma_y = 20$ MPa and is loaded with a constant axial force $N = -1000$ kN.

In Figs. 6a and 6b, the axial elongation and the rocking end rotation are shown for increasing values of the applied moment on the rocking end of the simply supported beam. Fig. 6a refers to the case of a beam with equal applied moments on both its ends, meaning that there is no shear force along the beam, while 6b refers to the case of an applied moment only on the rocking end of the beam, leading to the development of shear forces.

In both cases, it can be seen that the results of the macroelement are very close to the ones obtained using equivalent Abaqus models.

## 6 CONCLUSION

In this paper, the rocking macroelement formulation previously proposed by the authors, which referred to a member with elastic response, is extended to describe the response of members with yielding material in a monotonic motion. Specific steps of the original formulation are altered to take into account the different stress distributions on the rocking interface, as well as the limited region of the section that remains elastic.

The formulation is applied to solve two example problems. Comparisons of the results with equivalent Abaqus models show very good agreement with the theoretically correct solution.

## REFERENCES

[1] R. Skinner, R. Tyler, A. Heine, and W. Robinson, "Hysteretic dampers for the protection of structures from earthquakes," *Bulletin of the New Zealand National Society for Earthquake Engineering*, vol. 13, no. 1, pp. 22–36, 1980.

[2] N. M. Priestley, "Overview of PRESSS research program," *PCI journal*, vol. 36, no. 4, 1991.

[3] S. Sritharan, S. Aaleti, and D. J. Thomas, "Seismic analysis and design of precast concrete jointed wall systems," *ISU-ERI-Ames Report ERI-07404, Submitted to the Precast/Prestressed Concrete Institute*, 2007.

[4] W. Y. Kam, S. Pampanin, A. Palermo, and A. J. Carr, "Self-centering structural systems with combination of hysteretic and viscous energy dissipations," *Earthquake Engineering & Structural Dynamics*, vol. 39, no. 10, pp. 1083–1108, 2010.

[5] G. W. Housner, "The behavior of inverted pendulum structures during earthquakes," *Bulletin of the seismological society of America*, vol. 53, no. 2, pp. 403–417, 1963.

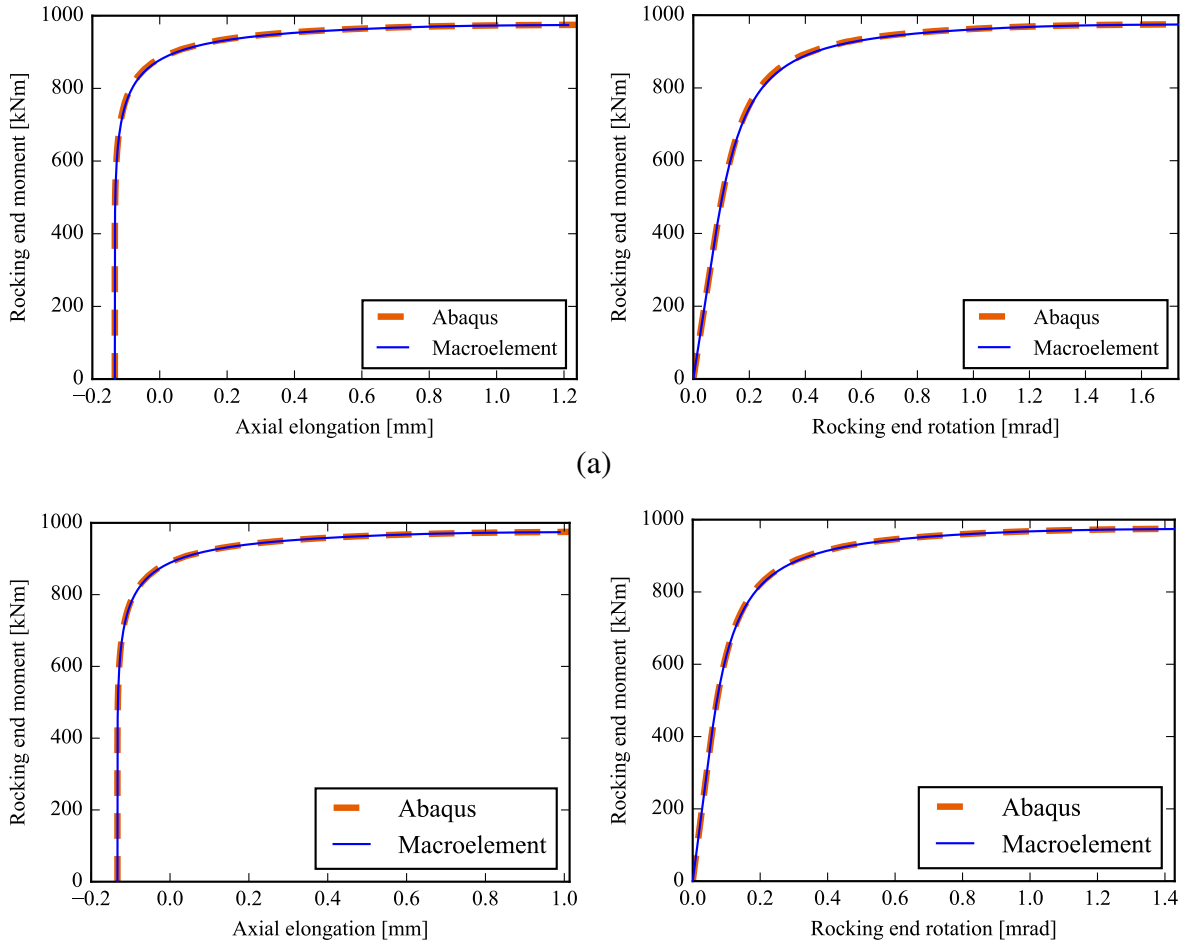


Figure 6: Axial elongation and rocking end rotation of a rocking simply supported beam and comparison with Abaqus, which is loaded with (a) equal moments on both its ends; (b) a moment only on its rocking end.

[6] C.-S. Yim, A. K. Chopra, and J. Penzien, "Rocking response of rigid blocks to earthquakes," *Earthquake Engineering and Structural Dynamics*, vol. 8, no. 6, pp. 565–587, 1980.

[7] J. Zhang and N. Makris, "Rocking response of free-standing blocks under cycloidal pulses," *Journal of Engineering Mechanics*, vol. 127, no. 5, pp. 473–483, 2001.

[8] E. G. Dimitrakopoulos and M. J. DeJong, "Revisiting the rocking block: closed-form solutions and similarity laws," in *Proceedings of the Royal Society of London A: Mathematical, Physical and Engineering Sciences*, vol. 468, pp. 2294–2318, The Royal Society, 2012.

[9] H. Roh and A. M. Reinhorn, "Analytical modeling of rocking elements," *Engineering Structures*, vol. 31, no. 5, pp. 1179–1189, 2009.

[10] H. Roh and A. M. Reinhorn, "Nonlinear static analysis of structures with rocking columns," *Journal of structural engineering, ASCE*, vol. 136, no. 5, pp. 532–542, 2009.

[11] S. Acikgoz and M. J. DeJong, "The interaction of elasticity and rocking in flexible structures allowed to uplift," *Earthquake Engineering & Structural Dynamics*, vol. 41, no. 15, pp. 2177–2194, 2012.

[12] C. B. Barthes, *Design of Earthquake Resistant Bridges Using Rocking Columns*. PhD thesis, University of California, Berkeley, California, United States, 2012.

[13] A. Belleri, M. Torquati, and P. Riva, "Finite element modeling of rocking walls," in *Proc., 4th ECCOMAS thematic conference COMPDYN*, 2013.

[14] A. Penna, S. Lagomarsino, and A. Galasco, "A nonlinear macroelement model for the seismic analysis of masonry buildings," *Earthquake Engineering & Structural Dynamics*, vol. 43, no. 2, pp. 159–179, 2014.

[15] M. F. Vassiliou, K. R. Mackie, and B. Stojadinović, "Dynamic response analysis of solitary flexible rocking bodies: modeling and behavior under pulse-like ground excitation," *Earthquake Engineering & Structural Dynamics*, vol. 43, no. 10, pp. 1463–1481, 2014.

[16] M. F. Vassiliou, R. Truniger, and B. Stojadinović, "An analytical model of a deformable cantilever structure rocking on a rigid surface: development and verification," *Earthquake Engineering & Structural Dynamics*, 2015.

[17] M. F. Vassiliou, K. R. Mackie, and B. Stojadinović, "A finite element model for seismic response analysis of deformable rocking frames," *Earthquake Engineering & Structural Dynamics*, 2016.

[18] E. Avgenakis and I. N. Psycharis, "Modeling of rocking elastic flexible bodies under static loading considering the nonlinear stress distribution at their base," *Journal of Structural Engineering, ASCE*, 2017.

[19] F. Gaydon and W. Shepherd, "Generalized plane stress in a semi-infinite strip under arbitrary endload," in *Proceedings of the Royal Society of London A: Mathematical, Physical and Engineering Sciences*, vol. 281, pp. 184–206, The Royal Society, 1964.

[20] Dassault Systemes, Providence, Rhode Island, United States, *Abaqus/CAE: User's Manual (6.11)*, 2011.

COMPDYN 2017
6th ECCOMAS Thematic Conference on
Computational Methods in Structural Dynamics and Earthquake Engineering
M. Papadrakakis, M. Fragiadakis (eds.)
Rhodes Island, Greece, 15–17 June 2017

# A SIMPIFIED PREDICTION METHOD FOR SEISMIC RESPONSES OF BUILDING FRAME STRUCTURES ALLOWED TO UPLIFT

**Tatsuya Azuhata**[1] **and Tadashi Ishihara**[2]

[1] International Institute of Seismology and Earthquake Engineering, Building Research Institute
Tsukuba, 305-0802, Ibaraki
e-mail: azuhata@kenken.go.jp

[2] Department of Production Engineering, Building Research Institute
Tsukuba, 305-0802, Ibaraki
e-mail: tishihar@kenken.go.jp

**Keywords:** Uplift, Rocking, Earthquake Response Reduction, Higher Modes, Response Spectrum.

**Abstract.** *Previous studies cleared that rocking behaviors can reduce seismic damages of some buildings. Based on this knowledge, some rocking structural systems which are allowed to uplift during earthquakes intentionally have been proposed as one of seismic energy dissipation systems. In this study, we propose a simplified prediction method for earthquake responses of such rocking structural systems.*

*To predict earthquake responses of the rocking systems, we need to evaluate effects of higher modes. We consider there are two sources to generate higher modes in the rocking systems. When a building starts uplift, higher modes simultaneously occur due to vertical inertial effects in the superstructure. Therefore, a dynamic overturning moment of the rocking systems surpasses that estimated statically. We evaluate this effect by using solutions of a free vibration of the target structure. Initial velocity for the free vibration can be specified if a velocity response spectrum is provided and the fundamental natural period, which is elongated after uplifting is appropriately estimated. Also, higher modes occur due to high-frequency components of an input earthquake ground motion. If the high-frequency components of the input motion are relatively large, performance for earthquake response reduction of the rocking structural system may deteriorate. These higher modes excited by the high-frequency components can be evaluated by using the response spectrum, too. We predict maximum earthquake responses of the rocking structural systems by combining the solution of free vibrations and higher mode responses of the corresponding fixed base model.*

## 1 INTRODUCTION

Previous studies cleared that rocking behaviors can reduce seismic damages of some buildings [For examples, 1-4]. Based on this knowledge, some rocking structural systems which are allowed to uplift during earthquakes intentionally have been proposed as one of seismic energy dissipation systems [For examples, 5-13]. In this study, we propose a simplified prediction method for earthquake responses of such rocking structural systems.

To predict earthquake responses of the rocking systems, we need to evaluate effects of higher modes. We consider there are two sources to generate higher modes in the rocking systems. When a building starts uplift, higher modes simultaneously occur according to vertical dynamic motion in the superstructure [1, 14, 15]. Therefore, a dynamic overturning moment of the rocking systems surpasses that estimated statically as shown in Fig.1.

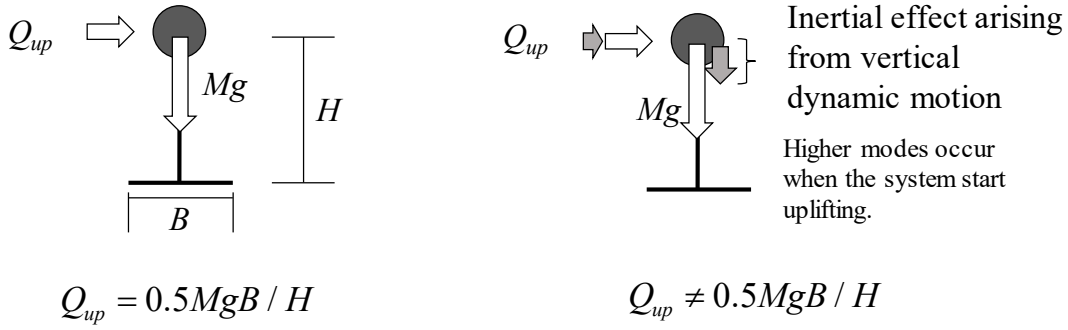


(a) Static (b) Dynamic

Figure 1: Inertial effect arising from vertical dynamic motion in rocking system

Also, higher modes occur due to high-frequency components of an input earthquake ground motion. If the high-frequency components of the input motion are relatively large, performance for earthquake response reduction of the rocking structural system may deteriorate [3].

We investigate such two effects of higher modes to seismic responses of rocking structural systems by free vibration analyses in chapter 3 and discuss a simplified method to predict seismic responses of them in chapter 4.

## 2 ANALYSIS MODEL AND TIME HISTORY RESPONSE ANALYSIS

### 2.1 System considered

In this study, we simulate earthquake responses of a frame allowed to uplift using a lumped mass system shown in Fig. 2. The height of superstructure is 30m and the width is footing beam is 7.5m. This system has two vertical springs under the footing beam. These springs can sustain only a compressive force. Initially, deformations of these springs are negative due to an effect of the self-wait of the system. When the deformation of either spring becomes zero under seismic loading, the system starts uplifting. The sway displacement is constrained. And we do not consider yielding of the super structure in this study. Mass of all mass points is equal. The story stiffness increases linearly from top to base. The ratio of stiffness of the top story to that of the base story is 0.5. These mass and stiffness of the superstructure are set so that the natural first period of it is equal to 1.0s.

The equations of motion of the system in horizontal, rotational and vertical directions are shown as the following Eq. (1) - (3), respectively.

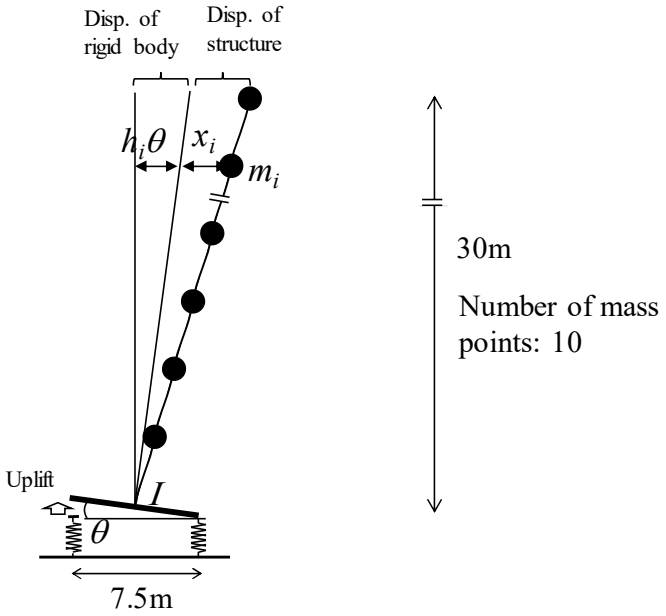


Figure 2: Lamped mass system for analyses

$$[M]\{\ddot{x}\}+[M]\{h_i\}\ddot{\theta}+[C]\{\dot{x}\}+[K]\{x\}=-[M]\{1\}\ddot{x}_g \tag{1}$$

$$\{h_i\}^T[\mathrm{M}]\{\ddot{x}\}+I\ddot{\theta}+R(t)=-\{h_i\}^T[\mathrm{M}]\{1\}\ddot{x}_g \tag{2}$$

$$\sum m\ddot{z}+V(t)=-\sum mg \tag{3}$$

where, [*M*], [*C*] and [*K*]: mass, damping and stiffness matrices of the super structure respectively, $\{h_i\}$: column vector consisting of height of each mass point, *I*: inertial moment of the footing beam, which is neglected in this study, $\Sigma m$: Total mass of the system, $R(t)$ and $V(t)$: rotational and vertical restoring forces by vertical springs under the footing beam.

We compose the [*C*] matrix setting damping factors, $h_i$, for all natural modes of the super structure to 2%.

The stiffness of soil springs varies according to the contact condition, that is whether the system is uplifting or not. Thus, $R(t)$ and $V(t)$ in Eq. (2) and (3) are affected by this condition. To make responses with impact stable, we include slight damping forces, which is probably negligible to comprehensive response characteristics, in the $R(t)$ and $V(t)$ by putting a dashpot in parallel with the spring. The dashpot is separated from the superstructure when the displacement of the vertical spring becomes zero.

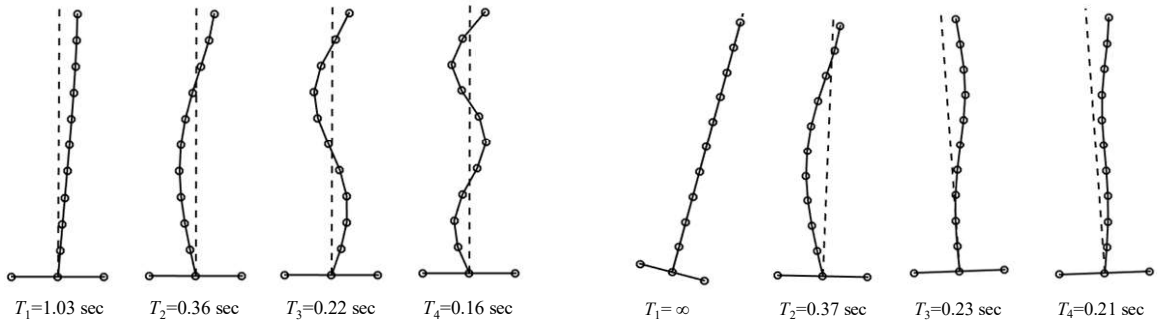


Figure 3: Natural modes and natural periods in contact and uplift phases

Figure 3 shows natural modes and natural periods of the contact and the uplift phases. The first natural period of the contact phase elongates from 1.0 s to 1.03s due to a flexibility effect of vertical springs. The first natural period of the uplift phase is infinity. The first natural mode of this phase is a rigid body mode. The second and third natural periods of the uplift phase are almost same as those of the contact phase.

## 2.2 Input ground motion

The input ground motion is an artificial ground motion (BCJ L2), which was proposed for structural design of high-rise buildings in Japan. The time duration is 120s and the peak ground velocity is about 0.5m/s. Velocity response spectra for two critical damping ratios, 2% and 5%, are shown in Fig.4. For free vibration analyses in chapter 3, we will use the maximum response velocity corresponding to the natural period of the contact phase estimated in this figure.

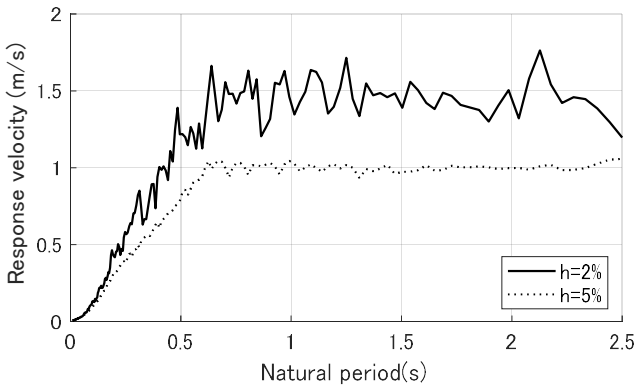


Figure 4: Velocity response spectra of input ground motion

## 2.3 Results of time history analysis

Figure 5 and 6 show time histories of roof displacements and uplifts on the base. The maximum roof displacement is about 70cm: the maximum uplift is about 15cm. Figure 7 shows a time history of base shear coefficient. We can see distinguished influence of higher modes to the base shear in the shape of wave. Figure 8 compares the maximum story shear coefficient of each story to that of the corresponding fixed base system. This results verify that shear forces can be reduced by allowing uplift to the structure. Figure 8 also shows the ultimate static shear forces for the rocking system by a broken line. These forces are estimated statically using seismic design lateral forces of Japanese seismic code. The dynamic results surpass the static estimation due to higher mode effects.

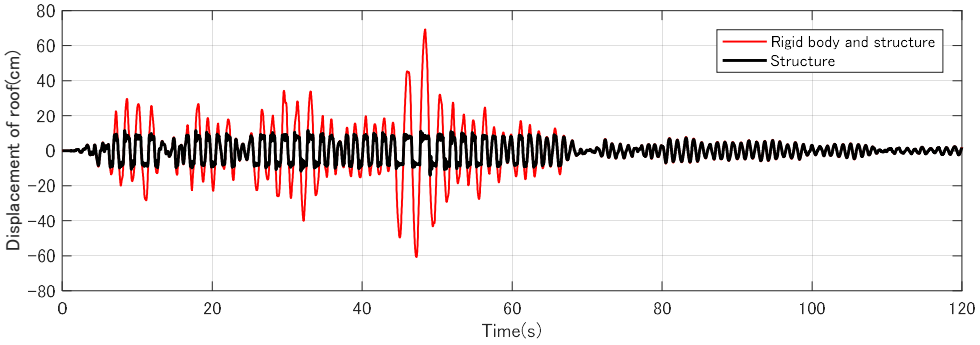


Figure 5: Time history of roof displacement

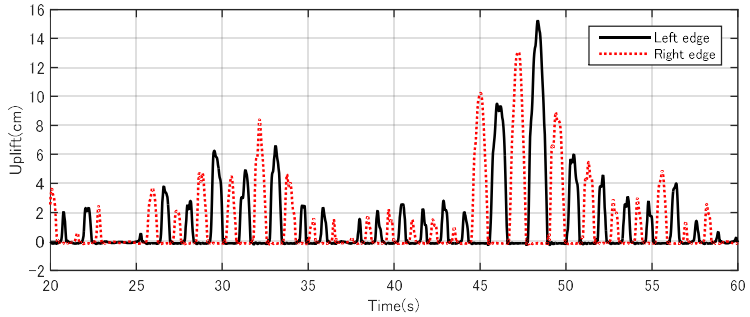


Figure 6: Time history of uplift

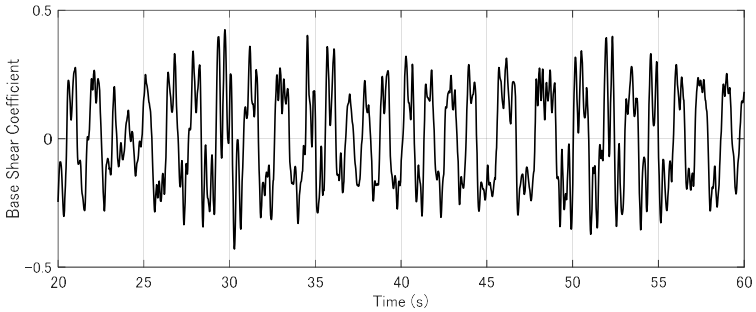


Figure 7: Time history of base shear

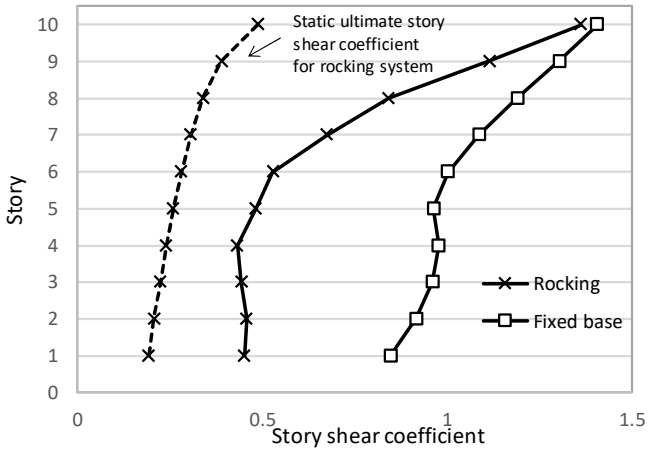


Figure 8: Comparison of shear coefficients of rocking system with those of fixed base system

## 3 FREE VIBRATION ANALYSES

### 3.1 Analysis procedure

We conduct free vibration analyses to investigate effects of higher modes to response characteristics of the rocking system. Initial velocity $\{V_0\}$ and displacement $\{D_0\}$ of each mass point for the free vibration analysis are determined by Eq. (4) and Eq. (5) respectively.

$$\{V_0\} = \sum \beta_i \{\varphi_i\} S_{vi} \cos\theta_i \tag{4}$$

$$\{D_0\} = \sum \beta_i \{\varphi_i\} S_{vi} \sin\theta_i / \omega_{ni} \tag{5}$$

where, $\beta_i\{\varphi_i\}$: participation vector in the contact phase, $S_{vi}$: the maximum response velocity of the equivalent one mass system, $\theta_i$: phase angle, $\omega_{ni}$: natural circular frequency in the contact phase.

We use first three modes to determine initial conditions. The $S_{vi}$ for each mode can be estimated by referring a response velocity spectra for $h$=2% in Fig. 2 as shown in Table 1. The first response period generally elongates when the system uplifts. However, the response velocity spectra in Fig.4 is constant in the range where natural periods are longer than 0.6s. Thus, we can neglect this elongation in this study and use the response velocity on the constant spectra as the $S_{vi}$ of the first mode.

The phase angle of each mode is set in the two ways as shown in Table 2. From this setting, we obtain two initial conditions shown in Fig.9.

Table 1: The maximum response velocity of equivalent one-mass system for each mode

| | Natural period (s) | $q_{vi}$ (m/s) |
|---|---|---|
| First mode | 1.03 | 1.50 |
| Second mode | 0.36 | 0.85 |
| Third mode | 0.22 | 0.50 |

Table 2: Phase angle $\theta_i$ of each mode

| | First mode | Second mode | Third mode |
|---|---|---|---|
| Initial condition - 1 | 0 | 0 | 0 |
| Initial condition - 2 | 0 | π /2 | π /2 |

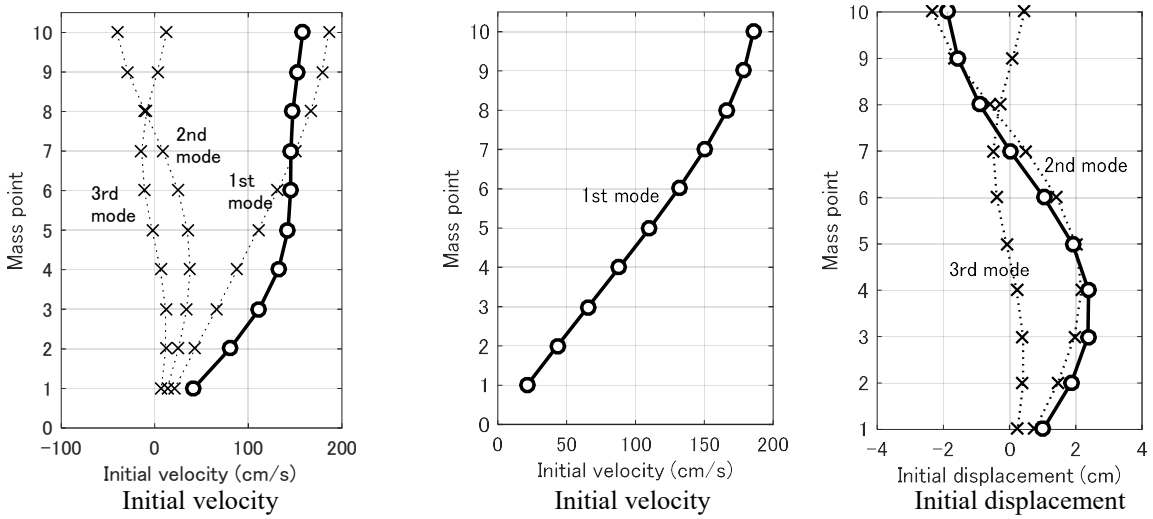


(a) Initial condition – 1 (b) Initial condition - 2

Figure 9: Initial conditions for free vibration analyses

Free vibration displacement response of a linear system can be expressed by Eq. (6), (7).

$$\{D(t)\} = \sum \{\varphi_i\} q_{di}(t) \tag{6}$$

$$q_{di}(t) = e^{-h_i \omega_{ni} t} \left\{ q_{di}(0) \cos \omega_{di} t + \frac{q_{vi}(0) + h_i \omega_{ni} q_{di}(0)}{\omega_{di}} \sin \omega_{di} t \right\} \tag{7}$$

where,

$$\omega_{di} = \sqrt{1 - h_i^2}\, \omega_{ni} \tag{8}$$

$$q_{di}(0) = \{\varphi\}^T [M] \{D_0\} / \{\varphi\}^T [M] \{\varphi\} \tag{9}$$

$$q_{vi}(0) = \{\varphi\}^T [M] \{V_0\} / \{\varphi\}^T [M] \{\varphi\} \tag{10}$$

The uplifting system is not a linear system. However, if we divide a whole response into some piecewise linear responses in the time domain, we can apply the general solution for the free

vibration like Eq. (6) - (10) for each one [14, 15]. When the system starts uplifting from the contact phase, we need to change natural modes and frequencies to those for the uplift phase and recalculate $q_{di}(0)$ and $q_{vi}(0)$ in Eq. (6), (7). When the system lands on the ground again, we need to reconstruct Eq. (6), (7) in the same way. We apply this piecewise linear method to solve free vibration problems of the uplift system. In this study, we estimate the viscous damping factor $h_i$ for each mode as 0.02 for all phases supposing the effect of damping forces in the $R(t)$ and $V(t)$ in Eq. (2) and (3) are negligible.

A. K. Chopra and R. K. Goel proposed the "uncoupled modal history response analysis" procedure to apply the classical modal history response analysis to non-linear systems [16]. Also, they presented the exact modal history response analysis procedure for the non-linear systems considering "the coupling of N equations in modal coordinate" [16]. We apply their concepts to free vibration analyses of the rocking system to extract effects of higher modes. The analysis procedure are as follows;

1) Separate initial conditions shown in Fig. 9 into the original three modal initial conditions which are expressed as $\beta_i \{\varphi_i\} q_{vi} \cos\theta_i$ and $\beta_i \{\varphi_i\} q_{vi} \sin\theta_i / \omega_{ni}$ in the right side of Eq. (4), (5),
2) Evaluate the separated free vibration response under each modal initial condition at the discretized analysis step,
3) Calculate summation of all separated free vibration responses to get a whole response at each step,
4) Judge whether the system starts uplifting or finishes it based on the whole response,
5) Reconstruct Eq. (6), (7) for all separated free vibration responses, if the system condition of uplifting varies,
6) Continue the analysis until response results for a sufficient time duration are obtained.

We refer to this analysis procedure as the "coupled modal free vibration analysis (CMFVA)" procedure here. Also, we refer to separated free vibration responses under the first, second and third modal initial conditions as "primary," "secondary" and "tertiary" responses respectively for convenience. These responses do not mean the pure modal responses. Especially, the primary response includes large affections by higher modes. Higher modes composing the primary response will be shown later.

### 3.2 Analysis results

Figures 10 to 13 compares results of the CMFVA analysis under the initial condition - 1 with those under the initial condition - 2. Figure 10 and 11 show shear coefficients of top story and base shear coefficients, respectively. In the case of the initial condition - 1, the primary, secondary and tertiary responses reach to their maximum almost simultaneously. Thus, whole responses, which are summation of all separated responses, under initial condition - 1 become larger than those under initial condition - 2.

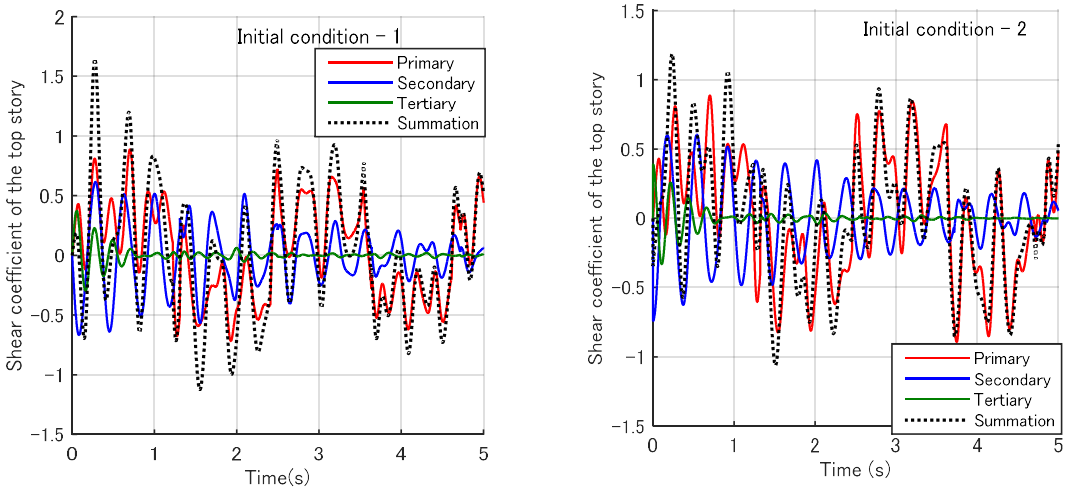


(a) Initial condition - 1 (b) Initial condition - 2

Fig.10: Comparison of shear coefficients of top story under different initial conditions (CMFVA)

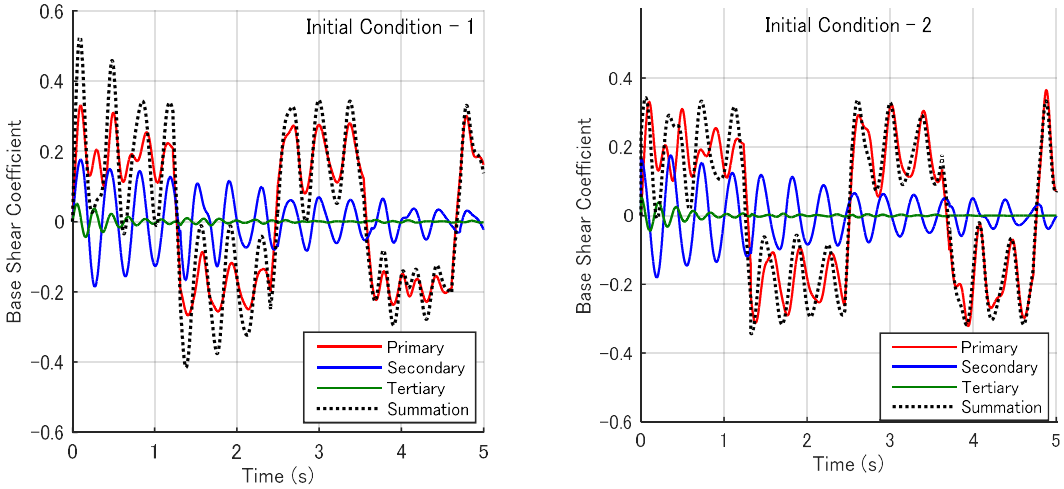


(a) Initial condition - 1 (b) Initial condition - 2

Fig.11: Comparison of base shear coefficients under different initial conditions (CMFVA)

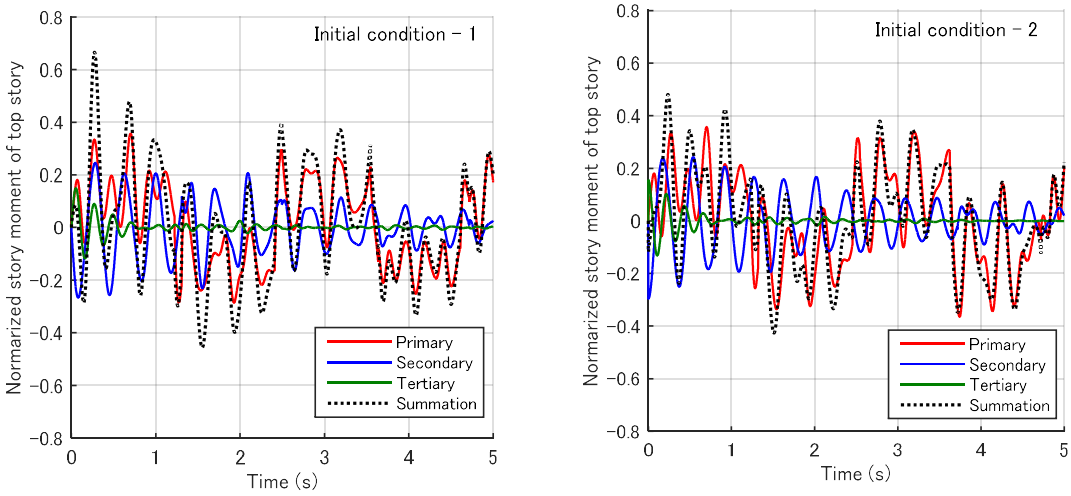


(a) Initial condition - 1 (b) Initial condition - 2

Fig.12: Comparison of normalized story moment of top story under different initial conditions (CMFVA)

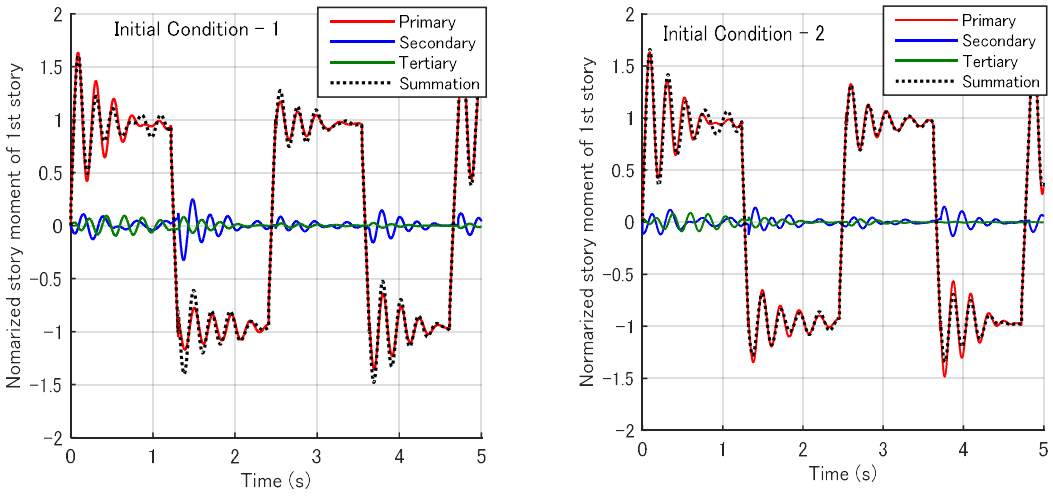


(a) Initial condition - 1 (b) Initial condition - 2

Fig.13: Comparison of normalized overturning moment under different initial conditions (CMFVA)

Figure 12 and 13 show normalized story moments, $Ms_i$, on the top and the base story which are calculated by the following equation, respectively. The story moment of the base story is the normalized overturning moment, $M_{OVT}$.

When $i<nst$,

$$Ms_i = \sum_{j=1}^{i} F_j \left( h_j - h_{i+1} \right) \Big/ 0.5\, w \sum_{j=1}^{i+1} m_j \tag{11}$$

When $i=nst$,

$$Ms_i = M_{OVT} = \sum_{j=1}^{i} F_j h_j \Big/ 0.5\, w \left( \sum_{j=1}^{i} m_j + m_{fb} \right) \tag{12}$$

where, $i$: number of story counted from the top, $j$: number of mass point counted from the top, $nst$: total number of stories, which is 10 in the case of the model shown in Fig.2, $F_j$: lateral force at the $j$-th math point, $h_j$: height of the $j$-th mass point, $w$: width of the system, $m_{fb}$: mass of footing beam.

As shown in Fig.12, the secondary and tertiary responses are relatively large in the story moment of the top story as well as in shear coefficients. In contrast, these responses become smaller in the overturning moment as shown in Fig.13. However, the overturning moment is amplified up to about 1.5 times static one by the vertical inertial effect explained in Fig.1.

Figure 14 shows time histories of base shear under the initial condition - 1 evaluated by the CMFVA comparing the uncoupled modal free vibration analysis (UCMFVA) which neglects “the coupling of N equations in modal coordinate” [16]. The results of the CMFVA and the UCMFVA are in good agreement. From the results shown in Fig 14. we can say that the secondary responses can be evaluated using the second natural mode of the contact phase. The primary response is more complicated than other responses because it is affected by higher modes arising from dynamic vertical motion. Figure 15 shows higher modes of the uplift phase which compose the primary response while the system is uplifting. These higher modes make the base shear fluctuate largely in this duration.

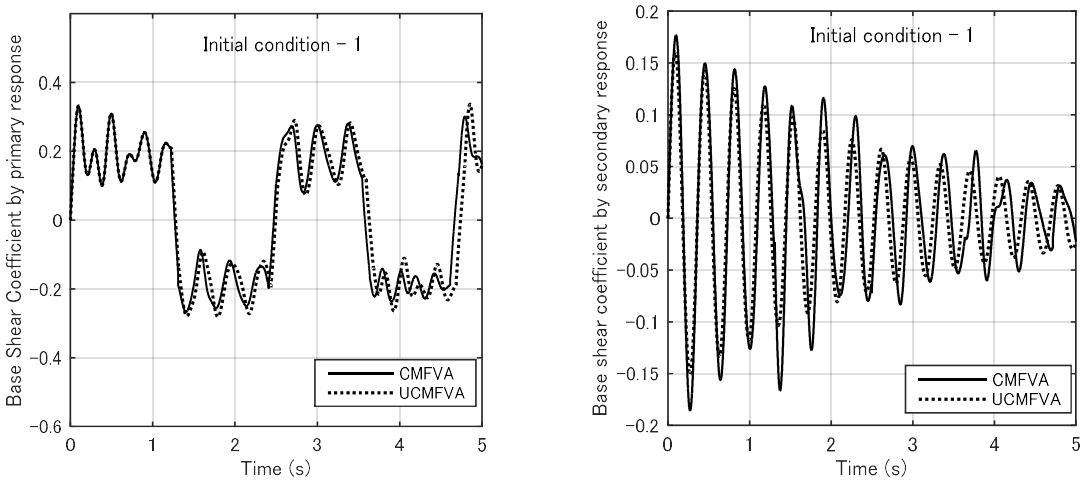


(a) Base shear coefficient by primary response (b) Base shear coefficient by secondary response

Fig.14: Comparison of CMFVA and UCMFVA

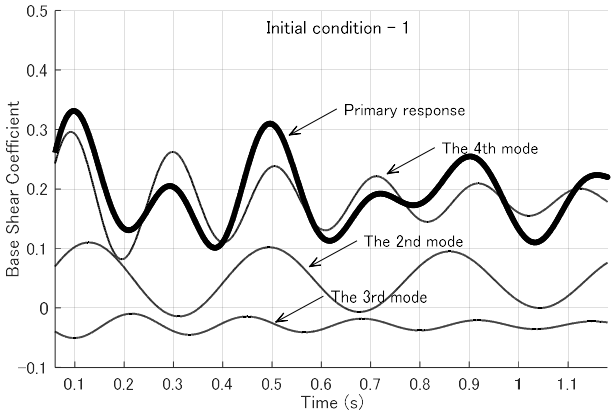


Figure 15: Higher modes composing the primary response for 0.1 - 1.1 sec. in Fig. 14

## 4 SIMPLIFIED MAXIMUM RESPONSE PREDICTION

To predict the maximum response values of the rocking system subjected to an earthquake ground motion simply, we suppose that they correspond to the maximum ones of free vibration responses. From the analysis results in the previous chapter, we can derive the following conclusions;

1) The maximum of primary response which is affected by higher modes arising from the dynamic vertical motion, which can be predicted by conducting the free vibration analysis under the first mode initial condition.
2) The maximums of secondary and tertiary responses are almost equal to those of systems in the contact phase which can be estimated by referring the response spectra of one mass system.

To predict the maximum responses, we need to combine the maximum ones of the primary, secondary and tertiary which are predicted by following the above-mentioned conclusions. In this study, we adopt the combination rule in the Steel Construction New Zealand guide in controlled rocking steel braced frames [17, 18]. The concept of this combination rule is expressed by the following equation.

$$R = R_P + \sqrt{R_2^2 + R_3^2} \tag{13}$$

where, $R$: the maximum response, $R_P$: the maximum of the primary response, $R_2$: the maximum of the secondary response, $R_3$: the maximum of tertiary response.
The notation of Eq. (13) is changed for application in this study.

Figure 16 compares predicted values with the maximum values of a time history analysis in chapter 2 and those of free vibration analyses (CMFVA) in chapter 3. These figures show the results of story shear coefficients and story moments respectively. In the both figures, the predicted values tend to surpass all response values in the middle stories. However, we can say that the proposed method can provide reasonable prediction as a whole.

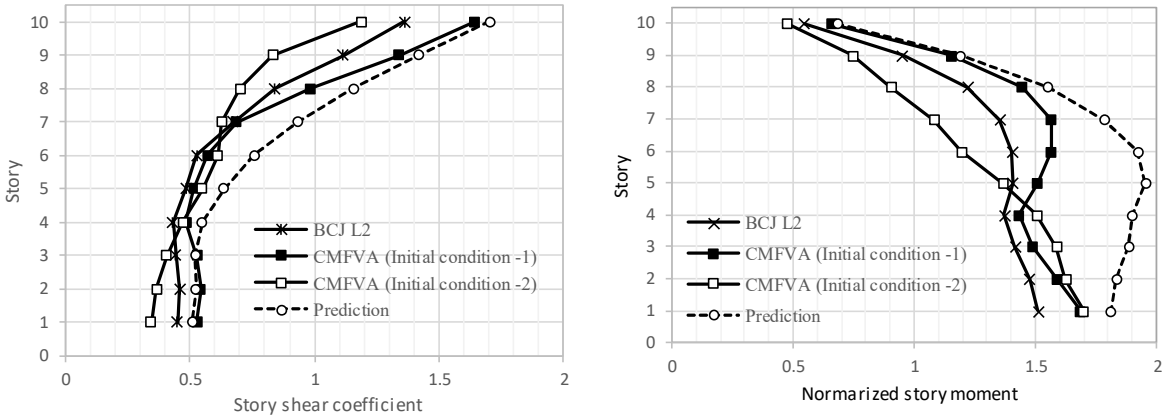


(a) Story shear coefficient (b) Normalized story moment

Figure 16: Comparison of predicted values with response values

## 5 CONCLUSIONS

To predict the maximum responses of the structures allowed to uplift, effects of higher modes were investigated by executing free vibration analyses. Free vibration responses were separated into the primary response, the secondary response and the tertiary response. Each separated response is determined by the corresponding modal initial condition.

The maximum of the primary response, which is affected by the higher modes arising from dynamic vertical motions during uplifting, can be predicted by a free vibration analysis under the first mode initial condition. The maximums of the secondary and the tertiary responses, which are amplified by high-frequency components of an earthquake ground motion, can be predicted by referring a response spectra of an earthquake ground motion.

Finally, it was presented that the maximum responses of the structures allowed to uplift can be predicted to combine the maximums of the three separated responses appropriately.

## ACKNOWLEDGEMENT

This work was supported by JSPS KAKENHI Grant Number JP16K06601.

## REFERENCES

[1] J. W. Meek, *Effects of foundation tipping on dynamic response*, Journal of Structural Engineering, Vol.101, No.ST7, ASCE: 1297-1311, 1975.

[2] A. Rutenberg, P. C. Jennings, G. W. Housner, *The response of Veterans Hospital Building 41 in the San Fernando Earthquake*, Earthquake Engineering and Structural Dynamic, 10(3), 359-379, 1982.

[3] Y. Hayashi, *Damage reduction effect due to basement uplift of buildings*, Journal of Structural and Construction Engineering. AIJ 485, 53-62, 1996. (In Japanese)

[4] Y. Hayashi, K. Tamura, M. Mori, I. Takahashi: *Simulation analysis of buildings damaged in the 1995 Kobe, Japan, earthquake considering soil-structure interaction*, Earthquake Engineering and Structural Dynamics, 28, 371-391, 1999.

[5] R. W. Clough, A. A. Huckelbridge, *Preliminary experimental study of seismic uplift of a steel frame*, Report No.UBC/EERC-77/22. EERC, University of California, Berkeley, CA., 1977.

[6] A. A. Huckelbridge, *Earthquake simulation tests of a nine story steel frame with columns allowed to uplift*, Report No.UBC/EERC-77/23. EERC, University of California, Berkeley, CA, 1977.

[7] M. Midorikawa, T. Azuhata, T. Ishihara, A. Wada, *Shaking table tests on seismic response of steel braced frames with column uplift*, Earthquake Engineering and Structural Dynamics, 35(14), 1767-1785, 2006.

[8] N. B. Chancellor, R. Sauce, J. M. Ricles, *Design and validation of steel self-centering concentrically-braced frames*, Proceeding of 16th WCEE, No. 2705, 2017.

[9] E. Tahmasebi, R. Sause, J. M. Ricles, *Probabilistic Seismic Damage Analysis of Steel Self-Centering Concentrically Braced Frame Systems*, Proceeding of 16th WCEE, No. 2811, 2017.

[10] T. C. Steele, L. D. A. Wiebe, *Collapse Assessment of Controlled Rocking Steel Braced Frames with different of rocking joint parameters*, Proceeding of 16th WCEE, No. 2963, 2017.

[11] M. Midorikawa, N. Kotani, T. Okazaki, T, Asari, T. Ishihara, T. Azuhata, *Seismic energy response of multi-story steel rocking frames allowing column mid-height at the first story*, Proceeding of 16th WCEE, No. 2986, 2017.

[12] M. Kovacs, L. Wiebe, *Controlled rocking heavy timber walls for regions of low to moderate seismicity*, Proceeding of 16th WCEE, No. 3253, 2017.

[13] J. Binder, C. Christopoulos, M. Gray, *Seismic response of hybrid ductile-rocking buckling restrained braced frames with cast steel supplement energy dissipation element*, Proceeding of 16th WCEE, No. 4450, 2017.

[14] T. Ishihara, M. Midorikawa, T. Azuhata, *Modal analysis of uplifting behavior of buildings modeled as uniform shear-beam*, Proceeding of 14th WCEE, Paper ID 05-06-0116, 2008.

[15] T. Ishihara, M. Midorikawa, T. Azuhata, *Modal properties and free vibration of uplifting behavior of multistory buildings modeled as uniform shear-beam*, Journal of Structural and Construction Engineering. Vol. 74, AIJ 640, 1055-1061, 2009. (In Japanese)

[16] A. K. Chopra, R. K. Goel: *A modal pushover analysis procedure for estimating seismic demands for buildings*, Earthquake Engineering and Structural Dynamics, 31, 561-582, 2002

[17] L. Wiebe, G. Sidwell, S. Gledhill, *Design guide for controlled rocking steel braced frames*, Steel Construction New Zealand, Manukau City, New Zealand, 2015.

[18] T. C. Steele, L. D. A. Wiebe, *Dynamic and equivalent static procedures for capacity design of controlled rocking steel braced frames*, Earthquake Engineering and Structural Dynamics, 45, 2349-2369, 2016.

COMPDYN 2017
6th ECCOMAS Thematic Conference on
Computational Methods in Structural Dynamics and Earthquake Engineering
M. Papadrakakis, M. Fragiadakis (eds.)
Rhodes Island, Greece, 15–17 June 2017

# DESIGN STRATEGY FOR THE ROCKING STABILITY OF HORIZONTALLY RESTRAINED MASONRY WALLS

**L. Giresini**[1]

[1] University of Pisa
Department of Energy, Systems, Territory and Constructions Engineering, Pisa, Italy
linda.giresini@unipi.it

**Keywords:** Horizontal restraint, rigid block dynamics, resonance, out-of-plane, masonry walls.

**Abstract.** *This paper investigates the pure rocking of a rigid block with horizontal restraints. The model simulates the behavior of a masonry wall connected to transverse walls and/or steel tie-rods, very frequently adopted as safety measures against seismic actions. From the system rotational stiffness, found for a Winkler-type model and for a single restraint, the resonance conditions of the horizontally restrained blocks are defined. The role of the horizontal restraint can be unilateral (acting only one direction of rotation) and/or bilateral (restraint with similar stiffness in both directions). Real earthquakes or Ricker's wavelets, representing near-fault ground motions, are assumed as input parameters. It is found that in the bilateral case the response is more predictable, as response spectra are monotonic curves whit a reduction of normalized rotation obtained for higher values of restraint stiffness. Moreover, the effect of horizontal restraints is beneficial for the range of frequency parameters valid for typical masonry walls. These considerations allow to define a design strategy to ensure the rocking stability of restrained masonry walls, through a self-centered rocking behavior.*

# 1 INTRODUCTION

The out-of-plane assessment of masonry walls is generally faced through kinematic approaches [1], [2] or global models where those modes are suggested by a specific deformation pattern of the structure [3]. Nevertheless, a rocking analysis cannot be neglected when assessing the seismic vulnerability of a masonry wall [4]. Rocking behavior is one of the reasons why many ancient structures survived for centuries in highly seismic areas. It can be indeed used as method for stabilizing rigid objects or free structures, in addition to traditional or innovative techniques of dissipation in masonry buildings [5]. Despite their apparent instability under horizontal ground motions, rocking structures exhibit earthquake resistance [6]. The stability condition of the rocking block can be different depending on its boundary conditions: it can be free-standing [7], vertically restrained [8] or horizontally restrained [9]. Moreover, external actions such as thrust of a roof on masonry panels can play a relevant role in the response [10]. The model of a block with horizontal restraints is based on two types of restraints [9]: (i) single spring at a certain depth of the block and (ii) Winkler-type spring bed. Case (i) is representative of anti-seismic devices such as steel tie-rods, very frequently used to impede out-of-plane movements of masonry walls [11], [12] . Case (ii) models the role of transverse walls connected to the rocking wall itself. In this paper, the effect of the horizontal restraints under sine pulse, Ricker wavelets and real seismic records is analyzed and discussed. Indeed, the response of the rocking block is particularly sensitive to the input motion. The period of the excitation significantly affects the response and the possibility of collapse: near-field ground motions, that contain long-period directivity pulses, might bring these structures to collapse [13]. Recently, numerical approaches were proposed to identify ground motions capable to cause 'rocking resonance' [14]–[16].

This paper illustrates the dynamics and the system stiffness of horizontally restrained rocking blocks, defining the resonance condition. The dimensionless variables $\Pi$, function of the spring bed and the single restraint stiffness, are also derived. Afterwards, the attention focuses on the analysis on a rocking façade under different typologies of pulses. By analyzing the behavior in unilateral and bilateral conditions and widening the analysis for different walls, a design strategy is conceived to reach a rocking behavior for which the response is more controllable and predictable.

# 2 DYNAMICS AND STIFFNESS OF THE HORIZONTALLY RESTRAINED ROCKING BLOCK

## 2.1 Equation of motion

The Housner block can be detained by two typologies of restraints: (i) single spring at a certain depth of the block and (ii) closely spaced independent flexible supports (Figure 1). Case (ii) is a simplification of transverse masonry walls connected to the rocking panel. This assumption is an approximation of the real mechanical behavior of transverse masonry walls: indeed, it ignores frictional and multidimensional elasticity effects. Let us assume that in the clockwise (CW) rotation the steel tie-rod is active, as in Figure 1, due to the tensile force acting on it. When the block rotates counter-clockwise (CCW), the tie-rod becomes inactive due to the buckling phenomenon. For what concerns transverse walls, the stiffness is different in CW and CCW rotations: in particular, in CW rotation it should take into account friction forces for the interlocking between the bricks of the rocking wall and those of the transverse walls. Nevertheless, this contribution is neglected and for CW rotation the transverse walls are assumed to not rotate. By contrast, in CCW these are active and offer a stiffening contribution limiting the rocking motion of the wall.

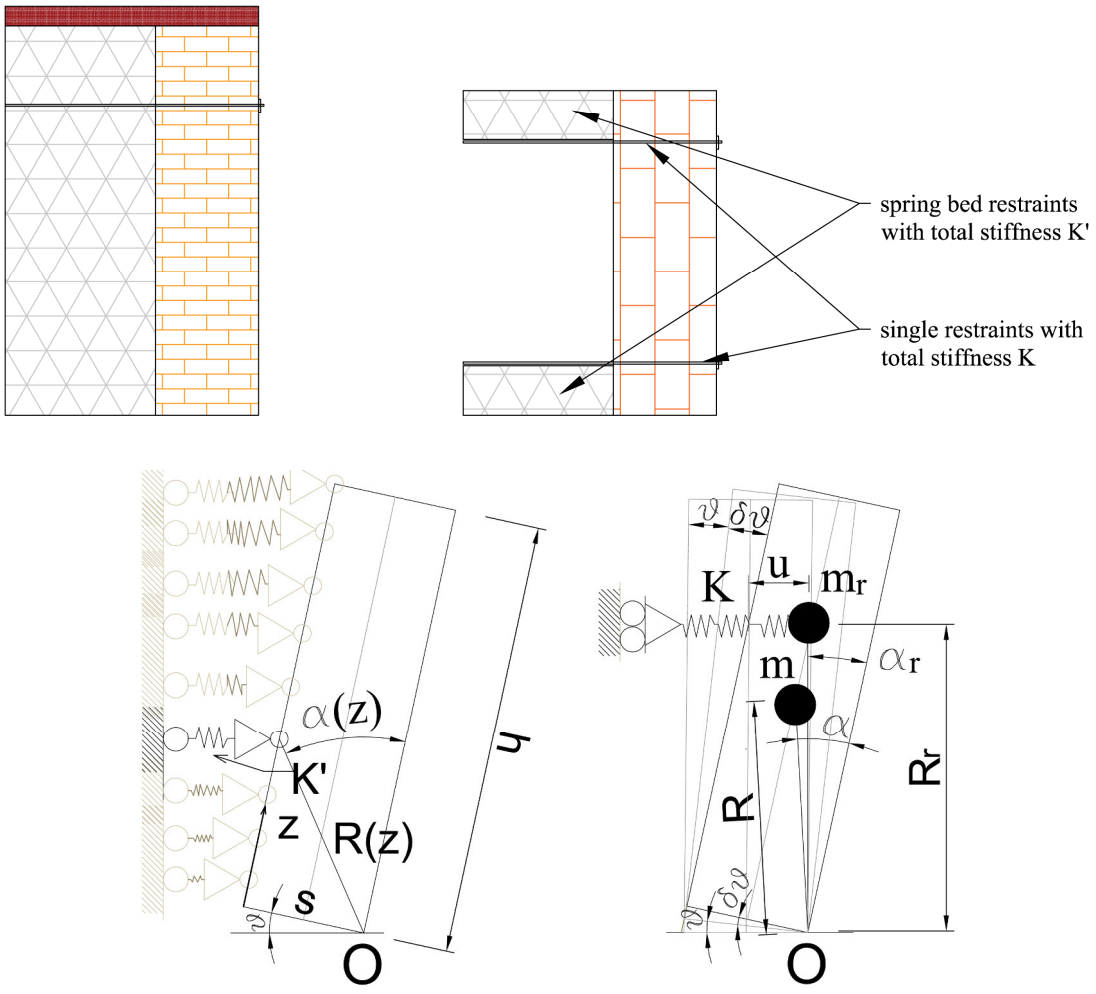


Active transverse walls (a) Active tie-rods (b)

Figure 1: Housner block simulating a masonry wall with transverse walls (a) and steel tie-rods (b). The two structural elements are modeled with closely spaced independent flexible supports smeared out through the depth of the block (a) and single spring with the radius vector $\beta R$ (b).

The complete equation of motion of the block restrained by a single restraint (of stiffness $K$) and by a spring bed (of stiffness $K'$) is:

$$I_0\ddot{\vartheta} + sgn(\vartheta)mgR\sin A_\vartheta + \\ +sgn(\vartheta)\,K\beta^2R^2\cos A_{r,\vartheta}\,[sin\,\alpha_r - \sin A_{r,\vartheta}] + sgn(\vartheta)\,K'\bar{h}\left(A + \frac{B\bar{h}}{2} + \frac{C\bar{h}^2}{3}\right) \\ - m\,\ddot{u}_g R\cos A_\vartheta = 0 \tag{1}$$

where:

$$A_\vartheta = \alpha - sgn(\vartheta)\vartheta \\ A_{r,\vartheta} = \alpha_r - sgn(\vartheta)\vartheta \tag{2}$$

$\alpha$ is the block radius vector, whereas $\alpha_r$ is the single spring radius vector. Moreover, $\bar{h}$ is the height along which the spring bed is effective. This value may obviously be lower than the block height $h$. $\ddot{u}_g$ is the seismic excitation and $\beta$ defines the single spring position.
This equation can be also expressed in function of the frequency ratio $p^2 = mgR/I_0$ by dividing it by $I_0$:

$$\ddot{\vartheta} = -sgn(\vartheta)\, p^2 \left\{ \sin A_\vartheta + \frac{K\beta^2 \mathrm{R}}{mg} \cos A_{r,\vartheta} \left[ sin\, \alpha_r - \sin A_{r,\vartheta} \right] + 2 \cos \alpha \frac{K'}{mg} \left( A + \frac{B\bar{h}}{2} + \frac{C\bar{h}^2}{3} \right) \right\} + p^2 \frac{\ddot{u}_g}{g} \cos A_\vartheta \tag{3}$$

where the terms multiplied by $K'$ are:
$A = sgn(\vartheta)\, s^2 \sin\vartheta\, \cos\vartheta\, (1 - \cos\vartheta)$;
$B = s\, (\sin^2\vartheta\, \cos\vartheta - \cos^3\vartheta + \cos^2\vartheta)$;
$C = sgn(\vartheta) \sin\vartheta\, \cos^2\vartheta$.

For values of radius vectors valid for masonry walls, namely $0 < R < 10$ m, where the larger values are typical of large façades of monumental buildings, the frequency ratio $p$, assuming rectangular block, varies as displayed in Figure 2.

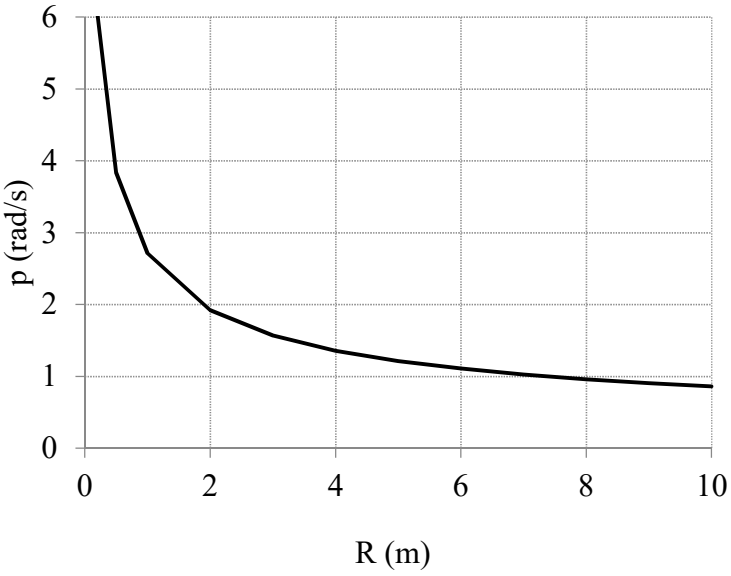


Frequency ratio p:
$p = \sqrt{mgR/I_0}$

For rectangular blocks:
$p = \sqrt{\frac{mgR}{\frac{4}{3}mR^2}} = \sqrt{\frac{3g}{4R}}$

Figure 2: Frequency ratio $p$ for rectangular blocks in the range of interest of $R$ values valid for masonry façades.

The integration of Equation (2) expresses the time-history response of the restrained rocking block, which is function of the following parameters:

$$\vartheta = \mathrm{f}\left[ p, \alpha, \alpha_r, \frac{K\beta^2 \mathrm{R}}{mg}, \frac{K'}{mg} \left( A + \frac{B\bar{h}}{2} + \frac{C\bar{h}^2}{3} \right) \right] \tag{4}$$

Those terms depend only on the geometry of the block and on the type of restraints, with the exception of $A, B, C$ (Equation (3)) that need to be further modified as reported in the following paragraph.

## 2.2 **Ricker wavelets and derivation of dimensionless terms for the restrained block**

The seismic action, enclosed in the term $\ddot{u}_g$ of Equation (2), generally has different frequency contents and amplitudes. Nevertheless, several authors considered the rocking response to pulses described as simple trigonometric functions and explained why rocking structures are particularly vulnerable to pulse-type earthquakes. In [17], it is observed that small blocks overturn with short period pulses, whereas larger blocks overturn due to the long-duration pulse.
The detrimental role of long-period pulses inherent in near-fault ground motions is also observed [18]. The Authors consider that under cycloidal pulses a free-standing block can overturn with two distinct modes: (1) by exhibiting one or more impacts; and (2) without exhibiting any impact. For the second mode, it can be determined a safe region that is located on the acceleration-frequency plane above the minimum overturning acceleration spectrum. The shape of this region depends on the restitution coefficient.
For pulse-type earthquakes, the use of dimensionless variables is very advantageous.
The Ricker wavelet [19] or its time derivative well approximate coherent pulses of several pulse-like ground motions [20]:

$$\psi(t) = \mathrm{a}_p \left(1 - \frac{2\pi^2 t^2}{T_p^2}\right) e^{-\frac{1}{2}\left(\frac{2\pi^2 t^2}{T_p^2}\right)} \tag{5}$$

where $a_p$ is the amplitude of the acceleration pulse. The value of $T_p = \frac{2\pi}{\omega_p}$ is the period that maximizes the Fourier spectrum of the wavelet, being $\omega_p$ the circular frequency of the acceleration pulse. A relevant value correlated to those parameters is the characteristic length scale of the ground excitation. This parameter, $L_p = a_p T_p^2$, gives a measure of the persistence of the most energetic pulse capable to generate inelastic deformation.
If one considers then pulse-type excitations, the response can be expressed in function of:

$$\vartheta = \mathrm{f}\left[p, \alpha, K, K', a_p, \omega_p, g\right] \tag{6}$$

assuming that, for the sake of simplicity, $\alpha = \alpha_r$ (slender blocks). The number of dimensionless products that completely describe the motion, according to the Vashy-Buckingham $\Pi$ theorem [8], [21], is given by the number of variables (8) minus the number of reference dimensions (2, namely the time and the length). One has then 6 dimensionless products, which are:

$$\Pi_\vartheta = \vartheta;\ \ \Pi_\omega = \frac{\omega_p}{p};\ \Pi_\alpha = \tan\alpha;\ \Pi_g = \frac{a_p}{g};\ \Pi_K = \frac{K\beta^2 R}{mg};\ \Pi_{K'} = \frac{K' R^2}{mg} \tag{7}$$

The validation of a MATLAB code used herein to generate the rocking curves and spectra solve a 4th-5th order is performed by comparing the results with those obtained by [8]. The integration of Equation (3) is performed with the Runge-Kutta method [22].
By considering the following dimensionless parameters:

$$\Pi_\omega = 1.0;\ \frac{\Pi_g}{\Pi_\alpha} = 2;\ \Pi_a = 0.176;\ \Pi_\gamma = 0 - 2;\ \Pi_K = \Pi_{K'} = 0, \tag{8}$$

it is possible to obtain rocking spectra. In Equation (8), $\Pi_\gamma$ refers to a rocking frame, made by a set of $N$ columns of mass $m_c$ and a cap beam of mass $m_b$. The frequency ratio of a rocking frame is given by $\hat{p} = p\sqrt{(1+2\gamma)/1+3\gamma}$, where $\gamma = m_b/(Nm_c)$ [23]. The dimensionless parameter $\Pi_\gamma$ correspond to the value of $\gamma$. The obtained rocking spectra are displayed in Figure 3.

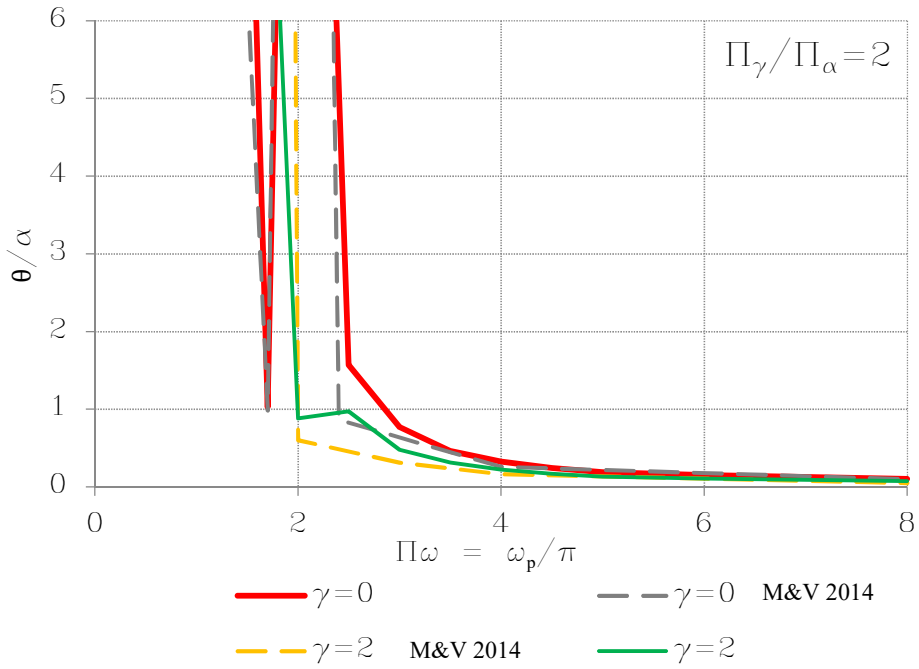


Figure 3: Rocking spectra for $\Pi_\omega = 1.0$; $\frac{\Pi_g}{\Pi_\alpha} = 2$; $\Pi_a = 0.176$; $\Pi_\gamma = 0 - 2$, results compared with Figure 3 of [8].

### 2.3 System rotational stiffness for smeared and single horizontal restraints

By expressing the work made by the springs in the two models, the resisting moment-rotation relationship is obtained, which is for case (i) [9]:

$$M_r(\vartheta) = mgR\sin(\alpha-\vartheta) + K\beta^2R^2\cos(\alpha-\vartheta)\,[sin\,\alpha - \sin(\alpha-\vartheta)] \tag{9}$$

By assuming a constant spring stiffness $K'$ smeared out through the whole depth of the block, the dimensionless resisting moment-rotation relationship for the spring bed model is [9]:

$$M_r(\vartheta) = mgR\sin(\alpha-\vartheta) + K'h\left(A + 2BR\cos\alpha + \frac{4CR^2\cos^2\alpha}{3}\right) \tag{10}$$

where:

$$\begin{gathered} A = sgn(\vartheta)\,s^2\sin\vartheta\,\cos\vartheta\,(1-\cos\vartheta); \\ B = s\,(\sin^2\vartheta\,\cos\vartheta - \cos^3\vartheta + \cos^2\vartheta); \\ C = sgn(\vartheta)\sin\vartheta\,\cos^2\vartheta \end{gathered} \tag{11}$$

The function $sgn(\vartheta)$ expresses the sign ± depending on the rotation sign, clockwise or counterclockwise. Let us assume here a positive rotation. Equations (9) and (10) are valid for any

rotation, whereas for small rotation, for which $\sin\vartheta \cong \vartheta$, $\cos\vartheta \cong 1$ and second order terms are neglected, the system rotational stiffness reads [9]:

$$K_{sys} = mgRcos\alpha \left(\frac{K\beta^2 R}{mg} cos\alpha - 1\right) \tag{12}$$

for the single spring model.

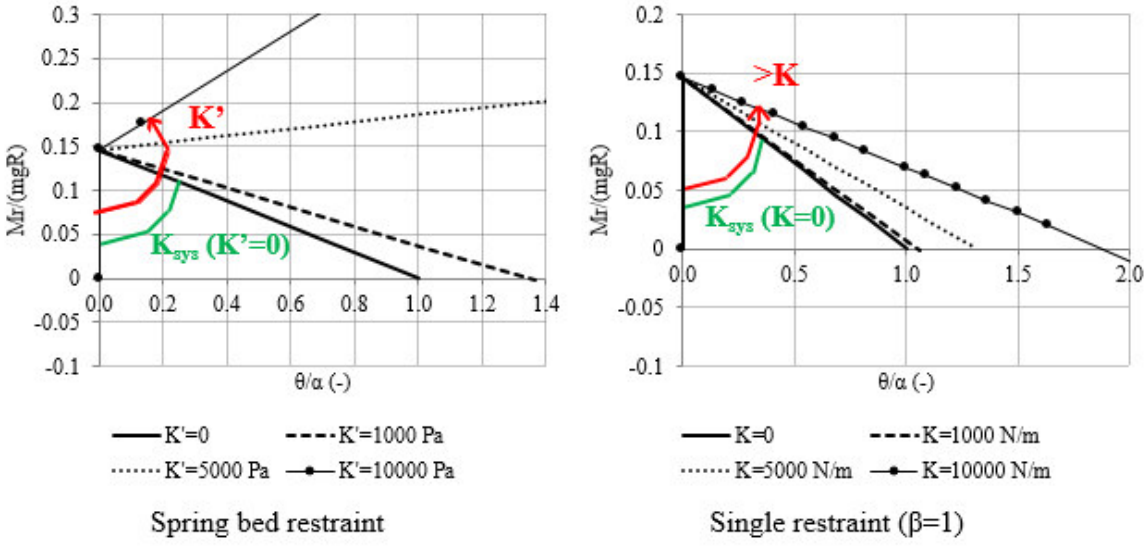


Figure 4: System rotational stiffness $K_{sys}$ in the dimensionless resisting moment-rotation relationship and curve variation with increased values of spring bed stiffness $K'$ and single spring stiffness $K$ (masonry wall with $\gamma$=18 kN/m$^3$, $\alpha$=0.15 rad and $R$=2.0 m), Equations (9) and (10).

In case of the spring bed model one has:

$$K'_{sys} = mgR\cos\alpha \left(\frac{8}{3}\frac{K'R^2}{mg}\cos^2\alpha - 1\right). \tag{13}$$

Both Equations (13) and (14) allow to express the moment-rotation law in a simplified way:

$$M_r(\vartheta) = M_r(0) + K_{sys}\,\vartheta \tag{14}$$
$$M_r(\vartheta) = M_r(0) + K'_{sys}\vartheta$$

where $M_r(0) = \text{mgR}\sin\alpha$. The rotational stiffness $K_{sys}$ or $K'_{sys}$ is the slope of the line in Figure 4, increasing for higher values of either $K$ or $K'$.
In the hypothesis of small rotations, one can easily define the value of the single spring stiffness in order to equate the two system rotational stiffness, by equating Equation (12) to Equation (13):

$$K_{sys} = K'_{sys} \rightarrow K = \frac{8}{3\beta^2}K' \cdot Rcos\alpha \tag{15}$$

Higher the spring bed stiffness, higher the stiffness of the single restraint. The latter is also proportional to the radius vector and to the cosine of the slenderness ratio. For what concerns the single spring position, lower the position (lower $\beta$), higher its stiffness value, as expected.

## 3 RESONANCE CONDITION

The resonance condition is obtained when the rotational frequency of the rocking block equates that of the excitation, namely $\omega_r = \omega_p$. In particular, for the case of spring bed the square of rotational frequency is:

$$\omega_r^2 = \frac{K'_{sys}}{I_0} = \frac{mgR\cos\alpha\left(\frac{8K'R^2}{3\ mg}\cos^2\alpha - 1\right)}{I_0} = p^2\cos\alpha\left(\frac{8}{3}\frac{K'R^2}{mg}\cos^2\alpha - 1\right). \tag{16}$$

Therefore:

$$\omega_r = p\sqrt{\cos\alpha\left(\frac{8}{3}\frac{K'R^2}{mg}\cos^2\alpha - 1\right)}\ \mathrm{M_r}(\vartheta) = \mathrm{mgR\sin(\alpha\text{-}\vartheta)} + \mathrm{K\beta^2R^2\cos(\alpha\text{-}\vartheta)\,[\sin\alpha\text{-}\sin(\alpha\text{-}\vartheta)]}. \tag{17}$$

For the single horizontal restraint one has:

$$\omega_r^2 = \frac{K_{sys}}{I_0} = \frac{mgR\cos\alpha\left(\frac{K\beta^2R}{mg}\cos\alpha - 1\right)}{I_0} = p^2\cos\alpha\ \left(\frac{K\beta^2R}{mg}\cos\alpha - 1\right) \tag{18}$$

and

$$\omega_r = p\sqrt{\cos\alpha\ \left(\frac{K\beta^2R}{mg}\cos\alpha - 1\right)}. \tag{19}$$

Both circular frequencies linearly depend on the frequency parameter $p$. For a slender column, $\cos\alpha \cong 1$ and the circular frequencies at resonance become:

$$\omega_{r,sm} = p\sqrt{\left(\frac{8}{3}\frac{K'R^2}{mg} - 1\right)}\ ;\ \omega_{r,single} = p\sqrt{\left(\frac{K\beta^2R}{mg} - 1\right)}\ . \tag{20}$$

That, in dimensionless terms, can be expressed as:

$$\Pi_{\omega,sm} = \sqrt{\frac{8}{3}\Pi_{K'} - 1}\ ;\ \Pi_{\omega,single} = \sqrt{\Pi_K - 1}\,, \tag{21}$$

respectively for smeared and single restraints. It is worthy to notice that these dimensionless terms do not depend on the slenderness ratio $\alpha$.

## 4 DYNAMIC RESPONSE WITH UNILATERAL OR BILATERAL RESTRAINTS

The dynamic response is strongly different if unilateral (mainly acting in one side of the block) or bilateral restraints (stiffness equal or at least of the same order of magnitude for both directions).

Let us assume a masonry façade connected with transverse walls, with analysis parameters reported in Table 1. The wall is the main façade of the Santa Gemma Church in Goriano Sicoli (L'Aquila), whose damage suggested a rocking motion during the L'Aquila earthquake [9].

To evaluate the influence of the horizontal restraints in the motion, the façade is subjected first to a sin pulse type action and then to a seismic-type excitation. The façade has two configurations: (a) spring bed modeling transverse walls acting only in one direction (non linear, NLin) and (b) spring bed with the same stiffness as that of the transverse walls in the two directions (linear, Lin).
A parametric analysis is performed by assuming a range of spring bed stiffness values $K'$ between 0 and 1E10 N/m$^2$ and three types of input action: sin pulse, real seismic records, Ricker wavelets. For all the analyses the restitution coefficient adopted is that of Housner, depending only on the slenderness ratio $\alpha$ [7].

| *Parameter* | *Value* | *Definition* |
|---|---|---|
| R (radius vector) | 5.726 m | Geometric survey |
| α (slenderness ratio) | 0.0778 rad | Geometric survey |
| s (thickness) | 0.89 m | Geometric survey |
| e (restitution coefficient) | 0.9909 | Derived by $e = 1 - \frac{3}{2}\sin^2\alpha$ [7] |
| L (depth of the wall) | 10.10 m | Geometric survey |
| $\gamma_{mas}$ (specific weight) | 18 kN/m$^3$ | Literature value (brick masonry, from [2]) |
| $E_y$ (vertical direction) | 1700 MPa | Masonry elastic modulus (in-situ flat jack test) |
| $E_x$ (horizontal direction) | 2125 MPa | Derived by $E_y$/0.8 [24]. |
| $K'_{TOT}$ (transverse stiffness of the spring bed) | 5.07E9 N/m$^2$ | Derived as in [9]. |

Table 1: Geometric and mechanical parameters of the analyzed masonry façade.

### 4.1 Response to sine pulse-type action

The pulse has an acceleration $a = 2.5\tan(\alpha)\, g \cdot \sin(\omega t)$ and duration of 1 sec, after which the motion is on free vibration. The response is displayed in Figure 5.
The frequency of the pulse is $\omega = 5.8$ rad/sec. The dynamic response is monitored for 10 seconds.
In the non-linear case (Figure 5a), the motion is oscillatory up to $K'$ values of about 1E6 N/m$^2$, whereas for higher values the rebound effect is clear. The rotation amplitude slightly decreases when the motion is oscillatory and the frequency increases for higher $K'$ values. This consideration is also valid for the linear case (Figure 5b), where the response is more controllable being symmetric. In this case the reduction of the rotation amplitude and of the vibration period are more evident. For instance, a value of $K'$ value of 1E6 N/m$^2$ is needed to obtain a reduction by 40% of the initial maximum rotation amplitude for the case without restraints. Correspondingly, a tripled frequency of vibration occurs. The measured value of transverse walls stiffness is about 5.07E9 N/m2 (calculated in elastic range). For this value, if one assumes the linear case, the normalized rotation is close to zero (Figure 5b). By contrast, in case of unilateral restraint, the maximum rotation amplitude is about the same as that without restraints ($\cong 0.7$) and the frequency of vibration is nearly the same ((Figure 5a).

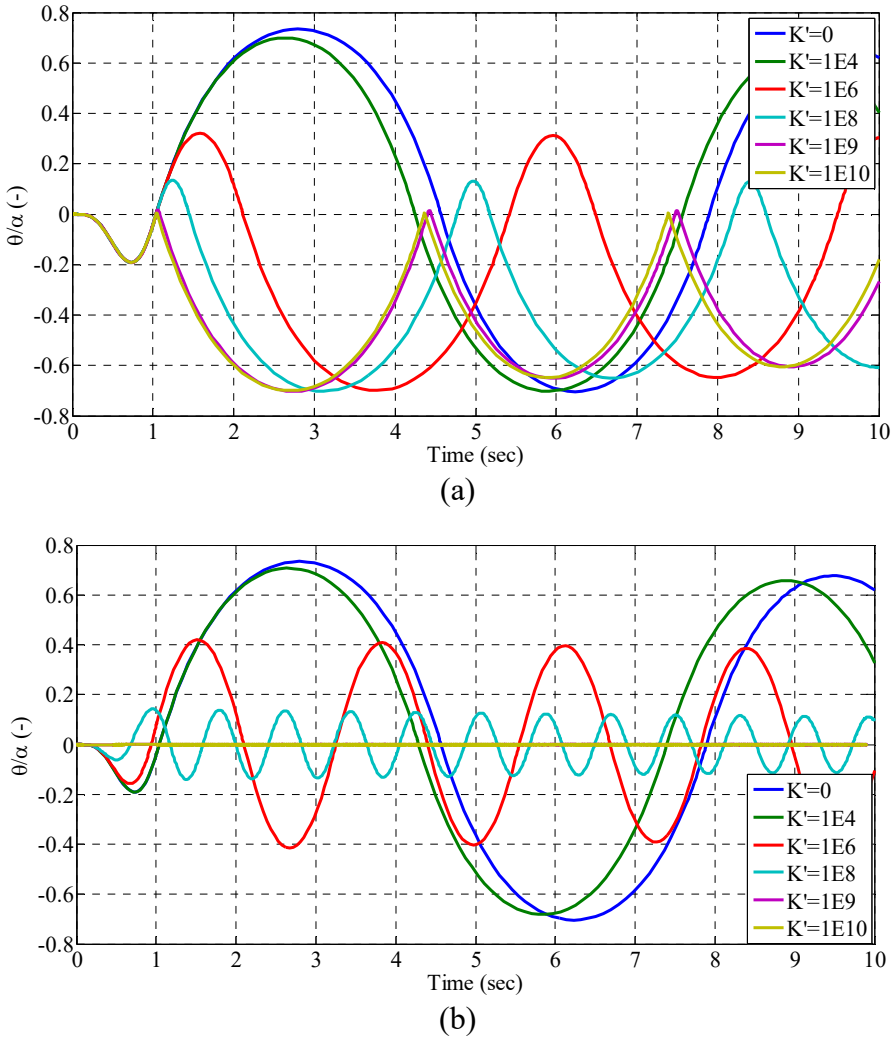


Figure 5: Normalized rotation time-history of the façade under a sin pulse-type action: (a) unilateral spring bed simulating transverse walls; (b) bilateral spring bed. Stiffness values are expressed in N/m$^2$.

### 4.2 Response to real seismic records

In this paragraph the response of the façade subjected to real earthquakes is discussed. The façade undergoes seismic records that it actually experienced during the L'Aquila main shock (Italy, 2009), whose acceleration time-histories are featured in [9]. The response of the façade is similar to that of the sine pulse for both unilateral and bilateral restraints. Indeed, if one considers the real case, that is unilateral restraints (spring bed with $\bar{h} = 4.90 \neq h$), the overturning is not predictable, as for some $K'$ ranges (e.g., $1E6 < K' < 1E7$ N/m$^2$, and $K' > 1E11$ N/m$^2$ - AQV record, Figure 6a) the façade overturns. The overturning phenomenon is due to a rebound effect due to the sensitive difference between restraints stiffness in the two directions of rotation. By contrast, when bilateral restraints participate to the motion, the behavior is much more predictable: a decreasing maximum amplitude ratio $\vartheta_{max}/\alpha$ can be observed for higher stiffness values (Figure 6b). This monotonic behavior suggests a design strategy for anti-seismic devices, based on reaching similar values of stiffness in the two directions of rotation.

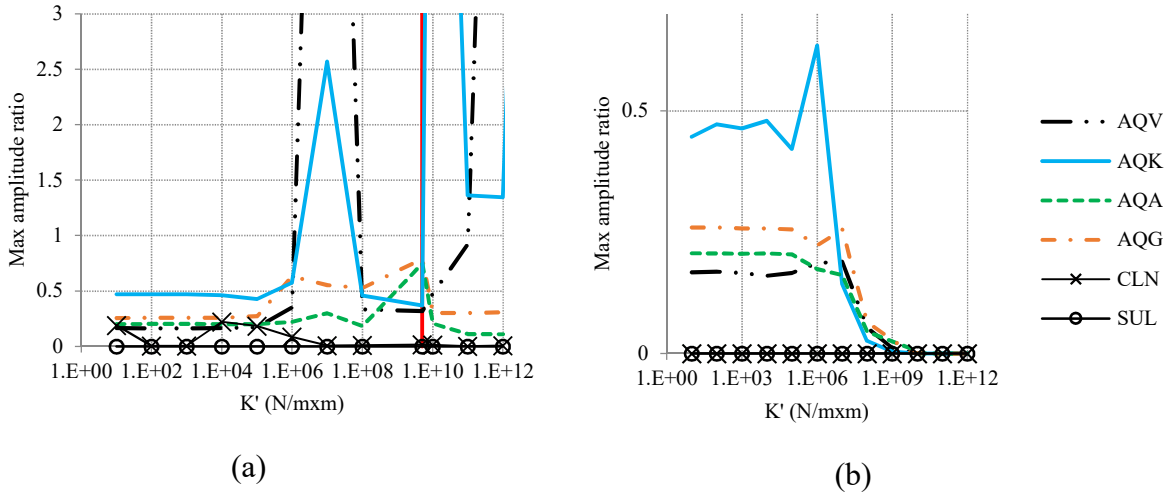


(a) (b)

Figure 6: Response of the masonry façade to real seismic records: (a) unilateral spring bed; (b) bilateral spring bed [9].

### 4.3 Response to Ricker wavelets

The façade frequency parameter $p$ is equal to 1.134 rad/s and $\Pi_a = 0.078$. To widen the results in case of Ricker wavelets, a parametric analysis is performed for the dimensionless parameters $\Pi_\omega = 0.5 - 8$ and $\frac{\Pi_g}{\Pi_\alpha} = 2 - 3$. Only the spring bed restraint is considered, varying the dimensionless $\Pi_{K'}$ values from 0 to 10. An oscillation motion is observed for the free rocking façade ($\Pi_{K'} = 0$) and in case of bilateral restraints, as shown in the response spectra of Figure 7a, the curves are monotonic and the overturning domain reduces for higher $\Pi_{K'}$ values. By contrast, when restraints act unilaterally (in only one direction it is $\Pi_{K'} \neq 0$, in the other one it is zero), the response is not so predictable, as for some values of $\Pi_{K'}$ (e.g. $\Pi_{K'}$ =+1.0, Figure 7), there is not a monotonic trend (Figure 7b).

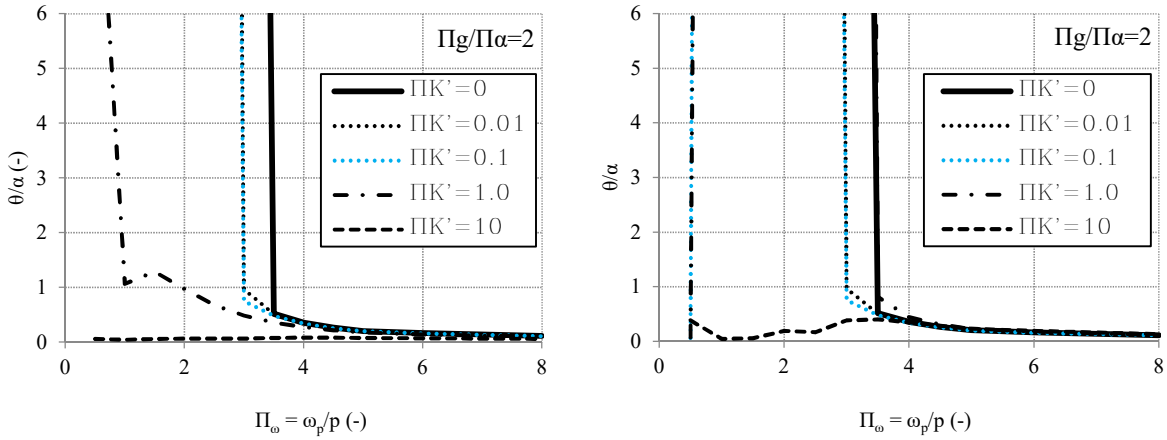


(a) (b)

Figure 7: Rocking spectra of the façade under Ricker wavelets with $\frac{\Pi_g}{\Pi_\alpha} = 2$: (a) bilateral case and (b) unilateral case.

Moreover, the beneficial role of horizontal restraints is valid only for a range of $\Pi_\omega$ lower than a limit value, in this case about 3.8 for both cases, inasmuch for higher values the response with and without horizontal restraints tends to be similar. An analogous results was found for the rocking response of panels with vertical restraints [8].

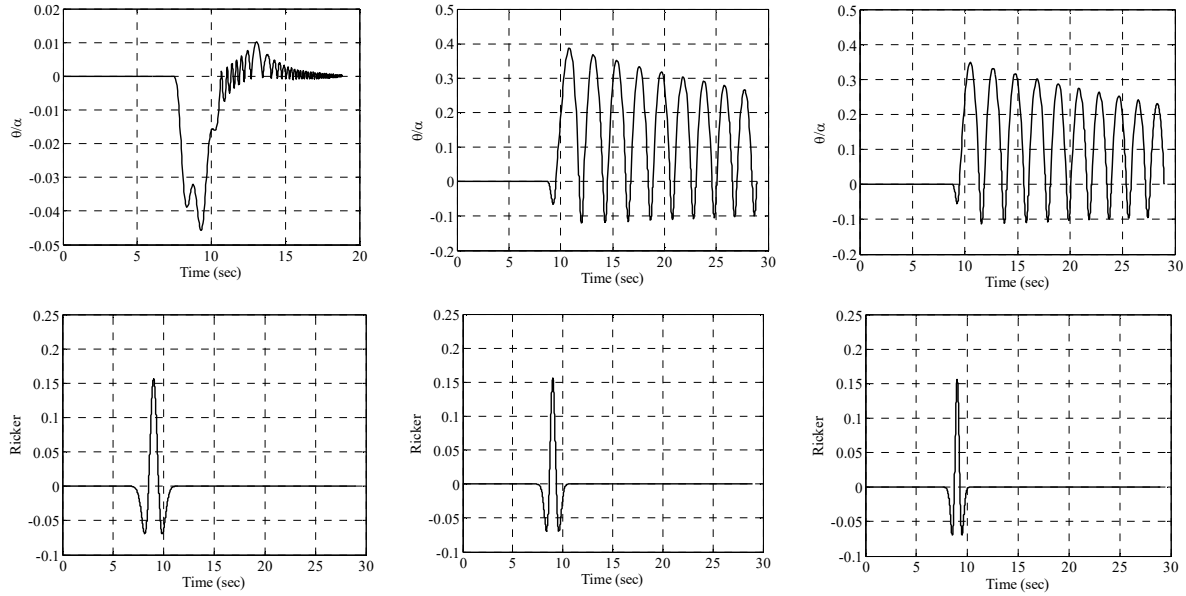


$\Pi_\omega = 2.5$ $\Pi_\omega = 3.5$ $\Pi_\omega = 4.5$

Figure 8: Response in unilateral case of the masonry façade to Ricker wavelets with $\frac{\Pi_g}{\Pi_\alpha} = 2$: $\Pi_{K'} = +10.0$.

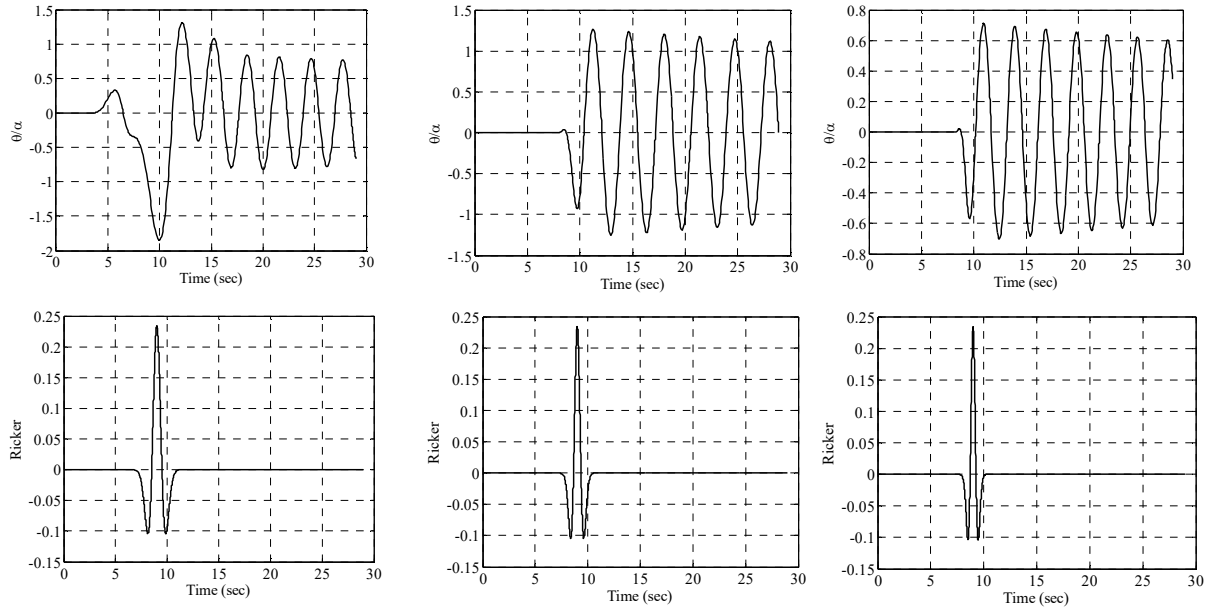


$\Pi_\omega = 2.5$ $\Pi_\omega = 3.5$ $\Pi_\omega = 4.5$

Figure 9: Response in bilateral case of the masonry façade to Ricker wavelets with $\frac{\Pi_g}{\Pi_\alpha} = 3$: $\Pi_{K'} = 1$. Resonance condition for $\Pi_\omega = 1.28$.

When a unilateral restraint is assumed, for $\frac{\Pi_g}{\Pi_\alpha} = 2$ the time-history rotation displayed in Figure 8 highlights that the rebound effect is clear but the value of stiffness is not such as to cause overturning.

If the same analysis is carried out by increasing the excitation amplitude to $\frac{\Pi_g}{\Pi_\alpha} = 3$, lower the spring bed stiffness value, higher the amplitude for the same frequency parameter $\Pi_\omega$ (Figure 9 for $\Pi_{K'} = 1$ and Figure 10 for $\Pi_{K'} = 10$) in case of bilateral restraints.

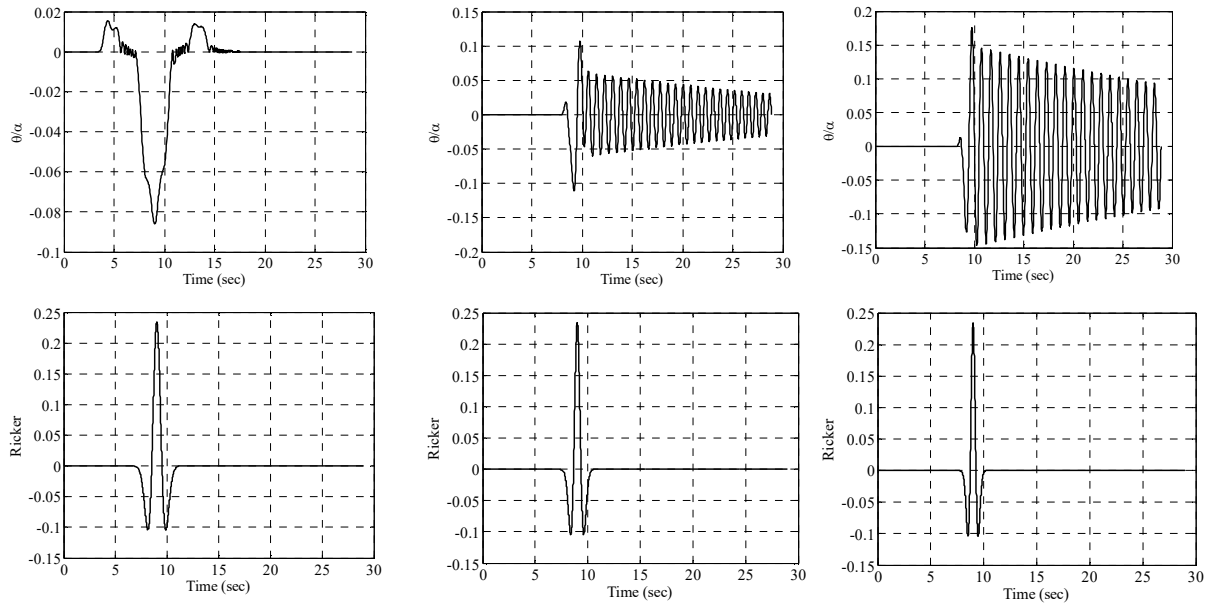


$\Pi_\omega = 2.5$ $\Pi_\omega = 3.5$ $\Pi_\omega = 4.5$

Figure 10: Response in bilateral case of the masonry façade to Ricker wavelets with $\frac{\Pi_g}{\Pi_\alpha} = 3$: $\Pi_{K'} = 10$. Resonance condition for $\Pi_\omega = 5.04$.

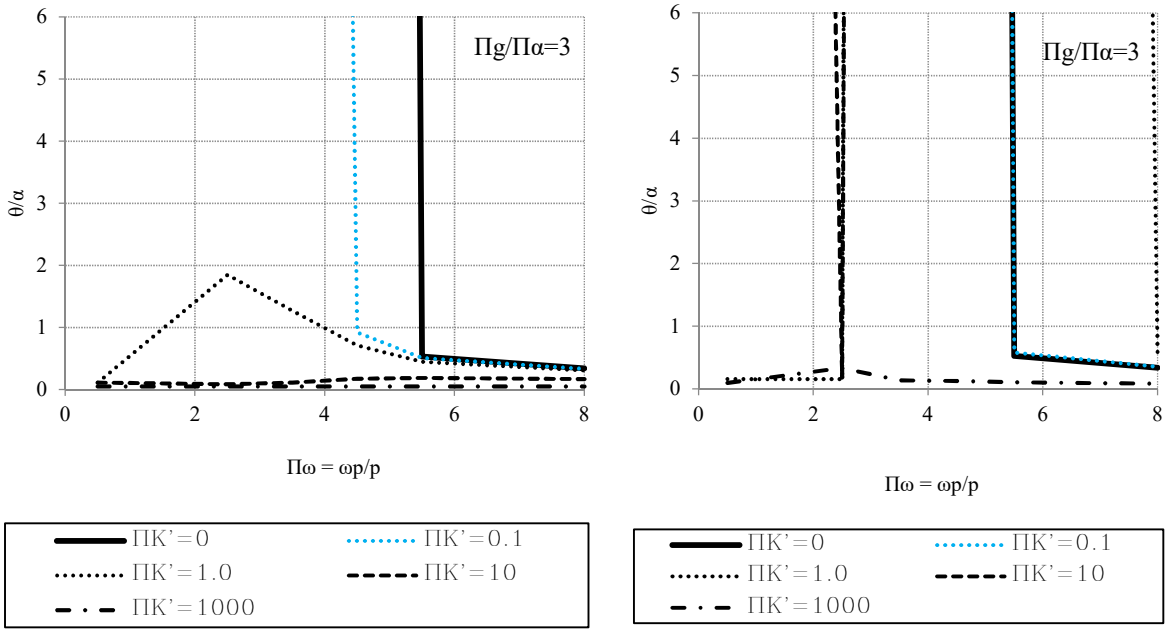


Figure 11: Rocking spectra of the façade under Ricker wavelets with $\frac{\Pi_g}{\Pi_\alpha} = 3$: (a) bilateral case and (b) unilateral case.

The value of $\Pi_\omega$ in resonance condition increases when higher stiffness value of $\Pi_K$, are assumed. However, an oscillatory motion is always registered for the bilateral restraints, while for unilateral restraints the difference of stiffness depending on the rotation sign causes the block overturning for rebound effect. In Figure 11 the response spectra of the façade under Ricker wavelets with $\Pi_g/\Pi_\alpha$ =3 are displayed. As occurred for the lower value of excitation amplitude, the response in the bilateral case is predictable with a monotonic trend, while in the unilateral case for some $\Pi_K$, values the façade overturns. In the case of bilateral restraints, the $\Pi_\omega$ value above which the restraints are not effective is about 5.5 (Figure 11a). In the unilateral case, the range of $\Pi_K$, included between 2.5 and 5.5 is associated to unstable conditions.

## 5 DESIGN STRATEGY: TARGET POINTS AND CONFIDENT RANGE

The use of Equation (15) is related to a possible design strategy for anti-seismic devices (such as steel tie-rods), whose stiffness is $K$. The following procedure can be adopted to define a $K$ value to have the same (or a similar value) system stiffness as that of the spring bed model. Once that the transverse stiffness of the wall is defined, depending on the radius vector and the slenderness ratio of the rocking wall, it is straightforward to determine the system stiffness from Equation (13). In a graph, valid for a specific value of slenderness ratio α, the radius vector $R$ of the block under examination intersects a curve (Equation (12)) describing the dimensionless system stiffness (on the ordinates) in function of $R$. This curve corresponds to the target value of the single restraint stiffness $K$ (Figure 12). From this value, it is therefore possible to easily calculate the diameter of the steel tie rods [9]. The position of the single restraint, denoted with β, is given by the curve itself (Equation (12)).
For instance, if one has a transverse walls stiffness equal to K'=5E7 N/m$^2$, R=4 m and α =0.15 rad, to get roughly the same system stiffness, a single restraint stiffness has to be about 1E8 N/m (Figure 13).
From these parametric curves one can obtain range of values of the single restraints stiffness associated to steel tie-rods able to ensure a predictable behavior of the masonry walls, searching for an oscillatory motion.

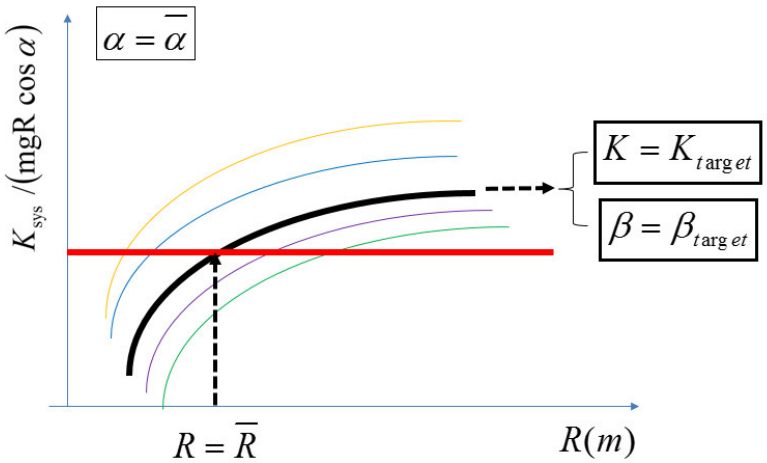


Figure 12 Procedure to define the value of the single restraint stiffness $K$ that equates the system stiffness $Ksys$ depending on an assigned spring bed stiffness $K'$.

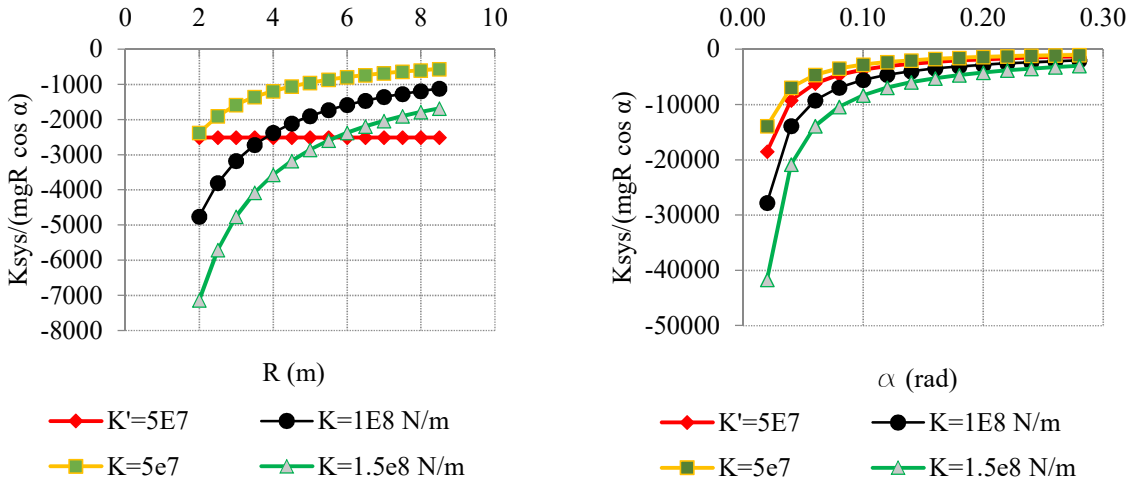


Figure 13: Variation of the system stiffness $K_{sys}$ depending on the geometric parameters and on the values of single spring K (β=1) or spring bed stiffness K': α=0.15 rad (a) and R=2.5 m (b).

## 6 LIMITATIONS OF THE METHOD

The illustrated method, for which it is possible to identify a target value of the single restraint stiffness to promote a self-centered (oscillatory) restrained motion, has some limitations, mainly related to correctly define the stiffness of transverse masonry walls. Indeed, the behavior of masonry is non-linear, but in this work only constant (for each sign of rotation) values of stiffness have been considered. Moreover, the determination of the elastic stiffness is not easy, inasmuch before an earthquake the diagonal cracks on transverse walls are generally unknown. Furthermore, if a portion of transverse walls rotates about a plastic hinge together with the rocking wall, their stiffness obviously does not affect motion. In this case, the role of transverse walls is only related to an increased masonry volume, an increased radius vector (of the complex system wall + transverse walls) and consequently a reduction of frequency parameter.

## 7 CONCLUSIONS

The model assumed in the paper simulates the behavior of a masonry wall connected to transverse walls and/or steel tie-rods, very frequently adopted as safety measure against out-of-plane modes due to seismic actions. From the system rotational stiffness, found for a Winkler-type model and for a single restraint, the resonance condition of the horizontally restrained block has been defined. The unilateral (restraint acting in only one direction of rotation) and the bilateral cases (restraints with similar stiffness in both directions) have been discussed. Real earthquakes, sine pulses or Ricker's wavelets were assumed as input parameters, obtaining results both for dimensionless parameters and for a real masonry façade. It is found that in the bilateral case the response is more predictable, as response spectra are generally monotonic curves able to enhance the response with a sensitive reduction of amplitude rotation. In particular, the effect of horizontal restraints is beneficial for the range of frequency parameters valid for typical masonry walls. These considerations allow to define a design strategy for ensure the rocking stability of restrained masonry walls, through a self-centered (oscillatory) rocking behavior. Indeed, once that the transverse stiffness of the wall is defined, it is straightforward to determine the value of $K$ that equates the normalized system stiffness. From this values, dynamic analyses

have to be performed to draw rocking spectra in order to estimate the safety coefficient reached with the anti-seismic intervention.

## ACKNOWLEDGEMENT

The Author thanks the sponsorship of the Italian Department of Civil Protection, in the framework of the RELUIS Project - Masonry Structures (2017).

## REFERENCES

[1] DMI, "Decreto del Ministro delle Infrastrutture 14 gennaio 2008. Approvazione delle nuove norme tecniche per le costruzioni." Gazzetta Ufficiale della Repubblica Italiana, n. 29 del 4 febbraio 2008, Supplemento Ordinario n. 30, 2008.

[2] CMIT, "Circolare del Ministro delle Infrastrutture e dei Trasporti 2 febbraio 2009, n. 617, contenente le Istruzioni per l'applicazione delle 'Nuove norme tecniche per le costruzioni' di cui al DM 14 gennaio 2008." Gazzetta Ufficiale della Repubblica Italiana n. 47 del 26 febbraio 2009, Supplemento Ordinario n. 27, 2009.

[3] L. Giresini, "Energy-based method for identifying vulnerable macro-elements in historic masonry churches," *Bull. Earthq. Eng.*, vol. 14, no. 3, pp. 919–942, 2016.

[4] L. Giresini, M. Fragiacomo, and P. B. Lourenço, "Comparison between rocking analysis and kinematic analysis for the dynamic out-of-plane behavior of masonry walls," *Earthq. Eng. Struct. Dyn.*, vol. 44, no. 13, pp. 2359–2376, Oct. 2015.

[5] M. Sassu, "The Reinforced Cut Wall (RCW): A Low-Cost Base Dissipator for Masonry Buildings," *Earthq. Spectra*, vol. 22, no. 2, pp. 533–554, 2006.

[6] I. N. Psycharis, D. Y. Papastamatiou, and A. P. Alexandris, "Parametric investigation of the stability of classical columns under harmonic and earthquake excitations," *Earthq. Eng. Struct. Dyn.*, vol. 29, no. 8, pp. 1093–1109, 2000.

[7] G. W. Housner, "The behavior of inverted pendulum structures during earthquakes," *Bull. Seismol. Soc. Am.*, vol. 53, no. 2, pp. 403–417, 1963.

[8] N. Makris and M. F. Vassiliou, "Dynamics of the Rocking Frame with Vertical Restrainers," *J. Struct. Eng.*, vol. 141, no. 10, 2015.

[9] L. Giresini and M. Sassu, "Horizontally restrained rocking blocks: evaluation of the role of boundary conditions with static and dynamic approaches," *Bull. Earthq. Eng.*, vol. 15, no. 1, pp. 385–410, 2017.

[10] L. Giresini, M. Fragiacomo, and M. Sassu, "Rocking analysis of masonry walls interacting with roofs," *Eng. Struct.*, vol. 116, pp. 107–120, Jun. 2016.

[11] A. De Falco, L. Giresini, and M. Sassu, "Temporary preventive seismic reinforcements on historic churches: numerical modeling of San Frediano in Pisa," *Appl. Mech. Mater.*, vol. 352, 2013.

[12] M. Andreini, A. De Falco, L. Giresini, and M. Sassu, "Collapse of the historic city walls of Pistoia (Italy): Causes and possible interventions," *Appl. Mech. Mater.*, vol. 351–352, 2013.

[13] I. N. Psycharis, M. Fragiadakis, and I. Stefanou, "Seismic reliability assessment of classical columns subjected to near-fault ground motions," *Earthq. Eng. Struct. Dyn.*, vol. 42, no. 14, pp. 2061–2079, 2013.

[14] C. Casapulla, "On the resonance conditions of rigid rocking blocks," *Int. J. Eng. Technol.*,

vol. 7, no. 2, pp. 760–771, 2015.
[15] C. Casapulla, P. Jossa, and A. Maione, “Rocking motion of a masonry rigid block under seismic actions: a new strategy based on the progressive correction of the resonance response,” *Ing. Sismica*, vol. 27, no. 4, pp. 35–48, 2010.
[16] C. Casapulla and A. Maione, “Free damped vibrations of rocking rigid blocks as uniformly accelerated motions,” *Int. J. Struct. Stab. Dyn.*, vol. 0, 2016.
[17] N. Makris and Y. S. Roussos, “Rocking response of rigid blocks under near-source ground motions,” *Geotechnique*, vol. 50, p. 243, 2000.
[18] J. Zhang and N. Makris, “Rocking Response of Free-Standing Blocks under Cycloidal Pulses,” *J. Eng. Mech.*, vol. 127, no. 5, 2001.
[19] N. Ricker, “Wavelet functions and their polynomials,” *Geophysics*, vol. 9, p. 314, 1944.
[20] M. Apostolou, G. Gazetas, and E. Garini, “Seismic response of slender rigid structures with foundation uplifting,” *Soil Dyn. Earthq. Eng.*, vol. 27, no. 7, pp. 642–654, 2007.
[21] G. I. Barenblatt, *Scaling, self-similarity, and intermediate asymptotics*. Mathematics, Cambridge Texts in Applied, series no 14, 1996.
[22] J. R. Dormand and P. J. Prince, “A family of embedded Runge-Kutta formulae,” *J. Comput. Appl. Math.*, vol. 6, no. 1, pp. 19–26, 1980.
[23] N. Makris and M. F. Vassiliou, “Planar rocking response and stability analysis of an array of free-standing columns capped with a freely supported rigid beam,” *Earthq. Eng. Struct. Dyn.*, vol. 42, p. 431, 2013.
[24] A. Brignola, S. Frumento, S. Lagomarsino, and S. Podestà, “Identification of Shear Parameters of Masonry Panels Through the In-Situ Diagonal Compression Test,” *Int. J. Archit. Herit.*, vol. 3, no. 1, pp. 52–73, 2008.

COMPDYN 2017
6th ECCOMAS Thematic Conference on
Computational Methods in Structural Dynamics and Earthquake Engineering
M. Papadrakakis, M. Fragiadakis (eds.)
Rhodes Island, Greece, 15–17 June, 2017

# VULNERABILITY ASSESSMENT OF FLAG-SHAPED HYSTERETIC ROCKING BRIDGE BENTS

**Anastasios I. Giouvanidis[1], Michalis Fragiadakis[2] and Elias G. Dimitrakopoulos[1]**

[1]Department of Civil and Environmental Engineering, The Hong Kong University of Science and Technology
Kowloon Bay, Hong Kong
e-mail: agiouvanidis@connect.ust.hk
e-mail: ilias@ust.hk

[2] School of Civil Engineering, National Technical University of Athens
GR 15780, Athens, Greece
e-mail: mfrag@mail.ntua.gr

**Keywords:** rocking, flag-shaped hysteretic behavior, prefabricated bridges, seismic resistant structures, fragility curves, vulnerability assessment.

**Abstract.** *Rocking motion implies that a structure under seismic loading exhibits rigid body rotation around pre-defined pivot points. Its stability primarily relies on utilizing the rotational inertia through (purposely) activated dynamic motion. This paper focuses on slender bridge frames that exhibit rigid planar rocking behavior. It examines rocking frames enhanced with elastic central tendons to provide supplemental re-centering capacity and buckling-restrained braces to dissipate seismic energy; transforming a freestanding frame into a hybrid rocking frame with flag-shaped hysteretic behavior. The objective of this study is twofold. Firstly, it investigates the existence of 'optimal' intensity measures for hybrid rocking structures by examining their 'practicality', 'efficiency' and 'sufficiency' with an appropriate engineering demand parameter. The analysis shows that the slenderness-based intensity measures reduce the scatter on the response and they exhibit independence from seismic hazard parameters. Further, this study also focuses on the seismic vulnerability assessment of the examined freestanding and hybrid rocking frames. To assess their seismic performance, the analysis employs a suite of recorded earthquakes and performs a parametric investigation in terms of the vulnerability of different structural configurations. This paper develops analytical fragility curves based on the most 'optimal' scalar intensity measures. The results reveal the mitigated fragility of the positive stiffness rocking frame compared to the other structural systems. For some intensity measures though, this seismic enhancement becomes marginal. Hence, a more sophisticated approach would require the introduction of a second engineering demand parameter tailored to the needs of hybrid rocking structures or an appropriate vector intensity measure.*

## 1 INTRODUCTION

Rocking as a means of seismic isolation is attracting research interest for almost a century (see e.g., [26] and references therein). Even though the existing rocking structures remain scarce (e.g., [38, 41] among others), currently, there is an increasing need to examine the response of freestanding [15, 39, 12, 2, 13, 46, 48, 19, 49] as well as controlled rocking structures [16, 21, 32, 17, 24] adopting classical or more sophisticated methods ([1, 47, 44, 3, 22] among others). From a practical point of view, the rocking frame of Fig. 1, proposed originally by Mander and Cheng [33] as a 'damage avoidance design', is gaining momentum in bridge engineering and its seismic behavior is extensively examined. In particular, [30, 31] showed that the stability of the rigid rocking bridge frame is enhanced, the more heavy its cap-beam is. Its stability primarily stems from the mobilization of its rotational inertia. Further, [11, 42] revealed that rocking piers can exhibit large drifts with minor damage and/or residual displacements. Recent experimental studies [43, 37] proved the negligible residual drifts of a posttensioned rocking column compared to the pertinent drifts of a conventional monolithic column ($0.4\%$ versus $6.8\%$ respectively). To minimize further the residual deformations many researchers (see e.g., [24] and references therein) combined the use of additional re-centering with energy dissipation devices, proposing 'hybrid rocking systems' which exhibit flag-shaped hysteretic behavior (FSHB). Giouvanidis and Dimitrakopoulos [24] revealed the diverse influence of the prestressing tendon's force. Prestressing the tendons might be beneficial for small rocking rotations, but could become detrimental for large rocking rotations; a counter-intuitive behavior.

Even though it is hard to overstate the significance of the deterministic methods in investigating the rocking behavior [15, 19], it is beneficial to complement them with a probabilistic evaluation of the (seismic) rocking response. In this context, Dimitrakopoulos and Paraskeva [18] proposed normalized fragility curves that estimate the overturning tendency of freestanding rocking structures and unveiled the existence of a critical peak ground acceleration, above and below which the rocking response scales differently. Building on previous work [23, 24], the present study: (i) investigates the existence of 'optimal' intensity measures (IMs) for hybrid rocking structures and (ii) compares the seismic fragility of hybrid rocking bridge frames with different post-uplift lateral stiffness (i.e., negative, zero, or positive) with the archetypal freestanding frame.

## 2 DYNAMICS OF THE HYBRID ROCKING BRIDGE FRAME

This section focuses on the analytical modelling of a rocking bridge frame which exhibits flag-shaped hysteretic behavior (FSHB). Consider the rocking frame of Fig. 1 enhanced with central (linear-elastic) slack (unbonded) tendons and (nonlinear-hysteretic) buckling restrained braces (BRBs) at the bottom of the piers (Fig. 1(c)). In the absence of a ground excitation, the frame remains in full contact with the ground (Fig. 1(a)). In the event of a ground shaking though, when the seismic demand (i.e., overturning moment due to the ground excitation) exceeds the static seismic resistance (i.e., restoring moment due to the gravity) the frame initiates rocking motion (Fig. 1(b)). In particular, rocking commences when the ground acceleration becomes $\ddot{u}_{g,\min} = g \tan \alpha$ [17, 24].

This study assumes (rigid) planar rocking motion. It also ignores the sliding between the contacting bodies and the fracture of the supplemental devices (i.e., tendons and/or dissipaters). Note that, the former is covered in [10] and the latter in [17].

Further, the Bouc-Wen model [9, 50] is adopted to describe the hysteretic behavior of the BRBs. The restoring dissipating force $F_D$ and the dimensionless hysteretic parameter $z(t)$ are

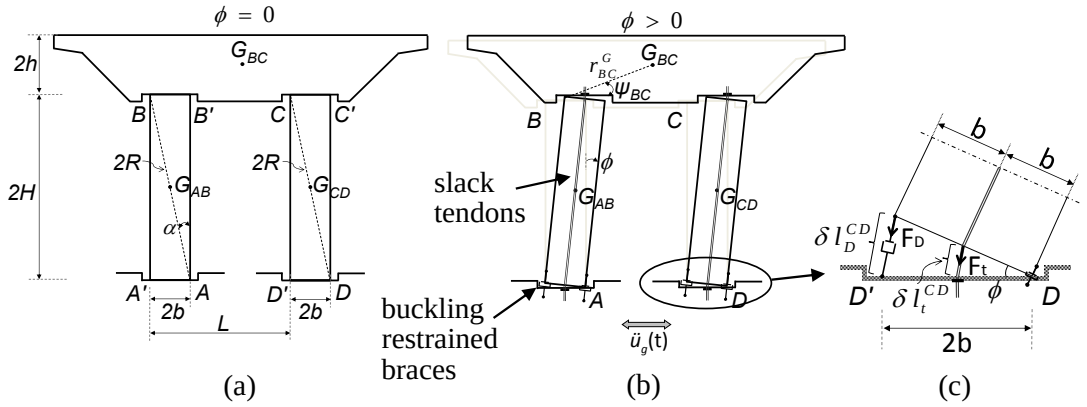


Figure 1: The examined rocking bridge frame (a) at rest position, (b) during clockwise (positive) rotation and (c) detail of the column-foundation connection.

expressed accordingly as [24]:

$$\begin{aligned} F_D &= \varepsilon k_d u\left(t\right) + \left(1-\varepsilon\right) k_d u_y z\left(t\right) \\ \dot{z}(t) &= \tfrac{1}{u_y}\left[\dot{u}(t) - \gamma\left|\dot{u}(t)\right| z(t)|z(t)|^{n-1} - \beta\dot{u}(t)|z(t)|^{n}\right] \end{aligned} \tag{1}$$

where $\varepsilon$ is the post-yield to pre-yield elastic stiffness ($k_d$) ratio of the BRBs and is taken equal to $\varepsilon = 0.025$ [8]. $u\left(t\right)$ is the axial deformation of the brace, $u_y$ is the yield deformation equal to $u_y = \delta l_{D_y} = 4b\sin\left(\phi_y/2\right)$ (Fig. 1(c)). $b$ is the half-width of the base of the column of the frame and $\phi_y$ is the yield rotation. Parameters $\beta, \gamma$ and $n$ control the shape of the hysteretic loop. The present work assumes $\beta = 0.55, \gamma = 0.45, n = 1$ [8].

When rocking initiates, the tendon deforms. The elongation of each tendon is equal to the sum of the elongations at the bottom and the top of each tendon: $\delta l_t = 4b\sin\left(\phi/2\right)$ (Fig. 1(c)). The equation of motion of the hybrid rocking frame is [24]:

$$\ddot{\phi} = -\frac{1+2\gamma_m}{1+3\gamma_m}p^2\left[\begin{array}{l} \sin\left(\alpha\mathrm{sgn}\left(\phi\right)-\phi\right) + \frac{\ddot{u}_g}{g}\cos\left(\alpha\mathrm{sgn}\left(\phi\right)-\phi\right) \\ +4\left(\rho_t+\varepsilon\rho_d\right)\sin\phi + 8\left(1-\varepsilon\right)\rho_d\sin\frac{\phi_y}{2}\cos\frac{\phi}{2}z\left(t\right) \end{array}\right] \tag{2}$$

where $\phi$ is the generalized coordinate which describes the rocking motion of the frame (Fig. 1). $p$ is the frequency parameter of the column of the frame which takes the form: $p = \sqrt{3g/4R}$ for rectangular columns, where $g$ is the acceleration of gravity and $R$ is the half-diagonal length of the column of the frame. $\alpha$ is the slenderness of the column (Fig. 1). $\mathrm{sgn}\left(\phi\right)$ is the sign function and $\gamma_m = m_{BC}/2m_{AB}$ is the mass ratio, with $m_{AB}$ and $m_{BC}$ the masses of the column $AB$ and the cap-beam $BC$ respectively. The dimensionless parameters $\rho_d = k_d b^2/\left(m_{AB}+m_{BC}\right)gR$ and $\rho_t = k_t b^2/\left(m_{AB}+m_{BC}\right)gR$ depend on the stiffness $k_d$ of the dissipater and $k_t$ of the tendon respectively. The present study assumes the stiffness $k_d$ of the dissipater is constant ($\rho_d = 3$), whereas the stiffness $k_t$ of the tendon, and subsequently the parameter $\rho_t$, varies within $0.001 \leq \rho_t \leq 0.55$ providing different hybrid frames with respect to their overall stiffness, i.e., negative, zero and/or positive post-uplift lateral stiffness [24] (Fig. 2).

During rocking, each time the rotation reverses, an impact occurs and energy is lost. This study adopts a coefficient $\eta$ equal to 0.92 to capture the energy loss at each impact. For a more careful analysis of the coefficient of restitution for various frame configurations the reader is referred to [17].

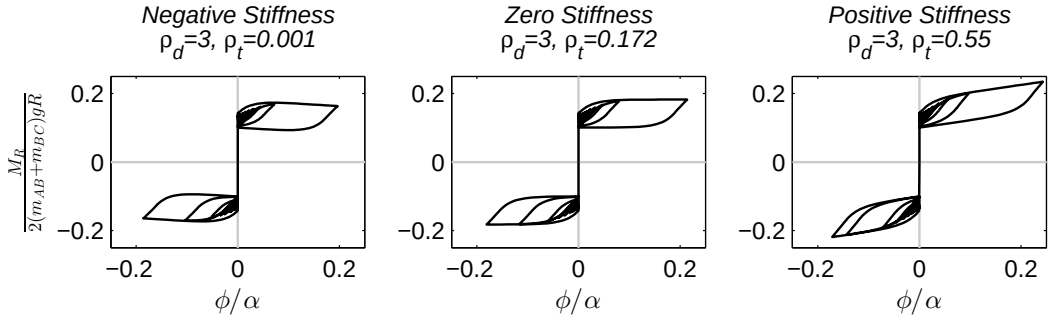


Figure 2: Flag-shaped hysteretic behavior of the rocking frame of Fig. 1 when subjected to an M&P pulse [34] with $\nu_g = 45°$, $\gamma_g = 2.0$, $\alpha_g/g = 0.6$ and $\omega_g/p = 5.0$. $M_R$ is the total restoring moment due to the forces from gravity, tendons and dissipaters, whereas the dimensionless parameters $\rho_d$ and $\rho_t$ depend on the stiffness of the dissipater and the tendon respectively [24].

## 3 SEISMIC VULNERABILITY ANALYSIS OF THE HYBRID ROCKING FRAME

### 3.1 Engineering demand parameter and intensity measures

This section investigates the seismic fragility of rocking bridge frames with different dynamic characteristics, i.e., negative, zero or positive post-uplift lateral stiffness when subjected to a suite of recorded earthquakes (Table 1). Consider the bridge frame of Fig. 1. Assume the frame has a cap-beam of 13 m width and $2h$ = 1 m height [33]. The two square columns have the same base-width $2b$ = 1 m, the same density and height $2H$ = 7 m [33, 17]. Both columns have the same slenderness $\alpha \simeq 8°$ and frequency parameter $p$ = 1.44 rad/s, while the distance between them is $L = 8$ m. The cap-beam/column mass ratio ($\gamma_m$) is 5 [33, 24]. Further, the tendons are assumed to be slack, anchored into the cap- and foundation-beam a depth of 0.75 m [33]. Following [8], the yield displacement ($u_y$) of the BRBs is taken as 3.5 mm, which corresponds to a yield rotation $\phi_y/\alpha \simeq 0.025$.

To effectively examine the seismic fragility of the rocking frame, this section: (i) introduces an appropriate engineering demand parameter (EDP) and the corresponding limit states (LSs) and (ii) investigates the existence of 'optimal' intensity measures (IMs) for hybrid rocking structures by investigating their 'practicality', 'efficiency' and 'sufficiency' [36, 28]. 'Practicality' is measured by the slope $b_R$ of the regression after conducting *cloud analysis* (as Fig. 3 shows later on). Specifically, the larger the $b_R$ the more 'practical' the IM [36]. An 'efficient' IM reduces the scatter (or dispersion) of the estimated structural demand [25, 28, 36]. On the other hand, a 'sufficient' IM offers an estimation of the structural demand independent of seismic hazard parameters, such as magnitude $M_w$, distance from the fault $R_{rup}$ [28], or epsilon $\epsilon$ [5].

***Engineering Demand Parameter (EDP)*:** According to the assumptions of the present study, an appropriate EDP to describe the motion of the rocking frame of Fig. 1 is the absolute value of the peak rotation $\phi_{max}$ normalized with the slenderness $\alpha$ of the column [18].

$$EDP = \frac{|\phi_{max}|}{\alpha} \tag{3}$$

This work also proposes three limit states (LSs) (Table 2). The exceedance of the first LS (EDP $> 0$) implies rocking initiation. The second LS corresponds to a design column drift

Table 1: Recorded earthquakes [45].

| No | Event | Station | $\phi^{\circ}$ [1] | Soil [2] | $M_w$ [3] | $R_{rup}$ [4] (km) | $PGA$ (g) |
|---|---|---|---|---|---|---|---|
| 1 | Loma Prieta, 1989 | Agnews State Hospital | 090 | C,D | 6.9 | 28.2 | 0.159 |
| 2 | Northridge, 1994 | LA, Baldwin Hills | 090 | B,B | 6.7 | 31.3 | 0.239 |
| 3 | Imperial Valley, 1979 | Compuertas | 285 | C,D | 6.5 | 32.6 | 0.147 |
| 4 | Imperial Valley, 1979 | Plaster City | 135 | C,D | 6.5 | 31.7 | 0.057 |
| 5 | Loma Prieta, 1989 | Hollister Diff. Array | 255 | –,D | 6.9 | 25.8 | 0.279 |
| 6 | San Fernando, 1971 | LA, Hollywood Stor. Lot | 180 | C,D | 6.6 | 21.2 | 0.174 |
| 7 | Loma Prieta, 1989 | Anderson Dam Downstrm | 270 | B,D | 6.9 | 21.4 | 0.244 |
| 8 | Loma Prieta, 1989 | Coyote Lake Dam Downstrm | 285 | B,D | 6.9 | 22.3 | 0.179 |
| 9 | Imperial Valley, 1979 | El Centro Array #12 | 140 | C,D | 6.5 | 18.2 | 0.143 |
| 10 | Imperial Valley, 1979 | Cucapah | 085 | C,D | 6.5 | 23.6 | 0.309 |
| 11 | Northridge, 1994 | LA, Hollywood Storage FF | 360 | C,D | 6.7 | 25.5 | 0.358 |
| 12 | Loma Prieta, 1989 | Sunnyvale Colton Ave | 270 | C,D | 6.9 | 28.8 | 0.207 |
| 13 | Loma Prieta, 1989 | Anderson Dam Downstrm | 360 | B,D | 6.9 | 21.4 | 0.24 |
| 14 | Imperial Valley, 1979 | Chihuahua | 012 | C,D | 6.5 | 28.7 | 0.27 |
| 15 | Imperial Valley, 1979 | El Centro Array #13 | 230 | C,D | 6.5 | 21.9 | 0.139 |
| 16 | Imperial Valley, 1979 | Westmoreland Fire Station | 090 | C,D | 6.5 | 15.1 | 0.074 |
| 17 | Loma Prieta, 1989 | Hollister South & Pine | 000 | –,D | 6.9 | 28.8 | 0.371 |
| 18 | Loma Prieta, 1989 | Sunnyvale Colton Ave | 360 | C,D | 6.9 | 28.8 | 0.209 |
| 19 | Superstition Hills, 1987 | Wildlife Liquefaction Array | 090 | C,D | 6.7 | 24.4 | 0.18 |
| 20 | Imperial Valley, 1979 | Chihuahua | 282 | C,D | 6.5 | 28.7 | 0.254 |
| 21 | Imperial Valley, 1979 | El Centro Array #13 | 230 | C,D | 6.5 | 21.9 | 0.139 |
| 22 | Imperial Valley, 1979 | Westmoreland Fire Station | 180 | C,D | 6.5 | 15.1 | 0.11 |
| 23 | Loma Prieta, 1989 | Halls Valley | 090 | C,C | 6.9 | 31.6 | 0.103 |
| 24 | Loma Prieta, 1989 | WAHO | 000 | -,D | 6.9 | 16.9 | 0.37 |
| 25 | Superstition Hills, 1987 | Wildlife Liquefaction Array | 360 | C,D | 6.7 | 24.4 | 0.2 |
| 26 | Imperial Valley, 1979 | Compuertas | 015 | C,D | 6.5 | 32.6 | 0.186 |
| 27 | Imperial Valley, 1979 | Plaster City | 045 | C,D | 6.5 | 31.7 | 0.042 |
| 28 | Loma Prieta, 1989 | Hollister Diff. Array | 165 | –,D | 6.9 | 25.8 | 0.269 |
| 29 | San Fernando, 1971 | LA, Hollywood Stor. Lot | 090 | C,D | 6.6 | 21.2 | 0.21 |
| 30 | Loma Prieta, 1989 | WAHO | 090 | –,D | 6.9 | 16.9 | 0.638 |

[1] Component [2] USGS, Geomatrix soil class [3] Moment magnitude [4] Closest distance to fault rupture

of 5% [33], which corresponds to a column rotation $\phi/\alpha \simeq 0.35$. This limit state indicates intermediate (observable) rocking action with potential local damage to the contact points, but without substantial danger of overturning. The third LS represents the maximum column drift of 11% [33], which corresponds to a column rotation $\phi/\alpha \simeq 0.8$, and herein is assumed that it leads to unstable configurations, potentially critical to the overturning (or failure) of the frame (Table 2).

Table 2: Proposed limit states.

| LSs [1] | EDP [2] | Capacity limit states | Description |
|---|---|---|---|
| LS1 | 0.0 | Rocking initiation | Uplifting |
| LS2 | 0.35 | Intermediate (observable) rocking action | Local damage due to contact |
| LS3 | 0.8 | Large rocking action | Unstable configuration (critical to overturning) |

[1] Limit States, [2] Engineering Demand Parameter

Table 3: Examined intensity measures.

| Category | Intensity Measure (IM) |
|---|---|
| Slenderness-based | $IM_1 = \frac{PGA}{g\tan\alpha}$, $IM_2 = \frac{pPGV}{g\tan\alpha}$, $IM_3 = \frac{p^2PGD}{g\tan\alpha}$, $IM_4 = \frac{\omega_m PGV}{g\tan\alpha}$, $IM_5 = \frac{A_{RMS}}{g\tan\alpha}$, $IM_6 = \frac{pCAV}{g\tan\alpha}$ |
| Frequency-based | $IM_7 = \frac{PGA}{pPGV}$ |
| Energy-based | $IM_8 = \frac{I_F}{p^{0.75}R}$, $IM_9 = \frac{L_e}{R}$ |

***Intensity Measures (IMs)*:** The identification of appropriate IMs for rocking structures is a far from trivial challenge. Dimitrakopoulos and Paraskeva [18] proposed 'optimal' IMs for (freestanding) rocking structures exhibiting negative post-uplift lateral stiffness. They showed the superior performance of the slenderness-based IMs compared to the frequency-based IMs. This paper, extends [18] and examines (hybrid) FSHB rocking frames with negative, zero and/or positive stiffness considering also energy-based IMs. Table 3 summarizes the examined IMs. $PGA$, $PGV$ and $PGD$ are the peak ground acceleration, peak ground velocity and peak ground displacement respectively. $CAV$ is the cumulative absolute velocity which equals the area under the (absolute) acceleration versus duration curve [27]. A strong ground motion parameter which includes the effects of the amplitude and frequency of a ground excitation is the root-mean-square acceleration $A_{RMS}$ [27]. $I_F$ is the Fajfar index which combines the peak ground velocity and the duration of strong motion [20]. $\omega_m$ denotes the mean frequency of the excitation [40], and $L_e$ is the energetic length-scale, firstly introduced for pulse-type ground motions [29] and later extended for non-distinct-pulse records [14].

### 3.2 Seismic analysis

This section employs the earthquake records of Table 1 and investigates the 'practicality', 'efficiency' and 'sufficiency' of the adopted IMs (Table 3) in capturing the behavior of the hybrid FSHB rocking frame of Fig. 1. Fig. 3 plots the EDP values $|\phi_{max}|/\alpha$ versus the examined IMs when the hybrid frames of Fig. 1 are subjected to the records of Table 1. This type of analysis is known as *cloud analysis*, where regression on IM-EDP plane is performed. The values

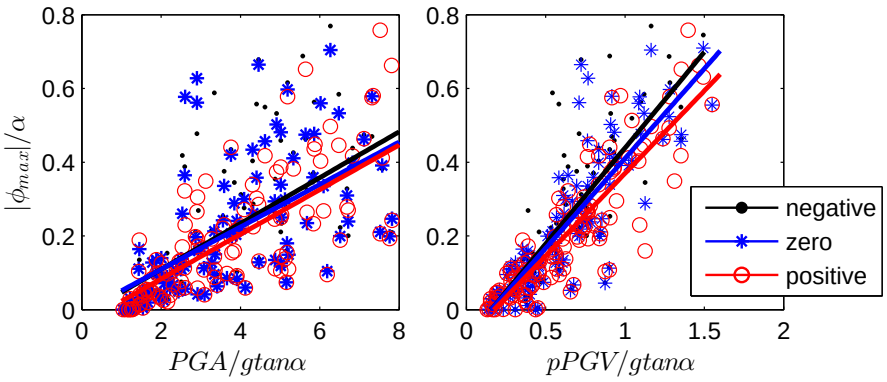


Figure 3: Cloud analysis of the 'safe rocking' cases of the hybrid FSHB rocking frames. Table 4 summarizes the results from the regression analysis for all the the examined IMs of Table 3.

Table 4: Results from cloud analysis of the different hybrid FSHB rocking frames of Fig. 1. $b_R$ denotes the slope of the linear regression and is a measure of 'practicality'. The larger the $b_R$ the more 'practical' the IM [36]. $R^2$ is the coefficient of determination and is an indication of 'efficiency', i.e., the larger the $R^2$ the smaller the scatter (or dispersion) on the response and hence the more 'efficient' the IM [28]. The values in the Table are determined after linear regression analysis in logarithmic scale.

| IMs [1] | Negative | | Zero | | Positive | |
|---|---|---|---|---|---|---|
| | $R^2$ | $b_R$ | $R^2$ | $b_R$ | $R^2$ | $b_R$ |
| $PGA/g\tan\alpha$ | **0.533** | **2.369** | **0.520** | **2.296** | **0.542** | **2.256** |
| $pPGV/g\tan\alpha$ | **0.490** | 2.282 | **0.497** | 2.226 | **0.507** | 2.137 |
| $p^2PGD/g\tan\alpha$ | 0.265 | 1.328 | 0.265 | 1.275 | 0.274 | 1.215 |
| $\omega_m PGV/g\tan\alpha$ | 0.436 | 2.054 | 0.435 | 2.008 | 0.461 | 1.987 |
| $A_{RMS}/g\tan\alpha$ | 0.486 | 2.334 | 0.473 | 2.251 | 0.498 | 2.217 |
| $pCAV/g\tan\alpha$ | **0.539** | **2.424** | **0.530** | **2.341** | **0.550** | **2.313** |
| $PGA/pPGV$ | 0.003 | 0.288 | 0.000 | 0.082 | 0.000 | 0.064 |
| $I_F/p^{0.75}R$ | **0.455** | 2.114 | **0.462** | 2.057 | **0.469** | 1.978 |
| $L_e/R$ | 0.254 | 1.103 | 0.257 | 1.075 | 0.256 | 1.018 |

[1] Intensity Measures (Table 3)

of the EDP in Fig. 3 correspond to the 'safe rocking' cases, i.e., where the EDP exceeds the LS1 but not the LS3 (Table 2)). To minimize the effects of scaling the amplitudes of the earthquake records of Table 1 are scaled up to a scale factor of 6. Table 4 summarizes the results from the linear regression analysis for all the proposed IMs. $R^2$ is the coefficient of determination which is considered as an indication of the 'efficiency', since the higher the $R^2$, the lower the $\beta_{ln(EDP)|IM}$ (or dispersion) and therefore the more 'efficient' the IM [28, 36]. Recall that, $b_R$ represents the slope of the linear regression analysis and it is a measure of 'practicality'; the higher the $b_R$ the more 'practical' the IM [36]. Table 4 shows that the more 'practical' IMs are the slenderness-based IMs, i.e., $IM_1 = PGA/g\tan\alpha$ and $IM_6 = pCAV/g\tan\alpha$, with the $IM_2 = pPGV/g\tan\alpha$ and $IM_5 = A_{RMS}/g\tan\alpha$ to show similar 'practicality'. Further, Table 4 also unveils that the normalized Fajfar index $IM_8 = I_F/p^{0.75}R$ together with most of the slenderness-based IMs maximize the coefficient of determination $R^2$, which is an indication of their 'efficiency'.

*Multi-stripe analysis* is an alternative to *cloud analysis* that provides a better indication of the 'efficiency' and 'sufficiency' of the proposed IMs (Fig. 3 and Table 3) [28]. Multi-stripe analysis scales the ground motions to a specified level of IM [6, 7]. For the purposes of the present section, the records of Table 1 are scaled with a factor between 0.4 and 6.5. Post-processing the EDP values we obtain results that are inherently conditional on the IM.

Fig. 4 plots the logarithmic standard deviation $\beta_{\ln(EDP)|IM}$ conditional on each IM level. In particular, it shows that the variation of the standard deviation $\beta_{\ln(EDP)|IM}$ among the different hybrid rocking frames is not significant. Therefore, under the assumptions of the present study, the 'efficiency' of the examined IMs remains unaffected by the different rocking frames. Further, Fig. 4 illustrates the 'inefficiency' of the frequency-based IM (i.e., $IM_7 = PGA/pPGV$), since it consistently predicts high dispersion on the response (i.e., $\beta_{\ln(EDP)|(PGA/pPGV)} > 1$). Similarly, $IM_9 = L_e/R$ also shows high $\beta_{\ln(EDP)|(L_e/R)}$, and hence it is regarded as 'insufficient' as well. On the contrary, the slenderness-based IMs (i.e., from $IM_1 = PGA/g\tan\alpha$ to $IM_6 = pCAV/g\tan\alpha$ in Table 3) and the energy-based $IM_8 = I_F/p^{0.75}R$ estimate the rocking response with low dispersion (i.e., $\beta_{\ln(EDP)|IM} < 1$), and therefore, they are considered as 'efficient'. Note in Fig. 4 that, for low IM levels the value of the EDP decreases, hence the

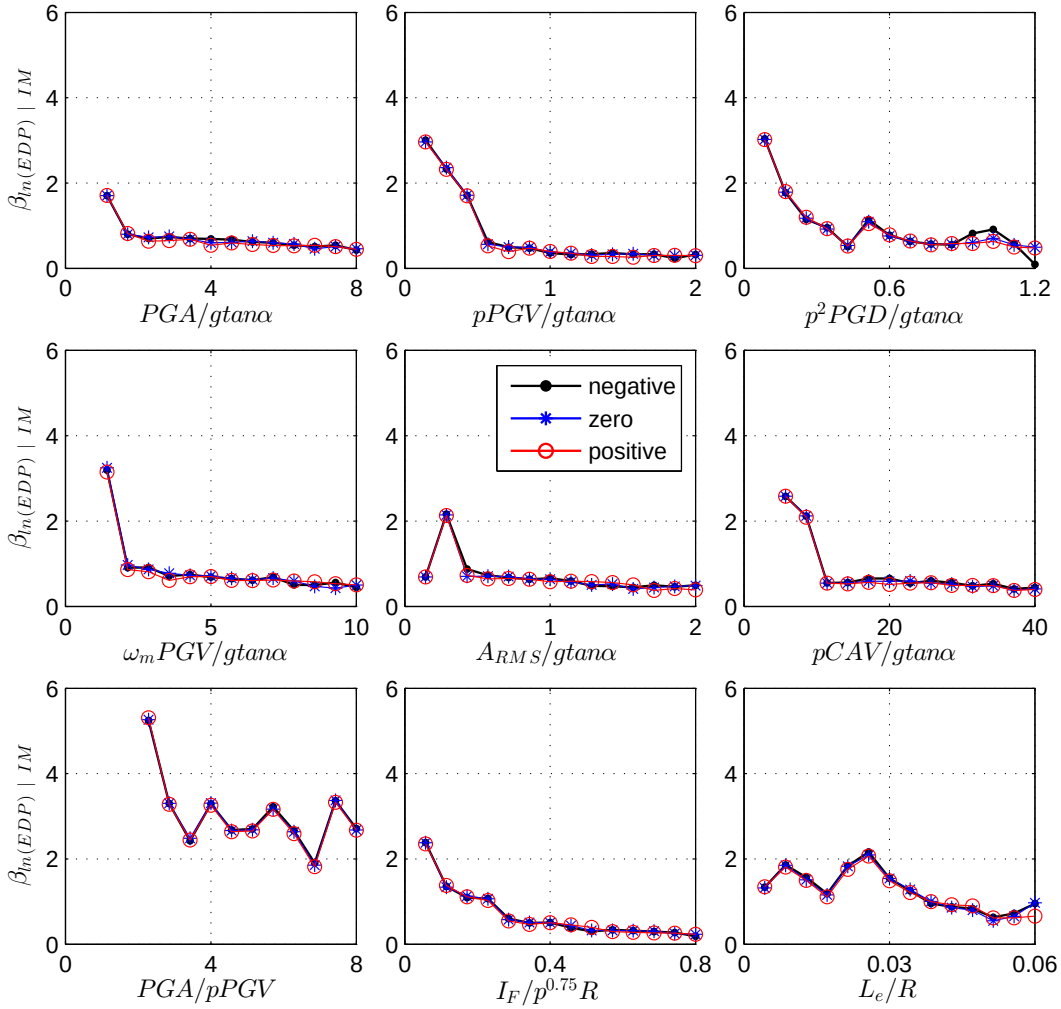


Figure 4: Logarithmic standard deviation $\beta_{\ln(EDP)|IM}$ conditional on each IM level of the 'safe rocking' cases of the hybrid frames of Fig. 1 with negative, zero and positive lateral stiffness. $\beta_{\ln(EDP)|IM}$ is a measure of 'efficiency' of every IM. The lower the $\beta_{\ln(EDP)|IM}$ the more 'efficient' the IM [28].

logarithmic standard deviation $\beta_{\ln(EDP)|IM}$ increases regardless of the examined IM.

On the other hand, 'sufficiency' provides an indication that an IM can be used independently of the seismological (or seismic hazard) parameters such as the magnitude $M_w$, the distance from the fault $R_{rup}$ [28] and/or epsilon $\epsilon$ [5]. Figs 5 to 7 plot the seismic response of the adopted hybrid FSHB rocking frames at various IM levels for all the examined IMs of Table 3 with respect to the distance from the fault $R_{rup}$ (Table 1). Constants $c_n$, $c_z$ and $c_p$ denote the slope of the regression analysis for the negative, zero and positive stiffness hybrid frames respectively. The closer the absolute value of the slope to zero, the more 'sufficient' the IM [28]. Note that, the present section investigates the 'sufficiency' of the IMs only with respect to the $R_{rup}$ and not e.g., the magnitude $M_w$ or the epsilon $\epsilon$ parameter. Specifically, Figs 5 and 6 plot the slenderness-based IMs, while Fig. (7) the frequency-based and the energy-based IMs of Table 3. Figs 5, 6, 7 show that the 'sufficiency' of an IM is not sensitive to the stiffness of the structure, at least for the structures considered herein, since for most cases the variation of the slope among the different frames is not substantial. Observe that, the examined IM levels are intentionally selected towards the left side of the fragility function, since ground motions with

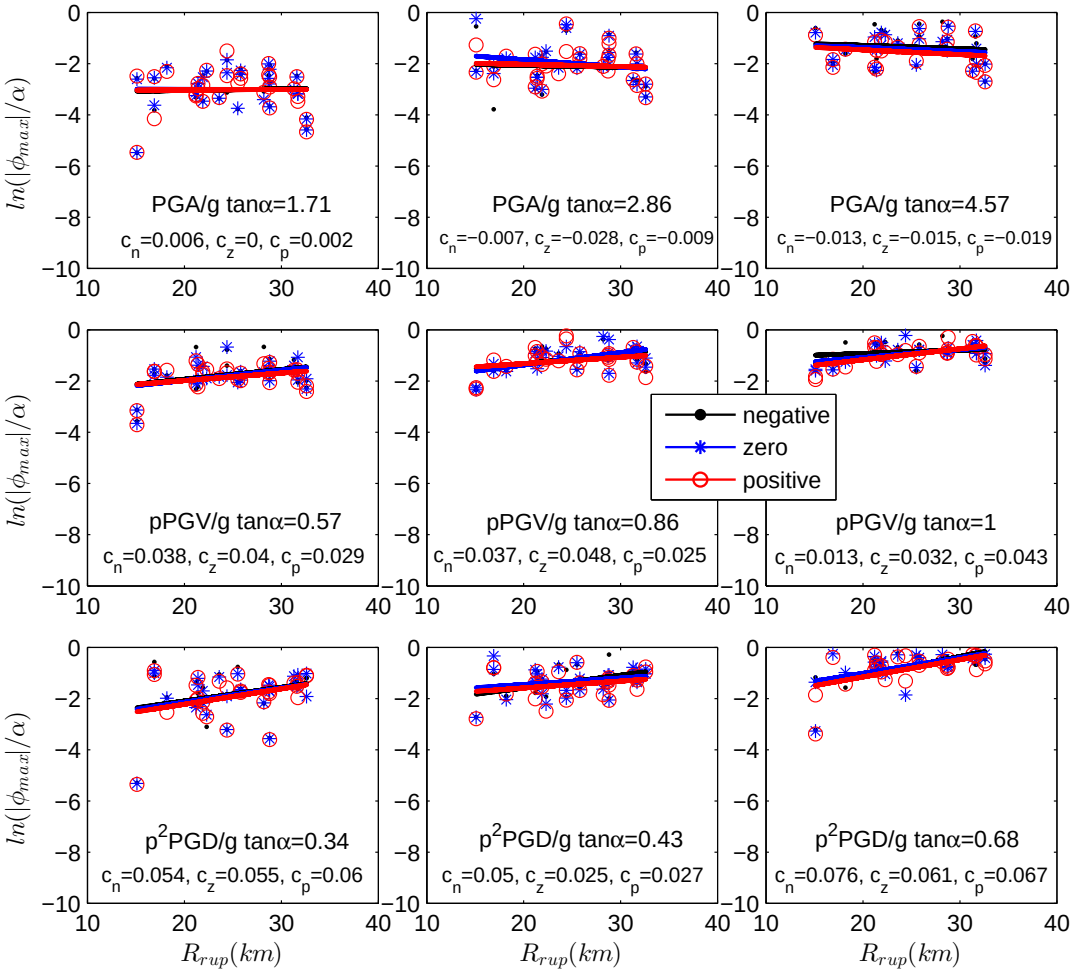


Figure 5: Regression analysis at various IM levels to examine the 'sufficiency' of the $IM_1 = PGA/g\tan\alpha$, $IM_2 = pPGV/g\tan\alpha$, $IM_3 = p^2PGD/g\tan\alpha$ of Table 3 with respect to the distance from the fault $R_{rup}$ (Table 1). Constants $c_n$, $c_z$ and $c_p$ represent the slope of the linear regression and the closer to zero the more 'sufficient' the IM [28].

low-to-middle IM levels occur much more frequently than ground motions with high IM levels [7]. In addition, more 'safe rocking' cases occur at these IM levels, improving the accuracy of the results. Exception is the $IM_7 = PGA/pPGV$ that 'safe rocking' action happens for higher $PGA/pPGV$ values. Among the slenderness-based IMs, Figs 5 and 6 show the 'insufficiency' of the $IM_3 = p^2PGD/g\tan\alpha$ and for some IM levels (i.e., $\omega_m PGV/g\tan\alpha = 2.14$) the 'insufficiency' of the $IM_4 = \omega_m PGV/g\tan\alpha$. On the contrary, $IM_1 = PGA/g\tan\alpha$ and $IM_5 = A_{RMS}/g\tan\alpha$ show great 'sufficiency' with respect to the distance $R_{rup}$. Fig. 7 illustrates the 'insufficiency' of both the freguency-based and the energy-based IMs (i.e., $IM_7 = PGA/pPGV$, $IM_8 = I_F/p^{0.75}R$ and $IM_9 = L_e/R$).

### 3.3 Fragility analysis

This section compares the seismic fragility of the different rocking frames (freestanding and hybrid) by calculating the total probability of failure $P_f$ that a ground motion with IM = x causes the exceedance of a limit state (i.e., EDP $>$ LS3) and subsequently collapse (or

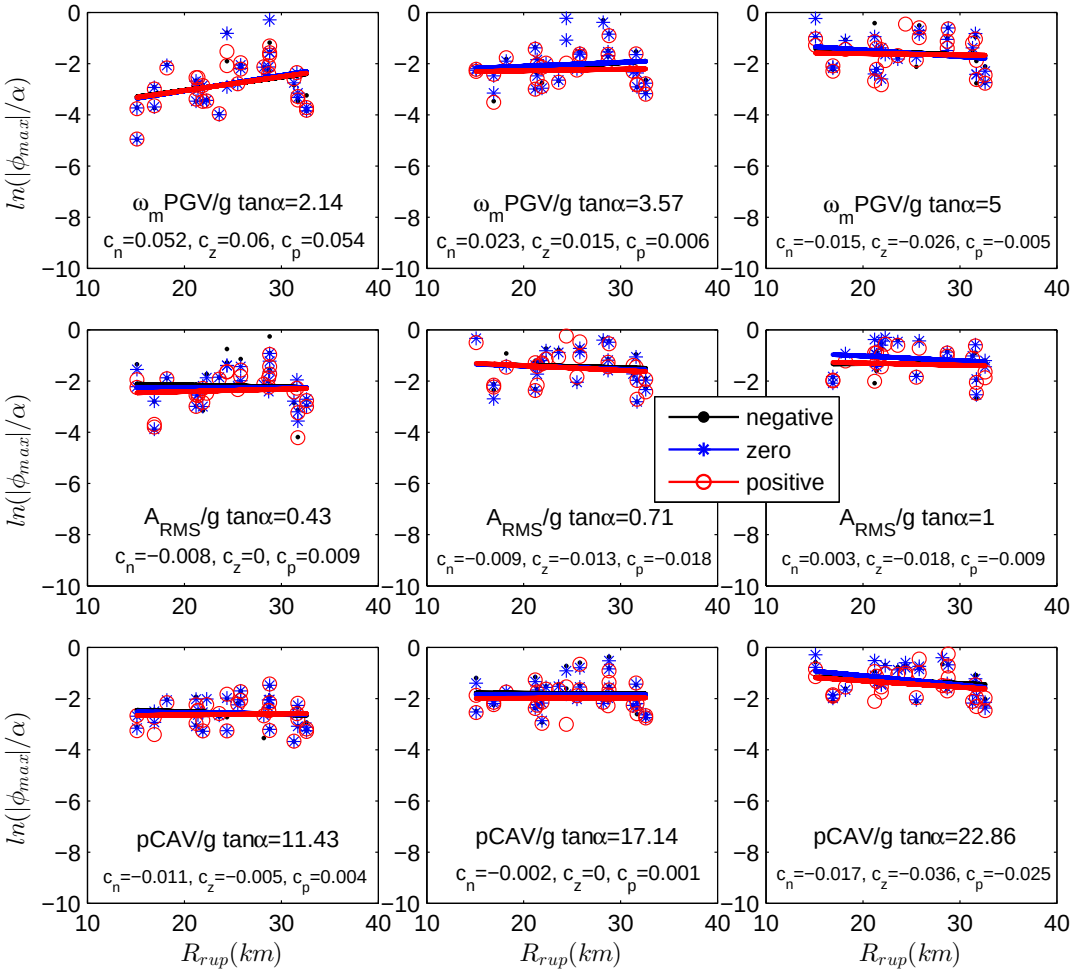


Figure 6: Regression analysis at various IM levels to examine the 'sufficiency' of the $IM_4 = \omega_m PGV/g \tan\alpha$, $IM_5 = A_{RMS}/g \tan\alpha$, $IM_6 = pCAV/g \tan\alpha$ of Table 3 with respect to the distance from the fault $R_{rup}$ (Table 1). Constants $c_n$, $c_z$ and $c_p$ represent the slope of the linear regression and the closer to zero the more 'sufficient' the IM [28].

overturning) of the structure occurs. Adopting the multi-stripe analysis method [5, 6], the limit state exceedance probability is calculated conditional on each intensity measure. To calculate the collapse probability, this study utilizes the logistic regression methodology. Note that, there are alternative methods to calculate the probability of collapse, e.g., the maximum likelihood estimation (MLE) [7]. Logistic regression, though, is consistent with maximum likelihood principles [7] and is commonly used to predict binary outcomes [35]. Specifically, since the structure either collapses or not (i.e., the EDP either exceeds the LS3 or not), collapse can be expressed with a 'categorical' variable [4]. This variable becomes zero when the structure does not collapse, and equal to one when it collapses.

Fig. 8 compares the seismic fragility of the hybrid FSHB rocking frames of Figs 1, 2 with the pertinent fragility of the archetypal freestanding frame for the most 'optimal' IMs based on the analysis in Section 3.2. Fig. 8 illustrates the mitigated fragility of the hybrid rocking frame with positive post-uplift lateral stiffness compared to the other rocking structural systems (freestanding and hybrid). In particular, the positive stiffness frame shows enhanced seismic

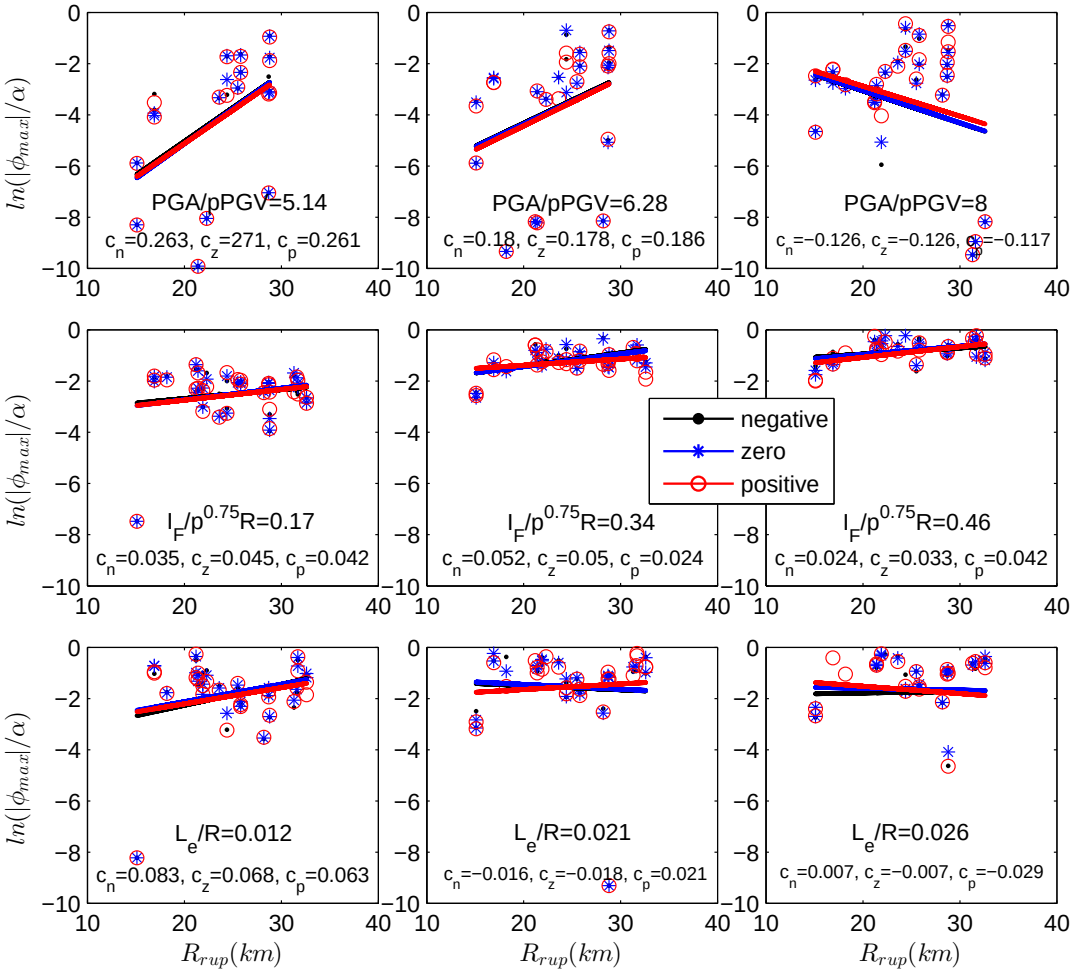


Figure 7: Regression analysis at various IM levels to examine the 'sufficiency' of the $IM_7 = PGA/pPGV$, $IM_8 = I_F/p^{0.75}R$, $IM_9 = L_e/R$ of Table 3 with respect to the distance from the fault $R_{rup}$ (Table 1). Constants $c_n, c_z$ and $c_p$ represent the slope of the linear regression and the closer to zero the more 'sufficient' the IM [28].

performance for all 'optimal' IMs. For some IMs though, the distinction among the hybrid frames becomes marginal (i.e., for $PGA/g\tan\alpha$, or as $A_{RMS}/g\tan\alpha$ increases). Recall that, the present study ignores the fatigue of the supplemental devices (i.e., tendons and buckling-restrained braces) and assumes that they continue to behave in a perfectly linear-elastic and nonlinear-hysteretic way respectively regardless of the number of rotation cycles. Another limitation is that it neglects the impact on the fragility of the accumulated energy dissipation by the BRBs. Giouvanidis and Dimitrakopoulos [24] showed that the enhanced seismic behavior of positive stiffness hybrid frames might come at the cost of higher energy demands by the dissipaters. A more complete approach would require the introduction of an additional EDP which characterizes the accumulated energy dissipation by the BRBs throughout the nonlinear response-history, or the consideration of a vector IM. This, however, is beyond the scope of the present work.

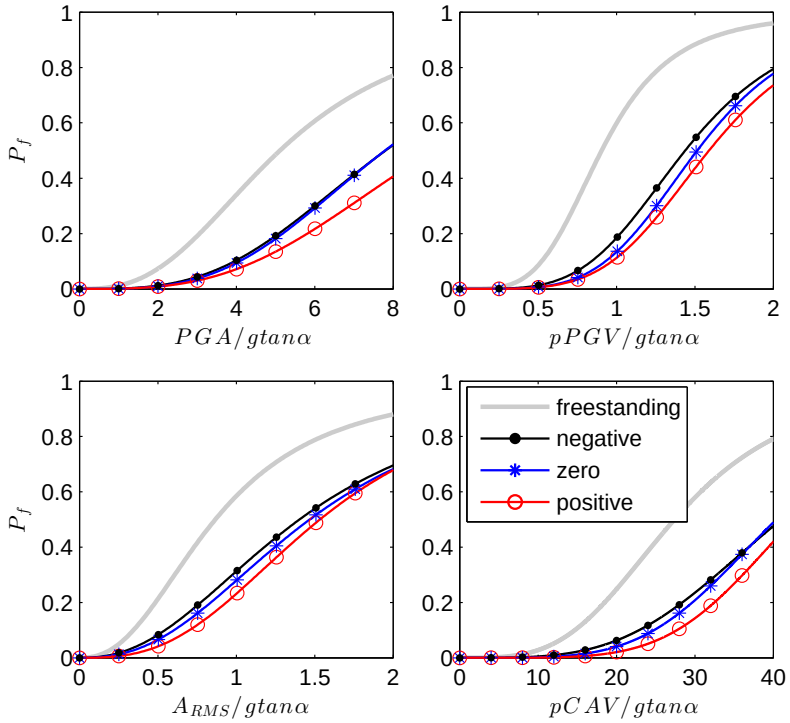


Figure 8: Failure prediction through seismic fragility curves of the freestanding and hybrid FSHB rocking frames for the most 'optimal' IMs adopting the logistic regression methodology.

## 4 CONCLUSIONS

This study investigates the existence of potentially 'optimal' intensity measures for hybrid rocking bridge frames by examining their 'practicality', 'efficiency' and 'sufficiency' with an appropriate engineering demand parameter. Specifically, this paper compares three categories of intensity measures, i.e., slenderness-based, frequency-based and energy-based IMs. The proposed slenderness-based IMs (e.g., $PGA/gtan\alpha$, $pPGV/gtan\alpha$, $A_{RMS}/gtan\alpha$ and $pCAV/gtan\alpha$) exhibit reduced scatter on the response, lower logarithmic standard deviation and independence from seismic hazard parameters such as the distance from the fault. Hence, the slenderness-based IMs show higher 'practicality', 'efficiency' and 'sufficiency' compared to the other proposed IMs. In addition, this work investigates the seismic fragility of slender rocking bridge frames with fundamentally different dynamic behavior. It compares the seismic performance of rocking frames with negative, zero and/or positive post-uplift lateral stiffness with the archetypal freestanding frame in terms of their seismic fragility when subjected to the same suite of recorded earthquakes. The results unveil the mitigated fragility of the positive stiffness frame compared to rocking structures of zero or negative stiffness. However, for some intensity measures the seismic enhancement (in terms of fragility) becomes marginal. A more sophisticated approach would require the introduction of a second engineering demand parameter tailored to the needs of hybrid rocking structures or the consideration of a vector intensity measure.

## REFERENCES


[1] Acikgoz, S., DeJong, M. J., The interaction of elasticity and rocking in flexible structures allowed to uplift. *Earthquake Engineering & Structural Dynamics*, **41**(15), 2177–2194, 2012.

[2] Acikgoz, S., DeJong, M. J., The rocking response of large flexible structures to earthquakes. *Bulletin of Earthquake Engineering*, **12**(2), 875–908, 2014.

[3] Acikgoz, S., DeJong, M. J., Analytical modelling of multi-mass flexible rocking structures. *Earthquake Engineering & Structural Dynamics*, **45**(13), 2103-2122, 2016.

[4] Agresti, A., *Categorical data analysis, 3rd Edition*. John Wiley & Sons, 2012.

[5] Baker, J. W., Cornell, C. A., A vector-valued ground motion intensity measure consisting of spectral acceleration and epsilon. *Earthquake Engineering & Structural Dynamics*, **34**(10), 1193–1217, 2005.

[6] Baker, J. W., Cornell, C. A., Vector-valued intensity measures incorporating spectral shape for prediction of structural response. *Journal of Earthquake Engineering*, **12**(4), 534–554, 2008.

[7] Baker, J. W., Efficient analytical fragility function fitting using dynamic structural analysis. *Earthquake Spectra*, **31**(1), 579–599, 2015.

[8] Black, C. J., Makris, N., Aiken, I. D., Component testing, seismic evaluation and characterization of buckling-restrained braces. *Journal of Structural Engineering*, **130**(6), 880–894, 2004.

[9] Bouc, R., Forced vibration of mechanical systems with hysteresis. *Proceedings of the 4th conference on non-linear oscillation*, Prague, Czechoslovakia, 1967.

[10] Brogliato, B., Zhang, H., Liu, C., Analysis of a generalized kinematic impact law for multibody-multicontact systems, with application to the planar rocking block and chains of balls. *Multibody System Dynamics*, **27**(3), 351–382, 2012.

[11] Cheng, C. T., Shaking table tests of a self-centering designed bridge substructure. *Engineering Structures*, **30**(12), 3426–3433, 2008.

[12] DeJong, M. J., Amplification of rocking due to horizontal ground motion. *Earthquake Spectra*, **28**(4), 1405–1421, 2012.

[13] DeJong, M. J., Dimitrakopoulos, E. G., Dynamically equivalent rocking structures. *Earthquake Engineering & Structural Dynamics*, **43**(10), 1543–1563, 2014.

[14] Dimitrakopoulos, E. G., Kappos, A. J., Makris, N., Dimensional analysis of yielding and pounding structures for records without distinct pulses. *Soil Dynamics and Earthquake Engineering*, **29**(7), 1170–1180, 2009.

[15] Dimitrakopoulos, E. G., DeJong, M. J., Revisiting the rocking block: closed-form solutions and similarity laws. *Proceedings of the Royal Society A: Mathematical, Physical and Engineering Science*, **468**(2144), 2294–2318, 2012.

[16] Dimitrakopoulos, E. G., DeJong, M. J., Overturning of retrofitted rocking structures under pulse-type excitations. *Journal of Engineering Mechanics*, **138**(8), 963–972, 2012.

[17] Dimitrakopoulos, E. G., Giouvanidis, A. I., Seismic response analysis of the planar rocking frame. *Journal of Engineering Mechanics*, **141**(7), 04015003, 2015.

[18] Dimitrakopoulos, E. G., Paraskeva, T. S., Dimensionless fragility curves for rocking response to near-fault excitations. *Earthquake Engineering & Structural Dynamics*, **44**(12), 2015-2033, 2015.

[19] Dimitrakopoulos, E. G., Fung, E. D. W., Closed-form rocking overturning conditions for a family of pulse ground motions. *Proceedings of the Royal Society A: Mathematical, Physical and Engineering Science*, **472**(2196), 20160662, 2016.

[20] Fajfar, P., Vidic, T., Fischinger, M., A measure of earthquake motion capacity to damage medium-period structures. *Soil Dynamics and Earthquake Engineering*, **9**(5), 236–242, 1990.

[21] Giouvanidis, A. I., Dimitrakopoulos, E. G., Seismic analysis of hybrid rocking bridge bents. *Proceedings of the 2nd European Conference on Earthquake Engineering and Seismology*, Paper No 2251, Istanbul, Turkey, 2014.

[22] Giouvanidis, A. I., Dimitrakopoulos, E. G., Nonsmooth dynamic analysis of sticking impacts in rocking structures. *Bulletin of Earthquake Engineering*, **15**(3), 2273-2304, 2017.

[23] Giouvanidis, A. I., Dimitrakopoulos, E. G., Seismic reliability assessment of rocking bridge bents with flag-shaped hysteretic behavior. *Proceedings of the 16th World Conference on Earthquake Engineering*, Paper No 1259, Santiago, Chile, 2017.

[24] Giouvanidis, A. I., Dimitrakopoulos, E. G., Seismic performance of rocking frames with flag-shaped hysteretic behavior. *Journal of Engineering Mechanics*, **143**(5), 04017008, 2017.

[25] Giovenale, P., Cornell, C. A., Esteva, L., Comparing the adequacy of alternative ground motion intensity measures for the estimation of structural responses. *Earthquake Engineering & Structural Dynamics*, **33**(8), 951–979, 2004.

[26] Housner, G. W., The behavior of inverted pendulum structures during earthquakes. *Bulletin of the Seismological Society of America*, **53**(2), 403–417, 1963.

[27] Kramer, S. L., *Geotechnical Earthquake Engineering*. Prentice-Hall International Series, 1996.

[28] Luco, N., Cornell, C. A.., Structure-specific scalar intensity measures for near-source and ordinary earthquake ground motions. *Earthquake Spectra*, **23**(2), 357–392, 2007.

[29] Makris, N., Black, C. J., Dimensional analysis of rigid-plastic and elastoplastic structures under pulse-type excitations. *Journal of Engineering Mechanics*, **130**(9), 1006–1018, 2004.

[30] Makris, N., Vassiliou, M. F., Planar rocking response and stability analysis of an array of free-standing columns capped with a freely supported rigid beam. *Earthquake Engineering & Structural Dynamics*, **42**(3), 431–449, 2012.

[31] Makris, N., Vassiliou, M. F., Are Some Top-Heavy Structures More Stable?. *Journal of Structural Engineering*, **140**(5), 06014001, 2014.

[32] Makris, N., Vassiliou, M. F., Dynamics of the rocking frame with vertical restrainers. *Journal of Structural Engineering*, **141**(10), 04014245, 2014.

[33] Mander, J. B., Cheng, C. T., *Seismic resistance of bridge piers based on damage avoidance design, Report No. NCEER-97-0014*, University at Buffalo, 1997.

[34] Mavroeidis, G. P., Papageorgiou, A. S., A mathematical representation of near-fault ground motions. *Bulletin of the Seismological Society of America*, **93**(3), 1099–1131, 2003.

[35] Neter, J., Kutner, M. H., Nachtsheim, C. J., Wasserman, W., *Applied linear statistical models*. McGraw-Hill, 1996.

[36] Padgett, J. E., Nielson, B. G., DesRoches, R., Selection of optimal intensity measures in probabilistic seismic demand models of highway bridge portfolios. *Earthquake Engineering & Structural Dynamics*, **37**(8), 711–725, 2008.

[37] Panagiotou, M., Trono, W., Jen, G., Kumar, P., Ostertag, C. P., Experimental seismic response of hybrid fiber-reinforced concrete bridge columns with novel longitudinal reinforcement detailing. *Journal of Bridge Engineering*, **20**(7), 04014090, 2014.

[38] Priestley, M. J. N., Seible, F., Calvi, G. M., *Seismic design and retrofit of bridges*. John Wiley & Sons, 1996.

[39] Psycharis, I. N., Fragiadakis, M., Stefanou, I., Seismic reliability assessment of classical columns subjected to near-fault ground motions. *Earthquake Engineering & Structural Dynamics*, **42**(14), 2061–2079, 2013.

[40] Rathje, E. M., Abrahamson, N. A., Bray, J. D., Simplified frequency content estimates of earthquake ground motions. *Journal of Geotechnical and Geoenvironmental Engineering*, **124**(2), 150–159, 1998.

[41] Routledge, P. J., Cowan, M. J., Palermo, A., Low-damage detailing for bridges - A case study of Wigram-Magdala bridge. *Proceedings, New Zealand Society for Earthquake Engineering 2016 Conference*, Christchurch, New Zealand, 2016.

[42] Thonstad, T., Mantawy, I. M., Stanton, J. F., Eberhard, M. O., Sanders, D. H., Shaking Table Performance of a New Bridge System with Pretensioned Rocking Columns. *Journal of Bridge Engineering*, **21**(4), 04015079, 2016.

[43] Trono, W., Jen, G., Panagiotou, M., Schoettler, M., Ostertag, C. P., Seismic response of a damage-resistant recentering posttensioned-hyfrc bridge column. *Journal of Bridge Engineering*, **20**(7), 04014096, 2014.

[44] Truniger, R., Vassiliou, M. F., Stojadinovic B., An analytical model of a deformable cantilever structure rocking on a rigid surface: experimental validation. *Earthquake Engineering & Structural Dynamics*, **44**(15), 2795–2815, 2015.

[45] Vamvatsikos, D., Fragiadakis, M., Incremental dynamic analysis for estimating seismic performance sensitivity and uncertainty. *Earthquake Engineering & Structural Dynamics*, **39**(2), 141–163, 2010.

[46] Vassiliou, M. F., Mackie, K. R., Stojadinovic B., Dynamic response analysis of solitary flexible rocking bodies: modeling and behavior under pulse-like ground excitation. *Earthquake Engineering & Structural Dynamics*, **43**(10), 1463–1481, 2014.

[47] Vassiliou, M. F., Truniger, R., Stojadinovic B., An analytical model of a deformable cantilever structure rocking on a rigid surface: development and verification. *Earthquake Engineering & Structural Dynamics*, **44**(15), 2775–2794, 2015.

[48] Vassiliou, M. F., Mackie, K. R., Stojadinovic B., A finite element model for seismic response analysis of deformable rocking frames. *Earthquake Engineering & Structural Dynamics*, **46**(3), 447-466, 2016.

[49] Vassiliou, M. F., Burger, S., Egger, M., Bachmann, J. A., Broccardo, M., Stojadinovic, B., The three-dimensional behavior of inverted pendulum cylindrical structures during earthquakes. *Earthquake Engineering & Structural Dynamics*, **doi:10.1002/eqe.2903**, 2017.

[50] Wen, Y.-K., Method for random vibration of hysteretic systems. *Journal of the Engineering Mechanics Division*, **102**(2), 249–263, 1976.

COMPDYN 2017
6th ECCOMAS Thematic Conference on
Computational Methods in Structural Dynamics and Earthquake Engineering
M. Papadrakakis, M. Fragiadakis (eds.)
Rhodes Island, Greece, 15–17 June 2017

# ENERGY DISSIPATION INVOLVED IN THE OUT-OF-PLANE RESPONSE OF UNREINFORCED MASONRY WALLS

**U. Tomassetti[1], F. Graziotti[1,2], A. Penna[1,2], and G. Magenes[1,2]**

[1] Dept. of Civil Engineering and Architecture, University of Pavia,
via Ferrata 3, 27100 Pavia, Italy.
umberto.tomassetti01@univeristadipavia.it

[2] European Centre for Training and Research in Earthquake Engineering,
via Ferrata 1, 27100 Pavia, Italy.
francesco.graziotti@unipv.it, andrea.penna@unipv.it, guido.magenes@unipv.it

**Keywords:** URM, out-of-plane, rocking, one-way bending, coefficient of restitution, elastic viscous damping ratio.

**Abstract.** *The assessment of the out-of-plane response of masonry has been largely investigated in literature assuming walls responding as rigid blocks or assemblies of rigid bodies. Several studies developed numerical integration of single-degree-of-freedom and multi-degree of freedom systems for the simulation of the OOP dynamic rocking response of simple mechanisms. Modelling the energy dissipation involved in such mechanisms is extremely important to capture the dependence of the damping phenomenon with the system frequency.*

*Some studies, recurring to the classical hypothesis of the impulsive dynamics, simulated the energy dissipation by means of the coefficient of restitution assuming as the overall reduction of energy were concentrated at the instant of the impact. In other works, the damping force has been modelled as a velocity dependent acting force through a constant, variable or stiffness proportional damping ratio.*

*The two damping models are compared highlighting advantages and shortcomings of each system. This paper proposes a numerical formulation for the direct equivalence of the two damping approaches for simple OOP one-way bending mechanisms assuming as force-displacement relationship nonlinear elastic tri-linear curves.*

## 1 INTRODUCTION

The high seismic vulnerability of unreinforced masonry (URM) structures has been highlighted in many studies in the literature [1-3]. The out-of-plane (OOP) behaviour of URM structures subjected to ground motion excitations has been extensively investigated by referring to the rocking dynamic of semi-rigid wall segments, characterised by consistent rotations, that impact each other. Such interpretation, confirmed by several experimental campaigns, could be considered acceptable under specific hypothesis and in case the masonry quality is good enough to ensure the formation of such mechanism. The understanding of this complex dynamic behaviour is essential in assessing the seismic performance of existing structures, for which an accurate prediction of displacement capacity and demand is essential in both safety verifications and risk analyses.

Housner [4] with a pioneer study derived a single degree of freedom (SDOF) equation of motion for dynamic response of slender rigid blocks (inverted pendulum structures) that could easily represent the one-way OOP response of a parapet wall (PW). Several studies [5-6], assuming that both end supports of the wall move simultaneously, derived SDOF equation of motion for the one-way vertical spanning strip walls (VSSW) displacing as an assembly of two rigid bodies. Dejong and Dimitrakopoulos [7] as well as Restrepo [8] extended the solution to include equivalent SDOF systems governing the dynamic behaviour of complex multi-block systems responding in rocking.

Makris and Konstantinidis [9] highlighted that the classical linear oscillator (regular pendulum) often adopted to analyse the OOP behaviour of masonry sub-structures, and the rocking block represent two fundamentally different dynamical systems. Rocking structures, indeed, do not have a fundamental period of vibration, the responding frequency is, hence, oscillation amplitude dependent [4-5]. Further differences between these two systems are also represented by restoring mechanisms, stiffness and characteristics of the damping phenomena. Therefore, equivalent stiffness methods based on the adoption of classical response spectra [10] cannot sufficiently predict the response of rocking structures. Makris and Konstantinidis proposed the derivation of rocking spectra as a more adequate approach to characterising the earthquake input. For these reasons, the solution proposed by several researchers to the challenging problem of assessing the OOP performance of URM structures has been to directly integrate the rocking equation of motion to reproduce their dynamic responses.

Recognising that the URM wall segments do not have infinite stiffness, researchers proposed bi-linear [11], tri-linear [6] and four-branch [12] non-linear elastic curves to model the force-displacement (F-u) relationship.

The energy dissipation in elastic non-linear systems (i.e. rocking structures) is of major importance to successfully simulate their dynamic behaviour, capturing the dependence of the damping phenomenon with the system frequency. Some studies, building off the classical hypothesis of the impulse dynamics, simulated the energy dissipation involved in such mechanisms by means of the coefficient of restitution assuming that the overall reduction of energy was concentrated at the instant of the impact [4-5]. In other works, the damping force has been modelled as a velocity dependent force through a constant [10] and variable (with cycle-to-cycle iterations) damping ratio [13]. The effectiveness of damping models acting on the system secant stiffness with a constant or linear damping ratio-frequency ($\xi$- $\omega$) relationship is also investigated [14].

The present study proposes a correlation between these different damping systems: elastic viscous dampers and coefficient of restitution focusing on the response of VSSW systems. The second section introduces the SDOF rigid body equation of motion. Section 3 reviews the tri-linear idealisation commonly used to simulate the static OOP force-displacement relationship

of a VSSW. The energy dissipation involved in this phenomenon is discussed in section 4 introducing both coefficient of restitution and velocity dependent damping force systems. Section 5 presents the numerical model developed from the present study. The results of the proposed equivalence and their experimental validation is discussed in section 6 and 7.

## 2 RIGID BODY SDOF EQUATION OF MOTION

Figure 1 shows the VSSW deformed shape responding in pure rocking behaviour characterised by the formation of the classical pivot interfaces at the wall top, bottom and mid-height. The resulting top and bottom rigid bodies rotate around such pivot (A'-B-C' in Figure 1) points impacting each other every time the system passes through mid-height horizontal rest-condition displacement ($u$=0 in Figure 1). $\alpha_2$ and $\alpha_1$ are geometric angles defining the slenderness of the two bodies; $W_2$ and $W_1$ represent the weight of the top and bottom bodies applied at the bodies centre of mass, $O$ is the overburden vertical force applied with eccentricity $e$, $t$ the thickness of the wall. $\theta_2$ and $\theta_1$ are the top and bottom body rotations equal to $u/h_2$ and $u/h_1$ respectively.

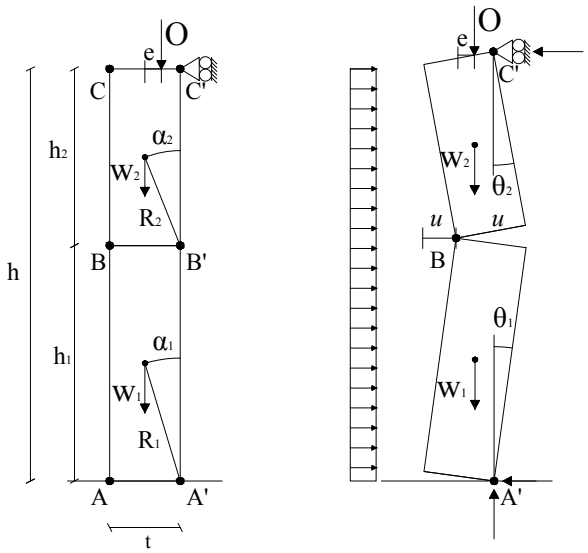


Figure 1: VSSW responding in Rocking behaviour: geometry at rest and deformed shape.

The equation of motion of this system responding in rocking can be derived directly from Lagrange's equation of motion. Under the hypothesis of no sliding, no bouncing effect, slender blocks (that allows us to linearize the equation) and assuming both supports moving simultaneously, similarly to Derakhshan *et al.* [15], the generic undamped SDOF equation of motion of a VSSW system can be written as follows:

$$m_{eff} \cdot \ddot{u}(t) + f_{bi}\,(u,t) = -\lambda \cdot m_{eff} \cdot \ddot{u}_g(t) \tag{1}$$

where $u$ represents the horizontal displacement associated to the wall mid-hinge location (shown in Figure 1), $m_{eff}$ is the effective mass of the system affected by the rotational moment of inertia of the two blocks (equation 2), $f_{bi}$ (u, $t$) is the bi-linear rigid restoring force relationship (equation 3) assuming a uniformly distributed lateral face load (considering uniform thickness and density along the wall height); $\lambda$ (equation 4) is the parameter that allow to mobilise the entire mass ($m_1$+$m_2$) in the excitation term (right side of the equation) with the ground acceleration ($\ddot{u}_g(t)$).

$$m_{eff} = \frac{2}{3}(m_1 + m_2) \tag{2}$$

$$f_{bi}(u,t) = \frac{2}{h_1} \cdot W \cdot (t - u(t)) + \frac{h}{h_1 \cdot h_2} \cdot O \cdot (t + 2e - u(t)) + \frac{2}{h_1} \cdot O \cdot (t - 2e) \quad (3)$$

$$\lambda = \frac{3}{2} \quad (4)$$

The resulting equation of motion is equivalent to those proposed by Sorrentino et al. [5], DeJong & Dimitrakopoulos [7]. The aforementioned studies described the rocking phenomena as function of the rotation of the lower body. Sorrentino *et al.* [5] have shown as the system frequency parameter considering $h_1/h$ ratios different from 0.5 may slightly affect $m_{eff}$ and $\lambda$. Experimental evidences have shown as this ratio could be addressed between 0.5 and 0.7 [16-17].

## 3 FORCE-DISPLACEMENT RELATIONSHIP

Before undergoing non-linear rocking behaviour through the formation of the classical pivot interfaces, URM walls are characterised by a linear response controlled by the masonry flexural stiffness till the attainment of the cracking force. Neglecting the wall un-cracked response may lead to a significant underestimation of the lateral capacity, especially for slender and slightly loaded walls, and an overestimation of the OOP displacement demand [6, 18].

The bi-linear curve relies on the assumption of wall responding as an assembly of two rigid bodies with an infinite initial stiffness and strength, representing an upper bound of the real OOP static resistance of a VSSW. The bi-linear curve could be identified by $F_0$ and $u_{ins}$ the defined according to the equations:

$$F_0 = \frac{2}{h_1}(W + O) \cdot t + \frac{O}{h - h_1}(t + 2e) \quad (5)$$

$$u_{ins} = \frac{2/h_1\,(W + O)t + O \cdot (t + 2 \cdot e)/(h - h_1)}{2/h_1\,(W + O) + 2O/(h - h_1)} \quad (6)$$

$K_0$ represents the negative stiffness of the system. The experimental *F-u* relationship of a VSSW could be more realistically represented by a tri-linear curve built on the rigid body bi-linear idealisation. Figure 2 illustrates the both the rigid-bilinear curve and the tri-linear relationships implemented in the model. The key parameters of the tri-linear relationship are $u_1$ ($=a_1 \cdot u_{ins}$) controlling the wall's initial cracked stiffness, and $F_y$ ($= b_1 \cdot F_0$) identifying a force plateau; the idealisations proposed in literature beyond $u_2$, generally located along the bi-linear curve ($u_2=u_{ins}-F_y/K_0$), drops to zero in some cases matching the bi-linear idealisation ($u_3=u_{ins}$ ), in some other cases with an higher negative stiffness ($u_3=a_3 \cdot u_{ins}$) taking into account the masonry compressive strength and the physical dimension of the hinges [19]. In this latter case, it may also be represented by a backward translation (with negative stiffness equal to $K_0$) of the last tri-linear branch causing a reduction of the $u_2$ value.

The values for $a_1$, $a_3$ and $b_1$ are strongly affected by aspects such as wall thickness, acting vertical overburden force and masonry mechanical properties [19]. Doherty [6] identified three stages of degradation: new, moderate and severe corresponding to $b_1$ values of 0.72, 0.60 and 0.50 and $a_1$ values of 0.06, 0.13 and 0.20, respectively. Other researchers later suggested $a_1$ values of 0.04 [18] and 0.05 [5] based on both experimental results of air-bag quasi-static tests and successful numerical modelling of the dynamic behaviour of VSSW systems. Derakhshan *et al.* [18] showed as $a_2$ value of 0.25 represents an upper bound level for this parameter. Their experimental work also suggested that the average ratio between the maximum lateral force resistance and the $F_0$ rigid force for two-leaf and three-leaf walls was around 0.81 suggesting $b_1$ values around 0.75 (1- $a_2$) [15]. A refined work on the characterisation of the *F-u* relationship of can be found in [19].

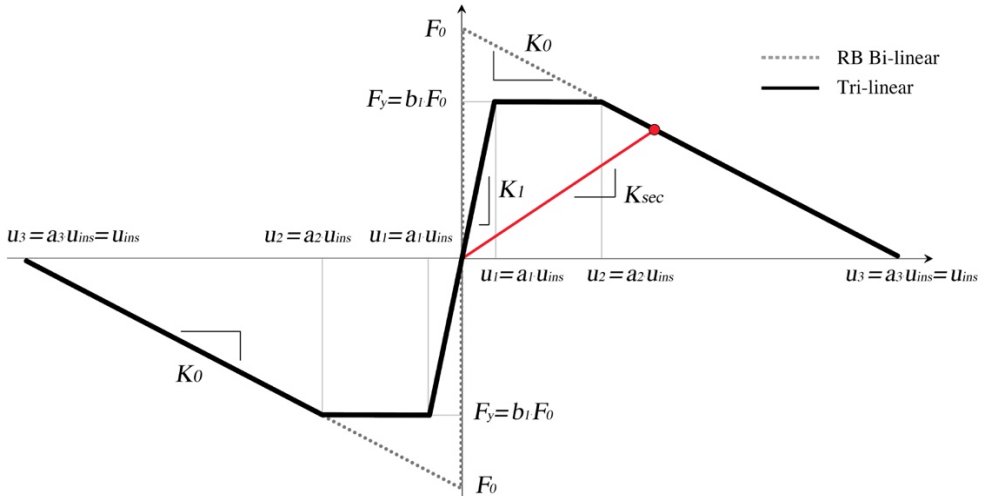


Figure 2: *F-u* relationship implemented: tri-linear configuration built on the bi-linear rigid body idealisation.

## 4 ENERGY DISSIPATION IN ROCKING STRUCTURES

The overall damping force acting in URM panels or assemblies responding in OOP rocking is given primarily by the energy dissipated through the impact of the wall during rocking in addition to a small contribution from the hysteretic energy dissipation, which both need to be considered in the model. A common approach, relying on the classical hypothesis of the impulse dynamics, is simulating the energy dissipation involved in such mechanisms through a coefficient of restitution [4-5, 20]. Another option is adopting an equivalent viscous damping approach defining a velocity dependent damping force through a constant, variable (with cycle-to-cycle iterations) and stiffness proportional damping ratio. The iterative procedure introduced by Doherty [6] and Lam *et al.* [13] consisted in evaluating the damping associated with each half-response cycle according to a calibration of Rayleigh damping against dynamic experimental $\xi$- $\omega$ data. This study will be focused only on non-iterative damping force model and systems adopting the coefficient of restitution. Both of these approaches are discussed in the following subsections.

### 4.1 The coefficient of restitution

Aslam *et al.* [21] defined the restitution coefficient as the direct ratio $e_{an}$ between angular velocities after ($\dot{\theta}_{n+1}$) and before ($\dot{\theta}_n$) the $n^{th}$ impact. Assuming an infinitesimal impact duration hence instant velocity variation, no displacement during impact and imposing the conservation of angular momentum around the rotational hinge by equating the angular momentum after and before the impact, a theoretical coefficient of restitution can be derived for a VSSW system as the ratio between the angular velocities after and before the impact [5]:

$$e_{an} = \frac{m_1 {R_1}^2 + I_{CM,1} - I_{CM,2}\frac{\tan\alpha_2}{\tan\alpha_1} - 2m_1 {R_1}^2 \sin^2\alpha_1 + m_2 {R_1}^2\left[2 + \frac{\sin\alpha_1\cos\alpha_1}{\tan\alpha_2} - \sin^2\alpha_1\left(4 + \frac{\tan\alpha_2}{\tan\alpha_1}\right)\right]}{m_1 {R_1}^2 + I_{CM,1} - I_{CM,2}\frac{\tan\alpha_2}{\tan\alpha_1} + m_2 {R_1}^2\left[2 + \sin\alpha_1\cos\alpha_1\left(\frac{1}{\tan\alpha_2} + \tan\alpha_2\right)\right]} \quad (7)$$

where $I_{CM,1}$ and $I_{CM,2}$ are the polar moment of inertia around the two blocks centre of mass for a VSSW system. Note that the coefficient of restitution depends on the system slenderness, the squatter the wall ($\alpha_1$) the higher is the energy dissipation (lower $e_{an}$). The coefficient of restitution experimentally observed is lower than $e_{an}$, and Sorrentino therefore proposed an experimental coefficient of restitution $e_{exp}$ that is $0.90 \cdot e_{an}$ for a VSSW [22]. Graziotti *et al.*

observed for a VSSW system values of coefficient of restitution between 0.90 and 0.84 (specimen slenderness around 27) [17]. Adopting the aforementioned definition, the coefficient of restitution acts in the numerical model by reducing the system velocity at each *n-th* impact (every time the horizontal displacement *u* passes through the null displacement) as follows:

$$\dot{u}_{n+1}(t + dt) = e_{exp} \cdot \dot{u}_n(t) \tag{8}$$

### 4.2 The Equivalent Viscous Damping

The energy dissipation can also be modelled through an equivalent viscous damping force. A classical damping model with a constant damping coefficient (CDC), assuming a constant damping ratio ($\xi$) acting on the system initial stiffness ($\omega_1$), is commonly adopted to simulate the dynamic response of rocking systems [10]. Moreover, two other damping systems have also been investigated and compared in order to capture the dependence of the damping phenomenon on the oscillation amplitude and on the current frequency of vibration of the system. Both damping models act on the instantaneous secant frequency $\omega(t)$ defined by the instantaneous secant stiffness $K_{sec}(t)$ of the system (slope of the red line in Figure 2) and presented in equation 9:

$$\omega(t) = \sqrt{\frac{K_{sec}(t)}{m_{eff}}} \tag{9}$$

The first one of the two associates a constant damping ratio through all the system frequencies, whereas the second one assumes a stiffness proportional term ($\xi$-$\omega$ linear relationship) identified by the damping ratio ($\xi_{in}$) corresponding to the frequency of the first branch of the tri-linear relationship ($\omega_1$ or $F_1$). The damping coefficient of the three damping models: CDC, constant damping ratio (CDR) and stiffness proportional damping ratio (SDR), is defined by equations 10, 11, 12 respectively:

$$C_{CDC} = 2 \cdot m_{eff} \cdot \omega_1 \cdot \xi \tag{10}$$

$$C_{CDR}(t) \cdot= 2 \cdot m_{eff} \cdot \omega(t) \cdot \xi \tag{11}$$

$$C_{SDR}(t) \cdot= 2 \cdot m_{eff} \cdot \omega(t) \cdot \xi(\omega(t)) \tag{12}$$

Figure 3 compares the three damping models in terms of damping ratio - frequency ($\xi$- $\omega$) relationship and distribution of the damping forces through the non-dimensional oscillation amplitude in matched rocking free vibration decays of a VSSW. Both CDR and SDR models, acting on the secant frequency, tend to concentrate the energy dissipation around the zero-oscillations amplitude, which correspond to the impact region, acting in a similar fashion of a coefficient of restitution. The area within the loops in Figure 3 representing the dissipated energy is the same for each damping model.

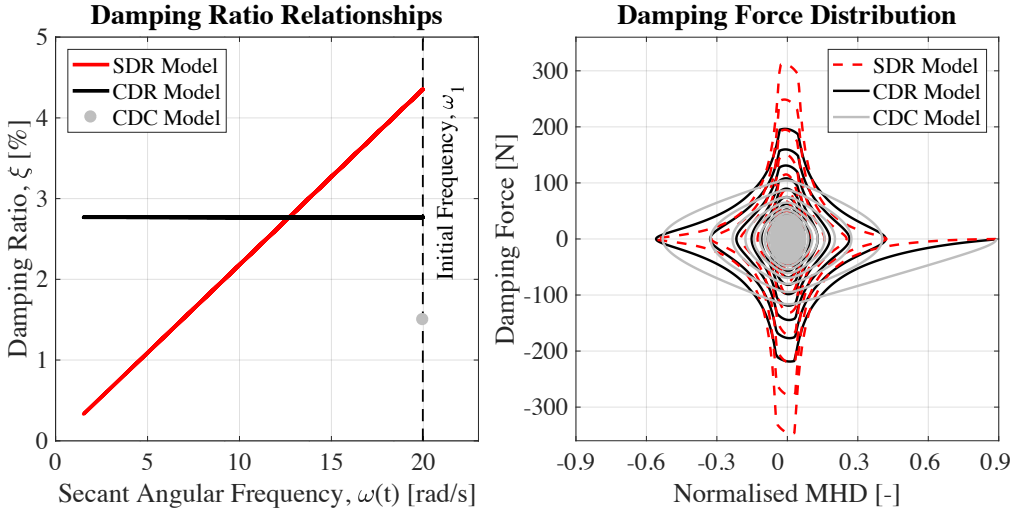


Figure 3: Left side: comparison between $\xi$- $\omega$ relationships of the three models. Independently from the actual or secant frequency of the system the CDC damp the system proportionally the initial angular frequency. CDR and SDR damping models associate to the current secant frequency a damping ratio according to a constant or a linear (defined by the $\xi$ value assigned to $\omega_1$) law; Right side: distribution of the damping force through the normalised oscillation amplitude of the three damping models: CDC, CDR, SDR.

### 4.3 An Equivalence between the Different Damping Systems

An equivalence between such different damping systems can be carried out by equating the energy losses provided by the different sources of damping. Generally, the coefficient of restitution, imposing a drop in the velocity at each impact, reduces the system kinetic energy. Considering half cycle of displacement between two successive response peaks (positive peak $u_p^+$ and negative peak $u_p^-$) of a system in free vibration phase, the energy loss due to impact, passing through displacement level equal to zero is given by the difference of kinetic energies after and before the collision:

$$\Delta T = T^+ - T^- = \frac{1}{2}\sum_{1}^{i} I_{CMi} \cdot \dot{\theta}_i^{+2} + m_i \cdot v_{CMi}^{+\,2} - \frac{1}{2}\sum_{1}^{i} I_{CMi} \cdot \dot{\theta}_i^{-2} + m_i \cdot v_{CMi}^{-\,2} \tag{13}$$

where $\dot{\theta}_i^+$ and $\dot{\theta}_i^-$ are the two bodies angular velocities after and before the impact defined by the rotations according to Figure 1, whereas $v_{CMi}^+$ and $v_{CMi}^-$ are the centre of mass velocities vectors composed by the two horizontal and vertical components (being the problem defined in 2D): $\dot{u}$ and $\dot{z}$.

The loss of energy due to an acting viscous damping force can be computed as the work done by the damping force in the considered response and time interval; this yields in the integral of equation 6:

$$\Delta E = \int_{u_p^+}^{u_p^-} \begin{matrix} C_{CDC} \\ C_{CDR}(t) \\ C_{SDR}(t) \end{matrix} \cdot \dot{u}\,(t) \cdot du \tag{14}$$

The integral in equation 14 does not have a trivial solution because the function present 6 discontinuities corresponding to the *F*-*u* corner points and the law characterising the different damping force depends on the displacement level achieved by the system. Adopting a similar approach, Giannini and Masiani [23] assuming a sine wave displacement rocking response for a rigid block (bi-linear *F*-*u* relationship), derived the following equivalence:

$$\xi = \frac{2 \cdot (1 - e)}{\pi \cdot (1 + e)} \tag{15}$$

Therefore, the work will be focused in studying the relationship between these two quantities for the presented viscous damping models and *F-u* relationship introduced.

## 5 IMPLEMENTED SDOF MODEL

The numerical model adopts the Newmark 'linear acceleration method' [24] integration scheme implemented in the non-iterative formulation version. It solves the SDOF equation introduced in equation 6 substituting the rigid bi-linear system restoring force $f_{bi}\ (u(t))$ with the tri-linear curve $f_{tri}\ (u(t))$ discussed in section 3. The implemented damped SDOF equation of motion in the three damping configurations studied follows:

$$m_{eff} \cdot \ddot{u}(t) + \begin{matrix} C_{CDC} \\ C_{CDR}(t) \\ C_{SDR}(t) \end{matrix} \cdot \dot{u}(t) + f_{tri}\ (u(t)) = -\lambda \cdot m_{eff} \cdot \ddot{u}_g(t) \tag{16}$$

The SDOF model adopting the coefficient of restitution lacks at the damping force terms reducing the system velocity by means of equation 8. In order to validate the numerical model Figure 4a shows the comparison between damped free vibration responses obtained with the implemented SDOF model and the SDOF proposed by Sorrentino *et al.* [5].

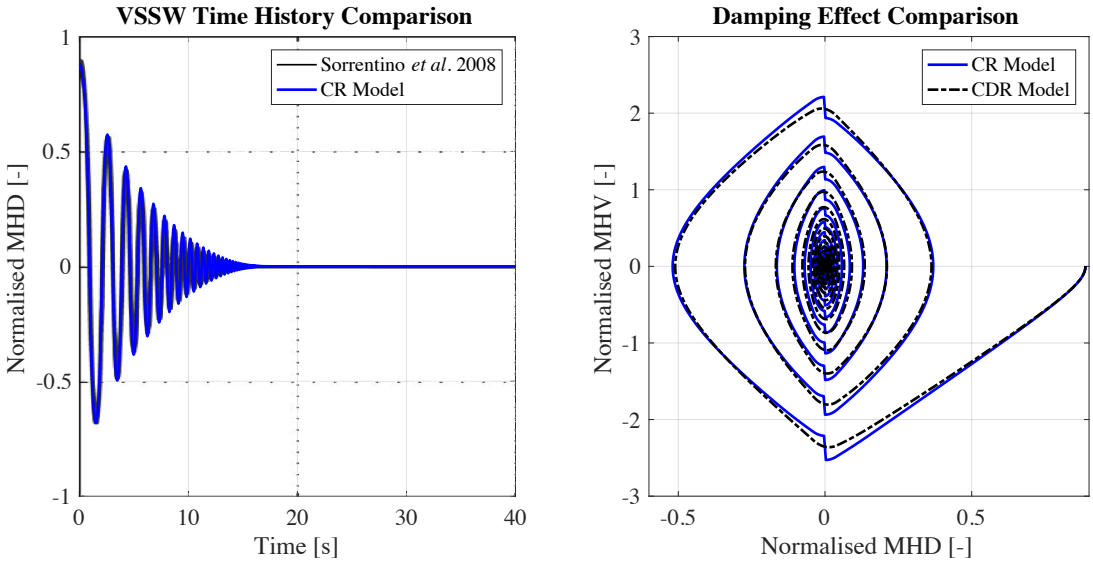


Figure 4: Left side: comparison between damped free vibration response time histories of a VSSW obtained by the presented SDOF and by Sorrentino *et al*. [5]. Details of the wall: *t*=0.4 m, *h*=4.0 m, *O*=0 N, $u_0$=0.9· $u_{ins}$, $\dot{u}_0$=0, $\ddot{u}_0$=0, *e*= $e_{an}$=0.955 (equation 7). Right side: comparison between matched damped free vibration responses in terms of normalised MHD and normalised MHV of a VSSW obtained by adopting the coefficient of restitution and a CDR model.

Figure 4b proposes instead a comparison between matched free vibration responses in terms of normalised mid-height displacement (MHD) and normalised velocity (MHV) obtained by adopting the coefficient of restitution CR and a constant damping ratio CDR model. It is worth noticing as in the impact region whereas the coefficient of restitution acts, reducing suddenly the system velocity, the CDR model decreases smoothly the velocity without inducing a clear discontinuity on it but acting at the same time similarly to a coefficient of restitution model.

## 6 DERIVATION OF THE EQUIVALENCE

The work consisted in analysing the damped free vibration response provided by the different damping systems and comparing them. The coefficient of restitution model has been taken as the reference damping systems. In order to ensure the equivalence between the energy dissipation provided by the different systems, satisfying the equivalence between equation 13 and 14, the damped free vibration decays provided by a velocity dependent acting force (CDC, CDR, SDR) have been matched with the ones provided by a SDOF adopting a coefficient of restitution. An error has been defined in order to proper select the damping ratio value that allowed to minimise the difference with the coefficient of restitution response for each system.

$$Err = \sum_{j=1}^{k} (|u_{CR}(j)| - |u_{DAF}(j)|)^2 \tag{17}$$

$Err$ represents the summation of absolute difference between the coefficient of restitution decay and the one provided by the models with a damping acting force (CDC, CDR, SDR) at each analysis time step for the entire length of the response ($k$).
Figure 5 plots the damping ratio values corresponding to each model that minimised the error for a specific VSSW and a defined set of coefficients of restitution. It is also shown the effect of the amplitude of oscillation releasing the VSSW from an initial imposed displacement equal to 0.9, 0.5 and 0.3 times the instability displacement. In general, all the models present a higher dispersion moving towards higher coefficients of restitution. The equivalence related to the CDC Model is the most sensitive to the oscillation amplitude while the CDR Model is only slightly affected by this variable. In both CDC and CDR models damped high oscillation amplitudes are associated to lower damping ratio values, while for the SDR Model the trend is reversed: slightly higher damping ratio values are associated to higher oscillations. This is associated to the nature of the SDR Model which tend to associate very low damping ratio values to oscillations close to collapse, consequently the request initial damping value to fit the response given by a CR Model is slightly higher.

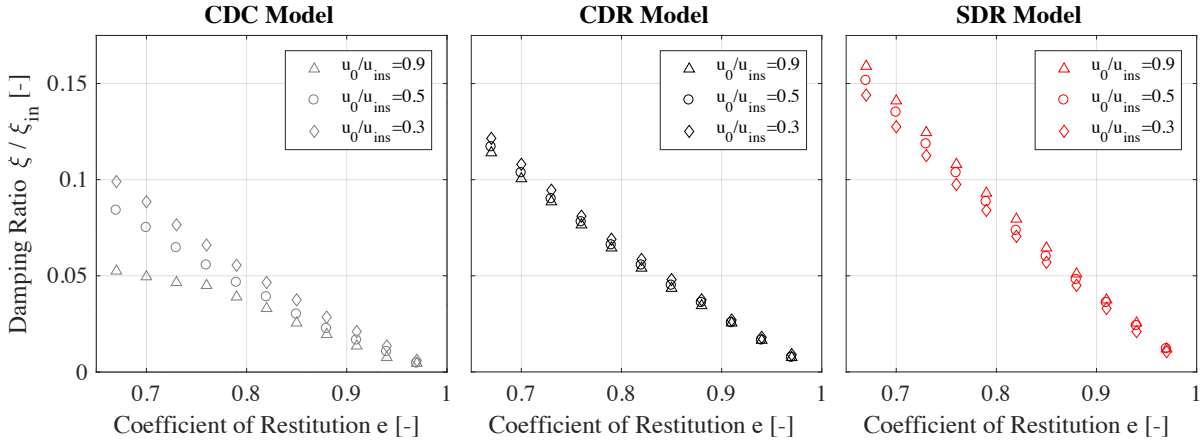


Figure 5: Comparison between CDC, CDR and SDR models in matching free vibration responses damped by a coefficient of restitution model. Details of the VSSW adopted for the comparison: $a_1$=0.04, $b_1$=0.85, $a_3$=1, $O$=0, $h_1/h$=0.7, $t$=0.3 and λ=15.

This finding confirm as a CDC model is not a good choose in simulating the energy dissipation involved in rocking mechanism. For the following comparisons, the authors considered as reference starting oscillation amplitude 0.5 the instability displacement. Figure 6 (top and centre rows) illustrates as the equivalence, once defined a specific tri-linear configuration in terms of

$a_1$, $a_3$ and $b_1$, is independent from the system slenderness and the acting axial load for all the damping models presented. On the contrary, the damping ratio values matching the coefficient of restitution response are affected by the chosen tri-linear $a_1$ parameter which controls the initial cracked stiffness (see Figure 6 bottom). Again, the most sensitive model to $a_1$ variations is the CDC one while the less affected is the CDR model. A higher initial stiffness leads to lower values of damping ratio for both CDC and CDR models, the SDR, instead, associates lower damping ratio values to lower $a_1$ parameters.

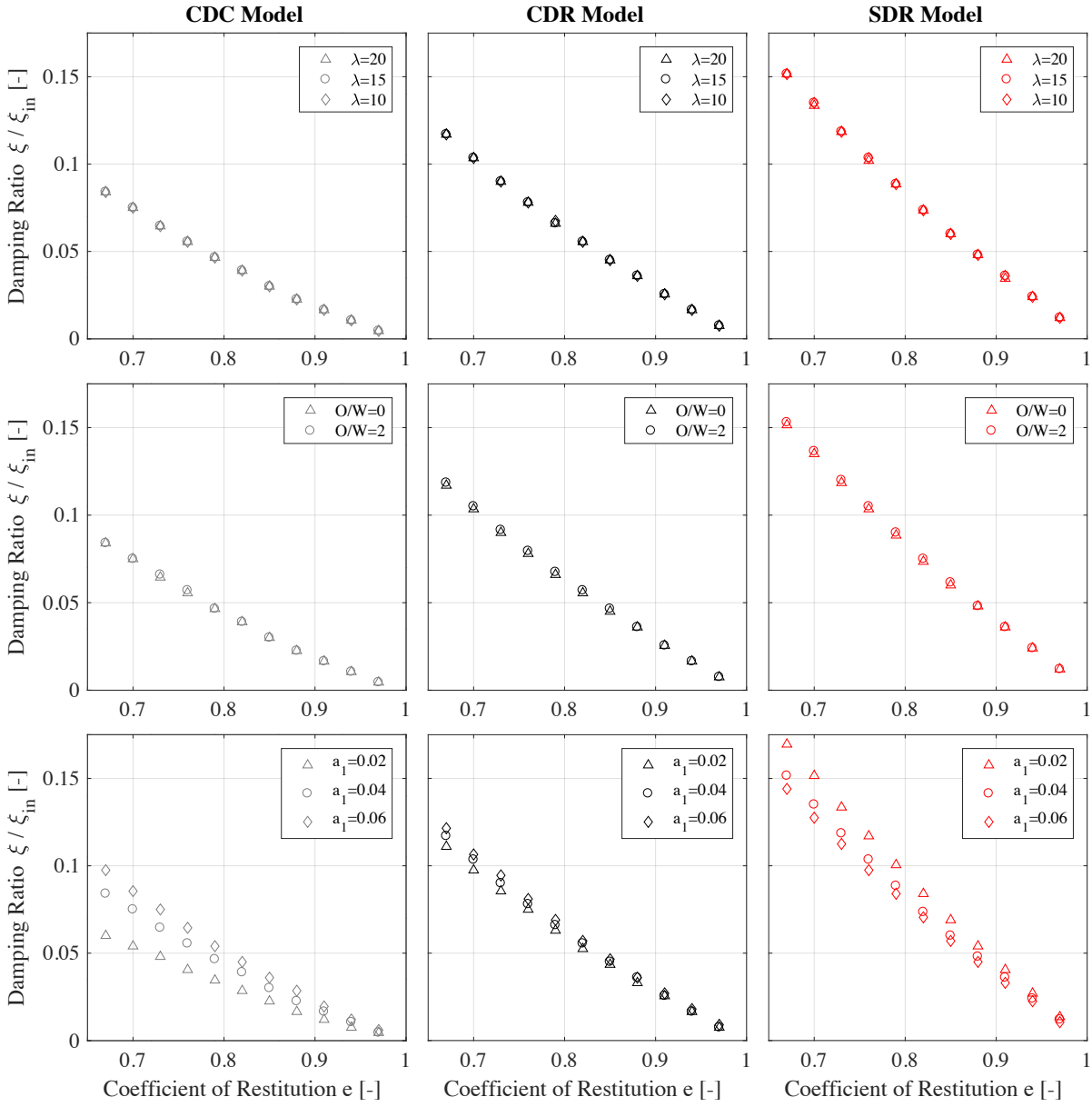


Figure 5: Comparison between CDC, CDR and SDR models in matching free vibration responses damped by a coefficient of restitution model. Details of the VSSW in the top row: $a_1$=0.04, $b_1$=0.85, $a_3$=1, $O$=0, $h_1/h$=0 and $t$=0.3. Details of the VSSW centre row: $a_1$=0.04, $b_1$=0.85, $a_3$=1, $h_1/h$=0, $t$=0.3 and λ=15. Details of the VSSW in the bottom row: $b_1$=0.85, $a_3$=1, $h_1/h$=0.7, $O$=0, $t$=0.3 and λ=15.

This is particularly evident for low values of $e$ that, causing a drop of the oscillation amplitudes, tends to concentrate the free vibration response in low amplitude oscillations, greatly

affected by $a_1$; the lower $a_1$ the quicker the oscillations decay and the higher the requested SDR damping.

Figure 6 plots the minimum errors defined in equation 17 associated to the best fit considering a specific VSSW configuration. The errors have been displaced in root due to their wide variation with coefficient of restitution: the lower $e$ the higher $Err$ is. Both damping models acting on the secant stiffness (CDR and SDR) presented lower errors compared to the CDC model. The CDR presented the lowest errors in matching free vibration decays controlled by the coefficient of restitution in a range of $e$ values between 0.91 and 0.8; the remaining coefficient of restitution decays have been simulated more efficaciously by a SDR model.

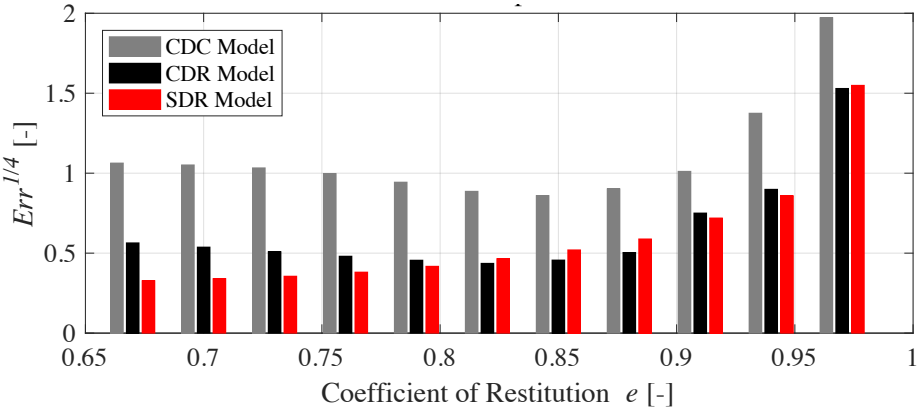


Figure 6: Comparison between errors associated to CDC, CDR and SDR models in matching free vibration responses damped by a CR. Details of the VSSW: $a_1$=0.04, $b_1$=0.85, $a_3$=1, $O$=0, $h_1/h$=0.7, $t$=0.3 and λ=15.

## 7 EXPERIMENTAL VALIDATION OF THE PROPOSED EQUIVALENCE

The results previously shown suggested that the cracked stiffness (controlled by parameter $a_1$) is the system characteristic that more affects the equivalence between velocity dependent acting force models and the coefficient of restitution. Figure 7 shows a second order polynomial fit of this dependence for each model compared to the one proposed by Giannini and Masiani [23]. CDC and SDR give damping ratio values lower and higher respectively than the ones provided by equation 15. The CDR model, instead, seems rather close to the equivalence proposed by Giannini and Masiani, with only slightly lower values and a reduced dependence on $a_1$.

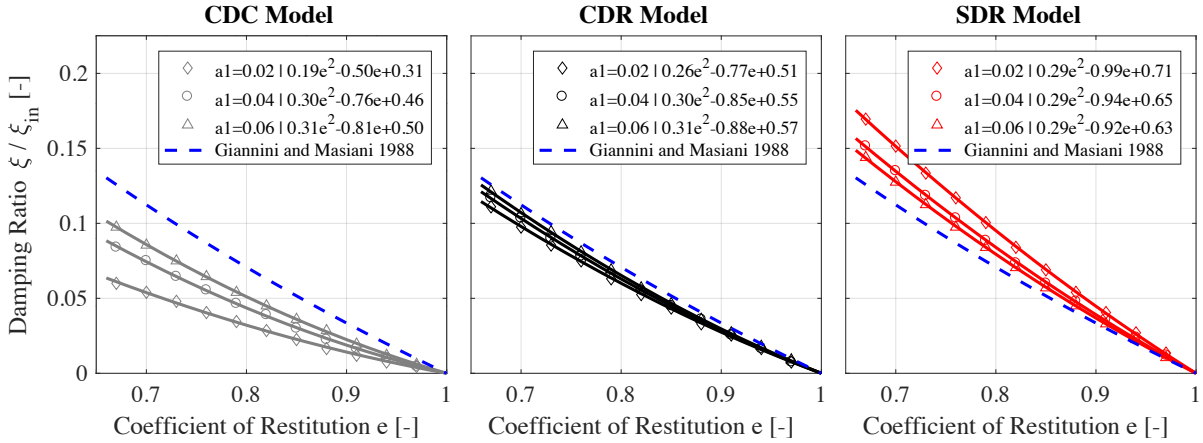


Figure 7: Comparison between proposed 2nd order polynomial fits and the relationship proposed by Giannini and Masiani [23]. Details of the VSSW: $b_1$=0.85, $a_3$=1, $h_1/h$=0.7, $O$=0, $t$=0.3 and λ=15.

In order to ensure the reliability of the proposed equivalence, a comparison between the performance of the different damping systems in simulating a dynamic OOP experimental response the is proposed. The reference experimental campaign is the one performed by Graziotti *et al.* and Tomassetti *et al.* [17, 25] consisting in series of shaking table tests on URM single leaf and cavity walls subjected to a pure OOP one-way bending action. Among the different signals a test performed adopting a 2 Hz Ricker Wave Acceleration input on the 0.3MPa-vertical-loaded specimen (i.e. SIN-03-00, test #2.4) has been selected for the comparison. It consisted of a particular acceleration pulse that induced a clear damped free vibration phase in the specimen, providing valuable information on the damping forces acting on the specimens. First of all, the experimental response has been calibrated selecting a reasonable tri-linear configuration and a coefficient of restitution equal to 0.835 close to the average value of 0.852 measured experimentally from peak response velocity ratio values [17]. The damping ratio values associated to each damping model have been calculated by averaging the values obtained by the equations in Figure 7 for $a_1$ values of 0.2 and 0.4 (having assumed to model the experimental response an $a_1$ value of 0.3). Figure 8 shows the comparison between experimental and numerical MHD histories.

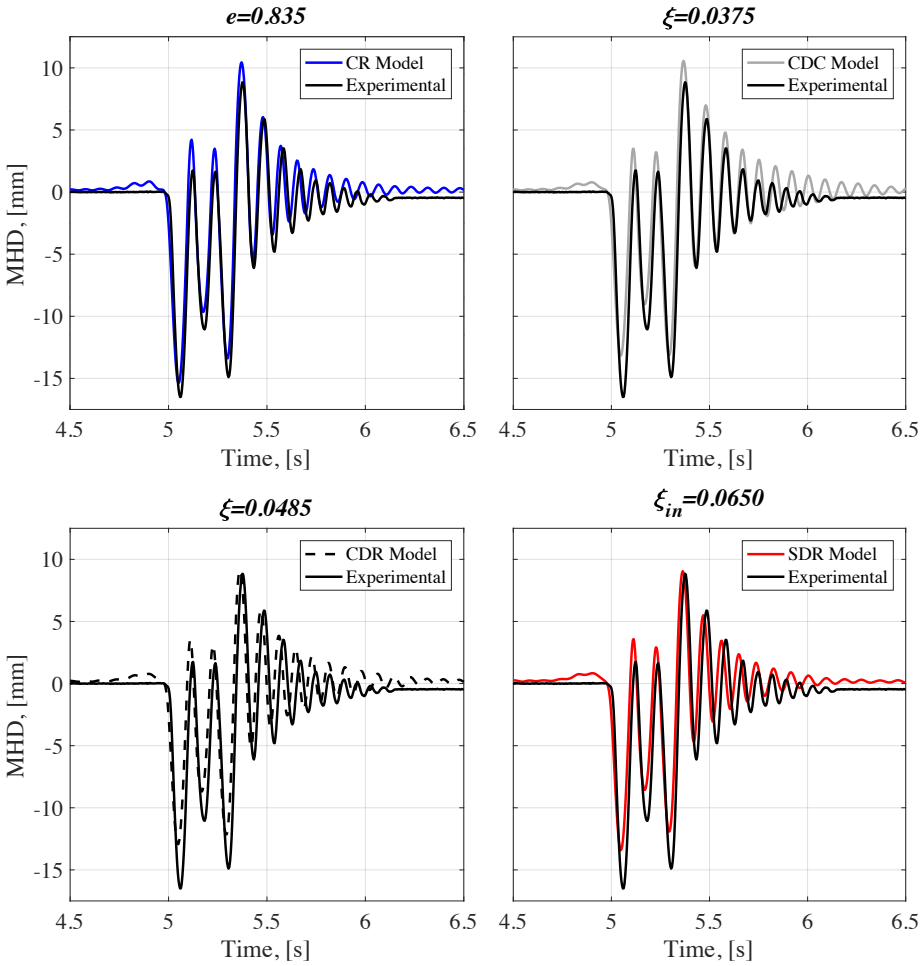


Figure 8: Comparison between numerical and experimental MHD histories of the different damping models. Details of the parameters necessary to simulate the SIN-03-00 response: $a_1$=0.03, $b_1$=0.80, $a_3$=1, $O/W$=6.2, $h_1/h$=0.57, $t$=0.102 and λ=27.

The SDR seems to damp the system slightly more than the other models. As the oscillation amplitude is lower (reduced $u_p/u_{ins}$), the SDR and the CDR tend to damp the system much more similarly each other due to the reduced contribution of the secant stiffness region. For this reason, low amplitudes test may slightly be overdamped if the polynomial fit presented in Figure 7, which has been derived for larger oscillation amplitudes (0.5 $u_p/u_{ins}$), is used. This is one of the shortcoming of adopting a SDR Model that, on the other hand, resulted the most effective in simulating the amplitude of response peaks during the decay.

## 8 CONCLUSIONS

The paper presents a simplified SDOF model for the evaluation of the out-of-plane one-way-bending dynamic response of URM walls. The model consists of a trilinear nonlinear elastic oscillator that could be associated with different damping models: coefficient of restitution, constant damping coefficient, constant damping ratio and stiffness proportional damping ratio both acting on the secant stiffness. The systems were calibrated against experimental results (procedure not reported in this work).

The final goal of the work was to define relationships between these numerical damping techniques. The coefficient of restitution model has been taken as the reference damping systems. In order to ensure the equivalence between the energy dissipation provided by the systems, the different damped free vibration decays have been matched with the ones provided by a SDOF model analyses adopting a coefficient of restitution.

Polynomial relationships were provided in order to directly correlate the different damping models with the coefficient of restitution. In general, these equivalences depend on the amplitude of oscillation and the relative initial stiffness of the systems. They were found to be substantially not dependent on the system slenderness and on the acting vertical overburden force. The constant damping ratio (CDR) model acting on the system secant stiffness, also considering its reduced dependence on oscillation amplitude and initial stiffness, resulted the most appropriate in simulating free vibration decays damped by a coefficient of restitution. In addition, the stiffness proportional damping ratio (SDR) model has shown rather good performances.

A further extension of the present work will be the validation of the proposed equivalences comparing the results of the different models subjected to a large sets of natural ground motions or more in general forced vibrations.

## REFERENCES

[1] A. Giuffrè, A mechanical model for statics and dynamics of historical masonry buildings. *Protection of the Architectural Heritage Against Earthquakes*, Springer-Verlag: Wien, 71-152, 1996.

[2] D. Dizhur, J. Ingham, L. Moon, M.C. Griffith, A. Schultz, I. Senaldi, G. Magenes, J. Dickie, S. Lissel, J. Centeno, C. Ventura, J. Leite, P. Lourenco. Performance of masonry buildings and churches in the 22 February 2011 Christchurch earthquake. *Bull. New Zealand Society for Earthquake Engineering,* **44**(4):279-296, 2011

[3] J. Ingham, M.C. Griffith, Performance of unreinforced masonry buildings during the 2010 Darfield (Christchurch, NZ) earthquake. *Australian Journal of Structural Engineering*., **11**(3): 207-224, 2011.

[4] G.W. Housner, The behavior of inverted pendulum structures during earthquakes. *Bull. Seismological Society of America*, **53**(2): 403–417, 1963.

[5] L. Sorrentino, R. Masiani, M.C. Griffith, The vertical spanning strip wall as a coupled rocking rigid body assembly, *Structural Engineering and Mechanics*, **29**: 433–453, 2008.

[6] K.T. Doherty, An investigation of the weak links in the seismic load path of unreinforced masonry buildings, PhD Thesis, University of Adelaide, Australia, 2000.

[7] M.J. DeJong, E.G. Dimitrakopoulos, Dynamically equivalent rocking structures, *Earthquake Engineering & Structural Dynamics*, **43**(10): 1543–1563, 2014.

[8] L.F. Restrepo Vélez, Seismic risk of unreinforced masonry buildings. PhD thesis, ROSE School, University of Pavia, Italy, 2004.

[9] N. Makris, D. Konstantinidis, The rocking spectrum and the limitations of practical design methodologies. *Earthquake Engineering & Structural Dynamics*, **32**(2):265–89, 2003.

[10] M.C. Griffith, G. Magenes, G. Melis, L. Picchi, Evaluation of out-of-plane stability of unreinforced masonry walls subjected to seismic excitation. *Journal of Earthquake Engineering*, **7**,141-169, 2003

[11] S. Lagomarsino, Seismic assessment of rocking masonry structures, *Bulletin of Earthquake Engineering*, **13**:97-128, 2014.

[12] T.M. Ferreira, A.A. Costa, R. Vicente, H. Varum, A simplified four-branch model for the analytical study of the out-of-plane performance of regular stone URM walls, *Engineering Structures*, **83**,140–153, 2015.

[13] N.T.K. Lam, M.C. Griffith, J. Wilson, K.T. Doherty, Time-history analysis of URM walls in out-of-plane flexure. *Engineering Structures*, **25**(6):743–754, 2003.

[14] U. Tomassetti, F. Graziotti, A. Penna, G. Magenes, A Single-Degree of Freedom Model for the Simulation of the Out-of-Plane Response of Unreinforced Masonry Walls, *Proc. 16th Italian Conf. on Earthquake Engineering*, L'Aquila, Italy, 2015.

[15] H. Derakhshan, D.Y. Dizhur, M.C. Griffith, J.M. Ingham, Seismic Assessment of out-of-plane loaded unreinforced masonry walls in multi-storey buildings, *Bulletin of New Zealand Society for Earthquake Engineering*, **47**(2): 119-138, 2014.

[16] ABK. Methodology for Mitigation of seismic hazards in existing unreinforced masonry buildings: wall testing, out of plane. *Topical Report 04*, c/o Agbabian Associates, El Segundo, California; 1981.

[17] F. Graziotti, U. Tomassetti, A. Penna, G. Magenes, Out-of-plane shaking table tests on URM single leaf and cavity walls, *Engineering Structures*, **125**, 455-470, 2016

[18] H. Derakhshan, M.C. Griffith, J.M. Ingham, Airbag testing of multi-leaf unreinforced masonry walls subjected to one-way bending. *Engineering Structures* **57**, 512-522, 2013

[19] H. Derakhshan, M.C. Griffith, J.M. Ingham, Out-of-plane behaviour one-way spanning unreinforced masonry walls. *Journal of Engineering Mechanics,* **139**(4): 409-417. 2013

[20] L. Sorrentino, O.A. Shawa, L.D. Decanini, The relevance of energy damping in unreinforced masonry rocking mechanisms. Experimental and analytic investigations. *Bulletin of Earthquake Engineering*, **9**(5):1617-1642, 2011.

[21] M. Aslam, W. Godden, D. Scalise, Rocking and overturning response of rigid bodies to earthquake motions. *Report University of California*, Berkeley, LBL-7539 UC-11, 1978.

[22] L. Sorrentino, Dinamica di muri sollecitati fuori del piano come sistemi di corpi rigidi. PhD thesis, Sapienza University of Rome, Italy, (in Italian), 2003.

[23] R. Giannini, R. Masiani, Dinamica delle oscillazioni dei blocchi rigidi, *IX Congresso nazionale dell'associazione italiana di meccanica teorica ed applicate*, (in Italian), 1988.

[24] N. M. Newmark, A method of computation for structural dynamics. *Journal of Engineering Mechanics*, ASCE, **85** (EM3) 67-94, 1959.

[25] U. Tomassetti, F. Graziotti, A. Penna, G. Magenes, Out-of-Plane Shaking Table Test on Unreinforced Cavity Walls. *Proceedings of 16th International Brick/Block Masonry Conference (IBMAC)*, Padua, Italy, 2016.

COMPDYN 2017
6th ECCOMAS Thematic Conference on
Computational Methods in Structural Dynamics and Earthquake Engineering
M. Papadrakakis, M. Fragiadakis (eds.)
Rhodes Island, Greece, 15–17 June, 2017

# PROBABILISTIC VALIDATION OF THE HOUSNER ROCKING MODEL

**Jonas A. Bachmann[1*], Mathias Strand[2], Michalis F. Vassiliou[1], Marco Broccardo[1], and Božidar Stojadinović[1]**

[1]ETH Zürich
Stefano-Franscini-Platz 5, 8093 Zürich, Switzerland
{bachmann, vassiliou, stojadinovic}@ibk.baug.ethz.ch

[2]NTNU Trondheim
Høgskoleringen 1, 7491 Trondheim, Norway
mathias0strand@gmail.com

**Keywords:** Rocking, uplifting structures, earthquake engineering, chaotic motion, probabilistic analysis.

**Abstract.** *The rocking oscillator has drawn the attention of many researchers since the publication of Housner's [1] seminal paper. As the response of the rocking oscillator is highly non-linear and exhibits negative stiffness [2] many researchers have suggested treating the rocking oscillator as a chaotic system, in the sense that small perturbations of its governing parameters result to widely diverging outcomes. Researchers that have tried to experimentally validate Housner's model have shown that, given the modelling uncertainty, it is hard to confidently predict the time history response of a rocking block to a specific ground motion. This makes practicing engineers hesitant to adopt rocking as an earthquake response modification strategy.*

*However, accurately predicting the response to a single ground motion would be ideal but it is not a necessary condition to trust a model: there is so much uncertainty in the expected ground motion that could overshadow the modelling uncertainty. To take the former uncertainty into account, in common practice, engineers use an ensemble of ground motions when they perform a time history analysis. Therefore, it is reasonable to try to compare numerical experimental testing results in terms of their statistics. If the numerical model is capable of capturing the statistics of the experimental testing, then, in terms of civil engineering design, the model is trustworthy. The first ones to adopt a probabilistic approach were Yim, Chopra and Penzien [3] who as early as in 1980 observed some order in rocking motion when they studied it from a probabilistic point of view. They observed specific trends in their numerical results when, instead of using only one, they used 10 synthetic ground motions. This paper compares the numerical and experimental response of a rigid rocking block when excited by an ensemble of 100 ground motions that share the statistical properties of original ground motion.*

## 1 INTRODUCTION

The rocking oscillator has drawn the attention of many researchers since the publication of Housner's [1] seminal paper. Rocking behavior has been studied to address three classes of structures:

a) large structures with underdesigned foundations that use uplift and rocking as a seismic response modification technique [4–15];

b) precious unanchored equipment and museum artifacts that are excited by earthquakes and whose overturning stability is important [16, 17]; and

c) ancient Greek and Roman temples [18, 19].

As the response of the rocking oscillator is highly non-linear, due to its negative stiffness [2], many have suggested treating the rocking oscillator as a chaotic system, in the sense that small perturbations of its governing parameters, be it the oscillator properties or the excitation, result to widely diverging outcomes. Researchers that have tried to experimentally validate Housner's model [20–26] have shown that, given the modelling uncertainty (especially of the one related to impact), it is difficult to confidently predict the time history response of a rocking block to a specific ground motion. Even if the coefficient of restitution is relatively well predicted, or determined via experiments, the response of the system to a ground motion is so sensitive that predicting the whole time history is practically impossible [27]. This has generated a lot of discussion about Housner's approach to determine the energy losses during impact and has resulted in various different energy dissipation models [28–37]. Moreover, it makes practicing engineers hesitant to adopt rocking as an earthquake response modification strategy, e.g. for bridges [8]. In contrast, Time History Analysis of yielding structures, where one has to model behaviors such as concrete cracking and spalling, rebar debonding or steel column buckling and connection failure, is accepted in engineering practice – even though research and "blind contests" show that predicting the response even of simple yielding structures is very sensitive to modelling assumptions [38] and that matching the experimental results is an extremely difficult task.

However, accurately predicting the response to a single ground motion would be ideal but it is not a necessary condition to trust a model (and the design solution it attempts to model): there is so much uncertainty in the expected ground motion that could overshadow the modelling uncertainty. In the cases where time history analyses are performed engineers commonly use an ensemble of ground motions to take the former uncertainty into account. Therefore, it is reasonable to try to compare numerical and experimental testing results in terms of their statistics. If the numerical model is capable of capturing the statistics of the experimental testing, then, regarding civil engineering design, the model is trustworthy. The first ones to adopt a probabilistic approach were Yim, Chopra and Penzien [3] who as early as in 1980 observed some order in rocking motion when they studied it from a probabilistic point of view. When, instead of using only one, they used 10 synthetic ground motions they observed specific trends in their numerical results. This shows that an order does exist in rocking motion.

This paper compares the statistics of the numerical and experimental response of a rigid rocking block when excited by an ensemble of 100 ground motions that have the similar spectral properties.

## 2 EMPLOYED NUMERICAL MODEL

The numerical model used in this study was kept as simple as possible, being the rigid rocking block on a rigid surface (Figure 1). It is assumed that the coefficient of friction is large enough to prevent sliding throughout the entire motion. The size and shape of the block are given by its semi-diagonal $R$, and its slenderness $\alpha$, defined as $\alpha = \text{atan}(B/H)$. When the block is subjected to a horizontal ground acceleration $\ddot{u}_g(t)$, and is rocking around O, or O' respectively, the non-linear equation of motion is ([3, 39–41] among others):

$$I_0\,\ddot{\theta}(t) + m_c g R[\alpha\,\text{sgn}\,\theta(t) - \theta(t)] = -m_c \ddot{u}_g(t) R\cos[\alpha\,\text{sgn}\,\theta(t) - \theta(t)] \tag{1}$$

Equation 1 can be expressed in a more compact form:

$$\ddot{\theta}(t) = -p^2\left(\sin[\alpha\,\text{sgn}\,\theta(t) - \theta(t)] + \frac{\ddot{u}_g}{g}\cos[\alpha\,\text{sgn}\,\theta(t) - \theta(t)]\right) \tag{2}$$

where $p$ is the frequency parameter defined as:

$$p = \sqrt{\frac{m_c g R}{I_0}} \tag{3}$$

To initiate rocking motion the ground acceleration $\ddot{u}_g$ must meet or exceed the value $g\tan\alpha$. For rectangular blocks the rotational inertia is $I_0 = 4/3 m_c R^2$, and $p$ simplifies to $p = \sqrt{(3g)/(4R)}$. The oscillation frequency $T$ of a rigid block under free vibration is not constant because it strongly depends on the vibration amplitude $\theta_0$ [1]. Nevertheless, the quantity $p$ is a measure of the dynamic characteristics of the block and is equal to the in-plane pendulum frequency of the block as if it were hanging from its rocking rotation point [42]. For a free-standing solid rectangular block with dimensions $10m \cdot 1.5m$ the frequency parameter yields $p = 1.2\,rad/s$.

Housner assumed that the impact is instantaneous and that the impact forces are concentrated at the new pivot point (O and O'). Under these assumptions, Conservation

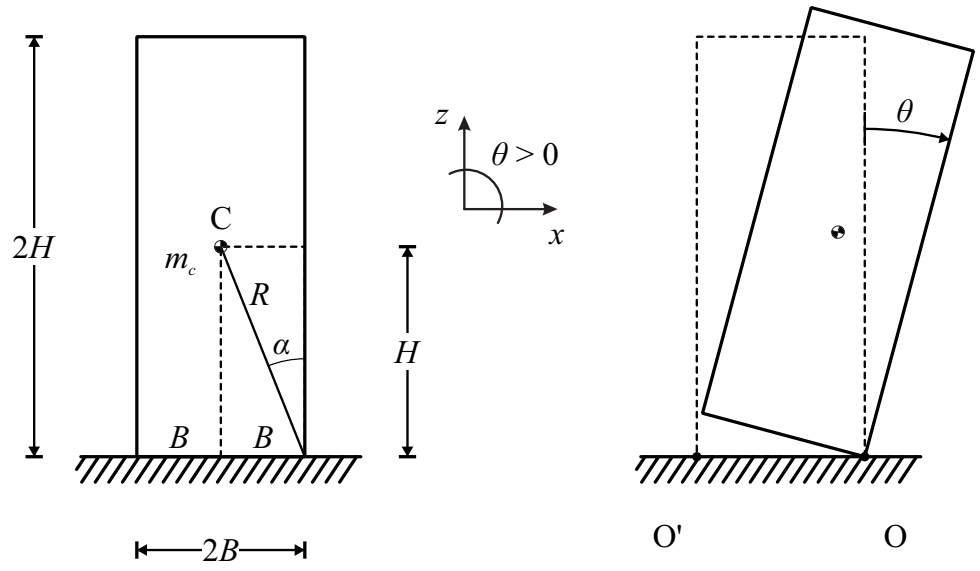


Figure 1: Rigid block rocking freely on a rigid surface.

of Angular Momentum (CoAM) an instant before the impact and immediately after the impact gives the coefficient of restitution:

$$r = \left(1 - 2\sin^2\alpha \frac{m_c R^2}{I_0}\right)^2 \tag{4}$$

Many researchers have revisited the above assumption [23, 25, 35, 43–45] and formulated more detailed expressions. In this study the Housner coefficient of restitution will be used due to the following:

i. the specimens used were engineered such that impact forces act as close as possible to the rocking corners.

ii. the Housner model is simple, and successful in identifying the most important energy dissipation factor: the slenderness $\alpha$ of the block.

The construction of the so called rocking spectra and the application of dimensional analysis to reduce the dimensionality of the problem are extensively described in [46–49], but are briefly described here for reasons of completeness:
When excited by an analytical pulse ground motion [50] of a specific shape, a given acceleration amplitude $a_p$, and dominant frequency $\omega_p$, the response $\theta$ of a rigid block is a function of five variables:

$$\theta = f\left(\alpha, R, g, a_p, \omega_p\right) \tag{5}$$

Since this function involves two reference dimensions ($[Length]$ and $[Time]$) it can be described by three dimensionless terms using Dimensional and Orientational Analysis [46–49] arguments:

$$\frac{\theta}{\alpha} = \phi\left(\alpha, \frac{\omega_p}{p}, \frac{a_p}{g\tan\alpha}\right) \tag{6}$$

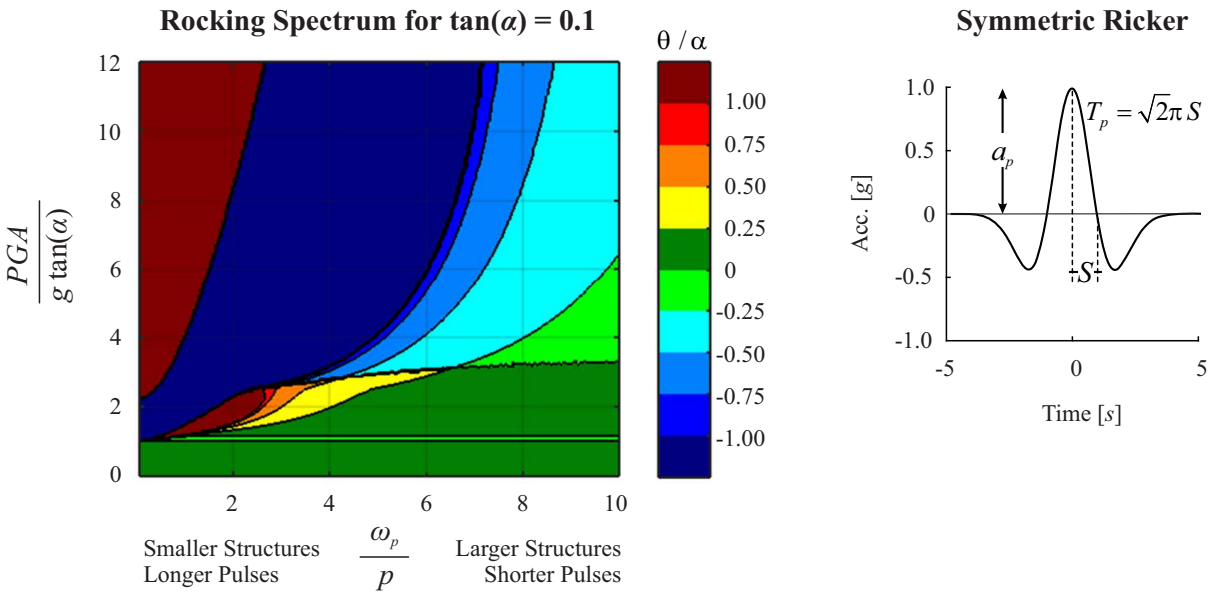


Figure 2: Rocking Spectrum (left) of a symmetric Ricker (right) analytical pulse ground motion.

Accordingly, rocking spectra (i.e. contour plots of $\theta/\alpha$ in the $\omega_p/p$ and $a_p/g\tan\alpha$ plane for a given slenderness $\alpha$ can be constructed. Figure 2 plots such a spectrum for $\tan\alpha = 0.1$. One can observe that for small structures or long period pulses (small $\omega_p/p$) the difference between the acceleration required to cause uplift ($\ddot{u}_g \geq g\tan\alpha$) and the acceleration required to overturn the block, is small. On the contrary, a larger structure (large $\omega_p/p$) has a larger range of pulse accelerations for which there is rocking but no overturning. It is for these structures that the study of rocking motion is meaningful, whereas for small structures a simple static analysis is enough.

An acceleration equal to $g\tan\alpha$ is enough to cause both uplift and overturn. Therefore, this paper is limited to the study of relatively large (in the prototype scale) rocking structures.

## 3 SPECIMENS AND TEST SETUP

### 3.1 Rocking Specimen

With reference to Figure 3, a specimen consists of an assembly of four wedges (Nr. 1), two linking plates (Nr. 2), and two hollow columns (Nr. 3). It presents symmetry with respect to three planes. All parts are made of aluminum and connected by aluminum bolts. The specimen's height ($\equiv 2H$) is $500mm$ and its depth is $400mm$. This specific depth of the specimen was chosen in order to avoid undesired out-of-plane motion. Previous tests using a specimen with equal width and depth revealed that, even for a weak 1D excitation, out-of-plane motion cannot be avoided.

The wedges used for the results presented in this manuscript had a total width of $82mm$, but the effective rocking width (distance between the center of rotations O and O' while rocking occurs) was $75mm$ resulting in an effective slenderness of $\tan\alpha = 75mm/500mm = 0.15$. To represent as closely as possible the Housner impact model

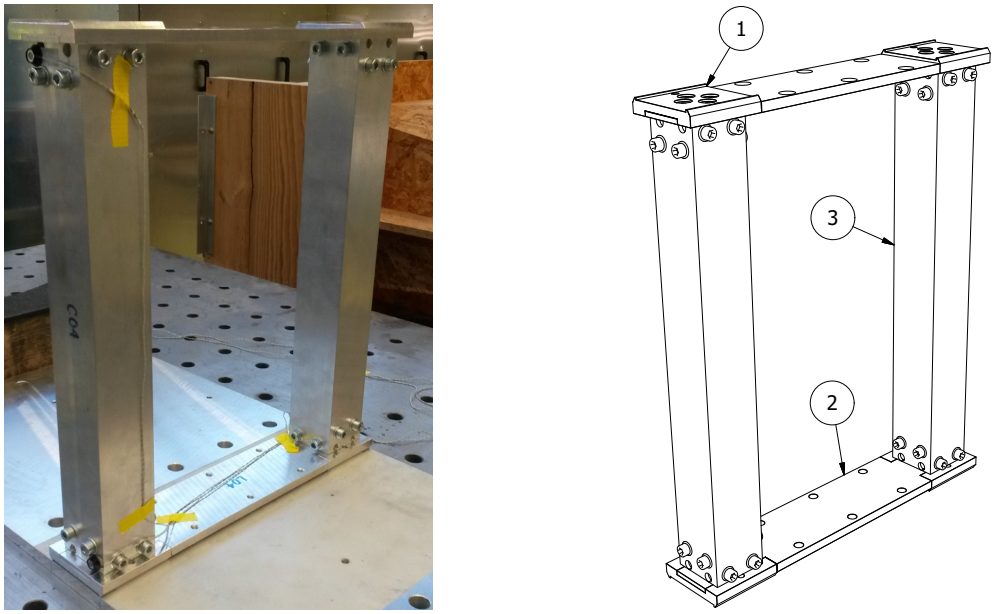


(a) Specimen in ETH laboratory (b) 3D model

Figure 3: Top: Specimen and 3D model

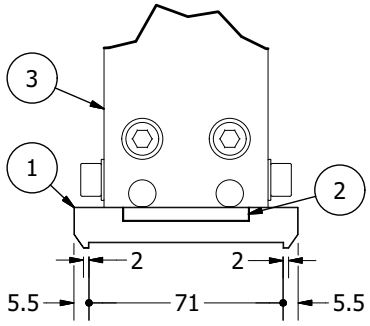


Figure 4: Close-up of wedges (units $[mm]$)

the center section of the wedges were carved out, leaving only a contact width of $2mm$ on each side (Figure 4). The setup was screwed together to allow for changes or replacements of specific parts while keeping the setup as simple as possible. The rocking column as shown in Figure 3a had a total weight of $3.94kg$. The natural eigenfrequency of the specimen was measured at $25Hz$ (corresponds to an eigenperiod of $0.04s$).

Recent research has questioned the Housner assumption regarding the point of action of the impact forces by either trying to determine the exact point of action of the impact forces [35] or by treating the location of the impact forces as a random variable [37]. The model examined herein does not focus on this problem which regards specimens with flat base. It represents structures that are designed to rock and their contact surfaces are designed such that the impact forces are concentrated as close to the corner as possible, in an effort both to increase damping and to decrease the uncertainty concerning the position of the impact forces. It has been shown [27] that, even if the impact forces are forced by design to act as close to the corner as possible, and even if this results to an excellent prediction of the coefficient of restitution, the rocking problem is so sensitive that it is impossible to predict the entire time history response. Thus, the need for probabilistic treatment arises.

### 3.2 Frequency Parameter and Coefficient of Restitution

In order to calibrate and validate the governing model parameters listed below, free vibration tests were performed in the ETH laboratory before the dynamic tests were executed.

i. frequency parameter $p$, defined by equation (3)

ii. coefficient of restitution $r$, defined by equation (4)

The frequency parameter $p$ takes into account size $R$ and rotational inertia $I_0$ and is therefore difficult to numerically accurately predict given the unequally distributed mass within the specimen, e.g. screws and bolts, linking plates etc. Therefore, $p$ was solely

| $p_{calibrated}$ | $r_{calibrated}$ | $r_{Housner}$ | $\frac{r_{calibrated} - r_{Housner}}{r_{calibrated}}$ |
|---|---|---|---|
| $4.8883s^{-1}$ | 0.9532 | 0.9465 | 0.70% |

Table 1: Calibrated and theoretical properties of the rocking specimen

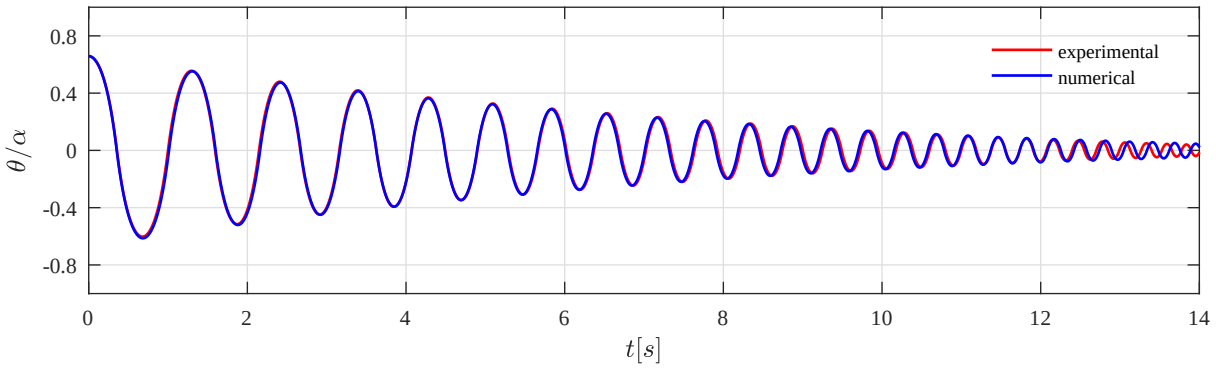


Figure 5: Free vibration: comparison between numerical ($p_{calibrated}$ and $r_{calibrated}$) and experimental data.

obtained from the laboratory and not compared to a computed numerical value. $p$ was calibrated as $4.8883s^{-1}$ using the non-linear relationship between the rocking period $T$ and the frequency parameter $p$ was used [1]:

$$\cosh \frac{pT}{4} = \frac{1}{1 - \theta_0/\alpha} \tag{7}$$

where $\theta_0$ is the maximum rocking angle for the half-cycle of duration $T/2$ ($\equiv$ time between two impacts). For every half-cycle $i$ a corresponding value $p_i$ can be determined. The resulting values for $p$ of the first 15 half-cycles were averaged to get $p_{calibrated}$. The influence of decreasing values for $\theta_0$ over time was accounted for empirically by a regression performed on numerical experiments.

The experimental coefficient of restitution was derived by relating total energies pre- and post-impact to compute the energy loss at every impact, given the assumptions that energy dissipation only takes place during impact, and that at rest ($\theta = 0$) the potential energy is zero. The maximum angle $\theta_{0,i}$ of each half-cycle $i$ was used to compute the corresponding increase of potential energy $\Delta V_i$, at which point the angular velocity $\dot{\theta}$ is zero and, thus, the potential energy is equal to the total energy.

Eventually, equation (8) describes the energy loss at impact $i$ and, therefore, the coefficient of restitution $c_i$ for the $i^{th}$ impact during a free vibration test.

$$c_i = \frac{\cos(\alpha - |\theta_{0,i+1}|) - \cos\alpha}{\cos(\alpha - |\theta_{0,i}|) - \cos\alpha} \tag{8}$$

Figure 5 plots the numerical and experimental outcome of the free vibration test after calibration ($p_{calibrated}$ was used), and Table 1 compares the calibrated parameter value for $c$ to the one predicted by applying Housner's assumptions. Noticeably, the two time histories compare well for more than 20 rocking cycles. Housner's assumption predicts the coefficient of restitution with an error $< 1\%$ and the free vibration response is captured excellently. However, as it will be shown in a next section, this does not suffice to predict the complete time history response to a ground motion.

### 3.3 Specimen Excitation and Shaking Table

The rocking response of the specimen was induced by dynamic excitation of its support. This was achieved by placing the specimen on the top of the ETH shaking table [51]. The

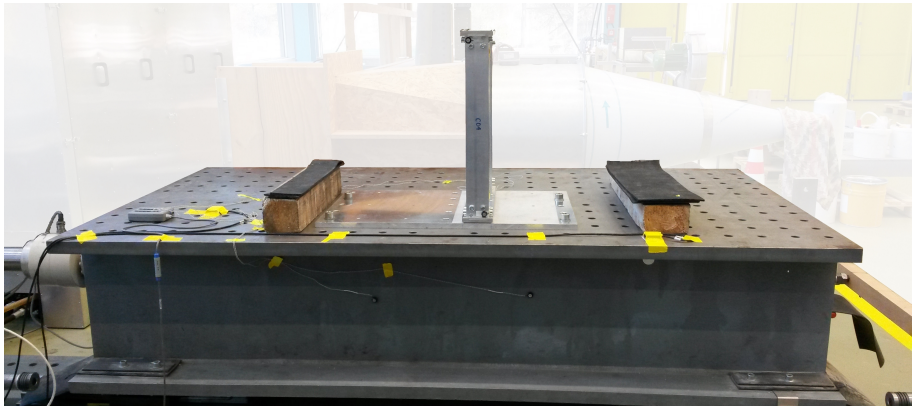

Figure 6: Experimental setup on the shaking table

shaking table platform is a stiff steel box that is placed on roller bearings and actuated using a servo-hydraulic actuator to move only in a uniaxial, horizontal direction. The stroke of the table is $250mm$ and the maximum velocity is $225mm/s$.

### 3.4 Data Acquisition System

Figure 6 shows the experimental and Figure 7 the schematic setup on the shaking table. The movement of the rocking column during the experimental tests was tracked with the Optotrak Certus System, manufactured by Northern Digital Inc. (NDI). In total four infrared-emitting diodes were placed as markers numbered from 1 to 4; two of them on the rocking specimen (Nr. 2 and 4), and two on the shaking table (Nr. 1 and 3). The markers recorded 3D position data with an accuracy of $0.1mm$. Additional output, recorded with the same sampling rate of $500Hz$, is the 2D-angle (in the plane $x-y$ of the NDI coordinate system) between the two lines 1–3 (going through the markers Nr. 1 and 3) and 2–4, respectively, and is computed by the software of the NDI system.

In the given configuration, respecting the feasible measurement window while allowing the shaking table to move to its maximum positions, the NDI camera allowed for recording angles with an error of $0.8mrad$ ($= 0.0053\alpha$). The initial and constant offset between the

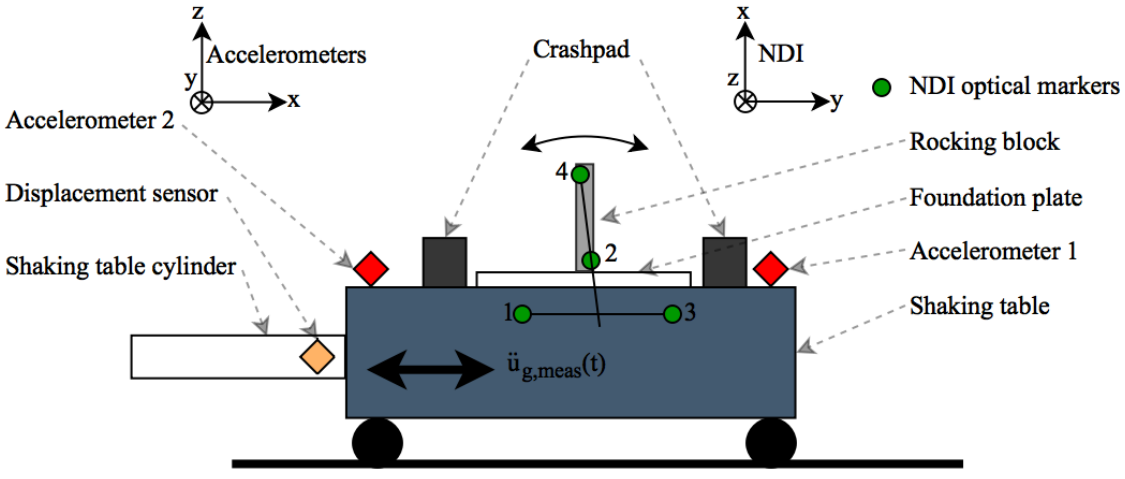


Figure 7: Schematic setup on the shaking table

Lines 1–3 and 2–4 was measured at rest (no rocking) and was subtracted during post processing. The NDI camera was positioned such that the y-axis of the NDI camera and the moving 1D-axis of the shaking table were parallel. Post processing of the 3D position data showed that this alignment was flawless.

## 4 DESCRIPTION OF THE SYNTHETIC GROUND MOTION GENERATION MODEL

In their pioneering work in 1980 Yim, Chopra and Penzien [3] used the 1968 model of Jennings *et al.* [52] to generate synthetic ground motions. Since then, more sophisticated models have been developed that produce simulated ground motions with similar elastic spectra characteristics to a given recorded ground motion. The Rezaeian and Der Kiureghian [53–55] stochastic ground motion model was used to create 100 synthetic ground motions for the longitudinal component of the 1940 El Centro Array #9 earthquake.

The set of 100 synthetic ground motion records was created such that it statistically matches the original motion. Figure 8a),b) shows the acceleration trace of the original ground motion as well as the elastic pseudo-acceleration response spectra of the generated

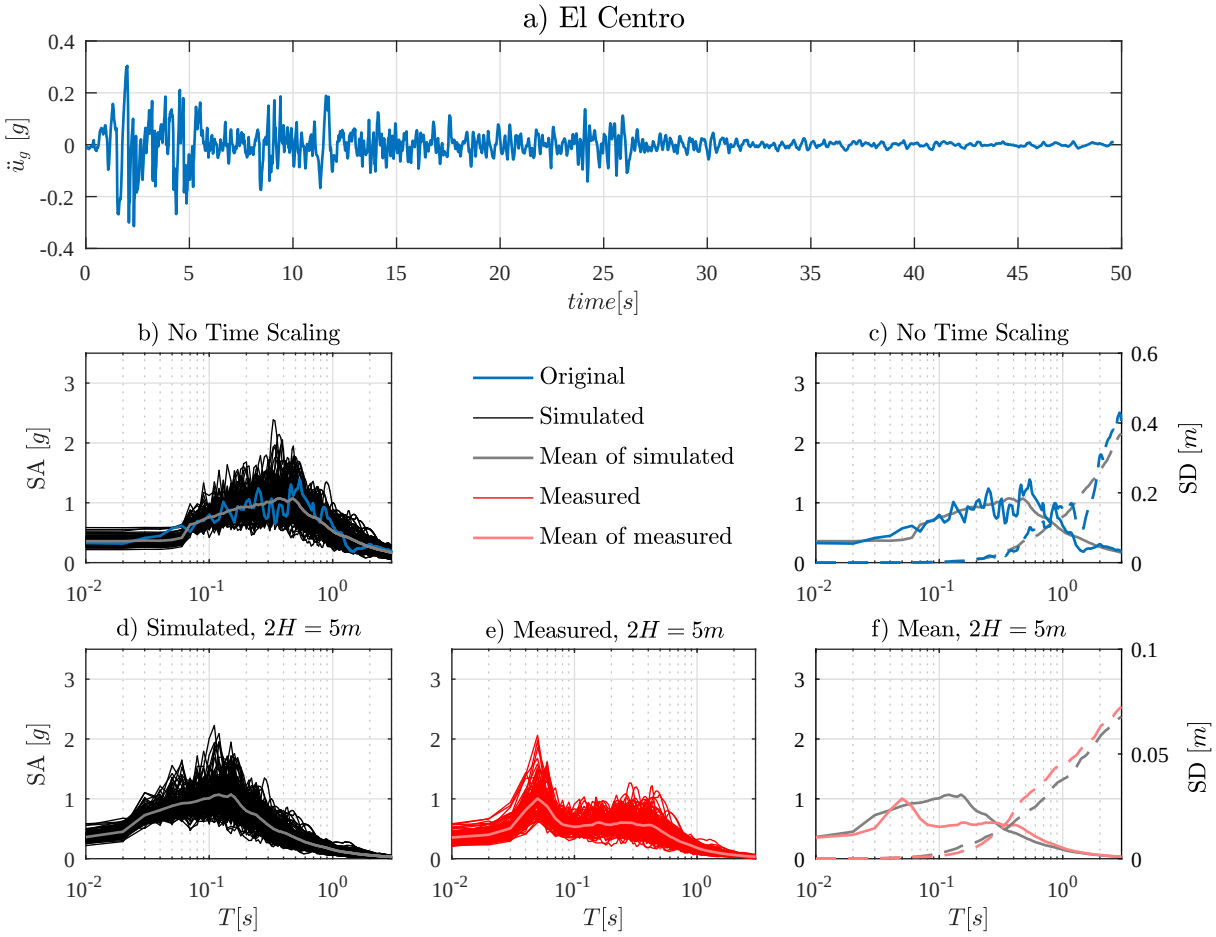


Figure 8: a) El Centro ground motion; b) Acceleration spectra of the recorded and the simulated ground motion (without time scaling); c) Mean acceleration and displacement spectra of the original and simulated ground motions d-f) Acceleration and displacement spectra of the simulated ground motions and their shake table realizations (with time scaling).

synthetic ground motion records.

Note that the simulated ground motions merely match the original ground motion in terms of selected response quantities of a linear elastic single-degree-of-freedom oscillator. This does not guarantee that structures with non-linear behavior, such as rocking structures, will have similar responses to individual ground motions in the generated ensemble. In fact, Vassiliou *et al.* [56] have shown that ground motions with identical elastic spectra can have very different rocking spectra. However, as there is no stochastic model to generate ground motions with same overturning potential, using ground motions with similar elastic spectra was adopted as a minimum precondition for the statistical comparison of the numerical and experimental results.

It is expected that the predictability of rocking motion will depend on the size of the rocking structure. From equation (6) it follows directly that to study this dependency, instead of using different specimens, one can change the time scale of the ground motion. Therefore, the dominant frequency of the input ground motions in the model scale will be:

$$\omega_{model} = \omega_{prototype}\sqrt{S} \tag{9}$$

where $S$ is the size scaling factor ($S = R_{prototype}/R_{model}$).

The prototype column that was tested had a total height $2H$ equal to $5m$. Given that in the model domain the size of the specimen is $0.5m$, the ground motions were scaled in time by a factor of $\sqrt{10}$ (i.e. their dominant frequency was increased). Note that the 100 simulated ground motions were produced in the prototype scale and afterwards they were scaled in time; not the vice versa.

Figure 8 compares the elastic spectra of the 100 simulated ground motions both in the prototype scale and when the ground motions are scaled in time. The spectra of both the simulated time histories (i.e. the input to the shaking table) and of the measured shaking table motion are shown. The mean of the displacement spectra of the 100 motions is also plot, as several researchers report that the maximum of the Elastic Displacement Spectrum is a good measure of the overturning potential of a ground motion [57–59].

One can observe that Rezeian's and Der Kiureghian's model succeeds in producing synthetic ground motions with similar elastic spectra to the recorded ones. A comparison between the spectra of the simulated ground motions and of the spectra of the motions measured on the shaking table shows that the shaking table generally failed to reproduce well the high frequency content of the input ground motions. However, this does not jeopardize the validity of the comparison between the response predicted by the numerical rocking model and the experimentally observed rocking response: The spectra of the *measured* ground motion still do not have a large dispersion. In any case, the numerical model uses the measured acceleration as excitation; and *not* the input to the shaking table controller.

## 5 DETERMINISTIC COMPARISON

Figure 9 shows the responses observed experimentally and determined numerically for the prototype model size of $5m$ to four randomly selected synthetic ground motions (out of the set of 100) of the original ground motion Lefkada. It demonstrates that, even though the experimentally measured frequency parameter, $p$, was used, Housner's model fails to

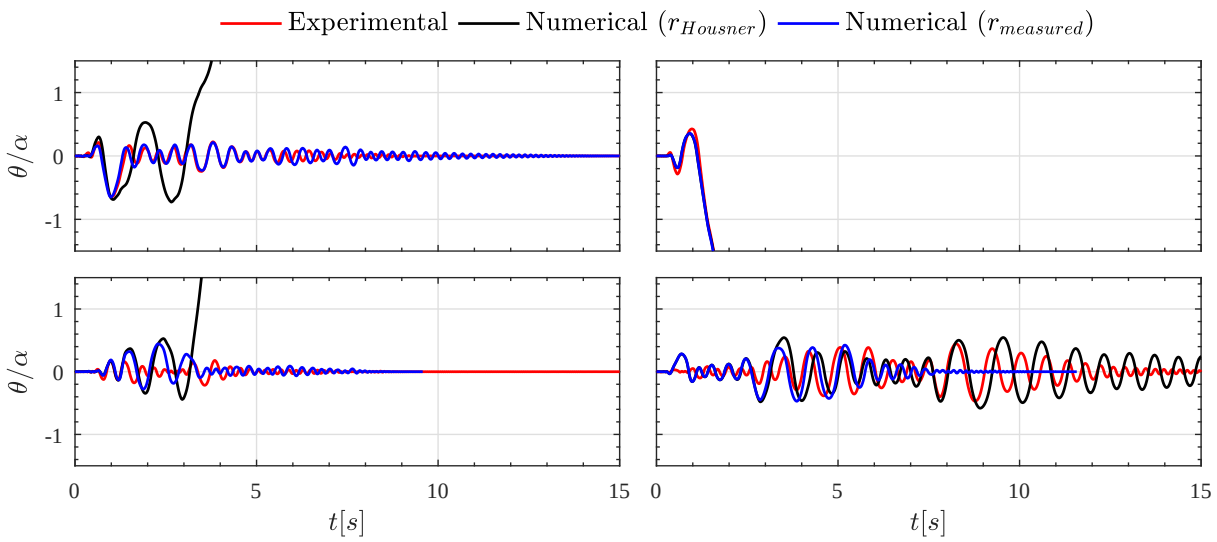


Figure 9: Deterministic comparison of time history responses to four randomly selected simulated ground motion: experimental vs. numerical (Housner) vs. numerical (empirical).

predict the response well. The results improve when the experimentally obtained coefficient of restitution is used. Nevertheless, the prediction in most cases is poor and there is not a consistent overestimation or underestimation of the maximum rocking response. Similarly, this can be observed in the other produced synthetic ground motions.

It can be concluded that the Housner rocking model, even when the coefficient of restitution is experimentally obtained with free vibration tests, is unable to confidently predict the response to a recorded earthquake ground motion. In an effort to estimate whether the model can predict the statistics of the response to an ensemble of ground motions (which is the actual design question) the next section adopts a probabilistic treatment.

## 6 STATISTICAL COMAPRISON

The experimental and the numerical response are compared in terms of their maximum rotation because this is the engineering parameter that is of interest to the designer.

Next, following [3] the maxima of $\theta/\alpha$ were arranged in ascending order and plotted in Figure 10 in the form of a cumulative probability distribution function (CDF). This plot shows the probability that the block will exhibit a response less than a specific value

| | $\theta_{num}$ | $\theta_{exp}$ | $\theta_{num} - \theta_{exp}$ | $\frac{\theta_{num} - \theta_{exp}}{\theta_{exp}}$ |
|---|---|---|---|---|
| percentile | $[\alpha]$ | $[\alpha]$ | $[\alpha]$ | [-] |
| $25^{\text{th}}$ | 0.37 | 0.36 | 0.01 | 0.03 |
| $50^{\text{th}}$ | 0.77 | 0.65 | 0.12 | 0.18 |
| $75^{\text{th}}$ | overturn | overturn | - | - |

Table 2: $25^{\text{th}}$, $50^{\text{th}}$ and $75^{\text{th}}$ percentile of the responses to the El Centro ground motion for the $5m$ tall prototype.

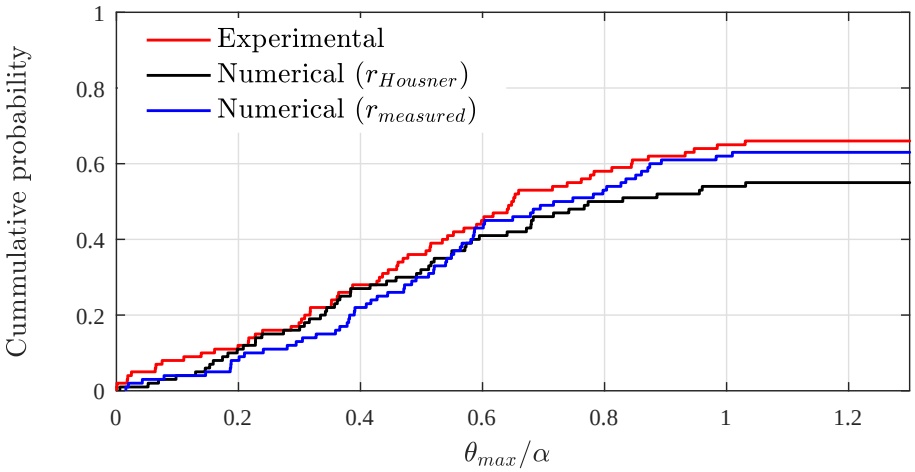


Figure 10: Cumulative distribution functions (CDF) of maximum tilt angle $\theta_{max}$ normalized by slenderness $\alpha$.

of $\theta/\alpha$. Table 2 shows that the numerical and the experimental models compare excellent in terms of the 25th, 50th and 75th percentile of $\theta/\alpha$ with a maximum relative error of 0.18. This is considered a good prediction, especially given the uncertainty in predicting the level of the ground motion intensity (however it is defined).

A comparison between the probabilities of overturning when the Housner coefficient of restitution and when the empirical coefficient of restitution are used reconfirms the 1980 finding of Yim *et al.* [3]:

*"From a probabilistic point of view, the coefficient of restitution influences the response [...] to a much lesser degree than the other system parameters."*

Therefore, for blocks with bases engineered to attract all the impact forces at the corners, it seems pointless (at least in terms of overturning probability) to try to revisit the coefficient of restitution proposed by Housner via sophisticated models. On the contrary, it is more useful to evaluate the stability of a rocking block probabilistically via the use of an ensemble of ground motions.

## CONCLUSIONS

The rocking response to a single ground motion is indeed very sensitive to all parameters and the prediction of the response of a rocking block to a single ground motion is a very difficult task. In that sense, it could be characterized as "chaotic". However, since the seismic problem is inherently stochastic (the ground motion is not known a priori and this induces uncertainty in the system), the modelling uncertainty should not be a reason to deter engineers from using rocking solutions. This paper compared experimental and numerical results of planar SDOF rocking. It showed that existing rigid rocking models are able to predict the statistics of the behavior of rigid rocking systems with an accuracy on the order of 18%, at least when their rocking surfaces are engineered in a way so that the impact forces are concentrated at the edges.

## REFERENCES


[1] G.W. Housner. The Behavior of inverted Pendulum Structures during Earthquakes. *Bulletin of the Seismological Society of America*, 53(2):403–417, 1963.

[2] Nicos Makris and Dimitrios Konstantinidis. The rocking spectrum and the limitations of practical design methodologies. *Earthquake Engineering & Structural Dynamics*, 32(2):265–289, feb 2003.

[3] Chik-Sing Yim, Anil K. Chopra, and Joseph Penzien. Rocking response of rigid blocks to earthquakes. *Earthquake Engineering & Structural Dynamics*, 8(6):565–587, 1980.

[4] John B Mander and Chin-Tung Cheng. Seismic resistance of bridge piers based on damage avoidance design. Technical report, 1997.

[5] Junichi Sakai and Stephen A Mahin. *Analytical investigations of new methods for reducing residual displacements of reinforced concrete bridge columns*. Pacific Earthquake Engineering Research Center, 2004.

[6] Chin-Tung Cheng. Shaking table tests of a self-centering designed bridge substructure. *Engineering Structures*, 30(12):3426–3433, 2008.

[7] Michalis F. Vassiliou. *Analytical investigation of the dynamic response of a pair of columns capped with a rigid beam and of the effect of seismic isolation on rocking structures*. PhD thesis, Doctoral dissertation, Dept. of Civil Engineering, Univ. of Patras, Greece (in Greek), 2010.

[8] Lijun Deng, Bruce L Kutter, and Sashi K Kunnath. Probabilistic seismic performance of rocking-foundation and hinging-column bridges. *Earthquake Spectra*, 28(4):1423–1446, 2012.

[9] Nicos Makris and Michalis F. Vassiliou. Planar rocking response and stability analysis of an array of free-standing columns capped with a freely supported rigid beam. *Earthquake Engineering & Structural Dynamics*, 42(3):431–449, mar 2013.

[10] Nicos Makris and Michalis F. Vassiliou. Are Some Top-Heavy Structures More Stable? *Journal of Structural Engineering*, 140(5):06014001, may 2014.

[11] Nicos Makris and Michalis F. Vassiliou. Dynamics of the Rocking Frame with Vertical Restrainers. *Journal of Structural Engineering*, 141(10):04014245, oct 2015.

[12] Elias G. Dimitrakopoulos and Anastasios I Giouvanidis. Seismic Response Analysis of the Planar Rocking Frame. *Journal of Engineering Mechanics*, 141(7):04015003, jul 2015.

[13] Anastasios I. Giouvanidis and Elias G. Dimitrakopoulos. Seismic Performance of Rocking Frames with Flag-Shaped Hysteretic Behavior. *Journal of Engineering Mechanics*, (accepted 5 OCT), 2016.

[14] Marianna Loli, Jonathan A Knappett, Michael J Brown, Ioannis Anastasopoulos, and George Gazetas. Centrifuge modeling of rocking-isolated inelastic RC bridge piers. *Earthquake engineering & structural dynamics*, 43(15):2341–2359, 2014.

[15] P. Kokkali, T. Abdoun, and I. Anastasopoulos. Centrifuge Modeling of Rocking Foundations on Improved Soil. *Journal of Geotechnical and Geoenvironmental Engineering*, 141(10):4015041, 2015.

[16] Amitabh Dar, Dimitrios Konstantinidis, and Wael W. El-Dakhakhni. Evaluation of ASCE 43-05 Seismic Design Criteria for Rocking Objects in Nuclear Facilities. *Journal of Structural Engineering*, page 04016110, jun 2016.

[17] Alessandro Contento and Angelo Di Egidio. Investigations into the benefits of base isolation for non-symmetric rigid blocks. *Earthquake Engineering & Structural Dynamics*, 38(7):849–866, jun 2009.

[18] Ioannis N. Psycharis, J. V. Lemos, D. Y. Papastamatiou, C. Zambas, and C. Papantonopoulos. Numerical study of the seismic behaviour of a part of the Parthenon Pronaos. *Earthquake Engineering & Structural Dynamics*, 32(13):2063–2084, nov 2003.

[19] Dimitrios Konstantinidis and Nicos Makris. Seismic response analysis of multidrum classical columns. *Earthquake Engineering & Structural Dynamics*, 34(10):1243–1270, aug 2005.

[20] MJN Priestley, RJ Evison, and AJ Carr. Seismic response of structures free to rock on their foundations. *Bulletin of the New Zealand National*, 1978.

[21] Mohammad Aslam, D Theodore Scalise, and William G Godden. Earthquake rocking response of rigid bodies. *Journal of the Structural Division*, 106(2):377–392, 1980.

[22] P. R. Lipscombe and S. Pellegrino. Free Rocking of Prismatic Blocks. *Journal of Engineering Mechanics*, 119(7):1387–1410, jul 1993.

[23] Fernando Peña, Francisco Prieto, Paulo B. Lourenço, A. Campos Costa, and J. V. Lemos. On the dynamics of rocking motion of single rigid-block structures. *Earthquake Engineering & Structural Dynamics*, 36(15):2383–2399, dec 2007.

[24] Quincy Tsun Ming Ma. *The mechanics of rocking structures subjected to ground motion*. PhD thesis, 2010.

[25] Rico E. Truniger, Michalis F. Vassiliou, and Božidar Stojadinović. An analytical model of a deformable cantilever structure rocking on a rigid surface: experimental validation. *Earthquake Engineering & Structural Dynamics*, 44(13), 2015.

[26] Rico E. Truniger, Michalis F. Vassiliou, and Božidar Stojadinović. Experimental Study on the Interaction between Elasticity and Rocking. In *10th U.S. National Conference on Earthquake Engineering*, 2014.

[27] Jonas A. Bachmann, Christoph Jost, Quentin Studemann, Michalis F. Vassiliou, and Bozidar Stojadinovic. An analytical model for the dynamic response of an elastic SDOF system fixed on top of a rocking single-story frame structure: experimental validation. In *ECCOMAS Congress 2016: 7th European Congress on Computational Methods in Applied Sciences and Engineering*, Heraklion, 2016.

[28] Giuseppe Oliveto, Ivo Caliò, and Annalisa Greco. Large displacement behaviour of a structural model with foundation uplift under impulsive and earthquake excitations. *Earthquake Engineering & Structural Dynamics*, 32(3):369–393, mar 2003.

[29] F. Prieto, P. B. Lourenço, and C. S. Oliveira. Impulsive Dirac-delta forces in the rocking motion. *Earthquake Engineering & Structural Dynamics*, 33(7):839–857, jun 2004.

[30] Sinan Acikgoz and Matthew J. DeJong. The interaction of elasticity and rocking in flexible structures allowed to uplift. *Earthquake Engineering & Structural Dynamics*, 41(11):1–18, mar 2012.

[31] Alessandro Baratta, Ileana Corbi, and Ottavia Corbi. Towards a seismic worst scenario approach for rocking systems: analytical and experimental set-up for dynamic response. *Acta Mechanica*, 224(4):691, 2013.

[32] Michalis F. Vassiliou, Rico E. Truniger, and Božidar Stojadinović. An analytical model of a deformable cantilever structure rocking on a rigid surface: development and verification. *Earthquake Engineering & Structural Dynamics*, 44(13), 2015.

[33] Sinan Acikgoz and Matthew J. DeJong. Analytical modelling of multi-mass flexible rocking structures. *Earthquake Engineering & Structural Dynamics*, 41(11):1549–1568, 2016.

[34] Anastasios I. Giouvanidis and Elias G. Dimitrakopoulos. Nonsmooth Dynamic Analysis of Sticking Impacts in Rocking Structures. *Bulletin of Earthquake Engineeringa*, (accepted 4 DEC), 2016.

[35] Dimitrios Kalliontzis, Sri Sritharan, and Arturo Schultz. Improved Coefficient of Restitution Estimation for Free Rocking Members. *Journal of Structural Engineering*, page 06016002, jul 2016.

[36] Michalis F. Vassiliou, Kevin R. Mackie, and Božidar Stojadinović. A finite element model for seismic response analysis of deformable rocking frames. *Earthquake Engineering & Structural Dynamics*, 2016.

[37] M N Chatzis, M Garcia Espinosa, and A W Smyth. Examining the Energy Loss in the Inverted Pendulum Model for Rocking Bodies. *Journal of Engineering Mechanics*, page 4017013, 2017.

[38] V Terzic, M J Schoettler, J I Restrepo, and S A Mahin. Concrete column blind prediction contest 2010: outcomes and observations. *PEER Rep. No*, 1, 2015.

[39] Jian Zhang and Nicos Makris. Rocking Response of Free-Standing Blocks under Cycloidal Pulses. *Journal of Engineering Mechanics*, 127(5):473–483, may 2001.

[40] Nicos Makris. The Role of the Rotational Inertia on the Seismic Resistance of Free-Standing Rocking Columns and Articulated Frames. *Bulletin of the Seismological Society of America*, 104(5):2226–2239, oct 2014.

[41] Nicos Makris and Georgios Kampas. Size Versus Slenderness: Two Competing Parameters in the Seismic Stability of Free-Standing Rocking Columns. *Bulletin of the Seismological Society of America*, 106(1):104–122, feb 2016.

[42] Elias G. Dimitrakopoulos and Matthew J. DeJong. Overturning of Retrofitted Rocking Structures under Pulse-Type Excitations. *Journal of Engineering Mechanics*, 138(8):963–972, aug 2012.

[43] Mohamed A. ElGawady, Quincy Tsun Ming Ma, John W. Butterworth, and Jason Ingham. Effects of interface material on the performance of free rocking blocks. *Earthquake Engineering & Structural Dynamics*, 40(4):375–392, apr 2011.

[44] Christine E. Wittich and Tara C. Hutchinson. Shake table tests of stiff, unattached, asymmetric structures. *Earthquake Engineering & Structural Dynamics*, 41(11):n/a–n/a, jun 2015.

[45] Tamás Ther and László P Kollár. Refinement of Housner's model on rocking blocks. *Bulletin of Earthquake Engineering*, pages 1–15.

[46] Elias G. Dimitrakopoulos and Matthew J. DeJong. Revisiting the rocking block: closed-form solutions and similarity laws. *Proceedings of the Royal Society A: Mathematical, Physical and Engineering Sciences*, 468(2144):2294–2318, aug 2012.

[47] Nicos Makris and Michalis F. Vassiliou. Sizing the slenderness of free-standing rocking columns to withstand earthquake shaking. *Archive of Applied Mechanics*, 82(10-11):1497–1511, oct 2012.

[48] Michalis F. Vassiliou and Nicos Makris. Analysis of the rocking response of rigid blocks standing free on a seismically isolated base. *Earthquake Engineering & Structural Dynamics*, 41(2):177–196, feb 2012.

[49] Michalis F. Vassiliou and Nicos Makris. Dynamics of the Vertically Restrained Rocking Column. *Journal of Engineering Mechanics*, 141(12):04015049, dec 2015.

[50] Michalis F. Vassiliou and Nicos Makris. Estimating time scales and length scales in pulselike earthquake acceleration records with wavelet analysis. *Bulletin of the Seismological Society of America*, 101(2):596–618, 2011.

[51] Hugo Bachmann, Thomas Wenk, Markus Baumann, and Pierino Lestuzzi. Der neue ETH-Erdbebensimulator. *Schweizer Ingenieur und Architekt*, 4, 1999.

[52] Paul C Jennings, George W Housner, and N Chien Tsai. Simulated earthquake motions. 1968.

[53] Sanaz Rezaeian and Armen Der Kiureghian. Simulation of synthetic ground motions for specified earthquake and site characteristics. *Earthquake Engineering & Structural Dynamics*, 39(10):1155–1180, 2010.

[54] Sanaz Rezaeian and Armen Der Kiureghian. A stochastic ground motion model with separable temporal and spectral nonstationarities. *Earthquake Engineering & Structural Dynamics*, 37(13):1565–1584, 2008.

[55] M Broccardo and A Der Kiureghian. Simulation of near-fault ground motions using frequency-domain discretization. In *Proceedings of the 10th National Conference on Earthquake Engineering. Anchorage, Alaska*, 2014.

[56] Michalis F. Vassiliou, Stefan Burger, Marius Egger, Jonas A. Bachmann, Marco Broccardo, and Božidar Stojadinović. The three-dimensional behavior of inverted pendulum cylindrical structures during earthquakes (under review). *Earthquake Engineering & Structural Dynamics*.

[57] Bidur Kafle, Nelson T. K. Lam, Emad F. Gad, and John Wilson. Displacement controlled rocking behaviour of rigid objects. *Earthquake Engineering & Structural Dynamics*, 40(15):1653–1669, dec 2011.

[58] F. Gelagoti, R. Kourkoulis, I. Anastasopoulos, and G. Gazetas. Rocking-isolated frame structures: Margins of safety against toppling collapse and simplified design approach. *Soil Dynamics and Earthquake Engineering*, 32(1):87–102, jan 2012.

[59] Vasileios Drosos and Ioannis Anastasopoulos. Shaking table testing of multidrum columns and portals. *Earthquake Engineering & Structural Dynamics*, 43(11):1703–1723, sep 2014.

COMPDYN 2017
6th ECCOMAS Thematic Conference on
Computational Methods in Structural Dynamics and Earthquake Engineering
M. Papadrakakis, M. Fragiadakis (eds.)
Rhodes Island, Greece, 15–17 June, 2017

# SIMPLE MODELS FOR THE SEISMIC RESPONSE OF RIGID OR FLEXIBLE BLOCKS

**S. Diamantopoulos**[1], **M. Fragiadakis**[2]

[1] Laboratory for Earthquake Engineering
National Technical University of Athens (NTUA)
9 Iroon Polytechniou 15780, Zografou Campus, Athens, Greece
e-mail: s_diam@outlook.com.gr

[2] Laboratory for Earthquake Engineering
National Technical University of Athens (NTUA)
9 Iroon Polytechniou 15780, Zografou Campus, Athens, Greece
e-mail: mfrag@mail.ntua.gr

**Keywords:** rocking structures, rigid blocks, flexible blocks, seismic response, FEM modeling, non-linear response history analysis.

**Abstract.** *The paper examines different approaches for modeling the seismic response of blocks that are either rigid or flexible. Simple models that are based on beam-column elements and can be implemented with common finite element (FE) software are developed. We first study rigid blocks and we compare our findings with results obtained solving directly the block's equation of motion as derived by Housner's theory. We compare different single-degree-of-freedom (SDOF) models which consist of a rigid beam connected to a zero-length, non-linear rotational spring with negative-stiffness, while different options for modelling energy dissipation are considered. The proposed models are compared using simple wavelets and natural ground motion records producing accurate results in all cases. The proposed FE approach allows to also study flexible blocks offering a modeling that is simple and able to provide very accurate solutions using tools that are widely available in existing software, or easy to implement in a FE code.*

## 1 INTRODUCTION

Free-standing slender blocks can uplift, rock or overturn [1, 2]. Rocking is the partial uplift of a rigid, or a flexible, structure from its base when the center of rotation changes. The solution of the rocking problem should take into account a wide range of non-linear phenomena such as impact, contact, sliding and uplift that occur during a rocking motion. As a result, many studies on the solitary rigid block have been presented for more than a century [3]. Research on the dynamic response of rocking structures is focused on developing methods that answer whether the structure will overturn or it will rock safely, while there are also many studies that propose means for the seismic protection of rocking structures. Several models and approaches for the numerical modeling of blocks have been proposed and are able to assess the rocking response of both rigid and flexible bodies (e.g. [4, 5]). Block flexibility complicates further the dynamic response of these structures, while many researchers, e.g. Psycharis [6], Apostolou et al. [7], and Acikgoz and Dejong [8] have studied their seismic response.

In this paper equivalent Single-Degree-of-Freedom (SDOF) models are proposed for solving the rocking block problem. The models include an elastic column (rigid or deformable) with a cross section similar to that of the block. The SDOF oscillator is connected to the ground with a zero-length, non-linear elastic rotation spring, as originally proposed by Vasilliou et al. [4]. We first consider only rigid blocks and we then extend the concept to the case of flexible systems. Moreover, energy dissipation in rocking bodies takes place instantaneously at every impact. Several finite element (FE) models use continuous viscous damping (e.g. Rayleigh damping) to quantify the energy dissipated by the structure during a ground motion [4]. This approach is not appropriate since energy dissipation is primarily instantaneous and takes place on every impact [9]. We propose instead an event-based damping scheme, which when combined with our simplified FE model it is able to produce accurate response estimates. Our approach correlates the coefficient of restitution with the angular velocity of the block and is validated against Housner's theory.

## 2 SEISMIC RESPONSE OF UNDAMPED RIGID ROCKING BLOCKS

A homogeneous rigid block with height $2h$ and width $2b$ is considered (Fig. 1). We assume that the coefficient of friction between the block and the rigid base is always big enough to prevent sliding. The block has weight $W$, mass $m$ and its moment of inertia about the point $O$ is $I_o$ (Fig. 1). Furthermore, $\theta$ is the response rotation, $\alpha = atan(b/h)$ is the block slenderness and $R = \sqrt{b^2 + h^2}$ is the size parameter of the block. The latter two parameters describe fully a block's geometry, while $g$ denotes the acceleration of gravity.

Taking into account that the body remains at the same position at the instant of impact, the equation of motion of a free-standing block under a horizontal ground acceleration $\ddot{u}_g$ is obtained from the equilibrium between the overturning and the restoring moment. If the restoring moment is $M_{rst} = I_o\ddot{\theta}(t) + mgR\sin[\alpha \mathrm{sgn}\theta(t) - \theta(t)]$ , and the overturning moment is given from the expression $M_{ovtn} = -m\ddot{u}_g(t)\,R\cos[\alpha \mathrm{sgn}\theta(t) - \theta(t)]$, the equation of motion will be [1, 10, 11, 12]:

$$I_o\ddot{\theta}(t) + mgR\sin[\alpha \mathrm{sgn}\theta(t) - \theta(t)] = -m\ddot{u}_g(t)\,R\cos[\alpha \mathrm{sgn}\theta(t) - \theta(t)] \tag{1}$$

The block will start rocking only when the ground acceleration exceeds a threshold value, i.e. when $\ddot{u}_g \geq (b/h)g = g\tan\alpha$. Moreover, for a rectangular block $I_o = 4/3mR^2$ and if we set $p = \sqrt{(3g)/(4R)}$, where $p$ is the parameter of frequency of the rocking block, the block's

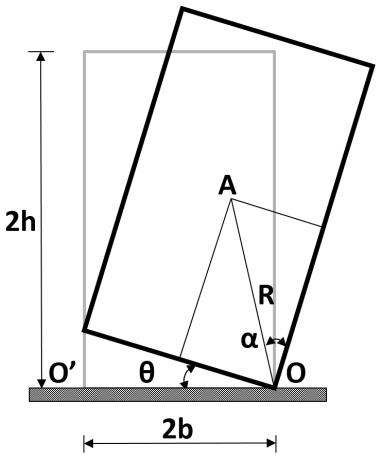


Figure 1: Rocking block geometry.

equation of motion takes the form:

$$\ddot{\theta}(t) = p^2 \left[ -\sin\left[\alpha \mathrm{sgn}\theta(t) - \theta(t)\right] - \ddot{u}_g(t)/g \cos\left[\alpha \mathrm{sgn}\theta(t) - \theta(t)\right]\right] \quad (2)$$

Assuming that $\theta$ and $\alpha$ are small we can linearize the equation of motion and simplify it:

$$\ddot{\theta}(t) = p^2 \left[ -\left[\alpha \mathrm{sgn}\theta(t) - \theta(t)\right] - \ddot{u}_g(t)/g\right] \quad (3)$$

The above expressions can be solved numerically using standard Ordinary Differential Equation (ODE) solvers. All results produced in this study were obtained with the aid of the ODE23s solver available in Matlab's [13] library.

## 3 SIMULATION OF ROCKING BLOCKS WITH SIMPLE SDOF MODELS

The need for a simple and robust solution algorithm for rigid block structures led us to the development of simplified single-degree-of-freedom (SDOF) models. These models can be implemented within finite element (FE) codes which are extensively used in engineering practice. Furthermore, this approach allows to easily handle flexible rocking bodies and can be extended to many other applications circumventing the need for specifically tailored analytical solutions. Following the concept originally proposed by Vassiliou et al. [4], we examine four simple SDOF models in order to calculate the motion of rigid rectangular blocks. The extension of this modeling to flexible blocks is also discussed. All models are based on an rigid/flexible SDOF oscillator with moment of inertia and modulus of elasticity identical to those of the block. The oscillator is connected at its base with a zero-length, non-linear rotational spring in order to simulate the restoring moment of the block (Fig. 2).

Figure 3a shows the moment-rotation relationship of the nonlinear spring during the rocking motion of a solitary free-standing rigid block. Moment equal to $M_o = mgb = mgR\sin\alpha$ is required for setting the block from its rest position ($\theta = 0$) to rocking motion. Once the block is set to rocking motion the restoring moment decreases (negative stiffness), reaching zero when the block overturns at $\theta = \alpha$. The moment-rotation relationship is introduced in the models setting the negative stiffness of the rocking block equal to $k_b = mgRsin(\alpha - \theta)$ according to Eq. 1. This expression can be simplified to $k_b = mgRsin\alpha(1 - \theta/\alpha)$, thus having a linear relationship for the negative stiffness. The two options are shown in Fig. 3a and b,

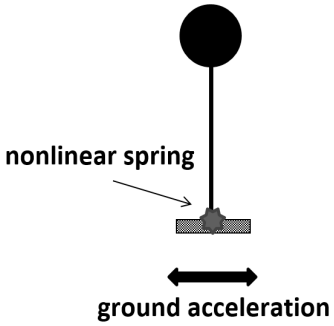


Figure 2: Single-degree-of-freedom (SDOF) rigid block model.

respectively. In both cases, unloading-reloading should follow exactly the same path, thus a pertinent material model should be available. A third option is using a rigid-perfectly plastic moment-rotation relationship with moment capacity equal to $M_o = mgR\sin\alpha$ (Fig. 3c) [4]. In this case the negative stiffness is introduced assuming full geometric non-linearity with second-order analysis.

All three options are possible thanks to the versatility of OpenSees [14] which offers pertinent material models and also can be used in large displacement-small strain problems. Furthermore, typically the first brach of most material models is linear elastic. If such a material model is adopted, a "yield" rotation defining a big initial stiffness value should be adopted. This can be easily achieved setting the "yield" rotation to very small values, e.g. $10^{-5} \div 10^{-12}$. Our parametric analyses have shown that the differences between the first two options of Fig. 3 (cases a, b) are negligible, while the third option (Fig. 3c) produces errors in some cases and depending on the model considered. In the remaining of this work our results have been obtained using the negative stiffness relationship assuming that the negative stiffness is constant, i.e. case b of Fig. 3, unless otherwise specified. The latter option is more easy to implement compared to first case and is also more stable compared to the third option.

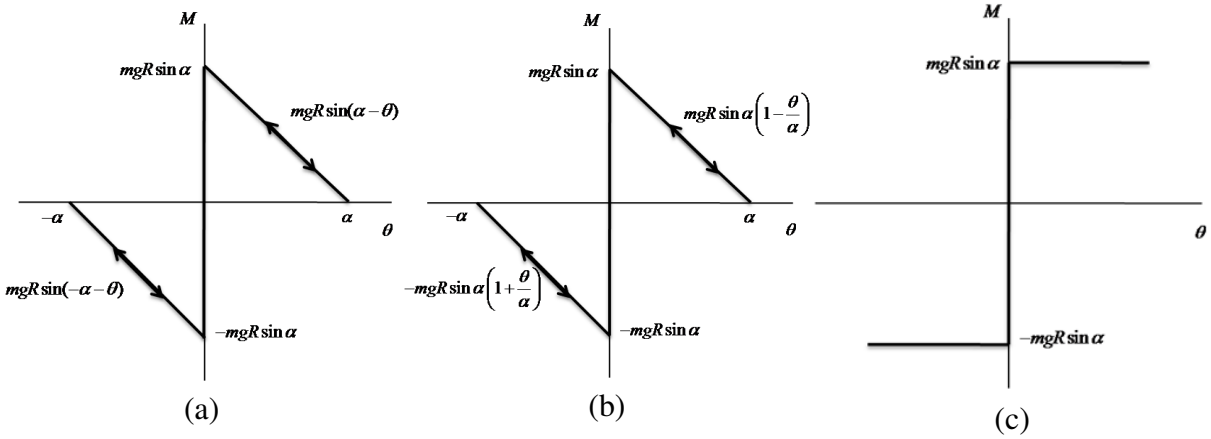


Figure 3: Moment-rotation relationships of the non-linear elastic rotation spring used in the SDOF models.

### 3.1 Spring Model 1 (SM1)

The first model considered is denoted as Spring Model 1 (SM1) and is shown conceptually in Figure 4. The model assumes that the block's mass is concentrated at its center (point $A$, Fig. 4). If the moment of inertia about the center $A$ is $I_A = (1/3)mR^2$, its value with respect to point $O$ (or $O'$) will be $I_o = 1/3mR^2 + mR^2 = 4/3mR^2$. The negative stiffness is taken into account through the stiffness of the spring.

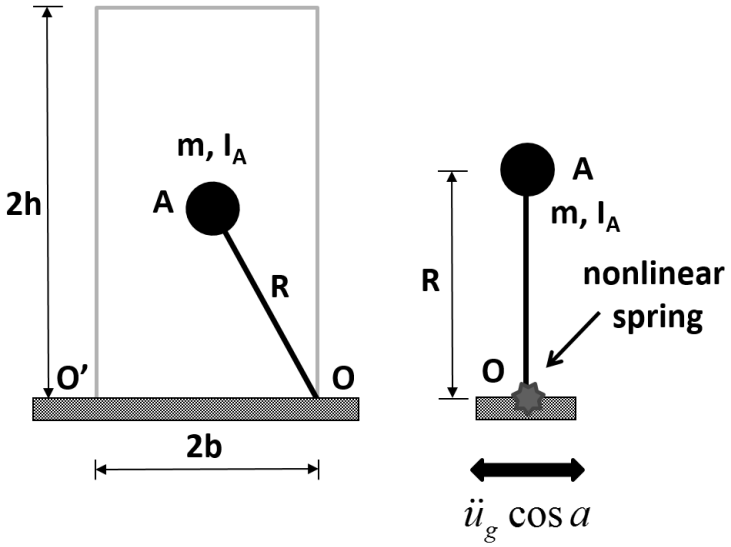


Figure 4: Single degree of freedom Spring Model 1 (SM1).

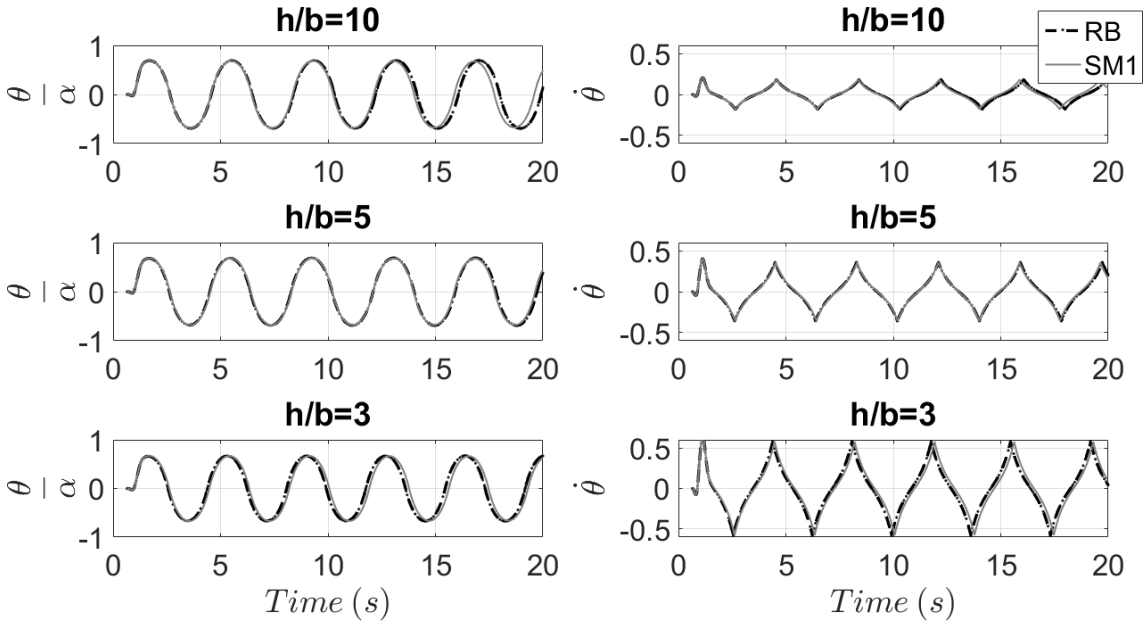


Figure 5: Comparison of rocking rotation and velocity response history between the rocking block (RB) and the SM1 model for a block with $R = 2m$ subjected to a symmetric Ricker pulse excitation with $\alpha_p = 3.6g\tan\alpha$ and $\omega_p = 3\pi$ rad/s.

For the three different moment-rotation relationships of Fig. 3, the equations of motion of the SM1 model are as follows:

$$I_o\ddot{\theta}(t) + mgR\sin[\alpha \mathrm{sgn}\theta(t) - \theta(t)] = -m(\ddot{u}_g(t)\cos\alpha)R\cos\theta(t) \quad (4)$$

$$I_o\ddot{\theta}(t) + mgR\sin\alpha \mathrm{sgn}\theta(t)\,[1 - \theta(t)\,\mathrm{sgn}\theta(t)/\alpha] = -m(\ddot{u}_g(t)\cos\alpha)R\cos\theta(t) \quad (5)$$

$$I_o\ddot{\theta}(t) + mgR[\sin\alpha \mathrm{sgn}\theta(t) - \sin\theta(t)] = -m(\ddot{u}_g(t)\cos\alpha)R\cos\theta(t) \quad (6)$$

Considering the exact matching of the restoring moments between the SM1 with the negative stiffness relationship and the RB, the only difference in the equations of motion arise from the overturning moment terms. The overturning moment of the rocking block (RB) is $M_{ovtn} = -m\ddot{u}_g(t)\,R\cos[\alpha \mathrm{sgn}\theta(t) - \theta(t)]$ while for the SM1 it is $M'_{ovtn} = -m\ddot{u}_g(t)\,R\cos\alpha\cos\theta(t)$. Figure 5 compares the rotation $\theta$, which is the response quantity of interest, versus the solution of the block's equation of motion (Eq. 1) with Matlab that will be here referred as "Rocking Block" (RB). The obtained results agree perfectly for slenderness values shown.

### 3.2 Spring Model 2 (SM2)

The second spring model (SM2) assumes that the mass of the block is concentrated at the pivot point (Fig. 6). This derivation is obtained comparing Eq. 1 with the equation of motion of a SDOF oscillator: $m\ddot{u} + c\dot{u} + ku = -m\ddot{u}_g$. In the case of the block, the d.o.f of interest is the rotation $\theta$ as opposed to the displacement $u$ of the SDOF oscillator. In rotational motion the mass is replaced by the moment of inertia $I_o = (4/3)mR^2$. The stiffness is considered through the stiffness of the spring. After manipulating the equation of motion, we find that the ground motion should be applied on the rotational degree-of-freedom multiplied with $3cos\alpha/4R$.

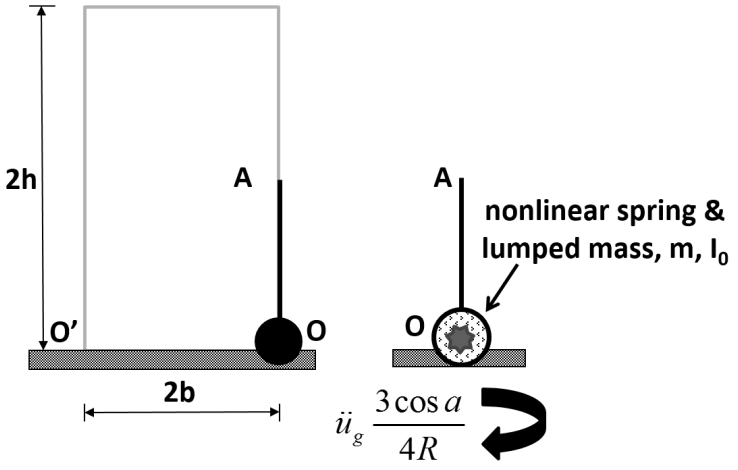


Figure 6: Single degree of freedom Spring Model 2 (SM2).

The equation of motion of the SM2 model, for each of the three moment-rotation relationships of Fig. 3, respectively, will be:

$$I_o\ddot{\theta}(t) + mgR\sin[\alpha \mathrm{sgn}\theta(t) - \theta(t)] = -I_o(\ddot{u}_g(t)\,3\cos\alpha/4R)\cos\theta(t) \quad (7)$$

$$I_o\ddot{\theta}(t) + mgR\sin\alpha \mathrm{sgn}\theta(t)\,[1 - \theta(t)\,\mathrm{sgn}\theta(t)/\alpha] = -I_o(\ddot{u}_g(t)\,3\cos\alpha/4R)\cos\theta(t) \quad (8)$$

$$I_o\ddot{\theta}(t) + mgR[\sin\alpha \mathrm{sgn}\theta(t) - \cos\alpha\sin\theta(t)] = -I_o(\ddot{u}_g(t)\,3\cos\alpha/4R)\cos\theta(t) \quad (9)$$

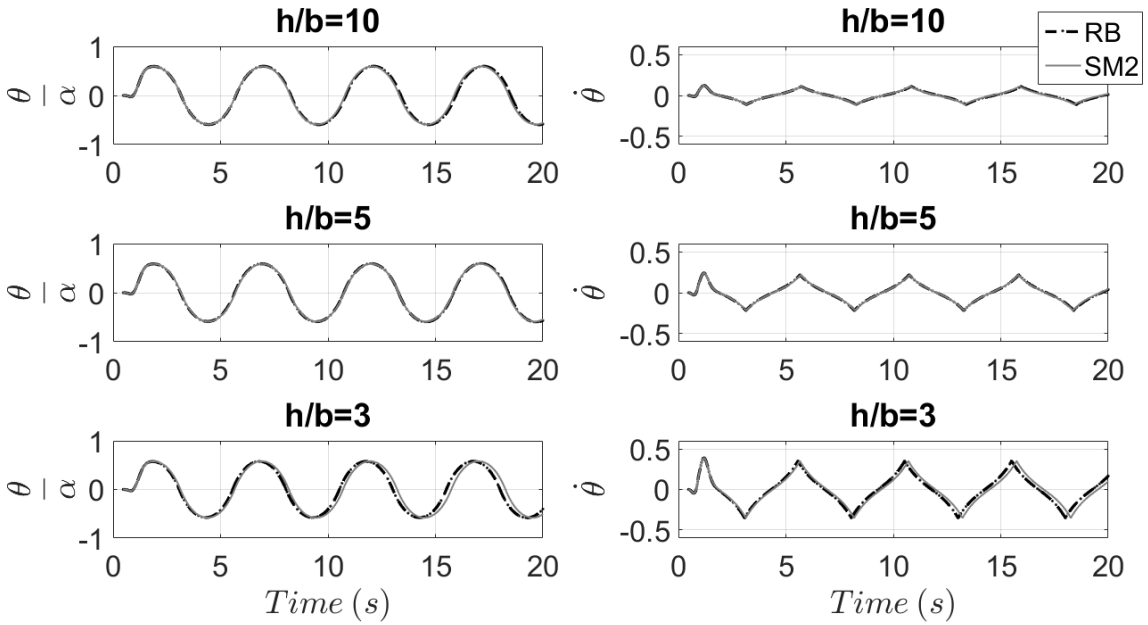


Figure 7: Comparison of rocking rotation and velocity response history between the rocking block (RB) and the SM2 model for a block with $R = 5m$ subjected to a symmetric Ricker pulse excitation with $\alpha_p = 3.6g\tan\alpha$ and $\omega_p = 2\pi$ rad/s.

If the negative stiffness is that of Fig. 3b, the restoring moments of SM2 and RB are identical. As a result, the only difference in the equations of motion is in the term of the overturning moments. The overturning moment of the rocking block is $M_{ovtn} = -m\ddot{u}_g(t)\,R\cos[\alpha\text{sgn}\theta(t) - \theta(t)]$ while for the SM2 it is $M'_{ovtn} = -I_o(\ddot{u}_g(t)\,3\cos\alpha/4R)\cos\theta(t) = -m\ddot{u}_g(t)\,R\cos\alpha\cos\theta(t)$. Figure 7 compares the response of the rocking block and SM2, when subjected to a symmetric Ricker pulse. Perfect agreement is observed for all slenderness values considered.

### 3.3 Spring Model 3 (SM3)

Spring Model 3 (SM3) assumes that the mass of the block is concentrated at the center of the block (point $A$), while the pivot point is its projection on the base (Fig. 8). The moment of inertia with respect to point $A$ is $I_A = 1/3mR^2 + mb^2$, while about $O$ it is $I_o = (1/3)mR^2 + mb^2 + mh^2 = \ldots = (4/3)mR^2$, thus equal to the moment of inertia of the block. Since the stiffness is considered through the stiffness of the spring, comparing with the equation of motion of the rocking block (Eq. 1), the only difference is in the overturning moment term since the overturning moment of the rocking block is $M_{ovtn} = -m\ddot{u}_g(t)\,R\cos[\alpha\text{sgn}\theta(t) - \theta(t)]$ while of the SM3 is $M'_{ovtn} = -m\ddot{u}_g(t)\,R\cos\alpha\cos\theta(t)$. The corresponding equations of motion that take into account the three moment-rotation relationships of Figure 3 are as follows:

$$I_o\ddot{\theta}(t) + mgR\sin[\alpha\text{sgn}\theta(t) - \theta(t)] = -m\ddot{u}_g(t)\,(R\cos\alpha)\cos\theta(t) \quad (10)$$

$$I_o\ddot{\theta}(t) + mgR\sin\alpha\text{sgn}\theta(t)\,[1 - \theta(t)\,\text{sgn}\theta(t)/\alpha] = -m\ddot{u}_g(t)\,(R\cos\alpha)\cos\theta(t) \quad (11)$$

$$I_o\ddot{\theta}(t) + mgR[\sin\alpha\text{sgn}\theta(t) - \cos\alpha\sin\theta(t)] = -m\ddot{u}_g(t)\,(R\cos\alpha)\cos\theta(t) \quad (12)$$

Rotation and velocity response histories for three different slenderness values ($h/b = 2, 5, 10$) and $R = 10m$ under a symmetric Ricker pulse are shown in Figure 9. Excellent agreement with the results of the rocking block theory is observed again.

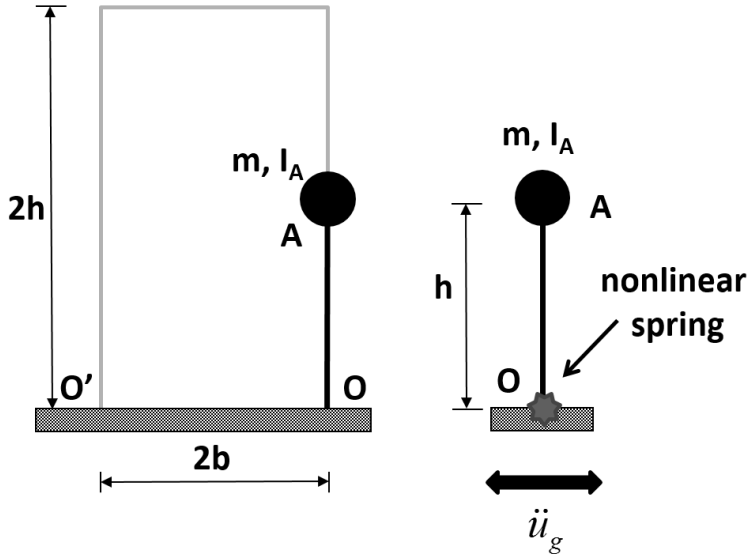


Figure 8: Single degree of freedom Spring Model 3 (SM3).

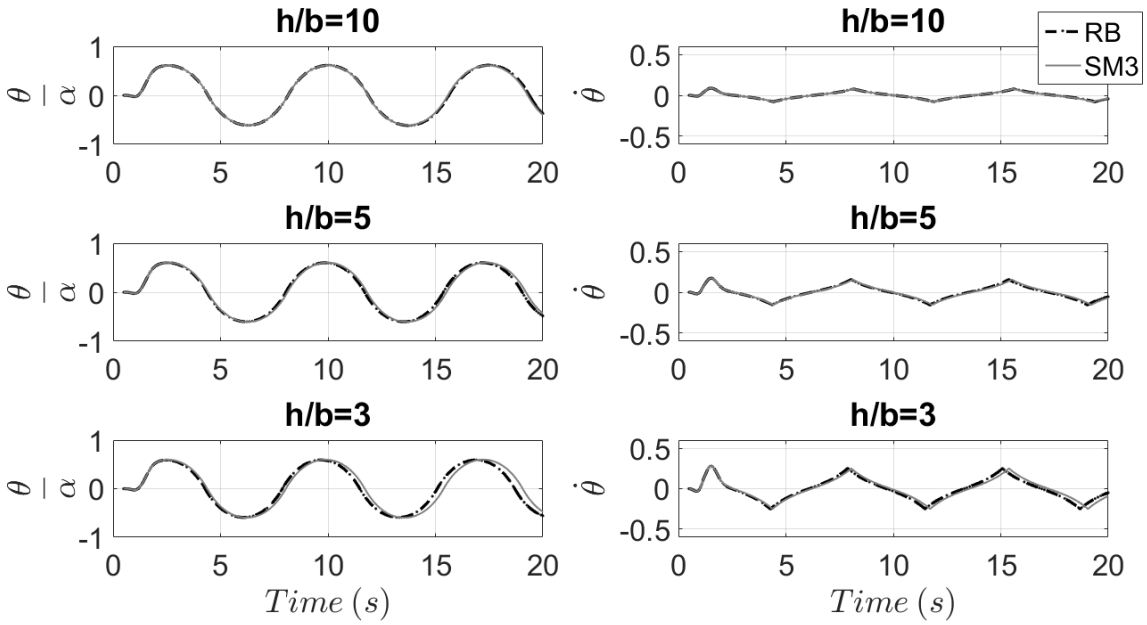


Figure 9: Comparison of rocking rotation and velocity response history between the rocking block (RB) and the SM3 model for a block with $R = 10m$ subjected to a symmetric Ricker pulse excitation with $\alpha_p = 3.6g\tan\alpha$ and $\omega_p = 1.4\pi$ rad/s.

### 3.4 Multi-mass Spring Model (mmSM)

We also consider as a fourth model option a multi-mass spring model, denoted as mmSM and shown in Fig. 10. This model is first examined for the rigid block case, but its purpose is for studying the rocking response of flexible bodies where the mass is distributed along the diagonal $2R$ of the block. The model consists of $n$ masses and is identical to a cantilever elastic column with moment of inertia about the pivot point $O$, equal to $I_o = (1/3)mL^2$, where $m$ is

the total mass and $L$ is the total length. Taking into account the above observation, the moment of inertia of a cantilever with distributed total mass $m$ and length equal to $2R$ about $O$ is: $I_o = (1/3)m(2R)^2 = (4/3)mR^2$ which is equal to the moment of inertia of the rocking block.

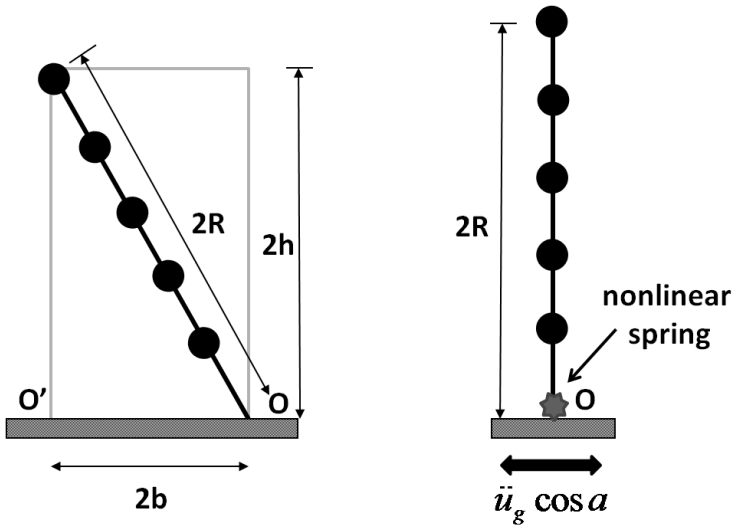


Figure 10: Multi-mass Spring Model (mmSM).

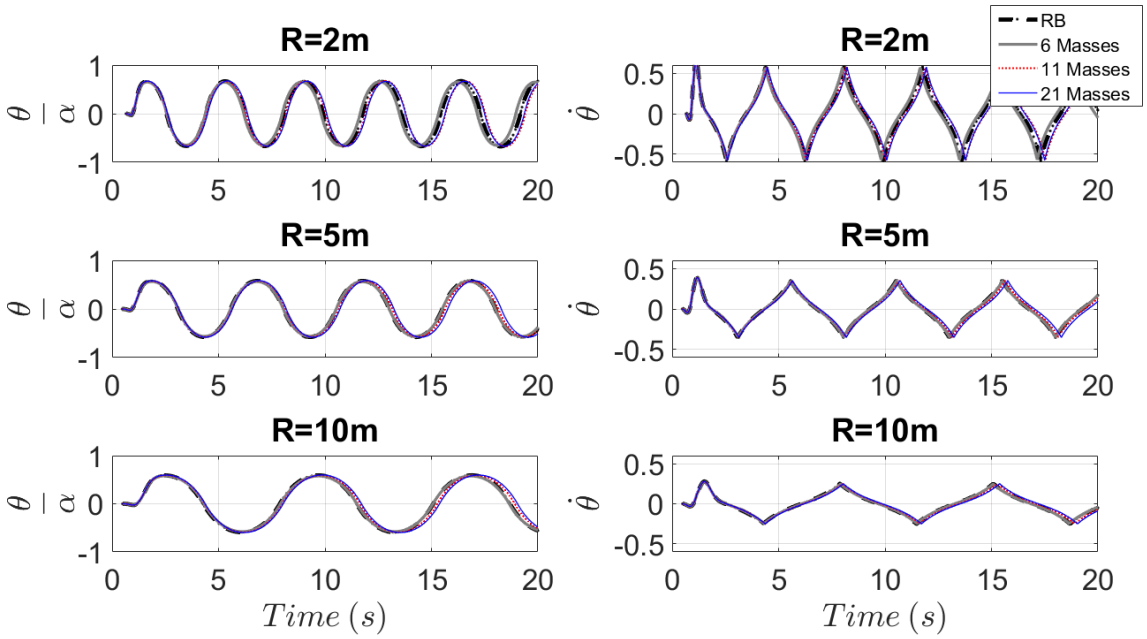


Figure 11: Sensitivity of mmSM for different number of masses considering different blocks with $R = 2, 5, 10m$ and $h/b = 3$ under a symmetric Ricker pulse with $\omega_p = 3\pi, 2\pi, 1.4\pi$ rad/s respectively.

The equations of motion for the mmSM model either taking into account the negative stiffness of the rocking block or considering explicitly second order effects are:

$$I_o\ddot{\theta}(t) + mgR\sin\left[\alpha \mathrm{sgn}\theta(t) - \theta(t)\right] = -m(\ddot{u}_g(t)\cos\alpha)R\cos\theta(t) \qquad (13)$$

$$I_o\ddot{\theta}\left(t\right)+mgR\sin\alpha\mathrm{sgn}\theta\left(t\right)\left[1-\theta\left(t\right)\mathrm{sgn}\theta\left(t\right)/\alpha\right]=-m(\ddot{u}_g\left(t\right)\cos\alpha)R\cos\theta\left(t\right) \quad (14)$$

$$I_o\ddot{\theta}\left(t\right)+mgR[\sin\alpha\mathrm{sgn}\theta\left(t\right)-\sin\theta\left(t\right)]=-m(\ddot{u}_g\left(t\right)\cos\alpha)R\cos\theta\left(t\right) \quad (15)$$

Fig. 11 compares the sensitivity to the number of masses for rigid blocks of the same slenderness $h/b=3$ but different size $R$. As expected for more stocky blocks and large rotations $\theta$ some small error is observed. Moreover, a model with six, or more masses (five and more elements) is sufficient for calculating the seismic response regardless of the block's size.

## 4 NON-LINEAR STATIC ANALYSIS

The different moment-rotation relationships used for modeling the restoring moments are examined through the pushover curves. When a horizontal force acts at the center of the block, the horizontal force-rotation curve for the rocking block (RB) is:

$$F=\frac{mgR\sin(\alpha-\theta)}{Rcos(\alpha-\theta)}\Rightarrow\frac{F}{mg}=\tan(\alpha-\theta) \quad (16)$$

In the models here proposed, the moment-rotation relationship was introduced taking into account the negative stiffness of the rocking block and is equal to:

$$F=\frac{mgR\sin(\alpha-\theta)}{R\cos\alpha\cos\theta}\Rightarrow\frac{F}{mg}=\frac{\sin(\alpha-\theta)}{\cos\alpha\cos\theta}=\tan\alpha-\tan\theta \quad (17)$$

Note that the above expression does not apply to SM2. Figure 12 compares the pushover curves of Equation 16 and 17 for four slenderness values. Overall, the errors observed are small and increase for small $h/b$ values. A similar comparison when a perfectly-plastic moment rotation

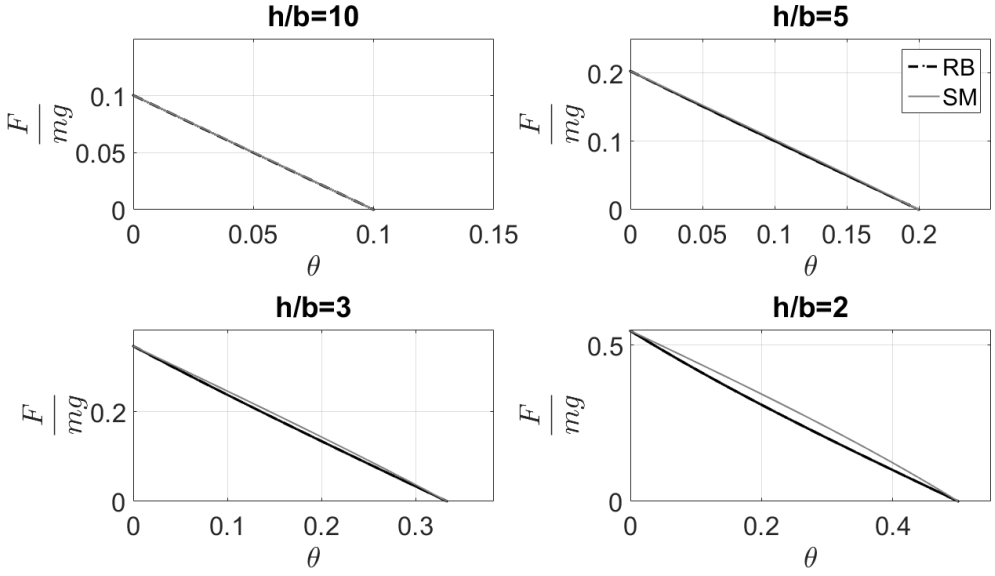


Figure 12: Force-rotation curves for the rocking block (RB) and the spring models (SM).

relationship is combined (Fig. 3c) with second-order effects is shown in Figures 13 and 14. The plots have adopted Equation 18 for SM1 and mmSM and Equation 19 for SM3.

$$F=\frac{mgR(\sin\alpha-\sin\theta)}{R\cos\alpha\cos\theta}\Rightarrow\frac{F}{mg}=\frac{\sin\alpha-\sin\theta}{\cos\alpha\cos\theta}=\frac{\tan\alpha}{\cos\theta}-\frac{\tan\theta}{\cos\alpha} \quad (18)$$

$$F=\frac{mgR(\sin\alpha-\cos\alpha\sin\theta)}{R\cos\alpha\cos\theta}\Rightarrow\frac{F}{mg}=\frac{\sin\alpha-\cos\alpha\sin\theta}{\cos\alpha\cos\theta}=\frac{\tan\alpha}{\cos\theta}-\tan\theta \quad (19)$$

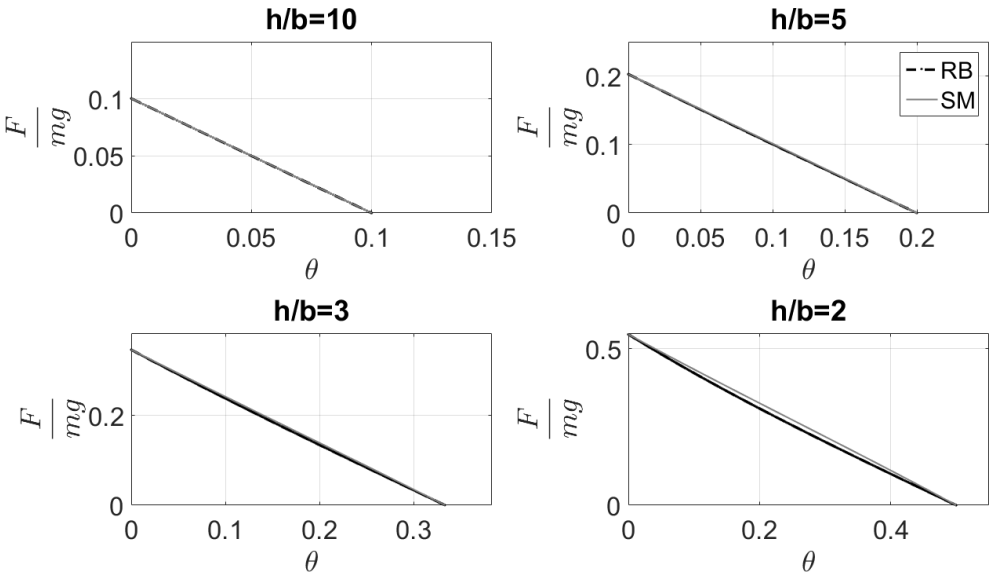


Figure 13: Force-rotation curves for the rocking block (RB) and the SM1 and mmSM.

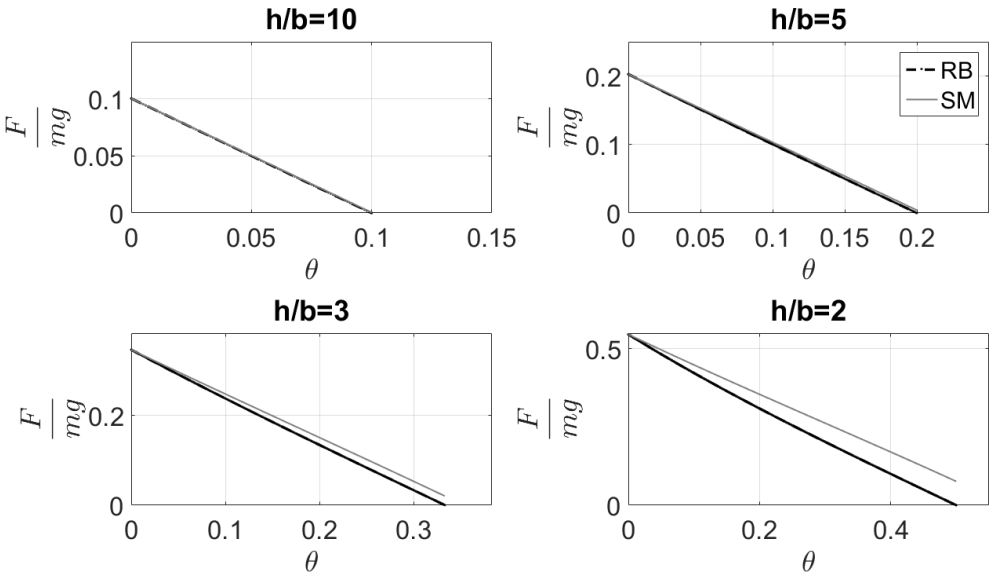


Figure 14: Force-rotation curves for the rocking block (RB) and the SM3.

Figures 13 and 14 show the pushover curves for four different slenderness values. The results are superior for SM1 and mmSM, while for SM3 some small error is observed which becomes more significant for stocky blocks.

It is interesting to also examine overturning moments. The equation of motion of the rocking block and the spring models was obtained from the equilibrium of the restoring and the overturning moment as already discussed. Figure 15 shows the ratio of $M_{ovtn}/(m\ddot{u}_g R)$ and $M'_{ovtn}/(m\ddot{u}_g R)$ for different slenderness values. The models work almost perfectly for slenderness values up to $tan\alpha = 0.2$ $(h/b = 5)$ and small rotations $\theta$.

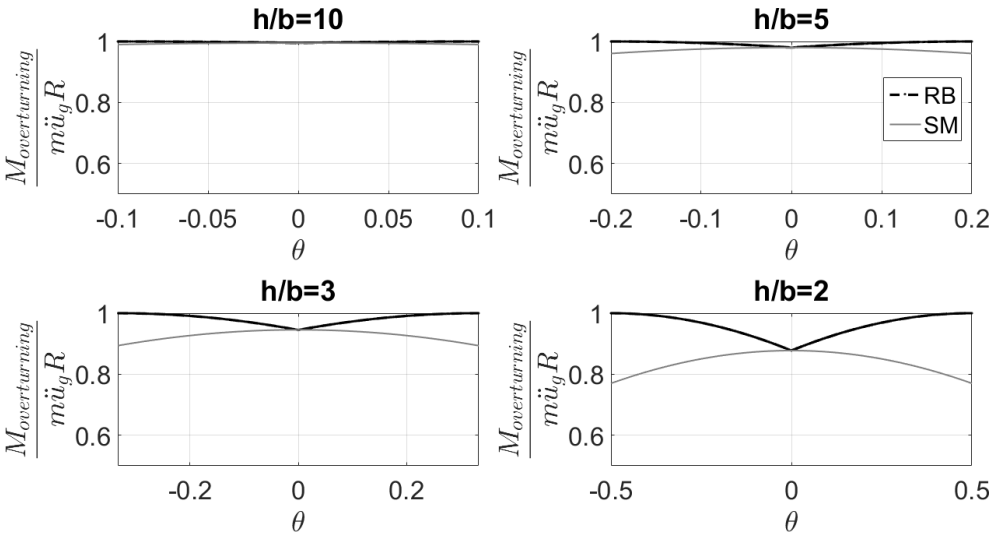


Figure 15: Error of overturning moments predicted by the Spring Models.

## 5 ROCKING ENERGY DISSIPATION

According to Housner [1], rocking bodies dissipate energy when impact occurs. The instant of the impact the sign of rotation is reversed and the block continues rocking with a new pivot point $O'$ [15]. The principle of conservation of angular momentum just before and right after impact implies:

$$I_o\dot{\theta_1} - m\dot{\theta_1}2bR\sin\alpha = I_o\dot{\theta_2} \tag{20}$$

where $\dot{\theta_1}$ and $\dot{\theta_2}$ is the angular velocity before impact and immediately after it, respectively. Simplifying the above relationship, the coefficient of restitution $\eta$ is defined as:

$$\eta = \frac{\dot{\theta_2}}{\dot{\theta_1}} = \frac{I_o - 2mR^2\sin^2\alpha}{I_o} = \left(1 - \frac{3}{2}\sin^2\alpha\right) \tag{21}$$

Therefore, the ratio of the kinetic energy before and after impact is estimated by the restitution factor $r$ as:

$$r = \frac{\frac{1}{2}I_o\dot{\theta_2}^2}{\frac{1}{2}I_o\dot{\theta_1}^2} = \left(1 - \frac{3}{2}\sin^2\alpha\right)^2 = \eta^2 \tag{22}$$

Combining the equation of motion of Eq. 1 with Eq. 21 we can solve the rocking-block problem numerically via a state-space formulation with standard ODE-solvers, as already discussed. This is a form of "event-based" energy dissipation, since energy is dissipated only when an impact ("event") occurs. Assuming that a body is rocking on a rigid surface, the coefficient of restitution that relates the post-impact with the pre-impact angular velocity can be easily introduced in the proposed models by pausing the analysis when impact is detected. The analysis is then resumed using as "initial" velocity of the subsequent time steps the product of the pre-impact angular velocity of every d.o.f. with the coefficient of restitution. The same procedure is repeated for every impact/event until the analysis is completed.

The results obtained with this practice, match perfectly the results obtained after solving directly the block's equation of motion as derived by Housner's theory. Figure 16 shows the

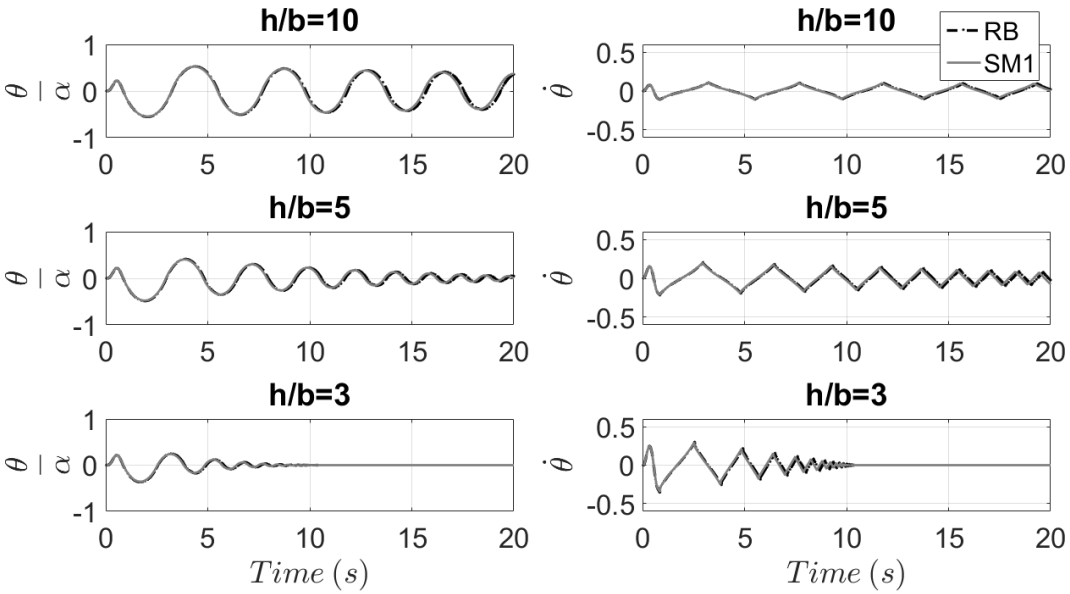


Figure 16: Comparison of rocking rotation and velocity response history between the rocking block (RB) and the event-based damped SM1 model for a block with $R = 5m$ subjected to a sine pulse excitation with $\alpha_p = 3.6g \tan\alpha$ and $\omega_p = 2.66\pi$ rad/s.

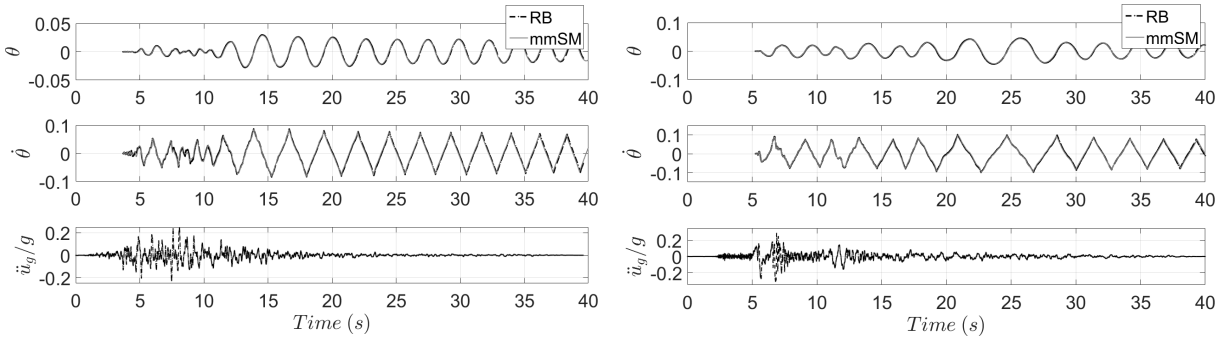


(a) (b)

Figure 17: Comparison of rocking rotation and velocity response history between the rocking block (RB) and the event-based damped mmSM model with six-masses for a block with $R = 5m$ and $\tan\alpha = 0.1$ subjected to (a) Loma Prieta's 1989 earthquake (Station: Anderson Dam Downstream, $\phi = 270^o$, $PGA = 0.235g$) and (b) Imperial Valleys' 1979 earthquake (Station: Cucapah, $\phi = 85^o$, $PGA = 0.309g$).

example of a block for three different $h/b$ values under a pulse-like excitation. Furthermore, Figures 17-19 present examples of blocks with three different $R$ values and two slenderness values subjected to natural records. All analyses confirm that the event-based damping assumption works perfectly and that the proposed FE models can assess the seismic response of a rigid rocking block on a rigid surface.

## 6 FLEXIBLE BLOCKS

Current research aims to model real structures made of concrete or other materials that are designed to resist seismic loading though rocking. Having studied thoroughly the rocking response of rigid structures, we extend the implementation to the case of flexible blocks. The effect of flexibility is significant when either the ratio $E/\rho g$ is small, or when the size parameter $R$ of the block is large enough. This is better understood from the expression for the first

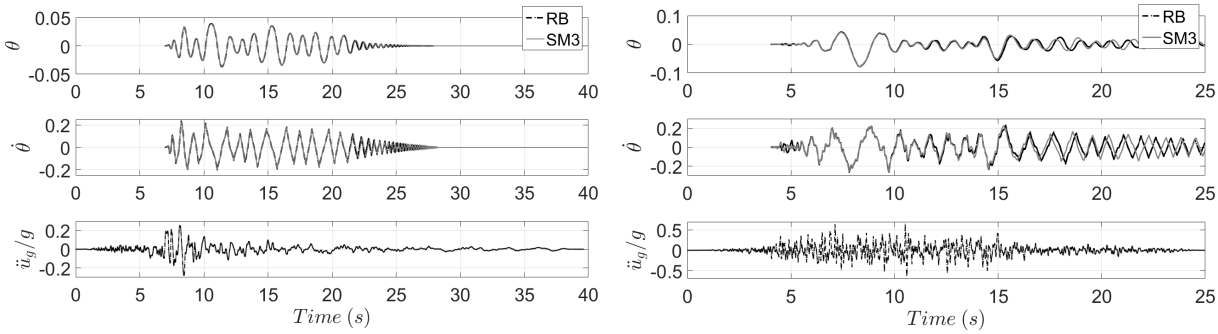


(a) (b)

Figure 18: Comparison of rocking rotation and velocity response history between the rocking block (RB) and the event-based damped SM3 model for a block with $R = 2m$ and $\tan\alpha = 1/6$ subjected to Loma Prieta's 1989 earthquake. (a) Station: Hollister Diff Array, $\phi = 255$, $PGA = 0.279g$ and (b) Station: Waho, $\phi = 90^o$, $PGA = 0.638g$.

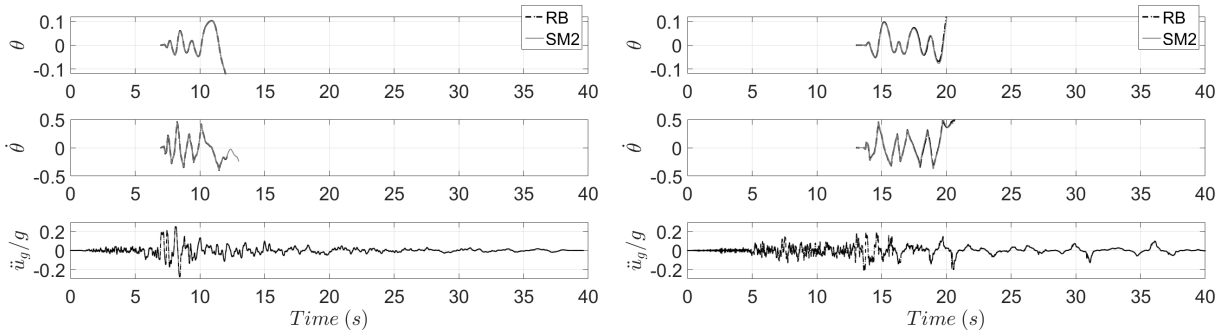


(a) (b)

Figure 19: Comparison of rocking rotation and velocity response history between the rocking block (RB) and the event-based damped SM2 model for a block with $R = 1m$ and $\tan\alpha = 1/6$ subjected to (a) Loma Prieta's 1989 earthquake (Station: Hollister Diff Array, $\phi = 255$, $PGA = 0.279g$) and (b) Superstition Hills' 1987 earthquake (Station: Wildlife Liquefaction Array, $\phi = 360^o$, $PGA = 0.20g$).

eigenperiod of flexible homogeneous rectangular blocks [4]:

$$T_1 = 12.38\sqrt{\frac{\rho}{E}}\frac{h}{\tan\alpha} \tag{23}$$

Flexibility increases the overturning acceleration due to the transformation of the rotational kinetic energy to bending vibrations at each rocking impact. Below we study the mmSM model for the modeling of flexible rocking blocks (FRB). For the case studies considered, the are made of concrete and have $E = 30GPa$ and $\rho = 2.5Mg/m^3$.

Figure 20 shows the response when the block is subjected to a sine pulse, while Figure 21 shows the response when a natural record is imposed (no damping). The flexible block was also modeled with a full mesh of quadrilateral elements in Abaqus [16]. The estimate of the top displacement of the column $u_{top} = u\cos\alpha$ is compared in Figures 20a and 21a. Figures 20b and 21b plot the top displacement of the column due to bending, $w_{top} = u_{top} - 2R\cos\alpha\sin\theta$, obtained as the difference between the total top displacement and the top displacement due to base rotation (similar to that of a rigid body). We observe that the effect of column flexibility is not significant for solitary blocks up to 30m tall, as already discussed in reference [4]. To confirm this, a rigid and a flexible block are compared in Figures 22 and 23 for different $R$ and $\alpha$ values.

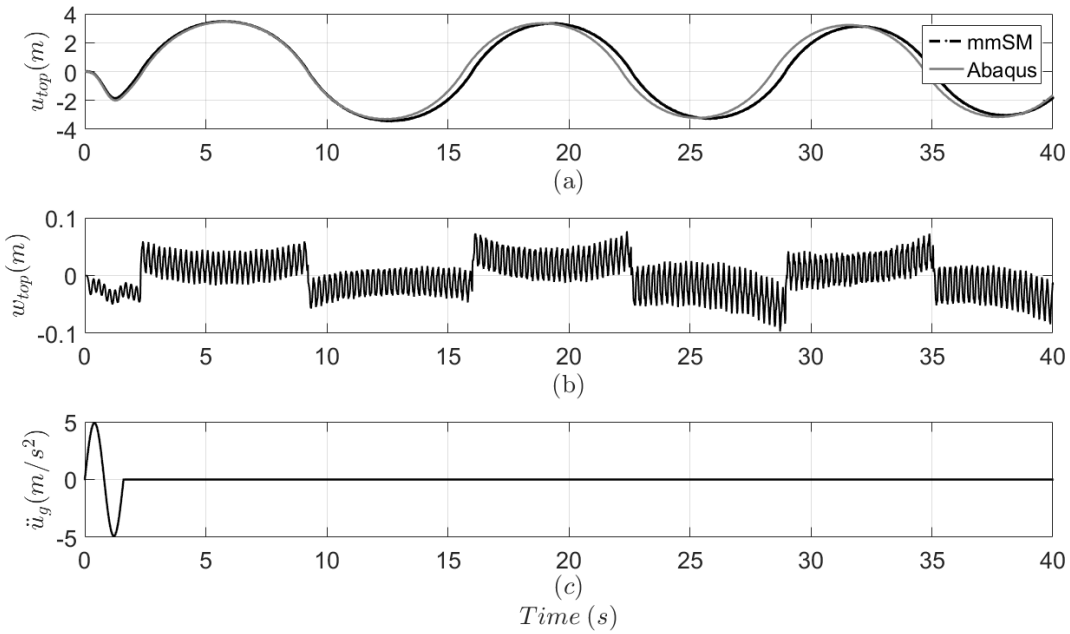


Figure 20: (a) Comparison of top displacement time history response between a flexible rocking block with $2h = 50m$ and $\tan\alpha = 0.1$ modeled in Abaqus and the proposed mmSM with six masses, (b) top displacement due to bending, and (c) the sine pulse excitation with $T_p = 1.6sec$ and $a_p = 5g\tan\alpha = 4.905m/sec^2$.

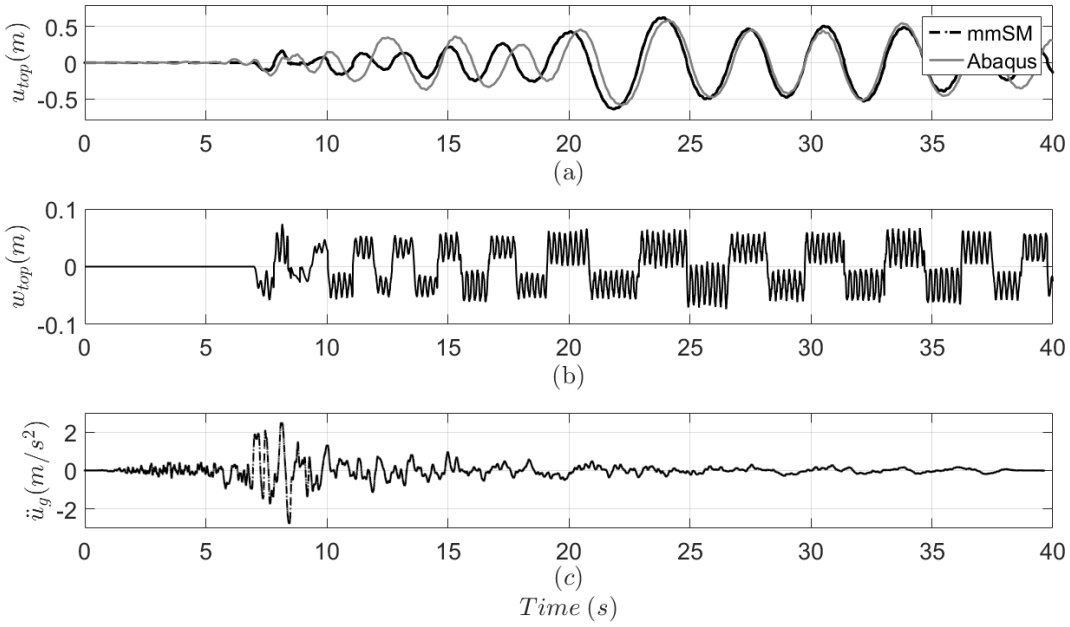


Figure 21: (a) Comparison of top displacement time history response between a flexible rocking block with $2h = 50m$ and $\tan\alpha = 0.1$ modeled in Abaqus and the proposed mmSM with six masses, (b) top displacement due to bending, and (c) the Loma Prieta's 1989 earthquake (Station: Hollister Diff Array, $\phi = 255^o$, $PGA = 0.279g$).

In Figures 22 and 23 we show the results of event-based damping using the coefficient of restitution obtained from Equation 21. Furthermore, Rayleigh damping is also applied on the flexible column using a damping ratio of $\zeta = 0.01$. We have chosen to apply only some minor damping since most of the energy dissipation is due to rocking. The first row of Figure 22

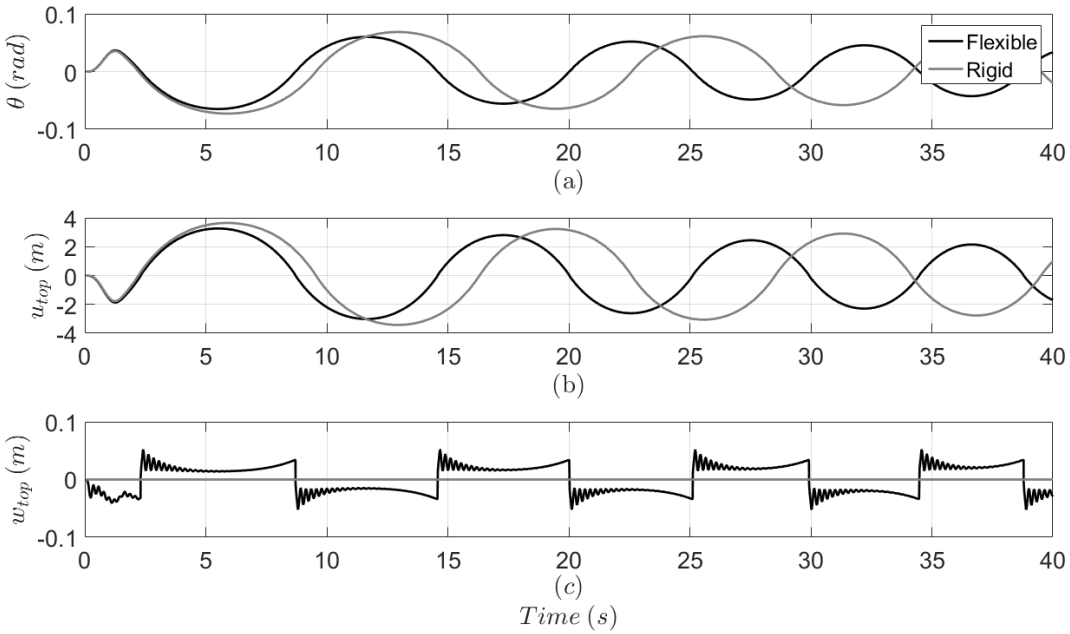


Figure 22: Comparison of (a) rotation, (b) top displacement and (c) top displacement due to bending time history response between a flexible and a rigid block with $2h = 50m$ and $\tan\alpha = 0.1$ subjected to a sine pulse excitation with $T_p = 1.6sec$ and $a_p = 5g\tan\alpha = 4.905m/sec^2$.

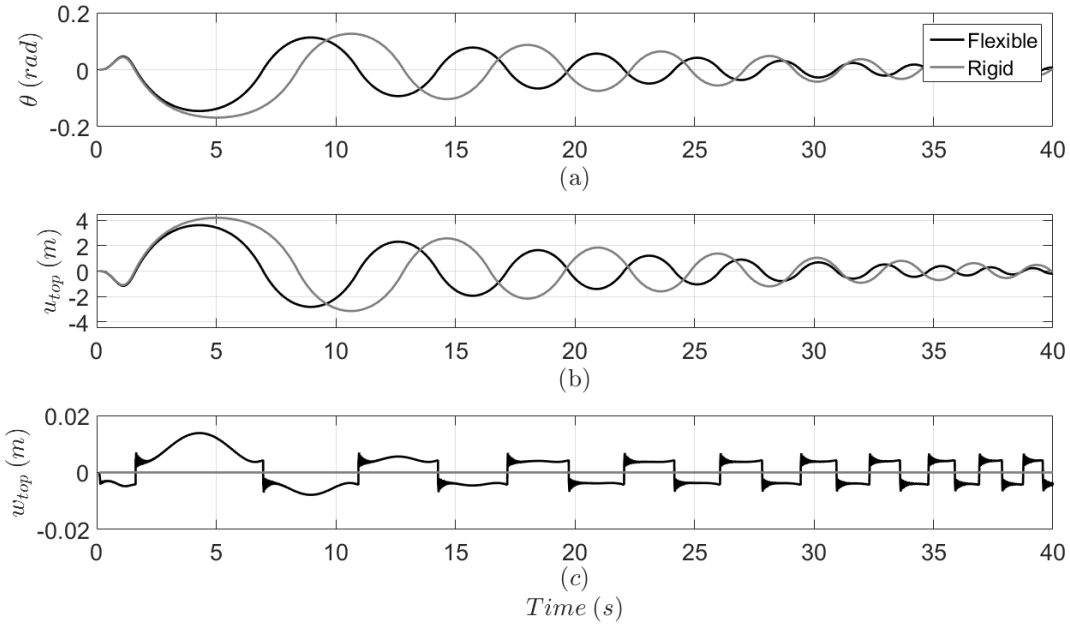


Figure 23: Comparison of (a) rotation, (b) top displacement and (c) top displacement due to bending time history response between a flexible and a rigid block with $2h = 25m$ and $\tan\alpha = 0.2$ subjected to a sine pulse excitation with $T_p = 1.6sec$ and $a_p = 2.7g\tan\alpha = 5.297m/sec^2$.

and 23 plot the rotation at the base of the column, the second row show the top displacement and the third row the top displacement due to bending. Top displacement due to bending is indeed negligible compared to the total displacement of the top (Fig. 23c) and for a block with $2h = 25m$. However, this may differ if a different seismic record is considered.

## 7 CONCLUSIONS

Different simple spring models for the analysis of rigid or flexible rocking bodies are considered. The models are first verified against the numerical solution of Housner's theory for a solitary rigid rocking block and the results were excellent. The response of flexible blocks were then examined and verified against the results of Abaqus. The seismic response assessment of rigid and flexible blocks led to the conclusions below:

- The rocking problem can be solved with single-degree-of-freedom finite element models based on beam-column elements connected to a zero-length elastic rotational spring.
- We have examined three different moment-rotation relationships and we studied their performance on different FE models.
- The primary source of error between the rocking block and the models is in the term of the overturning moment. The errors are acceptable and the models produce results almost identical to those of solving directly the block's equation of motion.
- A second goal is the assessment of the seismic response of flexible rocking blocks. A six-mass spring model was tested against the response obtained if the block was modeled with a full mesh of quadrilateral elements in Abaqus. The proposed model produced accurate results within a fraction of the required CPU time.
- "Event-based" damping is proposed as the safest and most accurate way to model energy dissipation for both rigid and flexible rocking systems.

## 8 ACKNOWLEDGEMENTS

The financial support provided by the European Research Council Advanced Grant "MASTER Mastering the computational challenges in numerical modelling and optimum design of CNT reinforced composites" (ERC-2011-ADG 20110209) is gratefully acknowledged.

## REFERENCES

[1] G.W. Housner, The behavior of inverted pendulum structures during earthquakes. *Bulletin of the Seismological Society of America*, **53(2)**, 404–417, 1963.

[2] N. Makris, D. Konstantinidis, The rocking spectrum and the limitations of practical design methologies. *Earthquake Engineering and Structural Dynamics*, **32**, 265–289, 2003.

[3] J. Milne, Seismic Experiments. *Transactions of the Seismological Society of Japan*, **8**, 1–82, 1885.

[4] M.F. Vassiliou, K.R. Mackie, B. Stojadinović, Dynamic response analysis of solitary flexible rocking bodies: modeling and behavior under pulse-like ground excitation. *Earthquake Engineering and Structural Dynamics*, **46(3)**, 447–466, 2016.

[5] M.F. Vassiliou, K.R. Mackie, B. Stojadinović, A finite element model for seismic response analysis of deformable rocking frames. *Earthquake Engineering and Structural Dynamics*, **43(10)**, 1463–1481, 2014.

[6] I.N. Psycharis, Dynamics of flexible systems with partial lift-off. *Earthquake Engineering and Structural Dynamics*, **11(4)**, 501–521, 1983.

[7] M. Apostolou, G. Gazetas, E. Garini, Seismic response of slender rigid structures with foundation uplifting. *Soil Dynamics and Earthquake Engineering*, **27(7)**, 642–654, 2007.

[8] S. Acikgoz, M.J. Dejong, The interaction of elasticity and rocking in flexible structures allowed to uplift. *Earthquake Engineering and Structural Dynamics*, **41(15)**, 2177–2194, 2012.

[9] A.K. Chopra, F. McKenna, Modeling viscous damping in nonlinear response history analysis of buildings for earthquake excitation. *Earthquake Engineering and Structural Dynamics*, **45(2)**, 193–211, 2016.

[10] C.S. Yim A. K. Chopra, J. Penzien, Rocking Response of Rigid Blocks to Earthquakes. *Earthquake Engineering and Structural Dynamics*, **8**, 565–587, 1980.

[11] M.J. DeJong, E.G. Dimitrakopoulos, Dynamically equivalent rocking structures. *Earthquake Engineering and Structural Dynamics*, **43**, 1543–1563, 2014.

[12] E.G. Dimitrakopoulos, M.J. DeJong, Revisting the rocking block: closed-form solutions and similarity laws. *Proceedings of the Royal Society of London A: Mathematical, Physical and Engineering Sciences*, 468, 2012.

[13] Matlab Version 2015b. The Language of Technical Computing.

[14] OpenSEES (Open System for Earthquake Engineering Simulations). opensees.berkeley.edu

[15] J. Zhang, N. Makris, Rocking response of free-standing blocks under cycloidal pulses. *Journal of Engineering Mechanics, ASCE*, **127(5)**, 473–483, 2001.

[16] Abaqus, Version 6.14, SIMULIA (ABAQUS Inc., Providence, USA).

COMPDYN 2017
6th ECCOMAS Thematic Conference on
Computational Methods in Structural Dynamics and Earthquake Engineering
M. Papadrakakis, M. Fragiadakis (eds.)
Rhodes Island, Greece, 15–17 June 2017

# DYNAMIC RESPONSE OF A RIGID SLAB SUPPORTED BY FOUR RIGID CYLINRICAL ROCKING AND WOBBLING COLUMNS

**Sharveen Rajah[1], Jonas A. Bachmann[2], Michalis F. Vassiliou[2], and Bozidar Stojadinovic[2]**

[1] Chair of Structural Dynamics and Earthquake Engineering, Institute of Structural Analysis, Swiss Federal Institute of Technology (ETH) Zurich, Stefano-Franscini-Platz 5, 8093 Zürich Switzerland
e-mail: srajah@student.ethz.ch

[2] Chair of Structural Dynamics and Earthquake Engineering, Institute of Structural Analysis, Swiss Federal Institute of Technology (ETH), Zurich Stefano-Franscini-Platz 5, 8093 Zürich Switzerland
{bachmann, vassiliou, stojadinovic}@ibk.baug.ethz.ch

**Keywords:** Earthquake Engineering, Rocking, Uplifting Structures, Wobbling, Bridges

**Abstract.** *Letting columns uplift has been proposed as an earthquake response modification strategy for bridges and other large structures. Uplift could be allowed along solely one direction of the structure or along both directions. In order for the latter approach to be implemented, the 3d behavior of systems allowed to uplift, rock and wobble should be studied. This paper studies the dynamic response of a rigid slab supported on 4 rigid cylindrical rocking and wobbling columns. The columns are constrained not to roll out of their initial position, which is a necessity for the system to be resilient. This system is the simplest 3d extension of the 2d rocking frame system.*

*The equations of motion are derived analytically and directly numerically integrated. Since the system has only 2DOFs it is computationally inexpensive and allows for extensive parametric analysis. Similar to the 2d rocking frame, it is found that the addition of the slab makes the investigated frame more stable than the individual columns.*

## 1 INTRODUCTION

According to the US Department of Transportation Federal Highway administration, "*Accelerated Bridge Construction (ABC) is bridge construction that uses innovative planning, design, materials, and construction methods in a safe and cost-effective manner to reduce the onsite construction time that occurs when building new bridges or replacing and rehabilitating existing bridges"*. In this context researchers [1-10] have developed concepts were precast elements are connected via ungrouted tendons and extra elements that work as dampers. The connections are dry, minimizing the on-site construction time.

The precast bridges could be allowed to uplift and rock freely (i.e. without tendons) taking advantage of the well- studied dynamic behavior of rocking structures. Indeed, a simple free-standing rocking block has been systematically studied for more than five decades both when the block is assumed rigid [11-26] and when it assumed deformable [27-37]. Small scale experiments have been also performed [38-51]. It has been proven that structures that rock in-plane (2d rocking) have remarkable dynamic stability. The uplift works as a mechanical fuse and limits the structure and the foundation design forces. Moreover, if the ends of the columns are protected, energy dissipation during rocking motion happens instantaneously when the column impacts the ground. After the ground motion excitation, structures with rocking columns return to their original, undeformed, position (if they do not overturn, i.e. collapse), without a residual displacement that inevitably occurs in a yielding fixed-base cantilever-like structures. This dynamic property of rocking structures contributes very significantly to improving their seismic performance for downtime and repair cost performance objectives. This behavior, as well as the survival of ancient Greek and Roman temples (that are essentially rocking structures) in high seismicity areas [52-55] has led researchers to suggest the use of rocking as a seismic response modification technique [56-68].

Even though there is a plethora of papers that study planar rocking as a seismic response modification strategy, it is only recently that the free (i.e. not constrained by tendons) 3d rocking motion was studied in the context of rocking structures [69, 70] (and not of the protection of equipment [71-76]). The main difference between the unintentional rocking for equipment protection and intentional structural column rocking, is that structures need to return to their original position. Therefore, their columns should not be allowed to roll out or strep out of their original position. There is recently published work on how to enforce that constraint in construction [10], and more ideas (such as a recess) that could be experimentally tested. This paper focuses on the development of a rocking model that can adequately describe the motion of a slab supported on 4 cylindrical columns allowed to uplift, rock and wobble, but not roll out of their original position. It hinges upon the recently published work that describes the motion of a rocking and wobbling rigid cylindrical solitary column [69, 70]. It can be seen as the simplest 3d extension of the rocking frame described in [60, 61].

## 2 REVIEW OF IN-PLANE ROCKING SOLITARY COLUMN AND FRAME MODELS

The equation of in-plane motion for a rigid rectangular rocking column (Figure 1) with slenderness $\alpha$ and a semi-diagonal of length $R$ is:

$$\ddot{\theta} = -p^2 \cdot \left( \sin\left[\pm\alpha - \theta\right] + \frac{\ddot{u}_g}{g} \cos\left[\pm\alpha - \theta\right] \right) \tag{1}$$

where

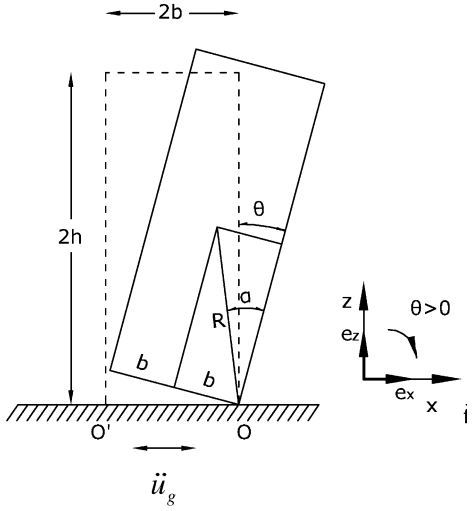


Figure 1. Geometric characteristics of the planar rigid rocking column.

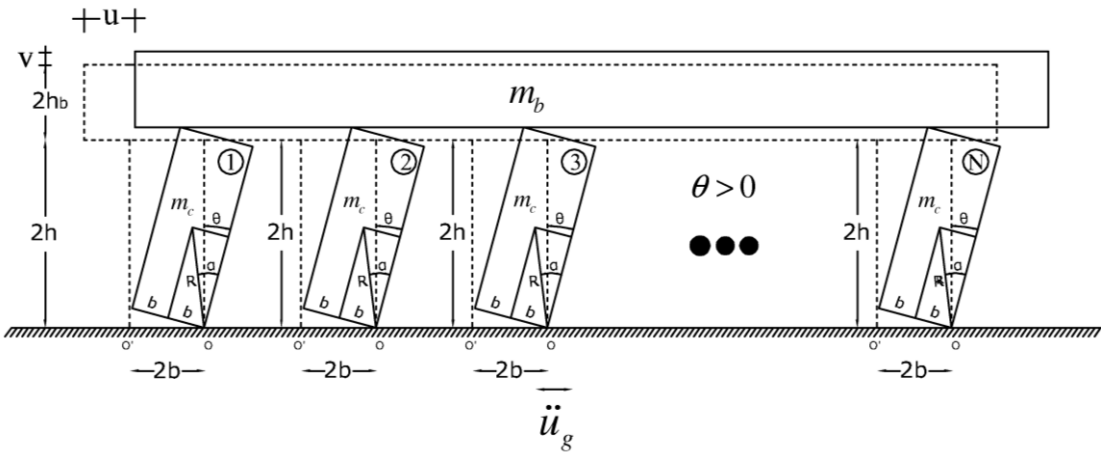


Figure 2. Geometric characteristics of the planar rigid rocking frame

$$p = \sqrt{(3g)/(4R)} \tag{2}$$

is the frequency parameter of the rocking column. The upper sign in front of $\alpha$ corresponds to a positive, and the lower to a negative rocking angle $\alpha$ with respect to the defined coordinate system (Figure 1).

Makris and Vassiliou [60] extended the rocking model of a solitary rigid rectangular column to a rocking frame comprised of a number of rigid columns capped by a rigid beam (Figure 2). Uplift of the columns is not restrained, but their sliding on the rocking surface is precluded. The corresponding equation of motion becomes:

$$\ddot{\theta} = -\hat{p}^2 \cdot \left( \sin\left[\pm\alpha - \theta\right] + \frac{\ddot{u}_g}{g} \cos\left[\pm\alpha - \theta\right] \right) \tag{3}$$

where the frequency parameter of the rocking frame is:

$$\hat{p} = \sqrt{\frac{1+2\gamma}{1+3\gamma}} \cdot \sqrt{\frac{3g}{4R}} \tag{4}$$

and $\gamma$ is the mass ratio of the mass of the cap beam divided by the mass of all $N$ columns:

$$\gamma = \frac{m_b}{Nm_c} \tag{5}$$

Since the frequency parameter of the rocking frame $\hat{p}$ (Equation 4) is smaller than the frequency parameter of a solitary column $p$, a comparison of Equations (1) and (3) shows that the response (tilt angle $\theta$) of the rocking frame is smaller than the response of the solitary column. As the mass of the cap beam increases, the mass ratio $\gamma$ increases, the frequency parameter $\hat{p}$ decreases, leading to a conclusion that rocking frames become more stable as the cap beam becomes more massive.

The response of the rocking frame is equal to the response of an equivalent solitary column which is geometrically similar to, yet larger than the columns of the frame. The size of the equivalent solitary rocking column is:

$$\hat{R} = \frac{1+3\gamma}{1+2\gamma} R \tag{6}$$

## 3 REVIEW OF THE SOLITARY COLUMN 3D ROCKING AND WOBBLING MODEL

Very recently, a 3d dynamic model of a rocking and wobbling rigid cylindrical column was presented [69, 70]. This model fulfills the constraint that the column should not roll out of its original position (Figures 4 and 5). The cylindrical column has a total mass $m$, base radius $b$ and height $2h$. Its semidiagonal is $R$ and its slenderness is $\alpha$ ($\tan\alpha = b/h$). The assumptions are:

a) The cylinder is considered rigid and homogeneous.
b) The supporting plane surface (ground) is considered rigid.
c) The contact between the cylinder and the ground is pointwise.
d) The cylinder is constrained not to roll-out of its initial position.
e) No sliding is allowed, i.e. the friction between the cylinder and the supporting plane surface is large.
f) The cylinder is always in contact with the support (i.e. it never flies). Therefore, the contact force is always compressive.
g) No damping mechanism is included. In [70] it is shown that damping has little influence on the seismic response of rocking and wobbling cylinders.

Given the above assumptions, the model has only two degrees of freedom: the tilt angle, $\theta$, and the rolling angle, $\varphi$. The latter determines the location of the contact point between the cylinder and the supporting plane (Figure 5).

The equations of motion of the model are:

$$\begin{aligned}\ddot{\theta} = &-p^2\left(\sin(\alpha-\theta)+\cos(\alpha-\theta)\left(\cos\varphi\cdot\frac{\ddot{u}_{gx}}{g}+\sin\varphi\cdot\frac{\ddot{u}_{gy}}{g}\right)\right)\\ &-\left(\begin{array}{l}\left(\dfrac{15\sin^2\alpha-16\cos^2\alpha}{12}\right)\cdot\cos\theta\cdot\sin\theta-\dfrac{3}{2}\sin^2\alpha\cdot\sin\theta-\\ -\cos\alpha\cdot\sin\alpha\cdot(1+\cos\theta)+2\cos\alpha\cdot\sin\alpha\cdot\cos^2\theta\end{array}\right)\cdot\frac{1}{\left(\dfrac{5}{4}+\dfrac{1}{12}\cos^2\alpha\right)}\dot{\varphi}^2\end{aligned} \tag{7}$$

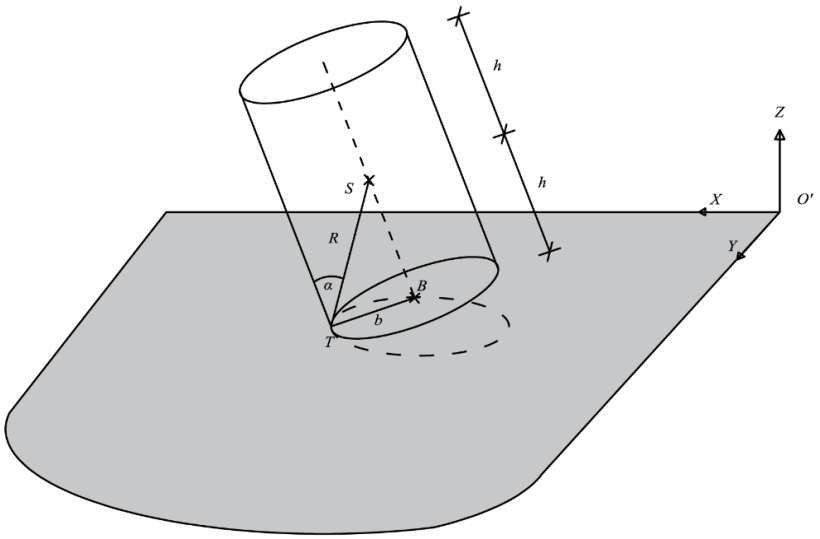


Figure.4 Geometry of the model: a rigid cylinder is allowed to uplift and wobble but is constrained not to roll-out of its original base.

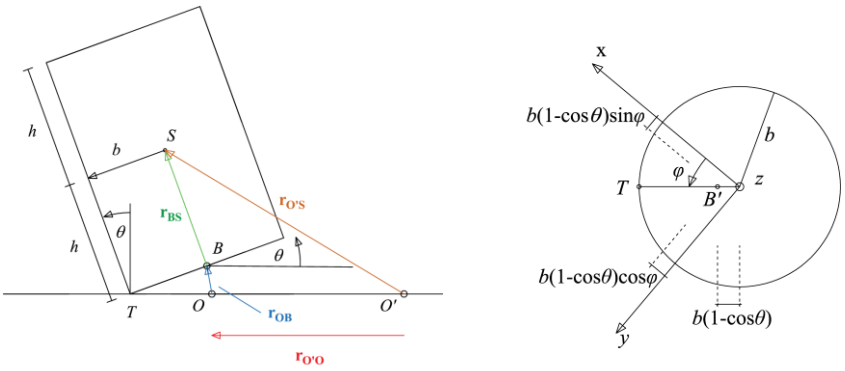


Figure 5 Left: Elevation passing through the center of mass of the rigid cylinder, S, and its contact point with the ground T, the pivot point; Right: Plan view: the circle is the original configuration of the cylinder and point B´ is the vertical projection of point B on the ground.

$$\left(\frac{1}{12}\left(-15\sin^2\alpha+16\cos^2 a\right)\cdot\sin^2\theta+3\sin^2 a\left(1-\cos\theta\right)+2\sin\alpha\cos\alpha\sin\theta\cdot\left(1-\cos\theta\right)\right)R\cdot\ddot{\varphi}+$$
$$\left(3\sin^2\alpha\sin\theta+\frac{1}{6}\left(-15\sin^2\alpha+16\cos^2\alpha\right)\sin\theta\cos\theta+2\cos\alpha\sin\alpha\left(2\sin^2\theta+\cos\theta-1\right)\right)R\cdot\dot{\varphi}\cdot\dot{\theta}= \quad (8)$$
$$=\left(\sin\alpha+\sin\left(\theta-\alpha\right)\right)\left(\ddot{u}_{gx}\sin\varphi-\ddot{u}_{gy}\cos\varphi\right)$$

where $p$ is the well-known frequency parameter used in the dynamic model of the 2d rocking block, here associated with the tilting motion of the cylinder:

$$p^2=\frac{mgR}{I_o}=\frac{12}{15+\cos^2\alpha}\frac{g}{R} \quad (9)$$

and:

$$R=\sqrt{h^2+b^2} \quad (10)$$

## 4 DESCRIPTION OF THE PROPOSED 3D MODEL

The proposed model extends the planar rocking frame model into the third dimension by adding a slab on top of 4 rocking and wobbling columns, as shown in Figure 6.

The slab has 3 degrees of freedom that correspond to the in plane rigid body horizontal translations and rotation about the slab vertical axis (yaw). The translation along the vertical direction and the pitch and roll of the slab are coupled with these three DOFs. Yaw is the extra DOF compared to rocking and wobbling solitary column model. Only pure torsion could be modeled within the scope of the proposed model, but this is not explored in this paper. As all model elements are assumed to be rigid, yaw coupled with horizontal translations would cause displacement incompatibility. However, yaw of the slab is not expected: the centers of mass and rigidity of the slab coincide because the re-centering force of every column is directly proportional to its bearing load. This phenomenon is not new: it appears in the case of the concave isolation bearings [79, 80]. Therefore, the yaw DOF is disregarded and it is expected that all columns under the slab undergo identical motion governed by the two horizontal translation DOFs of the slab.

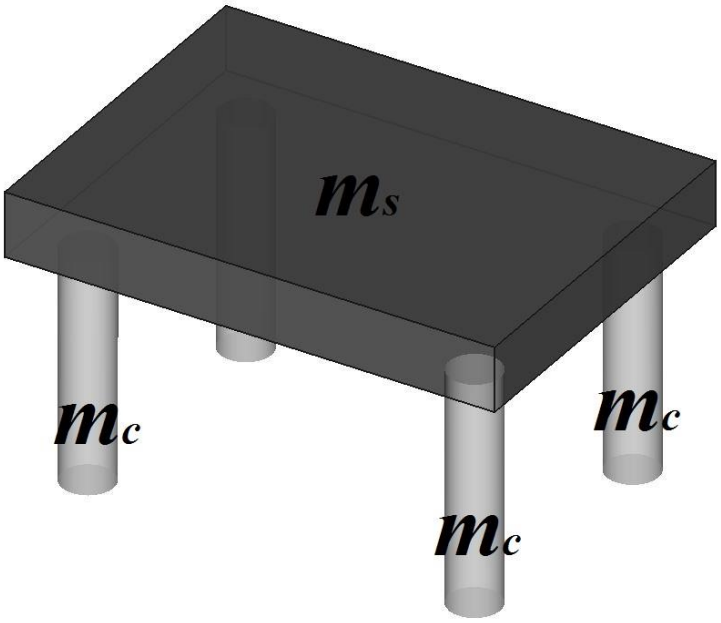


Figure 6. Rigid slab supported by four columns. The columns are allowed to uplift, rock and wobble, but not roll out of their original position..

Based on the assumption presented in section 3, the equations of motion of the system are:

$$\ddot{\theta} = -\hat{p}^2\left(\sin(\alpha-\theta)+\cos(\alpha-\theta)\left(\frac{\ddot{u}_g}{g}\cos\varphi+\frac{\ddot{v}_g}{g}\sin\varphi\right)\right)+$$
$$+\dot{\varphi}^2\left(\begin{array}{l}\sin\theta\sin^2\alpha\left(4\gamma+\frac{3}{2}\right)+\cos\alpha\sin\alpha(4\gamma+1)(1+\cos\theta-2\cos^2\theta)+\\ \sin\theta\cos\theta\left(\frac{4}{3}\cos^2\alpha-\frac{5}{4}\sin^2\alpha+4\gamma(\cos^2\alpha-\sin^2\alpha)\right)\end{array}\right)\frac{12}{48\gamma+15+\cos^2 a} \quad (11)$$

$$\left(\begin{array}{l}\left(\left(\frac{4}{3}\cos^2 a-\frac{5}{4}\sin^2\alpha+4\gamma\left(\cos^2\alpha-\sin^2\alpha\right)\right)\cdot\sin^2\theta+\\ (3+8\gamma)(1-\cos\theta)+2\sin\alpha\cos\alpha\sin\theta(1+4\gamma)\cdot(1-\cos\theta)\end{array}\right)\cdot\ddot{\varphi}+\right.$$

$$+\left(\begin{array}{l}(3+8\gamma)\sin^2\alpha\sin\theta+\left(\frac{8}{3}\cos^2\alpha-\frac{5}{2}\sin^2\alpha+8\gamma\left(\cos^2\alpha-\sin^2\alpha\right)\right)\sin\theta\cos\theta\\ +2\cos\alpha\sin\alpha(1+4\gamma)\left(2\sin^2\theta+\cos\theta-1\right)\end{array}\right)\cdot\dot{\varphi}\cdot\dot{\theta}= \tag{12}$$

$$=(2\gamma+1)\left(\sin\alpha-\sin(\theta-\alpha)\right)\frac{\left(\ddot{u}_{gx}\sin\varphi-\ddot{u}_{gy}\cos\varphi\right)}{R}$$

where

$$\hat{p}^2=\frac{12(2\gamma+1)}{48\gamma+15+\cos^2\alpha}\frac{g}{R} \tag{13}$$

and

$$\gamma=\frac{m_s}{4m_c} \tag{13}$$

For $\gamma = 0$ the equations yield the solitary rocking and wobbling rigid cylindrical column equations derived in [70]. It can also be seen that, unlike the case of a planar rocking frame, for which there is a formal and elegant equivalence with a geometrically similar, yet larger, column, in the 3d case there is no "equivalent solitary 3d column". However, if one keeps only the linear term of equations (7) and (11) the size of a quasi-equivalent solitary 3d column is:

$$\hat{R}=\frac{48\gamma+15+\cos^2\alpha}{(2\gamma+1)\left(15+\cos^2\alpha\right)}R \tag{14}$$

For slender columns (small $\alpha$) and for top heavy structures (large $\gamma$) $\hat{R}\to 1.5R$ (Figure 7), like in the case of the planar rocking frame [60, 61].

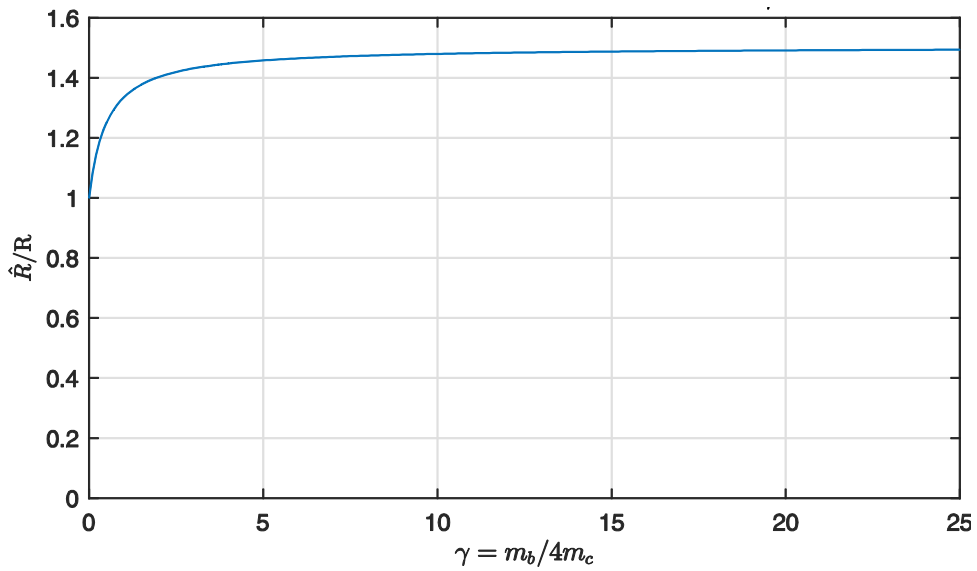


Figure 7 Equivalent solitary 3d column size as a function of mass ration $\gamma$.

## 5 RESPONSE TO GROUND MOTIONS

Figures 8 and 9 plot the time history response of a 3d slab-column system with column semidiagonal $R$=5m, column slenderness $\alpha$ = 0.2rad, and mass ratio $\gamma$ = 10 to the El Centro Array #9 (1940) and the Takatori, Kobe (1995) ground motions. When excited by the El Centro ground motion, the system uplifts and sustains wobbling motion without overturning. The Takatori ground motion overturns the system.

The same behavior as for the case of a solitary 3d column is observed: there are no pure impacts. The tilt angle $\theta$ takes values close to zero only during the first 5s of the response to the El Centro ground motion. During this time, "quasi-impacts" occur: there is a rapid change of the position of the contact point that results in spikes in column spin velocity $\dot{\varphi}$ [70].

## 6 ROCKING SPECTRA

In order to gain insight into the stability of the 3d slab-column system with different column sizes under earthquake ground motion excitation, rocking response spectra are constructed by scaling the two above mentioned ground motions. Figures 10 (a-c and e-g) plot the overturning spectra for El Centro ground motion (i.e. contour plots of maximum tilt angle, $\theta$), for a given column semidiagonal $R$ (on the abscissa), column slendernees $\alpha$=0.2 and mass ratios $\gamma$ = 1, 2 and 3. The ordinate defines the normalized peak ground acceleration, PGA/gtanα where PGA = $\max\left(\sqrt{u_{gx}{}^2 + u_{gy}{}^2}\right)$. Figures 10 (d and h) plot the minimum acceleration required to overturn a block of size $R$. Both components of the ground motion records were scaled equally. To overturn large size columns, large scaling factors were needed. Such large scaling of a single recorded ground motion is not ideal as it may produce ground motions with unrealistic properties. Nevertheless, the present pilot study adopts this scaling model.

The stability characteristic of rocking structures, that, for a given slenderness, larger structures are harder to overturn, holds for 3d slab-column systems. As in the case of the planar rocking frame, the addition of a slab on top of the columns increases their stability. Furthermore, the heavier the slab, the more stable the system. Moreover, even though there is no formal "equivalent column" as there is for planar rocking frames, the minimum acceleration spectra (Figure 10 d and g) for the 3d slab-column system have a similar form.

Figure 11 plots the overturning acceleration spectra when the equivalent size, $\hat{R}$, defined by equation (14) is used: different plots collapse to essentially one line. Therefore, even if an equivalence between the 3d slab-column system and a larger, yet geometrically similar, solitary column does not emerge naturally from the equations of motion (as it does for the planar rocking frame), numerical results show that such an equivalency does exist. Therefore, it can be stated that the response of a rigid slab supported by rigid cylindrical columns allowed to uplift and wobble can be approximated by the response of a solitary rigid cylindrical column, with same aspect ratio, yet larger size. The size of the equivalent column is given by equation (14). Since, the slab is expected to be much heavier than the columns, the mass ratio will be large and, based on Figure 7, one can state that the equivalent column is 1.5 times larger than the columns of the 3d slab-column system.

## 7 CONCLUSIONS

A model describing the motion of a rigid slab supported by 4 rigid cylindrical rocking and wobbling columns is developed and presented. Rocking spectra for 2 recorded ground motions are presented. It is shown that the addition of the slab increases the overturning stability of the columns. The dynamic behavior of the 3d slab-columns system is equivalent to a column of equal slenderness, yet larger in size than the individual system columns.

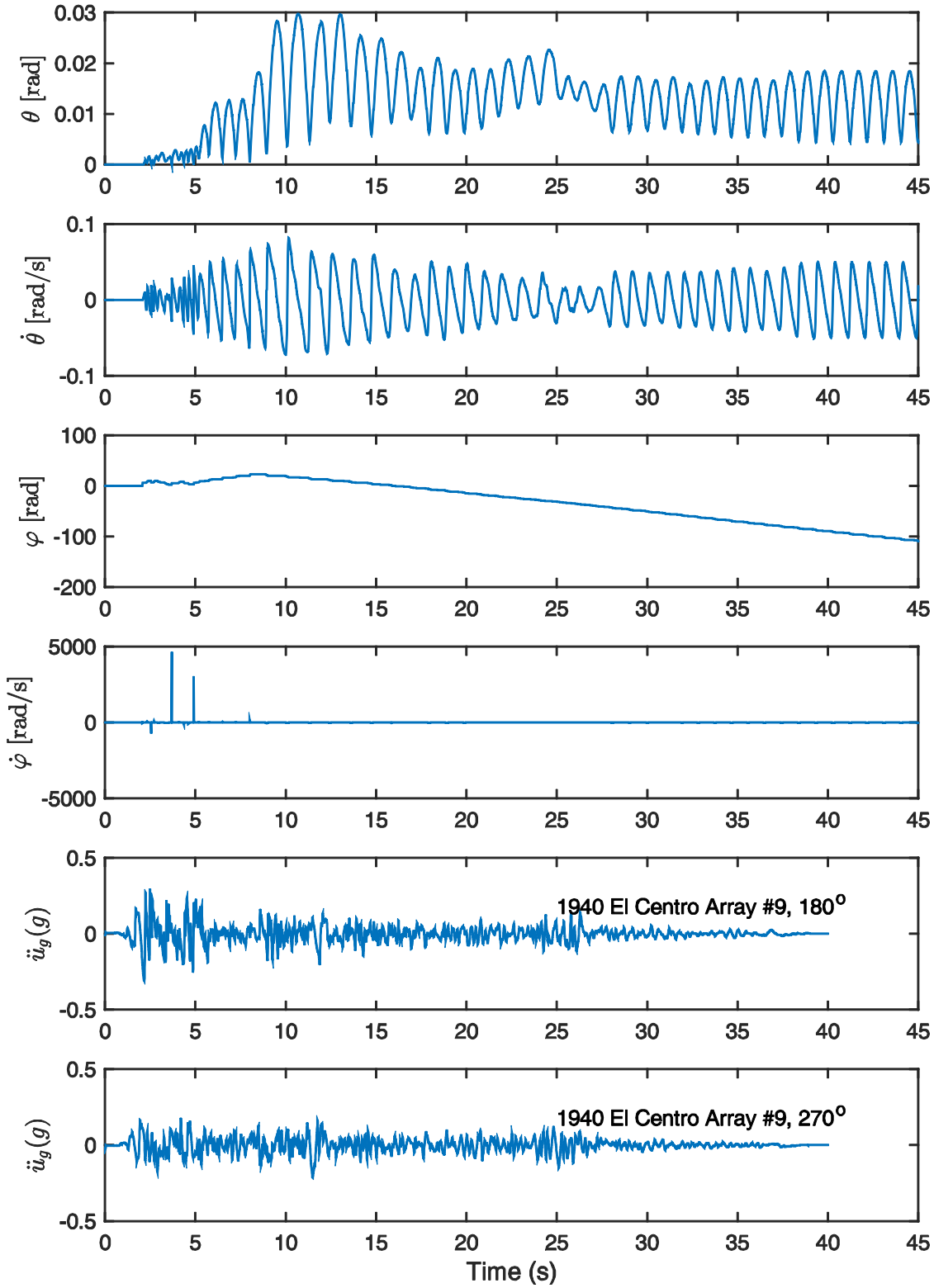


Figure 8 Response of a column-system slab with column slenderness α=0.2, column size R=5m, and mass ratio $\gamma = m_s/4m_c = 10$ to the 1940 El Centro Array #9 ground motion.

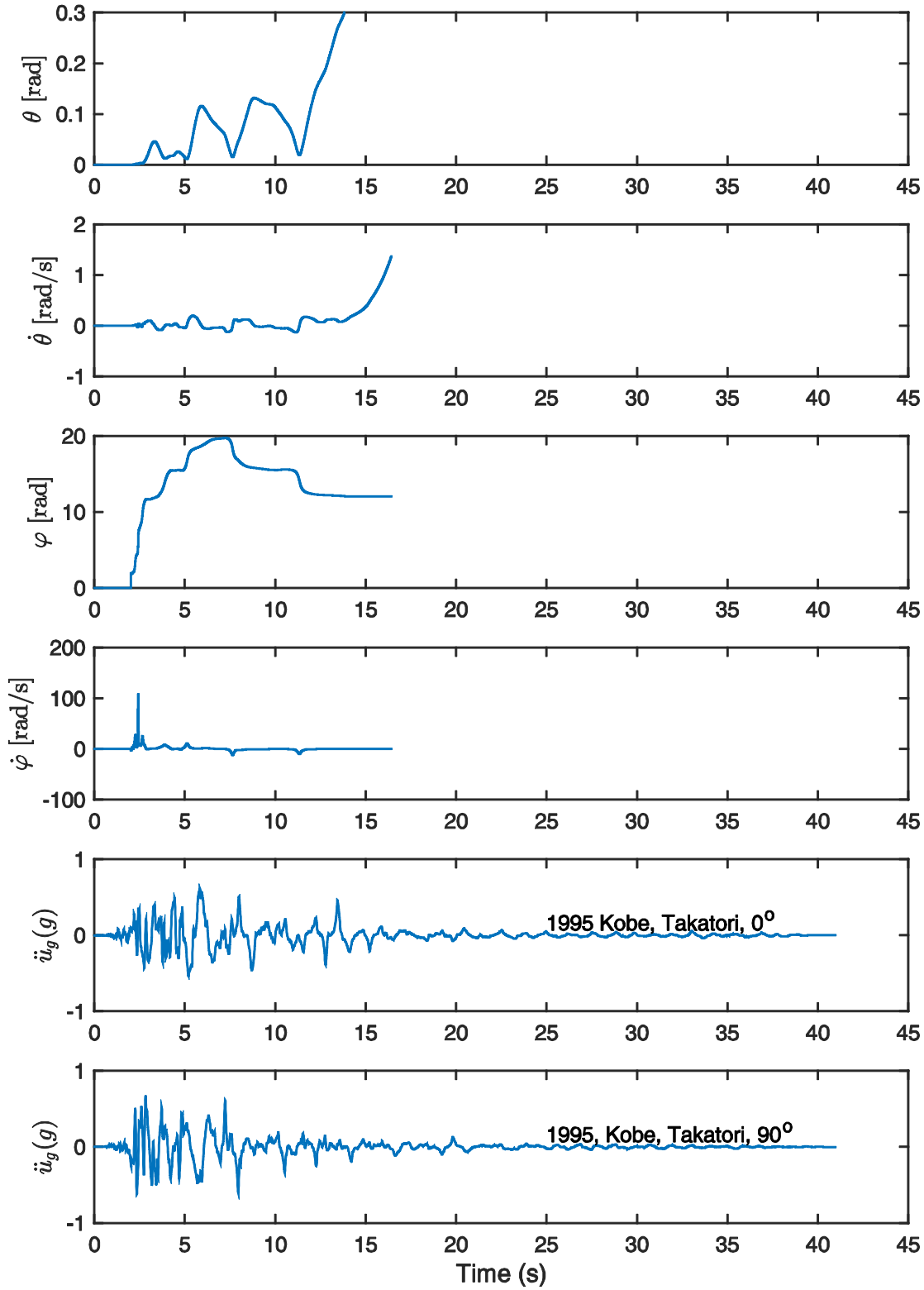


Figure 9 Response of a 3d slab-column system with column slenderness α=0.2, column size R=5m, and mass ratio $\gamma = m_s/4m_c = 10$ to the 1995 Kobe Takatori ground motion.

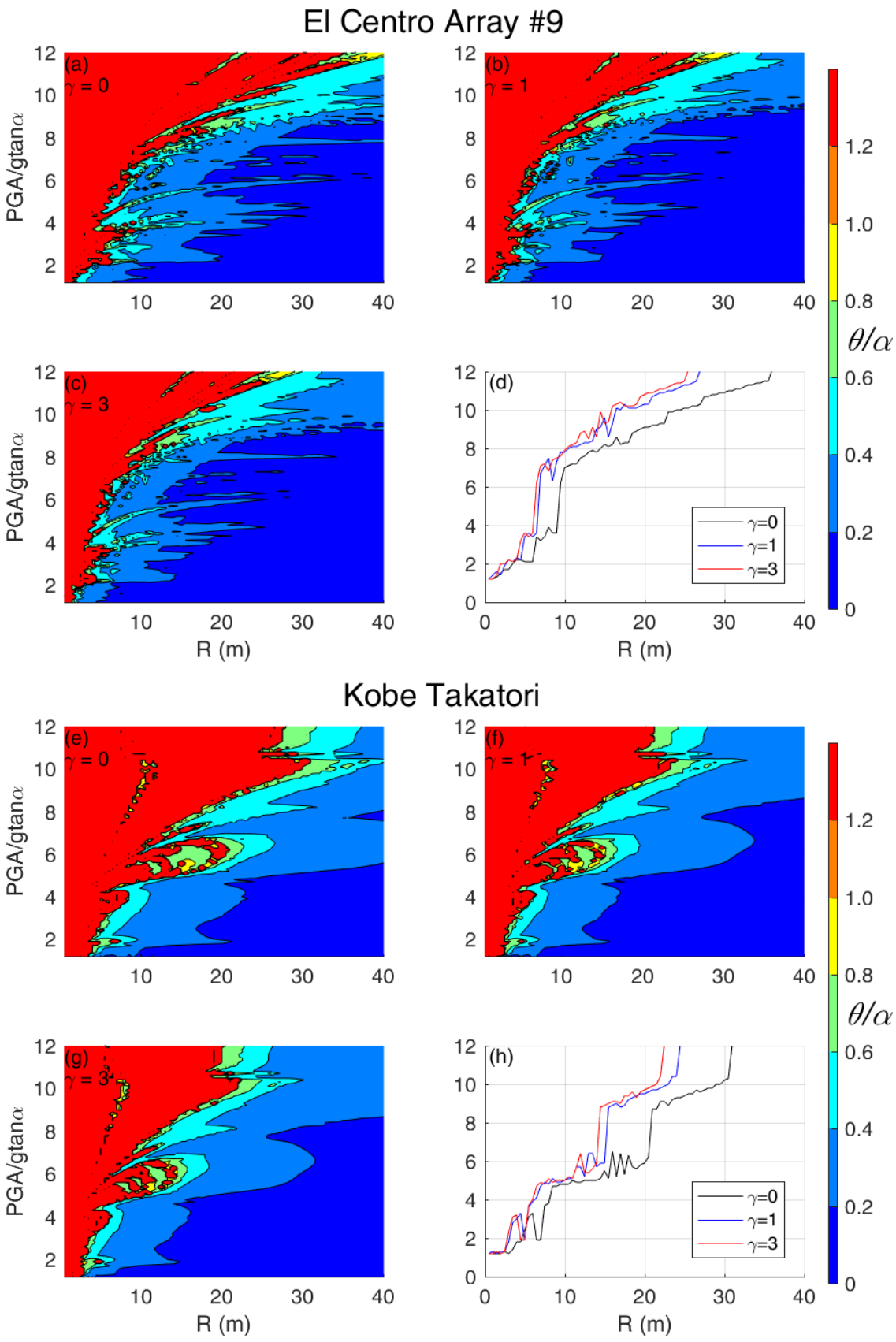


Figure 10 Rocking spectra for the 1940 El Centro Array #9 and 1995 Kobe Takatori ground motions. Column slenderness α=0.2.

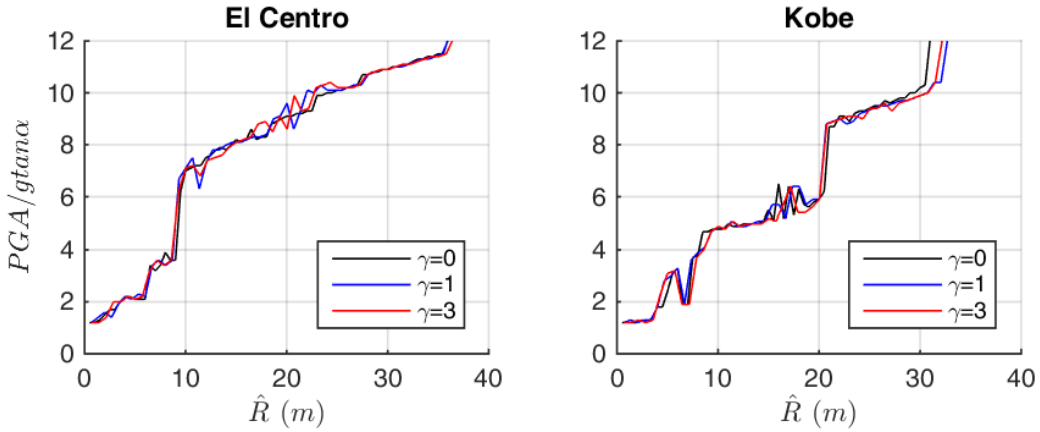


Figure 11 Overturning acceleration spectra for the 1940 El Centro Array #9 and 1995 Kobe Takatori ground motions using the equivalent column size $\hat{R}$ (slenderness α = 0.2).

## REFERENCES

[1] Mander, J. B., and Cheng, C.-T. (1997). ‘‘Seismic resistance of bridge piers based on damage avoidance design.’’ *Tech. Rep. No. NCEER- 97-0014, National Center for Earthquake Engineering Research, Dept. of Civil and Environmental Engineering, State Univ. of New York, Buffalo, NY.*

[2] Billington, S. L., & Yoon, J. K. (2004). Cyclic response of unbonded posttensioned precast columns with ductile fiber-reinforced concrete. *Journal of Bridge Engineering*, 9(4), 353-363.

[3] Sakai, J., and Mahin, S. (2004). “Analytical investigations of new methods for reducing residual displacements of reinforced concrete bridge columns.” *PEER Rep. 2004/02, Pacific Earthquake Engineering Research Center, Univ. of California, Berkeley, CA.*

[4] Wacker, J. M., Hieber, D. G., Stanton, J. F., and Eberhard, M. O. (2005). “Design of precast concrete piers for rapid bridge construction in seismic regions.” *Agreement T2695, Task 53, Federal Highway Administration, Washington, DC*

[5] Cohagen, L., Pang, J. B. K., Stanton, J. F., and Eberhard, M. O. (2008). “A precast concrete bridge bent designed to recenter after an earthquake.” *Research Rep., Federal Highway Administration, Washington, DC.*

[6] Liu, R., & Palermo, A. Pier to deck interaction and robustness of PRESSS hybrid rocking: issues affecting hammerhead pier bridges. *In Proceedings, New Zealand society for earthquake engineering 2016 conference. Christchurch.*

[7] Mantawy, I. M., Thonstad, T., Sanders, D. H., Stanton, J. F., & Eberhard, M. O. (2016). Seismic Performance of Precast, Pretensioned, and Cast-in-Place Bridges: Shake Table Test Comparison. *Journal of Bridge Engineering*, 21(10), 04016071.

[8] Routledge, P. J., Cowan, M. J., & Palermo, A. (2016). Low-damage detailing for bridges—a case study of Wigram–Magdala bridge. *In Proceedings, New Zealand society for earthquake engineering 2016 conference. Christchurch.*

[9] Thonstad, T., Mantawy, I. M., Stanton, J. F., Eberhard, M. O., & Sanders, D. H. (2016). Shaking table performance of a new bridge system with pretensioned rocking columns. Journal of Bridge Engineering, 21(4), 04015079.

[10] Mashal M, Palermo A, Experimental Testing of Emulative and Post-Tensioned Earthquake Damage Resistant Technologies for Accelerated Bridge Construction, *Proceedings of the 16th World Conference on Earthquake Engineering, 16WCEE 2017 Santiago Chile, January 9th to 13th 2017*

[11] Housner, G. W. (1963). The behavior of inverted pendulum structures during earthquakes. Bulletin of the seismological society of America, 53(2), 403-417.

[12] Yim, C. S., Chopra, A. K., & Penzien, J. (1980). Rocking response of rigid blocks to earthquakes. Earthquake Engineering & Structural Dynamics, 8(6), 565-587.

[13] Zhang J, Makris N. (2001) Rocking response of free-standing blocks under cycloidal pulses. *Journal of Engineering Mechanics*, ASCE; 127(5):473–483.

[14] Makris, N. and Konstantinidis, D. (2003), The rocking spectrum and the limitations of practical design methodologies. *Earthquake Engineering & Structural Dynamics*, 32, 265–289.

[15] Peña, F., Prieto, F., Lourenço, P. B., Campos Costa, A., & Lemos, J. V. (2007). On the dynamics of rocking motion of single rigid-block structures. *Earthquake Engineering & Structural Dynamics*, 36(15), 2383-2399.

[16] Dimitrakopoulos, E. G., & DeJong, M. J. (2012). Overturning of retrofitted rocking structures under pulse-type excitations. *Journal of engineering mechanics*, *138*(8), 963-972.

[17] Makris, N., & Vassiliou, M. F. (2012). Sizing the slenderness of free-standing rocking columns to withstand earthquake shaking. *Archive of Applied Mechanics*, 82(10-11), 1497-1511.

[18] Vassiliou, M. F., & Makris, N. (2012). Analysis of the rocking response of rigid blocks standing free on a seismically isolated base. Earthquake Engineering & Structural Dynamics, 41(2), 177-196.

[19] Dimitrakopoulos, E. G., & De Jong, M. J. (2013). Seismic overturning of rocking structures with external viscous dampers. In *Computational methods in earthquake engineering* (pp. 243-258). Springer Netherlands.

[20] DeJong, M. J., & Dimitrakopoulos, E. G. (2014). Dynamically equivalent rocking structures. *Earthquake engineering & structural dynamics*, *43*(10), 1543-1563.

[21] Dimitrakopoulos, E. G., & Paraskeva, T. S. (2015). Dimensionless fragility curves for rocking response to near-fault excitations. *Earthquake Engineering & Structural Dynamics*, *44*(12).

[22] Bachmann JA, Blöchlinger B, Wellauer M, Vassiliou MF, and Stojadinović B (2016), Experimental investigation of the seismic response of a column rocking and rolling on a concave base, ECCOMAS Congress 2016, VII European Congress on Computational Methods in Applied Sciences and Engineering, Crete Island, Greece, 5–10 June 2016

[23] Bakhtiary, E., & Gardoni, P. (2016). Probabilistic seismic demand model and fragility estimates for rocking symmetric blocks. Engineering Structures, 114, 25-34.

[24] Dimitrakopoulos EG, Fung EDW (2016) "Closed-form Rocking Overturning Conditions for a Family of Pulse Ground Motions"Proceedings of the Royal Society

[25] Giouvanidis AI, Dimitrakopoulos EG (2016) "Nonsmooth Dynamic Analysis of Sticking Impacts in Rocking Structures" Bulletin of Earthquake Engineering

[26] Makris, N., & Kampas, G. (2016). Size Versus Slenderness: Two Competing Parameters in the Seismic Stability of Free-Standing Rocking Columns. Bulletin of the Seismological Society of America.

[27] Chopra, A. K., & Yim, S. C. S. (1985). Simplified earthquake analysis of structures with foundation uplift. Journal of Structural Engineering, 111(4), 906-930.

[28] Psycharis, I. N. (1991). Effect of base uplift on dynamic response of SDOF structures. *Journal of Structural Engineering*, 117(3), 733-754.

[29] Oliveto, G., Caliò, I. and Greco, A. (2003), Large displacement behaviour of a structural model with foundation uplift under impulsive and earthquake excitations. *Earthquake Engng. Struct. Dyn*., 32: 369–393.

[30] Ma, Q. T. M. (2010). The mechanics of rocking structures subjected to ground motion (Doctoral dissertation, ResearchSpace@ Auckland).

[31] Acikgoz, S., & DeJong, M. J. (2012). The interaction of elasticity and rocking in flexible structures allowed to uplift. Earthquake Engineering & Structural Dynamics, 41(15), 2177-2194.

[32] Vassiliou, M. F., Mackie, K. R., & Stojadinović, B. (2013). Rocking response of slender, flexible columns under pulse excitation. In Proceedings of the 4th ECCOMAS Thematic Conference on Computational Methods in Structural Dynamics and Earthquake Engineering, Kos Island, Greece (pp. 12-14).

[33] Acikgoz, S., & DeJong, M. J. (2014). The rocking response of large flexible structures to earthquakes. *Bulletin of earthquake engineering*, *12*(2), 875-908.

[34] Vassiliou, M. F., Mackie, K. R., & Stojadinović, B. (2014). Dynamic response analysis of solitary flexible rocking bodies: modeling and behavior under pulse-like ground excitation. *Earthquake Engineering & Structural Dynamics* 43: 1463–1481

[35] Vassiliou, M. F., Truniger, R., & Stojadinović, B. (2015). An analytical model of a deformable cantilever structure rocking on a rigid surface: development and verification. *Earthquake Engineering & Structural Dynamics*, 44(15), 2775-2794.

[36] Makris, N., and Aghagholizadeh, M. (2016) The dynamics of an elastic structure coupled with a rocking wall. Earthquake Engng Struct. Dyn., doi: 10.1002/eqe.2838.

[37] Avgenakis E, Psycharis IN (2017), Modeling of rocking flexible bodies considering the deformability of their base, *Proceedings of the 16th World Conference on Earthquake Engineering, 16WCEE 2017 Santiago Chile, January 9th to 13th 2017*

[38] Makris, N., and Y. Roussos (1998*). Rocking response and overturning of equipment under horizontal pulse-type motions*, Rept. No. PEER-98/05, Pacific Earthquake Engineering Research Center, University of California, Berkeley, California.

[39] Ma, Q. T., & Khan, M. H. (2008). Free vibration tests of a scale model of the South Rangitikei Railway Bridge. In Proceedings of the New Zealand Society for Earthquake Engineering Annual Conference, Engineering an Earthquake Resilient NZ.

[40] Konstantinidis, D., & Makris, N. (2009). Experimental and analytical studies on the response of freestanding laboratory equipment to earthquake shaking.*Earthquake Engineering & Structural Dynamics*, *38*(6), 827-848.

[41] Konstantinidis, D., & Makris, N. (2010). Experimental and analytical studies on the response of 1/4-scale models of freestanding laboratory equipment subjected to strong earthquake shaking. *Bulletin of earthquake engineering*,*8*(6), 1457-1477.

[42] ElGawady, M. A., Ma, Q., Butterworth, J. W., & Ingham, J. (2011). Effects of interface material on the performance of free rocking blocks. Earthquake Engineering & Structural Dynamics, 40(4), 375-392.

[43] Drosos, V., & Anastasopoulos, I. (2014). Shaking table testing of multidrum columns and portals. *Earthquake Engineering & Structural Dynamics*, *43*(11), 1703-1723.

[44] Truniger, R., Vassiliou, M. F., & Stojadinovic, B. (2014). Experimental study on the interaction between elasticity and rocking. In *Proceedings of the 10th national conference in earthquake engineering, Earthquake Engineering Research Institute, Anchorage, AK*.

[45] Zhang, H., Brogliato, B., & Liu, C. (2014). Dynamics of planar rocking-blocks with Coulomb friction and unilateral constraints: comparisons between experimental and numerical data. *Multibody System Dynamics*, *32*(1), 1-25.

[46] Truniger, R., Vassiliou, M. F., & Stojadinović, B. (2015). An analytical model of a deformable cantilever structure rocking on a rigid surface: experimental validation. Earthquake Engineering & Structural Dynamics, 44(15), 2795-2815.

[47] Wittich, C. E., & Hutchinson, T. C. (2015). Shake table tests of stiff, unattached, asymmetric structures. Earthquake Engineering & Structural Dynamics, 44(14), 2425-2443.

[48] Kalliontzis, D., Sritharan, S., & Schultz, A. (2016). Improved coefficient of restitution estimation for free rocking members. Journal of Structural Engineering, 142(12), 06016002.

[49] Nikfar, F., and Konstantinidis, D. (2017) Shake table investigation on the seismic performance of hospital equipment supported on wheels/casters. *Earthquake Engng Struct. Dyn*., 46: 243–266. doi: 10.1002/eqe.2789.

[50] Dangol S, Maree A, Nielsen T, Ibarra L, Sanders D, Pantelides C. (2017) Experimental dynamic response of free-standing bodies under near field and far field ground motions, *Proceedings of the 16th World Conference on Earthquake Engineering, 16WCEE 2017 Santiago Chile, January 9th to 13th 2017*

[51] Maree A, Nielsen T , Dangol S , Sanders D , Ibarra L and Pantelides C, (2017), Sliding and rocking of free standing dry storage casks under earthquake excitation *Proceedings of the 16th World Conference on Earthquake Engineering, 16WCEE 2017 Santiago Chile, January 9th to 13th 2017*

[52] Konstantinidis, D., & Makris, N. (2005). Seismic response analysis of multidrum classical columns. *Earthquake engineering & structural dynamics*,*34*(10), 1243-1270.

[53] Papaloizou, L., & Komodromos, P. (2009). Planar investigation of the seismic response of ancient columns and colonnades with epistyles using a custom-made software. *Soil Dynamics and Earthquake Engineering*, *29*(11), 1437-1454.

[54] Psycharis, Ioannis N., Michalis Fragiadakis, and Ioannis Stefanou. "Seismic reliability assessment of classical columns subjected to near‐fault ground motions." *Earthquake Engineering & Structural Dynamics* 42.14 (2013): 2061-2079.

[55] Pappas, A., da Porto, F., & Modena, C. (2016). Seismic vulnerability assessment form for free-standing columns based on a simplified numerical analysis. *International Journal of Architectural Heritage*, 10(2-3), 281-299.

[56] Vassiliou, M. F. (2010). *Analytical investigation of the dynamic response of a pair of columns capped with a rigid beam and of the effect of seismic isolation on rocking structures* (Doctoral dissertation, Doctoral dissertation, Dept. of Civil Engineering, Univ. of Patras, Greece (in Greek)).

[57] Gelagoti, F., Kourkoulis, R., Anastasopoulos, I. and Gazetas, G. (2012), Rocking isolation of low-rise frame structures founded on isolated footings. *Earthquake Engng. Struct. Dyn*., 41: 1177–1197.

[58] Kourkoulis, R., Anastasopoulos, I., Gelagoti, F., & Kokkali, P. (2012). Dimensional analysis of SDOF systems rocking on inelastic soil. *Journal of Earthquake Engineering*, *16*(7), 995-1022.

[59] Antonellis, G., & Panagiotou, M. (2013). Seismic Response of Bridges with Rocking Foundations Compared to Fixed-Base Bridges at a Near-Fault Site. *Journal of Bridge Engineering*, *19*(5).

[60] Makris N. and Vassiliou M.F. (2013), Planar rocking response and stability analysis of an array of free standing columns capped with a freely supported rigid beam *Earthquake Engng. Struct. Dyn*, *42*(3), 431-449.

[61] Makris, N., & Vassiliou, M. F. (2014). Are Some Top-Heavy Structures More Stable?. *Journal of Structural Engineering*, 140(5).

[62] Dimitrakopoulos, E. G., & Giouvanidis, A. I. (2015). Seismic Response Analysis of the Planar Rocking Frame. *Journal of Engineering Mechanics,141*(7), 04015003.

[63] Makris, N., & Vassiliou, M. F. (2015). The dynamics of the rocking frame. In *Seismic Assessment, Behavior and Retrofit of Heritage Buildings and Monuments* (pp. 37-59). Springer International Publishing.

[64] Makris, N., & Vassiliou, M. F. (2015). Seismic Response and Stability of the Rocking Frame. In *Computational Methods, Seismic Protection, Hybrid Testing and Resilience in Earthquake Engineering* (pp. 249-273). Springer International Publishing.

[65] Giouvanidis AI, Dimitrakopoulos EG (2016) "Seismic Performance of Rocking Frames with Flag-Shaped Hysteretic Behavior" Journal of Engineering Mechanics

[66] Vassiliou, M. F., Mackie, K. R., and Stojadinović, B. (2017) A finite element model for seismic response analysis of deformable rocking frames. Earthquake Engng Struct. Dyn., 46: 447–466. doi: 10.1002/eqe.2799.

[67] Makris, N., & Vassiliou, M. F. (2014). Dynamics of the rocking frame with vertical restrainers. Journal of Structural Engineering, 141(10), 04014245.

[68] Vassiliou, M. F., & Makris, N. (2015). Dynamics of the Vertically Restrained Rocking Column. *Journal of Engineering Mechanics*, 141(12), 04015049.

[69] Burger S, Egger S, Bachmann JA, Vassiliou MF, Stojadinovic B, (2017) Behavior of inverted pendulum cylindrical structures that rock and wobble during earthquakes *Proceedings of the 16th World Conference on Earthquake Engineering, 16WCEE 2017 Santiago Chile, January 9th to 13th 2017*

[70] Vassiliou MF, Burger S, Egger M, Bachmann JA, Broccardo M, Stojadinovic B. (2017) The three-dimensional behavior of inverted pendulum cylindrical structures during earthquakes, *Earthquake Engineering & Structural Dynamics*.

[71] Koh AS and Hsiung CM (1991): Base isolation benefits of 3-D rocking and uplift. I: Theory. *Journal of engineering mechanics*, **117**(1), 1-18.

[72] Konstantinidis, D., & Makris, N. (2007). The dynamics of a rocking block in three dimensions. In *8th Hellenic Society for Theoretical and Applied Mechanics International Congress on Mechanics*.

[73] Zulli, D., Contento, A., & Di Egidio, A. (2012). 3D model of rigid block with a rectangular base subject to pulse-type excitation. *International Journal of Non-Linear Mechanics*, *47*(6), 679-687.

[74] Chatzis, M. N., & Smyth, A. W. (2012). Modeling of the 3D rocking problem. International Journal of Non-Linear Mechanics, 47(4), 85-98.

[75] Sextos, A., Nalmpantis, S., Faraonis, P., Skiada, D., & Stylianidis, K. (2013). Probabilistic seismic hazard assessment through geometrically non-linear back-analysis of byzantine and roman monuments. *10th HSTAM International Congress on Mechanics. Chania, Greece*.

[76] Sextos, A. G., Manolis, G. D., Athanasiou, A., & Ioannidis, N. (2017). Seismically induced uplift effects on nuclear power plants. Part 1: Containment building rocking spectra. Nuclear Engineering and Design.

[77] Anderson, E.L. (2003). Performance-Based Design of Seismically Isolated Bridges. Doctoral Dissertation, University of California, Berkeley.

[78] Becker, T. C., Keldrauk, E. S., Mieler, M. W., Mahin, S. A., & Stojadinovic, B. (2012). Effect of mass offset on the torsional response in friction pendulum isolated structures. In 15th World Conference on Earthquake Engineering, Lisboa, Portugal, paper (No. 752).

COMPDYN 2017
6th ECCOMAS Thematic Conference on
Computational Methods in Structural Dynamics and Earthquake Engineering
M. Papadrakakis, M. Fragiadakis (eds.)
Rhodes Island, Greece, 15–17 June 2017

# THE EFFECT OF HIGH IMPACT WHEELS ON RAIL FAILURE

**Harry Tournay**[1], **Semih Kalay**[2]

[1] Senior Scientist, Transportation Technology Center, Inc.
55500 DOT Road, PO Box 11130, Pueblo, CO, USA 81001
e-mail: harry_tournay@aar.com

[2] Sr. Vice President Technology, Transportation Technology Center, Inc.
55500 DOT Road, PO Box 11130, Pueblo, CO, USA 81001
e-mail: semih_kalay@aar.com

**Keywords:** Rail, Fracture, Failure, High Impact Wheels, Wheel Loads, Thermal Stress, Residual Stress, Reverse Bending, Indirect Loading, Head Defects, Transverse Defects, Base Defects, Fracture Mechanics, Wheel Impact Load Detectors, Track Modulus, Track Damping, Ties, Wheels.

**Abstract.** *Rail is subject to repeated load cycles and wear. These load cycles can induce fatigue and rail failure. As rail failure is less predictable, wear is the desirable failure mode and factors influencing rail failure are carefully managed by railroads. In North America, static wheel loads are limited to a nominal maximum of 159 KN; however, wheel treads can develop rolling contact fatigue resulting in so-called high impact wheels (HIW) that, before removal, can introduce high impact loads on the rail in excess of 700 KN.*

*Transportation Technology Center Inc. (TTCI) was tasked by the Association of American Railroads (AAR) to determine the effect of HIW on rail failure and ascertain whether more stringent removal criteria should be applied.*

*TTCI conducted extended high frequency strain measurements at a WILD site and related the measured strains to the dynamic impact loads by the WILD site. These measurements supported analytical models developed to simulate defect growth and rail failure.*

*Results of the analysis suggest that HIW have a minimal effect on rail failure because of:*

- *High attenuation of the bending wave under impact due to the high damping in the track.*
- *The low probability of repeated HIW cycles on specific elements within the rail.*

*This paper describes the measurement and analysis process as well as the development of the models and the interpretation of resulting data and conclusions drawn.*

## 1 INTRODUCTION

Rail is subject to fatigue and wear. Fatigue failure is unpredictable so wear is the desired rail replacement mode. Factors influencing rail life are carefully managed by North American railroads including the loads to which the rail is subjected. Nominal static axle loads are limited to 32t (159kN wheel load); however high impact wheels (HIW) can occur, resulting generally from rolling contact fatigue of the wheel tread. HIW are difficult to predict and are detected at wheel load impact detectors (WILD) and generally removed from service at a HIW load 400kN. Outliers, may, however, remain in service for a limited time.

The possible role of HIW in rail fracture together with the 400kN limit and potential restrictions on outliers is being questioned by the railroads. This paper reports on an investigation into the effect of HIW on fracture from transverse defects (TD) and, by implication, fracture from defects in the running surface of the rail. Investigations continue into the effect of HIW on fracture from under-head and base defects.

## 2 RAIL STRESSES

Rail is subject to three main stress regimes that can be of similar magnitude:

- Vertical and lateral stresses associated with wheel loads and the bending of the rail as a continuous beam on resilient supports.
- Thermal stresses. Continuously welded rail is laid at a so-called neutral temperature associated with climatic conditions and a compromise made between compressive stresses under high ambient temperatures that could result in track buckling and low ambient temperatures resulting in tensile stresses and the potential for rail breaks.
- Residual compressive and tensile stresses due to rail straightening after heat treatment during manufacture and residual compressive stresses due to wheel / rail rolling contact.

### 2.1 Stresses due to wheel loads

The rail forms a continuous beam on resilient foundations. Wheel loads result in bending directly under the wheel and so-called reverse bending both in advance of, and behind the wheel (Figure 1).

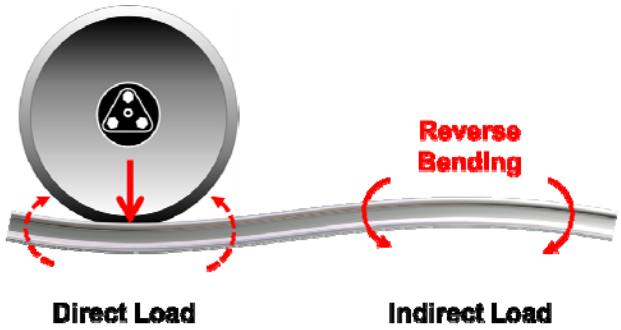


Figure 1. Direct loading and indirect loading (reverse bending) of the rail resulting from a single wheel load on a rail supported by an elastic foundation.

The rail is subjected, typically, to 5 nominal reverse bending cycles as each coupled pairs of wheels in typical railway bogies pass a point on the rail. Figure 2 shows a typical resulting bending moments in the rail due to nominal wheel loads.

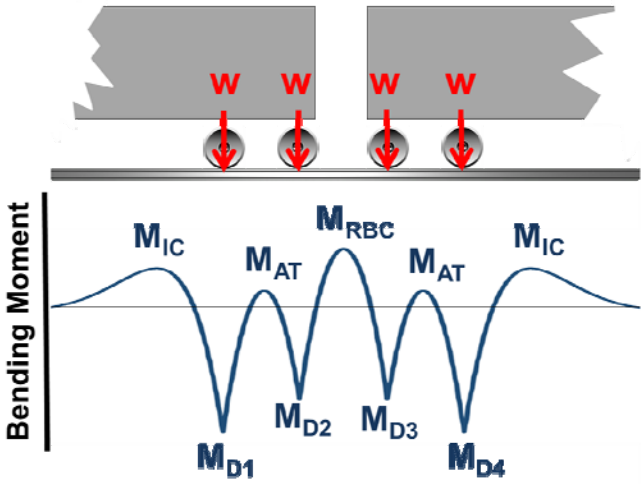


Figure 2. Typical bending moment distribution produced by four wheels across the ends of two coupled wagons.

Moments due to direct loading are a function of the wheel load; that is:

$$M_{DN} \approx f(W_{DN}) \quad \text{..... (1)}$$

Moments due to reverse bending are:

- $M_{RC}$ (reverse bending between bogies in a wagon)
- $M_{RT}$, (reverse bending between wheels in a bogie)
- $M_{RV}$ (reverse bending between coupled wagons)

These moments are a function of both the magnitude and proximity of adjacent wheel loads. The maximum reverse bending moment resulting in tension in the rail head (the driver of transverse defects in the head) occurs typically between cars (Figure 2).

As each coupled truck pair passes a point in the rail, alternating stress cycles are generated, ranging from tension through compression. These cycles are associated with rail fatigue (and crack growth if there is a defect).

The objective of this investigation was to determine the role of intermittent HIW on rail stresses and whether, possibly in combination with thermal and residual stresses (2.2 and 2.3 below), HIW can lead to premature rail fracture.

### 2.2 Thermal Stresses

Rail is laid at a neutral temperature (RNT) determined by the climate of the region of the track. Temperature differences between the RNT and ambient generate rail thermal stresses, $\sigma_t$, are assumed to be uniformly distributed through the rail section and approximately equal to:

$$\sigma_t = E\alpha\,\Delta T \quad \text{..... (2)}$$

where:

$\Delta T$ = temperature difference: ambient and RNT.

E = Young's Modulus for steel.

$\alpha$ = Coefficient of thermal expansion for steel.

### 2.3 Residual Stresses

Residual stresses can result from both initial manufacture (roller straightening) and in-service cold rolling due to repeated wheel loads. Roller straightening induces tension in the rail head and base (Figure 3) [1]. Repeated wheel loads can induce residual compression in the running surface of the rail (Figure 4) [4]. This leaves, generally, a region of tensile residual stress in the centre of the rail head.

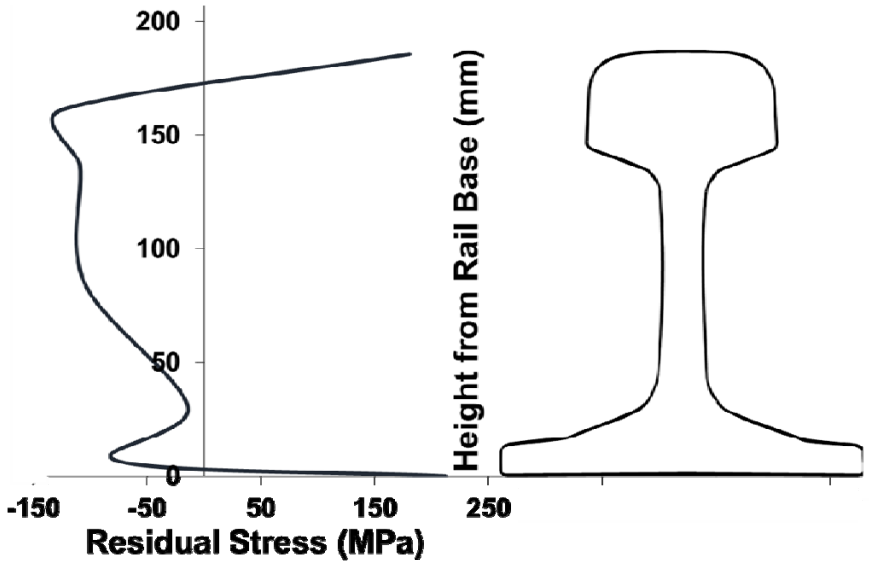


Figure 3. Measured residual stresses in the rail section due to roller straightening.

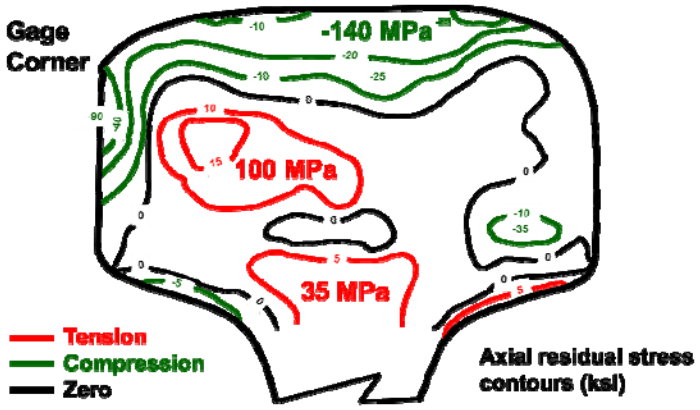


Figure 4. Axial residual stresses in the rail head due to roller straightening & service wheel loads.

## 3 STRESSES AT A POINT IN THE RAIL

### 3.1 Fatigue

In rail assumed to have no measurable macro-defects, rail fatigue is determined by the magnitude of the stress amplitude, $S_a$, where:

$$S_a = (S_{max} - S_{min}) / 2 \quad \text{..... (3)}$$

Figure 5 defines $S_{max}$ and $S_{min}$: and implies that rail fatigue is driven mainly by alternating stresses resulting from wheel loads and not by static thermal & residual stresses.

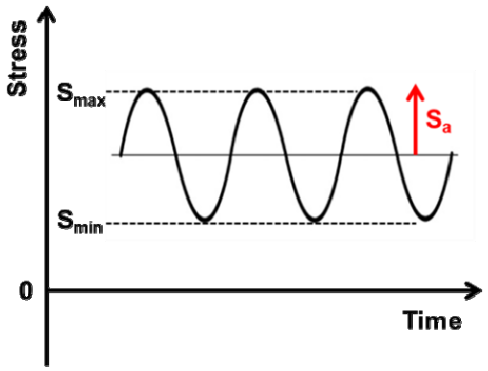


Figure 5. Variable stress amplitude, $S_a$ due to wheel loads is the driver of fatigue in a rail with no measurable defects.

### 3.2 Crack growth and fracture from a defect

When a defect is present in a rail, crack growth and ultimate fracture is driven by the stress at the crack tip and close vicinity. These tresses are driven by the combination of bending as well as thermal and residual stresses, Figure 6.

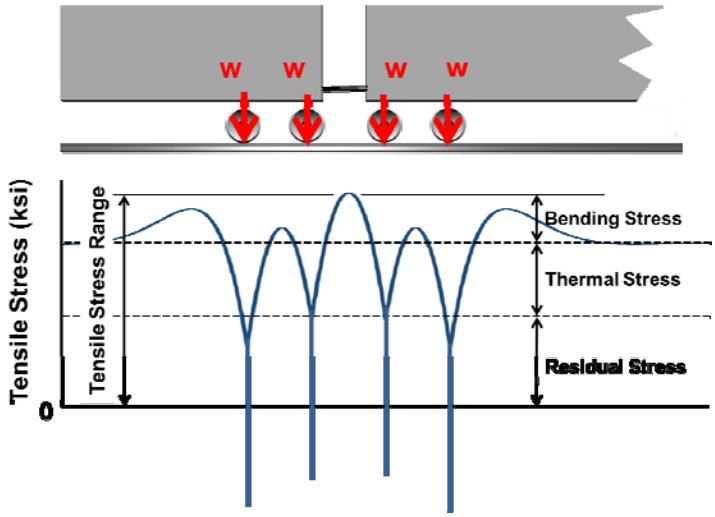


Figure 6. A combination of stresses due to wheel loads, and thermal and residual stresses is the driver of crack growth and fracture in a rail with a pre-existing defect

Fracture may occur when the stress intensity fracture ($K_I$) exceeds the critical stress intensity factor, or fracture toughness, $K_{IC}$. This is expressed as:

$$[\sigma_t + \sigma_r + \sigma_w] (\pi a)^{1/2} g - K_{IC} < 0 \quad \text{..... (4)}$$

Equation 4 is quoted in different forms in fracture mechanics literature (Kuna 2010) where:

$K_{IC}$ = Critical stress intensity factor, or fracture toughness of the rail material
$\sigma_t$ = Thermal stress
$\sigma_r$ = Residual stress
$\sigma_w$ = Stress from wheel loads
a = Defect / crack size
g = Factor describing the crack geometry

The basis for equation 4 may also be used to express crack growth rate.

Equation 4 suggests that crack growth and fracture occurs at a location where $[\sigma_t + \sigma_r + \sigma_w]$ are maximized in combination with g and defect size, a.

## 4 SERVICE TESTS

Wheel loads and associated rail stresses were measured at a typical WILD site on 97 km/h (60 mph) track with 67.5 kg/m (136RD) rail on concrete sleepers and Pandrol fasteners. A WILD site comprises three instrumented crib groups on each rail. Strain gages were placed between two instrumented crib groups as Figure 7 indicates. Gages were placed to measure longitudinal strains. Strains at the under-head locations (gage and field side) were monitored individually (Figure 8). Strain gages on the rail base were connected on a common circuit, producing an averaged strain signal.

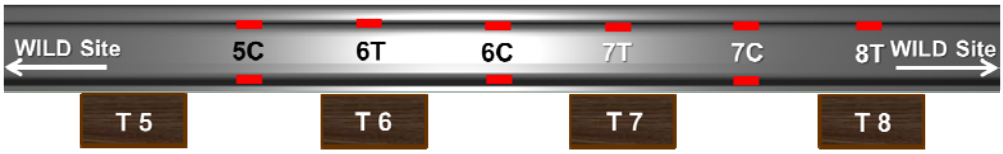


Figure 7. Gages placed between two instrumented groups

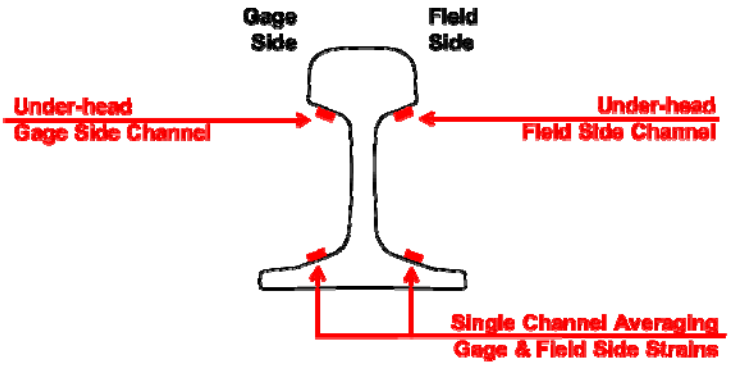


Figure 8. Strain gage locations over a crib

Strains were measured at an acquisition rate of 10K Hz and filtered at a frequency of 3 KHz. The WILD site vendor then provided dynamic wheel load data and the crib locations associated with each wheel load. TTCI then identified the loads (static and dynamic) bearing on the TTCI instrumented cribs. Wheel loads, W, and corresponding direct and indirect loading strains were then merged to produce strain profiles per wheel load.

Tests were conducted in:

– *Summer* when the track modulus was relatively soft (7–14 MPa). More than 17,000 wheelset passes were monitored; however, a limited number of HIW were measured as HIW are more prevalent in winter.

– *Winter* when the track modulus was at least 3 times harder (estimated from very approximate deflection measurements to be > 40 MPa). The ballast and formation was observed to be frozen with minimal rail vertical deflection. More than 96,000 wheelset passes were monitored in an attempt to capture as many and an increased number of HIW were measured.

Figure 9 shows the measured wheel load spectra.

Measured wheel load distributions were bi-modal, reflecting empty and loaded wagons, typical for North American WILD sites. The data also reflected the increased incidence of HIW in winter (typically > 200kN).

Measured stresses never exceeded approximately 90 MPa. Figure 10 shows an example of the summer and winter stress spectrum measured on the top of the base of the rail.

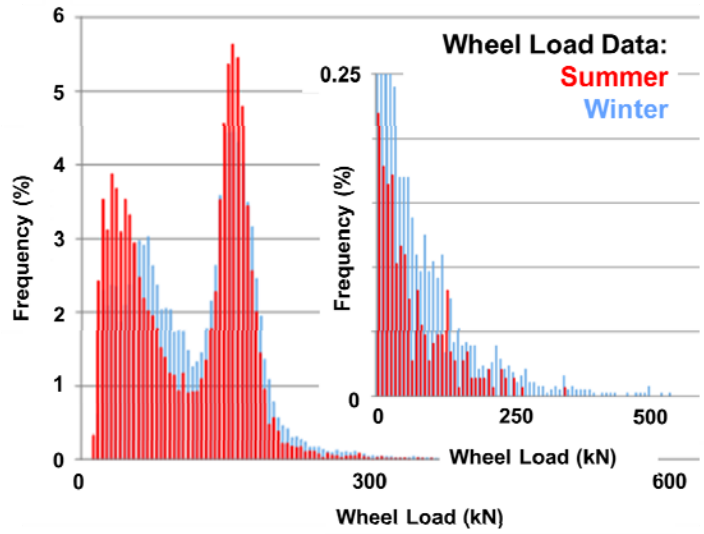


Figure 9. Summer and winter wheel load spectra at WILD site

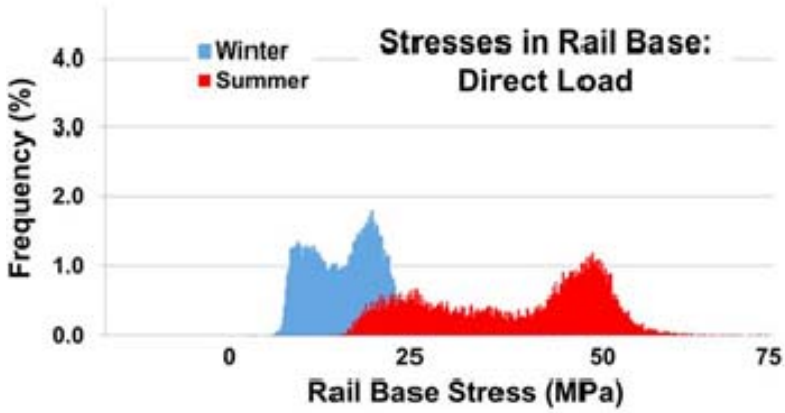


Figure 10. Example of rail stresses under the load spectrum indicated in Figure 9

It was concluded that the frequency and magnitude of the stresses due to HIW will not reduce the fatigue life of the rail beyond that attributed to nominal wheel loads.

Further observations from the service data suggest that the rail stresses under indirect load (reverse bending) reach a plateau beyond a wheel load of approximately 180kN (Figure 11).

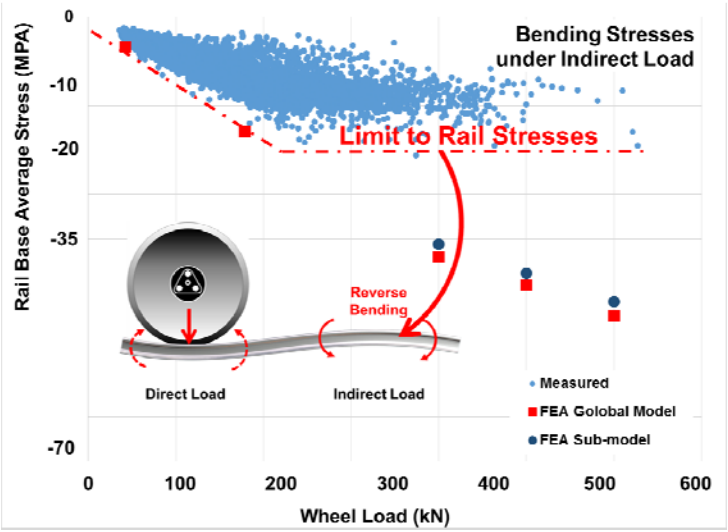


Figure 11. Measured stresses under indirect loading reach a maximum at a load of approximately 180kN

Stresses do not increase as predicted by the theory of a continuous beam on elastic foundation or the assumed bi-linear stiffness and hydraulic damping model in the track model used in the finite element analysis (FEA) of rail stresses (see data points associated with FEA global and sub-model in Figure 11).

Examination of the stress-time histories suggests that the root cause for this "plateauing effect" is the attenuation of the bending stresses.

Figure 12 shows the rail stresses under the impacting wheel at the time of impact. The influence if the impacting wheel is evident in relation to the stress peaks attributable to the "nominal" wheel loads.

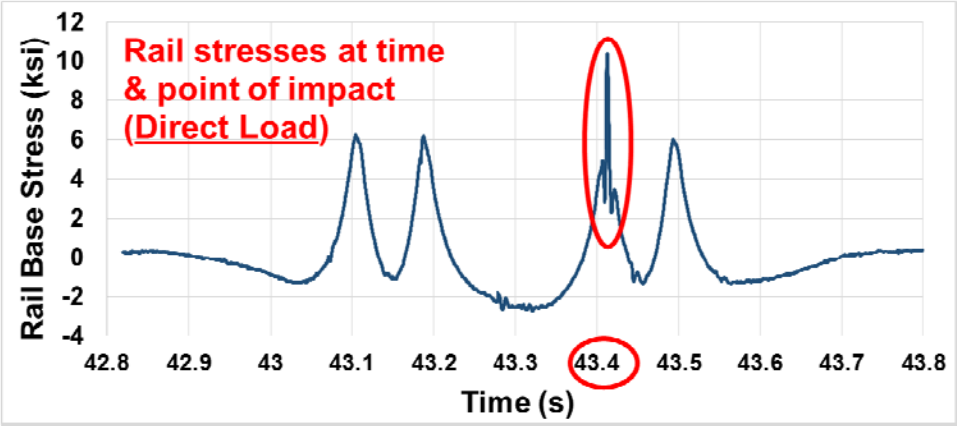


Figure 12. Rail stresses at point and time of impact of a HIW

Figure 13 shows the rail stresses at a point approximately 0.6 m away from the point of impact.

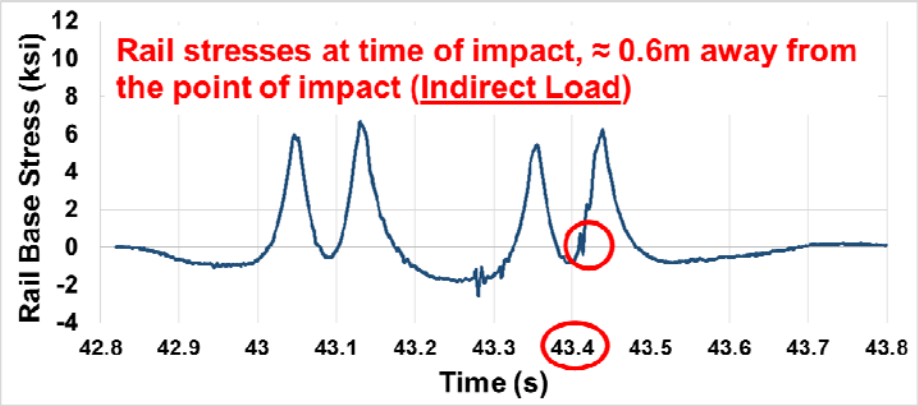


Figure 13. Rail stresses at time of impact shown in Figure 10, but approximately 0.6 m away from the point of impact

Two effects are apparent from Figures 10 and 11:

- The bending in the rail due to the impact load is almost completely attenuated.
- The little bending that is evident in the rail does not coincide with a peak bending due to a nominal wheel load. This is due to the difference in speed of the propagated bending wave due to the impact load and the speed of the wheels of the train producing the nominal wheel loads.

The significant conclusion to be drawn from these measurements is that the rail at the test site "sees" a HIW load in reverse bending very much as it "sees" a nominal wheel load. Consequently, transverse defects in the rail head that are subject to tensile stresses under reverse bending should not experience higher growth rates or fracture than that due to nominal wheel loads.

This finding may be generally true for rail on concrete ties in North America. However, it needs to be verified for the many different track types in North America and suggests the need for the development of a more complex track model to simulate HIW loads. This model probably needs to simulate at least sub-tie and rail pad stiffness and damping.

## 5 FRACTURE MECHANICS ANALYSES

Notwithstanding the findings on the limitations of the track model used, two fracture mechanics analyses were conducted using:

- A rail-specific fracture mechanics program called *RailGrow*. (Reference Section 5, Acknowledgements).
- A Finite Element Analysis of a penny-shaped crack simulating a transverse defect in the rail head.

### *5.1 RailGrow Analysis*

*RailGrow* is a fracture mechanics program that can simulate the growth rate of, amongst others, a transverse defect in a rail subject to bending stresses from wheel service load spectra, thermal stress spectra and assumed residual stress distributions in the rail head. Track modulus, rail sectional properties, and rail material are input together with fracture mechanics properties, defect size, shape, and position. Crack growth is predicted to failure under wheel and thermal overload conditions. The rail is assumed to be a continuous beam on elastic foundation, which was found to be over-predictive of the effect of HIW loads as discussed in Section 4.

Using *RailGrow*, a transverse defect was "grown" in the rail head under a specific load regime. At every 0.0254 mm of crack growth, the rail was subjected to a single HIW and a thermal overload. Critical crack sizes under the final fracture load applied in the laboratory were compared with a number of published laboratory test results, Igwemezie et al. 1993 (example: Figure 14).

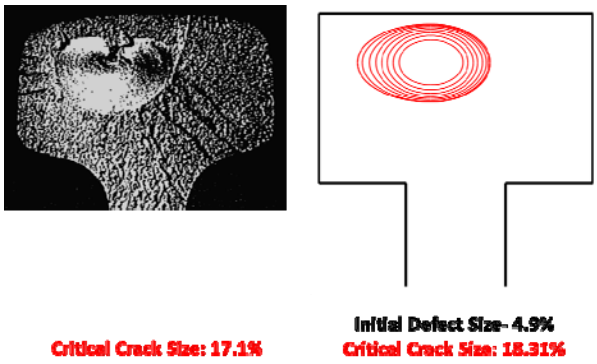


Figure 14. *RailGrow* simulated crack growth to failure "calibrated" against laboratory a test of fracture of a rail with pre-existing transverse defect under thermal and impact loads

The *RailGrow* model was then used to grow transverse defect cracks to critical sizes under different thermal and HIW overload conditions. Figure 15 shows the results of this analysis. The relationship between critical crack size of a transverse defect and the level of prevailing HIW is "flat" and is more a function of the temperature of the rail below the neutral laying temperature.

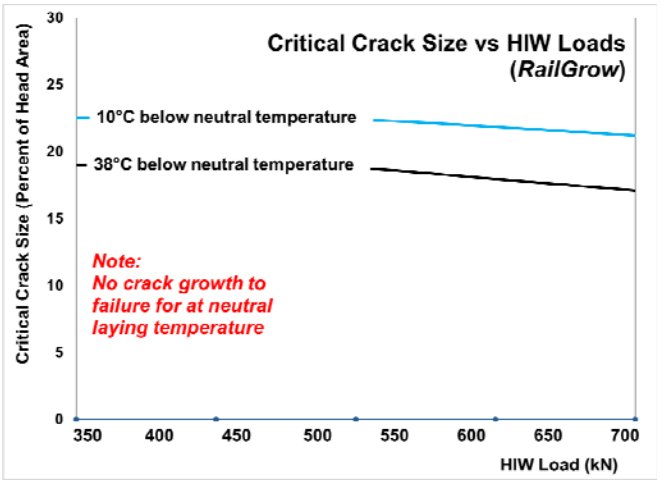


Figure 15. Critical crack size versus overload conditions predicted using RailGrow

## 5.2 Finite Element Analysis

Two basic finite element models of the rail were built:

– A so-called "global model" representing an approximately 25 m long section of rail subject to four point loads representing the wheel loading that Figure 2 depicts; one wheel simulating the HIW load, the other three point loads simulating nominal wheel loads.

– A shorter sub-model directly under the impacting wheel and including a section of rail under reverse bending. This model used boundary conditions developed from the global model with a segment of wheel being used to apply the HIW load.

The finite element model of the rail was supported at a typical tie spacing using a model that Figure 16 shows:

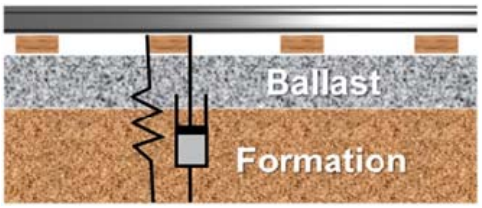


Figure 16. Track Model

The stiffness under each tie was modelled using a bi-linear spring / damper system in compression with different properties under uplift conditions.

A penny-shaped crack simulating a transverse defect was introduced in the sub-model (Figure 17) and crack tip stresses and KI values (crack tip energy in the axial tension mode) were determined for increasing HIW loads and rail; temperatures were below the rail neutral temperature.

As with the *RailGrow* analysis, the propensity for failure is "flat" with HIW load and more a function of the temperature below the rail neutral temperature (Figure 18).

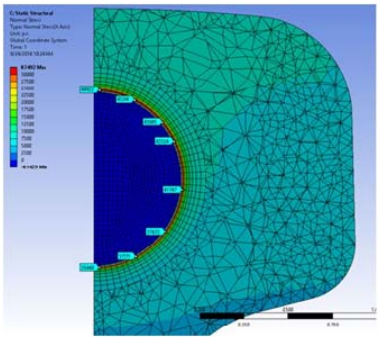

Figure 17. Example of mesh and output from the analysis of a penny-shaped crack in the rail head

Consequently, fracture mechanics analyses show no relationship between HIW and the fracture of rail from typical transverse defects in the rail head; this, even given that the fracture mechanics models over- predict the stresses in the rail head under reverse bending.

## CONCLUSIONS

TTCI has conducted extensive tests and analyses to determine the effect of HIW loads on rail failure from transverse defects in the head of the rail.

Measured stress maxima associated with HIW loads in revenue service were found to be too low and infrequent to reduce rail fatigue life and that any fracture must be initiated from pre-existing defects, for example, transverse defects.

Fracture from transverse defects in the rail head can only be activated by the reverse bending mode in the rail. This mode occurs both in advance and behind the wheel.

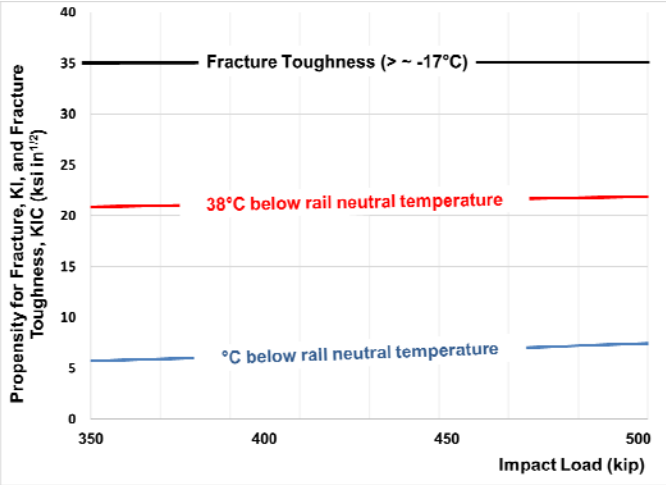


Figure 18. Plot of the energy at the tip of a penny-shaped crack in the rail head versus HIW load and temperature below the rail neutral laying temperature

Tests show that on track constructed of concrete sleepers on rail pads and secured with rail clips, the reverse bending mode is attenuated under dynamic wheel loads higher than 20kN. In other words, the rail "sees" a HIW load as any other service loaded wheel load of up to 20kN.

Two fracture mechanics models or approaches have been developed. These models have been shown not to simulate the attenuation measured in test and, consequently, will over-predict the effect of HIW loads. Both models show no effect of HIW on rail failure from transverse defects in the rail head.

Consequently, TTCI has found no evidence of an effect of HIW on rail failure from HIW.

## ACKNOWLEDGMENTS

The authors thank:

- Canadian National Railway and staff for facilitating the tests at Calrin WILD site.
- Retired Prof. Darrell Socie of the University of Illinois Urbana Champaign who developed the rail fracture mechanics program, *RailGrow*, under contract to TTCI and based on work done by the Volpe, The National Transportation Systems Center and funded by the office of the Federal Railroad Administration.
- Many TTCI staff in support of this project.

## REFERENCES

1. Gutscher, D. (2010, March). Railhead repair weld residual stress investigation. *Technology Digest* TD-10-007. Pueblo: AAR/TTCI.
2. Igwemezi, J. O., Kennedy, S. L., Feng, X., & Cai, Z. (1993, June). Defective rail fracture under dynamic, thermal and residual stresses. In *Proceedings of 5th Intl. Heavy Haul Conf, Beijing, China* (pp. 6-13).
3. Kuna, M. 2013. *Finite elements in fracture mechanics*. Dordrecht: Springer.
4. Orringer, O., Morris, J. M., & Steele, R. K. (1984). Applied research on rail fatigue and fracture in the United States. *Theoretical and Applied Fracture Mechanics*, *1*(1), 23-49, North Holland.

COMPDYN 2017
6th ECCOMAS Thematic Conference on
Computational Methods in Structural Dynamics and Earthquake Engineering
M. Papadrakakis, M. Fragiadakis (eds.)
Rhodes Island, Greece, 15–17 June 2017

# DYNAMIC RESPONSES OF RAILWAY ULTRA-HIGH-STRENGTH CONCRETE SLEEPERS UNDER EXTREME IMPACT LOADING

**Sakdirat Kaewunruen[1], Alex M Remennikov[2], and Shintaro Minoura[3]**

[1] Birmingham Centre for Railway Research and Education, School of Civil Engineering
The University of Birmingham, Edgbaston, B15 2TT UK
e-mail: s.kaewunruen@bham.ac.uk

[2] School of Civil, Mining and Environmental Engineering, University of Wollongong
Wollongong, NSW Australia
alexrem@uow.edu.au

[3] Structural Mechanics Laboratory, Railway Technical Research Institute
Tokyo, Japan
minoura.shintaro.51@rtri.or.jp

**Keywords:** Railway, Concrete Sleepers, Railroad Ties, Prestressing Tendons/Wires, Impact Analysis, Dynamic Responses, High Strength Concrete, Ultra High Performance, LS-Dyna.

**Abstract.** *Ultra high strength concrete has been adopted recently in construction industry. Prestressed concrete sleepers (or railroad ties) are designed usually using high strength concrete (around 50-80 MPa) in order to carry and transfer the wheel loads from the rails to the ground and to maintain rail guage for safe train travels. The sleepers are installed as the crosstie beam support in railway track systems. They are subjected to impact loading conditions that are resulted from train operations over wheel or rail abnormalities, such as flat wheels, dipped rails, crossing transfers, rail squats, corrugation, etc. The magnitude of the shock load relies on various factors such as axle load, types of wheel/rail imperfections, speeds of vehicle, track stiffness, etc. This paper demonstrates the development of finite element modelling to investigate the dynamic responses of prestressed concrete sleepers using ultra high strength materials (over 100 MPa), particularly under a variety of impact loads. The 3D finite element model of prestressed concrete sleeper has been developed using a finite element package, LS-Dyna. It has been verified by the experiments carried out using the high capacity drop-weight impact machine at the University of Wollongong, Australia. The experimental results provide very good correlation with numerical simulations. In this paper, the numerical studies are extended to evaluate the dynamic behaviors of high strength steel wires and ultra high strength concrete; as well as their nonlinear responses under different parameters. The outcome of this study can potentially lead to the utilization and design guideline of ultra high strength concrete for prestressed concrete sleepers.*

## 1 INTRODUCTION

In ballasted railway tracks, railway sleeper is a major structural component to transfer train axle loads from the rails to the underlying ballast and supporting system. Typical ballasted railway track and its components can be seen in Figure 1 [1]. Reportedly, it is chronically believed based on the industry practice that railway concrete sleepers possess reserved strength that are untapped. Accordingly, it is essential to evaluate the spectrum and amplitudes of forces applied to the railway track, in order to understand more clearly the behaviors in which track components respond to those forces, and to identify the processes whereby concrete sleepers in particular carry those force actions. Recent findings show that the nature of the majority of loading conditions on track structures is of dynamic impact [2]. Those loads are normally of short duration but of very high magnitude. They are ascribed to the wheel/rail interactions associated with irregularities, i.e. wheel burns, wheel flats, corrugations, non-uniform track modulus, and any other out-of-round wheel defects. Structural performance monitoring is an effective way to establish better understanding into the impact behaviors of prestressed concrete sleepers.

In addition, cracks in concrete sleepers have been visually observed by many railway organizations. As described in the review [3], the principal cause of cracking is the infrequent but high-magnitude wheel loads produced by a small percentage of "bad" wheels or railhead surface defects. For instance, the typical loading duration produced by wheel flats is about 1-10 msec, while the force magnitude can be over 400 kN per rail seat. Existing structural design concept for prestressed concrete sleepers in Australia is based on permissible stress principle taking into account only the static and quasi-static loads, which are unrealistic to the actual dynamic loads on tracks. However, it is inevitable to avoid those criteria in any consideration of rail track designs since even the standard quality ride of rail vehicles still involves with the low-velocity impact forces. In order to devise a new limit states design concept whereas the extreme loading conditions can be taken into account, the research efforts are required to perform comprehensive studies of the loading conditions, the static behaviour, the dynamic response, and the impact resistance of the prestressed concrete sleepers [4]. A collaborative research task between the University of Birmingham and University of Wollongong is to evaluate the dynamic responses of concrete sleepers under static and impact loads. There have been only a few studies related to the modelling of prestressed concrete sleepers. Most of them predicted the rail seat flexural behaviour of the concrete sleepers [5-6] using high strength concrete of 50-60 MPa. In contrast, the use of ultra high strength concrete for manufacturing railway sleepers has not been thoroughly evaluated.

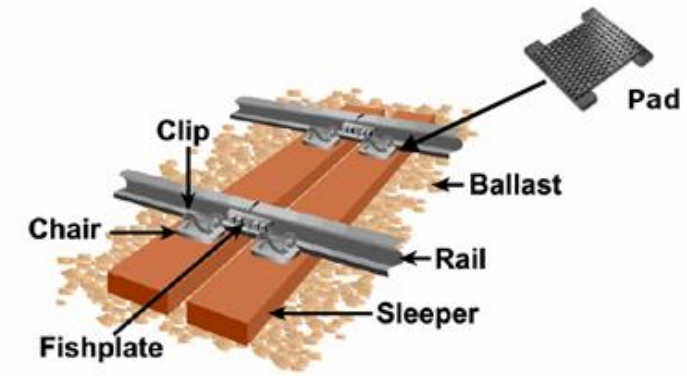


Figure 1: Typical ballasted railway track and its components [1]

This study has established a finite element model that can simulate and predict the responses of reinforced and prestressed concrete members. A three-dimensional non-linear finite element model of a railway prestressed concrete sleeper for static analysis was developed using the general-purpose finite element analysis package, ANSYS [7]. The concrete section was modelled using SOLID65 solid element where the compressive crushing of concrete and the concrete cracking in tension zone can be accommodated. In the current practice, the railway concrete sleeper is designed to resist prestressing force fully throughout the whole cross section as the force/moment redistribution can be seen in Figure 2. This makes the smeared crack analogy unsuitable for the replacement of prestressing tendons in the fully prestressed concrete sleeper. The use of a truss element, LINK8, for discrete reinforcement modelling, is then more practicable. An initial strain real-constant feature in ANSYS appropriately substituted the pre-tensioning forces in the tendon elements. However, it was assumed that perfect bonding between concrete and pre-stressing wires. The static full-scale experiment was conducted to validate this FE model [7]. The experimental details were based on the associated Australian Standards [8, 9].

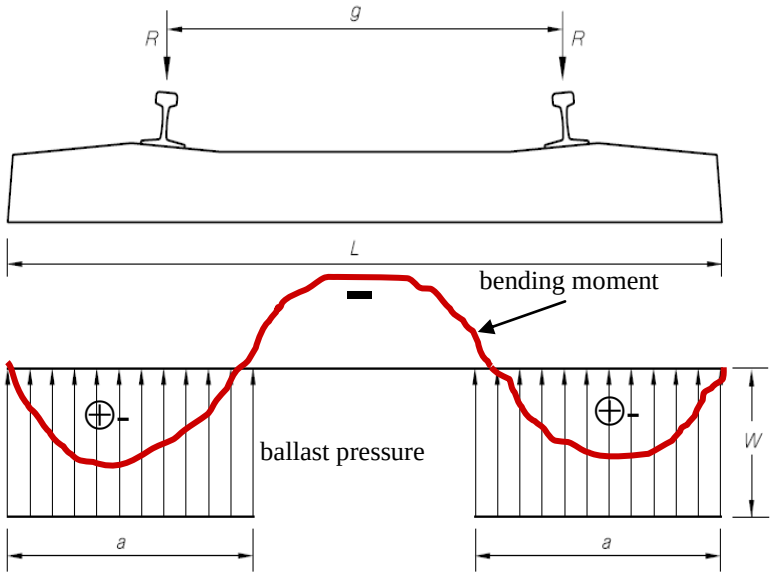


Figure 2: Moment distribution for standard gauge sleepers [8]

The calibrated finite element model has been extended to include ballast support and in situ boundary conditions. The extended model was linked to LS-Dyna [10] for impact analysis and validation against the drop impact tests. This paper investigates the impact responses of prestressed concrete sleepers using ultra high strength concrete (with compressive strength over 100 MPa). The highlights in this paper are the better understandings into the influence of concrete material on the impact behavior of railway prestressed concrete sleepers.

## 2 MODELLING OF IN SITU SLEEPER

In this investigation, the concrete part of the sleeper was modelled using a three-dimensional solid element, which has the material model to predict the failure of brittle materials [7]. This element is defined with eight nodes – each with three degrees of freedom: translations in nodal x, y, and z directions. To simulate the behaviour of prestressing wires, a truss element, were used to withstand the initial strain attributed to prestressing forces, by assuming

perfect bond between these elements and concrete. Note that this truss element cannot resist neither bending moments nor shear forces. Non-linear elastic behaviour of concrete can alternatively be defined by the multi-linear stress-strain relationships. The modulus of elasticity of concrete ( $E_c$ ) is esmiated based on AS3600 [11] using the compressive strengths (100, 200, and 1000 MPa).

For prestressing wires, the bi-linear elasto-plastic material models can be used as well as the multi-linear isotropic model from the manufacturer's data. The 0.2% proof stress is 1,700 MPa and the ultimate stress is 1,930 MPa. The static and dynamic elasticity of moduli of prestressing wire are 190,000 MPa.

The multi-linear isotropic dynamic stress-strain curve for the concrete and prestressing wires can be calculated based on the consideration of the effect of strain rate. Based on the assumption of perfect bond between prestressing wires and concrete, the dynamic material properties of concrete and prestressing wires can be determined as follows [12].

*Concrete:*

$$\sigma = f'_{c,dyn}\left[2\frac{\varepsilon}{\varepsilon_{c0,dyn}} - \left(\frac{\varepsilon}{\varepsilon_{c0,dyn}}\right)^2\right] \tag{1}$$

$$\frac{f'_{c,dyn}}{f'_{c,st}} = 1.49 + 0.268\log_{10}\dot{\varepsilon} + 0.035\left[\log_{10}\dot{\varepsilon}\right]^2 \tag{2}$$

$$\frac{\varepsilon_{c0,dyn}}{\varepsilon_{c0,st}} = 1.24 + 0.053\log_{10}\dot{\varepsilon} \tag{3}$$

where σ is the dynamic stress, $f'_{c,dyn}$ is the dynamic compressive strength, $f'_{c,st}$ is the static compressive strength of concrete, $\varepsilon$ is the dynamic strain, $\varepsilon_{c0,st}$ is the static ultimate strain, and $\dot{\varepsilon}$ is the strain rate in concrete fibre.

*Prestressing wires:*

$$\frac{f_{y,dyn}}{f_{y,st}} = 10^{0.38\log_{10}\dot{\varepsilon}^{-0.258}} + 0.993 \tag{4}$$

where $f_{y,dyn}$ is the dynamic upper yield point stress, $f'_{c,st}$ is the static upper yield point stress of prestressing wires (about 0.84 times proof stress), and $\dot{\varepsilon}$ is the strain rate in tendon.

A three-dimensional model of a typical railway prestressed concrete sleeper was developed initially in ANSYS [7] as illustrated in Figure 3. The dedicated solid bricks represent the concrete and the embedded three-dimensional spar elements are used as the prestressing wires. The pre-tensioning was modelled using an initial strain in the tendons corresponding to the prestressing forces at final stage (sustained prestressing force after all losses). For impact simulations, a FE model was extended to include rails, rail pads, ballast bed, and falling mass, as shown is Figure 4. The extended finite element model was calibrated using vibration data

[13-16]. The updated finite element model was then transferred to LS-Dyna. The simulation results were achieved by assigning the initial velocity to the drop mass to generate an impact event, similarly to the actual drop tests.

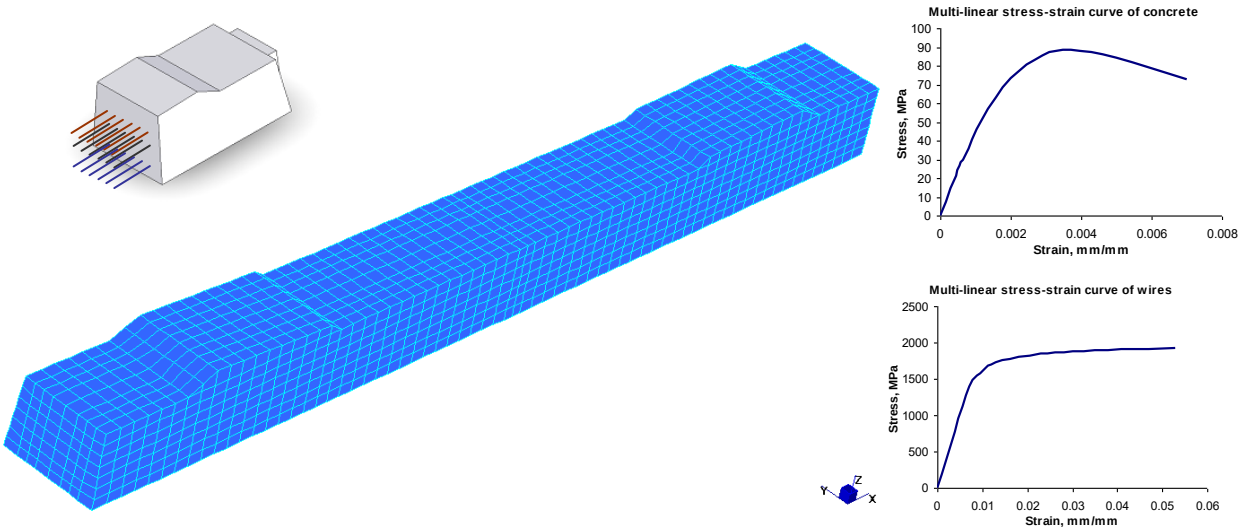


Figure 3: A three-dimensional model of full-scale railway sleeper [4]

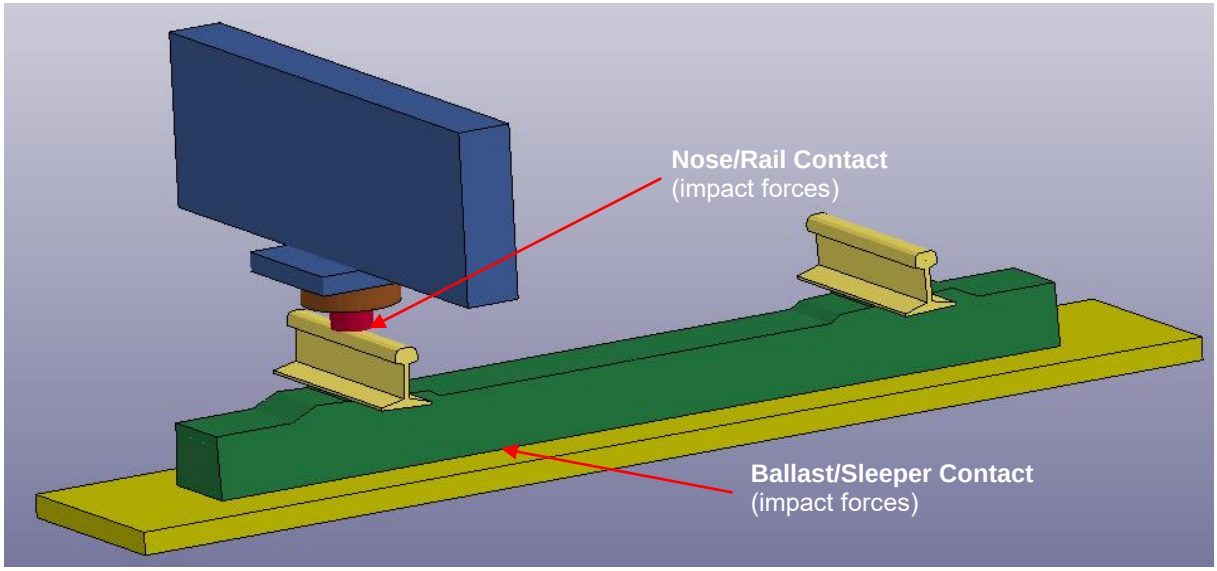


Figure 4: Extended finite element model of full-scale railway sleeper [4]

## 3 CALIBRATION OF FE MODEL

The prestressed concrete sleepers used in this study were kindly supplied by an Australian manufacturer, under a collaborative research framework funded by European Commission (H2020-RISE Project RISEN). A series of static tests on the concrete sleepers was performed at the University of Wollongong in accordance with the Australian Standards (which are similar to European Standards). The details of static responses, rotational capacity, post-failure mechanism, and residual load-carrying capacity of the prestressed concrete sleeper can be found in refs: [17-22].

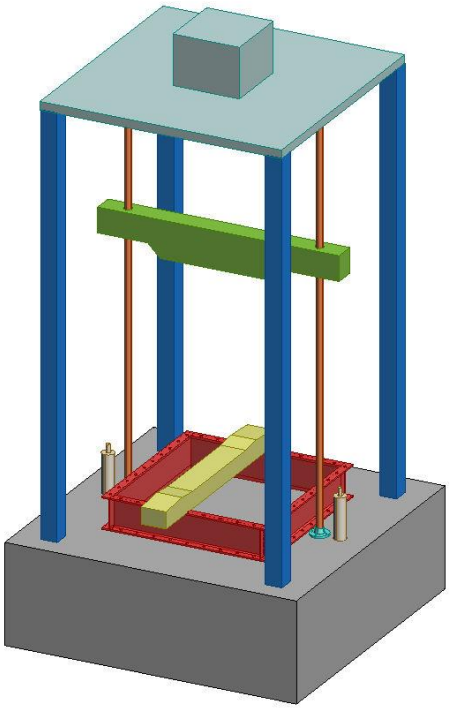

a) sketch of impact machine



b) impact test setup

Figure 5: Experimental overview

The high-capacity drop-weight impact-testing machine has been developed at the University of Wollongong, as depicted in Figure 5a. The drop mass assembled is 5.81 kN with the varied height from 0 to 6m in total, which provide the maximum capacity of 10m/s drop velocities. Experimental setup and impact tests were arranged in accordance with the Australian Standards, as shown in Figure 5b. The accelerometers have been used to measure the dynamic responses at mid-span and railseat. The contact impact force between impactor and rail was recorded using the dynamic load cell connected to the data acquisition system. For the verification purpose, the drop height used was 0.1m since there was the measurement limitation for the accelerometers employed. The in-situ conditions of railway concrete sleeper were replicated. Attempts to simulate impact loading actually occurred in tracks were succeeded experimentally and numerically. Comparison between numerical and experimental results can be found in Figure 6. It is found that the finite element model is fairly sufficient for use in predicting impact responses of the prestressed concrete sleepers. The trends of peak acceleration responses are quite close to each other, although there is certain phase difference.

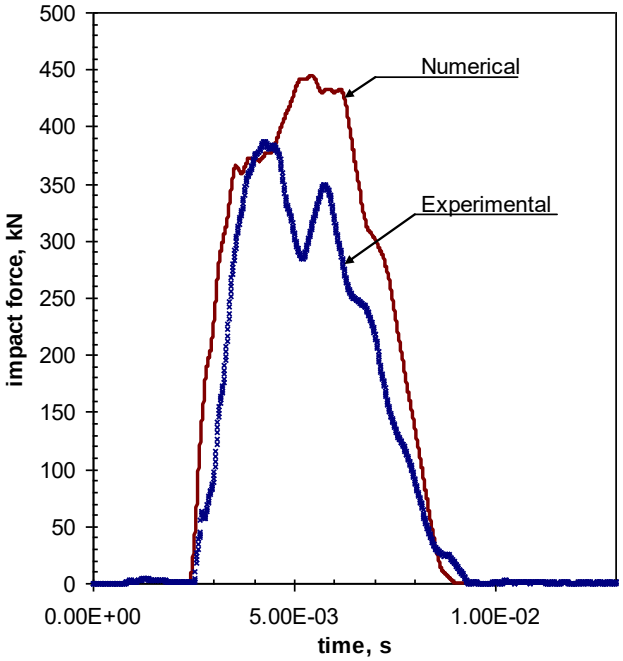


a) contact shock load

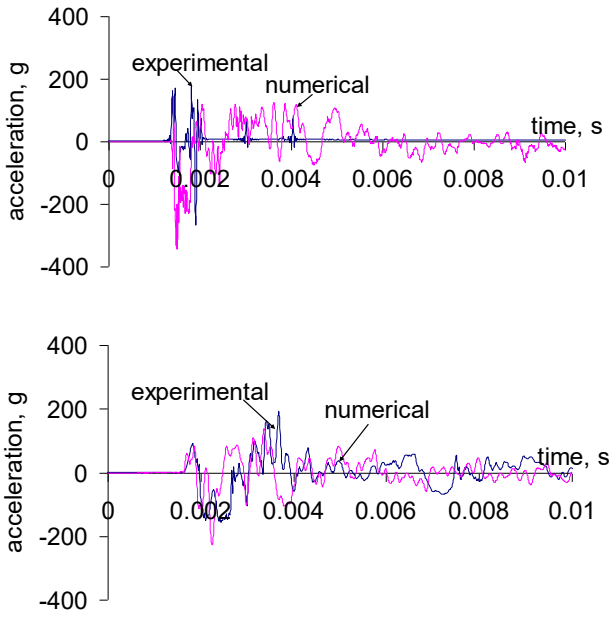


b) at railseat (top); at mid-span (bottom)

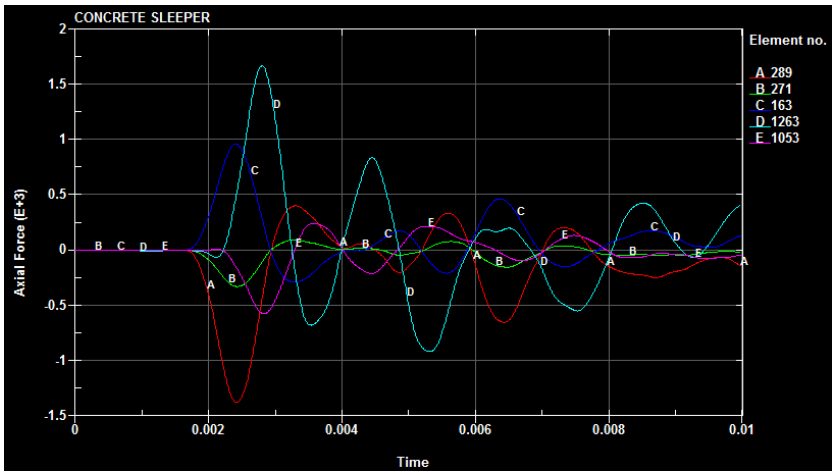


c) an example of prestressing force (at impact velocity 3 m/s)

Figure 6: Comparison of numerical and experimental results

## 4 EFFECT OF ULTRA HIGH STRENGTH OF CONCRETE

The relationship between compressive strength and elastic modulus of concrete is a complex topic. As shown in Figure 7, the modulus of concrete can vary from 50GPa to 100GPa (depending on the type of concrete mixes). In this analysis, the modulus of 50 GPa, 80GPa, and 100 GPa are considered for benchmarking analysis. In the finite element model, the drop velocity is also varied to evaluate the effect of drop heights on the impact force occurring on railway track structures. On the other hand, this analysis provides the insight into the effect of railway track environments on the contact impact forces due to the identical causes and the responses of concrete sleepers to such loading. For example, a wheel, with 10mm wheel flat on a specific vehicle and running at 300 km/h, generates different contact impact forces on tracks with different environments. However, this study focuses only on concrete parameters as they play key role on the interface impact force characteristics and flexural responses of sleepers under a low-velocity impact [20] as illustrated in Figure 8.

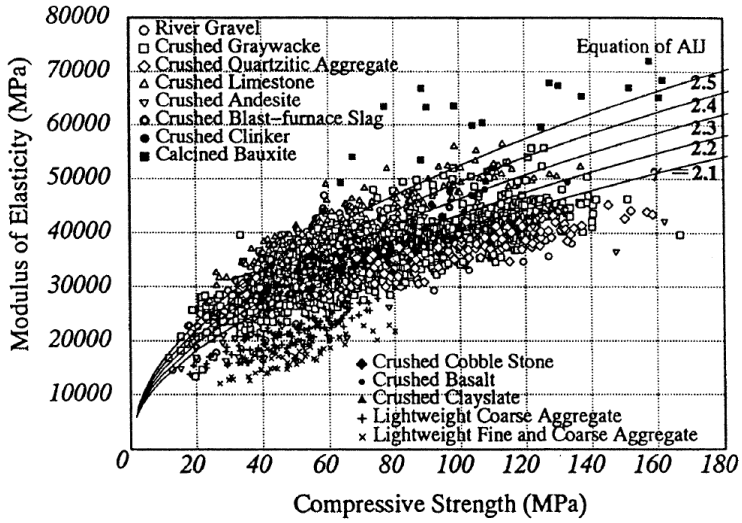


Figure 7: Compressive strength vs modulus of elasticity [22-25]

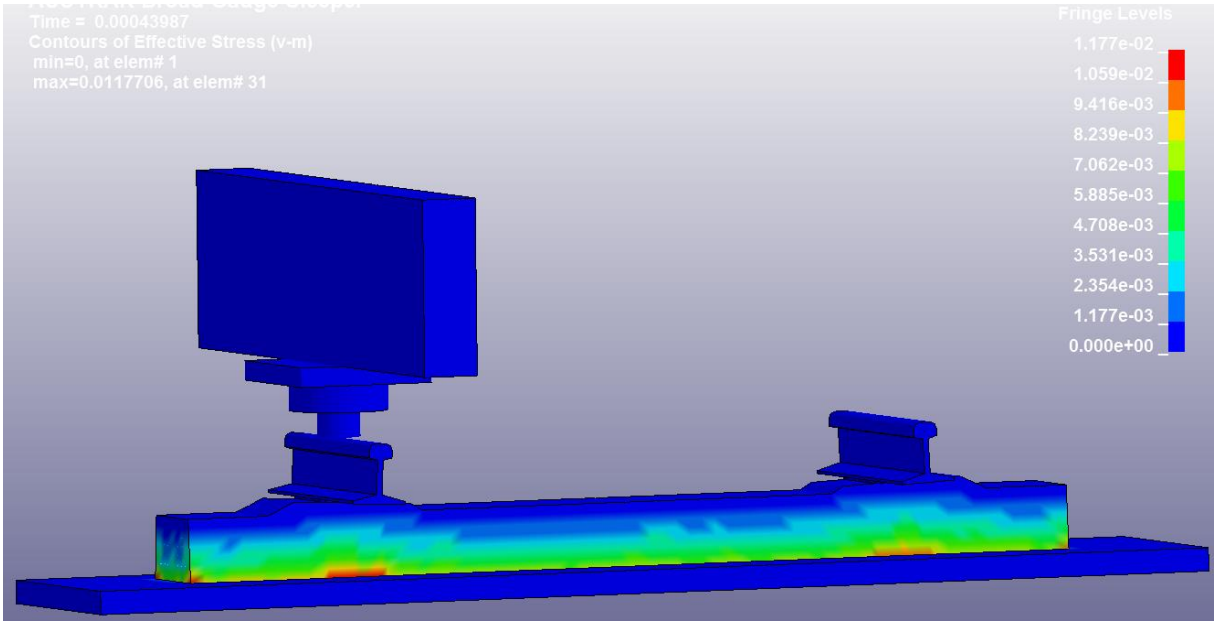


Figure 8: Impact von-misses stress in concrete sleeper (both railseats are firstly damaged)

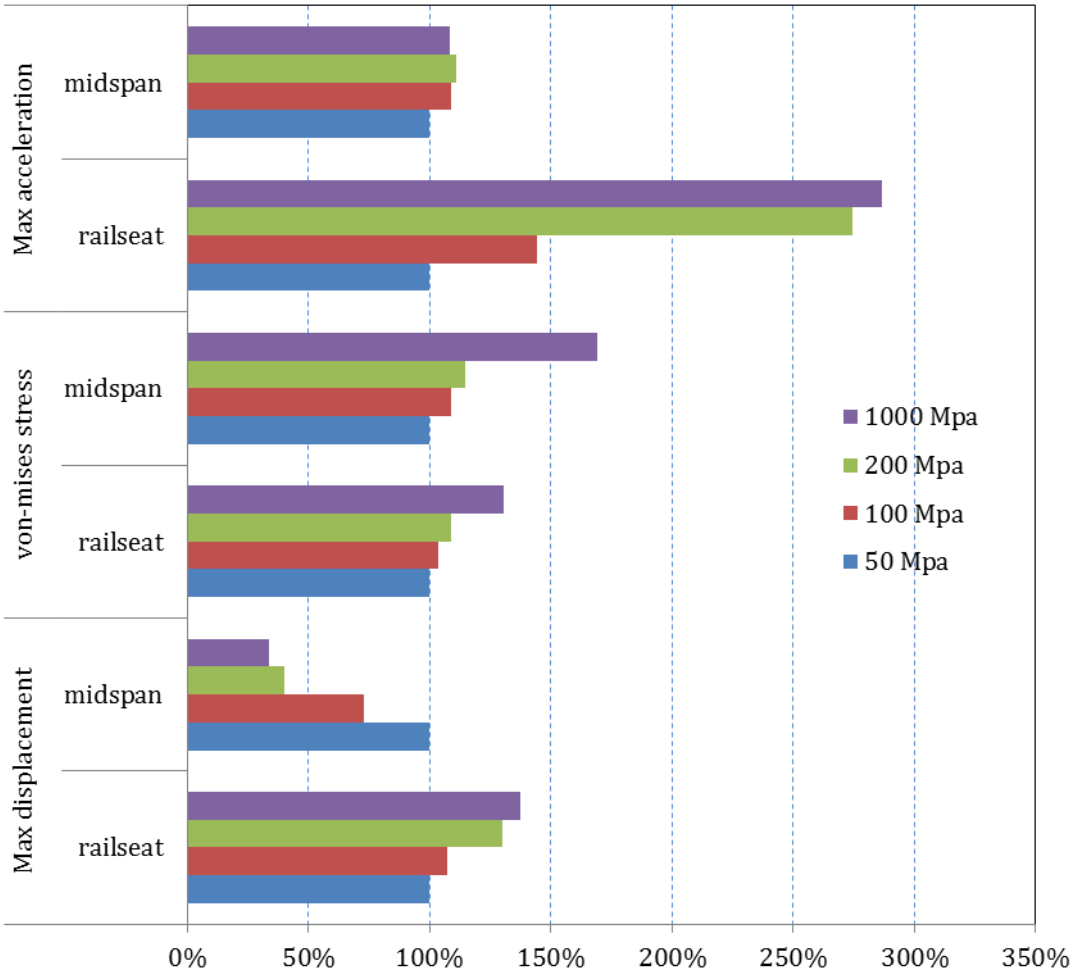


Figure 9: Effects of ultra-high-strength concrete on impact responses of railway sleepers

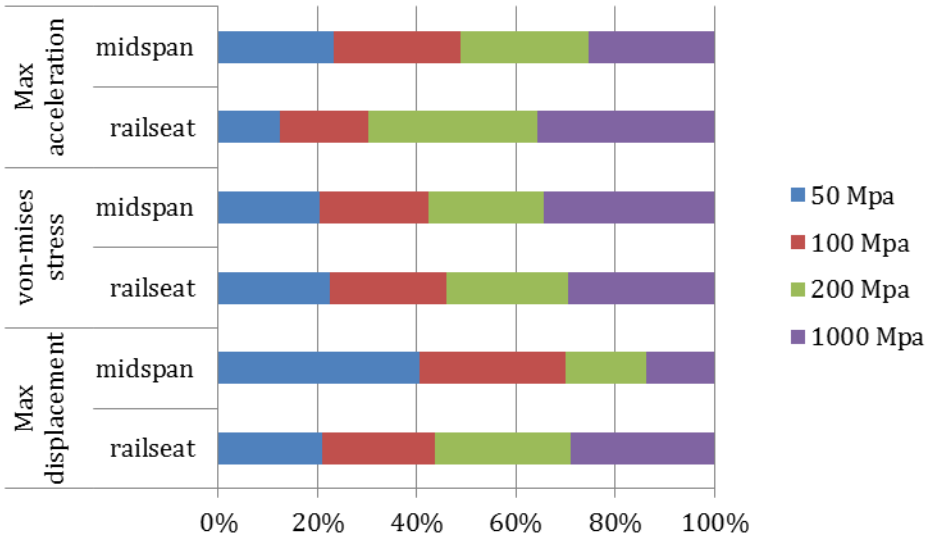


Figure 10: Influential analysis of ultra-high-strength concrete

Figures 9 and 10 demonstrate the dynamic effects of ultra-high-strength concrete on the impact responses of a railway sleeper. Using a normal high-strength concrete (50 MPa) as a baseline, it is clear that concrete strength plays an influential role in the maximum displacement, maximum acceleration and von-mises stress of the sleeper at both railseat and midspan zones. Especially at mid span, the von-mises stress can increase significantly due to the use of higher strength concrete. From Figure 10, it is clear that, in most cases, higher strength of concrete has more influence on the sleeper responses (except for the maximum displacement at mid span).

## 5 CONCLUSIONS

Ultra high strength concrete has recently been introduced in construction industry. Its application to railway environment has not been fully investigated. In this study, its use to manufacturing railway sleepers has been evaluated. The study is based on the experimental and numerical simulations of prestressed concrete sleepers subjected to impact loading. The three-dimensional finite element model have been established for investigate both static and dynamic behaviors of the railway sleepers. It has then been appended the track components to mimic in-situ conditions often found in actual tracks. A commercial finite element package, LS-Dyna, has been employed to extend the model for impact analysis and it has been validated against experimental drop impact tests. Nonlinear material properties under high strain rate effects were used. The emphasis of this study is placed on the effects of ultra-high-strength concrete on the dynamic responses of railway sleeper. This result illustrates dominant influences of concrete elastic moduli on the impact behavior of the sleeper. It is found that the ultra-high-strength concrete will increase stiffness of sleepers, then increase contact forces and dynamic responses of the sleepers.

## ACKNOWLEDGEMENT

The first author would like to gratefully acknowledge the University of Birmingham's BRIDGE Grant, which financially supports this work as part of the project "Improving damping and dynamic resistance in concrete through micro- and nano-engineering for sustainable and environmental-friendly applications in railway and other civil construction". This project is part of a collaborative BRIDGE program between the University of Birmingham and the University of Illinois at Urbana Champaign. The pre-stressed concrete sleepers were kindly provided by Austrak Ltd. The authors would also like to thank Alan Grant, Ian Bridge, Bob Roland, and Jason Knurst, for their assistance during the course of the experimental work. In addition, special thanks go to European Commission for financially sponsoring H2020-MSCA-RISE Project No. 691135 "RISEN: Rail Infrastructure Systems Engineering Network" (www.risen2rail.eu).

## REFERENCES

[1] Kaewunruen, S and Remennikov, AM, Non-destructive testing (NDT): A tool for dynamic health monitoring of railway track structures. *Materials Australia*, 39(6), 14-16 (invited), 2006.

[2] Remennikov, A.M. and Kaewunruen, S., A review on loading conditions for railway track structures due to train and track vertical interaction. *Structural Control and Health Monitoring*, 15, 207-234, 2008.

[3] Murray, M and Cai, Z, Literature review on the design of railway prestressed concrete sleeper. *RSTA Research Report*, Australia, 1998.

[4] Kaewunruen, S and Remennikov, AM, "Experimental and numerical studies of railway prestressed concrete sleepers under static and impact loads." *Civil Computing*, AIT-ACECOMS, inpress, 2007, (invited).

[5] Gustavson, R, "Static and dynamic finite element analyses of concrete sleepers*", Licentiate of Engineering Thesis*, Department of Structural Engineering, Chalmers University of Technology, Sweden, 2000.

[6] Gustavson, R, "Structural behaviour of concrete railway sleepers", *PhD Thesis*, Department of Structural Engineering, Chalmers University of Technology, Sweden, 2002

[7] Kaewunruen, S and Remennikov, AM, "Nonlinear finite element modelling of railway prestressed concrete sleeper", *Proceedings of the tenth East Asia-Pacific Conference on Structural Engineering & Construction (EASEC-10)*, Bangkok, Thailand, August 3-5, 2006, Vol. 4, pp. 323-328.

[8] Standards Australia, "Railway track material - Part 14: Prestressed concrete sleepers" *Australian Standard: AS1085.14-2003*, 2003a.

[9] Standards Australia, "Railway track material - Part 19: Resilient fastening assemblies" *Australian Standard: AS1085.19-2003*, 2003b.

[10] Livermore Software Technology Corporation, *LS-DYNA theoretical manual*. Livermore Software Technology Corporation, May 1998.

[11] Standards Australia, "Design of concrete structures" *Australian Standard: AS3600-2001*, 2001.

[12] Wakui H and Okuda H, "A study on limit-state design for prestressed concrete sleepers." *Concrete Library of JSCE* 33: pp. 1-25, 1999.

[13] Remennikov, AM and Kaewunruen, S, "Determination of dynamic properties of rail pads using instrumented hammer impact technique." *Acoustics Australia*, 33(2), 63-67, 2005.

[14] Remennikov, AM and Kaewunruen, S, "Experimental investigation on dynamic railway sleeper/ballast interaction." *Experimental Mechanics*, 46(1), 57-66, 2006.

[15] Kaewunruen, S and Remennikov, AM, "Sensitivity analysis of free vibration characteristics of an in-situ railway concrete sleeper to variations of rail pad parameters." *Journal of Sound and Vibration*, 298(1-2), 453-461, 2006.

[16] Kaewunruen, S and Remennikov, AM, "Effect of improper ballast tamping/packing on dynamic behaviors of on-track railway concrete sleeper." *International Journal of Structural Stability and Dynamics*, 7(1), 1-11, 2007.

[17] Kaewunruen, S and Remennikov, AM, "Post-failure mechanism and residual load-carrying capacity of railway prestressed concrete sleeper under hogging moment", *Proceedings of the International Conference on Structural Integrity and Failure (SIF-2006)*, Sydney, Australia, September 27-29, pp. 331-336, 2006.

[18] Remennikov, AM, Kaewunruen, S, and Ikaunieks, K, "Deterioration of dynamic rail pad characteristics." *Proceedings of Conference of Railway Engineering 2006*, Apr 30 - May 3, Melbourne, Australia, pp.173-179, 2006.

[19] Kaewunruen, S and Remennikov, AM, "Monitoring structural degradation of rail bearing pads in laboratory using impact excitation technique." *Proceedings of the 1st International Conference on Structural Condition Assessment, Monitoring, and Improvement*, Dec 12-14, Perth, Australia, pp. 399-405, 2005.

[20] Kaewunruen, S. and Remennikov, A., "Low-velocity impact analysis of prestressed concrete sleepers." *Concrete Institute of Australia's 23rd Biennial Conference 07*, October 18-20, Adelaide, Australia, 2007, [CD Rom].

[21] Kaewunruen, S. and Remennikov, A., "Impact responses of prestressing tendons in railway concrete sleepers in high speed rail environments." *Proceedings of the 5$^{th}$ Computational Methods in Structural Dynamics and Earthquake Engineering*, May 25-27, Crete Island, Greece, 2015, [CD Rom].

[22] Tomosawa, F., Noguchi, T., "Relationship between compressive strength and modulus of elasticity of high-strength concrete", *Journal of Structural and Construction Engineering* (Transactions of AIJ), 60(474), 1995.

[23] Kaewunruen, S., Meesit, R., Mondal, P., "Early-age dynamic moduli of crumbed rubber concrete for compliant railway structures", *Journal of Sustainable Cement-Based Materials*, 2017, in press. doi: 10.1080/21650373.2017.1280425

[24] Meesit, R., Kaewunruen, S., "Vibration characteristics of micro-engineered crumb rubber concrete for railway sleeper applications", *Journal of Advanced Concrete Technology* 15 (2), 55-66, 2017. doi: 10.3151/jact.15.55

[25] Kaewunruen, S., Meesit, R., "Sensitivity of crumb rubber particle sizes on electrical resistance of rubberised concrete", *Cogent Engineering*, 3 (1), 1126937, 2016.

COMPDYN 2017
6th ECCOMAS Thematic Conference on
Computational Methods in Structural Dynamics and Earthquake Engineering
M. Papadrakakis, M. Fragiadakis (eds.)
Rhodes Island, Greece, 15–17 June 2017

# NONLINEAR MODELLING AND ANALYSIS OF MOVING TRAIN LOADS ON INTERSPERSED RAILWAY TRACKS

**Sakdirat Kaewunruen[1], Tomasz Lewandrowski[2], and Kritditorn Chamniprasart[3]**

[1] Birmingham Centre for Railway Research and Education, School of Civil Engineering
The University of Birmingham, Edgbaston, B15 2TT UK
e-mail: s.kaewunruen@bham.ac.uk

[2] Military University of Technology in Warsaw
Warsaw, Poland
tomaszlewandrowski@gmail.com

[3] Department of Mechanical Engineering, Faculty of Engineering, Chulalongkorn University
Bangkok, Thailand
kritditorn.ch@gmail.com

**Keywords:** interspersed track, timber sleeper, concrete sleeper, moving load, envelop analysis, dynamic response, dynamic factor, nonlinear transient analysis, tensionless support.

**Abstract.** *The interspersed pattern sleeper of railway track, which is a replacement of old timber sleeper with concrete, is often used as a temporary maintenance for second or third class railway lines with aging timber sleepers. However, their negative effect on the railway has to be taken into an account. The numerical simulations of interspersed sleeper railway tracks are conducted as well as the plain ones using a finite element program, STRAND7, so that the precise numerical models can be established. Two moving point loads, 100 kN each, are simulated to represent a passenger train bogie moving along each rail in 2 dimensional plane. Dynamic displacements and accelerations of all sleepers are then evaluated. Sensitivity analyses are carried out by varying the speed of the moving train loads from 5 km/h to 120 km/h and by changing the type of the interspersed patterns to determine the dynamic behaviours that can cause any more rapid deterioration of the interspersed tracks compared with plain railway tracks. The results demonstrate the potential sources of structural vibrations that will swiftly degrade the interspersed railway tracks. The insight will help track engineers to plan predictive maintenance and inspection of the interspersed railway tracks in live operational networks.*

## 1 INTRODUCTION

Timber components have for a long time been used as railway sleepers for a railway track in many parts of railway networks around the world. As the timber sleeper life span is around 15-20 years depending on application and maintenance, such timber sleepers will be required for maintenance or even a huge replacement at certain point in time. Also, unless used in low speed operation, timber sleepers require a strengthening for enhancement in ability to withstand high velocity operations or to restrain longitudinal rail forces preventing a track buckling. "Interspersed" is a method that can be used as a measure against these problems. Interspersed railway track can be built by re-sleepering old and rotten timber sleepers and replace it with concrete sleepers [1]. Due to differential track stiffness, deterioration process, and operational parameter, many patterns of interspersed railway tracks have been introduced i.e. 1 in 2, 1 in 3, 1 in 4 and so on (which mean there is 1 concrete sleeper in every indicated number of sleeper such as 1 in 4 mean 1 concrete sleeper in every 4 sleepers including the concrete itself). It is important to note that this type of railway track mainly existed in a second or third class of railway tracks with low operational speeds.

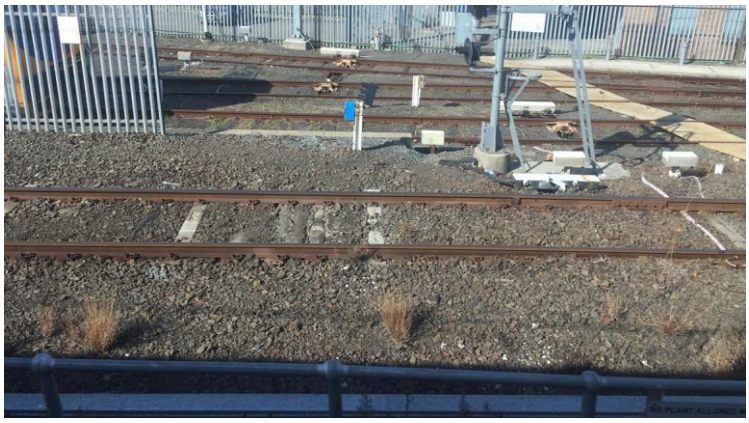

(TOP)



(BOTTOM)

Figure 1: Deteriorated interspersed railway track (Top: mud pumping, and Bottom: ballast pulverisation and ballast dilation)

The key reason is that this type of track has various flaws derived from how it is built. The replacement of old timber sleepers is frequently done over old and soft existed formation, which has been in services for so long, by installing new stiff concrete sleepers in its existing place. This can result in soil foundation failure, track stiffness inconsistency (as it made up of

both concrete and timber sleepers), and differential track decay rate [2]. These can impair the long-term performance of interspersed railway tracks as shown in Figure 1. Figure 1 shows the conditions of interspersed railway tracks under low-speed operations (<25 km/h). The tracks have been commissioned between 2006 and 2008 and have served as a link to maintenance junctions. The photos were taken in April 2016 during a site visit.

The serviceability limit state (or dynamic performance) has become the governing criteria for sleepers made of different material properties in the existing aged track systems. Note that this method is sometimes called 'spot replacement' or 'intersperse method'. It is important to note that a general recommendation (e.g. by Australian Office of Transport Safety Investigations) is to perform concrete sleeper installation only 'in-face' (i.e. the practice of installing the same sleeper type constinuously rather than interspersed with other sleepers in between, also referred to as 'on-face') [3-4]. This paper aims at investigating the nonlinear dynamic behaviours of the interspersed railway tracks. Based on critical literature review, this research has never been presented in open literature [3-6]. The insight into this practice will help rail track engineers to enable truly predictive track maintenance, enhance smarter track inspection regimes, and improve reliability of infrastructure assets in uncertain settings.

## 2 NONLINEAR FINITE ELEMENT MODELING

A 2D Timoshenko beam is selected as a beam model because it was found to be one of the most suitable options for modelling concrete sleeper [5]. For both rail track and sleeper they were designed as a beam element in finite model so shear and flexural deformation can be included in computation [6]. The rail pads at the rail seat are simulated by using series of spring dash-pot elements. In order to replicate ballast supports, non-linear tensionless beam support is used. The tensionless support can correctly demonstrate ballast under the sleeper as this attribute allow beam to lift over the support while the tensile support is omitted [6-8]. For train on the rail track, it is simplified to 2 points loads with 100kN in magnitude, 2m apart, on each side of the rail track (4 point loads in total), to enable envelop analysis (maximum responses). Figure 2 shows the illustration of the model.

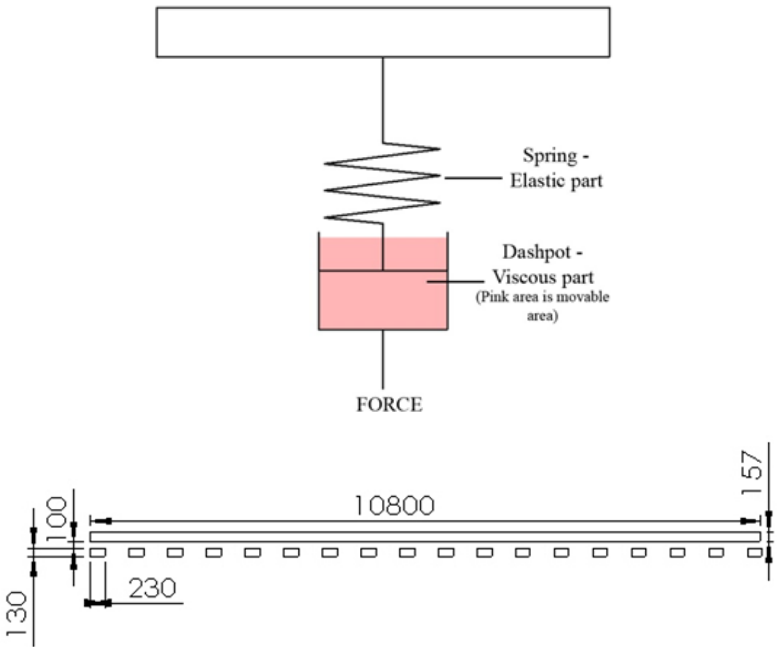


Figure 2: Schemetics of interspersed railway track modelling

The numerical simulation is conducted using non-linear transient dynamic solver in Strand7 to enable tensionless capability of ballast. The nonlinear iteration (Newton Raphson) has been used to compute the ballast contact and support. The model has been validated earlier using experimental parameters, field data and previous laboratory results [9-15].

## 3 DYNAMIC MOVING LOAD ANALYSIS

The effects of train velocity on the maximum responses of sleepers can be seen in Figure 3. The train speeds from 5 to 120 km/h have been investigated as shown in Figures 4 and 5. It is clear than the timber track has higher deformation. At rail seat, the relative uplifts of the sleepers tend to cause deteriorations of railway tracks over time. Figure 4 demonstrates the dynamic effects of interspersing methods coupled with train speeds on the maximum displacement responses of sleepers at mid spad. Considering the sleepers' responses, it is clear that timber sleepered tracks deform vertically lower than interspersed or concrete sleepered tracks. However, the concrete sleepers in either plain or interspersed tracks tend to deform significantly at their mid span. Such the deformations can cause centerbound problems or the issue with cracks at the midspan of sleepers. This issue is commonly found in railway tracks with poor maintenance. On this gound, the use of interspersed system will accelerate the centerbound problems in railway lines.

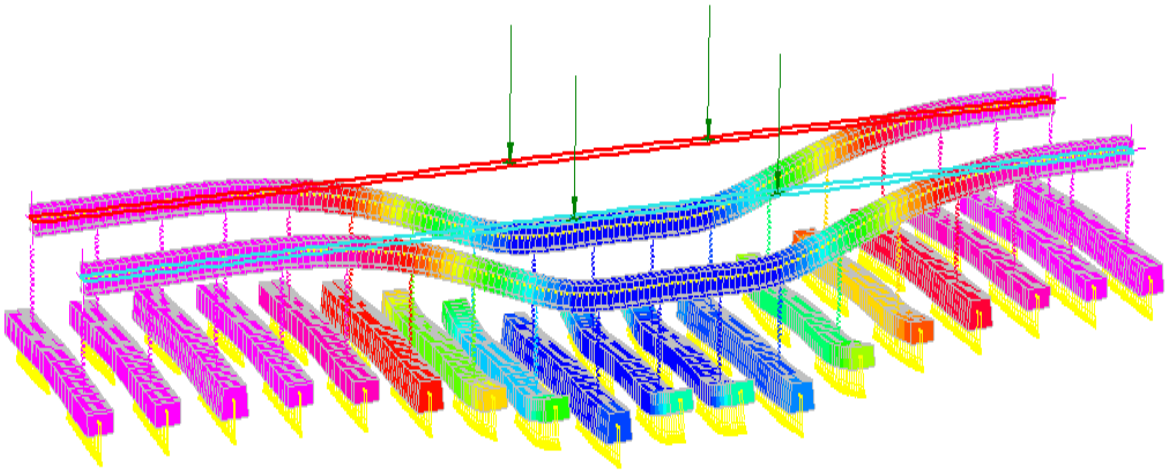

Figure 3: Dynamic responses of sleepers in the interspersed tracks

The dynamic effects of train velocity on the maximum uplift responses of sleepers can be seen in Figure 5. It is clear than the interspersed tracks have higher uplift deformation. The relative uplifts of the sleepers tend to cause deteriorations of railway tracks over time, such as ballast breakage, excessive dilation and densification, which can cause further track differential settlements. Figure 6 demonstrates the dynamic impact factor of interspersing methods coupled with train speeds on the maximum acceleration responses of the interspersed tracks. It is very clear that the heavy mass of concrete sleepers can suppress nonlinear vibration responses and secure the track through vibration control.

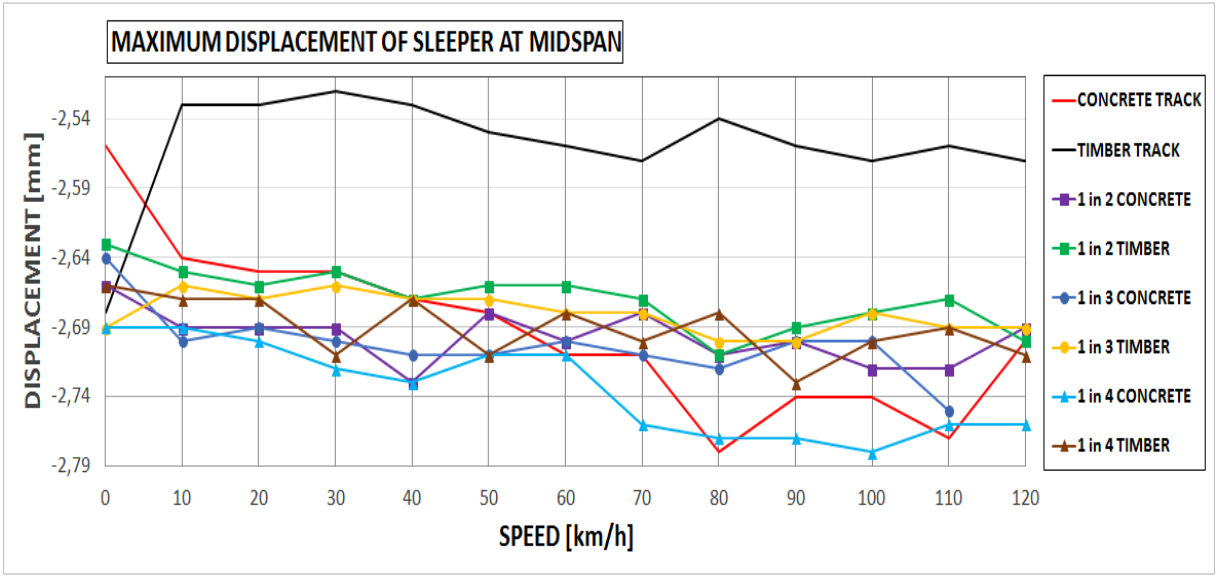


Figure 4: Maximum displacement of sleeper at midspan

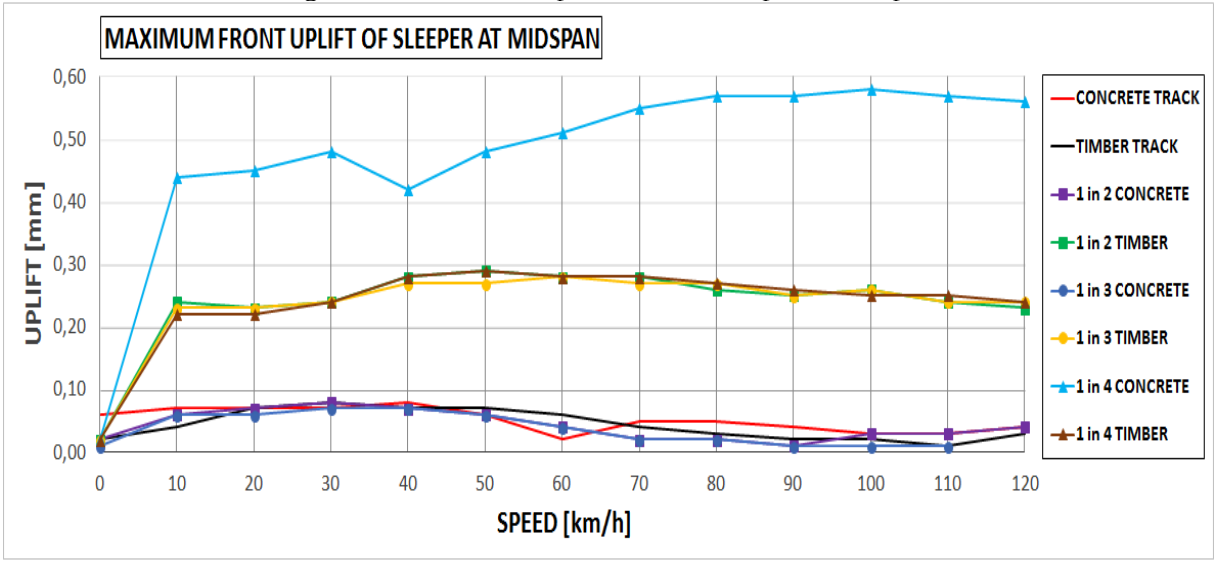


Figure 5: Maximum front uplift of sleeper at midspan

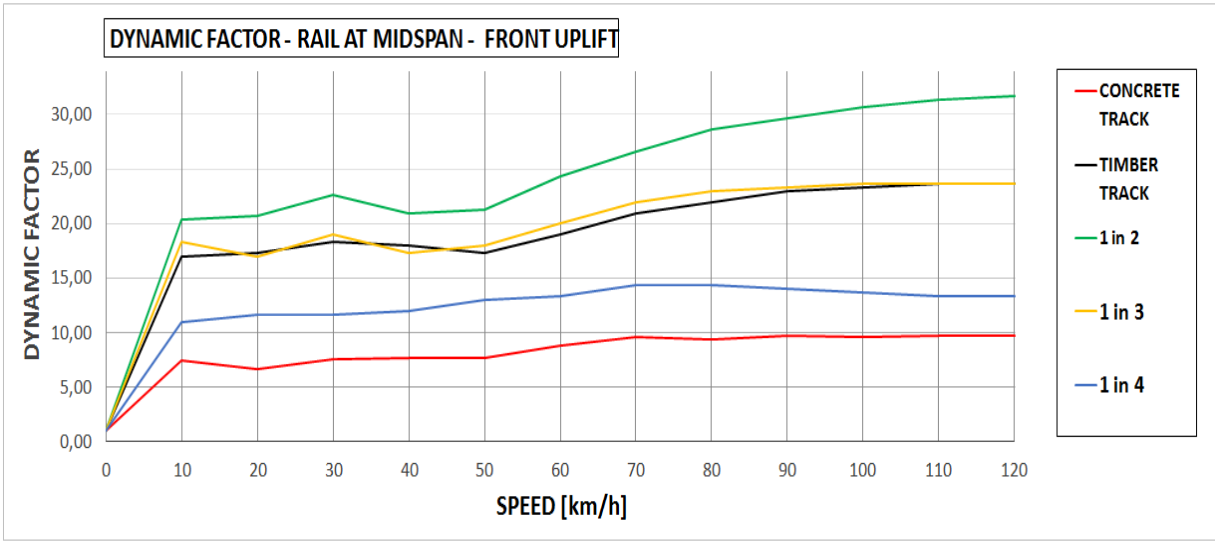


Figure 6: Dynamic factor of rail vibration at midspan (front uplift)

## 4 CONCLUSION

Railway industry in many countries around the world still adopts interspersed track system as a measure for spot replacement of decayed timber sleepers. Such practice is common for secondary or third class tracks where operations are not excessive. However, the practices can cause excessive track maintenance over time. This is because a cluster of timber sleepers with mixed quality could deteriorate faster than the others and the replacement by concrete sleepers could induce track stiffness inconsistency and aggravate loading conditions acting on the track. This paper is found to be the first to investigate nonlinear behaviours of the interspersed track due to a moving train load in order to understand the root cause of rapid track deterioration. A finite track models in three-dimensional space have been established and validated. The parametric studies have revealed the key insights into the actual source of track deterioration:

- Spot replacement of sleepers or interspersed tracks can deteriorate relatively faster than open-face tracks (i.e. pure concrete or timber sleepers). This is also evidenced by field monitoring.
- The cause of rapid deterioration such as track mud pumping, ballast pulverisation and ballast dilation is due to relative dynamic uplift responses of sleepers.
- Ballast dilation can be aggravated by concrete sleeper vibrations at resonance. The excessive ballast dilation can reduce lateral track stability.

## ACKNOWLEDGEMENT

The first author wishes to gratefully acknowledge the Japan Society for Promotion of Science (JSPS) for his JSPS Invitation Research Fellowship (Long-term), Grant No L15701, at Track Dynamics Laboratory, Railway Technical Research Institute and at Concrete Laboratory, the University of Tokyo, Tokyo, Japan. The JSPS financially supports this work as part of the research project, entitled “Smart and reliable railway infrastructure”. Special thanks to European Commission for H2020-MSCA-RISE Project No. 691135 “RISEN: Rail Infrastructure Systems Engineering Network” (www.risen2rail.eu). In addition, the sponsorships and assistance from CEMEX, Network Rail, RSSB (Rail Safety and Standard Board, UK) and G+D Computing (Dr Erik Kostson) with respect to STRAND7 are highly appreciated. Financial support from BRIDGE Grant (Collaboration between University of Birmingham and University of Illinois at Urbana Champaign) is also gratefully acknowledged.

## REFERENCES

[1] Kohoutek, R., “Dynamic and static performance of interspersed railway track,” Proceedings of Conference on Railway Engineering, Vol 1, pp.153-159, 1991.

[2] Kaewunruen S., Remennikov A.M., Akira A., Hirotaka S., 2014. “Free vibrations of interspersed railway track systems in three-dimensional space" Acoustics Australia, 42(1): 20-26, 2014.

[3] Lake, M, Ferreira, L, Murray, M., ‘Using simulation to evaluate rail sleeper replacement alternatives’. Transportation Research Record, 1785:58-63, 2002.

[4] Kaewunruen S, Mimoura S, Watanabe T, Remennikov AM, 'Remaining service life of railway prestressed concrete sleepers', International RILEM Conference on Materials, Systems and Structures in Civil Engineering, DTU, Denmark, 10p, 2016.

[5] Kaewunruen S, Remennikov AM., Investigation of free vibrations of voided concrete sleepers in railway track system, Proceedings of the Institution of Mechanical Engineers Part F Journal of Rail and Rapid Transit, 221(4): 495-508, 2007.

[6] Kaewunruen S, Remennikov AM., Effect of improper ballast packing/tamping on dynamic behaviours of on-track railway concrete sleeper, International Journal of Structural Stability and Dynamics 7(1): 167-177, 2007.

[7] Kaewunruen S, Remennikov AM., Sensitivity analysis of free vibration characteristics of an in-situ railway concrete sleeper to variations of rail pad parameters, Journal of Sound and Vibration 298(1-2): 453-461, 2006.

[8] Cai Z. Modelling of rail track dynamics and wheel/rail interaction, Ph.D. Thesis, Department of Civil Engineering, Queen's University, Ontario, Canada, 1992.

[9] Kaewunruen, S. and Chamniprasart, K., "Damage analysis of spot replacement sleepers interspersed in ballasted railway tracks", *Proceedings of the 29th Nordic Conference on Computational Mechanics*, Chalmers University of Technology, Gotenburg, Sweden, 2016.

[10] Kaewunruen, S., Lewandrowski, T. and Chamniprasart, K., "Dynamic responses of interspersed railway tracks to moving train loads", *International Journal of Structural Stability and Dynamics*, 18(1), 2017, in press.

[11] Kaewunruen S., Remennikov A.M., Nonlinear transient analysis of railway concrete sleepers in track systems. *International Journal of Structural Stability and Dynamics*, 8(3), 505-520, 2008.

[12] Kaewunruen S., Remennikov A.M., Dynamic properties of railway track and its components: Recent findings and future research direction, *Insight: Non-Destructive Testing and Condition Monitoring*, 52(1): 20-22, 2010.

[13] Kaewunruen S., Remennikov A.M., An alternative rail pad tester for measuring dynamic rail pad properties under large preloads, *Experimental Mechanics*, 48(1), 55-64, 2008.

[14] G+D Computing, *Using Strand7: Introduction to the Strand7 finite element analysis system*, Sydney, Australia, 2001.

[15] Kaewunruen S., Remennikov A.M., Effect of a large asymmetrical wheel burden on flexural response and failure of railway concrete sleepers in track systems, *Engineering Failure Analysis*, 15(8), 1065-1075, 2008.

COMPDYN 2017
6th ECCOMAS Thematic Conference on
Computational Methods in Structural Dynamics and Earthquake Engineering
M. Papadrakakis, M. Fragiadakis (eds.)
Rhodes Island, Greece, 15–17 June 2017

# DYNAMIC AMPLIFICATION FACTORS FOR RAILWAY TURNOUT BEARERS IN SWITCHES AND CROSSINGS

**Sakdirat Kaewunruen[1], Chayut Ngamkhanong[2], Rims Janeliukstis[3] and Ruilin You[4]**

[1] Birmingham Centre for Railway Research and Education, School of Civil Engineering
The University of Birmingham, Edgbaston, B15 2TT UK
e-mail: s.kaewunruen@bham.ac.uk

[2] Birmingham Centre for Railway Research and Education, School of Civil Engineering
The University of Birmingham, Edgbaston, B15 2TT UK
e-mail: chayut.ngam@gmail.com

[3] Department of Civil Engineering, Riga Technical University
Riga, Latvia
e-mail: rimas.j@inbox.lv

[3] Railway Engineering Institute, China Academy of Railway Sciences
Beijing, China
e-mail: youruilin0731@126.com

**Keywords:** Railway, Turnout bearers, Railroad bearers, Prestressing, Impact Analysis, Dynamic Responses, STRAND7.

**Abstract.** *Railway infrastructure is nonlinear by nature, scientifically proven by its behaviours, geometry and alignment, wheel-rail forces and operational parameters such as tractive efforts. It is often found that most train-turnout interaction models do not consider the time dependent ballast degradation. Such ballast degradation later causes differential settlement and aggravates impact forces acting on partial and unsupported sleepers and bearers. Furthermore, localised ballast breakages underneath any railseat increase the likelihood of centre-bound cracks in railway sleepers and bearers due to the unbalanced support. This paper presents a numerical simulation of a standard-gauge concrete bearer at crossing panel, taking into account the tensionless nature of ballast support. The finite element model was calibrated using static and dynamic responses using past experiments. In this paper, the influences of topologic asymmetry on dynamic amplification behaviours of crossing bearers under impact loading are firstly investigated. In addition, it is the first to demonstrate the effects of sleeper length on the design consideration of turnout bearers in crossing panel. The outcome of this study will improve the railway turnout construction and maintenance criteria in order to improve train-turnout interaction and ride comfort.*

## 1 INTRODUCTION

A typical ballasted railway track consists of many key components that form specific functional assets such as railway tracks, bridges, turnouts, overhead line structure, etc. Railway sleepers or bearers (also called 'railroad tie' in North America) are a vital structural element in the railway track systems. Railway sleepers are different to bearers in terms of topology, location, utilization, steel rail components they support, and the dynamic load condition they are subjected to. Their key role is quite similar to sleepers that they serve to redistribute loads from the rails to the underlying ballast bed, as well as to secure rails and crossings under live operations. Based on the current design approach, the design life span of the concrete sleepers is targeted at around 50 years in Australia and around 70 years in Europe [1-6], whilst turnout bearers tend to last just about half lives of sleepers in the field. There have been a number of previous investigations on the railway sleeper/bearer models [7-11]. Most of the models employed the concept of beam on elastic foundation where a sleeper is laid on the elastic support, acting like a series of springs. It is found that only vertical stiffness is sufficient to simulate the ballast support condition because the lateral stiffness seems to play an insignificant role in sleeper's bending responses [12-14]. In practice, the lateral force is less than 20% of vertical force and the anchorage of fastening has been designed to take care of lateral actions [12]. In fact, field measurements suggest a diverse range of sleeper flexural behaviors, which are largely dependent on the support condition induced by ballast packing and tamping [13-18]. However, it is still questionable at large whether modern ballast tamping process is effective and it could enable adequate symmetrical support for sleeper at railseat areas. In reality, the ballast is tamped only at the railseat areas. The ballast at the mid span is left loosening, with the intention to reduce negative bending moment effect on sleeper mid span, which is the cause of centre bound. Over time, the dynamic track settlement induces ballast densification and the sleeper mid-span comes into contact or is fully supported by ballast until the track geometry is restored by resurfacing activity (i.e. re-tamping).

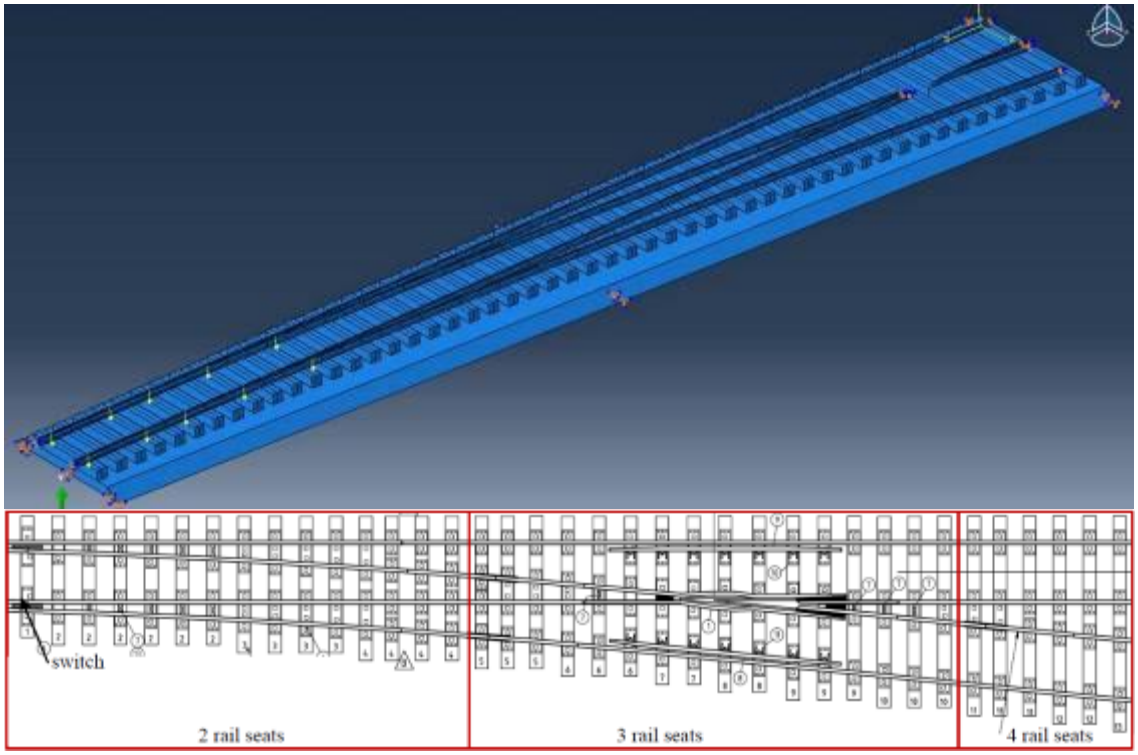


Figure 1: Typical turnout system layout (Sae Siew et al., 2016).

Based on a review of open literatures, the dynamic behavior of turnout bearers has not been fully investigated. As shown in Figure 1, a railway turnout system have generally been analysed the using a grillage beam method [19-20]. Although the simplification is very useful, such a method could not adequately assist in the failure analyses of turnout components. In some cases, the results using the grillage beam method seem to have discrepancies with the field observations where the maximum bending and shear forces were evident within the crossing panel [21]. A number of researches have been conducted to locate the critical section within a turnout, and many of which conclude that the critical section is located specifically at the crossing panel at either v-crossing or k-crossing [20]. Although it is clear that the turnout bearers are topological asymmetry, such the aspect has never been fully investigated. This paper presents an advanced turnout bearer modeling capable of nonlinear impact analysis into the dynamic effect of topological asymmetry of railway turnout bearers. It focuses on the nonlinear dynamic flexural responses of railway concrete sleepers subjected to a spectrum of ballast stiffness at the mid span, in comparison with the current design method in accordance with the design standards.

## 2 FINITE ELEMENT MODEL

In this study, a finite element model of concrete sleeper (optimal length) has been previously developed and calibrated against the numerical and experimental modal parameters [15]. The model is in very good agreement with previous extensive studies, which established that the two-dimensional Timoshenko beam model is the most suitable option for modeling concrete sleepers under vertical loads [7-9]. Figure 2 shows the two-dimensional finite element model for in-situ railway turnout bearers. Using a general-purpose finite element package STRAND7 [22], the numerical model included the beam elements, which take into account shear and flexural deformations, for modeling the concrete sleeper. The trapezoidal cross-section was assigned to the sleeper elements. The rails and rail pads at railseats were simulated using a series of spring. In this study, the bearer behaviour is stressed so that very small stiffness values were assigned to these springs. In reality, the ballast support is made of loose, coarse, granular materials with high internal friction. It is often a mix of crushed stone, gravel, and crushed gravel through a specific particle size distribution. It should be noted that the ballast provides resistance to compression only. It is noted that the use of elastic foundation in the current standards in Australia and North America [1, 18] does not well represent the real uplift behaviour of bearers in hogging moment region (or mid span zone of railway bearers). In this study, the support condition was simulated using the tensionless beam support feature in Strand7 [22]. This attribute allows the beam to lift or hover over the support while the tensile supporting stiffness is omitted. The tensionless support option can correctly represent the ballast characteristics in real tracks. Table 1 shows the geometrical and material properties of the finite element model. It is important to note that the parameters in Table 1 give a representation of a specific rail track in Europe. These data have been validated and the verification results have been presented elsewhere [15]. Also, the flexural influences on railway concrete bearers in a turnout system (switch and crossing) due to the variations of ballast support conditions together with the asymmetric topology of sleeper has not yet addressed by the past researchers [21]. Especially when the uplift behaviour due to ballast tensionless support in hogging region of sleepers is considered, a finite element analysis is thus required to supersede the simple manual calculation. For this study, the numerical simulations have been extended to conduct the analyses using the nonlinear solver in STRAND7. The effects of asymmetric topology of concrete bearers on their flexural responses in a turnout system can be evaluated. The length of bearer varies from 2.5m to 4.0m, which is practically common in the 2 and 3 rail-seats sections (see Figure 2).

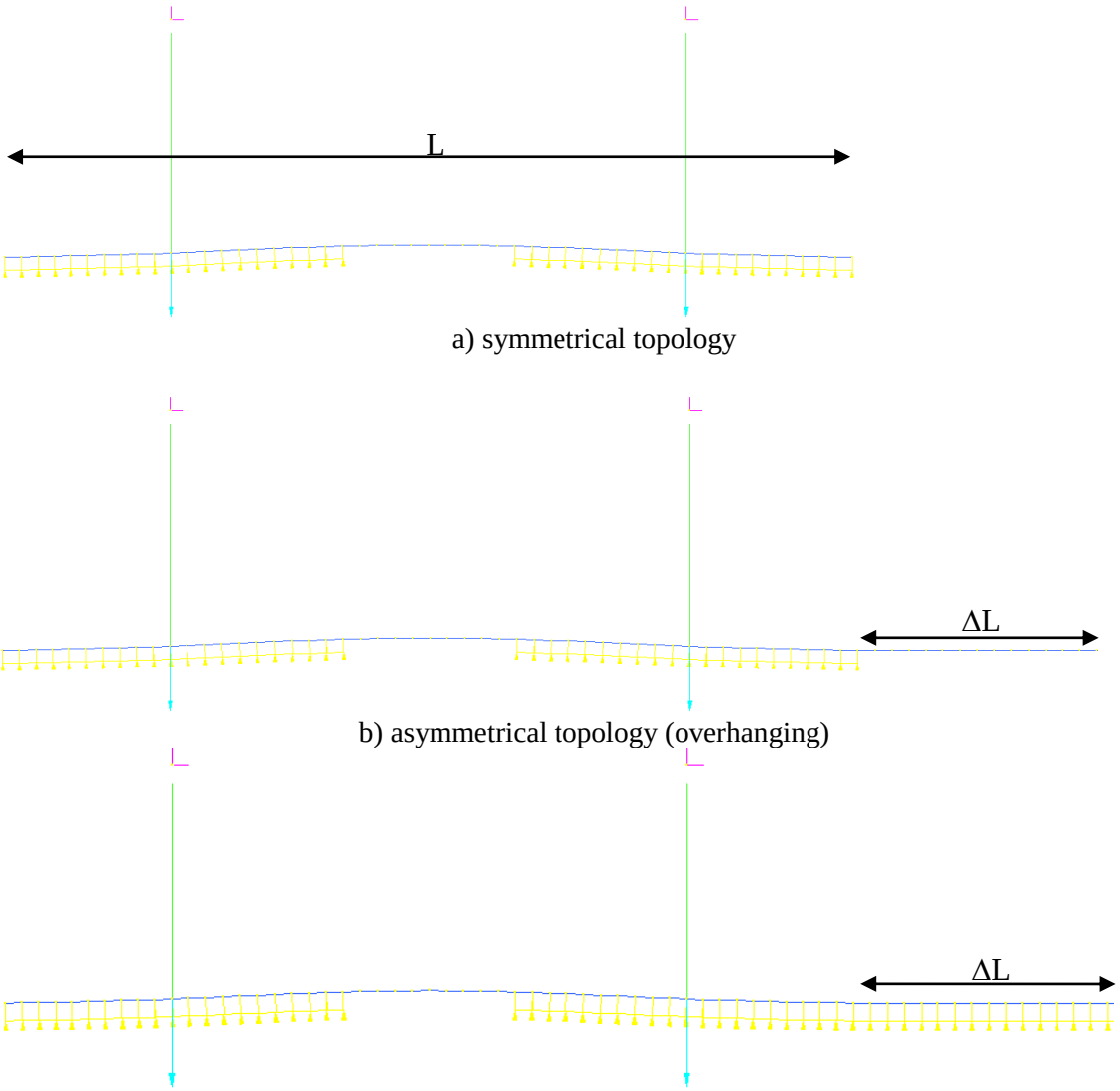


a) symmetrical topology

b) asymmetrical topology (overhanging)

c) asymmetrical topology (fully supported)

Figure 2. STRAND7 finite element model of a concrete bearer

Table 1 Engineering properties of the standard sleeper used in the modeling validation

| **Parameter lists** | | |
|---|---|---|
| Flexural rigidity | $EI_c$ = 4.60, $EI_r$ = 6.41 | MN/m$^2$ |
| Shear rigidity | $\kappa GA_c$ = 502, $\kappa GA_r$ = 628 | MN |
| Ballast stiffness | $k_b$ = 13 | MN/m$^2$ |
| Rail pad stiffness | $k_p$ = 17 | MN/m |
| Sleeper density | $\rho_s$ = 2,750 | kg/m$^3$ |
| Sleeper length | $L$ = 2.5 | m |
| Rail gauge | $g$ = 1.5 | m |

## 3 RESULTS AND DISCUSSION

The numerical simulations based on the design data in Table 1 enable Tables 2 and 3 that present the dynamic bending moment envelops along the bearer when subjected to the equal wheel load impulse of 100kN (3 ms) at both railseats, in comparison with the standard design moments. Based on AS1085.14 (Standards Australia, 2003), the design maximum positive bending moment at the rail seat = 12.50 kNm, while the centre negative design bending moment = 6.95 kNm (if considered half support) or =12.50 kNm (if considered full support). It is typical that the positive and negative moments are associated with the railseat and mid-span sections, respectively.

Table 2 Maximum bending moment of overhanging bearer

| **ΔL/L** (overhanging) | **At railseat (kNm)** | | **At mid span (kNm)** | |
|---|---|---|---|---|
| | M* | $\lvert M^*/M_{Design}\rvert$ | M* | $\lvert M^*/M_{Design}\rvert$ |
| 0 | + 13.81 | 1.1048 | +15.01 | 2.16 |
| 10% | +14.40 | 1.152 | - 8.01 | 1.15 |
| 20% | +18.65 | 1.492 | +9.30 | 1.34 |
| 30% | +14.46 | 1.1568 | +16.14 | 2.32 |
| 40% | +13.29 | 1.0632 | +14.34 | 2.06 |
| 50% | +14.69 | 1.1752 | +12.08 | 1.74 |
| 60% | +14.17 | 1.1336 | +10.09 | 1.45 |

Table 3 Maximum bending moment of fully-supported bearer

| **ΔL/L** (full support) | **At railseat (kNm)** | | **At mid span (kNm)** | |
|---|---|---|---|---|
| | M* | $\lvert M^*/M_{Design}\rvert$ | M* | $\lvert M^*/M_{Design}\rvert$ |
| 0 | + 13.81 | 1.10 | +15.01 | 2.16 |
| 10% | +14.40 | 1.15 | +9.35 | 1.35 |
| 20% | +18.69 | 1.50 | +9.50 | 1.37 |
| 30% | +14.51 | 1.16 | +16.50 | 2.37 |
| 40% | +13.30 | 1.06 | +14.85 | 2.14 |
| 50% | +14.73 | 1.18 | +12.75 | 1.83 |
| 60% | +14.21 | 1.14 | +10.00 | 1.44 |

Based on the static results in Tables 2 and 3, it is clear that the influence of the asymmetrical topology is more pronounced when there is a contact between bearer and ballast layer. Considering field investigation, such the contact could occur when there is a differential settlement on the mainline track (or run-through turnout road). Once the ballast-bearer contact establishes, the bearer will take additional bending moment at the inner railseat. Figures 3 and 4 demonstrate the dynamic amplification factors (DAF) for the turnout bearers. It can be seen that the common use of DAF around 2.5 (e.g. in Australian Standard and AREMA) is considered to be suitable for the turnout bearers, provided that the dynamic impact load amplitudes are retained at the same level. This also implies that if the train wheels or turnout crossings

are not properly maintained, the turnout bearers are likely to reach the structural capacity design under dynamic loading and are potentially be damaged.

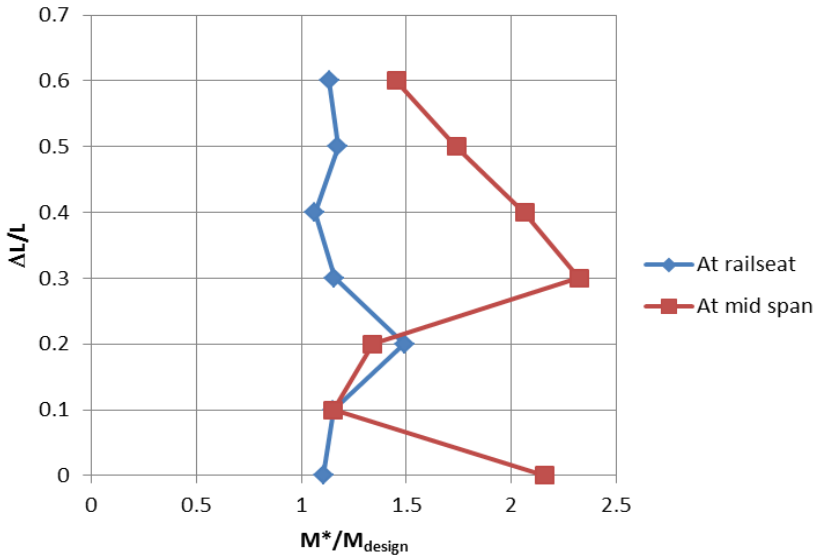


Figure 3. Dynamic amplification factor of concrete bearers under overhanging condition

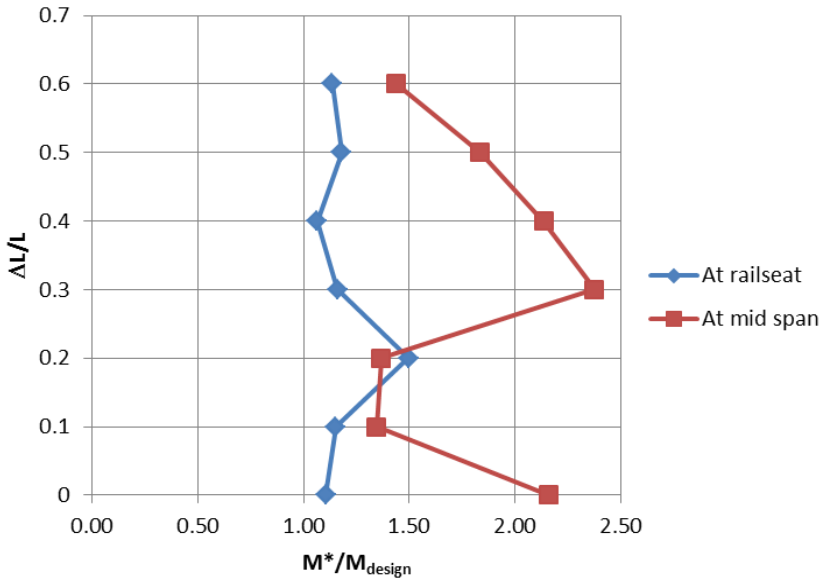


Figure4. Dynamic amplification factor of concrete bearers under ballast support condition

## 4 CONCLUSION

Railway turnout bearers are structural and safety critical components in railway turnout systems. This paper evaluates the critical dynamic transient effects of a variety of ballast conditions and asymmetric topology on the flexural responses of railway turnout bearers in a turnout system (switches and crossings) subjected to impact loading. The finite element model of bearers, which was established and calibrated earlier, is utilised in this study. The nonlinear solver in STRAND7 was employed to handle sleeper/ballast contact mechanics. Under dynamic impact conditions for overhanging and supported bearers, the numerical results exhibit that the bending moment resultants are considerably affected by topological aspects, es-

pecially when the ballast-sleeper contact is established. The standard design bending moments tend to be a fair estimate for both supported and overhanging conditions. Generally, positive bending moments at inner railseat of bearer have generally high sensitivity to the spectrum of ballast support conditions in comparison with the more pronounced influence of sleeper length. By understanding the impact behavior of turnout bearers, it is clear that the dynamic amplification factor of 2.5 is a minimum requirement in the design of turnout bearers. This implies that the turnout bearers are prone to damage under high-intensity impact loading, which could trigger and sweep through various resonant frequencies of the turnout bearers. The insight in this dynamic behavior of bearer has raised the awareness of track engineers for better design and maintenance of switch and crossing support structures.

## ACKNOWLEDGEMENTS

The first author wishes to gratefully acknowledge the Japan Society for Promotion of Science (JSPS) for his JSPS Invitation Research Fellowship (Long-term), Grant No L15701, at Track Dynamics Laboratory, Railway Technical Research Institute and at Concrete Laboratory, the University of Tokyo, Tokyo, Japan. The JSPS financially supports this work as part of the research project, entitled "Smart and reliable railway infrastructure". Special thanks to European Commission for H2020-MSCA-RISE Project No. 691135 "RISEN: Rail Infrastructure Systems Engineering Network" (www.risen2rail.eu). In addition, the sponsorships and assistance from CEMEX, Network Rail, RSSB (Rail Safety and Standard Board, UK) and G+D Computing (Dr Erik Kostson) with respect to STRAND7 are highly appreciated.

## REFERENCES

[1] Standards Australia, *Australian Standard: AS1085.14-2003 Railway track material - Part 14: Prestressed concrete sleepers*, Sydney, Australia, 2003.

[2] Kaewunruen, S., Ishida, T., Remennikov, A.M., "Numerical simulations of negative flexural responses (hogging) in railway prestressed concrete sleepers", *RILEM International Conference on Strategies for Sustainable Concrete*, Rio de Janeiro, Brazil, December 14-16, 2015.

[3] Kaewunruen, S., Ishida, T., Remennikov, A.M., "Impact analyses for negative flexural responses (hogging) in railway prestressed concrete sleepers", *International Conference on Recent Advances in Structural Dynamics*, Southampton, UK, July 3-6, 2016.

[4] Kaewunruen, S., Minoura, S., Watanabe, T., Remennikov, A.M., "Remaining service life of railway prestressed concrete sleepers", *Proceedings of International RILEM Conference on Materials, Systems and Structures in Civil Engineering*, 22-24 August 2016, Technical University of Denmark, Lyngby, Denmark, 2016.

[5] Kaewunruen, S. and Chamniprasart, K., "Damage analysis of spot replacement sleepers interspersed in ballasted railway tracks", *Proceedings of the 29th Nordic Conference on Computational Mechanics*, Chalmers University of Technology, Gotenburg, Sweden, 2016.

[6] Kaewunruen, S., Remennikov, A.M., "Nonlinear finite element modeling of railway prestressed concrete sleeper", *Proceedings of the 10th East Asia-Pacific Conference on*

*Structural Engineering and Construction, EASEC 2010*; Bangkok; Thailand; 3 August 2006 through 5 August, 2006.

[7] Grassie, S.L. Dynamic modelling of concrete railway sleepers. *Journal of Sound Vibration*, 187, 799-813, 1995

[8] Neilsen JCO., Eigenfrequencies and eigenmodes of beam structures on an elastic foundation, *Journal of Sound and Vibration*, 145, 479-487, 1991.

[9] Cai Z. Modelling of rail track dynamics and wheel/rail interaction, *Ph.D. Thesis*, Department of Civil Engineering, Queen's University, Ontario, Canada, 1992.

[10] Kassa, E. & Nielsen, J. C. O. Dynamic train–turnout interaction in an extended frequency range using a detailed model of track dynamics. *Journal of Sound and Vibration*, 320, 893-914, 2009.

[11] Remennikov, A.M. and Kaewunruen, S., Experimental load rating of aged railway concrete sleepers, *Engineering Structures*, 76(10), 147-162, 2014.

[12] Remennikov, A.M. and Kaewunruen, S., A review on loading conditions for , railway track structures due to wheel and rail vertical interactions, *Structural Control and Health Monitoring*, 15(2): 207-234, 2008.

[13] Kaewunruen S, Remennikov AM. Sensitivity analysis of free vibration characteristics of an in-situ railway concrete sleeper to variations of rail pad parameters, *Journal of Sound and Vibration* 298(1), 453-461, 2006.

[14] Kaewunruen S, Remennikov AM. Rotational capacity of railway prestressed concrete sleeper under static hogging moment, *Proceedings of the 10th East Asia-Pacific Conference on Structural Engineering and Construction*, Bangkok, Thailand, 2006.

[15] Kaewunruen S, Remennikov AM. Investigation of free vibrations of voided concrete sleepers in railway track system, *Proceedings of the Institution of Mechanical Engineers Part F Journal of Rail and Rapid Transit*, 221(4): 495-507, 2007.

[16] Sae Siew, J., Mirza, O., Kaewunruen, S., Nonlinear finite element modelling of railway turnout system considering bearer/sleeper-ballast interaction, *Journal of Structures*, 2015, http://dx.doi.org/10.1155/2015/598562

[17] Sae Siew, J., Mirza, O., Kaewunruen, S., Torsional effect on track support structures of rail turnouts crossing impact, *ASCE Journal of Transportation Engineering*, in press, 2016.

[18] Wolf, H.E., J.R. Edwards, M.S. Dersch and C.P.L. Barkan. Flexural Analysis of Prestressed Concrete Monoblock Sleepers for Heavy-haul Applications: Methodologies and Sensitivity to Support Conditions. In: *Proceedings of the 11th International Heavy Haul Association Conference*, Perth, Australia, June, 2015.

[19] Vu, M., Kaewunruen, S., Attard, M., Chapter 6 – Nonlinear 3D finite-element modeling for structural failure analysis of concrete sleepers/bearers at an urban turnout diamond, in *Handbook of Materials Failure Analysis with Case Studies from the Chemicals, Concrete and Power Industries*, p.123-160, Elsevier, the Netherlands. 2016, http://dx.doi.org/10.1016/B978-0-08-100116-5.00006-5

[20] Xiao, J., Zhang, F. & Qian, L. Numerical simulation of stress and deformation in a railway crossing. *Engineering Failure Analysis*, 18, 2296-2304, 2011.

[21] Manalo, A., Aravinthan, T., Karunasena, W., Stevens, N., "Analysis of a typical railway turnout sleeper system using grillage beam analogy", *Finite Elements in Analysis and Design*, 48(1): 1376-1391, 2012.

[22] G+D Computing, Using Strand7: Introduction to the Strand7 finite element analysis system, Sydney, Australia, 2001.

COMPDYN 2017
6th ECCOMAS Thematic Conference on
Computational Methods in Structural Dynamics and Earthquake Engineering
M. Papadrakakis, M. Fragiadakis (eds.)
Rhodes Island, Greece, 15–17 June 2017

# SEISMIC FRAGILITY OF HORIZONTAL PRESSURE VESSELS - EFFECTS OF STRUCTURAL INTERACTION BETWEEN INDUSTRIAL COMPONENTS

**J. Korndörfer, B. Hoffmeister and M. Feldmann**

Institute of Steel Construction
Mies-van-der-Rohe-Str. 1, 52074 Aachen, Germany
e-mail: korndoerfer@stb.rwth-aachen.de

**Keywords:** fragility surface, horizontal pressure vessel, cloud analysis, coupled systems, simplified model

**Abstract.** *The European project "INDUSE-2-SAFETY" aims at the development of a quantitative risk assessment methodology for seismic loss prevention of "special risk" petrochemical plants and components. To demonstrate the capabilities of this approach, a representative case study plant containing standard components is subjected to detailed investigation. Probabilistic seismic demand models are used to establish a relation between seismic demand and structural performance of the components with respect to relevant limit states. The resulting fragility curves are required as an input to the quantitative risk model.*

*The case study comprises of a LNG regasification plant which contains various components with extreme variability in structural and dynamic characteristics. Due to process flow related requirements, all of these components are interconnected by an extensive pipe network. In case of an earthquake, these interconnections may cause significant structural interaction effects. The influence of the coupling is hard to predict and thus often neglected or estimated inappropriately in a common structural design of a single plant component. Within this paper, the effects of structural interaction are assessed rigorously for a small part of the LNG plant using finite element methods. The subplant considered for this analysis consists of a horizontal pressure vessel, connected pipes and respective supporting structures.*

*Twenty-six natural seismic records are selected with respect to uniform site hazard spectra for three different return periods to account for a wide variability of earthquake characteristics such as magnitude, fault distance and wave content are considered in the analysis. Cloud analysis is employed to perform the probabilistic seismic demand analysis which yields the fragility of the horizontal pressure vessel. Besides the variability of the seismic input, the liquid filling level of the vessel as well as the direction of ground motion have been considered as additional sources of uncertainty.*

# 1 INTRODUCTION

Industrial plants can be of very complex nature due to a large number of possible components with extreme variability in structural and dynamic characteristics. In addition, process flow related interdependencies between the components govern the plant lay-out including interconnections by pipes and positions of supporting structures. It is, however, common practice to design the structures and components individually; the structural interaction between these subsystems is thus either neglected or taken into account only inappropriately, e.g. by provision of estimated forces without considering deformation compatibilities. These design methods might result in nonconservative assessment of the seismic performance of structures and components resulting in casualties and serious economic losses in case of earthquakes.

The study at hand focusses on the seismic performance of a horizontal pressure vessel, explicitly studying the effect of structural interaction with its surrounding components. The vessel is used for storage of liquefied natural gas (LNG) at an operating pressure of 6 bar. The component has an internal diameter of 2.6 m and a total length of 10.15 m (Volume of 51.2 m³). It is supported on two steel saddles (one free, one fixed in longitudinal direction) with a spacing of 6.3 m. The thickness of the vessel wall accounts to 8 mm and the material is SA240 Gr. 304 L. The vessel is part of a large LNG plant and is interconnected to several other industrial components by a piping system. For this purpose, two nozzles (DN 450/DN 500) are located on the top side of the vessel. The component under exam together with its surrounding is shown in Figure 1.

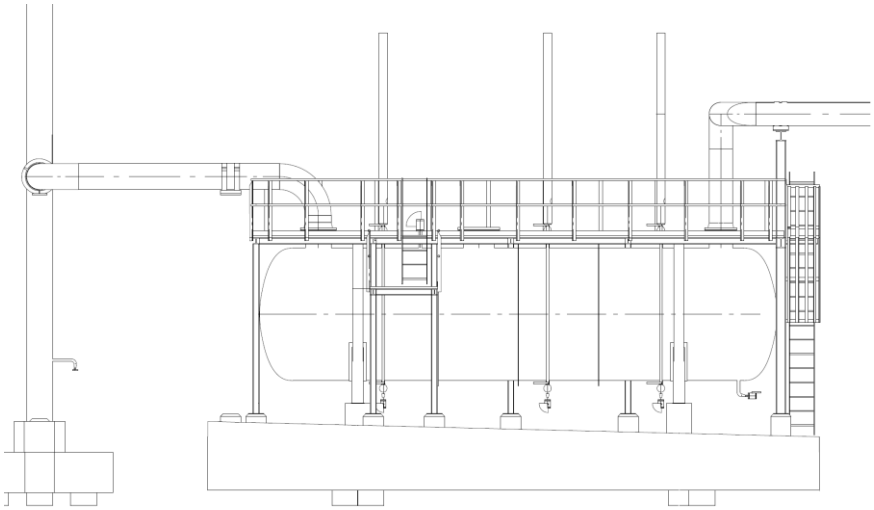

Figure 1: Horizontal pressure vessel under exam together with surrounding pipes and support structures

# 2 MODELLING APPROACH

## 2.1 Simplified modelling approach for horizontal pressure vessels

To derive fragilities of a structure numerically, dozens or even hundreds of dynamic transient simulations are required, depending on the probabilistic seismic demand model applied and on the amount of sources of uncertainties considered. Thus, simplified models are required to limit the computational effort and to efficiently assess the influence of different variables towards the fragility of the component under investigation. In the present study, a simplified model with only a few degrees of freedom, as shown in Figure 2, was used and implemented in ANSYS software to approximate the seismic response of the horizontal pressure vessel.

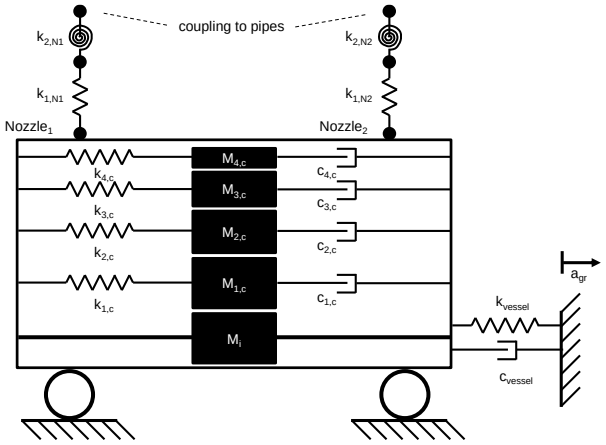


Figure 2: Sketch of the simplified model of the horizontal pressure vessel.

The simplified model is based on the assumption that deformations of the pressure vessel concentrate on the saddle region and the surrounding of the nozzles when subjected to seismic loading. Accordingly, the spring stiffnesses $k_{vessel}$ and $k_{i,Nj}$ have been calibrated to represent the nonlinear deformation behaviour as well as the dynamic structural response of the vessel. Approaches presented by Housner [1] and Karamanos [2] are adopted to take sloshing phenomena into account in a simplified way. The total mass of the pressure vessel is decomposed into an impulsive part (which incorporates the mass of the vessel and the impulsive component of the liquid) and four convective parts to account for the sloshing behaviour of the liquid filling (first four sloshing modes are considered). In the simplified model, the resulting masses are represented as lumped mass elements applied in their respective centre of gravity.

Three different limit states and associated engineering demand parameters (which are used to indicate whether or not the limit states are exceeded) were defined for the fragility analysis on the basis of nonlinear pushover simulations on a rigorous finite element model:

- LS 1: Rupture of vessel wall at saddle location
  ($EDP$: Base shear)
- LS 2: Rupture of vessel at nozzle transition'
  ($EDP$: Bending moment at the top of the nozzles)
- LS 3: Failure of the first anchor bolt
  ($EDP$: Base shear)

For more details on the derivation and verification of the simplified model as well as on the limit state analysis, please refer to [3].

## 2.2 Subplant model

The simplified model of the pressure vessel has been integrated into a realistic plant environment (coupled model) as indicated in Figure 1. Figure 3 shows the simplified model of the vessel (green) together with the pipes (red) that connect at both nozzle locations. Further, the supporting structure (blue) of the pipes is considered within the subplant.

The support structure consists of steel frames (S235) stiffened by diagonal X and V bracings. The structural elements are modelled using fibre section beam elements (BEAM188) with a bilinear elastic-plastic material behaviour (nominal stiffness/yield strength and 5% kinematic hardening). Additional dead and live loads are considered as nodal masses.

The pipes present in the subplant model are made of stainless steel SA Gr. 304 L which is identical to the material the pressure vessel itself is made of. One of them (DN 500) connects to nozzle 2 and leads to a ventilation stack. While this pipe is considered empty, the other three pipes are assumed to be filled with LNG. A DN 450 pipe connects to nozzle 1 of the pressure

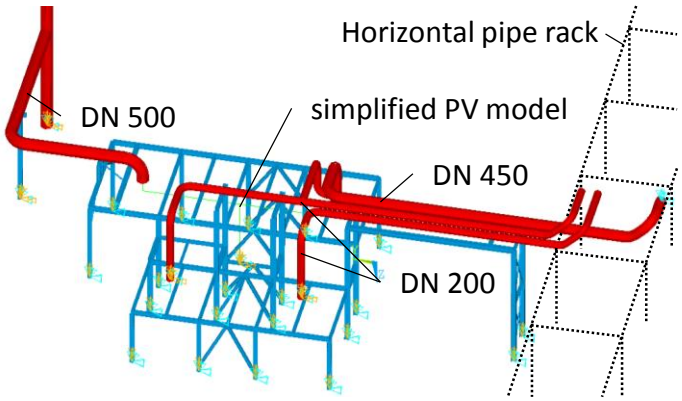


Figure 3: ANSYS model of the simplified pressure vessel model (green) coupled to surrounding pipes (red) and support structure (blue).

vessel whereas two smaller pipes (DN 200) are connected to another component, which is neglected in the model. The pipes continue to a horizontal pipe rack which is not considered in detail. Instead of explicitly modelling the pipe rack and the remaining components of the plant that are interacting with it, the dynamic characteristics of the surrounding of the subplant are taken into account as adjusted boundary conditions. For this in a first step, a modal analysis of the horizontal pipe rack was conducted to determine the decisive Eigenfrequencies of the structure and to estimate the participating masses in the respective modes. Then, single degree of freedom oscillators were employed in both horizontal directions and coupled to the end of the pipes to incorporate the dynamic response of the horizontal pipe rack. By following this approach, only the dominant modes in both directions are considered, while higher modes with low participation factors are neglected for simplicity reasons. The pipes were represented by pipe elements (PIPE288) with a bilinear elastic-plastic material behaviour ($E$=200000 N/mm²; $f_y$=200 N/mm²; $E_{hard}$=0.05·E).

## 3 FRAGILITY ANALYSIS

### 3.1 Fragility model

Within this study, fragility is defined with regards to seismic demands only. Thus, resulting fragilities represent the probability of exceeding a specific limit state at a specific level seismic intensity measure (IM) without considering uncertainties in the capacity of the system [4]:

$$F_{Rd}(x) = P[D \geq d^{LS} \mid IM = x] \tag{1}$$

where $D$ describes the seismic demand in terms of a suitable engineering demand parameter (e.g. base shear force, interstorey drift,…) and $d^{LS}$ represents the respective threshold value for the specific engineering demand parameter where the limit state is exceeded. Since uncertainties in the capacity of the system are not considered in a probabilistic manner, $d^{LS}$ is of deterministic nature. On the other hand, the seismic input is considered as a random variable, which means that the obtained seismic demand parameter $D$ is randomly distributed as well.

In a first step, the relation between seismic intensity measure (in the paper at hand, PGA has been adopted) and the seismic engineering demand parameter is established. The functional relationship between conditional median of the demand parameter $m_d$ and the seismic intensity measure $IM$ (probabilistic seismic demand model = PSDM) is generally assumed to follow a power law:

$$m_d = a(IM)^b \tag{2}$$

where $a$ and $b$ are regression parameters that are determined by a linear regression of the $ln(d_i)$ (maximum $EDP$ value observed during a seismic event) over $ln(IM_i)$ values (the index $i$ refers to the $i$-th seismic event), resulting from the probabilistic seismic demand analysis (e.g. incremental dynamic analysis or cloud analysis). The conditional logarithmic standard deviation of the fitted functional relationship between $m_d$ and $IM$ is calculated using eq. (3).

$$\beta_{d|IM} = \sqrt{\frac{\sum_{i=1}^{n}[ln(d_i) - ln(a(IM_i)^b)]^2}{n - df}} \tag{3}$$

where $n$ is the number of ground motions selected for the probabilistic seismic demand analysis and $df$ is the number of variables estimated in the linear regression (here, 2 variables are estimated – a and b, see equation (2)). Finally, the median $m_{Rd}$ as well as the dispersion $\beta_{Rd}$ of the demand fragility are calculated using the following equations:

$$m_{Rd} = \left(\frac{d^{LS}}{a}\right)^{1/b} \tag{4}$$

$$\beta_{Rd} = \frac{1}{b}\beta_{d|IM} \tag{5}$$

The seismic fragility is then expressed using a lognormal cumulative distribution function:

$$F_{Rd}(x) = P[D \geq d^{LS}|IM = x] = \Phi\left[\frac{\ln(x/m_{Rd})}{\beta_{Rd}}\right] \tag{6}$$

### 3.2 Probabilistic seismic demand model

Different methodologies for the probabilistic seismic demand analysis (PSDA) have been presented in literature [5]-[9]. The models most commonly used are the incremental dynamic analysis, the stripe analysis and the cloud analysis. In the present study, cloud analysis was selected for two reasons: Firstly, cloud analysis utilises the "bin" approach - instead of scaling up a single set of accelerograms to increase the intensity measure (which may not be realistic for higher scale factors), multiple sets of slightly scaled natural seismic records are used that have different characteristics (magnitude, fault distance, frequency content). Secondly, less records are usually needed in comparison to the incremental dynamic analysis approach to generate reasonable results. With respect to the computational resources required for transient analyses of the subplant, this is considered a decisive advantage. However, the assumption that the functional relationship between engineering demand parameter and seismic intensity measure follows a power law is not implicitly accurate. While good agreement is generally achieved for the range of intensities considered in the ground motion bins, the validity of results decreases when extrapolating equation (2) to higher intensities.

Within the project INDUSE-2-SAFETY, uniform hazard spectra with different target rates of exceedance for the location of the plant (soil class B) have been derived. Appropriate natural seismic records were selected from the PEER ground motion database and scaled to minimise

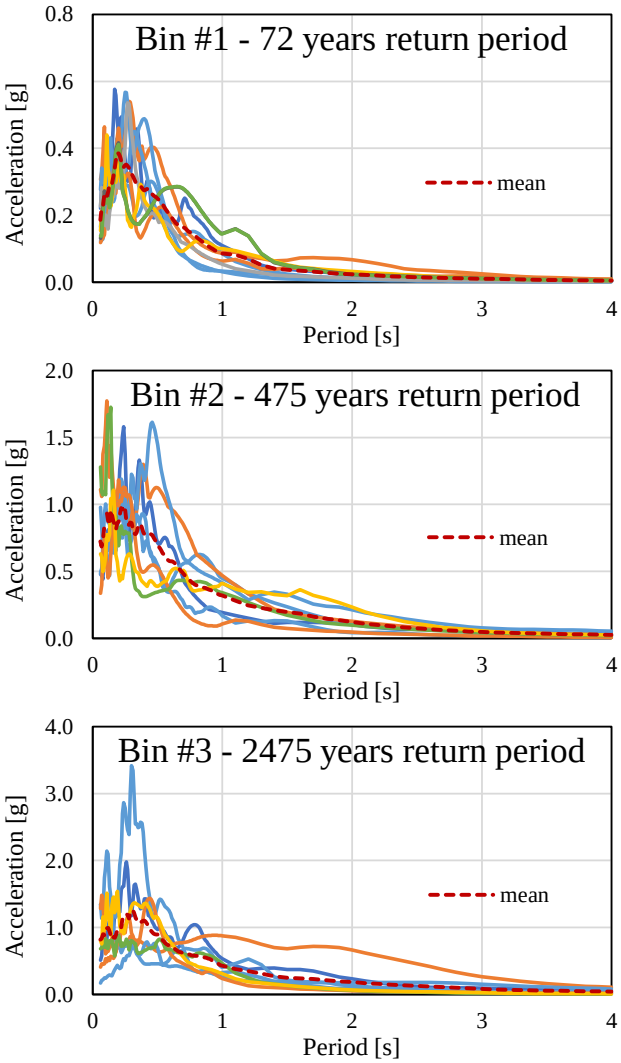


Figure 4: Spectra of seismic record selection

the deviation of mean spectral acceleration and uniform hazard spectra [10]. Three bins have been defined with return periods of 72, 475 and 2475 years. The spectra of the selected accelerograms are depicted in Figure 4. In total, 26 records are used for the PSDA. Bin #1 contains ten different accelerograms while bin #2 and bin #3 encompasses eight records, respectively.

The PSDA has been performed varying coupling conditions of the vessel (uncoupled/coupled), filling levels H and directions of ground excitation α. For the numerical simulations, structural damping was set to 2%, while sloshing modes were damped with 0.5% critical damping.

### 3.3 Fragility surfaces

In the following, the seismic fragility of the horizontal pressure vessel under investigation is illustrated. For each scenario (filling level H, direction of ground excitation α and coupling condition), the full set of seismic records has been applied and a fragility curve has been derived using cloud method as described earlier. In total, 34 scenarios have been defined which results in 34 fragility curves for each limit state and requires almost 900 transient simulations. To visualize the results (especially the influence of the filling level and the direction of ground motion), multiple fragility curves are merged into fragility surfaces that represent the probability of exceedance of a limit state for a certain level of PGA. For example, the surfaces shown in Figure 5 illustrate the probability of exceeding the limit state ‘rupture of vessel at saddle location’ for the uncoupled vessel (without considering the surrounding of the pressure vessel). The six surfaces represent different levels of PGA (starting at 0.6 g with incremental increase of 0.4 g in this case).

Obviously, the fragility of the vessel with respect to ‘rupture of vessel wall at saddle location’ depends significantly on the filling level H (0 corresponds to an empty vessel) and the direction of ground excitation α (0° corresponds to seismic excitation in transversal direction). Generally, the fragility increases with increasing filling level and angle of ground excitation. Seismic loading in longitudinal direction (α = 90°) seems to be more crucial than in axial direction. Comparing the fragility surfaces of the uncoupled vessel (Figure 5) with the coupled situation (Figure 6), probabilities of ‘rupture of vessel wall at saddle location’ are lower for most situations. Moreover, in the coupled scenario, the influence of the filling level seems to be negligible.

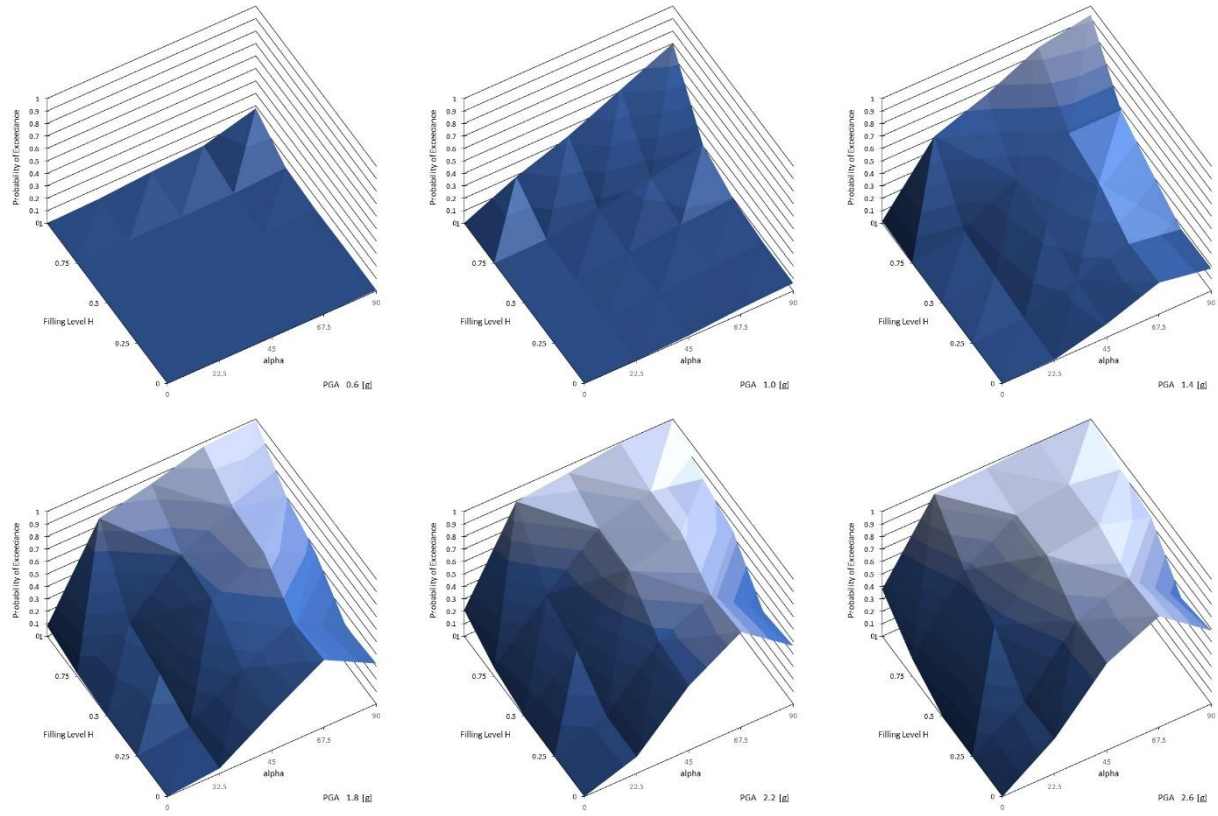


Figure 5: Fragility surface for LS ‘rupture of vessel wall at saddle location’, uncoupled state.

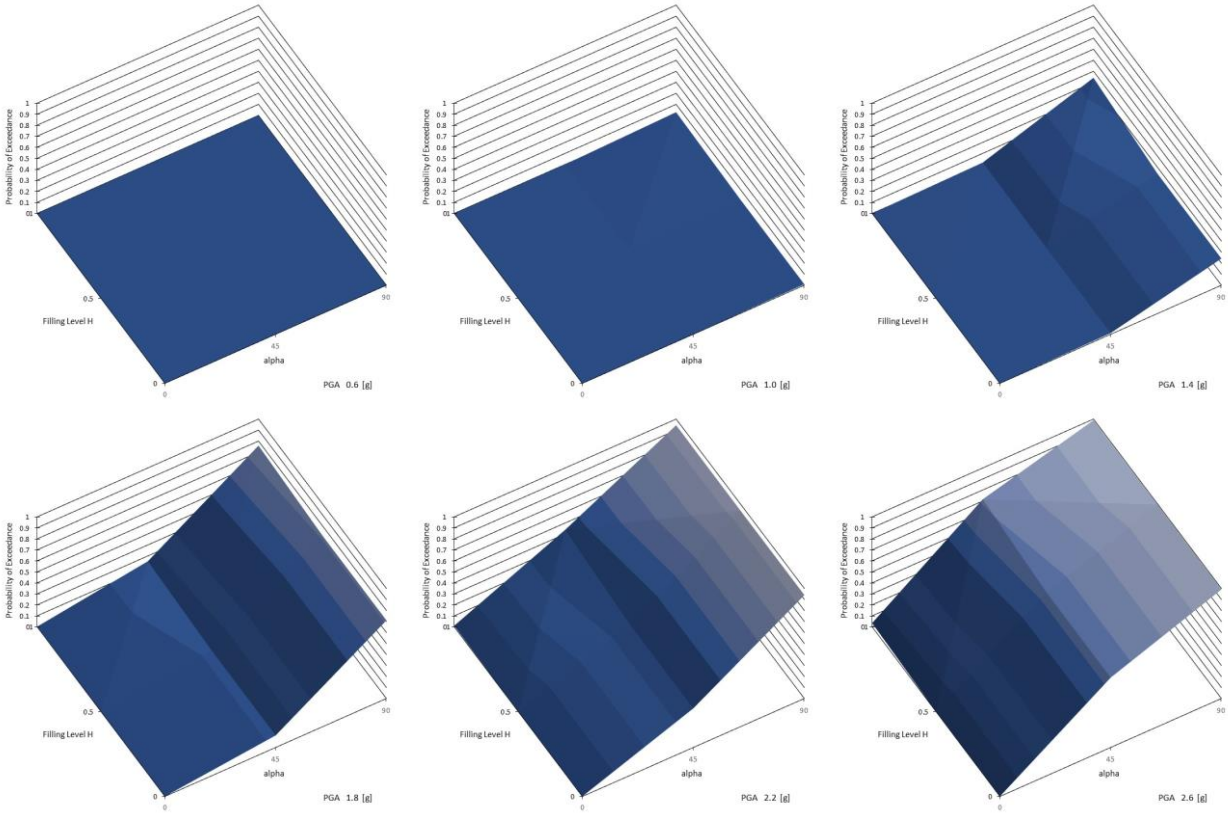


Figure 6: Fragility surface for LS ‘rupture of vessel wall at saddle location’, coupled state.

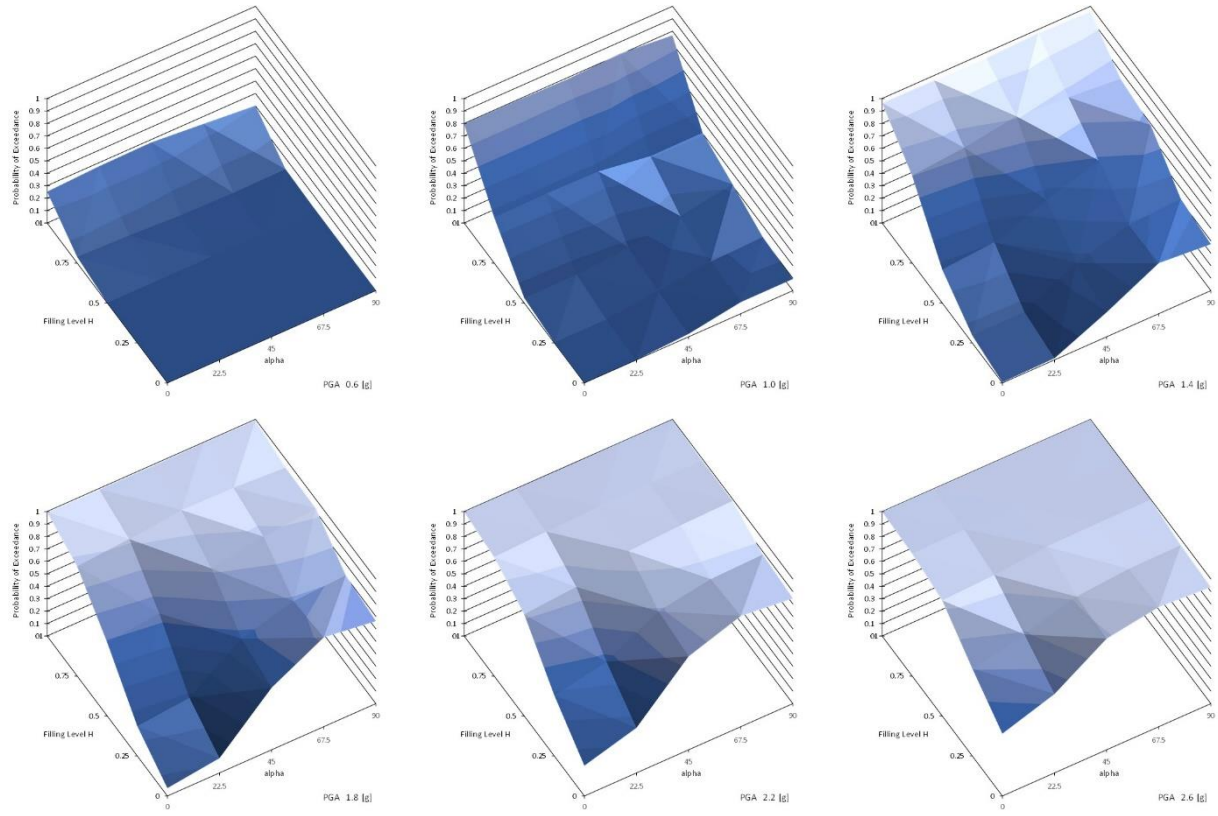


Figure 7: Fragility surface for LS ‘anchor bolt failure’, uncoupled state.

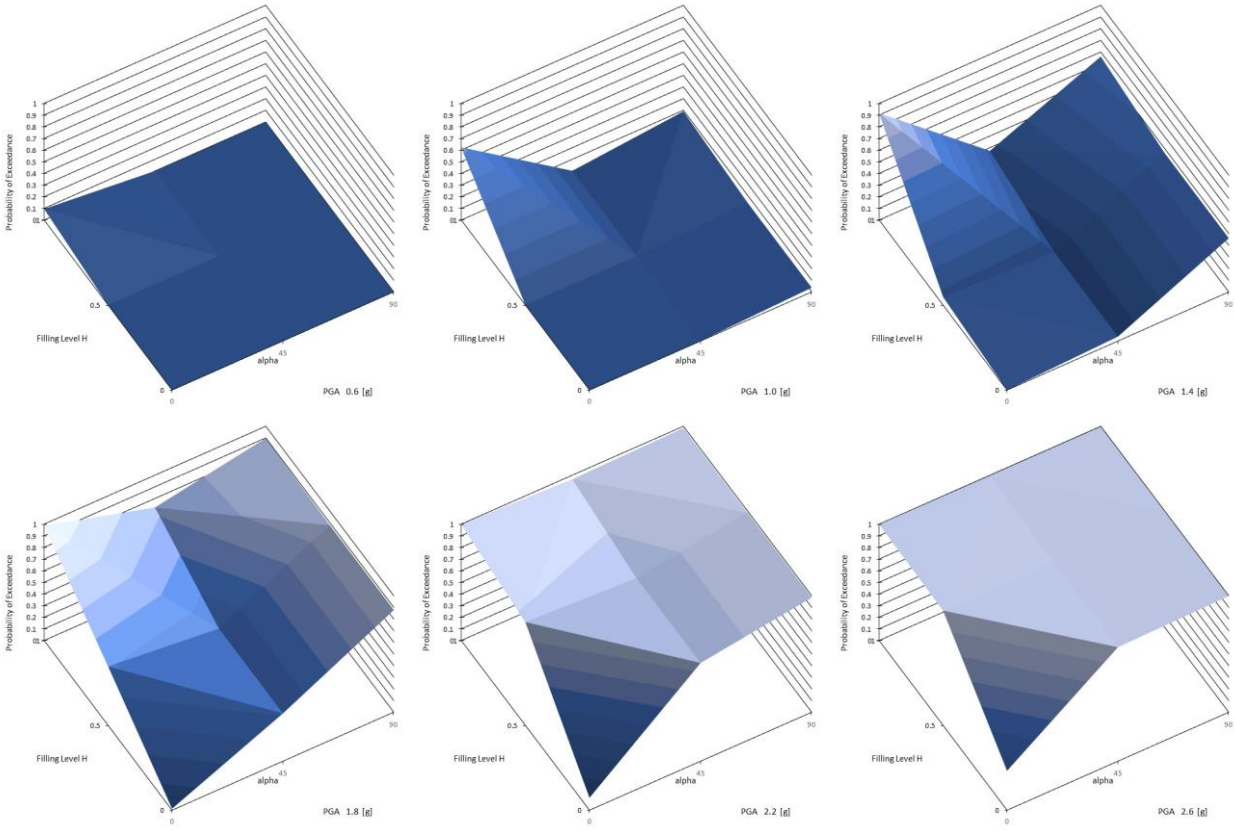


Figure 8: Fragility surface for LS ‘anchor bolt failure’, uncoupled state.

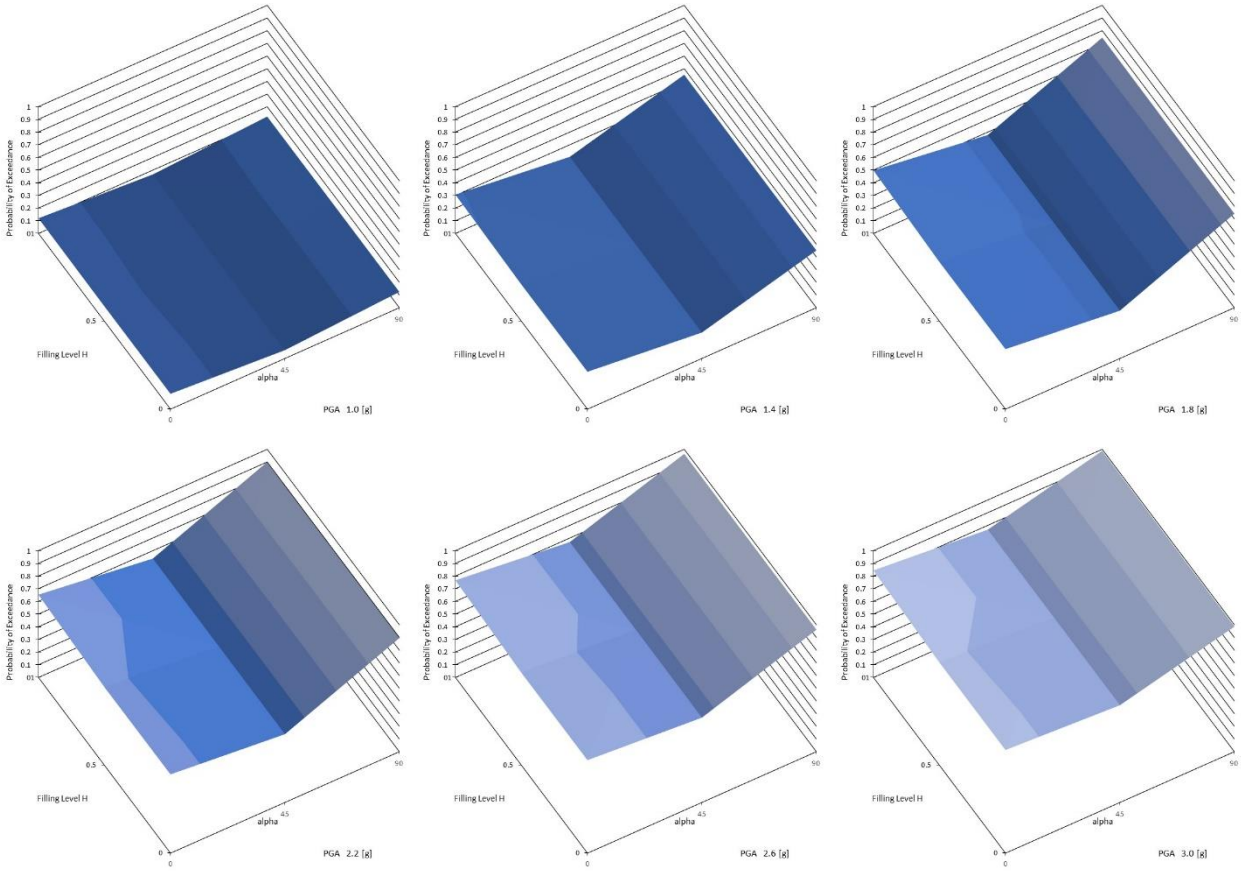


Figure 9: Fragility surface for LS ‘rupture at nozzle transition’, coupled state.

Figure 7 and Figure 8 depict fragility surfaces for the ‘anchor bolt failure’ limit state with and without considering the surrounding of the vessel. As already observed for the LS ‘rupture of vessel wall at saddle location’, the probability of failure decreases in case the coupling is accounted for properly. Independently of the coupling situation, the probability of exceeding ‘anchor bolt failure’ seems to be higher than exceeding the LS ‘rupture of vessel wall at saddle location’ (see Figure 5 and Figure 6). However, the fragility in the context of ‘anchor bolt failure’ can be easily reduced by replacing the existing bolts by higher strength/diameter ones.

Finally, fragility surfaces for the limit state ‘rupture at nozzle transition’ are shown in Figure 9. This limit state is only relevant for coupled scenarios, since the nozzles are free of load when not coupled to the surrounding piping system. Furthermore, only one of the nozzles (DN 450) is vulnerable to this limit state – the second nozzle has a higher resistance to this failure mode and is at the same time subjected to much lower bending moments. However, even the probability of exceeding the LS ‘rupture at nozzle transition’ at the DN 450 nozzle seems to be quite low compared to the exceedance of the other two limit states (consider the different level of PGA the surfaces are referencing to). Another observation is that the exceedance of this limit state does not depend on the filling level at all.

## 4 CONCLUSIONS

Within this study, a horizontal pressure vessel was investigated with respect to its seismic fragility varying the direction of seismic excitation and the filling level. Furthermore, special attention was given to the influence of the boundary conditions, by taking into account the surrounding of the vessel (piping system and support structure). To allow for extensive PSDA,

a simplified pressure vessel model, introduced in [3], was adopted for this study. Multiple fragility curves have been merged into fragility surfaces to illustrate the influence of the considered variables on the resulting fragility of the pressure vessel.

Three different limit states have been considered within this study, with 'anchor bolt failure' being the one with the highest probability of exceedance for most scenarios. It has also been shown that the probability of exceeding the two limit states 'anchor bolt failure' and 'rupture of vessel wall at saddle location' is significantly lower when the surrounding of the pressure vessel is taken into account properly. For the vessel, studied within this paper, 'rupture at nozzle transition' due to seismic loading has a very low probability of occurrence. However, it is expected that the probability of exceeding this limit state strongly depends on the layout of the coupled piping system.

## 5 ACKNOWLEDGEMENT

The work presented here is carried out as a research project by different European partners with a financial grant from the Research Fund for Coal and Steel (RFCS) of the European Community. The authors gratefully acknowledge the financial support.

## REFERENCES

[1] Housner, Dynamic Pressures on Accelerated Fluid Containers, *Bulletin of the seismological society of America*, 1955.

[2] Karamanos et al., Sloshing Effects on the Seismic Design of Horizontal-Cylindrical and Spherical Industrial Vessels, *Journal of Pressure Vessel Technology*, Vol. 128, pp. 328 – 340, 2005.

[3] Korndörfer et al., Fragility Analysis of Horizontal Pressure Vessels in the Coupled and Uncoupled Case, *Proceedings of the ASME 2016 PVP Conference*, Vancouver, 2016.

[4] Lu et al., Analytical Formulations of Fragility Functions with Applications to Probabilistic Seismic Risk Analysis, *Proceedings to the WCEE 15*, Lisboa, 2012.

[5] Cornell, Jalayer, Hamburger, Foutch, Probabilistic basis for 2000 SAC federal emergency management agency steel moment frame guidelines, *ASCE J. Struct. Eng*., Vol. 128, No. 4, pp. 526 – 33, 2002.

[6] Jalayer, Direct Probabilistic Seismic Anaysis: Implementing Non-linear Dynamic Assessments. Ph.D. dissertation, Dept. of Civil and Environmental Engineering, Stanford Univ., Stanford, CA, 2003.

[7] Jalayer, Cornell, Alternative non-linear demand estimation methods for probability-based seismic assessments, *Earthquake Engr. & Struct. Dynamics. J*., Vol. 38, No. 8, pp. 951 – 972, 2009.

[8] Vamvatsikos, Cornell, Incremental Dynamic Analysis, *Earthquake Engr. & Struct. Dynamics. J*., Vol. 31, No. 3, pp. 291 – 514, 2001.

[9] Mackie, Stojadinović, Comparison of Incremental Dynamic, Cloud and Stripe Methods for Computing Probabilistic Seismic Demand Models, *Proceeding to Structures Congress 2005*, p. 1 – 11, New York, 2005.

[10] Paolacci et al., Component fragility evaluation, seismic safety assessment and design of petrochemical plants under design-basis and beyond-design-basis accident conditions, *Deliverable 1.2*, INDUSE-2-SAFETY project, RFCS, 2015.

COMPDYN 2017
6th ECCOMAS Thematic Conference on
Computational Methods in Structural Dynamics and Earthquake Engineering
M. Papadrakakis, M. Fragiadakis (eds.)
Rhodes Island, Greece, 15–17 June 2017

# SHAKING TABLE TESTING OF CYLINDRICAL STEEL LIQUID STORAGE TANKS

**Ph. Mongabure[1], S. Vasic[2]**

[1] CEA
DM2S/SEMT/EMSI
91191 GIF SUR YVETTE
France
e-mail: philippe.mongabure@cea.fr

[2] CEA
DM2S/SEMT/EMSI
91191 GIF SUR YVETTE
France
e-mail: sandra.vasic@cea.fr

**Keywords:** seismic testing, shaking table, tanks

**Abstract.** This paper presents the experimental campaign carried out on cylindrical liquid storage steel tank specimens in CEA TAMARIS facility.

Two geometries of tanks have been tested on a shaking table under seismic conditions. The broad tank specimen (diameter 3 m, height 0.9 m) was dedicated to the study of sloshing and potential uplifting during the seism. This specimen was unanchored on the table and free to lift or slide. The influence of a floating roof on sloshing has been studied. The slender specimen (diameter 2 m, height 5 m) was dedicated to the foot buckling of the cylindrical shell. The slender specimen was anchored to the table. All the specimens were water filled.

All these specimens were strongly instrumented with inner pressure sensors and wave gauges and outer accelerometers and displacement sensors. In addition a new 3D scanner has been used to detect any residual deformation of the tanks by after / before tests comparisons. The purpose was to give to the calculating teams all the needed measurements and information to check their models.

Results acquired on one broad tank and one slender tank are presented here.

## 1 INTRODUCTION

In the framework of INDUSE2-SAFETY European project, CEA EMSI laboratory, hosting the seismic testing facility TAMARIS, has carried out experimental tests on tanks under seismic loadings. This experimental campaign formed the task 4.7 of the INDUSE-2-SAFETY project (called INDUSE2 in the following parts of this document).

The goals of this project are to study the petrochemical plants components fragility to improve the seismic safety assessment in EUROCODE 8. This project has received the grant agreement RFSR-CT-2014-00025 [1].

This article presents experimental results obtained on two tanks: a broad one (diameter 3 m, height 0.9 m) and a slender one (diameter 2 m, height 5 m).

## 2 TAMARIS EXPERIMENTAL FACILITY

The Seismic Mechanical Study Laboratory (EMSI), part of the Mechanical and Thermal Study Section in CEA-Saclay has been operating the TAMARIS experimental facility since 1991. This facility is composed of four shaking tables, a test pit and a reaction wall (Figure 1). These testing means are positioned in a huge reaction massif made of reinforced concrete. The tests carried out are intended to better understand the mechanical behavior of structures, equipment or devices under dynamic and seismic loadings.

Mostly, the tests are performed on the triaxial table AZALEE, which is capable of shaking specimens up to 100 tons and 1 g acceleration. It is a 6 x 6 $m^2$ metallic structure which is motioned in the three directions by eight actuators. The six Degrees Of Freedom (6 DOF, three translations and three rotations) can be monitored by a MTS control system.

Another interesting device is the VESUVE table. It is a simpler but efficient shaking table. It is moved by a unique horizontal actuator (1 DOF). The VESUVE table is monitored by a SERVOTEST control system.

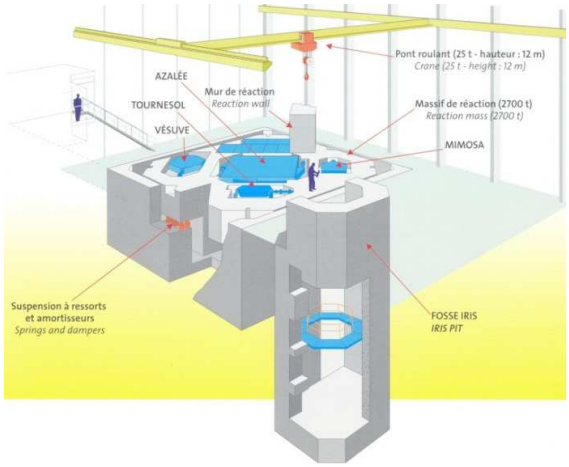


Figure 1: TAMARIS facility

The INDUSE2 tests on tanks have been conducted on the VESUVE table which has the following characteristics (Table 1).

| Table | DOF | Control | Dimensions (m x m) | Payload (tons) | Displacement (mm) | Seismic control frequency (for empty table) (Hz) |
|---|---|---|---|---|---|---|
| VESUVE | 1 | displacement | 3.1 x 3.8 | 20 | ±100 | 0 - 40 |

Table 1: VESUVE table characteristics

# 3 THE SPECIMENS

## 3.1 Initial configurations

Two configurations of steel tanks (Figure 2) are described in the INDUSE2 technical proposal [2]:

- a broad tank (unanchored, with or without floating roof),
- a slender tank (anchored).

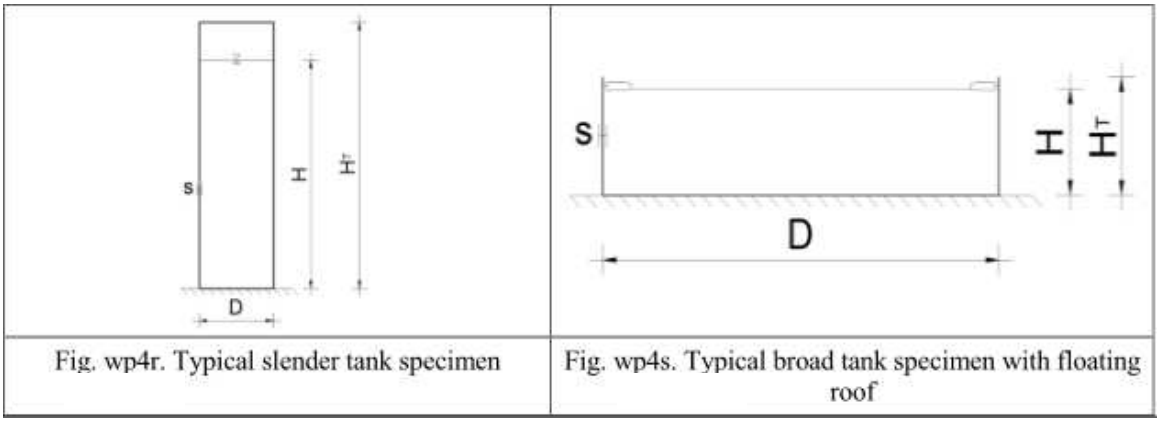


Fig. wp4r. Typical slender tank specimen

Fig. wp4s. Typical broad tank specimen with floating roof

Figure 2: Configurations of steel tanks [2]

## 3.2 Detailed design for the broad tank

The broad tank is scaled from a real tank (diameter 54 m, height 15 m). The scale ratio λ is 1/18. The specimen has a 3 m diameter and a 0.868 m height. It is formed by one cylindrical SS304 steel sheet 1 mm thick welded to a round bottom of the same material. A circular stiffener is welded to the top of the cylindrical shell. It has been fabricated by the Walter Tosto Company (Figure 3).

The broad tank was unanchored during the tests on the shaking table. It has been tested with a monoaxial seismic loading to study :

- the influence of a floating roof on sloshing created at low frequencies,
- the uplifting phenomenon induced by higher frequencies.

The estimated mass of the empty tank is 123 kg. Once filled with water at 90% of its height (0.781 m), the specimen mass was 5.6 tons.

A roof has been built in CEA from wood and rigid foam to ensure the buoyancy (Figure 3). 43 springs were fit around the roof in order to simulate the rigidity of the centering system of the roof in the real tank.

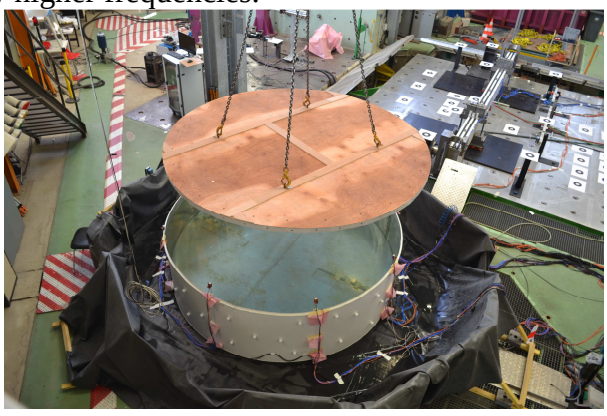

Figure 3: Broad tank with its roof

### 3.3 Detailed design for the slender tank

The slender tank is scaled from real tanks (diameter 8 m, height 20 m). Its scale ratio λ is 1/4. The specimen has a 2 m diameter and a 5 m height. It is formed by four cylindrical S355JR steel sheet 1.5 mm thick assembled by longitudinal and circumferential weldments to create a cylindrical shell. This one is welded to a massive basis. A circular stiffener is welded to the top of the cylindrical shell. The slender tank has been fabricated by the Walter Tosto Company (Figure 4).

Four glued outer flanges reinforced the tank's shell lower part without introducing any residual stress due to weldment. The slender tank has been tested with a monoaxial seismic signal to study the buckling of the cylindrical shell.

The basis has been designed to permit the bolting of the tank to an intermediate steel plate (2.3 x 2.3 $m^2$, 2100 kg). This plate was itself bolted to the shaking table's plate.

The mass of the empty tank was 2300 kg. Once filled with water at 90% of its height (4.5 m), the specimen mass was 16.4 tons. The total mass on the table was 18.5 tons.



Figure 4: Slender tank

### 3.4 Steels characterization

The two steels used for the tanks manufacture have been characterized according to the standard NF EN ISO 6892-1 A233. The laminating direction and the transverse direction have been discriminated. The results are shown in the following table (Table 2), where SST stands for Stainless Steel (SS304) Transverse, SSL for Stainless Steel Longitudinal, ST for Steel (S355JR) Transverse and SL for Steel Longitudinal.

| Tank | Steel | Thickness | Rp0.2 ($N/mm^2$) | Rm ($N/mm^2$) | A (%) |
|---|---|---|---|---|---|
| Broad | SST | 1.0 | 368 | 722 | 51.8 |
| Broad | SSL | 1.0 | 373 | 728 | 49.4 |
| Slender | ST | 1.5 | 420 | 452 | 26.7 |
| Slender | SL | 1.5 | 400 | 447 | 26.1 |

Table 2: Tanks steels mechanical characterization

### 3.5 Specimens testing position and orientation

The broad tank was positioned in the center of the table plate on an intermediate EPDM sheet (Figure 5). This rubber membrane increased the friction coefficient between tank base and the table to decrease sliding effect and protected the mechanical bearings and electrical circuits in case of water over topping.

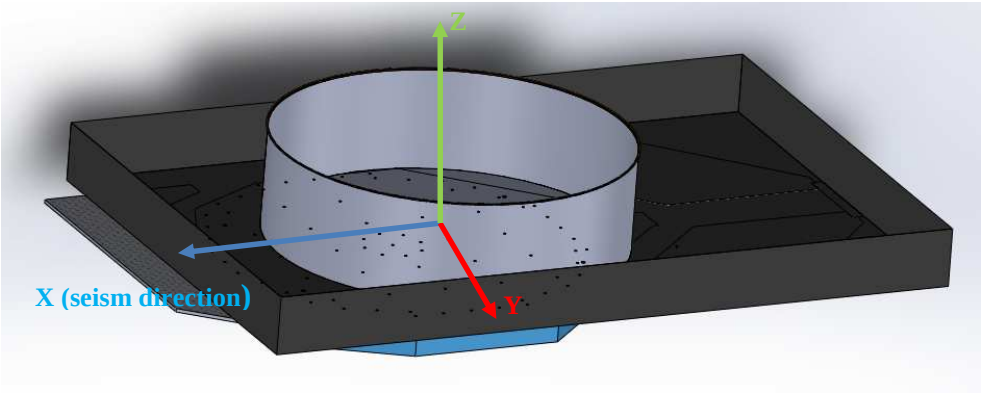


Figure 5: Broad tank on VESUVE table

The same implementation was reproduced for the slender tank, apart the anchoring of the tank in the VESUVE table, as previously described.

In both cases, the orientation reference was:

- X axis is the direction of the displacement, positive when the rod goes out,
- Y axis is transverse,
- Z axis is the vertical one positive towards the top.

The tanks were positioned taking into account the longitudinal welds of the cylindrical shell. These weldments were placed at 45° in respect of the X axis. Each tank had its own orientation and generatrixes were marked every 45° in trigonometric orientation. The 0°-180° axis was the seism axis, that is the X axis.

## 4 THE SEISMIC SIGNALS

The seismic signals used for the tests were natural acceleration signals chosen to maximize the mechanical effects on the tanks (Table 3, Figure 6):

- for the sloshing behaviour of broad tank,
- for the uplifting behaviour of broad tank,
- for the buckling behaviour of slender tanks.

The VESUVE table is controlled with displacement feedback. So, the seismic accelerograms have first been changed into displacement signals, and then a similitude has been applied for each type of test taking into account the scale of the specimen.

| Tank | Effect | Event | Country | Date | Component |
|---|---|---|---|---|---|
| Broad | Sloshing | Chichi | Taiwan | 21/09/1999 | |
| Broad | Sloshing | Düzce | Turkey | 12/11/1999 | |
| Broad | Uplifting | Northridge-01 | USA | 17/01/1994 | NORTHRx |
| Slender | Buckling | L'Aquila | ITALY | 06/04/2009 | IT0789xa |

Table 3: Signals used for the tanks

The most suitable similitude has been defined for each type of test (considering $\lambda < 1$):

- considering the sloshing behaviour on broad tank at low frequency, the Froude similarity was applied ($t/t_0 = \sqrt{\lambda}$ and $\gamma/\gamma_0 = 1$),
- considering the uplifting of a broad tank, an acceleration scaling was used ($t/t_0 = \lambda$ and $\gamma/\gamma_0 = 1$).
- considering the buckling of slender tanks, the velocity similarity was applied ($t/t_0 = \lambda$ and $\gamma/\gamma_0 = 1/\lambda$).

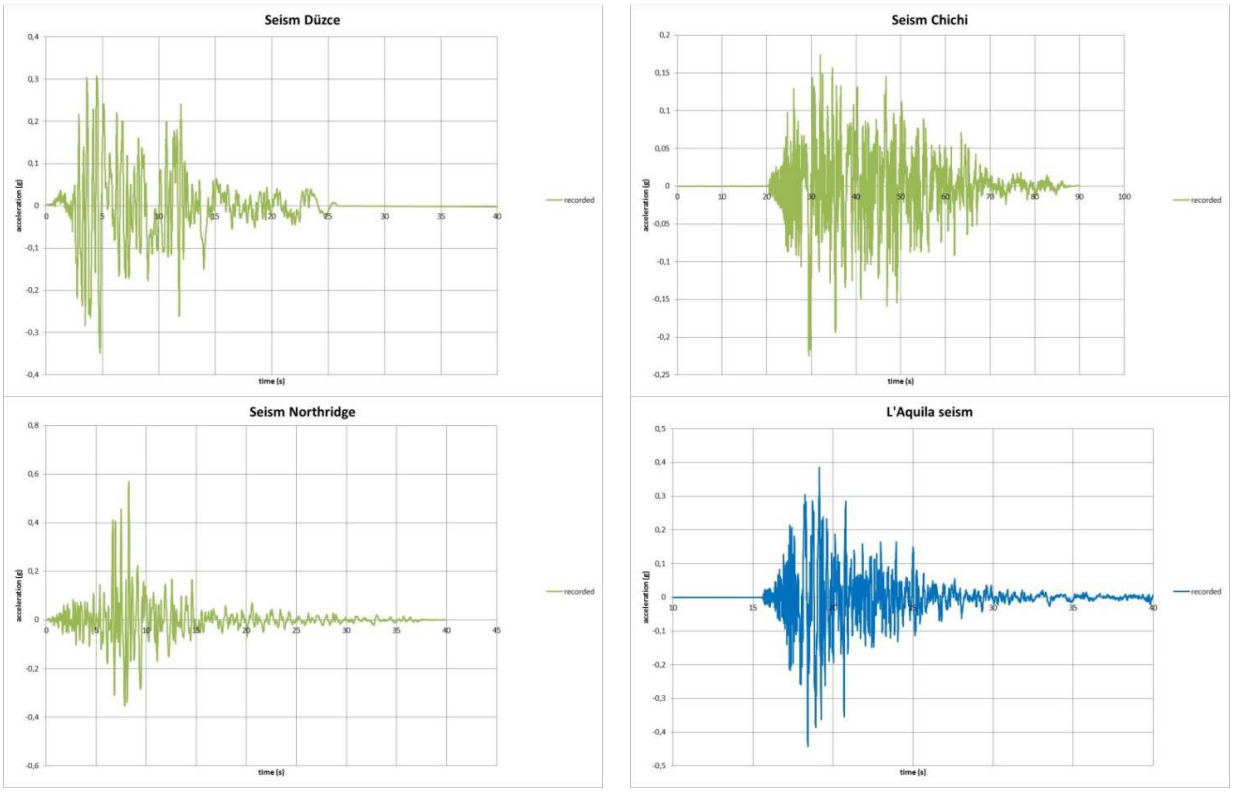


Figure 6: Natural seismic signals selected for the tests (accelerations in green for broad tanks, in blue for slender tank)

## 5 THE INSTRUMENTATION

The instrumentation placed on the tanks and on the table measured the mechanical inputs (accelerations, pressures) and the mechanical outputs (strain, displacements, water level) of the experimental system table + tank. The implementation of the instrumentation is shown in Figure 7 for the broad tank and in Figure 8 for the slender one. 120 sensors ca have been positioned on each tank.

### 5.1 Table instrumentation

A displacement sensor and a triaxial accelerometer measured the behavior of the table, i.e. the dynamic input at the foot of the tank.

## 5.2 Specimen instrumentation

Triaxial accelerometers were scattered on the outer surface of the tank in order to measure the accelerations distribution in regard to the height of the tank and the angle around the tank axis.

Pressure sensors measured the water pressure on the inner surface of the tank. They were scattered vertically and circumferentially in order to measure pressure variation versus time, that is the inner forces variation.

Level sensors measured the water level variations at the free surface of the tank. They were positioned around the top circumference of the tanks.

Local displacements, such as the uplifting of the tank base, were measured by vertical LVDT sensors fixed on the tank base and pointing on the table plate. Global displacements of the broad tank have been measured by cable displacement sensors placed between fixed point outside the table and the tank itself. For the slender tank due to its height, no traditional displacement sensors could be used. So an optical technique has been used. This one is presented in § 5.3.

Some strain gauges glued on the tanks measured relevant strains indicating that the desired phenomenon was triggered. They were positioned vertically on the outer surface of the slender tank's foot to detect the buckling of the tank foot. And they were positioned on the inner side of the broad tank's bottom plate to detect flexion triggered by the uplift.

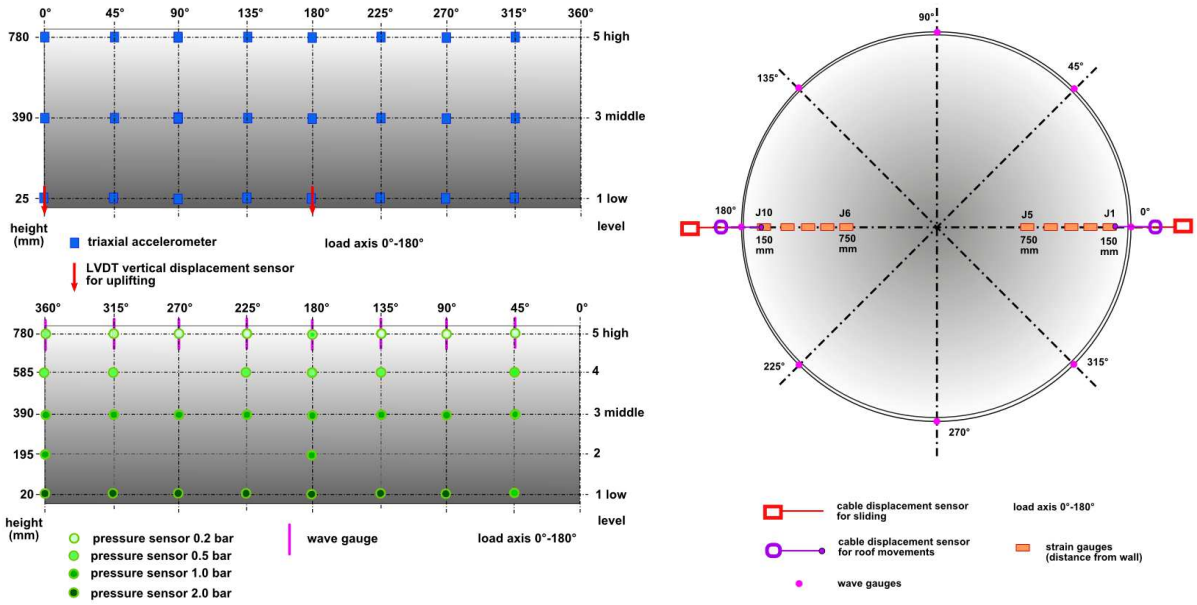


Figure 7: Instrumentation of broad tank

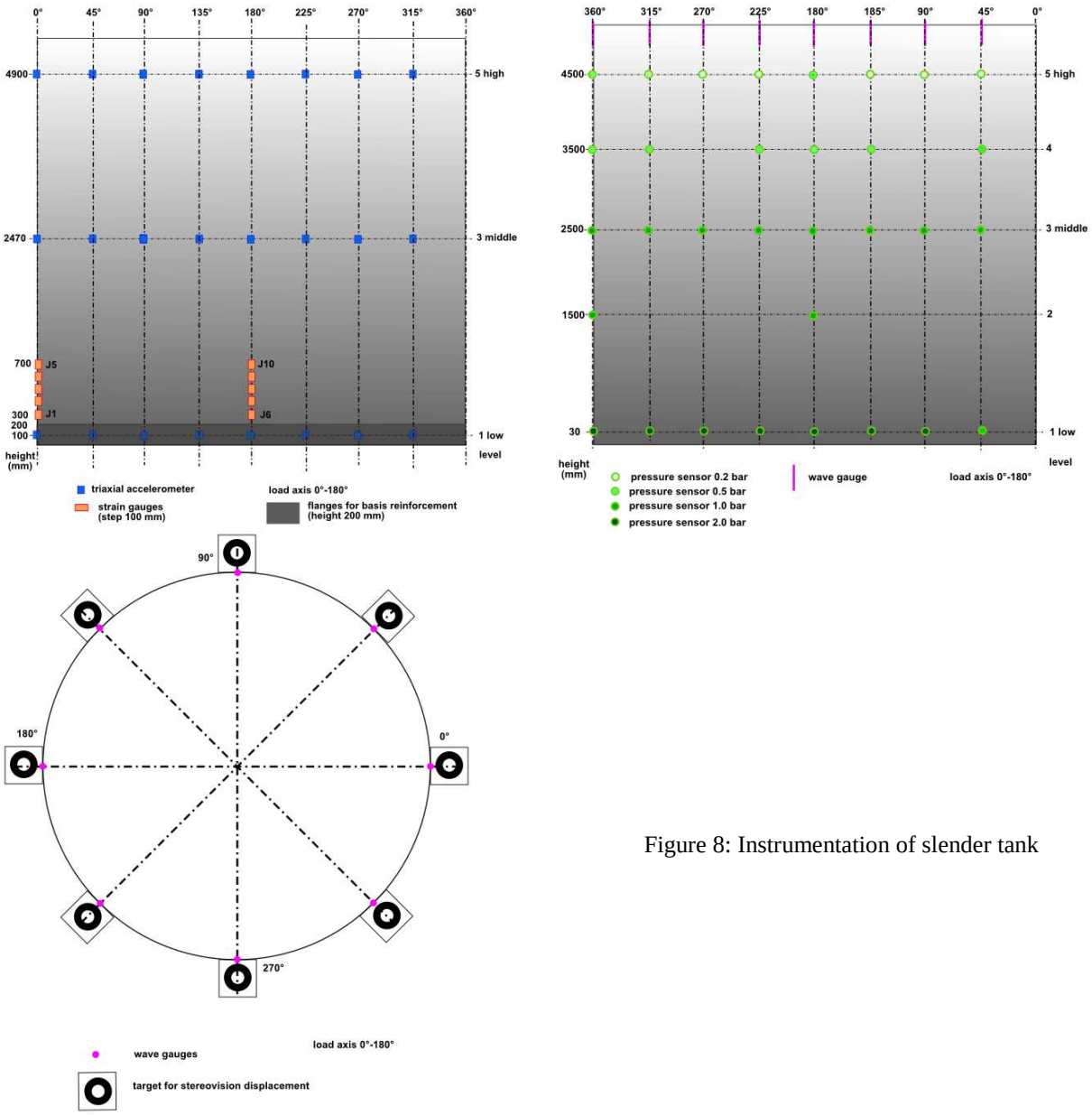


Figure 8: Instrumentation of slender tank

## 5.3 3D stereovision target tracking

To measure the displacement of the top of the slender tank, no conventional sensors could be used due to the height of the tank (5 m). A stereoscopic video technique, so called target tracking (Figure 9), has been implemented. This technique has been used for several years in EMSI laboratory. This system based on a stereoscopic rig and dedicated softwares for acquisition and post processing has been supplied by the VIDEOMETRIC Company (based in Clermont Ferrand, France).

The stereovision sensor is constituted of two CCD cameras encapsulated in a rigid carbon arm that produces twin stereoscopic images of the same object on which are positioned dedicated targets. It is linked to a computer with an acquisition software. The images stored (Figure 10) during a test at a 100 Hz frequency are post processed (i.e. targets are spotted, located and sorted in each image) to evaluate the targets displacements in all space directions versus time.

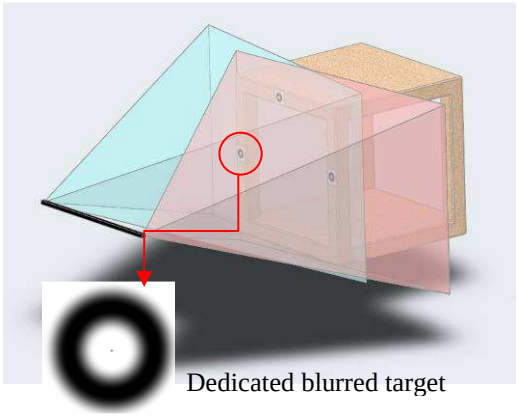


Figure 9: 3D target tracking principle



Figure 10: Stereoscopic view of SLENDER1 (top –down direction)

## 5.4 3D shape measurement

An optical technique for shape measurement has been used to compare the shape of the tanks before and after tests (Figure 11).

It is a structured light optical technique based on fringes pattern projection dedicated to tridimensional shape measurement. The fringes are projected by a conventional image projector. The illuminated surface is observed by a stereoscopic rig equipped with two high resolution cameras. This system has also been supplied by the VIDEOMETRIC Company.

The complete outer surface of a slender tank (ca 31 $m^2$) is the result of the assembly of ca 50 individual scans (ca 2 $m^2$ each). A sufficient overlap is necessary to be able to link all these individual scans. This operation is automatically performed by post processing using spherical markers scattered on the outer surface of a tank.

It was then possible to calculate the difference between pre and post-tests shapes, i.e. to calculate the residual deformations of the tanks.

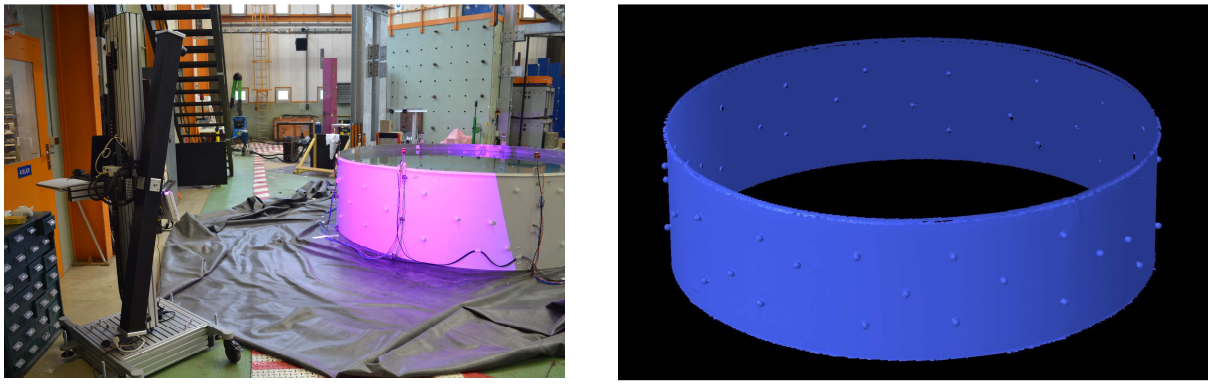

Figure 11: 3D shape measurement of a broad tank

## 6 TESTS ON BROAD TANK

Three seismic signals (Table 3) have been used on BROAD1 tank:

- For sloshing, Düzce, Turkey and Chi Chi, Taiwan,
- For uplifting, Northridge (USA).

### 6.1 Sloshing testing

The limit for the tests was the over topping of the water, that is a wave height of 87 mm. This has been reached for Düzce signal at a table displacement of ±30 mm. In Figure 12, several graphs show the consistency of measurement through different aspects:

(a) The measurements versus time of the waves every 90°, WG0 and WG180 being along the seism axis, show the phase opposite movement of the waves along the X axis. On the contrary, the perpendicular gauges WG90 and WG270 measured almost zero waves.

(b) Considering the wave height and bottom pressure repartition along the circumference, both measurements are coherent at two different times (high wave at 0°, low wave at 0°).

(c) The pressures along the 0° generatrix (P0_1 lowest sensor, P0_5 highest sensor) are coherent with the wave height measurements at 0°.

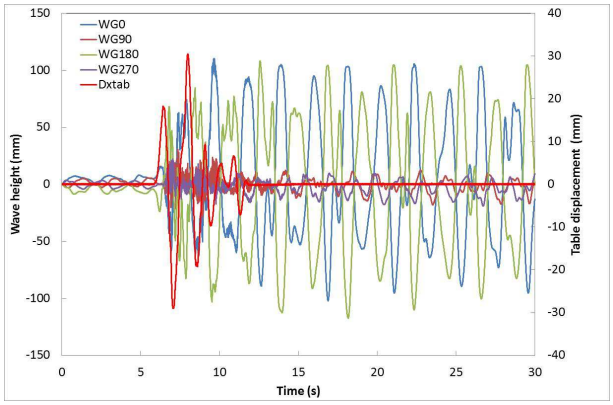


(a)

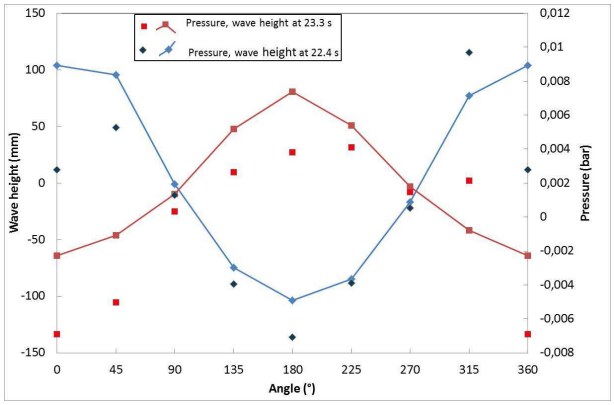


(b)

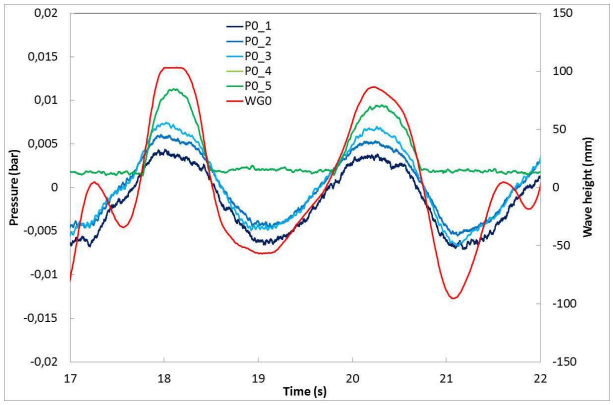


(c)

Figure 12: Some results for sloshing highest level (Düzce signal)

The over topping has been reached for Chi Chi signal at a table displacement of ±35 mm. In Figure 13, the same types of graphs as previously shown for the Düzce signal give the same quality of measurements.

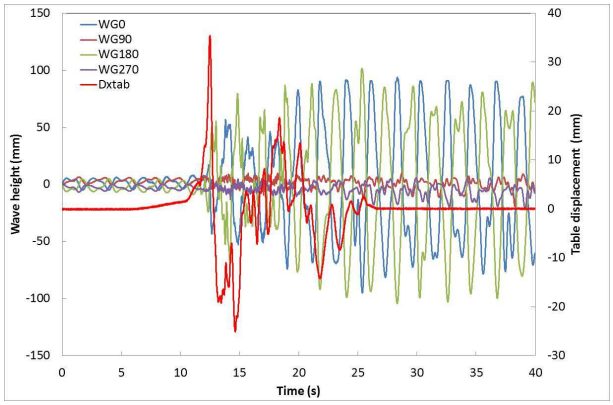


(a)

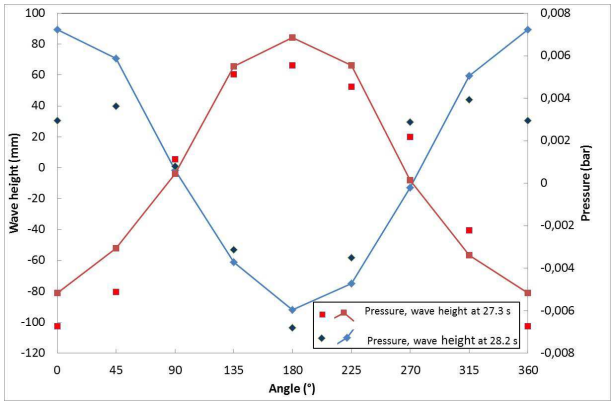


(b)

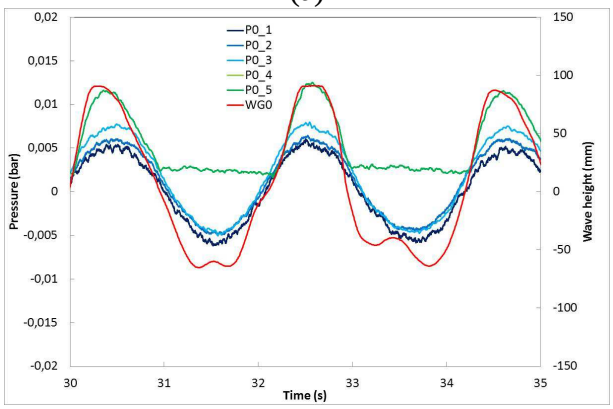


(c)

Figure 13: Some results for sloshing highest level (Chi Chi signal)

## 6.2 Influence of the roof for sloshing testing

The influence of the roof has been checked for the two signals. As expected, the roof creates a strong damping of the waves. In Figure 14, this damping is clearly shown by comparison with the measurements in Figure 12 (a), the input signal being the same (Düzce, ±30 mm).
This result has been checked for the Chi Chi signal as well.

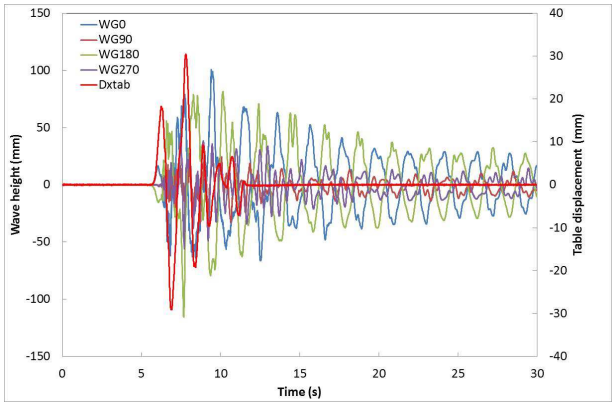


Figure 14: Wave height with the roof (Düzce signal)

## 6.3 Uplifting testing

The Northridge signal was used to trigger significant uplift on the broad tank. Some results are shown in Figure 15:

(a) An uplift of ca 40 mm was achieved at 180° for a -20 / +15 mm signal.
(b) This uplift was linked to a significant slide of the tank on the table (ca 70 mm). It was no use to increase the level of the signal for the slide effect was predominant on the uplift effect. 40 mm was the highest uplift achievable with this implementation.
(c) The strains measured by the gauges are consistent with the uplift. The highest strain was obtained close to the tank's wall, i. e. on J1 and J10. For example, J10 experienced a compression of 1100 µstrain.
(d) Finally, pressure measurements and uplift are also consistent. The pressure distribution along the circumference for the bottom sensors shows that a high pressure corresponds to low uplift whereas low pressure means high uplift.

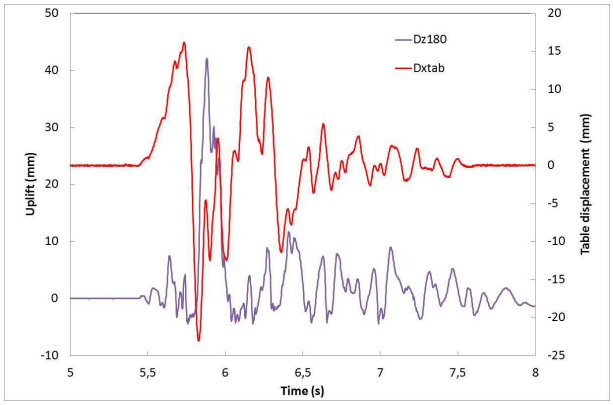


(a)

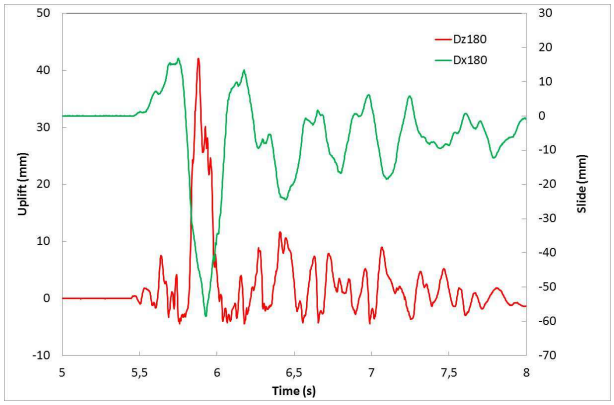


(b)

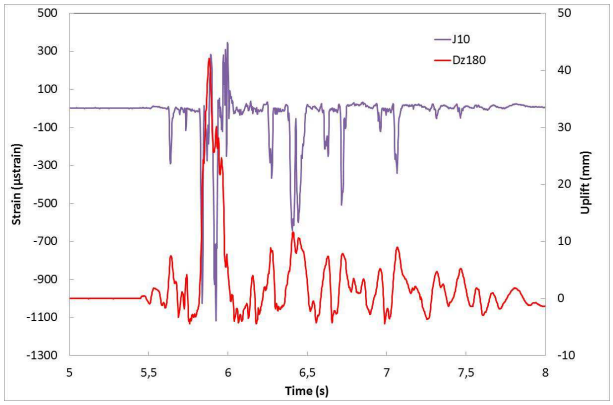


(c)

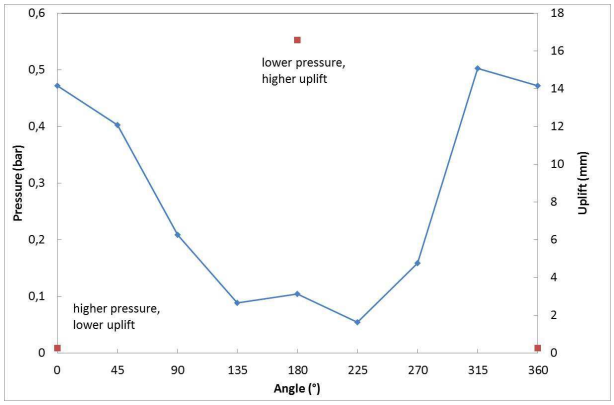


(d)

Figure 15: Some results for uplifting highest level (Northridge signal)

## 7 TESTS ON SLENDER TANK

One seismic signal has been used on SLENDER1 tank, the L'Aquila signal (Table 3). A ±15 mm signal level has been used at maximum which corresponds to a ±1 g on the table at the tank's foot. The buckling has not been achieved (Figure 16).

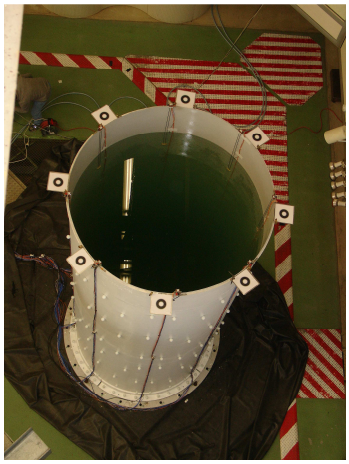

Figure 16: Slender tank ready to be tested

Several global facts can be shown from the time measurements:

(a) The highest drift (difference between top and foot) measured is ca 16 mm. A residual drift of ca 5 mm shows possible permanent deformation of the tank.

(b) An important amplification of the acceleration at the top gives measurement higher than 10 g for a table acceleration of 1 g.

(c) The comparison of the drift and strain gauge measurement shows a fine coherence of the local bending mechanism at 0°, a positive drift triggering a gauge tension.

(d) In the reverse, at 180° the positive drift triggers a gauge compression. The highest strain measured was a 1500 µstrain compression on J8 gauge.

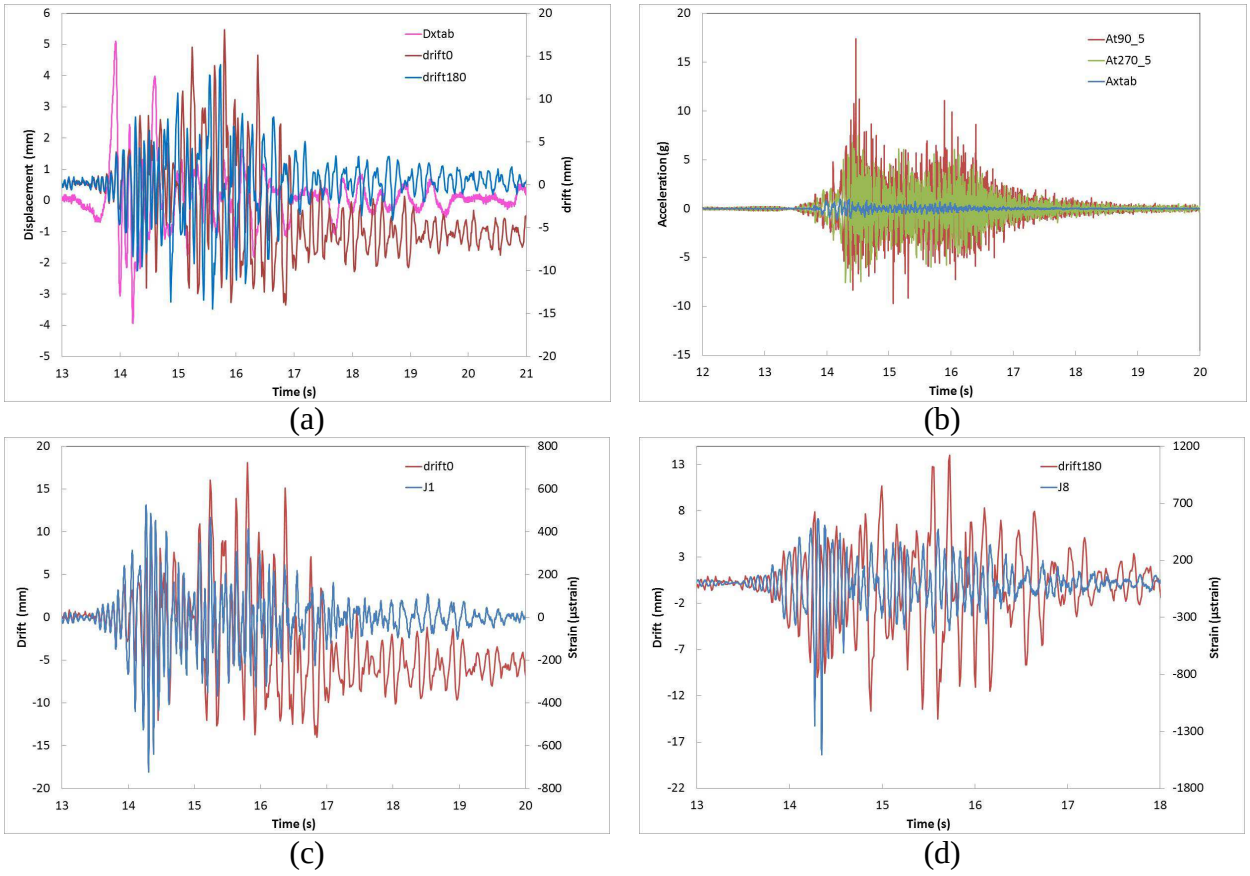


Table 4: Some results for SLENDER1 highest level (L'Aquila signal)

Drifts and local strain give some indications about the tank behavior (Figure 17):

(a) The drifts at 0° and 180° are first in the same direction and then in opposition. This means that the global behavior of the tank shifts from bending mode to shell deformation mode after the strong part of the signal.

(b) Strong local deformation occurs on the 180° generatrix. The local bending shifted to local shell deformation which could be a buckling initiation.

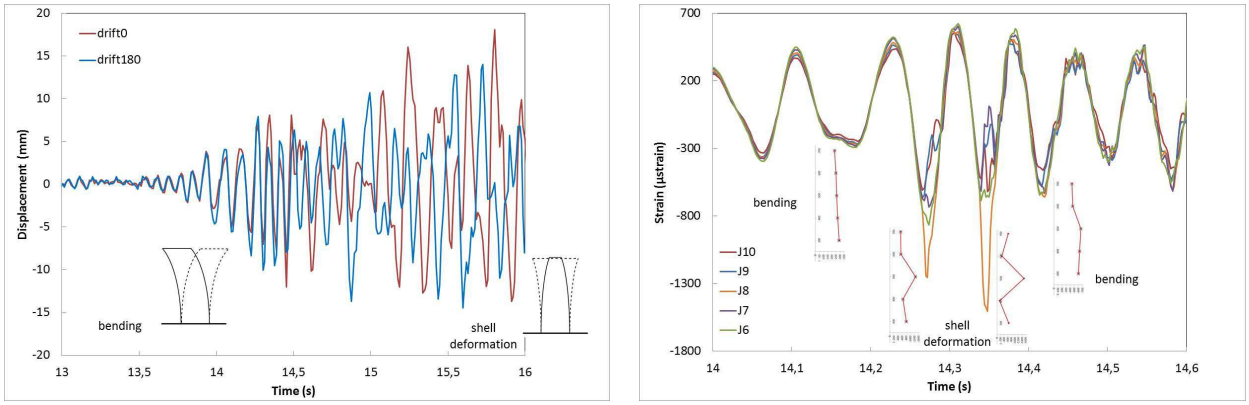


Figure 17: Behavior of slender tank

Finally, if we focus on the top of the tank:

- The displacements of the top of the tank are mainly radial displacement as shown by the in plane displacements (Figure 18) of the seven targets positioned every 45° at tank's top (the eighth one at 225° has fallen down).
- The residual deformations of SLENDER1 have been computed (Figure 19) as the geometrical distance between the posttest shape and the pretest shape, measured with the 3D scanner (see §5.4). This shows a four petals shape with ±8 mm amplitude, that is 0.8% residual radial strain.

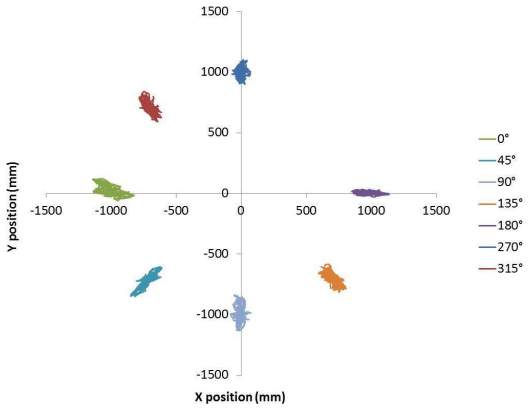


Figure 18: Displacements of targets around the top of the tank

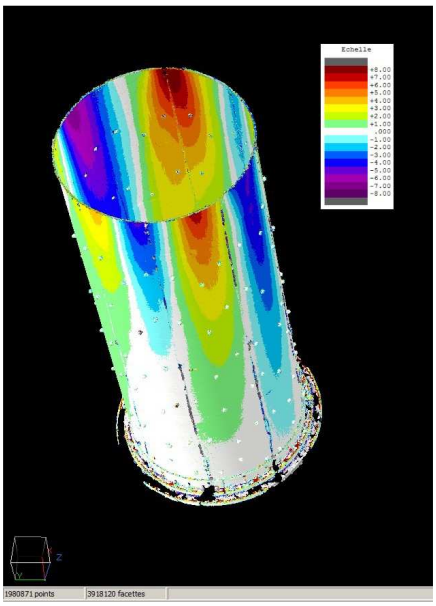

Figure 19: Difference of pretest / posttest shapes for SLENDER1

These measured deformations, at the foot (Figure 17) or at the top (Figure 18, Figure 19), are consistent with what can be observed on the videos shot during the tests.

## 8 CONCLUSIONS AND FUTURE WORK

The first analysis presented in this paper need to be strongly completed by some modal analysis, pre / posttest shape differentiation… All the intended goals have not been achieved in the study of the seismic behavior of tanks but the highly instrumented tanks gave a lot of measurements to be compared and analyzed.

A second slender tank will be tested in a close future. The goal is once more to trigger a significant buckling of its foot. The experience acquired in the first test will be used to achieve this goal.

## ACKNOWLEDGEMENTS

This work has been funded by the European Research Project INDUSE-2-SAFETY (Grant No. RFS-PR13056).

## REFERENCES

[1] 'INDUSE-2-SAFETY' Grant Agreement, *Component fragility evaluation and seismic safety assessment of 'special risk' petrochemical plants under design basis and beyond design basis accidents*, RFSR-CT-2014-00025, EC 12/6/2014.

[2] *B3-technical-annex INDUSE-2-SAFETY*, Trento University, 2013.

COMPDYN 2017
6th ECCOMAS Thematic Conference on
Computational Methods in Structural Dynamics and Earthquake Engineering
M. Papadrakakis, M. Fragiadakis (eds.)
Rhodes Island, Greece, 15–17 June, 2017

# DYNAMIC ANALYSIS AND COMFORT EVALUATION OF A FULL SUSPENSION BICYCLE EQUIPPED WITH A MR DAMPER

**A. Pascoal**[1], **J. Gonçalves** [1,2] **and M. Braz-César**[1,3]

[1] Polytechnic Institute of Bragança,Portugal
{pascoal,goncalves,brazcesar}@ipb.pt

[2] INESC-TEC, Portugal

[3] CONSTRUCT R&D Unit, FEUP, Portugal

**Keywords:** Suspension System, Bike, MR-Damper

**Abstract.** *Typical vehicle suspension systems are based on passive energy dissipation devices. This type of systems have proven to be a reliable and economic approach, however they are not capable to modify its behavior in accordance with the road conditions. On the other hand, active systems allow a continuous control of the suspension response although requiring sensors, actuators and controllers which represents a more complex and expensive system, usually demanding high power requirements. A middle-term vibration control approach is to use the so-called semi-active systems with the adaptability of active systems and lower energy consumption. This paper aims to evaluate the comfort ridding of a full suspension bicycle equipped with semi-active open loop controlled suspension system using a magneto-rheological (MR) damper. The assessment was carried out based on the analysis of real data, extracted from the instrumented bicycle prototype. The experimental tests were made in a smooth indoor pavement and a cobblestone road. Finally, the results obtained with the proposed semi-active suspension control system are presented and discussed.*

## 1 Introduction

In several engineering applications there is frequently the need to control and/or attenuate the vibrations of different mechanical systems, in order to promote the comfort increase of its users. Bicycles are typical mechanical systems, in which it is essential to control the vibrations that are transmitted to the passenger, while driving.

There are three main groups of control systems applied to attenuate the effects caused by unwanted vibrations, the passive, active and semi-active. The passive systems are the simpler and the more economical, since it is not necessary to use external power sources, actuating directly with the physical properties of the system. The main drawback of this systems is that they are not able to adapt to different road conditions and only actuate in a limited frequency bandwidth. The downsides of passive control systems can be avoided by using active control systems, but this systems require sensors, actuators, feedback control and external power source, making it complexer, more expensive to prototype and to produce and less economic while using. The solution for this problem is the use of semi-active control systems, that combine the characteristics of both passive and active control systems [1][2][3]. As in the passive control systems the control force is generated trough the energy dissipation of the system, yet, this force can be controlled. The force control implies power consumption, but much lower values when compared with the active control systems.

This paper aims to discuss the assessment of the comfort evaluation of an semi-active open controlled suspension system of a bicycle, that is equipped with a magneto-rheological damper [4][5][6][7]. The evaluation was carried based on the analysis of real data extracted from an instrumented bicycle prototype. The paper is structured as follows, initially the bicycle prototyping and its instrumentation are described, then the data extracted data is analyzed and discussed for several road and finally some conclusions and future work are pointed out.

## 2 Bicycle Prototyping and Instrumentation

The presented prototype was adapted from a standard commercial bicycle, that was originally equipped with a passive suspension system, being modified to use a MR damper instead of a typical shock absorber. These semi-active devices use MR fluid whose behavior can be controlled by a magnetic field in order to change the damping characteristics of the damper. This allows a passive or semi-active operation of the suspension controlled by keeping constant or varying the power of the electromagnet within the damper, respectively. Besides, they have as small power requirement, reliability and inexpensiveness to manufacture. These unique features makes them particularly appropriate to design advanced suspensions that can adapt the damping force according with the vehicle body motion (monitored through sensors in the vehicle) and road conditions. The bicycle prototype was equipped with accelerometers and with incremental encoders based on the Hall effect (applied to estimate displacement and velocity). The referred sensors provide valuable information in order to evaluate the ride comfort. The data was acquired at a $100$ Hz rate using an Arduino Mega Board and the data was sent to a laptop through a Serial Port connexion. The instrumented bicycle prototype can be observed in Figure 1.

## 3 Bicycle Comfort Analysis

Comfort is, in the cycling world, one of the topics that is subject to continuous research over the years [8][9]. In this case, acceleration measurements of the handlebar, seat and pedals are monitored and later applied in the performance evaluation for two input voltages 0.78 V




Figure 1: Bicycle Prototype

(0.35 A) and 1.56 V (0.70 A). To ensure that there are no differences between the experimental conditions, the velocity is kept constant during each test. The experimental tests were carried out in two types of horizontal road profiles: a smooth indoor pavement and a cobblestone road. The measurements taken during the tests, for each combination of voltage input and road profile, can be observed in Figures 2 to 5. A lower peak and RMS value signifies better performance or handling comfort.

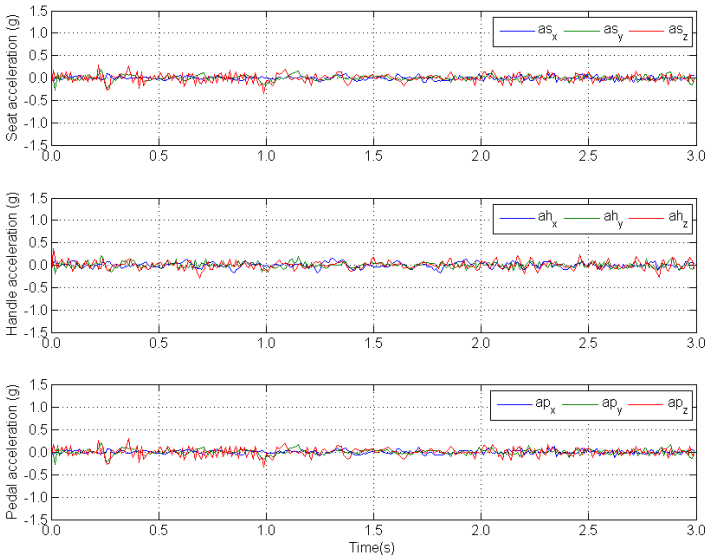


Figure 2: Indoor Pavement (0.78 V).

The damping properties or damping level of MR dampers can be modified using a voltage or a current based controller. The usual approach is to use a voltage signal created by a microcontroller or DAQ card to feed a voltage-to-current linear converter (WonderBox by Lord Co., USA) that is responsible to generate the operating current for the electromagnet within the device in order to change the magnetic field applied to the MR fluid. According with the

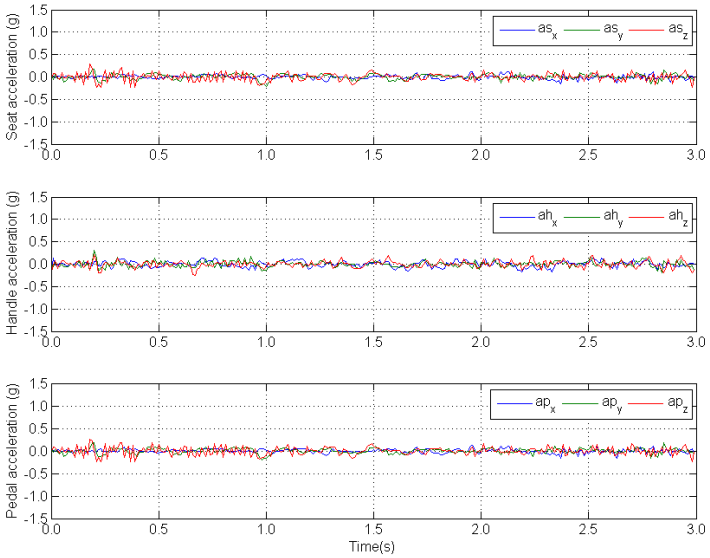


Figure 3: Indoor Pavement (1.56 V).

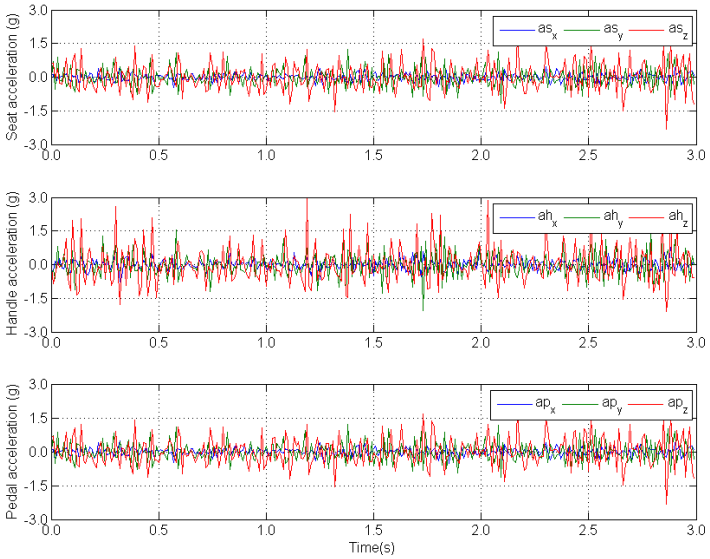


Figure 4: Cobblestone Pavement (0.78 V).

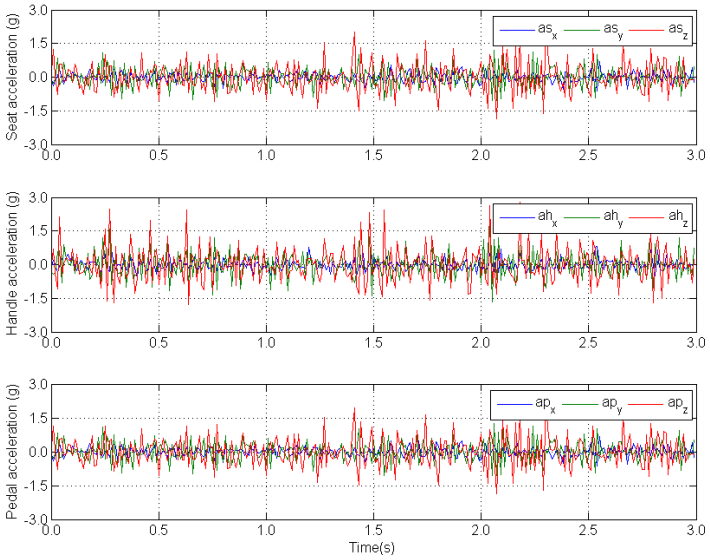


Figure 5: Cobblestone Pavement (1.56 V).

Table 1: Maximum Relative Accelerations

| | | Maximum Z-axis Acceleration (g) | | | Velocity m/s |
|---|---|---|---|---|---|
| Pavement | Input (V) | Handlebar | Pedals | Seat | |
| Indoor | 0.781 | 0.589 | 0.302 | 0.289 | 3.859 |
| | 1.56 | 0.207 | 0.259 | 0.291 | 3.683 |
| Cobblestone | 0.781 | 3.077 | 1.747 | 1.766 | 4.034 |
| | 1.56 | 2.801 | 2.251 | 2.219 | 3.869 |

device specifications, the RD-1005-3 series can operate within a current range from $0.0$ A up to $2.0$ A with a maximum recommended input value of $1.0$ A for continuous operation. Thus, the microcontroller generates a voltage input and the WonderBox provides the corresponding operating current for the electromagnet. As already has been specified, the operating current increases linearly with the voltage input.

The evaluation criteria are based on a comparison of the peak responses and also the root mean square (RMS) values for the z-axis acceleration. The results of this analysis are summarized in Tables 1 and 2.

As can be seen, the peak vertical acceleration in the handlebar for both road profiles is reduced as the voltage input or damping level increases. This mean that the vibration level

Table 2: Root Mean Square Relative Accelerations

| | | RMS Z-axis Acceleration (g) | | |
|---|---|---|---|---|
| Pavement | Input (V) | Handlebar | Pedals | Seat |
| Indoor | 0.781 | 1.261 | 1.252 | 0.089 |
| | 1.56 | 1.260 | 1.244 | 0.085 |
| Cobblestone | 0.781 | 1.505 | 1.384 | 0.629 |
| | 1.56 | 1.475 | 1.380 | 0.653 |

transmitted to the rider arms has been reduced and therefore the rider comfort and handling are improved. On the other hand, the peak values measured in the seat and pedals with a high voltage input are increased, which means that the damping effect provided by the MR damper is essentially focused on the bicycle handlebar. The results of the RMS values are consistent with the ones encountered for the peak accelerations, i.e., the higher the damping mode the lower the handlebar vibration level, although in this case there has been an improvement in almost all performance indexes indicating that the high voltage input or damping level is better for the rider comfort than the low voltage signal.

## 4 Conclusions and Future Work

Overall, it was verified that the MR damper is capable to improve the behavior of the bicycle suspension system providing a better riding experience. What particularly stands out from this analysis is that there is a large potential application of MR dampers to control the vibration level of a bicycle suspension system in order to improve the rider comfort and handling. It is recommended a further analysis using a closed-loop control system for different road profiles to demonstrate the effectiveness and robustness of the proposed controllable suspension system.

## REFERENCES

[1] A.S.Cherry, R.P.Jones, Fuzzy logic control of an automotive suspension system, IEEE, Vol: 142, No.2, pp. 149-160, 1995.

[2] Y. Jialing, C. Weiyi, C. Ning, A Review on the Development Status of Automotive Semi-active Suspension Systems, Automotive Engineering, 3, 276-280, 2006.

[3] Devdutt, M.L. Aggarwal, Fuzzy logic control of a semi-active quarter car system, International Journal of Mechanical, Industrial ScEngineering, Vol.8, No.1, 2014.

[4] B. Sapinski, Fuzzy Control for MR dampers in a Drivers Seat Suspension, Journal of Theoretical and Applied Mechanics, Vol. 43-1, pp. 179-201, 2005

[5] L.Cheng, Z. Qiang, Fuzzy Control of Vehicle Semi-active Suspension with MR Damper, 2010 WASE International Conference on Information Engineering (ICIE), Vol.3, pp. 426-429, 2010.

[6] B.F. Spencer Jr., S.J. Dyke, M.K. Sain, J.D. Carlson, Phenomenological model of a magnetorheological damper, Journal of Engineering Mechanics, 123, pp. 230.238, 1997.

[7] M. Braz Csar, R. Barros, Experimental behaviour and numerical analysis of MR dampers, 15WCEE - 15th World Conference on Earthquake Engineering, Lisbon, Portugal, 2012.

[8] S. Richard, Y. Champoux, Richard, Simon, and Yvan Champoux. "Evaluation of road bike comfort using classical and operational modal analysis." Proceedings of IMAC XXIII. 2005.

[9] BERTUCCI, W., PUEL, F., JARLOT, B., GRAPPE, F., DUC, S.. Evaluation of comfort: Acceleration transmissibility of different road bikes. Journal of Science and Cycling, North America, 4, dec. 2015. Available at: ¡http://www.jsc-journal.com/ojs/index.php?journal=JSCpage=articleop=viewpath

COMPDYN 2017
6th ECCOMAS Thematic Conference on
Computational Methods in Structural Dynamics and Earthquake Engineering
M. Papadrakakis, M. Fragiadakis (eds.)
Rhodes Island, Greece, 15–17 June 2017

# DEVELOPMENT OF AN OPTIMAL AND FUZZY SEMI-ACTIVE CONTROL SYSTEM FOR VEHICLE SUSPENSION

**K.F. Oliveira**[1], **M.T. Braz-César** [1], **J. Gonçalves** [1]

[1] Polytechnic Institute of Bragança
Campus de Santa Apolónia – Apt. 134 – 5301-857 Bragança - Portugal
e-mail: a25496@alunos.ipb.pt, {brazcesar, goncalves}@ipb.pt,

**Keywords:** Vibration control, MR damper, Fuzzy controller, optimal control system.

**Abstract.** *This paper aims to evaluate the performance of a semi-active controlled suspension system using a magneto-rheological (MR) damper to provide better ride comfort and safety to vehicle passengers than an uncontrolled or passive suspension system. Passive systems represent a conventional solution for vibration control of suspension systems. Although this system is a proven, reliable and economic technology, their parameters cannot be modified according to the road conditions. On the other hand, active systems allow a continuous control of the suspension motion, but require a complex and energy demanding actuator. The proposed suspension system has the adaptability of active systems with lower energy consumption, which constitute an economic and efficient option for vibration control in vehicle suspensions. The analysis was carried out with a set of numerical simulations in Matlab/Simulink using a 1/4 vehicle suspension model with two degrees of freedom for a passive system and two semi-active control modes based on fuzzy and optimal controllers.*

## 1 INTRODUCTION

As is well known, the purpose of automotive suspension systems is to minimize the effect of the road roughness in the vehicle to allow a comfort, safety and smooth drive. A large selection of vibration control system has been proposed to reduce unwanted vehicle vibrations. These systems are designed to reduce and dissipate quickly large oscillations and essentially they can be classified according with the control approach as passive, active and semi-active systems. Passive control systems use absorbing or dissipating energy devices operating in a passive mode, i.e., using the suspension motion to command the actuator. Thus, no external power source is required. Although they are simple and inexpensive when compared with other control approaches, they operate in a narrow frequency bandwidth since they cannot adjust the control mode for different road conditions. On the opposite side, active control systems are able to deal with modifications in the system properties including to road disturbances. However, complex actuators are often needed usually with high power requirements making them more complex and expensive than passive systems. In this context, semi-active control systems combining simple controllable or adjustable semi-active devices with low power requirements have been seen as a promising technology for automotive suspension systems with substantial advantages over both active and passive control systems.

Like active control systems, semi-active control approaches also require sensors, actuators and controllers to compute the control action, but the latter use simpler and therefore low-cost actuators which can operate with reduced power sources such as small batteries. The main issue is related with the selection of an effective controller to command the semi-active actuator. So far, a wide range of controllers have been proposed for semi-active vehicle suspension systems. While optimal controllers represent a well-known and simple classical vibration control approach, the hard dependence on the system model and lack of robustness can hinder their applicability to uncertain systems. On the other hand, fuzzy logic controllers seem to be a good approach to design advanced control systems due to its robustness to deal with the inherent uncertainty of automotive suspension systems [1-3].

This paper aims to evaluate the performance of a semi-active controlled suspension system using a magneto-rheological (MR) fluid based actuator. The analysis was carried out with a set of numerical simulations in Matlab/Simulink using a 1/4 vehicle suspension model with two degrees of freedom for a passive system and two semi-active control modes based on fuzzy and optimal controllers. The objective is to compare the effectiveness of each controller in increasing the ride comfort and road handling of a vehicle. The results obtained with the MR damper operating in a passive mode are compared with those obtained with semi-active control modes to assess the performance of the suspension control systems.

## 2 VEHICLE SUSPENSION

Typically, basic vehicle suspension systems are described by two masses: the body or vehicle mass and the suspension mass. Besides, suspension systems have a symmetric distribution over the car body that allows a simplified vibration response analysis using only one wheel or the so-called ¼ vehicle model shown in Figure 1 [4].

According with the two degrees-of-freedom (DOFs) mass system of the simplified model, the equations of motion of the system can be written as

$$m_1\ddot{x}_1 = F_s$$
$$m_2\ddot{x}_2 = F_t - F_s \quad (1)$$

in which $m_1$ is the sprung mass, $m_2$ is the unsprung mass, $F_s$ and $F_t$ are the suspension and tire forces, respectively, described by

$$F_s = k_1(x_2 - x_1) + c_1(\dot{x}_2 - \dot{x}_1)$$
$$F_t = k_2(x_0 - x_2) \tag{2}$$

where $x_1$ is the motion of the vehicle body and $x_2$ is the wheel displacement, $k_1$ is the suspension stiffness and $k_2$ the spring constant of the tire, and finally $c_1$ is the damping coefficient of the suspension system. In this case, $x_0$ represents the road disturbance.

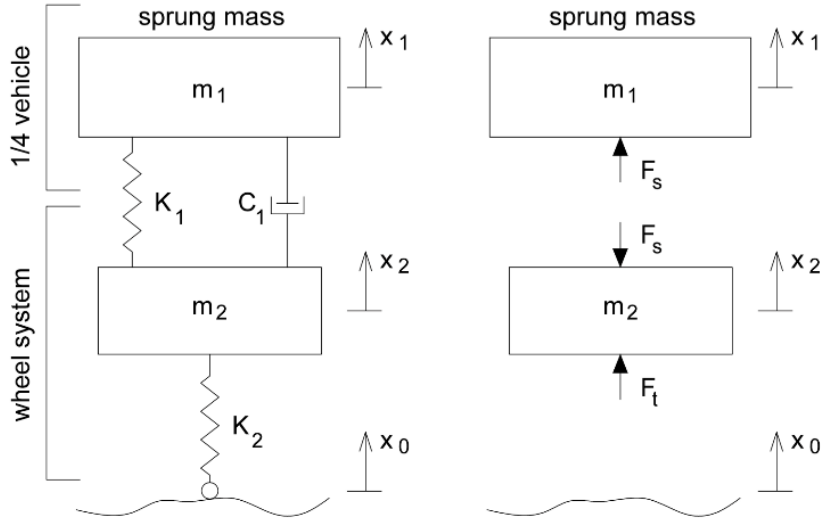


Figure 1 - ¼ vehicle suspension system (Two DOFs model).

The equations of motion of the suspension system can be rewritten as

$$\ddot{x}_1 = \frac{1}{m_1}[k_1(x_2 - x_1) + c_1(\dot{x}_2 - \dot{x}_1)]$$
$$\ddot{x}_2 = \frac{1}{m_2}[k_2(x_0 - x_2) - k_1(x_2 - x_1) - c_1(\dot{x}_2 - \dot{x}_1)] \tag{3}$$

which can be used to describe a state space model of the system as

$$\dot{X} = AX + Bx_0 \tag{4}$$

where $X$ is the state vector, $x_0$ is the input vector, matrix A given by

$$A = \begin{bmatrix} 0 & 0 & 1 & 0 \\ 0 & 0 & 0 & 1 \\ -\frac{k_1}{m_1} & \frac{k_1}{m_1} & -\frac{c_1}{m_1} & \frac{c_1}{m_1} \\ \frac{k_1}{m_2} & -\frac{(k_1+k_2)}{m_2} & \frac{c_1}{m_2} & -\frac{c_1}{m_2} \end{bmatrix} \tag{5}$$

is the state or system matrix and $B$ is the input vector given by

$$B = \left\{0, 0, 0, \frac{k_2}{m_2}\right\}^T \tag{6}$$

## 3 SEMI-ACTIVE MR SUSPENSION

Vehicle suspension system usually relies on passive dampers with constant damping characteristics to absorb and/or dissipate the kinetic energy generated by the wheel motion due to the road disturbance. These conventional shock absorbers can be replaced by active or semi-active actuators with real-time controllable damping and/or stiffness properties. Among these devices, MR fluid based dampers represent a novel technology that combines the simplicity of passive dampers with the adaptability of active actuators that have been widely used in advanced vehicle suspension systems. Basically, the MR fluid flow within the damper can be controlled using a magnetic field generated by an electromagnet located in the piston rod. This allows for a real-time modification of the rheological behavior of the MR fluid, which results in a modification of the damping force that can be adjusted in accordance with the vehicle motion and road condition. Besides, MR dampers allow a passive or semi-active operation of the vehicle suspension system by using a constant magnetic field or changing the power of the electromagnet, respectively.

The simplified model of a MR based semi-active suspension system is shown in Figure 2. The passive suspension stiffness $k_1$ and damping $c_1$ remain as constant values while the damping force represented by the variable damping c($t$) can be controlled in accordance with prescribed criteria or required operating settings.

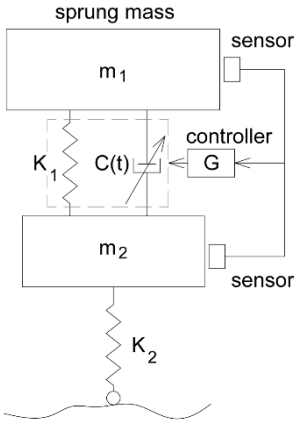


Figure 2 - Semi-active MR based vehicle suspension system.

In this case, the equations of motion are given by

$$\ddot{x}_1 = \frac{1}{m_1}[k_1(x_2 - x_1) + c_1(\dot{x}_2 - \dot{x}_1) + F]$$
$$\ddot{x}_2 = \frac{1}{m_2}[k_2(x_0 - x_2) - k_1(x_2 - x_1) - c_1(\dot{x}_2 - \dot{x}_1) - F] \quad (7)$$

where $F$ the control force of the suspension system generated by a MR damper located between the sprung and unsprung masses of vehicle suspension system. The corresponding state space model can be written as

$$\dot{X} = AX + Bx_0 + B_1F \quad (8)$$

where $B_1$ is the vector of the control force representing the effect of the actuator in the suspension system is given by

$$B_1 = \left\{0, 0, \frac{1}{m_1}, -\frac{1}{m_2}\right\}^T \tag{9}$$

and *F* is the damping force produced by the actuator. If only the MR damper is responsible by the damping in the suspension system, then $c_1$=0.

The damping force can be numerically simulated using a numerical model such as the modified Bouc-Wen model shown in Figure 3 [5].

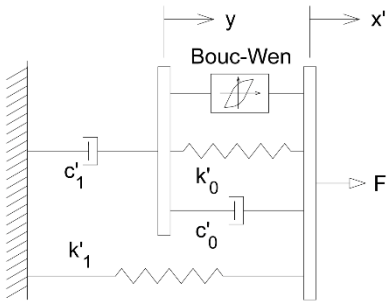


Figure 3 - Phenomenological model of the MR damper (modified Bouc-Wen model).

This model is able to represent the highly non-linear hysteretic behavior of MR dampers. According with the model depicted in Figure 4, the damper force *F* is obtained by

$$F = c_1'\dot{y} + k_1'(x' - x'_0) \tag{10}$$

where

$$\dot{y} = \frac{1}{c_0' + c_1'}\left[\alpha z + c_0'\dot{x}' + k_0'(x' - y)\right] \tag{11}$$

is dependent on the hysteresis effect given by the evolutionary variable

$$\dot{z}(t) = -\beta|\dot{x}'|z(t)|z|^{n-1} - \gamma\dot{x}'|z|^n + \delta\dot{x}' \tag{12}$$

Some of the modified Bouc-Wen parameters are current independent parameters (constant values) and frequently, α, $c_0'$ and $c_1'$ are current dependent parameter described by

$$\begin{aligned} \alpha(u) &= \alpha_a + \alpha_b u \\ c_0'(u) &= c_{0a}' + c_{0b}' u \\ c_1'(u) &= c_{1a}' + c_{1b}' u \end{aligned} \tag{13}$$

Besides, the dynamics involved in the MR fluid reaching equilibrium state is represented through first order filter given by

$$\dot{u} = -\eta(u - i) \tag{14}$$

in which the applied current *u* is described with a time delay relative to the desired current *i* and $\eta$ is a first-order filter time constant. The model parameters are determined based on experimental data.

In this study, a numerical model of a commercial MR damper (model RD-1005-3 by Lord Co., USA) is used to represent the damping force. A model parameter identification procedure was carried out and the following current independent parameters were found: δ=10.013, β=3.044 mm, γ = 0.103 mm, $k_0$ =1.121 N/mm, *f* = 40 N and n =2 [6].

It was also found that the current dependent parameters can be described by polynomial functions as follows

$$\alpha(u) = -826u^3 + 905u^2 + 412u + 38$$
$$c_0'(u) = -11.7u^3 + 10.5u^2 + 11.0u + 0.6 \quad (15)$$
$$c_1'(u) = -54.4u^3 + 57.0u^2 + 64.6u + 4.7$$

Finally, a first order filter with $\eta$= 130 sec$^{-1}$ was used to represent the first-order time lag involved in the current driver/electromagnet during a step command signal.

## 4 OPTIMAL CONTROLLER

The damping properties of MR dampers are frequently controlled using classical control algorithms in combination with a secondary or clipping unit that generates a bang-bang control operation. This approach represents a well-known semi-active control strategy for these devices known as Clipped-Optimal (CO) control algorithm. Besides, this controller has been shown to be very efficient in estimating the control signal and exploring the variable damping force of these semi-active actuators.

The basic idea is to append a force feedback loop to induce the device to produce approximately a desired control force. As has been said, this control strategy combines two controllers:

- A primary controller that includes an optimal control unit which is responsible for determining the optimal or desired control forces of an ideal active control system that should be applied to the structure to reduce the system response;

- A secondary controller. Since only the current/voltage applied to the current driver of the MR damper can be directly controlled, this controller has the function to generate the corresponding control signal in the form of a bi-state control output by clipping the optimal control forces. This accounts for the non-linear nature of MR dampers ensuring that they only produce dissipative forces (i.e., by adapting the ideal control to the semi-active nature of the actuator).

The Linear Quadratic Regulator (LQR) is a simple and well-known optimal controller that provides practical feedback gains. In these vibration control problems, the goal is to minimize the following quadratic cost function

$$\mathrm{J} = \int_0^\infty (X^T Q X + F^T R F)\, dt \quad (16)$$

in which the weighting parameter $Q$ is a diagonal semi-positive matrix that evaluates the state vector $X$ and the weighting parameter $R$ is a positive matrix that evaluates the control force $F$. The controller law is defined by a state feedback gain $G$ given by

$$G = R^{-1} B_2^T P \quad (17)$$

where $P$ represents the solution for the reduced Riccati equation

$$P A_1^T + \overline{A_1^T} P - P B_2 R^{-1} B_2^T P + Q = 0 \quad (18)$$

Thus, the optimal control problem is to find the feedback gain $G$ to obtain the corresponding optimal control force, which is given by

$$F = -GX \tag{19}$$

In this study, the weighting matrices $Q$ and $R$ were found by keeping $Q$ with a constant value and changing $R$ until the optimal control force is within the force range of the MR damper. The constant weighting matrix $Q$ is related with displacements and velocities of each mass and $R$ is a value that weights the importance of the damper force (there is only one actuator), which are defined as

$$Q = \begin{bmatrix} 1 & 0 & 0 & 0 \\ 0 & 0.5 & 0 & 0 \\ 0 & 0 & 1 & 0 \\ 0 & 0 & 0 & 0.5 \end{bmatrix}, \quad R = 10^{-8} \tag{20}$$

Then, the optimal state feedback gain $G$ can be found by solving the Riccati equation, which can be carried out using standard numerical tools in linear algebra. In this case, it follows that

$$G = [0.010 \quad -1.752 \quad 0.318 \quad -0.169] \tag{21}$$

## 5 FUZZY LOGIC CONTROLLER

Recently, soft computing and intelligent algorithms such as fuzzy logic based controllers (FLCs) have been proposed for semi-active vehicle suspension systems. This advanced modeling technique represents a powerful tool to deal with non-linear systems. FLC controllers use human-like reasoning through the use of fuzzy sets and linguistic variables related by a set of IF-THEN fuzzy rules. The design of a FLC requires the definition of membership functions (MFs) and the selection of appropriate fuzzy inference rules that relate the controller inputs and outputs. In this case, triangular MFs are used to represent both input and output variables as shown in Figures 4 and 5. The FLC inputs are the relative displacement and velocity across the MR damper, which represent state variables obtained via sensor measurements. The controller output is the control signal used to operate the MR damper.

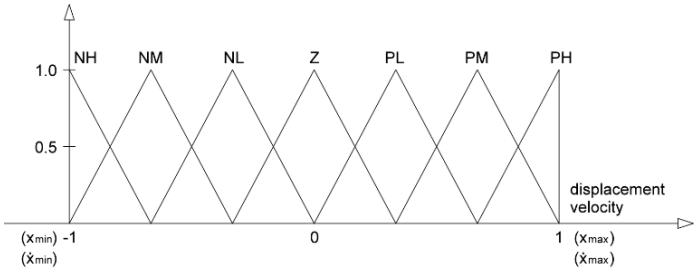


Figure 4 - MFs for displacement and velocity variables.

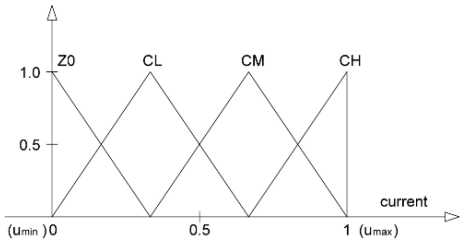


Figure 2 - MFs for the output variable (operating current).

As can be seen in Figure 4, seven linguistic variables were defined for each input as follows: NH- negative high, NM- negative medium, NL, negative low, Z- zero, PL- positive low, PM- positive medium, PH- positive high. The linguistic variables for the fuzzy controller output shown in Figure 5 are de-fined as: ZO- zero, CL- current low, CM- current medium and CH- current high.

| | | **Velocity** | | | | | | |
|---|---|---|---|---|---|---|---|---|
| | | **NH** | **NM** | **NL** | **Z** | **PL** | **PM** | **PH** |
| **Displacement** | **NH** | CH | CH | CM | PM | ZO | ZO | ZO |
| | **NM** | CH | CM | CM | PM | ZO | ZO | ZO |
| | **NL** | CM | CM | CL | ZO | ZO | ZO | ZO |
| | **Z** | CM | CM | CL | ZO | CL | CM | CM |
| | **PL** | ZO | ZO | ZO | ZO | CL | CM | CM |
| | **PM** | ZO | ZO | ZO | CM | CM | CM | CH |
| | **PH** | ZO | ZO | ZO | CM | CM | CH | CH |

Table 1 – Fuzzy rules of the proposed FLC.

The fuzzy inference system (FIS) must be defined assuming some knowledge about the system behavior. In this case, the following concept is used: if the displacement and velocity across the damper are very large, then the output is also large. The resultant fuzzy inference rule is shown in Table 1 [4].

## 6 NUMERICAL SIMULATION

A Matlab/Simulink model with the following parameters was used: $m_1$ = 350 kg; $m_2$ = 40 kg; $k_1$ = 50000 N/m; $k_2$ = 190000 N/m and $c_1$ = 500 N.s/m. The road disturbance is modeled as impulse signals as shown in Figure 6. In this case, two positive impulses with 5.0 mm alternated with a negative impulse with 2.5 mm are used.

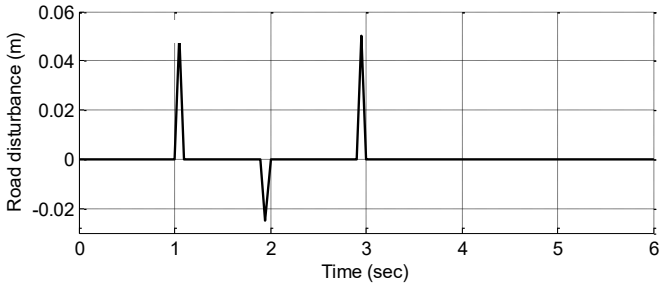


Figure 6 - Road disturbance - impulsive signals.

The clipped-optimal algorithm uses a clipping unit (or secondary controller) to adapt the control forces estimated by the primary optimal controller into a bi-state control signal (bang-bang/on-off controller) to command the MR damper. The damping forces generated by the actuator are dependent on the local responses of the structural system and therefore the device cannot always produce the desired optimal control force. Thus, the following command signal algorithm is applied

$$f_{MR} = \begin{cases} f_c, & f_c \cdot \dot{x} < 0 \\ 0, & \text{otherwise} \end{cases} \tag{22}$$

When the MR damper is delivering the desired optimal force, the operating current should remain the same. If the magnitude of the damper force is smaller than the magnitude of the desired optimal force and the two forces have the same sign, the voltage applied to the current driver is increased to the maximum level. Otherwise, the voltage is set to zero. The algorithm for selecting the command signal for the MR damper can be stated as

$$u = V_{max} H(f_c - f) f \tag{23}$$

where $V_{max}$ is the saturation voltage/current of the MR damper, fc is the desired optimal control force, f is the measured damper force and H is the Heaviside step function.

The results obtained with the two control approaches are shown in Figure 7 for the displacements of each mass and relative displacement between the two masses and Figure 8 for the acceleration of each mass.

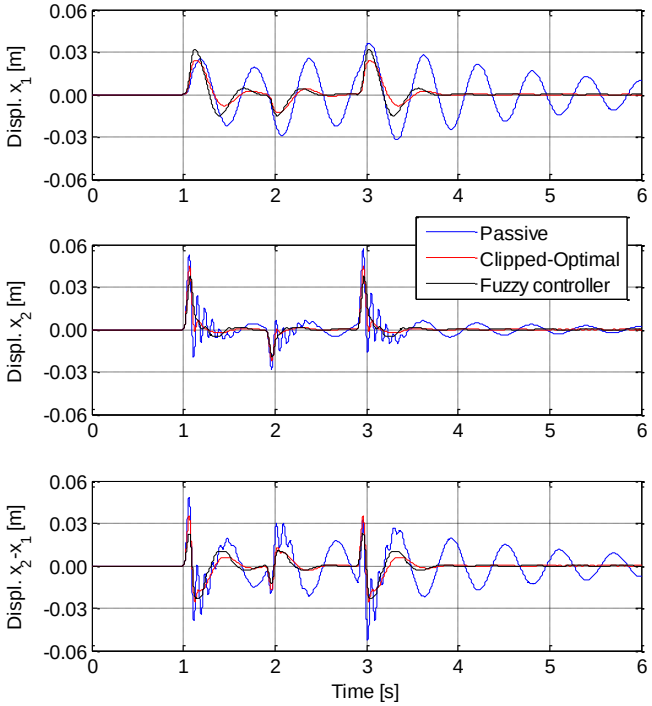


Figure 7 - Displacements (passive and semi-active modes).

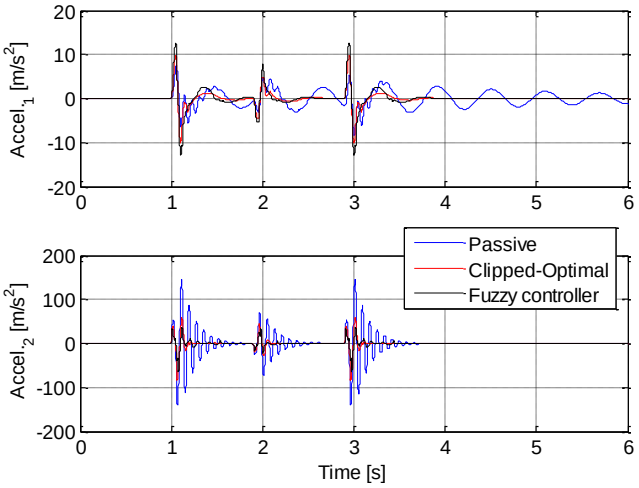


Figure 8 - Accelerations (passive and semi-active modes).

The semi-active control approach is more effective than the passive mode in eliminating the oscillation of the individual components. The effectiveness of the semi-active suspension system can be assessed measuring the root mean square (RMS) value of the body vertical motion ($m_1$) in both passive and semi-active control modes. The results are summarized in Table 2. Essentially, the results show that the proposed semi-active control system presents a higher performance in reducing the vehicle body vertical displacements and accelerations (clipped-optimal) than that obtained with the passive system.

| **Control system** | **RMS $x_1$** | **RMS $\ddot{x}_1$** |
|---|---|---|
| Passive | 0.0148 | 1.9369 |
| SA – optimal | 0.0062 | 1.5724 |
| SA – Fuzzy | 0.0073 | 2.1138 |

Table 2 – Controller evaluation (RMS criteria).

The semi-active fuzzy controller is less effective in reducing the peak vertical acceleration than the passive and clipped-optimal control mode, which is related with the fuzzy parameters used in this case. Searching procedures could be used to optimize the MFs and inference system in order to enhance the performance of the fuzzy controller.

## 7 CONCLUSION

In this study, a simplified model with two degree of freedom under impulsive road excitation was used to assess the performance of passive and semi-active suspension systems. The proposed semi-active suspension integrates a clipped-optimal and a fuzzy logic based controller in combination with a MR damper to reduce the motion of the vehicle body. Although the peak values of the body vertical acceleration are increased, the proposed clipped-optimal and fuzzy based control modes provide better ride comfort and safety reducing or attenuating the vibration level of the vehicle body when compared with the passive suspension system.

## REFERENCES

[1] L. Cheng, Z. Qiang, *Fuzzy Control of Vehicle Semi-active Suspension with MR Damper*, WASE International Conference on Information Engineering, Vol. 3, pp. 426-429, 2010.

[2] A. Cherry, R. Jones, *Fuzzy logic control of an automotive suspension system*, IEE, Vol. 142, No.2, pp. 149-160, 1995.

[3] B. Sapinski, *Fuzzy Control for MR dampers in a Driver's Seat Suspension*, Journal of Theoretical and Applied Mechanics, Vol. 43-1, pp. 179-201, 2005

[4] K. Oliveira, M. Braz-César, J. Gonçalves, *Fuzzy based Control of a Vehicle Suspension System using a MR Damper*, Series Lecture Notes in Electrical Engineering Vol. 402, pp. 571-582, 2016.

[5] B. Spencer Jr., S. Dyke, M. Sain, J. Carlson, *Phenomenological model of a magnetorheological damper*, Journal of Engineering Mechanics, Vol. 123, pp. 230.238, 1997.

[6] M. Braz-César, R. Barros, *Experimental behaviour and numerical analysis of MR dampers*, 15WCEE - 15th World Conference on Earthquake Engineering, 2012.

COMPDYN 2017
6th ECCOMAS Thematic Conference on
Computational Methods in Structural Dynamics and Earthquake Engineering
M. Papadrakakis, M. Fragiadakis (eds.)
Rhodes Island, Greece, 15–17 June 2017

# SEISMIC RESPONSE OF A CANTILEVERED HIGHWAY SIGN SUPPORT WITHOUT AND WITH A TMD DAMPER

**Fábio M. Paiva[1], Rui C. Barros[2]**

[1] CONSTRUCT Research Unit Collaborator, Dept Civil Engng, FEUP, Porto, Portugal
[2] Prof of Structural Engng with Habilitation at FEUP, Member of CONSTRUCT Research Unit, FEUP
R. Dr. Roberto Frias, 4200-465 Porto, Portugal
fabiopaiva.work@gmail.com ; rcb@fe.up.pt

***Keywords:*** seismic response, Eurocode 8-1, cantilevered sign support structure, TMD.

**Abstract.** *This work contributes to a better understanding of the seismic response of cantilevered sign support structures used in highways. For such, the present paper presents a comparative study of the seismic response of a cantilever sign support when subjected to earthquakes with and without a tuned mass damper (TMD). The paper starts with a brief summary of different methodologies to assess seismic input on structures. Some guidelines on the considered procedure for the selection of appropriate suites of accelerograms complying with Eurocode 8 prescription for Portugal (Faro) are presented. To mitigate earthquakes dynamic effects, the sign support structure can be equipped with a TMD with proven efficiency and ease of application and modelling, for the out-of-plane vibration control of the sign support in terms of displacements and accelerations reductions when the structure is subjected to series of real accelerograms compatible with the earthquake scenario of Eurocode 8-1.*

## 1. INTRODUCTION

As the present work intends to study the effectiveness of TMD, it is of major importance to describe the seismic input in the time domain. The purpose is to compare the structural response with and without a theoretical implementation of the TMD. For that linear elastic dynamic time history analysis will be conducted, which is also very useful when dominant modes are closely spaced or for multiply supported structures (bridges) where higher modes are expected to be excited, due to the asynchronous nature of incoming seismic waves [1]. Time-domain is prescribed in the majority of seismic codes around the world, as so in the Eurocode 8-1 (EC8-1) [2].

The aim of this paper is to present a structural model of a cantilevered sign structure in order to study the effect of real earthquake records and recommend passive control measures to limit the structure response (by TMD). Highway sign support structures have been studied previously by the authors, in the viewpoints of stability and design under [3] the Eurocode 3-1; moreover, some significant aspects of the wind response have also been addressed in other studies by the authors [4]. The following section pretends to detail the fundamentals of seismic-input selection on structures. Afterwards, the methodology to address the selection of real accelerograms complying with EC8-1 is presented. A theoretical implementation of TMD will be studied, and a comparative analysis of the structure response (displacements and accelerations) with and without TMD will be made

## 2. RECORD SELECTION IN EUROCODE 8-1

The structural seismic assessment requires earthquake loads to be represented either by response spectrum or by recorded acceleration time histories (accelerograms) as input to a linear or non-linear dynamic analysis. For that, input motions have to be selected so as to represent regional seismicity and must conform to expected earthquake (target spectrum), this mean they have to fulfill earthquake scenarios (as EC8-1 describes) in order to be used in the posterior dynamic analysis.

### 2.1 Elastic response spectra of Faro according with EC8

Contrary to general practice, the Portuguese National Annex of the EC8-1 adopts two zones (Figure 1), one for the near-source scenario and the other for a distant-source scenario. In the present work, Faro municipality has chosen for the location of the sign structure, because of the many studies available concerning its disaggregation seismic hazard. Faro is located in the south of Portugal, corresponding to zone 1.2 and 2.5 in Figure 1 (A1 and A2). In this study, and for the purpose of the TMD efficient assessment, only zone 1.2 will be study, which represents a severe earthquake and distant-source scenario.

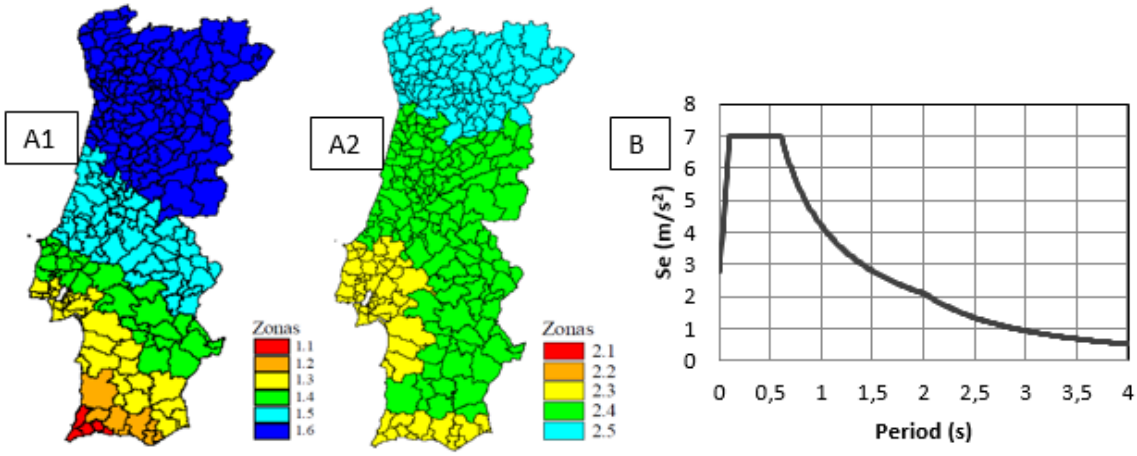


Figure 1: Seismic zonation for distant scenario (A1) and for nearby scenario (A2) in the EC8 Portuguese National Annex. Colors correspond to different PGA values, and at each site the higher of the two values is adopted. Elastic response spectrum for a ground type C in Faro, zone 1.2 (figure B)

In EC8-1 the seismic action on structures is defined after the acceleration elastic response spectrum. In Part 1, which applies for buildings, the spectral shapes are given for both horizontal and vertical components of motion. All shapes have a functional form which depends, a part of the soil class, on a single value, $a_g$, anchoring the spectrum to the seismicity of the site. The $a_g$ refers to the seismic classification of the territory in each country; it is basically related to the hazard in terms of peak ground acceleration (PGA) on rock for the site.

Recurring to EC8-1 Portuguese national annex, the resulting ag for zone 1.2 is 2.0 m/s$^2$. Adopting a ground type C ($S_{max}$=1.6, with S=1.4) and all the periods necessary to the construction of the elastic response spectrum, with TB=0.1, TC=0.6 and TD=2.0. The resulting elastic response spectrum ($\eta$=1.0) for Faro is represented in Figure1 B.

## 2.2 Identification of the critical earthquake scenario for Faro

Disaggregation of the seismic hazard for the Faro

The Cornell approach to probabilistic seismic hazard analysis (PSHA) is based on an area summation, covering all the relevant sources [5]. Restricting the summation to a given sub-area allows the estimation of the contribution of that sub-area to the total hazard. This notion is the basis of the technique known as hazard disaggregation [6], which allows the identification of the seismic sources making dominant contributions to the hazard at a particular site. This information can in turn be used to define the ground shaking scenarios (ex. magnitude and epicentral distance) that are relevant for earthquake risk mitigation at the site. Inadequate disaggregation of seismic hazard may be a distracting factor, focusing resources in sources that are not dominant and underestimate others.

Hazard disaggregation in Portugal (and Iberian Peninsula) was conducted in the works of [7]-[8], for example. Taking into account specific appreciations made in reference [9], the results of [8] were followed. In addition to that there is some information in the Portuguese National Annex EC8-1-5 [10], which provides representative magnitudes for a return period of 475 years. For Faro municipality the magnitude adopted according with EC8-1-5 was 7.5, and a distance (mean value) of 123 km, this consists in a distant-earthquake scenario with scattered seismicity around the Gulf of Cadiz and West Cape San Vicente as mentioned by Montilla et al [8].

## 2.3 Accelerograms selection rules according with EC8

Some issues can explain the difficulties experienced by common practitioners in dealing with code-based record selection. According with [11] these can be grouped on a twofold set: the first one derives from the fact that the determination of the design earthquakes may require hazard data often not readily available to engineers or may require seismological skills beyond their education (already mentioned); the second reason develops from matching a suite of real records to a design spectrum in a broad range of periods, which may be extremely unfeasible if appropriate tools are not available. The later situation has favored the use spectrum matching accelerograms, either artificial or through manipulation of real records. As generally recognized by many in the earthquake field, real records are considered the best representation of the seismic loading for structural assessment and design, so some computer aided tools have been developed for the record selection, as being that REXEL 3.5 [12], and other for spectral matching [13]. The REXEL computer software allows to build design spectra according EC8-1 or to user-defined target design spectra, and to search for sets of 7, 14, 21 groups of records (each group may be made of 1, 2 or 3 components ground motions), from the European Strong-motion Database (ESD) [14] and [15]. These sets are compatible to target spectra with respect to EC8-1 code prescriptions, but reflect also some seismological characteristics (magnitude, epicentral distance and EC8-1 soil site classification) relevant for the seismic structural analysis. In the case of spectrum seismic match, the record selection must be made outside of the program, in databases available online, and posteriorly matched to the target spectrum.

Once the reference spectrum has been defined, EC8-1 allows the use of any form of accelerograms for structural assessment; i.e., real, artificial or obtained by simulation of seismic source, propagation and site effects. To comply with Part 1 the set of accelerograms, regardless its type, should basically match the following criteria:

a) *a minimum of 3 accelerograms should be used*;

b) *the mean of the zero period spectral response acceleration values (calculated from the individual time histories) should not be smaller than the value of ag S for the site in question (S is the soil factor);*

c) *in the range of periods between 0.2T1 and 2T1, where T1 is the fundamental period of the structure in the direction where the accelerogram will be applied, no value of the mean 5% damping elastic spectrum, calculated from all time histories, should be less than 90% of the corresponding value of the 5% damping elastic response spectrum.*

The EC8-1, refers that in the case of spatial structures, the seismic motion shall consist of three simultaneously acting accelerograms representing the three spatial components of the shaking, then 3 of condition (a) shall be considered as the number of translational components of motion to be used (the two horizontal and the vertical one). Furthermore, the vertical component of the seismic action should be taken into account only for base-isolated structures, and for some special cases in regular buildings, if the design vertical acceleration for the A-type site class ($a_{vg}$) is greater than 0.25g. Finally, some prescriptions regarding duration are given for artificial accelerograms, and real or simulated records should be adequately qualified with regard to the seism genetic features of the sources and to the soil conditions appropriate to the site.

Section 4.3.3.4.3 of EC8-1, allows the consideration of the **mean effects on the structure**, rather than the **maximum**, if at least **seven nonlinear time-history analyses** are performed.

In [16] it was investigated whether it is possible to find unscaled real record sets fulfilling, as much as possible, the requirements of EC8-1. As a general conclusion it was found that prescriptions do not easily allow selecting suitable real record sets, factually favoring the use of records obtained either by computer techniques or manipulation of real records to have a spectral shape coincident to that of the reference in a broad range of periods.
The procedure for the selection of horizontal accelerograms according with EC8-1 for the life safety limit state (475 years return period) involves the next 4 steps:

1. Definition of the target spectrum, in this case the horizontal elastic response spectrum of Faro zone 1.2 (ground type C) that the set of records has to match on average. The present location demands the definition of two elastic response spectrum, zone 1.2 and 2.3, but was already mentioned, for Faro, the main earthquake hazard scenario correspond to a distant seismic source, so in this paper only zone 1.2 is studied.
2. Definition of the magnitude and distance bins for each of the two target spectra referred for the specific site class. For the type 1 (high and moderate seismicity regions) target spectrum the magnitude considered was $7.3<M<7.7$ and $80<R<160$. The reason for selecting the parameters magnitude, source-to-site distance and site class, is that important characteristics of the record such as frequency content, spectral amplitudes, spectral shape, and duration are correlated with the mentioned parameters [17]. For their case study [18] recommended a magnitude bin width +-0.20Mw and a distance bin +-40 km around the scenario value of 10 km, they recommend to relax the distance criterion if the search yields too few records. And in the case of insufficient records, they also suggest to be not too rigorous regarding the match of site class but to solely exclude records with very different site classification from that of the project site.
3. Assigning the period range where the average spectrum of the set has to be compatible with the target spectrum and tolerances acceptable. For the present case a minimum period of 0.14 s ($0.2*T1 \cong 0.14$ s, where T1=0.7s is the fundamental period of the cantilevered sign support) and maximum period of 2.0 ($2*T1=1.4$ but a larger value was adopted), the lower and upper spectral matching limits were respectively 10% and 30 %. The EC8 explicitly states that the average elastic spectrum must not underestimate the code spectrum, with 10% tolerance (lower limit), but does not provide any indication about the upper limit. Therefore, it is of economically importance to reduce as much as possible this overestimation of the spectrum, that's why the correspondent upper limit was chosen.
4. Running the search for combinations of seven records with two horizontal components of motion (14 records) and that, on average, match the design spectrum with parameters specified in step 3. REXEL 3.5 allows obtaining combinations of accelerograms compatible with target spectrum which does not need to be scale, but also permits choosing sets of accelerograms compatible with target spectrum if linearly scaled. This means that the list of spectra defined in step 2 are preliminarily normalized dividing the spectral ordinates to their Peak ground acceleration (PGA). Combinations of these spectra are compared to the non-dimensional code spectrum. This situation is for cases in which horizontal motion has to be applied in both direction of 3D structure, and where vertical acceleration can be ignored.

### 2.4 Accelerograms selection for Faro

In the first search none of the combinations available in the database complied with EC8 prescription, even with the scaled record option selected. In the subsequent search all ground types were considered for selection, hence a total of 3 earthquakes (possibly over-representing some events) were found acceptable (with 2x23 records from different stations).

The Figure 2 shows the 14 scaled records (7x e 7y) that are compatible with the EC8-1 target spectrum for Faro (zone 1). The program selects the records according with a parameter, which gives a measure how much the spectrum of an individual record deviates from the target spectrum of the code.

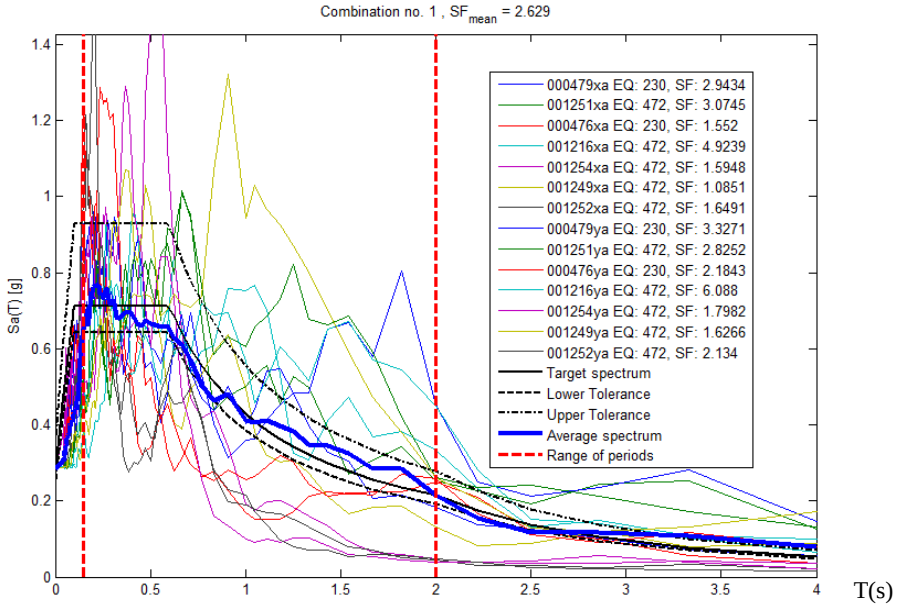

Figure 2 - Results of the 14 selected records, scaled response spectra and target spectrum

The average scale factor has 2.6, with a maximum 6.1 for the record 1216 in the y direction. The Figure 3 shows the 14 scaled accelerograms, 7 in the x direction (top) and 7 y direction (bottom).

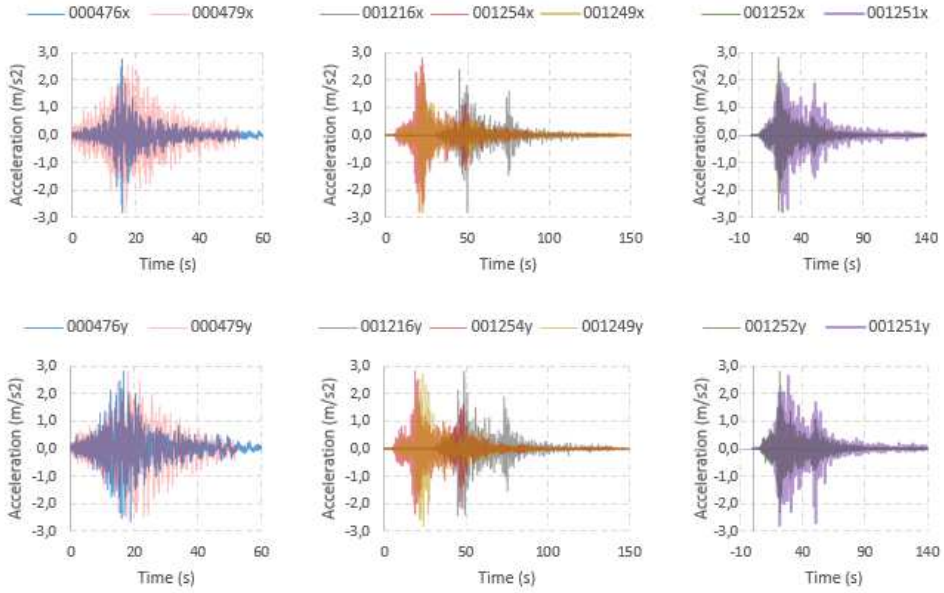

Figure 1: Scaled accelerograms, x direction (top graphics) and y direction (bottom graphics)

## 3. LINEAR DYNAMIC ANALYSIS OF A CANTILIVERED SIGN SUPPORT WITHOUT AND WITH A TMD DAMPER

### 3.1 Numerical Model Development and Modal Analysis

The Figure 4 represents a cantilevered sign support, constituted by a square hollow cross-section 250*250*8 mm (uniform member) in S355 strength steel. The column and the beam have a length of 6.5 m and 6.0 m, respectively. The signboard dimensions can also be seen in Figure 4. For in-depth information of the finite element model used in the dynamic analysis, the reader is referred to a paper from the authors [4]. In the same paper the reader can find the main results of the performed modal analysis.

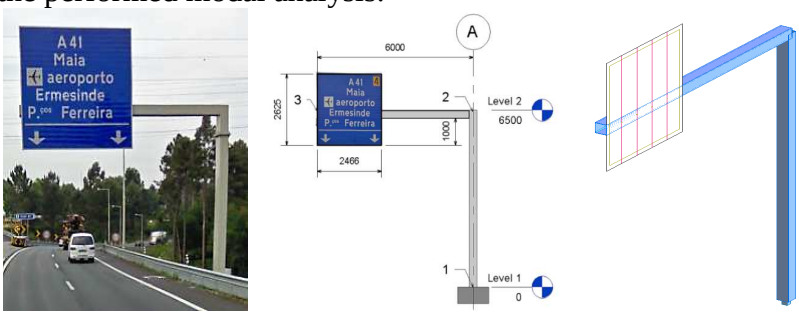


Figure 4 - Example of a cantilevered sign support structure (left) geometry of the design example (dimensions in mm, center) and numerical model of the cantilever sign support (right)

### 3.2 Results from Time History Analysis with and without a TMD for passive control of vibrations

The manner in which the two horizontal components of the accelerograms or ground motion (GM) are oriented when being applied to the structural model is extremely important and there is both little and inconsistent guidance on this aspect. In this work an original orthogonal orientation at 0º and then a 180º rotation of the GM was considered for the dynamic analysis (as indicated by the EC8-1).

The results in terms of displacements and accelerations were evaluated and compared for the computational structural model, without and with installed TMD vibrating bar. The Hilber-Hughes Taylor (HHT) method is used to solve dynamic equation of motion (with $\alpha$=-0.3 for an unconditionally stable scheme of integration). The HHT method is a very efficient algorithm for numerical integration that allows removing the unfavorable impact of high frequencies on the quality of a solution. A damping ratio of 0.5% and an integration time step of $\Delta t$=0.01/10 sec, for the 7 time series of two components (x and y) of seismic dynamic loads were applied (for each time series two directions were analyzed, 0º and 180º) and their mean, median and standard deviations results obtained in terms of displacements and accelerations.

The predication of the variability in structural response is important, because it helps to judge margins against undesirable performance. The record selection and scaling was based on a mean target spectrum, such as the uniform hazard spectrum. This means that no defined variability exists in the spectral values. The prediction of the structural response variability is statistically meaningless and will depend entirely on how the records were selected and scaled to match the target spectrum.

The Figure 5 shows the time variations of acceleration and displacement on the tip of the beam (node 3 in Figure 5) of the sign support, for the seismic input corresponding to 001251 time series in the cases without and with TMD.

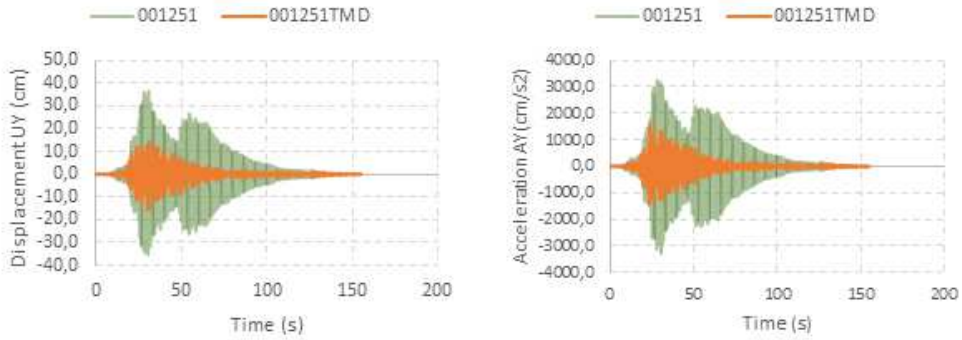


Figure 5: Displacements and accelerations (direction y) of node 3 of the beam (see Figure 4), without and with TMD modeled with mass ratio of 1% for the earthquake 001251 time series

Table 1 presents a summary of maximum values of displacements and accelerations on node 3 (horizontal direction), for the 7 the time series.

| Earthquake/ Time-series | Direction | 000476 | 000479 | 001216 | 001249 | 001251 | 001252 | 001254 | Mean | Median | Standard Deviation |
|---|---|---|---|---|---|---|---|---|---|---|---|
| Maximum displacement (cm) | x | 3,1 | 3,2 | 2,9 | 3,2 | 6,9 | 4,4 | 9,5 | 4,8 | 3,2 | 2,5 |
| | | **3,6** | **3,3** | **2,5** | **3,2** | **6,8** | **3,6** | **9,9** | **4,7** | **3,6** | **2,7** |
| | y | 8,1 | 29,5 | 13,1 | 18,1 | 36,6 | 14,7 | 11,1 | 18,7 | 14,7 | 10,4 |
| | | **9,2** | **13,4** | **11,5** | **13,2** | **15,8** | **16,4** | **14,5** | **13,4** | **13,4** | **2,5** |
| Maximum acceleration ($cm/s^2$) | x | 874,2 | 997,1 | 325,5 | 743,7 | 914,5 | 2636,3 | 1337,4 | 1118,4 | 914,5 | 734,5 |
| | | **917,1** | **1018,7** | **343,5** | **714,9** | **965,7** | **2521,8** | **1348,2** | **1118,6** | **965,7** | **690,3** |
| | y | 1332,2 | 2684,6 | 1223,3 | 1642,1 | 3282,4 | 2457,0 | 1742,5 | 2052,0 | 1742,5 | 768,9 |
| | | **1595,9** | **1263,5** | **1189,2** | **1270,9** | **1625,1** | **2021,7** | **1506,6** | **1496,1** | **1506,6** | **289,3** |

Table 1 – Maximum displacements and accelerations on node 3, for each of the time series (without TMD) and with TMD (bold format)

All the subsequent considerations are towards to the y direction, due to the TMD was tuned for the fundamental model vibration. In general, in the x direction, the TMD has produce no overall structural benefits. For the y direction, the maximum displacement and acceleration was found for the 001251 time-series, where in addition the TMD proved to be the most effective. The 000476 time-series displayed the minimum displacement and acceleration of all the 7 cases, in this particular situation the TMD has amplified slightly the response.

The efficiency on the use of the modeled TMD on the structure can be interpreted by the results of Table 1, here associated with mass ratio of 1%: reduction of maximum displacements and accelerations (mean values) in the y direction on the order of 28% and 14%, respectively. Another parameter that deserves attention is the standard deviation; for the case with TMD installed, there is a substantial reduction of the structural response variability (displacements and accelerations).

## 4. CONCLUSIONS

The paper introduces and describes a procedure for selecting and scaling natural records of earthquakes for the study of cantilevered sign support structures. The herein suggestions follows the EC8-1 (Portuguese National Annex) prescription for a particular sign support located in the south of Portugal (Faro).

Regarding the implementation of the TMD, it was concluded that this device is proving to be effective in terms of displacements and accelerations reductions when the structure is subjected to the scaled natural records, but only in the y direction (fundamental vibration mode). For the TMD modeled with the parameters calculated, it was concluded that in terms of maximum accelerations (mean values) reductions of the order of 28% can be achieved for a TMD with 1% mass ratio. For the maximum displacements (mean values) it was concluded that the structural reference system has proved less effective, achieving reductions of 14% for a TMD with 1% mass ratio. In the present paper, the implementation of the TMD was only considered the out-plane direction (y direction associated with the fundamental vibration mode), future studies should focus ways to provide effective damping in both directions, as a combination of two damping devices. From a structural system perspective, the in-plane and out-of-plane behaviors are almost uncoupled (modes of vibration); hence the movement (and suppression) can be considered independently and superimposed.

## ACKNOWLEDGMENTS

Although the co-authors are respectively collaborator and Member of Construct Research Unit of the Civil Engineering Department at FEUP, present lack of funds disabled Construct direct support of this R&D. So the authors solely acknowledge the Infrarisk Program PhD grant of the first co-author, and at the present moment the financial support received directly through the cost centre of the second co-author and associated with his overheads from past R&D multiple activities and consultancy services.

## REFERENCES

[1] Katsanos EI, Sextos AG, Manolus GD (2010): Selection of earthquake ground motion records: A state-of-the-art review from a structural engineering perspective. Soil dynamic and Earthquake Engineering 30, 157-167.

[2] CEN 2004. Eurocode 8: Design of structures for earthquake resistance- Part 1: General Rules, seismic actions and rules for buildings, Brussels, Belgium.

[3] Paiva F, Barros RC. Analysis of the stability and design of a cantilever sign support in highways. 4th International Conference on Integrity, Reliability & failure, Funchal, 23-27 June.

[4] Paiva FM, Barros RC. Comparisons of a cantilever sign support response subjected to natural wind gusts with and without a TMD. 4th ECCOMAS Thematic Conference on Computation Methods in Structural Dynamics and Earthquake Engineering (COMPDYN2013), Kos Island, Greece, 2013.

[5] Cornell C.A. (1968): Engineering Seismic Risk Analysis, Bull. Seismol. Soc. Am., 58, 1583-1606.

[6] Bazzurro P, Cornell CA (1999): Disaggregation of seismic hazard, Bull. Seismol. Soc. Am., 89, 501–520.

[7] Sousa M, Costa AC (2009): Ground motion scenarios consistent with probabilistic seismic hazard disaggregation analysis. Application to Mainland Portugal, Bull. Earthquake Eng., 7, 127-147.

[8] Montilla, J.A., Casado, CL, Romero, J.H (2002): Disaggregation in magnitude, distance, and azimuth in the South and West of the Iberian Peninsula. Bull. Seismol. Soc. Am., 6, 2177–2185.

[9] Fonseca JFBD, Vilanova SP (2012): Overview on current seismic hazard disaggregation studies for Western Iberia and Consequences for ground shaking scenarios for Lisbon, 15th World Conference on Earthquake Engineering, Lisbon, Portugal.

[10] CEN 2004. Eurocode 8: Design of structures for earthquake resistance- Part 5: Foundations, retaining structures and geotechnical aspects, Brussels, Belgium.

[11] Iervolino I, Cosenza E, Galasso C (2009): Shedding some light on seismic input selection in Eurocode 8, E. Conseza (ed.), Eurocode 8 Perspectives from the Italian Standpoint Workshop, 3-12, Doppiavoce, Naples, Italy.

[12] Iervolino I, Galasso C, Cosenza E (2010). REXEL: computer aided record selection for code-based seismic structural analysis. Bulletin of Earthquake Engineering.8:339-362, DOI 10.1007/s10518-009-9146

[13] http://www.seismosoft.com/seismomatch. 23/05/2016.

[14] Ambraseys N, Smit, P, Berardi R, Rinaldis D, Cotton F, Berge C (2000): Dissemination of European strong-motion data (Cd-Rom Collection). European Commission, Dgxii, Science, Research and Development, Bruxelles.

[15] Ambraseys NN, Douglas J, Rinaldis D, Berge-Thierry C, Suhadolc P, Costa G, Sigbjornsson R, Smit P (2004): Dissemination of European strong-motion data, Vol. 2, Cd-Rom Collection, Engineering and Physical Sciences Research Council, United Kingdom.

[16] Iervolino I, Maddaloni G, Cosenza E. (2008): Eurocode 8 compliant real record sets for seismic analysis of structures, Journal of Earthquake Engineering, 12(1): 54–90.

[17] Beyer K, Bommer JM, (2007): Selection and scaling of real accelerograms for bi-directional loading: A review of current practice and Code Provisions. Journal of Earthquake Engineering, 11:13-45, DOI: 10.1080/13632460701280013

[18] Bommer JJ, Acevedo AB (2004): The use of real earthquake accelerograms as input to dynamic analysis. Journal of Earthquake Engineering, Vol. 8:43-91, 2004. Special Issue, 1.

COMPDYN 2017
6th ECCOMAS Thematic Conference on
Computational Methods in Structural Dynamics and Earthquake Engineering
M. Papadrakakis, M. Fragiadakis (eds.)
Rhodes Island, Greece, 15–17 June 2017

# TUBULAR STEEL LATTICE TELECOMMUNICATION TOWERS, SUBJECTED TO WIND LOADING AND VORTEX SHEDDING

**Dário Vieira[1], Rui Carneiro Barros[2(*)]**

[1] Construct collaborator FEUP-Dept Civil Engng, PhD Student, Univ of Houston, Houston, USA
[2] Prof Structural Engng, Dept Civil Engng, Member of Construct, FEUP, Porto, Portugal
e-mail: rcb@fe.up.pt

***Keywords:*** lattice steel towers, wind vortex induced vibrations.

**Abstract.** *The main goal of this work was to evaluate the response of the diagonals members of steel lattice towers with circular cross-sections under the wind load determined according to the current regulation EN1991-1-4. For the purpose of this study a program in VBA using Excel was developed to evaluate the response of lattice steel towers to vortex shedding induced vibrations and possible failure due to fatigue. A design example was dealt with some possible detail.*

## 1. INTRODUCTION

The telecommunication tower design is strongly influenced by the project requirements. For lattice towers it is necessary to analyse the loading effects on its slender members as well as their resistance. One of the crucial analyses is related with the dynamic wind loading, which can lead to local failure of members and may create a chain of consecutive failures. This would lead to the tower structure loss of resistance and stability, leading eventually to global failure. Thus, wind related phenomenon like vortex shedding should and must be considered.
In the worst scenario, vortex shedding can create small medium and large amplitudes resonant vibrations corresponding to oscillations in the transversal direction, which may strongly lead to fatigue problems in some of the tower members.

The vortex shedding occurs in the diagonals of the telecommunication towers essentially because of the forms of their sections [1]. Although it is frequently not considered as a design verification in lattice towers, a considerable number of similar structures suffers failures due to vortex shedding. The non-linearity of the phenomenon, in addition to its complexity creates difficulties in its approach and study analysis. The aim of this work was to optimize the analysis of the vortex shedding on steel diagonals of lattice towers using a simple program to predict the potential elements at risk. Consequently, for the known diagonals that may experience some induced vibration problems, the final goal of this work is to further develop a method of minimizing the damage, which will be detailed in a letter research work. The results obtained may be useful for future projects and for lattice tower designs.

## 2. VORTEX SHEDDING

For bluff bodies, i.e., less aerodynamic, the wind action creates transversal vibrations due to vortex shedding [2]. This phenomenon is defined as the moment in which the flow of a fluid around an element creates an alternation of low pressures zones in its vicinity. This alternation causes the perpendicular vibration regarding the wind load direction [3]. As the fluid flow velocity reaches the critical velocity of the contact element, the dynamic force created by the shedding leads to higher vibrations (normal to the flow) in the zones where the dynamic force is more felt on the element perimeter [4]. Same as to say, it creates resonant vibration.

### 2.1 Lock-in

When the frequency of the vortex shedding and the natural frequency of the slender element are equal, the Lock-in is said to be created. In this instant, the element is subjected to higher vibrations, and its natural frequency controls the shedding [5] [6]. It is difficult to characterize the element response when the vortex shedding frequency value is far from the element frequency (the response type is random). This is way it is considered the scenario where the vibrations are of higher order in resonance. To simplify the analysis and calculations, it is considered a singular value of frequency where Lock-in occurs, but it is well established that in fact it occurs in a range of velocities of fluid flow (representing the frequencies) [4]. Thus, the following equation is used in the analysis:

$$V_{crit} = \frac{f_n D}{St} \tag{1.1}$$

## 3. VORTEX SHEDDING EVALUATION – EUROCODE EN1991-1-4 (2010)

The current Eurocode establishes that it should be verified two criterions for vortex shedding analysis necessity [7]:

- The ratio between the largest and the smallest dimension in the plane normal to the wind direction is greater than 6;
- The critical wind velocity in the considered mode of vibration, is less than 1.25 times the average wind velocity, at the cross-sectional level where the vortex shedding is triggered.

$$v_{crit,i} < 1{,}25 \cdot v_m \tag{2.1}$$

The average velocity is calculated using the equations and the conditions expressed in EN1991-1-4, for a giving base velocity and height (from the ground). For the case of lattice towers elements, the critical velocity is given for the first mode of vibration, since it's considered the mode that governs.

$$v_{crit,1} = \frac{b.n_{1,y}}{S_t} \tag{2.2}$$

Where b is the cross-section diameter, $n_{1,y}$ the frequency of the element for mode 1 and $S_t$ the Strouhal number, defined as a parameter that relates the vibrational forces and forces of inertia (body forces). For this study, the value of St is 0.18, for circular tubes.

For the vortex shedding calculations, the Eurocode presents two methods of analysis to calculate the maximum deflection. Calculating the maximum deflection, the resultant effect is given by:

$$F_w(s) = m(s) \cdot (2 \cdot \pi \cdot n_{i,y})^2 \cdot \phi_{i,y}(s) \cdot y_{F,máx} \tag{2.3}$$

Methods 1 and 2 are detailed in Appendix E of EN1991-1-4 [7]. It is necessary to determine another parameter to identify the type of flow [8], designated as Reynolds number, which influences the effect of the vortex shedding.

$$R_e(v_{crit}) = \frac{b \cdot v_{crit}}{\nu} \tag{2.4}$$

For the current code, the Reynolds number is used to determine the lift coefficient (for lateral movement) which is used in the deflection formula for method 1. Moreover, it is also used for the variables defined in Method 2.

## 4. FATIGUE ANALYSIS

The analysis used in the determination of number of cycles of excitation leading to damage is based on the rules and methods in the regulation EN1993-1-9 [9]. The initiation and crack propagation on a structural element is caused by a cyclic change of stress, this is way the code presents two types of safety verification for damage control: one based on range of equivalent stress in constant amplitude, and accumulative damage verification. The total number of cycles is given by [7]:

$$N = 2 \cdot T \cdot n_y \cdot \varepsilon_0 \cdot \left(\frac{v_{crit}}{v_0}\right)^2 \cdot \exp\left(-\left(\frac{v_{crit}}{v_0}\right)^2\right) \tag{3.1}$$

The number of cycles is a function of the critical velocity $v_{crit}$, the frequency of vibration $n_y$, the modal value of the wind velocity taking in account the Weibull distribution $v_0$, the life spam considered for the structural element T, and factor that describes the range of velocity in which vibrations occur $\varepsilon_0$.

For the equivalent stress in constant amplitude safety verification, the following condition must be verified:

$$\frac{\gamma_{Ff} \cdot \Delta\sigma_{E,2}}{\Delta\sigma_c / \gamma_{Mf}} \leq 1 \tag{3.2}$$

Where the variables related to stresses can be calculated using the formulas here expressed, in addition to using the graph of S-N curves for the resistance stress determination.

$$\Delta\sigma_{E,2} = \lambda \cdot \Delta\sigma_E \tag{3.3}$$

$$\lambda = \left( \frac{N}{2 \cdot 10^6} \right)^{\frac{1}{m}} \tag{3.4}$$

$$\Delta\sigma_E = 2 \cdot \sigma_{Comb.Freq} = 2 \cdot \sigma(\psi_1, \sigma_{máx}) \tag{3.1}$$

$$\sigma_{Comb.Freq} = \frac{\psi_1 \cdot M_{máx}}{I} \cdot \frac{D}{2} = \frac{0{,}2 \cdot M_{máx}}{I} \cdot \frac{D}{2} \tag{3.6}$$

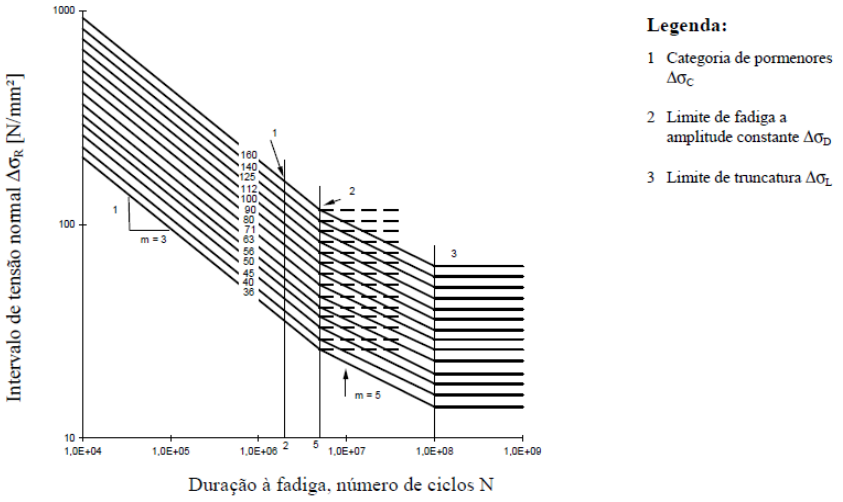


Figure 1 – S-N fatigue resistance curves for nominal stress range [9].

As for the safety verification based on the accumulative damaged, the code obliges that the ratio of the summation of the number of cycles associated to given range of stresses and the number of cycles associate to the resistant stress, must be less than 1.

$$D_d = \sum_i^n \frac{n_{Ei}}{N_{Ri}} \leq 1 \tag{3.7}$$

Furthermore, based on the EN1993-1-9 [9], the number of cycles until damage can be predicted by:

$$N = \frac{\Delta\sigma_C^m \cdot 2 \cdot 10^6}{\Delta\sigma_{Freq}^m} \tag{3.8}$$

Which can be converted to the period T related to it, which is a function of the frequency, the Weibull distribution, and the factor of range of velocities.

## 5. LATTICE TOWER - ANALYSIS

For this study it was analyzed a 200-meter-tall already designed lattice steel tower (figure 2) with different diagonals per section (depending on the height).

| Section number | Diagonals | |
|---|---|---|
| S | Tube elements | Steel Grade |
| 1 | Øx168,3x3,0 | 355 |
| 2 | Øx168,3x3,0 | 355 |
| 3 | Øx168,3x3,0 | 355 |
| 4 | Øx168,3x3,0 | 355 |
| 5 | Øx139,7x3,0 | 355 |
| 6 | Øx139,7x3,0 | 355 |
| 7 | Øx139,7x3,0 | 355 |
| 8 | Øx139,7x3,0 | 355 |
| 9 | Øx114,3x3,0 | 355 |
| 10 | Øx114,3x3,0 | 355 |
| 11 | Øx101,6x3,0 | 355 |
| 12 | Øx76,1x3,0 | 355 |
| 13 | Øx60,3x3,0 | 355 |
| 14 | Øx60,3x3,0 | 355 |
| 15 | Øx76,1x4,0 | 355 |
| 16 | Øx76,1x4,0 | 355 |
| 17 | Øx76,1x4,0 | 355 |
| 18 | Lx40x40x4 | 355 |
| 19 | Lx40x40x4 | 355 |
| 20 | Lx40x40x4 | 355 |

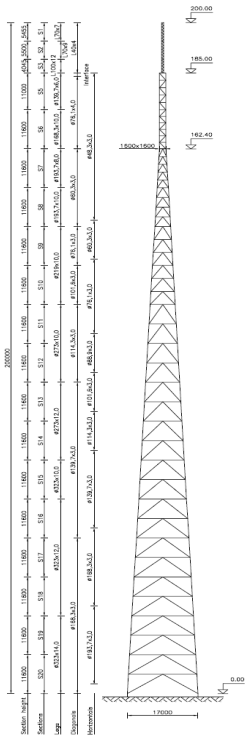


Figure 2 – Lattice tower geometry and diagonals sections.

To automate the process of analysis, it has been developed a program in VBA Excel for evaluation of both vibration induced by vortex shedding due to wind load, and the fatigue analysis for the lateral vibrations in the diagonals.

The program relies on the user input, and it is developed to work with a structural evaluation software, like Robot Structural Analysis from Autodesk. The user must provide all data required to run the program in excel. The program overview is simple and easy to use, with steps such that the user can follow the regulation guidelines (Figure 3).

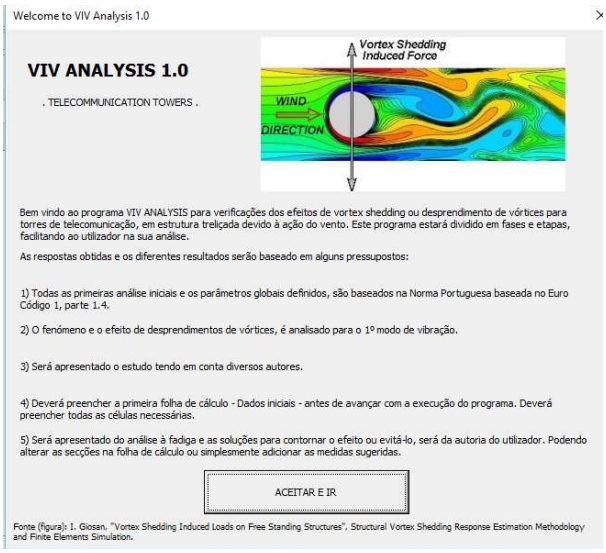


Figure 3 – Overview of the program (Vortex Induce Vibration Analysis) [10].

The output of the program will be all the variables necessary for vortex shedding evaluation, including potential diagonals at risk, and the results of fatigue safety verifications (Figure 4). Besides, the user can also choose to see the proposed measures of lateral vibration mitigation. This setup corresponds to adding steel fins of certain length (defined at the program) on the mid span of the element. It is used an equation based on an approximation of the alpha factor equation for reduction of the lift coefficient used in the Eurocode [11].

$$\alpha = \left(1 - \frac{l_s}{L}\right)^{9-\frac{d}{22}} \tag{4.1}$$

With the output information, it is possible to adapt the members if it is necessary, or if it fails the safety verifications.

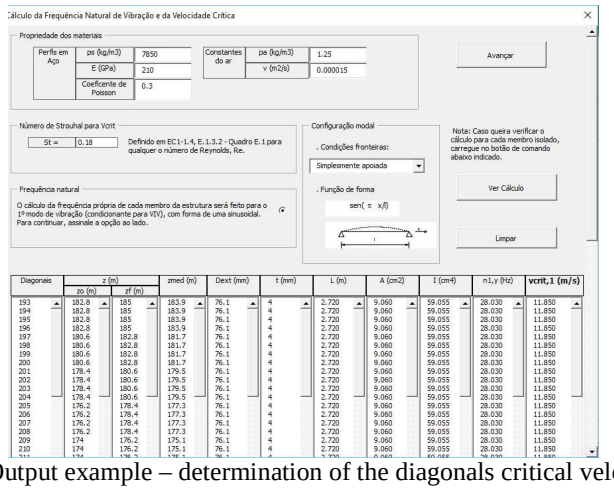


Figure 4 – Output example – determination of the diagonals critical velocities.

## 6. RESULTS

It is considered now one single element from the all structure, of the ones in the sections at risk of failure due to fatigue caused by vortex shedding. Using the program developed, the results for the diagonal 588 of section S15 are shown in table 1 and 2.

Table 1 – Properties of diagonal 588 S15.

| **Data** | |
|---|---|
| **z (mid section height)** | 66,7m |
| **Exterior diameter** | 139,7mm |
| **Thickness** | 3mm |
| **Span** | 7,981m |
| **Cross-sectional area** | 12,884cm$^2$ |
| **Inertia** | 301,090cm$^4$ |
| **Young's modulus** | 210GPa |
| Volumetric weight | 7850kg/m$^3$ |
| **Frequency of vibration (mode I)** | 6,167 Hz |

Table 2 – Lateral deflection due to vortex shedding and the resultant stress, given by the Eurocode.

| | **Method 1** | | **Method 2, considering turbulence effects** | | **Método 2, not considering turbulence effects** | |
|---|---|---|---|---|---|---|
| **Results of the parameters using the base values of table 8.4 EN1991-1-4** | - | - | Kv | 0,583 | - | - |
| | - | - | Ka | 1,166 | Ka | 2 |
| | clat | 0,70 | Cc | 0,02 | Cc | 0,02 |
| | Kw | 0,16 | al | 0,4 | al | 0,4 |
| | K | 0,10 | kp | 2,004 | kp | 1,490 |
| **ymáx (m)** | $3{,}99 \cdot 10^{-3}$ | | $4{,}45 \cdot 10^{-2}$ | | $5{,}92 \cdot 10^{-2}$ | |
| **σmáx (MPa)** | 14,233 | | 158,917 | | 211,428 | |

These results were used for the fatigue safety verification, and as shown in table 3 the element fails the condition of safety in method 2.

Table 3 – Fatigue safety verification, based on the equivalent stress in constant amplitude.

| Equivalent stress in constant amplitude safety verification | | |
|---|---|---|
| **Method** | **2, considering turbulence effects** | **2, not considering turbulence effects** |
| **vcrít (m/s)** | 4,786 | 4,786 |
| **vm (m/s)** | 36,915 | 36,915 |
| **N** | $8{,}17 \cdot 10^8$ | $8{,}17 \cdot 10^8$ |
| **$\Delta\sigma_c$ (MPa)** | 71 | |
| **$\Delta\sigma_{E,2}$ (MPa)** | 211,584 | 281,498 |
| $\frac{\gamma_{Ff} \cdot \Delta\sigma_{E,2}}{\Delta\sigma_c / \gamma_{Mf}}$ | 3,43 | 4,56 |

Table 4 – Results for the diagonal 588 of S15 related to failure prediction due to lateral vibrations.

| Method | 2, considering turbulence | 2, not considering turbulence |
|---|---|---|
| $v_{crít}$ (m/s) | 4,786 | 4,786 |
| $N_c$ | $2 \cdot 10^6$ | $2 \cdot 10^6$ |
| $\Delta\sigma_c$ (MPa) | 71 | |
| $\Delta\sigma_{Freq}$ (MPa) | 63,57 | 84,5712 |
| m (curve slope) | 3 | 3 |
| N (Resistant cycles) | $1{,}832 \cdot 10^6$ | $7{,}781 \cdot 10^5$ |
| Damage prediction | **41,5 days** | **17,6 days** |

As shown in table 4, not only the diagonal fails the safety check for fatigue analysis due to vibration in the lateral direction, but it can also be assumed that the members of this same section will fail in a short period. It is not possible to confirm that all members will fail in the time range calculated, but an alert notice is given for the design process.

For the entire structure the sections in blue can be defined as potential risk zones (figure 5).

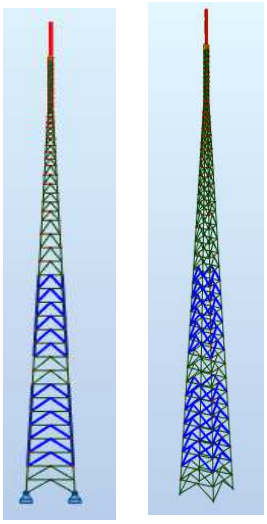

Figure 5 – Output example – determination of the diagonals critical velocities.

## 7. CONCLUSIONS

The second method of lateral vibration analysis for vortex shedding due to wind load presented in the Eurocode has a better approximation to similar cases where structural elements have failed. This is the reason way it is given special attention throughout the calculations of fatigue failure verifications. The risk of failure of the tower structural elements due to fatigue is as expected because for slender members in lower heights in which the wind turbulence is more felt, the promptness for transversal excitation is higher. Therefore, it should be taking into account adding bracing to the diagonals. The special software program in VBA using Excel that was developed for the purpose of this study, has great potential to be adapted to numerous scenarios and new features could be added for more complex cases. It is a valuable tool in accelerating the decision process and wind verifications.

**ACKNOWLEDGEMENTS**
Although the co-authors are respectively collaborator and Member of Construct Research Unit at FEUP, present lack of funds disabled Construct direct support of this R&D. So the authors solely acknowledge at the present moment the financial support received directly through the cost centre of the second co-author, and associated with his overheads from past R&D multiple activities and consultancy services.

**REFERENCES**
[1] Holmes, J.D., *Wind loading of structures*. 2001, London: Spon Press.
[2] Basu, R.I., *Aerodynamic forces on structures of circular cross-section. Part 2. The influence of turbulence and three-dimensional effects.* Journal of Wind Engineering and Industrial Aerodynamics, 1986. **24**(1): p. 33-59.
[3] Hansen, S.O., *Vortex-induced vibrations of structures*. 2007, Bangalore, India: Structural Engineers World Congress 2007. p. 20.
[4] Giosan, I., *Vortex Shedding Induced Loads on Free Standing Structures*, in *Structural Vortex Shedding Response Estimation Methodology and Finite Elements Simulation*. 2004.
[5] Blackburn, H. and R. Henderson, *Lock-in behavior in simulated vortex-induced vibration.* Experimental Thermal and Fluid Science, 1995.
[6] Robinson, R.W., et al., *A criterion for assessing wind induced crossflow vortex vibrations in wind sensitive structures*, in *Offshore technology report; OTH 92 379*. 1992: London: HMSO.
[7] IPQ, *NP EN 1991-1-4:2010/A1: 2010, Eurocódigo 1 Acções em estruturas Parte 1-4: Acções gerais. Acções do vento* 2010, Caparica: Instituto Português da Qualidade.
[8] Rudge, D. and C.-Y. Fei, *Response of Structural Members to Wind-Induced Vortex Shedding*. 1991, Massachusetts Institute of Technology.
[9] IPQ, *NP EN 1993-1-9: 2010, Eurocódigo 3 - Projecto de estruturas de aço Parte 1-9: Fadiga* 2010, Caparica: Instituto Português da Qualidade.
[10] Vieira, D., *Otimização de torres de telecomunicação metálicas tubulares treliçadas, sujeitas à ação do vento, incluindo o desprendimento de vórtices*, Master of Science thesis in Structural Civil Engineering (in Portuguese) 2016, FEUP - Faculdade de Engenharia da Universidade do Porto.
[11] CEN, E.C.F.S., *Eurocode 3 -Design of Steel strucutures - Part 3-2: Towers, masts and chimneys - Chimneys*. 2006.

COMPDYN 2017
6th ECCOMAS Thematic Conference on
Computational Methods in Structural Dynamics and Earthquake Engineering
M. Papadrakakis, M. Fragiadakis (eds.)
Rhodes Island, Greece, 15–17 June 2017

# APPROACH TO PREDICTION OF R/C BUILDINGS' SEISMIC DAMAGE AS PATTERN RECOGNITION PROBLEM USING ARTIFICIAL NEURAL NETWORKS

**K.E. Morfidis[1], and K.G. Kostinakis[2]**

[1] Assistant Researcher, Earthquake Planning and Protection Organization (EPPO-ITSAK)
Terma Dasylliou, 55535, Thessaloniki, Greece
e-mail: konmorf@gmail.com

[2] Post-Doc Researcher, Department of Civil Engineering, Aristotle University of Thessaloniki
Aristotle University campus, 54124, Thessaloniki, Greece
e-mail: kkostina@civil.auth.gr

**Keywords:** Seismic Damage Prediction, Artificial Neural Networks, Existing R/C Buildings, Structural Vulnerability Assessment, Seismic Response of Buildings, Pattern Recognition

**Abstract.** *In the present paper the investigation of the problem of reinforced concrete (r/c) buildings' seismic damage prediction is exhibited utilizing Artificial Neural Networks (ANN). More specifically, the problem is formulated and solved in terms of the Pattern Recognition Problem using Multilayer Feedforward Perceptron Networks (MFP). The networks are trained by the implementation of two training algorithms: the Scaled Conjugate Gradient algorithm (SCG) and the Resilient Back-Propagation algorithm (RP). The training data-set is created by means of Nonlinear Time History Analyses (NTHA) of 30 r/c buildings which are subjected to 65 earthquakes. The selected buildings have different heights, structural systems and structural eccentricities, and are designed on the basis of the suggestions of Eurocodes. The damage index which is used to describe the seismic damage state of buildings is the Maximum Interstorey Drift Ratio (MIDR). In the context of the present paper the influence of the number and the combination of seismic parameters which describe the level of impact of seismic excitations on the r/c buildings is also investigated. To this end, 8 different and widely used seismic parameters are utilized. Furthermore, the influence of the number of hidden layers, the number of neurons in the hidden layers, as well as the activation functions of neurons is also examined. The generalization abilities of the optimum configured ANNs are investigated through the assessment of their performance in the case of prediction of seismic damage state of the selected buildings subjected to 16 earthquakes different from the earthquakes which are used in the creation of the training data-set. The most significant conclusion that turned out is that the ANNs can reliably classify the r/c buildings into pre-defined damage classes if they are appropriately configured. More specifically, the parametric investigations prove that the most important factor for the effective ANNs' configuration is the activation functions of output layer's neurons (tansig function) as well as the number of the hidden layers (the utilization of two hidden layers leads to better results). As regards the examination of the optimum number and combination of seismic input parameters (using the "Stepwise" sensitivity analysis method) it is proved that are dependent on the utilized training algorithm.*

## 1 INTRODUCTION

The assessment of seismic damage level in case of r/c structures is at the core of the civil engineering research globally, since a large number of strong earthquakes that happened in the past have caused extensive structural damages and human losses. As a consequence, numerous researchers have published studies dealing with the methods that can be used in order to estimate the seismic vulnerability of existing buildings. The research studies can be classified into two general categories: a) studies dealing with the development of methods that can estimate the seismic performance of individual buildings and b) studies dealing with the development of methods that can rapidly assess the seismic vulnerability of groups of buildings with common structural characteristics. The research studies belonging to the first category resulted in analytical methodologies of assessment which are based on linear and nonlinear methods that have been adopted by modern seismic codes (e.g. [1, 2, 3]). Respectively, the researches belonging to the second category led to the development of methodologies that can accomplish the approximate assessment of the seismic vulnerability of buildings' groups with common structural characteristics (e.g. rapid screening methods; damage probability matrices; fragile curves, see for example [4, 5, 6]. These methods can be used in order to estimate the buildings' seismic vulnerability in a very short time comparing with the methods of the first category, with the price of losing accuracy. However, the merit of these approximate methods is important, since the use of them can lead to rapid and reliable decisions about the need for further investigation of buildings' seismic performance.

In the context of the direct (though approximate) assessment of the seismic vulnerability of buildings' groups with common structural characteristics, in the past 25 years many research studies have been conducted aiming to utilize the capacities of artificial intelligence, such as the Artificial Neural Networks (ANNs). The ANNs are complex computational structures, which attempt to mimic the operations of the biological (human or animal) brain and the central nervous system and are used for the solution of complex problems with the aid of computers using algorithms based on different philosophy than the conventional ones (see e.g. [7]). Although the ANNs have been developed on an idea that dates back to the 1940s [8], the first thorough investigation dealing with the use of them for the direct (in real time) estimation of the level of structural seismic damage was published in 1995 [9]. Since then, this approach has been the subject of numerous research studies (e.g. [10, 11]), which led to highly important and interesting results. These results designate the ability of ANNs to predict the potential seismic damage of buildings in an approximate but generally reliable way.

The aim of the present study is to further investigate the ability of ANNs to reliably predict the seismic damage level of r/c buildings. More specifically, the problem is formed and solved as a pattern recognition problem. Problems of this type can be solved reliably using ANNs. For the needs of the investigation, the training of the ANNs was achieved with the aid of a data set created using results from Nonlinear Time History Analyses of 30 r/c buildings with different heights, structural systems and structural eccentricities, subjected to 65 actual ground motions. The Maximum Interstorey Drift Ratio (MIDR), (e.g. [12]) was used as the damage index. As a consequence, 1950 (30 x 65) values of MIDR resulted from the analyses conducted. These values were categorized into five general damage levels, into which the investigated buildings were classified with the aid of the ANNs. The training of the ANNs was made by using both the Scaled Conjugate Gradient algorithm (SCG, [13]) and the Resilient Back-Propagation algorithm (RP, [14]). Moreover, the number and the combination of the seismic parameters leading to the strongest correlation between the analyses results and the results produced by the ANNs was investigated. To this end, 8 different and widely used seismic parameters were examined. Furthermore, the influence of the number of hidden layers,

the number of neurons in the hidden layers, as well as the activation functions of neurons was also examined. The prediction ability of the trained ANNs was checked through the prediction they made in the case of future earthquakes and it was demonstrated that they can extract especially reliable (though approximate) results.

## 2 THE ARIFICIAL NEURAL NETWORKS

It is well-known that the Artificial Neural Networks (ANNs) are complex computational structures which are capable to solve problems using the general rules of the human brain functions (see e.g. [7]). Thus, using ANNs it is feasible to approximate the solution of problems such as pattern recognition, classification and function approximation problem.

The ANNs' function is based on the combined action of interconnected processing units that are called artificial neurons (Figure 1(a)). The artificial neuron receives input signals ($x_1$, $x_2$,…., $x_m$) and transform them to an output signal ($y_k$) through the use of an adder (which adds the products of the input signals by the respective synaptic weights ($w_{k1}$, $w_{k2}$,…., $w_{km}$) of neuron's synapses), and the use of an activation function (which has as argument the $u_k$ that results from the adder and transform it to the output signal $y_k$).

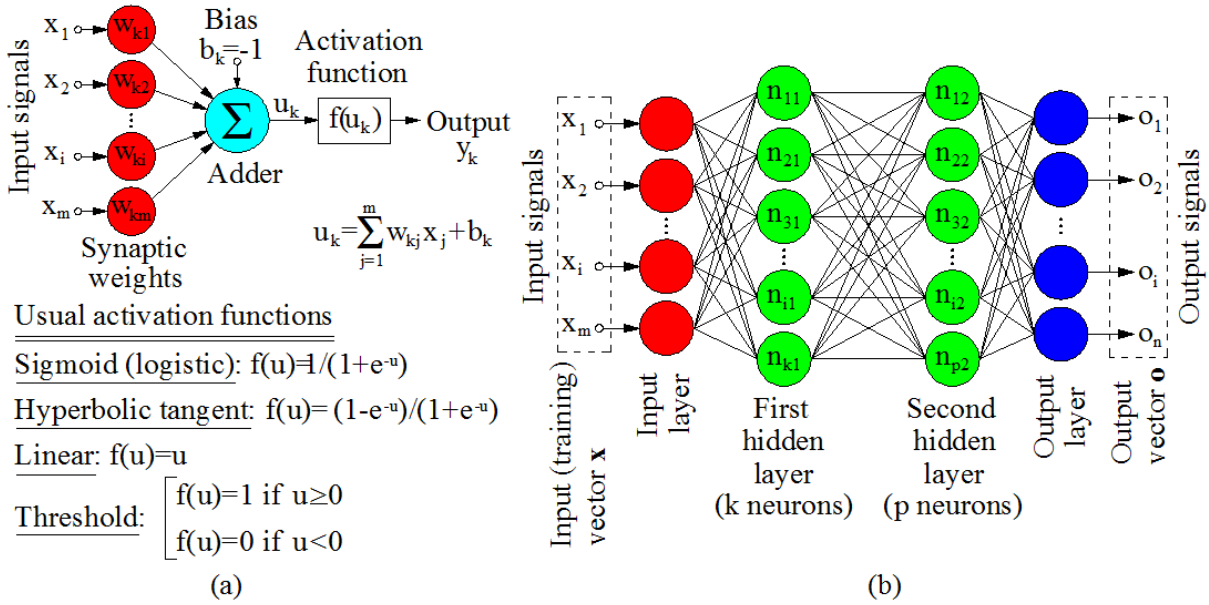


Figure 1: The artificial neuron (a), typical configuration of a multilayer feedforward perceptron ANN (b).

In Figure 1(b) the typical configuration of a Multilayer Feedforward Perceptron (MFP) type ANN with four layers of neurons (input layer, two hidden layers and output layer) is presented. MFP networks were selected for the analyses which were conducted in order to achieve the objective of the present investigation. The solution of problems through the utilization of ANNs is accomplished if they have been trained. The training of ANNs is achieved by procedures which are called training algorithms. These algorithms require a set of *n* input vectors **x** and the corresponding to them *n* output vectors **d** that called target vectors. The *n* pairs of vectors **x** and vectors **d** constitute the training data-set. During the training procedure, the values of the synaptic weights (w) are successively altered until the error vector **e**(**w**) [**e**(**w**)=**d**-**o**(**w**), where **o**(**w**) is the output vector] that is produced by the ANN is minimized.

## 3 FORMULATION OF THE SEISMIC DAMAGE PREDICTION PROBLEM AS A PATTERN RECOGNITION PROBLEM USING ANNs

As "pattern recognition" is defined the procedure of the detection and identification/classification of objects in specific categories (patterns). The solution of the pattern recognition problem is approached by the utilization of several methods (see e.g. [15]). One of these methods is based on the use of ANNs. In this section, it will be presented the procedure by which the problem of the r/c buildings' seismic damage prediction is formulated as a pattern recognition problem. The steps which are required for this formulation are illustrated in the flowchart of Figure 2. In this diagram the choices which were made for some of the problem's parameters in the current investigation are also presented. Detailed description of all selected parameters will be given in the following subsections.

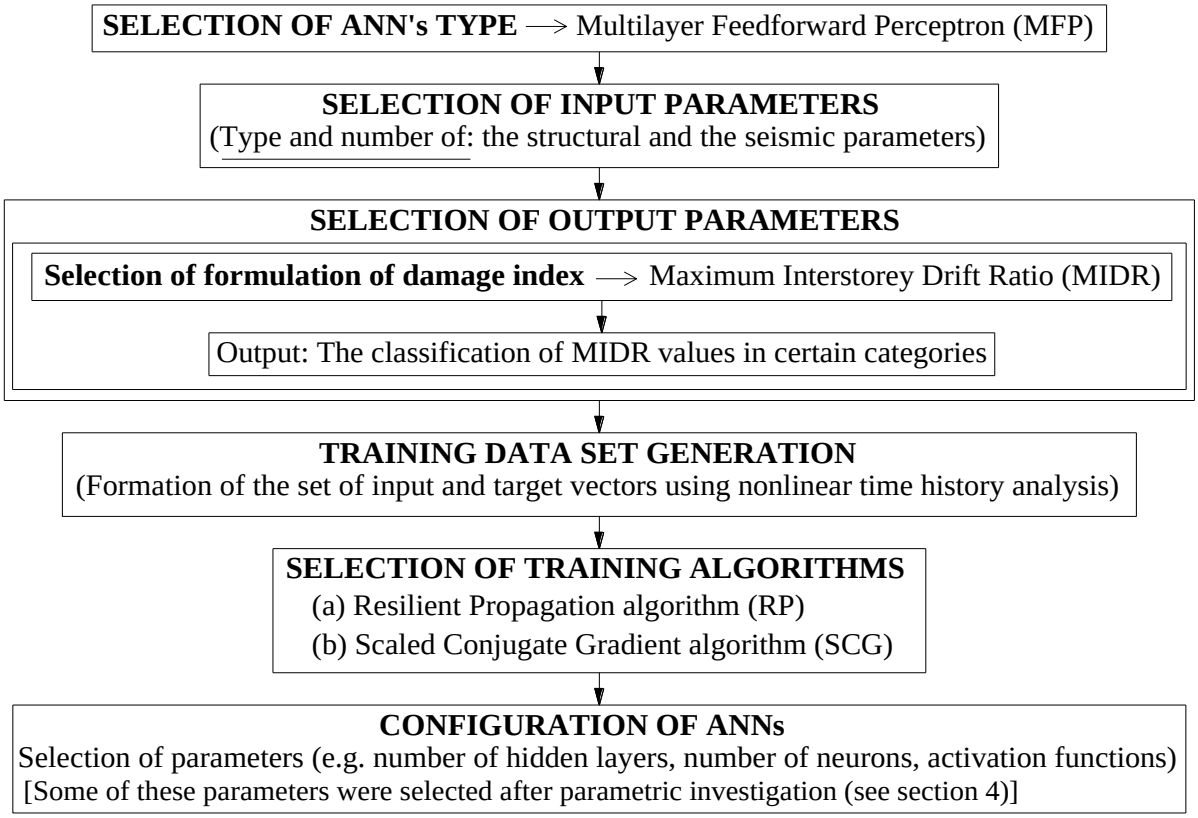


Figure 2: The procedure of the formulation of the pattern recognition problem.

### 3.1 Selection of the type of ANNs

As mentioned in the section 2, in the present investigation MFP networks were utilized. In the networks of this type, the neurons in any layer are connected to all neurons in the adjacent layer (Figure 1b). This choice was based on the fact that this type of ANNs was successfully used in many published investigations which are related to the subject of the present investigation (see e.g. [10, 11, 16, 17, 18]).

### 3.2 Selection of the input parameters

The ANNs are computational structures which are capable to handle and approach the solution of multiparametric problems. This feature gives the flexibility to select the number of the parameters (input parameters) through which a problem can be described. The parameters

which describe the problem of the prediction of the seismic damage of r/c buildings can be grouped in two categories: the structural parameters and the seismic parameters.

The structural parameters are used for the description of the buildings' response on earthquake excitations. In the case of the vulnerability assessment of existing r/c buildings, the widespread methods such as the fragility curves method (see e.g. [5, 6]) utilize macroscopic characteristics which are related to the geometric morphology and the structural system. In the present study 4 structural parameters were selected: the total height of buildings $H_{tot}$, the ratio of the base shear that is received by r/c walls (if exist) along two perpendicular directions x and y (ratio $n_{vx}$ and ratio $n_{vy}$), and the structural eccentricity $e_0$.

As regards the seismic parameters which are used to describe the seismic excitations and their impact to structures, there are many definitions which are resulted from the analysis of accelerograms records (see e.g. [19]). These parameters can be classified to: (a) seismic parameters determined from the time histories of the records; (b) seismic parameters determined from the response spectra of the records; (c) seismic parameters accounting for the earthquake's frequency content and (d) seismic parameters based on the earthquake's duration. For the investigation conducted in the present study, the 8 seismic parameters illustrated in Table 1 have been chosen.

| Ground Motion Parameter | Calculation procedure | Category |
|---|---|---|
| Peak Ground Acceleration: **PGA** | max\|a(t)\| | Seismic parameters determined from the time histories of the records. |
| Peak Ground Velocity: **PGV** | max\|v(t)\| | |
| Peak Ground Displacement: **PGD** | max\|d(t)\| | |
| Arias Intensity: $\mathbf{I_a}$ | $I_a = (\pi / 2g) \cdot \int_0^{t_{tot}} [a(t)]^2 dt$ | [a(t), v(t), d(t) are the acceleration, velocity and displacement time history respectively] |
| Acceleration Spectrum Intensity: **ASI** | $ASI = \int_{0.1}^{0.5} S_a(\xi = 0.05, T)dT$ | Seismic parameters determined from the response spectra of the records. |
| Housner Intensity: **HI** | $HI = \int_{0.1}^{2.5} PSV(\xi = 0.05, T)dT$ | ($S_a$ is the acceleration spectrum, PSV is the pseudovelocity spectrum, $\xi$ is the damping ratio) |
| $V_{max}/A_{max}$ (**PGV/ PGA**) | max\|v(t)\|/max\|a(t)\| | Seismic parameter accounting for the earthquake's frequency content. |
| Time of Uniform Duration: **TUD** | Special algorithm (e.g. [20]) | Seismic parameter based on the earthquake's duration. [TUD is the total time during which the ground acceleration is larger than a given threshold value (usually 5% of PGA)] |

Table 1: Examined ground motion parameters.

Thus, in the present study 12 input parameters (4 structural and 8 seismic) were selected. Therefore, the input vector of ANNs **x** has the general form which is given by the Eq. (1).

$$\mathbf{x} = \left[\mathbf{x}_{seism} \,|\, \mathbf{x}_{struct}\right]^T \tag{1}$$

$$\mathbf{x}_{seism} = \left[PGA \,|\, PGV \,|\, PGD \,|\, I_a \,|\, ASI \,|\, HI \,|\, PGV/PGA \,|\, TUD\right]^T, \quad \mathbf{x}_{struct} = \left[H_{tot} \,|\, e_0 \,|\, n_{vx} \,|\, n_{vy}\right]^T$$

However, it must be stressed that the dimension of the input vector **x** was not considered constant (12x1) in the analyses conducted in the present study. As will presented in the section 4, the number and the combination of the seismic parameters in the input vector **x** were investigated in order to accomplish the optimum performance of ANNs, i.e. the optimum prediction of the seismic damage. Thus, the dimension of the used input vectors was fluctuated between (5x1), i.e. 1 seismic parameter plus 4 structural parameters, and (12x1).

### 3.3 Selection of the output parameters

Due to the fact that the problem which is investigated in the present study is the r/c buildings' seismic damage prediction using ANNs, the first step in the procedure of the selection of the networks' output parameters is the choice of an appropriate damage index. As it is well-known, the damage indices are used for the numerical modeling of the damage level in the vulnerability assessment of structures, and can be grouped into categories based on whether they are local or global, deterministic or probabilistic, structural or financial (e.g. [21]). In the present study, the seismic damage of r/c buildings was expressed in terms of the Maximum Interstorey Drift Ratio (MIDR). The MIDR is a global and structural damage index which is generally considered as a reliable indicator of structural and nonstructural seismic damage of r/c buildings (e.g. [22]), and has been used for the evaluation of seismic response of structures (e.g. [23]). Indicative calculation of the MIDR value in the case of a n-storey building with a rectangular plan-view is shown in Figure 3.

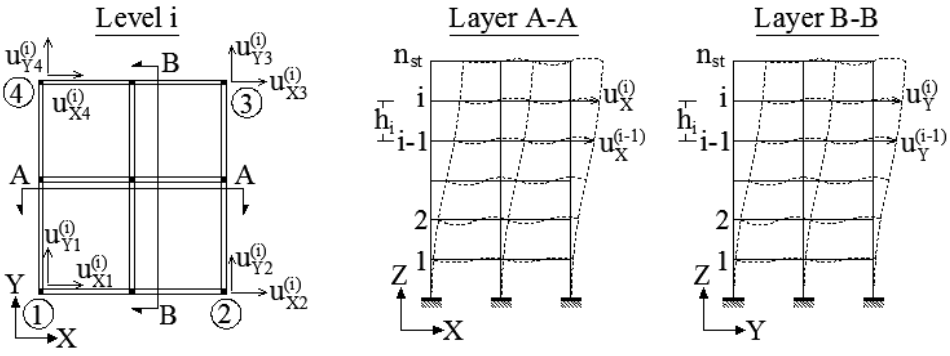


$$\boxed{MIDR=\max\{\max\Delta u_X;\max\Delta u_Y\}}$$

$$\max\Delta u_X=\max\{\max\Delta u_X^{(1)},...\max\Delta u_X^{(i-1)};..\max\Delta u_X^{(i)},...\max\Delta u_X^{(n_{st})}\}$$

$$\max\Delta u_Y=\max\{\max\Delta u_Y^{(1)},...\max\Delta u_Y^{(i-1)};..\max\Delta u_Y^{(i)},...\max\Delta u_Y^{(n_{st})}\}$$

$$\max\Delta u_X^{(i)}=\max\{|\Delta u_{X1}^{(i)}|;|\Delta u_{X2}^{(i)}|;|\Delta u_{X3}^{(i)}|;|\Delta u_{X4}^{(i)}|\}$$

$$\max\Delta u_Y^{(i)}=\max\{|\Delta u_{Y1}^{(i)}|;|\Delta u_{Y2}^{(i)}|;|\Delta u_{Y3}^{(i)}|;|\Delta u_{Y4}^{(i)}|\}$$

$$\underset{(j=1\text{-}4)}{\text{Point j}}:\ \Delta u_{Xj}^{(i)}=\max\left\{\frac{u_{Xj}^{(i)}(t)-u_{Xj}^{(i-1)}(t)}{h_i}\right\}_{t=0}^{t=t_{tot}};\ \Delta u_{Yj}^{(i)}=\max\left\{\frac{u_{Yj}^{(i)}(t)-u_{Yj}^{(i-1)}(t)}{h_i}\right\}_{t=0}^{t=t_{tot}}$$

($t_{tot}$= total duration of the seismic excitation)

Figure 3: Indicative calculation of the MIDR value in the case of a n-storey building with rectangular plan-view.

The formulation of the investigated problem as a pattern recognition problem requires the definition of classes into which a r/c building can be classified on the basis of its damage level after an earthquake. To this end, in the present study five damage states were defined using specific limit values of the MIDR. These damage states (valid for r/c buildings) are presented in the Table 2 (see e.g. [24]).

| **MIDR (%)** | <0.25 | 0.25-0.50 | 0.50-1.00 | 1.00-1.50 | >1.50 |
|---|---|---|---|---|---|
| **Degree of damage** | Null | Slight | Moderate | Heavy | Destruction |

Table 2: Relation between MIDR and damage state.

Using the five damage states which are defined in the Table 2 any r/c building which is subjected to an earthquake can be classified on the basis of its corresponding MIDR value. In terms of ANNs this means that any input vector **x** can be classified on the basis on its corresponding output vector **o** (or target vector **d** in the case in which the input vector is a training vector) in one of the five damage states of Table 2. Thus, the output vectors as well as the target vectors must have dimension (5x1). In other words, the number of outputs of ANNs in the present case is five. The general form of the output vectors is given (using an example) in Figure 4.

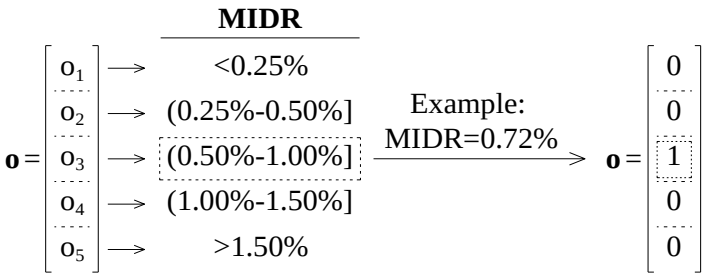


Figure 4: General form of output vectors **o**.

As it emerges from Figure 4, each element of a vector **o** represents one of the five classes/damage states of Table 2 and attains value equal to 1 if the corresponding MIDR belongs to the interval of values which define the specific damage state. Otherwise, it attains value equal to 0.

### 3.4 Training data-set generation

The procedure which is conducted for the generation of the training data-set is presented in the flowchart of the Figure 5. The steps of this procedure will be described subsequently.

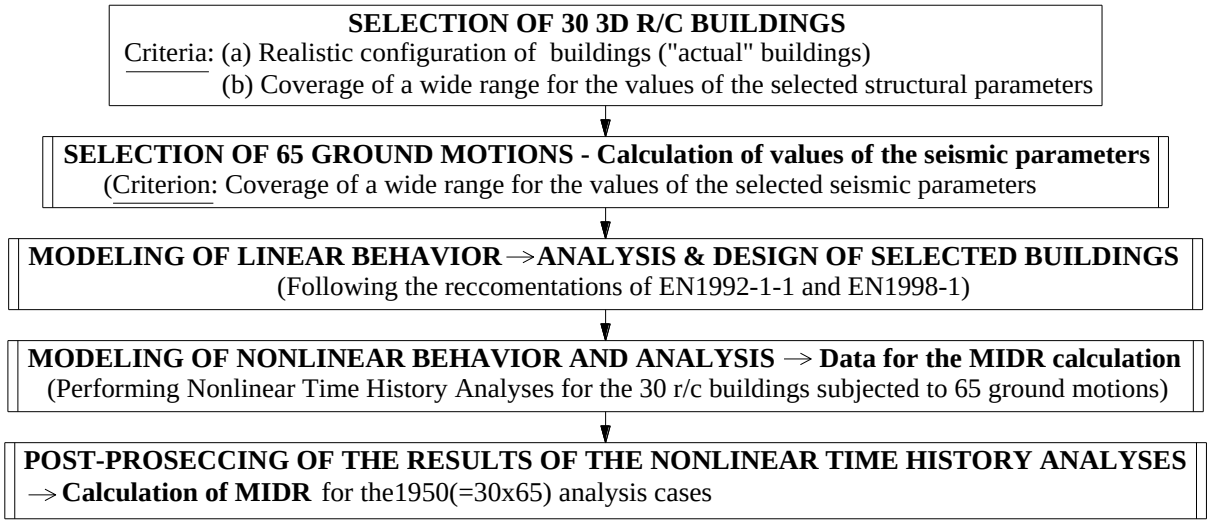


Figure 5: Procedure for the design and generation of the training data-set.

*(a) Selection of 30 r/c buildings:* The selected buildings (rectangular in plan and regular in elevation according to the criteria set by EN1998-1), differ in the total height $H_{tot}$, the structural eccentricity $e_0$ (=the distance between the mass center and the stiffness center of storeys), as well as the ratios of the base shear $n_{vx}$ and $n_{vy}$ that are received by the r/c walls (if they exist) along two perpendicular axes (axes x and y). The values of the above structural parameters for the selected buildings are given in Table 3.

| No. | $n_{st}$ | $L_x$ (m) | $L_y$ (m) | $e_o$ (m) | $n_{vx}$ (%) | $n_{vy}$ (%) | No. | $n_{st}$ | $L_x$ (m) | $L_y$ (m) | $e_o$(m) | $n_{vx}$ (%) | $n_{vy}$ (%) |
|---|---|---|---|---|---|---|---|---|---|---|---|---|---|
| 1 | 3 | 13.5 | 10.0 | 0.0 | 0.0 | 0.0 | 16 | 3 | 13.0 | 9.0 | 0.98 | 0.0 | 0.0 |
| 2 | 5 | 20.0 | 14.0 | 0.0 | 0.0 | 0.0 | 17 | 5 | 17.5 | 10.0 | 2.58 | 0.0 | 0.0 |
| 3 | 7 | 20.0 | 14.0 | 0.0 | 0.0 | 0.0 | 18 | 7 | 17.5 | 10.0 | 2.39 | 0.0 | 0.0 |
| 4 | 3 | 15.0 | 10.0 | 0.0 | 73.0 | 76.0 | 19 | 3 | 13.5 | 9.0 | 4.65 | 52.0 | 46.0 |
| 5 | 5 | 19.0 | 16.2 | 0.0 | 77.0 | 80.0 | 20 | 5 | 16.0 | 14.5 | 4.19 | 43.0 | 42.0 |
| 6 | 7 | 19.0 | 16.2 | 0.0 | 57.0 | 64.0 | 21 | 7 | 16.0 | 14.5 | 3.79 | 37.0 | 36.0 |
| 7 | 3 | 15.0 | 15.0 | 0.0 | 41.0 | 41.0 | 22 | 3 | 13.5 | 9.0 | 2.23 | 47.0 | 0.0 |
| 8 | 5 | 21.2 | 18.7 | 0.0 | 46.0 | 50.0 | 23 | 5 | 16.0 | 14.5 | 2.65 | 38.0 | 0.0 |
| 9 | 7 | 21.2 | 18.7 | 0.0 | 43.0 | 46.0 | 24 | 7 | 16.0 | 14.5 | 2.49 | 35.0 | 0.0 |
| 10 | 3 | 17.0 | 12.5 | 0.0 | 43.0 | 0.0 | 25 | 3 | 14.5 | 9.0 | 3.53 | 64.0 | 0.0 |
| 11 | 5 | 20.2 | 15.2 | 0.0 | 41.0 | 0.0 | 26 | 5 | 14.0 | 16.0 | 3.01 | 0.0 | 69.0 |
| 12 | 7 | 20.2 | 15.2 | 0.0 | 38.0 | 0.0 | 27 | 7 | 14.0 | 16.0 | 3.01 | 0.0 | 65.0 |
| 13 | 3 | 15.0 | 10.0 | 0.0 | 77.0 | 0.0 | 28 | 3 | 13.5 | 10.0 | 6.73 | 64.0 | 58.0 |
| 14 | 5 | 20.2 | 15.2 | 0.0 | 68.0 | 0.0 | 29 | 5 | 16.5 | 16.5 | 6.29 | 65.0 | 72.0 |
| 15 | 7 | 20.2 | 15.2 | 0.0 | 51.0 | 0.0 | 30 | 7 | 16.5 | 16.5 | 5.96 | 59.0 | 67.0 |

Table 3: Values of structural parameters of the selected r/c buildings.

In Table 3 $e_0=(e_{0x}^2+e_{0y}^2)^{1/2}$, where $e_{0x}$, $e_{0y}$ are the structural eccentricities along axes x and y.

*(b) Selection of ground motions:* A suite of 65 pairs of horizontal bidirectional earthquake ground motions obtained from the PEER [25] and the European strong-Motion database [26] was selected. The main criterion used for the selection of these excitations was to cover a large variety of realistic values for the 8 ground motion parameters considered in the present investigation (see Tables 1 and 4). The seismic parameters for each ground motion were determined as the geometric mean values of the parameters corresponding to the two horizontal components of each earthquake record.

| Ground Motion Parameter | Units | Minimum Value | Maximum Value |
|---|---|---|---|
| **PGA** | %g | 0.004 | 0.822 |
| **PGV** | cm/sec | 0.86 | 99.35 |
| **PGD** | cm | 0.36 | 60.19 |
| **$I_a$** | m/sec | ≈0.0 | 5.592 |
| **ASI** | g·sec | 0.003 | 0.633 |
| **HI** | cm | 3.94 | 317.6 |
| **PGV/PGA** | sec | 0. 036 | 0.336 |
| **TUD** | sec | ≈0.0 | 17.68 |

Table 4: Ranges of values of the selected seismic parameters.

*(c) Modeling of linear behavior, analysis and design of selected buildings:* The selected buildings (which were considered as Medium Ductility Class structures) were modeled, analyzed and designed based on the provisions of EN1992-1-1 [27] and EN1998-1 [28] (using the pro-

fessional analysis and design program RAF [29]). It must by stressed that in any case the choice of the dimensions of the r/c members' cross-sections, as well as of their reinforcement, was made while bearing in mind the optimum exploitation of steel (S500B) and concrete (C20/25).

*(d) Nonlinear modeling and analysis (Nonlinear Time History Analyses) – Calculation of Damage Index MIDR:* The buildings' nonlinear behaviour was modeled by means of lumped plasticity models at the column and beam ends, as well as at the base of the walls. The material inelasticity of the structural members was modeled with the aid of the Modified Takeda hysteresis rule [30]. The effects of the axial load-biaxial bending moments ($P$-$M_1$-$M_2$) interaction at column and wall hinges were taken into account by using the $P$-$M_1$-$M_2$ interaction diagram, which is implemented in the software adopted for the application of the analyses.

After the nonlinear modeling, the 30 selected r/c buildings were analyzed by Nonlinear Time History Analysis (NTHA) for each one of the 65 earthquake ground motion pairs. Thus, a total of 1950 NTHA (30 buildings x 65 earthquake records) were performed with the aid of the computer program Ruaumoko [31]. For each one of the 1950 analyses, the required data for the MIDR calculation were exported.

*(e) Post-processing of the results of NTHA – Calculation of MIDR:* The last step of the procedure for the training data-set generation (Figure 5) is the processing of the results of NTHA in order to calculate the MIDR values of the analyzed buildings. To this end, a computer code in Visual Basic was developed. This code calculates firstly the MIDR values following the procedure which is presented in Figure 3 and subsequently configures the target vectors **d** in the form which is given in Figure 4.

Thus, following the above procedure, 1950 training vectors **x** with dimension (12x1) which are described by Eq. (1) were created. Also, the corresponding 1950 target vectors **d** (dimension (5x1), Figure 4) were created.

### 3.5 Selection of training algorithms

Two training algorithms were adopted: the Resilient Backpropagation algorithm ("RP" algorithm, [14]) and the Scaled Conjugate Gradient algorithm ("SCG" algorithm, [13]). The RP algorithm constitutes a variation of methods which are based on variable learning rate and it is recommended for the quick and reliable solution of pattern recognition problems (see e.g. [32, 33]). The algorithm SCG belongs to the specific class of Conjugate Gradient (CG) methods, which can effectively handle large-scale problems. Furthermore, special features of the SCG algorithm are its fastness, as well as the fact that it does not contain user-dependent parameters.

### 3.6 Configuration of ANNs

The last step of the procedure for the formulation and solution of the seismic damage prediction problem as a pattern recognition problem using ANNs, is the configuration of the networks. More specifically, this step concerns the choice of the parameters which are required for the configuration of the used ANNs. These parameters are: (a) the number of the hidden layers; (b) the number of neurons in each hidden layer; (c) the activation functions of neurons; (d) the performance evaluation parameters; (e) the normalization functions of the input and output values and (f) the method for partitioning the data set in training, validation and testing subsets.

In the present study, specific choices for some of the aforementioned parameters were made, while for some others more than one choice were made. These choices are the following:

*(a)* *Number of the hidden layers*: ANNs with one or two hidden layers were selected.

*(b)* *Number of neurons in hidden layers*: The optimum number of neurons in hidden layers is not uniquely defined for all problems. Furthermore, there is no a direct method for its determination, so the trial and error method is always adopted. In the context of the present study, an investigation for the determination of the optimum number of neurons in hidden layers was conducted. More specifically, ANNs with a number of neurons in hidden layers that ranges between 10 and 60 were configured. Then, the number of neurons that led to the optimum results in each examined case was determined. In section 4, more details will be given.

*(c)* *Activation functions of neurons*: Two different types of activation functions for neurons were used: the sigmoid function (logistic - logsig) and the hyperbolic tangent function (tansig), (Figure 1(a)). The choice of using two activation functions (instead of using a single one) was made in order to investigate the optimum efficiency of the ANNs.

*(d)* *Performance evaluation parameters*: The performance evaluation parameters are indices which are used for the assessment of ANNs' prediction abilities. In the case of solution of a pattern recognition problem the most useful tools for the evaluation of ANNs are the Confusion Matrices - CM (see e.g. [32, 34]). The general form of a CM (for a three-class problem) is presented in Figure 6.

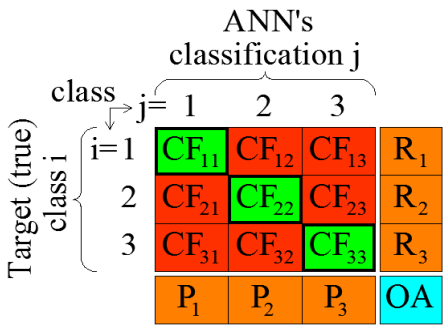


$CF_{ij}$ = the number of the input vectors whose true class is i and were classified by the ANN to class j

$R_i\,(\text{Recall}) = CF_{ii} / \sum_{j=1}^{3} CF_{ij}$

(the percentage of input vectors of true class i which were correctly classified by the ANN to class i)

$P_j\,(\text{Precision}) = CF_{jj} / \sum_{i=1}^{3} CF_{ij}$

(the percentage of input vectors which were classified by the ANN into class j, whose true class is j)

$OA\,(\text{Overall Accuracy}) = \sum_{i=1}^{3} CF_{ii} / N$

(the percentage of input vectors that correctly classified by the ANN)

(N=total number of input and target vectors)

Figure 6: General form of a confusion matrix for a three-class problem

On the basis of CMs three types of metrics for ANNs' prediction accuracy are defined, namely the "Recall" index, the "Precision" index and the "Overall Accuracy" index (Figure 6). In the present study, the "Overall Accuracy" or (OA) index was mainly used. However, for the evaluation of the several configurations of the ANNs which were examined the corresponding CMs are also presented and evaluated in section 4.

*(e)* *Normalization functions for the input and target vectors' elements*: The utilization of functions which normalize the values of the elements of input vectors **x** before these vectors introduced to ANNs is considered as necessary in order to optimize the training (e.g. [35]). The same transformation is also required for the elements of the target vectors **d**. A

function, through which the elements of input and the target vectors of the data set attain values in the range [-1,1], was selected in the present study [32].

*(f)* *Partition of the data-set*: The partition of the data-set in three sub-sets, namely the training, the validation and the testing sub-set is recommended in order to ensure good generalization of networks and to avoid the overfitting (e.g. [36]). In the present study, the partition of the data-set in training, validation and testing sub-sets was done in any case using the ratio 70%/15%/15% respectively. The training and target vectors, which consist of the three sub-sets, were chosen randomly [32].

## 4 PARAMETRIC INVESTIGATION FOR THE OPTIMUM PERFORMANCE OF ANNS

In this section the results of the parametric analyses which were conducted for the investigation of optimum ANNs' seismic damage prediction is exhibited. More specifically, the aim of these analyses was the investigation of the influence of:

(a) the number and the combination of seismic input parameters,
(b) the type of the neurons' activation functions,
(c) the training algorithms,
(d) the number of neurons in hidden layers, and
(e) the number of hidden layers

to the ANNs' performance.

This investigation was conducted in two parts. In the first part ANNs with one hidden layer were utilized. In this part the influence of the factors (a)-(d) were investigated. In the second part, ANNs with two hidden layers were used. It must be noted that in the second part of investigation, specific conclusions of the first part (such as conclusions about the influence of the number and the combination of seismic input parameters as well as the influence of the type of the neurons' activation functions) were taken into consideration in order to reduce the number of required training procedures, which is significantly more in the case of ANNs with two hidden layers. For example, in the case of ANNs with one hidden layer, the number of different combinations of activation functions' types in the hidden and output layer is 4 (i.e. logsig/logsig, tansig/tansig, logsig/tansig and tansig/logsig). The corresponding number in the case of ANNs with two hidden layers is 8. If we also take into consideration the fact that the investigation of the optimum number of neurons required training procedures for ANNs with different number of neurons in each hidden layer (10÷60 as it will be presented in the following subsections), it is clear that the total number of the required calculations in the case of ANNs with two hidden layers is significantly greater.

### 4.1 Investigation of optimum performance of ANNs with one hidden layer

The investigation of the optimum performance of ANNs with one hidden layer was conducted in three stages. In each stage, different number of seismic input parameters was considered:

(a) *Stage 1*: Each one of the 8 seismic input parameters of Table 1, and the 4 considered structural parameters were introduced into the input vectors **x** (Eq. 1). Therefore, eight different types of input vectors were formed (with dimension (5x1)).
(b) *Stage 2*: The 8 seismic input parameters of Table 1 were introduced simultaneously with the 4 structural parameters into the input vectors **x**. Therefore, one type of input vectors was formed (with dimension (12x1)).
(c) *Stage 3*: Using the two versions of "Stepwise" sensitivity analysis method [37, 38, 39] the number and the combination of seismic input parameters which lead to the optimum

ANNs' predictions for the seismic damage state of r/c buildings was investigated. Thus, in this stage input vectors with dimension between (5x1) and (12x1) were formed.

The Stages 1 and 2 were utilized for the detection of the optimum combination of neurons' activation functions in the hidden and the output layer between the 4 possible combinations. Thus, the analyses of the Stage 3 were conducted only for the optimum combination of these functions, but for both of the two training algorithms which were considered in the present study (RP and SCG). For the training of the investigated ANNs in Stages 1 and 2 a specific procedure was performed in order to detect the number of neurons in hidden layer which leads to the best predictions. This procedure is described in Figure 7.

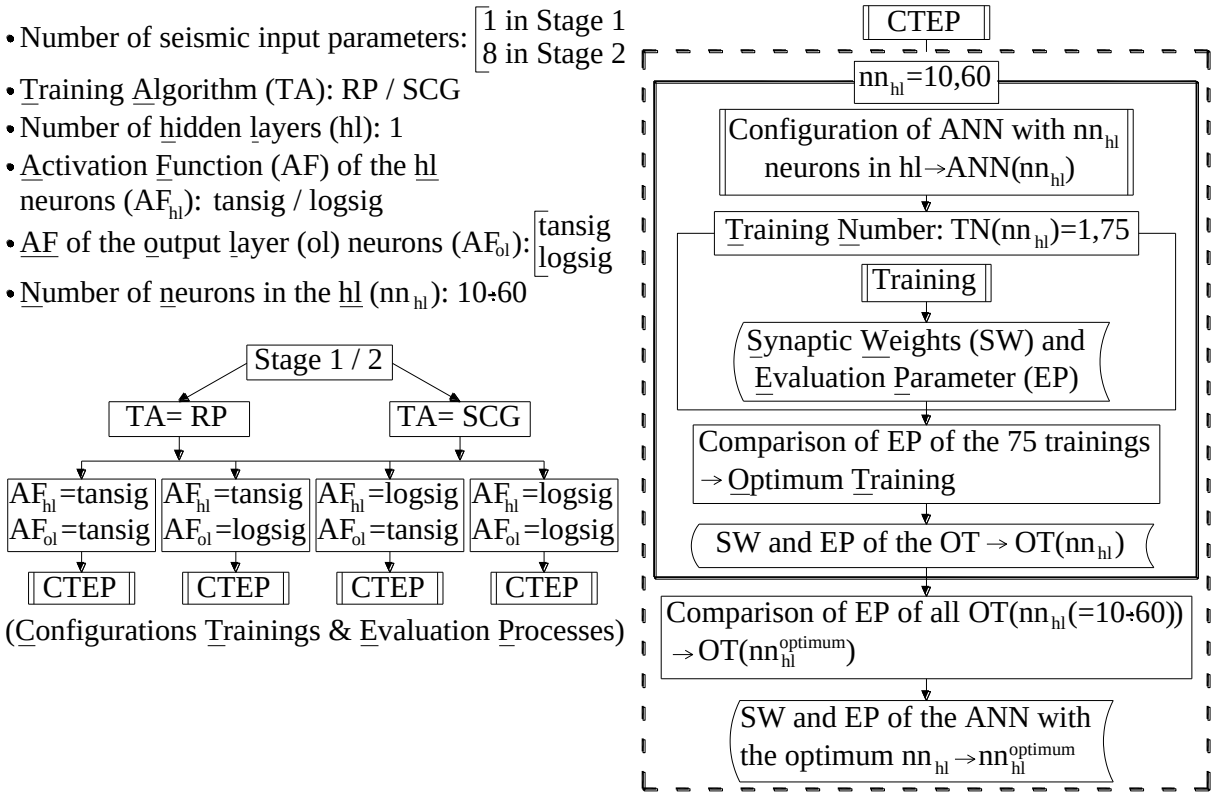


Figure 7: Calculations' procedure of Stages 1 and 2

It must be noted that the Evaluation Parameter (EP) in Figure 7 is the Overall Accuracy (OA) index which is defined in Figure 6. It must also be stressed that the Evaluation Parameter OA was calculated in any case on the basis of the samples which belong to the testing sub-set. This set, is used to control the generalization ability of the trained ANNs. Thus, the results of the current investigation have wider validity because they are exported from a data sub-set which is comprised of training and target vectors that are not used to optimize the values of ANNs' synaptic weights, but is comprised of unseen vectors. As turns out from the Figure 7, for each ANN which was configured, 75 training procedures were conducted. This is due to the fact that differences in the performance of the networks are caused by the initial values of the synaptic weights and biases (see e.g. [11]), and also due to the random composition of the three sub-sets of the data set (training, validation and testing data sub-sets). The best trained network (optimum trained network) for each one of the different ANN architectures was finally adopted in the procedure.

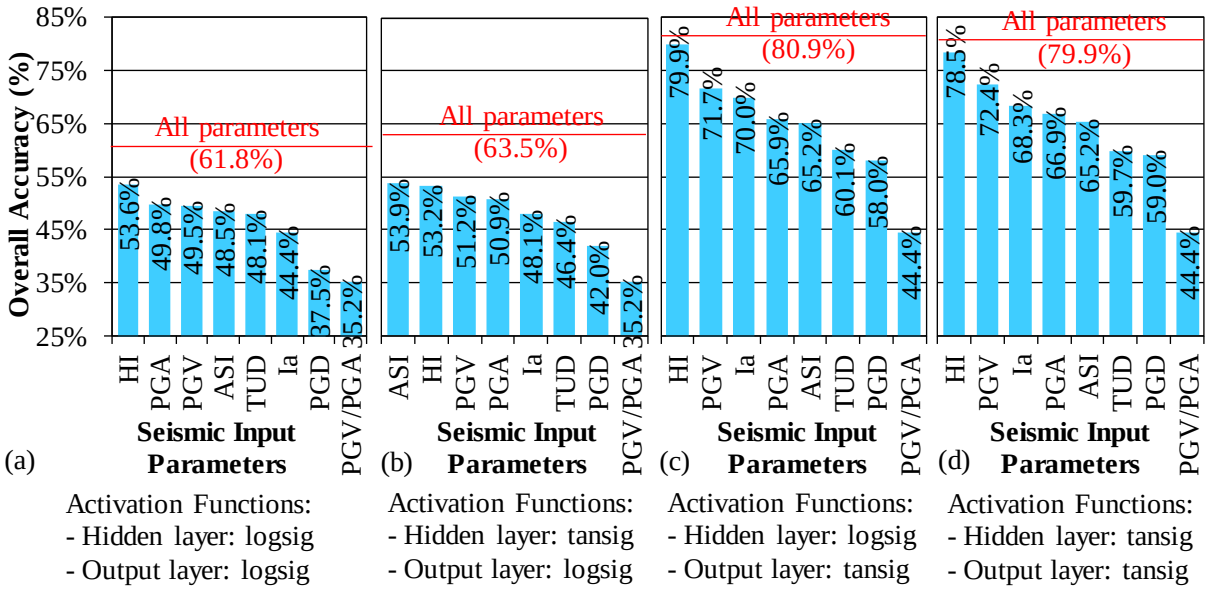


Figure 8: Overall Accuracy which is extracted from ANNs with one hidden layer and one seismic input parameter trained using the RP algorithm

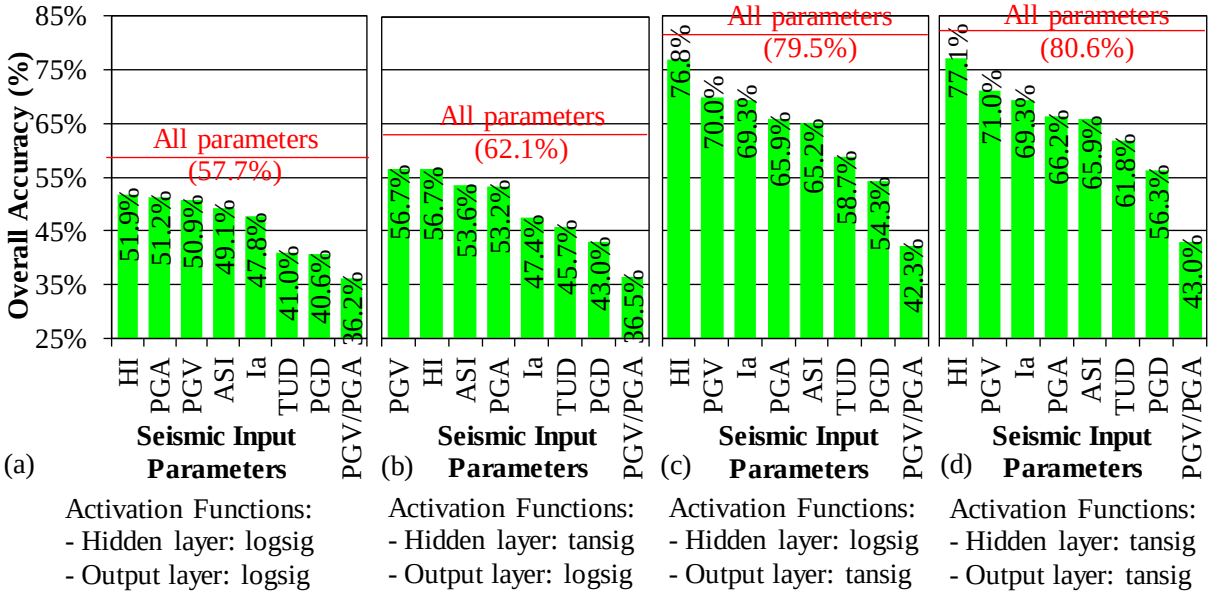


Figure 9: Overall Accuracy which is extracted from ANNs with one hidden layer and one seismic input parameter trained using the SCG algorithm

Figures 8 and 9 present the results of analyses of Stages 1 and 2. From these Figures, the following conclusions can be drawn:

- The ANNs in which the tansig function is used in the output layer extract higher values for OA index than the values which are extracted from ANNs with logsig function in this layer. This conclusion is valid either in cases in which one of the studied seismic input parameter is used or in the case in which all studied seismic input parameters are introduced to ANNs (horizontal red lines in Figures 8 and 9). For example, when the HI parameter is used as seismic input parameter the values of the OA index which are exported from ANNs with tansig function in their output layer fluctuate between 76.8% and 79.9%, whereas the cor-

responding fluctuation range in the case of the utilization of logsig function in the output layer is 51.9%-56.7%.

- The training algorithm has significantly less influence to the ANNs' prediction ability than the type of the output layer's activation function. For example, when all the studied seismic input parameters are introduced to networks the value of the OA index is equal to 80.9% in the case of utilization of RP algorithm and equal to 79.5% in the case of utilization of SCG algorithm for the training of ANNs with logsig function in the hidden layer and tansig function in the output layer (Figures 8(c) and 9(c)). Similar differences are observed for all the other combinations of activation functions in the hidden and the output layer.
- The ranking of the seismic input parameters concerning their importance (i.e. concerning the value of OA index which is extracted from ANNs when only one of them is imported to input vectors) is identical and independent of the training algorithm and of the type of hidden layer's activation functions only in the case of utilization of function tansig in the output layer (Figures 8(c), 8(d), 9(c), 9(d)).
- In almost all cases which are presented in Figures 8 and 9 the most effective seismic input parameter is the Housner Intensity (HI). Using this parameter as the only seismic input in the input vectors, values between 76.8% and 79.9% for the OA index are achieved in the case of utilization of the tansig activation function in the output layer. The corresponding values in the case of utilization of the logsig function range between 51.9% and 56.7%. On the contrary, the less effective seismic input parameters in all studied cases are the ratio PGV/PGA and the PGD. It must also be noted that the difference between the OA values which are extracted using the most effective seismic parameter and the corresponding values which are extracted using the less effective seismic parameter is almost double in the case in which the tansig function is used in the networks' output layer over the case in which the logsig function is used.
- The level of effectiveness of the HI parameter as the only seismic input parameter in input vectors approaches the corresponding level which is achieved when all seismic parameters are introduced in input vectors, mainly in the case of the utilization of tansig function in the output layer. As turns out from the Figures 8(c), 8(d), 9(c), 9(d) the OA values which are extracted using only the HI parameter in the input vectors are only 1.3%-4.2% smaller than the corresponding values which are extracted when all seismic parameters are introduced. Similar level of divergence is not observed if the logsig function is used in the output layer.

As mentioned above, in the Stage 3 of the investigation of one hidden layer ANNs' performance concerning to the seismic damage prediction, the optimum number and combination of seismic input parameters (i.e. the number and the combination of seismic input parameters which lead to the optimum ANNs' predictions for the seismic damage state) was investigated. To this end the two versions of the "Stepwise" sensitivity analysis method i.e. the "Forward Stepwise Method" (FSM), and the "Backward Stepwise Method" (BSM) were utilized. The "Stepwise" method is widely used for the investigation of importance of the parameters which affect multi-parametric problems with unknown mathematical formulation. The Stepwise Method consists of adding (FSM) or rejecting (BSM) step-by-step one input parameter of the network [37]. Thus, at each step, a new ANN is configured and is trained by the use of the available training data-set. The performance of the new network of each step is assessed (i.e. the OA index is calculated). On the basis of the changes of the performance parameter's values, the input parameters are ranked according to their importance. The sequence of FSM's and BSM's steps is presented in details by Morfidis and Kostinakis [40]. It must also be noted that the required procedure at each step of the Stepwise method (FSM or BSM) is the procedure which is described in the Figure 7. Thus, it is obvious that the amount of calculations

which are required for the complete implementation of the FSM and the BSM is significantly great. In order to make this statement clear it can be noted that in the present study (in which the influence of 8 seismic input parameters was examined) the full implementation of FSM and BSM required 8 steps each [40]. In each of these steps the procedure of Figure 7 was implemented. For this reason, in the present study the full implementation of the FSM and BSM was conducted only for ANNs with tansig function in the hidden and the output layer, but for the both of two training algorithms which were utilized (RP and SCG).

Figure 10 illustrates the results of the full implementation of the "Stepwise" method. More specifically, the maximum values of the OA index for each number of seismic input parameters between 1 and 8 in input vectors are presented. These values are the maximum OA index values which are exported from all the examined combinations of each method's step. In Figure 10 the numbers of neurons in the hidden layer of ANNs which export the maximum OA index values are also presented.

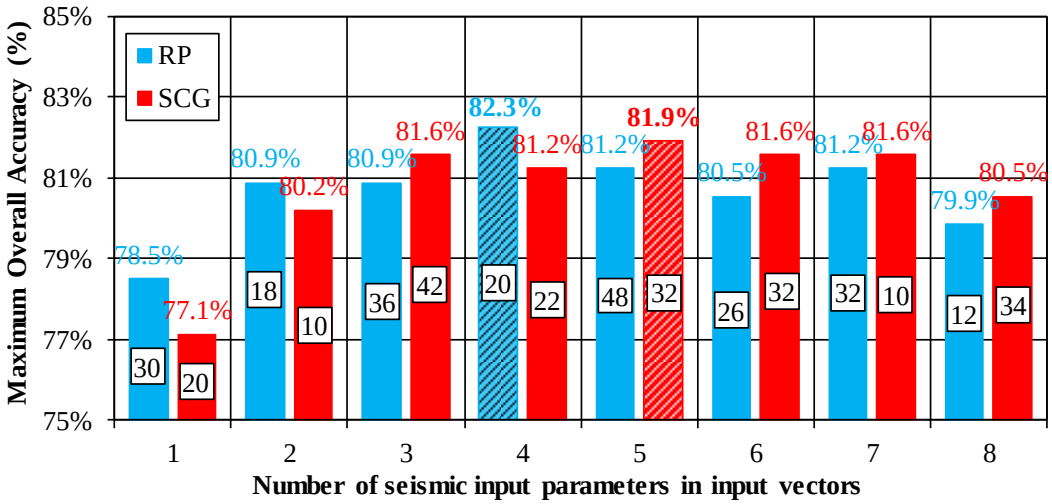


Figure 10: Maximum values of the Overall Accuracy index from the examined combinations of seismic input parameters in the context of the implementation of the "Stepwise" method

The main conclusions which arise from the Figure 10 are the following:

- With the exception of the case of only one seismic input parameter, in all other cases the maximum value of OA index fluctuates within a narrow range of values (2.39% in the case of utilization of RP algorithm and 1.71% in the case of utilization of SCG algorithm).
- The best performance of ANNs in the case of using the RP training algorithm is accomplished when 4 seismic parameters are introduced in input vectors (OA=82.3%). The corresponding number of seismic parameters in the case of use of the SCG algorithm is 5 (OA=81.9%).
- The optimum number of neurons in the hidden layer is altered randomly. This conclusion substantiates the nonexistence of a direct method for its calculation, and the recourse to the trial and error procedure.
- The two utilized training algorithms lead to results which do not differ significantly. Thus, the factor "training algorithm" is not considered as a critical factor in the present study.

In the Table 5 the optimum combinations of seismic input parameters for every number of seismic parameters which are introduced in input vectors are presented.

| | RP algorithm | SCG algorithm |
|---|---|---|
| **1** | HI | HI |
| **2** | HI-PGD | HI-PGV |
| **3** | HI-PGD-PGA | HI-PGV-PGD |
| **4** | HI-PGD-PGA-ASI | HI-PGV-PGD-PGA |
| **5** | HI-PGD-PGA-ASI-PGV/PGA | HI-PGV-PGD-PGA-PGV/PGA |
| **6** | HI-PGD-PGV-ASI-PGV/PGA-Ia | HI-PGV-PGD-PGA-PGV/PGA-Ia |
| **7** | HI-PGD-PGA-PGV-ASI-PGV/PGA-TUD | HI-PGV-PGD-PGA-PGV/PGA-Ia-ASI |

Table 5: Optimum combinations for each number of seismic input parameters – "Stepwise" method

From the combined study of the Figure 10 and the Table 5 it is concluded that the optimum combination of seismic parameters is consisted of the seismic parameters HI-PGD-PGA-ASI in the case of utilization of the RP algorithm, and of the seismic parameters HI-PGV-PGD-PGA-PGV/PGA in the case of utilization of the SCG algorithm.

(a)

| True (target) class \ ANN's classification | 1 | 2 | 3 | 4 | 5 | R |
|---|---|---|---|---|---|---|
| 1 | 42 | 4 | 1 | 0 | 0 | 89.4% |
| 2 | 5 | 20 | 4 | 0 | 0 | 69.0% |
| 3 | 0 | 15 | 55 | 14 | 3 | 63.2% |
| 4 | 0 | 0 | 8 | 24 | 2 | 70.6% |
| 5 | 0 | 0 | 0 | 7 | 89 | 92.7% |
| P | 89.4% | 51.3% | 80.9% | 53.3% | 94.7% | ***78.5%*** |

RP algorithm-tansig/tansig - 30 neurons in the hidden layer

| True (target) class \ ANN's classification | 1 | 2 | 3 | 4 | 5 | R |
|---|---|---|---|---|---|---|
| 1 | 37 | 4 | 0 | 0 | 0 | 90.2% |
| 2 | 3 | 23 | 10 | 3 | 0 | 59.0% |
| 3 | 0 | 5 | 54 | 8 | 3 | 77.1% |
| 4 | 0 | 0 | 11 | 36 | 12 | 61.0% |
| 5 | 0 | 0 | 1 | 8 | 75 | 89.3% |
| P | 92.5% | 71.9% | 71.1% | 65.5% | 83.3% | ***76.8%*** |

SCG algorithm-tansig/tansig -20 neurons in the hidden layer

(b)

| True (target) class \ ANN's classification | 1 | 2 | 3 | 4 | 5 | R |
|---|---|---|---|---|---|---|
| 1 | 40 | 9 | 0 | 0 | 0 | 81.6% |
| 2 | 6 | 22 | 10 | 0 | 0 | 57.9% |
| 3 | 0 | 6 | 47 | 7 | 1 | 77.0% |
| 4 | 0 | 0 | 5 | 39 | 7 | 76.5% |
| 5 | 0 | 0 | 0 | 8 | 86 | 91.5% |
| P | 87.0% | 59.5% | 75.8% | 72.2% | 91.5% | ***79.9%*** |

RP algorithm-tansig/tansig - 12 neurons in the hidden layer

| True (target) class \ ANN's classification | 1 | 2 | 3 | 4 | 5 | R |
|---|---|---|---|---|---|---|
| 1 | 43 | 10 | 0 | 0 | 0 | 81.1% |
| 2 | 6 | 34 | 3 | 0 | 0 | 79.1% |
| 3 | 0 | 0 | 53 | 7 | 2 | 85.5% |
| 4 | 0 | 0 | 12 | 26 | 8 | 56.5% |
| 5 | 0 | 0 | 0 | 9 | 80 | 89.9% |
| P | 87.8% | 77.3% | 77.9% | 61.9% | 88.9% | ***80.5%*** |

SCG algorithm-tansig/tansig -34 neurons in the hidden layer

(c)

| True (target) class \ ANN's classification | 1 | 2 | 3 | 4 | 5 | R |
|---|---|---|---|---|---|---|
| 1 | 44 | 6 | 0 | 0 | 0 | 88.0% |
| 2 | 3 | 26 | 5 | 0 | 0 | 76.5% |
| 3 | 0 | 5 | 36 | 8 | 2 | 70.6% |
| 4 | 0 | 0 | 10 | 42 | 10 | 67.7% |
| 5 | 0 | 0 | 0 | 3 | 93 | 96.9% |
| P | 93.6% | 70.3% | 70.6% | 79.2% | 88.6% | ***82.3%*** |

RP algorithm-tansig/tansig 20 neurons in the hidden layer

| True (target) class \ ANN's classification | 1 | 2 | 3 | 4 | 5 | R |
|---|---|---|---|---|---|---|
| 1 | 40 | 5 | 0 | 0 | 0 | 88.9% |
| 2 | 2 | 19 | 7 | 0 | 0 | 67.9% |
| 3 | 0 | 6 | 54 | 9 | 1 | 77.1% |
| 4 | 0 | 2 | 7 | 30 | 4 | 69.8% |
| 5 | 0 | 0 | 0 | 10 | 97 | 90.7% |
| P | 95.2% | 59.4% | 79.4% | 61.2% | 95.1% | ***81.9%*** |

SCG algorithm-tansig/tansig-32 neurons in the hidden layer

Figure 11: CMs of classifications made by the best trained (single-hidden layered) ANNs with: (a) one seismic input parameter (HI parameter), (b) eight seismic input parameters, (c) the optimum combination of the seismic input parameters

The evaluation of the performance of ANNs using the OA index is a procedure which leads directly to results (i.e. direct comparison between the results which are exported from various ANNs' configuration by means of only one index). However, more detailed study of the evaluation of the performance of ANNs in the pattern recognition problem's solution is accomplished through the study of the corresponding CMs and their related metrics (Figure 6). In Figure 11 the CMs of the classifications made by the best trained ANNs with one hidden layer are illustrated. In the blue colored cells of these matrices the OA index values which have been used above for the evaluation of the performance of ANNs are placed. The main characteristic of CMs is the information which they give about not only the total accuracy of predictions (this is given by the OA index) but also about the percentages of correct classifications of samples to the classes in which the examined objects can be classified. To this end the indices R (Recall index) and P (Precision index) are defined (Figure 6). Valuable information about the quality of the predictions of ANNs is also given by the configuration of CMs. More specifically, when the vast majority of the non-zero elements of a CM are located about the main diagonal means that the ANN achieves an acceptable classification. For example, if all the non-zero elements are located in the cells of the main diagonal and in the adjacent cells means that the objects are classified into correct classes and into classes which are adjacent to them (i.e. if the correct class for an object is the class i, the ANN classifies this object in the class i-1 or in class i+1). Therefore, all predictions/classifications about the expected damage states which are made by the ANN in this case are correct or nearby to the correct ones.

The main conclusions which can be drawn from the Figure 11 are the following:

- The difference of the quality of classification which is achieved by the ANNs trained using the RP algorithm and by the ANNs trained using the SCG algorithm is least and not clear.
- The vast majority of classifications in all cases which are presented in the Figure 11 are in the correct classes (green colored cells) or in classes adjacent to them (yellow colored cells). The classifications in categories which are not adjacent to the correct category (grey colored cells) are generally very few, especially in the cases in which all seismic parameters or their optimum combination are introduced to input vectors (Figures 11(b), 11(c)). For example, in the case of utilizing the RP algorithm, 4 classifications are made in classes not adjacent to correct ones when one seismic parameter (the HI parameter) was introduced in input vectors (Figure 11(a)). When the eight examined seismic parameters are introduced to input vectors, the corresponding number of classifications is 1 (Figure 11(b)).
- The percentages of correct classifications in each one of the 5 damage classes (values of indices R and P) are generally high. These percentages are significantly high in the case of classes 1 and 5 (with very little exceptions, they are greater than 85%). On the contrary relatively lower percentages of correct classifications in the classes 2, 3 and 4 are achieved, especially in the case of introduction of 1 seismic parameter (HI parameter) to input vectors.
- The quality of classification from the best trained ANNs with one hidden layer can be rated as acceptable, because, besides the achieved high percentages of correct classifications (OA=80%-82%), the approach which is accomplished for the damage state of the overall testing sample is very satisfactory.

### 4.2 Investigation of the influence of the second hidden layer to ANNs' performance

In the subsection 4.1 the results of the investigation for the optimum configuration of ANNs with one hidden layer (first part of the parametric investigation for the optimum performance of ANNs) were presented. As it was mentioned in the introduction of the section 4, the second part of the parametric investigation concerns the performance of networks with

two hidden layers. For reasons which were emphasized at that point, the investigation of ANNs with two hidden layers was based on the basic conclusions which were resulted from the corresponding investigation of the single layered ANNs. Thus, networks with tansig functions in the two hidden and the output layer were examined. Due to the fact that no clear conclusion was extracted about the more effective training algorithm between RP and SCG, both algorithms were utilized in the second part of investigation. Furthermore, the optimum combinations of the number of neurons in the two hidden layers were also examined. To this end, networks with all possible combinations of numbers of neurons in the two hidden layers between 10 and 60 were configured. Finally, as regards the seismic input parameters, three cases which correspond to the three stages of the investigation of the single layered ANNs were examined. The only difference is that at the 3rd stage it was not conducted analysis with the "Stepwise" method. Therefore, the results (i.e. the optimum seismic parameter combinations) of the "Stepwise" method which was conducted for the single layered networks were utilized. In the Figure 12 the procedure of the second part of the parametric investigation is illustrated.

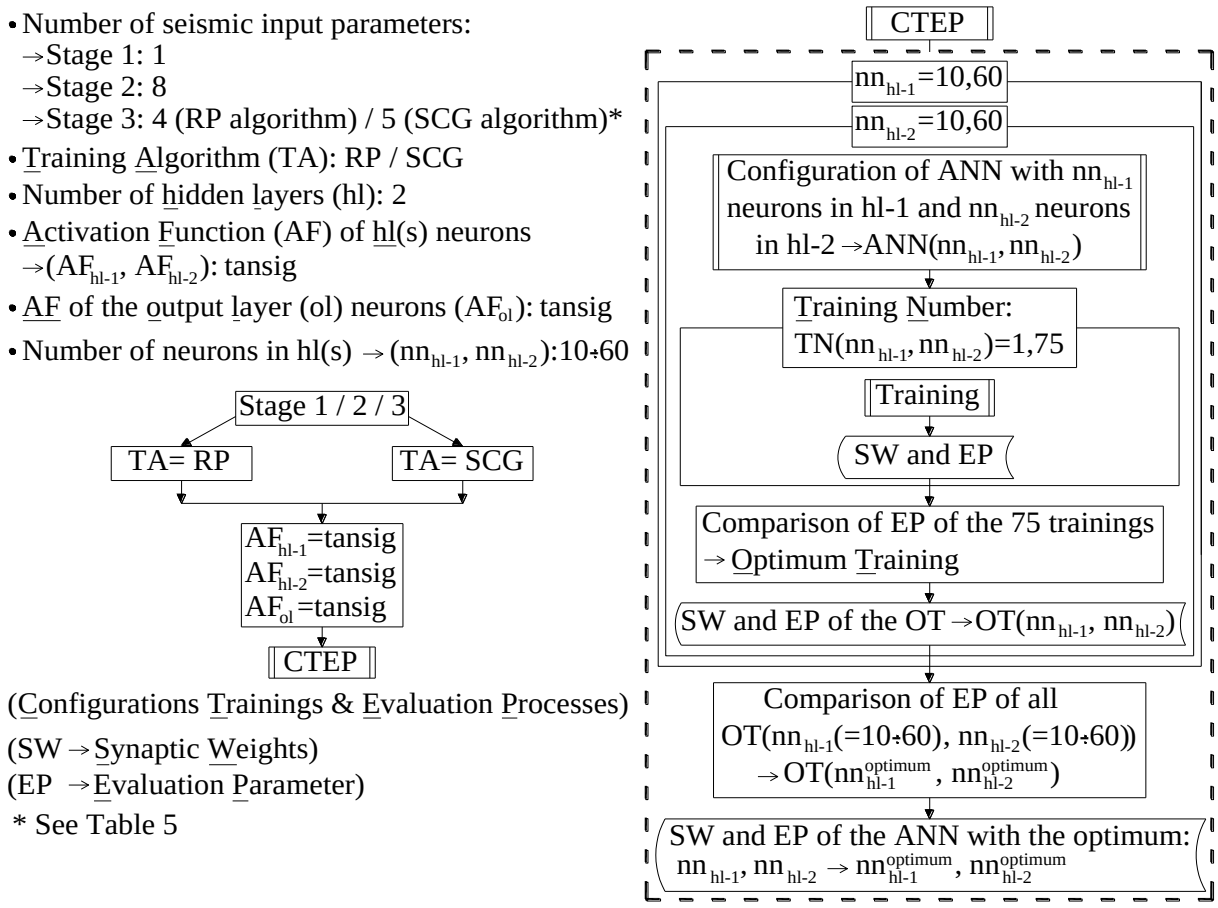


Figure 12: Calculations' procedure of the second part of parametric investigation (ANNs with two hidden layers)

Figure 13 illustrates the ranking of the examined seismic input parameters on the basis of their importance when ANNs with one and two hidden layers are utilized. In this Figure the numbers of neurons in hidden layers which export the maximum OA index values (the notation n/m states: n neurons in the first hidden layer and m neurons in the second hidden layer) are also presented.

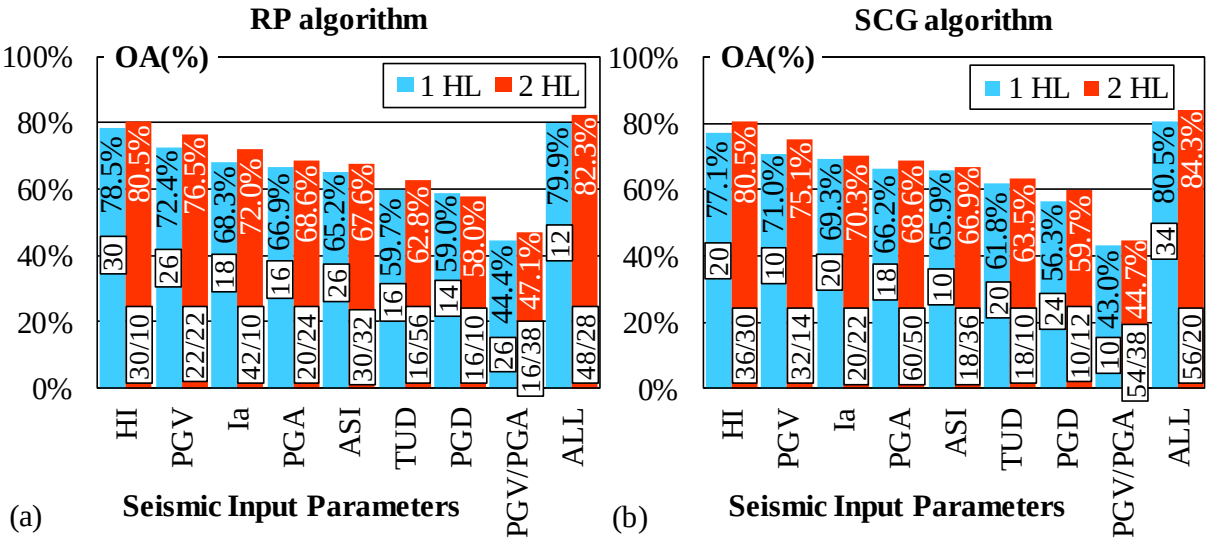


Figure 13: Ranking of the examined seismic input parameter which is resulted from ANNs with one and two hidden layers

The main conclusions which are extracted from the Figure 13 are the following:

- The ranking of the examined seismic parameters which is extracted using single layered ANNs or ANNs with two hidden layers is the same. This conclusion is valid in the case of networks with tansig function in all neurons' layers (hidden and output), and for both of two utilized algorithms.
- The use of two hidden layers increases the effectiveness of networks but not significantly. For example, the value of the OA index in the case in which one seismic parameter is introduced to input vectors (HI parameter) is 78.5% when a single layered network is used, while when a network with two hidden layers is utilized the corresponding value is 80.5% (Figure 13(a)). Hence, the use of a second hidden layer leads to increase of the OA value about 2.5% in the case of use of RP algorithm. The corresponding increase when the SCG algorithm is utilized is about 4.0% (Figure 13(b)). When all the examined seismic parameters are introduced to input vectors, the increase of the OA value due to the introduction of the second hidden layer is about 3.0% in the case of utilization of the RP algorithm and about 4.5% in the case of utilization of the SCG algorithm.
- The level at which the second hidden layer improves the classification quality does not depend on the utilized training algorithm, because in some cases the increase of the OA value is greater when the RP algorithm is used (for example when the parameter Ia or the parameter TUD introduced to input vectors), while in some others is greater when the SCG algorithm is utilized (for example if the parameter HI is introduced to the input vectors).

In Figure 14 the CMs of the classifications made by the best trained ANNs with two hidden layers are illustrated. The combined study of the Figures 11 and 14 indicates that, while the introduction of the second hidden layer does not increase significantly the value of the OA index, it improves the percentages of correct classifications in damage classes 2, 3, 4 which are not high in the case of utilization of single layered networks. More specifically, the relatively low values of the Recall and the Precision indices for these damage classes (for example about 50%-60% when the HI parameter is introduced in input vectors) when single layered networks are used, are increased up to 60% in the case of utilization of ANNs with two hidden layers. Moreover, in the case of introduction of all the examined seismic parameters in input vectors the most of values of the Recall and the Precision indices are greater than 75%.

(a)

ANN's classification

| True (target) class | 1 | 2 | 3 | 4 | 5 | R |
|---|---|---|---|---|---|---|
| 1 | 42 | 7 | 1 | 0 | 0 | 84.0% |
| 2 | 2 | 28 | 3 | 0 | 0 | 84.8% |
| 3 | 0 | 10 | 56 | 12 | 1 | 70.9% |
| 4 | 0 | 0 | 5 | 31 | 9 | 68.9% |
| 5 | 0 | 0 | 0 | 7 | 79 | 91.9% |
| P | 95.5% | 62.2% | 86.2% | 62.0% | 88.8% | ***80.5%*** |

RP algorithm - activation functions: tansig/tansig/tansig
30/10 neurons in hidden layers

ANN's classification

| True (target) class | 1 | 2 | 3 | 4 | 5 | R |
|---|---|---|---|---|---|---|
| 1 | 38 | 2 | 0 | 0 | 0 | 95.0% |
| 2 | 5 | 18 | 5 | 0 | 0 | 64.3% |
| 3 | 0 | 6 | 53 | 9 | 1 | 76.8% |
| 4 | 0 | 0 | 10 | 32 | 8 | 64.0% |
| 5 | 0 | 0 | 0 | 11 | 95 | 89.6% |
| P | 88.4% | 69.2% | 77.9% | 61.5% | 91.3% | ***80.5%*** |

SCG algorithm - activation functions: tansig/tansig/tansig
36/30 neurons in hidden layers

(b)

ANN's classification

| True (target) class | 1 | 2 | 3 | 4 | 5 | R |
|---|---|---|---|---|---|---|
| 1 | 35 | 5 | 1 | 0 | 0 | 85.4% |
| 2 | 5 | 39 | 3 | 0 | 0 | 83.0% |
| 3 | 0 | 4 | 46 | 8 | 0 | 79.3% |
| 4 | 0 | 0 | 12 | 36 | 5 | 67.9% |
| 5 | 0 | 0 | 0 | 9 | 85 | 90.4% |
| P | 87.5% | 81.3% | 74.2% | 67.9% | 94.4% | ***82.3%*** |

RP algorithm - activation functions: tansig/tansig/tansig
48/28 neurons in hidden layers

ANN's classification

| True (target) class | 1 | 2 | 3 | 4 | 5 | R |
|---|---|---|---|---|---|---|
| 1 | 42 | 3 | 0 | 0 | 0 | 93.3% |
| 2 | 8 | 32 | 3 | 0 | 0 | 74.4% |
| 3 | 0 | 8 | 55 | 5 | 1 | 79.7% |
| 4 | 0 | 0 | 3 | 47 | 10 | 78.3% |
| 5 | 0 | 0 | 0 | 5 | 71 | 93.4% |
| P | 84.0% | 74.4% | 90.2% | 82.5% | 86.6% | ***84.3%*** |

SCG algorithm - activation functions: tansig/tansig/tansig
56/20 neurons in hidden layers

(c)

ANN's classification

| True (target) class | 1 | 2 | 3 | 4 | 5 | R |
|---|---|---|---|---|---|---|
| 1 | 38 | 4 | 0 | 0 | 0 | 90.5% |
| 2 | 0 | 35 | 6 | 0 | 0 | 85.4% |
| 3 | 0 | 9 | 55 | 10 | 1 | 73.3% |
| 4 | 0 | 0 | 9 | 33 | 6 | 68.8% |
| 5 | 0 | 0 | 0 | 7 | 80 | 92.0% |
| P | 100% | 72.9% | 78.6% | 66.0% | 92.0% | ***82.3%*** |

RP algorithm - activation functions: tansig/tansig/tansig
10/34 neurons in hidden layers

ANN's classification

| True (target) class | 1 | 2 | 3 | 4 | 5 | R |
|---|---|---|---|---|---|---|
| 1 | 40 | 3 | 0 | 0 | 0 | 93.0% |
| 2 | 1 | 30 | 6 | 0 | 0 | 81.1% |
| 3 | 0 | 3 | 52 | 11 | 0 | 78.8% |
| 4 | 0 | 0 | 11 | 35 | 9 | 63.6% |
| 5 | 0 | 0 | 0 | 6 | 86 | 93.5% |
| P | 97.6% | 83.3% | 75.4% | 67.3% | 90.5% | ***82.9%*** |

SCG algorithm - activation functions: tansig/tansig/tansig
14/38 neurons in hidden layers

Figure 14: CMs of classifications made by the best trained (two-hidden layered) ANNs with: (a) one seismic input parameter (HI parameter), (b) eight seismic input parameters, (c) the optimum combination of the seismic input parameters

Finally, it must be noted that the number of classifications in classes which are not adjacent to the correct ones is least in the case of networks with two hidden layer. More specifically, in the case of introduction of HI in input vectors this number is 2 when the RP algorithm is used and 1 when the selected algorithm is the SCG. The corresponding number in the case of single layered networks is 4 and 7 respectively (Figure 11(a)). Additionally, in all cases which are illustrated in Figures 14(b), (c) the number of classifications to classes not adjacent to the correct ones is equal to 1 or 0.

In the Table 6 the configuration of the best trained networks which were used for the evaluation of ANNs' seismic damage predictions accuracy in the case of earthquakes that are not included to the training data-set is illustrated. The results of this evaluation are presented in the following section.

| ANN's name | Number of hidden layers | Number of neurons in hidden layers | Activation functions | Training algorithm | Number of seismic input parameters |
|---|---|---|---|---|---|
| N1-RP-20 | 1 | 20 | tan/tan | RP | 4* |
| N1-SCG-32 | 1 | 32 | tan/tan | SCG | 5* |
| N2-RP-48/28 | 2 | 48/28 | tan/tan/tan | RP | 8 |
| N2-SCG-56/20 | 2 | 56/20 | tan/tan/tan | SCG | 8 |

* The optimum combination of seismic input parameters of Table 5

Table 6: The configuration parameters of best trained ANNs

## 5 EVALUATION OF THE BEST TRAINED ANNS' SEISMIC DAMAGE PREDICTIONS FOR UNKOWN EARTHQUAKES

In the previous section were presented the investigation which was conducted for the definition of optimum configurations of ANNs' using as criterion the maximization of the percentage of the r/c buildings' correct classification into predefined seismic damage classes (Table 2). The ANNs' predictions accuracy was also evaluated using also the other metrics which are defined on the basis of the CMs (Figure 6). In the Table 6 the ANNs which achieved the best predictions/classifications of the seismic damage of the testing sub-set's buildings are illustrated.

In the current section the prediction ability of ANNs presented in Table 6 is further investigated using a set of samples which are not included to the training data-set. To this end, additional time history analyses were conducted using the 30 selected r/c buildings (Table 3) and 16 pairs of horizontal bidirectional ground motions (Table 7) different from the 65 ground motions which were used for the generation of the training data-set. Thus, a new testing set of 480(=30x16) samples was generated.

| Ground Motion Parameter | Units | Minimum Value | Maximum Value |
|---|---|---|---|
| **PGA** | %g | 0.014 | 1.20 |
| **PGV** | cm/sec | 1.14 | 123.44 |
| **PGD** | cm | 0.13 | 57.73 |
| **$I_a$** | m/sec | 0.003 | 11.07 |
| **ASI** | g·sec | 0.015 | 0.98 |
| **HI** | cm | 3.47 | 471.17 |
| **PGV/PGA** | sec | 0.04 | 0.29 |
| **TUD** | sec | ≈0.0 | 14.57 |

Table 7: Ranges of the selected seismic parameters' values corresponding to the 16 testing earthquakes

Then, the best configured ANNs (Table 6) were used to classify the 480 samples of the new testing set to the seismic damage classes of the Table 2. Similarly to the case of the investigation of the optimum ANNs' configuration, the OA index, as well as the other metrics which are related to the CMs, were utilized for the evaluation of the networks' performance in the current case.

In the Figure 15 the CMs of the classifications made by the best configured ANNs for the samples of the new testing set are illustrated.

(a)

| True (target) class \ ANN's classification | 1 | 2 | 3 | 4 | 5 | R |
|---|---|---|---|---|---|---|
| 1 | **110** | 2 | 0 | 0 | 0 | 98.2% |
| 2 | 16 | **43** | 40 | 0 | 0 | 43.4% |
| 3 | 0 | 7 | **43** | 21 | 5 | 56.6% |
| 4 | 0 | 0 | 7 | **13** | 10 | 43.3% |
| 5 | 0 | 0 | 0 | 11 | **152** | 93.3% |
| P | 87.3% | 82.7% | 47.8% | 28.9% | 91.0% | ***75.2%*** |

RP -tan/tan - 20 neurons in the hl - 4 seismic inputs

(b)

| True (target) class \ ANN's classification | 1 | 2 | 3 | 4 | 5 | R |
|---|---|---|---|---|---|---|
| 1 | **115** | 6 | 2 | 0 | 0 | 93.5% |
| 2 | 11 | **39** | 40 | 1 | 0 | 42.9% |
| 3 | 0 | 7 | **38** | 19 | 3 | 56.7% |
| 4 | 0 | 0 | 10 | **13** | 6 | 44.8% |
| 5 | 0 | 0 | 0 | 12 | **158** | 92.9% |
| P | 91.3% | 75.0% | 42.2% | 28.9% | 94.6% | ***75.6%*** |

SCG - tan/tan -32 neurons in the hl - 5 seismic inputs

(c)

| True (target) class \ ANN's classification | 1 | 2 | 3 | 4 | 5 | R |
|---|---|---|---|---|---|---|
| 1 | **115** | 9 | 0 | 0 | 0 | 92.7% |
| 2 | 11 | **38** | 40 | 0 | 0 | 42.7% |
| 3 | 0 | 5 | **42** | 16 | 3 | 63.6% |
| 4 | 0 | 0 | 8 | **16** | 4 | 57.1% |
| 5 | 0 | 0 | 0 | 13 | **160** | 92.5% |
| P | 91.3% | 73.1% | 46.7% | 35.6% | 95.8% | ***77.3%*** |

RP - tan/tan/tan - 48/28 neurons in hls - 8 seismic inputs

(d)

| True (target) class \ ANN's classification | 1 | 2 | 3 | 4 | 5 | R |
|---|---|---|---|---|---|---|
| 1 | **108** | 2 | 0 | 0 | 0 | 98.2% |
| 2 | 18 | **45** | 32 | 0 | 0 | 47.4% |
| 3 | 0 | 5 | **49** | 19 | 3 | 64.5% |
| 4 | 0 | 0 | 9 | **11** | 6 | 42.3% |
| 5 | 0 | 0 | 0 | 15 | **158** | 91.3% |
| P | 85.7% | 86.5% | 54.4% | 24.4% | 94.6% | ***77.3%*** |

SCG - tan/tan/tan -56/20 neurons in hls -8 seismic inputs

Figure 15: CMs of classifications made by the best trained ANNs for the samples of the new testing set: (a) N1-RP-20, (b) N1-SCG-32, (c) N2-RP-48/28, (d) N2-SCG-56/20

From the Figure 15, the following main conclusions can be drawn:

- The percentages of the correct classifications (i.e. the values of the OA index) for the samples of the new testing set are lower than the corresponding percentages which are extracted from the examined networks for the samples of the training data-set's testing sub-set. For example, the value of the OA index which is extracted from the network N1-RP-20 is 82.3% (Figure 11(c)) for the samples of the training data-set's testing sub-set, whereas the corresponding value for the samples of the new testing set is 75.2% (reduction 8.6%). Similar reductions arise for the other examined networks. This decrease of the values of the OA index is not significant if we take into consideration the fact that the input vectors of the new testing set include values of seismic parameters which are unknown to the used networks.
- Greater reductions than those of the OA index arise for the indices R and P especially for the damage classes 2, 3, 4, whereas the corresponding values of these parameters for the classes 1 and 5 remain in the same level. This conclusion is valid for all the examined networks and it is independent of the choice of the number of hidden layers and the utilized training algorithm.
- The general configuration of the CMs of the Figure 15 is similar to the configuration of the CMs which correspond to the classification of the testing sub-set's samples as regards the location of the non-zero elements. As mentioned in the section 4, the CMs in which the vast majority of the non-zero elements are located about the main diagonal (green and yellow colored cells) correspond to classifications which can be evaluated as acceptable. Therefore, the examined networks are capable to give a reliable vision of the expected damage state even for unknown earthquakes on the basis of their existing training. This conclusion is more valid in the case of networks with two hidden layers (only three samples are classified into classes not adjacent to the correct ones – see the grey colored cells in the Figures 15(c), (d)).

Finally, it must be stressed that the aforementioned reduction of the percentages of the overall correct classifications (OA index) as well as the reduction of the quality of classifications to the classes 2, 3, 4 can be attributed to the fact that the selection of the 16 testing earthquakes was done on purpose, in such a way in order to have values for seismic parameters which are out of the bounds of the corresponding parameters' values of the 65 seismic excitations which are used for the networks' training (see Table 4 and the red colored numbers in Table 7).

## 6 CONCLUSIONS

In the present paper it was investigated the ability of Artificial Neural Networks (ANN) to successfully approach the solution of the reinforced concrete (r/c) buildings' seismic damage prediction problem when it is formulated in terms of a pattern recognition problem. To this end, Multilayer Feedforward Perceptron Networks (MFP) were utilized. Two training algorithms, namely the Scaled Conjugate Gradient algorithm (SCG) and the Resilient Back-Propagation algorithm (RP), were used for the training of ANNs. The required training dataset was generated using results from Nonlinear Time History Analyses (NTHA) of 30 r/c buildings with different heights, structural systems and structural eccentricities, subjected to 65 actual ground motions. The selected r/c buildings were designed following the provisions of Eurocodes. In total, 1950 NTHA were conducted. From each one of them the damage index formulated in terms of Maximum Interstorey Drift Ratio (MIDR) was calculated. In order to investigate the optimum ANNs' performance several networks with different configurations were examined. More specifically, ANNs with different number of hidden layers (1 or 2), different number of neurons in the hidden layers (between 10 and 60), as well as different activation functions of neurons (sigmoid function (logsig) or hyperbolic tangent function (tansig)) were formed. Furthermore, the number and the combination of the seismic input parameters which lead to the optimum ANNs' predictions was investigated. To this end, 8 different and widely used seismic parameters were examined using the "Stepwise" sensitivity analysis method. Finally, the prediction ability of the best configured ANNs was further investigated using scenarios of future earthquakes. In the investigation procedure the ANNs' performance was evaluated in any case using the percentages of correct classifications of buildings into pre-defined damage classes (Overall Accuracy (OA) index) as well as the corresponding Confusion Matrices (CM). The basic conclusions that turned out from the present investigation are the following:

- The utilization of the tansig function in the output layer's neurons leads in all examined cases to much more exact predictions than those which are extracted when the function logsig is used.
- The used training algorithm affects the performance of ANNs but no clear conclusion is extracted about the more effective training algorithm between RP and SCG. Thus, the factor "training algorithm" is not considered as a critical factor in the present study.
- When only one seismic parameter is introduced to input vectors, the Housner Intensity (HI) parameter is the most effective one in almost all examined cases. This conclusion is valid in any case if the tansig function is used for the neurons of the output layer.
- The ranking of the seismic input parameters concerning their importance (i.e. concerning the value of OA) is identical and independent of the training algorithm, of the type of hidden layer's activation functions and of the number of hidden layers only in the case of utilization of function tansig in the output layer.
- The optimum number and combination of the seismic parameters depends on the used training algorithm, and on the activation functions of the hidden and output layer.

- The utilization of second hidden layer improves the quality of ANNs' predictions especially when the percentages of correct classifications into individual classes instead of the overall percentages of correct classifications are examined.
- The vast majority of classifications which are made by the ANNs correspond to the correct classes or to classes which are adjacent to the correct ones. This conclusion is valid in both cases of ANNs with one or two hidden layers. It also valid for the samples of the training data-set's testing sub-set, as well as for the samples of the data-set which is formed considering earthquakes unknown to the trained ANNs. Therefore, the examined networks are capable to give a reliable vision of the expected damage state even for unknown earthquakes on the basis of their existing training.

## REFERENCES

[1] FEMA-356, *Prestandard and Commentary for the Seismic Rehabilitation of Buildings.* Federal Emergency Management Agency, Washington DC, 2000.

[2] EN1998-3, *Design of structures for earthquake resistance – Part 3: Assessment and retrofitting of buildings*. European Committee for Standardization, Brussels, 2005.

[3] ASCE/SEI 41-06, *Seismic Rehabilitation of Existing Buildings*. American Society of Civil Engineers, ASCE, Virginia, 2009.

[4] FEMA-154, *Rapid visual screening of buildings for potential seismic hazards: A Handbook (FEMA-154)*. 2nd Edition, Washington DC, 2002.

[5] ATC, *Earthquake Damage Evaluation Data for California, ATC-13 Report*. Redwood City, CA: Applied Technology Council, 1985.

[6] A.J. Kappos, G. Panagopoulos, Ch. Panagiotopoulos, Gr. Penelis, A Hybrid Method for the vulnerability assessment of R/C and URM buildings. *Bulletin of Earthquake Engineering*, **4(4)**, 391-413, 2006.

[7] S. Haykin, *Neural Networks and Learning Machines, 3rd Edition*, Prentice Hall, 2009.

[8] M. McCulloch, W. Pitts, A logical calculus and the ideas immanent in the nervous activity. *Bulletin of Mathematical Biophysics*, **5**, 115-133, 1943.

[9] G. Molas, F. Yamazaki, Neural Networks for quick Earthquake Damage Estimation. *Earthquake Engineering and Structural Dynamics*, **24**, 505-516, 1995.

[10] N. Lagaros, M. Fragiadakis M, Fragility assessment of steel frames using neural networks. *Earthquake Spectra*, **23(4)**, 735-752, 2007.

[11] O.R. Lautour, P. Omenzetter, Prediction of seismic-induced structural damage using artificial neural networks. *Engineering Structures*, **31**, 600-606, 2009.

[12] S.L. Dimova, P. Negro, Seismic assessment of an industrial frame structure designed according to Eurocodes. Part 2: Capacity and vulnerability. *Engineering Structures*, **27(5)**, 724–735, 2005.

[13] M.F. Moller, A scaled conjugate gradient algorithm for fast supervised learning. *Neural Networks*, **6**, 525-533, 1993.

[14] M. Riedmiller, H. Braun, A Direct Adaptive Method for Faster Backpropagation Learning: The RPROP Algorithm. *Proceedings of IEEE*, San Francisco, 586-591, 1993.

[15] S. Asht, R. Dass, Pattern Recognition Techniques: A Review. *International Journal of Computer Science and Telecommunications*, **3(8)**, 25-29, 2012.

[16] B. Erkus, Utilization of Artificial Neural Networks in Building Damage Prediction. *MSc Thesis*. Middle East Technical University, Ankara, 1999.

[17] M.H. Arslan, An evaluation of effective design parameters on earthquake performance of RC buildings using neural networks. *Engineering Structures*, **32(7)**, 1888-1898, 2010.

[18] T.K. Šipoš, V. Sigmund, M. Hadzima-Nyarko, Earthquake performance of infilled frames using neural networks and experimental database. *Engineering Structures*, **51**, 113-127, 2013.

[19] S.L. Kramer, *Geotechnical Earthquake Engineering*. Prentice-Hall, 1996.

[20] SeismoSoft, *SeismoSignal v.5.1.0.*, 2015: www.seismosoft.com

[21] A.J. Kappos, Seismic damage indices for RC buildings: evaluation of concepts and procedures. *Construction Research Communications Limited ISSN 1365-0556*, 78-87, 1997.

[22] F. Naeim, *The seismic design handbook, 2nd edition*. Kluwer Academic, Boston, 2011.

[23] A. Elenas, K. Meskouris, Correlation study between seismic acceleration parameters and damage indices of structure. *Engineering Structures*, **23**, 698–704, 2001.

[24] A. Masi, M. Vona, M. Mucciarelli, Selection of Natural and Synthetic Accelerograms for Seismic Vulnerability Studies on Reinforced Concrete Frames. *J. Struct. Eng.*, **137**, 367-378, 2011.

[25] PEER (Pacific Earthquake Engineering Research Centre), Strong Motion Database, 2003. http://peer.berkeley.edu/smcat/

[26] European Strong-Motion Database,2003,http://www.isesd.hi.is/ESD Local/frameset.htm

[27] EN1992-1-1, *Design of Concrete Structures, Part 1-1: General rules and rules for buildings*. European Committee for Standardization, Brussels, 2005.

[28] EN1998-1, *Design of structures for earthquake resistance – Part 1: General rules, seismic actions and rules for buildings*. European Committee for Standardization, Brussels, 2005.

[29] T.O.L. - Engineering Software House, *RAF Version 4.4: Structural Analysis and Design Software*. Iraklion, Crete, Greece, 2014.

[30] A. Otani, Inelastic Analysis of RC frame structures. *Journal of the Structural Division, ASCE*, **100(7)**, 1433–1449, 1974.

[31] A.J. Carr, *Ruaumoko – A program for inelastic time-history analysis: Program manual. Department of Civil Engineering*. University of Canterbury, New Zealand, 2006.

[32] Matlab, *Neural networks toolbox user's guide*, 2013.

[33] H.M. Mushgil, H.A. Alani, L.E. George, Comparison between Resilient and Standard Back Propagation Algorithms Efficiency in Pattern Recognition. *International Journal of Scientific & Engineering Research*, **6(3)**, 773-778, 2015.

[34] T. Fawcett, An introduction to ROC analysis. *Pattern Recognition Letters*, **27**, 861–874, 2006.

[35] M.Y. Rafiq, G. Bugmann, D.J. Easterbrook, Neural network design for engineering applications. *Computers and Structures*, **79**, 1541-1552, 2001.

[36] M.T. Hagan, H.B. Demuth, M.H. Beale, *Neural Network Design*. MA: PWS Publishing, Boston, 1996.

[37] M. Gevrey, I. Dimopoulos, S. Lek, Review and comparison of methods to study the contribution of variables in artificial neural network models. *Ecological Modelling*, **160**, 249-264, 2003.

[38] G.R. Balls, D. Palmer-Brown, G.E. Sanders, Investigating microclimatic influences on ozone injury in clover (Trifolium subterraneum) using artificial neural networks. *New Phytologist*, **132**, 271-280, 1996.

[39] J.D. Olden, M.K. Joy, R.G. Death, An accurate comparison of methods for quantifying variable importance in artificial neural networks using simulated data. *Ecological Modelling*, **178**, 389–397, 2004.

[40] K. Morfidis, K. Kostinakis, Seismic parameters' combinations for the optimum prediction of the damage state of R/C buildings using neural networks. *Advances in Engineering Software*, **106**, 1-16, 2017.

COMPDYN 2017
6th ECCOMAS Thematic Conference on
Computational Methods in Structural Dynamics and Earthquake Engineering
M. Papadrakakis, M. Fragiadakis (eds.)
Rhodes Island, Greece, 15–17 June 2017

# Florence: seismic assessment of not-historical masonry buildings population

**Giulia Metelli[1], Tommaso Rotunno[1], Marco Tanganelli[1] and Stefania Viti[1]**

[1] Department of Architecture (DiDA), University of Florence
Via della Mattonaia 14, 50121 Firenze
e-mail: giulia.metelli.gm@gmail.com,; tommaso.rotunno@unifi.it;
marco.tanganelli@unifi.it; viti@unifi.it

**Keywords:** masonry buildings, site-specific analysis, …….

***Abstract.*** *The city of Florence, whose historic center has been declared a World Heritage Site by UNESCO in 1982, is known all over the world for its historical and artistic heritage. However, more than half of its buildings population was made in the XX century, therefore presenting the typical problems and weaknesses proper of pre-normative "recent" constructions. The XX century buildings population is made both by RC and masonry constructions. This work deals with the seismic assessment of masonry buildings made in Florence after the II world war. In those decades, in fact, a large number of masonry buildings has been made, both as private and public projects. The public interventions, belonging to housing national projects, were aimed at providing homes for needing citizens; they cover a large number of buildings, all over the town, having similar features and material. In the paper, a brief description of the development of the public housing in Florence has been presented, and some building—types have been assumed to represent the public buildings population. One of this buildings-type has been selected for an evaluation in terms of seismic assessment. To this purpose two case-studies, belonging to the same type, have been considered, and different assumptions, all consistent to the collected information, have been made about their masonry strength, elastic stiffness and floor weight, in order to represent a variety of possible situations compatible with the proposed classification. The seismic assessment of the case-studies has been made by performing a nonlinear static analysis, where the seismic input has been described according to the Italian current Technical Code. The obtained results evidence a safety level lower than expected for new constructions, whose acceptability depends on the model assumptions.*

## 1 INTRODUCTION

The city of Florence is known all over the world as representative of the Italian architecture, and symbol of Renaissance. However, more than half of its residential buildings population was made in the XX century, before the support of the recent technical seismic legislation. These buildings, secondary for importance but primary for number, are still in use, even if their safety level has never been checked.

By comparing the constructive activity in Florence to the one of the entire Country (Figure 1), it can be noted that in Florence the construction activity is gathered mostly in the beginning of the century, and it is made mostly by masonry buildings. Pre-normative masonry buildings, therefore, represent the large majority of the residential reality of the town.

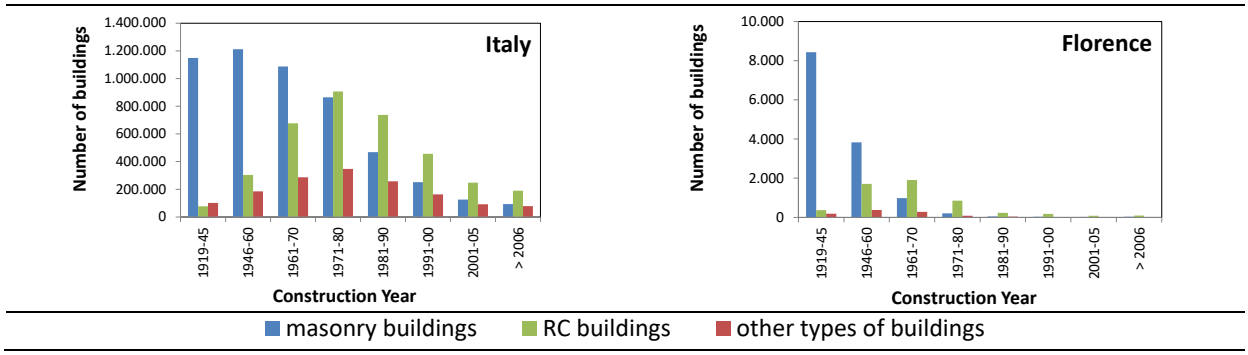


Figure 1. Construction activity in Italy and in Florence (ISTAT).

In the XX century many public housing interventions have been made in Florence, as well as in all over the country. They have been very important, since they comprehend a meaningful number of constructions, and their projects are, usually, more detailed and better preserved than the others. Furthermore, the buildings belonging to the public housing are more "homogenized" than the private ones, and they have settled a standard in morphology, mechanical properties and – consequently – performance; therefore they can be considered important in representing the XX century houses in Florence.

Even as regards the public housing interventions, the masonry buildings were much more numerous than the RC ones, as can be seen in Figure 2.

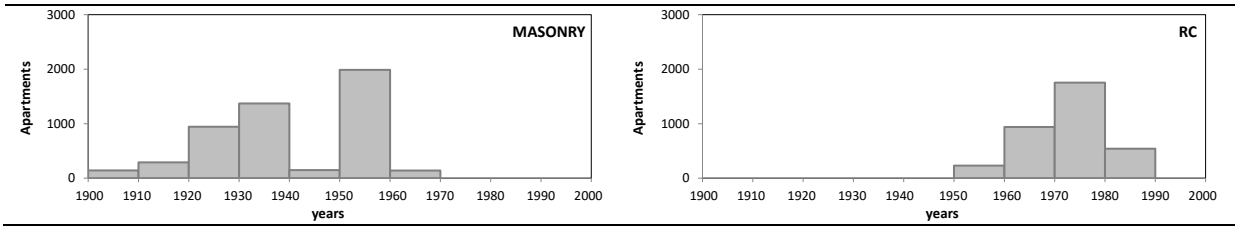


Figure 2. Public housing activity in the XX century.

This paper is focused on the evaluation of the seismic assessment of standard masonry buildings belonging to the public housing interventions made in Florence in the XX century. The study refers to two case-studies, assumed to represent a typical masonry building. The selection of the case-studies has been made after a careful survey on the buildings population belonging to the public housing interventions in Florence in the XX century. In the paper, a brief description of the development of the public housing in Florence has been presented (Section 2), in order to better frame the quantity and the properties of these residential buildings. In Section 3 the masonry main building types constituting the housing interventions in

Florence have been briefly presented, and one of them has been selected for the seismic assessment. Two different case-studies, differing for storey number and main walls disposition, have been selected and described. In Section 4 the seismic assessment of the case-studies, based on a nonlinear static analysis, has been presented and compared to the current safety standards.

## 2 MAIN HOUSING INTERVENTIONS IN FLORENCE

The first public housing intervention, in Florence, go back to 1849, when the SAE (anonymous housing society) built a house for workmen [1]. In the following years (1865-71) Florence became the Capital of Italy, and the housing polity was consequently affected by politic needs, like pursuing representativeness and security by replacing many old and tiny buildings with new middle-class constructions.

With the premature relocation of the Capital, Florence experienced a period of decline, and the city center become the refuge of the poorest part of the population. Many other anonymous interventions succeeded, to help the poorest population. One of the most representative was the housing committee "Comitato per le Case ad uso degli Indigenti", founded in 1855, which made 342 apartments (black circles in Figure 3) between 1886 and 1916.

At the beginning of the XX century, with the increasing of the industrial activity and the life standards, many new buildings, both private and public, were made. In 1903, with the first Code on the public housing [2], the public administration begin to make housing interventions, starting a process which lead, in 1909, to the institution of the IACP "Ente Autonomo per le Case Popolari" [1]. The first intervention consisted of 223 apartments, having good quality standards, according to the time (such as the supply of electricity and potable water). Such buildings had limited dimensions, and they were located in the suburban – and more inexpensive - areas. These constructions were very similar to the private houses, both for the plan organization and for the decorative choices. In the meantime, many private apartments were build (490 luxury, 3234 standard and 2212 working-class, respectively), usually without any order or urbanistic criterion. In order to limit the urbanistic disarrangement, a new plan was introduced in 1908, whose effects were compromised by the IWW.

After the war the housing activity restarted with the construction of new buildings in the suburban areas, whilst the central areas were left for middle-class housing and commercial use. Between 1922 and 1943, with the Fascist regime the housing emergency was faced by the "Istituto Autonomo Fascista Case Popolari", which made several buildings, with intensive occupational density and low standards. In 1935 the local Institutions merged in the National housing association (Consorzio Nazionale fra gli Istituti Autonomi per le Case Popolari), and new housing standards were set: higher buildings (4 storeys), smaller dimensions of rooms and a different plan-distribution. In the late '30 the quality of the apartments made for social housing became lower, together with the regime decline. Special attention should be paid to the house made for the soldiers families [1], which had higher standard quality and dimensions (6-10 rooms each) and presented a special arrangement, with buildings having a train-like aggregation.

After the IIWW the public housing had a further development. The tough economic situation generated a housing impasse, and the Office in charge was not able to face the situation; therefore the reconstruction projects were mostly private. In this situation, the birth of "INA-CASA" [3] represented a turning point in the public housing. INA-CASA was the building branch of the National Insurance Company (INA) [2]. Its aim was to construct houses to assign to the working class, adopting a ransom policy. INA-CASA cooperated with local companies: INPS and social security companies were in charge of the funding, the contractors

found the area for constructions, whilst IACP managed the buildings administration. In the years 1950-52 INACASA issued a framing regulation for the project of the first step of interventions (planned for the first 7 years of activity), in order to have homogeneous buildings all over the Country. The model was inspired to the Scandinavian experiences [1], with comprehensive quartiers, having all the devices and infrastructures for the inhabitants social and cultural life. A minimum surface was fixed for any apartment function, and few layouts were selected for all the interventions. The hallways were minimized to assure a minimum surface to the main rooms, and cloisters and courtyards were eliminated. Moreover, strict limits are assumed for the construction costs, with the effect of an extensive use of poor technology.

Due to the poor materials, the houses experienced a fast decline. Therefore, the next generation of guidelines (made in 1956-57 [4]) paid more attention to the quality and even the urban planning, the common areas, and the design coordination were improved. Starting from 1963, with the replacement of INA-CASA by GESCAL (Gestione Case per i Lavoratori), many further interventions were made in Florence, and many other actors, such as ATER and ARDSU, appeared in the scenario. Namely, ATER [2] managed the construction of around 12000 apartments, mainly still in use. The city itself built around 4000 units, while different – sometimes private - companies made around 6000 units.

As a results of the whole public housing activity occurred from 1849 to nowadays, more than 22000 apartments, corresponding to almost 15% of the total building population, have been made. Figure 3 shows the main interventions of public housing made in Florence. They have been classified after their years of construction, dimension and material (masonry or reinforced concrete, RC), besides the location inside the town area.

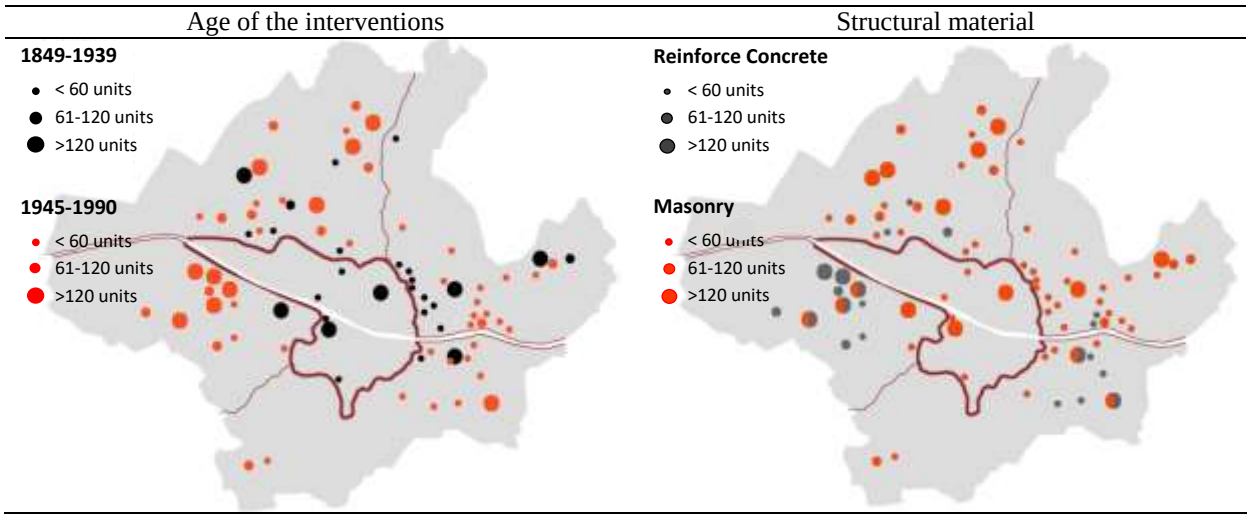


Figure 3. Main interventions of public housing made in Florence.

## 3 THE SELECTED CASE-STUDIES

### 3.1 Main types of buildings belonging to the public housing

As evidenced in Section 2, the buildings belonging to the public housing interventions present different properties, in terms of general features and mechanical properties, above all depending on age of construction, and on the general frame (technical, political and normative) of the time. The classification has been limited to the aggregation properties of masonry buildings, since the RC ones are beyond the scope of this paper. Table 1 shows the main in-

formation about the proposed classification, made after the aggregation geometry of the buildings. In this work the Type_1 has been selected for the seismic assessment.

Table 1. Main building-types made in the public housing masonry interventions

| | Buildings Types | Storey number | Construction years |
|---|---|---|---|
| 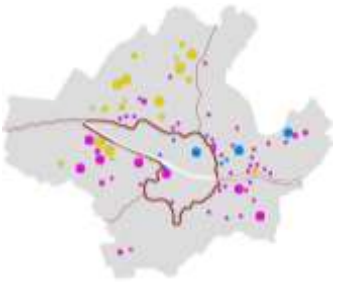 | Type_1: BLOCK  | 2-4 | late ‘800, 30s-today |
| | Type_2: LINE 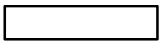 | 3-6 | 1870-1936, 30s-today |
| | Type_3: ANGLE 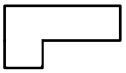 | 3-6 | 1800, 30s |

## 3.2 The considered building-type

The building-type selected for analysis is the one indicated as Type_1 in Table 1. The Type_1, together with the Type_2, is the most diffuse in Florence, and it can be found in different areas (see Table 1) and with different features. The peculiarities are the independency of each block, the rectangular plan with the stairs in the middle, which serve two apartments for each storey. The foundation is usually made by masonry walls, having the same geometry and larger depth than the upper ones. The hip roof is sustained by a proper perimeter concrete kerb.

In Florence many public intervention have adopted this type. Therefore, the buildings assumed to belong to this type can differ each other for material quality, walls disposition, floors orientation, number and type of storeys, etc. In this work, therefore, two different buildings, both belonging to the Type_1, have been considered.

## 3.3 The considered case-studies

Two different case-studies have been considered in this work, both classified as Type_1 and belonging to the same intervention, made between 1949 and 1951.

| Case-study #1 | Case-study #2 |
|---|---|
| 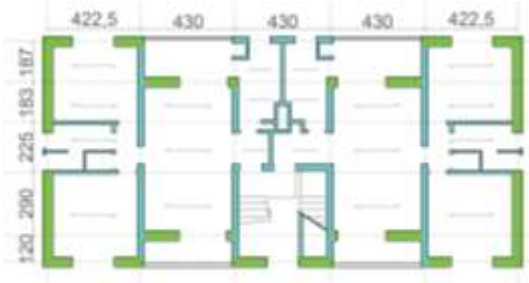  | 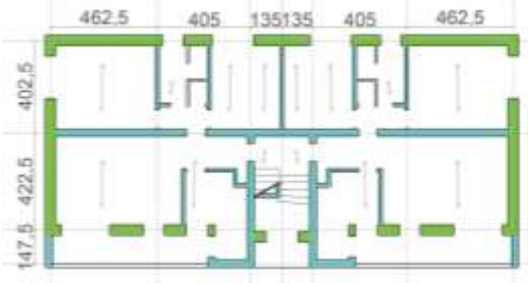  |
| Masonry A | Masonry B |
| Number of storeys: 4 | Number of storeys: 3 |
| Masonry walls: foundation: 55cm (A) | Masonry walls: foundation: 50 cm (A) |
| 1st, levels: 45 cm (A), 30 and 15 cm (B) | 1st level: 45 cm (A), 30 and 15 cm (B) |
| 2nd, 3rd, 4th levels: 30 and 15 cm (B) | 2nd and 3rd levels: 30 and 15 cm (B) |
| Main walls: *Y*-direction | Main walls: *X*-direction |

Figure 4. The two case-studies: plans and information.

An extensive information about the original projects has been collected, and the representation of the buildings has been made consequently. In Figure 4 the plans of the two case-studies are shown, together with the main assumptions made for the analysis. The two case-studies differ each other mainly for the direction of the main masonry walls and for the number of storeys. In Fig. 4 two different masonry types have been evidenced, respectively made of coursed rubble masonry (A) and plain brick one (B). The coursed rubble masonry is made of stones of various size and by horizontal courses, 1 meter spaced, made of bricks. The plain brick masonry, instead, is made with lime mortar.

The floors are made of RC joists alternated to hollow bricks, topped by a 4-cm concrete slab, and they have a thickness of 20 cm; the top storey floors, where there are not live loads, have the same technology but lower (12/16 cm) depth.

## 4 THE SEISMIC ANALYSIS

The seismic assessment has been made by performing a nonlinear static analysis, comparing the structural capacity of the case-study under horizontal loading to the seismic demand defined after the seismic classification of the site. In Section 4.1 the numerical models adopted for analysis are described, while in Sections 4.2 and 4.3 the capacity and the seismic demand of the case-study are presented, respectively. Finally Section 4.4 shows the obtained seismic assessment of the case-studies.

### 4.1 The models

The structural model has been made through the software 3Muri [5], which is the commercial version of the Tremuri computer code developed by [6]. The masonry have been represented as plane panels with a nonlinear beam-behavior [7]. A no-tension bilinear relationship has been assumed for the masonry, with a nonlinear reallocation of the compressive stress based on the stress-block model. The floors have been modelled through plane stiffness membranes having an equivalent thickness, two orthogonal elasticity moduli and an equivalent shear modulus. Therefore, the influence of the floor deformability has been considered in the global response of the structural system.

In Figure 5 the 3D views of the numerical models can be seen, while Tables 2 and 3 show the main values assumed for the mechanical properties of masonry, concrete and steel, respectively.

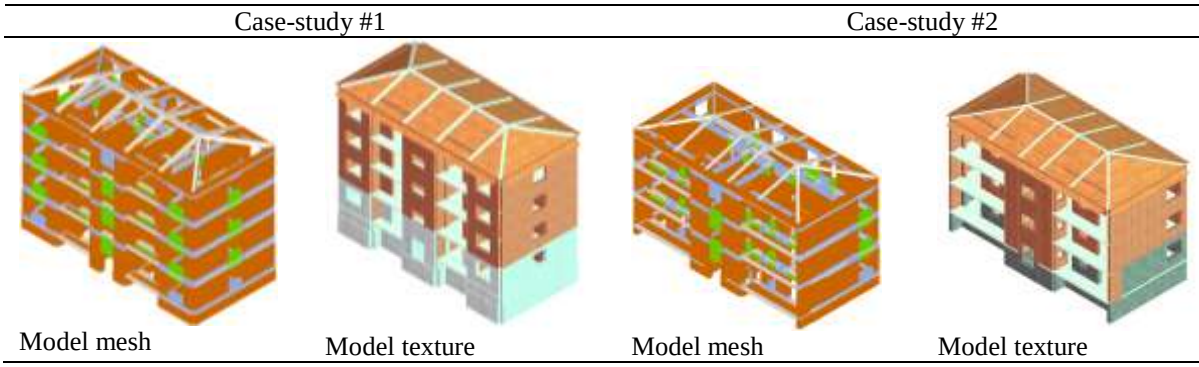


Figure 5. 3D views of the structural model.

The mechanical properties of masonry have been assumed according to the current Italian Technical Code [8], which provides two different values (minimum and maximum) for each

quantities. The value assumed for the masonry A refer to a "improvement coefficient" equal to 1.1, according to the instructions provided by the Code [8]. Furthermore, different safety factors (Confidence Factors, *CF*) can be assumed depending on the achieved knowledge level of the building. The masonry stress, therefore, has been described by the alternative values, respectively found as the maximum of the Code range, related to *CF*=1.00, and the minimum, related to *CF*=1.35.

Table 2. Mechanical quantities assumed for the masonry [8, C8A.2].

| | Masonry_A | | | | Masonry_B | | | |
|---|---|---|---|---|---|---|---|---|
| | symbol | unit | min value | max value | symbol | unit | min value | max value |
| Normal stress | $f_{m,A}$ | $N/cm^2$ | 260 | 380 | $f_{m,B}$ | $N/cm^2$ | 240 | 400 |
| Shear stress | $\tau_{0,A}$ | $N/cm^2$ | 5.6 | 7.4 | $\tau_{0,B}$ | $N/cm^2$ | 6.0 | 9.2 |
| Young modulus | $E_{m,A}$ | $N/mm^2$ | 1500 | 1980 | $E_{m,B}$ | $N/mm^2$ | 1200 | 1800 |
| Shear modulus | $G_{m,A}$ | $N/mm^2$ | 500 | 600 | $G_{m,B}$ | $N/mm^2$ | 400 | 600 |
| Specific weight | $\rho_A$ | $KN/m^3$ | 21 | | $\rho_B$ | $KN/m^3$ | 18 | |

Table 3. Mechanical quantities assumed for concrete and steel.

| | Concrete (class C20/25) | | | Steel (class "acciaio comune" [Verderame et al. 2011][9]) | | |
|---|---|---|---|---|---|---|
| quantity | symbol | unit | value | symbol | unit | value |
| Normal stress | $f_c$ | $N/mm^2$ | 24 | $f_c$ | $N/mm^2$ | 350 |
| Young modulus | $E_c$ | $N/mm^2$ | 28600 | $E_c$ | $N/mm^2$ | 206000 |

Even the masonry Young modulus has been represented through two alternative assumptions, which are assumed to describe the elastic stiffness of the uncracked (max $E_m$) and cracked (min $E_m$) masonry, respectively. Another variable has been introduced through the floors description. Indeed, two different types of floors have been considered, having different weight.

Since no specific information is available about the technology adopted for the floors, two different components, respectively normal and lighten, have been considered. The two floor types present the same structural behavior, changing only in their weight, with the lighten floor about 30% lighter than the other. In Table 4 the assumptions concerning the buildings representation are resumed, and the models adopted in the analysis have been named after them.

Table 4. Models adopted in the analysis.

| Model | Code | Masonry strength | Masonry stiffness | Floors weight |
|---|---|---|---|---|
| Weak and uncracked masonry, regular floors | W_UN_R | minimum | maximum | regular |
| Weak and cracked masonry, regular floors | W_CR_R | minimum | minimum | regular |
| Strong and uncracked masonry, regular floors | S_UN_R | maximum | maximum | regular |
| Strong and cracked masonry, regular floors | S_CR_R | maximum | minimum | regular |
| Weak and uncracked masonry, lighten floors | W_UN_L | minimum | maximum | lighten |
| Weak and cracked masonry, lighten floors | W_CR_L | minimum | minimum | lighten |
| Strong and uncracked masonry, lighten floors | S_UN_L | maximum | maximum | lighten |
| Strong and cracked masonry, lighten floors | S_CR_L | maximum | minimum | lighten |

## 4.2 The structural capacity

A pushover analysis has been performed on the case-studies, according to the instructions provided by the European [10] and Italian [11] Technical Codes. The adopted horizontal forces have two different patterns, respectively proportional to the mass distribution (*MP*) and to the first proportional mode (*1M*). For each direction of analysis, the forces have been applied - in both ways - to the mass center of each storey (with no eccentricity, *E0*), and to a distance corresponding to an eccentricity of +/- 5% (*E+*, *E-*), so that six analyses have been performed for each direction and horizontal pattern.

The obtained capacity curves have been represented through bilinear diagrams as required by NTC 2008, by *i)* imposing the areas equalization, and *ii)* assuming that the elastic tract includes the point of the original curve having the 60% of the maximum shear force.

In Figure 6 the pushover families provided by the nonlinear analysis have shown for the model W_UN_R. As can be noted, the buildings evidence a different strength in the two directions; in the case-study #1, which has the main masonry walls along the *Y*-direction, the capacity along the *Y*-direction is almost double than the other one. The case-study #2, instead, has a capacity slightly larger in the *X*-direction. In all cases, the two assumed horizontal patterns play an important role, with the capacity provided by the MP pattern higher and stiffer than the other. The introduced eccentricity, instead, does not affect significantly the obtained capacity. Figure 7 shows the capacity curves obtained for the two case-studies by introducing the considered assumptions about the material and the floors. For sake of simplicity, only the results referred to the cases *MP+E0* and *1M+E0*, i.e. by considering the horizontal forces along one way only and without any eccentricity, have been shown, to better evidence the effects related to the introduced assumptions.

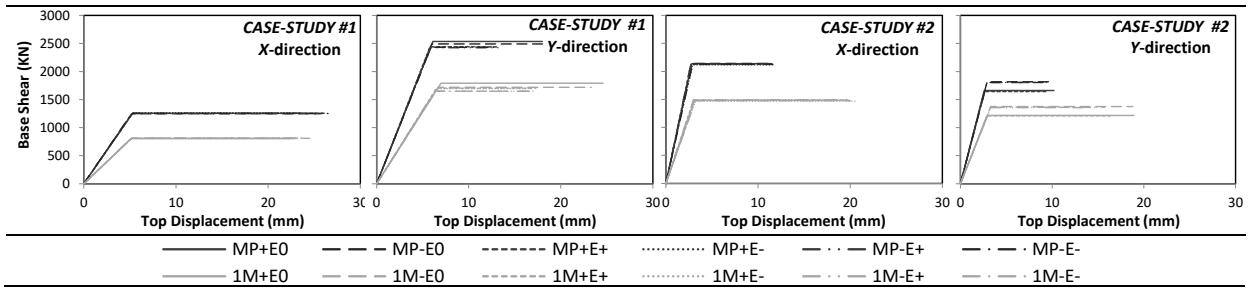


Figure 6. Capacity curves of the case-studies (model W_UN_R).

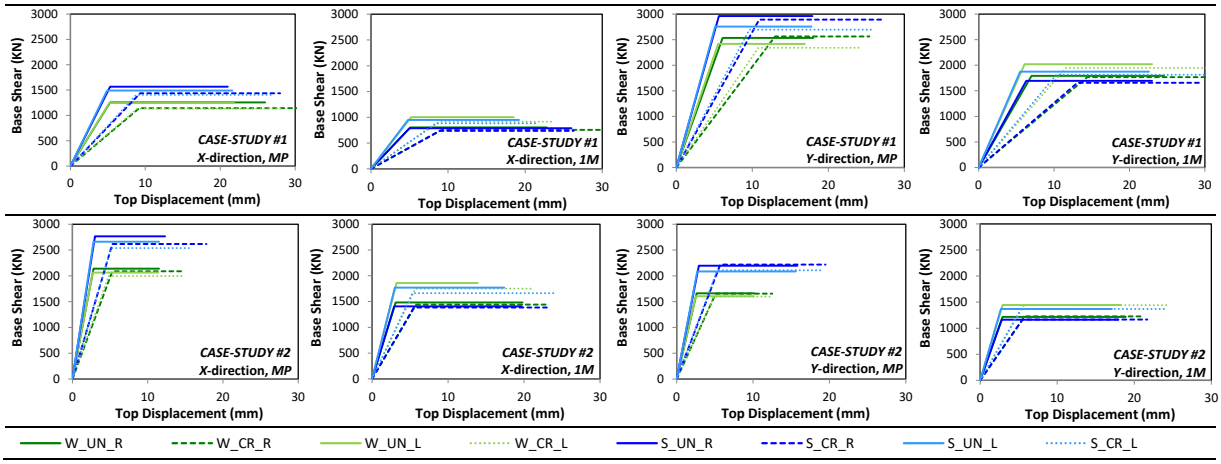


Figure 7. Capacity curves of the case-studies (no eccentricity).

As can be seen from the diagrams, the assumptions concerning the masonry behavior largely affect the obtained results, whilst the floor weight does not seem to play an important role in the seismic capacity of the case-studies.

### 4.3 The seismic demand

Florence has a PGA of 0,131g for a Return Period, *RP*, equal to 475 years, i.e. for a probability of occurrence equal to 10% in 50 years [12]. The seismic demand has been represented through the seismic spectrum provided by NTC 2008 for the Life Safety (LS) limit state, which is defined as a function of the soil classification, based on the uppermost 30 m shear-wave velocity ($v_{s,30}$). The elastic spectra provided by NTC 2008 slightly differ from the ones provided by EC8; in this work, therefore, the Italian Code has been preferred, since all the available information on the soil are compatible to such classification.

The soil classification of the case-study soil is not easy to achieve. Many investigations [13-15] have been made on the soil of the Florence area, providing a detailed knowledge of the lithostratigraphic subsurface, of the lithoid substrate profile and of the geotechnical properties of its soils. The survey included 1,850 drillings and 32 downhole tests, which provided, for the case-studies vicinity, different strathigraphies, varying in the steadiness of the soil and in the consequent uppermost $v_{s,30}$. As a consequence, different hypotheses regarding the soil classification can be made for area. In this work, therefore, three different hypotheses, all compatible to the available data, have been made, and three elastic spectra (referred to the soil-class B, C and D, respectively) have been considered. Figure 8 shows the elastic spectra considered for the case-studies, together with the information required for the spectra setting.

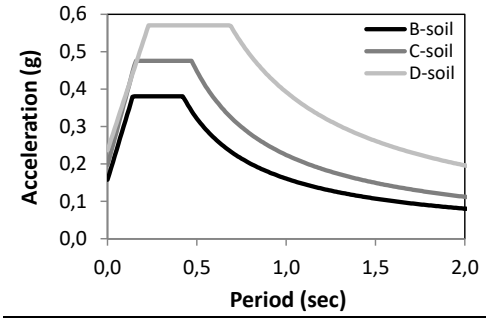


*Parameters for the seismic spectra setting*

| *class* | $T_R$ | $a_g$ | $F_0$ | $T^*_c$ | $S_T$ | $S_S$ | $Cc$ | $T_C$ | $T_B$ | $T_D$ |
|---|---|---|---|---|---|---|---|---|---|---|
| B | 475 | 0.131 | 2.41 | 0.30 | 1.0 | 1.2 | 1.397 | 0.442 | 0.141 | 2.215 |
| C | 475 | 0.131 | 2.41 | 0.30 | 1.0 | 1.5 | 1.558 | 0.471 | 0.157 | 2.215 |
| D | 475 | 0.131 | 2.41 | 0.30 | 1.0 | 1.8 | 2.274 | 0.687 | 0.229 | 2.215 |

$T_R$ = return period, $a_g$ = ground acceleration, $F_0$ = amplification factor on the rock-site, $T^*_C$ = beginning period of the velocity-constant branch, $S_T$ = topographic amplification factor, $S_S$ = stratigraphic amplification factor, $Cc$ = soil-type amplification, $T_C$ = period at the beginning of the velocity-constant branch for the assumed soil-type, $T_B$ = period at the beginning of the constant-acceleration branch, $T_D$ = period at the beginning of the displacement constant branch.

Figure 8. Elastic spectra representing the possible seismic input of the case-studies (*RP* = 475 years).

### 4.4 The seismic assessment

The seismic response of the case-studies has been found by intersecting the elastic seismic spectrum with the capacity curves, represented in the ADRS (Acceleration Displacement Response Spectrum) plane. Such transformation has been made by applying the N2 method [16]. According to Vidic *et al.* [17], the inelastic response has been assumed to coincide to the elastic one for intersection points belonging to the branch of the spectrum with periods over $T_C$, whilst, otherwise, it is opportunely amplified.

Figure 9 shows the intersection between the spectral capacity and the spectral demand for the two case-studies. As can be noted, the case-study #1 has a lower stiffness then the case-study #2. As a consequence, the case-study #1 intersects the seismic spectrum in the horizontal plateau only for the soil-type D (both directions) and C (*Y*-direction), while in the other cases the intersection occurs for lower ordinates. The case-study #2, instead, is much stiffer, with the effect of intersecting the seismic spectra in the plateau in all cases except for the soil-type D.

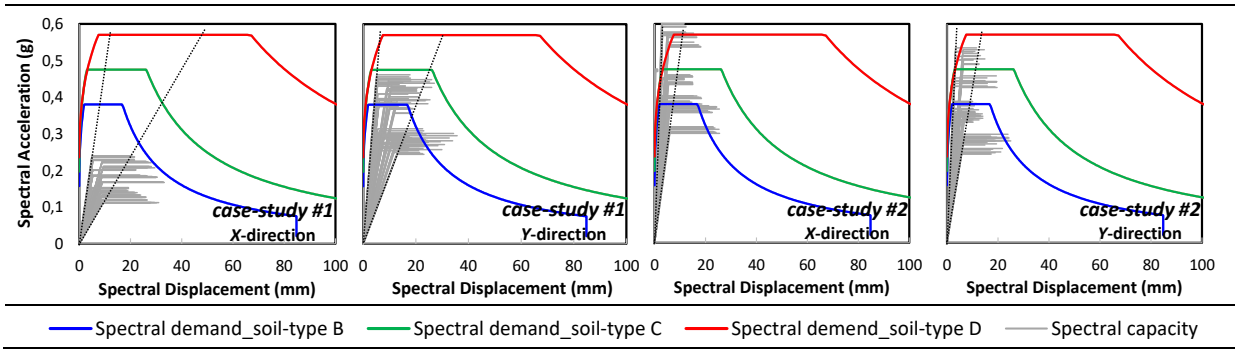


Figure 9. Spectral capacity and demand of the case studies.

The performance of the case-studies, i.e. their accomplishment of the safety level required by NTC 2008 has been expressed through a proper Performance Index (*PI*) as the ratio between the seismic capacity of each model and the corresponding demand. Figure 10 shows the *PI* found for the two case-studies through the adopted models.

As regards the case-study #1, the seismic performance in the *Y*-direction is much better than the one in the *X*-direction. However, when the B-soil is assumed, it results to be verified in almost all cases. At the opposite, *PI* is always lower than unity, i.e. the building does not accomplish the safety requirements, when the D-soil is considered. When the C-soil is assumed, instead, the PI is over the unity for excitations along the *Y*-direction only.

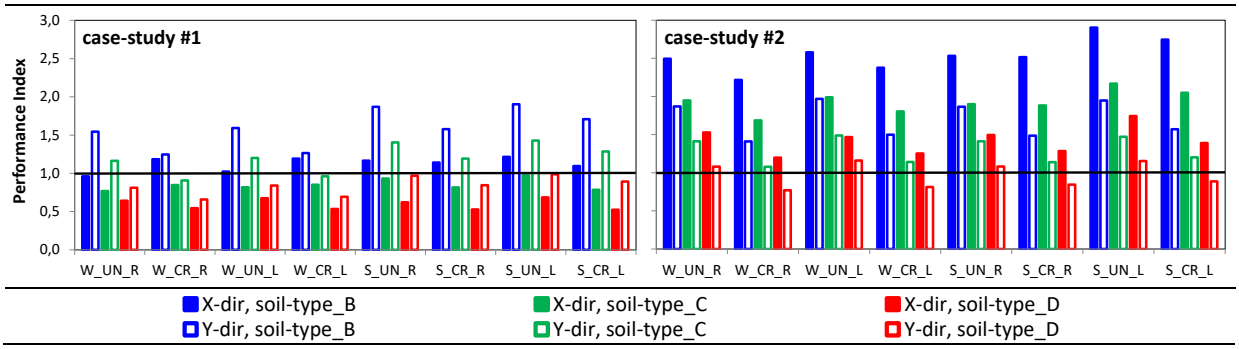


Figure 10. Performance Index of the two case-studies

The case-study #2 evidences higher values of *PI*, with the performance along the *X*-direction better than the one along the -direction. By assuming a soil-type B or C the building present an adequate safety level in all cases. When the D-soil is assumed, instead, the building performance along the *Y*-direction does not always comply to the safety requirements.

## 5 CONCLUSIVE REMARKS

In this paper the seismic assessment of masonry buildings representative of the XX century public housing interventions in Florence has been made. A classification of the buildings population belonging to the public housing activity has been proposed, based on aggregative criteria. One of the most common aggregation type consists of “block” buildings, rectangular in plan and with a number of storeys ranging between 2 and 4. Two case-studies have been selected to represent the block-type buildings family, having respectively 3 and 4 storey, and different orientation of floors and main masonry walls.

The seismic assessment of the case-studies has been made by performing a nonlinear static analysis, where the seismic input has been represented through the elastic spectra provided by the current Technical Code for a *Life Safety* limit state. Different soil classes, namely the B, C and D soil ones, have been assumed for setting the spectral demand, since the soil stratigraphy of the area presents a large variation due to the soil steadiness. Two different patterns, respectively proportional to the mass distribution and to the first vibrational mode, have been assumed for the pushover analysis. Furthermore, different hypotheses have been made regarding the strength and the stiffness of the masonry, and of the floor weight.

The analysis has evidenced a different performance of the two case-studies, with the case-study #2, having 3 storeys only, evidences a much better seismic performance. Furthermore, the assumptions made about the soil-type of the area plaid an important role in the seismic assessment of the buildings.

As regards the case-study #1, having the main walls along the *Y*-direction, the building is fully verified only for analysis in the *Y*-direction under the assumption of a B soil-type; at the opposite, when a D-soil is assumed for the area, the seismic performance is never satisfactory. For soil-class C, instead, the assessment depends on the assumptions made about the strength and the stiffness of the masonry. The variation in the floors weight, instead, does not affect the obtained results in any cases.

As regards the case-study #2, the safety requirement are satisfied in all cases in the hypothesis of soil-type B or C, while when the D-soil is assumed, the seismic performance of the building in the *X* direction.

The study has evidenced the possibility that the investigated buildings-type, i.e. the "block" masonry buildings, does not comply the current requirements concerning the seismic performance. Depending on *i)* the soil properties of the area, and *ii)* the specific features of the constructions, indeed, these buildings can be acceptable for their seismic performance. Their seismic assessment, therefore, should be investigated through more extensive analyses.

## REFERENCES

[1] Bertelli e Masini Bertelli M, Masini D (2002). Abitazioni popolari e locazioni urbane nella storia fiorentina, Sesto Fiorentino (FI), PLAN (in Italian).

[2] Pierini R. (2001). La città distante. Piani e progetti di edilizia residenziale pubblica, Pisa, Edizioni ETS.

[3] Legge 28 Febbraio 1949, n. 43. Provvedimenti per incrementare l'occupazione operaia, agevolando la costruzione di case per lavoratori. (GU Serie Generale n.54 del 7-3-1949).

[4] Beretta Angussola, L. (1963). I 14 anni del piano Ina Casa, Staderini, Roma.

[5] S.T.A. DATA (2012) 3Muri Software, release 4.0.3, S.T.A. DATA s.r.l., Torino. http://www.3muri.com

[6] Lagomarsino S, Penna A, Galasco A, Cattari S (2013) TREMURI program: an equivalent frame model for the nonlinear seismic analysis of masonry buildings. Eng. Struct. 56(11):1787–1799. doi:10.1016/j.engstruct.2013.08.002

[7] Galasco, A, Lagomarsino, S and Penna, A. (2006). On the use of pushover analysis for existing masonry buildings. Proc. of 1th European Conference on Erarthquake Engineering and Sismology, Geneva, Switzerland, 3-8 September 2006.

[8] Min. LL. PP. (2009) CIRCOLARE 2 febbraio 2009 , n. 617 Istruzioni per l'applicazione delle «Nuove norme tecniche per le costruzioni» di cui al decreto ministeriale 14 gennaio 2008. G.U. n. 47 del 26/02/2009, Supplemento Ordinario n. 27 (in Italian).

[9] Verderame G.M., Stella A., Cosenza E. (2001), Le proprietà meccaniche degli acciai impiegati nelle strutture in cemento armato realizzate negli anni ’60, *X Convegno Na*zionale "L'Ingegneria Sismica in Italia", Potenza e Matera 9-13 Settembre 2001.

[10] EC 8-3 (2005). Design of structures for earthquake resistance, part 3: strengthening and repair of buildings, European standard EN 1998-3. European Committee for Standardization (CEN), Brussels.

[11] NTC 2008. Norme tecniche per le costruzioni. D.M. Ministero Infrastrutture e Trasporti 14 gennaio 2008, G.U.R.I. 4 Febbraio 2008, Roma (in Italian).

[12] Montaldo, V., Meletti, C., Martinelli, F., Stucchi, M., and Locati, M. (2007). “On-Line seismic hazard data for the new Italian building code”. *Journal of Earthquake Engineering* 11, 119–132.

[13] M. Coli & P. Rubellini (2013). Geological anamnesis of the Florence area, Italy. Z. Dt. Ges. Geowiss. (German J. Geosci.), 164 (4), p. 581–589.

[14] M. Coli, L. Guerri & P. Rubellini (2015). Geotechnical characterization of the Florence (Italy) soils. *Proc. 5th Asian Regional Conference on Soil Mechanics and Geotechnical Engineering*, Fukuoka November 9-13, Japan.

[15] Lacanna G, Deguy P, Ripepe M, Coli M. Paoletti B, Tanganelli M, Viti S, De Stefano M (2016). Seismic vulnerability of urban areas: a case-study. Proc. ECCOMAS Congress. Crete Island, Greece 5-10 June 2016.

[16] Fajfar, P. 1999. Capacity spectrum method based on inelastic demand spectra. *Earthquake Engineering and Structural Dynamic* 28, 979-93.

[17] Vidic T., Fajfar P. e Fischinger M. (1994) .Consistent inelastic design spectra: strength and displacement. *Earthquake Engineering and Structural Dynamics* 23, pp. 502-521.

COMPDYN 2017
6th ECCOMAS Thematic Conference on
Computational Methods in Structural Dynamics and Earthquake Engineering
M. Papadrakakis, M. Fragiadakis (eds.)
Rhodes Island, Greece, 15–17 June 2017

# SEISMIC ASSESSMENT OF A RC CASE STUDY BUILDING USING THE SIMPLE LATERAL MECHANISM ANALYSIS, SLAMA, METHOD

**Roberto Gentile[1], Ciro Del Vecchio[2], Giuseppina Uva[1], and Stefano Pampanin[3]**

[1] Dipartimento di Ingegneria Civile, Ambientale, del Territorio, Edile e di Chimica, Politecnico di Bari
via Edoardo Orabona, 4, 70126 Bari, Italy
e-mail: roberto.gentile@poliba.it; giuseppina.uva@poliba.it

[2] Department of Structures for Engineering and Architecture, University of Napoli "Federico II",
via Claudio 21, 80125, Napoli, Italy
ciro.delvecchio@unina.it

[3] Department of Civil and Natural Resources Engineering, University of Canterbury,
Christchurch, New Zealand
stefano.pampanin@canterbury.ac.nz
[3] Department of Structural and Geotechnical Engineering, Sapienza University of Rome,
Via Eudossiana 18, Rome, Italy
stefano.pampanin@unroma1.it

**Keywords:** Seismic assessment; SLaMA; displacement-based; simplified tool; pushover.

***Abstract.*** The seismic assessment of an existing structure is a complex procedure. In the evaluation of the structural capacity, difficulties arise in the definition of the lateral resisting members, in the estimation of the lateral capacity from component to system level. The identification of the local and global mechanisms, depending on the hierarchy of strength at subassembly level, is a challenging task. Nowadays, advanced numerical analysis procedures, implemented in user-friendly commercial software, are commonly adopted in the current practice to overcome the difficulties in the use of non-linear analyses. Nevertheless, their accuracy strongly depends on the ability of the numerical model to capture all the probable failure mechanisms. To help the user in the assessment of the probable failure mechanism and to have a first estimation of the building lateral capacity, the Simple Lateral Mechanism Analysis (SLaMA) method has been recently developed and included in the NZSEE 2016 guidelines. SLaMA is a simple and reliable "by-hand" tool to derive the local and global mechanism of a structural system and the corresponding capacity curve. This paper deals with the application of the SLaMA to an existing RC building severely damaged during the Christchurch earthquake (2011, New Zealand). The lateral capacity of four 2D resisting systems was assessed following the SLaMA method. The results of a refined nonlinear numerical model were used to assess the accuracy and reliability of SLaMA. The good match confirmed that SLaMA can be a useful and simple tool to have a first estimation of the building lateral response. It allows to identify the main structural weaknesses driving the user to the development of more refined nonlinear models.

## 1 INTRODUCTION

High uncertainties characterize the seismic assessment procedures both at building and regional level [1]. Although significant advances were made to improve the procedures for the input selection and in the development of refined analysis methods, difficulties are still present. Nowadays, thanks to user-friendly commercial software, the use of non-linear analyses is common in the design practise. It is worth mentioning that, although the non-linear analysis are the most refined tools for the seismic assessment of existing buildings, their accuracy strongly depends on the ability of the numerical model to capture all the probable failure mechanisms.

For existing RC structures, characterising the lateral capacity of existing members (beams, columns, walls) that do not conform to modern seismic codes is challenging. This is because the lack of seismic detailing may lead to different failure mechanisms (flexure, shear, bar buckling, slip at the lap-splice of longitudinal reinforcement). Moreover, the lack of seismic detailing may have detrimental effects on the seismic capacity of beam-column joints. Indeed, recent earthquakes and relevant scientific studies ([7], [8]) outlined that the shear failure of poorly detailed beam-column joints significantly affects the structural seismic performances. High uncertainties are also related to the estimation of the probable material properties and to the influence of stiff-infill on the structural behaviour ([2], [3], [4], [5], [6]). As a result, the development of reliable numerical models to be employed in refined non-linear analysis is of paramount importance and the designers should have the chance to check the model accuracy. Nevertheless, the lack of simple tools to quickly assess the model accuracy or the influence of the modelling assumptions on the strength hierarchy, the failure mechanism and the global capacity curve makes the entire assessment procedure susceptible to large errors. In order to help the designers in the development of reliable nonlinear models, a step-by-step simplified analysis method named Simple Lateral Mechanism Analysis (SLaMA) was recently proposed in the New Zealand Society for Earthquake Engineering, NZSEE2016, guidelines for Detailed Seismic Assessment (DSA) of existing building [11]. As reported in the document: "*The onus is on the assessing engineer to understand the level of reliability available from the chosen assessment approach and to be able to articulate this to the end user of the DSA*".

In this paper, SLaMA is used to predict the lateral capacity of 2D lateral resisting systems extracted from a real building damaged by the 2011 Christchurch earthquake. In particular, the SLaMA method, which can be referred to as a "by-hand analytical pushover", is proposed as a reliable benchmark to assess the accuracy of a numerical model/analysis of a RC structure in predicting the main structural weaknesses and the capacity curve itself.

## 2 RESEARCH METHODOLOGY

A RC case study building damaged by the Christchurch earthquake (New Zealand, 2011) was selected for this study. The response of its main lateral resisting systems was assessed using both SLaMA and 2D refined nonlinear numerical models by using the FEM software Ruaumoko [12]. All the structural nonlinearities typical of the “non-conforming” RC structures, i.e. flexural-shear interaction, bar buckling, joint shear failure, possibility of soft-storey mechanisms, were properly considered. The results of the numerical model are directly compared with those predicted with SLaMA. The non-linear capacity curves and the plastic mechanism predicted at the ultimate limit state are compared and discussed.

The capability of SLaMA of predicting the actual hierarchy of strength and, hence, the plastic mechanism obtained from refined numerical pushover analyses is discussed. This confirmed that this simplified method can be used to have benchmark capacity curves useful to check the accuracy of refined numerical models.

## 3 CASE STUDY BUILDING

The case study building is an 8-storey RC building (approx. 24m tall) which was used as commercial office before the February 2011 Canterbury earthquake. It was built in 1974 and designed according to pre-70's practice when capacity design and seismic detailing were not yet introduced. The building was part of a reconnaissance project developed in the aftermath of the abovementioned earthquake and hence the observed damage state can be found in [13], [14].

Figure 1 shows the plan view of the ground level, taken from the original structural drawings, and the idealisation of the structure. The structural system consists of RC perimeter frames and a C-shaped structural wall, which is also connected to the corner columns through link beams, forming a frame-wall system. Assuming a decoupled behaviour of the web and the flanges of the C-wall, for the purpose of this work, the lateral resisting systems "extracted" from the building (see Figure 2) are the following:

- **Frame 1**: the RC frame on gridline 1 (N-S or y-direction);
- **Frame A**: the RC perimeter frame on gridline A, (E-W or x-direction). This is identical to the frame on gridline D;
- **Wall (flange only)**: two flanges of the RC C-shaped wall on the east side of the building;
- **Dual System**: the RC frame-wall system formed by the web of the C-wall connected to the corner columns through link beams (y-direction).

Building geometry, material properties, members dimensions, reinforcement detailing, load analysis and photographic report of the damage are widely discussed in [15] and [14].

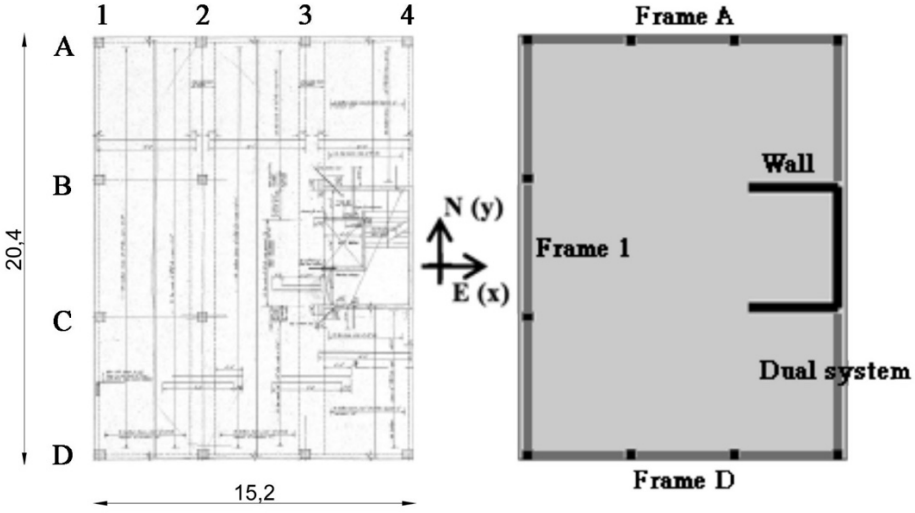


Figure 1: Original plan view of the ground level and idealisation of the structural system.

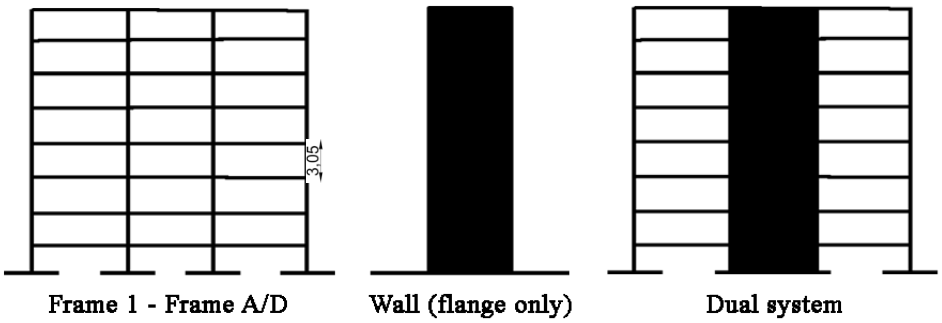


Figure 2: Schematic of the structural systems of the case study building.

# 4 SIMPLE LATERAL MECHANISM ANALYSIS

## 4.1 The method

The Simple Lateral Mechanism Analysis, introduced in the New Zealand code in 2006 [11] and significantly improved in the 2016 [24] version, can be referred to as a "by-hand analytical pushover" in which the structure capacity curve is calculated using basic principles. In line with the Direct Displacement Based Assessment (DDBA) approach, this method is a powerful instrument to assess the seismic performance (capacity-to-demand ratio in the ADRS domain) of relatively complex structures also considering 3D effects (inelastic torsion).

This paper deals with the application to 2D lateral resisting systems (see Figure 3Figure 4). A full example of the application of SLaMA, including detailed calculations and 3D effects is reported in detail in Del Vecchio et al. [15].

The starting point of the SLaMA method is the characterisation of the lateral capacity of each of the structural member (beams, columns, joints, walls) performing software-based sectional analyses (e.g. [18]) or by-hand simplified calculations. It is worth noting that this process would be carried out, in an identical way, to characterise the nonlinearities of a lumped plasticity numerical model. To avoid repetition, the details on this aspect are given in Section 5, when discussing the numerical models assumptions. The interaction between the members in each beam column joint subassembly is analysed (hierarchy of strength calculation, [25], see Figure 3). These results allow to assess the probable inelastic mechanism of the structure and calculate the related strength using equilibrium conditions. It is worth noting that, in order to compute the base shear strength, a full redistribution of the actions is assumed. Indeed, the fully exploit of the strength capacity of all the beam-column subassemblies is considered. The displacement capacity at the effective height, representative of the SDOF system, is calculated multiplying the minimum drift capacity of the RC members experiencing the first yielding or the ultimate failure by the effective height (which depends on the probable inelastic mechanism, see Figure 4). In this paper, the SLaMA is discussed with reference to Frame A, while the principles of the method is explained in details in the NZSEE guidelines [24] and applied on a worked example in Del Vecchio et al. [15].

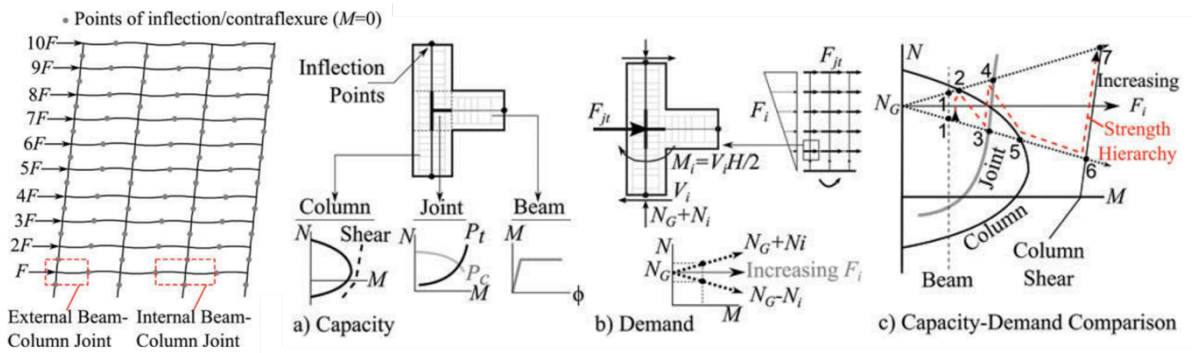


Figure 3: SLaMA application for a frame structure (Pampanin et al., 2002; Tasligedik et al., 2016).

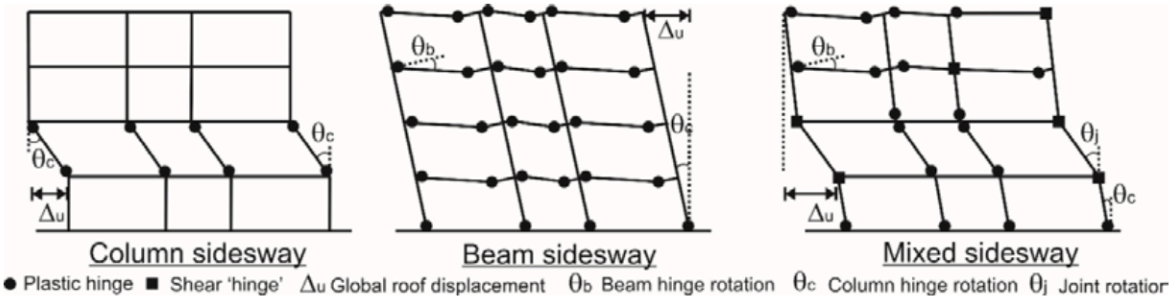


Figure 4: Possible plastic mechanisms (NZSEE 2016).

### 4.2 Results

The lateral resisting systems (LRSs) individuated in Section 3 were analysed using SLaMA, predicting both the capacity curve and the plastic mechanism at the ultimate limit state. It is worth noting that, considering the predicted plastic mechanisms, for all the LRSs the effective height was considered to be two thirds of the total height of the building.

Taking frame A as example, Figure 5 shows the derivation of its plastic mechanism based on the hierarchy of strength of the beam-column-joint subassemblies. The numerical analysis-based mechanism is also shown to avoid duplications, although it is discussed in Section 6. The results show that the predicted plastic mechanism is a beam sway, characterised by beam hinges in all the subassemblies. However, for a significant number of them, as for example joint D1 shown in Figure 5, the beam plastic hinge is predicted after the joint first shear cracking. The next mechanism in the hierarchy, the joint failure, cannot develop because of the limited beam hardening.

Although the first cracking in the joints does not influence the base shear capacity of the frame, it increases its deformability. For this reason, the capacity curve (Figure 6) was computed twice: first characterising the yield displacement considering the beam hinging and then considering the joint deformability at peak strength. The second curve is considered for the comparison in Section 6, since it is deemed to yield a more conservative estimation of the lateral capacity.

The capacity curve for the other analysed lateral resisting systems is shown in Figure 10 (in Section 6) in the context of the comparison with the numerical analyses results.

## 5 NUMERICAL ANALYSES AND NUMERICAL-ANALYTICAL COMPARISONS

### 5.1 Numerical modelling assumptions

A 2D numerical model was developed using the FEM software Ruaumoko [12] for each lateral resisting system. A displacement-control Pushover was carried out imposing a linear lateral force profile and neglecting P-delta effects. Figure 7 summarises the modelling assumptions and the nonlinear behaviour of structural components. A lumped plasticity approach was adopted using a Giberson one-component model for the frame elements [16] that concentrates the members nonlinearities at the end sections of beams and columns. Several studies ([7], [8], [9]) highlighted the importance of modelling the non-linear behaviour of poorly-detailed beam-column joints. For this reason, in this study they were modelled by means of rotational springs connecting the beam and column elements that converge in one node. The characterisation of the nonlinearities was based on the geometry, material and reinforcement details of the members reported in the original drawings.

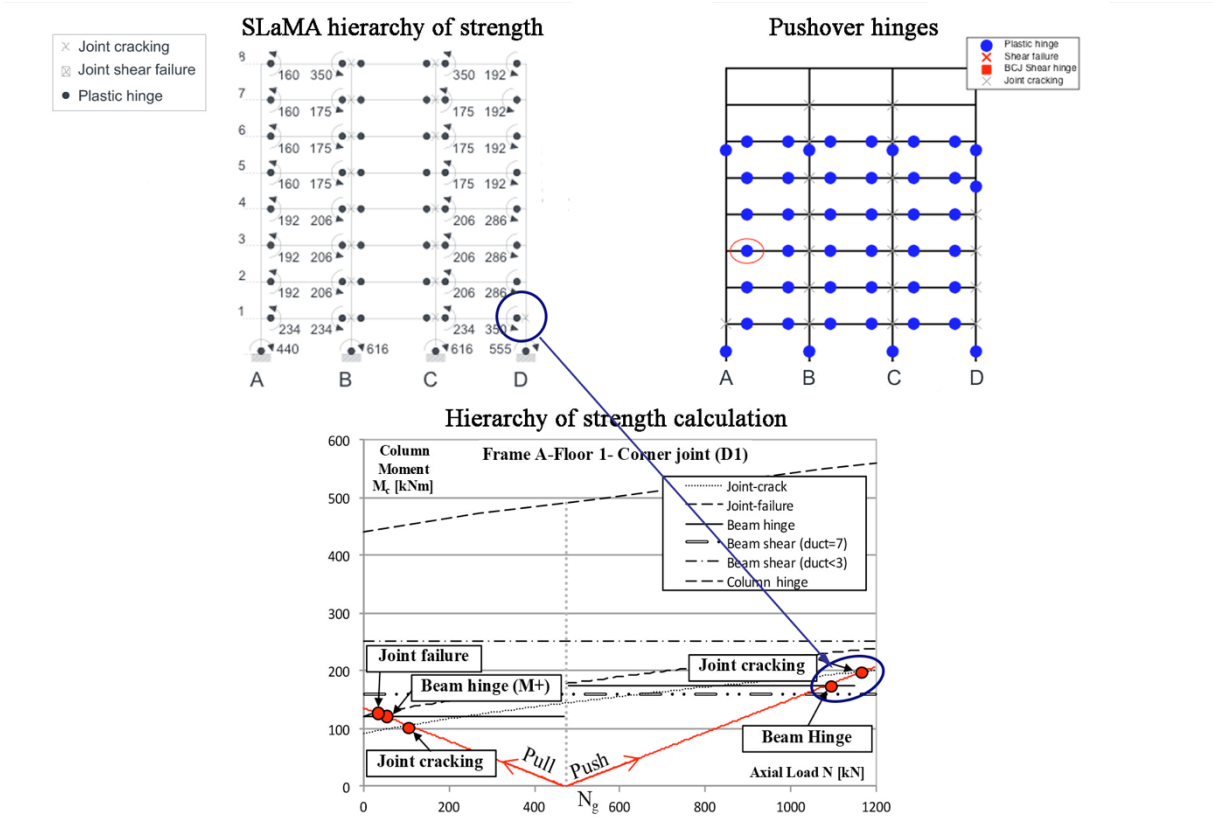


Figure 5: Plastic mechanism for frame A predicted through SLaMA and numerical pushover. On the bottom: hierarchy of strength of joint D1.

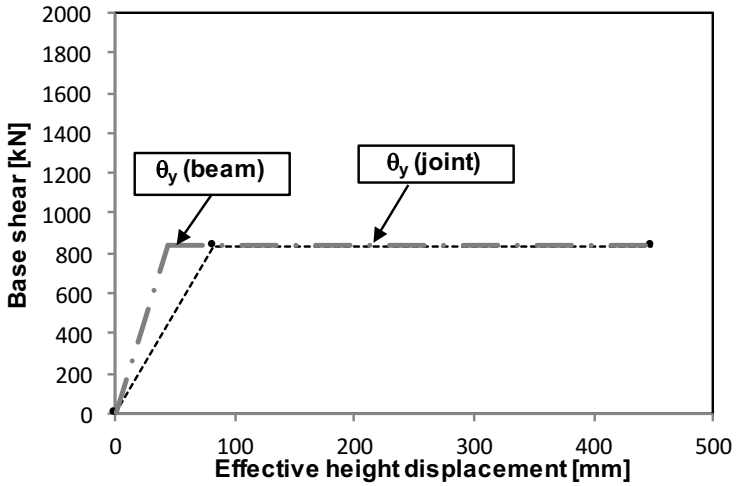


Figure 6: SLaMA capacity curve for Frame A.

In particular, the beams nonlinear behaviour was characterised basing on the equivalent plastic hinge length [17] and a bi-linear representation of the Moment-Curvature relationship calculated using the software CUMBIA [18] considering refined stress-strain relationships for concrete [19] and steel [20]. The approach proposed by Berry et al., 2005 [21] was used to check the buckling of the longitudinal bars. Finally, the shear degradation curve proposed by Kowalski and Priestley 2000 [22] was used to assess the possible shear failure limiting the drift capacity.

For columns, the same approach of beams was adopted, but in order to account for the influence of axial load on the moment capacity at different step of the analysis, the moment-axial

load interaction diagram was used. A similar approach was adopted for walls, for which the shear degradation curve proposed by Krolicki et al., 2011 [23] was adopted. Finally, the joints capacity was calibrated basing on a principal stress approach that allows to define the strength of the joint panel at the first cracking and at a severe damage limit state in terms of equivalent moment in the column (more details on the method are given in Pampanin et al., 2003 [8], together with the adopted deformation limit states). The joints rotational springs are hence modelled by means of equivalent column moment – axial load interaction diagram, which allows to capture the variation of strength with the axial load on the joint panel, defined for first cracking and severe damage limit states.

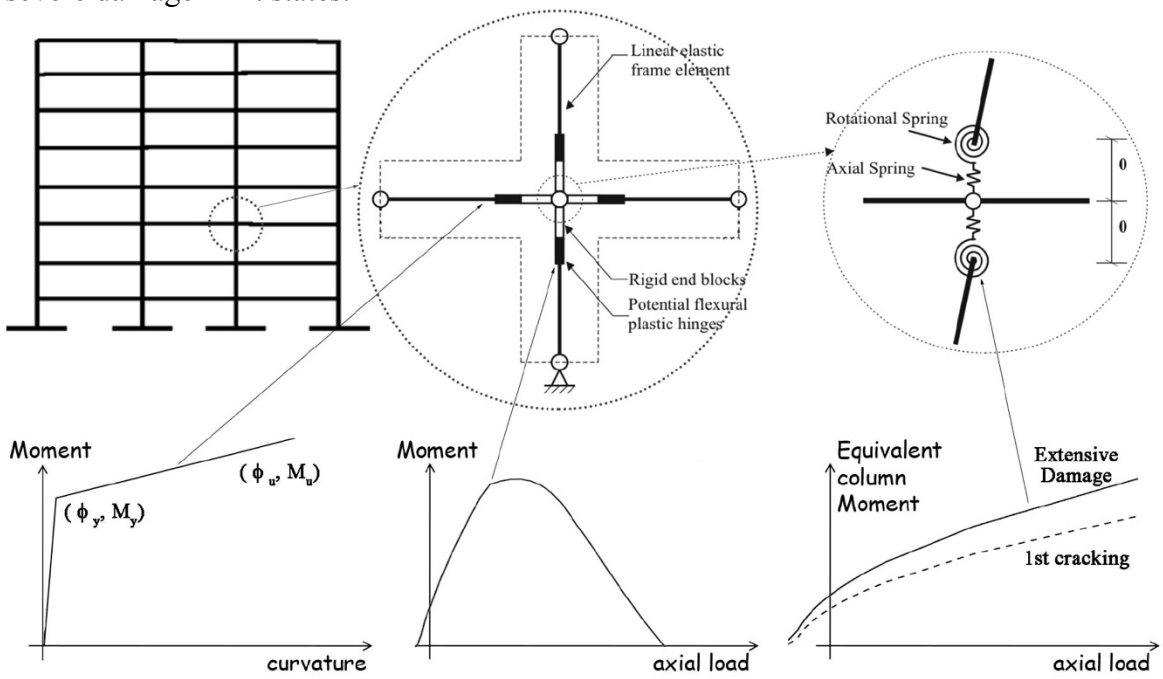


Figure 7: Numerical modelling assumptions and characterisation of the structural members.

## 5.2 Results

The capacity curves resulting from the pushover analyses, shown in Figure 8, are expressed in terms of base shear versus displacement at the effective height of the structural system (the adopted values for the effective height are discussed in Section 4.2) in order to represent the behaviour of an equivalent SDOF system. The ultimate point of the curves represents the step of the analyses in which the first member in the structural system reached its deformation capacity. A more detailed discussion on the numerical capacity curves is given in Section 6, in the context of the comparison with SLaMA. A snapshot of the formed hinges at the ultimate point is given in Figure 9, in which the members ductility demand is indicated and the member causing the ultimate limit state is highlighted with a circle. For the two frames, this indicates that the non-linear behaviour of the members is triggered up to the 6$^{th}$ level, avoiding the formation of a global mechanism and not allowing for the full redistribution of the internal actions. This phenomenon is detrimental for the base shear capacity of the two systems. Frame 1 plastic mechanism is characterised by a combination of beam hinges and shear failure in the joints (Mixed Sidesway) while mainly beam hinges form in frame A (Beam Sidesway). A Mixed Sidesway mechanism with full redistribution forms in the dual system while the flange of the C-wall is characterised by a flexural failure at the base level.

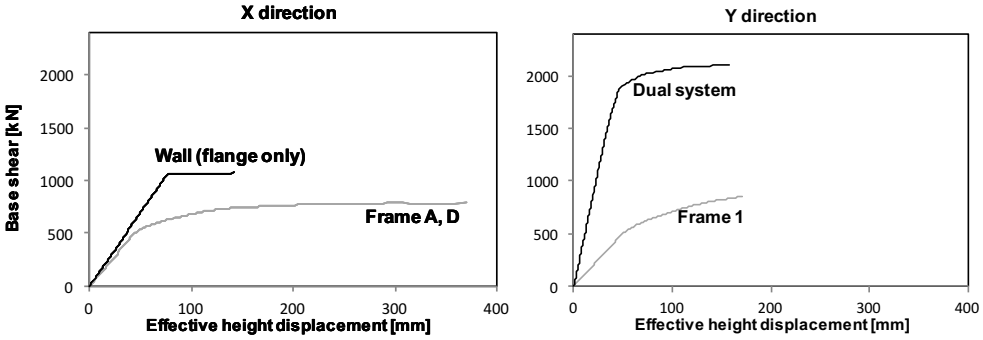


Figure 8: Pushover analyses results.

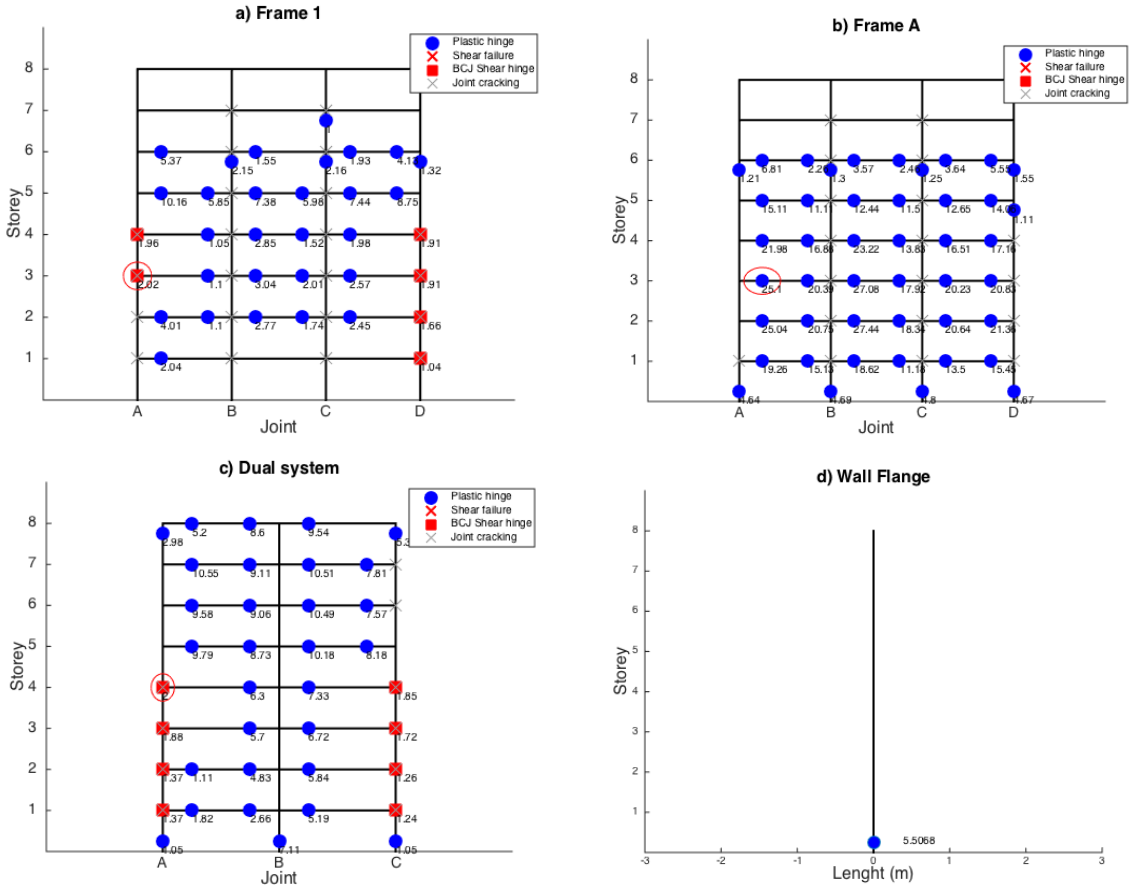


Figure 9: Plastic mechanism at ultimate limit state.

## 6 COMPARISON WITH SLaMA

For each lateral resisting systems (LRSs) individuated in Section 3, the SLaMA results are here compared with the ones of the numerical pushover analyses. The first fundamental comparison to make is based on the ability, in SLaMA, to properly capture the hierarchy of strength and, by extension, the plastic mechanism (with some degree of error). Figure 5 shows the comparison, only for frame A for brevity, of the plastic mechanism predicted with SLaMA (or, more precisely, the summary of the hierarchy of strength calculations) and the plastic mechanism extracted from the numerical analysis. As anticipated, there is high accuracy on the prediction of the hierarchy of strength in each subassembly. As an example, for the external joint D1 (indicated in Figure 5) the beam plastic hinge is predicted after the joint first shear cracking. This sequence replicates very well what is predicted in the numerical model. However, the numerical analysis indicates that the reaching of the drift capacity in the external beam at the 3$^{rd}$ floor

(highlighted in a red circle) does not allow a full redistribution of the internal actions in the frame and hence there is some discrepancy between the result of SLaMA and the numerical model in terms of plastic mechanism. This discrepancy also leads to an over estimation of the base shear capacity, with respect to the numerical analysis. This is reflected in the comparison of the SLaMA curve with the numerical one (see Figure 10.b).

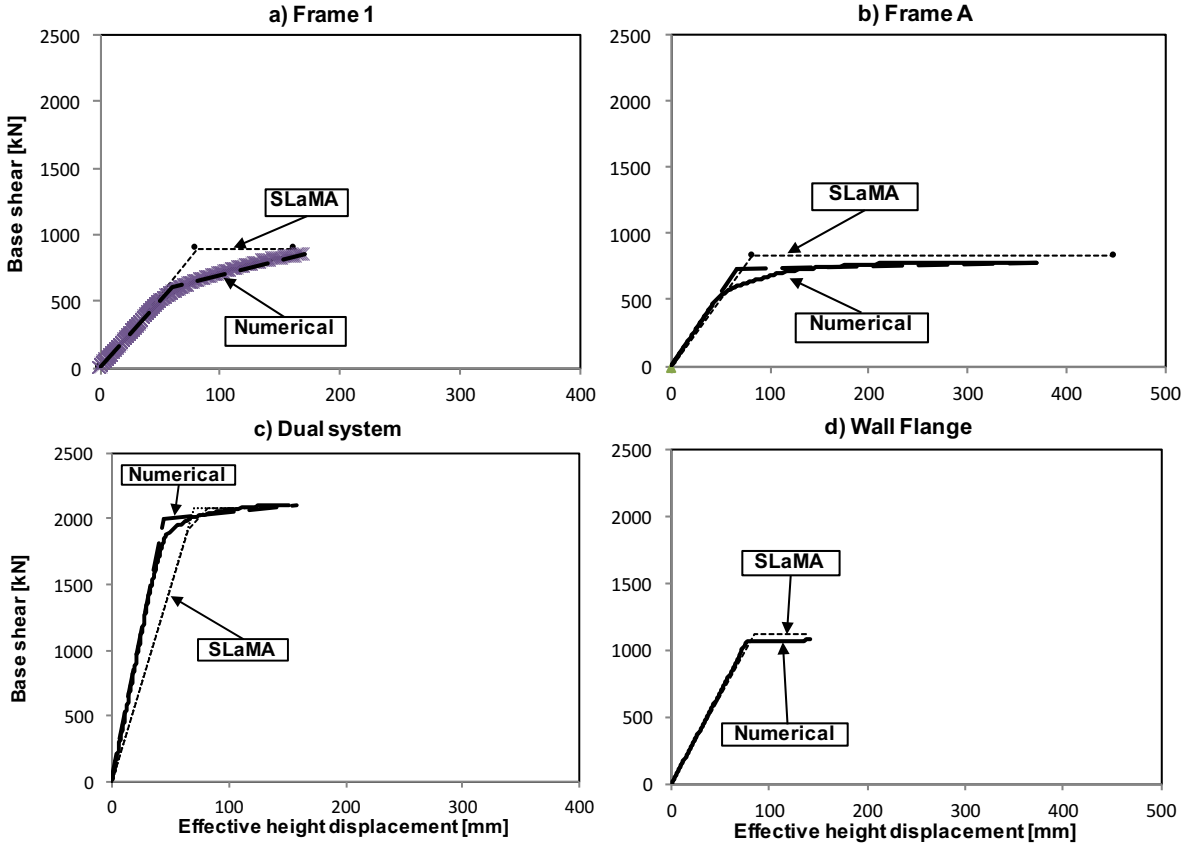


Figure 10: SLaMA vs Numerical capacity curve comparison for Frame 1, Frame A, dual system and wall.

The SLaMA-to-numerical comparison of the capacity curves is shown for all the selected lateral resisting systems in Table 1 and Figure 10, in which the bi-linear representation for the numerical curves is obtained according to ATC 1996 [26]. Satisfactory agreement is observed between the SLaMA and the numerical curves in terms of initial stiffness and ultimate strength and displacement. The main discrepancy is observed immediately after the first yielding (formation of the 1st plastic hinge). This is attributed to the approximation, in SLaMA, for which all the structural members reach the yielding for the same structure displacement. The over prediction on the ultimate base shear is caused by the assumption for which the internal actions are fully redistributed, which is not always observed in the numerical models (see Figure 9).

In terms of quantitative SLaMA-numerical comparison (given in Table 1), it is deemed that the most important parameters to consider are the ultimate displacement and the maximum base shear. In fact, these are directly affecting the seismic performance of the structure in the Acceleration-Displacement Response Spectrum (ADRS), in the context of the DDBA. Table 1 indicates that the ultimate base shear is often over predicted by SLaMA with respect to the numerical analysis, even though the maximum error is 6%. The only exception is the dual system, for which the comparison leads to almost no error. The base shear over prediction is to be attributed to the full actions redistribution hypothesis in SLaMA (see Section 4.1 and Figure 5). For what concerns the ultimate displacement, it is noted that, in this specific case, when this is

caused by a joint (frame 1, dual system) the result is an under prediction, while when it is caused by a beam (frame A) the result is an over-prediction. This interpretation is also based on a much greater number of case studies not published yet. Since in SLaMA the yielding point base shear is assumed to be equal to the ultimate one, there is always an over-prediction for this parameter. The error is smaller for walls and dual systems, for which the wall strongly governs the behaviour. Finally, the SLaMA-numerical comparison on the yield displacement is reported for completeness but not commented because of its different definition in SLaMA and in the bi-linear numerical pushover curve.

| LRS | ERR($d_y$) [%] | ERR($V_{by}$) [%] | ERR($d_u$) [%] | ERR($V_{bu}$) [%] |
|---|---|---|---|---|
| Frame 1 | 24.6 | 31.2 | -5.0 | 2.2 |
| Frame A | -30.7 | 18.9 | 21.0 | 6.2 |
| Dual System | 58.5 | 4.4 | -16.6 | -0.7 |
| Wall flange | 10.4 | 5.8 | -4.0 | 4.0 |

Table 1: SLaMA vs numerical discrepancy for all lateral resisting systems.

## 7 CONCLUSIONS

Four bi-dimensional lateral resisting systems of different typology (frame, cantilever wall, frame-wall dual system) were extracted from a real RC 8-storey building. Their lateral capacity, in terms of non-linear static capacity curve and plastic mechanism, was assessed by means of "by-hand" analytical predictions obtained with the Simple Lateral Mechanism Analysis (SLaMA). The results were compared with refined numerical models. The comparisons show that SLaMA is capable of reproducing the local interaction (actual hierarchy of strength) between the structural members. Moreover, the method allows to have an acceptable estimation of the plastic mechanism of the structure at the ultimate limit state (ULS) and of the lateral capacity curve. In fact, the match between the SLaMA and the numerical pushover analyses is satisfactory with a maximum discrepancy of about the 6% for the ULS base shear and 21% on the ULS displacement, for the cases analysed in this paper. It is worth mentioning that the qualitative trends outlined in this study are representative of different structural typologies and mechanisms. Nevertheless, further applications are needed to better quantify the limits of the SLaMA method and the range of the expected errors.

SLaMA is a useful tool to characterize any local/global failure mechanism characterizing the structural system which cannot be easily identified by using commercial software. The method can be employed to check the accuracy of the numerical models and to identify the main sources of errors. This allows to maintain a continuous control on the modelling procedure, improving the user confidence in the seismic assessment of the structural system. Furthermore, SLaMA allows to clearly identify the main structural weaknesses and to design proper retrofit solutions.

## ACKNOLEDGEMENTS

This study was partially funded by the Italian Department of Civil Protection, in the framework of PE 2014－2018 joint program DPC-ReLUIS, Task RS4: "Post-earthquake analysis: usability, damages, seismic design of repair and strengthening interventions" and by the "SAFER Concrete Technology" project, funded by the New Zealand Natural Hazard Research Platform (NHRP).

## REFERENCES


[1] Uva G., Sanjust C. A., Casolo S., Mezzina M., ANTAEUS project for the regional vulnerability assessment of the current building stock in historical centers. International *Journal of Architectural Heritage*, **10**(1), 20-43, 2016.

[2] Uva G., Porco F., Fiore A., Mezzina M., The assessment of structural concretes during construction phases. *Structural Survey*, **32**(3), 189-208, 2014. doi:10.1108/SS-06-2013-0023.

[3] Porco F., Uva G., Fiore A., Mezzina M., Assessment of concrete degradation in existing structures: a practical procedure. *Structural Engineering and Mechanics*, **52**(4), 701-721, 2014.

[4] Porco F., Porco G., Uva G., Sangirardi M., Experimental characterization of "non- engineered" masonry systems in a highly seismic prone area. *Construction and Building Materials*, **48**, 406-416, 2013.

[5] Fiore A., Porco F., Uva G., Effects of the yield and ultimate strengths of the equivalent strut models on the response of existing buildings with infill panels. *International Journal of Structural Engineering*, **6(2)**, 140-157, 2015.

[6] Porco F., Fiore A., Casolo S., Comparison between seismic retrofitting solutions for existing reinforced concrete buildings: a case study. *International Journal of Structural Engineering*, **5**(3), 242-261, 2014.

[7] Calvi GM, Magenes G, Pampanin S.: Relevance of beam-column joint damage and collapse in RC frame assessment. *Journal of Earthquake Engineering*, **6 (Special Issue 1)**, 75–100, 2002.

[8] Pampanin S, Magenes G, Carr A. Modelling of Shear Hinge Mechanism in Poorly Detailed RC Beam-Column Joints. In *fib Symposium "Concrete Str. in Seism. Reg.", May 2003. Paper n. 171.*

[9] Del Vecchio C, Di Ludovico M, Prota A, Manfredi G, Modelling beam-column joints and FRP strengthening in the seismic performance assessment of RC existing frames, *Composite Structures,* **142**, 107-116, 2016.

[10] Del Vecchio C, Di Ludovico M, Balsamo A, Prota A, Manfredi G, Dolce M.: Experimental investigation of exterior RC beam-column joints retrofitted with FRP systems. *ASCE Journal of Composites for Constructions*, **18(4)**, 1–13, 2014.

[11] New Zealand Society for Earthquake Engineering, The seismic assessment of existing buildings – Technical guidelines for engineering assessments. Revised draft, 10 October 2016.

[12] Carr, A.J. "Ruaumoko Program for Inelastic Dynamic Analysis – Users Manual", Carr Research Ltd., Christchurch, New Zealand, 2009.

[13] Pampanin, S., Kam, W.Y., Akguzel, U., Tasligedik, A.S., Quintana-Gallo, P., Seismic Performance of Reinforced Concrete Buildings in the Christchurch Central Business District: Part I – overview. *Natural Hazard Platform Recovery Project report*. 2012a.

[14] Pampanin, S., Kam, W.Y., Akguzel, U., Tasligedik, A.S., Quintana-Gallo, P., Seismic Performance of Reinforced Concrete Buildings in the Christchurch Central Business District: Part II – damage report. *Natural Hazard Platform Recovery Project report*. 2012b.

[15] Del Vecchio, C., Gentile, R., Pampanin, S., The Simple Lateral Mechanism Analysis (SLaMA) for the seismic performance assessment of a case study building damaged in the 2011 Christchurch earthquake. *University of Canterbury technical report*, New Zealand, 2017.

[16] Sharpe, R.D. The Seismic Response of Inelastic Structures. *Ph.D. Thesis*, Department of Civil Engineering, University of Canterbury, 1974.

[17] Priesley M.J.N., Calvi G.M., Kowalsky, M.J. *Displacement-Based Seismic Design of Structures*, IUSS Press, Pavia, Italy, 2007.

[18] Montejo, L., Kowalsky, M.J., Cumbia – set of codes for the analysis of concrete members, theory and user guide. *North Carolina state university technical report*. 2007.

[19] Mander, J.B., Priestley, M.J.N., Park, R., Theoretical stress strain model for confined concrete. *Journal of Structural Engineering,* **114**, 1804 – 1826, 1988.

[20] King, D.J., Priestley, M.J.N., Park., R., Computer programs for concrete column design. *University of Canterbury technical report*, New Zealand, 1986.

[21] Berry, P.B., Eberhard, M.O. Practical performance model for bar buckling. *ASCE Journal of structural engineering,* **131(7)**, 2005.

[22] Kowalsky, M.J., Priestley, M.J.N. Improved analytical model for shear strength of circular reinforced concrete columns in seismic regions. *ACI structural journal*, **97(3)**, 2000.

[23] Krolicki, J., Maffei, J. and Calvi, G.M. Shear Strength of Reinforced Concrete Walls Subjected to Cyclic Loading. *Journal of Earthquake Engineering*, **15(1)**, 30-71, 2011.

[24] New Zealand Society for Earthquake Engineering, Assessment and Improvement of the Structural Performance of Buildings in Earthquakes, New Zealand, 2006.

[25] Tasligedik, A.S., Agkuzel, U., Kam, W.Y., Pampanin, S., Strength Hierarchy at Reinforced Concrete Beam-Column Joints and Global Capacity. *Journal of Earthquake Engineering,* **0**, 1 – 34, 2016.

[26] Applied Technology Council (ATC), Seismic evaluation and retrofit of concrete buildings – Volume 1. Report SSC 96-01, 1996.

COMPDYN 2017
6th ECCOMAS Thematic Conference on
Computational Methods in Structural Dynamics and Earthquake Engineering
M. Papadrakakis, M. Fragiadakis (eds.)
Rhodes Island, Greece, 15–17 June 2017

# NOVEL MODELS AND TOOLS TO EVALUATE THE ECONOMIC FEASIBILITY OF RETROFITTING INTERVENTION

**M. Vona[1], M. Mastroberti[1], B. Manganelli[1]**

[1] School of Engineering – University of Basilicata
Potenza, Italy
{ marco.vona, monica.mastroberti, benedetto.manganelli } @unibas.it

**Keywords:** Seismic Performance, Fragility Curve, Repair Cost, Depreciation, Retrofitting Strategies

**Abstract.** *In order to mitigate the seismic risk, politician decision-makers, insurance companies, banks, professional engineers, private owners, (despite operating at different territorial scale and with different aims) need of accurate tools able to highlight the negative economic effects of an earthquake in terms of reduction of building economic value and earning power effective time. In this way, accurate seismic direct economic losses scenarios have a key role. In this paper, a new procedure for probabilistic, analytical seismic direct economic losses scenarios has been discussed and applied. Economic fragility curves for different existing building types (RC-MRF) have been defined. The economic feasibility of different form of retrofit interventions strongly depends by the entity of negative seismic damage economic effects, in terms of reduction of building economic value and earning power effective time. In this paper, a first attempt in estimation of building residual economic life after an earthquake has been performed. An innovative tool based on the integration of seismic direct losses models in building life-cycle cost value models has been presented and applied. This tool plays a fundamental role in promotion of a private seismic risk mitigation strategies, highlighted as accurate retrofitting intervention in peacetime could be able to minimize the negative seismic financial effects that is a primary objectives of owners-investors.*

## 1 INTRODUCTION

The high vulnerability of existing buildings is a crucial issue in modern earthquake engineering. This issue plays a fundamental role in seismic risk mitigation strategies and it should be strongly considered in all planning activities. The available studies are generally based on buildings stock and the possible seismic occurrence of earthquakes [1], [2], [3]. The main problem is the strong disproportion between the available public economic resources and the buildings that require retrofitting interventions.

For this reason, the accurate definition and the implementation of effective seismic risk mitigation strategies require a multidisciplinary approach based on new and effective tools. These tools should be based on accurate studies of seismic hazard, vulnerability, and economic consequence of earthquake. Unfortunately, these tools and studies are often remained an academic topics and their application is still largely unrealized [4].

Recently indirect actions able to grow the awareness of seismic risk, seismic vulnerability, and the importance of maintenance operations in the population have been implemented [5]. Actually, tools able to indirectly recall the owners to seismic issues could be identified developed and promoted. A private seismic risk mitigation process, differently to public one, could be moved also by economic-financial convenience criteria.

In this work, new approach to quantify the reduction of economic life due to seismic damage has been described. This approach is based on integration of seismic direct losses scenarios in building life-cycle economic value models. New and effective seismic direct losses scenarios for existing RC-MRF buildings is illustrated. The proposed approach has been also applied and validated.

## 2 METHODOLOGICAL APPROACH

Seismic direct losses scenarios play a key role in seismic risk mitigation. It provides information about the expected economic losses refer to all possible arriving earthquakes [3]. Generally, a seismic economic losses model could be referred to different kind of losses (direct and indirect). The direct losses are the repair costs necessary to restore the buildings pre-earthquake state [1].

In Figure 1, a flow chart illustrative of the built process for losses scenarios is reported. It is based on the convolution between fragility curves and repair cost functions. In next part of the section, several considerations and statements about the definition both of fragility curves and repair cost functions are reported.

The fragility curves are need in order to provide accurate information about the structural performance in a probabilistic way. The probability of exceeding for specific damage levels is evaluated. In several works, the advantages and disadvantages of different FCs built approaches and analyses methods have been discussed [6], [7], [8].

The accuracy of FCs mainly depends on Damage Model (DM) [9]. A Damage Model consisting in different damage levels, which should be characterized by a qualitative description of expected damage, a structural limit state, and a global engineered response parameter threshold. In order to define accurate seismic risk mitigation strategies the damage levels should be able to identify the building seismic safety level during and after the event. Consequently, limit states referred to structural performance of primary structural elements should be employed.

Based on FCs, a seismic direct losses scenario can be defined. It is a probabilistic tool able to provide information on direct economic losses when a given seismic intensity occurs.

Mathematically, a seismic direct losses scenario is computed through a probabilistic convolution operation between fragility curves and repair cost functions, as:

$$E\left[C_{r,r}\middle|I\right]=\sum_{i=1}^{n}E\left[C_{r,r}\middle|dl_{i|I}\right]P\left[DL=dl_i\middle|I\right] \quad (1)$$

Where $E_i\left[C_{r,r}\middle|dl_{i|I}\right]$ is the expected value of the repair cost function for a specific damage level $dl_{i|I}$ and intensity range $I$ . $P\left[DL=dl_i\middle|I\right]$ is the occurrence probability of damage level $dl_{i|I}$ for a specific seismic intensity value I, definable starting from the FCs.

In this work, the main efforts have been made in order to define the repair cost function in the more accurate way.

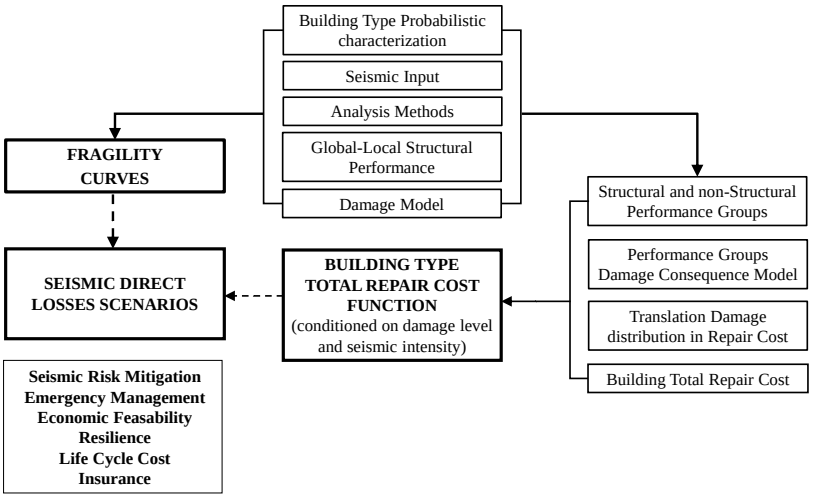


Figure 1. Procedure for analytical Seismic Direct Economic Losses Scenarios.

The strong variability in performance of each building type have been considered by FCs. Then, for same type the difference in damage distributions provides different consequent global repair costs. Repair Cost Functions have been defined for each building type, as different for each damage level and macro-seismic intensity range. For Repair Cost Functions a continue probability density function has been considered in order to be the best fit of discrete empirical frequency distribution of Ratio Cost.

The Ratio Cost ($C_{r,r}$) is the ratio between the total repair cost that are need to restore the pre-earthquake condition and the building replacement cost (including the demolition cost), [6]; it is ranging between 0 and 1.

Damage Consequence Models (DCM) for different performance groups have a key role in definition of building global ratio cost. DCMs are tools able to correlate the seismic damage of each structural and non-structural element to their repairing costs. As performance group, different components of building (such as column-beam, column-slab, shear wall, masonry wall etc.) could be considered. In this way, it is to be highlighted that accuracy of relation seismic damage of each structural and non-structural element to its repairing costs strongly depends on approach used to define FCs (in particular, modeling and analysis methods), as briefly reported in figure 2. Only accurate approach, based on macro-elements models, reliable behavior models, and structural analysis methods allow knowing the real damage state of each structural and non-structural elements.

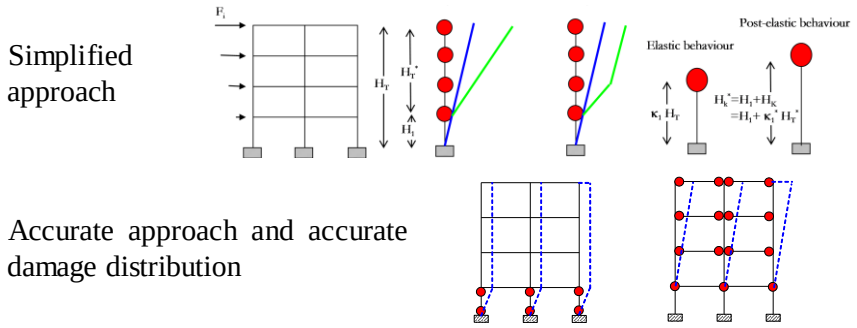


Figure 2. Accuracy of FCs and damage distribution analysis.

Damage states should be defined for each performance groups. Moreover, a relationship between damage states and damage levels of engineering demand parameters should be defined. In addition, detailed repair actions and associated repair costs should be identified for each performance group and damage states. Repair cost must be evaluated including all collateral, preliminary and supplementary works. Finally, for each investigated types total repair cost has been obtained combining the repair costs associating at each structural and structural components through specific DCM.

In order to evaluate the benefit of retrofitting, the building owner should be considered a consumer or production goods depending on the economic agents that require them to conform to the behavior all pattern of the consumer or investor [10]. This issue could be used also to prioritization strategies [11].

For many owners-investors the maintaining of building property economic value and the increasing of building economic life is the best goal. In this way, the interventions (such as extraordinary maintenance, repair, retrofitting, consolidation) must be able to meet also this objective, otherwise the intervention less frequently are realized. Therefore, the assessment the economic feasibility and the economic effects of an intervention are important questions.

In this way, building life cycle economic value model able to describe the temporal trend of building economic value during its lifetime, and provide indications on building economic life has a key role.

The property cost value may be split into two part: building and land cost value. Both vary in time following absolutely different dynamics [12]. The land value due to the land rent, normally, in time does not undergo any depreciation, indeed more readily, it grows. The first building part of deprecation is due to the age that determines a progressive achievement of service life. A second part of depreciation, always connected to physical degradation, is the income decay depreciation. Other forms of depreciations are linked to building obsolescence, that provide a decline in value not directly related to physical deterioration, but resulted from an outdated appearance and increased demands by occupants for a more efficient and controlled facilities. In [12] has been reported a simplified methodology for evaluation of temporal trend of cost value taking into account the deductions linked to the different forms of deprecation. In accordance with this procedure, the building is subdivided in functional elements (or homogeneous parts); for each of them the percentage of cost respect to total reconstruction cost and the depreciation functions must be evaluated.

The economic life concerns with earning power; without topics linked to cultural heritage, a building is often demolished before its physical life expiry to permit a more profitable use of the site, or because it is found cheaper to clear and rebuild rather than to adapt the building to the change requirement. Analytically, the end of building economic life corresponds with the point in which the depreciated building value is equal to zero. The above concepts are considered in this work in order to define the proposal.

## 3 APPLICATION AND RESULTS

In this section, a first application of the proposed approach is reported. Firstly, analytical FCs for several RC-MRF existing building types (Figure 3) have been defined from previous NLDAs numerical results [6] and following the improved approach of [8].

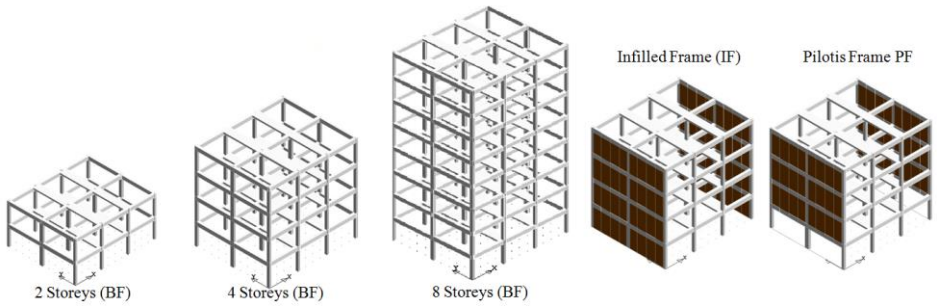


Figure 3. Considered building types: number of storey and infill distributions.

More detailed information about structural, geometrical, and mechanical characteristics of each considered building types and details about NLDAs are reported in [6], [8] and [9]. Fragility curves have been defined considering the Housner intensity.

Consequence Damage Models have been defined using the price list of Abruzzo Region of 2015. Wide set of results of experimental tests and real post-earthquake observations have been used to validate the model.

Damage consequence models for three performance groups have been built: beam-column joint, slab-column joint, masonry infill panel. The ductility ratio has been considered the most relevant parameter for beam-column joint and slab-column joint performance group. However, the interstorey drift ratio for masonry infill panel.

Four damage states have been considered for each performance groups. Each damage state has been characterized by a specific threshold value for the selected engineering response parameter, and a set of repair activities necessary to restore the components to its pre-earthquake state. In these latter were been included all necessary collateral works, such as installation of scaffoldings, installation of shoring to support gravity loads, demolition of partition and furnishing that obstruct the access to RC members that must be repaired, consequent replacement and restoration, technical costs etc. The damage consequent models have been also defined for masonry infill panels.

In Figure 4, for three types considered as example (BF-IF-PF 4 storey Old Code), the FCs and the associated repair cost functions are reported in terms of damage level and macro-seismic intensity grade. In this application, the EMS-98 intensity [14] has been considered as reference intensity. In this way, based on relationship between European macro-seismic scale EMS-98 and Housner intensity ($I_H$) proposed in [3] the equivalence between $I_H$ and EMS-98 has been defined.

A repair cost function coherent with near collapse condition suggested by the Italian and European seismic codes based on ultimate rotation ($3/4\ \theta_u < \theta < \theta_u$) has been defined. Moreover, an un-repairable collapse condition has been considered and a unitary ratio cost has been assigned. The Figure 4 synthetically characterizes the building types (BF-IF-PF 4 storey Old Code) structural fragility and their monetary consequence.

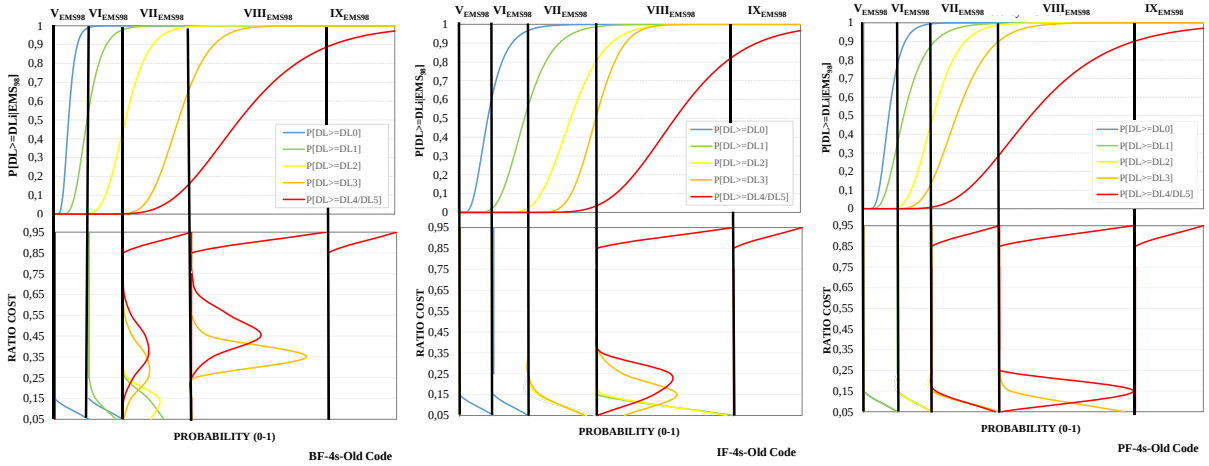


Figure 4. Fragility curves and Repair Cost Functions for RC-MRF Bareframe (BF) – Infillframe (IF) – Pilotisframe (PF) 4 storey - Old Code.

The repair cost functions reported in Figure 4 highlight difference both in mean and in variance value of repair cost for the same damage level (or seismic risk level) and seismic intensity range.

In particular, the BareFrame type is always characterized by mean values of ratio cost greater than those characterize Infilled and Pilotis type. A similar consideration is valid for variance values. These results are coherent with their different deformation capacity. This latter implies a different number of severe damaged non-structural elements and of structural elements at the same or low yield level.

A global relationship interstorey drift ratio – ratio cost has been defined for existing RC-MRF building types taking into account the structural performance variability in a large range of seismic intensity (Figure 5).

The global relation has been defined characterized all considered building types in terms of economic consequence of structural performance (employing the consequence damage models and a simple assembly procedure) and maximum interstorey drift ratio.

The Figure 5 shows a strong correlation between the interstorey drift ratio and ratio cost until infill panel collapse interstorey drift ratio (0.75-1%). The Figure 5 shows a step in interstorey drift ratio – ratio cost relation in correspondence of 0.75-1% interstorey ratio; this latter is due to the contribute of structural damage to ratio cost, that starts to be relevant. In particularly, for the same interstorey drift ratio, BF types ratio cost is greater than IF and PF ones.

Then, overlapping the infill panel collapse interstorey drift ratio, the relation depends by deformation capacity, which influences the entity and distribution of structural damage.

The deformation capacity also influence the occurrence of collapse; PF types have been characterized by unitary ratio cost soon after the collapse of few infill panels, in general at upper of pilotis storey.

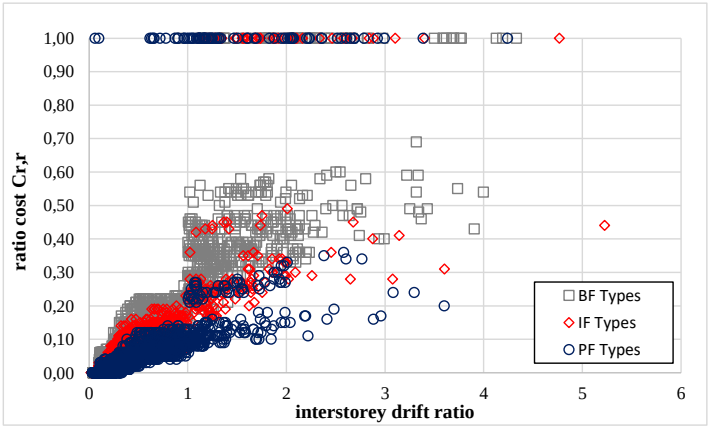


Figure 5. Analytical relationship interstorey drift ratio-ratio cost for existing RC-MRF building types.

The reliability of built consequence damage models and repair cost functions have been validated on the basis of L'Aquila earthquake reconstruction program and its resulting repair costs.

After L'Aquila earthquake (9 April 2009) several Ordinances of the Council Prime Minister [15], [16], have been issued in order to regulate the reconstruction process. In particular, they have established that the financial support of the Italian government to the reconstruction was given and it is managed by private owners. The financial available resource was based on the building usability rate, as defined by in situ inspections [13] and [17]. Assigned the usability rate for each damaged building, professional engineers were engaged by owners; repair and strengthening interventions have been defined and the corresponding costs have been computed. These projects have been the technical support in order to define the funding applications by the owners. These funding applications have allowed to collect a database containing information on 5775 residential buildings of several municipalities and located outside of the historical centre of the L'Aquila.

In order to validate the DCMs and consequent repair cost function the following correspondence between usability rating - damage level has been considered:

- Damage Level 1-2 \ usability rating B and C;
- Damage Level 3\ usability rating E-B (E treaty as B);
- Damage Level 4 \ usability rating E;

In Table 1, the obtained mean and standard deviation repair cost values for BF-IF-PF types 4 storey Old Code have been reported, and compared with those provide by statistics cost of L'Aquila reconstruction process [13] and [17].

| | BF - 4 storey - Old Code | | | | IF - 4 storey - Old Code | | | PF - 4 storey - Old Code | | | L'Aquila reconstruction process (9/4/2009) | |
|---|---|---|---|---|---|---|---|---|---|---|---|---|
| | VI $_{EMS}$ | VII $_{EMS}$ | VIII $_{EMS}$ | IX $_{EMS}$ | VI $_{EMS}$ | VII $_{EMS}$ | VIII $_{EMS}$ | VI $_{EMS}$ | VII $_{EMS}$ | VIII $_{EMS}$ | | |
| **DL1** RC mean (€/sqm) | 146 | 176 | -- | -- | 65 | 97 | 117 | 57 | 89 | -- | **B and C** RC mean (€/sqm) | 174 |
| **DL1** RC dev.st (€/sqm) | 30 | 29 | -- | -- | 34 | 43 | 15 | 26 | 21 | -- | | |
| **DL2** RC mean (€/sqm) | 158 | 184 | -- | -- | -- | 141 | 142 | 103 | 123 | 149 | **B and C** RC dev.st (€/sqm) | 118 |
| **DL2** RC dev.st (€/sqm) | 29 | 28 | -- | -- | -- | 18 | 19 | 21 | 22 | 12 | | |
| **DL3** RC mean (€/sqm) | -- | 221 | 250 | -- | -- | 162 | 195 | 134 | 157 | 198 | **E-B** RC mean (€/sqm) | 270 |
| **DL3** RC dev.st (€/sqm) | -- | 39 | 50 | -- | -- | 33 | 43 | 34 | 29 | 35 | **E-B** RC dev.st (€/sqm) | 141 |
| **DL4** RC mean (€/sqm) | -- | 255 | 321 | 358 | -- | -- | 289 | -- | 222 | 270 | **E** RC mean (€/sqm) | 426 |
| **DL4** RC dev.st (€/sqm) | -- | 55 | 46 | 63 | -- | -- | 52 | -- | 346 | 38 | **E** RC dev.st (€/sqm) | 178 |

Table 1. Comparison between analytical defined (for BF-IF-PF 4 storey Old Code types) and empirical (L'Aquila 9/4/2009 reconstruction process) repair cost (RC) for square meter (mean and standard deviation values).

The comparison highlights a good accordance between the mean value of repair costs (€/sq.m) analytically obtained and those provided by L'Aquila reconstruction process, in particular for Bareframe type. The main differences, especially in standard deviation values, are due to the lack in empirical data of distinction in terms of storey number, age construction, structural types, architectural features and maintenance state. For this reason, the comparison have been also conducted in a global point of view; the repair cost of all analysed building types have been considered without any distinction in terms of typological parameters.

The global comparison has been highlighted as the procedure and tools (DCMs) used in translation of an analytical damage distribution in a global ratio cost provide results similar to empirical ones. Therefore, the defined tools (Damage Consequence models) are able to provide a realistic estimation of expected repair cost based on a simple assignment and assembly methodology. However, the difference could be linked to characteristics of buildings compared, specific buildings conditions influencing the repair costs, such as accessibility, position iteration with others building, maintenance state, which in analytical process have been neglected, and the difference in damage models employed.

Based on a simple convolution between FCs and Repair Costs functions, expected direct economic losses models have been defined for each building types considered. Finally, economic fragility curves have been defined. In Figure 6 the obtained direct economic losses models for BF-IF-PF 4 storey Old Code types have been reported. The Seismic Direct Losses Models provide useful information on the total expected monetary losses resulting of building types structural fragility and taking into account the deformation capacity that influences the repair costs.

The defined Seismic Direct Losses Models have been highlighted as the expected ratio cost seems to be influenced by infill panel effectives and distribution. Bareframe and Pilotisframe types are responsible of similar monetary losses. On one hand the greatest fragility of Pilotis Frame is balanced by a less deformability that required less repair costs; on the other hand the less fragility of BareFrame (than Pilotis) is recovered by a greater deformability and so necessary repair costs. Infillframe type is responsible of lower monetary losses, due to the beneficial role of infill panels that positively influence both the strength and deformation capacity. Finally, the others typological parameters (such storey number, design code, material strength etc.) seem less influence the expected direct economic losses.

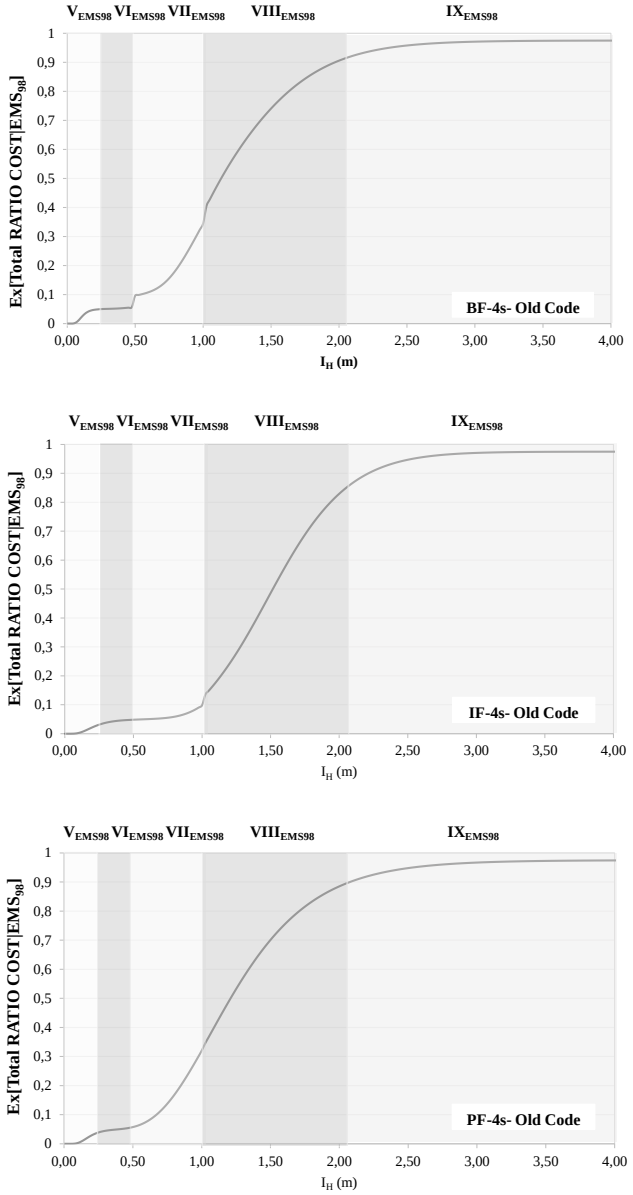


Figure 6. Seismic Direct Losses Models for RC-MRF Bareframe (BF) – Infillframe (IF) – Pilotisframe (PF) Old Code 4 storey.

Finally, in Figure 7, the temporal trends of the depreciated cost value (starting from the construction time), normalized then the total reconstruction cost, also called "life-cycle cost value model" for a residential existing RC building is reported. It is built using the information reported in technical manual of Italian building type costs. The two temporal trend have been defined assuming respectively the absence of extraordinary maintenance operations (black line) and occasional maintenance operations regarding few functional elements (grey line). The life-cycle cost value models highlight a building economic life equal to 55 years in absence of maintenances, whereas of 70 years with corrective maintenance operations. Building economic life is the time interval during which the depreciation runs from 0 to 100%.

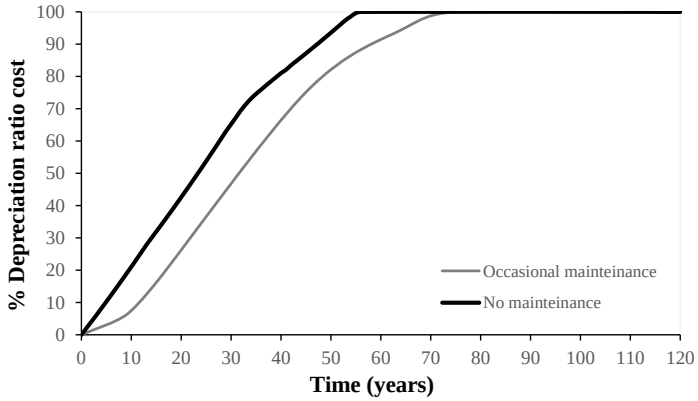


Figure 7. Life-Cycle Cost Value Models of an existing residential RC building considering two different maintenance processes.

The potential effect on residual economic life due to building seismic risk level for life safety performance level has been evaluated.

For example, a building situated in Italian seismic zone characterized by a reference macro-seismic intensity for life safety performance level of VIII ESM98 grade (10% of probability in 50 years), and characterized by vulnerability typical of BareFrame, InfillFrame, PilotisFrame 4 story Old-Code types respectively, has been considered.

In Figure 8, the effects on residual economic life resulting of building seismic risk level have been displayed. Mathematically, the modification of life-cycle cost value model has been obtained adding the expected value of ratio cost (related to VIII ESM98 seismic intensity range of seismic direct economic losses model) at a specific ordinate of building life-cycle cost value model (for example in this case at the sixteen year after the built). In this way, the cycle-life cost value move up of the expected ratio cost (repair cost/reconstruction cost), and the residual economic life proportionally reduces.

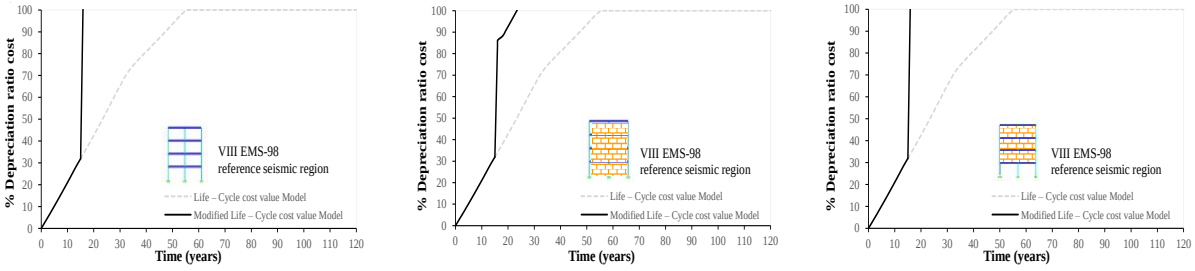


Figure 8. Life – Cycle cost value Model Modified taking into account the monetary losses resulting from seismic risk level for life safety performance level for BF-IF-PF 4 storey Old Code types.

The Figure 8 highlights as the seismic risk level of an existing RC building (BareFrame and PilotisFrame) designed only to gravity load implies an instantaneous and strong reduction of residual economic life after a reference earthquake. However, InfillFrame type highlights a less reduction of residual economic.

These integrated models represent a strong input for owners-investors to found themselves retrofitting interventions in peace-time, avoiding the economic disadvantages due to the reduction-annulment of building economic life as a result of seismic damage, that could be recovered only with high economic investment, in some cases even higher than that required for retrofitting.

## 4 CONCLUSION AND WORK IN PROGRESS

In this paper, a new procedure for definition of Seismic Direct Economic Losses Model has been presented and applied. The Seismic Direct Losses Models have been defined convolving Fragility Curves and Repair Cost Functions.

Novel Repair Cost Functions have been defined based on a translation process of analytical damage distribution in a global ratio cost. In this way have been defined Damage Consequence Models for the main performance groups

The translation process and the Damage Consequence Models have been empirical validated based on data of L'Aquila reconstruction process. Then, the defined DCMs and the simple assignment and assembly methodology are able tools to provide a realistic quantification of economic consequence of structural performance. In this way, the accuracy of structural performance play a key role.

The proposed approach for Seismic Direct Losses Models could be considered an improvement that the classic and convention ones based on expert vulnerability and damage-cost indexes. On the other hand, the novel approach is more easy and practical than those based on elements fragility curves.

In this work, a first attempt of using of Seismic Direct Economic Losses Model in evaluation of economic feasibility of retrofitting intervention on existing RC buildings has been presented. Innovative and strong multidisciplinary models based on integration of Life-Cycle Economic Value Model and Seismic Direct Economic Losses Model have been defined. These latter could be considered as innovative tools able to encourage the single owners-investors to be leader in mitigation process, in order to minimize the negative seismic financial effects that is one of their primary objectives.

In next work, further efforts and developments will be performed in order to obtain a better estimation of effect of seismic risk on building residual economic life.

## REFERENCES

[1] Dolce, M., Kappos, A.J., Masi, A., Penelis, G., and Vona, M. (2006). Vulnerability assessment and earthquake scenarios of the building stock of Potenza (Southern Italy) using the Italian and Greek methodologies. Engineering Structures, 28, 357-371.

[2] Dolce, M. (2009). Mitigation of Seismic Risk in Italy Following the 2002 S. Giuliano Earth-quake. WCCE – ECCE – TCCE Joint Conference Earthquake & Tsunami. Istanbul. Keynote lecture.

[3] Chiauzzi, L., Masi, A., Mucciarelli, M., Vona, M., Pacor, F., Cultrera, G., Gallovič, F., Emolo, A. (2012). Building damage scenarios based on exploitation of Housner intensity derived from finite faults ground motion simulations. Bulletin of Earthquake Engineering, 10(2), 517-545.

[4] Vona, M., Harabaglia, P., and Murgante, B. (2016). Thinking about resilient cities studying Italian earthquakes. Urban Design and Planning, 169 (4). http://dx.doi.org/10.1680/udap.14.00007.

[5] Dolce, M. (2012). *The Italian National Seismic Prevention Program*. 15 WCCE – Conference. Lisbona.

[6] Masi, A. and Vona, M. (2012). Vulnerability assessment of gravity-load designed RC buildings, evaluation of seismic capacity through nonlinear dynamic analyses. Engineering Structures, 45, 257–269.

[7] Borzi, B., Vona, M., Masi, A., Pinho, R., Pola, D. (2013). Seismic demand estimation of RC frame buildings based on simplified and nonlinear dynamic analyses. Earthquakes and Structures 4(2).

[8] Vona, M. (2014). Fragility Curves of Existing RC Buildings Based on Specific Structural Performance Levels, Open Journal of Civil Engineering, 4, 120-134.

[9] Vona, M., Mastroberti, M. (2016). A critical review of fragility curves for existing RC buildings. ECCOMAS Congress 2016. *VII European Congress on Computational Methods in Applied Sciences and Engineering.* Crete Island, Greece, 5-10 June, 2016.

[10] Manganelli, B. (2015). Real Estate Investing. *Springer International Publishing Switzerland*. 2015.

[11] Vona, M., Anelli, A., Mastroberti, M., Murgante, B., and Santa-Cruz S. (2017). Prioritization Strategies to reduce the Seismic Risk of the Public and Strategic Buildings. *Disaster Advances*, **10** (4).

[12] Vona, M. and Manganelli, B. (2015). Economic life prediction model of RC buildings based on fragility curves. *Lecture Notes in Computer Science* (including subseries Lecture Notes in Artificial Intelligence and Lecture Notes in Bioinformatics), 9157, pp771-781.

[13] Di Ludovico, M., Prota, A., Claudio, M., Manfredi, G., Dolce, M. (2016). Reconstruction process of damaged residential buildings outside historical centers after the L'Aquila earthquake: part I – "light damage" reconstruction. *Bulletin Earthquake Engineering*. DOI 10.10007/s10518-01-9877-8.

[14] Grunthal, G. (editor). European Macroseismic Scale 1998 (EMS-98). European Seismological Commission, sub commission on Engineering Seismology, working Group Macroseismic Scales. Conseil de l'Europe, *Cahiers du Centre Europeen de Geodynamique et de Seismologie*, vol. 15. Luxembourg; 1998.

[15] Ordinanza 09/07/2009 n. 3790 (Gazzetta ufficiale 20/07/2009 n. 166) Presidenza del Consiglio dei Ministri, Dipartimento della Protezione Civile - Ulteriori interventi urgenti diretti a fronteggiare gli eventi sismici verificatisi nella regione Abruzzo il giorno 6 aprile 2009 e altre disposizioni urgenti di protezione civile.

[16] Ordinanza 6/06/2009 n. 3779 (Gazzetta Ufficiale n. 132 del 10 giugno 2009). Presidenza del Consiglio dei Ministri, Dipartimento della Protezione Civile - Ulteriori interventi urgenti diretti a fronteggiare gli eventi sismici verificatisi nella regione Abruzzo il giorno 6 aprile 2009 e altre disposizioni urgenti di protezione civile.

[17] De Martino, G., Di Ludovico, M., Prota, A., Moroni, C., Manfredi, G., Dolce, M. (2017) Empirical damage and actual repair costs on RC private buildings after L'Aquila earthquake. 16th World Conference on Earthquake Engineering, 16 WCEE 2017, Santiago Chile, 9-13 Jenuary 2017. Paper n. 3757.

COMPDYN 2017
6th ECCOMAS Thematic Conference on
Computational Methods in Structural Dynamics and Earthquake Engineering
M. Papadrakakis, M. Fragiadakis (eds.)
Rhodes Island, Greece, 15–17 June 2017

# NEW SEISMIC RISK INDEX FOR EXISTING BUILDINGS

**M. Mastroberti[1], M. Vona[1]**

[1] School of Engineering – University of Basilicata
Potenza, Italy
{monica.mastroberti, marco.vona}@unibas.it

**Keywords:** Seismic Risk Mitigation; Existing RC buildings; Fragility Curves; Structural Performance; Seismic Risk Index.

**Abstract.** *The assessment of the seismic vulnerability of existing buildings (in particular for public or strategic) is frequently based on strongly simplified methods than those used for new or retrofitting design at least for the first evaluation. In particular, the seismic performances are often summarized by simple and poor indexes, incorrectly called seismic risk indexes. For example, the seismic risk index provided from several standard code or guidelines for practice are based on simplified and deterministic procedure. Moreover, the evaluation of the reference seismic intensity is generally based on simplified model. In this work, these limitations are highlighted and overcame. A new and probabilistic approach to define a more accurate Seismic Risk Index (SRI) for existing building is proposed. The novel SRI is based on reliable and analytical Fragility Curves.*

## 1 INTRODUCTION

In last years, the priority ranking for the retrofit of existing buildings has become a key issue in the mitigation of seismic risk [1]. The ranking lists are generally based on seismic risk of the buildings, which is defined based on several analysis methods and procedures.

The seismic risk index (SRI) can be considered as the most important parameter in planning of seismic risk mitigation strategies and in prioritization of retrofitting interventions [2], [3], [4]. Moreover, the SRIs are also useful tools for monitoring the changes in seismic risk through time and space [5].

The SRIs should be able to investigate and summarize the building safety level. Nevertheless, they are needed in order to investigate about the economic impact of the existing buildings vulnerability.

Unfortunately, there is not a standard method and definition of seismic risk indexes. Consequently, the significant differences could be lead to significant discrepancies in term of seismic risk strategies. The SRI is affected from a high number of factors, such as simple procedure providing inappropriate results.

The SRI should be defined starting from one or more goals, which are generally called Rehabilitation Objectives (RO), for example [6]. RO is based on a Target Performance Level and a Seismic Hazard Level. The Target Performance Level (PL) must be defined in terms of safety of the buildings and their occupants during and after the event.

In the last years, several studies have been carried out and different approaches have been proposed and reported in guidelines, standards, and codes. These last applications have been defined in order to provide better and simple procedure for practice engineers and decision makers in order to reduce the seismic risk of the communities.

In this work, the new procedure to define the Seismic Risk Index for existing buildings is defined. New SRI definition has been applied to existing reinforced concrete with moment resisting frames (RC-MRF) building types.

On the first, several existing approaches have been reported and described in order to investigate the main existing procedures to SRI evaluation. Different safety assessment procedures and SRI definitions are reported in very much guidelines and codes in other part of the world. In Table 1, only some approaches have been reported, those are considered the most interesting in order to comparison with the new proposal.

The first definition has been widely used in the past years in order to define the prioritization for public or strategic Italian buildings [2], [3]. The second can be considered as the actual evolution of the first and it is defined Italian and European codes in force.

The classic SRI is based on the simple comparison (as ratio) between the building capacity and demand, where the building capacity is expressed in a deterministic way. In this ratio, the comparison between capacity and demand is expressed in terms of seismic intensity parameters.

The seismic capacity of the existing buildings is expressed in terms of seismic intensity that marks out the achievement of Performance Level. However, the demand level is defined as the seismic intensity threshold compatible with the hazard level accepted for each performance level.

The above SRI must be used according to a deterministic or semi probabilistic structural behavior assessment procedures. This approach is coherent with knowledge factor defined in the Italian and European codes [9], [10].

Then, the classic seismic risk index measures the level of non-compliance to PL requirement (different between capacity and demand).

Consequently, in some cases the SRI values could be not representative of real building seismic safety state. In fact, in most cases the factors considered in the deterministic approach could be no able to take into account the uncertain and variability of real seismic behavior of the existing buildings, and could be representative of a singular and low probable failure behavior.

It to be highlight that in more recent Italian regulations [7], [8], SRI is based on the same concept. It used for distribution of economic funding for seismic risk mitigation and post event reconstruction.

| Code or Guidelines | SEISMIC RISK INDEX |
|---|---|
| O.P.C.M. 3274/2003 and subsequent guidelines | $\alpha_{LSi} = \frac{PGA_{PLi}}{PGA_{PLi\|HL}}$<br>$PGA_{LSi}$= seismic intensity that marks out the achievement of Performance Level ($PL_i$) compliance criteria.<br>$PGA_{LSi}$= maximum seismic intensity threshold in accordance with the Hazard Level associated to PL. |
| NTC08<br>EC8 | $\alpha_{LSi} = min\left\{\frac{\theta_{PLi}}{\max(\theta_{PLi\|HI})}, \frac{Vr_{PLi}}{max(V_{PLi\|HI})}\right\}$<br>$\max(\theta_{PLi\|HI})$ = maximum deformation of ductile elements achieved under a seismic intensity compatible with the Hazard Level associated to PL.<br>$\theta_{PLi}$= limit deformation for ductile elements required by Performance Level ($PL_i$).<br>$\max(V_{PLi\|HI})$ = maximum force of brittle elements achieved under a seismic intensity compatible with the Hazard Level associated to PL.<br>$V_{rPLi}$= limit force for brittle elements required by Performance Level ($PL_i$). |

Table 1: Seismic Risk Index definitions.

An improvement in seismic risk evaluation should be obtained dealing the performance assessment problem in a probabilistic way; the uncertainties are directly considered. In this way, it is to be highlighted that the classic expressions of SRI definitions are unsuitable to synthetically handle the results of probabilistic assessment procedure, and then a new definition should be defined.

## 2 METHODOLOGY

New Seismic Risk Index is integrated in a probabilistic performance assessment procedure, which directly take into account all the uncertainty sources in building behavior. The new SRI quantifies the level of seismic risk in terms of probability that the building capacity no fulfill the demand required by each limit state. This is the main difference with the existing considered approach. In fact, the new SRI is based on Fragility Curves and accurate characterization of Hazard Level required for each PL.

The Fragility Curves (FCs) approaches allow a complete probabilistic characterization of building performances. However, the seismic intensity corresponding to the Hazard Level assigned at each PL allows identifying the range or the ordinate of FC to consider; taking into account that each performance criteria must be verified for given reference intensity.

In Figure 1, the amounts involved in new Seismic Risk Index definition in reference a generic Performance Level are highlighted.

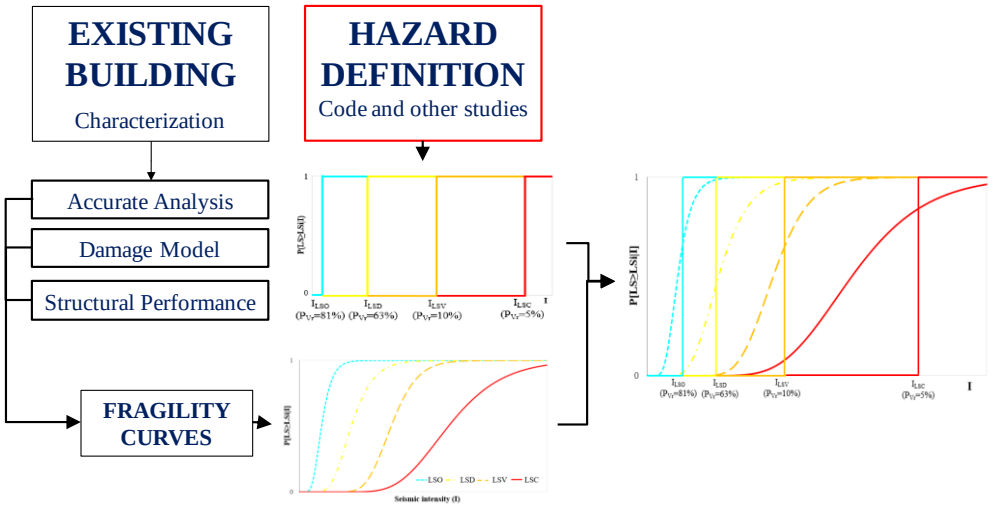


Figure 1. Framework to Seismic Risk Index definition.

New SRI definition is the follow:

$$\mathrm{SRI_{PLi}} = 1 - \frac{\int_{\mathrm{I_{PLi,i}}}^{\mathrm{I_{PLi,f}}} \mathrm{P[PL \geq PLi|I]dI}}{\int_{\mathrm{I_{PLi,i}}}^{\mathrm{I_{PLi,f}}} \mathrm{dI}} \tag{1}$$

In discrete way, the SRI become:

$$SRI_{PLi} = 1 - \frac{\sum_{I_{PLi,i}}^{I_{PLi,f}} P[PL \geq PLi|I]\Delta I}{\sum_{I_{PLi,i}}^{I_{PLi,f}} \Delta I} \tag{2}$$

SRI is equal or near to 1.0, if the considered building shows a good performances (or no achieves or exceeds the PL). For SRI less than 1.0, the considered building achieves or exceeds the PL requirements. The reliability of the new SRI strongly depends from accuracy of building fragility curves and hazard level characterization. In figure 2, a graphic representation of the formal definition of new SRI is reported.

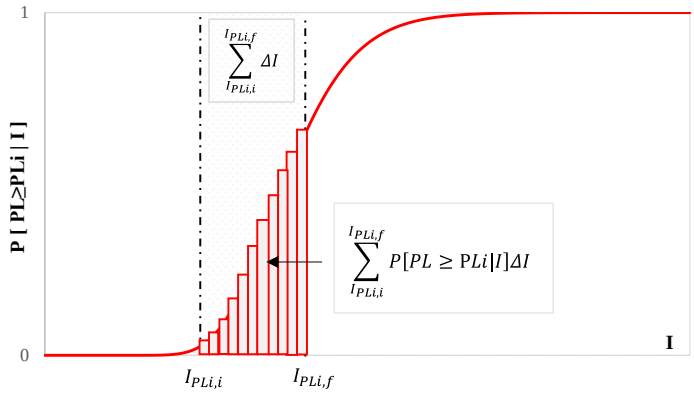


Figure 2: Graphic representation of new seismic risk index definition.

In the next section, a first application of new SRI is reported.

## 2.1 First application to existing RC-MRF buildings

As first application, in this work the proposed SRI definition has been applied to the most Italian and European widespread existing RC-MRF building types [11]. This application would provide a fast and reliable evaluation of the seismic safety level of considered building types with regard to the national Italian territorial scale. The application is based on previous studies [12], [13] and consequent Fragility Curves conditioned to Housener intensity.

On the first, it is to be highlighted that different approaches are available to FCs definition, base on different analysis methods, different damage models, different forms, and different intensity parameters; advantages and disadvantage have been discussed in other studies of the authors in order to define the optimal way [13], [14].

## 2.2 Seismic performance of investigated types

The considered types have been widely characterized in previous study [11]. The building types are low-mid-high rise (2-4-8 storey) and different infill panels distribution have been considered (frames without effective infills, BF; frames with regularly arranged of effective masonry infills IF; frames with effective masonry infills at the ground floor, PF). Based on the design code and construction age, other two different types have been considered. They can be considered as low-engineered buildings, designed with old codes and pre-modern seismic code typical of Southern Europe. The considered building types are briefly reported in Figure 3.

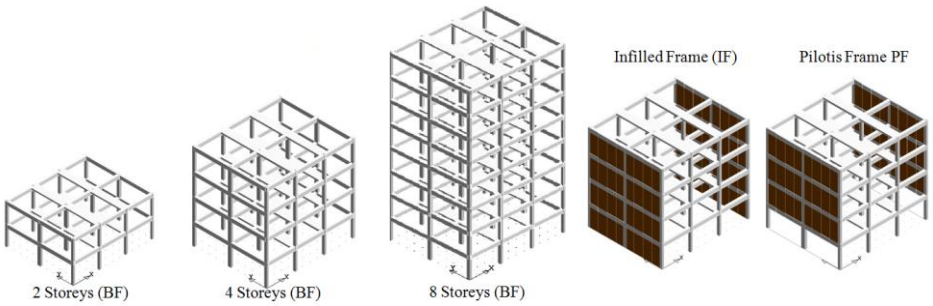


Figure 3. Considered building types: number of storey and infill distributions.

Structural performances have been evaluated using Non Linear Dynamic Analyses (NLDAs). More details about non linear models and analyses are reported in a previous study [11], [15].

The maximum performances have been summarized using global parameters (for example interstory drift ratio) and local ones (maximum, medium ductility ratio of beams and columns). These latter have been interpreted in terms of damage level based on a specific Damage Model [12], [13]. The considered damage levels are linked to four Performance Levels considered by Italian (NTC08) and European (EC8) code: Operatively PL, Light Damage PL, Life Safety PL and Collapse PL.

Each Damage Level (DL) has been characterized by a quantitative description addressed to section yield level of the more critical structural elements. In a synthetic way, the Figure 4 shows the structural elements flexural performance required by each Damage Level considered. Moreover, the Damage Level 0-1, is been linked also to interstorey drift ratio, that strongly influence the non-structural elements damage.

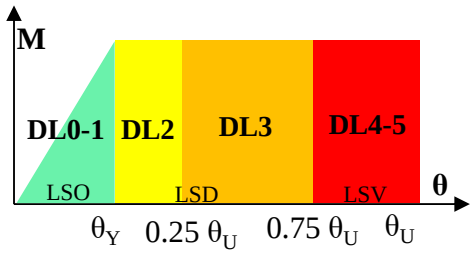


Figure 4: Structural element flexural performance required by each Damage Level.

According with Damage Model and the maximum damage distribution, base on the comparison between the achieved maximum structural performance by each primary structural element and non-structural element and the DL limit requirements, the achieved damage level has been identified.

## 2.3 Italian Life Safety Hazard level

With regard to methodology summarized in framework (Figure 1), seismic intensity range compatible with hazard levels required for each Performance Level have been identified. The Hazard Levels required by Italian seismic code in terms of probability of exceedance in a reference time interval of 50 years for each PL respectively have been considered.

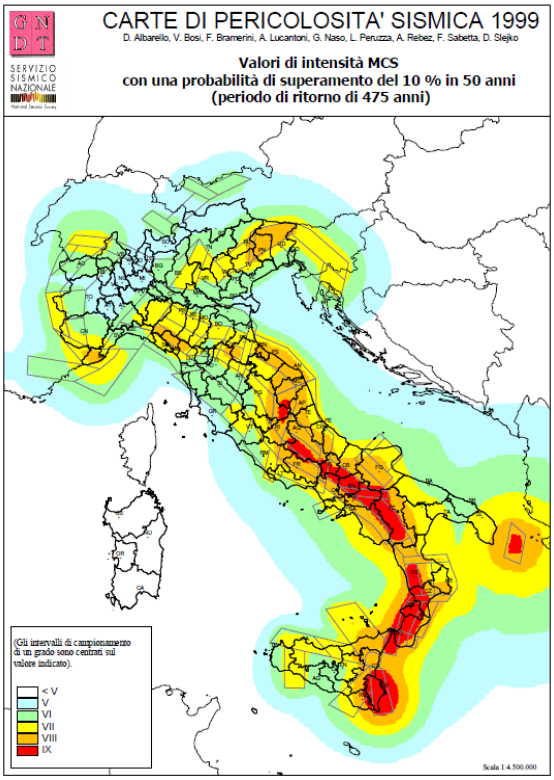


Figure 5: Italian Hazard map in MCS macro-intensity for an exceedance probability of 10% in 50 years.

In this study only the Life Safety Hazard Level has been characterized based on the Italian hazard map proposed in [16] in Mercalli-Cancani-Sieber macro-seismic intensity (MCS) for a return period of 475 years (Figure 5). The Figure 5 shows as the Italian territory could be splitted in six macro-seismic regions. Each of them is characterized by an expected macro-

seismic intensity (MCS) with a return period of 475 years or probability of exceedance of 10% in 50 years.

The map has been chosen due to the strong correlation between MCS macro-seismic scale and EMS-98 one. As reported in previous study [17], about the macroseismic intensity scale, a substantial equality between Mercalli–Cancani–Sieberg scale (MCS; Sieberg 1930) and the European definition of macroseismic intensities (MSK-76, EMS-92 and EMS-98) has been considered.

## 3 RESULTS

New Seismic Risk Index values have been evaluated for considered RC-MRF building types. In this application, the EMS-98 intensity [18] has been considered as reference intensity thus, SRIs have been evaluated based on the discrete expression (2) in regarding to a range of seismic intensity. In this way, based on relationship between European macro-seismic scale EMS-98 and Housner intensity ($I_H$) proposed in [17] equivalence between $I_H$ and EMS-98 has been defined. In Figure 6, the Fragility Curves for some building types considered have been reported. Moreover, the relation between $I_H$ and EMS-98 has been highlighted.

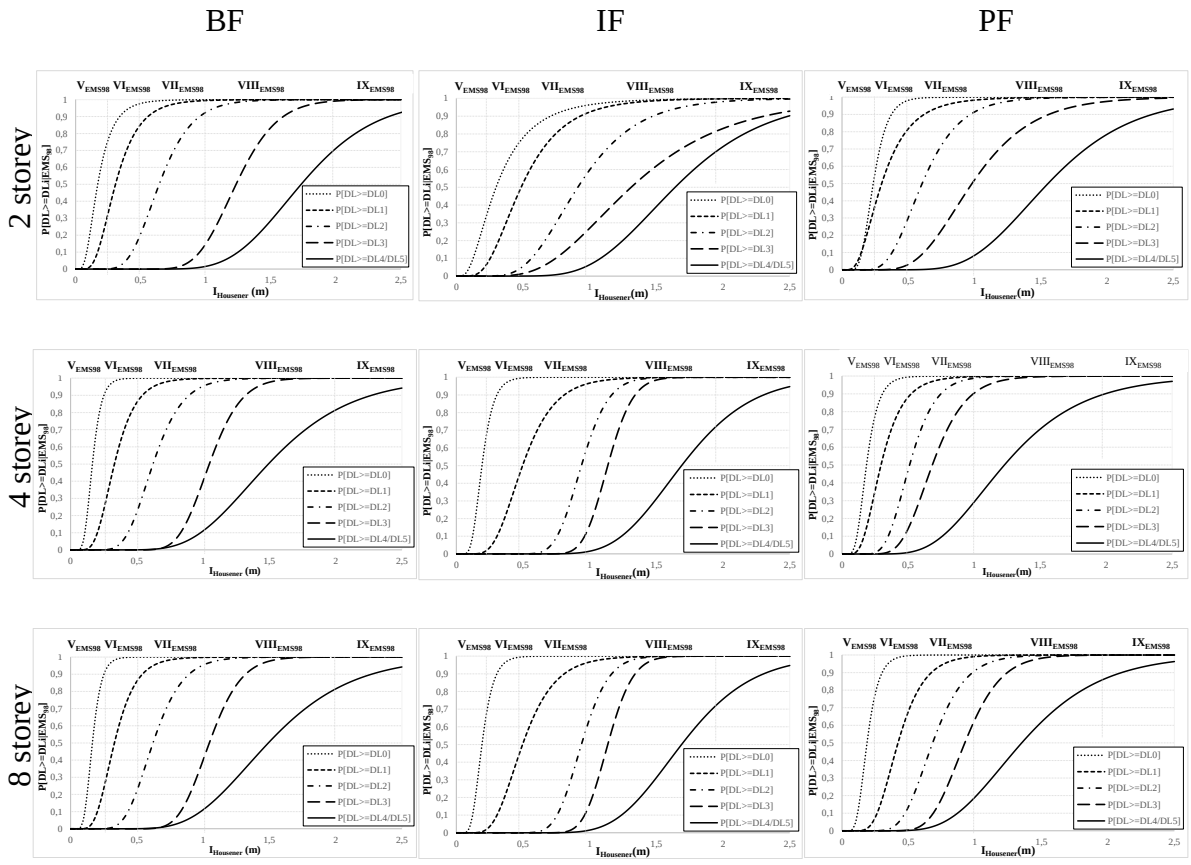


Figure 6: Fragility curves: Old Code for 2-4-8 storey types.

Different areas of fragility curve have been involved in SRIs quantification according with life safety hazard level intensity characterization. For each MCS Italian seismic area a different range of Fragility Curve has been considered. In order to clarify the application, in Figure 7 the areas of the fragility curve (for Life Safety LS) for each seismic region have been highlighted.

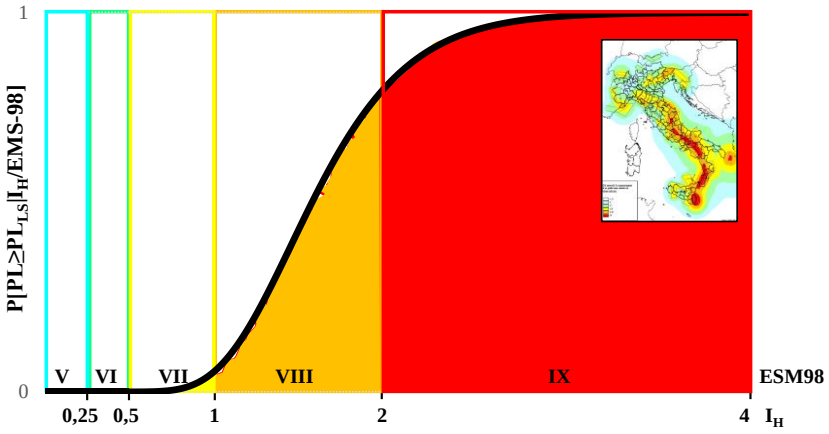


Figure 7: Fragility Curve and seismic intensity Hazard level characterization.

In Figure 8 are reported the SRIs values obtained for considered types for VII and VIII EMS98. SRIs have been classified in ascending order. For each Italian seismic region, types ranking lists for Life Safety PL have been obtained.

The Figure 8 (a) shows that the Old Code (OC) and PF types suffer the greater seismic risk level for $I_{EMS98}$ = VII (0,8 < SRI < 1). However, the Figure 8 (b) shows that all types are characterized by a high seismic risk level for $I_{EMS98}$ = VIII (0,3 < SRI < 0,63). Particularly, the typological ranking highlights as the Seismic Risk Index firstly depends by the infill panel distribution and effectiveness condition (PF-BF-IF). PF types are the most vulnerable types, following by BF and IF types.

For the same infill panel distribution and effectiveness condition, SRI is influenced by the design code. Building types designed in accordance with a no-seismic code (OC) are more vulnerable than those designed according to old seismic design code (PC). Finally, the Seismic Risk Index seems to be less influenced by the storey number.

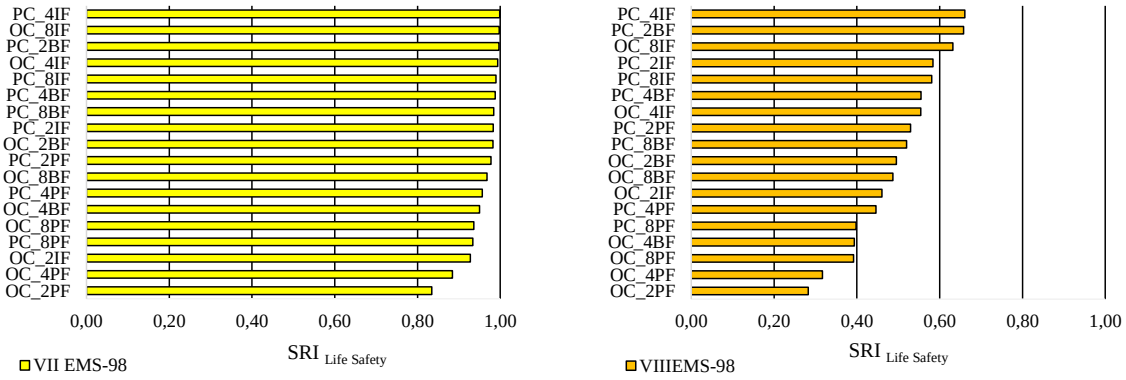


Figure 8: SRIs (for Life Safety PL) for each building types considered as situated in Italian seismic regions characterized by a reference macro-seismic intensity for Life Safety PL of VII, VIII EMS-98 intensity.

## 4 CONCLUSIONS

A new Seismic Risk Index based on the probabilistic approach has been defined in order to compare in a probabilistic way the performance of existing buildings with PL requirements. Specific Performance Level requirements have been proposed based on in force codes. It is

considered a more accurate way to seismic risk evaluation, than the conventional approach based on the simple and deterministic comparison between building capacity and required demand. The new SRI definition, based on a totally probabilistic approach (both in building characterized that in performance assessment), seems to provide different seismic risk index estimation than the conventional one. Then, it could be considered a useful tool for a more accurate and realistic estimation of building seismic risk index, based on the probability that a PL could be exceeded.

The new SRI requires a more accurate probabilistic building characterization and the definition of building FCs, which are the best way to represent the building seismic vulnerability.

The new SRI for the MRF-RC building types considered in this first study could be a reference for practice applications but only for building types or single building similar to those examined. Therefore, a more extensive use of the obtained information could be possible relying on the expert judgment of the analysts, which may revise the results in accordance with the peculiarities of analyzed buildings.

In future works, the effectiveness of new SRI than classic one will be further tested, based on recent post-earthquake scenario, and specify cases study.

## REFERENCES

[1] O.C. Zienkiewicz, R.C. Taylor, *The finite element method, Vol. I, 4th Edition*. McGraw Hill, 1989.

[2] J.T. Oden, T. Belytschko, I. Babuska, T.J.R. Hughes, Research directions in computational mechanics. *Computer Methods in Applied Mechanics and Engineering*, **192**, 913-922, 2003.

[3] J.H. Argyris, M. Papadrakakis, L. Karapitta, Elastoplastic analysis of shells with the triangular element TRIC. M. Papadrakakis, A. Samartin, E. Oñate eds. *4th International Colloquium on Computation of Shell and Spatial Structures (IASS-IACM 2000)*, Chania, Crete, Greece, June 4-7, 2000.

[1] Vona M, Harabaglia P and Murgante B. Thinking about resilience cities studying Italian earthquake. *Urban Design and Planning*, **169**(4), 185-199, 2016.

[2] Vona M, Anelli A, Mastroberti M, Murgante B and Santa-Cruz S, Prioritization Strategies to reduce the Seismic Risk of the Public and Strategic Buildings. *Disaster Advances*, **10** (4), 2017

[3] Vona M. and Murgante B., Evaluation of retrofitting policies of strategic buildings based on different multi-criteria decision-making (MCDM) methods, *IALCCE 2014 - Fourth International Symposium on Life-Cycle Civil Engineering*, Tokyo, Japan, 2014

[4] Masi A., Santarsiero G., Chiaussi L., Vulnerability assessment and seismic risk reduction strategies of hospital in Basilicata region (Italy), *15 WCEE* , Lisboa, 2012.

[5] Parsons M, Glavac S, Hastings P, Marshall G, McGregor J, McNeill P, Morley P, Reeve I, Stayner R. Top-down assessment of disaster resilience: A conceptual framework using coping and adaptive capacities. *International Journal of Disaster Risk Reduction*, **191**(11), 2015

[6] FEMA356, *Prestandard and Commentary for the Seismic Rehabilitation of Buildings*, 2000

[7] D.M. 28 febbraio 2017, n. 58 recante: *Sisma Bonus - Linee guida per la classificazione del rischio sismico delle costruzioni nonché le modalità per l'attestazione, da parte di professionisti abilitati, dell'efficacia degli interventi effettuati*. Ministero delle infrastrutture e dei trasporti (in Italian).

[8] DECRETO-LEGGE 17 ottobre 2016, n. 189. *Interventi urgenti in favore delle popolazioni colpite dal sisma del 24 agosto 2016*. (16G00205) GU Serie Generale n.244 del 18-10-2016. (in Italian).

[9] NTC 2008. *Norme Tecniche per le Costruzioni*. Decreto del Ministero delle infrastrutture, Supplemento Ordinario n.30 alla Gazzetta Ufficiale della Repubblica italiana, 29, 4/02/2008, Italy (in Italian).

[10] CEN Eurocode 8 2004, *Design Provisions for Earthquake Resistance of Structures*. European Prestandard ENV 1998, Brussels Belgium: ComitéEuropéen de Normalisation.

[11] Masi A. and Vona M., Vulnerability assessment of gravity-load designed RC buildings, evaluation of seismic capacity through nonlinear dynamic analyses. *Engineering Structures*, **45**, 257–269, 2012

[12] Vona M., Fragility Curves of Existing RC Buildings Based on Specific Structural Performance Levels, *Open Journal of Civil Engineering*, **4**. 120-134, 2014.

[13] Vona M., Mastroberti M, A critical review of fragility curves for existing RC buildings. ECCOMAS Congress 2016. *VII European Congress on Computational Methods in Applied Sciences and Engineering*. Crete Island, Greece, 5-10 June 2016

[14] Borzi B, Vona M, Masi A, Pinho R, Pola D. Seismic demand estimation of RC frame buildings based on simplified and nonlinear dynamic analyses, *Earthquakes and Structures*, **4**(2), 2013.

[15] Masi A, Vona M and Mucciarelli M., Selection of Natural and Synthetic Accelerograms for Seismic Vulnerability Studies on Reinforced Concrete Frames. *Journal of Structural Engineering*. 367, 2011.

[16] Albarello D, Bosi V, Bramerini F, Lucantoni A, Naso G, Peruzza L, Rebez A, Sabetta F, Slejko D. *Pericolosità sismica del territorio nazionale: carte di consenso GNDT e SSN*; 1999.

[17] Chiauzzi L, Masi A, Mucciarelli M, Vona M, Pacor F, Cultrera G, Gallovič F, Emolo A. Building damage scenarios based on exploitation of Housner intensity derived from finite faults ground motion simulations. *Bulletin of Earthquake Engineering*, **10**(2), 517-545, 2012

[18] Grunthal G. (editor). European Macroseismic Scale 1998 (EMS-98). European Seismological Commission, sub commission on Engineering Seismology, working Group Macroseismic Scales. Conseil de l'Europe, *Cahiers du Centre Europeen de Geodynamique et de Seismologie*, vol. 15. Luxembourg; 1998.

COMPDYN 2017
6th ECCOMAS Thematic Conference on
Computational Methods in Structural Dynamics and Earthquake Engineering
M. Papadrakakis, M. Fragiadakis (eds.)
Rhodes Island, Greece, 15–17 June 2017

# USING AN INSTRUMENTED VEHICLE TO ESTIMATE SURFACE ROUGHNESS OF A BRIDGE

**Ying Zhan, Francis T. K. Au**

The University of Hong Kong
The University of Hong Kong, Pokfulam, Hong Kong
{yingzhan, francis.au}@hku.hk

**Keywords:** Finite Element Modeling, Parameter Identification, Roughness Profile, Vehicle Bridge Interaction.

**Abstract.** *Bridge parameter identification based on vehicle-bridge interaction theory and data extracted from the vehicle response has many potential applications. However, its real application is restricted, partly due to the bridge surface roughness, which can significantly contaminate the vehicle response data and make parameter identification hard or even impossible. If the bridge surface roughness can be detected with satisfactory accuracy, then it is possible to eliminate its uncertain effect on the vehicle-bridge interaction, which will facilitate more accurate identification. This study aims to provide a way to estimate the surface roughness profile of a bridge using the acceleration data gathered from a vehicle running on the bridge twice with different masses. The mass-spring-damper model is used to simulate the moving vehicle. Finite element simulation results show that this method is able to estimate the surface roughness profile accurately.*

## 1 INTRODUCTION

Parameter identification is useful for estimating the dynamic properties of newly built bridges, detecting damage in existing bridges, and assessing the serviceability of old bridges. Various methods have been proposed for identifying various bridge parameters. One of the economical and convenient methods is the drive-by parameter identification approach.

The bridge and the vehicle running on can be considered as a coupled vibration system. The properties of a moving vehicle can be identified from the bridge vibration data [1]. Similarly, the bridge dynamic parameters can also be derived from the vibration data measured from an instrumented vehicle moving on a bridge [2, 3].

Using vehicles instrumented with sensors to detect bridge parameters is an indirect method that is both economical and convenient, and the disruption to normal traffic on the bridge can be minimized as compared to other methods [4]. However, this method is prone to environmental and other types of noise. In particular, the presence of surface roughness of the bridge can seriously affect the vehicle-bridge interaction phenomenon and contaminate the vehicle vibration data. Most of the theoretical research work has ignored the surface roughness. Some used simple waves to simulate the surface roughness, such as sinusoidal wave [5]; or considered in the vehicle-bridge interaction simulation but with an impractically small magnitude [6]. These methods are therefore incapable of dealing with real surface roughness. As a result, most of the experiments in related fields were conducted on bridge models with smooth surface in lab environment [7].

There were studies on road roughness detection with promising results, but their target and focus are different from those in this study. Their focus was on the statistical properties of road roughness, such as power spectral density, which is usually used for classification of road quality based on standards such as ISO 8608. This study, on the other hand, focuses on the estimation of surface roughness profile, which is useful in eliminating its uncertain effect on the vehicle-bridge interaction system.

## 2 THEORY

The vehicle-bridge interaction model with smooth surface is first examined, followed by another model with surface roughness. A method for estimating surface roughness profile is proposed accordingly based on the latter model.

### 2.1 Vehicle-bridge interaction dynamics for a smooth bridge

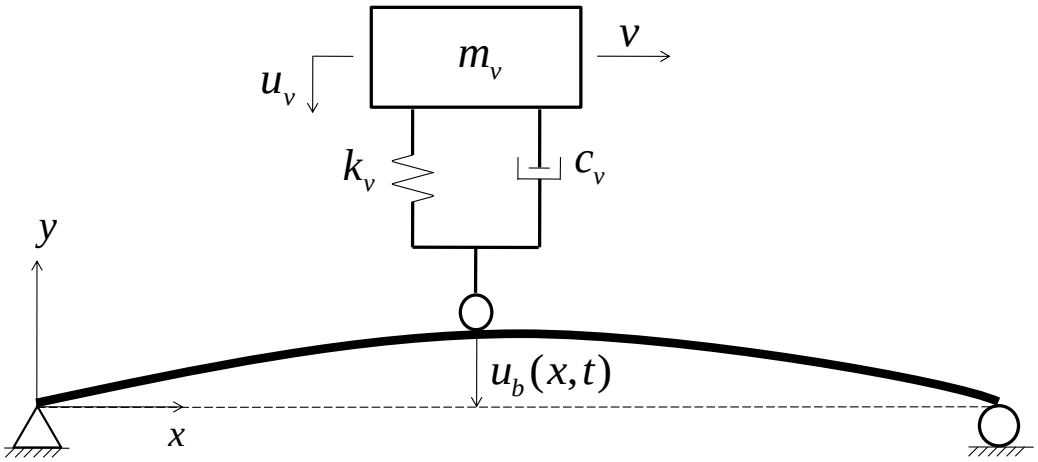


Figure 1: Vehicle-bridge interaction model

A vehicle is traveling on a simply supported uniform bridge with smooth surface as shown in Figure 1. The vehicle is modeled as a mass-spring-damper model, which captures the main features of the vehicle and is relatively simple to analyze. For this vehicle-bridge interaction system without surface roughness, the equation of motion of the bridge can be written as

$$\overline{m}\frac{\partial^2 u_b(x,t)}{\partial t^2}+c\frac{\partial u_b(x,t)}{\partial t}+EI\frac{\partial^4 u_b(x,t)}{\partial x^4}=F_c(t)\delta(x-vt) \tag{1}$$

where $\overline{m}$, $c$, $E$ and $I$ denote the mass per unit length, damping, elastic modulus and moment of inertia of the beam, respectively; $u_b(x,t)$ is the vertical displacement of the bridge at abscissa $x$ and time $t$; $F_c(t)$ is the contact force between the vehicle and bridge; $v$ is the speed of vehicle; and $\delta(x-vt)$ is the Dirac delta function to describe the movement of vehicle on the bridge mathematically, i.e.

$$\delta(x)=\begin{cases}+\infty, & x=0\\ 0, & x\neq 0\end{cases} \quad \text{and} \quad \int_{-\infty}^{+\infty}\delta(x)dx=1 \tag{2}$$

The equation of motion of the vehicle can be written as

$$m_v\frac{d^2u_v(t)}{dt^2}+c_v\left[\frac{du_v(t)}{dt}-\left.\frac{du_b(x,t)}{dt}\right|_{x=vt}\right]+k_v\left[u_v(t)-\left.u_b(x,t)\right|_{x=vt}\right]=0 \tag{3}$$

where $m_v$, $c_v$ and $k_v$ are the mass, damping and stiffness of the vehicle, respectively; $u_v(t)$ is the vertical displacement of the vehicle; $\left.\frac{du_b(x,t)}{dt}\right|_{x=vt}$ denotes the vertical velocity of the bridge at the contact point $x=vt$, which can be further split up in terms of the vibration velocity of the bridge caused by the vehicle load and the additional vertical velocity of the wheel caused by the horizontal movement of the wheel along the slope of the bridge due to vibration on the right-hand side respectively as

$$\left.\frac{du_b(x,t)}{dt}\right|_{x=vt}=\left.\frac{\partial u_b(x,t)}{\partial t}\right|_{x=vt}+v\left.\frac{\partial u_b(x,t)}{\partial x}\right|_{x=vt} \tag{4}$$

Since in reality bridges are very stiff, the slope caused by the vehicle load is very small. Moreover, the vehicle speed is not very high. Therefore, the second term on the left-hand side of Equation (3) can be ignored, thereby giving

$$m_v\frac{d^2u_v(t)}{dt^2}+c_v\left[\frac{du_v(t)}{dt}-\left.\frac{\partial u_b(x,t)}{\partial t}\right|_{x=vt}\right]+k_v\left[u_v(t)-\left.u_b(x,t)\right|_{x=vt}\right]=0 \tag{5}$$

The contact force between the bridge and vehicle is

$$F_c(t)=-m_vg+k_v\left[u_v(t)-\left.u_b(x,t)\right|_{x=vt}\right]+c_v\left[\frac{du_v(t)}{dt}-\left.\frac{\partial u_b(x,t)}{\partial t}\right|_{x=vt}\right] \tag{6}$$

The displacement of the bridge can be obtained as elaborated below.

Equation (1) is the equation of motion for the simply supported bridge and can be analyzed by mode superposition method [8]. The vertical displacement of bridge can be written as

$$u_b(x,t) = \sum_{i=1}^{\infty} \phi_i(x) Y_i(t) \tag{7}$$

where $\phi_i(x)$ is the *i*th mode shape of the bridge, and $Y_i(t)$ is the associated modal amplitude.

To evaluate the contribution of mode *i* to the bridge vertical displacement $u_b(x,t)$, substituting Equation (7) into Equation (1), multiplying both sides by $\phi_j(x)$ and integrating give

$$\begin{aligned} &\int_0^L \overline{m}\phi_j(x) \sum_{i=1}^{\infty} \left[ \phi_i(x) \frac{d^2 Y_i(t)}{dt^2} \right] dx + \int_0^L c\phi_j(x) \sum_{i=1}^{\infty} \left[ \phi_i(x) \frac{dY_i(t)}{dt} \right] dx + \\ &\int_0^L EI\phi_j(x) \sum_{i=1}^{\infty} \left[ \frac{d^4 \phi_i(x)}{dx^4} Y_i(t) \right] dx = \int_0^L F_c(t) \delta(x - vt) \phi_j(x) dx \end{aligned} \tag{8}$$

Assuming the damping of the bridge to be Rayleigh damping which satisfies the orthogonality condition, and applying the orthogonality condition, i.e.

$$\left.\begin{array}{c} \phi_i(x) \cdot m \cdot \phi_j(x) \\ \phi_i(x) \cdot c \cdot \phi_j(x) \\ \phi_i(x) \cdot EI \cdot \phi_j(x) \end{array}\right\} = 0 \quad \textbf{if} \quad i \neq j \tag{9}$$

in Equation (8) yield

$$\begin{aligned} &\overline{m} \frac{d^2 Y_j(t)}{dt^2} \int_0^L {\phi_j}^2(x) dx + c \frac{dY_j(t)}{dt} \int_0^L {\phi_j}^2(x) dx + EI \cdot Y_j(t) \int_0^L \phi_j(x) \frac{d^4 \phi_j(x)}{dx^4} dx \\ &= F_c(t) \phi_j(x = vt) dx \end{aligned} \tag{10}$$

where only one term of each infinite series remains on the left hand side. Hence the amplitude term $Y_j(t)$ can be obtained by solving this ordinary differential equation.

The mode of a simply supported beam is of sinusoidal shape given by

$$\phi_j(x) = \sin \frac{j\pi x}{L} \tag{11}$$

Substituting Equations (6) and (11) into Equation (10), and rearranging yields

$$\begin{aligned} &\frac{d^2 Y_j(t)}{dt^2} + 2\xi_{bj}\omega_{bj} \frac{dY_j(t)}{dt} + \omega_{bj}^2 Y_j(t) = \frac{2}{\overline{m}L} \sin \frac{j\pi vt}{L} \times \\ &\left\{ -m_v g + m_v \omega_v \left[ \omega_v u_v(t) + 2\xi_v \frac{du_v(t)}{dt} - \omega_v \sum_{k=1}^{\infty} \sin \frac{k\pi vt}{L} Y_k(t) - 2\xi_v \sum_{k=1}^{\infty} \sin \frac{k\pi vt}{L} \frac{dY_k(t)}{dt} \right] \right\} \end{aligned} \tag{12}$$

where $\omega_{bj}$ and $\xi_{bj}$ are the *j*th frequency and damping-ratio of the bridge respectively, i.e.

$$\omega_{bj} = \frac{j^2 \pi^2}{L^2} \sqrt{\frac{EI}{\overline{m}}}, \quad \xi_{bj} = \frac{c}{2\overline{m}\omega_{bj}} \tag{13}$$

Assuming the vehicle mass to be negligible in comparison with the bridge mass, i.e. $\frac{m_v}{\overline{m}L} << 1$, the terms in square brackets on the right-hand side of Equation (12) can be ignored, giving

$$\frac{d^2Y_j(t)}{dt^2} + 2\xi_{bj}\omega_{bj}\frac{dY_j(t)}{dt} + \omega_{bj}^2 Y_j(t) = \frac{-2m_v g}{\overline{m}L}\sin\frac{j\pi vt}{L} \tag{14}$$

Solving Equation (14) yields a solution for the modal amplitude $Y_j(t)$ as

$$\begin{aligned} Y_j(t) &= (M\cos\omega_{bjd}t + N\sin\omega_{bjd}t)^{-\xi_{bj}\omega_{bj}t} + \\ &\frac{\Delta_{bj}}{(1-\beta_j^2)^2 + (2\xi_{bj}\beta_j)^2}\left[(1-\beta_j^2)\sin\frac{j\pi vt}{L} - 2\xi_{bj}\beta_j\cos\frac{j\pi vt}{L}\right] \end{aligned} \tag{15}$$

where the constants $M$ and $N$ can be evaluated for any given initial conditions, $Y_j(0)$ and $\left.\frac{dY_j(t)}{dt}\right|_{t=0}$, the first term on the right-hand side accounts for the transient response that will damp out exponentially, and the second term represents the steady state harmonic response that will continue indefinitely. However, since the transient response damps out quickly, it is not the primary concern. Here the solutions under the initial condition $Y_j(0) = 0$ and $\left.\frac{dY_j(t)}{dt}\right|_{t=0} = 0$ are provided as an example. The *j*th frequency of the damped bridge $\omega_{bjd}$, the static vertical displacement of the *j*th mode caused by the vehicle loading $\Delta_{bj}$, the dimensionless speed parameter $\beta_j$, and constants $M$ and $N$ are given as follows

$$\omega_{bjd} = \omega_{bj}\sqrt{1-\xi_{bj}^2} \tag{16}$$

$$\Delta_{bj} = \frac{-2m_v gL^3}{j^4\pi^4 EI} \tag{17}$$

$$\beta_j = \frac{j\pi v}{L\omega_{bj}} \tag{18}$$

$$M = \frac{2\xi_{bj}\beta_j\Delta_{bj}}{(1-\beta_j^2)^2 + (2\xi_{bj}\beta_j)^2} \tag{19}$$

$$N = \frac{\Delta_{bj}}{(1-\beta_j^2)^2 + (2\xi_{bj}\beta_j)^2}\left[\frac{2j\pi\xi_{bj}\beta_j v - (1-\beta_j^2)\xi_{bj}\omega_{bj}L}{\omega_{bjd}L}\right] \tag{20}$$

Ignoring the transient responses in Equation (15) and substituting it into Equation (7), the vertical displacement of bridge can be obtained as

$$u_b(x,t) = \sum_{j=1}^{\infty}\frac{\Delta_{bj}}{(1-\beta_j^2)^2 + (2\xi_{bj}\beta_j)^2}\left[(1-\beta_j^2)\sin\frac{j\pi vt}{L} - 2\xi_{bj}\beta_j\cos\frac{j\pi vt}{L}\right]\sin\frac{j\pi x}{L} \tag{21}$$

Differentiating Equation (21) with respect to time $t$, the vertical velocity of the bridge is obtained as

$$\frac{\partial u_b(x,t)}{\partial t}=\sum_{j=1}^{\infty}\frac{\Delta_{bj}}{(1-\beta_j^2)^2+(2\xi_{bj}\beta_j)^2}\frac{j\pi v}{L}\left[(1-\beta_j^2)\cos\frac{j\pi vt}{L}+2\xi_{bj}\beta_j\sin\frac{j\pi vt}{L}\right]\sin\frac{j\pi x}{L} \quad (22)$$

Hence Equation (21) and (22) indicate that the vertical displacement as well as velocity of the bridge are linearly related to the mass of vehicle $m_v$.

### 2.2 2.2 Vehicle-bridge interaction model with surface roughness

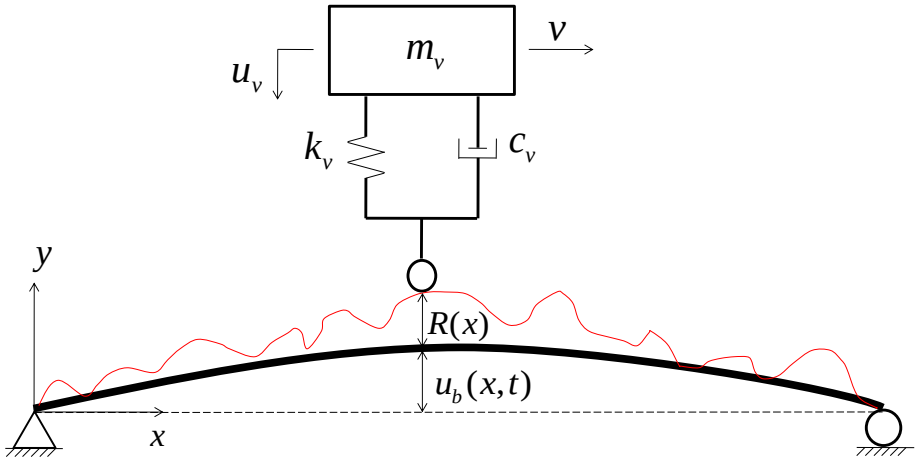


Figure 2 Vehicle-bridge interaction model with surface roughness

Two assumptions are made to establish the vehicle-bridge interaction model with surface roughness as shown in Figure 2. The wheel of the vehicle is always in contact with the bridge surface, i.e. the vehicle does not bounce on the bridge. The surface roughness profile remains unchanged during multiple passes in a short period.

Based on these two assumptions, the vertical displacement of the wheel of vehicle is equal to the sum of the vertical displacement of the bridge at the contact point and the surface roughness, i.e.

$$u_w(t)=u_b(x,t)\big|_{x=vt}+R(vt) \quad (23)$$

where $u_w(t)$ is the vertical displacement of the vehicle wheel, and $R(vt)$ is the surface roughness at the contact point $x=vt$. With the surface roughness taken into consideration, $u_b(x,t)\big|_{x=vt}$ in Equation (3) should be replaced by $u_w(t)$ in Equation (23), which yields

$$m_v\frac{d^2u_v(t)}{dt^2}+c_v\left\{\frac{du_v(t)}{dt}-\frac{d\left[u_b(x,t)\big|_{x=vt}+R(vt)\right]}{dt}\right\}+k_v\left\{u_v(t)-\left[u_b(x,t)\big|_{x=vt}+R(vt)\right]\right\}=0 \quad (24)$$

Substituting Equation (4) into Equation (24) and ignoring the additional vertical velocity of the wheel yields

$$m_v\frac{d^2u_v(t)}{dt^2}+c_v\frac{du_v(t)}{dt}+k_vu_v(t)=c_v\frac{\partial u_b(x,t)}{\partial t}\bigg|_{x=vt}+k_vu_b(x,t)\big|_{x=vt}+vc_v\frac{dR(vt)}{d(vt)}+k_vR(vt) \quad (25)$$

which is the equation of motion of the vehicle considering the effect of surface roughness.

### 2.3 Method for estimation of surface roughness profile

Based on Equation (25), a double-pass mass-addition technique is proposed to estimate the bridge surface roughness profile, as elaborated below.

Step 1: Let the test vehicle of mass $m_v$ with accelerometer installed on it move on the bridge at a constant speed $v$, and record its vertical acceleration response history $a_1(t)$.

Step 2: Add a certain mass on the vehicle so that the total vehicle mass becomes $\lambda m_v$ where $\lambda$ is a parameter slightly above unity, e.g. 1.1. Let the vehicle with added mass move on the bridge once more at the same speed $v$, and record its vertical acceleration response history $a_2(t)$.

Step 3: Calculate the following two time series $ans_1$ and $ans_2$ which are derived from Equation (25):

$$\begin{aligned} ans_1 &= c_v \left.\frac{\partial u_b(x,t)}{\partial t}\right|_{x=vt} + k_v u_b(x,t)\big|_{x=vt} + vc_v \frac{dR(vt)}{d(vt)} + k_v R(vt) \\ &= m_v a_1(t) + c_v v_1(t) + k_v u_1(t) \end{aligned} \tag{26}$$

$$\begin{aligned} ans_2 &= \lambda c_v \left.\frac{\partial u_b(x,t)}{\partial t}\right|_{x=vt} + \lambda k_v u_b(x,t)\big|_{x=vt} + vc_v \frac{dR(vt)}{d(vt)} + k_v R(vt) \\ &= \lambda m_v a_2(t) + c_v v_2(t) + k_v u_2(t) \end{aligned} \tag{27}$$

where $u_1(t)$ and $u_2(t)$ are the vertical displacement histories of the vehicle in the first and second passes respectively, $v_1(t)$ and $v_2(t)$ are the vertical velocity histories of the vehicle in the first and second passes respectively, which can be obtained by numerical integration of the acceleration histories $a_1(t)$ and $a_2(t)$.

Combining Equations (26) and (27) yields

$$vc_v \frac{dR(vt)}{d(vt)} + k_v R(vt) = ans_1 - \frac{1}{\lambda - 1}(ans_2 - ans_1) \tag{28}$$

which is an ordinary differential equation involving the surface roughness $R(vt)$, which can be solved numerically by methods such as Euler method or Runge–Kutta methods.

### 2.4 Differentiability of the surface roughness

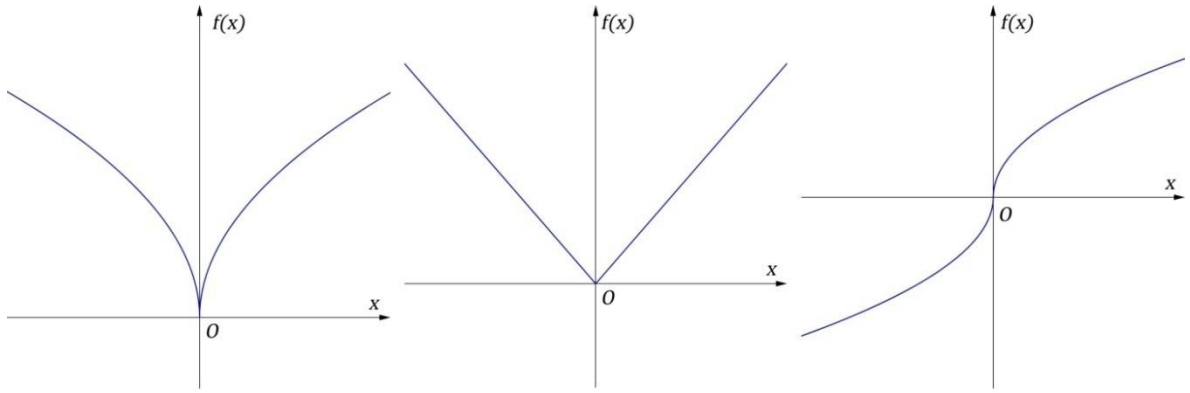


(a) Cusp at x = 0 (b) Corner at x = 0 (c) Vertical tangent at x = 0

Figure 3 Possible non-differentiable cases in surface roughness profile

In reality, the surface roughness can be of any shape. If it is described mathematically as a function of abscissa $x$, it might not be differentiable for any $x$. The surface roughness must be continuous without any removable or jump discontinuity, but in theory it could have vertical tangent points, corners and/or cusps, which make these points non-differentiable, as shown in Figure 3. This means that the transformation from Equation (23) to Equation (24) is not always mathematically feasible. However, the surface roughness is treated as a series of discrete points instead of a continuous curve in engineering. The interval between adjacent points is decided by the sampling rate or distance. The derivatives of series of discrete points can be obtained numerically, and therefore the differentiability of the surface roughness has no effect on the applicability of this method.

## 3 NUMERICAL VERIFICATION

The feasibility of the proposed method is verified numerically with different classes of surface roughness profile. Two error indicators are introduced to evaluate the performance of this method.

### 3.1 Generation of surface roughness for simulation

The standard ISO 8608 *Mechanical Vibration-Road Surface Profiles-Reporting of Measured Data* [9] classifies the surface profile into 5 categories based on their power spectral density and provides the following process to generate surface roughness for simulation purpose.

It is a commonly assumed hypothesis that the randomness of the road surface roughness can be represented by a normal zero-mean, real-valued stationary Gaussian process as

$$R(x) = \sum_{i=0}^{N} \sqrt{2G_d(n_i)\Delta n}\cos(2\pi n_i x + \phi_i) \tag{29}$$

where $N$ is the total number of harmonic waves used to construct the roughness profile, which usually varies from a few hundred to a few thousand; $\phi_i$ is the random phase angle uniformly distributed in the interval [0, 2π] (inclusive); and $G_d(n_i)$, $\Delta n$ and $n_i$ are defined as follows

$$G_d(n_i) = G_d(n_0)\left(\frac{n_i}{n_0}\right)^{-w} \tag{30}$$

$$\Delta n = \frac{n_u - n_l}{N} \tag{31}$$

$$n_i = n_l + i\Delta n \tag{32}$$

in which $n_u$ and $n_l$ are the upper and lower spatial frequency limits taken as 0.01 $m^{-1}$ and 10 $m^{-1}$ respectively, the reference spatial frequency $n_0$ is taken as 0.1 $m^{-1}$, the exponent is taken as $w = 2$, and the parameter $G_d(n_0)$ is determined based on the roughness class as shown in Table 1 according to the ISO standard [9].

To verify the effectiveness and applicability of the proposed method, three sets of surface roughness profile belonging to classes A, C and E are generated. The total number of sinusoidal wave used to form the roughness profile $N$ is taken as 1024. The generated surface roughness profile are shown in Figure 4 to Figure 6 respectively.

| Road class | Description | $G_d(n_0)$ ($10^{-6}$m$^3$) | | |
|---|---|---|---|---|
| | | Lower limit | Geometric mean | Upper limit |
| A | Very good | -- | 16 | 32 |
| B | Good | 32 | 64 | 128 |
| C | Average | 128 | 256 | 512 |
| D | Poor | 512 | 1024 | 2048 |
| E | Very poor | 2048 | 4096 | 8192 |

Table 1 Parameter $G_d(n_0)$ for different road classes

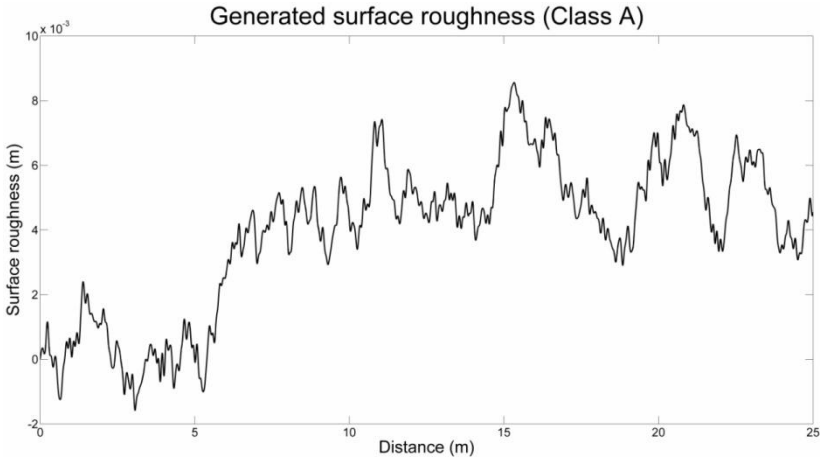


Figure 4 Generated surface roughness (Class A: Very good)

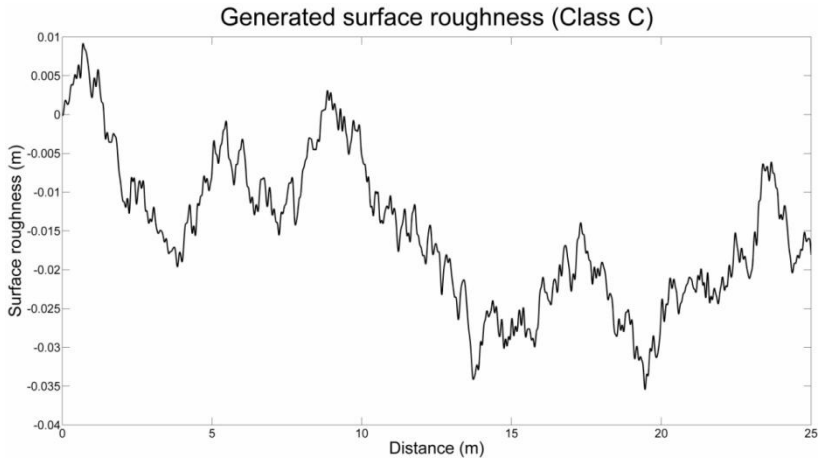


Figure 5 Generated surface roughness (Class C: Average)

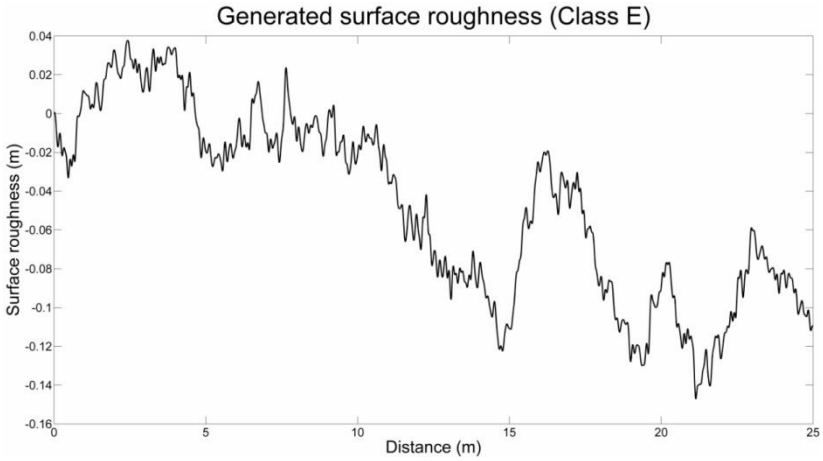


Figure 6 Generated surface roughness (Class E: Very poor)

### 3.2 Error indicator

To better evaluate the effectiveness of the proposed method, two error indicators, emphasizing on the absolute and relative errors respectively, are introduced.

Minkowski distance can be used to measure the difference between two series, i.e.

$$err_1 = \left( \sum_{i=1}^{n} |a_i - b_i|^p \right)^{\frac{1}{p}} \tag{33}$$

where $p > 1$. Here we adopt the most commonly used Minkowski distance with $p$ being 2, which is also known as the Euclidean distance. It is the distance between two points in Euclidean n-space, which can be used to measure the difference between two series. This indicator omits the absolute values of the two series and only focuses on their absolute difference. It has also an accumulative nature, and hence it cannot decrease as more terms are used in the series.

Since Minkowski distance cannot effectively measure the relative similarity of two series, the relative area difference is introduced, as

$$err_2 = \frac{\int |a(x) - b(x)| \, dx}{\int |b(x)| \, dx} \tag{34}$$

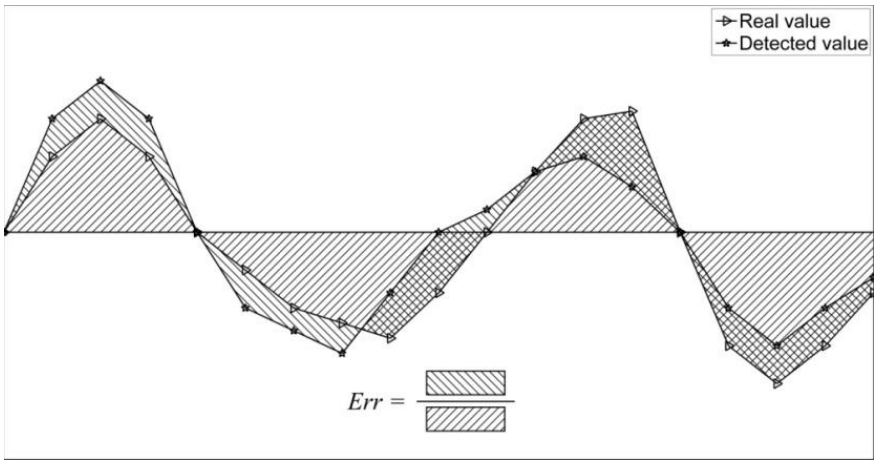


Figure 7 Relative area difference

Equation (34) can be construed as the ratio of the area between the detected value and the real value to the area of the real value as illustrated in Figure 7. This indicator takes the relative relationship between the detection error and the real value into account. Therefore, if the variation of the real value itself is higher, then the same relative area difference means a higher tolerance for the detected value.

### 3.3 Finite element simulation

The vehicle and bridge parameters used in the finite element simulation can be found in Table 2 and Table 3.

| Mass (kg) | Stiffness ($N \cdot m^{-1}$) | Damping ($N \cdot s \cdot m^{-1}$) | Speed ($m \cdot s^{-1}$) | Sampling Frequency ($s^{-1}$) | Added mass (kg) | Add mass ration λ |
|---|---|---|---|---|---|---|
| 1000 | $5 \times 10^4$ | 5000 | 10 | 1000 | 100 | 1.1 |

Table 2: Vehicle parameters for FE modeling

| Span (m) | EI ($N \cdot m^2$) | Mass ($kg \cdot m^{-1}$) | Damping ratio | | Element number |
|---|---|---|---|---|---|
| | | | 1st mode | 2nd mode | |
| 25 | $3.3 \times 10^9$ | 4800 | 0.02 | 0.02 | 25 |

Table 3 Bridge parameters for FE modeling

The simulation results for different surface roughness classes are shown in Table 4 and Figure 8 to Figure 10.

| Surface roughness class | $err_1$ ($10^{-3}$m) | $err_2$ (%) |
|---|---|---|
| A | $1.3 \times 10^{-3}$ | 0.49 |
| C | $4.8 \times 10^{-3}$ | 0.45 |
| E | $16.7 \times 10^{-3}$ | 0.46 |

Table 4 Results of error indicators

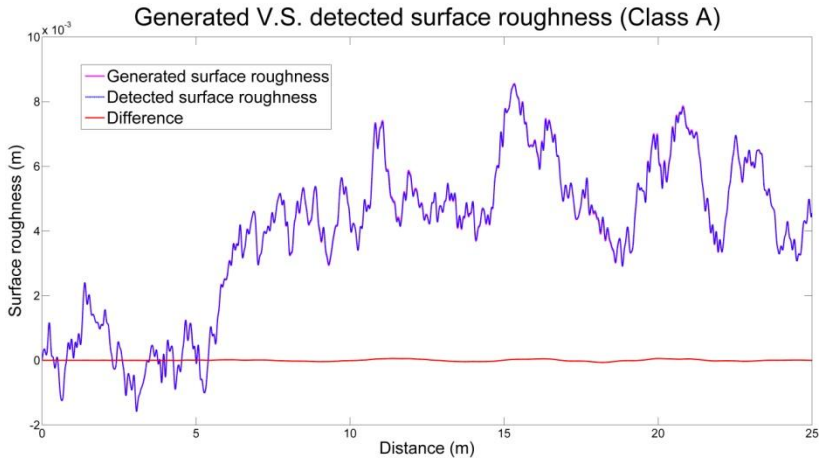


Figure 8 Surface roughness detection results (Class A: Very good)

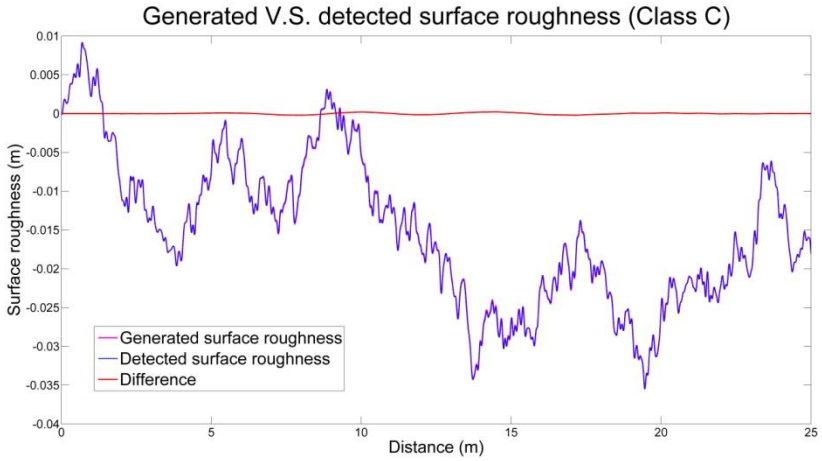


Figure 9 Surface roughness detection results (Class C: Average)

It can be concluded, both visually and based on the error indicators, that the simulation results are of satisfactory accuracy. The variation between the detected and generated surface roughness is very small compared to the variation of the generated surface roughness itself. As the variation of the generated surface roughness increases (the surface class becomes worse), the absolute detection error represented by $err_1$ also increases, but the relatively error represented by $err_2$ stays almost the same. Therefore, this method can be considered as effective for most bridges, whether their surface conditions are good or poor.

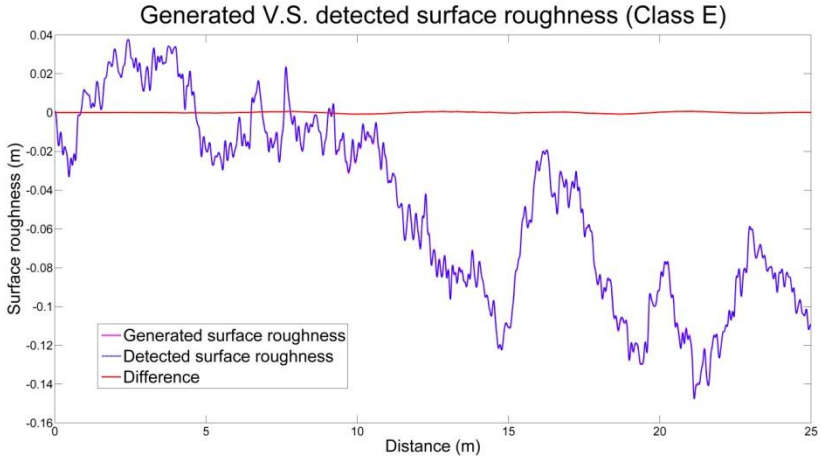


Figure 10 Surface roughness detection results (Class E: Very poor)

### 3.4 Discussion of errors

The error between the detected and generated surface roughness may be caused by various simplifying assumptions. Assuming the vehicle mass to be negligible in comparison with the bridge mass leads to several terms in Equation (12) being neglected. Ignoring the transient responses simplifies Equation (15) significantly but also introducing errors. The responses of the vehicle-bridge system obtained do not satisfy the governing equations exactly. The assumption of linear relationship between the bridge response and vehicle mass may also introduce some error. Further improvement can be achieved by boosting the accuracy of responses through iteration. Moreover, using numerical integration to calculate $u_v(t)$ and $v_v(t)$ from

$a_v(t)$ and the numerical solution of differential equations will inevitably cause a loss of accuracy.

## 4 CONCLUSION

In order to estimate the surface roughness of a bridge, this study presents a double-pass mass-addition method. The information required by this method includes the acceleration response histories extracted from an instrumented vehicle equipped with an accelerometer running on the bridge twice, with an added mass in the second time. Numerical simulation proves that this method is able to estimate the bridge surface roughness with satisfactory accuracy regardless of its surface quality.

This method is useful in reducing the uncertainties associated with surface roughness in vehicle bridge interaction and improving the accuracy of numerical simulation, which are helpful to the drive-by bridge parameter identification.

In order to get results with satisfactory accuracy, one should be mindful of the basic assumptions. The test vehicle should not be too heavy compared to the bridge mass, and the vehicle should not be too fast to avoid any loss of contact with the bridge.

## ACKONWLEDGEMENTS

The authors acknowledge financial support from the Hong Kong PhD Fellowship Scheme of the Hong Kong Research Grants Council for the first author.

## REFERENCES

[1] F.T.K. Au, R.J. Jiang, Y.K. Cheung, Parameter identification of vehicles moving on continuous bridges. *Journal of sound and vibration*, **269**, 91-111, 2004.

[2] Y.B. Yang, C.W. Lin, Vehicle–bridge interaction dynamics and potential applications. *Journal of sound and vibration*, **284**, 205-226, 2005.

[3] A. González, E.J. O'Brien, P. McGetrick, Identification of damping in a bridge using a moving instrumented vehicle. *Journal of Sound and Vibration*, **331**, 4115-4131, 2012.

[4] Z.H. Li, F.T.K. Au, Damage detection of a continuous bridge from response of a moving vehicle. *Shock and Vibration*, 2014.

[5] K.V. Nguyen, Comparison studies of open and breathing crack detections of a beam-like bridge subjected to a moving vehicle. *Engineering Structures*, **51**, 306-314, 2013.

[6] Y.B. Yang, Y.C. Li, K.C. Chang, Constructing the mode shapes of a bridge from a passing vehicle: a theoretical study. *Smart Structures and Systems*, **13**, 797-819, 2014.

[7] C.W. Kim, M. Kawatani, J. Hao, Modal parameter identification of short span bridges under a moving vehicle by means of multivariate AR model. *Structure and Infrastructure Engineering*, **8**, 459-472, 2012.

[8] R.W. Clough, J. Penzien, *Dynamics of Structures*. Computers & Structures Inc., 1995.

[9] ISO, ISO8608 *Mechanical vibration-Road surface profiles-Reporting of measured data*. International Organization for Standardization (ISO) Geneva, 1995.

COMPDYN 2017
6th ECCOMAS Thematic Conference on
Computational Methods in Structural Dynamics and Earthquake Engineering
M. Papadrakakis, M. Fragiadakis (eds.)
Rhodes Island, Greece, 15–17 June 2017

# ON THE ESTIMATION OF BRIDGE MODE SHAPES FROM DRIVE-BY MEASUREMENTS

**Abdollah Malekjafarian**[1], **and Eugene J. OBrien**[2]

[1] School of Civil Engineering, University College Dublin
Newstead Building, UCD, Belfield, Dublin 4, Ireland
e-mail: abdollah.malekjafarian@ucd.ie

[2] School of Civil Engineering, University College Dublin
Newstead Building, UCD, Belfield, Dublin 4, Ireland
e-mail: eugene.obrien@ucd.ie

**Keywords:** Bridge, Mode shape, Indirect methods, Drive-by, Vehicle bridge interaction.

***Abstract.*** *This paper summarizes the latest approaches proposed on indirect bridge monitoring and provides recommendations for future development. The possibility of the estimation of bridge mode shapes from indirect measurements, is investigated. The Hilbert transform is applied to the responses measured from two following axles to extract the amplitudes of the signals. The global bridge mode shapes are constructed by applying a re-scaling process to the local mode shapes obtained from the amplitudes. The performance of the proposed method is demonstrated using a numerical case study.*

## 1 INTRODUCTION

Improved condition monitoring of bridges is an important issue all over the world. The use of structural vibration data is one of the most popular Structural Health Monitoring (SHM) approaches. The concept is that if damage occurs in a structure, it causes measurable changes in its dynamic properties. In most vibration-based bridge health monitoring techniques, sensors are installed on the structure to monitor the dynamic properties. The on-site instrumentation tends to be costly, time-consuming, and may even have safety implications, depending on the location and type of bridge.

Bridge SHM using indirect measurements has been studied by many researchers in recent years [1, 2]. The concept is to instrument a vehicle passing over the bridge and identify bridge dynamic properties using the response measured on the vehicle. Malekjafarian et al. [3] provide a critical review of indirect methods published up tp 2015.

Identification of the bridge natural frequencies using indirect measurements has been extensively investigated by many researchers [4-6]. Yang and Chen [7] propose a modified version of the Stochastic Subspace Identification (SSI) method for estimating the bridge natural frequencies from the responses measured on a vehicle. It is shown that the method is more effective compared to conventional methods. Nagayama et al. [8] propose using a cross-spectrum of the accelerations measured from multiple vehicles to find the common vibration component. It is shown that the cross-spectrum provides a higher peak corresponding to the bridge natural frequency compared to the power spectral density (PSD) of the accelerations measured on a single vehicle.

Several attempts have been made for bridge damage detection using drive-by measurements. OBrien et al. [9] use empirical mode decomposition (EMD) of the accelerations measured on a passing vehicle for damage detection. It is shown that some components of the signal include the damage information. Hester and González [10] investigate using a wavelet transform of the drive-by measurements for the localization of bridge damage.

Estimation of the bridge mode shapes using indirect measurements has been investigated in a few studies [11-17]. Oshima et al. [13] propose a convoy truck-trailer system for estimating the bridge mode shapes. The estimated mode shapes are then used for bridge damage detection. The authors employ the truck to excite the bridge at a high level and a few trailers to measure the bridge response at many moving coordinates. The mode shape vectors of the bridge are identified from Singular Value Decomposition (SVD) of the measured signals. Short Time Frequency Domain Decomposition (STFDD) is proposed by Malekjafarian and OBrien [14] for identifying bridge mode shapes from a moving vehicle. In this method, the bridge is divided into a number of segments and the responses are measured on two following vehicles. Frequency Domain Decomposition (FDD) is applied to short signals related to each segment to identify the local mode shapes. The global bridge mode shapes are then obtained by a rescaling process. The STFDD method provides a better resolution of mode shapes compared to the method proposed by Oshima et al. The STFDD is improved by OBrien and Malekjafarian [15] to provide more resolution. The authors illustrate that the estimated mode shapes can be used for bridge damage detection. Yang et al. [11] theoretically prove that the vehicle response contains bridge mode shape information. The authors investigate the amplitude of the theoretical response of a moving sprung mass on a bridge using the Hilbert transform. It is shown that this amplitude at a frequency close to the bridge natural frequency, is an approximation of the bridge mode shape corresponding to that frequency.

Malekjafarian and OBrien [16] summarize the most recent methods for drive-by identification of bridge mode shapes. They conclude that a truck-trailer system equipped with an actuator can be an optimum vehicle for this case. In this paper, a recent method proposed by the

authors in [16], is explained and a discussion is elaborated about its limitations. An external excitation is employed to provide access to the energy of the bridge response at the key frequencies. It is discussed that this energy is not the bridge mode shape, but is correlated to the bridge mode shape at the time of measurement. It is shown that a rescaling process needs to be applied to obtain the bridge mode shapes from the Hilbert amplitudes. The first two mode shapes of the bridge are estimated with good accuracy and high resolution. This study provides important insights into the indirect identification of bridge mode shapes.

## 2 THE VBI MODEL

The truck-trailer vehicle shown in Fig. 1 is employed to excite the bridge and measure its responses. It consists of a truck towing two trailers. It is assumed that a controlled force, *F(t)*, can be applied to the fourth axle of the vehicle. The properties of the vehicle are given in Tables 1 and 2.

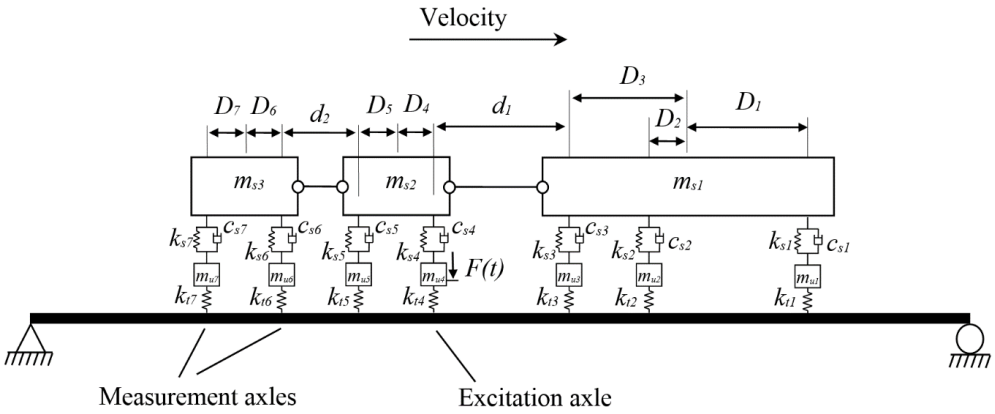


Figure 1: The truck-trailer model.

| | Unit | Symbol | Value |
|---|---|---|---|
| Body mass | kg | $m_{s1}$ | 27100 |
| Axle mass | kg | $m_{u1}$ | 700 |
| | | $m_{u2} = m_{u3}$ | 1100 |
| Suspension stiffness | N/m | $k_{s1}$ | $4\times10^5$ |
| | | $k_{s2} = k_{s3}$ | $1\times10^6$ |
| Suspension damping | Ns/m | $c_{s1}$ | $10\times10^3$ |
| | | $c_{s2} = c_{s3}$ | $20\times10^3$ |
| Tyre stiffness | N/m | $k_{t1}$ | $1.75\times10^6$ |
| | | $k_{t2} = k_{t3}$ | $3.5\times10^6$ |
| Moment of inertia | kg m$^2$ | $I_{s1}$ | $1.56\times10^5$ |
| Distance of axle to centre of gravity | m | $D_1$ | 4.57 |
| | | $D_2$ | 1.43 |
| | | $D_3$ | 3.23 |
| Body mass frequency | Hz | $f_{body,1}$ | 1.32 |
| Axle mass frequency | Hz | $f_{axle,1}$ | 8.82 |
| | | $f_{axle,2}$ | 10.17 |
| | | $f_{axle,3}$ | 10.20 |

Table 1. Properties of the truck.

| | Unit | Symbol | Value |
|---|---|---|---|
| Body mass | kg | $m_{s2}$ | 4000 |
| Axle mass | kg | $m_{u4} = m_{u5}$ | 50 |
| Suspension stiffness | N/m | $k_{s4} = k_{s5}$ | $4\times10^5$ |
| Suspension damping | Ns/m | $c_{s4} = c_{s5}$ | $10\times10^3$ |
| Tyre stiffness | N/m | $k_{t4} = k_{t5}$ | $1.75\times10^6$ |
| Moment of inertia | kg $m^2$ | $I_{s2}$ | 2401.67 |
| Distance of axle to centre of gravity | m | $D_4 = D_5$ | 1.25 |
| Body mass frequency | Hz | $f_{body,2}$ | 2.02 |
| Axle mass frequency | Hz | $f_{axle,4}$ | 33.01 |
| | | $f_{axle,5}$ | 33.04 |
| Gaps, truck-to-trailer and trailer-to-trailer | m | $d_1 = d_2$ | 1 |

Table 2. Properties of the trailers.

The bridge is a 15 m simply supported beam with a modulus of elasticity of 35000 MPa and second moment of area of 0.5273 $m^4$. The first two natural frequencies of the bridge are 5.65 and 22.62 Hz. The bridge is modeled using the finite element (FE) method using 20 beam elements. The global mass and stiffness matrices of the coupled vehicle bridge interaction (VBI) model are constructed at each time step.

## 3 NUMERICAL SIMULATIONS

The vehicle is assumed to pass over the bridge at the speed of 2 m/s. Two simulations are implemented with different excitation frequencies. An excitation force with an amplitude of 3 kN and frequency of 5.5 Hz is applied to the vehicle in the first simulation. This frequency is close to the first natural frequency of the bridge. The simulation is repeated with a new excitation frequency of 22.5 Hz. The acceleration responses are measured at the axles of the second trailer (Axles 6 and 7). The responses measured from the two simulations are shown in Fig. 2. It can be seen that the first mode of the bridge is dominant in the response shown in Fig. 2(a), while Fig. 2(b) shows a response where the second mode is dominant. The amplitudes of the measured signals correspond to the energy in them. As the bridge is excited at frequencies close to its natural frequencies, the energy of each signal is correlated to the bridge mode shapes. Although the amplitudes look like the bridge mode shapes, they are not exactly the mode shapes. For example, Fig. 2(b) gives different amplitudes for the same location from the two axles.

The amplitudes of the measured accelerations at two following axles are obtained using the Hilbert transform (Fig. 3). This figure clearly shows the difference between the amplitudes measured by different axles at the same location. For example, Fig. 3(a) shows the amplitudes of two following axles. They represent two different shapes which are not exactly the bridge first mode shape, but are correlated with it. Fig. 3(b) shows the amplitudes of the axles when the second mode is dominant in the responses.

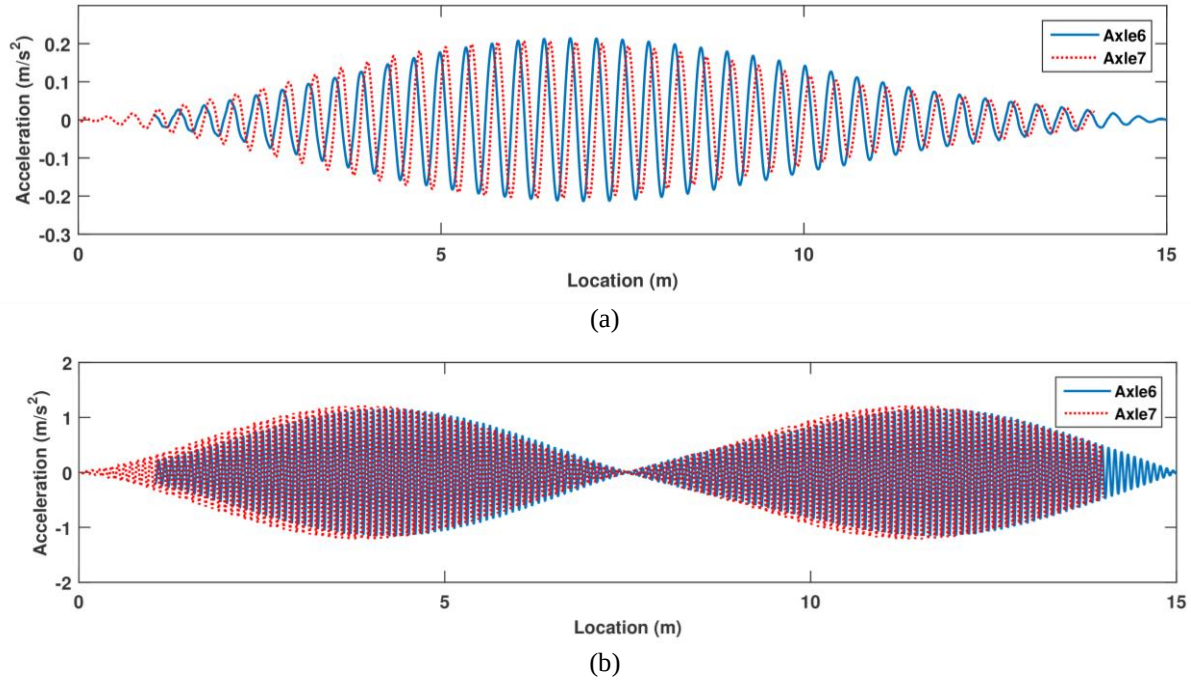


Figure 2: Acceleration responses measured at Axles 6 and 7; (a) excitation frequency of 5.5 Hz and (b) excitation frequency of 22.5 Hz.

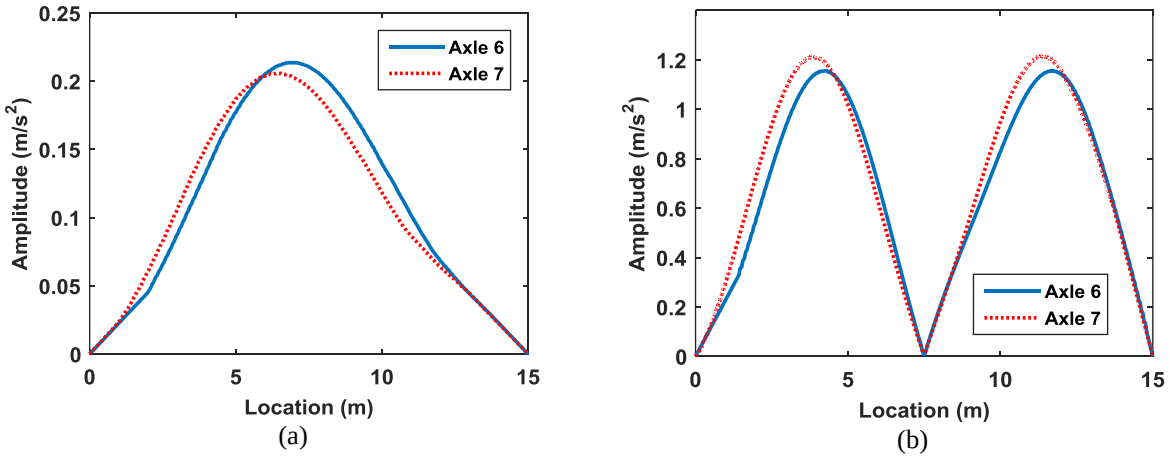


Figure 3: Amplitudes obtained from two following axles; (a) excitation frequency of 5.5 Hz and (b) excitation frequency of 22.5 Hz.

The amplitude for each axle represents how much the bridge is excited at the frequency of excitation. They are represented at two moving coordinates corresponding to the axle locations. However, as they are measured at the same time at different coordinates, the rescaling process proposed in [14] is used to find the global mode shape values. The bridge first and second mode shapes are estimated and compared to the FE mode shapes in Fig. 4. Fig. 4 (a) shows the first mode shape which is estimated by applying the rescaling process to the amplitudes shown in Fig. 3 (a). A similar procedure is used for the second mode shape shown in Fig. 4 (b). As the amplitude values shown in Fig. 3(b) have a positive sign, engineering judgment is used to infer the correct sign of the second mode shape components. It is shown that the mode shapes are estimated with good accuracy and high resolution.

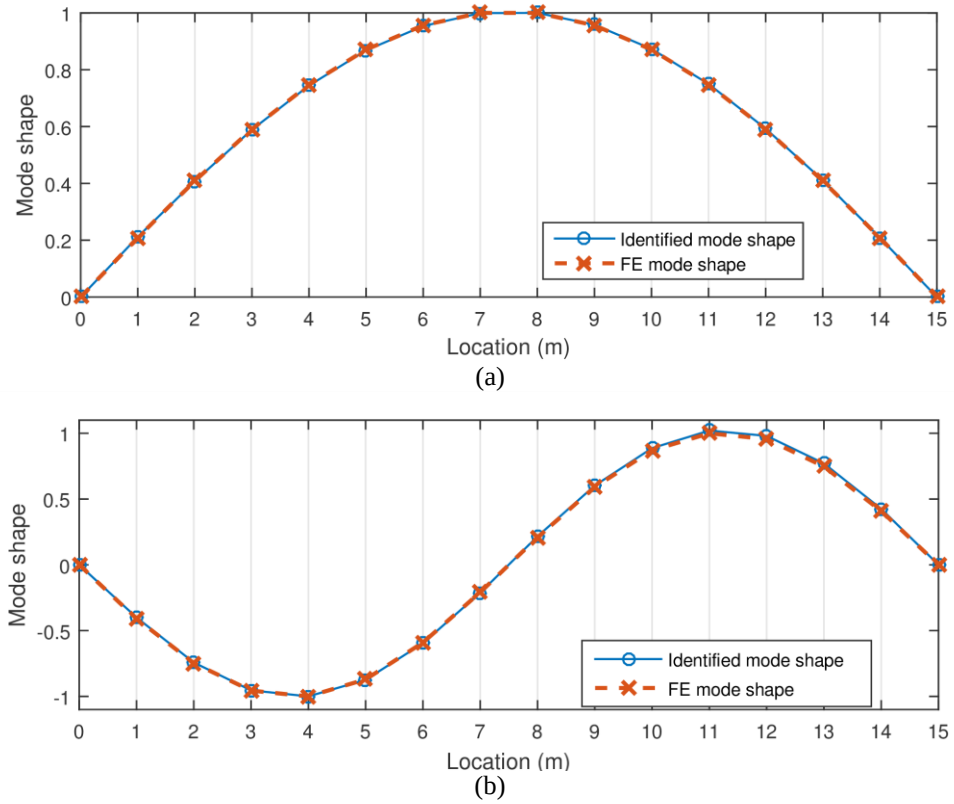


Figure 4: The normalized bridge mode shapes (a) the first mode, (b) the second mode.

## 4 DISCUSSION AND CONCLUSION

This paper provides a numerical study on the identification of bridge mode shapes with high resolution. It suggests using a truck-trailer system equipped with an actuator to artificially excite the bridge. It is proposed that the external excitation is useful for getting access to the energy of the bridge response at the key frequencies. Some of the previous studies assumed that this energy is a normalized bridge mode shape. In contrast, it is shown that the energy is not the bridge mode shape, but is correlated to the bridge mode shape at the time of measurement. To obtain the bridge mode shapes, a rescaling process is employed using the amplitude of the responses measured on two following axles. The study has gone some way towards enhancing understanding of the contribution of the bridge mode shapes to the measured response in a vehicle. There are many challenges that need to be tackled to use the idea in practice. More research is needed to overcome the challenge of the influence of road profile. In addition, the current work is based on acceleration measurements on the vehicle axle which is usually contaminated by measurement noise. On the other hand, using laser measurements on the vehicle provides many advantages compared to accelerometers. Therefore, future research should examine using such a measurement system. A Traffic Speed Deflectometer (TSD) device seems to be a promising instrumented vehicle which could be used successfully for indirect bridge monitoring.

## 5 ACKNOWLEDGMENT

The authors wish to express their gratitude for the financial support received from Science Foundation Ireland towards this investigation under the US-Ireland Partnership Scheme.

## REFERENCES

[1] Y.B. Yang, C.W. Lin, J.D. Yau, Extracting bridge frequencies from the dynamic response of a passing vehicle, Journal of Sound and Vibration, 272 (2004) 471-493.
[2] C.W. Lin, Y.B. Yang, Use of a passing vehicle to scan the fundamental bridge frequencies: An experimental verification, Engineering Structures, 27 (2005) 1865-1878.
[3] A. Malekjafarian, P.J. McGetrick, E.J. OBrien, A Review of Indirect Bridge Monitoring Using Passing Vehicles, Shock and Vibration, (2015).
[4] Y. Oshima, T. Yamaguchi, Y. Kobayashi, K. Sugiura, Eigenfrequency estimation for bridges using the response of a passing vehicle with excitation system, in: Proceedings of the fourth international conference on bridge maintenance, safety and management, 2008, pp. 3030-3037.
[5] Y.B. Yang, K.C. Chang, Extraction of bridge frequencies from the dynamic response of a passing vehicle enhanced by the EMD technique, Journal of Sound and Vibration, 322 (2009) 718-739.
[6] D.M. Siringoringo, Y. Fujin, Estimating Bridge Fundamental Frequency from Vibration Response of Instrumented Passing Vehicle: Analytical and Experimental Study, Advances in Structural Engineering, 15 (2012) 417-433.
[7] Y.B. Yang, W.F. Chen, Extraction of Bridge Frequencies from a Moving Test Vehicle by Stochastic Subspace Identification, Journal of Bridge Engineering, 21 (2016).
[8] T. Nagayama, A. Reksowardojo, D. Su, T.M.C. Zhang, Bridge Natural Frequency Estimation by Extracting the Common Vibration Component From the Responses of Two Vehicles, in: 6th International Conference on Advances in Experimental Structural Engineering, Urbana-Champaign, USA, 2015.
[9] E.J. OBrien, A. Malekjafarian, A. Gonzalez, Application of empirical mode decomposition to drive-by bridge damage detection, European Journal of Mechanics a-Solids, 61 (2017) 151-163.
[10] D. Hester, A. González, A discussion on the merits and limitations of using drive-by monitoring to detect localised damage in a bridge, Mechanical Systems and Signal Processing, 90 (2017) 234-253.
[11] Y.B. Yang, Y.C. Li, K.C. Chang, Constructing the mode shapes of a bridge from a passing vehicle: a theoretical study, Smart Structures and Systems, 13 (2014) 797-819.
[12] Y. Zhang, L.Q. Wang, Z.H. Xiang, Damage detection by mode shape squares extracted from a passing vehicle, Journal of Sound and Vibration, 331 (2012) 291-307.
[13] Y. Oshima, K. Yamamoto, K. Sugiura, Damage assessment of a bridge based on mode shapes estimated by responses of passing vehicles, Smart Structures and Systems, 13 (2014) 731-753.
[14] A. Malekjafarian, E.J. OBrien, Identification of bridge mode shapes using short time frequency domain decomposition of the responses measured in a passing vehicle, Engineering Structures, 81 (2014) 386-397.
[15] E.J. OBrien, A. Malekjafarian, A mode shape‐based damage detection approach using laser measurement from a vehicle crossing a simply supported bridge, Structural Control and Health Monitoring, 23 (2016) 1273-1286.
[16] A. Malekjafarian, E.J. OBrien, On the use of a passing vehicle for the estimation of bridge mode shapes, Journal of Sound and Vibration, DOI: 10.1016/j.jsv.2017.02.051 (2017).
[17] E.J. OBrien, A. Malekjafarian, Identification of bridge mode shapes using a passing vehicle, in: 7th International Conference on Structural Health Monitoring of Intelligent Infrastructure, Torino, Italy, July, 2015, 2015.

COMPDYN 2017
6th ECCOMAS Thematic Conference on
Computational Methods in Structural Dynamics and Earthquake Engineering
M. Papadrakakis, M. Fragiadakis (eds.)
Rhodes Island, Greece, 15–17June 2017

# COMPARATIVE ASSESSMENT OF STRUT MODELS FOR THE MODELLING OF IN-PLANE SEISMIC RESPONSE OF INFILL WALLS

**Laura Liberatore[1], Fabrizio Noto[1], Fabrizio Mollaioli[1] and Paolo Franchin[1]**

[1]Department of Structural and Geotechnical Engineering, Sapienza University of Rome
Via Gramsci 53, 00197 Rome, Italy
{laura.liberatore,fabrizio.mollaioli,paolo.franchin}@uniroma1.it
fabrizio.noto@gmail.com

**Keywords:** Masonry Infill, Strut Models, Lateral Strength, Lateral Stiffness, Equivalent Width.

**Abstract.** *The influence of infills on the seismic response of frame structures has long been recognised. Typically, stiffness and strength of the infill and connections between infill and frame are such that the infill affects the global seismic behaviour of the structure. Hence, the presence of infills should be considered in the analysis and design of new buildings and in the seismic assessment of existing ones. To this aim, simple models for infill walls, such as the equivalent diagonal no-tension strut model, have been developed in the last decades. The objective of the present study is to assess the validity of different strut models. To this aim, 162 experimental tests available in the literature are considered. The data set includes both reinforced concrete and steel frames, as well as confined masonry structures. The mechanical characteristics of masonry and the boundary conditions between frames and infills of the test specimens take into account a large set of situations, reflecting the great variability in the materials and in the construction techniques adopted in different countries. Moreover, the type of tests and the related results are not uniform; in some cases monotonic experiments are performed, whereas in other cases cyclic tests are carried out. As expected, the presence of different types of infill-frame systems results in a large scatter of the data. However, the comparison between experimental results and predictions show that, on the average, the infill strength can be adequately estimated by resorting to the strut model whereas major uncertainties are found for the stiffness prediction.*

## 1 INTRODUCTION

Damage observed after moderate and strong earthquakes highlighted the influence of infills on the seismic response of frame structures. Regularly distributed infills may significantly contribute to withstand seismic actions, reducing the deformation demand and enhancing the energy dissipation capacity [1,2]. On the contrary, irregular arrangement of infills may be strongly detrimental, producing unfavourable distribution of plastic hinges, high demand of inelastic deformations and brittle failures. Therefore, the presence of infills should be considered in the design of new buildings and in the seismic assessment of existing ones. For this reason, in the last decades, the issue concerning the modelling of infills has gained a growing attention and different methods have been proposed and developed [3,4]. Such methods may be divided roughly into two categories according to whether they are based on micro-modelling or on macro-modelling approaches.

The former is based on a finite element representation of the frame and the infill. The response of the frame, the infill and their interface are described by means of proper constitutive relations. To reproduce the shear sliding of masonry mortar, several plasticity-based continuous interface models have been developed [5]. In general, this approaches are quite complex due to the large amount of information required [6]. On the contrary, macro-models, even though unable to capture local phenomena, are characterized by an advantageous simplicity. The equivalent diagonal no tension strut is one of the most used macro-model, being often adopted for in-plane seismic assessment of frame structures. This model was initially based on the observation that the compressive path in the masonry panel, due to horizontal loads, develops mainly along its diagonal. Therefore, a way of representing the stiffening and strengthening effect of the masonry infill is replacing the panel with an equivalent no tension strut acting along the compressive path [7,8]. The strut model may also be used, with opportune modifications, for perforated infills [9]. The width of the strut depends on different features, such as the extension of the region of interaction between masonry and frame. The ultimate strength of the infills depends also on the failure mechanism, which is somewhat difficult to predict being affected by many factors, such as the material properties, the dimensions of the system and the vertical stress in the panel. Multiple strut configurations have also been proposed with the aim of capturing the interaction between the infill panel and the frame (e.g. [10,11]). The multiple strut approach allows to account for the shear transmission in critical regions but the calibration of the required parameters is somewhat complex. The use of these methods is recommended for building not designed for seismic loads, having insufficient shear reinforcement and strong infills.

In this study, a comparison between different single strut models is performed, based on 162 experimental tests available in the literature. The database includes both reinforced concrete and steel frames, as well as confined masonry structures. The mechanical characteristics of masonry and the boundary conditions between frames and infills of the test specimens take into account a large set of situations, reflecting the great variability in the materials and in the construction techniques adopted in different countries. In the following sections, the selected models and the considered experimental tests are briefly presented. Afterword, the comparison between experimental and predicted values is reported in terms of lateral stiffness and strength of the masonry infill.

## 2 STRUT MODELS

Various relationships have been proposed to calculate the lateral strength and stiffness of the equivalent strut. The former is strictly related to the infill failure mode, which depends on several parameters, such as the aspect and slenderness ratios, the mechanical characteristics of

masonry, the stiffness and strength of the surrounding frame. As observed by Haldar et al. [12], four main failure modes have been identified: i) shear failure due to bed-joint sliding; ii) cracking due to diagonal tension; iii) diagonal compression failure and iv) corner crushing of the infill. The predicted failure mode, the related strength and the stiffness change noticeably from one model to another [13].

In this study, five strut models have been taken into account (Table 1). Most of them takes into account different failure modes and are derived through comparisons with experimental results.

| Reference | $R_s^{(1)}$ | $R_{dt}^{(2)}$ | $R_{dc}^{(3)}$ | $R_{cc}^{(4)}$ |
|---|---|---|---|---|
| Decanini and Fantin [14] | Y | Y | Y | Y |
| Paulay and Priestley [15]<br>Priestley and Calvi [16] | Y | Y | Y | × |
| Saneinejad and Hobbs [17] | Y | Y | Y | Y |
| FEMA 306 [18] | Y | Y | × | Y |
| Panagiotakos and Fardis [19] | Shear strength | | | |

(1) Failure due to bed-joint sliding; (2) Cracking due to diagonal tension; (3) Failure due to diagonal compression; (4) Failure due to corner crushing

Table 1: Failure modes taken into account in the considered strut models.

Predictive equations for the strength are listed in Table 2, respectively. In the Table 2, the strut axial strength, *R*, is reported. The lateral strength, *H*, is then given by the following equation:

$$H = R\,cos(\theta) \tag{1}$$

In the model by Decanini and Fantin [14] four failure modes are considered (equation 2 to 5). In Table 2, $R_s$ is the strength in the bed-joint sliding failure mode; $R_{dt}$ is the strength in the diagonal tension failure mode; $R_{dc}$ is the strength in the diagonal compression failure mode and $R_{cc}$ is the strength in the corner compression failure mode; $d$ is the length of the strut; $t$ is the masonry thickness; $\theta$ is the strut angle of inclination; $f_m^{'}$ is the masonry compressive strength; $\tau_0$ is the basic shear strength of bed joints; $\tau_{m0}$ is the shear strength evaluated through diagonal compression tests; $\sigma_y$ is the vertical stress; $w$ is the width of the equivalent strut; $\lambda_h$ is a non-dimensional parameter and $k_1$ and $k_2$ are equation coefficients (see Table 3).

According to Paulay and Priestley [15] the strut force to initiate sliding in infill panels, $R_s$, depends on the shear friction stress and on the aspect ratio of the panel, the coefficient of friction is assumed equal to 0.3 (equation 6). The diagonal compression strength (equation 7) is function of the vertical contact length, *z*, between infill and column. In Priestley and Calvi [16] the diagonal tension cracking failure is also considered. This failure mode does not produce itself the infill collapse, however the in-plane damage due to cracking contributes to the out-of-plane expulsion of the panel. The diagonal force, which induces diagonal tension cracking, is evaluated using the relationship for tensile stress in a disk loaded along a diameter (equation 8).

| Reference | Strut Axial Strength | |
|---|---|---|
| Decanini and Fantin [14] | $R_s = \left[(1.2\ sen\ \theta + 0.45\ cos\ \theta)\tau_0\ + 0.3\ \sigma_y\right]\ t\ d$ | (2) |
| | $R_{dt} = \left(0.6\ \tau_{m0} + 0.3\ \sigma_y\right) t\ d$ | (3) |
| | $R_{dc} = \frac{1.16\ tan\ \theta}{\lambda_h} f_m^{'}\ t\ d$ | (4) |
| | $R_{cc} = \frac{1.12\ sen\ \theta\ cos\ \theta}{\lambda_h^{0.88}} f_m^{'}\ t\ d$ | (5) |
| Paulay and Priestley [15]<br>Priestley and Calvi [16] | $R_s = \frac{\tau_0}{1 - 0.3(h/l)}\ t\ d$ | (6) |
| | $R_{dc} = \frac{2}{3}\ z\ t\ f_m^{'}\ sec\ \theta \qquad z = \frac{\pi}{2}\frac{h}{\lambda_h}$ | (7) |
| | $R_{dt} = \frac{\pi}{2}\ t\ d\ f_{tm}^{'}$ | (8) |
| Saneinejad and Hobbs [17] | $R_s = min \begin{cases} \frac{\gamma\ \tau_0\ t\ d}{1 - 0.45\ tan\ \theta^{'}} \\ 0.83\ \gamma\ \ t\ d\ \ (0.83\ in\ MPa) \end{cases}$ | (9) |
| | $R_{dt} = 2\sqrt{2}\ t\ h_m f_t^{'}\ cos\ \theta$ | (10) |
| | $R_{dc} = \frac{0.5\ h_m\ t\ f_a}{cos\ \theta} \qquad f_a = 0.39 f_m^{'}\left[1 - \left(\frac{l_{eff}}{40\ t}\right)^2\right]$ | (11) |
| | $R_{cc} = \frac{(1 - \alpha_c)\alpha_c\ h\ t\ \sigma_c + \ \alpha_b\ l\ t\ \tau_b}{cos\ \theta}$ | (12) |
| FEMA 306 [18] | $R_s = \frac{\left(\tau_0 + \mu\ \sigma_y\right) l\ t}{cos\ \theta}$ | (13) |
| | $R_{dt} = 2\sqrt{2}\ t\ h_m f_t^{'}\ cos\ \theta$ | (14) |
| | $R_{cc} = w\ t\ f_{m90}^{'}$ | (15) |
| Panagiotakos and Fardis [19] | $R_s = \frac{1.3\ \ \tau_{cr}\ l_m\ t}{cos\ \theta}$ | (16) |

Table 2: Predictive equations for the strut axial strength.

In the analytical method developed by Saneinejad and Hobbs [17] all failure modes are considered. In equations 9 to 12 (Table 2), $\gamma$ is the load factor and $\theta^{'}$ is depicted in Figure 1. Diagonal cracking of the infill is regarded as a serviceability limit state; however, it may be related to a collapse limit state because presence of diagonal cracking in both diagonals accelerates the out-of-plane failure of the infill. For the cracking load, equation 10 is suggested,

where $f_t^{'}$ is the tensile strength of infill material. The diagonal compression strength is given by equation 11, where $f_a$ is the permissible stress, which takes into account the out-of-plane buckling and $l_{eff}$ is the effective length of the strut (Figure 1). From the above formula it results that the permissible stress is negative when the thickness of the infill is smaller than 2.5% of the effective length. Finally, in equation 12, $\alpha_c\ h$ and $\alpha_b\ l$ are the contact lengths between infill and columns and infill and beam, respectively, $\sigma_c$ and $\tau_b$ are the column-infill and beam-infill contact stresses.

Three potential in-plane failure modes are considered in FEMA 306 [18]. The Mohr-Coulomb failure criteria is used to assess the sliding-shear capacity of the infill, the corresponding strut resistance may be calculated by means of equation 13, where $\tau_0$ may be taken as 1/40 times the compressive strength and $\mu$ is the coefficient of friction along the bed joints. The diagonal tension strength in [18] is the same as suggested by Saneinejad and Hobbs, where $f_t^{'}$ may be taken as 1/20 of the compressive strength in the horizontal direction, $f_{m90}^{'}$. For corner compression failure, a modified version of the method proposed by Stafford-Smith and Carter [20] is suggested (equation 15).

Finally, Panagiotakos and Fardis [19] suggest calculate the infill ultimate strength by equation 16, where $\tau_{cr}$ is the masonry cracking strength as determined from diagonal compression tests.

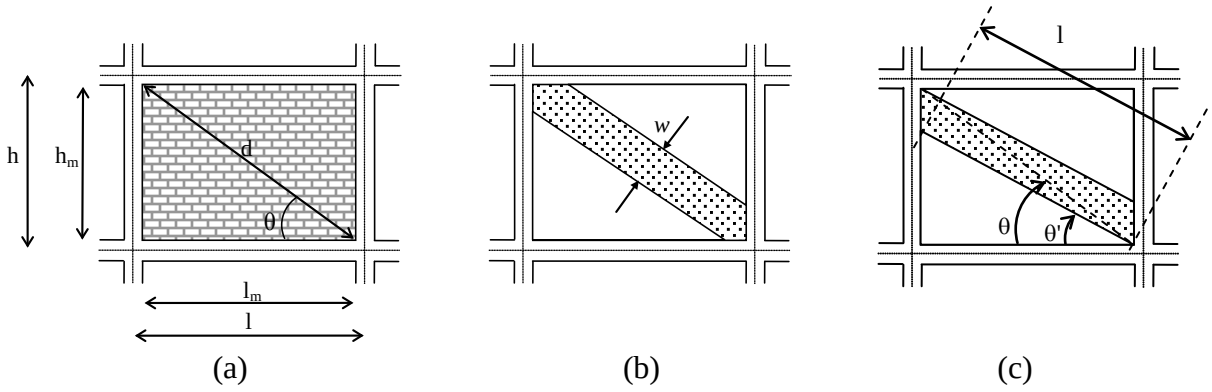


Figure 1: Equivalent strut model: a) in-plane geometrical features; b) equivalent strut; c) Saneinejad and Hobbs geometrical parameters [17].

The axial stiffness of the strut, *k*, is generally calculated as a function of the strut width, *w*, according to the following equation:

$$k = \frac{E_m\ t\ w}{d} \tag{17}$$

where $E_m$ is the modulus of elasticity of masonry, *t* is the panel thickness and *d* is the strut length. The lateral stiffness, $k_m$, can be calculated as:

$$k_m = \frac{E_m\ t\ w}{d} cos^2(\theta) \tag{18}$$

Equations proposed to estimate *w* are reported in Table 3. The parameter $\lambda_h$, used in some of these expressions, is a non-dimensional parameter introduced by Stafford-Smith [7] to take into account the influence of the relative stiffness of the frame and the infill:

$$\lambda_h\ = \sqrt[4]{\frac{E_m\ t\ sen\ 2\theta}{4EIh_m}}\, h \tag{19}$$

where: $E$ is the modulus of elasticity of the frame material and $I$ is the moment of inertia of columns (see above for definitions of other parameters).

| Reference | Equivalent strut width | |
|---|---|---|
| Decanini and Fantin [14] | $w = \left(\frac{k_1}{\lambda_h} + k_2\right) d$ (20) | for $\lambda_h < 3.14$ $k_1 = 1.3$ $k_2 = -0.178$<br>for $3.14 < \lambda_h < 7.85$ $k_1 = 0.707$ $k_2 = 0.01$<br>for $7.85 < \lambda_h$ $k_1 = 0.47$ $k_2 = 0.04$ |
| Paulay and Priestley [15]<br>Priestley and Calvi [16] | $w = \frac{d}{4}$ | (21) |
| Saneinejad and Hobbs [17] | $w = min\begin{cases} \frac{(1-\alpha_c)\alpha_c h \frac{\sigma_c}{f_c} + \alpha_b l \frac{\tau_b}{f_c}}{cos\,\theta} \\ 0.5 \frac{h_m \frac{f_a}{f_c}}{cos\,\theta} \end{cases}$ | (22) |
| FEMA 306 [18] | $w = 0.175\,(\lambda_h)^{-0.4} d$ | (23) |

Table 3: Predictive equations for the strut width.

The expression by Decanini and Fantin [14] provides the secant stiffness of the strut. The equation suggested by Paulay and Priestley [15], which gives a conservative value of the width, is recommended for a lateral force level of 50% of the ultimate capacity. The value suggested by Saneinejad and Hobbs [17] is related to the attainment of the resisting loads $R_{cc}$ and $R_{dc}$. The formula reported in FEMA 306 [18], which was initially proposed by Mainstone [21], was found suitable for the estimation of the infill secant stiffness if the masonry elastic modulus in the horizontal direction is used [19].

## 3 DATABASE USED IN THE STUDY

Experimental results available in the literature are used in this study to assess the selected strut models. The whole dataset, composed of 162 test specimens (Table 4), includes different types of frame-infill systems. With regard to reinforced concrete frames, both infilled frames and confined masonry structures are considered. In the infilled frames the masonry panel is built after the frame, whereas in confined masonry the panel is built earlier. The difference between confined masonry and infilled frame systems is twofold: i) in confined masonry, a stronger adherence between masonry and RC columns and beams develops compared to that present in infilled frames; ii) in confined masonry buildings the column and beam cross sections are generally smaller than in infilled frame buildings.

Concerning the walls, in 60% of the test specimens the masonry is made up of hollow units (vertical or horizontal hollows), in the other 40% the masonry is made up of solid bricks or blocks. The aspect and the slenderness ratios of the infills vary noticeably: the former is in the range 0.48-2.95, the latter varies between 5.33 and 25.78. However, in 80% of the specimens

the aspect and slenderness ratios are less than 1 and 15, respectively. This values can be considered representative of sizes present in common existing infilled framed buildings. Horizontal loads are applied monotonically or cyclically in 34 and 128 experimental tests, respectively. Cyclic loads are generally applied statically with force-controlled or, more often, displacement-controlled procedures. Pseudo-dynamic and dynamic tests are performed in 12 experimental tests.

The whole database is used to assess the capability of different strut models to estimate the infill strength. As for the assessment of the infill stiffness, only the tests for which the horizontal force versus horizontal displacement curves were available have been used. The reduced database includes 101 specimens.

| Reference | N. of test | Structure [(1)] |
|---|---|---|
| Benjamin and Williams, 1958, [22] | 8 | RC |
| Jorquera, 1964, [23] | 17 | CM |
| Leuchars and Scrivener, 1976, [24] | 2 | RC |
| Jurina, 1977, [25] | 3 | RC |
| Parducci et al., 1980 [26], 1982 [27] | 6 | RC |
| Liu et al., 1982, [28] | 9 | RC |
| Srinivasa Rao et al., 1982, [29] | 3 | RC (1), CM (2) |
| Gallegos and Casabonne, 1984, [30] | 2 | RC |
| Zarnic and Tomazevic, 1984 [31], 1986 [32] | 11 | RC |
| Decanini et al., 1985, [33] | 3 | CM |
| Michelini et al., 1986, [34,35] | 9 | CM |
| Valiasis and Stylianidis, 1989 [36] | 16 | RC |
| Pires, 1990, [37] | 6 | RC (3), CM (3) |
| Kato et al., 1992, [38] | 4 | CM |
| Meherabi et al., 1996, [39] | 10 | RC |
| Crisafulli, 1997, [11] | 2 | RC |
| Calvi e Bolognini, 2001, [40] | 8 | RC |
| Colangelo, 2005, [41] | 11 | RC |
| Hashemi and Mosalam, 2006, [42] | 1 | RC |
| Bergami, 2007, [43] | 2 | RC |
| Kakaletsis and Karayannis, 2008, [44] | 2 | RC |
| Stavridis, 2009, [45] | 2 | RC |
| Tasnimi and Mohebkhahb, 2011, [46] | 1 | Steel |
| Yuksel, 2011, [47] | 2 | RC |
| Sigmund and Penava, 2012, [48] | 1 | RC |
| Di Trapani, 2013, [49] and Cavaleri et al., 2005, [50] | 12 | RC |
| Markulak et al., 2013, [51] | 6 | Steel |
| Guidi et al., 2013, [52] | 1 | RC |
| Morandi et al., 2014, [53] | 2 | RC |

[(1)] RC=Reinforced Concrete, CM=Confined Masonry

Table 4: Experimental tests used in the study.

## 4 RESULTS AND DISCUSSION

Equations reported in Table 2 are used to predict the lateral strength of infills. The predictions are then compared with the experimental values of lateral strength. The experimental results always concern the infill-frame systems; therefore, a basic preliminary step was the estimation of the contribution of infill to the total lateral resistance. This is made herein by calculating the difference between the infilled frame and the bare frame. In those cases in which the bare frames were not available, an approximated frame backbone curve has been obtained using the model proposed by Haselton [54].

The ratio between predicted and experimental strength is calculated for the five strut models. The exponential of the logarithmic mean, $e^{\mu_{ln}}$, and the logarithmic standard deviation, $\sigma_{ln}$, of this ratio are then estimated. The former represents the median values under the hypothesis of a lognormal distribution, the latter approximates the coefficient of variation and gives a measure of the dispersion. These values are reported in Table 5 for the whole database and for data samples clustering different type of structures, i.e., infilled reinforced concrete frames, confined masonry systems and infilled steel frames.

The model proposed and Priestley [15] and Priestley and Calvi [16] provides, on the average, a good estimate of the actual values. However, with the exception of the steel frames set, a large dispersion is noted, being the logarithmic standard deviation between 0.453 and 0.534. The models proposed by Decanini and Fantin [14] and by Panagiotakos and Fardis [19] give, in general, the lowest dispersion for infilled RC frames and confined masonry, whereas the Paulay and Priestley [15] and Priestley and Calvi [16] model furnishes the best results for steel frames, in terms of both mean value and logarithmic standard deviation.

| | DF[(1)] | PF[(2)] | PPC[(3)] | SH[(4)] | FEMA[(5)] |
|---|---|---|---|---|---|
| Whole database | | | | | |
| $e^{\mu_{ln}}$ | 0.848 | 1.350 | 1.071 | 0.624 | 0.698 |
| $\sigma_{ln}$ | 0.407 | 0.409 | 0.517 | 0.580 | 0.571 |
| Infilled RC frames | | | | | |
| $e^{\mu_{ln}}$ | 0.871 | 1.389 | 1.010 | 0.652 | 0.708 |
| $\sigma_{ln}$ | 0.439 | 0.444 | 0.534 | 0.617 | 0.608 |
| Confined masonries | | | | | |
| $e^{\mu_{ln}}$ | 0.808 | 1.277 | 1.284 | 0.567 | 0.709 |
| $\sigma_{ln}$ | 0.294 | 0.285 | 0.453 | 0.472 | 0.456 |
| Infilled steel frames | | | | | |
| $e^{\mu_{ln}}$ | 0.701 | 1.151 | 1.045 | 0.517 | 0.492 |
| $\sigma_{ln}$ | 0.252 | 0.253 | 0.177 | 0.268 | 0.281 |

[(1)]Decanini and Fantin [14], [(2)]Panagiotakos and Fardis [19], [(3)]Paulay and Priestley [15] and Priestley and Calvi [16], [(4)]Saneinejad and Hobbs [17], [(5)]FEMA 306 [18].

Table 5: Predicted/experimental strength ratios: $e^{\mu_{ln}}$ = exponential of the logarithmic mean, $\sigma_{ln}$ = logarithmic standard deviation.

The predicted lateral strengths are plotted in Figure 2 versus the experimental ones. Different colours indicate different structural systems: blue markers are used for infilled reinforced concrete frames, red markers for confined masonries and black markers for infilled steel frames. Linear regression curves, related to the whole database, and coefficients of determination, $R^2$, are also reported in the figure.

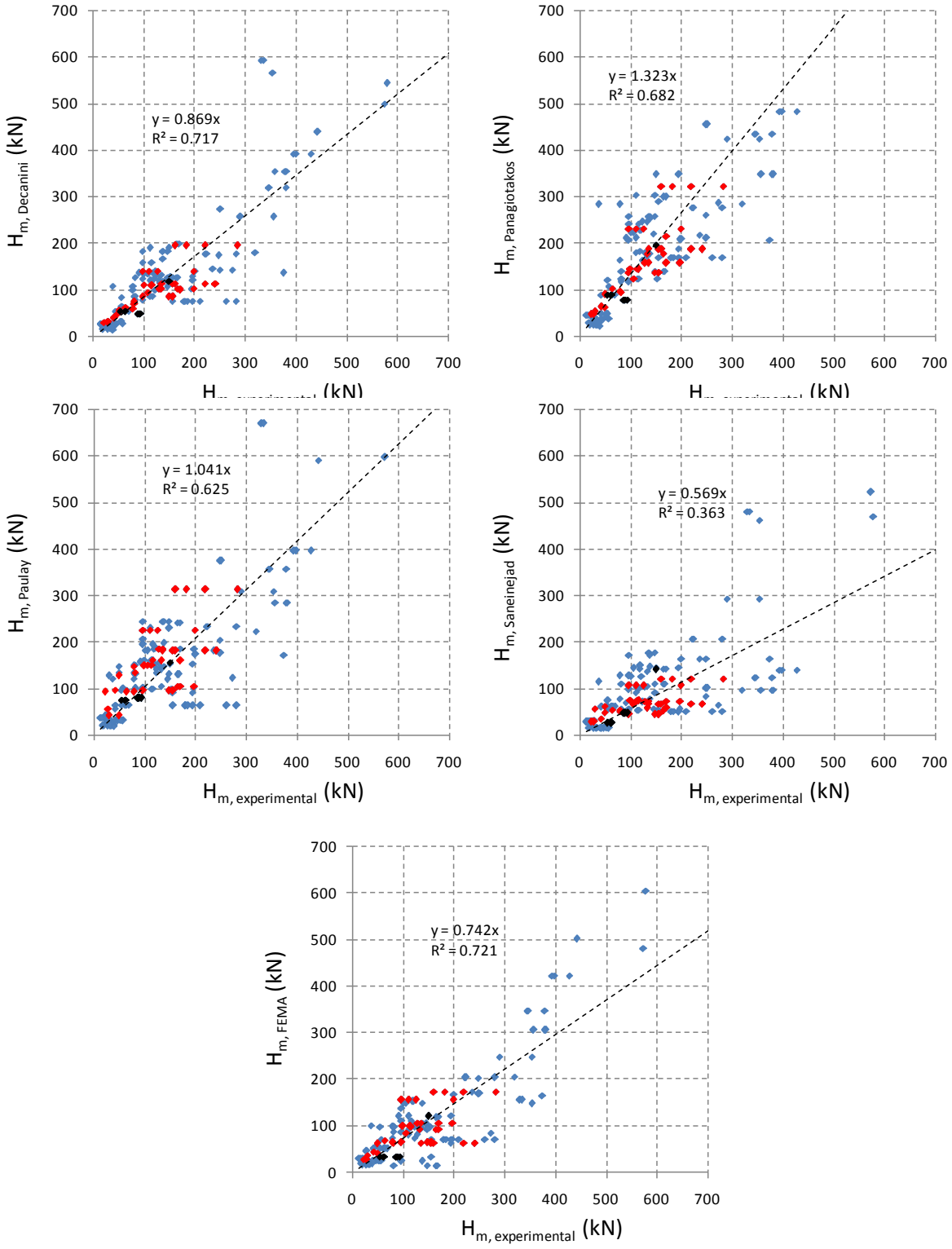


Figure 2: Lateral strength of infill: predictions vs. experimental values. Blue markers: infilled reinforced concrete frames; red markers: confined masonry; black markers: infilled steel frame.

It is noted that: strength values predicted by Panagiotakos and Fardis [19] are higher than the actual (experimental) ones; the model proposed by Paulay and Priestley [15] and Priestley and Calvi [16] is almost unbiased; the other models tend, on the average, to underestimate the

infill strength. The highest and the lowest coefficients of determination are obtained, considering the whole dataset, using the formulation proposed by the Decanini and Fantin [14] and Saneinejad and Hobbs [17], respectively.

The comparison between predicted and experimental lateral stiffness is made considering the reduced database. Formulas reported in Table 3 and equation 18 are used to calculate the predicted values. The experimental stiffness is calculated as the elastic stiffness of an equivalent bilinear system, obtained through the energy equivalence criterion up to the peak lateral load ($H_m$). Figure 3 shows the comparison between predicted and experimental results. The use of various formulas leads to different values of the equivalent width, and, therefore, of the strut stiffness. For example, the equation in FEMA [18] gives a much more deformable strut compared to the other models. Moreover, differences between predicted and experimental values are significant, showing that none of the considered models is able to predict the infill stiffness adequately. For the confined masonry frames, all of the models predict values of the stiffness lower than the actual ones. The dispersion of the data is noticeable, coefficient of variations varying between 1.7 and 2.0. These results show the great uncertainty in the assessment of infills stiffness.

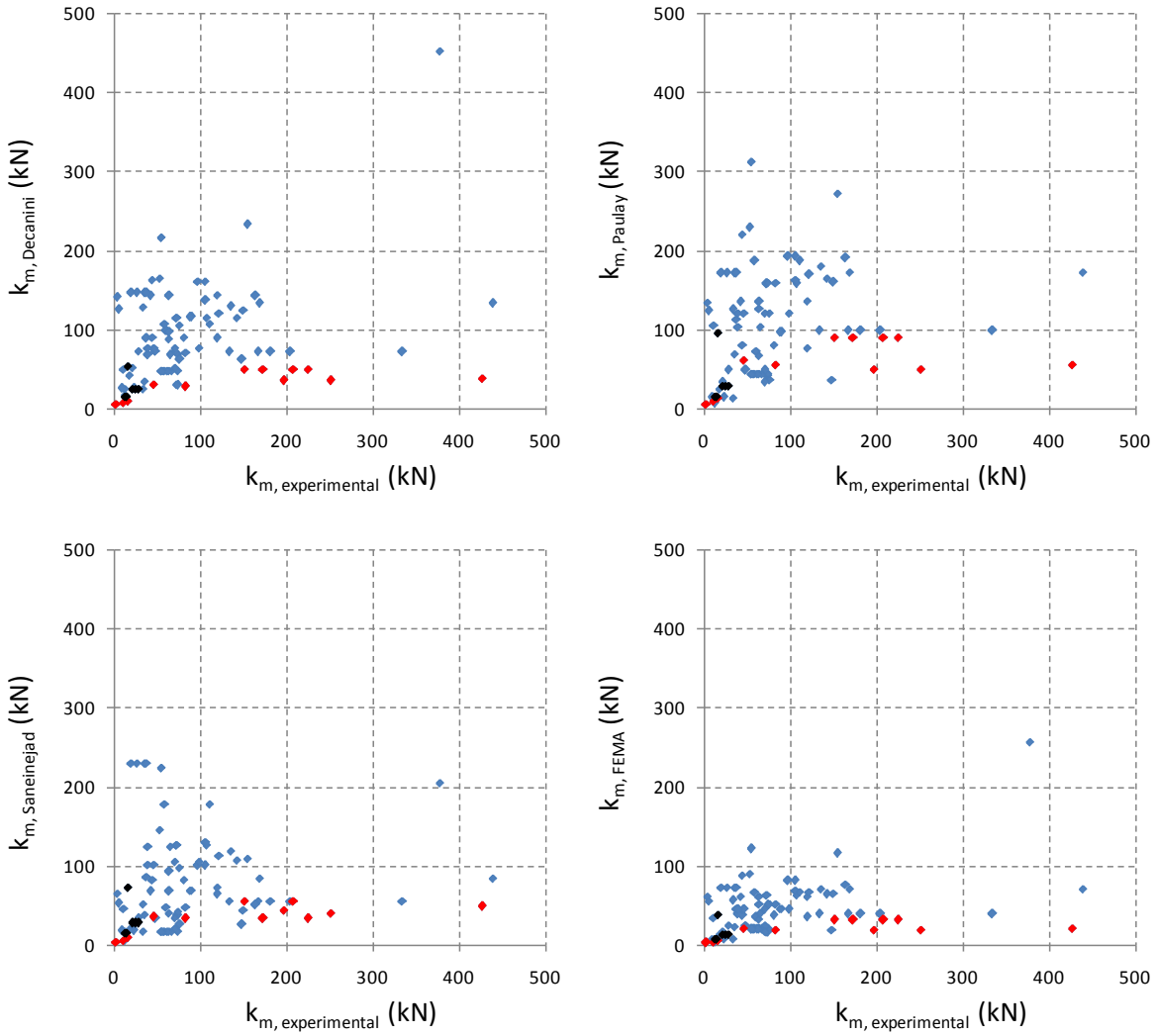


Figure 3: Lateral stiffness of infill: prediction vs. experimental values. Blue markers: infilled reinforced concrete frames; red markers: confined masonry; black markers: infilled steel frame.

## 5 CONCLUSIONS

In this work, 162 experimental tests have been considered to evaluate the adequacy of various strut models. The database includes different types of masonry walls, which are made of hollow or solid bricks or blocks, and different types of frame-infill systems: 116 infilled reinforced concrete frames, 39 confined masonry structures and 7 infilled steel frames.

The assessment of the contribution of infills to the lateral stiffness and strength of the experimental tests was a basic preliminary step. This assessment was made by calculating the difference between the infilled frame and the bare frame. In those cases in which the bare frame was not available, several assumptions, like for example that of rigid beams, have been made to calculate the bare frame backbone curves. Stiffness and strength predictions have been calculated considering five strut models. Such models require the knowledge of the geometrical and mechanical characteristics of the frame and the infill. In some cases, the required parameters were not assessed experimentally, such as the masonry shear strength and the horizontal compressive strength. When not available, these features have been calculated here by means of empirical equations.

The comparison between predicted and actual lateral strengths shows that the models by Paulay and Priestley [15], Priestley and Calvi [16] and Decanini and Fantin [14] give the best predictions, with the former having the advantage of being almost unbiased and the latter giving the lowest dispersion. The strength predicted by Panagiotakos and Fardis [19] is, on the average, higher than the actual one, while the other models ([17,18]) underestimate the infill strength. Concerning the stiffness, none of the models reproduce satisfactorily the actual values. Differences between predicted and experimental values are significant, showing the inadequacy of all the considered equations. Given the large differences obtained using different formulations, much attention should be paid in the model selection.

On the basis of the reported results, it can be concluded that the high variability of the material and the large number of parameters involved, make the reliability of the modelling very hard to obtain. However, the significant contribution of infill walls in the behaviour of infilled frames requires the continuation of research in this area. Finally, other aspects not taken into account in this study, such as the modelling of the hysteretic behaviour, need to be further investigated.

## ACKNOWLEDGEMENTS

The financial support of the Ministry of the Instruction, University and Research of Italy (MIUR) is gratefully acknowledged. This work has been partially carried out under the program “Dipartimento di Protezione Civile - Consorzio RELUIS 2017, Area Tematica 1”.

## REFERENCES

[1] L. Liberatore, L.D. Decanini, “Effect of infills on the seismic response of high-rise RC buildings designed as bare according to Eurocode 8”, *Ingegneria Sismica*, **28**(3): 7-23, 2011.

[2] L.D. Decanini, L. Liberatore, F. Mollaioli, “Damage potential of the 2009 L’Aquila, Italy, earthquake”, *Journal of Earthquake and Tsunami*, **6**(3), 1250032:1-32, 2012.

[3] F. Di Trapani, G. Macaluso, L. Cavaleri, M. Papia, “Masonry infills and RC frames interaction: literature overview and state of the art of macromodeling approach”, *European Journal of Environmental and Civil Engineering*, **19**(9), 1059-1095, 2015.

[4] N. Tarque, L. Candido, G. Camata, E. Spacone, "Masonry infilled frame structures: state-of-the-art review of numerical modelling", *Earthquakes and Structures*, **8**(3), 733-759, 2015.

[5] P.B. Shing, A.B. Mehrabi, "Behaviour and analysis of masonry-infilled frames", *Progress in Structural Engineering and Materials*, **4**(3), 320-331, 2002.

[6] L. Liberatore, M. Bruno, O. AlShawa O., M. Pasca, L. Sorrentino, "Finite-discrete element modelling of masonry infill walls subjected to out-of-plane loads", *7th European Congress on Computational Methods in Applied Sciences and Engineering (ECCOMAS)*, 3: 5219-5229, 2016.

[7] B. Stafford Smith, "Lateral stiffness of infilled frames", *Journal of Structural Division*, ASCE, **88**, no. ST6, 183-199, 1962.

[8] R.J. Mainstone, "On stiffness and strength of infilled frames", *Proceedings of Institution of Civil Engineers*, n. 7360, 57-90, 1971.

[9] L.D. Decanini, L. Liberatore, F. Mollaioli, "Strength and stiffness reduction factors for infilled frames with openings", *Earthquake Engineering and Engineering Vibration*, **13**(3), 437-454, 2014.

[10] V. Thiruvengadam, "On the natural frequencies of infilled frames", *Earthquake Engineering and Structural Dynamics*, **31**(2), 44-46, 1985.

[11] F.J. Crisafulli, *Seismic behaviour of reinforced concrete structures with masonry infills*, PhD Thesis, University of Canterbury, Christchurch, New Zealand, 1997.

[12] P. Haldar, Y. Singh, D.K. Paul, "Identification of seismic failure modes of URM infilled RC frame buildings", *Engineering Failure Analysis*, **33**: 97-118, 2013.

[13] L. Liberatore, F. Mollaioli, "Influence of masonry infills modelling on the seismic response of reinforced concrete frames", *15th International Conference on Civil, Structural and Environmental Engineering Computing (Civil-Comp Proceedings)*, **108**, n. 87, 2015.

[14] L.D. Decanini, G.E. Fantin, "Modelos simplificados de la mampostería incluida en porticos. Características de rigidez y resistencia lateral en estado límite", *Jornadas Argentinas de Ingenierìa Estructural*, 817-836, 1987.

[15] T. Paulay, M.J.N. Priestley, *Seismic design of reinforced concrete and masonry buildings*, John Wiley & Sons, Inc., 1992.

[16] M.J.N. Priestley, M. Calvi, "Towards a capacity-design assessment procedure for reinforced concrete frames", *Earthquake Spectra*, **7**(3), 413-437, 1991.

[17] A. Saneinejad, B. Hobbs, "Inelastic design of infilled frames", *Journal of Structural Engineering*, ASCE, **121**(4), 634-50, 1995.

[18] FEMA 306, *Evaluation of earthquake damaged concrete and masonry wall buildings - basic procedures manual*, prepared by The Applied Technology Council, 1998.

[19] T.B. Panagiotakos, M.N. Fardis, "Seismic response of infilled RC frames structures", *11th World Conference on Earthquake Engineering*, n. 225, 1996.

[20] B. Stafford-Smith, C. Carter, "A method of analysis for infilled frames", *Proceedings of the Institute of Civil Engineers*, **44**, 31-48, 1969.

[21] R.J. Mainstone, "Supplementary note on the stiffness and strength of infilled frames", *Building Research Station*, CP 13/74, Building Research Establishment, U.K., 1974.

[22] J.R. Benjamin, H.A. Williams, "The behavior of one-story brick shear walls", *Journal of the Structural Division*, Proc. ASCE, n. 1723, ST 4, 1958.

[23] L. Jorquera, "Estudio esperimental sobre la resistencia de muros de albanileria sometidos a cargas horizontales", *Revista de IDIEM*, **3**, 1964.

[24] J.M. Leuchars, J.C. Scrivener, "Masonry infill panels subjected to cyclic in-plane loading", *Bulletin of the New Zealand Society for Earthquake Engineering*, **9**(2):122-131, 1976.

[25] L. Jurina, "Pareti in muratura soggette ad azioni sismiche", *Costruire*, **100**: Tst/1-Tst/46, 1977.

[26] A. Parducci, M. Mezzi,. "Repeated horizontal displacements of infilled frames having different stiffness and connecting systems - experimental analysis", *7th World Conference on Earthquake Engineering*, Istanbul, Turkey, 1980.

[27] A. Parducci, A. Checchi, "Contributo delle tamponature di mattoni alla resistenza sismica delle strutture intelaiate", *6th International Brick Masonry Conference*, Rome, 1982.

[28] X. Liu, H. Zhang, J. Liu, L. Liu, "Experimental investigation and aseismic safety evaluation of brick masonry buildings with R/C tie columns", *7th European Conference on Earthquake Engineering*, , Athens, Greece, **5**: 197-204, 1982.

[29] P. Srinivasa Rao, H. Achyutha, R. Jagadish, N. Devanarayanan, "Influence of methods of construction on the behaviour of infilled frames", *6th International Brick and Block Masonry Conference*, Rome, Italy, 549-560, 1982.

[30] H. Gallegos, C. Casabonne, "Cyclic test of three different types of masonry walls", *Third International Symposium on Wall Structure*, Warsaw, Poland, 1984.

[31] R. Zarnic, M. Tomazevic, "The Behaviour of Masonry Infilled Reinforced Concrete Frames Subjected to Cyclic Lateral Loading", *8th World Conference on Earthquake Engineering*, San Francisco, p 863:870, 1984

[32] R. Zarnic, M. Tomazevic, T. Velechovsky, "Experimental study of methods for repair and strengthening of masonry infilled reinforced concrete frame", *8th European Conference on Earthquake Engineering*, Lisbon, Portugal, **5**: 11.1/41-48, 1986.

[33] L.D. Decanini, A. Payer, C. Serrano, R. Terzariol, "Investigacion experimental sobre el comportamiento sismorresitente de prototipos a escala natural de muros de mamposteria encadenada", *Memoria B Ingenieria Estructural*, colloquia 85, Tomo VI, 1985.

[34] R.J. Michelini et al. "Influencia de la acciòn vertical en el comportamiento estructural de paneles de mamposteria bajo el efecto de cargas orizontales", *4as Jornadas Chilenas de Sismologia e Ingenieria Antisismica*, Viña del Mar, Chile, Tomo 2: H119-138, 1986.

[35] R.J. Michelini, L.A. Olivencia, D.A. Forni, N.G. Maldonado, "Comportamiento ante acciones horizontales de mamposteria reparada", *4as Jornadas Chilenas de Sismologia e Ingenieria Antisismica*, Viña del Mar, Chile, Tomo 1: D96-115, 1986.

[36] T.N. Valiasis, K.C. Stylianidis, "Masonry Infilled R/C/ Frames under Horizontal Loading Experimental Results", *European Earthquake Engineering*, **3**: 10-20, 1989.

[37] F.M. Pires, *Influência das paredes de alvenaria no comportamento de estrututras reticuladas de betão armado sujeitas a acções horizontais*, PhD Thesis. Laboratorio Nacional de Engenharia Civil, Lisboa, 1990.

[38] H. Kato, T. Goto, H. Mizuno, M. Iiba, "Cyclic loading tests of confined masonry wall elements for structural design development of apartment houses in the Third World", *10th World Conference on Earthquake Engineering*, Madrid, Spain, p. 3539:3544, 1992.

[39] A.B. Mehrabi, P.B. Shing, M.P. Schuller, J.L. Noland, "Experimental evaluation of masonry-infilled RC frames", *Journal of Structural Engineering*, **122**(3):228-237, 1996.

[40] G.M. Calvi, D. Bolognini, "Seismic response of reinforced concrete frames infilled with weakly reinforced masonry panels", *Journal of Earthquake Engineering*, **5**:153-185, 2001.

[41] F. Colangelo, "Pseudo-dynamic seismic response of reinforced concrete frames infilled with non-structural brick masonry", *Earthquake Engineering and Structural Dynamics*, **34**(10):1219-1241, 2005.

[42] A. Hashemi, K.M. Mosalam, "Shake-table experiment on reinforced concrete structure containing masonry infill wall", *Earthquake Engineering and Structural Dynamics*, **35**:1827-1852, 2006.

[43] A.V. Bergami, *Implementation and experimental verification of models for nonlinear analysis of masonry infilled r.c. frames*, PhD Thesis, Roma Tre University, Rome, Italy, 2007.

[44] D.J. Kakaletsis, C.G. Karayannis, "Influence of masonry strength and openings on infilled R/C frames under cyclic loading", *Journal of Earthquake Engineering*, **12**(2):197-221, 2008.

[45] A. Stavridis, *Analytical and experimental study of seismic performance of reinforced concrete frames infilled with masonry walls*, PhD Thesis, University of California, San Diego, USA, 2009.

[46] A.A. Tasnimi, A. Mohebkhah, "Investigation on the behavior of brick-infilled steel frames with openings, experimental and analytical approaches", *Engineering Structures*, **33**: 968-980, 2011.

[47] E. Yuksel, P. Teymur, "Earthquake performance improvement of low rise RC buildings using high strength clay brick walls", *Bulletin of Earthquake Engineering*, **9**:1157-1181, 2011.

[48] V. Sigmund, D. Penava, "Experimental Study of Masonry Infilled R/C Frames with Opening", *15th World Conference on Earthquake Engineering*, Lisbon, Portugal, 2012.

[49] F. Di Trapani, *Masonry infilled RC frames: Experimental results and development of predictive techniques for the assessment of seismic response*, PhD Thesis, University of Palermo, Italy, 2013.

[50] L. Cavaleri, M. Fossetti, M. Papia, "Infilled frames: developments in the evaluation of cyclic behaviour under lateral loads", *Structural Engineering and Mechanics*, **21**(4):469-494, 2005.

[51] D. Markulak, I. Radić, V. Sigmund, "Cyclic testing of single bay steel frames with various types of masonry infill", *Engineering Structures*, **51**: 267-277, 2013.

[52] G. Guidi, F. da Porto, M. Dalla Benetta, N. Verlato, C. Modena, "Comportamento Sperimentale nel Piano e Fuori Piano di Tamponamenti in Muratura Armata e Rinforzata", *15th Convegno ANIDIS L'Ingegneria Sismica in Italia*, Padova, Italy, 2015.

[53] P. Morandi, S. Hak, G. Magenes, "In-plane Experimental Response of Strong Masonry Infills", *9th International Masonry Conference*, Guimarães, Portugal, 2014.

[54] C.B. Haselton, A.B. Liel, S.T. Lange, G.G. Deierlein, *Beam-Column Element Model Calibrated for Predicting Flexural Response Leading to Global Collapse of RC Frame Buildings*, PEER Report 2007/03, Pacific Earthquake Engineering Research Center, 2008.

COMPDYN 2017
6th ECCOMAS Thematic Conference on
Computational Methods in Structural Dynamics and Earthquake Engineering
M. Papadrakakis, M. Fragiadakis (eds.)
Rhodes Island, Greece, 15–17 June 2017

# FURTHER DEVELOPMENTS OF A SIMPLIFIED MODELLING OF INFILLED FRAMES FOR REINFORCED CONCRETE BUILDINGS

**Giuseppina Uva[1], Andrea Fiore[1,*], and Francesco Porco[1]**

[1]Politecnico di Bari, Dicatech
Via Orabona, 4 - 70126 Bari, Italy
giuseppina.uva@poliba.it
*andrea.fiore@poliba.it
francesco.porco@poliba.it

**Keywords:** Existing Building, Seismic Assessment, Reinforced Concrete, Infilled Frame, Equivalent Strut Method.

**Abstract.**
*The main proposals for the modelling of the infilled frames are calibrated on the results deriving from experimental testing data. In many cases, the experimental laws acquired that concern samples packaged with materials and executive methods (for frame-panel interface conditions, for mechanical properties ...) are extended to different with several uncertainties. Several researchers suggest approaches that ranging from the macro-scale to micro-scale analysis. The different proposals confirm the complexity to simulate the kinematic mechanism between constitutive elements (mortar and bricks) and between masonry panel and surrounding frame. Therefore, the great variability of models and available studies do not allow to apply a univocal model adaptable in all cases, (Except by adopting, micro-modelling approaches, increasing the computational effort). This raises the need to define simplified models that take into account the geometry, mechanical properties of the masonry walls and elements of the surrounding frame. For these purposes, the present study proposes a Rigid Blocks Method in a simplified format for simulating of the infilled frames in order to define the main parameters that characterize the simplified "Equivalent Strut model" (i.e. the macro-modelling of the infill walls). The method falls in the meso-scale approaches commonly used for analysis of masonry structures. The use of an equivalent rod for modelling the infill panels is simple and reduces the computational costs when it is need to evaluate the global behavior on building scale. In order to demonstrate its multiple advantages, the method is presented. The opportunity to simulate the behavior of the infilled frame varying the mechanical properties and modality to derive ad hoc constitutive laws in presence of openings are just some the potential of the method. With the help of numerical benchmarks having similar characteristics to those widespread into building heritage these results are widely discussed.*

## 1 INTRODUCTION

The numerical modelling of the infilled frames is affected by several variables, which makes the different models existing in the technical literature very variable and uncertain. For many years, in fact, the research goal of many researchers has been to reduce the influence of the many factors involved in the problem [1, 17]. Among the variables, first of all, it should be recalled the heterogeneity of the mechanical properties of the constituents (bricks and mortar) and the difficulty to obtain information and data about the masonry used in the infilled panels [26], the difficulty to simulate the frame-infill interaction or the impossibility to predict, at the design phase, the exact failure mode of the generic infilled frame.

A model that is particularly easy to use for this typology of studies is the "*Equivalent Strut Method*". In the field of the approaches of *macro* modelling, the Equivalent Strut is widely used to simulate the effects of infill panels on the global response of individual frames and / or buildings [2, 4, 11, 15, 19, 27]. These studies are important in order to establish the retrofit interventions needed to ensure the seismic safety to the deficient buildings [9, 10].

The model is based on the behaviour exhibited by an infilled frame subject to a horizontal load. In particular, by increasing the load, because of the detachment of masonry from the boundary reinforced concrete frame, the panel no longer behaves as a two-dimensional shear resistant element but as a "*one-dimensional equivalent beam*" element. The strut follows the distribution of the compressive forces along the diagonal of the panel and it acts as a strut in opposition to the horizontal action [3, 16, 18].

The described model is defined by the geometrical and mechanical characteristics and by the force-displacement constitutive law that governs the behaviour of the equivalent strut during the non-linear phase. The above parameters depend by models and experimental tests reported in the literature, which especially in the case of existing structures, cannot be generalized to all the possible cases, but are reliable only in few cases that are similar to those on which they were defined [4]. The laboratory tests cannot be generalized because are expensive. Therefore, it is necessary to employ computational procedures, more or less refined, by which the experimental tests on specimens of infilled frames are simulated numerically.

The aim of the present work is to define the Force-Displacement constitutive law of the *equivalent strut*. A simplified discrete model (falling within the family of the models, for *Rigid Block-analysis*) is used in this work and was implemented within a common commercial finite element software [5]. The definition of the *Rigid Blocks and Springs Model* (RBSM), in a simplified format, requires as input a few data on the geometry of the infilled frame and the mechanical parameters of the masonry panel. The purely numerical findings consist of capacity curves, in terms of shear base – interstorey drift. The characteristic branches of the constitutive law of the equivalent strut (the force-displacement relationship "$F_w$ - $d_w$") which regulates the elastic and plastic behaviour of the rod are obtained by means of a simplified procedure divided into three operating phases briefly recalled inside. The application of which, for the purposes of the present work only affect the third phase.

The procedure on a sampling of *#17* RBSM models with variable geometry was applied. For each of which the constitutive law of the equivalent rod was determined. With the seventeen force-displacement relationships, by means of numerical processing, the formulations for the parametric evaluation of the characteristic points of a single constitutive law of the entire sampling were defined. The generalized law so defined can be used to define an equivalent strut for building scale applications without having to resort to sophisticated modelling (having high computational costs) for each single infilled frame. Thence, the aim of this paper is to demonstrate how to perform extensive numerical experiments by RBSM models allows to obtain results useful for calibrating macro-models when it changes not only the geometry (as briefly

shown in this paper) but also, as future scenarios, when they change the mechanical characteristics of the panels. These results in terms of "approximate" laws are expressed. These laws define the parameters regulating the behaviour of the equivalent rods in non-linear field.

## 2 THE MESO-MODELING AND SIMPLIFIED PROCEDURE

The "*meso-scale*" models are usually referred to as "*discrete models*". If they are applied to structural systems that require a limited number of elements, they allow to reduce the computational burden required by the continuous or discontinuous approaches. The *Rigid Body Spring Model* (RBSM), consists in describing the masonry as a mechanism composed of the unitary cells constituted by of rigid blocks and elastic-plastic springs [6, 20] (Figure 1). Through this approach, it is possible to model the masonry panels at the "macro-scale" through a kinematic that takes into account the specific effects of masonry texture. It has been fruitfully applied, in the last few years, for modeling the behavior of masonry structures both in-plane and out-of-plane [21,22], allowing to perform the vulnerability assessment for whole masonry buildings [23,24,25].

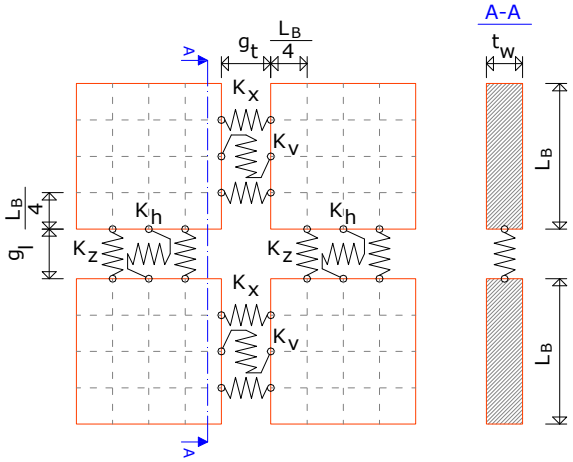


Figure 1: Simplified periodical cell describing the masonry texture.

The connection between the rigid blocks occurs by means of two axial springs (indicated with $K_x$ or $K_z$, depending on the direction) and a shear spring ($K_h$, $K_v$, depending on configuration) arranged along each of the common sides between the blocks at a distance equal, respectively, to $b_x$ and $b_z$. The hysteretic behaviour of the springs is obtained on the basis of the mechanical parameters of the constitutive elements of the panel (mortar and blocks) and takes account of the mechanical degradation of mortar joints in the cycles of loading and unloading.

In the simplified format, the use of a *meso-scale* modelling is an easy and quick step within the proposed procedure, aimed at defining some characteristic features of the global response of the infilled frame. For these reasons, the properties of the springs are defined according to a simplified approach. The elastic stiffness of each spring is estimated through the geometrical and mechanical properties of the infill, such as the *modulus of elasticity* of the masonry panel in horizontal and vertical direction ($E_{wh}$, $E_{wv}$), *shear modulus* ($G$), areas of influence of the axial spring ($A$), areas of influence of the shear spring ($A_T$), thickness of the head joint ($g_t$), thickness of the bed joint ($g_l$) and thickness of the masonry panel ($t_w$).

When the kinematic of the model is such as to engage the springs over the elastic response, force-displacement laws regulate the plastic behaviour of the system. As with the elastic behaviour, also for the decreasing behaviour of the stiffness has been adopted a simplified approach. Figure 2 shows the constitutive laws of the springs, respectively, axial and shear, used in the

present work. For both, three branches constitute the force-displacement law. In the figures, the subscript "*as*" indicates the axial spring, while "*ss*" the shear spring. The fundamental variables of the laws are calibrated with an approach depending on the material strengths: compression strength of the masonry in horizontal direction ($\sigma_{wh}$), compression strength of the masonry in vertical direction ($\sigma_{wv}$), tensile strength of the masonry ($\sigma_{wt}$), shear strength of the masonry along the bed joints ($\tau_{wh}$), shear strength of the masonry along the head joints ($\tau_{wv}$).

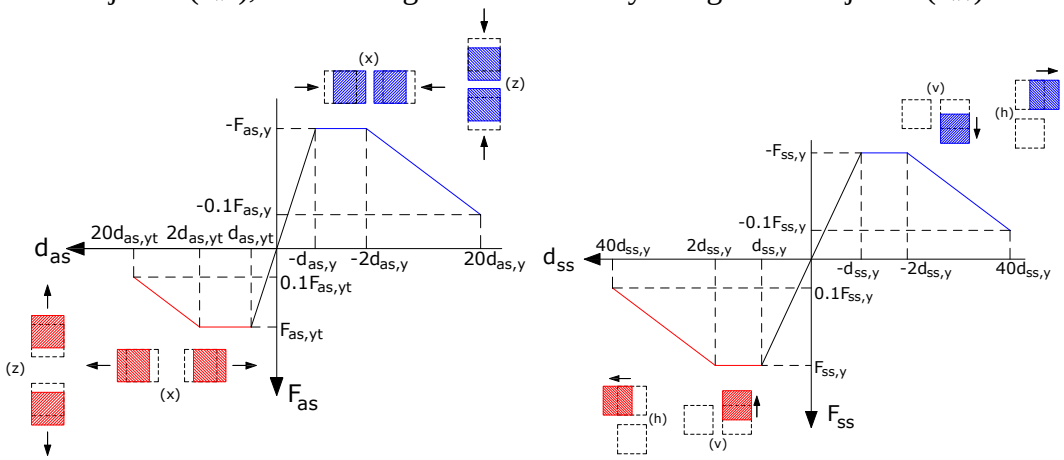


Figure 2: Constitutive laws of the axial and shear springs.

Three consequential step forms the simplified procedure (Figure 3).

1st step: *"meso-analysis of the infilled frame"*

The first step of the procedure is to assess the response of the infilled frame by a nonlinear static analysis (pushover). The model described in the previous section simulates the behaviour of the masonry panel. A *lumped-plasticity model* evaluated with plastic hinges arranged in five sections along the length of each element (beam and columns) describes the nonlinear behaviour of the concrete. The constitutive law adopted for the plastic hinges is in according to FEMA 273 [12]. In the case of existing structures, the evaluation of plastic hinges should take into account the effective strength values of materials in according to numerical approaches (in this context, the research developed by authors [13,14] are particularly interesting.)

2nd step: *"evaluation of the infill conribution without RC frame"*

The $F_h$-$d_h$ curve of the INF configuration is intended as the "*sum*" of two distinct contributions, respectively, due to the bare frame (B) and the masonry panel (MP). The first contribution is evaluated using a nonlinear static analysis on the model without infill panel. The second, however, is obtained by subtracting (in correspondence with each displacement value) from the response of the INF configuration, the share due to the bare frame B.

3rd step: *"Evaluation of the constitutive law of the Equivalent Strut"*

Once the response $F_w^{MP}$- $d_w^{MP}$ for masonry panel has been obtained, the constitutive law of the equivalent strut is built on the backbone of MP curve in order to define the ESM model. The law consists of four branches delimited by four characteristic points identified on the MP curve. The first branch describes the elastic response up to the yield point "*S*". The second branch describes the behaviour of the equivalent strut from when begins the plastic deformation up to achieve the point of maximum strength capacity "*M*". This is followed by the descending branch due to the propagation of crack in the panel such that induce a significant decrease of resistance until to the point "*D*". Finally, the fourth branch describes the force-displacement

relation until the failure (point "*R*") with a residual resistance maintained in order to ensure stability and convergence to the numerical solution. The *M* and *R* points are preliminarily identified. They coincide, respectively, with the maximum point and last point of the MP curve. While, *S* and *D* points are directly evaluated by an iterative approach that minimizes the difference between the subtended areas of the MP curve and the defined constitutive law.

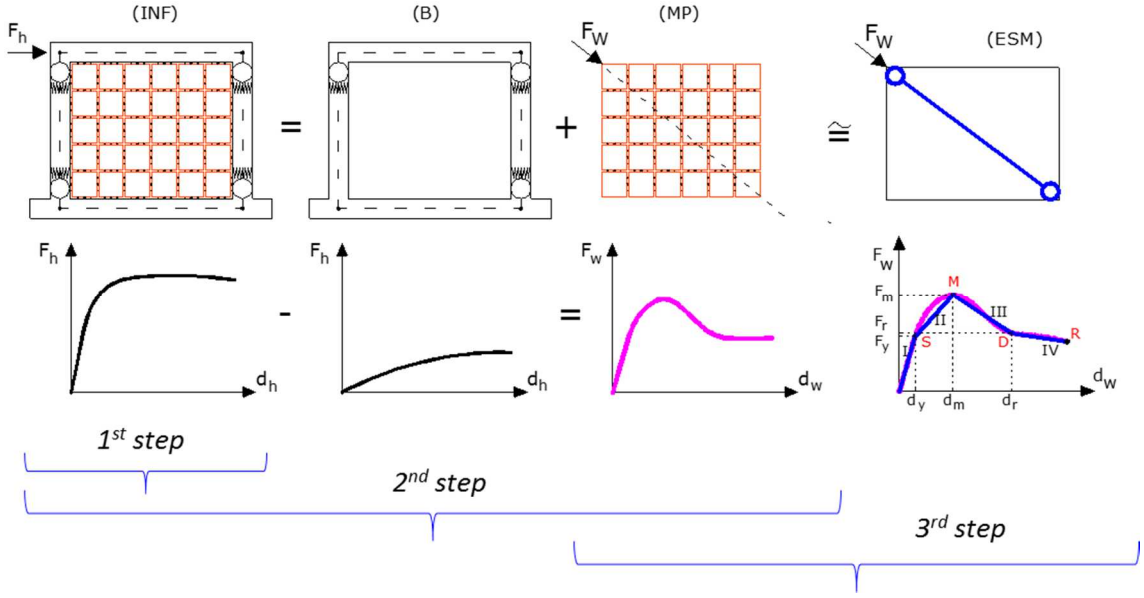


Figure 3: Graphical description of the simplified evaluation of the masonry panel response.

## 3 NUMERICAL TESTS

### 3.1 Description of the sampling and modeling

For the purposes of this study in software Sap2000 *#17* RBSM plane models were implemented. All models are listed in ascending order in Table 1 as a function of the *slenderness* "*λ*" equal to the ratio of height *H* and width *B* (defined in Figure 4) of the infilled frame (both measured than to the middle line of the sections). The thickness of the panel is equal to 30cm for all samples.

| n. | B [m] | L [m] | λ | n. | B [m] | L [m] | λ |
|---|---|---|---|---|---|---|---|
| 01 | 5.0 | 2.5 | 0.500 | 10 | 5.0 | 4.5 | 0.900 |
| 02 | 4.5 | 2.5 | 0.555 | 11 | 3.0 | 3.0 | 1.000 |
| 03 | 5.0 | 3.0 | 0.600 | 12 | 4.5 | 4.5 | 1.000 |
| 04 | 4.0 | 2.5 | 0.625 | 13 | 4.0 | 4.5 | 1.125 |
| 05 | 5.0 | 3.5 | 0.700 | 14 | 3.5 | 4.0 | 1.143 |
| 06 | 3.5 | 2.5 | 0.714 | 15 | 2.0 | 2.5 | 1.250 |
| 07 | 4.5 | 3.5 | 0.777 | 16 | 3.0 | 4.0 | 1.333 |
| 08 | 5.0 | 4.0 | 0.800 | 17 | 2.5 | 3.5 | 1.400 |
| 09 | 4.0 | 3.5 | 0.875 | | | | |

Table 1: Characteristics of sampling.

The boundary frame (the same for each sample) is reinforced concrete with conglomerate having class of resistance *C25/30*. It is constituted by two square columns with side equal to *30cm* and one beam with width *b=30cm* and height *h=50cm*. The longitudinal reinforcement

of the columns is equal to $8\phi16$ symmetrically along the sides distributed, while the beam presents in the centre span, longitudinal tension reinforcement *As* equal to $4\phi14$ and in compression reinforcement *As'* equal to $3\phi16$. Those quantities are inverted at the supports. The masonry panel is assumed made of brick blocks P700 type. They are characterized by a weight per unit of volume of about *700-760 kg/m*$^3$. Their physical and geometric characteristics are comply with the requirements established by Eurocode 6 [7] and fall among the elements classified as hollow bricks, with φ drilling percentage between 45% and 55%. Eurocode 6 provided the compression strength along the vertical direction, in the case of hollow blocks and ordinary mortar, with the Eq.1.

$$f_k = K \cdot f_b^{0.7} \cdot f_m^{0.3} \tag{1}$$

where:

- $f_k$ is the characteristic compressive strength, expressed in *MPa*. In the present treatment the average values of the resistances have been adopted. From experimental tests carried out on similar typologies of the blocks used, it is the average value obtained by multiplying the characteristic value by a factor equal to *0.8*.
- *K* is a constante qual to *0.45*.
- $f_b$ is the average compression resistance along the direction of loads, expressed in MPa.
- $f_m$ is the mortar compression strength, expressed in *MPa*.

As regards the compression strength in the horizontal direction, EC6 proposes the Eq.1, putting in place of *K* a coefficient $K_h = 0.5K$. The shear strength ($\tau_{wh} = \tau_{wv}$), with no vertical loads, it is assumed to *0.2MPa* assuming a mortar with bad features having M2.5 resistance class. The average value of the resistance, for non-linear analysis, is obtained by dividing the characteristic value to *0.7*. The mechanical characteristics are determined with the usual relations provided by the Italian Technical Standards [8]: $E=1000f_k$, $G=0.4E$ e $\nu=E(2G)^{-1}-1$.

The single RBSM model is constituted by a regular discretization of *n* two-dimensional plane elements (*4*-nodes *shell* elements) enclosed by a contour of the beam elements. The total degrees of freedom are *4n*. The behaviour perfectly rigid of blocks is guaranteed by assigning to *4*-nodes of each *shell* a "*Diaphragm*" internal constraint with Y rotational axis perpendicular to the OXZ reference system. The internal costraint connects the nodes of the shell element by means of ideal rigid rods devoid of mass and stiffness. The connections between rigid blocks is with "*NLlink*" elements of "*multilinear plastic*" typology (Figure 4). The nonlinear behaviour of *NLlink* elements is in according to constitutive laws shown in Figure 2, respectively, for the axial ($F_{as}$ - $d_{as}$) and shear ($F_{ss}$ - $d_{ss}$) springs.

At the interface between frame and masonry panel (i.e. between beam and *NLink* elements along the sides of the rigid blocks adjacent to the frame), are arranged *Rigid N*Link elements. The *rigid NLlink* maintain unchanged the relative distances between the nodes on axis line of the reinforced concrete element and the boundary line of the concrete, in order to simulate the material between them. The model is constrained to the ground by means of interlocking constraints at the base columns. In addition, the hinge constraints at the end nodes of the *rigid NLlink* elements simulate the position of specimen in the test device.

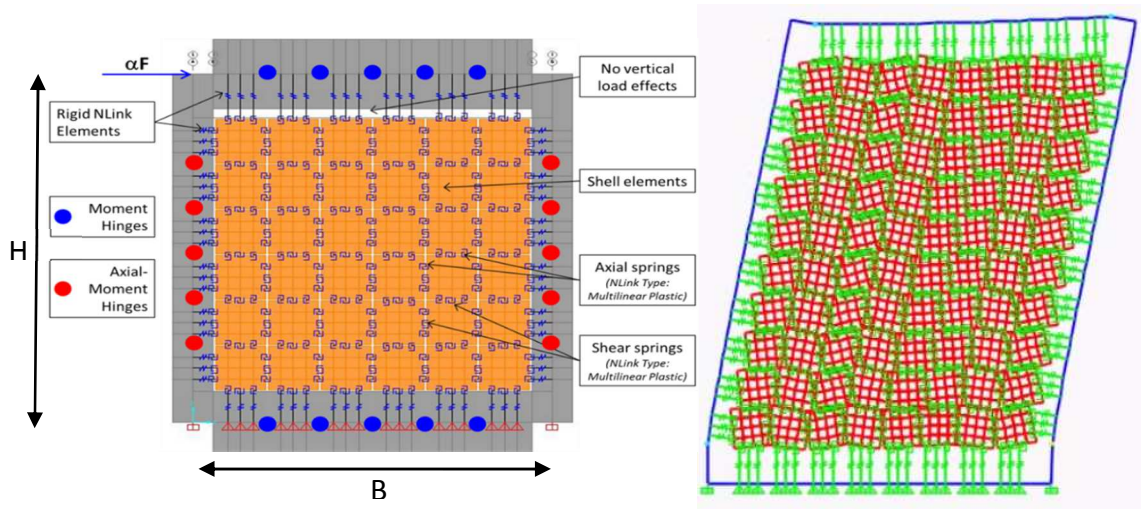


Figure 4: Extrude view of the finite element model with rigid blocks and springs implemented in Sap2000 (on the left); Deformed configuration for generic RBSM model (on the right).

### 3.2 Analysis by simplified procedure

The procedure described in §2 has been applied to the models listed in Table 1. For each model by starting from the nonlinear static analysis and its processing, the steps 2 and 3 lead to the definition of the law of the equivalent strut for the geometry of infilled frame considered. For example, the law of the equivalent rod for the model number 15 ($\lambda$=*1.25*) is represented in Figure 5.

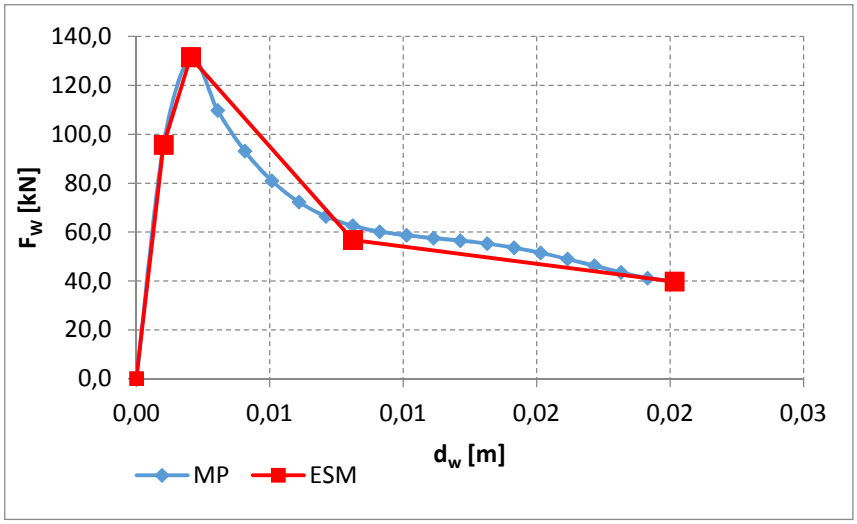


Figure 5: Force - displacement law for the sample with geometry 2,0m x 2,5m.

After determining the constitutive laws for all *17* models of the sampling, a numerical study was performed in order to obtain, as a function of the slenderness "$\lambda$", a univocal law of the entire sample. The aim is to define parametric formulations for the infill panels having similar mechanical properties to those of the sampling, which allow to determine the constitutive law of the equivalent rod, once known only the geometry of the infilled frame. To this end, bringing together the *17* constitutive laws, they were built of graphics to correlate the yield strength ($F_y$), the displacement at yield ($d_y$), the maximum strength ($F_{max}$) and the maximum displacement ($d_{max}$) to the shape parameter (in Figure 6 for the force $F_y$).

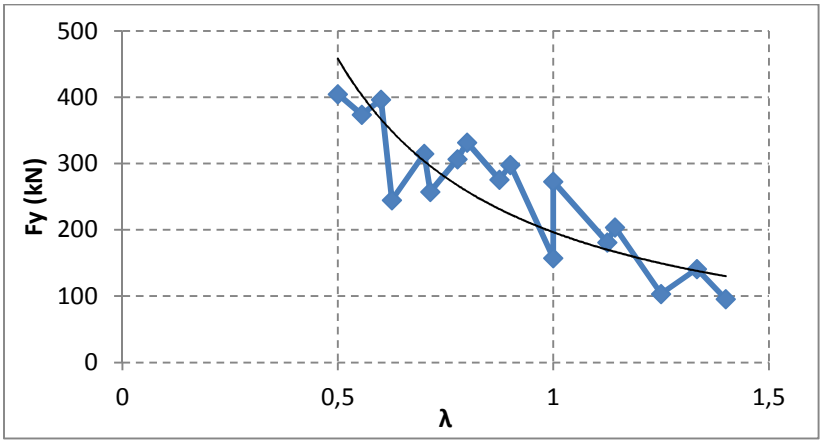


Figure 6: Exponential regression for the evaluation of $F_y$ as a function of the slenderness

The numerical regressions that approximate with lower margins of error are functions in the format, respectively, exponential and linear. The formulations obtained for the analysed sampling are shown below. The Eqs. 2 and 3 in exponential form, while Eqs. 4 and 5 in two variables linear.

$$F_y = 196.42 \cdot \lambda^{-1.223} \quad \& \quad d_y = 0.0012 \cdot \lambda^{-0.039} \tag{2}$$

$$F_{max} = 223.93 \cdot \lambda^{-1.039} \quad \& \quad d_{max} = 0.002 \cdot \lambda^{0.4183} \tag{3}$$

$$F_y = 11.389 + 99.667B - 44.97H \quad \& \quad d_y = -0.000105 + 0.000143B + 0.000233H \tag{4}$$

$$F_{max} = 52.384 + 91.45B - 41.09H \quad \& \quad d_{max} = -0.00147 + 0.000019B + 0.00034H \tag{5}$$

The D point that represents the maximum loss of strength of the panel when it is in the plastic phase is definable by the coordinates $\{3d_{max}; 0.3F_{max}\}$.

## 4 RESULTS

In order to validate the whole procedure, the results of the nonlinear analyses on *macro*-models and meso-models (RBSM) were compared. The geometries taken as a reference for the comparison are those having slenderness $\lambda$ equal, respectively, to *0.5*, *0.9* and *1.25*.

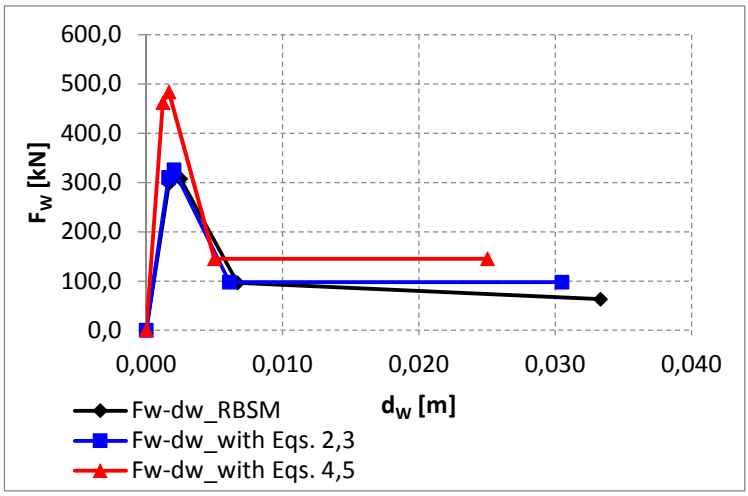


Figure 7: $F_w$-$d_w$ laws compared for sample having λ=0.9.

For all the three samples, the points of the force-displacement law of the equivalent strut was derived by applying the Eqs 2-5. For the geometry having $\lambda = 0.9$ in Figure 7 the $F_w$-$d_w$ laws are compared.

Subsequently, for each geometry under consideration for comparative purposes, two models with the Equivalent Strut Method (ESM) were implemented. The first with the equivalent rod having the $F_w$-$d_w$ law having main points defined by the eqs. 2 and 3. The second with strut that has $F_w$-$d_w$ law given by eqs. 4 and 5. For both models pushover analysis was performed. The capacity curves obtained from both models, in terms of *Base shear - Drift [%]* were compared with, respectively, the curves obtained with the RBSM models and the model relative to the bare frame. As an example, in Figure 8, the comparisons between results obtained for a geometry characterized by $\lambda=1.25$ are summarized.

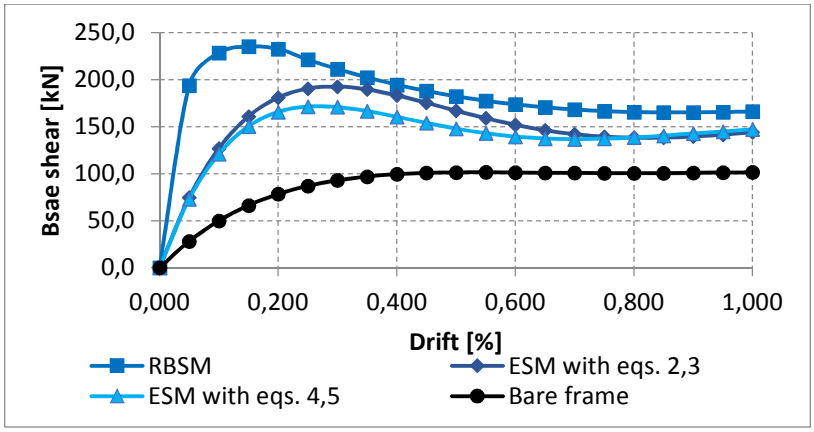


Figure 8: Comparison of results for geometry having $\lambda=1.25$.

The *macro*-models differ from the *meso*-scale model (RBSM), on average, by about *25%* in the range of *0<drift[%] <1*. In addition to the difference between the above models, the comparison between the models in terms of resistance increase with respect to the model representative of bare configuration (without infill) is very attractive. An increment of the base shear between *1.48* and *2.32* times the resistance explicated by the bare frame was encountered.

## 5 CONCLUSIONS

The main aim of this work is the calibration of the Equivalent Strut Method for modelling of infilled frames in *building*-scale application. The above calibration is proposed by means numerical experimental tests on discrete models (*Rigid Block and Spring Model* - RBSM), commonly used in the analysis of masonry structures, and subsequent application of a simplified procedure proposed by the authors.

The procedure aims to define the points of the nonlinear constitutive law of equivalent connecting rod by means of the use of numerical formulations expressed as a function of a geometrical shape parameter of the buffered frame. The formulations through the implementation of *#17* RBSM models having fixed mechanical characteristics and $\lambda$ that it varies between *0.5* and *1.4* were obtained.

By applying the procedure on the entire sampling and whereas for comparative purposes the results obtained for the geometries having the equal, respectively, to *0.5*, *0.9* to *1.25*, the following conclusions can be derived:

- The differences between RBSM models and models with equivalent struts having non-linear law obtained with generalized approximate formulations are equal to about 25%.
- The use of approximate formulations of exponential type for the definition of the non-linear law of the struts is closest to the results obtained with refined modelling RBSM, compared to the models with the struts defined with polynomial formulations.
- The results obtained, both preliminarily on the RBSM in its simplified form, both on the model with equivalent strut, show the significant contribution in strength provided by in-fills.

In the future, the definition of approximate laws for the calibration of the *macro*-models can be extended to infilled frames having different mechanical properties.

## ACKNOWLEDGEMENTS

The research presented in this article was partially funded by the Italian Department of Civil Protection in the framework of the national project DPC-ReLUIS 2014-2018.

## REFERENCES

[1] D. Celarec, P. Ricci, M. Dolšek. The sensitivity of seismic response parameters to the uncertain modelling variables of masonry-infilled reinforced concrete frames. *Engineering Structures*, **35**:165–177, 2012.

[2] A. Fiore, F. Porco, G. Uva. Effects of the yield and ultimate strengths of the equivalent strut models on the response of existing buildings with infill panels. *International Journal of Structural Engineering*, **6**(2):140-157, 2015. doi:10.1504/IJSTRUCTE.2015.069690

[3] B. Stafford Smith. Lateral Stiffness of infilled frames. Journal of Structural Division, ASCE, 6, 183-99, 1963.

[4] G. Uva, F. Porco, D. Raffaele, A. Fiore. On the role of equivalent strut models in the seismic assessment of infilled RC buildings. *Engineering Structures*, **42**, 83-94, 2012. doi:10.1016/j.engstruct.2012.04.005

[5] A. Fiore, F. Porco, A Multiscale approach for modelling of infilled frames. COMPDYN 2015 - 5th ECCOMAS Thematic Conference on Computational Methods in Structural Dynamics and Earthquake Engineering M. Papadrakakis, V. Papadopoulos, V. Plevris (eds.). Crete Island, Greece, 25–27 May 2015.

[6] S. Casolo, Macroscale modelling of microstructure damage evolution by a Rigid Body and Spring model. *Journal of Mechanics of Materials and Structures*, **4**(3), pp. 551-570, 2009. doi:10.2140/jomms.2009.4.551

[7] CEN. Eurocode 6 - Design of masonry structures - Part 1-1: General rules for reinforced and unreinforced masonry structures. Brussels. Belgium; 2005.

[8] DM 14/01/2008. Norme Tecniche per le Costruzioni (NTC 2008). Gazzetta Ufficiale n.29. Roma; 2008 *(in Italian)*.

[9] F. Porco, A. Fiore, S. Casolo. Comparison between seismic retrofitting solutions for existing reinforced concrete buildings: a case study. *International Journal of Structural Engineering*, **5**(3), 242-261, 2014. doi:10.1504/IJSTRUCTE.2014.063035

[10] F. Porco, A. Fiore, G. Uva, D. Raffaele. The influence of infilled panels in retrofitting interventions of existing reinforced concrete buildings: a case study. *Structure and Infrastructure Engineering*, **11**(2), 162-175, 2015. doi:10.1080/15732479.2013.862726

[11] A. Fiore, F. Porco, G. Uva, M. Sangirardi. The influence of uncertainties of infill panels relative to the seismic response of RC existing buildings, *WIT Transactions on the Built Environment*, **141**, 479–490, 2014. doi:10.2495/SUSI140411

[12] FEMA. Nerph guidelines for the seismic rehabilitation of buildings. FEMA-273, Washington, DC. 1997.

[13] G. Uva, F. Porco, A. Fiore, M. Mezzina, The assessment of structural concretes during construction phases", *Structural Survey*, **32**(3), 189-208, 2014. doi:10.1108/SS-06-2013-0023

[14] F. Porco, G. Uva, A. Fiore, M. Mezzina, Assessment of concrete degradation in existing structures: a practical procedure, *Structural Engineering and Mechanics*, **52**(4), 701-721, 2014. doi:10.12989/sem.2014.52.4.701

[15] P.G. Asteris, S.T. Antoniou, D.S. Sophianopoulos, C.Z. Chrysostomou, Mathematical macromodelling of infilled frames: state of the art. *Journal of Structural Engineering*, **137**(12), 1508–1517, 2011.

[16] G. Campione, L. Cavaleri, G. Macaluso, G. Amato, F. Di Trapani. Evaluation of infilled frames: an updated in-plane-stiffness macro-model considering the effects of vertical loads. *Bulletin of Earthquake Engineering*, **13**(8):2265-2281, 2014.

[17] M. Ercolino, P. Ricci, G. Magliulo, G. Verderame. Influence of infill panels on an irregular RC building designed according to seismic codes. *Earthquakes and Structures* **10**(2):261-291, 2016.

[18] R.J. Mainstone. Supplementary note on the stiffness and strength of infilled frames. Current paper CP13/74. *Building Research Establishment*. London, 1974.

[19] F.J. Crisafulli, A.J. Carr, R. Park, Analytical modelling of infilled frame structures - a general review. *Bulletin of the New Zealand Society for Earthquake Engineering* **33**(1), 30-47, 2000.

[20] S. Casolo and F. Peña, Modelling micro-structure aspects of masonry walls by a simplified approach, *Advances in Architecture* **15**, pp. 337-346, 2003.

[21] S. Casolo, G. Uva, Nonlinear analysis of out-of-plane masonry façades: Full dynamic versus pushover methods by rigid body and spring model, *Earthquake Engineering and Structural Dynamics*, 42: 499–521, 2013 - DOI: 10.1002/eqe.2224.

[22] S. Casolo, G. Uva, Out-of-plane seismic response of masonry façades: some comparisons among full dynamic and pushover analysis, *Ingegneria Sismica*, ISSN: 03931420, **27**:3, 33-54, 2010.

[23] S. Casolo, C.A. Sanjust, Seismic investigation on the Cathedral of Syracuse by finite elements and by a specific rigid body and spring model, *WIT Transactions on the Built Environment*, pp. 535, 2007. doi:10.2495/STR070501

[24] S. Casolo, A. Fiore, F. Porco, F., D. Raffaele, C.A. Sanjust, G. Uva. A multi-level approach for the numerical modelling of complex monumental buildings: Seismic assessment of the "Maniace Castle" of Syracuse. *Civil and environmental engineering:*

*Concepts, methodologies, tools, and applications*, pp. 1352-1379, 2016. doi:10.4018/978-1-4666-9619-8.ch061

[25] S. Casolo, G. Milani, C.A. Sanjust, A. Taliercio. Maniace castle in Syracuse, Italy: Comparison between present structural situation and hypothetical original configuration by means of full 3D FE models. *Open Civil Engineering Journal*, 6(SPEC.ISS.1), 173-187, 2012. doi:10.2174/1874149501206010173

[26] Porco, F., Porco, G., Uva, G., M. Sangirardi, Experimental characterization of "non-engineered" masonry systems in a highly seismic prone area. *Construction and Building Materials* **48**, pp. 406-416. 2013. doi:10.1016/j.conbuildmat.2013.07.028

[27] Perrone, D., Leone, M., Aiello, M. A. Evaluation of the infill influence on the elastic period of existing RC frames. *Engineering Structures*, 123, 419-433, 2016. doi:10.1016/j.engstruct.2016.05.050

-COMPDYN 2017
6th ECCOMAS Thematic Conference on
Computational Methods in Structural Dynamics and Earthquake Engineering
M. Papadrakakis, M. Fragiadakis (eds.)
Rhodes Island, Greece, 15–17 June 2017

# DEFINITION OF A FIBER MACRO-MODEL FOR NONLINEAR ANALYSIS OF INFILLED FRAMES

**F. Di Trapani[1]*, L. Cavaleri[2], G. Bertagnoli[1], G. Mancini[1], D. Gino[1], M. Malavisi[1]**

[1]Politecnico di Torino
Department of Structural, Geotechnical and Building Engineering
Corso Duca degli Abruzzi 24 - Torino
fabio.ditrapani@polito.it, gabriele.bertagnoli@polito.it, giuseppe.mancini@polito.it, diego.gino@polito.it, marzia.malavisi@polito.it

[2] University of Palermo
Dipartimento di Ingegneria Civile, Ambientale, Aerospaziale, dei Materiali
Viale delle Scienze 90128 - Palermo
liborio.cavaleri@unipa.it

**Keywords:** Infilled frames, fiber-section elements, micromodelling, macromodelling, FEM, stress-strain, correlations.

**Abstract.** *A common way to model infill-frame interaction is the use equivalent strut macro-models. In most cases these are compression only resistant truss elements defined with a multi-linear axial-force / axial-displacement law. The main difficulty in using this approach is to correctly calibrate such a force-displacement curve (slope of ascending and post-peak branches, critical yielding, peak and residual forces) because of the large number of variables (mechanical and elastic properties of materials) and the different possible damage mechanisms activated for the frame-infill system. Another possible way is using fiber-section elements as diagonal struts. In this case the force-displacement law is substituted by a stress-strain curve. In both cases a reliable definition of inelastic response of the strut, based on mechanical approaches, which are valid in general is not easy, as most of models provide rules valid for specific typologies of infills (e.g. weak or strong infills) and frames (e.g. concrete or steel frames). Based on this, the paper proposes the use of fiber-section diagonal struts with a concrete-type stress-strain relationship calibrated using a semi-empirical approach. The Kent-Scott-Park model, depending on four parameters, is used as reference constitutive law for the strut. Experimental data and additional numerical simulations are used to derive semi-empirical correlations linking geometrical and mechanical properties of the frame-infill system to the aforementioned parameters governing nonlinear response of the diagonal. Analytical expressions of the best fitting curves are finally provided and suggested as design equation.*

## 1 INTRODUCTION

Infilled frames are typically placed in framed structures as partition walls and to separate internal spaces from external environment. Although they are not commonly included in structural models, laboratory tests [e.g.1-4] and real observation of post-earthquake damage have demonstrated that masonry infills have a strong interaction with primary structures, influencing overall and local strength, stiffness and structural ductility [5-7]. Basically two different approaches are used to model infill-frame interaction. One is detailed finite element 2D or 3D modeling (e.g [8-10]) of the infill, the frame and the interface mortar [11-14]. Such a kind of approach is generally preferred for research purposes as it requires significant computational effort and expertise of the user. The other is macromodelling of the infill, which provides the use of one (or more) equivalent diagonal struts. This is approach is largely employed, especially when performing seismic assessments using nonlinear static or dynamic analyses. Since equivalent struts are an idealization of the real system, they have to undergo an identification process in order to effectively simulate the infill-frame interaction. A number of identification methods have been developed in the last 60 years. Some of these focused on the stiffening effects [15-19] produced by the infills on the overall response, other studies [e.g. 20-22] were addressed to the assessment of the inelastic in-plane response. More recently, equivalent strut macromodels have been updated to include the possibility to model the out-of-plane response of the infill wall, and its mutual interaction with the in-plane damaging. Studies [e.g. 23-25] have demonstrated that infills can develop a significant resistance against out-of-plane actions if they have adequate thickness and the frame is stiff enough. An updated literature review of macromodelling techniques can be found in [26].

Although, as it can be seen, a large literature is available, the uncertainty in the identification of the equivalents struts, in particular their inelastic response, still remains an open issue. This is due to the fact that the overall lateral response of the infilled frame basically depends on the damage mechanism occurring from time to time, which in turns, as summarized in [1], depends on the different possible assemblage of masonry infills and frames. Because of this, sliding of mortar joints, rather than corner crushing of units, of diagonal failure may occur. Moreover, in many cases, a combination of such mechanisms is also observed.

Such potential variability of failure mechanisms is not easy to predict a priori, and still constitutes the main unknown in the assessment of such systems. In fact, the identification strategies available in literature, which make use of mechanical approaches to predict the inelastic response are generally referred to special typologies of infilled frames or validated with reduced experimental testing. Consequently, a strategy to define the inelastic behaviour of the equivalent strut, which can be considered to be valid for any typology of masonry and any typology of frame, is not yet available in the literature. Today, the increasing need for a reliable assessment of seismic performance of new and existing buildings [27-32] moves the interest in finding models which are accurate in reproducing the inelastic response of structures.

Based on the aforementioned difficulties encountered in using mechanical approaches to define nonlinear behaviour of the equivalent struts, this paper proposes a calibration strategy making use of a semi-empirical definition of the parameters governing their inelastic response. The procedure is based on the use fiber-section elements to model equivalent struts, associating a concrete-type (Kent-Park [33]) stress-strain model for the fibers. This stress-strain model is basically governed by four parameters: peak strength, peak strain, ultimate strength and ultimate strain.

A comparison between real experimental test results of different typologies of specimens of infilled frames, and results of the associated equivalent strut models, allowed iteratively calibrating the four stress-strain parameters for several specimens. The same calibration pro-

cedure was repeated with the results of a detailed FE model. After, analytical correlation laws, based on the interpolation of data obtained, linking geometrical and mechanical features of an infilled frame and the stress-strain parameters were provided. The latter can be used as predictive tool for the identification of the stress strain law to assign to the equivalents struts.

## 2 PROPOSED MODELLING STRATEGY AND DETERMINATION OF THE STRESS-STRAIN PARAMETERS

The identification method proposed, is aimed at the definition of the stress-strain law to be assigned to the equivalent struts of a generic infilled frame. This implies that struts are modeled using fiber-section elements. The reference numerical models used in the paper are realized with OpenSees software platform [34]. The typical infilled frame model (Figure 1a-b) consists of nonlinear beam-column elements as beams and columns, and nonlinear compression only trusses as equivalent diagonal struts. The modeling scheme is shown in Figure 1b. The stress-strain law of the fibers composing the struts is a simple Kent-Park [33] concrete-type model. The latter depends on 4 parameters: peak strength ($f_{md0}$), peak strain ($\varepsilon_{md0}$), ultimate strength ($f_{mdu}$) and ultimate strain ($\varepsilon_{mdu}$) which regulate the ascending and descending branches. After the achievement of the ultimate strain the ultimate stress is maintained constant.

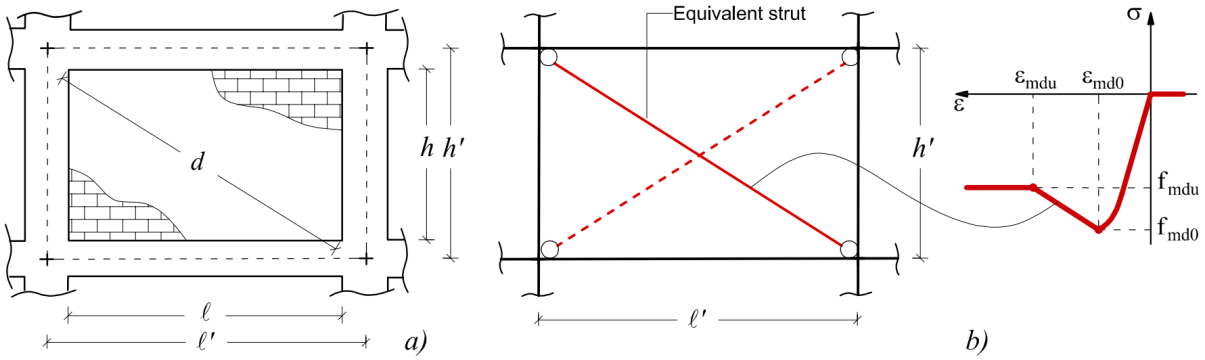


Figure 1: Modeling of an infilled frame: a) Real configuration; b) Equivalent strut model.

When using this approach to model equivalent struts, it should be noted that the four stress-strain parameters ($f_{md0}$, $\varepsilon_{md0}$, $f_{mdu}$, $\varepsilon_{mdu}$) are not coincident with those associated with the masonry constituting the infill. This is due to the fact that the lateral response of an infilled frame depends on the damage mechanism typology rather directly on masonry properties. As example, if the failure mechanism activated is the sliding of mortar joints, it is reasonable that compressive strength of masonry will be not achieved. For this reason, the stress-strain parameters, and the associated stress-strain relationship have to be intended as purely phenomenological. However, the stress-strain parameters cannot be thought as non-correlated with masonry properties, but more in general they depend on the geometrical and mechanical properties of the overall system.

The aim of the paper is then to find four analytical correlations which allow, starting from the basic geometrical and mechanical data of an infilled frame, to determine each of the stress-strain parameters. In this way once the infilled frame features are defined, the stress-strain curve of the struts can be evaluated through simple analytical calculations.

In order to derive the aforementioned correlations, the following procedure has been implemented:

1. Acquisition of experimental test data (force-displacement curves of in-plane monotonic or cyclic tests on infilled frames);
2. Definition of the numerical models of the infilled frames actually tested;
3. Calibration of the parameters $f_{md0}$, $\varepsilon_{md0}$, $f_{mdu}$, $\varepsilon_{mdu}$ iterating results of pushover curves up to the best matching with experimental curves;
4. Research of a correlation of between the stress-strain parameters obtained and the characteristics of the infilled frames.

Experimental calibration is considered the best way to derive stress-strain parameters, as it includes real phenomena which are not easily captured by analytical models. However, despite several researchers have conducted experiments on the in-plane response of infilled frames, only a few of these report detailed information on the preliminary tests on masonry (e.g. results of compressive tests on prisms, results of diagonal compressive tests, experimental evaluation of elastic and tangential moduli).

Because of this, in order to enlarge the data-set used to derive correlations, detailed FE models of the infilled frames actually testes were also realized. The FE models, once calibrated, were used to derive numerical predictions of the responses of the infilled frames with varying geometric and mechanical parameters of the infill. The subsequent procedure has been followed:

1. Calibration of a detailed FE model with experimental data;
2. Variation of geometrical and mechanical properties and derivation of numerical lateral force-displacement curves;
3. Definition of the OpenSees models of the infilled frames tested in FE simultions;
4. Calibration of the parameters $f_{md0}$, $\varepsilon_{md0}$, $f_{mdu}$, $\varepsilon_{mdu}$ iterating results of pushover curves up to the best matching with numerically generated curves;
5. Adding data to those obtained with experimental calibration.

Stress-strain parameters data-sets, one obtained from experimental tests, the other from numerical simulations of detailed FE models were then merged.

In the aforementioned process, the identification of the cross-section dimensions of the equivalent strut is carried is carried out using the procedure by Asteris et al. [19], which briefly summarized in the following. According to [19], the thickness ($t$) is equal to the actual thickness of the infill, while the width ($w$) is evaluated as:

$$w = k^{\gamma}\left(\frac{h}{l}\right)\frac{c}{\lambda^{*\beta}}d \tag{1}$$

where, with reference to Figure 1, $d$ is the length of the diagonal strut, $h$ and $l$ are the length and the height of the infill, $\kappa$ is a parameter accounting for the stiffening action exerted by vertical loads, defined as:

$$\kappa = [1 + (\lambda^{*} + 200)\varepsilon_{v}] \tag{2}$$

in which $\varepsilon_v$ is the axial strain on columns, calculated considering the total load $F_v$ acting on the 2 columns having cross-sectional area $A_c$ and elastic modulus $E_c$, as:

$$\varepsilon_{v} = \frac{F_{v}}{2E_{c}A_{c}} \tag{3}$$

The parameter $\lambda^{*}$ is calculated with the expression by Papia et al. (2003) [35]:

$$\lambda^* = \frac{E_{md}}{E_c}\frac{th'}{A_c}\left(\frac{h'^2}{l'^2}+\frac{1}{4}\frac{A_c}{A_b}\frac{l'}{h'}\right) \tag{4}$$

where $E_{md}$ is the Young modulus of the masonry infill along the diagonal direction and $A_b$ is the area of the beam cross-section. The other symbols appearing in Eq. (4) can be simply deduced from Figure 1.

The parameter $\gamma$ in Eq. (1) takes into account the combined effect of openings and aspect ratio with the following expression:

$$\gamma = 1 + 0{,}5\frac{r}{(l/h)^4} \tag{5}$$

being $r=1$ for in the case of solid infills.

Finally $c$ and $\beta$ depend on the Poisson's ratio $\nu_d$ of the masonry constituting the infill along the diagonal direction according to the following expressions:

$$\begin{aligned} c &= 0{,}249 - 0{,}0116\nu_d + 0{,}567\nu_d^{\,2} \\ \beta &= 0{,}146 - 0{,}0073\nu_d + 0{,}126\nu_d^{\,2} \end{aligned} \tag{6}$$

The determination of $E_d$ and $\nu_d$ starting from elastic moduli along the 2 orthogonal directions is described in [2]. In absence of experimental data in both directions the average Young's modulus and Poisson's ration along the vertical direction are used.

## 3 STRESS-STRAIN PARAMTERS FROM EXPERIMENTAL TESTS

Experimental test data from Cavaleri and Di Trapani (2014) [22], Mehrabi et al. (1996) [1], Kakaletsis and Karayannis [3], Papia et al. [35] were used as reference to derive stress-strain parameters. The choice of these studies was due to the completeness of their experimental programs, which included also detailed data of experimental tests on masonry constituting infills. Design details of specimens are reported in Table. 1.

The widths of the equivalent strut models associated to the specimens are also reported in Table 2 together with the parameters for their identification, calculated according to [19] and [35].

| Auth. | Spec. # | Masonry. Typol. | $t$ (mm) | $h$ (mm) | $h'$ (mm) | $l$ (mm) | $l'$ (mm) | $l/h$ | $d$ (mm) | $A_c$ (mm²) | $A_b$ (mm²) |
|---|---|---|---|---|---|---|---|---|---|---|---|
| [22] | S1A | Calc. | 200 | 1600 | 1800 | 1600 | 1800 | 1.0 | 2545.6 | 40000.0 | 80000.0 |
| [22] | S1B | Clay. | 150 | 1600 | 1800 | 1600 | 1800 | 1.0 | 2545.6 | 40000.0 | 80000.0 |
| [22] | S1C | LW conc. | 300 | 1600 | 1800 | 1600 | 1800 | 1.0 | 2545.6 | 90000.0 | 120000.0 |
| [1] | 4 | Brick | 92 | 1422 | 1536 | 2032 | 2210 | 1.43 | 2691.5 | 31684.0 | 34838.6 |
| [1] | 5 | Brick | 92 | 1422 | 1536 | 2032 | 2210 | 1.43 | 2691.5 | 31684.0 | 34838.6 |
| [1] | 11 | Brick | 92 | 1422 | 1536 | 2948 | 3126 | 2.07 | 3483.1 | 31684.0 | 34838.6 |
| [1] | 6 | Brick | 92 | 1422 | 1536 | 2032 | 2235 | 1.43 | 2712.3 | 41290.2 | 34838.6 |
| [3] | S | Brick | 60 | 800 | 900 | 1200 | 1350 | 1.5 | 1622.5 | 22500.0 | 20000.0 |
| [35] | S2A | Calc. | 200 | 1600 | 1800 | 1600 | 1800 | 1.0 | 2545.6 | 40000.0 | 80000.0 |
| [35] | S2B | Lat. | 150 | 1600 | 1800 | 1600 | 1800 | 1.0 | 2545.6 | 40000.0 | 80000.0 |

Table 1: Geometric details of specimens tested by [1], [3], [22], [35].

| Auth. | $F_v$ (kN) | $E_{md}$ (N/mm²) | $E_c$ (N/mm²) | $v_d$ - | $c$ - | $\beta$ - | $\varepsilon_v$ - | $\kappa$ - | $r$ - | $\gamma$ - | $h/l$ - | $\lambda^*$ - | $w$ (mm) |
|---|---|---|---|---|---|---|---|---|---|---|---|---|---|
| [22] | 400 | 5670 | 25000 | 0.15 | 0.260 | 0.150 | 0.00020 | 1.048 | 1 | 1.50 | 1.00 | 2.30 | 627.1 |
| [22] | 400 | 5719 | 25000 | 0.10 | 0.254 | 0.148 | 0.00020 | 1.046 | 1 | 1.50 | 1.00 | 1.74 | 636.4 |
| [22] | 400 | 3254 | 25000 | 0.18 | 0.264 | 0.151 | 0.00009 | 1.019 | 1 | 1.50 | 1.00 | 0.93 | 700.4 |
| [1] | 294 | 4600 | 17000 | 0.15 | 0.260 | 0.150 | 0.00027 | 1.059 | 1 | 3.08 | 0.70 | 0.98 | 587.1 |
| [1] | 294 | 8949 | 18064 | 0.15 | 0.260 | 0.150 | 0.00026 | 1.060 | 1 | 3.08 | 0.70 | 1.79 | 536.6 |
| [1] | 294 | 9604 | 18133 | 0.15 | 0.260 | 0.150 | 0.00026 | 1.059 | 1 | 10.24 | 0.48 | 1.66 | 726.7 |
| [1] | 294 | 4198 | 19856 | 0.15 | 0.260 | 0.150 | 0.00018 | 1.038 | 1 | 3.08 | 0.70 | 0.65 | 590.1 |
| [3] | 100 | 660 | 29961 | 0.15 | 0.260 | 0.150 | 0.00007 | 1.015 | 1 | 3.53 | 0.67 | 0.05 | 470.5 |
| [35] | 400 | 8317 | 23000 | 0.09 | 0.253 | 0.148 | 0.00022 | 1.058 | 1 | 1.50 | 1.00 | 3.66 | 577.4 |
| [35] | 400 | 5719 | 23000 | 0.10 | 0.254 | 0.148 | 0.00022 | 1.051 | 1 | 1.50 | 1.00 | 1.89 | 632.8 |

Table 2: Mechanical data of specimens and identification parameters.

The experimental tests were simulated with the OpenSees models, iterating the stress-strain parameters associated with the equivalent struts in order to best-fit the experimental backbone curves. The results obtained after the calibration of the equivalent struts are shown in Figures 2-5.

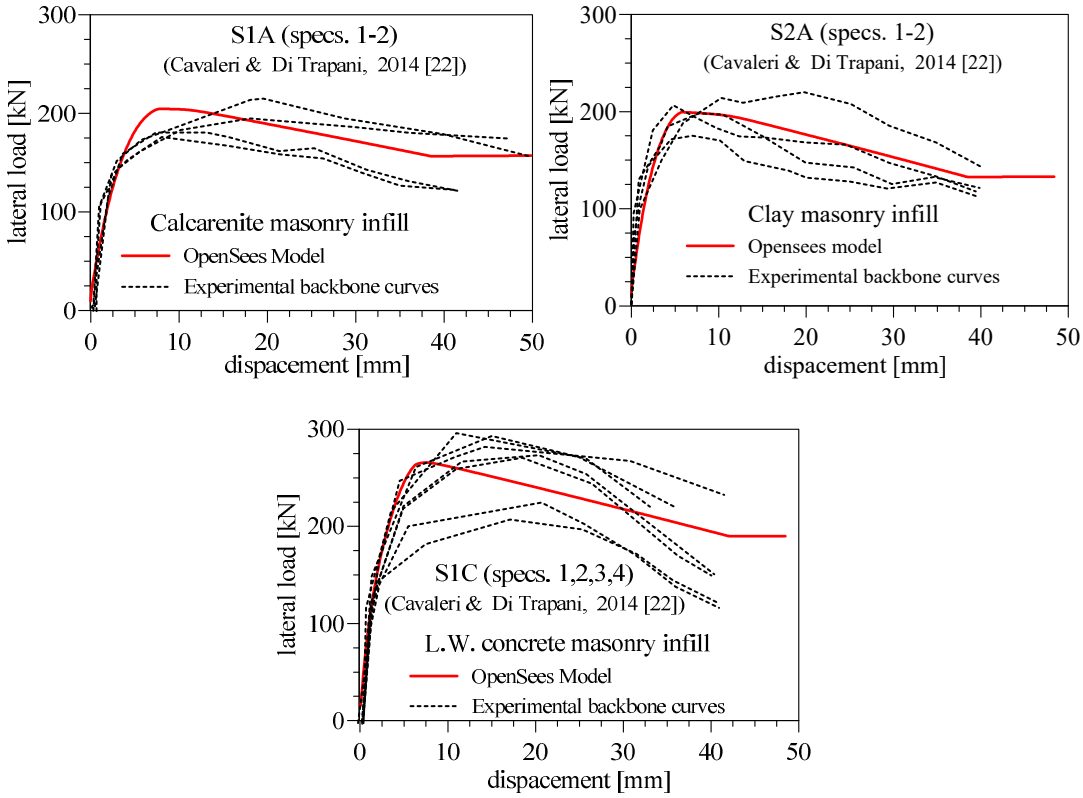


Figure 2: Experimental backbone curves of specimens by Cavaleri and Di Trapani, 2014 [22] and pushover curves of the OpenSees model at the end of the calibration.

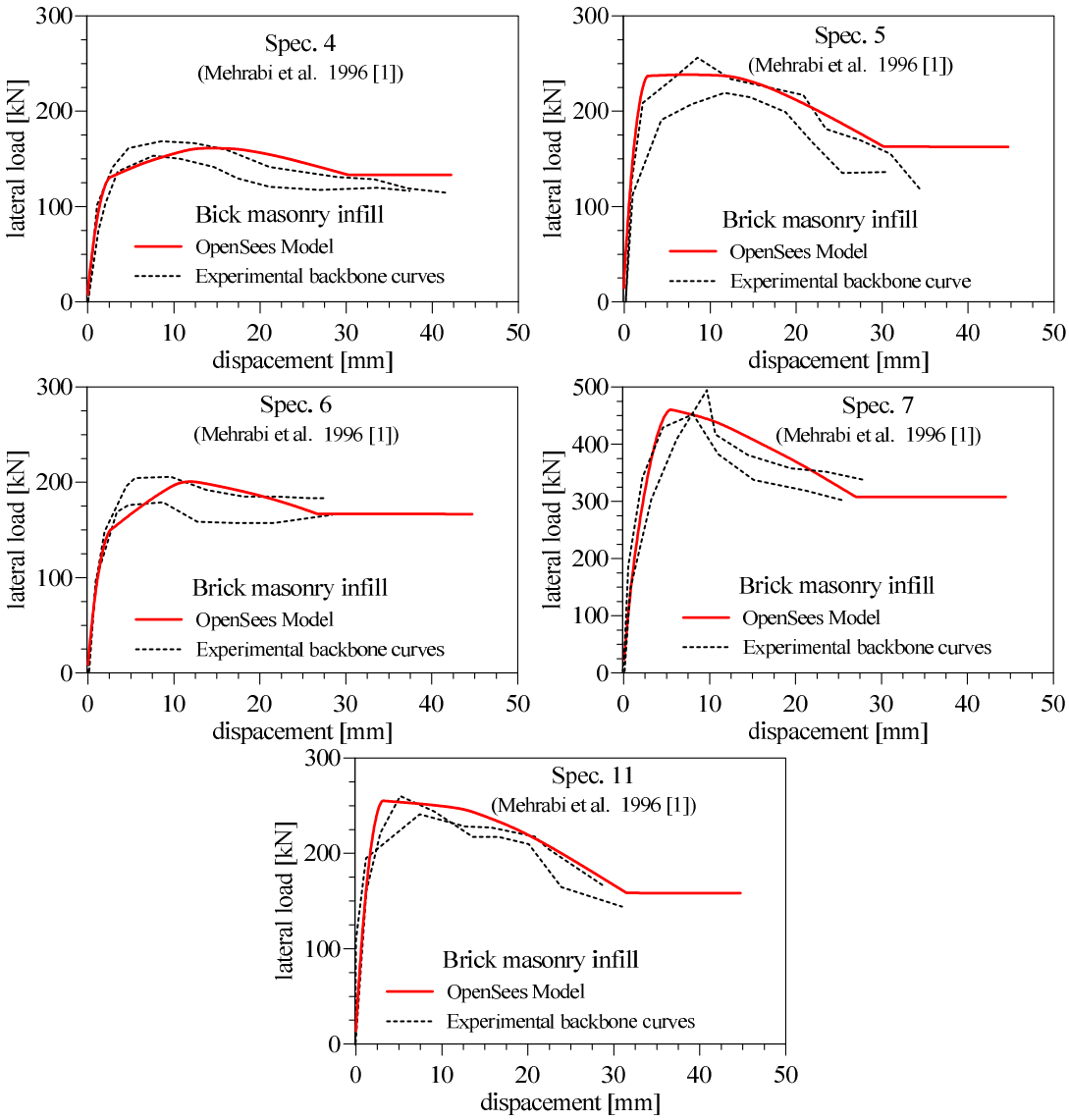


Figure 3: Experimental backbone curves of specimens by Mehrabi et al., 1996 [1] and pushover curves of the OpenSees model at the end of the calibration.

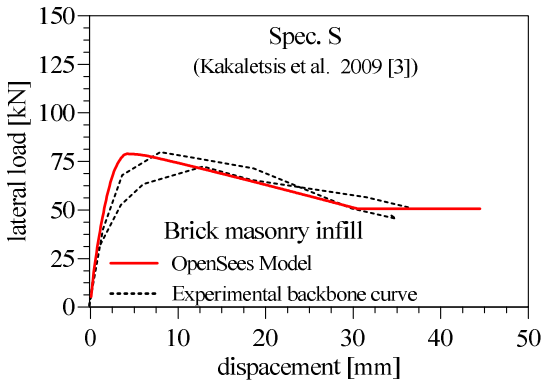


Figure 4: Experimental backbone curves of specimens by Kakaletsis et al., 2009 [3] and pushover curves of the OpenSees model at the end of the calibration.

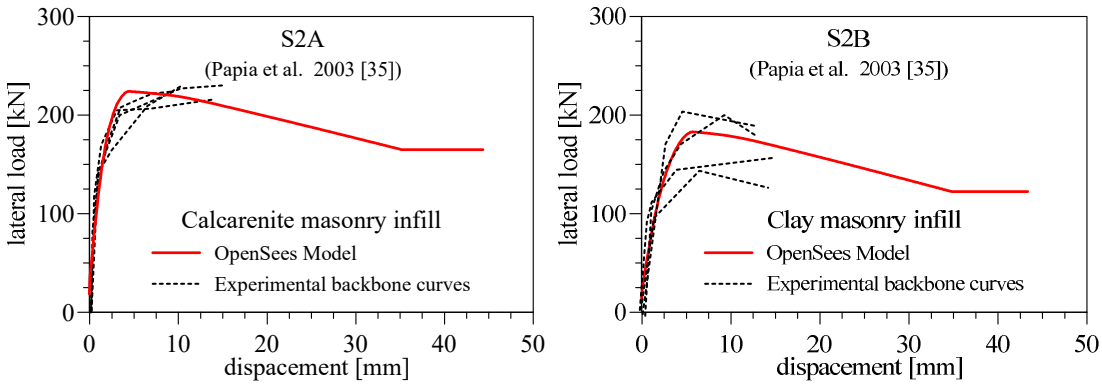


Figure 5: Experimental backbone curves of specimens by Papia et al., 2003 [35] and pushover curves of the OpenSees model at the end of the calibration.

The stress-strain parameters obtained for the models of the infilled frame specimens analyzed are reported in Table 3, together with the experimental values of shear and compressive strength of masonry infills. It can be observed, as before mentioned, that the compressive strength of diagonal struts ($f_{md0}$), which resulted after the calibration, was significantly lower than the actual compressive strength ($f_{mdu}$). This reduction ranged between -25% and -75% and depended on the different damage mechanism actually activated during the tests.

The experimental/numerical comparisons have also shown that the use of diagonal fiber-section struts with a concrete-type stress-strain law is particularly suitable to predict the response of infilled frames. In particular the proposed modeling approach resulted particularly accurate in predicting the ascending and descending branches, regulating initial and post-cracking stiffness and post-peak softening.

| **Auth.** | **Spec. #** | $f_{vm}$ | $f_m$ | $f_{md0}$ | $f_{mdu}$ | $\varepsilon_{md0}$ | $\varepsilon_{mdu}$ |
|---|---|---|---|---|---|---|---|
| | | N/mm² | N/mm² | N/mm² | N/mm² | - | - |
| [22] | S1A | 0.73 | 2.67 | 2.00 | 1.20 | 0.0018 | 0.0100 |
| [22] | S1B | 1.07 | 8.66 | 2.50 | 1.10 | 0.0015 | 0.0090 |
| [22] | S1C | 0.30 | 1.74 | 1.20 | 0.50 | 0.0015 | 0.0100 |
| [1] | 4 | 0.93 | 5.30 | 2.40 | 0.65 | 0.0008 | 0.0090 |
| [1] | 5 | 1.15 | 13.85 | 5.30 | 1.60 | 0.0008 | 0.0090 |
| [1] | 11 | 1.03 | 11.44 | 3.80 | 0.95 | 0.0008 | 0.0080 |
| [1] | 6 | 0.70 | 5.06 | 2.60 | 0.65 | 0.0008 | 0.0090 |
| [3] | S | 0.08 | 2.63 | 2.30 | 0.75 | 0.0030 | 0.0110 |
| [35] | S2A | 0.89 | 4.57 | 2.50 | 1.40 | 0.0010 | 0.0100 |
| [35] | S2B | 1.07 | 8.66 | 2.30 | 1.10 | 0.0015 | 0.0090 |

Table 3: Mechanical data of masonry and stress-strain parameters.

## 4 STRESS-STRAIN PARAMTERS FROM FE MODELS

In order to enlarge the data-set necessary to derive the correlations, additional tests were simulated with a detailed finite element model. The FE model was realized using ATENA 2D software platform which is based on a concrete smeared cracking model and also implements frictional interface elements. The reference specimens used for the simulation of the tests were specimens S1B [22]. Reinforced concrete elements were modeled using CCIsoQuad nonlinear elements with a SBeta material, defined with a uniaxial stress-strain concrete law and a biaxial failure criterion. The same material was used to model masonry units. Interface elements were used to model the contact surfaces between concrete and masonry and between masonry units. Interfaces were governed by Mohr-Coulomb failure surface with a specified friction coefficient and cohesion. Longitudinal reinforcement was included in the model using

rebar elements consisting in 1D truss with uniaxial steel (elasto-plastic with strain hardening law). For the transversal reinforcement a smeared reinforcement material was adopted. The numerical simulation of the tests consisted of two steps. First vertical loads at the tops of the column were applied. Then a lateral displacement was imposed up to the prescribed magnitude. The FE model and the assembly scheme are shown in Figure 6.

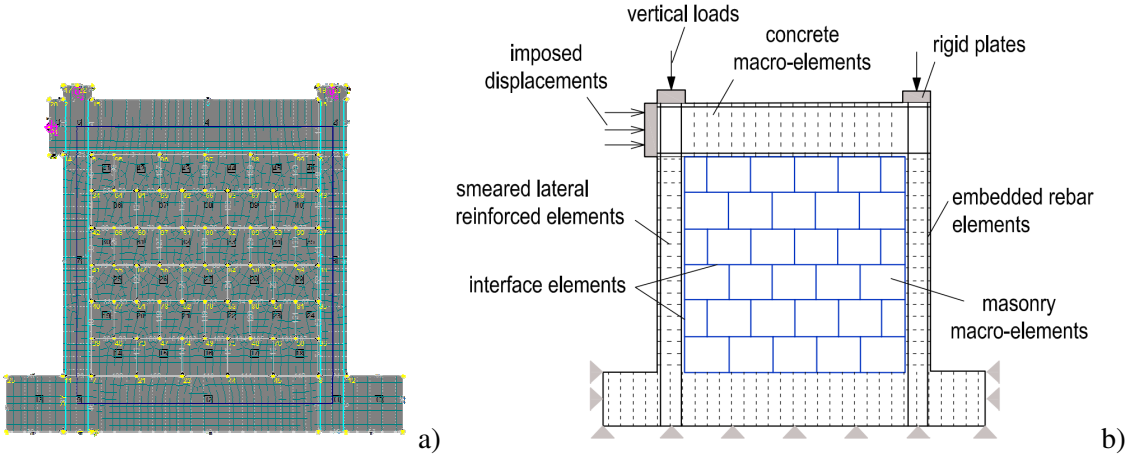


Figure 6: Definition of the FE model: a) FE model in ATENA; b)Scheme of the model assembly and application of loads.

The simulation of the tests of S1B specimen was iterated several times to obtain calibration parameters of the FE model. In the calibration process, mechanical data of materials (compressive and tensile strength of concrete and masonry) were those experimentally evaluated. The final result, after the calibration, is illustrated in Figure 7, where it can be noted the accuracy of the FE model in predicting the average initial stiffness and post-peak decay actually exhibited by the specimens. In Figure 8-a is shown the distribution of Von Mises stresses at the peak-load, while Figure 8-b and 8-c show the cracking pattern of the FE model at the peak and at the end of the test respectively. As it can be observed sliding of mortar joint was the dominant damage mechanism (as recognized in actual test), however this was associated with a diagonal cracking pattern involving masonry units. The calibration parameters determined for the reference FE model are reported in Table 4.

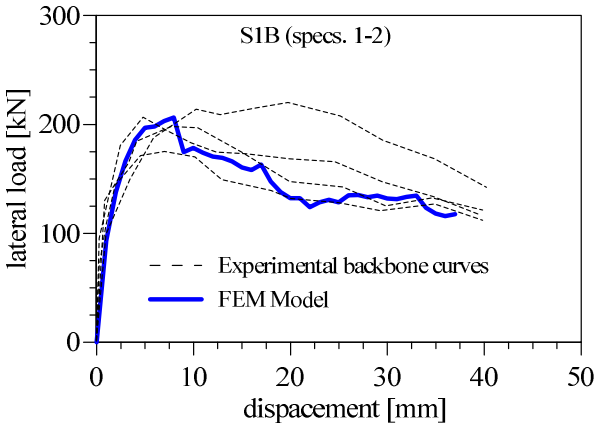


Figure 7: Experimental backbone curves of specimens S1B [35] and pushover curve of the FE model at the end of the calibration.

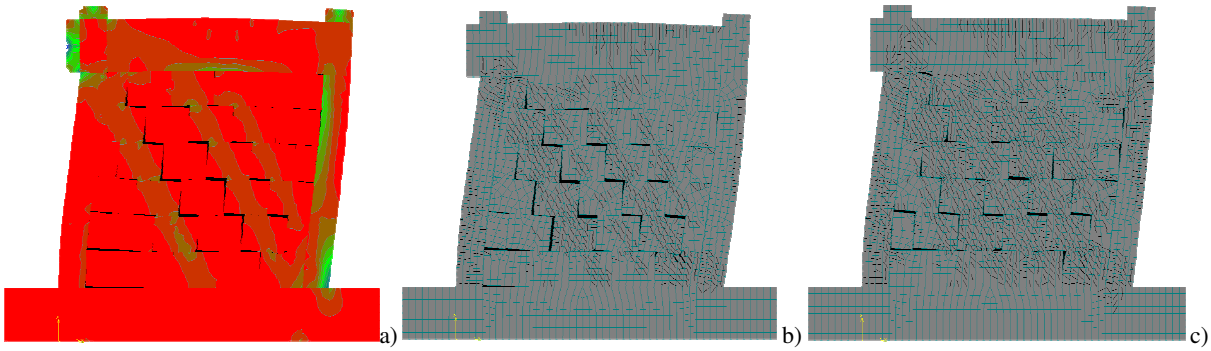

Figure 8: Results from FE model: a) Von Mises stresses at peak-load; b) cracking pattern at the peak-load; c) cracking pattern at end of the test.

| **Concrete** | | | | |
|---|---|---|---|---|
| Compressive strength | Tensile strength | Softening coefficient | Ultimate tensile strain | Shear retention factor |
| **$f_c$ [MPa]** | **$f_t$ [MPa]** | **-** | **-** | **-** |
| 25 | 0.25 | 0.20 | 0.001 | 0.20 |
| **Masonry** | | | | |
| Compressive strength | Tensile strength | Softening coefficient | Ultimate tensile strain | Shear retention factor |
| **$f_{cm}$ [MPa]** | **$f_{vm}$ [MPa]** | **-** | **-** | **-** |
| 8.66 | 1.07 | 0.20 | 0.001 | 0.15 |
| **Interface** | | | | |
| Normal stiffness | Tangential stiffness | Tensile strength | Cohesion | Friction coefficient |
| **$K_{nn}$ [MN/m]** | **$K_{tt}$ [MN/m]** | **$f_t$ [MPa]** | **c** | **μ** |
| 4000000 | 400000 | 0.4 | 1.0 | 0.7 |

Table 4: Mechanical data and calibration parameters of the reference FE model.

The FE model, after the calibration, was used to simulate supplementary tests by varying geometric and mechanical parameters of the infill. In particular the calibration parameters were fixed, as well as the geometry of the frame, while it was supposed to vary compressive and shear strength of masonry, infill thickness and masonry elastic modulus. The supplementary tests simulated are listed in Table 5, where the parameters each time varied are highlighted.

| **Spec. #** | **$f_{vm}$** N/mm² | **$f_m$** N/mm² | **$t$** N/mm² | **$E_m$** N/mm² |
|---|---|---|---|---|
| FEM-1S | **0.60** | **12.00** | 150 | 5719 |
| FEM-2S | **0.40** | **4.00** | 150 | 5719 |
| FEM-3S | **0.20** | **2.00** | 150 | 5719 |
| FEM-1T | 0.50 | 8.66 | **50** | 5719 |
| FEM-1T | 0.50 | 8.66 | **100** | 5719 |
| FEM-1T | 0.50 | 8.66 | **150** | 5719 |
| FEM-1T | 0.50 | 8.66 | **200** | 5719 |
| FEM-1E | 0.50 | 8.66 | 150 | **1200** |
| FEM-2E | 0.50 | 8.66 | 150 | **2000** |
| FEM-3E | 0.50 | 8.66 | 150 | **3850** |
| FEM-4E | 0.50 | 8.66 | 150 | **9000** |

Table 5: Geometric and mechanical data of numerical models generated from the reference S1B model.

The results of the tests simulated with the FE models are shown in Figure 9. Some general trends can be observed from the curves obtained, in particular: an increase of compressive and shear strength of masonry resulted in an global increase of the strength of the system, with a post-peak branch characterized by losses and regain of strength; an increase of the thickness of the infill resulted in an overall increase of strength, but this was less relevant as the thick-

ness increased, at the same time a post-peak loss of strength, progressively increasing, was recognized; an increase of Young's modulus of the infill resulted in a proportional increase of stiffness of the system and a significant reduction of the peak-displacement with a simultaneous reduction of the overall strength.

In Figure 9, results of the OpenSees models simulating FE tests are also reported. The parameters evaluated for the identification of the equivalent strut widths are reported in Table 6 together with the stress-strain parameters obtained after the calibration.

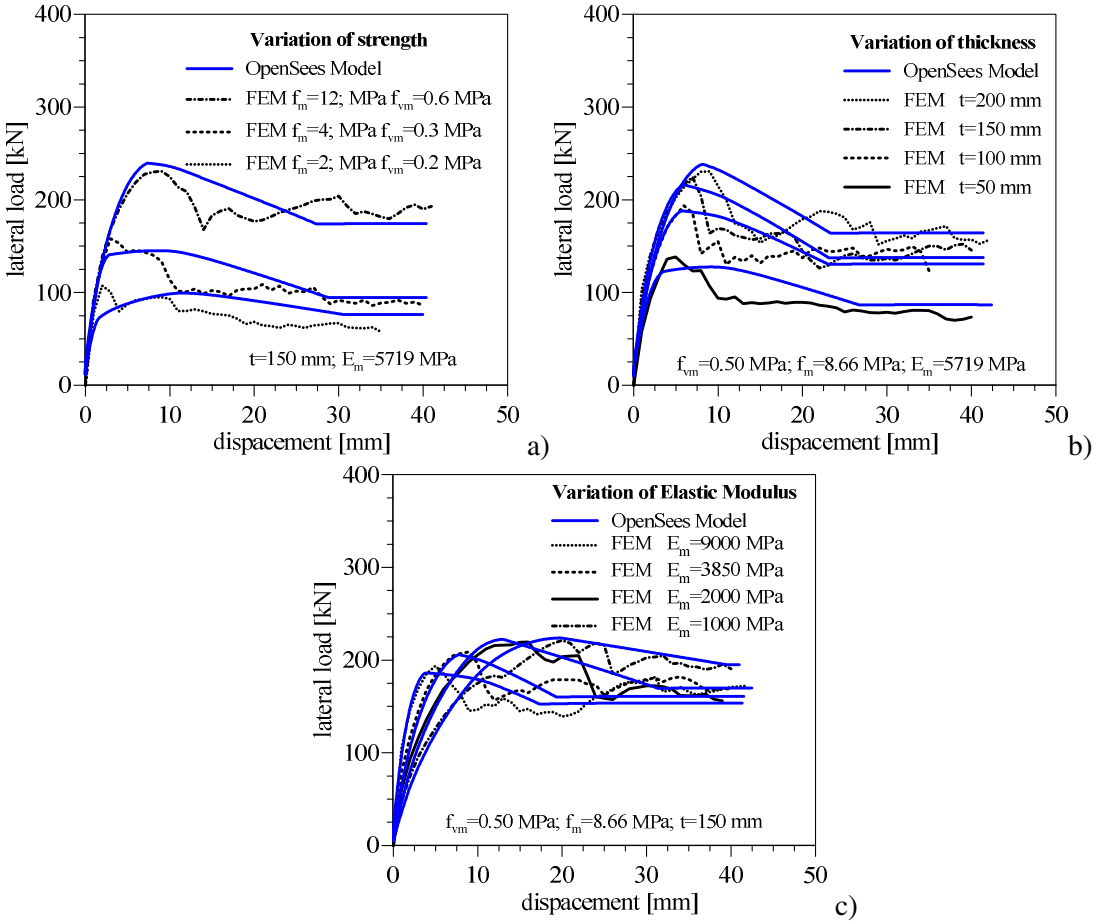


Figure 9: Results of FE model simulations and pushover curves of the OpenSees models at the end of the calibration: a) variation of strength; b) variation of thickness of the infill; c) variation of elastic Young's modulus.

| Spec. # | $k$ | $\gamma$ | $\lambda^*$ | $w$ | $f_{md0}$ | $f_{mdu}$ | $\varepsilon_{md0}$ | $\varepsilon_{mdu}$ |
|---|---|---|---|---|---|---|---|---|
| | - | - | - | mm | N/mm² | N/mm² | - | - |
| FEM-1S | 1.046 | 1.50 | 1.737 | 636.4 | 1.70 | 0.40 | 0.001 | 0.008 |
| FEM-2S | 1.046 | 1.50 | 1.737 | 636.4 | 2.90 | 1.50 | 0.002 | 0.007 |
| FEM-3S | 1.046 | 1.50 | 1.737 | 636.4 | 0.80 | 0.15 | 0.001 | 0.008 |
| FEM-1T | 1.042 | 1.50 | 0.579 | 744.3 | 3.50 | 0.70 | 0.001 | 0.008 |
| FEM-1T | 1.044 | 1.50 | 1.158 | 673.8 | 3.20 | 1.40 | 0.002 | 0.006 |
| FEM-1T | 1.046 | 1.50 | 1.737 | 636.4 | 2.70 | 1.10 | 0.002 | 0.006 |
| FEM-1T | 1.048 | 1.50 | 2.316 | 611.7 | 2.20 | 1.20 | 0.001 | 0.006 |
| FEM-1E | 1.042 | 1.50 | 0.608 | 739.2 | 2.20 | 1.40 | 0.003 | 0.008 |
| FEM-2E | 1.044 | 1.50 | 1.169 | 672.8 | 2.30 | 1.40 | 0.002 | 0.005 |
| FEM-3E | 1.041 | 1.50 | 0.304 | 817.7 | 2.00 | 1.60 | 0.005 | 0.010 |
| FEM-4E | 1.050 | 1.50 | 2.734 | 598.2 | 2.50 | 1.45 | 0.001 | 0.005 |

Table 6: Identification parameters of equivalents strut models and stress-strain patameters.

## 5 PROPOSED CORRELATIONS TO DETERMINE STRESS-STRAIN PARAMETERS

The stress-strain parameters obtained from the calibration of the equivalent strut models on real experimental tests and FE simulations were used to define direct semi-empirical correlations linking geometric and mechanical data of an infilled frame to the parameters defining the equivalent strut stress-strain law. If one sets the following quantities:

$$\alpha = \frac{f_m{}^2 \cdot w \cdot t \cdot \left(f_{vm} + \mu\sigma_n\right)}{\left(l/h\right) \cdot \lambda^{*0.4}} \tag{7}$$

$$\beta = \frac{f_{md0}{}^{0.8} \cdot w \cdot t}{E_{md}{}^{0.2} d} \tag{8}$$

$$\gamma = \left(\frac{f_{mdu}{}^2}{f_{md0}}\right)\left(\frac{E_c{}^{0.5}}{E_{md}{}^{1.5}}\right) \tag{9}$$

$$\delta = E_{md}{}^{0.15} \varepsilon_{md0} \tag{10}$$

where $\sigma_n$ is the average compressive stress on masonry due to vertical loads while the meaning of the other symbols has been already explained, the following trends (Figure 10) can be observed with respect to the normalized stress-strain parameters $f_{md0}/f_m$, $f_{mdu}/f_{md0}$, $\varepsilon_{md0}/\varepsilon_{m0}$, $\varepsilon_{md}/\varepsilon_{md0}$ ($\varepsilon_{m0}$ is set equal to 0.0015).

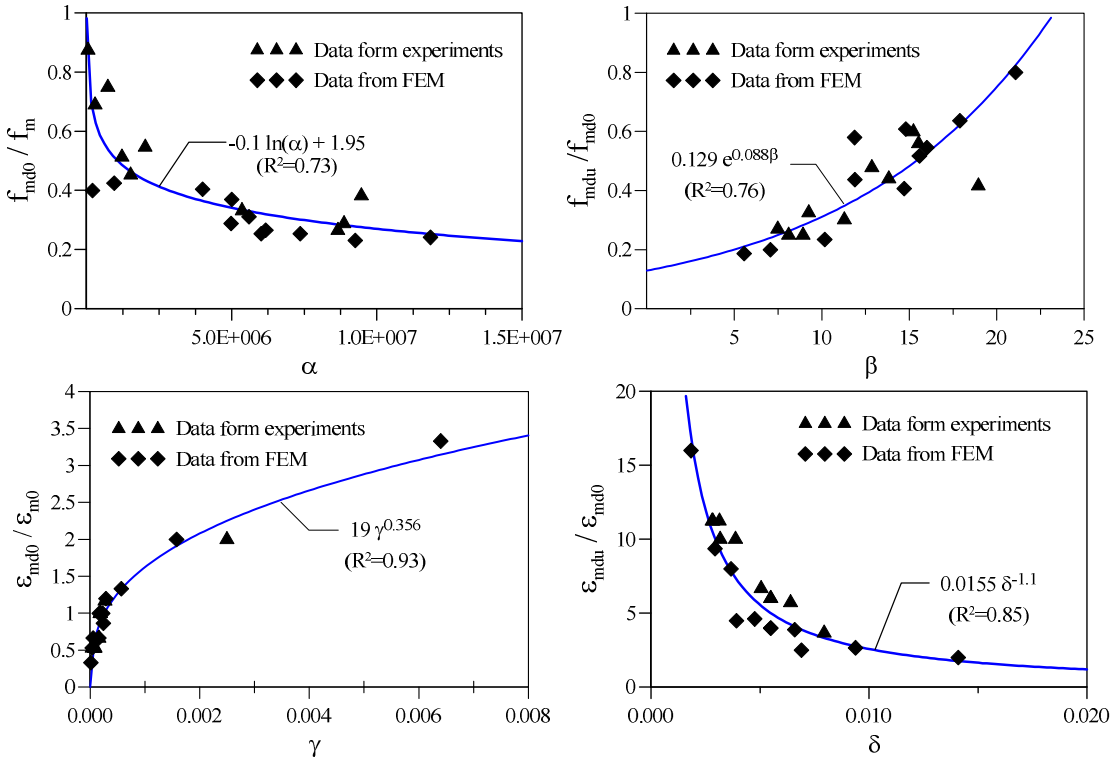


Figure 10: Relationship between parameters $\alpha$, $\beta$, $\gamma$ and $\delta$ and dimensionless stress-strain parameters and proposed analytical correlations.

Dimensionless stress-strain parameters resulted having a clear correlations with parameters $\alpha$, $\beta$, $\gamma$ and $\delta$ defined in Eqs. (7-10). These can be expressed by the following analytical relationships:

$$\frac{f_{md0}}{f_m} = -0.1 \cdot \ln(\alpha) + 1.95 \qquad (R^2 = 0.73) \tag{11}$$

$$\frac{f_{mdu}}{f_{md0}} = 0.129 \cdot e^{0.088\beta} \qquad (R^2 = 0.76) \tag{12}$$

$$\frac{\varepsilon_{md0}}{\varepsilon_{m0}} = 19 \cdot \gamma^{0.356} \qquad (R^2 = 0.93) \tag{13}$$

$$\frac{\varepsilon_{md0}}{\varepsilon_{mdu}} = 0.0155 \cdot \delta^{-1.1} \qquad (R^2 = 0.85) \tag{14}$$

The normalization of stress-strain parameters was adopted to highlight the relationship between the quantities. In this way the diagrams in Figure 10 give also the idea of the magnitude of variation between a stress-strain parameters and the entity used as normalizing factor.

In Eqs. (11-14) the coefficients of determination are also shown for each correlation. The latter range between 0.73 and 0.93, confirming an adequate reliability of the correlation laws proposed.

Stress-strain parameters of a generic infilled frame can be determined with Eqs. (7-10) and (11-14), which have to be used in the same order as they are listed. In fact paramter $\beta$ depends on $f_{md0}=f(\alpha)$, paramter $\gamma$ depends on $f_{mdu}=f(\beta)$ and parameter $\delta$ depends on $\varepsilon_{md0}=f(\gamma)$.

Eqs. (7-10), combined with Eqs. (11-14) can be used as an effective tool to predict the real complicated inelastic behaviour of an infilled frame subjected to lateral loads when using fiber-section equivalent strut macro models.

## 6 CONCLUSIONS

The identification of nonlinear behaviour of equivalent struts is still a major issue in the modeling process of infilled frames. This is due to the fact that the actual damage mechanisms activated in an infilled frame subjected to lateral loads can be really different and are not easy to be predicted a priori. Based on this, the paper proposes a method for the identification of the inelastic response of equivalents struts which starts from a semi-empirical approach oriented to the definition of concrete-type stress-strain relationship to be used for fiber-section modeling of equivalent struts. The parameters governing the equivalent strut stress-strain law, namely $f_{md0}$, $\varepsilon_{md0}$, $f_{mdu}$, $\varepsilon_{mdu}$, have been derived by iteratively calibrating a fiber-section equivalent strut model with real experimental tests and FE simulations. The stress strain-parameters have shown a distinct correlation with the quantities $\alpha$, $\beta$, $\gamma$ and $\delta$, depending on simple geometric and mechanical features of the infilled frames. Analytical expressions describing such a correlation have been determined for each parameter, and have shown an adequate degree of reliability. The latter allow, through the simple evaluation of parameters $\alpha$, $\beta$, $\gamma$ and $\delta$, to define the stress-strain parameters for a generic infilled frame. The identification strategy proposed on the paper can be used as a tool for the identification of the inelastic behaviour equivalents strut both for practical engineering and research purposes.

## REFERENCES


[1] A.B. Mehrabi, P.B. Shing, M.P. Schuler, J.L. Noland, Experimental evaluation of masonry-infilled RC frames, *J Struct Eng (ASCE)*, **122**, No. 3, 228-37,1996.

[2] L. Cavaleri, F. Di Trapani, G. Macaluso, M. Papia, P. Colajanni, Definition of diagonal Poisson's ratio and elastic modulus for infill masonry walls, *Mat. and Struct.*, **47**(1-2), 239-262, 2014.

[3] D.J. Kakaletsis, C.G. Karayannis, Experimental investigation of infilled reinforced concrete frames with openings, *ACI Structural Journal*, **102**, No. 2, 132-141, 2009.

[4] L. Cavaleri, F. Di Trapani, G. Macaluso, M. Papia, Reliability of code proposed models for assessment of masonry elastic moduli, *Ingegneria Sismica*, Anno XXIX n.1. 2012.

[5] M. Dolšek, P. Fajfar, The effect of masonry infills on the seismic response of four storey reinforced concrete frame - a deterministic assessment, *Eng. Structures*, **30**, No. 7, 1991-2001, 2008.

[6] P.G. Asteris, C.C. Repapis, A.K Tsaris, F. Di Trapani, L. Cavaleri, Parameters affecting the fundamental period of infilled RC frame structures, *Earthquake and Structures*, **9**(5), 999-1028, 2015.

[7] P.G. Asteris, A.K. Tsaris, L. Cavaleri, C. Repapis, A. Papalou, F. Di Trapani, D.F. Karypidis,. Prediction of the Fundamental Period of Infilled RC Frame Structures Using Artificial Neural Networks, *Computational Intelligence and Neuroscience*, Article ID 474106, http://dx.doi.org/10.1155/2016/5104907, 2015.

[8] P.G. Asteris, Lateral Stiffness of Brick Masonry Infilled Plane Frames, *J. Struct. Eng. (ASCE)*, **129**, No. 8, 1071-1079, 2003.

[9] M. Papia, Analysis of infilled frames using a coupled finite element and boundary element solution scheme, *Int J Numerical Methods in Engineering*, **26**, No.3, 731-742, 1988.

[10] L. Cavaleri, F. Di Trapani, Prediction of the additional shear action on frame members due to infills, *Bulletin of Earthquake Engineering*, **13**(5), 1425-1454, 2015.

[11] I. Koutromanos, A. Stavridis, P.B. Shing, K. Willam, Numerical modelling of masonry-infilled RC frames subjected to seismic loads, *Computers and Structures* **89**, 1026-1037, 2011.

[12] A.B. Mehrabi, P.B. Shing, Finite element modelling of masonry-infilled RC frames, *J. Struct. Eng.*, **123**, No. 5, 604-13, 1997.

[13] A. Spada, G. Giambanco, P. Rizzo, Damage and plasticity at the interfaces in composite materials and structures, *Computer Methods in Applied Mechanics and Engineering*, **198**, No. 49-52, 3884 – 3901, 2009.

[14] G. Giambanco, G. Fileccia Scimemi, A. Spada, The interphase element, *Computational Mechanics*, **50**, No. 3, 353-366, 2012.

[15] B. Stafford Smith, C. Carter , A method for analysis for infilled frames, *Proc. of Institution of Civil Engineers*, Paper No.7218, 31-48, 1969.

[16] R.J. Mainstone, Supplementary note on the stiffness and strength of infilled frames, *Building Research Station*, Current Paper CP 13/74, UK.

[17] M. Papia, L. Cavaleri, M. Fossetti, Infilled frames: developments in the evaluation of the stiffening effect of infills, *Structural engineering and mechanics*, **16**, No. 6, 675-93, 2003.

[18] G. Campione, L. Cavaleri, G. Macaluso, G.Amato, F. Di Trapani, Evaluation of infilled frames: an updated in-plane-stiffness macro-model considering the effects of vertical loads, *Bulletin of Earthquake Engineering*, **13**(8), 2265-2281, 2015.

[19] P.G. Asteris, L. Cavaleri, F. Di Trapani, V. Sarhosis, A macro-modelling approach for the analysis of infilled frame structures considering the effects of openings and vertical loads, *Structure and Infrastructure Engineering,* **12**(5), 551-566, 2016.

[20] A. Saneinejad, B. Hobbs, Inelastic design of infilled frames, *J Struct Eng (ASCE)*, **121**, No. 4, 634-50, 1995.

[21] T.B. Panagiotakos, M.N. Fardis, Seismic response of infilled RC frames structures, *XXI WCEE*, Acapulco, Mexico, 1996.

[22] L. Cavaleri, F. Di Trapani, Cyclic response of masonry infilled RC frames: Experimental results and simplified modeling, *Soil Dynamics and Earthquake Engineering,* **65**, 224–242, 2014.

[23] A. Hashemi, K.M. Mosalam, Seismic Evaluation of Reinforced Concrete Buildings Including Effects of Masonry Infill Walls, *PEER Report*, University of California, Berkeley, 2007.

[24] S. Kadysiewski, K.M. Mosalam, Modeling of Unreinforced Masonry Infill Walls Considering In-Plane and Out-of-Plane Interaction, *PEER Report 2008/102*, University of California, Berkeley, January 2009.

[25] P.G. Asteris, L. Cavaleri, F. Di Trapani, A.K. Tsaris, Numerical modelling of out-of-plane response of infilled frames: State of the art and future challenges for the equivalent strut macromodels, *Engineering Structures*, **132**, 110-122, 2017.

[26] F. Di Trapani, G. Macaluso, L. Cavaleri, M. Papia, Masonry infills and RC frames interaction: literature overview and state of the art of macromodeling approach, *European Journal of Environmental and Civil Engineering*, **19**(9), 1059-1095, 2015.

[27] G. Campione, L. Cavaleri, F. Di Trapani, G. Macaluso, G. Scaduto, Biaxial deformation and ductility domains for engineered rectangular RC cross-sections: A parametric study highlighting the positive roles of axial load, geometry and materials, *Engineering Structures*, **107**(15), 116-134, 2016.

[28] P. Castaldo, B. Palazzo, Della Vecchia, Life-cycle cost and seismic reliability analysis of 3D systems equipped with FPS for different isolation degrees, *Engineering Structures*, **125**, 349-363, 2016.

[29] P. Castaldo, B. Palazzo, T. Ferrentino, Seismic reliability-based ductility demand evaluation for inelastic base-isolated structures with friction pendulum devices, *Earthquake Engineering and Structural Dynamics*, DOI: 10.1002/eqe.2854, 2016.

[30] P. Castaldo, B. Palazzo, A. Mariniello, Effects of the axial force eccentricity on the time-variant structural reliability of aging R.C. cross-sections subjected to chloride-induced corrosion, *Engineering Structures*, **130**, 261-274, 2017.

[31] P. Castaldo, G. Amendola, B. Palazzo, Seismic fragility and reliability of structures isolated by friction pendulum devices: seismic reliability-based design (SRBD), *Earthquake Engineering and Structural Dynamics*, **46**(3), 425-446, 2017.

[32] P. Castaldo, M. Ripani, Optimal design of friction pendulum system properties for isolated structures considering different soil conditions, *Soil Dynamics and Earthquake Engineering,* **90**, 74-87, 2016.

[33] D.C. Kent, R. Park, Flexural Members with Confined Concrete, *Journal of Structural Division ASCE*, **97**(7), 1969-90, 1971.
[34] F. McKenna, G.L. Fenves, M.H. Scott, *Open system for earthquake engineering simulation*, University of California, Berkeley, CA, 2000.
[35] M. Papia, L. Cavaleri, M. Fossetti, Infilled frames: developments in the evaluation of the stiffening effect of infills, *Structural engineering and mechanics*, **16**, No. 6, 675-93, 2003.

COMPDYN 2017
6th ECCOMAS Thematic Conference on
Computational Methods in Structural Dynamics and Earthquake Engineering
M. Papadrakakis, M. Fragiadakis (eds.)
Rhodes Island, Greece, 15–17 June 2017

# NONLINEAR STATIC ANALYSIS OF INFILLED RC FRAMES: A NOVEL SIMPLIFIED PROCEDURE

**C. Lima, C. Faella, and E. Martinelli**

DICiv – Department of Civil Engineering, University of Salerno
via Giovanni Paolo II, 132 – Fisciano (SA), Italy
e-mail: clima@unisa.it, c.faella@unisa.it, e.martinelli@unisa.it

**Keywords:** Seismic assessment, RC frames, masonry infill, Nonlinear static analysis, N2 Method.

**Abstract.** *Masonry walls are generally utilized in Reinforced Concrete (RC) structures, either as external infills or as internal partitions. Although the interaction between them and structural members significantly affects the seismic response of structures, infills are usually not included in the structural models and, hence, their mechanical contribution is neglected in seismic analysis and assessment of existing structures. However, additional strength provided by infills may either play a beneficial role or affect the resulting structural capacity. Although several proposals are currently available for simulating the nonlinear response of masonry infills in structural analysis, no well-established methods emerged so far for evaluating the global response of infilled RC frames.*
*This paper proposes a simplified procedure based on Nonlinear Static (NLS) analysis and an extension of the well-known N2 Method. A statistical assessment and validation is also presented with the aim to confirm accuracy and reliability of the proposed analysis procedure.*

## 1 INTRODUCTION

In the last fifty years, Reinforced Concrete (RC) frames have been widely realized also in seismic areas, such as the Mediterranean region. In these structures, masonry walls are generally used as both internal partitions and external infills.

Although the behaviour of masonry infills may significantly affect the overall structural response as well observed in recent seismic events [1], only RC members are considered in practice-oriented structural analysis, while masonry infills are considered to contribute to the structural response by mean of their weight and mass only [2]. However, such a simplification, generally accepted for new structures designed according to the Capacity Design rules in which the stiffness of columns is higher than the one of masonry, may affect the response of existing RC structures characterized by strong infill walls and weak columns [3].

Plenty of researches have been developed on this subject by the scientific community. Specifically, simulating the actual dynamic behaviour of infills and evaluating their influence on the global seismic response of RC structures is the main investigated issues [4][5]: nevertheless, no procedures capable to take into account the contribution of masonry infills in practice-oriented seismic analyses of RC frames have been established so far. As a matter of fact, Nonlinear Static (NLS) analyses are commonly employed nowadays for evaluating the seismic response of both new and existing structures. They are generally performed on bare frame models, but recent developments aiming at introducing the effect of masonry infills have been recently proposed in the scientific literature. One of those procedures is based on formulating a specific R–μ–T relationship [6] for partially dissipative systems. It aims at to consider the effects of a the significant softening response induced by the progressive damage affecting masonry walls during the seismic shaking. Moreover, further improvements have been achieved for assessing the seismic capacity of infilled frames within the framework of the Capacity Spectrum Method (CSM) and the Coefficient Method [7].

Although, such procedures generally result in accurate predictions of the actual seismic response of infilled RC frames, their analytical definitions are formally complicated and based on several parameters whose determination is not generally straightforward. Moreover, if "weak" infills are considered, they do not clearly reduce (as, in principle, one should expect) to the well-known N2 Method widely accepted for bare structures [8].

Therefore, the challenge of formulating a simple, accurate and reliable procedure for determining the performance point of masonry infilled RC structures by means of NLS analysis is still a relevant issue within the scientific community.

A possible extension of the N2 Method to the masonry infilled structures has been recently proposed by Martinelli et al. in 2015 [9]. Specifically, they analysed the capacity curves of both bare and infilled configurations of a series of parametric structures and proposed a scalar "shape" parameter aimed at simply correlating the displacement of the infilled structure to the one of the bare configuration evaluated via the N2 Method.

In the present paper, the aforementioned procedure is firstly presented, then a further validation of such a proposal is outlined based on a parametric set of structure wider than the one originally used by the Authors [9]. Specifically, NonLinear Time History (NLTH) and NLS analyses performed on two- four- and six-storey structures are herein integrated by considering one-, three- and five-storey buildings in which the monotonic and cyclic response of infill walls is simulated through the computationally convenient approach based on the "equivalent strut" concept [10]. Finally, a sample application on an existing frame considered as a relevant case study is reported.

## 2 OVERVIEW OF THE SIMPLIFIED PROCEDURE

Martinelli et al. [9], based on the results of several numerical experiments and comparisons between the capacity curves of bare and infilled structures, suggested a direct estimation of the displacement demand of infilled frames via NLS analyses. Specifically, the top displacement of a framed structure with masonry infills can be obtained from the one evaluated via N2 Method [8] for the corresponding bare structure:

$$\Delta_{top,infill}^{NLS} = \alpha \cdot \Delta_{top,bare}^{NLS}, \tag{1}$$

where $\alpha$ is a parameter defining the "shape" of the two capacity curves corresponding to the infilled frame and the corresponding bare one. Specifically, the shape parameter $\alpha$ is defined as the ratio between the areas beneath the two aforementioned capacity curves, up to a displacement equal to the demand determined through the N2 Method on the bare structure:

$$\alpha = \frac{A_{bare}^{NLS}}{A_{infill}^{NLS}}. \tag{2}$$

As a matter of fact, the nonlinear behaviour of a structure with and without infills is captured by the capacity curves reported in Figure 1. The proposed procedure is based on evaluating the displacement demand of the bare configuration through the well-know and widely accepted N2 Method (Figure 1,a). Thus, the parameter $\alpha$ is determined by means of eq. (2) (Figure 1,b) and the displacement demand of the infilled structure is obtained through eq. (1).

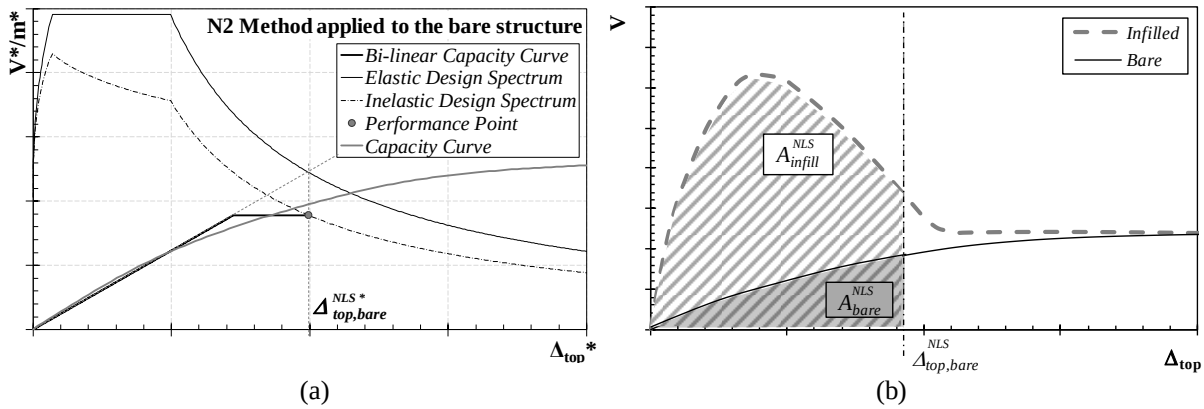


(a) (b)

Figure 1: Seismic demand evaluation on the bare structure (a) and comparison between capacity curves (b).

Actually, as it clearly emerges from its definition, the parameter $\alpha$ ranges between 0 and 1. Specifically, values close to *0* are obtained for "strong" masonry walls and/or "low" seismic actions, while values close to the unit denotes "weak" masonry infills and/or "strong" seismic actions. Moreover, the proposed procedure reduces to the widely accepted and validated N2 Method if the gap between the two curves tends to close and, hence, $\alpha$ tends to *1*.

## 3 THE STRUCTURES FOR THE PARAMETRIC ANALYSIS

Two-, four- and six-storey 3D frames, generated through a simulated design inspired to codes and practices in force in 1960s in Italy [11], are considered in a parametric analysis intended at investigating the mechanical contribution of masonry infills on the resulting response of RC frames. The 3D frames are characterised by three-bays along the y-direction and either three- or five-bays along the x-direction. Further geometric and mechanical properties are omitted herein and can be found in a previous work [9].

As a matter of fact, the simulated design only considers gravitational; it was originally developed for the six-storey frame, whereas two- and four-storey structures were firstly obtained by removing the lower levels [9]. In the present study, three further structures are generated by adopting the same criteria: specifically, one, three and five floors are removed from the six-storey frame in order to obtain one-, three- and five-storey structures. Moreover, only analysis along the x-direction are performed and presented in this paper with the aim to further validate the procedure proposed in [9].

Infilled frames are analysed considering three different distributions of masonry walls. Specifically, type A denotes fully infilled structures in which masonry walls are located in all the , type B refers to structures in which infills are inserted alternatively by bay, while type C indicates frames in which the first storey is not infilled [9].

Moreover, since openings can significantly affect the behaviour of infills, and then the global structural response, different opening ratios are considered. As matter of fact, according to the model by Papia et al. [12], the role of openings is taken into account by reducing with a parameter $\lambda_0$ both strength and stiffness of the equivalent strut which simulate infills:

$$\lambda_0 = 1 - 1.5 \cdot a \geq 0 \quad where \quad a = l_v / l_w \,. \tag{3}$$

in which $l_v$ and $l_w$ are the horizontal lengths of the opening and the wall, respectively. As previously defined, the parameter a can range between 0 (for which $\lambda_0=1$) corresponding to infill walls without openings and a=0.667 which means to not consider the infill wall in the structural model ($\lambda_0=0 \rightarrow$ bare structure) due to its weak expected response. Consequently, opening ratios a ranging between 0 and 0.60 were considered.

Finally, two levels of the seismic intensity are considered in the parametric analysis. Values of Peak Ground Acceleration (PGA) equal to 0.10 g and 0.35 g are taken into account in order to simulate both low and medium-to-strong seismic shakings. As matter of principle, these two levels of intensity are intended at reproducing the seismic input required for serviceability and ultimate limit states in medium-to-strong seismic areas, according to EC8 [13] and the Italian code [14]. The corresponding two Linear Elastic Design Spectra (LEDS) needed for performing NLS analyses are obtained according to EC8 provisions [13] considering a soil category A and a spectrum type A for buildings. Furthermore, NLTH analyses are developed taking into account two sets of seven unscaled natural accelerograms selected from the European Strong Motion Database [15] which are compatible with the two aforementioned LEDS.

Further details about the seismic input, as well as the characteristics of structures and infills are herein omitted for sake of brevity and can be found in Martinelli et al. [9].

| Seismic intensity | 0.10 g | | | 0.35 g | | |
|---|---|---|---|---|---|---|
| Storeys | 1 | 2 | 3 | 4 | 5 | 6 |
| Bays along x-direction | 3 | | | 5 | | |
| Infill distribution | A | B | | C | | bare |
| Infill openings (a) | 0.00 | 0.20 | 0.40 | 0.60 | | (a=0.667) |

Table 1: Matrix of the cases considered in the parametric analyses.

Table 1 reports the matrix of the cases analyses in the parametric study. A total number of 148 structures is analysed against two different levels of the seismic intensity. Specifically, considering that in NLTH analyses two sets of seven accelerograms are taken into account, 148x14=2072 nonlinear dynamic analyses are performed on 3D models. Moreover, 148x2=296 pushover analyses are conducted according to EC8 [13] by applying two different horizontal force patterns (referred to as “modal” and “uniform”) to the structure under investigation.

### 3.1 Modelling RC frames and masonry infill walls

The RC frames described are modelled in OpenSEES [16] by employing force-based distributed plasticity elements (namely "*nonlinearbeamcolumn"*) available in the software for simulating RC elements. Both cover and core concrete are modelled by adopting the *Concrete01* material [16], which does not consider tension strength of the material, while *Steel01* stress-strain law with hardening ratio equal to 1% is considered for rebars. The models take into accounts both mechanic and geometrical nonlinearity adopting the *"P-Delta geometric transformation"* command included in the software.

Truss elements are used for modelling the "equivalent struts" simulating the masonry infills made of artificial blocks of expanded clay with thickness equal to 30 cm. Specifically, two diagonal equivalent struts which can carry loads only in compression are defined according to the model by Dolsek and Fajfar [17]. Hence, the infill walls are macro-modelled by means of a tri-linear relationship representing their horizontal force-displacement behaviour (Figure 2).

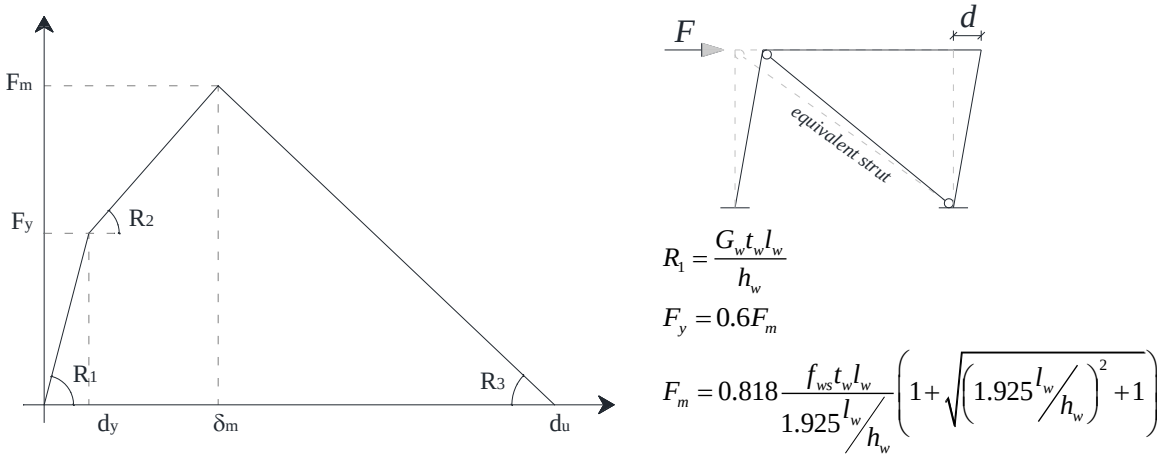


Figure 2: Force-displacement law of the diagonal strut in along the horizontal direction.

Figure 2 shows the force-displacement relationship adopted for modelling the two diagonal trusses simulating the masonry wall with the following meaning of symbols:

- $G_w$ = shear modulus of the masonry;
- $t_w$ = thickness of the wall;
- $f_{ws}$ = shear strength of masonry.

Figure 3 reports some examples of force-displacement curves adopted in this study for simulating the behaviour of masonry infills.

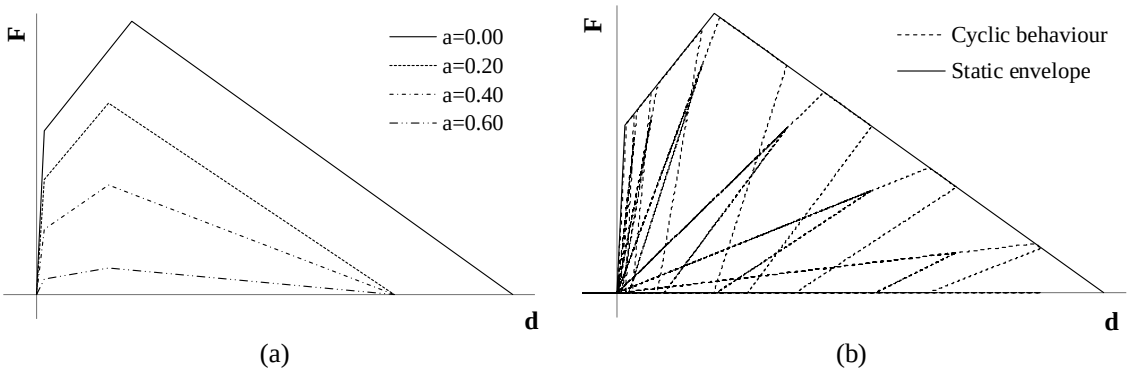


(a) (b)

Figure 3: Force-displacement law of the diagonal strut in along the horizontal direction.

The horizontal displacement $d_m$ corresponding to the maximum force $F_m$ depends on different limitations of the storey drift, assumed equal to 0.2% for short walls, 0.15% for long walls with a window and 0.10% for walls with a door opening. The post-peak negative stiffness of the softening branch is obtained considering an ultimate displacement $d_u=5d_m$ which corresponds a residual strength equal to zero. The presence of openings is taken into account by duly reducing $R_1$ and $F_m$ through the coefficient $\lambda_0$ defined in eq. (3) (Figure 3,a).

The nonlinear response of the simulated equivalent struts was carefully calibrated against experimental results available in the scientific literature [9] and is defined by adopting the "Pinching04" model available in OpenSEES which cyclic behaviour is depicted in Figure 3,b. The cyclic behaviour of the truss clearly demonstrates that such an element only responds in compression.

## 4 RESULTS OF THE PARAMETRIC ANALYSIS

NonLinear Time History and NLS analyses are carried out on the aforementioned structures considering the two sets of natural accelerograms and the LEDS outlined and the section 3.

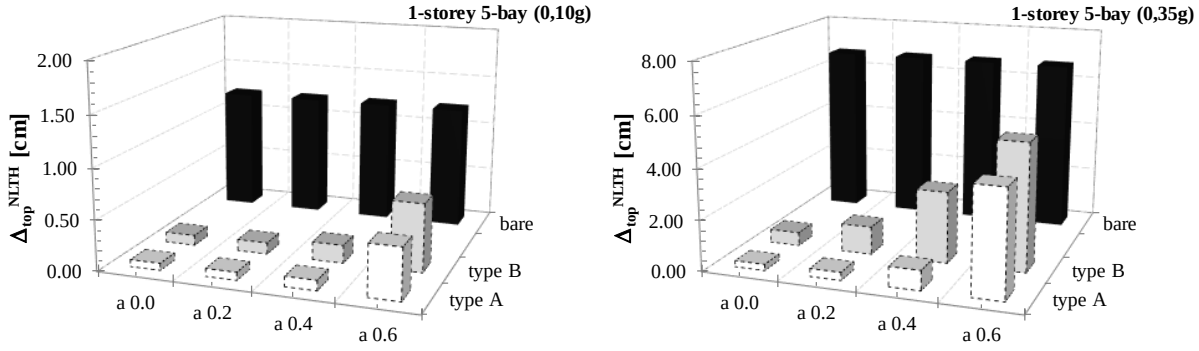


Figure 4: Top displacement demand obtained through NLTH analyses for the one-storey five-bay structures.

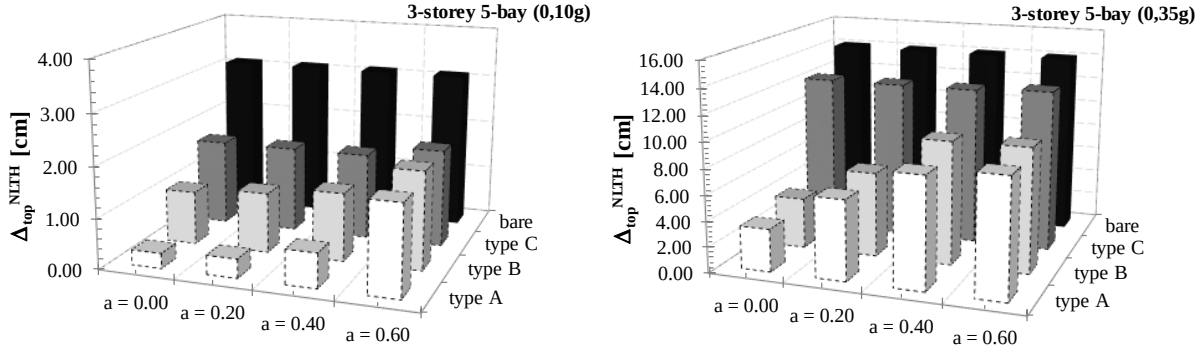


Figure 5: Top displacement demand obtained through NLTH analyses for the three-storey five-bay structures.

The results of NLTH analyses are presented in terms of top absolute displacement demands $\Delta_{top}^{NLTH}$, which represent the average value of the maximum response obtained for the seven accelerograms that simulate the seismic intensity (Figure 4 to Figure 6). Specifically, due to space constraints, only results of the structures with five bays are shown herein, being the ones obtained for three-bay frames very similar to them. Furthermore, it is worth highlighting that results obtained for two-, four- and six-storey frames are not shown herein as they have been already outlined by Martinelli et al. [9], while the new contribution of the present work is represented by the analyses of the one-, three- and five-storey structures.

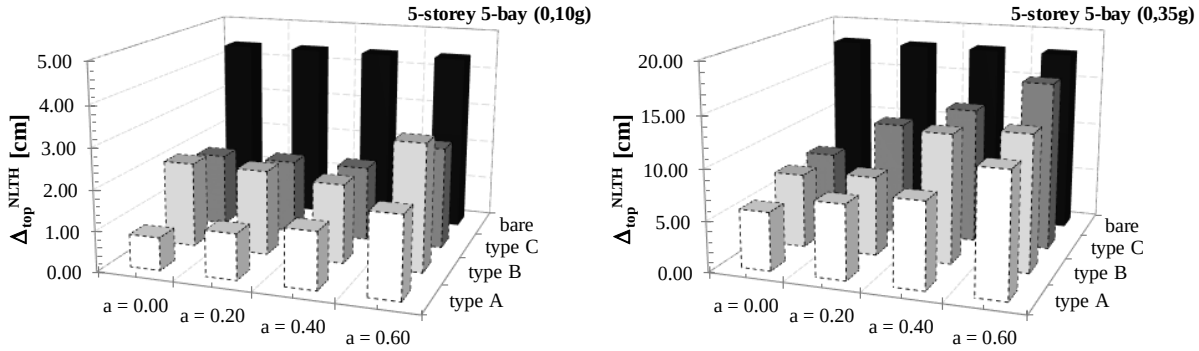


Figure 6: Top displacement demand obtained through NLTH analyses for the five-storey five-bay structures.

As expected, NLTH analyses demonstrate that top displacements of infilled frames are generally smaller than ones obtained in bare structures. Moreover, the $\Delta_{top}^{NLTH}$ values reduce with the opening ratio a, as a clear effect of the stiffness of infill which contribute to the lateral capacity of the structure. Although masonry infill walls reduce the displacement demand on RC frames, it is worth to highlight that the results herein presented cannot be merely summarised by claiming that masonry infill walls play a "beneficial" effect on the seismic response of RC frames. In fact, the internal distribution of forces as well as the total force transferred to foundations can be significantly different (and often higher) than the corresponding values determined for a bare RC frame resulting in premature brittle failure of columns and joints which reduces the displacement capacity [18].

### 4.1 Application of the proposed procedure

NonLinear Static (NLS) analyses are carried out on the same set of frames analysed via NLTH analyses, in both bare and infilled configurations. The representation of the capacity curves derived for both "modal" and "uniform" distribution is herein omitted for sake of brevity. As expected, a significant variation in terms of both lateral stiffness and maximum strength is induced by openings of increasing dimensions [18].

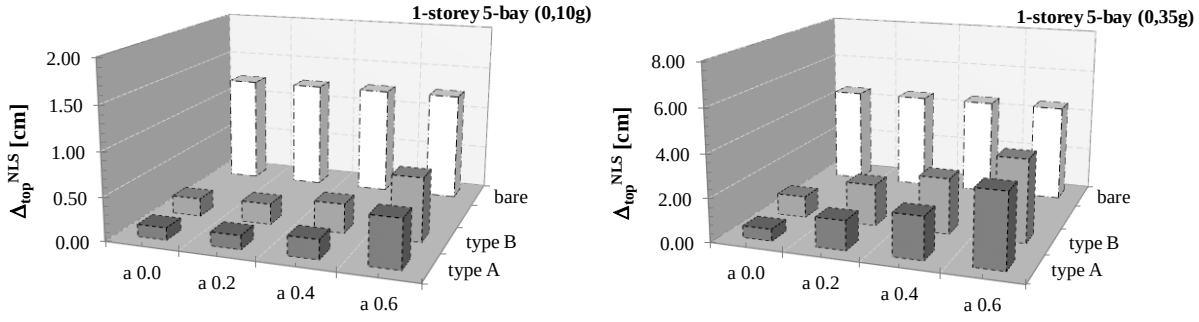


Figure 7: Top displacement demand obtained through the novel procedure for the one-storey five-bay structures.

Then, the values of the top displacement demand of the RC bare frames are obtained by applying the well-known N2 Method [8] and the parameter $\alpha$ is defined according to eq. (2) by considering the "shape" of the two capacity curves corresponding to the infilled frame and the corresponding bare one (Figure 1). Finally, the displacement demand $\Delta_{top,infill}$ of infilled structures is evaluated by means of equation (1) and, according to EC8 [13] provisions, the displacement demand of the structures evaluated through NLS analysis is taken equal to the maximum value between the ones obtained by applying the two different horizontal force distributions ("modal" and "uniform"). Figure 7 to Figure 9 report the top absolute displacement demands

$\Delta_{top}^{NLS}$ evaluated by applying the procedure proposed by Martinelli et al. [9] for infilled structures and the N2 Method for the corresponding bare frame. The results about one- three- and five-storey structures are outlined in the same shape already used for presenting the top displacement demand evaluated via NLTH analyses (Figure 4 to Figure 6), while the representation of $\Delta_{top}^{NLS}$ for frames with two, four and six storeys is omitted herein for the sake of brevity.

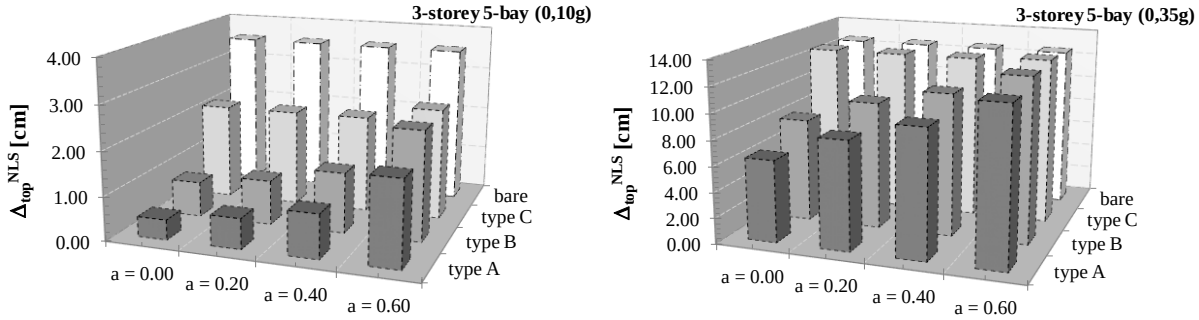


Figure 8: Top displacement demand obtained through the novel procedure for the three-storey five-bay structures.

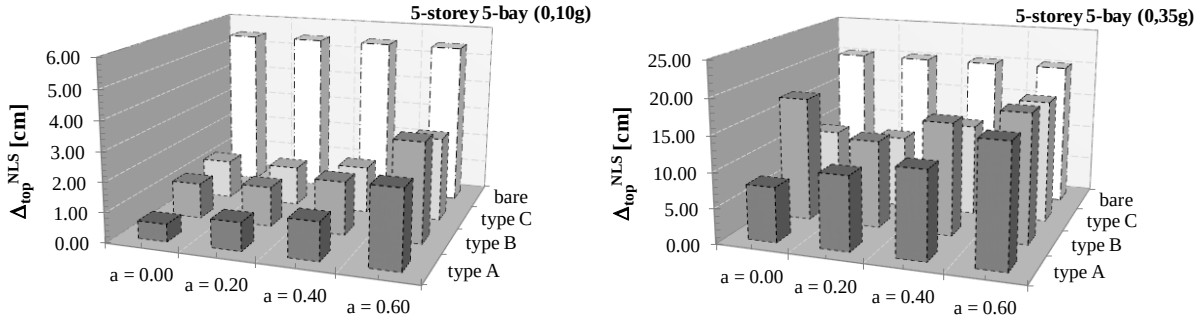


Figure 9: Top displacement demand obtained through the novel procedure for the five-storey five-bay structures.

Figure 7 to Figure 9 demonstrate that top displacements of infilled frames evaluated through the proposed procedure are always smaller than the ones obtained in bare structures. The $\Delta_{top}^{NLS}$ values are in agreement with the general trend already observed for NLTH analyses. Specifically, they reduce with the opening ratio a, as a clear effect of the higher stiffness provided by masonry infill.

## 4.2 Validation against NLTH results and accuracy of the proposed procedure

Martinelli et al. [9] performed a validation of the proposed procedure considering the same two-, four- and six-storey frames used for calibrating and formulating the novel method. They obtained a very high correlation and accuracy of the results compared with ones derived with NLTH analyses. Herein, the results originally obtained from the Authors are enriched by considering one-, three- and five-storey structures with three and five bays, characterised by different distribution of masonry walls and openings. Specifically, the results obtained by applying the novel procedure are compared with the ones evaluated through NLTH analyses.

Figure 10 shows the comparison between the top displacement demand evaluated via NLTH analyses (average value of seven accelerograms) and the corresponding value determined through the proposed procedure. The two charts are divided for outlining the influence of the two level of seismic intensity under consideration. It is worth to highlight that the following comparisons include results obtained for three- and five-bay structures, but they are not explicitly depicted as similar results are obtained for both types of frames demonstrating that the number of bays is a parameter that does not affect the accuracy of the proposed procedure.

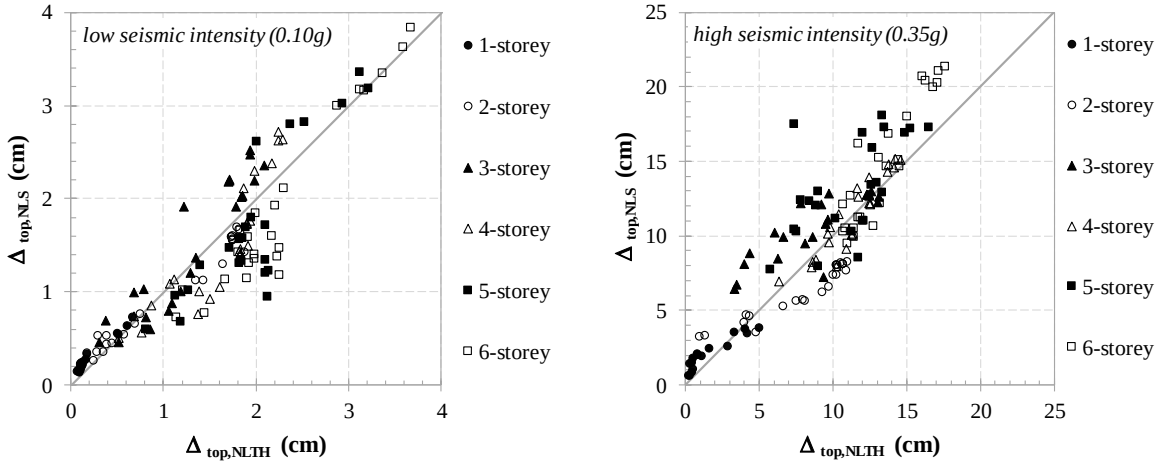


Figure 10: Comparison of the proposed procedure against NLTH analyses.

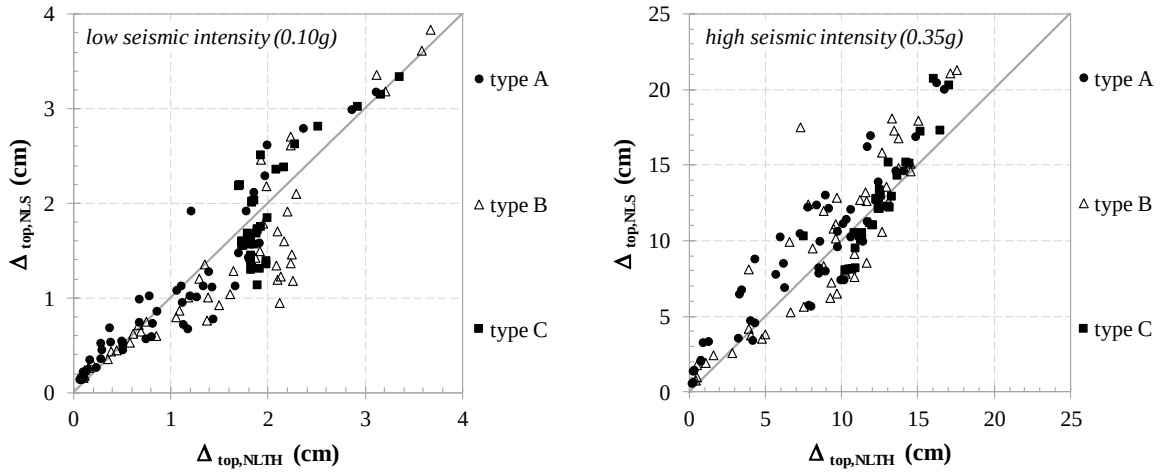


Figure 11: NLS proposed procedure vs. NLTH analyses: structures grouped against the infill distribution.

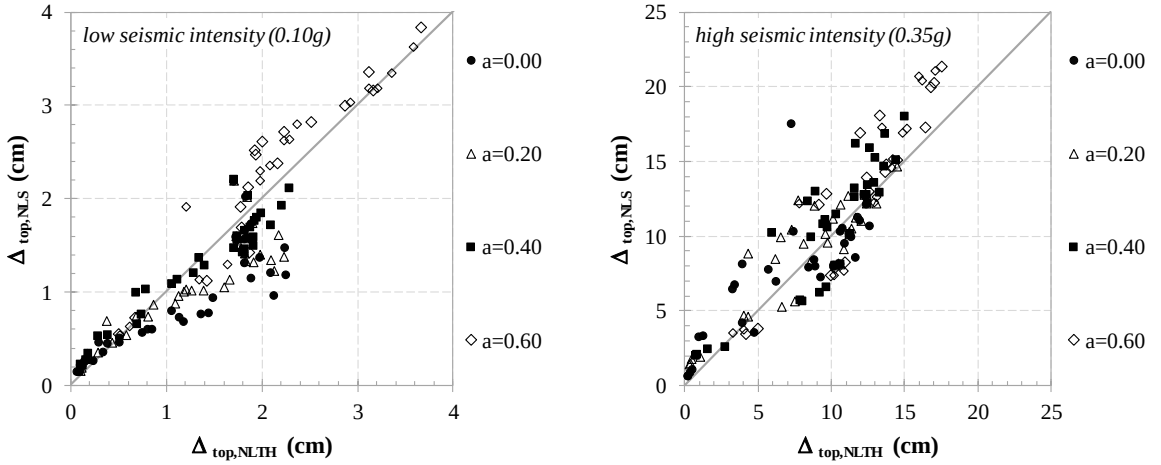


Figure 12: NLS proposed procedure vs. NLTH analyses: structures grouped against the infill opening ratios.

Further comparisons are depicted in Figure 11 and Figure 12 in which results are grouped considering the infill distribution (Type A, B and C) and the opening ratios (a from 0 to 0.60).

The significant level of accuracy of the novel procedure emerges in Figure 13, which reports the comparison of results for all the analysed structures as a whole and the two level of seismic

intensity under investigation. Figure 13 also reports the value of the correlation factor $R^2=0.92$ and the distribution of the ratio between the displacement demand evaluated trough the novel procedure and the corresponding value obtained via NLTH analysis.

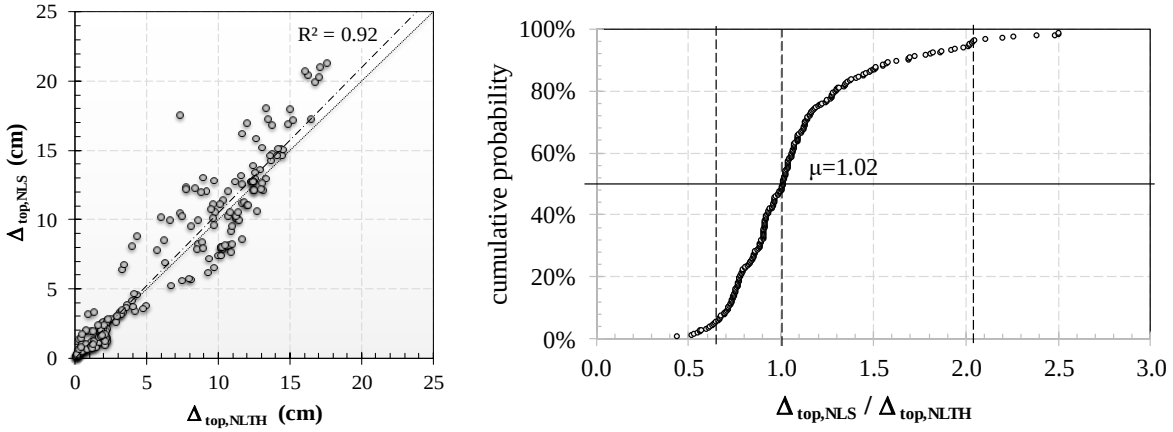


Figure 13: Accuracy of the proposed NLS procedure.

The comparisons demonstrate the very good agreement between the results estimated through the proposed procedure and the ones of NLTH analyses. The coefficient of determination $R^2$, originally evaluated equal to 0.934 by Martinelli et al. [9] for a database of structures smaller than the one considered in this study, is very close to the unit yet confirming the accuracy of the proposed procedure. Moreover, the median value of the displacement ratio of the entire database of structures as a whole is equal to 1,02 resulting in slightly conservative estimation of the displacement demand (median value of $\overline{\Delta_{top}^{NLS}}$ is greater than $\overline{\Delta_{top}^{NLTH}}$). This result confirms an accuracy greater than the one originally evaluated by Martinelli et al. [9] on a smaller parametric field.

Finally, it is worth to highlight that the standard deviation of the ratio $\Delta_{top}^{NLS} / \Delta_{top}^{NLTH}$ is equal to 0.49 resulting in medium-to-low values of uncertainties introduced by the novel procedure. As expected, such a value is slightly higher than the one originally evaluated by Martinelli et al. [9] as it is derived considering a parametric field of structures wider than the one originally used for calibrating the procedure.

## 5 CASE STUDY

The present section reports an application of the proposed procedure to an seven-story building considered as a relevant case study. Specifically, an existing masonry infilled RC structure located in Southern Italy and designed for only gravitational loads according to codes of practice in force in the 1970's.

Masonry infills are made of artificial blocks of clay forming a wall with thickness equal to 35 cm and the following mechanical properties:

- specific weight: $\gamma_w = 8.00$ kN/m$^3$;
- compressive strength: $f_m = 4.00$ N/mm$^2$;
- shear strength: $\tau_0 = 0.30$ N/mm$_2$;
- elastic modulus: E = 3600 N/mm$^2$;
- shear modulus: G = 1080 N/mm$^2$.

The concrete cylindrical strength is equal to 20.75 MPa, while $f_{sm}$=220 MPa is considered for the yielding strength of steel bars. , Figure 14 represents further details, taken from the original design documents.

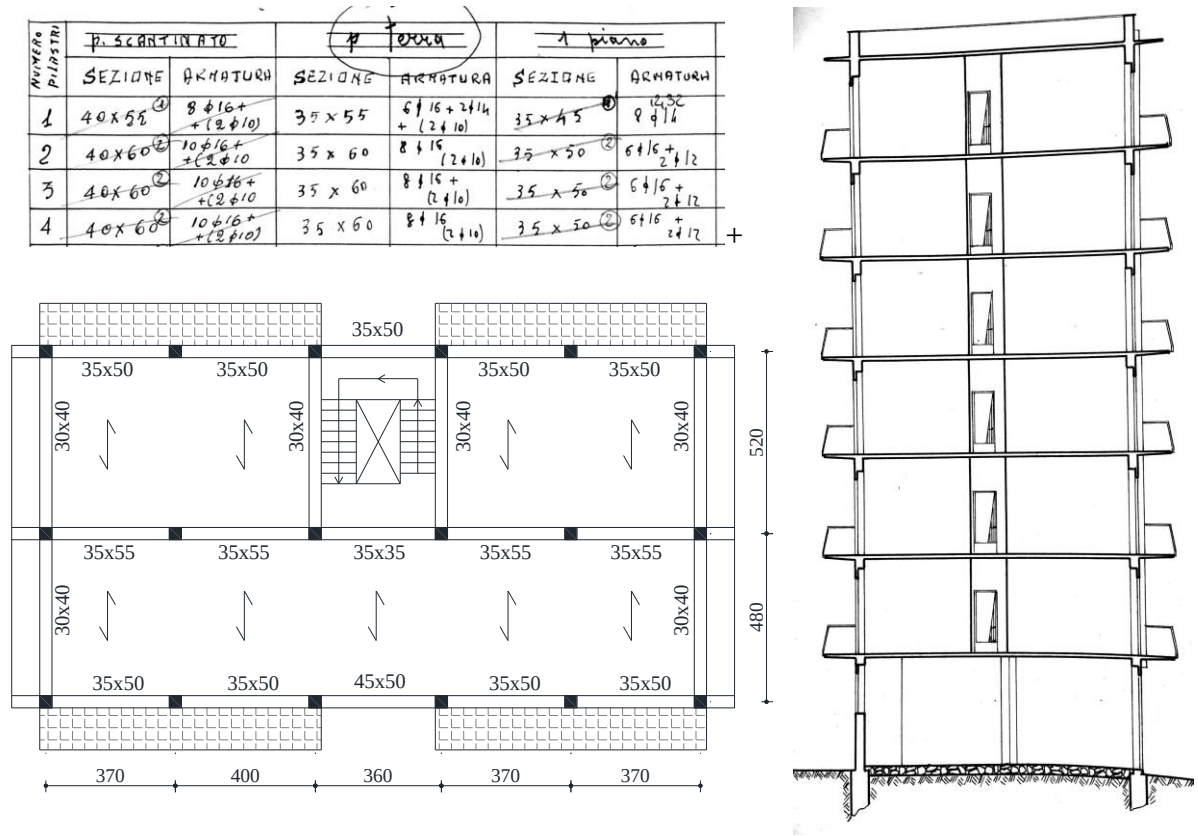


Figure 14: Details of the analyzed structure.

The structure is modelled in OpenSEES [16] with Concrete01 and Steel01 laws simulating the nonlinear behaviour of materials. Beam and column are modelled through distributed plasticity force-based elements (namely *"nonlinearbeamcolumn"*), while masonry infill walls are simulated adopting the equivalent strut model by Dolsek and Fajfar [17] described in section 3 and already used within the parametric analysis presented above. Specifically, the real distribution of openings within infills is taken into account considering the opening ratio defined in section 3. Figure 15 shows the horizontal force-displacement relationships of the masonry infill under investigation. Opening ratios equal to a=0.00 (solid wall), a=0.40 and a=0.60 are considered in order to modelling infills with increasing dimensions of windows and doors, while infills at the first storey are not included within the structural model as very large doors are present at that level. Moreover, the strain-stress relationship of the equivalent strut simulating infills is depicted in Figure 15. This relationship is modelled in OpenSEES by adopting the *Pinching04* material assigned to truss element with cross sectional area equal to $A_{truss}=1\ mm^2$.

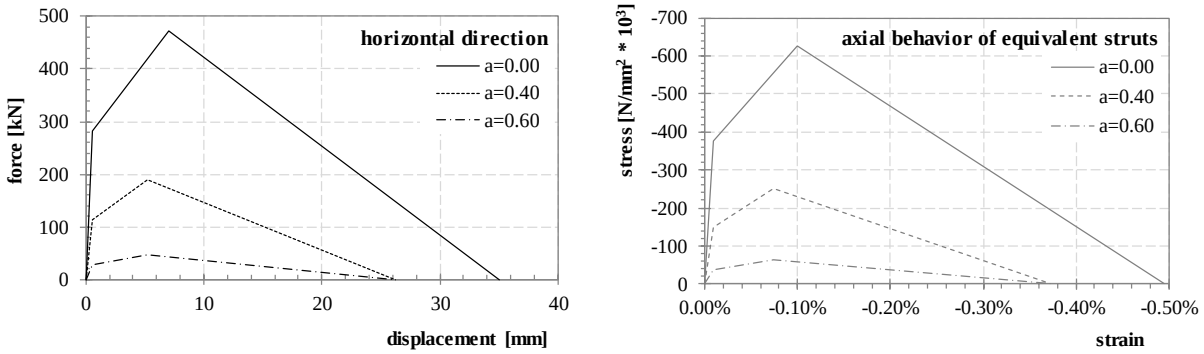


Figure 15: Nonlinear behaviour of the equivalent struts simulating masonry infill walls.

Both Nonlinear Static (NLS) and NLTH analyses are performed. According to the current Italian code [14], two levels of seismic intensity related to the Limit State of Damage Preservation (SLD) and of Life Safety (SLV) are considered. Figure 16 shows the two Linear Elastic Demand Spectra (LEDS) considered in NLS analyses along with the spectra of the two sets of seven natural accelerograms used in NLTH analyses.

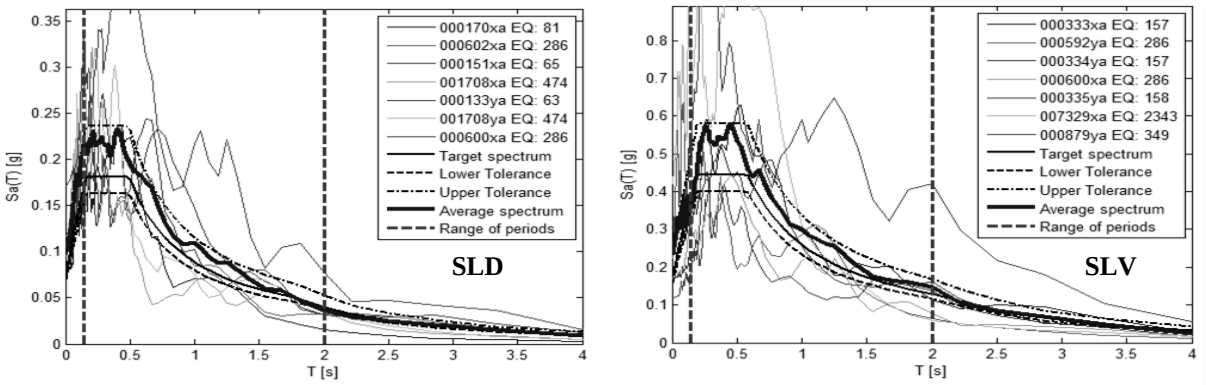


Figure 16: Spectra representing the seismic input levels of NLS and NLTH analyses.

NLS analyses are performed on the infilled structure and the corresponding bare one in the two-main directions; both "uniform" and "modal" patterns are considered. Figure 17 shows the eight capacity curves obtained for the infilled model along with the curves of the bare frame.

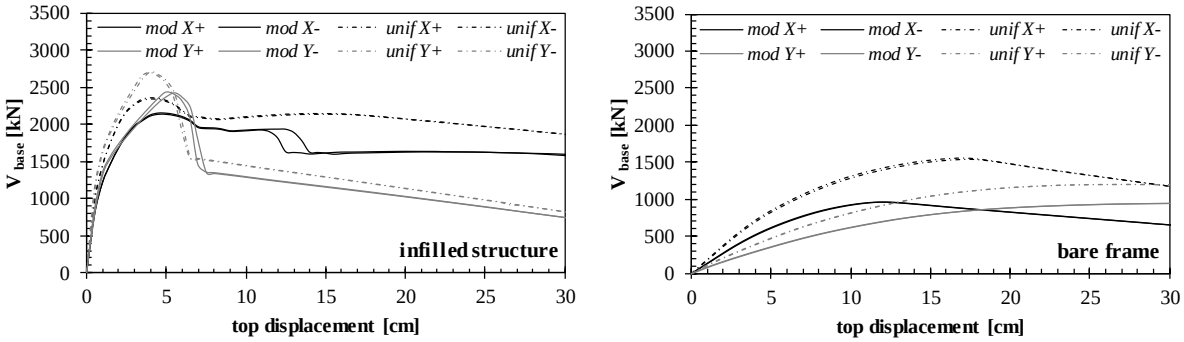


Figure 17: Capacity curves of the infilled structure and the corresponding bare one.

The response of the structure in the negative verse is quite similar to the positive one in both x- and y-direction. Moreover, the presence of infills significantly increases both stiffness and strength of the analysed model. The N2 Method is applied based on the capacity curves of the bare structure and the displacement demand $\Delta_{top,bare}^{NLS}$ is evaluated. Then, the proposed novel procedure is adopted as described in Section 2 with the aim to evaluate the top displacement demand of the structural model including masonry infills.

Moreover, NLTH analyses are also performed in order to compare the results obtained through the proposed procedure with the ones provided by the dynamic analysis. These results are reported in Table 2 and Table 3 for the Limit State SLD and SLV, respectively, along with the values of the shape parameter $\alpha$ and of the areas beneath the capacity curves, up to a displacement demand of the bare structure determined through the N2 Method. The displacement demands obtained via NLTH analyses are intended as average values of seven numerical simulations related to the seven natural accelerograms. Specifically, the column denoted as $\Delta_{top,bare}^{NLS}$ reports the displacement demand evaluated via N2 Method on the bare frames, while the other two columns ( $A_{bare}^{NLS}$ and $A_{\text{infill}}^{NLS}$ ) report the areas beneath the capacity curves, up to a displacement

demand $\Delta_{top,bare}^{NLS}$. The shape parameter $\alpha$ is evaluated through eq. (2) and the column $\Delta_{top,\text{infill}}^{NLS}$ reports the valued of the top displacement demand of infilled structures determined adopting the proposed procedure. Moreover, the maximum displacement demand for each direction is highlighted and compared to the one obtained via NLTH analysis.

| Direction | | NLS analysis bare (N2 Method) $\Delta_{top,bare}^{NLS}$ [cm] | $A_{bare}^{NLS}$ | infilled $A_{\text{infill}}^{NLS}$ | α | $\Delta_{top,\text{infill}}^{NLS}$ [cm] | max | NLTH analysis bare $\Delta_{top,bare}^{NLTH}$ [cm] | infilled $\Delta_{top,\text{infill}}^{NLTH}$ [cm] |
|---|---|---|---|---|---|---|---|---|---|
| X | mod X+ | 5.089 | 1.78E+05 | 8.72E+05 | 0.204 | 1.038 | 1.038 | 3.518 | 1.079 |
| | mod X- | 5.025 | 1.80E+05 | 8.76E+05 | 0.205 | 1.032 | | | |
| | unif X+ | 4.046 | 1.64E+05 | 7.65E+05 | 0.214 | 0.865 | | | |
| | unif X- | 3.987 | 1.65E+05 | 6.50E+05 | 0.254 | 1.014 | | | |
| Y | mod Y+ | 5.846 | 1.25E+05 | 1.03E+06 | 0.121 | 0.705 | 0.705 | 3.191 | 1.037 |
| | mod Y- | 5.846 | 1.24E+05 | 1.04E+06 | 0.119 | 0.698 | | | |
| | unif Y+ | 4.081 | 9.28E+04 | 8.46E+05 | 0.110 | 0.448 | | | |
| | unif Y- | 4.081 | 9.24E+04 | 8.44E+05 | 0.109 | 0.447 | | | |

Table 2: Numerical results of the analyses for the Limit State SLD.

| Direction | | NLS analysis bare (N2 Method) $\Delta_{top,bare}^{NLS}$ [cm] | $A_{bare}^{NLS}$ | infilled $A_{\text{infill}}^{NLS}$ | α | $\Delta_{top,\text{infill}}^{NLS}$ [cm] | max | NLTH analysis bare $\Delta_{top,bare}^{NLTH}$ [cm] | infilled $\Delta_{top,\text{infill}}^{NLTH}$ [cm] |
|---|---|---|---|---|---|---|---|---|---|
| X | mod X+ | 15.197 | 1.05E+06 | 2.73E+06 | 0.383 | 5.827 | 5.827 | 9.256 | 4.014 |
| | mod X- | 15.052 | 1.05E+06 | 2.78E+06 | 0.378 | 5.691 | | | |
| | unif X+ | 12.452 | 1.07E+06 | 2.48E+06 | 0.432 | 5.376 | | | |
| | unif X- | 12.343 | 1.08E+06 | 2.49E+06 | 0.434 | 5.358 | | | |
| Y | mod Y+ | 19.481 | 1.07E+06 | 2.80E+06 | 0.381 | 7.426 | 7.598 | 10.796 | 3.634 |
| | mod Y- | 19.481 | 1.11E+06 | 2.84E+06 | 0.390 | 7.598 | | | |
| | unif Y+ | 13.601 | 7.96E+05 | 2.41E+06 | 0.330 | 4.489 | | | |
| | unif Y- | 13.601 | 7.95E+05 | 2.40E+06 | 0.331 | 4.498 | | | |

Table 3: Numerical results of the analyses for the Limit State SLV.

Finally, Figure 18 demonstrates a good agreement between the proposed procedure and the NLTH analyses considered in this study, the former being slightly conservative at the SLV.

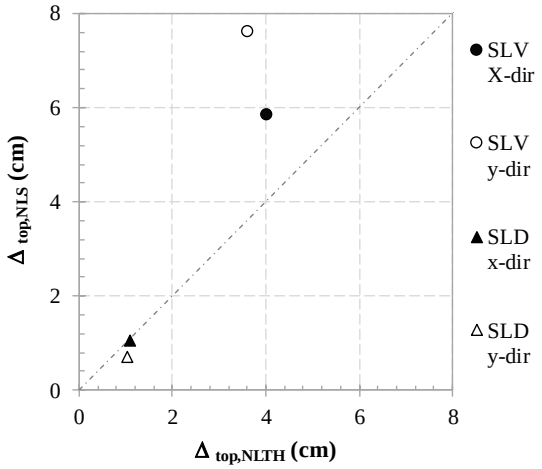


Figure 18: Comparison of the proposed procedure against NLTH analyses for the case of study.

## 6 CONCLUSIONS

This paper has proposed a further validation of a simplified procedure recently formulated by the Authors for simulating seismic response and determining displacement demand on masonry infilled RC frames. A wide parametric analysis has been proposed with the aim to support the proposed formulation, which is further validated on a relevant case study.

The proposed analyses point out that simplicity is the key attractive features of the proposed procedure, which prove to be also very accurate, as demonstrated in a wide number of applications covering a significant set of relevant quantities (in a total of 148 structures) and their variability in a wide range of values. Moreover, the procedure has been assessed in two different levels of seismic intensity (with PGA of 0.10g and 0.35g) corresponding to two relevant limit states in medium-seismicity regions.

Finally, further validations will be presented in the future with the aim to assess the stability of the proposed procedure with respect to several typologies of structural members and masonry types.

## ACKNOWLEDGMENTS

This study is part of the DPC-ReLUIS 2014-2018 Research Project. Moreover, the Authors wish to acknowledge the financial support of the University of Salerno, as part of the FARB 2014 Research Programme.

## REFERENCES

[1] G.M. Verderame, I. Iervolino, P. Ricci, Report on the damages on buildings following the seismic event of the 6th April 2009 V1.20. *ReLUIS Report*, (http://www.reluis.it), 2009.

[2] G.G. Penelis, A.J. Kappos, *Earthquake-resistant concrete structures, 1st ed.* Abington, Oxon (UK), Taylor & Francis, 1997.

[3] T. Paulay, M.J.N. Priestley, *Seismic design of reinforced concrete and masonry buildings*. John Wiley & Sons, inc., ISBN: 978-0-471-54915-4, New York, USA, 1992.

[4] I. Koutromanos, A. Stavridis, P.B. Shing, K. Willam, Numerical modeling of masonry-infilled RC frames subjected to seismic loads. *Computer and Structures*, **89**, 1026–1037, 2011.

[5] C.G. Karayannis, M. Favvata, D. Kakaletsis, Seismic behaviour of infilled and pilotis RC frame structures with beam–column joint degradation effect. *Engineering Structures*, **33**, 2821–2831, 2011.

[6] M. Dolsek, P. Fajfar, Simplified non-linear seismic analysis of infilled reinforced concrete frames. *Earthquake Engineering and Structural Dynamics*, **34**, 49–66, 2005.

[7] M. Favvata, M.C. Naoum, C.G. Karayannis, Limit states of RC structures with first floor irregularities. *Struct Eng Mech*, **47**(6), 791–818, 2013.

[8] P. Fajfar, Capacity spectrum method based on inelastic demand spectra. *Earthquake Engineering and Structural Dynamics*, **28**, 979–93, 1999.

[9] E. Martinelli, C. Lima, G. De Stefano, A simplified procedure for Nonlinear Static analysis of masonry infilled RC frames. *Engineering Structures*, **101**, 591–608, 2015.

[10] G. Campione, L. Cavaleri, G. Macaluso, G. Amato, F. Di Trapani, Evaluation of infilled frames: an updated in-plane-stiffness macro-model considering the effects of vertical loads. *Bulletin of Earthquake Engineering*, **13**(8), 2265-2281, 2015.

[11] L. Santarella, *Prontuario del Cemento Armato (in Italian), XXV Edizione*. Hoepli, Milano (Italy), 1966.

[12] M. Papia, L. Cavaleri, M. Fossetti, Infilled frames: developments in the evaluation of the stiffening effect of infills. *Structural Engineering Mechanics*, **16**(6), 675–93, 2003.

[13] European Committee for Standardization C.E.N., *Eurocode 8: Design of Structures for Earthquake Resistance, EN 1998-1-6:2005*. Brussels (BE), 2005.

[14] Ministerial Decree, *Nuove norme tecniche per le costruzioni (in Italian)*. Ordinary Supplement n. 30 to the Italian Official Journal of February 04, 2008.

[15] I. Iervolino, C. Galasso, E. Cosenza, REXEL: computer aided selection for code based seismic structural analysis. *Bulletin of Earthquake Engineering*, **8**(2), 339–362, 2010.

[16] S. Mazzoni, F. McKenna, M.H. Scott, G.L. Fenves, et al., *OpenSEES Open System for Earthquake Simulation, Command Language Manual*. Pacific Earthquake Engineering Research Center, 2007.

[17] M. Dolsek, P. Fajfar, The effect of masonry infills on the seismic response of a four storey reinforced concrete frame – a deterministic assessment. *Engineering Structures*, **30**(11), 1991–2001, 2008.

[18] C. Lima, E. Martinelli, G. De Stefano, Seismic response of infilled RC frames: practice-oriented models and open issues. *Earthquakes and Structures*, **6**(4), 409–436, 2014.

COMPDYN 2017
6th ECCOMAS Thematic Conference on
Computational Methods in Structural Dynamics and Earthquake Engineering
M. Papadrakakis, M. Fragiadakis (eds.)
Rhodes Island, Greece, 15–17 June 2017

# INELASTIC RESPONSE OF MASONRY INFILLED REINFORCED CONCRETE STRUCTURES

**Alkis Fotos[1], Filippos Foskolos[1], Athanasios K. Tsaris[1], Constantinos C. Repapis[2], Panagiotis G. Asteris[1]**

[1] Computational Mechanics Laboratory, School of Pedagogical and Technological Education
Heraklion, GR 14121, Athens, Greece
panagiotisasteris@gmail.com

[2] Department of Civil Engineering, Piraeus University of Applied Sciences
250 Thivon and Petrou Ralli Str., Aigaleo 122 44, Athens, Greece
crepapis@puas.gr

**Keywords:** Inelastic Analysis, Infill walls, Masonry, Mathematical Modeling, Pushover Analysis, Reinforced Concrete, Seismic Response.

**Abstract.** *It is well known that masonry infill walls, although non-engineered and considered as non-structural, may provide most of the earthquake resistance and prevent collapse of relatively flexible and weak RC structures. The objective of this study is to investigate the effect of masonry infill walls with openings on the performance of reinforced concrete frames under lateral loads. Specifically, this study is concerned with the evaluation of inelastic parameters of masonry infilled reinforced concrete buildings. Buildings with various heights are selected and designed according to EC8. Inelastic pushover analyses are performed and local and global strength and inelastic deformation characteristics are evaluated. The influence of various parameters, such as the number of storeys, the distribution of infill walls, their strength and their opening percentage on the seismic response of the buildings is thoroughly examined. The results from nonlinear pushover analyses indicate that the overstrength and ductility of RC buildings can be higher than the values considered in the design. The presence of infill walls increases considerably the stiffness of the structures and their global resistance to lateral loads. However, the irregular distribution of infills (soft storey – case of pilotis) significantly reduces the capacity of the structure*.

# 1 INTRODUCTION

Reinforced concrete (RC) frames with unreinforced masonry infill walls are commonly used worldwide. Masonry infill walls are non-structural elements and are usually ignored in the design of the structures. However, the infill walls significantly influence the seismic response of a structure since they may interact with bounding frames when the structure is subjected to strong lateral loads induced by seismic load. In many cases infills may provide most of the earthquake resistance, improve the behaviour of the structure and prevent collapse of relatively flexible and weak RC structures. Nevertheless, an irregular distribution of infill walls may have negative effects on the structure's performance.

There is a complex interaction between primary structures and masonry infill panels and it is well known that in the presence of lateral actions masonry infills partially detach from the surrounding frame, remaining in contact with this only in correspondence of two opposite corners. A significant bracing action, affecting both the strength and stiffness, originates by this mechanism, as demonstrated by a large number of experimental investigations [1-13] and analytical-numerical studies [14-32]. However, despite several modelling strategies available in the literature, going from pinned equivalent struts macromodeling to FE micromodeling [33-38], masonry infills are generally not accounted for in models because of the large amount of uncertainties arising during their structural identification.

In this study, the effect of masonry infill walls with openings on the performance of reinforced concrete frames under lateral loads is investigated using inelastic pushover analyses. To this end, buildings with various heights and infill wall opening percentages are selected.

# 2 DESCRIPTION OF THE STRUCTURES

## 2.1 Building forms and infill walls parameters

In this study, the seismic response of masonry infilled reinforced concrete buildings is investigated. Buildings examined have 4, 6, 8 and 10 storeys. The storey height for all buildings is kept constant and equal to 3.0 m. All buildings have 4 spans with 6 m length. In the perpendicular direction the span length has been kept constant and equal to 5 m for all cases.

Both bare-frame structures as well as structures with fully or partially unreinforced masonry infilled frames with or without openings are analysed, in order to examine the influence of infill walls. Infill panels are 0.25 m thick, following the conventional construction double leaf walls with a masonry panel strength equal to 3.0 MPa, which represents a good clay masonry. Young's modulus $E_w$ of masonry is 3.0 GPa. Four different cases for infill wall openings are studied. These are: fully infilled walls (0% openings), infill walls with small and large openings (25% and 50% openings) and bare frames (100% openings). Infill walls are uniformly distributed in all spans of the frame. Moreover, the case of an open storey at the ground floor (pilotis) is examined for each infilled frame.

In total, 28 different cases of infilled RC frames were analysed in order to investigate the influence of several parameters on the seismic response of infilled frame structures.

## 2.2 Design of structures

The frames are designed according to Eurocode standards using the software FESPA [39]. Modal response spectrum analysis was also performed. The frames were designed for seismic zone I with reference peak ground acceleration on type A ground, $a_{gR}$ = 0.16 g, importance factor $\gamma_I$ equal to 1.0, ground type B with soil factor $S$ equal to 1.2, according to Eurocode 8, medium ductility class (DCM) and behaviour factor, $q$, equal to 3.45. Concrete strength class C25/30 was used for beams and columns, while steel grade B500c was used for the rein-

forcement steel bars. The dead load was 1.50 kN/m$^2$ plus 0.90 kN/m$^2$ to include interior partition walls in the mass of the building. Live load was 3.5 kN/m$^2$. Slabs were 150 mm thick for all cases. Beams were 250/600 mm for all frames. Square column sections were used for all frames. For the 10-storey frame, columns had dimensions ranging from 650x650 [mm] at the ground floor to 500x500 [mm] at the roof. For the 4-storey frame, column dimensions are 550x550 [mm] at the first three storeys and 500x500 [mm] at the roof. Column longitudinal reinforcement ratio was kept low and ranged between 1.0% and 1.5%, with most cases being under 1.15%.

## 3 MODELLING OF INFILL STRUCTURES

### 3.1 Modelling of infill walls

The response of composite infilled framed structures is modelled using diagonal compressive struts with appropriate geometrical and mechanical characteristics (Figure 1). As it is widely accepted, diagonal struts can adequately model the inelastic behaviour of infills with low computational cost. In Figure 1, *w* is the width of the diagonal strut, *d* is the diagonal length of the masonry panel, *L* is the distance between the centres of two columns, and *z* is the contact length of the diagonal strut to the column.

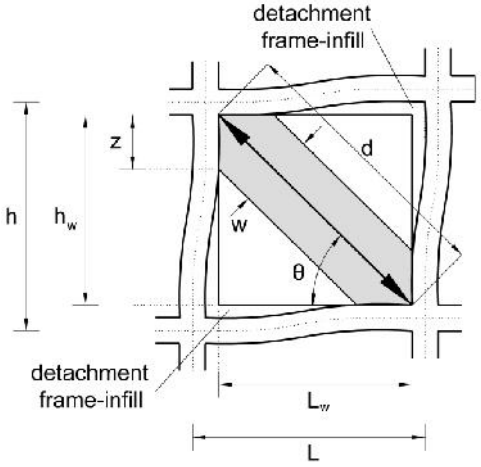


Figure 1: Masonry infill frame sub-assemblage.

Mainstone and Weeks [40] and Mainstone [41] based on experimental and analytical data, proposed the following empirical equation for the calculation of the equivalent strut width *w*, which was later included in FEMA-274 [42] for the analysis and rehabilitation of buildings as well as in FEMA-306 [43]:

$$\frac{w}{d} = 0.175 \lambda_h^{-0.4} \tag{1}$$

where *d* is the diagonal length of the masonry panel and $\lambda_h$ is given by the following equation,

$$\lambda_h = h \sqrt[4]{\frac{E_w t_w \sin 2\theta}{4EIh_w}} \tag{2}$$

where $E_w$ is the modulus of elasticity of the masonry panel, *EI* is the flexural rigidity of the columns, $t_w$ the thickness of the infill panel and equivalent strut, *h* the column height between

centerlines of beams, $h_w$ the height of infill panel, and $\theta$ the angle, whose tangent is the infill height-to-length aspect ratio, being equal to:

$$- = \tan^{-1}\left(\frac{h_w}{L_w}\right) \tag{3}$$

where $L_w$ is the length of infill panel. All the above parameters are explained in Figure 1.

In case of openings in the infills, the infill wall stiffness can be multiplied with the following reduction factor $\lambda$, proposed by Asteris [44]:

$$\lambda = 1 - 2\alpha_w^{0.54} + \alpha_w^{1.14} \tag{4}$$

where $\alpha_w$ is the ratio of the area of opening to the area of infill wall. The above coefficient is used in the current study to find the equivalent width of a strut for the case of an infill with opening by multiplying the width obtained using Eq. (1) by the relevant reduction factor.

### 3.2 Modelling of RC structures

All buildings were modelled as plane frames using Seismostruct [45]. A plastic-hinge element has been adopted for beams and columns, with concentrated inelasticity within a fixed length at each member's end. The Mander et al. [46] model, later modified by Martinez-Rueda and Elnashai [47], has been assumed for the core and the unconfined concrete, while Menegotto-Pinto steel model has been adopted for the reinforcement steel [48]. Concrete compressive strength was equal to 25 MPa and the yield strength of the steel equal to 500 MPa. Mass was calculated using the seismic load combination, namely dead loads plus 30% of the live loads.

Masonry is modelled using the inelastic infill panel element. This is an equivalent strut nonlinear cyclic model proposed by Crisafulli [49] for the modelling of the nonlinear response of infill panels in framed structures. Each panel is represented by six strut members. Each diagonal direction features two parallel struts to carry axial loads across two opposite diagonal corners and a third one to carry the shear from the top to the bottom of the panel (Figure 2). The struts act only across the diagonal that is on compression, hence, its "activation" depends on the deformation of the panel. The axial load struts use the masonry strut hysteresis model, while the shear strut uses a dedicated bilinear hysteresis rule, as described by Crisafulli [49].

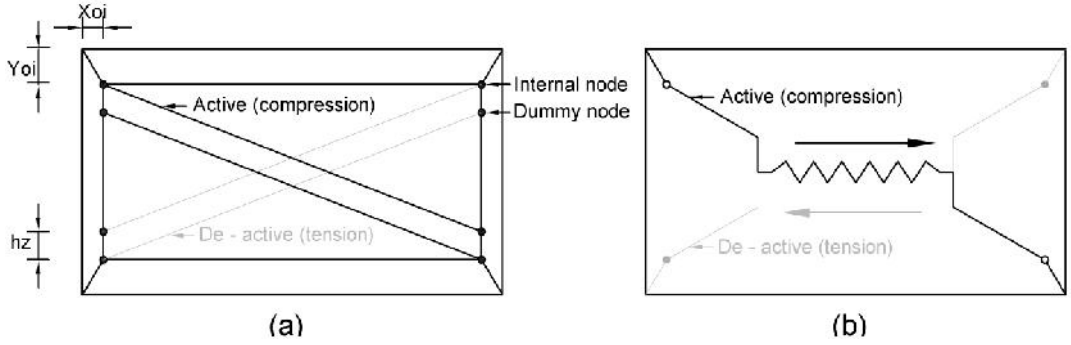


Figure 2: Infill panel element proposed by Crisafulli [49]. a) Compression/Tension Struts, b) Shear Strut.

### 3.3 Performance criteria

Local or global failure definition criteria are adopted, in order, to estimate the limiting lateral deformation capacity and corresponding limit resistance, global deformability and ductility of the infilled RC structures. In the present study, it is assumed that local failure occurs

only when a column fails, thereby, assuming that beam failure cannot cause a brittle catastrophic type of failure of the entire structure, due to the expected redistribution of loads that takes place in this case. The following criteria are evaluated for every structure:

a) local inelastic rotation capacities at the end critical regions of beams and columns according to EC8-3,
b) local shear force capacity of the individual members according to EC8-3 and
c) failure of the compression struts of the infill masonry walls for the infilled frames

### 3.4 Target Point

Target displacement is evaluated according to EC8 procedure for three performance levels. The idealized elasto-perfectly plastic force displacement relationship is determined in such a way that the areas under the actual and the idea1ized force deformation curves are equal and the yield force of the idealized system is equal to the base shear force at the formation of the plastic mechanism.

## 4 INELASTIC ANALYSES

Pushover analyses with two distributions of lateral loads (uniform and triangular) were performed for all the frames. The predicted base shear – roof displacement characteristics are shown in Figures 3 to 6. On each capacity curve, the bilinear approximation and the target point for limit state of significant damage (SD) are also shown. In this study, failure is considered when at least one of the performance criteria described above is reached.

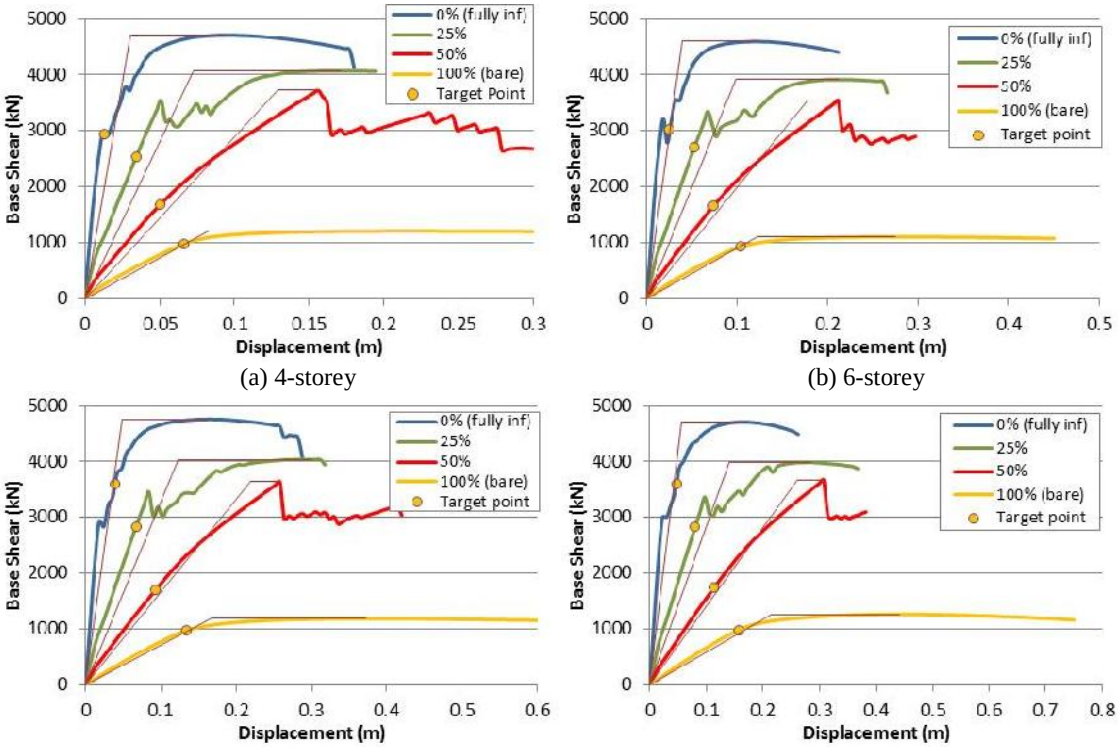


(a) 4-storey (b) 6-storey

(c) 8-storey (d) 10-storey

Figure 3: Capacity curves of examined frames.

In Figure 3 the capacity curves of frames with 4, 6, 8 and 10 storeys are shown, for the fully infilled frame (0% openings), the frames with 25% and 50% infill opening ratios and the

bare frame (100% openings). As expected, masonry infills significantly influence the seismic response of the frames. For fully-infilled frames, the stiffness of the frame increases considerably compared to the bare frame. This increase is smaller for frames with 25% and 50% opening ratio. As also shown in previous studies [50-51] for opening ratios above 80% the influence is insignificant.

Total displacement and interstorey drifts of the infilled frames decrease compared to bare frames. Target displacement also decreases. Consequently, both ductility capacity and demand decrease with the presence of infill walls. On the contrary, overstrength significantly increases with the presence of infill walls. The capacity strength of the examined fully-infilled frames increased by 374% to 417% compared to the strength of the bare frames. However, after the failure of the infills the strength reduces.

The capacity curves of the bare frames and the fully-infilled frames with different number of storeys are shown in Figure 4. It can be seen, that higher frames have smaller initial stiffness and higher target displacement for both bare and infilled frames. The predicted base shear – roof displacement characteristics with uniform and triangular lateral loads are compared in Figure 5 for the 6-storey bare and fully-infilled frame. The maximum strength from pushover with uniform lateral loads is higher, while the target displacement is smaller, compared to the capacity curve with triangular distribution of lateral loads.

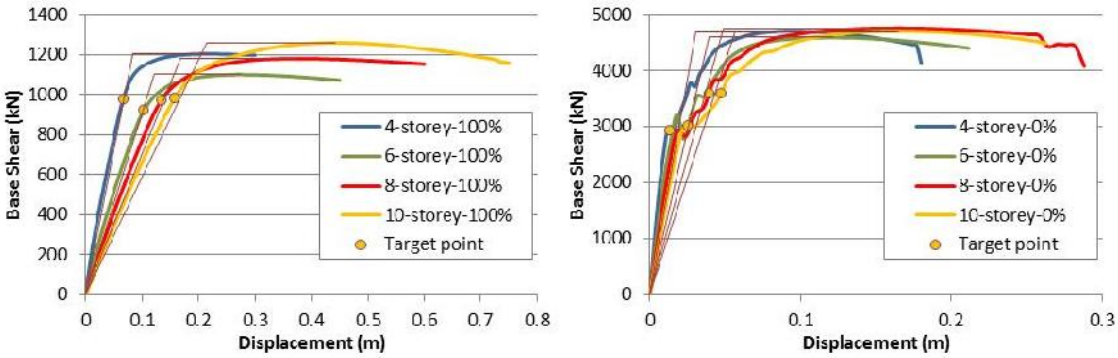


(a) Bare frame (b) Fully infilled

Figure 4: Capacity curves of 4, 6, 8 and 10-storey (a) bare and (b) fully-infilled frames.

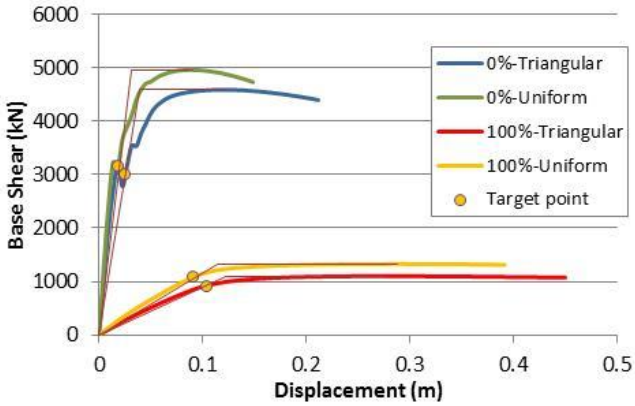


Figure 5: Capacity curves of 6-storey bare and fully-infilled frame with uniform and triangular lateral loads.

Capacity curves for bare, fully infilled frames and frames with soft storey are compared in Figure 6 for the 8 and 10-storey frames. The deformed shape of these frames is shown in Figure 7. In the same figure, the performance criteria are shown for the members of the frames.

Yield is indicated in green, flexural failure in red and shear failure of the members in blue. In the structures with a soft storey at the first floor, infills do not reach their strength degrading branch since inelastic energy absorption concentrates to the columns of the open storey. On the contrary, infills in the lower part of the fully infilled frames do reach their maximum resistance. Fully-infilled frames having regularly distributed infills, exhibit reduced local deformation demands and therefore behave in a desirable manner.

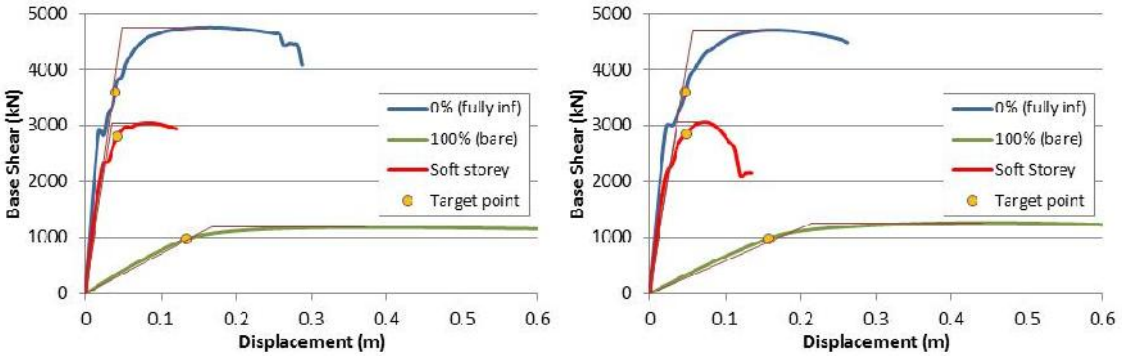


(a) 8-storey (b) 10-storey

Figure 6: Capacity curves of the 8 and 10-storey bare, soft storey and fully-infilled frame.

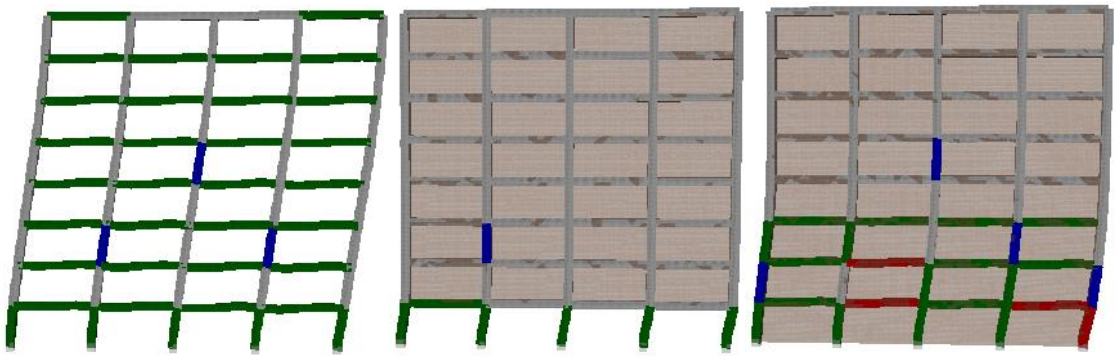

Figure 7: Deformed shape and performance criteria of the 8-storey bare, soft storey and fully-infilled frame (green: yield, red: flexural failure, blue: shear failure).

## 5 CONCLUSIONS

The influence of the masonry infill walls on the seismic performance of reinforced concrete frames is investigated in this study. Buildings with four to ten storeys are initially designed according to EC8. Static pushover analyses are subsequently performed for bare and infilled frames with various opening ratios. Based on the results of these analyses, the following are concluded:

- Results from static pushover analyses confirm the significant influence of the infills on the seismic response of the structures. Thus, infill walls should be included in the model.
- Infill walls increase the stiffness and overstrength of the structure but reduce its deformability and thus its ductility.
- A non-uniform distribution of infills, like an open first storey, results in a concentration of damage at this storey, creating a soft-storey response mechanism. The irregular distribution of infills significantly reduces the capacity of the structure which necessitates their inclusion

in the structural model. On the other hand, regularly distributed infills significantly reduce the deformation and ductility demand in structural elements, with the frames exhibiting an improved performance.

- As the opening percentage of the infills increases, the stiffness and overstrength decreases and the behaviour of the frame approaches that of the bare frame. For opening ratios above 75% the influence of the infills is insignificant.

## REFERENCES


[1] S.V. Polyakov, On the interaction between masonry filler walls and enclosing frame when loading in the plane of the wall. *Translation in earthquake engineering*, Earthquake Engineering Research Institute, San Francisco, 36-42, 1960.

[2] A.B. Mehrabi, P.B. Shing, M. Schuller, J. Noland, Experimental evaluation of masonry-infilled RC frames. *ASCE Journal of Structural Engineering*, **122**(3), 228-237, 1966.

[3] B.S. Smith, Behavior of square infilled frames. *ASCE Journal of the Structural Division*, **92(**ST1), 381-403, 1966.

[4] B.S. Smith, C. Carter, A method of analysis for infilled frames. *Institution of Civil Engineers*, **44**(1), 31-48, 1969.

[5] R.E. Klingner, V.V. Bertero, Earthquake resistance of infilled frames. *ASCE Journal of the Structural Division*, **104**(6), 973–989, 1978.

[6] S.G. Buonopane, R.N. White, Pseudodynamic testing of masonry infilled reinforced concrete frame. *Journal of Structural Engineering*, ASCE, **125**(6), 578-589, 1999.

[7] M. Dolšek, P. Fajfar, Mathematical modelling of an infilled RC frame structure based on the results of pseudo-dynamic tests. *Earthquake engineering & structural dynamics*, **31**(6), 1215-1230, 2002.

[8] L. Cavaleri, M. Fossetti, M. Papia, Infilled frames: developments in the evaluation of cyclic behaviour under lateral loads. *Structural Engineering and Mechanics*, **21**(4), 469-494, 2005.

[9] C.G. Karayannis, D.J. Kakaletsis, M.J. Favvata, Behavior of bare and masonry infilled R/C frames under cyclic loading: Experiments and analysis. *WIT Transactions on The Built Environment*, **81**, 2005

[10] M.H. Santhi, G.M.S. Knight, K. Muthumani, Evaluation of seismic response of soft-storey infilled frames. *Computers and Concrete*, **2**(6), 423-437, 2005.

[11] D.J. Kakaletsis, C.G. Karayannis, Experimental investigation of infilled reinforced concrete frames with openings. *ACI Structural Journal*, **106**(2), 132-141, 2009.

[12] J. Zovkić, V. Sigmund, I. Guljaš, Testing of R/C frames with masonry infill of various strength. *Proceedings of the 15th World Conference on Earthquake Engineering*, Lisbon, Portugal, January 2012.

[13] L. Cavaleri, F. Di Trapani, Cyclic response of masonry infilled RC frames: Experimental results and simplified modelling, *Soil Dynamics and Earthquake Engineering*, **65**, 224-242, 2014.

[14] C.Z. Chrysostomou, *Effects of degrading infill walls on the nonlinear seismic response of two-dimensional steel frames*. Ph.D. Dissertation, Cornell University, Ithaca, New York, 1991.

[15] M. Dolšek, P. Fajfar, Soft storey effects in uniformly infilled reinforced concrete frames. *Journal of Earthquake Engineering*, **5**(1), 1-12, 2001.

[16] C.Z. Chrysostomou, P. Gergely, J.F. Abel, A six-strut model for nonlinear dynamic analysis of steel infilled frames. *International Journal of Structural Stability and Dynamic*, **2**(3), 335-353, 2002.

[17] P.G. Asteris, Lateral stiffness of brick masonry infilled plane frames. *ASCE Journal of Structural Engineering*, **129**(8), 1071-1079, 2003.

[18] E. Vintzileou, C. Zeris, C. Repapis, Seismic Behaviour of Infilled Existing RC Buildings, *ICCES'04 Symposium: Earthquake Structural Engineering*, Madeira, Portugal, July 2004.

[19] P.G. Asteris, Closure to "Lateral stiffness of brick masonry infilled plane frames" by P.G. Asteris. *ASCE Journal of Structural Engineering*, **131**(3), 523-524, 2005.

[20] C. Repapis, C. Zeris, E. Vintzileou, Evaluation of the Seismic Behaviour of Existing RC Buildings: II. A Case Study for Regular and Irregular Buildings, *Journal of Earthquake Engineering*, Imperial College Press, **10**(3), 429-452, 2006.

[21] M. Dolšek, P. Fajfar, The effect of masonry infills on the seismic response of a four-storey reinforced concrete frame – a deterministic assessment. *Engineering Structures*, **30**(7), 1991-2001, 2008.

[22] M. Dolšek, P. Fajfar, The effect of masonry infills on the seismic response of a four storey reinforced concrete frame – a probabilistic assessment. *Engineering Structures*, **30**(11), 3186-3192, 2008.

[23] P.G. Asteris, Finite element micro-modeling of infilled frames. *Electronic Journal of Structural Engineering*; **8** (8), 1-11, 2008.

[24] H.A. Moghaddam, Lateral load behavior of masonry infilled steel frames with repair and retrofit. *ASCE Journal of Structural Engineering*, **130** (1), 56-63, 2004.

[25] D.J. Kakaletsis, C.G. Karayannis, Influence of masonry strength and openings on infilled R/C frames under cycling loading. *Journal of Earthquake Engineering*, **12**(2), 197-221, 2008.

[26] D. Kakaletsis, Analytical modeling of masonry infills with openings. *Structural Engineering and Mechanics*, **31**(4), 423-437, 2009.

[27] L. Cavaleri, M. Papia, A new dynamic identification technique: application to the evaluation of the equivalent strut for infilled frames. *Engineering Structures*, **25**(7), 889–901, 2003.

[28] D. Celarec, P. Ricci, M. Dolšek, The sensitivity of seismic response parameters to the uncertain modelling variables of masonry-infilled reinforced concrete frames. *Engineering Structures*, **35**, 165-177, 2012.

[29] L. Cavaleri, M. Papia, An output-only stochastic parametric approach for the identification of linear and nonlinear structures under random base excitations: Advances and comparisons. *Probabilistic Engineering Mechanics*, **35**, 11–21, 2014.

[30] L. Cavaleri, F. Di Trapani, Prediction of the additional shear action on frame members due to infills, *Bullettin of Earthquake Engineering*; **13**(5), 1425–1454, 2015. DOI: 10.1007/s10518-014-9668-z.

[31] G. Campione, L. Cavaleri, G. Macaluso, G. Amato, F. Di Trapani, Evaluation of infilled frames: an updated in-plane-stiffness macro-model considering the effects of vertical loads. *Bullettin of Earthquake Engineering*, 13(8), 2265-2281, 2014. DOI: 10.1007/s10518-014-9714-x.

[32] A.I. Kritikos, G.D. Ntasis, D.G. Zitouniatis, M.E. Lemonis, P.G. Asteris, Lateral response evaluation of steel frame structures with masonry infills, M. Papadrakakis, M. Fragiadakis eds., *6th ECCOMAS Thematic Conference on Computational Methods in Structural Dynamics and Earthquake Engineering (COMPDYN 2017),* Rhodes Island, Greece, June 15–17, 2017.

[33] H.A. Moghaddam, P.J. Dowling, *The State of the Art in Infilled Frames*. ESEE Research Report No. 87-2, Imperial College of Science and Technology, Civil Engineering Department, London, U.K, 1987.

[34] M. Papia, L. Cavaleri, M. Fossetti, Infilled frames: developments in the evaluation of the stiffening effect of infills. *Structural engineering and mechanics*, **16**(6), 675-93, 2003.

[35] P.G. Asteris, S.T. Antoniou, D.S. Sophianopoulos, C.Z. Chrysostomou, Mathematical macromodeling of infilled frames: State of the art. *ASCE Journal of Structural Engineering*, **137** (12), 1508-1517, 2011.

[36] P.G. Asteris, D.M. Cotsovos, C.Z. Chrysostomou, A. Mohebkhah, G.K. Al-Chaar, Mathematical micromodeling of infilled frames: State of the art. *Engineering Structures*, **56**, 1905-1921, 2013.

[37] A. Mohyeddin, S. Dorji, E.F. Gad, H.M. Goldsworthy, Inherent limitations and alternative to conventional equivalent strut models for masonry infill-frames. *Engineering Structures*, **141**, 666–675, 2017.

[38] Chrysostomou, C.Z., Asteris, P.G. On the in-plane properties and capacities of infilled frames. *Engineering Structures*, **41**, 385-402, 2012.

[39] LH logismiki. *FESPA 10 for windows*, v.5.4.0.100. Athens, Greece, 2013

[40] R.J. Mainstone, G.A. Weeks, The influence of bounding frame on the racking stiffness and strength of brick walls. *2nd International Brick Masonry Conference*, Building Research Establishment, Watford, England, 165-171, 1970.

[41] R.J. Mainstone, Supplementary note on the stiffness and strengths of infilled frames. Current Paper CP 13/74, Building Research Station, Garston, Watford, U.K., 1974.

[42] FEMA-274. NEHRP Commentary on the Guidelines for the Seismic Rehabilitation of Buildings, Washington (DC), Federal Emergency Management Agency, 1997.

[43] FEMA-306. Evaluation of earthquake damaged concrete and masonry wall buildings: basic procedures manual, Washington (DC), Federal Emergency Management Agency, 1998.

[44] P.G. Asteris, Lateral stiffness of brick masonry infilled plane frames. *ASCE Journal of Structural Engineering*, **129** (8), 1071-1079, 2003.

[45] SeismoSoft. *SeismoStruct 2016 - A computer program for static and dynamic nonlinear analysis of framed structures*. Seismosoft Ltd., Pavia, Italy. http://www.seismosoft.com [09 February 2016].

[46] J.B. Mander, M.J.N. Priestley, R. Park, Theoretical stress-strain model for confined concrete. *ASCE Journal of structural engineering*; **114** (8), 1804–1826, 1988.

[47] J.E. Martinez-Rueda, A.S. Elnashai, Confined concrete model under cyclic load. *Materials and Structures*; **30** (3), 139-147, 1997.

[48] M. Menegotto, P.E. Pinto, Method of analysis for cyclically loaded R.C. plane frames including changes in geometry and non-elastic behaviour of elements under combined normal force and bending. *Symposium on the Resistance and Ultimate Deformability of Structures Acted on by Well Defined Repeated Loads*, International Association for Bridge and Structural Engineering, Zurich, Switzerland, 15-22, 1973.

[49] F.J. Crisafulli, *Seismic behaviour of reinforced concrete structures with masonry infills*. Ph.D. Dissertation, University of Canterbury, New Zealand, 1997.

[50] P.G. Asteris, C.C. Repapis, A.K. Tsaris, F. Di Trapani, L. Cavaleri, Parameters affecting the fundamental period of infilled RC frame structures. *Earthquakes and Structures*, **9**(5), 999-1028, 2015.

[51] P.G. Asteris, C.C. Repapis, E.V. Repapi, L. Cavaleri, Fundamental period of infilled reinforced concrete frame structures. *Structure and Infrastructure Engineering*, 1-13, 2016.

COMPDYN 2017
6th ECCOMAS Thematic Conference on
Computational Methods in Structural Dynamics and Earthquake Engineering
M. Papadrakakis, M. Fragiadakis (eds.)
Rhodes Island, Greece, 15–17 June 2017

# LATERAL RESPONSE EVALUATION OF STEEL FRAME STRUCTURES WITH MASONRY INFILLS

**Antonios I. Kritikos, Georgios D. Ntasis, Dimitrios G. Zitouniatis, Minas E. Lemonis, and Panagiotis G. Asteris**

Computational Mechanics Laboratory, School of Pedagogical and Technological Education
Heraklion, GR 14121, Athens, Greece
panagiotisasteris@gmail.com

**Keywords:** Steel frames, Infill walls, Masonry, Analytical model, Pushover Analyses, Seismic Behavior, Seismic Design.

**Abstract.** *An established practice for the design of steel frame structures is to ignore the contribution of non-structural elements, such as masonry infilled walls. Even though this is considered a pro-safety simplification, it removes the opportunity to predict more realistically the actual structural response, on one hand, and to evaluate non-structural damage, particularly under less severe earthquakes, on the other. This study attempts to evaluate the contribution of masonry infills to the response of typical steel frames. In particular, a selection of multi-storey frames designed according to Eurocode 3 and 8, ignoring the presence of infills, is examined. The infills are then modeled, using an equivalent diagonal strut scheme. Their contribution to the structural response is evaluated through both linear and nonlinear analyses, for variable ratio of wall openings and number of storeys. The response characteristics are compared with the respective ones of the bare steel frames. The results reveal a significant increase in stiffness, as well as improved lateral resistance. Moreover, in regard to damage limitation requirements, the effectiveness of the infilled frames is significantly enhanced.*

## 1 INTRODUCTION

The contribution of non-structural elements in the analysis and design of steel frame structures is normally ignored, partly due to the inherent uncertainties on masonry materials and construction. However, it has been indicated by experimental and analytical studies [1, 2] that the impact of masonry infill in the seismic response of frame structures, can become significant both in terms of stiffness and resistance and therefore necessary to be accounted for.

For the modeling of masonry infills under global frame analysis, two practical approaches have emerged: micro-modeling and macro-modeling. With micro-modeling, the interaction between every brick unit and the mortar is included in a discrete form, with characteristics that are directly connected to the mechanical properties of the materials. This approach is considered the most accurate one, but unfortunately can prove time consuming and hard to implement. With macro-modeling on the other hand, the influence of the infill is represented with sets of equivalent struts, reflecting infill failure modes and characteristics that are normally estimated through analytical or empirical methods. Macro-modeling has evolved from single diagonal strut implementations [3] to multi-strut assemblies that are capable to capture the corner interactions between masonry and frame members [4-8]. Even though multi-strut models are more accurate than single ones, they are also less intuitive and require much more parameters to be properly setup. Detailed and in-depth state-of-the art works can be found in Asteris et al. 2011 & 2013 [9-10], and Mohyeddin et al. 2017 [11].

An aspect of the infill geometry that greatly affects in-plane behavior is the presence of openings. Mosalam et al. (1997) [12] studied experimentally the response of infilled frames with openings under cyclic loading. Also, Kakaletsis and Karayannis (2008) [13] examined experimentally the earthquake response of RC infilled frames with openings and suggested an equivalent strut scheme. Tasnimi and Mohebkhah (2011) [14] studied experimentally steel frames and suggested analytical models for infills with window and door openings. Asteris et al. (2012) [15] have proposed a reduction factor for the stiffness of infills with openings.

In this work the performance of steel moment-resisting frames, with variable ratio of openings and number of storeys, that were designed as usual, ignoring the influence of masonry infills, is evaluated under lateral loading conditions, using diagonal strut infill modeling.

## 2 DESCRIPTION OF EXAMINED STEEL FRAMES

A parametric analysis has been undertaken in order to investigate the in-plane influence of masonry infills in the response of 2D moment-resisting steel frames. Specifically, four regular frame designs were considered, with 4, 8, 10 and 12 storeys, each 3m high. The number of bays has been kept constant to three, with each bay 5m long. The frames were designed for both gravity and seismic loading according to Eurocodes 3 and 8 [16,17], ignoring masonry infills completely, as typically is done in practice. For lateral stability, moment resisting framing was selected, which relies on the rotational stiffness and the bending resistance of the beam-to-column joints to successfully transfer lateral loads to the ground.

The design process has been performed through the commercially available program SAP2000 [18], with the following design parameters: steel grade: S355, uniform dead load: 15 KN/m, uniform live load: 20 KN/m, seismic ground acceleration: 0.24g, soil type: B, seismic behaviour factor: 5.0.

In Figure 1, the four designed frames are displayed. Selection of the beam cross sections was dictated by the gravity loading. Column profiles on the other hand, were determined by the joint resistance requirements and more specifically, by the requirement of the joint component column web panel in shear. This component can be reinforced through a supplementary web plate that is welded upon the column web, but according to EN1993-1-8 [19], the

thickness of this plate cannot be bigger than the thickness of the column web itself. Therefore, the capacity of the joint to transfer gravity or seismic forces is directly linked to column size.

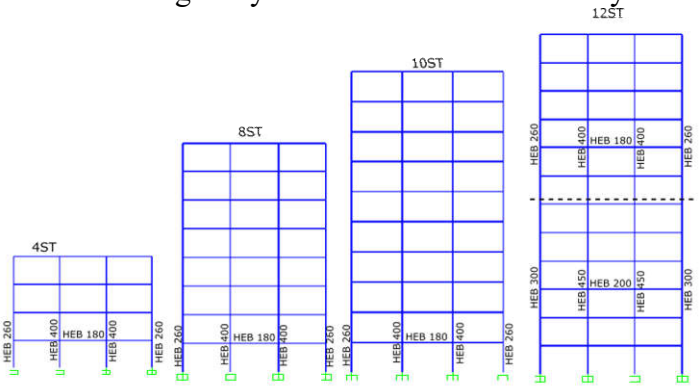


Figure 1: Steel frames that were examined.

## 3 EVALUATION OF FRAME BEHAVIOR WITH MASONRY INFILLS

### 3.1 General

In this work, the modeling of the infills was accomplished using single diagonal compression struts, as a balanced compromise between accuracy and required effort to prepare a full scale model, with commonly available frame analysis software. In particular, the main shortcoming of single strut modeling is the representation of shear and bending moment interactions between the infill and the surrounding members. However, it requires significantly less parameters for input and its performance against experimental pseudo-dynamic tests [15] has been found less accurate than multi-strut models, but in satisfactory agreement with them.

In Figure 2, the 4-storey frame is displayed, with diagonal compressive springs applied to every panel. The member elements are positioned along their centerlines and the length of each spring element is defined by the nodal distance of diagonally opposite beam-to-column joints. The additional time for the preparation of such a model was minimal and comparable to modeling with bracings, provided that the force-deformation characteristic of the springs is previously established. This is considered a decisive factor for a more wide-spread implementation of such an approach by the steel construction industry.

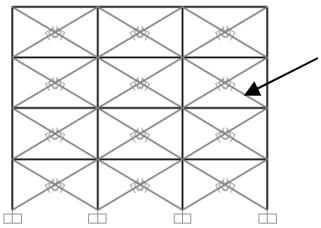


| Masonry properties | |
|---|---|
| Thickness $t_w$ | 180 mm |
| Compressive strength $f_m$ | 4.1 MPa |
| Young's Modulus $E_w$ | 2.3 GPa |

Figure 2: Steel frame model with diagonal struts for the simulation of infills and masonry properties

The force-deformation characteristic of the springs is nonlinear, with only the compressive path being active, as illustrated in Figure 3. The initial segment of the characteristic corresponds to the elastic linear range with initial stiffness $S_{ini}$. The firstly encountered limit corresponds to the first crack on the masonry that occurs for a strut force $F_{cr}$, and deformation $\delta_{cr}$. Subsequently, the ultimate load limit, occurs at force $F_m$ and deformation $\delta_m$, after which the response deteriorates, up to a residual force level, denoted with force $F_r$ and deformation $\delta_u$.

The minimum required parameters for the complete description of the force-displacement characteristic are $S_{ini}$, $F_m$, $k$, $a$, $b$ and $m$, according to the following relationships:

- $S_{\text{sec}} = kS_{ini}$
- $F_{cr} = aF_m$
- $F_r = bF_m$
- $\delta_u = m\delta_m$

Parameter $a = F_{cr} / F_m$ is taken equal to 0.8, similar to existing literature practices [7,20], while parameter $b = F_r / F_m$ usually ranges between 0.02-0.4 [4,7,20] and a value equal to 0.2 is adopted here. The parameter $k$ that relates secant stiffness towards the ultimate load, $S_{\text{sec}}$, with the initial stiffness, $S_{ini}$, is taken equal to 0.5, based on the characterization of experimental data [21] and available analytical modeling [4]. For the needs of estimating the ultimate displacement $\delta_u$, the negative stiffness of the third branch of the force-deformation law has been approximated in a range of 0.01-0.1 of initial stiffness [22], with value 0.1 corresponding to quite brittle masonry with weak framing. Conservatively, a value of $m$ equal to 5 is considered here. The determination of $S_{ini}$ and $F_m$ is described in the next two sections.

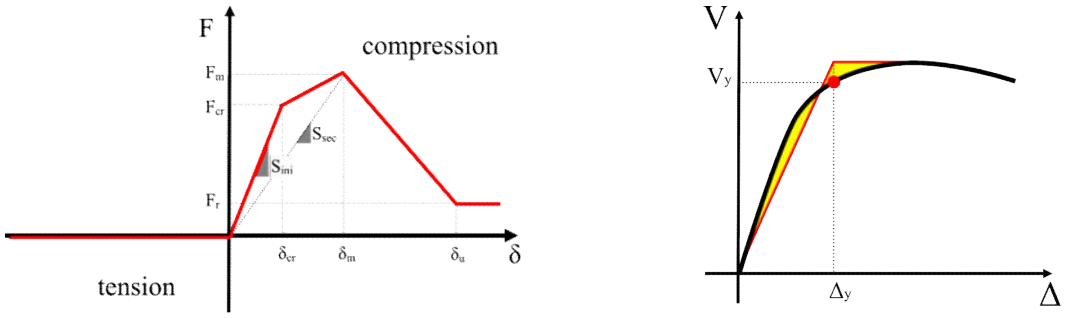


Figure 3: Force-deformation law of the diagonal struts (left) and capacity curve yield point definition (right).

### 3.2 Initial Stiffness

The width $w$ of an equivalent diagonal strut may be found according to equation 1, which was first proposed by Mainstone and Weeks (1971) [3] and was included in FEMA-306 [2]:

$$w = 0.175\lambda_h^{-0.4} d \tag{1}$$

where, $d$ is the diagonal length of the masonry infill and $\lambda_{\text{h}}$ given by the following equation:

$$\lambda_h = \sqrt[4]{\frac{E_w t_w \sin 2\theta}{4EIh_w}} \cdot h \tag{2}$$

where $E_w$ is the modulus of elasticity of the masonry infill, $t_w$ its thickness, $h_w$ the net height of infill panel, $EI$ the flexural rigidity of the columns, $h$ their height, measured between beam centrelines, and $\theta$ the angle, so that, $\tan\theta = h_w / L_w$, where $L_{\text{w}}$ the net length of infill.

When openings exist in the infills, the thickness of the equivalent diagonal strut is modified, by multiplying the value found from equation 1, with a reduction factor $\lambda$, that has been proposed by Asteris et al. (2012) [15], and is shown in the following equation:

$$\lambda = 1 - 2a_w^{0.54} + a_w^{1.14} \tag{3}$$

where $\alpha_w$ is the ratio of the openings relative to the total infill panel area.

### 3.3 Strength

The resistance of masonry infills is rather complicated to predict analytically. Several failure mechanisms can be realized and the ultimate load that can be sustained for each one is not only dependent on the infill characteristics, but also on detailing and construction quality. Typical in-plane failure mechanisms include [2] compression failure, diagonal tension failure, shear sliding failure and general shear failure. Only the compression strength has been considered for our evaluation, which, in the diagonal direction, can be expressed as:

$$V_c = wt_w f'_{m90} \tag{4}$$

where $f'_{m90}$ the masonry compressive strength in the horizontal direction, that can be assumed 50% of the respective stacked prism strength, and the parameters $w$, $t$ as before.

### 3.4 Modeling of members of the steel frame

Steel columns and beams members were modeled taking into account material and geometric nonlinearity. For material nonlinearity, a lumbed plasticity approach has been adopted, with the properties of individual plastic hinges determined through discretization of the cross-sections to fiber layers. Offset distance from centerline joints, equal to 5% of the member length were designated for the location of plastic hinges.

## 4 RESULTS AND DISCUSSION

The four test frames were analysed in SAP2000[18], using static pushover analysis with uniform lateral loading, for six cases of infill opening ratios $a_w$: 0, 0.1, 0.25, 0.5, 0.75 and 1. The case $a_w$=1 corresponds to the bare frame while $a_w$=0 to solid infills without any opening. The normalized capacity curves (base shear to building weight ratio $V/W$ vs. roof drift to building height ratio $\Delta/H$) are shown in Figure 4. The red dot on each curve, marks the yield point, which is calculated from the yield displacement of the bilinear approximation (Figure 3), which is regressed until the areas between the bilinear and the actual curve are balanced out. For this calculation, the actual curve is considered up to its maximum capacity or its capacity at 10% drift, whichever is bigger.

The masonry infills significantly influence the response both in terms of initial stiffness $K$ and capacity. Specifically, the increase of initial stiffness, compared to the bare frames, is depicted in Figure 5 and proves quite drastic, reaching levels of 16x magnification for $a_w$=0, while for $a_w$=0.25~0.5 the increase ranges between 1.8 and 4.4, which is still considered remarkable. For $a_w$=0.75 on the other hand, the change is insignificant. The described behavior is uniform for all different number of storeys. Also, similar increase, but slightly smaller, can be observed for the secant stiffness targeting the yield point.

In terms of capacity, a substantial increase is also observed for the frames with infills. As shown in Figure 5, the yield base shear for $a_w$=0 becomes 2-3 times larger compared to the bare frames, and for $a_w$=0.25 the increase lies between 1.15 and 1.40, while for larger $a_w$ it becomes rather insignificant. This increase however is accompanied with a notable change of the shape of the capacity curve, the appearance of limit point, after which the capacity drops to a rather stable residual capacity, which for small $a_w$ remains quite higher, than the bare frame. This post-critical capacity drop proves more severe for frames with more storeys.

The drifts on the other hand, typically decrease due to masonry infills. The comparison of the roof drifts at yield of the infilled frames relative to the bare frame ones, reveal a close to linear increase with the infill opening ratio $a_w$, as can be seen in Figure 5. For $a_w$=0, the yield roof drift becomes approximately five times smaller than the drift of the bare frame. The be-

havior remains uniform for all different frames. The reduced drifts can prove valuable for the verification against damage limitation seismic requirements [17]. Specifically, damage limitation is satisfied when design intestorey drift ratios are smaller than 1%, in buildings with non-structural brittle materials attached to the structure. In this context, the ratios of required base shear to induce a 1% roof drift ratio (RDR), relative to the bare frame, are depicted in Figure 5, for all different frames and infill openings. It is evident that substantially bigger base shear is needed (approximately 4 times if $a_w$=0, and 2 times if $a_w$=0.25), to exceed the 1% RDR in infilled frames. The relationship proves quite close for all different frames.

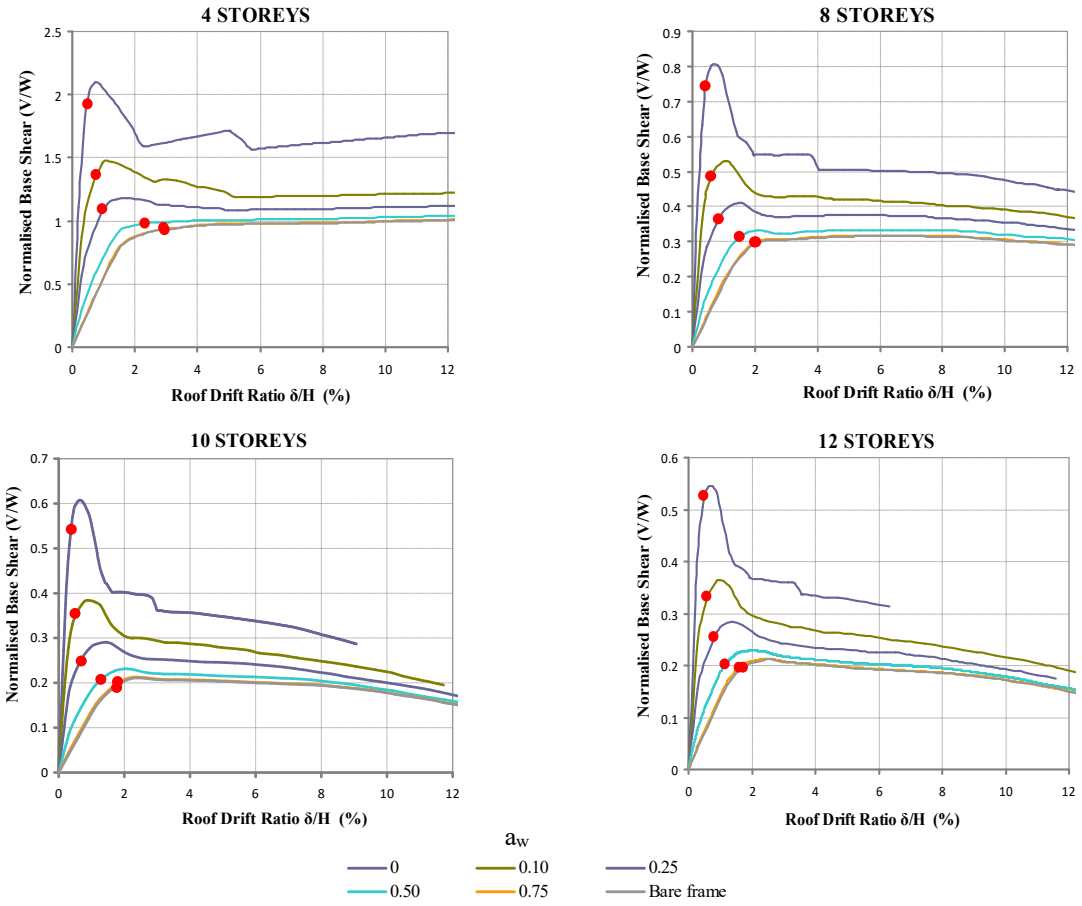


Figure 4: Normalized capacity curves of the examined frames for various ratios of openings $a_w$.

## 5 CONCLUSIONS

An investigation of the response of typical moment-resisting steel frames with masonry infills and variable ratio of openings has been performed, using nonlinear static analyses. The results revealed an improved behavior for the frames with infills, however some points of concern have been observed as outlined below.

- Up to yielding, the response of the frames with infills, improves drastically, both in terms of initial stiffness and drifts. In particular, for performance level of 1% roof drift ratio, the increased stiffness offers the possibility to surpass the damage limitation requirements for the seismic design of the structure.
- The post-yield behavior seems also improved, in terms of yield and maximum capacity, but a critical point of the response can emerge, after which strength degradation is observed that is quite severe for infills with small or no openings.
- When the opening ratio exceeds 50% in every frame panel, no significant improvement of the infilled frame response has been detected.

- All infilled frames managed to reach high drift ratios (above 5%), while at the same time exceeding the sustained base shear of the bare frame. However, the improvement of the capacity at these levels of drift ratios is not equally impressive as in a pre-yield state. Specifically, at 5% roof drift ratio, which can be considered appropriate for no collapse requirements, a 1.7x magnification of capacity has been recorded for infills with no openings and 1.15x for infills with 25% openings.

The drastically increased pre-yield stiffness of the infilled frames should raise awareness, for the potential consequences when using a fundamental period under seismic design, based on the bare frame alone. For the frames examined in this work, the fundamental periods of the bare frames were found more than triple of those of the infilled frames with $a_w$=0. Using the same seismic design parameters, the errors in the calculation of the design seismic base shear, from EN1998 [17] spectrum, using the bare frame period instead of the infilled frame one, have been calculated and are shown in Figure 6. An extreme underestimation of the design base shear, up to -77%, has been found, for the higher storey frames with fewer openings.

Before practical design recommendation can be made, further research is required, towards the impact of irregularities and post-yield masonry-frame interactions, particularly under dynamic loading conditions.

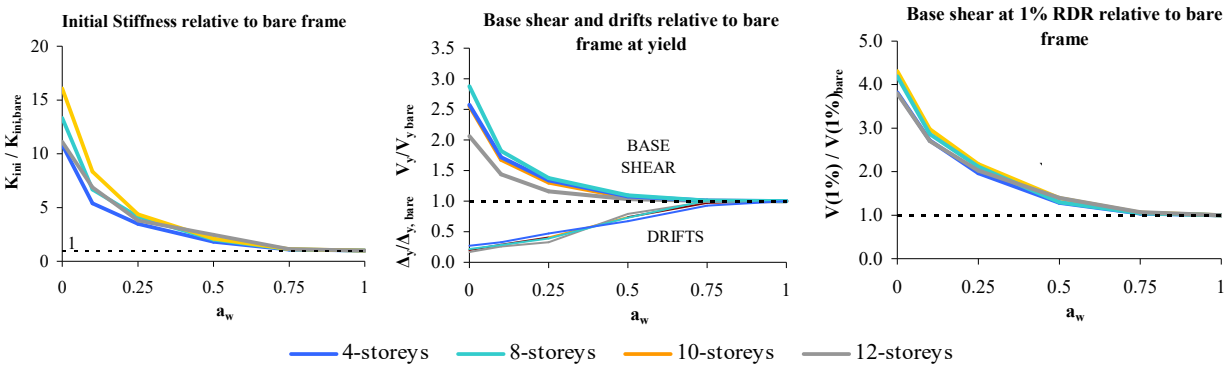


Figure 5: Response characteristics of the examined frames versus the infill openings ratio $a_w$.

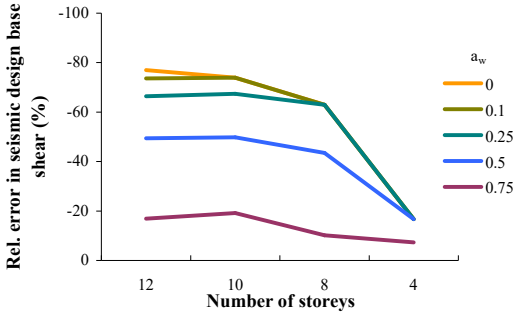


Figure 6: Relative error in the estimation of seismic base shear according to EN1998 when ignoring infills

## REFERENCES

[1] J.B. Mander, B. Nair, K. Wojthowski, J. Ma, *An experimental study on the seismic performance of brick-infilled steel frames with and without retrofit. Technical report.* NCEER 93–0001, 1998.

[2] FEMA 306, *Evaluation of earthquake damaged concrete and masonry wall buildings*. Applied technology council, 1998.

[3] R.J. Mainstone, G.A. Weeks, The Influence of a Bounding Frame on the Racking Stiffnesses and Strengths of Brick Walls. *Proceedings of the 2nd International Brick Masonry Conference, Building Research Establishment*, Watford, England, 1970.

[4] A. Madan, A.M. Reinhorn, J.B. Mander R.E. Valles, Modeling of masonry infill panels for structural analysis. *Journal of Structural Engineering*, **123**(10), 1295-1302, 1997.

[5] W.W. El-Dakhakhni, M. Elgaaly, A.A. Hamid, Three-strut model for concrete masonry-infilled steel frames. *Journal of Structural Engineering*, **129**(2), 177-185, 2003

[6] A. Furtado, H. Rodrigues, A. Arêde, Modelling of masonry infill walls participation in the seismic behaviour of RC buildings using OpenSees. *International Journal of Advanced Structural Engineering (IJASE)*, **7**(2), 117-127, 2015

[7] I., Radić, D. Markulak, V. Sigmund, Analytical modelling of masonry-infilled steel frames. *Tehnički vjesnik*, **23**(1), 115-127, 2016.

[8] A. Fotos, F. Foskolos, A.K. Tsaris, C.C. Repapis, P.G. Asteris, Inelastic response of masonry infilled reinforced concrete structures, M. Papadrakakis, M. Fragiadakis eds., *Proc. of 6th ECCOMAS Thematic Conference on Computational Methods in Structural Dynamics and Earthquake Engineering,* Rhodes Island, Greece, June 15–17, 2017.

[9] P.G. Asteris, S.T. Antoniou, D.S. Sophianopoulos, C.Z. Chrysostomou, Mathematical macromodeling of infilled frames: State of the art. *Journal of Structural Engineering*, **137**(12), 1508-1517, 2011.

[10] P.G. Asteris, D.M. Cotsovos, C.Z. Chrysostomou, A. Mohebkhah, G.K Al-Chaar, Mathematical micromodeling of infilled frames: State of the art. *Engineering Structures*, **56**, 1905-1921, 2013.

[11] A. Mohyeddin, S. Dorji, E.F. Gad, H.M. Goldsworthy, Inherent limitations and alternative to conventional equivalent strut models for masonry infill-frames. *Engineering Structures*, **141**, 666–675, 2017.

[12] K.M. Mosalam, R.N. White, P. Gergely, Static response of infilled frames using quasi-static experimentation. *Journal of Structural Engineering*, **123**(11), 1462-4169, 1997.

[13] D. J. Kakaletsis, C. G. Karayannis, Influence of masonry strength and openings on infilled R/C frames under cycling loading. *Journal of Earthquake Engineering*, **12**(2), 197-221, 2008.

[14] A.A. Tasnimi, A. Mohebkhah, Investigation on the behavior of brick-infilled steel frames with openings, experimental and analytical approaches. *Engineering Structures*, **33**(3), 968-980, 2011.

[15] P.G. Asteris, I.P. Giannopoulos, C.Z. Chrysostomou, Modeling of infilled frames with openings. *Open Construction & Building Technology Journal*, **6**(1), 81-91, 2012.

[16] European Committee for Standardization (CEN), EN1993-1-1 - Eurocode 3: Design of steel structures - Part 1-1: General rules and rules for buildings, 2005.

[17] European Committee for Standardization (CEN), EN1998-1 - Eurocode 8: Design of structures for earthquake resistance- Part 1: General rules, seismic actions and rules for buildings, 2004.

[18] Computers and Structures Inc., SAP2000, Berkeley, California, 2015.

[19] European Committee for Standardization (CEN), EN1993-1-8 - Eurocode 3: Design of structures for earthquake resistance- Part 1-8: Design of joints, 2005.

[20] D. Celarec, P. Ricci, M. Dolšek, The sensitivity of seismic response parameters to the uncertain modelling variables of masonry-infilled reinforced concrete frames. *Engineering Structures*, **35**, 165-177, 2012.

[21] A.V. Bergami, C. Nuti, Compression Tests on Masonry Walls Realized with a Single or Double Masonry Panel. *Journal of Civil Engineering and Architecture Research*, **2**(7), 802-809, 2015.

[22] T.B. Panagiotakos, M.N. Fardis, Seismic response of infilled RC frames structures. *11th world conference on earthquake engineering,* June, 1996,

COMPDYN 2017
6th ECCOMAS Thematic Conference on
Computational Methods in Structural Dynamics and Earthquake Engineering
M. Papadrakakis, M. Fragiadakis (eds.)
Rhodes Island, Greece, 15–17 June 2017

# DIRECTIONAL EFFECTS ON COMBINED IN-PLANE AND OUT OF PLANE SEISMIC BEHAVIOR OF MASONRY INFILLS

**Marco Donà[1], Giovanni Tecchio[1], Luca Domenicale[1], Elisa Saler[1], Massimiliano Minotto[1] and Francesca da Porto[1]**

[1] Dept. of Civil, Environmental and Architectural Engineering (ICEA), University of Padova
Via Marzolo 9, 35131 Padova, Italy
{marco.dona, giovanni.tecchio, luca.domenicale,
elisa.saler, massimiliano.minotto, francesca.daporto}@dicea.unipd.it

**Keywords:** Infilled RC Frames, nonlinear static analysis, masonry infills, in plane and out of plane interaction of infills.

**Abstract.** *Unreinforced masonry (URM) infill walls affect both the strength and the stiffness of reinforced concrete (RC) frame structures undergoing lateral loads. Despite being classified as non-structural elements and often neglected in design numerical models, URM infills have a relevant influence on the seismic behaviour of structures. The brittle nature of URM determines a swift degradation of stiffness, strength, and low energy dissipation capacity once the panels are damaged or fail in the one of the in-plane direction failure modes.*

*The aim of this work is to adopt and calibrate a macro-model for masonry infill walls that considers simultaneous in-plane and out-of-plane actions, and apply it to the nonlinear pushover analysis of RC frame structures representative of traditionally and seismically designed buildings. To this scope, a recently proposed URM infill macro-model with in-plane out-of-plane interaction is calibrated with existing experimental data from quasi-static tests performed on two types of clay masonry infill walls that are commonly found both in Italy and other Mediterranean countries. The calibrated elements are included in planar numerical models of RC framed structures representative of the Italian building stock, considering both traditionally and newly designed frames. Nonlinear static pushover analyses are performed on the frames with simultaneous static forces acting on the walls elements in the out-of-plane direction. Results confirm that increasing the out-of-plane loads on the panels induces both cracking and failure of the walls at lower lateral drifts of the buildings. The global force-displacement curves of the frames are also affected.*

# 1 INTRODUCTION

Unreinforced masonry (URM) infill walls affect both the strength and the stiffness of reinforced concrete (RC) frame structures undergoing lateral loads. When an earthquake strikes, in particular, infill walls increase the global lateral stiffness and strength of the structure and they can contribute to the energy dissipation of the structure, if damage is limited to acceptable levels. However, in many cases masonry infill panels have also played a negative role on the seismic response of buildings; in fact, damage and failures to URM infill walls has been linked to heavy socio-economic consequences, including human casualties, unusable buildings and high repair costs. Several negative phenomena impact the seismic response of both old and newly constructed buildings. The interaction between infill walls and frame elements, as an example, can also be the source of localized damage to structural components, activating undesirable failure modes. Moreover, the brittle nature of URM determines a swift degradation of stiffness, strength, and low energy-dissipation capacity once the panels are damaged or they fail (El-Dakhakhni *et al.* 2003) [1].

In addition to in-plane (IP) failures modes, infill walls can also suffer the expulsion in the out-of-plane (OOP) direction, posing a serious hazard to human safety. Studies dedicated to the behaviour of URM infill walls in the out-of-plane direction have been historically less numerous, compared to those regarding the in-plane behaviour, and fewer studies have discussed the effects of a combination of in-plane and out-of-plane actions, which is the most realistic action on infill walls during an earthquake. URM infills are usually classified as non-structural elements and often neglected in design numerical models. Moreover, although a number of simple and more refined models for infill walls have been proposed in the past few decades, most of them consider only in-plane actions.

Several studies about macro-modelling of infilled frame structures have been proposed in recent years (Asteris et al. in 2011 [2], Jeselia et al. in 2013 [3] and Tarque et al. in 2015 [4]), in which different models have been analyzed, classifying macro-model in single diagonal strut models and more complex multi-strut models. Macro-models require less computational effort compared to micro-models, which instead involve non-linear finite element modelling of the RC frame, the infill panels and the interface between the frame and the wall. Therefore macro-models are more suitable to represent the global behavior of structures.

The representation of the masonry infill wall through an equivalent diagonal element was introduced in 1960s, who proposed a truss diagonal element characterized by the same material and thickness of the panel, but considering an “equivalent width”. In the following years, Smith provided a more sophisticated formulation for the equivalent element width, which is a function of the ratio between the frame and panel stiffness.

Multiple-strut models were proposed with the aim of better simulating both the effect of the panel and the internal forces distribution on the frame members.

Since 1997 Crisafulli [5] carried out some studies to compare the performance of one, two and three-strut models. According to those studies, a single-strut model cannot properly represent the internal forces generated on the frame members, although its simplicity and ability to correctly represent the lateral stiffness of the infilled frame and the axial stresses induced from lateral forces; therefore, a 2-struts model at least should be used for a more appropriate modelling, considering also a 3-struts model to minimize the errors for the bending and shear stresses.

Regarding the IP/OOP interaction, in 2004 Calvi et al. [6] studied the resisting arch-mechanism of the masonry walls, depending on the slenderness (the ratio between height and thickness). In particular they referred to Flanagan & Bennett (1999) [7] and Angel-Abrams (1994) [8] studies. Flanagan & Bennett have demonstrated that the IP damage influence

depends on the ratio of slenderness of the infill walls and not on the ultimate load capacity. Angel-Abrams have demonstrated experimentally that, for high levels of slenderness, the reduction of the OOP resistance due to the IP damage can be evaluated at about 50%. More recently, other authors who have been studied the influence of the IP damaging on the OOP behavior through a numerical model are Furtado and Rodrigues (2015) [9] and Najafgholipour et al. (2013) [10], while several studies and an experimental campaign on URM infill walls have been made by da Porto et al. [11], in particular considering thick panels. This study instead aims to consider the simultaneous combined IP/OOP action. In 2015 Mosalam & Gunay [12] proposed a macro-model (MG-model) to consider the IP/OOP interaction, calibrated according to the following expression:

$$\left(\frac{P_{il}}{P_{ic}}\right)^{3/2}+\left(\frac{P_{ol}}{P_{oc}}\right)^{3/2}=1 \tag{1}$$

where $P_{il}$ and $P_{ol}$ are respectively the in-plane and out-of-plane loads, instead $P_{ic}$ and $P_{oc}$ are the in-plane and out-of-plane capacities. This model (Figure 1) represents the infill by means of a diagonal element based on two bi-directional domains (Figure 2), which govern respectively the yielding and the removal criteria of the element itself. In particular, this element consists of two elastic beams with a plastic hinge in the contact point, where an inelastic fiber section with fibers spaced in the out-of-plane direction is defined: in this way, they withstand to axial force as well as to bending moment, combining the IP/OOP response; the fibers are defined through their area $A_i$, location $z_i$ related to the central axes, yielding stress $f_{vi}$ and yielding deformation $\varepsilon_{vi}$. Yielding condition is given by a IP-Axial Force/OOP-Bending Moment diagram (Figure 2a) derived from Eq. (1), and a similar domain is used to remove the element during the analysis when it is exceeded by the displacement of the central node. The model use a simple elastic-plastic constitutive law for the fibers, which means that, once the element yields, it maintains its capacity until the element removal occurs.

Starting from the MG-model, taken as reference, the paper proposes a more appropriate macro-model to consider simultaneous IP and OOP actions, calibrated on the basis of previous experimental campaings [6[11], with the aim to assess the influence of the seismic action directionality on the response of the infilled R.C. frame. For this purpose, a parametric non-linear pushover analysis was carried out in OpenSees, involving different direction of the load pattern, differrent configurations of R.C. frames, traditionally and seismically designed, and two types of infill, thin and thick, representative of the Italian building stock. Results are presented in terms of pushover curves, energy indexes and inter-storey drift profiles.

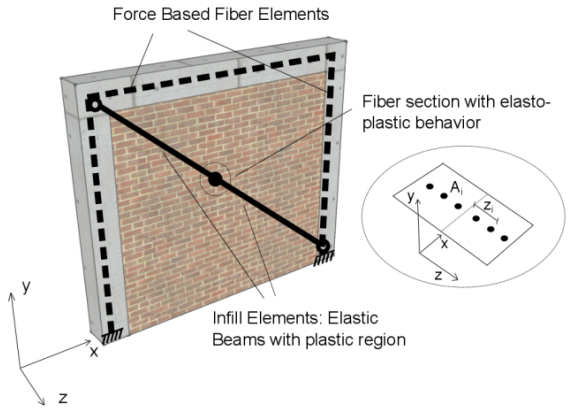


Figure 1. Infilled Frame Modelling according to Mosalam & Gunay [12]. Infills were modelled by using elastic beams with a plastic fiber region to simulate the In-Plane/Out-of-Plane interaction.

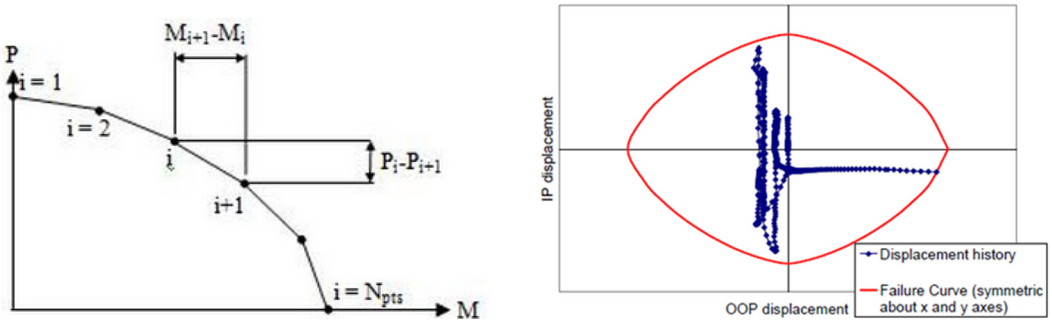


a) b)

Figure 2. a) IP-Force (P)/OOP-Moment (M) domain for the yielding condition of the fibers and (b) IP/OOP displacement domain for the element removal, from Mosalam & Gunay[12].

## 2 CALIBRATION OF THE F.E. MODELS THROUGH IP/OOP TEST RESULTS

### 2.1 Presentation of the reference tests

The available experimental results regard two different types of infill panel tested both in-plane and out-of-plane at the University of Padova (da Porto *et al.* 2013) [11] and Pavia (Calvi *et al*. 2004) [6]. These masonry panels have similar length and height but two different thicknesses, in order to assess the seismic behavior of both thick and thin infills. The walls tested by da Porto *et al.* [11] were full-scale panels made of clay units with vertical holes. Infills built with this thick units have become more common in recent years, because they can improve thermal insulation and are generally more robust, especially against earthquakes. However, thin walls made of clay units with horizontal holes have been the typical light enclosure system used since 1960s and are widespread in existing buildings. These infills were studied, still through full-scale tests, by Calvi et al. [6]. The characteristics of the experimental sets and the main results are shown respectively in Table 1 and Figure 3 and 4.

Looking at Figure 4, a progressive stiffness and strength degradation is observed in the OOP direction increasing the IP damage and the following points can be identified on the capacity curves:

- a *Damage Limit State* (DLS) corresponding to a first important variation of the slope;
- an *Ultimate Limit State* (ULS), corresponding to the peak strength;
- a *Collapse Point* (CP), which identifies the moment (determined also by test observations) of sudden strength degradation, which anticipates the out-of-plane collapse of the panel.

| | | *Type Padova (PD)* | *Type Pavia (PV)* |
|---|---|---|---|
| *RC frame* | Column section | 300x300 mm | 300x300 mm |
| | Beam section | 250x500 mm | 250x500 mm |
| | Frame height | 3200 mm | 3250 mm |
| | Frame length | 4750 mm | 4800 mm |
| | Concrete compressive strength | 30 MPa | 30 MPa |
| | Concrete elastic modulus | 25000 MPa | 25000 MPa |
| | Steel yield strength | 450 MPa | 560 MPa |
| | Steel elastic modulus | 200000 MPa | 195000 MPa |
| *Masonry infill* | Infill thickness | 300 mm | 115 mm |
| | Infill height | 2650 mm | 2750 mm |
| | Infill length | 4150 mm | 4200 mm |
| | Masonry compressive strength | 6.0 MPa | 4.5 MPa |
| | Masonry elastic modulus | 6000 MPa | 4500 MPa |

Table 1. Geometrical and material properties for the two infilled RC frames tested.

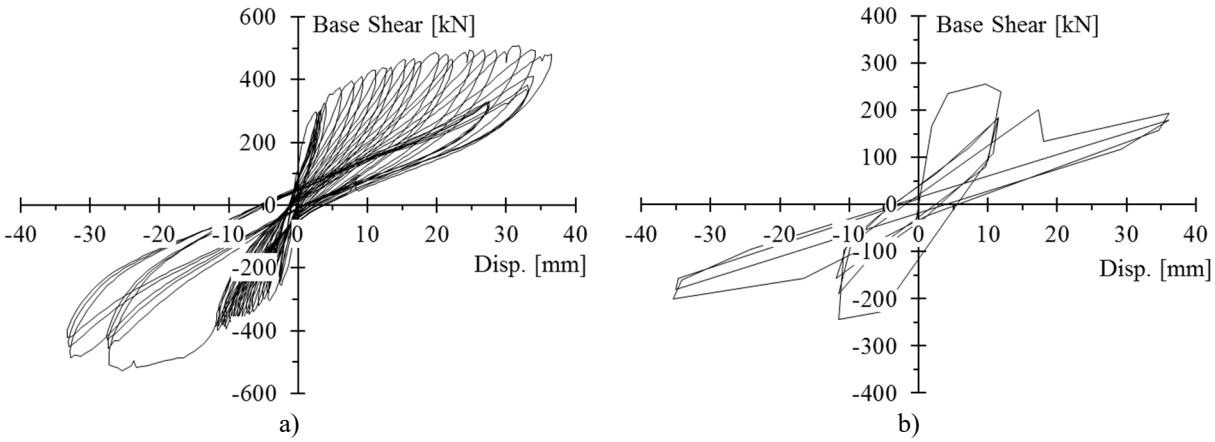


Figure 3. IP hysteretic cycles of infilled frames tested at the University of Padova (a) and Pavia (b).

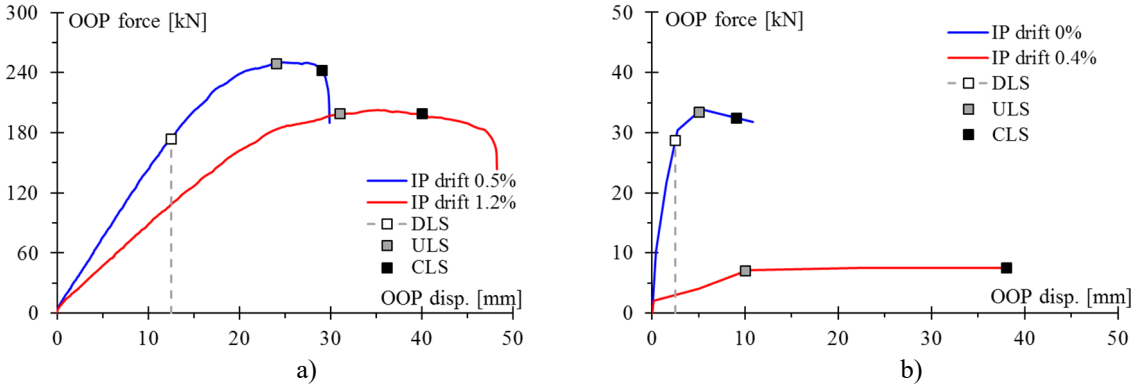


Figure 4. OOP test results starting from different IP damages: (a) thick panel (Padova), (b) thin panel (Pavia).

| *IP Limit States* | *Thick panel (Padova)* | *Thin panel (Pavia)* |
|---|---|---|
| *DLS* | 0.5 % | 0.4 % |
| *ULS* | 1.2 % | 1.0 % |
| *CLS* | 2.5 % | 1.4 % |

Table 2. IP limit drifts, associated to the principal limit states, for the two analyzed infill panels.

Finally, the IP limit states, directly derived from test observations, are reported in Table 2 (with the same meaning of those presented for the OOP direction).

## 2.2 Presentation of the F.E. model

In the proposed F.E model (see Figure 5), implemented in OpenSees, RC members were modelled using force based beam-column elements with non-linear fiber sections, using five integration points. The Kent-Scott-Park [13] constitutive law, with added linear tension softening, was considered for the concrete, while Mander's model was adopted to evaluate the confinement parameters for the core and cover concrete. For the steel bars, an elasto-plastic behaviour with strain hardening was used, as proposed by Menegotto & Pinto[14]. These material laws, calibrated through the previous test results, are shown in Figure 6a),b),c).

In order to confer a realistic OOP stiffness to the frame planar models, elastic springs with OOP stiffness were placed on the frame nodes which would be connected to the frames in the orthogonal direction. The stiffness values of these fictitious springs were iteratively calibrated for each model so as to obtain similar first periods of vibration in both OOP and IP directions.

The infill panels are modelled by means of two equivalent struts, each of them is defined similarly to the element of the MG-model [12], but with half IP/OOP resistance: the same fiber section, composed by 10 fibers symmetrically placed out-of-plane with respect to the strut axis, is used to consider the IP-OOP interaction, but a different hysteretic law is defined to represent the degradation of the masonry strength and stiffness. In particular, the "Hysteretic material" (from OpenSees material library) was used to simulates the infill experimental behavior and was calibrated, for each of the 5 different fibers, as shown in Figure 6d. The calibration of the "yielding point" (maximum strength) of the fibers was done in accord to MG model, with the only difference that the same "yield strain" (calculated as the medium yield stress of the fibers divided the masonry Young's modulus) was assumed for all the fibers, thus using different elastic moduli for the fibers (calculated as the yield stress of the specific fiber divided the yield strain), but such that their mean value is the elastic modulus of the masonry; considering a material with strength and stiffness degradation, this was necessary to increase the controllability of the model for the following calibrations.

The contact length, which define the distance between the struts, was appropriately calculated according to Stafford Smith (1966) [15].

The in-plane inertial masses include both the frame masses and the infill ones and they are represented as lumped masses at each beam-column joint. Instead, the out-of-plane mass is considered only for the masonry infill, because of the bi-dimensional model, and this is concentrated only in the central point of the two struts, equally subdivided between the struts. In the out-of-plane direction, the two central nodes of the struts are rigidly connected.

The calibrated hysteretic laws of Figure 6d) allow to better predict the real seismic behaviour of the masonry panels with respect to the MG model. Moreover, if for the MG model the removal domain is necessary to cut the capacity of the yielded panel, simulating the loss of the total IP and OOP strength of the panel after its collapse, in the proposed modified MG model (mMG) the same domain, corresponding to the Collapse Limit State (CLS) domain in Figure 7, is effectively used to describe only the real out-of-plane collapse of the panel, which corresponds to a sudden reduction of the infilled-frame IP resistance, equal to the residual IP strenght of the panel. Thus, the removal condition for the IP direction is not used, because the model already simulates the stiffness and strength degradation up to zero. The main differences between the MG model and that proposed are summarized in Table 3.

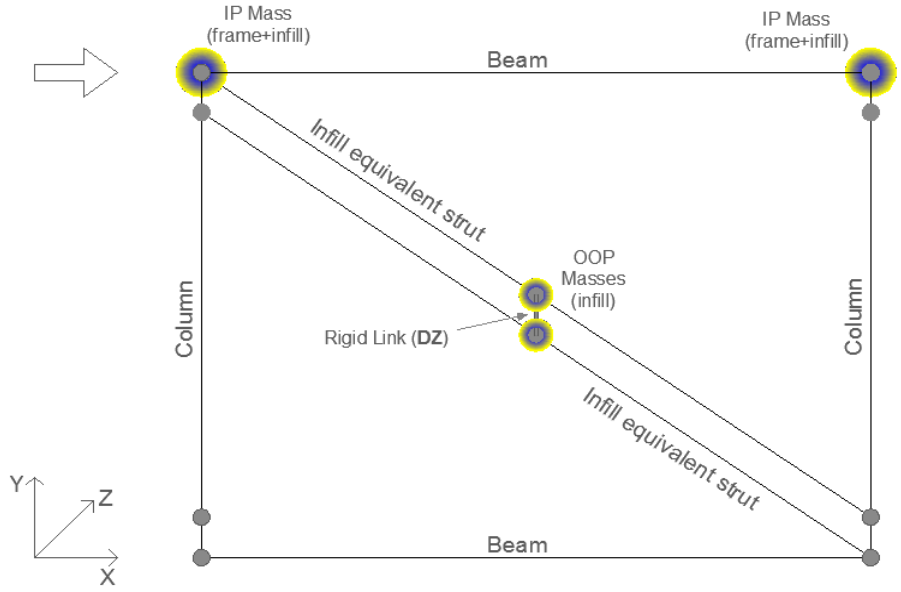


Figure 5. Model proposed by the authors, or modified Mosalam-Günay (mMG) model.

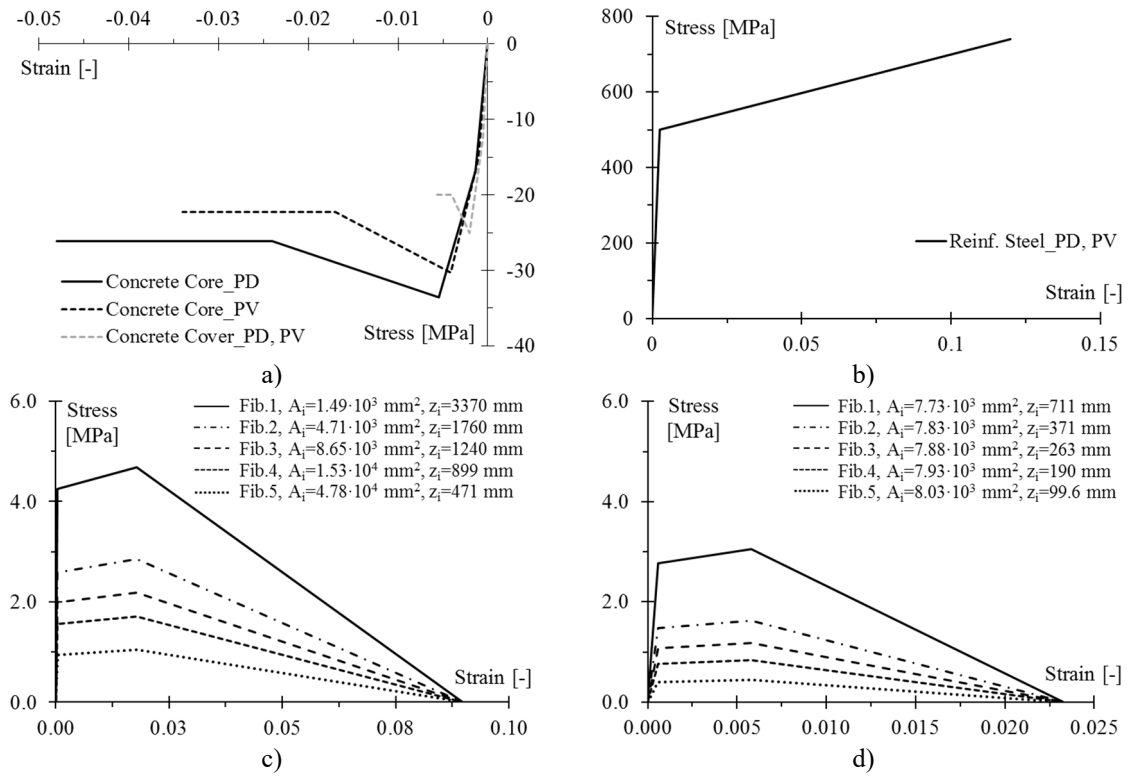


Figure 6. Constitutive laws, associated to the fibers, of the materials implemented in the F.E. analysis: a) concrete; b) reinforcing steel; c) infill type Padova; d) infill type Pavia.

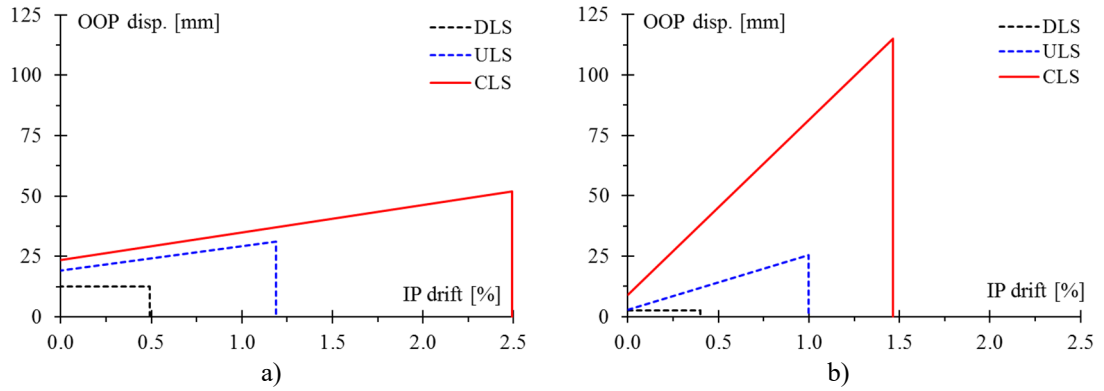


Figure 7. IP-drift/OOP-displacement domains for the principal limit states: a) thick panel; b) thin panel.

| *Differences* | *Mosalam-Günay model (MG)* | *Proposed model (mMG)* |
|---|---|---|
| *1* | One diagonal strut | *Two diagonal struts*, to improve the evaluation of the infill effects on the frame, according to Crisafulli [5] |
| *2* | Elasto-plastic behaviour | *Hysteretic behaviour* with softening |
| *3* | IP-Force/OOP-Moment domain for the yielding criterion plus IP/OOP displacement domain for the infill removal according to a 3/2 power law | *OOP (only) displacement domain* for the infill removal, *calibrated* from test results |

Table 3. Main differences between the original MG model and the modified one (mMG) proposed by authors.

Similar displacement domains, with the only purpose to assess the damage level reached by the infill panels during the IP/OOP numerical analyses, were calibrated for the Damage Limit State (DLS) and Ultimate Limit State (ULS), as shown in Figure 7. These domains, actually IP - drift/OOP - displacement domains, are obtained through a linear interpolation of

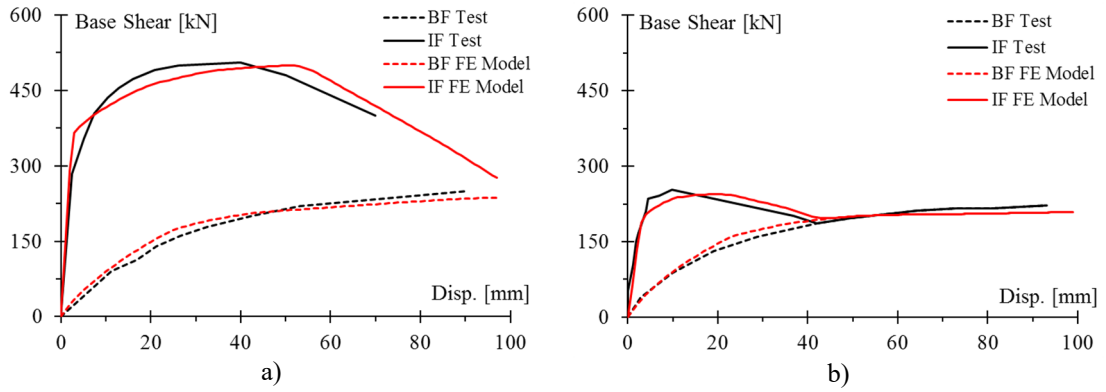


Figure 8. In-plane calibration results: a) thick panel (type Padova); b) thin panel (type Pavia).

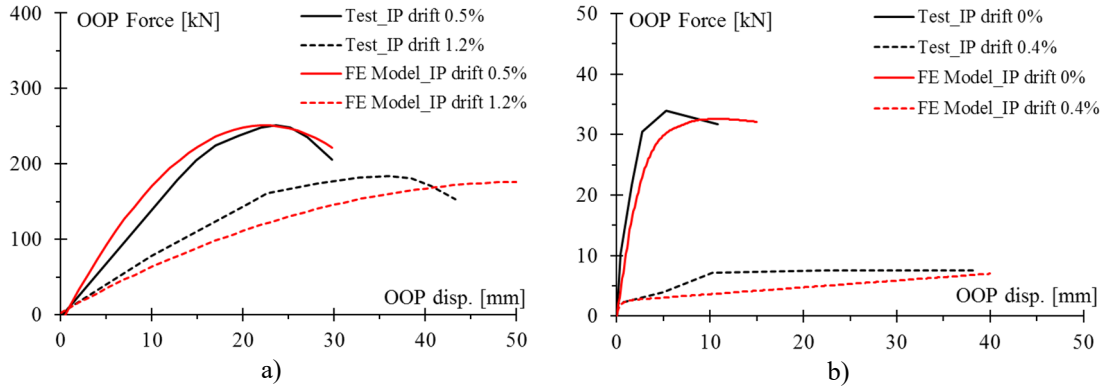


Figure 9. Out-of-plane calibration results for different levels of IP damage: a) thick panel; b) thin panel.

the OOP limit states, function of the in-plane damage, and the IP limit states presented in Figure 4 and Table 2 respectively, both deriving from experimental evidences.

The results of the model calibration, considering the tests related to both thick (Padova) and thin (Pavia) panels, are reported in Figure 8 and Figure 9, respectively for the IP behavior of the bare and infilled frames and for the OOP behavior of the infills at different IP damage.

## 3 PARAMETRIC ANALYSIS

A parametric non-linear static analysis was performed in OpenSees using the proposed model. Pushover analyses were initially carried out on the bare frame (BF) models, as reference, and then on the infilled frame (IF) models, considering both infill types previously calibrated, type Padova (PD) or thick and type Pavia (PV) or thin.

For the IP/OOP load pattern, the force distribution proportional to masses and heights was chosen, according to the Italian [16] and European codes [17], applying concentrated loads in each mass of the structural model. To consider various intensity ratios between OOP and IP forces acting on the panel, different inclination $\alpha$ of the seismic action were considered, specifically: 0°, 15°, 30°, 45°, 60°. In particular, the IP load pattern, applied to each beam-column node, is multiplied by $cos\alpha$, while the OOP load pattern, acting on the central nodes of the equivalent struts, is multiplied by $sin\alpha$.

The set of frames reported in Table 4, representing some of the most common Italian R.C. buildings, was analyzed in the parametric study, considering for each frame two different types of design: only for gravity loads, or traditional design (TD), and for both gravity and seismic forces, or seismic design (SD). The material characteristics and sections of these frames, with the longitudinal and transverse reinforcement, are reported in Table 5.

In particular, for SD frames a steel B450C and a concrete C30/35 were used according to

| Squat | Regular | Slender |
|---|---|---|
| 3x2 | 2x3 | 1x3 |
| 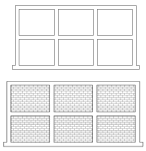 | 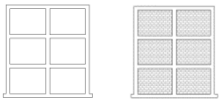 | 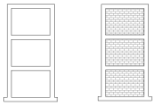 |
| 5x2 | 3x3 | 2x5 |
| 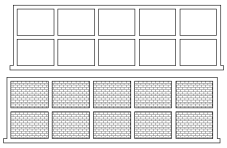 | 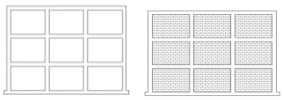 | 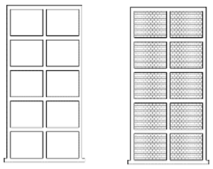 |
| *Frame for PD infill*: bay length 4.55 m; storey height 2.85 m | | |
| *Frame for PV infill*: bay length 4.60 m; storey height 2.95 m | | |

Table 4. Sample set considered in the parametric study, representative of the Italian R.C. frames.

| | Seismic Design (SD) | Traditional Design (TD) |
|---|---|---|
| *Concrete* | C30/35<br>$f_{ck} = -30\ MPa$<br>$E_c = 27386\ MPa$<br>$f_{ct} = 2.9\ MPa$<br>$E_{ct} = 1450\ MPa$ | C20/25<br>$f_{ck} = -20\ MPa$<br>$E_c = 22361\ MPa$<br>$f_{ct} = 2.2\ MPa$<br>$E_{ct} = 1100\ MPa$ |
| *Steel* | B450C<br>$f_{yk} = 450\ MPa$<br>$f_{ym} = 500\ MPa$<br>$f_u = 620\ MPa$<br>$E_s = 205000\ MPa$ | AQ50<br>$f_{yk} = 370\ MPa$<br>$f_{ym} = 410\ MPa$<br>$f_u = 550\ MPa$<br>$E_s = 195000\ MPa$ |
| *Column* | 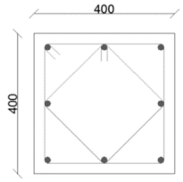<br>Long. reinforcement: 8 Φ18 | 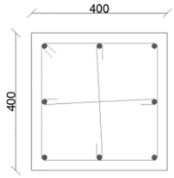<br>Long. reinforcement: 8 Φ16 |
| *Beam* | 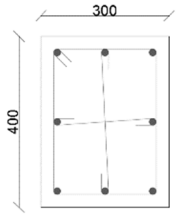<br>Long. reinforcement: 8 Φ16 | 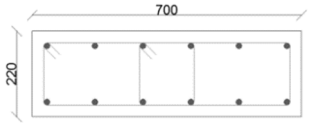<br>Long. reinforcement: 12 Φ16 |

Table 5. Materials, sections and reinforcement details of the R.C. elements of the frames analyzed.

NTC08 [16], while for TD frames a steel AQ50-60 and a concrete C20/25 were chosen following some common Italian design criteria of the 50-80s (Cristofaro *et al.* [18]).

For the evaluation of the structural damage level during the analysis, some Performance Levels (PLs) and Limit States were defined also for the R.C. frame. In particular, the PLs considered, which were verified step-by-step of the analysis, are:

- *colYM* (*column Yield bending Moment*), calculated from a paramtric moment-curvature analysis where the parameter is the vertical axial load N on the section; a function of the nominal yield curvature $\chi_y$ depending on *N* was derived and is reported in Figure 10;

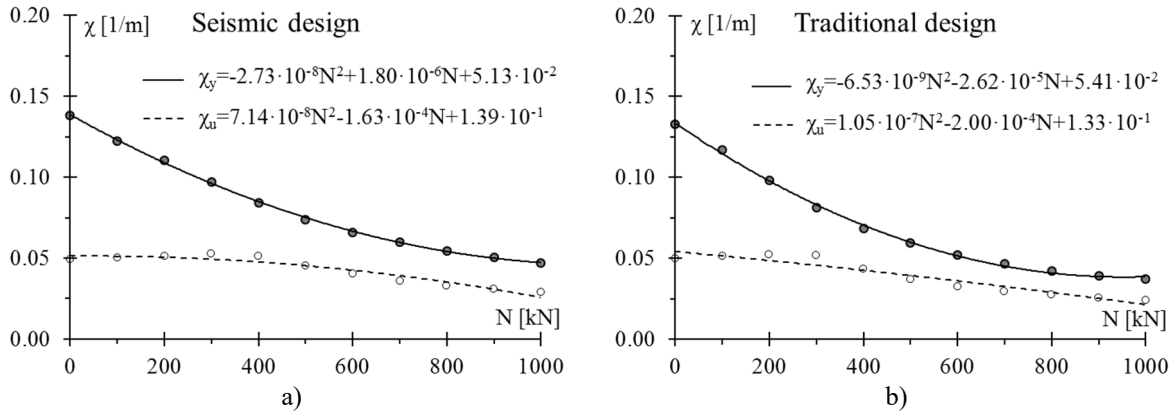


Figure 10. Nominal $\chi_y$ and ultimate $\chi_u$ curvature as function of axial load $N$, for both column sections of Table 5.

- *colUM* (*column Ultimate bending Moment*), calculated as *colYM;* a function of the ultimate curvature $\chi_u$ depending on $N$ was derived and is shown in Figure 10;
- *colSF* (*column Shear Failure*), calculated according to the R.C. shear strength formulation of Sezen [19], which takes into account the section ductility;
- *colNF (column Nodal Failure*), obtained by the node rotation capacity defined in NTC08.

The Limit States (LS) of the frame (*fr*), yielding and ultimate LS, are therefore defined as:

$$\begin{aligned} frYield &= colYM \\ frULS &= \min\left\{colUM;\ colSF;\ colNF\right\} \end{aligned} \tag{2}$$

## 4 RESULTS

### 4.1 Pushover Curves

The pushover curves from Figure 11 to Figure 13 report the total in-plane shear force at the base versus the maximum displacement at the top of some frame configurations analysed. Each graph compares the pushover curves obtained for the bare frame (BF) and infilled frame in-plane (IP) to the ones obtained considering different directions of the load pattern, OOP15, OOP30, OOP45, OOP60 where the number is the inclination $\alpha$ of the seismic force. Furthermore, each curve reports the Performance Levels and Limit States reached by both frame and panel.

The principal outcomes from the pushover curves are briefly summarized below.

- The resistance of the bare frame (BF) is clearly different for the two designs, seismic (SD) or traditional (TD), resulting higher in the case of SD of about 1.2 to 1.4 times, depending on the frame type.
- For the infill type Padova, the maximum strength contribution of the panel to the infilled frame system in-plane (IP) (i.e. the maximum distance between the IP curve and the BF one) is between 1.5 and 2 times that provided by the infill type Pavia, depending on the frame type (for frame with the same number of floors, it increases with increasing number of bays).
- The infilled frames present a maximum strength much greater than that of the bare frames and, in the case of thick panel, this is about 1.8 times that of the related infilled frame with thin panel; this result is not inconsistent with the previous note, because the maximum strength of the infilled frame is reached at difference displacements for the two infill types.
- The pushover curves of the infilled frame with thick panel present a wide plastic branch, generally with strain hardening (at least for SD frames), while those relating to the thin panel present a softening branch.

- About the Performance Levels, it is possible to observe that their order of occurrence and position vary in function of infill type and design type of the frame. For example:
• in case of thick panel, its Ultimate Limit State occurs close or just after the frame yielding while, for the thin panel, all its limit states (also the collapse) anticipate the frame yielding;

**Slender building (2x5)**

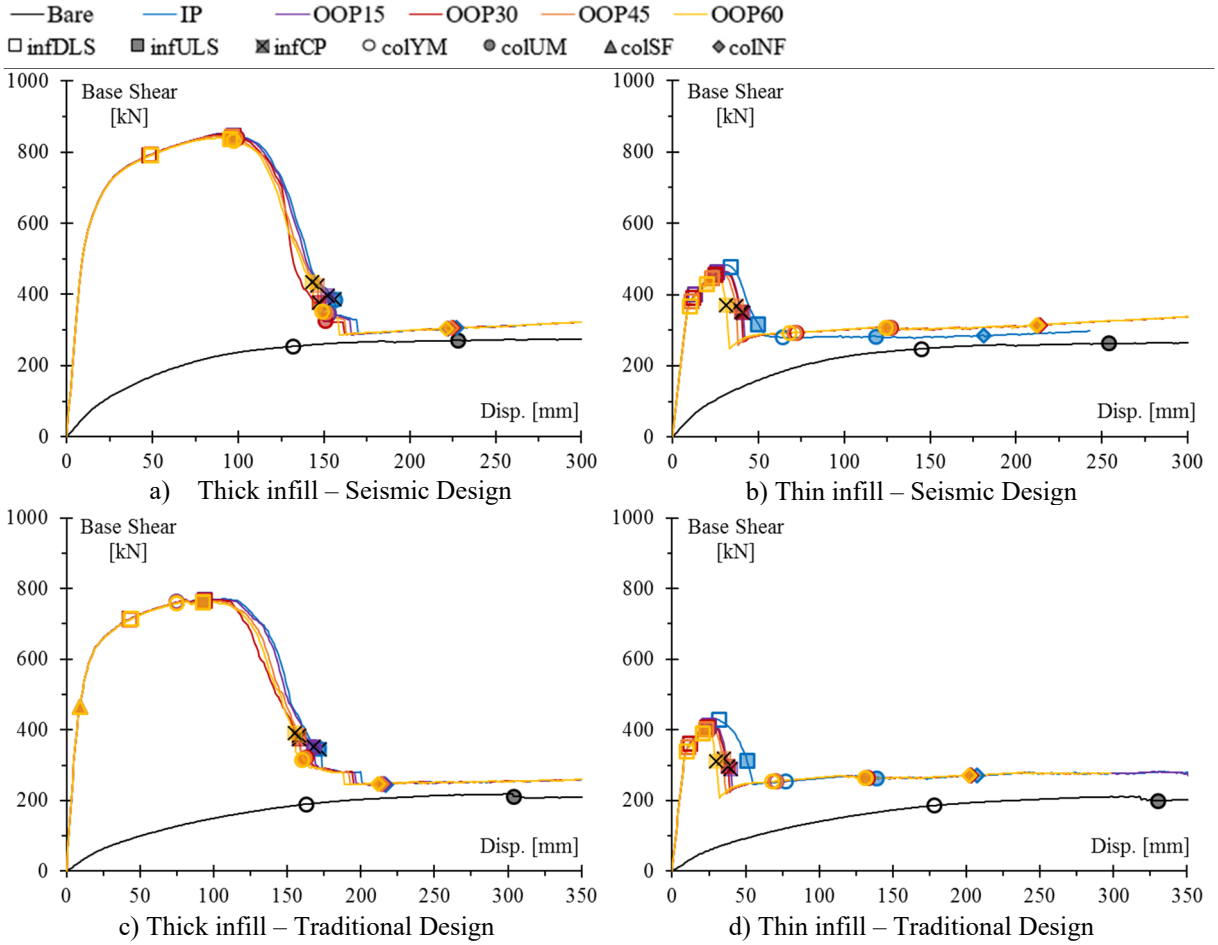


a) Thick infill – Seismic Design
b) Thin infill – Seismic Design
c) Thick infill – Traditional Design
d) Thin infill – Traditional Design

Figure 11. Pushover curves of bare (BF) and infilled frame (IP, OOP at 15°, 30°, 45°, 60°): slender frame (2x5).

**Regular building (2x3)**

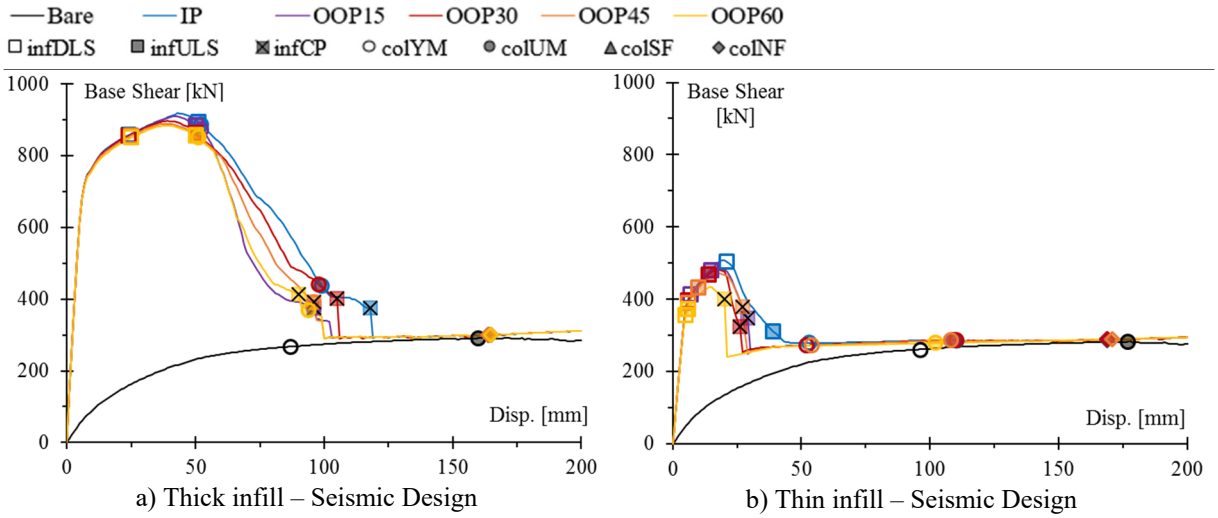


a) Thick infill – Seismic Design
b) Thin infill – Seismic Design

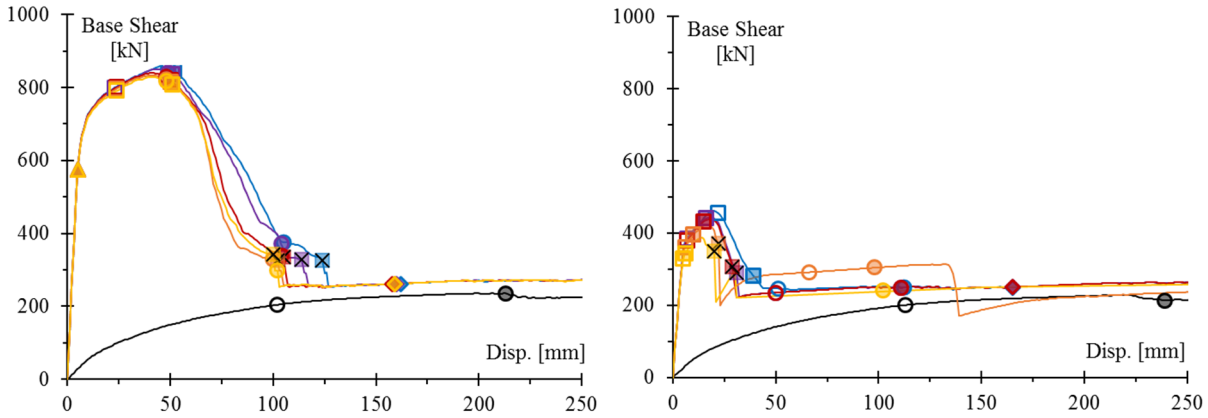


c) Thick infill – Traditional Design d) Thin infill – Traditional Design

Figure 12. Pushover curves of bare (BF) and infilled frame (IP, OOP at 15°, 30°, 45°, 60°): regular frame (2x3).

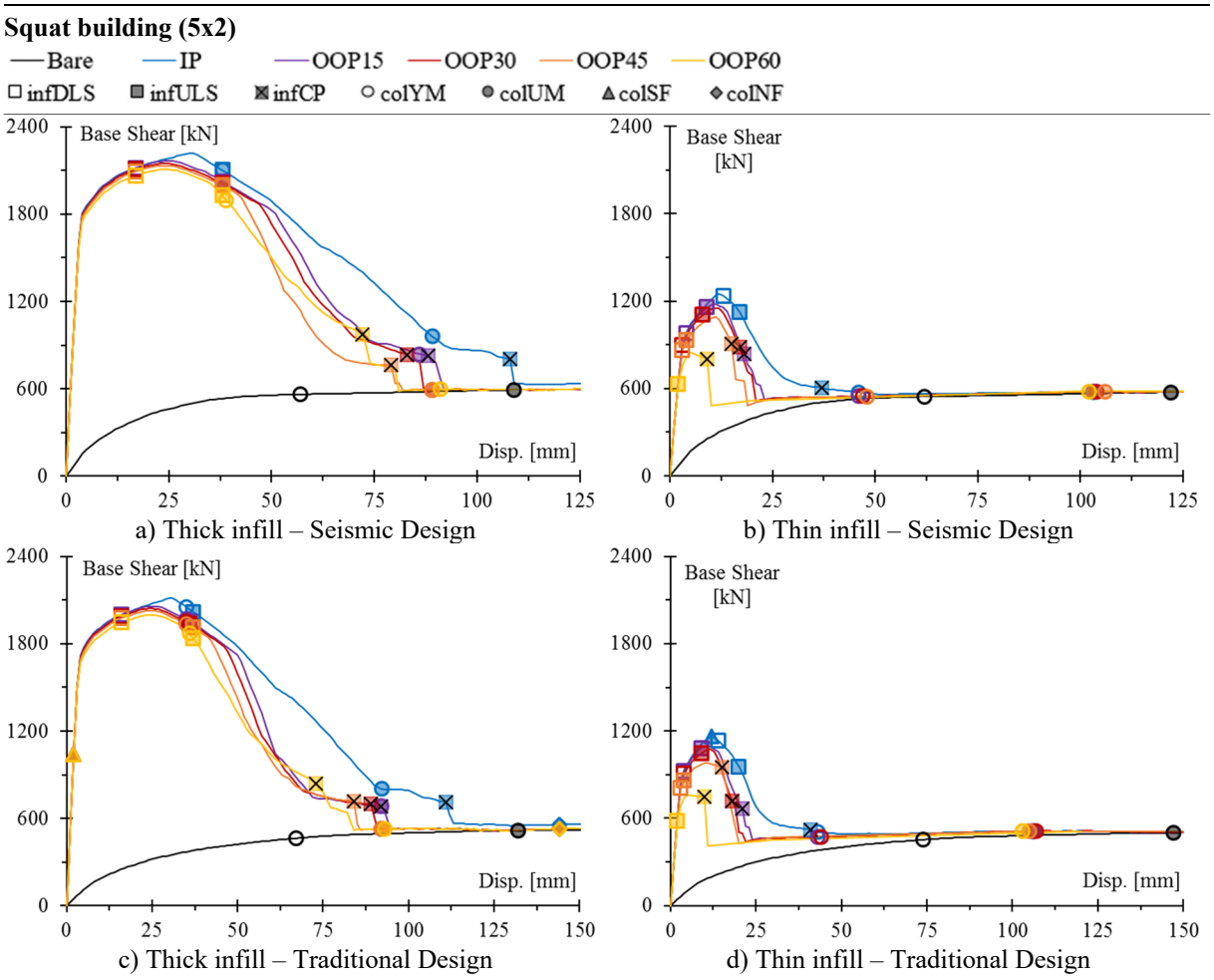


a) Thick infill – Seismic Design b) Thin infill – Seismic Design

c) Thick infill – Traditional Design d) Thin infill – Traditional Design

Figure 13. Pushover curves of bare (BF) and infilled frame (IP, OOP at 15°, 30°, 45°, 60°): squat frame (5x2).

- the performance levels of the frame are generally anticipated in case of traditional design and thick panel, in fact, a thicker panel increases the bracing effect leading to smaller displacements but higher stresses on the frame; in these cases, furthermore, columns experience the shear failure and thus the ULS is suddenly reached in the elastic branch of the pushover curve.

- Increasing the ratio OOP/IP of the load pattern, through an increment of the inclination $\alpha$ of the seismic action, the collapse of the panels is generally anticipated, with a consequent reduction of the overall in-plane resistance (capacity curve) of the infilled frame. But while for the case of thick panel the OOP effects only slightly affect the width of the plastic branch of the pushover curve and the softening phase, negligibly influencing the limit states, for the case of thin panel it can be observed, increasing the OOP action, a significant reduction of the maximum resistance as well as an anticipation of the infill limit states.

## 4.2 Energy indexes

The graphs reported in Figure 14 show the values of the energy index $E$ (or area under the pushover curve) for the in-plane deflection of the infilled frame, up to reach the ULS of both

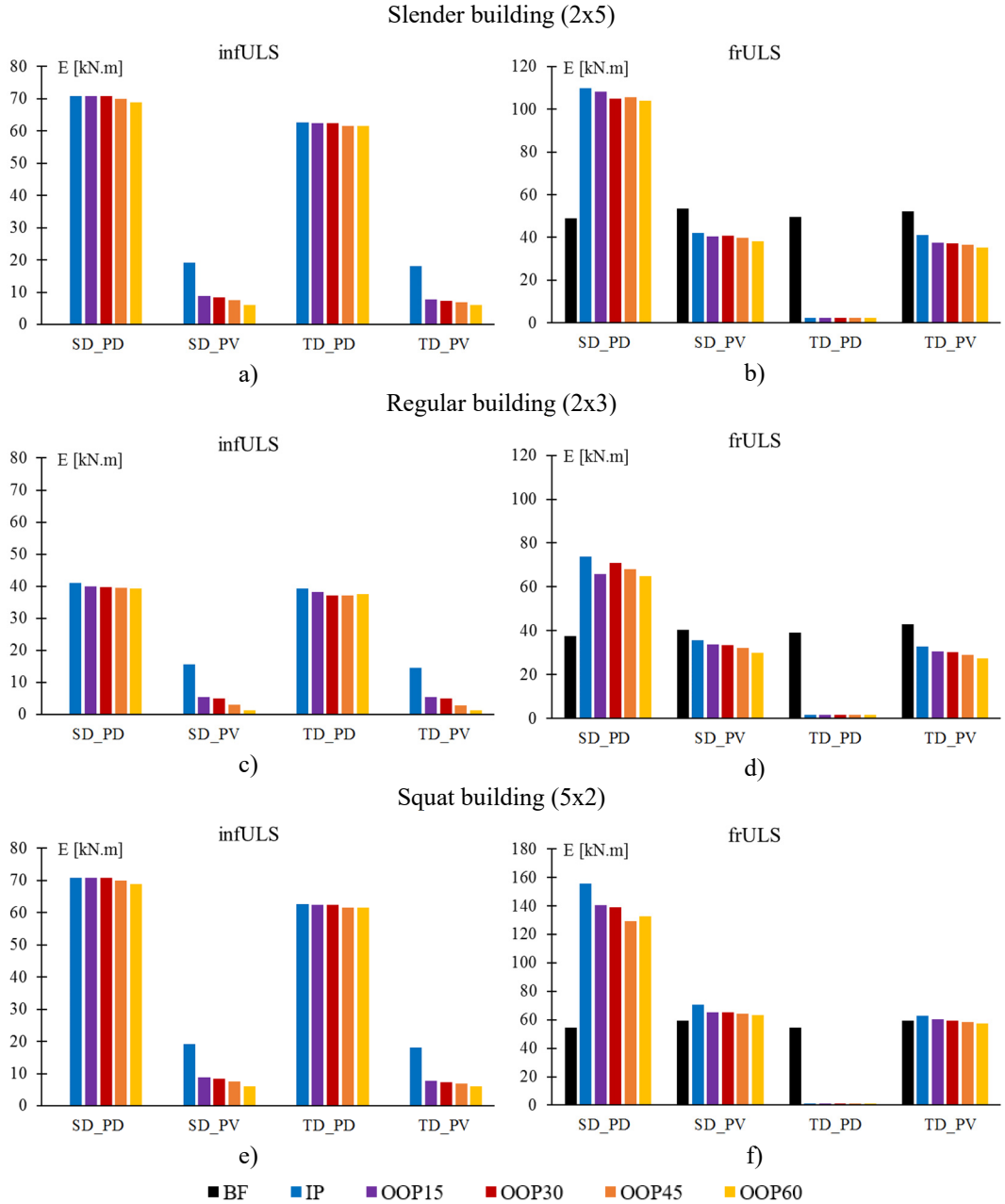


Figure 14. Energy index or area under the pushover curve, related to the ULS of the infill (a, c, e) and frame (b, d, f), for different inclinations (OOP) of the seismic action.

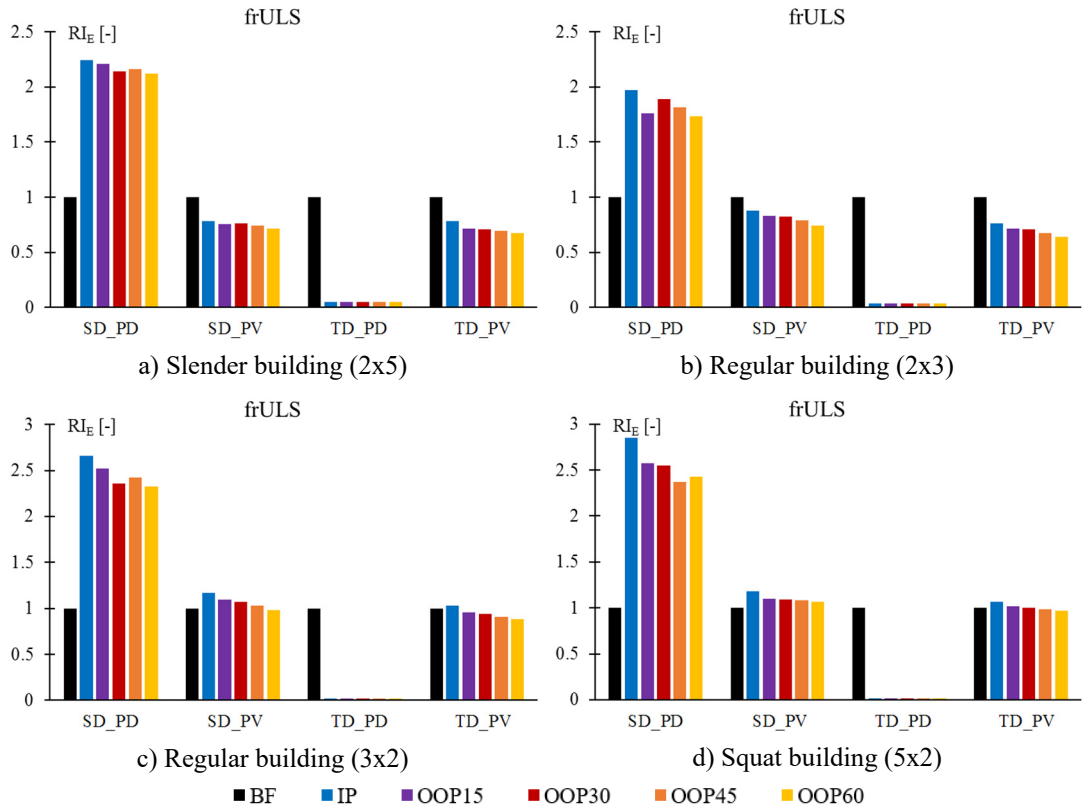


Figure 15. Energy robustness index related to the frame ULS, for different inclinations of the seismic action.

infill and frame. Figure 15, instead, shows the energy robustness index $RI_E$, calculated as the ratio between the energy dissipated by the infilled frame and that dissipated by the associated bare frame (BF): from this definition, it is clear that $RI_E$, which do not exist for the infill ULS but only for that of the frame, quantifies in terms of energy the beneficial contribution of the infill relatively to the BF.

The principal results from Figure 14 and Figure 15 are summarized hereinafter.

- The values of the energy index ($E$) associated to the infill ULS are strongly affected by the OOP actions only in the case of thin panel: in this case, respect to the thick panel, $E$ is much smaller and decreases rapidly with increasing load pattern inclination.
- About the ULS of the frame, it is possible to do the following considerations:
  - the use of a thick panel greatly increases the energy dissipated by the building in case of seismic design of the frame while, in case of traditional design, because of the possibility of a brittle collapse, this index shows minimum values;
  - using a thin panel, instead, the infill effects on the energy dissipation of the building are slightly advantageous only in the case of squat frames, since in the other cases (slender and regular) the small energy contribution of this type of infill is not able to compensate the reduction of energy due to the anticipation of the ULS respect to the bare frame.
- Finally, using thin panel, the energy dissipated at the ULS by the seismically designed frame is slightly higher than that dissipated by the traditional frame.
- The energy robustness index ($RI_E$), which is 1 (by definition) for the bare frame, explicitly shows the beneficial or not effects of the infills in increasing the energy dissipated by the infilled frame to reach the ULS of the frame. The previous remarks about the energy index are still valid for the energy robustness index.

### 4.3 Inter-storey drift

Figure 16 to Figure 19 show the in-plane inter-storey drift profiles along the building height, for different case studies, at the following limit states: damage and ultimate limit states of the infill (infDLS and infULS respectively) and yielding and ultimate limit states of the frame (frYield and frULS respectively). The principal remarks are listed hereinafter.

- Regarding the case with thick panel, the inter-storey drift profiles at the infill limit states are not affected by the OOP actions, as well as the ones at the frame yielding, which generally occurs very close to the infill ULS. The profiles at the frame ULS, also, are only slightly influenced by the OOP actions, in particular at the first floor. The presence of a thick panel, regarding the frame limit states and with respect to the bare frame, tends to reduce drift values of the upper floor and to concentrate the deformation at the first level where, for the slendernest buildings, the drift value becomes higher than that of the bare frame.
- In case of thin panel, instead, the drift profiles at the infill DLS and ULS greatly depend on the inclination of the load pattern and the drift values from the IP-OOP analyses are very smaller than those obtained by the IP only analysis. At the frame limit states, instead, similar conclusions to those for the thick panel can be done for squat configuration while, for regular (2x3 TD) and slender (2x5) frame configurations it is possible to observe an interesting phenomeno: starting from a drift profile due to IP actions that concentrates the deformation at the first level, increasing the OOP effects on the infills, the soft storey moves from the first to the second floor.

Finally, for the various configuration analysed, Figure 20 reports the IP inter-storey drifts, related to the achievement of the infill limit states, versus the inclination of the seismic action. This figure clearly shows what already seen previously, namely that the OOP actions, in the

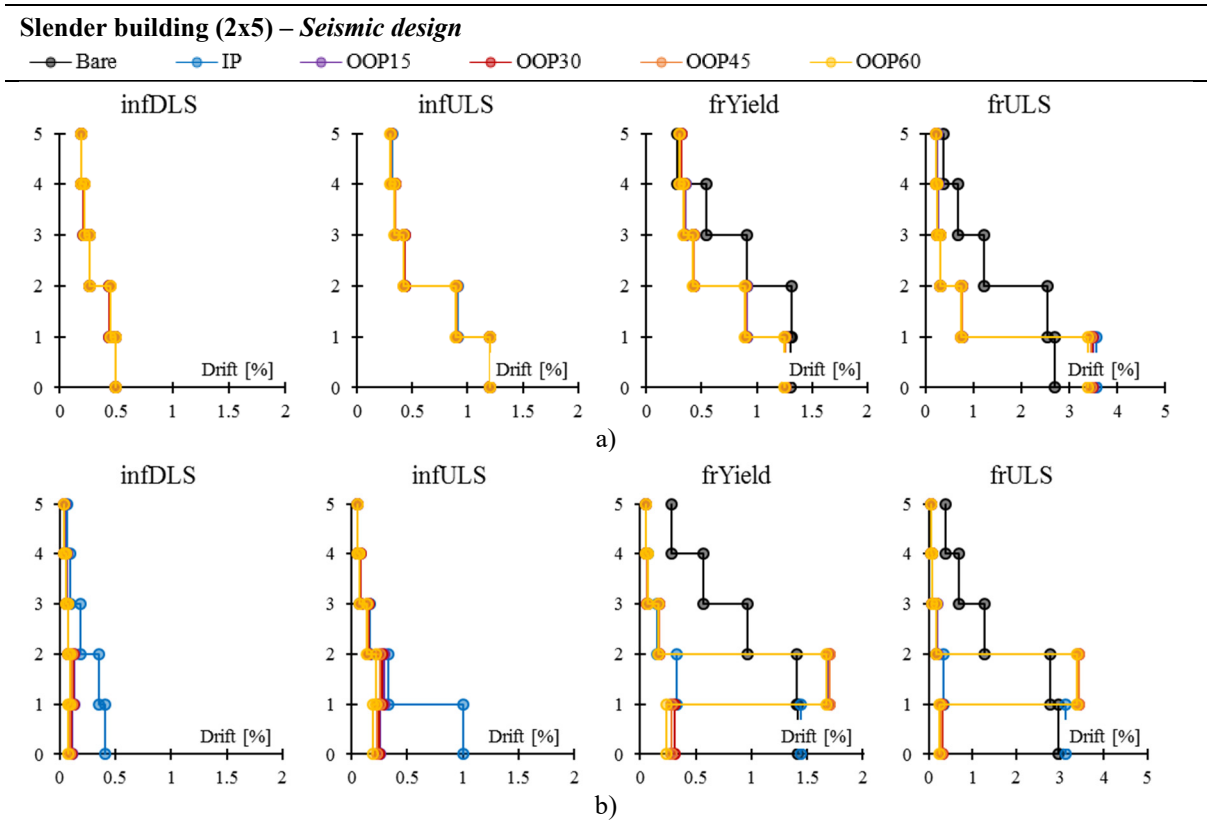


Figure 16. Inter-storey drift profiles for the SD frame (2x5), for different inclinations of the seismic action and at the various limit states of infill and frame: a) thick panel (type Padova); b) thin panel (type Pavia).

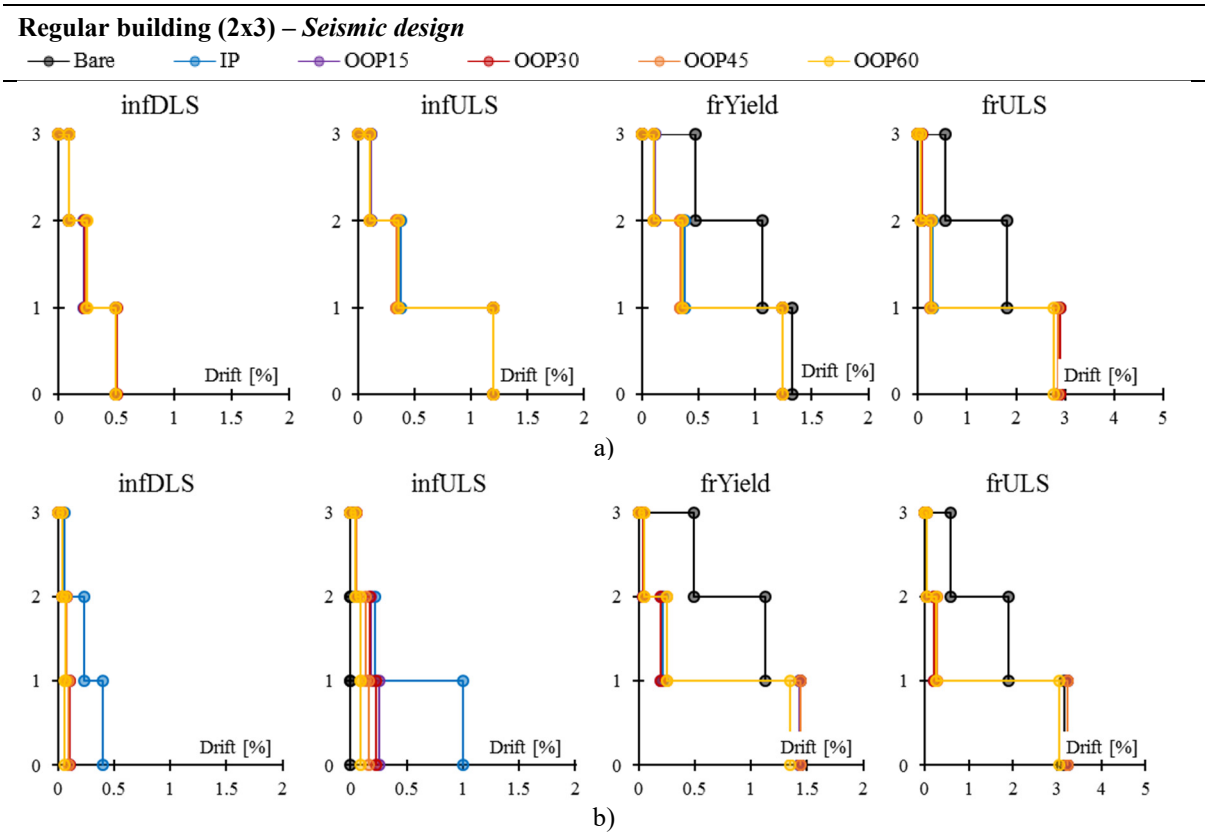


Figure 17. Inter-storey drift profiles for the SD frame (2x3), for different inclinations of the seismic action and at the various limit states of infill and frame: a) thick panel (type Padova); b) thin panel (type Pavia).

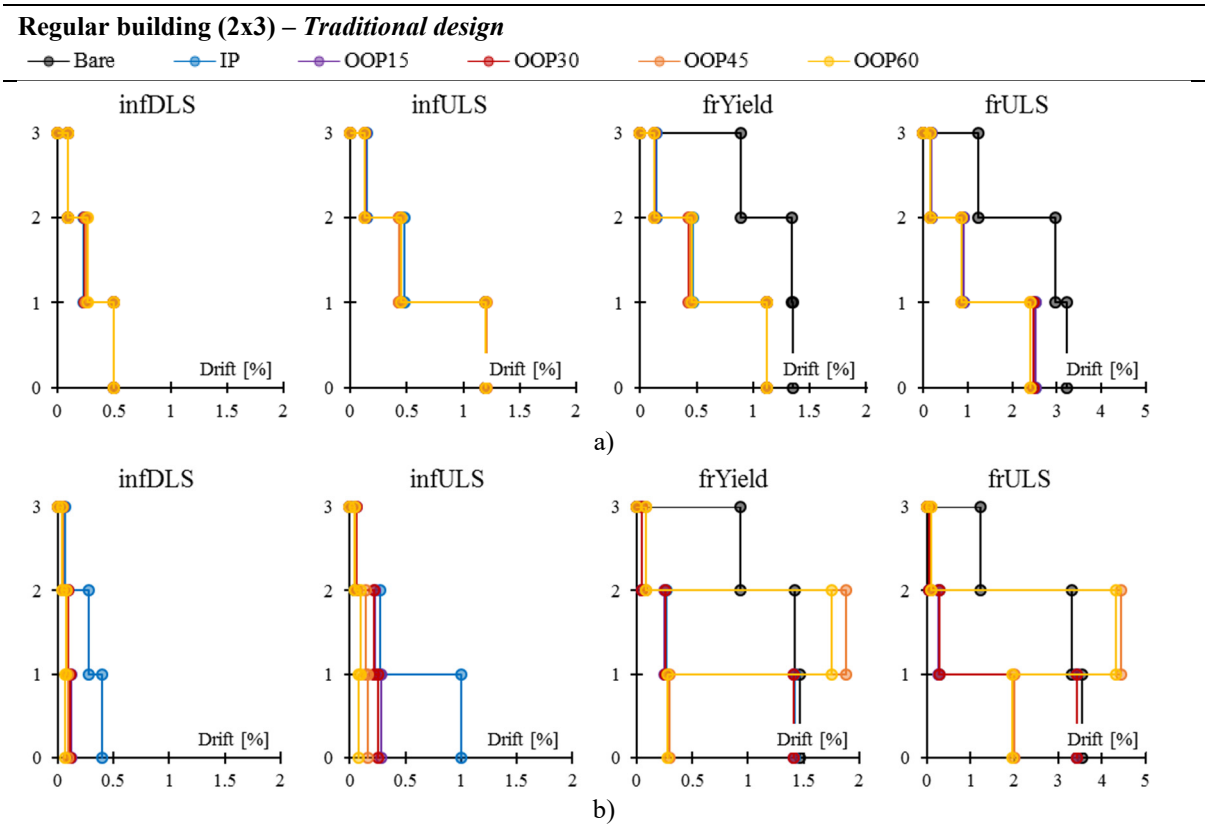


Figure 18. Inter-storey drift profiles for the TD frame (2x3), for different inclinations of the seismic action and at the various limit states of infill and frame: a) thick panel (type Padova); b) thin panel (type Pavia).

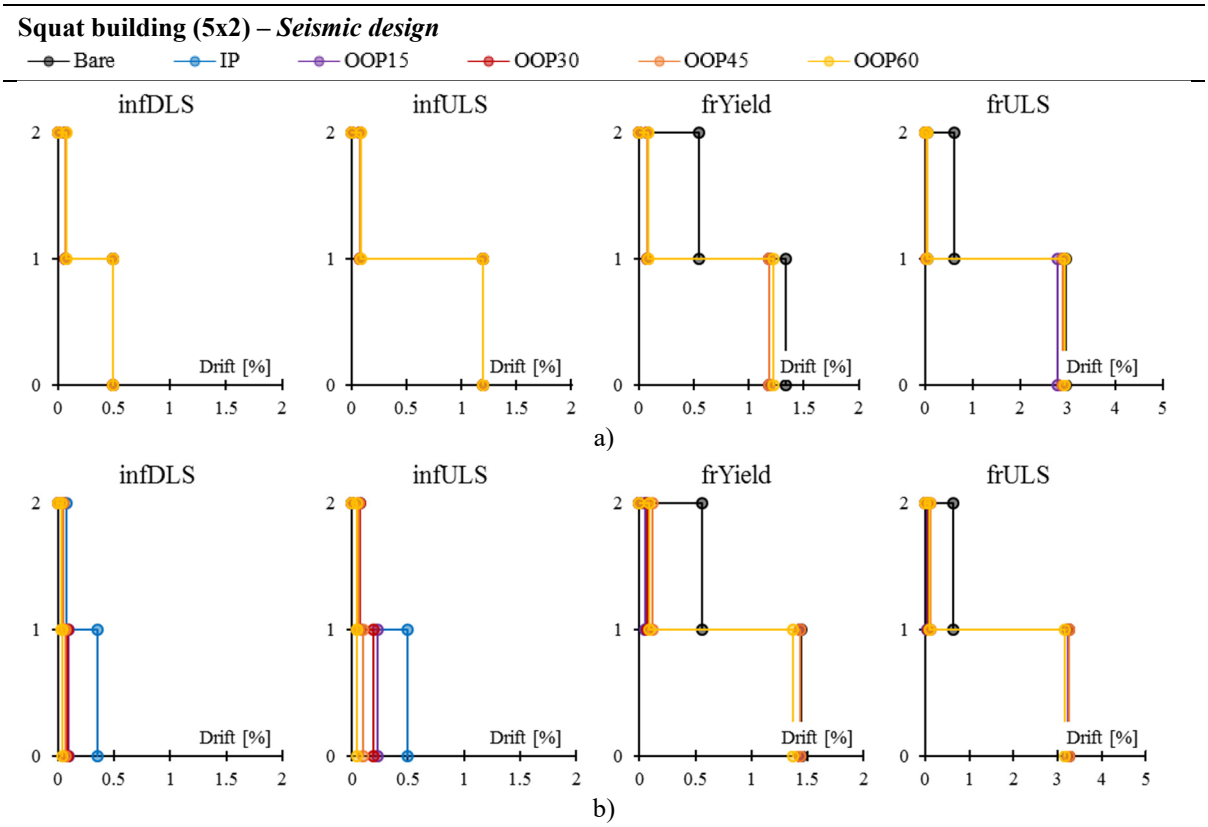


Figure 19. Inter-storey drift profiles for the SD frame (5x2), for different inclinations of the seismic action and at the various limit states of infill and frame: a) thick panel (type Padova); b) thin panel (type Pavia).

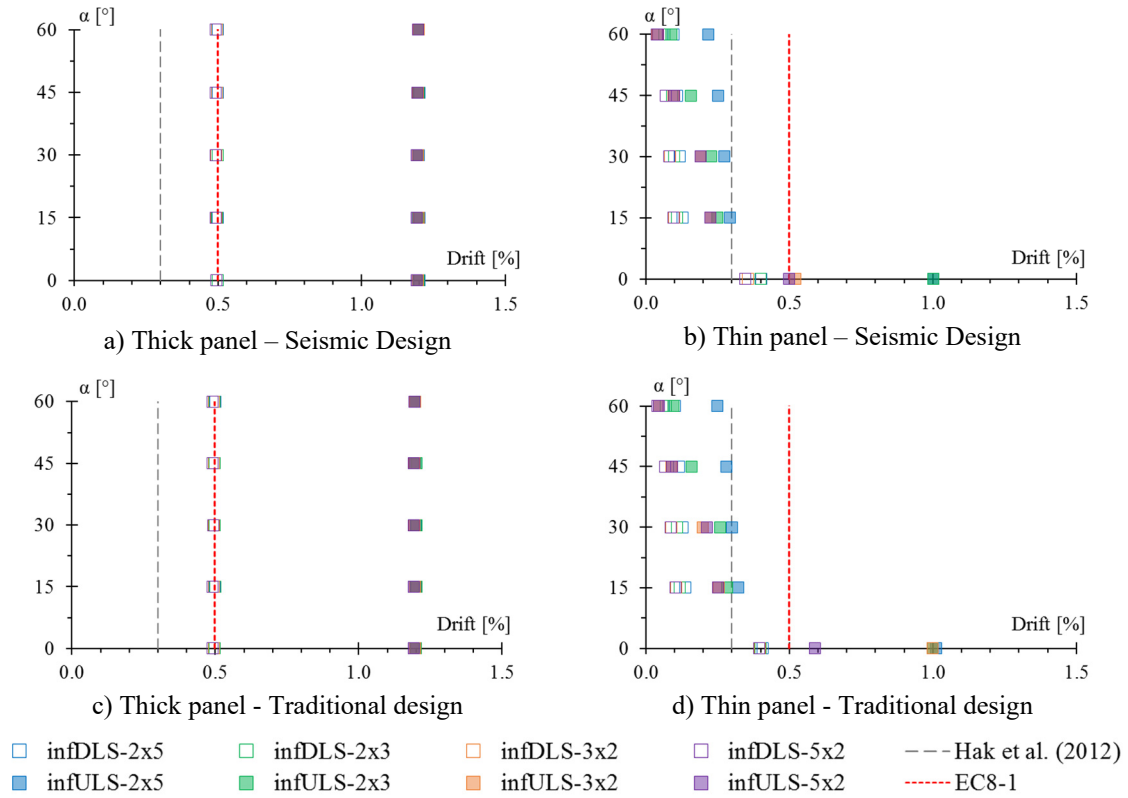


Figure 20. IP inter-storey drift values, at the infill DLS and ULS, versus the seismic action inclination (α), for the different case studies analysed; indication of the EC8 drift limit and of a suggested value by Hak et al.[20].

case of thin panel, strongly affect the value of the IP inter-story drift at which the DLS or ULS of the panel is reached, while are unimportant for the case of thick panel. For this reason, the EC8 [17] drift limit of 0.5% (in case of non-structural components not specifically designed to withstand seismic forces) can be considered appropriate only if a thick panel (type Padova) is used; the same limit was already shown to be not conservative in case of thin masonry panel, type Pavia, by Hak et al.[20], who suggested a more conservative limit of 0.3%. However, considering the IP/OOP interaction effects, also this drift value becomes not appropriate at all for the thin panels, which can reach the DLS at drift values (measured in plane) also much smaller. Finally, a similar dependence of the trend of the drift values on the inclination of the seismic force can be observed for both DLS and ULS of the same infill type.

## 5 CONCLUSIONS

- The paper presented a new FE macromodel to simulate the interaction between the in-plane (IP) and out-of-plane (OOP) behaviour of masonry infills in R.C. frames. The model was calibrated for two different types of masonry infill, thick and thin, through test results obtained from previous experimental campaigns on real scale infilled frame.
- The model was implemented in a parametric pushover analysis in OpenSees, with the aim to assess the influence of the directionality of the seismic action on the lateral response of different R.C. infilled frames. In particular, six frame configurations (squat, regular and slender) and, for each of these, two types of design (for gravitational loads only and for seismic actions) were considered in the analysis, studing the cases of bare frame, infilled frame with thick panel and infilled frame with thin panel.
- The main influences of the OOP forces on the infilled frame seismic behaviour are presented through pushover curves (with the indication of the principal performance levels and limit states) and energy indexes, drift profiles and drift values related to the achivement of the various limit states (for both infill and frame).
- Some of the principal conclusions from this numerical study are:
  - IP/OOP interaction of the infill considerably affects the structural response of the infilled frame in case of thin panel (type Pavia), reducing the global resistance and anticipating the infill limit states;
  - the peak resistance, higher in case of thick panel and seismic design of the frame, reduces increasing the inclination of the seismic action;
  - infilled frames with thick panels present pushover curves with a wide plastic branch, generally with strain hardening, while those related to infilled frames with thin infills show a softening branch (so the firsts present a more ductile behaviour);
  - the infill ULS is achieved close to the frame yielding in case of thick panel; for the thin panel, instead, all the limit states (including the collapse) are reached before;
  - considering the regular frame configurations analysed in this study, if the in-plane seismic action generally leads the soft storey to be localized at the first level of the infilled frame, for both infill panels, the out-of-plane effects, in case of thin panel, move this soft storey to the second floor;
  - thin panels are greatly influenced by the OOP forces: the inter-storey drifts of the infilled frame, registered in-plane, required to reach the infill limit states, strongly decrease with increasing inclination of the seismic action; for this reason, the current drift limit proposed by EC8, i.e. 0.5% (in case of non-structural components not specifically designed to withstand seismic forces), can be considered appropriate only if the panel is thick (type Padova), which is negligibly influenced by the IP/OOP interaction effects.

## REFERENCES

[1] El-Dakhakhni, Wael W., Mohamed Elgaaly, and Ahmad A. Hamid. "Three-strut model for concrete masonry-infilled steel frames." Journal of Structural Engineering 129.2 (2003): 177-185.

[2] Asteris, P. G., et al. "Mathematical macromodeling of infilled frames: state of the art." Journal of Structural Engineering 137.12 (2011): 1508-1517.

[3] Jeselia Catherin M., Jayalekshmi B. R., and Katta Venkataramana, "Modeling of Masonry infills - A review," American Journal of Engineering Research (AJER) 2, 59-63, 2013.

[4] Tarque Nicola, Candido Leandro, Camata Guido, and Spacone Enrico, "Masonry infilled frame structures: state-of-the-art review of numerical modelling," Earthq. Struct., vol. 8, no. 3, pp. 733–759, 2015.

[5] Crisafulli, Francisco Javier. "Seismic behaviour of reinforced concrete structures with masonry infills." (1997).

[6] Calvi, G. Michele, Davide Bolognini, and Andrea Penna. "Seismic performance of masonry-infilled RC frames: benefits of slight reinforcements." Invited lecture to "Sísmica 6 (2004): 14-16.

[7] Flanagan, Roger D., and Richard M. Bennett. "Bidirectional behavior of structural clay tile infilled frames." Journal of structural engineering 125.3 (1999): 236-244.

[8] Angel, Richard et al. Behavior of reinforced concrete frames with masonry infills. University of Illinois Engineering Experiment Station. College of Engineering. University of Illinois at Urbana-Champaign., 1994.

[9] Furtado, André, et al. "Simplified macro-model for infill masonry walls considering the out-of-plane behaviour." Earthquake Engineering & Structural Dynamics 45.4 (2016): 507-524.

[10] Najafgholipour, M. A., Mahmoud R. Maheri, and Paulo B. Lourenço. "Capacity interaction in brick masonry under simultaneous in-plane and out-of-plane loads." Construction and building materials 38 (2013): 619-626.

[11] Da Porto, Francesca, et al. "Combined in-plane/out-of-plane experimental behaviour of reinforced and strengthened infill masonry walls." 12th Canadian Masonry Symposium, Vancouver, British Columbia. 2013.

[12] Mosalam, Khalid M., and Selim Günay. "Progressive collapse analysis of reinforced concrete frames with unreinforced masonry infill walls considering in-plane/out-of-plane interaction." Earthquake Spectra 31.2 (2015): 921-943.

[13] Kent, Dudley Charles, and Robert Park. "Flexural members with confined concrete."*Journal of the Structural Division* (1971).

[14] Menegotto, M. and Pinto P. "Method of Anaysis for Cyclically Loaded Reinforced Concrete Plane Frames Including Changes in Geometry and Non-Elastic Behavior of Elements under Combined Normal Force and Bending. IABSE Symp. of Resistance and Ultimate Deformability of Structures Acted on by Well Defined Repeated Loads." (1973).

[15] Smith, Bryan Stafford. "Behavior of square infilled frames." *Journal of the Structural Division* 92.1 (1966): 381-404.

[16] Decreto Ministeriale del 14/01/2008 (DM 14/01/2008), 2008. Approvazione delle nuove norme tecniche per le costruzioni, G.U. n. 29 del 4/2/2008 (in Italian)

[17] CEN. "Eurocode 8–Design of Structures for earthquake resistance–Part 1: General rules, seismic actions and rules for buildings." *European Standard NF EN* 1 (1998): 2005.

[18] Cristofaro, M.T., D'Ambrisi, A., De Stefano, M., Pucinotti, R., Tanganelli, M. Caratterizzazione Meccanica Di Calcestruzzi Estratti Da Edifici Esistenti Con Il Metodo Sonreb. Presented at the Conferenza Nazionale sulle prove non Distruttive Monitoraggio Diagnostica, Associazione Italiana Prove non Distruttive Monitoraggio Diagnostica; Firenze (2011).

[19] Sezen, Halil. *Seismic Behavior and Modeling of Reinforced Concrete Building Columns*. Diss. Civil and Environmental Engineering)--University of California, Berkeley, 2002.

[20] Hak, Sanja, et al. "Damage control for clay masonry infills in the design of RC frame structures." *Journal of Earthquake Engineering* 16.sup1 (2012): 1-35.

COMPDYN 2017
6th ECCOMAS Thematic Conference on
Computational Methods in Structural Dynamics and Earthquake Engineering
M. Papadrakakis, M. Fragiadakis (eds.)
Rhodes Island, Greece, 15–17 June 2017

# DEVELOPMENT OF A THREE-DIMENSIONAL COMPUTATIONAL MODEL FOR THE IN-PLANE AND OUT-OF-PLANE ANALYSIS OF MASONRY-INFILLED REINFORCED CONCRETE FRAMES

**F. Anić[1], D. Penava[1], and V. Sarhosis[2]**

[1] Josip Juraj Strossmayer University of Osijek
Faculty of Civil Engineering Osijek
3 Vladimir Prelog Street, HR - 31000 Osijek, Republic of Croatia
{fanic, davorin.penava}@gfos.hr

[2] Newcastle University
School of Civil Engineering and Geosciences
NE1 7RU, Newcastle upon Tyne, United Kingdom
vasilis.sarhosis@newcastle.ac.uk

**Keywords:** Computational modelling, masonry-infilled frames, structural analysis, Atena 3D.

**Abstract.** *Structural frames, constructed either by steel or reinforced concrete (RC), are often infilled with masonry panels. In design, they are usually treated as non-structural elements, and their interaction with the bounding frame is often ignored. However, recent studies have demonstrated that infilled frame can be superior to a bare frame in terms of stiffness, strength and energy dissipation, when the structure is subjected to strong lateral loads including earthquakes. Today, several models have been developed to evaluate infilled structures. Nevertheless, such models have been validated with limited experimental data, and they have demonstrated different performances when compared with test results. This paper presents the development of a three-dimensional computational model based on the finite element method (FEM) that has been used to study the in-plane and out-of-plane behaviour of masonry infilled RC frames containing openings. Masonry infill walls were modelled as an assemblage of stiff yet deformable bricks while mortar joints as zero thickness interfaces. Initially, the material and interface parameters were determined by carrying out a series of small scale tests. The computational model was then used to predict the in-plane and out-of-plane behaviour of a series of full scale infill wall panels constructed in the laboratory using a similar brick and mortar combination. From the results analysis, it was shown that the FE model was capable of capturing the mode of failure and the load carrying capacity of the masonry-infilled RC frame with sufficient accuracy.*

## 1 INTRODUCTION

Structural frames, constructed either by reinforced concrete are often infilled with masonry panels/walls. However, in design, the presence of masonry infill for the analysis of the structure is usually ignored. The complexity and interaction mechanism between the masonry infill and the RC frame leads structural engineers to completely disregard this structural component from the analysis [1]. So, it is common practice that the panel and the frame of the structure to be designed separately. However, this results a possible change of the seismic demand due to the significant reduction in the natural period of the composite structural system [2–4]. Also, by doing so, the interaction effects between the two structural components are completely ignored. Recent research [5] demonstrated that the two components complement each other and provide a more efficient structural system. Despite research dating back to the 1950s, there is still lack in the full understanding of the interaction behaviour of masonry infilled steel frames which deem further investigation. Over the last three decades, both full scale experimental testing [6] and various types of computational analyses [7] have been carried out to investigate this interaction and gain a better understanding and representation of the detailed behaviour (i.e. crack patterns) of such systems. Today, there has been a significant development in computational models which have been used for the research of such structural systems. These are becoming increasingly popular due to large costs associated with full-scale experiments and data acquisition systems required to gather all necessary information. However, the biggest hurdle is to identify the correct material parameters to be inputted into masonry constitutive models and produce accurate and reliable models which can simulate the actual behaviour of the structure subjected to various external linear and non-linear loads [8].

So far, it is well understood that an infill wall acts as a diagonal strut connecting the two loaded corners under lateral loads. However, this is a case only applicable when infill walls does not contain any openings (e.g. doors, windows, etc.) interfering the diagonal distribution of stresses. However, there is limited research on the influence of the significance of the location and the size of the opening in infilled frames [9]. Also, masonry infilled RC frames subjected to seismic excitations suffer a combined in- and out-of-plane response. Yet, most calibrated in-plane models are done using 2D methods of analysis where the out-of-plane behaviour of the frame is impossible to be captured and understood. Therefore, the development of accurate 3D micromodel able to predict the in-plane and out-of-plane behaviour of masonry infilled frames is vital.

This paper presents the development of a three-dimensional computational model based on the finite element method (FEM) that has been used to study the in-plane and out-of-plane behaviour of masonry infilled RC frames containing openings. Masonry infill walls were modelled as an assemblage of stiff yet deformable bricks while mortar joints as zero thickness interfaces. Initially, the material and interface parameters were determined by carrying out a series of small scale tests [10]. The computational model was then used to predict the in-plane and out-of-plane behaviour of a full scale infill wall panels constructed in the laboratory using a similar brick and mortar combination. From the results analysis, it was shown that the FE model was capable of capturing the load carrying capacity of the masonry-infilled RC frame as well as the different stages of behaviour from initial crack development, crack propagation at stages of in-creased loading and the mode of failure.

## 2 EXPERIMENTAL TESTING

Ten masonry infilled RC frames were tested at a scale of 1:2.5 by one of the authors [11]. Frames were designed as medium ductility frames (DCM) in compliance with EN 1992-1-1 [12] and EN 1998-1 [1]. Masonry infill walls were made by Group 2 hollow clay masonry units (Figure 1). Mortar joints were M5 designation according to EN 1996-1-1 [13] and nominal 10 mm thick. A quasi-static cyclic lateral loading applied at the beam-ends. Each infilled frame specimen was also subjected to vertical pre-compression which applied on top of the columns and was equal to 365 kN (Figure 1). According to DG 3- EMS 98, static pushover loading was applied after large cracks in the infill occurred [14, 23]. A detailed description of the test-rig, the structural material properties, as well as of the loading scheme, can be found in [15].

Six infilled frame configurations were studied in this research. These are presented in Table 1 and include: a) II/1 RC frame without infill; b) II/2 RC frame with full infill; c) I/1 RC frame with centric door opening in the infill; d) I/2 RC frame with centric window opening in the infill; e) I/3 RC frame with eccentric door opening in the infill; and f) I/4 RC frame with eccentric window opening in the infill. Also, in Table 1, $A_o$ is the area of an opening and is equal to $h_o \times l_o$, $A_i$ is the area of masonry infill wall and is equal to $h_i \times l_i$, $l_o$ is the opening length, $h_o$ is the opening height, $h_\mathrm{i}$ is 1.3 m and is the infill wall height, $l_\mathrm{i}$ is 1.8 m and is the infill wall length, $e_\mathrm{o}$ is the opening eccentricity, $t_\mathrm{i}$ is 0.12 m and is the infill wall thickness and $P$ is the parapet wall height. Experimental testing of the masonry infilled RC frames were divided into three groups. The first group consisted of four masonry infilled RC frames containing an unconfined opening (e.g. door or window) centrically or eccentrically positioned. The second group had vertical tie-column elements around the opening. The third group had two reference specimens, i.e., infilled frames without an opening and a bare reinforced-concrete frame. The opening area ($A_o$) was selected to be 2.0 m$^2$ which falls within the range (i.e., $A_o > 1.5$ m$^2$ and $A_o > 2.5$ m$^2$) defined by EN 1998-1, [16] & [17].

The experimental test results are presented by the resistance envelope curves (peaks of the second cycles), values of the secant stiffness at characteristic drifts and observed failure mechanisms. Characteristic damage grades of the infilled frame specimens were observed as being 0.1 % for Slight (DG1), 0.2 to 0.3 for Moderate (DG 2), 0.5 for Heavy (DG 3) and 1.0 % for Pre-collapse (DG 4). These damage grades are in compliance with the EMS-98 damage scale [14], and they occurred at the masonry infill. Also, the experimental tests showed that there were two notable features of the behaviour of the masonry infill walls with and without openings. First, bed-joint sliding above the opening observed. This was due to weakened horizontal planes caused by the presence of the opening. Then, diagonal tensile or bed-joint sliding failure occurred at the masonry piers.

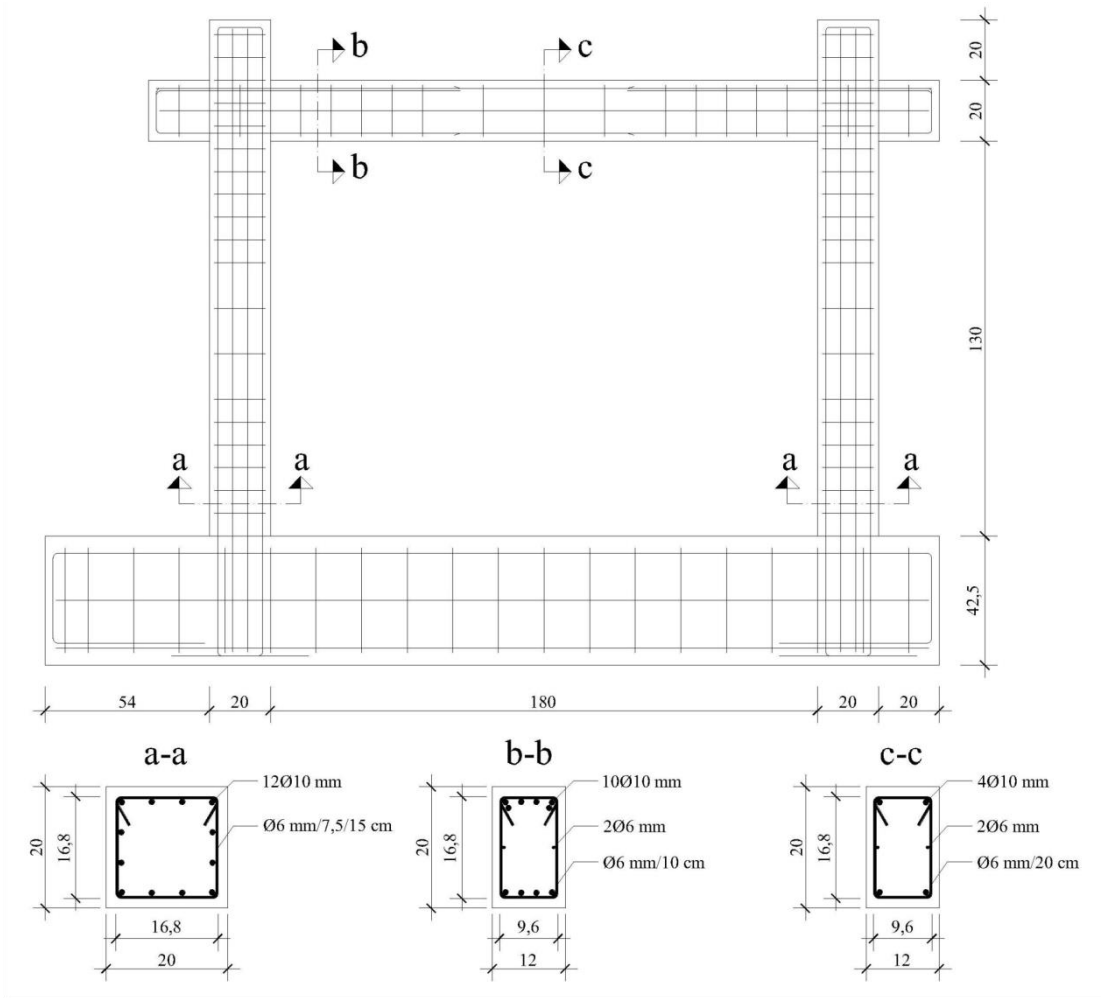




Figure 1: Tested infilled frames [11, 15]

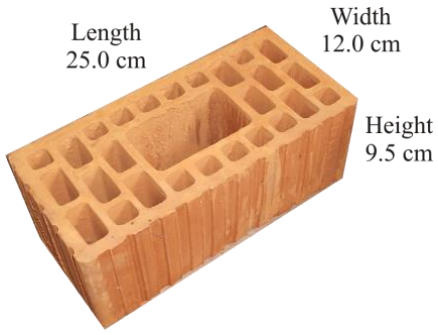


Figure 2: Hollow clay block used

By comparing the measured resistance envelope curves between the infilled frames and the bare frame, significant increases in secant stiffness and a load carrying capacity of up to three times have been observed.

| Specimen | | Appearance of the specimen | Opening | | Description |
|---|---|---|---|---|---|
| Group | Mark | | Type and area | Position | |
| I | 1 | 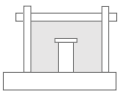 | Door<br>$l_o/h_o$=0.35/0.90 m<br>$A_o$=0.32 m$^2$<br>$A_o/A_i$=0,14 | Centric<br>$e_o$= $l_i$/2 =0.90 m | Specimens without confinement |
| | 2 | 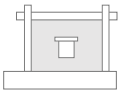 | Window<br>$l_o/h_o$=50.0/60.0 cm<br>$A_o$=0.30 m$^2$<br>$A_o/A_i$=0,13 | Centric<br>$e_o$= $l_i$/2 =0.90 m<br>$P$=0.40 m | |
| | 3 | 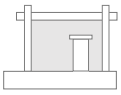 | Door<br>$l_o/h_o$=0.35/0.90 m<br>$A_o$=0.32 m$^2$<br>$A_o/A_i$=0,14 | Eccentric<br>$e_o$=$h_i$/5+$l_o$/2=0.44 m | |
| | 4 | 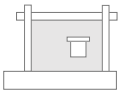 | Window<br>$l_o/h_o$=50.0/60.0 cm<br>$A_o$=0.30 m$^2$<br>$A_o/A_i$=0,13 | Eccentric<br>$e_o$=$h_i$/5+$l_o$/2=0.44 m<br>$P$=0.40 m | |
| II | 1 | 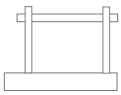 | - | - | Reference specimens |
| | 2 | 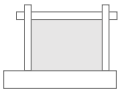 | - | - | |

Table 1: Classification and description of the specimens

## 3 COMPUTATIONAL MODELLING OF MASONRY INFILLED FRAMES

Three dimensional computational models representing bare and masonry infilled RC frames tested in the laboratory were developed using the Atena3D software [18]. Concrete frame, lintel, steel plates and masonry units were modelled using 3D solid constituents. Also, concrete rebar modelled by 1D truss elements with perfect bond assigned to the concrete. Mortar joints were modelled as a zero thickness interfaces. The modelling constituents and boundary conditions used in the analyses are shown at Figure 3. A mesh size of 4 cm was used for the analysis [10]. *CCIsoTetra* mesh elements were used for steel plates while *CCIso-Brick* was used for all the other elements of the masonry infilled RC frame.

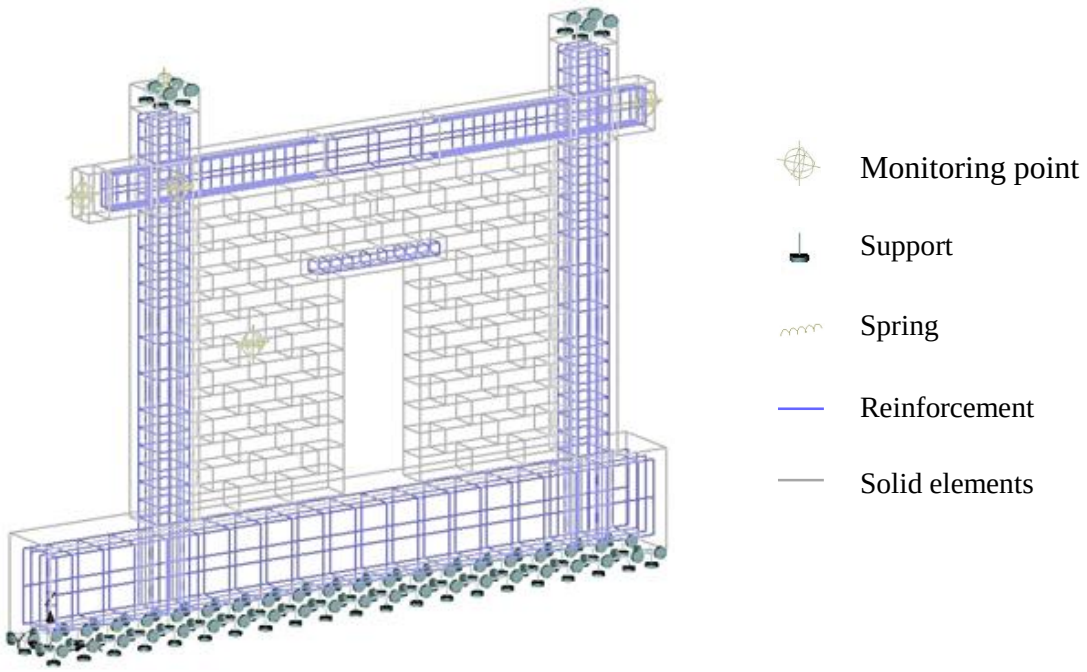


Figure 3: Typical infilled frame developed in Atena 3D (Case I/1)

A constant pre-compression equal to 365 kN assigned at the column ends. Due to large vertical pre-compression, friction could not be undermined. Friction coefficient for sliding the steel roller ($\mu_F$) was taken as 0.03 [19]. Hence, the friction force ($T_F$) for one column end was calculated using eq. 1.

$$T_F = \mu_F \times 365 \approx 10 \text{ kN} \quad (1)$$

For introducing friction force onto the numerical model, a non-linear surface spring was set on the beams end on the opposite side of the in-plane applied loading. Spring stiffness calculated by eq. 2.

$$K_s = \frac{2T_F}{A_{beam}} = 0.83 \text{ MPa} \quad (2)$$

Figure 4b shows the spring's non-linear relationship. The concrete frame, lintel and masonry units simulated using "*3D non-linear cementitious"* material model (Table 1). Reinforcement simulated using the "*bilinear reinforcement"* material model shown in Table 2 and the mortar joints simulated using the "*3D interface"* material model (Table 3). Material model parameters were adopted from [10] and are described in detail in [20].

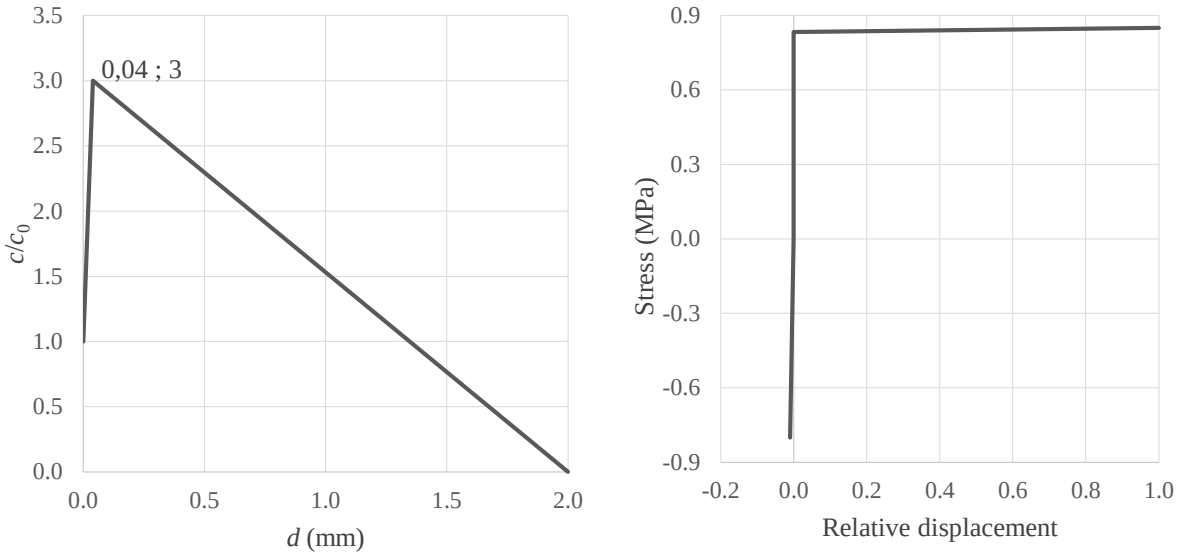


a) Mortar interlock b) Spring non-linear function

Figure 4 Material functions

| Description | Symbol | Frame concrete Value | Concrete lintel Value | Clay block Value | Unit |
|---|---|---|---|---|---|
| Elastic modulus | $E$ | 4.100 E+04 | 3.032 E+04 | 5.650 E+03 | MPa |
| Poisson's ratio | $\mu$ | 0.200 | 0.200 | 0.100 | / |
| Tensile strength | $f_t$ | 4.000 | 2.317 | 1.800 | MPa |
| Compressive strength | $f_c$ | -5.800 E+01 | -2.550 E+01 | -1.750 E+01 | MPa |
| Specific fracture energy | $G_f$ | 1.200 E-04 | 5.739 E-05 | 4.500 E-04 | MN/m |
| Crack spacing | $s_{max}$ | 0.125 | 0.125 | -5.000 E-04 | m |
| Tensile stiffening | $c_{ts}$ | 0.400 | 0.400 | -1.358 E-03 | / |
| Critical compressive disp. | $W_d$ | -1.010 E-03 | -5.000 E-04 | / | / |
| Plastic strain at $f_c$ | $\varepsilon_{cp}$ | -1.417 E-03 | -8.411 E-04 | / | / |
| Reduction of $f_c$ due to cracks | $r_{c.lim}$ | 0.800 | 0.800 | 0.800 | / |
| Crack shear stiffness factor | $S_F$ | 20.000 | 20.000 | 20.000 | / |
| Aggregate size | | 1.600 E-02 | 2.000 E-02 | / | m |
| Fixed crack model coefficient | | 1.000 | 1.000 | 1.000 | / |

Table 1: Non-linear cementitious 2 material properties for each constituent

| Description | Symbol | Value | Unit |
|---|---|---|---|
| Elastic modulus | $E$ | 2.10 E+05 | MPa |
| Yield strength | $\sigma_y$ | 5.50 E+02 | MPa |
| Tensile strength | $\sigma_t$ | 6.50 E+02 | MPa |
| Limited ductility of steel | $\varepsilon_{lim}$ | 0.01 | / |

Table 2: Bilinear steel reinforcement material properties

| Description | Symbol | Mortar bedjoint | Mortar head-joint | Unit |
|---|---|---|---|---|
| | | Value | Value | |
| Normal stiffness | $K_{nn}$ | 5.65 E+05 | 8.50 E+04 | MN/m$^2$ |
| Min. normal stiffness | $K_{nn.min}$ | 5.65 E+02 | 8.50 E+01 | MN/m$^2$ |
| Tangential stiffness | $K_{tt}$ | 2.57 E+05 | 3.86 E+04 | MN/m$^2$ |
| Min. tangential stiffness | $K_{tt.min}$ | 2.57 E+02 | 3.86 E+01 | MN/m$^2$ |
| Tensile strength | $f_t$ | 0.20 | 0.20 | MPa |
| Cohesion | $c$ | 0.35 | 0.35 | MPa |
| Friction coefficient | | 0.24 | 0.24 | / |
| Interlock function | | see fig. 1a | / | |

Table 3: Interface material properties

According to Eurocode 8 [1], the allowable minimum damage ($d_r$) for no-collapse scenario for non-structural elements (3rd Class) made of brittle materials can be estimated by 0.10 $h$; where h is the height of the specimen. In favour of satisfying the stated requirement with the specimen's height of 140 cm, the inter-storey drift ratio ($d_r$) has to be $\leq$ 14 mm. Thus, during the numerical simulations, all frames were allowed to deform up to 28 $mm$ ($e.g.\ 2 \times d_r$) so that the 1% $d_r$ to be evaluated. Furthermore, depending on the location of the application of the monotonic load, frames with eccentric openings would behave differently mechanically. Subsequently, two additional models were developed for the case I/3 (e.g. I/3a & I/3b) and two for the case I/4 (e.g. I/4a & I/4b). All loads were applied as point loads onto the steel plates. It should be mentioned that steel plates had enough thickness to neglect St. Venant's principle and a perfect connection to the frame. Vertical load was applied in 5 steps (i.e. 73 kN per step). Horizontal forces applied as a prescribed deformation of 0.20 mm in 140 steps to achieve a total displacement equal to 28 mm.

## 4 RESULTS AND DISCUSSION

Figure 5 & 6 show the computational and experimental values with respect to displacement ($d$), drift ratio ($d_r$), shear force ($V_R$) and shear force ratio ($V_R/V_{R.max}$). A shear force ratio equal to 1.0 allowed for the maximum experimental shear force value ($V_{R.max}$).

Figure 5 shows the crack pattern and minimal principal stresses for in-plane deformations in the order of 28 mm. The minimal crack width was 0.1 mm [21]. Hairline cracks are in the order of 0.1 mm and in many cases represent insignificant damage. However, according to [22, 23], hairline cracks can signal moderate or higher level of damage. Also, Table 5 presents a comparison of the $V_R/d$ and the drift ratio. In Table 5, the deviation of computational against the experimental results calculated using the eq. 3.

$$\Delta = 1 - \frac{Computational\ value}{Experimental\ value} \qquad 3$$

From Table 5 and Figures 5& 6, we can conclude that:

a) The response of monotonic static and cyclic quasi – static models (Figure 6 & Table 5) are within expected range [16] especially with regards to initial stiffness. Large differences occurred after cyclic quasi - static models reached plasticity as monotonic static models have a greater bearing capacity [16]. Plasticity in cyclic quasi–static models

develops around 0.25% $d_r$ and around 4 times larger i.e. 1.25% $d_r$ for the monotonic static models (Figure 6).

b) From Figure 7 and for all models, the failure mechanism can be characterized by a shear development in the toe area, damage at the frame and in the diagonal of the masonry infill.
c) The differences between computational models with eccentric openings (I/3a & I/3b, I/4a & I/4b) loaded from different ends are not extensive as the average difference in stiffness is 8% (Table 5).
d) The positive and negative experimental cyclic results differ by 15% on average. In some cases (e.g. the stiffness of I/1 model at 0.50% $d_r$), the difference could be in the order of 52% (Table 5). Consequently, the monotonic static model results are in majority of cases between the positive and negative curve (Figure 6) with a larger tendency to the positive curve.
e) Considering the large variability of masonry constituents [10,11], the developed model based on the micro-scale modelling approach was able to capture the experimental behaviour of the masonry infill RC frame with sufficient accuracy.
f) The model was subjected to nonlinear static (monotonic) approach and the results comparison with experimental data showed high quality compatibility in failure mechanism description and response in initial stage. As anticipated, after the initial stage the model showed higher response resistance.

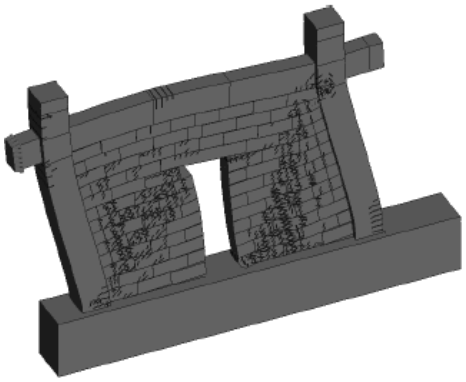

(a) Crack pattern I/1 model

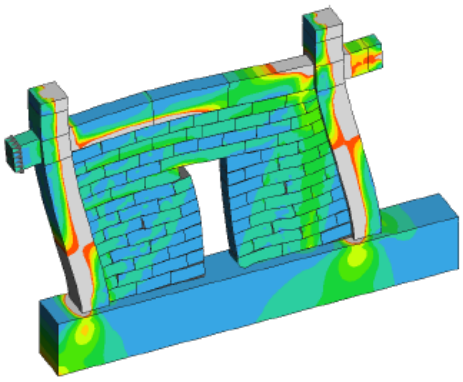

(b) Min. principal stress isolines I/1 model

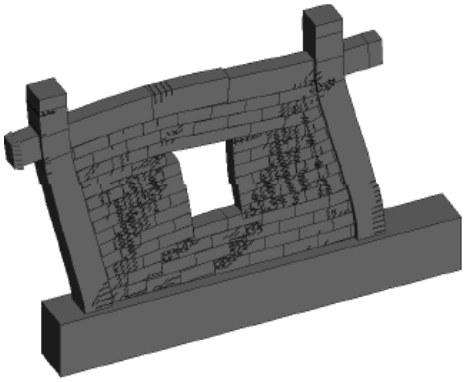

(c) Crack pattern I/2 model

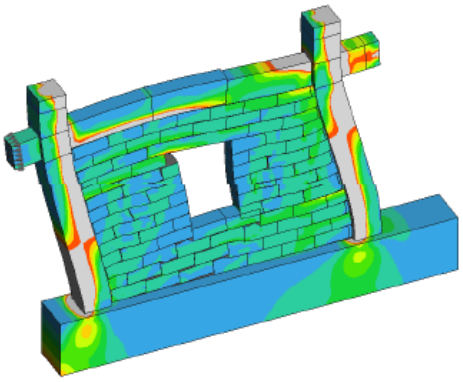

(d) Min. principal stress isolines I/3a model

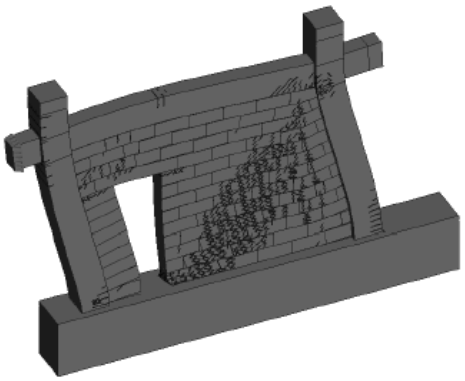

(e) Crack pattern I/3a model

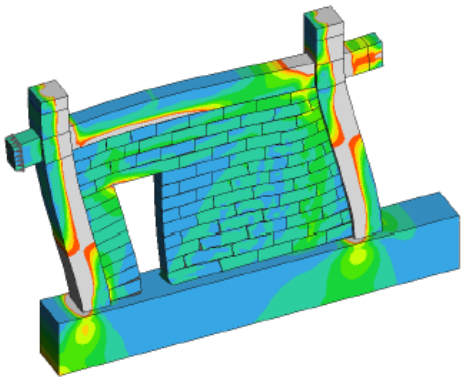

(f) Min. principal stress isolines I/3a model

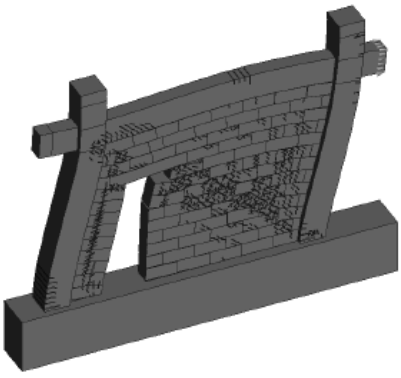

(g) Crack pattern I/3b model

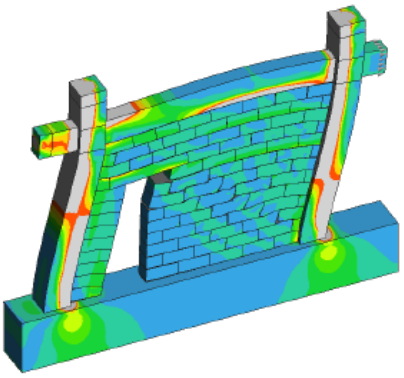

(h) Min. principal stress isolines I/1b model

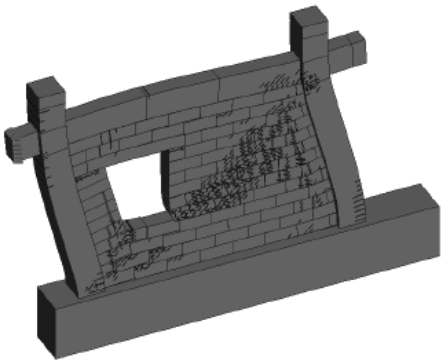

(i) Crack pattern I/4a model

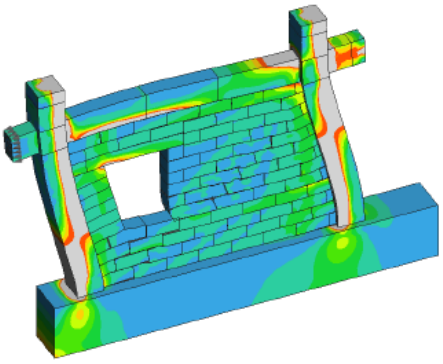

(j) Min. principal stress isolines I/4a model

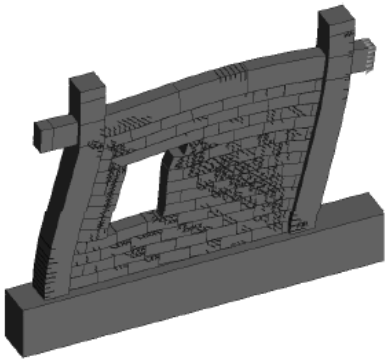

(k) Crack pattern I/4b model

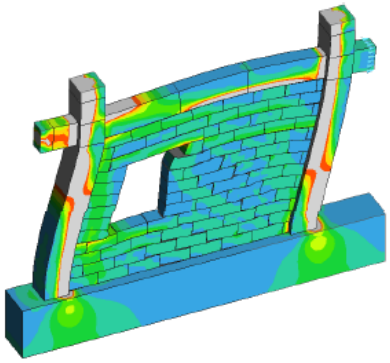

(l) Min. principal stress isolines I/4b model

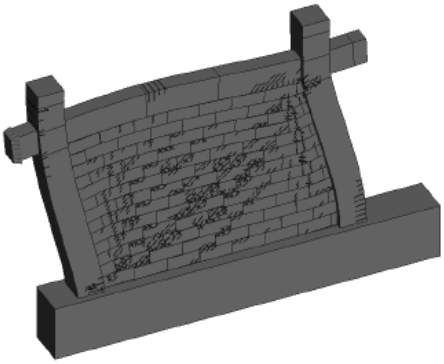

(m) Crack pattern III/2 model

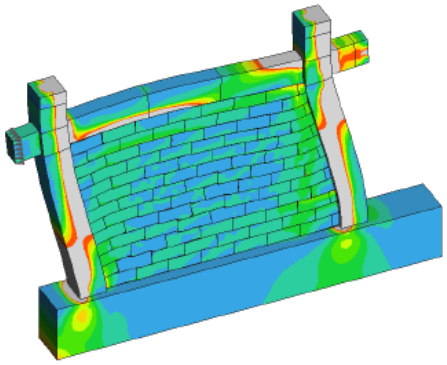

(n) Min. principal stress isolines III/2 model

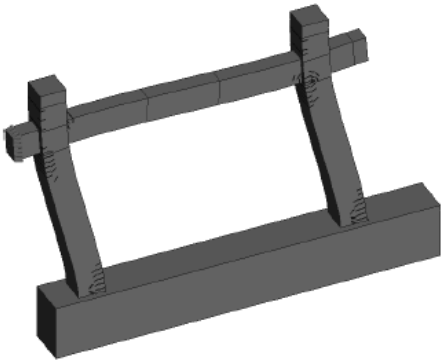

(o) Crack pattern III/1 model

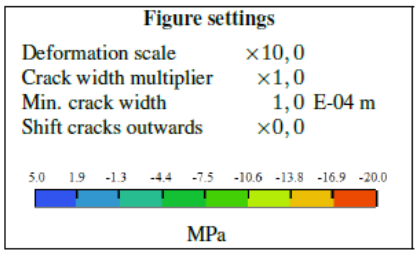


Figure 5: Principal stress and crack patterns for the models developed by Atena 3D software (deformation at 28 mm)

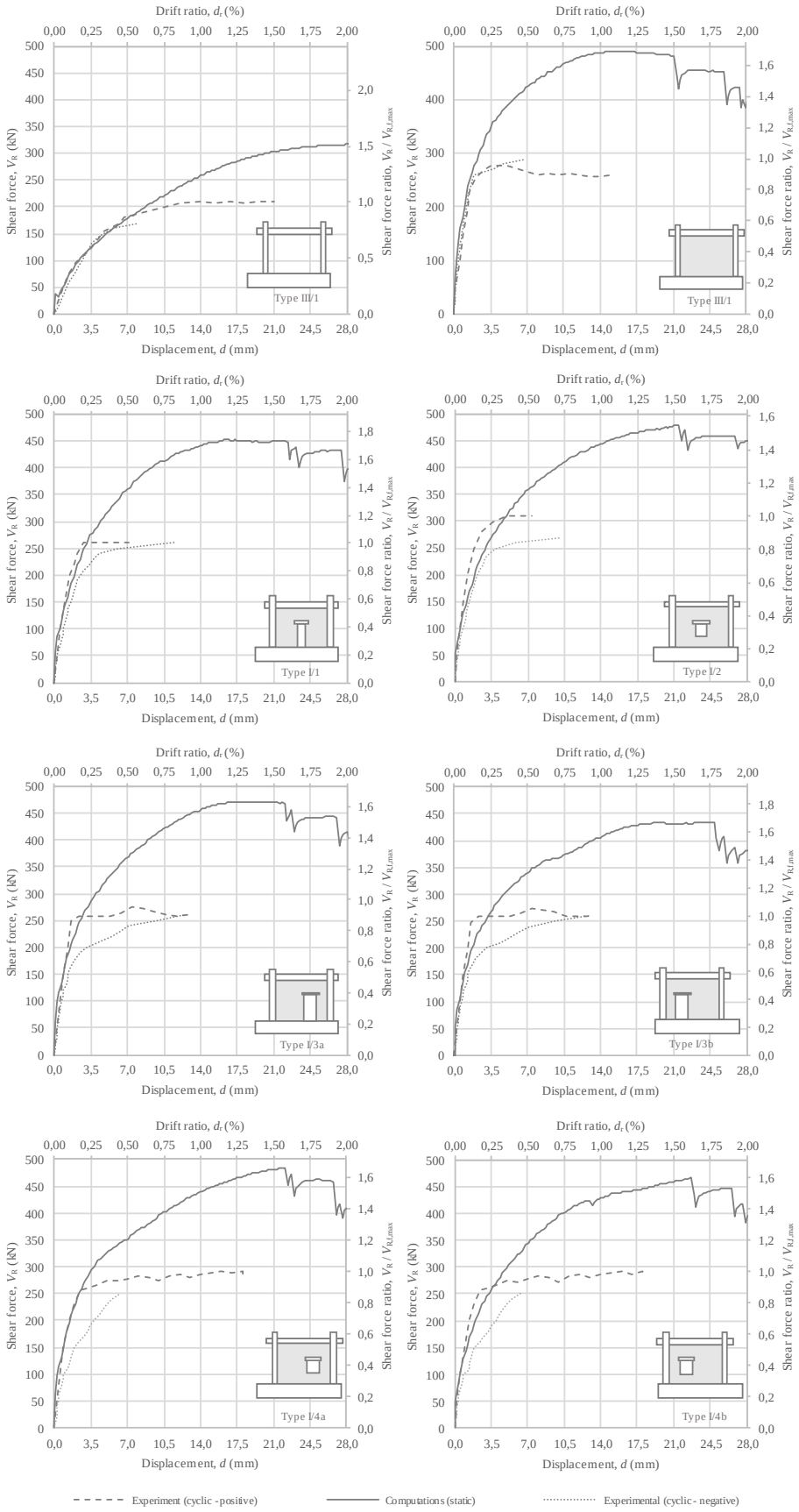


Figure 6: Comparison of experimental and numerical shear force vs displacement curves

| Test type | Storey drift ratio | Stiffnes ($V_R$ / $d$) by model type (kN/mm) | | | | | | | | | Difference from the computational model (%) | | | | | | | | |
|---|---|---|---|---|---|---|---|---|---|---|---|---|---|---|---|---|---|---|---|
| | | I/1 | I/II | III/1 | III/2 | I/3 | | I/4 | | | I/1 | I/II | III/1 | III/2 | I/3 | | I/4 | | |
| | | | | | | a | b | a | b | | | | | | a | b | a | b | |
| Experimental cyclic - positive | 0.25 | 74.29 | 83.68 | 35.29 | 77.72 | 73.85 | | 75.23 | | Experimental cyclic - positive | -7.36 | 7.04 | -1.42 | -26.79 | -8.53 | -3.84 | -9.33 | 2.37 | |
| | 0.50 | 74.29 | 44.22 | 25.98 | 36.71 | 38.60 | | 39.65 | | | 30.54 | -15.54 | 1.51 | -66.26 | -34.65 | -25.39 | -27.63 | -23.11 | |
| | 0.75 | n/a | n/a | 19.00 | 24.77 | 24.44 | | 26.48 | | | n/a | n/a | -10.50 | -79.81 | -64.58 | -45.57 | -45.14 | -45.00 | |
| | 1.00 | n/a | n/a | 14.90 | 18.37 | n/a | | 20.46 | | | n/a | n/a | -23.34 | -88.82 | n/a | | -53.58 | -49.39 | |
| | 1.50 | n/a | n/a | 9.94 | n/a | n/a | | n/a | | | n/a | n/a | -44.95 | n/a | n/a | | n/a | | |
| | 2.00 | n/a | n/a | n/a | n/a | n/a | | n/a | | | n/a | n/a | n/a | n/a | n/a | | n/a | | |
| Experimental cyclic - negative | 0.25 | 66.15 | 69.47 | 36.59 | 77.14 | 57.91 | | 55.11 | | Experimental cyclic - negative | -20.56 | -11.98 | 2.20 | -27.74 | -38.41 | -32.42 | -49.24 | -33.26 | |
| | 0.50 | 35.95 | 37.50 | 23.71 | n/a | 34.09 | | n/a | | | -43.53 | -36.23 | -7.90 | n/a | -52.45 | -41.97 | n/a | | |
| | 0.75 | 24.51 | n/a | n/a | n/a | 24.00 | | n/a | | | -59.59 | n/a | n/a | n/a | -67.61 | -48.24 | n/a | | |
| | 1.00 | n/a | n/a | n/a | n/a | n/a | | n/a | | | n/a | n/a | n/a | n/a | n/a | n/a | n/a | | |
| | 1.50 | n/a | n/a | n/a | n/a | n/a | | n/a | | | n/a | n/a | n/a | n/a | n/a | n/a | n/a | | |
| | 2.00 | n/a | n/a | n/a | n/a | n/a | | n/a | | | n/a | n/a | n/a | n/a | n/a | n/a | n/a | | |
| Computational static | 0.25 | 79.75 | 77.79 | 35.79 | 98.54 | 80.16 | 76.69 | 82.25 | 73.44 | Average difference | 13.96 | 2.47 | 0.39 | 27.26 | 23.47 | 18.13 | 29.29 | 15.44 | |
| | 0.50 | 51.60 | 51.09 | 25.59 | 61.03 | 51.97 | 48.40 | 50.60 | 48.81 | | 6.49 | 25.88 | 3.20 | n/a | 43.55 | 33.68 | n/a | | |
| | 0.75 | 39.11 | 38.95 | 20.99 | 44.54 | 40.23 | 35.58 | 38.43 | 38.39 | | n/a | n/a | n/a | n/a | 66.10 | 46.90 | n/a | | |
| | 1.00 | 31.60 | 31.78 | 18.38 | 34.68 | 32.52 | 28.95 | 31.42 | 30.56 | | n/a | n/a | n/a | n/a | n/a | | n/a | | |
| | 1.50 | 21.33 | 22.73 | 14.41 | 22.94 | 22.47 | 20.62 | 22.80 | 21.92 | | n/a | n/a | n/a | n/a | n/a | | n/a | | |
| | 2.00 | 14.09 | 16.09 | 11.33 | 14.21 | 18.28 | 13.61 | 14.61 | 13.98 | | n/a | n/a | n/a | n/a | n/a | | n/a | | |

Table 5: Stiffness difference

## 5 CONCLUSIONS

A three-dimensional computational model based on the finite element method of analysis has been developed. The computational model was able to predict the in-plane and out-of-plane behaviour of masonry infilled RC frames containing openings. Use was made of the commercial software Atena3D. Within Atena 3D, the masonry infill walls were modelled as an assemblage of stiff yet deformable bricks. Mortar joints were represented as zero thickness interfaces. Initially, the brick and interface parameters were determined by carrying out a series of small scale tests. The computational model was then used to predict the in-plane and out-of-plane behaviour of a full scale infill wall panels constructed in the laboratory using a similar brick and mortar combination. From the results analysis, it was shown that the FE model was capable of capturing the load carrying capacity of the masonry infilled RC frame as well as the different stages of mechanical behaviour of masonry infilled RC frames with sufficient accuracy. Both experimental and numerical results showed that there were two notable features of the behaviour of masonry infilled RC frames. These are: a) initial bed-joint sliding above the opening; followed by b) diagonal tensile or bed-joint sliding failure at the masonry piers of masonry infill walls. The computational model was also able to capture the load against displacement characteristics of the masonry infilled RC frames with sufficient accuracy. Hence, it has been demonstrated that Atena 3D can be used successfully to predict the in plane and out-of-plane mechanical behaviour of a masonry infilled RC frames with and without opening when subjected to a nonlinear static procedure.

## ACKNOWLEDGMENTS

The research presented in this paper is a part of the research project FRAmed-MAsonry Composites for Modelling and Standardization (FRAMA), which is supported by the Croatian Science Foundation. This support is gratefully acknowledged.

## REFERENCES

[1] CEN. *Eurocode 8: Design of Structures for Earthquake Resistance - Part 1: General Rules, Seismic Actions and Rules for Buildings (EN 1998-1:2004)*. Brussels: European Committee for Standardization, 2004.

[2] W.W. El-Dakhakhni, M. Elgaaly,A.A. Hamid. Three-Strut Model for Concrete Masonry-Infilled Steel Frames. *J Struct Eng* **129**, 177–185, 2003.

[3] Kose MM. Parameters affecting the fundamental period of RC buildings with infill walls. *Eng Struct*, **31**, 93–102, 2009.

[4] P.G. Asteris, C.C. Repapis, L. Cavaleri, V. Sarhosis, A. Athanasopoulou. On the fundamental period of infilled RC frame buildings. *Struct Eng Mech*, **54**, 1175–1200, 2015.

[5] D.J. Dowrick. *Earthquake Resistant Design and Risk Reduction*. 2nd ed. John Wiley & Sons Ltd, 2009.

[6] C. Wang, J.P. Forth, N. Nikitas, V. Sarhosis. Retrofitting of masonry walls by using a mortar joint technique; experiments and numerical validation. *Eng Struct*; **117,** 58–70, 2016.

[7] P.G. Asteris, L. Cavaleri, F. Di Trapani, V. Sarhosis. A macro-modelling approach for the analysis of infilled frame structures considering the effects of openings and vertical loads. *Struct Infrastruct Eng*; **12,** 551–566, 2016.

[8] V. Sarhosis, Y. Sheng. Identification of material parameters for low bond strength masonry. *Eng Struct*; **60,** 100–110, 2014.

[9] A. Mohebkhah,A. Tasnimi. Distinct Element Modeling of Masonry-Infilled Steel Frames with Openings. *Open Constr Build Technol J,* **6**, 42–49, 2012.
[10] D. Penava, V. Sigmund, I. Kožar. Validation of a simplified micromodel for analysis of infilled RC frames exposed to cyclic lateral loads. *Bull Earthq Eng*; **14**, 2779–2804 2016.
[11] D. Penava. *Influence of openings on seismic response of masonry infilled reinforced concrete frames*. Osijek, Josip Juraj Strossmayer University of Osijek: Doctoral dissertation, 2012.
[12] CEN. *Eurocode 2: Design of concrete structures - Part 1-1: General rules and rules for buildings (EN 1992-1-1:2004)*. Brussels: European Committee for Standardization, 2004.
[13] CEN. *Eurocode 6: Design of masonry structures - Part 1-1: General rules for reinforced and unreinforced masonry structures (EN 1996-1-1:2005)*. Brussels: European Committee for Standardization, 2005.
[14] G. Grünthal, R.M.W. Musson, J. Schwarz, et al. *European macroseismic scale 1998*. Luxembourg, 1998.
[15] V. Sigmund, D. Penava. Influence of openings, with and without confinement, on cyclic response of infilled r-c frames — an experimental study. *J Earthq Eng*, **18**, 113–146, 2014.
[16] M. Tomaževič. *Earthquake-Resistant Design of Masonry Buildings*. London: Imperial College Press, 1999.
[17] E. Neufert, P. Neufert. *Architects' data*. 4th ed. Wiley-Blackwell, 2012.
[18] s.r.o. CC. ATENA for Non-Linear Finite Element Analysis of Reinforced Concrete Structures.
[19] M. Hirt, J-P. Lebet. *Steel Bridges: Conceptual and Structural Design of Steel and Steel-Concrete Composite Bridges*. CRC Press, 2013.
[20] V. Cervenka, L. Jendele, Cervenka J. *ATENA Program Documentation Part 1 Theory*. Prague: Cervenka Consulting Ltd., 2012.
[21] J.B. Burland, B.B. Broms, V.F.B. De Mello. Behaviour of foundations and structures: state-of-the art report. In: *Proc. of the 9th International Conference on Soil Mechanics and Foundation Engineering*, Tokyo, Japan, 495–546, 1977.
[22] ATC. *Evaluation of earthquake damaged concrete and masonry wall buildings: basic procedures manual (FEMA 306)*. Redwood City, California, 1998.
[23] V. Sarhosis, K.D. Tsavdaridis, I. Giannopoulos. Discrete element modelling (DEM) for masonry infilled steel frames with multiple window openings subjected to lateral load variations. Open Construction and Building Technology Journal, 8, 93-103, 2014.

COMPDYN 2017
6th ECCOMAS Thematic Conference on
Computational Methods in Structural Dynamics and Earthquake Engineering
M. Papadrakakis, M. Fragiadakis (eds.)
Rhodes Island, Greece, 15–17 June 2017

# SIMPLIFIED MODELING OF MASONRY INFILL WALLS WITH HORIZONTAL SLIDING JOINTS

**V. Bolis [1], M. Preti [2], A. Stavridis[3]**

[1] PhD, Department of Civil, Architectural, Environmental and Land Planning Engineering, University of Brescia, via Branze, 43 – 25123 Brescia, Italy. E-mail: v.bolis@unibs.it
(corresponding author) Phone 0039.030.371.5496.

[2] Assistant Professor, Department of Civil, Architectural, Environmental and Land Planning Engineering, University of Brescia, via Branze, 43 – 25123 Brescia, Italy. E-mail: marco.preti@ing.unibs.it

[3]Assistant Professor, Department of Civil, Structural and Environmental Engineering – University at Buffalo, Buffalo, USA. E-mail: astavrid@buffalo.edu

**Keywords:** infilled frame design, deformable infill, analytical formulation, strut model, in-plane response, column shear action.

***Abstract.*** *The vulnerability of masonry infilled frame structures has been demonstrated by many recent earthquakes and research studies and it is often triggered by the in-plane interaction between the flexible frame and the masonry infill (characterized by an inherent higher stiffness). Among the different solutions studied to mitigate such issue, a deformable infill typology with horizontal sliding joints has been proposed and tested by the authors in previous studies, capable of reducing the infill-frame interaction and of limiting the damage in the masonry, so that also the out of plane infill stability is maintained.*

*This paper proposes a simplified approach to assess the seismic performance of this innovative masonry infill typology. Analytical formulations, based on geometrical and mechanical properties, are proposed to describe the in-plane response of the infill and its interaction with the bounding frame. Thanks to these formulations, a simplified numerical model for the infill, adopting an equivalent strut approach, is calibrated to be used in the non-linear analysis of infilled frame structures, accounting for their cyclic response. The reliability of the method is validated trough the comparison of the estimated infill resistance and shear demand on the column with those obtained from an extensive experimental campaign and numerical study based on refined finite element models. The results show the efficiency of the proposed simplified model in estimating the response of the infilled RC frame, in particular the shear action in the frame columns, which are the critical element of the structure.*

## 1. INTRODUCTION

Over the last decades, several research studies [1]–[7] and field evidence[8], [9] stressed the seismic vulnerability of masonry infilled reinforced concrete (RC) structures. In these structures the seismic response is highly affected by the presence of stiff masonry infills, which significantly modify the RC bare frame response, triggering, in many cases, brittle and unexpected collapse. Due to the heterogeneity of the masonry infills and their scattered material properties, the infill-frame interaction modeling is still a rather challenging task for practicing engineers, so that in most cases the structural effect of the infills is ignored in the seismic design of the structures.

In the last years, several authors have focused on the masonry infill vulnerability and different innovative solutions have been proposed with the aim of reducing the infill-frame interaction, as reducing the forces transferred between the frame and the infill can reduce both the structural element vulnerability and the infill damage. The proposed solutions reached the aim with different approach: (i) partitioning of the infill wall [10]–[16]; (ii) adopting alternative joints instead of mortar (dry or plastic joints) [17]–[21]; (iii) using deformable materials for the construction of the infill [22], [23].

This paper deals with the in-plane response of masonry infill with horizontal sliding joints, subdividing the wall into sub-portions, as proposed in [12], [13]. A simplified numerical model, adopting an equivalent strut approach, is presented and validated. The model is proportioned on an analytical model first presented in [23], which is based on simple equilibrium equations. The calibration of the strut model is based on the parametric study of an infilled RC frame performed in [24], modelled with refined FEM according to [25]. In literature [26]–[28] different configurations of equivalent strut have been suggested to reproduce the effects of the infill-frame interaction. Both single or multiple diagonal struts, oriented to the frame joints or eccentric, were proposed, the latter meant to reproduce the shear action in the columns or beams.

In this study two different configurations have been calibrated: (i) one with a single strut per diagonal, spanning between the frame joints, (Model A, in the following) and (ii) the other with one single strut per direction, linked with the columns at a calibrated distance (Model B, in the following), in order to reproduce the column shear action produced by the infill-frame interaction.

The comparison with the experimental and numerical results of single-bay, single-story frames [13], [24]. shows that the proposed approach can fairly reproduce both the important features of the infill response (including the initial stiffness, peak strength, and post-yielding behavior) and the effects of the infill-frame interaction, in terms of maximum column shear.

## 2. INFILL TYPOLOGY AND PERFORMANCES

The innovative construction technique proposed and experimentally assessed in [12], [13] consists in partitioning the infill wall into several sub-portions by the introduction of horizontal sliding joints at selected locations along the height (Figure 1a, b). Such solution increases the deformability of the infill, associated to the in-plane relative sliding between the infill sub-portions. To reduce the contact forces along the columns-infill interface and delay crushing of the masonry, deformable elements are placed on both the sides of the infill. In addition, a small gap is maintained between the infill and the beam above to avoid their contact and the consequent interaction.

The in-plane cyclic response of an infill prototype, tested in a confining steel frame with the hinged at the column-beam joints, is reported in Figure 1a, showing a ductile response

characterized by a low strength and stiffness. Moreover, the infill showed only minor damage in some masonry sub-portion, after exceeding 2% drift.

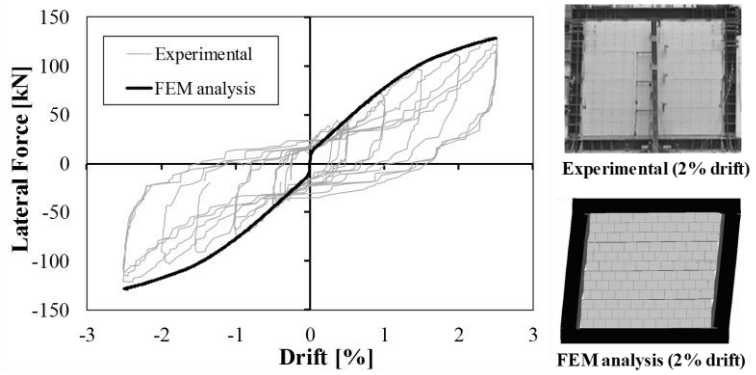


(a) steel frame infilled with a masonry wall partitioned by horizontal sliding joints: test layout and results (adapted from [13])

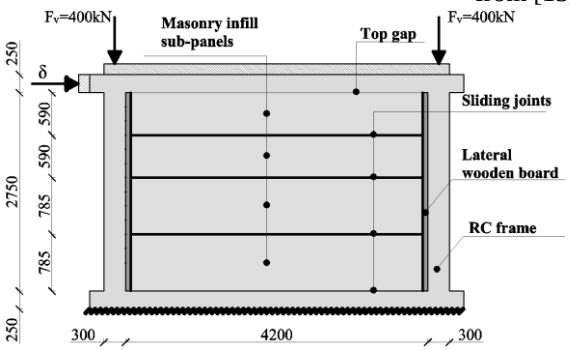


(b) layout of the RC infilled-frame object of the finite element modeling (FEM) (dimensions in mm)

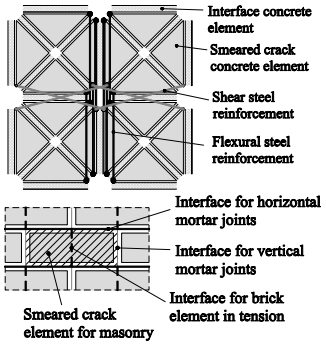


(c) concrete and masonry FEM schematic

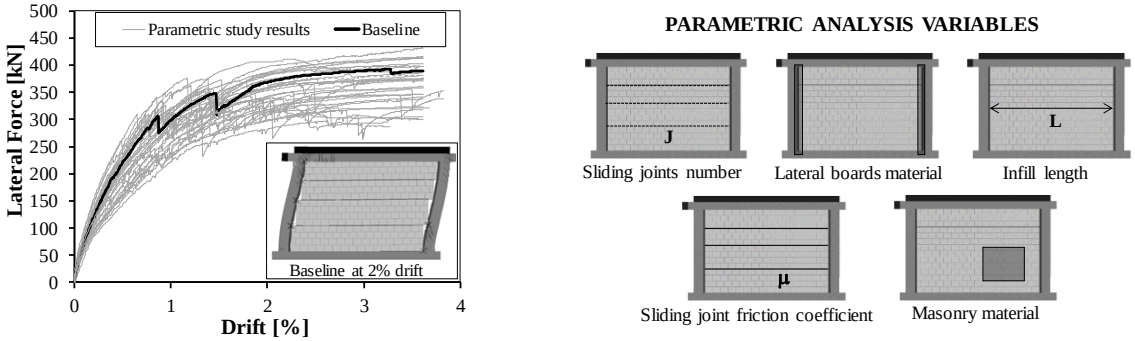


(d) results of the parametric analysis on the masonry infilled RC frame(adapted from [24])

Figure 1. Synthesis of the results of previous research works on infilled frame with horizontal sliding joints and schematic of the finite element modeling (FEM) adopted.

The efficiency of such an infill typology in the application to reinforced concrete (RC) frames was extensively tested in [11] and numerically assessed in [24] by means of a refined finite element based on smeared crack and interface elements (Figure 1b, c), calibrated on the experimental mechanical properties of the different components. Such numerical model allowed to perform a parametric study investigating the role of mechanical and geometrical properties of the infill. The main results of the study are recalled in Figure 1d. Moreover, these analyses quantified the contact

forces transferred by the infill to the frame columns, at the subpanel corners, which increase the shear forces acting on the RC columns compared to the bare frame response. It was observed that the shear actions on the columns increase as the imposed inter-story drift increases, and for drifts larger than 1% the shear demand on the column can have similar intensity as that in the case of traditional solid masonry infills. Therefore, despite the severe reduction of the infill stiffness and vulnerability due to the infill partitioning the design of the RC frame columns has to take this shear demand into account.

## 3. ANALYTICAL MODEL FOR THE INFILL

The analytical model here presented stems from a first analytical interpretation of the experimental response of an infilled steel frame presented in [23], then developed in [24], [29], [30], supported by the results of a refined finite element model. The proposed formulations provide an estimate of the infill net contribution ($\Delta F_s$) to the frame lateral strength, based on simple equilibrium equations, that, added to the bare frame lateral strength, provides the overall infilled frame resistance.

The contact forces to be considered in the equilibrium to rotation around the column base hinge result from the superposition of the effects of two different resisting mechanisms in the infill: the compression of the sub-portion along their diagonal ("strut mechanism",) and the friction activating by the sliding of the masonry sub-portion on the horizontal joints ("frictional mechanism"). The graphical illustration of the two mechanisms is reported in Figure 2 and the infill lateral strength can be expressed as the sum of the two contributions ($\Delta F_s = \Delta F_s^{strut} + \Delta F_s^{frict}$).

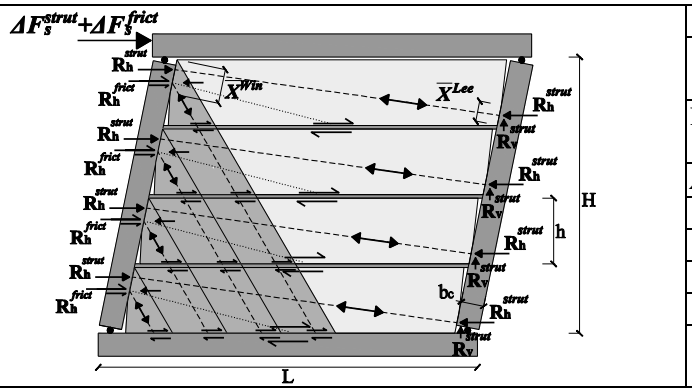


| | |
|---|---|
| $\Delta F_s$ | Infill strength contribution |
| $R_n$ | Resultant of the contact forces in the n$^{th}$ infill sub-portion |
| $R_{h,n}$ , $R_{v,n}$ | Horizontal and vertical components of the contact force $R_n$ |
| $\bar{X}_n$ | Contact length |
| h | Sub-portion heigth |
| H | Infill heigth |
| $b_c$ | Column width |
| L | Infill length |
| Apex "*Lee*" and "*Win*" refers to Windward and Leeward columns, respectively. | |

Figure 2. Static scheme adopted in the analytical model with details of the contact forces between the frame columns and the masonry infill.

Equation (1) provides the infill strength contribution due to the "strut" mechanism, obtained considering both the pertaining horizontal and vertical components of the contact forces on the columns. Such formulation is obtained under the hypothesis that, per each sub-portion, the horizontal components ($R_{h,n}^{strut} = \sigma_c \cdot \beta \cdot \overline{X}^{Lee} \cdot t$) have the same intensity on the two columns. In contrast, the vertical ones ($R_{v,n}^{strut}$) differs: on the windward column, they are proportional to the horizontal component through the contact friction coefficient ($\mu_c$), while on the leeward side the vertical contact force component is smaller as the resultant is oriented along the sub-portion diagonal (with inclination $\alpha$).

$$\Delta F_s^{strut} = \sigma_c \cdot \beta \cdot \overline{X}^{Lee} \cdot t \cdot \left[ \left( 1 - \beta \cdot \frac{\overline{X}^{Lee}}{h} \right) + \frac{b_c}{2h} \left( \mu_c + \tan \alpha \right) \right] \tag{1}$$

$$\Delta F_s^{fric} = \frac{1}{2} \cdot \left[ W + N \cdot R_{h,n}^{strut} \cdot \left( \mu_c - \tan \alpha \right) \right] \cdot \left( \frac{1}{1 - \mu_j \cdot \mu_c} \right) \cdot \mu_j \tag{2}$$

This difference of the two vertical contact forces increases the normal stress on the horizontal sliding joints, thus affecting also the "frictional mechanism". Therefore, the analytical formulation for the contribution to the infill lateral strength due to the "frictional mechanism" results in Equation (2), where the unbalanced vertical contact force is summed to the sub-portion self-weight.

According to Equations (1) and (2), the lateral strength of the infill can be estimated once geometrical and material properties of the infill are known, except for the contact length ($\bar{X}_n$). In detail the required parameters are: the infill-column contact compression strength ($\sigma_c$), the infill thickness ($t$), the sub-portion height ($h$), the column width ($b_c$), the friction coefficient along the infill-column contact ($\mu_c$) and along the horizontal sliding joints ($\mu_j$), the sub-portion diagonal inclination ($\alpha$), the infill self-weight ($W$) and the number of sub-portions ($N$). The only parameter not a-priori defined is the contact length between the columns and the infill sub-portions ($\bar{X}_n$). The quantification of such parameter, varying the imposed lateral drift and the number of sub-portions, can be estimated with Equation (3), which was calibrated on the parametric study presented in [24]. It is worth noting that in Equation (1) a stress block approach for the estimate of the contact stress is adopted, assuming a reduction coefficient ($\beta$) for the contact length, taken equal to 0.8.

$$\begin{cases} \overline{X} = \left[ 0.3 - 0.019 \cdot \left( N - 4 \right) \right] \cdot Drift[\%] & Drift \le 1\% \\ \overline{X} = 0.3 \cdot \sqrt[3]{Drift[\%]} - 0.019 \cdot \left( N - 4 \right) & Drift > 1\% \end{cases} \tag{3}$$

### 3.1. Evaluation of the maximum column shear action in moment resisting frames

The same superposition approach adopted for the infilled frame lateral resistance allows to quantify the shear action in the columns, accounting for the infill-frame interaction, with acceptable approximation. The additional column shear due to the infill-frame interaction can be obtained after the quantification of the contact forces. The shear developing in the column due to the transfer of the bending moments at the frame joints is quantified considering the response of the bare frame, as a function of the drift.

Figure 3 shows the static scheme for the equilibrium Equations (4), proposed for the evaluation of the columns' shear located at their top or bottom end. Equation (5) specifies the calculation of the column shear action for the windward column top end, which is typically the most stressed section. $R_{h,n}$ is the horizontal components of the contact forces for the n$^{th}$ sub-portion, $h_n$ is the distance between $R_{h,n}$ and the base hinge, while $M_{col}^{top}$ and $M_{col}^{bottom}$ are the beam-column joint bending moments. Since the vertical component of the contact stresses plays a secondary role, its contribution is neglected in Equation (4).

The values of the contact forces to be adopted in the equations are those provided in the previous paragraph, considering that, on the windward column both the "strut" and "frictional" mechanism contribute to the contact force, while on the leeward column only the "strut" mechanism is involved. Equations (7) and (8) quantify the relevant contributions to the column shear actions.

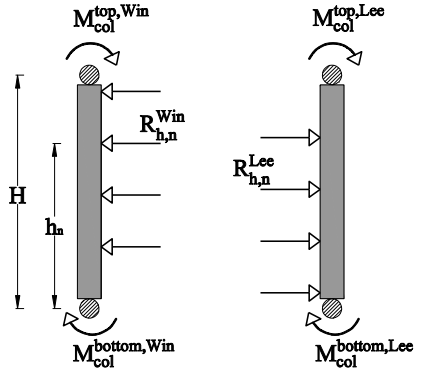


Figure 3. Static scheme for the analytical evaluation of the columns shear action for a moment resisting frame infilled with horizontal sliding panels.

$$V = V^{\inf} + V^{bare} = V^{\inf} + \frac{M_{col}^{top} + M_{col}^{bottom}}{H} \tag{4}$$

$$V_{top}^{\inf,Win} = \frac{\sum R_{h,n}^{Win} \cdot h_n}{H} = V_{top}^{strut,Win} + V_{top}^{frict,Win} \tag{5}$$

$$V_{bottom}^{\inf,Lee} = V_{top}^{strut,Win} \tag{6}$$

$$V_{top}^{strut,Win} = \frac{1}{H_{col}} \sum_{n=1}^{N} \left[ R_{h,n}^{strut} \cdot \left( n \cdot h - 0.4 \overline{X}^{Lee} \right) \right] = R_{h,n}^{strut} \cdot \left( \frac{N+1}{2} - 0.4 \frac{\overline{X}^{Lee}}{h} \right) \tag{7}$$

$$V_{top}^{frict,Win} = \frac{1}{H_{col}} \sum_{n=1}^{N} \left[ R_{h,n}^{frict} \cdot \left( n \cdot h - \frac{1}{2} h \right) \right] = R_{h,n}^{frict} \frac{N}{2} \tag{8}$$

## 4. SIMPLIFIED EQUIVALENT STRUT MODEL

The analytical model presented in the previous chapter allows for the calibration of a simplified strut model to be used for the analysis of multi-story buildings, for which a refined FE model would be too much time-consuming in design practice. The proposed approach models the infill by means of one compression-only truss element per infill diagonal (Figure 4a), calibrated to reproduce the previously described "strut" and "frictional" mechanisms. To this aim, each diagonal strut is equipped with three parallel non-linear spring elements with the constitutive laws reported in Figure 4a: Spring 1 has an elastic-perfectly-plastic behavior with an initial rigid branch, accounting for the "frictional" contribution provided by the sole self-weight; Spring 2 is characterized by a slip bilinear hysteretic law, calibrated to account for the hardening in the "frictional" mechanism, due to the "strut" mechanism; Spring 3 has a slip bilinear hysteretic rule, obtained with reference to the analytical contribution of the "strut" mechanism or simply by subtraction of the response of Spring elements 1 and 2 from the analytical total infill capacity curve.

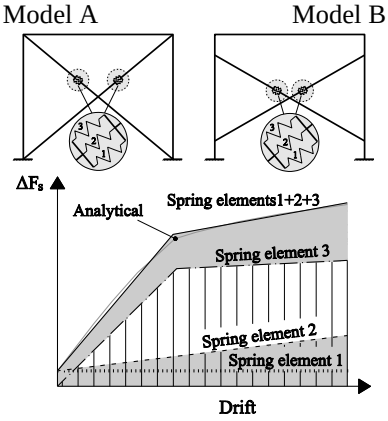


(a) monothonic response and spring elements layout

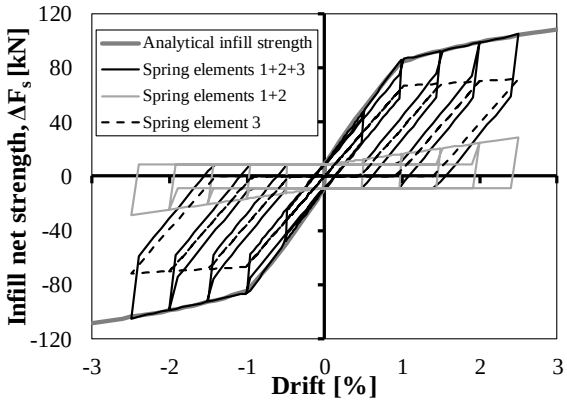


(b) cyclic response

Figure 4. Net lateral strength contribution of the infill equivalent strut model, and details of the different non-linear spring elements response.

The cyclic response provided by the selected set of springs is reported in Figure 4b, and is capable of reproducing the cyclic degradation associated to the strut mechanism.

The strut model is here proposed in two different configurations (Figure 4a): the first ("Model A") has the diagonal struts linked to the frame joints, while in the second ("Model B") the diagonals are eccentric to the joints. Both the models are suitable for reproducing the lateral strength contribution of the infill, but only Model B can capture the shear increase on the frame columns due to the infill-frame interaction.

The model parameters are assessed according to Figure 5. The spring axial behavior ($N/\Delta d$) is calibrated to reproduce the target infill lateral force-drift curve ($\Delta F_s$-$\Delta$) by means of Equations (9) to (14), where $d$ and $d'$ are the un-deformed and deformed diagonal length, $\vartheta$ is the diagonal strut inclination, $z$ is the distance of the strut from the nearest frame node, $H$ and $L$ are the bay height and length, $\Delta_1$ and $\Delta_2$ are the horizontal displacement of the two opposite strut-to-column connections. In Model B, Equation (15) quantifies the maximum shear action in the columns produced by the strut ($V_{\max}^{col}$). The choice of the $z$ value targets both the shear action ($V_{\max}^{col}$) on the columns and the net infill lateral strength ($\Delta F_s$), as obtained from the analytical model for a selected design target drift (Equation (16)).

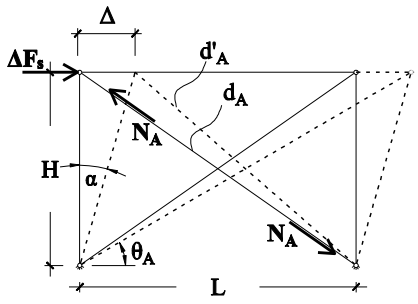


$$N_A = \Delta F_s \cdot \sqrt{1+\left(\frac{H}{L}\right)^2} \quad (9)$$

$$\Delta d_A = \Delta \cdot \cos\theta_A \quad (10)$$

$$k_A = \frac{N_A}{\Delta d_A} \quad (11)$$

(a)

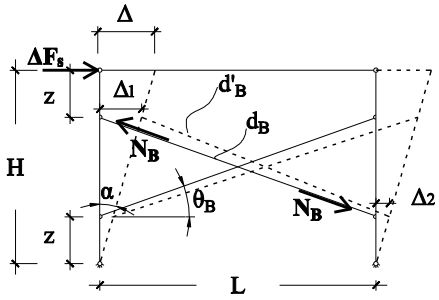


$$N_B = \frac{\Delta F_s \cdot \sqrt{1+\left(\frac{H-2z}{L}\right)^2}}{\left(1-\frac{2z}{H}\right)} \quad (12)$$

$$\Delta d_B = (\Delta_1 - \Delta_2)\cdot\cos\theta_B = \frac{\Delta}{H}(H-2z)\cdot\cos\theta_B \quad (13)$$

$$k_B = \frac{N_B}{\Delta d_B} \quad (14)$$

$$V_{\max}^{col} = N_B \cdot \cos\theta_B \cdot \left(1-\frac{z}{H}\right) \quad (15)$$

(b)

Figure 5. Static scheme for Model A (a) and Model B (b) adopted in the simplified model of the infilled frame.

$$z = h\frac{V_{\max}^{col} - \Delta F_s}{2V_{\max}^{col} - \Delta F_s} \quad (16)$$

## 4.1. Validation of the strut model

The efficiency of the proposed strut model in reproducing the infilled frame response is validated through the comparison with the results of the experimental specimen described in [13] and those obtained from the numerical study presented in [24]. For the two case studies, the adopted

parameters for the springs, adopting both Model A and Model B, are summarized in Table 1. For Model B, a 2% target drift is chosen for the calibration of *z*.

Table 1. Equivalent strut parameters calibrated on the analytical model to capture the experimental response of the infilled steel frame ([13]) and the numerical results of the infilled RC frame ([24]).

| | | Horizontal component at the beam level ($\Delta F_s$) | Simplified strut model (Model A) | Simplified strut model (Model B) |
|---|---|---|---|---|
| **EXPERIMENTAL INFILLED STEEL FRAME [Preti et al.2015]** | | | | |
| **Geometry** | **Bay** | H=2.43m; L=2.93m | | |
| | **Infill** | | θ=40.5° | z=0.827m; θ=14.8° |
| **Spring Calibration** | **Spring element 1** ***(W=17.09kN, $\mu_j$=0.5)*** | $F_y$= W $\mu_j$= 8.54 kN<br>$k_{in}$=43000 kN/m<br>$k_2$=0 kN/m | $N_y$= 11.10 kN<br>$k_{in}$=1442057 kN/m<br>$k_2$=0 kN/m | $N_y$= 27.69 kN<br>$k_{in}$=8972360 kN/m<br>$k_2$=0 kN/m |
| | **Spring element 2** | $F_y$= 0.00001 kN<br>$k_{in}$=inf kN/m<br>$k_2$=341.65 kN/m | $N_y$= 0.00001 kN<br>$k_{in}$= inf<br>$k_2$=577 kN/m | $N_y$= 0.00001 kN<br>$k_{in}$= inf<br>$k_2$=3588 kN/m |
| | **Spring element 3** | $F_y$=67.66 kN (at 1% drift)<br>$k_{in}$=2784 kN/m<br>$k_2$=147 kN/m | $N_y$= 87.9 kN (at 1% drift)<br>$k_{in}$= 4699 kN/m<br>$k_2$= 249 kN/m | $N_y$= 219.26 kN (at 1% drift)<br>$k_{in}$= 29240 kN/m<br>$k_2$= 1549 kN/m |
| **NUMERICAL INFILLED RC FRAME [Bolis et al.2016]** | | | | |
| **Geometry** | **Bay** | H=2.8m; L=4.2m | | |
| | **Infill** | | θ=33.7° | z=0.901m; θ=13.4° |
| **Spring Calibration** | **Spring element 1** ***(W=28.22kN, $\mu_j$=0.5)*** | $F_y$= W $\mu_j$= 14.112 kN<br>$k_{in}$=141120 kN/m<br>$k_2$=0 kN/m | $N_y$= 16.96 kN<br>$k_{in}$= 2038400 kN/m<br>$k_2$=0 kN/m | $N_y$= 40.70 kN<br>$k_{in}$= 11737657 kN/m<br>$k_2$=0 kN/m |
| | **Spring element 2** | $F_y$= 0.00001 kN<br>$k_{in}$=inf kN/m<br>$k_2$=260.48 kN/m | $N_y$= 0.00001 kN<br>$k_{in}$= inf<br>$k_2$=376 kN/m | $N_y$= 0.00001 kN<br>$k_{in}$= inf<br>$k_2$=2167 kN/m |
| | **Spring element 3** | $F_y$=49.78 kN (at 1% drift)<br>$k_{in}$=1778 kN/m<br>$k_2$=60.9 kN/m | $N_y$= 59.83 kN (at 1% drift)<br>$k_{in}$= 2568 kN/m<br>$k_2$= 88 kN/m | $N_y$= 143.56 kN (at 1% drift)<br>$k_{in}$= 14787 kN/m<br>$k_2$= 507 kN/m |

The diagonal struts are applied into a frame modeled with beam elements and lumped plasticity, representing both flexural and shear non-linear behavior.

Figure 6 shows the comparison between the cyclic capacity curve of the simplified model and the result of the cyclic quasi-static test on the infilled steel frame ([13]). Both the proposed configurations (Model A and Model B) provide a fairly good approximation of the experimental curve, with only a slight underestimation of the dissipation capacity. In this case, no experimental data on the column shear action are available for comparison.

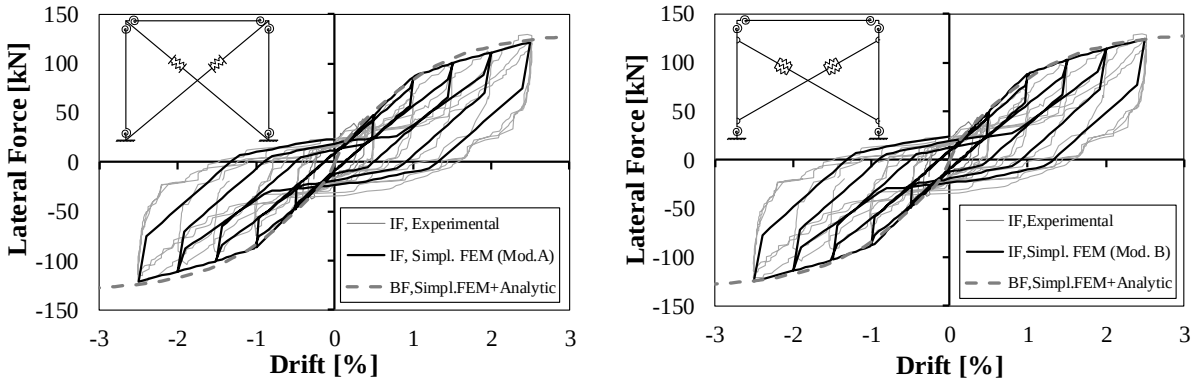


(a) Model A (b) Model B

Figure 6. Simplified model of the experimental infilled steel frame with sliding joints tested by Preti et al. (2015)

Figure 7a,b show the comparison between the capacity curves obtained with the simplified ("Simpl.FEM") and the refined ("Refined FEM") numerical model for the bare ("BF") and infilled ("IF") frame studied in [24]. Similarly to the comparison with the experimental steel frame, both

the proposed configurations of the strut model (Model A and B) offer results well matching those of the refined numerical model results. As for the shear in the columns, Figure 7c highlights a safe-sided slight over-estimation obtained with the strut model (Model B). For completeness, Figures 6 and 7 report also the analytical prediction of the monothonic response, obtained from the superposition of the analytical infill contribution to the bare frame response.

Below, the validation of the simplified strut model has been extended with the comparison with some of the results of the parametric study reported in [24]. Figure 8 shows the results of the comparison for 9 different case studies, whose properties are reported in Table 2. The results of both the simplified model (Model A and Model B) are reported, normalized over the refined FEM results.

Also in these cases the result of the superposition of the analytical infill contribution to the bare frame is reported, for comparison.

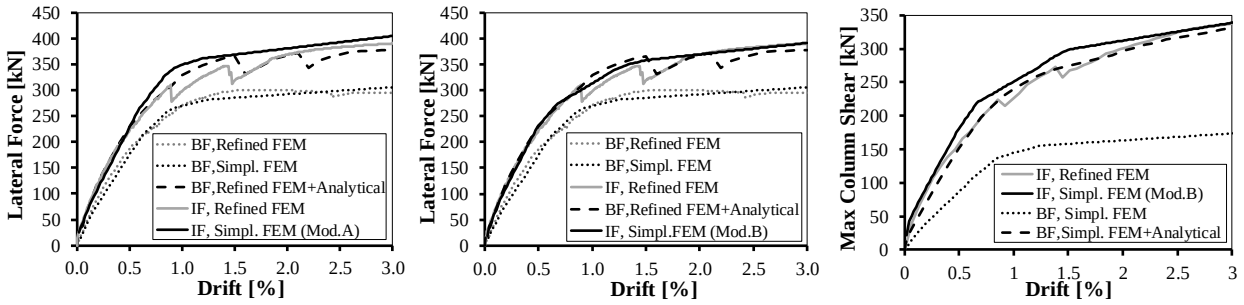


(a) Force-vs.-Drift curve (Model A) (b) Force-vs.-Drift curve (Model A) (c) Max.column shear-vs.-Drift curve (Model B)

Figure 7. Comparison of the simplified and refined modeling of the reference infilled RC frame.

Table 2. Properties of the studied cases in the parametric comparison between the refined numerical model, the analytical model and the simplified models.

| **Parameters** | | **Case 1 (Baseline)** | **Case 2** | **Case 3** | **Case 4** | **Case 5** | **Case 6** | **Case 7** | **Case 8** | **Case 9** |
|---|---|---|---|---|---|---|---|---|---|---|
| N° infill sub-panel | N | 4 | 7 | 14 | 4 | 4 | 4 | 4 | 4 | 4 |
| Friction coefficient | $\mu_j$ | 0.5 | 0.5 | 0.5 | 0.05 | 1 | 0.5 | 0.5 | 0.5 | 0.5 |
| Infill length | L [m] | 4.2 | 4.2 | 4.2 | 4.2 | 4.2 | 3 | 6 | 4.2 | 4.2 |
| Contact yielding stress | $\sigma_c$ [kN/m$^2$] | 2200 | 2200 | 2200 | 2200 | 2200 | 2200 | 2200 | 1040 | 3210* |

*the masonry yielding stress is adopted (2700 MPa)

On the first line of Figure 8 the comparison is reported in terms of infilled frame in-plane response for three different drift levels (0.5%, 1%, and 2%). It can be observed that at small drifts such as 0.5%, the comparison shows an approximation with an error lower than 20% except when the contact material located at the column-infill interface is stronger than masonry (Case 9). However, for larger drift, the error diminishes below 15% for all cases, with the tendency of overestimation as the drift grows to 2%. On the second line of Figure 8, the evaluation of the maximum column shear action is reported for the same three drift levels. As observed for the lateral strength, the error remains below 25% in the worst case, for 0.5% drift. The error reduces below 15% for 1% and 2% drift and shows the tendency for a safe-sided overestimation as the drift gets larger.

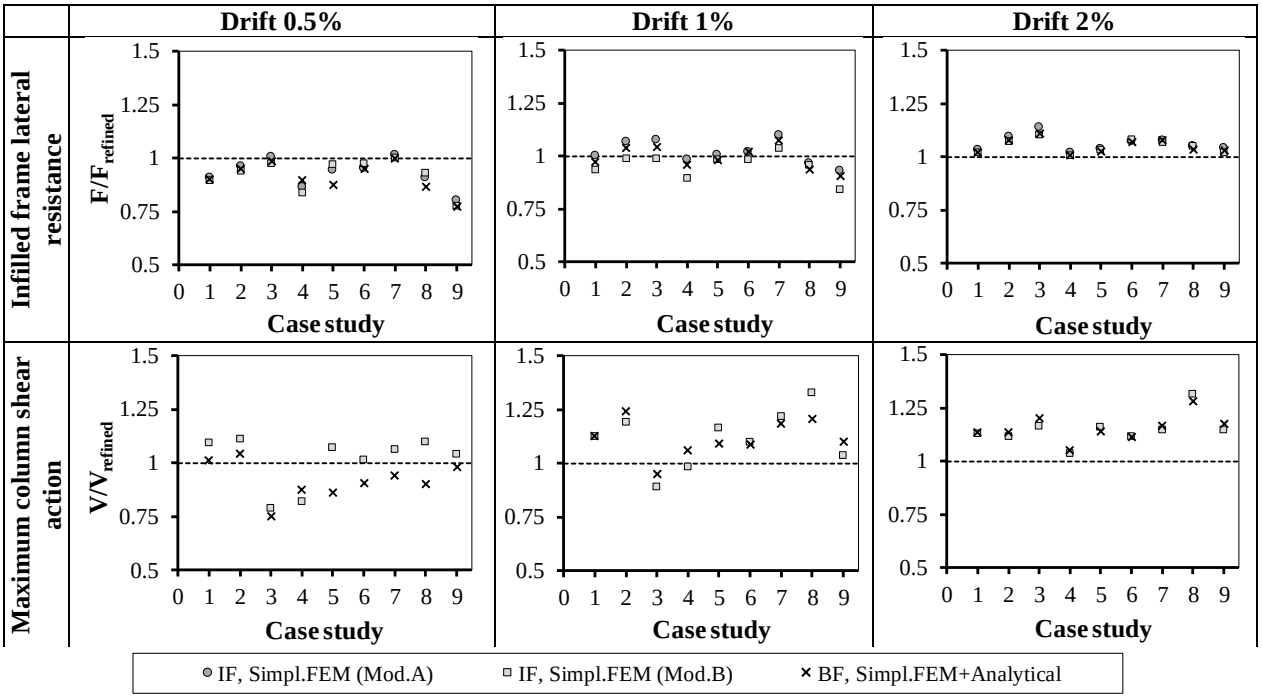


Figure 8. Results of the parametric analysis performed with the analytical and equivalent strut models, normalized on the values obtained from the refined FEM analyses, in terms of infilled frame lateral strength (F) and column shear action (V).

## 5. CONCLUSIONS

In this paper a simplified modeling approach is presented for the estimate of the infill-frame in-plane interaction when a masonry infill partitioned with horizontal joints is adopted. The approach is based on an equivalent strut numerical macro-model, calibrated on analytical formulations, capable of reproducing both the infill lateral strength contribution and the maximum column shear produced by the interaction.

The proposed analytical formulations originate from simple equilibrium equations based on few geometrical and mechanical properties of the infill, namely the infill geometry and weight, the number of sliding joints and their friction coefficient, the column-infill contact yielding stress. A basic parameter is the length of such contact, whose analytical estimate is proposed, as a function of the interstorey drift.

Based on these analytical formulations, a simplified macro-model suitable for numerical analyses of multi-story buildings is proposed and calibrated. The model reproduces the interaction of the infill with the structural frame by means of diagonal struts. Two different configurations have been proposed: the first (Model A) is only capable of reproducing the interaction in terms of contribution of the infill in the frame lateral strength; the second (Model B) allows also to reproduce the maximum shear action in the columns during the in-plane response.

The validation of the proposed models is performed by means of the comparison of their results with those obtained experimentally and numerically in previous works on infilled portal frames. The comparison of the capacity curves (monotonic and cyclic) shows a good reliability of the proposed approach, with an error that, in the worst cases, remains below 25% up to a 2% interstorey

drift. As for the shear action in the column, a tendency of the simplified model to overestimate the maximum value is observed, compatible with a safe-sided design.

Moreover, the obtained results validate the adopted approach for the evaluation of the infilled frame response, based on the simple superposition of the infill contribution to the bare frame response. Such effectiveness is supported by the limited interaction with the frame ensured by the infill with sliding joints, compared to that of traditional masonry infill.

## 6. ACKNOWLEDGEMENTS

The presented study was developed in the research program financed by the "Presidenza del Consiglio dei Ministri - Dipartimento della Protezione Civile" within the Reluis research program; the present publication, however, does not necessarily reproduce the Department position and judgments.

## 7. REFERENCES

[1] P. B. Shing and A. Stavridis, "Analysis of seismic response of masonry-infilled RC frames through collapse," *ACI Structural Journal*, vol. 297, pp. 1–20, 2014.

[2] G. Al-Chaar, M. Issa, and S. Sweeney, "Behavior of masonry-infilled nonductile reinforced concrete frames," *Journal of Structural Engineering*, vol. 128, no. 8, pp. 1055–1063, 2002.

[3] S. H. Basha and H. B. Kaushik, "Behavior and failure mechanisms of masonry-infilled RC frames (in low-rise buildings) subject to lateral loading," *Engineering Structures*, vol. 111, pp. 233–245, Mar. 2016.

[4] H.-S. Lee and S.-W. Woo, "Effect of masonry infills on seismic performance of a 3-storey R/C frame with non-seismic detailing," *Earthquake engineering & structural dynamics*, vol. 31, no. 2, pp. 353–378, 2002.

[5] L. Decanini, F. Mollaioli, A. Mura, R. Saragoni, and others, "Seismic performance of masonry infilled R/C frames," in *13th World Conference on Earthquake Engineering*, 2004.

[6] M. N. Fardis, S. N. Bousias, G. Franchioni, and T. B. Panagiotakos, "Seismic response and design of RC structures with plan-eccentric masonry infills," *Earthquake Engng. Struct. Dyn.*, vol. 28, no. 2, pp. 173–191, Feb. 1999.

[7] M. Dolšek and P. Fajfar, "The effect of masonry infills on the seismic response of a four-storey reinforced concrete frame — a deterministic assessment," *Engineering Structures*, vol. 30, no. 7, pp. 1991–2001, Jul. 2008.

[8] EERI, "The MW 6.3 Abruzzo, Italy, Earthquake of April 6, 2009." EERI Special Earthquake Report, Jun-2009.

[9] K. Goda *et al.*, "The 2015 Gorkha Nepal earthquake: insights from earthquake damage survey," *Frontiers in Built Environment*, vol. 1, p. 8, 2015.

[10] M. Mohammadi and V. Akrami, "An engineered infilled frame: Behavior and calibration," *Journal of Constructional Steel Research*, vol. 66, no. 6, pp. 842–849, Jun. 2010.

[11] P. Morandi, R. R. Milanesi, and G. Magenes, "Innovative seismic solution for clay masonry infills with sliding joints: Principles and details," in *Proceedings of the 16th International Brick and Block Masonry Conference (IBMAC 2016)*, Padova, Italy, 2016.

[12] M. Preti, N. Bettini, and G. Plizzari, "Infill Walls with Sliding Joints to Limit Infill-Frame Seismic Interaction: Large-Scale Experimental Test," *Journal of Earthquake Engineering*, vol. 16, no. 1, pp. 125–141, Jan. 2012.

[13] M. Preti, L. Migliorati, and E. Giuriani, "Experimental testing of engineered masonry infill walls for post-earthquake structural damage control," *Bull Earthquake Eng*, vol. 13, no. 7, pp. 2029–2049, Nov. 2014.
[14] M. Preti and V. Bolis, "Masonry infill construction and retrofit technique for the infill-frame interaction mitigation: Test results," *Engineering Structures*, vol. 132, pp. 597–608, Feb. 2017.
[15] A. S. Tasligedik and S. Pampanin, "Rocking Cantilever Clay Brick Infill Wall Panels: A Novel Low Damage Infill Wall System," *Journal of Earthquake Engineering*, vol. 0, no. 0, pp. 1–27, Jul. 2016.
[16] N. Verlato, G. Guidi, F. Da Porto, and C. Modena, "Innovative systems for masonry infill walls based on the use of deformable joints: Combined in-plane/out-of-plane tests." 2016.
[17] I. S. Misir, O. Ozcelik, S. C. Girgin, and S. Kahraman, "Experimental work on seismic behavior of various types of masonry infilled RC frames," *Structural Engineering and Mechanics*, vol. 44, no. 6, pp. 763–774, Dec. 2012.
[18] M. Vailati and G. Monti, "Earthquake-Resistant and Thermo-Insulating Infill Panel with Recycled-Plastic Joints," in *Earthquakes and Their Impact on Society*, S. D'Amico, Ed. Springer International Publishing, 2016, pp. 417–432.
[19] C. E. Adamis, E. Vintzileou, and V. Palieraki, "In-plane and out-of-plane response of a mosonry infill divided into smaller wallettes," in *Proceedings of the 16th International Brick and Block Masonry Conference (IBMAC 2016)*, Padova, Italy, 2016.
[20] Y. Nakamura, H. Derakhshan, G. Magenes, and M. C. Griffith, "Influence of Diaphragm Flexibility on Seismic Response of Unreinforced Masonry Buildings," *Journal of Earthquake Engineering*, vol. 0, no. 0, pp. 1–26, Jul. 2016.
[21] L. Silva, G. Vasconcelos, P. B. Lourenço, and F. Akhoundi, "Experimental evaluation of a constructive system for earthquake resisting masonry enclosure walls," in *Proceedings of the 16th International Brick and Block Masonry Conference (IBMAC 2016)*, Padova, Italy, 2016.
[22] D. Markulak, I. Radić, and V. Sigmund, "Cyclic testing of single bay steel frames with various types of masonry infill," *Engineering Structures*, vol. 51, pp. 267–277, Jun. 2013.
[23] M. Preti, N. Bettini, L. Migliorati, V. Bolis, A. Stavridis, and G. A. Plizzari, "Analysis of the in-plane response of earthen masonry infill panels partitioned by sliding joints," *Earthquake Engng Struct. Dyn.*, vol. 45, no. 8, pp. 1209–1232, Jul. 2016.
[24] V. Bolis, A. Stavridis, and M. Preti, "Numerical Investigation of the In-Plane Performance of Masonry-Infilled RC Frames with Sliding Subpanels," *Journal of Structural Engineering*, vol. 0, no. 0, 2016.
[25] A. Stavridis and P. B. Shing, "Finite-element modeling of nonlinear behavior of masonry-infilled RC frames," *Journal of structural engineering*, vol. 136, no. 3, pp. 285–296, 2010.
[26] P. G. Asteris, S. T. Antoniou, D. S. Sophianopoulos, and C. Z. Chrysostomou, "Mathematical Macromodeling of Infilled Frames: State of the Art," *Journal of Structural Engineering*, vol. 137, no. 12, pp. 1508–1517, 2011.
[27] F. J. Crisafulli, A. J. Carr, and R. Park, "Analytical modelling of infilled frame structures-a general review," *Bulletin-New Zealand Society for Earthquake Engineering*, vol. 33, no. 1, pp. 30–47, 2000.
[28] A. Madan, A. M. Reinhorn, J. B. Mander, and R. E. Valles, "Modeling of Masonry Infill Panels for Structural Analysis," *Journal of Structural Engineering*, vol. 123, no. 10, pp. 1295–1302, 1997.

[29] V. Bolis, “Seismic performance of RC frames infilled with engineered walls with sliding panels,” PhD Thesis, University of Brescia, Brescia, Italy, 2016.
[30] M. Preti, V. Bolis, and A. Stavridis, “Infill-frame interaction of masonry walls partitioned with horizontal sliding joints: analysis and simplified modeling,” *Journal of Earthquake Engineering*, vol. (submitted for publication), 2017.

COMPDYN 2017
6th ECCOMAS Thematic Conference on
Computational Methods in Structural Dynamics and Earthquake Engineering
M. Papadrakakis, M. Fragiadakis (eds.)
Rhodes Island, Greece, 15–17 June 2017

# EMPIRICAL-BASED INFILL MODEL ACCOUNTING FOR IN-PLANE/OUT-OF-PLANE INTERACTION APPLIED FOR THE SEISMIC ASSESSMENT OF EC8-DESIGNED RC FRAMES

**Paolo Ricci**[1], **Mariano Di Domenico**[1], **Gerardo M. Verderame**[1]

[1] University of Naples Federico II
Department of Structures for Engineering and Architecture
Via Claudio 21 – 80125 – Naples – Italy
{paolo.ricci, mariano.didomenico, verderam}@unina.it

**Keywords:** URM infill wall, out-of-plane, incremental dynamic analyses, seismic assessment, in-plane/out-of-plane interaction, macro-model.

**Abstract.** *In the Mediterranean area, Reinforced Concrete (RC) buildings are usually provided of Unreinforced Masonry (URM) infill wall panels. When subjected to seismic action, these non-structural elements are sensitive to the displacements produced in the In Plane (IP) direction and to the acceleration in the Out Of Plane (OOP) direction. The damage due to IP displacements reduce the OOP capacity and vice-versa: this phenomenon is called IP-OOP interaction. Proposed empirical-based formulations both for predicting infills OOP strength and for modeling the effects of IP displacement demand on OOP behavior and vice versa are illustrated. A new lumped-plasticity macro-model based on the proposed empirical formulations and conceived to represent the IP and the OOP behavior taking into account the mutual interaction effects is defined. Part of the proposed modelling strategy is a routine that removes the whole infill panel from the structural model in case of its IP or OOP collapse. In this paper, the proposed model is described and applied to model the infills of case-study infilled RC frames designed according to Eurocode 8 and different for design PGA at Life Safety Limit State. The results of non-linear time-history analyses are presented and discussed in order to show the effects of taking into account or neglecting the IP-OOP interaction phenomena in assessing the seismic response of the case-study buildings.*

## 1 INTRODUCTION

In the Mediterranean area, Reinforced Concrete (RC) buildings are usually provided of Unreinforced Masonry (URM) infill wall panels. When subjected to the seismic action, these non-structural elements are sensitive to the displacements produced in the In Plane (IP) direction and to the acceleration in the Out Of Plane (OOP) direction [1]. IP displacements can damage infill walls and produce the attainment of the Damage Limitation Limit State (DL), with significant effects in terms of repairing costs for RC buildings after earthquakes. OOP acceleration can produce infills' collapse by their overturning, which is a great risk for life safety as well as an obstacle to escape/rescue operations during seismic emergency [2]: in this sense, the OOP collapse of infill walls is associable to the attainment of the Life Safety Limit State (LS). A great number of experimental and analytical works concerning the IP behaviour of URM infills is available in literature ([3-6], among many others) and some analytical and experimental works have been proposed about their OOP behaviour, especially in recent years ([7-15], among others), and concerning the IP-OOP interaction phenomena, i.e., the effects of IP actions on the OOP behaviour and vice versa. For instance, several authors showed through analytical and experimental studies how the IP displacement demand affects the OOP response of infills in terms of capacity and demand acting on them.

In this work, a state of art concerning URM infills modelling strategies accounting for their OOP behaviour and the IP-OOP interaction is reported. An empirical-based URM infill macro-model accounting for the IP-OOP interaction implemented in OpenSEES is introduced. Then, two case study RC buildings designed in accordance with Eurocodes 2 and 8 recommendations, different for design PGA at LS (0.15 and 0.35 g), are described. The case-study bare frames are infilled with a single-wythe thick and strong infill wall. Incremental Dynamic Analyses (IDAs) are carried out on the infilled case-study buildings in order to define in a non-linear incremental framework the different seismic capacity assessed with and without accounting for the IP-OOP interaction phenomena.

## 2 STATE OF ART

In [16] Hashemi and Mosalam proposed a strut and tie macro-model of infills based on the results of FEM analyses. In this model, the infill is represented by eight no-tension truss elements joined in the center by a no-compression truss element. Mechanical and geometric characteristics of struts and tie are calibrated in order to obtain an interaction domain of IP OOP action which follows the one obtained through FEM analyses.

In [11] Kadysiewski and Mosalam introduced a macro-model in which the infill is modelled through one diagonal beam element pinned at the edges provided of a lumped mass in the center active only in the OOP direction. The OOP behaviour is assumed as elastic-plastic. To account for the IP-OOP interaction, the authors introduce interaction domains in terms of yielding force and collapse displacements derived from numerical analyses. Integral part of the discussed model is a routine that removes from the structural model the elements representative of the infill when their IP-OOP displacement history exceeds the convex interaction domain in terms of ultimate displacement.

Furtado et al. [17] defined a "Kadysiewski and Mosalam-based" macro-model in which the infill is represented by 4 diagonal rigid elements joined in the center by one element which takes into account the non-linearity of the infill behaviour. The central element is joined to the diagonal struts through 2 nodes in which the OOP mass is lumped. Also in this case, part of the model is an algorithm that removes the elements representative of the infill from the structural model if its IP-OOP displacement history exceeds a linear interaction domain in terms of ultimate displacement. A macro-model based on the one defined by Kadysiewski and Mosal-

am was also proposed by Longo et al. [18]. Shing et al. [19] proposed a macro-model in which the infill wall is represented by two fiber-section diagonals accounting for the IP-OOP interaction and through a vertical and a horizontal element accounting for the bi-directional arching action.

An infill wall model accounting for the IP-OOP interaction was proposed by Oliaee and Magenes [20]. The infill is represented by 2 diagonals, each one divided into 2 non-interacting in-series no-tension elements, an inelastic truss representing IP behaviour and a distributed inelasticity fiber element representing OOP behaviour. The IP-OOP interaction is introduced through the updating of the strain at peak load of the material assigned to fibers (OOP stiffness reduction) and through the reduction of the fiber elements' thickness (OOP strength reduction) depending on the maximum IP displacement registered.

## 3 EMPIRICAL-BASED URM INFILL MODEL ACCOUNTING FOR IP-OOP INTERACTION

Experimental tests aimed at assessing the OOP behaviour of URM infills and the effects of IP displacement demand on the OOP capacity were performed by different authors ([7-15], among others). In a companion paper [21], the Authors of this study collected in a database the values of secant stiffness and lateral force registered for the above test specimens at first macro-cracking and peak load, as well as the value, if provided, of their ultimate OOP displacement. The application of code and literature provisions aimed at predicting stiffness, force and displacement associated to the significant points of the OOP backbone of URM infills showed that:

1) Timoshenko's formula [22] for the calculation of the lateral stiffness of an elastic isotropic plate provides a good estimation of URM infills secant stiffness at first macro-cracking point (Equation 1).

$$K_{crack} = \frac{bD}{\alpha a^3} \tag{1}$$

In Eq. 1, a and b are the shorter and longer dimensions of the infill, respectively, while D is the plate flexural stiffness and α is a parameter accounting for the infill aspect-ratio and boundary conditions.

2) Dawe and Seah's [9] formulation accounting for two-way arching action exhibits good performances in predicting the OOP strength of URM infills, as well as Kadysiewski and Mosalam approach [11] based on the first vibration frequency of a distributed-mass cracked beam pinned at edges produces good predictions of their secant stiffness at peak load (Equation 2).

$$K_{max} = 6.562E \frac{w}{(h/t)^3} \tag{2}$$

In Eq. 2, E is the infill elastic modulus in the vertical direction, w, h and t are the infill width, height and thickness, respectively.

3) No literature or code provision is applicable to obtain a good prediction of URM infills OOP collapse displacement.

In order to define a tri-linear OOP backbone for infills, in an empirical-based framework, a least square linear regression was carried out on the experimental uniformly distributed first cracking loads, $q_{crack}$, reported in the collected database. Moreover, to obtain a more reliable prediction of the uniformly distributed peak load, $q_{max}$, with respect to the one provided by

applying Dawe and Seah's relationship, a least square linear regression was carried out on the experimental values of $q_{max}$, too. The obtained relationships are:

$$q_{crack} = 0.31 \ f_m'^{0.05} \frac{t}{h^{2.66}} \tag{3}$$

$$q_{max} = 1.95 \ f_m'^{0.35} \frac{t^{1.59}}{h^{2.96}} \tag{4}$$

$K_{crack}$ and $K_{max}$ should be calculated by applying equations (1) and (2), respectively.

Based on experimental evidences (Angel et al. [8], Guidi et al. [14], Calvi and Bolognini [13], Griffith and Vaculik [12]), a plastic post-peak behaviour is assumed and the collapse OOP displacement is assumed equal to 3.7 times the predicted displacement at peak load.

Based on experimental evidences, relationships aimed at predicting secant stiffness and lateral strength at first cracking and peak load degradation due to IP damage represented by the maximum IDR attained during the IP loading normalized with respect to the IDR corresponding to the complete loss of IP loads bearing capacity by the infill, $IDR_u$, were defined.

$$\frac{P_{dam}}{P_{undam}} = \begin{cases} \min\left\{1 \ ; \ \alpha\left(\frac{IDR}{IDR_u}\right)^{\beta}\right\} & \text{if } IDR < IDR_u \\ 0 & \text{if } IDR \geq IDR_u \end{cases} \tag{5}$$

In Eq. 5, $P_{dam}$ is the observed variable for the infill that underwent a maximum IP displacement represented by the IDR, $P_{undam}$ is the same observed variable for the undamaged infill, and the α and β coefficients are determined through a linear least squares regression in the log-log plan (Table 1). Clearly, $P_{dam}/P_{undam}$ cannot be higher than 1 and must be equal to 0 if $IDR \geq IDR_u$, i.e., the OOP capacity drops to zero at the infill IP collapse, as shown in Figure 1.

| | $K_{crack,dam}/K_{crack,undam}$ | $F_{crack,dam}/F_{crack,undam}$ | $K_{max,dam}/K_{max,undam}$ | $F_{max,dam}/F_{max,undam}$ |
|---|---|---|---|---|
| α | 0.07 | 0.11 | 0.12 | 0.27 |
| β | -0.76 | 0.89 | -0.69 | -0.37 |

Table 1. α and β values for Equation 5.

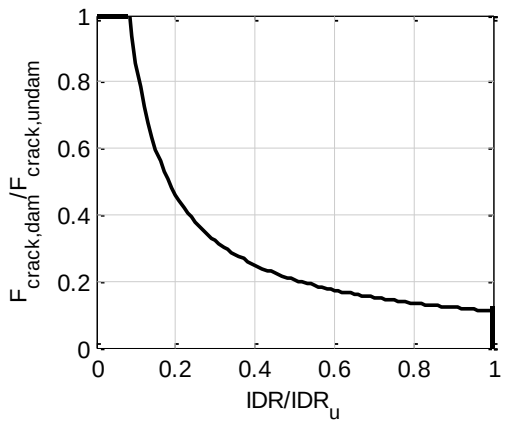


(a)

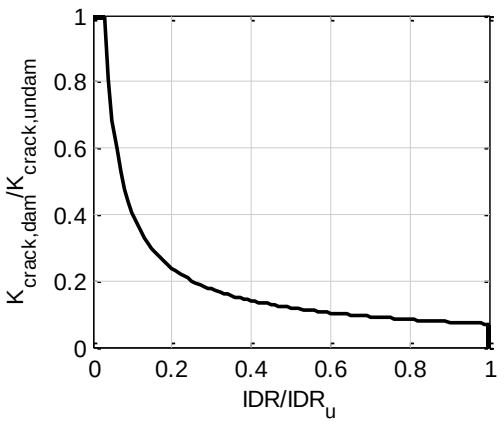


(b)

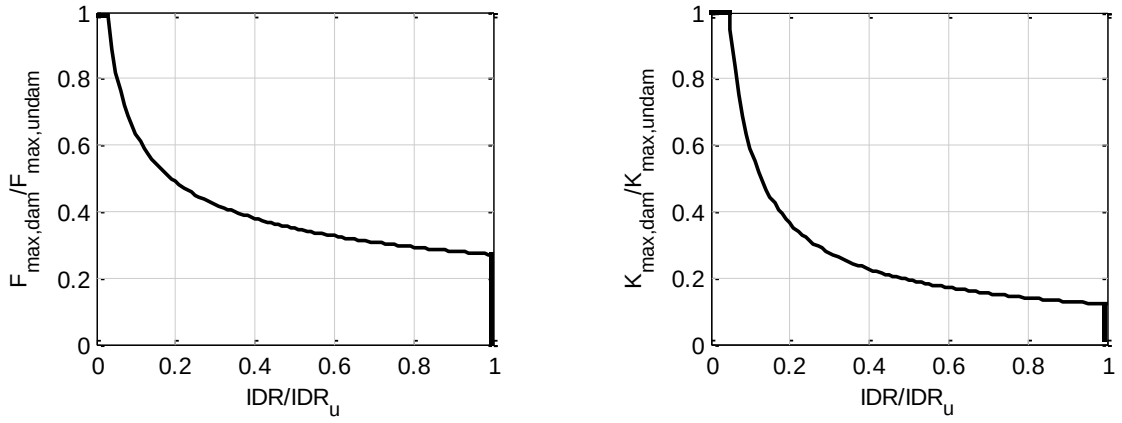


Figure 1. Degradation of first macro-cracking force (a) and secant stiffness (b) and of peak load force (c) and secant stiffness (d) due to IP damage represented by the current IDR normalized with respect to IP collapse IDR, $IDR_u$.

Based on the only reliable experimental datum provided on this issue in literature by Furtado et al. [15], it is assumed that the $d_{u,dam}/d_{u,undam}$ ratio decreases linearly at increasing $IDR/IDR_u$. Note that this approach is consistent with the proposal of Fardis in section 3.5 of [23].

$$\frac{d_{u,dam}}{d_{u,undam}} = 1 - \frac{IDR}{IDR_u} \tag{6}$$

IP load bearing capacity reduction due to OOP displacements was reconstructed based on Flanagan and Bennett's [24] combined IP-OOP test performed on specimen 23. Based on these experimental evidences, if the infill has been damaged by the OOP action represented by the OOP maximum displacement $d_{OOP}$, the IP force that produces the IP displacement $d_{IP}$, $F_{IP,dam}(d_{IP}, d_{OOP})$ can be expressed through a simplified linear relationship as:

$$\frac{F_{IP,dam}(d_{IP}, d_{OOP})}{F_{IP,undam}(d_{IP})} = 1 - \frac{d_{OOP}}{d_{OOP,u}} \tag{7}$$

in which $F_{IP,undam}(d_{IP})$ is the IP force that produces the IP displacement $d_{IP}$ of the undamaged panel and $d_{OOP,u}$ is the undamaged infill ultimate OOP displacement.

The proposed empirical-based model has been implemented in OpenSEES [25]. First, the OOP force-displacement behaviour relationship should be defined for the undamaged panel through the semi-empirical approach described in this section. Hereafter, the above-defined OOP behaviour relationship will be mentioned as the IDR=0 backbone. Then, *n* IDRs ($IDR_i$, with *i*=1, …, *n*) should be set as discrete IP damage thresholds. Through the degradation-modelling relationships, it is possible to define *n* OOP backbones, corresponding to the *n* IDRs: each one of these curves, which will be mentioned hereafter as $IDR=IDR_i$ backbone, represents the OOP behaviour that the infill will exhibit from the moment the IP IDR demand exceeds the damage threshold represented by $IDR_i$ (see Figure 2).

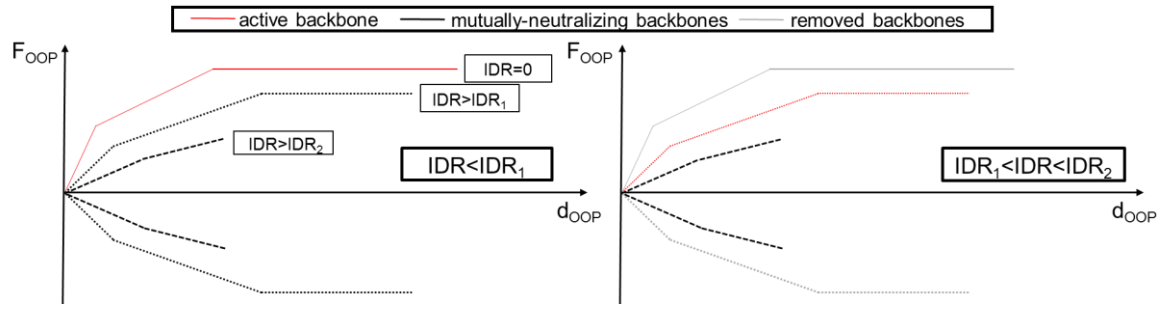


(a) (b)

Figure 2. Proposed modelling strategy of the IP-OOP interaction. Active and mutually-neutralizing OOP backbones for IDR<$IDR_1$ (a); active, mutually-neutralizing and removed backbones for IDR between $IDR_1$ and $IDR_2$ (b).

As shown in Figure 3, each infill should be represented by a diagonal element representing the IP behaviour of the infill. Each of these elements is connected through a pinned joint to the surrounding frame and is provided of a central node connected to a second central node in which the mass participating to the first OOP vibration mode of the infill is lumped: generally, it can be assumed equal to the 81% of the panel total mass [11]. The connection between these central nodes is ensured by $2n+1$ plastic hinges. First, a plastic hinge carrying the IDR=0 backbone must be defined (in the following example, a Hysteretic Material is used to this aim). Then, for each IDR=$IDR_i$ backbone, a couple of plastic hinges must be defined: the first one, which will be called "*i*-th real plastic hinge", models the OOP behaviour defined by the considered $IDR_i$ backbone; the second one, which will be called "*i*-th auxiliary plastic hinge", behaves according to the force-displacement relationship defined by the IDR=$IDR_i$ backbone mirrored with respect to the displacements axis. This goal can be achieved in OpenSEES by defining the "auxiliary" backbones through a Parallel Material that is referred, with scale factor equal to -1, to the constitutive relationship used to define the corresponding "real" backbone. This means that the OOP force for a given OOP displacement in the *i*-th real plastic hinge is always equal and opposite to the OOP force at the same displacement in the *i*-th auxiliary plastic hinge. This also means that as long as all plastic hinges are part of the infill model, the panel OOP behaviour is the one defined by the IDR=0 backbone, while the effects of the other plastic hinges are mutually neutralizing.

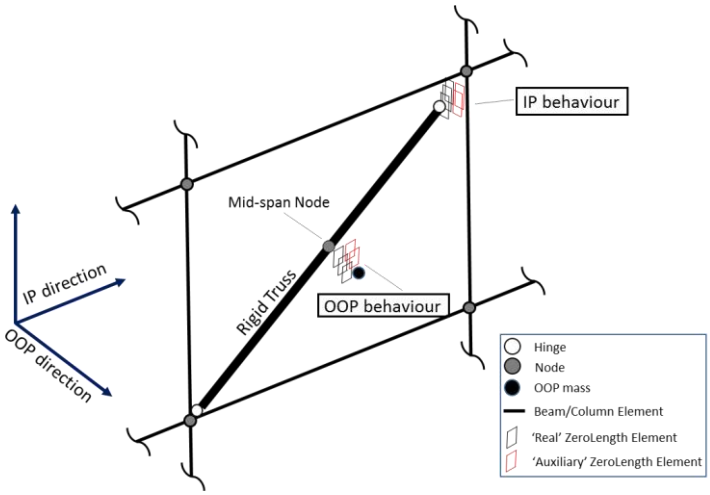


Figure 3. Graphical representation of the proposed modelling strategy.

Integral part of the proposed model is a routine that removes from the structural model the $IDR_{i-1}$ real plastic hinge and the $IDR_i$ auxiliary plastic hinge when the IP IDR exceeds the previously defined damage threshold represented by $IDR_i$. In this way, as soon as the IDR exceeds $IDR_i$ and as long as the IDR is lower than the successive IP damage threshold $IDR_{i+1}$, the panel OOP behaviour is defined by the $IDR=IDR_i$ backbone "contained" in the *i*th real plastic hinge, while the effects of the remaining plastic hinges are still mutually neutralizing. Moreover, if the OOP displacement exceeds the ultimate displacement associated to the $IDR=IDR_i$ backbone, all the elements representative of the infill wall are removed from the structural model. An explanatory version of the removal routine is shown in Figure 4.

```
PRIOR TO THE STRUCTURAL ANALYSIS

for each Infill Wall modeled
    set CF1, a control flag for the element removal, to 0
    for each ZeroLength element (ZL) carrying a "real" OOP backbone
        set IPLD, the value of the IP displacement at which the ZL must be removed
        set CF2, a control flag for the ZL removal, to 0
        set OOPUD, the value of the ultimate OOP displacement associated to the ZL
    end
end

DURING THE STRUCTURAL ANALYSIS, AT EACH STEP CONVERGED

for each Infill Wall modeled
    set IPD to the current in-plane displacement
    set OOPD to the current out-of-plane displacement
    if (element not already removed, i.e., CF1==0)
        if OOPD>OOPUD
            remove the whole infill wall
            set CF1 to 1
        else
            for i that skims each ZL carrying a "real" OOP backbone
                if (the i-th ZL not already removed, i.e., CF2==0)
                    if IPD>IPLD
                        remove the i-th ZL carrying the "real" OOP backbone
                        remove the ZL carrying the i+1-th "auxiliary" OOP backbone
                        set CF2 to 1
                    end
                end
            end
        end
    end
end
```

Figure 4. Removal routine simplified schema.

The IP strength and stiffness degradation can be controlled through the ratio between the OOP displacement demand and the OOP displacement capacity of the undamaged panel. It can be modelled, together with the whole infill removal due to the attainment of the IP ultimate displacement, through a procedure very similar the one explained in the previous lines for the modelling of the infill OOP behaviour.

## 4 CASE-STUDY RC BUILDINGS

### 4.1 RC frames

Hereafter, the design of 2 RC case-study buildings with rectangular plan is presented (Figure 5). The buildings are provided of 5 and 3 bays in the X and Z direction, respectively. All bays spans are 4.5 m long while the inter-storey height is always equal to 3 m. Each building has been designed for gravity and seismic loads by applying the Response Spectrum Analysis method according to EC2 [26] and EC8 [27]. The case-study buildings designed are distinguished for different values of the design PGA at LS (0.15 g and 0.35 g). The materials used for the building design are class C28/35 concrete and reinforcing steel with yielding stress equal to 450 $N/mm^2$. The buildings were designed on a stiff and horizontal type A soil. EC8 Type 1 elastic spectrum, which is recommended for high-seismicity zones, was used to

evaluate horizontal seismic actions. A behaviour factor equal to 4.68 was applied to reduce spectral pseudo-accelerations. All designed buildings resulted regular in plan while not regular elevation due to a non-gradual stiffness reduction along their height. P-δ effects resulted negligible. The longitudinal and transverse reinforcement for beams and columns were determined accordingly to force demands assessed through RSA and by applying capacity design rules. In order to perform non-linear dynamic analyses, the RC elements non-linearity is modelled through a tri-linear moment-chord rotation backbone provided of the cracking point and perfectly plastic after yielding point. These points are determined through a section analysis and by applying the dispositions about yielding chord rotation given by the Annex A of EC8, part 3 [28].

In the following, each case-study building is defined through an acronym, such as 8P*X*, in which *X* is the design PGA at LS expressed in g/100 (15 or 35).

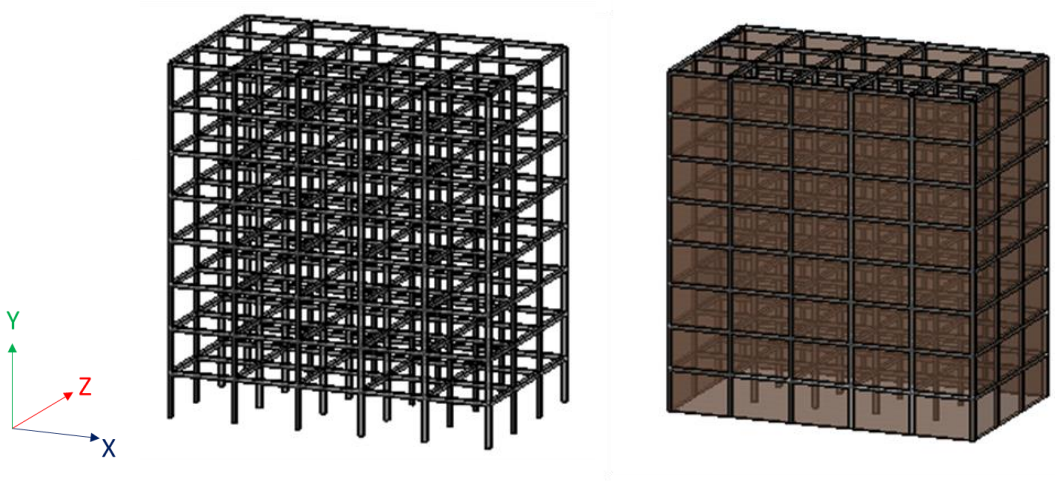


Figure 5. Representation of the bare and infilled case-study buildings.

## 4.2 Infill walls

A one-leaf 300 mm thick, 4500 wide and 3000 mm high URM infill wall is modelled. Its mechanical properties are the ones calculated for the masonry wallets tested by Guidi et al. [14] (Table 2). The value of the masonry shear strength was set to 0.30 N/mm$^2$ according to Table 3.4 of EC6 [29].

| | | | | vertical (parallel to holes) | | horizontal (perpendicular to holes) | |
|---|---|---|---|---|---|---|---|
| h/t | m [t] | G [N/mm$^2$] | $\tau_{cr}$ [N/mm$^2$] | E [N/mm$^2$] | $f_m$ [N/mm$^2$] | E [N/mm$^2$] | $f_m$ [N/mm$^2$] |
| 10 | 3.3 | 788 | 0.30 | 1767 | 1.19 | 4312 | 6 |

Table 2. Geometric and mechanical features of the case-study infill.

Each infill wall was introduced in the structural model through a single equivalent strut whose non-linear behaviour is modelled based on Panagiotakos and Fardis proposal [3-4]. The ratio of the softening over the elastic stiffness, α, was set to -3.6%. These assumption lead to predictions of the softening stiffness and ultimate IP displacement in good accordance with the experimental evidences shown by Guidi et al. (specimen URM-U). The OOP behaviour was modelled accordingly to the empirical-based approach discussed in the previous section.

The IP and OOP behaviour characteristic points and the OOP vibration period of the case-study infill, $T_a$, are reported in Table 3.

| IP behaviour | | | OOP behaviour | | |
|---|---|---|---|---|---|
| $F_{crack}$ | [kN] | 405.0 | $F_{crack}$ | [kN] | 73.9 |
| $K_{crack}$ | [kN/mm] | 354.6 | $K_{crack}$ | [kN/mm] | 83.9 |
| $d_{crack}$ | [mm] | 1.14 | $d_{crack}$ | [mm] | 0.9 |
| $F_{max}$ | [kN] | 526.5 | $F_{max}$ | [kN] | 281.2 |
| $K_{max}$ | [kN/mm] | 40.8 | $K_{max}$ | [kN/mm] | 63.6 |
| $d_{max}$ | [mm] | 12.9 | $d_{max}$ | [mm] | 4.4 |
| α | [%] | -3.6 | $d_u$ | [mm] | 16.3 |
| $d_u$ | [mm] | 54.1 | $T_a$ | [s] | 0.035 |
| $IDR_u$ | [%] | 1.80 | | | |

Table 3. IP and OOP behaviour of the case-study infill.

The infill wall behaviour degradation was modelled through the proposed empirical approach: for instance, the IP degradation was modelled with backbones defined at steps of 0.05 times the $d_{OOP,u}$ displacement while the OOP degradation was modelled with backbones defined at steps of 0.05 times the $IDR_u$.
The PGA associated to the first OOP collapse ($PGA_C$) for the case-study buildings assessed through a "code-based approach" on the bare frames, i.e., by matching the infill OOP strength calculated accordingly to EC6 §6.3.2 and the OOP demand acting on them calculated accordingly to EC8 §4.3.5, are reported in Table 5.

| | 8P15 | 8P35 |
|---|---|---|
| $PGA_C$ [g] | 0.41 | 0.38 |

Table 4. PGA at first OOP infill collapse accordingly to an EC-based approach

## 5 RECORDS SELECTION FOR INCREMENTAL DYNAMIC ANALYSES AND ANALYSIS PROCEDURE

Seven ground motions were selected among the records of seven different European earthquakes collected in the Engineering Strong-Motion (ESM) Database [30] in order to perform Incremental Dynamic Analyses (IDAs) [31]. Significant characteristics of the selected ground motions are reported in Table 6.

| | **ESM ID** | **Country** | **Date** | **M** | **$R_{epi}$ [km]** | **PGA – NS [g]** | **PGA – EW [g]** |
|---|---|---|---|---|---|---|---|
| 1 | ME-1979-0006 | Montenegro | 15/04/1979 | 5.8 | 22.7 | 0.092 | 0.080 |
| 2 | IT-1984-0005 | Italy | 11/05/1984 | 5.5 | 19.2 | 0.025 | 0.015 |
| 3 | IT-1997-0004 | Italy | 26/09/1997 | 5.7 | 24.2 | 0.023 | 0.024 |
| 4 | IT-1998-0103 | Italy | 09/09/1998 | 5.6 | 18.0 | 0.161 | 0.156 |
| 5 | GR-1999-0001 | Greece | 07/09/1999 | 5.9 | 19.7 | 0.108 | 0.119 |
| 6 | TK-1999-0294 | Turkey | 13/09/1999 | 5.8 | 13.8 | 0.074 | 0.317 |
| 7 | IT-2009-0102 | Italy | 07/04/2009 | 5.5 | 15.6 | 0.131 | 0.089 |

Table 5. Selected Ground Motions for Incremental Dynamic Analyses.

The selection of records was performed searching among the bidirectional registration of stations based on EC8 type A soils, consistently with the design soil type. Consistently with the choice of using EC8 Type I design spectrum, only earthquakes with magnitude between 5.5 and 7 and only registration of stations with epicentral distance between 10 and 30 km were considered. The 5%-damped response spectra of the selected records are reported in Figure 6a (North-South component) and 6b (East-West component). Both horizontal components of the selected records were simultaneously matched to the 5%-damped EC8 design spectrum at LS using wavelets through the RspMatchBi software by Grant [32]. So, two different record-set were defined after matching: a first record-set (R15) used for IDAs on buildings designed for a PGA at LS of 0.15 g, a second record-set (R35) used for IDAs on buildings designed for a PGA at LS of 0.35 g. The response spectra of the R15 and R35 records are shown in Figure 6c and 6d, respectively, together with their mean spectrum and the EC8 target response spectrum.

IDAs were performed by scaling each selected and matched record for a set of predetermined scale factors in order to obtain for each horizontal direction an incremental PGA (selected as Intensity Measure) vs maximum IDR (selected as Engineering Demand Parameter) curve. Moreover, a bisection procedure was implemented in order to define the PGA associated to the first OOP infill collapse and removal from the structural model with a precision equal to +/- 0.01 g. Note that IDAs were performed on a W/ model, in which the degradation of IP and OOP backbones due to interaction was implemented, together with the infill removal routine, and on a W/O model in which only the infill removal routine at the attainment of the IP or OOP collapse displacement was implemented.

The analyses were carried out by applying mass- and tangent stiffness-proportional Rayleigh damping rules for two control vibration modes. A “global” and a “local” mode were selected as control modes. For instance, the first control mode corresponds the first natural frequency of the infilled structure, while the second control mode corresponds to the mode associated to the frequency closer to the infill natural frequency in the OOP direction. The assigned damping ratio is equal to 2% both for the first global and for the second local control mode: the last choice is due to the lack of exhaustive studies on this topic, which is worth to be investigated in the future.

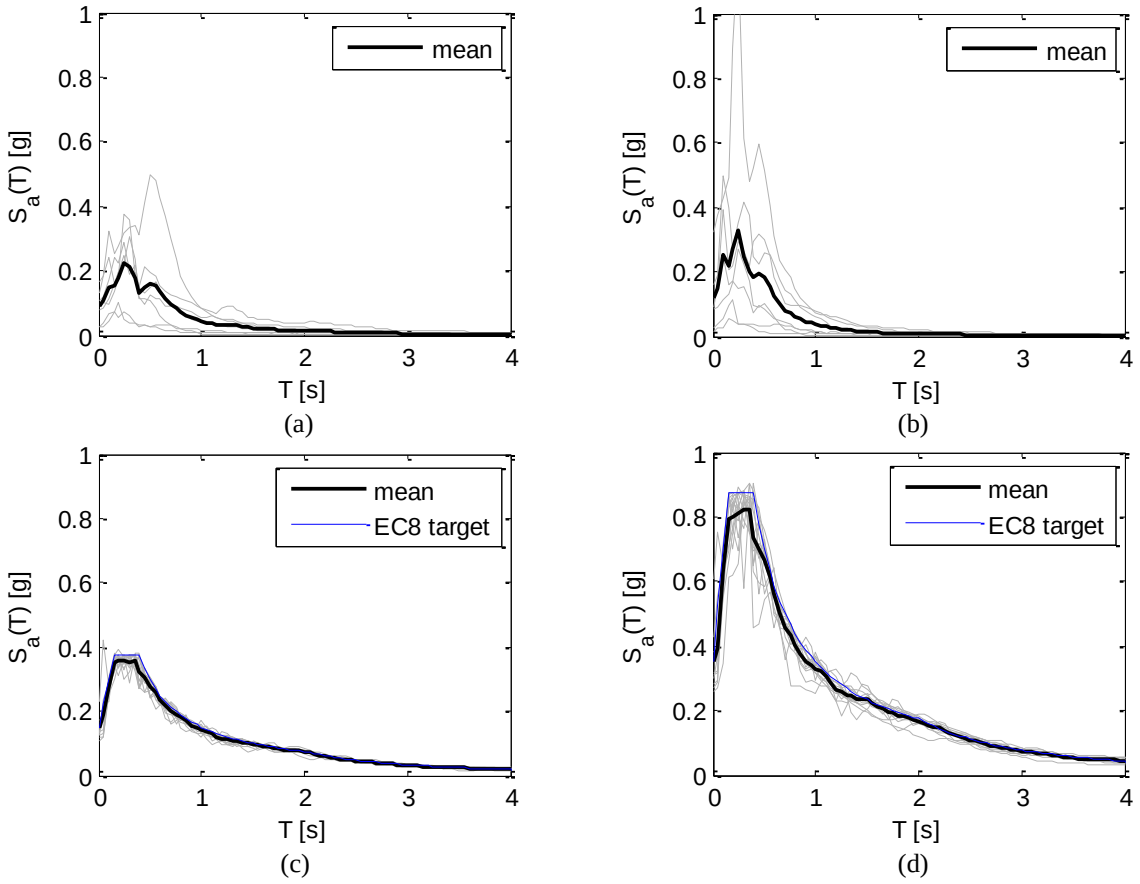


Figure 6. Selected records response spectra for NS component (a), EW component (b). Response spectra of the selected records matched to EC8 design spectrum at LS for PGA=0.15 g (c) and PGA=0.35 g (d).

## 6 ANALYSES RESULTS

Incremental Dynamic Analyses were performed on the case-study buildings using the OpenSEES software. IDA curves for all case-study buildings are shown for both W/ and W/O models in Figure 7. Median IDA curves for W/ and W/O models are compared in Figure 8.

As expected, IDR demands are greater in the Z direction (less stiff direction of the buildings) and for the W/ model of all case-study buildings. For instance, the maximum IDR demand is underestimated by neglecting IP-OOP interaction especially for buildings designed for a 0.15 g PGA at LS, while building designed for a LS PGA of 0.35 g are provided of structural members with greater inertia properties and are, so, stiffer with respect to horizontal actions. Accounting for IP-OOP interaction seems to be necessary in order to not underestimate displacement demands during seismic analyses.

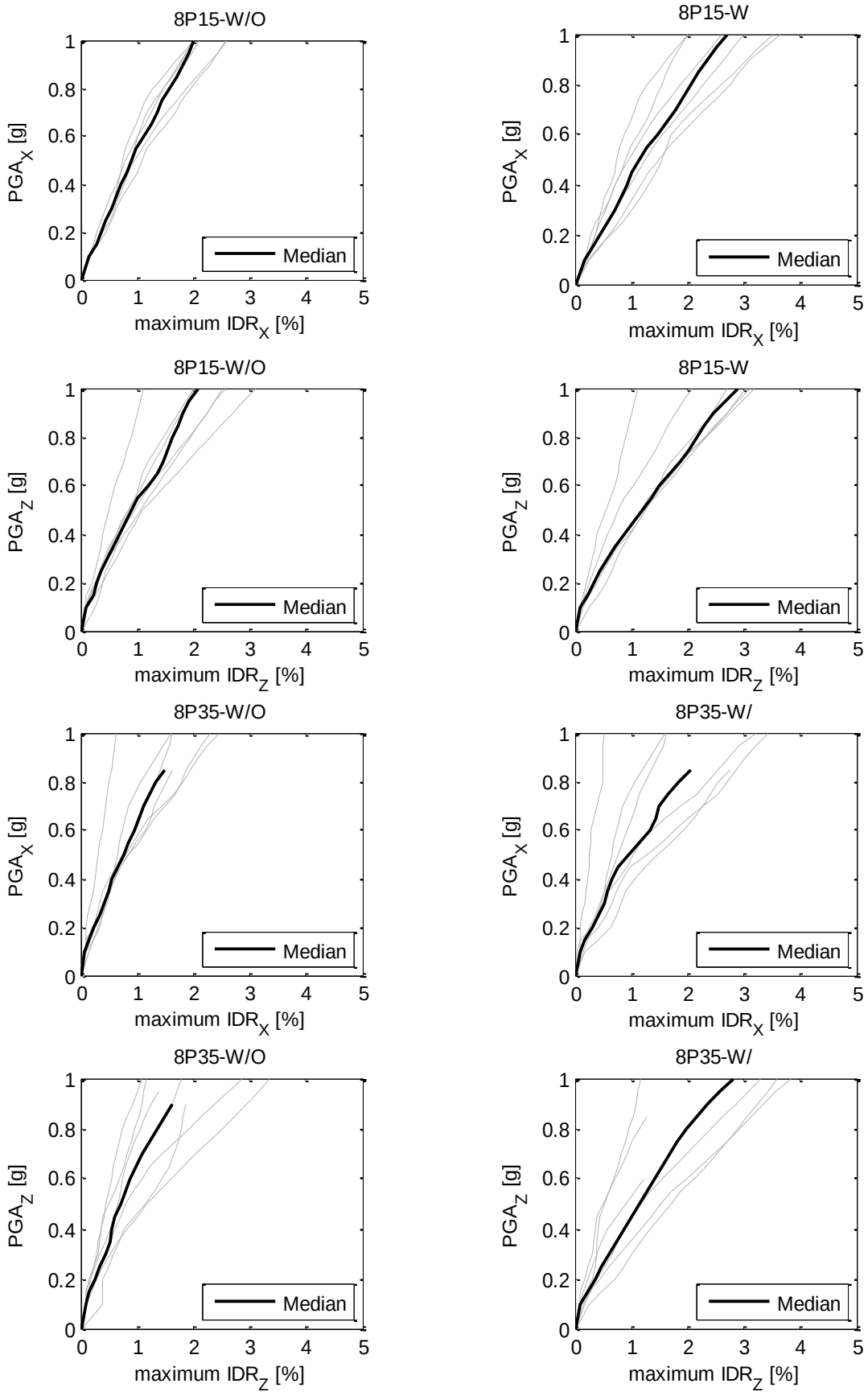


Figure 7. IDA curves for all case-study buildings (grey) together with their median IDA curve (black).

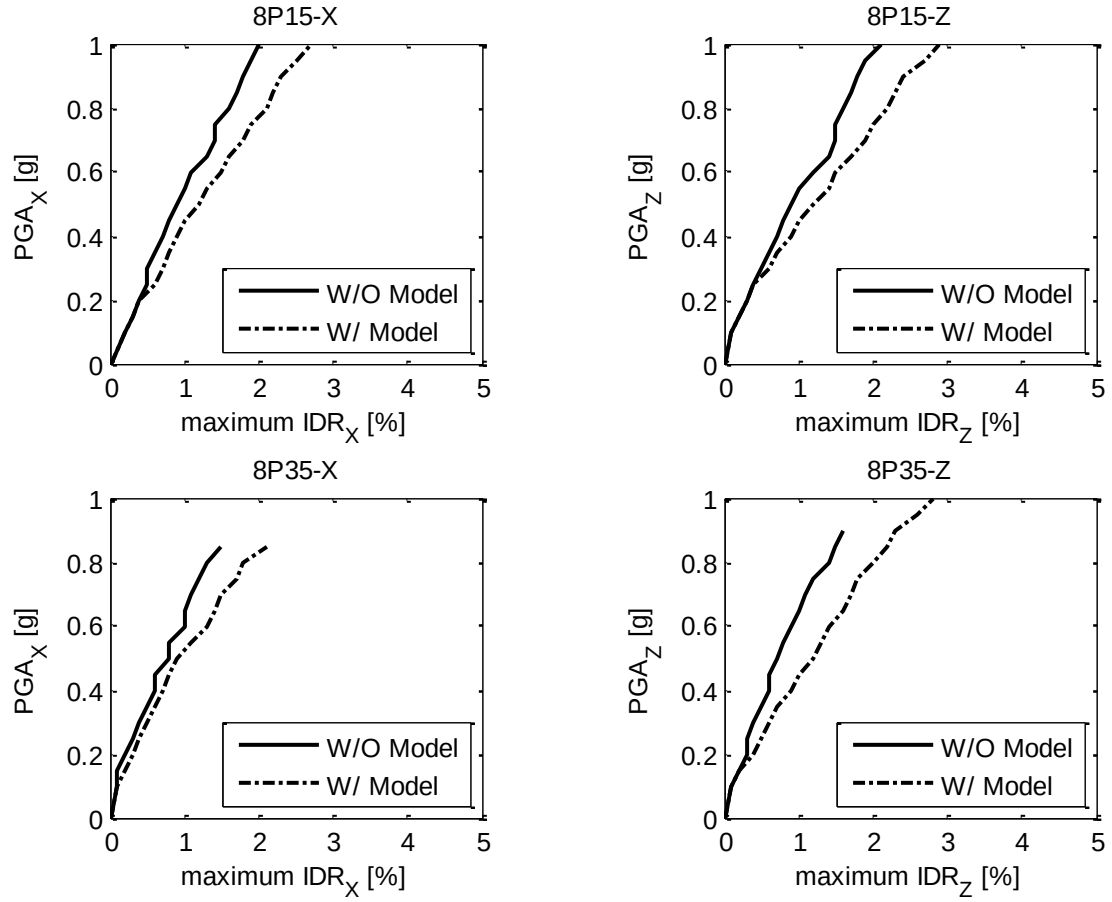


Figure 8. Comparison of median IDA curves for W/O (continuous line) and W/ (dotted line) models of all case-study buildings.

In Table 6, the mean PGA at first OOP collapse for all case-study buildings are reported, together with the lower (L) and higher (H) storey at which the first OOP collapse occurred.

| | W/O Model | | W/ Model | |
|---|---|---|---|---|
| | PGA [g] | Storey (L/H) | PGA [g] | Storey (L/H) |
| 8P15 | 0.28 | 6/7 | 0.16 | 3/4 |
| 8P35 | 0.25 | 6/8 | 0.14 | 3 |

Table 6. First OOP collapse mean PGA for all case-study buildings.

Generally speaking, they are, as expected, lower for W/ models. In fact, in W/O models the OOP collapse is attained for a fixed OOP collapse displacement equal to 16 mm, while in W/ models the OOP collapse displacement reduces due to IP action. The ratio of the infill natural period in the OOP direction, $T_a$, over the case-study buildings' vibration period in the same direction, $T_1$, is always lower than 1. This means that for stiffer buildings designed for higher PGA at LS, and so provided of lower natural vibration period, the $T_a/T_1$ ratio is closer to unit than for buildings designed for a lower PGA. For this reason, higher OOP actions are expected for infills in stiffer buildings and so a lower PGA at first OOP collapse is as well expected for buildings designed for a 0.35 g PGA at LS.

Collapse PGAs assessed through dynamic analyses, which accounts for IP-OOP interaction and structural non-linearity, is extremely higher that collapse PGAs evaluated through a code-based approach (Table 4). For instance, the overestimation of OOP collapse PGAs ranges

from 46% (W/O model of 8P15 building) to 132% (W/ model of 8P35 building). Moreover, a code-based approach predicts the first OOP infill collapse at the last storey, while it is expected due to IP-OOP interaction, based on the results of the above described analyses, between the third and the fourth floor. In fact, at intermediate storeys the maximum combined effect of higher IDR demands (increasing from higher to lower storeys) and higher OOP demands (increasing from lower to higher storeys) is expected. Without accounting for IP-OOP interaction, the first OOP collapse is expected at higher storeys (sixth to eighth): in fact, in this case, the OOP collapse is only due to higher OOP demands, which reach their maximum at the higher storeys. Probably, higher modes effects make the maximum OOP demand occur not always at the last storey.

Simplified methods accounting at least for IP-OOP interaction in a linear elastic framework during OOP safety check of infills should be implemented in order to provide an accurate estimate of the OOP collapse PGA, which is often lower than design PGA at LS. Note that at §2.2.2(6)P, EC8 [27] states that at LS: "*it shall be verified that under the design seismic action the behaviour of nonstructural elements does not present risks to persons and does not have a detrimental effect on the response of the structural elements*". The OOP collapse of infills presents enormous risks for life safety and, in this sense, case-study buildings with first OOP collapse PGA lower than the design PGA (8P35) are not EC8-compliant in the safety check at LS, even if their structural members were designed according to EC8 provisions.

Fragility curves relating the probability of exceeding the DL (maximum IDR demand equal or greater than 0.5%) or the "First OOP Collapse Limit State" (PGA equal to the first OOP collapse PGA) to PGAs for W/ and W/O models are shown in Figure 9.

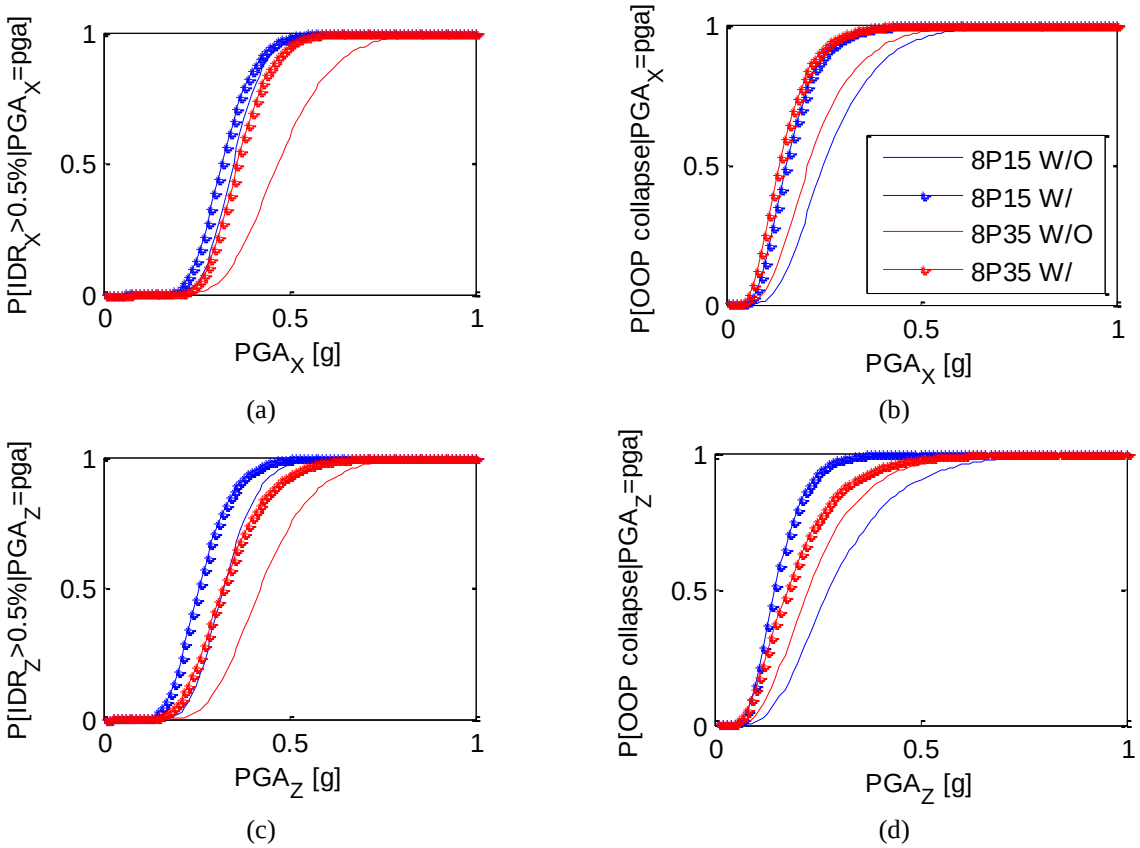


Figure 9. Fragility curves for all case-study buildings in X (a-b) and Z (c-d) directions, with respect to the attainment of DL (a-c) or of the 1st OOP infill collapse (b-d). Legend reported in (b).

First DL exceedance always occurred in the Z direction, while first OOP collapse always involved infills along disposed along Z direction for seismic demand acting along X direction.

Based on the results above discussed in terms of IDA and median IDA curves, the probability of DL exceedance is underestimated for W/O models due to the underestimation of IP displacement demands caused by the effects of OOP demand on the IP infill behaviour, which are neglected if the IP-OOP interaction is neglected. The design at higher PGA at LS produces structural elements with higher inertia properties. For this reason, at equal upper-limit PGA, a noticeably lower probability of DL exceedance is expected and observed for 8P35 case-study building. The probability of OOP collapse activation is, as expected, underestimated for W/O models. Values closer to unit for the ratio of the infill OOP vibration period over the supporting structure vibration period, which lead to a higher dynamic amplification of OOP demands along the building height are expected for stiffer buildings. For this reason, at equal upper-limit PGA, a noticeably higher probability of first OOP occurrence is expected, in general, for stiffer buildings, such as those designed for a higher PGA at LS, and is observed for the 8P35 case-study building.

## 7 CONCLUSIONS

This research paper is focused on the out-of-plane (OOP) behaviour of URM infills walls and on the effects on it of the in-plane (IP) displacement demand and vice-versa, i.e., the IP-OOP interaction effects. Modelling infills accounting for their OOP behaviour and for the IP-OOP interaction is the main topic of this work. For instance, Incremental Dynamic Analyses were carried out on two Eurocodes-conforming 8-storeys RC buildings designed for two different PGA acceleration at Life Safety Limit State (0.15 and 0.35 g), in order to analyze the effects of taking or not taking account of the IP-OOP interaction effects in the case-study buildings seismic assessment.

First, a state-of-the-art on the OOP infills behaviour and on the IP-OOP interaction modelling is presented. Then, a novel empirical-based model for URM infills accounting for OOP behaviour and IP-OOP interaction implemented in OpenSEES is presented. The proposed model is applied to model the thick infills of the case-study buildings, whose characteristics are briefly described. 7 bidirectional ground motions were selected among the records of strong European records. The ground motion components were simultaneously matched to the design spectrum at Life Safety Limit State (LS) of the case-study buildings. IDA curves for all records, their median curve and fragility curves with respect to the attainment of Damage Limitation Limit State (DL) and of the first OOP infill collapse are shown to summarize dynamic analyses' results, together with the mean of PGAs at first OOP collapse assessed during analyses for all case-study buildings.

The analyses results showed that the IP displacement demand is noticeably underestimated if the IP-OOP interaction is neglected, especially for buildings designed for lower PGA at LS and so constituted of structural members provided of low inertial properties. If IP-OOP interaction is neglected, the probability of DL exceedance is underestimated for all PGA demands. PGA associated to the first OOP collapse is underestimated if IP-OOP interaction is neglected, especially for stiffer buildings designed for higher PGA at LS. Moreover, an EC-based approach in assessing the PGA associated to the first infill OOP collapse could overestimate that PGA up to 132%. In order to not overestimate RC buildings' performances with respect to both DL and LS Limit States, IP-OOP interaction modelling seems unavoidable.

In future works, further analyses should be carried out involving a greater number of case-study buildings, different for number of storeys and design PGAs. Different infills' layout should be also considered. Simplified methods aimed at assessing the OOP capacity of infills accounting for IP-OOP interaction phenomena in a code-based framework should be defined.

## ACKNOWLEDGEMENTS

This work was developed under the financial support of METROPOLIS (*Metodologie e tecnologie integrate e sostenibili per l'adattamento e la sicurezza di sistemi urbani - PON Ricerca e Competitività 2007-2013*) and *ReLUIS-DPC 2014-2018 Linea Speciale RS12 Tamponature*, funded by the Italian Department of Civil Protection (DPC). These supports are gratefully acknowledged.

## REFERENCES

[1] A. Filiatrault, T. Sullivan, Performance-based seismic design of nonstructural building components: The next frontier of earthquake engineering. *Earthquake Engineering and Engineering Vibration*, **13.1,** 17-46, 2014.

[2] S. Taghavi, E. Miranda, Seismic performance and loss assessment of nonstructural building components. *Proceedings of 7th National Conference on Earthquake Engineering*, Boston, United Stated of America, July 21-25, 2002.

[3] M.N. Fardis, T.B. Panagiotakos, Seismic design and response of bare and masonry-infilled reinforced concrete buildings. Part II: infilled structures. *Journal of Earthquake Engineering*, **1.3,** 475-503, 1997.

[4] T.B. Panagiotakos, M.N. Fardis, Seismic response of infilled RC frames structures. *11th World Conference on Earthquake Engineering*, Acapulco, Mexico, June 23-28, 1996.

[5] A. Saneinejad, B. Hobbs, Inelastic design of infilled frames. *Journal of Structural Engineering*, **121.4**, 634-650, 1995.

[6] R.J. Mainstone, On the stiffness and strength of infilled frames. *Proc., Supplement (IV), Paper 7360S, Instn. of Civ. Engrs.*, London, England, 1971.

[7] E.L. McDowell, K.E. McKee, E. Sevin, Arching action theory of masonry walls. *Journal of the Stuctural Division*, **82.2**, 1-8, 1956.

[8] R. Angel, D.P. Abrams, D. Shapiro et al., *Behaviour of reinforced concrete frames with masonry infills*. University of Illinois Engineering Experiment Station. College of Engineering. University of Illinois at Urbana-Champaign., 1994.

[9] J.L. Dawe, C.K. Seah, Out-of-plane resistance of concrete masonry infilled panels. *Canadian Journal of Civil Engineering*, **16.6**, 854–864, 1989.

[10] R.D. Flanagan, R.M. Bennett, Arching of masonry infilled frames: Comparison of analytical methods. *Practice Periodical on Structural Design and Construction*, **4.3**, 105-110, 1999.

[11] S. Kadysiewski, K.M. Mosalam, *Modelling of unreinforced masonry infill walls considering in-plane and out-of-plane interaction*. Pacific Earthquake Engineering Research Center, 2009.

[12] M.C. Griffith, J. Vaculik, N.T.K. Lam et al., Cyclic testing of unreinforced masonry walls in two-way bending. *Earthquake Engineering & Structural Dynamics*, **36.6**, 801-821, 2007.

[13] G.M. Calvi, D. Bolognini, Seismic response of reinforced concrete frames infilled with weakly reinforced masonry panels. *Journal of Earthquake Engineering*, **5.2**, 153-185, 2001.

[14] G. Guidi, F. da Porto, M. Dalla Benetta et al., Comportamento sperimentale nel piano e fuori piano di tamponamenti in muratura armata e rinforzata. *Proceedings of the XV ANIDIS, L'Ingegneria Sismica in Italia*, Padua, Italy, June 30 – July 4, 2013 (in Italian).

[15] A. Furtado, H. Rodrigues, A. Arêde, H. Varum, Experimental evaluation of out-of-plane capacity of masonry infill walls. *Engineering Structures*, **111**, 48-63, 2016.

[16] S.A. Hashemi, K.M. Mosalam, *Seismic evaluation of reinforced concrete buildings including effects of infill masonry walls*. Pacific Earthquake Engineering Research Center, 2007.

[17] A. Furtado, H. Rodrigues, A. Arede, H. Varum, Simplified macro-model for infill masonry walls considering the out-of-plane behaviour. *Earthquake Engineering & Structural Dynamics*, **45.4**, 507-524, 2015. DOI: 10.1002/eqe.2663.

[18] F. Longo, G. Granello, G. Tecchio, F. da Porto, C. Modena, A masonry infill wall model with in-plane out-of-plane interaction applied to pushover analysis of RC frames. *Brick and Block Masonry: Proceedings of the 16th International Brick and Block Masonry Conference*, Padua, Italy, June 26-30, 2016.

[19] P.B. Shing, L. Cavaleri, F. Di Trapani, Prediction of the out-of-plane response of infilled frames under seismic loads by a new fiber-section macro-model. *Brick and Block Masonry: Proceedings of the 16th International Brick and Block Masonry Conference*, Padua, Italy, June 26-30, 2016.

[20] M. Oliaee, G. Magenes, In-plane out-of-plane interaction in the seismic response of masonry infills in RC frames. *Brick and Block Masonry: Proceedings of the 16th International Brick and Block Masonry Conference*, Padua, Italy, June 26-30, 2016.

[21] M. Di Domenico, P. Ricci, G.M. Verderame, Empirical unreinforced masonry infill macro-model accounting for in-plane/out-of-plane interaction. *COMPDYN 2017*, Rhodes Island, Greece, June 15-17, 2017.

[22] S.P. Timoshenko, S. Woinowsky Krieger, *Theory of plates and shells*. McGraw-Hill, New York, 1959.

[23] M.N. Fardis (editor), *Experimental and numerical investigations on the seismic response of RC infilled frames and recommendations for code provisions, ECOEST/PREC8 Report No.6*, Laboratorio Nacional de Engenharia Civil Publications, Lisbon, 1996.

[24] R.D. Flanagan, R.M. Bennett, Bidirectional behaviour of structural clay tile infilled frames. *Journal of Structural Engineering*, **125.3**, 236-244, 1999.

[25] F. McKenna, G.L. Fenves, M.H. Scott, *Open system for earthquake engineering simulation*. University of California, Berkeley, CA, 2000.

[26] Eurocode 2 (ENV 1992-1-1). Design of concrete structures. 1: General rules and rules for buildings, Brussels, 2004.

[27] Eurocode 8 (ENV 1998-1-1). Design provisions for earthquake resistance of structures. Brussels, Belgium: European Committee for Standardization, 2003.

[28] Eurocode 8 (ENV 1998-3). Design provisions for earthquake resistance of structures. Brussels, Belgium: European Committee for Standardization, 2003.

[29] EN 1996-1-1 Eurocode 6: Design of masonry structures - Part 1-1: General rules for reinforced and unreinforced masonry structures, 2005.

[30] L. Luzi, R. Puglia, E. Russo, ORFEUS WG5, Engineering Strong Motion Database, version 1.0. Istituto Nazionale di Geofisica e Vulcanologia, Observatories and Research Facilities for European Seismology. DOI: 10.13127/ESM.

[31] D. Vamvatsikos, C.A. Cornell, Incremental dynamic analysis. *Earthquake Engineering and Structural Dynamics*, **31.3**, 491-514, 2002.

[32] D.N. Grant, Response spectral matching of two horizontal ground-motion components. *Journal of Structural Engineering*, **137.3**, 289-297, 2010.

COMPDYN 2017
6th ECCOMAS Thematic Conference on
Computational Methods in Structural Dynamics and Earthquake Engineering
M. Papadrakakis, M. Fragiadakis (eds.)
Rhodes Island, Greece, 15–17 June 2017

# INFLUENCE OF IN-PLANE AND OUT-OF-PLANE INTERACTION OF INFILL WALLS ON GLOBAL COLLAPSE RESISTANCE CAPACITY OF INFILLED RC FRAME

**Jianping Han[1], Zhenlong Zhang[2], Linjie Huang[3], and Xiaoyun Sun[2]**

[1] Key Laboratory of Disaster Prevention and Mitigation in Civil Engineering of Gansu Province, Lanzhou University of Technology
287 Langongping Rd., Lanzhou 730050, China
e-mail: jphan@lut.cn

[2] School of Civil Engineering, Lanzhou University of Technology
287 Langongping Rd., Lanzhou 730050, China
zlzhang1990@126.com, sxyhuining@163.com

[3] School of Civil Engineering, Southeast University
2 Sipailou Street, Nanjing 210096, China
15095428282@163.com

**Keywords:** In-Plane and Out-of-Plane Interaction, Infill Walls, Infilled RC Frame, Incremental Dynamic Analysis, Global Collapse Resistance capacity.

**Abstract.** *Firstly, the model using beam-column elements with fiber discretization to consider in-plane and out-of-plane interaction of infill walls was elaborated. Then, in order to validate the proposed model, a shaking table test model of a 4-storey infilled RC frame was modeled and analyzed via the finite element software, OpenSees. Comparison with the experimental and simulated results indicates that the numerical model considering in-plane and out-of-plane interaction of unreinforced masonry infill walls is valid for modeling the infilled RC frame structure. Then, based on the calibrated numerical model, a three-dimensional model of an infilled RC frame teaching building was established via OpenSees. And static pushover analysis and incremental dynamic analysis under 24 suites of ground motion records were carried out on the model with and without considering in-plane and out-of-plane interaction of unreinforced masonry infill walls. Furthermore, incremental dynamic analysis results were used to evaluate the global collapse resistance capacity of the structure with 50% collapse probability. Analytical results show in-plane and out-of-plane interaction of infill walls has a significant influence on the seismic behavior of the structure. The model without considering in-plane and out-of-plane interaction of infill walls shows obvious degradation. Without accounting for in-plane and out-of-plane interaction of infill walls, the global collapse resistance capacity of the structure will be underestimated obviously.*

## 1 INTRODUCTION

The Great Wenchuan Earthquake in 2008 in China and the Haiti earthquake in 2010 caused serious casualties and property losses due to the collapse of structures [1, 2]. Therefore, how to evaluate the collapse resistance capacity of the structure subjected to strong or catastrophic earthquakes has become an important issue in the earthquake engineering [3]. Nowadays, the researches on global collapse resistance capacity evaluation mainly focused on the bare frame of the building. And the influence of some nonstructural components such as infill walls was not well included. For analyzing and designing the infilled RC frame structure, only the influence of infill walls to lateral stiffness of structures was considered. The interaction between infill walls and the main structure was neglected.

The mechanism of the interaction between the main structure and infill walls is complicated and it is also influenced by many factors, so there is still no consensus on how to deal with this issue rationally [4-6]. Based on the Strut and Tie model, Hashemi proposed an approach to model both the in-plane (IP) and out-of-plane (OOP) response of the infill, as well as the interaction between IP and OOP capacities. But this model is only appropriate for an analysis based on small displacement, and it is not appropriate when the model is subjected to large in-plane load and out-of-plane displacement. Based on these concerns, infill model using beam-column elements with fiber discretization is proposed by Kadysiewski, which can obtain relatively stable numerical simulation results [7].

In this paper, the model using beam-column elements with fiber discretization to consider the IP and OOP interaction of infill walls was elaborated firstly. Then, in order to validate the proposed model, a shaking table test model of a 4-storey infilled RC frame was modeled and analyzed via the finite element software, OpenSees. Based on the calibrated numerical model, a three-dimensional model of an infilled RC frame teaching building was established. And static pushover analysis and incremental dynamic analysis under 24 suites of ground motion records were carried out on the model with and without considering the IP and OOP interaction of unreinforced masonry infill walls. Furthermore, incremental dynamic analysis results were used to evaluate the global collapse resistance capacity of the structure with 50% collapse probability.

## 2 THE INFILL WALL MODEL ACCOUNTING FOR IP AND OOP INTERACTION

An infill model using beam-column elements with fiber discretization is shown in Figure 1 [7]. For each infill panel, representing a single bay in a single story, the model consists of one diagonal member. That member is composed of two beam-column elements, jointed at the midpoint node. This node is given a lumped mass along the OOP direction.

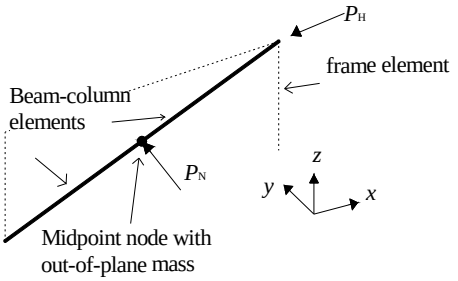


Figure 1: The infill model using beam-column elements with fiber discretization.

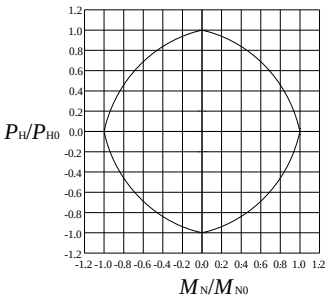


Figure 2: *P-M* interaction curve of typical infill panel.

Based on a nonlinear finite element model of the infill panel, Hashemi and Mosalam indicated that there is an interaction between IP and OOP capacities. In that study the interaction was expressed as the *P-M* interaction curve of typical infill panel, as shown in Figure 2. The function was expressed as a third-degree polynomial, as shown in following:

$$\left(\frac{M_{\mathrm{N}}}{M_{\mathrm{N0}}}\right)^{\frac{3}{2}}+\left(\frac{P_{\mathrm{H}}}{P_{\mathrm{H0}}}\right)^{\frac{3}{2}}\le 1.0 \tag{1}$$

where, $M_{\mathrm{N}}$ is the OOP bending strength in the presence of IP force, and $M_{\mathrm{N0}}$ is the OOP bending strength without IP force. $P_{\mathrm{H}}$ is the IP capacity in the presence of OOP force, and $P_{\mathrm{H0}}$ is the IP capacity without OOP force.

## 3 VALIDATION OF THE INFILL WALL MODEL ACCOUNTING FOR IN-PLANE AND OUT-OF-PLANE INTERACTION

### 3.1 The model structure by shaking table test and its numerical model

The investigated building is a 4-storey gallery-type teaching building of infilled RC frame with 4 storeys and 2 bays, which was designed according to current Chinese seismic design code for the 7 degree of seismic fortification with a peak ground acceleration of 0.10g. The 1/5 scaled model shown in Figure 3 was built for shaking table test. The height of the first story of this model is 780 mm, the height of other storeys are 600 mm.

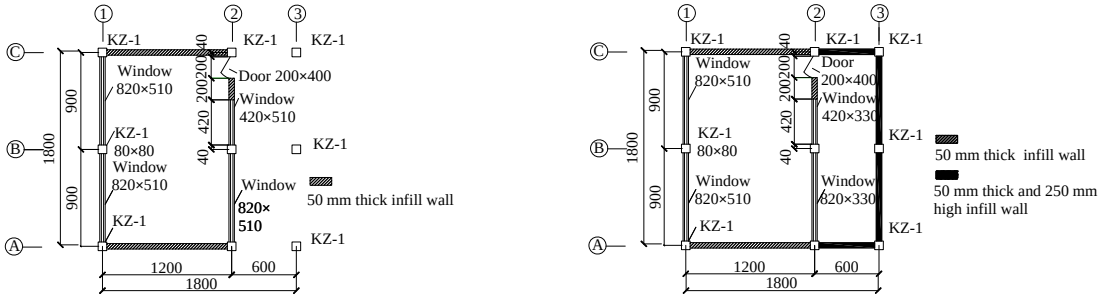


(a) Ground floor plan (b) Standard floor plan

Figure 3: The shaking table test model of 4-storey RC planar frame structure.

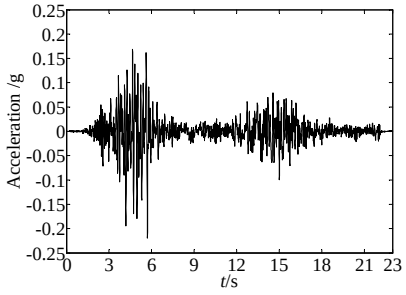


Figure 4: Table excitation of the shaking table test.

The table excitation shown in Figure 4 was taken as input to predict the top displacements. Taking the coincidence degree between stimulating results and test results as evaluation

criteria, the error of mean square root, $error_{\mathrm{RMS}} = \sqrt{\frac{1}{N} \times \sum_{i=1}^{n} \left( F_{\mathrm{comp_i}} - F_{\mathrm{exp_i}} \right)^2}$ , was used to judge the numerical results .

The numerical model was modeled via OpenSees. The beams and columns are modeled using Displacement-Based Beam-Column Element, in which the $P$-$\Delta$ effect of columns are considered by using P-Delta transformation. The hysteretic of beams and columns are modeled through the fiber sections, in which the fiber for reinforcing steels and concrete are defined as ReinforcingSteel constitutive model and Concrete02 constitutive model respectively [8-10]. The beam-column element of relatively stable fiber discretization was used for infilled walls model, and the two beam with hinge elements based on fiber section were applied to consider the IP and OOP interaction of infill walls [7].

### 3.2 Comparison of test results and numerical simulation results

The time history curves of top displacement from test and numerical simulation with and without considering the IP and OOP interaction of infill walls are shown in Figure 5. The maximum value of top displacement obtained from test is 6.34 mm, the maximum value of top displacement obtained from the model considering the IP and OOP interaction of infill walls is 6.96 mm, and $error_{\mathrm{RMS}} = 1.72$. And the maximum value of top displacement obtained from model without considering the IP and OOP interaction of infill walls is 9.84mm, $error_{\mathrm{RMS}} = 2.83$. The numerical results with considering the IP and OOP interaction of infill walls are more consistent with the test results than without considering the IP and OOP interaction of infill walls. The results indicate that the numerical model considering the IP and OOP interaction of unreinforced masonry infill walls is valid for modeling the infilled RC frame structure.

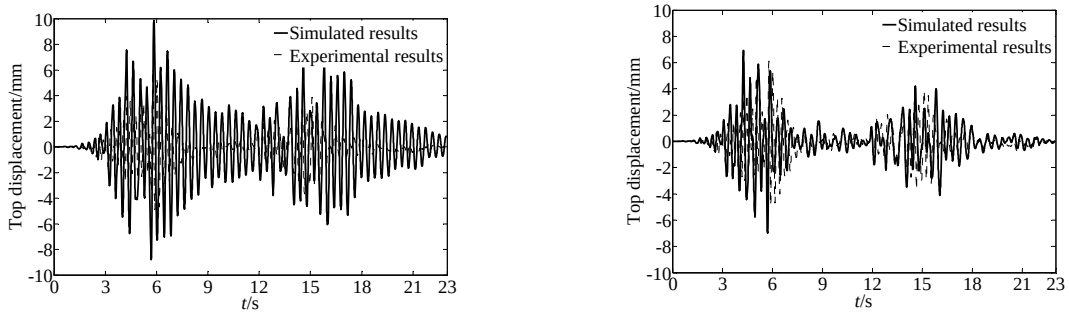


(a) Without considering the IP and OOP interaction of infill walls

(b) With considering the IP and OOP interaction of infill walls

Figure 5: Comparison of the top displacement curves.

## 4 EVALUATION OF COLLAPSE RESISTANCE CAPACITY WITH CONSIDERING IN-PLANE AND OUT-OF-PLANE INTERACTION OF INFILL WALLS

### 4.1 The investigated structures and numerical models

As shown in Figure 6, the investigated structure is a primary school teaching building, a 6-storey infilled reinforced concrete frame, which is located in the region with seismic fortification 8 degree. The height of the first story of this model is 4000 mm, the height of other storeys are 3600 mm. The main objective is to investigate the influence of the IP and

OOP interaction of infill walls on collapse resistance capacity of the structure. Two analytical models were modeled respectively, namely, with and without considering the IP and OOP interaction of infill walls were modeled respectively.

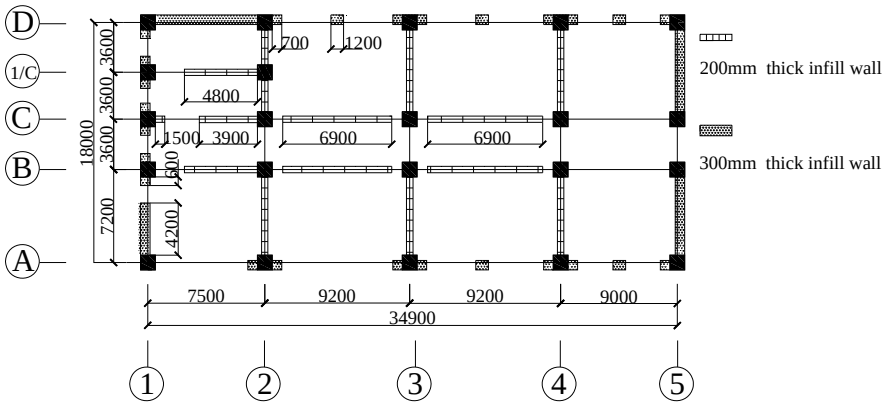


Figure 6: The model of 6-storey infilled RC frame.

The fiber section model is developed via the OpenSees nonlinear analysis software platform. The Displacement-Based Beam-Column Element is used for column and beam component and each component sets five integration points. P-Delta transformation is used as coordinate geometric transformation, which takes into consideration $P-\Delta$ effect. The concrete of column and beam section is divided into a certain number of rectangular grids and each grid is assumed to be a fiber. Reinforcing steels are also defined as fibers and is defined by ReinforcingSteel constitutive model [8]. In order to reflect the confinement effect of stirrup, the concrete of column and beam section is divided into cover concrete and core concrete and each is defined by the corresponding constitutive parameters of Concrete02 constitutive model [8-10].

## 4.2 Nonlinear static analysis of the structure

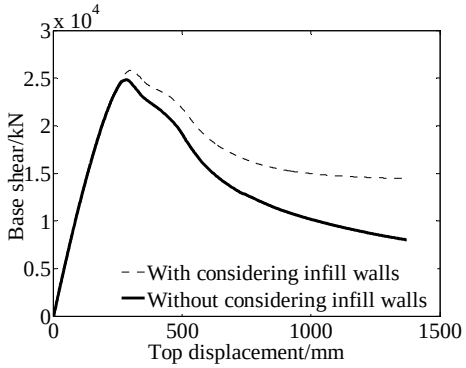


Figure 7: Comparison of pushover curves.

The pushover curves of the two models are shown in Figure 7. When the top displacement is less than 280 mm, the pushover curves obtained from the two models are almost coincident. For the models with and without considering the IP and OOP interaction of infill walls, the models begin to enter yield stage when the top displacement exceeds 300mm and 280 mm respectively. As the increase of top displacement, the curve without considering the IP and OOP interaction of infill walls descends faster than the one with considering the IP and OOP interaction of infill walls. The results demonstrate that without considering the IP and OOP interaction of infill walls, the degradation characteristic of the structure will be underestimated.

### 4.3 Incremental dynamic analysis of the structure

As shown in Table 1, 22 far field ground motion records from PEER earthquake records database and 2 ground motion records from the Wenchuan Earthquake are selected for incremental dynamic analysis [5, 7].

The IDA curves of two analytical models with and without considering the IP and OOP interaction of infill walls are shown in Figure 8 and Figure 9 respectively. When the maximum interstory drift ratio $\theta_{\max}$ is less than 0.01, the results from the two models are almost identical. When the maximum interstory drift ratio $\theta_{\max}$ is between 0.01 and 0.05, the IDA curves become different. Corresponding to the same spectral acceleration $S_a(T_1, 5\%)$, the maximum interstory drift ratio obtained from the analytical model with considering the IP and OOP interaction of infill walls is obvious less than the maximum interstory drift ratio from the analytical model without considering the IP and OOP interaction of infill walls. Therefore, collapse resistance capacity would be underestimated if the IP and OOP interaction of infill walls is not taken into account.

Table 1 Selected ground motion records

| No. | Earthquake events | | | Station | Component |
|---|---|---|---|---|---|
| | Name | Magnitude | Year | | |
| 1 | Northridge, USA | 6.7 | 1994 | BeverlyHills-Mulhol | NORTHR/MUL279 |
| 2 | Northridge, USA | 6.7 | 1994 | Canyon Country-WLC | NORTHR/LOS270 |
| 3 | Duzce, Turkey | 7.1 | 1999 | Bolu | DUZCE/BOL090 |
| 4 | Imperial Valley, USA | 6.5 | 1979 | Delta | IMPVALL/H-DLT352 |
| 5 | Imperial Valley, USA | 6.5 | 1979 | EI Centro Array #11 | IMPVALL/H-E11230 |
| 6 | Kobe, Japan | 6.9 | 1995 | Nishi-Akashi | KOBE/NIS090 |
| 7 | Kobe, Japan | 6.9 | 1995 | Shin-Osaka | KOBE/SHI090 |
| 8 | Kocaeli, Turkey | 7.5 | 1999 | Duzce | KOCAELI/DZC270 |
| 9 | Kocaeli, Turkey | 7.5 | 1999 | Arcelik | KOCAELI/ARC090 |
| 10 | Landers, USA | 7.3 | 1992 | Yermo Fire Station | LANDERS/YER360 |
| 11 | Landers, USA | 7.3 | 1992 | Coolwater | LANDERS/CLW-TR |
| 12 | Loma Prieta, USA | 6.9 | 1989 | Gilroy Array #3 | LOMAP/GO30090 |
| 13 | Loma Prieta, USA | 6.9 | 1989 | Coyote Lake Dam (SW Abut) | LOMAP/CYC285 |
| 14 | Superstition Hills, USA | 6.5 | 1987 | EI Centro Imp.Co | SUPERST/B-ICC090 |
| 15 | Superstition Hills, USA | 6.5 | 1987 | Poe Road (temp) | SUPERST/B-POE360 |
| 16 | Cape Mendocino, USA | 7.0 | 1992 | Rio Dell Overpass | CAPEMEND/RIO360 |
| 17 | Chi-Chi, Taiwan | 7.6 | 1999 | CHY101 | CHICHI/CHY101-N |
| 18 | Chi-Chi, Taiwan | 7.6 | 1999 | CHY041 | CHICHI/CHY041-N |
| 19 | Tabas, Iran | 7.4 | 1978 | Dayhook | TABAS/DAY-TR |
| 20 | San Fernando, USA | 6.6 | 1971 | LA-Hollywood Stor | SRERNPEL180 |
| 21 | Friuli, Italy | 6.5 | 1976 | Tolmezzo | FRIULI/A-TMZ270 |
| 22 | Imperial Valley, USA | 7.0 | 1940 | EI Centro Array #9 | IMPVALL/I-ELC180 |
| 23 | Wenchuan, China | 8.0 | 2008 | 51AXT | EW |
| 24 | Wenchuan, China | 8.0 | 2008 | 51JYZ | EW |

The IDA curves of two analytical models with and without considering the IP and OOP interaction of infill walls are shown in Figure 8 and Figure 9 respectively. When the maximum interstory drift ratio $\theta_{\max}$ is less than 0.01, the results from the two models are almost identical. It indicates that with and without considering the IP and OOP interaction of

infill walls can obtain the same seismic response of the structure when the structure remains elastic or the structure is not damaged seriously. When the maximum interstory drift ratio $\theta_{\max}$ is between 0.01 and 0.05, the IDA curves become different. Corresponding to the same spectral acceleration $S_a(T_1,5\%)$ , the maximum interstory drift ratio obtained from the analytical model with considering the IP and OOP interaction of infill walls is obvious less than the maximum interstory drift ratio from the analytical model without considering the IP and OOP interaction of infill walls. Therefore, collapse resistance capacity would be underestimated if the IP and OOP interaction of infill walls is not taken into account.

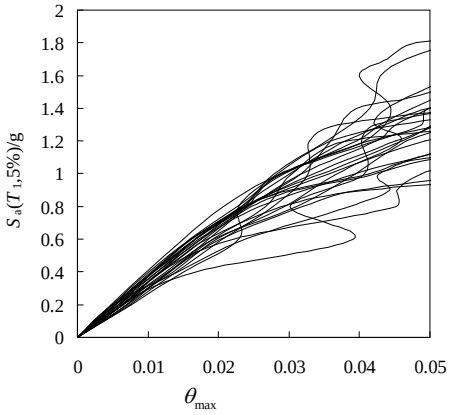


Figure 8: IDA curves without considering the IP and OOP interaction of infill walls.

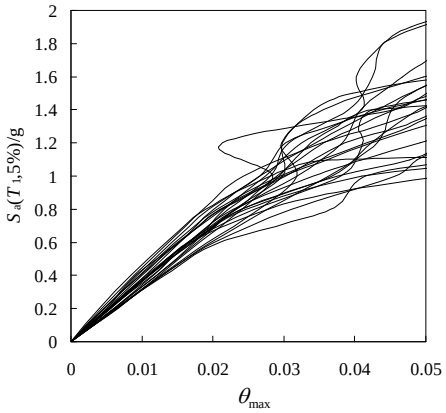


Figure 9: IDA curves with considering the IP and OOP interaction of infill walls.

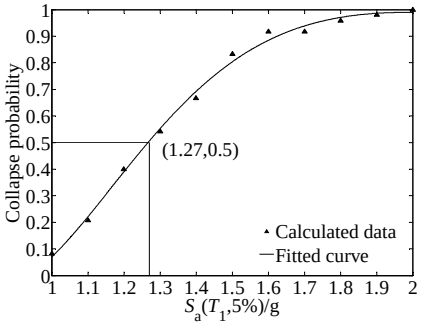


Figure 10: Collapse probability curves without considering the IP and OOP interaction of infill walls.

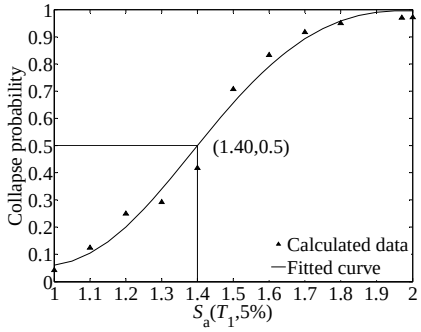


Figure 11: Collapse probability curves with considering the IP and OOP interaction of infill walls.

Taking $S_a(T_1,5\%)$ as random variable, the collapse probability curves without and with considering the IP and OOP interaction of infill walls, which are shown in Figure 10 and Figure 11 respectively, were obtained by using normal distribution parameter estimation. The index $S_a(T_1,5\%)_{50\%\text{Collapse}}$ , corresponding to 50% collapse probability, is also shown in Figure 10 and Figure 11. The collapse probability of the model without considering the IP and OOP interaction of infill walls is less than the value of the model with considering the IP and OOP interaction of infill walls. The collapse resistance capacity of the model without considering the IP and OOP interaction of infill walls is $S_a(T_1,5\%)_{50\%\text{Collapse}}=1.27\text{g}$ . For the model with considering the IP and OOP interaction of infill walls, it is $S_a(T_1,5\%)_{50\%\text{Collapse}}=1.40\text{g}$ . It indicates that collapse resistance capacity will be significantly underestimated without considering the IP and OOP interaction of infill walls.

## 5 CONCLUSIONS

In order to simulate and evaluate the global collapse resistant capacity of structure accurately and reliably, the analytical model should not only consider the characteristics of structural components adequately, but also take into account the behavior of nonstructural components properly. So it is very important to consider the influence of in-plane and out-of-plane interaction of infill walls on the global collapse resistance capacity. The case study results of a three-dimensional model of an infilled 6-storey RC frame teaching building show that global collapse resistance capacity would be significantly underestimated if the in-plane and out-of-plane interaction of infill walls is not taken into account in the analytical model.

## REFERENCES

[1] Civil and Structural Groups of Tsinghua University, Xinan Jiaotong University and Beijing Jiaotong University, Analysis on seismic damage of buildings in the Wenchuan earthquake. *Journal of Building Structures*, **29(4)**, 1-9, 2008.

[2] M. O. Eberhard, S. Baldridge, J. Marshall, W. Mooney, G. J. Rix, *The Mw 7.0 Haiti earthquake of January 12, 2010: USGS/EERI Advance Reconnaissance Team report*. U.S. Geological Survey Open-File Report 2010-1048, 2010.

[3] Y. Wang, M. Gao, L. Ye, X. Lu, J. Qian, Research strategy of building seismic design method based on collapse probability under great earthquakes. *Journal of Civil, Architectural & Environmental Engineering*, **32(S2)**, 291-297, 2010.

[4] H. B. Kaushik, D. C. Rai, S. K. Jain, Code approaches to seismic design of masonry-infilled reinforced concrete frames: A state-of-the-art review. *Earthquake Spectra*, **22**, 961-983, 2006.

[5] M. Dolšek, P. Fajfar, The effect of masonry infills on the seismic response of a four-storey reinforced concrete frame—a deterministic assessment. *Engineering Structures*, **30**, 1991-2001, 2008.

[6] S. Pujol, D. Fick, The test of a full-scale three-story RC structure with masonry infill walls. *Engineering Structures*, **32**, 3112-3121, 2010.

[7] S. Kadysiewski, K. M. Mosalam, *Modeling of unreinforced masonry infill walls considering in-plane and out-of-plane interaction*. Report No. PEER 2008/102, Pacific Earthquake Engineering Research Center, University of California, Berkeley, 2009.

[8] S. K. Kunnath, Y. A. Heo, J. F. Mohle, Nonlinear uniaxial material model for reinforcing steel bars. *Journal of Structural Engineering*, **135**, 335-343, 2009.

[9] J. Han, J. Yang, Investigation on global collapse resistance capacity of RC frame under severe earthquake considering deterioration characteristic of structural components. *Earthquake Engineering and Engineering Dynamics*, **32(6)**, 11l-122, 2012.

[10] Information on http://opensees.berkeley.edu.

[11] Applied Technology Council, FEMA P695, *Quantification of building seismic performance factors*. Redwood City, California, 2009.

compdybCOMPDYN 2017
6th ECCOMAS Thematic Conference on
Computational Methods in Structural Dynamics and Earthquake Engineering
M. Papadrakakis, M. Fragiadakis (eds.)
Rhodes Island, Greece, 15–17 June 2017

# IN-PLANE SEISMIC PERFORMANCE OF RC STRUCTURES WITH AN INNOVATIVE MASONRY INFILL WITH SLIDING JOINTS THROUGH NON-LINEAR ANALYSES

**A. Rossi[1], P. Morandi[2], R.R. Milanesi[2], and G. Magenes[1,2]**

[1] IUSS Pavia
Piazza della Vittoria 15, Pavia, Italy
andrea.rossi@iusspavia.it

[2] Dep. of Civil Engineering and Architecture of the University of Pavia and EUCENTRE
Via Ferrata 1/3, Pavia, Italy
paolo.morandi@unipv.it
riccardo.milanesi@unipv.it
guido.magenes@unipv.it

**Keywords:** Innovative infill with sliding joints, in-plane seismic response, performance levels, macro-modelling, non-linear analyses on infilled structures.

**Abstract.** *Within the European FP7 Project "INSYSME", the research unit of the University of Pavia has conceived a new seismic resistant masonry infill system with sliding joints, which allows in-plane damage control of the masonry and the reduction of the detrimental effects due to the panel-frame interaction. The system proposed ([1] and [2]) has been subjected to an extensive experimental campaign and both the in-plane and out-of-plane seismic behaviour of RC frames with the innovative infills with and without opening have been examined ([3] and [4]) In this paper, a study on the in-plane seismic performance of RC structures with the newly developed infills has been conducted through nonlinear static and dynamic analyses. The experimental cyclic in-plane response has been calibrated through numerical simulations of the tests by representing the masonry infill as two compressive diagonal struts pinned at its ends to the intersection of beam and column centrelines. Nonlinear analyses on 6-storey 3-bay RC frames designed for different levels of PGA have been conducted. Bare and infilled frames have been taken into account and various infilled configurations have been considered, also examining the case with and without openings. The results have permitted to study the influence of the infill on the global in-plane behaviour of the structure, in particular in terms of displacement and inter-storey drift demands and their reduction as respect to bare configurations. The definition of specific performance levels at the infill level according to the amount of damage attained in the cyclic in-plane tests ([3] and [4]), has allowed determining a consistent criterion for the attainment of the limit state conditions at the level of the building, considering the actual performance of the infills in the structures in terms of the drift demand versus capacity. Finally, a comparison between the results of the non-linear analyses on the structural configurations infilled with the innovative solution and with a "traditional" infill typology (double-leaf masonry in adherence at the RC structure [7]) has been performed, clearly highlighting the improvement of the in-plane seismic response of the newly developed system.*

## 1 INTRODUCTION

Since more than fifty years, many researchers have studied the seismic behavior of masonry infills and analyzed their interaction with the surrounding RC frame structures. A large amount of experimental tests and numerical analyses has been carried out with the aim of reducing the vulnerability of masonry infills subjected to seismic actions. The main goal of these studies is to find a cost-effective technological solution able to limit the damage in the infills and guarantee their lateral stability, while the thermal, acoustic and durability performances are not compromised.

In accordance with the "traditional" construction solution, masonry infills and the surrounding RC frames are completely in contact. The infills are usually built after the casting and hardening of the RC frame, and no gaps or any particular connections are inserted in between these elements. The traditional masonry infill solution has a series of critical aspects, related to both in-plane and out-of-plane seismic response, pointed out by the outcomes of several experimental tests and by the experience in post-seismic surveys [2].

In order to improve the seismic response of the infills and to control the damage and the stability of the panels, the research unit of University of Pavia, within the European FP7 Project "INSYSME" [5], has conceived a new seismic resistant masonry infill system with sliding joints within the wall and flexible joints around the wall-frame interface. The sliding joints divide the infill into horizontal stripes and are designed specifically to allow the relative in-plane movement of these stripes. The detrimental interaction of the infill with the surrounding RC frame is limited by the flexible joints, avoiding the direct impact of the infill against the frame and absorbing part of the energy generated during the shake. Therefore, the local stress concentration in the joints is limited by both the flexible joints at the wall-frame interface and the sliding joints. The out-of-plane stability of the infill is ensured by properly designed "shear keys" attached to the column. Figure 1a shows the details of the innovative masonry infills proposed by University of Pavia and Figure 1b shows the sketch of the in-plane deformed infilled frame; an exhaustive description of the system is reported in Morandi et al. in [1] and [2].

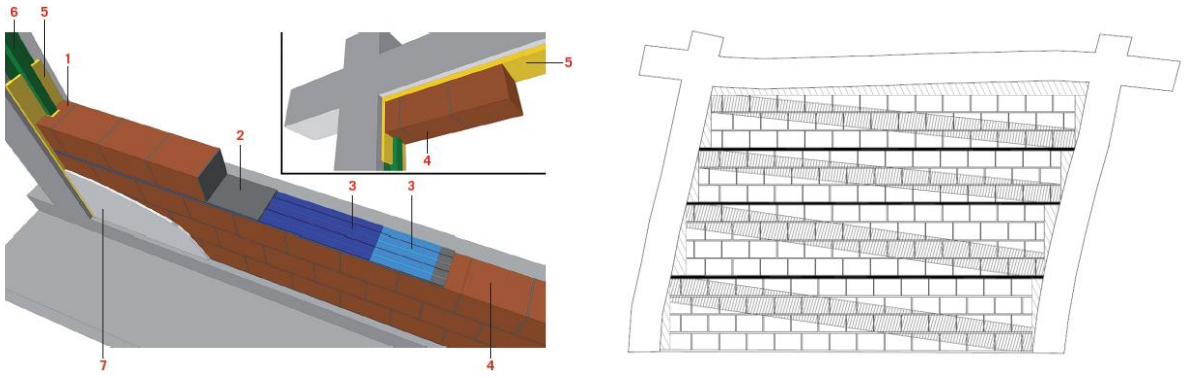


(a) (b)

Figure 1: (a) Details of the innovative masonry infill with sliding joints: 1.C-shape units; 2. mortar bed-joints; 3. Sliding joints; 4. clay units; 5. interface joints; 6. shear keys; 7. Plaster. (b) Sketch of the compressive struts and the deformed frame with the infill with sliding joints

The main objective of this work is to study the in-plane performance of the innovative infill system and its influence in the overall seismic response of RC buildings, also in comparison with the results on a traditional infill solution constituted by a double-leaf wall of horizontally perforated weak clay units.

A series of numerical non-linear static and dynamic analyses were performed on different types of newly designed RC plane frame structures, considering two typologies of innovative infills (with and without opening) and the traditional one without opening, in various infill configurations. A macro-modelling approach was adopted, since the focus of this work is the damage on infills, which is governed essentially by inter-storey drift, and since the large amount of non-linear analyses require a high computational burden; this simplified approach was considered the best solution giving reliable results within reasonable time. The software adopted to perform the non-linear analyses is Ruaumoko2D, a finite element program specifically for non-linear static and dynamic analysis ([6]).

A proper calibration of the numerical macro-model of the innovative infill system proposed by University of Pavia was possible thanks to the results of the experimental tests performed on this infill typology within the European FP7 Project "INSYSME", reported in Milanesi et al. ([3]) and Morandi et al. ([4]).

## 2 CASE STUDIES

The in-plane cyclic experimental response of the innovative infill system was evaluated by means of in-plane static cyclic tests, within an extensive test campaign executed at the University of Pavia within the European FP7 Project ([5]).

Three full-scale specimens were tested in-plane: a single story - single bay RC bare frame called “TNT”), a fully infilled frame (“TSJ1”) and a partially infilled RC frame with a 1.42 m wide central opening at the entire height (“TSJ2”). The geometry of the RC frame surrounding the innovative infills was the same for the three frames. The concrete class was C28/35 and the steel adopted for the steel reinforcement was of type B450C. The masonry was made up by vertically hollowed plain clay units (length x height x thickness = 30 x 19 x 25 cm) and general-purpose mortar, being the overall thickness of the wall equal to 29 cm (25 cm thick units with 2 cm thick plaster at both sides). Figure 2 shows a schematic representation of the three tested specimens along with the reinforcement details of the RC frames.

In addition to the innovative infills, a traditional infill system, constituted by a double-leaf wall of horizontally perforated weak clay units (length x height x thickness = 25 x 25 x 12 cm) cast in complete adherence to the RC frame (see Figure 3) has been taken into account to establish a comparison with a commonly adopted infill typology. This masonry infill (called “T2”) has been suitably calibrated by Hak et al. ([7]), on in-plane cyclic tests carried out by Calvi and Bolognini ([8]).

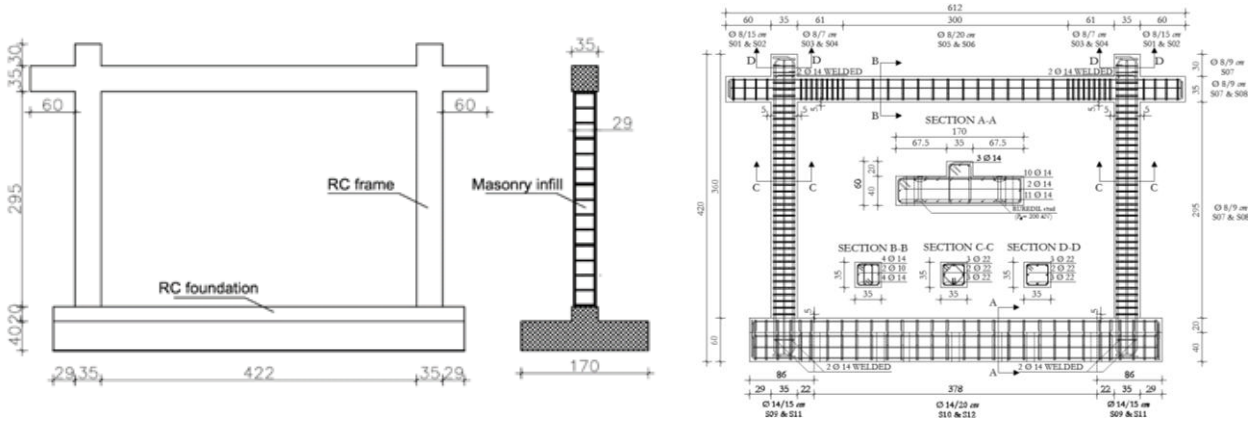


(a) (b)

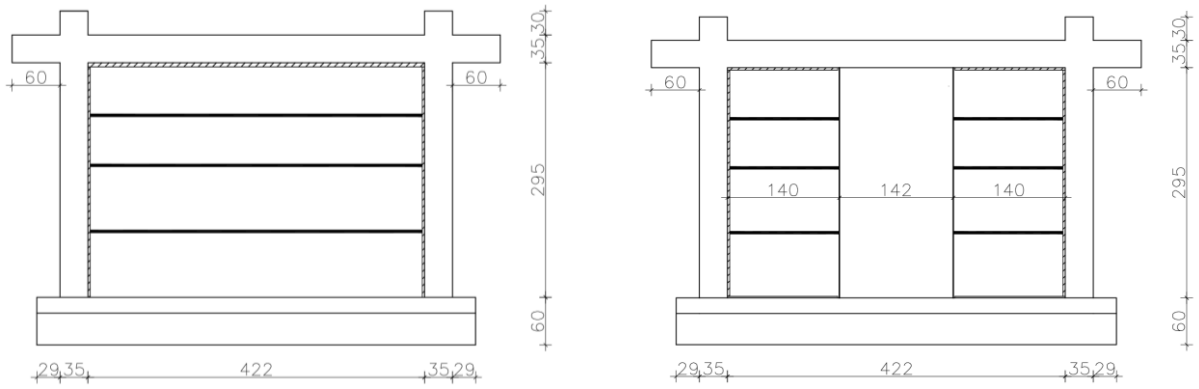


(c) (d)

Figure 2: Frame configurations: a) RC bare frame (TNT); b) reinforcement details of the RC frame; fully infilled frame (TSJ1); d) partially infilled frame (TSJ2).

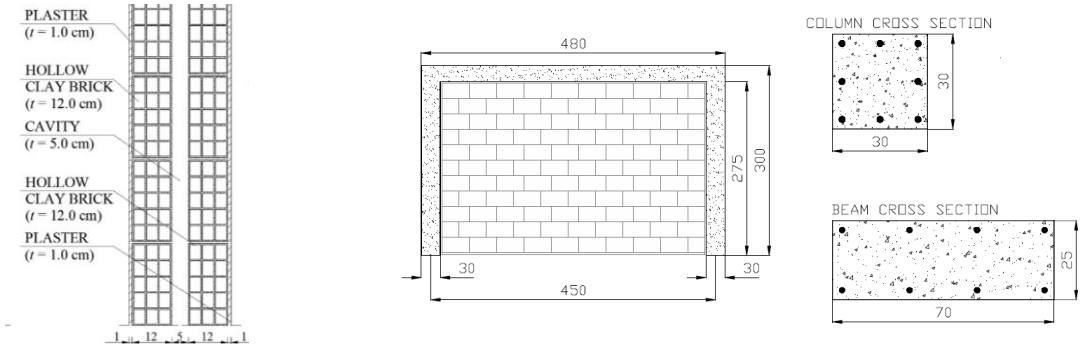


(a) (b)

Figure 3: (a) "Traditional" infill type: vertical section of the double-leaf wall [7]; (b) Geometry of the frames tested by Calvi and Bolognini [8]

In order to evaluate the influence of the infills in terms of overall in-plane response of RC buildings, six-storey RC frame structures were chosen to be representative of typical infilled buildings in the European context. The height of each storey was 3.0 m and the building was composed by four RC plane frames internally spaced of 5.0 m, each of them consisting of three bays of 5.0 m, 2.0 m and 5.0 m, respectively. The case study selected to be analyzed is the internal plane frame shown in Figure 4. The materials used for the building are concrete of class C28/35 and reinforcement steel of class B450C.

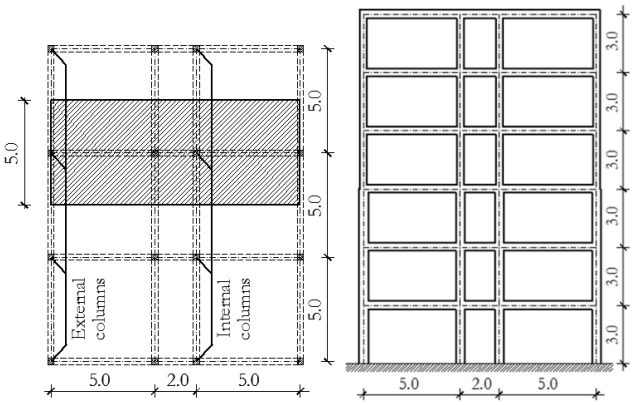


Figure 4: Plan and elevation of two-dimensional prototype structure.

The building was designed according to Eurocode 2 [9], Eurocode 8 [10] and NTC 2008 [11], with reference to the results of multimodal dynamic response spectrum analyses performed on linear bare frame models. The elastic gross stiffness of RC elements was reduced of 50% to account for the effect of cracking. The buildings were designed for three levels of seismicity, having a peak ground acceleration on ground type A, $a_g$, equal to 0.10g, 0.25g and 0.35g and founded on ground type B ($a_g$ was multiplied by the soil factor *S*, equal to 1.35 for $a_g$=0.10g and *S*=1.2 in the other two cases). The ductility class of the building was "high" (DCH) and, in accordance with the code recommendation, the behavior factor of this regular structure, *q*, was equal to 5.85. The parameters of the elastic and design spectra at the Ultimate Limit State for each of the three values of PGA have been selected according to Eurocode 8 [10] (response spectrum Type 2 has been adopted for the seismicity level with $a_g$ of 0.10g, response spectrum Type 1 has been used for the other two cases). The members of RC frames were dimensioned following the design capacity principles with strong columns and weak beams, in order to avoid "shear failure". The dimensions and the longitudinal reinforcement of the two-dimensional case-study frames are shown in Table 1, Table 2 and Table 3. The two structures designed for a PGA of 0.10g·S and 0.25g·S resulted to be the same, due to the geometry and steel reinforcement minimum requirements given by the codes. Further design details are discussed in Hak et al. in [7].

| **$a_g$** | **Storey** | **Cross sectional width/height [*cm*]** | |
|---|---|---|---|
| 0.10 g – 0.25 g | 1st - 3rd | 45/45 | Columns |
| | 4th – 6th | 35/35 | |
| 0.35 g | 1st - 3rd | 55/55 | |
| | 4th – 6th | 45/45 | |
| 0.10 g – 0.25 g – 0.35 g | 1st – 6th | 30/45 | Beams |

Table 1: Dimensions of the beams and the columns of the RC frame.

| **Storey** | **$a_g$ =0.10 g - 0.25 g** | | **$a_g$ =0.35 g** | |
|---|---|---|---|---|
| | Exterior column | Interior column | Exterior column | Interior column |
| 1st- 3rd | 8 Φ18 | 8 Φ18 | 12 Φ18 | 12 Φ18 |
| 4th- 6th | 8 Φ18 | 12 Φ18 | 8 Φ18 | 12 Φ18 |

Table 2: Longitudinal reinforcement of the columns.

| **Storey** | **$a_g$ =0.10 g - 0.25 g** | | | | **$a_g$ =0.35 g** | | | |
|---|---|---|---|---|---|---|---|---|
| | Exterior beam | | Interior beam | | Exterior beam | | Interior beam | |
| | Top | Bottom | Top | Bottom | Top | Bottom | Top | Bottom |
| 1st- 2nd | 4 Φ18 | 2 Φ18 | 3 Φ18 | 2 Φ18 | 4 Φ18 | 2 Φ18 | 4 Φ18 | 3 Φ18 |
| 3rd- 4th | 4 Φ18 | 2 Φ18 | 2 Φ18 | 2 Φ18 | 4 Φ18 | 2 Φ18 | 3 Φ18 | 2 Φ18 |
| 5th | 4 Φ18 | 2 Φ18 | 2 Φ18 | 2 Φ18 | 4 Φ18 | 2 Φ18 | 2 Φ18 | 2 Φ18 |
| 6th | 3 Φ18 | 2 Φ18 | 2 Φ18 | 2 Φ18 | 3 Φ18 | 2 Φ18 | 2 Φ18 | 2 Φ18 |

Table 3: Longitudinal reinforcement of the beams.

## 3 MASONRY INFILLS SEISMIC PERFORMANCES

As better specify in Hak et al. [7], different limit states can be evaluated in terms of drift attained to a correspondent level of damage derived from in-plane cyclic tests on infills. An operational limit state (OLS), a damage limit state (DLS) and a life safety limit state (LSS or ULS) are defined specifically for infill performance. At OLS the infill is considered undamaged or slightly damaged, at DLS the infill is damaged, but can be effectively and economi-

cally repaired, whereas at LSS/ULS the infill is considered severely damaged and reparability is economically questionable, but lives are not threatened.

In Table 4, the in-plane drift capacity corresponding to the different limits states for each infill system has been reported, as defined by Morandi et al. [4] for the innovative infills and by Hak et al. [7] for the traditional double-leaf infill.

| LIMIT STATE | Solid infill – Sliding joints TSJ1 | Infill with opening - Sliding joints TSJ2 | Traditional Infill - Double leaf T2 |
|---|---|---|---|
| ***Drift OLS*** | 0.50% | 0.40% | 0.20% |
| ***Drift DLS*** | 3.00% | 0.90% | 0.30% |
| ***Drift LSS or ULS*** | > 3.00% | > 3.00% | 1.00% |

Table 4: Drift limit states of the considered infills ([4], [7]).

## 4 NUMERICAL CALIBRATION

The numerical-macro models representing the innovative infills were calibrated taking, as reference, the in-plane cyclic tests carried out at the University of Pavia. The results of the in-plane cyclic tests were more largely reported by Morandi et al. ([4]), along with the mechanical properties of the materials obtained from tests of characterization. The in-plane tests were conducted applying a displacement-controlled loading history at increasing drift levels up to very large values, with three reverse cycles performed for each target displacement. The results of the experimental tests were compared to the response of the numerical macro-models in terms of force-displacement curves for the entire displacement history.

The purpose of the calibration was to reproduce numerically the in-plane experimental behavior of the frames with the innovative infill systems, which it was, in turn, necessary to obtain reliable models to be used in the subsequent non-linear analyses at the "building scale".

The infilled frames were modelled using a macro-element approach, using Ruaumoko2D program ([6]). Three models, the simple bare-frame portal, the fully infilled and the one with the central opening, were defined as reported in Figure 5.

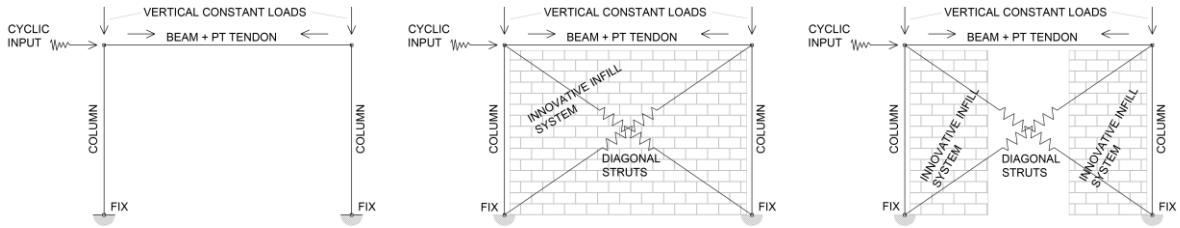


Figure 5: Scheme of the three in-plane cyclic tested specimens.

In the structural models, the RC members of the frames were defined as one-component Giberson elements ([12]) with concentrated plasticity at their ends. Assuming that the design of the frame was properly performed, the possibility of shear failures in the structural members was not taken into account. In accordance with the recommendations of Pristley et al. in [13], the region of intersection between the beam and the columns were characterized by perfectly elastic short elements. The hysteresis rule adopted to simulate the RC behavior of the section of the columns was the Schoettler-Restrepo rule ([6]), while the non-linear behavior of the beam was defined by the Fukada rule ([14]), as shown in Figure 6.

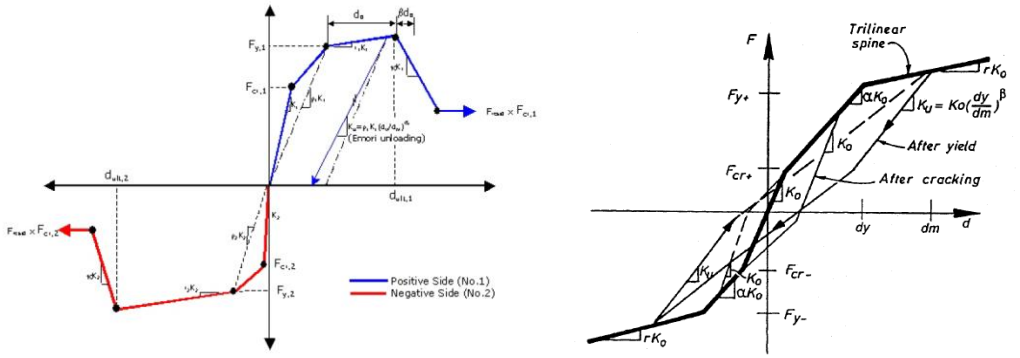


Figure 6: (a) Backbone curve of Schoettler-Restrepo rule [6]; (b) Fukada degrading Tri-linear hysteresis rule [14]

Considering the infilled frame cases, two diagonal non-linear springs that represent the innovative infill system have been considered. These elements were pinned to the extreme nodes of the frame and work only in compression ("no tension" elements). The hysteresis rule associated to the non-linear behaviour of the two diagonal struts representing the infills was the one proposed by Crisafulli in [15], as reported in Figure 7. The innovative infill with the opening was modelled following the same principles of the fully infill. According to the experimental results, the two diagonal spring defined by the Crisafulli hysteresis rule was capable to represent both the configurations of the innovative system, with and without opening.

The springs elements, defined by the Crisafulli hysteresis rule, are defined by an elastic modulus ($E_{mo}$), a compressive strength ($f'_m$) and an initial stiffness ($K_D$) equal to ($E_{mo}$)·(*AREA1*)/(element length). The area of the section of the element is assumed to be dependent on the deformation, *AREA1* at displacement *R1*, and *AREA2* at displacemet *R2*. The shape of the envelope of the hysteretic cycles was assumed to be parabolic. The peak of the curve was defined by the point ($\varepsilon'_m$, $f'_m$) and the intersection with the x-axis occurs at the value of deformation $\varepsilon_u$. The slope of the descending branch of the curve was determined by the factor $\gamma_{un}$, while the reloading factor $\alpha_{re}$ defines the point at which the reloading curves attain the strength envelope. The closing strain, $\varepsilon_{cl}$, corresponds to the partial closing of the cracks where the compressive stresses could be developed.

The final parameters of the calibrated diagonal macro-elements, representig the innovative infill system, are listed in Table 5, both for the case of fully infill and infill with opening.

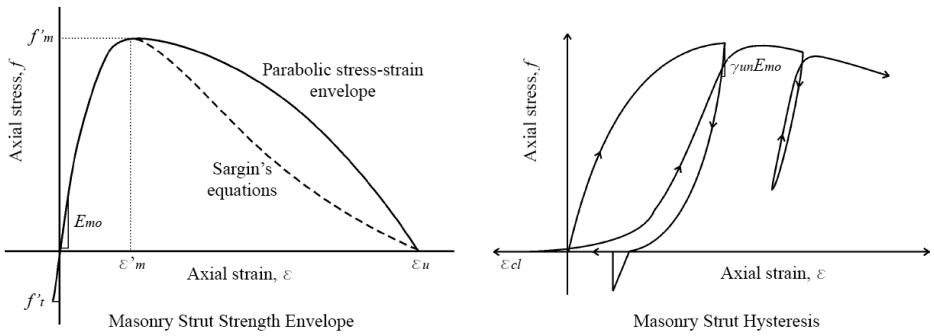


Figure 7: Masonry Strut Strength Envelope and Masonry Strut Hysteresis for Crisafulli rule [6].

| Parameters of the element | | Fully infill | Infill with opening | |
|---|---|---|---|---|
| $K_D$ | kN/m | 81371 | 54644 | *initial diagonal stiffness* |
| $f'_m$ | kPa | -1297 | -1372 | *compressive strength* |
| $\varepsilon'_m$ | - | -0.00047 | -0.0005 | *strain at* $f'_m$ |
| $\varepsilon_u$ | - | -0.99 | -0.99 | *ultimate strain* |
| $\varepsilon_{cl}$ | - | 0.47 | 0.5 | *closing strain* |
| $E_{mo}$ | MPa | 2967 | 2967 | *initial masonry modulus* |
| $\gamma_{un}$ | - | 5 | 2 | *stiffness unloading factor* |
| $\alpha_{re}$ | - | 0.12 | 0.01 | *strain reloading factor* |
| ***AREA1*** | $m^2$ | 0.1518 | 0.102 | *initial strut cross-sectional area* |
| ***AREA2*** | $m^2$ | 0.1053 | 0.065 | *final strut cross-sectional area* |
| ***R1*** | m | -0.0024 | -0.0028 | *displacement at 1* |
| ***R2*** | m | -0.0073 | -0.028 | *displacement at 2* |

Table 5: Parameters of the diagonal struts.

Figure 8(a), Figure 8(b) and Figure 8(c) show the comparison, in terms of force-displacement curve, between the in-plane cyclic tests (black line) and the numerical models (red line) on the bare frames and on the frames infilled with the innovative system (with and without opening). Figure 8(d) also reports the comparison of the three envelope numerical curves. The input of the numerical-model was given by the loading history of the displacement effectively applied at the half-height of the top-beam during the pseudo-static cyclic tests. The plots show that the force-displacement curves of the numerical models match very well the experimental ones, during all the cycles.

In the cases of the infilled frames (both with and without opening), it was also possible to evaluate the energy dissipated during each cycle. Figure 9 shows the comparison between the energy dissipated by the frames during the in-plane cyclic tests and the one of the numerical models, which fit very well. Based on these results, it is possible to consider this macro-modeling approach accurate enough for the purpose of the present work.

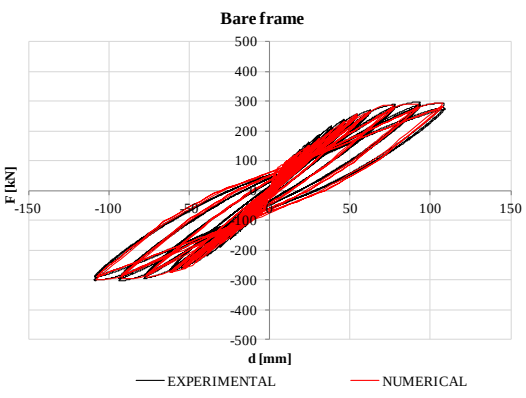


(a)

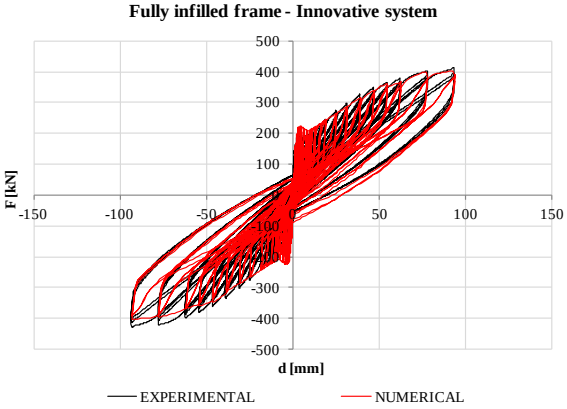


(b)

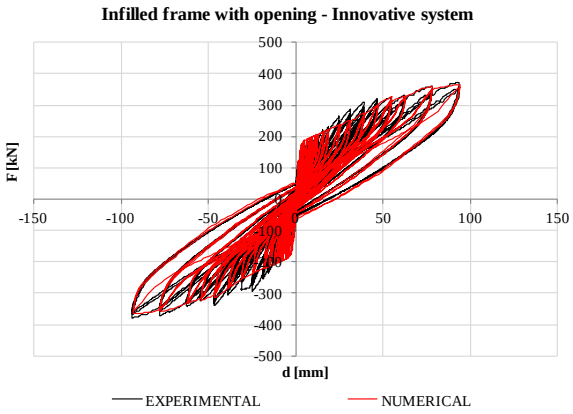


(c)

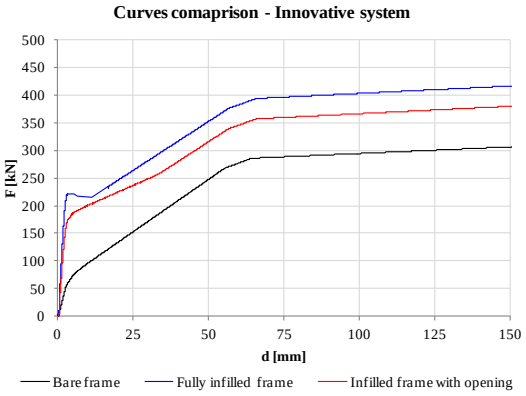


(d)

Figure 8: Comparison between the force-displacement experimental and numerical curves: (a) bare frame; (b) fully infilled case; (c) partially infilled case. (d) envelope comparison between the three calibrated models.

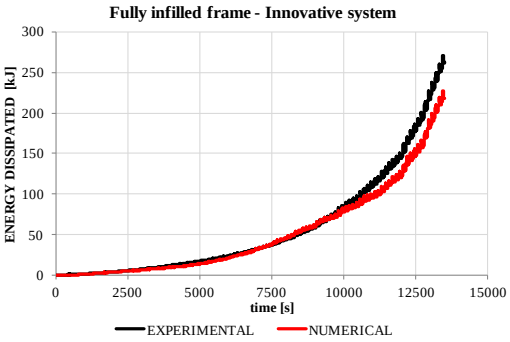


(a)

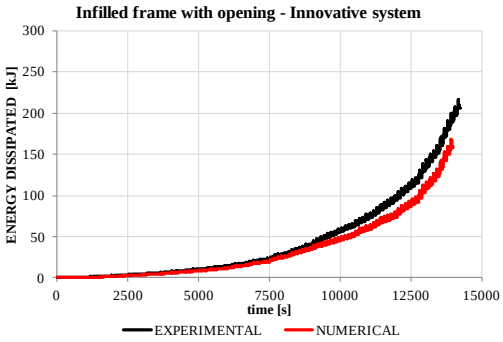


(b)

Figure 9: Comparison between the energy dissipation of the in-plane cyclic tests and the numerical models: (a) fully infilled case; (b) partially infilled case.

Moreover, in Figure 10(a), the macro-model hysteretic response of the double-leaf "traditional" infill (cyclic in-plane response and its envelope) is shown. The infill is modeled with two diagonal struts with the envelope and the hysteretic laws by Crisafulli ([15]), evaluating the stiffness and the strength with the criteria proposed by Decanini et al. ([17]), as indicated in Hak et al. in [7].

Figure 10(b) finally reports the comparison between the innovative systems and the traditional one in terms of the numerical infill contribution envelopes.

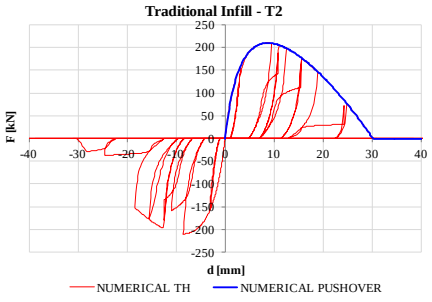


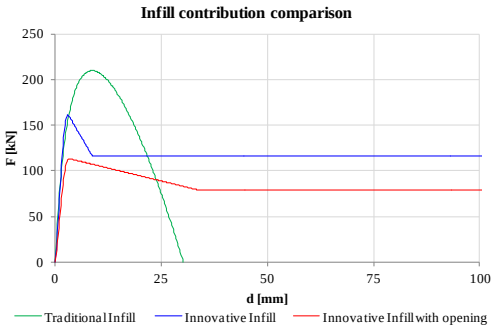


Figure 10: (a) Macro-model calibration of the double-leaf traditional infill (cyclic in-plane response and envelope); (b) envelope of the infill contributions between the innovative systems and the traditional one.

## 5 NON-LINEAR ANALYSES ON BARE AND INFILLED BUILDINGS

A series of non-linear static ("pushover") and dynamic time-history analyses have been performed on the case-study building, with different infill configurations, in order to evaluate the influence of the infills in the seismic response of the structures. A macro-modeling approach using the program Ruaumoko, as defined for the numerical calibration of the single infilled frames, was adopted. Three case-study frames were defined, one per each level of design PGA: 0.10g·S, 0.25g·S and 0.35g·S. In the case of the innovative infill solution with sliding joints, for each of the three case-study frames, five different configurations were considered, one bare and four infilled, as reported in Figure 11. In the case of the "traditional" infills, only two configurations have been taken into account: the partially infilled frame (Figure 11b) and the one side partially infilled frame (Figure 11d).

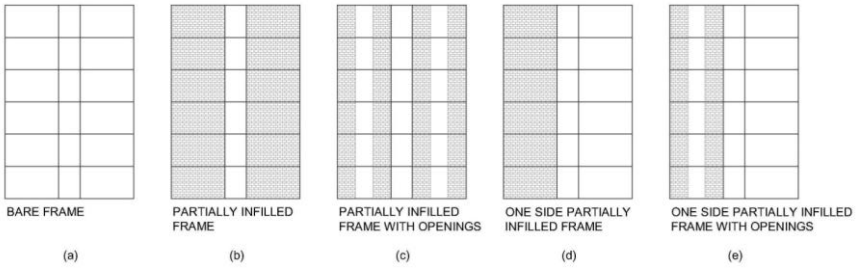


Figure 11: Different infilled configurations for the six-storey building.

As for the case of the simple portal-frame described before, the macro-modelling of the case-study frames was based on a concentrated-plasticity modeling approach (Figure 12a), where the RC beams and the columns were represented by Giberson elements and the behavior of the rotational springs at the RC member ends was assumed to be defined by the Takeda hysteresis rule [18] (Figure 12b), with no strength degradation. The stiffness corresponding to unloading and reloading is characterised through the definition of coefficients $\alpha$ and $\beta$ ($\alpha$ = 0.5 for both beams and columns; $\beta$ = 0.3 for beams and $\beta$ = 0.0 for columns), while the ratio between initial and post-yielding stiffness is defined by the Ramberg-Osgood moment-curvature bi-linear factor $r$ ($r$ = 0.01 for beams and columns) (Figure 12c). Also in this case, the possibility of shear failure occurrence in the structural elements is not considered, supposing the frames are properly designed and detailed according to modern seismic design code provisions. The gross stiffness of the RC structural members was reduced and the ratio of the effective to elastic initial stiffness was set equal to 0.25 for beams and 0.35 for columns. In the regions of intersection between beams and columns the, finite-length elastic elements were introduced. The viscous damping was represented by a tangent stiffness Rayleigh model. Following the recommendations by Priestley et al. ([13]) the damping corresponding to the fundamental mode of vibration was reduced and a value of 3.0% is adopted, while 5.0% damping was assumed in the second mode. The masses of the structure were lumped in the central nodes between the beams and the columns.

The models used for the infills are those evaluated in the calibration of the in-plane cyclic tests on the single storey-single bay infilled frames.

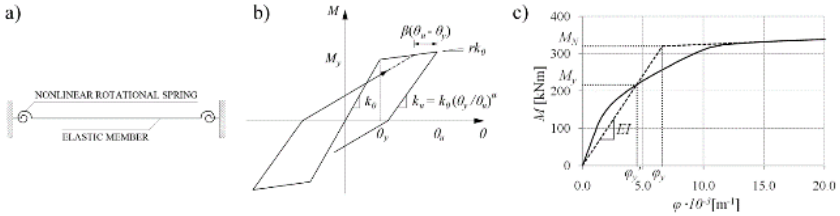


Figure 12: Concentrated-plasticity frame member; (b) Modified Takeda hysteretic rule; (c) Moment-curvature bilinear idealization.

## 5.1 Pushover analyses

In the non-linear static analyses, the horizontal action was given by means of equivalent horizontal loads applied at each mass of the structure. The intensity of the forces has increased monotonically, while their distribution was kept constant and proportional to the first modal shape of the structure. The capacity curves obtained from the pushover analyses (base shear vs roof displacement) on the configurations with the innovative infills are reported in Figure 13. On the capacity curves, the steps corresponding to the first attainment of the different limit states (OLS, DLS and LSS/ULS) in the first infill of the buildings with the drift capacity defined in Section 3, has been indicated.

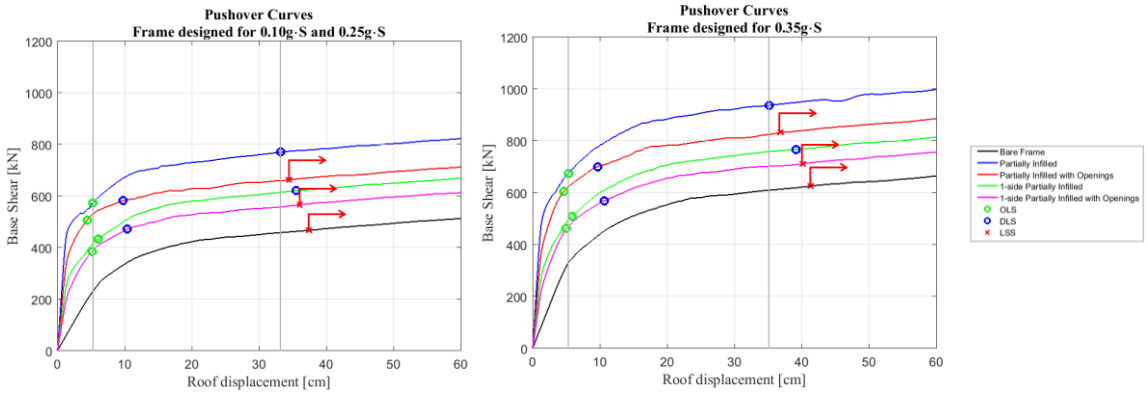


Figure 13: Capacity curves for the bare ad infilled (innovative system) frames.

For what concerns the buildings with the innovative infills, Figure 13 shows that no strength degradation on the capacity curve is found. The frame-models are therefore capable to attain large levels of displacements without reducing the base shear resistance. The shape and the trend of the curves are similar each other, and, as expected, the frame designed for higher level of PGA reach higher values of base shear. In addition, the curves of the infilled frames show higher values of base shear respect to the curves relative to the bare frame. In particular, the partially infilled frame system is the one capable to withstand higher level of horizontal forces. This difference is more evident in the initial part of the plot, in which also the stiffness reaches larger values. After the elastic range, the slope of the curves decreases and the curves keep themselves almost parallel to each other. The partially infilled frame reaches 3.0% of drift in correspondence of a value of roof displacement smaller than the others system. Moreover, it is possible to notice that the more the system is rigid and capable to withstand higher forces, the more the system shows smaller value of top displacement in correspondence of the same level of maximum inter-storey drift. In order to compare numerically in terms of resistance the different pushover curves, the base shear correspondent to the values of displacements related to the performance levels of the infill as reported in Section 3 was evaluated (see the gray vertical lines in Figure 13). Finally, it is interesting to notice that the

opening in the infill walls does not weaken the system significantly before the attainment of the OLS in comparison with the case without opening. The increase of base shear of the infilled structures is smaller for RC frames designed for higher seismic actions since the contribution of the infills in the global strength of the building affects to a lesser extent for more resistant and stiff RC structures.

A comparison in terms of the initial stiffness of the innovative system has also been performed, evaluating it as the secant stiffness at 50% of 0.6 times the base shear level reached at the life safety limit state (Figure 14). The reason of this choice is that, commonly, the bilinear idealization of a pushover curve pass through the point at $0.6 \cdot V_{max}$ ($V_{max}$: maximum value of base shear). The reduction of 50% is needed to catch the behavior of the system in the initial phase, in which the elements still behave elastically. The partially infilled frame system is the stiffest one and the partially infilled frame with opening is more rigid than the 1-side infilled frame. As expected, the presence of the infills increases the overall rigidity of the structure, compared to the bare frame configuration. It is interesting to note that the increase in stiffness of the infilled structures is smaller for RC frames designed for higher seismic actions since the contribution of the infills in the global stiffness of the building affects to a lesser extent for more resistant and stiff RC structures.

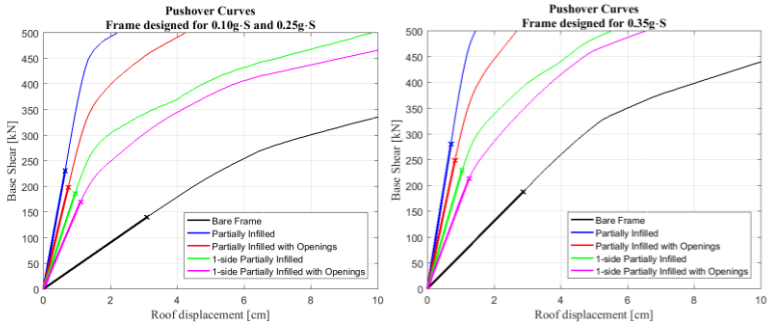


Figure 14: Initial part of the capacity curves for the bare and infilled frames with innovative infill.

Figure 15 shows the differences between the traditional and innovative infill systems, considering the infills in one side of the frame or in both sides, without taking into account the presence of an opening. The traditional system has a similar initial stiffness of the innovative one, but after the reaching of a peak in terms of base shear, a fast force degradation occurs until the attainment of a certain level of force that corresponds to the LSS (red dots); this limit is reached at very low level of roof-displacement respect to the innovative solution. At larger values of displacements, after the exceed of the ultimate conditions of the infills, the overall behavior of these structures tends to approximate (regardless by numerical instability) the response of the RC bare frames. On the other side, the buildings with the innovative infills do not show any strength degradation on the capacity curve and are able to attain much larger levels of displacement capacity before reducing the base shear resistance, as respect to the traditional ones.

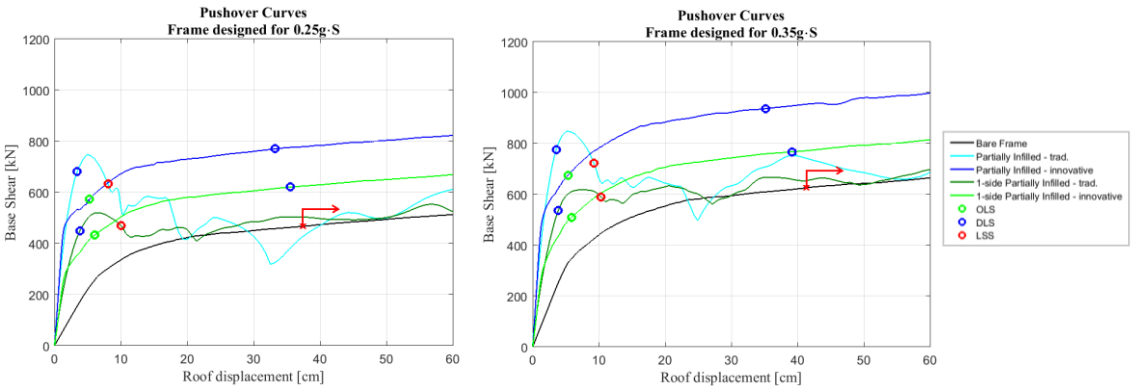


Figure 15: Capacity curves for the bare ad infilled (innovative and traditional systems) frames.

## 5.2 Non-linear dynamic analyses

Non-linear dynamic analyses were performed on each case-study frame for each configuration defined previously. The input ground motions were scaled to the DLS and to the ULS.

The selection of the earthquake records was done based on the recommendation of previous studies ([19]) on natural ground motions scaled to specified levels of seismicity. Ten earthquake input ground motions were considered per each group of analyses relative to a specific frame model, which is a number larger than the minimum number of seven records given by the European seismic codes ([10], [11]) to consider average response quantities from all the analyses. The software REXEL [20] was adopted to select the earthquakes from the European database. The average value of the ten records was matched with the target spectrum (±10%) in a range between $0.2 \cdot T_1$ and $2 \cdot T_1$, where $T_1$ is the fundamental period of the structure. The selected spectrum compatible records were scaled to the design value of PGA of the case-study frames. The records compatible to EC8 spectrum Type 1 are relative to the case-study frames designed for PGA equal to 0.25g·S and 0.35g·S, while the ground motions compatible to EC8 spectrum Type 2 are related to the case-study frames designed for PGA = 0.10g·S. In accordance with the design procedure, to obtain records compatible with the spectrum corresponding to the damage limitation limit state, the reduction factor $\nu = 0.5$ was applied. Only earthquakes recorded on soil class B are considered, with magnitudes between 5.5 and 8.0 for Type 1 and between 3.5 and 5.5 for Type 2 spectra. In Figure 16, the spectrum compatible earthquake records at the ULS with PGA equal to 0.10g·S and 0.25g·S have been reported.

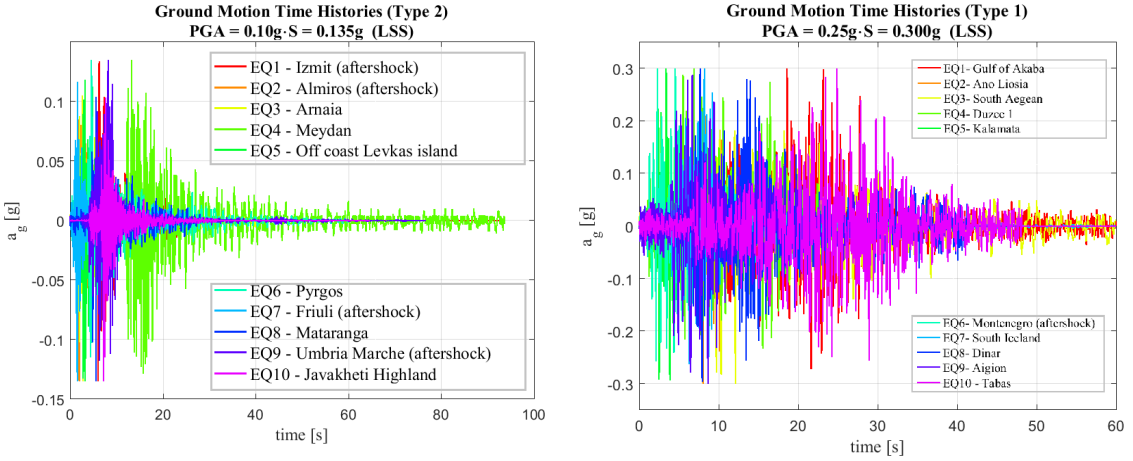


Figure 16: Design spectrum compatible earthquake records at the ULS: (a) PGA=0.10g·S; (b) PGA=0.25g·S.

The floor displacements and inter-storey drifts coming from the dynamic non-linear analyses have been evaluated. The selection of the input ground motion has a great influence in the response on the structures, also considering that different frame typologies, both infilled and bare, with different modes of vibrations, behave differently to the same earthquake. Nevertheless, considering that the sets of input ground motion adopted in the analyses were composed by ten spectrum compatible accelerograms, the quantities related to the response of the structure were analyzed in terms of average values. The following figures (from Figure 17 to Figure 20) summarize the displacement and drift profiles for each set of accelerograms, considering the bare frames, the four configurations with the innovative infills and the two with the traditional infills. Displacement profiles are obtained for each frame type and for each ground motion record corresponding to the instant of a maximum displacements obtained in any of the storeys. The lines in the displacement-plots (Figure 17 and Figure 18) represent the average values of the displacement for the specific set of accelerograms. Drift profiles are obtained for each frame type and for each ground motion record corresponding to the instant of a maximum drift obtained in any of the storeys. The lines in the drift-plots (Figure 19 and Figure 20) represent the average values of the maximum drifts for the specific set of accelerograms.

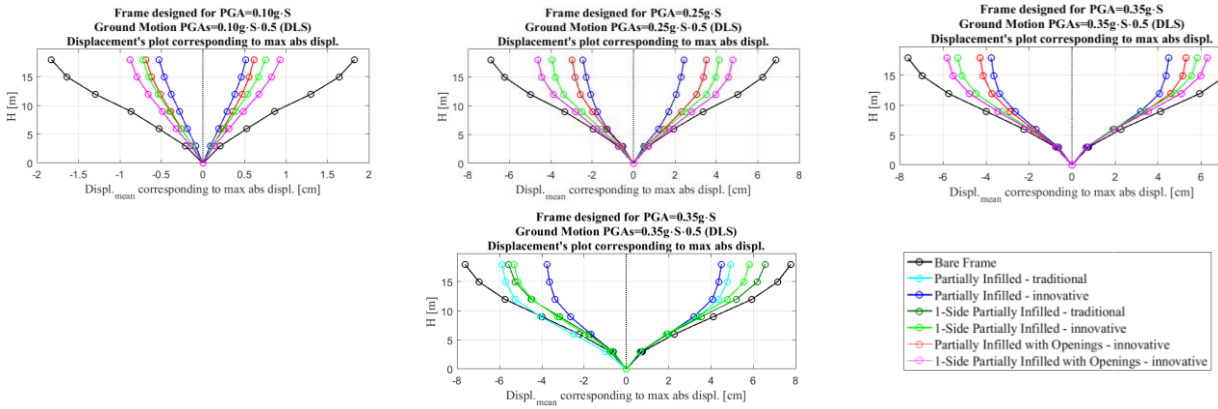


Figure 17: Displacement profiles at the DLS.

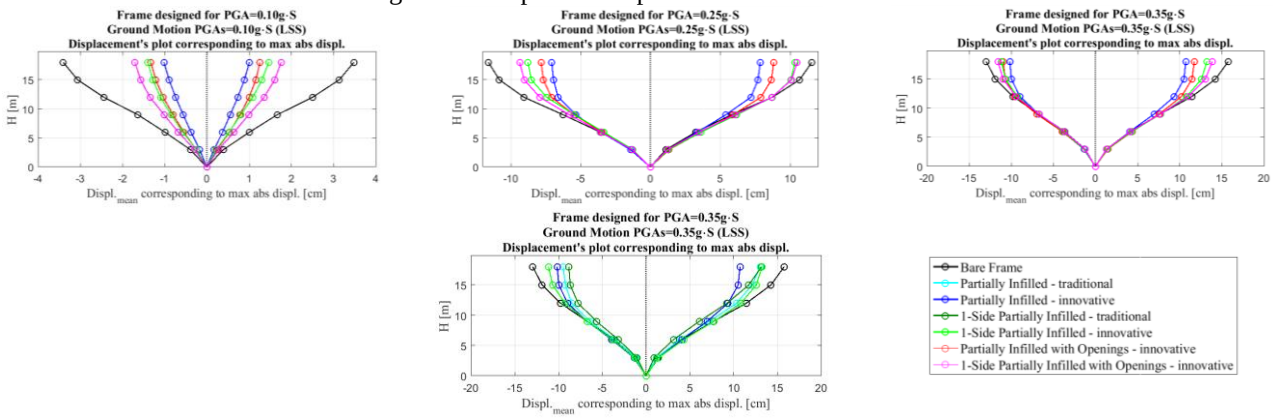


Figure 18: Displacement profiles at the LSS (ULS)

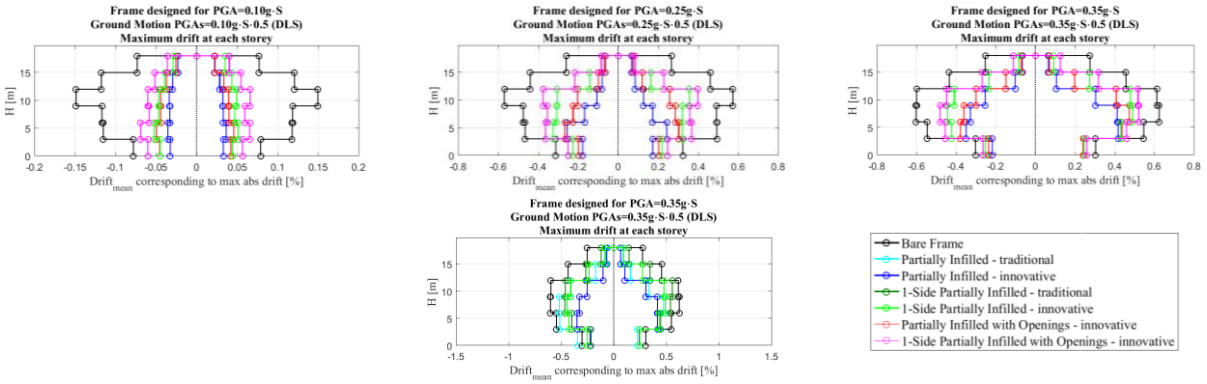


Figure 19: Inter-storey drift profiles at DLS.

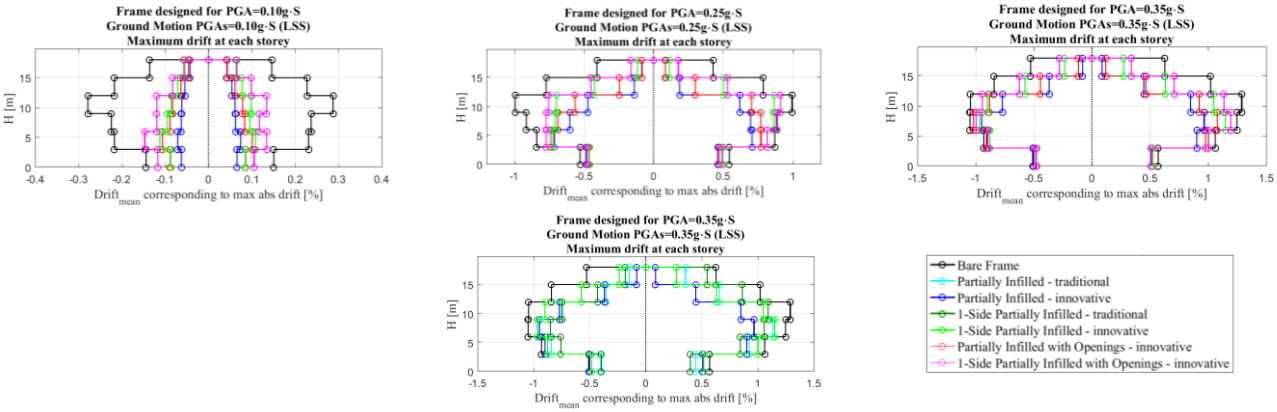


Figure 20: Inter-storey drift profiles at LSS (ULS).

Looking at the response in terms of displacements of the structures (Figure 17 and Figure 18), it is possible to notice that the maximum absolute displacement is always the one relative to the upper floor and therefore no higher mode of vibrations occur; the displacement shapes relative to the achievement of the maximum displacement is almost the same for all the configurations (approximately linear with the exception of the upper floors).

As expected, the presence of the infills (both the innovative and traditional ones) in the frames reduces considerably the maximum value of displacement demand as respect to the bare structures and, in particular, the partially infilled frames configuration exhibits the lowest values of displacements.

Another series of considerations can be done looking at the drift profiles (Figure 19 and Figure 20). Besides the fact that the drift demands are larger for the bare frames than for the infilled configurations, the drift profile of the frames without infills is quite different from the configurations with walls. Moreover, it is possible to notice that the maximum drift for the bare frame configuration is reached in correspondence of the fourth storey, while in the other cases it is located between the second and the third floor. In some cases, the buildings with traditional infills have reached higher drift demands respect to the ones with innovative infills due to their brittle behavior having a sharp descending branch after the peak force and, therefore, providing a smaller contribution to the overall in-plane response of the buildings that lead to a performance more similar to the one of a bare frame.

Comparing the three different structures designed for the three levels of PGA, the difference in terms of drifts and displacements between the bare frame and infilled frames configurations diminish with the increase of PGA level. This effect was expected since the properties of the infills remain the same while the sections of beams and columns change.

Furthermore, for all the cases considered, from observations on the displacement and drift profiles, no occurrence of any soft-storey mechanisms appears.

In the case of traditional infills, the reduction of drift demands appears to be more significant at DLS than at ULS, due to the fact that, subjected to the design seismic action at ULS, the traditional are severely damage, as better specified in the following section.

Interestingly, the results also illustrate that, at the DLS, storey drifts for the bare frames in some cases exceed the design limit of 0.5%, suggesting that the current code approach is unable to fully control the response of traditional infills rigidly attached to the structure. The fact that drifts are larger than expected can be attributed in part to the EC8 recommendation to use 50% of the gross section flexural and shear stiffness for the section stiffness when in fact the cracked section stiffness is often lower, and in part to the fact that the frames enter into the inelastic response range also under the DLS seismic action, and consequently the displacements are higher than predicted by a linear analysis with initial stiffness.

## 6 SEISMIC PERFORMANCE OF THE INFILLED BUILDINGS

The distribution of in-plane damage due to the action of selected earthquake records is evaluated from the results of dynamic non-linear analyses for each considered frame type and infill typology at the different limit states. The damage of a single infill is assessed through the maximum achieved drift. In particular, the frames are assumed to fulfil the performance criteria if the requirements defined in Table 6 are satisfied for more than 50% of the earthquake records (at least 6 out of 10).

| | **Fully infill with sliding joints** | **Infill with sliding joints with opening** | **Traditional Infill - Double leaf T2** |
|---|---|---|---|
| | $Drift_{_max_storey_i} < 0.5\%$ (OLS) | $Drift_{_max_storey_i} < 0.4\%$ (OLS) | $Drift_{_max_storey_i} < 0.2\%$ (OLS) |
| | $0.5\% \leq Drift_{_max_storey_i} < 3.0\%$ (DLS) | $0.4\% \leq Drift_{_max_storey_i} < 0.9\%$ (DLS) | $0.2\% \leq Drift_{_max_storey_i} < 0.3\%$ (DLS) |
| | $Drift_{_max_storey_i} \leq 3.0\%$ (LSS=ULS) | $0.9\% \leq Drift_{_max_storey_i} \leq 3.0\%$ (LSS=ULS) | $0.3\% \leq Drift_{_max_storey_i} \leq 1.0\%$ (LSS=ULS) |
| | $Drift_{_max_storey_i} > 3.0\%$ | $Drift_{_max_storey_i} > 3.0\%$ | $Drift_{_max_storey_i} > 1.0\%$ |

Table 6: Performance levels of the infills ([4], [7]).

From Figure 21 to Figure 22, the in-plane damage distribution obtained for each configuration of the infilled frames designed for PGA=0.35g·S is displayed. The colors of the infills indicate if a certain limit state is exceeded or not according to the procedure of Table 6.

***INNOVATIVE INFILL - PGA= 0.35g·S - input ground motion scaled at DLS***

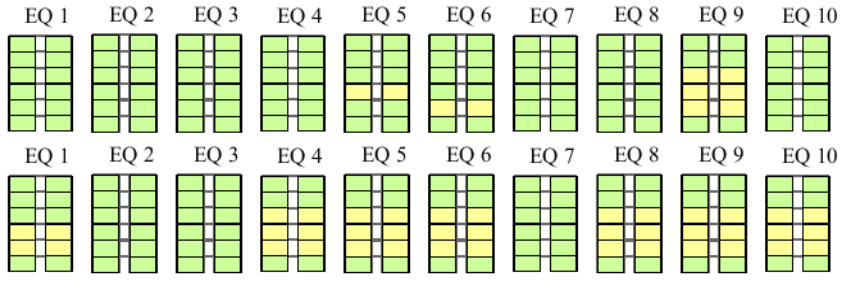


*Partially infilled frame*

*Partially infilled frame with opening*

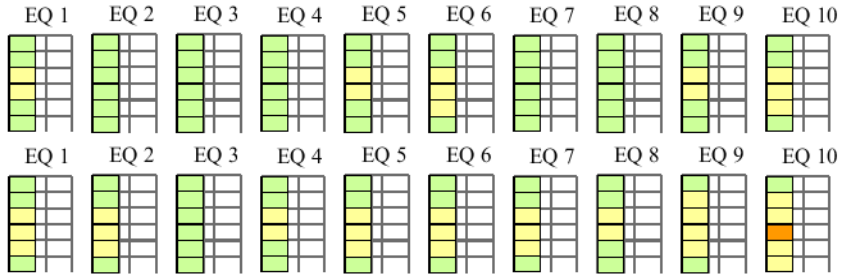


Figure 21: Damage distribution of dynamic analyses of infilled frame designed for PGA=0.35g·S and subjected to the input ground motions scaled to DLS: PGA=0.35g·S·0.5.

***INNOVATIVE INFILL - PGA= 0.35g·S - input ground motion scaled at LSS (ULS)***

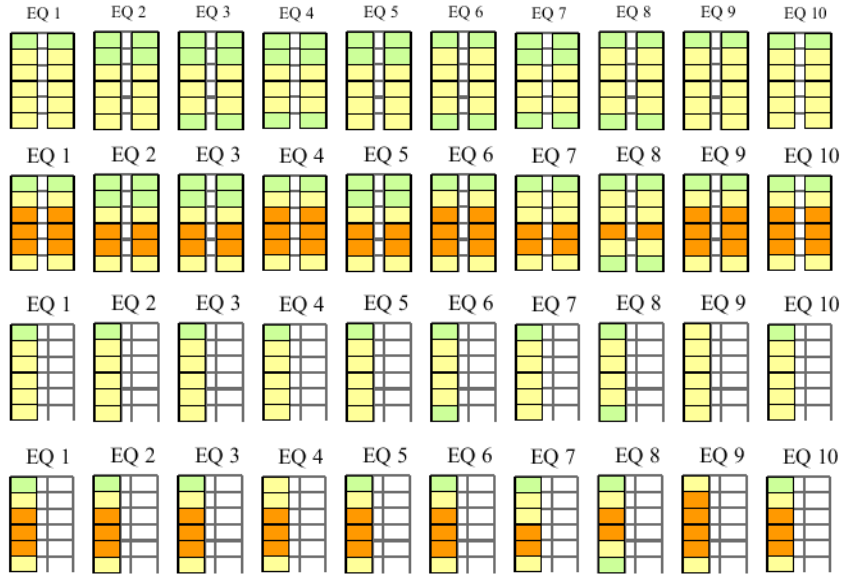


Figure 22: Damage distribution of dynamic analyses of infilled frame designed for PGA=0.35g·S and subjected to the input ground motions scaled to LSS: PGA=0.35g·S.

All the configurations with the innovative infills largely satisfy the performance criteria at ULS and DLS for all the applied levels of PGA (the largest value applied was 0.35·S g).

In particular, the drift limits related to the life safety limit state (LSS/ULS) are never exceeded in any of the infill configuration and frame typology. In the case of frames designed for a PGA=0.10·S g, no input ground motion set, even if it is scaled to its relative ULS, has caused the exceeding of OLS. In the case of frame designed for a PGA=0.25·S g, if the input ground motions are scaled to the DLS, the DLS drift limit is never achieved. If the input accelerograms are scaled to the LSS, the DLS is exceeded in some cases, but only in the configurations in which the infills have the opening. In the case of frames designed for a PGA=0.35·S g, if the ground motions are scaled to the DLS, only one of the one-side infilled frames with the openings exceeds the drift limit at the DLS. In case of accelerograms scaled to LSS, the drift at DLS is achieved by the frame models with the infills with the openings but, on the other hand, the frames with the infills without openings never reach this limit.

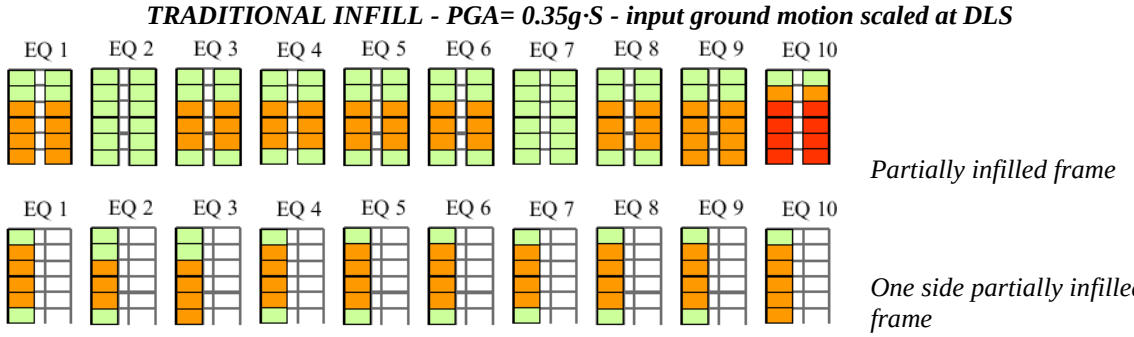


Figure 23: Damage distribution of dynamic analyses of traditional infilled frame designed for PGA=0.35g·S and subjected to the input ground motions scaled to DLS: PGA=0.35g·S·0.5.

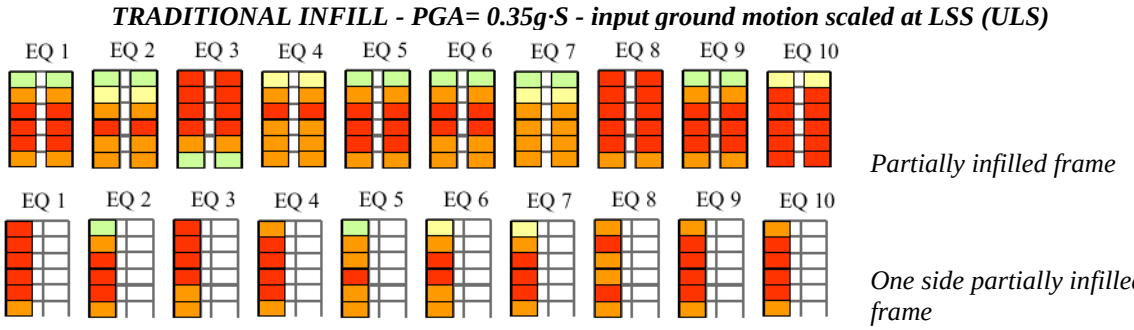


Figure 24: Damage distribution of dynamic analyses of traditional infilled frame designed for PGA=0.35g·S and subjected to the input ground motions scaled to LSS: PGA=0.35g·S.

The traditional infills, for both configurations that have been taken into account, show a lower seismic performance respect to the innovative system. The values of drifts at DLS and at ULS reported in Table 6 have been always exceeded for ground motions scaled at DLS and ULS, respectively. Therefore, considering the analyses performed within the case studies taken into account, the respect of the limit states is never fulfilled, due to the fact that the drift limitations of the bare frame imposed by the standards at the design levels are not safe-sided for the traditional infills, as concluded by Hak et al in [7].

## 7 CONCLUSIONS

Within the European FP7 Project "INSYSME" ([5]) the research unit of the University of Pavia has conceived a new seismic resistant masonry infill ([1], [2]), with sliding joints within the wall and deformable joints at the panel/frame interface which, through an extensive experimental campaign, has showed a strong reduction of the level of damage respect to the traditional completely adherent solutions.

The present work has been focused on the in-plane seismic performance of the innovative infill and its influence in the overall in-plane behaviour of RC buildings. The in-plane seismic behaviour of the innovative infills (with and without opening) has been calibrated on in-plane cyclic tests ([3], [4]) by modelling the infill with macro-elements composed by two diagonal non-linear struts pinned at two edges according to the Crisafulli hysteretic rule ([15]).

RC frame buildings have been designed to three different PGA levels and various infill configurations have been taken into account in order to perform 2D nonlinear static and dynamic analyses on several distinct case studies. Moreover, considering the results on a previous research ([7]), a comparison with the results with traditional double leaf masonry infills

has been conducted. Focusing on parameters such as the displacement profile, the inter-storey drift and the base shear, the overall in-plane seismic response of the buildings has been discussed as a function of the infill type and configuration, also in comparison with the bare frame case.

As expected, the presence of the infills modifies the global behaviour of the structure, and the differences to the bare frame configuration are more pronounced in the case of buildings designed for lower levels of PGA and infilled with the traditional system.

The buildings with the innovative infills have always widely satisfied the "life safety" (ULS), the "damage limitation" (DLS) and the "operational" performance limit states both for the case of the infill with and without opening. In the case of the infilled configurations without opening, no analyses have ever even reached any inter-storey drift limit at ULS and DLS in any storey with ground motions scaled at ULS and DLS, respectively. Therefore, based on these results applied on the considered case studies, it is possible to infer that the performance of the infill system with sliding joints proposed by the University of Pavia is excellent at any limit state (OLS, DLS and ULS) with the applied seismic actions.

The results also exhibit a significant improvement of the in-plane performance compared to a commonly adopted "traditional" infill system constituted by a double leaf wall of a horizontally perforated clay unit masonry.

This research is only a first step for a full understanding of the overall in-plane seismic behaviour of RC buildings infilled with the innovative solution and further numerical investigation should be performed in order to carry out a larger number of non-linear time-history analyses applied to a wider range of PGA levels and structural configurations with different infill distribution.

## AKNOLEDGEMENTS

This study has been carried out the University of Pavia and EUCENTRE within the project INSYSME "Innovative Systems for earthquake resistant Masonry Enclosures in rc buildings", grant FP7-SME-2013-2-GA606229, 2013-2016 and the Executive Project DPC-RELUIS 2010-2013. The financial support received is gratefully acknowledged.

## REFERENCES

[1] P. Morandi, R.R. Milanesi, G. Magenes, Soluzione innovativa per tamponatura antisismica in laterizio a giunti scorrevoli [in Italian], *XVI ANIDIS,* L'Aquila, Italy, September 13-17, 2015.

[2] P. Morandi, R.R. Milanesi, G. Magenes, Innovative seismic solution for clay masonry infills with sliding joints: principles and details, *16th IBMAC,* Padova, Italy, June 26-30, 2016.

[3] R.R. Milanesi, P. Morandi, G. Magenes, Innovative seismic solution for clay masonry infills with sliding joints: experimental tests, *16th IBMAC,* Padova, Italy, June 26-30, 2016.

[4] P. Morandi, R.R. Milanesi, C.F. Manzini, G. Magenes, Experimental tests of an engineered seismic solution of masonry infills with sliding joints, *16th WCEE,* Santiago de Chile, Chile, January 9-13, 2017.

[5] INSYSME "Innovative Systems for earthquake resistant Masonry Enclosures in RC building", European project, grant FP7-SME-2913-2-GA606229, 2013-2016.

[6] A.J. Carr, Ruaumoko Manual, University of Canterbury, Cristchurch, New Zealand, 2007.

[7] S. Hak, P. Morandi, G. Magenes, T. Sullivan, Damage control for clay masonry infills in the design of RC frame structures, *Journal of Earthquake Engineering*, vol. 16, S1, pp. 1-35, 2012.

[8] G.M. Calvi, D. Bolognini, Seismic response of RC frames infilled with weakly reinforced masonry panels, *Journal of Earthquake Engineering*, Vol. 5, No. 2, pp. 153-185, 2001.

[9] CEN *Eurocode 2 - Design of concrete structures, Part 1-1: General rules and rules for buildings*, European Committee for Standardisation, ENV 1992-1-1, Brussels, Belgium, 2004.

[10] CEN *Eurocode 8 - Design of structures for earthquake resistance*, *Part 1: General rules, seismic actions and rules for buildings*, EN 1998-1, European Committee for Standardisation, Brussels, Belgium, 2004.

[11] NTC08 *Norme Tecniche per le costrutioni* (in Italian), Ministero delle Infrastrutture e dei Trasporti, Roma : Decreto Ministeriale of 14th January 2008, 2008

[12] M.F. Giberson, The response of nonlinear multi-story structures subjected to earthquake excitation, *EERL Report*, California Institute of Technology, Pasadena, California, 1967.

[13] Priestley, M.J.N., Calvi, G.M., and Kowalsky, M.J., Displacement-Based Seismic Design of Structures, *IUSS Press*, Pavia, Italy, 2007.

[14] Y. Fukada, Study on the restoring force characteristics of reinforced concrete buildings *[in Japanese]*, *Proceedings Kanto District Symposium*, Architectural Institute of Japan, Tokyo, Japan, No. 40, 1969.

[15] F.J., Crisafulli, Seismic behaviour of reinforced concrete structures with masonry infills, *PhD Dissertation*, Department of Civil Engineering, University of Canterbury, New Zealand, 1997.

[16] R.R. Milanesi, Seismic performance of a newly conceived masonry infill with sliding joints, *PhD Dissertation*, UMESchool, University of Advanced Studies IUSS Pavia, Italy, 2016.

[17] L. Decanini, F. Mollaioli, A. Mura, R. Saragoni, Seismic performance of masonry infilled RC frames, *Proceedings of the 13th World Conference of Earthquake Engineering*, Vancouver, Canada, 2004.

[18] S. Otani, Nonlinear dynamic analysis of reinforced concrete building structures, *Canadian Journal of Civil Engineering*, Vol. 7, pp. 333-344, 1980

[19] I. Iervolino, G. Maddaloni, E. Cosenza, Eurocode 8 complian real record sets for seismic analysis of structures, *Journal of Earthquake Engineering*, Vol. 12, pp. 54-90, 2008.

[20] I. Iervolino, C. Galasso, E. Cosenza, REXEL: computer aided record selection for code-based seismic structural analysis, *Bulletin of Earthquake Engineering*, Vol. 8, pp. 339-362, 2010.

COMPDYN 2017
6th ECCOMAS Thematic Conference on
Computational Methods in Structural Dynamics and Earthquake Engineering
M. Papadrakakis, M. Fragiadakis (eds.)
Rhodes Island, Greece, 15–17 June 2017

# SEISMIC BEHAVIOR OF PRESTRESSED PRECAST SHEAR WALL BUILDINGS USING MULTIPLE ROCKING JOINTS

**Boya Yang**[1], **Xilin Lu**[1]

[1] State Key Laboratory of Disaster Reduction in Civil Engineering, Tongji University
Shanghai 200092, China
0301yangboya@tongji.edu.cn

**Keywords:** Self-centering, Multiple Rocking Joints, Structural Dynamics, Prestressed Precast Concrete Structures, OpenSEES.

**Abstract.** *The use of prestressed precast concrete shear walls (PPCW) as the primary lateral force resisting system in seismic regions has been studied in previous researches. The PPCW structures could concentrate the deformation at the joints and use the unbonded prestressed tendons to provide restoring force to achieve self-centering capacity, thus the residual drift is rather small. In this paper, analytical models of 16-story PPCW frame-shear wall structures designed using displacement-based approaches were established using OpenSEES to study the influence of location of joints and number of joints under both cyclic loading and earthquake loading. Case study buildings were analyzed under three levels of seismic hazards. The comparison was made between the behavior of the PPCW structures and the conventional cast-in-place concrete shear wall (CIPW) structures including the inter-story drifts, shear force distribution, base moment distribution and concrete crushing stress at contact edges of rocking sections. The results indicated that higher mode effects were mitigated on shear and moment actions and residual drifts of buildings were negligible.*

## 1 INTRODUCTION

Resilient structural design is a recent development in earthquake-resistant structural systems. Self-centering structure is a branch of earthquake resilient structures. In comparison with traditional structures, self-centering structures characterize less energy dissipation, negligible structural damage and smaller residual deformation under severe earthquakes [1-2]. This system is featured by a softening force displacement response with minimal damage as a result of geometric nonlinearity. Self-centering capability, especially when combined with replaceable energy-dissipating elements, provide structures higher performance levels than conventional seismic lateral force resisting systems.

Prestressed precast concrete shear wall (PPCW) structures belong to self-centering structures. Figure 1 shows the typical details of a PPCW schematically. The PPCW structure is normally constructed by precast wall panels across horizontal joints at the floor levels using unbonded post-tensioned prestressing (PT) tendons. Debonded mild steel reinforcement crossing the wall joints, which is referred to as energy dissipation (ED) steels in this paper, is provided to enhance the hysteretic energy dissipation of the structure. To prevent significant gap opening at the upper joints, mild steel should be designed crossing these joints to make the joints strong enough. The adoption of PT tendons allows the precast wall panels to open at the base and also minimizes the residual drift by providing a restoring force, resulting in a flag shaped hysteresis loop. A series of experimental and analytical studies conducted on the unbonded PPCWs have demonstrated the excellent seismic performance of PPCW structures [3-7].

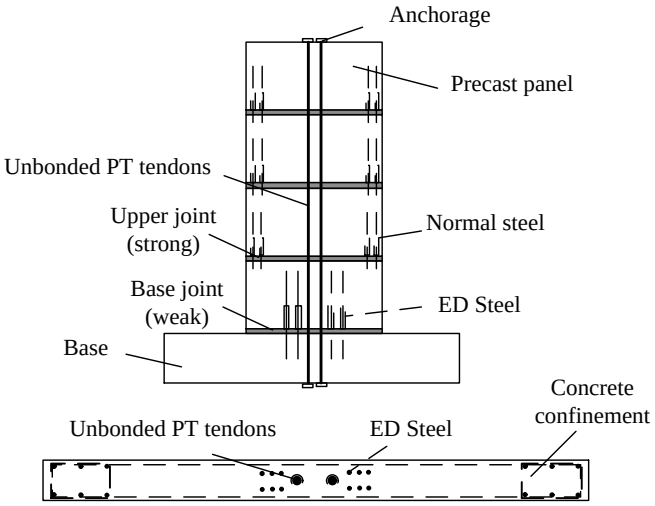


Figure 1: Schematic representation of a PPCW

Wiebe et al. [8] investigated the seismic performance of multiple rocking sections over the height of one single shear wall models. The results showed that the bending moment envelope was proved to be significantly reduced by providing multiple rocking sections, while maintaining the inter-story drifts within permissible limits. Khanmohammadi et al. [9] employed multiple rocking systems for PPCW systems and all rocking sections were equally designed by strength. The results indicated a great reduction of seismic shears and overturning moments along the vertical height with negligible residual drifts.

In order to investigate the behavior of multiple rocking systems in high-rise buildings, two alternatives of rocking joints design (only base, base & mid height) were considered. For comparison with the conventional design, for each building, corresponding cast-in-place shear wall structures designed by the current design code [10-12] were also established. Criteria in-

cluding peak drifts, inter-story drift, distribution of shear force and bending moment ratio, and concrete stress strains at base rocking sections were evaluated and compared with the traditional design building to discover the effect of multiple rocking sections over height on the structural response.

## 2 NUMERICAL MODELING VERIFICATION

### 2.1 Test Description

The experimental program investigating the behavior of precast concrete walls utilizing unbonded PT tendons conducted by Perez *et al*. [4] was selected to validate the simulation method. The test setup is shown in Figure 2. Specimen TW1 were tested under monotonic loading and TW2 was tested under cyclic loading. Material properties are listed as below: compressive strength of the unconfined concrete $f_c$=52Mpa; compressive strength of the confined concrete $f_{cc}$=110Mpa; yielding stress of the PT tendons $f_{py}$=951MPa; initial stress of PT tendons $f_{pi}$=0.6$f_{pu}$ (design ultimate stress $f_{pu}$=1102MPa).

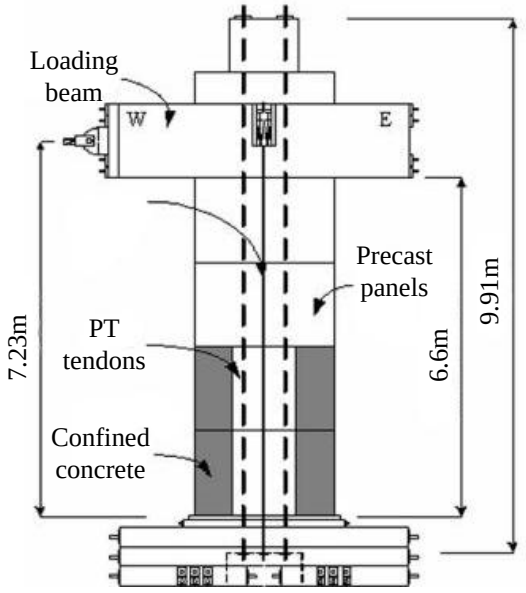


Figure 2: Test set up

### 2.2 Simulation Method

Figure 3 illustrates a schematic view of the methodology used for simulation of the experimental PPCW specimen in OpenSEES. It is assumed that no sliding-slip exists between the contact surfaces. The proposed simulation model included a bed of truss elements at the base of wall where the gap-opening is expected, corotational elements for the PT tendons, and fiber force-based beam-column elements for the precast wall panel. In beam-column elements, each section is discretized into unconfined concrete fibers, confined concrete fibers, and steel fibers. One force-based element per story with five integration points was used for the walls and the columns. For concrete material, Concrete02 material model is used in which the modified Kent and Park model is used in compression, an initial linear elastic branch together with a linear softening branch up to zero stress is used in tension. For reinforcing steel, Steel02 material model is used. Concrete fibers were modeled with no tensile capacity which is achieved by combined the traditional material and the Elastic-No-Tension material in series. A truss bed height of twice the length of plastic hinge is recommended ($h_{spring}$=2$l_p$). Plastic hinge

length $l_p$=min ($2t_w^{"}, 2a^{"}$), where $t_w^{"}$ is thickness of confined concrete, and $a^{"}$ is depth of the equivalent compression stress block excluding cover thickness. The "PDelta" algorithm is used to consider the effect of large deformations.

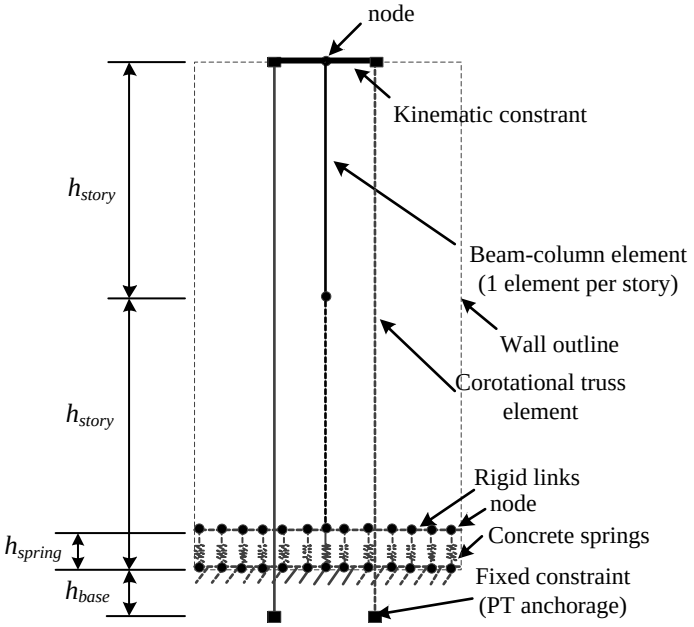


Figure 3: Modeling of PPCW

## 2.3 Results of Numerical Analyses

Figure 4(a) compares the experimental results of the lateral response for TW1 with the analytical results, which shows that the initial stiffness and base shear of TW1 are well captured. Figure 4(b) compares length of contact between the wall base panel and foundation. Figure 5 compares the results of the lateral response for TW2. A good agreement between analytical and experimental response was found in the results pertaining to both hysteretic curves and uplifts. The results indicated that the bed of truss elements using the uniaxial concrete stress-strain material model accurately captured the wall-to-foundation rocking interface. Analysis based on fiber section elements is accurate enough to predict both the global and local response of concrete structures although shear-flexure interaction was not considered.

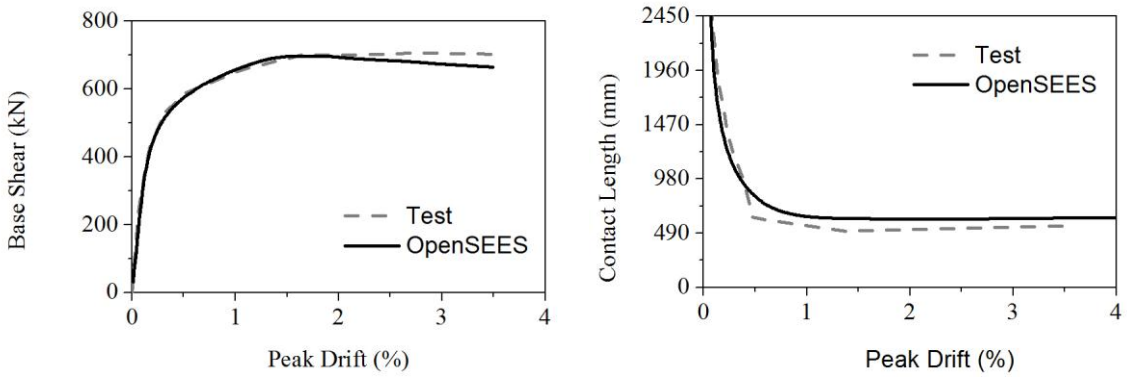


(a) (b)

Figure 4: Comparison of the analytic model with experimental results for TW1: (a) Wall lateral response; (b) Contact Length

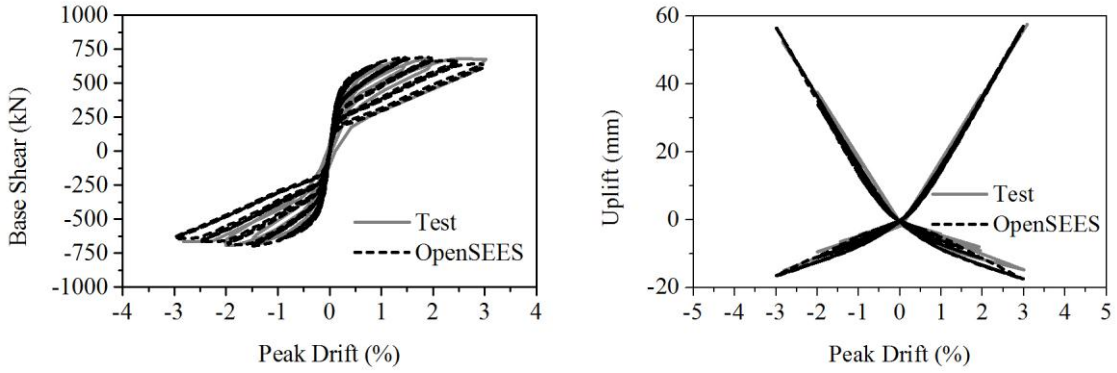


(a) (b)

Figure 5: Comparison of the analytic model with experimental results for TW2: (a) Wall lateral response; (b) Uplift of wall ends

## 3 CASE STUDY STRUCTURE

A group of 16-story buildings of rectangular plan used for office buildings were evaluated. The buildings of the first group were designed by the conventional provisions, and those of the second group using PPCW structural system were designed following the direct displacement-based design (DDBD) [13]. The buildings were almost identical in geometry. In addition to rocking system at the base, double rocking joints (one at the base and the other at mid-height) were also considered. The 16-story PPCW buildings allowing gap-opening only at base is designated as PPCW-16-1, while allowing gap-opening at base and mid-height is designated as PPCW-16-2 (Figure 6). Similar notation is adopted for CIPW buildings.

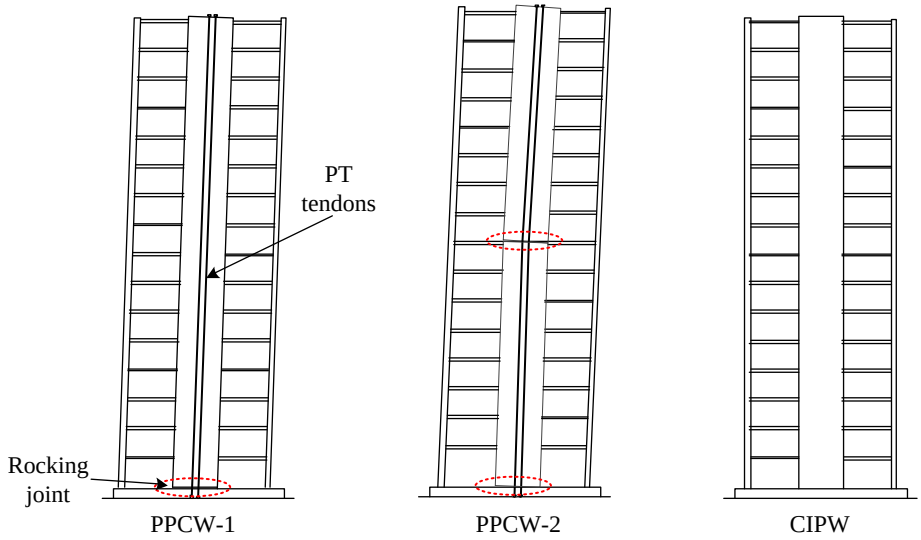


Figure 6: Schematic representation of considered opening joints

The lateral force resisting system of the buildings consists of a frame-wall system in the NS direction and a moment-resisting frame system in the EW direction. The plan of the considered buildings with a dimension of 36m×18m and a story height of 4.0m is illustrated in Figure 7. The dead load (*DL*) and live load (*LL*) is 5kPa and 2kPa, respectively [10]. Gravity load combination is assumed to be 1.00*DL*+0.50*LL*. The seismic site design is Group 2 and Site Class IV according to the related design criteria [11].

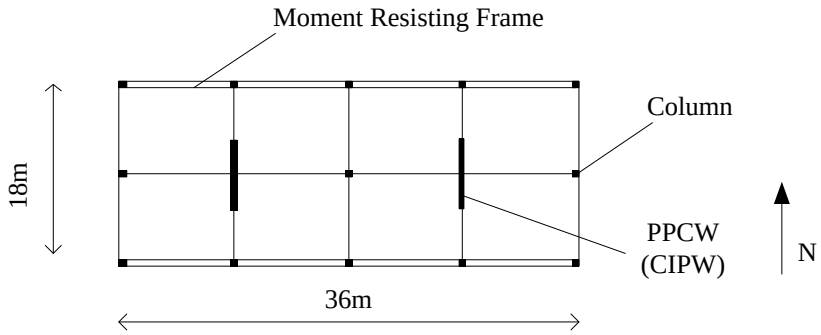


Figure 7: Building plan for the case study structure

### 3.1 Design of PPCW buildings

The PPCW structural structures were designed following the DDBD approach. Each wall consists of one precast concrete wall panel each story, post-tensioned to the foundation with unbonded high strength PT tendons. The beam-column connection is designed as hybrid precast ductile connections following the recommendations given by El-Sheikh et al. [14]. Column-foundation connection is similar with the wall-foundation connection. The connection between the floors and the precast wall panels is assumed to be a vertical sleeved-type connection to allow the lateral forces to be transmitted from the floor to the wall while preventing any vertical actions to be transmitted from the wall panel to floor [15]. A listing of the important features of PPCW buildings is provided in Table 1 and Table 2.

| Story Number | Column (mm×mm) | $\rho_{ptc}$ (%) | Beam(NS) (mm×mm) | $\rho_{ptbNS}$ (%) | Beam(EW) (mm×mm) | $\rho_{ptbEW}$ (%) |
|---|---|---|---|---|---|---|
| 1-4 | 800×800 | 1.09 | 600×300 | 0.58 | 900×300 | 0.58 |
| 5-8 | 750×750 | 1.24 | | | | |
| 9-12 | 700×700 | 1.43 | 600×300 | 0.66 | 900×300 | 0.58 |
| 13-16 | 650×650 | 1.66 | | | | |

Note: $\rho_{ptc}$ = area ratio of PT steel in columns; $\rho_{ptb}$ = area ratio of PT steel in beams; Beam(NS) means beams in NS direction; Beam(EW) means beams in EW direction.

Table 1: Member sizes of PPCW buildings

| $l_w$ (mm) | $t_w$ (mm) | $\rho_{ptw}$ (%) | $\rho_s$ (%) | $l_{hoop}$ (mm) | $l_{debonded}$ (mm) |
|---|---|---|---|---|---|
| 8500 | 500 | 0.053 | 0.52 | 2000 | 1000 |

Note: $l_w$ =wall length; $t_w$ =wall thickness; $\rho_{ptw}$ = area ratio of PT steel in wall; $\rho_s$ = area ratio of ED steel; $l_{hoop}$ = confinement region length; $l_{debonded}$ = unbonded length of ED steel.

Table 2: Design details of precast walls used in PPCW buildings

### 3.2 Design of CIPW buildings

In addition to PPCW buildings, the third model was considered with the cast-in-place shear wall (CIPW) buildings. The CIPW buildings were almost identical to PPCW buildings in geometry. The CIPW buildings were designed by the seismic provisions in China. Detailed size information of the CIPW building is listed in Table 3 and Table 4.

| Story Number | Column (mm ×mm) | $\rho_c$ (%) | Beam(NS) (mm ×mm) | $\rho_{bNS}$ (%) | Beam(EW) (mm ×mm) | $\rho_{bEW}$ (%) |
|---|---|---|---|---|---|---|
| 1-4 | 800 ×800 | 1.42 | 800 ×300 | 0.7 | 900 ×400 | 0.72 |
| 5-8 | 750 ×750 | 1.35 | | | | |
| 9-12 | 700 ×700 | 1.24 | 700 ×300 | 0.71 | 800 ×300 | 0.74 |
| 13-16 | 650 ×650 | 1.26 | | | | |

Note: $\rho_c$ = area ratio of longitudinal steel in columns; $\rho_b$ = area ratio of longitudinal steel in beams.

Table 3. Member sizes of CIPW buildings

| $l_w$ (mm) | $t_w$ (mm) | $\rho'$ (%) | $\rho''$ (%) | $\rho_t$ (%) | $l_{hoop}$ (mm) |
|---|---|---|---|---|---|
| 8500 | 500 | 1.25 | 0.35 | 0.13 | 2000 |

Note: $\rho'$= ratio of longitudinal boundary reinforcement area to gross section area of wall boundary; $\rho''$= ratio of volume of transverse confining steel to gross concrete area of web; $\rho_t$ = volumetric ratio of transverse reinforcement; $l_{hoop}$ = confinement region length.

Table 4. Design details of shear walls used in CIPW buildings

## 4 GROUND MOTIONS

| ID No. | Record Seq. | Year | $M_w$ | Event | Recording Station | $R_{rup}$ (km) | Record Component |
|---|---|---|---|---|---|---|---|
| 1 | 169 | 1979 | 6.5 | Imperial Valley | Delta | 22.03 | IMPVALL_H-DLT262<br>IMPVALL_H-DLT352 |
| 2 | 741 | 1989 | 6.9 | Loma Prieta | BRAN | 10.72 | LOMAP_BRN000<br>LOMAP_BRN090 |
| 3 | 1106 | 1995 | 6.9 | Kobe, Japan | KJMA | 0.96 | KOBE_KJM000<br>KOBE_KJM090 |
| 4 | 1120 | 1995 | 6.9 | Kobe, Japan | TAKATORI | 1.47 | KOBE_TAK000<br>KOBE_TAK090 |
| 5 | 1158 | 1999 | 7.5 | Kocaeli, Turkey | Duzce | 15.37 | KOCAELI_DZC180<br>KOCAELI_DZC270 |
| 6 | 1244 | 1999 | 7.6 | Chi-Chi, Taiwan | CHY101 | 9.94 | CHICHI_CHIY101-E<br>CHICHI_CHIY101-N |
| 7 | 1605 | 1999 | 7.1 | Duzce, Turkey | Duzce | 6.58 | DUZCE_DZC180<br>DUZCE_DZC270 |

Table 5: Details of the selected input accelerations for the nonlinear time history analysis

The seismic fortification intensity of the case study buildings site is assumed to be 8, which means the peak ground motion (PGA) under frequent, basic, and rare level of seismic hazard is 0.07g, 0.2g, and 0.4g respectively [10]. Structures are designed to be elastic under frequent level of seismic hazard. Thus except for basic and rare level earthquake (PGA=0.2g and 0.4g), severe level earthquake was considered, which has a PGA of 0.6g. A total of seven earthquake records (Table 5) were selected from the PEER Ground Motion Database. The magnitude of the selected earthquake $M_w$ is greater than 6.5.

The mean acceleration response spectrum with 5% damping of the scaled ground motion records under rare level of seismic hazard is shown in Figure 8. The bold line is design acceleration response spectrum provided in Chinese seismic code GB50011-2010.

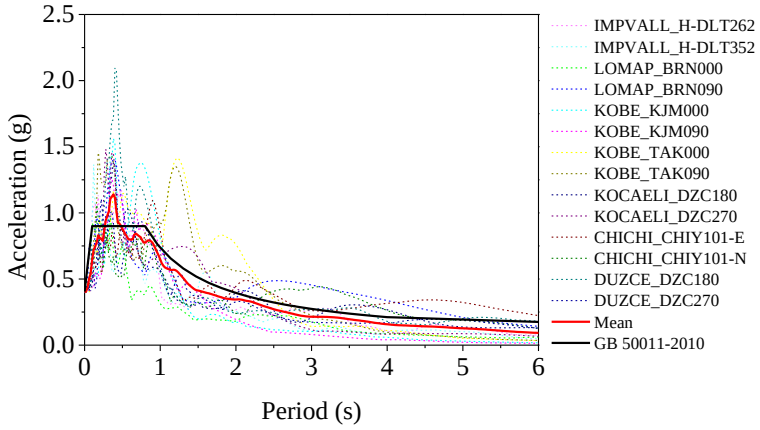


Figure 8: Code-specified design acceleration spectrum and median response spectrum $S_a$ of selected input ground motion records

## 5 RESULTS OF ANALYSES

Three-dimensional analytical models for the two designs were created, and nonlinear static and dynamic time history analyses were carried out under bidirectional excitations. The ratio of PGA(NS) to PGA(EW) should be fixed as 1:0.85 according to the Chinese seismic code.

### 5.1 Nonlinear static analyses

A total of 50 contact springs were used to model the gap-opening interface of precast walls in the 16-story PPCW buildings. Nonlinear pushover analyses of the case study buildings were conducted adopting inverted triangular distribution of lateral forces. The response of case study buildings under monotonic loading is shown in Figure 9(a). Figure 9(b) compares hysteretic energy dissipation for PPCW and CIPW structures. Hysteresis curve of the CIPW building is fuller, which indicates the possibility of large residual deformations after an earthquake and better energy dissipation. As expected, the hysteresis curves of the PPCW buildings show significant ‘flag-shape’ characteristic. Energy dissipation of PPCW buildings is smaller and results in minor residual inter-story drifts.

### 5.2 Nonlinear dynamic analyses

Modal analysis was carried out first to evaluate the natural characteristics of the case study buildings. The vibration periods calculated using OpenSEES are shown in Table 6. The Rayleigh damping of the PPCW and CIPW structures were considered 3% and 5%, respectively. Base uplift due to rocking eliminates the development of concrete tensile stresses at the wall base and provides a ‘base isolation effect’ through the elongation of the system’s structural period.

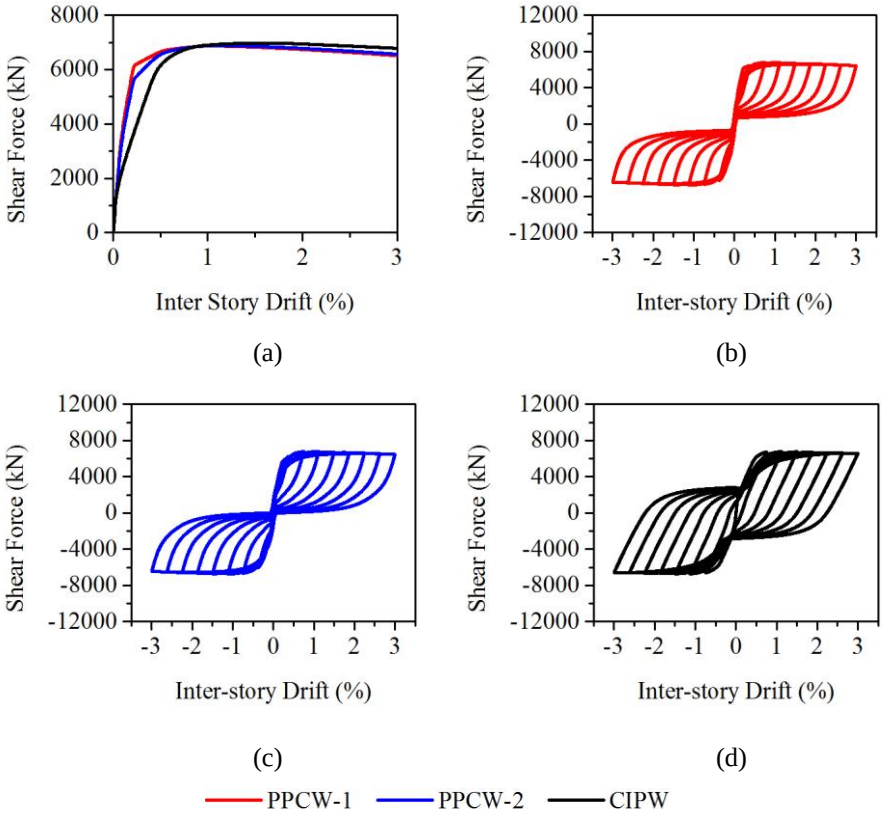


Figure 9: Static response of case study buildings: (a) monotonic loading; (b) cyclic loading of PPCW-1; (c) cyclic loading of PPCW-2; (d) cyclic loading of CIPW

| | 1st Mode Period (s) | 2nd Mode Period (s) |
|---|---|---|
| PPCW-1 | 1.39 | 0.24 |
| PPCW-2 | 1.38 | 0.24 |
| CIPW | 1.35 | 0.23 |

Table 6: Fundamental periods of PPCW and CIPW buildings in NS direction

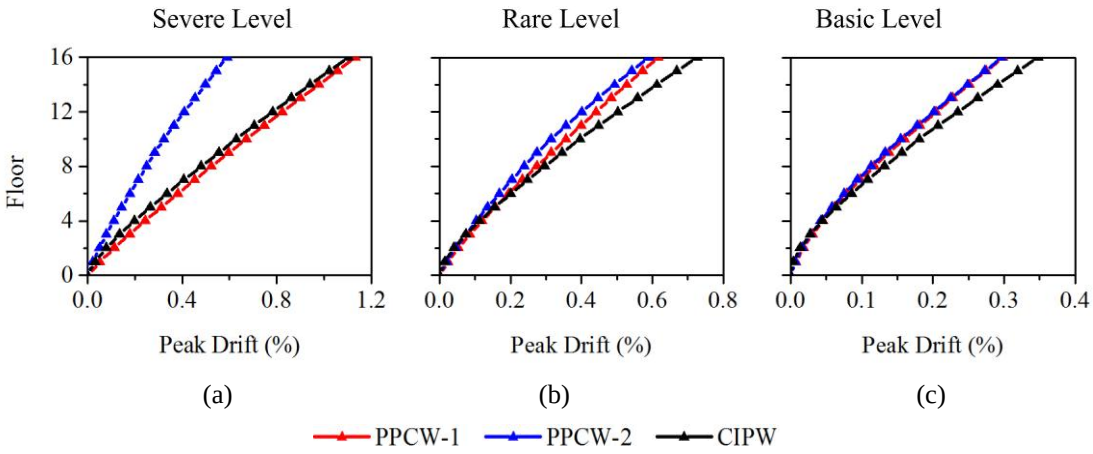


Figure 10: Mean values of inter-story drift under seismic loading

The effects of gap-opening at the different locations of the precast shear wall on the maximum peak roof drifts are investigated, as shown in Figure 10. The results indicate that be-

cause of the joint opening at mid height, the peak drift is significantly reduced by nearly 50% at severe level seismic hazard. In rare and basic level seismic hazard, the peak drift of PPCW-2 building is approximately equal to that of PPCW-2 building, but still less than CIPW buildings.

In Figure 11, results of the maximum inter-story drift are presented. Results of drifts in PPCW buildings did not exceed 1% under rare level ground motions, which is the design drift value in the conventional seismic code designs, the outcome results were acceptable from design point of view. The PPCW buildings have a more uniform distribution of inter-story drift ratio (IDR) compared with the corresponding CIPW buildings. Under the basic level ground motions, the inter-story drifts of PPCW-1 and PPCW-2 buildings are nearly the same. Development of rocking joints over height caused the drift to increase in the upper half and decrease in the lower half parts. With the increase of input amplitude of ground motions, inter-story drift of PPCW-2 buildings reduces significantly compared to PPCW-1 building.

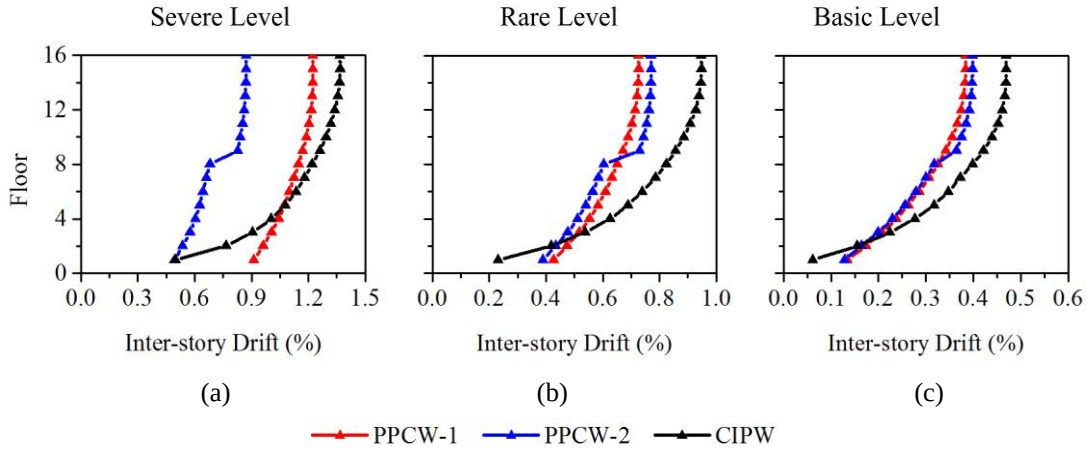


Figure 11: Mean values of inter-story drift under seismic loading

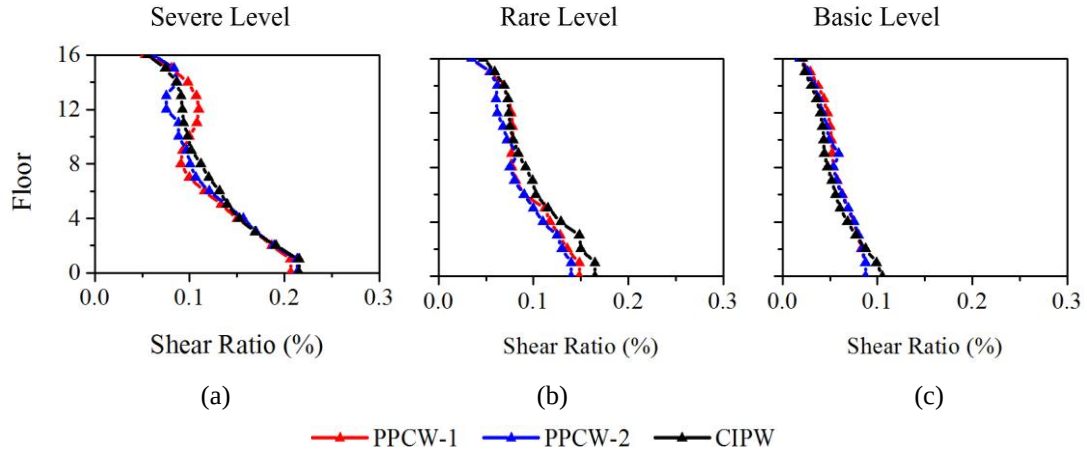


Figure 12: Mean values of shear force ratio under seismic loading

The distribution of shear forces is important in the performance-based design approaches. Distribution of shear force ratios along height under three level of seismic hazard are shown in Figure 12. To compare the results straightforward, the shear force ratios were normalized by the total weight of the building. With adding one more rocking joint at mid-height, shear forces were smaller than CIPW building, which in turn represented that the current design codes and shape of shear force distribution were more regular than those without the second

increase in upper half-height. With developing rocking sections, the amounts of shear forces through upper half part of the buildings tended to be larger than PPCW-1 building.

Figure 13 shows distribution of maximum bending moment under three level ground motions. The results were normalized by the product of the building height and weight which was a moment that can be regarded as overturning moment by applying a concentrated force to the roof with the value of the total seismic weight of the structure. Values of the moment demands related to CIPW models are more than those of the PPCW model, particularly at lower parts of buildings. The maximum bending moment of PPCW-2 building at mid height was reduced by 54 and 79% compared with PPCW-1 building under severe and rare ground motions, respectively.

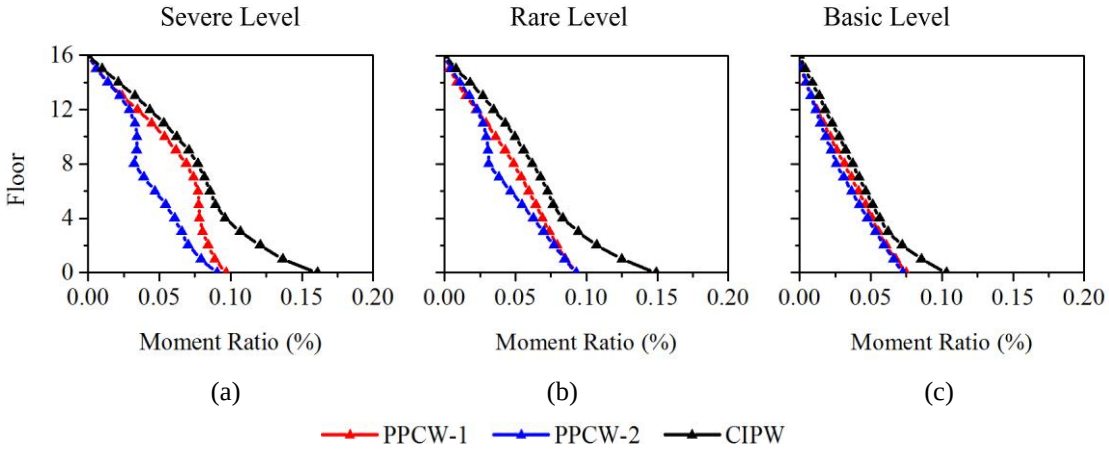


Figure 13: Mean values of moment ratio under seismic loading

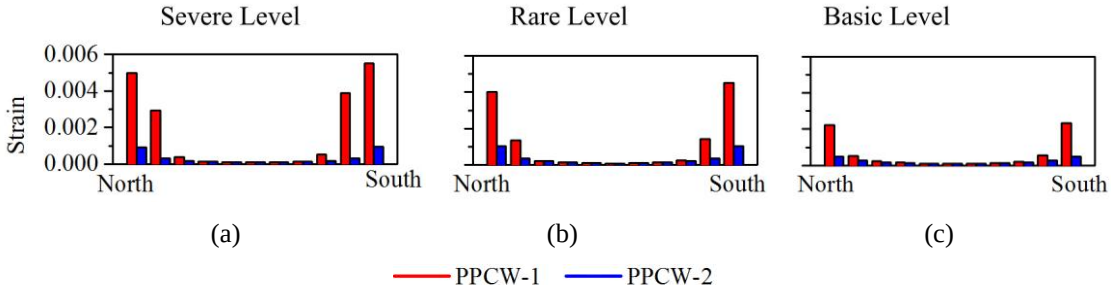


Figure 14: Concrete compressive strain on base rocking joints of PPCW buildings

The maximum suffered concrete compressive strains of the PPCW buildings are in the base-to-foundation section, which are presented in Figure 14. Unlike cast-in-place shear walls, damage to PPCWs is often featured by crushing of confined core concrete at the wall toes [3-5, 16]. As expected, the maximum concrete compressive strains are found around the wall toes, and the observed concrete compressive strains are lower than design ultimate concrete compressive strains (0.02 for confined concrete; 0.004 for unconfined concrete). The concrete strain is greatly alleviated in all cases, which means the adding joint at mid-height is a good protection of toes of concrete walls. The results showed that the concrete of the rocking sections did not reach the yielding point in any of the models under three levels of seismic hazard. No crushing of confined concrete wall toes is expected in PPCW buildings.

## 6 CONCLUSIONS

- The proposed fiber model based on OpenSEES of a PPCW is simple to conduct. Comparisons with the experimental results demonstrated that the simulation method can capture the nonlinear hysteretic response characteristics of PPCW reasonably well under both monotonic loading and cyclic loading. The model estimated the wall uplift and change in neutral axis accurately. The rationality of the model is verified.
- The PPCW buildings have a more uniform distribution of inters-tory drift ratio compared with the corresponding CIPW buildings and thus preventing undesirable weak story failure pattern.
- The higher mode effects on shear and moment action demands were mitigated using multiple rocking joints.
- By using multiple joint, compressive strains of the concrete at wall toes are significantly reduced and severe damage of the wall is alleviated.

## 7 ACKNOWLEDGMENT

This research is sponsored by Natural Science Foundation of China (NSFC) (51638012). The support is gratefully acknowledged.

## REFERENCES

[1] N.B. Chancellor, M.R. Eatherton, D.A. Roke, et al, Self-Centering Seismic Lateral Force Resisting Systems: High Performance Structures for the City of Tomorrow. *Buildings*, **4(3)**, 520-548, 2014.

[2] X. Lu, Y. Mao, Y. Chen, J. Liu, Y. Zhou, New structural system for earthquake resilient design. *Journal of Earthquake and Tsunami*, **7(03)**, 1350013, 2013.

[3] T. Holden, J. Restrepo, J.B. Mander, Seismic Performance of Precast Reinforced and Prestressed Concrete Walls. *Journal of Structural Engineering*, **129**, 286-296, 2003.

[4] F.J. Perez, R. Sause, S. Pessiki, Analytical and Experimental Lateral Load Behavior of Unbonded Post-Tensioned Precast Concrete Walls. *Journal of Structural Engineering*, **133**, 1531-1540, 2007.

[5] B. Erkmen, A.E. Schultz, Self-centering behavior of unbonded, post-tensioned precast concrete shear walls. *Journal of Earthquake Engineering*, **13(7)**, 1047-1064, 2009.

[6] B.J. Smith, Y.C. Kurama, M.J. McGinnis. Design and measured behavior of a hybrid precast concrete wall specimen for seismic regions. *Journal of Structural Engineering* **137(10)**, 1052-1062, 2011.

[7] H. Wu, X. Lu, H. Jiang, Experimental study on seismic performance of prestressed precast concrete shear walls. *Journal of Building Structures*, **37(5)**, 208-217, 2016. (in Chinese)

[8] L. Wiebe, C. Christopoulos, Mitigation of Higher Mode Effects in Base-Rocking Systems by Using Multiple Rocking Sections, *Journal of Earthquake Engineering*, **13(sup1)**, 83-108, 2009.

[9] M. Khanmohammadi, S. Heydari, Seismic behavior improvement of reinforced concrete shear wall buildings using multiple rocking systems. *Engineering Structures*, **100**, 577-589, 2015.

[10] CMC. Load Code for the Design of Building Structures (GB 50009-2012). China Building Industry Press: Beijing, 2012. (in Chinese).

[11] CMC. Code for Seismic Design of Buildings (GB 50011-2010), China Building Industry Press: Beijing, 2010. (in Chinese).

[12] CMC. Code for Design of Concrete Structures (GB 50010-2010). China Building Industry Press: Beijing, 2010. (in Chinese).

[13] M.J.N. Priestley, Direct displacement-based design of precast/prestressed concrete buildings. PCI Journal, 47(6), 66-79, 2002.

[14] M.T. El-Sheikh, R. Sause, S. Pessiki, L.W. Lu, Seismic Behavior and Design of Unbonded Post-Tensioned Precast Concrete Frames. PCI Journal, 44(3), 54-71, 1999.

[15] M.J. Schoettler, A. Belleri, D. Zhang, J.I. Restrepo, R.B. Fleischman, Preliminary results of the shake-table testing for the development of a diaphragm seismic design methodology. PCI Journal, 54(1), 100-124, 2009.

[16] X. Lu, X. Dang, J. Qian , Y. Zhou , H. Jiang. Experimental study of self-centering shear walls with horizontal bottom slits, Journal of Structural Engineering, 04016183-1, 2016. doi: 10.6052/j.issn.1000-4750.2015.12.1021. (on line)

COMPDYN 2017
6th ECCOMAS Thematic Conference on
Computational Methods in Structural Dynamics and Earthquake Engineering
M. Papadrakakis, M. Fragiadakis (eds.)
Rhodes Island, Greece, 15–17 June 2017

# INFLUENCE OF RIGID FLOOR ASSUMPTION IN SEISMIC ANALYSIS OF RC EXISTING BUILDINGS

**Francesco Porco**[1], **Sergio Ruggieri**[2], **and Domenico Raffaele**[3]

[1] Dep. Dicatech, Politecnico di Bari, Via Orabona, 4 – 70126, Italy
f.porco@poliba.it

[2] Dep. Dicatech, Politecnico di Bari, Via Orabona, 4 – 70126, Italy
sergio.ruggieri@poliba.it

[3] Dep. Dicatech, Politecnico di Bari, Via Orabona, 4 – 70126, Italy
d.raffaele@poliba.it

**Keywords:** RC existing building, seismic assessment, FEM, structural irregularity

**Abstract.** *The study concerns with the seismic analysis of reinforced concrete (RC) building, with particular attention to the role played by floor system. The rigid-floor assumption is often used for RC existing buildings' vulnerability assessment, in order to simplify the study of their structural behavior. Seismic codes (EC8, NZS4203, FEMA-273) provide a set of quantitative criteria related to deformation of diaphragm and average drift of the associated storey and qualitative criteria related to the shape of diaphragm. Despite in many cases this hypothesis can be considered sufficiently accurate, it is not always valid because it is related to several features of structure as floor geometry and materials, relative stiffness between floor system and vertical structural elements, shape of building, etc. In fact, unlike new structures, the main problem of RC existing buildings is not having geometrical and mechanical regular features (for example, in a ribbed slab, the irregular depth of the top concrete slab) as well as to present irregular dynamic parameters.*

*When the floor system cannot be considered rigid, it may be studied as flexible slab with the increment of uncertainty related to stress states of structural elements.*

*In order to understand how the floor system influences the structural behavior, it has been investigated the seismic performance of several applications, extrapolated from real RC existing buildings, through numerical methods, with and without the rigid-floor assumption.*

## 1 INTRODUCTION

Existing RC buildings are mostly characterized by an unsatisfactory level of the technical design (mainly because the reference building codes are very obsolete), and the development of vulnerability studies is one of the main research focus that the scientific community has explored in the last years at different scales of analyses [1, 2, 3, 4]. These studies, together with the observation of post-seismic damage after recent earthquakes, have clearly shown that the seismic risk of existing RC buildings is very high, confirming the need of systematically assessing their safety level and to develop to this aim not only proper techniques for the modeling and analysis but also for the monitoring and control, especially in the case of strategic structures [5, 6]. In fact, on the one hand, existing buildings were designed by engineers through old codes, which do not take in exam the seismic actions, on the other hand existing buildings are often characterized by meaningful historical and artistic value.

Modern seismic codes, as Eurocode 8 [7] and consequently Italian NTC [8], suggest a performance based approach and guidelines that engineers can use in order to analyze the real behavior of existing structure and to choose the most suitable retrofit solutions. One of most important steps of the abovementioned performance approach is the nonlinear analysis of the structural model, static or dynamic, in order to define the structural capacity and compare it to seismic demand.

In this phase, a correct estimate of capacity is only possible through a correct finite element method (FEM) model, even if simplified, which takes into account a series of hypothesis on materials, geometry, loads, etc…

The FEM model, even on geometric regular existing building, must consider a presence of irregularity factors, which can change results of analysis. With this regard, a particular attention in analysis results has to be taken when the influence of in situ materials strength is included in FEM model, as shown in Uva et al., 2014 [9] and Porco et al., 2014 [10]; or when the influence of secondary structural elements as infill panels is considered, as shown in Porco et al., 2013 [11] and 2015 [12]; Fiore et al., 2014 [13] and 2015 [14]; Casolo et al., 2013 [15].

Clearly, these influence factors cause strong behavior difference on buildings analyzed, regarding to elements stiffness, masses and modal parameters.

In this paper, the attention is focused on one of these irregularity factors: a floor in-plane deformability. The influence of this factor, in the evaluation of seismic behavior of RC existing building, has been evaluated.

## 2 STATE OF THE ART

In RC buildings, floor system is a bi-dimensional structure loaded orthogonally to its plane by gravity loads and it distributes seismic actions among structural vertical elements. Generally, buildings are designed using the assumption of rigid floor, which is justified when floor is stiffer than vertical elements. To design new RC buildings, modern codes as Eurocode (consequently in Italian code) provides technological rules for several typologies of rigid floor. For example, to obtain an in-plane rigid behavior, a floor system must have a thickness of top concrete slab larger than 4 cm, as show in Figure 1 where a ribbed slab is represented:

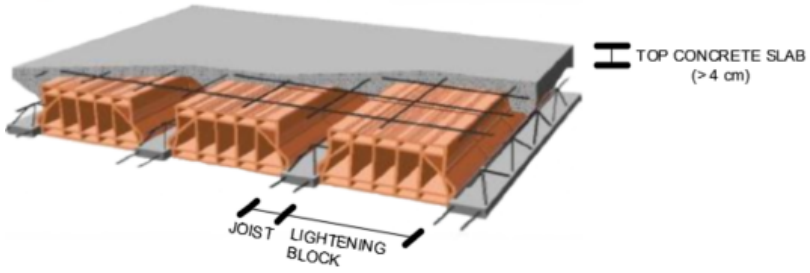


*Figure 1 – example of rigid floor, according to Italian NTC*

Some cases of South Italian existing RC buildings have no top concrete slabs (SAP slab), as shown in figure 2. In other cases, top concrete slab has a low thickness because of the presence of hydraulic or electrical systems or because of human mistakes.



*Figure 2 – SAP slab (without top concrete slab)*

The rule of top concrete slab thickness cannot be enough to define a rigid floor: its stiffness must be compared to the stiffness of structural vertical elements. With this regard, FEMA (1997) [16] provides a quantitative criterion which defines floor as either flexible, stiff or rigid. In particular way, it defines a factor λ as ratio between the maximum to minimum lateral in-plane deflection of floor, caused by horizontal actions. The ratio is shown in Eq.1, where X and Y are depicted in figure 3:

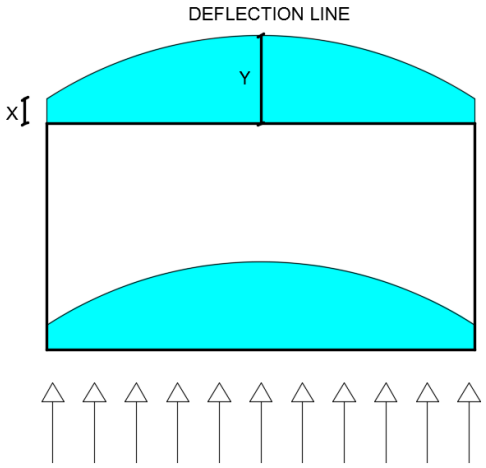


*Figure 3 – In-plane displacement of slab, without the rigid floor assumption*

$$\lambda = Y/X \tag{1}$$

If λ is larger than 2, the floor is deformable while if λ is lower than 0.5, the floor is rigid. If λ is included between 0.5 and 2, the floor is "stiff" (neither flexible nor rigid).

Eurocode 8 provides a qualitative criterion to define the rigid floor: the floor system is taken as being rigid if, when it is modeled with its actual in-plane flexibility, its horizontal displacements nowhere exceed those resulting from the rigid floor assumption by more than 10% of the corresponding absolute horizontal displacements in the seismic design situation.

As well as Eurocode 8, even NZS 4203 [17] provides a qualitative criterion, such as indications of rigid floor assumption invalidity, for instance abrupt discontinuities, major variations in in-plane stiffness or major re-entrant corners in diaphragms.

Moeni e Rafezy, 2011 [18], analyzed the rigid floor assumption on buildings with irregular shape in-plan, evaluating results in terms of Deflect/Drift ratio through qualitative and quantitative criteria provided by several international codes, such as those aforementioned. Authors tested the efficiency and accuracy of all indications available in the matter of floor deformability.

Previously, several studies have been carried out in order to study the deformability of floor and its effect on the structural behavior.

Saffarini and Qudaimat, 1992 [19], analyzed several RC buildings to compare the difference between rigid floor and flexible-floor analyses. They found that the rigid-floor assumption is accurate for buildings without shear walls, but it can cause errors for building systems with shear walls. The study made up of a numerical model where some parameters were varied, such as number of stories, story height, slab type, building-plan aspect ratio, regularity of building plan, openings in the slab, the sizes and spacing of columns and shear walls.

Kunnath et al., 1991 [20], studied the effect of deformable floor system on irregular buildings, using a simplified macro modeling scheme which included an inelastic behavior. Results of research showed that, the base shear is larger when the floor is flexible, rather than when it is rigid and elastic. However, incrementing the number of ways and floors, interior frames have a higher base shear with a larger strength and ductility demand.

Dolce et al., 1994 [21], studied the inelastic dynamic response of a large number of floor systems simple models. On their cases studied, they analyzed the variability of the ratio $k_{floor}/k_{vert}$, using a spring model and varying elements stiffness. They obtained that, when the stiffness distribution of structural vertical elements is uniform, the flexibility of floor system is negligible, while when the structures have important re-entrances, the deformability effect is relevant.

Other authors studied this problem (Ju and Lin, 1999 [22]; Fleishman and Farrow, 2001 [23], Lee at al., 2002 [24]; Fouad at al., 2012 [25]; Bakar et al. [26], 2014; Tena-Colunga et al., 2015 [27]), observing the differences of results of modal parameters and stresses, obtained by different modeling methods and using the hypothesis of rigid floor or not.

Relying on results obtained by the abovementioned authors and using indications provided by international seismic codes, the aim of this paper is to show the differences of simple numerical applications' structural behavior, on the basis of a variation of the FEM model, which take or not into account the rigid floor assumption.

## 3 STRUCTURAL FEM MODELS

In order to study the influence of the floor deformability, two FEM models are carried out using FEM software SAP2000 [28].

The reference case is a single storey RC frame building, which has one bay in both direction, dimension in plan of 3 x 6 m and height of 3 m. Beams and columns have dimension of 30 x 30 cm and floor is constituted by a ribbed slab with joists of ordinary dimension (10 x 20 cm). Top concrete slab has a thickness of 4 cm, minimum value which Italian code considers to assume the hypothesis of rigid floor. Strength class of concrete is 25/30, according to [4]. In the reference case, it is considered only dead load, neglecting non-structural and accidental loads.

The first model is a "frame model" which considers a rigid floor hypothesis by applying a constrain "diaph" at every nodes of plane. Dead loads are inserted on a shell "none" which is linked to every nodes of plane.

The second model is a "solid model" which does not consider a rigid floor hypothesis. In this case, columns are modeled as frames while beams and slab are modeled using solid elements, meshed each centimeter, in order to modify both thickness of edge beams and thickness of concrete slab.

The two above mentioned models are shown in Figure 4.

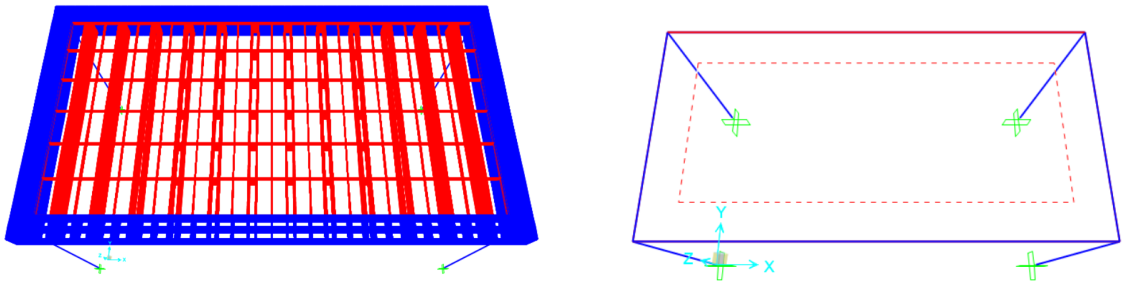


*Figure 4 – Reference models*

In both models, one dimension of vertical elements is varied, from a ratio between section sides of 1:1 to 1:4, in order to vary the ratio between floor stiffness and structural vertical element stiffness. In addition, columns have been replaced by shear walls (modeled through shell elements), with thickness which varying from 20 cm to 40 cm. For each models, it is evaluated the difference of period and participating mass, through a modal analysis, which compare the two FEM model typology.

Moreover, same comparison is carried out for same models with 3 and 5 storeys. In Figures 5-6-7 histograms of the differences aforementioned are shown. Periods and participating mass of the solid models are indicated in green while same parameters of the diaph models in grey.

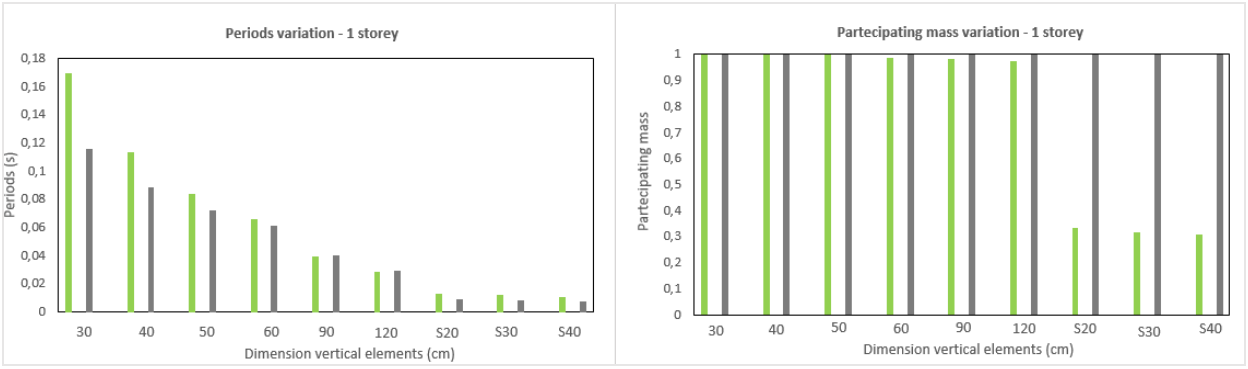

*Figure 5 – 1 storey models variations*

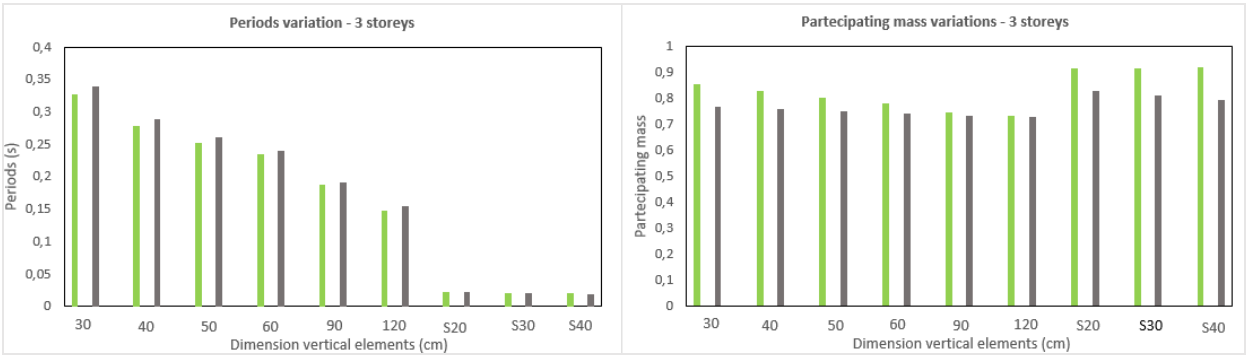


*Figure 6 – 3 storeys models variations*

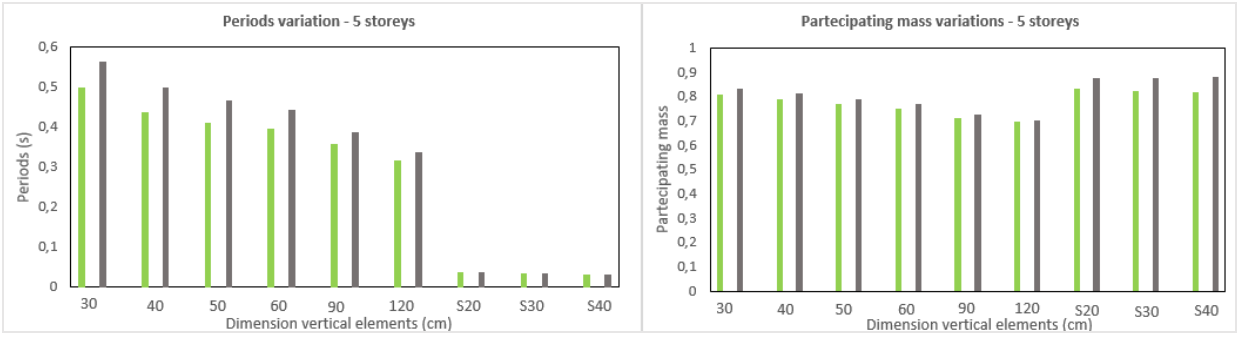


*Figure 7 – 5 storeys models variations*

Subsequently, modal analyses are carried out on a single storey RC frame building, which has one bay and doubling dimension in plan (3 x 12 m) and height of 3 m. Histograms of the differences of periods and participating mass are shown in figure 8, using same colors for model typology.

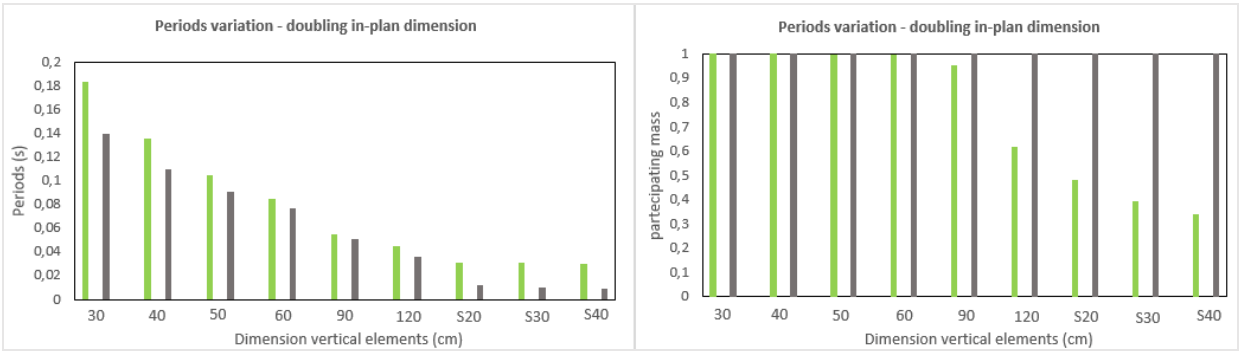


*Figure 8 – 1 storey models variations – doubling in-plan dimensions*

Using solid models, it is possible to study if the floor is rigid or deformable. Particularly, relying on the quantitative criteria provided by [5], maximum deflection and interstorey drift for reference model has been monitored and the ratio between them has been calculated (ratio Deflect/Drift). In the same way, this ratio has been calculated, increasing the number of sto-

reys and the ratio of dimension in plan. In figure 9 histograms show these ratios, even considering the variation of structural vertical elements dimension. In blue are represented the cases with columns for structural vertical element while in red are represented the cases with shear wall. When the values exceed 2, the floor is deformable. When the number of storeys increases, the ratio is always calculated on the first floor, because in that plane is detected the maximum ratio Deflect/Drift.

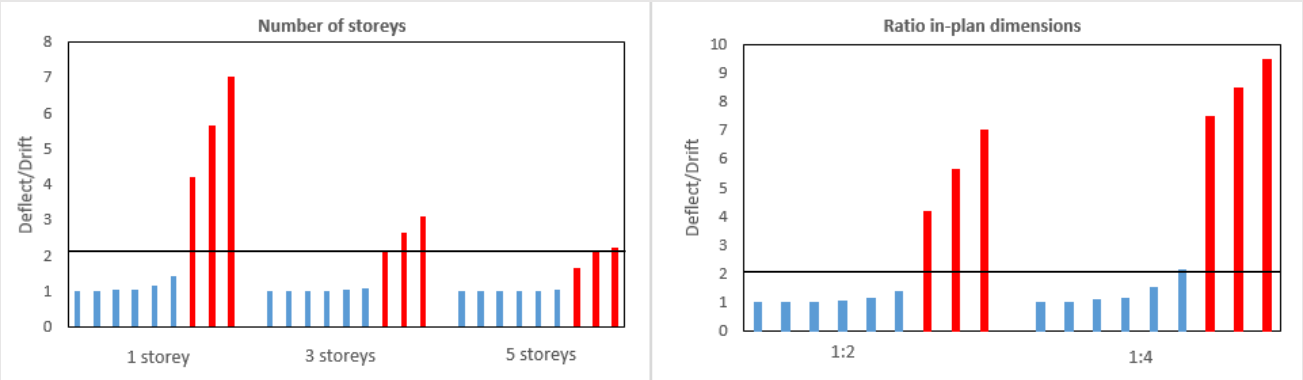


*Figure 9 – Deflection/Drift ratio variations, increasing number of storeys and in-plan dimensions*

## 4 NUMERICAL APPLICATIONS

In order to understand when the floor can be deformable in RC existing building, two numerical applications, extrapolate from two real case study, have been analyzed using solid models. For this purpose, a single storey RC frame building is assumed as new reference model. It has dimension in plan of 6 x 12 m. and height of 3 m. Beams and columns have dimension of 30 x 30 cm. It has one bay in long direction and two bays in short direction, in order to simulate the resistant frames in one way, as in RC existing building designed without using of seismic codes. The new reference model is shown in Figure 10a.

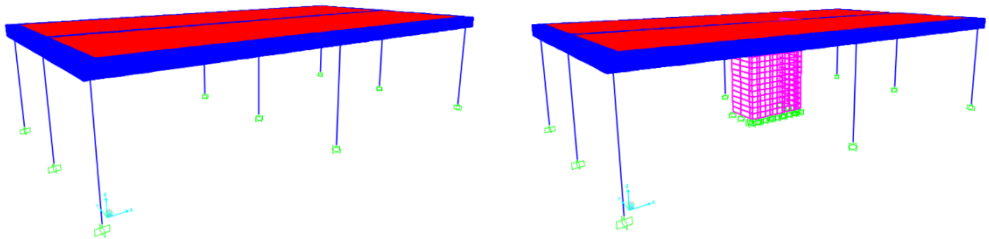

*Figure 10a – 10b – 1st application*

In first application, the new reference model is compared with a same model, which has a C-shape shear walls instead of the central column, in which there is an elevator, as shown in Figure 10b. Clearly, in a floor there is an opening. The ratio Deflect/Drift is evaluated increasing the thickness of walls from 20 cm to 40 cm, keeping constant the opening dimension. The histogram of figure 11b shows the results: the comparisons among each model and new reference model. In Figure 11a is displayed a typical deformed shape of this application, where Deflection is the maximum displacement in-plane and Drift is the minimum displacement in-plane.

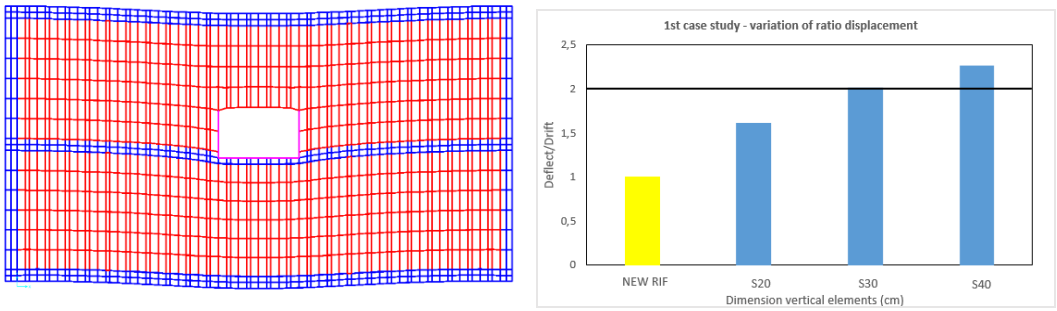


*Figure 11a – 11b – Deflect/Drift ratio results of 1st case study*

In second application, the new reference model is compared with the same model, where are varied the dimensions of external columns under central beam and the dimensions of other structural elements is not varied. Specifically, one dimension of columns taken in exam, is increased up to obtain a ratio between them section sides of 1:4. This application is representative of the typical case in which a possible way to retrofit a RC existing building is taken into account, regularizing its dynamic behavior. Figure 12, in terms of ratio Deflect/Drift, exhibits the results.

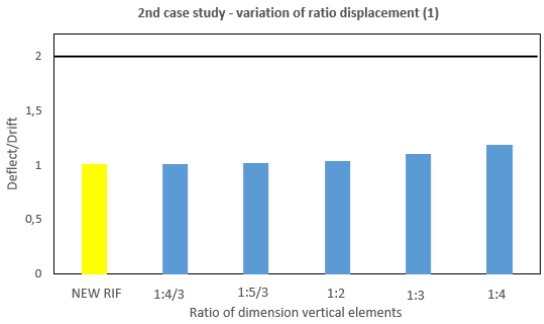


*Figure 12 - Deflect/Drift ratio results of 2nd application – increment of ratio dimensions columns*

Subsequently, the external columns under central beam have been substituted with shear walls of 30 cm and the variation of ratio Deflect/Drift is evaluated, increasing the length of walls from 1.30 m to 4.30 m. A comparison between new reference model and modified model is illustrated in Figure 13.

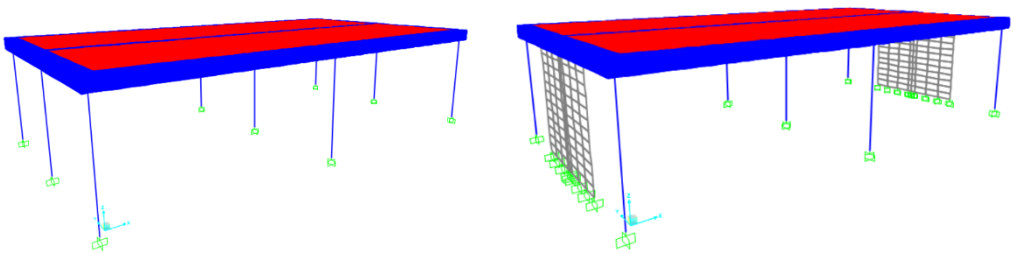

*Figure 13 - 2nd case study – shear walls length increment*

The results, in terms of ratio Deflect/Drift, and the deformed shape in-plane are explained in figure 14.

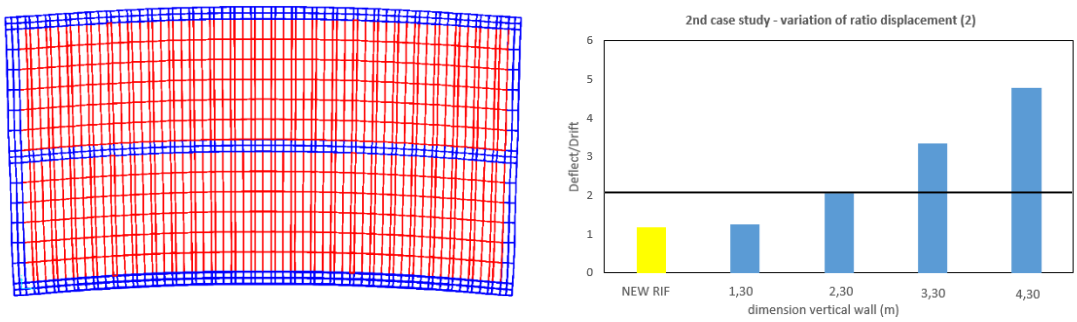


*Figure 14 - Deflect/Drift ratio results of 2nd application - increment of shear walls length*

## 5 CONCLUSIONS

In this paper, simple models of RC existing building are analyzed in order to evaluate structural behavior, using or not the rigid floor assumption. These analyses have been achieved varying the ratio between floor stiffness and structural vertical element stiffness. For considering the rigid floor hypothesis, “frame models” are carried out using a constraint on each point of plane. These models have been compared to analogues “solid models” and modal parameters differences have been evaluated. Furthermore, for each models, ratio Deflect/Drift has been evaluated, varying on the reference model, the number of storeys and the dimension in plan.

Same analyses have been accomplished on the two numerical application. The first case study compares a new reference model with same model having a C-shape shear wall, the second one compares the new reference model with same model, having some columns whose dimensions in thickness and length was varied.

Results are summarized as follow:

- The two different types of modeling have shown that on the same model, when the structural vertical elements are columns, variations of modal parameters (periods and participating mass) are negligible, rather when the model has shear walls, same parameters have high variations;
- Increasing reference model’s storeys number, the results, in terms of Deflect/Drift ratio, show that the rigid floor assumption is more and more appropriate;
- Increasing in-plan dimension of the reference model, the results, in terms of Deflect/Drift ratio, shown that the rigid floor assumption is less and less appropriate;
- The two numerical applications analyzed shown that rigid floor assumption cannot be always considered correct. In the first case, the presence of C-shape shear wall, at constant opening in the floor, as soon as the thickness increases, the floor becomes more deformable. In the same way, in the second case, the addition of shear walls on the structure perimeter, as soon as their length increases, the plane becomes more deformable.

Future aims of the research are study the floor behavior, under seismic actions, when the thickness of top concrete slab is smallest of 4 cm and when changing the edge beam dimensions.

## ACKNOWLEDGEMENTS

The research presented in this article was partially funded by the Italian Department of Civil Protection in the framework of the national project DPC-ReLUIS 2014-2018.

## 6 REFERENCES

[1] D. Perrone, M. A. Aiello, M. Pecce, F. Rossi., Rapid visual screening for seismic evaluation of RC hospital buildings. *Structures,* **3**, 57-70, 2015. doi:10.1016/j.istruc.2015.03.002.

[2] I. Iervolino, G. Manfredi, M. Polese, G. M. Verderame, G. Fabbrocino, Seismic risk of R.C. building classes. *Engineering Structures*, **29**(5), 813-820, 2007. doi:10.1016/j.engstruct.2006.06.019.

[3] G. M. Verderame, M. Polese, E. Cosenza, Vulnerability of existing R.C. buildings under gravity loads: A simplified approach for non sway structures. *Engineering Structures*, **31**(9), 2141-2151, 2009. doi:10.1016/j.engstruct.2009.03.014.

[4] G. Uva, C. A. Sanjust, S. Casolo, M. Mezzina, ANTAEUS project for the regional vulnerability assessment of the current building stock in historical centers. International *Journal of Architectural Heritage*, **10**(1), 20-43, 2016. doi:10.1080/15583058.2014.935983.

[5] S. Hans, C. Boutin, E. Ibrahim, P. Roussillon, In situ experiments and seismic analysis of existing buildings. part I: Experimental investigations. *Earthquake Engineering and Structural Dynamics*, **34**(12), 1513-1529, 2005. doi:10.1002/eqe.502.

[6] G. Uva, G. Porco, F. Porco, A. Fiore, Monitoring and safety for prestressed bridge girders by SOFO sensors. *Journal of Civil Structural Health Monitoring*, **3**, 3-18, 2013. doi: 10.1007/s13349-012-0029-9.

[7] CEN. Eurocode 8: Design of structures for earthquake resistance. Part 3: Assessment and retrofitting of buildings. Brussels, 2005.

[8] DM 14/01/2008, Norme Tecniche per le Costruzioni. Gazzetta Ufficiale n. 29. Rome 2008.

[9] G. Uva, F. Porco, A. Fiore, M. Mezzina, The assessment of structural concretes during construction phases. *Structural Survey*, **32**(3), 189-208, 2014. doi:10.1108/SS-06-2013-0023.

[10] F. Porco, G. Uva, A. Fiore, M. Mezzina, Assessment of concrete degradation in existing structures: a practical procedure. *Structural Engineering and Mechanics*, **52**(4), 701-721, 2014. doi:10.12989/sem.2014.52.4.701.

[11] F. Porco, A. Fiore, G. Uva, D. Raffaele. The influence of infilled panels in retrofitting interventions of existing reinforced concrete buildings: a case study. *Structure and Infrastructure Engineering*, **11**(2), 162-175, 2015. doi:10.1080/15732479.2013.862726.

[12] F. Porco, G. Porco, G. Uva, M. Sangirardi, Experimental characterization of "non-engineered" masonry systems in a highly seismic prone area. *Construction and Building Materials*, **48**, 406-416, 2013. doi:10.1016/j.conbuildmat.2013.07.028.

[13] A. Fiore, F. Porco, G. Uva., Effects of the yield and ultimate strengths of the equivalent strut models on the response of existing buildings with infill panels. *International Jour-*

*nal of Structural Engineering*, **6**(2), 140-157, 2015. doi:10.1504/IJSTRUCTE.2015.069690.

[14] A. Fiore, F. Porco, G. Uva, M. Sangirardi, The influence of uncertainties of infill panels relative to the seismic response of RC existing buildings, *WIT Transactions on the Built Environment*, **141**, 479–490, 2014. doi:10.2495/SUSI140411.

[15] F. Porco, A. Fiore, S. Casolo. Comparison between seismic retrofitting solutions for existing reinforced concrete buildings: a case study. *International Journal of Structural Engineering*, **5**(3), 242-261, 2014. doi:10.1504/IJSTRUCTE.2014.063035.

[16] Federal Emergency Management Agency (1998), National Earthquake Hazard Reduction Program Guidelines for Seismic Rehabilitation of Buildings, FEMA-273, Washington, D.C..

[17] Standards Association of New Zealand [1992] Code of practice for general design and design loading for buildings: NZS 4203, Wellington, New Zealand.

[18] M. Moeni, B. Rafezy., Investigation into the Floor Diaphragms Flexibility in Reinforced Concrete Structures and Code Provision. *Global Journal of Researches in Engineering*, **11**(1), 25-35, 2011. ISSN: 0975-5861.

[19] H. Saffarini, M. Qudaimat, In-plan e floor deformations in RC structures. *Journal of Structural Engineering*, **118**(11), 3089- 3102, 1992. ISSN 0733-9445.

[20] S. K. Kunnath, N. Panahshahi, A. M. Reinhorn, Seismic response of RC buildings with inelastic floor diaphragms. *Journal of Structural Engineering ASCE*, 117(4), 1218-1237, 1991. ISSN 0733-9445.

[21] M. Dolce, V.D. Lorusso, A. Masi, Seismic response of building structures with flexible inelastic diaphragm. *The structural design of tall buildings*, **3**, 87- 106, 1994.

[22] S. H. Ju, M. C. Lin, Comparison of building analyses assuming rigid or flexible floor. *Journal of Structural Engineering ASCE*, **125**, 25-39, 1999. http://dx.doi.org/10.1061.

[23] R. B. Fleischman, K. T. Farrow, Dynamic behaviour of perimeter lateral-system structures with flexible diaphragms. *Earthquake engineering and structural dynamics*, **30,** 745–763, 2001. doi: 10.1002/eqe.36.

[24] D. Lee, H.Kim, Efficient seismic analysis of high-rise building structures with the effects of floor slabs. E*ngineering Structures*, **24**(5), 613-623, 2002. http://dx.doi.org/10.1016/S0141-0296(01)00126-2

[25] K.Fouad, Z. Ali, R. Mustapha, Structural Analyses with Flexibility Effect of the Floor Slabs. 15 World Conference on Earthquake Engineering, Lisbon, 2012.

[26] M. Ahmadi, S. A. Bakar, H. S. Abbas, Investigation into diaphragm flexibility using shear wall. *Journal of the Croatian Association of Civil Engineers - Građevinar*, **66**(9), 831-836, 2014. doi: 10.14256/JCE.1049.2014

[27] A. Tena-Colunga, K.L. Chinchilla-Portillo, G. Juarez-Luna, Assessment of the diaphragm condition for floor systems used in urban buildings. *Engineering Structures*, **93**, 70–84, 2015. http://dx.doi.org/10.1016/j.engstruct.2015.03.025

[28] Computer and Structures I. SAP2000, Advanced 18. Structural Analysis Program–Manual – Computer and Structures, Inc, Berkeley, California, USA, 2015.

COMPDYN 2017
6th ECCOMAS Thematic Conference on
Computational Methods in Structural Dynamics and Earthquake Engineering
M. Papadrakakis, M. Fragiadakis (eds.)
Rhodes Island, Greece, 15–17 June, 2017

# DEVELOPMENT OF A CURVILINEAR HYSTERESIS MODEL FOR REINFORCED CONCRETE STRUCTURES

**Daisuke KITAGAWA**[1] **and Hisashi UMEMURA**[2]

[1]Graduate school of Nagoya Institute of Technology
Gokiso-cho, Showa-ku, Nagoya-shi, Japan
e-mail: 28415032@stn.nitech.ac.jp

[2] Graduate School of Nagoya Institute of Technology
Gokiso-cho, Showa-ku, Nagoya-shi, Japan
e-mail: h.umemura@nitech.ac.jp

**Keywords:** Reinforced Concrete Structure, Curvilinear Hysteresis Model, Force-Displacement Relation, Genetic Algorithm, Hysteresis Model Capability Evaluation

**Abstract.** *Multilinear hysteresis models such as the Clough model are generally used for earthquake response analysis of reinforced concrete (RC) structures, while force-deformation relations obtained in experimental studies are curvilinear. Other hysteresis models are developed to consider features such as strength degradation at large deformation regions, stiffness degradation due to cyclic loading or inverted S-shaped slip property. However, these models are generally not widely used because most use many rules to express all the features and require many parameters, which makes the model complicated. In this study, a curvilinear hysteresis model for RC structures is developed with relatively simple rules and a small number of parameters. The model consists of only two functions, the skeleton curve and the inner loop, and nine model parameters. The developed model is applicable to various types of RC beams and columns, including strength deterioration at large deformation regions, stiffness degradation due to cyclic loading or inverted S-shaped slip property. A method to evaluate the capability of hysteresis model is developed using the minimized error index based on genetic algorithm to obtain the best parameter which will reproduce the force-displacement relations. Force-displacement relations of RC specimens are collected from previous experimental studies and the error indices are calculated. The developed model are capable of reproducing force-displacement relations well compared to other hysteresis models for RC structures.*

## 1 INTRODUCTION

In general, multi-linear hysteresis models such as the Clough or Takeda model are used to describe the restoring force characteristics of reinforced concrete(RC) structures, although force-displacement relations obtained in experiments of RC members are curvilinear. On the other hand, curvilinear hysteresis models are developed for wooden structures[1][2], which reproduce experiments well using relatively simple rules with a small number of parameters. The same approach may be applicable for RC structures that include slip or stiffness degradation due to cyclic loadings.

In this study, a curvilinear hysteresis model for RC structures is developed. Force-displacement relations obtained in previous experimental studies are reproduced to evaluate the capability of the developed model.

## 2 HYSTERESIS MODEL

The outline of the developed model is shown in Figure 1, which consists of only two rules, the skeleton curve(I) and the unload-reload curve(II).

### 2.1 Skeleton curve

The skeleton curve is simply defined by one function

$$f = A_0 \frac{\tanh((\alpha/d_m) \cdot d)}{d^\beta + d_0} \tag{1}$$

where $f$ is the force, $d$ is the displacement, $\alpha$ and $\beta$ are parameters to control the shape of the curve. The maximum force point $(d_m, f_m)$ are determined by the following equations.

$$A_0 = f_m \cdot \frac{{d_u}^\beta + d_0}{\tanh(\alpha)} \tag{2}$$

$$d_0 = \frac{(0.5\beta \sinh(2\alpha) - \alpha) \cdot d_m}{\alpha} \tag{3}$$

The influences of the shape parameters $\alpha$ and $\beta$ are shown in Figure 2, in which the maximum force point$(d_m, f_m)$ is fixed at (0.3, 14.0). The parameter $\alpha$ controls the initial stiffness and strength deterioration and $\beta$ influences the strength deterioration after the maximum force point.

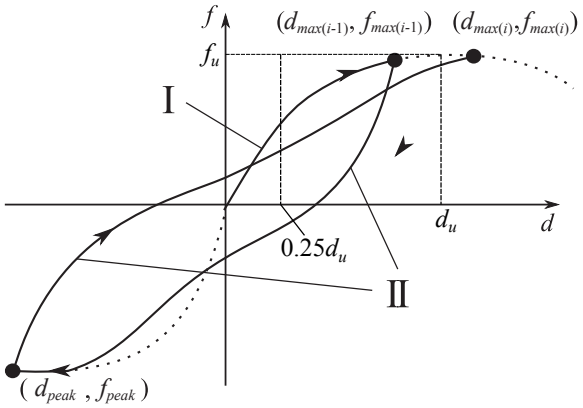


Figure 1: Model outline

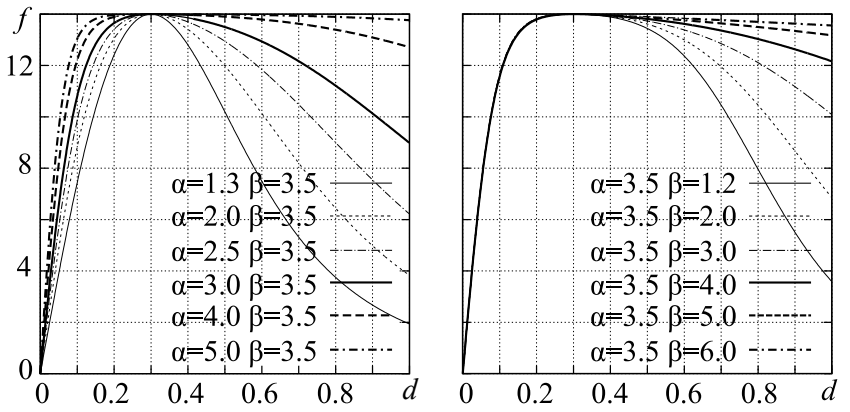


(a) Shape factor $\alpha$ (b) Strength deterioration factor $\beta$

Figure 2: Influences of the skeleton shape parameters

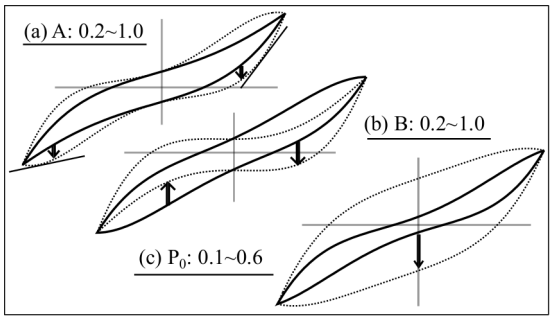


Figure 3: Influences of the inner loop parameters

When the velocity direction is reversed and the absolute maximum displacement exceeds the elastic limit ($0.25d_u$), the hysteresis enters the unload-reload curve (rule II).

## 2.2 Unload-reload curve

The following function expresses a loop ranging from a spindle-shape loop to a slip-type loop

$$F_{bottom}^{top} = \mp AD^4 + BD^3 \mp (P_0 - A)D^2 + (1 - B)D \pm P_0 \tag{4}$$

where $A$, $B$ and $P_0$ are parameters to control the shape of the curve. $F$ and $D$ are normalized force and displacement with values of -1 or +1 at the unloading point or the maximum/minimum point on the other side of the unloading point using scale factors.

The influences of the parameters $A$, $B$ and $P_0$ on the inner loop are illustrated in Figure 3. The parameter $A$ controls stiffness variation level, $B$ controls slip characteristics and $P_0$ controls loop area, respectively.

$P_0$ is the ratio of the force at $D = 0$ to the peak force $f_{peak}$. According to the load-displacement curves obtained in previous experimental studies, the parameter $P_0$ cannot be fixed as a constant value, but varies depending on the peak displacement. In many cases, $P_0$ increases as peak displacement increases as shown in Figure 4(a). Three examples of relations between peek displacements and $P_0$ are shown by the points in Figure 4(b). Based on the characteristics of these relations, $P_0$ is formulated as follows

$$P_0 = \frac{-1}{1 + r_{pzc} \cdot \left(\frac{d_{peak}}{d_u}\right)^{\gamma}} + 1 \tag{5}$$

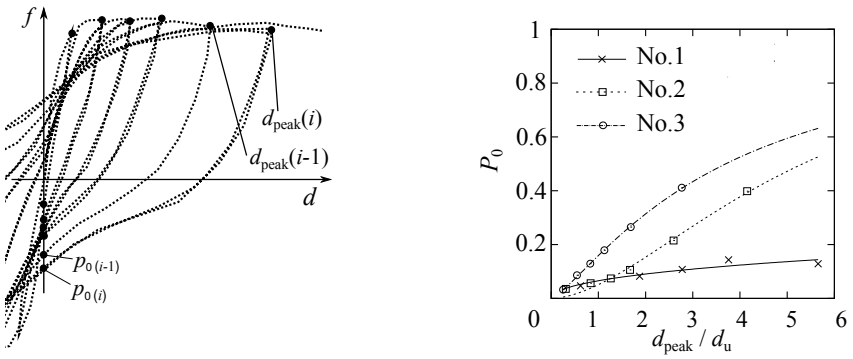


(a) Reading $P_0$ from experimental data (b) Examples of $P_0 - d_{peak}$ relations [5]

Figure 4: Relations between unloading displacement ($d_{peak}$) and the force at zero displacement ($P_0$)

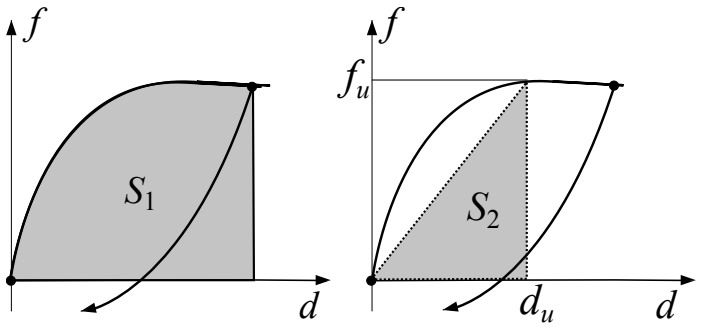


Figure 5: Hysteretic area $S_1$ and base area $S_2$

where $r_{pzc}$ and $\gamma$ are model parameters to determine $P_0$. The displacement $d_{peak}$ is normalized by the displacement at the maximum force $d_u$.

For the three examples shown by the points in Figure 4(b), the $P_0$ values calculated by Equation 5 are illustrated by the lines. The experimental $P_0$ values are well expressed by the equation with appropriate values for the parameters $r_{pzc}$ and $\gamma$.

### 2.3 Stiffness degradation

Stiffness degradation due to cyclic loading is expressed by increasing the hysteretic maximum displacement, as shown in Figure 1. When the velocity direction is reversed, the unload-reload curve function (Equation 4) scale factors are determined to aim for the previous peak point ($d_{max(i-1)}, f_{max(i-1)}$). The target peak point is moved from ($d_{max(i-1)}, f_{max(i-1)}$) to ($d_{max(i)}, f_{max(i)}$) on the skeleton curve to consider the stiffness degradation. The amount of movement of the maximum experienced displacement is based on the energy dissipation, determined by the following equation with the previous hysteretic area (S1) normalized by the basic area (S2)

$$d_{max(i)} = d_{max(i-1)} \cdot \left(1 + r_s \cdot \frac{S_1}{S_2}\right) \tag{6}$$

where $S_1$ and $S_2$ are dissipated energy area and basic energy area in the previous hysteresis loop (Figure 5), respectively, and $r_s$ is a model parameter to determine the amount of stiffness degradation due to cyclic loading.

### 2.4 Model outline

The required model parameters are listed in Table 1.

Table 1: Model parameters

| Model parameter | Variable |
|---|---|
| Maximum force | $f_u$ |
| Deformation at the maximum force | $d_u$ |
| Skeleton curve shape factor | $\alpha$ |
| Skeleton curve strength deterioration factor | $\beta$ |
| Inner loop shape factor | $A$ |
| Inner loop slip factor | $B$ |
| Inner loop swelling factor | $r_{pzc}$ |
| Inner loop swelling index | $\gamma$ |
| Stiffness degradation factor | $r_s$ |

A summary of the developed hysteresis model is given below:

- Until the absolute maximum displacement exceeds the elastic limit, restoring force is determined by the skeleton curve function (Equation 1).
- After the displacement exceeds the elastic limit and the velocity direction is reversed, restoring force is calculated by the unload-reload curve (Equation 4). The scale factors for both displacement and force are determined so that the normalized displacement and force take a value of 1 or -1 at unloading point ($d_{peak}$, $f_{peak}$) and maximum point at the opposite direction ($d_{max}$, $f_{max}$).
- To consider stiffness degradation, the maximum experienced point at the opposite direction ($_{max}$, $f_{max}$) is increased based on energy consumption in the previous loop.
- If the velocity is reversed in unload-reload state, new scale factors are calculated for the new unloading point and target at the opposite direction.
- The absolute maximum deformations are saved for both directions. When the absolute displacement exceeds the maximum value, restoring force is calculated by the skeleton curve function.

## 3 REPRODUCING LOAD-DEFORMATION RELATIONS FROM PREVIOUS EXPERIMENTAL STUDIES

Load-deformation relations are collected from previous experimental studies for reproduction using the developed model.

The normalized error of the reproduction is calculated by the following equation

$$E = \frac{1}{f_m}\sqrt{\frac{1}{N}\sum_{i=1}^{N}(f_{exp}(i) - f_{model}(i))^2)} \tag{7}$$

where $f_{exp}(i)$ and $f_{model}(i)$ are the forces at ith step in the experiment and model reproduction and $N$ is the total step number. The error is normalized by the maximum force $f_m$ in the experiment.

The best values of the parameter sets are determined using genetic algorithm to minimize the normalized error. During optimization, both the skeleton curve strength deterioration factor $\beta$

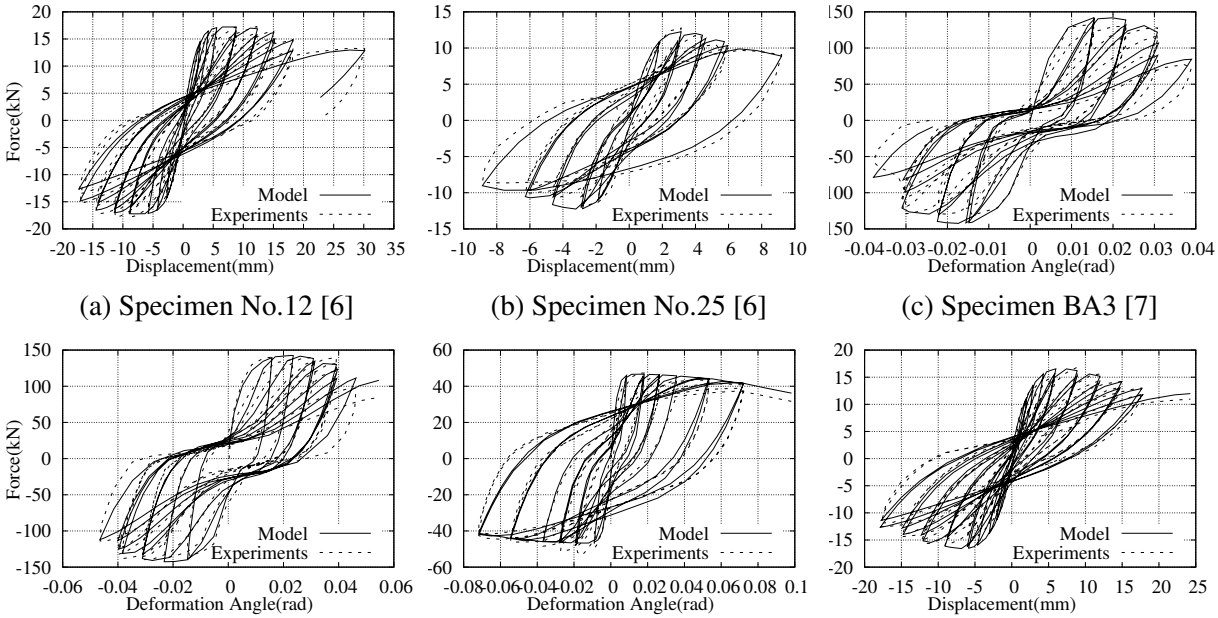


(a) Specimen No.12 [6] (b) Specimen No.25 [6] (c) Specimen BA3 [7]

(d) Specimen BA11 [7] (e) Specimen No.17 [8] (f) Specimen B04R [9]

Figure 6: Force-displacement relations in experiments and model reproductions

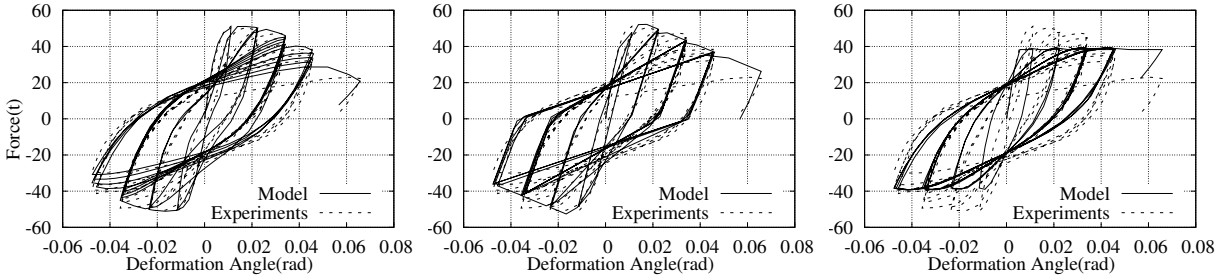


(a) Developed model (b) Takeda model (c) NCL model

Figure 7: Reproduction comparison with other hysteresis models (Specimen[8] No12)

and the stiffness degradation factor $r_s$ influence strength deterioration at the large displacement region, which makes it difficult to get stable values for the parameters. Therefore, the envelope curves are extracted from experimental data and the skeleton parameters, $f_u$, $d_u$, $\alpha$ and $\beta$, are optimized first before determining the other parameters.

Examples of the reproductions for the best model parameters to fit load-deformation relations in the experiments are shown in Figure 6, where the dotted lines are experiments and solid lines are model reproductions. From spindle-shaped force-displacement relations (ex.(e)) to slip-type ones (ex.(c)), the force-displacement relations are well reproduced including strength deterioration at the large deformation area and stiffness degradation due to cyclic loadings.

The same methodology is applied to other hysteresis models, the Takeda model[3], the most frequently used multi-linear model for RC structures in Japan, and the NCL model[4], a curvilinear model for RC structures, with the results for an experiment shown in Figure 7. In Takeda model, stiffness degradation due to cyclic loading is not considered which may lead to overestimation of the energy dissipating capacity of structures. In NCL model, unload-reload curves are not well reproduced in the first and last several cycles because the force at zero-displacement ($P_0$ in the developed model) is constant.

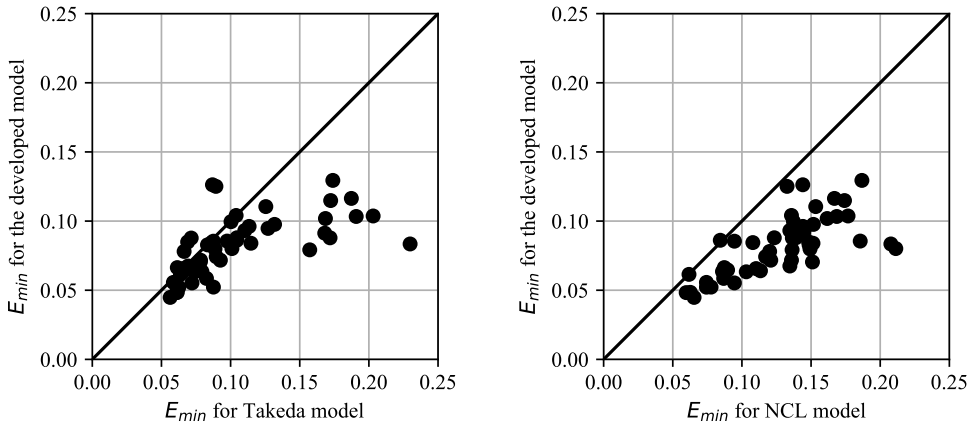


(a) vs Takeda model (b) vs NCL model

Figure 8: Comparison of minimized error with other hysteresis models [6]-[13]

## 4 MODEL CAPABILITY EVALUATION

To evaluate the capability of the developed model, the error index of the model $E_{min}$ is defined as the minimized normalized error. In other words, the best parameter set is obtained by genetic algorithm for each reproduction and the minimized error is used to assess model capability. Smaller minimized error ($E_{min}$) means better capability of the hysteresis model to reproduce force-displacement relations.

Fifty-one force-displacement relations of RC beam or column specimens are collected from previous experimental studies with various kinds of failure such as shear failure, flexural failure or shear failure after flexural yielding published in the *Proceedings of the Japan Concrete Institute* or *Journal of Structural and Construction Engineering*. The minimized errors defined above are calculated for each specimen for the developed model, Takeda model and NCL model. The results are compared in Figure 8. In most experiments, the $E_{min}$ for the developed model is smaller than that for Takeda model or NCL model, which shows that the developed model is more capable of reproducing experimental RC force-deformation relations.

## 5 CONCLUSIONS

A curvilinear hysteresis model for reinforced concrete structures is developed. The developed model is relatively simple and requires a smaller number of parameters even though it considers many features such as strength deterioration at large displacement regions, stiffness degradation due to cyclic loading and inverted S-shaped slip property.

Various force-displacement relations from previous RC member experiments were reproduced by the developed model and compared to other models. The model parameters were determined using genetic algorithm to best reproduce the experimental results. The reproduction can be quite good if the parameters are set appropriately.

The model capability is evaluated using minimum normalized error calculated for 51 force-displacement relations obtained in previous experimental studies and compared to other RC structure hysteresis models. In most cases, the reproduction of the developed model are better than the other models. The developed model showed high capability in reproducing experimental RC force-deformation relations.

## REFERENCES

[1] H. Umemura, *Curvilinear Hysteresis Model for Wooden Structures*, Summaries of technical papers of Annual Meeting Architectural Institute of Japan. C-1, Structures III, pp. 133-134, 2008 (In Japanese)

[2] H. Matsunaga, Y, Miyazu and S. Soda, *Time History Seismic Response Analysis for Wooden Structure Applied Extended NCL Model*, Summaries of technical papers of Annual Meeting Architectural Institute of Japan. C-1, Structures III, pp. 181-182, 2008 (In Japanese)

[3] Takeda, T. , M.A. Sozen and N.N. Nielsen, *Reinforced Concrete Response to Simulated Earthquakes*, Journal, Structural Division, ASCE, Vol.96, No.ST12, pp.2557-2573, 1970

[4] S. Tani, S. Nomura, T. Nagasawa and A. Hiramatsu, *Restoring Force Characteristics of Reinforced Concrete Aseismatic Elements (Part 1): Restoring Force Characteristics and Modelization*, Journal of Structural and Construction Engineering, AIJ, Vol.202, pp.11-19, 1972 (In Japanese)

[5] Y. Kumazawa, K. Ito, K. Nakano, Y. Matsuzaki, Y. Sonobe and T.Kiyohara, *Experimental Study on Structual Performance of Reinforced Concrete Column using High Strength Shear Reinforcement of 785N/mm2 class and High Strength Conrete : Part1 Outline and Results of Experiment*, Summaries of technical papers of Annual Meeting Architectural Institute of Japan. C-2, Structures IV, pp.839-840, 1999 (In Japanese)

[6] T. Okanishi, K. Katori, S. Hayashi and S. Kokusho, *Deformability of Reinforced Concrete Column Subjected to High Axial Force*, Journal of Structural and Construction Engineering, AIJ, Vol.461, pp.65-74, 1994 (In Japanese)

[7] J. LEE and F. Watanabe, *The Prediction of Ductility of RC Beams Under Reversed Cyclic Shear and Flexure*, Journal of structural and construction engineering, AIJ, Vol.520, pp.93-100, 1999 (In Japanese)

[8] K. Yoshioka, T. Okada and T. Takeda, *Stusy on Improvement of Earthquake-resisrant Behaviors of Reinforced Concrete Column : Part 1 Experimental Study on the Arrangement of Main Bars and Web Reinforcement to Give Columns Large Ductility*, Transactions of the Architectural Institute of Japan. Vol.279, pp.53-63, 1979 (In Japanese)

[9] S. Kokusho, Y. Matsuzaki, K. Takiguchi, A. Wada, S. Hayashi, M. Fukuhara and T. Saegusa, *Study of Aseismic Performance of Reinforced Concrete Column Under High Axial Load (Part 3)*, Summaries of technical papers of annual meeting Architectural Institute of Japan. Structures, pp.2113-2114, 1983 (In Japanese)

[10] H. Shikano, K. Nakano, T. Ota, H. Maeda, Y. Matsuzaki and M. Konomi *Experimental Study on Structual Performance of Reinforced Concrete Column using High Strength Shear Reinforcement : Part 1 Outline and Results of Experiment*, Summaries of technical papers of Annual Meeting Architectural Institute of Japan. C-2, Structures IV, pp.419-420, 2002 (In Japanese)

[11] F. Watanabe, M. Nishiyama, H. Muguruma *Strength and ductility of ultra high strength concrete column*, Journal of structural and construction engineering, AIJ, Vol. 446, pp.99-106, 1993 (In Japanese)

[12] S. Kokusho, Y. Matsuzaki, K. Takiguchi, A. Wada, S. Hayashi, M. Hukuhara, T. Saegusa, *Study of aseismic performance of reinforced concrete column under high axial load (Part 4)*, Summaries of technical papers of annual meeting Architectural Institute of Japan. ,Structures, pp.2115-2116, 1983 (In Japanese)

[13] K. Nara, T. Fujinaga, Y. SUN, *The Experimental Study on Behavior of Damaged RC Beam-columns after Retrofitting*, Summaries of technical papers of Annual Meeting Architectural Institute of Japan. C-2, Structures IV, pp. 563-564, 2010 (In Japanese)

COMPDYN 2017
6th ECCOMAS Thematic Conference on
Computational Methods in Structural Dynamics and Earthquake Engineering
M. Papadrakakis, M. Fragiadakis (eds.)
Rhodes Island, Greece, 15–17 June 2017

# MRFs DESIGNED ACCORDING TO THE THEORY OF PLASTIC MECHANISM CONTROL VS CODE RULES

**Roberta Muscati**[1]

[1]Ph. D. student, Department of Civil Engineering, University of Salerno – Italy

E-mail: rmuscati@unisa.it

**Keywords:** Global Mechanism, Reinforced Concrete Frames, Hierarchy criteria.

***Abstract.*** *In this paper the aim is to show a comparison between two design methodologies. In the following is reported the design of a reinforced concrete frame according code rules i.e. adopting the hierarchy criteria and the same frame designed by the Theory of Plastic Mechanism Control (TPMC).*
*The TPMC, based on the application of the kinematic theorem of plastic collapse, is a more sophisticated design procedure because it works in full compliance with codes recommendations considering that it respects the hierarchy criteria. These last, in fact, are fundamental to avoid dangerous collapse mechanisms such as "soft-storey" mechanism but they are not sufficient to guarantee the exploitation of the maximum dissipation capacity of the frame.*
*In addition push-over analyses have been made to investigate the actual collapse mechanism of the designed structure. All the obtained results confirm the ability of the design procedure to obtain a collapse mechanism of global type.*

## 1 INTRODUCTION

The optimization of the seismic structural response represents the primary purpose of every designer. This aim consists in the possibility to avoid dangerous and unsatisfactory collapse mechanism, in terms of energy dissipation capacity i.e. in the possibility to control the typology of collapse mechanism.

A perfect design should lead to the collapse of the structure according to the global mechanism, characterized by the development of plastic hinges in all the beam ends and at the base sections of the first storey columns.

To this scope in 1970s, in New Zealand [1-4], born the concept of capacity design i.e. the awareness that to reach the maximum dissipation capacity of the structures is necessary to design the different elements with several resistances. In fact, the basic principles of capacity design approach impose to differentiate on one hand, dissipative zones, designed according to the internal actions arising from the seismic forces provided by the codes, and on the other hand non-dissipative zones, proportioned on the maximum internal actions transmitted by the dissipative zones.

In a seismic resistant concrete frame this means designing structures with strong columns and weak beams. These design criteria are nowadays present in all the modern seismic codes, included the Eurocode 8 [5], under the name of the so called beam-column hierarchy criterion.

Unfortunately this approach is only able to prevent the development of a partial collapse mechanism but does not assure a collapse mechanism of global type because it isn't a rigorous application of the capacity design's criteria. Even if different strategies have been developed in order to improve the seismic behaviour of concrete moment resisting frames [6-18], considering also the influence of the soil conditions [19], a more sophisticated design procedure has been developed starting form an idea presented in 1997 [20] with reference to steel moment resisting frames. Starting from this first work, the "Theory of Plastic Mechanism Control" (TPMC) has been obtained as a powerful tool for the seismic design. In particular, it consists on the extension of the kinematic theorem of plastic collapse to the concept of mechanism equilibrium curve. This design approach was successively extended to a large variety of structural typologies [21-37]. In 2015 TPMC was developed also with reference to the reinforced concrete frames [38-40].

The strength of this method is its simplicity that will be emphasized by means of a worked example. The aim of this paper is to show the comparison of this methodology with that recommended by the codes in term of dissipation capacity. To this purpose a static inelastic analysis has been carried out for both design procedures.

## 2 DESIGN ACCORDING MODERN SEISMIC CODES

The Eurocode 8 suggest to design according to the hierarchy of strengths of the various structural components, in particular according to the beam to column hierarchy criterion.

In multi-storey buildings, formation of a soft storey plastic mechanism shall be prevented, as such a mechanism might entail excessive local ductility demands in the columns of the soft

storey. To satisfy that requirement, in frame buildings with two or more storeys, the sum of the design values of resistance moments of the column framing the joint must be greater than the sum of the design values of the moments of resistance of the beams framing the same joint, multiplied by an over strength factor ($\gamma_{Rd}$ = 1,3).

$$\sum M_{Rc} \geq \gamma_{Rd} \sum M_{Rb} \tag{1}$$

Exception is made for the roof level.

Unfortunately this method, based on a simple joint equilibrium, in most cases cannot achieve the design goal i.e. the development of a global type mechanism.

## 3 THEORY OF PLASTIC MECHANISM CONTROL FOR MRC FRAMES

To guarantee an accurate design method able to assure the development of a collapse mechanism of global type, in 1997, has been presented a new rigorous methodology "Theory of Plastic Mechanism Control" [20], indicated in the following with the acronym TPMC.

It is based on the upper bound theorem of plastic collapse extended to the concept of mechanism equilibrium curve. According to the theory of limit analysis, the assumption of a rigid-plastic behavior of the structure until the development of a collapse mechanism is made.

Given the above, in general, the structures can exhibit three main collapse mechanism typologies: these mechanisms, depicted in Figure 1, are to be considered undesired because they do not involve all the dissipative zones.

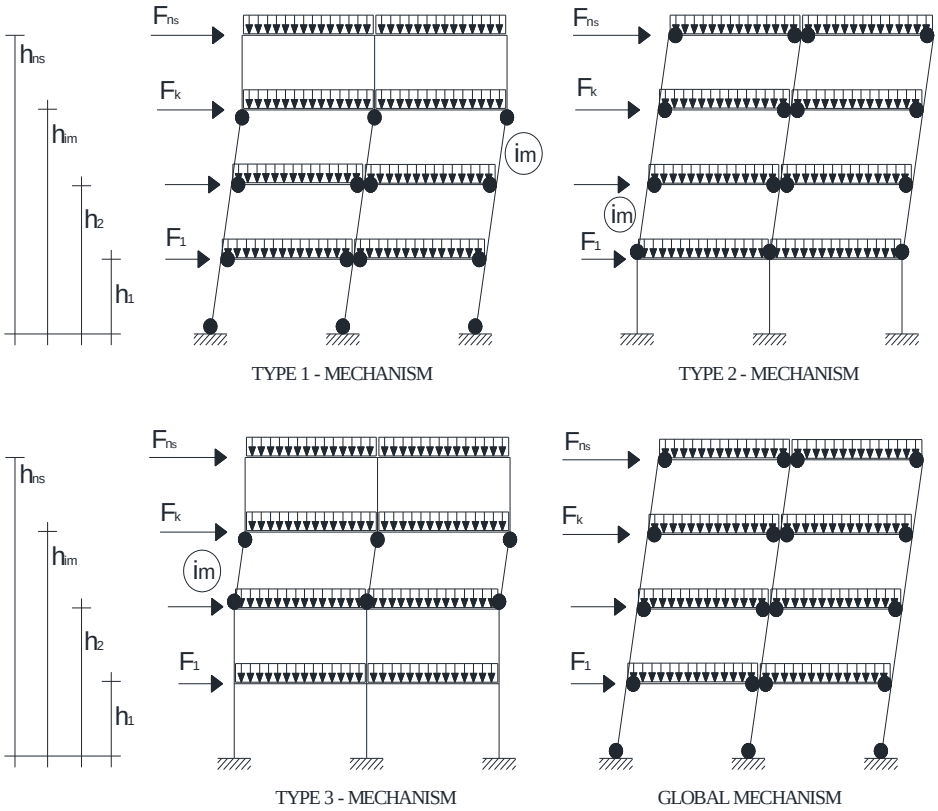


Figure 1: Collapse mechanism typologies

The TPMC is able to assure that plastic hinges develop only at beam ends while all the columns remain in elastic range with the only exception of the base sections at first storey columns. In this method is of paramount importance the introduction of the concept of linearized mechanism equilibrium curve for each considered mechanism.

The mathematical expression of this curve is represented by the Eq. (2).

$$\alpha = \alpha_0 - \gamma\delta \tag{2}$$

where $\alpha_0$ is the kinematically admissible multiplier of horizontal forces and $\gamma$ is the slope of the mechanism equilibrium curve. For any given collapse mechanism, according to a kinematic approach, the mechanism equilibrium curve can be easily derived by equating the external to the internal work.

However, the simple application of the upper bound theorem of plastic collapse is not sufficient to assure the desired collapse mechanism because the high horizontal displacements occur before the complete development of the kinematic mechanism. These displacements give rise to significant second order effects which cannot be neglected in the seismic design of structures. In order to account for second-order effects, the external second-order work due to vertical load is also evaluated.

For the better comprehension of the adopted notation, reference is made to Table 1.

| | | | |
|---|---|---|---|
| $n_c$ | number of columns | $M_{c,i,im}$ | plastic moment of the i-th column at $i_m$-th storey |
| $n_b$ | number of bays | $M_{c,im} = \sum_{i=1}^{n_c} M_{c,i,im}$ | sum of plastic moments of columns at $i_m$-th storey |
| $n_s$ | number of storeys | $M_V = \sum_{k=1}^{n_s} V_k h_k$ | second-order work due to vertical loads in global mechanism |
| $i_m$ | index of mechanism | $M_F = \sum_{k=1}^{n_s} F_k h_k$ | external work due to horizontal forces in the global mechanism |
| $H_o$ | sum of the interstorey heights of the storeys involved by the generic mechanism | $F = \sum_{k=1}^{n_s} F_k$ | sum of the horizontal forces |
| $h_k$ | height of the k-th storey (with k=1, 2, .., $n_s$) | $M_{b.jk}$ | plastic design resistance of beam at j-th bay of the k-th storey |
| e | index of beam ends (e=L=left end, e=R=right end) | $M_{b,Rd,e} = \sum_{k=1}^{n_s}\sum_{j=1}^{n_b} M_{b.jk}$ | sum of the plastic design resistances of beam ends (for e end) in the global mechanism |

Table 1: Notation

In the following will be reported the main relations; for complete equations of this method is possible to refer to previously, specific paper [39].

Therefore, the application of the virtual work principle provides the kinematically admissible multiplier that, for LR (from Left to Right) and RL (from Right to Left) earthquake, can be written as reported in Eqs. (3) and (4), respectively.

$$\alpha_{0,LR}^{(g)} = \frac{\left[M_{c,1} + M_{b,Rd,L}^{+} + M_{b,Rd,R}^{-}\right]}{M_F} \tag{3}$$

$$\alpha_{0,RL}^{(g)} = \frac{\left[M_{c,1} + M_{b,Rd,L}^{-} + M_{b,Rd,R}^{+}\right]}{M_F} \tag{4}$$

The sign "+" is used to indicate that the bending moment produces tension in lower fibers of the beam section and compression in the upper fibers, while the sign "–" is used to indicate the opposite case.

In order to compute the slope of the mechanism equilibrium curve $\gamma$, it is necessary to evaluate the second-order work due to vertical loads.

In the case of global mechanism it is given by Eq. (5).

$$\gamma^{(g)} = \frac{\frac{1}{H_o} M_V}{M_F} = \frac{\frac{1}{h_{n_s}} M_V}{M_F} \tag{5}$$

Is possible to obtain a mechanism equilibrium curve for each considered mechanism.

In particular, for the $i_m$-th mechanism ($i_m = 1, 2, \dots, n_s$) of the $t$-th mechanism typology ($t = 1, 2, 3$), the application of kinematic theorem of plastic collapse provides through the Eq. (6) for LR earthquake and the Eq. (7) for RL earthquake, the evaluation of the mechanism equilibrium curves.

$$\alpha_{im,LR}^{(t)} = \alpha_{0,im,LR}^{(t)} - \gamma_{im}^{(t)} \tag{6}$$

$$\alpha_{im,RL}^{(t)} = \alpha_{0,im,RL}^{(t)} - \gamma_{im}^{(t)} \tag{7}$$

$\alpha_{0,im}^{(t)}$ and $\gamma_{im}^{(t)}$ represent, respectively, the kinematically admissible multiplier and the slope of mechanism equilibrium curve of the $i_m$-th mechanism of the $t$-th mechanism typology.

Beam sections are designed to resist vertical loads so, the unknowns of the design problem, are the column sections. They could be determined by means of design conditions i.e. the equilibrium curve corresponding to the global mechanism has to lie below those corresponding to all other mechanisms for each value of the displacement $\delta$, up to a selected ultimate displacement $\delta_u$ (Figure 2).

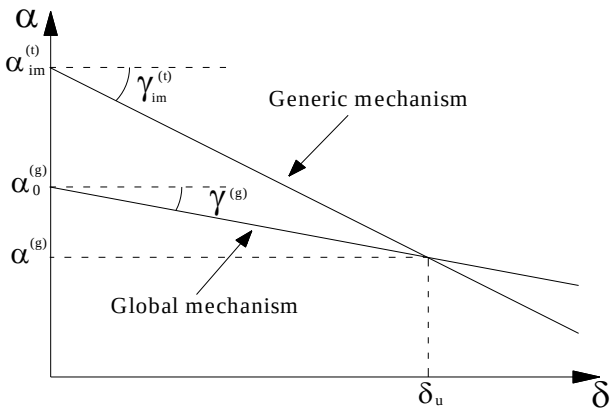


Figure 2: Design condition

Therefore, there are $6n_s$ design conditions to be satisfied for a structural scheme having $n_s$ storeys. With reference to $i_m$-th mechanism of type-1, the kinematically admissible multiplier of seismic horizontal forces is given, for LR earthquake, by:

$$\alpha_{0,i_{m,LR}}^{(1)} = \frac{M_{c,1} + \sum_{k=1}^{i_m-1}\sum_{j=1}^{n_b} M_{b.jk,L}^{+} + \sum_{k=1}^{i_m-1}\sum_{j=1}^{n_b} M_{b.jk,R}^{-} + M_{c,im}}{\sum_{k=1}^{i_m} F_k h_k + h_{i_m}\sum_{k=i_m+1}^{n_s} F_k} \tag{8}$$

and for RL earthquake by:

$$\alpha_{0,i_{m,RL}}^{(1)} = \frac{M_{c,1} + \sum_{k=1}^{i_m-1}\sum_{j=1}^{n_b} M_{b.jk,L}^{-} + \sum_{k=1}^{i_m-1}\sum_{j=1}^{n_b} M_{b.jk,R}^{+} + M_{c,im}}{\sum_{k=1}^{i_m} F_k h_k + h_{i_m}\sum_{k=i_m+1}^{n_s} F_k} \tag{9}$$

while the slope of the mechanism equilibrium curve is the same for both directions:

$$\gamma_{i_m}^{(1)} = \frac{1}{h_{i_m}} \frac{\sum_{k=1}^{i_m} V_k h_k + h_{i_m}\sum_{k=i_m+1}^{n_s} V_k}{\sum_{k=1}^{i_m} F_k h_k + h_{i_m}\sum_{k=i_m+1}^{n_s} F_k} \tag{10}$$

With reference to $i_m$-th mechanism of type-2 the kinematically admissible multiplier of seismic horizontal forces is given, for LR earthquake, by:

$$\alpha_{0,i_{m,LR}}^{(2)} = \frac{M_{c,im} + \sum_{k=i_m}^{n_s}\sum_{j=1}^{n_b} M_{b.jk,L}^{+} + \sum_{k=i_m}^{n_s}\sum_{j=1}^{n_b} M_{b.jk,R}^{-}}{\sum_{k=i_m}^{n_s} F_k (h_k - h_{i_m-1})} \tag{11}$$

and for RL earthquake by:

$$\alpha_{0,i_{m,RL}}^{(2)} = \frac{M_{c,im} + \sum_{k=i_m}^{n_s}\sum_{j=1}^{n_b} M_{b.jk,L}^{-} + \sum_{k=i_m}^{n_s}\sum_{j=1}^{n_b} M_{b.jk,R}^{+}}{\sum_{k=i_m}^{n_s} F_k (h_k - h_{i_m-1})} \tag{12}$$

while the slope of the mechanism equilibrium curve is:

$$\gamma_{i_m}^{(2)} = \frac{1}{h_{n_s} - h_{i_m-1}} \frac{\sum_{k=i_m}^{n_s} V_k \left(h_k - h_{i_m-1}\right)}{\sum_{k=i_m}^{n_s} F_k (h_k - h_{i_m-1})} \tag{13}$$

It is useful to note that, for $i_m = 1$ Eqs. (11), (12) and (13) are coincident with Eq. (3), (4) and (5) respectively, because in such case the mechanism is coincident with the global one. In addition, these relations for $i_m = 1$ include the term $h_{i_m-1} = h_0$ which is to be assumed equal to zero. Finally, with reference to $i_m$-th mechanism of type-3, the kinematically admissible multiplier of horizontal forces, is given by:

$$\alpha_{0,i_m}^{(3)} = \frac{2M_{c,im}}{\left(h_{i_m} - h_{i_m-1}\right)\sum_{k=i_m}^{n_s} F_k} \tag{14}$$

In this case the expression is the same for both directions of earthquake because the beams are not involved in this collapse mechanism.
In addition, the corresponding slope of the mechanism equilibrium curve is given by:

$$\gamma_{i_m}^{(3)} = \frac{\sum_{k=i_m}^{n_s} V_k}{\left(h_{i_m} - h_{i_m-1}\right)\sum_{k=i_m}^{n_s} F_k} \tag{15}$$

It is important to underline that, for any given geometry of the structural system, the slope of mechanism equilibrium curve attains its minimum value when the global type mechanism is developed. In fact, it is easy to check that $\gamma^{(g)}$, which is equal to $\gamma_1^{(2)}$, is always the minimum value among all the $\gamma_{i_m}^{(t)}$.

## 4 WORKED EXAMPLE

The structural scheme in Figure 3 consists of five-bay six-storey moment resisting frame.

The interstorey height is equal to 3m. The characteristic values of the vertical loads acting on the beams are equal to 10.7 kN/m and 4 kN/m for permanent ($G_k$) and live ($Q_k$) actions, respectively. The structural materials adopted are concrete C25/30 and reinforcement of steel grade B450C.

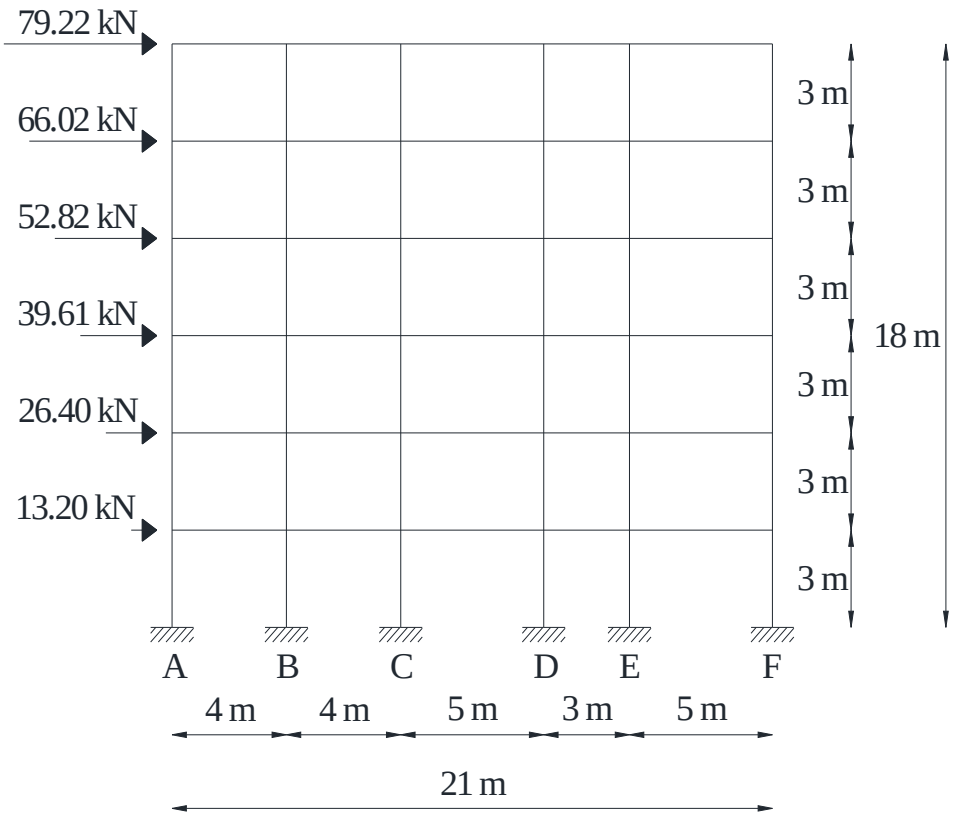


Figure 3: Structural scheme of the designed frame

According to Eurocode 8, the value of the period of vibration used for preliminary design is:

$$T = 0.075\,H^{3/4} = 0.075 \cdot 18^{3/4} \approx 0.65\,s \tag{16}$$

where $H$ is the total height of the frame.

With reference to the design spectrum for stiff soil conditions (soil class A of Eurocode 8) and by assuming a behaviour factor q equal to 3.9, the horizontal seismic forces are those depicted in Figure 3. The design requirements are that the beams should remain elastic and the columns should provide the required ductility by plastic hinges. In this specific case, has been considered a DCM (medium ductility) building.

Regarding the structural modelling, the mechanical non-linearities have been concentrated at beam and column ends by means of plastic hinge elements. The constitutive law of such plastic hinge is provided by a rigid plastic moment-rotation curve. The type of hinge depends on the element considered i.e. by its internal action. In fact, for the beams and the columns M3 and P-M3 hinge type have been considered, respectively. In case of P-M3 hinge type, the interaction domain P-M has been evaluated for each column and used in SAP2000 computer program [41].

In order to evaluate the inelastic behaviour of the designed structure, a push-over static analysis, has been conducted for both design procedures.

### 4.1 Results of the TPMC design procedure

In the TPMC procedure the first step is the selection of the maximum top sway displacement up to which the global mechanism has to be assured.

$$\delta_u = \theta_u \cdot h_{ns} = 0.01 \cdot h_{ns} = 0.01 \cdot 18 = 0.18\,m \tag{17}$$

The reinforcement at the beam ends is the same at all the storeys; the values are reported in Table 2.

| PART OF SECTION | $L_{AB}$ = 4m | | $L_{BC}$ = 4m | | $L_{CD}$ = 5m | | $L_{DE}$ = 3m | | $L_{EF}$ = 5m | |
|---|---|---|---|---|---|---|---|---|---|---|
| | e = L | e = R | e = L | e = R | e = L | e = R | e = L | e = R | e = L | e = R |
| Top | 4 ϕ16 | 4 ϕ16 | 4 ϕ16 | 4 ϕ16 | 4 ϕ16 | 4 ϕ16 | 4 ϕ16 | 4 ϕ16 | 4 ϕ16 | 4 ϕ16 |
| Bottom | 4 ϕ16 | 4 ϕ16 | 3 ϕ16 | 4 ϕ16 | 4 ϕ16 | 4 ϕ16 | 3 ϕ16 | 4 ϕ16 | 3 ϕ16 | 4 ϕ16 |

Table 2: Reinforcement at the beam ends (L = left and R = right).

In Table 3 the axial forces $N_q$, due to vertical loads, for both directions of earthquake, are reported for each storey and for each column.

| Storey | Column A | | Column B | | Column C | | Column D | | Column E | | Column F | |
|---|---|---|---|---|---|---|---|---|---|---|---|---|
| $i_m$ | $N_{q,LR}$ [kN] | $N_{q,RL}$ [kN] | $N_{q,LR}$ [kN] | $N_{q,RL}$ [kN] | $N_{q,LR}$ [kN] | $N_{q,RL}$ [kN] | $N_{q,LR}$ [kN] | $N_{q,RL}$ [kN] | $N_{q,LR}$ [kN] | $N_{q,RL}$ [kN] | $N_{q,LR}$ [kN] | $N_{q,RL}$ [kN] |
| 1 | 143.2 | 143.2 | 286.5 | 286.5 | 322.3 | 322.3 | 286.5 | 286.5 | 286.5 | 286.5 | 179.1 | 179.1 |
| 2 | 119.4 | 119.4 | 238.8 | 238.8 | 268.6 | 268.6 | 238.8 | 238.8 | 238.8 | 238.8 | 149.2 | 149.2 |

| | | | | | | | | | | | | |
|---|---|---|---|---|---|---|---|---|---|---|---|---|
| 3 | 95.52 | 95.52 | 191.0 | 191.0 | 214.9 | 214.9 | 191.0 | 191.0 | 191.0 | 191.0 | 119.4 | 119.4 |
| 4 | 71.64 | 71.64 | 143.2 | 143.2 | 161.1 | 161.1 | 143.2 | 143.2 | 143.2 | 143.2 | 89.55 | 89.55 |
| 5 | 47.76 | 47.76 | 95.52 | 95.52 | 107.4 | 107.4 | 95.52 | 95.52 | 95.52 | 95.52 | 59.70 | 59.70 |
| 6 | 23.88 | 23.88 | 47.76 | 47.76 | 53.73 | 53.73 | 47.76 | 47.76 | 47.76 | 47.76 | 29.85 | 29.85 |

Table 3: Axial forces acting in the columns related to the vertical loads for both directions of earthquake

In Table 4 are reported the axial loads related to the shear actions due to the plastic hinges, developed at the beam ends $N_{M,LR}$ ($N_{M,RL}$), for LR earthquake (for RL earthquake).

| Storey | Column A | | Column B | | Column C | | Column D | | Column E | | Column F | |
|---|---|---|---|---|---|---|---|---|---|---|---|---|
| $i_m$ | $N_{M,LR}$ [kN] | $N_{M,RL}$ [kN] | $N_{M,LR}$ [kN] | $N_{M,RL}$ [kN] | $N_{M,LR}$ [kN] | $N_{M,RL}$ [kN] | $N_{M,LR}$ [kN] | $N_{M,RL}$ [kN] | $N_{M,LR}$ [kN] | $N_{M,RL}$ [kN] | $N_{M,LR}$ [kN] | $N_{M,RL}$ [kN] |
| 1 | -326.62 | 326.62 | 40.08 | -12.00 | 25.24 | -65.21 | -120.76 | 174.04 | 152.82 | -174.14 | 229.23 | -261.20 |
| 2 | -272.18 | 272.18 | 33.40 | -10.00 | 21.04 | -54.34 | -100.63 | 145.03 | 127.35 | -145.11 | 191.03 | -217.67 |
| 3 | -217.75 | 217.75 | 26.72 | -8.00 | 16.83 | -43.47 | -80.51 | 116.03 | 101.88 | -116.09 | 152.82 | -174.14 |
| 4 | -163.31 | 163.31 | 20.04 | -6.00 | 12.62 | -32.60 | -60.38 | 87.02 | 76.41 | -87.07 | 114.62 | -130.60 |
| 5 | -108.87 | 108.87 | 13.36 | -4.00 | 8.41 | -21.74 | -40.25 | 58.01 | 50.94 | -58.05 | 76.41 | -87.07 |
| 6 | -54.44 | 54.44 | 6.68 | -2.00 | 4.21 | -10.87 | -20.13 | 29.01 | 25.47 | -29.02 | 38.21 | -45.53 |

Table 4: Axial forces acting in the columns related to the shear actions for both directions of earthquake

Applied the design procedure, prevented the technological condition (checking that the column section does not increase along the height) and optimized the reinforcement in the column; the definitively values of required bending moment for each column $M_{c,i,1}$, the section, the upper and lower reinforcement and the axial force, for both directions of the earthquake are reported in Table 5.

| Storey | Column | $M_{c,im,LR}$ [kNm] | $M_{c,im,RL}$ [kNm] | b x h | $A_s = A'_s$ | $N_{LR}$ [kN] | $N_{RL}$ [kN] |
|---|---|---|---|---|---|---|---|
| 1° | A | 153.63 | 164.05 | 30x60 | 3 Φ 28 | -183.34 | 469.90 |
| | B | | | 50x30 | 2 Φ 28 | 326.64 | 286.44 |
| | C | | | 50x30 | 2 Φ 28 | 347.62 | 257.17 |
| | D | | | 50x30 | 2 Φ 28 | 165.80 | 460.60 |
| | E | | | 50x30 | 2 Φ 28 | 439.38 | 112.42 |
| | F | | | 30x70 | 3 Φ 28 | 408.33 | -82.10 |
| 2° | A | 178.87 | 202.80 | 30x60 | 4 Φ 28 | -152.79 | 391.58 |
| | B | | | 50x30 | 2 Φ 28 | 272.2 | 238.70 |
| | C | | | 50x30 | 2 Φ 28 | 289.69 | 214.31 |
| | D | | | 50x30 | 2 Φ 28 | 138.17 | 383.83 |
| | E | | | 50x30 | 2 Φ 28 | 366.15 | 93.69 |
| | F | | | 30x70 | 4 Φ 28 | 340.28 | -68.42 |
| 3° | A | 250.61 | 276.58 | 30x60 | 5 Φ 28 | -122.23 | 313.27 |
| | B | | | 50x30 | 3 Φ 28 | 217.76 | 190.96 |
| | C | | | 50x30 | 3 Φ 28 | 231.75 | 171.45 |
| | D | | | 50x30 | 3 Φ 28 | 110.53 | 307.07 |
| | E | | | 50x30 | 3 Φ 28 | 292.92 | 74.95 |
| | F | | | 30x70 | 5 Φ 28 | 272.22 | -54.74 |

| | | | | | | | |
|---|---|---|---|---|---|---|---|
| 4° | A | 281.75 | 307.20 | 30x60 | 4 Φ 32 | -91.67 | 234.95 |
| | B | | | 50x30 | 3 Φ 28 | 163.32 | 143.22 |
| | C | | | 50x30 | 3 Φ 28 | 173.81 | 128.59 |
| | D | | | 50x30 | 3 Φ 28 | 82.90 | 230.30 |
| | E | | | 50x30 | 3 Φ 28 | 219.69 | 56.21 |
| | F | | | 30x70 | 5 Φ 32 | 204.17 | -41.05 |
| 5° | A | 258.75 | 280.27 | 30x60 | 5 Φ 28 | -61.11 | 156.63 |
| | B | | | 50x30 | 3 Φ 28 | 108.88 | 95.48 |
| | C | | | 50x30 | 3 Φ 28 | 115.87 | 85.72 |
| | D | | | 50x30 | 3 Φ 28 | 55.27 | 153.53 |
| | E | | | 50x30 | 3 Φ 28 | 146.46 | 37.47 |
| | F | | | 30x60 | 5 Φ 28 | 136.11 | -27.37 |
| 6° | A | 168.09 | 181.41 | 30x50 | 3 Φ 28 | -30.56 | 78.32 |
| | B | | | 40x30 | 3 Φ 28 | 54.44 | 47.74 |
| | C | | | 40x30 | 3 Φ 28 | 57.94 | 42.86 |
| | D | | | 40x30 | 3 Φ 28 | 27.63 | 76.77 |
| | E | | | 40x30 | 3 Φ 28 | 73.23 | 18.74 |
| | F | | | 30x50 | 4 Φ 28 | 68.06 | -13.68 |

Table 5: Design of column sections at each storey for earthquake

In order to validate the designed frame a pushover analysis has been carried out in SAP2000 computer program.

The results of the push-over analysis are mainly constituted by base shear – top sway displacement curve, for both direction of earthquake, that are depicted in Figure 4.

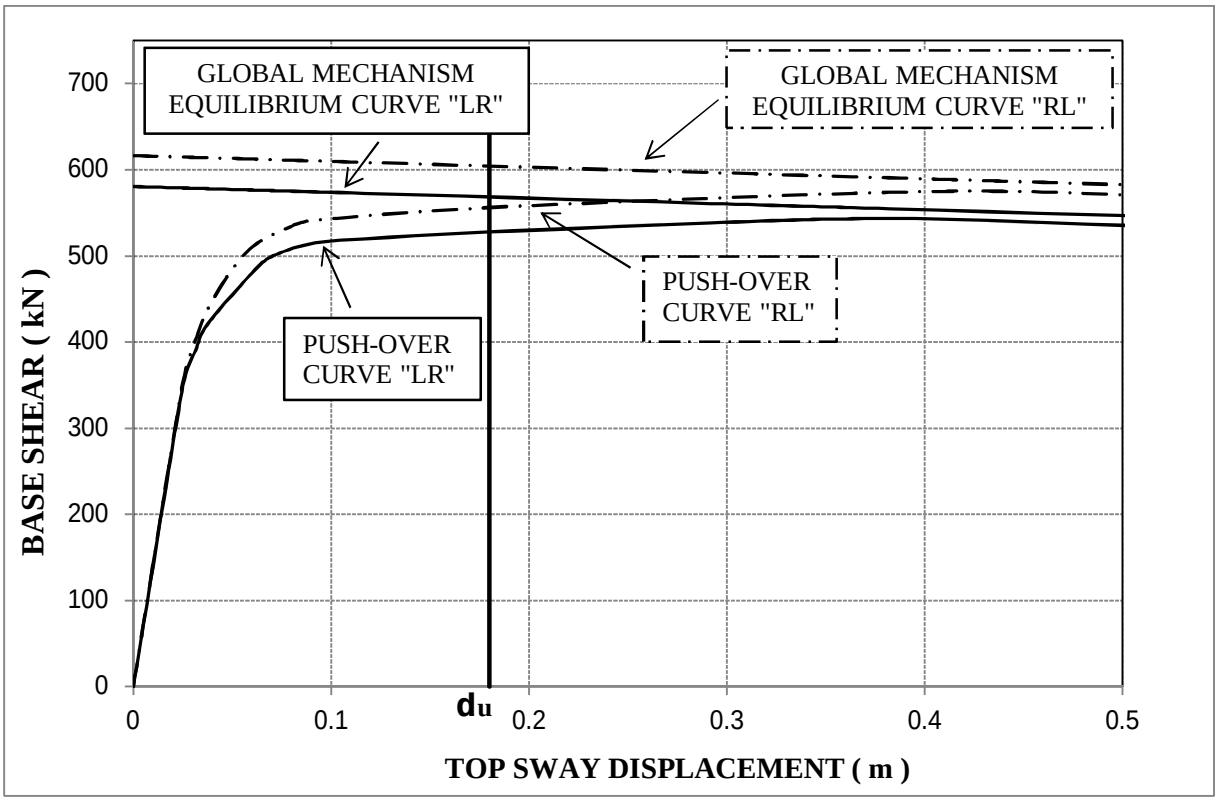


Figure 4: Overlap of the push-over curve with the global mechanism equilibrium curve.

As is possible to observe the seismic response of the designed frame confirms the development of the desired collapse mechanism typology.

In the same figure the mechanism equilibrium curve of global mechanism, both for LR and RL earthquake, is very close and parallel to the corresponding push-over curve. In the following has been reported the equations of these curves.

$$\alpha_{LR}^{(g)} = 2.0938 - 0.002435\,\delta \tag{18}$$

$$\alpha_{RL}^{(g)} = 2.2233 - 0.002435\,\delta \tag{19}$$

A further confirmation, of the fulfilment of the design objective, are reported in Figure 5.

The distribution of the pattern of yielding, developed at the occurrence of the design ultimate displacement, corresponding to both seismic direction is, in fact, in perfect agreement with the global mechanism.

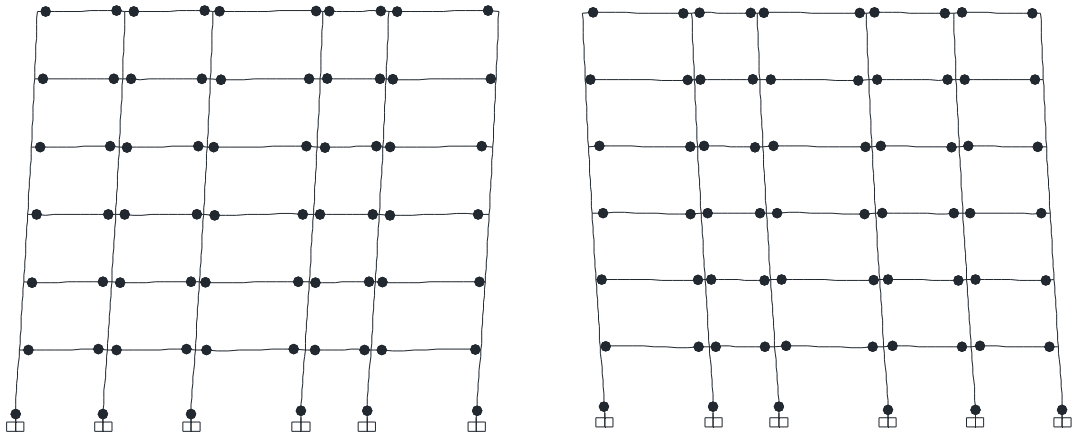

Figure 5: Pattern of yielding of the designed frame at $\delta = \delta_u$ for LR and RL earthquake direction.

An appropriate design will require to concentrate the attention on the control and limitation of displacements that could occur during the earthquake.

According to the limit reported in the Eurocode 8, the interstorey drift have been checked; in particular the considered limit refers to buildings having non structural elements of brittle materials attached to the structure:

$$d_r\,\nu \leq 0.005\,\mathrm{h} \tag{20}$$

In Table 7 the final results are reported.

| STOREY | $d_s$ [cm] | $d_r$ [cm] | $\upsilon$ | $d_r\,\upsilon$ | 0.005 h |
|---|---|---|---|---|---|
| 6° | 9.4871 | 1.0253 | 0.5 | 0.5126 | 1.5 |
| 5° | 8.4617 | 1.2506 | | 0.6253 | 1.5 |
| 4° | 7.2111 | 1.6513 | | 0.8256 | 1.5 |
| 3° | 5.5598 | 1.9617 | | 0.9808 | 1.5 |
| 2° | 3.5980 | 2.0957 | | 1.0478 | 1.5 |
| 1° | 1.5022 | 1.5022 | | 0.7511 | 1.5 |

Table 6: Limitation of interstorey drift for TPMC frame.

If this serviceability requirement is not verified, the structural stiffness can be improved by increasing the beam sections or the ultimate design displacement. In fact, in both cases the final results will be a more rigid structure with respect to the one obtained in the worked example herein presented.

### 4.2 Frame designed in accordance with Eurocode 8

The same five-bay six-storey moment resisting frame, previously presented, has been designed even in accordance with Eurocode 8. It is clear that the formation of soft-storey, whereby plastic hinges can develop simultaneously at the top and bottom end of columns in a storey, is unacceptable in multi-storey framed buildings.

Therefore columns of storeys must be stronger than the beams that frame into them.

Designed the structure, applying the beam-column hierarchy criterion, the definitively values of the section, the upper and lower reinforcement are reported in Table 7.

| STOREY | Column | b x h | $A_s = A'_s$ |
|---|---|---|---|
| 1° | A | 30x30 | 4 Φ 16 |
| | B | 40x30 | 4 Φ 16 |
| | C | 40x30 | 4 Φ 16 |
| | D | 40x30 | 4 Φ 16 |
| | E | 40x30 | 4 Φ 16 |
| | F | 30x30 | 4 Φ 16 |
| 2° | A | 30x30 | 5 Φ 16 |
| | B | 40x30 | 5 Φ 16 |
| | C | 40x30 | 4 Φ 16 |
| | D | 40x30 | 5 Φ 16 |
| | E | 40x30 | 5 Φ 16 |
| | F | 30x30 | 4 Φ 16 |
| 3° | A | 30x30 | 5 Φ 16 |
| | B | 40x30 | 5 Φ 16 |
| | C | 40x30 | 5 Φ 16 |
| | D | 40x30 | 5 Φ 16 |
| | E | 40x30 | 5 Φ 16 |
| | F | 30x30 | 5 Φ 16 |
| 4° | A | 30x30 | 5 Φ 16 |
| | B | 40x30 | 6 Φ 16 |
| | C | 40x30 | 6 Φ 16 |
| | D | 40x30 | 6 Φ 16 |
| | E | 40x30 | 6 Φ 16 |
| | F | 30x30 | 5 Φ 16 |
| 5° | A | 30x30 | 5 Φ 20 |
| | B | 40x30 | 5 Φ 20 |
| | C | 40x30 | 5 Φ 20 |
| | D | 40x30 | 5 Φ 20 |
| | E | 40x30 | 5 Φ 20 |
| | F | 30x30 | 5 Φ 20 |

| | | | |
|---|---|---|---|
| 6° | A | 30x30 | 5 Φ 20 |
| | B | 40x30 | 5 Φ 24 |
| | C | 40x30 | 5 Φ 24 |
| | D | 40x30 | 5 Φ 24 |
| | E | 40x30 | 5 Φ 24 |
| | F | 30x30 | 5 Φ 20 |

Table 7: Design of column sections at each storey for earthquake

In order to validate the designed frame, in Figure 6 are reported the pattern of yielding corresponding to both seismic direction, obtained through a pushover analysis.

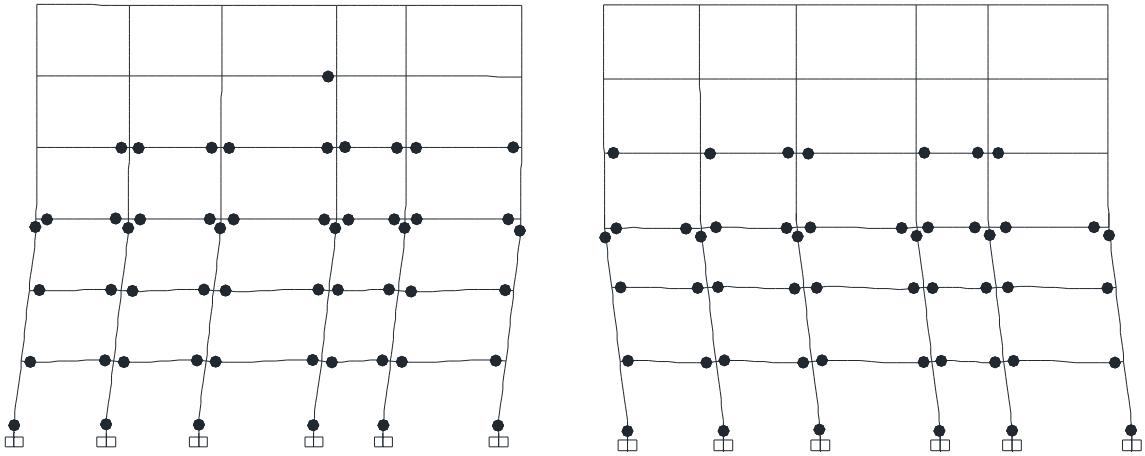

Figure 6: Pattern of yielding in the frame designed in according with Eurocode 8, for both earthquake directions.

As is possible to observe from Figure 6, the structure exhibits a Type 1 collapse mechanism, extended to the third storey of the frame.
Therefore, the fulfilment of the strong-column/weak-beam principle is fundamental to avoid soft-storey mechanism but it is no sufficient to guarantee the development of the maximum number of plastic hinges. Even in this case is very important to verify the serviceability requirements, expressed through the (20). In Table 8 the final results are reported.

| STOREY | $d_s$ [mm] | $d_r$ [mm] | $\upsilon$ | $d_r\,\upsilon$ | 0.005 h |
|---|---|---|---|---|---|
| 6° | 9.7710 | 0.7558 | 0.5 | 0.3779 | 1.5 |
| 5° | 9.0151 | 1.3036 | | 0.6518 | 1.5 |
| 4° | 7.7114 | 1.7522 | | 0.8761 | 1.5 |
| 3° | 5.9591 | 2.0783 | | 1.0391 | 1.5 |
| 2° | 3.8808 | 2.2281 | | 1.1140 | 1.5 |
| 1° | 1.6526 | 1.6526 | | 0.8263 | 1.5 |

Table 8: Limitation of interstorey drift for EC8 frame.

## 1. CONCLUSIONS

In this paper a comparison between two design procedure, for reinforced concrete moment resisting frames, has been presented.

The procedure called “Theory of Plastic Mechanism Control”, based on the extension of the kinematic theorem of plastic collapse to the concept of mechanism equilibrium curve, allows to evaluate the sum of plastic moments of the columns required at each storey in order to develop a collapse mechanism of global type.

Beams are designed in order to bear external loads, while columns are designed according to the maximum internal actions transmitted by the dissipative zones, in this way TPMC constitutes a rigorous application of the capacity design principles.

On the other hand has been presented the design carried out through the beam-column hierarchy criterion, commonly suggested by seismic codes.

Unfortunately the beam-column hierarchy criterion is not sufficient to assure the development of the flexural plastic hinges at the ends of all the beams, combined with the only base column.

In conclusion, the closed form solution of the design conditions that makes the TPMC procedure very easy to be applied even by means of hand calculations, it could also be suggested for code purpose to definitely solve the problem of collapse mechanism control whose importance in seismic design is universally recognised. Therefore, is important to underline that the TPMC method is in perfect agreement with that recommended by the code. Finally, it is important to underline that also the joists influence should be accounted for [42]. This is a possible development of future research.

## REFERENCES

[1] New Zealand Standard Code of Practice for the Design of Concrete Structures, NZS 3101: Part 1; Commentary NZS 3101: Part 2; Standard Association of New Zealand, Wellington, New Zealand, 1982.

[2] Paulay T., “Capacity design of earthquake resisting ductile multistorey reinforced concrete frames”, Proc.3rd Canad, conf. on earthquake eng., Montreal, Vol. 2, pp. 917-948, 1979.

[3] Paulay T., “Seismic design of ductile moment resisting reinforced concrete frames, columns: evaluation of actions”, Bull. New Zealand Natl. Soc. Earthquake Eng., 10, 85-94, 1977.

[4] Paulay T., “Deterministic Design Procedure for Ductile Frames in Seismic Areas”, ACI Publication SP-63, American Concrete Institute, Detroit, pp. 357-381, 1980.

[5] EN 1998-1, “Eurocode 8: Design of Structures for Earthquake Resistance – Part 1: general Rules, Seismic Actions and Rules for Buildings”, CEN, 2004.

[6] Castaldo, P., Amendola, G., Palazzo, B., 2017 Seismic fragility and reliability of structures isolated by friction pendulum devices: seismic reliability-based design (SRBD), Earthquake Engineering and Structural Dynamics, 46(3), 425-446.

[7] Castaldo, P., Palazzo, B., Della Vecchia, P. 2016 Life-cycle cost and seismic reliability analysis of 3D systems equipped with FPS for different isolation degrees, Engineering Structures 125, pp. 349-363.

[8] Formisano, A., Lombardi, L. “Perforated shear panels for seismic rehabilitation of existing reinforced concrete buildings” (2015) Civil-Comp Proceedings, 108..

[9] Formisano, A., Sahoo, D.R. “Steel shear panels as retrofitting system of existing multi-story RC buildings: Case studies” (2015) Advances in Structural Engineering: Mechanics, Volume One, pp. 495-512. DOI: 10.1007/978-81-322-2190-6_41

[10] Castaldo, P., Palazzo, B., Ferrentino, T., 2016, Seismic reliability-based ductility demand evaluation for inelastic base-isolated structures with friction pendulum devices, Earthquake Engineering and Structural Dynamics, DOI: 10.1002/eqe.2854.

[11] Palazzo B., Castaldo P., Marino I., The Dissipative Column: A New Hysteretic Damper,” Buildings 5(1), 163-178, 2015, doi:10.3390/buildings5010163.

[12] De Iuliis M., Castaldo P., An energy-based approach to the seismic control of one-way asymmetrical structural systems using semi-active devices, Ingegneria Sismica - International Journal of Earthquake Engineering XXIX(4):31-42, 2012.

[13] Castaldo, P., Palazzo, B., Ferrentino, T., Petrone, G.. Influence of the strength reduction factor on the seismic reliability of structures with FPS considering intermediate PGA/PGV ratios. Composites Part B: Engineering, 2016, http://dx.doi.org/10.1016/j.compositesb.2016.09.072.

[14] Formisano, A., Lombardi, L., Mazzolani, F.M. “Perforated metal shear panels as bracing devices of seismic-resistant structures” (2016) Journal of Constructional Steel Research, 126, pp. 37-49. DOI: 10.1016/j.jcsr.2016.07.006

[15] Castaldo, P., Palazzo, B., Perri F. FEM simulations of a new hysteretic damper: the dissipative column, Ingegneria Sismica - International Journal of Earthquake Engineering, Anno XXXIII – Speciale CTA- 2015- Num. 1-2:34-45.

[16] Castaldo P., De Iuliis M., Optimal integrated seismic design of structural and viscoelastic bracing-damper systems, Earthquake Engineering and Structural Dynamics, 43(12), 1809–1827, 2014, DOI: 10.1002/eqe.2425.

[17] Castaldo P., Integrated Seismic Design of Structure and Control Systems. Springer International Publishing: New York, 2014 . DOI 10.1007/978-3-319-02615-2.

[18] Formisano, A., Lombardi, L., Mazzolani, F.M. “Full and perforated metal plate shear walls as bracing systems for seismic upgrading of existing rc buildings” (2015) Ingegneria Sismica, 33 (1-2), pp. 16-34.

[19] Castaldo, P., Ripani, M. 2016 Optimal design of friction pendulum system properties for isolated structures considering different soil conditions, Soil Dynamics and Earthquake Engineering 90, 74-87.

[20] Mazzolani F. M., Piluso V., “Plastic Design of Seismic Resistant Steel Frames”, Earthquake Engineering and Structural Dynamics, Vol. 26, pp. 167-191, 1997.

[21] Longo A.; Montuori R.; Piluso V., “Theory of Plastic Mechanism Control for MRF-CBF dual system and its validation”. Bulletin of Earthquake Engineering (BEEE), 2014.

[22] Longo A., Montuori R., Piluso V. “Failure mode control of X-braced frames under seismic actions”. Journal of Earthquake Engineering, 12: 728-759, 2008.

[23] Montuori R., Nastri E., Piluso V., “Theory of Plastic Mechanism Control for Eccentrically Braced Frames with inverted Y-scheme”. Journal of Constructional Steel Research, Volume 92, pp. 122-135, 2014.

[24] Montuori R., Nastri E., Piluso V., “Rigid-plastic analysis and moment–shear interaction for hierarchy criteria of inverted Y EB-Frames”. Journal of Constructional Steel Research, vol. 95 pp.71-80, 2014.

[25] Montuori R., Nastri E., Piluso V., “Advances in Theory of Plastic Mechanism Control: Closed Form Solution for Mr-Frames”, Earthquake Engineering & Structural Dynamics, Volume 44, Issue 7, Pages 1035–1054, June 2015.

[26] Montuori R., Nastri E., Piluso V., “Seismic Design of MRF-EBF Dual Systems with Vertical Links: Ec8 Vs Plastic Design”. Journal of Earthquake Engineering, 2015.

[27] Montuori R., Nastri E., Piluso V., “Seismic Response of EB-Frames with Inverted Yscheme: TPMC Versus Eurocode Provisions”. Earthquakes and Structures, 2015.

[28] Longo, A., Montuori, R., Piluso, V.“Moment frames – concentrically braced frames dual systems: analysis of different design criteria” (2016) Structure and Infrastructure Engineering, 12 (1), pp. 122-141. DOI: 10.1080/15732479.2014.996164

[29] Longo, A., Montuori, R., Piluso, V.“Seismic design of chevron braces cupled with MRF fail safe systems” (2015) Earthquake and Structures,8(5),pp.1215-1239.DOI: 10.12989/eas.2015.8.5.1215

[30] Longo, A., Montuori, R., Nastri, E., Piluso, V.“On the use of HSS in seismic-resistant structures”(2014) Journal of Constructional Steel Research, 103, pp. 1-12. DOI:10.1016/j.jcsr.2014.07.019

[31] Montuori, R., Nastri, E., Piluso, V. “Theory of plastic mechanism control for the seismic design of braced frames equipped with friction dampers” (2014) Mechanics Research Communications, 58, pp. 112-123. DOI: 10.1016/j.mechrescom.2013.10.020

[32] Montuori, R., Nastri, E., Piluso, V. “Theory of plastic mechanism control for eccentrically braced frames with inverted y-scheme” (2014) Journal of Constructional Steel Research, 92, pp. 122-135. DOI: 10.1016/j.jcsr.2013.10.009

[33] Montuori, R., Troisi, M., Piluso, V. “Theory of plastic mechanism control of seismic-resistant MR-frames with set-backs” (2012) Open Construction and Building Technology Journal, 6, pp. 404-413. DOI: 10.2174/1874836801206010404

[34] Giugliano, M.T., Longo, A., Montuori, R., Piluso, V. “Seismic reliability of traditional and innovative concentrically braced frames” (2011) Earthquake Engineering and Structural Dynamics, 40 (13), pp. 1455-1474. DOI: 10.1002/eqe.1098

[35] Giugliano, M.T., Longo, A., Montuori, R., Piluso, V. “Failure mode and drift control of MRF-CBF dual systems” (2010) Open Construction and Building Technology Journal, 4, pp. 121-133. DOI: 10.2174/1874836801004010121.

[36] Longo, A., Montuori, R., Piluso, V. “Seismic reliability of chevron braced frames with innovative concept of bracing members” (2009) Advanced Steel Construction, 5 (4), pp. 367-389.

[37] Longo, A., Montuori, R., Piluso, V. “Seismic reliability of V-braced frames: Influence of design methodologies” (2009) Earthquake Engineering and Structural Dynamics, 38 (14), pp. 1587-1608. DOI: 10.1002/eqe.919

[38] Montuori R., Muscati R., “Plastic Design of Seismic Resistant Concrete Frame”. Earthquakes and Structures, Vol. 8, No. 1, pp. 205-224, January 2015.

[39] Montuori R., Muscati R., “A general design procedure for failure mechanism control of reinforced concrete frames”. Engineering Structures, Volume 118, 1 July 2016, Pages 137-155.

[40] Montuori, R., Muscati, R. “Smart and simple design of seismic resistant reinforced concrete frame” (2016) Composites Part B: Engineering, Article in Press. DOI: 10.1016/j.compositesb.2016.09.05.

[41] CSI 2007. SAP 2000: Integrated Finite Element Analysis and Design of Structures. Analysis Reference. Computer and Structure Inc. University of California, Berkeley.

[42] Montuori, R., Nastri, E., Piluso, V. “Modelling of floor joists contribution to the lateral stiffness of RC buildings designed for gravity loads”, (2016) Engineering Structures, 121, pp. 85-96. DOI: 10.1016/j.engstruct.2016.04.046

COMPDYN 2017
6th ECCOMAS Thematic Conference on
Computational Methods in Structural Dynamics and Earthquake Engineering
M. Papadrakakis, M. Fragiadakis (eds.)
Rhodes Island, Greece, 15–17 June 2017

# NONLINEAR FEA OF SOIL-STRUCTURE-INTERACTION EFFECTS ON RC SHEAR WALL STRUCTURES

**Mohammad AlHamaydeh, Ph.D., P.E.[1], George Markou, Ph.D.[2], and Dina Saadi[1]**

[1] American University of Sharjah
PO Box 26666, Sharjah, United Arab Emirates
e-mail: malhamaydeh@aus.edu, g00037041@aus.edu

[2] ALHOSN University
PO Box 38772, Abu Dhabi, United Arab Emirates
e-mail: g.markou@alhosnu.ae

**Keywords:** Nonlinear, FEA, Reinforced Concrete, Soil-Structure-Interaction.

**Abstract.** *Considering Soil-Structure-Interaction (SSI) in Finite Element Analysis (FEA) is accounted for through explicit representation of the soil domain allowing for departures from fixed base conditions and constraints. The performance evaluation of a six-story reinforced concrete (RC) shear wall with and without SSI is presented in this paper. The soil domain and Reinforced Concrete (RC) elements including walls, slabs, and foundations are modeled using 3D 8-noded hexahedral brick elements. Furthermore, longitudinal and transverse reinforcement are modeled as embedded rod elements while the cracking of concrete is modeled via the smeared crack approach. Nonlinear pseudo-static and cyclic pushover analyses are carried out on fixed and flexible base models. The soil in the flexible base model represents a site class E soil type according to ASCE7-10. A parametric study is performed on different pushover loading profiles prior to the comparison between fixed and flexible base systems. The performance evaluation of the two systems is done through direct comparison of pushover curves, displacement, strain locations and cracking patterns. Based on the numerical findings, the RC wall in the SSI model is found to exhibit higher lateral displacements yet lesser levels of strain concentrations for the any given horizontal deformation. Additionally, the superstructure toughness developed in the fixed base model is higher than the SSI model due to the vertical displacement of the soil medium. Finally, cracks in the slabs are found to be more prominent in the SSI model at the upper floors due to the accumulated lateral displacement of the wall and the overall more flexible behavior of the model. In conclusion, soil flexibility (SSI) is found to have a considerable effect on the overall structural system behavior.*

## 1 INTRODUCTION

Considering soil flexibility during analysis for any structural system will result in different stress distributions and displacement profiles. Soil-Structure Interaction (SSI) evaluates the structural system response taking into account the soil as a support condition. Soil deformability often leads to releasing stresses in footings that will increase lateral displacements. The extent of soil deformability depends on many parameters, such as bearing capacity, shear wave velocity, cohesion, etc.

Two mechanisms have to be considered when studying the impact of SSI on the seismic response of structures, kinematic interaction and inertial interaction. Kinematic interaction is the mechanism that occurs due to difference in movement between the soil and foundation. Inertial interaction is the mechanism induced from the relative displacement between the soil and foundation due to the inertial forces. Inertial forces cause base shear and moments at the foundation level that could cause displacement to the soil [1].

The simulation of the soil medium by using Finite Element Analysis (FEA) is essential when considering the SSI phenomenon. To obtain accurate results, the soil element mesh size has to be optimized in order to obtain accurate results with reasonable computational demand. Similarly, the extent of the soil medium and its representative depth has to be wisely chosen if large models and excessive computational demands are to be avoided.

Tabatabaiefar et al. [2] used 2D Finite Element (FE) modeling in order to study the seismic behavior of a ten-story building with a moment-resisting frame considering SSI effects. Their SSI model included the discretization of the soil depth utilizing shell elements, while the building's frame was modeled through the use of beam-column linear elements. The used software was FLAC2D, which is a 2D FE software that can model the soil profile with different shear wave velocities representing soil classes such as Ce, De and Ee according to the Australian code. Likewise, a nonlinear elasto-plastic constitutive SSI model was investigated by Torabi and Rayhani [1] by using a 3D FE model. Different embedment depths and aspect ratios were considered when discretizing the soil domain so as to account for SSI. The 3D modeling of soil medium was done in Opensees with 8-noded brick elements with total depth of 30m. The superstructure was modeled as lumped mass SDOF beam-column element for simplicity and computational efficiency purposes.

A more recent work was presented by Markou and AlHamaydeh [3] and Makrou et al. [4], in the latter, the full-scale five-story RC building was modeled under pseudo-static push over loads. The soil domain, the raft slab and half of the ground floor of the structure were modeled through the use of the 8-noded solid elements, while the remaining part of the superstructure was modeled through the use of the beam-column finite element that incorporates the fiber approach and the natural mode method. This type of simulation is known as hybrid modeling (HYMOD) which allows for the decrease of the computational demand without losing the required numerical accuracy during the analysis.

Nonlinear FEA (NLFEA) is pivotal to earthquake engineering [5]–[18] and failure analysis [19], [20]. The available tools for the structural engineering community vary significantly in complexity and capability. Since high fidelity NLFEA is typically very demanding computationally, brilliant simplifications are always sought after. Some of the common and widely accepted methods are macromodel-based formulations which implement comprehensive elements capable of exhibiting nonlinear characteristics. Macromodel-based formulations either incorporate fiber models to calculate member properties, they are based on mechanics of typical structural members. Common nonlinearities that are accommodated by such techniques are:

linear or uniform flexibility, as well as concentrated or distributed plasticity with yield penetration, etc. Many existing analysis platforms employ such modeling capabilities. e.g. IDARC-2D [21], [22], OpenSees [23]–[25], ZeusNL [26] and SeismoStruct [27].

## 2 PROBLEM DESCRIPTION

### 2.1 Structure properties

This paper will focus on examining the lateral response of a six-story RC shear wall including the associated tributary areas of the slabs, and considering SSI effects. Two FE models are investigated herein, a fixed base model and a flexible base model. Figure 1 shows the fixed base model. The FE model includes a shallow foundation, the shear wall, six slabs and a soil medium (for the case of the flexible base model; see Figure 2). Furthermore, the wall and slab reinforcement are discretized and modeled as shown in Figure 1b. The considered RC wall was designed and detailed as ordinary RC wall in accordance to the ASCE7-10 standard [28]. The design and detailing of the RC wall was adopted from a previously conducted investigation [12]. The RC wall is 2.5 m long in-plan and 24 m in height (six floors at 4 m). Table 1 summarizes the remaining design specifics. The considered building, from which the representative RC shear wall is used herein, was designed to sustain a superimposed dead load of 3.6 kPa (75psf), live load of 2.4 kPa (50psf), and partition wall load of 0.72 kPa (15psf). The FE modeling and analysis are carried out using the ReConAn FEA solver [29].

**Table 1- Design details for the RC shear wall**

| Element/Floors | Compressive Strength (MPa) | In-Plan Length x Thickness (mm) | Vertical (Flexural) Reinforcement | Horizontal (Shear) Reinforcement |
|---|---|---|---|---|
| Walls/4-6 | 38 | 2500x200 | T12@450mm | T12@450mm |
| Walls/1-3 | 38 | 2500x250 | T25@200mm | T16@300mm |
| Slabs/1-6 | 28 | 200 | T16@150mm top and bottom | |

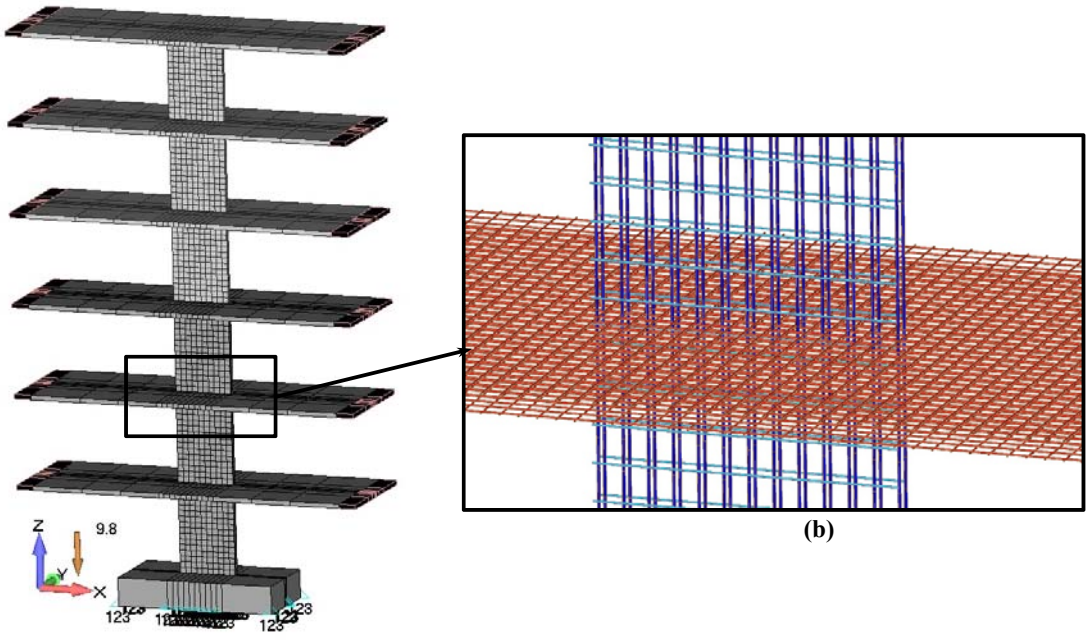


**Figure 1- Finite Element Mesh of the fixed base model (a) Concrete hexahedral elements, (b) Embedded rebar elements**

## 2.2 Soil properties

The soil extent is taken as two times the foundation in-plan dimensions in the lateral and longitudinal directions as recommended in the literature [30]. The foundation footprint is 3.5 m by 7 m, and 1.25 m deep. Based on the adopted soil domain dimensions, the model included a total soil depth equal to 10 m. Figure 2 illustrates the discretization of the soil medium created in order to account for the SSI effects in the flexible base model. The top of foundation is matching the top of soil and does not assume any above-foundation soil, a simplified conservative modeling approach.

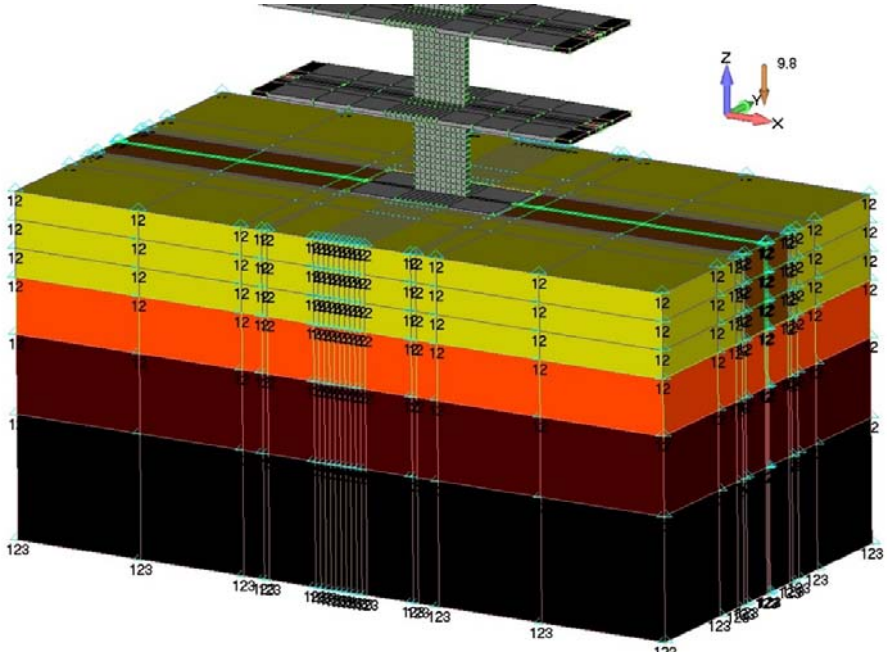


**Figure 2- Finite element mesh of the flexible base model**

In regards to the soil parameters, Table 20.3-1 of ASCE7-10 [28] was used where the soil characteristics (shear wave velocity and standard penetration resistance) of site class E were adopted. Using basic soil parameters, the bearing capacity and modulus of elasticity of the soil are calculated using equations 1 through 4 [31] (see Table 2).

$$G = {v_s}^2 \times \rho \tag{1}$$

$$E = 2(1+\mu)G \tag{2}$$

$$\emptyset\ (\text{deg}) = 27.1 + 0.3\text{N}_{60} - 0.00054\ (\text{N}_{60})^2 \tag{3}$$

$$q_u = q \times N_q + 0.5 \times \gamma \times B \times N_\gamma \tag{4}$$

| | | | | | |
|---|---|---|---|---|---|
| G | Shear modulus | $\emptyset$ | Soil internal friction angle | $\gamma$ | Soil unit weight |
| E | Modulus of elasticity | $\text{N}_{60}$ | Standard penetration resistance | $B$ | Footing width |
| $v_s$ | Shear wave velocity | $N_q$ /$N_\gamma$ | Terzaghi's bearing capacity factors | $q_u$ | Soil bearing capacity |
| $\rho$ | Soil density | $q$ | Soil pressure underneath footing | $\mu$ | Poisson's ratio |

**Table 2- Soil parameters for site class E**

| Soil Parameter | G | E | $\emptyset$ | $q_u$ |
|---|---|---|---|---|
| Value | 25.3 MPa | 65.7 MPa | 28.9° | 0.964 MPa |

## 3 VALIDATION MODEL

The validation process was performed through numerical calibration of the FEA model against published experimental results. The SSI problem that was adopted in this investigation was adopted from Lin et al. [32], where the effects of biogrouting on concrete piles embedded in sandy soils was investigated. In one experiment, a 76 mm-diameter concrete pile was embedded in sandy soil medium extending 1.1m by 1.1 m and 1.55 m deep. The pile was pushed down along the gravity direction until failure. The soil had sensors in different locations to capture stresses and displacements. The vertical load versus the vertical displacement plot for a non-treated pile was compared with the curve obtained from the simulation model developed in this presented research. Figure 3a shows the FE model of the concrete pile embedded in soil, while Figure 3b illustrates the displacement of the concrete pile inside the soil medium. The soil elements that were connected to the pile were modeled assuming a low compressive strength and modulus of elasticity in an attempt to capture the shear stresses that are transferred from the pile to the sand domain through friction.

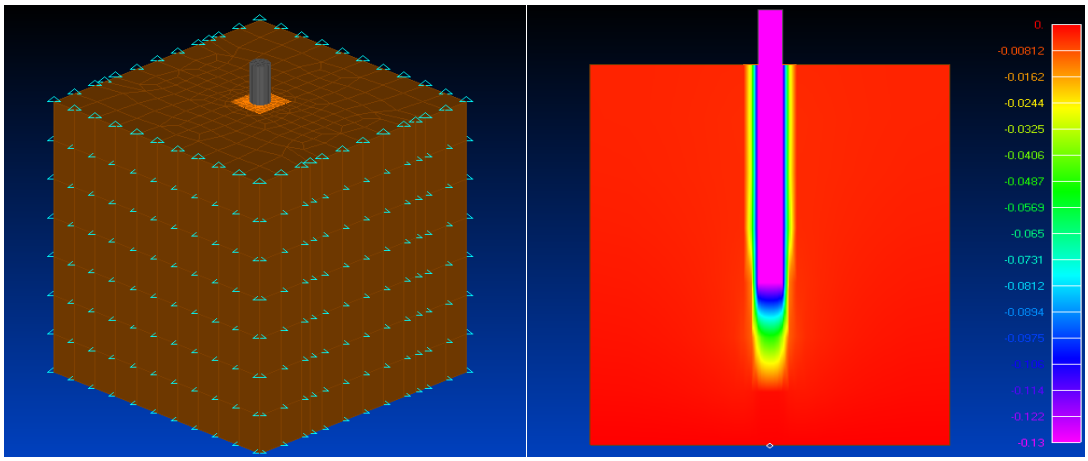


**(a)** **(b)**

**Figure 3- Concrete pile embedded in sand domain (a) 3D mesh of pile and soil medium, (b) displacement contour just prior to failure**

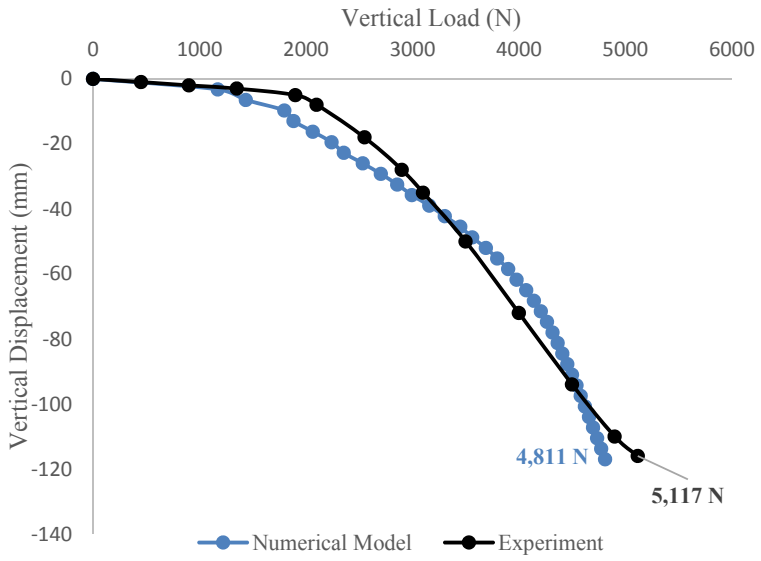


**Figure 4- Comparison between the numerical and experimental for vertical load vs pile displacement**

The comparison between the experimental and numerical results is shown in Figure 4. From the comparison is clearly observed that the numerical model captures the essence experimentally reported mechanical behavior.

## 4 NONLINEAR FEA

### 4.1 Modeling assumptions

In order to account for the continuity of slabs and avoid cantilever-type deformations, the tributary area associated with the wall is modeled with roller restraints around the edges. Figure 5 shows the restraints assigned to the slabs where the same boundary conditions were applied at all floors. Given that the horizontally applied displacements and forces during the analyses, were along the x-axis of the model, the z- and y-axis Degrees Of Freedom (DOFs) were fixed along the edges of the short span of the slabs (parallel to the y-axis), while the edges found on the long span of the slabs were restrained in the y-axis in order to avoid any out of plane deformations.

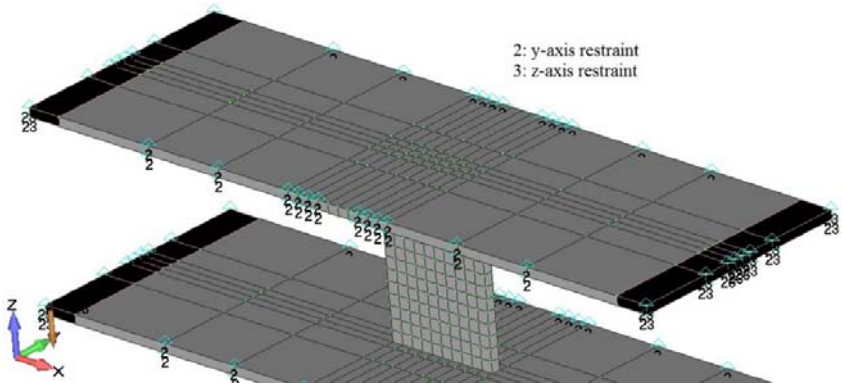


**Figure 5- Slab boundary conditions**

### 4.2 Loading protocol

The modeled structure was loaded with lateral displacements along the x-axis (displacement-control) and the members' own weights were accounted for by the software automatically. Superimposed gravity loads (dead and live) were applied as distributed loads on the slabs. Displacement-controlled pushover analysis was performed so as to evaluate the overall system's seismic response (Soil-Foundation-Wall). Since the seismic loads originate at the slab center of mass and then are transmitted to the lateral forces-resisting system (wall), the imposed displacements were assigned at the floor levels. The relative magnitudes of the assigned displacements were kept constant and proportional to floor elevations, so as to simulate the induced inertial forces during seismic events [33]. In this presented research work the building is pushed laterally for a maximum roof displacement of 2.5% of its total height (600 mm). Since the distribution of the prescribed seismic loads/displacements greatly influences the capacity estimates for the structure at question, a parametric study was performed. It is generally recommended to consider at least two different profiles [33]. Therefore, four different displacement profiles were considered in an effort to shed light on any design weaknesses that static analyses are incapable of detecting. Equation 5 describes the displacement applied at each floor for all considered profiles, where ($\boldsymbol{x}$) is the floor elevation from ground level, ($\boldsymbol{L}$) is the total building height and ($\boldsymbol{k}$) is the profile power factor ranging from 1 to 2. Specifically, the four profiles had the following power factors: 1 (linear first fundamental vibrational mode), 1.2 (profile used for the

original design), 1.5 and 2 (typical cases to be considered representing higher mode effects to different extents). This sensitivity analysis exercise was performed on the fixed-base model only for brevity.

$$Floor\ Displacement = (\frac{x}{L})^k \tag{5}$$

The pushover curves were compared as shown in Figure 6. For k = 1 and 2, the profiles were deemed not very suitable, as the former uncooperatively exaggerates the capacity while the latter unrealistically underestimates the capacity since it is associated with extreme higher-modes-dominated behavior. For k = 1.2 and 1.5, they are deemed appropriate seismic capacities for the structural system. The k value of 1.2 is chosen as it is consistent with the design stage profile for the original building [12].

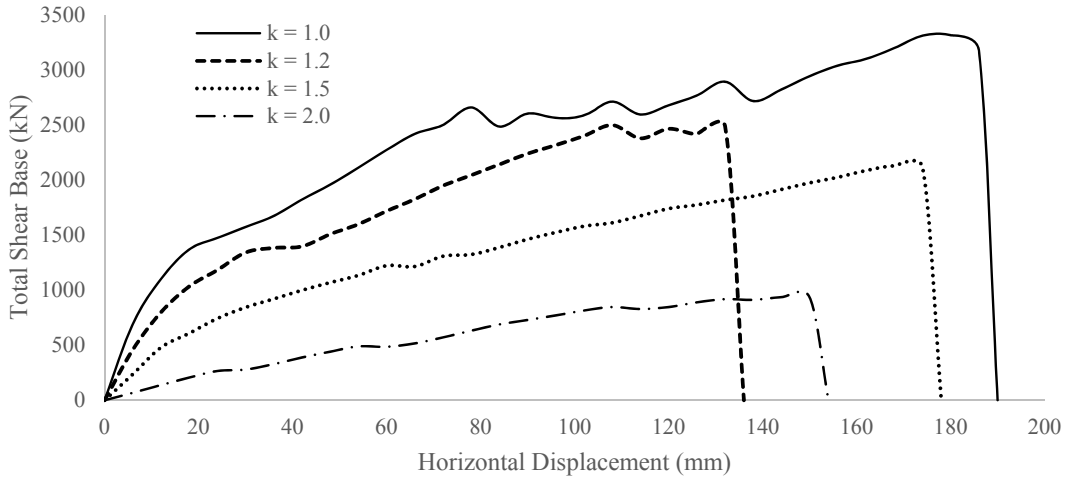


**Figure 6 - Pushover curves for different displacement profiles**

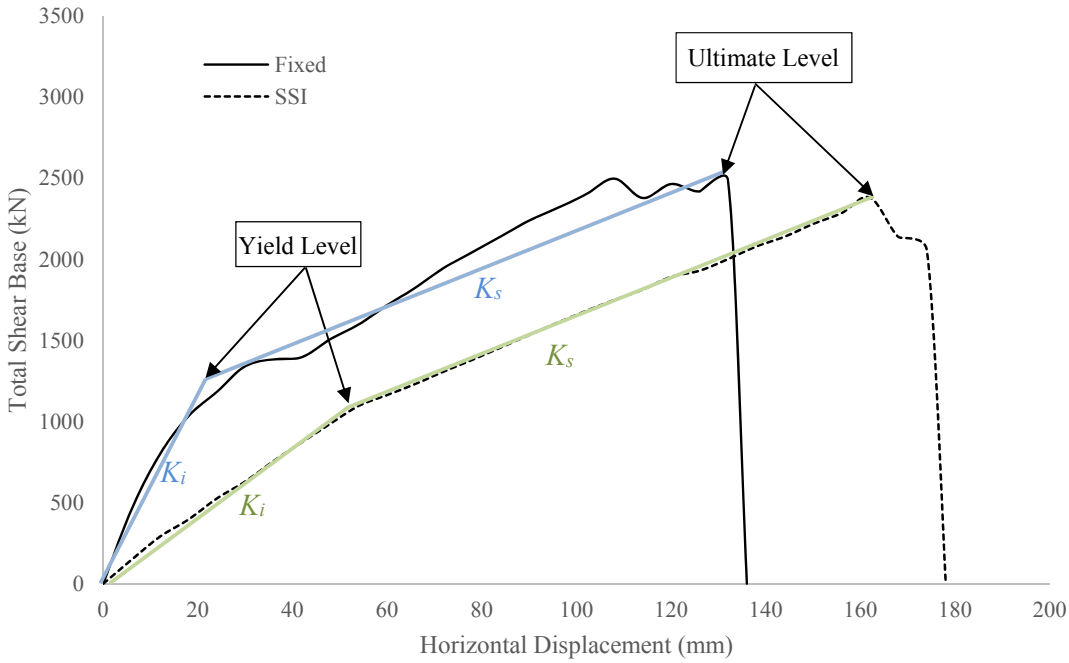


**Figure 7 – Base shear vs horizontal displacement curves for the fixed base and SSI models**

The following comparisons between the fixed base and flexible base models including displacements, strains and cracking patterns, are based on the k = 1.2 displacement profile. Figure 7 demonstrates the pushover curves of two models as they were subjected to the same displacement-controlled pseudostatic protocol.

## 5 DISCUSSION OF RESULTS

### 5.1 Pseudostatic Pushover Loading

#### 5.1.1. Force-Deflection Response

Changing the fixed boundary conditions applied at the foundation level with hexahedral finite elements (soil base) allows the isolated footing to compress the soil resulting in a more flexible structural response. Consequently, rotation is allowed at the base which leads to increased lateral displacements (corresponding to some internal stresses relieves) in the superstructure. In this article, the pushover analysis was performed using displacement-controlled approach where the building was pushed laterally to 2.5% of the total height, which is 0.025 x 24m = 0.6m. The imposed displacement was applied through the use of 100 displacement increments and an energy-based convergence criterion tolerance equal to $10^{-5}$. Referring to the pushover curves in Figure 7, the fixed base model demonstrates higher resistance for any specific imposed displacement value. Key response parameters, such as the initial stiffness ($\boldsymbol{K_i}$) and secondary stiffness ($\boldsymbol{K_s}$) for the fixed base and SSI models are evaluated and listed in Table 3.

$$K_i = \frac{Fy}{\Delta y} \tag{6}$$

$$K_s = \frac{Fu - Fy}{\Delta u - \Delta y} \tag{7}$$

Where $Fy$ is the yield force, $Fu$ is the ultimate force, $\Delta y$ and $\Delta u$ are the yield and ultimate displacements, respectively.

Generally, the SSI model exhibits more flexible behavior in comparison to the fixed base model (higher displacements corresponding to lower forces). For example, the yield displacement is 225% higher for the SSI model, and the initial stiffness is 41% lesser, compared to their fixed base counterparts. Since lesser stress and strain demands are typically undergone in the SSI model, the yield force is also lesser, but the secondary stiffness is higher. This is indicative of lesser superstructure inelastic demands exhibited through higher post-yielding stiffness. Moreover, the superstructure toughness is reduced by 16%.

**Table 3- Key response parameters from Figure 7**

| Parameter | SSI Model | Fixed Base (FB) Model | SSI/FB |
|---|---|---|---|
| $Fy$ | 1,098 kN | 1,183 kN | 0.93 |
| $\Delta y$ | 0.054m | 0.024m | 2.25 |
| $K_i$ | 20,333 kN/m | 49,292 kN/m | 0.41 |
| $Fu$ | 2,382 kN | 2,488 kN | 0.96 |
| $\Delta u$ | 0.162m | 0.132m | 1.23 |
| $K_s$ | 11,889 kN/m | 12,083 kN/m | 0.98 |
| $K_s \,/\, K_i$ | 0.585 | 0.245 | 2.39 |
| Toughness | 235 kJ | 249 kJ | 0.94 |

Figure 8 shows the numerically predicted deformed shapes for the two models at the ultimate loading conditions. As it can be seen the fixed base model failed at a total horizontal displacement of 136 mm, where the corresponding displacement for the case of the SSI model was 169 mm (24.3% larger displacement prior to failure).

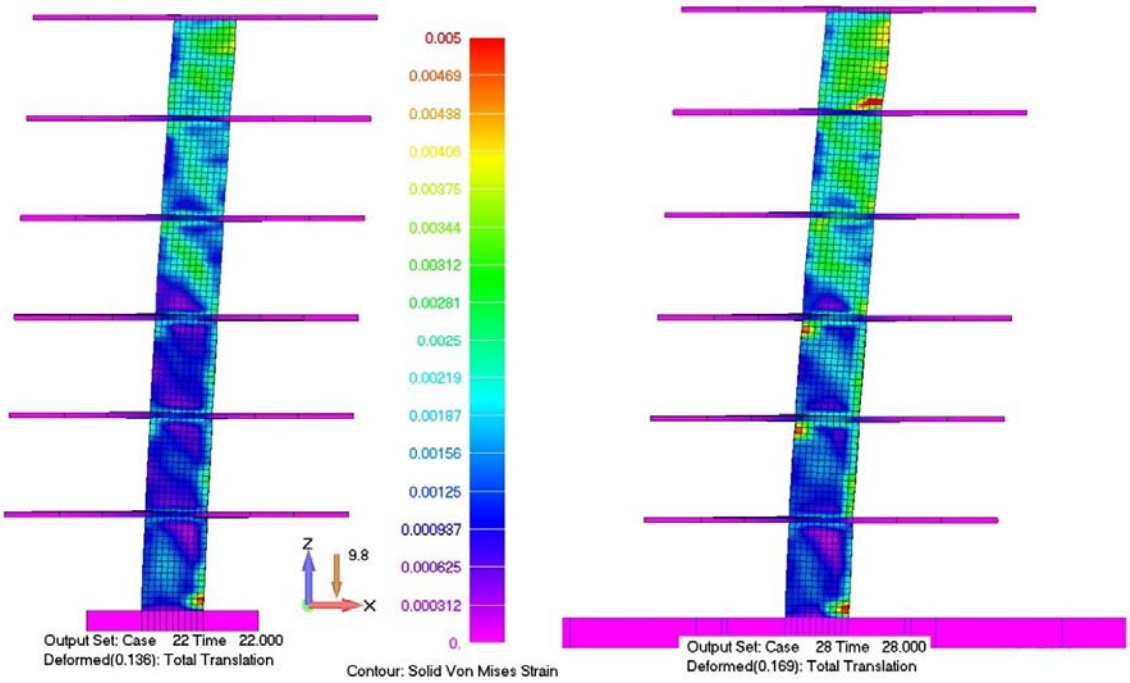


**(a)** **(b)**

**Figure 8 – Von Mises strain contours on deformed shape prior to failure of the (a) SSI model (b) fixed base model.**

### 5.1.2. Strain levels

Based on the numerical findings, the strain concentrations in the RC wall of the fixed model were found to be higher in the fixed base model due to their high stiffness. This is expected given the boundary conditions that were applied at the foundation level which does not allow for any rotation. Figure 8 illustrates the differences in strain levels prior to failure for the two models. As it can be seen, for the case of the SSI model the lower floors exhibited lower strain concentrations in comparison to the fixed model at the stage of the maximum horizontal displacement. This is attributed to the ability of the SSI model to allow the isolated footing to develop rotations (Figure 8b). The strains shown in indicate the high demands from the pushover analysis, as strain values above 0.003 indicates that the concrete sections are tension-controlled and exhibiting significant yielding according to ACI318-11, Chapter 9 [34].

Moreover, the numerical investigation showed that the fixed base model exhibited a cracking pattern that is dominated by horizontal and diagonal cracks at the bottom region of the RC wall due to the full rotational restraint of the base. At the point where the maximum horizontal displacement was applied, the isolated footing developed tensile cracks as well. The full restraint of the foundation creates high moments that cause cracking of concrete due to tensile stress concentrations. Whereas in the SSI model, the crack development in the slabs was found to be higher. This finding could be attributed to the increased lateral wall displacements as a direct result of the rotational flexibility of its base. i.e. the additional sway of the wall adds more bending demands on the slabs given the relative rigidly of the wall.

## 5.2 Cyclic Loading

### 5.2.1. Force-Deflection Response

Cyclic displacement-controlled analysis was performed to further investigate the overall effect of the SSI phenomenon in terms of the overall structural behavior of the considered system. The lateral displacement protocol that was imposed on the structure pictorially illustrated in Figure 9. The resulting hysteretic loops obtained from the analysis can be seen in Figure 10. It is observed that the force-deformation curves in Figure 10 indicate a somewhat similar seismic response to that presented in Figure 7. The deterioration in the structural response after the first two cycles, can be easily noticed. The cyclic structural toughness (area enclosed in hysteresis loops) the fixed base and SSI models were found to be 677.45 kJ and 643.27 kJ, respectively. The 5% reduction in the cyclic structural toughness is evidently a direct consequence of the increased flexibility of the SSI model.

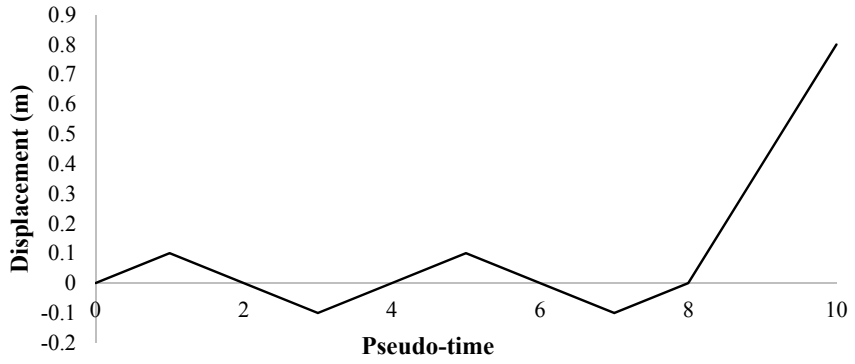


**Figure 9- Cyclic lateral displacement protocol**

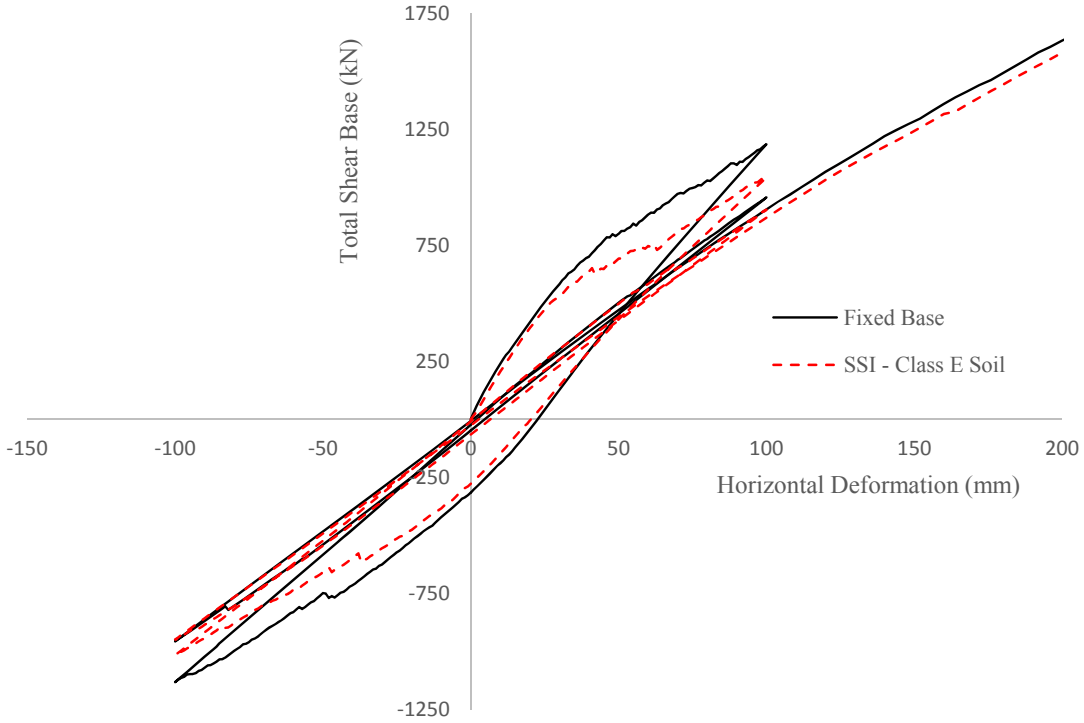


**Figure 9- Hysteresis curve for fixed base and flexible base models**

Figures 11 illustrate the Von Mises strain levels for the cyclic analysis of flexible base model at a roof displacement of 0.2m. The cyclic analysis material models that were used to perform this numerical investigation were based on the work presented by Mourlas et al. [35].

### 5.2.1. Soil Stress-Strain Response

The soil's contribution to the overall structural behavior was evident for the analyses performed with the SSI model. Stress concentrations at various locations were captured throughout the cyclic analysis. As it can be seen in Figures 12 and 13, the von Mises stresses that were developed under the foundation were not larger than 200 kPa, which indicates that the soil domain behaved in a linear manner throughout the analysis. In addition to that, it is easy to observe that the stress contours in the soil medium are controlled by the deformation state of the shear wall structure and its foundation.

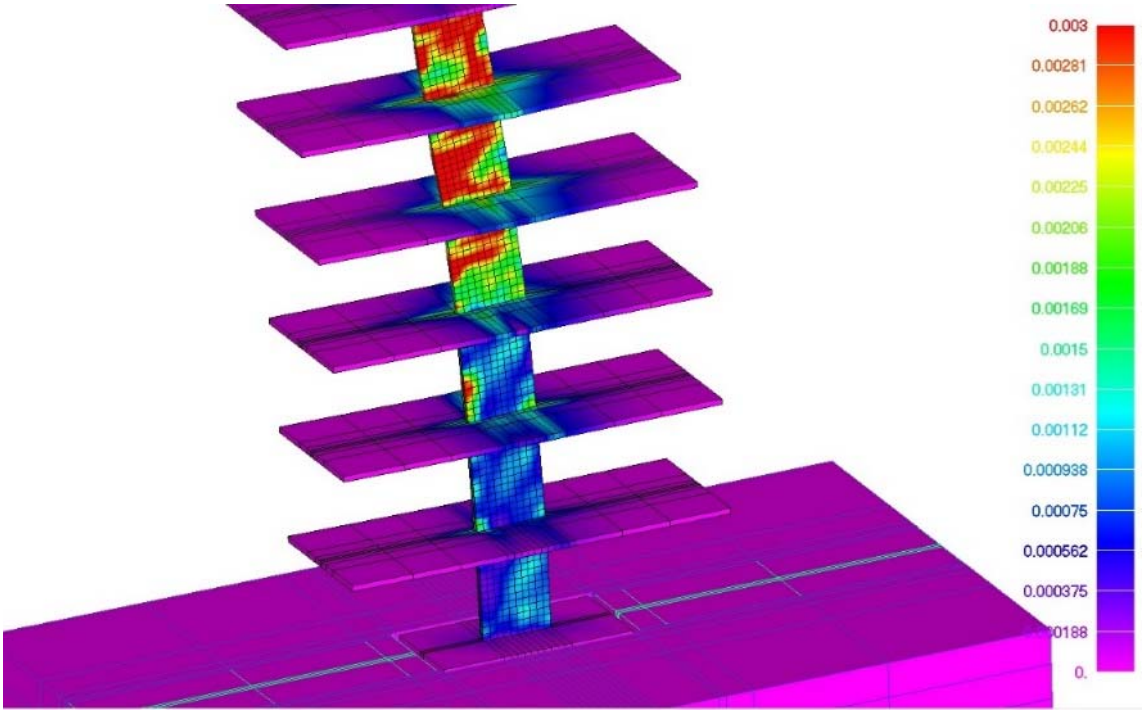


**Figure 10- Von Mises strain contours for the SSI model at the 0.2m roof displacement step.**

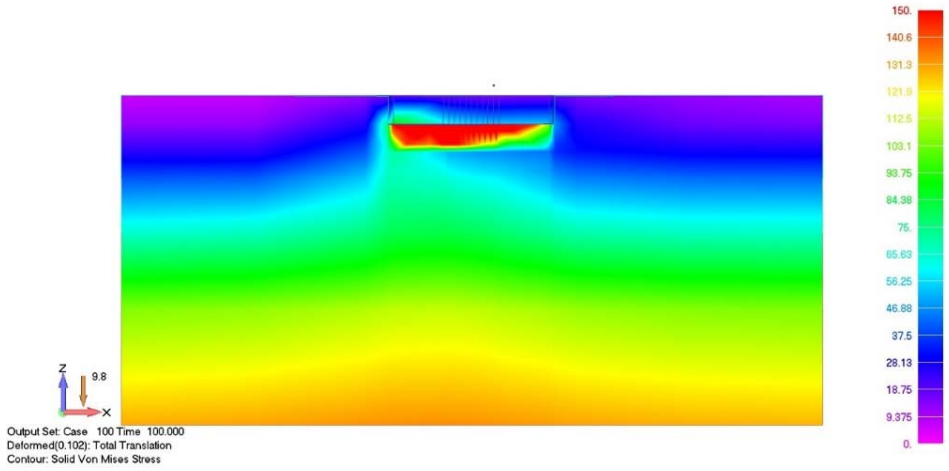


**Figure 11- Von Mises stress contours for the soil domain at increment 100 (δ = 100 mm)**

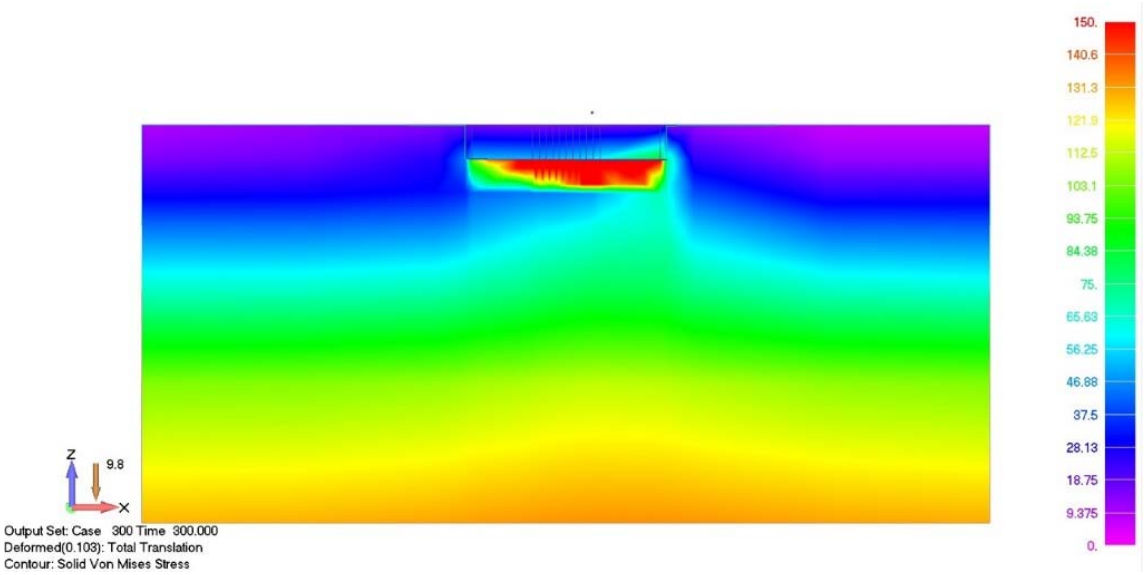


**Figure 12- Von Mises stress contours for the soil domain at increment 300 (δ = -100 mm)**

Based on the numerical findings, it was found that the isolated foundation did not develop any uplift thus the structure was compressing the soil medium-foundation interface throughout the cyclic analysis.

## 6 CONCLUSIONS

Based on the performed nonlinear FEA, the following may be concluded:

- The SSI affects the lateral response of structures by increasing lateral displacement. The weaker the soil, the higher the rotational release which the system will experience is. Thus, the difference in displacement between fixed and flexible base systems (for the same base shear) might not be felt if the soil is very stiff. i.e. when the soil is very stiff, the footing will not encounter relative displacement that will allow it to rotate.
- Regions of high strain concentrations shift when considering SSI effects. In fixed base systems, strains are higher at the bottom of the walls due to rotational fixity. Whereas in SSI system, walls behave in a more flexible manner deriving lower strain concentrations. However, the slabs will experience higher bending demands as the wall exhibits higher lateral displacements. Higher strain concentrations within the RC structural elements results in yielding of steel reinforcement, which is a limit state that requires further investigation.
- The shear wall of the SSI model develops lower strain concentrations in comparison to the fixed base model for the same horizontal deformation levels. This numerical finding could be attributed to the excess flexibility of the SSI model. This additional flexibility stems from the compressibility of the soil beneath the footing in response to the overturning effects of the imposed lateral displacements.
- The soil domain did not develop any nonlinearities throughout the cyclic analysis, and the footing did not develop any uplifts. The stress concentrations within the soil medium was found to be relatively low, highlighting the efficient footing design that did not allow for any high stress concentrations during the cyclic analysis.

## 7 REFERENCES


[1] H. Torabi and M. T. Rayhani, "Three dimensional Finite Element modeling of seismic soil–structure interaction in soft soil," *Computers and Geotechnics*, vol. 60, pp. 9–19, 2014.

[2] F. Behnamfar and M. Banizadeh, "Effects of soil-structure interaction on distribution of seismic vulnerability in RC structures," *Soil Dynamics and Earthquake Engineering*, vol. 80, pp. 73–86, 2016.

[3] G. Markou and M. AlHamaydeh, "3D Finite Element Modeling of GFRP-Reinforced Concrete Deep Beams without Shear Reinforcement," *International Journal of Computational Methods*, no. 1850001, DOI: 10.1142/S0219876218500019, 2017.

[4] G. Markou, R. Sabouni, F. Suleiman, and R. El-Chouli, "Full-Scale Modeling of the Soil-Structure Interaction Problem Through the use of Hybrid Models (HYMOD)," *International Journal of Current Engineering and Technology*, vol. 55, no. 22, pp. 2277–4106, 2015.

[5] M. AlHamaydeh, S. Yehia, N. Aly, A. Douba, and L. Hamzeh, "Design Alternatives for Lateral Force-Resisting Systems of Tall Buildings in Dubai, UAE," *International Journal of Civil and Environmental Engineering*, vol. 6, pp. 185–188, 2012.

[6] M. AlHamaydeh and G. Al-Shamsi, "Development of Analytical Fragility Curves for Representative Buildings in Dubai, United Arab Emirates," in *The International Conference on Earthquake Engineering; Skopje Earthquake - 50 Years of European Earthquake Engineering (SE-50EEE), May 29-31*, 2013.

[7] M. AlHamaydeh, N. Aly, and K. Galal, "Effect of Diverse Seismic Hazard Estimates on Design and Performance of RC Shear Wall Buildings in Dubai, UAE," in *The 2015 World Congress on Advances in Structural Engineering and Mechanics (ASEM15), August 25-29*, 2015.

[8] M. Al Satari and J. Anderson, "Estimating Inelastic Seismic Demands by Elastic Analysis for Reinforced Concrete (RC) Framed Structures," in *The 75th SEAOC Annual Convention, September 13-16*, 2006, pp. 153–167.

[9] M. Al Satari, *Estimation of Seismic Response Demands for R/C Framed Structures: An Insight Into The Nonlinear Seismic Behavior*. VDM Verlag, Saarbrücken, Germany, 2008.

[10] M. H. Al Satari, "Estimation of Seismic Response Demands for RC Framed Structures," University of Southern California, 2005.

[11] M. AlHamaydeh, K. Galal, and S. Yehia, "Impact of Lateral Force-Resisting System and Design/Construction Practices on Seismic Performance and Cost of Tall Buildings in Dubai, UAE," *Earthquake Engineering and Engineering Vibration*, vol. 12, no. 3, pp. 385–397, 2013.

[12] M. AlHamaydeh, N. Aly, and K. Galal, "Impact of Seismicity on Performance and Cost of RC Shear Wall Buildings in Dubai, UAE," *ASCE, Journal of Performance of Constructed Facilities*, no. DOI: 10.1061/(ASCE)CF.1943-5509.0001079, 2017.

[13] M. AlHamaydeh, J. Abdalla, S. Abdalla, A. Al-Rahmani, and A. Mostafa, "Inelastic Seismic Demands For Reinforced Concrete Frames In Dubai," in *The 14th European Earthquake Engineering Conference (14EEEC), Aug. 30-Sept. 3*, 2010.

[14] J. Anderson, V. Bertero, and M. Al Satari, "Inelastic Seismic Response of a Tilt-up Wall Building and Design Implications," in *The 74th SEAOC Annual Convention, Sept. 28-Oct. 1*, 2005.

[15] M. Al Satari and J. Anderson, "Nonlinearity Effects on the Seismic Behavior of RC Framed Structures," in *The 76th SEAOC Annual Convention, September 26-29*, 2007.

[16] M. AlHamaydeh, S. Abdullah, A. Hamid, and A. Mustapha, "Seismic design factors for RC special moment resisting frames in Dubai, UAE," *Earthquake Engineering and Engineering Vibration*, vol. 10, no. 4, pp. 495–506, 2011.
[17] J. C. Anderson, V. V. Bertero, M. Kargahi, and M. Al Satari, "Seismic Performance of an Instrumented Tilt-up Wall Building," Pacific Earthquake Engineering Research Center, Berkeley, California, USA, 2004.
[18] M. AlHamaydeh, N. Ibrahim, D. Kaloti, O. Alhasan, and A. Aisha, "Structural Design of Steel Plate Shear Wall Systems in Dubai, UAE," in *CYRUS Institute of Knowledge (CIK) conference, "West-Meets-East: Exploring Sustainable Development, Innovation, and Entrepreneurship Opportunities, January 9-11*, 2014.
[19] M. AlHamaydeh, F. Abed, and A. Mostafa, "Finite Element Simulation of Different Failure Modes for Buckling-Restrained Braces under Cyclic Loading," in *The 9th International Conference on Composite Science and Technology (ICCST-9), April 24-26*, 2013.
[20] M. AlHamaydeh, F. Abed, and A. Mustapha, "Key parameters influencing performance and failure modes for BRBs using nonlinear FEA," *Journal of Constructional Steel Research*, vol. 116, pp. 1–18, Jan. 2016.
[21] A. M. Reinhorn, H. Roh, M. Sivaselvan, S. K. Kunnath, R. E. Valles, A. Madan, C. Li, R. Lobo, and Y. J. Park, "IDARC2D Version 7.0: A Program for the Inelastic Damage Analysis of Structures," 2009.
[22] M. AlHamaydeh, M. Najib, and S. Alawnah, "INSPECT: A Graphical User Interface Software Package for IDARC-2D," *SoftwareX*, vol. 5, pp. 243–251, 2016.
[23] F. McKenna, G. Fenves, and M. Scott, "OpenSees – Open System for Earthquake Engineering Simulation, ver. 2.5.0." Pacific Earthquake Engineering Research Center (PEER), http://opensees.berkeley.edu/, Berkeley, California, USA, 2016.
[24] A. Schellenberg, T. Yang, and E. Kohama, "OpenSees Navigator ver. 2.5.5." Pacific Earthquake Engineering Research Center (PEER), http://openseesnavigator.berkeley.edu/, Berkeley, California, USA, 2015.
[25] S. Mazzoni, "BuildingTcl/BuildingTclViewer." Pacific Earthquake Engineering Research Center (PEER), http://opensees.berkeley.edu/wiki/index.php/BuildingTcl, Berkeley, California, USA, 2010.
[26] A. S. Elnashai, V. Papanikolaou, and D. Lee, "ZEUS NL – A system for Inelastic Analysis of Structures, User's Manual, ver. 1.9.0." Mid-America Earthquake (MAE) Center, Department of Civil and Environmental Engineering, University of Illinois at Urbana-Champaign, http://mae.cee.illinois.edu/software/software_zeusnl.html, Urbana-Champaign, Illinois, USA, 2011.
[27] SeismoSoft Inc., "SeismoStruct 2016 – A Computer Software for Static and Dynamic Nonlinear Analysis of Framed Structures, ver. 7." SeismoSoft, Inc., http://www.seismosoft.com/SeismoStruct_2016_Release-4_ENG, 2016.
[28] ASCE/SEI, "Minimum Design Loads for Buildings and Other Structures (ASCE/SEI 7-10)," American Society of Civil Engineers/Structural Enginnering Institute, 2010.
[29] G. Markou, "ReConAn - Finite Element Analysis Software, v1.00." Institute of Structural Analysis and Seismic Research, National Technical University of Athens, 2010.
[30] M. Ghandil and F. Behnamfar, "The near-field method for dynamic analysis of structures on soft soils including inelastic soil-structure interaction," *Soil Dynamics and Earthquake Engineering*, vol. 75, pp. 1–17, 2015.
[31] B. M. Das, *Principles of geotechnical engineering*. Cengage Learning, 2010.
[32] H. Lin, M. T. Suleiman, H. M. Jabbour, D. G. Brown, and E. Kavazanjian, "Enhancing

the Axial Compression Response of Pervious Concrete Ground Improvement Piles Using Biogrouting," *Journal of Geotechnical and Geoenvironmental Engineering*, vol. 142, no. 10, p. 4016045, Oct. 2016.

[33] A. S. Elnashai and L. Di Sarno, *Fundamentals of Earthquake Engineering*, First Edit. John Wiley & Sons Ltd, 2008.

[34] ACI Committee 318, *Building Code Requirements for Structural Concrete (ACI 318M-11)*. 2011.

[35] C. Mourlas, M. Papadrakakis, and G. Markou, "A Computationally Efficient Model For The Cyclic Behavior Of Reinforced Concrete Structural Members," pp. 1–40, 2017.

COMPDYN 2017
6th ECCOMAS Thematic Conference on
Computational Methods in Structural Dynamics and Earthquake Engineering
M. Papadrakakis, M. Fragiadakis (eds.)
Rhodes Island, Greece, 15–17 June 2017

# SEISMIC FINITE ELEMENT ANALYSIS OF AN EXISTING OLD CONCRETE STRUCTURE BY USING MULTIFIBER BEAMS: INTRODUCTION OF AN ADAPTIVE PUSHOVER METHOD

**A. Omar[1], S. Grange[2], and F. Dufour[3]**

[1] AZM University – Grenoble Alpes University
Fouad Chehab Boulevard, Tripoli, Lebanon
e-mail: aomar@azmuniversity.edu.lb

[2] INSA Lyon
Univ Lyon, INSA-Lyon, SMS-ID, F-69621, France
stephane.grange@insa-lyon.fr

[3] Grenoble Alpes University
Univ. Grenoble Alpes, 3SR, F-38041 Grenoble, France
frederic.dufour@3sr-grenoble.fr

**Keywords:** Modal Analysis, Non-linear Dynamic Behavior, Adaptive Pushover Analysis, Reinforced Concrete Structures, Ambient vibration.

**Abstract.** *The study of the seismic vulnerability of existing structures is an important issue. Many researches have been developed in order to investigate the structural behavior of these structures, and extract the basic informations needed to establish retrofitting guidelines in order to reduce the seismic risk to acceptable levels. The most accurate analysis procedure for the structures subjected to strong ground motions is the time-history analysis. This method is time-consuming though for application in all practical purposes. The necessity for faster methods that would ensure a reliable structural assessment or design of structures subjected to seismic loading led to the pushover analysis. Pushover analysis is a non-linear static analysis based on the assumption that structures oscillate predominantly in the first mode or in the lower modes of vibration during a seismic event. The present work deals with seismic vulnerability assessment of an old existing reinforced concrete structure – Perret tower – located in Grenoble, France. After a brief description of the structure in exam, a preliminary computation of the mass of the building and the definition of every existing section are performed. A simplified 3D numerical model is carried out using a finite element code based on multifiber beams approach. Firstly, a non-linear temporal dynamic analysis is performed, then a conventional and adaptive pushover analysis is carried out. The results obtained of the studied cases are then compared: it is observed that the conventional pushover analysis should be adjusted in order to take into account the change of dynamic characteristics due to the formation of plastic mechanisms. Finally, the tower critical levels in term of damage are highlighted.*

## 1 INTRODUCTION

The seismic vulnerability assessment of existing structures and buildings is an important issue nowadays. In general terms, vulnerability expresses the propensity of a system of elements exposed to hazards to suffer damage. Many researches have been developed in order to investigate the behavior of these structures, and extract the basic informations needed to establish retrofitting guidelines in order to reduce the risks to acceptable levels. Numerous types of structures can be subjected to seismic risks and require a particular attention, such as buildings, towers, bridges, dams and nuclear power plants. In this matter, the seismic loading is due to well known "ground shaking" that can lead to a significant damage and/or collapse of the structure.

In seismic regions, a majority of old structures have been only designed to withstand gravity loads or to sustain seismic risks according to outdated seismic codes. These structures were designed and built without considering adequately earthquakes provisions constituting therefore an important source of risks. Recently, major earthquakes around the world have clearly proved that these old structures require an appropriate analysis to predict accurately their seismic behavior and evaluate their vulnerability. This allows proposing guidelines for the retrofitting procedure which is necessary for reducing seismic damage to allowable levels.

The process of analysis and design of a new structure is quite different from the case of an existing old structure. The design procedure objective is not the same in both cases indeed. When designing a new structure, the behavior is considered as ductile as the brittle failure modes are avoided. However, the failure modes characterizing an existing structure are mainly considered as brittle. This difference must be taken into account during the analysis phase.

The prediction of seismic behavior of existing structures has attracted some attention in the last decades [1, 2, 9, 11]. Several codes such as the Japanese Standard for Evaluation of Seismic Capacity of Existing Reinforced Concrete buildings [7] and Eurocode 8 [6] have addressed strengthening and rehabilitation of existing structures.

The numerical modeling represents a quite powerful and economic tool to assess accurately the seismic vulnerability of structures. The main objective of this paper is to present the numerical seismic analysis of the Perret tower located in Grenoble, France. Firstly, the description of the tower structure will be shown. Then it will be followed by a linear and non-linear analysis by mean of a 3D simplified finite element modeling using multifiber beams. Thirdly, the results of the non-linear temporal dynamic analysis will be compared with those obtained by carrying out a non-linear static pushover analysis. In this matter, an adaptive pushover method will be then described in order to improve the numerical behavior accuracy. And finally, conclusions and perspectives will be discussed.

## 2 PRESENTATION OF PERRET TOWER

Perret tower is a reinforced concrete structure constructed between 1924 and 1925, currently located in the park Mistral in Grenoble, France. This tower, which is the first tall reinforced concrete building in Europe, with a height of 83 m approximately, was specifically built by the architect Auguste Perret. It has been completed in 1925 for the “Houille Blanche” and tourism exhibition in downtown Grenoble, France. Its main purpose was to be a panoramic observation point and was opened for public until 1960. It consists of a framework mainly made up of 8 piles joined together by three ring-shaped shear walls at 3 different levels (Figure 1). The screen walls are made of perforated concrete. The different constitutive levels of the tower are the following:

- A crown located at 3 m above the ground;

- At level 51.8 m, there is a platform elevator above it rises a second tower consisting of three terraces:
  - A platform for visitors at 60 m
  - A terrace at 71 m (summit platform); Figure 3.1 section at the base
  - terrace at 78 m (2 summit arcs and a ball)

Elevators and helical stairs give access to the platform, and another stair leads to the top of the tower. The tower is lying on a shallow foundation supported by 72 deep inclusions. At the level of the platform for visitors, a discontinuity in the section of the tower appears, where the columns above this level rest on a small cantilever beam. Figure 3.a shows clearly the details of this zone. Moreover, the columns are tapered and have a section quite similar to T shape (Figure 3.b).

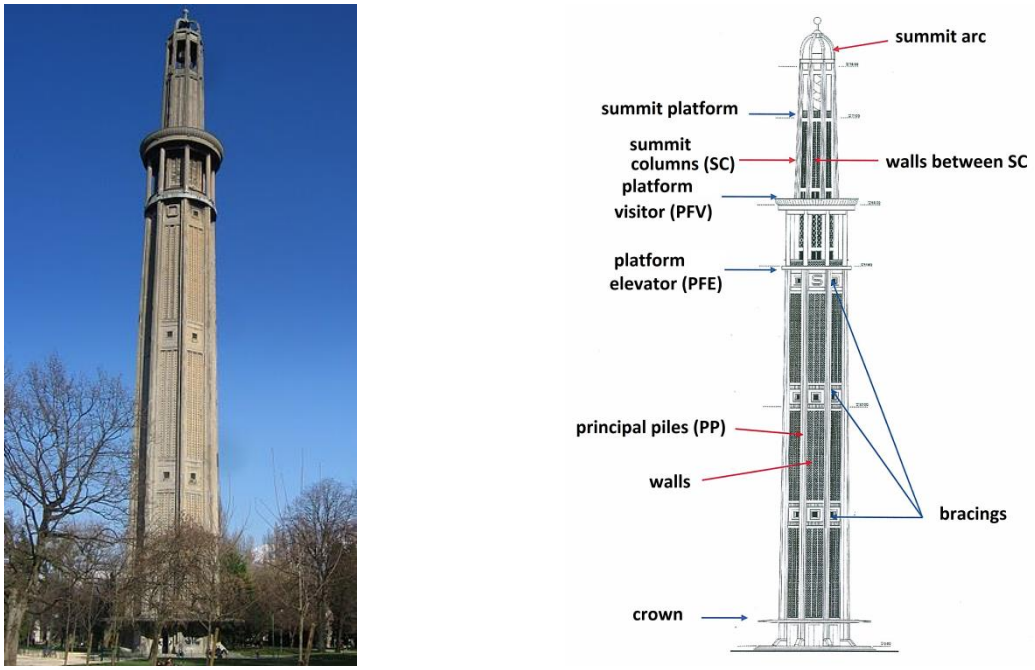


(a) (b)

Figure 1: (a) Overview of the Perret tower in Grenoble, (b) the detailed structure's description

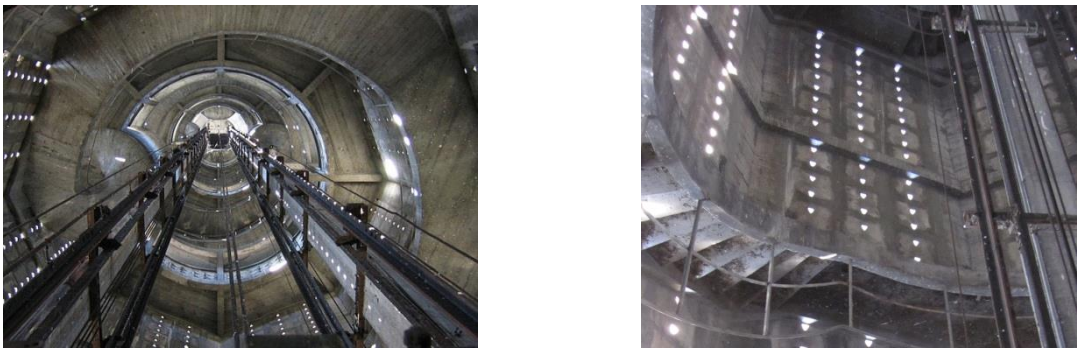

(a) (b)

Figure 2: (a) Interior view showing the helicoidal stair and the elevators, (b) Screen walls

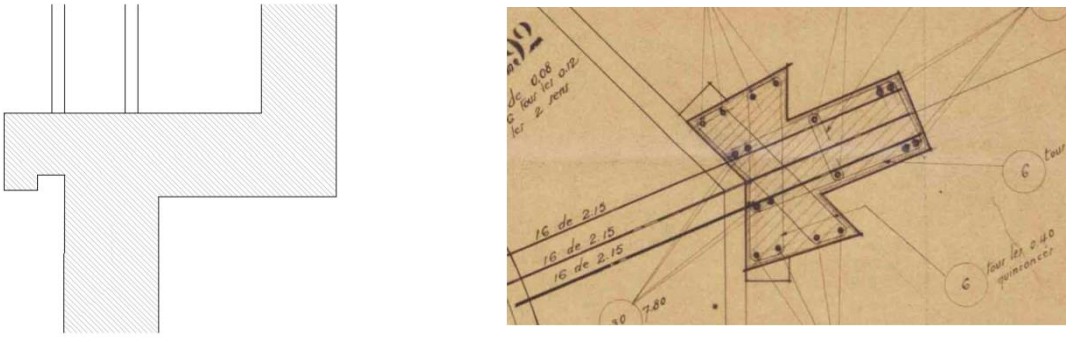


(a) (b)

Figure 3: (a) Interior view showing the helicoidal stair and the elevators, (b) Screen walls

## 3 NUMERICAL MODELING

The structure is composed of eight piles confined together by three ring shaped shear walls which keep them together as unique structure. So the structure can be considered as a monolithic vertical beam. At the opposite, the screen walls seem to be only decorative as they are weakly linked to the columns. In this matter, the junctions contain very few corroded steel rebars. Thus, these elements do not participate to the structural stiffness. At the same time, there is an important concrete degradation of the spiral stairs which bring only mass to the tower and therefore their stiffness is negligible.

A numerical modeling is proposed hereafter to try reproducing the linear behavior of the tower as a first step which will be followed by a non-linear analysis. The eight piles will be considered as belonging to the same section of one beam clamped at the base and SSI was not taken into account. The total mass of the tower (1677tons) has been modeled by mean of concentrated masses distributed over 23 sections along the height of the tower. Numerical computations were performed with multifiber Timoshenko beam elements [10, 13], introduced in the finite-element code FEDEASLab (a MATLAB toolbox) [8]. This finite element strategy allows reproducing in a simplified manner the cyclic behavior of concrete as this numerical approach is suitable for slender structures. 1D non-linear constitutive behavior laws can be used for modeling concrete and steel fibers. The details of the numerical modeling data and results will be treated in the following paragraphs.

### 3.1 FE mulitifiber beam modeling

This approach is used to simplify the modeling of a structure versus a full 3D approach. Each element of the structure (columns, beams...) is decomposed into several beam elements with a node at each end. The section of a multifiber beam element is decomposed into several parallel fibers to the axis of the beam (Figure 4.a). For each fiber, a uniaxial constitutive law can be applied; this allows representing different materials in one section. The beam can follow Bernoulli or Timoshenko kinematics then each behavior law requires only a uniaxial writing.

The section of each column is discretized into 8 fibers of concrete and 3 fibers of steel (equivalent to the real section of steel), so at all the section of the beam contains 64 fibers of concrete and 24 fibers of steel (Figure 4.b). The simple model is equivalent to a simple beam

fixed at the base in the ground whose section and stiffness vary with height. The model is discretized along the height into 22 elements and 23 nodes.

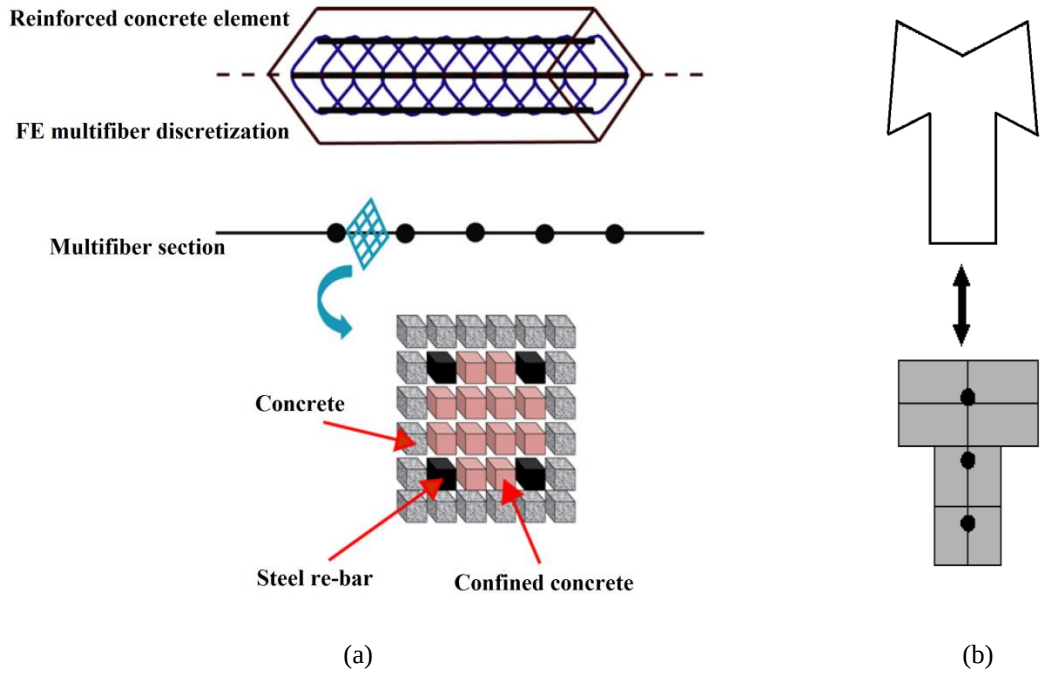


Figure 4: (a) Multifiber beam modeling, (b) Piles section discretization

### 3.2 Constitutive models for concrete and steel materials under cyclic loadings

The major feature of the used material models is to describe each material only by one uniaxial law, which constitutes a significant simplification compared to a 2D or 3D description. The mechanical characteristics of the concrete have been determined by mean of experimental testing performed on specimen extracted from the tower. However, steel properties were not available at the time of the study so they were fixed on conservative values.

The behavior of concrete is described by the unilateral La Borderie model [12]. This local model based on damage mechanics follows the thermodynamics of irreversible processes and allows to take into account phenomena on opening and closure of cracks under cyclic loading for concrete (Figure 5.a). Quantification of damage distinguishing tension and compression through the corresponding two damage variables is a very interesting feature for the seismic analysis of a structure. The results obtained with this model in previous numerical simulations of structure under dynamic loading have also shown its good performance [5]. The model's general formulation is tridimensional (3D), but only the uniaxial (1D) version is used herein. The mechanical properties are fixed considering a compressive strength of 25 MPa measured in situ, tensile strength of 2 MPa calculated based on EC8, Young's modulus of 30 GPa and a poisson's ratio of 0.17.

The behavior of steel is represented by the modified model of Menegotto-Pinto [14] (Fig. 5.b). This uniaxial cyclic law reproduces a kinematic hardening and the buckling of the bars in compression when the transverse ones or stirrups are not sufficiently brought closer. Due to the lack of data about the steel properties used in the past when the tower was built, we supposed that the steel is smooth round of construction whose yield stress is supposed 235 MPa, Young's modulus about 190 GPa and a poisson's ratio of 0.3.

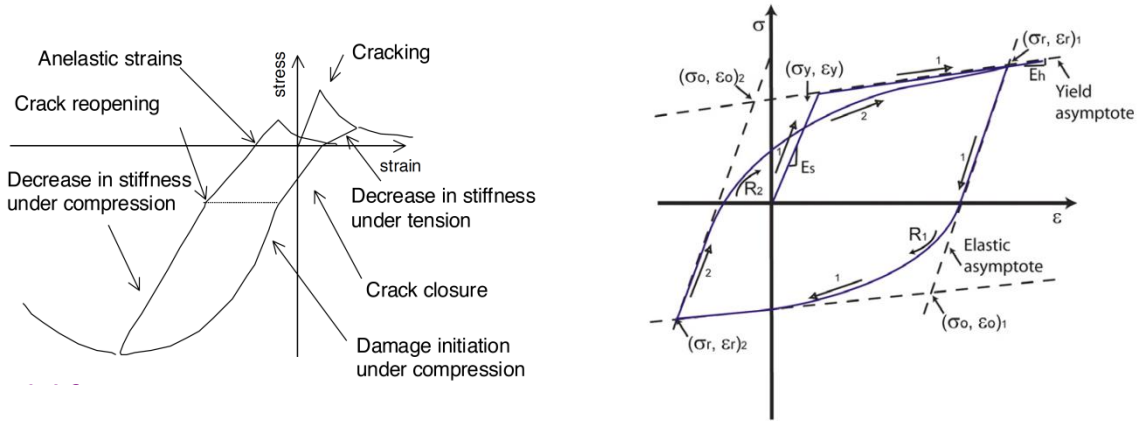


(a) (b)

Figure 5: (a) La Borderie's 1D cyclic model, (b) Menegotto–Pinto's 1D cyclic model

### 3.3 Modal analysis using experimental data from ambient noise

The tower has been monitored by nine accelerometric stations (Figure 6). Four have been placed at the base of the structure, four additional at the level of the visitor platform and another one at the top of the tower. This in-situ modal analysis campaign has been performed on the Perret Tower in 2011 by the French company Miage Sarl by mean of the ambient noise technique [4]. The experimental results are provided into the table 1.

| **Modes** | **EW direction f (Hz)** | **NS direction f (Hz)** |
|---|---|---|
| 1st longitudinal | 0.81 | 0.75 |
| 2nd longitudinal | 2.88 | 2.56 |
| 3rd longitudinal | 4.88 | 4.69 |

Table 1: Experimental modal analysis of the Perret tower: resonance frequencies in the different directions using the FDD method with ambient noise.

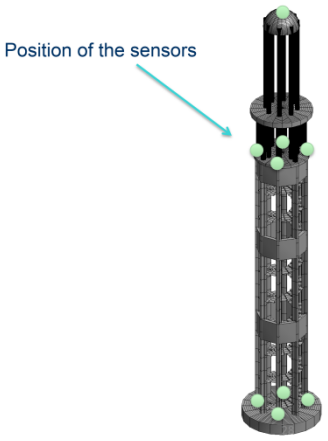


Figure 6: Positions of the accelerometric stations used in the ambient noise in-situ measurements

### 3.4 Numerical modal analysis

The results of the modal analysis carried out by taking into account only the structural parts of the tower (eight columns and three ring-shaped shear walls) are provided in table 2. The first three modes (Figure 7) correspond to bending effect. The results show that the numerical fundamental mode frequency is congruent with the value measured in-situ. However, the second and third modal frequencies obtained numerically are higher than in-situ values. This can be due to the numerical section rigidity which is higher than the reality due to the assumptions of the infinitely stiff three ring-shaped shear walls. By calculating the modal participation factor of the first 4 modes, we found that the fundamental mode is not predominant by large percentage (57.1%) as in the case of regular structures, and at the same time the higher modes have an important modal participation. The sum of modal participation factors for the first 4 modes is about 90%. This is due firstly to the non-uniform repartition of masses along the height of the structure which is heavier at the base than at higher levels, and secondly to the infinitely stiff braces in the model which promote the formation of bends and consequently activating the higher modes.

| **Modes** | **Numerical f (Hz)** |
|---|---|
| 1st longitudinal | 0.78 |
| 2nd longitudinal | 3.44 |
| 3rd longitudinal | 7.81 |

Table 2: Numerical modal frequencies

A sensitivity analysis has been carried out by [3] in order to identify the most accurate numerical model to be used for the Perret tower. It allowed to better understand the contribution to the global stiffness given by the "secondary" structural components and mainly the screen walls. The numerical results showed that taking into account the screen walls allows to match the in-situ analysis results, with high accuracy. Although, the severe conditions of degradation of these decorative elements authorize to hypothesize, for them, a low-strength and fragile behavior under true seismic loading




Figure 7: Representation of the three first fundamental modes of the Perret tower

### 3.5 Non-linear temporal dynamic analysis

The main idea of the study is to simulate the effects of a possible earthquake on the tower. Eurocode 8 spectrum has been used to calibrate the accelerograms assumed acting in 3 directions (Figure 8). Three difference sets of accelerograms have been used to have a better idea of the tower response. These signals have been artificially generated by the ISTerre (Institut des sciences de la terre) in Grenoble.

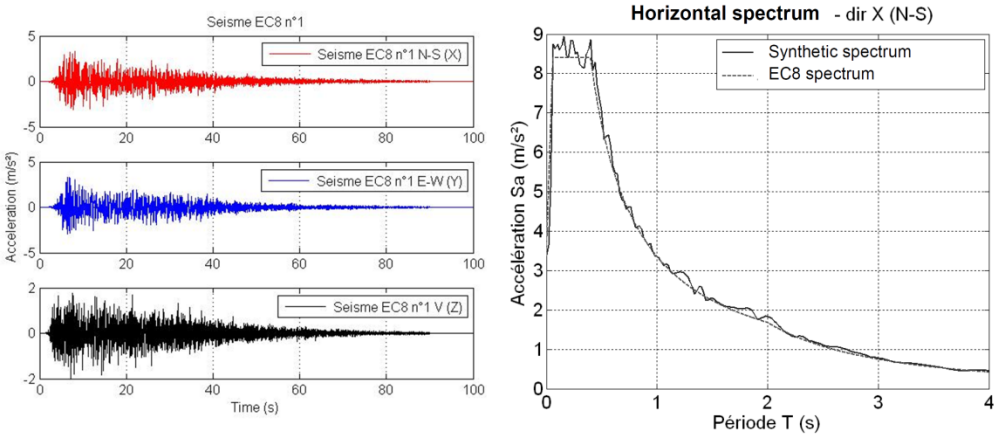


Figure 8: Set of accelerograms and spectrum of the X ones compared to the EC8 spectrum required

The amplitude of horizontal displacements of the numerical model of the Perret tower subjected to the EC8 earthquake in the EW direction reaches 20 cm while vertical displacements are negligible (< 6 mm) (Figure 9). In terms of solicitations at the base of the structure, the maximum shear force is 3087 KN and the maximum bending moment is 94390 KN.m.

Under the effect of the tri-directional earthquake the behaviour of the structure becomes nonlinear. Figures 10,11 and 12 show the results of numerical analysis in terms of damage and plastic strain in the steel rebars. Specifically, the behaviour of structure is mainly of flexion type, without adverse effects of torsion. This confirms that multi-fibre Timoshenko beams can be used.

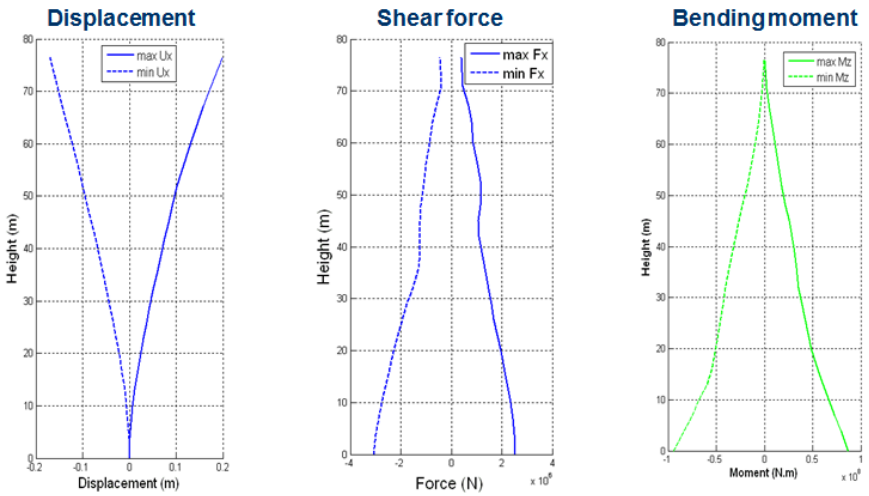


Figure 9: Non-linear temporal dynamic analysis results

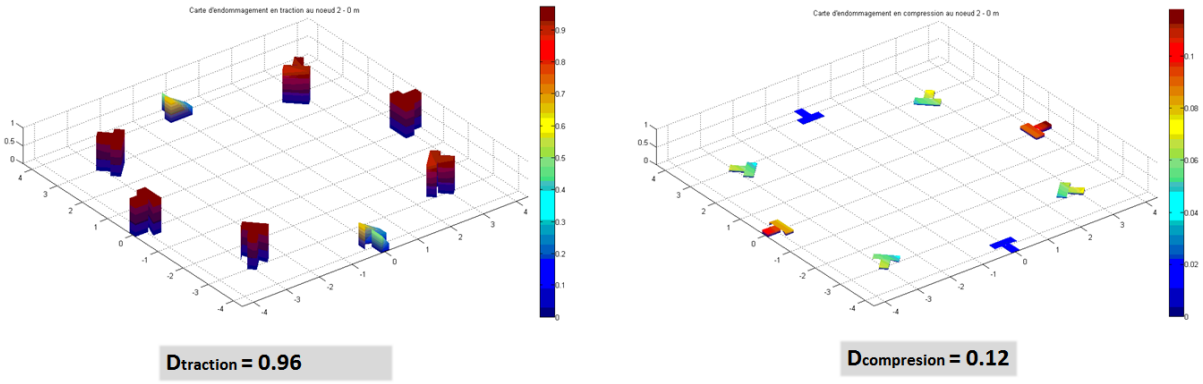


Figure 10: Tensile and compressive damages at 0 m level

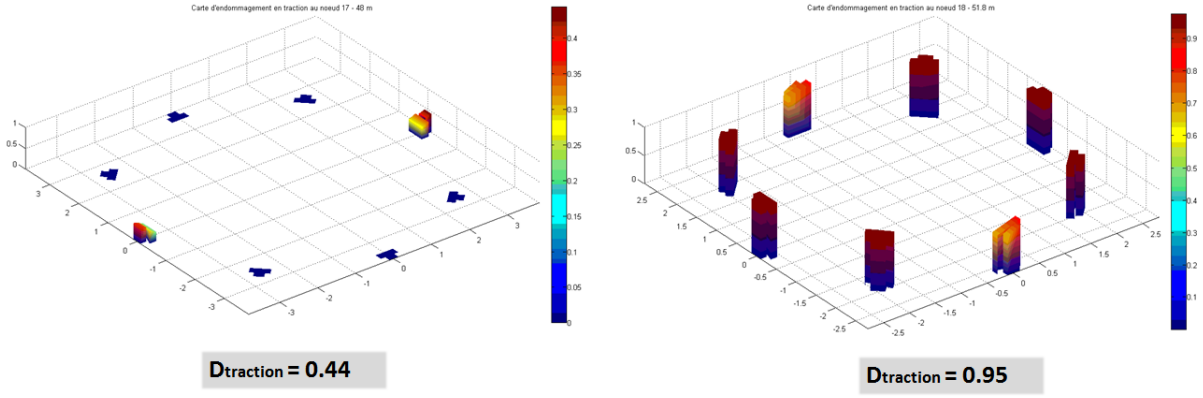


Figure 11: Tensile damage at 50.9 m (left) and 51.8 m (right) levels

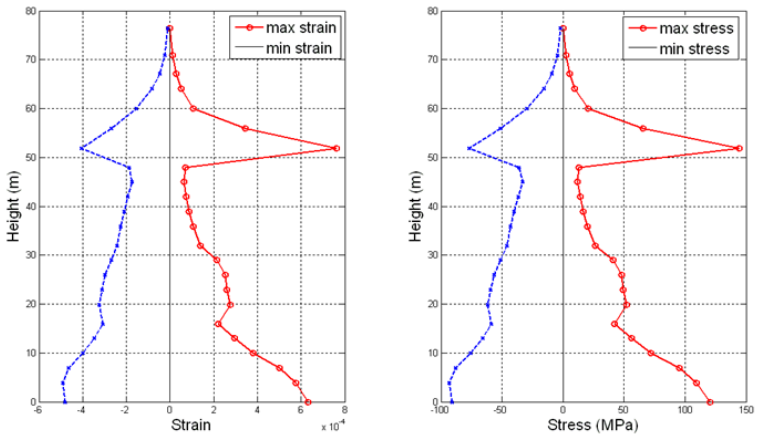


Figure 12: Repartition of maximum and minimum stresses and strains of rebars along the height of the tower

The objective of this work is the numerical evaluation of structural disorders which will be used to quantify the level of global damage of the structure. In other term, the damage is defined as irreversible degradations resulting from a dynamic stress modifying the later behavior of the structure. Within the framework of a reinforced concrete structure, such as Perret tower, whose dynamic behavior is expressed primarily in bending, the concept of damage relates to the cracking of the concrete in traction, spalling of the concrete in compression and the plasticization of the steel reinforcements, the three aspects being closely interrelated. With the numerical tools used, we have indicators of damage (damage variable in the sense of damage mechanics).

The damage in traction of concrete leads to the dissipation of energy, which can influence the behavior of the structure. Thus, the study of this damage brings an indication on the dynamic operation of the structure. A chart of damage makes it possible to visualize the damaged zones corresponding to a strong localization of the deformations "cracking of concrete". Those concentrate at the base of the tower and at the level of the discontinuity of section at 51.8 m. The maximum damage in traction is about: 0.96 at the base (Figure 10), 0.44 at 50.9 m just before the discontinuity (Figure 11) and 0.95 just after the discontinuity (Figure 11). We conclude that the critical zone at 51 m is strongly damaged in traction.

The main risk of the damage of the concrete in compression is related to spalling which induces the ruin by buckling of the steel reinforcements. However, this kind of risk is not observed on the structure of Perret tower as the maximum compressive is at the base and its value (0.12) is low (Figure 10).

By looking to Figure 12, we find that there is no plastification of steel rebars. The maximum stress and strain values are localized at the level of the section's discontinuity (51m) where the maximum stress is 145 MPa which is less than the yielding stress value (235 MPa), as for the maximum strain 0.76‰ which is less than the value of yielding stress (1.2‰). Therefore, the steel behavior remains in the elastic domain with no yielding,

### 3.6 Pushover analysis

The purpose of the pushover analysis is to assess the structural performance by estimating the strength and deformation capacities using static, nonlinear analysis and comparing these capacities with the demands at the corresponding performance levels. Traditionally, conventional pushover method has been used and implemented in design codes.

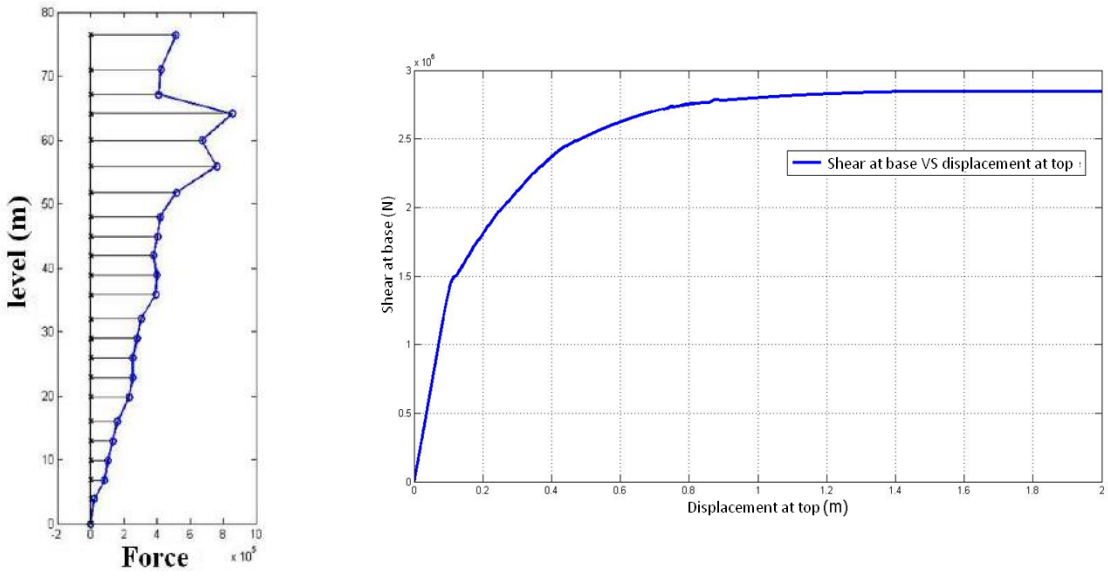


(a) (b)

Figure 13: Pushover analysis for the fundamental mode of Perret tower (a) lateral force distribution (b) capacity curve

Traditional pushover analysis is based on the assumption that the dynamic response of the MDOF (Multi-Degree-Of-Freedom) system is determined by a single mode only and that the shape of that mode is constant, throughout the time-history, regardless of the level of deformation. The response of the structure is supposed controlled by the first mode of

vibration and mode shape, or by the first few modes of vibration. The structure is subjected to a lateral load that is equivalent approximately to the relative inertia forces generated at the locations of substantial masses such as floor levels (Figure 13.a). The outcome of the analysis is the global force-displacement curve or capacity curve of the structure (Figure 13.b). This capacity curve provides valuable information about the response of the structure because it approximates how it will behave after exceeding its elastic limit.

The plateau of the capacity curve is reached for an asymptote corresponding to a value of shear at base about 2800 KN. This plateau corresponds to the mechanism of plastification which appears in the structure by several aspects like cracking of the concrete, plastification of steel and apparition of plastic hinges.

Secondly, the capacity curve is transformed to the ADRS (Acceleration Displacement Response Spectrum) (Figure 14), and an iteration process must be carried to find the performance point of the structure which corresponds to the equality between the capacity and demand ductility of the structure

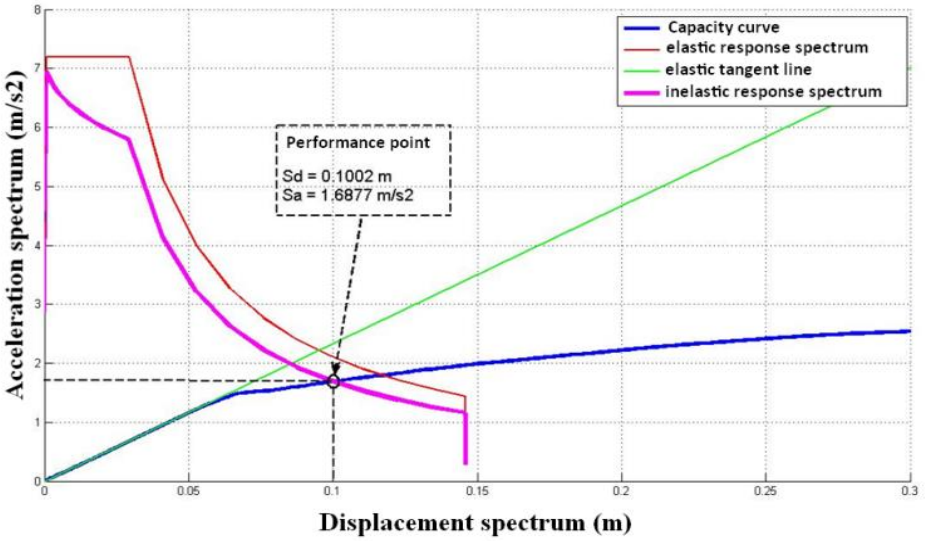


Figure 14: Pushover analysis of Perret tower: Finding the performance point of the structure

Table 3 shows the Pushover analysis results. By comparing the obtained values with those obtained in temporal dynamic analysis, we find that the results are not accurate especially in terms of shear force where the error is important ($\approx$ 46 %). That means that carrying out pushover analysis for the fundamental mode only is not sufficient to provide accurate results and good estimation of dynamic behavior by an alternative static pushover approach. It can be explained also by the fact that the modal participation factor of the first mode is not high sufficiently (57 %) to govern the dynamic response of the tower. In other terms, higher modes are activated during the dynamic process and need to be taken into account during pushover analysis. In the following, a non-linear multimodal pushover analysis will be presented.

| Displacement at top (cm) | Shear force at base (KN) | Bending moment at base (kN.m) |
|---|---|---|
| 16.22 | 1661 | 80332 |

Table 3: Pushover mode 1 – values of top displacement and solicitations at the base of the tower

### 3.7 Non-linear multimodal pushover analysis

An improved non-linear multimodal pushover analysis method is presented to incorporate contributions of multiple modes and the effects of their interactions to the responses. The key step for the method is to obtain and equivalent seismic force for the important vibration modes. After launching pushover analysis for each mode apart, the results of different analysis must be combined to take into account the interactions between the responses. The combination is based on the SRSS method (Square Root of the Sum of the Square):

$$u_i^{SRSS} = \sqrt{\sum_{j=1}^{n} u_{i,j\ max}^2} \quad (1)$$

This formula can be applied for all variables such as displacements, forces and moments. The obtained results are shown in table 4.

| | **Displacement at top (cm)** | **Shear force at base (kN)** | **Bending moment at base (kN.m)** |
|---|---|---|---|
| **Combining 2 modes** | 17.04 | 1877 | 80353 |
| **Combining 3 modes** | 17.22 | 2219 | 83930 |
| **Combining 4 modes** | 17.23 | 2305 | 84000 |

Table 4: variation of displacement at top and solicitations at base with the number of modes included in the multimodal pushover analysis

Table 4 shows that by increasing the number of modes combined in multimodal pushover analysis, the values of displacement at top and solicitations at the base become closer to those obtained by the non-linear temporal dynamic analysis. However, the error still important in terms of base. By comparing the values of displacements, we found that 17.23 cm (value obtained by multimodal pushover analysis) represents about 85% of the value obtained by dynamic analysis (20 cm). This value was determined by considering the combination of the first 4 modes which have a modal participation of 90%. This difference between values can be interpreted by the phenomenon of damage evolution of the structure. The structure damage increases with the evolution of dynamic process under seismic loading, which can influence the dynamic characteristics of the structure (modal frequencies, modal shapes).

### 3.8 Effect of damage on the dynamic characteristics of the structure

The dynamic analysis is a complex phenomenon including several mechanisms (yielding, opening and closure of cracks...). The damage of the concrete in traction increases with time under seismic effect. By investigating the evolution of the tensile damage of concrete fibers during the non-linear dynamic temporal simulation, we found that in a specified phase (between 5s and 7.5s) (Figure 15) the damage of concrete fibers increases by an important rate. After carrying out modal analysis at each instant of dynamic process, we draw the evolution of modal frequencies of the first 4 modes (Figure 15), and we conclude that at the same phase there is a falling of the values of frequencies. In this matter, at each instant, we created a numerical model of the tower and we considered that the new value of Young's modulus of is affected by the tensile damage value $D_1$:

$$E_{damaged} = (1 - D_1)E_{initial} \quad (2)$$

Figure 15 shows clearly that the modal frequencies decreased by a percentage of 35% during the evolution of dynamic process, that's prove the effect of damage of concrete on the modal frequencies of the studied structure.

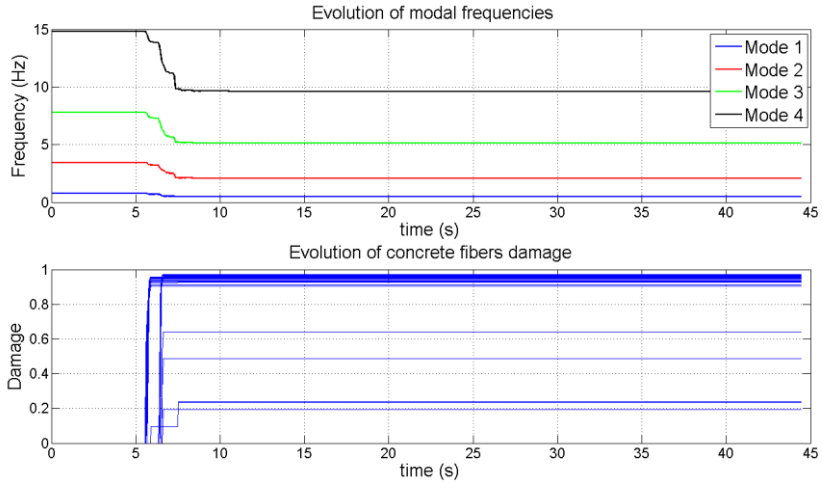


Figure 15: Evolution of damage in traction of concrete and of the modal frequencies during the non-linear dynamic simulation

### 3.9 Adaptive pushover analysis of Perret tower

Although conventional pushover analysis provides crucial information on response parameters of the structure, this method is not exempt from some limitations such as the inability to include progressive stiffness degradation. Therefore, the need for an adaptive procedure that overcomes the noted deficiency. The adaptive pushover analysis procedures are mostly concerned with an appropriate estimation of the force vector that is going to 'push' the structure at each static force increment. The monitoring of the change in the incremental force vector could ensure that the stiffness degradation or strength deterioration of the structure is counted to be more realistic than conventional nonlinear static analysis. Once the new lateral force distribution has been determined, the remaining steps of the adaptive pushover analysis follow those of the conventional.

After executing multimodal pushover analysis (for the first five modes) and taking into account the new distribution of lateral forces by considering the modal shapes of the damaged structure, we found the new values of displacement at top and solicitations at base (Table 5). We could conlude that the value of displacement at top became closer to those obtained by the temporal dynamic analysis. But in terms of shear force and bending moment at base of the tower, the differences between the corresponding dynamic and static pushover results are still important. This can be explained by the inability of adaptive pushover analysis used in the analysis to take into account the formation of plastic mechanism in the structure during dynamic process under seismic loading.

| | **Dynamic analysis** | **Adaptive pushover** |
|---|---|---|
| **Displacement at top (cm)** | 20 | 18.76 |
| **Shear force at base (kN)** | 3087 | 2490 |
| **Bending moment at base (kN.m)** | 94390 | 85616 |

Table 5: Comparison of the results of dynamic and static adaptive pushover analysis

## 4 CONCLUSIONS

The main objectives of this research were (i) to investigate numerically the seismic vulnerability of the Perret tower by mean of simplified 3D model and compare the linear behavior results with those obtained in-situ, (ii) to explore the critical structural zones of the tower which are the most affected by an earthquake, (iii) to discuss and access different methodologies for dynamic behavior of the tower like non-linear temporal dynamic analysis and pushover methodology, (iv) to explore the deficiencies presented in the conventional pushover method which is a practical engineering tool, and (v) to evaluate the level of damage of the tower under an earthquake.

The simplified 3D modeling used gives a good estimation of the behavior of the Perret tower in terms of solicitations and displacement. Under seismic loading, the concrete is almost cracked at the base and the level of section discontinuity (51m) with no yielding of steel which supports the efforts elastically.

Pushover analysis can provide good results as a static alternative of dynamic analysis. In terms of displacements and solicitations, the obtained results are still little bit far from the ones obtained by non-linear temporal dynamic analysis. It can provide an insight into the structural aspects which control performance during severe earthquakes, and data on the strength and ductility of the structure which cannot be obtained in an elastic analysis.

Furthermore, the non-linear static procedure based on pushover analysis is restricted with a single or few modes response. Then it is valid for low-rise buildings where the behavior is dominated by fundamental vibration mode. It is required to take into account of higher modes effects in pushover analysis of tall buildings. Moreover, conventional pushover procedure is based on a very restrictive assumption, i.e. invariant lateral force distribution without considering progressive stiffness degradation.

Therefore, the future research should continue developing the adaptive pushover analysis that overcomes the deficiencies above cited. It should take into account the structural weakness which may be generated when the structure's dynamic characteristics change after the formation of the first local plastic mechanism. The redistribution of inertia forces due to structural yielding should be investigated also in the adaptive procedure.

## REFERENCES

[1] C. Desprez, P. Kotronis, J. Mazars, Seismic vulnerability assessment of a RC structure before and after FRP retrofitting. *Bulletin of Earthquake Engineering*, Springer Verlag, 13 (2), pp.539-564, 2015.

[2] M. Zeinoddinia, A. Dabiria, Seismic Analytical Model for Retrofitted Old Reinforced Concrete Structures. *The 2nd International Conference on Rehabilitation and Maintenance in Civil Engineering*, Procedia Engineering, 54, 188 – 206, 2013.

[3] M. De Biasio, S. Grange, F. Dufour, The role of model calibration in seismic FE analysis: the case study of an old reinforced concrete structure by using ambient vibration noise modal analysis, *Proceedings of 15th World Conference on Earthquake Engineering*, Lisbon, Portugal, Paper 3547, 2012.

[4] C. Michel, P. Gueguen, S. El Arem, J. Mazars, P. Kotronis, Full-scale dynamic response of an RC building under weak seismic motions using earthquake recordings, ambient vibrations and modeling. *Earthquake Engineering and Structural Dynamics*, 39:419–441, 2010.

[5] X. H. Nguyen, J. Mazars, P. Kotronis, Simplified 3D modelling of dynamic behaviour of reinforced concrete structures, *Revue européenne de génie civil*, vol 10, no 3, p 361-373. 2006.

[6] Eurocode 8, *European norm on "seismic structural calculations",* NF EN 1998-1, 2005.

[7] A. Takahashi, S. Tago, A. Ilki, T. Okada, Seismic capacity evaluation of existing reinforced concrete buildings in turkey (effect of retrofit), *13th World Conference on Earthquake Engineering*, Vancouver, B.C., Canada August 1-6, Paper No. 3477, 2004.

[8] F. C. Filippou, M. Constantinides, FEDEASLab Getting Started Guide and Simulation Examples, *Technical Report NEESgrid-2004-22*, 2004.

[9] P. E. Pinto, Assessment and redesign of existing structures: current developments in Europe. *Proceedings 11th World Conference on Earthquake Engineering*, Acapulco, Mexico. Paper no 2123. New York: Elsevier Science, 1996.

[10] E. Spacone, F. C. Filippou, F. Taucer, Fibre beam-column model for non-linear analysis of R/C. frames. Part 1: Formulation. *Earthquake Engineering and Structural Dynamics*; 25:711–725, 1996.

[11] A. Corsanego, Performance indices and field seismic capacity assessment. *Proceedings 10th European Conference on Earthquake Engineering*, Vienna, Austria. Vol 2. Rotterdam: Balkema. 2715–2721, 1994.

[12] C. La Borderie, J. Mazars, G. Pijaudier-Cabot, Damage mechanics model for reinforced concrete structures under cyclic loading. In: Gerstle W, Bazant ZP, editors. A.C.I, vol. 134, p. 147–172, 1994.

[13] J. Guedes, P. Pegon, A. V. Pinto. A fibre Timoshenko beam element in Castem 2000. *Special Publication No 1.94.31 ELSA*, European Joint Research Center (Ispra, Italy), 1994.

[14] M. Menegotto, P. Pinto, Method of analysis of cyclically loaded reinforced concrete plane frames including changes in geometry and non-elastic behaviour of elements under combined normal force and bending. *IABSE Symposium on resistance and ultimate deformability of structures acted on by well-defined repeated loads, final report*, Lisbon, Portugal, 1973.

COMPDYN 2017
6th ECCOMAS Thematic Conference on
Computational Methods in Structural Dynamics and Earthquake Engineering
M. Papadrakakis, M. Fragiadakis (eds.)
Rhodes Island, Greece, 15–17 June 2017

# SEISMIC DESIGN OF ABOVEGROUND STORAGE TANKS CONTAINING LIQUID

**Martin Sivy**[1], **Milos Musil**[1]

[1] Slovak University of Technology, Faculty of Mechanical Engineering
Namestie slobody 17, 812 31 Bratislava, Slovakia
e-mail: {martin.sivy, milos.musil}@stuba.sk

**Keywords:** Liquid Storage Tanks, Earthquake, Seismic Vulnerability, Seismic Characteristics, Simplified Models, Eurocode 8.

**Abstract.** *Liquid storage tanks are important components of liquid transmission and distribution systems and should be properly designed to withstand dynamic loadings which can take several forms. One of them is the investigation of tanks subjected to a seismic excitation. During seismic activity, a specific interaction between the tank and the liquid occurs. It is expressed as a vibration of the tank, its walls and contained liquid. The impulsive (lower) portion of the liquid moves in unison with the structure while the convective (upper) portion represents the free surface moving against a wall which results in a sloshing effect. The procedure for the design of tank-liquid systems for earthquake resistance is covered in various international and national standards. The paper deals with the seismic analysis of the aboveground vertical liquid storage tanks of circular cross section with different slenderness parameters (from broad to tall tanks) intended to compute the dynamic properties (natural frequencies and respective modes of oscillation) and the response of the flexible tank – liquid system to seismic loading using the response spectrum method. The paper also focuses on the comparison of dynamic properties of the tank-liquid system when it is resting on a rigid or flexible foundation. For tanks supported on softer soils, the dynamic response may be significantly different from those supported on rigid foundations. In addition to the seismic analysis, the paper is dedicated to comparing the acquired results from analyses computed by FE method (in ANSYS Multiphysics) with the results from analytical calculations of a tank containing liquid introduced in Eurocode 8.*

## 1 INTRODUCTION

In contemporary global industrial development and improvement of production efficiency, emphasis must be given to the improvement of safety in facilities using new and advanced technical resources that will ensure effective prevention of large industrial accidents. In a broader context, the word "safety" can be expressed by the term loss prevention so as to prevent the loss of human life and in doing so, also ensuring the integrity of property, production and the environment [1].

There are some quantitative and qualitative methods in hazard identification (HAZOP, DOW index, fault tree analysis, selection method, etc.) to prevent negative consequences of transmission and processing systems (e.g., heat exchangers, evaporators, drying devices, cooling system, etc.) in ordinary operation (more introduced in [2]).

On the other hand, the systems must withstand external loadings of different nature (static, dynamic) as well. Requirements for the suppression of possible loading in future operation must be reflected in the design process of the device which are mostly included in various international, national or company standards and/or guidelines. One of the most critical external events affecting safety and operation efficiency of systems is seismic excitation (e.g., seismic testing of structures is described in [3]).

Large capacity tanks and vessels are one such device which is assessed in terms of vulnerability against seismic effects. Tank-liquid systems are commonly used in the storage of various liquids in various sectors of industry (e.g., nuclear, chemical, food, etc.). Seismic analysis of liquid storage tanks requires special considerations which take into account time-dependent hydrodynamic forces and pressure exerted by the liquid on the tank wall and bottom. Knowledge of these hydrodynamic effects is essential in the seismic design of tanks. Inadequately designed tanks in the past exposed to strong ground motions led to damage, ruptures and failures of tank accessories. Furthermore, when tanks store flammable or toxic liquids, disastrous effects, such as uncontrolled fire, explosion or toxic dispersion arose [2]. Therefore, tanks must be designed to maintain their integrity before, during and after a seismic event to prevent negative future effects.

Based on experimental research and analytical results of G. W. Housner [4, 5, 6], A. S. Veletsos [7, 8], P. K Malhotra [9] and others, different provisions for seismic resistance of different tank-liquid systems (e.g., aboveground, buried, elevated, etc.) have been developed. Some of them were adopted in international codes and guidelines dedicated to a seismic resistance of these systems, e.g., AWWA, ACI, API, Eurocode 8 and NZSEE.

## 2 BASIC CONCEPT

Evaluation of hydrodynamic forces due to lateral base excitation requires modeling and dynamic analyses of the tank-liquid systems. The complexity of the investigated liquid storage tanks may be simplified by mechanical models. The most used equivalent mechanical model is the one proposed by G. W. Housner [4] which converts investigated tank-liquid system into a spring-mass system. Housner's model or eventually its modification is introduced in the codes aimed at the structural design for earthquake resistance (e.g., in Eurocode 8 [10]).

This mechanical analogy assumes that the contained liquid can be divided into two regions. The first, impulsive portion of the liquid moves in unison with the tank as a rigid body and induces impulsive hydrodynamic pressure on the tank wall and its base. In the equivalent model, it is replaced by an impulsive mass $m_{\mathrm{i}}$ rigidly attached to the tank walls at a height $h_{\mathrm{i}}$ ($h_{\mathrm{i}}{}'$). A second or convective portion of the liquid represents the free surface which undergoes sloshing motion and exerts convective hydrodynamic pressure on the tank wall and base. In the simplified model, this zone is substituted by an infinite number of convective masses $m_{cn}$

attached to the tank wall at height $h_{cn}$ ($h_{cn}'$) by a spring of stiffness $k_{cn}$. Each convective mass represents the effective liquid mass that oscillates in each particular slosh mode [11].

Parameters introduced in Fig. 1 like liquid masses and heights are used in basic seismic characteristics such as base shear, overturning moment and hydrodynamic pressure. Procedure for parameters calculation for cylindrical storage tanks can be found e.g. in [10, 12].

Mechanical models were first developed for tanks with rigid walls which were modified for short and slender tanks. Subsequently, Haroun and Housner [6] and Veletsos [7] developed models for flexible tanks. Malhotra [9] further simplified models proposed by Veletsos [7]. Observing and comparing the parameters of the rigid and flexible tank-liquid systems it was concluded there is no significant difference in the results obtained from these models [13].

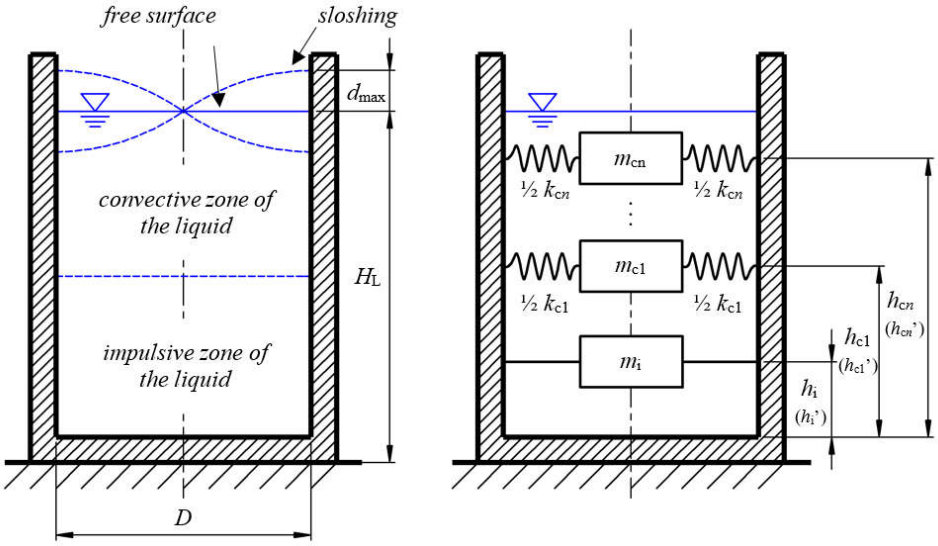


Figure 1: Equivalent spring-mass mechanical model

In addition to spring-mass models, other equivalent models were developed in which the convective liquid can be substituted by a system of simple pendulums, each of mass $m_{cn}$, and length $l_{cn}$. For observing nonlinear phenomena (e.g. at sloshing frequencies), the aforementioned linear models do not provide an adequate representation of the liquid free-surface. Therefore, models capable of describing relatively large amplitudes (spherical pendulum model) or strongly nonlinear motion (pendulum describing impacts with the tank walls) must be employed [12].

Analytical methods are suitable only for the simplest systems. For complex structures, analytical approach may be insufficient and inaccurate. Therefore, numerical approaches have been developed. The most widely used is the method based on finite elements (FEM). This interaction can be investigated by applying elements based on different formulation, such as the added mass concept, Lagrangian or Eulerian methods. Using fluid elements, a definition of fluid-structure interaction (FSI) at interface between structure and fluid is required to couple their displacements.

## 3 SEISMIC RESPONSE OF ABOVEGROUND LIQUID STORAGE TANKS

The paper is focused on the seismic analysis of aboveground vertically oriented liquid storage tanks with circular cross section and differing slenderness parameters $\gamma$ (liquid height to tank radius – 0.5, 1 and 2). The investigated models are of radius $R$ (5 m), wall thickness $t$ (5e-3 m) and heights $H$ (4, 6 and 11 m). The tanks are filled with liquid (water) with free surface

heights $H_L$ (2.5, 5 and 10 m). The aim is to calculate dynamic properties such as impulsive and convective frequencies and respective modes of oscillation. Subsequently, a seismic response to a given earthquake loading is calculated using a response spectrum method.

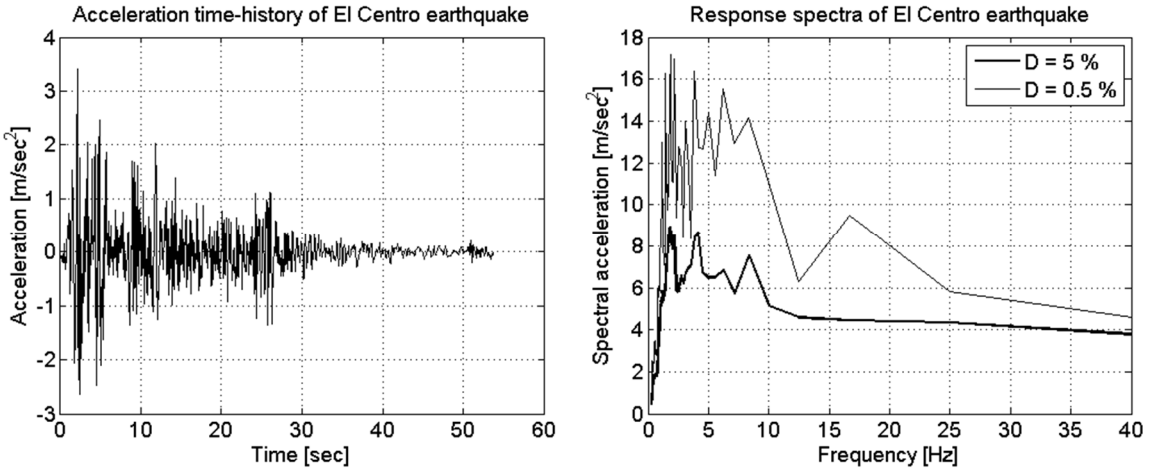


Figure 2: El Centro earthquake

For the seismic input, data recorded from the El Centro earthquake (1940) with a PGA of 3.417 m/sec$^2$ at 2.14 sec was used. Acceleration time-history of the earthquake and its response spectra for proportional damping of 0,5 % (liquid) and 5 % (structure) are presented in Fig. 2.

### 3.1 Impulsive vibration

Impulsive mode of oscillation corresponds to the lateral mode of a tank-liquid system. It refers to a situation when the tank oscillates in unison with its content (liquid). The lateral force acting on the tank depends on the respective impulsive frequency. Tank flexibility affects the impulsive component of hydrodynamic effects, hence impulsive frequency of the assumed system as well. In Eurocode 8, there is a procedure for the determination of impulsive frequency at which this unfavourable response occurs. The equation was proposed by Malhotra [9] and is expressed as

$$f_i = \frac{1}{C_i}\frac{\sqrt{t/R}\sqrt{E}}{\sqrt{\rho_L}H_L} \tag{1}$$

where $\rho_L$ is the density of the liquid, $E$ is Young's modulus of elasticity of the tank material and $C_i$ represents coefficients for respective slenderness parameter $H_L$ / $R$ which are presented e.g. in [9, 10].

| Slenderness parameter $\gamma$ | Eurocode 8 | ANSYS Multiphysics |
|---|---|---|
| 0.5 | 23.68 Hz | 21.06 Hz |
| 1 | 14.41 Hz | 14.20 Hz |
| 2 | 7.38 Hz | 7.28 Hz |

Table 1: Comparison of impulsive natural frequencies

Tab. 1 presents calculated impulsive natural frequencies for investigated tank-liquid systems by analytical approach (Eurocode 8) and compared by numerical computations in ANSYS. Fig. 3 represents computed unfavourable responses for various tanks containing liquid at natural frequencies listed in Tab. 1.

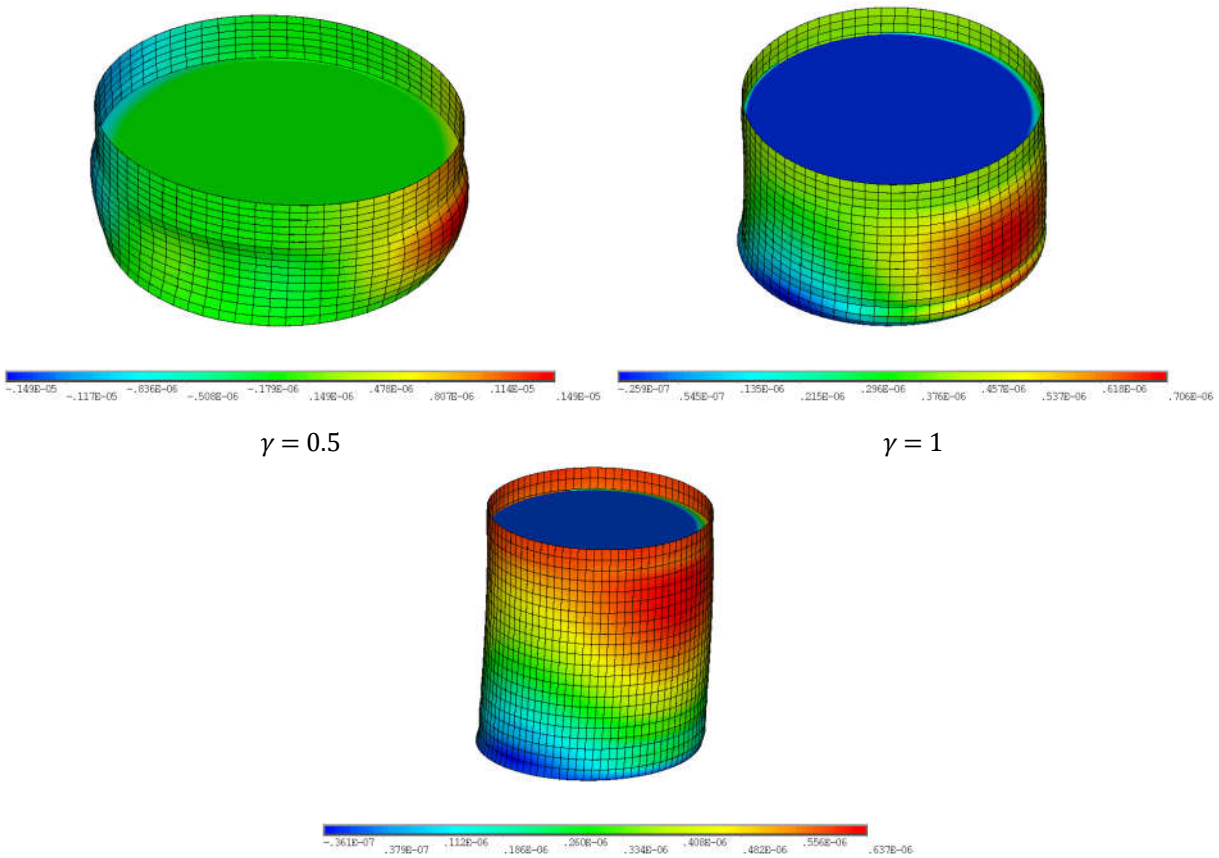


Figure 3: Impulsive modes of oscillation

For tanks supported on softer soils, the dynamic response may be significantly different from those supported on the rigid foundation. In addition to the lateral component of motion, the foundation motion may include a rocking component. If the response of the structure is dominated by its impulsive mode, the soil-structure interaction effects may result in a decrease in the natural impulsive frequency of investigated tank-liquid system. This decrease depends on the flexibility of the foundation soils.

| Slenderness parameter $\gamma$ | ANSYS Multiphysics |
|---|---|
| 0.5 | 19.40 Hz |
| 1 | 9.24 Hz |
| 2 | 3.12 Hz |

Table 2: Impulsive natural frequencies influenced by foundation flexibility

In Tab. 2, impulsive natural frequencies of investigated tank-liquid systems supported on a flexible foundation are presented. In FE analysis, the Winkler's foundation model is used with foundation stiffness of $k = 10\text{e}7\text{N/m}^3$. When comparing results with frequencies from Tab. 1, soil-structure interaction decreased values of original impulsive natural frequencies.

### 3.2 Convective vibration

The upper (convective) portion of the liquid (Fig. 1) does not move as a rigid body with the tank walls but experiences a sloshing motion. Convective effects are associated with oscillations of much shorter frequency than the impulsive effects. These two components are weakly coupled and each effect is insensitive in characteristics of the other.

Convective oscillations can be expressed as a linear combination of the corresponding natural modes of the liquid. Slosh modes of the free surface in a vertical cylindrical vessel of a circular cross-section are usually formulated analytically by the Helmholtz equation. Using polar coordinates, the Helmholtz equation can be expressed as

$$\left(\frac{\partial^2}{\partial r^2} + \frac{1}{r}\frac{\partial}{\partial r} + \frac{1}{r^2}\frac{\partial^2}{\partial \theta^2} + k_m^2\right) S_m = 0 \tag{2}$$

where $k_m$ is a wave number of a respective mode of oscillation and $S_m$ is a function describing the amplitude of the response depending on the location of the oscillating free surface. The solution for each slosh mode of (2) can be expressed by the Bessel function of the first kind

$$S_{n,m} = J_n\left(\lambda_{n,m}\frac{r}{R}\right)\cos n\theta \tag{3}$$

where $J_n$ represents the Bessel function of the first kind and $\lambda_{n,m}$ is the $m$th zero of $J_n'(\lambda_{n,m})$.

The natural frequency of the convective liquid with respective wave number may be calculated as follows

$$f_{\text{c}(n,m)} = \frac{1}{2\pi}\sqrt{\lambda_{n,m}\frac{g}{R}\tanh\left(\lambda_{n,m}\frac{H_\text{L}}{R}\right)} \tag{4}$$

Eurocode 8 standard introduces (4) for calculation of natural convective frequencies but the expression is modified only for modes antisymmetric about the axis of rotation, i.e. modes of oscillation are described by the Bessel function of the first kind and first order.

Fig. 4 shows three selected slosh modes of oscillation which are computed analytically using (4) for the investigated model of the liquid storage tank (with slenderness ratio equal to one) and subsequently compared with sloshing waves computed by FEM in ANSYS.

The natural frequencies corresponding to the selected modes of oscillation are introduced in Tab. 3. Analytically calculated convective frequencies are compared with those obtained from FE analysis.

| Mode of oscillation | Analytical approach | ANSYS Multiphysics |
|---|---|---|
| (1,1) | 0.30 Hz | 0.30 Hz |
| (1,2) | 0.51 Hz | 0.52 Hz |
| (2,3) | 0.70 Hz | 0.71 Hz |

Table 3: Comparison of selected convective natural frequencies

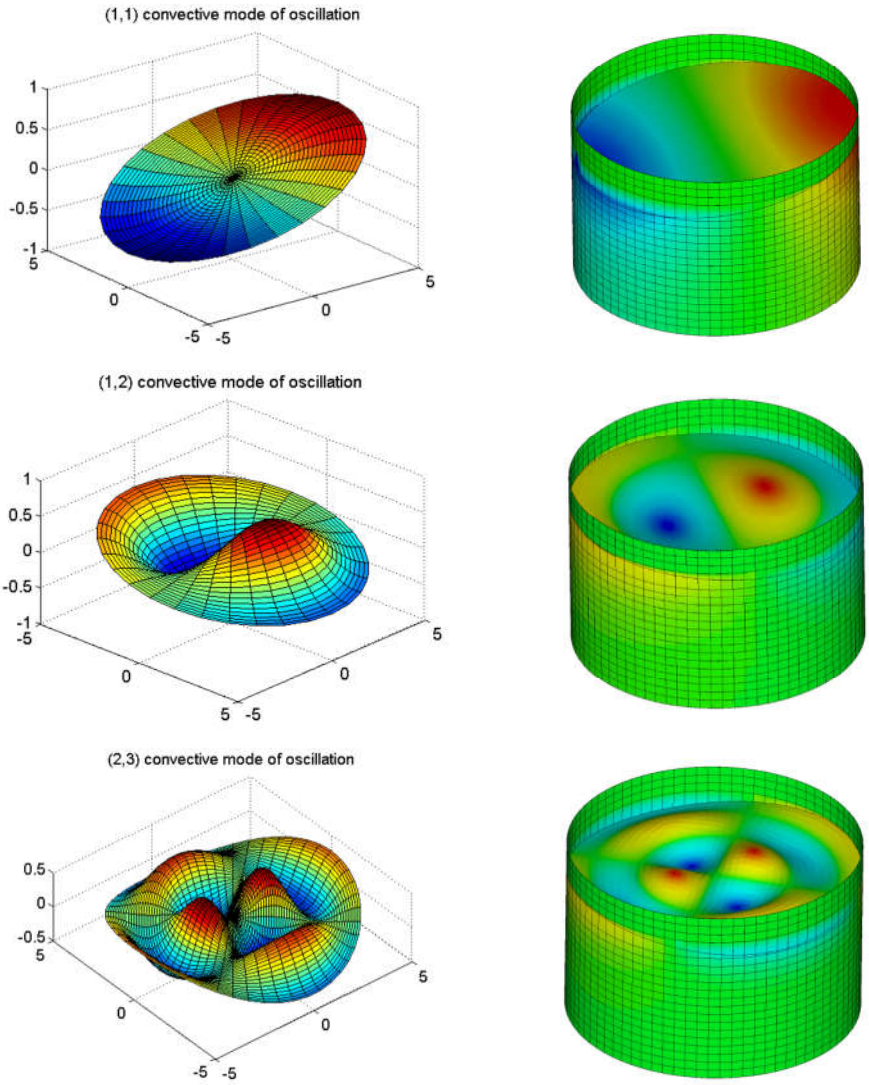


Figure 4: Selected convective modes of oscillation

For most tanks, the first impulsive and first convective modes account for 85–98% of the total liquid mass in the tank. The remaining mass of the liquid vibrates primarily in higher impulsive modes in tall tanks, and higher convective modes for broad tanks [9]. Therefore, only first oscillating frequency and mode is considered for design purposes. Eurocode 8 introduces the expression for the calculation of the first convective frequency in the simplified procedure for fixed base cylindrical tanks.

$$f_c = \frac{1}{C_c\sqrt{R}} \tag{5}$$

where $C_c$ represents coefficients for respective slenderness (e.g., in [9, 10]).

Fig. 5 gives the values of the first convective frequency as a function of the most used slenderness parameters $\gamma$. The figure presents the sloshing frequencies for $\gamma$ assuming constant radii $R$ of the investigated tank (5 m) whilst the liquid heights are changing. As it can be seen, frequencies become almost independent of $\gamma$ (for $\gamma$ larger than about 1). Frequencies show good correlation between analytical and numerical calculations.

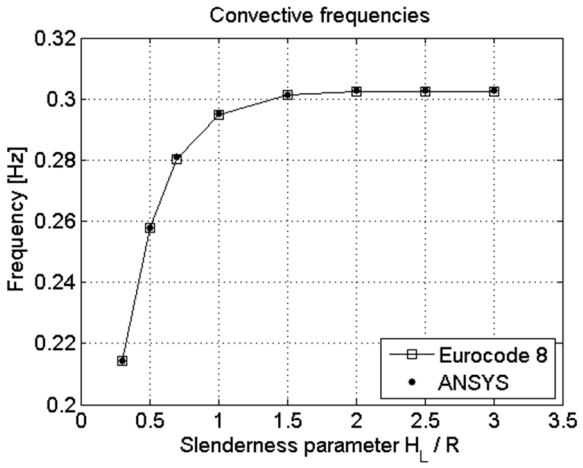


Figure 5: Convective frequencies for various slenderness parameters

When investigating an influence of flexible foundation on convective components, effects of soil-structure interaction are expected to be small due to weak coupling between convective and impulsive components (the convective effects are associated with oscillations of much shorter frequency than those characterizing the impulsive effects) and may be neglected [7].

### 3.3 Sloshing wave height

When investigating open tanks filled with liquid, the maximum vertical displacement of the free liquid surface is observed. Oscillation of the convective liquid in the containers may lead to negative effects, such as deformations of the tank walls (closed tanks) or liquid spilling (tanks without roofs). Therefore, sufficient freeboard between the free surface and the top of the tank must be designed.

The sloshing wave height may be given from the following expression

$$d(r,\theta,t) = R\sum_{n,m=1}^{\infty} \frac{2}{\lambda_{n,m}^2 - 1} \frac{J_n\left(\lambda_{n,m}\frac{r}{R}\right)}{J_n(\lambda_{n,m})} \frac{S_e(f_{c(n,m)})}{g} \cos n\theta \tag{6}$$

where $S_e(f_c)$ is the convective spectral acceleration, obtained from a 0,5 %-damped elastic response spectrum.

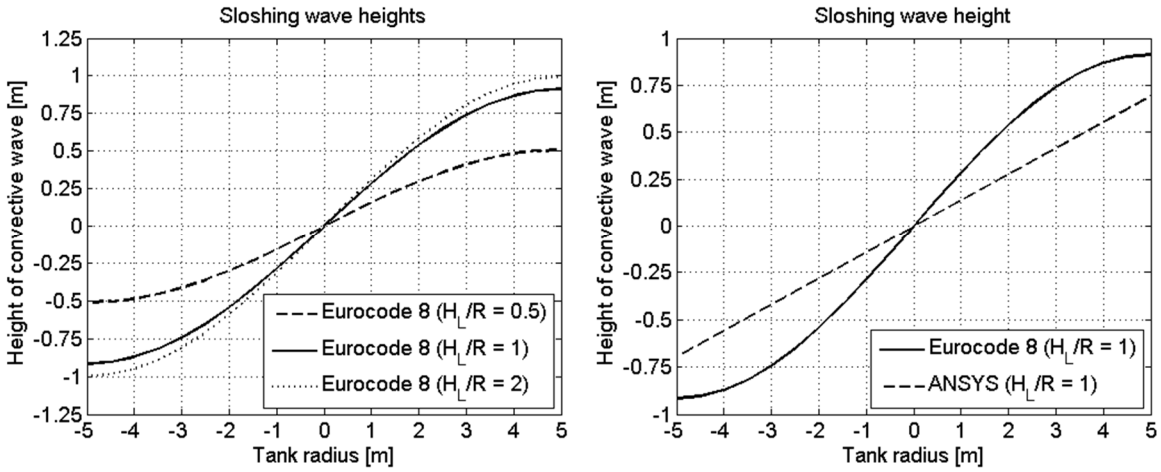


a) b)

Figure 6: Sloshing wave height

In Eurocode 8, the wave height is calculated by assuming only the first mode of oscillation and the procedure is reduced for specifying the maximum height at the tank wall. Peak value of the wave height at the edge may be expressed as

$$d_{\max} = 0{,}84 \ \frac{RS_{\mathrm{e}}(f_{\mathrm{c}1,1})}{g} \tag{7}$$

For calculation of the vertical displacements for tank models, only the first convective mode is considered with spectral acceleration values from the respective response spectrum (Fig. 2). In Fig. 6a surface displacements along tank radius are shown. For the tank of $\gamma$ equal to one, maximum vertical displacement is 0.70 m using (6) or (7) and 0.91 m using ANSYS (Fig. 6b).

### 3.4 Response spectrum analysis

Response spectrum method (spectrum analysis) is a significant method for seismic analysis of structures and equipment. It is mainly used in place of a time-history analysis to determine the response of structures to time-dependent loading. A spectrum analysis is one in which the results of a modal analysis are used with a response spectrum to calculate displacements and stresses in the model. The structures and equipment components are modeled usually as multi-degree-of-freedom systems on the base of finite element method [14].

The modal solution is required because the structure's mode shapes and frequencies must be available to calculate the spectrum solution. The sufficient number of modes characterizing the structure's response in the frequency range of interest must be extracted. The ratio of the effective mass to the total mass greater than 0.9 (more than 90% of the mass is included) is generally considered acceptable [15].

When investigating tank-liquid system using FEM and considering a fluid-structure interaction, the modal analysis uses as the mode-extraction method unsymmetric matrix formulation. If the unsymmetric eigensolver is used, right and left eigenvectors must be computed. The effective mass for the *i*th mode can be expressed as

$$\mathbf{M}_{\mathrm{e}i} = (\mathbf{d}_{\mathrm{s}})^{\mathrm{T}}\mathbf{K}_{\mathrm{s}}\boldsymbol{\phi}_{\mathrm{s}i}^{\mathrm{R}}\frac{(\boldsymbol{\phi}_i^{\mathrm{L}})^{\mathrm{T}}\mathbf{M}\mathbf{d}}{\omega_i^2} \tag{8}$$

where $\mathbf{d}_{\mathrm{s}}$ is the direction vector of the excitation (structural DOFs only), $\mathbf{K}_{\mathrm{S}}$ is the stiffness matrix of the structural part, $\boldsymbol{\phi}_{\mathrm{s}i}^{\mathrm{R}}$ is the *i*th right eigenvector (structural DOFs only).

The equation of motion for the system subjected to the ground motion $\ddot{u}_{\mathrm{g}}(t)$ is written as

$$\mathbf{M}\ddot{\mathbf{u}}(t) + \mathbf{C}\dot{\mathbf{u}}(t) + \mathbf{K}\mathbf{u}(t) = -\mathbf{M}\mathbf{d}\ddot{u}_{\mathrm{g}}(t) \tag{9}$$

where $\mathbf{d}$ is a vector of excitation direction (direction cosines).

The response of the structure is represented in terms of a linear superposition of mode shapes

$$\mathbf{u}(t) = \sum_{i=1}^{n}\boldsymbol{\phi}_i \mathrm{w}_i\,(t) \tag{10}$$

where $\mathrm{w}_i(t)$ are called normal coordinates and are functions of the time variable $t$.

When using the unsymmetric eigensolver, the matrices are unsymmetric. Both left and right normalized eigenmodes are used to decouple the modal equations as follows

$$(\boldsymbol{\phi}^{\mathrm{L}})^{\mathrm{T}}\mathbf{M}(\boldsymbol{\phi})\ddot{\mathbf{w}}(t) + (\boldsymbol{\phi}^{\mathrm{L}})^{\mathrm{T}}\mathbf{C}(\boldsymbol{\phi})\dot{\mathbf{w}}(t) + (\boldsymbol{\phi}^{\mathrm{L}})^{\mathrm{T}}\mathbf{K}(\boldsymbol{\phi})\mathbf{w}(t) = -(\boldsymbol{\phi}^{\mathrm{L}})^{\mathrm{T}}\mathbf{M}\mathbf{d}\ddot{u}_{\mathrm{g}}(t) \tag{11}$$

The participation factor for a given excitation direction, if the unsymmetric eigensolver is used, is defined as

$$\gamma_i = \left(\boldsymbol{\phi}_i^{\mathrm{L}}\right)^{\mathrm{T}} \mathbf{M}\mathbf{d} \tag{12}$$

Equation (11) leads to the modal coordinate equation

$$\ddot{\mathrm{w}}_i(t) + 2\omega_i\xi_i\dot{\mathrm{w}}_i(t) + \omega_i^2\mathrm{w}_i(t) = -\gamma_i\ddot{u}_{\mathrm{g}}(t) \tag{13}$$

In the modal superposition method, (12) is solved to obtain the time histories of the normal coordinates $\mathrm{w}_i(t)$ which with (10) gives the history of the relative displacement vector $\mathbf{u}(t)$.

This concept may be used to apply the response spectrum method to the MDOF structure. If the response spectrum of the given earthquake is known (e.g. acceleration response spectrum) it can be used in the calculating the maximum response of the system. Maximum displacement vector in the *i*th mode can be written

$$\mathbf{u}_{i\max} = \frac{\gamma_i S_{\mathrm{A}i}}{\omega_i^2}\boldsymbol{\phi}_i \tag{14}$$

where $\mathrm{S}_{\mathrm{A}i}$ represents the spectral acceleration for the *i*th mode.

Given displacement vector (14) represents the maximum value of any response of interest. The overall response of the system is calculated by combining the maximum modal responses specified by one of the mode combination methods (SRSS, CQC, GRP, etc.).

A general rule for modal response combination can be defined as

$$R = \pm\sqrt{\varepsilon_{i,j}R_iR_j} \tag{15}$$

where $R_i$, $R_j$ are the *i*th and *j*th modal response respectively and $\varepsilon_{i,j}$ is a combination matrix whose shape and values are based on the chosen modal response combination.

A response spectrum method for determining the overall responses of the investigated tank-liquid systems fixed to a rigid foundation was performed. the seismic response was described by two response spectrum curves, one with 5 % proportional damping of the structure while the latter had 0,5 % for the liquid (Fig. 2). Fig. 7 shows the overall responses of liquid storage tanks to the El Centro earthquake. Tab. 4 presents results of the response spectrum method for the investigated liquid storage tanks.

| Slenderness parameter $\gamma$ | Maximum displacement | Maximum sloshing wave |
|---|---|---|
| 0.5 | 0.304e-3 m | 0.526 m |
| 1 | 0.683e-3 m | 0.694 m |
| 2 | 0.005 m | 0.712 m |

Table 4: Summary of results from response spectrum method

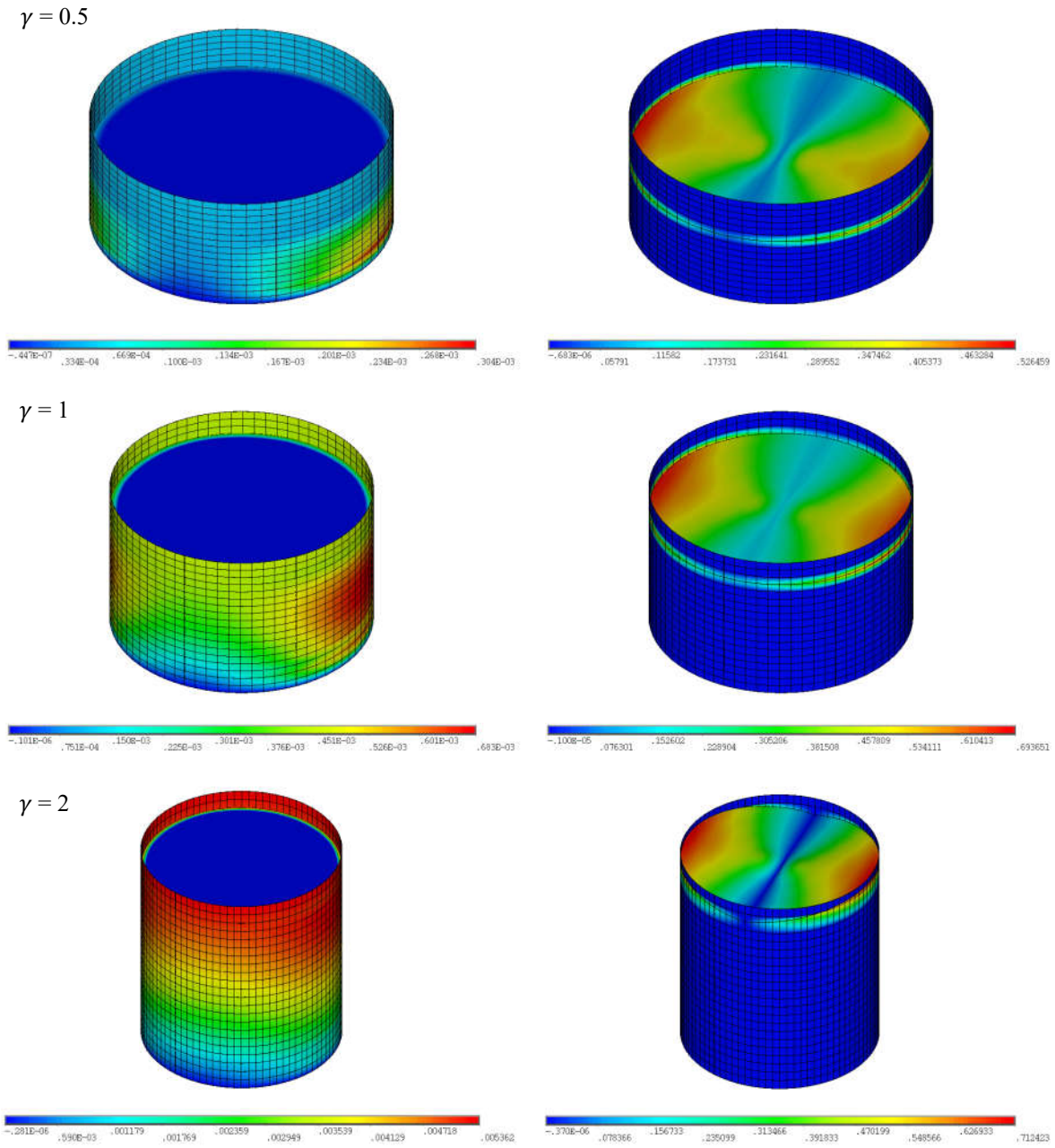


Figure 7: Overall responses of liquid storage tanks to El Centro earthquake

## 4 CONCLUSIONS

The continuing development of technologies in each industry requires increased attention to operational safety and protection of the environment. Liquid storage tanks serve as reservoirs for a variety of liquids (e.g., storage tanks in nuclear power plants), which are usually vulnerable to seismic effects (past earthquakes e.g., in Fukushima, San Fernando, etc.). Therefore, their safe operation is desirable. Seismic analysis is one method which should be carried out to provide satisfactory performance of tanks, especially in earthquake prone regions.

The aim of the paper was to perform a seismic design for various tank-liquid systems (from broad to tall tanks) and determine the dynamic effects such as impulsive and convective frequencies and modes of oscillation, which may result in unison vibration and sloshing

respectively, and the overall response to the seismic loading. In addition to the aforementioned dynamic effects, some seismic characteristics (e.g., base shear, overturning moment, hydrodynamic pressure etc.) used in the seismic design were not covered in this paper, since they were given attention in other publications of the authors, e.g. in [11, 16, 17].

For the calculation of dynamic characteristics, analytical models according to Eurocode 8 standard and numerical approach (finite element method) were used. Some seismic characteristics calculated analytically were compared with results obtained in ANSYS Multiphysics and Matlab software. Results between each solution represented good conformity.

## 5 ACKNOWLEDGMENTS

This work was supported by the grant from the Grant Agency of VEGA no. 1/0742/15 entitled *Analysis for Seismic Resistance of Liquid Storage Tanks with Nonlinear and Time-Dependent Parameters* and by the Slovak Research and Development Agency under the contract no. APVV-15-0630 entitled *Extension of the Validity of the Computation Standards for the Seismically Resistant Liquid Storage Tanks, in terms of Safety at NPPs and Other Industrial Areas*.

## REFERENCES

[1] M. Musil, M. Sivy, O. Chlebo and O. Prokop, Seismic Response of Elevated Liquid Storage Tanks, *Aplimat 2017 Proceedings of the 16th Conference on Applied Mathematics*, Bratislava, Slovakia, January 31 – February 2, 2017.

[2] P. Peciar, R. Fekete, M. Peciar, *Process Engineering II*, Vydavatelstvo STU, 2016.

[3] S. Ziaran, M. Cekan, O. Chlebo, M. Musil, Analysis of Seismic Response on the Excitation of Support Structures, *Proceedings of the 43rd International Congress on Noise Control Engineering* (*Inter-Noise 2014*), Toowong DC, The Australian Acoustical Society, 2014.

[4] G. W. Housner, Dynamic Pressures on Accelerated Fluid Containers, *Bulletin of the Seismological Society of America*, **47**(1), 1987.

[5] G. W. Housner, *Earthquake Pressures on Fluid Containers*, Eighth Technical Report under Office of Naval Research, California Institute of Technology, Pasadena, California, 1954.

[6] M. A. Haroun, G. W. Housner, Seismic Design of Liquid Storage Tanks, *Journal of the Technical Councils of ASCE*, **107**(1), pp. 191-207, 1981.

[7] A. S. Veletsos, *Seismic Response and Design of Liquid Storage Tanks, Guidelines for the Seismic Design of Oil and Gas Pipeline Systems*, Technical Council on Lifeline Earthquake Engineering (ASCE), pp. 255-370, 1984.

[8] A. S. Veletsos, J. Y. Yang, Earthquake Response of Liquid-Storage Tanks, *Advances in Civil Engineering through Engineering Mechanics*, North Carolina State University, Raleigh, North Carolina, USA, 1977.

[9] P. K. Malhotra, T. Wenk, M. Wieland, Simple Procedure for Seismic Analysis of Liquid-Storage Tanks, *Structural Engineering International*, **10**(3), pp. 197-201, 2000.

[10] EN 1998-4, *Eurocode 8 – Design of Structures for Earthquakes Resistance, Part 4 – Silos, Tanks and Pipelines*, CEN, 2006.

[11] M. Sivy, M. Musil, Seismic Resistance of Storage Tanks Containing Liquid in Accordance with Principles of Eurocode 8 Standard, *Strojnicky casopis – Journal of Mechanical Engineering*, **66**(2), pp. 79-88, 2016.

[12] R. A. Ibrahim, *Liquid Sloshing Dynamics Theory and Applications*, Cambridge University Press, 2005.

[13] O. R. Jaiswal, *Review of Code Provisions on Seismic Analysis of Liquid Storage Tanks*, Report No. IITK-GSDMA-EQ-01-V1.0, Indian Institute of Technology Kanpur, India, 2004.

[14] PNM34080183 – *Requirements on Evaluation of Seismic Resistance of Structures, Systems and Components of Mochovce NPP*, 2009.

[15] A. K. Gupta, *Response Spectrum Method in Seismic Analysis and Design of Structures*, Blackwell Scientific Publications, 1990.

[16] M. Sivy, M. Musil, Procedure for Seismic Analysis of Liquid Storage Tanks using FEM Approach and Analytical Models, *Advances in Mechanism Design II: Proceedings of the XII International Conference on the Theory of Machines and Mechanisms*, Springer, 2017.

[17] M. Musil, M. Sivy, Influence of Wall Flexibility of Liquid Storage Tanks on Hydrodynamic Pressures Induced During Seismic Activity, *Engineering Mechanics 2016*: *Book of Full Texts,* 22nd International Conference, Svratka, Czech Republic, May 9 – 12, 2016.

COMPDYN 2017
6th ECCOMAS Thematic Conference on
Computational Methods in Structural Dynamics and Earthquake Engineering
M. Papadrakakis, M. Fragiadakis (eds.)
Rhodes Island, Greece, 15–17 June 2017

# TORSION EFFECT DUE TO ASYMMETRIC POUNDING BETWEEN MULTISTORY RC BUILDINGS

**Christos G. Karayannis**[1], **Maria C. Naoum**[2]

[1] Prof., Civil Engineering Dept.
Democritus University of Thrace, Xanthi 67100, Greece
karayan@civil.duth.gr

[2] PhD student, Civil Engineering Dept.
Democritus University of Thrace, Xanthi 67100, Greece
mnaoum@ civil.duth.gr

**Keywords:** Asymmentric structural pounding, multistory reinforced concrete structures, non-linear dynamics analysis, Earthquake Engineering.

**Abstract.** *Earthquake induced collisions between adjacent structures have been repeatedly reported in the literature as a frequent case of damage. It is quite usual seismic induced oscillations of a structure in a block of buildings to be partly restrained in lateral displacements and therefore a torsional movement to be introduced in the building during an earthquake excitation. Further it has been repeatedly observed that torsion is a critical factor leading in many occasions to major structural damage or even complete collapse during strong ground motions. Seismic damage surveys and relevant analyses conducted on modes of failure of building structures during past severe earthquakes have concluded that among the most damage susceptible structures are those that exhibit torsional behavior. In this work the case of reinforced concrete multistory buildings that suffer pounding in a non-symmetric way is studied. Pounding occurs only in one (case 1) or two (case 2) columns of the structure whereas the other columns are free to move without restrictions. This way torsional oscillations are introduced in the structural system during a seismic excitation. Nonlinear dynamic step-by-step analysis and special purpose elements are employed for the needs of this study. More than fifty pounding cases with torsional effect between structures with different total height for three excitations are studied and results in terms of displacements, torsional rotations, ductility requirements are presented and commented. The influence of the size of the gap distance between the adjacent structures on the torsion effect is also investigated. The results clearly show that high capacity requirements in terms of torsional moments, column shear strength and ductility are developed due to the asymmetric pounding.*

## 1 INTRODUCTION

The earthquake induced collisions between structural systems that are in contact or in close proximity to each other is commonly referred to as structural pounding. Based on reports of field observations after numerous destructive earthquakes all over the world, it can be concluded that pounding is frequently observed when strong earthquakes strike big cities and densely populated urban areas [1], [2], [3]. Further false code application lead sometimes to building separations that are inadequate and inconsistent with the philosophy of modern codes that imply large deformations can occur during major earthquakes due to inelastic response. Moreover the high cost of land in densely populated metropolitan cities and the small lot sizes make the seismic separation requirements not always easy to apply.

Karayannis and Fotopoulou (1998) examined various cases of structural pounding [4] between multistory reinforced concrete structures designed according to the Eurocodes 2 and 8. The work is based on non-linear dynamic step-by-step analysis and its purpose was to present initial results for the influence of some critical pounding parameters on the ductility requirements of the columns and to examine the possibility of taking into account the pounding effect during the design process according to EC2 to EC8.

Furthermore in city centers with large blocks densely filled with buildings the land lots are mostly not equal nor alike in plan geometry henceforth it is very likely adjacent buildings in a block to be partly and in a non-symmetric way in contact to each other. Consequently it is quite usual seismic induced oscillations of a structure in a block to be partly restrained in lateral displacements and therefore a torsional movement to be introduced in the building during an earthquake excitation. Therefore it can be concluded that in these cases pounding between adjacent structures may introduce significant plan asymmetry in the building in terms of lateral stiffness distribution.

On the other hand it is well known that buildings due to inherent asymmetries may exhibit torsional behavior during seismic excitations. Further it has been repeatedly observed that torsion is a critical factor leading frequently to major structural damage or even complete collapse during strong ground motions.

In this work forty eight pounding cases each one for three earthquake excitations have been studied. These cases are sorted into two series based on the level of the asymmetry introduced in an 8-story building due to pounding. In series 1 pounding cases with high asymmetry are included since pounding takes place between only one external column of the 8-story building and one column of the adjacent short and stiff structure. In series 2 pounding takes place between two columns of the 8-story building and two columns of the adjacent short and stiff structure. Both series include asymmetric pounding cases between the 8-story and an adjacent structure with $n_s$ =1, 2, 3, 4, 5, 6, 7 and 8 stories. Each pounding case first is examined considering that the interacting structures are in contact from the beginning (gap distance $d_g$=0) and further it is examined considering that there is a gap distance equal to 1 or 2 cm ($d_g$=1 and 2 cm) between the structures. Nonlinear dynamic step-by-step analysis and special purpose elements are employed for the needs of this study.

## 2 MODEL IDEALIZATION OF POUNDING

In this work the pounding between adjacent structures with different total heights that are partly in contact to each other in a non-symmetric way is studied (fig. 1). This configuration implies that the seismic induced oscillations of the tall building is laterally partly restrained by the other structure and therefore a torsional movement is introduced in the building during an

earthquake excitation. Therefore in the examined cases pounding between adjacent structures introduces significant plan asymmetry in the building in terms of lateral stiffness distribution.

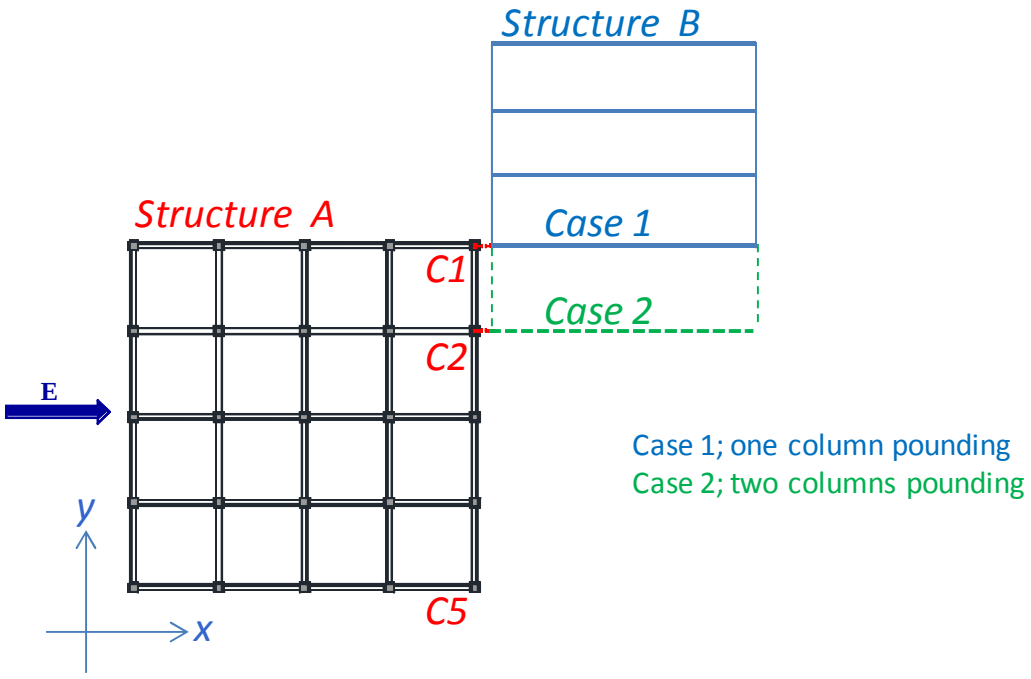


Figure 1: Plan view. Asymmetric pounding.

It is considered that one flexible multistory building (Structure A in fig. 1) is in contact or in close proximity to one less flexible shorter structure (Structure B in fig. 1). If there is a gap distance between these structures collisions can only occur when the lateral displacements of the structures exceed the pre-defined gap distance ($d_g$). The influence of the gap size on the pounding effects is also investigated.

As it can be shown in fig. 1 two cases of asymmetric pounding are examined. In case 1 the lateral displacement of one column (column C1) of the 8-story building (structure A) is restrained in the x-direction only towards the adjacent structure (structure B); whereas in case 2 the lateral displacements of two columns (columns C1 and C2) are restraint. In both cases torsional movement is introduced in the structure under consideration (structure A) due to the plan asymmetry caused by the restraints imposed by the pounding between the adjacent structures.

The heights of the story levels of the two structures are equal (Fig. 2). Actual condition and the model idealization of this pounding case are shown in Fig. 2.

Contact points are taking into account at the levels of the floor slabs of the short structure (Fig. 2). Nevertheless, from the analyses of the examined pounding cases it has been found that the response of the interacting structures is mainly influenced by the position and the characteristics of the contact point at the short structure's top floor. The influence of the other contact points on the results proved to be negligible in the examined cases. The same conclusion also holds, more or less, for the examined cases with non-zero initial distance gap.

Nevertheless, in the following analyses and results, the influence of the pounding effect through all floor contact point on the behaviour of the structures and on the response and ductility requirements of the columns is examined.

Seismic analyses have been performed using time steps in the range of 1/1000 sec to 1/10000 sec in order to maintain equilibrium during the integration.

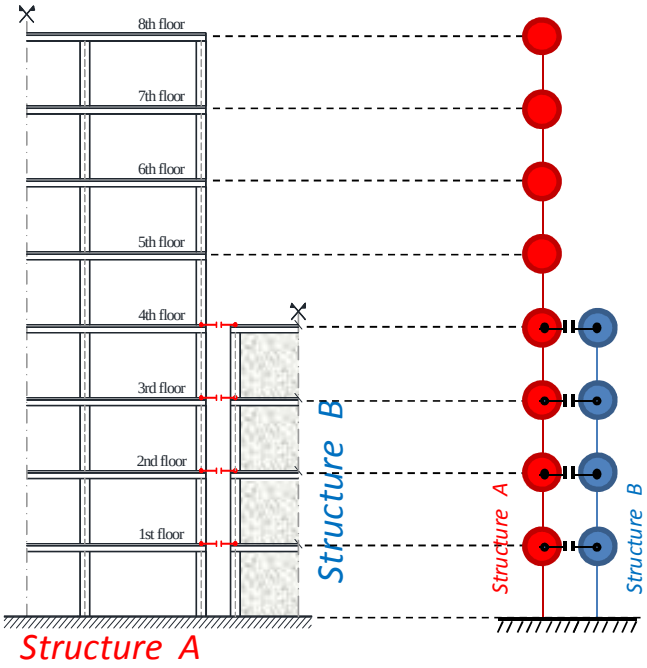


Figure 2: Pounding between buildings with different total heights. The heights of the stories of the two structures are alike.

## 3 CONTACT ELEMENT

Collisions are simulated using special purpose contact elements that become active when the corresponding nodes come into contact.

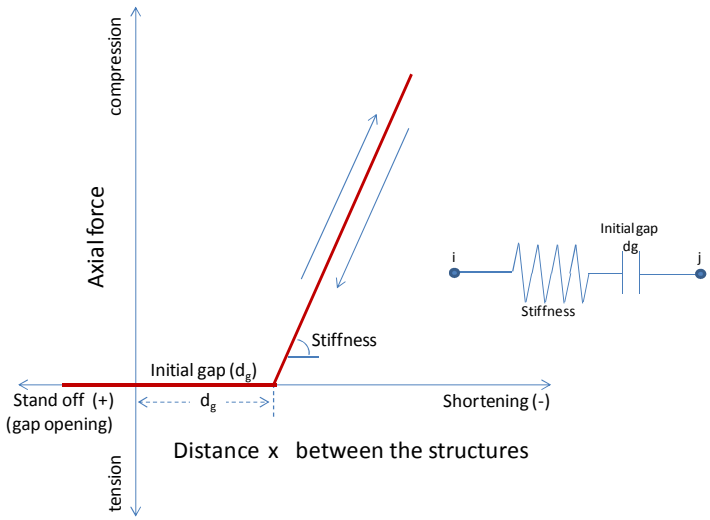


Figure 3: Contact elements

The response of the contact elements is shown in Fig.3. The negative direction of the X-axis represents the condition that the buildings move away from each other. In the positive direction of the X-axis there are two parts in order to simulate the actual behaviour of the structures in case there is an initial small gap distance ($d_g$) between them. It is possible that the structures move one towards the other but the displacements are small and the existing gap is not covered. In this case the contact element remains non-active and the buildings continue

to vibrate independently. In the case that the structures move one towards the other and the sum of the displacements of the two structures bridge the existing gap or the structures are in contact from the beginning ($d_g$=0) then the contact element responds as a spring with large stiffness.

## 4 ANALYSIS MODEL OF STRUCTURES

The frame structural system of the tall structure consists of beams and columns. Each structure is modeled as a 3D assemblage of non-linear elements connected at nodes. Each node has six degrees of freedom. The mass is lumped at the mass center of each floor. Each structure responds dynamically and vibrates independently. Collision occurs when the lateral displacements of the structures at the floor levels exceed the predefined gap distance ($d_g$) between the two structures.

The computer program used in this work is the program package ETABS2000. The finite element mesh used here for the modeling of each structure utilizes an one-dimensional element for each structural member. The element is a common lumped plasticity beam-column model that considers the inelastic behaviour concentrated in zero-length "plastic hinges" at the element's ends. An interaction 3D surface N-$M_x$-$M_y$ is employed for the check of the elastic or plastic response of the zero-length plastic hinges.

## 5 POUNDING CASES

More than fifty pounding cases have been studied for the needs of this work. Each one is subjected to three different natural seismic excitations having been selected so that their spectra fit properly with the design spectrum used for the design of the 8-story building.

The examined cases are sorted into two series based on the level of the asymmetry that is induced in the 8-story building due to the pounding.

Series 1 includes pounding cases with high asymmetry (case 1 in fig. 1) where pounding takes place between only one column of the 8-story building (column C1 in fig. 1) and one column of the adjacent short and stiff structure. In series 2 (case 2 in fig. 1) pounding takes place between two columns of the 8-story building (columns C1 and C2 in fig. 1) and two columns of the adjacent short and stiff structure.

Thus both series include asymmetric pounding cases between the 8-story and an adjacent structure which has $n_s$ story level where $n_s$ =1, 2, 3, 4, 5, 6, 7 and 8 stories.

Pounding cases of the 8-story building with an adjacent single story structure with different period values (not very stiff) are also examined and results are presented herein.

Each one of the pounding cases of both series first is examined considering that the interacting structures are in contact from the beginning (gap distance $d_g$=0); further each pounding case is examined considering that between the interacting structures there is a gap distance equal to 1 and 2 cm ($d_g$=1 and 2 cm).

## 6 RESULTS AND COMMENTS

The results and the conclusions deduced from the analyses of each series include the observed overall response of the multistory frame in terms of the induced torsional behavior and its repercussions on the developing capacity requirements of the columns. Therefore results for the shear demands and shear capacity of the columns are also presented and commented

upon. Special attention has been given to the response of the columns of the story of the multistory frame where the pounding takes place.

### 6.1 Torsional behavior

Torsional movement is observed in the 8-story building due to the asymmetric pounding that occurs between it and the adjacent shorter and stiff structure. The time history of the developing torsional moment at the base floor of the 8-story building during the seismic excitation due to case 1 asymmetric pounding (fig. 1) with a 3-story very stiff structure is presented in figure 4.

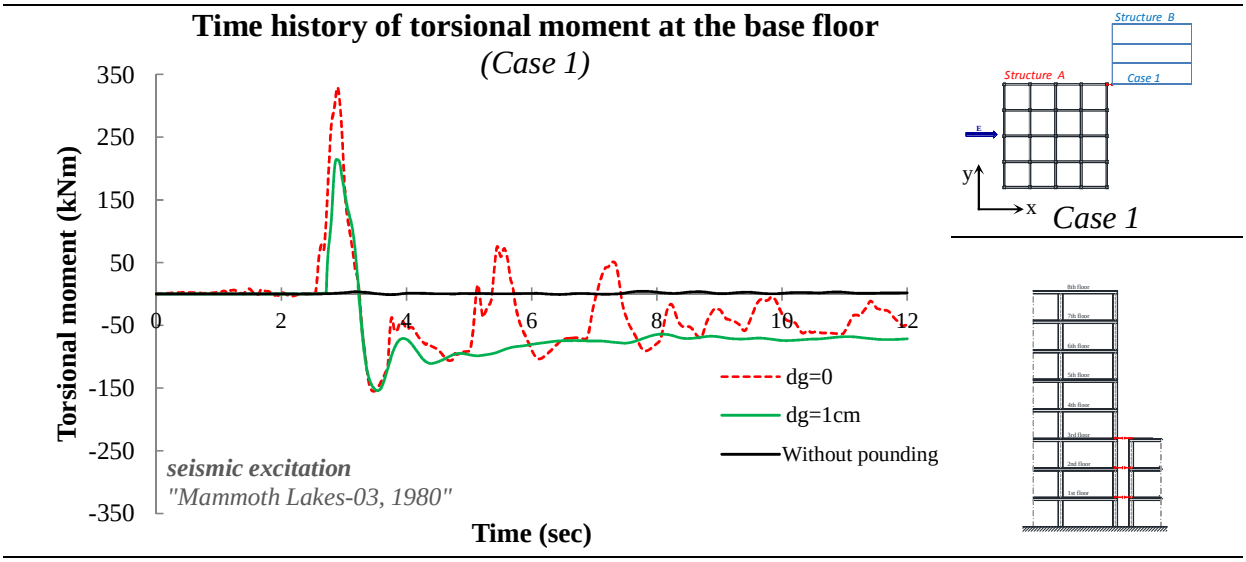


Figure 4: Time history of the torsional moment at the base floor due to asymmetric pounding case 1 between the 8-story building and a 3-story stiff structure.

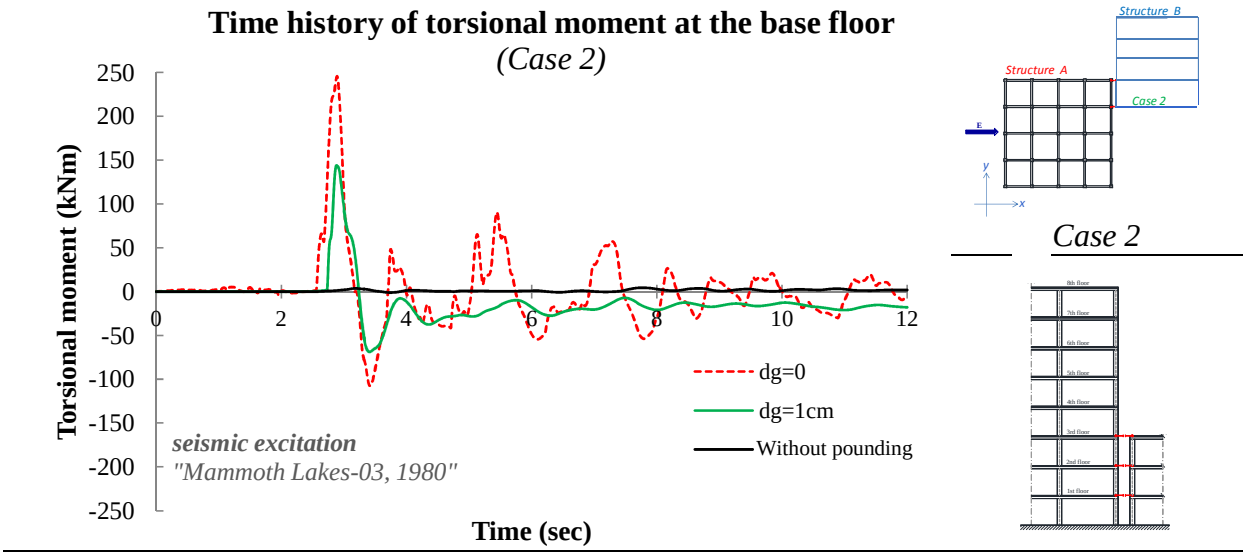


Figure 5: Time history of the torsional moment at the base floor due to asymmetric pounding case 2 between the 8-story building and a 3-story stiff structure.

Further the time history of the torsional moment at the base floor of the 8-story building during the seismic excitation due to case 2 asymmetric pounding (fig.1) with a 3-story very stiff structure is presented in figure 5. From these figures (figures 4 and 5) it can be deduced that asymmetric type of pounding causes significant torsional movement and high value tor-

sional moments in the 8-story building although its plan view is symmetric and in the cases it vibrates without the pounding effect it presents no torsional moment and consequently no torsional movement.

From the results it can also be deduced that the developing torsion of the 8-story building also depends on the height of the adjacent stiff structure. In Fig. 6 the time histories of the developing torsional moment for the four cases of pounding are presented. In particular the pounding case between the 8-story building (8RC) and a single story building (1RC), a three story building (3RC), a five story building (5RC) and an eight story building (8RC) are included and compared to each other. From these comparisons it can be observed that in general the developing torsion increases as the height (the number of the stories) of the adjacent stiff structure increases.

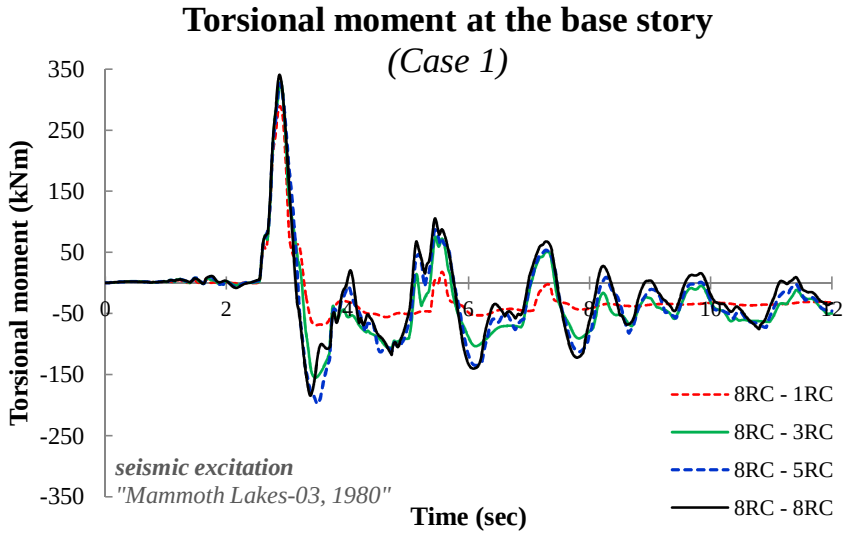


Figure 6: Influence of the number of stories (total height) of the adjacent structure on the developing torsional moment of the 8-story building (8RC) as observed at the base floor due to asymmetric pounding (case 1).

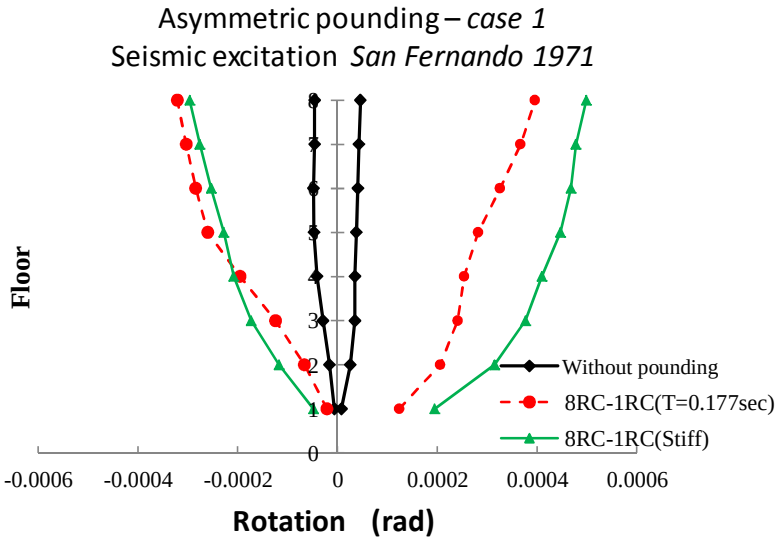


Figure 7: Influence of the period of the adjacent single story structure (1RC) on the developing torsional oscillations (maximum observed rotations of all stories) of the 8-story building (8RC) due to asymmetric pounding (*case 1*).

Furthermore the developing torsion of the 8-story building is also influenced by the period of the adjacent structure. In Fig. 7 the maximum observed rotations of the all floors of the 8-story structure are presented for the cases (a) free vibration without pounding, (b) pounding case 1 with a single story structure exhibiting period in the direction of the seismic excitation equal to T=1.77s and (c) pounding case 1 with single story very stiff structure.

From Fig. 7 it can be observed that the period of the adjacent single story structure influences the pounding of the buildings and it seems that the stiffer single story structure induces higher values of rotation in the 8-story building.

### 6.2 Column shear forces

As expected the torsional movement of the examined building highly influences the distribution of the developing shear forces in the columns. In Fig. 8 the time history of the developing shear forces of column C1 of the 3rd floor is for the pounding case 1 between the 8-story building and a 3-story stiff structure.

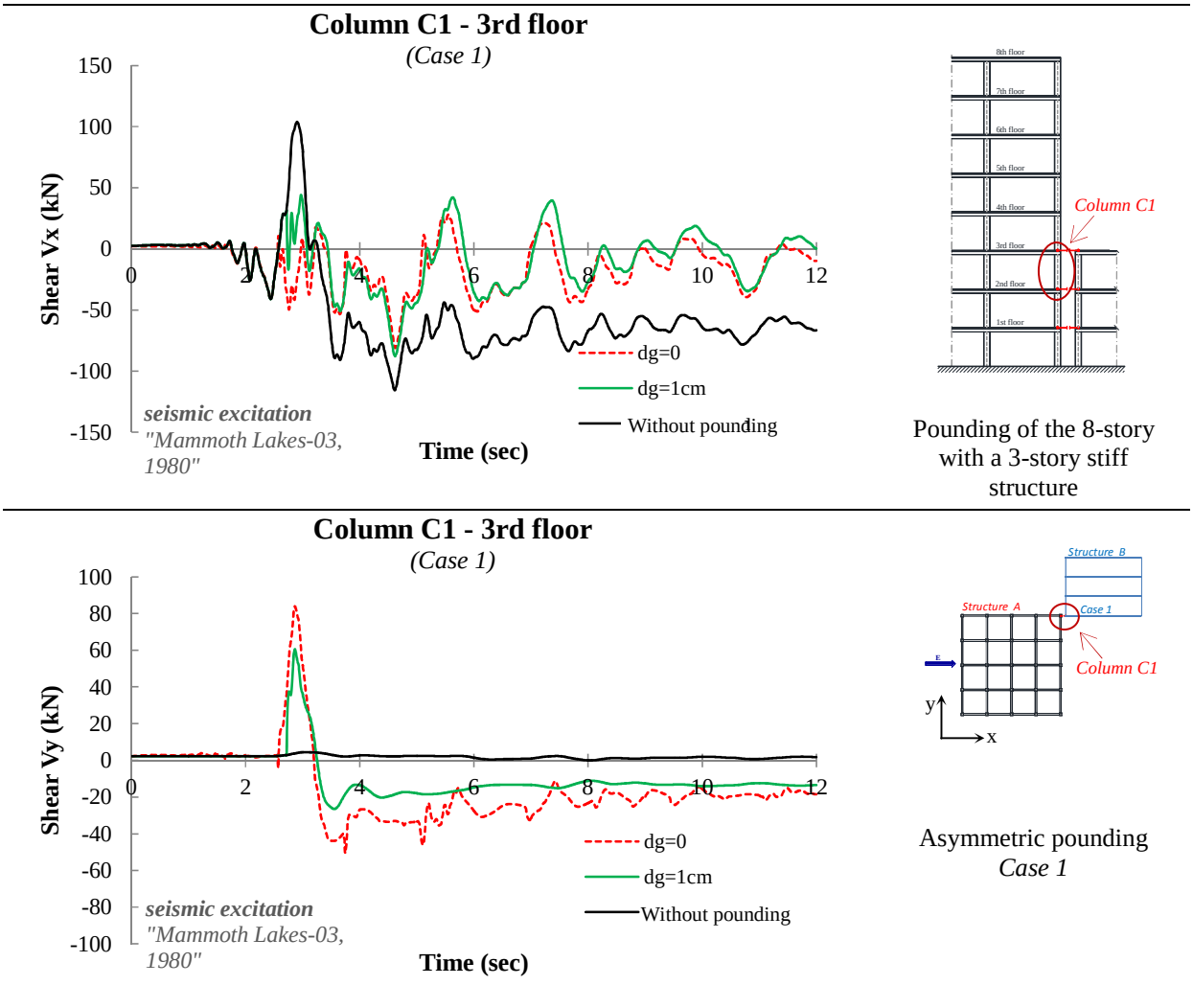


Figure 8: Shear time history for column C1 of the 3rd floor in the two directions for seismic excitation acting in the x-direction. It is stressed that high shear is developed in the normal direction (y-direction) due to the torsional movement induced by the asymmetric pounding.

It can be seen the shear forces of the column C1 in the direction of the earthquake excitation (x-direction) decrease due to the movement restraint provided by the adjacent 3-story structure at this point of the building whereas at the same time significant shear forces are developed in the normal direction (y-direction).

The ratios $r_v$ of the maximum shear force ($maxV_y$) of column C1 at the base floor developing normal to the direction of the earthquake excitation to the maximum shear force ($maxV_x$) of the same column developing in the direction of the earthquake excitation for the pounding between the 8-story building and the single story stiff structure are presented in table 1 for pounding cases 1 and 2.

| $r_v=maxV_y/maxV_x$ *seismic excitation* | *Case 1* | *Case 2* |
|---|---|---|
| Borego Mtn (4/9/1968) | 0.98 | 0.56 |
| San Fernando (2/9/1971) | 0.76 | 0.63 |
| Mammoth Lakes-03 (5/25/1980) | 1.11 | 0.61 |

Table 1: Ratios $r_v$ for column C1 at the base floor. Pounding between 8-story and single story structures.

The ratios $r_v$ of the maximum shear force ($maxV_y$) of column C1 at the 3rd floor developing normal to the direction of the earthquake excitation to the maximum shear force ($maxV_x$) of the same column developing in the direction of the earthquake excitation (x-direction) for the pounding between the 8-story building and the 3-story stiff structure are presented in table 2 for pounding cases 1 and 2.

| $r_v=maxV_y/maxV_x$ | $d_g$ = 0 | | $d_g$ = 1 cm | |
|---|---|---|---|---|
| *seismic excitation* | *Case 1* | *Case 2* | *Case 1* | *Case 2* |
| Borego Mtn (4/9/1968) | 0.85 | 0.66 | 0.46 | 0.37 |
| San Fernando (2/9/1971) | 0.71 | 0.70 | 0.41 | 0.31 |
| Mammoth Lakes-03 (5/25/1980) | 1.03 | 0.94 | 1.37 | 0.50 |

Table 2: Ratios $r_v$ for column C1 at the 3rd floor. Pounding between 8-story and 3-story structures.

The ratios $r_v$ of the maximum shear force ($maxV_y$) of column C1 at the 5th floor developing normal to the direction of the earthquake excitation to the maximum shear force ($maxV_x$) of the same column developing in the direction of the earthquake excitation (x-direction) for the pounding between the 8-story building and the 5-story stiff structure are presented in table 3 for pounding cases 1 and 2.

| $r_v=maxV_y/maxV_x$ | $d_g$ = 0 | | $d_g$ = 1 cm | |
|---|---|---|---|---|
| *seismic excitation* | *Case 1* | *Case 2* | *Case 1* | *Case 2* |
| Borego Mtn (4/9/1968) | 1.00 | 0.54 | 0.83 | 0.74 |
| San Fernando (2/9/1971) | 0.99 | 1.25 | 0.88 | 0.84 |
| Mammoth Lakes-03 (5/25/1980) | 1.21 | 1.01 | 1.08 | 1.23 |

Table 3: Ratios $r_v$ for column C1 at the 5th floor. Pounding between 8-story and 5-story structures.

From tables 1, 2 and 3 it can be seen that significant shear forces are developed in the direction normal to the direction of the seismic excitation. This conclusion holds for all seismic excitations used in this study. Thus for pounding case 1 and $d_g$=0 (structures in contact) for the pounding cases examined in this study ratio $r_v$ shows that the shear force developed nor-

mal to the excitation direction is more or less equal to the shear force developed in the direction of the seismic excitation. Further though it can be observed that in cases an initial seismic gap ($d_g$=1cm) exists from the beginning between the interacting structures an essential mitigation of the phenomenon is observed.

### 6.3 Ductility requirements

Pounding induced torsional vibration changes significantly the ductility requirements of the columns and rather increases the ductility requirements of columns that experience high displacement due to the rotational movement of the structure and especially of column C5.

In Fig. 9 the ductility requirements of column C5 of the 8-story building (see Fig. 1) in all floor levels for pounding case 1 and $d_g$=0 are presented and compared with the corresponding ones of the same column for the same seismic excitation without pounding effect. It can be observed that column C5 in the levels above the contact level exhibits increased ductility requirements in comparison with the ones of the same column for the same excitation without pounding effect.

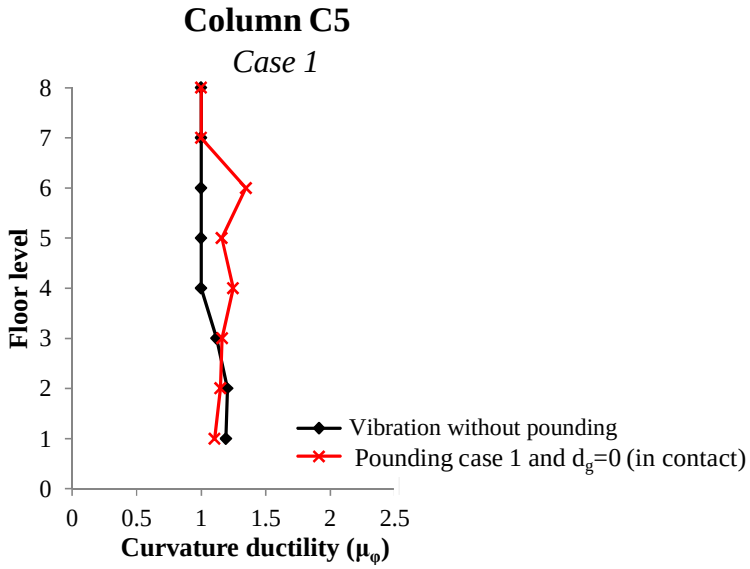


Figure 9: Maximum ductility requirements of column C5 in all floor levels. Comparisons of ductility requirements between pounding (case1) of the 8-story building with a single story structure and the free vibration of the 8-story building (without pounding effect).

## 7 CONCLUSIONS

- Seismic induced interaction between adjacent buildings that are partly and in a non-symmetric way in contact may introduce significant torsional oscillations. This type of structural interaction may be referred as asymmetric pounding.
- Asymmetric pounding between an 8-story reinforced concrete building with symmetric plan view and an adjacent shorter structure that has $n_s$ floor levels is investigated for $n_s$=1,2,3,4,5,6,7 and 8 stories. Interaction cases with high (case 1) and medium (case 2) asymmetric pounding are included in the present study. It has been observed that in general the developing torsion increases as the height (the number of the stories) of the adjacent stiff structure increases.

- The examined asymmetric type of pounding causes significant torsional movement and high value torsional moments in the 8-story building. The developing torsion increases as the height of the adjacent shorter structure increases.
- The period of the adjacent structure influences the severity of the pounding. In the case of pounding between the 8-story with a single story structure it seems the stiffer the single story structure is the higher values of rotation is induced in the 8-story building.
- From the presented study it can be concluded that the torsional movement which is induced due to the asymmetric pounding highly influences the distribution of the developing shear forces in the columns. High shear forces are developed in the columns in the direction normal to the earthquake direction although the plan view of the building is symmetric in both directions.
- Pounding induced torsional vibration changes significantly the ductility requirements of the columns and rather increases the ductility requirements of columns that experience high displacement due to the rotational movement of the structure.

## REFERENCES

[1] C. Arnold, R. Reitherman, *Building Configuration and Seismic Design.* Wiley, New York, 1982.

[2] E. Rosenblueth, R. Meli., The 1985 earthquake: Causes and effects in Mexico City. *Concrete International (ACI)*, **8(5)**, 23-24, 1986.

[3] V.V. Bertero, Observationon structural pounding. *Proceedings of the International Conference on Mexico Earthquakes*, ASCE, 264-287, 1986.

[4] C.G. Karayannis, M.G. Fotopoulou, Pounding of multistorey RC structures designed to EC8 and EC2. *11th European Conference on Earthquake Engineering (Proceedings in CD form)*, Balkema, ISBN 90-5410-982-3, 1998.

[5] C.G. Karayannis, M.C. Naoum, Inter-story pounding and torsional effect due to interaction between adjacent multistory RC buildings. *COMPDYN 2017, 6th ECCOMAS Thematic Conference on Computational Mechanics in Structural Dynamics and Earthquake Engineering, Rhodes Island, Greece, 15-17 June, 2017* .

COMPDYN 2017
6th ECCOMAS Thematic Conference on
Computational Methods in Structural Dynamics and Earthquake Engineering
M. Papadrakakis, M. Fragiadakis (eds.)
Rhodes Island, Greece, 15–17 June 2017

# DYNAMIC ANALYSIS OF BRIDGE GIRDERS UNDER MOVING LOADS CONSIDERING WARPING AND MASS EFFECTS: NUMERICAL AND ANALYTICAL BEAM MODELS

**João Serra[1], Ricardo Vieira[2], and Francisco Virtuoso[2]**

[1] Instituto Superior Técnico
Lisbon
e-mail: joao.a.serra@tecnico.ulisboa.pt

[2] Instituto Superior Técnico
Lisbon
{ricardo.figueiredo.vieira,francisco.virtuoso}@tecnico.ulisboa.pt

**Keywords:** Vibrations, Dynamic Analysis, Thin-Walled Beams, Torsion, Warping, Bridges, High-Speed Railways, Moving Masses.

**Abstract.** *In order to perform efficient dynamic analyses of continuous high-speed railway bridges, a numerical and an analytical beam models are proposed in the present work. The behaviour of the bridge girder is described by a three-dimensional Euler-Bernoulli beam element, where an additional degree-of-freedom is considered at each beam-end, representing the cross-sectional warping. The structural response is determined by considering a modal analysis along with a direct integration scheme. The natural frequencies and vibration mode shapes are determined by the developed models. The trains are modeled as series of moving masses acting eccentrically at constant speed, allowing the corresponding inertial effects to be considered besides the gravitational force of mass.*

## 1 INTRODUCTION

In the design of high-speed railway bridges, special consideration must be given to the torsional response of thin-walled girders. Therefore, warping of the cross-sections cannot be neglected in the structural dynamic analysis.

Performing dynamic analyses of bridges using shell finite element models allows to obtain accurate results, as long as detailed geometrical and material descriptions of the structures are known. However, using such models in early design stages is time consuming, which renders the evaluation of several structural solutions cumbersome. The use of beam models can minimize the time needed to calculate structural responses and prove good agreement with shell models. In the present work, a numerical and an analytical beam models are prosed.

The coupled governing equations of thin-walled beams were derived by applying the Hamilton's principle along with the Vlasov's beam theory.

In the developed numerical model, the behaviour of the bridge girder is described by a three-dimensional Euler-Bernoulli beam finite element, where an additional degree-of-freedom is considered to represent the cross-sectional warping. Lisi, [1], recently developed a beam finite element model for the static and the dynamic analysis of thin-walled beams under the action of a single eccentric moving force. The present work extends Lisi's study towards the inclusion of arrays of moving masses. Other relevant studies on coupled lateral bending-torsional vibrations of beams under moving loads are those of Michaltsos et al., [2][3][4].

The proposed analytical model allows to obtain the structural response of continuous beams with bending-torsional coupling in an exact sense. The formulation presented is based on the work done by Chan and Ashebo, [5], where the problem of uncoupled bending vibrations was solved exactly. This method was also used by Graça, [6], to model the dynamic response of continuous bridge girders, despite coupled bending-torsional motion was not considered.

The trains are modelled as series of moving masses acting eccentrically at constant velocity. Thus, the corresponding inertial effects of the moving loads are considered besides the gravitational force of mass.

Both models are suitable for computational implementation and automation of the design process.

## 2 THE GOVERNING EQUATIONS OF COUPLED THIN-WALLED BEAMS

The governing equations that describe the static and the dynamic behaviour of thin-walled beams with arbitrary cross-section were derived by applying the Hamilton's principle, yielding

$$\begin{aligned}&\rho\left(A\ddot{\xi}_z + S_z^P\ddot{\phi}\right) - \rho\left(-S_y\ddot{\xi}_x' + I_{yy}\ddot{\xi}_z'' + I_{yz}\ddot{\xi}_y'' + I_{y\omega}\ddot{\phi}''\right) + \\ &+E\left(-S_y\xi_x''' + I_{yy}\xi_z''''+ I_{yz}\xi_y''''+ I_{y\omega}\phi''''\right) = f_z\end{aligned} \tag{1}$$

$$\begin{aligned}&\rho\left(A\ddot{\xi}_y - S_y^P\ddot{\phi}\right) - \rho\left(-S_z\ddot{\xi}_x' + I_{zy}\ddot{\xi}_z'' + I_{zz}\ddot{\xi}_y'' + I_{z\omega}\ddot{\phi}''\right) + \\ &+E\left(-S_z\xi_x''' + I_{zy}\xi_z''''+ I_{zz}\xi_y''''+ I_{z\omega}\phi''''\right) = f_y\end{aligned} \tag{2}$$

$$\begin{aligned}&\rho\left(S_z^P\ddot{\xi}_z - S_y^P\ddot{\xi}_y + I_0^P\ddot{\phi}\right) - \rho\left(-S_\omega\ddot{\xi}_x' + I_{\omega y}\ddot{\xi}_z'' + I_{\omega z}\ddot{\xi}_y'' + I_{\omega\omega}\ddot{\phi}''\right) + \\ &+E\left(-S_\omega\xi_x''' + I_{\omega y}\xi_z''''+ I_{\omega z}\xi_y''''+ I_{\omega\omega}\phi''''\right) - GJ\phi'' = m_x\end{aligned} \tag{3}$$

where primes indicate differentiation with respect to the spatial coordinate $x$ and dots represent derivatives with respect to time $t$. The variable $E$ represents the modulus of elasticity,

$G$ is the shear modulus, $J$ is the torsion constant, $A$ is the cross-section area, $S_i$ and $I_{ij}$ are respectively the first and second moments of inertia, with $\{i,j\}=\{y,z\}$, and $S_\omega$ and $I_{\omega\omega}$ correspond to the first and the second sectorial moments, respectively. The generalized displacements $\xi_x$, $\xi_z$, $\xi_y$ and $\phi$ and the applied loading $f_z$, $f_y$ and $m_x$ are illustrated in Figure 1.

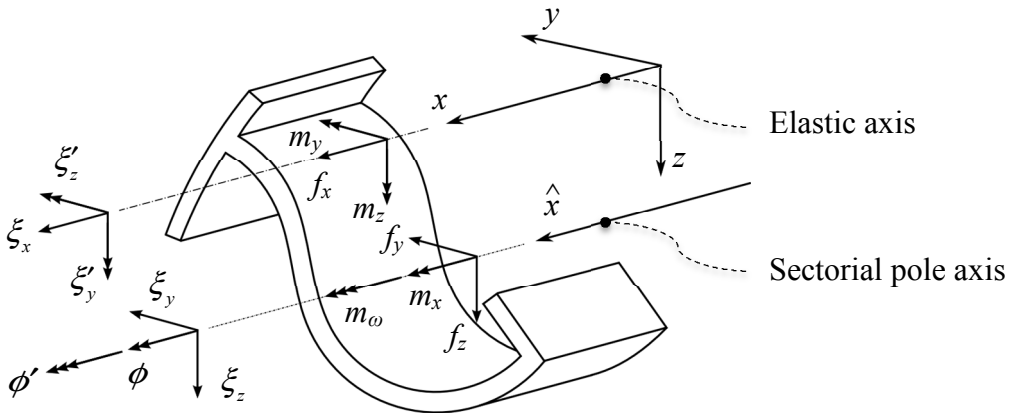


Figure 1: Element loading and generalized displacements.

For mono-symmetric cross-sections, being $z$ the axis of symmetry, and considering the principal global coordinate system ($x$,$y$,$z$), the principal sectorial pole $P$ and origin $O$, the dynamic equilibrium of the bridge's girder is given by

$$\rho A\ddot{\xi}_z + EI_{yy}\xi_z'''' = f_z \tag{4}$$

$$\rho\left(A\ddot{\xi}_y - S_y^P\ddot{\phi}\right) + EI_{zz}\xi_y'''' = f_y \tag{5}$$

$$\rho\left[-S_y^P\ddot{\xi}_y + \left(I_{zz}^P + I_{yy}^P\right)\ddot{\phi}\right] + EI_{\omega\omega}\phi'''' - GJ\phi'' = m_x \tag{6}$$

being the warping effect included and the rotary inertia of the cross-sections neglected.

## 3 FINITE ELEMENT SOLUTION

The developed beam finite element considers the six nodal degrees-of-freedom of a three-dimensional Euler-Bernoulli beam and an additional warping degree-of-freedom. This represents the out-of-plane displacements of the cross-sections when a beam is loaded in torsion. As depicted in Figure 2, the generalized displacements are referred to the centre of gravity, which motivates the presence of coupling terms in the element matrices.

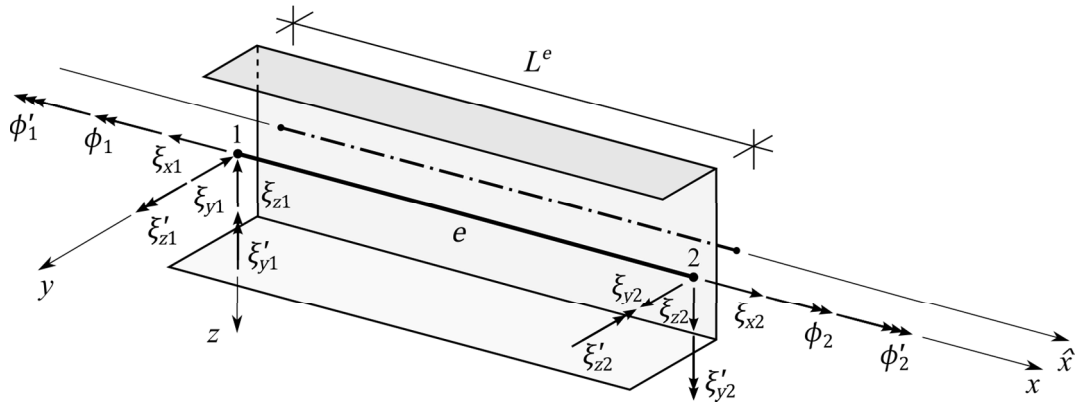


Figure 2: Beam element and the corresponding nodal degrees-of-freedom referred to the centre of gravity.

The element axial displacements $\xi_x^e$ are approximated by Lagrange's interpolation functions, whilst Hermite's cubic interpolation functions are suitable to the bending displacements $\xi_z^e$ and $\xi_y^e$ and to the torsional rotations $\phi$.

By applying the Galerkin's method, the governing equations are restated in the matrix form as follows:

$$\mathbf{M}^e\ddot{\boldsymbol{u}}^e + \mathbf{C}^e\dot{\boldsymbol{u}}^e + \mathbf{K}^e\boldsymbol{u}^e = \mathbf{f}^e \tag{7}$$

where $\mathbf{M}^e$ is the element mass matrix, $\mathbf{C}^e$ is the element damping matrix, $\mathbf{K}^e$ is the element stiffness matrix and $\mathbf{f}^e$ is the element external force vector. In [7], these matrices are thoroughly derived, being therein presented explicit expressions for their calculation.

The structural response to a time-dependent loading involves the solution of the differential equation (7) in time. To this end, the Newmark's $\beta$ method is used, [8].

## 4 ANALYTICAL SOLUTION

In this section, it is proposed an analytical model to perform the dynamic analysis of continuous thin-walled beams with mono-symmetric cross-section. The natural frequencies and the corresponding mode shapes of vibration are met exactly and the modal superposition method is used to determine the structural response to moving loads. The Newmark's $\beta$ method is applied to integrate of the governing equations in time.

The developed formulation considers an $N$-span bridge of total length $L$, as depicted in Figure 3, subjected to moving loads $f_z$, $f_y$ and $m_x$ of the form

$$f_z(x,t) = \sum_k^{n_{load}} \delta\left(x - x_k(t)\right) V_{zk}(t) \tag{8}$$

$$f_y(x,t) = \sum_k^{n_{load}} \delta\left(x - x_k(t)\right) V_{yk}(t) \tag{9}$$

$$m_x(x,t) = \sum_k^{n_{load}} \delta\left(x - x_k(t)\right) M_{xk}(t) \tag{10}$$

being $x_k(t)$ the position of the $k$-th load, $\delta(t)$ the Dirac delta function, $n_{load}$ the number of loads, $V_{ik}$ the $k$-th force parallel to the $i$-axis and $M_{xk}$ the resulting torsion moment.

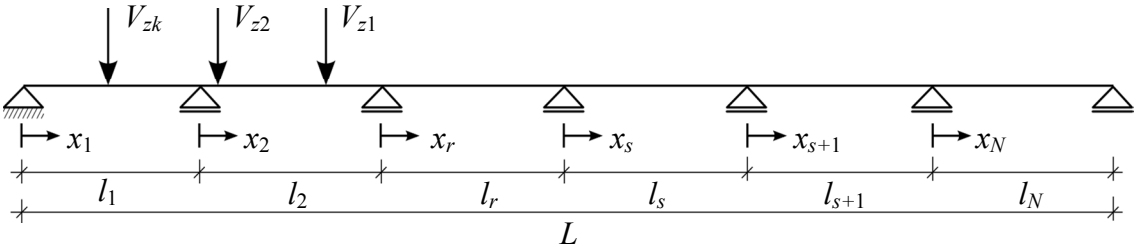


Figure 3: Model of the $N$-span bridge considered in the analytical formulation.

Considering that the generalized displacements are approximated by harmonic functions, the homogeneous solution of the equations (4)-(6) is given by

$$-\rho A p^2 \Xi_z(x) + EI_{yy}\Xi_z''''(x) = 0 \tag{11}$$

$$-\rho A p^2 \Xi_y(x) + \rho S_y^P p^2 \Phi(x) + EI_{zz}\Xi_y''''(x) = 0 \tag{12}$$

$$\rho S_y^P p^2 \Xi_y(x) - \rho\left(I_{zz}^P + I_{yy}^P\right) p^2 \Phi(x) + EI_{\omega\omega}\Phi''''(x) - GJ\Phi''(x) = 0 \tag{13}$$

being $\Xi_z$, $\Xi_y$ and $\Phi$ the shape functions of the vertical displacement $\xi_z$, lateral displacement $\xi_y$ and torsional rotation $\phi$, respectively, and $p$ is a circular frequency.

In the case of mono-symmetric cross-sections, being $z$ the axis of symmetry, the bending vibrations in the $xz$-plane are decoupled. Thus, the equation (11) reduces to

$$-\lambda^4 \Xi_z(x) + \Xi_z''''(x) = 0 \tag{14}$$

where the frequency parameter $\lambda$ is obtained by

$$\lambda^4 = \frac{\rho A p^2}{EI_{yy}} \tag{15}$$

The solution $\Xi_z$ of the equation (11) is given in trigonometric and hyperbolic terms by

$$\Xi_z(x) = \mathcal{A}_1 \cosh(\lambda x) + \mathcal{A}_2 \sinh(\lambda x) + \mathcal{A}_3 \cos(\lambda x) + \mathcal{A}_4 \sin(\lambda x) \tag{16}$$

being the $\mathcal{A}_j$ constants such that the boundary conditions are satisfied. This allows expressing three of the constants $\mathcal{A}_j$ as functions of the fourth, which represents an arbitrary amplitude of the mode shape.

For the case of coupled bending-torsional vibrations in the $xy$-plane, the solutions $\Xi_y$ and $\Phi$ of the equations (12)-(13) involve some mathematical treatment. By combining these two equations into one equation, eliminating either $\Xi_y$ or $\Phi$, [9], it is possible to obtain the following ordinary differential equation:

$$\left[ dD^8 - D^6 - \left(a + bd\right) D^4 + bD^2 + abc \right] \chi(x) = 0 \tag{17}$$

being $\chi$ either $\Xi_y$ or $\Phi$, $D$ is a differential operator in order to $x$, and the remaining parameters given by

$$a = \left( I_{zz}^P + I_{yy}^P \right) \frac{\rho p^2}{GJ} \qquad b = \frac{\rho A p^2}{EI_{zz}} \qquad c = 1 - \frac{S_y^{P2}}{A\left( I_{zz}^P + I_{yy}^P \right)} \qquad d = \frac{EI_{\omega\omega}}{GJ} \tag{18}$$

Considering an exponential solution for the differential equation (17) and performing a change of variables, the following quartic polynomial is obtained:

$$d\eta^4 - \eta^3 - \left(a + bd\right)\eta^2 + b\eta + abc = 0 \tag{19}$$

Since, for a physical problem, the coefficients $a$, $b$, $c$ and $d$ are always positive reals, being $c$ less than one, it is possible to show, [10] that all eight roots of the polynomial (19) are

$$\alpha, \quad -\alpha, \quad \beta, \quad -\beta, \quad \gamma, \quad -\gamma, \quad \delta \text{ and } \quad -\delta \tag{20}$$

where

$$\alpha = \sqrt{\eta_1}, \quad \beta = \sqrt{\eta_2}, \quad \gamma = \sqrt{\eta_3}, \quad \delta = \sqrt{\eta_4} \quad \text{and} \quad i = \sqrt{-1} \tag{21}$$

being $\eta_1$, $\eta_2$, $-\eta_3$ and $-\eta_4$ the four real roots of equation (19).

Thus, obtaining the solution $\chi$ of the equation (17), the lateral bending displacement $\Xi_y$ and the torsional rotation $\Phi$ are defined as follows:

$$\Xi_y(x) = \mathcal{B}_1\cosh(\alpha x) + \mathcal{B}_2\sinh(\alpha x) + \mathcal{B}_3\cosh(\beta x) + \mathcal{B}_4\sinh(\beta x) + \\ + \mathcal{B}_5\cos(\gamma x) + \mathcal{B}_6\sin(\gamma x) + \mathcal{B}_7\cos(\delta x) + \mathcal{B}_8\sin(\delta x) \tag{22}$$

$$\Phi(x) = \mathcal{C}_1\cosh(\alpha x) + \mathcal{C}_2\sinh(\alpha x) + \mathcal{C}_3\cosh(\beta x) + \mathcal{C}_4\sinh(\beta x) + \\ + \mathcal{C}_5\cos(\gamma x) + \mathcal{C}_6\sin(\gamma x) + \mathcal{C}_7\cos(\delta x) + \mathcal{C}_8\sin(\delta x) \tag{23}$$

The relations between the two sets of constant $\mathcal{B}_j$ and $\mathcal{C}_j$ are given by

$$\mathcal{C}_1 = \kappa_\alpha \mathcal{B}_1, \quad \mathcal{C}_2 = \kappa_\alpha \mathcal{B}_2, \quad \mathcal{C}_3 = \kappa_\beta \mathcal{B}_3, \quad \mathcal{C}_4 = \kappa_\beta \mathcal{B}_4, \\ \mathcal{C}_5 = \kappa_\gamma \mathcal{B}_5, \quad \mathcal{C}_6 = \kappa_\gamma \mathcal{B}_6, \quad \mathcal{C}_7 = \kappa_\delta \mathcal{B}_7, \quad \mathcal{C}_8 = \kappa_\delta \mathcal{B}_8, \tag{24}$$

where the coefficients $\kappa_\alpha$, $\kappa_\beta$, $\kappa_\gamma$ and $\kappa_\delta$ are defined as follows:

$$\kappa_\alpha = \frac{\rho A p^2 - EI_{zz}\alpha^4}{\rho S_y^P p^2}, \quad \kappa_\beta = \frac{\rho A p^2 - EI_{zz}\beta^4}{\rho S_y^P p^2}, \quad \kappa_\gamma = \frac{\rho A p^2 - EI_{zz}\gamma^4}{\rho S_y^P p^2}, \quad \kappa_\delta = \frac{\rho A p^2 - EI_{zz}\delta^4}{\rho S_y^P p^2} \tag{25}$$

In order to obtain the *n*-th frequency of vibration of the considered structure, the equations (16), (22) and (23) are applied to each span *s* along with the corresponding boundary conditions, as illustrated in Figure 4. The frequency of vibration is given by the equations that define the static boundary conditions at the last support of the span *N*. This assembly procedure was used by Chan and Ashebo, [5], being extended in the present work to coupled vibrations.

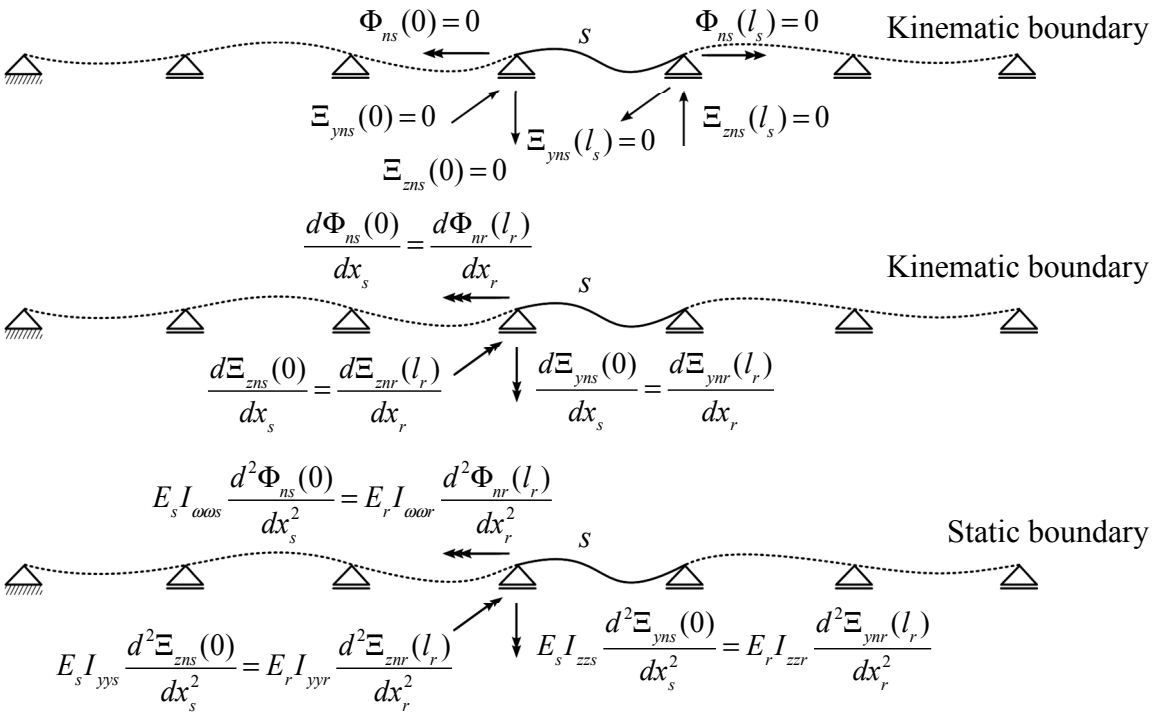


Figure 4: Boundary conditions at the supports of a generic span *s*.

The constants $\mathcal{A}_{jns}$ and $\mathcal{B}_{jns}$, resulting from the application of shape functions to the *s*-th span, are calculated by imposing the following static and kinematic boundary conditions at the corresponding supports:

$$\Xi_{zns}(0)=0, \quad \Xi_{zns}(l_s)=0, \quad \Xi_{yns}(0)=0, \quad \Xi_{yns}(l_s)=0, \quad \Phi_{ns}(0)=0, \quad \Phi_{ns}(l_s)=0 \tag{26}$$

$$\frac{d\Xi_{zns}(0)}{dx_s}=\frac{d\Xi_{znr}(l_r)}{dx_r},\quad \frac{d\Xi_{yns}(0)}{dx_s}=\frac{d\Xi_{ynr}(l_r)}{dx_r},\quad \frac{d\Phi_{ns}(0)}{dx_s}=\frac{d\Phi_{nr}(l_r)}{dx_r} \tag{27}$$

$$E_sI_{yys}\frac{d^2\Xi_{zns}(0)}{dx_s^2}=E_rI_{yyr}\frac{d^2\Xi_{znr}(l_r)}{dx_r^2},\quad E_sI_{zzs}\frac{d^2\Xi_{yns}(0)}{dx_s^2}=E_rI_{zzr}\frac{d^2\Xi_{ynr}(l_r)}{dx_r^2}$$
$$\text{and}\quad E_sI_{\omega\omega s}\frac{d^2\Phi_{ns}(0)}{dx_s^2}=E_rI_{\omega\omega r}\frac{d^2\Phi_{nr}(l_r)}{dx_r^2} \tag{28}$$

The case of decoupled vertical bending vibrations is firstly considered. By substituting the corresponding boundary conditions (26)-(28) in the equation (16), and considering that one of the four $\mathcal{A}_{jn1}$ constants, relative to the first span, represent an arbitrary amplitude of the shape function $\Xi_{zn1}$, yields

$$\mathcal{A}_{1n1}=0,\quad \mathcal{A}_{2n1}=1,\quad \mathcal{A}_{3n1}=0,\quad \mathcal{A}_{4n1}=-\frac{\sinh(\lambda_{n1}l_1)}{\sin(\lambda_{n1}l_1)} \tag{29}$$

and for the *s*-th inner span

$$\mathcal{A}_{1ns}=\frac{1}{2}\frac{E_rI_{yyr}}{E_sI_{yys}}\frac{\lambda_{nr}^2}{\lambda_{ns}^2}\left[\mathcal{A}_{1nr}\cosh(\lambda_{nr}l_r)+\mathcal{A}_{2nr}\sinh(\lambda_{nr}l_r)-\mathcal{A}_{3nr}\cos(\lambda_{nr}l_r)-\mathcal{A}_{4nr}\sin(\lambda_{nr}l_r)\right] \tag{30}$$

$$\mathcal{A}_{2ns}=\frac{\lambda_{nr}}{\lambda_{ns}}\left[\mathcal{A}_{1nr}\sinh(\lambda_{nr}l_r)+\mathcal{A}_{2nr}\cosh(\lambda_{nr}l_r)-\mathcal{A}_{3nr}\sin(\lambda_{nr}l_r)-\mathcal{A}_{4nr}\cos(\lambda_{nr}l_r)\right]\times$$
$$\times\frac{\sin(\lambda_{ns}l_s)}{\sin(\lambda_{ns}l_s)-\sinh(\lambda_{ns}l_s)}-\mathcal{A}_{1ns}\frac{\cos(\lambda_{ns}l_s)-\cosh(\lambda_{ns}l_s)}{\sin(\lambda_{ns}l_s)-\sinh(\lambda_{ns}l_s)} \tag{31}$$

$$\mathcal{A}_{3ns}=-\mathcal{A}_{1ns} \tag{32}$$

$$\mathcal{A}_{4ns}=\frac{\lambda_{nr}}{\lambda_{ns}}\left[\mathcal{A}_{1nr}\sinh(\lambda_{nr}l_r)+\mathcal{A}_{2nr}\cosh(\lambda_{nr}l_r)-\mathcal{A}_{3nr}\sin(\lambda_{nr}l_r)+\mathcal{A}_{4nr}\cos(\lambda_{nr}l_r)\right]-\mathcal{A}_{2ns} \tag{33}$$

Imposing the boundary condition on the bending moment at the last support of the span *N*, the following equation is obtained:

$$\mathcal{A}_{1nN}\cosh(\lambda_{nN}l_N)+\mathcal{A}_{2nN}\sinh(\lambda_{nN}l_N)-\mathcal{A}_{3nN}\cos(\lambda_{nN}l_N)-\mathcal{A}_{4nN}\sin(\lambda_{nN}l_N)=0 \tag{34}$$

which roots give the natural frequencies for the decoupled vertical bending motion. In the work of Chan and Ashebo, [5], the equation (34) is not presented, being the procedure of finding the natural frequencies unclear.

The frequencies of the coupled lateral bending-torsional vibrations are determined through a similar procedure. By substituting the remaining boundary conditions (26)-(28) in the equations (22)-(23), the eight $\mathcal{B}_{jn1}$ constants of the first span are given by

$$\mathcal{B}_{1n1}=0,\quad \mathcal{B}_{3n1}=0,\quad \mathcal{B}_{5n1}=0,\quad \mathcal{B}_{7n1}=0 \tag{35}$$

$$\mathcal{B}_{6n1}=\frac{\mathcal{B}_{2n1}\sinh(\alpha_{n1}l_1)(\kappa_{\delta1}-\kappa_{\alpha1})+\mathcal{B}_{4n1}\sinh(\beta_{n1}l_1)(\kappa_{\delta1}-\kappa_{\beta1})}{\sin(\gamma_{n1}l_1)(\kappa_{\gamma1}-\kappa_{\delta1})} \tag{36}$$

$$\mathcal{B}_{8n1} = \frac{\mathcal{B}_{2n1}\sinh(\alpha_{n1}l_1)(\kappa_{\alpha1}-\kappa_{\gamma1}) + \mathcal{B}_{4n1}\sinh(\beta_{n1}l_1)(\kappa_{\beta1}-\kappa_{\gamma1})}{\sin(\delta_{n1}l_1)(\kappa_{\gamma1}-\kappa_{\delta1})} \tag{37}$$

For the generic inner span $s$ the expressions of the eight constants $\mathcal{B}_{jns}$ may be easily obtained using symbolic algebra software. Once computed the explicit expressions for the constants $\mathcal{B}_{jns}$, it is straightforward to apply the presented analytical procedure to girders with any number of spans.

The $n$-th frequency of vibration is obtained by imposing the boundary conditions on the bending moment and the bimoment at the last support of the span $N$. These conditions can be written as functions of $\mathcal{B}_{2n1}$ and $\mathcal{B}_{4n1}$, yielding

$$\begin{bmatrix} S_{22} & S_{24} \\ S_{42} & S_{44} \end{bmatrix} \begin{Bmatrix} \mathcal{B}_{2n1} \\ \mathcal{B}_{4n1} \end{Bmatrix} = \mathbf{0} \tag{38}$$

where the matrix components $S_{kl}$ are determined by making $\mathcal{B}_{kn1}$ and $\mathcal{B}_{ln1}$ equal to zero and one, respectively, when the first span is evaluated, i.e., in equations (35)-(37). By giving $\mathcal{B}_{2n1}$ a unit value, the $\mathcal{B}_{jn1}$ constants are rewritten as follows:

$$\mathcal{B}_{1n1}=0, \quad \mathcal{B}_{3n1}=0, \quad \mathcal{B}_{5n1}=0, \quad \mathcal{B}_{7n1}=0, \quad \mathcal{B}_{2n1}=1, \quad \mathcal{B}_{4n1}=-\frac{S_{22}}{S_{24}} \tag{39}$$

$$\mathcal{B}_{6n1} = \frac{S_{24}\sinh(\alpha_{n1}l_1)(\kappa_{\delta1}-\kappa_{\alpha1}) + S_{22}\sinh(\beta_{n1}l_1)(\kappa_{\beta1}-\kappa_{\delta1})}{S_{24}\sin(\gamma_{n1}l_1)(\kappa_{\gamma1}-\kappa_{\delta1})} \tag{40}$$

$$\mathcal{B}_{8n1} = \frac{S_{24}\sinh(\alpha_{n1}l_1)(\kappa_{\alpha1}-\kappa_{\gamma1}) + S_{22}\sinh(\beta_{n1}l_1)(\kappa_{\gamma1}-\kappa_{\beta1})}{S_{24}\sin(\delta_{n1}l_1)(\kappa_{\gamma1}-\kappa_{\beta1})} \tag{41}$$

Finally, the $n$-th frequency of vibration for the coupled bending-torsional motion is calculated be seeking for the roots of the equation

$$\det\left(\begin{bmatrix} S_{22} & S_{24} \\ S_{42} & S_{44} \end{bmatrix}\right) = 0 \tag{42}$$

Once the frequencies of vibration have been calculated, the $m$- and the $n$-th mode shape, in which the continuous beam is said to respond when vibrates with a frequency $p_m$ or $p_n$, is established by the explicit expressions

$$\Xi_{zm}(x) = \sum_{s=1}^{N}\left[\mathrm{H}(x-\sum_{r=1}^{s-1}l_r) - \mathrm{H}(x-\sum_{r=1}^{s}l_r)\right]\Xi_{zms}(x_s) \tag{43}$$

$$\Xi_{yn}(x) = \sum_{s=1}^{N}\left[\mathrm{H}(x-\sum_{r=1}^{s-1}l_r) - \mathrm{H}(x-\sum_{r=1}^{s}l_r)\right]\Xi_{yns}(x_s) \tag{44}$$

$$\Phi_{n}(x) = \sum_{s=1}^{N}\left[\mathrm{H}(x-\sum_{r=1}^{s-1}l_r) - \mathrm{H}(x-\sum_{r=1}^{s}l_r)\right]\Phi_{ns}(x_s) \tag{45}$$

being H the Heaviside step function.

To quantify the damping properties, it is established a proportional relation to the modal mass properties. Considering the modal superposition method, the beam's generalized displacements $\xi_z$, $\xi_y$ and $\phi$ are redefined as

$$\xi_z(x,t) = \sum_k^{\infty} \Xi_{zk}(x)\, \Psi_k(t) \tag{46}$$

$$\xi_y(x,t) = \sum_l^{\infty} \Xi_{yl}(x)\, \Upsilon_l(t) \tag{47}$$

$$\phi(x,t) = \sum_l^{\infty} \Phi_l(x)\, \Upsilon_l(t) \tag{48}$$

where $\Psi_k$ and ®$_l$ are the time-varying amplitudes of the $k$-th and the $l$-th vibration modes.

By applying the Betti's law, the orthogonality conditions of the vibration mode shapes $m$ and $n$ with respect to mass yield

$$\int_0^L \Xi_{zm}(x)\, \Xi_{zn}(x)\, dx = 0 \tag{49}$$

$$\int_0^L \left[ \rho A\, \Xi_{ym}(x)\, \Xi_{yn}(x) + \rho \left( I_{zz}^P + I_{yy}^P \right) \Phi_m(x)\, \Phi_n(x) \right] dx = 0 \tag{50}$$

The decoupling of the governing equations (4)-(6) is accomplished by considering the modal coordinate expressions (46)-(47), leading to

$$M_{zm} \ddot{\Psi}_m(t) + C_{zm} \dot{\Psi}_m(t) + p_m^2 M_{zm} \Psi_m(t) = P_{zm}(t) \tag{51}$$

$$M_{y\phi n} \ddot{\Upsilon}_n(t) + C_{y\phi n} \dot{\Upsilon}_n(t) + p_n^2 M_{y\phi n} \Upsilon_n(t) = P_{y\phi n}(t) \tag{52}$$

where

$$M_{zm} = \rho A \int_0^L \Xi_{zm}^2(x)\, dx, \quad C_{zm} = 2\zeta_{zm} p_m M_{zm}, \quad P_{zm} = \int_0^L \Xi_{zm}(x) f_z(x,t)\, dx \tag{53}$$

$$\begin{aligned} &M_{y\phi n} = \int_0^L \left[ \rho A\, \Xi_{yn}^2(x) + \rho \left( I_{zz}^P + I_{yy}^P \right) \Phi_n^2(x) \right] dx, \quad C_{y\phi n} = 2\zeta_{y\phi n} p_n M_{y\phi n} \\ &\text{and} \quad P_{y\phi n} = \int_0^L \left[ \Xi_{yn}(x) f_y(x,t) + \Phi_n(x) m_x(x,t) \right] dx \end{aligned} \tag{54}$$

being $\zeta_{zm}$ and $\zeta_{y\phi n}$ the modal viscous damping ratios of each vibration mode.

The dynamic response of the structure under the action of moving loads is obtained by applying the Newmark's $\beta$ method to the equations (51)-(52).

## 5 DYNAMIC RESPONSE OF CONTINUOUS BEAMS UNDER MOVING LOADS

In the sequel, the proposed numerical and the analytical beam models are applied in order to perform the dynamic analysis of a multi-span bridge eccentrically traversed by moving vehicles. The longitudinal model is shown in Figure 5 and the prescribed boundary conditions at the supports are listed in Table 2. The dynamic responses are obtained by taking into account the high-speed universal trains HSLM-A10 proposed by the EN 1991-2, [11], travelling at 80 and 120 ms$^{-1}$. The mass effect of the moving loads is also considered.

An open double-T cross section is considered, being the material and the geometrical properties presented in Table 1.

| $E$ (kN/m$^2$) | $G$ (kN/m$^2$) | $\rho$ (ton/m$^3$) | $A$ (m$^2$) | $J$ (m$^4$) | $I_{yy}$ (m$^4$) | $I_{zz}$ (m$^4$) | $I_{z\omega}$ (m$^5$) |
|---|---|---|---|---|---|---|---|
| 33000 | 13750 | 2.55 | 9.51 | 1.22 | 9.16 | 122.37 | 175.74 |

Table 1: Material and geometrical properties of the cross-section considered in the examples.

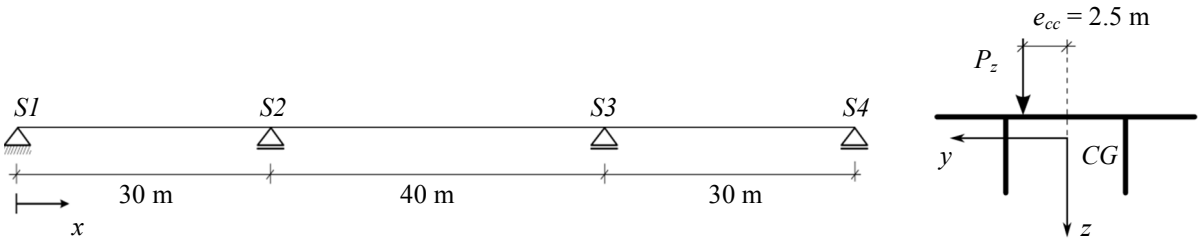


Figure 5: Longitudinal model of the considered three-span girder.

| Support | Nodal Coordinate | Kinematic Boundary Conditions | Static Boundary Conditions |
|---|---|---|---|
| *S1* | $x = 0$ m | $\xi_z(x)=\xi_y(x)=\phi(x)=0$ | $\xi_z''(x)=\xi_y''(x)=\phi''(x)=0$ |
| *S2* | $x = 30$ m | $\xi_z(x)=\xi_y(x)=\phi(x)=0$<br>$\xi_z'(x^-)=\xi_z'(x^+)$ | $\xi_z''(x^-)=\xi_z''(x^+)$<br>$\xi_y''(x^-)=\xi_y''(x^+)$ |
| *S3* | $x = 70$ m | $\xi_y'(x^-)=\xi_y'(x^+)$<br>$\phi'(x^-)=\phi'(x^+)$ | $\phi''(x^-)=\phi''(x^+)$ |
| *S4* | $x = 100$ m | $\xi_z(x)=\xi_y(x)=\phi(x)=0$ | $\xi_z''(x)=\xi_y''(x)=\phi''(x)=0$ |

Table 2: Prescribed boundary conditions at the supports of the three-span girder.

The natural frequencies calculated by the two beam models are compared in Table 3 with the values given by the shell finite element model.

The dynamic influence lines of the vertical displacements and accelerations at the track's mid-point of the central span are presented in Figure 6 and Figure 7.

| Frequencies of Vibration in the plane *xz* (Hz) | | | |
|---|---|---|---|
| Frequency Number | Model of Analysis | | |
| | Numerical | Analytical | Shell FEM |
| 1 | 4.58 | 4.59 | 4.43 |
| 2 | 7.48 | 7.52 | 7.05 |
| 3 | 8.97 | 9.02 | 8.19 |
| 4 | 17.07 | 17.29 | 15.05 |
| 5 | 25.84 | 26.40 | 22.20 |
| 6 | 28.18 | 28.78 | 23.31 |

| Frequencies of Vibration in the plane *xy* (Hz) | | | |
|---|---|---|---|
| Frequency Number | Model of Analysis | | |
| | Numerical | Analytical | Shell FEM |
| 1 | 4.87 | 4.89 | 4.76 |
| 2 | 7.41 | 7.45 | 7.10 |
| 3 | 8.53 | 8.57 | 7.91 |
| 4 | 15.78 | 15.93 | 14.11 |
| 5 | 17.17 | 18.11 | 12.74 |
| 6 | 23.55 | 23.94 | 20.46 |

Table 3: Natural frequencies of vibration of the considered girder.

In the next, the mass effect of the moving vehicles is taken into account in the dynamic response of the three-span girder. Therefore, the considered loading is written as follows:

$$f_z(x,t)=\sum_k^{n_{load}} \delta\big(x-x_k(t)\big)\left[V_{zk}(t)-m_k\frac{d^2v_k}{dt^2}\right] \quad \text{and} \quad m_x(x,t)=f_z(x,t)\,e_{cc} \tag{55}$$

being $x_k(t)$ the position and $m_k$ the mass of the $k$-th load, $v_k$ is the vertical displacement of the moving mass $m_k$, $\delta$ the Dirac delta function, $n_{load}$ the number of loads and $e_{cc}$ is the eccentricity of the track's position.

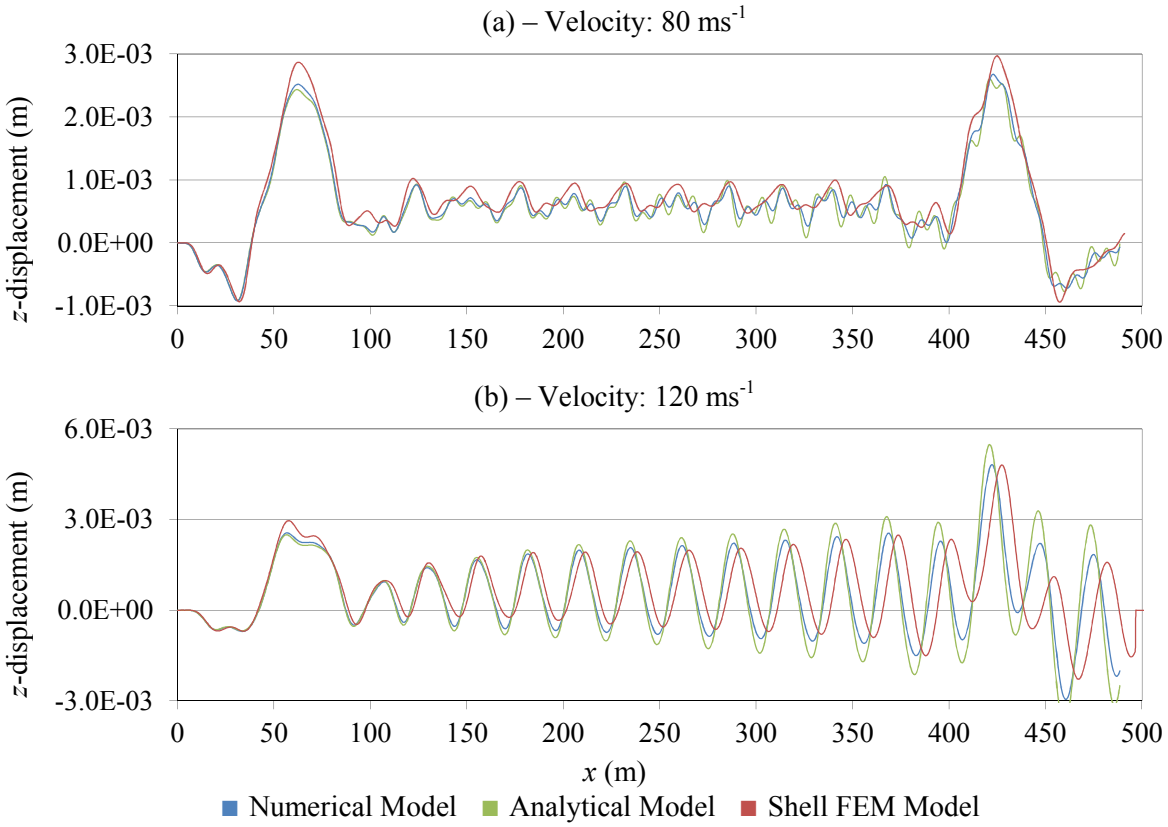


Figure 6: Dynamic influence lines of the $z$-displacement at the track's mid-point of the central span.

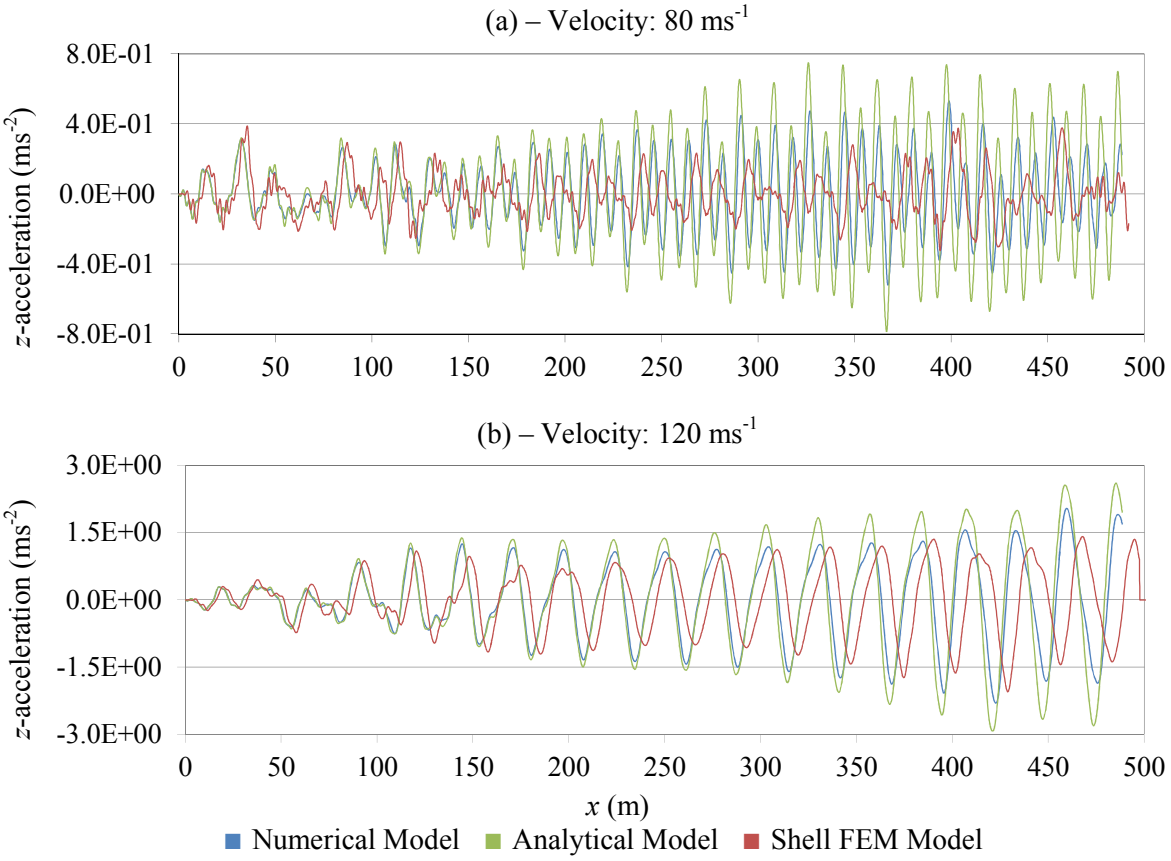


Figure 7: Dynamic influence lines of the $z$-acceleration at the track's mid-point of the central span.

Since the load is acting on a moving coordinate, $v_k$ and its derivatives with respect to time $t$ are given as follows, [12]:

$$v_k(t)=\xi_z(ct,t)\,,\quad \frac{dv_k}{dt}=\frac{\partial\xi_z}{\partial t}+c\frac{\partial\xi_z}{\partial x}\,,\quad \frac{d^2v_k}{dt^2}=\frac{\partial^2\xi_z}{\partial t^2}+2c\frac{\partial\xi_z}{\partial t}\frac{\partial\xi_z}{\partial x}+c^2\frac{\partial^2\xi_z}{\partial x^2} \tag{56}$$

where $c$ represents the velocity of the moving masses. Notice that it is assumed that the masses do not separate from the beam during their travel and vertical vibration.

In Figure 8 the dynamic response considering the mass of the vehicles is represented. The influence of constrained warping is also evaluated by using the numerical model. It is observed that both the displacements and accelerations in the $z$ direction are lower than when the warping effect is considered.

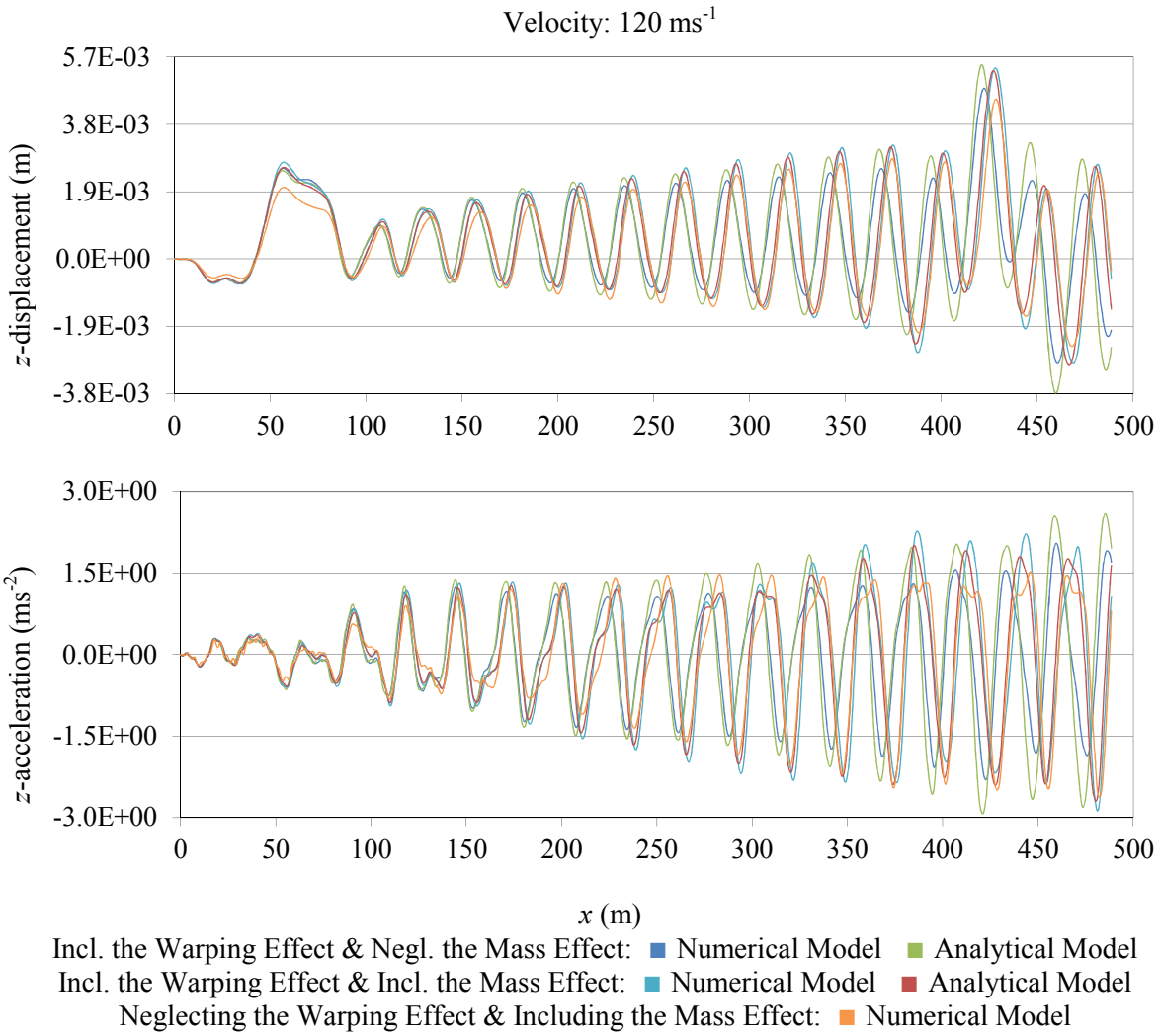


Figure 8: Influence of the mass effect on the influence lines of the $z$-displacement at the track's mid-point of the central span.

## 6 CONCLUSION

The main objective of the present work was to provide two beam models capable of performing dynamic analyses of railway bridges, being considered the warping displacements and the mass effects of the moving loads.

In the previous sections, a *numerical* and an *analytical* beam models were developed and applied to the analysis of an open cross-section girder. The torsional response was shown to be significantly influenced by the warping deformations.

The developed beam models gave good results, being in good agreement with the shell finite element model implemented in commercial software. Thus, the developed models perform efficient dynamic analyses that consider the warping effect, which may be very useful at early design stages.

The presented models could serve as a starting point for further in-depth study of the subject and may be considered as a first step tending to more complete formulations accounting for other aspects that have not been considered.

## REFERENCES

[1] D. Lisi, *A Beam Finite Element Model Including Warping – Application to the Dynamic and Static Analysis of Bridge Decks*, IST, Técnico Lisboa, 2011.

[2] D.S. Sophianopoulos and G.T. Michaltsos, Combined torsional-lateral vibrations of beams under vehicular loading – I: formulation and solution techniques, *Automatic Control & Robotics*, 2, 877-886, 1999.

[3] L.T. Stayridis and G.T. Michaltsos, Eigenfrequency analysis of thin-walled girders curved in plan, *Journal of Sound and Vibration*, 227, 383-396, 1999.

[4] G.T. Michaltsos, E. Sarantithou and D.S. Sophianopoulos, Flexural-torsional vibration of simply supported open cross-section steel beams under moving loads, *Journal of Sound and Vibration*, 280, 479-494, 2005.

[5] T.H.T. Chan and D.B. Ashebo, Theoretical study of moving force identification on continuous bridges, *Journal of Sound and Vibration*, 295, 870-883, 2006.

[6] A. Graça, *Modelação da Resposta em Pontes Devido à Passagem de Comboios de Alta Velocidade – formulação e implementação computacional de um modelo para simulação do efeito da passagem de comboios de alta velocidade em pontes*, Master Dissertation, IST, Técnico Lisboa, 2011.

[7] J. Serra, *Dynamic Analysis of Bridge Girders Subjected to Moving Loads – Numerical and Analytical Beam Models Considering Warping Effects*, IST, Técnico Lisboa, 2014.

[8] W. Wunderlich and W.D. Pilkey, *Mechanics of Structures – Variational and Computational Methods*, Second Edition, CRC Press, 2003.

[9] J.R. Banerjee, S. Guo and W.P. Howson, Exact dynamic stiffness matrix of a bending-torsion coupled beam including warping, *Computers & Structures*, 59(4), 613-621, 1996.

[10] R.E.D. Bishop, S.M. Cannon and S. Miao, On coupled bending and torsional vibration of uniform beams, *Journal of Sound and Vibration*, 131(3), 457-464, 1989.

[11] EN 1991-2: Actions on structures – Part 2: Traffic loads on bridges, CEN – European Commitee for Standardization.

[12] H. Ouyang, Moving-load dynamic problems: A tutorial (with brief overview), *Mechanical Systems and Signal Processing*, 25, 2039-2060, 2011.

COMPDYN 2017
6th ECCOMAS Thematic Conference on
Computational Methods in Structural Dynamics and Earthquake Engineering
M. Papadrakakis, M. Fragiadakis (eds.)
Rhodes Island, Greece, 15–17 June 2017

# DYNAMICAL BEHAVIOR OF A WIND TURBINE POWER TRAIN CONSIDERING A ROTOR-GEARBOX-GENERATOR COUPLED MODEL

**Rafael M. Teixeira[1], Flavia M. Ohara[2], Matheus D. Milhomens[3], Aline S. de Paula[4]**
Universidade de Brasília, Department of Mechanical Engineering 70.910.900 - Brasília-DF, Brazil
rafaelm.teixeira@hotmail.com
fla_mo@hotmail.com
mdmilhomens@gmail.com
alinedepaula@unb.br

**Keywords:** Wind turbine, electromechanical dynamics, power train, rotor, gearbox, generator.

**Abstract.** *The world's energy demand is growing with increasing population and development in emerging markets. Electricity generation from fossil fuels, which represent the main source of energy in the world, is responsible for a significant amount of land, water and air pollution due to CO2 production as well as other greenhouse gases emissions. In this context, the use of renewable energy sources has gained a lot of attention in the last decades, as solar, biomass and wind energies. Considering the high wind energy potential worldwide, wind turbine modeling and analysis has been studied by several authors recently. The goal is to have a better understanding of the system behavior in order to increase the efficiency in the energy conversion and reduce the cost. The electromechanical dynamics of power train- which is composed mainly by the rotor, gearbox and generator - plays an important role on the turbine performance. In the literature, it is usual to focus on the modeling of one of these three elements and consider simplified dynamics to the others. In this paper, a complete model is considered, named rotor-gearbox-generator coupled model, where the three elements are focused on with the goal of obtaining a more realistic representation of wind turbines power train. The gear box considered in this work consists in a two-stage planetary with epicyclicgearing, while a permanent magnet synchronous generator is considered. The dynamical behavior is evaluated for different loads showing system behaviorand energy conversion efficiency.*

## 1 INTRODUCTION

The challenges posed by the need to implement policies that ensure sustainable development are particularly relevant in the field of energy. Increasingly it is faced the need to find in renewable energy a real and feasible way of electricity production when comparable to conventional energy sources, whose are responsible for serious environmental threats.

Wind power is a clean and renewable alternative to the production of electricity, which is aligned with the goals proposed by the Kyoto Protocol, since its use contributes to the reduction of greenhouse gases,especially in countries whose energy matrix is predominantly fossil. Unlike hydroelectric plants, wind farms do not cause expropriation areas and relocation of people.Thus, wind energy is well accepted in social and environmental points of view[6].

A wind turbine is a system composed basically of a rotor, a low-speed input shaft, a gearbox (speed multiplier), a high-speed output shaft and a generator. Figure 1 shows the components of the turbine.

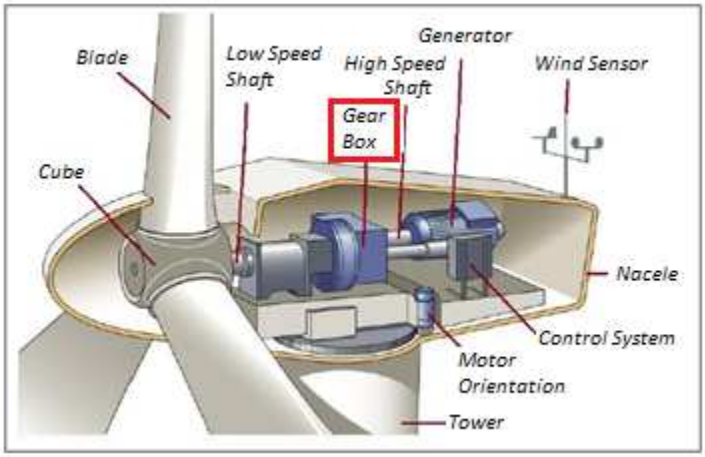


Figure1. Components of a wind turbine.

Wind turbines are devices capable of converting kinetic energy of the wind into electrical energy. Its operation consists in the rotation of rotor blades due to the force of the wind, which is connected to a low speed shaft. This shaft is then coupled to a multiplier box in order to obtain a high speed shaft, which is responsible for driving an electrical generator.

One of the most important components in the wind turbines is the Gear Box, highlighted in Figure 1, which is responsible for increasingthe shaft rotation providing appropriate speed to the generator.

Several research papers on wind turbines are currently being published.However, it is usual to focus on the modeling of one of the three principal elements (rotor, gear box, generator) and consider simplified dynamics to the others.

Betz [3],Heir[7], Busawon [4] and Johnson [9] presentedstudies related to the dynamics of the wind turbine rotor. Still related to the rotor, Manyoge [12] presented a mathematical model to describe the power coefficient behavior, which is used in the present work. Peeters [16][17], Todorov [18], WeiShi[20], Datong [5], Wang [21] and Helsen [8]studied mathematical models related to the gearbox of wind turbines (the mechanical part of the power train). Regarding the generator, Marques [13], Bernardes [2], Ming Yin [14], Bastos [1] and Lei [11]studied mathematical models related to the generator. Vásques [19] developed mathematical models of permanent magnet synchronous generators for hydrokinetic systems. Given the similarity with wind systems, the model is perfectly feasible to wind turbines and is used in the present work.

From the literature, there is a clear separation between works that considers mechanical and electrical analysis. The goal of this work is to analyze the dynamics of the power train considering a complete electromechanical model, that contemplates the coupled dynamics of rotor, gearbox and generator.

## 2 ROTOR-GEARBOX-GENERATOR MODEL

### 2.1 Rotor

The rotor is the component responsible for transforming the kinetic energy of the wind into rotational mechanical energy. Considering rotor configuration, there are two types of wind turbines: upwind and downwind. In the upwind turbines, the rotor is positioned in front of the tower. Unlike the downwind, where the rotor stays behind the tower.

Rotors with 3 blades are more common because they present a good relation between power ratio, cost and speed of rotation, as well as better aesthetics compared to 2-bladed turbines. This work is based on an upwind rotor with 3 blades.

#### 2.1.1 Power extracted from the wind

The power extracted from the winds depends on several variables such as air density, wind speed, rotor rotation and rotor geometry. The definition of extracted power, given by Busawon [4], is shown un Eq. (1) and represents the mechanical power related to the rotational behavior of the rotor.

$$P_{mec} = \frac{1}{2}\rho\pi r^2 V_0^3 C_p(\lambda,\beta) \tag{1}$$

where $\rho$ is the air density, $r$is the radius of the rotor, $V_0$ is the wind speed, and $C_p$is the power coefficient, which depends on the blade tip velocity ratio$\lambda$, the rotor blade geometry and the number of Reynolds of the flow in relation to the diameter of the rotor [18].

There are expressions for $C_p$determined numerically, as the one presented by Heier [7], that brings an approximation in terms of $\lambda$ and $\beta$, as follows:

$$C_p(\lambda,\beta) = a_1\left(\frac{a_2}{\lambda_i} - a_3\beta - a_4\beta^{a_5} - a_6\right)e^{-\frac{a_7}{\lambda_i}} \tag{2}$$

where the term $\lambda_i$ is given by:

$$\lambda_i = \frac{1}{\frac{1}{\lambda + a_8\beta} - \frac{a_9}{\beta^{3+1}}} \tag{3}$$

The constants $a_i$ with $i = 1,\ldots,9$ can be modified according to the type of turbine to be analyzed for better adjustment.

Once the extracted power is determined by Eq. (1), the mechanical input torque of the turbine is given as presented in Eq.(4).

$$T_{mec} = \frac{P_{mec}}{\omega_{rot}} \tag{4}$$

where $\omega_{rot}$is the speed of the output shaft of the rotor.

## 2.2 Gearbox

The multiplier box of the wind turbines is responsible for transmitting the mechanical energy delivered by the rotor shaft to the generator and is necessary for the input speed to be multiplied to suit the speed required for the electric generator. They are usually made up of shafts, drive gears and couplings.

The gearbox model developed in this work, shown in Fig. 2, is a commercial model of the company TGM, with a multiplication system composed of two stages in series of epicyclic trains.

One train is composed of four planets gears and while the other has three. Fig.2 shows a schematic picture of the gearbox, whose symbol $J_i$ refers to the moment of inertia, $Z_i$ the number of teeth of the gears, $m_i$ the masses of the planets gears, $r_{c.i}$ the radius of the Carrier arms , and $\varphi_i$ the absolute angular displacement of a fixed coordinate. The index $i = 1, 2, 3, 4, R_1, 5, 6, 7, R_2, 8$ correspond to the rotor, carrier (2), planet gears, sun gear and ring gear of the first stage, carrier (5), planet gears, sun gear and ring gear of the second stage and the generator, respectively. $K_1$, $K_2$, $K_3$refers to the stiffness of each shaft.

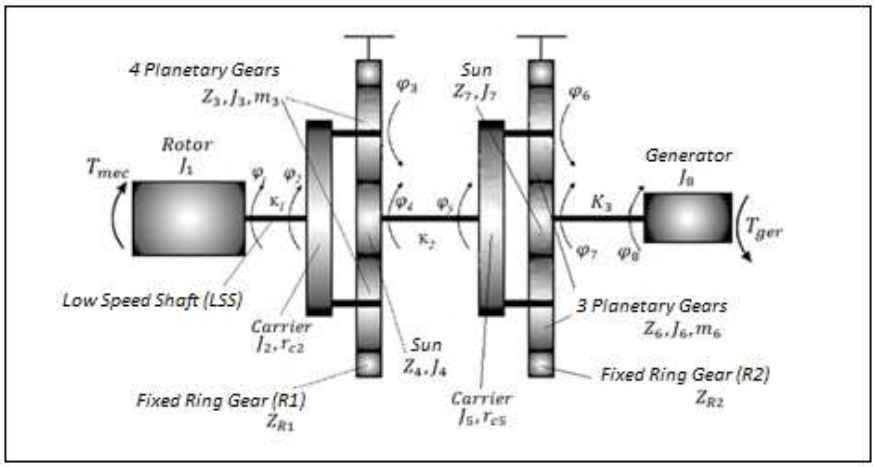


Figure 2. Schematic drawing of the gearbox TGM.

Mathematical modeling is performed by applying the Lagrange equations, and considering totally rigid bodies (except axles) and all rotational only motions (except planetary gears that have tangential translation movements to the sun gears).

Considering the gear ratios $\gamma$, using the number of teeth$Zr$and$Z$of the gears shown in Eq. 5, we have the kinematic relations (Eq. 6), used in the system model [15].

$$\begin{aligned} \gamma_1 &= 1 - (Zr1/Z3)\gamma_2 = 1 + (\mathrm{Zr1/Z4}) \\ \gamma_3 &= 1 - (Zr2/Z6)\gamma_4 = 1 + (Zr2/Z7) \end{aligned} \tag{5}$$

$$\dot{\varphi}_3 = \gamma_1\dot{\varphi}_2\dot{\varphi}_4 = \gamma_2\dot{\varphi}_2$$
$$\dot{\varphi}_6 = \gamma_3\dot{\varphi}_5\dot{\varphi}_7 = \gamma_4\dot{\varphi}_5 \quad (6)$$

Simplifying the equations of the system, using the relations shown in Eq. 6, we obtain the system of only 4 degrees of freedom.

Eq. (7) shows the four equations of motion for the multiplier set.

$$\varphi_1: J_1\ddot{\varphi}_1 + K_1\varphi_1 - K_1\varphi_2 = T_{mec} - \mu_1\text{atan}\,(\dot{\varphi}_1 e^6) - C_1\dot{\varphi}_1 + C_1\dot{\varphi}_4$$

$$\varphi_2: [J_2 + 4m_3r_{c2}^2 + 4J_3\gamma_1^2 + J_4\gamma_2^2]\ddot{\varphi}_2 + [K_1 + \gamma_2^2K_2]\varphi_2 - K_1\varphi_1 - \gamma_2K_2\varphi_5 = -\mu_2\text{atan}\,(\dot{\varphi_2 e^6}) - C_1\dot{\varphi}_2 - (C_1 + \gamma_2^2C_2)\varphi_5$$

$$\varphi_5: [J_5 + 3m_6r_{c5}^2 + 3J_6\gamma_3^2 + J_7\gamma_4^2]\ddot{\varphi}_5 + [K_2 + \gamma_4^2K_3]\varphi_5 - \gamma_2K_2\varphi_2 - \gamma_4K_3\varphi_8 = -\mu_3\text{atan}\,(\dot{\varphi_5 e^6}) + C_2(\gamma_2\dot{\varphi}_5) - C_2 + \gamma_4^2C_3 + C_3(\gamma_4\dot{\varphi}_8)$$

$$\varphi_8: J_8\ddot{\varphi}_8 + K_3\varphi_8 - \gamma_4K_3\varphi_5 = T_{ger} - \mu_4\text{atan}\,(\dot{\varphi}_8 e^6) - C_3\dot{\varphi}_8 + C_3(\gamma_4\dot{\varphi}_6) \quad (7)$$

## 2.3 Generator

The generator considered in this work is asynchronous generator of permanent magnets (permanent magnet synchronous generator, PMSG). These generators have high performance and have no slip rings or windings, that are replaced by magnetic elements [2].

Using the mathematical model that defines the dynamics of the generator (synchronous of three-phase protruding poles), the equations of movement of the generator as a function of $i_d$ e $i_q$can be represented by Eq. (8), as detailed by Vásques [19].

$$i_d = (L_L + L_d)\frac{di_d}{dt} = -(R_L + R_S)i_d + \left(L_L + L_q\right)\frac{N_P}{2}\omega_{mec}i_q$$
$$i_q = \left(L_L + L_q\right)\frac{di_q}{dt} = -(R_L + R_S)i_q - (L_L + L_d)\frac{N_P}{2}\dot{\varphi}_8 i_d - \frac{N_P}{2}\omega_{mec}\psi_{pm} \quad (8)$$

where$i_d$ and$i_q$are the currents in the direct axis and the quadrature axis of the generator respectively, $\omega_{mec}$is the velocity of the output shaft of the multiplier and $\psi_{pm}$ é is the magnetic coupling flux of the generator.

In a wind turbine, a value of much interest in the project is the power generated. The active power of the generator is given by Eq. 9:

$$P_{ativ} = \frac{3}{2}(V_d i_d + V_q i_q) \quad (9)$$

Another important value is the electrical power that was actually converted from the mechanical power. The electromechanical power of the generator is given by the expression, Eq. (10):

$$P_{ele} = \frac{3}{2}\omega_e(\psi_d i_q - \psi_q i_d) \quad (10)$$

where$\omega_e$is the electric angular velocity and $\psi_d$and$\psi_q$are the direct and quadrature magnetic fluxes respectively.

The power generated is the product of the mechanical speed $\omega_{mec}$with the electric torque$T_{ger}$.

In this way, the expression for the generator torque shown in Eq.11:

$$T_{ger} = \frac{3N_p}{4}\left[\psi_{pm} i_q + \left(L_d - L_q\right) i_d i_q\right] \tag{11}$$

## 3 ROTOR-GEARBOX-GENERATOR MODEL COUPLED

Attaching the mechanical (Eqs. 4 e 6) and electrical (Eqs. 8 e 11) parts and considering the state variables$\{x_1, x_2, x_3, x_4, x_5, x_6, x_7, x_8, x_9, x_{10}\} = \{\varphi_1, \dot{\varphi}_1, \varphi_2, \dot{\varphi}_2, \varphi_5, \dot{\varphi}_5, \varphi_8, \dot{\varphi}_8, i_d, i_q\}$, the equations of motion can be rewritten as a set of first-order differential equations, Eq. (12). Note that the angular velocity $\omega_{mec}$ is variable $\dot{\varphi}_8$ while the speed of the rotor,$\omega_{\mathrm{rot}}$, is variable $\dot{\varphi}_1$.

$$\begin{aligned}
\dot{x}_1 &= x_2 \\
\dot{x}_2 &= \frac{-C_1 x_2 + C_1 x_4 - \mu_1 \mathrm{atan}\,(x_2 e^6) - K_1 x_1 + K_1 x_3 + T_{mec}}{J_1} \\
\dot{x}_3 &= x_4 \\
\dot{x}_4 &= \frac{-C_1 x_2 - (C_1 + \gamma_2^2 C_2) x_4 + \gamma_2 x_6 C_2 - \mu_2 \mathrm{atan}\,(x_4 e^6) - [K_1 + \gamma_2^2 K_2] x_3 + K_1 x_1 + \gamma_2 K_2 x_5}{J_2 + 4m_3 r_{c2}^2 + 4J_3 \gamma_1^2 + J_4 \gamma_2^2} \\
\dot{x}_5 &= x_6 \\
\dot{x}_6 &= \frac{\gamma_2 x_4 C_2 - (C_2 + \gamma_4^2 C_3) x_6 + \gamma_4 x_8 C_3 - \mu_3 \mathrm{atan}\,(x_6 e^6) + \gamma_2 K_2 x_3 - [K_2 + \gamma_4^2 K_3] x_5 + \gamma_4 K_3 x_7}{J_5 + 3m_6 r_{c5}^2 + 3J_6 \gamma_3^2 + J_7 \gamma_4^2} \\
\dot{x}_7 &= x_8 \\
\dot{x}_8 &= \frac{C_3 \gamma_4 x_6 - C_3 x_8 - \mu_4 \mathrm{atan}\,(x_8 e^6) - K_3 x_7 + K_3 \gamma_4 x_5 - T_{ger}}{J_8} \\
\dot{x}_9 &= \frac{-(R_L + R_S) x_9 + (L_L + L_q) \frac{N_P}{2} x_8 x_{10}}{(L_L + L_d)} \\
\dot{x}_{10} &= \frac{-(R_L + R_S) x_{10} - (L_L + L_d) \frac{N_P}{2} x_8 x_9 - \frac{N_P}{2} x_8 \psi_{pm}}{\left(L_L + L_q\right)}
\end{aligned} \tag{12}$$

The efficiency of the system is also a very important parameter of analysis in the design of a wind turbine. It indicates how much electrical energy can be obtained given an input power. Efficiency is obtained by calculating the ratio of the active power $P_{ativ}$, given by Eq. 9, and the mechanical input power,$P_{mec}$, as shown in Eq. 13.

$$\eta = \frac{P_{ativ}}{P_{mec}} \tag{13}$$

## 4 DYNAMIC ANALYSIS OF THE COMPLETE SYSTEM

Analysis is carried out by numerical integration of Eq. (12)using Runge-Kutta of 4th order. Gearbox parameters are provided by TGM and presented in Table 1. Generator parameters are the same used by Tucunaré project [19], as presented in Table 2.

| Element | Mass (kg) | Total Inertia (kg.m²) | Diameter (mm) | Stiffness (N/m) | Viscous Damping (N/m) |
|---|---|---|---|---|---|
| Input axis 1 | -- | -- | -- | $1.468210^8$ | $7.3411x10^4$ |
| Carrier 2 | -- | J2=160.9612 | 676 | -- | -- |
| Gears Planets 3 | 20.64 | J3=8.7649 | -- | -- | -- |
| Solar gear 4 | -- | J4=2.2026 | -- | -- | -- |
| Axis 2 | -- | -- | -- | $0.4203x10^8$ | $2.1015x10^4$ |
| Carrier 5 | -- | J5=53.0721 | 588 | -- | -- |
| Gears Planets 6 | 11.0867 | J6=3.2232 | -- | -- | -- |
| Solar gear 7 | -- | J7=0.1765 | -- | -- | -- |
| Axis 3 | -- | -- | -- | $0.0483x10^8$ | $0.2417x10^4$ |
| Generator | -- | J8=22.2548 | -- | -- | -- |

Table 1.TGM gearbox Components information.

| Gearbox efficiency $\eta$ | Gear ratio | Inductance $L_d$ | Resistance $R_s$ | Magnetic Flux $\psi_{pm}$ | Number of pole pairs |
|---|---|---|---|---|---|
| 1 | 10 | 0,00899995 H | 0,0218463 ohm | 4,759 Wb | 12 |

Table 2.Input data for the generator [19].

Initially the frequency response is evaluated by the Fast Fourier Transform (FFT) considering the free response of the system. Four different cases are simulated, two considering the mechanical part alone (one with high and other with low damping) and two for the complete model described previously (one with high and other with low damping). The idea of considering at first only the mechanical part is analyze the influence of coupling the electrical part.

For each case, 4 simulations of the free system with respect to the time are performed. In each simulation one of the initial displacements (related to $J_1, J_2, J_5, J_8$) has a nonzero value

equal to 1 radian. The frequency response is calculated to each one of the 4 free responses and the results consists in the sum of all FFTs.

Considering only the mechanical part alone, Figure 3 presents the frequency response to high (A) and low (B) damping. Low damping is considered as 1% of the high damping. From Figure (B) we observe 3 peaks related to natural frequencies, as expected (the zero frequency related to rigid body motion was not activated). When the damping is higher, second and third peaks become together and smaller in amplitude and only one peak is pronounced.

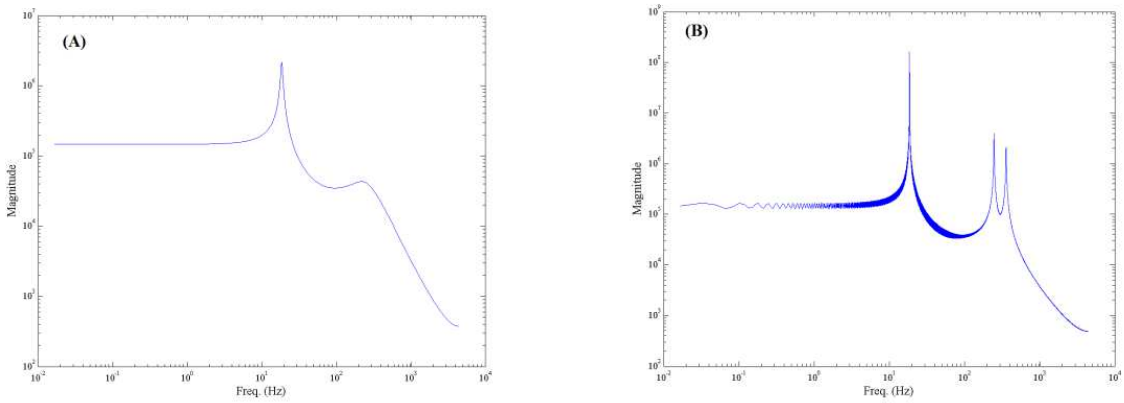


Figure 3. FFT of mechanical alone: (A) High damping; (B) low damping.

Figure 4 shows frequency response for the complete model considering the same damping coefficients used in the results obtained in Figure 3. For the coupled model with smaller damping coefficient, one can observe the presence of some small peaks between the natural frequencies as highlighted in Figure 4B. Note that natural frequency refers to the model that considers only the mechanical part alone. The presence of these small peaks is due to the electric coupling of the generator, that presents nonlinearity.

The results presented in Figures 3 and 4 are one preliminary. Note that system response was considered free, thus, the generator is not really operating. By considering the frequency response when the system is operational, we guess that the influence on the frequency response will be accentuated.

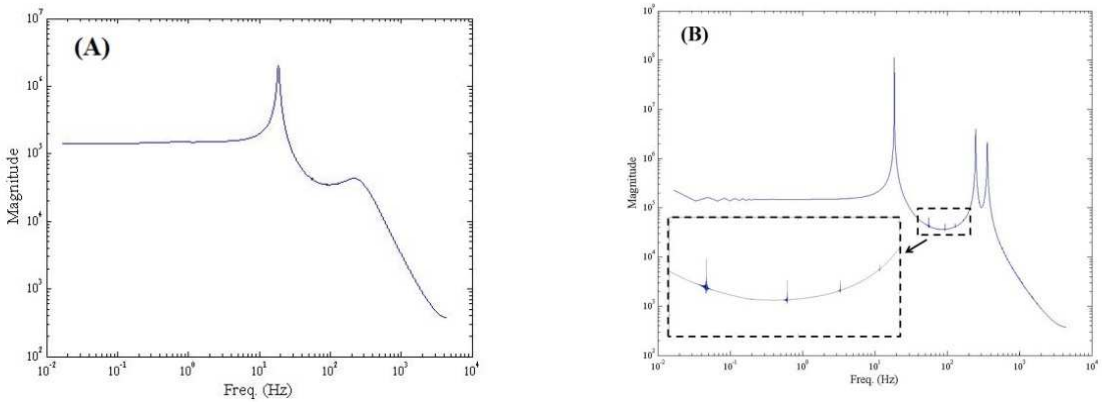


Figure 4. FFT of complete system: (A) high damping; (B) low damping .

At this point, the dynamic behavior of the complete system is of concern. It is considered a wind speed input as shown in Figure 4. In addition, zero initial conditions are considered for

all state variables except for the rotor angular velocity,$\dot{\varphi_1}$, equal to 2,35m/s, corresponding to the velocity that generates the maximum$C_p$for the angle $\beta = 5°$and a wind speed of 15m/s. Figures 6 and 7 show the angular displacements and velocities of the transmission system components for the wind profile considered in Figure 5. Figure 8 shows mechanical and electrical torques presented by the rotor and the generator, respectively, while Figure 9 shows mechanical, active and electromechanical power. Figures 10 and 11 show the efficiency of the transmission system and the power coefficient,$C_p$. Finally, Figures 12 and 13 show the currents and voltages in the quadrature axes *q*and direct axis *d*, respectively, of the generator.

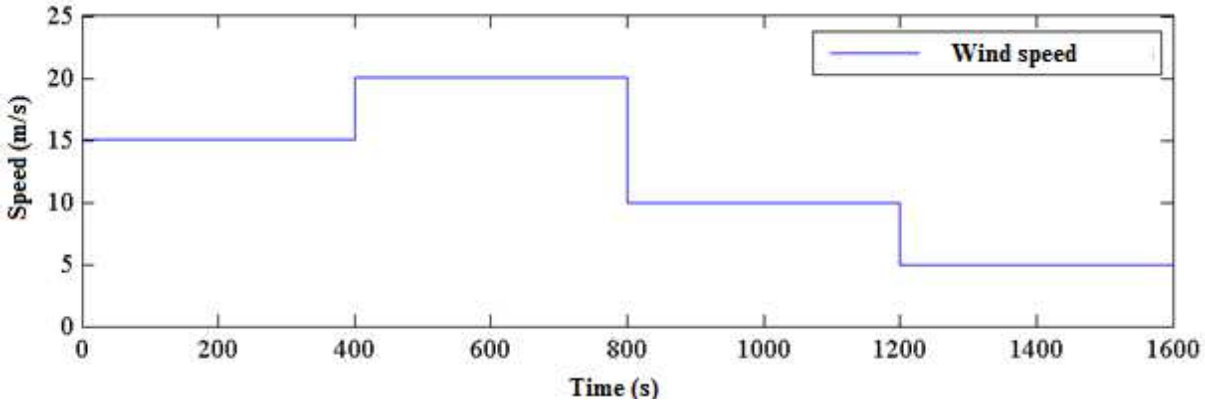


Figure 5. Wind speed input.

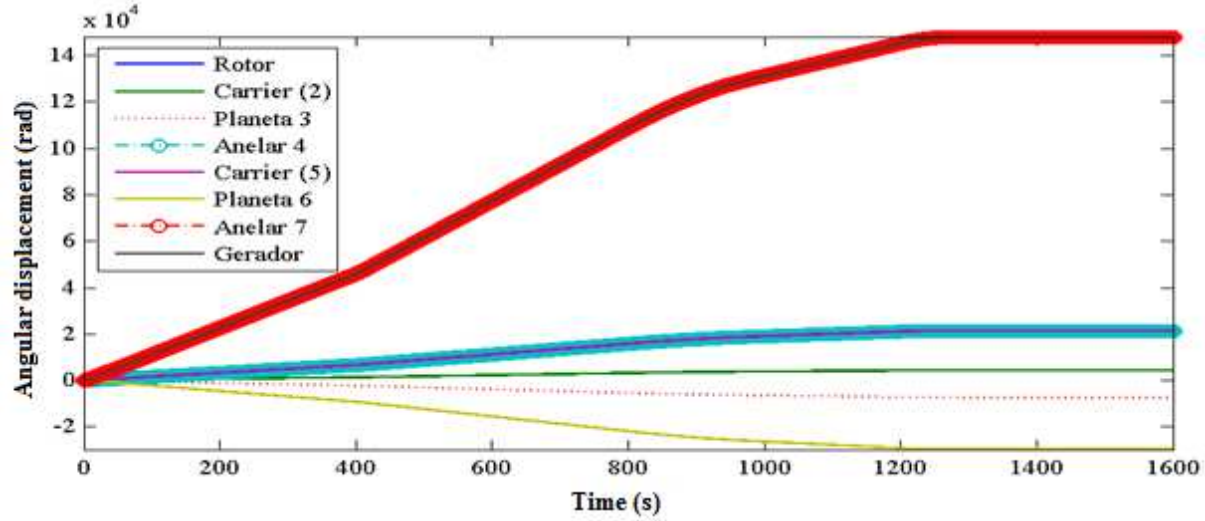


Figure6. Angular displacement of transmission system components.

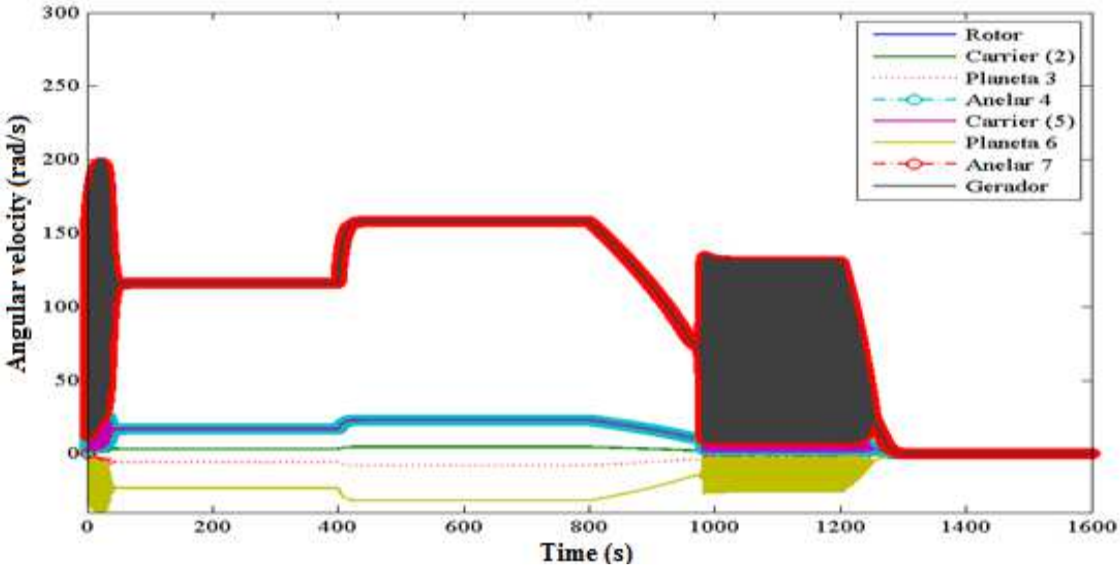


Figure7. Angular velocity of the transmission system components.

It is observed that for wind velocities of 15 to 20m/s, the turbine presents a satisfactory operation after a transient period, as shown in Figure 7. When the speed decreases to 10m/s, the turbine does not stabilize and the angular speeds of the casing components oscillate, resulting in undesired behavior.When the wind speed decreases further, now to 5m/s, the inlet torque becomes insufficient to keep the turbine running.

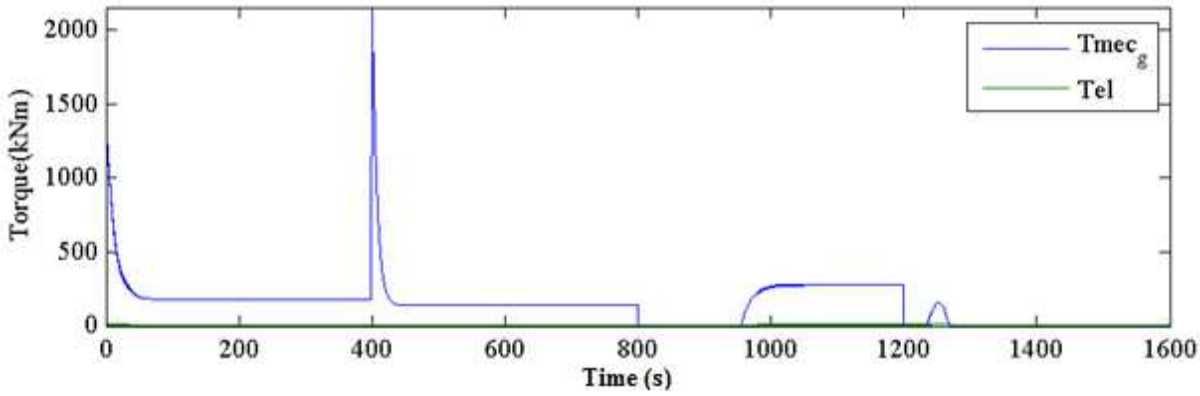


Figure 8.Mechanical and electrical torques of the complete model.

We observed in Fig. 9 that between 800 and 1000 seconds, where the wind speed is 10m/s, the active power is greater than the mechanical input power. This results in an efficiency greater than 1, indicating a physical incoherence.

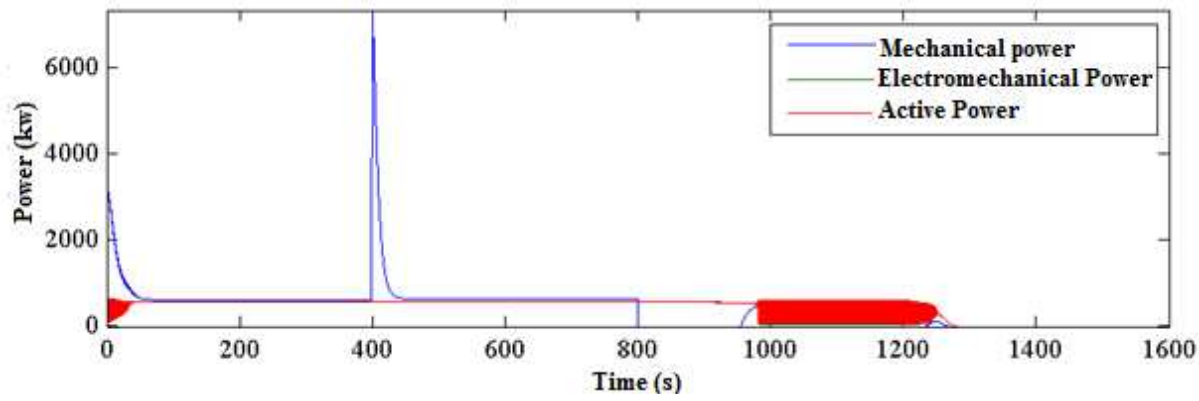


Figure 9.Mechanical, electrical and active powers of the complete model.

It is observed from Fig. 10 that the efficiency of the turbine is higher in the case of wind velocity equal to 15m/s than when it is 20m/s, showing that not always the higher wind speed results in a higher power coefficient.

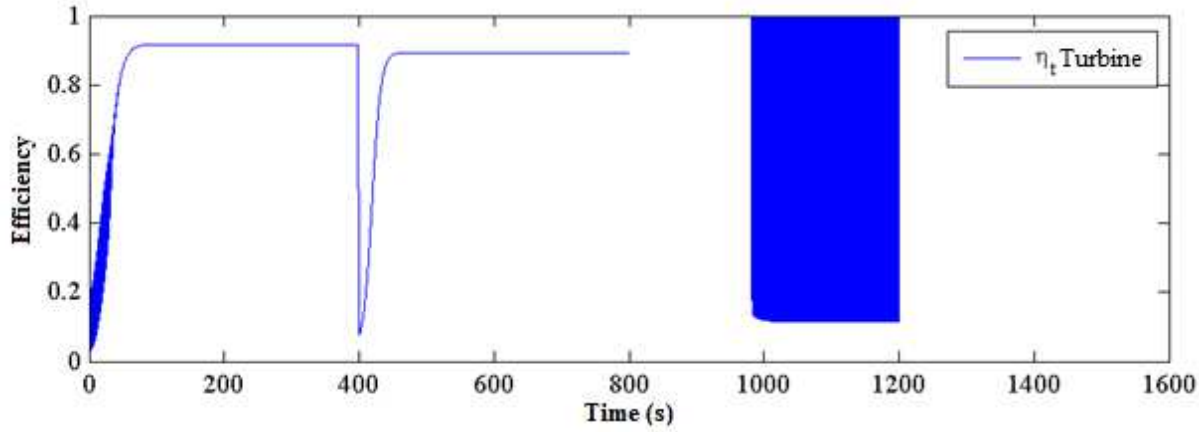


Figure10. Efficiency of the transmission system.

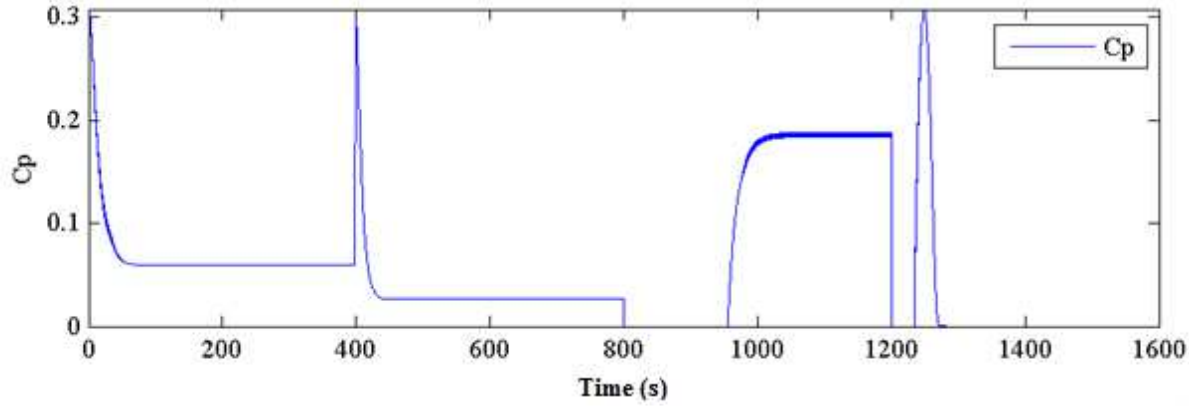


Figure11. Power Coefficient $C_p$.

In Fig.11 we observe that $C_p$ stabilizes in very low values, less than 0.3. It is possible to improve the performance of the system by applying appropriate control to obtain an ideal blade tip speed, $\lambda$.

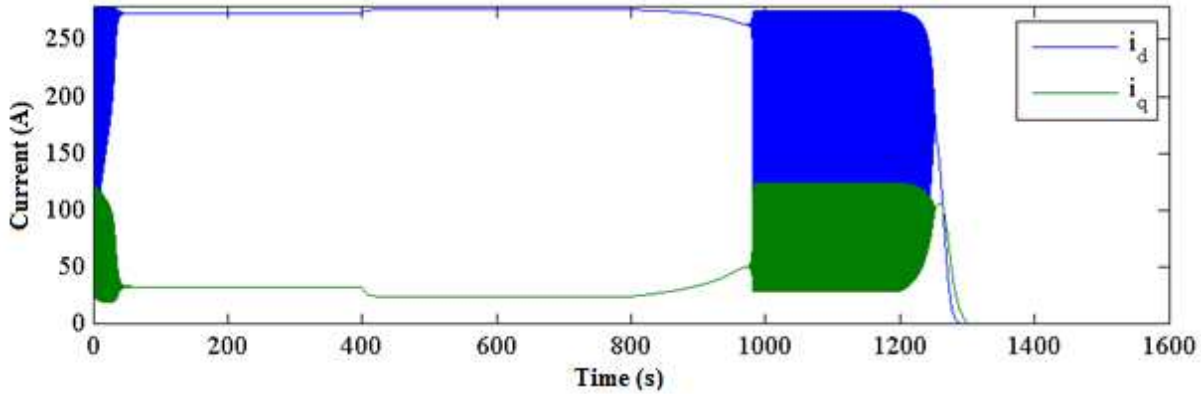


Figure12. Currents$i_d$ e $i_q$for the complete model

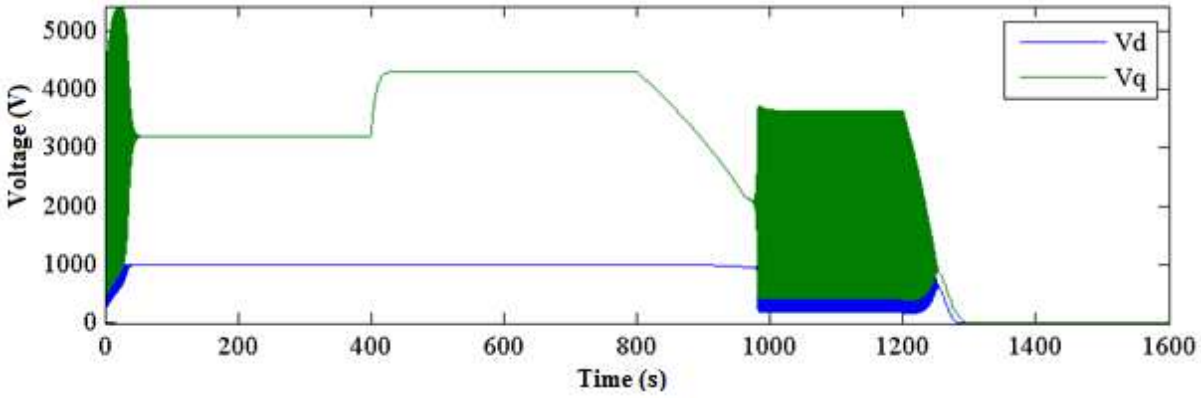


Figure13. Voltages $v_d$ e $v_q$for the complete model

From Figs. 12 and 13, we observe that the currents and voltages remain stable for the first two wind speed variations. Near 1000 seconds of analysis, it is observed that the system destabilizes until it stops when the wind speed reaches 5m/s.

## 5 CONCLUSION

This paper presents a mathematical model for the electromechanical transmission system of a wind turbine, including three main components: rotor, multiplier gearbox and generator. From the analysis in the frequency domain, we observe that when the electrical part is coupled to the mechanical, small peaks appears between the natural frequencies (being natural frequency related to the linear model that considers only the mechanical part).The nonlinearity that comes with the electrical coupling may be responsible for these peaks. The dynamical analysis in time allow a detailed analysis of each component of the system. The development of the complete model allows a more realistic dynamic analysis

## REFERENCES

[1] Bastos A.F., Cota E.F., Silva S.R., Pereira H.A., Use a newton's method for rotor resistence control of wind turbine generators. In: International conference on renewable energies and power quality – ICREPQ. EA4EPQ; 2012.

[2] Bernardes T.A. Análise e Controle de Gerador Síncrono a Imã Permanente Aplicado a Sistema de Conversão de Energia Eólica. Dissertação (Mestrado) - Universidade Federal de Santa Catarina, Santa Maria, 2009.
[3] Betz. A.,1919, Wind-EnergieundihreAusnutzungdurchWindmühlen.
[4] Busawon, K., Dodson, L., Jovanovic, M., 2005, Estimation of the power coefficient in a wind conversion system, Decision and Control, IEEE Conference on , pp.3450-3455.
[5] Datong Q., Jianhong W., Qingwei z., "A study on the dynamic behavior of drive train in horizontal wind turbine by a flexible multibody model (Submitted).
[6]Felippes R.A., Análise e Desenvolvimento de Aerogeradores com Pás Compósitas,Dissertação de Mestrado em Ciências Mecânicas, Departamento de Engenharia Mecânica, Universidade de Brasília, Brasília, 2012.
[7] Heier, S., 2006, Grid Integration of Wind Energy Conversion Systems. 2ª Ed., John Wiley & Sons, London, Inglaterra.
[8] Helsen J., Vanhollebeke F., Vandepitte D., Desmet W., "Multibody modelling of varying complexity for modal behaviour analysis of wind turbine gearboxes. Volume 36, Issue 11, November 2011, Pages 3098–3113
[9] K. E. Johnson, Adaptive Torque Control of Variable Speed Wind Turbines, NREL/TP-500-36265, August 2004.
[10] Lees, A.W., Friswell, M.I. &Litak, G. (2011), “Torsional Vibration of Machines with GearErrors”, Journal of Physics: Conference Series,v.305 (012020).
[11] Lei Y., Mullane A., Lightbody G., Yacamini R., Modeling of the wind turbine with a doubly fed induction generator for grid integration studies. IEEE Transactions on Energy Conversion, vol. 21, no. 1, March 2006.
[12] Manyonge, A., Ochieng, R. M., Onyango, F. N., Shichikha, J. M., 2012. Mathematical Modelling of Wind Turbine in a Wind Energy Conversion System: Power Coefficient Analysis. AppliedMathematicalSciences, v. 6, n. 4527 - 4536.
[13]Marques, J., 2004, Turbinas Eólicas: Modelo, Análise e Controle do Gerador de Indução com Dupla Alimentação, Universidade Federal de Santa Maria, RS.
[14] Ming Yin, Li. G,Zhou, Zhao, C., Modeling of the Wind Turbine With a Permanente Magnet Synchronous Generator for Integration, 1-4244-1298-6/07/2007 IEEE.
[15]Shigley, J. E., Mischke, C. R., Budynas, R.G., 2005, Projeto de Engenharia Mecânica, 7ª Ed., Bookman, São Paulo, SP.
[16] Peeters R. H.; Vandepitte, D.; Sas, P. Analysis of Internal Drive Train Dynamics in a Wind Turbine. Wiley Interscience, Leuven, p. 1-21, Set. 2005.
[17] Peeters, J., 2006, Simulation of Dynamic Drive Train Loads in a Wind Turbine, UniversidadeCatólica de Leuven – Bélgica.
[18] Todorov, M., Dobrev, I., Massouh, F, 2009, Analysis of Torsional Oscillation of Drive Train in Horizontal-Axis Wind Turbine, Electromotion-2009, EPE Chapter Electric Drives, Lille, France, 7 p.
[19]Vásques, F.A.M., Oliveira, T. F., Brasil, A. C. P., "On the electromechanical behavior of hydrokinetic turbines" Energy Conversion and Management 115 (2016) 60–70
[20] Wei Shi, Kim C.W., Park H.C., Dynamic Modeling and Analysis of a Wind Turbine Drivetrain Using the Torsional Dynamic Model, International Journal of Precision engineering and manufacturing, Vol. 14, no. 1, pp. 153-159 January 2013.
[21] Wang J., Qin D., Ding Y., Dynamic behavior of wind turbine by a mixed flexible-rigid multi-body model. Journal of System Design and Dynamics, Vol3, Nº3, 2009.

COMPDYN 2017
6th ECCOMAS Thematic Conference on
Computational Methods in Structural Dynamics and Earthquake Engineering
M. Papadrakakis, M. Fragiadakis (eds.)
Rhodes Island, Greece, 15–17 June 2017

# INTER-STORY POUNDING AND TORSIONAL EFFECT DUE TO INTERACTION BETWEEN ADJACENT MULTISTORY RC BUILDINGS

**Christos G. Karayannis**[1], **Maria C. Naoum**[2]

[1] Prof., Civil Engineering Dept.
Democritus University of Thrace, Xanthi 67100, Greece
karayan@civil.duth.gr

[2] PhD student, Civil Engineering Dept.
Democritus University of Thrace, Xanthi 67100, Greece
mnaoum@ civil.duth.gr

**Keywords:** Inter-story pounding, asymmetric structural pounding, multistory reinforced concrete structures, nonlinear dynamics analysis, earthquake engineering.

**Abstract.** *The influence of the structural pounding on the seismic behaviour of reinforced concrete structures designed to EC2 and EC8 with non-equal story heights is investigated. In these cases the slabs of the diaphragms of the short stiffer structure hit the columns of the other adjacent structure at points within their deformable heights. Further it is quite usual seismically induced oscillations of a structure in a block of buildings in city center to be partly restrained in lateral displacements and therefore torsional behaviour to be introduced during an earthquake excitation. In this work the case of an 8-story reinforced concrete building that suffers inter-story pounding in a non-symmetric way is studied. Pounding occurs only in one (case 1) or in two (case 2) columns of the structure whereas the other columns are free to move without restrictions and therefore a torsional behavior is produced. The slabs of the short stiff structure hit the columns of an 8-story frame structure at a height equal to 2/3 of their deformable length. Nonlinear dynamic step-by-step analysis and special purpose elements are employed for the needs of this study. Pounding cases with torsional effect between structures with non-equal story levels and different total heights for three excitations are studied and results in terms of displacements, torsional rotations, shear forces, ductility requirements are presented and commented. The results clearly show that high capacity requirements in terms of torsional moments and column shear strength are developed due to the asymmetric inter-story pounding. Furthermore from the results it can also be deduced that the columns that suffer the hit develop high shear requirements that exceed the available capacity during the step-by-step seismic response of the structures.*

## 1 INTRODUCTION

Based on reports of field observations after numerous destructive earthquakes all over the world, it can be concluded that pounding is frequently observed when strong earthquakes strike big cities and densely populated urban areas [1],[2],[3]. Moreover the high cost of land in densely populated metropolitan cities and the small lot sizes make the seismic separation requirements not always easy to apply.

Karayannis and Fotopoulou (1998) [4] examined various cases of structural pounding between multistory reinforced concrete structures designed according to the Eurocodes 2 and 8. The work is based on non-linear dynamic step-by-step analysis and its purpose was to present initial results for the influence of some critical pounding parameters on the ductility requirements of the columns and to examine the possibility of taking into account the pounding effect during the design process according to EC2 to EC8.

Further in city centers with large blocks densely filled with buildings the land lots are mostly not equal nor alike in plan geometry henceforth it is very likely adjacent buildings in a block to be partly and in a non-symmetric way in contact to each other. Consequently it is quite usual seismically induced oscillations of a structure in a block to be partly restrained in lateral displacements and therefore a torsional movement to be introduced in the building during an earthquake excitation. This phenomenon can be referred to as asymmetric pounding.

Considering that (i) pounding is a frequent cause of structural damage that under certain conditions it can lead to collapse initiation, (ii) the problem has not yet been studied effectively especially for the case of colliding structures with non-equal inter-story heights, (iii) according to the new design codes (Eurocodes 2 and 8, ACI 318) flexible frame structures prone to structural pounding can be designed and (iv) seismically induced oscillations of a structure in a block of buildings in a city center is likely to be partly restrained in lateral displacements and therefore torsional behaviour to be introduced; in this paper an attempt to study the influence of the asymmetric structural pounding on the ductility and shear requirements for reinforced concrete structures with different story heights is presented. This phenomenon can be referred to as asymmetric inter-story pounding.

The examined structures are multistory reinforced concrete frames with unequal total heights and different story heights designed according to the codes EC2 and EC8. In these very common pounding cases the slabs of the diaphragms of the short stiffer structure hit the columns of the other structure at a point within the deformable height.

In this work more than fifty pounding cases for three different seismic excitations each are examined. The examined cases include pounding cases between an 8-story reinforced structure designed to EC2 and EC8 and a shorter structure with $n_s$ stories where $n_s$=1,2,3,4,5,6,7 and 8. The heights of the story levels of the multistory structures are not the same with the ones of the second structure. These cases are sorted into two series based on the level of the asymmetry introduced in an 8-story building due to pounding. In series 1 pounding cases with high asymmetry are included since pounding takes place between only one external column of the 8-story building and one column of the adjacent shorter structure. In series 2 pounding takes place between two columns of the 8-story building and two columns of the adjacent shorter structure. Each pounding case first is examined considering that the interacting structures are in contact from the beginning (gap distance $d_g$=0) and further it is examined considering that there is a gap distance equal to 1 or 2 cm ($d_g$=1 and 2 cm) between the structures. Nonlinear dynamic step-by-step analysis and special purpose elements are employed for the needs of this study.

The results clearly show that high capacity requirements in terms of torsional moments and column shear strength are developed due to the asymmetric inter-story pounding. Furthermore

from the results it can also be deduced that the columns that suffer the hit develop high shear requirements that exceed the available capacity during the step-by-step seismic response of the structures.

## 2 MODEL IDEALIZATION OF POUNDING

The pounding between adjacent structures with different total heights that are partly in contact to each other in a non-symmetric way is studied (fig. 1a). This configuration implies that the seismic oscillations of the tall building is laterally only partly restrained by the other structure and therefore a torsional movement is introduced in the building during an earthquake excitation. Henceforth in the examined cases pounding between adjacent structures introduces significant plan asymmetry in the building in terms of lateral stiffness distribution.

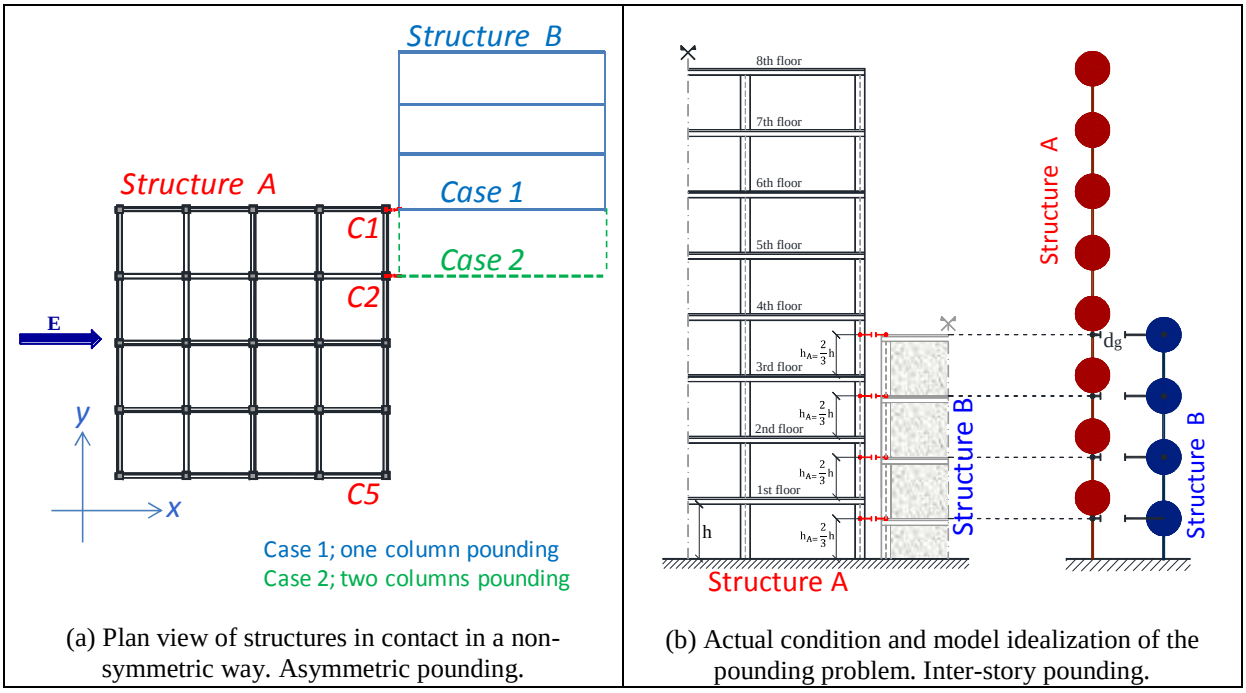


(a) Plan view of structures in contact in a non-symmetric way. Asymmetric pounding.

(b) Actual condition and model idealization of the pounding problem. Inter-story pounding.

Figure 1: Plan view of structures in contact in a non-symmetric way and model idealization of the pounding between buildings with different story heights. Asymmetric inter-story pounding.

It is considered that one flexible multistory building (Structure A in fig. 1) is in contact or in close proximity to one less flexible shorter structure (Structure B in fig. 1). If there is a gap distance between these structures collisions can only occur when the lateral displacements of the structures exceed the pre-defined gap distance ($d_g$). The influence of the gap size on the pounding effects is also investigated.

As it can be shown in fig. 1a two cases of asymmetric pounding are examined. In case 1 the lateral displacement of one column (column C1) of the 8-story building (structure A) is restrained in the x-direction only towards the adjacent structure (structure B); whereas in case 2 the lateral displacements of two columns (columns C1 and C2) are restraint. In both cases torsional movement is introduced in the structure under consideration (structure A) due to the plan asymmetry caused by the restraints imposed by the pounding between the adjacent structures.

The heights of the storey levels of the two structures are not equal (figure 1b). In this very common case the slabs of the diaphragms of each structure hit the columns of the other struc-

ture at a point within their deformable height. This phenomenon is especially intense at the contact point of the upper storey level of the short stiffer structure with the corresponding column of the tall building. The actual condition and the model idealization of this pounding case are shown in fig. 1b. Contact points are taken into account at the levels of the floor slabs of the short structure. Analyses have been performed using time steps of the order of 1=1000 to 1=10000 in order to achieve numerical stability and to adequately reproduce higher mode response excited by the short-duration impacts. Contact points are taking into account at the levels of the floor slabs of the short structure (fig. 1b). Nevertheless, from the analyses of the examined pounding cases it has been found that the response of the interacting structures is mainly influenced by the position and the characteristics of the contact point at the short structure's top floor. The influence of the other contact points on the results proved to be negligible in the examined cases. The same conclusion also holds, more or less, for the examined cases with non-zero initial distance gap.

Nevertheless, in the following analyses and results, the influence of the pounding effect through all floor contact point on the behaviour of the structures and on the response and ductility requirements of the columns is examined.

## 3 CONTACT ELEMENT

Collisions are simulated using special purpose contact elements that become active when the corresponding nodes come into contact.

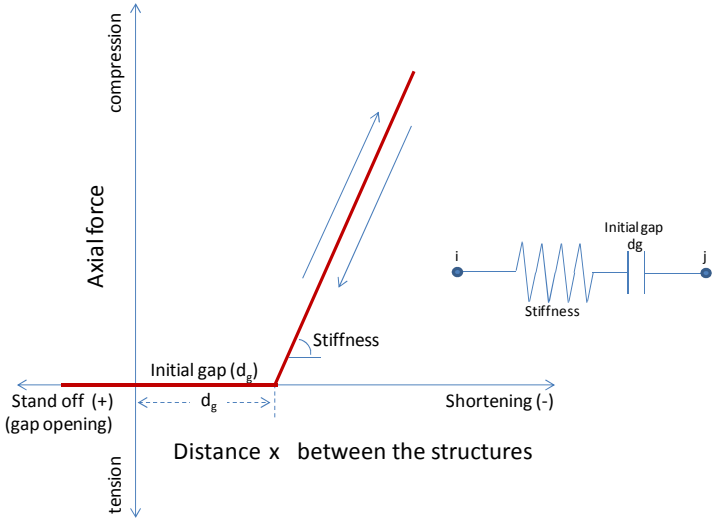


Figure 2: Contact elements

The response of the contact elements is shown in fig.2. The negative direction of the X-axis represents the condition that the buildings move away from each other. In the positive direction of the X-axis there are two parts in order to simulate the actual behaviour of the structures in case there is an initial small gap distance ($d_g$) between them. It is possible that the structures move one towards the other but the displacements are small and the existing gap is not covered. In this case the contact element remains non-active and the buildings continue to vibrate independently. In the case that the structures move one towards the other and the sum of the displacements of the two structures bridge the existing gap or the structures are in contact from the beginning ($d_g$=0) then the contact element responds as a spring with large stiffness.

## 4 ANALYSIS MODEL OF STRUCTURES

The frame structural system of the tall structure consists of beams and columns. Each structure is modeled as a 3D assemblage of non-linear elements connected at nodes. Each node has six degrees of freedom. The mass is lumped at the mass center of each floor. Each structure responds dynamically and vibrates independently. In the cases the interacting structures have equal story heights collisions occur when the lateral displacements of the structures at the floor levels exceed the predefined gap distance ($d_g$) between the two structures. In the cases that the heights of the interacting structures are not equal (inter-story pounding) the slabs of the shorter structure hit the corresponding columns of the 8-story building at points within their deformable length (fig. 1).

The computer program used in this work is the program package ETABS2000. The finite element mesh used here for the modeling of each structure utilizes an one-dimensional element for each structural member. The element is a common lumped plasticity beam-column model that considers the inelastic behaviour concentrated in zero-length "plastic hinges" at the element's ends. An interaction 3D surface N-$M_x$-$M_y$ is employed for the check of the elastic or plastic response of the zero-length plastic hinges.

## 5 POUNDING CASES

More than fifty pounding cases have been studied for the needs of this work. Each one is subjected to three different natural seismic excitations having been selected so that their spectra fit properly with the design spectrum used for the design of the 8-story building.

In the inter-story pounding cases it is considered that the pounding takes place at points of the deformable height of the columns of the more flexible 8-storey frame structure. It is expected that the important problem in the case of inter-floor pounding of reinforced concrete structures is the development of critical shear state, since in these cases the demands of flexural ductility can more safely be satisfied. Furthermore, the fact that the failure of reinforced concrete members due to shear is brittle led the investigation of inter-floor pounding to the examination of the developing shear forces and their comparisons to the corresponding shear strength. Pounding at the mid-height of the column produces two column parts with equal flexural moments that may be flexurally critical parts. Further in any case the two parts of the column (the upper and the down part) suffer the same shear force which is equal to half of the impact force. Thus pounding cases at points of the column different to the mid-height creates a long part that may be flexurally critical and leads to a short shear critical column part. Therefore the contact points of the two structures in the examined cases lie at 2/3 of the height of the columns of the 8-story building; thus $h_A = 2/3\ h$ in Fig. 1b.

The examined cases are sorted into two series based on the level of the asymmetry that is induced in the 8-story building due to the pounding.

Series 1 includes pounding cases with high asymmetry (case 1 in fig. 1a) where pounding takes place between only one column of the 8-story building (column C1 in fig. 1a) and one column of the adjacent short and stiff structure. In series 2 (case 2 in fig. 1a) pounding takes place between two columns of the 8-story building (columns C1 and C2 in fig. 1a) and two columns of the adjacent short and stiff structure.

Thus both series include asymmetric pounding cases between the 8-story and an adjacent very stiff structure which has $n_s$ story levels; where $n_s$ =1, 2, 3, 4, 5, 6, 7 and 8 stories.

Each one of the pounding cases of both series first is examined considering that the interacting structures are in contact from the beginning (gap distance $d_g$=0); further each pounding case is examined considering that between the interacting structures there is a gap distance equal to 1 and 2 cm ($d_g$=1 and 2 cm).

## 6 RESULTS AND COMMENTS

The results and the conclusions deduced from the analyses of each series include the observed overall response of the multistory frame in terms of the induced torsional behavior and its repercussions on the developing capacity requirements of the columns. Therefore results for the shear demands and shear capacity of the columns are also presented and commented upon. Special attention has been given to the response of the columns of the story of the multistory frame where the pounding takes place.

### 6.1 Torsional behavior

Torsional oscillation is observed in the 8-story building due to the asymmetric inter-story pounding that occurs between it and the adjacent shorter and stiff structure. The time histories of the developing torsional moment at the base floor of the 8-story building during the seismic excitation due to asymmetric inter-story pounding (fig. 1) with a single-story very stiff structure for pounding cases 1 and 2 are presented in fig. 3. Similarly the time histories of the developing torsional moment at the base floor of the 8-story building due to asymmetric inter-story pounding with a 3-story very stiff structure for pounding cases 1 and 2 are presented in fig. 4.

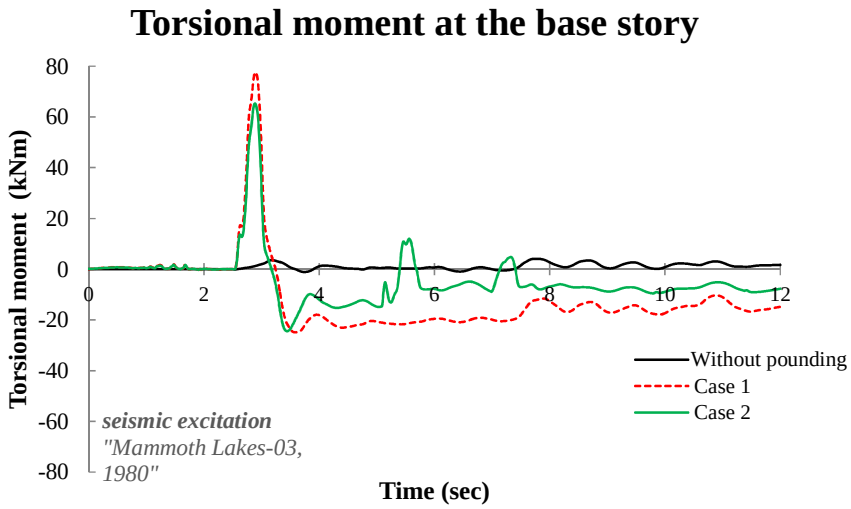


Figure 3: Time history of the torsional moment at the base floor due to asymmetric inter-story pounding for cases 1 and 2 between the 8-story building and a single story stiff structure.

Further in figs. 3 and 4 the time history of the corresponding torsional moment at the base floor of the 8-story building during the same seismic excitation without pounding is also included for comparison reasons. From this figures (fig. 3 and 4) it can clearly be deduced that asymmetric type inter-story pounding causes significant torsional movement and high value torsional moments in the 8-story building although its plan view is symmetric and in the cases it vibrates without the pounding effect it presents insignificant torsional moment and consequently no torsional movement.

From the results it is also deduced that the torsional movement which is induced due to the asymmetric pounding highly influences the distribution of the developing shear forces in the columns [5]. High shear forces are developed in the columns in the direction normal to the earthquake direction although the plan view of the building is symmetric in both directions.

In fig. 5 the observed maximum torsional rotations of all stories of the 8-story building (8RC) due to asymmetric pounding cases 1 and 2 are presented.

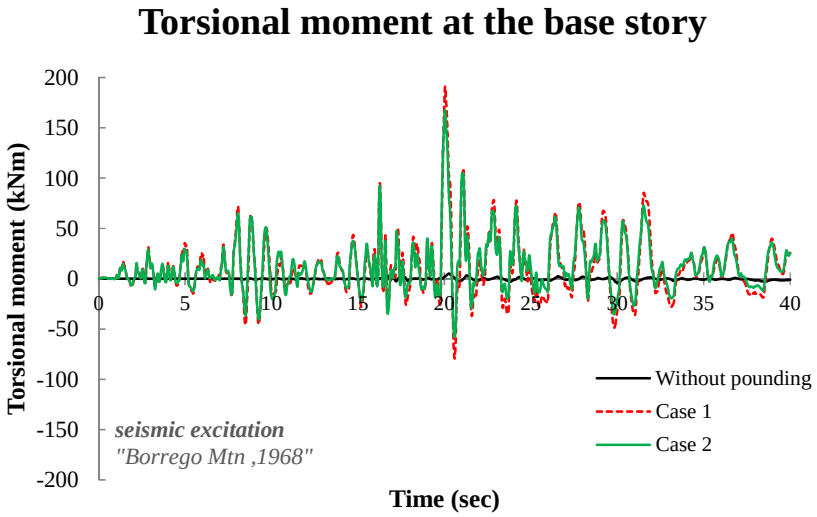


Figure 4: Time history of the torsional moment at the base floor due to asymmetric inter-story pounding for cases 1 and 2 between the 8-story building and a 3-story stiff structure.

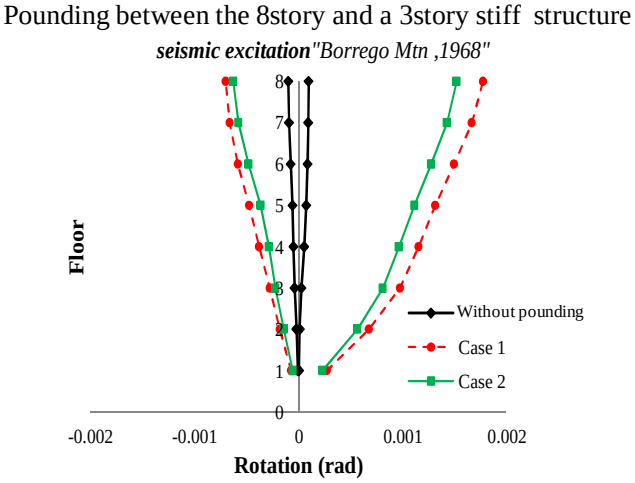


Figure 5: Maximum Torsional rotations of all stories of the 8-story building (8RC) due to asymmetric pounding (*cases 1 and 2*).

## 6.2 Columns that suffer the pounding - Shear force time histories

Time history for the developing shear force of the column C1 that suffers the pounding hit at the base floor of the 8-story building for pounding case 1 between the 8-story and a single story very stiff structure is presented in fig. 6 and is compared to the shear force time history of the same column for the response of the building without pounding. It can easily be concluded from fig. 6 that the developing shear forces in the case of inter-story pounding are significantly higher than the corresponding ones in the case that the building responds without pounding problems.

The ratio $p_v$ of the maximum shear force $V_{x,max,ip}$ developing in the x-direction in the case of asymmetric inter-story pounding (ip) to the maximum shear force $V_{x,max}$ in the case that the building responds without pounding effect may point out the significance of problem. Thus the ratio $p_{v1}$ for the case 1 and the ratio $p_{v2}$ for the case 2 are 8.8 and 5.7, respectively.

Based on these values it can easily be obtained that when inter-story pounding occurs the developing shears are very high compared to the expected ones without the pounding problem.

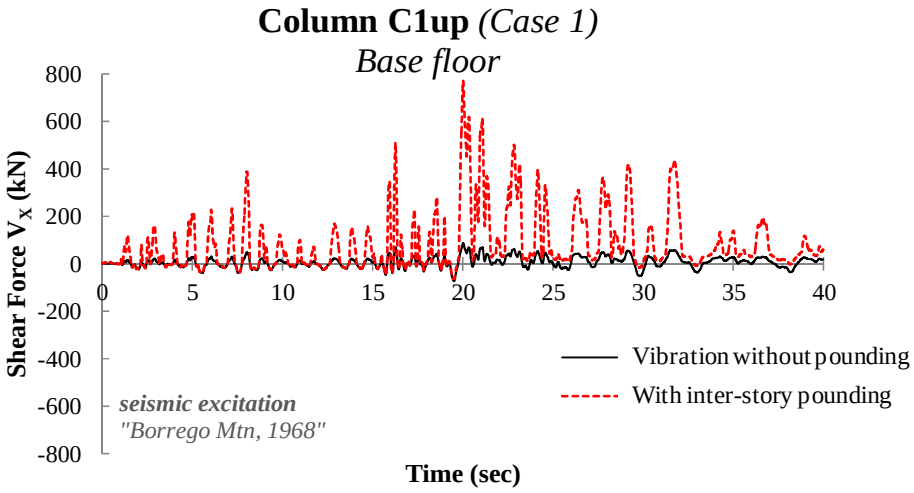


Figure 6: Time history of the shear force of Column C1 that suffers the hit (upper part) at the base floor due to asymmetric inter-story pounding for case 1 between the 8-story building and a single story stiff structure.

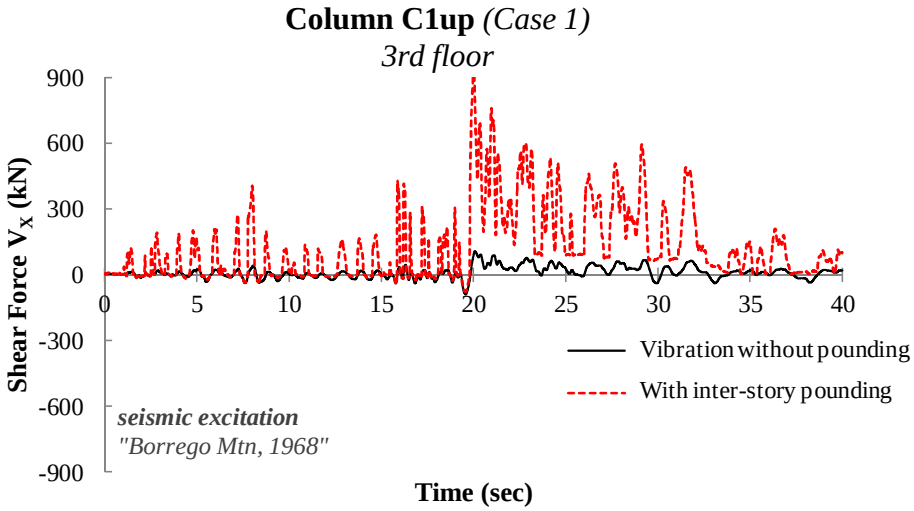


Figure 7: Time history of the shear force of Column C1 that suffers the hit (upper part) at the 3rd floor due to asymmetric inter-story pounding for case 1 between the 8-story building and a 3- story stiff structure.

Furthermore in fig. 7 time history for the developing shear force of the column C1 that suffers the pounding hit at the 3rd floor of the 8-story building for pounding case 1 between the 8-story and a 3-story stiff structure is presented in fig. 7 and is compared to the shear force time history of the same column for the response of the building without pounding. It can easily be concluded from fig. 7 that the developing shear forces in the case of inter-story pounding are significantly higher than the corresponding ones in the case that the building responds without pounding problems.

The ratio $p_{v1}$ for the case 1 and $p_{v2}$ for the case 2 are 9.2 and 3.5, respectively. Based on these values it can easily be obtained that when inter-story pounding occurs the developing shears are very high compared to the expected ones without the pounding problem.

### 6.3 Columns that suffer the pounding - Shear force capacity

In figs. 8a and b the developing shear force values at the upper part of the column C1 at the base floor of the 8-story building for pounding with a single story stiff structure and for cases 1 and 2, respectively, are presented and compared to the ones of the available shear strength. In these figures the pairs of the observed shear force V - axial force N for all the time steps of the performed dynamic step-by-step analysis are presented and compared to the limits of the available strength. The red line represents the strength limits for each pair of V - N for the limit state of Significant Damage (SD) whereas the blue line the strength limits for the Near Collapse (NC) limit state.

It can be observed that in both asymmetric pounding cases (case 1 and case 2) there are pairs V - N values that lie outside the line limit of the available strength. It means that there are time periods during the seismic response of the building within which the developing shear forces exceed the available shear capacity and therefore a potential of a local shear brittle failure can be expected.

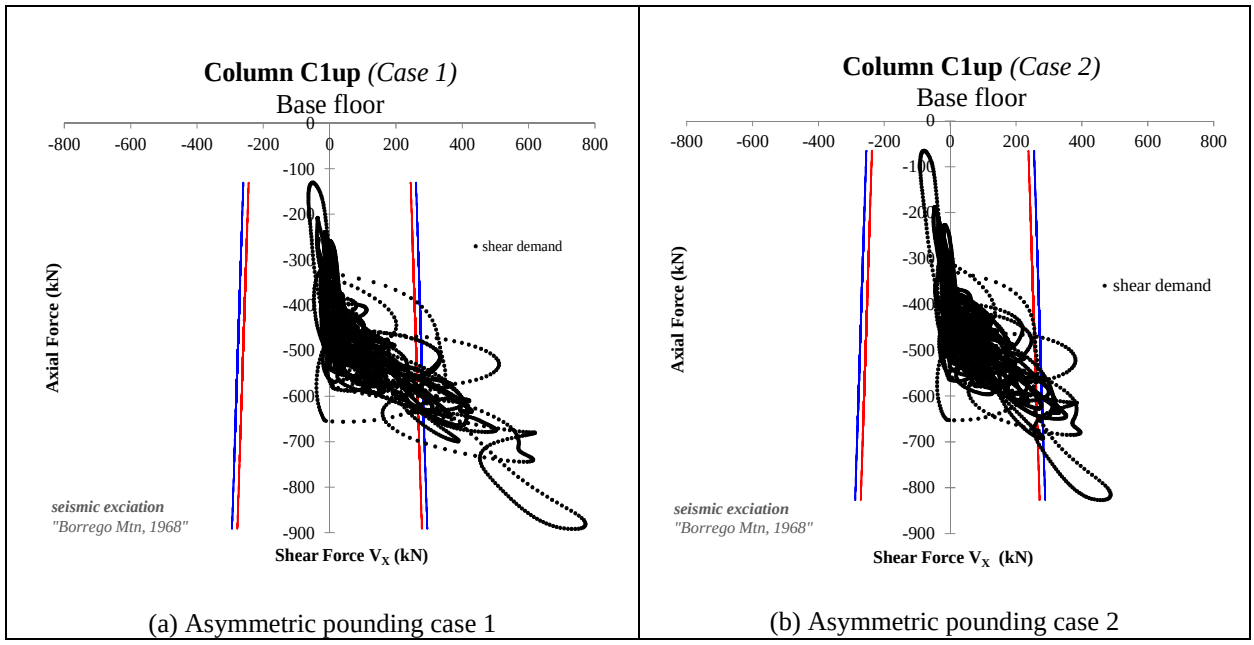


(a) Asymmetric pounding case 1

(b) Asymmetric pounding case 2

Figure 8: Asymmetric inter-story pounding between the 8-story building and a single story very stiff structure. Shear force V - axial force N pairs of observed values for all the time steps of the performed dynamic step-by-step analysis are presented and compared to the limits of the available strength.

Similarly in figs. 9a and b the developing shear force values at the upper part of the column C1 that suffers the hit at the 3rd floor of the 8-story building for pounding with a 3-story stiff structure for the cases 1 and 2, respectively, are presented and compared to the ones of the available shear strength.

It can be observed that in both asymmetric pounding cases (case 1 and case 2) there are pairs V - N values that lie outside the line limit of the available strength. It means that there are time periods during the seismic response of the building within which the developing shear forces exceed the available shear capacity and therefore a potential of a local shear brittle failure can be expected.

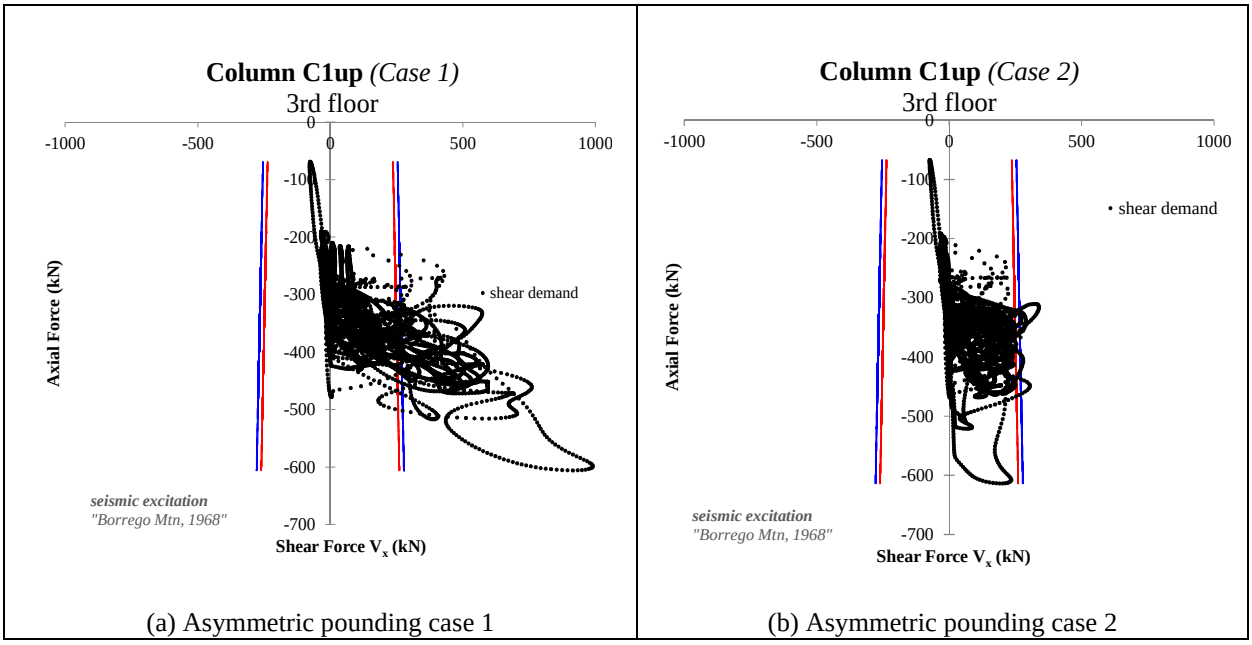


(a) Asymmetric pounding case 1 (b) Asymmetric pounding case 2

Figure 9: Asymmetric inter-story pounding between the 8-story building and a 3-story story very stiff structure. Shear force V - axial force N pairs of observed values for all the time steps of the performed dynamic step-by-step analysis are presented and compared to the limits of the available strength.

## 6.4 Ductility requirements

Pounding induced torsional vibration changes the ductility requirements of the columns and significantly increases the ductility requirements of the column that experiences the hit due to the inter-story pounding between the adjacent structures.

The ductility requirements of column C1 of the 8-story building in all floor levels for inter-story pounding with a single story stiff structure are presented in fig. 10. The presented results are for pounding cases 1 and 2 and the structures are in contact ($d_g$=0) from the beginning of the excitation.

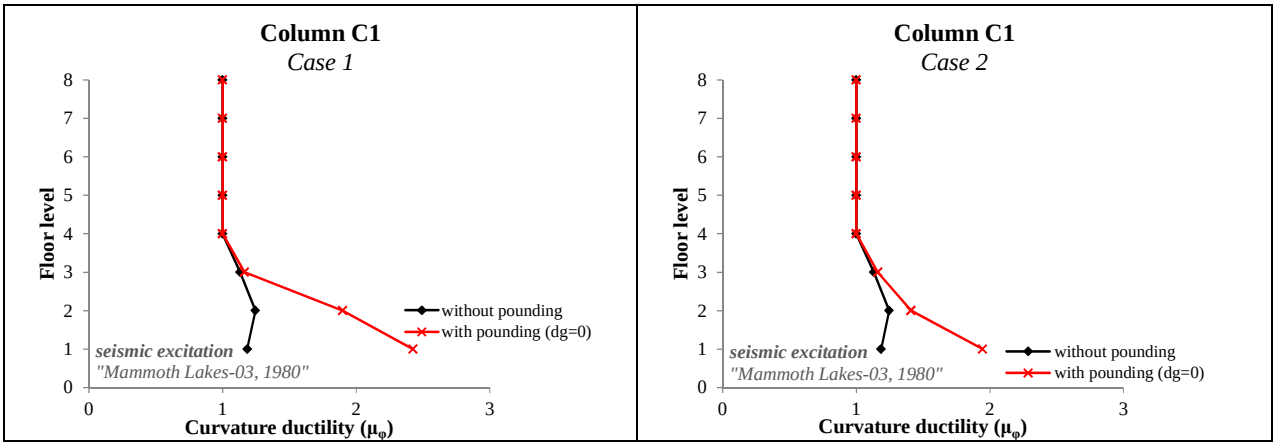


Figure 10: Maximum ductility requirements of column C1 in all floor levels. Comparisons of ductility requirements between pounding (case1) of the 8-story building with a single story structure and the free vibration of the 8-story building (without pounding effect).

The contact points lie at 2/3 of the height of the columns of the 8-story building (inter-story pounding); thus $h_A$ = 2/3 h in Fig. 1b. The results are compared with the corresponding ones of the same column for the same seismic excitation without pounding effect.

It can be observed that column C1 at the base floor where pounding takes place exhibits significantly increased ductility requirements in comparison with the ones of the same column for the same excitation without pounding effect.

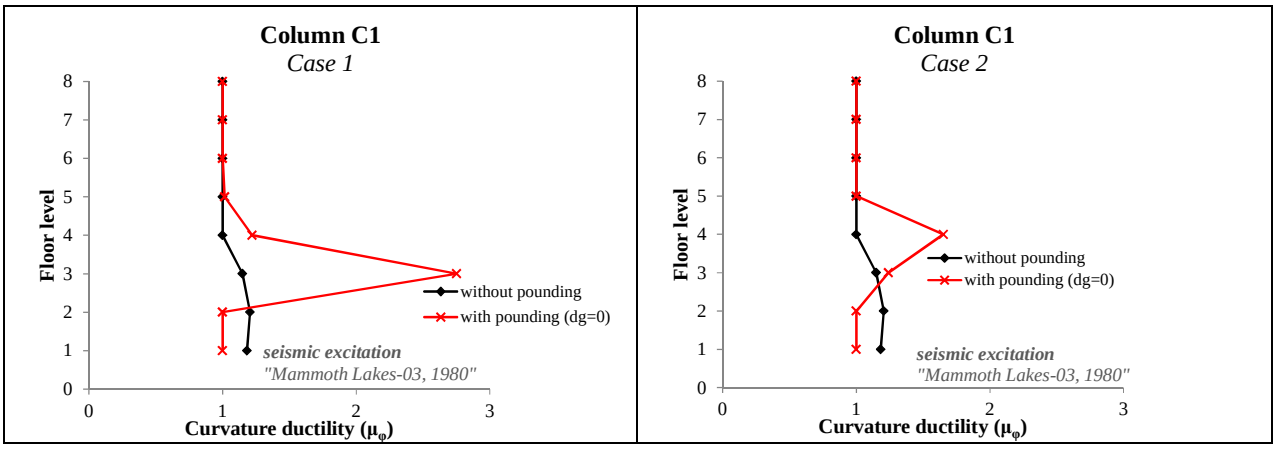


Figure 11: Maximum ductility requirements of column C1 in all floor levels. Comparisons of ductility requirements between pounding (case1) of the 8-story building with a 3-story structure and the free vibration of the 8-story building (without pounding effect).

Similarly in Fig. 11 the ductility requirements of column C1 of the 8-story building in all floor levels for inter-story pounding with a 3-story stiff structure, case 1 and $d_g$=0, are presented and compared with the corresponding ones of the same column for the same seismic excitation without pounding effect. Also in this case it can be observed that column C1 at the floor where pounding takes place exhibits significantly increased ductility requirements in comparison with the ones of the same column for the same excitation without pounding effect.

Furthermore it is observed that the column C1 at the 3rd level that suffers the hit exhibits higher ductility requirements in pounding cases where high asymmetric pounding (case 1) takes place in comparison with the ones in the cases where medium asymmetric pounding (case 2) occurs.

Nevertheless it has to be noted that the ductility requirements in the examined cases although substantially high in the cases that pounding takes place do not really exceed the usual available ductility capacity of reinforced concrete columns designed to Eurocodes 2 and 8.

## 7 CONCLUSIONS

- Seismically induced interaction between adjacent buildings that are partly and in a non-symmetric way in contact may introduce significant torsional oscillations. Furthermore in cases that the story heights of the interacting structures are not equal then the slabs of the diaphragms of the one structure hit the columns of the other structure at a point within their deformable height. This type of structural interaction may be referred to as asymmetric inter-story pounding.
- Asymmetric pounding between an 8-story reinforced concrete building with symmetric plan view and an adjacent shorter structure that has $n_s$ floor levels is investigated for $n_s$=1,2,3,4,5,6,7 and 8 stories. Interaction cases with high (case 1) and medium (case 2) asymmetric pounding are included in the present study. It has been observed that in general the developing torsion increases as the height (the number of the stories) of the adjacent stiff structure increases.

- From the presented study it can be concluded that the torsional movement which is induced due to the asymmetric pounding highly influences the distribution of the developing shear forces in the columns. Furthermore high shear forces are developed in the columns in the direction normal to the earthquake direction although the plan view of the building is symmetric in both directions.
- Pounding induced torsional vibration changes the ductility requirements of the columns and significantly increases the ductility requirements of the column that experiences the hit due to the inter-story pounding between the adjacent structures.
- It is stressed that in all the examined inter-story asymmetric pounding cases during the step-by-step analyses a great number of time steps have been observed within which the pairs of the developing shear force - axial force (V - N) values lie well outside the line limit of the available strength. It means that there are time periods during the seismic response of the building within which the developing shear forces well exceed the available shear capacity and therefore a potential local shear brittle failure is expected.

## REFERENCES

[1] C. Arnold, R. Reitherman, *Building Configuration and Seismic Design.* Wiley, New York, 1982.

[2] E. Rosenblueth, R. Meli., The 1985 earthquake: Causes and effects in Mexico City. *Concrete International (ACI),* **8(5)**, 23-24, 1986.

[3] V.V. Bertero, Observationon structural pounding. *Proceedings of the International Conference on Mexico Earthquakes,* ASCE, 264-287, 1986.

[4] C.G. Karayannis, M.G. Fotopoulou, Pounding of multistorey RC structures designed to EC8 and EC2. *11th European Conference on Earthquake Engineering (Proceedings in CD form),* Balkema, ISBN 90-5410-982-3, 1998.

[5] C.G. Karayannis, M.C. Naoum, Torsion effect due to asymmetric pounding between multistory RC buildings. *COMPDYN 2017, 6th ECCOMAS Thematic Conference on Computational Mechanics in Structural Dynamics and Earthquake Engineering, Rhodes Island, Greece, 15-17 June, 2017* .

COMPDYN 2017
6th ECCOMAS Thematic Conference on
Computational Methods in Structural Dynamics and Earthquake Engineering
M. Papadrakakis, M. Fragiadakis (eds.)
Rhodes Island, Greece, 15–17 June 2017

# NUMERICAL SIMULATION OF SOIL-STRUCTURE INTERACTION: A PARAMETRIC STUDY

**Maria Giovanna Durante[1], Luigi Di Sarno[2], Armando Lucio Simonelli[2]**

[1] University of California, Los Angeles
Department of Civil and Environmental Engineering
2270 Boelter Hall, Los Angeles, CA 90095-1593
mgdurante@ucla.edu

[2]University of Sannio
Department of Engineering
Piazza Roma, 21, 82100 Benevento, IT
{ldisarno, alsimone}@unisannio.it

**Keywords:** Soil-Structure Interaction, Numerical simulation, Experimental validation, Parametric analysis.

**Abstract.** *Soil Structure Interaction (SSI) is a complex phenomenon that may radically change the earthquake response of structural systems, as consequence of the variation of the natural frequency and the damping ratio. One of the most effective means for evaluating SSI is the use of physical models. In this study the physical model considered is formed by an oscillator founded on a group of piles embedded in a horizontally layered deposit of dry sand. The benchmark experimental campaign was carried out at the Bristol Laboratory for Advanced Dynamics Engineering (BLADE) at the University of Bristol (UK), financed by the Seismic Engineering Research Infrastructures for European Synergies (SERIES). An accurate parametric numerical study is performed and the results are discussed. The study investigates the effects of the dynamic properties of the oscillator on the period elongation and piles response. By means of advanced numerical analyses the outcomes of the present work provide insights into the quantitative evaluation of period elongation and the strength of inertial contribute to the bending moment at the pile head, when the system approaches resonance conditions.*

## 1 INTRODUCTION

The complex interaction between soil, foundation and superstructure is usually called Soil-Structure-Interaction (SSI). In dynamic conditions the effects of such interaction may cause significant variations of the system response due to the modification of dynamic properties of both structure and soil as a consequence of the shaking. The main effects of SSI on deep foundations include: (*i*) kinematic bending applied along the piles – even in the absence of a superstructure; (*ii*) the variation between the free-field ground motion and the motion at the pile top, that is at the base of the superstructure. From a structural point of view, SSI causes mainly period elongation and variation of the damping ratio.

An effective way for evaluating SSI is the use of earthquake simulator for testing physical models, and the employment of such results for the validation of numerical models. In this paper the numerical model adopted has been validated by means of 1-g shaking table results from and experimental campaign carried out at the Bristol Laboratory for Advanced Dynamics Engineering (BLADE) at the University of Bristol (UK). This experimental effort was funded by the Seismic Engineering Research Infrastructures for European Synergies (SERIES). In order to investigate the effects of the oscillator properties on the SSI, a parametric analysis has been carried out. The inputs considered have been selected from the recent 2016 and 2017 Central Italy sequence and scaled in frequency at the model size. The configuration considered in the parametric study is formed by an oscillator connected to the central pile. The outcomes of the numerical simulations are presented in terms of period elongation, maximum relative displacement for the oscillator and bending moments for the pile connected to the oscillator and the neighboring pile. The parametric study shows that the resonance of the system soil-foundation, oscillator and input drives the response of all the component of the system.

## 2 PHYSICAL MODEL

The physical model considered in this work is formed by a Single-Degree-Of-Freedom (SDOF) founded on a pile embedded in a bi-layer deposit. This configuration has been selected among others available from an experimental shaking-table campaign carried out at 3mx3m 1-g shaking table of the Bristol Laboratory for Advanced Dynamics Engineering (BLADE) at the University of Bristol (UK) [1].

### 2.1 Experimental setup

The physical model (Figure 1) was formed by a group of five piles embedded in a bi-layer of dry Leighton Buzzard (LB) sand fraction E ($D_r$ = 28%, $\gamma_d$ = 13.63 kN/m$^3$) for the top layer and a mix of 85% of fraction B and 15% of fraction E ($D_r$ = 41%, $\gamma_d$ = 17.46 kN/m$^3$) for the bottom one. The initial stiffness contrast ($G_{bottom}/G_{top}$), computed experimentally [2], was equal to 3. Piles were formed by an alloy aluminum tube ($E$ = 7e10 Pa) with thickness t = 0.71 mm, outer diameter D = 22.23 mm and length L = 750 mm. The response of the model was monitored using accelerometers, Linear Variable Displacement Transformer (LVDT) and strain gauges. More details about the experimental campaign can be found in Durante et al. [3].

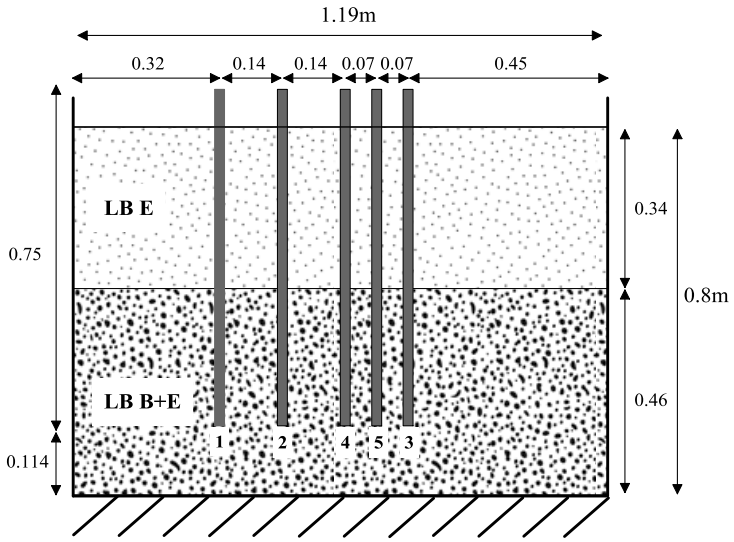


Figure 1: Model details (after Durante et al., 2016)

## 2.2 Numerical model

Based on the physical model described in the previous section, a numerical model has been developed and implemented in the finite difference element code FLAC2D v.5 [4]. In such numerical model (Figure 2), soil deposit is modeled using a user-defined hysteretic Ramberg-Osgood constitutive model [5]. The two model parameters of the model are obtained fitting the model response with experimental Vucetic and Dobry $G(\gamma)$ and $D(\gamma)$ curves for zero plasticity index [6]. The structural elements are modeled by means of pile (for the foundation) and beam elements (for all the SDOF components) implemented in FLAC2D. Pile elements interact with the soil by means of non-linear normal and shear coupling springs. The normal springs are defined using the Georgiadis et al. [7] analytical method, while the shear springs properties are obtained from the soils properties [4]. More details about the numerical model and its validation against the shaking table results can be found in [8].

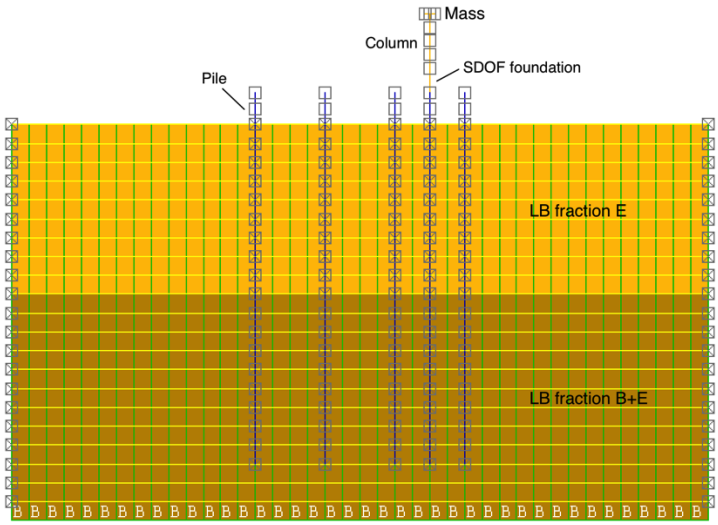


Figure 2: Numerical model (after Durante et al. 2015 [8])

## 2.3 Parametric analysis

In order to investigate the effects of the dynamic properties of the oscillator on the period elongation and on piles response, a parametric study has been performed. In do doing, two different sections have been considered for the column (SEC1 and SEC2) and seven different masses for a total of eight different oscillators (Table 1). The oscillators are connected to the central pile (Pile 5, Figure 1) and subjected to three scaled ground motion records (Figure 3, Table 2). The latter strong motion records were selected from the recent seismic sequence of Central Italy earthquakes (e.g. [9] among others]. The oscillators have been carefully selected so that the range of variation of the wave parameter ($1/\sigma = f_{fix} \cdot h/V_s$ [10]) is 0.01 – 0.6. The latter mechanical parameter can be considered as a synthetic index of the structure and soil relative stiffness, in which $f_{fix}$ is the theoretical natural frequency of the fixed base oscillator, $h$ is the height of the column and $V_s$ is the shear wave velocity of the deposit in the active length of the pile. It should be noted that SEC1 was assumed equal to the actual section adopted for the oscillators in the experimental campaign. The Scaling Factor (SF) for the ground motions is assumed equal to 12, in accordance with the scaling law adopted in the experimental campaign [11].

| | Total added mass [g] |
|---|---|
| SEC1 (3x12mm, h=100mm, E=7e10Pa) | 600 |
| | 150 |
| | 50 |
| SEC2 (20x20mm, h=50mm, E=7e10Pa) | 1300 |
| | 550 |
| | 320 |
| | 200 |
| | 150 |

Table 1: Oscillator details

| ID | Event | Magnitude | PGA [g] |
|---|---|---|---|
| NRC | 24 August 2016 (Norcia Station) | 6.1 | 0.37 |
| CNE | 30 October 2016 (Castel Sant'Angelo Station) | 6.5 | 0.29 |
| AQF | 18 January 2017 (L'Aquila –V. Aterno –Ferriera Station) | 5.5 | 0.13 |

Table 2: Ground motions adopted

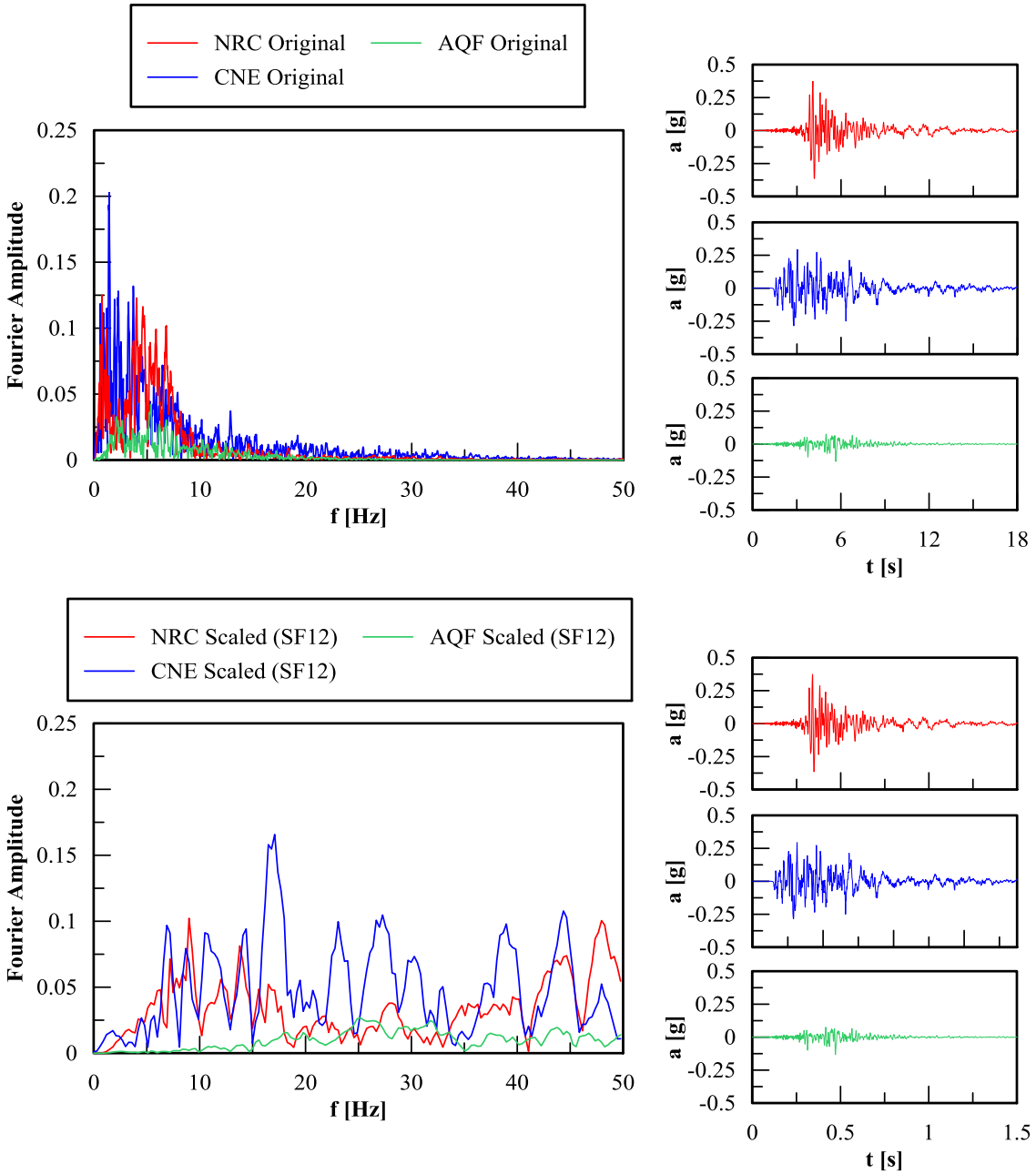


Figure 3: Original and scaled input adopted (FFTs and time series)

## 3 MAIN RESULTS

The main results obtained from the parametric analyses are discussed. In the following sections the SSI effects are reported in terms of period elongation and piles response.

### 3.1 Soil-Structure-Interaction effects

In this work, the elongated period of the oscillator ($T_{SSI}$) is obtained from the Transfer Functions (TFs) computed between the displacements recorded at the top of the oscillator and the one on the free-field surface. The wave parameter is computed considering the shear wave velocity that corresponds to the level of deformation for the ground motion considered.

The variation of the period elongation ($T_{SSI}/T_{fix}$) with the wave parameter are reported in Figure 4. As expected, the increasing of the period elongation is proportional to the wave pa-

rameter with a linear variation. It should be noted that it is possible to fit the data using two different linear equations, one for each group of oscillator considered in this study (SEC1 and SEC2, Table 1). The linear equation for SEC1 is the same that was obtained experimentally in [3], while the equation for SEC2 is characterized by the same slope but different constant term. This outcome suggests that, if it is assumed a linear trend between $T_{SSI}/T_{fix}$ and $1/\sigma$, the slope of the equation is affected by the soil-foundation system, while the constant term is influenced by the column characteristics. This aspect is still under investigation and it will further discussed in future publications.

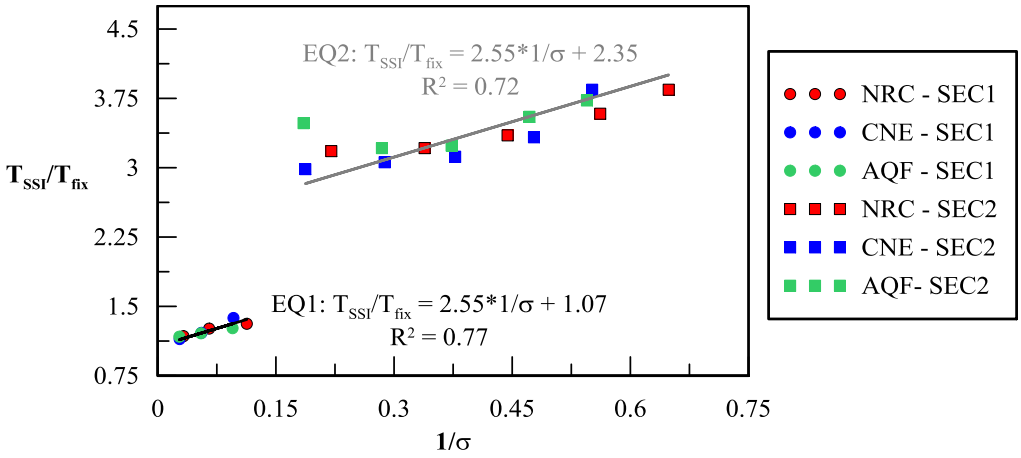


Figure 4: Period elongation versus wave parameter

Figure 5 shows the variation of the maximum relative displacement of the oscillator, computed as the difference in the time domain between the response at the top and the base of the oscillator, with the wave parameter. The relative displacement increases with the wave parameter with a different slope for each input. The strong motion that generates the most rapid increasing of the relative displacement with the wave parameter is CNE, which possesses the intermediate value of PGA. The observed behavior is related to the frequency content of the input (Figure 3): the high intensity around the soil deposit frequency (around 30 Hz) induces effects of resonance that affect the oscillator response.

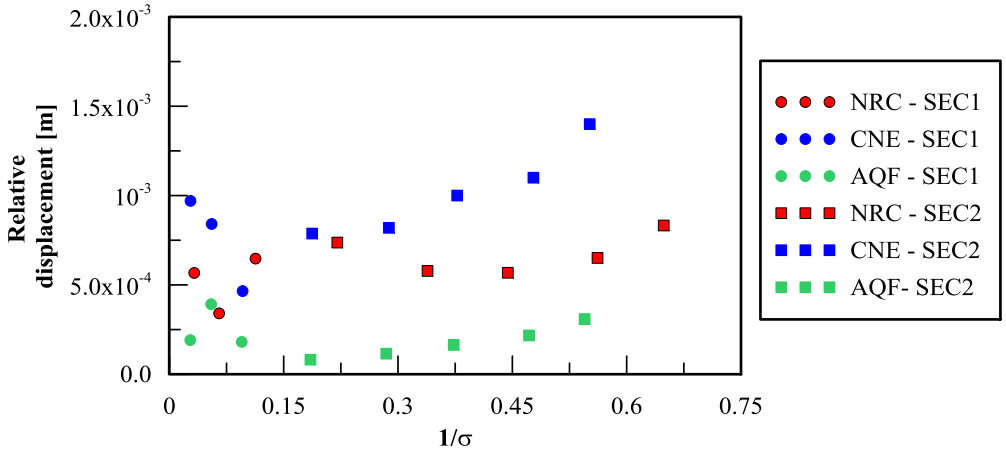


Figure 5: Oscillator elative displacement versus wave parameter

### 3.2 Geotechnical response

The effects of the SSI on piles response are presented in this section with reference to the pile directly connected to the oscillator (Pile 5, Figure 1) and the lateral pile not connected to the oscillator (Pile 4, Figure 1) but within the area of influence of pile 5 (the ratio between the spacing among the piles for the small group ($s$) and the pile diameter ($D$) is around 3).

Soil response in the free-field condition for all the configurations is reported in Figure 6 in terms of absolute maximum acceleration along the depth. The soil response is function only of the input considered and so the kinematic interaction on the piles is not changing with the oscillator.

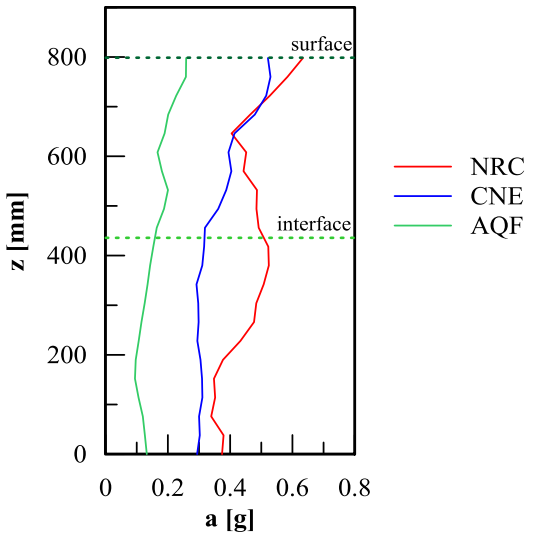


Figure 6: Envelope of absolute acceleration versus depth for the selected ground motions

Figure 7 shows the envelope of the absolute bending moments along depth for Piles 4 and 5 for the configuration considered together with the pure piles kinematic response (Free Head Pile configuration without oscillator – FHP). Figure 7a shows that despite Pile 4 is not connected to the oscillator, its response is changing with the configuration considered, due to the short distance to the oscillator ($s/D$=3). As a result, Pile 4 experiences either an increasing or decreasing of the response respect to the pure kinematic response (FHP response) depending to the oscillator considered. This phenomenon is related to the complex combination of resonance effects with soil non-linearity and for this reason it is not trivial to provide a general rule able to predict such response. This aspect requires further investigations. However, it is worth noticing that in both piles analyzed the response after the pile active length (that falls in the first layer of the deposit) results not affected by the inertial interaction at the pile head.

Figures 8 and 9 show the envelope of the absolute bending moments along depth for Piles 4 and 5 for the configuration considered together with the pure piles kinematic response for the records CNE and AQF, respectively. When considering CNE, the response of Pile 4 (Figure 8a) seems to be affected by the inertial effects of the oscillator only in the top part of it, but it is not able to affect the kinematic response at the interface between the two layers as it happens for the motion AQF (Figure 9a). The response of Pile 5 (Figures 7b, 8b and 9b) shows that: (*i*) the inertial contribution to the pile response is dissipated at different depths for the different motion but always within the first layer; and (*ii*) the oscillator that generates higher inertial effects is different for each ground motion because of the combination between the dynamic properties of oscillators and ground motions.

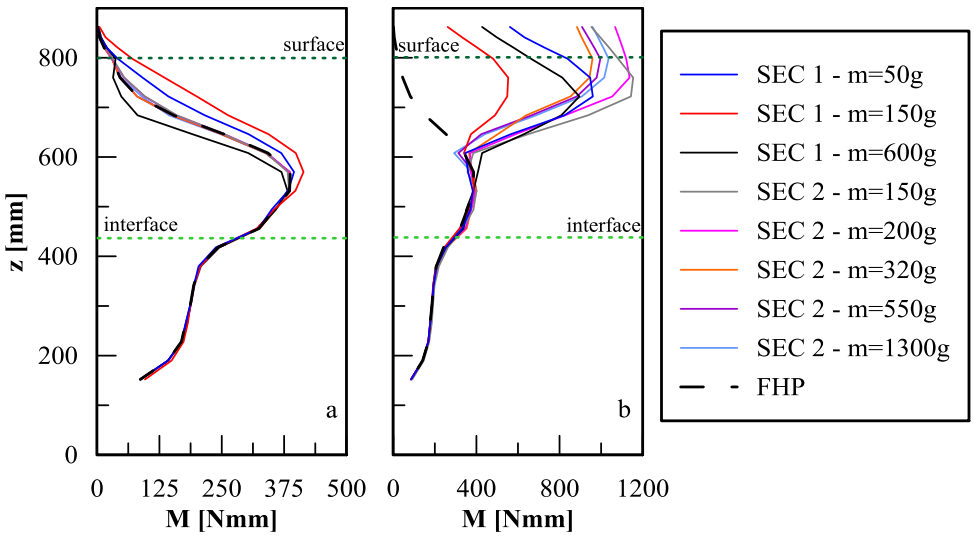


Figure 7: Envelope of bending moment along Piles 4 (a) and 5 (b) for NRC ground motion

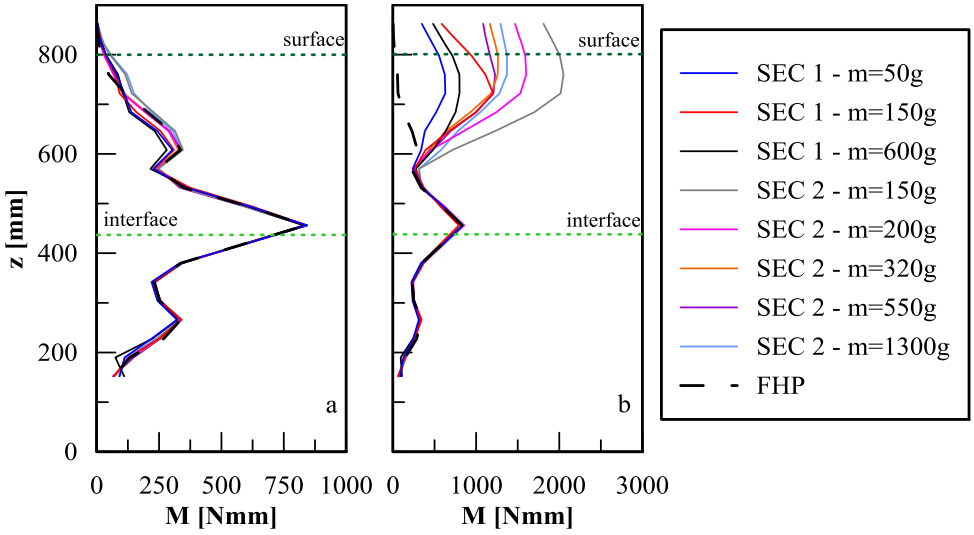


Figure 8: Envelope of bending moment along Piles 4 (a) and 5 (b) for CNE ground motion

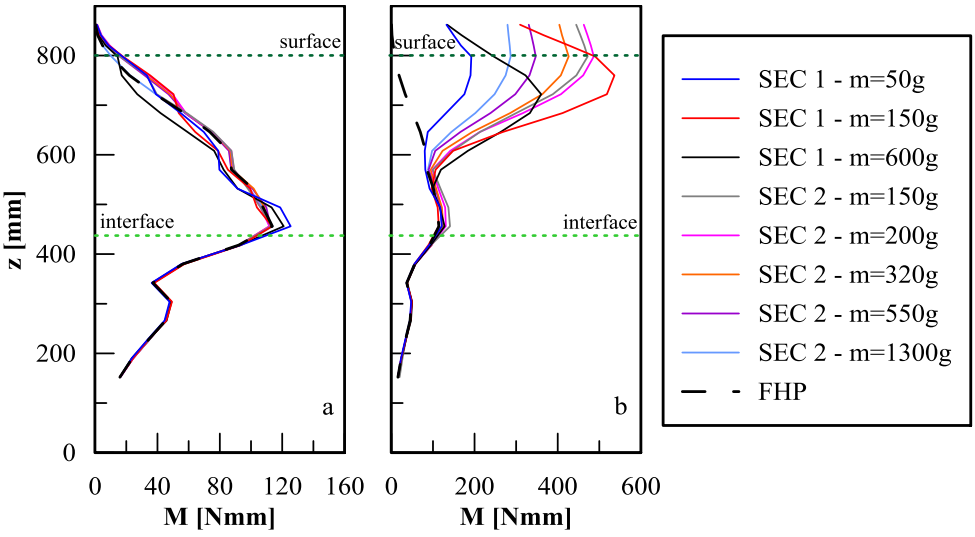


Figure 9: Envelope of bending moment along Piles 4 (a) and 5 (b) for AQF ground motion

## 4 CONCLUSIONS

A parametric analysis was performed by means of an advance two-dimensional model in the finite difference element code FLAC2D. The numerical model was based on a physical model tested on the shaking table of the BLADE laboratory at the University of Bristol. The physical model was formed by a group of five piles embedded in a bi-layer with several oscillators connected to the central pile. The numerical model accounts for hysteretic constitutive model for the soil and non linear connection between piles and soil. Three different scaled ground motion from the recent central Italy earthquake sequence were selected as input in the numerical model. The main outcomes of this work are:

- The numerical results of the Soil-Structure-Interaction in terms of $T_{SSI}/T_{fix}$ and $1/\sigma$ are in good agreement with the experimental results;
- For the evaluation of the Soil-Structure-Interaction, the relation between $T_{SSI}/T_{fix}$ and $1/\sigma$ can be considered linear for each group of section considered. The equations obtained from the fitting of the numerical results show that the slope coefficient of the equation is affected by the soil-foundation system, while the constant term is influenced by the column characteristics;
- The relative displacement of the oscillator increases with the wave parameter with a different slope for each ground motion, with the maximum response for the input with a significant frequency content around the natural frequency of the deposit;
- For Pile 4 the comparison between the FHP configuration with the configuration with the oscillator shows that the inertial effect affects its response for a depth that is related to the ground motion considered but always within the active length of the pile (first layer);
- For Pile 5 the inertial effects caused by the oscillators are dissipated at different depths for each ground motion (within the first layer) and the resonance mechanisms activated for each test generates different responses in terms of bending moment at the pile head.

## ACKNOWLEDGEMENTS

The research leading to these results has received funding from the European Union Seventh Framework Programme (FP7/2007-2013) under grant agreement n° 227887, SERIES. The financial support provided by the project ReLUIS (Task MT2) funded by the Italian Civil Protection is also appreciated. The authors would like to acknowledge also all the contributors to the SERIES project.

## REFERENCES

[1] Simonelli A.L., Di Sarno L., Durante M.G., Sica S., Bhattacharya S., Dietz M., Dihoru L., Taylor C.A., Cairo R., Chidichimo A., Dente G., Modaressi A., TodoBom L.A., Kaynia A.M., Anoyatis G., Mylonakis G. *Chapter 26: Experimental Assessment of Seismic Pile-Soil Interaction*. Seismic Evaluation and Rehabilitation of Structures, Geotechnical, Geological and Earthquake Engineering 2014; **Volume 26**: 455-475, 2014.

[2] Durante M.G., Karamitros D., Di Sarno L., Sica S., Taylor C.A., Mylonakis G., Simonelli A.L. *Characterisation of shear wave velocity profiles of non-uniform bi-layer soil*

*deposits: analytical evaluation and experimental validation.* Soil Dynamics and Earthquake Engineering **75**: 44–54. DOI: dx.doi.org/10.1016/j.soildyn.2015.03.010, 2015.

[3] Durante M.G., Di Sarno L., Taylor C. A., Mylonakis G., Simonelli A. L. *Soil– pile–structure interaction: experimental outcomes from shaking table tests.* Earthquake Engineering and Structural Dynamics, **45 (7)**, 1041–1061, 2016. DOI: 10.1002/eqe.2694, 2016.

[4] Itasca. *FLAC – Fast Lagrangian Analysis of Continua – Version 5.0*. Itasca Consulting Group, Inc., Minneapolis, USA, 2005.

[5] Karamitros D. *Development of a numerical algorithm for the dynamic elastoplastic analysis of geotechnical structures in two (2) and three (3) dimensions.* PhD Thesis, National Technical University of Athens, Athens, 2010.

[6] Vucetic M., Dobry R. *Effect of soil plasticity on cyclic response*. Journal of Geotechnical Engineering, ASCE; Vol. **117 (1)**, pp. 89-107, 1991.

[7] Georgiadis M., Anagnostopoulos C., Saflekou S. *Centrifugal Testing of laterally loaded piles in sand.* Canadian Geotechnical Journal, **29**, pp. 208-216, 1992.

[8] Durante M.G., Di Sarno L., Taylor C.A., Mylonakis G., Simonelli A.L. *Soil-pile-structureinteraction: experimental results and numerical simulations.* Proc. of COMPDYN 2015, 5th ECCOMAS Thematic Conference on Computational Methods in Structural Dynamics and Earthquake Engineering. Crete Island, Greece, 2015.

[9] Stewart J.P., Lanzo G., Aversa S., Bozzoni F., Dashti S., Di Sarno L., Durante M.G., Simonelli A.L., Penna A., Foti S., Chiabrando F., Grasso N., Di Pietra V., Franke K., Reimschiissel B., Galadini F., Falcucci E., Gori S., Kayen R.E., Kishida T., Mylonakis G., Katsiveli E., Pagliaroli A., Giallini S., Pelekis P., Psycharis I., Vintzilaiou E., Fragiadakis M., Scasserra G., Santucci de Magistris F., Castiglia M., Fierro T., Mignelli T., Sextos A., Alexander N., De Risi R., Sica S., Mucciacciaro M., Silvestri F., d'Onofrio A., Chiaradonna A., De Silva F., Tommasi P., Tropeano G., Zimmaro P. *Engineering Reconnaissance of the 24 August 2016 Central Italy Earthquake. Version 2*, Zimmaro P. and Stewart J.P. editors – Geotechnical Extreme Event Reconnaissance (GEER) Association Report No. GEER-050B. DOI:10.18118/G61S3Z, 2016.

[10] NIST. *Soil–structure interaction for building structures. National Institute of Standards and Technology*. U.S. Department of Commerce, Washington D.C. Project Technical Committee: Stewart JP (Chair), Crouse CB, Hutchinson T, Lizundia B, Naeim F, Ostadan F., Report No. NIST GCR 12-917-21., 2012.

[11] Muir Wood D., Crewe A., Taylor C.A. *Shaking table testing of geotechnical models.* IJPMG - International Journal of Physical Modelling in Geotechnics; **1(2002)**:01–13, 2002.

COMPDYN 2017
6th ECCOMAS Thematic Conference on
Computational Methods in Structural Dynamics and Earthquake Engineering
M. Papadrakakis, M. Fragiadakis (eds.)
Rhodes Island, Greece, 15–17 June 2017

# SEISMIC ANALYSIS OF A HISTORIC WATER TOWER: A FLUID-STRUCTURE-SOIL INTERACTION PROBLEM

**Angeliki Zanni[1], Michail Spyridis[2], and Dimitris L. Karabalis[3]**

Department of Civil Engineering, University of Patras, 26504 Rio, Patras, GREECE
aggelikhzannh@gmail.com[1]
spiridis.mixalis@gmail.com[2]
karabali@upatras.gr[3]

**Keywords:** Fluid-Structure-Soil Interaction, Hollow Tanks, Seismic Analysis, Water Tower.

**Abstract.** *The dynamic analysis of a historic water is attempted taking into consideration the fluid-structure-soil interaction. The water tank is cylindrical with a concentric manhole and rests on a relatively flexible structure and a ring of surface foundations. A FEM model of the tower and the structure is developed preserving all the details of the original structure. Extensive parametric studies, undertaken in the context of this work, resulted in a discrete model for the hollow water tank along the lines of the convective-impulsive mass concept. Related non-dimensional charts are shown herein. In addition, a discrete spring-mass-damper model is used for the simulation of soil-structure interaction. The full model of the water tower is subjected to seismic excitation and the results obtained by this rigorous numerical model are compared to other simplified approaches.*

## 1 INTRODUCTION

The water tower under investigation was designed by the famous Italian engineer Pier Luigi Nervi for the Santa Maria Novella Station in Florence, introducing several innovations in comparison to other similar structures of the same era. It was constructed in 1930 and is still in use. Figure 1 shows a view of the structure and representative plans [1,2].

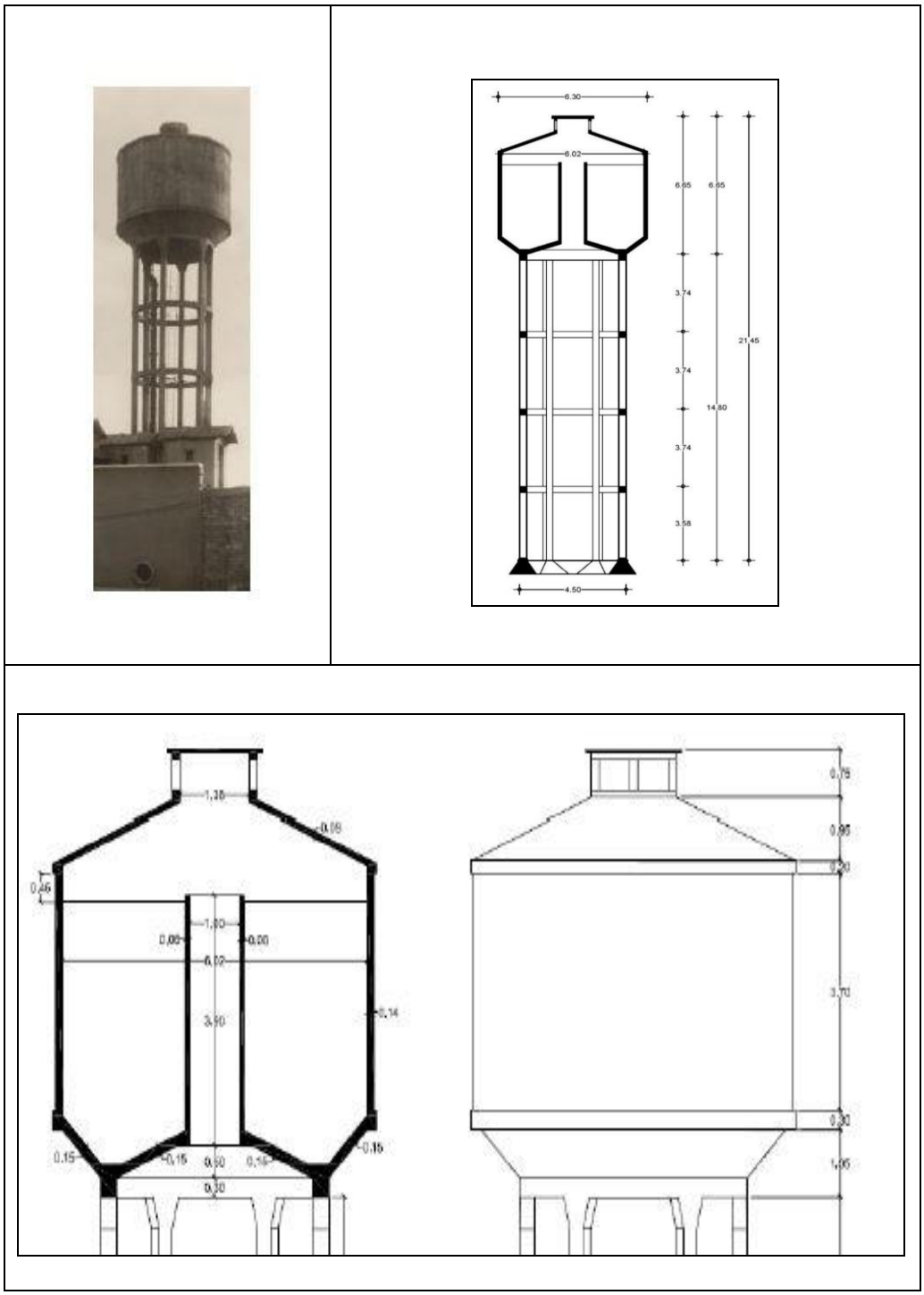


Figure 1. View and plans of the water tower at Santa Maria Novella Station in Florence [1,2].

The motivation for this study comes from a similar work by Sorace, Terenzi & Mori [2] and the particular way they model the circular water tank with the coaxial manhole, although this was not the focus of their work. They based their model on the discrete impulsive-convective Housner [3,4] approach for circular tanks, without manhole. To this, they added some arbitrary modifications, i.e. subtracting the volume of the manhole from the total water volume and, thus, calculating an equivalent water mass corresponding to an idealized circular tank of reduced water content. Although this approximation appears, more or less, adequate for the geometry and water level of the particular structure, it certainly violates the intrinsic hydrodynamic characteristics of such structures, in general, since the physical presence of the manhole is ignored. With this in mind, the authors of this work set out to perform a parametric study for water tanks with coaxial manholes based on a rigorous FEM model. The results of this study are compared to those obtained in [2] and some interesting conclusions are drawn. Finally, a complete analysis of the water tower at the Santa Maria Novella Station is presented (a) using a rigorous FEM model for the structure and the water-structure interaction and (b) taking in addition into account the interaction of the above system with the soil. The results of this analyses are also compared to those obtained using the approximate approach presented in [2].

## 2 DYNAMIC ANALYSIS OF CIRCULAR TANKS WITH COAXIAL MANHOLES

The geometry and a FEM model of a circular, full water tower with a manhole are shown in figure 2. In all cases examined in this eigenanalysis, the concrete walls of the outside and the inside (manhole) shells are considered rigid and, for the purposes of this parametric study aiming at computing the dynamic characteristics of the liquid content, of negligible mass.

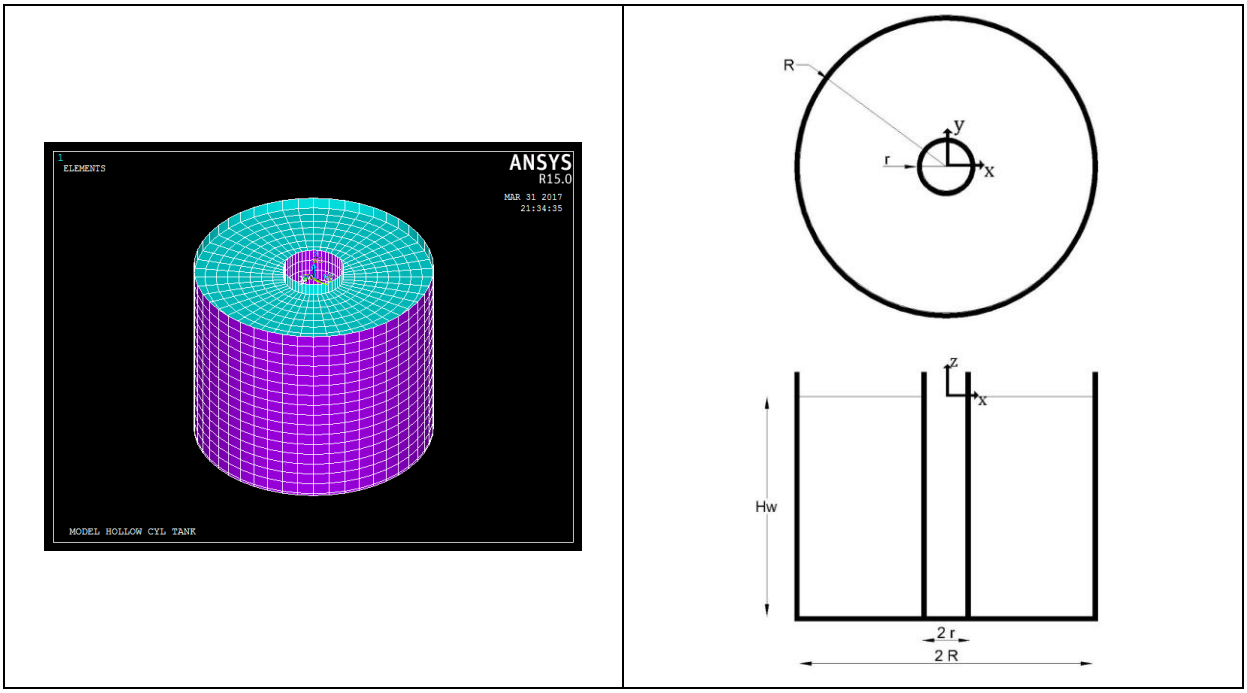


Figure 2. Geometry and FEM model of circular water tank with manhole.

The results of the modal analysis of the tank are shown in figure 3, where (a) the 1st eigenfrequency of the water, (b) the 1stconvective mass $M_1$, and (c) the corresponding con-

vective mass height $H_1$ are plotted in a non-dimensional form versus the ratio r/R, i.e. the radius of the manhole to the that of the tank, as shown in figure 2. In all cases, g is the acceleration of gravity, $M_w$ is the total mass of water and $H_w$ the total height of water in the tank. The results obtained by the rigorous FEM model are plotted along with those of the approximate approach used in [2]. In an effort to verify the accuracy of the above solutions, results for r=0, i.e. a cylindrical tank without a manhole, as obtained from the analytic solution provided in Ref. [5], are also shown in figure 3, for all ratios of $H_w$/R.

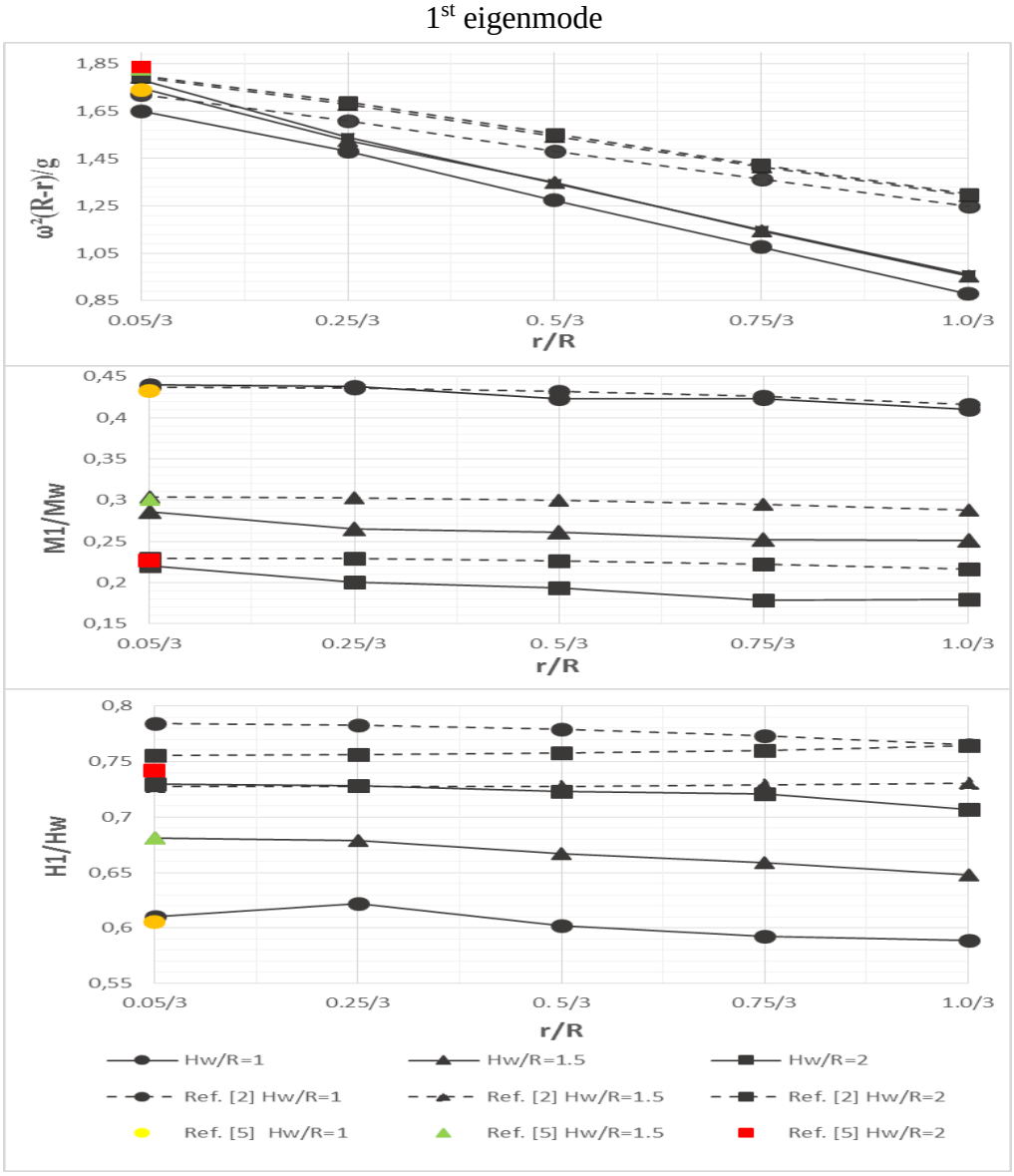


Figure 3. Non-dimesional of 1st eigenfrequency and corresponding convective mass and convective mass height versus the ratio of r/R for several values of $H_w$/R.

On the basis of the results shown in figure 3 it is concluded that (a) as it should be expected, the difference between the rigorous FEM model and the approach adopted in Ref. [2] increases as the ratio r/R increases, (b) the differences between the two approaches also increase as the height $H_w$ of the water increases in comparison to the radius R of the tank. These differences are in all cases substantial, except for $H_w/R=1$ where a good agreement between the ratio $M_1/M_w$ appears for all values of r/R. Of course, both approaches converge well at the limit value of r/R=0.05/3 to those provided in Ref. [5] for simple cylindrical tanks. However, for the particular water tank resting on the tower at the Santa Maria Novella Station, where r/R=0.5/3 and $H_w/R=1.2$ (approximately) the approximate approach of Ref. [2] presents an error, as compared to the rigorous FEM model, of about 23% with respect to the 1st eigenfrequency, 15% with respect to the ratio $M_1/M_w$, and 10% as far as the ratio $H_1/H_w$ is concerned.

## 3 SEISMIC RESPONSE OF WATER TOWER AT SANTA MARIA NOVELLA STATION

As a first step towards a practical seismic analysis, the entire water tower at Santa Maria Novella Station, actual structure and full water tank, is subjected to a horizontal seismic excitation. The seismic record chosen is an artificial accelerogram compatible with the design spectrum of Eurocode 8 for soil category C and damping 5%, with PGA=0.4g and duration 20sec. The fitting of the artificial accelerogram to the target spectrum is made via the iterative procedure introduced in [6]. A 6% of critical damping is assumed for the concrete structure. The analysis is performed using (a) a full FEM model, including the fluid in the tank, and (b) a FEM model for the concrete structure and the approximate discrete model proposed in [2] for the fluid. The 1st period of the structure is computed at 2.87sec using the FEM model and 2.58 sec using the approach in Ref. [2]. Certainly the high value of the 1st period is attributed to the convective fluid mass which accounts for about 30% of the total water mass, and the remaining impulsive mass, since the 1st period of the rather flexible concrete structure, with an empty tank, is 0.94sec. The response versus time of the water tower, in terms of displacement at the top of the structure and base shear, is shown in figure 4.

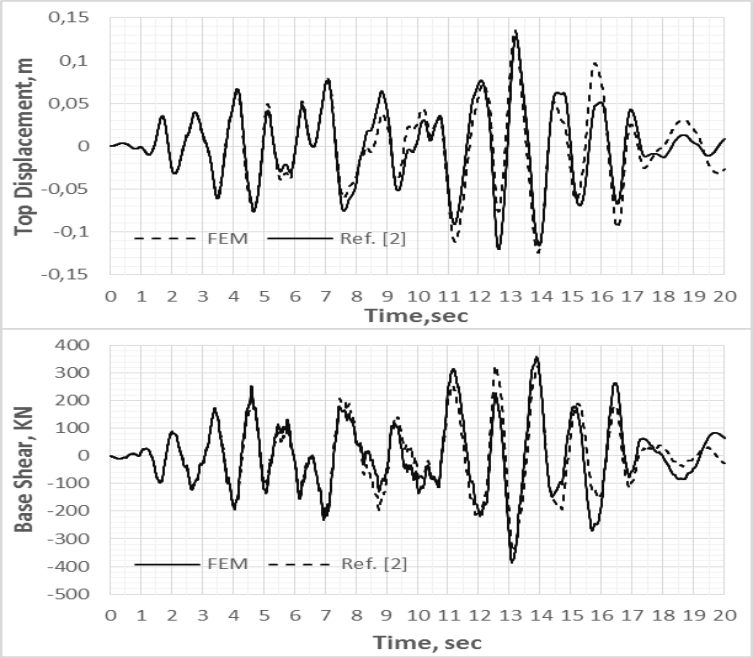


Figure 4. Displacement at the top and base shear of the water tower at Santa Maria Novella Station versus time due to a seismic excitation compatible with the design spectra of EC-8.

Although for this structure, the differences in peak absolute values in terms of displacements and base shear do not seem large, the differences in the dynamic characteristics used by the two approaches (see discussion in previous section) become evident. Of course, the FEM model takes effectively into consideration all eigenmodes of the sloshing fluid (at least those "allowed" by the particular choice of time step) while in the approximate discrete model of Ref. [2] only the 1st mode is included. As it is shown in the literature, e.g. Refs [5,7], the 2nd and higher sloshing modes are of negligible importance and can safely be ignored for all practical purposes.

In a second step, the effect of soil-structure interaction is considered. To this extend, a discrete spring-mass system is introduced at the base of the foundation of the FEM model. The water tower under investigation is supported by 6 footings, at the base of each column, closely arranged and connected rigidly at their top by circular beam. For the purposes of this study, the foundation is simulated as a rigid circular ring resting on a soil medium with shear wave velocity around 280m/sec (an arbitrary guess for the actual soil conditions). The spring and damping constants are computed following the approach proposed in Ref. [8]. Further details for the FEM simulation of the structure and the foundation model can be found in Ref. [9]. The same artificial accelerogram is used as in the previous paragraph. As it is expected, a relative increase in the top displacement and a decrease in the base shear, as compared to fixed base conditions, are observed when the SSI phenomenon is taken into account.

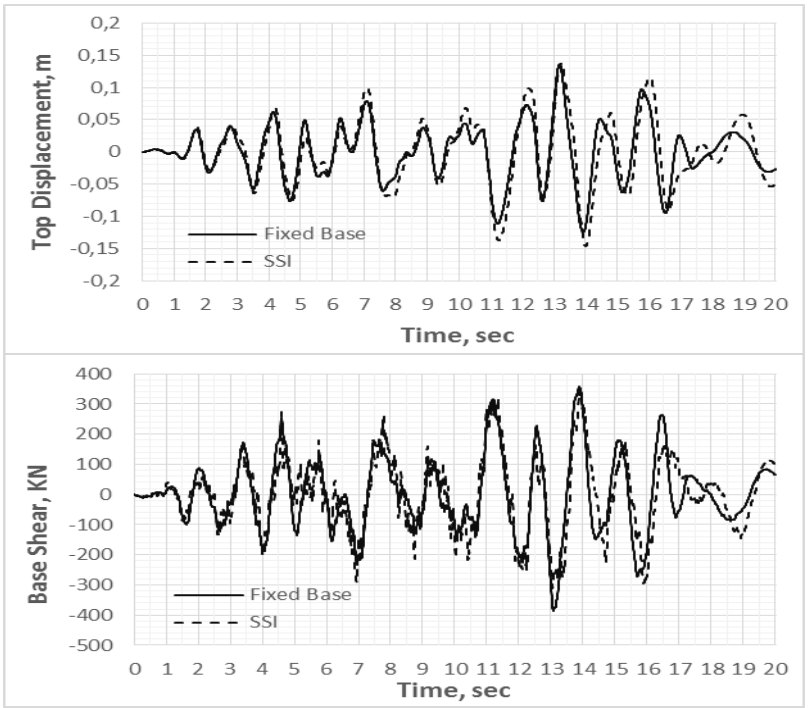


Figure 4. A comparison study between fixed base and SSI conditions in terms of displacement at the top and base shear of the water tower at Santa Maria Novella Station due to a seismic excitation compatible with the design spectra of EC-8.

## 4 CONCLUSIONS

A FEM rigorous model is developed for the study of the structure-fluid interaction of cylindrical tanks with a coaxial manhole. The results of these analyses are compared to those obtained by an approximate approach where the hydrodynamic effects due to structural geometry are ignored. The conclusions drawn on the basis of these parametric studies are as follows:

- The 1st eigenperiod of the tank increases monotonically as the radius of the manhole increases in comparison to that of the tank ratio (r/R), and it is almost independent of the water level $H_w$/R.
- The differences of eigenanalysis characteristics, i.e. 1st eigenfrequency and the corresponding convective mass and convective mass height, between the two approaches increase substantially as the radius of the manhole increases in comparison to that of the tank, for all levels of water fill.
- A seismic analysis of the historic water tower at Santa Maria Novella Station using both approaches results to minor differences between them. This is attributed to the particular geometric and structural characteristics of the tower under investigation.
- Hydrodynamic effects caused by a particular structural geometry, such as internal holes, should not be ignored, in general, for structures in which a large portion of the vibrating mass is in fluid form and is located at a high elevation with respect to the rest of the structure, e.g. water towers.
- Approximate approaches ignoring hydrodynamic effects are not in a position to consider certain important effects related to sloshing, e.g. wave height and overspilling.
- SSI for structures with large fundamental period does not play an important role in their seismic response. However, it could become detrimental for seismic motions of low frequency and soft soil conditions.

## REFERENCES

[1] S. Sorace, Private correspondence, 2015.

[2] S. Sorace, G. Terenzi, C. Mori, Passive energy dissipation-based retrofit strategies for R/C frame water towers, *Engineering Structures*, **106**, 385-398, *2016.*

[3] G.W. Housner, Dynamic behavior of water tanks, *Bulletin of the Seismological Society of America*, **53(2)**, 381-387, 1963.

[4] M.A. Haroun, G.W. Housner, Seismic design of liquid storage tanks, ASCE Journal of Technical Councils, **107(1)**, 191-207, 1981.

[5] A.S. Veletsos, P. Shivakumar, Tanks containing liquids or solids, Chapter 15, D.E. Beskos, S.A. Anagnostopoulos eds., *Computer Analysis and Design of Earthquake Resistant Structures A Handbook*, Advances in Earthquake Engineering, Computational Mechanics Publications, Southampton, 1997.

[6] D.L. Karabalis, G.J. Cokkinides, D.C. Rizos, J.S. Mulliken, Simulation of earthquake ground motions by a deterministic approach, *Advances in Engineering Software*, **31**, 329-338, 2000.

[7] G.C. Drosos, A.A. Dimas, D.L. Karabalis, Discrete models for seismic analysis of liquid storage tanks of arbitrary shape and fill height, *Journal of Pressure Vessel Technology*, **130**, 1-12, 2008.

[8] T. L. Karavasilis, D.C Rizos, D.L. Karabalis, Seismic analysis of spherical tanks including fluid-structure-soil interaction, *13th World Conference on Earthquake Engineering*, Vancouver, B.C., Canada, August 1-6, 2004.

[9] A. Zanni, Dynamic analysis of a water tower including soil-structure interaction, Diploma Thesis, Department of Civil Engineering, University of Patras, Greece, 2016.

COMPDYN 2017
6th ECCOMAS Thematic Conference on
Computational Methods in Structural Dynamics and Earthquake Engineering
M. Papadrakakis, M. Fragiadakis (eds.)
Rhodes Island, Greece, 15–17 June 2017

# DEVELOPMENT OF AMPLIFIED SEISMIC RESPONSE SPECTRA FOR STRUCTURAL ANALYSIS OF DECOUPLED SMALL BORE PIPES

**Anders Blom**[1]

[1] AREVA NP Uddcomb
Garnisonsgatan 7, 25466 Helsingborg, Sweden
e-mail: anders.blom@areva.com

**Keywords:** Amplified Response Spectrum, Decoupled Small Bore Pipes, Modal Analysis, Piping Analysis, Seismic Loads.

**Abstract.** *In various applications, not at least within the nuclear industry, piping systems are required to be structurally verified for seismic loads. Piping systems often have connected small bore pipes which also have requirements for seismic qualification. If the ratio of run-to-branch pipe moment of inertia is large, the small bore pipes can often be decoupled from the main pipes when performing the structural analysis. There are many reasons why decoupling is preferred in comparison to performing a coupled analysis. Firstly, from a project perspective, it is desirable to finish the design and verification of the main pipes before the work on the small bore pipes is started. Secondly, with decoupled pipes the analysis models become smaller, meaning reduced analysis time and reduced risk of encountering convergence difficulties for dynamic loads. Finally, decoupling the small bore pipes makes it possible to distinguish between primary and secondary loads, which will take away unnecessary conservatism in the evaluation of the small bore pipes. Though there are advantages of decoupling, the analyst will be faced with the question of how to consider the impact of the main pipe oscillations in the analysis of the small bore pipe. Seismic loads are generally applied to pipes as response spectrum loads derived in a seismic analysis of the supporting building structure. A clear disadvantage of a response spectrum analysis is that it only calculates bounds for forces, moments, displacements and accelerations and that it does not result in any frequency dependent quantities. There is no established industrial practice how the impact on the small bore pipe from the main pipe should be considered at the decoupling point and in many cases simplifications that give non-conservative results are made. This study presents a method to create an amplified response spectrum at the small bore piping connection point making use of modal analysis results and response spectrum input data. The method is validated by comparison with results from coupled analyses. The benefit of the proposed method is also demonstrated by applying it in evaluation of a small bore pipe.*

## 1 INTRODUCTION

In various applications, not at least within the nuclear industry, piping systems are required to be structurally verified for seismic loads. Generally, the seismic loads are applied to pipes as response spectrum loads derived in a seismic analysis of the supporting building structure. The structural behavior of the piping is then obtained by performing a response spectrum analysis in which the modal responses of the piping system are combined.

Piping systems often have connected small bore pipes which also have requirements for seismic qualification. If the ratio of run-to-branch pipe moment of inertia is large, the small bore pipes can often be decoupled from the main pipes when performing the structural analysis.

There are many reasons why decoupling is preferred in comparison to performing a coupled analysis. Firstly, from a project perspective, it is desirable to finish the design and verification of the main pipes before the work on the small bore pipes is started. Secondly, with decoupled pipes the analysis models become smaller, meaning reduced analysis time and reduced risk of encountering convergence difficulties for dynamic loads. If the small bore pipe is very small in comparison to the main pipe, the modal analysis could also result in twin modes and an unrealistically high response can be obtained if an unsigned modal combination method is used, a phenomenon addressed in [1]. Finally, decoupling the small bore pipes makes it possible to distinguish between primary and secondary loads, which will take away unnecessary conservatism in the evaluation of the small bore pipes.

Though there are advantages of decoupling, the analyst will be faced with the question of how to consider the impact of the main pipe oscillations in the analysis of the small bore pipe. A clear disadvantage of a response spectrum analysis is that it only calculates bounds for forces, moments, displacements and accelerations and that it does not result in any frequency dependent quantities.

While different decoupling criteria have been developed for systems and subsystems in general and main and small bore pipes in particular and considerable attention is given to their accuracy, the main focus is always on the main system or pipe. No guidance how the impact from the main system on the subsystem or small bore pipe should be considered is given. The lack of guidance for the analysis of subsystems is also pointed out in [2], in which an overlap approach is proposed as an alternative to decoupling. Antaki [3], also points out the lack of uniform industrial practice and that the practice is to model the connection point as an anchor and apply anchor motions and an envelope of the spectra for the main pipe supports at this point.

It is obvious that the latter method is inexact and in most cases non-conservative. The accuracy of the method becomes lower, the more flexible the main pipe is. In the overlapping method, the main pipe is included up to a point at which each of the three translational directions has been blocked at least twice. Though the validity of this method is justified in [2], it has other drawbacks. It is not a pure analysis decoupling since there are still needs for modelling of the main pipe. In some cases a rather large part of the main pipe needs to be modelled in order to fulfil the blocking criteria. Furthermore, with the overlapping method, it is not possible to distinguish between primary and secondary loads in the small bore pipe.

The purpose of this study is to present a method to create amplified response spectra to be used as input for analyzing decoupled small bore pipes. The method has been developed as a research project involving an M.Sc. thesis project resulting in [4].

## 2 DESCRIPTION OF THE METHOD

### 2.1 Construction of a response spectrum

A response spectrum is derived by looking at the response of a single degree-of-freedom (SDOF) oscillator (illustrated in Figure 1) subjected to an input motion. There are many books and articles describing the derivation of response spectra. Chopra [5], for example, presents the following stepwise procedure for deriving a response spectrum for a given input motion $\ddot{u}_g(t)$:

1. Numerically define $\ddot{u}_g(t)$
2. Select natural frequency $\omega_n$ and damping $\zeta$ of a SDOF oscillator
3. Compute the deformation response $u(t)$ of this SDOF system due to the input motion $\ddot{u}_g(t)$
4. Determine $u_0$, the peak value of $u(t)$
5. Calculate the spectral ordinates $D = u_0$, $V = \omega_n D$ and $A = \omega_n^2 D$
6. Repeat steps 2 to 5 for a range of $\omega_n$ and $\zeta$ values covering all possible systems of engineering interest
7. Plot *D*, *V* or *A* vs $\omega_n$

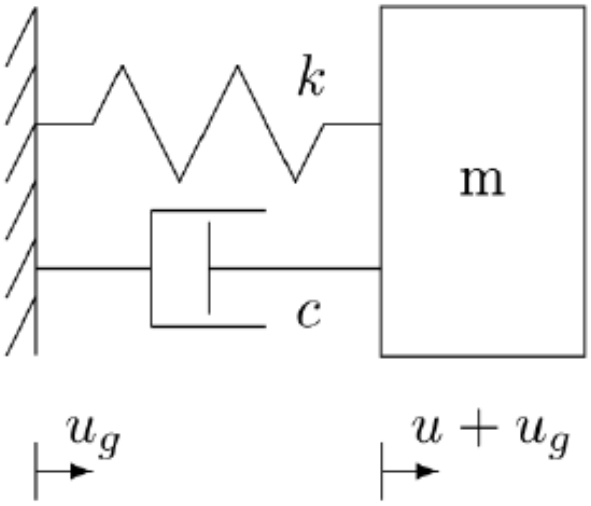


Figure 1: Single degree-of-freedom oscillator.

### 2.2 Computation of the deformation response

For the connection point of a small bore pipe, the pipe motions would be the input for generating response spectra. Since the main pipe seismic loads are given as response spectra, no time history is available. However, the mode shapes of the main pipe eigenmodes are known and each eigenmode can be considered as an oscillation of the form

$$u_g(t) = u_{g0} \sin(\omega t) \tag{1}$$

For an oscillator with natural frequency $\omega_n$, the dynamic amplification based on the relative motion of the mass can be expressed as

$$\frac{u_0}{u_{g0}} = \frac{\left(\frac{\omega}{\omega_n}\right)^2}{\sqrt{\left(1-\frac{\omega^2}{\omega_n^2}\right)^2 + \left(2\zeta\frac{\omega}{\omega_n}\right)^2}} \tag{2}$$

The dynamic amplification calculated by this expression is shown in Figure 2.

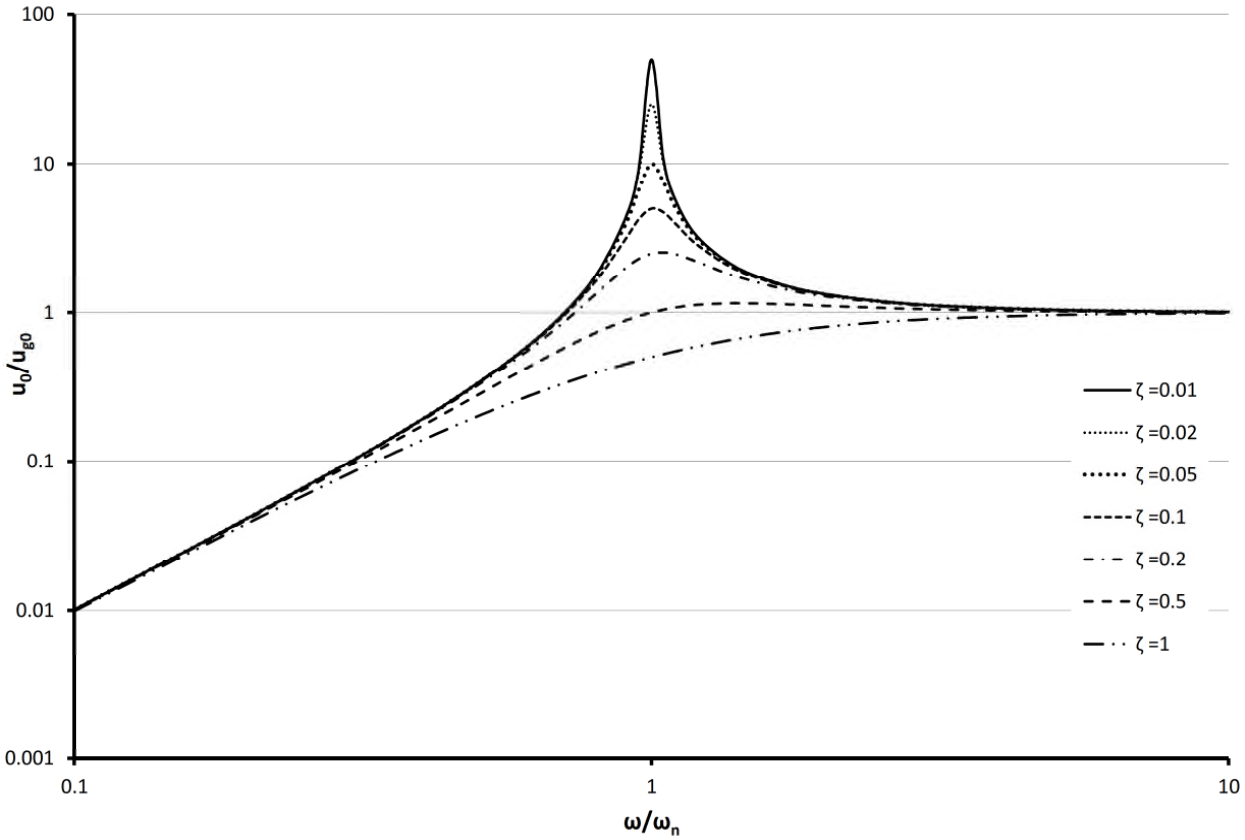


Figure 2: Dynamic amplification based on relative motion.

Hence, for each pair of main pipe natural frequency $\omega_i$ and subsystem frequency $\omega_n$ and damping ratio $\zeta$ a dynamic amplification factor $DF(\omega_n, \omega_i, \zeta)$ can be computed as

$$DF(\omega_n, \omega_i, \zeta) = \frac{\left(\frac{\omega_i}{\omega_n}\right)^2}{\sqrt{\left(1-\left(\frac{\omega_i}{\omega_n}\right)^2\right)^2 + \left(2\zeta\left(\frac{\omega_i}{\omega_n}\right)\right)^2}} \tag{3}$$

The peak value $u_0$ of the deformation of an oscillator with frequency $\omega_n$ due to a main pipe harmonic oscillation with amplitude $u_{g0}$ may be expressed as

$$u_0 = DF \cdot u_{g0} \tag{4}$$

For a system with all pipe mode shapes in the same coordinate direction subjected to a uniform response spectrum, the maximum displacement of the main pipe in the *i*th mode is obtained by

$$\{\mathrm{u}\}_i = \{\Phi\}_i \Gamma_i \frac{1}{\omega_i^2} A_i \tag{5}$$

where $\{\Phi\}_i$ is the mode shape of mode *i*, $\Gamma_i$ is the participation factor of mode *i* and $A_i$ is the spectral acceleration corresponding to mode *i* obtained from the response spectrum exciting the main pipe. At the decoupling point, where the input motion for generation of a response spectrum is denoted $u_g$, the maximum displacement the *i*th mode thus becomes

$$u_{g0,i} = u_{\Phi,i} \Gamma_i \frac{1}{\omega_i^2} A_i \tag{6}$$

where $u_{\Phi,i}$ is the mode shape coordinate of mode *i* at the decoupling point. The maximum deformation response for any oscillator eigenmode *n* with natural frequency $\omega_n$ can thus be calculated as

$$u_{0,i} = DF(\omega_n, \omega_i, \zeta) u_{\Phi,i} \Gamma_i \frac{1}{\omega_i^2} A_i \tag{7}$$

In this way the maximum response for any pair of main pipe frequency $\omega_i$ and oscillator frequency $\omega_n$ can be calculated. Normally, several modes contribute to the main pipe response. To obtain the maximum response for a subsystem frequency $\omega_n$ considering a main pipe response to which several modes contribute, a combination of the oscillator responses $u_{0,i}$ due to all contributing main pipe modes *i* has to be made. Several methods for combining modes exist, some of which are described in paragraph 2.5. Normally the combination methods are expressed in terms of a general modal quantity $R_i$ which can be displacement, force, acceleration etc. for mode *i*. Let the maximum combined modal response regardless of combination method be

$$R_{\mathrm{mod}} = \sum_{i=1}^{1} R_{i,\max} \tag{8}$$

where the summation in this case does not mean algebraic summation but summation according any method. If Eq. (8), which is written in terms of the general modal quantity is rewritten as the deformation response for the oscillator as given by Eq. (7), the combined response for a subsystem of frequency $\omega_n$ can be expressed as

$$u_0 = \sum_{i=1}^{I} u_{0,i} = \sum_{i=1}^{I} DF(\omega_n, \omega_i, \zeta) u_{\Phi,i} \Gamma_i \frac{1}{\omega_i^2} A_i \tag{9}$$

The deformation response thus calculated corresponds to step 4 in the procedure for constructing a response spectrum described in paragraph 2.1. Table 1 shows in an illustrative way how the oscillator deformation response is constructed for a number of oscillator frequencies

for a chosen damping ratio $\zeta$. For each oscillator frequency the spectral ordinates *D*, *V* and *A* can be calculated according to step 5 in paragraph 2.1 and plotted vs frequency to obtain a plot of the response spectrum. The procedure can be repeated for any damping ratio $\zeta$.

| **Oscillator frequency** | **Deformation response of oscillator** | | | | |
|---|---|---|---|---|---|
| | $u_0(\omega_{i=1})$ | $u_0(\omega_{i=2})$ | $u_0(\omega_{i=...})$ | $u_0(\omega_{i=I})$ | $u_0$ |
| $\omega_{n=1}$ | $DF(\omega_{n=1},\omega_{i=1})$ $\cdot u_{\Phi,1}\Gamma_1\frac{A_1}{\omega_{i=1}^2}$ | $DF(\omega_{n=1},\omega_{i=2})$ $\cdot u_{\Phi,2}\Gamma_2\frac{A_2}{\omega_{i=2}^2}$ | ... | $DF(\omega_{n=1},\omega_{i=I})$ $\cdot u_{\Phi,I}\Gamma_I\frac{A_I}{\omega_{i=I}^2}$ | $\sum_{i=1}^{I} DF(\omega_{n=1},\omega_i)$ $\cdot u_{\Phi,i}\Gamma_i\frac{A_i}{\omega_i^2}$ |
| $\omega_{n=2}$ | $DF(\omega_{n=2},\omega_{i=1})$ $\cdot u_{\Phi,1}\Gamma_1\frac{A_1}{\omega_{i=1}^2}$ | $DF(\omega_{n=2},\omega_{i=2})$ $\cdot u_{\Phi,2}\Gamma_2\frac{A_2}{\omega_{i=2}^2}$ | ... | $DF(\omega_{n=2},\omega_{i=I})$ $\cdot u_{\Phi,I}\Gamma_I\frac{A_I}{\omega_{i=I}^2}$ | $\sum_{i=1}^{I} DF(\omega_{n=2},\omega_i)$ $\cdot u_{\Phi,i}\Gamma_i\frac{A_i}{\omega_i^2}$ |
| $\omega_{n=...}$ | | | ... | | |
| $\omega_{n=N}$ | $DF(\omega_{n=N},\omega_{i=1})$ $\cdot u_{\Phi,1}\Gamma_1\frac{A_1}{\omega_{i=1}^2}$ | $DF(\omega_{n=N},\omega_{i=2})$ $\cdot u_{\Phi,2}\Gamma_2\frac{A_2}{\omega_{i=2}^2}$ | ... | $DF(\omega_{n=N},\omega_{i=I})$ $\cdot u_{\Phi,I}\Gamma_I\frac{A_I}{\omega_{i=I}^2}$ | $\sum_{i=1}^{I} DF(\omega_{n=N},\omega_i)$ $\cdot u_{\Phi,i}\Gamma_i\frac{A_i}{\omega_i^2}$ |

Table 1: Tabular construction of oscillator response

## 2.3 Excitation and response in three directions

For a general case with mode shapes in the three dimensional space and spectrum excitation in all three directions an oscillator in each coordinate direction can be simulated by extending Eq. (4) to

$$\{\mathrm{u}_0\} = \begin{Bmatrix} x_0 \\ y_0 \\ z_0 \end{Bmatrix} = DF \cdot \{\mathrm{u}_{g0}\} = DF \cdot \begin{Bmatrix} x_{g0} \\ y_{g0} \\ z_{g0} \end{Bmatrix} \tag{10}$$

The corresponding maximum modal deformation response for each mode then becomes

$$\{\mathrm{u}_0\}_{i,d} = DF(\omega_n,\omega_i,\zeta)\{\mathrm{u}_\Phi\}_i \Gamma_{i,d}\frac{1}{\omega_i^2}A_{i,d} \tag{11}$$

where $d$ denotes the direction of spectrum excitation (*x*, *y* or *z*), $\{\mathrm{u}_0\}_{i,d} = \{x_{0,d} \quad y_{0,d} \quad z_{0,d}\}_i^T$ is the deformation response for mode $i$ and load application direction $d$, $\{\mathrm{u}_\Phi\}_i = \{x_\Phi \quad y_\Phi \quad z_\Phi\}_i^T$ is the mode shape coordinates at the decoupling point, $\Gamma_{i,d}$ is the participation factor of mode $i$ under loadings in direction $d$ and $A_{i,d}$ is the spectral acceleration for mode $i$ in direction $d$. Combining the modal the response according to Eq. (8) gives

$$\{u_0\}_d = \sum_{i=1}^{I} \{u_0\}_{i,d} = \sum_{i=1}^{I} DF(\omega_n, \omega_i, \zeta) \{u_\Phi\}_i \Gamma_{i,d} \frac{1}{\omega_i^2} A_{i,d} \tag{12}$$

The contribution from the three directions of load application can then be combined by square root of sum of square (SRSS) combination:

$$\{u_0\} = \begin{Bmatrix} x_0 \\ y_0 \\ z_0 \end{Bmatrix} = \begin{Bmatrix} \sqrt{x_{0,x}^2 + x_{0,y}^2 + x_{0,z}^2} \\ \sqrt{y_{0,x}^2 + y_{0,y}^2 + y_{0,z}^2} \\ \sqrt{z_{0,x}^2 + z_{0,y}^2 + z_{0,z}^2} \end{Bmatrix} \tag{13}$$

The above expression gives the maximum deformation response for each direction. By varying the oscillator frequency the spectral ordinates *D*, *V* and *A* can be computed for each direction and plotted vs frequency.

### 2.4 Multi-level excitation

So far the method presented is based on a uniform spectrum application or single point spectrum analysis. The same method can be applied to a multi-point spectrum analysis. The maximum modal deformation response for each mode *i*, direction *d* and level *l* can be obtained as

$$\{u_0\}_{i,d,l} = DF(\omega_n, \omega_i, \zeta) \{u_\Phi\}_i \Gamma_{i,d,l} \frac{1}{\omega_i^2} A_{i,d,l} \tag{14}$$

where $\Gamma_{i,d,l}$ is the participation factor for spectrum excitation of *i* under loadings in direction *d* at level *l*. $A_{i,d,l}$ is the spectral acceleration for mode *i* in direction *d* at level *l*. Depending whether the support points (levels) are considered to move in phase, stochastically independent, or counter phase, the combination of different levels is made by algebraic, square root of summed squares (SRSS) or absolute summation. For *L* levels of independent support excitations, the combination of level responses becomes

$$\{u_0\}_{i,d} = \sum_{l=1}^{L} \{u_0\}_{i,d,l} \tag{15}$$

where the summation in this case does not mean algebraic summation but summation according any method. The results from Eq. (15) can then be inserted in Eq. (12). Using these results in Eq. (13) finally gives the total response and the procedure to create response spectra can be continued.

### 2.5 Modal combination method

To obtain the maximum response for a subsystem frequency $\omega_n$ considering a main pipe response to which several modes contribute, a combination of the subsystem responses $u_{g0,i}$ due to all contributing main pipe modes *i* has to be made. Since all information on time and sign relations between modes are lost in a response spectrum analysis, combinations are usually made by statistical methods. Several methods exist. A few common methods are described below expressed in terms of a general modal quantity $R_i$ which can be displacement, force, acceleration etc. for mode *i*.

1. **Absolute summation:** All modes are assumed to have their maxima at the same time which will be an upper bound for the response. The combined modal response can be expressed as

$$R_{\text{mod}} = \sum_{i=1}^{I} \left| R_{i,\max} \right| \tag{16}$$

where $I$ is the highest mode considered to contribute to the response.

2. **Square root of sum of squares (SRSS):** The modes are considered to be statistically independent, i.e. no correlation between the individual modal responses:

$$R_{\text{mod}} = \sqrt{\sum_{i=1}^{I} R_{i,\max}^2} \tag{17}$$

3. **NRC ten percent method:** In this method, defined in [6], modes $k$ with frequencies separated by more than 10% of each other are combined with SRSS as above. However, modes whose frequencies are spaced within 10% of each other are combined by absolute summation. This can be expressed as

$$R_{\text{mod}} = \sqrt{\sum_{k=1}^{I} R_{k,\max}^2 + 2\sum \left| R_{i,\max} R_{j,\max} \right|} \quad i \neq j \tag{18}$$

where $1 \leq i \leq j \leq I$. The first summation is done for modes with separated frequencies and the second summation is done for modes with closely spaced frequencies. Closely spaced modes $i$ and $j$ are defined as modes with frequencies within 10% of each other according to

$$\frac{\omega_j - \omega_i}{\omega_i} \leq 0.1 \tag{19}$$

4. **Complete quadratic combination (CQC):** A modal correlation coefficient between each pair of modes is considered in the summation of responses according to:

$$R_{\text{mod}} = \sqrt{\left( \sum_{i=1}^{I} \sum_{j=1}^{I} R_{i,\max} \rho_{ij} R_{i,\max} \right)} \tag{20}$$

where $i$ and $j$ are any two modes up to the highest contributing mode $I$ and $i \neq j$. $\rho_{ij}$ is the correlation coefficient. A few different methods for calculating the correlation coefficient exist of which the methods according to Rosenblueth and Der Kiureghian are the most frequently used. In [7], Rosenblueth defines the following equations for the correlation coefficient:

$$\rho_{ij} = \frac{1}{1+\epsilon_{ij}^2} \tag{21}$$

where

$$\epsilon_{ij} = \frac{\omega_i\sqrt{1-\zeta_i^2} - \omega_j\sqrt{1-\zeta_j^2}}{\zeta_i'\omega_i + \zeta_j'\omega_j} \qquad \zeta_i' = \zeta_i + \frac{2}{\omega_i s} \tag{22}$$

and $s$ is the duration of the strong phase of the earthquake excitation. $\zeta_i$ and $\zeta_j$ are the modal damping ratios for mode $i$ and $j$.
The correlation coefficient according to Der Kiureghian [8] is

$$\rho_{ij} = \frac{8\left(\zeta_i\zeta_j\omega_i\omega_j\right)^{1/2}\left(\zeta_i\omega_i + \zeta_j\omega_j\right)\omega_i\omega_j}{\left(\omega_i^2 - \omega_j^2\right)^2 + 4\zeta_i\zeta_j\omega_i\omega_j\left(\omega_i^2 + \omega_j^2\right) + 4\left(\zeta_i^2 + \zeta_j^2\right)\omega_i^2\omega_j^2} \tag{23}$$

The choice of method may be governed by design codes or it can be based on engineering judgement for the application in consideration. However, for obtaining the total subsystem response it would be reasonable to use the same method as used to obtain the main pipe response.

## 2.6 Order of combination

In paragraph 2.4, it was shown how the total response could be obtained by combining the level response followed by modal combination and finally combining the directional responses. If the modal combination is performed with the CQC method for which the sign of the modal responses is required, this order of combination is only possible if the level responses are combined algebraically. For other combination methods, the modal combination needs to be performed first according to

$$\{u_0\}_{d,l} = \sum_{i=1}^{I}\{u_0\}_{i,d,l} \tag{24}$$

Then the levels can be combined:

$$\{u_0\}_{d} = \sum_{l=1}^{L}\{u_0\}_{d,l} \tag{25}$$

Finally the results of this summation can be inserted in in Eq. (13) for combination of the loading directions.

## 2.7 Residual rigid response

It is not practical to calculate all mode shapes and frequencies for piping systems. For high frequencies, the modes behave rigid and are not excited by support motions. The frequency above which modes can be considered rigid is normally referred to as Zero Period Acceleration (ZPA) frequency and the corresponding acceleration is called ZPA. Hence, this frequency is normally used as cut-off frequency when performing modal extraction and modal combination. However, the mass associated with the modes above the cut-off frequency is then missing in the calculation of the response. To account for this, the residual rigid response of the missing mass can be obtained in a static analysis in which the missing mass is multiplied by the spectrum ZPA. This residual rigid response or missing mass correction can then be added to the solution from the combination of modal responses performed according to the methods described in paragraph 2.5 to obtain the complete system response.

Since amplified response spectra are created for frequencies up to the ZPA, the missing mass term will not affect the results. However, it will be included in the analysis examples in Section 3 and 4.

## 3 VERIFICATION

To verify the method, results from a decoupled analysis and a coupled analysis are compared. The model of the piping system is shown in Figure 3. The model consists of a main pipe with an outer diameter of 275 mm and a thickness of 20 mm. It has a small bore pipe with an outer diameter of 48.26 mm and a thickness of 5.08 mm attached to it.

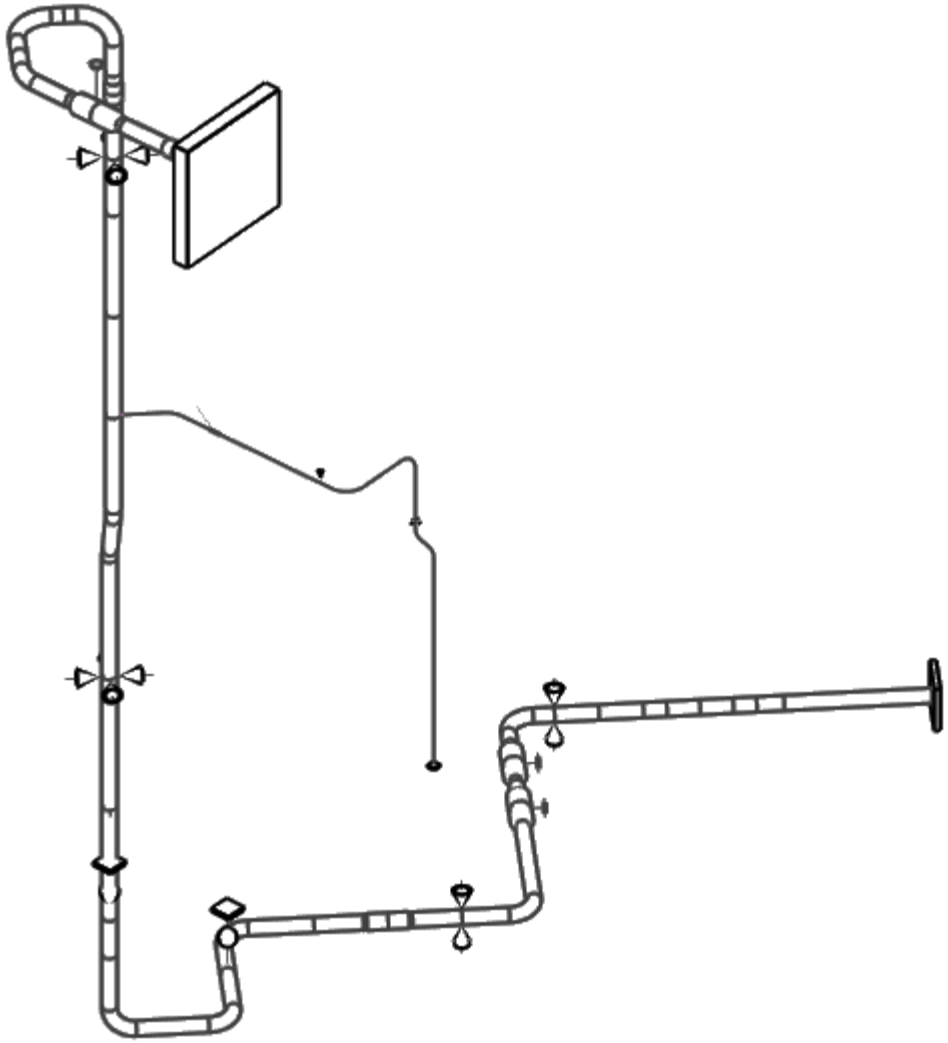

Figure 3: Model of coupled piping system.

### 3.1 Loads and analysis procedure

The system is supported at several points by restraints, spring hangers and fix supports at its terminal ends and subjected to four different levels of earthquake excitation making it a multi-level spectrum analysis. The applied response spectra are shown in Figure 4 and Figure 5. These are spectra for 5% damping, which is considered in the analysis. Levels LV=2 and LV=5 act on the main pipe supports whereas levels LV=3 and LV=4 act on the small bore pipe supports. The analysis is performed with a cut-off frequency of 60 Hz. The modes are

combined by the CQC method with correlation coefficients according to Der Kiureghian. The contributions of the different levels are combined by absolute summation and the spectral directions by the SRSS method. Finally, the residual response is added although in this case, it is very small.

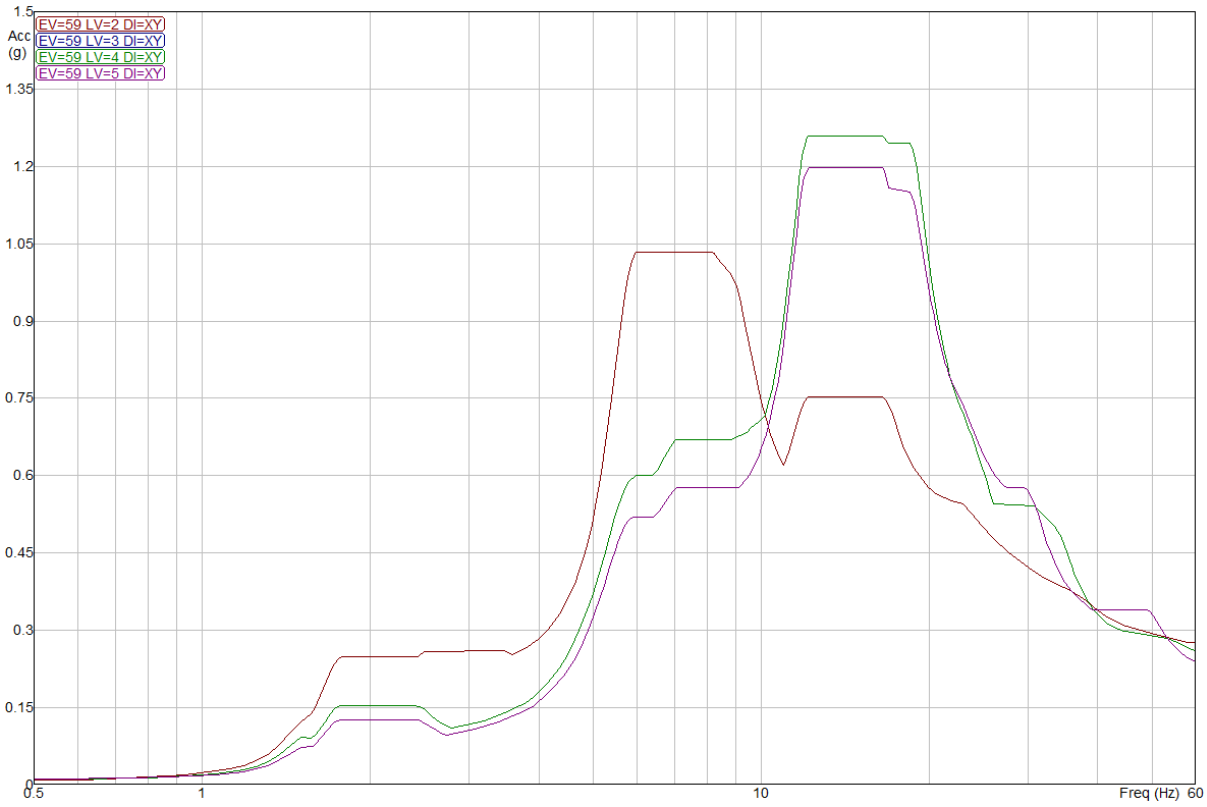


Figure 4: Applied response spectra in *x* and *y* directions.

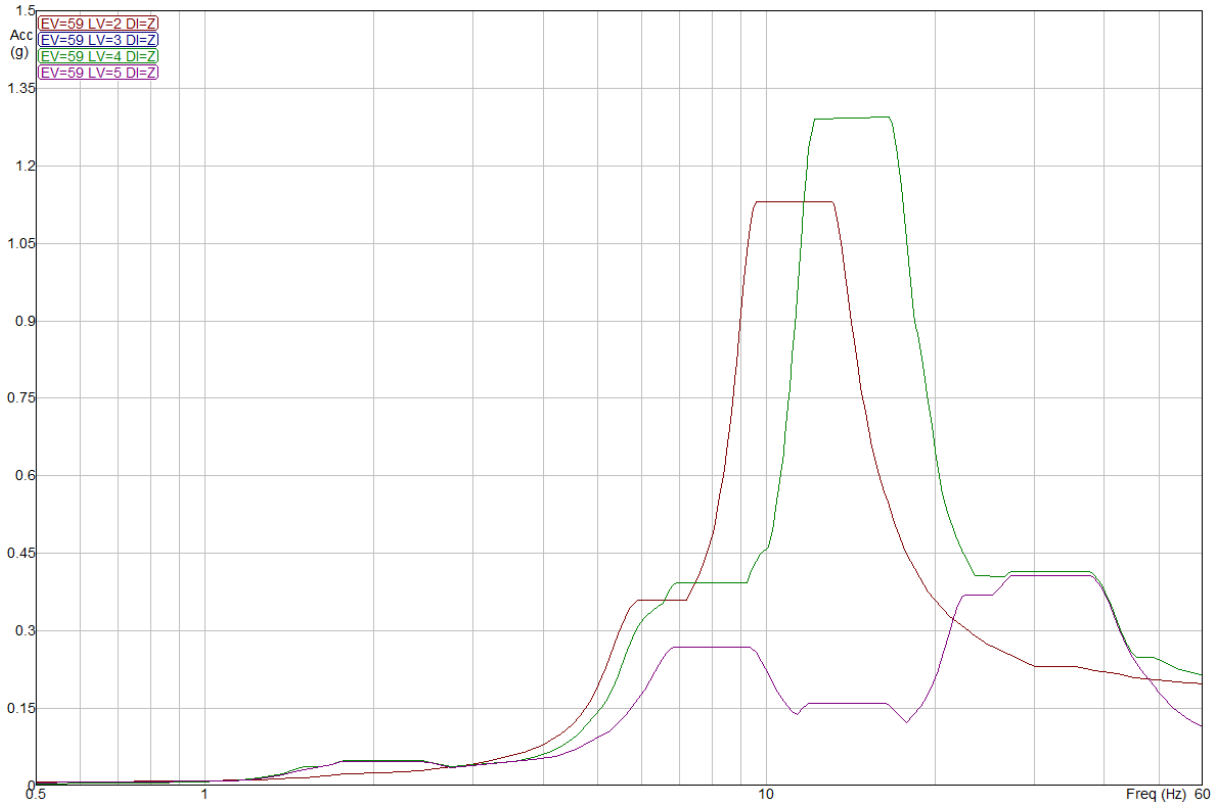


Figure 5: Applied response spectra in *z* direction.

In the decoupled analysis, the main pipe is analyzed first. The model is the same as for the coupled analysis though with the small bore pipe removed. Using the modal results a response spectrum for each direction is constructed for 5% damping according to the procedure in Section 2. The same combination methods are used as in the coupled analysis. The spectra thus generated are shown in Figure 6. Normally spectrum peaks are broadened in the frequency direction to account for inaccuracies in the calculation of natural frequencies. A plot of the generated spectra with peaks broadened ±15% is shown in Figure 7. Since there is no broadening effect in the main pipe excitation of the small bore pipe in the coupled analysis, a comparison using unbroadened spectra at the decoupling point would be of interest. Hence, the comparison is based both on results obtained by broadened and unbroadened amplified response spectra.

The model of the decoupled small bore pipe is the same as for the coupled analysis though with the main pipe removed. The decoupling point is modelled as a fix point. To simulate the stiffness of the omitted main pipe, the diagonal elements of the stiffness matrix of the main pipe have been calculated for force and moments applied at the decoupling point. These stiffness values have been applied to the fix point of the decoupled small bore pipe model. The model of the decoupled small bore pipe is shown in Figure 8, where also point labelling has been included.

In the coupled analysis, the small bore pipe behavior is a combination of inertial response and quasi-static response due to the motion of the main pipe. When the small bore pipe is analysed separately by applying response spectrum loads at the decoupling point, only the inertial response is obtained. In order to compare the results, the maximum displacements obtained at the decoupling point of the main pipe model have been applied in the analysis of the decoupled small bore pipe. The quasi-static results are then added to the inertial response by SRSS summation.

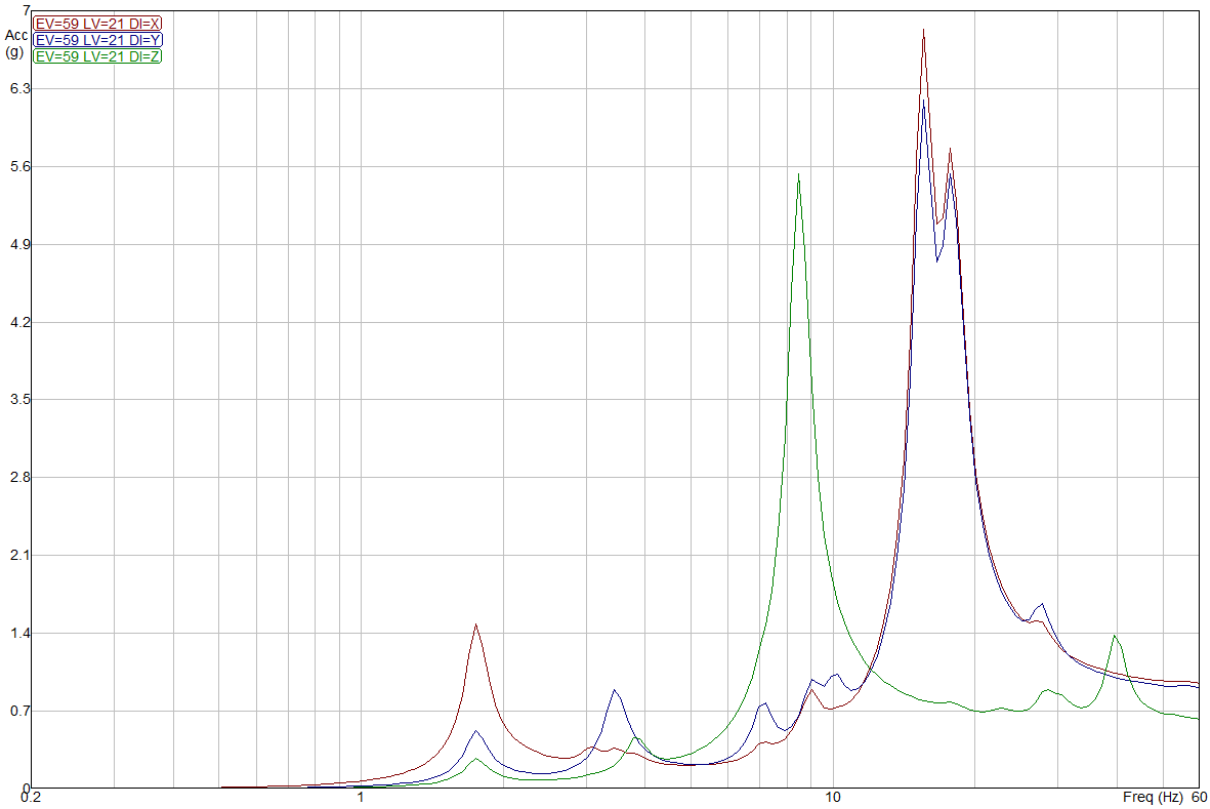


Figure 6: Generated amplified spectra at decoupling point.

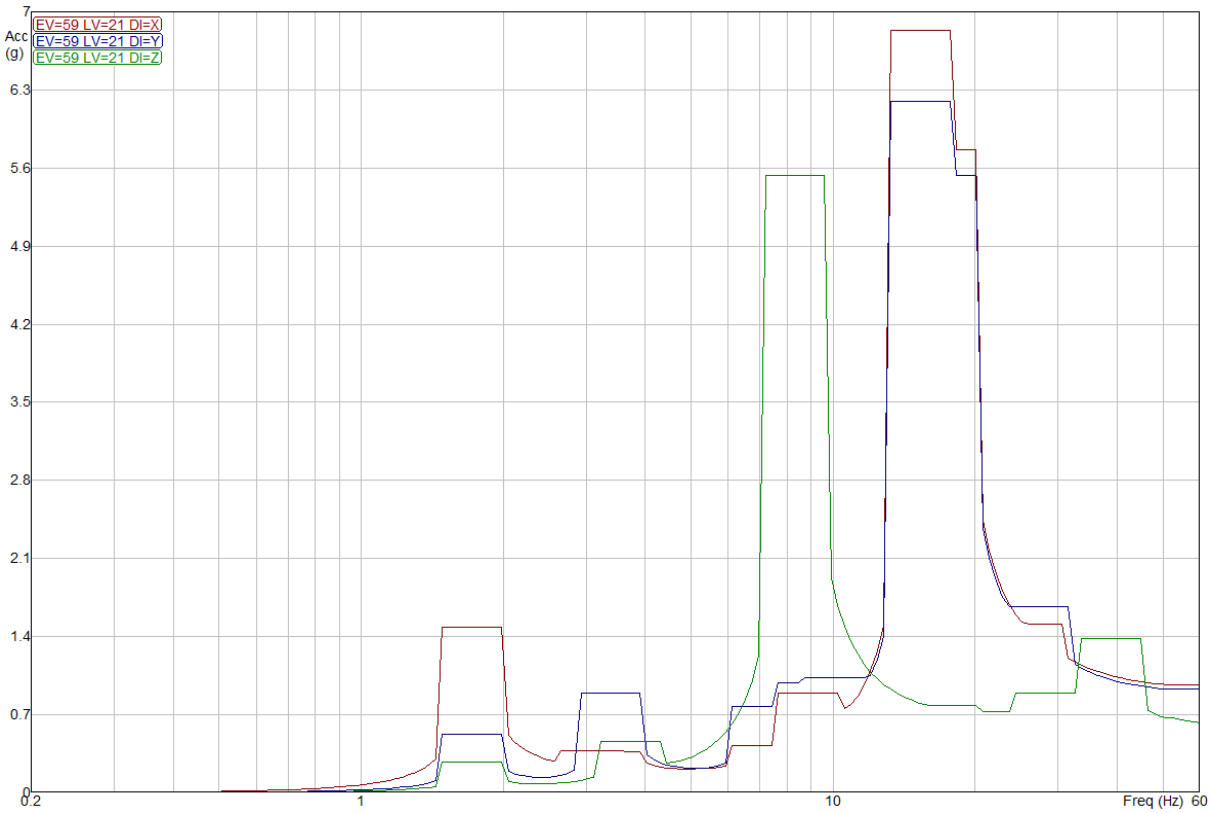


Figure 7: Generated amplified spectra at decoupling point with 15% peak broadening.

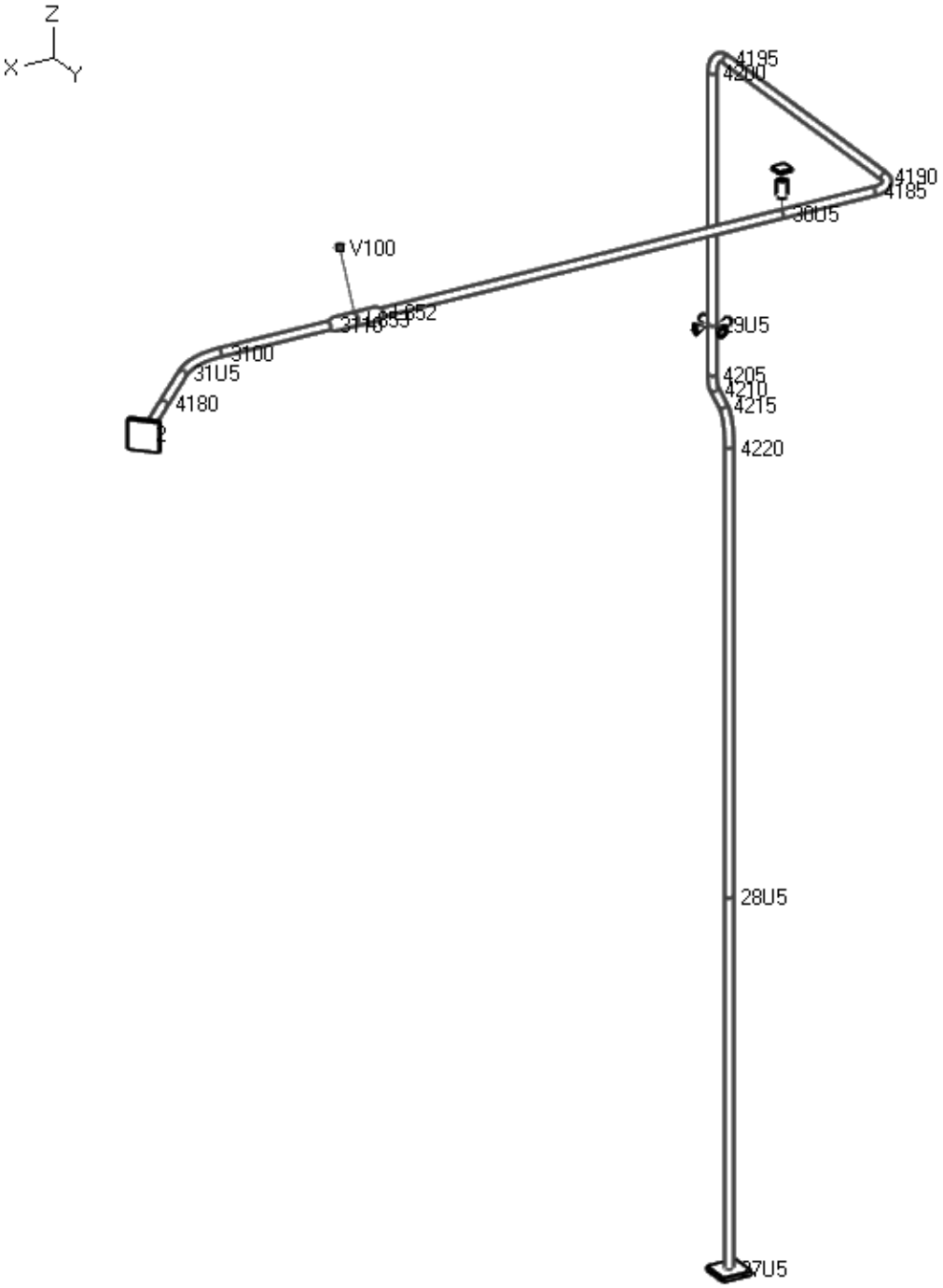


Figure 8: Model of decoupled small bore pipe.

## 3.2 Results

The results are compared by looking at the displacements at the points indicated in Figure 8. Table 2 shows the directional displacements $u_x$, $u_y$ and $u_z$ for each point in the coupled analysis and the decoupled analysis with unbroadened spectra applied at the decoupling point. Also the resultant displacements $r_c$ for the coupled model and $r_d$ for the decoupled model are presented. The difference between the resultant displacements is presented both as displacement values and as a percentage. Table 3 shows the same comparison but based on the analysis with broadened spectra applied at the decoupling point.

| Point | Coupled model | | | | Decoupled model | | | | $\Delta r$ [mm] | $\Delta r / r_c$ [%] |
|---|---|---|---|---|---|---|---|---|---|---|
| | $u_x$ [mm] | $u_y$ [mm] | $u_z$ [mm] | $r_c$ [mm] | $u_x$ [mm] | $u_y$ [mm] | $u_z$ [mm] | $r_d$ [mm] | | |
| **2** | 8.26 | 6.07 | 4.82 | 11.32 | 8.26 | 6.07 | 4.82 | 11.32 | 0.00 | 0 |
| **3100** | 10.90 | 6.43 | 7.45 | 14.69 | 9.63 | 7.25 | 6.73 | 13.81 | -0.88 | -6.00 |
| **3110** | 10.90 | 6.53 | 9.64 | 15.95 | 9.63 | 8.20 | 8.27 | 15.11 | -0.83 | -5.23 |
| **4180** | 9.08 | 5.91 | 5.31 | 12.07 | 8.55 | 6.27 | 5.15 | 11.78 | -0.29 | -2.36 |
| **4185** | 10.91 | 5.41 | 7.53 | 14.32 | 9.63 | 5.63 | 6.32 | 12.82 | -1.50 | -10.44 |
| **4190** | 10.89 | 6.11 | 5.89 | 13.80 | 9.56 | 5.97 | 5.21 | 12.42 | -1.39 | -10.05 |
| **4195** | 12.30 | 6.11 | 1.99 | 13.87 | 10.40 | 5.96 | 2.04 | 12.16 | -1.72 | -12.37 |
| **4200** | 9.31 | 5.02 | 1.39 | 10.67 | 7.71 | 4.74 | 1.22 | 9.13 | -1.54 | -14.41 |
| **4205** | 1.04 | 0.69 | 1.39 | 1.87 | 0.87 | 0.64 | 1.22 | 1.63 | -0.24 | -12.86 |
| **4210** | 2.54 | 1.62 | 0.88 | 3.14 | 2.17 | 1.52 | 0.76 | 2.75 | -0.39 | -12.47 |
| **4215** | 3.01 | 2.12 | 0.48 | 3.71 | 2.58 | 1.95 | 0.41 | 3.26 | -0.45 | -12.19 |
| **4220** | 4.25 | 3.15 | 0.01 | 5.29 | 3.63 | 2.90 | 0.01 | 4.64 | -0.65 | -12.23 |
| **27U5** | 0.00 | 0.00 | 0.00 | 0.00 | 0.00 | 0.00 | 0.00 | 0.00 | 0.00 | - |
| **28U5** | 6.07 | 4.81 | 0.00 | 7.74 | 4.72 | 3.94 | 0.00 | 6.15 | -1.59 | -20.56 |
| **29U5** | 0.00 | 0.00 | 1.39 | 1.39 | 0.00 | 0.00 | 1.22 | 1.22 | -0.17 | -12.48 |
| **30U5** | 10.91 | 5.51 | 7.94 | 14.57 | 9.63 | 6.24 | 6.74 | 13.31 | -1.26 | -8.67 |
| **31U5** | 10.30 | 6.14 | 6.32 | 13.56 | 9.24 | 6.71 | 5.90 | 12.85 | -0.70 | -5.19 |
| **L852** | 10.90 | 6.33 | 10.46 | 16.38 | 9.63 | 8.49 | 8.86 | 15.60 | -0.78 | -4.79 |
| **L853** | 10.90 | 6.43 | 10.06 | 16.17 | 9.63 | 8.35 | 8.57 | 15.36 | -0.81 | -4.99 |
| **V100** | 11.06 | 8.73 | 9.64 | 17.07 | 10.69 | 9.47 | 8.18 | 16.46 | -0.62 | -3.62 |

Table 2: Displacement comparison between coupled and decoupled analysis results for unbroadened spectra.

| Point | Coupled model | | | | Decoupled model | | | | $\Delta r$ [mm] | $\Delta r/ rc$ [%] |
|---|---|---|---|---|---|---|---|---|---|---|
| | $u_x$ [mm] | $u_y$ [mm] | $u_z$ [mm] | $r_c$ [mm] | $u_x$ [mm] | $u_y$ [mm] | $u_z$ [mm] | $r_d$ [mm] | | |
| 2 | 8.26 | 6.07 | 4.82 | 11.32 | 8.26 | 6.07 | 4.82 | 11.32 | 0.00 | 0.00 |
| 3100 | 10.90 | 6.43 | 7.45 | 14.69 | 10.02 | 7.76 | 7.59 | 14.77 | 0.08 | 0.55 |
| 3110 | 10.90 | 6.53 | 9.64 | 15.95 | 10.02 | 8.86 | 9.95 | 16.67 | 0.72 | 4.54 |
| 4180 | 9.08 | 5.91 | 5.31 | 12.07 | 8.65 | 6.37 | 5.28 | 11.97 | -0.10 | -0.83 |
| 4185 | 10.91 | 5.41 | 7.53 | 14.32 | 10.02 | 6.48 | 8.12 | 14.43 | 0.11 | 0.80 |
| 4190 | 10.89 | 6.11 | 5.89 | 13.80 | 10.41 | 6.58 | 6.24 | 13.80 | 0.00 | 0.01 |
| 4195 | 12.30 | 6.11 | 1.99 | 13.87 | 12.96 | 6.58 | 2.13 | 14.68 | 0.81 | 5.84 |
| 4200 | 9.31 | 5.02 | 1.39 | 10.67 | 10.01 | 5.37 | 1.45 | 11.45 | 0.78 | 7.31 |
| 4205 | 1.04 | 0.69 | 1.39 | 1.87 | 1.10 | 0.73 | 1.46 | 1.97 | 0.10 | 5.17 |
| 4210 | 2.54 | 1.62 | 0.88 | 3.14 | 2.64 | 1.79 | 0.91 | 3.32 | 0.17 | 5.57 |
| 4215 | 3.01 | 2.12 | 0.48 | 3.71 | 3.08 | 2.29 | 0.50 | 3.88 | 0.16 | 4.44 |
| 4220 | 4.25 | 3.15 | 0.01 | 5.29 | 4.33 | 3.37 | 0.01 | 5.49 | 0.19 | 3.66 |
| 27U5 | 0.00 | 0.00 | 0.00 | 0.00 | 0.00 | 0.00 | 0.00 | 0.00 | 0.00 | - |
| 28U5 | 6.07 | 4.81 | 0.00 | 7.74 | 6.20 | 4.94 | 0.00 | 7.92 | 0.18 | 2.37 |
| 29U5 | 0.00 | 0.00 | 1.39 | 1.39 | 0.00 | 0.00 | 1.46 | 1.46 | 0.06 | 4.38 |
| 30U5 | 10.91 | 5.51 | 7.94 | 14.57 | 10.02 | 7.20 | 8.73 | 15.11 | 0.54 | 3.72 |
| 31U5 | 10.30 | 6.14 | 6.32 | 13.56 | 9.54 | 7.01 | 6.38 | 13.45 | -0.11 | -0.81 |
| L852 | 10.90 | 6.33 | 10.46 | 16.38 | 10.02 | 9.11 | 10.91 | 17.39 | 1.01 | 6.15 |
| L853 | 10.90 | 6.43 | 10.06 | 16.17 | 10.02 | 8.99 | 10.44 | 17.03 | 0.87 | 5.37 |
| V100 | 11.06 | 8.73 | 9.64 | 17.07 | 11.57 | 11.31 | 9.78 | 18.90 | 1.82 | 10.69 |

Table 3: Displacement comparison between coupled and decoupled analysis results for broadened spectra.

### 3.3 Discussion of the results

First, it should be pointed out that an exact match of results would never be expected since information is always lost when decoupling is made. For example, adding the quasi-static solution to the dynamic response is an approximation in comparison to the coupled analysis which gives an exact solution. In spite of this, the comparisons show fairly good agreement. The decoupled analysis based on unbroadened spectra underestimates the response in the entire model with a maximum deviation of 21%. The decoupled analysis based on broadened spectra produce results similar to the coupled analysis or somewhat overestimates the results. The maximum deviation is 11%. Upon decoupling, there will never be an exact match of natural frequencies in comparison with the coupled analysis. With narrow peaks in the response spectrum, a small deviation in frequency will have a significant impact on the response. With broadened decoupled spectra, the effect of deviating natural frequencies due to approximations in the modelling can be accounted for.

This verifying example shows that the proposed method for generating and using amplified response spectra can be used when decoupling is desired. However, it is important to broaden the amplified spectra to account for deviations in natural frequencies. Even though broadened spectra are used, sources for errors should be reduced as much as possible. Hence, it is recommended to implement stiffness values at the decoupling point.

## 4 ANALYSIS EXAMPLE

One of the benefits of decoupling is the possibility to separate primary stresses from secondary in the stress evaluation. This will be shown in the following sample stress evaluation, which is performed on a coupled and decoupled system.

### 4.1 Code criteria

Several piping design codes exist and in many cases the equations for stress evaluation are similar. For this example, the class 2 criteria of the nuclear section of the ASME Boiler and Pressure Vessel Code [9] will be used. For dynamic loads, evaluation criteria exist both for non-reversing and reversing dynamic loads. Earthquake loads can be considered as reversing dynamic loads so the criteria for reversing dynamic loads are used. The earthquake considered is a safe shutdown earthquake which is a faulted condition event (Level D). Sub-paragraph NC-3654.2(b) of the code gives the following equations for stress evaluation:

$$B_2 \frac{D_0}{2I} M_W \leq 0.5 S_h \tag{26}$$

$$B_1 \frac{P_E D_o}{2t} + B_2' \frac{D_o}{2I} M_E \leq 3 S_h \tag{27}$$

$$C_2 \frac{M_{AM} D_o}{2I} < 6 S_h \tag{28}$$

$$\frac{F_{AM}}{A_M} < S_h \tag{29}$$

where Eq. (26) limits the sustained stress due to weight loading, Eq. (27) limits the stress due to weight and inertial loading (primary stress) whereas Eqs. (28) and (29) limits the stresses due to dynamic anchor motions (secondary stresses). For a coupled analysis, the secondary stresses cannot be separated from the primary stresses so they will be included in the evaluation w.r.t. Eq. (27) and no evaluation will be made w.r.t. Eqs. (28) and (29).

### 4.2 Analysis models and loads

The same analysis models as were used in the validation in Section 3 are used for the stress evaluation. However, in this analysis more severe response spectra are applied to the model. The spectra derived for application at the decoupling point are broadened. As an interesting comparison, also envelopes of the spectra acting on the main pipe are derived and applied at the decoupling point. Both the amplified and enveloped spectra are shown in Figure 9.

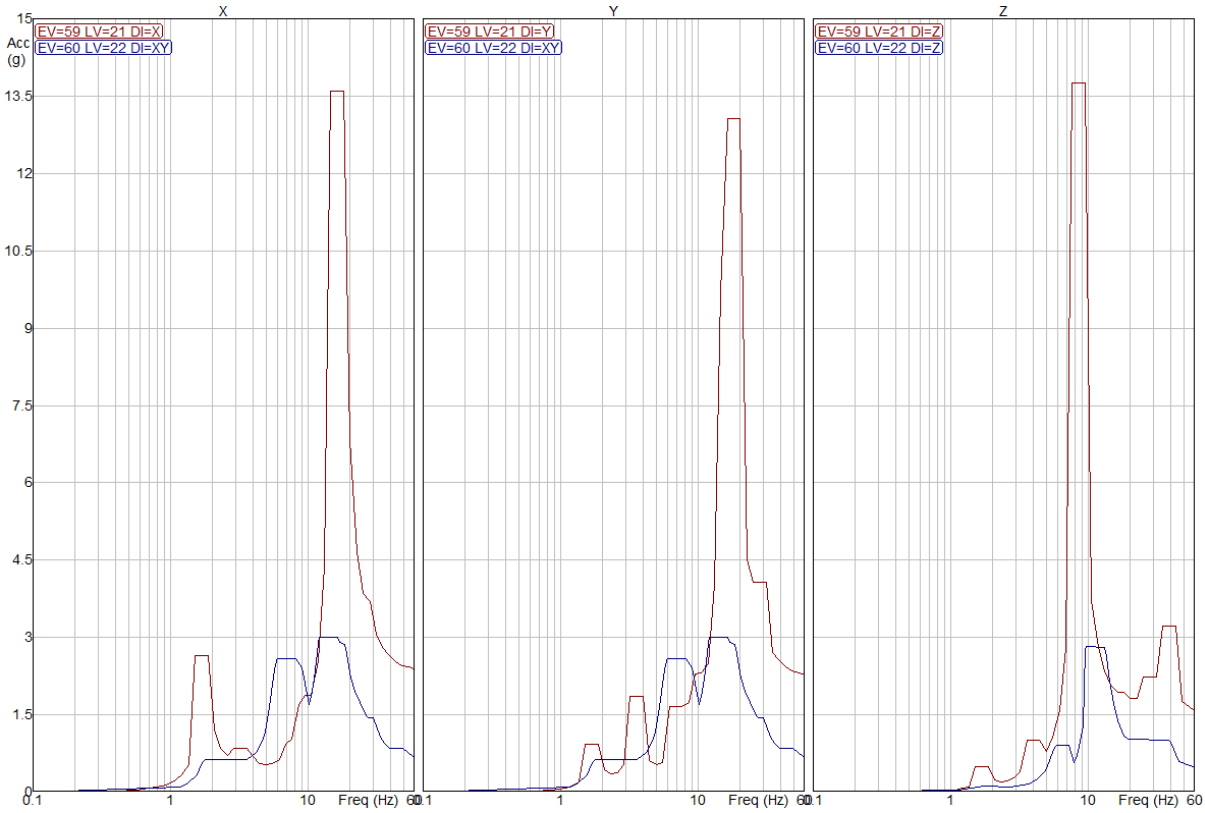


Figure 9: Amplified response spectra (EV=59) and enveloped response spectra (EV=60).

## 4.3 Analysis results

The highest stress results from the analyses are shown in Table 4. For each equation, the results are shown as stress usage ratios, i.e. the stress calculated according to any of the equations divided by the allowable stress. Hence, a stress usage ratio above 1.0 means failure to qualify the system. In the coupled analysis, Eq. (27) is not fulfilled. The reason for this is the fact that the stress in the coupled analysis is not only due to inertial loading since it also includes the stress in the small bore pipe caused by the movement of the main pipe . By decoupling, the primary and secondary stresses can be separated and assessed w.r.t. the appropriate equations. This results in a qualified system. Not unsurprisingly, the amplified spectra give higher results than the envelope spectra.

| **Analysis** | **Stress usage ratio** | | | |
|---|---|---|---|---|
| | **Eq. (26)** | **Eq. (27)** | **Eq. (28)** | **Eq. (29)** |
| Coupled | 0.89 | 1.11 | N/A | N/A |
| Decoupled with amplified spectra | 0.94 | 0.92 | 0.28 | 0.05 |
| Decoupled with envelope spectra | 0.94 | 0.72 | 0.28 | 0.05 |

Table 4: Results from the example analysis.

## 4.4 Discussion

The results of the analysis works a good example showing that decoupling can be useful in qualifying a piping system since the separation in primary and secondary stresses can be made.

The practice to model the connection point as an anchor and apply anchor motions and an envelope of the spectra for the main pipe supports at this point as was stated in [3] clearly underestimates the stress and gives non-conservative results. Looking at the stress only due to the inertial response and not together with pressure and weight stress as in Eq. (27), the difference between the amplified and envelope methods is even greater. This is not surprising if the spectra in Figure 9 are compared. The spectral peaks are significantly higher in the amplified spectra and the frequency contents are different. The amplified spectra reflect the dynamic characteristics of the main pipe whereas envelope spectra lack influence of the main pipe on the small bore pipe response. No validating proof supporting the envelope method exists; it is only used for convenience reasons. However, this example clearly shows that it is not a suitable method since the risk is high that it will give non-conservative results.

## 5 CONCLUSION

The method to create amplified response spectra at the small bore piping connection point shows good agreement when applied in a decoupled analysis and comparing the results with a coupled analysis. However, it is recommended to broaden the spectra to account for modelling errors when decoupling.

Any errors in decoupled analyses are most likely due to the decoupling and not due to the generation of amplified response spectra. Existing decoupling criteria mainly focus on the influence of the small bore pipe on the main pipe and not the opposite. More investigations will be needed to provide decoupling criteria that are appropriate for response spectrum analysis of small bore pipes.

When it can be justified to decouple small bore pipes, it is a useful technique since secondary stresses can be separated from primary stresses and unnecessary conservatism can be removed from the analysis. However, it is important to create amplified spectra. The practice to apply envelope of the spectra acting on the main pipe at the decoupling point is not a suitable method. It is clearly shown in the example analysis that this is not a conservative method.

## REFERENCES

[1] R. Houdart, J Hennart and M. Urbano, Advanced Twin Mode Rotation, *5th International Conference on Nuclear Engineering*, Nice, 1997.

[2] L.H. Geraets, J.P. Forget, Criteria for Decoupling and Overlap of Piping Systems - Procedure and Application, *Transactions of the 8th International Conference on Structural Mechanics in Reactor Technology*, Vol. F1 5/6, 175-179, 1985.

[3] G.A. Antaki, Analytical Considerations in the Code Qualification of Piping Systems (U), *1995 ASME/JSME Pressure & Piping Conference*, Honolulu, USA, July 23-27, 1995.

[4] K. Bondesson, *Development of Methodology for Generating Response Spectra for Decoupled Smallbore Piping*, Master's Dissertation, Div. of Structural Mechanics, LTH, Lund University, 2014.

[5] A.K. Chopra, *Dynamic of Structures - Theory and Applications to Earthquake Engineering*, 4th Edition, Prentice Hall, Upper Saddle River, New Jersey, 2012.

[6] U.S. Nuclear Regulatory Commission, *Combining Modal Responses and Spatial Components in Seismic Response Analysis*, Regulatory Guide 1.92, Revision 1, February 1976.

[7] E. Rosenblueth and J. Elorduy, Responses of Linear Systems to Certain Transient Disturbances, *Proceedings of the 4th World Conference on Earthquake Engineering*, Santiago, Chile, January 13–18, Volume I, 185–196, 1969.

[8] E.L. Wilson, A. Der Kiureghian and E.P. Bayo, A Replacement for the SRSS Method in Seismic Analysis, *Earthquake Engineering and Structural Dynamics*, Vol. 9, No. 2, 187–192, John Wiley & Sons, New York, March–April 1981.

[9] The American Society of Mechanical Engineers, *ASME Boiler and Pressure Vessel Code*, Section III: Division 1 – Subsection NC, 2015 Edition.

COMPDYN 2017
6th ECCOMAS Thematic Conference on
Computational Methods in Structural Dynamics and Earthquake Engineering
M. Papadrakakis, M. Fragiadakis (eds.)
Rhodes Island, Greece, 15–17 June 2017

# COMPARISON OF 1D EQUIVALENT-LINEAR AND NONLINEAR SEISMIC SITE RESPONSES IN DEEP SEDIMENT LAYERS

**Zhu Jiao**[1], **Chen Guoxing**[1], **and Zhao Kai**[1]

[1] Institute of Geotechnical Engineering, Nanjing Tech University
Nanjing 210009, China
e-mail: zhujiao90@163.com, gxchen@njtech.edu.cn, zhaokaiseu@aliyun.com

**Keywords:** Deep Sediment Layers, Seismic Site Response, Equivalent Linear, Nonlinear, Ground Motion Parameters.

**Abstract.** *A reasonable description of soil hysteretic constitutive relation has a significant impact on the evaluation of design ground motion parameters. These parameters play an important role in predicting seismic damage and taking further effective anti-seismic measures. In this study, based on the 200m-deep-borehole profiles in Suzhou region (China), the 1-D seismic site responses are compared by two analysis methods. One is an equivalent linear analysis (ELA) modeling in frequency domain, the other is a nonlinear analysis (NLA) using a multi-degree-of-freedom, lumped mass model in term of the modified Matasovic constitutive modeling in time domain. The effects of bedrock motion characteristics (amplitude, frequency content and duration) on the predictions from the two site response analyses in deep sediment layers have also been analyzed. Using the results from a broad range of bedrock motions, we can find the difference between the two site response analyses in different strain levels. Specifically, the surface peak ground acceleration (PGA) calculated by ELA increases monotonically as the PGA of bedrock motion increases. However, the surface PGA calculated by NLA first increases rapidly and then decreases gradually or keeps constant. Moreover, the surface acceleration response spectra (Sa) for short periods computed using ELA and NLA are significantly different. The high-frequency contents of bedrock motions exhibit obvious filtering in ELA while the high-frequency contents in NLA first magnify and then attenuate as the PGA of bedrock motion increases. In addition, for the medium or strong bedrock motions, the surface ground motion duration is not only related to bedrock motion characteristics, but also closely related to the cyclic behavior of nonlinear soil medium. The influence of bedrock motion intensity on the duration prolongation of surface ground motion can be reasonably evaluated using NLA.*

## 1 INTRODUCTION

Many site investigations and theoretical researches indicate that local site conditions have a profound influence on surface ground motions and seismic damage distribution [1-3]. Reliable predictions of seismic site response and design ground motion parameters play an important role in predicting seismic damage and taking further effective anti-seismic measures. The propagation of seismic waves through soil deposits depends on the intensity and frequency content of input ground motions, the seismic wave dispersion and absorption due to soil deposits and cyclic soil constitutive model. The stress-strain relationship of soil under cyclic loading is nonlinear, hysteretic and deformation cumulative. A reasonable description of the dynamic behavior of soil is vital for improving the accuracy of site response analysis.

Based on a large amount of experimental results, Seed and Idriss [4] first found that large strain in soil induced by strong earthquakes was the major factor leading to nonlinear effects of soils, which draw extensive attention to nonlinear soil behavior in the field of geotechnical engineering [5, 6]. Furthermore, seismic damage investigation records of destructive earthquake events such as the 1985 $M_S$ 8.1 Mexico earthquake, 1989 $M_S$ 7.1 Loma Prieta earthquake, 1995 $M_S$ 7.2 Kobe earthquake in Japan, and 1999 Chi-Chi earthquake in Taiwan also showed remarkable soil nonlinearity. Based on comparison of site response analyses performed by the equivalent linear analysis (SHAKE) and nonlinear (DEEPSOIL and LS-DYNA) analysis methods, Bolisetti et al. [7] found there were significant differences between predictions from the two analysis methods especially for large strains and higher frequencies; the equivalent linear method is unable to reproduce the high frequency acceleration response, resulting in almost constant spectral accelerations in the short period range. Kaklamanos et al. [8] compared the recorded ground motions of vertical seismometer arrays in Japan with the predictions from corresponding linear, equivalent linear and nonlinear site response models to obtain the strain levels at which the models break down respectively. When the peak shear strains were 0.01%-0.1%, the linear site response models failed to accurately predict short-period ground motions; when the peak shear strains were greater than 0.05%, nonlinear models exhibited a closer prediction to record data than equivalent linear models.

The equivalent linear model, due to its simplicity and low calculation effort, is the most frequently employed model in engineering practice to approximate nonlinear soil behavior. However, the comparisons of predictions from equivalent linear model with recorded data in vertical arrays demonstrate that, during strong earthquakes, the equivalent linear site response analyses filter out high frequency components of the input motion and almost underestimate the surface peak ground acceleration. Therefore, in this study, based on two typical deep borehole profiles in Suzhou region, the comparisons of 1D equivalent linear and nonlinear seismic site responses are performed within the industry-standard site response program DEEPSOIL, in order to gain insight into the effects of analysis methods on seismic site responses in deep sediment layers.

## 2 ENGINEERING GEOLOGICAL CHARACTERISTICS

Suzhou is located at the southern margin of the Yangtze river delta in china, and is covered by extensive soft clayey soil, saturated silt and silty fine sand belonging to the sedimentary of marine and alluvial lacustrine facies. Deep overburden layers exist in this region, and the general strata are characterized as multi-sedimentary rhythms. Two typical borehole profiles (profile No. 1 and 2), with the overburden thickness over 200 m, as shown in Figure 1, are selected to perform seismic site responses. According to the China Code for Seismic Design of Buildings GB50011-2010 [9], both the sites belong to the Ⅲ category. The sediment for-

mation is characterized as alternate deposition of fluvial, lacustrine and marine facies. The typical deposits in Suzhou region are fill, silty clay, silty sand, clay and silty fine sand.

The natural frequency of deposit is closely related to the shear wave velocity of soil [10]. Thus, it is necessary to use the measured shear wave velocities at different depths of the two profiles. Due to the limitation of test condition, the depth of measured shear wave velocity for profile No. 2 is only 167 m. The shear wave velocities of soil at deeper depths are obtained by extrapolating the fitting curve of shear wave velocities with depth. Figure 1 shows the soil distribution characteristics and corresponding shear wave velocities for borehole profile No. 1 and 2.

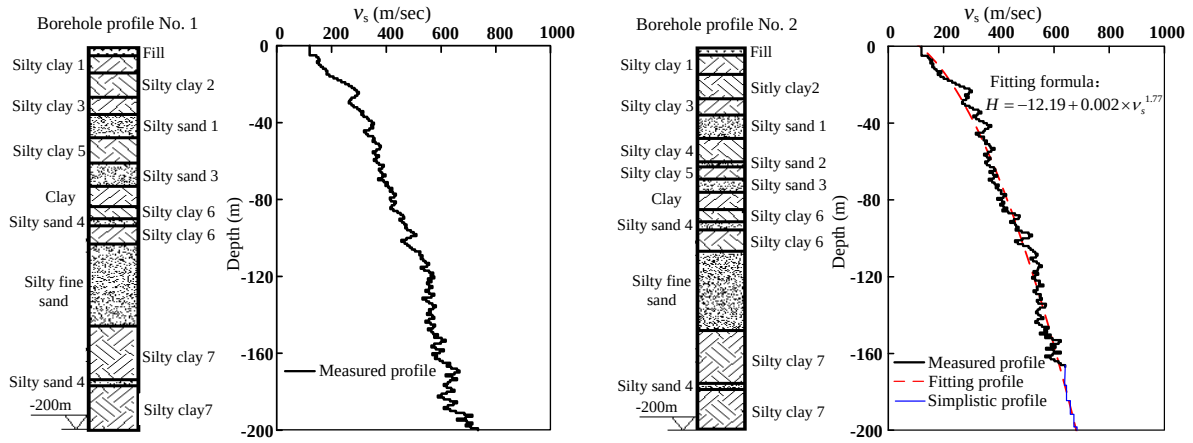


Figure 1: Soil profiles and corresponding shear wave velocity profiles used in the analysis

## 3 NONLINEAR CYCLIC BEHAVIORS OF SOILS

The accuracy of predicted surface ground motions depends on the rationality of the soil hysteretic constitutive relation and the corresponding parameters. The equivalent linear method implemented in DEEPSOIL is similar to that in SHAKE [11], in which the seismic site response is simplified as the one-dimensional wave problem of vertical incident S wave in horizontally layered soil deposit. The equivalent linear viscoelastic model is employed to approximate nonlinear soil behavior, which is not only stable in numerical calculation, but also can consider frequency dependent characteristics such as damping due to the scattering of waves and surface wave propagation, and perform a deconvolution analysis. The layer properties in this method are adjusted through an iterative process involving a series of linear analyses. The linear analysis is first performed using the strain dependent shear modulus and damping obtained directly from the laboratory tests, and the iterations are continued until the calculated shear strains match within a pre-defined tolerance. The equivalent linear method can generally reflect the nonlinear and hysteresis of the dynamic stress-strain relationship of soil. In nonlinear analysis implemented in DEEPSOIL, the geologic column is discretized into individual layers using multi-degree-of freedom lumped parameter model. Each individual layer is represented by a corresponding mass, non-linear spring, and dashpot for viscous damping. Lumping half the mass of each of two consecutive layers at their common boundary forms the mass matrix. The stiffness matrix is updated at each time increment to incorporate nonlinearity of the soil. Hashash et al. (2016) incorporate the nonlinear pressure dependent cyclic soil model in DEEPSOIL. The model is an extension of the modified hyperbolic model developed by Matasovic, and accounts for the influence of confining pressure on strain dependent modulus and damping of soil. The extended Masing criteria define unloading-reloading criteria and behavior under irregular loading conditions. The backbone curve for the model is described by the following equation [11]:

$$\tau = \frac{G_{mo}\,\gamma}{1+\beta\left(\frac{\gamma}{\gamma_r}\right)^s} \tag{1}$$

Where

$$\gamma_r = \gamma_{ref}\left(\frac{\sigma'}{\sigma_{ref}}\right)^b \tag{2}$$

Where $\tau$ is the shear stress; $\gamma$ is the shear strain; $\beta$ and $s$ are dimensionless parameters; $G_{mo}$ is the initial shear modulus; $\gamma_r$ is the reference shear strain; $b$ is the correction coefficient of $\gamma_r$ at different depth; $\sigma'$ is the effective vertical stress; $\sigma_{ref}$ is the reference effective vertical stress at which $\gamma_r$ is equal to $\gamma_{ref}$ .

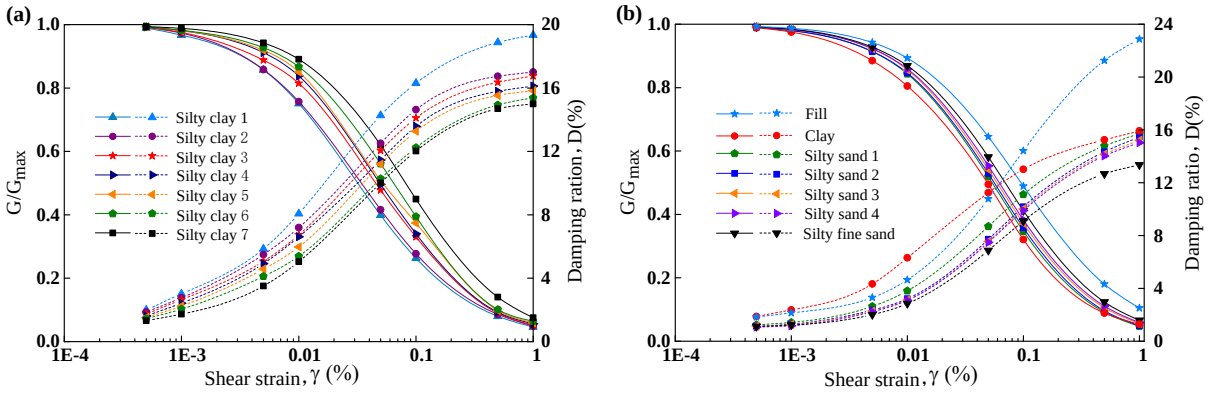


Figure 2: G/Gmax and damping ratio D curves versus shear strain amplitude γ for soils in Suzhou region: (a) Silty clay; (b) Fill, Clay, Silty sand and Silty fine sand.

According to the borehole data, as well as the resonant column test results for typical soil samples of depth less than 100 m in Suzhou, Figure 2 shows the normalized shear modulus degradation and damping ratio curves as functions of the shear strain. The nonlinear behavior of soil decreases with increasing depth, namely, shallow soils are more nonlinear than deep soils. Moreover, the damping ratio of soil increases with increasing shear strain. The damping ratio is very small at small strain. In DEEPSOIL, the model parameters can be determined by fitting the inputted modulus-reduction and damping curves. For soils of depth less than 100 m, due to the layers are thin, the shear modulus degradation and damping ratio curves are directly given by laboratory experiments. However, for silty fine sand, silty clay 7 and silty sand 4 of depth more than 100 m, the corresponding curves are given by the correction method considering the effect of confining pressure. The correction coefficient b is equal to 0.5 for silty fine sand and silty sand 4, and 0.5 for silty clay 7 [12]. In nonlinear analysis, the thickness of the layer $i$ is determined by the maximum frequency that can be propagated:

$$h_i = \frac{(v_s)_i}{4\,f_{\max}} \tag{3}$$

Where $h_i$ is the thickness of each layer, $(v_s)_i$ is the shear wave velocity, $f_{\max}$ is the maximum frequency that the layer $i$ can propagate. Generally, for all layers, the maximum frequency should be of 25-50 Hz, therefore, the thickness of each layer was of 1-4 m. An elastic bedrock was taken as the seismic bedrock interface of input motions, and the Rayleigh damping at 2nd modes was employed as viscous damping. To ensure the calculation results have high accuracy, the number of iterations was selected as 20 in equivalent linear analysis, while in nonline-

ar analysis, the flexible sub-incrementation scheme with $\Delta\gamma_{max}=10^{-6}$ was used to control increment step. In addition, the interface of elastic homogeneous bedrock and nonhomogeneous soil is taken as the seismic bedrock interface of input motion. However, the depth of seismic bedrock interface has a significant effect on design ground motion parameters. Hence, for deep site in Suzhou region, the soil layer with shear velocity not less than 700 m/s was selected as the seismic bedrock interface [13].

## 4 SELECTION OF INPUT EARTHQUAKE RECORDS

Many studies have shown that bedrock motion characteristics have an important impact on the seismic site response. Therefore, in this paper, a suite of three horizontal acceleration records were selected as the bedrock motion to cover a wide range of amplitudes, frequency contents, and durations, including the ground motion records on Montebello-Bluff site during the 1994 Ms 6.7 Northridge earthquake in America, Feltre site during the 1976 Ms 6.5 Friuli earthquake in Italy, and Jingning site during the 2008 Ms 8.0 Wenchuan earthquake in china. The intensity of bedrock motion is characterized by peak ground acceleration (PGA) and Arias intensity (AI) [14]; the frequency content is characterized by predominant period ($T_p$), and the duration is characterized by significant duration between 5% and 95% of the AI ($D_{5\text{-}95}$). These main characteristics of input ground motions are summarized in Table 1. The acceleration time histories and Fourier spectra of bedrock motions are shown in Figure 3. The cumulative energy curves of bedrock motions in frequency domain are shown in Figure 4. In the Montebello -Bluff Rd record, 90% of the energy is present in a narrower frequency band (0.1-4.9 Hz). in the Feltre record, the mid- and high-frequency components are abundant, 90% of the energy is present in the frequency band of 0.2-13.8 Hz. In addition, the energy cumulated in the frequency band of 10.0-13.8 Hz is as much as 45% of the total energy. However, in the

Table 1: Details of input ground motions used for site response analysis.

| Event (Year) | Ms | Station name | Epicentral distance (km) | Component | PGA (g) | AI (m/s) | $T_p$ (s) | $D_{5\text{-}95}$ (s) | Sample rate (Hz) |
|---|---|---|---|---|---|---|---|---|---|
| Northridge (1994) | 6.7 | Montebello–Bluff Rd | 46.21 | S26W | 0.179 | 0.323 | 0.24 | 10.58 | 100 |
| Friuli (1976) | 6.5 | Feltre | 108.56 | EW | 0.038 | 0.014 | 0.08 | 12.34 | 200 |
| Wenchuan (2008) | 8.0 | Jingning | 552 | EW | 0.025 | 0.021 | 0.7 | 33.02 | 200 |

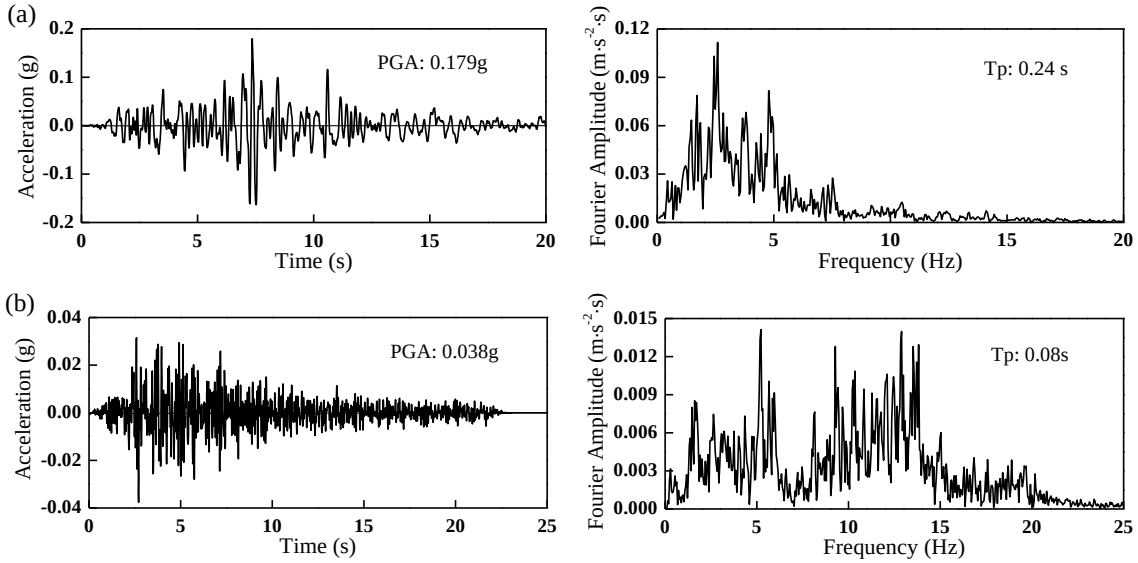

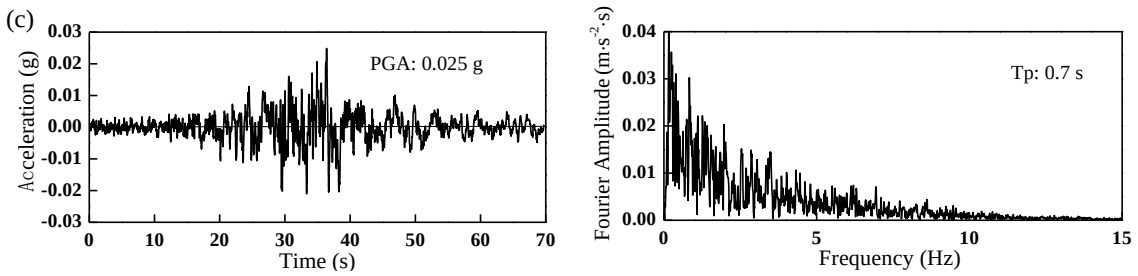


Figure 3: Time histories of acceleration and Fourier spectra of bedrock motions: (a) Montebello-Bluff Rd record; (b) Feltre record and (c) Jingning record.

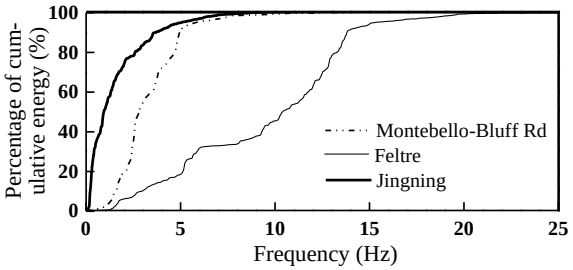


Figure 4: Cumulative energies of bedrock motions in frequency domain

Jingning record, the low frequency component is extremely abundant, 90% of the energy is present in the narrower frequency band (0.1-3.8 Hz), and the energy cumulated in the frequency band of 0.1-0.9 Hz is as much as 50% of the total energy.

## 5 SITE RESPONSE ANALYSIS RESULTS

In what follows, we study the effect of input motion in terms of intensity and frequency content on the resulting surface ground motion. To model different levels of intensity, the PGA values of the seismic records were adjusted to 0.01, 0.025, 0.05, 0.10, 0.15, 0.20, 0.25 and 0.3 g, respectively. Input motions with PGA$\leqslant$0.05 g, PGA=0.10 - 0.20 g, PGA$\geqslant$0.25 g are defined as low-level earthquakes, moderate-level earthquakes, high-level earthquakes, respectively. We perform equivalent linear frequency domain site response analyses (ELA) and nonlinear time domain site response analyses (NLA) using DEEPSOIL.

### 5.1 Peak shear strain

Figure 5 shows the variations of peak shear strain $\gamma_{max}$ with soil depth for borehole profile No. 1 calculated by ELA and NLA under bedrock motions of Montebello-Bluff Rd record and Feltre record with different intensities. Bedrock motion characteristics and site response analysis methods have significant effect on $\gamma_{max}$, however, the maximum values of $\gamma_{max}$ are approximately presented at the same depth. The depth is approximately 9.5 m. The $\gamma_{max}$ at depth of 9.5 m for borehole profile No.1 under different bedrock motions are shown in figure 6. It can be seen that the $\gamma_{max}$ values of shallow soils computed using ELA and NLA are significantly different, and this difference increases with the increase of bedrock motion intensity. When the bedrock PGA is less than or equal to 0.05 g, the $\gamma_{max}$ values of shallow soils, which just reach the order of $10^{-4}$ only in a few cases, are almost in the order of $10^{-5}$. The $\gamma_{max}$ values calculated by ELA are close to those calculated by NLA, the state of soil is in nonlinear elastic range or just reaches nonlinear range. When the bedrock PGA is between 0.1g and 0.2g, the $\gamma_{max}$ values of shallow soils are in the order of $10^{-4}$ under Feltre record with abundant high frequency, the state of soil is in nonlinear range; however, the corresponding $\gamma_{max}$ values reach the order of $10^{-3}$ under Jingning record with abundant low frequency, the soils exhibit strong

nonlinearity. In this case, seismic site response under low frequency earthquake is much larger than that under high frequency earthquake. When the bedrock PGA is more than or equal to 0.25 g, the $\gamma_{max}$ values of shallow soils are all in the order of $10^{-3}$ under different bedrock motions, the soils exhibit strong nonlinearity. Moreover, the difference between $\gamma_{max}$ values calculated by ELA and NLA is significant.

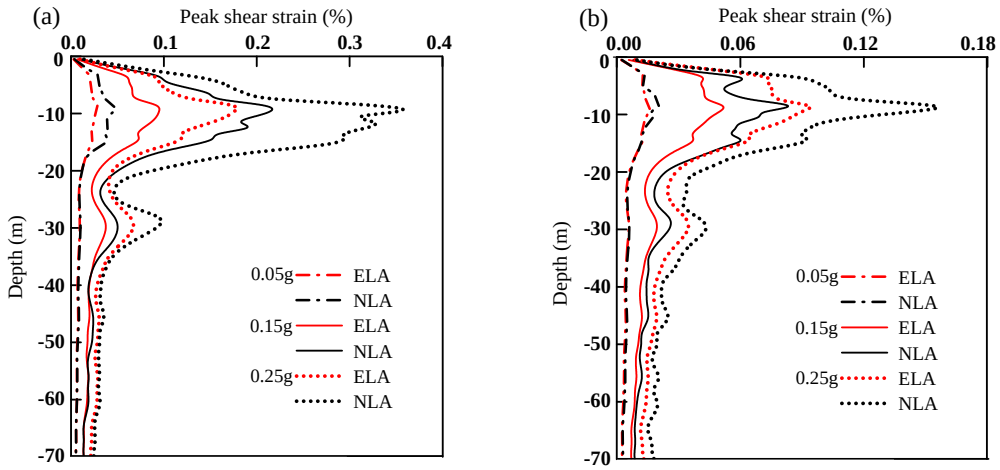


Figure 5: Variation of peak shear strain with soil depth for borehole profile No. 1 under different input motions with PGA=0.05g, 0.15g and 0.25g: (a) Montebello-Bluff Rd record and (b) Feltre record.

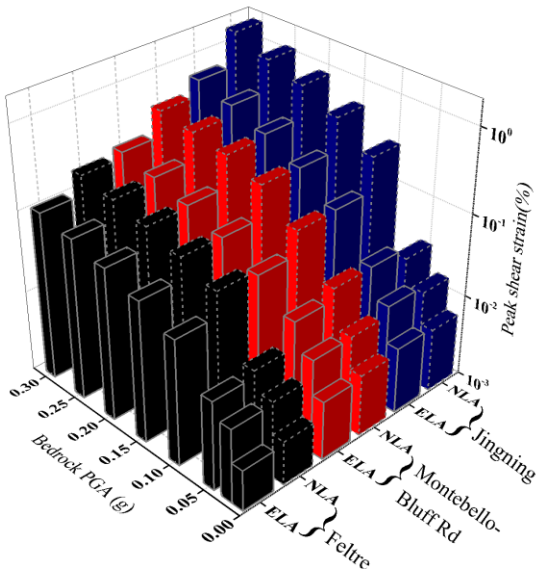


Figure 6: Peak shear strain at depth of 9.5 m for borehole profile No. 1 under bedrock motions with different intensities and frequency spectrum characteristics

## 5.2 Effect of bedrock motion intensities on surface PGAs

The surface PGAs of borehole profiles No. 1 and 2 under different seismic bedrock motion levels calculated by ELA and NLA are shown in figure 7(a) and (b), respectively. Surface PGAs calculated by ELA increase monotonically as the PGAs of bedrock motion increase. However, surface PGAs calculated by NLA first increase rapidly and then decrease gradually or keep constant. When the bedrock PGA is equal or lesser than 0.05g, the soil layer is approximately linear elastic, and thus the surface PGAs given by the two methods are very close. When the bedrock PGA is between 0.1g and 0.2g, the nonlinear effect of soil layer is remarkable. Accordingly, surface PGAs computed by ELA and NLA are significantly different, the

surface PGAs in NLA are much greater than those in ELA. However, the surface PGAs given by the two methods both increase with the increase of bedrock PGAs. In addition, surface PGAs are closely related to the spectral characteristics of bedrock ground motions. Specifically, the more abundant the low frequency contents of bedrock ground motions are, the larger the surface PGAs are. However, the difference between surface PGAs calculated by ELA and NLA increases as the high frequency contents of bedrock ground motions become richer. Namely, the difference is the largest when inputting the Feltre record with rich high frequency contents, which is followed successively by inputting Montebello-Bluff Rd record and Jingning record with rich low frequency contents. When the bedrock PGA is larger than or equal to 0.25g, the shallow soil layer shows strong nonlinearity. The nonlinear constitutive model can reflect the yield of the soil at large strain level (>$10^{-3}$). In this condition, the surface PGAs given by NLA are close to or even smaller than those given by ELA. The deep sediment layers have significant high-frequency contents filtering and low frequency contents amplification effects on bedrock ground motions. As the transient tangent stiffness of soil is greater than the secant stiffness of soil in strong nonlinearity range, the high frequency contents of bedrock ground motions given by NLA are amplified. In other words, the nonlinear seismic effect of deep layer during large earthquake is a comprehensive reflection of these two effects.

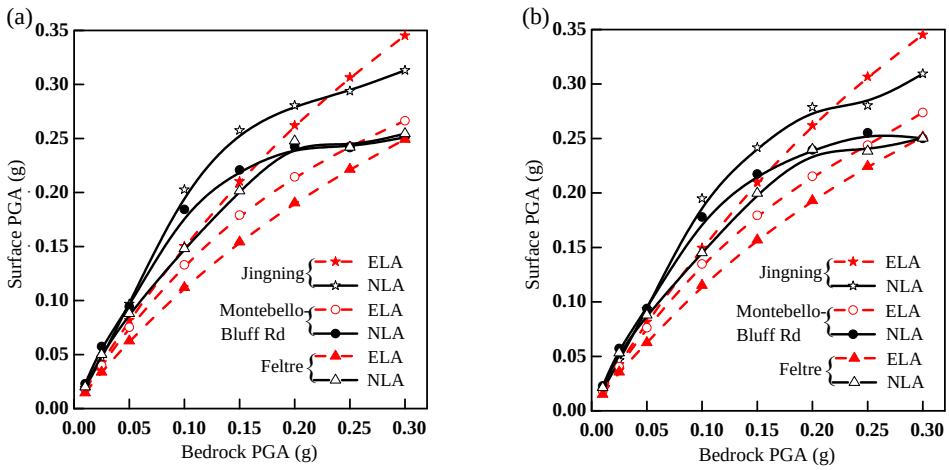


Figure 7: Effect of bedrock motion intensities on PGAs at the surface of: (a) borehole profile No. 1 and (b) borehole profile No. 2

## 5.3 Effect of bedrock motion characteristics on surface spectral acceleration

Figure 8 shows the surface Sa spectra of borehole profile No. 1 under bedrock motions of Feltre record and Jingning record. Compared with the bedrock Sa spectra, the amplification effect of surface Sa spectra at short periods computed using ELA reduces significantly as the PGAs of bedrock motions increase, and the predominant periods move to long periods. Thus, during low-level earthquakes with PGAs equal to 0.01 and 0.05 g, moderate-level earthquakes with PGA equal to 0.15 g ,and high-level earthquakes with PGA equal to 0.3 g, the predominant periods of surface ground motions are 0.08s, 0.19s, 0.19s, and 0.63s for Feltre record, respectively; and the corresponding predominant periods are 0.34s, 0.7s, 0.7s and 1.22s for Jingning record. It is obvious that the long period components of ground motions become richer and the high frequency components are filtered out. Although the spectrum shapes of Sa computed by NLA exhibit different trend, but the corresponding predominant periods are roughly identical to those computed by ELA. In NLA, the high frequency components first magnify and then attenuate as the PGAs of bedrock motion increase. When the bedrock PGA

is equal or lesser than 0.05g, the $\gamma_{max}$ values of soils are in the order of $10^{-5}$-$10^{-4}$. Thus, the soils exhibit nonlinear elastic behavior, and the different frequency components of ground motions have different amplifications. In general, the spectrum shapes of surface Sa given by the two methods are the similar in a wide period range, however, the Sa values computed by NLA in the short period range of T<0.5 s are larger than those computed by NLA. When the intensity of input ground motion increases, such as the input PGA=0.15 g, the $\gamma_{max}$ values of soils are approximately in the order of $10^{-4}$-$10^{-3}$. Thus, the strong nonlinearity of soils has significant filtering effect on the high frequency components of ground motion. The surface Sa spectra computed by ELA are smaller than the bedrock Sa spectra in the short period range

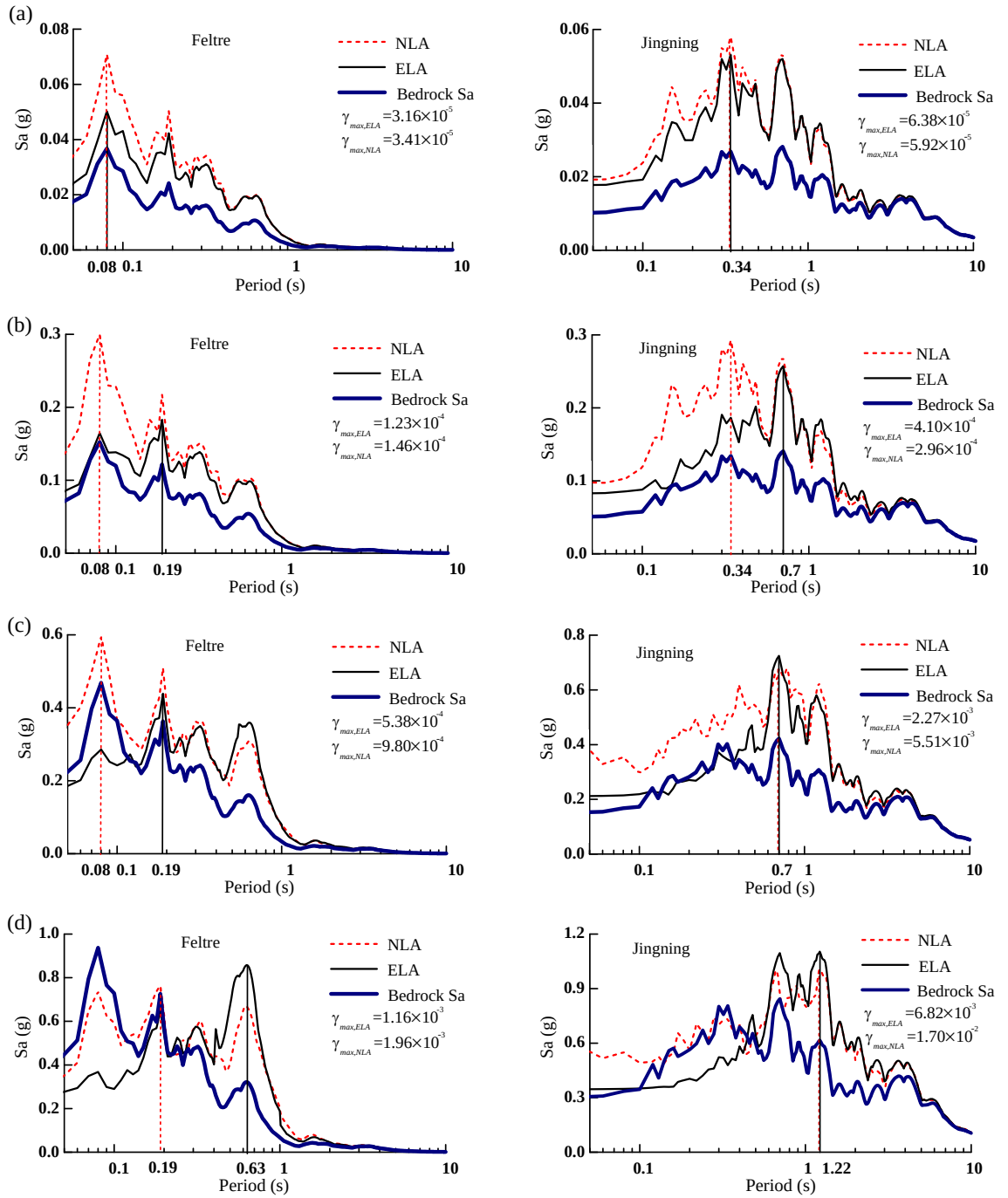


Figure 8: Surface acceleration response spectra under bedrock motions with different intensities for borehole profile No.1: (a) PGA = 0.01 g; (b) PGA = 0.05 g; (c) PGA = 0.15 g and (d) PGA = 0.3 g

of T<0.12 s. In general, the surface Sa spectra computed by NLA are larger than those computed by ELA in a wide period range. However, at the period of approximate 0.6 s, the surface Sa spectra computed by ELA are larger than those computed by NLA. When the bedrock PGA is 0.3 g, the $\gamma_{max}$ values of soils are in the order of $10^{-3}$-$10^{-2}$. The shallow soils exhibit strong nonlinearity. Therefore, the high frequency components of the ground motion are greatly filtered, and the long period components are significantly amplified. Compared with the bedrock spectra, the surface Sa spectra at middle and long periods exhibit different magnification effects.

### 5.4 Duration of ground motion

Ground motion duration is an important parameter to characterize the ground motion. The prolongation of duration will increase the cumulative deformation of the structure, or even result in the loss of local structural strength due to low cycle fatigue [15]. Figure 13 shows the ground motion duration prolongation values $\Delta D_{5\text{-}95}$ for borehole profile No. 1 calculated by ELA and NLA under different seismic bedrock motions. The value is defined as:

$$\Delta D_{5-95} = D_{5-95,\text{surf}} - D_{5-95,\text{bedr}} \tag{4}$$

Where $\Delta D_{5\text{-}95,\text{surf}}$ and $\Delta D_{5\text{-}95,\text{bedr}}$ are the durations of surface and bedrock ground motions between the 5% and 95% Arias intensity, respectively.

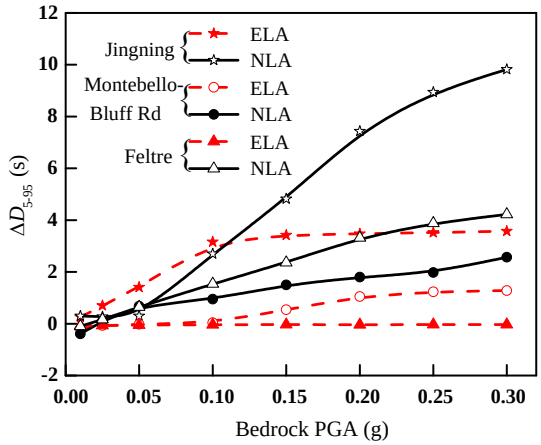


Figure 9: Prolongations of the ground motion duration for standard profile No. 1

The ground motion duration is not only related to the characteristics of bedrock motion [16], but also closely related to seismic site response analysis methods. And these correlations are enhanced with the increase of bedrock motion intensity. When the bedrock PGA is more than 0.05 g, the $\Delta D_{5\text{-}95}$ values calculated by ELA are the largest when inputting Jingning record, which are followed successively by inputting Montebello-Bluff Rd record and Feltre record. The $\Delta D_{5\text{-}95}$ values calculated by NLA are also the largest when inputting Jingning record, however, followed successively by inputting Feltre record and Montebello-Bluff Rd record. This may be because the energy of Feltre record is mainly concentrated in high frequency band, and the energy in this frequency band will be filtered out by using ELA method. Therefore, when the Feltre record is inputted as bedrock motion, the durations of surface ground motion calculated by ELA are even reduced, that is, the $\Delta D_{5\text{-}95}$ values are negative. In addition, with the increase of the bedrock motion intensity, the $\Delta D_{5\text{-}95}$ values given by ELA increase rapidly to a value that is basically constant; however, the corresponding $\Delta D_{5\text{-}95}$ values given by NLA continue to increase, while the gradients decrease gradually.

## 6 CONCLUSIONS

Based on typical borehole profiles in Suzhou region, the seismic site responses in deep sediment layers are performed and compared by ELA and NLA methods. The conclusions are as follows:

1. The surface PGAs calculated by ELA increase monotonically with the increase of bedrock motion intensity. However, the surface PGAs calculated by NLA first increase rapidly and then decrease gradually or keep constant. In addition, the surface PGA is closely related to the spectral components of the bedrock ground motion, and the difference between surface PGAs computed by ELA and NLA increases as the high frequency components of the bedrock ground motions become richer.

2. As the intensity of bedrock motion increases, the amplification effect of surface Sa spectra at short periods computed using ELA reduces significantly, and the predominant periods move to long periods. However, the spectrum shapes of surface Sa spectra computed by NLA exhibit different trend. Specifically, the high frequency components of bedrock motions first magnify and then attenuate.

3. The surface ground motion duration is not only related to the characteristics of bedrock motion, but also closely related to the cyclic behavior of nonlinear soil medium. And these correlations increase with the increase of bedrock motion intensity. Generally, the influence of bedrock motion intensity on the duration prolongation of surface ground motion can be reasonably evaluated using NLA.

## REFERENCES

[1] S.E. Hough, J.R. Altidor, D. Anglade, D. Given, M.G. Janvier, J.Z. Maharrey, M. Meremonte, B.S.-L. Mildor, C. Prepetit, A. Yong, Localized damage caused by topographic amplification during the 2010 M 7.0 Haiti earthquake. *Nature Geoscience*, **3**, 778-782, 2010.

[2] G. Lanzo, F. Silvestri, A. Costanzo, A. d'Onofrio, L. Martelli, A. Pagliaroli, S. Sica, A. Simonelli, Site response studies and seismic microzoning in the Middle Aterno valley (L'aquila, Central Italy). *Bulletin of Earthquake Engineering*, **9**, 1417-1442, 2011.

[3] G.X. Chen, J.Y. Zhan, J.D. Liu, X.J. Li, Parameter study on ground motion design of deep soft site under far-field large earthquake. *Chinese Journal of Geotechnical Engineering*, **35**, 1591-1599, 2013.

[4] H.B. Seed, I.M. Idriss, Soil moduli and damping factors for dynamic response analyses. *Report No. EERC 70-10*, University of California, Berkeley, 1970.

[5] T. Satoh, M. Horike, Y. Takeuchi, T. Uetake, H. Suzuki, Nonlinear behaviour of scoria soil sediments evaluated from borehole records in eastern Shizuoka prefecture, Japan. *Earthquake Engineering & Structural Dynamics*, **26**, 781-795, 1997.

[6] C. Gélis, L.F. Bonilla, Influence of a sedimentary basin infilling description on the 2-D P-SV wave propagation using linear and non-linear constitutive models. *Geophysical Journal International*, **198**, 1684-1700, 2014.

[7] C. Bolisetti, A.S. Whittaker, H.B. Mason, I. Almufti, M. Willford, Equivalent linear and nonlinear site response analysis for design and risk assessment of safety-related nuclear structures. *Nuclear Engineering and Design*, **275**, 107-121, 2014.

[8] J. Kaklamanos, L.G. Baise, E.M. Thompson, L. Dorfmann, Comparison of 1D linear, equivalent-linear, and nonlinear site response models at six KiK-net validation sites. *Soil Dynamics and Earthquake Engineering*, **69**, 207-219, 2015.

[9] Chinese Standard, Code for Seismic Design of Buildings issued by Ministry of Housing and Urban-Rural Development of the People's Republic of China, Beijing, *GB50011-2010*, 19-20, 2010.

[10] Y.M.A. Hashash, D. Park, Non-linear one-dimensional seismic ground motion propagation in the Mississippi embayment. *Engineering Geology*, **62**, 185-206, 2001.

[11] Y.M.A. Hashash, M.I. Musgrove, J.A. Harmon, D.R. Groholski, C.A. Phillips, D. Park, *DEEPSOIL 6.1, User Manual*, 2016.

[12] T. Jiang, H.L. Xing, A simple method considering effects of confining pressure on dynamic shear moduli and damping ratio. *Chinese Journal of Rock Mechanics and Engineering*, **26**, 1432-1437, 2007.

[13] J. Zhu, G.X. Chen, H.G. Xu, Effect of seismic bedrock interface depth on surface motion parameters of deep site. *Chinese Journal of Geotechnical Engineering*, **37**, 2079-2087, 2015.

[14] A. Arias, A measure of earthquake intensity. *Seismic Design for Nuclear Power Plants*, R. J. Hansen(Editor), MIT Press, Cambridge, Massachusetts, 438-483, 1970.

[15] J. Hancock, J.J. Bommer, Using spectral matched records to explore the influence of strong-motion duration on inelastic structural response. *Soil Dynamics and Earthquake Engineering*, **27**, 291-299, 2007.

[16] G.X. Chen, D.D. Jin, J. Zhu, J. Shi, X.J. Li, Nonlinear analysis on seismic site response of Fuzhou Basin, China. *Bulletin of the Seismological Society of America*, **105**, 928-949, 2015.

COMPDYN 2017
6th ECCOMAS Thematic Conference on
Computational Methods in Structural Dynamics and Earthquake Engineering
M. Papadrakakis, M. Fragiadakis (eds.)
Rhodes Island, Greece, 15–17 June 2017

# A PLASTICITY MODEL FOR 1D SOIL RESPONSE ANALYSIS

**Maria Anthi**[1], **Panagiota Tasiopoulou**[2] **and Nikos Gerolymos**[3]

[1] National Technical University of Athens, Greece
9, Heroon Polytechniou Str., Polytechnic Campus, Zografos P.C 15780
e-mail: anthimaria@hotmail.com

[2] National Technical University of Athens, Greece
9, Heroon Polytechniou Str., Polytechnic Campus, Zografos P.C 15780
e-mail: ptasiopoulou@gmail.com

[3]National Technical University of Athens, Greece
9, Heroon Polytechniou Str., Polytechnic Campus, Zografos P.C 15780
e-mail: gerolymos@gmail.com

**Keywords:** 1D plasticity model, nonlinear site response analysis, hysteretic response, cyclic loading

**Abstract.** *A plasticity model is presented for the non-linear ground response analysis of layered sites. The model is the one-dimensional version of that recently proposed by Tasiopoulou and Gerolymos (2016) for sand behavior, designated as TA-GER sand model. Critical state compatibility for monotonic and cyclic loading, anisotropic plastic flow rule and Bouc-Wen motivated hardening law are among the key-features of the developed 1D model, offering considerable flexibility in representing complex patterns of cyclic behavior such as stiffness decay and increase in strength due to build-up of pore-water pressure. Implemented through an explicit finite–difference algorithm into an in-house computer code which performs integration of the wave equations to obtain the nonlinear response of layered soil deposits, the model is first calibrated to match published experimental shear modulus and damping curves and is then validated against results from two wave-propagation codes available in literature.*

## 1 INTRODUCTION

Several constitutive models and numerical codes have been proposed over the last decades for 1D seismic response analysis of horizontally layered soils subjected to vertically-polarized S waves. In general, they can be categorized into three major groups: (a) The equivalent linear viscoelastic models (e.g. [1], [2]), (b) the nonlinear hysteretic (or phenomenological) models (e.g. [3], [4], [5]), and (c) the plasticity-based models (e.g. [6], [7]).

Equivalent linear models are the most popular owing to their computational convenience and simplicity. Their main limitations include their inability to efficiently predict the behavior of a nonlinear system under strong ground motions where large cyclic shear strains dominate the response and the violation of the principle of physical causality [8]. Well identified features of cyclic soil behaviour, such as: densification, cyclic mobility, stiffness decay and loss of strength due to pore pressure generation, asymmetric response with loading direction are inherently impossible to be reproduced.

Hysteretic models are plausible alternatives to plasticity-based models, but, while capable of overcoming most of the aforementioned limitations, the calibration process is often an arduous task in which the physical meaning of the model parameters is often jeopardized in favour of case-specific accuracy. The absence of a physical law for relating volumetric with shear strains is the main source of this drawback.

This paper presents a downscale version of the recently developed plasticity-based model by Tasiopoulou and Gerolymos for sand behavior [9], [10]. A methodology for the calibration of the model parameters is developed, so that the constitutive stress–strain loops are consistent with experimental shear modulus and damping curves available in the literature. The finite difference wave-propagation code, into which the aforementioned model was implemented, is validated through comparison with results from the equivalent-linear code STRATA [2] and the nonlinear hysteretic code NL-DYAS [4], [5].

## 2 BRIEF MODEL DESCRIPTION

Tasiopoulou and Gerolymos [9], [10] developed a new plasticity-based model for sand behaviour formulated in the 6-dimenional stress-strain space. In this paper, a 2-dimensional (in p-q space) version of the model is presented for the 1D seismic response analysis of layered soils. According to this version, the incremental stress-strain relationship is given in the following matrix form:

$$\begin{bmatrix} dp \\ dq \end{bmatrix} = \eta \begin{bmatrix} K - \dfrac{-K^2 M_s d}{-KM_s d + 3G}\zeta_a^{\,n} & \dfrac{3KGd}{-KM_s d + 3G}\zeta_a^{\,n} \\ \dfrac{-3KGM_s}{-KM_s d + 3G}\zeta_a^{\,n} & 3G - \dfrac{9G^2}{-KM_s d + 3G}\zeta_a^{\,n} \end{bmatrix} \begin{bmatrix} d\varepsilon_p \\ d\varepsilon_q \end{bmatrix} \tag{1}$$

in which $K$ and $G$ are the elastic (small strain) bulk modulus and shear modulus respectively, $d$ is the ratio of the plastic volumetric strain increment $d\varepsilon_p{}^{\mathrm{p}}$, over the plastic deviatoric strain increment $d\varepsilon_q{}^{\mathrm{p}}$ and is based on Rowe's dilatancy theory as it depends on the distance of the current stress ratio $q/p$ from the phase transformation line. $M_{pt}$ and $M_s$ is the failure stress ratio representing the ultimate strength. Parameter $\zeta_a$ is a hysteretic dimensionless quantity that

provides the loading and unloading rule and is a function of the Bouc–Wen parameter $\zeta$, while the exponent $n$ controls the rate of transition from the elastic state to the perfectly plastic one. Finally, $\eta$ is inserted as a multiplier of the hardening elastoplastic matrix expressing the dissipated hysteretic energy. It is expressed in a ductility based form as it is a function of $\mu$ which is a reference ductility defined in terms of shear strain, as follows:

$$\eta = \frac{s_1}{s_1 + \mu^{s_2}} \tag{2}$$

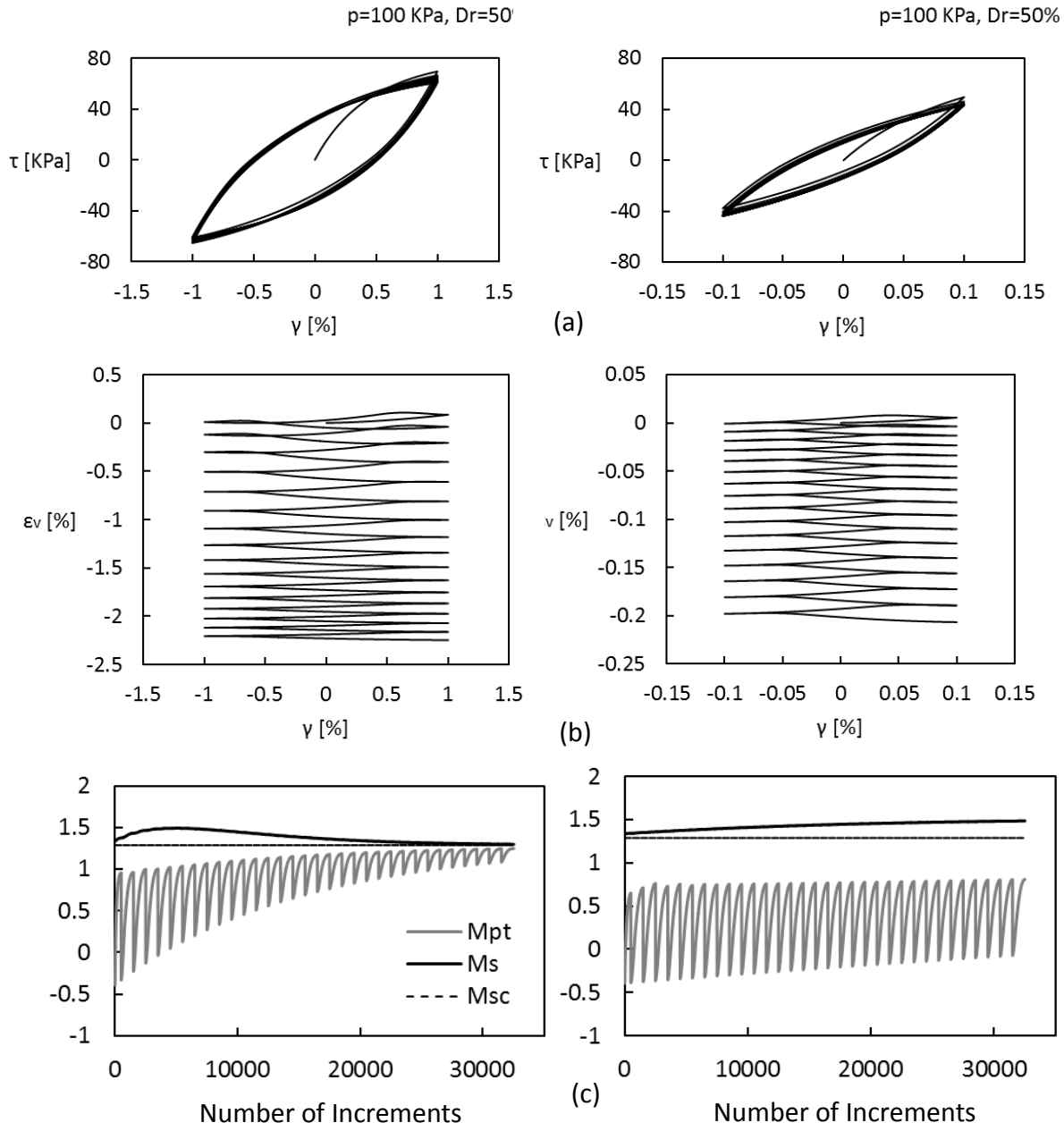


Figure 1: (a) Stress-strain hysteretic loops (b) Volumetric strain ep (c) Evolution of Mpt and Ms parameters vs shear strain for Dr=50%, p=1000KPa and maximum shear strain γ=1% and γ=0.1%

where $s_1$ and $s_2$ are model parameters. Indicative model predictions are shown in Fig. 1 for characteristic values of the aforementioned parameters. The shear stress – strain loops as well as the volumetric strain vs. shear strain are presented for a relative density $D_r$ = 50% and a mean effective stress $p$ = 100 KPa, for two different strain amplitudes $\gamma$ = 1% and $\gamma$ = 0.1%. The figure also depicts the evolution of the phase transformation and the ultimate strength parameters $M_{pt}$ and $M_s$, from their initial values to their critical state value $M_{sc}$ for the large amplitude excitation.

## 3 PARAMETERS CALIBRATION

To determine the parameters of the model (Eq. 2), $G_{max}$ is first obtained (e.g., from resonant column tests, crosshole / downhole tests, etc.); then, the parameters $n$, $s_1$ , and $s_2$ must be assessed.The calibration is then based on matching some established experimental G : γ and ξ : γ curves from the literature. To this end, the Lavenberg–Marquardt optimization procedure is used, available in mathematical code MATLAB. Two published families of G : γ , ξ : γ curves have been utilized: (a) the Vucetic & Dobry curves for sand [11] and (b) the pressure ($\sigma'_0$)-dependent curves of Darendeli et al. [12].

Starting from the Vucetic & Dobry (1991) curves, the results of the calibration are illustrated in **Fig. 2**. The agreement between computed and experimental curves is quite satisfactory. Small discrepancies are observed for small strain levels.

Darendeli et al. [12] recommended a new family of normalized shear modulus and material damping curves, as functions of plasticity index and mean effective stress. Four confining pressures *($\sigma'_0$ = 25, 100, 400, 1600 kPa)* are examined herein. Comparison of the predicted with the experimental curves is depicted in Fig 3.

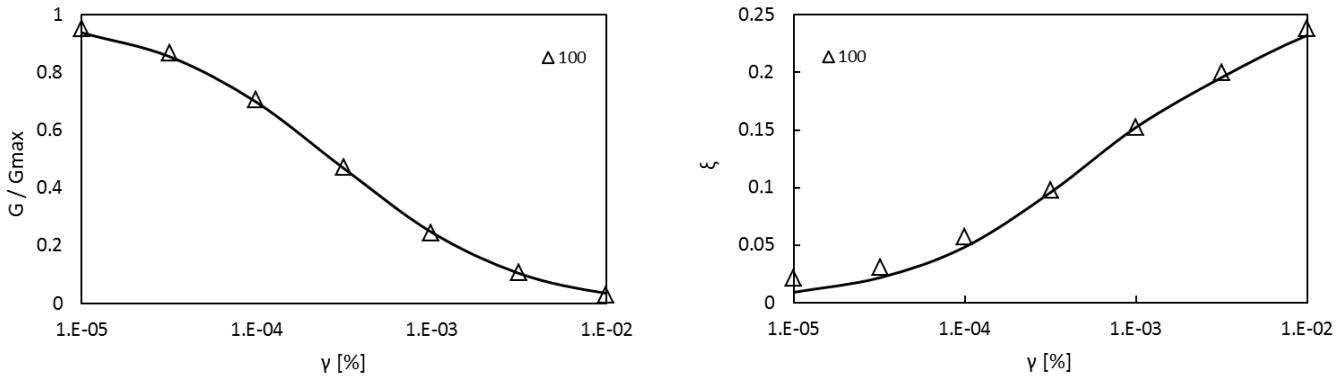


Figure 2: Approximation of the Vucetic and Dobry (1991) shear modulus and damping curve for sand (PI=0) of confinement pressure p=100 KPa. Published data is depicted with markers; model results with continuous lines.

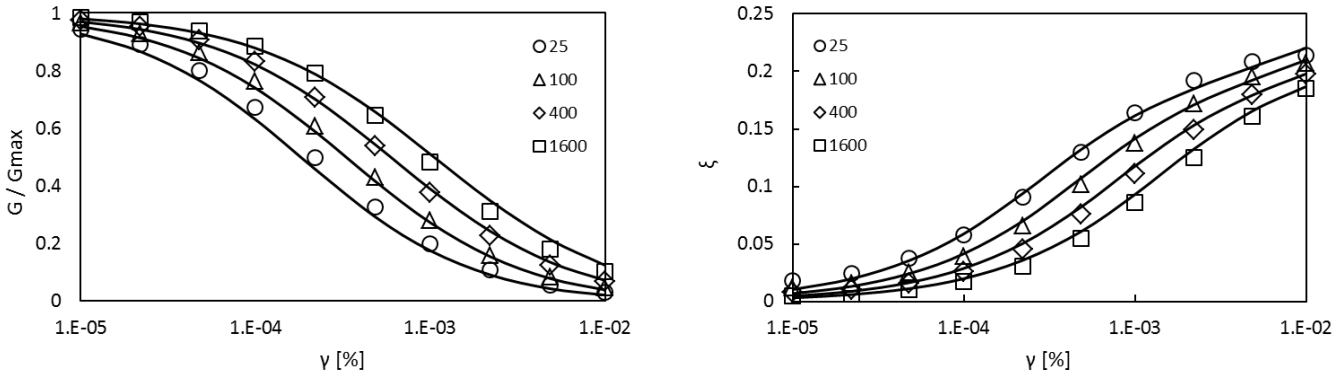


Figure 3: Approximation of the Darendeli shear modulus and damping curves for sands (PI=0) of various confinement pressure levels. Published data is depicted with markers; model results with continuous lines.

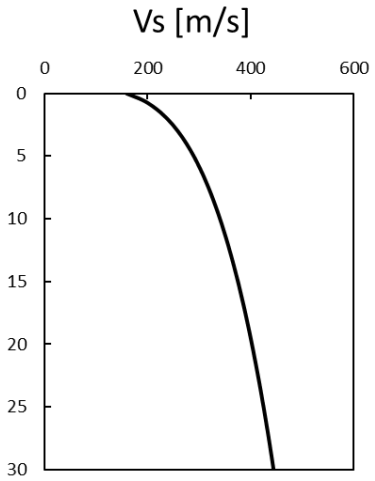


Figure 4: Shear wave velocity distribution of the examined soil profile

## 4 COMPARISON WITH OTHER METHODS

The 2-dimensional version of the TA-GER sand model [9], [10] is implemented into a computer code which uses the explicit finite-difference technique to integrate the equations of motion for the nonlinear one-dimensional ground response analysis of layered sites.

The effectiveness of the proposed model is checked against the hysteretic model by Gerolymos and Gazetas [4] implemented in the finite difference code NL-DYAS ([4], [5]).

To compare NL-DYAS with TA-GER, a 30-m deep *dense sand* profile with density $\rho$ = 2.1 Mg/m$^3$, constant with depth, and shear wave velocity distribution (Fig 4), is excited at its base and its response is calculated.

A strong motion, the JMA 090 record from the Kobe (1995) earthquake and a moderate one from Kalamata 1986 earthquake are used as excitations at the base of the soil column. We consider the sand to behave according to the Derendeli curves.

To serve as a yardstick, an equivalent linear soil response analysis was also carried out with the use of code STRATA [2] — one of the current state-of-practice soil amplification codes.

The results of the three analyses (TA–GER, NL-DYAS, STRATA) are portrayed in terms of : (a) the acceleration time histories at the ground surface (Figs 5 and 9), (b) the distributions with depth of the peak values of acceleration, displacement, shear strain, and shear stress (Figs 6 and 10), (c) the stress–strain hysteresis loops of the two nonlinear models at the depth of 5m and 15m (Figs 7 and 11), and (d) the corresponding acceleration response spectra (Figs 8 and 12). The following conclusions can be drawn:

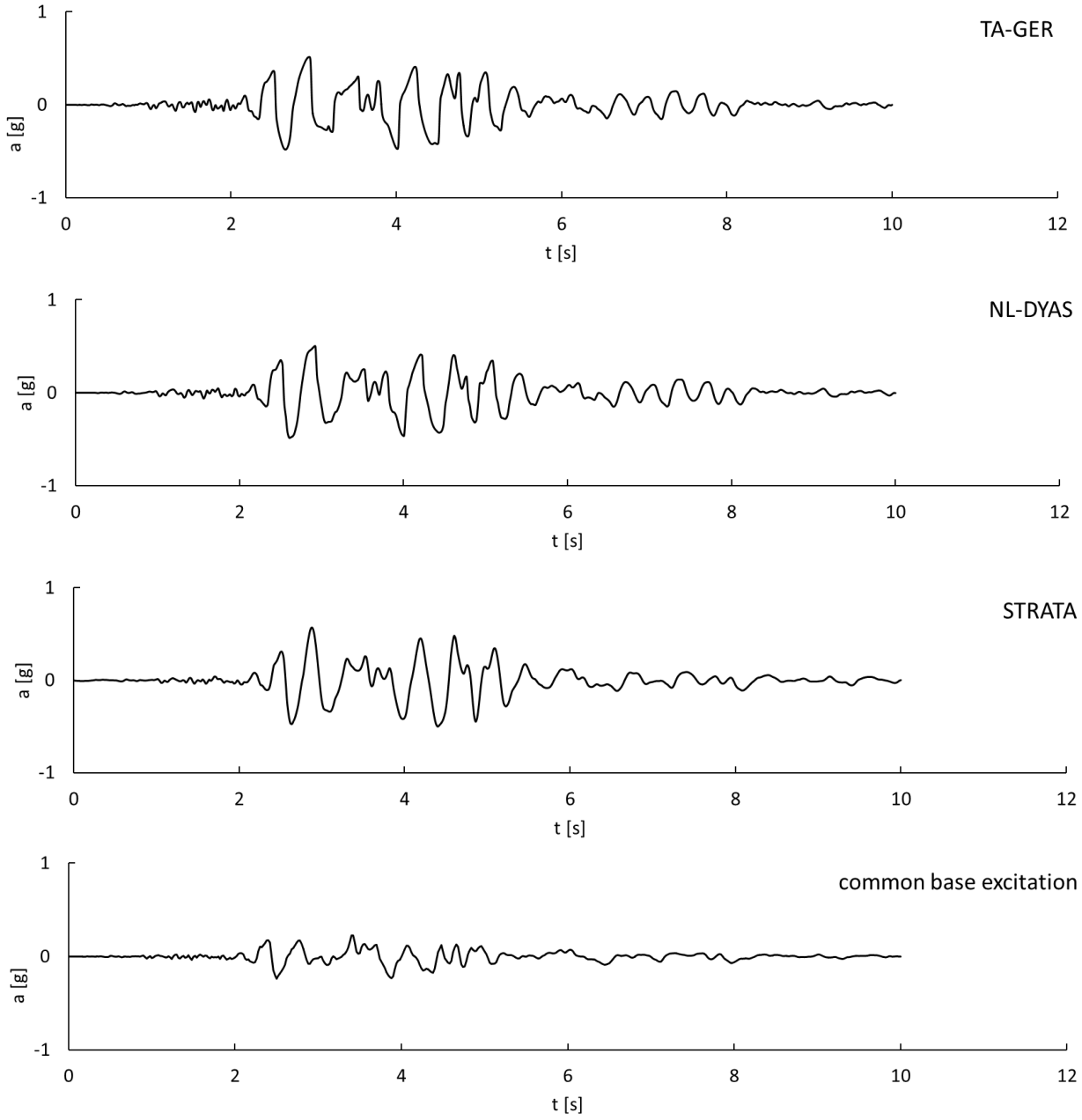


Figure 5: Comparison of acceleration time histories at the surface computed with the three models. Shaking with Kalamata 1986 record

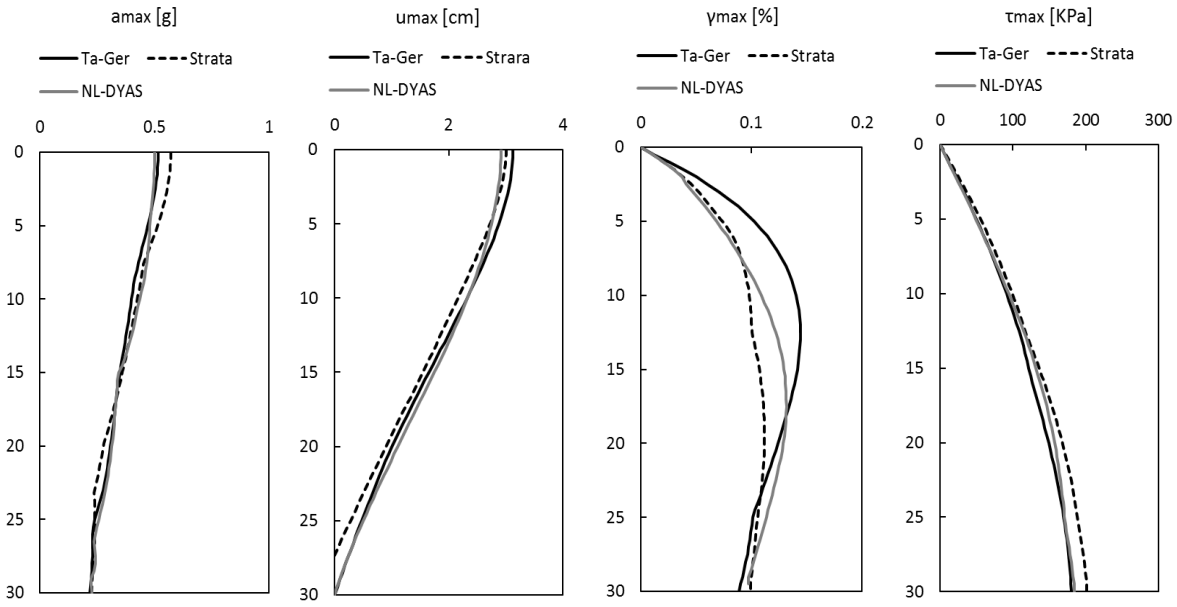


Figure 6: Distributions with depth of the peak values of acceleration, displacement, shear strain, and shear stress. Shaking with Kalamata 1986 record

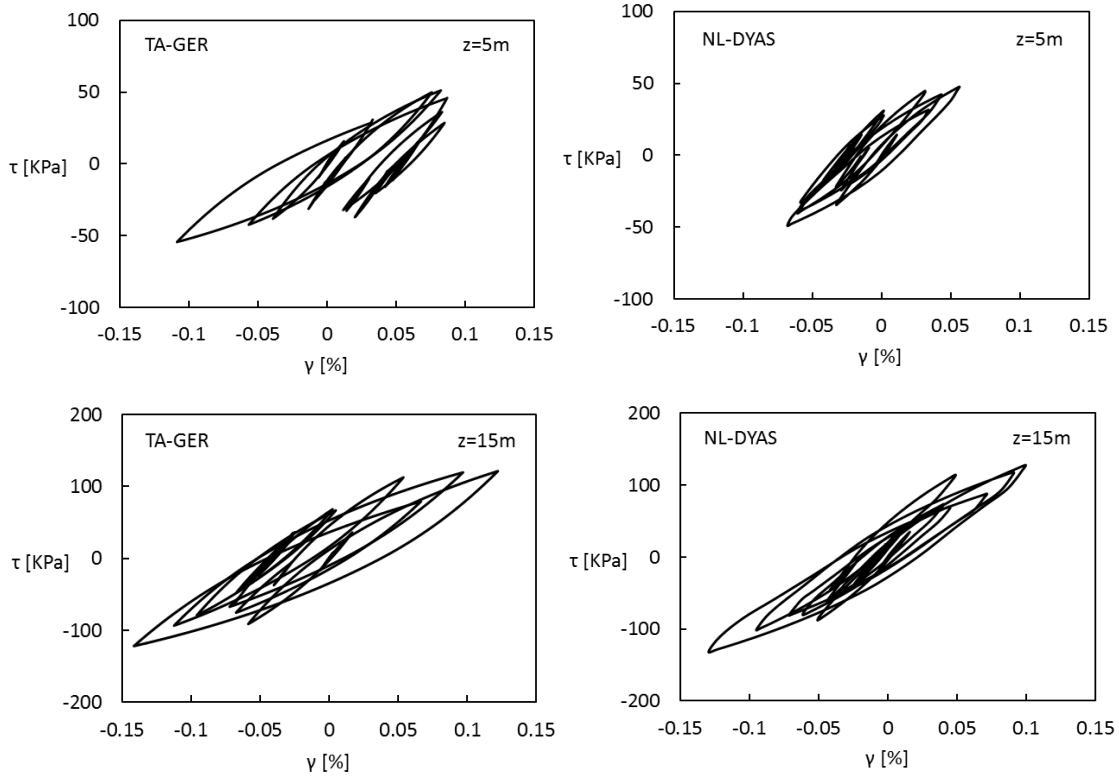


Figure 7: Comparison of stress – strain loops computed with TA- GER and NL – DYAS at z=15m and z=5m. Shaking with Kalamata 1986 record

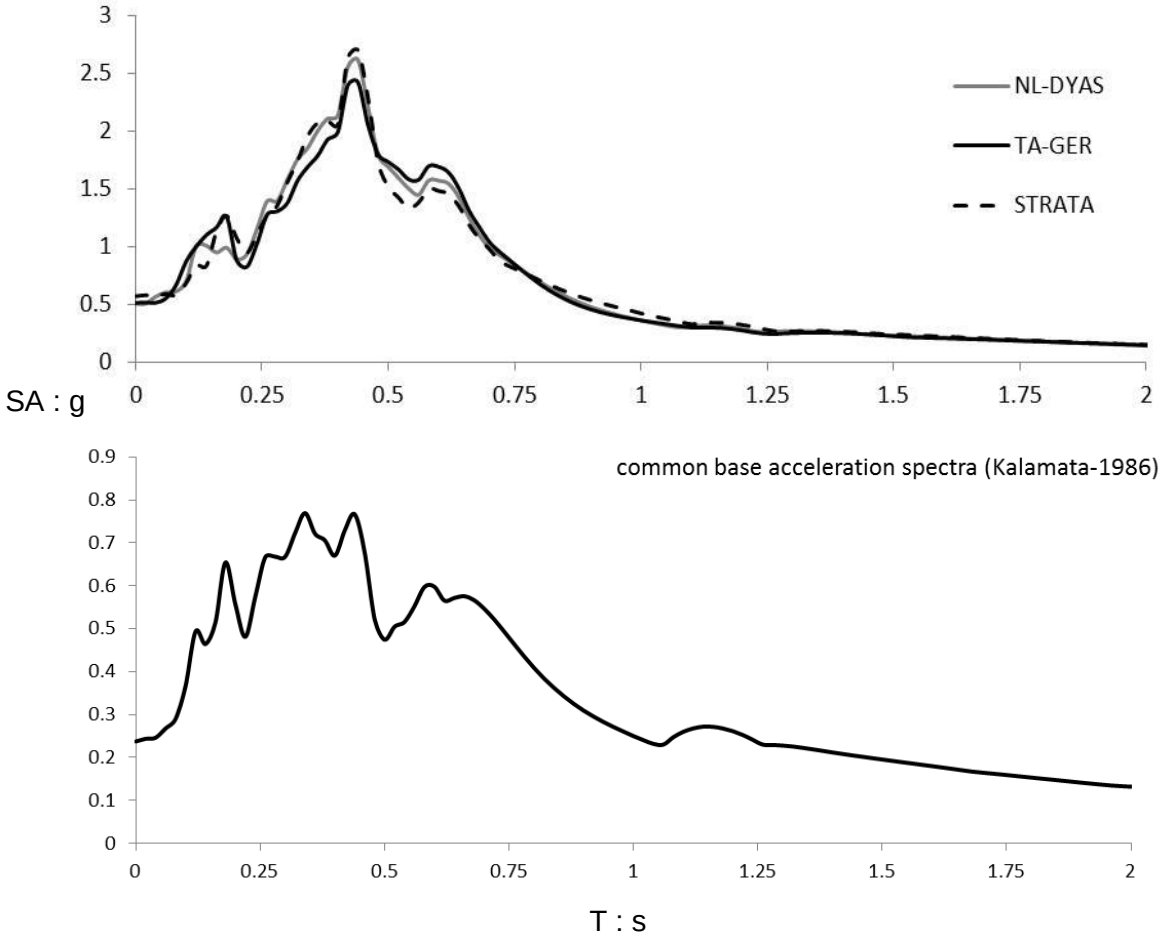


Figure 8: Acceleration response spectra at the surface calculated with the three models

- For the moderate excitation, all three codes (and corresponding soil models) predict similar response in terms of distributions with depth and quite similar acceleration time histories, with STRATA exhibiting slightly higher amplitudes.
- Regarding the strong seismic excitation, a fairly similar response is predicted by the two non-linear models. On the other hand, STRATA significantly exaggerates the long-period pulses, while it depresses the high-frequency components — a performance within expectations, as such "depression" of high frequencies has been already noted in the literature (e.g. [13], [14], [15], [16]). The response acceleration spectra from the three codes reinforce this conclusion: whereas the two inelastic soil models produce almost identical spectra, the equivalent-linear analysis, having filtered-out the short-period components, underpredicts the spectral values for periods less than 0.45 sec. It is worth mentioning that an improved equivalent-linear method that avoids the overdamping of high frequencies has been developed by Assimaki and Kausel [14]. Such overdamping stems from the facts that damping is a function of strain amplitude and that high frequencies are usually associated with small amplitudes of motion; thus, these components experience substantially less damping than the dominant frequencies and are artificially suppressed when hysteretic damping is taken as constant. The overestimation of the long period spectral accelerations by the equivalent linear method is due to resonance phenomena that take place in a linear analysis. Such phenome-

na cannot be developed when nonlinearity is accounted for, as the shear modulus, therefore the natural periods of soil, are not fixed but change over time.

- The distributions with depth of the peak values of acceleration, shear stress, and horizontal displacement computed with the two nonlinear models for the JMA 090 record are in well agreement, considerably deviating from those of the equivalent linear method. The similarity between the $\tau - \gamma$ diagrams of TA-GER and NL-DYAS analyses is evident for the moderate motion. There are sharp differences for the strong seismic excitation, however, with the TA-GER model predicting broader hysteresis loops that are more regular in shape.

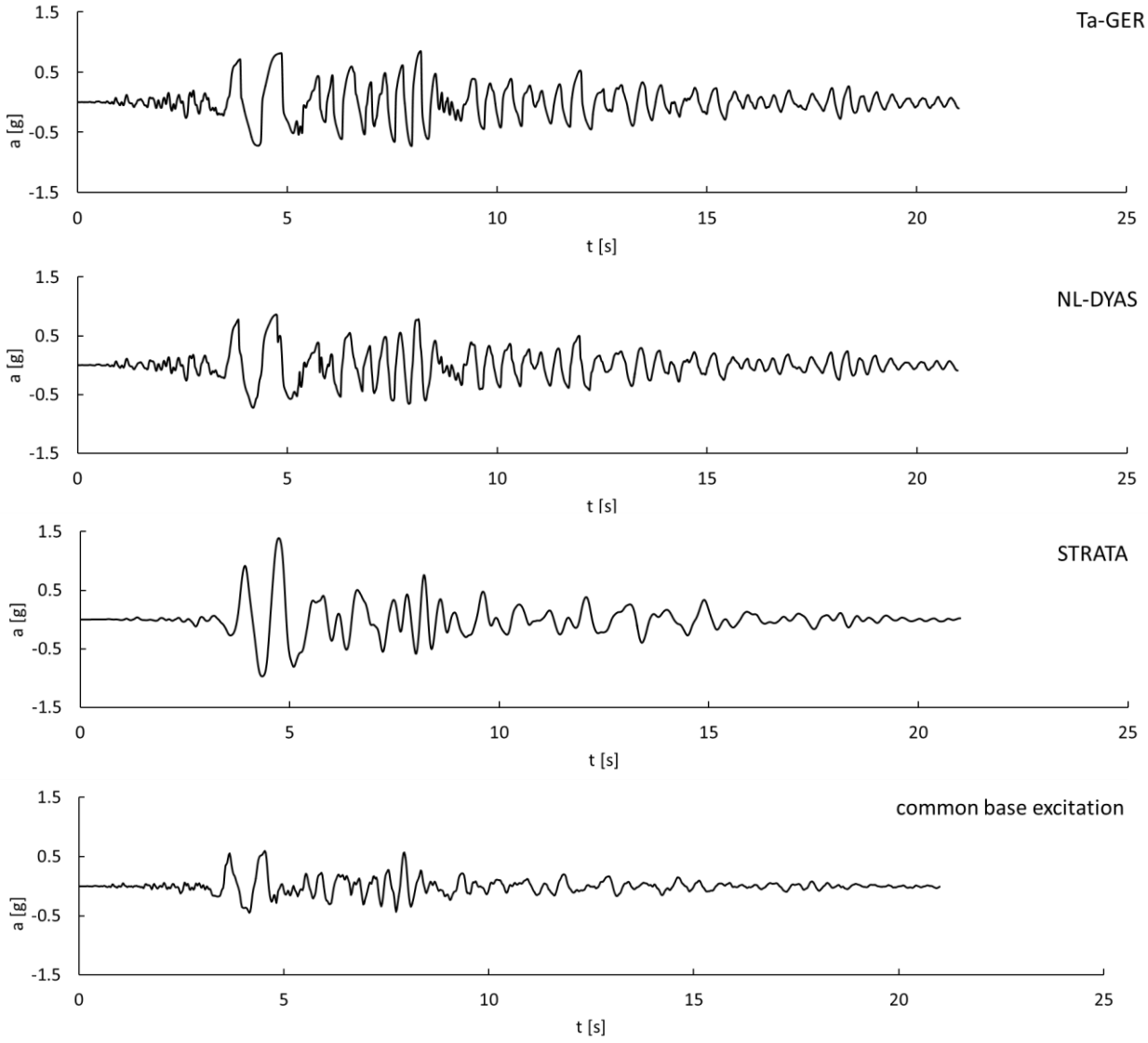


Figure 9: Comparison of acceleration time histories at the surface computed with the three models. Shaking with Kobe JMA 090 1995 record

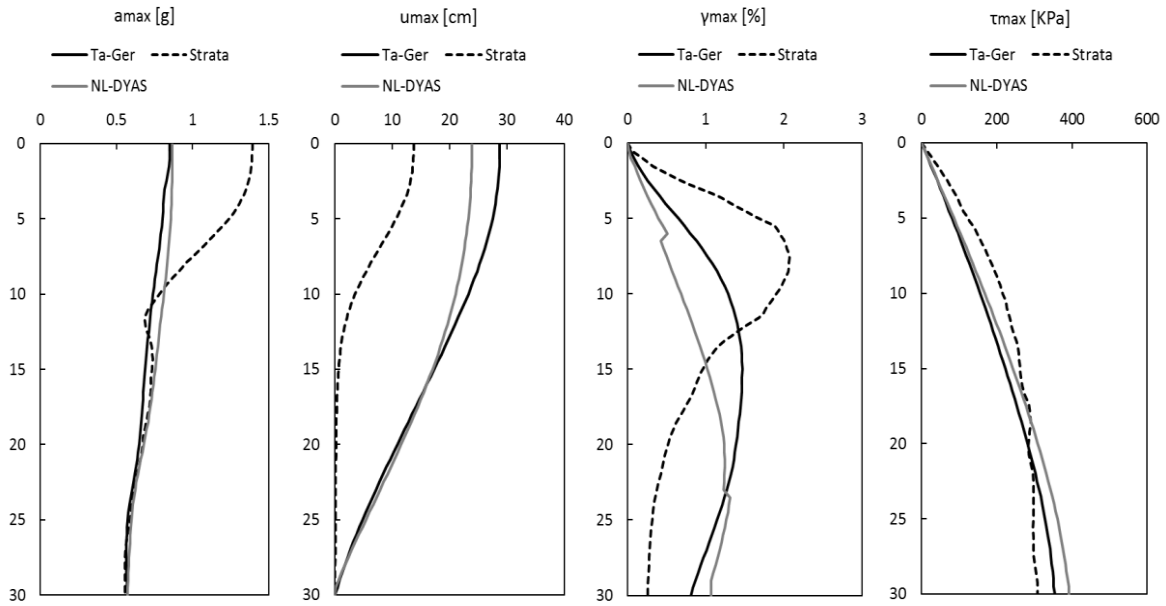


Figure 10 Distributions with depth of the peak values of acceleration, displacement, shear strain, and shear stress. Shaking with Kobe JMA 090 1995 record

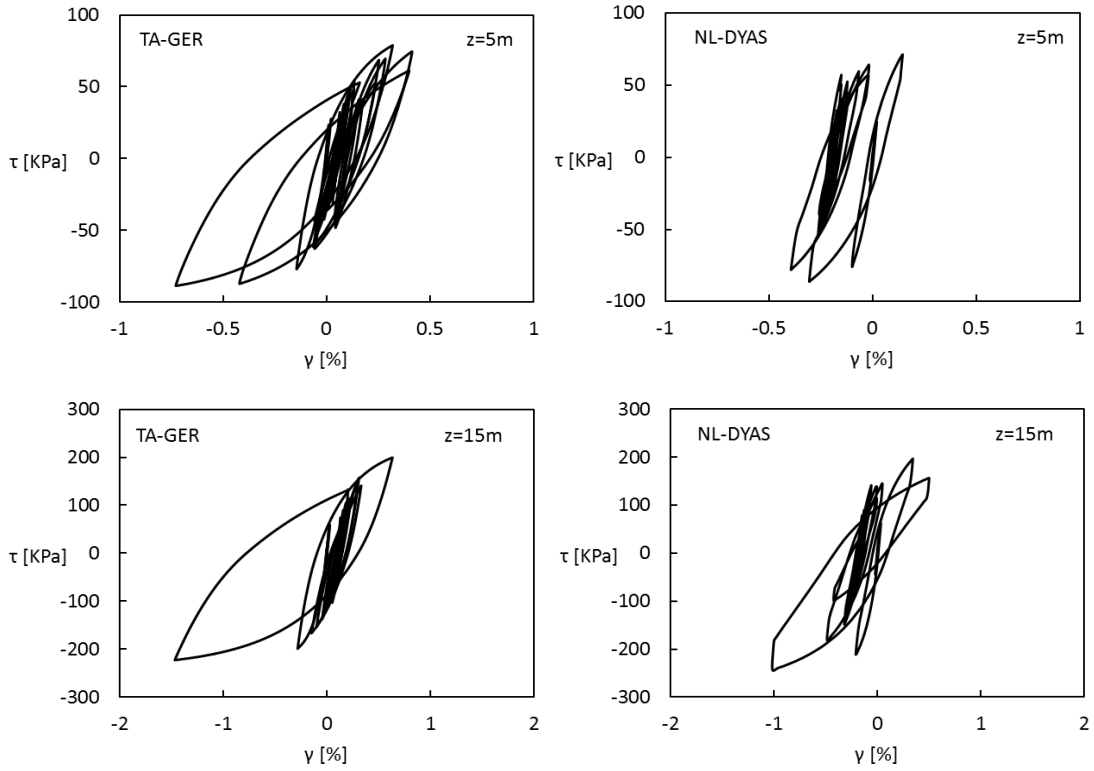


Figure 11 Comparison of stress – strain loops computed with Ta- Ger and NL – DYAS at z=15m and z=5m. Shaking with Kobe JMA 090 1995 record

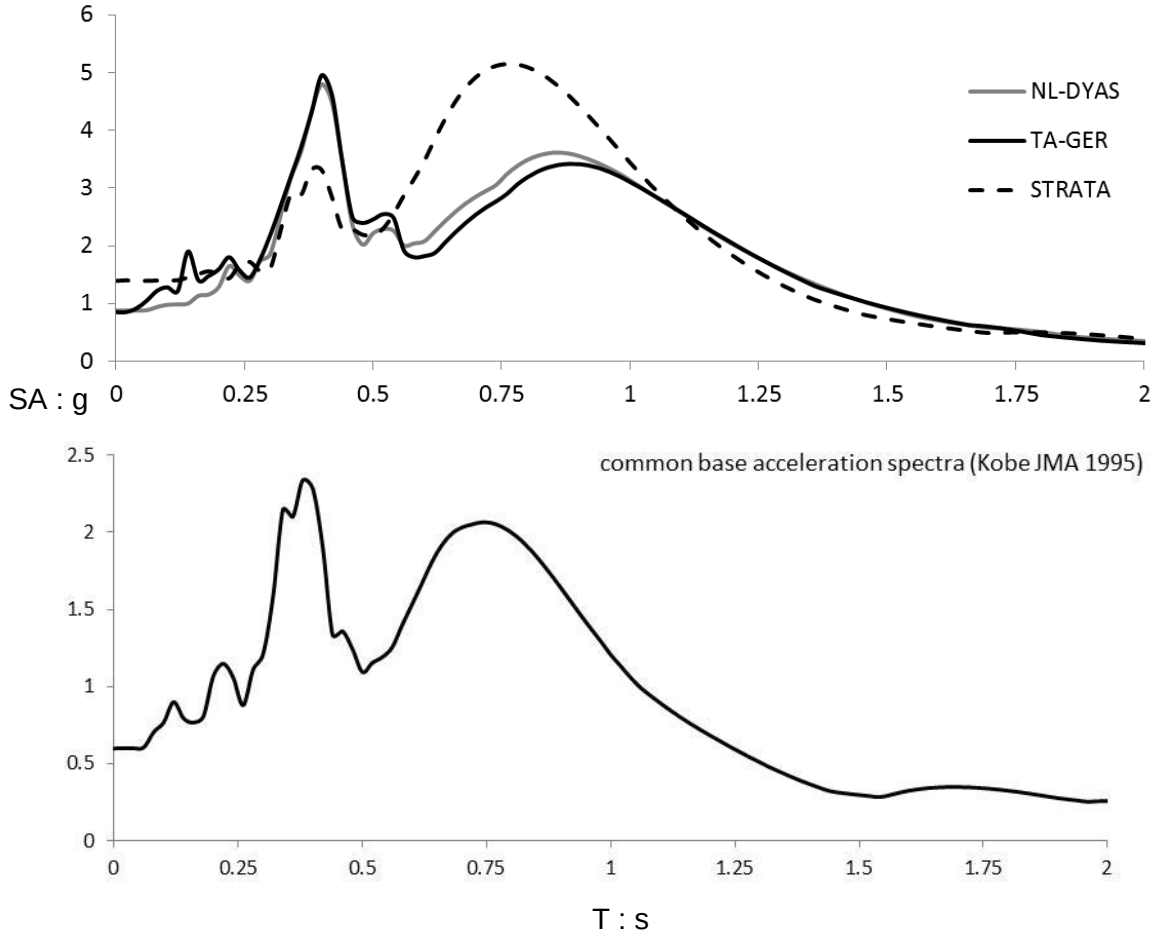


Figure 12: Acceleration response spectra at the surface calculated with the three models

## 5 CONCLUSIONS

A plasticity-based model implemented into a finite differences computer code was presented in this paper and found capable of predicting efficiently the 1D nonlinear site response. The model is a simplified version of that originally proposed by Tasiopoulou and Gerolymos [9], [10]. The few model parameters were calibrated against experimental results in terms of the shear modulus reduction and damping ratio increase curves available in the literature. The capability of the model in simulating the nonlinear response of horizontally layered deposits was checked through comparison with two codes available in the literature: NL-DYAS and STRATA. While the three codes exhibited similar results for the moderate seismic excitation case, validating the proposed plasticity-based model, the equivalent linear method fails to yield satisfactory results for the strong motion case, significantly underestimating the high-frequency components of the ground response and overestimating the low-frequency ones.

## REFERENCES

[1] Schnabel PB, Lysmer J and Seed HB. "SHAKE: A computer program for earthquake response analysis of horizontally layered sites," Rep. EERC 72-12, Univ. of California, Berkeley, 1972.

[2] Rathje, E.M., Ozbey, M.C., and Kottke, A. 2006. “Site Amplification Predictions using Random Vibration Theory,” Proceedings, First European Conference on Earthquake Engineering and Seismology, Paper No. 337, Geneva, Switzerland, September (CD-ROM).

[3] Lee MKW and Finn WDL. "DESRA-2, Dynamic effective stress response analysis of soil deposits with energy transmitting boundary including assessment of liquefaction potential," Soil Mechanics Series No. 38, University of British Columbia, 1978.

[4] Gerolymos N, Gazetas G. Constitutive model for 1-D cyclic soil behavior applied to seismic analysis of layered deposits. Soils Found 2005; 45(3):147–59.

[5] Drosos V, Gerolymos N, Gazetas G. Constitutive model for soil amplification of ground shaking: Parameter calibration, comparisons, validation. Soil Dyn Earthq Eng 2012; 42:255–74

[6] Hashash, Y.M.A. and Park D. (2001). "Non-linear one-dimensional wave propagation in the Mississippi Embayment". Engineering Geology, v. 62 (1-3), 185-206.

[7] Yang, Z., Lu, J., and Elgamal, A. (2004). "A Web-Based Platform for Computer Simulation of Seismic Ground Response." Advances in Engineering Software, 35(5), 249-259.

[8] Ching JY and Glaser SD. "1D time-domain solution for seismic ground motion prediction," *Journal of Geotechnical and Geoenvironmental Engineering*, ASCE, 36-47, 2001.

[9] Tasiopoulou P, Gerolymos N. (2016), “Constitutive modeling of sand: Formulation of a new plasticity approach”, Soil Dynamics and Earthquake Engineering 82, pp. 205-221.

[10] Tasiopoulou P., Gerolymos N. (2016), “Constitutive Modelling of Sand: A Progressive Calibration Procedure accounting for Intrinsic and Stress-Induced Anisotropy”, Geotechnique 66(9), 1-17.

[11] Vucetic, M. and Dobry, R. (1991) “Effect of soil plasticity on cyclic response.” *Journal of Geotechnical Engineering*, 117(1), 89–107.

[12] Darendeli, M.B., Stokoe, K.H., II, Rathje, E.M. and Roblee, C.J. (2001) “Importance of Confining Pressure on Nonlinear Soil Behavior and Its Impact on Earthquake Response Predictions of Deep Sites.” *Proc., 15th International Conference on Soil Mechanics and Geotechnical Engineering*, August 27-31, Istanbul, Turkey

[13] Constantopoulos, I.V., Roesset J.M., and Christian, J.T. (1973) "A comparison of linear and exact nonlinear analysis of soil amplification," *Proc., 5th World Conference on Earthquake Engineering*, vol. 2, 1806–1815.

[14] Assimaki, D. and Kausel, E. (2002) “An equivalent linear algorithm with frequency- and pressure-dependent moduli and damping for the seismic analysis of deep sites.” Soil Dynamics and Earthquake Engineering, 22, 959–965.

[15] Rathje, E.M., and Kottke, A.R. (2011) “Relative differences between equivalent linear and nonlinear site response methods.” *Proc., 5th International Conference on Earthquake Geotechnical Engineering*, January 10 – 13, Santiago, Chile.

[16] Travasarou, T. and Gazetas, G. (2004) “On the linear seismic response of soils with modulus varuing as a power of depth – the Maliakos marine clay.” *Soils and Foundations*,44(5), 85–93.

COMPDYN 2017
6th ECCOMAS Thematic Conference on
Computational Methods in Structural Dynamics and Earthquake Engineering
M. Papadrakakis, M. Fragiadakis (eds.)
Rhodes Island, Greece, 15–17 June 2017

# STEADY-STATE AND TRANSIENT DYNAMIC VISCO-ELASTIC RESPONSE OF CONCRETE AND EARTH DAMS DUE TO DAM-RESERVOIR INTERACTION

**Loizos Pelecanos[1], Stavroula Kontoe[2], and Lidija Zdravković[2]**

[1]Department of Architecture & Civil Engineering, University of Bath,
Claverton Down, Bath, BA2 7AY, United Kingdom.
e-mail: L.Pelecanos@bath.ac.uk

[2] Department of Civil & Environmental Engineering, Imperial College London
Skempton Building, Exhibition Road, London, SW7 2AZ, United Kingdom
{stavroula.kontoe, l.zdravkovic}@imperial.ac.uk

**Keywords:** Dam, Reservoir, Interaction, Earthquake Engineering, Finite elements, Structural Dynamics.

**Abstract.** *The aim of this study is to investigate the effects of dam–reservoir interaction on the dynamic response of dams. Both thin rectangular concrete cantilever and large trapezoidal earth dams are considered with empty and full reservoir.*

*It has recently been shown by Pelecanos et al. [32] that the amplification of accelerations at the crest of the dam depends on the combinations of the frequency of the harmonic acceleration load and the fundamental frequencies of the dam and the reservoir. This study considers transient dynamic loading and selected scenarios of different combinations of the above-mentioned frequencies are examined under random seismic acceleration load.*

*It is shown that for certain cases the amplification of accelerations of the dam can be affected by the presence of the upstream reservoir. In general, thin rectangular concrete cantilever dams are found to be considerably more sensitive to dam–reservoir interaction than large trapezoidal earth dams. Therefore, this investigation examines the significance of dam–reservoir interaction and when this interaction should be taken into consideration or it could be neglected.*

## 1 INTRODUCTION

The dynamic behaviour of a dam with a full reservoir is different from the behaviour of a dam with an empty reservoir. The motion of the reservoir affects the motion of the dam (because of the induced hydrodynamic pressures [7, 8]) and vice-versa. This phenomenon is called dynamic dam-reservoir interaction (DRI) and it could be catastrophic in cases of resonance, i.e. when the two domains (dam and reservoir) are vibrating in phase.

The early studies on the effects of the reservoir on the response of dams considered a stiff and undeformable dam of various geometries [40, 39, 41, 2, 5] and concentrated on the prediction of the hydrodynamic pressures on the upstream dam face [28, 11, 12, 26]. Later studies considered a flexible dam [7, 25] and investigated the vibrations of both the reservoir and the dam structure. Over time various closed-form analytical solutions were proposed [40, 41, 6] for simplified problems, while more advanced numerical models [32, 18, 40] were adopted to consider the complicated interaction between the dam and the reservoir by discretising both domains. The latter were generally based on Finite [16, 34, 30] and/or Boundary Element [38] approaches.

Previous studies of DRI [5, 7, 17, 21, 20, 19] showed that the effects of DRI are more pronounced in concrete dams than in earth dams. For this reason, seismic analyses of earth dams have traditionally neglected DRI effects [31]. The early fundamental work of Chopra [7] is of particular interest, as it studied a model concrete gravity dam vibrating in its fundamental mode and examined its response for various combinations of the circular frequency of the applied harmonic load and the fundamental circular frequencies of the dam and the reservoir. The effects of this interaction are mainly focused on (a) the fundamental period of vibration of the dam-reservoir system (DRS) and (b) the magnitude of the dynamic response of the dam. It is generally believed that DRI firstly causes the DRS to soften, elongating its fundamental period of vibration, and secondly it alters the dam's response by amplifying or de-amplifying the seismic motion. Finally, monitoring data from forced vibration tests on real concrete gravity dams [8] showed that the measured natural period of vibration of dams was larger for a full reservoir than a partly filled reservoir [9, 15, 16, 35].

A recent study by Pelecanos et al. [32] investigated the fundamental behavior of dam-reservoir systems under harmonic loads and examined the amplification of accelerations at steady-state conditions. Two general cases were considered of simplified model concrete cantilever and trapezoidal earth. The amplification of accelerations at the crest of the dam was explored under harmonic acceleration load for various combinations of the frequency of the harmonic load and the fundamental frequencies of the dam and the reservoir. It was found that DRI affects both the fundamental period of the dam and the amplification of accelerations within the dam structure and that these DRI effects are more pronounced for concrete cantilever dams than trapezoidal earth dams.

This paper describes a further investigation of reservoir-dam interaction and its influence on the dynamic acceleration response of dams. It builds on the work of Pelecanos et al. [32] and extends that work to transient dynamic acceleration loads by considering seismic input motions. Similar to the study of Pelecanos et al. [32], both rectangular cantilever and trapezoidal earth dams are considered. In all the performed analyses, both the dam and the reservoir rest on a stiff undeformable ground and therefore the effects of dam- reservoir-foundation interaction are not considered.

## 2 PROBLEM DEFINITION

The problem under study is shown in Figure 1. A dam (1) rests on the ground (in this work, a stiff and undeformable foundation) (3) and retains a large amount of water in the reservoir

(2). Under seismic (or general dynamic) conditions, an acceleration motion from the ground (such as at point A) causes movement of both the dam structure and the reservoir.

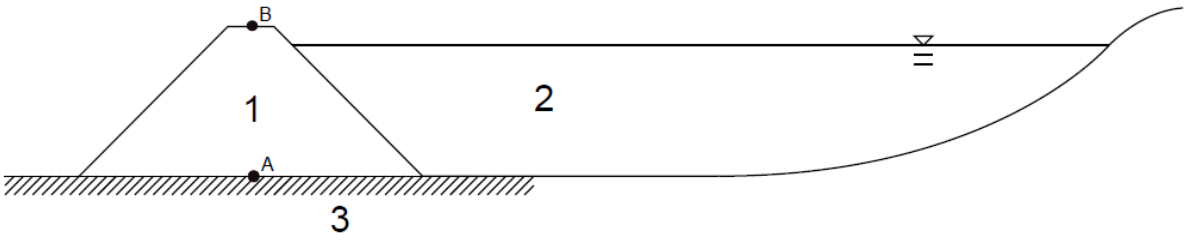


Figure 1: Geometry of the dam-reservoir-foundation system: (1) Dam, (2) Reservoir, (3) Foundation.

The critical question is how the motion of each domain (dam structure and reservoir) will be affected by the motion of the neighbouring domain, i.e. what is the effect of reservoir-dam interaction, especially on the accelerations of the dam crest (point B). Therefore, in this investigation, acceleration input motions are applied at the dam base (such as point A) and the accelerations at the crest of the dam (point B) are monitored and examined for different cases, with a full and an empty reservoir.

In all the analyses presented in this paper, the reservoir domain is modelled with 8-noded isoparametric displacement-based solid elements according as elaborated in Pelecanos et al. [30]. All the analyses carried out are two-dimensional plane-strain dynamic in the time-domain using the FE software ICFEP (Imperial College Finite Element Program) [33]. The time-integration scheme employed is the generalised α-method of Chung & Hulbert [10] which is able to use numerical damping to selectively filter high frequencies (spectral radius at infinity, $\rho_\infty$ = 9/11, see Kontoe et al. [23].

## 3 FINITE ELEMENT MODELS

### 3.1 Rectangular concrete dam

The first case considers a simple rectangular cantilever dam. The geometry of the cantilever dam is shown in Figure 2. The region A-B-C-D represents the upstream reservoir, A-B-F-E represents the cantilever dam and F-G-H-C represents the foundation. The height of the dam is taken as, H=60m, the width of the dam is W=18m, the length of the reservoir, L=300m and the thickness of the foundation, T=18m. The reservoir length to height ratio is taken as, L/H = 5 according to the suggestions of Pelecanos et al. [30] for stiff dams with a vertical upstream face.

The material properties of the dam are taken as follows: Poisson's ratio, ν=0.3 and mass density, ρ=2500 kg/m$^3$. Damping, ξ, of the Rayleigh type [8] is specified in the dam with a target value of 5%. The values for the two natural circular frequencies of Rayleigh damping, $\omega_1$ and $\omega_2$, are taken as equal to the fundamental circular frequency of the dam, $\omega_d$, and the circular predominant frequency of the input excitation ω. The foundation is modelled as rigid and a high bulk modulus value is assigned, K = $10^8$ $K_w$ = 2.2 $10^{14}$ kPa (where, $K_w$ = 2.2 $10^6$ kPa is the bulk modulus of water) and a Poisson's ratio ν =0.4.

The reservoir water is assumed to behave as a linear material with a bulk modulus, $K_w$=2.2·$10^6$ kPa (the exact value for water) and a nominal value of shear modulus, $G_w$=100 kPa [30]. The fundamental circular frequency of the reservoir, $\omega_r$ is given by Equation 1 [5] (where, $V_p$=1483 m/s is the p-wave velocity of water).

$$\omega_r = 0.25\frac{V_p}{H} \quad (1)$$

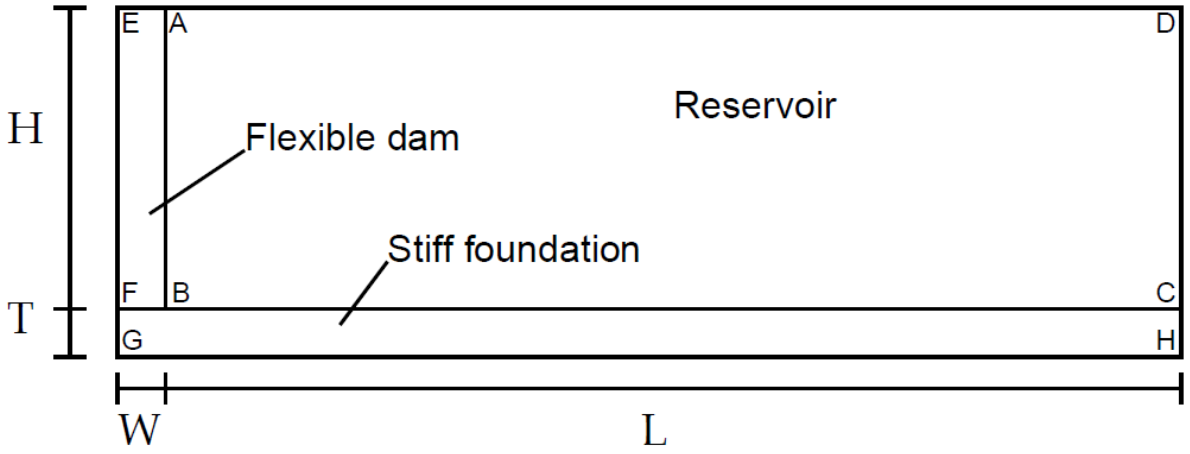


Figure 2: Geometry of the rectangular dam.

It should be noted that the value of the elastic Young modulus, E, is altered in each analysis so that specific combinations of ω, $\omega_r$ and $\omega_d$ are achieved. This is discussed in more detail in Section 5.1. The fundamental frequency of the dam may be obtained from the Euler-Bernoulli or Timoshenko bending equations [35].

Zero-thickness isoparametric interface elements [13][33] are placed along the interface of the dam and the reservoir (A-B) and the interface of the reservoir and the foundation (B-C). The values assigned for the normal and shear stiffness of the interface elements are $K_N=10^8$ kN/m and $K_S=1$ kN/m respectively [30].

The applied boundary conditions include: zero displacements in the vertical direction along the bottom boundary (G-H), and prescribed values of acceleration in the horizontal direction. Zero displacements are specified in the vertical direction on the upstream reservoir boundary, whereas the horizontal boundary condition applied on the upstream reservoir boundary (C-D) is the standard viscous boundary [22][24] which is described by Equation 2 [30].

$$\sigma = \rho V_p \dot{u} \tag{2}$$

where σ is a normal stress on the boundary, ρ is the density of the material the BC has been applied to (i.e. water in this case), $V_p$ is the p-wave velocity of the water (=1483 m/s) and ů is the velocity in the horizontal direction. More details about this BC may be found in Kontoe et al. [24].

### 3.2 Trapezoidal earth dam

The geometry of the examined earth dam is shown in Figure 3. The region A-B-C-D represents the upstream reservoir, A-B-F-E represents the earth dam and F-G-H-C represents the foundation. The height of the dam is taken as H=60m, the width of the crest of the dam W=18m, the breadth of the dam shoulders B=180m, the length of the reservoir L=300m and the thickness of the foundation T=18m. Note that the slope ratio, B/H = 1/3. The L/H ratio is taken as equal to 5 according to the suggestions of [30] for trapezoidal earth dams.

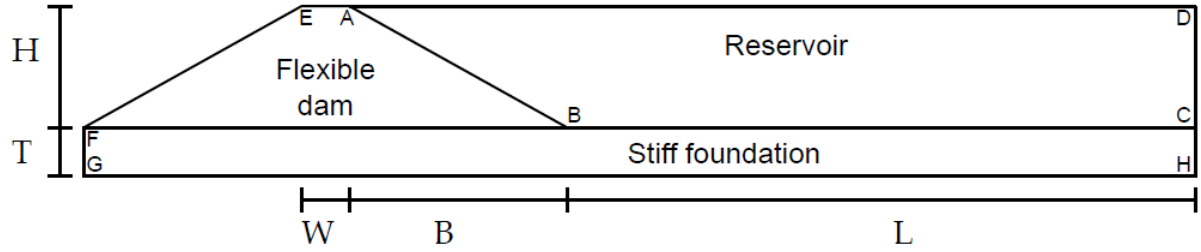


Figure 3: Geometry of the trapezoidal earth dam considered.

The material properties of the dam are as follows: Poisson's ratio, ν=0.3 and mass density, ρ=2000 kg/m$^3$. Similarly to the cantilever dam, damping, ξ of the Rayleigh type [8] is specified in the dam with a target value of 5% and the foundation is again modelled to behave as a rigid material. The boundary conditions are the same as the cantilever dam case: zero displacements are specified in the vertical direction along the bottom boundary (G-H), whereas the acceleration input motion is specified in the horizontal direction.

The value of the shear wave velocity, $V_s$, is altered in each analysis so that specific combinations of ω, $\omega_r$ and $\omega_d$ are achieved. This is discussed in more detail in Section 5.2. The fundamental frequency of the dam may be obtained from the Ambraseys [1] equation [37].

Again, interface elements are placed at the interface of the dam and the reservoir (A-B) and the interface of the reservoir and the foundation (B-C). Finally, the same boundary conditions are applied on the bottom (F-G) and the upstream reservoir (C-D) boundaries as with the previous case of the cantilever dam.

## 4 DAM-RESERVOIR INTERACTION UNDER HARMONIC LOADING

Pelecanos et al. [32] studied the response of both concrete cantilever and trapezoidal earth dams under harmonic loads. For both cases the amplification of accelerations at the crest of the dam was explored under harmonic acceleration load for various combinations of the frequency of the harmonic load, ω, and the fundamental frequencies of the dam, $\omega_d$, and the reservoir, $\omega_r$. To achieve these different combinations, the values of the elastic modulus, E, and of the shear wave velocity, $V_s$, were altered in the case of the concrete cantilever dam and the trapezoidal earth dam respectively, to provide some specific values of the ratio of the fundamental circular frequency of the reservoir over the fundamental circular frequency of the dam, $\omega_r/\omega_d$, over the range of 0.25 to 4.

The applied boundary conditions included: zero displacements in the vertical direction along the bottom boundary (G-H), and prescribed values of harmonic acceleration in the horizontal direction, as given by Equation 3. Different values of circular frequency, ω, were considered, for constant amplitude $\alpha_0$= 1 m/s$^2$ and for 40 cycles, in order to reach a steady-state response.

$$\alpha(t) = a_0 \cos \omega t \tag{3}$$

where, α is the input acceleration, $\alpha_0$ is the amplitude of the harmonic load, ω is the circular frequency of the harmonic loading and t is the time.

Regarding the rectangular cantilever dam, Figure 4 (from Pelecanos et al. [32]) shows the amplification of the accelerations at the dam crest, |F| with respect to the ratio of the circular frequency of the harmonic load to the fundamental circular frequency of the dam, $\omega/\omega_d$, for various values of the ratio of the fundamental circular frequency of the reservoir to the fun-

damental circular frequency of the dam, $\omega_r/\omega_d$. On the same figure, the corresponding amplification of a dam with an empty reservoir is plotted with a dashed line for comparison.

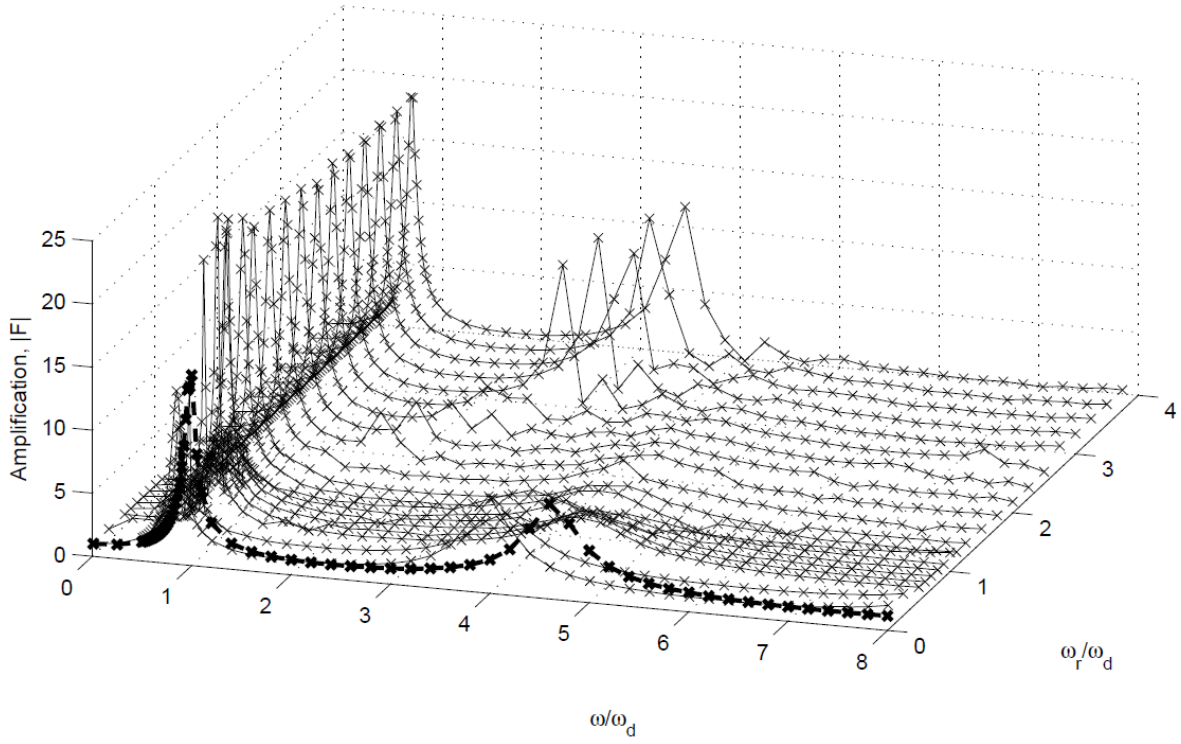


Figure 4: Amplification of acceleration, |F| at the crest of the rectangular concrete dam for various values of the frequency ratios $\omega/\omega_d$ and $\omega_r/\omega_d$ (After Pelecanos et al. [32]).

The amplification spectrum (|F| - $\omega/\omega_d$) follows a similar trend for all the values of the examined $\omega_r/\omega_d$ ratio. Namely, there are generally two peak values of the amplification as observed for the empty reservoir case. However, the magnitude of the peak values of the amplification and the value of the $\omega/\omega_d$ ratio at which they occur is different for different values of the $\omega_r/\omega_d$ ratio.

Moreover, it is shown that the maximum value of amplification occurs in the region where $\omega/\omega_d \approx \omega_r/\omega_d \approx 1$, i.e. where $\omega \approx \omega_d \approx \omega_r$. This is due to resonance between the harmonic load, the dam and the reservoir. There are also large values of amplification for $\omega/\omega_d \approx \omega_r/\omega_d$ (shown diagonally in the figure), i.e. where $\omega \approx \omega_r$. The value of amplification for the latter case ($\omega \approx \omega_r$) can be larger than the amplification corresponding to the second mode of vibration (i.e. close to $\omega/\omega_d \approx 4.7$). However, it seems that in some cases (e.g. close to $\omega/\omega_d \approx \omega/\omega_r \approx 3$) there is a combined effect of (a) $\omega \approx \omega_r$ and (b) the second natural mode of vibration of the dam.

Regarding the trapezoidal earth dam, Figure 5 (from Pelecanos et al. [32]) shows the amplification of acceleration, |F|, at the dam crest with respect to the ratio of the circular frequency of the harmonic load to the fundamental circular frequency of the dam, $\omega/\omega_d$ for various values of the ratio of the fundamental circular frequency of the reservoir to the fundamental circular frequency of the dam, $\omega_r/\omega_d$. The amplification of a dam with an empty reservoir is also plotted with a dashed line for comparison.

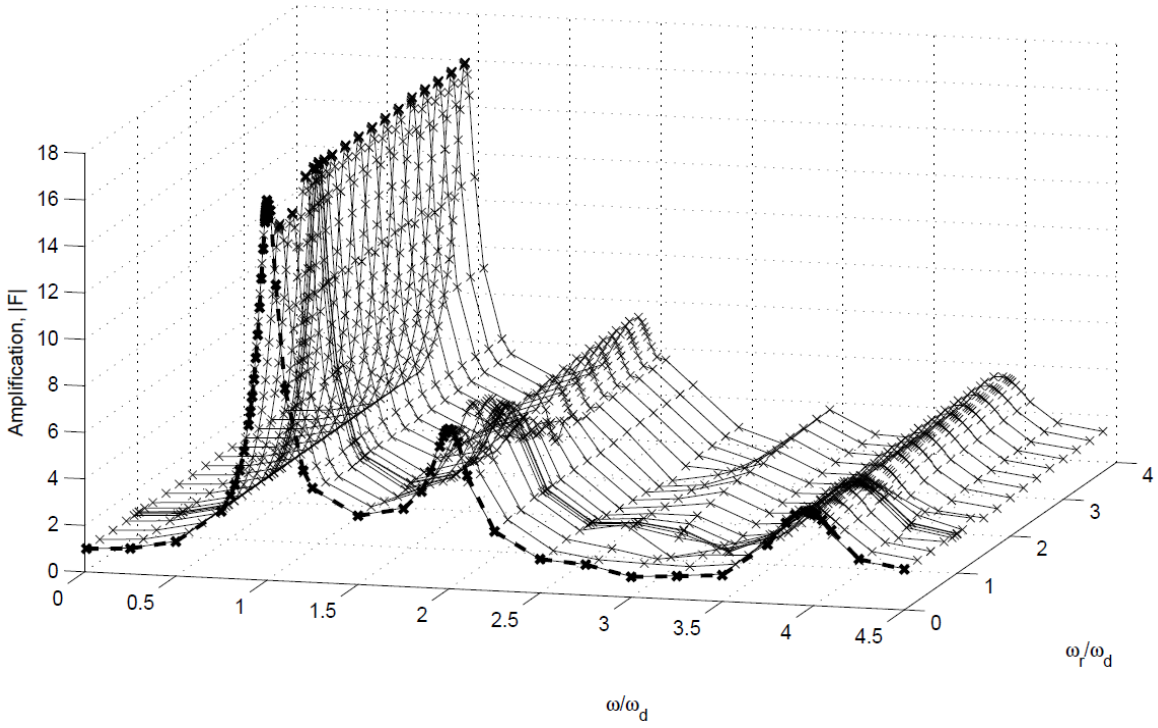


Figure 5: Amplification of acceleration, |F| at the crest of the earth dam for various values of the frequency ratios $\omega/\omega_d$ and $\omega_r/\omega_d$ (After Pelecanos et al. [32]).

Similar to the case of the cantilever dam, the amplification spectrum (|F| - $\omega/\omega_d$) follows a similar trend for all the values of the $\omega_r/\omega_d$ ratio. Namely, for each $\omega_r/\omega_d$ ratio three main peaks can be identified in the amplification response, which correspond to the three first modes of vibration of the dam. In contrast to the case of the cantilever dam, the magnitude of the peak values of the amplification and the value of the $\omega/\omega_d$ ratio at which they occur does not seem to depend significantly on the $\omega_r/\omega_d$ ratio. Overall, there are very small differences between the amplification spectra for different values of the $\omega_r/\omega_d$ ratio. This suggests that the presence of the reservoir does not affect significantly the amplification (and hence the dynamic response) of the dam, for any value of the $\omega_r/\omega_d$ ratio.

## 5 DAM-RESERVOIR INTERACTIOM UNDER SEISMIC LOADING

The investigation of Pelecanos et al. [32] was restricted to a harmonic load shaking a dam-reservoir system. However, since in reality dams are subjected to transient shaking, this study is concerned with seismic loading of reservoir-dam systems. The horizontal acceleration record of the El Centro (Imperial Valley, 1940) earthquake is used as the input motion. The acceleration time history of this motion is shown in Figure 6, and the corresponding 5% damped response spectrum is shown in Figure 7. As it is shown in the latter figure, there are two distinct peaks of spectral acceleration, $S_a$ for periods of 0.27s and 0.52s. The period for which the maximum value of $S_a$ occurs is considered to be the dominant period of the seismic load and it is $T_{EQ}$ = 0.52s.

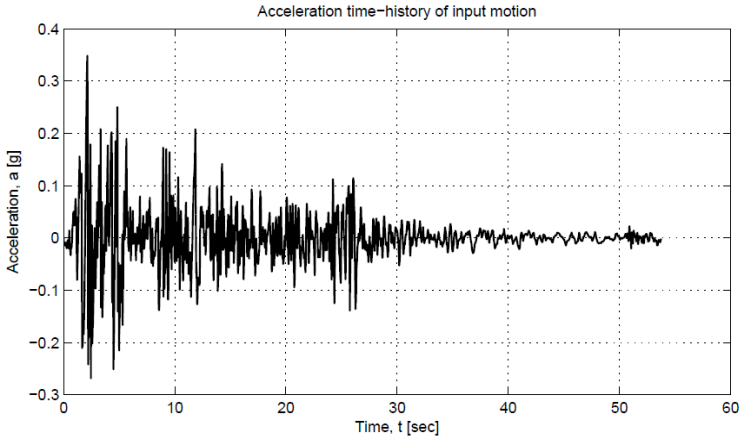


Figure 6: Acceleration time-history of the El-Centro (1940) earthquake record.

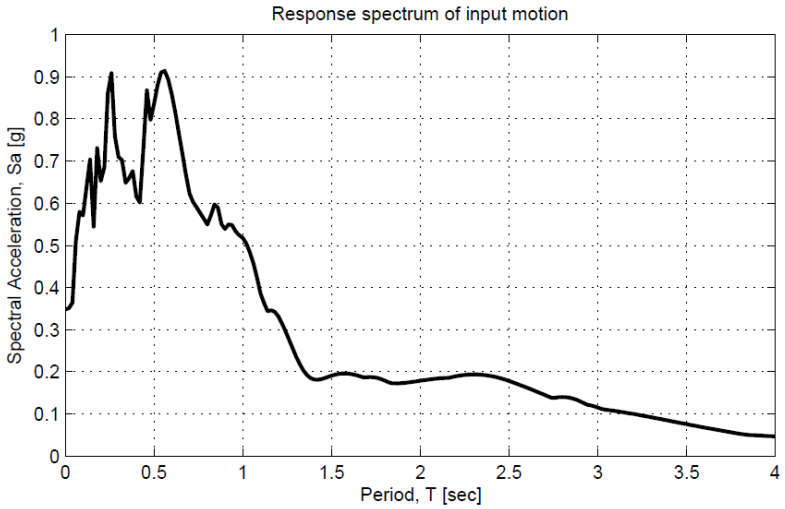


Figure 7: Response spectrum of the El Centro (1940) earthquake record for damping ξ=5%.

Table 1: Cases of combinations of $\omega/\omega_d$ and $\omega_r/\omega_d$ frequency ratios examined for seismic loading.

| CASE | $\omega/\omega_d$ | $\omega_r/\omega_d$ |
|---|---|---|
| A | 1 | 1 |
| B | 3 | 3 |
| C | 1 | 3 |
| D | 1/3 | 1 |
| E | 1/3 | 1/3 |

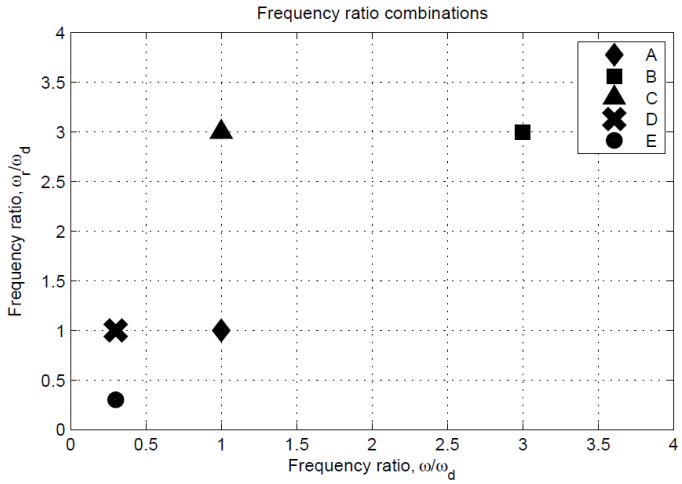


Figure 8: Cases of combinations of $\omega/\omega_d$ and $\omega_r/\omega_d$ frequency ratios examined under seismic loading.

Following the investigation of Pelecanos et al. [32] for harmonic loading, both a cantilever and a trapezoidal earth dam are again considered. For each of the dam types, five cases are examined for various combinations of the frequency ratios $\omega/\omega_d$ and $\omega_r/\omega_d$, as listed in Table 1 and shown graphically in Figure 8. These combinations are chosen based on the observations of Pelecanos et al. [32] concerning harmonic loading, i.e. large amplification of accelerations is expected for Cases A-D, whereas smaller amplification of the accelerations is expected for Case E.

## 5.1 Rectangular concrete dam

For the case of the cantilever dam, the model geometry shown in Figure 2 is employed. The imposed boundary conditions are described in Section 3.1. All five cases (Table 2) are analysed twice, with a full and an empty reservoir. In all cases, the elastic modulus, E, is varied for each case as listed in Table 2, to achieve the combinations of frequencies listed in Table 1.

Table 2: Material and geometric properties of the rectangular concrete dam cases considered under seismic loading.

| CASE | Height, H [m] | Thickness, t [m] | Elastic modulus, E [kPa] |
|---|---|---|---|
| A | 180 | 18 | $1.2 \cdot 10^9$ |
| B | 180 | 18 | $1.4 \cdot 10^8$ |
| C | 60 | 6 | $1.4 \cdot 10^8$ |
| D | 60 | 6 | $1.2 \cdot 10^9$ |
| E | 180 | 18 | $1.2 \cdot 10^{10}$ |

Figure 9 shows the acceleration time-histories at the crest of the dam (for both full and empty reservoirs), whereas Figure 10 shows the corresponding 5% damped response spectra. For the dam with a full reservoir and for all 5 cases (A, B, C, D and E), the peak value of amplification occurs at a value of the $\omega/\omega_d$ ratio smaller than the corresponding for the dam with an empty reservoir (see Figure 10). This suggests that the fundamental period of the dam is larger when reservoir-dam interaction is considered. The latter conclusion is in agreement with the earlier observation of Pelecanos et al. [32] (see also Figure 4) for harmonic load, i.e. the load resonates with the dam-reservoir system at a smaller value of natural circular frequency,

therefore the fundamental period of the dam-reservoir system (i.e. dam with a full reservoir) is larger than that of a dam with an empty reservoir.

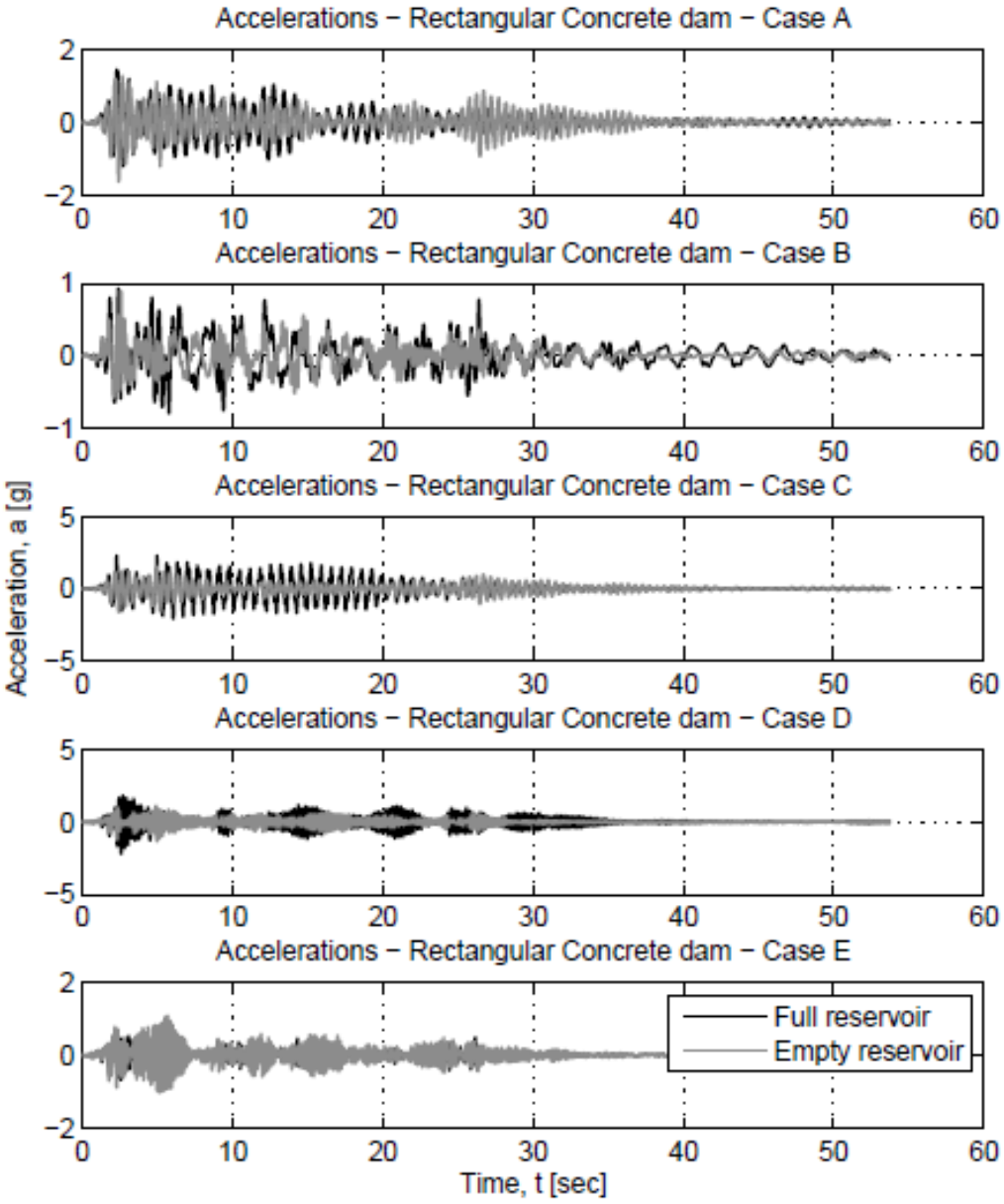


Figure 9: Acceleration time-histories at the crest of the rectangular concrete dam.

Moreover, the value of amplification of accelerations is larger for cases A-D with a full reservoir than those with an empty reservoir (Figure 10). This is again in agreement to the investigation of Pelecanos et al. [32] using harmonic loading (see Figure 4), where higher values of amplification were observed for the frequency combinations of cases A-D for the dam with a full reservoir.

Besides, for case E (i.e. for $\omega/\omega_d = \omega_r/\omega_d = 1/3$), the amplification of accelerations is found to be smaller for a dam with a full reservoir than that for a dam with an empty reservoir (Figure 10). This is again in agreement with the previous investigation regarding harmonic loading (see Figure 4), where the amplification for $\omega/\omega_d = \omega_r/\omega_d = 1/3$ was smaller in a dam with a full reservoir than a dam with an empty reservoir.

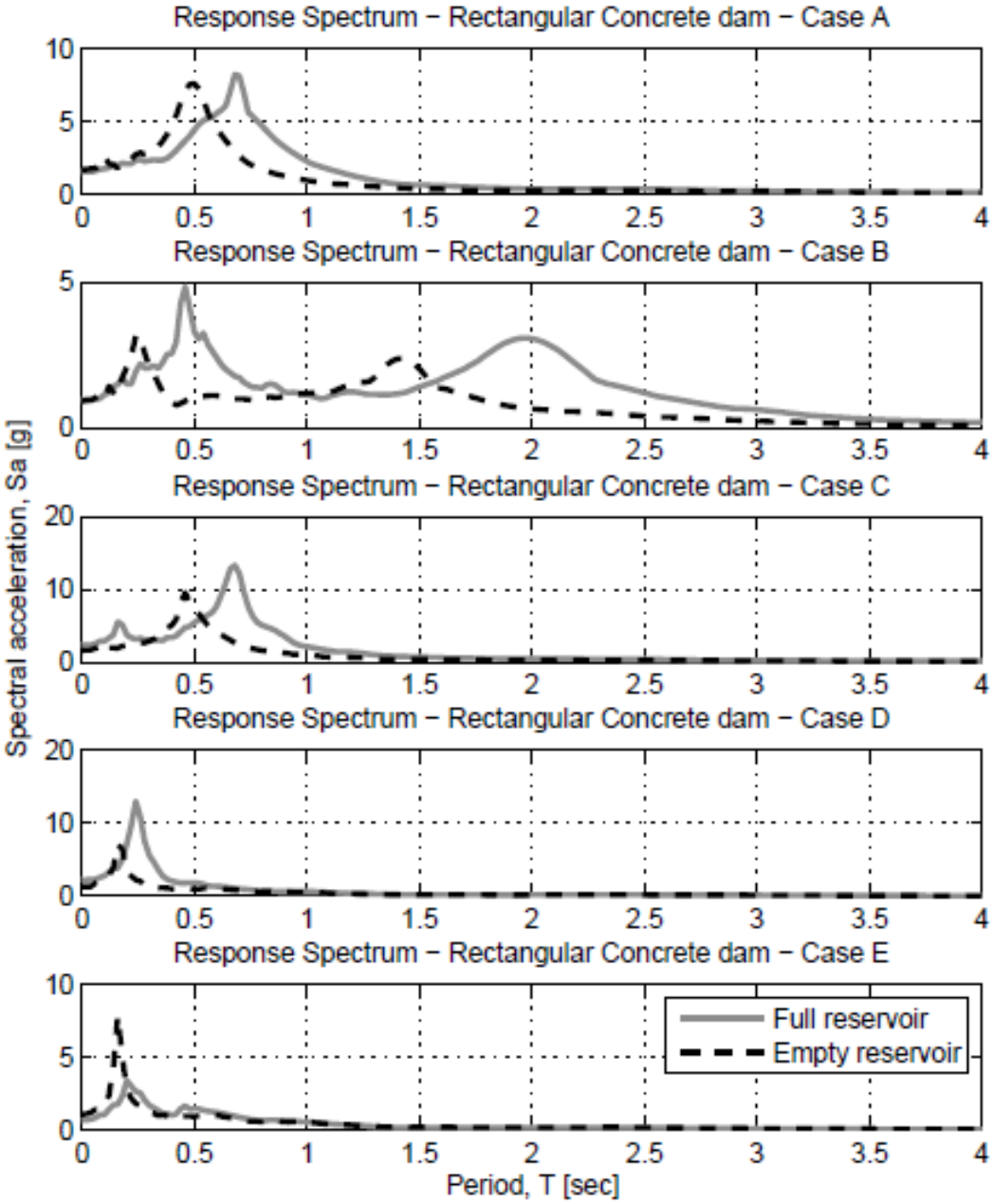


Figure 10: Response spectra (for damping $\xi$=5%) of the acceleration at the crest of the rectangular concrete dam.

## 5.2 Trapezoidal earth dam

For the case of the earth dam, the model geometry shown in Figure 3 is employed. The boundary conditions imposed are described in Section 3. Again, all five cases (Table 1) are analysed twice, with a full and empty reservoir. The shear wave velocity, $V_s$, is changed in each case as listed in Table 3, to achieve the combinations of frequencies listed in Table 1, but in all cases keeping the value of the p-wave velocity of the reservoir constant, $V_p$ = 1483 m/s.

Table 3: Material and geometric properties of the trapezoidal earth dam cases considered under seismic loading.

| CASE | Height, H [m] | Shear wave velocity, $V_s$ [m/s] |
|---|---|---|
| A | 900 | 4500 |
| B | 900 | 1500 |
| C | 300 | 1500 |
| D | 300 | 4500 |
| E | 900 | 13500 |

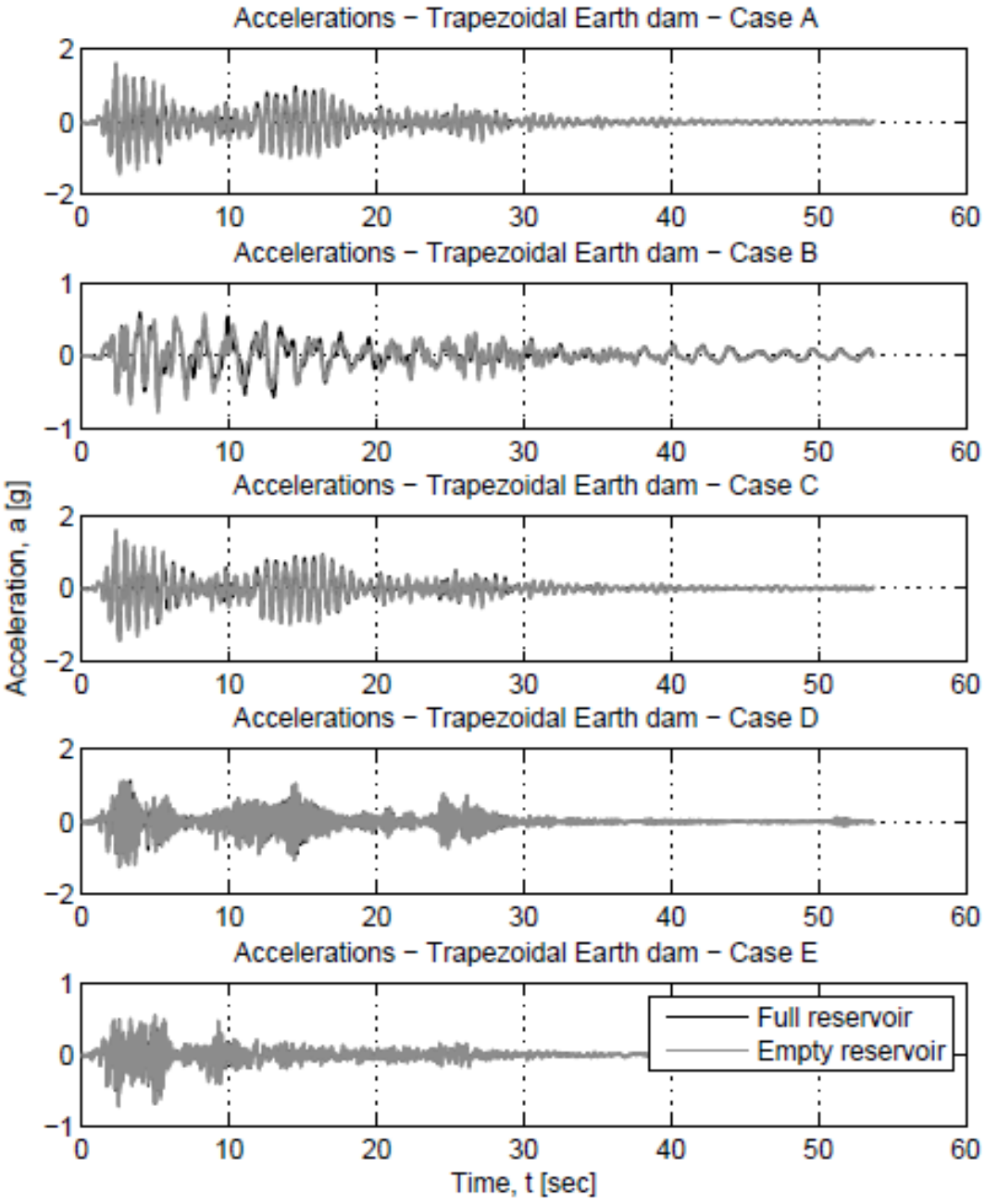


Figure 11: Acceleration time-histories at the crest of the earth dam.

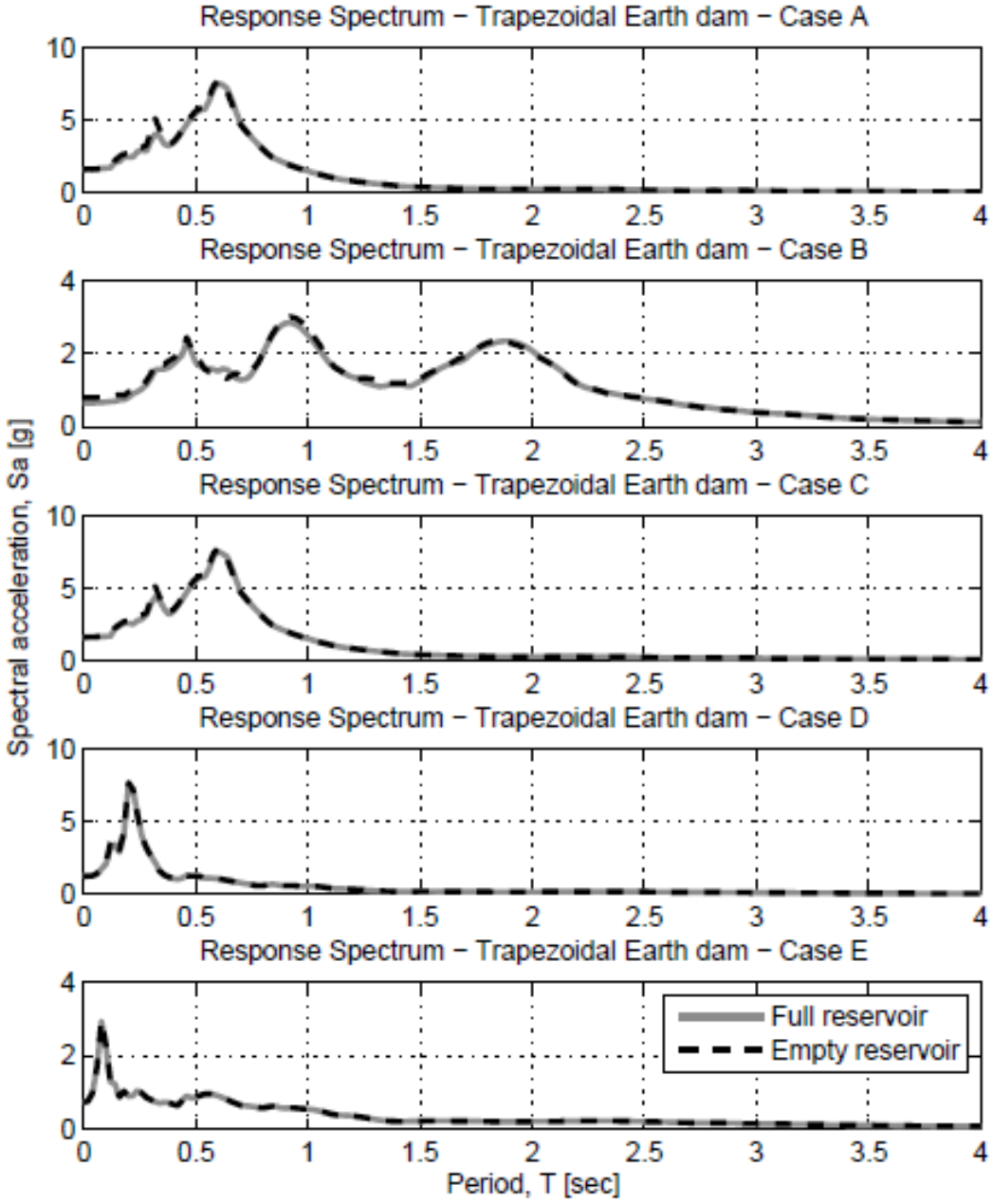


Figure 12: Response spectra (for damping ξ=5%) of the acceleration at the crest of the earth dam.

Figure 11 shows the acceleration time-histories at the crest of the dam (for both full and empty reservoirs), whereas Figure 12 show the corresponding 5% damped response spectra. It may be observed from all figures that the observations for the cantilever dam case do not apply to the earth dam. Although some minor differences between the full and empty reservoir cases may be noticed in the acceleration time-histories (Figure 11), no major differences exist in the response spectra (Figure 12). This means that both the frequency content and the value of amplification are not significantly affected by the presence of the reservoir, for all cases A-E, i.e. for various combinations of the frequency ratios. The previous conclusion of the negligible influence of the reservoir on the dynamic response of earth dams under harmonic loading from Pelecanos et al. [32] is therefore confirmed for seismic loading case as well.

The effects or DRI (both softening and amplification) are found to be insignificant for earth dams. This may be attributed to (a) the sloped upstream face and (b) the large volume of an earth dam. The hydrodynamic pressures induced on a sloped upstream dam face are smaller than those on a vertical dam face [42]. Moreover, the inertial effects from the additional mass from the reservoir are small compared to the inertia of a large earth dam. The second peak value of $S_a$ did not affect the results of this section, as no resonance was expected for the cases chosen.

## 6 CONCLUSIONS

This paper describes an investigation carried out to assess the effects of reservoir-dam interaction on the transient dynamic (seismic) behaviour of dams. The main aim is to examine whether the presence of an upstream reservoir alters the response of a dam and to identify the cases in which the dynamic reservoir-dam interaction may have detrimental effects. Both rectangular cantilever and trapezoidal homogeneous earth dams are considered under seismic loading. This study is an extension of the work of Pelecanos et al. [32] who considered harmonic loads of a wide range of frequencies. The main conclusions of this study may be summarised as follows:

- The effects of dam-reservoir interaction (DRI) under seismic load are very similar to the DRI effects under harmonic loads at steady-state and therefore this study confirms the findings of Pelecanos et al. [32].
- The effects of DRI are mainly related to (a) change of the fundamental period of the dam and (b) change in the amplification of accelerations within the dam structure.
- DRI effects, in terms of both amplification of accelerations and change in the fundamental period, are more pronounced for cantilever dams. This could have an application on various water retaining structures with a slender cross-sectional geometry, such as arch dams, canal locks etc.
- Generally, the presence of the reservoir "softens" the response of the dam, i.e. it results in a larger fundamental period, $T_d$ of the dam. This may be attributed to the added mass, m (see also Westergaard [40]) of the reservoir which vibrates with the dam. In contrast, the reservoir does not provide any additional (shear or bending) stiffness, k to the dam ($T_d = 2 \pi \sqrt{(m/k)}$).
- The amplification of the input acceleration in a dam with a reservoir can be either higher or lower than the amplification in a dam with an empty reservoir. This depends on the relative magnitude of the dominant circular frequency of the load, $\omega$, and the fundamental circular frequencies of the dam and reservoir, $\omega_d$ and $\omega_r$ respectively.

## ACKNOWLEDGEMENTS

This work was part of the PhD research of the first author at Imperial College London, funded by EPSRC. This support is gratefully appreciated. The assistance of Dr M. Latheef and Ms E. Skiada in the numerical analyses is also acknowledged.

## REFERENCES

[1] Ambraseys, N. N., 1960, On the shear response of a two-dimensional truncated wedge subjected to arbitrary disturbance, Bull. Seism. Soc. Am., 50, 1, 45-56.

[2] Bustamante, J. I., Rosenblueth, E., Herrera, I., Flores, A., 1963, Presion hidrodinamica en presas y depositos. Boletin Sociedad Mexicana de Ingenieria Sismica, 1, 2.
[3] Calcina, S. V., Eltrudis, L., Piroddi, L., Ranieri, G., 2014, Ambient Vibration Tests of an Arch Dam with Different Reservoir Water Levels: Experimental Results and Comparison with Finite Element Modelling, The Scientific World Journal, 692709, 1-12.
[4] Chopra, A. K., 1966, Earthquake effects on dams, PhD Thesis, University of California, Berkeley.
[5] Chopra, A. K., 1967, Earthquake response of earth dams, J. Soil Mech. Found. Div., ASCE, 93, SM2, 1399-1412.
[6] Chopra, A. K., 1967, Hydrodynamic pressures on dams during earthquakes, J. Engrg. Mech. Div., ASCE, 93, EM6, 205-223.
[7] Chopra, A. K., 1968, Earthquake behavior of reservoir-dam systems, J. Engrg. Mech. Div., ASCE, 94, EM6, 1475-1500.
[8] Chopra, A. K., 1995, Dynamics of structures: Theory and application to earthquake engineering, Prentice-Hall, New Jersey.
[9] Chopra, A. K., Gupta, S., 1978, Hydrodynamic and foundation interaction effects in frequency response functions for concrete gravity dams, Earthq. Engrg. and Struct. Dyn., 10, 1, 89-106.
[10] Chung, J., Hulbert, G. M., 1993, A time integration algorithm for structural dynamics with improved numerical dissipation: the generalised-α method, J. Appl. Mech., 60, 371-375.
[11] Chwang, A. T., 1978, Hydrodynamic pressures on sloping dams during earthquakes. Part 2: Exact theory, J. Fluid Mech., 87, 2, 343-348.
[12] Chwang, A. T., Housner, G. W., 1978, Hydrodynamic pressures on sloping dams during earthquakes. Part 1. Momentum method, J. Fluid Mech., 87, 2, 335-341.
[13] Day, R. A., Potts, D. M., 1994, Zero thickness interface elements - Numerical stability and application, Int. J. for Num. Anal.Meth. Geomech., 18, 10, 689-708.
[14] Darbre, G. R., de Smet, C. A. M., Kraemer, C., 2000, Natural frequencies measured from ambient vibration response of the arch dam of Mauvoisin, Earthquake Engng. Struct. Dyn., 29, 5, 577-586.
[15] Duron, Z. H., Hall, J. F., 1988, Experimental and finite element studies of the forced vibration response of morrow point dam, Earthq. Engrg. and Struct. Dyn., 16, 7, 1021-1039.
[16] Fenves, G. L., Mojtahedi, S., Reimer, R. B., 1992, Effect of contraction joints on earthquake response of an arch dam, J. Struct. Engrg, ASCE, 118, 4, 1039-1055.
[17] Hall, J. F., Chopra, A. K., 1980, Dynamic response of embankment, concrete-gravity and arch dams including hydrodynamic interaction, Earthquake Engineering Research Centre, University of California, Berkeley, EERC-80/39.
[18] Hall, J. F., Chopra, A. K., 1982, Two-dimensional dynamic analysis of concrete gravity and embankment dams including hydrodynamic effects, Earthq. Engrg. and Struct. Dyn., 10, 2, 305-332.
[19] Hall, J. F., Chopra, A. K., 1982, Hydrodynamic effects in earthquake response of embankment dams, J. Geotech. Engrg. Div., ASCE, 108, GT4, 591-597.
[20] Hall, J. F., Chopra, A. K., 1982, Hydrodynamic effects in the dynamic response of concrete gravity dams, Earthq. Engrg. and Struct. Dyn., 10, 2, 333-345.
[21] Hall, J. F., Chopra, A. K., 1982, Hydrodynamic effects in earthquake response of embankment dams, J. Geotech. Engrg. Div., ASCE, 108, GT4, 591-597.
[22] Kellezi, L. X., 2000, Local transmitting boundaries for transient elastic analysis, Soil Dyn. and Earthq. Engrg., 19, 7, 533-547.
[23] Kontoe, S., Zdravkovic, L., Potts. D.M., 2008, An assessment of time integration schemes for dynamic geotechnical problems, Comput. And Geotech., 2008, 35, 253-264.

[24] Kontoe, S., Zdravkovic, L., Potts. D. M., 2009, An assessment of the domain reduction method as an advanced boundary condition and some pitfalls in the use of conventional absorbing boundaries, Int. J. for Num. Anal. Meth. Geomech., 33, 309-330.
[25] Lee, G. C., Tsai, C.S., 1991, Time domain analyses of dam-reservoir system. Part I: exact solution, J. Engrg. Mech. Div., ASCE, 117, 9, 1990-2006.
[26] Liu, P. L. F., 1986, Hydrodynamic pressures on rigid dams during earthquakes, J. Fluid Mech., 165, 131-145.
[27] Lysmer, J., Kuhlemeyer, R. L., 1969, Finite dynamic model for infinite media, J. Engrg. Mech. Div., ASCE, 95, 4, 859-877.
[28] Newmark, N. M., Rosenblueth, E., 1971, Fundamentals of Earthquake Engineering, Prentice-Hall Inc., Enlewood Cliffs, New Jersey.
[29] Pelecanos, L., 2013, Seismic response and analysis of earth dams, PhD thesis, Imperial College London.
[30] Pelecanos, L., Kontoe, S., Zdravkovic, L., 2013, Numerical modelling of hydrodynamic pressures on dams, Comput. and Geotech., 53, 68-62.
[31] Pelecanos, L., Kontoe, S., Zdravkovic, L., 2015, A case study on the seismic performance of earth dams. Géotechnique 65 (11), 923-935
[32] Pelecanos, L., Kontoe, S., Zdravkovic, L., 2016, Dam–reservoir interaction effects on the elastic dynamic response of concrete and earth dams. Soil Dynamics and Earthquake Engineering 82, 138-141
[33] Potts, D. M., Zdravkovic, L., 1999, Finite element analysis in geotechnical engineering: Theory, Thomas Telford, London.
[34] Saini, S. S., Bettess, P., Zienkiewicz, O. C., 1978, Coupled hydrodynamic response of concrete gravity dams using finite and infinite elements, Earthq. Engrg. and Struct. Dyn., 6, 4, 363-374.
[35] Tan, H., Chopra, A. K., 1996, Dam-Foundation Rock Interaction Effects in Earthquake Response of Arch Dams, Earthq. Engrg. and Struct. Dyn., 122, 5, 528-538.
[36] Timoshenko, S. P., Goodier, J. N., 1934, Theory of Elasticity, Mc-Graw Hill, New York.
[37] Tsiatas, G., Gazetas, G., 1982, Plane-strain and shear-beam free vibration of earth dams, Soil Dyn. and Earthq. Engrg., 1, 4, 150-160.
[38] Von Estorff O., Antes H., 1991, On FEM-BEM coupling for fluid-structure interaction analyses in the time domain, Int. J. for Num. Meth. Engrg., 31, 6, 1151-1168.
[39] von Karman, T., 1933, Discussion on Water Pressures on Dams During Earthquakes, Transactions, ASCE, 98, 1, 434-436.
[40] Westergaard, H. M., 1933, Water pressures on dams during earthquakes, Transactions, ASCE, 98, 1, 418-433.
[41] Wilson, E. L., Khalvati, M., 1983, Finite elements for the dynamic analysis of fluid-solid systems, Int. J. for Num. Meth. Engrg., 19, 11, 1657-1668.
[42] Zangar, C. N., 1953, Hydrodynamic pressures on dams due to horizontal earthquakes, Proc. Soc. Exp. Stress Anal., 10, 93-102.

**NOMENCLATURE**

| | |
|---|---|
| $a_o$ | amplitude of harmonic acceleration load |
| a(t) | acceleration load time history |
| E | Young's elastic modulus |
| \|F\| | amplification of acceleration |
| $G_w$ | shear modulus of water |
| H | height of the dam |

| | |
|---|---|
| $I$ | moment of inertia |
| $k$ | stiffness |
| $K_d$ | bulk modulus of the dam materials |
| $K_N$, $K_S$ | normal and shear stiffness values of the interface elements |
| $K_w$ | bulk modulus of water |
| $L$ | length of the reservoir |
| $m$ | mass |
| $S_a$ | spectral acceleration |

COMPDYN 2017
6th ECCOMAS Thematic Conference on
Computational Methods in Structural Dynamics and Earthquake Engineering
M. Papadrakakis, M. Fragiadakis (eds.)
Rhodes Island, Greece, 15–17 June 2017

# INVESTIGATING THE EFFECT OF USING SOIL BENTONITE WALL ON DAMAGE MITIGATION OF STEEL BURIED PIPELINES SUBJECTED TO REVERSE FAULT RUPTURE

**Farnoud Farzanegan Pour**[1], **Meysam Fadaee**[2]

[1] M.Sc. Student of Earthquake Engineering, Department of Civil Engineering, Science and Research branch, Islamic Azad University, Tehran, Iran
Farnoud.Farzaneganpour@srbiau.ac.ir

[2] Assistant Professor, Department of Civil Engineering, Science and Research branch, Islamic Azad University, Tehran, Iran
Fadaee@srbiau.ac.ir

**Keywords:** Steel Buried Pipeline, Reverse Fault Rupture, Three Dimensional Finite Element Model, Soil Bentonite Wall, Damage Mitigation

***Abstract.*** *As pipelines pass from large geographical regions, their passage through areas with active faults in seismic regions might be inevitable. On the other hand, map of active faults is faced with many uncertainties and it is not possible to estimate the precise place of fault, angle of fault and the fault line. Thus, as lifelines, pipelines are vulnerable to great dangers during an earthquake and resulting permanent ground deformations known as PGD. The previous earthquakes such as Chi-Chi (1999) and Wenchuan (2008) showed a wide ranges of damages caused to various structures subjected to reverse fault rupture. The aim of this study is to investigate the effect of using soft deformable wall (in order to diverting rupture path and absorbing the tectonic deformation) in the response of buried pipelines subjected to reverse fault rupture considering two cases: a) pipeline parallel to fault line b) pipeline perpendicular to fault line.*

*In this method, a thick diaphragm-type soil bentonite wall (SBW) is used in the fault diversion path in order to absorb the fault movements. Three-dimensional finite element model including steel buried pipe in dense sand subjected to reverse fault rupture is considered. The results indicate that using soil bentonite wall can remarkably mitigate the damages caused to pipeline in parallel case. In perpendicular case, the location of damages on buried pipeline is confined in a small area around the SBW which is of great importance in quick discovery of pipeline's damaged section location in order to quick repair and return of pipeline to service.*

## 1 INTRODUCTION

In today societies, While the distribution of vital material is developed, pipelines are accounted as one of the most important and infra-structural facilities of every country. Water, gas, oil and other liquids are remarkably transferred into the long distances path through pipelines. Pipelines are installed in two forms of surface and buried which generally executed buried due to the immunity to environmental hazards. But as buried pipelines encompassed wide areas along its path, it fraught in various geotechnical dangers. One of the most important of these dangers is earthquake and its consequences. During the investigation carried out by O'Rourke and Liu, damages caused to pipelines mostly occurred by permanent ground deformation (PGD) resulted from earthquakes [1]. This matter is of a great importance regarding the fact that (PGD) happens in a short length of pipelines in comparison with transient ground deformation (inferred of earthquake waves) and shows the importance of pipeline behavior subjected to PGD. The PGD that caused by landslide, liquefaction or surface rupture can remarkably apply damages on buried pipelines.

The report of the damages caused to water and gas pipelines in the past earthquakes of Manjil (1990) [2], Northridge (1994) [3], Chi-Chi (1999) [4], Kokaeli (1999) [5] and Chili (2010) [6], are shown/showed the leakage and the stop of service of pipelines and in severe cases, explosion and fire of gas pipelines.

Fault rupture is one of the most common types of PGD and can occur in various types. Apparat from different types of fault rupture, Some of the important factors in the amount of damages applied to pipelines are: The ratio of buried depth to pipe dimeter (H/D), ratio of diameter to pipe thickness (D/t), soil types, fault angle ($\psi$ figure 1) and pipe crossing angle with respect to fault line ( $\beta$ in figure 1).

The investigation carried out by Joshi et al on the effects of reverse fault rupture on buried pipelines showed that the capacity of buried pipeline to accommodate the reverse fault rupture could be increased if the pipe crossing angle with respect to fault line became near-parallel [7]. On the other hand, with current knowledge, it is not always possible to determine the precise place of fault and its path and therefore pipe crossing angle with respect to fault line ($\beta$). Moreover, even the passage of buried pipeline parallel to fault line (figure 1a) which was recommended by joshi et al [7], can cause severe damages to buried pipelines in some critical conditions.

In this research, by inspiring from researches of Fadaee et al [8], [9] with using a thick diaphragm-type soil bentonite wall (SBW) in a specific distance with buried pipelines which is parallel with fault line (figure 1a), SBW absorbs the deformation resulted from any possible reverse fault rupture and mitigates the damages caused to pipelines cross section (figure 2). More details about the performance of SBW in reverse fault rupture are shown in [8], [9].

In this paper, the effect of using SBW on buried pipelines crossing fault line in normal orientation (Figure 1b) in investigated.

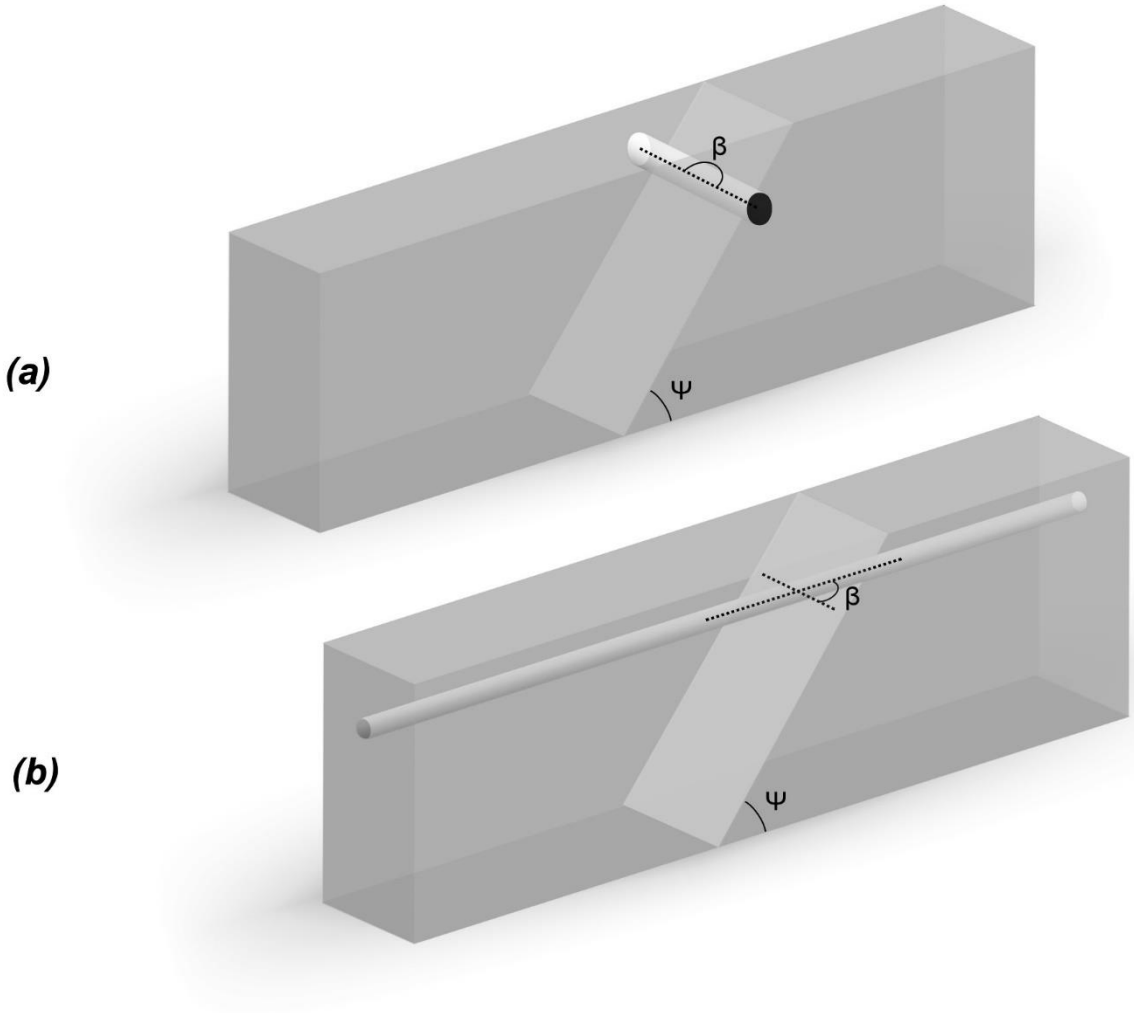


Figure 1. a schematic view of fault's angle ($\psi$) and pipeline crossing angle with fault line (β). a) Pipeline parallel to fault line (β =180). b) Pipeline perpendicular to pipeline ($\beta = 90$)

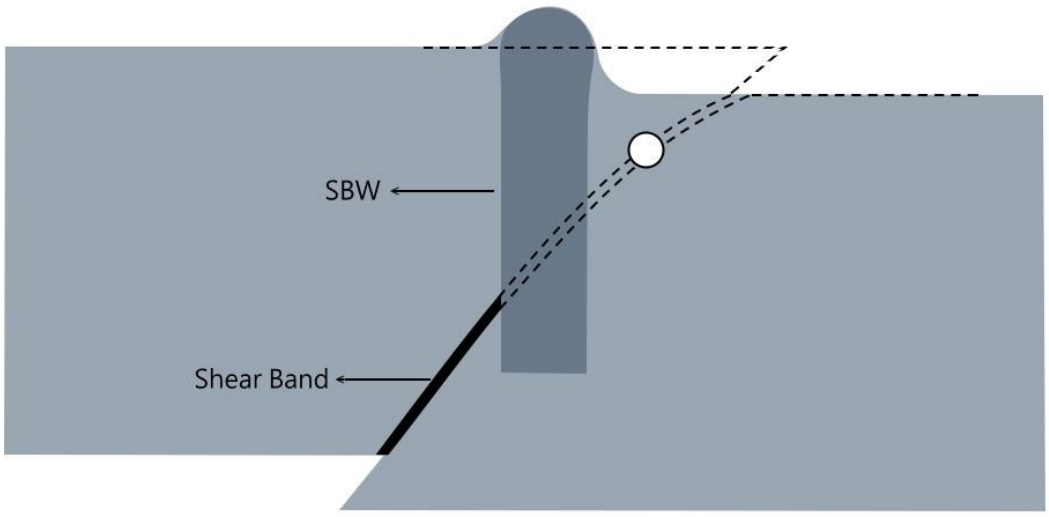


Figure 2. a schematic view of SBW performance in case of reverse fault rupture

## 2 NUMERICAL MODELING

A steel continuous buried pipeline was subjected to reverse fault rupture in two forms: a) Pipeline parallel to fault line (figure 3). b) pipeline perpendicular to fault line (figure 4). To do so, the finite element (FE) method was employed for numerical simulation of the problem. Apart from some limits in exact simulation of shear band formation, FE modeling has been shown to be able of competently reproducing fault rupture propagation in the free field [10], as well as under shallow and deep foundations [11], and pipelines. An essential prerequisite is the usage of a refined mesh and appropriate constitutive model for soil. Based on the findings of previous studies [10], an elastoplastic constitutive model with Mohr Coulomb failure criterion and isotropic strain softening are selected. the details of constitutive soil model are shown in [10].

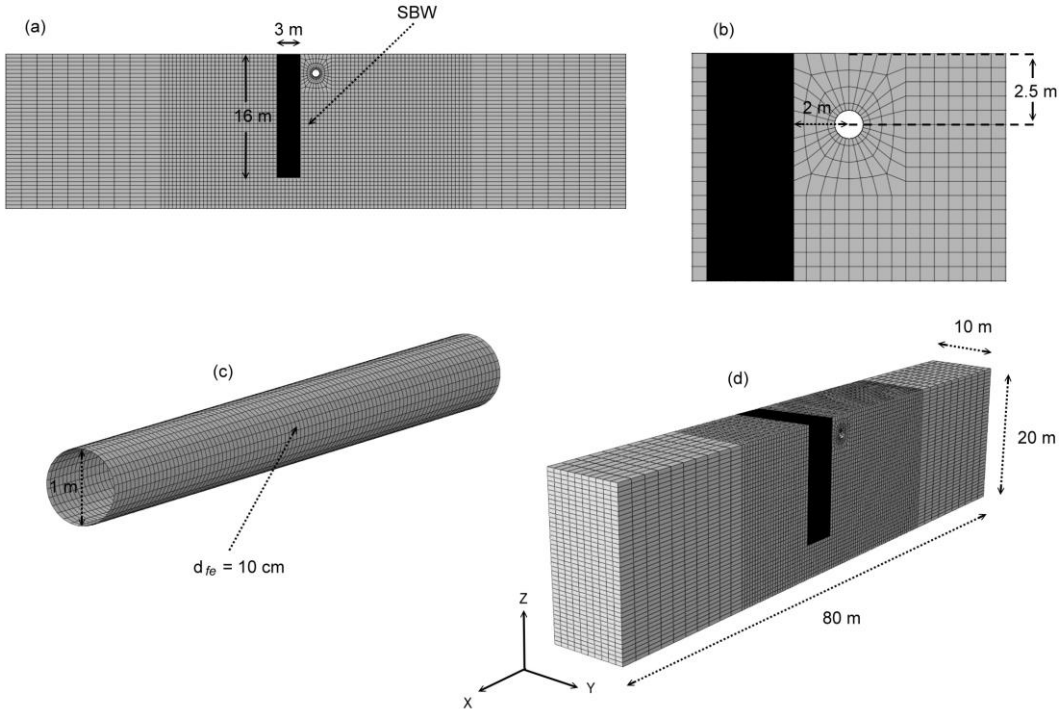


Figure 3. Details of FE model in parallel case a) The location of soil bentonite wall b) Pipe's burial depth and distance of SBW to pipe c) Details of pipe mesh d) Dimensions of soil blocks

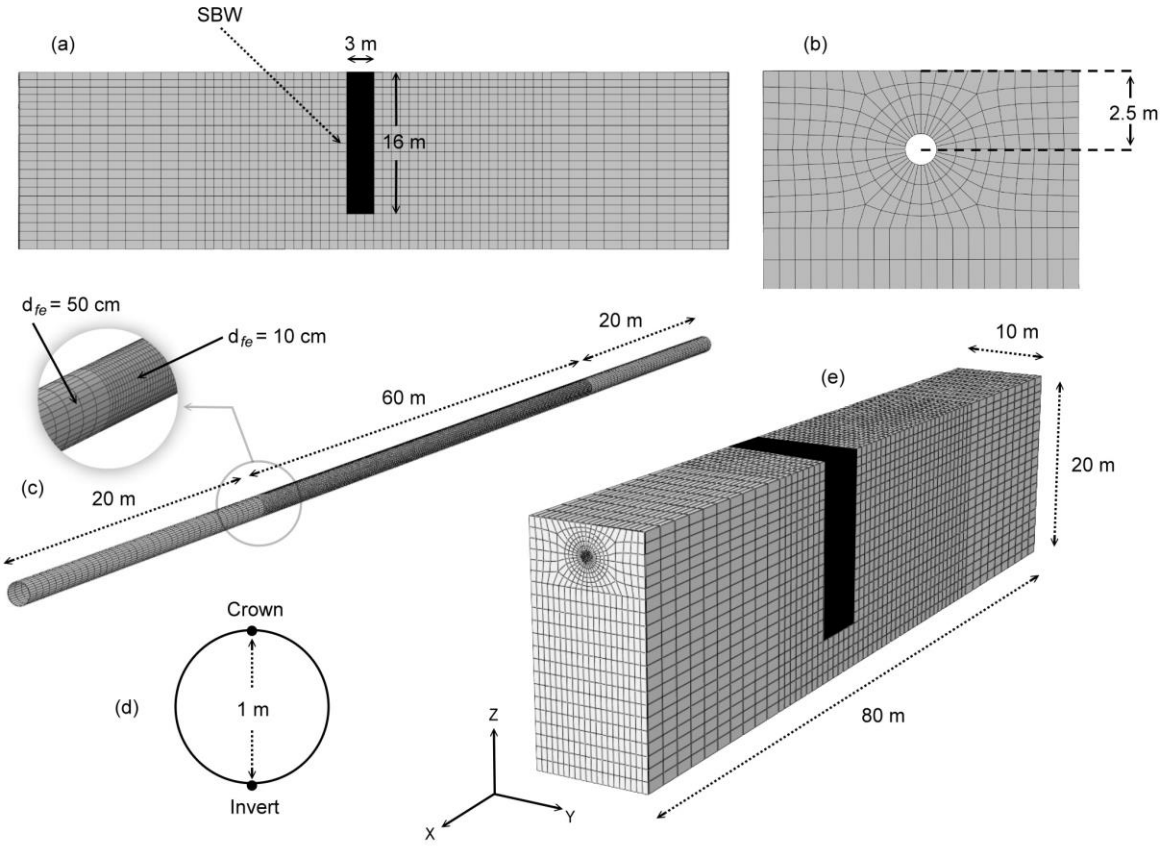


Figure 4. Details of FE model in perpendicular mode a) The location of soil bentonite wall b) Pipe's burial depth and distance of SBW to pipe c) Details of pipe mesh d) Dimensions of soil blocks

Dense sand was used in this research which was calibrated and verified in previous research [9]. Table 1 shows the soil property.

| | |
|---|---|
| E (first layer, kPa) | 12000 |
| E (last layer, kPa) | 50000 |
| $\emptyset_p$ | 42 |
| $\emptyset_{res}$ | 32 |
| $\psi_p$ | 12 |
| $\psi_{res}$ | 1 |
| $\gamma_f$ | 0.165 |
| $\rho$ (t/$m^3$) | 1.8 |

Table 1- summary of soil property

Elastoplastic behavior for pipe was considered too. The pipe which used was constructed from API/5L X65 which is commonly used in oil and gas industries. A large-strain $J_2$ flow (von Mises) plasticity model with isotropic hardening is employed for describing the mechanical behavior of the steel pipe material.

Figure 4 shows the stress-strain curve obtained from uniaxial tensile test done by Vazouras et al [13].

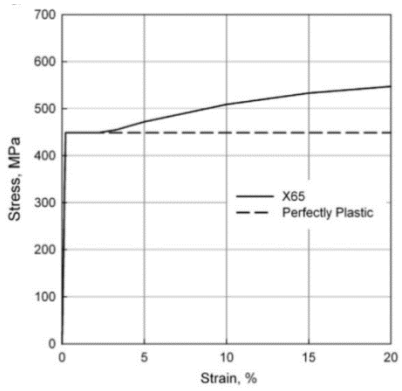


Figure 4. Uniaxial nominal stress-engineering strain curve, APL-5L-X65 [13]

Soil block dimension as shown in figure 3&4 was chosen as below:

depth of 20 meters, length of 80 meters and the width of the model, based on the sensitive analysis was considered as 10 meters.

A burial depth of 2.5 meters was chosen for steel pipe. For modeling of pipeline, four–node reduced-integration shell elements (type S4R) was used in order to observe the wrinkle, local buckling and ovalization of pipe's cross-section, whereas eight-node reduced-integration "brick" elements (C3D8R) was used for simulation of surrounding soil.

The dimension of soil mesh was also considered equal to $d_{FE}$=1 based on the recommendations of Anastasopoulos in the rupture area [10]. The dimensions of SBW and its distance from pipe (for parallel mode) was chosen equal to 3, 16 and 2 meters for width, depth and distance from pipe, respectively based on sensitive analysis.

A contact algorithm was considered to simulate the interface between the outer surface of the steel pipe and the surrounding soil. To this end, interface friction was taken into account for the algorithm, using a coulomb friction criterion and also allows for the separation of the soil medium and pipe surface. According to Yimsiri et al [14], The friction coefficient, μ ,was computed based on the reduced interface friction angle between the soil and the pipe equal to 2/3∅, which ∅ is soil internal friction. So based on given soil property is table 1, for the selected soil, μ, was set to 0.52.

The analysis was conducted in two consecutive steps:

a) Application of gravity loading to simulate the initial stress state in the soil
b) Application of reverse faulting motion

The bottom boundary of the model represents the interface between the soil and the underlying bedrock. Therefore, it was divided in two parts, one on the right representing the footwall which remains motionless, and the other on the left been subjected to the tectonic movement of the hanging wall.

## 3 MODELLING RESULTS

### 3.1 Pipeline parallel to fault line

In this section, by using expressed numerical modeling, at first, the effects of reverse fault rupture in the angles of $\psi = 30°$ and $\psi = 45°$ on buried pipelines in parallel case without using SBW is investigated. Then, the effects of using SBW in reducing damages caused to pipeline is examined. For this purpose, several analysis with different fault line distance from pipeline in both angles of $\psi = 30°$ and $\psi = 45°$ performed and the most critical ones selected. These sensitive analyses showed that the most critical situation happens when the shear band formed in soil due to fault movement, is passed from pipe cross section. In fact,

pipe section is placed between footwall and hanging wall. Figure 5 shows a schematic view of critical situation.

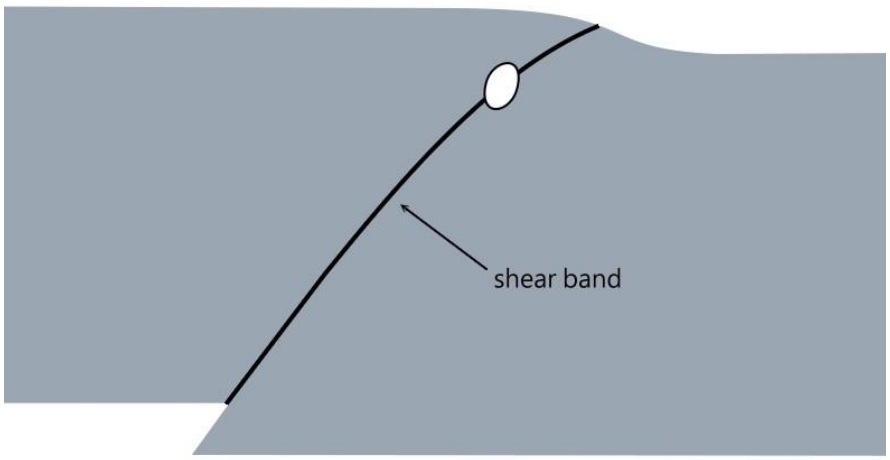


Figure 5. schematic view of critical condition of pipeline parallel to reverse fault rupture.

The factor of ovalization and pipe movement is also investigated. The ovalization of pipe section is of great importance from the standpoint of performance reduction. Moreover, in gas pipeline which is undergone inside pressure, this ovilization can lead to severe dangers. Finally, the influence of SBW in fault rupture deviation and its effects on pipeline movements is examined.

### 3.1.1 Pipe strains

The figure 6 and 7 compares the maximum compressive and tensile strains in pipe cross section under the fault angles of 30° & 45° in two modes of with SBW and without SBW. It can be clearly seen that with using SBW, pipe's strains are remarkably decreased. A closer look at these two figures shows that using SBW can reduce tensile and compressive strains up to 90%.

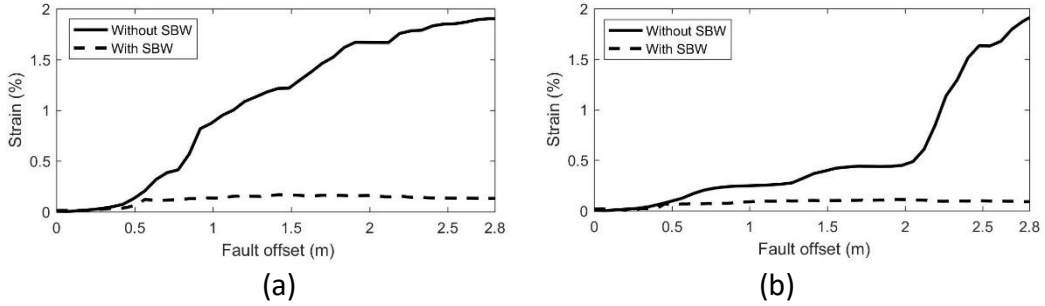


Figure 6. comparison of maximum compressive strains. A) $\psi = 45°$ B) $\psi = 30°$

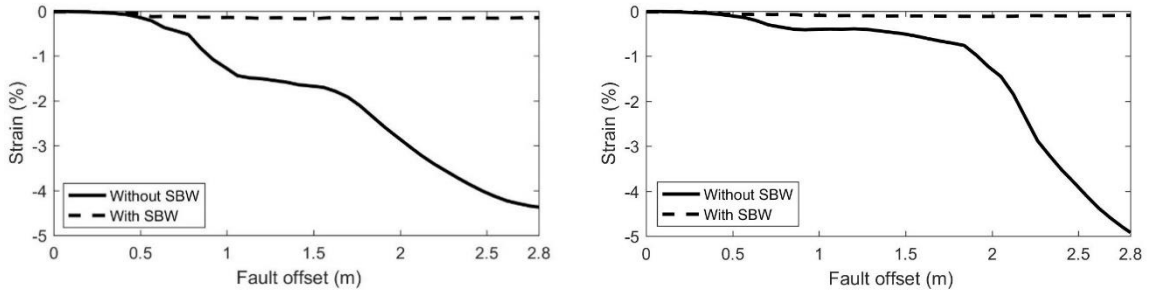


Figure 7. comparison of maximum tensile strains. A) $\psi = 45°$ B) $\psi = 30°$

### 3.1.2 Pipe's cross-Section deformations

As pipes are modeled by using shell elements of S4R, the pipe's cross-section deformations can be seen. Also, factor of ovality which is defined in Eq. (1), [15] as a representation of the degree of distortion of pipe's cross-section can be monitored. $f_o$, $D_{max}$, $D_{min}$ are factor of ovality, maximum diameter and minimum diameter of pipe cross section, respectively.

$$f_o = \frac{D_{max} - D_{min}}{D_{max} + D_{min}} \quad (1)$$

Figure 8 shows the changes of $f_o$ by increasing fault offset for the fault angles of 30° and 45°, respectively in two modes of with and without SBW.

As it is expected, using SBW has remarkable effects on the reduce of pipe's cross-section ovalization. The precise investigation shows that using SBW can lead to reduction of up to 90% in factor of ovality.

Figure 9 shows deformed shape of pipe cross-section for two modes of with and without SBW after 2.8m fault offset for fault angles of 45° & 30°. The results indicate that using SBW is hugely effective in preventing pipe cross-section deforming.

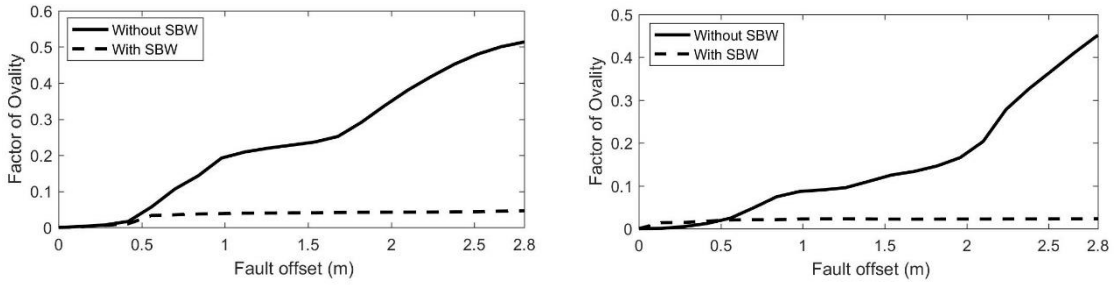


Figure 8. changes of $f_o$ A) $\psi = 45°$ B) $\psi = 30°$

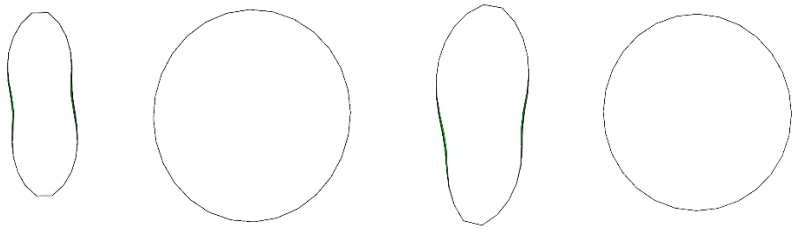

(a) (b) (c) (d

Figure 9. pipe cross-section deformation at 2.8 m fault offset. a) Without SBW, $\psi = 45°$ b) With SBW, $\psi = 45°$ c) Without SBW, $\psi = 30°$ d) With SBW, $\psi = 30°$

### 3.1.3 Pipe movements

As discussed earlier, in parallel form, critical situation happens when the pipeline placed between hanging wall and footwall (figure 5). So the pipeline movement in the direction of soil movement is inevitable. These movements can lead to some issues in pipe joints and welds as a result of fault offsets.

Figure 10 shows the pipe movements for different fault offsets for two fault angles of 30° and 45°. In $\psi$ =30°, until the fault offset of 0.5m, the movement of pipeline with and without SBW is approximately equal, but after 0.5m fault offset, pipe movements increases with an almost constant trend without using SBW and in the fault offset of 2.8m, pipe moves 1.8 m. While by using SBW, the pipe almost remains stable. For comparison, at 2.8 m fault offset, pipe movement reaches 0.4m which is less than 25% of pipe movement without using SBW.

The trend is almost the same For $\psi$ =45°.

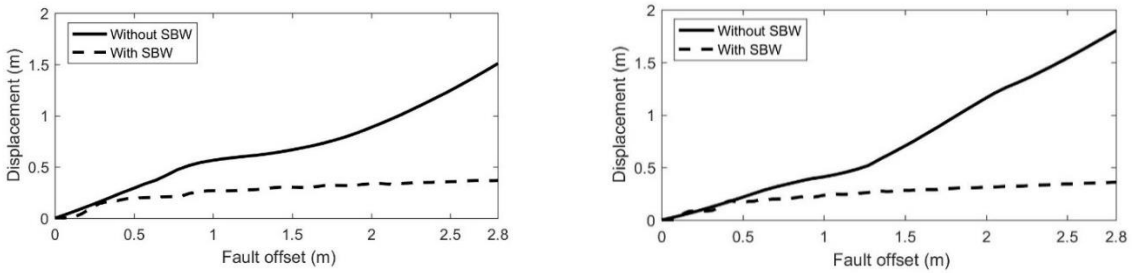


(a) (b)

Figure 10. Pipeline movement: A) $\psi = 45°$ B) $\psi = 30°$

## 3.2 Pipeline perpendicular to fault line

In this section, another case is investigated where the pipe crosses fault line perpendicularly (figure 4). In this case the fault angle is considered to be 45°. SBW with the same dimensions is used. In order to investigate the effect of SBW, like previous case, at first, a model without SBW is subjected to reverse fault rupture and then, the response of pipeline with SBW wall which is placed in fault dispersion path (X=37 to X=40) compares to each other.

### 3.2.1 Localizing pipe damages

Figure 11 shows the location of pipe strains along the pipe length for different fault movements away from the wall. As can be seen, the location of pipe damages is localized in

2m from left side of the SBW to 3m from right side of the SBW for various fault lines away from the SBW.

So considering existing uncertainties in the exact determination of fault line location and Regarding the fact that the SBW absorbs deformations of reverse fault rupture, with using SBW, the location of damages subjected to pipeline can be localized in a small area around the SBW. So that in case of reverse fault rupture on buried pipelines and subsequent damages (like pipe rupture and leakage which is inevitable in large fault offsets), the process of repair and return of pipeline to service can be done more rapidly. It should be noted that in case of not using SBW, the location of pipe damages is not clear and it may cause delays in repairing the pipeline.

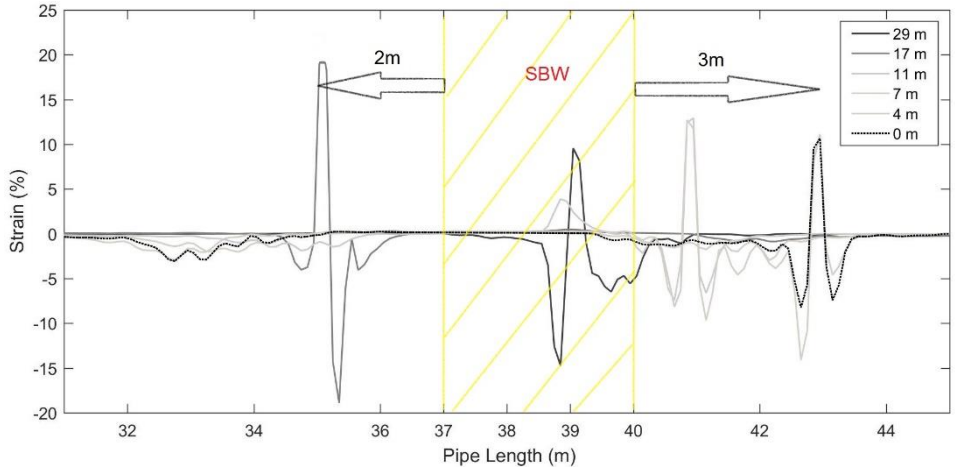


Figure 11. Location of crown strains for different fault lines away from SBW

## 4 CONCLUSION

In this research, the effect of using soil bentonite wall (SBW) on damage mitigation caused to pipeline subjected to reverse fault rupture in two cases of pipeline parallel to fault line and pipeline perpendicular to fault line by using 3D FE method is investigated. The analyses are carried out on dense sand and steel pipeline. The results are as follows:

1- In parallel case, using SBW with the dimensions of 3*16m distanced 2m away from pipe center, can remarkably reduce damages when subjected to reverse fault rupture. The results of investigation show that using SBW with mentioned dimension, after low fault offset (0.5m) with fault angles 30° and 45°, the pipe cross-section strains, factor of ovality and pipe movements remains minor and constant throw different fault offsets. The comparison of pipeline responses with and without using SBW indicates the reduction of up to 90% in pipe strains and factor of ovality and up to 70% reduction in pipe movements with/ using SBW.

2- Comparison of pipe responses with two fault angles of 30° and 45° shows with using of SBW, the effect of fault angle eliminates and the pipe responses remains the same.

3- For perpendicular case, with a matter of fact that SBW absorbs the deformation of reverse fault rupture and inevitable severe pipe damages subjected to large reverse fault offsets, using SBW can confine the area of damages subjected to pipeline in a small zone around the SBW. So in case of earthquake and subsequent reverse fault rupture, the location of pipe which needs to be repaired is obvious. This is of great importance in terms of quick repair and service of pipeline as lifelines.

## REFERENCES


[1] O'Rourke, M.J., and Liu, X. (2012). "Seismic Design of Buried and Offshore Pipelines," Monograph MCEER12-MN04, Buffalo, N.Y., USA.

[2] Towhata I. Geotechnical earthquake engineering. Springer series in geomechanics and geoengineering. 2010. p. 684.

[3] O'Rourke TD, Palmer MC. Earthquake performance of gas transmission pipelines. Earthq Spectra 1996;12(3):493–527.

[4] Earthquake Engineering Research Institute. The Chi Chi, Taiwan earthquake of September 21, 1999. EERI special earthquake report; December 1999

[5] Japan Society of Civil Engineers. The 1999 Kocaeli earthquake, Turkey, investigation into the damage to civil engineering structures, JSCE earthquake engineering committee; December, 1999

[6] Ayala AG, O'Rourke MJ. Effects of the 1985 Michoacán Earthquake on Water Systems and Other Buried Lifelines in Mexico, NCEER-89-0009; 1989.,136 p.

[7] Joshi S, Prashant A, Deb A, Sudhir K. Jain., (2011), "Analysis of buried pipelines subjected to reverse fault motion," Soil Dynamics and Earthquake Engineering, Vol. 31, pp. 930–940

[8] Fadaee M, Anastasopoulos I, Gazetas G, Jafari M.K, Kamalian M, (2013), "Soil bentonite wall protects foundation from thrust faulting: analyses and experiment", Earthquake Engineering and Engineering Vibration, Vol.12, pp. 473-486

[9] Fadaee M, Ezzatyazdi P, Anastasopoulos I, Gazetas G, (2016), "Mitigation of reverse faulting deformation using a soil bentonite wall: Dimensional analysis, parametric study, design implications", Soil Dynamics and Earthquake Engineering, Vol. 89, pp. 248–261

[10] Anastasopoulos I, Gazetas G, Bransby F, Davies MCR and El Nahas A (2007), "Fault Rupture Propagation through Sand: Finite Element Analysis and Validation through Centrifuge Experiments," Journal of Geotechnical and Geo Environmental Engineering, ASCE, 133(8): 943−958.

[11] Anastasopoulos I, Gazetas G, Bransby MF, Davies MCR and El Nahas A (2009), "Normal Fault Rupture Interaction with Strip Foundations," Journal of Geotechnical and Geoenvironmental Engineering, ASCE, 135(3): 359–370

[12] Bray JD (1990), "The Effects of Tectonic Movements on Stresses and Deformations in Earth Embankments," PhD Dissertation, University of California, Berkeley.

[13] Vazouras P, Karamanos SA, Dakoulas P. (2010) "Finite element analysis of buried steel pipelines under strike-slip fault displacements," Soil Dynamics and Earthquake Engineering,30 (11):1361–76.

[14] Yimsiri S, Soga K, Yoshiaki K, Dasari GR, O'Rourke TD. "Lateral and upward soil–pipeline interactions in sand for deep embedment conditions," J Geotech Geoenviron Eng 2003;130(8):830–41

[15] Hojat Jalali H, Rahimzadeh Rofooei F, Attari NKA, Samadian M. (2016), "Experimental and finite element study of the reverse faulting effects on buried

continuous steel gas pipelines," Soil Dynamics and Earthquake Engineering, Vol.86, pp.1-14

COMPDYN 2017
6th ECCOMAS Thematic Conference on
Computational Methods in Structural Dynamics and Earthquake Engineering
M. Papadrakakis, M. Fragiadakis (eds.)
Rhodes Island, Greece, 15–17 June 2017

# GENERATING ARTIFICIAL TIME HISTORIES USING A NEW COMPUTER-BASED ENVIRONMENTAL PLATFORM: OPENSIGNAL

**Marco Baglio[1], Sebastiano Marasco[2], Gian Paolo Cimellaro[1]**

[1] Department of Structural, Geotechnical & Building Engineering (DISEG),
Politecnico di Torino, ITALY
e-mail: gianpaolo.cimellaro@polito.it

[2] Department of Structural, Geotechnical & Building Engineering (DISEG),
Politecnico di Torino, ITALY
e-mail: sebastiano.marasco@studenti.polito.it

**Keywords:** Conditional mean Spectrum, Signal Processing, synthetic ground motions, artificial ground motions.

**Abstract.** *The paper is presenting a new artificial time-histories generation model which uses spectrum compatible time-histories, created using a new envelope function that can be used in regions characterized by subduction earthquakes with long duration period and paucity of earthquake records data. The method has been implemented in a new computer-based platform for ground motion processing and selection. The platform is organized into three main modules as follows: Signal Processing is designed for data processing; it allows to open raw data downloaded from main databases all over the world acquiring the principal seismic parameters. Seismic Records Selection evaluates a set of spectra or time-histories data. Various attenuation laws and correlation models are implemented to compute the Conditional Mean Spectrum and the Predicted Mean Spectrum. Real time-histories can be selected and downloaded by PEER and ESMD databases using waveform matching, spectrum matching or energetic methods. A physics-based stochastic model is implemented for the generation of synthetic time-histories as well as a wavelet-based stochastic models for artificial time-histories. Site Response Analysis concerns modelling the local site effects of the ground motion propagation using a hybrid approach based on an equivalent linear model. The soil behavior is modeled assuming that both shear modulus and damping ratio vary with shear strain amplitude. Hence, the hysteretic behavior of the soil is described using the shear modulus degradation and damping ratio curves.*

## 1 INTRODUCTION

The exponential increment of computational power is progressively moving the state-of-practice in earthquake engineering toward the use of dynamic non-linear time history analysis with respect to response spectrum analysis. All these methods need as prerequisite the selection of a proper suite of earthquake ground motions to be reliable. In fact, among all possible sources of uncertainty (e.g., structural material properties, modelling approximations, design and analysis assumptions, etc.), the selection of earthquake ground motion has the highest effect on the variability of the structural response [1] [2] . Two selection criteria are mainly used for such aim: (i) researches based on parameters obtained by disaggregated seismic hazard maps at a specific site, such as the magnitude, $M$, and the source-to-site distance, $R$, the soil type, $V_{s30}$, the source mechanism and the duration, (ii) researches based on spectral matching , such as design code spectrum (DS), seismic scenario determined from a ground motion prediction relationship (PMS) [3], uniform hazard spectrum (UHS), and conditional mean spectrum (CMS) [4]. Using DS and UHS might bring to over-softening and overdamping during the analysis [5]; therefore, a matching procedure based on the CMS has been developed and presented for the Italian territory in this paper. The lack of real records in several areas of the world leads to cases studies where is necessary resorting to artificial or synthetic time-histories. Three methods have been implemented: according to the grade of knowledge, records can be generated starting from (i) the target spectrum, (ii) the seismic parameters ($M$, $R$, $V_{s30}$), (iii) the geometric spreading and $Q$ function. The local seismic response has been modelled using an equivalent linear model, assuming that both the shear modulus and the damping ratio vary with the shear strain amplitude. So, the hysteretic behaviour of the soil is described using the shear modulus degradation and damping ratio curves. A large number of computer programs, public and commercial, are available at the Observatories and Research Facilities for European Seismology (ORFEUS) data center1, such as SMARTS 2.0, Shake-91, DIMAS, and PickEv 2000, and at the Pacific Earthquake Engineering research center2, such as SIMQKE-I and SIMQKE-II. Most of existing public signal processing software are developed to analyse a single seismic earthquake record at a time (e.g., Seismosignal – available at http://seismosof.com/or view wave available at http://iisee.kenken.go.jp/staff/kashima/viewwave.html). For multiple records analysis, commercial software are needed, such as Bispec [5], but they have the inconvenient that they are not freely available in the market. Iervolino et al. [6] developed a Matlab-based software called REXEL, which allows ground motion selection using the Italian database, Itaca [7]; however, the proposed software is not able to perform multiple signal processing and it is not able to build the CMS on the Italian territory automatically, by using as input the GIS coordinates. Similar software have also been developed by Corigliano et al. [8] who implement a software called ASCONA for the selection of compatible natural ground motions. Recently, also Katsanos and Sextos [9] developed a Matlab-based software environment integrating finite element analysis with earthquake records selection which works with the PEER database. The presented platform includes many features, which are not available in the programs mentioned above: signal processing, soil response analysis, the computation of the Conditional Mean Spectra. This paper presents the application of CMS in a classic power spectrum-based model with the innovation of random envelope functions in order to generate spectrum-compatible ground motions. The method has been applied in a software called OPENSIGNAL [10] for processing and selection of seismic records, freely available at the following link:

http://areeweb.polito.it/ricerca/ICRED/Software/OpenSignal.php

## 2 SIGNAL PROCESSING

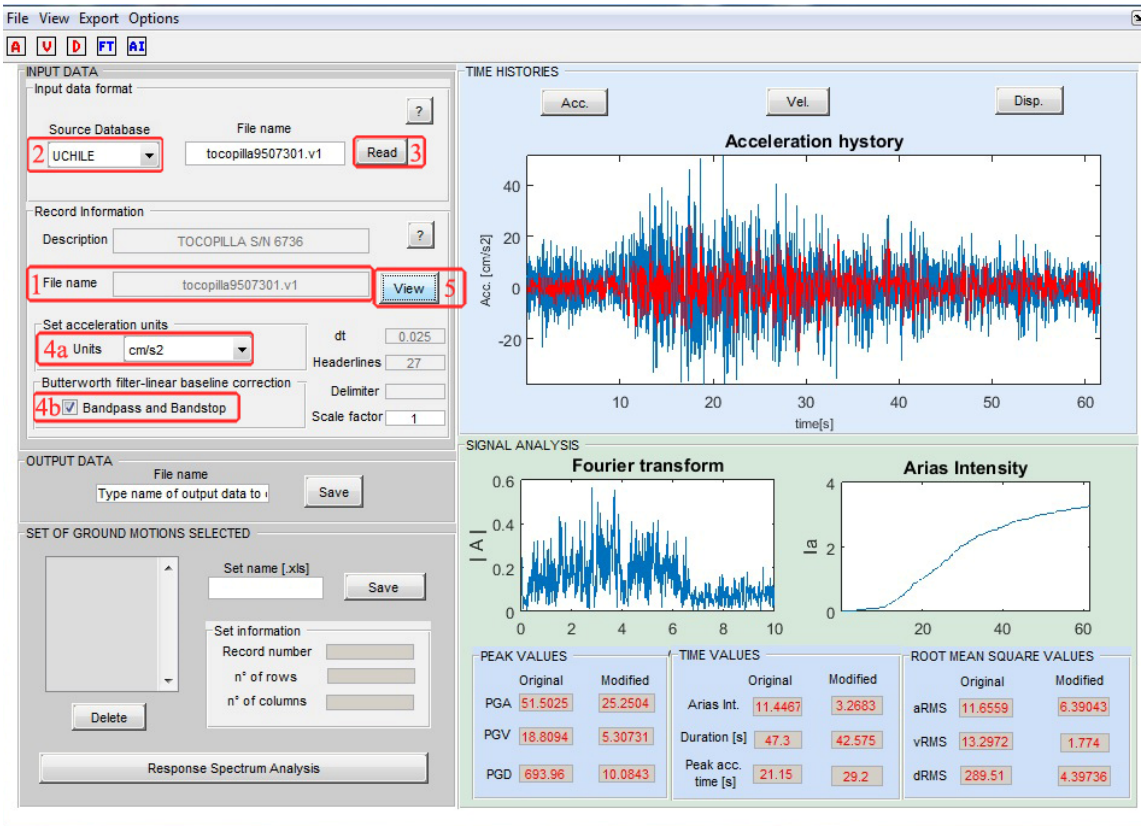


Figure 1 Signal Processing window.

Many ground motion parameters, such as peak displacements and velocities, are used often in different field of earthquake and geotechnical engineering [11]; however, their values are affected by the noise of the earthquake ground motion. The influence of noise in ground motion records is evident at low and high frequencies where the signal-to-noise ratio is usually lower compared to the mid spectrum. Then, filtering operations became the primary tool for correcting the ground motion records and consequentially it has become standard practice to cut low and high frequencies by looking at the spectra of the Fourier amplitude spectra and the signal-to-noise ratio. The Butterworth filter is the most used in seismic applications and it is designed to have a flat frequency response in the pass-band range, while it is equal to 0 in the stop-band range. Analytically, the frequency response amplitude of the Butterworth filter is given by

$$|H(\omega)| = \frac{1}{\sqrt{1+\left(\frac{\omega}{\omega_c}\right)^{2N}}} \tag{1}$$

where $\omega$ is the generic angular frequency, $\omega_c$ represents the cut-off frequency, and $N$ is the order of the filter. The source of this error as mentioned above, is generated by the high and low frequency noise which contaminates the signal. Baseline corrections can be applied using different techniques, in the time domain to remove unwanted trends and in the frequency domain to remove unwanted frequencies. In the frequency domain, the noise is most easily removed by the use of a bandpass filter, like the low-pass filter which is set up to values <0.1.

In addition, the effect of aliasing can be eliminated by filtering the original ground motion beyond the Nyquist frequency (12.5 Hz). In most of the databases, ground motion records are already filtered, but there might be cases in which some records are unfiltered and in that case, the filtering option in the environmental platform can be used. **Error! Reference source not found.** shows *Signal Processing* window of computer environment. The number identifies the steps to be followed in order to obtain a correct processing procedure and they are summarized below:

1. Import the record with "Open" or insert the name.dat of the file.
2. Select the correct database.
3. Push "Read" for reading the file and extracting of the main information.

4a. Select the measure units for the accelerations.

4b. Tip the "Bandpass and Bandstop" for filtering the signal.

5. Push "View" for loading the acceleration history and plotting the signal properties and the time histories.

In the *Input Data Format* (upper left), the records are uploaded and read automatically for the selected ground motion databases (PEER, ESMD, UCHILE and ITACA) or using the option "free format." The Butterworth filter by modifying can be set according to minimum frequency, $f_{min}$, maximum frequency, $f_{max}$, and order, $n$. The effect of the filter is shown in *Time Histories* panel where the time histories of accelerations, velocities, and displacements, both filtered and unfiltered are displayed. In the *Signal Analysis* block (low right corner in Figure 1), the main parameters of earthquake records (e.g., peak ground acceleration, velocity and displacement, duration, etc.) both peak and root mean square values are calculated and saved both for filtered and unfiltered data; Arias Intensity and Fourier Transform graphs are plotted in specific frames . Finally, all processed data and records can be exported in other common formats, such as MS Excel and txt (bottom left in Figure 1).

### 2.1 Response Spectral Analysis

Once the set of ground motions are selected and filtered, the Elastic Response Spectra (acceleration, velocity, displacement, etc.) can be computed for a given value of damping ratio. Furthermore, the mean and median acceleration response spectra of the uploaded set of records with the associated range of dispersion ($\pm\sigma$) can be also evaluated and plotted using also log and semi-log scales.

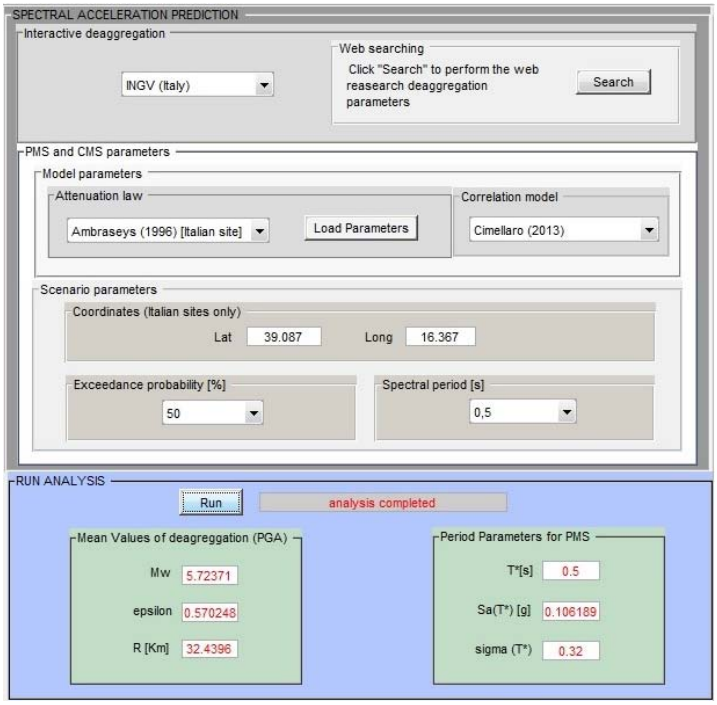


Figure 2 Computation of CMS in Italian territory; scenario parameters panel allows its computation according to GIS coordinates. CMS for other countries is available with several attenuation laws and correlational models [12][21].

## 3 TARGET SPECTRA

Different types of target spectrum can be defined during the ground motion selection process. The design spectrum (*DS*) can be evaluated according to the Italian seismic standards, the NTC 2008 [13] for any point in the Italian territory, once the parameters are defined (e.g., nominal life, soil category, damping ratio, over strength factor q to describe the inelastic behaviour, etc.). Additionally, the *DS* according to the European seismic standard, EC8 [14], and to the US standards [15] can be evaluated inserting the proper parameters. Furthermore, the platform allows evaluating for a given probability of exceedance the *UHS*, and the Predicted Mean Spectrum (*PMS*) using different ground motion prediction equations (GMPE), which are currently available: Ambraseys et al., Campbell and Bozorgnia, Boore and Atkinson, and Chiou and Youngs [3][16][17][18]. Two additional attenuation laws have been recently inserted to define the *CMS* for Chilean sites [19] and the Regional Indian attenuation equations for Indian sites [20]. However, the novelty of the proposed system architecture is that it allows evaluating the CMS [21][22] for the first time on the entire Italian territory automatically knowing the GIS coordinates (Figure 2) and in any other site worldwide knowing the proper parameters.

## 4 REAL TIME-HISTORIES SELECTION

Ground motion selection and scaling procedures are applied in order to obtain a set of motions that are usually used in dynamic elastic and even non-linear response history analysis. The proposed framework retrieves records from the PEER-NGA strong motion database (PEER – available at http://ngawest2.berkeley.edu/), the European strong motion database (ESMD – available at http://www.isesd.hi.is/ESD_Local/frameset.htm). Three selection criteria are available: Waveform Matching, Spectral Matching, Energetic criteria.

Waveform Matching can be obtained selecting some specific seismological parameters obtained by the disaggregated seismic hazard maps at a specific site, such as the moment magnitude, Mw, the fault distance or Joyner–Boor distance (R or RJB, expressed in kilometer), the fault mechanism, the soil type according to EC8, and the waveform parameters (e.g., peak ground acceleration, peak ground velocity, peak ground displacement).

Spectral Matching requires an additional step, the definition of the target spectrum and the type of matching to be carried out. The current available options in the platform are three: (i) Single period, (ii) Multi periods (up to three values), and (iii) Mean Deviation. A selected percentage error is defined in all cases to vary the number of earthquakes selected. The second step is the selection of the Target Spectrum among the CMS, the DS, the UHS, the PMS, or any User Defined (UDS) response spectrum. After the selection of the target spectrum, the search of the records between the ground motion databases available in the computer environment is performed. Both horizontal and vertical components of ground motion can be considered in both research methods. Spectrum-compatible records can be located among the last research on Waveform matching.

## 5 SYNTHETIC TIME-HISTORIES SELECTION

The combination of seismological models of the spectral amplitude of ground motion with the engineering notion that high-frequency motions are basically random [23] is the basis of *SMSIM* code. Following the generic formulation proposed in [23], the total spectrum of the motion at a site can be divided into contributions from earthquake source ($E$), path ($P$), site ($G$) and type of motion ($I$):

$$Y(M_0, R, f) = E(M_0, f)P(R, f)G(f)I(f) \tag{2}$$

Referring to [23] for detailed information about the meaning and formulation of each contribute, Figure 3 illustrates the window of selection of input parameters. Beta is the shear-wave velocity in the vicinity of the source. Geometric spreading is represented by three linear segment, described by three slopes and two points in common. Spectrum control is controlled by the choice of source type (single or double corner), Sigma is the stress drop related to the magnitude Mr and Mf the derivate of log(sigma) with respect to magnitude, fb/fa is the ratio between corner frequencies. The whole path-attenuation is given by a piecewise continuous set of three straight lines in log Q and log f space (s1 and s2 are the slopes of first and third lines that have values Qr1 and Qr2 at frequencies fr1 and fr2, ft1 and ft2 are the transition frequencies). Wfa and Wfb defines the weight of fa and fb concerning the source duration. The diminution factors regard the application of a filter. Parameters for Western North America and Eastern North America are uploaded and available by default. The site amplification is fixed with a generic formulation for generic rock site. An arbitrary number of independent Time-histories can be generated; for each time-history, several parameters are computed and displayed (e.g. velocity, displacement, Fourier amplitude, Arias intensity).

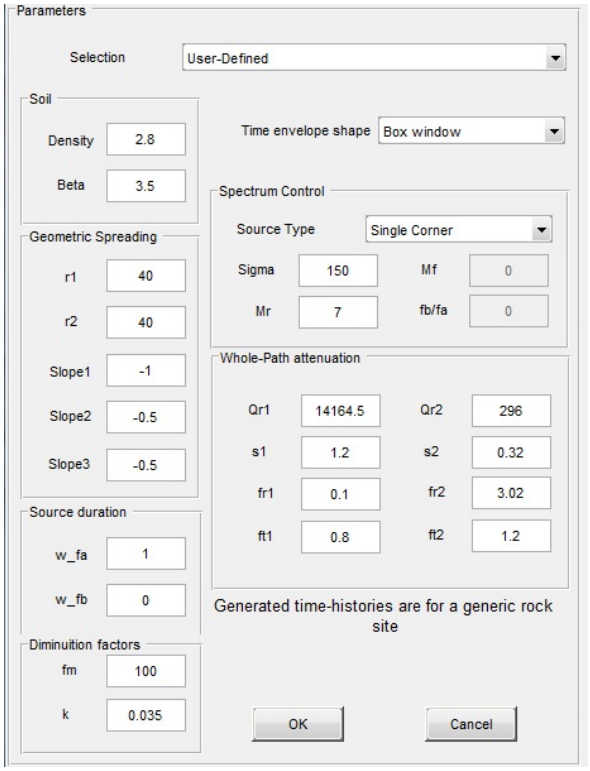


Figure 3 Required parameters for generation of synthetic time-histories.

## 6 ARTIFICIAL TIME-HISTORIES SELECTION

### 6.1 Wavelet-based method

The decomposition of ground motion time-histories into wavelet packets and the reconstruction of time-histories from wavelet packets has been applied in the creation of a stochastic ground-motion model [24]. The wavelet packet is defined as

$$c_{j,k}^{i} = \int_{-\infty}^{\infty} x(t)\psi_{j,k}^{i}(t)dt \tag{3}$$

The inverse wavelet packet is

$$x(t) = \sum_{i=1}^{2^j} \sum_{k=1}^{2^{N-j}} c_{j,k}^{i}\, \psi_{j,k}^{i}(t) \tag{4}$$

Employing two groups of wavelet packets, 13 parameters quantify time and frequency characteristics of the acceleration time histories. Such parameters are predicted as a function of

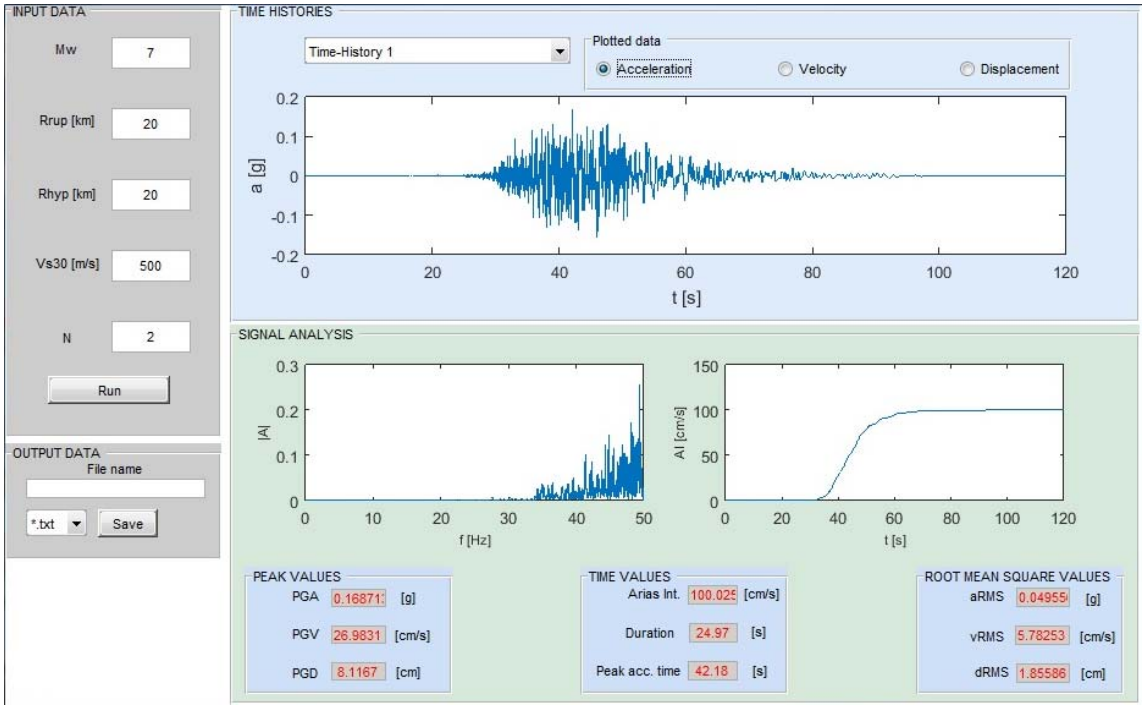


Figure 4 Window of generation of artificial time-histories. Synthetic time-histories share a coincident layout with few differences in the INPUT DATA panel.

four predictor variables: the moment magnitude (Mw), the hypocentral distance (Rhyp), rupture distance (Rrup), and average shear-wave velocity within 30 m depth (VS30). In turn, the predictor variables are obtained by a two-stage regression analysis. In Yamamoto [24] it has been proposed a range of values that provides a good match from the GMPEs; those values are reported and recommended inside the code. As in synthetic time-histories, the generation of independent time-histories is unlimited and the signal processing is analogous (Figure 4).

### 6.2 Power spectral density based method

Spectrum-compatible ground motions are generated by the power spectral density PSD, which is related to a target spectrum [25]:

$$PSD(\omega_n) = \frac{1}{\omega_n\left(\frac{\pi}{4\varsigma} - 1\right)}\left(\frac{\omega_n^2 S_V^2}{r_{s,p}^2} - \int_0^{\omega_n} PSD(\omega_n)d\omega\right)^{1/2} \tag{5}$$

where $\omega_n$ is the natural pulse, $r_{s,p}$ is the peak factor for a ground motion of duration $s$ and probability $p$, $\varsigma$ is the damping factor. Referring to [25] for detailed information about the formulation of peak factor, PSD can be used for generation of stationary time-histories:

$$A_n(\omega_n) = \sqrt{2PSD(\omega_n)\Delta\omega} \tag{6}$$

$$z(t) = \sum_n A_n \sin(\omega_n t + \phi_n) \tag{7}$$

A stationary ground motion is obtained by summing several sine functions with a random phase $\phi_n$, which provides independence among several generated ground motions. Non-

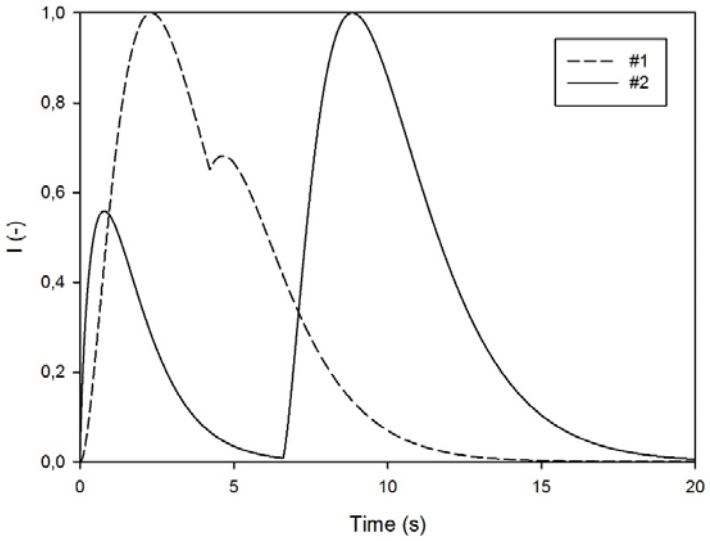


Figure 5 Two examples of implemented random envelope functions. They are generated by random shifting and scaling the second curve in a selected range and overall scaling of the whole function.

stationarity is achieved by an envelope function *I(t)* multiplied for the stationary time-history. The novelty of the procedure is a code generating envelope functions (Figure 5) from overlapping two or more Saragoni and Hart functions [26] in order to taking into account the random shape of real ground motions. A process of iterative adjustment improves the spectral matching by

$$PSD(\omega_n)^{i+1} = PSD(\omega_n)^i \left(\frac{S_V}{S_V^i}\right)^2 \tag{8}$$

Such procedure is implemented into the software by selecting the target among the available spectra with a signal-processing equal to other synthetic and artificial models, providing a useful tool for generating realistic spectrum-compatible time-histories (e.g. regions with undersized source databases).

## 7 SITE RESPONSE ANALYSIS

The proposed method uses an equivalent linear model (hybrid approach), which describes the soil behavior assuming that both the shear modulus and the damping ratio vary with the shear strain amplitude. Therefore, the hysteretic behavior of the soil is described using the shear modulus degradation curve (G - γ) and the damping ratio curve (ξ - γ). In the proposed platform, clay, sand, and rock degradation curves are available by default [27].

The dynamic equations of the system:

$$[M]\{\ddot{u}\} + [C]\{\dot{u}\} + [K]\{u\} = -[M]\{I\}\ddot{u}_g \tag{9}$$

(9)(10) is solved using Newmark method:

$$\dot{u}_{i+1} = \dot{u}_i + [(1-\gamma)\Delta t]\ddot{u}_i + (\gamma\Delta t)\ddot{u}_{i+1} \tag{10}$$

$$u_{i+1} = u_i + \Delta t\dot{u}_i + \left[\left(\frac{1}{2} - \beta\right)\Delta t^2\right]\ddot{u}_i + \beta\Delta t^2\ddot{u}_{i+1} \tag{11}$$

Where [M], [C], and [K] are the mass, damping, and stiffness matrices, while $\{\ddot{u}\}$, $\{\dot{u}\}$ and $\{u\}$ are the vectors of absolute nodal accelerations, velocities, and displacements; $\Delta t$ defines the time step, $\beta$ and $\gamma$ are both assumed equal to 1/4. Evaluating the nodal displacements and the corresponding shear deformations γ at a given time instant t, the γ values are inserted in the curves to update the shear modulus G and the damping ratio ξ, which are used to define the new stiffness and damping matrices defined at the same time instant t. The proposed method has some limitation at large shear strain deformations, because in that case, the soil presents a non-linear behavior and both stiffness and damping depend on the number of loading–unloading cycles. Nevertheless, it was observed that at medium deformations, the non-linear behavior of the soil is not significantly influenced by the load path [28]. Thus, the proposed hybrid approach can lead to reliable results for the range of medium deformations.

## 8 CONCLUSION

The paper presents a new model of generation of artificial time-histories. Employing a classic method based on the analysis of the power spectrum density, an arbitrary number of independent stationarity artificial spectrum-compatible time-histories are generated.

The novelty of the method consists in two features: (i) the application of the Conditional Mean Spectrum, which leads to an improvement of the energetic content, (ii) the achievement of non-stationarity obtained by random envelope functions, which provide realistic shape to the final time-histories. The random envelope functions are created by the overlapping of two or more envelope functions and varying the shape and position of these. Such model is implemented in a software platform for processing and selection of seismic records, called "OPENSIGNAL," freely available for the public. The platform consists of a number of modules, integrated in a unified environment and aimed for: selection of ground motion records, signal processing, response spectra analysis, soil spectra analysis and generation of synthetic/artificial time-histories.

## ACKNOWLEDGEMENTS

The research leading to these results has received funding from the European Research Council under the Grant Agreement n° ERC_IDEAL RESCUE_637842 of the project IDEAL RESCUE-Integrated Design and Control of Sustainable Communities during Emergencies.

## REFERENCES

[1] Padgett, Jamie Ellen, and Reginald DesRoches. "Sensitivity of seismic response and fragility to parameter uncertainty." Journal of Structural Engineering 133.12 (2007): 1710-1718.

[2] G.P. Cimellaro, A.M. Reinhorn, A. D'Ambrisi, and M. De_Stefano. Fragility Analysis and Seismic Record Selection. *Journal of Structural Engineering, ASCE*, 137(3), 379-390, 2011

[3] Campbell, Kenneth W., and Yousef Bozorgnia. "NGA ground motion model for the geometric mean horizontal component of PGA, PGV, PGD and 5% damped linear elastic response spectra for periods ranging from 0.01 to 10 s." Earthquake Spectra 24.1 (2008): 139-171.

[4] Baker, Jack W. "Conditional mean spectrum: Tool for ground-motion selection." Journal of Structural Engineering 137.3 (2010): 322-331.

[5] Hachem, M. (2003). BISPEC Program Description and User's Manual. Available at: http://www.ce.memphis.edu/7137/PDFs/BispecHelpManual.pdf.

[6] Iervolino, I., Galasso, C., and Cosenza, E. (2010). REXEL: computer aided record selection for code-based seismic structural analysis. Bull. Earthq. Eng. 8, 339–362. doi:10.1007/s10518-009-9146-1

[7] Luzi, L., Hailemikael, S., Bindi, D., Pacor, F., Mele, F., and Sabetta, F. (2008). ITACA (ITalian ACcelerometric Archive): a web portal for the dissemination of Italian strong-motion data. Seismol. Res. Lett. 79, 716–722. doi:10.1785/gssrl.79.5.716

[8] Corigliano, M., Lai, C., Rota, M., and Strobbia, C. (2012). ASCONA: automated selection of compatible natural accelerograms. Earthq. Spectra 28, 965–987. doi:10.1193/1.4000072

[9] Katsanos, E. I., and Sextos, A. G. (2013). ISSARS: an integrated software environment for structure-specific earthquake ground motion selection. Adv. Eng. Software 58, 70–85. doi:10.1016/j.advengsof.2013.01.003.

[10] G.P. Cimellaro, and S. Marasco. A computer-based environment for processing and selection of seismic ground motion records: OPENSIGNAL. *Frontiers in Built Environment*, 1:17, 2015

[11] Boore, D. M., and Bommer, J. J. (2005). Processing of strong-motion accelerograms: needs, options and consequences. Soil Dyn. Earthq. Eng. 25, 93–115. doi:10.1016/j.soildyn.2004.10.007

[12] Cimellaro, G. P. (2013). Correlation in spectral accelerations for earthquakes in Europe. Earthq. Eng. Struct. Dyn. 42, 623–633. doi:10.1002/eqe.2248

[13] NTC-08. (2008). Nuove Norme Tecniche per le Costruzioni (NTC08) (in Italian). Gazzetta Ufciale Della Repubblica Italiana. Rome: Consiglio Superiore dei Lavori Pubblici, Ministero delle Infrastrutture, 29.

[14] CEN. (2004). Eurocode 8: Design of Structures for Earthquake Resistance Part 1: General Rules, Seismic Actions and Rules for Buildings. Brussels: European Committee for Standardization.

[15] FEMA. (2009). NEHRP Recommended Seismic Provisions for New Buildings and Other Structures. Federal Emergency Management Agency (FEMA P-750). Washington, DC: Federal Emergency Management Agency.

[16] Ambraseys, N. N., Simpson, K. A., and Bommer, J. (1996). Prediction of horizontal response spectra in Europe. Earthq. Eng. Struct. Dyn. 25, 371–400. doi:10.1002/(SICI)1096-9845(199604)25:4<401::AID-EQE551>3.0.CO;2-B

[17] Boore, D. M., and Atkinson, G. M. (2008). Ground-motion prediction equations for the average horizontal component of PGA, PGV, and 5%-damped PSA at spectral periods between 0.01 s and 10.0 s. Earthq. Spectra. 24, 99–138. doi:10.1193/1.2830434

[18] Chiou, B. S.-J., and Youngs, R. R. (2008). An NGA model for the average horizontal component of peak ground motion and response spectra. Earthq. Spectra. 24, 173–215. doi:10.1193/1.2894832

[19] Contreras, V., and Boroschek, R. (2012). “Strong ground motion attenuation relations for Chilean subduction zone interface earthquakes,” in 15 WCEE (Lisbon).

[20] Iyengar, R. N., Chadha, R. K., Rao, K. B., and Kanth, S. T. G. R. (2010). “Development of probabilistic seismic hazard map of India,” in The National Disaster Management Authority, ed. R. N. Iyengar (New Delhi: Government of India), 86 p.

[21] Baker, J. W., and Jayaram, N. (2008). Correlation of spectral acceleration values from NGA ground motion models. Earthq. Spectra 24, 299–317.

[22] Baker, J. W., and Cornell, C. A. (2006). Spectral shape, epsilon and record selection. Earthq. Eng. Struct. Dyn. 35, 1077–1095. doi:10.1002/eqe.571

[23] Boore, David M. "Simulation of ground motion using the stochastic method." Seismic Motion, Lithospheric Structures, Earthquake and Volcanic Sources: The Keiiti Aki Volume. Birkhäuser Basel, 2003. 635-676.

[24] Yamamoto, Yoshifumi, and Jack W. Baker. "Stochastic model for earthquake ground motion using wavelet packets." Bulletin of the Seismological Society of America 103.6 (2013): 3044-3056.

[25] Gasparini, Dario Ambrose, and Erik Hector Eugene Joseph Vanmarcke. Simulated earthquake motions compatible with prescribed response spectra. Massachusetts Institute of Technology, Department of Civil Engineering, Constructed Facilities Division, 1976.

[26] Rodolfo Saragoni, G., and Gary C. Hart. "Simulation of artificial earthquakes." Earthquake Engineering & Structural Dynamics 2.3 (1973): 249-267.

[27] Bardet, J., Ichii, K., and Lin, C. (2000). EERA: A Computer Program for EquivalentLinear Earthquake Site Response Analyses of Layered Soil Deposits. Los Angeles, CA: Department of Civil Engineering; University of Southern California.

[28] Jardine, R., Potts, D., Fourie, A., and Burland, J. (1986). Studies of the influence of nonlinear stress-strain characteristics in soil structure interaction. Geotechnique 36, 377–396. doi:10.1680/geot.1986.36.3.377

COMPDYN 2017
6th ECCOMAS Thematic Conference on
Computational Methods in Structural Dynamics and Earthquake Engineering
M. Papadrakakis, M. Fragiadakis (eds.)
Rhodes Island, Greece, 15–17 June 2017

# NUMERICAL SIMULATIONS WITH CUSHIONING MATERIAL INSTALLED BEHIND THE RETAINING WALL FOR RESILIENT STRUCTURES

**Kazuhiro Kaneda [1], Hiroyuki Yamazaki [2], and Satoru Ohtsuka [3]**

[1] Takenaka Corporation
1-5-1, Ohtsuka, Inzai, Chiba, Japan, 270-1395
kaneda.kazuhiro@takenaka.co.jp

[2] Port and Airport Research institute
3-1-1, Nagase, Yokosuka, Kanagawa, Japan, 239-0826
yamazaki@pari.go.jp

[3] Nagaoka University of Technology
1603-1, Kamitomioka, Nagaoka, Niigata, Japan, 940-2188
ohtsuka@nagaokaut.ac.jp

**Keywords:** Retaining wall, Cushioning material, Earth pressure, Dynamic simulation, Quasi-active state.

**Abstract.** *Following the Hyogoken Nanbu earthquake in 1995, the design earthquake wave was larger. After the Tohoku chihou Taiheiyouoki earthquake in 2011, the tsunami was focused after earthquake. In the future large earthquakes are expected to occur in Japan. We are required to design more resilient structures that can withstand these events.*
*We conducted a numerical simulation of the reduction of earth pressure in a sandy backfill. When a cushioning material was placed behind the retaining wall, the earth pressure was reduced, because the backfill sand moved to the active earth pressure state. It is possible that the design section of the gravity caisson became smaller. In the dynamic approach, shaking table tests were performed and the earth pressure acting on the retaining wall was seen to reduce. However, the mechanism of earth pressure reduction was not clear in the dynamic tests. Therefore in this study, the mechanism of earth pressure reduction during an earthquake was clarified using a numerical simulation. From the simulation results, the residual horizontal displacement in the case of sand is larger than that in the case of cushioning material. It is cleared that in the cushioning material the inertial force of backfill sand was absorbed for the friction force toward to the foundation ground beside the effect of quasi-active state.*

# 1 INTRODUCTION

The mechanism of earth pressure reduction in a backfill with cushioning material behind the retaining wall is herein discussed. The influences of Poisson's ratio and the elastic modulus of the cushioning material on the reduction of earth pressure against a retaining wall were examined by assuming the material to be an elastic body. Numerical simulations revealed that the attainment of the active state in the sandy backfill was due mainly to the lower Young's modulus and Poisson's ratio of the cushioning material in the static condition. Under static loading, the soil in the vicinity of a wall enters the active state, or what has also been called a "quasi-active state," in which it is deformed by the cushioning material buffer. The concept of the quasi-active state was first introduced by Hazarika and Okuzono (2004), in which EPS was used as a compressible inclusion to reduce the dynamic earth pressure against the retaining wall. Hazarika et al. (2008) extended the cushioning technique to reduce the dynamic earth pressure against the retaining wall and validated the approach by conducting shaking table tests on gravity type retaining structures. However, the mechanism of earth pressure reduction was not clear in the dynamic case. Therefore, in this study, the mechanism of earth pressure reduction during an earthquake was clarified using a numerical analysis. First, the mechanism of earth pressure reduction was explained for the static case. Subsequently, the deformation of the retaining wall with earth pressure reduction was discussed for the dynamic case.

# 2 STATIC CASE

## 2.1 Simulation condition

Numerical simulations were performed in order to simulate the static and dynamic cases. The FEM program code MuDIAN, developed by Takenaka Corporation (Shiomi et al., 1993) was used in the simulation. The numerical mesh in the case of the cushioning material and boundary conditions are indicated in Figure 1. A sandy foundation ground of 2 m and a sandy backfill 2 m high and 10 m wide was constructed in the plane strain condition. The bottom of foundation ground was kept fixed. Two cases were simulated. One case was simulated with sand at the backfill, while the other had a 0.5 m thick layer of cushioning material at the backfill. The Mohr Coulomb failure criterion of the soil was used as the constitutive model in this study. Table 1 shows the material constants of sand and the cushioning material used in the simulation. The cushioning material and the retaining wall were considered elastic bodies. The friction angle of soil was set at 40°. The stiffness of the foundation ground was greater than that of the backfill sand. The cushioning material was assumed to be tier chips (Kaneda. et.al. 2011); its elastic modulus and Poisson's ratio were small compared with those of the soil. The retaining wall was assumed to be composed of concrete. The slip between the retaining wall and soil or cushioning material was not considered in this simulation. Initial calculations were performed using the self-weight of the soils. Then, an additional load of 50 $kN/m^2$ was applied at the top (red part in Fig.1).

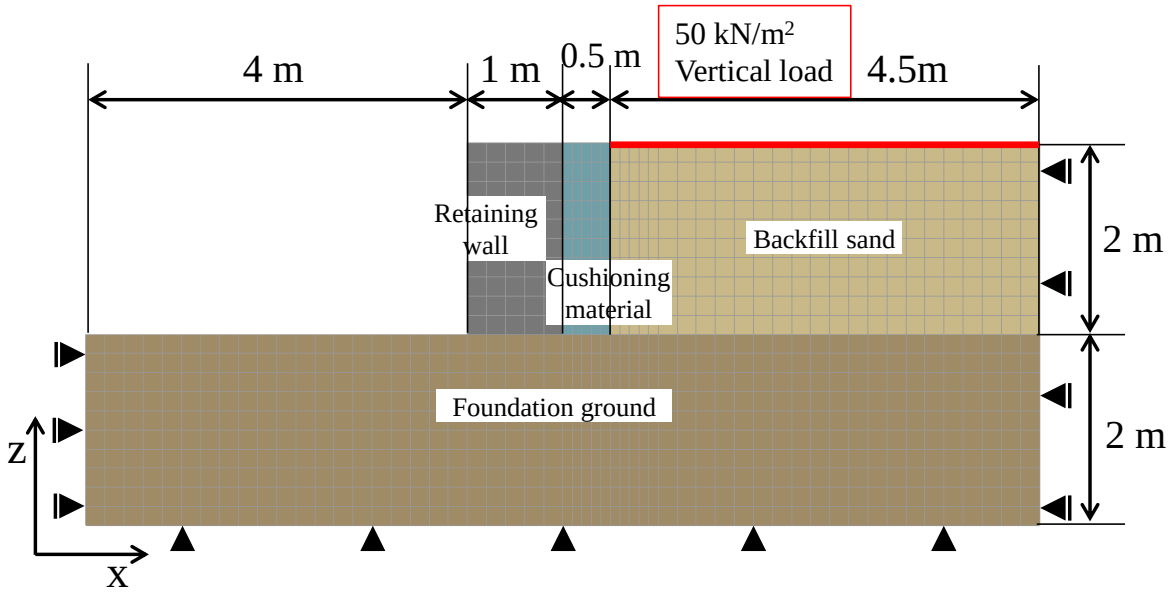


Figure 1: Boundary conditions.

| | Foundation ground | Backfill sand | Retaining wall | Cushioning material |
|---|---|---|---|---|
| Elastic modulus ($kN/m^2$) | 112000 | 56000 | 24400000 | 200 |
| Poisson ratio | 0.3 | 0.3 | 0.2 | 0.2 |
| Unit weight ($kN/m^3$) | 16.62 | 16.62 | 23.03 | 8.82 |
| Cohesion ($kN/m^2$) | 1 | 1 | | |
| Friction angle (Degree) | 40 | 40 | | |

Table 1: Material constants.

## 2.2 Simulation results and considerations

Figure 2 shows the stress distribution in the vertical direction (compressive stress) acting on the retaining wall from the sand or the cushioning material after loading. In the case of sand, the compressive stress from the sandy backfill was transmitted to the retaining wall. In the case of the cushioning material, the compressive stress is smaller than that in the case of sand at the total. Figure 3 shows the equivalent shear strain distributions after loading. The shear strain in the cushioning material case is larger than that in the sand case. Figure 4 shows the mechanism of earth pressure reduction in the static condition (Kaneda. et.al. 2011). When cushioning material is present in the backfill and the backfill sand underwent deformation, the cushioning material entered the passive state and the stress increased. On the other hand, the backfill sand entered the active state and the stress decreased with deformation. The equilibrium state is the intersection between the passive cushioning material and the active backfill sand. Thus, earth pressure reduction is the difference between the stress values at the point of intersection and the initial force. See the references in detail. (Kaneda. et.al. 2011).

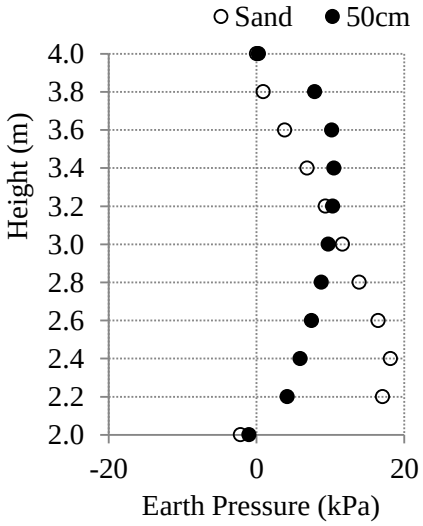


Figure 2: Stress distributions in the vertical direction acting on the retaining wall.

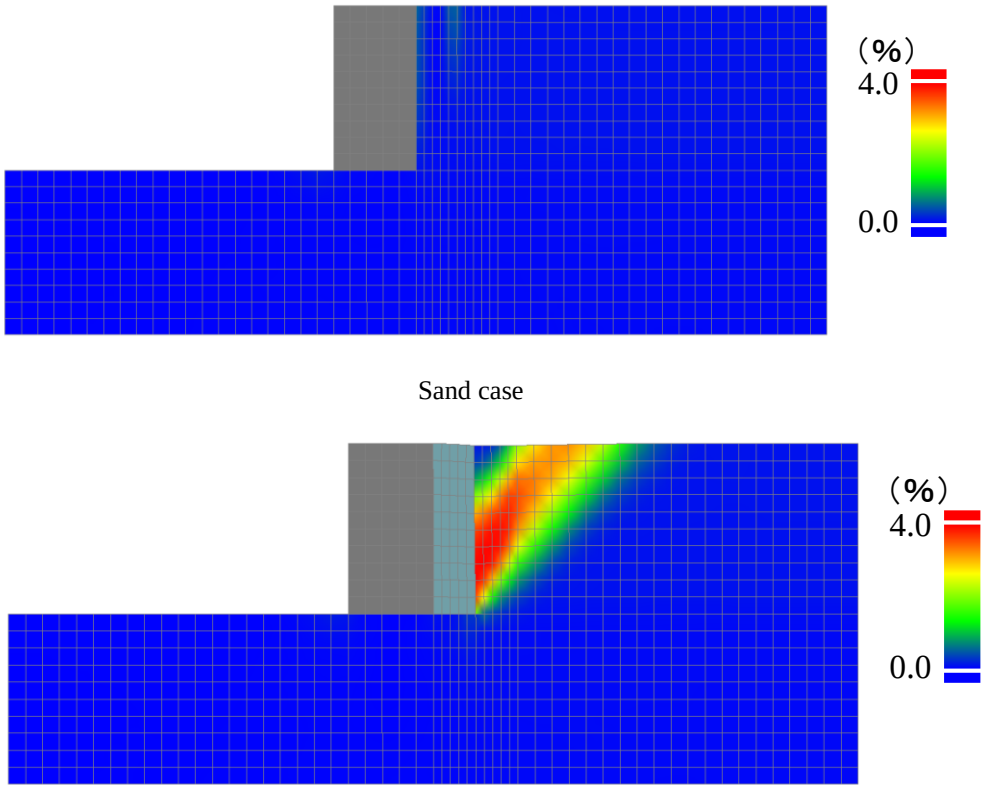


Figure 3: Equivalent shear strain distributions.

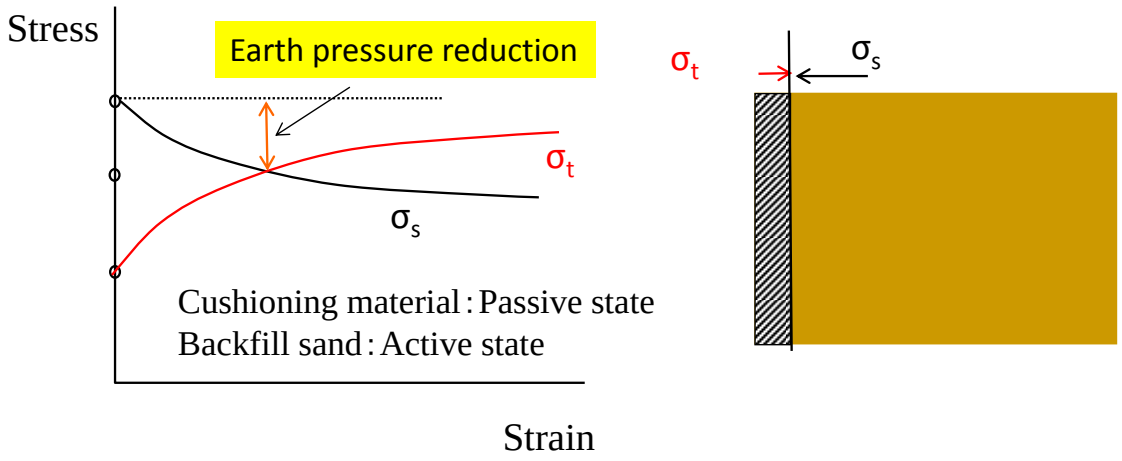


Figure 4: Mechanism of earth pressure reduction.

## 3 DYNAMIC CASE

### 3.1 Simulation condition

Figure 5 shows the numerical mesh in the case of the cushioning material and boundary condition in dynamic case. A sandy foundation ground of 8 m, a sandy backfill of 2 m high and 40 m wide is constructed in plane strain condition. There are three simulation cases, one with only sand, and the other two with 0.2 m and 0.5 m cushioning material. The bottom of the mesh was set to be a viscos boundary and both the sides were connected to the free field, which has a huge mass. The soil constitutive equation was obtained from the Yoshida mode. See the reference for details. (Yoshida. et. al. 1993)

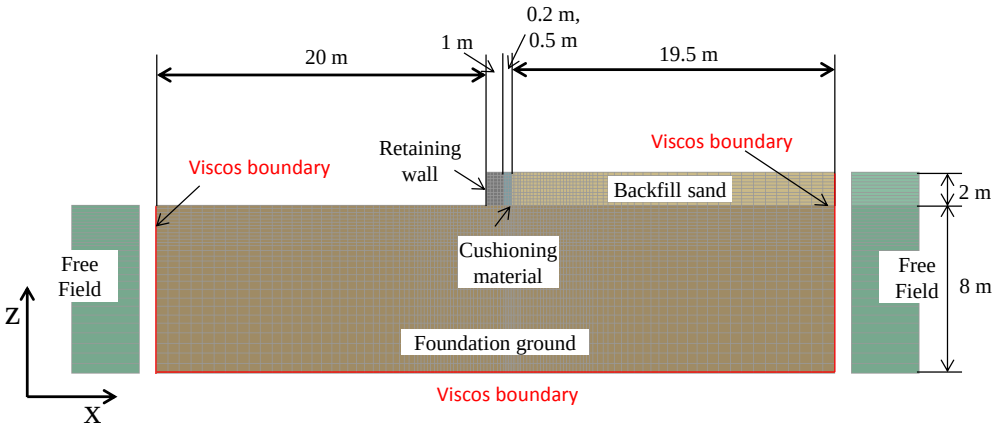


Figure 5: Boundary conditions.

The dynamic deformation characteristic ($G/G_0$) and damping ratio $h$ are calculated from equations (1) and (2). For the soil ground, $h_{max}$ is assumed to be 21.0%.

$$\frac{G}{G_0} = \frac{1}{1+\frac{\gamma}{\gamma_r}} \tag{1}$$

$$h = h_{\max}\left(1-\frac{G}{G_0}\right) \tag{2}$$

where $G$: shear stiffness, $G_0$: initial shear stiffness, $\gamma_r$ : reference strain, $h$: dumping, $h_{\max}$: maximum dumping

Table 2 lists the material constants. The hyperbolic model at $\gamma_r = 0.1$ was used for sand. The material constants of both the Retaining wall and Cushioning material are the same as the static case. Figure 6 shows the $G/G_0$, $h$~$\gamma$ curve in sand in this research.

| | Foundation ground | Backfill sand | Retaining wall | Cushioning material |
|---|---|---|---|---|
| Elastic modulus(kN/m$^2$) | 112000 | 56000 | 24400000 | 200 |
| Poisson ratio | 0.3 | 0.3 | 0.2 | 0.2 |
| Unit weight (kN/m$^3$) | 16.62 | 16.62 | 23.03 | 8.82 |
| Reference strain $\gamma_r$ | 0.1 | 0.1 | | |
| Maximum dumping $h_{\max}$(%) | 21 | 21 | | |

Table 2: Material constants.

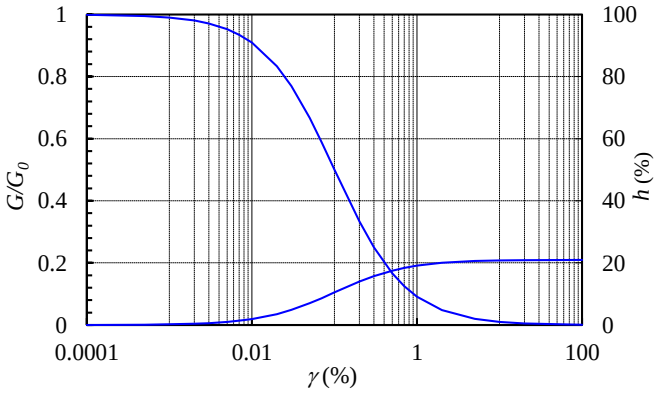


Figure 6: $G/G_0$, $h$~$\gamma$ curve.

Similar to the static case, the self-gravity analysis was performed first, followed by the dynamic analysis. Rayleigh damping was adopted for both structures and soils. Table 3 shows the Rayleigh damping coefficient. The α and β were determined by f1=1Hz, f2=5Hz and h=2%, respectively. Figure 7 shows the input motion. The bottom had an input of 2E with the viscos boundary. Table 4 shows the viscos parameters. The slip between the retaining wall and soil or cushioning material was also not considered in this simulation, as in the static case.

| | α | β |
|---|---|---|
| damping | 0.209440 | 0.001061 |

Table 3: Rayleigh damping.

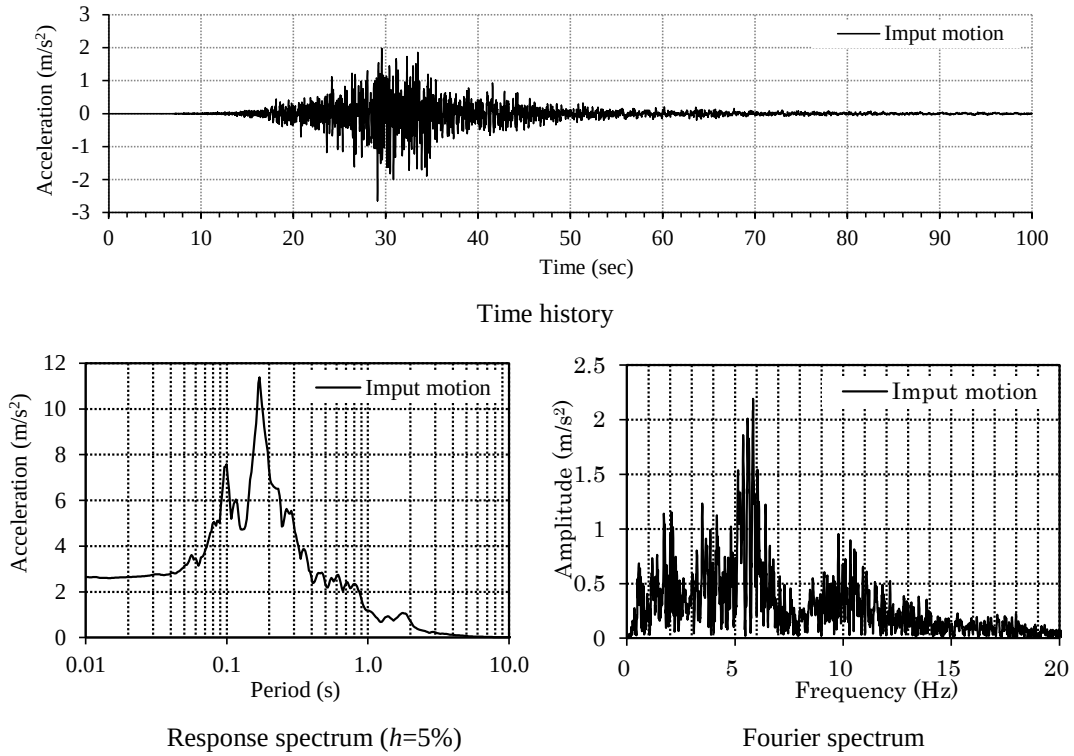


Figure 7: Input motion.

| | |
|---|---|
| Unit weight (kN/m$^3$) | 17.64 |
| Vp(m/s) | 2000 |
| Vs(m/s) | 340 |

Table 4: Viscos parameters.

### 3.2 Eigen value analysis

Table 5 shows the results of the eigen value analysis. Figure 8 shows the first eigen value mode. The horizontal mode was observed as the first eigen value mode.

| | Mode | Frequency (Hz) | Period (s) | |
|---|---|---|---|---|
| Sand | 1 | 3.210 | 0.312 | Horizontal mode |
| | 2 | 4.390 | 0.228 | Horizontal mode |
| | 3 | 5.880 | 0.170 | Vertical mode |
| 20 cm cushioning material | 1 | 3.200 | 0.312 | Horizontal mode |
| | 2 | 4.380 | 0.228 | Horizontal mode |
| | 3 | 5.880 | 0.170 | Vertical mode |
| 50 cm cushioning material | 1 | 3.200 | 0.312 | Horizontal mode |
| | 2 | 4.380 | 0.228 | Horizontal mode |
| | 3 | 5.880 | 0.170 | Vertical mode |

Table 5: Eigen value.

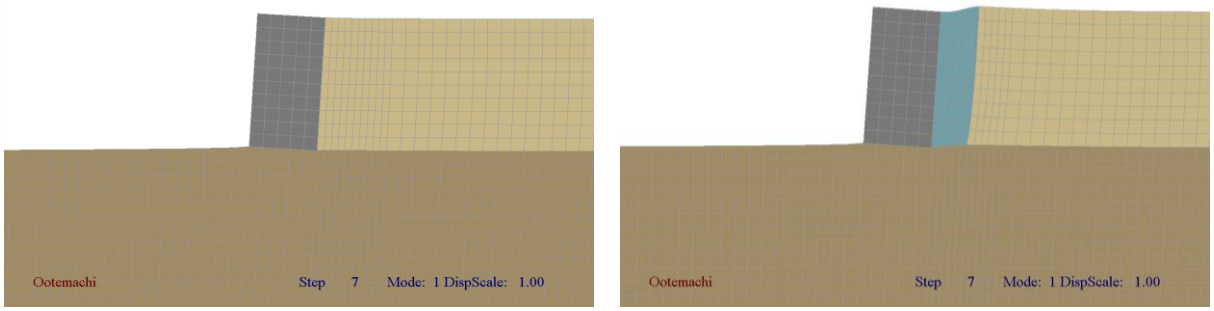


Sand 50 cm cushioning material

Figure 8: First eigen value mode.

### 3.3 Simulation results

Figure 9 shows the x direction time history from the retaining wall point (red circle). All cases move to the left after 30 s. In the sand case, the deformation was the largest on the left side. In the 0.5 m cushioning material case, it was the smallest. It was shown that displacement is smaller when cushioning material is attached. Figure10 shows the earth pressure at the retaining wall at both 29.1 s and 100 s (final). In the sand case, the earth pressure occurred at the retaining wall. However, in the case of 50 cm cushioning material case, the earth pressure did not occur. At the trend in the final case is also same. Figure 11 shows the equivalent shear strain distributions at both 29.1 s and 100 s (final). At the 29.1 s mark, in the sand case, the shear strain of the foundation ground in front of retaining wall occurred for the forward deformation. In the 0.5 m cushioning material case, there was shear strain on the lower backfill sand. In the final case, there was more shear strain of the foundation ground in front of retaining wall in the sand case. In the 0.5m cushioning material case, the shear strain occurred for both, the lower backfill and its underlying foundation ground. In the sand case, for the inertial force of the backfill sand, the retaining wall was pushed with the lower left of the retaining wall acting as a fulcrum. On the other hand, in the 0.5 m cushioning material case, while there was shear stain of the foundation ground in front of retaining wall, for the cushioning, the inertial force of backfill sand was absorbed for the friction force toward to the foundation ground as shown by the shear strain of foundation ground. As a result, it is considered that the earth pressure at the retaining wall was small. Like the static, it is also considered that the effect of the quasi-active state existed for the reduction of earth pressure.

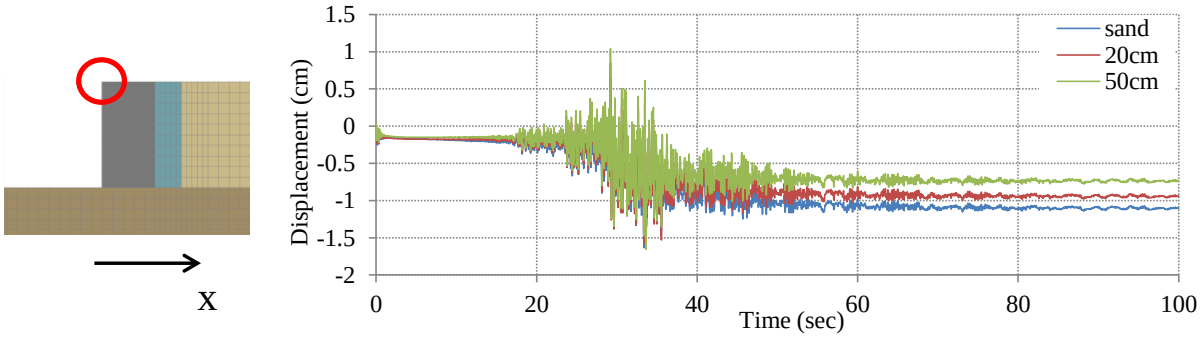


Figure 9: X direction time history.

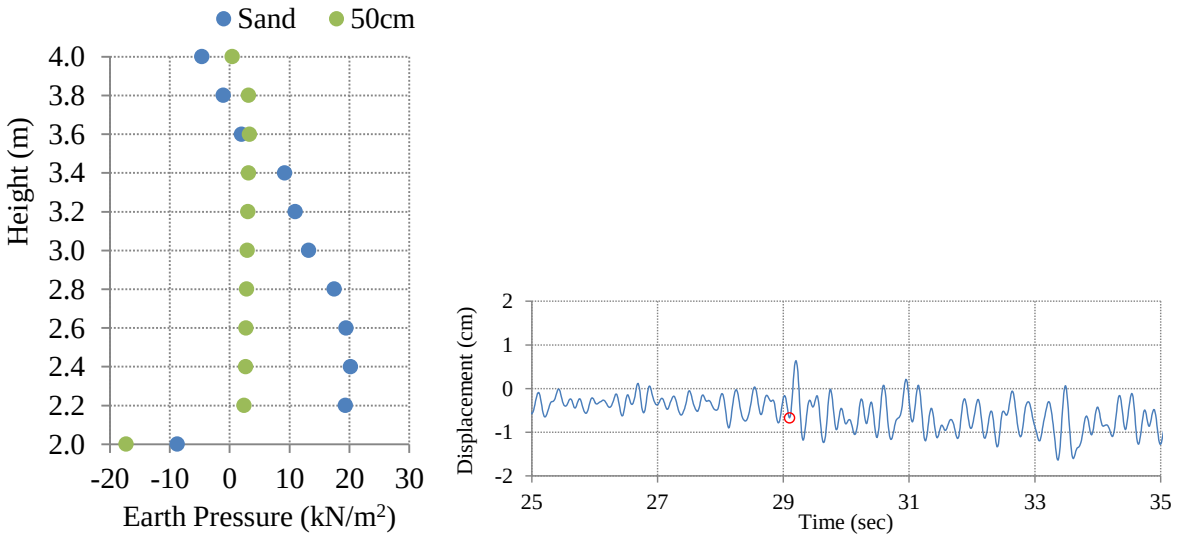


29.10 sec

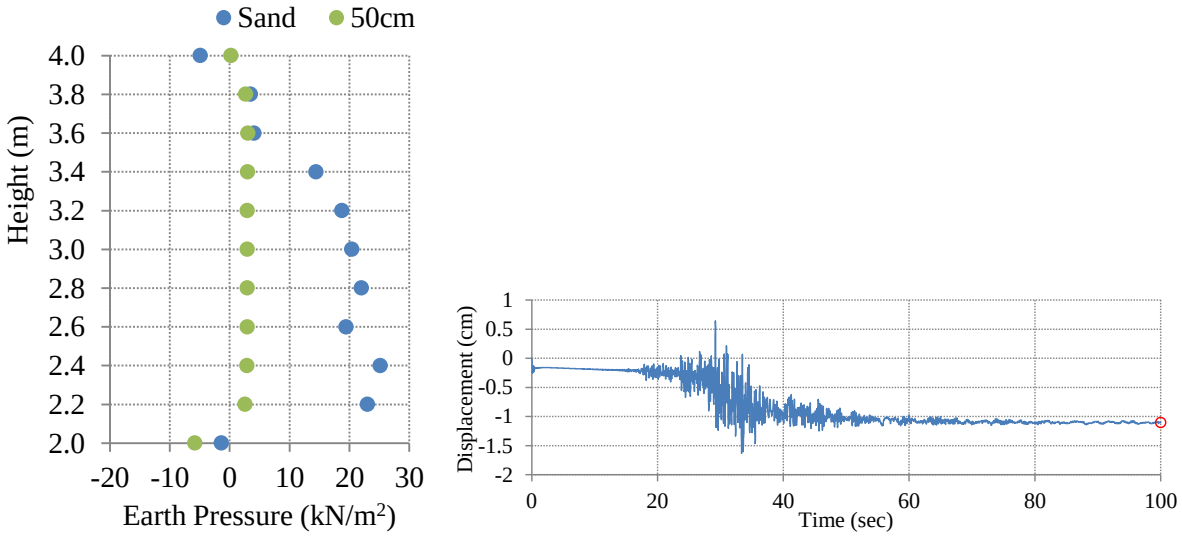


100 sec(final)

Figure 10: Earth pressure at retaining wall.

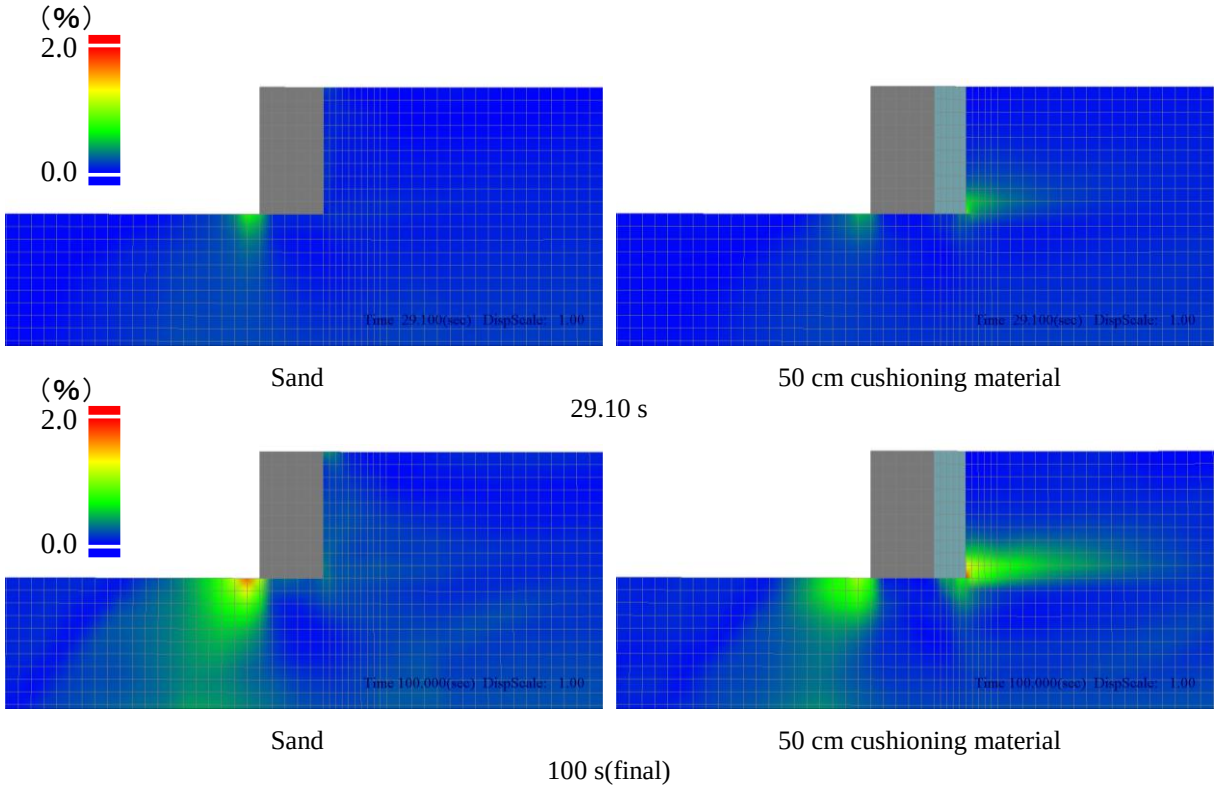


Figure 11: Equivalent shear strain distributions.

## 4 CONCLUSIONS

Earth pressure reduction of the retaining wall with cushioning material was conducted using numerical simulations. In the static case, further reduction of earth pressure was observed in the cushioning material as compared to the sand case. This is likely due to the backfill sand turning into the active state in the cushioning material case (quasi-active state). In the dynamic case, a smaller deformation of the retaining wall was observed in the cushioning material as compared to the sand case. It is considered that in the cushioning material, the inertial force of backfill sand was absorbed by the friction force toward to the foundation ground in addition to the effect of the quasi-active state.

Finally, in this simulation, the slip between the retaining wall and the cushioning material or sand backfill was not considered. However, the effect of slip is important for the deformation in the dynamic analysis. In the future, we would like to include the slip effect in numerical simulations.

## REFERENCES

[1] Hazarika, H. and Okuzono, S., Modeling the Behavior of a Hybrid Interactive System Involving Soil, Structure and EPS Geofoam, *Soils and Foundations, Japanese Geotechnical Society*, Vol. 44, No. 5, 149-162., 2004.

[2] Hazarika, H., K.ohama, E. and Sugano, T., Underwater Shaking Table Tests on Waterfront Structures Protected with Tire chips Cushion, *Journal of Geotechnical and Geo Environmental Engineering*, ASCE, Vol. 134, No. 12, 1706-1719., 2008

[3] Shiomi, T., Shigeno, Y. and Zienkiewicz, O. C., Numerical prediction for model No.1, Verification of Numerical Procedures for the Analysis of Soil Liquefaction Problems (eds. By Arulanandan and Scott), Balkema, pp.213-219., 1993

[4] Kaneda, K, Hazarika, H. and Yamazaki, H, Mechanism of Earth Pressure Reduction Using Tire Chips in Sand Backfill, The 14th Asian Regional Conf. on Soil Mechanics and Geotechnical Engineering, Hong Kong, CD-ROM., 2011

[5] Yoshida, N. and S. Tsujino, "A simplified practical stress-strain model for the multi-dimensional analysis under repeated loading." The 28th Japan national conference on soil mechanics and foundation engineering., 1993

COMPDYN 2017
6th ECCOMAS Thematic Conference on
Computational Methods in Structural Dynamics and Earthquake Engineering
M. Papadrakakis, M. Fragiadakis (eds.)
Rhodes Island, Greece, 15–17 June, 2017

# AN ENERGY-MOMENTUM FORMULATION FOR NONLINEAR DYNAMICS OF PLANAR CO-ROTATING BEAMS

**Sophy Chhang[1,2], Mohammed Hjiaj[1], Jean-Marc Battini[2] and Carlo Sansour[1]**

[1]Structural Engineering Research Group /LGCGM , INSA de Rennes, Université Bretagne Loire, 20 Avenue des Buttes de Coësmes, 35708 Rennes Cédex 7, France
e-mail: Sophy.Chhang@insa-rennes.fr, Mohammed.Hjiaj@insa-rennes.fr, Carlo.Sansour@nottingham.ac.uk

[2]Department of Civil and Architectural Engineering, KTH, Royal Institute of Technology, SE-10044 Stockholm, Sweden
e-mail: Jean-Marc.Battini@byv.kth.se

**Keywords:** Corotational formulation; energy-momentum method; conserving energy; nonlinear dynamic; 2D Beams

**Abstract.** *This article presents an energy-momentum integration scheme for the nonlinear dynamic analysis of planar Bernoulli/Timoshenko beams. The co-rotational approach is adopted to describe the kinematics of the beam and Hermitian functions are used to interpolate the local transverse displacements. In this paper, the same kinematic description is used to derive both the elastic and the inertia terms. The classical midpoint rule is used to integrate the dynamic equations. The central idea, to ensure energy and momenta conservation, is to apply the classical midpoint rule to both the kinematic and the strain quantities. This idea, developed by one of the authors in previous work, is applied here in the context of the co-rotational formulation to the first time. By doing so, we circumvent the nonlinear geometric equations relating the displacement to the strain which is the origin of many numerical difficulties. It can be rigorously shown that the proposed method conserves the total energy of the system and, in absence of external loads, the linear and angular momenta remain constant. The accuracy and stability of the proposed algorithm, especially in long term dynamics with a very large number of time steps, is assessed through two numerical examples.*

## 1 INTRODUCTION

The co-rotational method is a very attractive approach to derive highly nonlinear beam elements [1, 4, 3, 2, 5, 6, 7, 8, 9, 10, 11, 12]. The fundamental idea is to decompose the motion of the element into rigid body and pure deformational parts through the use of a local system which continuously rotates and translates with the element. The deformational response is captured at the level of the local reference frame, whereas the geometric nonlinearity induced by the large rigid-body motion, is incorporated in the transformation matrices relating local and global quantities. The main interest is that the pure deformational parts can be assumed as small and can be represented by a linear or a low order nonlinear theory.

Regarding the inertia terms in the co-rotational context, Crisfield et al. [1, 2] used linear local interpolations although they took local cubic interpolations to derive the elastic terms. Then, the inertia terms are easily derived and the classical constant Timoshenko mass matrix is obtained. However, Le at al. [3] adopted the Interdependent Interpolation element (IIE) formulation [13], and hence cubic shape functions, to derive both the inertia and elastic terms. This leads to a formulation that requires a less number of elements but also to more complicated expressions for the inertia force vector and tangent dynamic matrix. The formulation was then extended to 3D beams without [8, 9] and with [10] warping.

Another important issue in the context of non-linear dynamics is the choice of the time stepping method. In commercial finite element programs, the Alpha method [14] is usually used. However, this approach introduces numerical dissipations and consequently, the energy in the system is not conserved [15, 16]. In the last decades, it has been recognized that energy conservation is a key for the stability of time-stepping algorithms in the dynamics of solids and structures. Simo and Tarnow [16] were the first authors to design energy momentum algorithms that inherit the conservation of momenta and energy for geometrically nonlinear problem involving quadratic Green- Lagrange strains. Much effort was devoted then to develop energy momentum methods for nonlinear rod dynamics [17, 19, 18, 20, 21]. Sansour et al. [22, 23] developped an energy-momentum method applicable to any nonlinear shell and to any nonlinear complexities involved in the strain-displacement relations. It has been extended to arbitrary continuum formulations [24] and to geometrically exact Bernoulli beam model [19]. Based on the generalization of the method in [24], Gams et al. [18] developed the for the geometrically exact planar Reissner beam. Besides, it has been applied to the problem of the dissipation of high frequency oscillations associated to energy-momentum methods [25].

In the co-rotational context, there have been some efforts to develop energy-momentum methods as well. Crisfield and Shi [11] proposed a mid-point energy-conserving time algorithm for two-dimensional truss elements. This concept was further developed by Galvanetto and Crisfield [5] for planar beam structures. Various end- and mid-point time integration schemes for the nonlinear dynamic analysis of 3D co-rotational beams are discussed in [1]. The authors concluded that the proposed mid-point scheme can be considered as an approximately energy conserving algorithm. Salomon et al. [12] showed the conservation of energy and momenta in the 2D and 3D analyses for the simulation of elastodynamic problems. They mentioned that, for some cases, the angular momentum is asymptotically preserved and a priori estimate is obtained. However, despite of all these works, the design of an effective time integration scheme for co-rotational elements that inherently fulfils the conservation properties of energy and momenta is still an open question.

In this paper, an energy momentum method in the context of co-rotational shear flexible 2D beam elements is proposed. The IIE cubic shape functions [13] are used together with a shallow

arch beam thoery for the co-rotational framework. Based on the previous works of Sansour et al. [22, 23], the main idea is to apply the midpoint rule not only to nodal displacements, velocities and accelerations but also to the strain fields. It means that the strains are updated by using the strain velocities instead of by using directly the strain-displacement relation. The midpoint velocities are applied to the kinematic variables as well. The conservation of energy, linear and angular momentum are then validated by the numerical applications.

The paper is organized as follows: the beam kinematics and strain definitions are presented in Section 2. Section 3 is devoted to Hamilton's principle and conserving properties. The energy-momentum method is then developed in Section 4. In order to assess the numerical performances of the proposed method, two numerical applications are presented in Section 5. Finally, conclusions are presented in Section 6.

## 2 BEAM KINEMATICS AND STRAIN DEFINITIONS

### 2.1 Beam kinematics

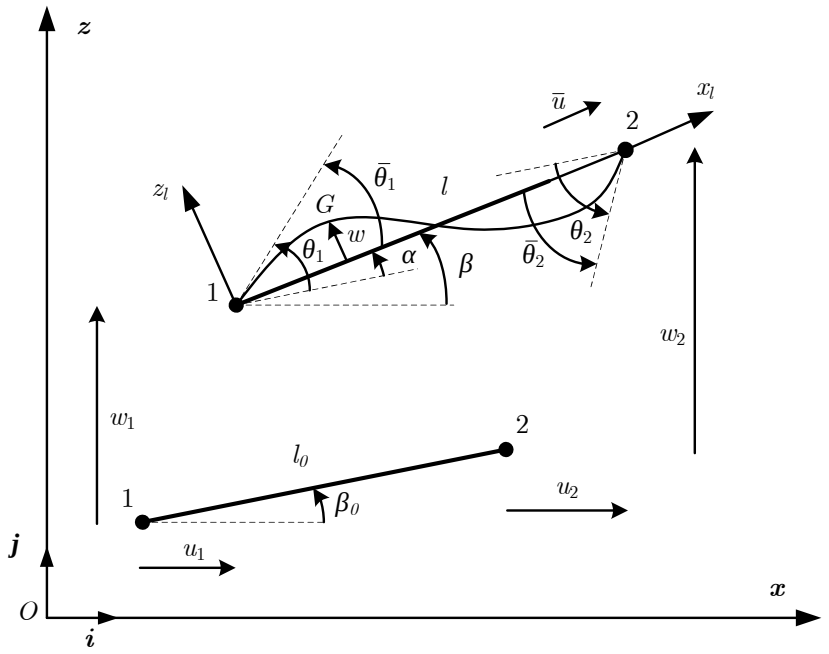


Figure 1: Beam kinematics.

The kinematics of the beam and all the notations used in this section are shown in Figure 1. The motion of the element is decomposed in two parts. In a first step, a rigid body motion is defined by the global translation ($u_1$,$w_1$) of the node 1 as well as the rigid rotation $\alpha$. This rigid motion defines a local coordinate system ($x_l$, $z_l$) which continuously translates and rotates with the element. In a second step, the element deformation is defined in the local coordinate system. Assuming that the length of the element is properly selected, the deformational part of the motion is always small relative to the local co-ordinate systems. Consequently, the local deformations can be expressed in a simplified manner.

The vectors of global and local displacements are defined by

$$\boldsymbol{q} = \left[ \begin{array}{cccccc} u_1 & w_1 & \theta_1 & u_2 & w_2 & \theta_2 \end{array} \right]^{\mathrm{T}} \tag{1}$$

and

$$\bar{\boldsymbol{q}} = \left[ \begin{array}{ccc} \bar{u} & \bar{\theta}_1 & \bar{\theta}_2 \end{array} \right]^{\mathrm{T}} \tag{2}$$

Explicitly, the components of $\bar{\boldsymbol{q}}$ are given by

$$\bar{u} = l - l_0 \tag{3}$$
$$\bar{\theta}_1 = \theta_1 - \alpha \tag{4}$$
$$\bar{\theta}_2 = \theta_2 - \alpha \tag{5}$$

where $l_0$ and $l$ denote the initial and current lengths of the element, respectively:

$$l_0 = \sqrt{(x_2 - x_1)^2 + (z_2 - z_1)^2} \tag{6}$$
$$l = \sqrt{(x_2 + u_2 - x_1 - u_1)^2 + (z_2 + w_2 - z_1 - w_1)^2} \tag{7}$$

The current angle of the local system with respect to the global system is denoted as $\beta$ and is given by

$$c = cos\beta = \frac{1}{l}\left(x_2 + u_2 - x_1 - u_1\right) \tag{8}$$
$$s = sin\beta = \frac{1}{l}\left(z_2 + w_2 - z_1 - w_1\right) \tag{9}$$

From Figure 1, the components $u_G$, $w_G$ of the global positions of the centroid G and the global rotation $\theta_G$ of the cross section are obtained as

$$u_G = N_1\left(x_1 + u_1\right) + N_2\left(x_2 + u_2\right) - w\,\mathrm{sin}\beta \tag{10}$$
$$w_G = N_1\left(z_1 + w_1\right) + N_2\left(z_2 + w_2\right) + w\,\mathrm{cos}\beta \tag{11}$$
$$\theta_G = \theta + \alpha \tag{12}$$

where $w$ is the local transversal displacement, $\theta$ is the local rotation of the cross-section and the linear interpolations $N_1$, $N_2$ are

$$N_1 = 1 - \frac{x}{l_0} \tag{13}$$
$$N_2 = \frac{x}{l_0} \tag{14}$$

### 2.2 Strain definitions

The shape functions of the IIE are used together with a shallow arch beam theory for the local formulation. The shallow arch longitudinal and shear strains are given by

$$\varepsilon_{11} = \varepsilon - \kappa\, z \tag{15}$$
$$\gamma = \frac{\partial w}{\partial x} - \theta \tag{16}$$

in which the axial strain $\varepsilon$ and the curvature $\kappa$ are defined by

$$\varepsilon = \frac{1}{l_0}\int_{l_0}\left[\frac{\partial u}{\partial x} + \frac{1}{2}\left(\frac{\partial w}{\partial x}\right)^2\right]\mathrm{d}x \tag{17}$$
$$\kappa = \frac{\partial^2 w}{\partial x^2} \tag{18}$$

The shape functions of the IIE element [13] are based on the exact solution of the homogeneous form of the equilibrium equations for a Timoshenko beam. Consequently, the IIE element retains the accuracy inherent to the cubic interpolation including the bending and shear deformation. It should be noted that, in Eq.(18), the axial strain is averaged over the element in order to avoid membrane locking. The local axial displacement $u$, the local transversal displacement $w$ and the local rotation $\theta$ are calculated by

$$u = N_2\,\bar{u} \tag{19}$$
$$w = N_3\,\bar{\theta}_1 + N_4\,\bar{\theta}_2 \tag{20}$$
$$\theta = N_5\,\bar{\theta}_1 + N_6\,\bar{\theta}_2 \tag{21}$$

where the shape functions of the IIE element are given by

$$N_3 = \mu\,x\left[6\,\Omega\left(1-\frac{x}{l_0}\right)+\left(1-\frac{x}{l_0}\right)^2\right] \tag{22}$$
$$N_4 = \mu\,x\left[6\,\Omega\left(\frac{x}{l_0}-1\right)-\frac{x}{l_0}+\frac{x^2}{l_0^2}\right] \tag{23}$$
$$N_5 = \mu\left(1+12\,\Omega-\frac{12\,\Omega\,x}{l_0}-\frac{4\,x}{l_0}+\frac{3\,x^2}{l_0^2}\right) \tag{24}$$
$$N_6 = \mu\left(\frac{12\,\Omega\,x}{l_0}-\frac{2\,x}{l_0}+\frac{3\,x^2}{l_0^2}\right) \tag{25}$$
$$\Omega = \frac{EI}{k_s\,GA\,l_0^2} \tag{26}$$
$$\mu = \frac{1}{1+12\,\Omega} \tag{27}$$

with $E$ is Young's modulus; $G$ is the shear modulus of the material; $A$ is the area of the cross-section; $I$ is the inertia moment of the cross-section and $k_s$ is the shear correction coefficient. For a rectangular cross-section, $k_s$ is equal to $5/6$.

For the dynamic terms, $\Omega$ is taken to $0$ because this simplification does not affect the numerical results. In addition with $\Omega = 0$, the Hermitian shape functions of the classical Bernoulli element are recovered.

## 3 HAMILTON'S PRINCIPLE

Hamilton's principle states that the integral of the Lagrangian between two specified time instants $t_1$ and $t_2$ of a conservative mechanical system is stationary

$$\delta\int_{t_1}^{t_2}\mathcal{L}\,\mathrm{d}t = 0 \tag{28}$$

The Lagrangian $\mathcal{L}$ is given by

$$\mathcal{L} = \mathsf{K} - \mathsf{U}_{int} - \mathsf{U}_{ext} \tag{29}$$

with $\mathsf{K}$ is the kinetic energy. $\mathsf{U}_{int}$ and $\mathsf{U}_{ext}$ are respectively the internal and the external potential energies. The body is non-conducting linear elastic solid and thermodynamic effects are not

included in the system. The kinetic energy is the sum of the translational and rotational kinetic energies:

$$\mathsf{K} = \frac{1}{2}\int_{l_0} \rho A\, \dot{u}_G^2 \,\mathrm{d}x + \frac{1}{2}\int_{l_0} \rho A\, \dot{w}_G^2 \,\mathrm{d}x + \frac{1}{2}\int_{l_0} \rho I\, \dot{\theta}_G^2 \,\mathrm{d}x \tag{30}$$

The internal potential is defined as

$$\mathsf{U}_{int} = \frac{1}{2}\int_{l_0} EA\, \varepsilon^2 \mathrm{d}x + \frac{1}{2}\int_{l_0} EI\, \kappa^2 \mathrm{d}x + \frac{1}{2}\int_{l_0} k_s GA\, \gamma^2 \,\mathrm{d}x \tag{31}$$

The external potential is defined as

$$\mathsf{U}_{ext} = -\sum_{i=1}^{6} P_i\, q_i \tag{32}$$

where $\rho$ is the density of the material. $P_i$ is the $i$ component (concentrated forces and moments at the nodes) of external force vector $\boldsymbol{P}$.

By introducing Eqs.(30) to (32), the variation of Eq.(28) can be written as

$$\begin{aligned} &\int_{t_1}^{t_2} \left( \int_{l_0} \rho A\, \dot{u}_G\, \delta\dot{u}_G \,\mathrm{d}x + \int_{l_0} \rho A\, \dot{w}_G\, \delta\dot{w}_G \,\mathrm{d}x + \int_{l_0} \rho I\, \dot{\theta}_G\, \delta\dot{\theta}_G \,\mathrm{d}x \right) \mathrm{d}t \\ - &\int_{t_1}^{t_2} \left( \int_{l_0} EA\, \varepsilon\, \delta\varepsilon \,\mathrm{d}x + \int_{l_0} EI\, \kappa\, \delta\kappa \,\mathrm{d}x + \int_{l_0} k_s GA\, \gamma\, \delta\gamma - \sum_{i=1}^{6} P_i\, \delta q_i \right) \mathrm{d}t = 0 \end{aligned} \tag{33}$$

By using part integration for the first three terms of (33), the previous equation can be reformulated

$$\begin{aligned} &\int_{t_1}^{t_2} \left( \int_{l_0} \rho A\, \ddot{u}_G\, \delta u_G \,\mathrm{d}x + \int_{l_0} \rho A\, \ddot{w}_G\, \delta w_G \,\mathrm{d}x + \int_{l_0} \rho I\, \ddot{\theta}_G\, \delta\theta_G \,\mathrm{d}x \right) \mathrm{d}t \\ + &\int_{t_1}^{t_2} \left( \int_{l_0} EA\, \varepsilon\, \delta\varepsilon \,\mathrm{d}x + \int_{l_0} EI\, \kappa\, \delta\kappa \,\mathrm{d}x + \int_{l_0} k_s GA\, \gamma\, \delta\gamma \,\mathrm{d}x - \sum_{i=1}^{6} P_i\, \delta q_i \right) \mathrm{d}t = 0 \end{aligned} \tag{34}$$

The above equation is the starting point for further developments. The above Hamiltonian system exhibits the following properties. If external loads are conservative, the total energy of the beam element can be written as

$$\mathsf{K} + \mathsf{U}_{int} + \mathsf{U}_{ext} = \mathsf{constant} \tag{35}$$

The linear momentum is defined by

$$\mathsf{L} = \begin{bmatrix} \mathsf{L}_u \\ \mathsf{L}_w \end{bmatrix} = \int_{l_0} \rho A \begin{bmatrix} \dot{u}_G \\ \dot{w}_G \end{bmatrix} \mathrm{d}x \tag{36}$$

and the angular momentum by

$$\mathsf{J} = \int_{l_0} \rho A \begin{bmatrix} u_G \\ w_G \\ 0 \end{bmatrix} \times \begin{bmatrix} \dot{u}_G \\ \dot{w}_G \\ 0 \end{bmatrix} \mathrm{d}x + \int_{l_0} \rho I \begin{bmatrix} 0 \\ 0 \\ \dot{\theta}_G \end{bmatrix} \mathrm{d}x \tag{37}$$

In the above equations, $\dot{u}_G$, $\dot{w}_G$ and $\dot{\theta}_G$ are the global velocities of the centroid G of the cross-section.
The time derivative of the two momenta define the equations of motion:

$$\frac{\mathrm{d}}{\mathrm{d}t}\mathsf{L} = \begin{bmatrix} P_1 + P_4 \\ P_2 + P_5 \end{bmatrix} \tag{38}$$

and

$$\begin{aligned} \frac{\mathrm{d}}{\mathrm{d}t}\mathsf{J} &= (x_1 + u_1)\, P_2 - (z_1 + w_1)\, P_1 + (x_2 + u_2)\, P_5 \\ &- (z_2 + w_2) P_4 + P_3 + P_6 = M_{ext} \end{aligned} \tag{39}$$

from which it can be seen that, with vanishing external load, the linear momentum is a constant and, with vanishing external moments, the angular momentum is a constant. It should be noted that the expression "external load" refers to all possible loading conditions including reactions forces.

## 4 ENERGY-MOMENTUM METHOD

The classical midpoint time integration scheme is defined by the following equations:

$$\boldsymbol{q}_{n+\frac{1}{2}} = \frac{\boldsymbol{q}_{n+1} + \boldsymbol{q}_n}{2} = \boldsymbol{q}_n + \frac{1}{2}\Delta\boldsymbol{q} \tag{40}$$

$$\dot{\boldsymbol{q}}_{n+\frac{1}{2}} = \frac{\dot{\boldsymbol{q}}_{n+1} + \dot{\boldsymbol{q}}_n}{2} = \frac{\boldsymbol{q}_{n+1} - \boldsymbol{q}_n}{\Delta t} = \frac{\Delta\boldsymbol{q}}{\Delta t} \tag{41}$$

$$\ddot{\boldsymbol{q}}_{n+\frac{1}{2}} = \frac{\ddot{\boldsymbol{q}}_{n+1} + \ddot{\boldsymbol{q}}_n}{2} = \frac{\dot{\boldsymbol{q}}_{n+1} - \dot{\boldsymbol{q}}_n}{\Delta t} = \frac{2}{\Delta t^2}\Delta\boldsymbol{q} - \frac{2}{\Delta t}\dot{\boldsymbol{q}}_n \tag{42}$$

By extension of the classical midpoint rule, the average midpoint strains are developed in the context of energy-momentum method. This idea has been introduced in [22, 23]. The midpoint velocities are applied to both the kinematic fields and the strains because the nonlinear terms arise from both fields. This gives:

$$\int_{t_n}^{t_{n+1}} f(t)dt = f(t_{n+\frac{1}{2}})\Delta t = f_{n+\frac{1}{2}}\Delta t \tag{43}$$

$$f_{n+\frac{1}{2}} = f_n + \frac{\Delta t}{2}\dot{f}_{n+\frac{1}{2}} \tag{44}$$

where the function $f$ can represent both the kinematic $(u_G, w_G, \theta_G)$ and deformational quantities $(\varepsilon, \kappa, \gamma)$.

The application of the midpoint rule (43) to the Hamilton's principle (34) gives

$$\begin{aligned} \Delta t \;& \left( \int_{l_0} \rho A\, \ddot{u}_{G,n+\frac{1}{2}}\, \delta u_{G,n+\frac{1}{2}}\, \mathrm{d}x + \int_{l_0} \rho A\, \ddot{w}_{G,n+\frac{1}{2}}\, \delta w_{G,n+\frac{1}{2}}\, \mathrm{d}x + \int_{l_0} \rho I\, \ddot{\theta}_{G,n+\frac{1}{2}}\, \delta\theta_{G,n+\frac{1}{2}}\, \mathrm{d}x \right. \\ + \;& \int_{l_0} EA\, \varepsilon_{n+\frac{1}{2}}\, \delta\varepsilon_{n+\frac{1}{2}}\, \mathrm{d}x + \int_{l_0} EI\, \kappa_{n+\frac{1}{2}}\, \delta\kappa_{n+\frac{1}{2}}\, \mathrm{d}x + \int_{l_0} k_s GA\, \gamma_{n+\frac{1}{2}}\, \delta\gamma_{n+\frac{1}{2}}\, \mathrm{d}x \\ - \;& \left. \sum_{i=1}^{6} P_{i,n+\frac{1}{2}}\, \delta q_{i,n+\frac{1}{2}} \right) = 0 \end{aligned} \tag{45}$$

As the variation $\delta \boldsymbol{q}^{\mathrm{T}}$ is arbitrary, the dynamic equilibrium at time $n+\frac{1}{2}$ is obtained from the previous equation

$$\begin{aligned}
\boldsymbol{f}_{R,n+\frac{1}{2}} &= \int_{l_0} \rho A\, \ddot{u}_{G,n+\frac{1}{2}} \left(\frac{\partial u_{G,n+\frac{1}{2}}}{\partial \boldsymbol{q}_{n+\frac{1}{2}}}\right)^{\mathrm{T}} \mathrm{d}x + \int_{l_0} \rho A\, \ddot{w}_{G,n+\frac{1}{2}} \left(\frac{\partial w_{G,n+\frac{1}{2}}}{\partial \boldsymbol{q}_{n+\frac{1}{2}}}\right)^{\mathrm{T}} \mathrm{d}x \\
&+ \int_{l_0} \rho I\, \ddot{\theta}_{G,n+\frac{1}{2}} \left(\frac{\partial \theta_{G,n+\frac{1}{2}}}{\partial \boldsymbol{q}_{n+\frac{1}{2}}}\right)^{\mathrm{T}} + \int_{l_0} EA\, \varepsilon_{n+\frac{1}{2}} \left(\frac{\partial \varepsilon_{n+\frac{1}{2}}}{\partial \boldsymbol{q}_{n+\frac{1}{2}}}\right)^{\mathrm{T}} \mathrm{d}x \\
&+ \int_{l_0} EI\, \kappa_{n+\frac{1}{2}} \left(\frac{\partial \kappa_{n+\frac{1}{2}}}{\partial \boldsymbol{q}_{n+\frac{1}{2}}}\right)^{\mathrm{T}} \mathrm{d}x + \int_{l_0} k_s GA\, \gamma_{n+\frac{1}{2}} \left(\frac{\partial \gamma_{n+\frac{1}{2}}}{\partial \boldsymbol{q}_{n+\frac{1}{2}}}\right)^{\mathrm{T}} \mathrm{d}x \\
&- \boldsymbol{P}_{i,n+\frac{1}{2}} = 0
\end{aligned} \tag{46}$$

With the help of the second and third of Eqs. (40), the accelerations at midpoint are obtained as

$$\ddot{u}_{G,n+\frac{1}{2}} = \frac{2}{\Delta t}\, \dot{u}_{G,n+\frac{1}{2}} - \frac{2}{\Delta t}\, \dot{u}_{G,n} \tag{47}$$

$$\ddot{w}_{G,n+\frac{1}{2}} = \frac{2}{\Delta t}\, \dot{w}_{G,n+\frac{1}{2}} - \frac{2}{\Delta t}\, \dot{w}_{G,n} \tag{48}$$

$$\ddot{\theta}_{G,n+\frac{1}{2}} = \frac{2}{\Delta t}\, \dot{\theta}_{G,n+\frac{1}{2}} - \frac{2}{\Delta t}\, \dot{\theta}_{G,n} \tag{49}$$

and the strains at $n+\frac{1}{2}$ are obtained from Eq.(44) as

$$\varepsilon_{n+\frac{1}{2}} = \varepsilon_n + \frac{\Delta t}{2}\, \dot{\varepsilon}_{n+\frac{1}{2}} \tag{50}$$

$$\kappa_{n+\frac{1}{2}} = \kappa_n + \frac{\Delta t}{2}\, \dot{\kappa}_{n+\frac{1}{2}} \tag{51}$$

$$\gamma_{n+\frac{1}{2}} = \gamma_n + \frac{\Delta t}{2}\, \dot{\gamma}_{n+\frac{1}{2}} \tag{52}$$

The total tangent matrix is defined by

$$\mathbf{K}_{\mathrm{T}} = \frac{\partial \boldsymbol{f}_{R,n+\frac{1}{2}}}{\partial \boldsymbol{q}_{n+1}} \tag{53}$$

It can be observed that by updating the strains by integrated the strain velocity, see Eqs. (50)–(52), the obtained strains at $n+1$ are not equal to the strains (Eqs.(16)–(18)) determined from the total displacements and rotations at $n+1$. The similar concept is also applied to the acceleration quantities, see Eqs. (47)–(49). However, only these updated quantities by integrating from velocity guarantee energy conservation and also stability of the integration method.

## 5 NUMERICAL EXAMPLES

Two numerical examples are presented in this section. The first purpose is to verify that the proposed algorithm conserves the total energy of the system and remain stable even if a very large number of time steps are applied. The second purpose is to show that the proposed algorithm conserves the linear and angular momenta in the absence of applied external loads.

### 5.1 Simple beam

A simply-supported beam depicted in Figure 2 is subjected to a vertical concentrated load $P = 4.1$ MN at mid-span. The length of the beam is $L = 1$ m. The cross-section width and depth are $b = 0.20$ m and $h = 0.15$ m. The material parameters are: elastic modulus $E = 1$ GPa, Poisson's ratio $\nu = 0.3$, density $\rho = 7850$ kg/m$^3$. The number of elements in this example is 8. The time step size is $\Delta t = 10^{-4}$ s. The interest of this example is that, for this short beam, the shear effect is important.

The horizontal displacement at the right end and the vertical displacement at mid-span are depicted in Figures 3 and 4. Therefore, large displacements can be observed. In Figure 5, it is shown that the proposed energy-momentum method conserves the total energy of the system ,and that the solutions remain stable for one million time steps.

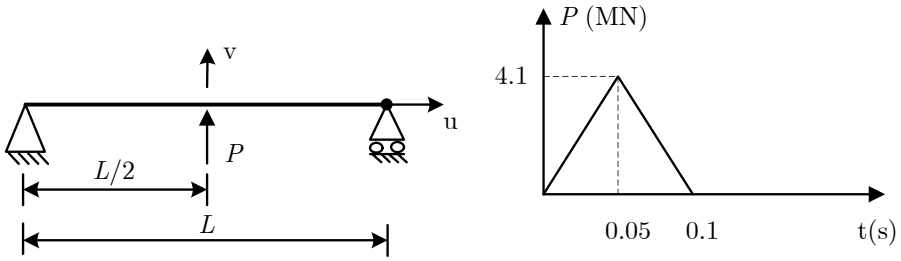


Figure 2: Geometry and loading of simple beam

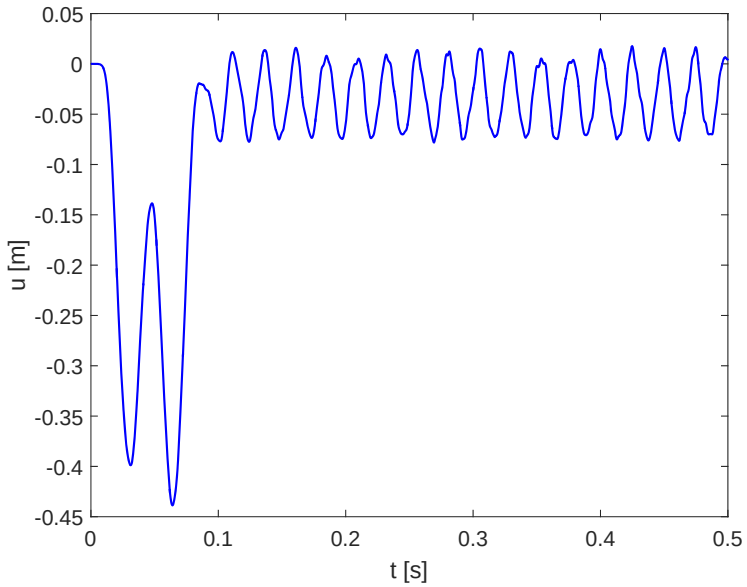


Figure 3: Horizontal displacement u [m] of simple beam

### 5.2 Free fly beam

Consider a free fly beam without support subjected to a triangle load $P = 3 \times 10^5$ N, see Figure 6. The length of the beam is $L = 3$ m, the cross-sectional area is $A = 0.02$ m$^2$ and the moment of inertia $I = 66.67 \times 10^{-8}$ m$^4$. The material properties are: elastic modulus $E = 200$

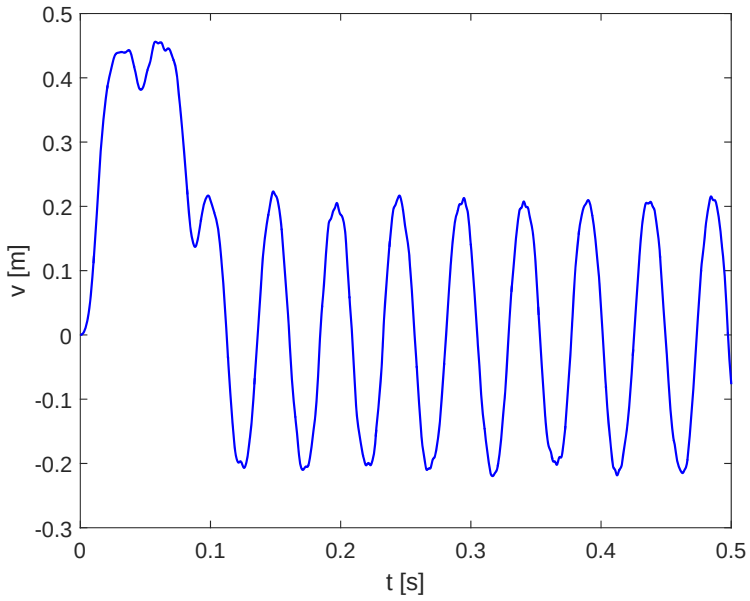


Figure 4: Vertical displacement v [m] of simple beam

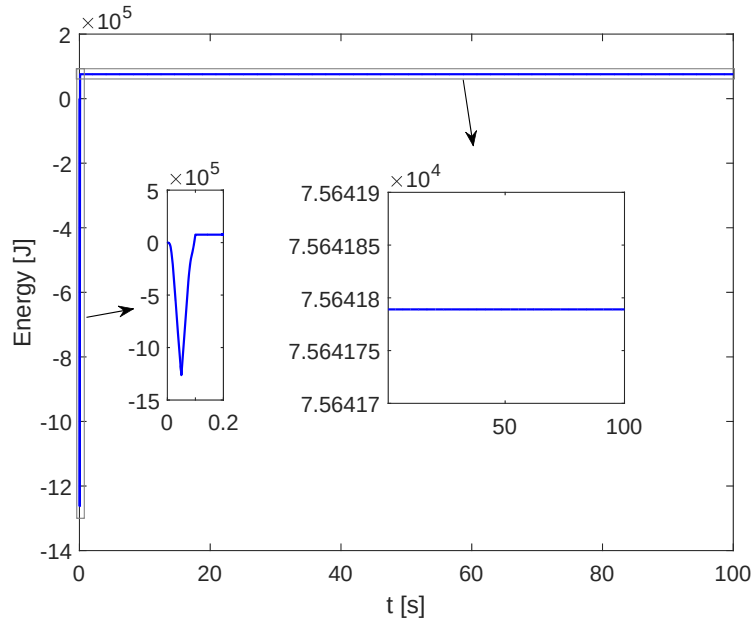


Figure 5: Energy [J] of simple beam

GPa, Poisson's ratio $\nu = 0.3$, density $\rho = 48831$ kg/m$^3$. The number of elements is $4$ and the time step size is $\Delta t = 10^{-4}$ s.

In Figure 7, the vertical displacement at mid-span is depicted. It is shown that the beam moves in a long distance $2045$ m at $100$ s with the speed $73.62$ km/h. In addition, the result in Figure 8 shows the conservation of the total energy even if one million time steps are applied.

The interest of this problem is to study the conservation of the linear and angular momenta after the time $0.4$s because no forces and moments are then applied to the beam. Since only vertical loads are applied at the beginning, the linear momentum Lu in the horizontal direction should be zero. As shown in Figure 9, the linear momentum Lu is almost zeros with the maxi-

mum value of $2 \times 10^{-5}$. Moreover, Figures 9 and 10 show the conservation of linear momentum Lw in the vertical direction and angular momentum for one million time steps.

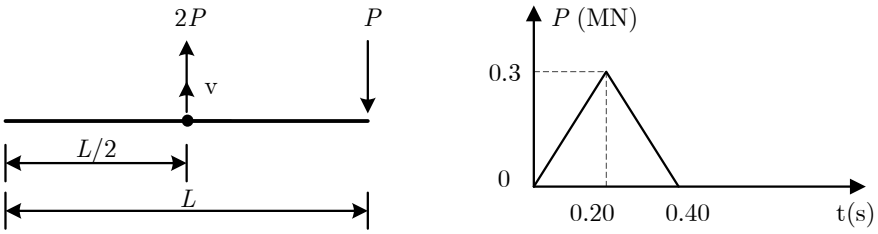


Figure 6: Geometry and loading of free fly beam

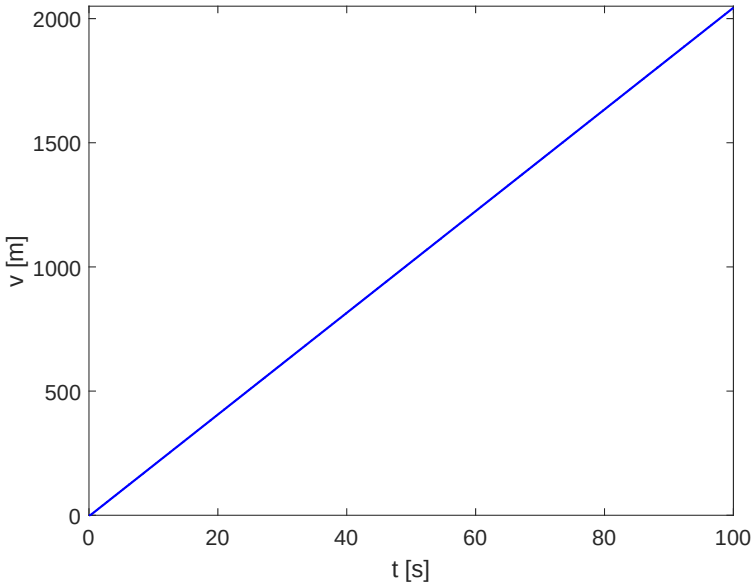


Figure 7: Vertical displacement [m] of free fly beam

## 6 CONCLUSION

This paper has presented an energy-momentum method for co-rotational planar shear flexible beams. The main idea is to use the classical midpoint rules for both the kinematic and strain quantities. The advantage of the proposed algorithm is that it conserves the total energy of the system and remains stable and accurate even if a very large number of time steps are applied. Besides, in the absence of applied external loads, the linear and angular momenta are constant. These characteristics have been proved numerically by using two numerical applications.

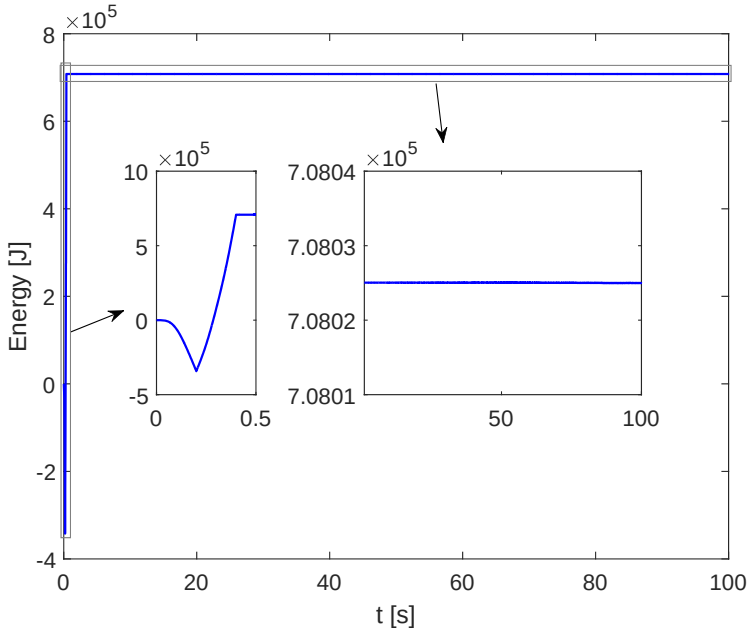


Figure 8: Energy [J] of free fly beam

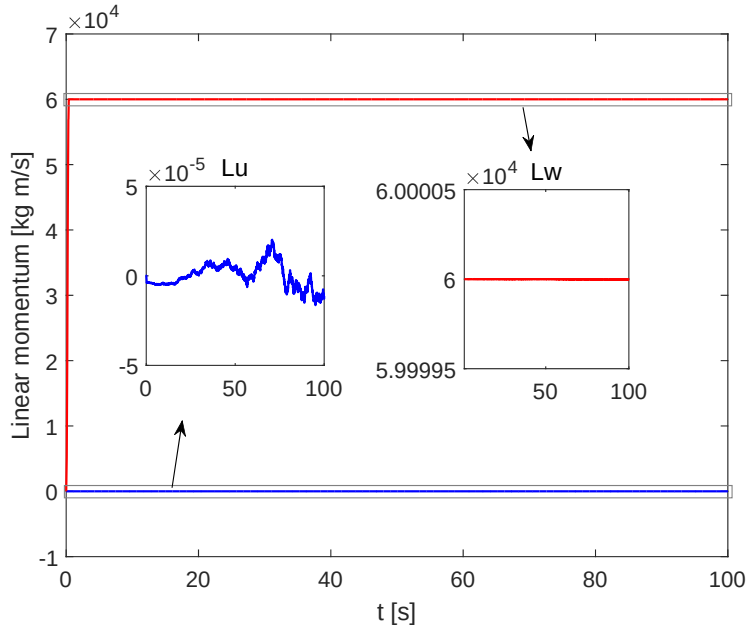


Figure 9: Linear momentum [kg m/s] of free fly beam

## ACKNOWLEDGEMENTS

The first and the second authors gratefully acknowledge financial support by the European Commission (Research Fund for Coal and Steel) through the project RobustImpact under grant agreement RFSR-CT-2012-00029 and the financial support of the region of Brittany (France) through the ARED funding scheme.

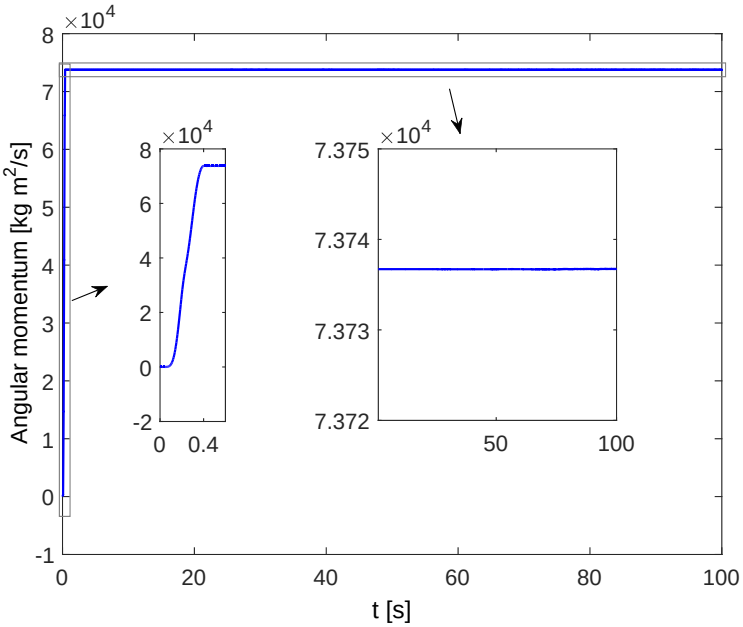


Figure 10: Angular momentum J [kg $m^2$/s] of free fly beam

## REFERENCES

[1] M.A. Crisfield, U. Galvanetto, G. Jelenić, Dynamics of 3-D co-rotational beams. *Computational Mechanics*, **20**, 507–519, 1997.

[2] M.A. Crisfield, J. Shi, An energy conserving co-rotational procedure for non-linear dynamcis with finite elements. *Nonlinear Dynamics* **9**, 37–52, 1996.

[3] T.-N. Le, J.-M. Battini, M. Hjiaj, Efficient formulation for dynamics of corotational 2D beams. *Computational Mechanics*, **48**, 153–161, 2011.

[4] M. Iura, S.N. Atluri, Dynamic analysis of planar flexible beams with finite rotaions by using inertial and rotating frames. *Computers and Structures*, **55**, 453–462, 1995.

[5] U. Galvanetto, M.A. Crisfield, An energy-conserving co-rotational procedure for the dynamics of planar beam structures. *International Journal for Numerical Methods in Engineering*, **39**, 2265–2282, 1996.

[6] K.M. Hsiao, J.Y. Lin, W.Y. Lin, A consisten co-rotational finite element formulation for geometrically nonlinear dynamic analysis of 3-D beams. *Computer Methods in Applied Mechanics and Engineering*, **169**, 1–18, 1999.

[7] Y. Urthaler, J.N. Reddy, A corotational finite element formulation for the analysis of planar beams. *Communications in Numerical Methods in Engineering*, **21**, 553–570, 2005.

[8] T.-N. Le, J.-M. Battini, M. Hjiaj, Dynamics of 3D beam elements in a corotational context: A comparative study of established and new formulations. *Finite Elements in Analysis and Design*, **61**, 97–111, 2012.

[9] T.-N. Le, J.-M. Battini, M. Hjiaj, A consistent 3D corotational beam element for nonlinear dynamic analysis of flexible structures. *Computer Methods in Applied Mechanics and Engineering*, **269**, 538–565, 2014.

[10] T.-N. Le, J.-M. Battini, M. Hjiaj, Corotational formulation for nonlinear dynamics of beams with arbitrary thin-walled open cross-sections. *Computers and Structures*, **134**, 112–127, 2014.

[11] M.A. Crisfield, J. Shi, A co-rotational element/time-integration strategy for non-linear dynamics. *International Journal for Numerical Methods in Engineering*, **37**, 1897–1913, 1994.

[12] J. Salomon, A.A. Weiss, B.I. Wohlmuth, Energy-conserving algorithms for a corotational formulation. *SIAM Journal on Numerical Analysis*, **46**, 1842–1866, 2008.

[13] J.N. Reddy, On locking-free shear deformable beam finite elements. *Computer Methods in Applied Mechanics and Engineering*, **149**, 113–132, 1997.

[14] H.M. Hilber, T.J.R. Hughes, R.L. Taylor, Improved numerical dissipation for time integration algorithms in structural dynamics. *Earthquake Engineering Strucuture Dynamic*, **5**, 282–292, 1977.

[15] M. Geradin, A. Cardona, *Flexible Multibody Dynamics. A Finite Element Approach*. John Wiley and Sons, 2001.

[16] J.C. Simo, N. Tarnow, The discrete energy-momentum method. Conserving algorithms for nonlinear elastodynamics. *Journal of Applied Mathematics and Physics*, **43**, 757–792, 1992.

[17] J.C. Simo, N. Tarnow, M. Doblar, Non-linear dynamics of three-dimensional rods: Exact energy and momentum conserving algorithms. *International Journal for Numerical Methods in Engineering*, **38**, 1431–1473, 1995.

[18] M. Gams, I. Planic, M. Saje, Energy conserving time integration scheme for geometrically exact beam. *Computer Methods in Applied Mechanics and Engineering*, **196**, 2117–2129, 2007.

[19] C. Sansour, T.-L. Nguyen, M. Hjiaj, An energy-momentum method for in-plane geometrically exact Euler-Bernoulli beam dynamcis. *International Journal for Numerical Methods in Engineering*, **102**, 99–134, 2015.

[20] I. Romero, F. Armero, An objective finite element approximation of the kinematics of geomtrically exact rods and its use in the formulation of an energy-momentum conserving scheme in dynamics. *International Journal for Numerical Methods in Engineering*, **54**, 1683–1716, 2002.

[21] D. Kuhl, M.A. Crisfield, Energy-conserving and decaying algorithms in non-linear structural dynamics. *International Journal for Numerical Methods in Engineering*, **45**, 569–599, 1999.

[22] C. Sansour, W. Wagner, P. Wriggers, J. Sansour, An energy momentum integration scheme and enhanced strain finite elements for the non-linear dynamics of shells. *International Journal of Non-linear Mechanics*, **37**, 951–966, 2002.

[23] C. Sansour, P. Wriggers, J. Sansour, Nonlinear dynamics of shells: theory finite element formulation, and integration schemes. *Nonlinear Dynamics*, **13**, 279–305, 1997.

[24] C. Sansour, P. Wriggers, J. Sansour, On the design of energy-momentum integration schemes for arbitrary continuum formulations. Applications to classical and chaotic motion of shells. *International Journal for Numerical Methods in Engineering*, **60**, 2419–2440, 2004.

[25] M. Gams, I. Planinc, M. Saje, A heuristic viscosity-type dissipation for high frequency oscillication damping in time integration algorithms. *Computational Mechanics*, **41**, 17–29, 2007.

COMPDYN 2017
6th ECCOMAS Thematic Conference on
Computational Methods in Structural Dynamics and Earthquake Engineering
M. Papadrakakis, M. Fragiadakis (eds.)
Rhodes Island, Greece, 15–17 June 2017

# NUMERICAL STUDY ON SEISMIC RESPONSE ANALYSIS OF THE PLATE GIRDER BRIDGE DAMAGED BY THE 2016 KUMAMOTO EARTHQUAKE

**MYA NAN AYE[1], AKIRA KASAI[2], and ZHIPENG LIU[1]**

[1]Graduate School of Science and Technology, Civil and Environmental Engineering, Kumamoto University
Kurokami 2-39-1, Chuo-ku, Kumamoto City, 860-8555, Japan, Tel: 096-342-3579
e-mail: 154d9410@st.kumamoto-u.ac.jp, 169d8837@st.kumamoto-u.ac.jp

[2]Associate Professor, Faculty of Advanced Science and Technology, Division of Materials Science, Kumamoto University
Kurokami 2-39-1, Chuo-ku, Kumamoto City, 860-8555, Japan, Tel: 096-342-3579
e-mail: kasai@kumamoto-u.ac.jp

**Keywords:** Seismic response analysis, 2016 Kumamoto earthquake, Local buckling behavior, Damage survey, Tawarayama Bridge

**Abstract.** *In 2016 Kumamoto Earthquake, many buildings, embankment structures and transportation infrastructures have been damaged. This paper presents damage survey of a plate girder bridge, namely Tawarayama Bridge which is situated on Kumamoto Prefectural road No 28, Tawarayama bypass, where the damage related to the bridge is enormous and elucidates the damage mechanism that can occur in that type of bridge due to earthquake with epicenter which is very close to bridge.*

*At first, the parts of Tawarayama Bridge are investigated in order to find out the damages and examine the factors of occurrence. Then, seismic response analysis of Tawarayama Bridge subjected to 2016 Kumamoto earthquake motion is carried out. In observing the damages, the local buckling behavior of steel main girders are found. So shell elements are applied in finite element model to consider local buckling behavior. Frequency analysis is carried out to grasp the vibration characteristics and after that, the time history response analyses are performed using earthquake ground motion in both longitudinal and transverse directions to investigate the dynamic response of the bridge. The predicted earthquake motion simulated by* Professor Yoshiya Hata from Osaka University *is applied for dynamic response analysis. Finally, the results for comparison of numerical results with real disasters are discussed.*

## 1 INTRODUCTION

On 2016 April 14, an earthquake of magnitude 6.5 (JMA seismic intensity of 7) hit the Kumamoto region, Japan. That earthquake is the fore shock followed by main shock which hit on 2016 April 16 with the magnitude of 7.3 (JMA seismic intensity of 7). There are more than 140 aftershocks within 2 days including at least 11 with magnitude of 4.5 and one with 6. Mashiki town and Higashi ward of Kumamoto are severely effected as the epicenters are located there. Due to the effect of these earthquakes, many buildings and transportation infrastructures are damaged.

## 2 SUMMARY OF EARTHQUAKE DATA

According to JMA (Japanese Meteorological Agency), 7 earthquakes with large intensity (4 with magnitude 5.4 to 5.9, 2 with 6.4 to 6.5 and one with 7.3) are occurred in same area from April 14 to 16. Table 1 shows the magnitude, maximum seismic intensity, ground surface acceleration and depth of two main shocks and Figure 1 is the location map of Kumamoto, Mashiki and Mount Aso.

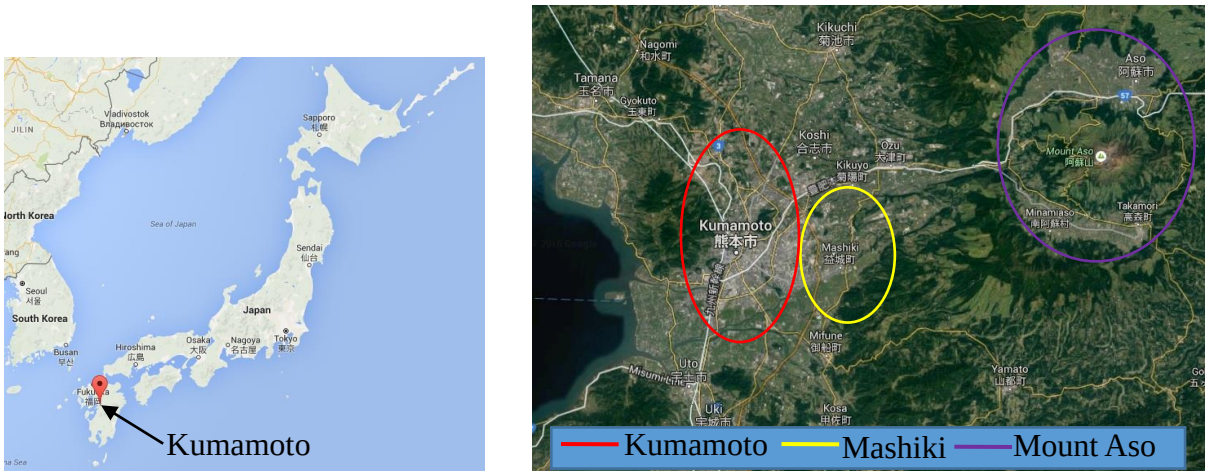


Figure 1. Location of Kumamoto, Mashiki and Mount Aso

| Earthquake Name | Magnitude | Maximum Seismic Intensity | Acceleration (N-S or E-W) | Depth |
|---|---|---|---|---|
| 2016 April 14, 21:26 (Fore Shock) | 6.5 | 7 (Mashiki)<br>6 (Kumamoto) | 925 cm/s$^2$ (Mashiki)<br>574 cm/s$^2$ (Kumamoto) | 10 km |
| 2016 April 16, 01:25 (Main Shock) | 7.3 | 7 (Mashiki, Nishihara)<br>6 (Kumamoto) | 1156 cm/s$^2$ (Mashiki)<br>827 cm/s$^2$ (Kumamoto) | 10 km |

Soure: JMA (Japan Meteorological Agency)

Table 1. Magnitude, Maximum Seismic Intensity, Acceleration and Depth of Main Shocks

## 3 OVERVIEW OF BRIDGE DAMAGES

Among 3000 bridges in Kumamoto Prefecture, about 40 bridges, including Aso Bridge and Minami-Aso Bridge, are severely affected by the earthquake and others 70 bridges under Kumamoto Prefecture administration are damaged also. Apart from these, JR Kyushu Shinkansen (Bullet Train) has been suspended due to damage of bridge on Kyushu Expressway.

Although most bridge piers are not damaged after foreshock, many bridges are severely damaged after main shock. In Kumamoto region, the phenomenon of pier settlements is found as characteristic damage. By looking the location of damage bridges on map, it is clear that most of the bridges that damaged are concentrated near fault.

Bridges on Tawarayama bypass which is an important route that connects the Kumamoto Prefecture and Miyazaki Prefecture are also damaged. This paper will mainly focus on damages of Tawarayama Bridge which is plate girder bridge and numerical study on seismic analysis of that bridge.

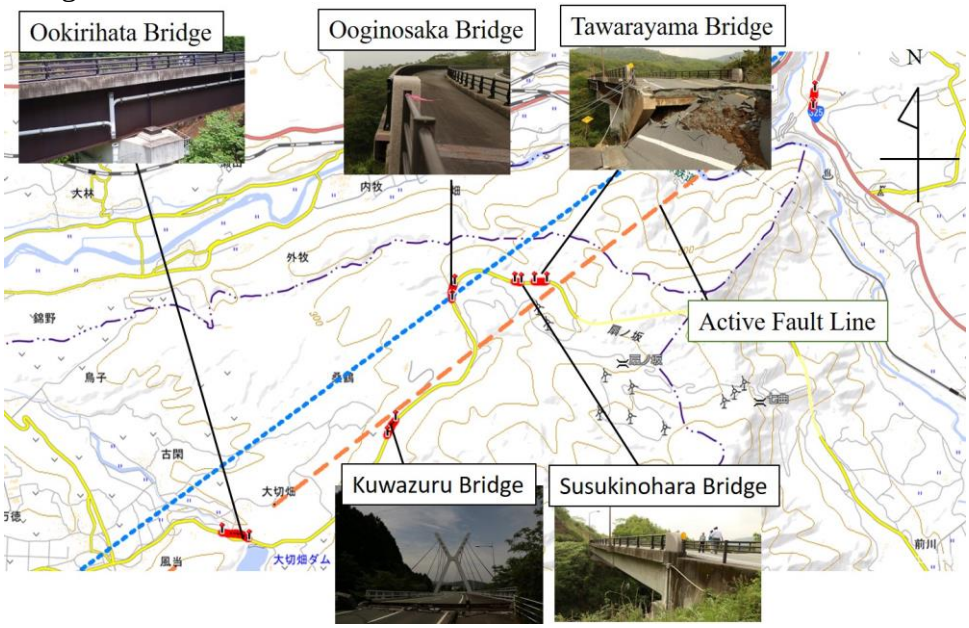


Figure 2. Location of damage bridges on Tawarayama bypass

## 4 OVERVIEW OF TAWARAYAMA BRIDGE

Tawarayama Bridge is a 3-span girder bridge of total length 140 m with maximum span length of 61.5m and effective width of 8.5 m. Substructure consists of inverted T type abutment (A1, A2) and overhang pier (P1, P2) and foundation consists of caisson pile. Figure 3 shows the longitudinal profile of the bridge. Figure 4 is the plan view of bridge in which A1 represents abutment of Kumamoto side and A2 represents that of Takamori side.

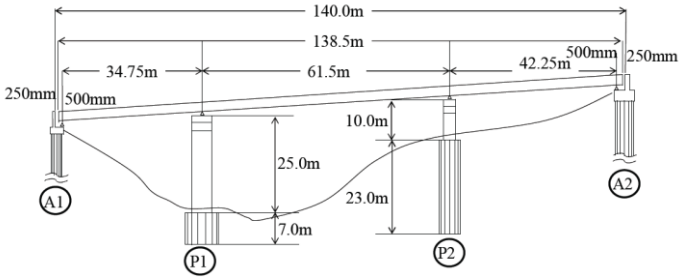


Figure 3. Longitudinal profile

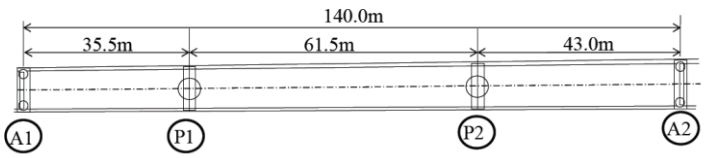


Figure 4. Plan view

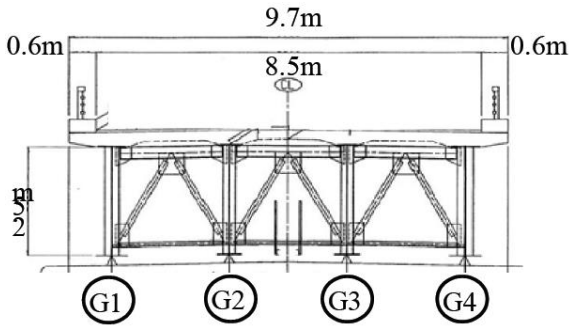


Figure 5. Cross section of superstructure

For the piers, it is represented as P1 and P2 from Kumamoto side. Figure 5 shows the cross-section of superstructure. A1 and A2 abutments are constructed as single column with deep foundation. The bridge is nearly straight and adopted the cable type girder prevention structure which connects the girder and the bridge abutment parapet as a bridge collapse prevention structures. Rubber bearing is used and side block is provided at the girder ends only.

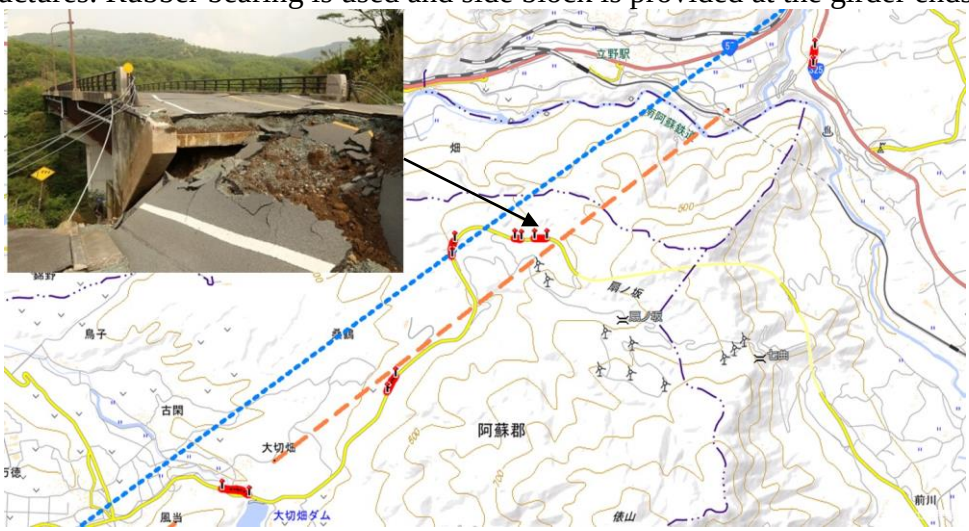


Figure 6. Location of Tawarayama Bridge

## 5 DAMAGE SURVEY OF TAWARAYAMA BRIDGE

Tawarayama Bridge which situate on Tawarayama bypass is also damaged by the 2016 Kumamoto earthquake as it is very near to active fault line. The deformation of the whole bridge can be seen in Figure 7 which was produced by 3D scanner technique. The damages of the bridge is found as follows.

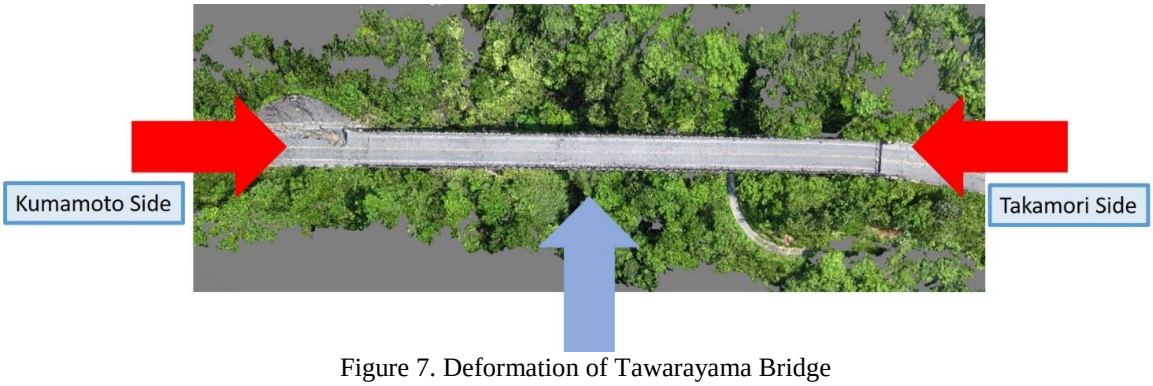


Figure 7. Deformation of Tawarayama Bridge

The settlement of deck slab is occurred at the east side (A2 side) of the bridge due to the girders falling off from the rubber bearings and the abutment tilting. The deck slab settlement of 53cm was seen as shown in Figure 8.

At the west side (A1 side), it is seen that road embankment has collapsed due to the soil movement and caused exposing of the pile foundation under the abutment. It may be due to large compressive force and future consideration should be made for specific result.



Figure 8. Damage of A2 abutment (East side)



Figure 9. Damage of A1 abutment (West side)



Figure 10. Deformation of main girder

Figure 10 shows the deformation of main girder and P1 pier seen from A1 side. The deformation can be found about 20 m from A1 side while moving towards P1. The deformation of G3 girder is shown in Figure 11. It has confirmed that the bucking in the vicinity of the lower lateral structure is occurred. The impinging of lower horizontal members buckling may be due to acting of compressive force on the bridge deck from both the A1 and A2 abutments, or, approaching of the abutments towards the bridge girder.



Figure 11. Deformation of girder 3

In this paper, this fact is raised as the most important destructive mechanism. The extent of compressive force which should be assumed for the seismic design of bridge girder, has not verified yet. In addition, the ground motion was larger than assumed so it is needed to identify the sites ground motion. According to this survey, it can be suggested that in future, seismic design of bridge girder should be considered based on the buckling phenomenon of bridge girder in response of seismic intensity 7 ground motion, especially at the vicinity of the girder ends.

## 6 SEISMIC RESPONSE ANALYSIS

ABAQUS software is used to create finite element model of Tawarayama Bridge. In this model, shell elements are applied to take account the local buckling behavior as such behavior of steel main girders are found in observing the damages. In addition, beam elements are used for considering whole buckling behavior. L-beam, T-beam and I-beam are used for cross-bracing, top and bottom chord, and cross-beams respectively. Solid elements for pier and abutment, and spring elements for bearing are applied in FE model. The material properties of the model used in the numerical analysis were, SM490 with yield stress ($\sigma_y$) of 400MPa and Young Modulus (E) of 205GPa for steel and concrete with Young Modulus (E) of 30.35GPa.

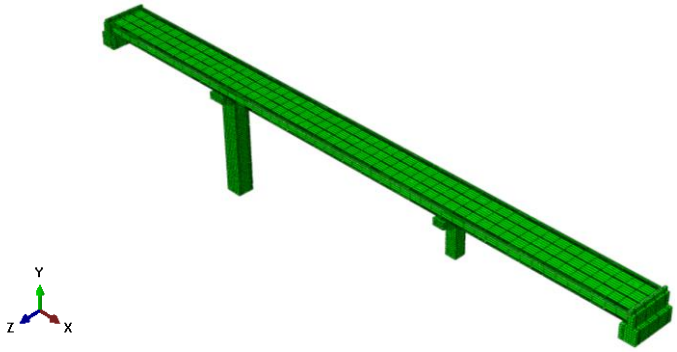


Figure 12. Finite Element Model of Tawarayama Bridge

### 6.1 Calculation of spring stiffness from properties of rubber bearing

In modeling Tawarayama Bridge, spring element is used for rubber bearing and the spring stiffness to be applied are calculated from properties of damper by using following formulae.

For horizontal direction,

$$K_{so} = (G_0 A)/(\sum t_e) \quad (1)$$

$$K_{st} = (G_0 A)/(\sum t_e) \quad (2)$$

For vertical direction,

$$K_v = (EA)/(\sum t_e) \quad (3)$$

where,

$$E = (3+6.58S^2)\ (0.5 \le b/a \le 2) \quad (4)$$

$$S = ab/(2(a+b)\ t_e) \quad (5)$$

$$E = (4+3.29S^2)\ (b/a<0.5,\ b/a>2) \quad (6)$$

$$S = a/2t_e \quad (7)$$

$K_{so}$, $K_{st}$, $K_v$ = spring stiffness in horizontal and vertical direction
$G_0$ = shear modulus
A = area of rubber bearing
$t_e$ = thickness of laminated rubber
E = Young's modulus
S = shape factor
a = width of rubber bearing
b = length of rubber bearing

The springs are installed at A1, P1, P2 and A2 between abutments or piers and girders. At each abutment and piers, 4 springs are installed under each girder. The values of each parameter used and calculated spring stiffness are shown in Table 2.

| Part | $G_0$ ($N/mm^2$) | a (mm) | b (mm) | A ($mm^2$) | $t_e$ (mm) | n | $\Sigma t_e$ (mm) | S | E ($N/mm^2$) | $K_{so}$ (Nm/mm) | $K_{st}$ (tf/cm) | $K_v$ (tf/cm) |
|---|---|---|---|---|---|---|---|---|---|---|---|---|
| A1 | 0.785 | 450 | 450 | 202500 | 12 | 17 | 204 | 9.375 | 456.064 | 794.117 | 794.117 | 461637 |
| P1 | 1.177 | 600 | 650 | 390000 | 22 | 5 | 110 | 7.091 | 392.883 | 4252.54 | 4252.54 | 1420410 |
| P2 | 1.177 | 750 | 750 | 562500 | 36 | 3 | 108 | 5.208 | 213.555 | 6250 | 6250 | 1134190 |
| A2 | 0.785 | 450 | 450 | 202500 | 13 | 11 | 143 | 8.654 | 388.961 | 1132.87 | 1132.87 | 561661 |

Table 2. Properties of rubber bearing and spring stiffness

## 6.2 Eigenvalue analysis

To grasp the vibration characteristics, the eigenvalue analysis was carried out. Natural periods and effective mass ratios of each predominant mode obtained from ABAQUS are presented in Table 3.

According to eigenvalue analysis result, it is observed that the 1st mode is translation in transverse direction (Z-axis), 2nd mode is vertical rotation, 3rd mode is translation in longitudinal direction (X-axis) and 4th mode is deflection. Maximum value of effective mass ratio for x, y and z component, longitudinal, tranverse and in plane direction, are found at mode 3, 9 and 1 respectively. That for x, y, z rotation are found at mode 8, 2 and 9.

| MODE | Eigenvalue | Frequency (Cycle/time) | Effective Mass Ratio | | | | | |
|---|---|---|---|---|---|---|---|---|
| | | | X-component | Y-component | Z-component | X-rotation | Y-rotation | Z-rotation |
| 1 | 33.829 | 0.92568 | 0.00000 | 0.00000 | 0.37221 | 0.03130 | 0.08588 | 0.00000 |
| 2 | 41.597 | 1.0265 | 0.00000 | 0.00000 | 0.26612 | 0.04693 | 0.71332 | 0.00000 |
| 3 | 42.606 | 1.0389 | 0.67256 | 0.00000 | 0.00000 | 0.00000 | 0.00190 | 0.00084 |
| 4 | 195.3 | 2.2242 | 0.00107 | 0.17451 | 0.00000 | 0.04119 | 0.00000 | 0.08490 |
| 5 | 202.44 | 2.2645 | 0.00000 | 0.00001 | 0.00008 | 0.00070 | 0.00009 | 0.00000 |
| 6 | 353.1 | 2.9907 | 0.00000 | 0.00000 | 0.11648 | 0.05998 | 0.03159 | 0.00000 |
| 7 | 410.55 | 3.2248 | 0.32490 | 0.00045 | 0.00000 | 0.00010 | 0.00094 | 0.00452 |
| 8 | 418.66 | 3.2565 | 0.00000 | 0.00000 | 0.17497 | 0.41388 | 0.04317 | 0.00000 |
| 9 | 611.62 | 3.9361 | 0.00058 | 0.35867 | 0.00000 | 0.08484 | 0.00000 | 0.73175 |
| 10 | 846.23 | 4.6298 | 0.00000 | 0.00000 | 0.00041 | 0.05812 | 0.00118 | 0.00000 |

Table 3. Eigen value analysis result

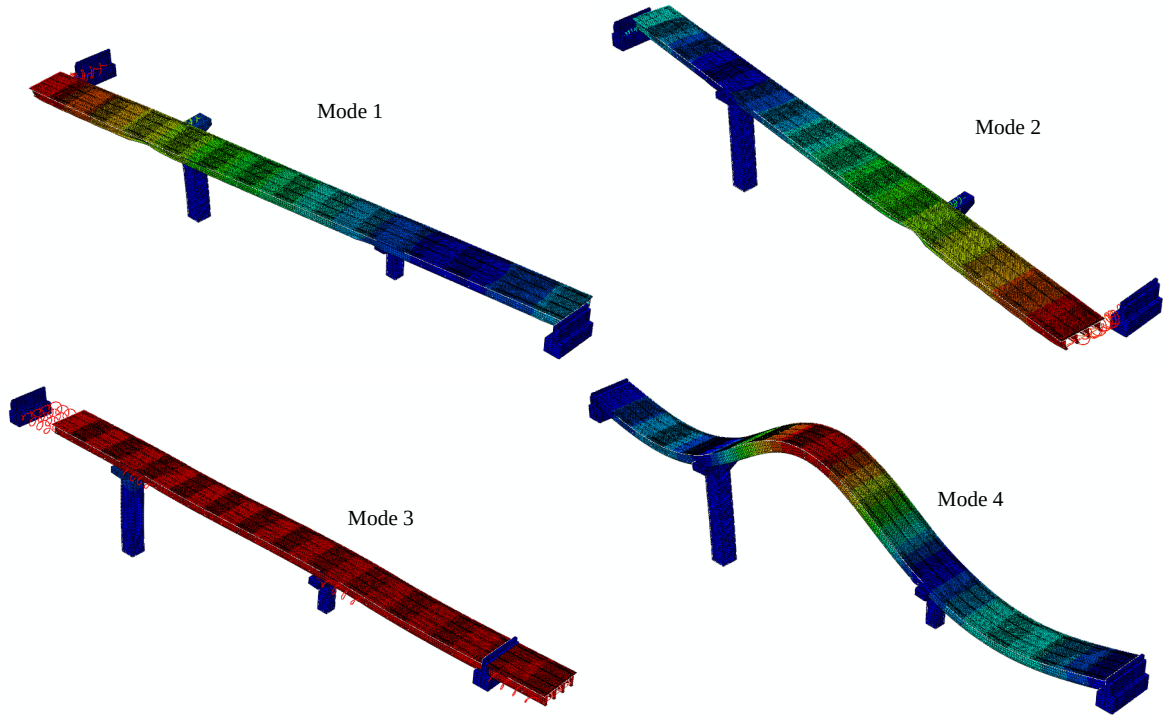


Figure 13. Mode shapes

## 6.3 Seismic input data

The predicted ground motion simulated by Professor Yoshiya Hata from Osaka University is used as seismic input data and that earthquake acceleration waves for East-West direction and North-South direction are illustrated in Figure 14 and 15. In Tawarayama Bridge, East-West is longitudinal direction and North-South is the transverse direction. Both longitudinal and transverse directions are considered to investigate the dynamic response of the bridge.

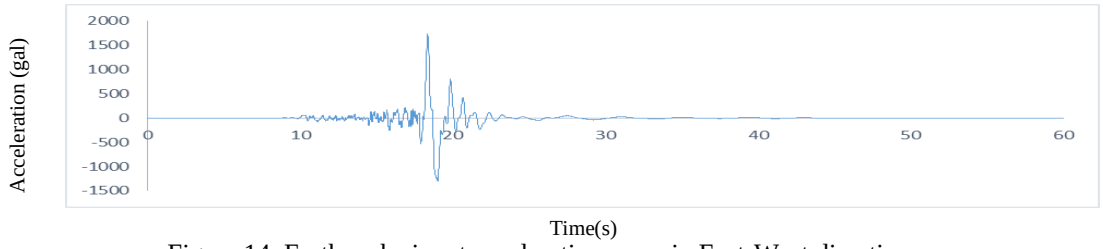


Figure 14. Earthquake input acceleration wave in East-West direction

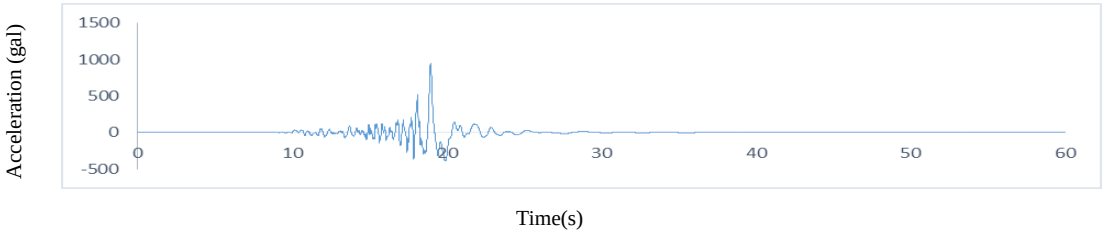


Figure 15. Earthquake input acceleration wave in North-South direction

### 6.4 Numerical analysis

For the numerical analysis, constant time step of 0.01sec is utilized. The seismic response analysis with ground acceleration input and a constant dead load is performed using the FEM ABAQUS program.

## 7 RESULTS AND DISCUSSION

### 7.1 Deformation of spring elements

This section will be discuss the deformation of spring elements used for rubber bearings. The load-displacement relationship curve of spring elements at each location are presented in longitudinal and transverse direction.

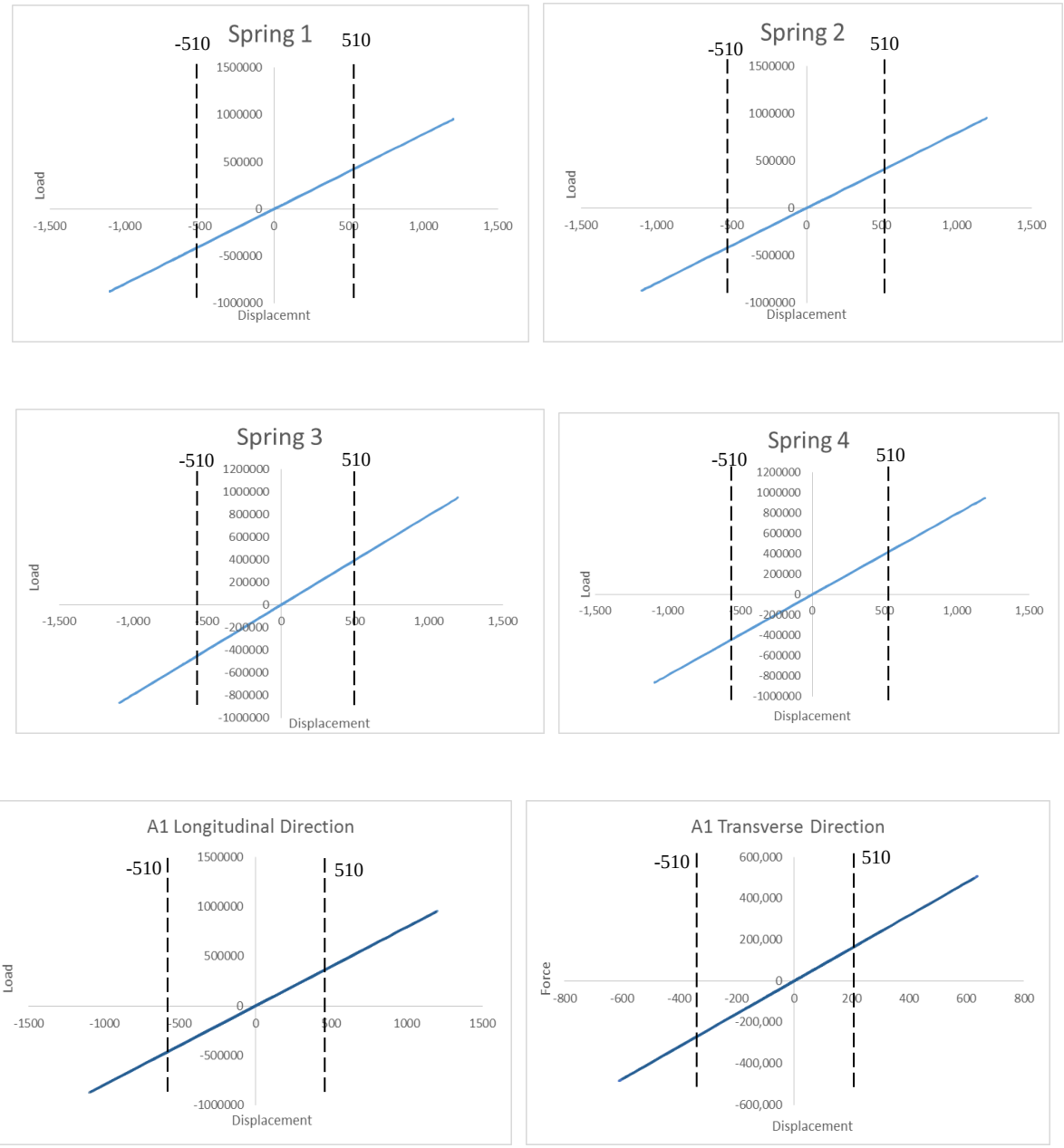


Figure 16. Stress-strain curves for spring at A1 abutment

The displacement in longitudinal direction found to be maximum for all springs. For the longitudinal direction, the value of displacement decrease from G4 to G1 in all A1, P1, P2 and A2. In transverse direction, the displacement decrease in the order G2, G3, G4 to G1 in abutments and decrease in order G2, G3, G1 to G4 in piers.

It is found that the displacement of all springs exceeds their displacement criteria except springs at P2 in transverse direction. The dotted lines in the Figure 16-19 shows the displacement criteria of spring elements from the theoretical point of view.

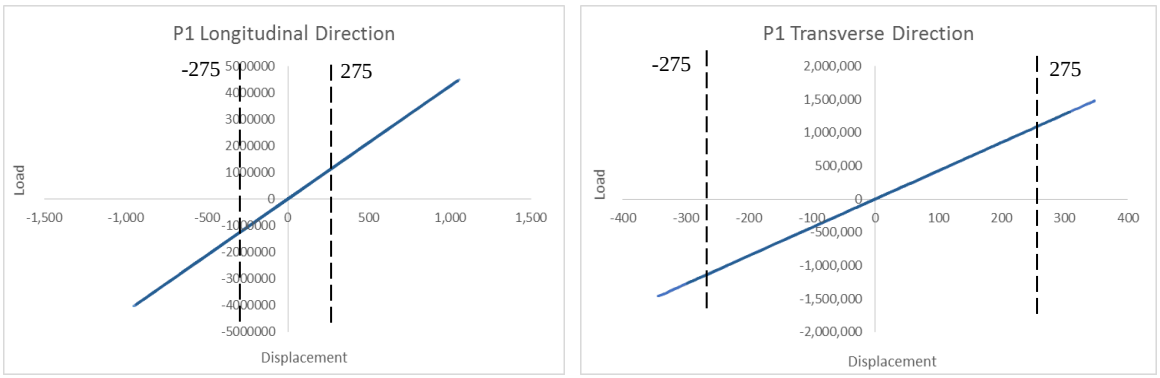


Figure 17. Stress-strain curves for spring at P1 pier

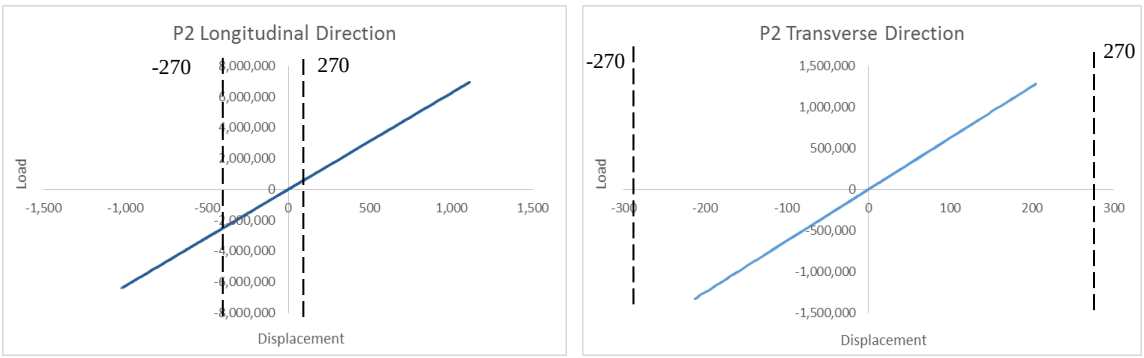


Figure 18. Stress-strain curves for spring at P2 pier

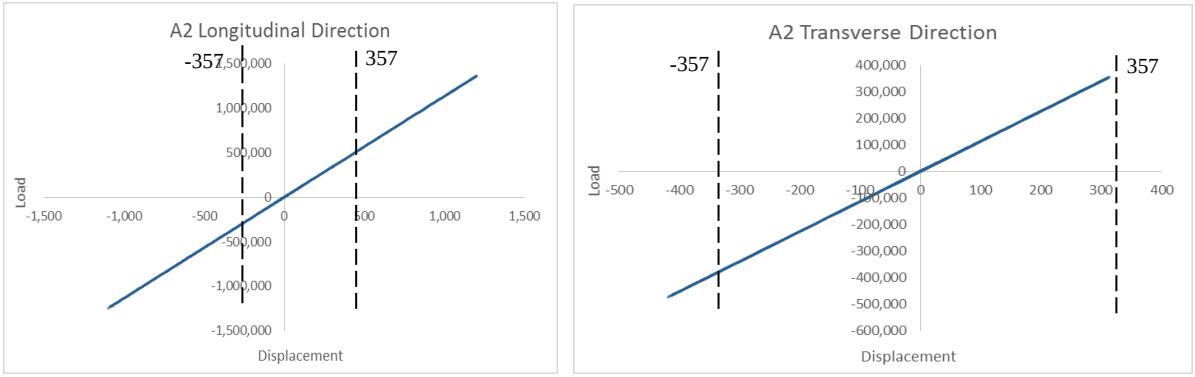


Figure 19. Stress-strain curves for spring at A2 abutment

## 7.2 Buckling of lower lateral members

Buckling of lower lateral members will be presented in this section. According to the Euler's buckling formula, buckling load can be presented by the following formula.

$$P_{cr} = \pi^2 EI/L_e^2 \quad (7)$$

The member section used for lower lateral members in Tawarayama Bridges is T 95 x 152 x 8 x 8 and the yield stress of the steel is 400 MPa. The following table describe the Euler's buckling loads according to the boundary conditions and the yield load of member used for lower lateral members.

| | Pinned-Pinned | Fixed-Free | Fixed-Fixed | Fixed-Pinned |
|---|---|---|---|---|
| K | 1 | 2 | 0.5 | 0.7 |
| E (GPa) | 205 | 205 | 205 | 205 |
| I ($mm^4$) | 4684000 | 4684000 | 4684000 | 4684000 |
| $L_e$ (mm) | 2600 | 5200 | 1300 | 1820 |
| A ($mm^2$) | 1912 | 1912 | 1912 | 1912 |
| Yield load (N) | 764800 | 764800 | 764800 | 764800 |
| $P_{cr}$ (N) | 1401922 | 350480 | 5607687 | 2861065 |

Table 4. Yield load and Euler's buckling according to boundary condition

Figure 20 shows the location of buckled members which are in most serious condition and labelled as 1 to 6 so as to clear for further explanation. These members are found buckled in actual condition also.

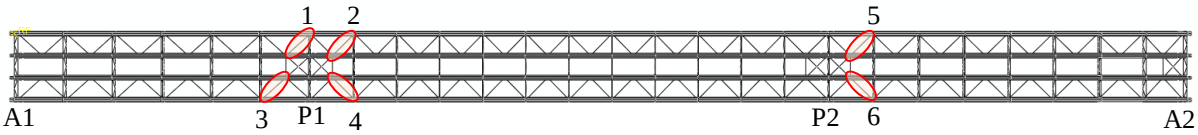


Figure 20. Location of buckled members

According to the displacement time history response, it is clear that displacement in longitudinal direction is greater than that in transverse direction. Displacement response according to time history is almost the same at ends and center position although noticeable differences are found in some members like in transverse direction of member 3 and 4. The maximum member forces of all members except member 1 in compression and tension are approximately 760000 N which is close to yield stress of the members. That of member 1 is around 400000 N which is much less than yield stress.

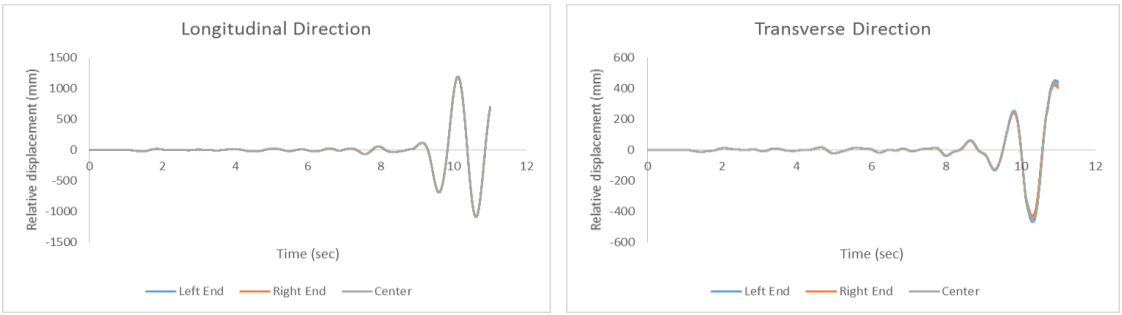


Figure 21. Displacement time history response of Member 1 in X and Y directions (Longitudinal and Transverse)

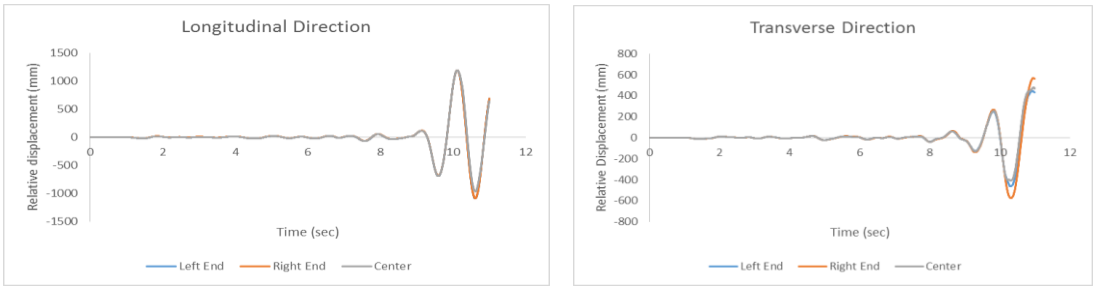


Figure 22. Displacement time history response of Member 2 in X and Y directions (Longitudinal and Transverse)

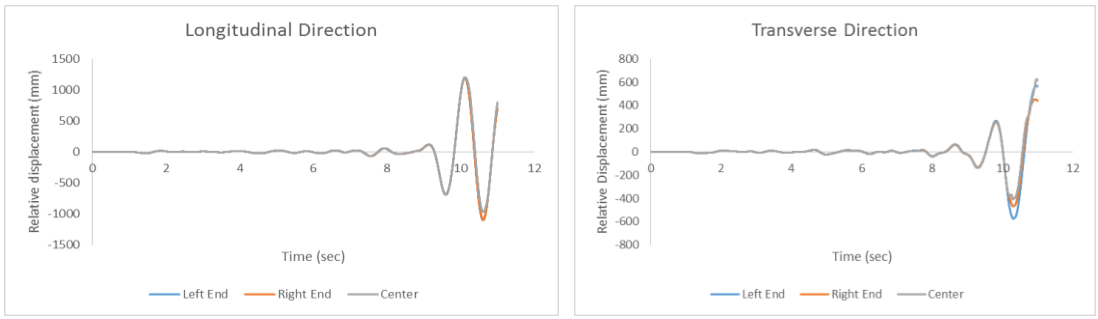


Figure 23. Displacement time history response of Member 3 in X and Y directions (Longitudinal and Transverse)

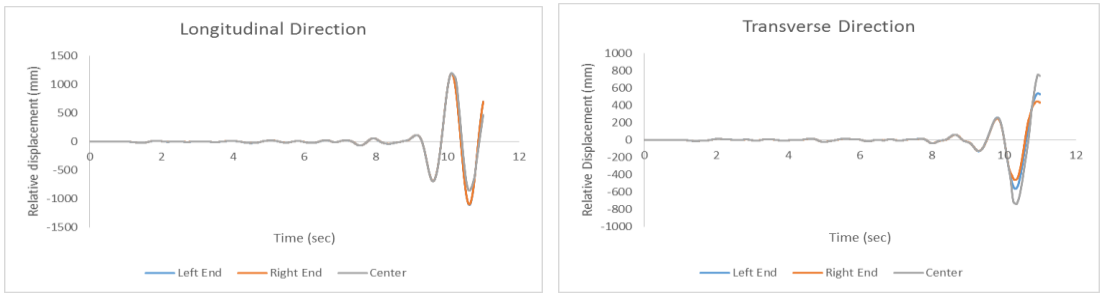


Figure 24. Displacement time history response of Member 4 in X and Y directions (Longitudinal and Transverse)

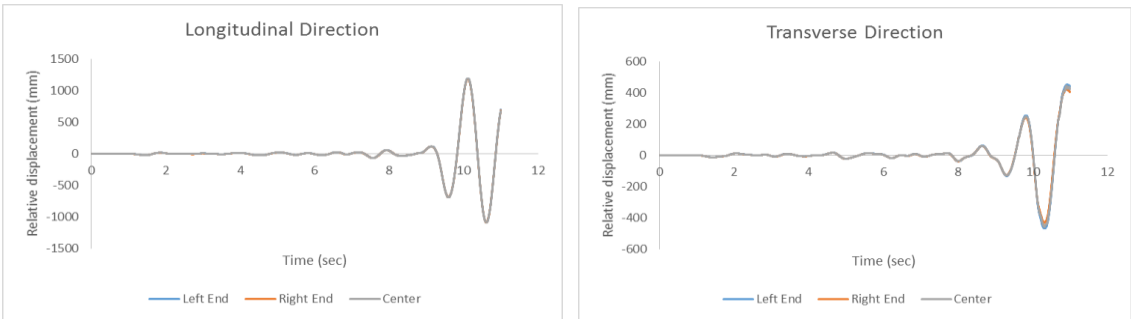


Figure 25. Displacement time history response of Member 5 in X and Y directions (Longitudinal and Transverse)

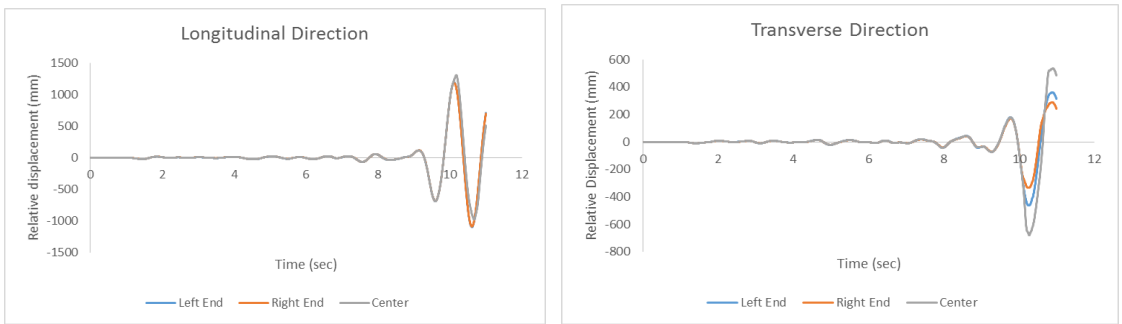


Figure 26. Displacement time history response of Member 6 in X and Y directions (Longitudinal and Transverse)

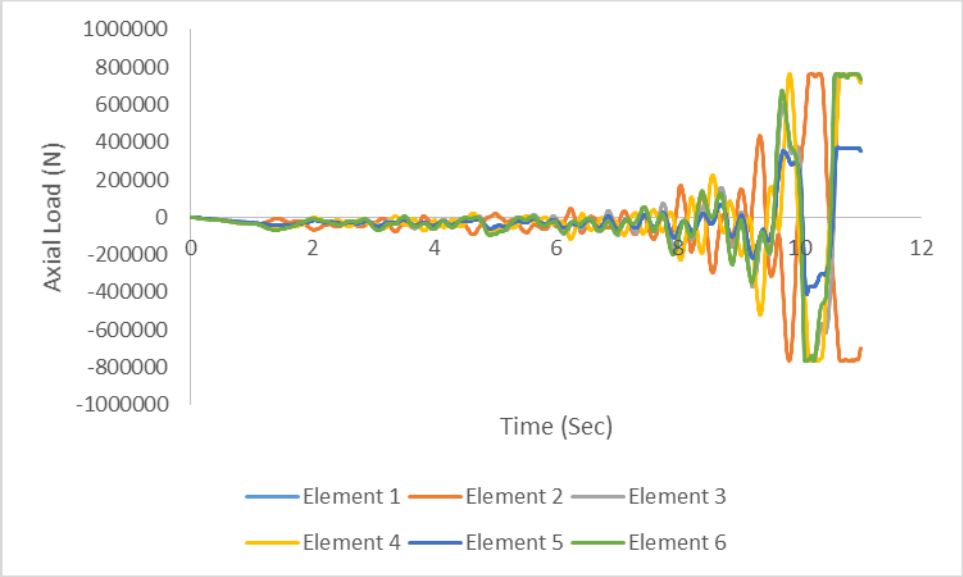


Figure 27. Load time history response in X and Y directions (Longitudinal and Transverse)

The load-deformation cure is too complex and the reasons for that behavior is under consideration. To investigate that behavior the simplify FE model using beam elements will be created in future.

## 8 SUMMARY AND CONCLUSIONS

Field surveys of Tawarayama Bridges are carried out to review the actual conditions and dynamic response analysis subjected to ground motion in longitudinal and transverse directions is also performed to investigate the seismic behavior of the bridge. The current findings and conclusions of this study are summarized as follows:

1. From field surveys

- A large ground deformation near Tawarayama bridge
- Moving of bridge towards Takamori side along longitudinal direction as well as towards valley side along transverse direction
- Settlement of girder
- Deformation of bridge girder due to compression force
- Buckling of lower lateral members
- Swaying of dampers and broken of damper

2. From dynamic response analysis

- Displacement in both longitudinal and transverse directions (displacement in longitudinal direction is more dominant)
- Deformation of main girder
- Buckling of lower lateral members
- Displacement of springs which exceeds the displacement criterial especially in longitudinal axis

By seeing these results, the following can be said that

- The displacement of bridge in real situation and the displacement results from dynamic analysis are similar although the values results from analysis is larger. This may due to inconsideration of contact between girder and abutment in FE model.
- In both field survey and analysis, the deformation of main girder near piers can be found.
- The lower lateral members that are buckled in real situation also shows buckling behavior during analysis.
- In actual condition, swaying of damper are more dominant in longitudinal direction and the spring elements used for rubber dampers displaced in longitudinal direction more than in transverse direction.

Even though, there are similar facts from field survey and dynamic response analysis, it is needed to upgrade the FE model for the following facts to get the better results.

- Applying fine mesh where thorough investigation is needed
- Considering contact behavior between main girders and abutments
- Considering damped condition

## REFERENCES

[1] Dassault Systèmes Simulia Corp., Providence, RI, USA, ABAQUS 6.14 Documentation, 2014.

[2] Japan Road Association, Specifications for Highway Bridges, Part I - Steel Bridge and Part V - Seismic Design, Japan, 2002.

[3] Akira Kasai, Lessons from the 2016 Kumamoto Earthquake, Study Group of Structures in Tokai, The Symposium on considering how to keep bridges performance in Chubu region, pp 9-16, August, 2016.

[4] Akira Kasai, Mya Nan Aye, Damage survey of 2016 Kumamoto earthquake and the present state preservation in the suffered bridges using UAV, German Japanese Bridge Symposium 2016 (GJBS 2016), Osaka, Japan, August 30-31, 2016.

[5] Mya Nan Aye, Akira Kasai, Damage Survey of Bridges during the 2016 Kumamoto Earthquake and Numerical Analysis of Plate Girder Bridge subjected to the Kumamoto Earthquake, Japan-US Joint Workshop, The international Workshop on the 2016 Kumamoto Earthquake, Fukuoka, Japan, March 6, 2016.

COMPDYN 2017
6th ECCOMAS Thematic Conference on
Computational Methods in Structural Dynamics and Earthquake Engineering
M. Papadrakakis, M. Fragiadakis (eds.)
Rhodes Island, Greece, 15–17 June, 2017

# DISSIPATING EFFECT OF GLAZED CURTAIN WALL STICK SYSTEM INSTALLED ON HIGH-RISE MEGA-BRACED FRAME-CORE BUILDINGS UNDER NONLINEAR SEISMIC EXCITATION

**Lorenzo Casagrande[1,2], Antonio Bonati[1], Ferdinando Auricchio[2], Antonio Occhiuzzi[1]**

[1] Construction Technologies Institute (ITC) - National Research Council (CNR)
viale Lombardia 49, MI 20098 ITALY
e-mail: {Casagrande,Bonati,Occhiuzzi}@itc.cnr.it

[2] University of Pavia - Civil Engineer and Architectural Department
via Ferrata 3, PV 27100 ITALY
e-mail: {Casagrande,Auricchio}@unipv.it

**Keywords:** High-rise Structures, Mega-braced Frames, Non-structural Elements, Glazed Curtain Walls, Nonlinear Dynamics, Earthquake Engineering

**Abstract.** *The results derived from the investigation on the dynamic behavior of glazed curtain wall non-structural stick systems installed in modern high-rise mega-frame prototypes is herein summarized. The supporting steel structures, designed in accordance with European rules, consisted of planar frames extracted from reference three-dimensional steel Moment Resisting Frame (MRF), respectively having thirty- and sixty-storey height. To limit interstorey drift and second order effects, outriggers trusses were placed every fifteen stories, whilst a CBF system was chosen as internal core. The characterization of non-structural façade elements was performed through experimental full-scale crescendo-tests on aluminium/glass curtain wall units. Deriving experimental force-displacement curves, it was possible to calibrate three-dimensional inelastic FE models, capable to simulate the interaction between glass panels and aluminium frame. Subsequently, equivalent nonlinear links were calibrated to reproduce the dynamic behaviour of tested glazed unit, and implemented in the thirty- and sixty-storey structural planar frames FE models. Nonlinear time history analyses (NLTHAs) were performed to quantify local and global performance, investigating the enhanced combination of stiffness and strength generated through the implementation of glazed curtain wall on the numerical FE models. Results will be shown in terms of inter-storey drift profiles and displacement peaks, axial force curves and percentage peak variation, showing the sensitivity to the structure height. Trends were discussed to show that, if accurately designed, omitting non-structural elements from the seismic assessment of high-rise prototypes conduct to a sensible underestimation of dynamic dissipation capacity of the building.*

## 1 INTRODUCTION

Tall and super-tall buildings have become popular in urbanized areas due to the growing use of high-strength and smart materials, innovative construction techniques and cost effectiveness [1, 2, 3]. Moreover, the increasing demand for business and residential space have denoted the scarcity of land, constraining the wide use of high-rise structures in modern cities and facing relatively new criticalities, such as inappropriate ground typologies and areas of severe seismicity. Due to their intrinsic complex features and large dimensions [4, 5], several peculiar characteristics shall be considered during the design phase, ensuring the achievement of certain performance levels (i.e. collapse prevention, moderate damage, serviceability) and the evaluation of the characterizing mechanical aspects such as higher mode and longer periods in earthquake assessment [1, 6]. The strength decrease induced by geometric and material nonlinearities, local buckling or steel member fracture can lead to permanent damages or catastrophic collapses, while P-$\Delta$ effects can endanger such modern and more flexible buildings, posing challenges for seismic design in terms of stiffness and stability.

Generally, while mid-rise structures undergo to a combination of strength and stiffness design criteria, stiffness and stability usually govern the design phase in high-rise buildings. Since the design shall balance human safety and economic causes, governed by the variability of the background inputs and the structural assumptions, detailed analyses and ad-hoc studies are required to predict the seismic performance, such as scaled shaking table tests [7, 8] and advanced finite element (FE) simulations [1, 6]. The adoption of the performance-based design has shown that the synergy between structural and non-structural element performance becomes vital, since failure of architectural elements can decrease the performance level of the entire building. As observed during recent earthquakes, non-structural components represent the higher percentage in cost reparation, being the major initial investment. In particular, the large use of glazed curtain wall systems as external enclosures in high-rise modern buildings, has stimulated the researchers to examine the dynamic non-linear response of these non-structural elements. However, in comparison to structural elements, limited information has been collected on the dynamic design of non-structural members.

In light of this scenario, the present paper summarizes the results carried out through nonlinear modelling of high-rise moment resisting frame (MRF) steel systems: crescendo tests on full-scale glazed curtain wall system were performed to investigate to what extent façade elements affect structural frame global and local seismic response.

## 2 NONLINEAR DYNAMIC ANALYSES

In order to predict the dynamic behavior of the structural prototypes, nonlinear time history analyses (NLTHa) were performed, representing a robust and efficient tool to determine global and local seismic performances in structures. Since pushover analyses present specific limitations and inadequacies in high-rise MRFs design, principally the deficiency in safely estimation of the higher-mode effects in recent adaptive modal combinations (AMC) solutions [9, 10], nonlinear dynamic analyses have become the most attractive technique. Whereas different scale and peculiar responses of mechanical and physical idealizations are involved in façade-structure interaction, both detailed brick- and fiber-based FE models were assumed. On one hand, brick-based FE models give more knowledge on complex phenomena than equivalent mechanical representation [11, 12], being able to reproduce their local response in terms of time-dependent stress/strain concentration. On the other hand, the insight on the well-known physical phenomena allows their easy calibration into classical fiber-based FE models, saving

significant computational time. In this light, since a three-dimensional approach would be extremely onerous to investigate the full-scale mega-frame dynamic response, the contribution of the resisting frame system was easily incorporated into classical fibre force-based [13] FE models, able to represent bolted [14, 15, 16, 17, 18] and welded [11, 19, 20, 21] connections, and the other members besides. By contrast, aiming to develop a qualified façade numerical model and to understand the phenomena underpinning the mechanical global behavior, detailed brick-based FE simulations were performed in order to assess the aluminium frame deformability, the interaction between glass panels and aluminium frame, the gasket mechanical distortion and the transom-to-mullion connection stiffness. Finally, fiber-based link elements were calibrated from standard glazed curtain wall unit subjected to laboratory test and the relative three-dimensional FE model, in order to simulate their seismic response. In this scenario, the modeling assumptions and simulation techniques will be given, after a brief introduction on the main geometric and mechanical properties of both the examined planar frames and the tested façade.

### 2.1 Description of the case-study buildings

The two prototypes consisted on 6 x 6-bay buildings extracted from reference thirty- and sixty-storey three-dimensional structures, respectively named MF-01 and MF-02, designed in accordance with current European seismic standards [25] and considering high seismicity (i.e. PGA = 0.40 g) on soil class C (i.e. 180 m/s $<$ Vs $<$ 360 m/s).

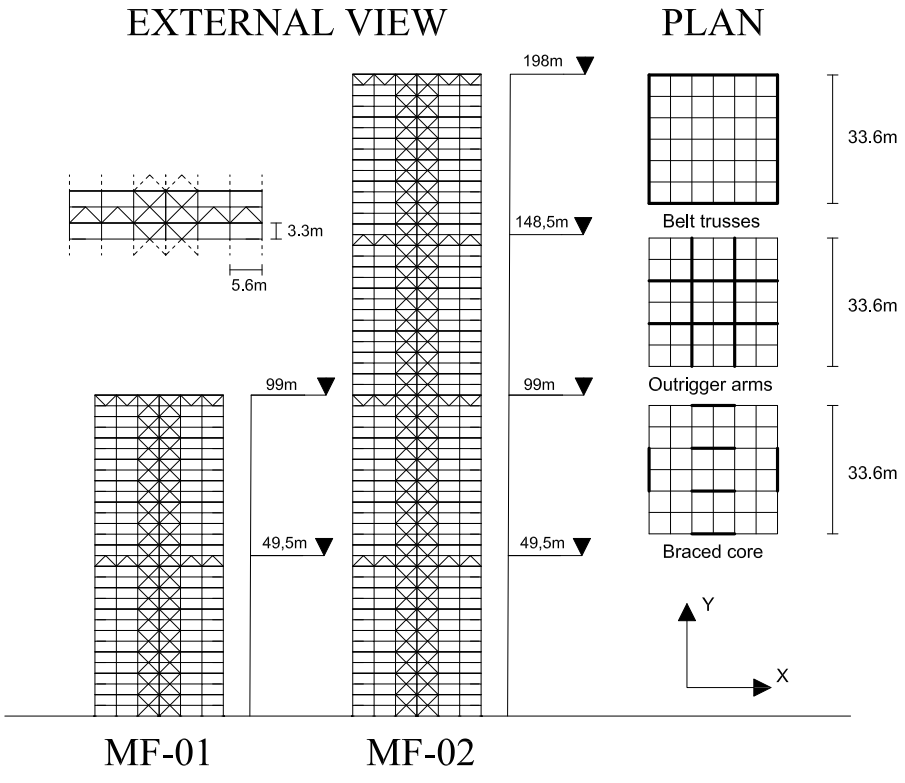


Figure 1: Structural scheme and geometric details of the reference thirty- and sixty-storey planar frames.

In addition to the permanent non-structural internal weight, dead and live loads were considered to be 2kN/m$^2$ and 4kN/m$^2$, respectively. According to ASCE-7 05 provisions [22], the lateral wind pressure was calculated considering the speed at the ground equal to 37 m/s (84

mph). The software used in the first-stage analyses and design were SAP 2000 [23] and MIDAS GEN [24], where a series of response spectrum analyses (RSAs) were performed on the MRF models. As shown in Figure 1, where a sketch of plan and elevation is provided, the complex lateral-force resisting system (LFRS) was constituted by a central 5.6 x 5.6m CBF core, connected with HD columns and perimetral CBF through one-storey height orthogonal outriggers, placed every fifteen stories to limit inter-storey drifts and second order effects. External belt trusses rang the structure. The behaviour factor (q) adopted for V bracing systems was conservatively assumed to be equal to 2, as specified in section 6.3 of EC8 [25], while medium ductility class (DCM) was considered according to EC8 prescriptions [25]. The beam span was set to 5.6 m, defining a uniform column spacing on the in-plane principal directions; accordingly with the tested façade geometry, the inter-storey height was set at 3.3 m, implying a global structural height of 99 m and 198 m for MF-01 and MF-02, respectively. Member sizes and mechanical properties adopted for the structural members were derived from the design phase, according to EC8 guidelines [25]. In detail, HD tapered profiles were used for the columns, while IPE400 beams were adopted for both prototypes in each storey, except for outrigger floors where HD steel sections were chosen. Hollow structural section (HSS) profiles were assumed as brace sections, decreasing in size along the height of the structure. According to [11], steel grade S275, S450 and S700 were used for beams, columns and braces, respectively. Figure 2 displays an example of welded gusset-plate and bolted beam-to-column connection. In Figure 2 (left), the HSS brace was welded to the gusset plate through fillet welds, while full penetration welds (FPW) were provided to connect the flanges of the columns and beams to the gusset plate.

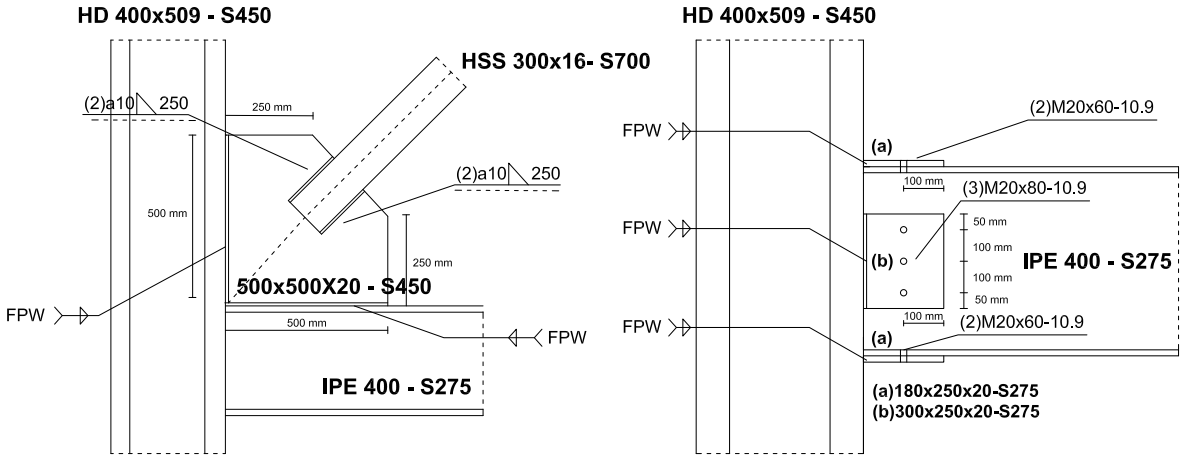


Figure 2: Example of designed gusset-plate (left) and beam-to-column (right) connections.

Furthermore, gusset plate design for each storey in MF-01 and MF-02 prototypes, was performed according to the prescription in [25, 11]. Figure 2 (right), shows the partially-restrained joint obtained through two M20x80-10.9 bolts used to connect the flange of the beam to a 180x250x20 mm plate, welded by FPW to the flange of the column in accordance with the prescriptions of [19]. Three M20x80-10.9 bolts were used to bolt the web of the beam to the shear tab. In the end, the structure was considered to be fixed to the ground, both during the design process and the numerical simulations. The fundamental period (T1) was determined to be equal to 1.75 s for MF-01 and 4.16 s for MF-02 prototypes.

## 2.2 Description of the test performed on the commercial stick curtain wall

This paper focuses on previously performed experimental data, achieved by full-size in-plane tests led at the laboratory of the Construction Tecnologies Institute (ITC) of the Italian National Research Council (CNR) [26]. The seismic response of a commercial full-scale stick curtain wall was evaluated, comparing the integrity of results with past studies [27, 28, 29, 30, 31].

### 2.2.1 Experimental setup and equipment

The experimental setup consisted in a 5.720 x 7.370 mm steel frame, where three rigid beams were installed at different height, representing the principal structure slabs and adaptable to different curtain wall geometries. Furthermore, horizontal displacement could be imposed to the rigid beams in order to simulate seismic-induced lateral drifts [32, 33]; however, during the test only the median beam was activated, while the upper and lower beam were rigidly fixed to the supporting frame. In particular, a hydraulic actuator (General Hydraulic, stroke $\pm$ 600mm, maximum load 200 kN) was fixed to an external rigid reaction system and pushed in the horizontal in-plane direction, in correspondence to the beam-mullion connection, performing the force-control test. The instrumentation was composed by a 50 kN LeBow load cell, capable to measure the applied force, and two linear potentiometric displacement transducers (LVDT) to measure horizontal displacement of the median beam; a 10 Hz continuous data acquisition collected load and displacement during the tests. Figure 3 shows the test set-up and the aluminium member cross-section geometries.

### 2.2.2 Description of the façade specimen

Consistently with the designed mega-frame steel structure geometry, the investigated façade was 7200 mm high and 5600 mm wide, with 3300 mm inter-storey height. The test unit had six transoms and five mullions, while three different profile cross-sections were used for mullions and three for transoms (Figure 3). In particular, transoms of the external bays displayed a cross-section with lower inertia respect to the other spans. EN-AW 6060-T6 was the commercial aluminium alloy adopted for the members, with E = 69 GPa as Young Modulus, $\sigma_y$ = 150MPa and $\sigma_u$ = 190MPa as yield and ultimate stress. The insulated glazing panel thickness was 8+8.2+16+6mm, constituted by a tempered glass characterized by E = 70 GPa and supported on the edges by silicone gaskets. Two mechanical connections were recognizable into the test unit: the transom-to-mullion and the glass-to-frame connection. The former, realized by a U-shaped steel joint, was connected to the alluminium members by four steel screws, resulting in a reduced rotational stiffness with respect to the fully-fixed configuration. The latter, was obtained distributing an internal and external silicone gaskets layer along the contact edges. The clearance between the mullion/transom elements and the glass panels was 5mm.

### 2.2.3 Experimental activity and results

Initially, a quasi-static test was performed increasing the force applied to the central rigid beam until a specific drift was monitored on the opposite mullion. Consequently, the force was set to zero, highlighting the amount of residual plastic deformations. Since the specimen had an opening window impossible to re-close after the first cycle, due to the shear deformations of the frame, the subsequent cycles were performed with opened window. However, repeating the first cycle was possible to observe the incidence of a single window loss, showing that the missing

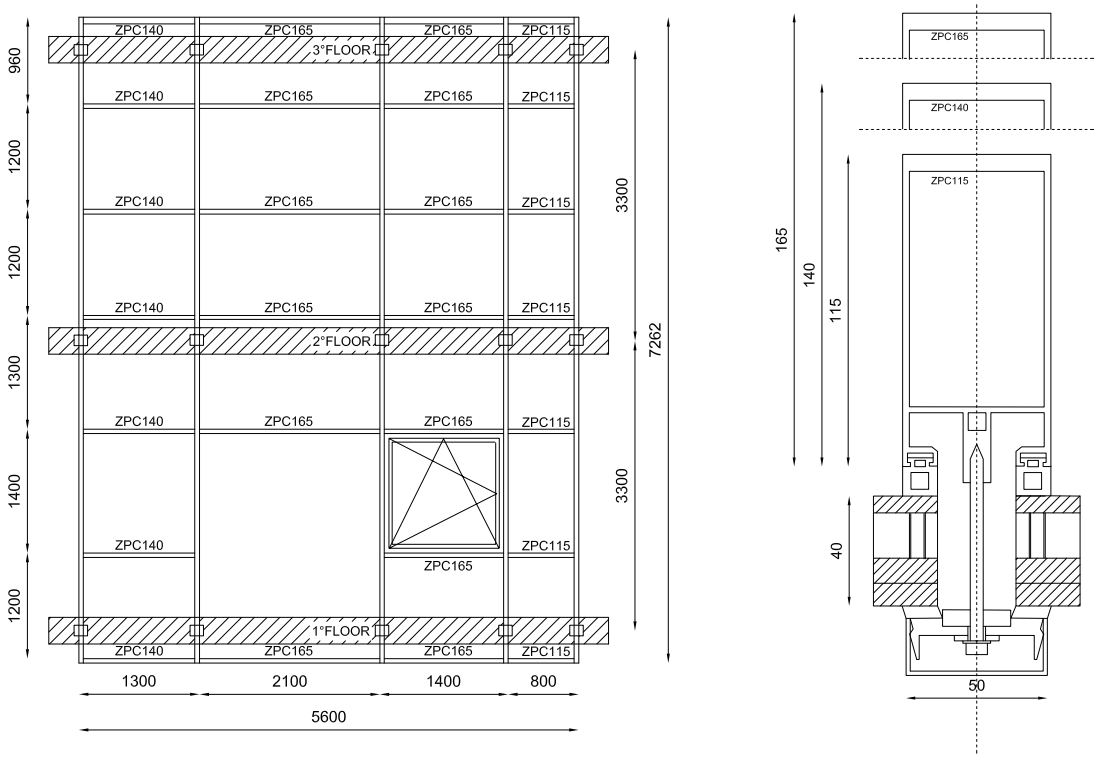


Figure 3: Façade geometry (left) and transom/mullion cross-sections (right). Note: dimensions in mm.

glass panel did not modified the façade response. The force-to-drift results are displayed in Figure 8, in accordance with Caterino et al. [26].

### 2.3 Finite Element modelling approach

In order to investigate the effect of glazed curtain walls on structural seismic behavior when applied to mega-tall buildings, a three-stages FE modeling approach was implemented. First-stage modelling aimed to reproduce nonlinear fibre-based simulations of the building case-studyies, subjected to NLTHAs deriving from a set of ten natural records [34, 35]. These accelerograms (EQs) were spectrum-compatible in displacement according to EC8 prescriptions [25], selected a Type 1 spectrum with PGA equal to 0.4g, soil Type C and $T_D$=8s (Figure 4). Second-stage advanced modelling investigated the dynamic behaviour of the façade through nonlinear brick-based models, simulating the test results. Finally, third-stage modelling aimed to calibrate equivalent nonlinear links, representing the glazed curtain wall response to be implemented on first-stage fibre-base FE models.

#### 2.3.1 Fibre-based modelling approach for MRF structure

In order to analyze the local and global seismic response of the MF-01 and MF-02 reference structures, detailed fiber-based models were implemented on the open source platform OpenSees [36], based on conceptual modeling by Brunesi et al. [42]. Structural members were modeled through inelastic force-based fiber elements, simulating the propagation of inelasticity over the member length through a bilinear stress-strain behavior with isotropic strain hardening. In particular, the Menegotto-Pinto [37] material model was adopted, while material and geometrical nonlinearities were considered through distributed plasticity approach and classi-

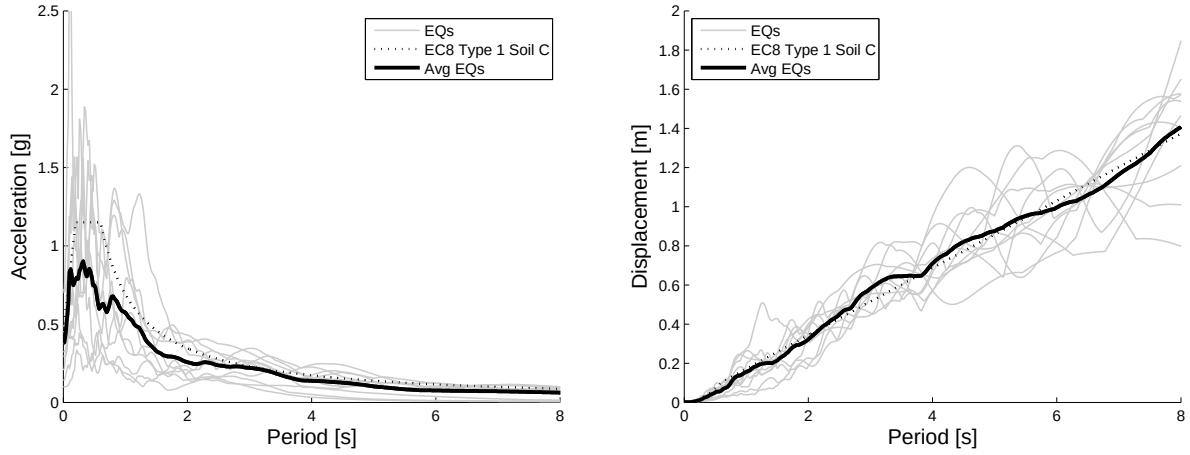


Figure 4: Seismic input as acceleration (left) and displacement (right) elastic response spectra.

cal corotational transformation [38]. Schematics of the modelling idealization adopted for brace and gusset plate mechanical connections are showed in Figure 5. The enhanced stiffness due to the gusset-plate welding into the beam-column conjunction, that confine the extremity of inelastic force-based beam-column portions, was adduced introducing a set of rigid elements [11, 19]. Along the end of the brace, in order to capture the potential progression of plastic hinges, an additional $2t$-length force-based beam-column element was selected from the gusset plate - where $t$ is the thickness of the gusset plate - [11, 19, 43]. Prospective buckling mechanisms in both braces and gusset plates were considered applying an out-of-plane imperfection equal to 0.1% of the length at its midspan. Similarly, according to [12, 14, 15, 16, 18, 39, 40, 42], the T-stub bolted joint mechanical idealization was assumed to reproduce the hysteresis behavior, as a partially restrained connection. Accordingly to the Grant and Priestley paradigm [41], when considering the tangent stiffness-proportional Rayleigh damping, the stiffness-proportional matrix multiplying coefficient used to perform nonlinear dynamic analyses was correlated to the damping ratio associated to the fundamental period of the structure [38, 41, 42, 43].

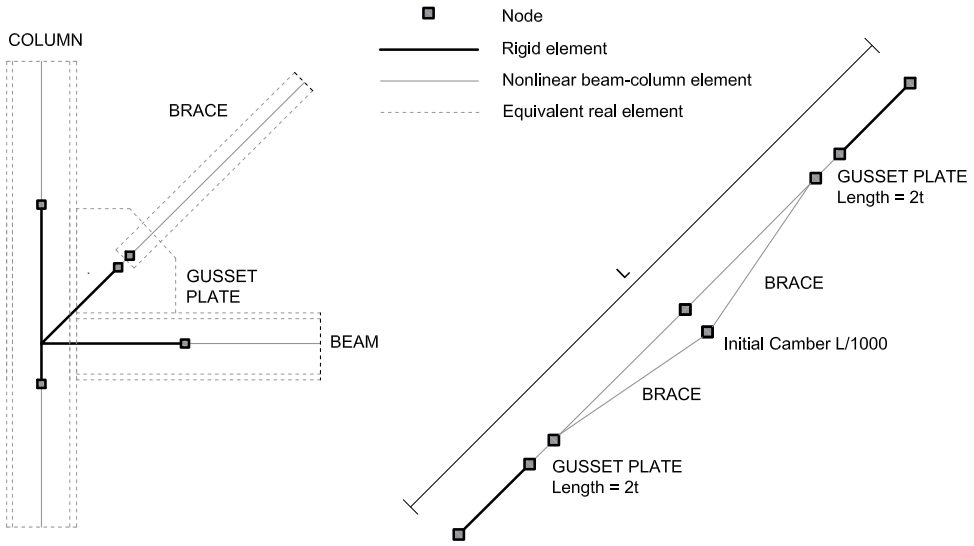


Figure 5: Modeling idealization for brace and gusset-plate connections.

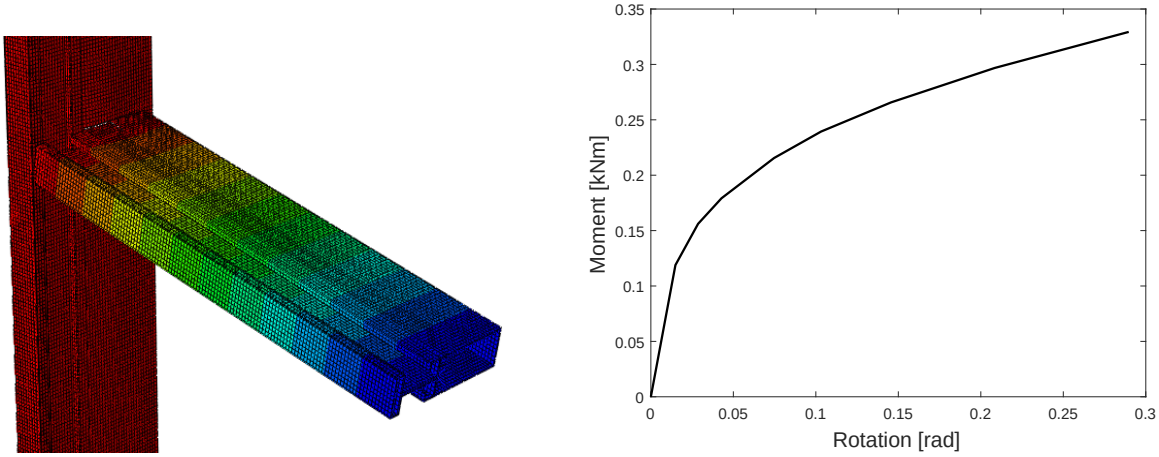


Figure 6: Three-dimensional modelling (left) and moment-rotation diagram (right) of the transom-to-mullion connections.

### 2.3.2 Three-dimensional solid-based modelling approach for façade

Advanced numerical simulations were performed to reproduce the dissipative behavior of the tested glazed curtain wall unit. In particular, four parameters were recognized as main responsible of the lateral response of the façade: *(i)* the geometry of aluminium frame and the rotational stiffness of transom-to-mullion connections; *(ii)* the clearance between aluminium frame and glass panels; *(iii)* the mechanical behavior of gaskets; *(iv)* the local interaction between glass and frame [32, 33, 31]. Three-dimensional brick-based models were analysed in ABAQUS 6.14 [44] in order to capture the local mechanisms and the interactions between each parameter affecting the overall response. Therefore, equivalent nonlinear link-elements were calibrated to explicitly reproduce the rotational stiffness of transom-to-mullion connections and the combined effect of glass-to-gaskets slippage, considering potential impacts between the glazed surface and the aluminium frame, as in Figure 6-7, in line with a computational time-saving approach [45, 46]. In fact, these connectors were implemented on a full-scale model, as on Figure 8, reducing the FE formulation variables and reproducing the global tested response.

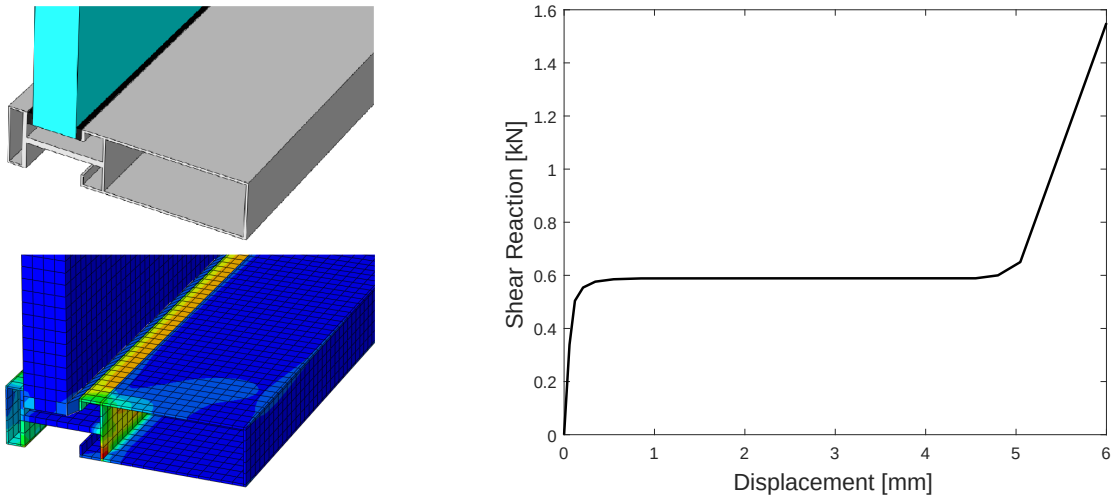


Figure 7: Three-dimensional modelling (left) and shear-displacement diagram (right) of the glass-to-gasket connections.

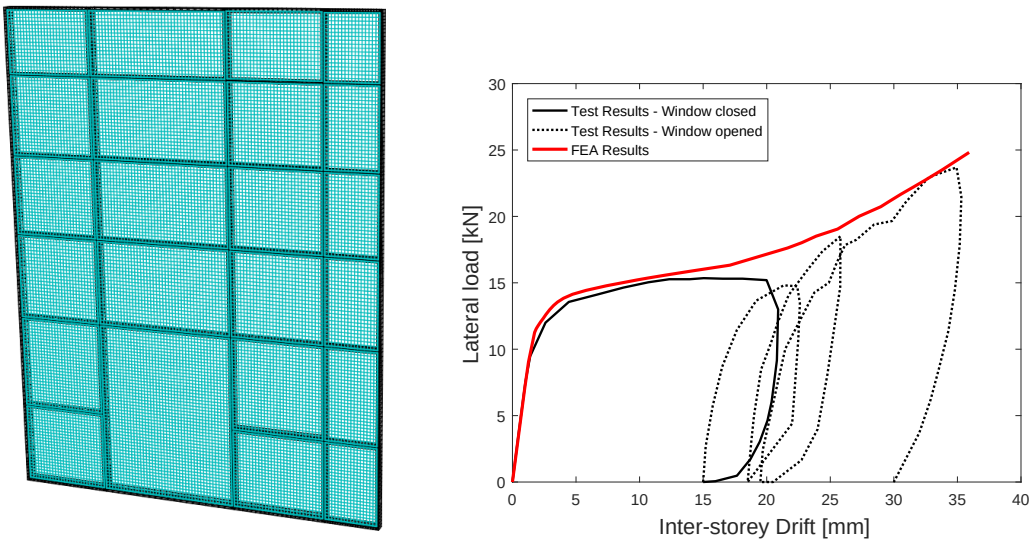


Figure 8: Three-dimensional modelling (left) and force-displacement diagram (right) of tested façade.

Figure 6 displays a high-fidelity FE model calibrated to investigate the moment-rotation relationship of transom-to-mullion connection. Three-dimensional deformable isoparametric solids were adopted to model each connection component, accounting for finite strain and rotation in large-displacement analysis. Fist-order elements were adopted, i.e. 8-node linear brick (C3D8R), with reduced integration through Barlow points and hourglass control methods of Flanagan and Belytschko. Both geometrical and material nonlinearities were considered. The classical rate-independent Von Mises model for metal plasticity with associated yield surface for isotropic materials and strain hardening was assumed to faithfully reproduce the cyclic stress-strain relationship of the steel members during the applied loading-unloading history. Since the U-shaped connecting steel joint presented higher stiffness and strength respect to the aluminium members, it was considered that the joint rotational capacity was mainly due to the deformation of the frame. Therefore, the simulation remained accurate properly representing bolted connections through equivalent nonlinear frictional parameters and constraining the effect of slipperiness between the U-shaped joint and the aluminum members. Figure 7 presents a robust brick-based FE modeling developed to study the glass-to-gaskets interaction, at a local scale. While the same mechanical and physical assumptions for aluminum members were considered, the constitutive laws for glass and gaskets were herein introduced. According to Memari et al. [46], the glass panel was considered as an equivalent full-section isotropic elastic three-dimensional element (C3D8R), evaluating the maximum stress response. The glass-to-gasket nonlinear friction effect and the mechanical deformation of the gasket were modeled by elasto-plastic relationship with isotropic hardening, connecting the nodes on the glass panel boundary to the the frame nodes. The calibration of the equivalent stress-strain constitutive laws was conducted in accordance with [46, 47, 48] and the experimental tests carried out at the Institute of Construction Technology. Since numerous in-plane racking tests [29, 45, 46] have shown that glass damage propagates when glass-to-frame contact occurs along glass-panel edges in corner regions, the stiffening interaction due to the impact was directly incorporated onto gasket constitutive laws, through a validated parametric campaign of FEM analyses. Figure 8 shows the advanced three-dimensional modeling of the tested façade and the accurate matching between the simulation and experimental results. Equivalent nonlinear links were calibrated to represent the seismic response of the glazed curtain wall in OpenSees high-rise reference structures.

## 3 RESULTS AND COMPARISONS

In this chapter, the main results will be displayed in terms of NLTHa global and local performance, of the two reference high-rise structures MF-01 and MF-02. In particular, the influence of the glazed curtain wall system will be shown, illustrating to which extent this affects the overall seismic response when façades are considered acting on the LFRSs. Initially, each section will display the comparison between NLTHa average response (NLTHA Avg), carried out from the structures with glazed curtain walls, respect to the correspondent bare MRF. Consequently, the percentage variation between both component will be shown. Individual earthquake (EQs) acceleration result, referred to the MRF with non-structural elements, will be shown in grey.

### 3.1 Global performance

Figure 9 summarizes the global response of the two mega-frame buildings in terms of peak displacement and inter-storey drift, together with their average values, respectively for MF-01 (left) and MF-02 (right). Peak displacements, achieved in the most extreme records, were 0.58 m and 1.72 m, while medium values up to 0.41 m and 0.88 m were obtained. The response assumed a rough cantilevered shape with soft discrepancy in correspondence to the outrigger; as will be discussed in the following, this aspect was more pronounced in the inter-storey drift prediction (Figure 9).

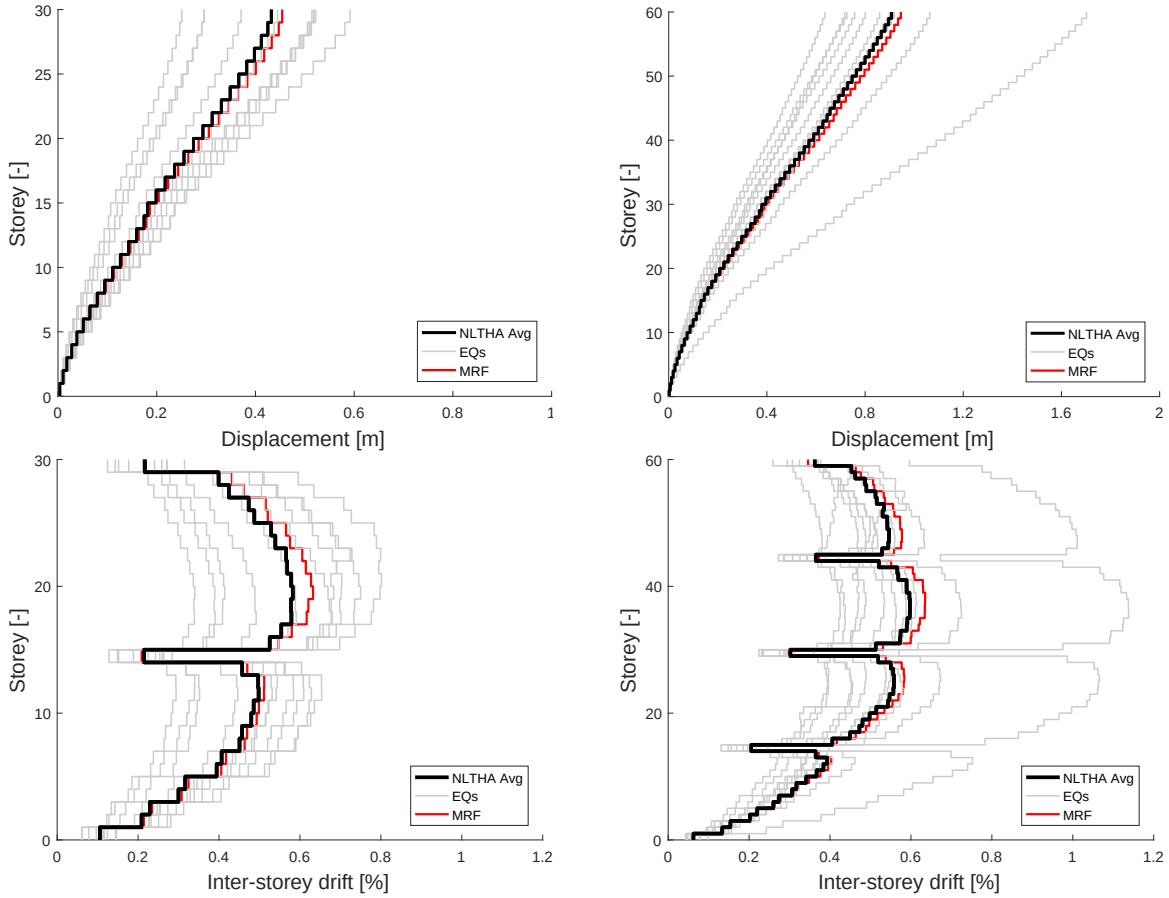


Figure 9: Displacement profile and Inter-storey drift of MF-01 (left) and MF-02 (right).

The stiffening enhancement procured by the outriggers was significantly visible for both structure, as a prominent peak inter-storey drifts reduction (up to 57%). By contrast, significant

acceleration were experienced during dynamic simulations, i.e. 0.59g and 0.35g for both MF-01 and MF-02, respectively, underlining the stiffest behavior of the former (as also evidenced by fundamental periods discrepancy, i.e. 1.75 s vs. 4.16 s). The series of NLTHa have shown that, if properly designed to induce a good balance between acceleration and deformation demands, this structural system supply an optimum combination of global stiffness and strength in high-rise structures. Moreover, since MRF contribution was greater than NLTHA Avg (Figure 9), this illustrates that the MRF structure was more flexible without considering the external façades.

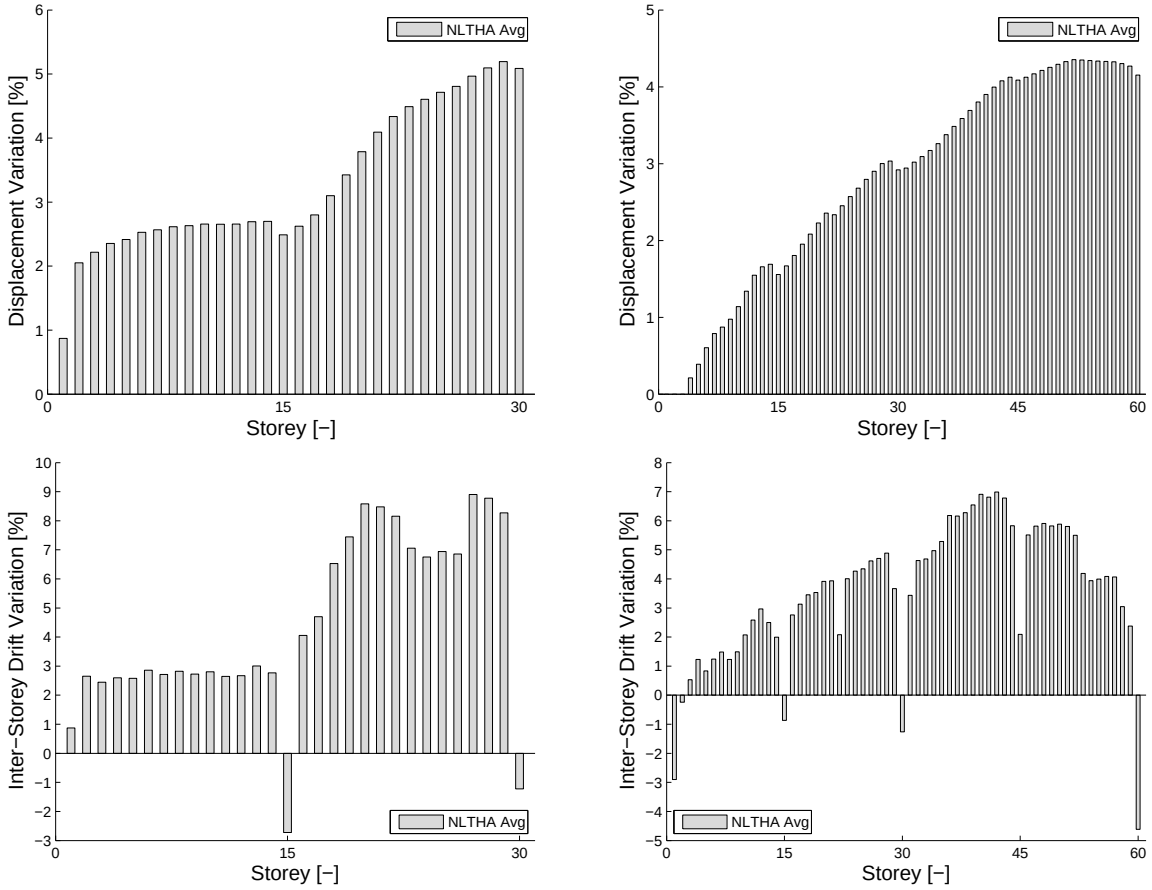


Figure 10: Displacement profile and Inter-storey drift variation of MF-01 (left) and MF-02 (right).

In fact, Figure 10 shows to what extent the variation between the overall structural response of the MRF with glazed façades differed from the bare MRF. Peak discrepancies were accounted for 5.45% and 4.53% as top average displacement, respectively for MF-01 and MF-02, while 9.23% and 7.47% represented the inter-storey drift profile in average. The shape of the displacement variation reflected the tendency of the displacement diagram, assuming a fairly-cantilevered progression. It was clearly visible the outrigger influence in inter-storey drift profiles, showing a trend reversal, while on the displacement variation profile the effect attenuates.

## 3.2 Local performance

According to Brunesi et al. [42, 43], the key components advocated to resist seismic actions in this structural system are columns, braces and outriggers. Response in term of axial load peak profiles in critical members will be shown. In addition, the percentage variation between the MRF with external cladding and bare MRF results will be computed.

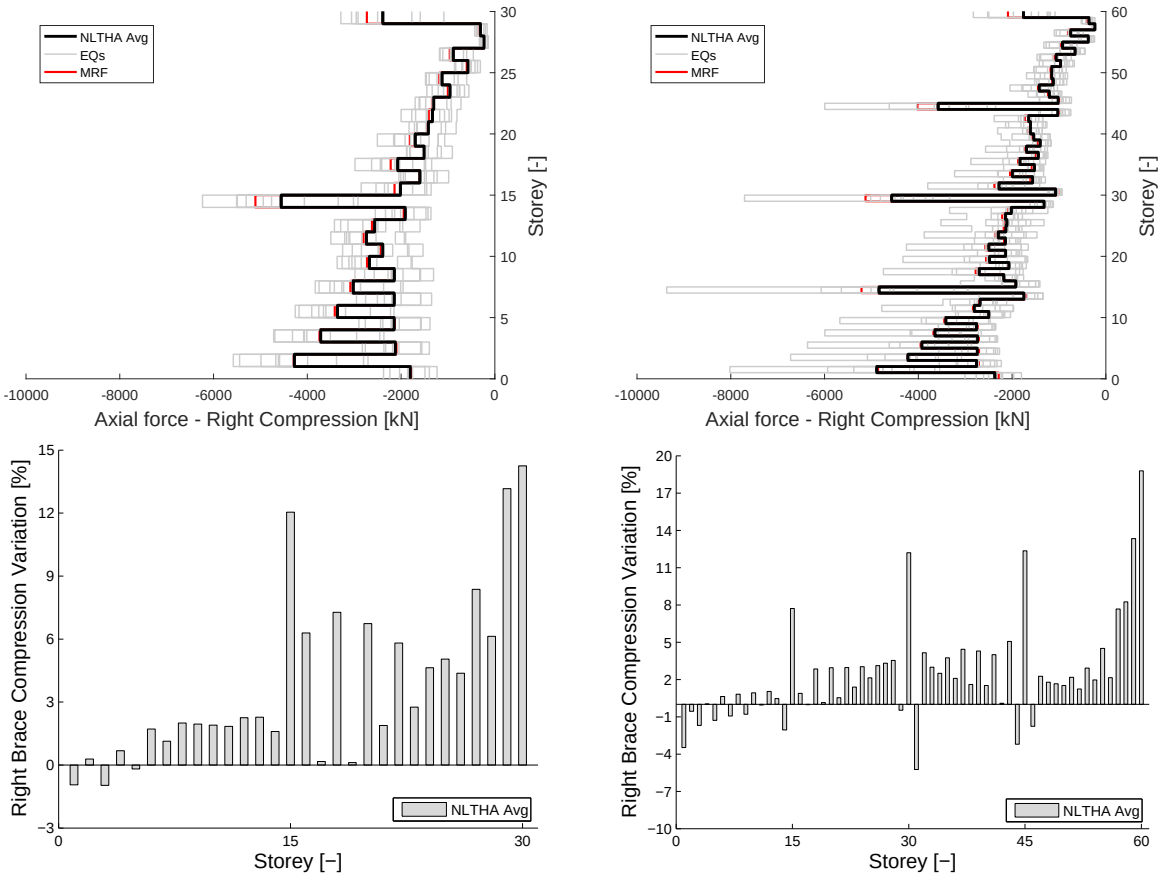


Figure 11: Axial force profile in reference braces and compression variation, in MF-01 (left) and MF-02 (right).

In Figure 11 the comparison between compressive peak forces in the most critical brace is displayed. Average loads of up to 4500 kN and 5000 kN were obtained, respectively for MF-01 and MF-01. A similar demand was obtained in correspondence to the outriggers floors, as a consequence of the increment in terms of floor acceleration [42, 43], where was demonstrated that modelling the structure without the curtain walls conduced to overestimate NLTHAs results up to 20%. Figure 12 summarizes the seismic peak axial loads predicted by NLTHAs in the outrigger braces, placed at the $15^{th}$ and $30^{th}$ storey of the thirty- and sixty- storey case study building, since they resulted to be the most critical storeys (see Figure 11). The diagrams present a comparison between the forces observed considering the MRF with the external façade and the supporting structure alone: peak compression was almost stable along the height, reaching a maximum of 4250kN and 4500kN, in MF-01 and MF-02, respectively. However, a larger mismatch between axial force percentage variation was determined in the outriggers placed at the top of MF-01 and at mid-height of MF-02, of up to approximately 25%. Being the discrepancy between the response of MRF with cladding and the bare MRF higher in that braces than that observed in other structural members, particular care has to be paid to the earthquake-induced demand evaluation during the design phase of these elements and the related connections. As a result of the outriggers in-plane rotation, earthquake-induced compressive overloads were experienced by the external core-columns [42, 43]. Figure 13 collects the seismic axial forces transferred to the leftmost core-column of the thirty- and sixty-storey structures, accounting for the façade system, their average and the equivalent on the bare MRF. This reflected on the discrepancy between forces, up to approximately 14% in MF-01 and 18% in MF-02.

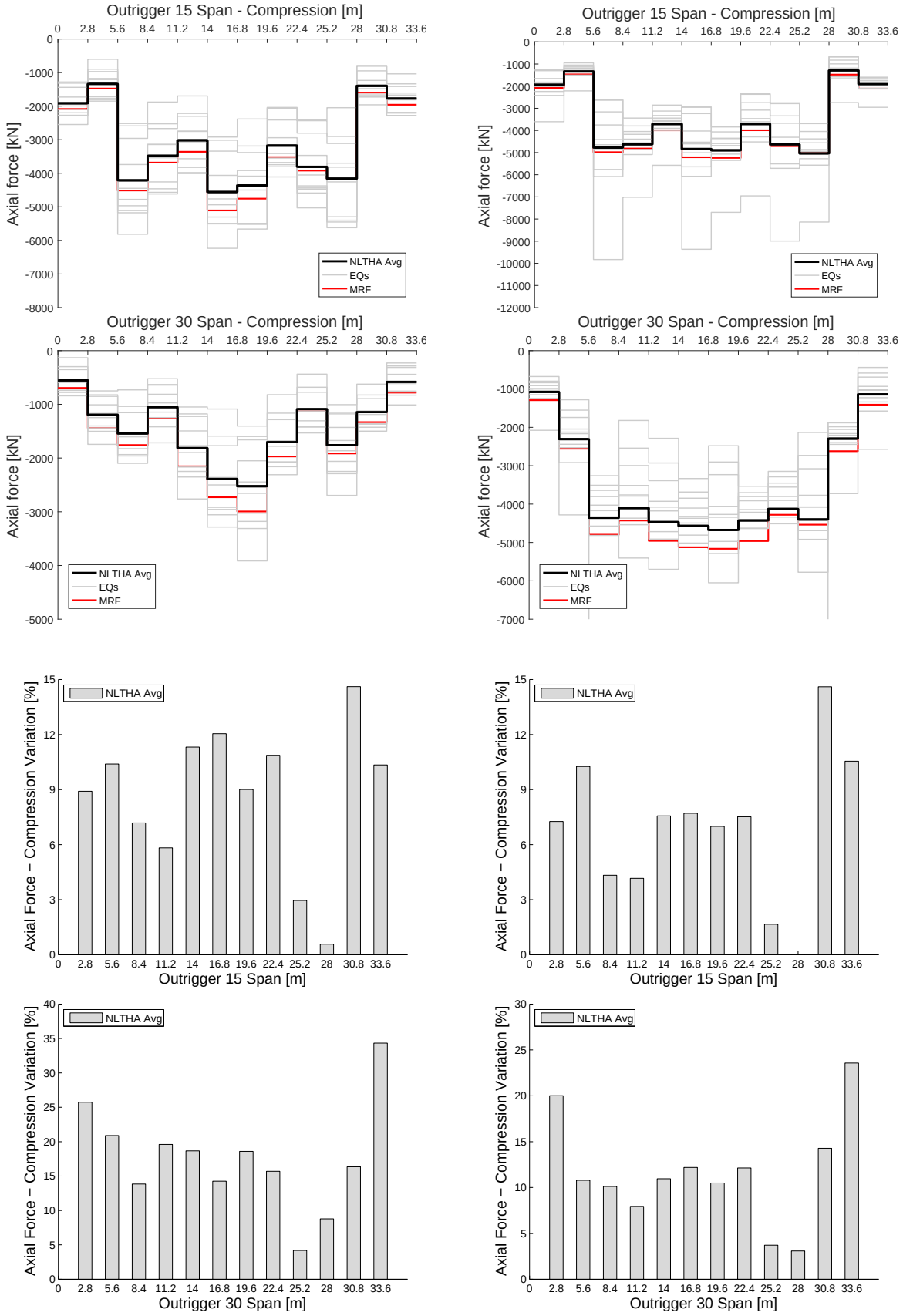


Figure 12: Axial force profile in outrigger braces and compression variation, in MF-01 (left) and MF-02 (right).

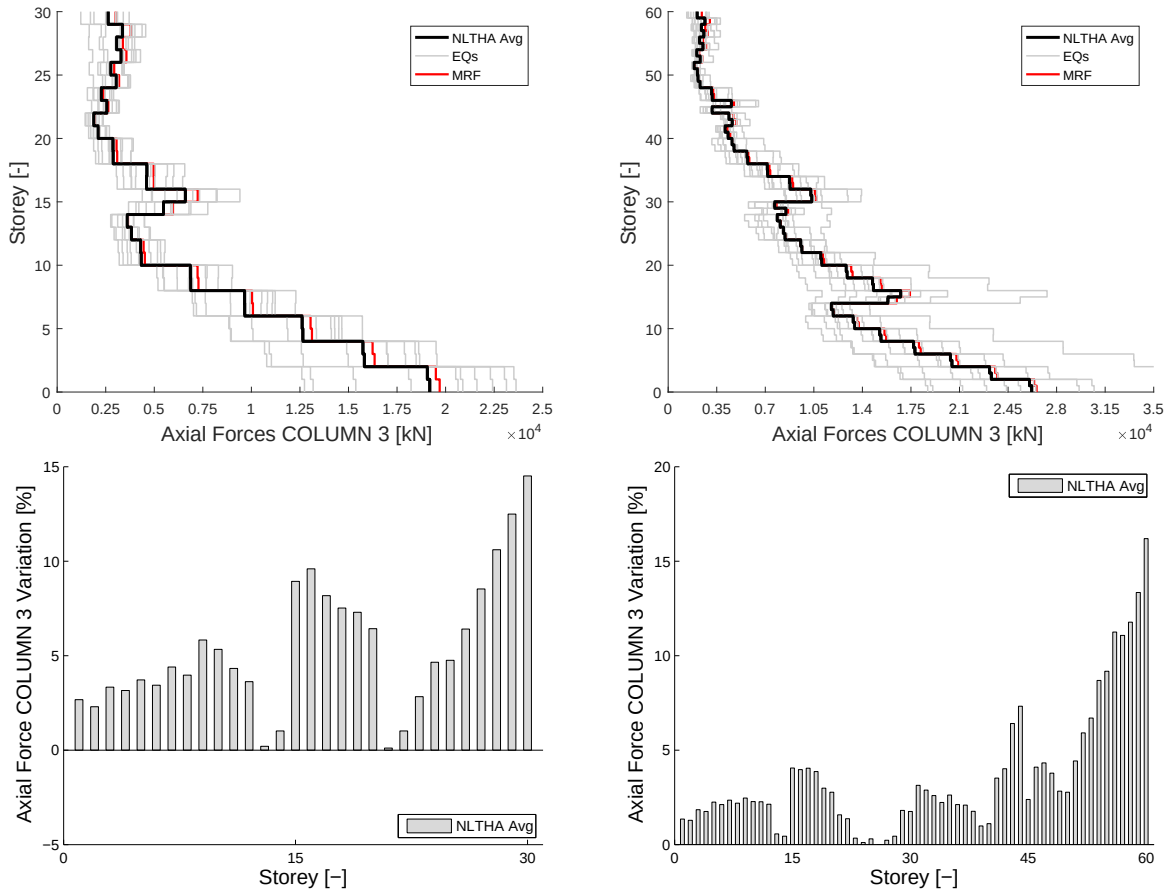


Figure 13: Axial force peak profile in the lefmost core column and compression variation, in MF-01 (left) and MF-02 (right).

## 4 CONCLUSIONS

This paper summarizes the NLTHAs results performed on two reference thirty- and sixty-storey planar prototypes, extracted from a high-rise mega-braced frame structures with outriggers and belt trusses, and designed according to European prescriptions. In detail, the research focuses on the dynamic of glazed curtain walls, i.e. to what extent is plausible consider façades interacting with the LRFS during a severe earthquake event, altering the structural seismic response. The main observations acquired from the numerical analysis results are synthesized:

- Effects caused by façade dissipation were proven to be not negligibly on the LRFS and on the key components of both prototypes, reflecting dissimilarities up to 9.23% and 34.2% as local and global response, respectively. Fundamental period decremented up to 14.3% in MF-01 and 11.3% in MF-02, considering the glazed curtain wall dissipation.
- Response profiles and peak variations were characterized by an approximately linear increasing trend along the height, with pronounced discontinuities in correspondence to the outriggers, due to their overall stiffening effect.
- External outrigger braces resulted to be the most influenced by the cladding dissipation.
- Sensitivity to the structure height was investigated as a result of glazed curtain wall response, showing that façades mainly influence global and local response with a reverse fashion respect to the structural height.

## REFERENCES


[1] H. Fan, Q.S. Li, A.Y. Tuan, L. Xu, Seismic analysis of the world's tallest building, *J Constr Steel Res 2009*, **65**, 1206-15.

[2] X. Lu, X. Lu, H. Guan, W. Zhang, L. Ye, Earthquake-induced collapse simulation of a super-tall mega-braced frame-core tube building, *J Constr Steel Res 2013*, **82**, 59-71.

[3] X. Lu, X. Lu, H. Sezen, L. Ye, Development of a simplified model and seismic energy dissipation in a super-tall building, *Eng Struct 2014*, **67**, 109-22.

[4] G.M. Montuori, E. Mele, G. Brandonisio, A. De luca, Secondary bracing systems for diagrid structures in tall buildings, *Eng Struct 2014*, **75**, 477-88.

[5] G.M. Montuori, E. Mele, G. Brandonisio, A. De luca, Design criteria for diagrid tall buildings: stiffness versus strength, *Struct Des Tall Spec Build 2014*, **23**, 1294-314.

[6] T.S. Jan, M.W. Liu, Y.C. Kao, An upper-bound pushover analysis procedure for estimating the seismic demands of high-rise buildings, *Eng Struct 2004*, **26**, 117-28.

[7] C.S. Li, S.S.E. Lam, M. Z. Zhang, Y. L. Wong, Shaking table test of a 1:20 scale high-rise building with a transfer plate system, *J Struct Eng ASCE 2006*, **132**, 1732-44.

[8] X.L. Lu, Y. Zou, W.S. Lu, B. Zhao, Shaking table model test on Shangai world financial center tower. *Earthq Eng Struct Dyn 2007*, **36**, 439-57.

[9] H. Krawinkler, G.D.P.K. Seneviratna, Pros and cons of pushover analysis of seismic performance evaluation, *Eng Struct 1998*, **20**, 452-62.

[10] A.K. Chopra, R.K. Goel, A modal pushover analysis procedure to estimate seismic demand for unsymmetric-plan buildings, *Earthq Eng Struct Dyn 2004*, **33**, 903-27.

[11] R. Nascimbene, G.A. Rassati, K.K. Wijesundara, Numerical simulation of gusset-plate connections with rectangular hollow section shape brace under quasi-static cyclic loading, *J Constr Steel Res 2011*, **70**, 177-79.

[12] E. Brunesi, R. Nascimbene, M. Pagani, D. Belic, Seismic performance of storage steel tanks during the May 2012 Emilia, Italy, earthquakes, *J Perform Constr Fac ASCE 2015*, **29**(5), 04014137.

[13] E. Spacone, F.C. Filippou, F.F. Taucer, Fibre beam-column model for non-linear analysis of RC frames: Part 1. Forumlation, *Earthq Eng Struc Dyn 1996*, **25**, 711-25.

[14] E. Brunesi, R. Nascimbene, G.A. Rassati, Response of partially-restrained bolted beam-to-column connections under cyclic loads, *J Constr Steel Res 2014*, **97**, 24-38.

[15] E. Brunesi, R. Nascimbene, G.A. Rassati, Evaluation of the response of partially restrained bolted beam-to-column connection subjected to cyclic pseudo-static loads, *Structure Congress, Pittsburg, Pennsylvania, May 2-4, 2013*, p. 2310-21.

[16] E. Brunesi, R. Nascimbene, G.A. Rassati, Seismic response of MRFs with partially-restrained bolted beam-to-column connections through FE analyses, *J Constr Steel Res 2015*, **107**, 37-49.

[17] E. Brunesi, R. Nascimbene, G.A. Rassati, Seismic performance of steel MRF with partially-restrained bolted beam-to-column connections through FE simulations, *Structures Congress 2014, Boston, Massachussets, April 3-5, 2014*, p. 2640-51.

[18] G.A. Rassati, R.T. Leon, S. Noe, Component modeling of partially restrained composite joints under cyclic and dynamic loading, *J Struct Eng ASCE 2004*, **130**, 343-51.

[19] S. Santagati, D. Bolognini, R. Nascimbene, Strain life analysis at low-cycle fatigue on concentrically braced steel structures with RHS shape braces, *J Earthq Eng 2012*, **16**, 107-37.

[20] K.K Wijesundara, R. Nascimbene, T.J. Sullivan, Equivalent viscous damping for steel concentrically braced frame structures, *Bull Earthq Eng 2011*, **9**, 1535-58.

[21] K.K Wijesundara, R. Nascimbene, G.A. Rassati, Modeling of different bracing configurations in multi-storey concentrically braced frames using a fiber-beam based approach, *J Constr Steel Res 2014*, **101**, 426-36.

[22] ASCE 7-05. Minimum design loads for buildings and other structures, *Reston (VA): American Society of Civil Engineers 2006*.

[23] SAP2000. Linear and nonlinear static and dynamic analysis and design of three-dimensional structures, *Berkeley (CA): Computers and Structures Inc. (CSI)*.

[24] MIDAS GEN: Integrated Design system for Buildings and General Structures, *Korea: MIDAS Information Technology Co., Ltd.*.

[25] Eurocode 8. Design of structures for earthquake resistance - Part 1: General rules, seismic actions and rules for buildings, *EN 1998-1-1. Brussels (Belgium) 2005*.

[26] N. Caterino, M. Del Zoppo, G. Maddaloni, A. Bonati, G. Cavanna, A. Occhiuzzi, Seismic assessment and finite element modelling of glazed curtain walls, *Struct Eng and Mech 2017*, **61**(1), 77-90.

[27] S.J. Thurston, A.B. King, Two-directional cyclic racking of corner curtain wall glazing, *Building Research Association of New Zeland (BRANZ) 1992*.

[28] C.P. Pantelides, R.A. Behr, Dynamic in-plane racking tests of curtain wall glass elements, *Earthq Eng Struc Dyn 1994*, **23**(2), 211-228.

[29] R.A. Behr, A. Belarbi, J.H. Culp, Dynamic racking tests of curtain wall glass elements with in-plane and out-of-plane motions, *Earthq Eng Struc Dyn 1995b*, **24**(1), 1-14.

[30] R.A. Behr, Seismic performance of architectural glass in mid-rise curtain wall, *J Arch Eng 1998*, **4**(3), 94-98.

[31] H. Sucuoĝlu, C.G. Vallabhan, Behaviour of window glass panels during earthquakes, *Eng Struc 1997*, **19**(8), 685-694.

[32] J.G. Bouwkamp, J.F. Meehan, Drift limitations imposed by glass, *Proceedings of the Second World Conference on Earthquake Engineering, Tokyo, Japan, 1960*.

[33] J.G. Bouwkamp, Behavior of windows panels under in-plane forces, *Bull Seism Soc Am 1961*, **51.1**, 85-109.

[34] T.J. Sullivan, Direct displacement-based seismic design of steel eccentrically braced frame structures, *Bull Earthq Eng 2013*, **11**, 2197-231.

[35] T.J. Maley, R. Roldán, A. Lago, T.J. Sullivan, Effects of response spectrum shape on the response of steel frame and frame-wall structures, *Pavia (Italy): IUSS Press 2012*.

[36] OpenSees. Open system for earthquake engineering simulation, *Berkeley (CA): Pacific Earthquake Engineering Research Center, University of California*.

[37] F.C. Filippou, E.P. Popov, V.V. Bertero, Effects of Bond Deterioration on Hysteretic Behavior of Reinforced Concrete Joints *Earthquake Engineering Research Center, University of California, Berkeley 1983*, Report EERC 83-19.

[38] E. Brunesi, R. Nascimbene, Extreme response of reinforced concrete buildings through fiber force-based finite element analysis, *Eng Struct 2014*, **69**, 206-15.

[39] A. Braconi, W. Salvatore, R. Tremblay, O.S. Bursi, Behaviour and modelling of partial-strength beam-to-column composite joints for seismic applications, *Earthq Eng Struct Dyn 2007*, **36**, 142-61.

[40] M. Latour, V. Piluso, G. Rizzano, Cyclic modeling of bolted beam-to-column connections: component approach, *J Earthq Eng 2011*, **15**, 537-63.

[41] M.J.N. Priestley, D.N. Grant, Viscous damping in seismic design and analysis, *J Earthq Eng 2005*, **9**, 229-55.

[42] E. Brunesi, R. Nascimbene, L. Casagrande , Seismic analysis of high-rise mega-braced frame-core buildings, *Eng Struct 2016*, **115**, 1-17.

[43] E. Brunesi, R. Nascimbene, G.A. Rassati, L. Casagrande , Seismic performance of high-rise steel MRFs with outrigger and belt trusses through nonlinear dynamic FE simulations, *COMPDYN2015, 5$^{th}$ ECCOMAS Thematic Conference on Computational Methods in Structural Dynamics and Earthquake Engineering, Crete Island, Greece 25-27, 2015*.

[44] ABAQUS 6.14 Documentation, *Dassault Systmes Simulia Corp., Providence, RI, USA, 2016*

[45] S. Sivanerupan, J.L. Wilson, E.F. Gad, N.T.K. Lam, Seismic Assessment of Glazed Façade Systems, *Proceedings of the Annual Technical Conference of the Australian Earthquake Engineering Society, Newcastle, 2009*.

[46] A.M. Memari, A. Shirazi, P.A. Kremer, Static finite element analysis of architectural glass curtain walls under in-plane loads and corresponding full-scale test, *Struc Eng and Mech 2007*, **25**(4), 365-382.

[47] J. Kimberlain, L. Carbary, C. D. Clift, P. Hutley, Advanced Structural Silicone Glazing, *International Journal of High-Rise Buildings 2013*, **2**(4), 345-354.

[48] W. Lu, B. Huang, K.M. Mosalam, S. Chen, Experimental evaluation of a glass curtain wall of a tall building, *Earthq Eng Struc Dyn 2016*, **45**, 1185-1205.

COMPDYN 2017
6th ECCOMAS Thematic Conference on
Computational Methods in Structural Dynamics and Earthquake Engineering
M. Papadrakakis, M. Fragiadakis (eds.)
Rhodes Island, Greece, 15–17 June, 2017

# A DISCONTINUOUS GALERKIN MATERIAL POINT METHOD (DGMPM) FOR THE SIMULATION OF IMPACT PROBLEMS IN SOLID MECHANICS

**A. Renaud**[1], **T. Heuzé**[1]

[1] Research Institute in Civil and Mechanical Engineering (GeM, UMR 6183 CNRS)
Ecole Centrale de Nantes
1 rue de la Noë, Nantes
e-mail: {adrien.renaud,thomas.heuze}@ec-nantes.fr

**Keywords:** Material Point Method, Discontinuous Galerkin, dynamic impact, elastic solid, hyperelastic solid.

**Abstract.** *The material point method is extended in this work to the Discontinuous Galerkin approximation framework for the simulation of impacts on elastic and hyperelastic solids. The formulation is based on the weak form of conservation laws on each cell of an eulerian grid in which volume integrals are discretized on a set of material points lying in that cell, and on the computation of Godunov fluxes at cells faces. The resulting method is first derived within the small strains framework and illustrated on a one-dimensional and a two-dimensional problem of impact on an elastic media. Then a one-dimensional hyperelastic problem of a solid undergoing large strains is presented, and a comparison is performed with an analytical solution.*

## 1 INTRODUCTION

The numerical simulation of hyperbolic initial boundary value problems (IBVP) in solid mechanics has been and is again mainly performed with the finite element method (FEM). Despite its well-known advantages, this method becomes less efficient and accurate for problems involving large strains because of mesh tangling and hence, the required re-meshing and projection steps. Meshless methods have been developed to circumvent these shortcomings. Among them, the material point method [1] (MPM) uses a collection of particles that can move in an eulerian grid to represent a continuum with a lagrangian description. The material points carry all the fields of the problem while the grid is only used to compute gradients and solve the discrete equations. Fields travel from material points to nodes and *vice versa*, and since history is known at every single particle, the grid can be discarded and reconstructed for convenience.

Hyperbolic IBVP including extreme loading conditions such as impacts require the ability to accurately track the wave front of shock waves to provide a better understanding of physical phenomena occurring in dynamic forming processes such as electromagnetic forming. However, classical time integrators used with the FEM introduce high frequency noise in the vicinity of discontinuities which is hard to remove without loss of accuracy. Furthermore, the MPM space discretization leads to a decrease of the Courant number that prevents the capture of discontinuities. The discontinuous galerkin finite element method (DGFEM) has been developed for the neutron transport equation [2] and is now used in fluid and solid mechanics [3]. This extension of classical finite element method is based on the discontinuous Galerkin (DG) approximation in which shape functions are discontinuous across elements boundaries. The continuity of fields is not enforced on the whole mesh but only element-by-element and it allows to capture sharp solutions like shocks. Moreover, the characteristic structure of hyperbolic problems can be introduced within the numerical scheme as what has been first done with the finite volume method [4]. Hence, the DG approximation is well-suited to accurately capture wave fronts but is still limited by mesh tangling in a lagrangian approach where large deformations occur.

The purpose of this work is to develop a numerical method which allows to accurately follow wave fronts in a solid that is subjected to large deformations in a lagrangian framework. The eulerian grid of MPM can be used as a support for the DG approximation and the DGMPM introduced here aims at meeting advantages of both MPM and DG methods while freeing of their respective limits. We first derive the DGMPM formulation within the large strain framework with a total lagrangian formulation which is then linearized to apply to small strains framework. Then, we focus on the computation of interface fluxes resulting from the weak form. The method is finally illustrated on one-dimensional and two-dimensional problems, and comparisons are performed with the material point method, the finite element method and the analytical solution when it is known.

## 2 THE HYPERELASTIC DYNAMIC CONTINUUM PROBLEM

Let $\Omega_0 \in \mathbb{R}^3$ denote the reference position of a continuum body, with reference coordinates system $\boldsymbol{X}$, and $\Omega_t \in \mathbb{R}^3$ the position of the same body at a different time with the current coordinates system $\boldsymbol{x}$. The motion of the body is described by the smooth function $\boldsymbol{\varphi}(\boldsymbol{X}, t)$ which gives the position $\boldsymbol{x}$ at time $t$ of a particle initially located at $\boldsymbol{X}$. The mapping between current and reference configurations is $\boldsymbol{x} \equiv \boldsymbol{\varphi}(\boldsymbol{X}, t)$. The deformation gradient tensor and the

velocity vector are defined as :

$$\boldsymbol{F}(\boldsymbol{X},t) := \frac{\partial \boldsymbol{\varphi}(\boldsymbol{X},t)}{\partial \boldsymbol{X}} \tag{1}$$

$$\boldsymbol{v}(\boldsymbol{X},t) := \dot{\boldsymbol{\varphi}}(\boldsymbol{X},t) \tag{2}$$

where the superposed dot denotes the material time derivative. Combination of equations (1) and (2) yields :

$$\dot{\boldsymbol{F}}(\boldsymbol{X},t) = \frac{\partial \boldsymbol{v}(\boldsymbol{X},t)}{\partial \boldsymbol{X}} \tag{3}$$

The solid must satisfy locally the conservation of linear momentum written in the reference configuration within the time interval of interest $t \in ]0,T]$, and with neglected body forces :

$$\frac{\partial \rho_0 \boldsymbol{v}}{\partial t} - \boldsymbol{\nabla}_X \cdot \boldsymbol{\Pi} = \boldsymbol{0} \quad \forall \boldsymbol{X} \in \Omega_0 \tag{4}$$

where $\rho_0(\boldsymbol{X}) = \rho(\boldsymbol{x}, t=0)$ is the reference mass density, $\boldsymbol{\Pi}$ is the first Piola-Kirchhoff stress tensor and $\boldsymbol{\nabla}_X \cdot (\bullet)$ is the divergence vector with respect to reference coordinates. The Plohr and Sharp formulation [5] consists in viewing equation (3) as a conservation law in order to write the following homogeneous system of partial differential equations :

$$\frac{\partial \boldsymbol{q}}{\partial t} + \sum_{l=1}^{3} \frac{\partial \boldsymbol{\mathcal{F}}_l}{\partial X_l} = \boldsymbol{0} \tag{5}$$

where $\boldsymbol{q}$ is the vector of conserved quantities and $\boldsymbol{\mathcal{F}}_l$ the $l^{th}$ flux vector :

$$\boldsymbol{q} = \begin{Bmatrix} \boldsymbol{F}\cdot\boldsymbol{e}_1 \\ \boldsymbol{F}\cdot\boldsymbol{e}_2 \\ \boldsymbol{F}\cdot\boldsymbol{e}_3 \\ \rho_0\boldsymbol{v} \end{Bmatrix} \quad ; \quad \boldsymbol{\mathcal{F}}_l = -\begin{Bmatrix} (\boldsymbol{v}\otimes\boldsymbol{e}_1)\cdot\boldsymbol{e}_l \\ (\boldsymbol{v}\otimes\boldsymbol{e}_2)\cdot\boldsymbol{e}_l \\ (\boldsymbol{v}\otimes\boldsymbol{e}_3)\cdot\boldsymbol{e}_l \\ \boldsymbol{\Pi}\cdot\boldsymbol{e}_l \end{Bmatrix} = \boldsymbol{\mathcal{F}}\cdot\boldsymbol{e}_l \tag{6}$$

In the particular case of linear elasticity within the small strains framework, the system is built by replacing equation (3) with the geometrical compatibility equations $\dot{\boldsymbol{\varepsilon}} = \frac{1}{2}(\boldsymbol{\nabla}\boldsymbol{v} + \boldsymbol{\nabla}\boldsymbol{v}^T)$, that can also be combined with the elastic constitutive equation $\boldsymbol{\sigma} = \mathbb{H} : \boldsymbol{\varepsilon}$, where $\mathbb{H}$ is the fourth-order elasticity tensor. The vectors expressions are :

$$\boldsymbol{q} = \begin{Bmatrix} \boldsymbol{\sigma}\cdot\boldsymbol{e}_1 \\ \boldsymbol{\sigma}\cdot\boldsymbol{e}_2 \\ \boldsymbol{\sigma}\cdot\boldsymbol{e}_3 \\ \rho\boldsymbol{v} \end{Bmatrix} \quad ; \quad \boldsymbol{\mathcal{F}}_l = -\begin{Bmatrix} \mu(v_1\boldsymbol{e}_l + v_i\boldsymbol{e}_i) + \lambda v_l\boldsymbol{e}_1 \\ \mu(v_2\boldsymbol{e}_l + v_i\boldsymbol{e}_i) + \lambda v_l\boldsymbol{e}_2 \\ \mu(v_3\boldsymbol{e}_l + v_i\boldsymbol{e}_i) + \lambda v_l\boldsymbol{e}_3 \\ \boldsymbol{\sigma}\cdot\boldsymbol{e}_l \end{Bmatrix} \tag{7}$$

with $\boldsymbol{\sigma}$ being the Cauchy stress tensor, $\boldsymbol{\varepsilon}$ the linearized strain tensor, and $(\lambda, \mu)$ are Lamé's coefficients.

## 3 THE DISCONTINUOUS GALERKIN MATERIAL POINT METHOD

A continuum body $\Omega_t$ is described by a set of $P$ material points in an eulerian grid composed of $N$ quadrangular 4-nodes elements (or cells) such that the volume covered by the grid is $\mathcal{V} = \cup_{e=1}^{N} \mathcal{V}_e$ with $\mathcal{V}_i \cap \mathcal{V}_j = \emptyset \; \forall \, i, j$ (fig. 1).

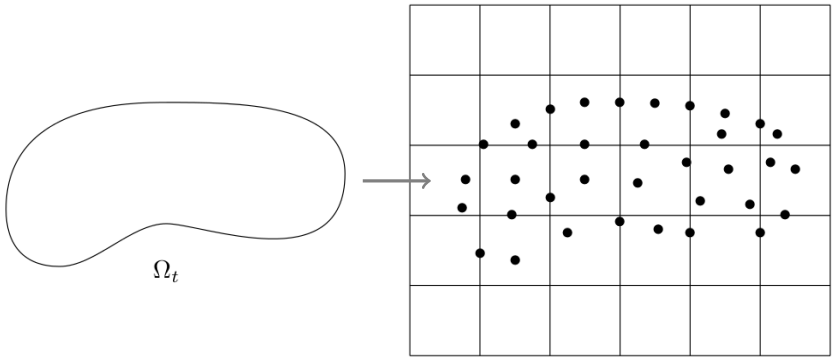


Figure 1: Representation of a continuum body by a set of material points in $\mathbb{R}^3$.

### 3.1 Weak form of equation of motion

The discontinuous galerkin approach relies on approximation functions that are discontinuous at cells interfaces and hence, the weak form of equation (5) is written on each element of the grid [3]:

$$\int_{\mathcal{V}_e} \frac{\partial \boldsymbol{q}}{\partial t} \cdot \boldsymbol{w} \, dV + \int_{\mathcal{V}_e} \sum_l \frac{\partial \boldsymbol{\mathcal{F}}_l}{\partial X_l} \cdot \boldsymbol{w} \, dV = 0 \quad \forall \, \boldsymbol{w}, \forall \, \mathcal{V}_e \tag{8}$$

Integration by parts leads to :

$$\int_{\mathcal{V}_e} \frac{\partial \boldsymbol{q}}{\partial t} \cdot \boldsymbol{w} \, dV - \int_{\mathcal{V}_e} \sum_l \boldsymbol{\mathcal{F}}_l \cdot \frac{\partial \boldsymbol{w}}{\partial X_l} \, dV + \int_{\Gamma_e} (\boldsymbol{\mathcal{F}} \cdot \boldsymbol{n}) \cdot \boldsymbol{w} \, d\Gamma = 0 \quad \forall \, \boldsymbol{w}, \forall \, \mathcal{V}_e \tag{9}$$

where $\boldsymbol{n}$ is the outward normal vector to the boundary and $\boldsymbol{\mathcal{F}} \cdot \boldsymbol{n} = \boldsymbol{\mathcal{F}}_n$ denotes a normal flux at cell faces (which computation is developed in section 4). We introduce *specific* quantities that will be injected in the weak form (9) :

$$\boldsymbol{q}^s = \rho_0 \boldsymbol{q} \quad ; \quad \boldsymbol{\mathcal{F}}_k^s = \rho_0 \boldsymbol{\mathcal{F}}_k \tag{10}$$

Moreover, a particular representation of mass density based on material points mass is used :

$$\rho\left(\boldsymbol{x}, t\right) = \sum_{\alpha=1}^{P} m_\alpha \delta\left(\boldsymbol{x}_\alpha - \boldsymbol{x}\right) \Longrightarrow \rho_0\left(\boldsymbol{X}\right) = \rho(\boldsymbol{x}, 0) = \sum_{\alpha=1}^{P} m_\alpha \delta\left(\boldsymbol{X}_\alpha - \boldsymbol{X}\right) \tag{11}$$

where $\delta$ is the delta dirac distribution and $m_\alpha$ is the mass of the $\alpha^{th}$ material point. Such a discretization of the reference mass density combined with the writing of conservation laws (5) leads to a total lagrangian formulation. Equation (9) thus reads :

$$\int_{\mathcal{V}_e} \rho_0 \frac{\partial \boldsymbol{q}^s}{\partial t} \cdot \boldsymbol{w} \, dV - \int_{\mathcal{V}_e} \rho_0 \sum_l \boldsymbol{\mathcal{F}}_l^s \cdot \frac{\partial \boldsymbol{w}}{\partial X_l} \, dV + \int_{\Gamma_e} \boldsymbol{\mathcal{F}}_n \cdot \boldsymbol{w} \, d\Gamma = 0 \quad \forall \, \boldsymbol{w}, \forall \, \mathcal{V}_e \tag{12}$$

which, with delta dirac integration properties transforms to :

$$\sum_{\alpha=1}^{P} \left( m_\alpha \frac{\partial \boldsymbol{q}^s\left(\boldsymbol{X}_\alpha\right)}{\partial t} \cdot \boldsymbol{w}(\boldsymbol{X}_\alpha) - \sum_l \boldsymbol{\mathcal{F}}_l^s\left(\boldsymbol{X}_\alpha\right) \cdot \frac{\partial \boldsymbol{w}\left(\boldsymbol{X}_\alpha\right)}{\partial X_l} \right) + \int_{\Gamma_e} \boldsymbol{\mathcal{F}}_n \cdot \boldsymbol{w} \, d\Gamma = 0 \quad \forall \, \boldsymbol{w}, \forall \, \mathcal{V}_e \tag{13}$$

### 3.2 Nodes to material points mapping

As in MPM we need to transfer fields from nodes to material points and we use shape functions which support reduces to only one cell :

$$\boldsymbol{q}^s(\boldsymbol{X}_\alpha) = \sum_{i=1}^{N} S_{i\alpha}\boldsymbol{q}_i^s \tag{14}$$

where $S_{i\alpha}$ denotes the shape functions attached to the $i^{th}$ node evaluated at $\boldsymbol{X} = \boldsymbol{X}_\alpha$, and $\boldsymbol{q}_i^s$ the specific vector of conserved quantities at node $i$. Once introduced in (13), it comes :

$$\boldsymbol{w}_i \cdot \sum_{\alpha=1}^{P} S_{i\alpha} m_\alpha S_{j\alpha} \frac{\partial \boldsymbol{q}_j^s}{\partial t} - \boldsymbol{w}_i \cdot \sum_l \frac{\partial S_{i\alpha}}{\partial X_l} m_\alpha S_{i\alpha} \boldsymbol{\mathcal{F}}_{l,j}^s + \boldsymbol{w}_i \cdot \int_{\Gamma_e} S_i(\boldsymbol{X}) \boldsymbol{\mathcal{F}}_n \, d\Gamma = 0 \quad \forall\, \boldsymbol{w}_i \tag{15}$$

$$\Leftrightarrow M_{ij} \frac{\partial \boldsymbol{q}_j^s}{\partial t} - \sum_{l=1}^{3} K_{ij}^l \boldsymbol{\mathcal{F}}_{l,j}^s + \boldsymbol{\mathcal{F}}_j^* = \boldsymbol{0} \tag{16}$$

which is the semi-discrete system that must be solved on the grid. Time discretization is performed with an explicit algorithm (*forward Euler, Runge-Kutta 2*), leading to discrete equations.

**Remark :** In particular configurations of material points, the consistent mass matrix $M_{ij}$ can be singular [6] and it is avoided by lumping this matrix : $M_i^L = \sum_j M_{ij}$.

### 3.3 Material points to nodes mapping

In order to solve system (16), fields have to be defined at nodes and an interpolation of conserved quantity is performed :

$$\boldsymbol{q}_i = M_i^L \boldsymbol{q}_i^s = \sum_{\alpha=1}^{P} S_{i\alpha} m_\alpha \boldsymbol{q}_\alpha^s \tag{17}$$

to be solved for each $\boldsymbol{q}_i^s$. This mapping is a mass weighted interpolation that stabilized the MPM.

**Remark :** Every fields are defined at nodes in DGMPM and constitutive equations are integrated in fluxes contained in volume and surface integrals whereas in MPM, velocity is updated at nodes and constitutive equations are integrated at material points.

## 4 INTERFACE FLUXES COMPUTATION

Fields continuity is relaxed across elements boundary and interface fluxes appear in the weak form. They can be used to introduce the characteristic structure of hyperbolic problems in the numerical scheme. One possibility is to solve a Riemann problem normal to each edge of a given cell and to compute the *Godunov* flux corresponding to the stationary solution ($x/t = 0$) of the Riemann problem [7]. For the two-dimensional case (fig 2), the problem at a given edge consists in finding the solution of the auxiliary initial value problem (IVP):

$$\frac{\partial \tilde{\boldsymbol{q}}}{\partial t} + \frac{\partial \boldsymbol{\mathcal{F}}_n}{\partial \xi} = \boldsymbol{0}, \quad \xi = \boldsymbol{X} \cdot \boldsymbol{n} \ \in ]-\infty, \infty[, \quad t > 0 \tag{18}$$

$$\tilde{\boldsymbol{q}}(\xi, 0) = \begin{cases} \tilde{\boldsymbol{q}}_L \text{ if } \xi < 0 \\ \tilde{\boldsymbol{q}}_R \text{ if } \xi > 0 \end{cases} \tag{19}$$

where $L$ and $R$ denote states belonging to the *Left* cell and the *Right* cell to the edge respectively. These states are constructed by averaging the values defined at nodes for each side (remind that the DG approximation gives one nodal field value for each cell connected to a given node). The

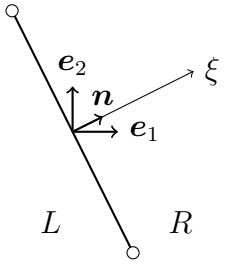


Figure 2: Edge separating two cells indexed $L$ (left) and $R$ (right). A local coordinate $\xi$ and a normal vector $\boldsymbol{n}$ are defined.

normal flux vector can be decomposed with the consideration that $\boldsymbol{n} = n_1 \boldsymbol{e}_1 + n_2 \boldsymbol{e}_2$ :

$$\boldsymbol{\mathcal{F}}_n = \boldsymbol{\mathcal{F}} \cdot \boldsymbol{n} = n_1 \boldsymbol{\mathcal{F}}_1 + n_2 \boldsymbol{\mathcal{F}}_2 \tag{20}$$

The conservation laws system (18) combined with (20) yields :

$$\frac{\partial \tilde{\boldsymbol{q}}}{\partial t} + \sum_p n_p \frac{\partial \boldsymbol{\mathcal{F}}_p}{\partial \xi} = \boldsymbol{0}$$

$$\frac{\partial \tilde{\boldsymbol{q}}}{\partial t} + \sum_p n_p \frac{\partial \boldsymbol{\mathcal{F}}_p}{\partial \tilde{\boldsymbol{q}}} \cdot \frac{\partial \tilde{\boldsymbol{q}}}{\partial \xi} = \boldsymbol{0}$$

$$\frac{\partial \tilde{\boldsymbol{q}}}{\partial t} + \sum_p n_p \boldsymbol{A}^p \cdot \frac{\partial \tilde{\boldsymbol{q}}}{\partial \xi} = \boldsymbol{0}$$

The characteristic analysis of this system written with vectors (6) can be conducted with the study of the jacobian matrix $\boldsymbol{\mathcal{J}} = \sum_p n_p \boldsymbol{A}^p$. In two dimensions :

$$\boldsymbol{A}^p = \begin{bmatrix} \boldsymbol{0} & \boldsymbol{0} & -H_{ip1j} \boldsymbol{e}_i \otimes \boldsymbol{e}_j \\ \boldsymbol{0} & \boldsymbol{0} & -H_{ip2j} \boldsymbol{e}_i \otimes \boldsymbol{e}_j \\ -\frac{\delta_{1p}}{\rho_0} \boldsymbol{1} & -\frac{\delta_{2p}}{\rho_0} \boldsymbol{1} & \boldsymbol{0} \end{bmatrix} \tag{21}$$

and $H_{klmn}$ are the fourth-order material elasticity tensor components. The eigenvalues and eigenvectors of the Jacobian matrix are used to obtain the solution of the Riemann problem for linear (elastic) problems, or to build an approximate Riemann Solver [7] for hyperelastic nonlinear problems. The solution is used to compute Godunov fluxes at cells interfaces $\boldsymbol{\mathcal{F}}_n \left( \tilde{\boldsymbol{q}}(x/t = 0) \right)$.

# 5 NUMERICAL RESULTS

## 5.1 One dimensional compression wave in a bar (small strain)

Let us consider an elastic bar of length $l = 6m$ made of a linear elastic material with Young's modulus $E = 2.10^{11}\,Pa$, density $\rho = 7800 kg.m^{-3}$ and unit cross section area $S$. The left end of the bar is suddenly loaded with a surface force $T^d = 1.10^9\ Pa$. The bar is discretized with 150 regular grid cells (each containing one single centered material point) and the time integration is carried out with an explicit Euler scheme. This problem has been solved with DGMPM and a comparison is performed with MPM and the analytical solution [8] for different time steps (fig 3).

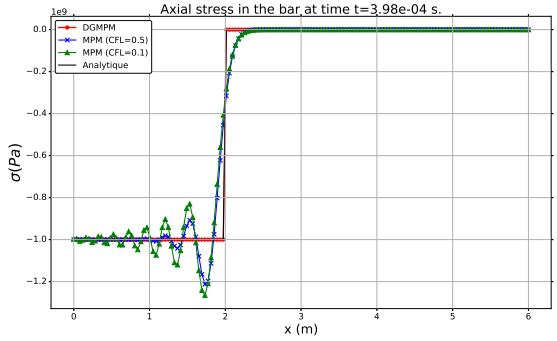


(a)

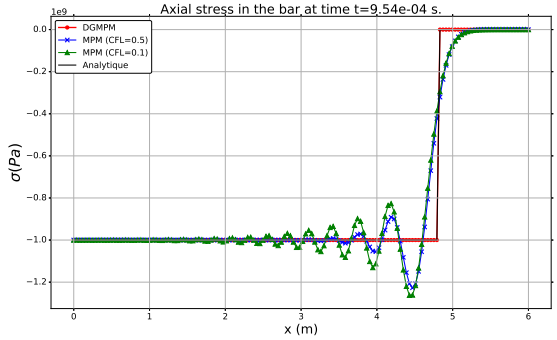


(b)

Figure 3: Axial stress in a bar at different times. Comparison of DGMPM, MPM and analytical solution.

The solution consists of a discontinuous elastic disturbance propagating rightward at speed $c = \sqrt{\frac{E}{\rho}}$ and is here accurately captured by the DGMPM solution. It is known that a numerical scheme is able to capture a discontinuity providing the Courant number be one without loss of stability ($\alpha = c\frac{\Delta t}{\Delta x}$). The MPM is unstable with $\alpha = 1$ and hence, it is unable to track discontinuities. The stability analysis of DGMPM will not be developed here, but it can be shown that when a single material point is located in each cell, the Courant number can be equal to one and a wave front can be represented. This property is lost with more points in each cell but it can be improved by using a Runge-Kutta 2 time integrator.

### 5.2 Two dimensional partial impact on a plate (small strain)

We are now interested in two-dimensional plane strains cases and the problem treated concerns a linear elastic rectangular plate undergoing an impact on a part of its left boundary (fig 4). The plate dimensions are $l$ x $h$ = 4 x 3 $m^2$ discretized with 33 x 25 material points, and the width of impact area is $a = 1\ m$. A velocity Dirichlet boundary condition is enforced on material points directly in the MPM while ghost nodes are used in the DGMPM grid [4]. The problem has been solved with the finite element code Cast3M [9] (explicit time integration), the material point method and its discontinuous Galerkin extension and the comparison is shown in fig 5 for one point per cell.

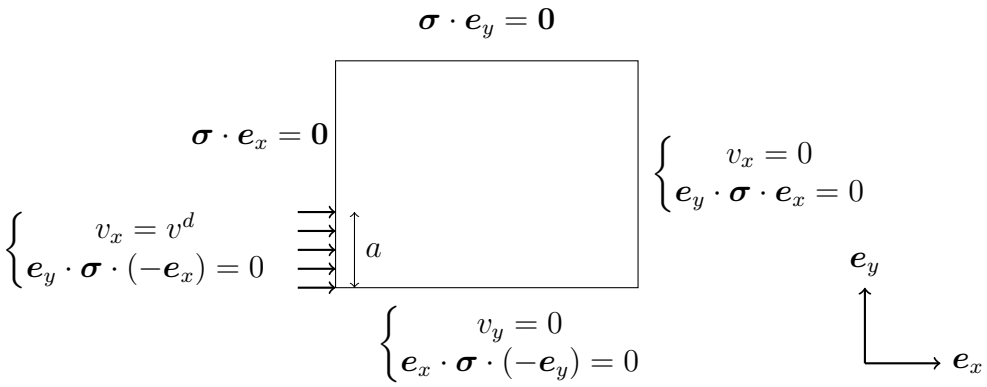


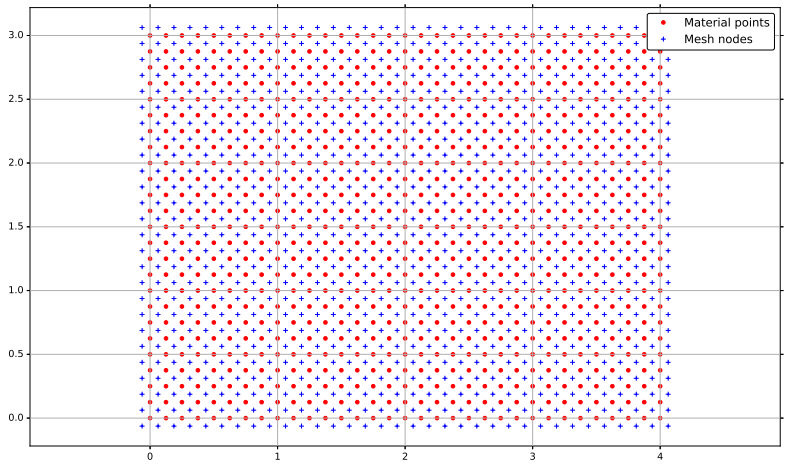


Figure 4: Elastic plate undergoing a compressive impact on a part of its left boundary. Parameters : $E = 2.10^{11}\,Pa$, $\nu = 0.3$, $\rho = 7800\ kg \cdot m^{-3}$, $v^d = 5m.s^{-1}$.

As mentioned above about FEM and MPM, the time integration used involves oscillations in the solution and the Courant condition ($\alpha < 1$) introduces numerical diffusion. This two

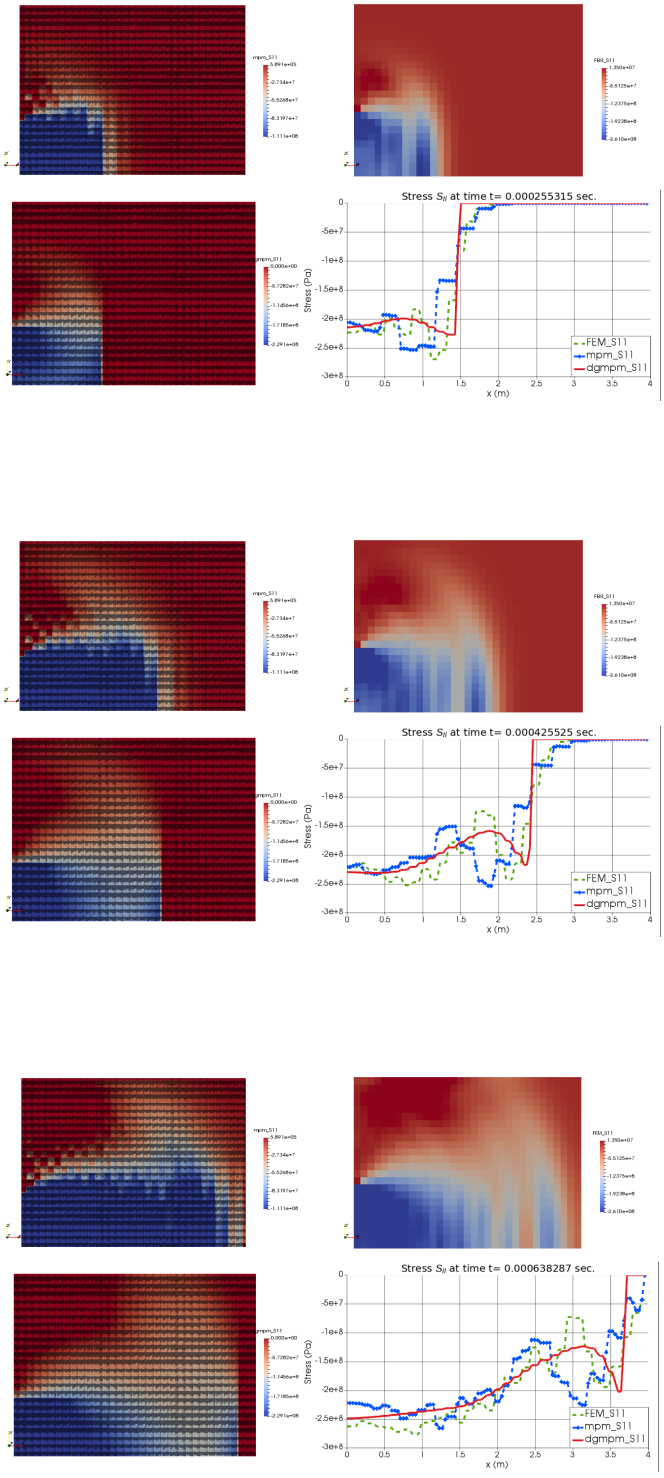


Figure 5: Longitudinal stress profile resulting from MPM (top left), FEM (top right) and DGMPM (bottom left) and superposed plot along the bottom boundary of the plate at different times for DGMPM and MPM and FEM (bottom right). $\alpha_{MPM} = 0.5$, $\alpha_{FEM} = 0.9$, $\alpha_{DGMPM} = 1$

dimensional problem involves two families of waves : tensile/compression waves traveling at celerity $c_p = \sqrt{(\lambda + 2\mu)/\rho}$ and shear waves traveling at celerity $c_s = \sqrt{\mu/\rho}$. These waves can make the DGMPM solution scheme unstable when the Courant number equals one. To avoid it, a transverse Riemann solver based on the Corner Transport Upwind method [4] has been used and sharp solutions can be captured more accurately. These results confirm that the extension of MPM to DG framework provides a better wave front tracking.

### 5.3 One dimensional compression wave in a hyperelastic bar (large strain)

The last numerical test is an extension of the first one to the large strains framework. The bar is now made of a hyperelastic Saint-Venant-Kirchhoff material for which the constitutive equation is :

$$\boldsymbol{\Pi} = 2\mu \boldsymbol{F} \cdot \boldsymbol{E} + \lambda \,\mathrm{trace}\,(\boldsymbol{E})\boldsymbol{F} \tag{22}$$

where $\boldsymbol{E} = \frac{1}{2}(\boldsymbol{F}^T \cdot \boldsymbol{F} - \mathbf{1})$ is the Green-Lagrange strain tensor and $\boldsymbol{\Pi}$ is the first Piola-Kirchhoff stress tensor. For a one-dimensional bar, this relation reduces to : $\Pi_{xx} = \frac{E}{2} F_{xx}(F_{xx}^2 - 1)$. The bar is suddenly loaded on its left side ($T^d = 8.10^8 Pa$). In figure 6, the upper subplot shows the material points positions at different times updated with the velocity solution. The bottom one shows the Piola-Kirchhoff stress from MPM, DGMPM (both in total Lagrangian formulation) and an analytical solution.

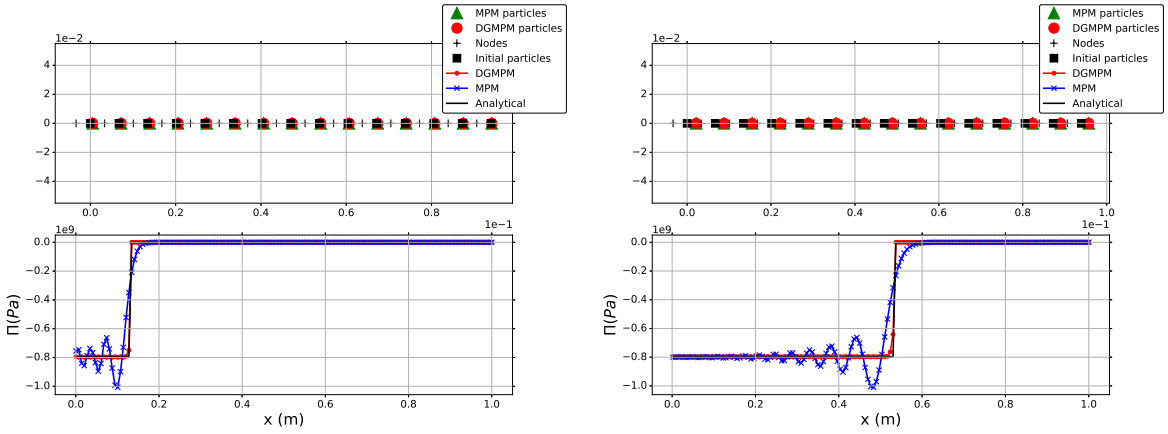


Figure 6: Saint-Venant-Kirchhoff hyperelastic bar undergoing large deformations (positions - Piola stress) plot at different times. Material parameters are the same as in the linear elastic case.

The DGMPM is no longer exactly on the analytical solution of this nonlinear problem and the reason might be the use of an approximate Riemann solver instead of the nonlinear one (which is more expensive). Once again classical MPM fails to represent the discontinuity and introduces oscillations in the results.

## 6 CONCLUSION

In this work, the Material Point Method has been extended to the Discontinuous Galerkin approximation framework in order to improve wave front tracking. This extension is based on the use of shape functions defined element-by-element and discontinuous across cells interfaces.

The weak form of the problem within the large strains framework is written for the equation of motion (4) and for the lagrangian kinematic equation (3). The DGMPM hyperbolic system is built with a total lagrangian formulation (13) and contains numerical fluxes at cells interfaces which are computed with the solution of a Riemann problem. The main difference with the original scheme is that the constitutive equations are contained in nodal fluxes and the characteristic structure of hyperbolic problems can be introduced in the numerical solution, providing a better description of discontinuities.

## REFERENCES

[1] D. Sulsky, S.-J. Zhou, and H. L. Schreyer, "Application of a particle-in-cell method to solid mechanics," *Computer Physics Communications*, vol. 87, no. 12, pp. 236 – 252, 1995.

[2] W. H. Reed and T. Hill, "Triangular mesh methods for the neutron transport equation," *Los Alamos Report LA-UR-73-479*, 1973.

[3] J. S. Hesthaven and T. Warburton, *Nodal discontinuous Galerkin methods: algorithms, analysis, and applications*. Springer Science & Business Media, 2007.

[4] R. J. Leveque, *Finite volume methods for hyperbolic problems*. Cambridge university press, 2002.

[5] B. J. Plohr and D. H. Sharp, "A conservative eulerian formulation of the equations for elastic flow," *Advances in Applied Mathematics*, vol. 9, no. 4, pp. 481 – 499, 1988.

[6] E. Love and D. Sulsky, "An unconditionally stable, energymomentum consistent implementation of the material-point method," *Computer Methods in Applied Mechanics and Engineering*, vol. 195, no. 3336, pp. 3903 – 3925, 2006.

[7] E. F. Toro, *Riemann solvers and numerical methods for fluid dynamics: a practical introduction*. Springer Science & Business Media, 2013.

[8] L. Wang, *Foundations of stress waves*. Elsevier, 2011.

[9] *Cast3M. User's manual*, 2016.

COMPDYN 2017
6th ECCOMAS Thematic Conference on
Computational Methods in Structural Dynamics and Earthquake Engineering
Y. Guzel, G. Elia, M. Rouainia
Rhodes Island, Greece, 15–17 June 2017

# THE EFFECT OF INPUT MOTION SELECTION STRATEGIES ON NONLINEAR GROUND RESPONSE PREDICTIONS

**Yusuf Guzel[1], Gaetano Elia[2] and Mohamed Rouainia[3]**

[1] Newcastle University
NE1 7RU Newcastle upon Tyne
y.guzel@newcastle.ac.uk

[2] Newcastle University
NE1 7RU Newcastle upon Tyne
gaetano.elia@ncl.ac.uk

[3] Newcastle University
NE1 7RU Newcastle upon Tyne
mohamed.rouainia@ncl.ac.uk

**Keywords:** Ground response analysis, bedrock motion, selection strategy, spectral response, design response spectrum

**Abstract.** *Ground response prediction is a key tool in the seismic design of earth structures. The prediction is mainly governed by three factors, namely the bedrock motions, the nonlinear characteristics of the soil deposit and the corresponding initial shear wave velocity profile. This study focuses on the first factor by analysing the effect of five different earthquake selection/scaling strategies on the results of nonlinear ground response. The analyses are interpreted in terms of spectral response and engineering demand parameters (EDPs) at ground surface, including the relative horizontal displacement, the peak ground acceleration (PGA) and the spectral acceleration at the first natural period of the soil deposit ($Sa(T_1)$). An ideal 50 m soft clay deposit is analysed using a kinematic hardening soil constitutive model implemented in a fully coupled finite element procedure. The results of the advanced nonlinear ground response analyses indicate that, for two different seismic intensity levels, all the selection strategies lead to similar spectral responses at around $T_1$, with the exception of PGA scaling. Furthermore, the spectral matching strategy leads to a smaller variability in the EDP results. It is also found that the design response spectrum proposed by EC8 for a soft soil deposit does not seem to be fully representative of the possible future earthquake events, thus requiring a revision.*

## 1 INTRODUCTION

The alteration of the earthquake characteristics from the bedrock to the surface due to local site conditions is of great interest for the engineering communities dealing with seismic design. The common way of predicting local site effects on wave propagation processes is to propagate seismic input motions through horizontally layered soil deposits by means of simple or advanced numerical methods enabling to assess the surface acceleration time histories, response spectra, amplification factors (AFs), soil stiffness degradation and associated hysteretic damping in response to the shear strains induced by a possible earthquake event [1].

Ground response analyses are mainly governed by the bedrock motion, the nonlinear dynamic features of the soil deposit and its initial shear wave velocity profile. These components sustain some uncertainties attributed to, for example, i) the ambiguity in the selection of a probable earthquake event with specific features from a database (i.e. magnitude, distance, fault mechanism), ii) the possible variability in the measurement of the shear wave velocity profile due to the heterogeneity of the soil deposit and iii) the soil disturbance affecting laboratory tests used to determine the material nonlinear dynamic properties [2]. These uncertainties may ultimately cause bias in site response predictions if they are not properly accounted for in the analysis [3].

Several studies have dealt with the above uncertainties to quantify their possible effects on ground response predictions. For this purpose, Monte Carlo simulations have been conducted with linear or nonlinear soil models by varying site properties [1, 3-5]. While these studies explicitly indicate the importance of accounting for the shear wave velocity, stiffness degradation and damping level variabilities in ground response analyses, they also recognise the impact of the bedrock motion selection on the accuracy of the site response results. Different input motion selection and modification methods, such as peak ground acceleration (PGA) scaling, spectral matching and the mean squared error (MSE) approach, have been proposed in the structural engineering literature [6-9], but their application to geotechnical earthquake engineering problems is limited [10].

This paper examines the impact of different earthquake selection and scaling strategies on the free-field ground response of an ideal soft soil deposit. Sets of seven bedrock motions are used for each selection strategy, considering two seismic intensity levels of 0.15 g and 0.35 g. Advanced time-domain nonlinear ground response analyses are performed with SWANDYNE II [11], a fully coupled finite element (FE) code incorporating the kinematic hardening soil model proposed by Rouainia and Muir Wood [12]. The results of the simulations are firstly interpreted in terms of engineering demand parameters (EDPs) at surface, i.e. relative horizontal displacement, PGA and spectral acceleration at the first natural period of the soil deposit ($Sa(T_1)$). The comparison with EC8 in terms of amplification factors is subsequently presented to highlight the inability of the EC8 prescriptions to fully capture site effects occurring in soft soil deposits.

## 2 FINITE ELEMENT MODEL

An ideal 50 m deep soft clay deposit is modelled in SWANDYNE II using a 5 m wide column discretised with 250, 1×1 m isoparametric quadrilateral finite elements with 8 solid nodes and 4 fluid nodes. In the dynamic analyses the bottom of the mesh is assumed to be rigid, while the nodes along the vertical sides are characterized by the same displacements (i.e. tied-nodes lateral boundary conditions). The selected input records are directly applied to the solid nodes at the base of the mesh as prescribed horizontal displacement time histories. The Rouainia and Muir Wood (RMW) advanced soil constitutive model is adopted to simulate the dynamic clay behaviour during the seismic excitation. RMW has been successfully employed

to predict the dynamic performance of different earth structures [13, 14], as it has been shown to be able to reproduce the decay of the shear stiffness with strain amplitude, the corresponding increase of hysteretic damping and the related accumulation of excess pore water pressure and structure degradation under undrained conditions. In this work, the model parameters, reported in Table 1, are determined by conducting a series of undrained cyclic simple shear test simulations under controlled strain levels in order to produce normalized shear modulus and damping curves representative of a soft soil material [15].

| Parameter/ symbol | Physical contribution/meaning | Value |
|---|---|---|
| $M$ | Critical state stress ratio for triaxial compression | 1.35 |
| $\lambda^*$ | Slope of normal compression line in ln $v$-ln $p$ compression plane | 0.252 |
| $\kappa^*$ | Slope of swelling line in ln $v$-ln $p$ compression plane | 0.0297 |
| $R$ | Ratio of size of bubble and reference surface | 0.1 |
| $B$ | Stiffness interpolation parameter | 8.0 |
| $\psi$ | Stiffness interpolation exponent | 1.0 |
| $\boldsymbol{\eta}_0$ | Anisotropy of initial structure | **0** |
| $r_0$ | Initial degree of structure | 1.75 |
| $A^*$ | Parameter controlling relative proportion of distorsional and volumetric destructuration | 0.494 |
| $k$ | Parameter controlling rate of loss of structure with damage strain | 0.5 |
| $\nu$ | Poisson's ratio | 0.25 |

Table 1: RMW model parameters.

The initial stiffness profile of the deposit is obtained using the well-known equation proposed by Viggiani and Atkinson [16] for the dependency of the small-strain shear modulus $G_0$ on the mean effective stress, $p'$, and overconsolidation ratio, $OCR$:

$$\frac{G_0}{p_r} = A\left(\frac{p'}{p_r}\right)^n OCR^m \tag{1}$$

In this work, the dimensionless stiffness parameters $A$, $m$ and $n$ are set equal to 1050, 0.27 and 0.84, respectively, and $p_r$ is a reference pressure (equal to 1 kPa). In the initialisation phase of the FE model, an overconsolidation ratio of 1.5 is assumed constant with depth. The resulting shear wave velocity profile has an average value in the top 30 m of the column equal to 140 m/s, thus classifying the deposit as a soil class D according to EC8 [9]. The first natural period ($T_1$), calculated using the elasticity theory, is equal to 1.17 s.

## 3 SELECTION STRATEGIES

Five different strategies for selecting and modifying bedrock input motions recorded on soil class A are employed in this work. Specifically, PGA scaling, Sa($T_1$) scaling, $0.2T_1$-$2T_1$ scaling, spectral matching and mean squared error (MSE) scaling are investigated. PGA scaling focuses only on the compatibility of the bedrock motions, on an average, with the target response spectrum (i.e. the EC8 5% damping design response spectrum for soil class A) at zero period. Sa($T_1$) scaling seeks for an average compatibility with the target response spectrum at $T_1$ only. According to the $0.2T_1$-$2T_1$ scaling strategy proposed by EC8, the average

compatibility with the target response spectrum is achieved within the $0.2T_1$-$2T_1$ period range with lower tolerance of 10% and the average PGA is not less than that of the target response spectrum. MSE scaling considers the total difference between the natural logarithmic spectral acceleration of the event and the target response spectrum over a specified period range of interest. Finally, the spectral matching strategy achieves the full matching of the bedrock motions with the target response spectrum by modifying the frequency content of the input motions.

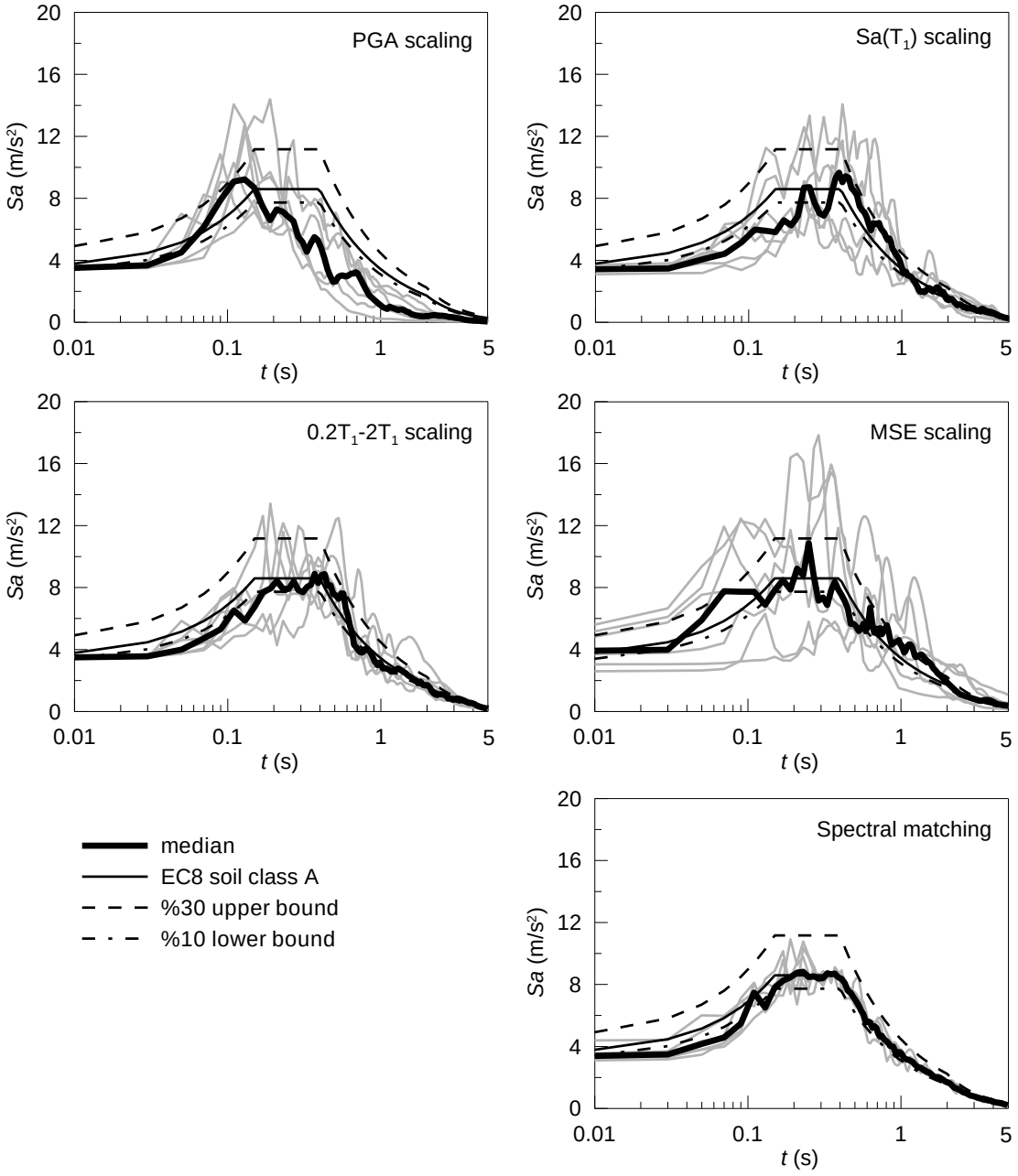


Figure 1: Response spectra of bedrock motions selected according to different strategies for the 0.35 g seismic intensity level.

For each selection strategy, seven motions are chosen from the earthquake database [8, 17] to evaluate the average dynamic response of the FE column in accordance with EC8. In addition, two different seismic intensity levels of 0.15 g and 0.35 g are considered to highlight the

effect of soil nonlinearity on the wave propagation process. The selection of the bedrock motions according to the first three strategies is conducted by using the computer program REXEL [17]. SEISMOMATCH [18] is instead used to perform the spectral matching approach, while MSE scaling is obtained using the PEER Ground Motion Database website [8]. Figure 1 presents the response spectra of the five sets of input motions selected according to the different strategies for the stronger intensity level case, together with the comparison between the median and target response spectra for each selection strategy.

## 4 RESULTS AND DISCUSSION

### 4.1 Response spectra at ground surface

The median site response spectra predictions obtained at surface using the five different sets of bedrock motions are presented in Figure 2 for the two seismic intensity levels. It is clear that, in all cases, the first and the second natural modes of the soil deposit contribute in the seismic oscillation. Moreover, the predictions of site response based on PGA scaling are significantly different from those obtained with the remaining selection strategies, resulting in an average response spectrum positioned well below the EC8 one for both the intensity levels investigated. For the seismic intensity level of 0.15 g, the five selection strategies give similar response spectra at surface, in particular at around $T_1$, with the exception of PGA scaling. It can be observed, however, that $0.2T_1$-$2T_1$ and $Sa(T_1)$ scaling strategies give slightly higher spectral responses at the second natural period of the deposit. In the case of the higher seismic intensity level (i.e. 0.35 g), $0.2T_1$-$2T_1$ scaling and spectral matching strategies result in higher spectral accelerations at shorter periods. In this case, the MSE scaling strategy produces surface response spectra diverging considerably from the other response predictions at the shorter periods. This might be due to the greater dispersion in the spectral peaks over the entire period range of the individual input motions at bedrock (Figure 1). This issue is not investigated in this research but the reader can refer to the study of Mazzoni *et al*. [19] for more information. Again, the spectral predictions at around $T_1$ are quite similar, with the exception of PGA scaling.

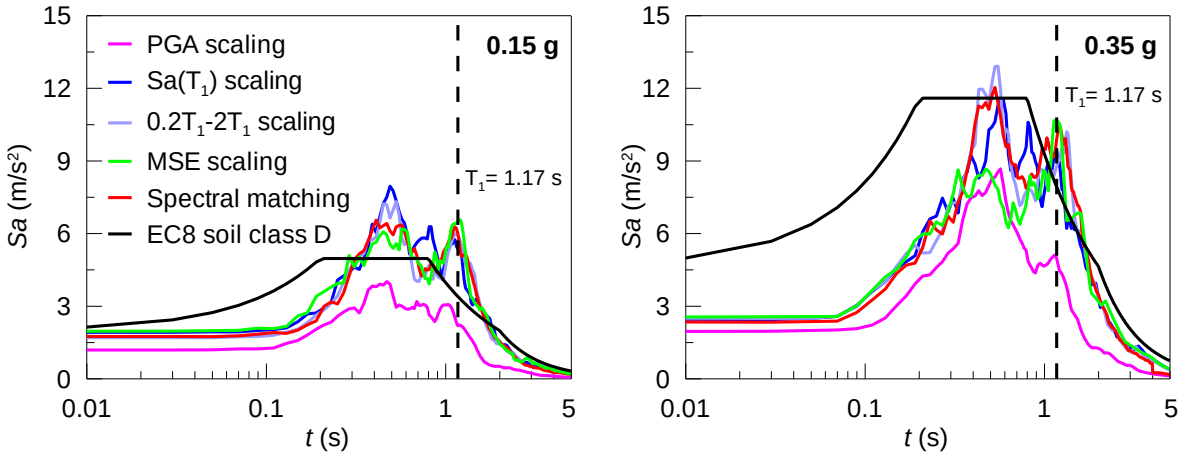


Figure 2: Median site response spectra predictions at surface for the 0.15 g (left) and 0.35 g (right) seismic intensity levels.

### 4.2 EDPs at ground surface

The impact of the different earthquake selection strategies on the results of the advanced ground response analyses is investigated here with respect to the EDPs obtained at ground

surface for both seismic intensity levels. The results are shown in Figure 3 for the individual motions (triangles), together with the mean values (squares) and mean plus/minus one standard deviation (circles) for each selection strategy.

Scaling the input motion records at the same PGA leads to relative horizontal displacements, peak ground accelerations and spectral accelerations at $T_1$ considerably lower, on average, than those obtained with the other selection strategies. Interestingly, $Sa(T_1)$ scaling introduces similar (or even less) variability in the EDPs at ground surface in comparison with the one obtained with $0.2T_1$-$2T_1$ scaling.

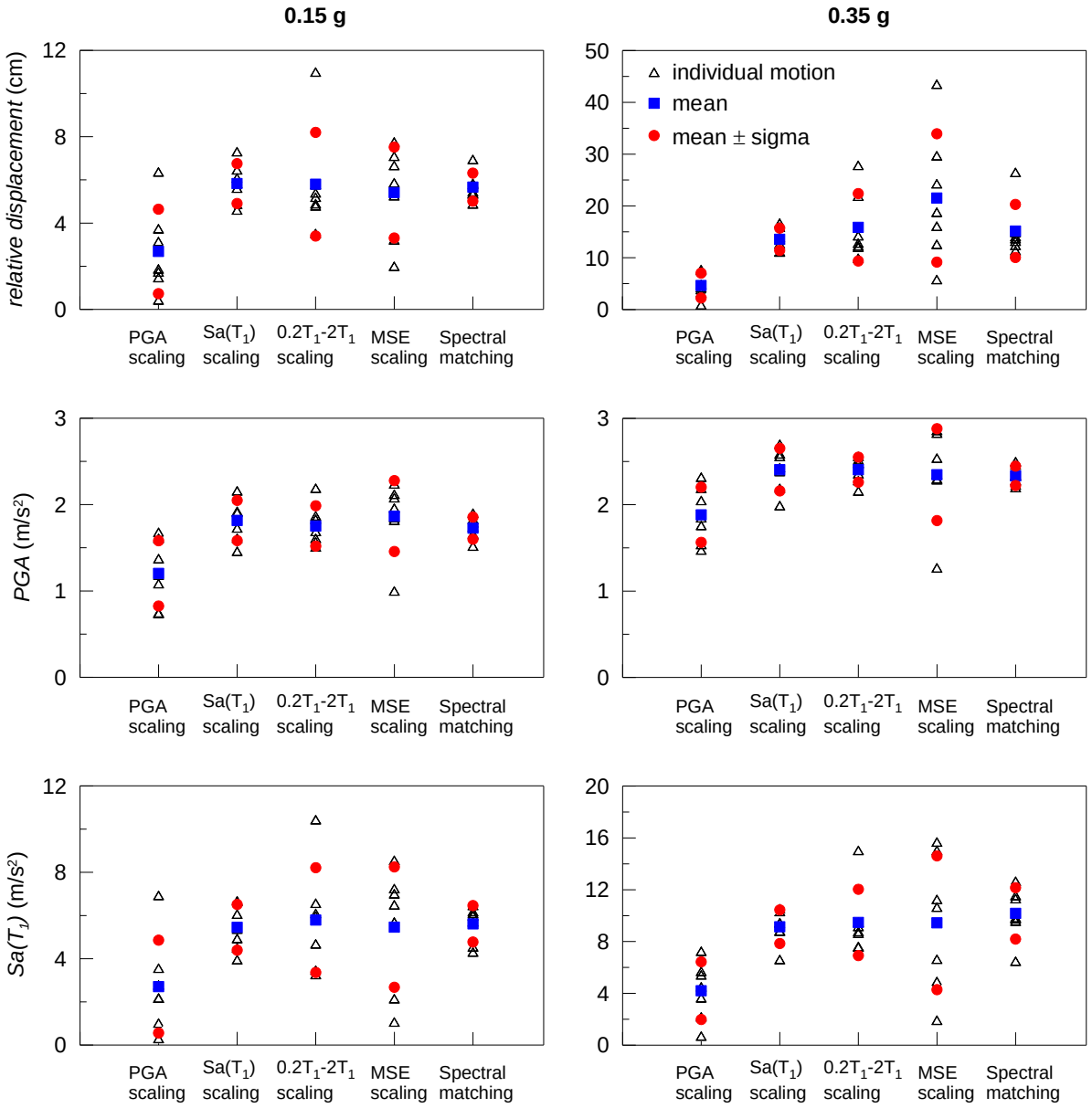


Figure 3: EDPs obtained for the 0.15 g (left) and 0.35 g (right) seismic intensity levels, including mean and mean plus/minus one standard deviation.

The MSE scaling strategy is characterised by the higher dispersion of values around the mean (i.e. the higher standard deviation), especially at the higher intensity level. The cause of this level of dispersion, as explained earlier, can be attributed to the greater scattering of the spectral peaks of the individual bedrock input motions. On the contrary, the EDPs obtained

with the spectral matching strategy are the least scattered at both seismic intensity levels. This is due to the fact that, in this case, the bedrock motions are fully matched with the target response spectrum, thus producing more stable and robust results at ground surface.

### 4.3 Comparison with the EC8 design response spectrum

From Figure 2 it is clear that the EC8 spectral shape does not capture well the amplification, which takes place at the first natural period of the soil deposit for the lower seismic intensity level. Nevertheless, in the case of earthquake events with higher intensity level, the EC8 design spectrum becomes a better proxy of the predicted surface response spectra, even though the amplification at around $T_1$ is still not fully captured. This observation is consistent with the results presented by Pitilakis *et al*. [20] and Rey *et al*. [21]. The same trend is observed when presenting the results of the ground response analyses in terms of amplification factors (Figure 4). Although the scope of this research is not to recommend new soil factors or a new spectral shape in the design code prescriptions, nonetheless the work highlights the necessity of revisiting the EC8 design response spectrum for soft soil deposits.

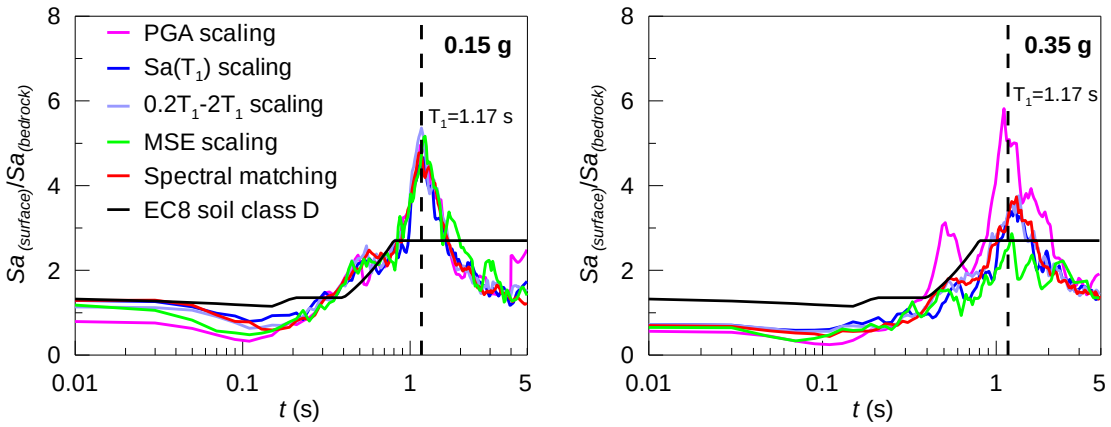


Figure 4: Amplification factors obtained from each selection strategy at 0.15 g and 0.35 g seismic intensity levels.

In the case of a low seismic intensity level, the five selection strategies give similar amplification factors between 0.3 s and 5 s, with PGA scaling producing an overall de-amplification of the peak ground acceleration at surface. For the higher intensity level, instead, the PGA scaling strategy gives considerably high amplification factors between 0.4 s and 2 s, i.e. in the range corresponding to the first two natural periods of the deposit.

## 5 CONCLUSIONS

Five different earthquake selection and scaling strategies are chosen in this study to analyse the effect of the input motion characteristics on the results of free-field ground response analyses of an ideal soft clay deposit. A fully coupled effective stress based FE code is employed in the dynamic simulations in conjunction with an advanced soil constitutive model. For each selection strategy, sets of seven bedrock motions for two different seismic intensity levels are generated using freely available computer programs (i.e. REXEL, SEISMOMATCH and PEER Ground Motion Database). The principal findings of this work are that:

- Simply scaling the ground motion records at the same PGA does return EDP results that are not consistent with those obtained with more advanced scaling strategies. This is due to the importance of the spectral shape in nonlinear response, as PGA is not a good indicator of the strength and frequency content of the ground motion.

- The level of variability of the site response in the form of standard deviation of the resultant EDPs at ground surface is significantly reduced when using the spectral matching strategy. A robust and stable mean value of the EDPs can be estimated by using spectrally matched accelerograms.
- The spectral shape proposed by EC8 for soft soils does not seem to capture well the predicted surface response spectra for the lower seismic intensity levels, while it becomes a better proxy at higher intensity levels. Although the aim of this research is not to propose a new spectral shape for design prescriptions, the work highlights the necessity of revisiting the EC8 design response spectrum for soft soils.

## REFERENCES

[1] E.M. Rathje, A.R. Kottke, W.L. Trent, Influence of input motion and site property variabilities on seismic site response analysis. *Journal of Geotechnical and Geoenvironmental Engineering*, **136**(4), 607-619, 2010.

[2] K.-K. Phoon, F.H. Kulhawy, Characterization of geotechnical variability. *Canadian Geotechnical Journal*, **36**(4), 612-624, 1999.

[3] W. Li, D. Assimaki, Site-and motion-dependent parametric uncertainty of site-response analyses in earthquake simulations. *Bulletin of the Seismological Society of America*, **100**(3), 954-968, 2010.

[4] P. Bazzurro, C.A. Cornell, Ground-motion amplification in nonlinear soil sites with uncertain properties. *Bulletin of the Seismological Society of America*, **94**(6), 2090-2109, 2004.

[5] J.P. Stewart, A.O. Kwok, Nonlinear seismic ground response analysis: code usage protocols and verification against vertical array data. *Geotechnical Engineering and Soil Dynamics IV*. ASCE Geotechnical Special Publication No. 181, 2008.

[6] N. Shome, C.A. Cornell, P. Bazzurro, J.E. Carballo, Earthquakes, Records, and Nonlinear Responses. *Earthquake Spectra*, **14**(3), 469-500, 1998.

[7] J. Hancock, J. Watson-Lamprey, N.A. Abrahamson, J.J. Bommer, A. Markatis, E. McCoy, R. Mendis An improved method of matching response spectra of recorded earthquake ground motion using wavelets. *Journal of Earthquake Engineering*, **10**(spec01), 67-89, 2006.

[8] T.D. Ancheta, R.B. Darragh, J.P. Stewart, E. Seyhan, W.J. Silva, B.S.J. Chiou, K.E. Wooddell, R.W. Graves, A.R. Ko-Ttke, D.M. Boore, *PEER NGA-West2 Database, PEER Report 2013/03*. Pacific Earthquake Engineering Research Center, University of California, Berkeley, 2013.

[9] CEN, *Eurocode 8: Design of structures for earthquake resistance–Part 1: General rules, seismic actions and rules for buildings*. CEN Brussels, 2005.

[10] A. Kottke, E.M. Rathje, A semi-automated procedure for selecting and scaling recorded earthquake motions for dynamic analysis. *Earthquake Spectra*, **24**(4), 911-932, 2008.

[11] A.H.C. Chan, *User Manual for DIANA-SWANDYNE II*. University of Birmingham, 1995.

[12] M. Rouainia, D. Muir Wood, A kinematic hardening constitutive model for natural clays with loss of structure. *Géotechnique*, **50**(2), 153-164, 2000.

[13] G. Elia, M. Rouainia, Seismic performance of earth embankment using simple and advanced numerical approaches. *Journal of Geotechnical and Geoenvironmental Engineering*, **139**(7), 1115-1129, 2013.

[14] G. Elia, M. Rouainia, Performance evaluation of a shallow foundation built on structured clays under seismic loading. *Bulletin of Earthquake Engineering*, **12**(4), 1537-1561, 2014.

[15] M. Vucetic, R. Dobry, Effect of soil plasticity on cyclic response. *Journal of Geotechnical Engineering*, **117**(1), 89-107, 1991.

[16] G.M.B. Viggiani, J.H. Atkinson, Stiffness of fine-grained soil at very small strains. *Géotechnique*, **45**(2), 249-265, 1995.

[17] I. Iervolino, C. Galasso, E. Cosenza, Rexel: computer aided record selection for code-based seismic structural analysis. *Bulletin of Earthquake Engineering*, **8**(2), 339-392, 2010.

[18] Seismosoft, *SeismoMatch 2016 – A computer program for spectrum matching of earthquake records*, 2016.

[19] S. Mazzoni, M. Hachem, M. Sinclair, An Improved Approach for Ground Motion Suite Selection and Modification for Use in Response History Analysis. *15th World Conference on Earthquake Engineering*, Lisbon, 2012.

[20] K. Pitilakis, E. Riga, A. Anastasiadis, Design spectra and amplification factors for Eurocode 8. *Bulletin of Earthquake Engineering*, **10**(5), 1377-1400, 2012.

[21] J. Rey, E. Faccioli, J.J. Bommer, Derivation of design soil coefficients (S) and response spectral shapes for Eurocode 8 using the European Strong-Motion Database. *Journal of Seismology*, **6**(4), 547-555, 2002.

COMPDYN 2017
6th ECCOMAS Thematic Conference on
Computational Methods in Structural Dynamics and Earthquake Engineering
M. Papadrakakis, M. Fragiadakis (eds.)
Rhodes Island, Greece, 15–17 June 2017

# STUDY ON IMPACT LOAD RESPONSE OF THE PC SLEEPER FOR RAIL JOINT USING THREE-DIMENSIONAL NUMERICAL ANALYSIS MODEL

**Shintaro Minoura [1*], Tsutomu Watanabe[1], Kodai Matsuoka[1], Hiroshi Yamane[2]**

[1] Railway Technical Research Institute
2-8-38 Hikari-cho, Kokubunji-shi, Tokyo 185-8540 Japan
minoura.shintaro.51@rtri.or.jp, watanabe.tsutomu.30@rtri.or.jp, matsuoka.kodai.13@rtri.or.jp

[2]West Japan Railway Company
4-24, Shibata 2-chome, Kita-ku, Osaka 530-8341 Japan
hiroshi-yamane4@westjr.co.jp

**Keywords:** Prestressed Concrete Sleeper, Railway Track, Rail Joint, LS-DYNA, Impact Load, Dynamic Interaction

**Abstract.** *The purpose of this study is to clarify the influence of impact load due to train passing through the rail joint on the prestressed concrete sleeper (PC sleeper).The design of PC sleeper has been carried out in consideration of the influence of the impact load. Impact loads are caused by rail joints, irregularities of rail welded joints, rail corrugation, and wheel flat (damages generated on the wheel treads when the wheels slide on the rail running surface). Among them, the impact loads due to the rail joint and the wheel flats tend to be relatively large. In Japan, from the beginning of the development of the PC sleepers, the wheel flats have been recognized as one of the biggest factors of the impact load, and the studies on the influence of the impact load caused by the wheel flats on PC sleepers have been actively conducted. On the other hand, there have been few studies on the influence of the impact load caused by the rail joint on PC sleepers. In this study, we constructed a three-dimensional FE model of the PC sleeper which is able to simulate the nonlinear behavior of the PC sleeper. Using this analytical model, the influence of the impact load caused by the rail joint on the maximum bending moment and the stress generated in PC sleeper for various amounts of rail irregularity and various train speeds was quantitatively evaluated. In addition, the influence of parameters such as the amount of prestressing force, abrasion of PC sleeper, corrosion of PC steel wire were clarified. In the future, we plan to develop on optimum design method for PC sleeper for the rail joint considering the impact load caused by the rail joint using the result of the analysis.*

# 1 INTRODUCTION

The design of PC sleeper is carried out in consideration of the influence of the impact load. Impact loads are caused by rail joints, irregularities of rail welded joints, rail corrugation, and wheel flat (damages generated on the wheel treads when the wheels slide on the rail running surface). Among them, the impact loads due to the rail joint and the wheel flats tend to be relatively large. In Japan, from the beginning of the development of the PC sleepers, the wheel flats have been recognized as one of the biggest factors of the impact load and studies on the influence of the impact load caused by the wheel flats on PC sleepers have been actively conducted [1]. On the other hand, there have been few studies on the influence of the impact load caused by the rail joint on PC sleepers.

In the previous study, the numerical analysis with the beam model was executed, and the effect of the impact load due to the rail joint on PC sleeper was evaluated [2]. This previous study indicates that the supporting condition of the PC sleeper has the significant influence on the generated bending moment of the PC sleeper.

However, studies on the cracks generated in the PC sleeper due to the impact load, the effect of the wear of the bottom surface of the PC sleepers, the effect of the prestressing force and the effect of the corrosion of the PC steel wire are inadequate. To evaluate these effects with numerical analysis, it is necessary to construct a three-dimensional FE model considering nonlinearity of the material of the PC sleeper.

Based on the above background, we focused on the rail joint and constructed a nonlinear three-dimensional FE model reproducing the PC sleeper for the rail joint. Using this model, the influence of the various parameters on the bending moment and the stress of the PC sleeper for the rail joint were quantitatively evaluated.

# 2 ANALYSIS METHOD

## 2.1 Target PC sleeper

Figure 1 shows the target PC sleeper and rail joint section. The weight of the rail in this section is 60kg per meter and there are rail joints every 25m. The PC sleeper just under the rail joint is “PC sleeper for the rail joint” prescribed in Japanese Industrial Standards (JIS). Other sleepers are “type 6 PC sleeper” prescribed in JIS. Number of PC sleepers is 14 per 25m. The section is in a transition curve.

Figure 2 shows the attachment positions of the strain gauges, and Figure 3 shows the measurement method of the vibration mode of the PC sleeper. In order to compare the measurement results of the actual PC sleeper with the results of the numerical analysis, the bending moment and the vibration mode of the PC sleepers at the time of the train passing were measured. For the measurement of the bending moment, the strain gauges were attached to the

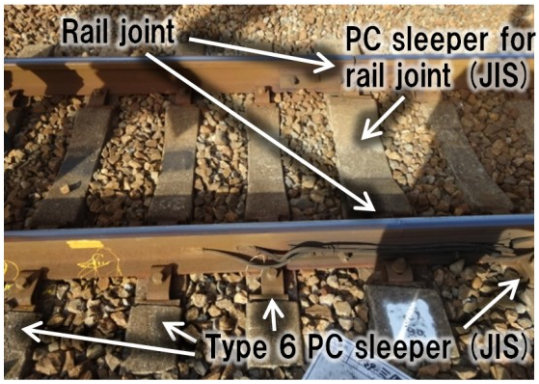


Figure 1: Target track structure

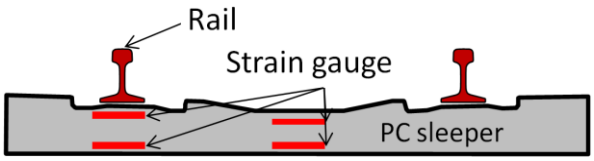


Figure 2: Attachment position of the strain gauge

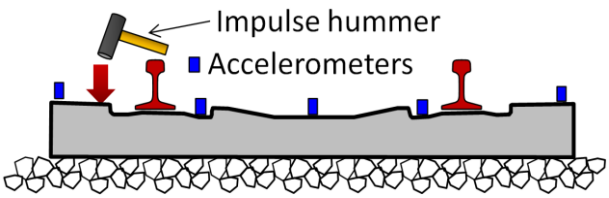


Figure 3: Measurement method of the vibration mode

cross section at the rail position and the center cross section, and the bending moment calculated from the measured strain. In the measurement of the vibration mode, five piezoelectric accelerometers (Rion PV-85) were placed at the positions shown in Figure 3, and the free vibration response by the impulse hammer was measured. The identification method of vibration mode is ERA (Eigensystem Realization Algorithm) method [3]. The running trains are the commuter vehicles for the 1067mm gauge line (wheel load of about 50kN).

## 2.2 Analysis model

Figure 4 shows the outline of the numerical analysis model and Figure 5 shows the analysis model of PC sleeper for the rail joint (JIS). In the analysis, three-dimensional nonlinear FEM analysis was performed using the structural analysis software LS-DYNA (Ver. R 8.0.0). For vehicles, car body, bogie and wheel axle are modeled as rigid. These rigid bodies are connected with springs and dampers. The rail is modeled with beam elements. Around the rail joint, there are 30 rail elements between the adjacent rail fastening devices. For other sections, there are 6 rail elements between the adjacent rail fastening devices. The PC sleeper for the rail joint is modeled as hexahedral solid element. PC steel wire and stirrup are modeled as beam elements. Concrete elements of the PC sleeper and PC steel wires and stirrups are modeled to be completely adhered to each other. The type 6 PC sleeper is modeled as a beam element. The prestressing force of the PC sleeper is reproduced by giving the initial stress in the axial direction to the PC steel wire. The number of elements in the FE model was 10792 elements, and the number of nodes is 13271 nodes.

Figure 6 shows rail surface irregularities at the rail joint section. In order to study the influence of the impact force generated due to the irregularities of the surface of the rail, irregularities of the rail surface around the rail joint were measured using a measuring machine having a length of 1m. The irregularities of the rail surface measured were input to the analysis model.

Table 1 shows the material properties used in the analysis. Properties of the respective materials are based on the design standards for Japanese railway structures and track components [4] [5]. From the vibration mode of the PC sleeper and the measurement results of the generated bending moment, the spring constant of the track pad was set to twice the nominal value

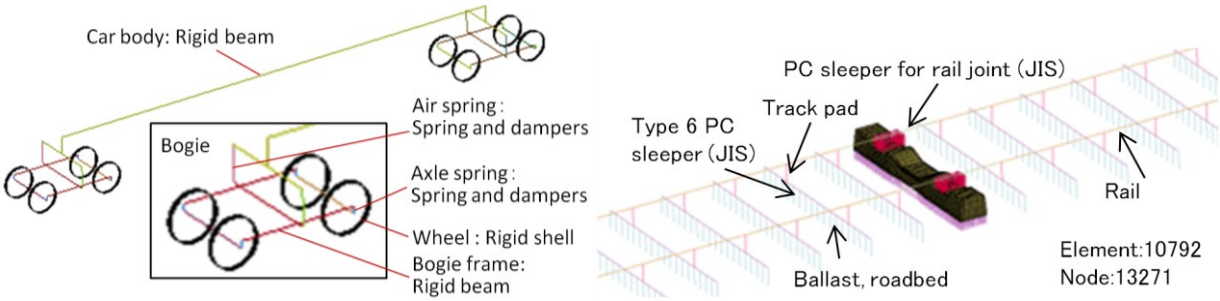


(a) Analysis model of train (b) Analysis model of track structures

Figure 4: Outline of numerical analysis model

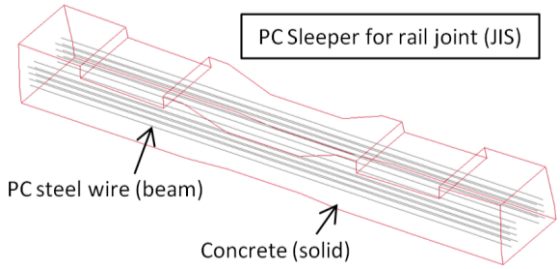


Figure 5: Analysis model of PC sleeper for rail joint

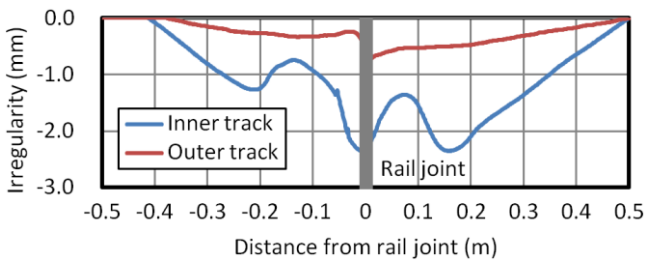


Figure 6: rail surface irregularities at the rail joint section

and the spring constant of the support of the PC sleeper was set to the value corresponding to the center supported state in which the spring constant of the support of PC sleeper at the center is larger than that of the support of PC sleeper at the rail position. Nearly a year has elapsed since the last implementation of maintenance work of the target PC sleeper and the rain joint section. So, it is considered that the compaction state of the ballast below the PC sleeper at the rail position loosened due to the impact of the train load and the support state of the PC sleeper shifted from the uniform support state to the center support state. In the section of 300mm in length around the center of the PC sleeper, twice the design value was used for spring constant of the support of the PC sleeper. The range of 300mm is a value estimated from the consistency between the actual measurement result and the analysis result concerning the vibration mode and the generated bending moment.

### 2.3 Analysis case

Table 2 shows the details of the analysis case. In this study, we evaluated the effect of the irregularity of the rail surface, prestressing force of the PC sleeper, wear of the bottom surface of the PC sleeper and corrosion of PC steel wires. The influence of the train speed on the irregularity of the rail surface was also evaluated. The irregularity of the rail surface is based on the measured value (the maximum amount of irregularity is 0.72mm for the outer rail,

| | |
|---|---|
| Rail | Type: 60kg Rail (JIS)<br>Young's modulus $E_S$ : 200MPa |
| Track Pad | Spring Constant $D_P$ : 220MN/m |
| Type 6 PC sleeper (JIS) | PC steel wire:dia.2.9mm*3 stranded wire, 12<br>Length $L_P$:2000mm, Bottom width $B_P$:240mm<br>Height $H_P$:170mm(rail), 150mm(center)<br>Young's modulus (concrete) $E_C$:49.5GPa |
| PC sleeper for rail joint (JIS) | PC steel wire:dia.2.9mm*3 stranded wire, 16<br>Length $L_P$:2000mm, Bottom width $B_P$:300mm<br>Height $H_P$:170mm(rail), 145mm(center)<br>Young's modulus (concrete) $E_C$:49.5GPa<br>Tensile strength of concrete:3.08MPa |
| Ballast | Ballast thickness $h$:250mm<br>Spring constant $D_B$:180MN/m(for 1 rail) |
| Roadbed | Ground reaction force coefficient $K_{30}$:110MN/m$^3$<br>Spring constant $D_S$:111MN/m(for 1 rail) |

(In the range of 300 mm length near the center of the sleepers, spring constant of ballast spring and roadbed spring are doubled.)

Table 1: Material properties used in the analysis

| | |
|---|---|
| Train speed $V$ | 30～130km/h （87km/h for basic case） |
| Rail surface irregularity $\delta$ | • Measured value (maximum 0.72mm for outer rail, maximum 2.35mm for inner rail),<br>• Twice as measured value<br>• Three times as measured value<br>• Four times as measured value |
| Prestressing force | Ratio to the design value<br>100%, 50%, 30%, 20%, 10%, 0% |
| Wear of bottom surface | 0mm, 10mm, 20mm |
| Corrosion of PC steel wire | • No corrosion<br>• PC steel wire in the upper end of PC sleeper<br>• PC steel wire in the lower end of PC sleeper |

(Underlined value is for base case)

Table 2: Analysis case

2.35mm for the inner rail). In addition, the analysis was executed for the cases which the irregularity of the rail surface increased to double, three times and four times as large as the actual amount of the irregularity. As for the influence of the corrosion of the PC steel wires, the analysis was performed using the model without PC steel wire in the lower part of PC sleeper. It is assumed that the steel material corrodes due to cracks in the PC sleeper and becomes ineffective. As for the influence of the bottom wear, the analysis was carried out by deleting the solid element on the bottom surface and changing the size of the PC sleepers. The train running speed in the base case was set to 87km/h which is the speed at the time of the actual measurement.

## 3 ANALYSIS RESULTS

### 3.1 Vibration mode of the PC sleeper

Table 3 shows the comparison between the actual measurement result and the analysis result of the vibration mode and the frequency of the PC sleeper for the rail joint. Figure 7 shows the vibration mode forms of the PC sleeper for the rail joint. For the PC sleeper for the rail joint, 101Hz as the translation mode in the vertical direction, 74Hz in the rotation mode, 202Hz in the first bending mode, 534 Hz in the second bending mode, and 907 Hz in the third bending mode were obtained. Comparing the natural frequencies of the actual measurement and the analysis, excluding the rotation mode, the differences between the natural frequencies of the measured value and the analysis results were within about 5%.

### 3.2 Bending moment of the PC sleeper

Figure 8 shows a comparison between the actual measurement results and the numerical analysis results with respect to the time history waveform of the bending moment of the PC sleeper for the rail joint when the train is passing. As shown in the figure, the maximum value of the negative bending moment at the center of the PC sleeper is larger than the positive bending moment at the rail position of the outer track side. From Figure 8 we can see that,

| Vibration mode | Vertical translation | Rotation | 1st mode | 2nd mode | 3rd mode |
|---|---|---|---|---|---|
| Measured (Hz) | 101 | 74 | 202 | 534 | 907 |
| Analysis (Hz) | 99 | 89 | 199 | 513 | 925 |

Table 3: Comparison between the measurement and the analysis of vibration mode of the PC sleeper for the rail joint

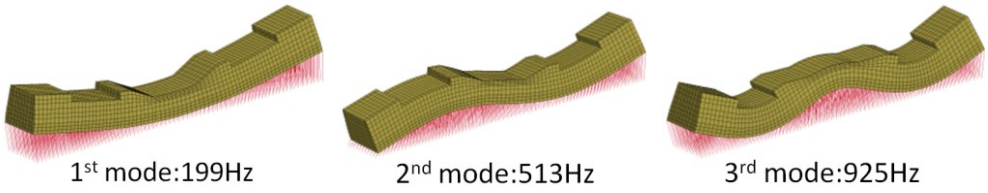


Figure 7: Vibration mode form of the PC sleeper for the rail joint

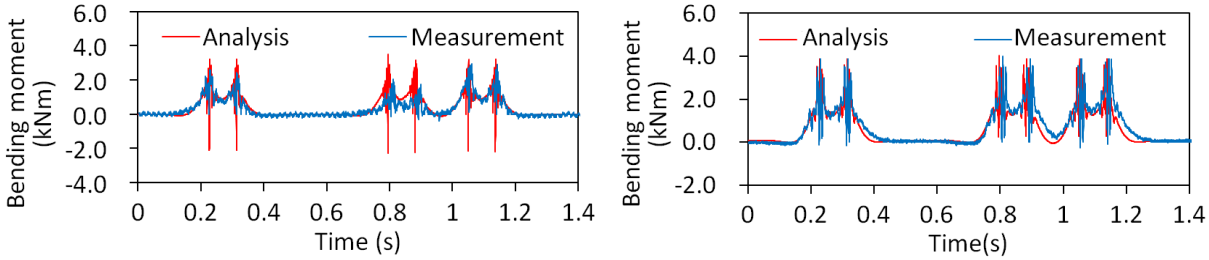


(a) Positive bending at rail position (outer rail) (b) Negative bending at the center of the sleeper

Figure 8: Comparison between the measurement and the numerical analysis

although the negative moment instantaneously occurs at the rail position in the analysis, the analysis results and the actual measurement results generally agree with each other.

### 3.3 Effect of parameters

Figure 9 shows the effect of the irregularities of the rail surface on the maximum bending moment. The figure also shows the decompression moment and the crack generation moment used in the design for both the positive bending at the rail position and the negative bending at the center of the sleeper. From the figure, it is confirmed that the maximum moment increases as the irregularity becomes larger in all the cases. Moreover, the generated moment at the rail position of the inner rail side exceeds the crack generation moment to be considered in the design when irregularity of rail surface is 3 times or more as large as the actual measurement value. For the bending moment at the rail position cross section on the inner rail side, the generated moment in the case when the irregularities of the rail surface is four times as large as the actual value is smaller than that in the case where the irregularity is three times as large as the actual value. This is thought to be the influence of the train speed as described later.

Figure 10 shows the effect of each parameter on the maximum stress generated at the outermost edge of the PC sleepers. The stress value is positive for tension and negative for the compression. For the positive bending at the rail position cross section, the maximum stress at the bottom surface of the PC sleepers is shown in the figure, and for the negative bending at the center of the PC sleeper, the maximum stress at the top surface of the PC sleepers is shown in the figure. From the figure, it is confirmed that the crack generation stress is reached at the rail position cross section of the inner rail side in case where the irregularities of the rail

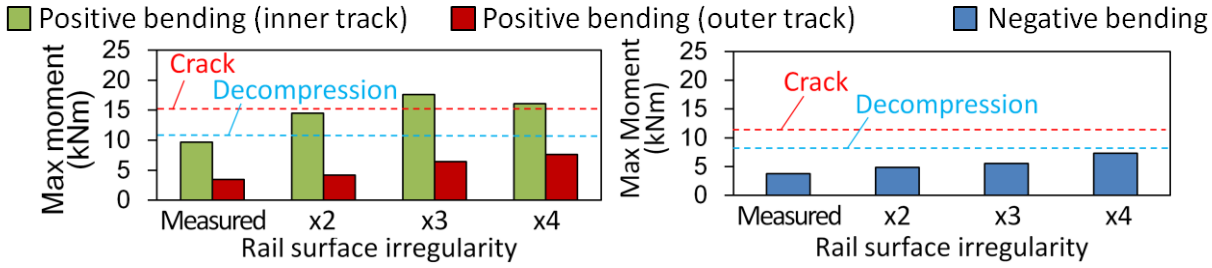


(a) Positive bending at rail position (b) Negative bending at the center of the sleeper

Figure 9: Effect of the irregularities of rail surface on the maximum bending moment

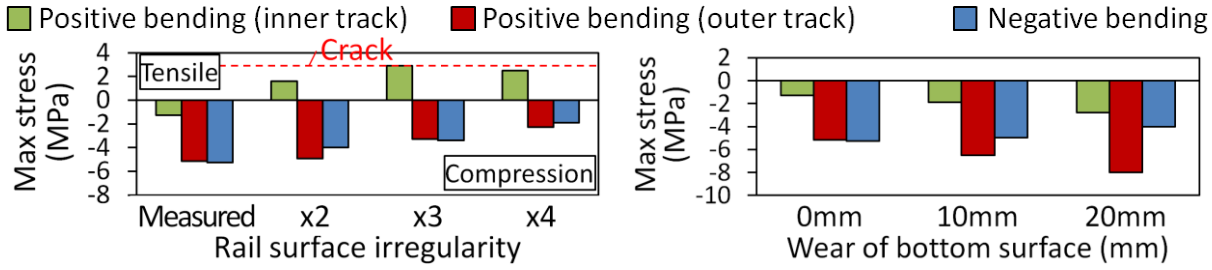


(a) Effect of the rail surface irregularity (b) Effect of the wear of the bottom surface

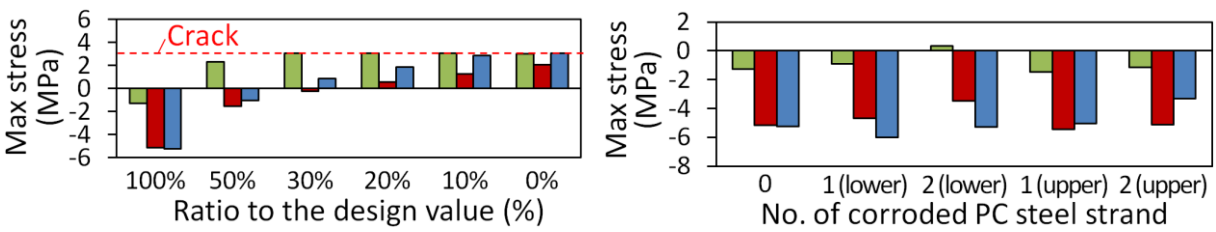


(c) Effect of the prestressing force (d) Effect of the corrosion of the PC steel wire

Figure 10: Effect of each parameter on the maximum stress

surface are tripled (the maximum irregularity on the inner rail side: 7.05mm).

For the bottom surface wear, it is confirmed that the maximum stress of negative bending increases due to the increase in amount of the wear. For the negative bending, the distance from the compressed edge of the PC sleeper to the PC steel wires is shortened with the increase of the wear of the bottom surface of the PC sleeper.

For the influence of prestressing force, if the prestressing force reduces to 30% of the initial prestressing force, cracks occur at the rail position on the inner race side, and cracks occur at the center of the PC sleeper if the prestressing force reduces to 10%.

For the influence of the corrosion of PC steel wires, the maximum stress in positive bending increases when the lowermost PC steel wire is removed, and the maximum stress of the positive bending at the rail position increases when the uppermost PC steel wire is removed.

Figure 11 shows the influence of the train running speed on the maximum bending moment for the various amounts of irregularity of the rail surface.

From the figure, the maximum bending moment tends to increase with the increase of irregularity of the rail surface and the train speed. However, for the maximum bending moment on the inner rail side, there is a peak observed at the running speed of around 70 km/h in the basic case, and there are peaks observed at the running speed around 30km/h, 70km/h, 120km/h in the case where the irregularity of the rail surface is 4 times as large as the actual measured value. It is confirmed from this fact that there is speed dependence with respect to the bending moment.

Although the profile of the measured irregularity of the rail surface of the inner rail is not a simple shape, it can be regarded that rail surface drops 2.35mm of the end of the length of rail of about 0.4m. Therefore, when the time at which the wheel takes to freely fall by 2.7 mm and the time at which the train takes to move by 0.4m along the rail coincide with each other, the amount of drop of the wheel becomes the maximum and the generated maximum moment is expected to increase. The train speed corresponding to the case is about 65km/h for the measured rail irregularity, about 46km/h for the case where the rail irregularity is twice as large as the measured value, and about 33km/h for the case where the rail irregularity is four times as large as the measured value. In each analysis case, since the peak appears at these speeds, the maximum moment of generated is considered to be influenced by the shape of the irregularity of the rail surface.

## 4 CONCLUSIONS

In this study, we constructed a nonlinear three-dimensional FE model reproducing the PC sleeper for the rail joint. Using this model, the influence of the various parameters on the bending moment and the stress of the PC sleeper for the rail joint were quantitatively evaluated.

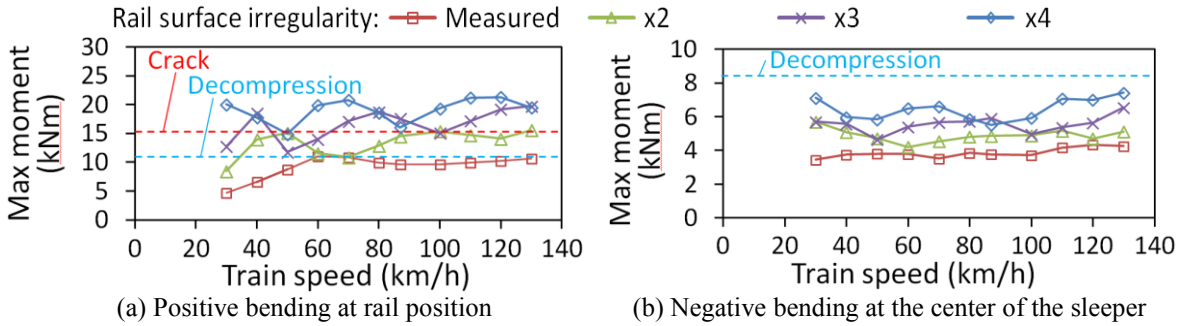


(a) Positive bending at rail position (b) Negative bending at the center of the sleeper

Figure 11: Influence of the train running speed on the maximum bending moment for the various amounts of irregularity of the rail surface

- According to the numerical analysis using the measured irregularity of the rail surface, the crack generates due to the train running at the speed of 87km/h when the irregularity of the rail surface is as three times as large as the measured value (the maximum amount of the irregularity on the inner rail side: 7.05mm)
- According to the analysis evaluating the effect of the corrosion of the PC steel wire, the generated maximum stress of the negative bending at the center of the sleeper increases in the case where the PC steel wire is removed assuming the bottom wear and corrosion of the steel wire at the upper end of the PC sleeper. In addition, the maximum stress of the positive bending at the rail position increases according to the analysis for the case where the PC steel wire at the bottom end of the PC sleeper is removed.
- According to the analysis, the cracks generated at the rail position of the inner track side in the case where the prestressing force is reduced to 30% of the initial prestressing force and the crack generated at the center of the PC sleeper in the case where prestressing force is reduced to 10% of the initial prestressing force.
- The bending moment of the PC sleeper has the characteristics of the speed dependency which is regarded as effect of the irregularity of the rail surface.

We will take these findings into the consideration in the design of the PC sleeper and to build an optimum design method of PC sleeper for the rail joint to cope with the impact load by the rail joint in the future research.

## REFERENCES

[1] H. Wakui, H. Okuda, A study on limit state design method for prestressed concrete sleepers, *Concrete library of JSCE*, No. 33, 1–25, June, 1999.

[2] T. Watanabe, K Matsuoka, S. Minoura, H. Yamane, Dynamic Response Characteristic of Prestressed Concrete Sleeper at Rail Joint, *Proceedings of the Japan Concrete Institute*, Vol.38, No.2, pp.985-990, 2016.(in Japanese)

[3] K. Matsuoka, K. Kaito, H. Ishii, Statistical consideration regarding the vibration characteristics and variation factors of 24-span steel railway bridge in 86 years in service, *Journal of Japan Society of Civil Engineers F4*, Vol.68, No.3, pp.157-174, 2012. (in Japanese)

[4] Railway Technical Research Institute, Design Standards for Railway Structures and Commentary (Track Structures), Maruzen Publishing Co. Ltd, 2004. (in Japanese)

[5] Railway Technical Research Institute, Design Standards for Railway Structures and Commentary (Concrete Structures), Maruzen Publishing Co. Ltd, 2004. (in Japanese)

COMPDYN 2017
6th ECCOMAS Thematic Conference on
Computational Methods in Structural Dynamics and Earthquake Engineering
M. Papadrakakis, M. Fragiadakis (eds.)
Rhodes Island, Greece, 15–17 June 2017

# RESONANCE PHENOMENA IN SYSTEMS WITH HYSTERETIC NONLINEARITIES

**Mikhail E. Semenov[1,2,3], Olga O. Reshetova[2], Olesya I. Kanishcheva[1], Peter A. Meleshenko[1,2] and Evgeniya G. Kabulova[4]**

[1] Zhukovsky--Gagarin Air Force Academy
Starykh Bolshevikov st. 54 ``A", 394064, Voronezh, Russia
e-mail: mkl150@mail.ru, melechp@yandex.ru, oleka_olesya@mail.ru

[2] Voronezh State University
Universitetskaya sq. 1, 394006, Voronezh, Russia
mkl150@mail.ru, melechp@yandex.ru, tribunskih1993@mail.ru

[3] Voronezh State University of Architecture and Civil Engineering
XX-letiya Oktyabrya st. 84, 394006 Voronezh, Russia
mkl150@mail.ru

[4] Stary Oskol Technological Institute, National University of Science and Technology, MISIS
Mikroraion im. Makarenko 42, 309516, Stary Oskol, Russia
evgenia791@mail.ru

**Keywords:** Unbounded solutions, Hysteresis, Viscous and Coulomb friction.

**Abstract.** *The work is dedicated to study of the dynamics of model systems that are described by differential equations with additive hysteretic nonlinearities in the case when a hysteretic loop bypass clockwise. In particular, for the model of the harmonic oscillator with hysteretic external force the conditions for existence of unbounded solutions are obtained. For the model of harmonic oscillator with a dry (Coulomb) and viscous friction under external hysteretic affection we obtained a set of conditions that ensure the self-oscillation mode. The numerical examples that illustrate the results of this work are also presented.*

## 1 INTRODUCTION

Appearance of mathematical models of hysteretic phenomena is connected with the wide set of applied problems, generally in the theory of automatic control (see, e.g., [1,2,3] and related references). In these systems the sources with hysteretic properties can not be considered separately, but should be considered as a part of some complex system [1,4]. In this way the hysteretic nonlinearity should be taken into account on the step of modeling and should be included to the system of differential equations that describe the system under consideration. Here we should take a following note. In order to make an adequately description of the dynamics of real physical and mechanical systems, it is necessary to take into account the effects of hysteretic nature such as "backlash", "stops" etc. For example, the backlashes inevitably appear in the mechanical systems during its long operation due to "aging" of the materials. The hysteretic phenomena (especially in the form of control parameters) play an important role in such fields as physics, chemistry, biology, economics etc. It should also be pointed out that the hysteretic phenomena (taking into account its physical nature) are insufficiently known in our days. This fact leads to exciting and interesting problems even in the well-studied classical systems.

Investigation of hysteretic phenomena has a long history. First works on the systems with hysteretic parts were made by A.A. Andronov in 1946. However the rigorous mathematical theory of hysteresis was formulated in the monography of M.A. Krasnoselskii and A.V. Pokrovskii [3] where the hysteretic phenomena are considered in the frame of the system's theory. Namely, the hysteretic converters are treated as operators (such operators parametrically depend on its initial state) defined on a sufficiently rich functional space (for example, in the space of continuous functions). The dynamics of such converters are described by the relation of "input-state" and "state-output".

An important problem is the study of resonance in systems with hysteresis [4]. In this way we note a well-known fact: in the presence of viscous friction the harmonic resonance is not realized (for details see, e.g., [6]). In particular, in [6] it is considered the dynamics of the oscillator with strong nonlinearity (authors studied its phase portrait and the trajectory). It is proved that the form of periodic solutions depends on the "origin" of strong nonlinearity. The main result of [6] is the fact that, for a class of equations that describe the harmonic oscillations with resonance external force and hysteretic operator in the right part of equation, the presence or absence of unbounded solutions depend on the amplitude of the external affection.

In this paper we study the resonance properties of systems in which the energy pumping in the system due to the presence of hysteresis level. Examples of such systems are the oscillations of the ferromagnetic ball in a magnetic field, oscillations of the system of coupled oscillators when the "connection force" has a hysteretic nature [7]. It should also be pointed out that these systems can be considered as an effective models in the solid state physics in the modeling of interatomic interactions taking into account various types of dislocations that arise due to material's aging. Also such a model can be applied for the problem of viscoelasticity.

## 2 MODEL

Let us consider a system whose dynamics is described by the following equation with the corresponding initial conditions:

$$\begin{aligned} &\ddot{x} + \omega^2 x = R[\omega_0]x, \\ &x(0) = x_0,\ \dot{x}(0) = x_1. \end{aligned} \tag{1}$$

where $R$ is an non-ideal relay operator with the negative spin and $\omega_0$ is an initial state of the operator (see Figure 1).

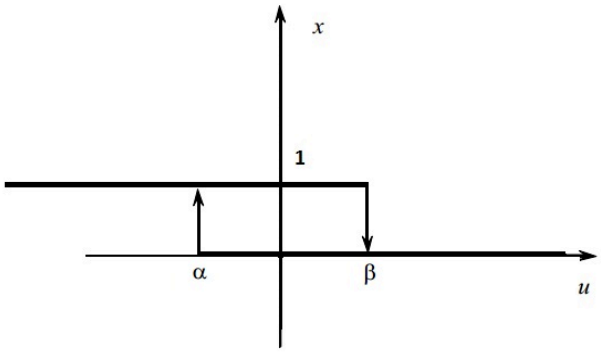


Figure 1: Non-ideal relay with negative spin

**Theorem:** Let the initial value satisfies the condition $x_0 \notin [\alpha;\beta]$. Then, the corresponding solutions are unbounded.

**Proof:** Let us assume that the initial conditions obey the following inequality $x_0 > \beta$, then at a certain initial period of time $(t \geq 0)$ the solution of the equation (1) will have the form $x_0(t) = A_1 \cos(t + \varphi_0) + 1, 0 \leq t \leq t_1$, where $t_1$ is the time at which the equality $x(t_1) = \alpha$ is obeyed. It is clearly that this moment exists. The solution of equation (1) at interval $[t_1 : t_2]$ will be determined by the relation $x_1(t) = A_1 \cos(t + \varphi_1) - 1$. Here $t_2$ is the moment at which the equality $x_1(t_2) = 1$ will be obeyed. It is also clearly that such a moment exists etc.

Thus, in the absence of switching the solution of the equation (1) is sewn of the functions defined by the following relations: for even $n$ we have $x_n(t) = A_n \cos(t + \varphi_n) + 1$, and for odd $n$ we have $x_{n+1}(t) = A_{n+1} \cos(t + \varphi_n) - 1$.

Using the continuity conditions for solution and its derivative at the point $t_n$ we obtain the following equality

$$\begin{cases} A_n \cos\varphi_n + 1 = A_{n+1} \cos\varphi_{n+1} - 1, \\ -A_n \sin\varphi_n = -A_{n+1} \sin\varphi_{n+1}, \\ A_n \cos\varphi_n + 1 = 1. \end{cases} \tag{2}$$

Squaring and summing the first two equalities we obtain:

$$\begin{cases} {A_n}^2 \cos^2\varphi_n + 4A_n \cos\varphi_n + 4 = {A_{n+1}}^2 \cos^2\varphi_{n+1}, \\ {A_n}^2 \sin^2\varphi_n = {A_{n+1}}^2 \sin^2\varphi_{n+1}, \\ A_n \cos\varphi_n = 0. \end{cases}$$

Or

$$\begin{cases} {A_n}^2 + 4A_n \cos\varphi_n + 4 = A_{n+1},^2 \\ A_n \cos\varphi_n = 0. \end{cases}$$

Finally we obtain:

$$A_n^{\,2} + 4 = A_{n+1}^{\,2}. \tag{3}$$

Similarly, for the next interval, at the point at which the solution has the value $-1$, we have:

$$\begin{cases} A_{n+1}\cos\varphi_{n+2} = A_{n+2}\cos\varphi_{n+3} + 1, \\ -A_{n+1}\sin\varphi_{n+2} = -A_{n+2}\sin\varphi_{n+3}, \\ A_{n+1}\cos\varphi_{n+2} = -1. \end{cases}$$

Squaring the first two equalities

$$\begin{cases} A_{n+1}^{\,2}\cos^2\varphi_{n+2} - 2A_{n+1}\cos\varphi_{n+2} + 1 = A_{n+2}^{\,2}\cos^2\varphi_{n+3}, \\ A_{n+1}^{\,2}\sin^2\varphi_{n+2} = A_{n+2}^{\,2}\sin^2\varphi_{n+3}, \\ A_{n+1}\cos\varphi_{n+2} = -1. \end{cases}$$

Then summarize them

$$\begin{cases} A_{n+1}^{\,2} - 2A_{n+1}\cos\varphi_{n+2} + 1 = A_{n+2}^{\,2}, \\ A_{n+1}\cos\varphi_{n+2} = -1. \end{cases}$$

Finally we get:

$$A_{n+2}^{\,2} = A_{n+1}^{\,2} + 3. \tag{4}$$

Then from (3) and (4) it follows: $A_{n+2}^{\,2} = A_n^{\,2} + 4$.

In other words, if the initial value is such that the hysteretic element "works", then the corresponding solution is unbounded.

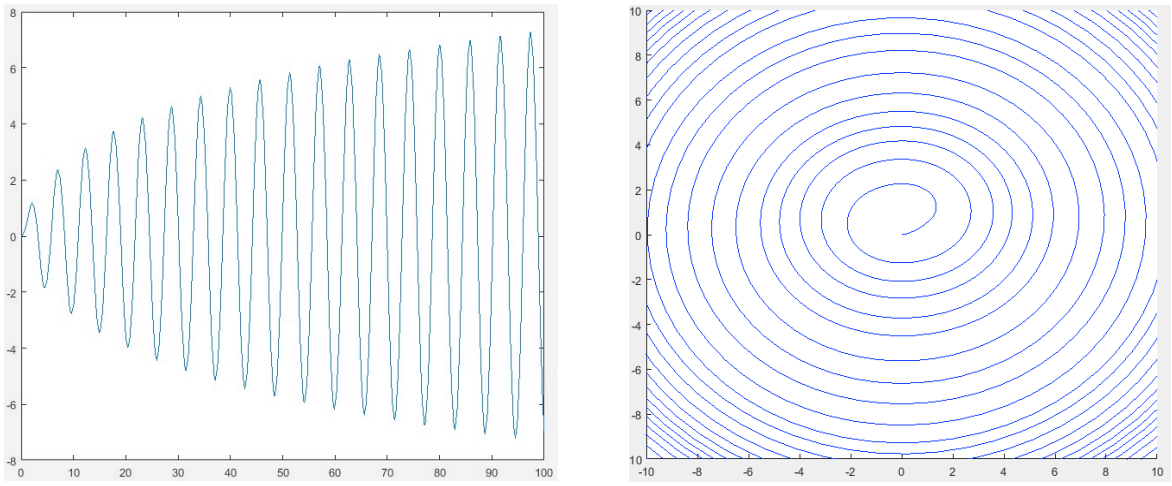

Figure 2: Solution (left panel) and phase portrait (right panel) of equation (1) with the given initial conditions

**Note 1.** Let us note that the solution oscillates and the rate of growth of amplitude is proportional to $\sqrt{t}$.

**Note 2.** The theorem remains valid for other types of hysteretic nonlinearities. Main requirement is the positiveness of the loop's area.

If the initial value lies on the segment $[\alpha;\beta]$, then the corresponding solution is limited on the whole positive time interval.

## 3 VISCOUS AND COULOMB FRICTION

Let us consider the various kinds of friction. The dynamics of oscillator with a viscous friction can be described by the equation:

$$\ddot{x} + 2\xi\dot{x} + \omega^2 x = R[\omega_0]x. \tag{5}$$

In the following consideration we assume that the threshold numbers of non-ideal relay are symmetric relative to origin. Considering the dynamics of the solution it should be noted that once the amplitude of the solution becomes high enough, the work of the friction force balances the energy obtained by the oscillator from the hysteretic element. Let us consider two cases related to the different kind of the roots of characteristic equation of the linear part of the equation (5).

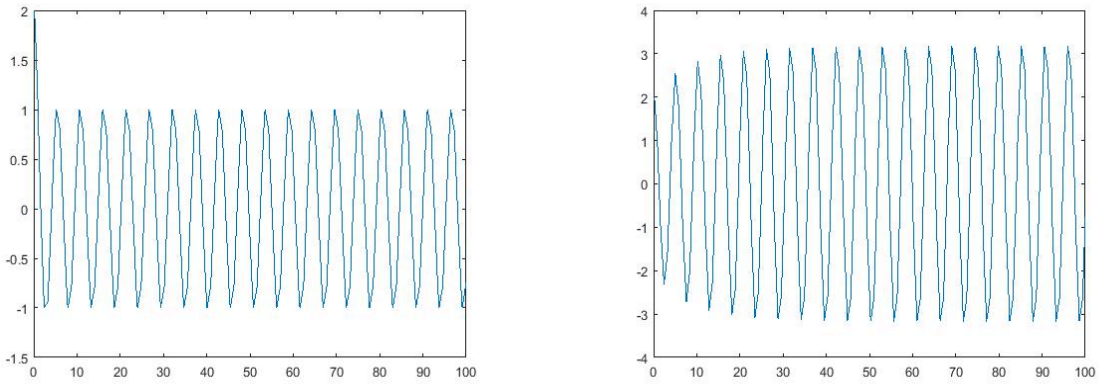

Figure 3: Oscillations in the system (5) at $\xi = 0.1; \xi = 1$ (left and right panels, respectively)

A qualitative change in the nature of the solution (compare the figures 3 and 4) becomes due to the fact that at $\xi = 2$ the roots of the characteristic equation are real. The nature of the oscillations has remained stable with the changed period.

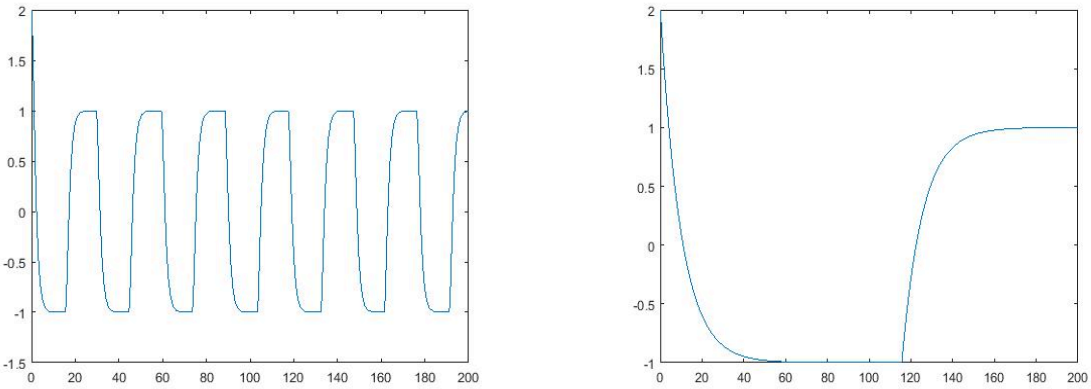

Figure 4: Oscillations in the system (5) at $\xi = 2.1; \xi = 10$ (left and right panels, respectively)

The dynamics of oscillator with the Coulomb friction under external hysteretic affection is described by the equation

$$\ddot{x} + \eta\,\mathrm{sgn}\,\dot{x} + x = R[\omega_0]x. \tag{6}$$

Multiplying both sides of (6) on $\dot{x}$ and integrating over the period $T$ we obtain:

$$\int_0^T \frac{1}{2}\frac{d}{dt}\left(\dot{x}^2 + x^2\right) = -\eta(\operatorname{sgn}\dot{x})\dot{x} + \dot{x}R[\alpha,-\alpha]x, \tag{7}$$

$$\Delta E = -\eta\int_0^T |\dot{x}|dt + S_{loop}. \tag{8}$$

From the equation (5) it follows that the energy gain will be positive if the work of friction forces will be smaller than the loop's area (otherwise it will be negative). In this way the considered system can be treated as a system with the negative feedback. Let us note that at steady-state regime the condition $2\left(x_{\max} - x_{\min}\right)\eta = S_{loop}$ is satisfied. This means that the amplitude of the oscillation is such that the work of frictional forces on the period is equal to the loop's area. These result illustrates the figure 5.

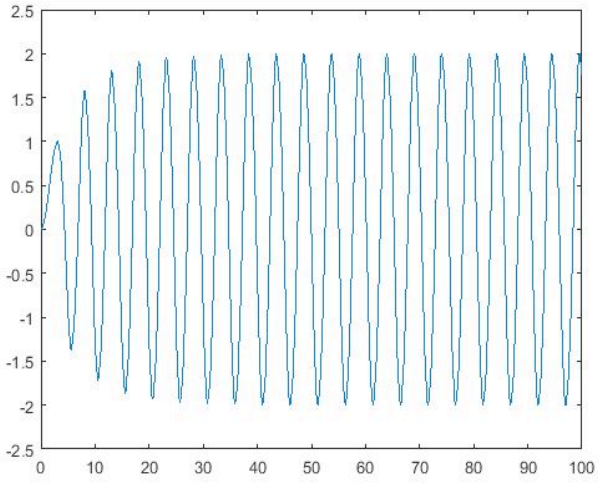


Figure 5: Oscillations in the system (6) at $\eta = 0.5$

## 4 CONCLUSIONS

In this paper we found that in the dynamical model of harmonic oscillator under external hysteretic affection (force with a hysteretic nature) with a negative spin the unbounded oscillations occur. It is shown also, that in the models of the harmonic oscillator with Coulomb and viscous frictions under hysteretic external force with negative spin the stable self-oscillations are realized.

## ACKNOWLEDGEMENTS

This work is supported by the RFBR grant No 16-08-00312-a

## REFERENCES

[1] V. Hassani, T. Tjahjowidodo, T. N. Do, A survey on hysteresis modeling, identification and control, *Mechanical Systems and Signal Processing*, **49**, 209-233, 2014.

[2] B. Carboni, W. Lacarbonara, Nonlinear dynamic characterization of a new hysteretic device: experiments and computations, *Nonlinear Dynamics*, **83**, 23-39, 2016.

[3] M.E. Semenov, A.M. Solovyov., P.A. Meleshenko, Elastic inverted pendulum with backlash in suspension: stabilization problem, *Nonlinear Dynamics*, **82**, 677-688, 2015.

[4] M.A. Krasnosel'skii, A.V. Pokrovskii, *Systems with Hysteresis,* Springer Verlag, 1989.

[5] M.E. Semenov, P.A. Meleshenko, H.T.T. Nguyen, et al., Radiation of Inverted Pendulum with Hysteretic Nonlinearity, *PIERS Proceedings*, August 25-28, Guangzhou, 1442 - 1445, 2014.

[6] A.M. Krasnosel'skii, A.V. Pokrovskii, Dissipativity of a nonresonant pendulum with ferromagnetic friction, *Automation and Remote Control*, **67**, 221-232, 2006.

[7] M.E. Semenov, P.A. Meleshenko, A.M. Solovyov, A.M. Semenov, Hysteretic Nonlinearity in Inverted Pendulum Problem, *Springer Proceedings in Physics*, **168**, 463-507, 2015.

COMPDYN 2017
6th ECCOMAS Thematic Conference on
Computational Methods in Structural Dynamics and Earthquake Engineering
M. Papadrakakis, M. Fragiadakis (eds.)
Rhodes Island, Greece, 15–17 June, 2017

# FLUTTER ANALYSIS OF COMPOSITE LAMINATES WITH CURVILINEAR FIBRES

**Hamed Akhavan and Pedro Ribeiro**

DEMec/INEGI, Faculdade de Engenharia, Universidade do Porto
Rua Dr. Roberto Frias, s/n 4200-465, Porto, PORTUGAL
e-mail: {hamed,pmleal}@fe.up.pt

**Keywords:** Flutter, Composite Plate, Piston Theory, Curvilinear Fibres, Variable Stiffness.

**Abstract.** *In this investigation, the authors intend to study the dynamic instability (flutter) of variable stiffness composite laminates (VSCLs) in the presence of supersonic flow. In the type of VSCL considered here, plies have curvilinear fibres and, consequently, the stiffness is variable in a macroscopic view. The plates considered are rectangular. In each ply, a reference fibre path, represented by a function of horizontal coordinate x, is defined. The reference fibre path orientation changes linearly from $T_0$ at the centre to $T_1$ at both vertical edges of the ply; the other fibre paths are defined shifting the reference path in direction y. The displacement and rotations are defined using a Third-order Shear Deformation Theory, and then they are discretised by a p-version finite element model that applies to VSCL plates. Piston theory is employed to model the aerodynamic force of the upstream flow in direction x. Flutter airspeeds are investigated for VSCL plates with different fibre angles. Changes of flutter speed are evaluated in two different regimes of steady and unsteady flow.*

## 1 INTRODUCTION

The traditional fibrous composite panels consist of fibres placed with various angles (orientations) in the matrix of each ply. From a macroscopic point of view, the in-plane and the bending stiffness of the panel do not change from one point to the other. In complex structures where fibrous composite panels are used, load and stress distributions in different regions of the panel are not uniform. To reinforce the regions of high stress, two methods were before used: increasing the thicknesses or mounting stiffeners. These two techniques alter the final shape of the design by occupying more space and increasing the weight. The variable stiffness concept using curvilinear fibres [1, 2, 3] can propose a panel with different, and under-controlled stiffness. This concept suggests to rotate fibre orientation in a region with high stress.

The promising capabilities of composite laminates with curvilinear fibre paths based on their linear vibration behaviour [4, 5, 6], static behaviour [7, 8], stress re-distribution and (post)buckling [9, 10], and non-linear vibrations [11, 12] are already demonstrated. These references reported higher natural frequencies, less static deflection, different stress re-distribution and different dynamics of composite plates consisting of curvilinear fibre paths. Also, higher buckling loads and failure onsets are predicted using this type of fibre paths. As far as aeroelasticity is concerned, there are not enough studies explaining the flutter modes and behaviour of such plates. In some investigations [13, 14], flutter of wings have been controlled by adding curvilinear stiffeners. About the composite laminates with curvilinear fibres, [15] used a genetic algorithm to find the impact of various tailoring choices including curvilinear fibre orientation and stacking sequence upon the flutter.

As it is understood, the use of curvilinear fibres to control flutter has received relatively little attention in the literature. In this paper, supersonic flutter of a variable stiffness composite laminate (VSCL) - composite laminates with curvilinear fibres - is investigated. The target is to search for improvements in flutter of such plates against constant stiffness composite plates (CSCL) where straight fibres are used. A third-order shear deformation theory is used to model the displacements of the plate. Displacements and rotation of a general point in the mid-plane are discretised using a *p*-version finite element [16, 17]. The plate is in the presence of a supersonic flow. To model the aerodynamic force of the upstream flow, Piston theory [18] is employed. The equations of motion, in the form of an eigenvalue problem, are solved to find the flutter speed. The eigenvalues of such system are complex.

Flutter speeds of VSCLs with different boundary conditions including clamped and free boundaries against various tow orientations are evaluated. VSCLs with other boundaries are under investigation. The aim of this study is to investigate how does the flutter speed vary in VSCLs with diverse fibre angles at the centre and edges of the plates.

## 2 EIGENVALUE PROBLEM OF VSCL PLATES WITH PISTON THEORY

Figure 1a displays the schematic of the plate. The rectangular VSCL has length $a$, width $b$, and thickness $h$, where a right-handed three-dimensional Cartesian coordinate system $x, y, z$ is adopted, with the origin of the coordinate system located in the geometric centre of the undeformed plate. The laminate is symmetric about its middle surface, consisting of 12 composite layers with curvilinear fibre paths. The reference fibre path is defined in the form of

$$\theta\left(x\right) = 2\left(T_1 - T_0\right)\frac{|x|}{a} + T_0 \tag{1}$$

where $T_0$ and $T_1$ are the fibre path angles in the centre and vertical edges of the ply (Figure 1b). The angle of the reference fibre path, $\theta$, is a linear function of the $x$-coordinate and, in order to define the other fibre paths, this reference fibre path is shifted in $y$-direction [2].

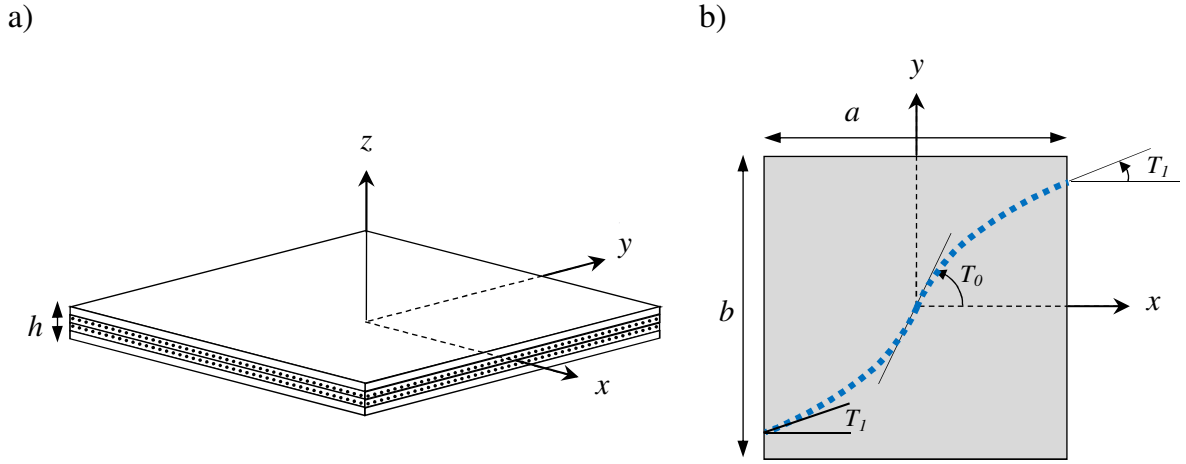


Figure 1: a) geometry of the laminate and b) curvilinear fibre path.

**Fig 1.** A symmetric laminate including a reference curvilinear fibre path in a flat ply.

A displacement field based on third-order shear deformation theory [19, 20] is used as follows

$$u\left(x,y,z,t\right)=u^{0}\left(x,y,t\right)+z\phi_{x}\left(x,y,t\right)-cz^{3}\left(\phi_{x}\left(x,y,t\right)+\frac{\partial w^{0}\left(x,y,t\right)}{\partial x}\right) \tag{2}$$

$$v\left(x,y,z,t\right)=v^{0}\left(x,y,t\right)+z\phi_{y}\left(x,y,t\right)-cz^{3}\left(\phi_{y}\left(x,y,t\right)+\frac{\partial w^{0}\left(x,y,t\right)}{\partial y}\right)$$

$$w\left(x,y,z,t\right)=w^{0}\left(x,y,t\right)$$

Here, $u$, $v$, and $w$ are the displacement components in the $x$, $y$, and $z$ directions; $u^0$, $v^0$, and $w^0$ are their values at the mid-plane and $\phi_x$ and $\phi_y$ are the independent rotations of the normal to the middle surface about the $y$ and $x$ axis, respectively. $t$ is time and $c=4/3h^2$. Mid-plane displacements and rotations are discretised using a *p*-version finite element as

$$\left\{\begin{array}{c} u^{0}\left(x,y,t\right) \\ v^{0}\left(x,y,t\right) \\ w^{0}\left(x,y,t\right) \\ \phi_{x}\left(x,y,t\right) \\ \phi_{y}\left(x,y,t\right) \end{array}\right\}=\left[\begin{array}{ccccc} \mathbf{N^{u}}\left(x,y\right)^{T} & \mathbf{0} & \mathbf{0} & \mathbf{0} & \mathbf{0} \\ \mathbf{0} & \mathbf{N^{u}}\left(x,y\right)^{T} & \mathbf{0} & \mathbf{0} & \mathbf{0} \\ \mathbf{0} & \mathbf{0} & \mathbf{N^{w}}\left(x,y\right)^{T} & \mathbf{0} & \mathbf{0} \\ \mathbf{0} & \mathbf{0} & \mathbf{0} & \mathbf{N^{\phi_{x}}}\left(x,y\right)^{T} & \mathbf{0} \\ \mathbf{0} & \mathbf{0} & \mathbf{0} & \mathbf{0} & \mathbf{N^{\phi_{y}}}\left(x,y\right)^{T} \end{array}\right]\left\{\begin{array}{c} \mathbf{q_{u}}\left(t\right) \\ \mathbf{q_{v}}\left(t\right) \\ \mathbf{q_{w}}\left(t\right) \\ \mathbf{q_{\phi_{x}}}\left(t\right) \\ \mathbf{q_{\phi_{y}}}\left(t\right) \end{array}\right\} \tag{3}$$

where $\mathbf{N^{i}}\left(x,y\right)$ are vector of shape functions and $\mathbf{q_{i}}\left(t\right)$ are generalised displacement vectors (**i**= **u**, **v**, **w**, $\phi_{\mathbf{x}}$, and $\phi_{\mathbf{y}}$) [16, 17].

The stress-strain relation (in material coordinates i.e. the fibre direction and perpendicular to the fibre direction) of an orthotropic lamina is valid in each arbitrary point of the ply made of curvilinear fibres. Because of the rotation of the fibre path $\theta(x)$, the stresses and strains can be rotated from their material coordinates to the global coordinates ($x$ and $y$) using transformation matrix [1]. The strain displacement relations in the linear regime are considered here.

The flutter pressure - pressure on upper surface of the plate while the lower surface has static pressure - due to a supersonic flow (highly unsteady) is introduced by Piston theory [18]

$$\Delta P\left(x,y,t\right) = -\frac{\rho_\infty {U_\infty}^2}{M}\left(\frac{1}{U_\infty}w_{,t} + w_{,x}\right) \tag{4}$$

in which $\rho_\infty$ is upstream far-field density, $U_\infty$ velocity of the flow, and $M$ local Mach number. By removing the derivative in terms of time $w_{,t}$, the analysis is is in the steady regime. Substituting terms of shape functions and generalized coordinates, Equation 3, in flutter pressure of Equation 4 and subsequently using the principle of virtual work gives the equations of motion as

$$\begin{bmatrix} \mathbf{M}^{11} & \mathbf{0} & \mathbf{0} & \mathbf{0} & \mathbf{0} \\ & \mathbf{M}^{22} & \mathbf{0} & \mathbf{0} & \mathbf{0} \\ & & \mathbf{M}^{33} & \mathbf{M}^{34} & \mathbf{M}^{35} \\ & & & \mathbf{M}^{44} & \mathbf{0} \\ sym & & & & \mathbf{M}^{55} \end{bmatrix} \begin{Bmatrix} \ddot{\mathbf{q}}_\mathbf{u} \\ \ddot{\mathbf{q}}_\mathbf{v} \\ \ddot{\mathbf{q}}_\mathbf{w} \\ \ddot{\mathbf{q}}_{\boldsymbol{\phi}_\mathbf{x}} \\ \ddot{\mathbf{q}}_{\boldsymbol{\phi}_\mathbf{y}} \end{Bmatrix} + \begin{bmatrix} \mathbf{K}_\mathbf{L}^{11} & \mathbf{K}_\mathbf{L}^{12} & \mathbf{K}_\mathbf{L}^{13} & \mathbf{0} & \mathbf{0} \\ & \mathbf{K}_\mathbf{L}^{22} & \mathbf{K}_\mathbf{L}^{23} & \mathbf{0} & \mathbf{0} \\ & & \mathbf{K}_\mathbf{L}^{33} & \mathbf{K}_\mathbf{L}^{34} & \mathbf{K}_\mathbf{L}^{35} \\ & & & \mathbf{K}_\mathbf{L}^{44} & \mathbf{K}_\mathbf{L}^{45} \\ sym & & & & \mathbf{K}_\mathbf{L}^{55} \end{bmatrix} \begin{Bmatrix} \mathbf{q}_\mathbf{u} \\ \mathbf{q}_\mathbf{v} \\ \mathbf{q}_\mathbf{w} \\ \mathbf{q}_{\boldsymbol{\phi}_\mathbf{x}} \\ \mathbf{q}_{\boldsymbol{\phi}_\mathbf{y}} \end{Bmatrix} \tag{5}$$

$$+ \begin{bmatrix} \mathbf{0} & \mathbf{0} & \mathbf{0} & \mathbf{0} & \mathbf{0} \\ & \mathbf{0} & \mathbf{0} & \mathbf{0} & \mathbf{0} \\ & & \mathbf{F}_{unsteady}^{33} & \mathbf{0} & \mathbf{0} \\ & & & \mathbf{0} & \mathbf{0} \\ sym & & & & \mathbf{0} \end{bmatrix} \begin{Bmatrix} \dot{\mathbf{q}}_\mathbf{u} \\ \dot{\mathbf{q}}_\mathbf{v} \\ \dot{\mathbf{q}}_\mathbf{w} \\ \dot{\mathbf{q}}_{\boldsymbol{\phi}_\mathbf{x}} \\ \dot{\mathbf{q}}_{\boldsymbol{\phi}_\mathbf{y}} \end{Bmatrix} + \begin{bmatrix} \mathbf{0} & \mathbf{0} & \mathbf{0} & \mathbf{0} & \mathbf{0} \\ & \mathbf{0} & \mathbf{0} & \mathbf{0} & \mathbf{0} \\ & & \mathbf{F}_{steady}^{33} & \mathbf{0} & \mathbf{0} \\ & & & \mathbf{0} & \mathbf{0} \\ sym & & & & \mathbf{0} \end{bmatrix} \begin{Bmatrix} \mathbf{q}_\mathbf{u} \\ \mathbf{q}_\mathbf{v} \\ \mathbf{q}_\mathbf{w} \\ \mathbf{q}_{\boldsymbol{\phi}_\mathbf{x}} \\ \mathbf{q}_{\boldsymbol{\phi}_\mathbf{y}} \end{Bmatrix} = \mathbf{0}$$

In simplified notation, the equations of motion including viscous damping may be written in the form of $\mathbf{M}\ddot{\mathbf{q}}\left(t\right) + \left(\mathbf{F}_{unsteady} + \alpha\mathbf{M} + \beta\mathbf{K}\right)\dot{\mathbf{q}}\left(t\right) + \left(\mathbf{K_L} + \mathbf{F}_{steady}\right)\mathbf{q}\left(t\right) = \mathbf{0}$. Using $\dot{\mathbf{q}}\left(t\right) = \mathbf{y}\left(t\right)$, the second-order differential equations of motion can be transformed to first-order differential equations of motion as follows

$$\begin{bmatrix} \mathbf{M} & \mathbf{0} \\ \mathbf{0} & -\mathbf{M} \end{bmatrix} \begin{Bmatrix} \dot{\mathbf{y}}\left(t\right) \\ \dot{\mathbf{q}}\left(t\right) \end{Bmatrix} + \begin{bmatrix} \mathbf{F}_{unsteady} + \alpha\mathbf{M} + \beta\mathbf{K} & \mathbf{K_L} + \mathbf{F}_{steady} \\ \mathbf{M} & \mathbf{0} \end{bmatrix} \begin{Bmatrix} \mathbf{y}\left(t\right) \\ \mathbf{q}\left(t\right) \end{Bmatrix} = \begin{Bmatrix} \mathbf{0} \\ \mathbf{0} \end{Bmatrix} \tag{6}$$

By taking $\mathbf{q}\left(t\right) = \mathbf{q_0}^{i\omega t}$, the eigenvalue problem below is achieved,

$$i\omega \begin{bmatrix} -\mathbf{M} & \mathbf{0} \\ \mathbf{0} & \mathbf{M} \end{bmatrix} \begin{Bmatrix} \mathbf{y}\left(t\right) \\ \mathbf{q}\left(t\right) \end{Bmatrix} = \begin{bmatrix} \mathbf{F}_{unsteady} + \alpha\mathbf{M} + \beta\mathbf{K} & \mathbf{K_L} + \mathbf{F}_{steady} \\ \mathbf{M} & \mathbf{0} \end{bmatrix} \begin{Bmatrix} \mathbf{y}\left(t\right) \\ \mathbf{q}\left(t\right) \end{Bmatrix} \tag{7}$$

Here, $\mathbf{F}_{unsteady}$ represents the aerodynamic damping. Solving this eigenvalue problem results in flutter speed in the unsteady regime of flow. Neglecting the term $\mathbf{F}_{unsteady}$ gives the steady results for flutter speed. $\omega$ will be found as conjugate pairs whose real parts represent frequency and imaginary parts damping. Flutter happens if the imaginary part of at least one $\omega$ is less than zero.

## 3 FLUTTER OF COMPOSITE LAMINATES WITH CURVINEAR FIBRES

12-layer laminates with fibre configurations $[\langle 45^\circ + \varphi_0, 45^\circ + \varphi_1 \rangle, \langle -45^\circ - \varphi_0, -45^\circ - \varphi_1 \rangle, \langle 0^\circ + \varphi_0, 0^\circ + \varphi_1 \rangle, \langle 0^\circ - \varphi_0, 0^\circ - \varphi_1 \rangle, \langle 90^\circ + \varphi_0, 90^\circ + \varphi_1 \rangle, \langle -90^\circ - \varphi_0, -90^\circ - \varphi_1 \rangle]_{sym}$ are analysed. The fibre orientations are introduced in this way: in the first layer, $T_0 = 45^\circ + \varphi_0$ and $T_1 = 45^\circ + \varphi_1$; in the second layer, $T_0 = -45^\circ - \varphi_0$ and $T_1 = -45^\circ - \varphi_1$; and so forth. Mechanical properties of the VSCL are as follows: major and minor Youngs moduli, $E_1 = 126.3$ GPa and $E_2 = 8.765$ GPa, shear moduli $G_{12} = G_{13} = 4.92$ GPa and $G_{23} = 3.35$ GPa, Poisson's ratio $\nu_{12} = 0.334$ and density $\rho = 1557$ kg/m$^3$. The length and width of the plate are equal to 0.5 m. The total thickness is 0.006 m and all the layers have equal thickness. It should be mentioned that when $\varphi_0$ and $\varphi_1$ angles are not equal, these fibre configurations represent VSCLs. When $\varphi_0$ and $\varphi_1$ angles are equal (e.g. 0°), the configuration represents a CSCL. For the VSCL plates analysed in the following figures, flutter speeds with changing $\varphi_0$ - shown with red star in the figures - and with changing $\varphi_1$ - shown with black diamond in the figures - are calculated in the range of fibre angle from $0^\circ$ to $45^\circ$. If $\varphi_0$ is changing then $\varphi_1 = 0^\circ$ and vice versa. The analysis is performed for VSCL with different clamped and free boundary conditions. In this study, seven one-dimensional shape functions, equal to 245 DOF, is used in the *p*-version finite element. The coefficients of viscous damping $\alpha$ and $\beta$ are extracted from experiments [21] and are equal to $8.2 \times 10^{-5}$ and -0.505, respectively.

### 3.1 All edges clamped

Figure 2 displays the flutter speed (shown in the vertical axis) of the clamped VSCL plates in three various situations: steady regime without viscous damping, unsteady regime without viscous damping and unsteady regime with viscous damping. It shows that performing the analysis in unsteady regime of flow - taking into consideration $w_{,t}$ in Equation 4 - increases the flutter speed. Although adding the viscous damping reduces the flutter speed in CSCL (i.e. $\varphi_0 = \varphi_1 = 0^\circ$), this effect changes slightly in VSCLs. In all three cases, increasing $\varphi_0$ ($\varphi_1 = 0^\circ$) or $\varphi_1$ ($\varphi_0 = 0^\circ$) reduces the flutter speed. From this point of view and in the range of investigated VSCLs, using the curvilinear fibres has no advantage.

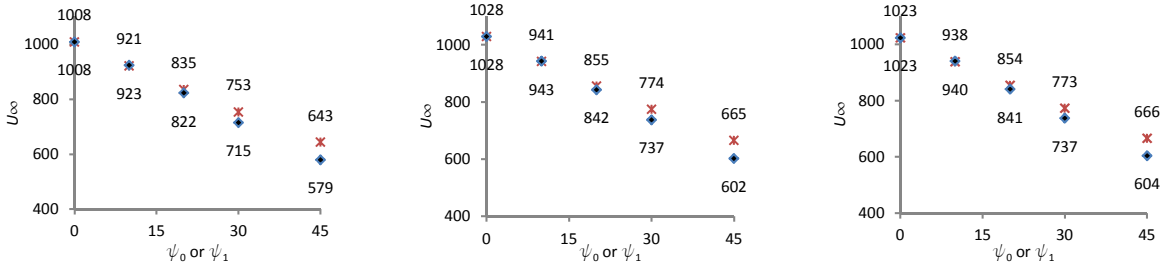


a) b) c)

Figure 2: Flutter speed of the clamped plate in a) steady regime without viscous damping, b) unsteady regime without viscous damping and c) unsteady regime with viscous damping.

### 3.2 All edges free

In order to include aerodynamic and structural damping into account, in free boundary condition, only flutter speeds in the unsteady regime of flow and in the presence of viscous damping

are displayed. In the free plates, given in Figure 3, flutter speed always decreases with the increase of fibre angle at the centre of the plate $\varphi_0$. But, increasing $\varphi_1$ has a different effect: it first reduces the flutter speed and then leads higher flutter speeds. In the range of investigated plates, the best design in terms of flutter speed, is the CSCL with 653 $m/s$. The fact that increasing the fibre angle at the edges of the plate improves the flutter speed needs more investigation. Understanding different effects of fibre angles at the centre and the edges on flutter concept can help the researchers to evaluate VSCLs with other types of boundary condition or fibre angle ranges to exploit their potentials better.

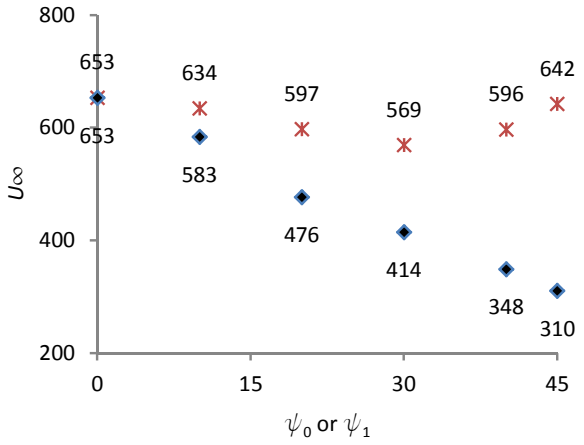


Figure 3: Flutter speed of the free plate in the unsteady regime with viscous damping.

## 4 CONCLUSIONS

A VSCL plate with curvilinear fibres was introduced where the fibre angle changes linearly from the centre of the ply to the edges. The flutter speed of such plate subjected to a supersonic upstream was evaluated in the steady and in the unsteady regimes of flow. A structural viscous damping proportional to the mass and the stiffness matrix was applied. Piston theory was used to model the aerodynamic pressure of the flow. The analysis was carried out for different boundary conditions including clamped and free plates. It was shown that in clamped and free VSCL plates, the flutter speed always decreases with the increase of the fibre angles at the centre of the plate. In other words, the clamped and free composite laminates with curvilinear fibres at the centre did not show any advantage in comparison to laminates with straight fibres. As far as free plate is concerned, only with increasing the fibre angle at the edges ($\varphi_1 > 30°$) the flutter speed increases. The potential possibilities to increase the flutter speed of VSCL plates with the concept of curvilinear fibres requires to be uncovered with consideration of different boundary conditions and various range of fibre angle orientations.

## ACKNOWLEDGEMENTS

The authors gratefully acknowledge the funding of Project NORTE-01-0145-FEDER-000022 - SciTech - Science and Technology for Competitive and Sustainable Industries, cofinanced by Programa Operacional Regional do Norte (NORTE2020), through Fundo Europeu de Desenvolvimento Regional (FEDER).

## REFERENCES


[1] H. Akhavan, *Non-linear vibrations of tow placed variable stiffness composite laminates*. PhD Thesis, University of Porto, Portugal, 2015.

[2] C. Waldhart, *Analysis of tow-placed, variable-stiffness laminates*. Master Thesis, Virginia Polytechnic Institute and State University, VA, 1996.

[3] S.T. IJsselmuiden, *Optimal design of variable stiffness composite structures using lamination parameters*. PhD Thesis, Delft University of Technology, The Netherlands, 1996.

[4] H. Akhavan, P. Ribeiro, Natural modes of vibration of variable stiffness composite laminates. *Composite Structures*, **93**, 3040–3047, 2011.

[5] M.M. Abdalla, S. Setoodeh, Z. Gürdal, Design of variable stiffness composite panels for maximum fundamental frequency using lamination parameters. *Composite Structures*, **81**, 283–291, 2007.

[6] A.W. Blom, S. Setoodeh, J.M.A.M Hol, Z. Gürdal, Z, Design of variable-stiffness conical shells for maximum fundamental eigenfrequency. *Computers & Structures*, **86**, 870–878, 2008.

[7] S. Yazdani, P Ribeiro, Geometrically non-linear static analysis of unsymmetric composite plates with curvilinear fibres: p-version layerwise approach. *Composite Structures*, **118**, 74–85, 2014.

[8] S. Yazdani, P Ribeiro, J.D. Rodrigues, A p-version layerwise model for large deflection of composite plates with curvilinear fibres. *Composite Structures*, **108**, 181–190, 2014.

[9] B.F. Tatting, Z. Gürdal, *Automated finite element analysis of elastically-tailored plates*. NASA contractor report no NASA/CR-2003-212679, 2003.

[10] B.F. Tatting, Z. Gürdal, *Design and manufacture of elastically tailored tow placed plates*. NASA contractor report no NASA/CR-2002-211919, 2002.

[11] H. Akhavan, P. Ribeiro, Free geometrically nonlinear oscillations of perfect and imperfect laminates with curved fibres by the shooting method. *Nonlinear Dynamics*, **81**, 949–965, 2015.

[12] H. Akhavan, P. Ribeiro, Non-linear forced periodic oscillations of laminates with curved fibres by the shooting method. *International Journal of Non-Linear Mechanics*, **76**, 176–189, 2015.

[13] B.K. Stanford, C.V. Jutte, Comparison of curvilinear stiffeners and tow steered composites for aeroelastic tailoring of aircraft wings. *Computers & Structures*, **183**, 48–60, 2017.

[14] R.R. Fernandes, A.Y. Tamijani, Flutter analysis of laminated curvilinear-stiffened plates. *57th AIAA/ASCE/AHS/ASC Structures, Structural Dynamics, and Materials Conference*, San Diego, United States, January 4-8, 2016.

[15] B.K. Stanford, C.V. Jutte, W.K. Chauncey, Aeroelastic benefits of tow steering for composite plates. *Composite Structures*, **118**, 416–422, 2014.

[16] W. Han, M. Petyt, K.M. Hsiao, An investigation into geometrically nonlinear analysis of rectangular laminated plates using the hierarchical finite element method. *Finite Elements in Analysis and Design*, **18**, 273–288, 1994.

[17] P. Ribeiro, *Geometrical nonlinear vibration of beams and plates by the hierarchical finite element method*. PhD Thesis, University of Southampton, UK, 1998.

[18] E.H. Dowell, R. Clark, D. Cox, *A modern course in aeroelasticity*. Dordrecht: Kluwer academic publishers, 2004.

[19] J. Reddy, *Mechanics of laminated composite plates and shells: theory and analysis*. CRC Press, 2004.

[20] B. Vlasov, On the equations of bending of plates. *Dokla Ak Nauk Azerbeijanskoi-SSR*, **3**, 955–979, 1957.

[21] J. Rodrigues, P. Ribeiro, H. Akhavan, Experimental and finite element modal analysis of variable stiffness composite laminated plates. *Proceedings of the 11th Biennial International Conference on Vibration Problems (ICOVP-2013)*, Lisbon, Portugal, 2013.

COMPDYN 2017
6th ECCOMAS Thematic Conference on
Computational Methods in Structural Dynamics and Earthquake Engineering
M. Papadrakakis, M. Fragiadakis (eds.)
Rhodes Island, Greece, 15–17 June 2017

# ON THE DYNAMIC BEHAVIOR OF A NONLINEAR OSCILLATOR WITH SOFTENING CHARACTERISTICS ATTACHED TO AN ELECTRO-DYNAMIC ACTUATOR

**Alfonso Cutuli**[1], **Rosario Aiello**[1] **and Gianluca Gatti**[1]

[1] University of Calabria
Dept. of Mechanical, Energy and Management Eng., V. P. Bucci 46C, 87036 Rende, Italy
e-mail: alfonsocutuli@gmail.com, rio88_@hotmail.it, gianluca.gatti@unical.it

**Keywords:** Nonlinear Vibration, Nonlinear Oscillator, Vibration Control.

**Abstract.** *This paper presents an investigation on the dynamics involved in a two degrees of freedom system consisting of a nonlinear oscillator attached to the moving head of a linear electro-dynamic shaker. The effective stiffness of the nonlinear attachment is realized to achieve a softening force-deflection curve characteristics, and magnets are exploited to this purpose. The shaker is modelled as a linear spring-mass-damper system excited by a harmonic force with a varying excitation frequency. The attached oscillator consists of a cantilever beam with a specified mass on its tip, and it behaves linearly in the given domain of investigation. The nonlinearity is then introduced by adopting magnets in an attractive configuration acting on the tip of the beam. This has the twofold effect of reducing the linear effective stiffness and adding a negative stiffness of cubic type. The equations of motion of the system are presented, and an analytical solution in terms of amplitude-frequency equation is reported. This allows to explore the role of the key parameters involved in the system dynamics, and their effects is investigated in terms of the frequency response curve. The relationship among the non-dimensional, dimensional and physical parameters of an equivalent mechanical prototype is presented.*

## 1 INTRODUCTION

The dynamics of two degree-of-freedom (DOF) nonlinear oscillators has been extensively reported in the literature, and the main applications have been related to the passive control of vibration, e.g. as vibration absorber [1] and energy sink [2].

A coupled system with springs of a linear-plus-cubic characteristics was investigated in [3], showing that the presence of the nonlinearity can result in amplification rather than reduction of the vibration amplitude. Reduction of the vibration amplitude can be obtained by a proper selection of the parameters in a system with nonlinear damping and nonlinear springs [4]. The theoretical investigation on the system behaviour in the vicinity of a main resonance was reported in [5], where possible quasi-periodic response was highlighted. In [6] such a nonlinear system was investigated for vibration mitigation and absorption, the local bifurcations of the periodic solutions was illustrated via frequency-response curves (FRCs), and their evolution with an increase of the excitation amplitude was shown. The performance and characteristics of a nonlinear neutralizer acting on a linear host structure were investigated in [7], and distinguishable features, such as closed detached resonance curves, have been predicted either inside [8] or outside [9,10] the main FRC. Experimental evidence of those features have been reported in [11,12]. In the majority of these studies, nonlinearity is concentrated on the suspension stiffness, which is modelled as a linear plus a cubic spring with a hardening characteristics. A static force-deflection curve of this type can be physically realized by assembling linear springs in a specific geometric configuration [12].

Other studies reported on the use of nonlinear springs with softening characteristics to achieve a quasi-zero stiffness effect for vibration isolation purposes [13-15]. The combination of mechanical springs and magnets has been exploited in [16].

In this paper we analyse an experimental setup in which an electro-dynamic shaker is used to excite a nonlinear system which has a much smaller mass than that of the shaker. The system is modelled as a nonlinear softening oscillator coupled to a linear system, representing the shaker, which also provide the harmonic force excitation. Because the system is softening, the resonance frequency due to the nonlinear system bends to lower frequencies and determines multi-valuedness of the amplitude response at some given frequencies of excitation. An analytical solution to the amplitude-frequency relation is reported, and a theoretical investigation on the effect of the system parameters on the response, has revealed coexisting steady-states regimes with detached resonance curves appearing inside the amplitude-frequency diagrams.

## 2 EXPERIMENTAL TEST-RIG

### 2.1 System description

The experimental test-rig under consideration in this work is illustrated in Fig. 1(a), and a schematic model is reported in Fig. 1(b). It consists of a large electro-dynamic shaker, on the moving head of which a support structure is attached. This is used to hold a cantilever beam, which is clamped at one extreme on the support and it is free to move at the other extreme. At the free end, two magnets are attached on each side of the beam and they act as a concentrated mass at the tip. They are also used to induce an auxiliary nonlinear stiffness component when they interact with their corresponding counter-parts on the support structure. If the magnets are arranged so that those on the tip of the beam are attracted by those on the support structure, the overall effect is to reduce the linear stiffness due to the slender beam alone, and add a nonlinear component of softening type. The physical parameters of the system and their corresponding values are reported in Table 1.

In the frequency range of interest, the beam with concentrated mass on its tip may be considered as a single DOF oscillator with effective stiffness and mass given by [17]

$$k_{1_beam} = \frac{3EI}{L^3}$$
$$m = 0.2357 m_{beam} + m_{tip} \tag{1}$$

where $I$ is the second moment of area of the beam section and $m_{beam}$ is the beam mass.

Preliminary experimental tests were performed to estimate the frequency response function (FRF) of the system due to random excitation. An LMS Scadas III system was used for data acquisition and signal processing, and an accelerometer (PCB 352C22) was attached on the tip of the beam. Magnets on the support structure are removed so as to avoid any magnetic interaction with the beam, and the system was thus considered to behave as a two DOF linear oscillator. Result is reported in Fig. 2 as solid line and normalised to the maximum value. It can be seen that the resonance frequency at about 20 Hz due to the shaker is very highly damped, and the resonance frequency of the beam with attached tip mass is at about 34 Hz, as predicted by adopting the effective stiffness and mass in Eq. (1). To investigate the softening effect on the FRF, magnets are attached on the support structure in an attractive arrangement and at a specified distance, as reported in Table 1. It is reasonably assumed that the effect of the weight of the magnets on the mass of the excited main oscillator was negligible. The normalised result in this case is reported as dashed line in Fig. 2, where it can be noted that the overall effect, when using a linear FRF estimate, is to move the resonance peak to the lower frequencies, which is the case of a softening stiffness.

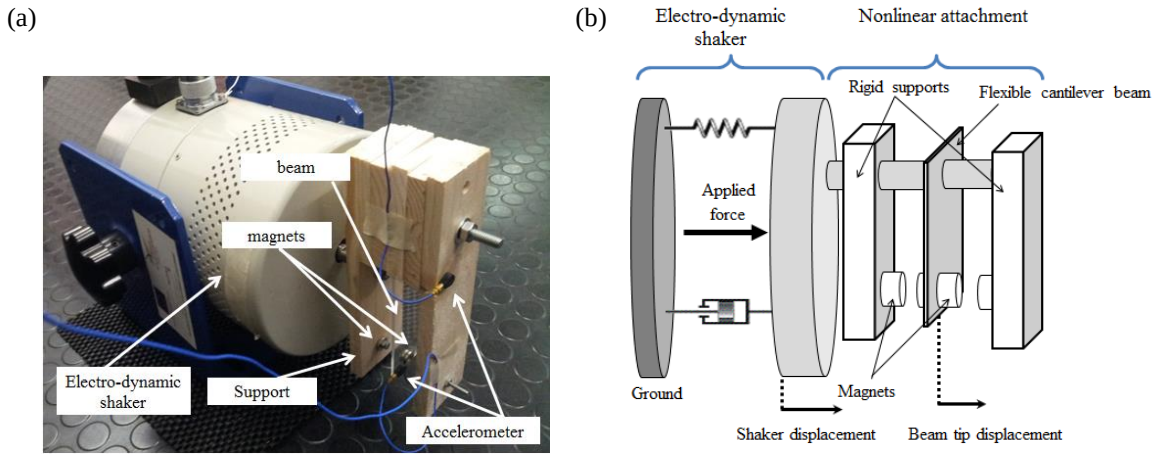


Figure 1. Two DOF system under study: (a) photograph and (b) schematic model.

| Description | Parameter | Value | Description | Parameter | Value |
|---|---|---|---|---|---|
| Shaker stiffness [N/m] | $k_{shaker}$ | 9000 | Beam width [mm] | $a$ | 30 |
| Shaker moving mass [kg] | $m_{shaker}$ | 0.45 | Beam thickness [mm] | $s$ | 2 |
| Support mass [kg] | $m_{supp}$ | 0.15 | Beam length [mm] | $L$ | 90 |
| Magnet mass [g] | $m_{mag}$ | 1.2 | Beam density [kg/m$^3$] | $\rho$ | 850 |
| | | | Beam Young's modulus [N/m$^2$] | $E$ | 1.95e9 |
| | | | Distance between magnets [mm] | $b$ | 10 |

Table 1: Physical parameters of the experimental system.

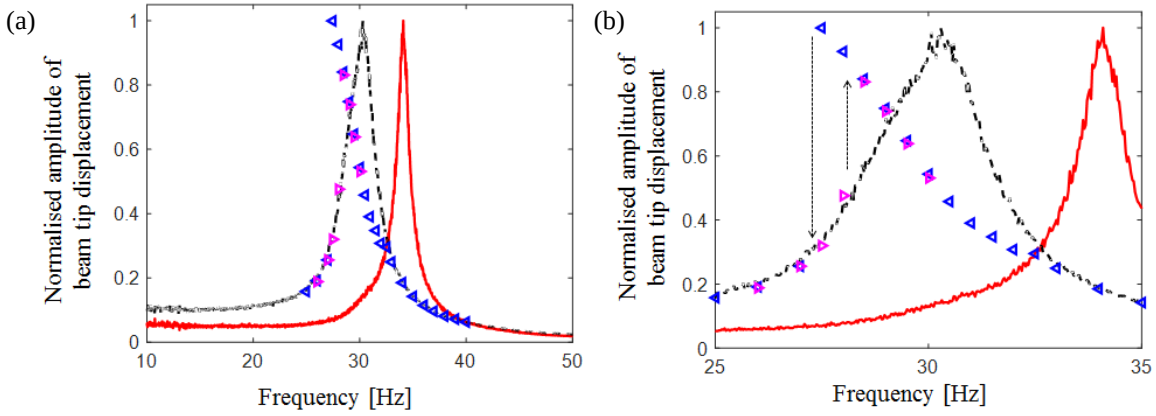


Figure 2. (a) Measured amplitude of beam tip displacement normalised to the maximum value, and (b) close-up. Linear FRF estimate without (solid line) and with (dashed line) magnets. Right (left) -pointing triangles indicate the FRC obtained by measuring the response at each frequency when increasing (decreasing) frequency of excitation.

For a better insight on the dynamic response of the system due to harmonic excitation, the shaker was driven with constant amplitude at each frequency, using a signal generator and a power amplifier. The system response in time was then measured using the accelerometer, and the spectrum of the corresponding signal was estimated by the frequency analyser. The amplitude of the spectrum at the excitation frequency is considered to reconstruct the frequency response curve (FRC), and this is normalised and plotted in Fig. 2 as well, using markers: left-pointing triangles are used to indicate the case where the excitation frequency is decreased from 40 to 25 Hz; right-pointing triangles indicate the case where the excitation frequency is increased from 25 to 30 Hz. Despite higher order harmonics were present around the resonance, it can be clearly noted that actual FRC presents a bending of the resonance peak to the lower frequencies, and this determines multi-valuedness and jump phenomena in the FRC. These latter are indicated in the close-up of Fig. 2(b) by vertical arrows pointing upwards for jump-up, or pointing downwards for jump-down.

## 2.2 Magnetic interaction

To quantify the magnetic interaction, an experimental setup, as illustrated in Fig. 3(a,b), was assembled and used to estimate the force-deflection characteristics. To this purpose, one magnet was constrained on a horizontal surface and a second magnet was attached on the base of a non-metallic cylinder, in such a way that it was set in a repelling arrangement to the previous magnet. A plastic tube was used to constrain the non-metallic cylinder to a vertical motion, when located on top of the magnet attached to ground. The force-deflection curve of magnetic interaction was then estimated by measuring the change in displacement for each additional weight applied on top of the non-metallic cylinder. Results of this test are reported in Fig. 3(c) as markers, and a fitting curve to the experimental data is also overlapped. A reasonably good fitting was achieved using the following equation

$$F_{mag} = \frac{C_{mag}}{y^n} \tag{2}$$

where $C_{mag} = 0.104$ Nm$^{1/3}$ and $n = 1/3$.

The total magnetic force acting on the tip of the beam is then given by the following relation

$$F_{mag_tip} = -\frac{C_{mag}}{(b-z)^n} + \frac{C_{mag}}{(b+z)^n} \tag{3}$$

where $b$ is given in Table 1, and $z = x_s - x$ is the relative displacement between the support, $x_s$, and the beam tip, $x$, as depicted in Fig. 4(a). Equation (3) may be expanded in McLaurin's series to the third order to give

$$F_{mag_tip} \approx k_{1_mag} z + k_{3_mag} z^3 \tag{4}$$

where

$$\begin{aligned} k_{1_mag} &= -2\,C_{mag} / 3b^{4/3} \\ k_{3_mag} &= -28 C_{mag} / 81 b^{10/3} \end{aligned} \tag{5}$$

Equation (3) and (4) are plotted in Fig. 4(b), where it is noted that the cubic-type approximation in Eq. (4) (solid line) well approximates the expression in Eq. (3) (dashed line). The approximation is reasonable for relative displacements up to about half of the distance, $b$, between magnets at rest.

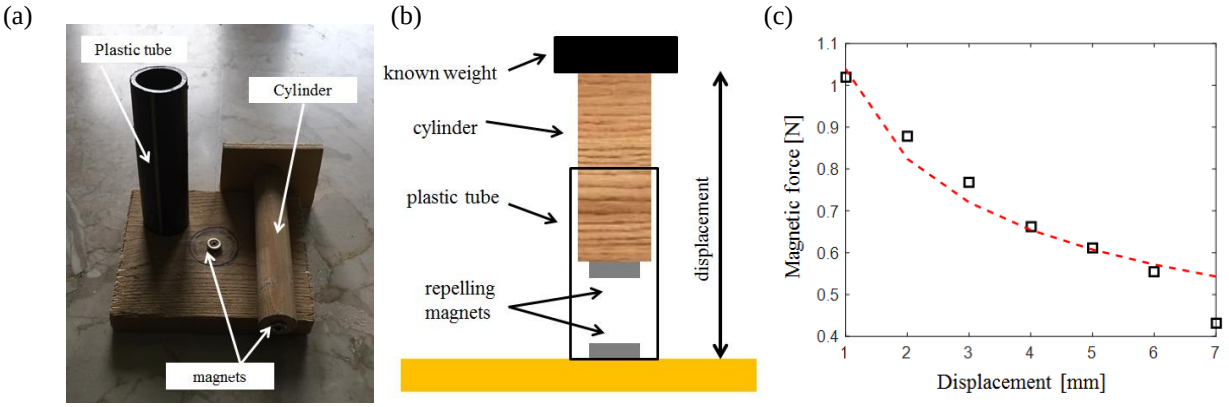


Figure 3. Experimental rig used to estimate the force-deflection curve characteristics of magnetic interaction: (a) photograph and (b) schematics. (c) Measured characteristics (markers) and fitting curve (dashed line).

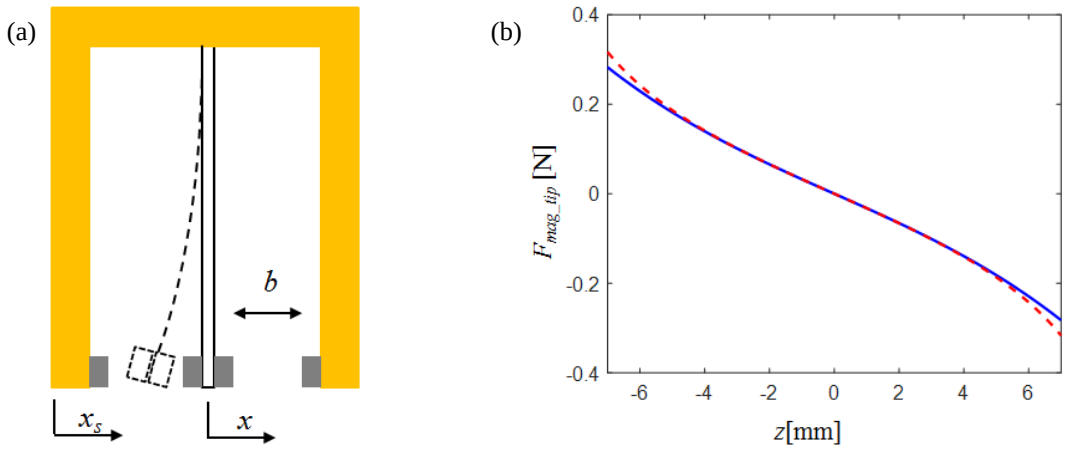


Figure 4. Magnetic force at tip: (a) close-up, (b) net force from Eq. (3) (dashed line) and Eq. (4) (solid line).

## 3 SYSTEM MODELLING

A simplified model for the system described in the previous section is reported in Fig. 5(a), and the corresponding equations of motion are given as

$$\begin{aligned} &m_s\ddot{x}_s + c_s\dot{x}_s + k_s x_s + c_1\dot{z} + k_1 z + k_3 z^3 = F\cos(\omega t) \\ &m\ddot{x}_s - m\ddot{z} - c_1\dot{z} - k_1 z - k_3 z^3 = 0 \end{aligned} \tag{6}$$

where parameters are indicated in Fig. 5(a). In particular it is

$$\begin{aligned} k_1 &= k_{1_beam} + k_{1_mag} = \frac{3EI}{L^3} - \frac{2C_{mag}}{3b^{4/3}} \\ k_3 &= k_{3_mag} = -\frac{28C_{mag}}{81b^{10/3}} \end{aligned} \tag{7}$$

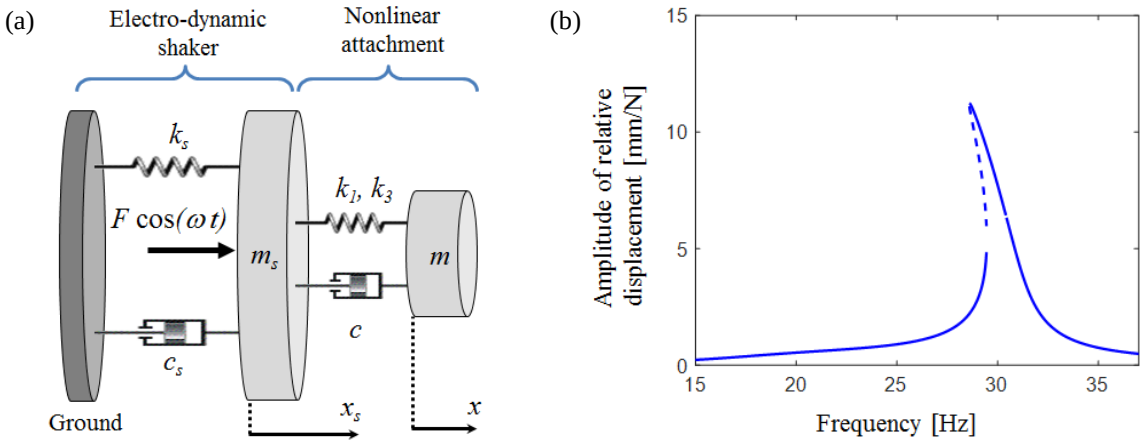


Figure 5. (a) Simplified model of the system in Fig. 1. (b) Example of FRC with stable (solid line) and unstable (dashed line) solutions.

In the assumption that the mass of the shaker and the attached support is much larger than the effective mass of the nonlinear oscillator, which is the actual case in Fig. 1, the non-dimensional form of Eqs. (6) simplifies to [10]

$$\begin{aligned} &y_s'' + 2\zeta_s y_s' + y_s = \cos(\Omega\tau) \\ &w'' + 2\zeta w' + \Omega_0^2 w + \gamma w^3 = y_s'' \end{aligned} \tag{8}$$

and the following non-dimensional parameters are defined

$$\begin{aligned} &y_s = \frac{x_s}{x_0}, \quad w = \frac{z}{x_0}, x_0 = \frac{F}{k_s}, \omega_s = \sqrt{\frac{k_s}{m_s}}, \omega_1 = \sqrt{\frac{k_1}{m}}, \tau = \omega_s t, \\ &\mu = \frac{m}{m_s}, \gamma = \frac{k_3}{\mu k_s} x_0^2, \zeta_s = \frac{c_s}{2m_s\omega_s}, \zeta = \frac{c}{2m\omega_s}, \Omega_0 = \frac{\omega_1}{\omega_s}, \Omega = \frac{\omega}{\omega_s} \end{aligned} \tag{9}$$

It is noted form Eq. (8) that the assumption of a small mass ratio, $\mu$, implies that the shaker is not affected by the smaller nonlinear system, while this latter is affected by the former. A

solution for the relative displacement amplitude in Eq. (8) is reported from [10] in terms of the amplitude-frequency response as

$$\frac{9}{16}\gamma^2 W^6 + \frac{3}{2}\gamma W^4\left(\Omega_0^2 - \Omega^2\right) + W^2\left(\Omega^4 + 4\zeta^2\Omega^2 + \Omega_0^4 - 2\Omega_0^2\Omega^2\right) - \frac{\Omega^4}{\left(1-\Omega^2\right)^2 + 4\zeta_s^2\Omega^2} = 0 \quad (10)$$

which is a cubic polynomial equation in terms of $W^2$ (i.e. the relative displacement amplitude squared), and thus admits three solutions, two of which are stable and one is unstable. The FRC of the relative displacement amplitude is plotted in Fig. 5(b) for the values of parameters listed in Table 1, assuming $\zeta = 0.02$, $\zeta_s = 0.3$ and $F = 4$ N. It can be noted that Fig. 5(b) qualitatively predicts a similar peak bending as that seen in the experimental results of Fig. 2.

The experimental case reported in this paper was particularly unfavourable, mainly due to the high damping of the shaker. In case of lighter damping, the FRC exhibits more interesting phenomena, such as resonance interactions and appearance of detached curves inside the main FRC. For a softening attachment, this happens because its resonance peak bends to the lower frequencies and interacts with the resonance peak due to the shaker with attached support, as can be seen in Fig. 6(a) and (b), where a damping $\zeta_s$ of 0.03 and 0.01 is used, respectively.

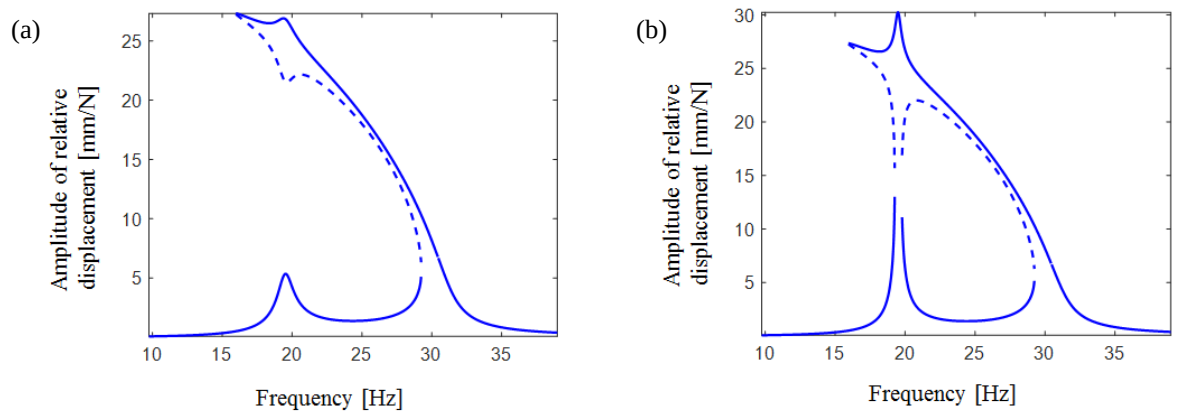


Figure 6. FRC when a light damping in the shaker is considered: (a) $\zeta_s = 0.03$, (b) $\zeta_s = 0.01$. Stable solutions (solid line) and unstable solutions (dashed line).

## 4 CONCLUSIONS

Based on the design and on some experimental tests performed on a nonlinear oscillator with softening spring characteristics driven by a shaker, this paper has shown some interesting dynamic effects appearing when the resonance peak of the nonlinear oscillator interacts with the resonance peak of the shaker: inner detached resonance curves manifest in the main frequency response curve for relatively light damping of the shaker. Although this was not shown experimentally due to the high damping of the actual shaker used in this work, the theoretical model predicts those features.

Understanding the complex dynamics involved in the type of system described in this paper, could be valuable not only for the tests of softening oscillators using an electro-dynamic shaker, but it could advance knowledge in the behaviour of two degrees of freedom nonlinear oscillators, and eventually foster pioneering engineering applications for vibration isolation, vibration absorption and vibration energy harvesting.

## REFERENCES


[1] T. Detroux, G. Habib, L. Masset, G. Kerschen, Performance, robustness and sensitivity analysis of the nonlinear tuned vibration absorber. *Mechanical Systems and Signal Processing*, **60-61**, 799-809, 2015.

[2] Y. Starosvetsky, O.V. Gendelman, Vibration absorption in systems with a nonlinear energy sink: Nonlinear damping. *Journal of Sound and Vibration*, **324**, 916-939, 2009.

[3] J. Shaw, S.W. Shaw, A.G. Haddow, On the response of the non-linear vibration absorber. *International Journal of Non-linear Mechanics*, **24**, 281-293, 1989.

[4] S.J. Zhu, Y.F. Zheng, Y.M. Fu, Analysis of non-linear dynamics of a two-degree-of-freedom vibration system with non-linear damping and non-linear spring. *Journal of Sound and Vibration*, **271**, 15-24, 2004.

[5] O.V. Gendelman, E. Gourdon, C.H. Lamarque, Quasiperiodic energy pumping in coupled oscillators under periodic forcing. *Journal of Sound and Vibration*, **294**, 651-662, 2006.

[6] Y. Starosvetsky, O.V. Gendelman, Response regimes of linear oscillator coupled to nonlinear energy sink with harmonic forcing and frequency detuning. *Journal of Sound and Vibration*, **315**, 746-765, 2008.

[7] M.J. Brennan, G. Gatti, The characteristics of a nonlinear vibration neutralizer. *Journal of Sound and Vibration*, **331**, 3158-3171, 2012.

[8] G. Gatti, Uncovering inner detached resonance curves in coupled oscillators with nonlinearity. *Journal of Sound and Vibration*, **372**, 239-254, 2016.

[9] N.A. Alexander, F. Schilder, Exploring the performance of a nonlinear tuned mass damper. *Journal of Sound and Vibration*, **319**, 445-462, 2009.

[10] G. Gatti, M.J. Brennan, On the effects of system parameters on the response of a harmonically excited system consisting of weakly coupled nonlinear and linear oscillators. *Journal of Sound and Vibration*, **330**, 4538-4550, 2011.

[11] A.D. Shaw, T.L. Hill, S.A. Neild, M.I. Friswell, Periodic responses of a structure with 3:1 internal resonance. *Mechanical Systems and Signal Processing*, **81**, 19-34, 2016.

[12] G. Gatti, M.J. Brennan, Inner detached frequency response curves: an experimental study. *Journal of Sound and Vibration*, http://dx.doi.org/10.1016/j.jsv.2017.02.008.

[13] S.E. Woodard, J.M. Housner, Nonlinear behavior of a passive zero-spring-rate suspension system. *Journal of Guidance, Control, and Dynamics*, **14**, 84-89, 1991.

[14] P. Alabuzhev, A. Gritchin, L. Kim, G. Migirenko, V. Chon, P. Stepanov, *Vibration Protecting and Measuring Systems with Quasi-Zero Stiffness*, Hemisphere, New York, 1989.

[15] T. Mizuno, M. Takasaki, D. Kishita, K. Hirakawa, Vibration isolation system combining zero-power magnetic suspension with springs. *Control Engineering Practice*, **15**, 187-196, 2007.

[16] A. Carrella, M.J. Brennan, T.P Waters, K. Shin, On the design of a high-static–low-dynamic stiffness isolator using linear mechanical springs and magnets. *Journal of Sound and Vibration*, **315**, 712-720, 2008.

[17] S.S. Rao, *Mechanical Vibrations*, Prentice Hall, 2011.

COMPDYN 2017
6th ECCOMAS Thematic Conference on
Computational Methods in Structural Dynamics and Earthquake Engineering
M. Papadrakakis, M. Fragiadakis (eds.)
Rhodes Island, Greece, 15–17 June 2017

# MODELLING COCNCRETE MATERIAL BEHAVIOUR UNDER HIGH LOADING RATES

**Alaa O. Swesi**[1] **, Ali A. Abbas**[2]**, Demetris M. Cotsovos**[3]

[1] PhD Student, Institute of Infrastructure and Environment,

Heriot-Watt University, Edinburgh EH14 4AS, UK

e-mail: aos1@hw.ac.uk

[2] Senior Lecturer in Structural Engineering, School of Architecture,

Computing and Engineering, University of East London, London E16 2RD, UK
e-mail: abbas@uel.ac.uk

[3] Assistant Professor, Institute of Infrastructure and

Environment, School of the Built Environment, Heriot-Watt

University, Edinburgh EH14 4AS, UK

e-mail: d.cotsovos@hw.ac.uk

**Keywords:** Concrete, Material Properties, Cracking, Loading Rate, Finite-Element Analysis, Software Packages, Nonlinear Dynamic Analysis, Brittle Behaviour

**Abstract.** *The present work sets out to investigate numerically, by means of dynamic Non-linear Finite-Element Analysis (NLFEA), the effect of the strain-rate exhibited under high loading rates (associated usually with blast and impact problems) on the material properties of structural concrete and the ensuing cracking process it undergoes. The numerical predictions obtained were initially validated against relevant published data obtained from tests on plain concrete prismatic and cylindrical specimens under increasing loading rates under direct or indirect tension, uniaxial compression and flexure. The numerical studies reveal that the responses under impact loading differ significantly from those under static loading once certain thresholds of loading rates are exceeded. The study builds on previous work [1-3], which has shown that the commonly observed stress-strain relationship of plain concrete specimens under high rates of loading actually describes dynamic structural response rather than material behaviour. A couple of finite element packages were used, in the present study, which adopt different approaches for modelling concrete material behaviour. The comparative analysis of the predictions obtained reveals that when realistically accounting for the brittle nature and the triaxiality which characterise concrete material behavior, the experi-*

*mentally and numerically observed variation in specimen behaviour (under increasing loading rates) is primarily attributed to parameters associated with structural response and not, as widely considered, to strain-rate sensitivity of the material properties of structural concrete. Furthermore, it is shown that strain-rate sensitivity in concrete is based on an interpretation of the experimental evidence through the use of material models the analytical formulation of which depends heavily on parameters associated with post-failure mechanisms (i.e. strain softening, tension stiffening, shear-retention ability, etc) which attribute ductile characteristics to concrete material behaviour that is not compatible with its brittle nature. The response is also affected by the nature of the problem at hand (a wave propagation problem within a highly nonlinear material). Therefore, it is concluded that at the material level the numerical study shows that the effect of high loading rates on the behaviour of concrete is mainly linked to the development of inertia forces rather than strain-rate sensitivity of its material properties. Overall the aim of the present study is to provide insight into the effect of loading-rate on the mechanics underlying RC structural dynamic response under impact loading.*

## 1 INTRODUCTION

It has been well established, both experimentally and numerically, that the behaviour of plain concrete specimens (with a low moisture content) differs considerably from that under static loading, once certain thresholds of applied loading-rates are surpassed [4-7]. Nevertheless, there has been considerable debate concerning the reasons that trigger this shift. There is a consensus that inertia has a significant effect on the behaviour exhibited by plain concrete specimens under high-rate loading. However, considerable disagreement exists regarding the influence of strain-rate sensitivity on the material properties of structural concrete. Many researchers consider that the *material* properties of concrete are dependent on the rate of deformation (i.e. strain-rate dependency), a view which until recently was widely accepted and incorporated into the framework of existing military codes for the design and analysis of RC structures under blast and impact. Lately however, an increasing number of researchers [8-10] have expressed the opposite view, stating that the *material* properties of structural concrete (characterised by a low moisture content) are essentially strain-rate independent and that the observed changes in specimen behaviour with increasing loading rates is the result of (a) parameters affecting *structural* response, (b) the brittle nature and triaxiality characterising concrete material behaviour and (c) the nature of the problem at hand (a wave propagation problem within a highly nonlinear material).

The present study builds on previous research work [1-3], which has shown that the commonly observed stress-strain relationship of plain concrete specimens under high rates of loading actually describes dynamic *structural* response rather than *material* behaviour. The present study aims at investigating numerically, via dynamic nonlinear finite element analysis (NLFEA) of plain concrete prismatic specimens under increasing loading rates under uniaxial compression and tension. Emphasis is mainly focused on investigating the effect of loading rate on specific aspects of specimen behaviour, such as the maximum sustained load as well the variation of the stress-displacement within the specimen during the loading process. This is carried out in order to identify the true reasons that trigger the observed shift in specimen behaviour with increasing loading rates, which is a necessary prerequisite for developing an effective method (both in terms of safety and economy) for assessing RC structural response under high loading rates. Thus, the work will have implications for impact-resistant design.

For the numerical investigation, two finite element analysis (FEA) software packages were considered, both capable of carrying out three-dimensional (3D) nonlinear static and dynamic analyses, namely ABAQUS [11] and and RC-FINEL [12,13]. The latter study [1] is essentially assessed in the present work using ABAQUS. To realistically describe the nonlinear behaviour of concrete under high loading rates it is imperative that the material models, incorporated into any FEA package, are capable of accurately describing concrete material behaviour under both static and dynamic loading. ABAQUS incorporate concrete constitutive models the analytical formulation of which is based on continuum mechanics theories and relies heavily on the use of *post*-failure concrete characteristics (i.e. strain softening, tension stiffening and shear-retention). On the other hand, RC-FINEL incorporates a fully brittle empirical [13] material law describing concrete behaviour under triaxial loading while at the same time adopting a unique iterative solution strategy capable of compensating for the numerical instabilities stemming from the brittle concrete material law adopted [13]. The present and previous studies [1-3] have shown that the *material* properties of structural concrete are essentially strain-rate independent and that any effect of loading-rate on specimen behaviour is clearly attributed to parameters associated with the dynamic response of the specimen (acting as a *structure*). This sheds doubt on the applicability of such post-failure responses for the purposes of impact-resistant design.

## 2 MATERIAL BEHAVIOUR OF CONCRETE UNDER STATIC LOADING

Concrete is a heterogeneous material since its basic components (aggregate, cement paste and free water) have considerably different material properties [14]. Even in an unloaded state, it contains voids and discontinuities in the form of microcracks [13]. As a result, when an external load is applied on a concrete specimen, a complex internal stress field develops. The behaviour of concrete in uniaxial tension is mainly determined by testing plain concrete prisms in direct, or indirect (splitting) tension and flexure. Based on the available experimental data it is observed that concrete essentially behaves elastically until it reaches its tensile strength and then fails in a brittle manner suffering an abrupt loss of load carrying capacity. The behaviour of concrete under uniaxial compression is determined mainly by testing plain concrete cylinders or prisms (see Figure 1a) and is described through the typical stress-strain curves presented in Figure 1b. These curves describe the deformation behaviour of the concrete specimen parallel and normal to the direction of loading. Such curves comprise an ascending and a subsequent descending branch. Based on available experimental data [12,13,15-18], the descending branch does not describe *material* behaviour but the interaction between specimen and testing device. This interaction is the result of frictional forces developing at the interface between the specimen and the steel platens normally used to apply the external load. As a result the specimen is subjected to lateral confinement close to its supports (see Figure 1a). Another important aspect of concrete behaviour in compression is that it exhibits an abrupt increase of the rate of the lateral expansion when the load approaches the peak level. The latter level corresponds to the minimum volume level marking the beginning of a drastic volume dilation leading rapidly to failure. The variation of the volume of concrete under increasing compression is also shown in Figure 1b. Similar trends of behaviour are also observed under triaxial compression states of stress.

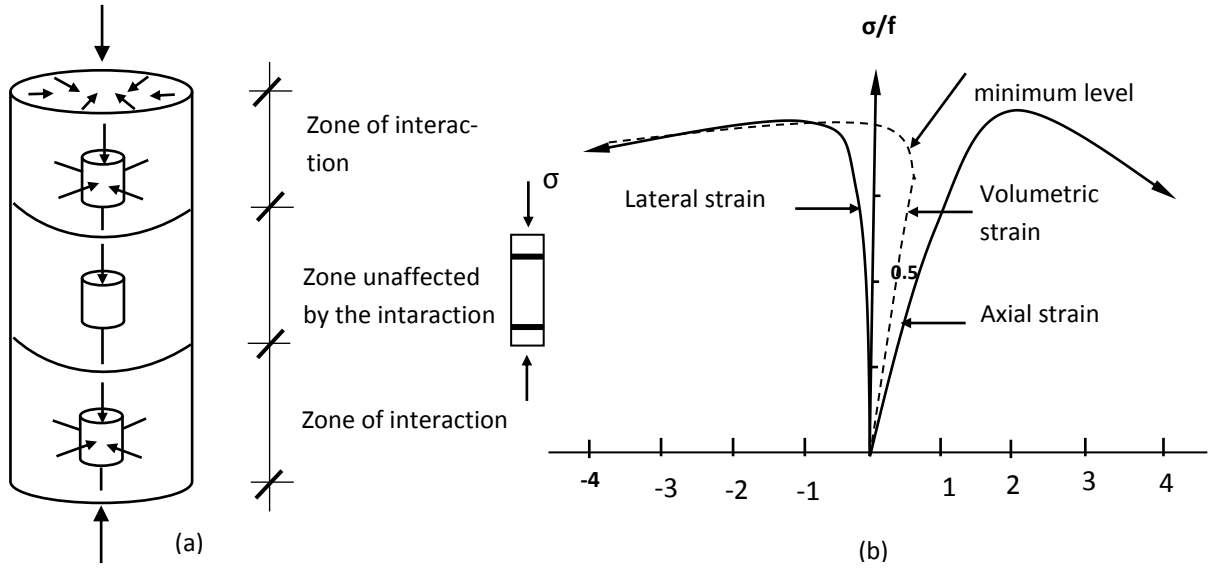


Figure 1: Stress state within the concrete cylinder specimen under uniaxial compression [13]

## 3 EFFECT OF LOADING RATE ON CONCRETE BEHAVIOUR

To date, a large number of experiments have been carried out to examine the behaviour of concrete (prismatic or cylindrical) specimens under high rates of uniaxial compression, direct or indirect tension [1,8,10]. The observed shift in specimen behaviour with increasing loading rates primarily takes the form of an increase in the maximum sustained load. This change be-

comes more pronounced with increasing loading rates and intensity. A summary of available experimental data is presented in Figure 2, expressing the relationship between the maximum sustained load max$P_d$ (normalised with respect to its load carrying capacity under static loading max$P_s$) and the rate of axial defamation exhibited by the specimen expressed as strain-rate in compression (Figure 2a) or tension (Figure 2b).

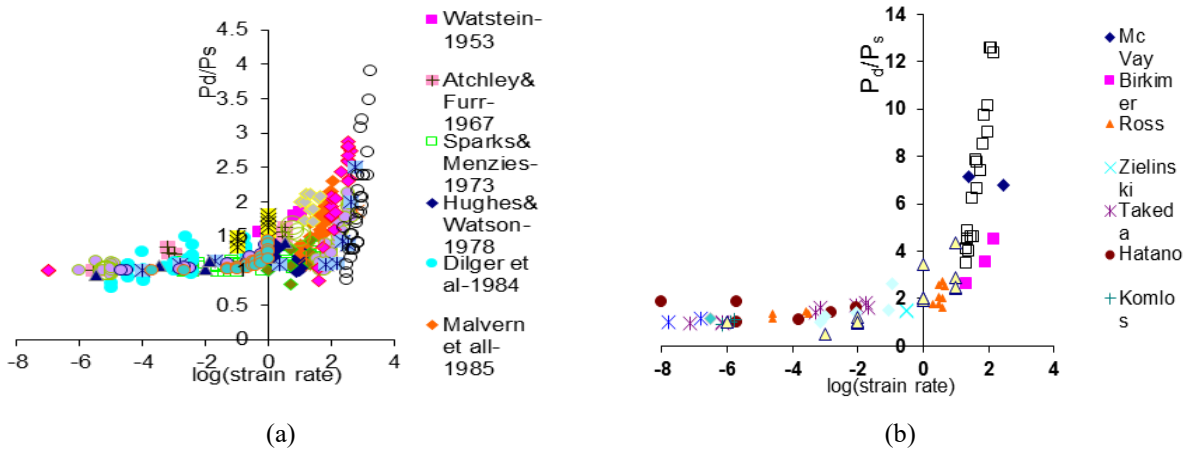


(a) (b)

Figure 2: Experimental data for strength increase under different strain rates for concrete specimens under (a) compression and (b) tension [1]

Based on the available test data and the use of regression-analysis a number of curves have been proposed to date describing the increase of specimen strength under uniaxial compression (Figure 3a) and tension (Figure 3b) with increasing loading rates. However, it is evident that the behaviour of the concrete specimens under high-rate loading differs considerably compared to that established under static loading the experimental data cannot provide the reasons that trigger this shift. Furthermore, when inspecting the available experimental data it is clear that it is characterised by considerable scatter. This scatter is linked to a wide range of parameters which vary from experiment to experiment and include the experimental techniques implemented, the geometry and moisture content of the specimens, the different types of concrete used, etc [1,8]. As a result the available test data can only provide a *qualitative* description of the effect of loading-rate on the specimen behaviour.

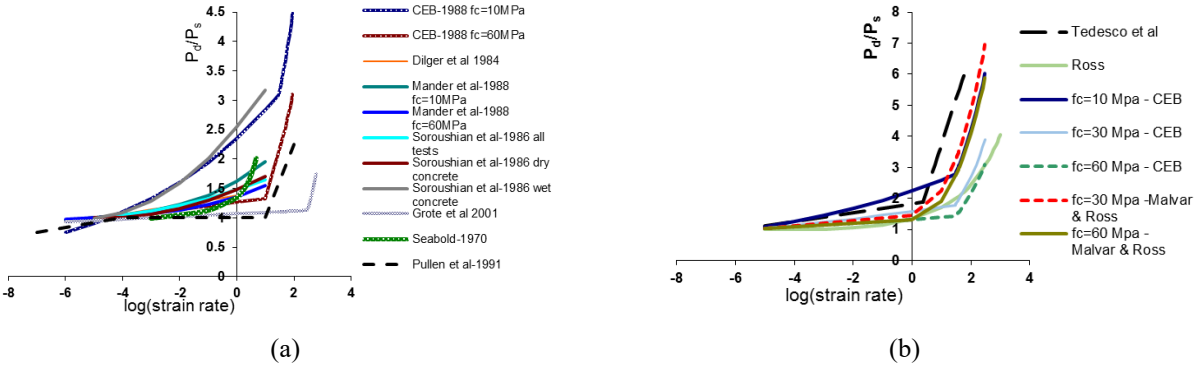


(a) (b)

Figure 3: Regression-analysis curves for strength increase under different strain rates for concrete specimens under (a) compression and (b) tension [1]

In order to gain insight into the behaviour of concrete under high loading rates and to quantify the effects of various parameters on the dynamic response of plain concrete specimens, nonlinear finite-element analysis (NLFEA) was employed [19]. Through a comparison of the numerical predictions with the available experimental data, in a previous study, it was shown [1] that concrete specimens under impact loading must be viewed as *structures* and not as *material* units form which average material properties can be determined because their behaviour is directly linked to the inertia effect of their mass as well as to their geometry and the imposed boundary conditions. The present numerical study extends the previous one by using ABAQUS software.

## 4 CONSTITUTIVE MODELLING OF CONCRETE MATERIAL BEHAVIOUR

The formulation of analytical constitutive models describing the material behaviour of concrete is based mainly on the analysis of experimental data gathered from tests since the early 70's in which concrete specimens (cylinders or cubes) were subjected to uniaxial, biaxial or triaxial loading conditions. A review of the test data obtained is presented by [12, 13, 18]. Based on the preceding tests, stress-strain relationships are obtained describing the material behaviour under multiaxial stress-states as well as failure criteria. However, it should be noted that this data is characterised by considerable scatter due to heterogeneous nature of concrete as well as the variation of various parameters from test to test such as concrete mix, curing conditions, static uniaxial compressive strength of concrete $f_c$, the experimental techniques used, as well as the shape and size of the specimens [13].

The models of concrete behaviour may be broadly classified into two categories: those directly derived directly from regression analyses of experimental data (so-called empirical models) and those relying on continuum mechanics theories (such as, nonlinear elasticity, plasticity, visco-plasticity, damage mechanics) for their development, although the latter also remain dependent on the use of experimental data for their calibration. The resulting formulations usually incorporate a number of parameters, the evaluation of which is essential for achieving a close correlation between the model-predicted behaviour and its experimentally-established counterpart. These parameters, which are usually linked to post-peak strength concrete characteristics in both compression and tension (such as, for example, strain softening, tension stiffening, shear-retention ability) coupled with strain-rate sensitivity when high-rate loading conditions are considered, are often established through calibration based on the use of experimental information at the *structural*, rather than at the *material* level.

The application of FEA software packages in practical structural analysis has shown that the majority of constitutive relationships are case-study dependent, since the solutions obtained are realistic only for particular types of problems. The extension of the applicability of these packages to a different set of problems requires modifications, sometimes significant, of the constitutive relationships. The vast majority of constitutive models describing the behaviour of concrete under dynamic loading assume that there is a link between the constitutive properties of concrete and the strain rate at which the material is loaded and, consequently, the external loading rate. Although this seems to be the case for low loading rates, where creep plays a significant role in material behaviour, it has been proposed that for the case of high loading rates there is no need to change the static value of Young's modulus [1,7-10].

### 4.1 RC-FINEL and ADINA

RC-FINEL has been found to provide realistic predictions of a wide range of different concrete structural forms under static (monotonic and cyclic) [13] and dynamic (earthquake and impact) [12] loading conditions. It incorporates a brittle material model, which describes

the behaviour of concrete under triaxial loading conditions [13], as well as a unique nonlinear strategy the formulation of which allows for the brittle nature of the material model employed, while at the same time it provides a realistic description of the cracking process and minimizes the likelihood of numerical instabilities associated with this process [10-12]. The material model of concrete behaviour adopted is characterised by both simplicity (fully brittle, with neither strain-rate nor load-path dependency, fully defined by a single material parameter - the uniaxial cylinder compressive strength $f_c$) and attention to the actual physical behaviour of concrete in a structure (unavoidable triaxiality which is described on the basis of experimental data of concrete cylinders under definable boundary conditions).

Crack formation is modelled by using the smeared-crack approach. A crack forms when the stress developing in a given part of the structure corresponds to a point in the principal stress space that lies outside the surface defining the failure criterion for concrete, thus resulting in localized material failure. This failure takes the form of a crack and is followed by immediate loss of load-carrying capacity in the direction normal to the plane of the crack. Concurrently, the shear stiffness is also considered to reduce drastically to a very small percentage of its previous (i.e. uncracked) value. However, it is not set to zero in order to minimize the risk of numerical instabilities during the execution of the solution procedure, as explained elsewhere [12,13]. A procedure for crack closure is also provided and full description of the triaxial constitutive model and numerical formulations used in RC-FINEL software is provided elsewhere [12,13]. It should be noted that ADINA software package [20] now includes the same triaxial model by Kotsovos and Pavlovic [13] that is used in RC-FINEL, although there some differences in the non-linear solution strategy.

### 4.2 ABAQUS

The concrete damaged plasticity model is offered in ABAQUS for the analysis of concrete at low confining pressures (less than four or five times the ultimate compressive stress in uniaxial compression loading). It is based on the models proposed by Lubliner et al. [21] and Lee and Fenves [22], with the assumption of scalar (isotropic) damage and is designed for applications in which the concrete is subjected to arbitrary loading conditions. The model takes into consideration the degradation of the elastic stiffness induced by plastic straining both in tension and compression. There are two failure mechanisms for the mechanical response of the concrete include tensile cracking and compressive crushing. The evolution of failure is controlled by two hardening variables, which are referred to as equivalent plastic strains in tension and compression, respectively. The model assumes that the uniaxial tensile and compressive response of concrete is characterized by damaged plasticity, adopting a post-peak branch on the corresponding stress-strain curves.

## 5 RESULTS AND DISCUSSION

### 5.1 Dynamic problem investigated

The present numerical investigation uses a concrete prism, similar to the specimens usually tested to determine the material properties of concrete under static loading. The prisms were subjected to uniaxial compression and tension, for which the prisms were assumed to be fixed at their bottom face and are subjected to an axial load applied at their upper face, through a rigid element (mimicking steel platen in experiment) with the same cross-section (see Figure 4) in order for the external load to be distributed uniformly on the upper face of the concrete prism. It is assumed that the concrete prismatic specimen and the rigid element on top are fully bonded at their interface. The prism height is 253mm and its cross-section

forms a square with a width of 100mm whereas the rigid element has a height of 200mm. Because of the double symmetry of the problem at hand, one quarter of the actual specimen was modeled with suitable boundary conditions. The uniaxial compressive strength of concrete $f_c$ is 30MPa. In all cases the external load is applied incrementally as a force with its value increasing linearly at a constant rate until the load-carrying capacity of the RC specimen is reached and failure occurs. Initially the static problem is investigated to effectively calibrate the model and this is followed by the investigation of the dynamic problems at higher loading rates.

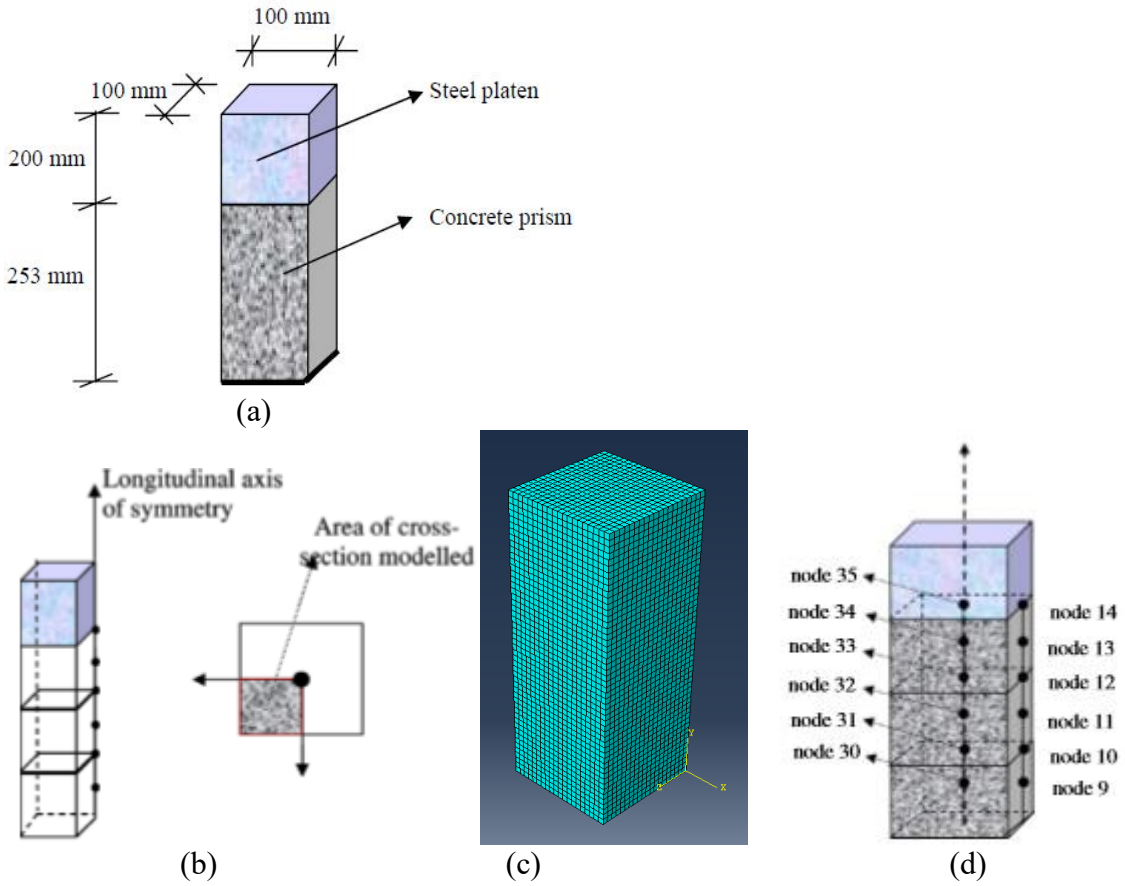


**Figure 4:** (a) Details of the prism specimen modelled, (b) symmetrical arrangement and coarse mesh adopted by Cotsovos and Pavlovic [1], (c) finer mesh used in current study and (d) nodes where values of axial (30-35) and lateral (9-14) displacements were examined

## 5.2 Modelling of the dynamic problem

In the previous numerical study by Cotsovos and Pavlovic [1], a coarse mesh of three 27-noded brick elements (see Figure 4b) was used. This follows the philosophy upon which the FE model used in that study was based, which does not employ small finite elements [13]. This is because the latter material model is based on experiments on concrete cylindrical specimens (subjected to various triaxial loading conditions) and thus these cylinders constitute a "material unit" for which average material properties are obtained. Hence the volume of these cylinders was used to provide a reasonable guideline to the order-of-magnitude of the size of the FE which should be used for concrete modelling. In the present study, on the other hand, the same concrete specimen was modelled using a finer mesh with an element size of 5 mm as shown in Figure 4c. A different constitutive model for concrete was also used, i.e. plastisticity-based as opposed to the brittle one used previously. The present study aims to investigate the capability of the FE model developed using ABAQUS software [11] to simulate the be-

haviour of concrete prism under high rates of axial compressive and tensile loading. A reduced integration scheme is adopted for the element formulation to avoid numerical problems due to locking. The load was applied as uniform pressure directly on the prism top surface.

### 5.3 Discussion of results under high rate of compressive loading

A comparison was carried out between the previous study (adopting macro modelling) using FINEL software [1] and the present research work (utilising much smaller elements) using ABQUS software, under increasing rates of both compressive and tensile loading. The results for the compressive loading are depicted in Figure 5, which show that the axial stress-displacement curves for both studies are in good agreement. It can also be seen that the response of the concrete prism under static and low rates of loading (lower than 200,000 MPa/sec) are similar. But, the numerical stress-displacement curves begin to differ from their static counterparts as the applied loading rate increased (above 200,000 MPa/sec). It can be concluded that, as the rate of loading becomes higher, the load-carrying capacity and sustained maximum axial strain exhibited by the specimen increase.

The variation of the load-carrying capacity max$P_d$ (normalised with respect to its value under static loading max$P_s$) at the maximum sustained load versus the stress and strain rates are shown in Figure 6(a) and (b), respectively.

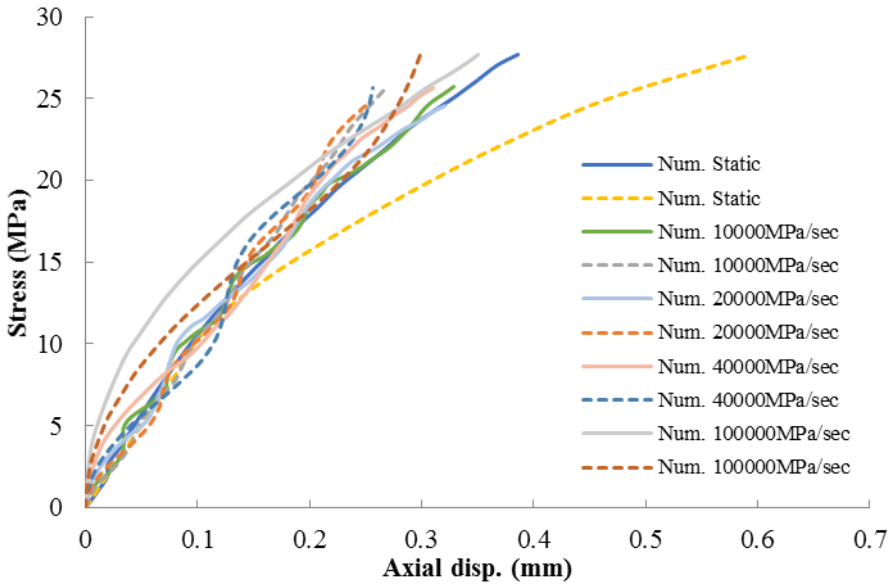


(a)

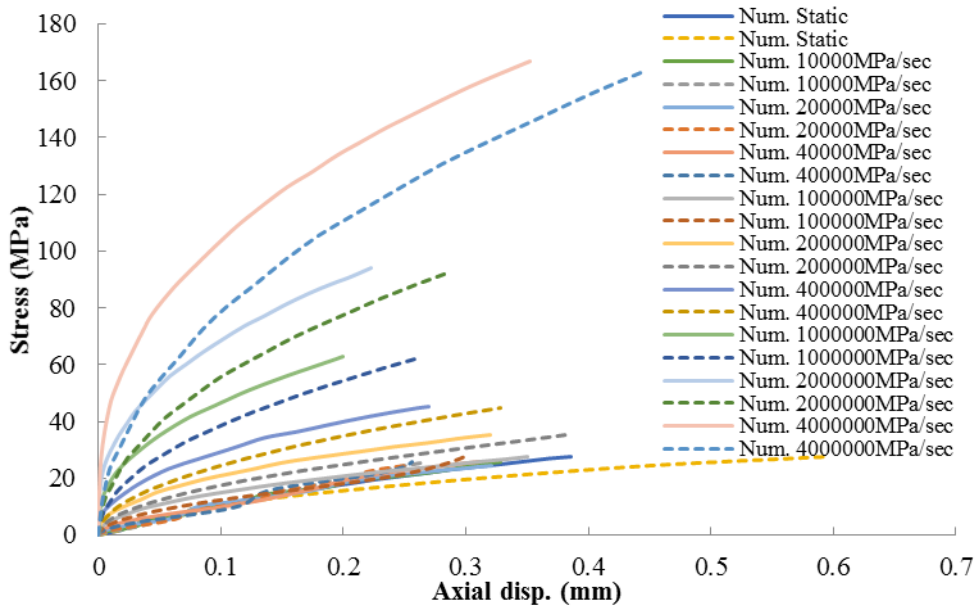


(b)

**Figure 5:** Comparison between numerical stress-displacement curves from previous study [1] (continues line) with current numerical study (dashed line) for concrete prism under different stress rates up to (a) 100,000 and (b) 4,000,000 MPa/sec

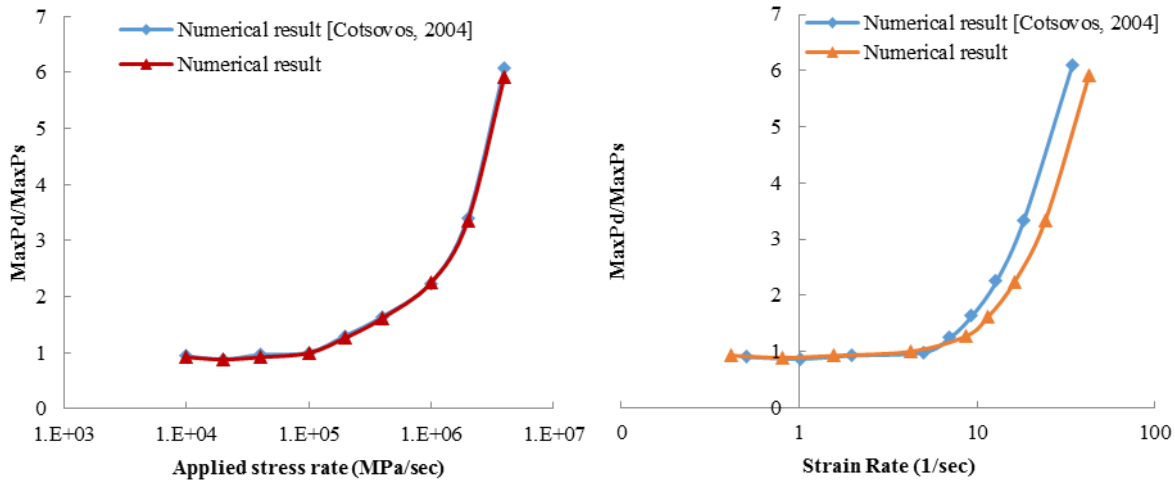


**Figure 6:** Comparison of the numerical DIF expressed as (a) max$P_d$/max$P_s$ and (b) max$\varepsilon_d$/max$\varepsilon_s$ for different applied stress rate based on previous study [1] and current numerical study

Axial and lateral displacement were measured at different nodes along the height of the specimen and the relevant nodes are highlighted in Figure 4d. The ensuing numerical results presented in Figure 7 show that both axial and lateral displacements of the nodes close to the bottom of the specimen gradually decrease as the rate of loading increases (over the value of 200,000 MPa/sec). This displacement becomes very small (even negligible) as compared with the displacements at the upper part of the specimen in the case of very high rates of loading (over 400,000 MPa/sec). In addition, the numerical results presented in Figure 7 show that the axial displacement in static case is linear, while the displacement at the nodes in the lower

part of the specimen becomes negligible in the case of high rate of loading. This was true for both the previous and current numerical studies, which are in good agreement. Figure 8 depicts a schematic representation of the axial and lateral deformations under both low- and high-rate loading. Figure 8 indicate that, as the rate of loading increases, the portion of the height ($h_{eff}$) of the prism mostly affected by the applied load reduces. For relatively high rates of loading, this *effective* length is confined in the region of the prism in the proximity of the applied load (at the upper face) and extending downwards, whereas the remainder of the specimen (i.e. the bottom portion) remains practically unaffected by the applied load. Therefore, under high rates of loading, the prism behaviour is essentially characterized by $h_{eff}$. This explains the apparent increase in load-carrying capacity and confirming that it is not an intrinsic *material*, but is due to the specimen responding as a *structure* with different *effective* lengths.

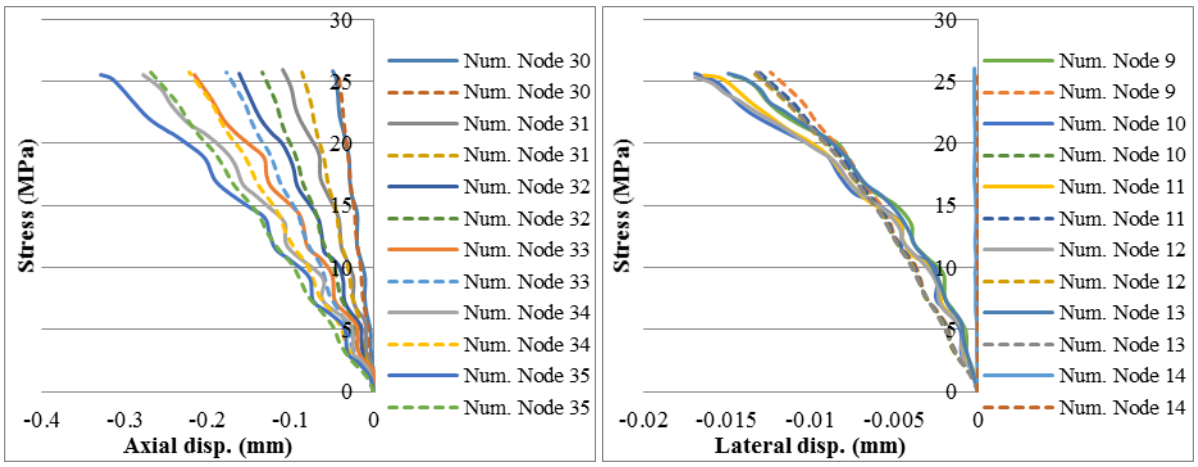


**10,000 MPa/sec**

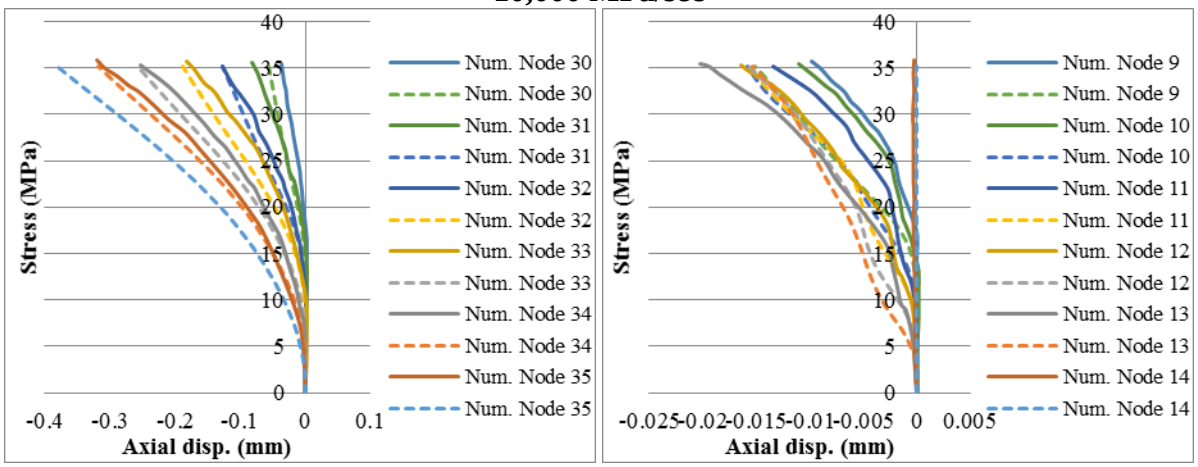


**200,000 MPa/sec**

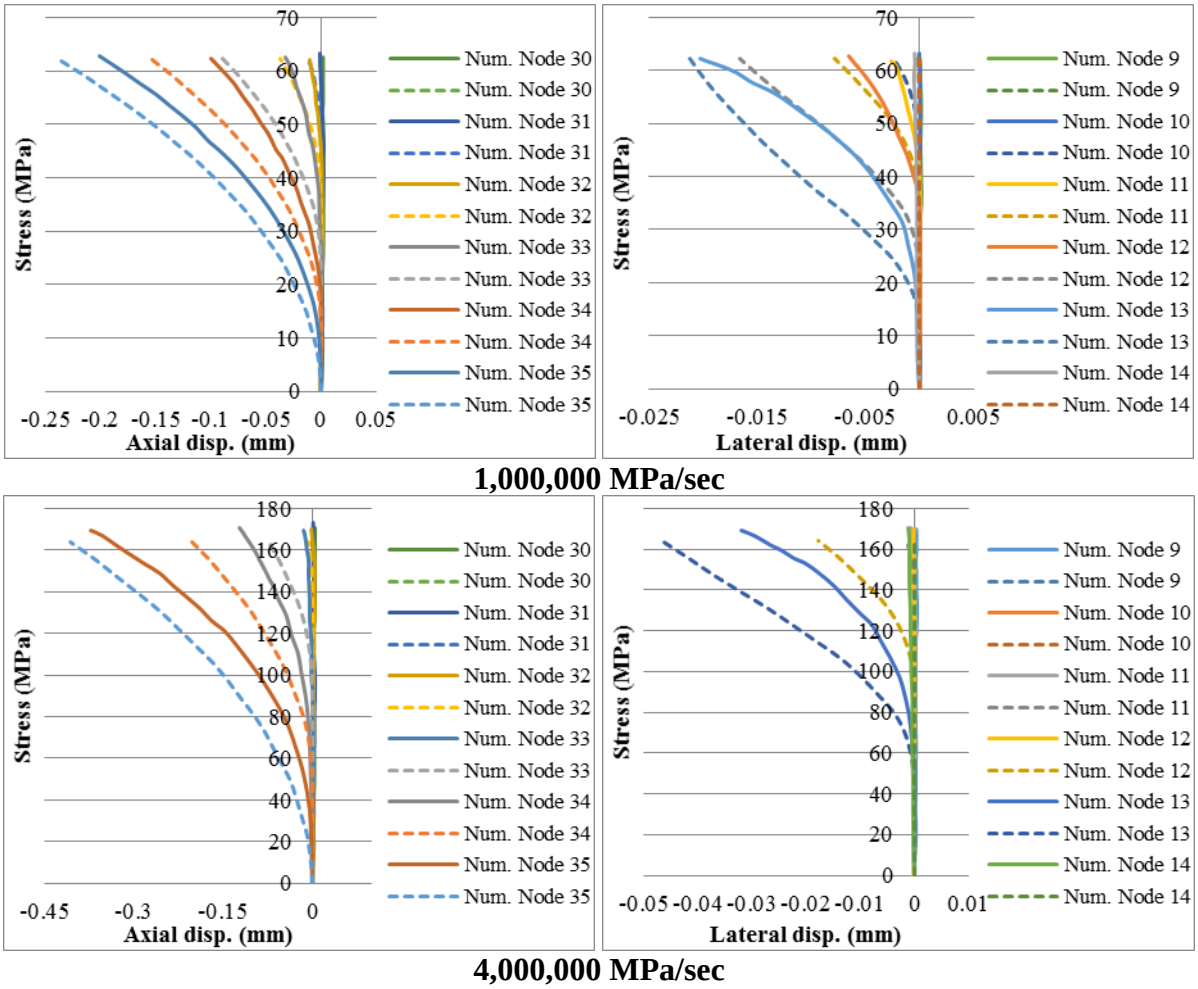


**Figure 7:** Comparison of numerical axial stress-axial displacement and -lateral displacement curves at different stress rates, with the results measured at different distances from the top face of the specimen based on previous study [1] (continues line) and current numerical study(dashed line)

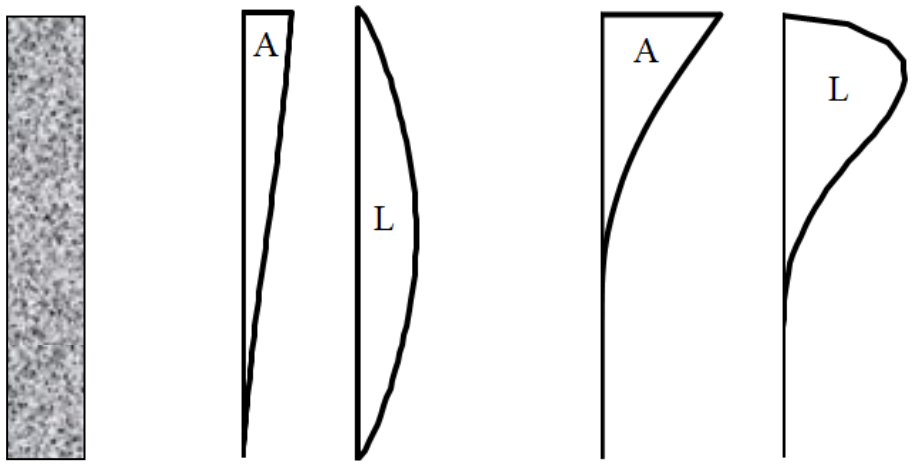


**Figure 8:** A schematic representation of the distribution of axial displacement (A) and lateral displacement (L) along the longitudinal axis of the concrete prism prior to failure

### 5.4 Discussion of results under high rate of tensile loading

Similarly to the case with compressive loading, the responses of the specimen under tensile loading (see Figure 9) shows that the axial stress-displacement curves of the concrete prism under static and low rates of loading (lower than 200,000 MPa/sec) are similar. At higher loading rates, on the other hand, curves begin to differ from their static counterparts as the applied loading rate increased. Thus, it can be concluded that, as the rate of loading becomes higher, the load-carrying capacity and sustained maximum axial strain exhibited by the specimen increase. This is confirmed in Figure 10, which shows the variation of the axial reaction with the stress rate. The results of the previous FINEL-based and the current ABAQUS-based study were also in good agreement.

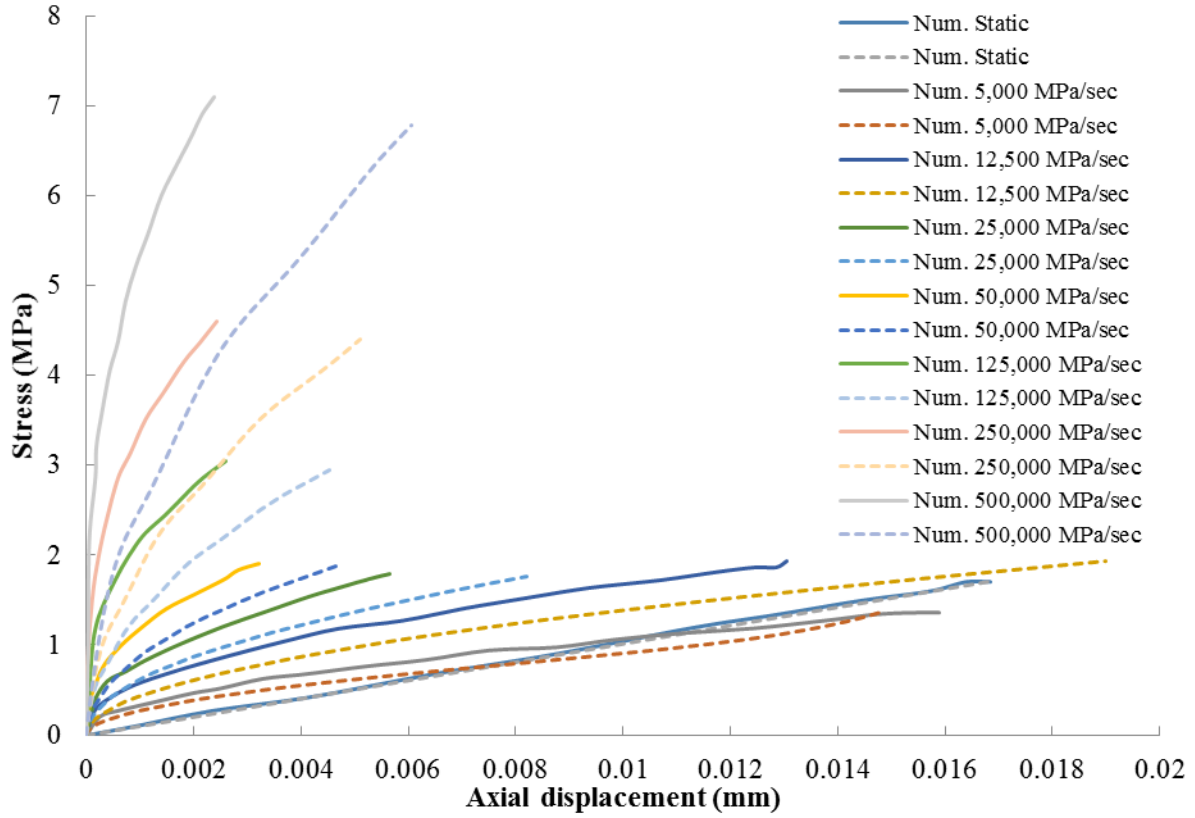


**Figure 9:** Comparison between axial tensile stress-axial displacement curves for concrete prism under different stress rates based on previous study [1] (continues line) with current numerical study (dashed line)

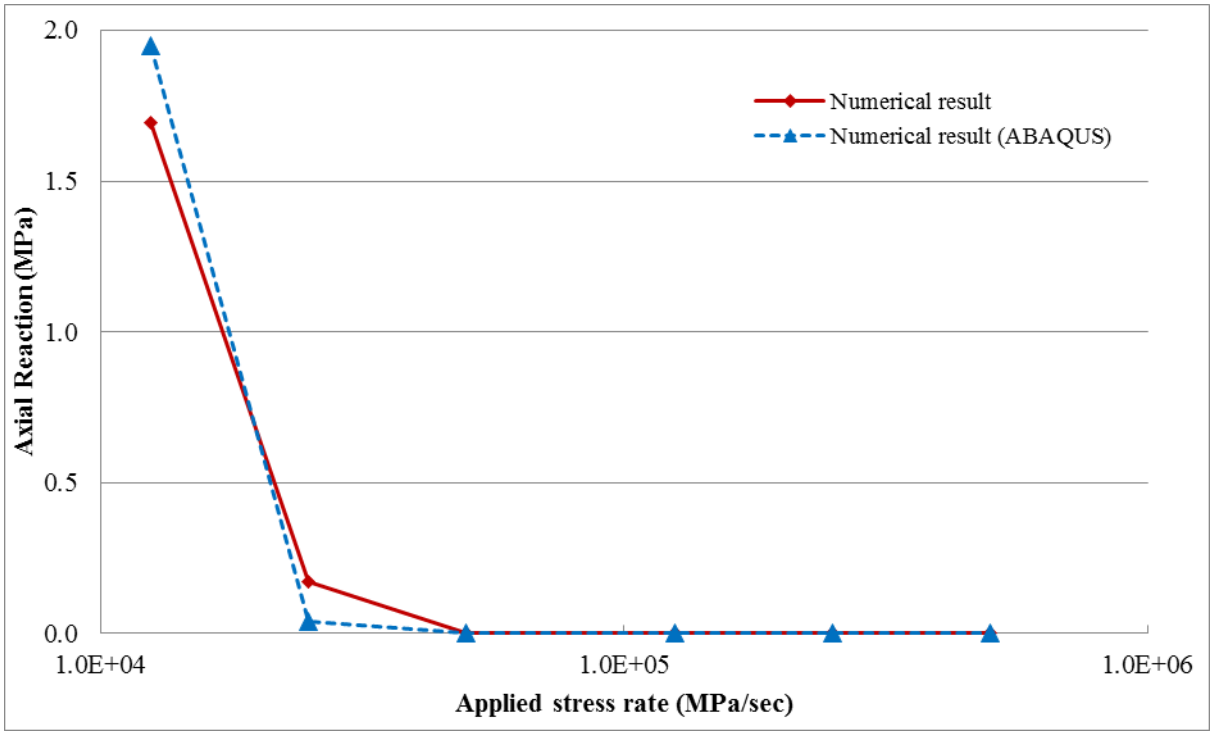


**Figure 10:** Comparison of the numerical results of the variation of the axial reaction with stress rate at the bottom of the specimen (dashed line) with previous study [1] results (continues line)

## 6 CONCLUSIONS

- Concrete specimens under impact loading need to be viewed as *structures* and not as *material* units form which average material properties can be determined (i.e. only correct under static loading).
- Specimen behaviour is directly linked to the *inertia* effect of their mass as well as to their geometry and the imposed boundary conditions.
- Impact problem should be considered as a wave propagation problem within a highly nonlinear material as the application of the external loads leads to the development of stress waves which propagate through the concrete medium, away from the area where the load is imposed.
- The propagation speed of these waves depends on the material properties of concrete and the level of damage (cracking) sustained by the concrete medium, while their intensity level depends on the rate of loading and the magnitude of the applied load.
  - In the case of low loading rates, the stress waves generated, travel through the whole length of the specimen.
  - Under high rates of loading the numerical results reveal that the specimen exhibits a *localised* response as failure occurs prior to the stress waves being able to travel the full length of the specimen.
  - As a result *only* the region of the concrete specimen close to the point of loading deforms whereas the rest remains practically unaffected.

- Under high rates of uniaxial compression, high rates of axial and lateral deformation are also exhibited which trigger the development of significant *inertia* forces in these directions. These forces have a *confining* effect on the concrete prism and tend to restrict the deformations both axially and laterally, thus essentially confining the concrete specimen (*inertial confinement*) and slowing down the cracking process it undergoes compared to that established under static testing.
- The confinement effect allows the prism to exhibit higher load-carrying capacities and maximum values of strain compared to those established under static loading.

## REFERENCES

[1] D.M. Cotsovos, M.N. Pavlovic, Numerical investigation of concrete subjected to compressive impact loading. Part 1: A fundamental explanation for the apparent strength gain at high loading rates. *Computers & Structures,* **86**,145-163, 2008.

[2] A.A. Abbas, A.D. Pullen and D.M. Cotsovos, Structural response of RC wide beams under low-rate and impact loading. *Magazine of Concrete Research*, **62**, 723-740, 2010.

[3] AA Abbas and D.M.Cotsovos, Numerical investigation of the behaviour of RC wide beams under impact loads, M. Papadrakakis, V. Papadopoulos, V. Plevris eds. *5th ECCOMAS Thematic Conference on Computational Methods in Structural Dynamics and Earthquake Engineering (COMPDYN 2015),* Crete Island, Greece, 25–27 May 2015.

[4] G. Hughes and D. Spiers, *An investigation on the beam impact problem*. Cement and Concrete Association, Technical Report 546, 1982.

[5] N. Kishi, H. Mikami, K.G. Matsuoka, T. Ando, Impact behaviour of shear- failure-type RC beams without shear rebar. *International Journal of Impact Engineering,* **27**, 955-968, 2002.

[6] S. Saatci, F.Vecchio, Effects of shear mechanisms on impact behavior of reinforced concrete beams. *ACI Structural Journal,* **106**, 1, 78-86, 2009.

[7] D.M. Cotsovos, M.N. Pavlovic, Modelling of RC Beams under Impact Loading. *ICE Proceedings, Structures & Buildings,***165**, 2, 77-94,2012.

[8] D.M. Cotsovos, N.D. Stathopoulos, C. Zeris, Fundamental behaviour of RC beams subjected to high rates of concentrated loading. *ASCE Journal of Structural Engineering,* **134**, 1839-1851, 2008.

[9] D.M. Cotsovos, M.N. Pavlovic, Numerical investigation of concrete subjected to compressive impact loading. Part 2: Parametric investigation of factors affecting behaviour at high loading rates. *Computers & Structures,* **86**,164-180, 2008.

[10] D.M. Cotsovos and M.N. Pavlovic, Numerical investigation of concrete subjected to high rates of uniaxial tensile loading. *International Journal of Impact Engineering,* **35**, 319-335, 2008.

[11] ABAQUS Version 6.12-3 Documentation, Available online at http://www.3ds.com/products-services/simulia/products/abaqus (accessed 29/02/2016).

[12] M.D. Kotsovos, *Finite-Element Modelling of Structural Concrete: Short-Term Static and Dynamic Loading Conditions*, 1st Edition, CRC Press, 2015.

[13] M.D. Kotsovos, M.N. Pavlović, *Structural concrete, Finite-element analysis for limit-state design*. Thomas Telford, London, UK, 1995.

[14] A.A. Neville, *Properties of concrete, 5th Edition*. Prentice Hall, 2011.

[15] P.M. Zisopoulos, M.D. Kotsovos, M.N. Pavlovic, Deformational behaviour of concrete specimens in uniaxial compression under different boundary conditions. *Cement and concrete research*, **30**(1), 153-159, 2000.

[16] M.D. Kotsovos, Effect of testing techniques on the post-ultimate behaviour of concrete in compression. *Material Structures RILEM*,**16**,3-12, 1983.

[17] J.G.M. Van Mier, *Strain-softening of concrete under multiaxial loading conditions*. PhD thesis, Eindhoven University of Technology, 1984.

[18] J.G.M. Van Mier, S.P. Shah, M. Armand, J.P. Balayssac, A. Bascoul, S. Choi, et al. Strain softening of concrete in uniaxial compression. *Material Structures RILEM*, **30**, 195-209, 1997.

[19] O.C. Zienkiewicz, R.L., Taylor, *Vol. 2: The Finite Element Method for Solid and Structural Mechanics, 6th Edition*. Butterworth-Heinemann, Oxford, UK, 2005.

[20] ADINA. Theory and Modeling Guide. Volume I: ADINA Solids & Structures. Available online at http://www.adina.com/adinadownloads/docs/primer_89.pdf (accessed 02/05/2017).

[21] J. Lubliner, J. Oliver, S. Oller and E. Oñate, A Plastic-Damage Model for Concrete. *International Journal of Solids and Structures*, **25**(3), 299-326, 1989.

[22] J. Lee and G.L. Fenves, Plastic-damage model for cyclic loading of concrete structures. *ASCE Journal of Engineering Mechanics*, **124**(8), 892-900, 1998.

COMPDYN 2017
6th ECCOMAS Thematic Conference on
Computational Methods in Structural Dynamics and Earthquake Engineering
M. Papadrakakis, M. Fragiadakis (eds.)
Rhodes Island, Greece, 15–17 June, 2017

# NUMERICAL ANALYSIS OF FLUTTER INSTABILITY IN SIMPLIFIED BLADE CASCADE

**Jan Vimmr[1], Ondřej Bublík[1], Aleš Pecka[1], and Luděk Pešek[2]**

[1]European Centre of Excellence NTIS - New Technologies for the Information Society,
Faculty of Applied Sciences, University of West Bohemia
Univerzitní 8, Pilsen, CZ-306 14, Czech Republic
e-mail: jvimmr@kme.zcu.cz, {obublik, pecka}@ntis.zcu.cz

[2] Institute of Thermomechanics AS CR, v.v.i., Academy of Sciences of the Czech Republic
Dolejškova 1402/5, Prague, CZ-182 00, Czech Republic
e-mail: pesek@it.cas.cz

**Keywords:** simplified blade cascade, flutter assessment, ALE formulation, discontinuous Galerkin method, aerodynamic damping parameter, travelling wave mode

**Abstract.** *In this paper the occurrence of flutter in a simplified blade cascade is analysed. The simplified blade cascade is formed by three flat plates, which perform a kinematic harmonic motion, each with a different inter-blade phase angle. The inter-blade phase angles are chosen in order for travelling wave mode of vibration to be present. The aim of the simulations is to determine the aerodynamic damping coefficients caused by the aerodynamic forces acting on the flat plates, which show whether flutter occurs. The non-linear system of Favre-averaged Navier-Stokes equations in ALE formulation completed by the Spalart-Allmaras turbulence model was chosen as the mathematical model. The simulations were performed using the developed in-house CFD software based on the discontinuous Galerkin method, which offers high order of accuracy.*

## 1 INTRODUCTION

In the forties of the 20th century, first papers focused on the aero-elasticity of blades in axial turbines appeared, e.g. [1]. An empirical criterion for the presence of flutter based on a reduced blade frequency for bending blade vibration was introduced in [2]. The criterion states that if the reduced blade frequency is less than 0.33, the flutter is not excited. However, other influences such as geometric configuration of blade cascade and angle of attack can influence the occurrence of flutter. The problem of aero-elasticity is still a subject of interest since modern turbines are designed to withstand high operational temperatures and flow rates [3].

Originally, the term flutter was established for flow attached to the vibration of blade when phase displacement between blade motion and induced aerodynamic forces occurs. Depending on the time shift between the moving structure and unsteady aerodynamic forces acting on the structure, following cases can occur:

i) the kinetic energy of the blade is absorbed by the flow,

ii) the kinetic energy of the flow is transmitted to the blade.

In the first case, we talk about damped vibration from the aero-elasticity point of view. In the second case, the extra energy added to the blades results in the increase of amplitudes, in other words in unstable vibration, which we call flutter. It has been shown, see [4], that the critical flutter point, i.e. the highest aero-dynamical excitation, arises for a particular inter-blade phase angle. Most aerodynamic studies are based on the so called travelling wave mode of vibration, where one assumes that all blades vibrate at the same frequency, amplitude and inter-blade phase angle. Other aerodynamic studies use the influence coefficient technique which is based on calculating the aerodynamic forces of vibrating blade acting on non-vibrating adjacent blades.

For the purpose of this study, we choose the travelling wave mode approach. Following [4] we consider an unsteady flow through a simplified blade cascade formed by three flat plates. All the flat plates in the cascade perform a harmonic motion with given inter-blade phase angles so that their mutual movement creates travelling waves. In our paper [5], this problem was solved only for one inter-blade phase angle. The aim of this numerical study is to evaluate aerodynamic forces acting on the flat plates in the simplified cascade for the whole range of the inter-blade phase angles from $-\pi$ to $\pi$. Furthermore, the aerodynamic damping parameter is calculated out of the aerodynamic forces on which basis it is inferred whether flutter occurs. The upcoming simulations are performed using the developed in-house CFD software based on the discontinuous Galerkin method. The in-house CFD software is validated on two test problems described in section 4. In section 5 we present numerical results of unsteady compressible viscous fluid flow through the simplified blade cascade for various inter-blade phase angles.

## 2 MATHEMATICAL MODEL

A two-dimensional compressible viscous fluid flow in a time-varying computational domain $\Omega(t) \in \mathcal{R}^2$ with boundary $\partial\Omega$ is described by the non-linear system of Favre-averaged Navier-Stokes equations which, in the dimensionless arbitrary Lagrangian-Eulerian (ALE) formulation,

can be written as

$$\begin{aligned}
&\frac{D^A\bar{\varrho}}{Dt}+\frac{\partial(\bar{\varrho}\tilde{u}_j)}{\partial x_j}-U_j\frac{\partial\bar{\varrho}}{\partial x_j}=0,\\
&\frac{D^A}{Dt}(\bar{\varrho}\tilde{u}_i)+\frac{\partial}{\partial x_j}(\bar{\varrho}\tilde{u}_i\tilde{u}_j+\bar{p}\delta_{ij})-U_j\frac{\partial(\bar{\varrho}\tilde{u}_i)}{\partial x_j}=\frac{1}{Re}\frac{\partial}{\partial x_j}(\tilde{t}_{ij}+\tau_{ij}),\\
&\frac{D^A}{Dt}(\bar{\varrho}\tilde{e})+\frac{\partial}{\partial x_j}(\bar{\varrho}\tilde{e}\tilde{u}_j+\bar{p}\tilde{u}_j)-U_j\frac{\partial(\bar{\varrho}\tilde{e})}{\partial x_j}=\\
&\qquad=\frac{1}{Re}\frac{\partial}{\partial x_j}\left[(\tilde{t}_{ij}+\tau_{ij})\tilde{u}_i+\frac{\kappa}{\kappa-1}\left(\frac{\mu}{Pr}+\frac{\mu_t}{Pr_t}\right)\frac{\partial}{\partial x_j}\left(\frac{\bar{p}}{\bar{\varrho}}\right)\right],
\end{aligned}\tag{1}$$

where $i,j=1,2$, $\bar{\varrho}$ and $\bar{p}$ are dimensionless time-averaged values of density and pressure, $\tilde{u}_i$ are dimensionless mass-averaged Cartesian components of velocity vector, $\tilde{e}$ is mass-averaged energy, $Re$ is the Reynolds number, $Pr$ is the Prandtl number, $\mu$ and $\mu_t$ are dimensionless dynamic and turbulent viscosities and $U_j$ are dimensionless components of the mesh velocity. The turbulent Prandtl number for flow around flat plate is $Pr_t=0.89$. Furthermore, the dimensionless mass-averaged stress tensor and the Reynolds stress tensor are given by

$$\tilde{t}_{ij}=2\mu\bar{S}_{ij},\ \tau_{ij}=2\mu_t\bar{S}_{ij},$$

where

$$\bar{S}_{ij}=\frac{1}{2}\left(\frac{\partial\tilde{u}_i}{\partial x_j}+\frac{\partial\tilde{u}_j}{\partial x_i}\right)-\frac{1}{3}\delta_{ij}\frac{\partial\tilde{u}_k}{\partial x_k}.$$

The equation of state for ideal gas is considered as

$$\bar{p}=(\kappa-1)\left[\bar{\varrho}\tilde{e}-\frac{1}{2}\bar{\varrho}\sum_{i=1}^{2}\tilde{u}_i^2\right].$$

Note that the symbol $\frac{D^A}{Dt}$ denotes the ALE derivative [6].

To include the influence of turbulent fluctuations on the mean flow a one-equation turbulence model of Spalart and Allmaras [7] is used. This turbulent model was designed specifically for aerospace applications (external flows) and therefore it seems to be an appropriate choice for the problem considered in this paper, which is described in section 5. The model is given by the transport equation for the dimensionless eddy viscosity $\tilde{\nu}$ written in the dimensionless ALE form as

$$\begin{aligned}
\frac{D^A(\bar{\varrho}\tilde{\nu})}{Dt}+\frac{\partial(\bar{\varrho}\tilde{\nu}\tilde{u}_j)}{\partial x_j}-U_j\frac{(\partial\bar{\varrho}\tilde{\nu})}{\partial x_j}=\frac{1}{Re}\frac{1}{\sigma}\left[\frac{\partial}{\partial x_j}\left((\mu+\bar{\varrho}\tilde{\nu})\frac{\partial\tilde{\nu}}{\partial x_j}\right)+\bar{\varrho}c_{b2}\frac{\partial\tilde{\nu}}{\partial x_j}\frac{\partial\tilde{\nu}}{\partial x_j}\right]+\\
+c_{b1}\bar{\varrho}\tilde{S}\tilde{\nu}-\frac{1}{Re}c_{w1}f_w\frac{1}{\bar{\varrho}}\left(\frac{\bar{\varrho}\tilde{\nu}}{D}\right)^2
\end{aligned}\tag{2}$$

and completed by the following relations

$$\mu_t=\bar{\varrho}\tilde{\nu}f_{v1},\ \ \tilde{S}=\bar{\Omega}+\frac{1}{Re}\frac{\tilde{\nu}}{\kappa^2D^2}f_{v2},\ \ f_w=g\left(\frac{1+c_{w3}^6}{g^6+c_{w3}^6}\right)^{\frac{1}{6}},\ \ g=r+c_{w2}\left(r^6-r\right),$$

$$r=\min\left(\frac{\tilde{\nu}}{Re\,\tilde{S}\kappa^2D^2},10\right),\ \ f_{v1}=\frac{\chi^3}{\chi^3+c_{v1}^3},\ \ \chi=\frac{\tilde{\nu}}{\nu},\ \ f_{v2}=1-\frac{\chi}{1+\chi f_{v1}}$$

with commonly used constants $c_{b1} = 0.1355,\ c_{b2} = 0.622,\ \sigma = \frac{2}{3},\ \kappa = 0.41,\ c_{w1} = \frac{c_{b1}}{\kappa^2} + \frac{1+c_{b2}}{\sigma},\ c_{w2} = 0.3,\ c_{w3} = 2.0,\ c_{v1} = 7.1$, $D$ is the distance to the nearest wall and $\bar{\Omega}$ is the magnitude of vorticity.

The non-linear system of Favre-averaged Navier-Stokes equations (1) and the transport equation for eddy viscosity (2) are numerically solved as a single coupled system, which can be written in a dimensionless compact flux vector form as follows

$$\frac{D^A \boldsymbol{w}}{Dt} + \sum_{j=1}^{2} \left( \frac{\partial}{\partial x_j} \boldsymbol{f}_j(\boldsymbol{w}) - U_j \frac{\partial \boldsymbol{w}}{\partial x_j} \right) = \frac{1}{Re} \sum_{j=1}^{2} \frac{\partial}{\partial x_j} \boldsymbol{f}_j^v(\boldsymbol{w}, \nabla \boldsymbol{w}) + \boldsymbol{p}(\boldsymbol{w}, \nabla \boldsymbol{w}), \tag{3}$$

where $\boldsymbol{w}$ is the vector of flow variables, $\boldsymbol{f}_j(\boldsymbol{w})$ are the inviscid fluxes, $\boldsymbol{f}_j^v(\boldsymbol{w}, \nabla \boldsymbol{w})$ are the viscous fluxes and $\boldsymbol{p}(\boldsymbol{w}, \nabla \boldsymbol{w})$ is the production term. The vectors take the form

$$\boldsymbol{w} = \begin{bmatrix} \bar{\varrho} \\ \bar{\varrho}\tilde{u}_1 \\ \bar{\varrho}\tilde{u}_2 \\ \bar{\varrho}\tilde{e} \\ \bar{\varrho}\tilde{\nu} \end{bmatrix},\ \boldsymbol{f}_1(\boldsymbol{w}) = \begin{bmatrix} \bar{\varrho}\tilde{u}_1 \\ \bar{\varrho}\tilde{u}_1^2 + \bar{p} \\ \bar{\varrho}\tilde{u}_1\tilde{u}_2 \\ \tilde{u}_1(\bar{\varrho}\tilde{e} + \bar{p}) \\ \bar{\varrho}\tilde{\nu}\tilde{u}_1 \end{bmatrix},\ \boldsymbol{f}_2(\boldsymbol{w}) = \begin{bmatrix} \bar{\varrho}\tilde{u}_2 \\ \bar{\varrho}\tilde{u}_1\tilde{u}_2 \\ \bar{\varrho}\tilde{u}_2^2 + \bar{p} \\ \tilde{u}_2(\bar{\varrho}\tilde{e} + \bar{p}) \\ \bar{\varrho}\tilde{\nu}\tilde{u}_2 \end{bmatrix},$$

$$\boldsymbol{f}_1^v(\boldsymbol{w}, \nabla \boldsymbol{w}) = \begin{bmatrix} 0 \\ \tilde{t}_{11} + \tau_{11} \\ \tilde{t}_{12} + \tau_{12} \\ \sum_{i=1}^{2} \tilde{u}_i(\tilde{t}_{i1} + \tau_{i1}) + \frac{\kappa}{\kappa - 1} \left( \frac{\mu}{Pr} + \frac{\mu_t}{Pr_t} \right) \frac{\partial}{\partial x_1} \left( \frac{\bar{p}}{\bar{\varrho}} \right) \\ \frac{1}{\sigma} (\mu + \bar{\varrho}\tilde{\nu}) \frac{\partial \tilde{\nu}}{\partial x_1} \end{bmatrix},$$

$$\boldsymbol{f}_2^v(\boldsymbol{w}, \nabla \boldsymbol{w}) = \begin{bmatrix} 0 \\ \tilde{t}_{12} + \tau_{12} \\ \tilde{t}_{22} + \tau_{22} \\ \sum_{i=1}^{2} \tilde{u}_i(\tilde{t}_{i2} + \tau_{i2}) + \frac{\kappa}{\kappa - 1} \left( \frac{\mu}{Pr} + \frac{\mu_t}{Pr_t} \right) \frac{\partial}{\partial x_2} \left( \frac{\bar{p}}{\bar{\varrho}} \right) \\ \frac{1}{\sigma} (\mu + \bar{\varrho}\tilde{\nu}) \frac{\partial \tilde{\nu}}{\partial x_2} \end{bmatrix},$$

$$\boldsymbol{p}(\boldsymbol{w}, \nabla \boldsymbol{w}) = \begin{bmatrix} 0 \\ 0 \\ 0 \\ 0 \\ \frac{1}{Re} \frac{1}{\sigma} \bar{\varrho} c_{b2} \left( \frac{\partial \tilde{\nu}}{\partial x_1} \frac{\partial \tilde{\nu}}{\partial x_1} + \frac{\partial \tilde{\nu}}{\partial x_2} \frac{\partial \tilde{\nu}}{\partial x_2} \right) + c_{b1} \bar{\varrho} \tilde{S} \tilde{\nu} - \frac{1}{Re} c_{w1} f_w \frac{1}{\bar{\varrho}} \left( \frac{\bar{\varrho}\tilde{\nu}}{D} \right)^2 \end{bmatrix}.$$

## 3 DISCRETIZATION

The spatial discretization of equations (3) is performed using the discontinuous Galerkin finite element method (DGFEM), see for example [8], [9], [10]. Let $\mathcal{T}_h = \{\Omega_k : \bigcup_k \overline{\Omega}_k = \overline{\Omega} \ \wedge \ \bigcap_k \Omega_k = \emptyset,\ k = 1, \ldots, K\}$ be a triangulation of the time-varying computational domain $\Omega(t) \in \mathcal{R}^2$ boundary of which is denoted by $\partial\Omega$. Note that each element may vary in time, i.e. $\Omega_k = \Omega_k(t)$. Let $\Gamma^{int}$ and $\Gamma^b \subset \partial\Omega$ be the sets of interior and boundary edges of elements in $\mathcal{T}_h$. In order to discretize the non-linear system of equations (3) the infinite dimensional function space is replaced by the finite dimensional function space $\mathbf{S}_h = [S_h]^4$, where

$$S_h = \{g \in L^2(\Omega) :\ g|_{\Omega_k} \in \mathcal{P}^q(\Omega_k) \quad \forall \Omega_k\} \tag{4}$$

and $\mathcal{P}^q(\Omega_k)$ is the space of polynomials of degree $q$ on $\Omega_k$.

Multiplying the system of equations (3) by a test function $\boldsymbol{v} \in \mathbf{S}_h$, integrating it over $\Omega_k$ and applying Green's theorem and the Reynolds transport theorem, the following integral identity is obtained

$$\begin{aligned}\frac{\mathrm{d}}{\mathrm{d}t}\int_{\Omega_k} \boldsymbol{w}\cdot\boldsymbol{v}\,\mathrm{d}\Omega\; &- \int_{\Omega_k}\sum_{j=1}^{2}(\boldsymbol{f}_j(\boldsymbol{w})-U_j\boldsymbol{w})\cdot\frac{\partial \boldsymbol{v}}{\partial x_j}\,\mathrm{d}\Omega + \oint_{\partial\Omega_k}\sum_{j=1}^{2}(\boldsymbol{f}_j(\boldsymbol{w})-U_j\boldsymbol{w})n_j\cdot\boldsymbol{v}\,\mathrm{d}l = \\ &= \frac{1}{Re}\oint_{\partial\Omega_k}\sum_{j=1}^{2}\boldsymbol{f}_j^v(\boldsymbol{w},\nabla\boldsymbol{w})n_j\cdot\boldsymbol{v}\,\mathrm{d}l - \frac{1}{Re}\int_{\Omega_k}\sum_{j=1}^{2}\boldsymbol{f}_j^v(\boldsymbol{w},\nabla\boldsymbol{w})\cdot\frac{\partial\boldsymbol{v}}{\partial x_j}\,\mathrm{d}\Omega + \\ &+ \int_{\Omega_k}\boldsymbol{p}(\boldsymbol{w},\nabla\boldsymbol{w})\cdot\boldsymbol{v}\,\mathrm{d}\Omega.\end{aligned}$$

The key part of the method is the approximation of curve integrals. In case of the discontinuous Galerkin method, this procedure is analogous to the finite volume approach. In particular, the inviscid fluxes are evaluated as

$$\sum_{j=1}^{2}\boldsymbol{f}_j(\boldsymbol{w})n_j \approx \boldsymbol{\mathcal{H}}(\boldsymbol{w}^+,\boldsymbol{w}^-)\ \text{ on }\ \Gamma^{int},$$

$$\sum_{j=1}^{2}\boldsymbol{f}_j(\boldsymbol{w})n_j \approx \boldsymbol{\mathcal{H}}(\boldsymbol{w}^b,\boldsymbol{w}^-)\ \text{ on }\ \Gamma^{b},$$

where $\boldsymbol{n} = [n_1, n_2]^T$ is the outer unit normal vector, $\boldsymbol{w}^-$ and $\boldsymbol{w}^+$ are respectively the left and right limits of $\boldsymbol{w}$ on the edges of $\Gamma^{int}\cup\Gamma^b$ and $\boldsymbol{w}^b$ is the value of $\boldsymbol{w}$ at the boundary $\partial\Omega$ evaluated out of the prescribed boundary condition. As the numerical flux $\boldsymbol{\mathcal{H}}$, the Lax-Friedrichs flux, see [11],

$$\boldsymbol{\mathcal{H}}(\boldsymbol{w}^+,\boldsymbol{w}^-) = \frac{1}{2}\left(\sum_{j=1}^{2}\left(\boldsymbol{f}_j(\boldsymbol{w}^+)+\boldsymbol{f}_j(\boldsymbol{w}^-)\right)n_j - \lambda\left(\boldsymbol{w}^+-\boldsymbol{w}^-\right)\right)$$

is considered, where $\lambda = |\sum_{j=1}^{2}\tilde{u}_j n_j| + \bar{a}$ is the maximal eigenvalue and $\bar{a} = \sqrt{\kappa\bar{p}/\bar{\varrho}}$ is the local speed of sound. Similarly, the viscous fluxes are evaluated using appropriate numerical fluxes. In the present paper, the approximation known as interior penalty method is chosen, see [10] for more details.

The discontinuous Galerkin method is stable under the $L^2$-norm, however it does not provide TVD stability. For this reason the undesirable oscillations can occurs in the presence of shock waves or in the regions with high gradients. In these cases, a small amount of the artificial viscosity is added into the right hand side of the system of equations (3) through the term

$$\epsilon\frac{\partial^2\boldsymbol{w}}{\partial x_j\partial x_j}, \tag{5}$$

where $\epsilon = I_s\frac{\lambda h}{q}$ and $\lambda$ is the maximum eigenvalue, $h$ is the minimum element diameter, $q$ is the degree of basis polynomials and $I_s$ is a parameter determined by the shock wave indicator. In this paper, the shock wave indicator proposed in [12] is chosen. Following [12] the density $\bar{\varrho}$ is expressed as a linear combination of basis functions up to degree $q$ and up to degree $(q-1)$

$$\bar{\varrho}_k = \sum_{i=1}^{N(q)}\bar{\varrho}_{k,i}\varphi_{k,i}(\boldsymbol{x}), \qquad \hat{\bar{\varrho}}_k = \sum_{i=1}^{N(q-1)}\bar{\varrho}_{k,i}\varphi_{k,i}(\boldsymbol{x}),$$

respectively. Consequently, the value of the smoothness indicator is defined for each element $\Omega_k$ as

$$S_{e,k} = \frac{(\bar{\varrho}_k - \hat{\bar{\varrho}}_k,\ \bar{\varrho}_k - \hat{\bar{\varrho}}_k)}{(\bar{\varrho}_k,\ \bar{\varrho}_k)},$$

where $(\cdot,\ \cdot)$ is the standard $L^2$ inner product on $\Omega_k$. Finally, the value $I_s$ is set to

$$I_s = \begin{cases} 0 & \text{if } \ s_{e,k} < s_0 - \gamma, \\ \frac{1}{2}\left[1 + \sin\left(\frac{\pi(s_{e,k}-s_0)}{2\gamma}\right)\right] & \text{if } \ s_0 - \gamma \leq s_{e,k} \leq s_0 + \gamma, \\ 1 & \text{if } \ s_{e,k} > s_0 + \gamma, \end{cases}$$

where $s_{e,k} = \log_{10} S_{e,k},\ s_0 = 1/q^4$ and $\gamma$ is a chosen constant. See [12] for more details.

Let $\boldsymbol{w}_k$ be the restriction of $\boldsymbol{w}$ on $\Omega_k$ and let $\varphi_{k,i} \in \mathcal{P}^q(\Omega_k)$ be the $i$-th basis function on $\Omega_k$. In this study, linear Lagrange polynomials are chosen as the basis functions $\varphi_{k,i}$. The $m$-th component $w_k^m$, $m = 1, 2, ..., 4$, of $\boldsymbol{w}_k$ can be expressed as a linear combination of basis functions as follows

$$w_k^m(\boldsymbol{x}, t) = \sum_{i=1}^{N(q)} w_{k,i}^m(t)\varphi_{k,i}(\boldsymbol{x}). \tag{6}$$

Expanding the solution as a linear combination of basis functions and evaluating the volume and curve integrals using Gaussian quadrature of appropriate order the following system of ordinary differential equations is obtained

$$\frac{\mathrm{d}(\mathbf{MW})}{\mathrm{d}t} = \mathbf{R}(\mathbf{W}), \tag{7}$$

where the vector $\mathbf{W}$ consists of unknown coefficients of linear combination (6) and $\mathbf{M}$ is the mass matrix.

The time integration of (7) is performed using the implicit backward Euler method and the resulting system of non-linear algebraic equations is solved by Newton's method

$$\begin{aligned} &\boldsymbol{W}^{s=0} = \boldsymbol{W}^n, \\ &\left[\frac{\boldsymbol{M}^{n+1}}{\Delta t} - \frac{\partial \boldsymbol{R}}{\partial \boldsymbol{W}}(\boldsymbol{W}^s)\right]\Delta \boldsymbol{W} = \boldsymbol{R}(\boldsymbol{W}^s) - \frac{\boldsymbol{M}^{n+1}\boldsymbol{W}^s - \boldsymbol{M}^n\boldsymbol{W}^n}{\Delta t}, \\ &\boldsymbol{W}^{s+1} = \boldsymbol{W}^s + \Delta \boldsymbol{W}, \\ &\boldsymbol{W}^{s+1} \longrightarrow \boldsymbol{W}^{n+1}. \end{aligned} \tag{8}$$

The system of linear equations (8) is solved iteratively using the GMRES method with the block diagonal Jacobi preconditioner.

## 4 VALIDATION OF THE IN-HOUSE CFD CODE

Before moving on to the numerical simulation of the fluid flow through the simplified blade cascade, which is the central target of the paper, it is necessary to validate the developed CFD code. Since the experimental data for the simplified blade cascade is not available yet, two test problems commonly studied in literature are chosen, see [13].

Firstly, comparisons are made for simulations of an inviscid compressible steady fluid flow around the NACA0012 airfoil at Mach number 0.8 for angles of attack varying between $\pm 4^\circ$. The computational mesh with 10905 elements is shown in Figure 1 in the vicinity of the airfoil.

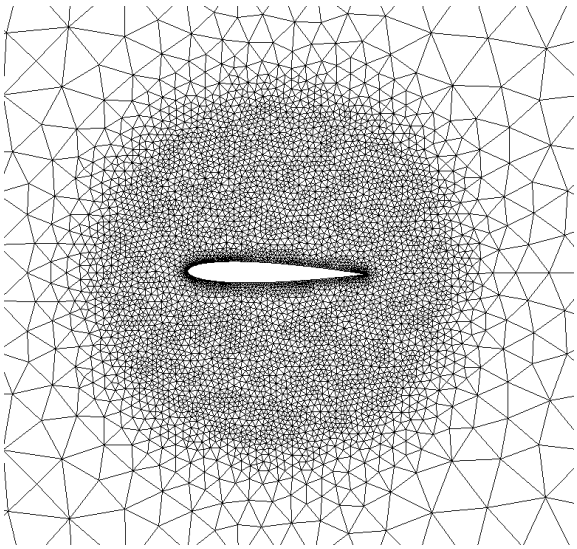

Figure 1: Computational mesh in the vicinity of the NACA0012 airfoil.

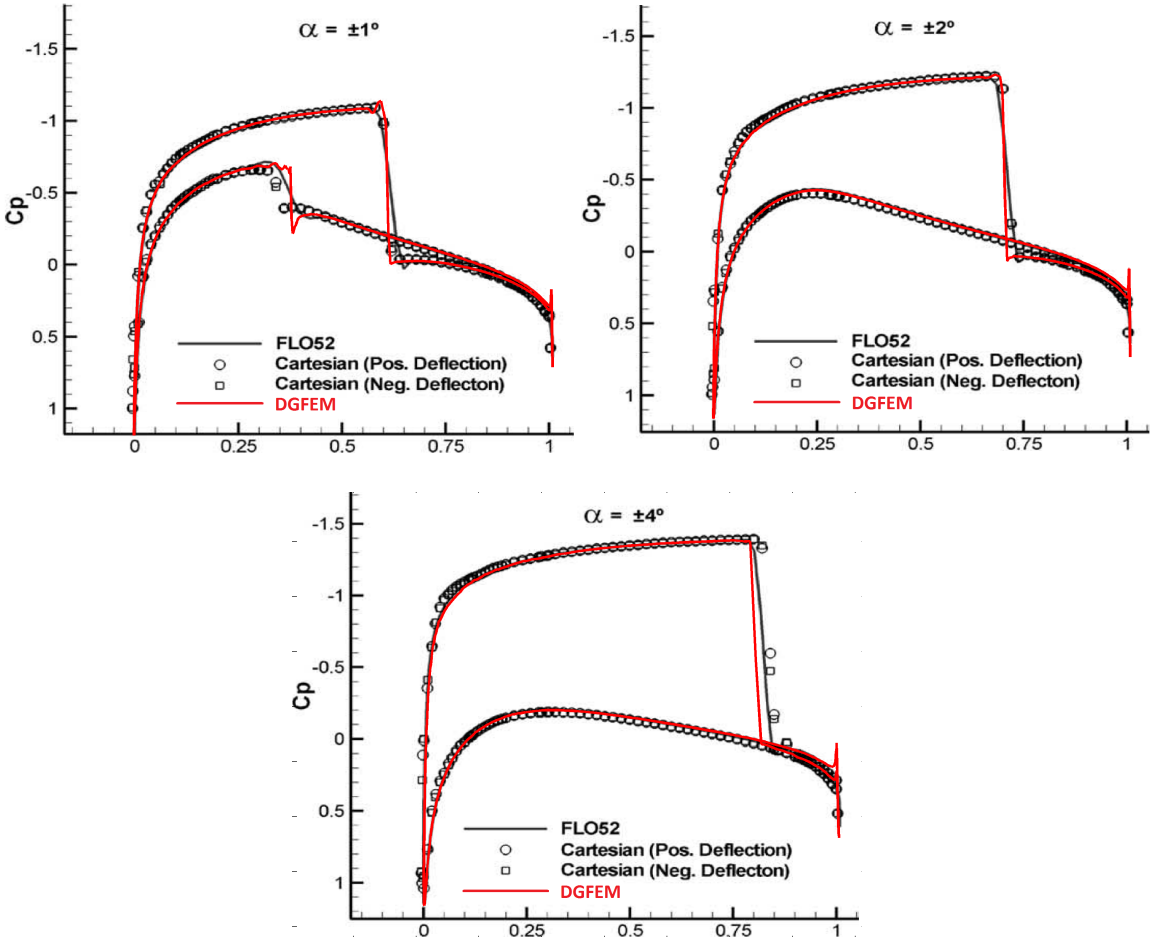


Figure 2: Distribution of $c_p$ coefficient along the airfoil chord for various angles of attack $\alpha$.

The resulting $c_p$ coefficient on the surface of the airfoil computed by the developed DGFEM code (colored red) along with the data taken from [13] (colored black) is shown in Figure 2.

The second test case for validation is an inviscid compressible unsteady fluid flow around oscillating NACA0012 airfoil for a free stream Mach number $M_\infty = 0.755$. The instantaneous

motion of the airfoil is given as a function of time

$$\alpha(t) = \alpha_m + \alpha_o \sin(\omega\, t),$$

which defines the angle of tilt of the airfoil. Here the mean angle $\alpha_m = 0.016°$ and the amplitude of oscillation $\alpha_o = 2.51°$. The angular velocity is defined as $\omega = 2ku_\infty/c$, where reduced frequency $k = 0.0814$, profile chord length $c = 1$ and $u_\infty$ is a free-stream velocity. The coordinates of reference point of rotation are $x_{ref} = [0.25, 0]$. The Figure 3 show a comparison of obtained numerical results (red) by the developed code with the results published in [13] and [14] (black). A reasonably good agreement is apparent from both of the test problems, which confirms a correct implementation of the implicit DGFEM solver along with the ALE approach.

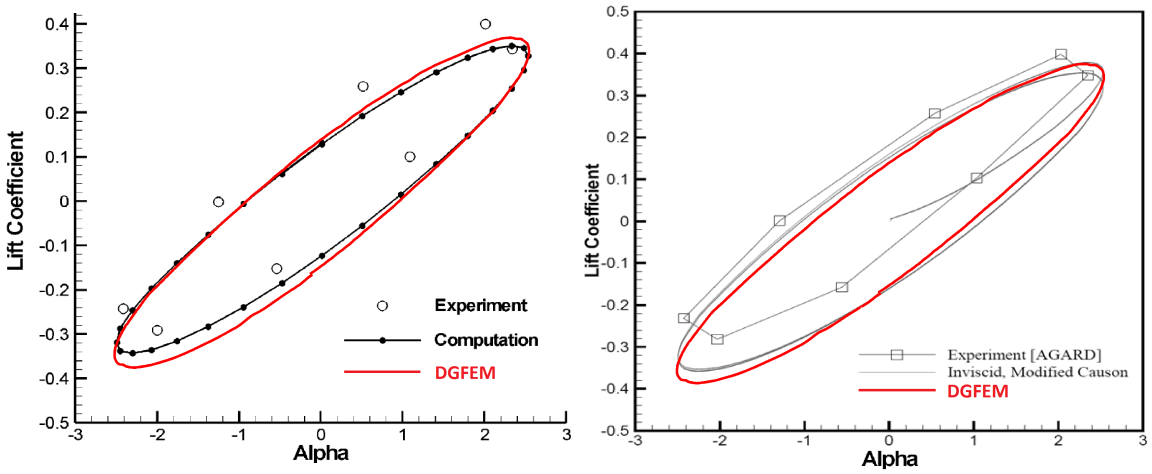


Figure 3: Dependence of the lift coefficient $c_L$ on the angle of the airfoil. Comparison with the numerical and experimental results published in [13] (left) and [14] (right).

## 5 NUMERICAL RESULTS

The developed in-house CFD software based on the discontinuous Galerkin method was used to simulate compressible viscous fluid flow through a simplified blade cascade with prescribed harmonic motion. The geometric configuration of the simplified blade cascade and the angle of attack of the flow were adopted from [4], test case no. 3, where it was experimentally studied. The only difference is that the thin airfoils of the test cascade from [4] were replaced by 3 millimetres thick flat plates. The geometric configuration of the simplified test cascade is shown in Figure 4.

The considered two-dimensional computational domain and the corresponding unstructured triangular mesh with 11932 elements is shown in Figure 5 (left). The detailed view of the mesh in the vicinity of the three flat plates is shown in Figure 5 (right). For the computation of the deformed coordinates of mesh nodes, the blending function approach is used, see [15], [16]. In this paper the blending function is generalized for three independently moving flat plates, Figure 4. Let us look at the computation of the deformed mesh in more detail. Let $\boldsymbol{x}_0$ denote the vector of initial coordinates of all mesh nodes. For each blade ($i = 1, 2, 3$) the vector $\boldsymbol{x}_0$ of initial coordinates is transformed into a new vector $\boldsymbol{y}_i$ using the following formula:

$$\boldsymbol{y}_i = \boldsymbol{p}_i + \mathbf{T}(\alpha)_i \boldsymbol{x}_0, \tag{9}$$

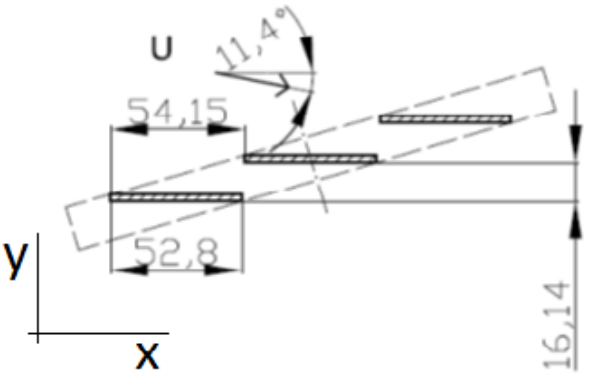


Figure 4: The geometric configuration of the simplified cascade which consists of three oscillating flat plates. The dimensions are in millimetres. The width of the plates is 80 mm.

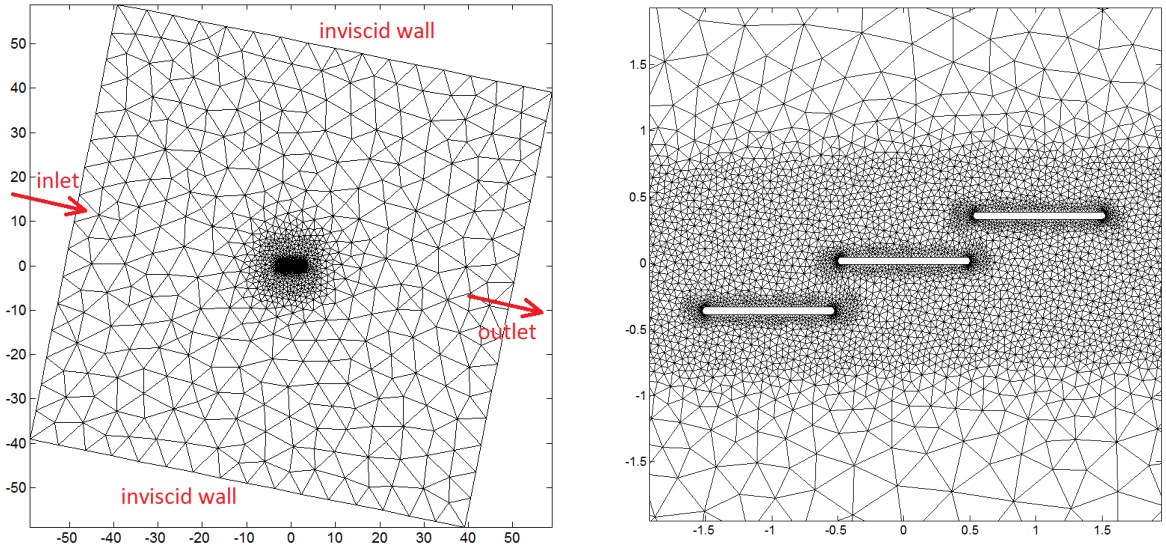


Figure 5: Computational domain and triangular mesh (left), computational mesh in the vicinity of simplified cascade (right).

where $\boldsymbol{p}_i = \boldsymbol{p}_i(t)$ is the time dependent translation vector and $\mathbf{T}(\alpha)_i = \mathbf{T}(\alpha(t))_i$ is the time dependent rotation matrix of $i$-th blade. The vector $\boldsymbol{x} = \boldsymbol{x}(t)$ of new coordinates is computed by applying the blending function $b_i$ as follows

$$\boldsymbol{x} = \frac{1}{n}\sum_{i=1}^{n}(b_i(\boldsymbol{x}_0)\boldsymbol{x}_0 + (1 - b_i(\boldsymbol{x}_0))\boldsymbol{y}_i). \tag{10}$$

The key part of this algorithm is to determine the blending functions $b_i$, which must satisfy two basic properties:

1. $b_i = 0$ on the boundary of the $i$-th blade,
2. $b_i = 1$ on the boundary of the $j$-th blade and on the boundary of the computational domain.

A blending function $b_i$, which fulfils the two properties, can be obtained by solving the equation

$$\frac{\partial^2 b_i}{\partial x^2} + \frac{\partial^2 b_i}{\partial y^2} = 0, \tag{11}$$

equipped with the boundary condition $b_i = 0$ on the $i$-th blade and $b_i = 1$ on the rest of the boundary. The solution to the boundary value problem (11) for the considered three flat plates defined in Figure 4 is shown in Figure 6.

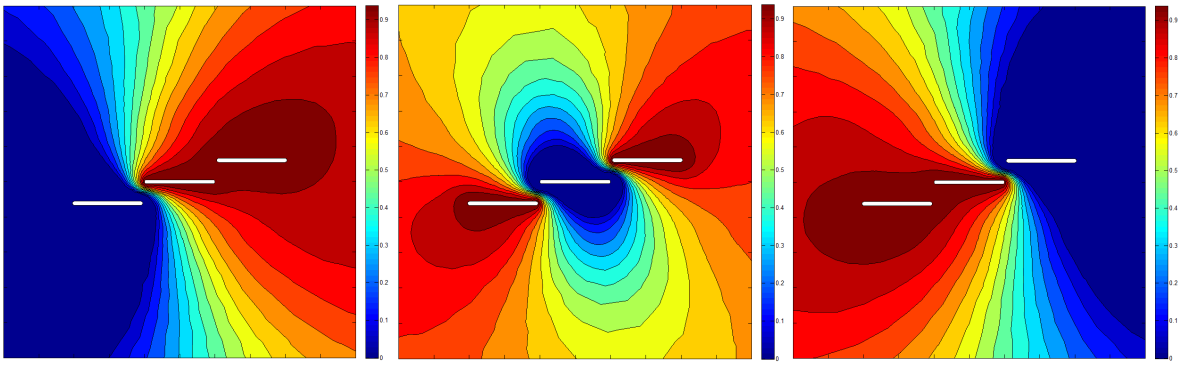

Figure 6: Solution to the boundary value problem (11) for bottom plate (left), middle plate (middle) and top plate (right) in viscinity of the three flat plates.

Each plate performs kinematic harmonic motion in y-direction $y = A\sin(2\pi ft + \phi)$ with an inter-blade phase angle $\phi = +\varphi$ for the upper plate, $\phi = 0$ for the middle plate and $\phi = -\varphi$ for the bottom plate. The amplitude and the frequency of the harmonic motion is $A = 0.003\,\mathrm{m}$ and $f = 20\,\mathrm{Hz}$, respectively. In [5], this problem was solved only for $\varphi = \pi/2$. Here, the analysis of the problem is extended to angles $\varphi = \{-3/4\pi, -1/2\pi, -1/4\pi, 1/4\pi, 1/2\pi, 3/4\pi, \pi\}$.

At the inlet of the computational domain, see Figure 5, the stagnation pressure $\bar{p}_{01} = 101325\,\mathrm{Pa}$, the stagnation temperature $\bar{T}_{01} = 293.15\,\mathrm{K}$ and the angle of attack $\alpha = 11.4°$ were prescribed. At the outlet, the static pressure $\bar{p}_2 = 95520\,\mathrm{Pa}$ was prescribed. The value of $\bar{p}_2$ was calculated out of the free stream velocity $\tilde{u}_\infty = 100\,\mathrm{ms}^{-1}$ under the consideration of standard sea level air conditions.

Figure 7 shows phase diagrams where the $y$-component of aerodynamic force acting on the middle plate is plotted depending on $y$-component of the displacement for various inter-blade phase angles $\varphi$. The obtained y-components of aerodynamic forces acting on the middle plate were analysed for all inter-blade face angles and consequently the aerodynamic damping parameter

$$\sigma = -\frac{c_w}{\pi A^2}$$

was determined. The variable

$$c_w = \int F_y dy$$

denotes the work of aerodynamic forces acting on the middle plate preformed during one cycle of harmonic motion with time period $T$. The resulting aerodynamic damping parameter $\sigma$ depending on inter-blade face angle $\varphi$ is shown in Figure 8. The parameter $\sigma$ has the following meaning. If the value of $\sigma$ is positive, than the kinetic energy of the flat plate is transmitted to the flow and the oscillation is damped. In this case the flutter most likely does not occur. If the value of $\sigma$ is negative, than the kinetic energy of the flow is transmitted to the flat plate and thus the flutter phenomena can occur.

## 6 CONCLUSION

The CFD solver based on the discontinuous Galerkin method was developed for the numerical solution of compressible viscous flow problems in domains with moving boundaries. The

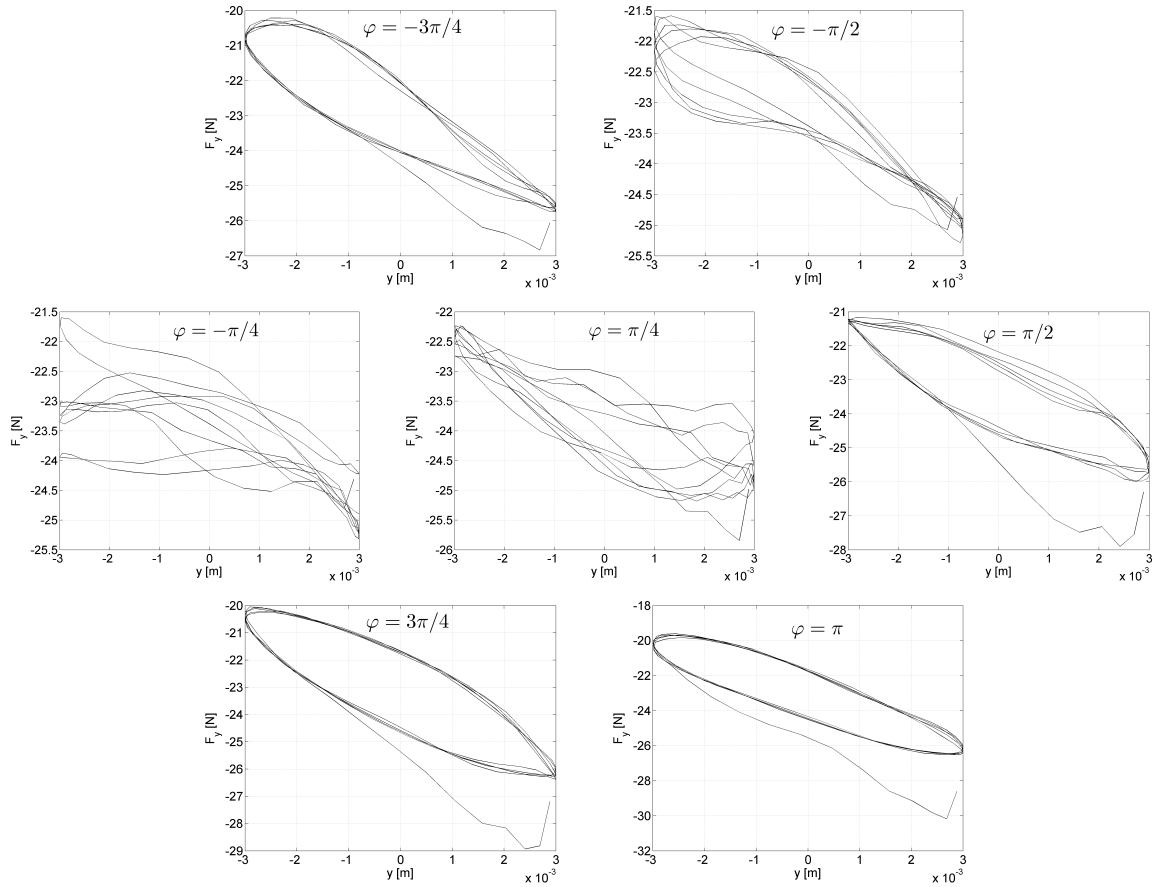


Figure 7: Phase diagrams of y-component of aerodynamic force acting on the middle plate depending on y-component of displacement for various inter-blade phase angles $\varphi$.

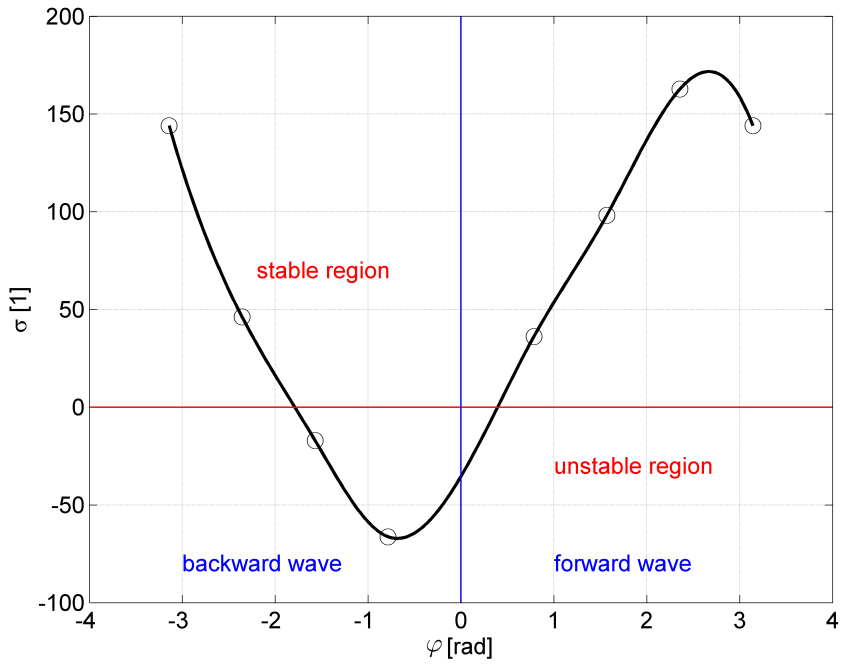


Figure 8: Aerodynamic damping parameter $\sigma$ depending on the inter-blade phase angle $\varphi$.

solver was validated on two test problems and consequently it was applied to numerical simulation of compressible viscous fluid flow through the simplified blade cascade formed by three flat plates with prescribed harmonic motion.

The presented results of flow field were analysed with regard to the flutter occurrence. The theory of the simplified blade cascade [3] as well as the results presented in this paper, Figure 8, suggest that the flutter occurs for the backward travelling wave mode. An experimental validation of results presented in this paper is planned in the near future in the Institute of Thermomechanics of the Czech Academy of Sciences.

## ACKNOWLEDGEMENTS

The authors appreciate the kind support by the grant GA16-04546S *"Aero-elastic couplings and dynamic behaviour of rotational periodic bodies"* of the Czech Science Foundation.

## REFERENCES

[1] H.M. Owens, W.E. Trumpler, Mechanical Design and Testing of Long Steam Turbine Blanding. *ASME Paper*, **49-A-64**, 1949.

[2] E.K. Armstrong, R.E. Stevenson, Some Practical Aspect of Compressor Blade Vibration. *Journal of the Royal Aeronautical Society*, **64** (591), 117-130, 1960.

[3] R. Kielb, J. Barter, O. Chernycheva, T. Fransson, Flutter of low pressure turbine blades with cyclic symmetric modes: A preliminary design method. *Journal of Turbomachinery, Transactions of the ASME*, **126**, 306-309, 2004.

[4] D. Schlafli, *Experimental investigation of transient flow in oscillating ring lattices*, Ph.D. Thesis no. 800, Lausanne, 1989. (in German)

[5] J. Vimmr, O. Bublík, H. Prausová, J. Hála, L. Pešek, Numerical simulation of fluid flow through simplified blade cascade with prescribed harmonic motion using discontinuous Galerkin method. *EPJ Web of Conferences*, 2017. (in press)

[6] M. Feistauer, J. Česenek, Space-Time Discontinuous Galerkin Finite Element Method for Convection-Diffusion Problems and Compressible Flow. *Numerical Methods and Applications, Lecture Notes in Computer Science*, **6046**, 1-13, 2011.

[7] P.R. Spalart, S.R. Allmaras, A One-Equation Turbulence Model for Aerodynamic Flows. *AIAA Paper*, **92-439**, 1992.

[8] W.H. Reed, T.R. Hill, Triangular mesh methods for the neutron transport equation. *Los Alamos Scientific Laboratory Report*, **LA-UR-73-479**, 1973.

[9] B. Cockburn, C.-W. Shu, Runge-Kutta Discontinuous Galerkin Methods for Convection-Dominated Problems. *Journal of Scientific Computing*, **16** (3), 173-261, 2001.

[10] V. Dolejší, M. Holík, J. Hozman, Efficient solution strategy for semi-implicit discontinuous Galerkin discretization of the Navier-Stokes equation. *Journal of Computational Physics*, **230** (11), 4176-4200, 2011.

[11] E.F. Toro, *Riemann Solvers and Numerical Methods for Fluid Dynamics*. Springer, Heidelberg, 1999.

[12] P.-O. Persson, J.Peraire, Sub-Cell Shock Capturing for Discontinuous Galerkin Methods. *44th AIAA Aerospace Sciences Meeting and Exhibit*, Reno, Nevada, January 9-12, 2006.

[13] D.J. Kirshman, F. Liu, Flutter prediction by an Euler method on non-moving Cartesian grids with gridless boundary conditions. *Computers and Fluids*, **35** (6), 571-586, 2006.

[14] J. Fürst, K. Kozel, P. Furmánek, High order finite volume schemes for numerical solution of 2D and 3D transonic flows. *Kybernetika*, **45** (4), 567-579, 2009.

[15] P.-O. Persson, J. Bonet, J. Peraire, Discontinuous Galerkin solution of the Navier-Stokes equations on deformable domains. *Computer Methods in Applied Mechanics and Engineering*, **198** (17-20), 1585-1595, 2009.

[16] O. Bublík, J. Vimmr, A. Jonášová, Comparison of discontinuous Galerkin time integration schemes for the solution of flow problems with deformable domains. *Applied Mathematics and Computation*, **267**, 329-340, 2015.

COMPDYN 2017
6th ECCOMAS Thematic Conference on
Computational Methods in Structural Dynamics and Earthquake Engineering
M. Papadrakakis, M. Fragiadakis (eds.)
Rhodes Island, Greece, 15–17 June 2017

# HYSTERETIC MODEL FOR THE EXPLICIT MATERIAL POINT METHOD

**Christos D. Sofianos**[1], **Vlasis K. Koumousis**[1]

[1] National Technical University of Athens
Institute of Structural Analysis & Aseismic Research
Zografou Campus, 15780 Athens, Greece
e-mail: sofianoschristos@yahoo.gr, vkoum@central.ntua.gr

**Keywords:** Material Point Method, Hysteresis.

**Abstract.** *The material point method (MPM) is an advancement of particle in cell method (PIC), in which Lagrangian bodies are discretized by a number of material points that hold all the properties and the state of the material [1]. All internal variables, stress, strain, velocity etc., that specify the current state and are required to advance the solution are stored in the material points. A background grid is employed to solve the governing equations by interpolating the material point data to the grid. The derived momentum conservation equations are solved at the grid nodes and information is transferred back to the material points and the background grid is reset. In this work the standard explicit MPM is extended to account for elastoplastic material behavior. The stress-strain constitutive law is determined according to the strain decomposition rule [2] where the strain rates are uncoupled into an elastic and a plastic part. In order to account for the different phases during elastic loading or unloading and yielding two Heaviside type functions are introduced [3]. These act as switches and incorporate the yield function [8]. The final form of the constitutive stress-strain relation incorporates the tangent modulus of elasticity, which now includes the Heaviside functions and gathers all of the governing behavior, facilitating considerably the solution. Numerical results are presented that validate the proposed formulation in the context of the MPM and in comparison with Finite Element Method.*

## 1 INTRODUCTION

The Material Point Method (MPM) is an extension of the Particle in Cell (PIC) [9] method that was first developed for fluid mechanics problems. Many of the inherent numerical problems associated with PIC were alleviated in the fluid implicit particle method (FLIP) [10]. MPM was originally conceived as an extension of FLIP in solid mechanics. The most noticeable difference however, is that in MPM the description of motion and governing equations are derived from the weak form of the updated Lagrangian formulation.

The MPM utilizes both an Eulerian background grid and a Lagrangian discretization of the domain. It can be divided into two phases. First the material domain is represented by a set of particles (material points). All the information of the subdomain that each particle represents is hold in the material points (such as mass, momentum, velocity, strain or stresses etc.). This Lagrangian phase is followed by an Eulerian phase where a background grid is employed. Information is then transferred into the nodes of the grid where the governing equations are solved. After this convective phase the material point variables are updated and the background grid is reset to its original form. This means that the grid is not attached to the material points and does not follow the deformation. In addition, one of the advantages of the MPM is that the background grid can be arbitrarily chosen for convenience.

## 2 MPM MODEL

If $\Omega$ is the domain of the material, it can be represented by $N_p$ number of material points (or particles) as in Figure 1.

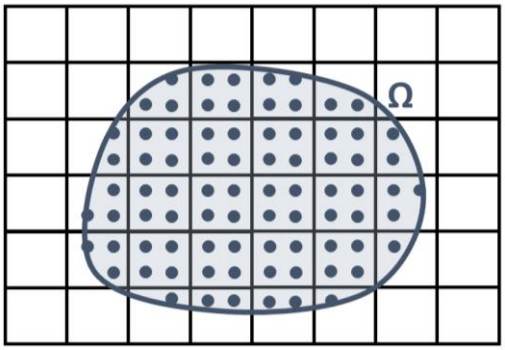


Figure 1: MPM discretization.

The material points are assigned a mass $m_p$, position $x_p$, velocity $v_p$ and stress $\sigma_p$. Since the total mass is divided into the material point set and the material points have constant mass through the simulation, the mass conservation is fulfilled. Conservation of momentum is:

$$p\frac{dv}{dt} = \nabla\sigma + pb \tag{1}$$

where $v$ is the velocity field, $\sigma$ is the Cauchy stress tensor, $p$ is the density and $b$ is the specific body force. In the previous relation $\nabla\sigma$ is the internal force while $pb$ is the external forces acting on the body. Moreover, if $E$ is the mechanical energy and $\varepsilon$ the strain tensor, the mechanical energy conservation equation is defined as:

$$p\frac{dE}{dt} = \sigma : \frac{dE}{dt} + pv \cdot b \tag{2}$$

The strain rate is expressed in terms of the gradient velocity as:

$$\frac{dE}{dt} = \frac{1}{2}\left(\nabla v + \left(\nabla v\right)^T\right) \tag{3}$$

and for the linear elastic case the constitutive equation relating stresses and stresses can be expressed using the elasticity tensor $D$ as:

$$\frac{d\sigma}{dt} = D\frac{d\varepsilon}{dt} \tag{4}$$

The plane stress elasticity matrix $D$ is defined as:

$$D = \begin{bmatrix} \frac{E}{\left(1-\nu^2\right)} & \frac{E\nu}{\left(1-\nu^2\right)} & 0 \\ \frac{E\nu}{\left(1-\nu^2\right)} & \frac{E}{\left(1-\nu^2\right)} & 0 \\ 0 & 0 & \frac{E}{2\left(1+\nu\right)} \end{bmatrix} \tag{5}$$

where $E$ is the Young's modulus and $\nu$ is the Poisson ratio.

In the Material Point Method each particle represents a sub-domain of the whole domain $\Omega$. Using the Dirac delta function the mass density can be expressed as a function of the material point masses and the material point positions as:

$$p = \sum_{i=1}^{N_p} m_p \delta\left(x - x_p\right) \tag{6}$$

Similar to the Finite Element method the material gradients are calculated on a background computational grid. Shape functions are used to approximate the solution and the velocity and acceleration of any material point are expressed in terms of the nodal accelerations of the grid as:

$$v\left(x_p\right) = \sum_{i=1}^{N} v_i N_i \tag{7}$$

and:

$$\alpha\left(x_p\right) = \sum_{i=1}^{N} \frac{dv_i}{dt} N_i \tag{8}$$

where in both relations the summation refers to the nodes of the element of the background grid that the material point resides in. In this work the shape functions used are cubic B-Splines [4], [5]. They have been shown to reduce the quadrature errors and the grid crossing errors associated with discontinuous shape functions. Applying the Galerkin method and using the previous relations in the momentum equation integrals are replaced by sums over all the material points and the momentum equation now reads:

$$\sum_{i=1}^{N} m_i \frac{dv_i}{dt} = F_i^{\text{int}} + F_i^{ext} \tag{9}$$

The internal and the external forces are defined as:

$$F_i^{\text{int}} = -\sum_{i=1}^{N_p} \frac{m_{p,i}}{p} \sigma_{p,i} \nabla N_i \tag{10}$$

and:

$$F_i^{ext} = \tau_i + b_i \tag{11}$$

where the subscript $p,i$ denotes the material point $i$.
Although many implementations are possible the main algorithm of the MPM is described below:

Map mass, momentum and internal forces from the particles to the background grid nodes:

$$\begin{aligned} m_i &= \sum_{p=1}^{N_p} M_p N_i \\ (mv)_i &= \sum_{p=1}^{N_p} (Mv)_p N_i \\ F_i^{\text{int}} &= -\sum_{p=1}^{N_p} \frac{M_p}{p_p} \sigma_p \nabla N_i \end{aligned} \tag{12}$$

Compute the nodal force vector and apply the boundary conditions:

$$F_i = F_i^{ext} + F_i^{\text{int}} \tag{13}$$

Update nodal momenta at the nodes:

$$(mv)_i = (mv)_i + F_i dt \tag{14}$$

Update particle positions and velocities:

$$\begin{aligned} v(x_p) &= v(x_p) + \left( \sum_{i=1}^{N} \frac{F_i N_i}{m_i} \right) dt \\ x_p &= x_p + \left( \sum_{i=1}^{N} \frac{(mv)_i N_i}{m_i} \right) dt \end{aligned} \tag{15}$$

Employing the Modified Update Stress Last (MUSL) scheme the final step is to recalculate the grid nodal momentum based on the new particle velocities and from there calculate the particle strain and stress increments as:

$$\begin{aligned} (mv)_i &= \sum_{p=1}^{N_p} M_p v(x_p) N_i \\ v_i &= \frac{(mv)_i}{m_i} \\ \Delta\varepsilon_p &= \sum_{i=1}^{N} v(x_p) \nabla N_i dt \\ \Delta\sigma_p &= E \Delta\varepsilon_p \end{aligned} \tag{16}$$

## 3 HYSTERETIC MODEL

Based on the theory of classical plasticity the governing equations of plasticity are the flow rule, the yield condition, the consistency condition and the hardening rule. In this work kinematic hardening is considered. The plastic strain tensor $\{\dot{\varepsilon}^p\}$ can be expressed in terms of the flow rule $\Phi$ as:

$$\{\dot{\varepsilon}^p\} = \dot{\lambda}\frac{\partial\Phi(\{\sigma\})}{\partial\{\sigma\}} \tag{17}$$

where $\dot{\lambda}$ is the plastic multiplier and $\{\sigma\}$ is the stress tensor. The Kuhn-Tucker optimality conditions state that:

$$\dot{\lambda} \geq 0 \quad \Phi \leq 0 \quad \dot{\lambda}\Phi = 0 \tag{18}$$

Using the additive decomposition of the strain rates we derive:

$$\{\dot{\varepsilon}\} = \{\dot{\varepsilon}^{el}\} + \{\dot{\varepsilon}^{pl}\} \tag{19}$$

The elastic part of the strain rates is connected to the stress rate tensor with the use of the elasticity tensor as:

$$\{\dot{\sigma}\} = [D]\{\dot{\varepsilon}^{el}\} \tag{20}$$

Substituting equation (17) to (20) with the use of (19) we can write:

$$\{\dot{\sigma}\} = [D]\left\{\{\dot{\varepsilon}\} - \dot{\lambda}\frac{\partial\Phi(\{\sigma\})}{\partial\{\sigma\}}\right\} \tag{21}$$

Using the Kuhn-Tucker optimality condition in (18) and relation (21) and since at yield $\dot{\Phi} = 0$ and $\dot{\lambda} \geq 0$ the following relation can be derived [8]:

$$\left(\frac{\partial\Phi(\{\sigma\})}{\partial\{\sigma\}}\right)^T \{\dot{\sigma}\} + \left(\frac{\partial\Phi(\{\sigma\})}{\partial\{\sigma\}}\right)^T \{\dot{\eta}\} = 0 \tag{22}$$

Finally, the expression for the plastic multiplier becomes [8]:

$$\dot{\lambda} = \left(-C + \left(\frac{\partial\Phi(\{\sigma\})}{\partial\{\sigma\}}\right)^T [D]\frac{\partial\Phi(\{\sigma\})}{\partial\{\sigma\}}\right)^{-1} \left(\frac{\partial\Phi(\{\sigma\})}{\partial\{\sigma\}}\right)^T [D]\{\dot{\varepsilon}\} \tag{23}$$

The previous equations hold when yielding has occurred. In order to smooth the transition from the elastic to the inelastic regime and generalize the plastic multiplier in the whole domain of the strain tensor as in [6] and [7], the following Heaviside functions are introduced:

$$H_1 = \begin{cases} 1 & \Phi = 0 \\ 0 & \Phi < 0 \end{cases}, \qquad H_2 = \begin{cases} 1 & \dot{\Phi} = 0 \\ 0 & \dot{\Phi} < 0 \end{cases} \tag{24}$$

This way a single expression is used for the plastic multiplier neglecting the need for a piece wise approach for the domains of the Kuhn-Tucker condition.

$$\dot{\lambda} = H_1 H_2 \left( -C + \left( \frac{\partial \Phi(\{\sigma\})}{\partial \{\sigma\}} \right)^T [D] \frac{\partial \Phi(\{\sigma\})}{\partial \{\sigma\}} \right)^{-1} \left( \frac{\partial \Phi(\{\sigma\})}{\partial \{\sigma\}} \right)^T [D] \{\dot{\varepsilon}\} \tag{25}$$

The Heaviside functions are smoothed according to the following relations [3]:

$$H_1 = \left| \frac{\Phi}{\Phi_0} \right|^n \quad , \qquad H_2 = 0.5 + 0.5 sign\left( \{\varepsilon\}^T \{\dot{\sigma}\} \right) \tag{26}$$

Finally substituting the plastic multiplier into equation (21) the following relation can be obtained relating stress and strain rates:

$$\begin{gathered} \{\dot{\sigma}\} = [E_t] \{\dot{\varepsilon}\} \\ [E_t] = [D] \left( [I] - \left| \frac{\Phi}{\Phi_0} \right|^n \left( 0.5 + 0.5 sign\left( \{\varepsilon\}^T \{\dot{\sigma}\} \right) \right) [R] \right) \end{gathered} \tag{27}$$

This tangent elasticity modulus can now be incorporated in the MPM framework in relation (16) and the updated stresses can be calculated using the explicit scheme.

## 4 NUMERICAL EXAMPLES

### 4.1 Cantilever beam

In this example a cantilever beam subject to a point load on its free end is analyzed. The material is steel with *E=210GPa*, *v=0.3* and $s_y$*=240MPa*. The beam has a length of *1m* and a height of *0.1m* while its width is *0.05m*. The material point discretization is shown in Figure 2. For the beam discretization 360 material points were used. The load is applied gradually over time in order to simulate a quasi-static conditions. The force-displacement diagram of the free end of the beam are presented in Figure 3 and are compared with results from Finite Element codes. Finally, the Von Mises stresses are presented in Figure 4. Results are in good agreement and the hysteretic MPM model can accurately predict both the displacement history of the beam as well as its stress state.

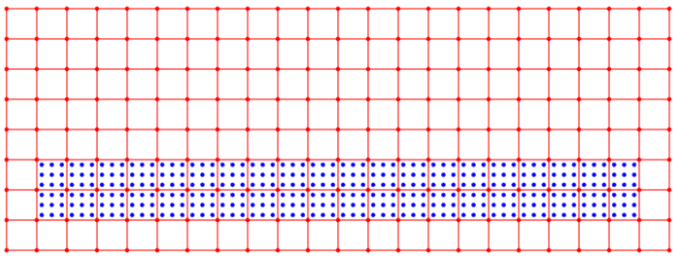

Figure 2: MPM discretization of cantilever beam with 360 material points.

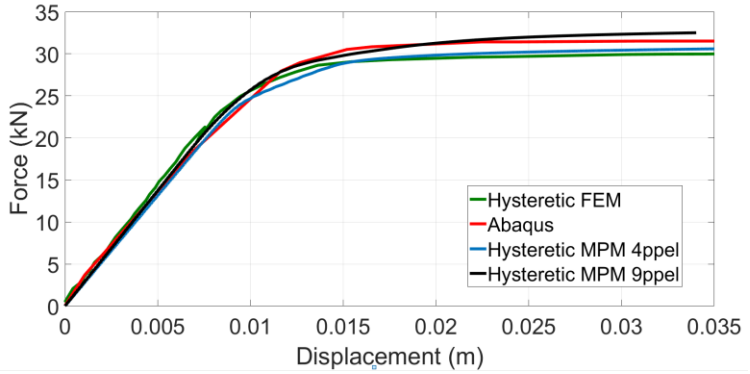


Figure 3: Force-displacement diagrams at the free end.

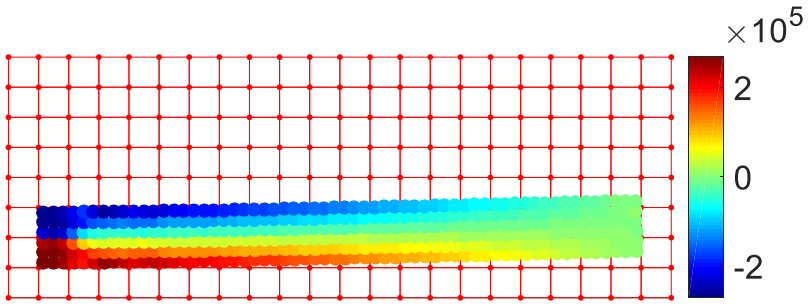


Figure 4: Von Mises stresses.

### 4.2 Dynamic load cantilever beam

For this second example another cantilever beam is considered with dimensions 1x0.2m. The beam thickness is 0.02m. Material is steel S235 and 5% hardening is considered. The beam is loaded at its free end with a sinusoidal load of 75kN. In Figure 5 the history of the displacement of the free end of the beam is presented and compared with results from ANSYS Finite Element code. Plastic regions were developed in the support of the beam. Results are in good agreement verifying the proposed formulation in quasi-static and dynamic conditions.

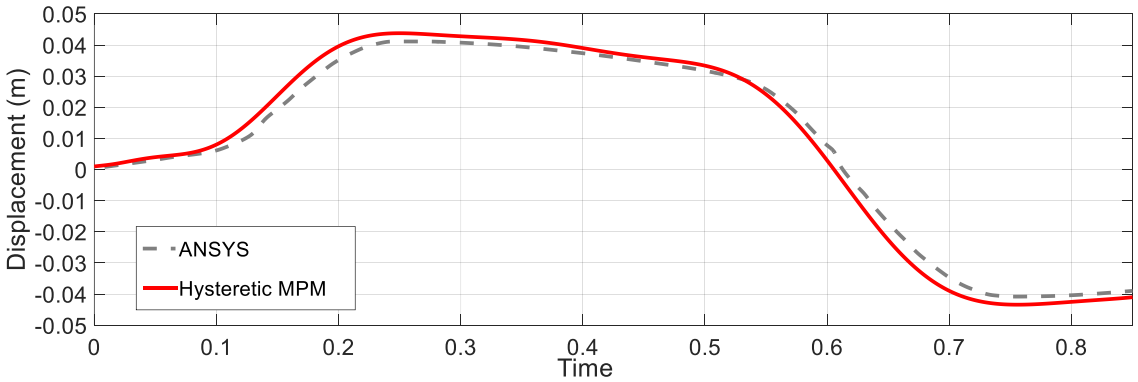


Figure 5: Free end displacement history.

## 5 CONCLUSIONS

- The Material Point Method is used in an explicit formulation to model dynamic or quasi-static loadings accounting for the inelastic behavior.

- An hysteretic model has been presented for nonlinear analysis that accounts for smooth transition from the elastic to the inelastic regime.
- The hysteretic model has been efficiently incorporated into the MPM framework by modifying the tangent modulus of elasticity.
- High order cubic B-Splines have been used to minimize the grid crossing error and improve the accuracy of the MPM method.
- Numerical examples are compared with existing finite element codes and verify the proposed model ability to simulate hysteretic phenomena in the framework of MPM.

## ACKNOWLEDGMENTS

The authors would like to acknowledge the support from the "RESEARCH PROJECTS FOR EXCELLENCE IKY/SIEMENS".

## REFERENCES

[1] D. Sulsky, Z. Chen and H. L. Schreyer, A particle method for history-dependent materials, *Comput. Methods, Appl. Mech.* Eng. **118**,179 (1994).

[2] Lubliner J. Plasticity theory. New York. Dover Publications, Inc, 2008

[3] Bouc R. "Forced vibration of mechanical system with hysteresis", Proc. 4th Conf. on Nonlinear Oscillation, Prague

[4] Andersen S., Andersen L., Analysis of spatial interpolation in the material-point method. *Computers and Structures* **88** (2010), 506-518.

[5] Steffen M, Kirby RM, Berzins M. Analysis and reduction of quadrature errors in the material point method (MPM). *International Journal for Numerical Methods in Engineering*;**76**:(2008), 922–48

[6] Triantafyllou S., Koumousis V., Bouc-Wen Hysteretic Plane Stress Element, *Journal of Engineering Mechanics*, **138** (2012), 235-246.

[7] Casciati F. (1995) Stochastic dynamics of hysteretic media. In: Krée P., Wedig W. (eds) Probabilistic Methods in Applied Physics. Lecture Notes in Physics, vol 451. Springer, Berlin, Heidelberg.

[8] Triantafyllou S.P., Koumousis V.K., An hysteretic quadrilateral plane stress element, *Arch Appl Mech*, **82** (2012), 1675-1687.

[9] Harlow F.H., The particle-in-cell computing method for fluid dynamics, *Methods for Computational Physics*, **3** (1964), 319–43.

[10] Brackbill J.U., Ruppel H.M., FLIP: A method for adaptivelyzoned,particle-in-cellcalculations of fluid flows in two dimensions. *Journal of Computational Physics*,**65**(2), (1986), 314–343.

COMPDYN 2017
6th ECCOMAS Thematic Conference on
Computational Methods in Structural Dynamics and Earthquake Engineering
M. Papadrakakis, M. Fragiadakis (eds.)
Rhodes Island, Greece, 15–17 June 2017

# THE EVALUATION APPROACH OF SPENT NUCLEAR FUEL INTERGRITY BY USING FINITE ELEMENT METHOD

**K. H. Kim[1], Y. I. Yoo[2], O C. Kwon[2], J. K. Park[2], K. B. Eom[2], S. K. Lee[2], and J. S. Yoo[2]**

[1] R&D Center, KEPCO Nuclear Fuel Co.
989 beon-gil 242, Daedock-daero, Yuseong-gu, Daejeon, Korea
e-mail: kyounghong@knfc.co.kr

[2] R&D Center, KEPCO Nuclear Fuel Co.
989 beon-gil 242, Daedock-daero, Yuseong-gu, Daejeon, Korea
{yiyoo, ockwon, jkpark, kbeom, skilee, jsyoo}@knfc.co.kr

**Keywords:** Spent Nuclear Fuel, Structural Integrity, Drop Simulation

**Abstract.** *In Korea, the storage capability for Spent Nuclear Fuel(SNF) in the nuclear power plants will be expected to be saturated in the near future. SNF have to transfer from spent pool in the plants to another area by using the safety way. Handling and transportation of SNF are common key processes for the SNF management. During this activity, SNF is required to evaluate structural integrity by using the proven evidences of the tests or other reliable methodologies. The SNF test, however, is accompanied by very high cost and safety issues because of handling irradiation object. Alternatively, the computational methodologies(ex: Finite Element Method, Numerical Method, etc.) are usually employed as a technical solution based on the information of other effects. In this paper, the simulations for analyzing the fuel integrity is conducted by using verified finite element model during the regulated normal and postulated conditions. At first, the model is designed as the many beam elements considering full size. Second, the verification process was performed for having the mechanical properties and dynamic characteristic at the model. At the end, SNF drop was simulated at the several conditions. In the result of this paper, SNF has stress within elastic zone at 0.3 m drop but SNF is expected to be damaged result from free drop simulation of 9.0 m.*

## 1 INTRODUCTION

In 1978, Kori 1 began commercial operation as first nuclear power plant in Korea. Since then, the nuclear power industry has developed. In today, a total of 25 nuclear power plants are currently in operation. Nuclear power generation uses principle of converting from heat energy of nuclear fuels to electricity. At this time, fission products are generated at the fuels loaded in the reactor inevitably. For that reason, evaluating integrity of nuclear fuel assemblies is an essential process to be ensured confining uranium and irradiated products to fuel rods during handling and transportation, including operation of the power plants. To evaluat-

ing the integrity of nuclear fuels, it is important to identify the material/mechanical properties and to estimate the fuel behavior under those conditions.

Nuclear fuel assemblies consist of fuel rods containing uranium pellets, grids with complex shapes for supporting the rods, top / bottom nozzle connected to reactor structures, and guide tubes which control rods for controlling the heat output are inserted. The manufactured nuclear fuel assemblies are installed in new fuel transport containers for transporting to nuclear power plants without any damage. Generally, the transported fuel assemblies are loaded into the reactor by a crane and produce heat in harsh environmental conditions of high temperature and high pressure for five years. During the loading period, the metal materials constitute oxidized, hydrogenated, and deteriorated through the chemical reaction with the cooling water. After the power generation, they wait in the spent pool at the power plants until they are post-treated or disassembled.

Due to the spent fuel in standby, the storage capacity of the spent pool will soon be saturated at the nuclear power plant in Korea. SNFs have to be transported by using the safety way to the other area. Therefore, the handling and transportation of SNF for post-treatment is a rising issue faced by the Korea's nuclear industry [1, 2].

In order to confirm the safety of the handling and transportation of the un-irradiated fresh nuclear fuel, it can be explained by reflecting the material and mechanical characteristics and analyzing each accident condition for predicting nuclear fuel behavior in advance. For this purpose, various mechanical tests about unirrdiated fuel assemblies are conducted by mechanical test facility when developing nuclear fuel [3]. Investigating irradiated nuclear fuel assemblies are also a very good way to determine mechanical properties includes all effects. But it is difficult in reality due to important issue connected with radiation shielding of the facility and tester safety. Alternatively, the classical mechanics method and finite element analysis are widely used to predict the behavior of nuclear fuel assemblies in nuclear reactors based on test result and logical deduction [4, 5].

For safety of SNF transportation, radiation shielded containers are required. In order to prove the integrity of the container, 10CFR71 [6] of US Federal Regulations define normal accidents and postulated conditions of various cases. Several studies have been conducted to determine that these requirements are met. The US Department of Energy's research institutes assessed their integrity in consideration of the characteristics of the SNF and selected representative SNF to carry out integrity analysis together with the transport container. The one research regarding rail way transportation of SNF conducted by US nuclear fuel companies and research institutes[7, 8].

Prior to this study, the two studies were performed by KEPCO NF to selecting the representative nuclear fuel, which is expected to be the most damaged among many type of nuclear fuels supplied to Korea. The one is the hand calculation considering of geometry data and the other is the finite element analysis through the simplified single beam reflected dynamic characteristics [9, 10]. Both models are designed from several hundred fuel rods with another components to one beam. These models are useful to come to a rough conclusion in the short time. However, the hand calculation model is difficult to describe the behavior of the nuclear fuel according to the time and estimate impact force under regulated normal and postulated conditions. In case of simplified single beam model, dynamic behavior of the fuel can be obtained by solving numerical equations. The stress of fuel rod estimated by reflecting displacement of the beam model results under assumption that is rod motion is equal to the fuel model. Therefore, simplified single model is limit to analyzing stress at the each part for evaluation of integrity.

In this paper, the model was designed as many beam elements considering full size to describe the motion of the nuclear fuel and evaluate the integrity of the fuel rods under handling

and transportation. At first, the representative nuclear fuel selected previous studies was modeled by using geometry data of un-irradiated condition. To the next, the model was verified by comparing with result of mechanical test. The some parameters was changed in the model to make the SNF conditions. And drop simulations were performed under selected conditions for finding maximum stress and damage area of the model.

## 2 MODELING AND MODEL VERIFICATION

### 2.1 Nuclear fuel model

In previous studies, impact simulations were performed on a single beam with multiple lumped masses by using finite element model verified dynamic characteristics compare with the test results. The beam model can describe the dynamic and impact behavior of the un-irradiated fresh nuclear fuel from a macroscopic point of view. However, if one characteristic (e.g., contact condition with fuel rods and grids, temperature effect of material, etc.) is changed in the nuclear fuel, the model is difficult to predict the exactly fuel motions during impact simulations since the changed effect is not to directly reflected in the model. For estimating the behaviors of spent nuclear fuel, it is necessary to full scale model that is modeling by several components. In this study, the FE model as shown in figure 1 (a) was designed by the components and the FE model of the nuclear fuel consists mainly of beam elements and analyzed by ANSYS 16.0.

### 2.2 Verification process

To verify the actual assemblies with the dynamic characteristics of the fuel model considered in Section 2.1, the following sequence was performed. Firstly, mass was checked comparing with the actual nuclear fuel and analytical model weight. And the model analysis was performed to confirm natural frequencies and mode shapes of the FE model. Lateral free vibration test result was used for energy dissipation of the model in time domain. Finally, some parameters of the model were controlled for matching with the lateral and the axial impact test.

### 2.3 Vibration characteristics

The mass of the fuel modeled as shown in Figure 1 (a) was matched to within 0.35 %. The natural frequencies and mode shapes were extracted as shown in Table 1 and Figure 1 (b) to (f) by the modal analysis results. It can be confirmed that the natural frequency difference between the test and analysis result within about 10 %, but Mac value is decreased at the 3$^{rd}$ mode due to difference of joint connection mechanism of grids and guide tubes.

| Mode number | 1 | 2 | 3 | 4 | 5 |
|---|---|---|---|---|---|
| Frequency difference (%) | 0.30 | 10.02 | 0.20 | 3.57 | 2.76 |
| Mac value | 0.92 | 0.81 | 0.59 | 0.70 | 0.83 |

Table 1: Mode frequency between the test and the analysis

Figure 2 (a) shows the data obtained by free oscillation result from initial displacement of mid grid in the lateral direction. Nuclear fuel has decrease amplitude according to increasing time due to energy dissipation mechanism such as frictional force between grid and rod contact, material damping, impact of fuel tube and uranium pellet, etc. The results of the finite element analysis and the test results agree well in the first cycle. But after second peak, there was a large error due to the difference of some nonlinear characteristics between test and model result. However, since most of the impact behavior occurs before the first peak ap-

proach, it is enough for estimating fuel behavior in the time domain. And the displacement of the model at the first peak is larger than test so that the model is conservative in terms of impact simulations.

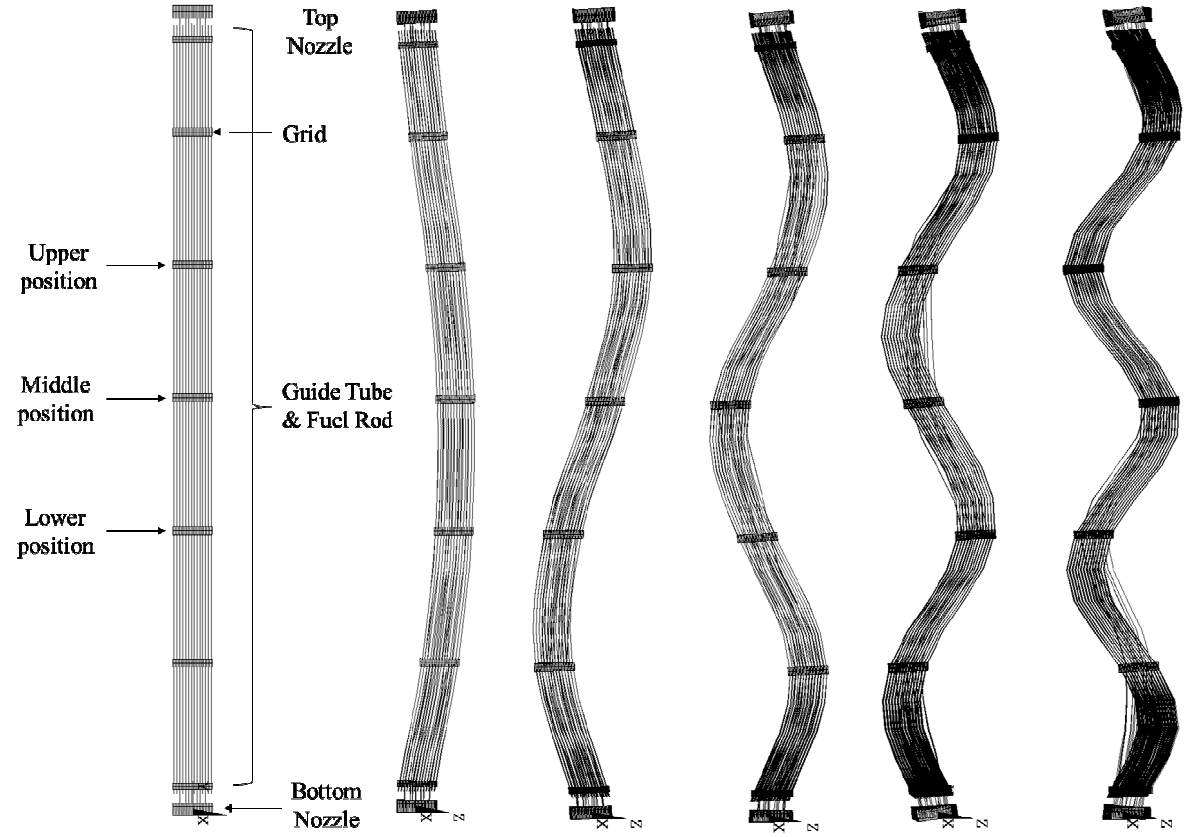


Figure 1: Finite Element(FE) model and Mode shape

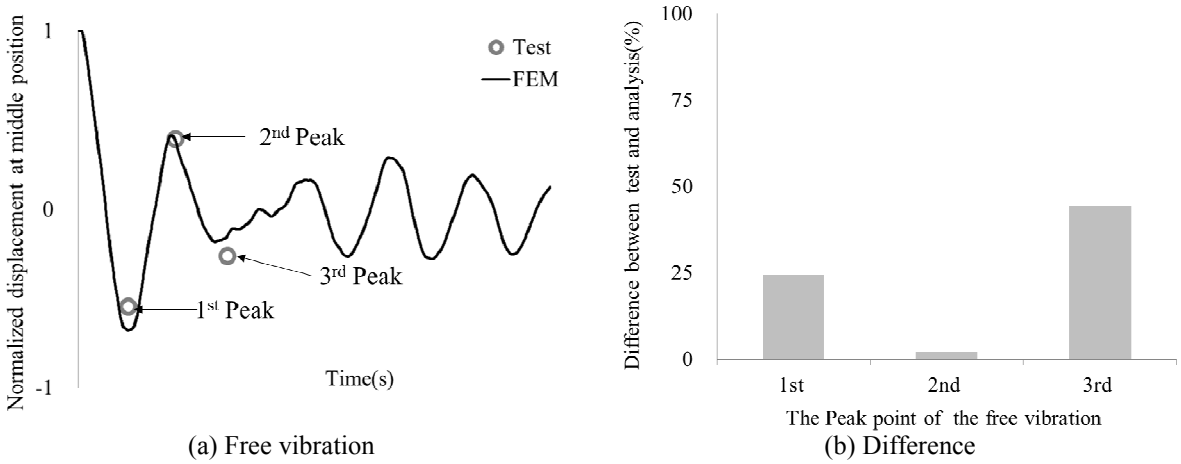


Figure 2: Lateral free vibration of the nuclear fuel

## 2.4 Impact characteristics

Nuclear fuel is exposed to various environments during operating, handling and transportation. To prove integrity of nuclear fuel from the damage cause by external force, impact tests were carried out at the time of nuclear fuel development. Figure 3 (a), (b) and (c) show the

impact force characteristics when three grids are collided with the surface of a wall according to initial displacement of the mid gird. The impact force in the graph was normalized by maximum force generated in the lateral impact test. The force was measured caused by free drop from constant distances and shown in Figure 3 (d). The value was normalized by maximum axial impact force obtained during the axial drop test. In the case of the finite element model, the lateral and axial characteristics were large difference to compare with test data at the small displacements but the difference is decreased within 20 % as the displacement increased.

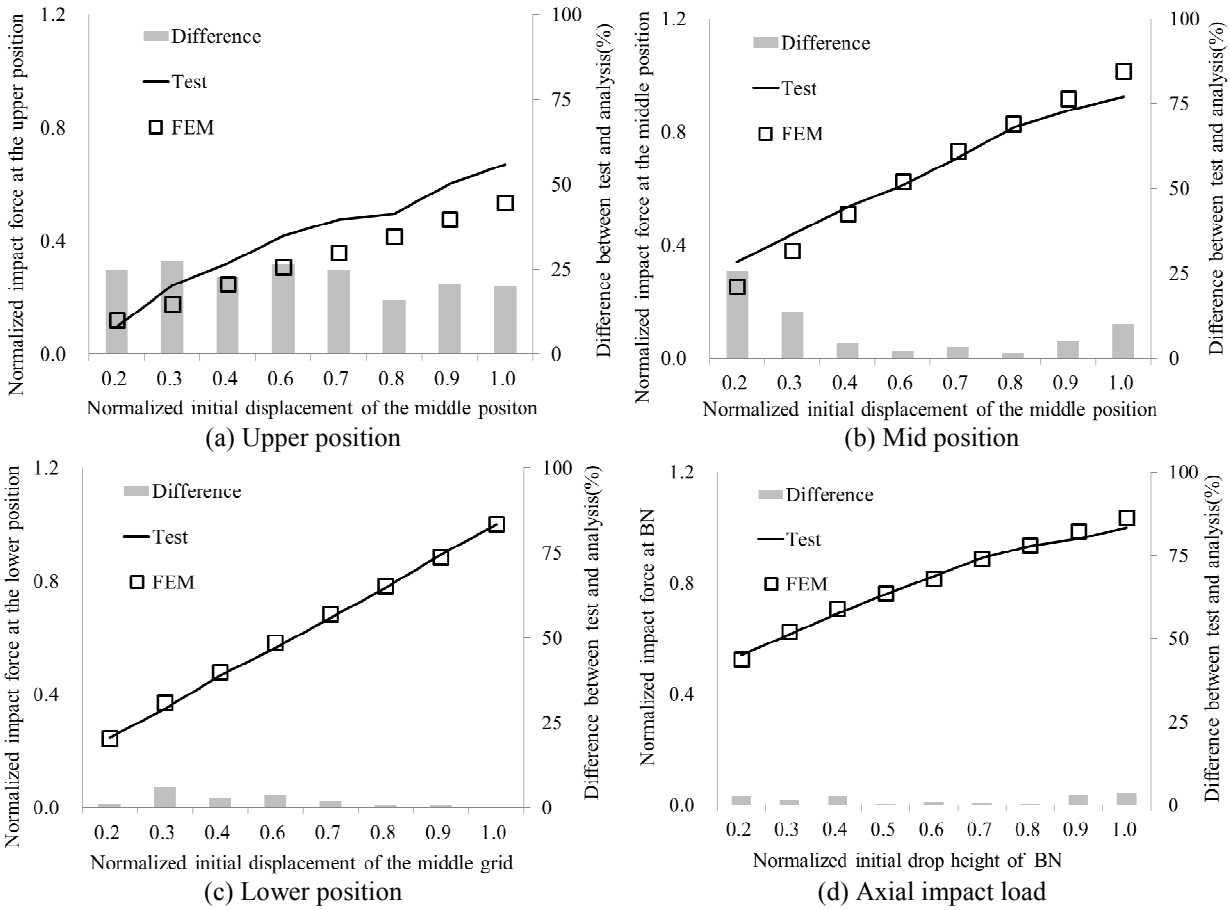


Figure 3: Impact results of the tests and analyses

## 2.5 Consideration of EOL condition

Nuclear fuel assemblies are loaded into the reactor and exposed to cooling water for a long time under high temperature and pressure conditions, resulting in creep, hydrogenation of materials, and irradiation effect. Especially, the lateral stiffness of the fuel is decreased cause by the relaxation of the spring and the dimple supporting the fuel rod. At the Beginning Of Life(BOL), the loads of spring and the dimple are acting on the fuel rods for keeping the distance between fuel rods and then the loads are removed at a high temperature and growth of the grids by irradiation or thermal relaxations and the diameter reduction of the fuel rod by high pressure. The gaps between the grid and fuel rods occur, and the stiffness of the spring and the dimple is also changed by irradiation effect. Therefore, some of the parameters were adjusted in the finite element model to describe the End Of Life(EOL) condition, which was verified by considering only the contact conditions except the material properties. As a result, the lateral stiffness and energy dissipation(e.g., hysteresis loss, etc.) were reduced because the frictional loads are removed from the EOL model in the ideal state as shown in Fig. 4, and the

mode frequency of the EOL model was also reduced when the mode shape of the fuel rod is only considered.

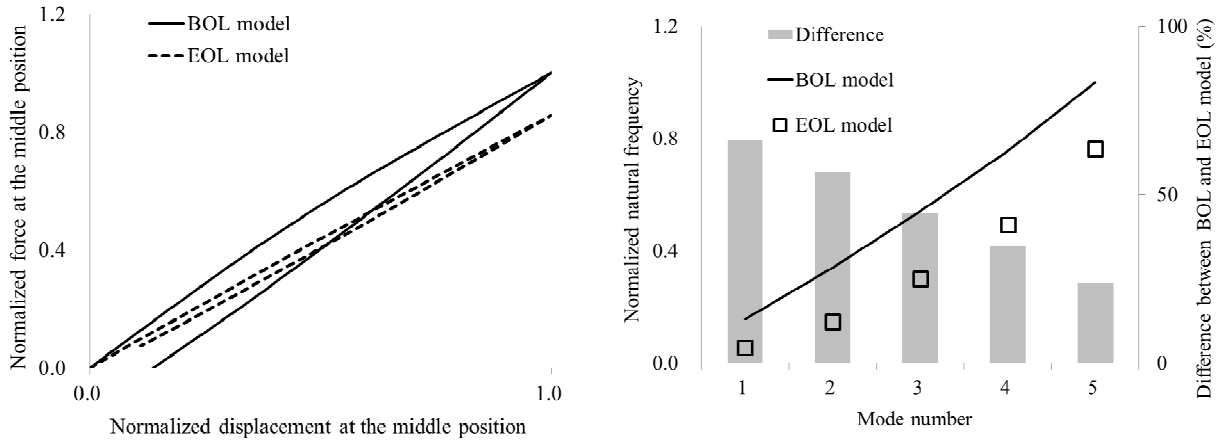


(a) Hysteresis of lateral axis (b) Mode frequency

Figure 4: analytical characteristic of the EOL model

## 3 DROP SIMUALTION DURING HANDLING AND TRANSFORTATION

### 3.1 Drop condition

When the cask containing SNF assemblies is dropped according to normal / hypothetical scenarios during handling and transport, and impact force is acted on SNF. This can cause large stresses on the fuel rods supported by the fuel skeleton and expose the radioactive material due to fuel rod damage. Therefore, the 10CFR 71 of US federal regulations contains various terms for the prevention of serious fuel rod damage and release of radioactive material from the packaging under normal and postulated accident conditions. The height of free drop is 0.3 m considering total weight including cask at the normal condition and 9 m drop height is required at the postulated accident. In these analyses, the drop simulations were performed at 0.3 m and 9.0 m for one fuel, assuming that the cask has rigid body motion without any deformation.

### 3.2 Drop result

Figure 5 (a) shows the deformed fuel shape when the impact force reaches the maximum value during the drop simulation. The grids and top/bottom nozzle as well as fuel rods are crashed with the ground surface. So, impact forces acted on the fuel rod directly. Figure 5 (b) shows the impact force on the top/bottom nozzle and the grids under each drop condition, based on the maximum force generated in the lateral impact test in section 2.4. In the case of 0.3 m drop, impact force was generated almost uniformly on the fuel, but in 9.0 m drop condition, the impact force on the fuel rod portion was largely affected. Figure 5 (c) shows the load in the time domain during the axial drop. When the nuclear fuel was dropped from 9.0 m, the force was generated about 17 times higher than the maximum force occurred in the axial impact test.



(a) Deformed shape after impact(Displacement scale factor: 5)

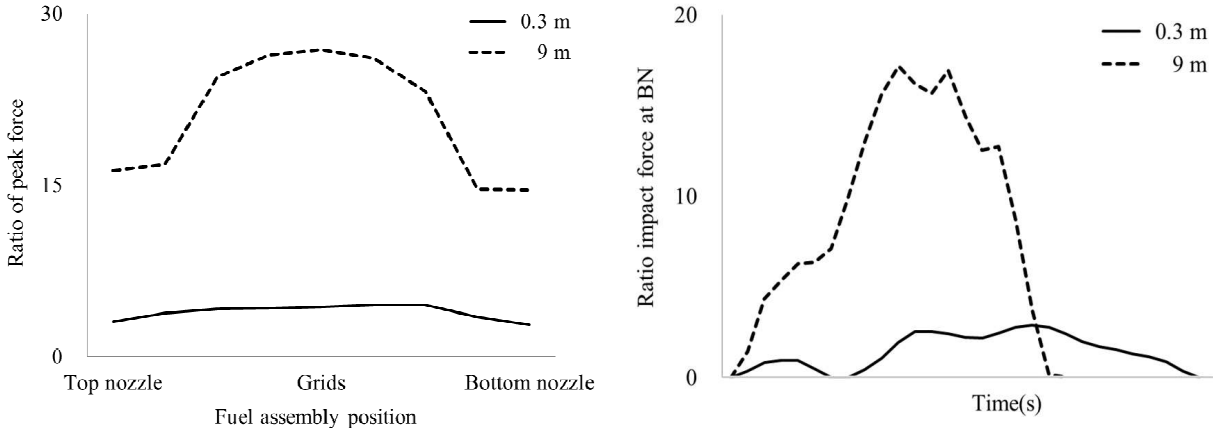


(b) Maximum impact force of lateral drop (c) Impact force of axial drop

Figure 5: Deformation and impact force of the drop simulation

## 4 EVALUATION OF STRUCTUAL INTEGRITY

In the previous study, the integrity of the fuel rod was evaluated by reflecting the deformation of simplified beam model to the rod model. In this paper, Table 2 shows the maximum stresses form fuel scale model acting on the guide tube and the fuel rod based on the yield stress of the material. In the case of 0.3 m drop, the stresses of the guide tubes and the fuel rods did not exceed the yield stress. However, when falling at 9.0 m, the maximum stress of the fuel rods and the guide tubes exceed the yield stress. It is possible to cause breakage or damage. Also, the guide tube showed that the maximum stress near the impact surface in the axial drop simulation exceeded the yield stress, and the fuel rod showed maximum stress in the section where the maximum moment occurred in the lateral drop simulation.

| Drop height | Component | Lateral drop | Axial drop |
|---|---|---|---|
| 0.3 m | Fuel rod | 0.49 | 0.08 |
| | Guide tube | 0.06 | 0.04 |
| 9.0 m | Fuel rod | **3.20** | 0.45 |
| | Guide tube | 0.52 | **1.15** |

Table 2: Ratio of the maximum stress to the yield stress

## 5 CONCLUSIONS

- Verification process was performed to describe unique mechanical characteristics of the nuclear fuel.
- The impact forces and stresses of each component were estimated under drop conditions.
- By analyzing the drop simulation of this model, it is possible to select the section where the maximum stress is expected to occur.
- A lateral drop can produce the greatest stress on the fuel rod, and maximum stress occurs at guide tubes in the axial drop.

## REFERENCES


[1] S. K. Lee, S. Y. Kim, Y. S. Jung, *Spent fuel status in Korea and integrity evaluation*, Proceedings of the 17th International Symposium on the Packaging and Transportation of Radioactive Materials(PATRAM 2013), San Francisco, CA, USA, Aug. 18-23, 2013

[2] S. Y. Kim, S. K. Lee, B. S. Choi, K. S. Choi, C.J. Lim, *The approach of used fuel integrity evaluation during transportation and storage*, The European Forum to discuss Nuclear Technology Issues, Opportunities & Challenges(ENC 2012), Manchester, United Kingdom, December 9-12, 2012

[3] K.W. Kim, K.L. Jeon, Y. K. Jang, J. H. Park, Y. H. Koo, *Progress in nuclear fuel technology in Korea, Korea Nuclear Society*, Nuclear Engineering and Technology, Vol. 41, No.4, 493-520, May, 2009

[4] K. S. Lee, S. Y. Jeon, H. K. Kim, *Development of the simplified fuel assembly model for the fuel assembly SSE and LOCA analysis*, Transaction of International Association for structural mechanics in reactor technology(SMiRT20), Espoo, Finland, Aug. 9-14, 2009

[5] P.Petkevich, V.Abramov, V. Yuremenko, V. Piminov, V. Makarov, A. Afanasiev, Simulation of the nuclear fuel assembly drop test with LS-DYNA, Transaction of International Association for structural mechanics in reactor technology(SMiRT21), New Delhi, India, November 6-11, 2011

[6] *Part71-Packging and transportation of radioactive material*, United States Nuclear Regulatory Commission(U.S.NRC), January 30, 2017

[7] Thomas L. Sanders, Kevin D. Seager, Yusef R. Rashid, Peter R. Barrett, Anthony P. Malinauskas, Robert E. Einzinger, Hans Jordan, Thomas A. Duffey, Stephen H. Sutherland, Philip C. Reardon, *A method for determining the spent-fuel contribution to transport cask containment requirements*, Sandia report(SAND90-2406), Nov., 1992

[8] Scott Sanbron, Brian Koeppel, Nichilas Klymyshyn, Harold Adkins, Kennth Geelhood, *Assembly level modeling and transportation damage prediction of used nuclear fuel(UNF) cladding-14569*, Proceeding of Waste Management conference(WM 2014), March 2-6, Phoenix, Arizona, USA, 2014

[9] W. Zhao, Z. Karoutas, P. Evans, O. McRae, *LS-DYNA® Application in simulating impact tests of nuclear fuel spacer grids and drop tests of fuel shipping packages*, 12th International LS-DYNA User Conference, Dearborn, Micigan, USA, June 3-5, 2012

[10] J. J. Kim, K. B. Eom, N. G. Park, S. K. Lee, J. S. Yoo, *Structural characteristic analysis for R-SNF selection during transportation and handling*, Spring Proceedings of Korean Radioactive Waste Society, May 25-27, Mokpo, Korea, 2016

[11] O C. Kwon, S. Y. Kim, Y. I. Yoo, N. G. Park, S. K. Lee, J. K. Yoo, *R&D activities of spent nuclear fuel integrity evaluation during handling and transportation for long-term storage*, Proceedings of the 18th International Symposium on the Packaging and Transportation of Radioactive Materials(PATRAM 2016), Kobe, Japan, Sep. 18-23, 2016

[12] Billerey, A. *Evolution of fuel rod support under irradiation-Impact on the mechanical behavior of fuel assembly*, IAEA, Nuclear Fuel Cycle and Materials Section, 101-111, July, 2005

COMPDYN 2017
6th ECCOMAS Thematic Conference on
Computational Methods in Structural Dynamics and Earthquake Engineering
M. Papadrakakis, M. Fragiadakis (eds.)
Rhodes Island, Greece, 15–17 June, 2017

# NUMERICAL SIMULATION OF IMPACTS ON ELASTIC-VISCOPLASTIC SOLIDS WITH THE FLUX-DIFFERENCE SPLITTING FINITE VOLUME METHOD

**T. Heuzé**[1]

[1]Research Institute in Civil and Mechanical Engineering (GeM, UMR 6183 CNRS)
École Centrale de Nantes, 1 rue de la Noë, F-44321 Nantes, France
e-mail: thomas.heuze@ec-nantes.fr

**Keywords:** Flux difference splitting finite volume method, Elastic-viscoplastic solids, Dynamic impact, Curvilinear structured meshes.

**Abstract.** *A finite volume method is used and extended for the numerical simulation of impacts on elastic-viscoplastic solids with bidimensional curvilinear structured meshes. The formulation is based on the flux-difference splitting method [1], has second order accuracy through flux limiters, embeds the corner transport upwind method, and uses the second order accurate Strang splitting method to handle the right hand side of the system of balance laws. The approach is here derived with a Chaboche-type [2] elastic-viscoplastic solid within the small strain framework, and is illustrated on a problem of impact on a heterogeneous volume containing an inclusion. A comparison is performed with a finite element solution obtained with the finite element code Cast3M [3].*

## 1 INTRODUCTION

The numerical simulation of hyperbolic initial boundary value problems including extreme loading conditions such as impacts requires the ability to accurately capture and track the wave front of shock waves induced in the medium. Indeed, this permits to correctly follow the path of waves and hence understand the mechanical phenomena occuring within that medium. For solid-type media, it allows also for an accurate assessment of the plastic strain field and hence that of residual stresses and distortions within the structure. High speed forming processes like electromagnetic material forming are some application examples of severe loading conditions in which the track of wave fronts is important both for understanding the development of plastic strain in the workpiece and optimizing its final shape. Hence, these problems require numerical schemes able to meet high orders of accuracy and a high resolution of discontinuity without any spurious oscillations.

The numerical simulation of impacts on dissipative solids has been and is again mainly performed with the classical finite element method coupled with centered differences or Newmark finite difference schemes in time [4]. Though this approach has well-known advantages, classical time integrators introduce high frequency noise in the vicinity of discontinuities which is hard to remove with artificial viscosity without destroying the accuracy of the numerical solution. The finite volume method, initially developed for the simulation of gas dynamics [1], has gained recently more and more interest for problems involving impacts on solid media [5, 6, 7, 8]. This method shows some advantages to achieve an accurate tracking of wavefronts; among others (i) continuity of fields is not enforced on the mesh in its cell-centered version, that allows for capturing discontinuous solutions, (ii) the characteristic structure of hyperbolic equations can be introduced within the numerical solution, either through the explicit solution of a Riemann problem at cell interfaces, or in a implicit way through the construction of the numerical scheme, (iii) the amount of numerical viscosity introduced can be controlled locally as a function of the local regularity of the solution, so that to permit the elimination of spurious numerical oscillations while preserving a high order of accuracy in more regular zones.

We are here interested in elastic-viscoplastic systems, leading to a non-homogeneous system of partial differential equations, generating a system of weakly discontinuous waves beyond the viscoplastic yield, following a discontinuous (elastic) wave due to the transition between elastic and elastic-viscoplastic ranges. In this work, we use and extend a finite volume method applied to these dissipative media with bidimensional curvilinear structured meshes of quadrangles. The formulation is based on the flux-difference splitting method [1], has second order spatial accuracy through flux limiters, embeds the corner transport upwind method, and uses the second order accurate Strang splitting method to handle the right hand side of the system of balance laws. The approach is here derived with a Chaboche-type [2] elastic-viscoplastic solid within the small strain framework, and is illustrated on a problem of impact on a heterogeneous volume containing an inclusion. A comparison is performed with a finite element solution obtained with the finite element code Cast3M [3].

## 2 ELASTIC-VISCOPLASTIC INITIAL BOUNDARY VALUE PROBLEM

Let's consider an elastic-viscoplastic solid with an Odqvist creep law [2] (or Chaboche-type model) and a linear kinematic hardening, the associated constitutive equations written within

the small strain framework are summarized below:

$$\dot{\boldsymbol{\varepsilon}} = \dot{\boldsymbol{\varepsilon}}^e + \dot{\boldsymbol{\varepsilon}}^p \tag{1}$$

$$\dot{\boldsymbol{\sigma}} = \mathbf{C} : \dot{\boldsymbol{\varepsilon}}^e \tag{2}$$

$$f = \sigma_{\text{eq}}(\boldsymbol{\xi}) - \sigma_y \; ; \quad \sigma_{\text{eq}} = \sqrt{\frac{3}{2}\boldsymbol{\xi} : \boldsymbol{\xi}} \; ; \quad \boldsymbol{\xi} = \mathbf{s} - \mathbf{X} \; ; \quad \mathscr{C} = \{(\boldsymbol{\sigma}, \mathbf{X}, \dot{\boldsymbol{\varepsilon}}^p) | f \leq 0\} \tag{3}$$

$$\dot{\boldsymbol{\varepsilon}}^p = \frac{3}{2}\dot{p}\frac{\boldsymbol{\xi}}{\sigma_{\text{eq}}} \tag{4}$$

$$\dot{\mathbf{X}} = \frac{2}{3}D\dot{\boldsymbol{\varepsilon}}^p \tag{5}$$

$$\dot{p} = \left\langle \frac{f}{K} \right\rangle^n \tag{6}$$

where equations (1), (2), (3), (4), (5) and (6) respectively refer to the additive partition of the strain rate ($\dot{\boldsymbol{\varepsilon}}$) into elastic ($\dot{\boldsymbol{\varepsilon}}^e$) and viscoplastic ($\dot{\boldsymbol{\varepsilon}}^p$) parts, the elastic law, the yield criterion $f$ (or viscous stress) associated to Mises' norm and the elastic convex $\mathscr{C}$, the viscoplastic flow rule, the evolution law of the kinematic hardening and the creep law. One defines $\boldsymbol{\xi} = \mathbf{s} - \mathbf{X}$, where $\mathbf{s}$ is the deviatoric part of Cauchy stresses $\boldsymbol{\sigma}$, $\mathbf{X}$ the variable defining the center of the elastic convex, $\langle x \rangle = (x + |x|)/2$ the positive part of $x$, $\mathbf{C}$ the elastic stiffness tensor, $\dot{p}$ the rate of cumulated viscoplastic strain, and $D$ the hardening parameter.

To these constitutive equations, are added the equations of motion and the relations between the linearized strain rate tensor $\dot{\boldsymbol{\varepsilon}}$ and the velocity field. One can show that we obtain the following non-homogeneous system of partial differential equations, written here for the bidimensional plane strain case:

$$\frac{\partial \mathbf{u}}{\partial t} + \frac{\partial \mathbf{f}_x}{\partial x} + \frac{\partial \mathbf{f}_y}{\partial y} = \mathbf{S}(\mathbf{u}) \qquad \forall (\mathbf{x} \times t) \in (\Omega \times ]0, t_{\text{end}}]) \tag{7}$$

defined within a domain $\Omega$ and a time interval of duration $t_{\text{end}}$, and has to be supplemented with appropriate initial and boundary conditions. The vector of unknowns $\mathbf{u}$, fluxes $\mathbf{f}_x$ and $\mathbf{f}_y$, and the right hand side $\mathbf{S}(\mathbf{u})$ are defined as follows:

$$\mathbf{u} = \begin{bmatrix} \sigma_{xx} \\ \sigma_{yy} \\ \sigma_{xy} \\ u \\ v \end{bmatrix} \; ; \quad \mathbf{f}_x = \begin{bmatrix} -(\lambda + 2\mu)u \\ -\lambda u \\ -\mu v \\ -\sigma_{xx}/\rho \\ -\sigma_{xy}/\rho \end{bmatrix} \; ; \quad \mathbf{f}_y = \begin{bmatrix} -\lambda v \\ -(\lambda + 2\mu)v \\ -\mu u \\ -\sigma_{xy}/\rho \\ -\sigma_{yy}/\rho \end{bmatrix} \; ; \quad \mathbf{S}(\mathbf{u}) = -3\frac{\mu}{\sigma_{\text{eq}}} \left\langle \frac{f}{K} \right\rangle^n \begin{bmatrix} \xi_{xx} \\ \xi_{yy} \\ \xi_{xy} \\ 0 \\ 0 \end{bmatrix} \tag{8}$$

where $\lambda$ and $\mu$ denote the Lamé's parameters, $u$ and $v$ the velocity components, and $\rho$ the mass density. The eigen-analysis of the jacobian matrix associated to the homogeneous part of (7)

$$\mathcal{J} = \frac{\partial(\mathcal{F} \cdot \mathbf{n})}{\partial \mathbf{u}} = \frac{\partial \mathbf{f}_x}{\partial \mathbf{u}} n_x + \frac{\partial \mathbf{f}_y}{\partial \mathbf{u}} n_y = \mathbf{A} n_x + \mathbf{B} n_y = - \begin{bmatrix} 0 & 0 & 0 & n_x(\lambda + 2\mu) & \lambda n_y \\ 0 & 0 & 0 & n_x \lambda & n_y(\lambda + 2\mu) \\ 0 & 0 & 0 & n_y \mu & n_x \mu \\ \frac{n_x}{\rho} & 0 & \frac{n_y}{\rho} & 0 & 0 \\ 0 & \frac{n_y}{\rho} & \frac{n_x}{\rho} & 0 & 0 \end{bmatrix} \tag{9}$$

gives the characteristic speeds $\lambda_1 = -c_L$, $\lambda_2 = c_L$, $\lambda_3 = -c_s$, $\lambda_4 = c_s$, $\lambda_5 = 0$, where $c_L = \sqrt{(\lambda + 2\mu)/\rho}$ and $c_s = \sqrt{\mu/\rho}$ are the celerities associated to tensile/compression and shear waves respectively; and associated characteristic directions (eigenvectors) $\mathbf{K}^{(p)}$, $1 \leq p \leq 5$.

## 3 FINITE VOLUME METHOD

The finite volume method is based on subdividing the computational domain in elementary cells within which, for the cell-centered version, an approximation $\mathbf{U}_i$ of the field $\mathbf{u}$ is defined in the cell $i$ by integral averaging. This approximation is updated by means of balance laws (7) written in integral form on each grid cell, coupled to an explicit time integration scheme.

### 3.1 Strang splitting for the right hand side

The solution procedure to account for the right hand side of the differential system (7) can be carried out by means of a splitting algorithm [1]. For first order accuracy (Godunov splitting), a first step consists in solving the homogeneous part of (7) on the time step associated to the initial condition known at time $t_n$ ($n$ referring to the time step number). The obtained solution $\bar{\mathbf{u}}^{n+1}$ is then used as an initial condition for the following initial value problem:

$$\begin{aligned} &\frac{d\mathbf{u}}{dt} = \mathbf{S}(\mathbf{u}) \\ &\mathbf{u}(0) = \bar{\mathbf{u}}^{n+1} \end{aligned} \tag{10}$$

This decomposition is exact for a linear advection-reaction equation. For the nonlinear system considered here, it is an approximation. Naming $C$ et $S$ operators associated to the solution of homogeneous and non-homogeneous parts, the update of the unknown field reads

$$\mathbf{u}^{n+1} = S^{(\Delta t)} C^{(\Delta t)} \mathbf{u}^n \tag{11}$$

In order to improve the accuracy of the computed viscoplastic strains, the second order accurate Strang splitting algorithm is used here:

$$\mathbf{u}^{n+1} = S^{(\Delta t/2)} C^{(\Delta t)} S^{(\Delta t/2)} \mathbf{u}^n \tag{12}$$

### 3.2 Flux-difference splitting formulation

We use here a finite volume formulation based on flux-difference splitting [1], applied to curvilinear structured meshes of quadrangles. This version falls within the class of total variation non-increasing methods, that allow to meet both a high order of accuracy in zones where the solution field is regular and a high resolution of discontinuities without spurious numerical oscillations. Their strength relies on their ability to introduce a controlled amount of numerical viscosity locally, so that to adapt to the local regularity of the solution. This formulation is applied to the homogeneous part of the differential system (7) so that to be in accordance with a non-increasing total variation.

Let's consider the grid cell $i$ shown in figure 1, of area $|A_i|$, which edge $s$ ($1 \leq s \leq 4$) joining points $P_s$ and $P_{s+1}$ is of length $L_s$, has an outward unit normal $\mathbf{n}_s$, and has left $(L)$ and right $(R)$ states known at time $t_n$. The update of the cell state at time $t_{n+1}$ reads:

$$\mathbf{U}_i^{n+1} = \mathbf{U}_i^n - \frac{\Delta t}{|A_i|} \left( \sum_{k=1}^{P} L_k \mathcal{A}_k^+ \Delta \mathbf{U}_k + \sum_{l=1}^{Q} L_l \mathcal{A}_l^- \Delta \mathbf{U}_l \right) - \frac{\Delta t}{|A_i|} \left( \sum_{k=1}^{P} L_k \tilde{\mathbf{F}}_k^{\text{out}} - \sum_{l=1}^{Q} L_l \tilde{\mathbf{F}}_l^{\text{in}} \right) \tag{13}$$

The above formula consists of two groups of terms which are detailed below.

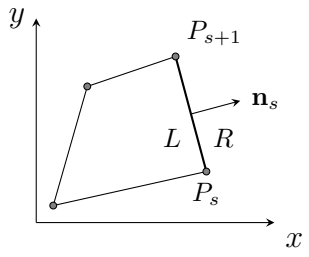


Figure 1: Quadrangular finite volume

### 3.2.1 Godunov flux

The *first* group of terms in equation (13) shows *fluctuations*, denoted by operators $\mathcal{A}_k^{\pm}\Delta\mathbf{U}_k$:

$$\mathcal{A}_k^{\pm}\Delta\mathbf{U}_k = \sum_{p=1}^{M_w} \lambda_p^{\pm}\mathcal{W}_k^{(p)} = \sum_{p=1}^{M_w} \lambda_p^{\pm}\alpha_k^{(p)}\mathbf{K}_k^{(p)} \tag{14}$$

quantifying the effect of all waves travelling rightward or leftward respectively in the local frame of edge $k$. Theses fluctuations are defined with positive and negative parts of characteristic speeds $\lambda_p^{\pm}$, and associated characteristic directions $\mathbf{K}_k^{(p)} \equiv \mathbf{K}^{(p)}(\mathbf{n}_k)$. Each wave is weighted with a coefficient $\alpha_k^{(p)}$ determined by the projection of the jump of the unknown vector $\Delta\mathbf{U}_k = (\mathbf{U}_R - \mathbf{U}_L)_k$ across the edge $k$ onto the characteristic basis $\mathbf{K}_k^{(p)}$ ($1 \leq p \leq M_w$, $M_w = 5$ here):

$$\Delta\mathbf{U}_k = \sum_{p=1}^{M_w} \mathcal{W}_k^{(p)} = \sum_{p=1}^{M_w} \alpha_k^{(p)}\mathbf{K}_k^{(p)} = \mathbf{K}\boldsymbol{\alpha}_k \tag{15}$$

The wavestrength is defined by $\mathcal{W}_k^{(p)} = \alpha_k^{(p)}\mathbf{K}_k^{(p)}$. This projection amounts to solve a (linear) Riemann problem associated to edge $k$. The fluctuations associated to each edge are summed to compute the contribution of first order terms to the update of grid cell $i$; this summation is performed on negative fluctuations for edges having an outward normal, and on positive fluctuations for edges having an inward normal, so that $P + Q = N$, $N$ being the number of edges of grid cell $i$. The formulation with fluctuations is actually equivalent [1] to applying the Godunov's method which interface fluxes are computed with the steady part ($x/t = 0$) of the Riemann problem solution.

### 3.2.2 Additional fluxes

The *second* group of terms in equation (13) involve additional fluxes defined at edges, either inward (in) or outward (out) depending on the edge normal, that consist of two types of contributions

$$\tilde{\mathbf{F}}_l^{\text{in}} = \tilde{\mathbf{F}}_l^{\text{HO}} + \tilde{\mathbf{F}}_l^{\text{tran}}. \tag{16}$$

**High order fluxes**

The first contribution allows to reach a higher order (HO) of accuracy (order two here),

defined with wavestrength $\mathcal{W}_l^{(p)}$ that have been limited, hence denoted $\tilde{\mathcal{W}}_l^{(p)} = \tilde{\alpha}_l^{(p)}\mathbf{K}_l^{(p)}$:

$$\tilde{\mathbf{F}}_l^{\text{HO}} = \frac{1}{2}\sum_{p=1}^{M_w} |\lambda_l^{(p)}| \left(1 - \frac{\Delta t}{\Delta s_l}|\lambda_l^{(p)}|\right) \tilde{\mathcal{W}}_l^{(p)} \tag{17}$$

where $\Delta s_l$ refers to the distance between barycenters of grid cells sharing edge $l$. Waves are limited based on an upwind ratio $\theta_l^{(p)}$ defined for wave $p$ on edge $l$ as:

$$\theta_l^{(p)} = \frac{\mathcal{W}_J^{(p)} \cdot \mathcal{W}_l^{(p)}}{\|\mathcal{W}_l^{(p)}\|^2} \tag{18}$$

where $J$ denotes the upwind edge, that is the opposed edge to $l$ belonging to grid cell $L$ located to the left in the local frame of edge $l$ (see figure 1) if $\lambda_l^{(p)} > 0$, or the opposed edge belonging to grid cell $R$ located to the right if $\lambda_l^{(p)} < 0$. However, for noncartesian quadrangles upwind and downwind edges do not necessarily have the same normal. Thus, the computation of the upwind ratio (18) has to be performed with wavestrengths computed in a same local reference frame, that of edge $l$. Wavestrengths $\mathcal{W}_J^{(p)}$ are hence computed with weighting coefficients $\alpha_J^{(p)}$ recomputed in the local frame of edge $l$:

$$\alpha_J^{(p)} = \mathbf{K}^{-1}(\mathbf{n}_l) \cdot \Delta\mathbf{U}_J \tag{19}$$

where $\Delta\mathbf{U}_J$ denotes the jump across edge $J$ of the unknown vector. The upwind ratio (18) can be understood as a certain measure of the local regularity of the solution, the wavestrength of wave $p$ associated to edge $l$ is then limited by means of a limiting function $\phi(\theta_l^{(p)})$:

$$\tilde{\alpha}_l^{(p)} = \phi(\theta_l^{(p)})\alpha_l^{(p)} \tag{20}$$

Many limiting functions exist and permit to obtain different known finite volume schemes [9]. Some of them enable the numerical scheme to satisfy a non-increasing total variation, so that the appearance of spurious numerical oscillations can be avoided in the vicinity of discontinuities. The limiter Superbee defined by $\phi(\theta) = \max(0, \min(1, 2\theta), \min(2, \theta))$ falls in this family, and is used in this work. More generally, the limitation of wavestrength amounts to add locally some numerical viscosity, and to locally lower the order of accuracy to properly capture discontinuities. In zones where the solution field is more regular, the limitation is not active and an accuracy of order two can be reached.

**Transverse fluxes**

The second contribution to additional fluxes (16) enables to improve the stability of the numerical scheme, so that the Courant number can be set at one. These fluxes allows to account for informations travelling in bias with respect to the considered grid cell; this is the contribution to the grid cell to be updated of a cell only sharing a node (but not an edge) with it. This method is called the *Corner Transport Upwind (CTU) method* [1]. These fluxes are of great importance to ensure numerical stability for elastic media; indeed elasticity couples strain components through Poisson's effect, so that a transverse information to the considered grid cell should be introduced in the numerical scheme.

Let's consider the patch of grid cells shown in figure 2. One focuses on the edge denoted $(i)$ which local frame $(\mathbf{n}_i, \mathbf{t}_i)$ is shown. This edge gives rise to the computation of normal

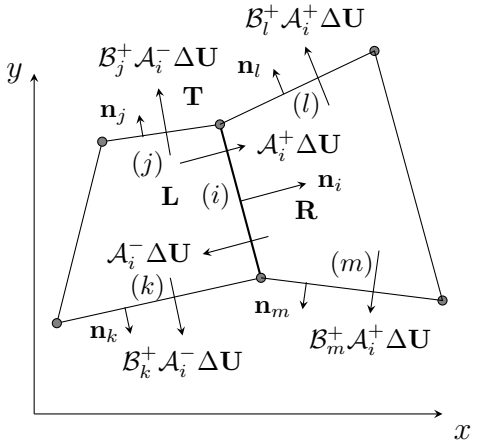


Figure 2: Normal and transverse fluctuations defined from edge $i$.

fluctuations $\mathcal{A}_i^+\Delta\mathbf{U}$ and $\mathcal{A}_i^-\Delta\mathbf{U}$ contributing to grid cells $R$ et $L$ respectively. These normal fluctuations leads to the computation of transverse fluctuations giving contribution to neighboring cells across edges $(j)$ and $(k)$ for cell $L$, and across edges $(m)$ and $(l)$ for cell $R$. These transverse fluctuations are computed by projecting normal fluctuations on the characteristic basis associated to the Riemann problem defined on the adjacent edge; it appears as a transverse Riemann solver. For instance the negative normal fluctuation is decomposed on the characteristic basis associated to edge $(j)$ as

$$\mathcal{A}_i^-\Delta\mathbf{U} = \sum_{p=1}^{M_w} \beta_p \mathbf{K}_j^{(p)} = \mathbf{K}_j\boldsymbol{\beta} \tag{21}$$

where $\mathbf{K}_j$ accounts here for the normal $\mathbf{n}_j$ of edge $(j)$, but also of different material properties between grid cells $L$ and $T$. Coefficients $\beta_p$ are determined analytically for bidimensional plane strain elasticity equations. For outward normals shown in figure 2, the transverse fluctuations are computed with the positive operator $\mathcal{B}^+$, that is only waves with positive characteristic speeds will contribute to this transverse fluctuation

$$\mathcal{B}_j^+\mathcal{A}_i^-\Delta\mathbf{U} = c_L\mathcal{W}^{(2)} + c_s\mathcal{W}^{(4)} \tag{22}$$

An additional numerical flux defined at edges is hence built from these transverse fluctuations:

$$\tilde{\mathbf{F}}_j^{\text{tran}} = \frac{\Delta t}{2\Delta s_j}\mathcal{B}_j^+\mathcal{A}_i^-\Delta\mathbf{U}_i \tag{23}$$

which contributes to grid cell $T$. The flux $\tilde{\mathbf{F}}_l^{\text{tran}}$ associated to edge $l$ appearing in equation (16) thus denotes transverse contributions from adjacent grid cells to cell $i$. More generally, this finite volume scheme is linked to a Taylor expansion of the solution in the vicinity of a grid cell. In this framework, Godunov fluxes are first order terms, high order fluxes are second order terms, and transverse fluxes correspond to cross-derivatives.

## 4 SUDDEN VELOCITY LOADING AND UNLOADING OF A HETEROGENEOUS VOLUME

Let's consider a square heterogeneous volume, of side length $2a$, with an inclusion of circular cross-section of radius $R$ centered within the volume, which mesh is shown in figure 3.

This volume in an initial natural state is suddenly loaded on its left side at time $t = 0$ with a constant first component of velocity $\bar{u}$. After time $\tau$, the applied velocity is set to zero. Normal velocity components at the top and bottom sides of the volume are set to zero while transmittive boundary conditions have been set on the right side. We assume an arbitrary heterogeneous material, that consists of an inclusion in aluminium embedded in a matrix made of steel. The analysis is carried out in plane strain. Numerical data used for computations are summarized in table 1.

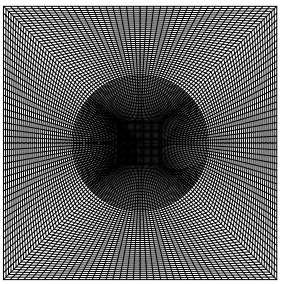

Figure 3: Mesh

| Geometry | Matrix | Inclusion |
|---|---|---|
| $a = 10^{-3}$m | $E_M = 200$GPa | $E_I = 700$GPa |
| $R = 5 \times 10^{-3}$m | $\nu_M = 0.3$ | $\nu_I = 0.34$ |
| Loading | $\rho_M = 7800$kg.m$^{-3}$ | $\rho_I = 2700$kg.m$^{-3}$ |
| $\bar{u} = 40$m.s$^{-1}$ | | $\sigma_{y_I} = 350$MPa |
| $\tau = 7 \times 10^{-8}$s | | $D = 2$GPa |

Table 1: Numerical data used for computations.

The matrix is assumed to remain elastic, only the inclusion undergoes viscoplastic strains. For comparison purpose, a finite element solution is obtained with the finite element code Cast3M [3], computed with an implicit time discretization and bilinear quadrangular finite elements. This numerical solution is compared to the finite volume one in figures 4, 5, and 6 at times $1 \times 10^{-7}$, $1.9 \times 10^{-7}$ et $3 \times 10^{-7}$ seconds respectively. The Courant number has been set at 0.9, the same time step being used for both numerical solutions. The comparison is performed on

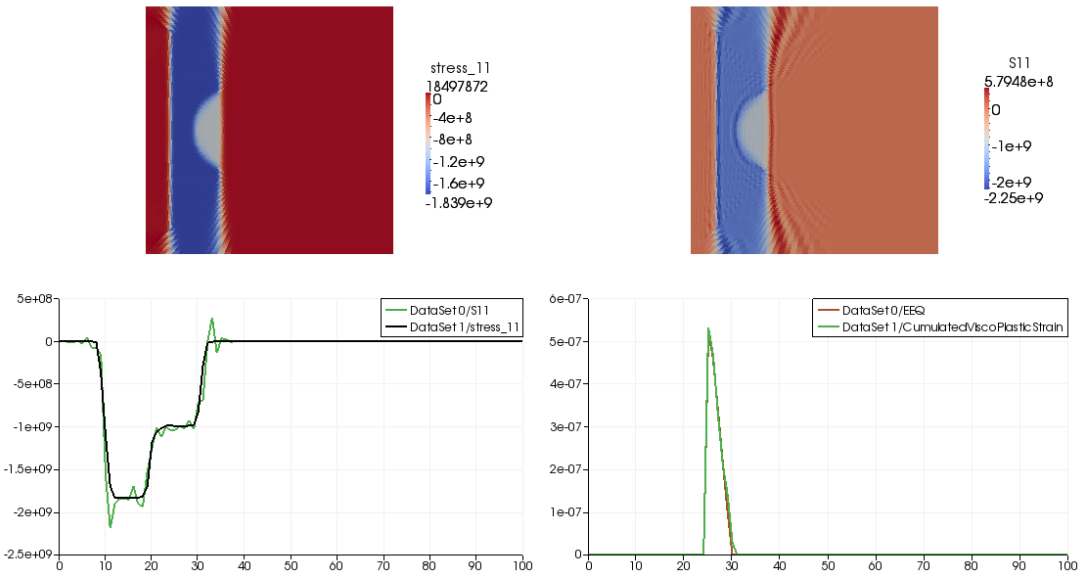


Figure 4: Time $t = 1 \times 10^{-7}$s

the component $\sigma_{11}$ (in Pa) of the stress field and on the cumulated viscoplastic strain $p$. These two quantities are plotted along the horizontal median line, and superposed for the finite volume solution (DataSet0) and the finite element solution (DataSet1). Isovalues on the top left of figures 4 to 6 are associated to the finite volume solution while these at the top right are associated

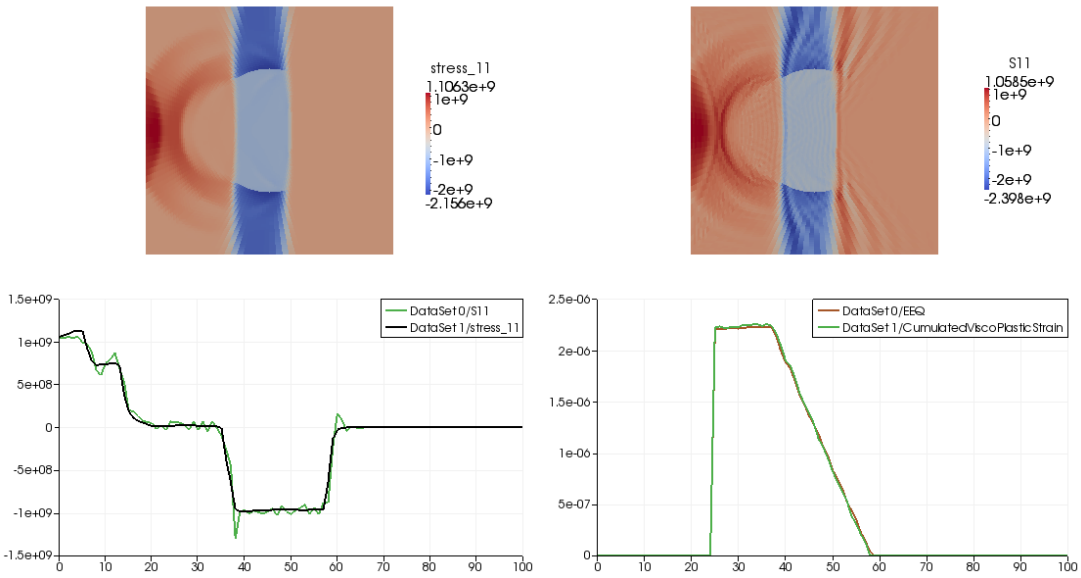


Figure 5: Time $t = 1.9 \times 10^{-7}$s

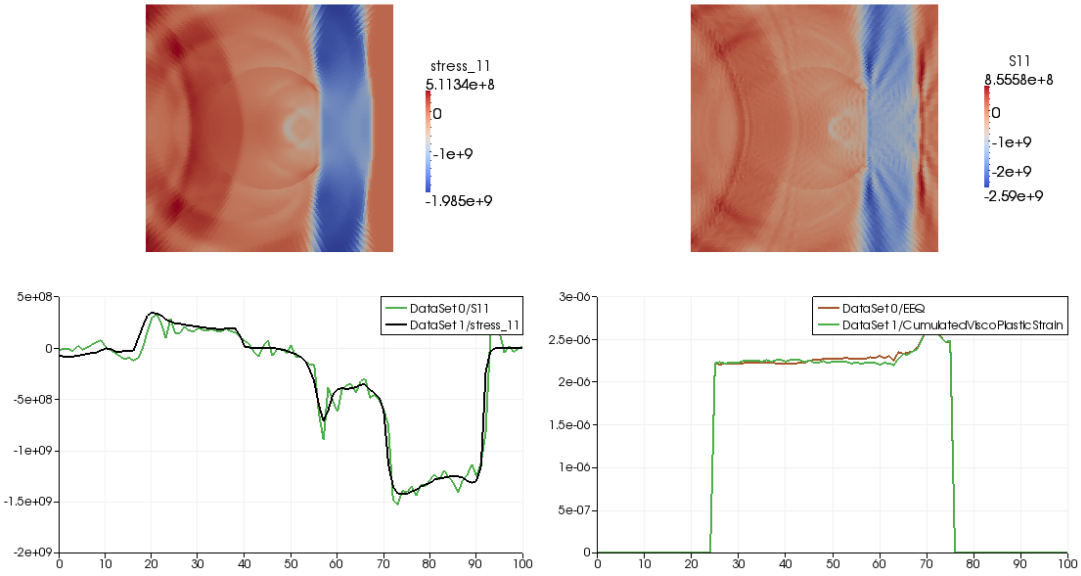


Figure 6: Time $t = 3 \times 10^{-7}$s

to the finite element solution. One can observe in figure 4 the slot of negative normal stress formed by the prescribed horizontal velocity on the left side. Its falling front has interacted with the front interface between the matrix and the inclusion, and has been both reflected and transmitted, generating an intermediate state of higher stress (lower in absolute value) and a higher first component of velocity since the impedance of the matrix is higher than that of the inclusion. The finite element stress field shows spurious numerical oscillations in the vicinity of discontinuities, especially close to the top and bottom sides where tensile spurious stress states appear. Cumulated viscoplastic strain are almost identical for both numerical solutions.

In figure 5, one can see that the reflected wave has been transformed into tensile wave after the interaction with the increasing stress front associated to velocity unloading; then has been reflected on the left side of the volume. The cumulated viscoplastic strains propagation is delayed with respect to the propagation of the negative stress slot, which is due to viscoplasticity. At last, one can see in figure 6 that this slot has interacted with the back side of the inclusion interface, generating intermediate states of normal compression stress, while cumulated viscoplastic strains grow more importantly close to this area. Generally speaking, the finite volume solution

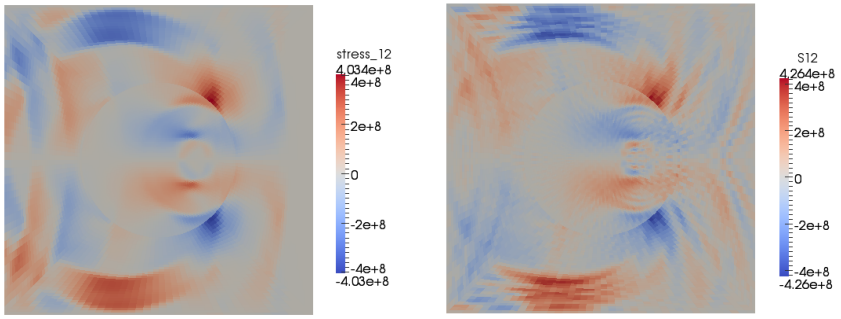


Figure 7: Shear stress component $\sigma_{12}$ at time $t = 3 \times 10^{-7}$s

allows to obtain the same viscoplastic strains than these of the finite element solution without the spurious numerical oscillations on stresses obtained with the finite element solution. Figure 7 shows the comparison of the shear component of stress $\sigma_{12}$ at time $t = 3 \times 10^{-7}$s, on which these oscillations are visible.

## 5 CONCLUSIONS

It has been presented in this work the use and extension of a finite volume method for elastic-viscoplastic solids with curvilinear structured meshes of quadrangles. The formulation is based on the flux-difference splitting method, and uses the second order accurate Strang splitting approach for the computation of the right hand side of the differential system of equations. Comparison is performed with a finite element solution obtained with the finite element code Cast3M [3] on a suddenly loaded then unloaded heterogeneous volume. The comparison shows identical cumulated viscoplastic strains computed. However, the finite volume solution enables to overcome spurious numerical oscillations on the stress and velocity fields thanks to flux limiters, applied on the homogeneous part of (7), satisfying a non-increasing total variation.

## REFERENCES

[1] R. Leveque. *Finite volume methods for hyperbolic problems.* Cambridge University PressMcGraw Hill, 2002.

[2] J. Lemaitre, J.L. Chaboche. *Mechanics of solid materials*. Cambridge university press, 1994.

[3] Cast3M. User's manual. www.cast3M-cea.fr, 2016.

[4] T. Belytschko, W.K. Liu, B. Moran. *Nonlinear finite elements for continua and structures.* Wiley, 2000.

[5] P.T. Barton, D. Drikakis, E.I. Romenskii. A high order eulerian godunov method for elastic-plastic flow in solids, *International Journal for Numerical Methods in Engineering*, **81**, 453-484, 2010.

[6] A.L. Ortega, M. Lombardini, D. Pullin, D. Meiron, Numerical simulation of elastic-plastic solid mechanics using an eulerian stretch tensor approach and HLLD Riemann solver. *Journal of Computational Physics*, **257**, 414-441, 2014.

[7] N. Favrie, S. Gavrilyuk. Mathematical and numerical model for nonlinear viscoplasticity. *Phil. trans. R. Soc. A*, **369**, 2864-2880, 2011.

[8] S. Ndanou, N. Favrie, S. Gavrilyuk. Multi-solid and multi-fluid diffuse interface model: applications to dynamic fracture and fragmentation, *Journal of Computational Physics*, **295**, 523-555, 2015.

[9] P.K. Sweby. High resolution schemes using flux limiters for hyperbolic conservation laws, *SIAM Journal on Numerical Analysis*, **21**, 995-1011, 1984.

COMPDYN 2017
6th ECCOMAS Thematic Conference on
Computational Methods in Structural Dynamics and Earthquake Engineering
M. Papadrakakis, M. Fragiadakis (eds.)
Rhodes Island, Greece, 15–17 June 2017

# AN INTEGRATED PROCEDURE FOR SEISMIC RESPONSE ANALYSIS OF STRUCTURES USING DIFFERENTIAL QUADRATURE METHOD

**Hongjing Li, Xijun Kong, and Haojie Xing**

College of Civil Engineering, Nanjing Tech University
30 South Puzhu Road, Nanjing 211816, China
e-mail: hjing@njtech.edu.cn

**Keywords:** Seismic response, Time-stepping procedure, Differential quadrature method, Multi-degree-of-freedom system, Computational effort.

**Abstract.** *The current linear and nonlinear seismic response analysis approaches are based generally on the numerical approximation step-by-step procedures in practice, and huge computational effort is usually required in order to achieve the desired level of accuracy over the range of time for which the response is needed. However, higher efficiency is the final objective developing the analysis procedures in the same requirements of numerical stability and numerical accuracy. In this paper, a numerical time-stepping procedure is developed for the solution of equations governing the motion of a multi-degree-of-freedom system subjected to earthquake induced ground acceleration on the basis of the differential quadrature (DQ) rule. Initially the history of the seismic ground motion and the structural dynamic responses are divided into a sequence of time intervals in which the DQ analysis procedure will be carried out for evaluation of the seismic response, and the ground acceleration function is constructed over each interval by piecewise linear interpolations. Then each interval is divided into a set of time step once again, and the final responses of velocity and acceleration are expressed approximately as a weighted linear sum of the initial conditions and the response of displacement at the discrete points over the interval by using the DQ rule. The formulae for the quadrature solution of the differential equations of motion are deduced so that the history of the dynamic response of the system could be calculated in the time-stepping procedure using the DQ method. Finally a two-story shear frame structure is employed for numerical illustration, results show that this DQ analysis procedure may achieve a high order of accuracy when the lengths of the time intervals and the discrete points over each interval are chosen properly.*

## 1 INTRODUCTION

It is important to evaluate the dynamic behavior of a code-designed structure during a strong earthquake, and the time-stepping procedures may provide a tool for implementation of this purpose. Among the different time-stepping methods, Newmark beta methods are more general and applied frequently in the field of earthquake engineering. It is noted that a practical structure is usually system with a huge number of degree of freedom, and the seismic response must be calculated within a very short time interval because of demands of the numerical stability and accuracy. This means that the time history of the seismic response can only be obtained by computations repeatedly many times according to the different time-stepping approaches established generally on the numerical approximation step-by-step procedures, so huge computational efforts are usually required. However, the higher efficiency is the final objective developing the analysis procedures in the same requirements of numerical stability and numerical accuracy.

Differential quadrature method (DQM) proposed by Bellman and his associates [1, 2] is a numerical solution technique for the initial and/or boundary value problems of ordinary and partial differential equations. The main idea of the DQM is that the values of derivatives at each sampling grid point are expressed approximately as weighted linear sums of the function values at all sampling grid points within the domain under consideration, and it is recognized production of the high accurate solutions with a minimal computational effort [3]. In engineering field, the DQM is usually applied for solving of time-invariant problems such as static analysis or natural vibration analysis [4-17], that means the DQM is used for the approximation of the derivatives to spatial coordinates and the solutions of various engineering boundary value problems have been provided by this method. Earthquake induced ground motion is a kind of time varying excitation for structures, and obviously the problem of seismic response analysis belongs to the initial value problem after the discretization of spatial domain and the boundary conditions of the structure are carried out by certain numerical method such as the finite element method and the differential equations governing the motions of the structure are established. A method solving the initial value problems using the differential quadrature rule has been developed by Fung [18, 19] and Liu et al. [20], in this paper, it is extended to evaluate the dynamic response of the structure subjected to excitation of ground acceleration induced by an earthquake. Because the seismic ground acceleration is a wave process with complicated frequency components and practically expressed as a discrete time function with thousands of sampling grid points during duration of the earthquake, the differential quadrature rule cannot be used directly for the time derivatives approximation to achieve the solution of the governing equations of the structure. Based on reference [21], an integrated procedure that the seismic time history analysis is transformed into a sequence of initial value problems and the differential quadrature rule is applied step by step within a short time interval to avoid distortion of the weighting coefficient matrix is presented, the purpose is to provide a high accuracy numerical approach for structural response analysis due to earthquake excitation.

## 2 DIFFERENTIAL QUADRATURE RULE

The DQM approximates the values of the derivatives at each sampling grid point for a function as a weighted linear sum of function values at all given sampling grid points. A differential quadrature approximation at the *i*-th discrete point is given by

$$f_i' = \sum_{j=0}^{n} w_{ij} f_j \quad \text{for } i = 0, 1, 2, \cdots, n \tag{1}$$

in which $n$ denotes the number of discrete points considered in the domain; $f_i = f(x_i)$ and $f_i' = f'(x_i)$ are the function value and its derivative at the point $x = x_i$, respectively; $w_{ik}$ is the corresponding weighting coefficient, they are written in matrix form as

$$\boldsymbol{w} = \begin{bmatrix} w_{00} & w_{01} & \cdots & w_{0n} \\ w_{10} & w_{11} & \cdots & w_{1n} \\ \vdots & \vdots & & \vdots \\ w_{n0} & w_{n1} & \cdots & w_{nn} \end{bmatrix} \tag{2}$$

Generally the form of the function $f(x)$ is taken as

$$f(x) = x^k, \ k = 0, 1, 2, \cdots, n \tag{3}$$

then the weighting coefficient matrix can be calculated, i.e.

$$\boldsymbol{w} = \begin{bmatrix} 1 & x_0 & \cdots & x_0^n \\ 1 & x_1 & \cdots & x_1^n \\ \vdots & \vdots & & \vdots \\ 1 & x_n & \cdots & x_n^n \end{bmatrix} \begin{bmatrix} 0 & 1 & & \\ & 0 & \ddots & \\ & & \ddots & n \\ & & & 0 \end{bmatrix} \begin{bmatrix} 1 & x_0 & \cdots & x_0^n \\ 1 & x_1 & \cdots & x_1^n \\ \vdots & \vdots & & \vdots \\ 1 & x_n & \cdots & x_n^n \end{bmatrix}^{-1} \tag{4}$$

or

$$\boldsymbol{w} = \boldsymbol{V}\boldsymbol{A}\boldsymbol{V}^{-1} \tag{5}$$

where $x_0, x_1, x_2, \cdots, x_n$ are the co-ordinates of the n+1 discrete points; $\boldsymbol{V}$ represents a Vandermonde matrix which consists of elements of $x_j^k$ and always has an inverse.

For numerical computational problems, it is convenient to choose the discrete points with equal spacing, and this choice is performed practically in most time-stepping procedures. But in DQM, the accuracy and the stability characteristic of the quadrature solutions are dictated by the choice of the locations of the sampling grid points, and basically the non-uniform grids have been considered instead of the equally spaced grids. However, an issue of the sampling grid points for differential quadrature solution to give unconditionally stable higher-order accurate time step integration algorithms is introduced by Fung [18], in which independent variables $x$ may be determined by solving the following equation:

$$x^m - W_1 - W_2 x - W_3 x^2 - \cdots - W_m x^m = 0 \tag{6}$$

where

$$W_k = \frac{(-1)^{m-k} m!\, m!\, (m + k - 2)!}{(k-1)!\,(k-1)!\,(m+1-k)!\,(2m)!} \frac{2[m + \mu(k-1)]}{1+\mu} \tag{7}$$

## 3 SEISMIC RESPONSE ANALYSIS BY DQ RULE

### 3.1 Dynamic response of the MDOF systems

The differential equations governing the response of a multi- degree-of-freedom system to earthquake-induced ground motion can be expressed as

$$\boldsymbol{m}\ddot{\boldsymbol{u}} + \boldsymbol{c}\dot{\boldsymbol{u}} + \boldsymbol{k}\boldsymbol{u} = -\boldsymbol{m}\boldsymbol{\iota}\, \ddot{u}_g \tag{8}$$

that satisfies the initial conditions

$$\boldsymbol{u} = \boldsymbol{u}(0), \ \dot{\boldsymbol{u}} = \dot{\boldsymbol{u}}(0) \tag{9}$$

where $\boldsymbol{k}$, $\boldsymbol{c}$ and $\boldsymbol{m}$ are the stiffness, damping and mass matrices, respectively; $\boldsymbol{\iota}$ is the influence vector; $\ddot{u}_g(t)$ is the ground acceleration induced by the earthquake.

The displacement $\boldsymbol{u}$ of an $N$-DOF system can be expressed as the superposition of the modal contributions, that is

$$\boldsymbol{u}(t) = \sum_{j=1}^{N} \boldsymbol{\Phi}_j q_j(t) \tag{10}$$

in which $\boldsymbol{\Phi}_j$ is $j$-th natural mode of the system without damping, and $q_j$ corresponding modal co-ordinates.

Using this equation, the coupled equations (8) in $\boldsymbol{u}(t)$ can be transformed to a set of uncoupled equations with $q_j(t)$ as the unknowns if the system has classical damping. Substituting Eq. (10) in Eq. (8) gives

$$\sum_{i=1}^{N} \boldsymbol{m}\boldsymbol{\Phi}_i \ddot{q}_i(t) + \sum_{i=1}^{N} \boldsymbol{c}\boldsymbol{\Phi}_i \dot{q}_i(t) + \sum_{i=1}^{N} \boldsymbol{k}\boldsymbol{\Phi}_i q_i(t) = -\boldsymbol{m}\boldsymbol{\iota}\, \ddot{u}_g \tag{11}$$

Premultiplying each term in this equation by $\boldsymbol{\Phi}_j^T$ and using the orthogonality property of the modes gives

$$\ddot{q}_j + 2\zeta_j \omega_j \dot{q}_j + \omega_j^2 q_j = -\eta_j \ddot{u}_g \text{ for } j = 1, 2, \cdots, N \tag{12}$$

where $\omega_j$ and $\zeta_j$ are the natural frequency and damping ratio of the $j$-th mode of the MDOF system, respectively. $\eta_j$ is the modal participation factor, calculated by

$$\eta_j = \frac{\boldsymbol{\Phi}_j^T \boldsymbol{m}\boldsymbol{\iota}}{\boldsymbol{\Phi}_j^T \boldsymbol{m}\boldsymbol{\Phi}_j} \tag{13}$$

It is noted that the $N$ uncoupled equations in (12) are independent each other, therefore they can be solved individually by any analytical or numerical methods. Once the modal co-ordinates $q_j(t)$ have been determined, the solutions of the system, i.e. $\boldsymbol{u}$, $\dot{\boldsymbol{u}}$ and $\ddot{\boldsymbol{u}}$, are also obtained.

### 3.2 Seismic response analysis within a time step by DQ rule

For the dynamic equation excited by the earthquake, it is practical to determine the solution by numerical methods. Considering the seismic response within a time interval of $[t_i, t_j]$, in which $t_i$ and $t_j$ are two different discrete time instants at time axis. For differential quadrature analysis of seismic response, the time interval of $[t_i, t_j]$ is defined as a time step in which the responses will be determined. Obviously the length of the step, $\Delta t_{ij}$, can be obtained as

$$\Delta t_{ij} = t_j - t_i \tag{14}$$

It is unnecessary to take $\Delta t_{ij}$ be constant, in fact, the length of each step is usually not equal in differential quadrature analysis because of the property of higher accuracy of this method, so that benefits of less computational efforts can be obtained.

Establishing a local coordinate system shown in Fig.1 over the step, then Eq. (12) becomes a set of the ordinary differential equations to coordinate $\tau$, it is rewritten by omitting the subscript $j$ as

$$\ddot{q}(\tau) + 2\zeta\omega\dot{q}(\tau) + \omega^2 q(\tau) = -\eta\ddot{u}_g(\tau) \tag{15}$$

Introducing a state vector consisting of $q(\tau)$ and $\dot{q}(\tau)$ as follows:

$$\boldsymbol{y} = \begin{Bmatrix} q \\ \dot{q} \end{Bmatrix} \tag{16}$$

then Eq. (15) may be formed in the state space, that is

$$\boldsymbol{M}\dot{\boldsymbol{y}} + \boldsymbol{K}\boldsymbol{y} = -\boldsymbol{M}\boldsymbol{I}\,\ddot{u}_g \tag{17}$$

with the initial condition

$$\boldsymbol{y} = \boldsymbol{y}(0) = \begin{Bmatrix} q_0 \\ \dot{q}_0 \end{Bmatrix} \tag{18}$$

where

$$\boldsymbol{M} = \begin{bmatrix} -\omega^2 & 0 \\ 0 & 1 \end{bmatrix},\ \boldsymbol{K} = \begin{bmatrix} 0 & \omega^2 \\ \omega^2 & 2\zeta\omega \end{bmatrix},\ \boldsymbol{I} = \begin{Bmatrix} 0 \\ 1 \end{Bmatrix} \tag{19}$$

It is noted that both $\boldsymbol{M}$ and $\boldsymbol{K}$ are symmetrical in Eq. (17) and an identical equation has been introduced. Compared with Eq. (15), the order of Eq. (17) reduced to one order but number of equations increased twice.

The DQ rule proposed in Eq. (1) will be used to achieve the solutions of Eq. (17). In order to apply the DQ rule, the time step under consideration is divided into *n* parts including separate nodes with coordinates of $\tau_k$ $(k = 0, 1, 2, \cdots, n)$. Let the initial point $\tau_0$ and the final point $\tau_n$ be at the two terminals of the time step, respectively, see Fig. 1. These mini-intervals within the time step are generally not equal in length owing to demands of the numerical accuracy and stability.

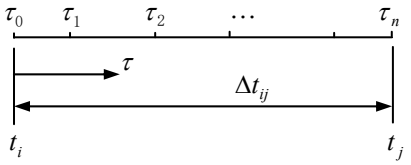


Figure 1: Local coordinate system.

Introducing the following notations:

$$\boldsymbol{y}_k = \boldsymbol{y}(\tau_k),\ \dot{\boldsymbol{y}}_k = \dot{\boldsymbol{y}}(\tau_k),\ \ddot{\boldsymbol{y}}_k = \ddot{\boldsymbol{y}}(\tau_k) \tag{20}$$

therefore

$$\boldsymbol{y}_0 = \boldsymbol{y}(\tau_0) = \begin{Bmatrix} q(t_i) \\ \dot{q}(t_i) \end{Bmatrix},\ \boldsymbol{y}_n = \boldsymbol{y}(\tau_n) = \begin{Bmatrix} q(t_j) \\ \dot{q}(t_j) \end{Bmatrix} \tag{21}$$

It is obvious that $\boldsymbol{y}(\tau)$ is a function about $\tau$, hence the DQ rule formulated in the expression (1) may be used to give approximately the derivatives at each discrete grid points by the weighted sums of the function values at all grid points over the whole time step, i.e.

$$\dot{\boldsymbol{y}}_k = \sum_{r=0}^{n} w_{kr}\boldsymbol{y}_r \quad \text{for } k = 0, 1, 2, \cdots, n \tag{22}$$

It is noted that total $n$ equations are included in Eqs. (22), they can be also expressed in form of matrix, this leads to

$$\dot{\boldsymbol{Y}} = \boldsymbol{Y}\boldsymbol{w}^T \tag{23}$$

where

$$\boldsymbol{Y} = \left[\boldsymbol{y}_0, \boldsymbol{y}_1, \cdots, \boldsymbol{y}_n\right] \tag{24}$$

Substituting Eq. (23) in Eq. (17) gives

$$\boldsymbol{A}\boldsymbol{X} + \boldsymbol{X}\boldsymbol{B} = \boldsymbol{C} \tag{25}$$

in which $\boldsymbol{X}$ is a matrix assembled compactly by a set of unknown vectors, $\boldsymbol{y}_1, \boldsymbol{y}_2, \cdots, \boldsymbol{y}_n$, which would be solved for the solution of seismic response. The form of matrix $\boldsymbol{X}$ is

$$\boldsymbol{X} = \left[\boldsymbol{y}_1, \cdots, \boldsymbol{y}_n\right] \tag{26}$$

$\boldsymbol{A}$ and $\boldsymbol{B}$ are the coefficient matrice, $\boldsymbol{C}$ is also a matrix corresponding to discrete values of earthquake-induced ground acceleration at different time instants. They can be calculated by

$$\boldsymbol{A} = \boldsymbol{M}^{-1}\boldsymbol{K} = \begin{bmatrix} 0 & -1 \\ \omega^2 & 2\zeta\omega \end{bmatrix}, \tag{27a}$$

$$\boldsymbol{B}^T = \begin{bmatrix} w_{11} & w_{12} & \cdots & w_{1n} \\ w_{21} & w_{22} & \cdots & w_{2n} \\ \vdots & \vdots & \ddots & \vdots \\ w_{n1} & w_{n2} & \cdots & w_{nn} \end{bmatrix} = \begin{bmatrix} 1 & \tau_1 & \cdots & \tau_1^{n-1} \\ 1 & \tau_2 & \cdots & \tau_2^{n-1} \\ \vdots & \vdots & \ddots & \vdots \\ 1 & \tau_n & \cdots & \tau_n^{n-1} \end{bmatrix} \begin{bmatrix} 1 & & & \\ & 2 & & \\ & & \ddots & \\ & & & n \end{bmatrix} \begin{bmatrix} \tau_1 & \tau_1^2 & \cdots & \tau_1^n \\ \tau_2 & \tau_2^2 & \cdots & \tau_2^n \\ \vdots & \vdots & \ddots & \vdots \\ \tau_n & \tau_n^2 & \cdots & \tau_n^n \end{bmatrix}^{-1} \tag{27b}$$

$$\boldsymbol{C} = -\boldsymbol{I}\ddot{\boldsymbol{u}}_{\boldsymbol{g}} - \boldsymbol{y}_0\boldsymbol{w}_0 \tag{27c}$$

$$\ddot{\boldsymbol{u}}_{\boldsymbol{g}} = \left\{\ddot{u}_{g1}, \ddot{u}_{g2}, \cdots, \ddot{u}_{gn}\right\}, \ \boldsymbol{w}_0 = \left\{w_{10}, w_{20}, \cdots, w_{n0}\right\}$$

It may be observed that the coefficient matrice of $\boldsymbol{A}$, $\boldsymbol{B}$ and $\boldsymbol{C}$ are definite in the Eq. (25), and the modal coordinates $q_k$ and $\dot{q}_k$ will be determined by solving the matrix equation (25), then the seismic response vector $\boldsymbol{y}$ is also obtained in discrete form

## 4 EXPRESSION OF GROUND ACCELERATION

The earthquake induced ground acceleration is a complicated time history process with abundant frequency components, and it can be only defined by numerical value at discrete time instants. If the accelerogram of the strong ground shaking within certain duration $T$ has been instrumented during an earthquake, the discrete values of the ground acceleration will be known as

$$\ddot{u}_{gl} = \ddot{u}_g(t_l), \ t_l \in [0, T], \ l = 1, \cdots, m \tag{28}$$

where $T$ is duration of the strong ground motion, $m$ is the number of sampling grid points within the domain interval under consideration, usually the accelerogram is recorded with equal spacing, that means all the length of each step within the time interval of $[0, T]$, i.e. $\Delta t = t_{l+1} - t_l$, is equal.

But in DQM, the unequally spaced grids has generally been chosen to enhance the accuracy of the quadrature solutions, this will lead to the result that the discrete points used in the DQ rule must not be coincident with the sampling grid points at the recorded accelerogram, so the values of the ground acceleration at some discrete points will be unknown probably when

the DQM is employed to evaluate the seismic response of the system according to Eq. (15). Obviously, the sampling values at each discrete grid point within the given time step may be utilized to construct the time function of the ground acceleration by any interpolation approach. In fact, it is natural and convenient to form the acceleration function based on the piecewise linear interpolations. Over each time step $t_i \le t \le t_j$, the acceleration function is given by

$$\ddot{u}_g(\tau) = \ddot{u}_{gi} + \sum_{l=1}^{k} \alpha_l \Delta t + \alpha_{k+1}(\tau - k\Delta t) \tag{29}$$

in which $\alpha_k$ is the constant slope of the assumed linearly varying acceleration over the *k*-th mini-interval during the time step under consideration, it can be calculated according to

$$\alpha_k = \frac{\ddot{u}_{g,k+1} - \ddot{u}_{gk}}{\Delta t} \tag{30}$$

Thus, the earthquake induced ground acceleration $\ddot{u}_g(t)$ is expressed by a time function constituted from a sequence of piecewise linear functions. This treatment process is shown as Figure 2.

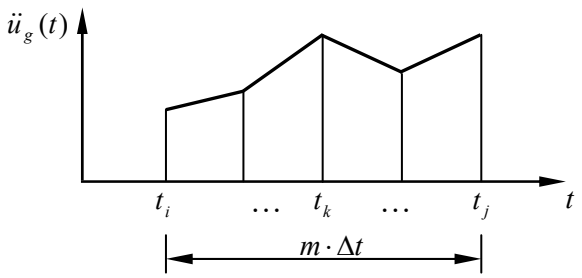


Figure 2: Function of earthquake induced ground acceleration.

## 5 THE DQ PROCEDURE FOR SEISMIC RESPONSE ANALYSIS

It is assumed that there totally are *m* sampling grid points spaced equally for time history of the ground acceleration within certain time step of $\Delta t_{ij}$, obviously we obtain

$$\Delta t_{ij} = m \cdot \Delta t \tag{31}$$

Over the time step $\Delta T_i$, the non-uniform discrete points serving the DQ rule will probably not coincide with the original sampling points spaced equally for the recorded accelerogram. After the function expression of the ground acceleration is formed according to formula (29), the value of the ground acceleration at any time instant will be determined.

The DQ analysis procedure for seismic response may be established as follows:

(1) Determining the duration defining the time domain for seismic response analysis;

(2) Constucting the function expression of the earthquake induced ground acceleration within the duration domain by the piecewise linear interpolation method;

(3) Dividing the duration domain into a sequence of time steps, it is unnecessary that the beginning and terminal points of the interval coincide with the original sampling points for the record of strong ground motion;

(4) Over each time step, a sequence of grid points is chosen for dissection of the interval by using any proper discrete scheme, for example, the choice of the Chebyshev-Gauss-Lobatto points;

(5) Evaluating the seismic response over each time step according to the DQ analysis method mentioned above, so the time history of seismic response may be obtained by combining computational results during all the steps.

This procedure is shown briefly in Figure 3.

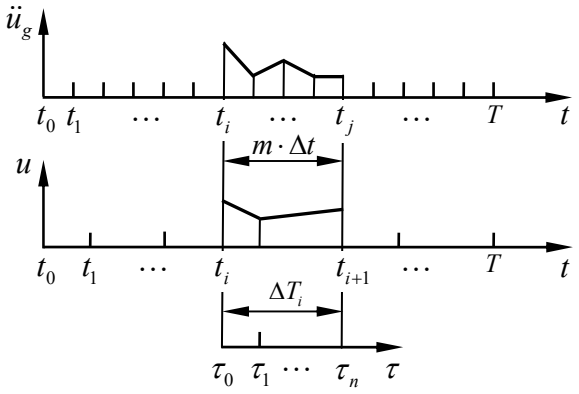


Figure 3: Illustration of the DQ analysis procedure.

It is noticed that re-divided time steps over the duration domain (step 3) are significant in the DQ analysis procedure. It is unnecessary to divide the duration domain in equal length for each step, but the dissection should be implemented by considerations of both characteristics of the seismic ground motion and dynamic properties of the system.

## 6 NUMERICAL EXAMPLE

In this section, a two-story shear frame shown in Fig. 4 is employed for numerical illustration of the DQ analysis procedure. The dynamic properties of the two-DOF system are listed in Table 1, in which the damping properties are kind of Rayleigh damping with 5 percent modal damping ratio.

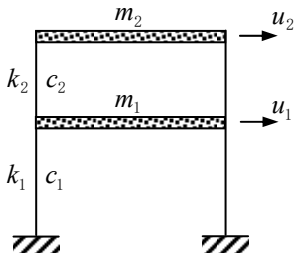


Figure 4: Case structure.

| Stiffness properties [kN·m$^{-1}$] | | Mass properties [kN·s$^2$·m$^{-1}$] | | Damping properties [kN·s·m$^{-1}$] | | Natural periods [s] | |
|---|---|---|---|---|---|---|---|
| $k_1$ | $k_2$ | $m_1$ | $m_2$ | $c_1$ | $c_2$ | $T_1$ | $T_2$ |
| $9.0\times10^4$ | $6.75\times10^4$ | $4.0\times10^2$ | $3.0\times10^2$ | $6.0\times10^2$ | $4.5\times10^2$ | 0.6378 | 0.2751 |

Table 1: Characteristics of the case structure.

The accelerogram recorded at #9 El Centro Array during the Imperial Valley earthquake, America of 19$^{th}$ May, 1940 is selected for excitation of the system. The time history of the ground acceleration and corresponding earthquake response spectrum are shown in Fig. 5 and Fig. 6.

In order to verify effect of the DQ procedure for seismic response analysis, the dynamic responses of the system due to given earthquake excitation are computed first by modal superposition method. All terms of modal contributions are calculated via Duhamel's integral and the results will be the standard for comparison, and called it 'exact' solution.

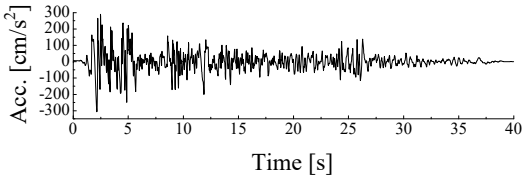


Figure 5: Time history of the ground acceleration.

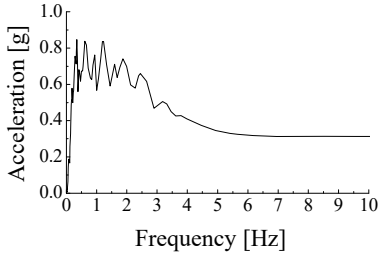


Figure 6: Response spectrum of the ground acceleration

The seismic responses of the system are calculated by the time-stepping analysis procedure using DQ rule, the calculated results are shown in Fig. 7 in which exact solution is expressed by the actual line and the DQ results the discrete circles. It is noticed that the sampling periods for the ground acceleration is taken in 0.01 second, and the intervals with same length are also chosen for quadrature integration computation. Only the responses within first 25 seconds are drawn because the main dynamic behaviors of the system have been included. It has been founded that the calculated dynamic responses by DQ analysis procedure are very close to the exact solution when the length of the time interval is selected short enough.

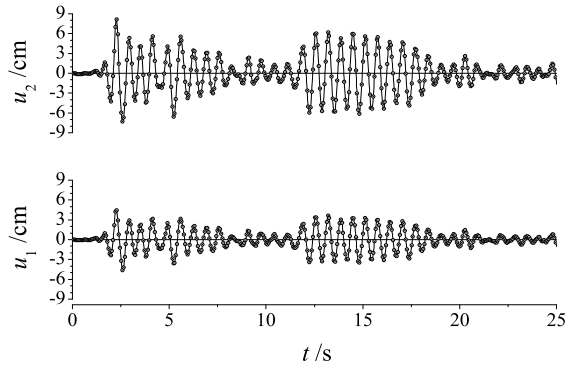


Figure 7: Calculated results of seismic responses during 0-25 seconds.

If the length of the time step is enlarged, for example, from 0.01 second to 0.02, 0.04 and 0.08 second, and information according to original sampling period is omitted, the computational efforts will be reduced. Fig. 8 and Fig. 9 show the calculated results of dynamic response using DQ analysis procedure based on the time step with the length of 0.02 second and 0.08 second, respectively. Furthermore, Newmark beta method generally applied for linear and nonlinear seismic response analysis is employed under the same condition with DQ analysis procedure to evaluate the dynamic responses of this system for comparison. The actual line is still the exact solution calculated in the sampling period of 0.01 second, and the results by DQ procedure and Newmark beta method are expressed in the line of dashes and the dotted line, respectively.

It can be founded from Fig. 8 and Fig. 9 that difference between the calculated results from DQ analysis and Newmark method, respectively is very small if the time steps are taken short enough (the length is 0.02 second shown in Fig. 8), all the two approaches can achieve good

accuracy. But in the condition of large interval, the calculated results by DQ analysis procedure are obviously better than those by Newmark method.

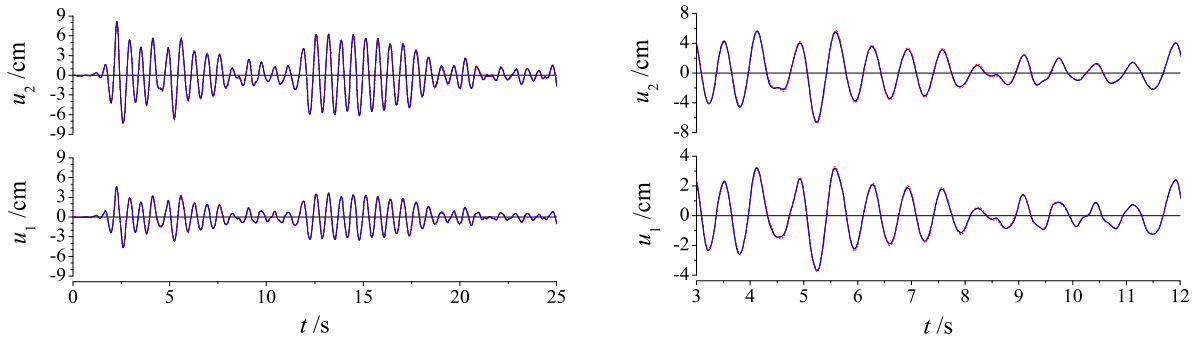


(a) (b)

Figure 8: Comparison of calculated results using DQM and Newmark-β method while $\Delta t$ = 0.02s, where (b) is the local zoom of (a).

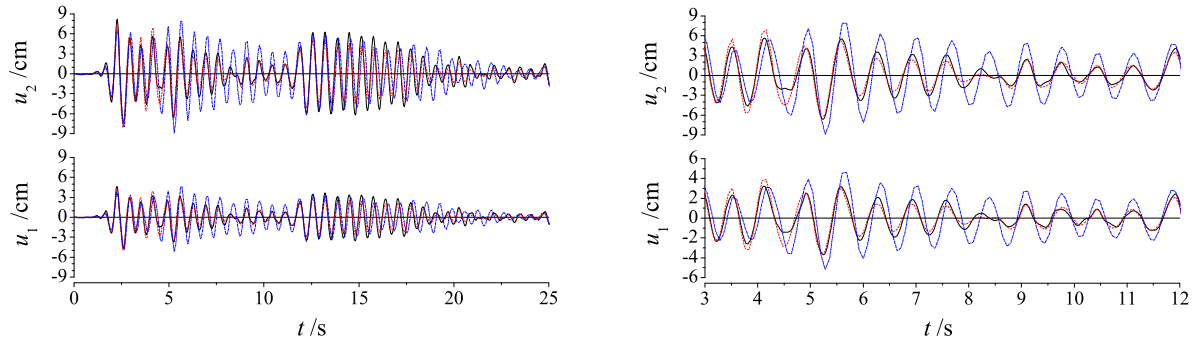


(a) (b)

Figure 9: Comparison of calculated results using DQM and Newmark-β method while $\Delta t$ = 0.08s, where (b) is the local zoom of (a).

## 7 CONCLUSIONS

In this paper, the differential quadrature rule is applied to discretization of time domain and an integrated time-stepping procedure is presented for dynamic response analysis of system subjected to earthquake induced ground motion. The time history of the ground acceleration expressed by a set of discrete values is constructed as a function to time using piecewise linear interpolations, so that all the values of the ground acceleration at any time instants may be obtained. This leads to DQ rule could be used over a time interval with not long length and finite discrete points selected unnecessarily the original sampling grid points for the ground acceleration. Because the time coordinate is one dimensional system, difficulties existed in the settlement of boundary conditions are naturally overcome, and accuracy for computation will be increased through proper choice of positions of the discrete points within each interval. Results from numerical analysis show that the proposed quadrature procedure can still achieve an excellent analysis for the time history of the seismic response even when the length of the time interval is selected a little larger. So the computational efficiency would be improved by using the proposed quadrature procedure for seismic response analysis in time domain, because a relative larger length of the discrete interval may be selected in practice so that the actual computer efforts will decrease greatly.

## ACKNOWLEDGEMENTS

This work was supported by the National Natural Science Foundation of China under Grant No. 51478222 and Specialized Research Fund for the Doctoral Program of Higher Education under Grant. 20123221110011. These supports are gratefully acknowledged.

## REFERENCES

[1] R. Bellman, J. Casti, Differential quadrature and long-term integration, *Journal of Mathematical Analysis and Applications*, **34**, 235-238, 1971.

[2] R. Bellman, B. G. Kashef, J. Casti, Differential quadrature: a technique for the rapid solution of nonlinear partial differential equations, *Journal of Computational Physics*, **10**, 40-52, 1972.

[3] C. W. Bert, M. Malik, Differential quadrature method in computational mechanics: a review, *Applied Mechanics Reviews*, **49**, 1-28, 1996.

[4] C. W. Bert, S. K. Jang, A. G. Striz, Two new approximate methods for analyzing free vibration of structural components, *AIAA Journal*, **26**, 612-618, 1988.

[5] C. W. Bert, X. Wang, A. G. Striz, Differential quadrature for static and free vibration analysis of anisotropic plates, *International Journal of Solids and Structures*, **30**, 1737-1744, 1993.

[6] C. W. Bert, M. Malik, The differential quadrature method for irregular domains and application to plate vibration, *International Journal of Mechanical Sciences*, **38**, 589-606, 1996.

[7] C. W. Bert, M. Malik, Differential quadrature: a powerful new technique for analysis of composite structures, *Composite Structures*, **39**, 179-189, 1997.

[8] A. N. Sherbourne, M. D. Pandey, Differential quadrature method in the buckling analysis of beams and composite plates, *Computers & Structures*, **40**, 903-913, 1991.

[9] S. K. Jang, C. W. Bert, A. G. Striz, Application of differential quadrature to static analysis of structural components, *International Journal for Numerical Methods in Engineering*, **28**, 561-577, 1989.

[10] K. Kang, C. W. Bert, A. G. Striz, Vibration analysis of shear deformable circular arches by the differential quadrature method, *Journal of Sound and Vibration*, **181**, 353-360, 1995.

[11] K. Kang, C. W. Bert, A. G. Striz, Vibration analysis of horizontally curved beams with warping using DQM, *Journal of Structural Engineering*, ASCE, **122**, 657-662, 1996.

[12] A. G. Striz, S. K. Jang, C. W. Bert, Nonlinear bending analysis of thin circular plates by differential quadrature, *Thin-Walled Structures*, **6**, 51-62, 1988.

[13] K. M. Liew, J. B. Han, Z. M. Xiao, et al. Differential quadrature method for Mindlin plates on Winkler foundations, *International Journal of Mechanical Sciences*, **38**, 405-421, 1996.

[14] K. M. Liew, J. B. Han, Z. M. Xiao, Differential quadrature method for thick symmetric cross-ply laminates with first-order shear flexibility, *International Journal of Solids and Structures*, **33**, 2647-2658, 1996.

[15] X. Wang, C. W. Bert, A. G. Striz, Differential quadrature analysis of deflection, buckling, and free vibration of beams and rectangular plates, *Computers & Structures*, **48**, 473-479, 1993.

[16] X. Wang, A. G. Striz, C. W. Bert, Buckling and vibration analysis of skew plates by the differential quadrature method, *AIAA Journal*, **32**, 886-889, 1994.

[17] H. Zeng, C. W. Bert, A differential quadrature analysis of vibration for rectangular stiffened plates, *Journal of Sound and Vibration*, **241**, 247-252, 2001.

[18] T. C. Fung, Solving initial value problems by differential quadrature method – part 1: first-order equations, *International Journal for Numerical Methods in Engineering*, **50**, 1411-1427, 2001.

[19] T. C. Fung, Solving initial value problems by differential quadrature method – part 2: second- and higher-order equations, *International Journal for Numerical Methods in Engineering*, **50**, 1429-1454, 2001.

[20] J. Liu, X. Wang, An assessment of the differential quadrature time integration scheme for nonlinear dynamic equations, *Journal of Sound and Vibration*, **314**, 246-253, 2008.

[21] T. Wang, Differential quadrature analysis method for seismic time history response of curved girder bridges (in Chinese), *master dissertation*, Nanjing Tech University, 2009.

COMPDYN 2017
6th ECCOMAS Thematic Conference on
Computational Methods in Structural Dynamics and Earthquake Engineering
M. Papadrakakis, M. Fragiadakis (eds.)
Rhodes Island, Greece, 15–17 June 2017

# DYNAMICAL PROCESSES ANALYSIS IN THE LOAD BEAMS AFTER PARTIAL DESTRUCTION

**Vladimir A. Gordon, Olga V. Pilipenko**

Orel State University named after I.S. Turgenev
95, Komsomolskaya str., Orel, 302026, Russia
e-mail: gordon1312@mail.ru

**Keywords:** Beam on elastic foundation, partial damage to the foundation, sudden structural changes, transient dynamic processes, the dynamic increments of strain and stress.

**Abstract.** *The study of dynamic processes in loaded constructions at sudden changes in their structure and (or) design scheme, due to various reasons, is an urgent task as part of the solution to the problem to ensure reliable and safe operation of facilities. This paper considers the stress-strain state at the ends of a double hinged beam with rectangular cross section in a state of pure bending. It is assumed that at some point the beam is separated from a layer of a certain thickness, which induces a sudden change in the area, moments of inertia and strength of the cross-section. Moreover, the instantaneous partial destruction, changing the calculation scheme of the beam is simulated. Before the formation of the structural damage, the reaction of the construction is defined by a static exposure. The sudden formation of a defect leads to lower overall stiffness of the structure, which no longer provides a static equilibrium of the system. Inertial and dissipative forces, which have suddenly emerged, cause a dynamic response. The beam is set in motion, in which the maximum stresses exceed the stresses developing in a quasi-static layer separation. Mathematically, the problem reduces to the integration of the inhomogeneous differential equation of the 4th order with inhomogeneous boundary conditions for the given initial conditions. The novelty of the approach lies in the fact that the solution is based on the decomposition of the movement on the modes of the natural oscillation of a damaged beam, but the initial conditions are formulated for an undamaged beam. The effect of the layer sudden separation is characterized quantitatively by coefficients such as a ratio of maximum dynamic stress to the maximum static stress and to the stress, developing at the quasi-static transition of a solid beam to a partially damaged one. These coefficients and the time to reach maximum values of stress are determined depending on the degree of damage to a beam (thickness of a separated layer). These quantitative results demonstrate a significant excess (8-fold while reducing by half the height of the cross section) of stresses in a statically loaded beam with a sudden change in the cross-sectional area by reducing its height. The study of the parameters of additional stresses and time of their occurrence can be useful when assessing the vitality of a structure and its elements and time of evacuation in an emergency.*

## 1 INTRODUCTION

One of the most important tasks of modern structural mechanics is the problem of sensitivity analysis of developed systems and constructions to changes in their projects, imperfections in manufacture, variations of external influences, structural changes under load, degradation of support devices and other factors of different nature and origin.

Information about the sensitivity is very important and allows solving effectively complex problems of optimization and support of the survivability and reliability of a construction and its elements. The sensitivity analysis in designing the structure means establishing the nature of the relationship between design variables, which are available to an engineer, and state variables, which are determined by the laws of mechanics, i.e. the construction response. The dependence of the construction response measured by such variables as displacement, deformation, tension, etc., from the design variables, such as physical and mechanical properties of materials, dimensions, geometric characteristics and forms of constructions, supporting communication, etc., is implicitly defined by the equations of equilibrium (motion) of the construction mechanics. Sudden failures of constructive elements can lead to changes of the calculating scheme of the construction and create the risk of a progressive (avalanche) collapse [1, 2]. Before the formation of a defect the construction response is determined by the static effects. The sudden formation of a defect leads to a decrease in overall stiffness of the construction, which no longer provides a static equilibrium of the system.

The normative documents for the design of load-bearing structures practically have no recommendations for the calculation of buildings and structures on the survivability in case of a sudden impact, which is not foreseen by the project [3]. Therefore, in the framework of solving the problems of ensuring reliable and safe operation of buildings, the study of dynamic processes in structurally nonlinear systems, which suddenly change, due to various reasons, its structure and the calculating scheme under the load, is an urgent problem. Obtaining such information for real structures requires improvement of known methods and development of new ones for their calculation.

The analysis of modern engineering literature shows that the formulations and methods of solving the problems of durability and survivability, which would take into account sudden changes in a constructive and calculating schemes of the elements of the construction, and operational structural damage, are a few and imperfect. Today, there are a number of works devoted to studies of the dynamic processes initiated in the loaded beams and plates by the sudden formation of various structural changes and damage. Here is a brief overview of some of them.

In papers [4-6] the problem of stress-deformation state of rods in a sudden shutdown of the supporting connections was solved; the possible mechanism of the avalanche development of damage leading to the loss of bearing capacity or destruction was shown. In result of the sequence of transformations of the boundary conditions the location and magnitude of maximum stresses and deformations are changing. The effect of variable stiffness and cross-sectional shape on a stress-strain state of a beam in the course of a dynamic process caused by a sudden change of resistance conditions was studied in papers [7, 8]. Sphenoid and cone-shaped beams with rectangular, circular and triangular cross section were considered. Vibrations of a single-span beam with clamped and hinged ends loaded by a distributed load at the sudden removal of a hinged support were being studied [9, 10]. The problem was solved taking into account the energy dissipation in the vibrations. The decrease in the level of maximum stresses and strains taking into account the viscosity of the material of the beam was shown. Papers [11-13] analyze the dynamic processes occurring in circular and annular plates of a variable along the radius thickness with a central rigid inclusion at a sudden conversion

of pinching the inner contour into the free support. The research used the analytical method of integration of differential equations in Cartesian and polar coordinates with arbitrary variable coefficients [14-16]. Papers [17-19] are dedicated to the solution to the task of defining dynamic additional load in the elements of space frame-rod systems, modeling spatial frames of multi-storey buildings and their fragments at a sudden change of their structure. The method of analyzing the dynamic phenomena in constructions subjected to sudden structural rearrangements covers the study of the processes in the loaded elastic beams in case of sudden formation of transverse cracks [20, 21] and longitudinal stratifications [22-24]. The physical model of a beam with a crack experiencing bending vibrations is a construction consisting of two beam segments connected by a torsion spring located in the section with a crack [25]. Longitudinal stratification is interpreted as a sudden distraction of shear connections between layers while maintaining cross connections. Instead of a monolithic rod (plate), a layered package of rods (plates) is formed, and it allows mutual sliding of layers. In this case, the bending rigidity of an object is decreasing and vibration amplitudes are increasing. Paper [26] investigates the redistribution of stresses in the stretched-reinforced rods in a sudden breakage of the reinforcement or the destruction of the matrix. The mechanism of vibration stimulation in case of an accident is due to the fact that at the destruction of one of the components of the composite, the tensile strength, which is statically attached thereto, goes to the preserved material by impact (blow). Mathematical models for the transverse vibrations of a beam on an elastic base, which are initiated by full or partial destruction of the base [27-28]. Spectrum of natural frequencies of bending vibrations of a beam on a partially destructed base is determined by the frequency equation, obtained by the procedure similar to that used in the finite element method in constructing the stiffness matrix of the finite element. Four-vectors of the section condition are introduced: the deflection, the angle of the rotation of the cross section, the bending moment and the cross section force. In a matrix form, dependences of state vectors in an arbitrary section from a vector of initial parameters are obtained. State vectors are a set of blocks, including kinematic and power parameters. Due to this, the matrix of the initial cross-section effect on an arbitrary one becomes a cell matrix, always of size 4x4. The use of state vectors and initial parameters reduces the order of matrix effects up to the fourth at any number of the conjugating parts of the beam, which significantly reduces the calculations complexity. All these papers, with the participation of the authors of this article use the same method for solving homogeneous and nonhomogeneous differential equations describing dynamic processes in loaded elastic bodies, when developing pulse changes in loads, support conditions, dimensions and shapes of the cross sections, the partial destruction of a beam and (or) ground at a sudden cracking and other structural rearrangements of the construction. The solutions are constructed using the Fourier method of separation of variables, decomposition of dynamic movements, the initial static deformations and loads in the modes of natural vibrations of damaged constructions with the use of Duhamel's integral.

The problem of estimating the tension-strain state of a loaded elastic beam is being considered below, and its calculating scheme changes suddenly due to the reduction in cross sectional area. This change is accompanied by a dynamic process, during which deformation and tension greatly exceeds the static performance and in general can lead to loss of bearing capacity and destruction.

## 2 QUASI-STATIC SEPARATION OF LAYER

Let us consider the tension-deformation state of a double hinged beam with rectangular cross section which is loaded at the ends by concentrated moments $\mu$. The calculating scheme and the size of the structure are shown in figure 1.

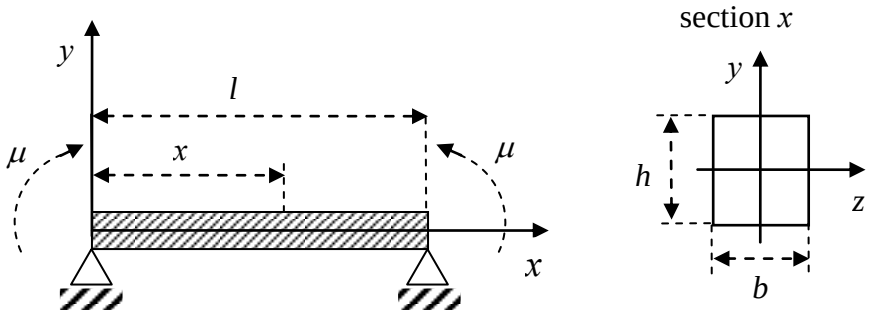


Figure 1: The beam calculating scheme.

The beam is in pure bending, the bending moment in an arbitrary cross-section *x* is equal to $\mu$, and the maximum pressure

$$\sigma_{st_{\max}} = \frac{\mu}{W_z},$$

where the resistance moment of the cross section is $W_z = \frac{2J_z}{h}$, the axial moment of the section inertia is $J_z = \frac{bh^3}{12}$.

The deflection of the beam *w* in the result of the static effect of moments $\mu$ are determined by the solution of the differential equation

$$\frac{d^2\bar{w}_{st}}{d\xi^2} = \bar{\mu}, \tag{2.1}$$

where $\xi = \frac{x}{l}$, $\bar{w}_{st} = \frac{w_{st}}{l}$, $\bar{\mu} = \frac{\mu l}{E J_t}$ are dimensionless variables and parameters.

The solution of equation (2.1) with boundary conditions

$$\bar{w}_{st}(0) = 0, \quad \bar{w}_{st}(1) = 0 \tag{2.2}$$

has the form

$$w_{st} = -\frac{\bar{\mu}}{2}\xi(1-\xi), \ 0 \le \xi \le 1. \tag{2.3}$$

It is further assumed that at some point the layer with thickness $\alpha h$ $(0 \le \alpha \le 1)$ suddenly separates from the beam, and it means a sudden change in the height of the cross section to the value of $h_1$ (figure 2).

$$h_1 = (1-\alpha)h. \tag{2.4}$$

The moments of the section inertia and resistance are respectively

$$J_{z_1} = J_z(1-\alpha)^3;$$
$$W_{z_1} = W_z(1-\alpha)^2.$$

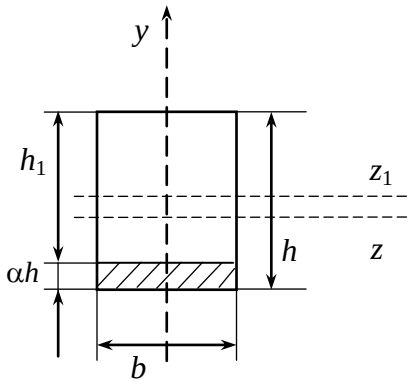


Figure 2: The cross section of the damaged beam.

The maximum tension $\sigma_{st_{\max 1}}$ at the quasi-static separation of the layer $\alpha h$ is the following

$$\sigma_{st_{\max 1}} = \frac{\sigma_{st_{\max}}}{(1-\alpha)^2}$$

or, in the dimensionless form

$$\overline{\sigma}_{st_{\max 1}} = \frac{\sigma_{st_{\max 1}}}{\sigma_{st_{\max}}} = \frac{1}{(1-\alpha)^2}.$$

The dependence $\overline{\sigma}_{st_{\max 1}}$ on parameter α is shown in figure 3.

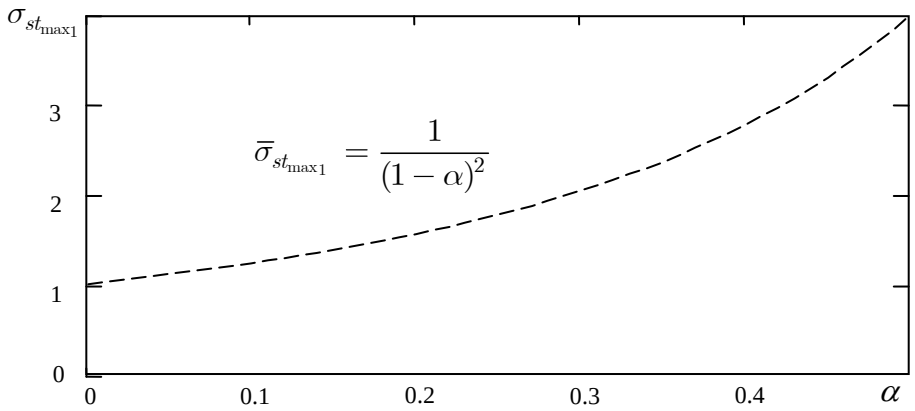


Figure 3: The influence of the thickness of the quasi-statically separated layer at the maximum tension.

## 3 FORMULATION OF PROBLEM OF THE SUDDEN SEPARATION OF LAYER

In case of the sudden separation of layer $\alpha h$ the transition dynamic process occurs in which the maximum stress at some point exceeds the stress developing under the layer quasi-static separation. The following is the calculation of the parameters of this process in the ideal case, i.e. without attenuation of resulting elastic vibrations.

Bending elastic vibrations emerging after the separation of the layer $\alpha h$ are described by the differential equation

$$EJ_{z_1}\frac{\partial^4 w}{\partial x^4} + \rho A_1 \frac{\partial^2 w}{\partial t^2} = 0, \tag{3.1}$$

where $w = w(x,t)$ are the deflections of the beam vibrations;

$t$ – time;

$\rho$, $E$ – are respectively, the density and the modulus of the material elasticity;

$A_1 = bh_1 = bh(1-\alpha)$ is the beam cross-sectional area after the separation of layer $\alpha h$.

The unknown function $w = w(x,t)$ must satisfy the limit states:

1) boundary

$$\begin{aligned} w(0,t) &= 0, \qquad EJ_{z_1} w''(0,t) = \mu; \\ w(l,t) &= 0, \qquad EJ_{z_1} w''(l,t) = \mu. \end{aligned} \tag{3.2}$$

2) initial

$$w(x,0) = w_{st}(x), \qquad \left.\frac{\partial w}{\partial t}\right|_{x,0} = 0. \tag{3.3}$$

Conditions (3.3) imply that the motion of a beam in case of the sudden separation of layer $\alpha h$ starts from the condition (2.3) created by the static deformation (kinematic stimulation of vibrations).

Thus, the mathematical problem is reduced to the integration of the homogeneous equation (3.1) with inhomogeneous boundary conditions (3.2) at initial conditions (3.3).

Let's write down problem (3.1)-(3.3) in the dimensionless form, in addition, introducing to (2.1) the following variables and parameters

$$\tau = \frac{t(1-\alpha)}{l^2}\sqrt{\frac{EJ_z}{\rho A}}, \qquad \overline{w} = \frac{w}{l}, \qquad \overline{\mu}_1 = \frac{\mu l}{EJ_z(1-\alpha)^3}.$$

Then the equation (3.1) takes a form

$$\frac{\partial^4 \overline{w}}{\partial \xi^4} + \frac{\partial^2 \overline{w}}{\partial \tau^2} = 0, \tag{3.4}$$

boundary conditions

$$\begin{aligned} \overline{w}(0,\tau) &= 0, \qquad \left.\frac{\partial^2 \overline{w}}{\partial \xi^2}\right|_{0,\tau} = \overline{\mu}_1; \\ \overline{w}(1,\tau) &= 0, \qquad \left.\frac{\partial^2 \overline{w}}{\partial \xi^2}\right|_{1,\tau} = \overline{\mu}_1. \end{aligned} \tag{3.5}$$

initial conditions

$$\overline{w}(\xi,0) = -\frac{\overline{\mu}}{2}\xi(1-\xi), \qquad \left.\frac{\partial \overline{w}}{\partial \tau}\right|_{\xi,0} = 0. \tag{3.6}$$

## 4 METHOD FOR SOLVING THE DYNAMIC PROBLEM

We seek a solution of equation (3.4) in the form

$$\overline{w} = \overline{w}_0(\xi,\tau) + f(\xi). \tag{4.1}$$

Substituting the submission (4.1) in equation (3.4), we obtain an inhomogeneous differential equation for the function $\overline{w}_0(\xi,\tau)$

$$\frac{\partial^4 \overline{w}_0}{\partial \xi^4} + \frac{\partial^2 \overline{w}_0}{\partial \tau^2} = -\frac{d^4 f}{d\xi^4}. \tag{4.2}$$

The function $f(\xi)$ is chosen so that the boundary conditions for equation (4.2) would become homogeneous

$$\begin{aligned} &\overline{w}_0(0,\tau) = 0, \qquad \left.\frac{\partial^2 \overline{w}_0}{\partial \xi^2}\right|_{0,\tau} = 0; \\ &\overline{w}_0(1,\tau) = 0, \qquad \left.\frac{\partial^2 \overline{w}_0}{\partial \xi^2}\right|_{1,\tau} = 0. \end{aligned} \tag{4.3}$$

For this, function $f(\xi)$ must satisfy the following requirements

$$\begin{aligned} &f(0) = 0, \qquad \left.\frac{d^2 f}{d\,\xi^2}\right|_0 = \overline{\mu}_1; \\ &f(1) = 0, \qquad \left.\frac{d^2 f}{d\,\xi^2}\right|_1 = \overline{\mu}_1. \end{aligned} \tag{4.4}$$

The function that satisfies requirements (4.4) has the form

$$f(\xi) = -\frac{\overline{\mu}_1}{2}\,\xi(1-\xi) = \frac{\overline{w}_{cm}(\xi)}{(1-\alpha)^3}. \tag{4.5}$$

It follows that the right part of equation (4.2) is equal to 0, that is equation (4.2) is homogeneous. Separating the variables in equation (4.2) by submission

$$\overline{w}_0 = \overline{W}_0(\xi)T(\tau), \tag{4.6}$$

we get two ordinary differential equations for the functions $\overline{W}_0(\xi)$ and $T(\xi)$

$$\frac{d^4 \overline{W}_0}{d\xi^4} - w^2 \overline{W}_0 = 0. \tag{4.7}$$

$$\frac{d^2 T}{d\tau^2} + w^2 T = 0, \tag{4.8}$$

where $w$ is the dimensionless frequency of a beam proper vibrations.

The general solutions to equations (4.7) and (4.8) have the form, respectively

$$\overline{W}_0 = C_1 \sin\sqrt{w}\xi + C_2 \cos\sqrt{w}\xi + C_3 sh\sqrt{w}\xi + C_4 ch\sqrt{w}\xi. \tag{4.9}$$

$$T = A\sin w\tau + B\cos w\tau, \tag{4.10}$$

where $A$, $B$, $C_i$ $(i = \overline{1,4})$ are the constants of integration.

Separating variables in the boundary conditions (4.3), we obtain

$$\begin{aligned} &\bar{W}_0(0) = 0, \qquad \left.\frac{d^2\bar{W}_0}{d\,\xi^2}\right|_0 = 0; \\ &\bar{W}_0(1) = 0, \qquad \left.\frac{d^2\bar{W}_0}{d\,\xi^2}\right|_1 = 0. \end{aligned} \tag{4.11}$$

Satisfying the boundary conditions (4.11), we obtain from (4.9) the system of algebraic equations for $C_i$ $(i = \overline{1,4})$

$$\begin{cases} C_2 + C_4 = 0 \\ -C_2 + C_4 = 0 \\ C_1 \sin\sqrt{w} + C_2 \cos\sqrt{w} + C_3 sh\sqrt{w} + C_4 ch\sqrt{w} = 0 \\ -C_1 \sin\sqrt{w} - C_2 \cos\sqrt{w} + C_3 sh\sqrt{w} + C_4 ch\sqrt{w} = 0, \end{cases} \tag{4.12}$$

whence it follows that $C_2 = C_4$ and

$$\begin{cases} C_1 \sin\sqrt{w} + C_3 sh\sqrt{w} = 0 \\ -C_1 \sin\sqrt{w} + C_3 sh\sqrt{w} = 0. \end{cases} \tag{4.13}$$

The condition for the existence of nonzero solutions to the system of homogeneous equations (4.13) is its determinant equality to zero

$$\begin{vmatrix} \sin\sqrt{w} & sh\sqrt{w} \\ -\sin\sqrt{w} & sh\sqrt{w} \end{vmatrix} = 0.$$

We obtain the frequency equation after disclosure of the determinant

$$2\sin\sqrt{w}\; sh\sqrt{w} = 0,$$

where

$$\sin\sqrt{w} = 0. \tag{4.14}$$

The roots of the equation (4.14) give the spectrum of frequencies of proper bending vibrations

$$w_n = (n\pi)^2, \quad (n = 1, 2, ...). \tag{4.15}$$

Each proper frequency corresponds to a form of proper vibrations

$$\bar{W}_{0n} = \sin\sqrt{w_n}\xi + \chi_n sh\sqrt{w_n}\xi, \tag{4.16}$$

where it is indicated $\chi_n = -\dfrac{\sin\sqrt{w_n}}{sh\sqrt{w_n}}$.

Further, according to (4.6), taking into account (4.10) and (4.16), we obtain

$$\bar{w}_0 = \sum_{n=1}^{\infty} (A_n \sin w_n\tau + B_n \cos w_n\tau)(\sin\sqrt{w_n}\xi + \chi_n sh\sqrt{w_n}\xi). \tag{4.17}$$

We find coefficients $A_n$ and $B_n$, thus satisfying initial conditions (3.6)

$$\bar{w}(\xi,0)=\bar{w}_0(\xi,0)+f(\xi)=\sum_{n=1}^{\infty}B_n(\sin\sqrt{w_n}\xi+\chi_n sh\sqrt{w_n}\xi)+\frac{\bar{w}_{st}}{(1-\alpha)^3}=\bar{w}_{st}. \quad (4.18)$$

$$\left.\frac{\partial\bar{w}}{\partial\tau}\right|_{\xi,0}=\left.\frac{\partial\bar{w}_0}{\partial\tau}\right|_{\xi,0}=\sum_{n=1}^{\infty}A_n(\sin\sqrt{w_n}\xi+\chi_n sh\sqrt{w_n}\xi)=0.$$

From the second the ratio (4.18) follows $A_n=0$. We describe the first the ratio (4.18) in the form

$$\sum_{n=1}^{\infty}B_n\bar{W}_{0n}(\xi)=\beta(\alpha)\bar{w}_{cm}(\xi), \quad (4.19)$$

where it is indicated $\beta(\alpha)=1-\frac{1}{(1-\alpha)^3}$.

Using the orthogonality property forms of the proper vibrations (4.16)

$$\int_0^1\bar{W}_{0i}(\xi)\bar{W}_{0j}(\xi)\,d\xi=\begin{cases}0, & if \quad i\neq j\\ 1, & if \quad i=j,\end{cases}$$

multiplying (4.19) and integrating from 0 to 1, we obtain a formula for calculating coefficients $B_i$ $(i=1,2,...,n,...)$

$$B_i=\beta(\alpha)\frac{\int_0^1\bar{w}_{cm}(\xi)\bar{W}_{0i}(\xi)\,d\xi}{\int_0^1\bar{W}_{0i}^2(\xi)\,d\xi}. \quad (4.20)$$

According to (4.1), we calculate the deflections in the process of vibrations

$$\bar{w}(\xi,\tau)=\sum_{n=1}^{\infty}B_n\bar{W}_{0n}(\xi)\cos w_n\tau-\frac{\bar{\mu}}{2(1-\alpha)^3}\xi(1-\xi). \quad (4.21)$$

By the successive differentiation of a deflections function (4.21), we obtain the rotation angles of cross sections $\frac{\partial\bar{w}}{\partial\xi}$ and curvature $\frac{\partial^2\bar{w}}{\partial\xi^2}$:

$$\frac{\partial\bar{w}}{\partial\xi}=\sum_{n=1}^{\infty}B_n\frac{d\bar{W}_{0n}}{d\xi}\cos w_n\tau-\frac{\bar{\mu}}{2(1-\alpha)^3}(1-2\xi),$$

$$\frac{\partial^2\bar{w}}{\partial\xi^2}=\sum_{n=1}^{\infty}B_n\frac{d^2\bar{W}_{0n}}{d\xi^2}\cos w_n\tau+\frac{\bar{\mu}}{(1-\alpha)^3}. \quad (4.22)$$

## 5 NUMERICAL ANALYSIS

The highest stresses in the dynamic process after the separation of layer $\alpha h$ because of the symmetry of the problem will develop in the dangerous section $\xi=\frac{1}{2}$ at time $\tau=\tau_1$.

$$\gamma_{dyn.\max} = \frac{M\ \frac{1}{2},\tau_1}{W_z(1-\alpha)^2} = \frac{EJ_z(1-\alpha)}{W_z l}\frac{\partial^2\overline{w}}{\partial\xi^2}\Big|_{\frac{1}{2},\tau_1}$$

or in a dimensionless form, taking into account (4.22), (4.20) and (2.3)

$$\overline{\sigma}_{dyn.\max} = \frac{1}{(1-\alpha)^2}\left[1 - \frac{(1-\alpha)^3 - 1}{2}\sum_{n=1}^{\infty}\frac{\int_0^1(\xi-1)\overline{W}_{0n}(\xi)d\xi}{\int_0^1\overline{W}_{0n}^2 d\xi}\cdot\frac{d^2\overline{W}_{0n}}{d\xi^2}\Big|_{\frac{1}{2}}\cos w_n\tau_1\right],$$

where it is indicated $\overline{\sigma}_{dyn.\max} = \frac{\sigma_{dyn.\max}}{\mu}W_z$.

The effect of the sudden separation of layer $\alpha h$ quantifies the ratio $K_{dyn.1(\alpha)}$, calculated as the ratio of maximum dynamic tension $\overline{\sigma}_{dyn.\max}$ to maximum tension $\overline{\sigma}_{st_{\max 1}}$, which develops at a quasi-static transition of the intact beam to the damaged one

$$K_{dyn.1}(\alpha) = \frac{\overline{\sigma}_{dyn.\max}}{\overline{\sigma}_{st_{\max 1}}} = 1 - \frac{(1-\alpha)^3 - 1}{2}\sum_{n=1}^{\infty}\frac{\int_0^1\xi(\xi-1)\overline{W}_{0n}(\xi)d\xi}{\int_0^1\overline{W}_{0n}^2(\xi)d\xi}\cdot\frac{d^2\overline{W}_{0n}}{d\xi^2}\Big|_{\frac{1}{2}}\cdot\cos w_n\tau_1. \quad (5.1)$$

Taking into account the first five summands in the sum (5.1) takes the form

$$K_{dyn.1}(\alpha) = 1 + \frac{4}{\pi}\left[1-(1-\alpha)^3\right]\left[\cos\pi^2\tau_1 - \frac{1}{3}\cos 9\pi^2\tau_1 + \frac{1}{5}\cos 25\pi^2\tau_1\right]. \quad (5.2)$$

We find moment $\tau_1$ as a point of extremum of the function $\overline{\sigma}_{dyn.\max}\left(\frac{1}{2},\tau\right)$ and, consequently, of the function $\frac{\partial^2\overline{w}}{\partial\xi^2}\Big|_{\frac{1}{2},\tau}$ (4.22). Differentiating (4.22) according to $\tau$ and equating the derivative to zero, we find the first nonzero root of the obtained transcendental equation

$$\frac{\partial^3\overline{w}}{\partial\xi^2\partial\tau} = -\sum_{n=1}^{\infty}w_n B_n\frac{d^2\overline{W}_{0n}}{d\xi^2}\Big|_{\frac{1}{2}}\cdot\sin w_n\tau_1 = 0. \quad (5.3)$$

Taking into account five summands in the left part of equation (5.3) we get

$$\tau_1 = 0{,}010756. \quad (5.4)$$

The comparison of the signs of the derivative of function (4.22) according to the time left (+) and right (–) from the extremum of (5.4) shows that if $\tau_1 = 0{,}010756.$ the function $\overline{\sigma}_{dyn.\max}\left(\frac{1}{2},\tau\right)$, indeed, reaches a maximum.

In addition to the ratio $K_{dyn.1}$ the transition process can be characterized, as well, by a coefficient $K_{dyn.}$, indicating how many times the maximum stress in the dynamic process after the separation of layer $\alpha h$ $\bar{\sigma}_{dyn.\max}$ exceeds the maximum stress in the original static state

$$K_{dyn.} = \frac{\bar{\sigma}_{\max_{dyn.}}}{\sigma_{st_{\max}}} = \frac{K_{dyn.1}}{(1-\alpha)^2}. \tag{5.5}$$

Figures 4 *a* and *b* show the dependence graphics of coefficients $K_{dyn.1}$ (5.2) and (5.5), respectively, on parameter $\alpha$ characterizing the damage degree of the beam.

Note that the true time $t_1$ to reach the value maximum stress depends on the parameter of damage of the beam $\alpha$ (figure 5).

We also note that the problem has been solved without taking into account energy dissipation during the dynamic process as a result of a sudden change in the size of the beam. It is acceptable for the problem of estimating the degree of stress increase when we need to determine the value of the first maximum stresses at $\tau = \tau_1$.

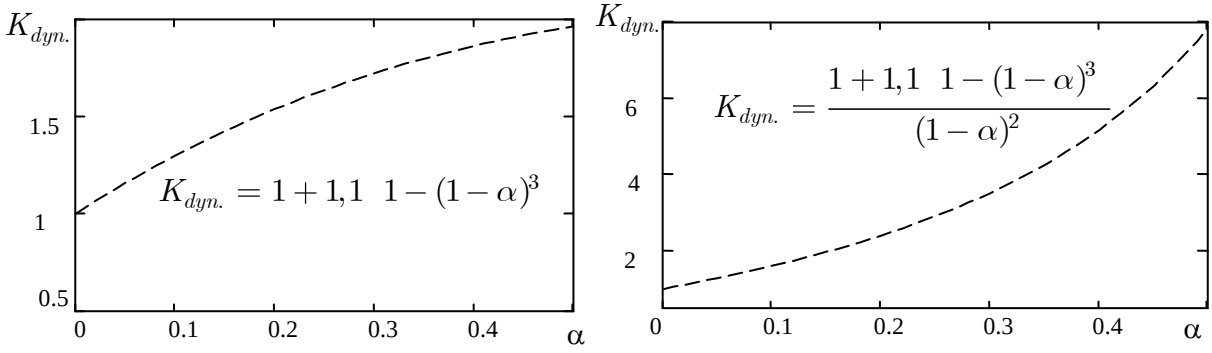


Figure 4: The coefficients characterizing the increase of the maximum stresses depending on the extent of damage to the beam.

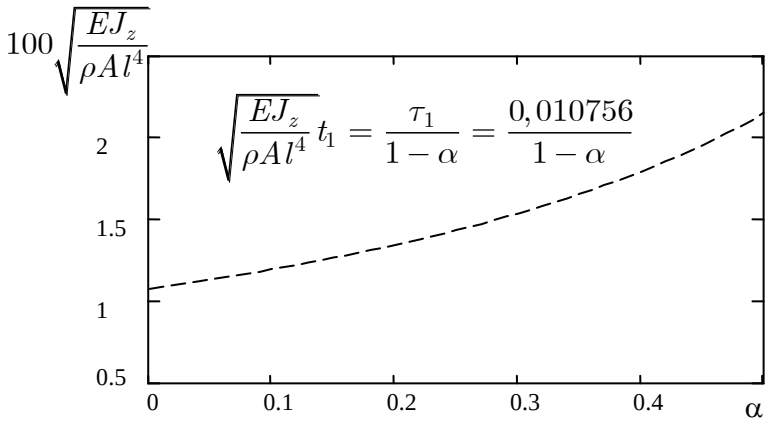


Figure 5: The dependence of the time of the first maximum stress on the parameter of damage α.

## 6 CONCLUSIONS

Thus, the simplest example a single span simply supported beam has demonstrated significant excess of the stresses in a statically loaded structure at a sudden change in its geometrical parameters (in particular, changes in the area and the axial moment of inertia of the rectangu-

lar cross-section by reducing its height). The approach can be applied to the sensitivity analysis for designed building constructions and their elements to sudden structural changes under load.

## REFERENCES


[1] Yu.P. Nazarov, Basmannyj rynok: analiz konstruktivnyh reshenij i vozmozhnyh mehanizmov razrushenija zdanija [Basmanny market: the analysis of construction solutions and possible mechanisms of the building destruction]. *Stroitel'naja mehanika i raschjot sooruzhenij* [Structural mechanics and calculation of constructions], **2**, 17-19, 2007.

[2] P.G. Eremeev, Predotvrashhenie lavinoobraznogo (progressirujushhego) obrushenija nesushhih konstrukcij unikal'nyh bol'sheproletnyh sooruzhenij pri avarijnyh vozdejstvijah [Preventing of avalanche (progressive) collapse of bearing constructions of unique long-span structures under accidental impacts]. *Stroitel'naja mehanika i raschjot sooruzhenij* [Structural mechanics and calculation of constructions], **2**, 65-72.

[3] G.D. Geniev, V.I. Kolchunov, N.V. Klueva, A.I. Nickulin, K.P. Pyatikrestovsky, Concrete structural strength and deformation at design impact. Publishing House ASV, Moscow, 216 p., 2004.

[4] V.A. Gordon, T.A. Pavlova, Dinamicheskie javlenija v balke pri lavinoobraznom processe vykljuchenija svjazej v oporah [Dynamic phenomena in a beam while the avalanche process of the disconnection in the supports]. *Vibracionnye mashiny i tehnologii*: sbornik nauchnyh trudov [Vibrating machines and technology: collection of scientific papers]. P.1. Kursk, Russia, 166-169, 2005.

[5] V. Gordon, Y. Stepanov, P. Anokhin, Transitional processes in the constructions with the sudden structural reconstructions. *Proc. 15th Intern. Congress on Sound and vibration*, July 06-10, Daejeon, Korea, 2008.

[6] T.A. Pavlova, Development of the method of calculation of building structures on the survivability of the sudden structural changes (Candidate Thesis). Orel: Orel State Technical University, 2006.

[7] V.A. Gordon, T.A. Pavlova, Stress-strain state in a spheroid-shaped beam in case of sudden elimination of support. *Proceedings* of *the 3rd International Symposium «Impact vibration systems, machines, and technology»*, Orel, Russia, 95-98, 2006.

[8] T.A. Pavlova, Sravnenie dinamicheskih javlenij v balke pri vnezapnyh izmenenijah uslovij opiranija [Comparison of dynamic phenomena in the beam with a sudden change of support conditions]. *Vibracionnye mashiny i tehnologii*: sbornik nauchnyh trudov [Vibrating machines and technology: collection of scientific papers]. P.1. Kursk, Russia, 94-99, 2005.

[9] T.V. Poturaeva, Perehodnyj dinamicheskij process v sterzhnevoj konstrukcii pri vnezapnom izmenenii uslovij opiranija [The transition dynamic process in a rod construction at the sudden change of support conditions]. *Fundamental and applied problems of engineering and* technology, **4**, 27-31, 2008.

[10] Y. Stepanov, V. Gordon, V. Shorkin, Concept for estimation of structural safety of bar systems. *Proc. 12th Intern.Congress on Sound and vibration*, Lisbon, Portugal, July 11-14, 120-126, 2005.

[11] V.A Gordon, V.I. Brusova, Axisymmetric vibrations of a circular plate at a sudden change in support conditions. *Proc.* of *Science and innovation in construction: The International Congress*, Voronezh, Russia, **3**, 105-110, 2008.

[12] V.A. Gordon, N.V. Klyueva, V.I. Brusova, Osesimmetrichnye kolebanija kol'cevoj plastinki pri vnezapnom izmenenii uslovij opiranija [Axisymmetric vibrations of a circular plate subjected to a sudden change of support conditions]. *Stroitel'naja mehanika i raschjot sooruzhenij* [Structural mechanics and calculation of constructions], **1**, 41-43, 2009.

[13] V.I. Brusova, Transition processes in circular discs and beams under certain beyond-construction impacts (Candidate Thesis), Orel: Orel State Technical University, 2009.

[14] V. Gordon, S. Ovsiannikova, L.Shmarkova, The analytical decision of a problem of vibrations one-dimensional non-homogeneous elastic bodies. *Proc. 6th Intern. Congress on Sound and vibration*, Copenhagen, Denmark, July 5-8, 1999.

[15] V.A. Gordon, O.V. Pilipenko, Analytical solutions to the problems of mechanics of inhomogeneous bodies. LAP Lambert Academic Publishing, Deutschland, 174 p., 2014.

[16] V.I. Brusova, V.A. Gordon, T.V. Poturaeva, The asymptotic method integration of differential equations with variable coefficients in polar coordinates. Orel: publishing house of the OSTU, 77 p., 2010.

[17] A.D. Kholodov, Dynamic phenomena in core systems at the change of their structure (Candidate Thesis), Tula: Tula State University, 2009.

[18] N.V. Kljueva, V.A. Gordon, Raschjot dinamicheskih dogruzhenij v sterzhnevoj prostranstvennoj sisteme s vnezapno vykljuchajushhimisja jelementami [Calculation of dynamic loading in the rod spatial system with suddenly switched off elements]. *Stroitel'naja mehanika i raschjot sooruzhenij* [Structural mechanics and calculation of constructions], **4**, 72-79, 2008.

[19] V.A. Gordon, N.V. Kljueva, T.V. Poturaeva, Raschjot dinamicheskih usilij v konstruktivno-nelinejnyh jelementah sterzhnevyh sistem pri vnezapnyh strukturnyh izmenenijah [Calculation of dynamic effort in a constructive nonlinear elements of rod systems at sudden structural changes]. *Stroitel'naja mehanika i raschjot sooruzhenij* [Structural mechanics and calculation of constructions], **6**, 26-30, 2008.

[20] T.V. Poturaeva, V.A. Gordon, Dinamicheskoe dogruzhenie svobodno opertoj nagruzhennoj balki, iniciirovannoe vnezapnym obrazovaniem treshhiny [Dynamic additional loading by freely supported loaded beam, initiated by a sudden formation of cracks]. *Stroitel'stvo i rekonstrukcija* [Construction and reconstruction], **4**, 28-33, 2009.

[21] V.A. Gordon, T.V. Poturaeva, Chastoty sobstvennyh izgibnyh kolebanij svobodno opertoj balki s treshhinoj [Frequencies of natural vibrations of a feerely supported beam with a crack]. *Stroitel'naja mehanika i raschjot sooruzhenij* [Structural mechanics and calculation of constructions], **3**, 19-23, 2009.

[22] O. Pilipenko, V. Gordon, Dynamic loading of composite beam with the sudden longitudinal stratification. *Proc. 10th HSTAM Intern. Congress on Mechanics*, Chania, Crete, Greece, May 25-27, 2013.

[23] V.A. Gordon, O.V Pilipenko, E.V. Bruma, Dynamic additional loading of a beam at stratification. LAP Lambert Academic Publishing, Deutschland, 94 p., 2016.

[24] V.A. Gordon, E.A. Kravtsova, Dinamicheskie dogruzhenija v balke s raznourovnevymi prodol'nymi rassloenijami [Dynamic loading in a beam with longitudinal multi-level stratifications]. *Stroitel'stvo i rekonstrukcija* [Construction and reconstruction], **6**, 17-27, 2012.

[25] Y. Bamnios, E. Douka, A. Trochidis, Identification of cracks in single and double cracked beams using mechanical impedance. *Proc. 10th Intern. Congress on Sound and vibration*, Stockholm, Sweden, July 7-10, 2003.

[26] V.A. Gordon, A.G. Tamrazyan, T.V. Savostikova, Dinamicheskie naprjazhenija v armirovannom sterzhne pri vnezapnom obrazovanii treshhin [The dynamic stresses in reinforced rob/core at the sudden formation of cracks]. *Vestnik Nauchno-issledovatel'skogo centra «Stroitel'stvo»* [Messenger of the research center «Construction»], **2**, 167-176, 2010.

[27] V. Gordon, O. Pilipenko, Vibration of loaded beam initiated by fully or partially destruction of the elastic foundation. *Proc. 22nd Intern. Congress on Sound and vibration*, Florence, Italy, July 12-16, 2015.

[28] V. Gordon, O. Pilipenko, T. Gasimov, Beam dynamic stresses increments after partial deconstruction of foundation. *Proc. European Congress on Computational Methods in Applied Sciences and Engineering*, Crete, Greece, June 05-10, 2016.

COMPDYN 2017
6th ECCOMAS Thematic Conference on
Computational Methods in Structural Dynamics and Earthquake Engineering
M. Papadrakakis, M. Fragiadakis (eds.)
Rhodes Island, Greece, 15–17 June 2017

# MODAL ANALYSIS PROCEDURE USING COMPLEX LEFT AND RIGHT EIGENVECTORS OF NON-PROPORTIONALLY DAMPED STRUCTURES

**E. Stanoev**[1]
[1] Chair of Wind Energy Technology,
Faculty of Mechanical Engineering and Marine Technology,
University of Rostock, Albert-Einstein-Str. 2, 18059 Rostock, Germany
*e-mail: evgueni.stanoev@uni-rostock.de*

***Keywords:*** modal decomposition of the equations of motion, modal transformation method, left and right complex eigenvectors, complex eigenvalue problem, proportional/non-proportional damping.

**Abstract.** *In the general case of non-proportionally damped structural model the associated quadratic eigenvalue problem leads to complex eigenvalues and eigenvectors. The modal decomposition of the equations of motion is usually to be performed in complex space.*
*In this paper are presented possible variants of a general method [2] - [5] for modal transformation of damped multi-degree-of-freedom-systems (MDOFS) with non-modal symmetric damping matrix. The assembly of a modal transformation matrix in real space is based either on the conjugated complex left eigenvectors, or on the right eigenvectors, or on a combination of the left and right eigenvectors of the system. The eigenvector normalization can be performed with respect to the general mass or to the general stiffness matrix. The equations of motion are stated in state-space formulation. The developed real-space modal transformation matrix is always built by a combination of two complex transformations. Analytically expressions for all presented variants of the modal transformation basis are developed be the aid of computer algebra software. Those formulas operate with the real and the imaginary parts of the eigenvectors and the associated eigenvalues. All variants of the suggested modal procedure retain the common advantages of the classic modal decomposition of the equations of motion.*
*The vibrations of a rotor blade of a wind turbine subjected to wind thrust loads have been calculated in two variants to demonstrate the performance of the presented modal analysis procedures. The initial computation of the complex eigenvalue solution of the FEM beam model and all subsequent computations are done by the aid of computer algebra software. The suggested procedures can be applied in structural systems containing different damping and energy-loss mechanism in various parts of the structure, described by non-proportional damping matrix.*

## 1 INTRODUCTION

The classic modal transformation of the equations of motion of multi-degree-of-freedom-systems (MDOFS) is applied to systems without damping. Fully real free frequencies and eigenvectors are the solution of the associated linear eigenvalue problem. The inclusion of damping in the equations of MDOFS leads to a quadratic eigenvalue problem with corresponding complex conjugate pairs of eigenvalues and eigenvectors. The modal decomposition of the equations has to be performed in complex space.

The damping can be account for in a simple way by use of the Rayleigh damping assumption – this leads to proportional damping matrix. In this special case the real eigenvectors of the undamped system are also eigenvectors of the system with proportional damping. The corresponding modal matrix, to be used for modal decomposition of the equations of motion, is fully real. In the general case of viscous damping, represented by non-proportional symmetric damping matrix, we have to deal with complex conjugate pairs of eigenvectors. This case is considered in the present paper.

There are presented three variants of a new modal transformation procedure for structural models with non-proportional symmetric damping matrix. The first one, briefly outlined in Sec. 2, is based on the complex right eigenvectors, normalized with respect to the mass matrix. A more detailed presentation of this procedure is given in [2] – [4]. The second variant, developed in a similar way to the first one, operates with the complex right eigenvectors too, but they are normalized with respect to the stiffness matrix. The procedure is described in details in Sec. 3.

In Sec. 4 is presented the third variant of the suggested procedure. Here we operate with both the right and the left complex eigenvectors of the MDOFS, the normalization is with respect to the stiffness matrix.

The main subject in all variants is to avoid the modal decomposition in complex arithmetic by assembling of a new modal transformation matrix in real space, belonging to the "state space" form of the equations of motions. The columns of the matrix are developed analytically by a combination of two complex transformations. Considering the proportional damping case which is also included, an analytical formula for the constant phase lag/lead of free vibrations is derived in both procedures presented in Sec. 2 and Sec. 3.

In all variants of the suggested procedure the complex eigenvectors and eigenvalues of the structural model should be computed first. In the presented example in Sec. 5 – vibration of a rotor blade of a wind generator - computer algebra software was applied to solve the eigenvalue problem. In real life applications of the presented method to high dimensional problems it must be available a reliable eigenmode solver for large complex eigenvalue computations. There are many literature references for large scaled problems with various solution strategies, see [10] – [12]. The author has used an implicitly restarted Arnoldi/Lanczos method [11], [12] to solve the complex eigenvalue problem in an application of the method to a fluid-structure-foundation interaction problem, see more details in [1] - [3].

In Sec. 5 the proposed modal analysis method, presented in Section 4, has been applied to a rotor blade beam structure with 54 DOF. The numerical example demonstrates the performance of the method for the general case of non-proportional damping. In this case the damping matrix of the system contains a stiffness proportional (Rayleigh) damping and aerodynamic (non-proportional) damping parts. In the second variant of the solution – with proportional damping matrix, the formula for the constant phase of the resonance modes is verified numerically.

## 1.1 Free vibrations of a viscously damped system

The equations of motion of a damped MDOFS are

$$\mathbf{M}\ddot{\mathbf{V}} + \mathbf{D}\dot{\mathbf{V}} + \mathbf{K}\mathbf{V} = \mathbf{p}(t) \tag{1.1}$$

where **M**, **D** and **K** are, respectively the (n x n) mass, damping and stiffness matrices, and **V**, $\dot{\mathbf{V}}$ are the (n x 1) displacement and velocity vectors and **p**(t) is the (n x 1) excitation vector.

In structural mechanics problems we consider the **M** and **K** matrices to be real, symmetric and positive definite, excluding the presence of rigid body modes. The matrix **D**, presenting a non-proportional damping**,** is assumed to be symmetric and non-negative.

With the assumed free vibration in the form

$$\mathbf{V} = \mathbf{X}e^{\lambda t}, \qquad \dot{\mathbf{V}} = \lambda\,\mathbf{X}e^{\lambda t}, \tag{1.2}$$

the associated quadratic eigenvalue problem is

$$\left(\lambda_j^2\,\mathbf{M} + \lambda_j\mathbf{D} + \mathbf{K}\right)\mathbf{X}_j = \mathbf{0} \qquad \forall\,(j = 1, \cdots, n) \tag{1.3}$$

In Eq. (1.3) the j[th] eigenvalue $\lambda_j$ and the corresponding eigenmode $\mathbf{X}_j$ appear in complex conjugate pairs (index j omitted):

$$\lambda = \lambda_r + i\lambda_i\,, \qquad \overline{\lambda} = \lambda_r - i\lambda_i \tag{1.4a}$$

$$\mathbf{X} = \mathbf{X}_r + i\mathbf{X}_i\,, \qquad \overline{\mathbf{X}} = \mathbf{X}_r - i\mathbf{X}_i \tag{1.4b}$$

The dynamic equilibrium of a **viscously damped single oscillator** is governed by

$$m\ddot{v}(t) + c\dot{v}(t) + kv(t) = q(t) \qquad \text{or} \tag{1.5a}$$

$$\ddot{v}(t) + 2\eta\omega\dot{v}(t) + \omega^2 v(t) = p(t) \tag{1.5b}$$

where $\ddot{v}$ is acceleration,
$\dot{v}$ - velocity,
$\omega = \sqrt{\frac{k}{m}}$ - free vibration frequency,
$\eta = \frac{c}{2m\omega}$ - Lehr's damping ratio and $p(t) = \frac{q(t)}{m}$.

The exponential solution $x\,e^{\lambda t}$, introduced into the homogenous form of the differential equation (1.5b), yields the eigenvalue problem

$$\lambda^2 + 2\eta\omega\,\lambda + \omega^2 = 0 \tag{1.6}$$

The eigenvalue solution (assuming $\eta \ll 1$, subcritical damping) of Eq. (1.6) is a complex conjugate pair:

$$\lambda_{1/2} = \underbrace{-\eta\omega}_{\lambda_r} \pm i\underbrace{\omega\sqrt{1-\eta^2}}_{\lambda_i = \omega_D} = \lambda_r \pm i\lambda_i \qquad \text{where} \quad \omega_D = \omega\sqrt{1-\eta^2} \tag{1.7}$$

### 1.2 The constant phase lag problem

Introducing the single-oscillator-eigenvalues (1.7) into (1.4a), we can express the j[th] free vibration of the MDOFS as linear combination of the two complex conjugate eigenpairs (1.4b):

$$\mathbf{V} = \mathbf{X}\, e^{\lambda t} = \mathbf{X}\, e^{\left(-\eta\omega \pm i\omega\sqrt{1-\eta^2}\right)t} =$$
$$= e^{-\eta\omega t}[(\mathbf{X}_r + i\mathbf{X}_i)(cos\,\omega_D t + i\sin\omega_D t) + (\mathbf{X}_r - i\mathbf{X}_i)(cos\,\omega_D t - i\sin\omega_D t)]$$

$$= e^{-\eta\omega t}\left[\underbrace{2\mathbf{X}_r}_{\mathbf{F}\cos\varphi}\ cos\,\omega_D t - \underbrace{2\mathbf{X}_i}_{\mathbf{F}\sin\varphi}\ \sin\omega_D t\right] \tag{1.8}$$

The last relation leads to the real form of a damped free oscillation for every k[th] DOF:

$$V_k = e^{-\eta\omega t}[F_k\, cos(\omega_D t + \varphi_k)] \tag{1.9}$$

where $\varphi_k = arctan\frac{(X_i)_k}{(X_r)_k}$ : phase lag/lead for the k[th] DOF (1.10)

Since the viscous damping is assumed to be non-proportional, the free vibration solution (1.9) represents non-synchronous damped oscillation (i.e. the phase $\varphi_k$ is different for each k[th] DOF). In the case of proportionally damped system we have to deal with synchronous free oscillation – i.e. the phase $\varphi_k$ is constant - the same for all DOF ($\varphi_k = 0$ for undamped systems) – see [6], [7], p.118.

The features, showed in Eq.(1.9), (1.10) are well known and used in modal analysis, see for example [6]. In Sec. 2 and 3 of the present paper the constant phase lag in the proportional damping case is expressed analytically. The developed formulas are in dependence of the normalization of the modal matrix.

## 2 MODAL ANALYSIS PROCEDURE BASED ON THE MASS NORMALIZED COMPLEX RIGHT EIGENVECTORS

The procedure, briefly reviewed here, has been presented in details in [2] – [4].

### 2.1 The single mass oscillator

The equation of motion of a damped single degree of freedom system (SDOFS) (1.5b) can be written in the extended form

$$\underbrace{\begin{bmatrix}1 & 0\\ 0 & -\omega^2\end{bmatrix}}_{\mathbf{m}}\underbrace{\begin{bmatrix}\dot{w}(t)\\ \dot{v}(t)\end{bmatrix}}_{\dot{\mathbf{q}}} + \underbrace{\begin{bmatrix}2\eta\omega & \omega^2\\ \omega^2 & 0\end{bmatrix}}_{\mathbf{k}}\underbrace{\begin{bmatrix}w(t)\\ v(t)\end{bmatrix}}_{\mathbf{q}} = \underbrace{\begin{bmatrix}p(t)\\ 0\end{bmatrix}}_{\mathbf{p}(t)} \tag{2.1a}$$

$$\mathbf{m}\dot{\mathbf{q}} + \mathbf{k}\mathbf{q} = \mathbf{p} \tag{2.1b}$$

with the velocity

$$w = \dot{v} \tag{2.2}$$

The exponential approach $\mathbf{q} = \mathbf{x}e^{\lambda t}$, $\dot{\mathbf{q}} = \lambda \mathbf{x} e^{\lambda t}$, introduced into the homogenous form of the differential equation (2.1), leads to the quadratic eigenvalue problem

$$\dot{\mathbf{q}} + \underbrace{(\mathbf{m}^{-1}\mathbf{k})}_{\boldsymbol{a}}\mathbf{q} = \mathbf{0} \quad \rightarrow \quad (\mathbf{a} + \lambda_j \mathbf{e})\mathbf{r}_j = \mathbf{0} \quad (j = 1,2) \tag{2.3}$$

The solution are two complex conjugate eigenvalues ($\eta << 1$, subcritical damped system):

$$\lambda_{1/2} = -\eta\omega \pm \sqrt{(\eta\omega)^2 - \omega^2} = \underbrace{-\eta\omega}_{\lambda_r} \pm \underbrace{i\omega\sqrt{1-\eta^2}}_{\lambda_i} = \begin{cases} \lambda = \lambda_r + i\lambda_i \\ \overline{\lambda} = \lambda_r - i\lambda_i \end{cases} \tag{2.4a}$$

where $\omega = \sqrt{(\lambda_r)^2 + (\lambda_i)^2}$, $\eta = -\dfrac{\lambda_r}{\omega}$, (2.4b)

and two corresponding complex conjugate right eigenvectors

$$\mathbf{r}_j = \begin{bmatrix} \lambda_r \pm i\lambda_i \\ 1 \end{bmatrix} \quad (j = 1,2) \tag{2.5}$$

The eigenvectors are normalized with respect to the mass matrix

$$[\mathbf{r}_1 \quad \mathbf{r}_2]^T \cdot \mathbf{m} \cdot [\mathbf{r}_1 \quad \mathbf{r}_2] = \begin{bmatrix} g_1 & \\ & g_2 \end{bmatrix} \quad \rightarrow \quad \varphi_j = \frac{\mathbf{r}_j}{\sqrt{g_j}} \quad (j = 1,2) \tag{2.6}$$

and then combined into a modal matrix $\varphi$:

$$\varphi = [\varphi_1 \quad \varphi_2] \tag{2.7}$$

Due to the mass normalization - Eq. (2.6), the orthogonality relationships (2.8), (2.9) can be derived:

$$\varphi^{\mathbf{T}}\mathbf{m}\varphi = \varphi^{\mathbf{T}}\begin{bmatrix} 1 & 0 \\ 0 & -\omega^2 \end{bmatrix}\varphi = \begin{bmatrix} 1 & 0 \\ 0 & 1 \end{bmatrix} \quad \leftrightarrow \quad \varphi^{-\mathbf{T}}\begin{bmatrix} 1 & 0 \\ 0 & 1 \end{bmatrix}\varphi^{-\mathbf{1}} = \begin{bmatrix} 1 & 0 \\ 0 & -\omega^2 \end{bmatrix} \tag{2.8}$$

$$\varphi^{\mathbf{T}}\mathbf{k}\varphi = \varphi^{\mathbf{T}}\begin{bmatrix} 2\eta\omega & \omega^2 \\ \omega^2 & 0 \end{bmatrix}\varphi = \begin{bmatrix} -\lambda & 0 \\ 0 & -\overline{\lambda} \end{bmatrix} \leftrightarrow \quad \varphi^{-\mathbf{T}}\begin{bmatrix} -\lambda & 0 \\ 0 & -\overline{\lambda} \end{bmatrix}\varphi^{-\mathbf{1}} = \begin{bmatrix} 2\eta\omega & \omega^2 \\ \omega^2 & 0 \end{bmatrix} \tag{2.9}$$

The inverse of the complex modal matrix $\varphi(\omega,\eta)$ can be expressed analytically using computer algebra software:

$$\varphi^{-1} = \frac{1}{2\sqrt{1-\eta^2}}\begin{bmatrix} (-Z_1 - iZ_2) & P - iQ \\ (-Z_1 + iZ_2) & P + iQ \end{bmatrix} \tag{2.10}$$

where

$$Z_1 = \sqrt{\sqrt{1-\eta^2} + (1-\eta^2)} \qquad Z_2 = \sqrt{\sqrt{1-\eta^2} - (1-\eta^2)} \tag{2.11a}$$

$$P = \omega\left(\sqrt{1-\eta^2}\, Z_2 - \eta Z_1\right) \qquad Q = \omega\left(\sqrt{1-\eta^2}\, Z_1 + \eta Z_2\right) \tag{2.11b}$$

## 2.2 The damped multi-degree-of-freedom-system

The equations of motion (1.1) of damped MDOFS (n DOF) will be written in the state-space form:

$$\underbrace{\begin{bmatrix}\mathbf{M} & \\ & -\mathbf{K}\end{bmatrix}}_{\mathbf{M_G}}\underbrace{\begin{bmatrix}\dot{\mathbf{W}} \\ \dot{\mathbf{V}}\end{bmatrix}}_{\dot{\mathbf{Q}}}+\underbrace{\begin{bmatrix}\mathbf{D} & \mathbf{K} \\ \mathbf{K} & \end{bmatrix}}_{\mathbf{K_G}}\underbrace{\begin{bmatrix}\mathbf{W} \\ \mathbf{V}\end{bmatrix}}_{\mathbf{Q}}=\underbrace{\begin{bmatrix}\mathbf{p}(t) \\ \end{bmatrix}}_{\mathbf{P}} \quad ; \qquad \dot{\mathbf{V}}=\mathbf{W} \tag{2.12a}$$

$$\mathbf{M_G}\,\dot{\mathbf{Q}}+\mathbf{K_G}\,\mathbf{Q}=\mathbf{P}\ , \tag{2.12b}$$

where $\mathbf{M_G}$ and $\mathbf{K_G}$ are, respectively the (2n x 2n) symmetric generalized mass and the generalized stiffness matrices.

With the exponential solution $\mathbf{V}=\mathbf{X}e^{\lambda t}$ the quadratic eigenvalue problem (1.3) can be written in the 2n-dimensional form

$$\left(\lambda\mathbf{M_G}+\mathbf{K_G}\right)\begin{bmatrix}\lambda\mathbf{X} \\ \mathbf{X}\end{bmatrix}=\mathbf{0}\ , \tag{2.13}$$

where

$$\lambda^{(j)}=\lambda_r^{(j)}+i\lambda_i^{(j)} \quad \rightarrow\begin{bmatrix}\lambda^{(j)}\mathbf{X}^{(j)} \\ \mathbf{X}^{(j)}\end{bmatrix}; \qquad \overline{\lambda}^{(j)}=\lambda_r^{(j)}-i\lambda_i^{(j)} \quad \rightarrow\begin{bmatrix}\overline{\lambda}^{(j)}\overline{\mathbf{X}}^{(j)} \\ \overline{\mathbf{X}}^{(j)}\end{bmatrix}; \quad \left(j=1,2\ldots n\right) \tag{2.14}$$

are the corresponding n complex conjugate eigenpairs.

Each j[th] eigenvector-pair $\mathbf{X}^{(j)}$, $\overline{\mathbf{X}}^{(j)}$ is normalized (index (j) omitted) with respect to the general mass matrix $\mathbf{M_G}$:

$$\begin{bmatrix}\lambda\mathbf{X} \\ \mathbf{X}\end{bmatrix}^T\mathbf{M_G}\begin{bmatrix}\lambda\mathbf{X} \\ \mathbf{X}\end{bmatrix}=A+iB \qquad \rightarrow \quad \mathbf{\Phi}=\frac{\mathbf{X}}{\sqrt{A+iB}}=\mathbf{\Phi_r}+i\,\mathbf{\Phi_i}\,, \tag{2.15a}$$

$$\begin{bmatrix}\overline{\lambda}\overline{\mathbf{X}} \\ \overline{\mathbf{X}}\end{bmatrix}^T\mathbf{M_G}\begin{bmatrix}\overline{\lambda}\overline{\mathbf{X}} \\ \overline{\mathbf{X}}\end{bmatrix}=A-iB \qquad \rightarrow \quad \overline{\mathbf{\Phi}}=\frac{\overline{\mathbf{X}}}{\sqrt{A-iB}}=\mathbf{\Phi_r}-i\,\mathbf{\Phi_i}\,, \tag{2.15b}$$

Due to the normalization (2.15) we have the orthogonality relationships (2.16), (2.17) – expressed in terms of the j[th] eigenvector-pair (index (j) omitted):

$$\begin{bmatrix}\lambda\mathbf{\Phi} & \overline{\lambda}\overline{\mathbf{\Phi}} \\ \mathbf{\Phi} & \overline{\mathbf{\Phi}}\end{bmatrix}^T\underbrace{\begin{bmatrix}\mathbf{M} & \\ & -\mathbf{K}\end{bmatrix}}_{\mathbf{M_G}}\begin{bmatrix}\lambda\mathbf{\Phi} & \overline{\lambda}\overline{\mathbf{\Phi}} \\ \mathbf{\Phi} & \overline{\mathbf{\Phi}}\end{bmatrix}=\begin{bmatrix}1 & \\ & 1\end{bmatrix} \tag{2.16}$$

$$\begin{bmatrix}\lambda\mathbf{\Phi} & \overline{\lambda}\overline{\mathbf{\Phi}} \\ \mathbf{\Phi} & \overline{\mathbf{\Phi}}\end{bmatrix}^T\underbrace{\begin{bmatrix}\mathbf{D} & \mathbf{K} \\ \mathbf{K} & \end{bmatrix}}_{\mathbf{K_G}}\begin{bmatrix}\lambda\mathbf{\Phi} & \overline{\lambda}\overline{\mathbf{\Phi}} \\ \mathbf{\Phi} & \overline{\mathbf{\Phi}}\end{bmatrix}=\begin{bmatrix}-\lambda & \\ & -\overline{\lambda}\end{bmatrix} \tag{2.17}$$

The (2n x 2n) complex modal matrix $\mathbf{\Phi_G}$ is make up of the n eigenvector-pairs (2.15):

$$\mathbf{\Phi_G} = \begin{bmatrix} \lambda^{(1)}\,\mathbf{\Phi}^{(1)} & \overline{\lambda}^{(1)}\,\overline{\mathbf{\Phi}}^{(1)} & \dots & \dots & \lambda^{(n)}\,\mathbf{\Phi}^{(n)} & \overline{\lambda}^{(n)}\,\overline{\mathbf{\Phi}}^{(n)} \\ \mathbf{\Phi}^{(1)} & \overline{\mathbf{\Phi}}^{(1)} & \dots & \dots & \mathbf{\Phi}^{(n)} & \overline{\mathbf{\Phi}}^{(n)} \end{bmatrix} \tag{2.18}$$

By use of the orthogonality properties (2.16), (2.17) a modal decomposition of the equations of motion (2.12) can be performed:

$$\underbrace{\mathbf{\Phi}_G^T \begin{bmatrix} \mathbf{M} & \\ & -\mathbf{K} \end{bmatrix} \mathbf{\Phi_G}}_{\mathbf{E}} \dot{\mathbf{A}} \quad + \quad \underbrace{\mathbf{\Phi}_G^T \begin{bmatrix} \mathbf{D} & \mathbf{K} \\ \mathbf{K} & \end{bmatrix} \mathbf{\Phi_G}}_{diag\{-\lambda^{(j)}\}} \mathbf{A} \quad = \quad \mathbf{\Phi}_G^T \begin{bmatrix} \mathbf{p}(t) \\ \end{bmatrix} \tag{2.19}$$

where

$$\begin{bmatrix} \mathbf{W} \\ \mathbf{V} \end{bmatrix} = \mathbf{\Phi_G} \cdot \mathbf{A} = \mathbf{\Phi_G} \cdot \left[ a^{(1)}\; b^{(1)} \quad \cdots \quad a^{(n)}\; b^{(n)} \right]^T \tag{2.20}$$

$a^{(j)}$ , $b^{(j)}$ : new complex variables, belonging to the j$^{th}$ eigenpair

In regard to Eqs.(2.8), (2.9) and (2.4b), the differential equations (2.19) can be transformed **in pairs** into the real form of SDOFS-equation (index (j) omitted):

$$\underbrace{\varphi^{-\mathbf{T}} \begin{bmatrix} 1 & 0 \\ 0 & 1 \end{bmatrix} \varphi^{-\mathbf{1}}}_{} \cdot \begin{bmatrix} \dot{x} \\ \dot{y} \end{bmatrix} + \underbrace{\varphi^{-\mathbf{T}} \begin{bmatrix} -\lambda & 0 \\ 0 & -\overline{\lambda} \end{bmatrix} \varphi^{-\mathbf{1}}}_{} \cdot \begin{bmatrix} x \\ y \end{bmatrix} = \underbrace{\varphi^{-\mathbf{T}} \begin{bmatrix} \lambda \mathbf{\Phi}^T\,\mathbf{p}(t) \\ \overline{\lambda}\,\overline{\mathbf{\Phi}}^T\,\mathbf{p}(t) \end{bmatrix}}_{}$$

$$\begin{bmatrix} 1 & 0 \\ 0 & -\omega^2 \end{bmatrix} \cdot \begin{bmatrix} \dot{x} \\ \dot{y} \end{bmatrix} + \begin{bmatrix} 2\eta\omega & \omega^2 \\ \omega^2 & \end{bmatrix} \cdot \begin{bmatrix} x \\ y \end{bmatrix} = \begin{bmatrix} g(t) \\ h(t) \end{bmatrix} \tag{2.21}$$

where $x^{(j)}$ , $y^{(j)}$ are real modal coordinates for each j$^{th}$ eigenpair.

The matrix $[\varphi(\omega,\eta)]^{-1}$ of the corresponding j$^{th}$ eigenvalue pair $\lambda^{(j)} = \lambda_r^{(j)} \pm i\lambda_i^{(j)}$ can be computed by Eqs. (2.4), (2.5), (2.10), (2.11).

The new (2n x 2n) transformation basis $\mathbf{Y}$ in real space can be defined by combination of two complex transformations (2.19), (2.21):

$$\begin{bmatrix} \mathbf{W} \\ \mathbf{V} \end{bmatrix} = \mathbf{\Phi_G} \cdot \underbrace{\begin{bmatrix} \left(\varphi^{(\mathbf{1})}\right)^{-\mathbf{1}} & & \\ & \dots & \\ & & \left(\varphi^{(\mathbf{n})}\right)^{-\mathbf{1}} \end{bmatrix}}_{\mathbf{\Psi}^{-\mathbf{1}}} \cdot \underbrace{\begin{bmatrix} x_1 \\ y_1 \\ \dots \\ x_n \\ y_n \end{bmatrix}}_{\mathbf{X}} = \underbrace{\mathbf{\Phi_G} \cdot \mathbf{\Psi}^{-\mathbf{1}}}_{\mathbf{Y}} \cdot \mathbf{X} = \mathbf{Y} \cdot \mathbf{X} \tag{2.22}$$

By the aid of the relationship (2.22) the equations of motion (2.12) will be transformed into n real uncoupled SDOFS block equations as follows:

$$\underbrace{\mathbf{Y}^{\mathrm{T}}\cdot\begin{bmatrix}\mathbf{M} & \\ & -\mathbf{K}\end{bmatrix}\cdot\mathbf{Y}}_{\begin{bmatrix}1 & & & & \\ & -\omega_1^2 & & & \\ & & \cdots & & \\ & & & 1 & \\ & & & & -\omega_n^2\end{bmatrix}}\cdot\underbrace{\begin{bmatrix}\dot{x}_1\\ \dot{y}_1\\ \cdots\\ \dot{x}_n\\ \dot{y}_n\end{bmatrix}}_{\dot{\mathbf{x}}}+\underbrace{\mathbf{Y}^{\mathrm{T}}\cdot\begin{bmatrix}\mathbf{D} & \mathbf{K}\\ \mathbf{K} & \end{bmatrix}\cdot\mathbf{Y}}_{\begin{bmatrix}2\eta_1\omega_1 & \omega_1^2 & & & \\ \omega_1^2 & 0 & & & \\ & & \cdots & & \\ & & & 2\eta_n\omega_n & \omega_n^2\\ & & & \omega_n^2 & 0\end{bmatrix}}\cdot\underbrace{\begin{bmatrix}x_1\\ y_1\\ \cdots\\ x_n\\ y_n\end{bmatrix}}_{\mathbf{x}}=\underbrace{\mathbf{Y}^{\mathrm{T}}\cdot\begin{bmatrix}\mathbf{p}\end{bmatrix}}_{\begin{bmatrix}g_1\\ h_1\\ \cdots\\ g_n\\ h_n\end{bmatrix}} \tag{2.23}$$

It can be shown that the $\mathbf{Y}$-matrix and all „load"-vectors $[g(t)\quad h(t)]^T$ in Eq. (2.23) are purely real. After component multiplication of the analytically expressed terms of $\boldsymbol{\Phi}_{\boldsymbol{G}}$ and of $\boldsymbol{\Psi}^{-1}$ all imaginary parts cancel each other, see details in [3], [4].

To each j[th] eigenvector-pair in the real (2n x 2n) matrix $\mathbf{Y}$ are belonging two columns, denoted like

$$\mathbf{Y}=\begin{bmatrix}\cdots & \mathbf{Y}_{\mathrm{x}}^{(\mathrm{j})\mathbf{W}} & \mathbf{Y}_{\mathrm{y}}^{(\mathrm{j})\mathbf{W}} & \cdots\\ \cdots & \mathbf{Y}_{\mathrm{x}}^{(\mathrm{j})\mathbf{V}} & \mathbf{Y}_{\mathrm{y}}^{(\mathrm{j})\mathbf{V}} & \cdots\end{bmatrix}$$

Their components can be expressed analytically using Eqs.(2.10), (2.11):

$$\begin{aligned}
\mathbf{Y}_{\mathrm{x}}^{(\mathrm{j})\mathbf{W}} &= \frac{1}{\sqrt{1-\eta^2}}\left\{\left(Z_2\,\omega\sqrt{1-\eta^2}+\eta\omega Z_1\right)\boldsymbol{\Phi}_{\mathbf{r}}+\left(Z_1\,\omega\sqrt{1-\eta^2}-\eta\omega Z_2\right)\boldsymbol{\Phi}_{\mathbf{i}}\right\}\\
\mathbf{Y}_{\mathrm{y}}^{(\mathrm{j})\mathbf{W}} &= \frac{1}{\sqrt{1-\eta^2}}\left(\omega^2 Z_1\boldsymbol{\Phi}_{\mathbf{r}}-\omega^2 Z_2\boldsymbol{\Phi}_{\mathbf{i}}\right)\\
\mathbf{Y}_{\mathrm{x}}^{(\mathrm{j})\mathbf{V}} &= \frac{1}{\sqrt{1-\eta^2}}\left(-Z_1\boldsymbol{\Phi}_{\mathbf{r}}+Z_2\boldsymbol{\Phi}_{\mathbf{i}}\right)\\
\mathbf{Y}_{\mathrm{y}}^{(\mathrm{j})\mathbf{V}} &= \frac{1}{\sqrt{1-\eta^2}}\left\{\left(Z_2\,\omega\sqrt{1-\eta^2}-\eta\omega Z_1\right)\boldsymbol{\Phi}_{\mathbf{r}}+\left(Z_1\,\omega\sqrt{1-\eta^2}+\eta\omega Z_2\right)\boldsymbol{\Phi}_{\mathbf{i}}\right\}
\end{aligned} \tag{2.24a-d}$$

The two components of the associated "load" vector, Eq. (2.23), are purely real too:

$$g(t)=\frac{\omega}{\sqrt{1-\eta^2}}\left\{\left(Z_2\sqrt{1-\eta^2}+Z_1\eta\right)\boldsymbol{\Phi}_{\mathbf{r}}^{\mathbf{T}}+\left(Z_1\sqrt{1-\eta^2}-Z_2\,\eta\right)\boldsymbol{\Phi}_{\mathbf{i}}^{\mathbf{T}}\right\}\mathbf{p}(t) \tag{2.25a}$$

$$h(t)=\frac{\omega^2}{\sqrt{1-\eta^2}}\left\{Z_1\boldsymbol{\Phi}_{\mathbf{r}}^{\mathbf{T}}-Z_2\,\boldsymbol{\Phi}_{\mathbf{i}}^{\mathbf{T}}\right\}\mathbf{p}(t) \tag{2.25b}$$

In [5] has been shown that in the case of proportional damping all coordinates of $\mathbf{Y}_{\mathrm{y}}^{(\mathrm{j})\mathbf{W}}$ and $\mathbf{Y}_{\mathrm{x}}^{(\mathrm{j})\mathbf{V}}$ have to be equal to zero:

$$\mathbf{Y}_{\mathbf{y}}^{\mathbf{W}}=\frac{1}{\sqrt{1-\eta^2}}\left(\omega^2 Z_1\boldsymbol{\Phi}_{\mathbf{r}}-\omega^2 Z_2\boldsymbol{\Phi}_{\mathbf{i}}\right)=\mathbf{0}\quad\rightarrow\quad -Z_1\boldsymbol{\Phi}_{\mathbf{r}}+Z_2\boldsymbol{\Phi}_{\mathbf{i}}=\mathbf{0} \tag{2.26}$$

The relationship (2.26) leads to

$$\rightarrow\quad\frac{\Phi_{i(k)}}{\Phi_{r(k)}}=\frac{Z_1}{Z_2}=\frac{\sqrt{\sqrt{1-\eta^2}+(1-\eta^2)}}{\sqrt{\sqrt{1-\eta^2}-(1-\eta^2)}}=\frac{\eta}{1-\sqrt{1-\eta^2}}=const. \tag{2.27}$$

for all k[th] DOF of the j[th] eigenmode pair ($\mathbf{\Phi_r} \pm i\mathbf{\Phi_i}$) with corresponding eigenvalue ($\lambda_r \pm i\lambda_i$). This is the analytical proof of the statement of a constant phase lag/lead, see Eq. (1.9), (1.10). In the case of proportionally damped system each free vibration is a synchronous motion of all DOF. This special case is considered more detailed in [5], Sec. 3.

### 2.3 Solution of the modal equations and back transformation

Each SDOFS block equation in (2.23) can be solved eliminating the modal coordinate $x^{(j)}$ to obtain the usual form of the SDOFS equation of motion (index (j) omitted):

$$x = \dot{y} + \frac{1}{\omega^2} h(t) \tag{2.28a}$$

$$\ddot{y} + 2\eta\omega\,\dot{y} + \omega^2 y = g(t) - \frac{2\eta}{\omega} h(t) - \frac{1}{\omega^2}\dot{h}(t) \tag{2.28b}$$

A usual step-by-step integration of Eq. (2.28b) yields the modal response $y^{(j)}(t)$. The final time series of the original n DOFs are calculated by superposition of the modal coordinates $x^{(j)}$, $y^{(j)}$ (assembled in **X**) in accordance to Eq. (2.22).

## 3 MODAL ANALYSIS PROCEDURE BASED ON THE STIFFNESS NORMALIZED COMPLEX RIGHT EIGENVECTORS

The procedure presented here, is a new variant of the method from Sec. 2. For this reason only the differences in comparison to the first variant are described.

### 3.1 The single mass oscillator

We operate with the same two corresponding complex conjugate eigenvectors $\varphi_{1/2}$, but now they are normalized with respect to the stiffness matrix **k**, see Eq. (2.1), (2.6):

$$[\mathbf{r}_1 \quad \mathbf{r}_2]^T \cdot \mathbf{k} \cdot [\mathbf{r}_1 \quad \mathbf{r}_2] = \begin{bmatrix} h_{11} & \\ & h_{22} \end{bmatrix} \quad \rightarrow \quad \varphi_j = \frac{\mathbf{r}_j}{\sqrt{h_{jj}}} \qquad (j = 1,2) \tag{3.1}$$

The normalization with respect to **k** leads now to the orthogonality relationships (3.2), (3.3):

$$\varphi^{\mathbf{T}}\mathbf{m}\,\varphi = \varphi^{\mathbf{T}}\begin{bmatrix} 1 & 0 \\ 0 & -\omega^2 \end{bmatrix}\varphi = \begin{bmatrix} -\frac{1}{\lambda} & 0 \\ 0 & -\frac{1}{\bar{\lambda}} \end{bmatrix} \quad \leftrightarrow \quad \varphi^{-\mathbf{T}}\begin{bmatrix} -\frac{1}{\lambda} & 0 \\ 0 & -\frac{1}{\bar{\lambda}} \end{bmatrix}\varphi^{-\mathbf{1}} = \begin{bmatrix} 1 & 0 \\ 0 & -\omega^2 \end{bmatrix} \tag{3.2}$$

$$\varphi^{\mathbf{T}}\,\mathbf{k}\,\varphi = \varphi^{\mathbf{T}}\begin{bmatrix} 2\eta\omega & \omega^2 \\ \omega^2 & 0 \end{bmatrix}\varphi = \begin{bmatrix} 1 & 0 \\ 0 & 1 \end{bmatrix} \quad \leftrightarrow \quad \varphi^{-\mathbf{T}}\begin{bmatrix} 1 & 0 \\ 0 & 1 \end{bmatrix}\varphi^{-\mathbf{1}} = \begin{bmatrix} 2\eta\omega & \omega^2 \\ \omega^2 & 0 \end{bmatrix} \tag{3.3}$$

The analytical expression for the inverse of the complex modal matrix $\varphi(\omega,\eta)$ is now:

$$\varphi^{-1} = \frac{1}{2\sqrt{1-\eta^2}}\begin{bmatrix} W_2 - iW_1 & Q + iP \\ W_2 + iW_1 & Q - iP \end{bmatrix} \tag{3.4}$$

where

$$W_1 = \sqrt{\omega\sqrt{1-\eta^2}\left(1-2\eta\sqrt{1-\eta^2}\right)}\,, \quad W_2 = \sqrt{\omega\sqrt{1-\eta^2}\left(1+2\eta\sqrt{1-\eta^2}\right)} \tag{3.5a}$$

$$P = \omega\left(W_2\sqrt{1-\eta^2} - \eta W_1\right), \qquad Q = \omega\left(W_1\sqrt{1-\eta^2} + \eta W_2\right) \tag{3.5b}$$

### 3.2 The multi-degree-of-freedom-system with damping

The state-space form of equations of motion and the associated eigenvalue problem – Eq. (2.12) - (2.14) remain. The difference now is the normalization of the eigenvectors with respect to the general stiffness matrix $\mathbf{K_G}$**:**

$$\begin{bmatrix}\lambda\mathbf{X}\\ \mathbf{X}\end{bmatrix}^T \mathbf{K_G} \begin{bmatrix}\lambda\mathbf{X}\\ \mathbf{X}\end{bmatrix} = A+iB \qquad \rightarrow \quad \boldsymbol{\Phi} = \frac{\mathbf{X}}{\sqrt{A+iB}} = \boldsymbol{\Phi}_\mathbf{r} + i\,\boldsymbol{\Phi}_\mathbf{i}\,, \tag{3.6a}$$

$$\begin{bmatrix}\overline{\lambda}\,\overline{\mathbf{X}}\\ \overline{\mathbf{X}}\end{bmatrix}^T \mathbf{K_G} \begin{bmatrix}\overline{\lambda}\,\overline{\mathbf{X}}\\ \overline{\mathbf{X}}\end{bmatrix} = A-iB \qquad \rightarrow \quad \overline{\boldsymbol{\Phi}} = \frac{\overline{\mathbf{X}}}{\sqrt{A-iB}} = \boldsymbol{\Phi}_\mathbf{r} - i\,\boldsymbol{\Phi}_\mathbf{i}\,, \tag{3.6b}$$

Due to the normalization (3.6) we have the orthogonality relationships (3.7), (3.8) – expressed in terms of the j[th] eigenvector-pair (index (j) omitted):

$$\begin{bmatrix}\lambda\boldsymbol{\Phi} & \overline{\lambda}\,\overline{\boldsymbol{\Phi}}\\ \boldsymbol{\Phi} & \overline{\boldsymbol{\Phi}}\end{bmatrix}^T \underbrace{\begin{bmatrix}\mathbf{M} & \\ & -\mathbf{K}\end{bmatrix}}_{\mathbf{M_G}} \begin{bmatrix}\lambda\boldsymbol{\Phi} & \overline{\lambda}\,\overline{\boldsymbol{\Phi}}\\ \boldsymbol{\Phi} & \overline{\boldsymbol{\Phi}}\end{bmatrix} = \begin{bmatrix}-\frac{1}{\lambda} & \\ & -\frac{1}{\overline{\lambda}}\end{bmatrix} \tag{3.7}$$

$$\begin{bmatrix}\lambda\boldsymbol{\Phi} & \overline{\lambda}\,\overline{\boldsymbol{\Phi}}\\ \boldsymbol{\Phi} & \overline{\boldsymbol{\Phi}}\end{bmatrix}^T \underbrace{\begin{bmatrix}\mathbf{D} & \mathbf{K}\\ \mathbf{K} & \end{bmatrix}}_{\mathbf{K_G}} \begin{bmatrix}\lambda\boldsymbol{\Phi} & \overline{\lambda}\,\overline{\boldsymbol{\Phi}}\\ \boldsymbol{\Phi} & \overline{\boldsymbol{\Phi}}\end{bmatrix} = \begin{bmatrix}1 & \\ & 1\end{bmatrix} \tag{3.8}$$

The modal matrix $\boldsymbol{\Phi}_\mathbf{G}$ is build up according to Eq. (2.18). By the aid of $\boldsymbol{\Phi}_\mathbf{G}$ the modal decomposition of the equations of motions is performed to:

$$\underbrace{\boldsymbol{\Phi}_G^T \begin{bmatrix}\mathbf{M} & \\ & -\mathbf{K}\end{bmatrix} \boldsymbol{\Phi}_G}_{\begin{bmatrix}-\frac{1}{\lambda^{(1)}} & & \\ & \cdots & \\ & & -\frac{1}{\overline{\lambda}^{(n)}}\end{bmatrix}} \dot{\mathbf{A}} + \underbrace{\boldsymbol{\Phi}_G^T \begin{bmatrix}\mathbf{D} & \mathbf{K}\\ \mathbf{K} & \end{bmatrix} \boldsymbol{\Phi}_G}_{\begin{bmatrix}1 & & \\ & \cdots & \\ & & 1\end{bmatrix}} \mathbf{A} = \boldsymbol{\Phi}_G^T \begin{bmatrix}\mathbf{p}(t)\end{bmatrix} \tag{3.9}$$

In regard to Eqs. (3.2), (3.3) the complex differential equations (3.9) can be transformed **in pairs** into the real form of SDOFS-equation, corresponding to the j[th] eigenpair (index (j) omitted):

$$\underbrace{\varphi^{-\mathbf{T}}\begin{bmatrix} -\frac{1}{\lambda} & \\ & -\frac{1}{\overline{\lambda}} \end{bmatrix}\varphi^{-\mathbf{1}}}_{\begin{bmatrix} 1 & 0 \\ 0 & -\omega^2 \end{bmatrix}} \cdot \begin{bmatrix} \dot{x} \\ \dot{y} \end{bmatrix} + \underbrace{\varphi^{-\mathbf{T}}\begin{bmatrix} 1 & \\ & 1 \end{bmatrix}\varphi^{-\mathbf{1}}}_{\begin{bmatrix} 2\eta\omega & \omega^2 \\ \omega^2 & \end{bmatrix}} \cdot \begin{bmatrix} x \\ y \end{bmatrix} = \underbrace{\varphi^{-\mathbf{T}}\begin{bmatrix} \lambda\,\mathbf{\Phi}^T\,\mathbf{p}(t) \\ \overline{\lambda}\,\overline{\mathbf{\Phi}}^T\,\mathbf{p}(t) \end{bmatrix}}_{\begin{bmatrix} g(t) \\ h(t) \end{bmatrix}} \tag{3.10}$$

The matrix $[\varphi(\omega,\eta)]^{-1}$ in (3.10) for the j[th] eigenvalue pair $\lambda^{(j)} = \lambda_r^{(j)} \pm i\lambda_i^{(j)}$ can be computed by Eqs. (3.4),(3.5).

The (2n x 2n) transformation basis **Y** is now defined formally equal to (2.22), but here by use of the complex transformations (3.9), (3.10):

$$\begin{bmatrix} \mathbf{W} \\ \mathbf{V} \end{bmatrix} = \mathbf{\Phi_G} \underbrace{\begin{bmatrix} \left(\varphi^{(1)}\right)^{-1} & & \\ & \cdots & \\ & & \left(\varphi^{(n)}\right)^{-1} \end{bmatrix}}_{\mathbf{\Psi}^{-1}} \underbrace{\begin{bmatrix} x_1 \\ y_1 \\ \cdots \\ x_n \\ y_n \end{bmatrix}}_{\mathbf{X}} = \underbrace{(\mathbf{\Phi_G}\mathbf{\Psi}^{-1})}_{\mathbf{Y}}\,\mathbf{X} = \mathbf{Y}\,\mathbf{X} \tag{3.11}$$

By the aid of the modal transformation basis **Y** from (3.11) the modal form of the equations of motion (2.23) remains.

In this case the components of two columns in the real matrix **Y**, belonging to the j[th] eigenvector-pair, are - see also Eq. (3.5a-b):

$$\begin{aligned}
\mathbf{Y}_{\mathrm{x}}^{(\mathrm{j})\mathbf{W}} &= \frac{\omega}{\sqrt{1-\eta^2}}\left[\left(-\eta\,W_2 + \sqrt{1-\eta^2}\,W_1\right)\mathbf{\Phi_r} - \left(\eta\,W_1 + \sqrt{1-\eta^2}\,W_2\right)\mathbf{\Phi_i}\right] \\
\mathbf{Y}_{y}^{(\mathrm{j})\mathbf{W}} &= \frac{\omega^2}{\sqrt{1-\eta^2}}\left[\left(-\eta\,Q - \sqrt{1-\eta^2}\,P\right)\mathbf{\Phi_r} + \left(\eta\,P - \sqrt{1-\eta^2}\,Q\right)\mathbf{\Phi_i}\right] \\
\mathbf{Y}_{x}^{(\mathrm{j})\mathbf{V}} &= \frac{1}{\sqrt{1-\eta^2}}\left[W_2\mathbf{\Phi_r} + W_1\mathbf{\Phi_i}\right] \\
\mathbf{Y}_{y}^{(\mathrm{j})\mathbf{V}} &= \frac{\omega}{\sqrt{1-\eta^2}}\left[Q\mathbf{\Phi_r} - P\mathbf{\Phi_i}\right]
\end{aligned} \tag{3.12a-d}$$

The two components of the associated "load" vector are now – by use of Eq.(3.5a-b):

$$\begin{aligned}
g(t) &= \frac{\omega}{\sqrt{1-\eta^2}}\left[\left(-\eta\,W_2 + \sqrt{1-\eta^2}\,W_1\right)\mathbf{\Phi_r^T} - \left(\eta\,W_1 + \sqrt{1-\eta^2}\,W_2\right)\mathbf{\Phi_i^T}\right]\mathbf{p}(t) \\
h(t) &= \frac{\omega^2}{\sqrt{1-\eta^2}}\left[\left(-\eta\,Q - \sqrt{1-\eta^2}\,P\right)\mathbf{\Phi_r^T} + \left(\eta\,P - \sqrt{1-\eta^2}\,Q\right)\mathbf{\Phi_i^T}\right]\mathbf{p}(t)
\end{aligned} \tag{3.13a-b}$$

The numerical solution of each SDOFS block equation and the final back transformation to the original DOFs remain the same like in Sec. 2 – in accordance to Eqs. (2.28), (3.11).

The phase angle $\varphi_k = arctan\frac{\Phi_{i(k)}}{\Phi_{r(k)}}$ in the special case of proportional damping can be determine from the restriction that all coordinates of $\mathbf{Y}_{\mathbf{x}}^{(\mathrm{j})V}$ have to be equal to zero, see [5]:

$$\mathbf{Y}_x^V = \frac{1}{\sqrt{1-\eta^2}}(W_2\boldsymbol{\Phi}_\mathbf{r} + W_1\boldsymbol{\Phi}_\mathbf{i}) = \mathbf{0} \tag{3.14}$$

The relationship leads together with (3.5a,b) to

$$\rightarrow \quad \frac{\Phi_{i(k)}}{\Phi_{r(k)}} = -\frac{W_2}{W_1} = \frac{1+2\eta\sqrt{1-\eta^2}}{2\eta^2-1} = const. \tag{3.15}$$

Comparing this result to Eq.(2.27), the constant phase lag depends obviously on the kind of the eigenmode normalization.

## 4 MODAL ANALYSIS PROCEDURE BASED ON BOTH THE COMPLEX RIGHT AND LEFT EIGENVECTORS

The procedure described in this section has been presented in [3] in slightly different form. The variant here will be developed without normalization of the eigenvectors of the SDOFS.

### 4.1 The single mass oscillator

The form (2.3) of the general eigenvalue problem and his solution – Eq. (2.4), (2.5), remain the same. The eigenvectors $\mathbf{r}_\mathbf{j}\ (j=1,2)$ are **right eigenvectors** of the matrix $\mathbf{a} = \mathbf{m}^{-1}\mathbf{k}$.

In order to determine the left eigenvectors of the matrix $\mathbf{a}$ the substitution

$$\underbrace{\begin{bmatrix} f_w \\ f_v \end{bmatrix}}_{\mathbf{f}} = \underbrace{\begin{bmatrix} 2\eta\omega & \omega^2 \\ \omega^2 & 0 \end{bmatrix}}_{\mathbf{k}} \underbrace{\begin{bmatrix} w \\ v \end{bmatrix}}_{\mathbf{q}} \tag{4.1a}$$

$$\mathbf{f} = \mathbf{k}\mathbf{q}, \qquad \dot{\mathbf{f}} = \mathbf{k}\dot{\mathbf{q}} \tag{4.1b}$$

has been introduced. The equation of motion (2.1b) is transformed to

$$\underbrace{\mathbf{k}\dot{\mathbf{q}}}\ + \ \mathbf{k}(\mathbf{m}^{-1}\underbrace{\mathbf{k}})\underbrace{\mathbf{q}} \ = \ \mathbf{k}\mathbf{m}^{-1}\mathbf{p}$$

$$\dot{\mathbf{f}} \ + \ \mathbf{k}\mathbf{m}^{-1}\mathbf{f} \ = \ \mathbf{k}\mathbf{m}^{-1}\mathbf{p}$$

$$\underbrace{\begin{bmatrix} 1 & 0 \\ 0 & 1 \end{bmatrix}}_{\mathbf{e}} \underbrace{\begin{bmatrix} \dot{f}_w \\ \dot{f}_v \end{bmatrix}}_{\mathbf{f}} + \underbrace{\begin{bmatrix} 2\eta\omega & -1 \\ \omega^2 & 0 \end{bmatrix}}_{\mathbf{k}\mathbf{m}^{-1}} \underbrace{\begin{bmatrix} f_w \\ f_v \end{bmatrix}}_{\mathbf{f}} = \underbrace{\begin{bmatrix} 2\eta\omega & -1 \\ \omega^2 & 0 \end{bmatrix}}_{\mathbf{k}\mathbf{m}^{-1}} \underbrace{\begin{bmatrix} p(t) \\ 0 \end{bmatrix}}_{\mathbf{p}(t)} \tag{4.2}$$

The corresponding eigenvalue problem is formulated assuming

$$\mathbf{f} = \mathbf{x}e^{\lambda t}, \qquad \dot{\mathbf{f}} = \lambda\mathbf{x}e^{\lambda t} \tag{4.3}$$

$$\rightarrow \quad \left( \underbrace{\mathbf{k}\mathbf{m}^{-1}}_{\mathbf{a}^{\mathbf{T}}} + \lambda \mathbf{e} \right) \mathbf{x} = \mathbf{0} \qquad \rightarrow \quad \left( \mathbf{a}^{\mathbf{T}} + \lambda \mathbf{e} \right) \mathbf{x} = \mathbf{0} \tag{4.4}$$

where

$$\mathbf{a}^{\mathbf{T}} = \left( \mathbf{m}^{-1}\mathbf{k} \right)^{\mathbf{T}} = \mathbf{k}^{\mathbf{T}} \left( \mathbf{m}^{-1} \right)^{\mathbf{T}} = \mathbf{k}\,\mathbf{m}^{-1} = \begin{bmatrix} 2\eta\omega & -1 \\ \omega^2 & 0 \end{bmatrix} \tag{4.5}$$

due to the symmetry of the matrices **k** and **m**. The two eigenvalues $\lambda_{1/2}$ of (4.4) remain the same - Eq. (2.4), but the corresponding complex conjugate eigenvectors are now

$$\mathbf{x}_{1/2} = \mathbf{x}_r \pm i\mathbf{x}_i = \begin{bmatrix} \frac{\eta \mp i\sqrt{1-\eta^2}}{\omega} \\ 1 \end{bmatrix} \tag{4.6}$$

The formulation

$$\mathbf{x}^{\mathbf{T}} \left( \mathbf{a} + \lambda \mathbf{e} \right) = \mathbf{0} \qquad \rightarrow \quad \left( \mathbf{a}^{\mathbf{T}} + \lambda \mathbf{e} \right) \mathbf{x} = \mathbf{0} \quad \rightarrow \quad \left( \mathbf{a}^{\mathbf{T}} + \lambda_j \mathbf{e} \right) \mathbf{l}_{\mathbf{j}} = \mathbf{0} \tag{4.7}$$

shows that **x** represents here the **left eigenvectors** of the matrix $\mathbf{a} = \mathbf{m}^{-1}\mathbf{k}$ (respectively, the right eigenvectors of the matrix $\mathbf{a}^{\mathbf{T}} = \mathbf{k}\,\mathbf{m}^{-1}$), i.e. $\mathbf{x}_{\mathbf{j}} = \mathbf{l}_{\mathbf{j}}$ (j=1,2) .

In this variant the modal matrix is defined without normalization by

$$\varphi^{\mathrm{L}} = [\mathbf{l}_1 \quad \mathbf{l}_2] = \begin{bmatrix} \frac{\eta - i\sqrt{1-\eta^2}}{\omega} & \frac{\eta + i\sqrt{1-\eta^2}}{\omega} \\ 1 & 1 \end{bmatrix} \tag{4.8}$$

The eigenvalue problem in the „left“ formulation (4.7) may be rewritten using the $\varphi^{\mathbf{L}}$ modal matrix as:

$$\mathbf{a}^{\mathbf{T}}\varphi^{\mathrm{L}} + \varphi^{\mathrm{L}}\boldsymbol{\lambda} = \mathbf{0} \tag{4.9}$$

where $\boldsymbol{\lambda} = \begin{bmatrix} \lambda & \\ & \overline{\lambda} \end{bmatrix}$ (4.10)

represents the spectral matrix of $\mathbf{a}^{\mathbf{T}}$. From Eq. (4.9) the diagonalization of the $\mathbf{a}^{\mathbf{T}}$ matrix and the inverse relation can be developed:

$$\mathbf{a}^{\mathbf{T}} \;=\; \varphi^{\mathbf{L}} \cdot \left( -\boldsymbol{\lambda} \right) \cdot \left( \varphi^{\mathbf{L}} \right)^{-\mathbf{1}} \qquad \leftrightarrow \qquad -\boldsymbol{\lambda} \;=\; \left( \varphi^{\mathbf{L}} \right)^{-\mathbf{1}} \cdot \mathbf{a}^{\mathbf{T}} \cdot \left( \varphi^{\mathbf{L}} \right) \tag{4.11}$$

The inverse matrix $\left( \varphi^{\mathbf{L}} \right)^{-\mathbf{1}}$ is calculated now to:

$$(\varphi^{\mathrm{L}})^{-1} = \frac{1}{2\sqrt{1-\eta^2}} \begin{bmatrix} i\omega & \sqrt{1-\eta^2} - i\eta \\ -i\omega & \sqrt{1-\eta^2} + i\eta \end{bmatrix} \tag{4.12}$$

## 4.2 Modal decomposition of a multi-degree-of-freedom-system with damping

The state-space form of equations of motion (2.12) is transformed in two variants using the substitution

$$\mathbf{F} = \mathbf{K_G}\,\mathbf{Q}\ , \qquad \dot{\mathbf{F}} = \mathbf{K_G}\,\dot{\mathbf{Q}} \tag{4.13}$$

1) $$\dot{\mathbf{Q}} + \underbrace{\mathbf{M_G^{-1}} \cdot \mathbf{K_G}}_{\mathbf{A}} \cdot \mathbf{Q} = \mathbf{M_G^{-1}} \cdot \mathbf{P} \tag{4.14a}$$

2) $$\begin{aligned} \underbrace{\mathbf{K_G}\,\dot{\mathbf{Q}}} \quad &+ \quad \mathbf{K_G}\,\mathbf{M_G^{-1}}\underbrace{\mathbf{K_G}\,\mathbf{Q}} \quad = \quad \mathbf{K_G}\,\mathbf{M_G^{-1}}\,\mathbf{P} \\ \dot{\mathbf{F}} \quad &+ \quad \mathbf{K_G}\,\mathbf{M_G^{-1}}\,\mathbf{F} \quad = \quad \mathbf{K_G}\,\mathbf{M_G^{-1}}\,\mathbf{P} \end{aligned} \tag{4.14b}$$

Because of the symmetry of $\mathbf{M_G}$ and $\mathbf{K_G}$ we receive the relationship

$$\mathbf{K_G}\,\mathbf{M_G^{-1}} = \mathbf{K_G^T}\left(\mathbf{M_G^{-1}}\right)^{\mathbf{T}} = \left(\underbrace{\mathbf{M_G^{-1}}\mathbf{K_G}}_{\mathbf{A}}\right)^{\mathbf{T}} = \mathbf{A^T} \tag{4.15}$$

Here we need the right and the left eigenvectors of the matrix **A**, to be calculated from the form (4.14a) resp.(4.14b):

$$\left(\mathbf{A} + \lambda_j \mathbf{E}\right)\mathbf{R}_j = \mathbf{0} \qquad \text{resp.} \qquad \left(\mathbf{A}^T + \lambda_j \mathbf{E}\right)\mathbf{L}_j = \mathbf{0} \tag{4.16a-b}$$

The formulations (4.14a) and (4.14b) yield directly the relationship between an arbitrary $j^{th}$ right and left eigenvector

$$\mathbf{L_j} = \mathbf{K_G}\ \mathbf{R_j} \tag{4.17}$$

The right and the left modal matrix, respectively, are complete sets of the corresponding n eigenpairs

$$\mathbf{R} = \left[\mathbf{R_1}\ \overline{\mathbf{R}}_1 \quad \ldots \quad \mathbf{R_n}\ \overline{\mathbf{R}}_n\right] \tag{4.18a}$$

$$\mathbf{L} = \left[\mathbf{L_1}\ \overline{\mathbf{L}}_1 \quad \ldots \quad \mathbf{L_n}\ \overline{\mathbf{L}}_n\right] \tag{4.18b}$$

The orthogonality property of the eigenvectors leads to

$$\mathbf{R^T L} = \mathbf{R^T K_G R} = \begin{bmatrix} \gamma_{11} & & & & \\ & \overline{\gamma}_{11} & & & \\ & & \cdots & & \\ & & & \gamma_{nn} & \\ & & & & \overline{\gamma}_{nn} \end{bmatrix} \tag{4.19}$$

Using the main diagonal components $\gamma_{kk}$ from Eq. (4.19) the modal matrices $\mathbf{R}$, $\mathbf{L}$ are normalized with respect to the general stiffness matrix $\mathbf{K_G}$:

$$\mathbf{\Phi}_k^{\mathbf{R}} = \frac{1}{\sqrt{\gamma_{kk}}}\mathbf{R_k} \qquad \rightarrow \quad \mathbf{\Phi^R} = \left[\mathbf{\Phi}_1^{\mathbf{R}}\ \ \overline{\mathbf{\Phi}}_1^{\mathbf{R}} \quad \ldots \quad \mathbf{\Phi}_n^{\mathbf{R}}\ \ \overline{\mathbf{\Phi}}_n^{\mathbf{R}}\right] \tag{4.20a}$$

$$\mathbf{\Phi}_k^{\mathbf{L}} = \frac{1}{\sqrt{\gamma_{kk}}}\mathbf{L_k} \quad \rightarrow \quad \mathbf{\Phi}^{\mathbf{L}} = \left[\mathbf{\Phi}_{\mathbf{1}}^{\mathbf{L}} \;\; \overline{\mathbf{\Phi}}_{\mathbf{1}}^{\mathbf{L}} \quad \ldots \quad \mathbf{\Phi}_{\mathbf{n}}^{\mathbf{L}} \;\; \overline{\mathbf{\Phi}}_{\mathbf{n}}^{\mathbf{L}}\right] \tag{4.20b}$$

Due to (4.19) and the chosen type of normalization (4.20) we receive the relationships

$$\left(\mathbf{\Phi}^{\mathbf{L}}\right)^{\mathbf{T}} \cdot \mathbf{\Phi}^{\mathbf{R}} = \left(\mathbf{\Phi}^{\mathbf{R}}\right)^{\mathbf{T}} \cdot \mathbf{\Phi}^{\mathbf{L}} = \mathbf{E} \tag{4.21}$$

$$\mathbf{\Phi}^{\mathbf{R}} = \left[\left(\mathbf{\Phi}^{\mathbf{L}}\right)^{\mathbf{T}}\right]^{-\mathbf{1}} = \left(\mathbf{\Phi}^{\mathbf{L}}\right)^{-\mathbf{T}} \quad \leftrightarrow \quad \left(\mathbf{\Phi}^{\mathbf{R}}\right)^{\mathbf{T}} = \left(\mathbf{\Phi}^{\mathbf{L}}\right)^{-\mathbf{1}} \tag{4.22}$$

where **E** is a (2n x 2n) identity matrix.

The eigenvalue problem (4.16b) may be rewritten using the $\mathbf{\Phi}^{\mathbf{L}}$ - modal matrix:

$$\left(\mathbf{A}^{\mathbf{T}} + \lambda_k \mathbf{E}\right)\mathbf{\Phi}_k^{\mathbf{L}} = \mathbf{0} \quad \rightarrow \quad \mathbf{A}^{\mathbf{T}} \cdot \mathbf{\Phi}^{\mathbf{L}} + \mathbf{\Phi}^{\mathbf{L}} \cdot \mathbf{\Lambda} = \mathbf{0} \tag{4.23}$$

where

$\mathbf{\Lambda} = diag\{\lambda_j\}$ $(j = 1, \ldots, 2n)$ : spectral matrix

From Eq. (4.23) can be derived the diagonalization of the $\mathbf{A}^{\mathbf{T}}$-matrix and the associated inverse relationship:

$$\mathbf{A}^{\mathbf{T}} = \mathbf{\Phi}^{\mathbf{L}} \cdot (-\mathbf{\Lambda}) \cdot \left(\mathbf{\Phi}^{\mathbf{L}}\right)^{-\mathbf{1}} \quad \leftrightarrow \quad -\mathbf{\Lambda} = \left(\mathbf{\Phi}^{\mathbf{L}}\right)^{-\mathbf{1}} \cdot \mathbf{A}^{\mathbf{T}} \cdot \mathbf{\Phi}^{\mathbf{L}} \tag{4.24}$$

The modal decomposition of the system equations (4.14b) is based on the modal superposition relationship

$$\mathbf{F} = \mathbf{\Phi}^{\mathbf{L}} \cdot \underbrace{\left[a_1 \quad b_1 \quad \ldots \quad a_n \quad b_n\right]^T}_{\mathbf{B}^{\mathbf{L}}} = \mathbf{\Phi}^{\mathbf{L}} \cdot \mathbf{B}^{\mathbf{L}} \tag{4.25a}$$

where

$$\mathbf{B}^{\mathbf{L}} = \left[a_1 \quad b_1 \quad \ldots \quad a_n \quad b_n\right]^T \quad \text{: new modal complex coordinates} \tag{4.25b}$$

The equations of motion (4.14b) are transformed into a set of 2n uncoupled complex equations:

$$\underbrace{\left(\mathbf{\Phi}^{\mathbf{L}}\right)^{-\mathbf{1}} \mathbf{E} \mathbf{\Phi}^{\mathbf{L}}}_{\begin{bmatrix} 1 & & \\ & \ldots & \\ & & 1 \end{bmatrix}} \dot{\mathbf{B}}^{\mathbf{L}} \quad + \quad \underbrace{\left(\mathbf{\Phi}^{\mathbf{L}}\right)^{-\mathbf{1}} \overbrace{\left(\mathbf{K}_{\mathbf{G}} \mathbf{M}_{\mathbf{G}}^{-\mathbf{1}}\right)}^{\mathbf{A}^{\mathbf{T}}} \mathbf{\Phi}^{\mathbf{L}}}_{\begin{bmatrix} -\lambda_1 & & & & \\ & -\bar{\lambda}_1 & & & \\ & & \ldots & & \\ & & & -\lambda_n & \\ & & & & -\bar{\lambda}_n \end{bmatrix}_{-\mathbf{\Lambda}}} \mathbf{B}^{\mathbf{L}} \quad = \quad \underbrace{\left(\mathbf{\Phi}^{\mathbf{L}}\right)^{-\mathbf{1}} \mathbf{A}^{\mathbf{T}} \mathbf{P}}_{\begin{bmatrix} p_{a1}^L \\ p_{b1}^L \\ \ldots \\ p_{an}^L \\ p_{bn}^L \end{bmatrix}_{\mathbf{P}^{\mathbf{L}}}} \tag{4.26}$$

Each j-th pair of the n uncoupled equations (4.26) can now be transformed using Eq. (4.11) (index (j) omitted):

$$\underbrace{\varphi^{\mathbf{L}}\begin{bmatrix}1 & 0\\ 0 & 1\end{bmatrix}\left(\varphi^{\mathbf{L}}\right)^{-1}}_{\begin{bmatrix}1 & 0\\ 0 & 1\end{bmatrix}} \cdot \begin{bmatrix}\dot{x}\\ \dot{y}\end{bmatrix}^{L} + \underbrace{\varphi^{\mathbf{L}}\begin{bmatrix}-\lambda & 0\\ 0 & -\bar{\lambda}\end{bmatrix}\left(\varphi^{\mathbf{L}}\right)^{-1}}_{\left(\mathbf{a}^{T}\right)} \cdot \begin{bmatrix}x\\ y\end{bmatrix}^{L} = \underbrace{\varphi^{\mathbf{L}}\begin{bmatrix}p_a^{L}\\ p_b^{L}\end{bmatrix}}_{\begin{bmatrix}g_L\\ h_L\end{bmatrix}} \qquad \begin{bmatrix}2\eta\,\omega & -1\\ \omega^2 & \end{bmatrix} \tag{4.27}$$

The free vibration frequency $\omega^{(j)}$ and the modal damping ratio $\eta^{(j)}$ for the j[th] eigenpair $\left(\lambda^{(j)} = \lambda_r + i\lambda_i\ ,\quad \bar{\lambda}^{(j)} = \lambda_r - i\lambda_i\right)$ are to be computed according to Eq. (2.4). The corresponding matrices $\varphi^{\mathrm{L}}, (\varphi^{\mathrm{L}})^{-1}$ can be evaluated by Eq. (4.8), (4.12).

A purely real transformation basis $\mathbf{Y_L}$ will be built up by combination of the complex transformations (4.26) and (4.27):

$$\mathbf{F} = \mathbf{K}_{\boldsymbol{G}}\begin{bmatrix}\mathbf{W}\\ \mathbf{V}\end{bmatrix} = \boldsymbol{\Phi}^{\mathbf{L}}\underbrace{\begin{bmatrix}\left(\varphi^{\mathrm{L}(1)}\right)^{-1} & & \\ & \cdots & \\ & & \left(\varphi^{\mathrm{L}(n)}\right)^{-1}\end{bmatrix}}_{(\boldsymbol{\Psi}_{\mathrm{L}})^{-1}}\begin{bmatrix}x_1\\ y_1\\ \cdots\\ x_n\\ y_n\end{bmatrix}_{\mathrm{L}} = \underbrace{\boldsymbol{\Phi}^{\mathbf{L}}\,(\boldsymbol{\Psi}_{\mathrm{L}})^{-1}}_{\mathbf{Y_L}}\mathbf{X_L} = \mathbf{Y_L}\,\mathbf{X_L} \tag{4.28}$$

In the product of the two complex matrices $\boldsymbol{\Phi}^{\mathbf{L}} \cdot \left(\boldsymbol{\Psi}_{\mathbf{L}}\right)^{-1}$, Eq.(4.28), the imaginary parts cancel each other, the resulting transformation matrix $\mathbf{Y_L}$ is purely real – see Eq. (4.30). The same applies to all "load" vectors $\begin{bmatrix}g_L & h_L\end{bmatrix}^T$ in Eq. (4.27).

Finally the equations of motion (4.14b) can be uncoupled by means of the transformation basis $\mathbf{Y_L}$ into n SDOFS block equations in real arithmetic:

$$\underbrace{\left(\mathbf{Y_L}\right)^{-1}\cdot\mathbf{E}\cdot\mathbf{Y_L}}_{\begin{bmatrix}1 & & & \\ & 1 & & \\ & & \cdots & \\ & & & 1\end{bmatrix}}\cdot\dot{\mathbf{X}}_{\mathbf{L}}(t) + \underbrace{\left(\mathbf{Y_L}\right)^{-1}\cdot\mathbf{A}^{\mathbf{T}}\cdot\mathbf{Y_L}}_{\begin{bmatrix}2\eta^{(1)}\omega^{(1)} & -1 & & & & \\ \left(\omega^{(1)}\right)^2 & 0 & & & & \\ & & \cdots & & & \\ & & & \cdots & & \\ & & & & 2\eta^{(n)}\omega^{(n)} & -1 \\ & & & & \left(\omega^{(n)}\right)^2 & 0\end{bmatrix}}\cdot\underbrace{\mathbf{X_L}(t)}_{\begin{bmatrix}x_1\\ y_1\\ \cdots\\ x_n\\ y_n\end{bmatrix}_L} = \underbrace{\left(\mathbf{Y_L}\right)^{-1}\cdot\mathbf{A}^{\mathbf{T}}\cdot\mathbf{P}(t)}_{\begin{bmatrix}g_L^{(1)}\\ h_L^{(1)}\\ \cdots\\ g_L^{(n)}\\ h_L^{(n)}\end{bmatrix}} \tag{4.29}$$

The components of $\mathbf{Y_L}$, which belong to the j[th] eigenvector-pair, are the following two columns - see (4.28), (4.12):

$$\left[\cdots\quad (\mathbf{Y}_x)^{(j)}\quad \left(\mathbf{Y}_y\right)^{(j)}\quad \cdots\right] = \left[\boldsymbol{\Phi}_{\mathrm{r}}^{\mathbf{L}} + i\boldsymbol{\Phi}_{\mathrm{i}}^{\mathbf{L}}\quad \boldsymbol{\Phi}_{\mathrm{r}}^{\mathbf{L}} - i\boldsymbol{\Phi}_{\mathrm{i}}^{\mathbf{L}}\right]\cdot\frac{1}{2\sqrt{1-\eta^2}}\begin{bmatrix} i\omega & \sqrt{1-\eta^2} - i\eta\\ -i\omega & \sqrt{1-\eta^2} + i\eta\end{bmatrix}$$

$$= \frac{1}{\sqrt{1-\eta^2}}\left[\cdots\quad -\omega\,\boldsymbol{\Phi}_{\mathrm{i}}^{\mathbf{L}}\qquad \left(\boldsymbol{\Phi}_{r}^{\mathbf{L}}\sqrt{1-\eta^2} + \boldsymbol{\Phi}_{\mathrm{i}}^{\mathbf{L}}\,\eta\right)\quad \cdots\right] \tag{4.30}$$

The associated two components of the "load" vector from (4.29) are calculated - with regard to (4.8) - to be fully real too:

$$\begin{bmatrix} \dots \\ g_L \\ h_L \\ \dots \end{bmatrix} = (\mathbf{Y_L})^{-1}\mathbf{A}^{\mathrm{T}}\mathbf{P} = \mathbf{\Psi_L}\underbrace{(\mathbf{\Phi^L})^{-1}}_{(\mathbf{\Phi^R})^{\mathbf{T}}}\mathbf{A}^{\mathrm{T}}\mathbf{P} = \begin{bmatrix} \dots \\ \frac{2}{\omega}\left(\eta\,(\mathbf{\Phi}_{\mathrm{r}}^{\mathbf{R}})^{\mathrm{T}} + \sqrt{1-\eta^2}\left(\mathbf{\Phi}_{\mathrm{i}}^{\mathbf{R}}\right)^{\mathrm{T}}\right) \\ 2(\mathbf{\Phi}_{\mathrm{r}}^{\mathbf{R}})^{\mathrm{T}} \\ \dots \end{bmatrix}\mathbf{A}^{\mathrm{T}}\mathbf{P} \tag{4.31}$$

### 4.3 Solution of the modal equations and back transformation

The solution of each j[th] SDOFS block equation in (4.29) is performed eliminating first the modal coordinate $x^{(j)}$ (index (j) omitted):

$$\begin{bmatrix} 1 & 0 \\ 0 & 1 \end{bmatrix}\begin{bmatrix} \dot{x} \\ \dot{y} \end{bmatrix} + \begin{bmatrix} 2\eta\,\omega & -1 \\ \omega^2 & 0 \end{bmatrix}\begin{bmatrix} x \\ y \end{bmatrix} = \begin{bmatrix} g_L(t) \\ h_L(t) \end{bmatrix} \tag{4.32}$$

The second equation

$$x = -\frac{\dot{y}}{\omega^2} + \frac{h_L}{\omega^2} \tag{4.33a}$$

should be introduced into the first one:

$$\ddot{y} + 2\eta\omega\,\dot{y} + \omega^2\,y = -\omega^2\,g_L + 2\eta\omega\,h_L + \dot{h}_L \tag{4.33b}$$

The modal response $y(t)$ is easy determined by step-by-step integration of Eq. (4.33b), then the $x(t)$ according to (4.33a). The final time series of the original n DOFs are calculated by superposition of the modal coordinates in accordance to Eq. (4.28):

$$\begin{bmatrix} \mathbf{W} \\ \mathbf{V} \end{bmatrix} = (\mathbf{K_G})^{-1}\,\mathbf{Y_L}\,\mathbf{X_L} \tag{4.34}$$

# 5 NUMERICAL EXAMPLE

## 5.1 Structural system, stiffness and geometry data

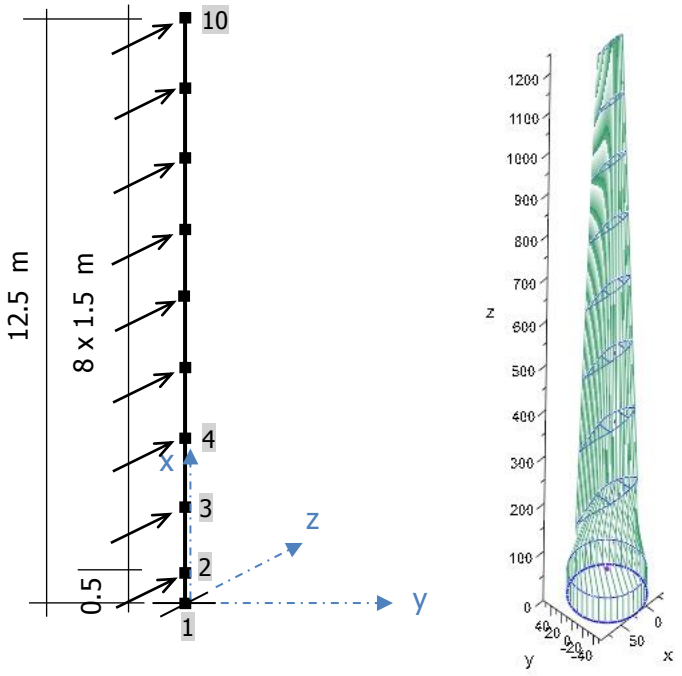


Fig. 1 Rotor blade beam model subjected to wind loads

The stiffness data of the blade thin wall cross sections have been calculated in [14]. The generic aerodynamic blade geometry has been derived from real blade data.

The finite element solution is based on the numerical integration of the system of differential equations for the Bernoulli-beam. The reference axis of the beam model coincides with the centre of the circular-section at the root – it is the real rotational axis of the rotor blade. Thereby the differential equations and all cross section stiffness data are referred to this axis, accounting for the eccentric mass application.

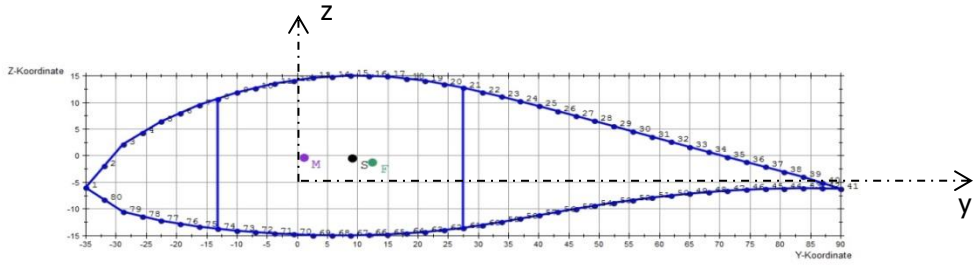


Fig. 2 Rotor blade sections at 2.0 m – thin wall cross section model

## 5.2 Wind loads

The wind loads are calculated according to the formula for the aerodynamic lift force per unit length of an aerofoil, see [13] p.59:

$$L = \frac{1}{2}\rho \cdot c(r) \cdot W^2 \cdot C_L \tag{5.1}$$

where: $W$ : air velocity relative to the aerofoil
$\rho$ : air density = 1.225 [kg/m$^3$]
$c(r)$ : chord of the aerofoil
$C_L$ : lift coefficient $C_L = 2\pi\,\alpha = 2\pi\left(\frac{\pi}{180}6.0\right) = 0.658$,
the flow angle $\alpha$ is assumed to be 6.0 [deg]

The air velocity $W$ is the vector sum of the rotational speed Ω (assumed to reach 60 rpm in the initial four seconds) and the wind speed $u$, incident on the aerofoil in accordance with the Betz-theory:

$$W = \sqrt{(\Omega\, r)^2 + \left(\frac{2}{3}u\right)^2} \qquad \text{where } \Omega = \left(\frac{60}{30}\pi\right) \text{ in [rad/s]} \tag{5.2}$$

The wind speed time series $u(t)$, used for calculation of the wind thrust force, is shown in fig.3 :




Fig. 3 Wind speed time series

The resulting wind thrust loads T($t$) per unit length along the x-axis of the rotor blade can be determined as function of the wind speed $u(t)$. In the structural model the wind thrust loads are acting as summarized nodal forces.




Fig. 4 Wind thrust function acting on the rotor blade at 12.5 m

### 5.3 Relationships and data for the damping approach

Starting point of the computation are the equations of motion

$$\begin{bmatrix} \mathbf{M} & \mathbf{0} \\ \mathbf{0} & -\mathbf{K} \end{bmatrix} \begin{bmatrix} \dot{\mathbf{W}} \\ \dot{\mathbf{V}} \end{bmatrix} + \begin{bmatrix} \mathbf{D} & \mathbf{K} \\ \mathbf{K} & \mathbf{0} \end{bmatrix} \begin{bmatrix} \mathbf{W} \\ \mathbf{V} \end{bmatrix} = \begin{bmatrix} \mathbf{P}(t) \\ \mathbf{0} \end{bmatrix} \tag{5.3}$$

where $\mathbf{P}(t)$ is the nodal force vector, representing the wind thrust according to Sec. 5.2.

The system equations (5.3) will be solved applying the proposed modal analysis method in Sec. 3 for two cases: non-proportional and proportional damping.

The lowest four free-vibration frequencies and associated periods for the undamped system are calculated to

$$\begin{aligned} f_1 &= 2.643\ [s^{-1}] & T_1 &= 0.378\ [s] \\ f_2 &= 4.622\ [s^{-1}] & T_2 &= 0.216\ [s] \\ f_3 &= 7.942\ [s^{-1}] & T_3 &= 0.126\ [s] \\ f_4 &= 16.650\ [s^{-1}] & T_4 &= 0.060\ [s] \end{aligned} \tag{5.4}$$

Stiffness proportional damping as a special case of Rayleigh damping has been assumed:

$$\mathbf{D_p} = \beta\, \mathbf{K} \tag{5.5a}$$

where $$\beta = \frac{2\eta}{\omega_1} = \frac{\eta\, T_1}{\pi} = 0.000964[s] \tag{5.5b}$$

In Eq. (5.5b) the damping ratio $\eta = 0.008$ for the first natural period $T_1$ has been taken in accordance with [13] p. 249.

The non-proportional symmetric damping matrix $\mathbf{D_{np}}$ is build adding to the $\mathbf{D_p}$-matrix a new matrix $\mathbf{D_a}$, which represents the aerodynamic damping. The formulation is based on a

simple expression for the aerodynamic damping coefficient $c_d(r)$ per unit length, given in [13], p. 247:

$$c_d(r) = \frac{1}{2}\rho \cdot \Omega r \cdot c(r) \cdot \frac{dC_L}{d\alpha} \quad \left[\frac{kg}{s}\frac{1}{m}\right], \quad \text{where} \quad \frac{dC_L}{d\alpha} = 2\pi \tag{5.6}$$

In accordance with Eq. (5.1), (5.2), the corresponding damping coefficients $c_d(r)$ along the x-axis of the rotor blade are calculated to

| r [m] | $c(r)$ [m] | $c_d(r)$ [kg/s.m] |
|---|---|---|
| 0 | 1.1 | 0 |
| 0.5 | 1.1 | 13.2993 |
| 2.0 | 1.25 | 60.4513 |
| 3.5 | 1.15 | 97.3266 |
| 5.0 | 1.05 | 126.948 |
| 6.5 | 0.95 | 149.315 |
| 8.0 | 0.85 | 164.428 |
| 9.5 | 0.75 | 172.286 |
| 11.0 | 0.65 | 172.891 |
| 12.5 | 0.55 | 166.241 |

The coefficients $c_d(r)$, which represent the aerodynamic damping, are active for vibration in z-direction of the cross-section coordinate system, see Fig. 2. The associate symmetric damping matrix for the Bernoulli-beam element is derived by analogy with the method used to derive the finite element mass matrix, see [15]. Finally the symmetric system damping matrix, $\mathbf{D_{np}}$, is assembled in a finite-element manner, including structural (proportional) and aerodynamic damping:

$$\mathbf{D_{np}} = \mathbf{D_p} + \mathbf{D_a} \tag{5.7}$$

## 5.4 Non-proportional damped system

We use here the matrix $\mathbf{D_{np}}$ – Eq.(5.7). The vector of the first ten complex conjugate eigenvalue pairs of the matrix $\mathbf{A} = \mathbf{M_G^{-1}} \cdot \mathbf{K_G}$, see Eq.(4.16), is

$$\begin{pmatrix} -5.56181 + 15.7652\,i \\ -5.56181 - 15.7652\,i \\ -0.40981 + 29.0336\,i \\ -0.40981 - 29.0336\,i \\ -6.33469 + 49.2454\,i \\ -6.33469 - 49.2454\,i \\ -9.53814 + 104.542\,i \\ -9.53814 - 104.542\,i \\ -5.43041 + 105.219\,i \\ -5.43041 - 105.219\,i \\ -20.7608 + 185.185\,i \\ -20.7608 - 185.185\,i \\ -22.1068 + 207.402\,i \\ -22.1068 - 207.402\,i \\ -27.8796 + 238.91\,i \\ -27.8796 - 238.91\,i \\ -45.8047 + 292.379\,i \\ -45.8047 - 292.379\,i \\ -63.5216 + 353.962\,i \\ -63.5216 - 353.962\,i \end{pmatrix} \tag{5.8}$$

The number of modes considered in the modal transformation is limited to the first four eigenvector pairs. The structural system in Fig. 1 has 54 DOF. The corresponding (108x8) modal matrix $\mathbf{\Phi_G}$ with stiffness normalized eigenvectors – Eq.(3.6a,b), is computed to (only the first ten rows are printed)

$$\begin{pmatrix}
-3.49\,10^{-7}-5.71\,10^{-7}\,i & -3.49\,10^{-7}+5.71\,10^{-7}\,i & 9.6\,10^{-5}+1.89\,10^{-8}\,i & 9.6\,10^{-5}-1.89\,10^{-8}\,i & -3.85\,10^{-8}+5.43\,10^{-7}\,i & -3.85\,10^{-8}-5.43\,10^{-7}\,i & -3.83\,10^{-6}-2.72\,10^{-5}\,i & -3.83\,10^{-6}+2.72\,10^{-5}\,i \\
-4.4\,10^{-7}-7.21\,10^{-7}\,i & -4.4\,10^{-7}+7.21\,10^{-7}\,i & 1.21\,10^{-4}+2.39\,10^{-8}\,i & 1.21\,10^{-4}-2.39\,10^{-8}\,i & -4.74\,10^{-8}+6.9\,10^{-7}\,i & -4.74\,10^{-8}-6.9\,10^{-7}\,i & -5.13\,10^{-6}-3.48\,10^{-5}\,i & -5.13\,10^{-6}+3.48\,10^{-5}\,i \\
3.38\,10^{-5}+5.85\,10^{-6}\,i & 3.38\,10^{-5}-5.85\,10^{-6}\,i & 2.66\,10^{-6}+7.94\,10^{-7}\,i & 2.66\,10^{-6}-7.94\,10^{-7}\,i & -8.14\,10^{-5}+2.24\,10^{-6}\,i & -8.14\,10^{-5}-2.24\,10^{-6}\,i & 1.53\,10^{-4}-5.7\,10^{-6}\,i & 1.53\,10^{-4}+5.7\,10^{-6}\,i \\
4.53\,10^{-6}+4.29\,10^{-6}\,i & 4.53\,10^{-6}-4.29\,10^{-6}\,i & 8.18\,10^{-7}+3.09\,10^{-7}\,i & 8.18\,10^{-7}-3.09\,10^{-7}\,i & -3.35\,10^{-5}-1.27\,10^{-6}\,i & -3.35\,10^{-5}+1.27\,10^{-6}\,i & 1.21\,10^{-4}+9.28\,10^{-7}\,i & 1.21\,10^{-4}-9.28\,10^{-7}\,i \\
-1.34\,10^{-4}-2.3\,10^{-5}\,i & -1.34\,10^{-4}+2.3\,10^{-5}\,i & -1.05\,10^{-5}-3.13\,10^{-6}\,i & -1.05\,10^{-5}+3.13\,10^{-6}\,i & 3.19\,10^{-4}-9.05\,10^{-6}\,i & 3.19\,10^{-4}+9.05\,10^{-6}\,i & -5.92\,10^{-4}+2.25\,10^{-5}\,i & -5.92\,10^{-4}-2.25\,10^{-5}\,i \\
-1.74\,10^{-6}-2.85\,10^{-6}\,i & -1.74\,10^{-6}+2.85\,10^{-6}\,i & 4.8\,10^{-4}+9.48\,10^{-8}\,i & 4.8\,10^{-4}-9.48\,10^{-8}\,i & -2.36\,10^{-7}+2.72\,10^{-6}\,i & -2.36\,10^{-7}-2.72\,10^{-6}\,i & -2.0\,10^{-5}-1.36\,10^{-4}\,i & -2.0\,10^{-5}+1.36\,10^{-4}\,i \\
-6.15\,10^{-5}-1.66\,10^{-5}\,i & -6.15\,10^{-5}+1.66\,10^{-5}\,i & 0.00129-1.0\,10^{-6}\,i & 0.00129+1.0\,10^{-6}\,i & 1.13\,10^{-4}+1.86\,10^{-6}\,i & 1.13\,10^{-4}-1.86\,10^{-6}\,i & -2.22\,10^{-4}-2.9\,10^{-4}\,i & -2.22\,10^{-4}+2.9\,10^{-4}\,i \\
-1.59\,10^{-4}-8.49\,10^{-5}\,i & -1.59\,10^{-4}+8.49\,10^{-5}\,i & 0.011-4.88\,10^{-7}\,i & 0.011+4.88\,10^{-7}\,i & 2.38\,10^{-4}+4.97\,10^{-5}\,i & 2.38\,10^{-4}-4.97\,10^{-5}\,i & -8.16\,10^{-4}-0.00269\,i & -8.16\,10^{-4}+0.00269\,i \\
0.00737+0.00119\,i & 0.00737-0.00119\,i & 1.58\,10^{-4}+1.66\,10^{-4}\,i & 1.58\,10^{-4}-1.66\,10^{-4}\,i & -0.0157+5.98\,10^{-4}\,i & -0.0157-5.98\,10^{-4}\,i & 0.026-0.00105\,i & 0.026+0.00105\,i \\
2.0\,10^{-4}+1.9\,10^{-4}\,i & 2.0\,10^{-4}-1.9\,10^{-4}\,i & 3.59\,10^{-5}+1.36\,10^{-5}\,i & 3.59\,10^{-5}-1.36\,10^{-5}\,i & -0.00147-5.38\,10^{-5}\,i & -0.00147+5.38\,10^{-5}\,i & 0.00524+3.57\,10^{-5}\,i & 0.00524-3.57\,10^{-5}\,i
\end{pmatrix} \tag{5.9}$$

The matrix $\mathbf{\Psi}^{-1}$ is now calculated in the case of four involved eigenmodes according to Eq. (3.11), (3.4):

$$\mathbf{\Psi}^{-1} = \begin{bmatrix}
\left(\varphi^{(1)}\right)^{-1} & & & \\
& \left(\varphi^{(2)}\right)^{-1} & & \\
& & \left(\varphi^{(3)}\right)^{-1} & \\
& & & \left(\varphi^{(4)}\right)^{-1}
\end{bmatrix} =$$

$$\begin{pmatrix}
2.6857-1.2849\,i & 35.194+35.194\,i & 0 & 0 & 0 & 0 & 0 & 0 \\
2.6857+1.2849\,i & 35.194-35.194\,i & 0 & 0 & 0 & 0 & 0 & 0 \\
0 & 0 & 2.7322-2.6561\,i & 78.236+78.236\,i & 0 & 0 & 0 & 0 \\
0 & 0 & 2.7322+2.6561\,i & 78.236-78.236\,i & 0 & 0 & 0 & 0 \\
0 & 0 & 0 & 0 & 3.9601-3.0574\,i & 175.65+175.65\,i & 0 & 0 \\
0 & 0 & 0 & 0 & 3.9601+3.0574\,i & 175.65-175.65\,i & 0 & 0 \\
0 & 0 & 0 & 0 & 0 & 0 & 5.5787-4.6458\,i & 538.89+538.89\,i \\
0 & 0 & 0 & 0 & 0 & 0 & 5.5787+4.6458\,i & 538.89-538.89\,i
\end{pmatrix} \tag{5.10}$$

Finally the (108x8) real transformation matrix $\mathbf{Y}$ is computed according to (3.11) – here only the first ten rows:

$$\mathbf{Y} = \begin{pmatrix}
0 & 0.000002 & 0.000022 & 0 & 0 & -0.000009 & 0 & 0.001258 \\
0 & 0.000003 & 0.000028 & 0 & 0 & -0.000012 & 0 & 0.001609 \\
0.000008 & -0.000017 & 0.000001 & -0.000005 & -0.000028 & 0.000027 & 0.000067 & -0.000011 \\
0.000001 & -0.000018 & 0 & -0.000002 & -0.000011 & 0.000049 & 0.000053 & -0.000259 \\
-0.000033 & 0.000066 & -0.000002 & 0.000021 & 0.00011 & -0.000103 & -0.000259 & 0.000027 \\
0 & 0.000012 & 0.000111 & 0 & 0 & -0.000047 & -0.000001 & 0.00628 \\
-0.000015 & 0.000058 & 0.000297 & 0.000009 & 0.000039 & -0.000124 & -0.00008 & 0.013754 \\
-0.000035 & 0.000337 & 0.00255 & 0.00002 & 0.000079 & -0.001052 & -0.000202 & 0.125274 \\
0.001819 & -0.003317 & 0.000036 & -0.001111 & -0.005438 & 0.002459 & 0.011388 & 0.001937 \\
0.000038 & -0.000796 & 0.000008 & -0.000091 & -0.000501 & 0.002123 & 0.002276 & -0.011014
\end{pmatrix}$$

(5.11)

After the modal transformation the time-dependent "load" vector is calculated to be a function of the wind speed time series, see Fig. 3 :

$$\begin{bmatrix} g_1(t) \\ h_1(t) \\ \cdots \\ g_3(t) \\ h_3(t) \end{bmatrix} = \mathbf{Y}^{\mathrm{T}} \cdot \begin{bmatrix} \mathbf{p} \end{bmatrix} = \begin{pmatrix} 5.788\,u^2 \\ 1.359\,u^2 \\ 0.1244\,u^2 \\ -1.915\,u^2 \\ 1.734\,u^2 \\ -32.53\,u^2 \\ 0.9771\,u^2 \\ -15.46\,u^2 \end{pmatrix} \tag{5.12}$$

The resultant four uncoupled SDOFS block equations from type of Eq. (3.10), prepared in the form (2.23), are solved by step-by-step integration:

$$\begin{bmatrix} 1 & & & & \\ & -\omega_1^2 & & & \\ & & \cdots & & \\ & & & 1 & \\ & & & & -\omega_n^2 \end{bmatrix} \cdot \underbrace{\begin{bmatrix} \dot{x}_1 \\ \dot{y}_1 \\ \cdots \\ \dot{x}_n \\ \dot{y}_n \end{bmatrix}}_{\dot{\mathbf{x}}} + \begin{bmatrix} 2\eta_1\,\omega_1 & \omega_1^2 & & & \\ \omega_1^2 & 0 & & & \\ & & \cdots & & \\ & & & 2\eta_n\,\omega_n & \omega_n^2 \\ & & & \omega_n^2 & 0 \end{bmatrix} \cdot \underbrace{\begin{bmatrix} x_1 \\ y_1 \\ \cdots \\ x_n \\ y_n \end{bmatrix}}_{\mathbf{x}} = \begin{bmatrix} g_1 \\ h_1 \\ \cdots \\ g_n \\ h_n \end{bmatrix}, \qquad (n = 4) \tag{5.13}$$

where $[\omega_i] =$ ( 16.7175 29.0365 49.6511 104.976 )

$[\eta_i] =$ ( 0.332693 0.0141136 0.127584 0.0908603 ) (5.14a,b)

The effect of the implied additional aerodynamic damping results evidently in the large damping ratio $\eta_i = 0.33269$ for the first free vibration.

The vibration-response has been determined in the time 0… 25.6 s, the time step length for the applied Newmark integration method is 0.03665 s.

The time response of the modal coordinates $y_j(t), x_j(t),\ (j = 1,2,3)$ are shown in the figures 5a-c:

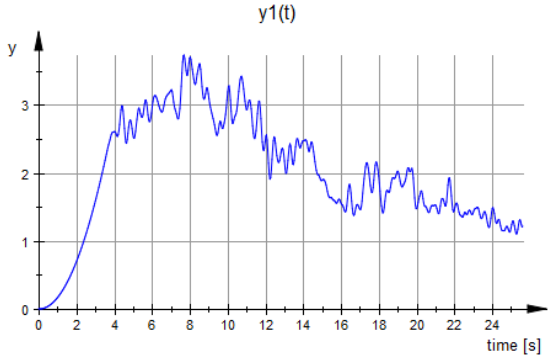


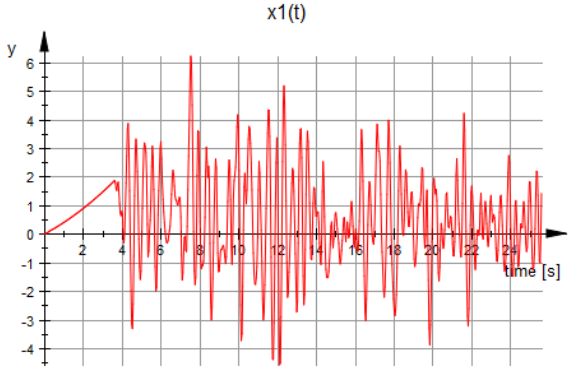

Fig. 5a Time response of the modal coordinates $y_1(t), x_1(t)$ for the case "non-proportional damping"

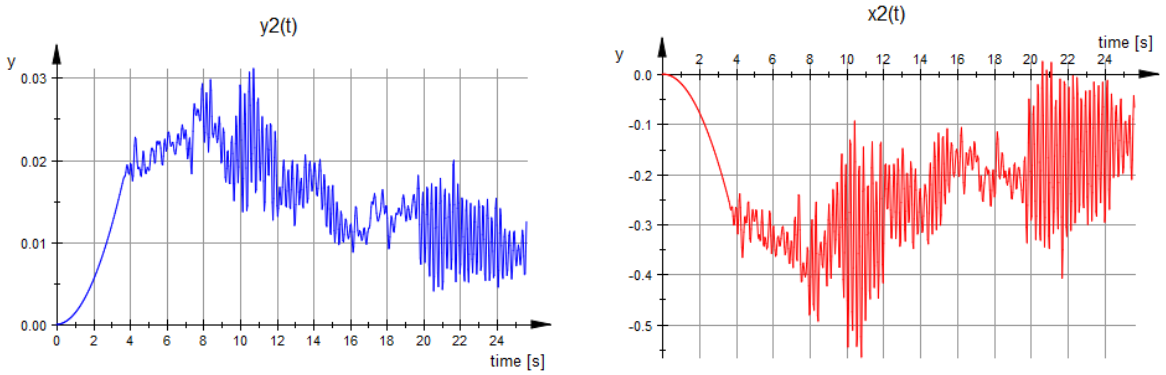


Fig. 5b Time response of the modal coordinates $y_2(t), x_2(t)$ for the case "non-proportional damping"

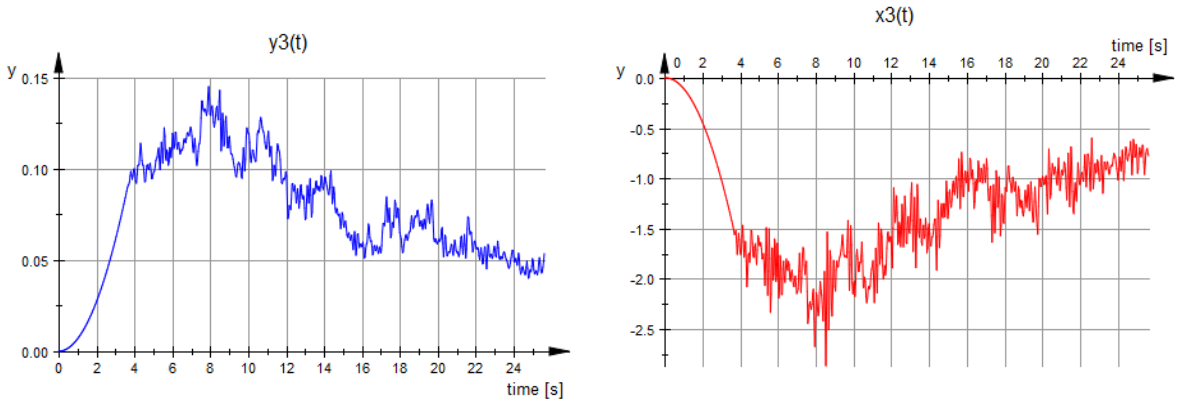


Fig. 5c Time response of the modal coordinates $y_3(t), x_3(t)$ for the case "non-proportional damping"

By a back transformation according to Eq. (3.11) the total response $\mathbf{V}(t)$ is obtained - see Figs. 6, 7 (vibration components at the rotor blade tip node #10).

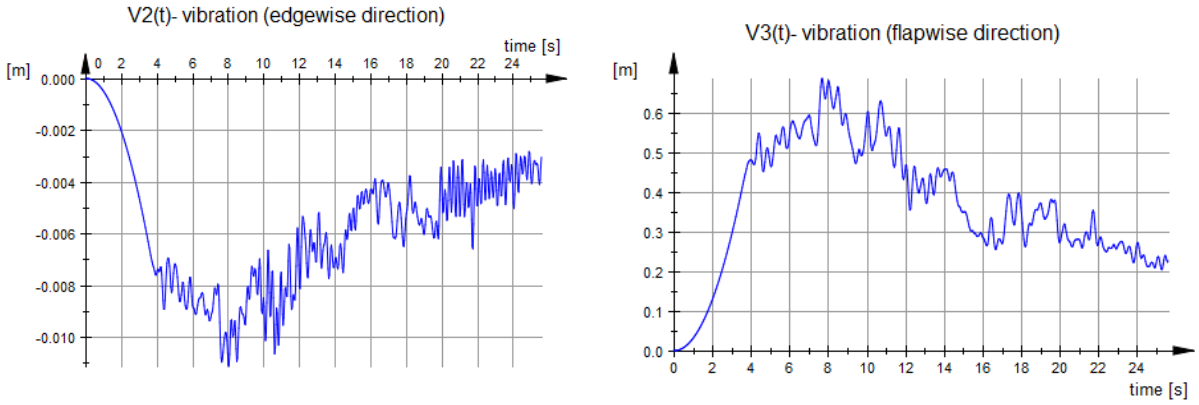


Fig.6 Total vibrations $u_2(t), u_3(t)$ $[m]$ (y- and z-direction, see fig.2) at the rotor blade tip - node #10

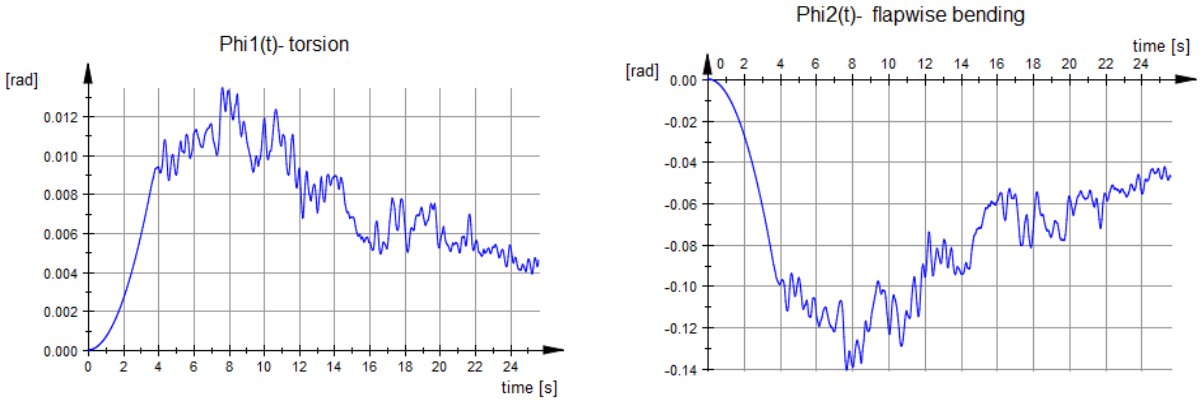


Fig.7 Total rotation $\varphi_1(t),\ \varphi_2(t)\ [rad]$ at the rotor blade tip (about x- and y-axis at node #10)

The vibration responses, computed by direct step-by-step integration of the equations (5.3), are practically identical to those in Fig. 6,7.

### 5.5 Proportional damped system

In this case we use the derived symmetric damping matrix $\mathbf{D_p}$ – Eq.(5.7). The first ten lowest complex conjugate eigenvalue pairs, resulting from Eq. (2.13), are now:

$$\begin{pmatrix} -0.132832+16.6035\,i \\ -0.132832-16.6035\,i \\ -0.406268+29.0352\,i \\ -0.406268-29.0352\,i \\ -1.19966+49.8844\,i \\ -1.19966-49.8844\,i \\ -5.27314+104.483\,i \\ -5.27314-104.483\,i \\ -5.39463+105.676\,i \\ -5.39463-105.676\,i \\ -16.7361+185.622\,i \\ -16.7361-185.622\,i \\ -20.9751+207.591\,i \\ -20.9751-207.591\,i \\ -27.8753+238.91\,i \\ -27.8753-238.91\,i \\ -42.2056+292.945\,i \\ -42.2056-292.945\,i \\ -62.3277+354.226\,i \\ -62.3277-354.226\,i \end{pmatrix} \tag{5.15}$$

The corresponding (108x8) $\mathbf{\Phi_G}$ modal matrix – Eq. (2.18), comprises the first four complex conjugate eigenvector pairs, normalized with respect to the stiffness matrix – see Eq.(3.6a,b). In order to verify the derived relationship for the constant phase lag, see (3.15), we compute this ratio for all components of the involved $(\mathbf{\Phi_r} \pm i\mathbf{\Phi_i})^{(j)}\ (j = 1, \ldots 4)$ eigenvectors (for instance the first ten rows only):

$$\begin{pmatrix} -1.01613 & -1.02838 & -1.04928 & -1.1063 \\ -1.01613 & -1.02838 & -1.04928 & -1.1063 \\ -1.01613 & -1.02838 & -1.04928 & -1.1063 \\ -1.01613 & -1.02838 & -1.04928 & -1.1063 \\ -1.01613 & -1.02838 & -1.04928 & -1.1063 \\ -1.01613 & -1.02838 & -1.04928 & -1.1063 \\ -1.01613 & -1.02838 & -1.04928 & -1.1063 \\ -1.01613 & -1.02838 & -1.04928 & -1.1063 \\ -1.01613 & -1.02838 & -1.04928 & -1.1063 \\ -1.01613 & -1.02838 & -1.04928 & -1.1063 \end{pmatrix} \leftrightarrow \begin{pmatrix} -1.01613 \\ -1.02838 \\ -1.04928 \\ -1.1063 \end{pmatrix} = \frac{1+2\eta_j\sqrt{1-\eta_j^2}}{2\eta_j^2-1}\ , \quad (j = 1, \ldots 4) \tag{5.16}$$

The corresponding damping ratios $\eta_j$ are computed in accordance with Eq. (2.4b).

The (108x8) real transformation matrix **Y**, computed in regard with Eq. (3.11), (3.12), has now the form (only the first twenty rows are printed):

$$\mathbf{Y} = \begin{pmatrix}
0 & 0 & 0.000022 & 0 & 0 & 0 & -0.000053 & 0 \\
0 & 0 & 0.000028 & 0 & 0 & 0 & -0.000068 & 0 \\
0.000009 & 0 & 0.000001 & 0 & -0.000028 & 0 & 0.00005 & 0 \\
0.000002 & 0 & 0 & 0 & -0.000011 & 0 & 0.000038 & 0 \\
-0.000035 & 0 & -0.000003 & 0 & 0.00011 & 0 & -0.000195 & 0 \\
-0.000001 & 0 & 0.000111 & 0 & 0 & 0 & -0.000265 & 0 \\
-0.000017 & 0 & 0.000297 & 0 & 0.000039 & 0 & -0.000642 & 0 \\
-0.000053 & 0 & 0.002549 & 0 & 0.000082 & 0 & -0.005423 & 0 \\
0.001935 & 0 & 0.000051 & 0 & -0.005447 & 0 & 0.008771 & 0 \\
0.000069 & 0 & 0.00001 & 0 & -0.000499 & 0 & 0.001632 & 0 \\
-0.002448 & 0 & -0.000063 & 0 & 0.006585 & 0 & -0.010006 & 0 \\
-0.000067 & 0 & 0.00314 & 0 & 0.000099 & 0 & -0.006234 & 0 \\
-0.00004 & 0 & 0.000568 & 0 & 0.000073 & 0 & -0.00092 & 0 \\
-0.000223 & 0 & 0.009905 & 0 & 0.000305 & 0 & -0.017838 & 0 \\
0.007945 & 0 & 0.000182 & 0 & -0.019879 & 0 & 0.027365 & 0 \\
0.000184 & 0 & 0.000025 & 0 & -0.001282 & 0 & 0.003913 & 0 \\
-0.005433 & 0 & -0.00011 & 0 & 0.011877 & 0 & -0.012914 & 0 \\
-0.000156 & 0 & 0.006512 & 0 & 0.00018 & 0 & -0.009482 & 0 \\
-0.000067 & 0 & 0.000826 & 0 & 0.000081 & 0 & -0.000752 & 0 \\
-0.000542 & 0 & 0.022556 & 0 & 0.00058 & 0 & -0.031471 & 0
\end{pmatrix} \tag{5.17}$$

The time-dependent "load" vector in the general modal transformed equations (2.23) is now calculated according to Eq. (3.13):

$$\begin{bmatrix} g_1(t) \\ h_1(t) \\ \cdots \\ g_4(t) \\ h_4(t) \end{bmatrix} = \begin{pmatrix} 5.691\,u^2 \\ 0 \\ 0.1578\,u^2 \\ 0 \\ 1.864\,u^2 \\ 0 \\ 0.8032\,u^2 \\ 0 \end{pmatrix} \tag{5.18}$$

The time dependence is expressed through the time series for $u(t)$ in fig. 3. Note that in the special case of proportionally damped system $x_j = \dot{y}_j$, i.e. $h_j(t) = 0$.

In the resultant four uncoupled SDOFS block equations from type (3.10), the free frequencies and the modal damping ratios are:

$$[\omega_i] = \begin{pmatrix} 16.604 & 29.0381 & 49.8988 & 104.616 \end{pmatrix}$$

$$[\eta_i] = \begin{pmatrix} 0.008 & 0.0139909 & 0.0240418 & 0.0504049 \end{pmatrix} \tag{5.19a,b}$$

After step-by-step integration of the four modal equations, the time series of the modal coordinates $x_j(t)$, $y_j(t)$, $(j = 1,...4)$, are obtained – Fig. 8:

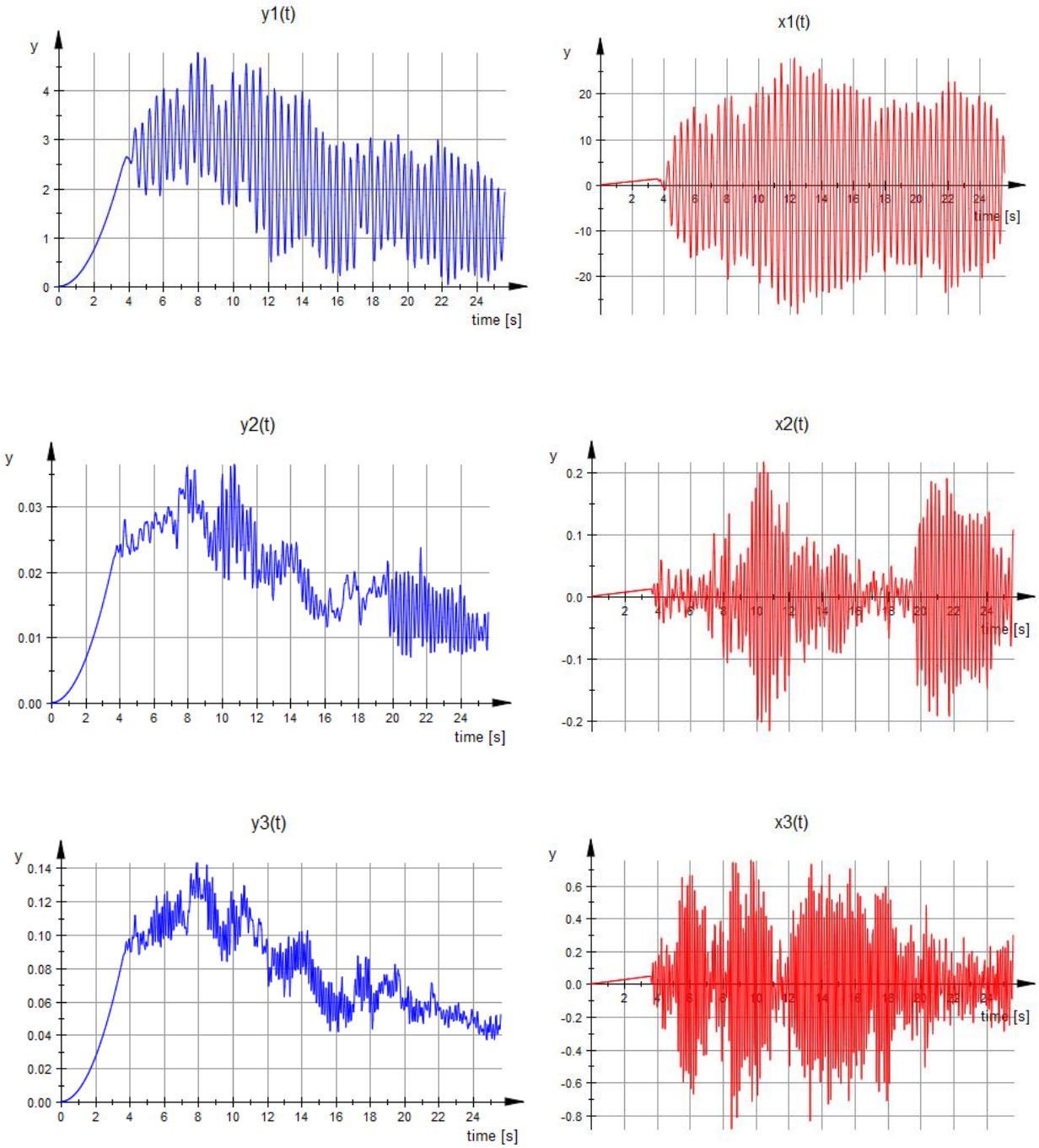


Fig. 8 Time response of the modal coordinates $y_j(t), x_j(t)$ $(j = 1,2,3)$ for the case "proportional damping"

The total responses $\mathbf{V}(t)$ are computed by a back transformation according to Eq. (3.11) – see Figs. 9a-d (here in the time range of 0 – 10 sec):

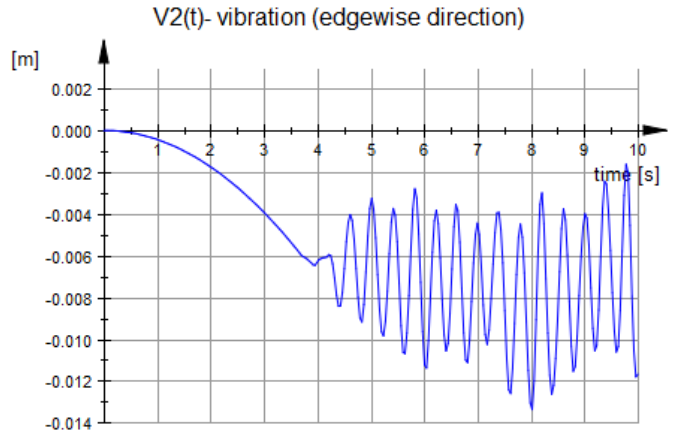


Fig 9a - Total vibration $u_2(t)\ [m]$ at the rotor blade tip (y-direction at node #10) for the case "proportional damping"

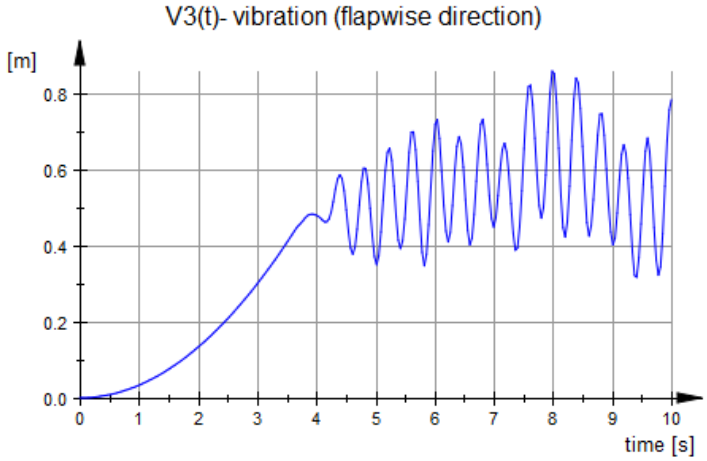


Fig 9b - Total vibration $u_3(t)\ [m]$ at the rotor blade tip (z-direction at node #10) for the case "proportional damping"

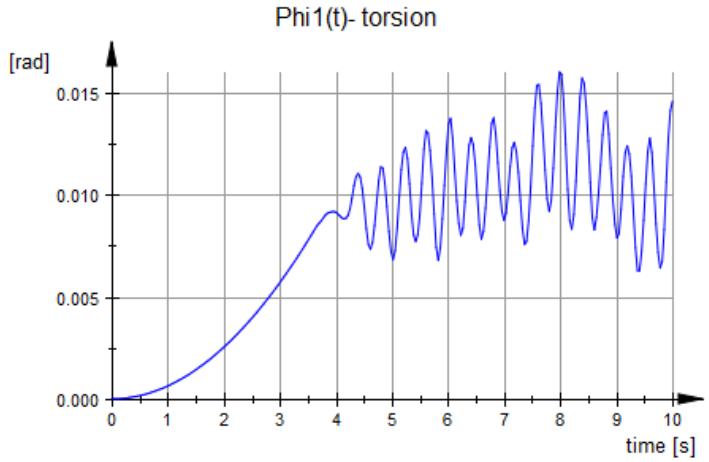


Fig 9c - Total torsion $\varphi_1(t)\ [rad]$ about x-direction at node #10 for the case "proportional damping"

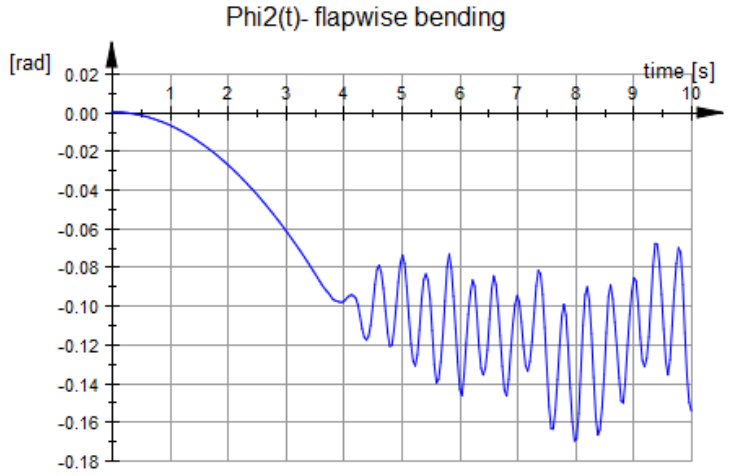


Fig 9d - Total rotation $\varphi_2(t)\ [rad]$ about y-axis at node #10 for the case "proportional damping"

The time series for the DOF calculated by direct step-by-step integration of the equations (5.3) are practically identical to the vibrations shown in Fig. 9a-d. The only difference occurs in the torsional vibration, see fig.10. The deviations may be explained by the absence of a torsional eigenmode in the four employed eigenvectors in the modal matrix.

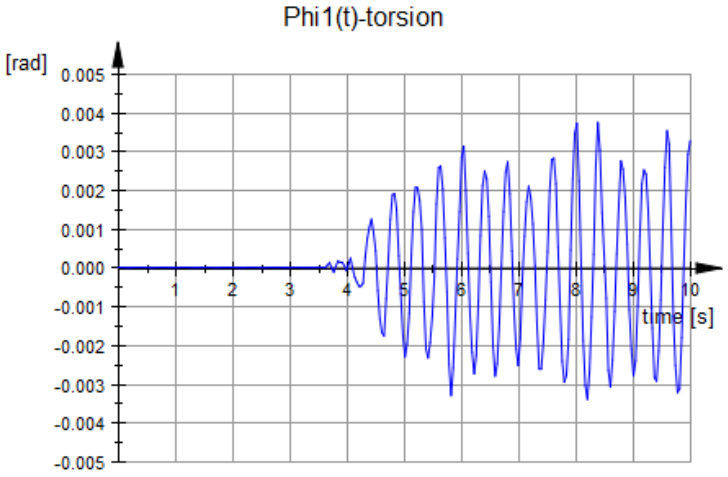


Fig 10 - Total torsion $\varphi_1(t)\ [rad]$ at node #10, calculated by direct step-by-step integration ("proportional damping")

## 6 CONCLUSIONS

- A general modal decomposition method for MDOFS with non-proportional damping is presented in three variants. In general, all of them are based on the complex eigenvalue solution of a structural model with symmetric non-proportional damping matrix. The complex conjugate eigenpairs – eigenvalues and the corresponding eigenvectors – are to be computed first for the "state space" form of the equations of motion. By combining of two complex transformations, connected to the eigenvalue problems of the SDOFS and the MDOFS, three different kinds of a modal transformation matrix **Y** in real space are

developed analytically to perform a modal decomposition of the equations of motion in real arithmetic.

- The first variant of the suggested procedure is described in Sec. 2. The real transformation matrix **Y** is assembled employing the right complex conjugate eigenvector pairs, normalized in both the SDOFS and MDOFS cases with respect to the corresponding mass matrix. The difference in the second variant, described in Sec. 3, is the normalization of the both modal matrices with respect to the corresponding stiffness matrices. In Sec. 4 has been presented the third variant, based on both the right and the left complex eigenvector pairs. In this version the complex conjugated eigenvectors for the MDOFS are normalized with respect to the stiffness matrix, the "left" modal matrix for the SDOFS don't need normalization.
- All variants of the presented modal procedure retain the common advantages of the classic modal decomposition of the equations of motion. Usually an uncomplete modal transformation should be performed by use of a few eigenmodes. Employing only the lowest few *(k)* eigenvector pairs in the **Y** -basis *(k<<n)* is leading with sufficient numerical accuracy to the total time response of all n DOF. The equations of motion are transformed into *k* uncoupled SDOFS block equations.
- The *k* uncoupled modal equations are easily numerically integrated like a SDOFS-equation – the result is the time response of the modal coordinates. Finally a back transformation to the original DOF has to be performed using the suggested new real **Y** –basis.
- The applications of the first and the second variants of the suggested method to the special case of proportionally damped system (employing a Rayleigh damping matrix) is leading to a simple analytical expression for the constant ratio $\frac{\Phi_{i(k)}}{\Phi_{r(k)}}$ for all k$^{th}$ DOF of each considered eigenmode $(\mathbf{\Phi_r} \pm i\mathbf{\Phi_i})$. This is an indirect proof of the statement for synchronous free vibrations in the case of proportional damping. For more detailed investigations on this topic see [5].
- In Sec. 5 a numerical example – vibration of a rotor blade with 54 DOF - demonstrates the performance of the presented modal procedure in the variant of Sec. 3 for two cases – non-proportional and proportional (Rayleigh) damping. In the first variant the damping matrix of the system contains a stiffness-proportional part and a simple approximated aerodynamic damping part. In the second variant the formula for the constant phase of the resonance modes is verified numerically.
- Real life applications of the proposed modal analysis method and possible numerical complications are discussed more widely in [4], [5]. The present paper is a briefly overview of some possible variants of the suggested new modal transformation procedure in real space for viscous non-proportionally damped structural models.

## REFERENCES

[1] H. Cramer, E. Stanoev, Zur modalen Analyse bei gedämpften Mehrmassensystemen.

*10. Dresdner Baustatik-Seminar: Neue Bauweisen – Trends in Statik und Dynamik,* TU Dresden, Lehrstuhl für Statik, Dresden, 2006, p. 81-90

[2] H. Cramer, E. Stanoev, Ein Verfahren zur modalen Analyse gedämpfter Systeme der Strukturmechanik. *Rostocker Berichte aus dem Institut für Bauingenieurwesen, Heft 19,* Universität Rostock, Institut für Bauingenieurwesen, 2008, ISSN 1438-7638, p. 83-107

[3] E. Stanoev, A modified modal analysis method for damped multi-degree-of-freedom-systems in structural mechanics. *Zeitschrift für angewandte Mathematik und Mechanik (ZAMM)*, 2013, 1 – 23 (2013), http://onlinelibrary.wiley.com/doi/10.1002/zamm.201300061/abstract

[4] E. Stanoev, A modal analysis method for structural models with non-modal damping, *MS "Multibody system dynamics and modal reduction" in the frame of 11th World Congress on Computational Mechanics (WCCM XI), 5th European Conference on Computational Mechanics (ECCM V),* 20-25 Juli 2014, Barcelona, ISBN: 978-84-942844-7-2, Tomo IV, p. 3034-3045

[5] E. Stanoev, A real-space modal analysis method for non-proportional damped structures, *MS 918 "Computer algebra systems in modelling static and dynamic problems in mechanics of solids" in the frame of the ECCOMAS Congress 2016 (VII European Congress on Computational Methods in Applied Sciences and Engineering)*, 5-10 Juni 2016, Crete Island, Greece, https://www.eccomas2016.org/proceedings/ pdf/5682.pdf

[6] H. J. Peters, P. Tiso, J.F.L. Goosen, F. van Keulen, Modifying resonance modes of dissipative structures using magnitude and phase information, *11th World Congress on Computational Mechanics (WCCM XI), 5th European Conference on Computational Mechanics (ECCM V),* 20-25 Juli 2014, Barcelona, ISBN: 978-84-942844-7-2, Tomo II, p. 489-500

[7] M. Géradin, D. Rixen, *Mechanical vibrations – theory and applications to structural dynamics*, John Wiley & Sons Ltd, 1997

[8] K. Meskouris, *Baudynamik – Modelle, Methoden, Praxisbeispiele*, Ernst & Sohn, 1999

[9] A.K. Chorpa, *Dynamics of Structures. Theory and Applications to Earthquake Engineering*, Pearson Prentice Hall, New Jersey, 2007

[10] M.-C. Kim, L.-W. Lee, Eigenproblems for large structures with non-proportional damping. *Earthquake Engng. Struct. Dyn*, 28, 157-172, 1999

[11] D. C. Sorensen, Implicitly Restarted Arnoldi/Lanczos Methods for Large Scale Eigenvalue Calculations. *Dep. Comp. Appl. Math*., Rice University, Houston, 1995

[12] R. Lehoucq, D. C. Sorensen, Implicitly Restarted Lanczos Method. (Section 4.5,7.6) : Z. Bai, J. Demmel, J. Dongarra, A. Ruhe and H. van der Vorst, editors, *Templates for the Solution of Algebraic Eigenvalue Problems: A Practical Guide*, SIAM, Philadelphia, 2000, 67-80, 166-184

[13] T. Burton, N. Jenkins, D. Sharpe, E. Bossanyi, *Wind Energy Handbook*, John Wiley & Sons, 2011, chapter 5.7, 5.8

[14] Nan Li, *Berechnung der Querschnittssteifigkeiten des Rotorblatts einer WEA durch ein FE-Verfahren für dünnwandige mehrzellige Profile mit Einsatz von MATLAB*, Studienarbeit, University of Rostock, Chair of Wind Energy Technology, 2015

[15] E. Stanoev, Eine alternative FE-Formulierung der kinetischen Effekte beim räumlich belasteten Stab. *Rostocker Berichte aus dem Institut für Bauingenieurwesen, Heft 17*, Universität Rostock, Institut für Bauingenieurwesen, 2007, ISSN 1438-7638, p.143-161

COMPDYN 2017
6th ECCOMAS Thematic Conference on
Computational Methods in Structural Dynamics and Earthquake Engineering
M. Papadrakakis, M. Fragiadakis (eds.)
Rhodes Island, Greece, 15–17 June 2017

# ISOGEOMETRIC METHODS IN DYNAMIC ANALYSIS OF CURVED BEAMS INCLUDING WARPING AND DISTORTIONAL EFFECTS

**I.N. Tsiptsis[1], and E.J. Sapountzakis[2]**

[1] Institute of Structural Analysis and Antiseismic Research
School of Civil Engineering
National Technical University of Athens, Greece
e-mail: mrtsip@hotmail.com

[2] Institute of Structural Analysis and Antiseismic Research
School of Civil Engineering
National Technical University of Athens, Greece
e-mail: cvsapoun@central.ntua.gr

**Keywords:** Analog equation method-AEM, Boundary element method-BEM, Finite element method-FEM, distortion, warping, curved beams, vibration, splines, NURBS, Isogeometric analysis.

**Abstract.** *In this research effort, Isogeometric tools are employed either in the Analog Equation Method (AEM), a boundary element based method, or in the Finite Element Method for the analysis of curved homogenous beams of arbitrary cross section (thin- or thick- walled) taking into account nonuniform warping, shear deformation effects (shear lag due to both flexure and torsion) and distortion. A set of distortional (in-plane warping) parameters have been considered and multiplied by the corresponding distortional functions, which constitute together with the warping ones the Navier equations for 2-D elasticity problem. One-dimensional boundary value problems described by second-order differential equations are formulated with respect to the displacement and rotation components as well as to the independent in- and out-of-plane warping parameters and solved. The in- and out-of-plane warping functions as well as the geometric constants including the additional ones due to warping and distortion (stiffness matrices) are evaluated employing a pure BEM approach. In order to derive the differential equations of motion with respect to the kinematical components, the terms of inertia contributions have to be added in the previous ones and, thus, the spatial mass matrix can be derived. Numerical results are worked out to illustrate the method, designate its efficiency, accuracy and computational cost, as well as verify its integrity comparing with the results of 3-D FEM (Finite Element Method) models.*

## 1 INTRODUCTION

Refined models either straight or curved with shell or solid elements are widely used in structures, such as for example the deck of a bridge with a thin-walled cross section, for stress or strain analysis. The analysis of such members employing the so-called "Higher-Order Beam Theories" [1-3] is of increased interest due to their important advantages over more elaborate approaches based on shell or solid finite elements [4], which are mainly incorporated in commercial software.

In-plane deformations, such as distortion, occurring when thin-walled sections undergo bending and torsional deformations can considerably weaken the flexural and torsional stiffness of thin-walled beams. Even though distortion is larger in magnitude near the beam's ends, it does not remain local (exponentially decays away from the support) and thus it should be considered over the entire domain of the beam to account for its stiffness-weakening effect. Schardt [5-6] developed an advanced formulation known as Generalized Beam Theory (GBT) which is a generalization of the classical Vlasov beam theory in order to incorporate flexural and torsional distortional effects. Further developments of GBT avoid some of its cumbersome procedures through eigenvalue cross sectional analysis [7-12]. Ferradi and Cespedes [2] presented the formulation of a 3D beam element solving an eigenvalue problem for the distortional behavior of the cross section (in-plane problem) and computing warping functions separately by using an iterative equilibrium scheme. Finally, Dikaros and Sapountzakis [13] presented a general boundary element formulation for the analysis of composite beams of arbitrary cross section taking into account the influence of generalized cross sectional warping and distortion due to both flexure and torsion. In this proposal, distortional and warping functions are evaluated by the same eigenvalue problem and in order of importance.

Regarding horizontally curved beams subjected to vertical or radial loads, they inherently exhibit a more complex behavior comparing to straight formulations due to the fact that the effects of primary and secondary torsion are always coupled to those of bending and cross section distortion either for centered or eccentric loads. Petrov and Geradin [14] employing the same concept with El Fatmi and Ghazouani [3] for straight beams formulated a theory for curved and pre-twisted beams of arbitrary homogeneous cross sections, covering geometrically nonlinear range as well. Kim and Kim [15] developed a theory for thin-walled curved beams of rectangular cross section by extending the theory developed earlier for straight beams taking into account warping and distortional deformations. Park et al. [16] expanded their previous work [17], which was limited to straight box girder bridges, to curved formulations. They developed a curved box beam element which was employed in order to develop design charts for adequate spacing of the intermediate diaphragms of curved bridges. Flexural and torsional displacement functions have been based on those proposed for doubly symmetric cross section by Kang and Yoo [18] while distortional functions have been derived for a mono-symmetric cross section [19]. Yoo et al. [20] applied the concept of the BEF analogy for the analysis of distortional stresses of horizontally curved box-girders. The proposed procedure is capable of handling simple or continuous single cell box girders (or separated multi-cell box girders) with rigid or deformable interior diaphragms or cross-frames. Towards establishing a more general theory, Arici and Granata [21] employed the Hamiltonian Structural Analysis Method for the analysis of straight and curved thin-walled structures on elastic foundation extending the so-called GBT. To the authors' knowledge, there are no research efforts that introduce a unified distortional and warping eigenvalue analysis of arbitrarily shaped cross sections to the analysis of curved beams.

As far as the free vibration and dynamic response is concerned, it has been noticed in studies of the last decades, mainly for straight beam formulations, that the thin-walled members' behavior can be highly affected by cross section's in-plane (distortion) deformations. There are a number of investigations with various approaches in order to determine the cross sectional deformations which are either restricted to quadrilateral cross sections [22-23] or to the evaluation of two distortional modes that are roughly approximated by cubic polynomials [24]. Thin-walled closed piecewise straight beams with angled joints were also studied by Jang and Kim [25], but arbitrarily shaped sections were not investigated. More recently, Petrolo et al. [26] as well as Carrera and Varello [27] developed a beam formulation which can be exploited for the analyses of compact, thin-walled structures and bridge-like cross-sections. However, this approach is only capable of handling problems that involve a limited range of deformation types due to the fact that the displacement field, which is based on, is not formulated in the most general way. In addition to these, Jang et al. [28] and Bebiano et al. [29] developed more refined beam models with open- or closed-shaped cross section for the vibration problem. However, their cross sectional analyses are based on beam-frame and plate models for the discretization of the cross section. However, these approaches depend on the section's shape, the nodal topology and the number of intermediate nodes employed which make the procedure cumbersome while deformation mode selection becomes important for the analysis. Regarding vibration analysis of curved beams including distortional effects, few research efforts have taken into account the complete coupling of torsion, warping, and distortion deformations together with the curvature effect. Zhu et al. [30] provided a dynamic theory for the spatial vibration analysis of horizontally curved thin-walled rectangular box-shaped beams based on the displacement fields proposed by Kim and Kim [22]. Thus, to the authors' knowledge, there is no study on the vibration problem of curved beams with arbitrary cross section including in- and out-of-plane deformations.

In modern regulations and design specifications, the importance of torsional and distortional effects in stress or strain analysis of structural members is recognized. Particularly, in sub-sections 6.2.7.1 and 6.2.7.2 of EN 1993-2, Eurocode 3: Design of steel structures - Part 2: Steel bridges, regarding torsion, the designer is obliged to keep the distortional stresses under a specific limiting value or follow some general design rules in case of neglecting distortion. It should also be noted that most of the provisions of Eurocode 3 regarding torsion are valid only when distortional deformation can be neglected. Special attention is paid for distortion by the following bridge design specifications. The Guide Specifications for Horizontally Curved Highway Bridges by the American Association of State Highway and Transportation Officials – AASHTO (1993) specify the maximum spacing of the intermediate diaphragms through an approximate formula. The Hanshin Expressway Public Corporation of Japan provides the Guidelines for the Design of Horizontally Curved Girder Bridges – HEPCJ (1988) specifying the maximum spacing of the intermediate diaphragms in curved box girder with respect to that in straight box girders multiplied by a reduction factor. It should be noted here that the boundary conditions and the cross section shape are not taken into account directly for both specifications. Finally, up to the 1980s the design of a bridge structure was based on static analysis, corrected by a dynamic amplification factor which is based on the first natural frequency. An extensive effort was made by Hamed and Frosting [31] to introduce the effects of warping and distortion of bridge cross-sections. An analytical model is developed in their works where the bridge is idealized as being made of panels which behave as plates in the transversal direction and as Euler–Bernoulli beams in the longitudinal direction [26].

In this study, the static and dynamic analysis of horizontally curved beams of arbitrary cross section, loading and boundary conditions including generalized cross sectional warping

and distortional effects due to both flexure and torsion is presented. The aim of this Chapter is to propose a new formulation by enriching the beam's kinematics both with out-of- and in-plane deformation modes and, thus, take into account both cross section's warping and distortion in the final 1D analysis of curved members, towards developing GBT further for curved geometries while employing independent warping parameters, which are commonly used in Higher Order Beam Theories (HOBT). The approximating methods and schemes proposed by Dikaros and Sapountzakis [13, 32] are employed and extended in this study. Adopting the concept of end-effects and their exponential decay away from the support [3], appropriate residual strains are added to those corresponding to rigid body movements. Further, applying Hooke's stress-strain law and employing the equilibrium equations of 3D elasticity, a system of partial differential equations can be derived for each material over the 2D cross section's domain together with the corresponding boundary and initial conditions. Consequently, a coupled two-dimensional boundary value problem is formulated, with or without considering Poisson ratio. Applying a proper discretization scheme for the cross section, the above mentioned problem will lead to the formulation of an eigenvalue problem which the eigenvalues and the corresponding eigenvectors, for a desired number of modes, can be extracted from. The obtained set of modes contains axial, flexural and torsional modes in order of significance without distinction between them. To avoid the additional effort needed in order to recognize the most significant modes, the iterative local equilibrium scheme described in the work of Dikaros and Sapountzakis [32] is adopted until the error due to residual terms becomes minimal. The functions derived are evaluated employing 2D BEM [33]. The coefficient matrices containing the geometric and mass properties of the cross section can now be calculated. Thus, a set of boundary value problems are formulated with respect to the unknown kinematical components (displacements, rotations and independent parameters) for each time instant, the number of which is defined by the user depending on the accuracy of the results. This linear system is solved using Isogeometric tools, either integrated in the Finite Element Method (FEM) [34] or in the Analog Equation Method (AEM) [35], which is BEM based. Employing the principal of virtual work the new equilibrium equations are derived. Additionally, by employing a distributed mass model system accounting for longitudinal, transverse, rotatory, torsional, warping and distortional inertia, free vibration characteristics and responses of the stress resultants and displacements to static and moving loading can be evaluated. The results obtained from the beam element will be compared to those obtained from finite 3D solutions. Numerical examples are presented to illustrate the efficiency and the accuracy of this formulation. To the authors' knowledge, the numerical procedures previously mentioned have not been reported in the literature for the analysis of curved beams including distortional effects.

The essential features and novel aspects of the formulation that will be presented in the following compared with previous ones are summarized as follows.

i. The developed beam formulation is capable of the dynamic analysis of spatial curved beams of arbitrary composite cross section with one plane of constant curvature considering warping and distortional effects (in addition to the previous formulations) that are introduced in the same boundary value problem which describes the cross section's deformations.

ii. The cross sectional analysis is based on an iterative equilibrium scheme which results in a numerical procedure with less computational effort and complexity comparing to traditional eigenvalue analysis reported in the literature for similar problems. Particularly, modes attributed to different structural phenomena can be separated directly and make the supervision of the results easier. In addition to this, the data post-processing and the iterative

procedure become faster due to the fact that warping and distortional functions are calculated separately.

iii. The accuracy level of the numerical method proposed can be decided by the user by setting the desirable number of the modes taken into account and, thus, increasing the number of higher modes added in the final solution.

iv. The numerical solution of the curved advanced beam is based on B-splines [36-37] and NURBS (Isogeometric Analysis) offering the advantage of integrating computer aided design (CAD) in the analysis.

## 2 S TATEMENT OF THE PROBLEM

Let us consider a straight or curved prismatic element of length $L$ (Fig. 1) with an arbitrarily shaped composite cross section of $m$ homogenous, isotropic and linearly elastic materials with modulus of elasticity $E_m$, shear modulus $G_m$ and and Poisson ratio $\nu_m$, occupying the region $\Omega_m$ of the $yz$ plane with finite number of inclusions (Fig. 2). Let also the boundaries of the regions $\Omega_m$ be denoted by $\Gamma_m$. This boundary curve is piecewise smooth, i.e. it may have a finite number of corners. In Fig. 2 $CXYZ$ is the principal bending coordinate system through the cross section's centroid $C$, while $y_C$, $z_C$ are its coordinates with respect to $Sxyz$ reference coordinate system through the cross section's shear center $S$. It holds that $y_C = y - Y$ and $z_C = z - Z$. The initial radius of curvature, denoted by $R$ is considered constant and it is parallel to $Y$ axis. The displacement vector $\bar{u}(x,y,z)$ of an arbitrary point of the cross section is obtained as the sum of SV solution vector corresponding to the rigid body motion combined with a residual (index R) displacement vector due to end-effects which are responsible for the generation of self-equilibrating stress distributions:

$$\begin{aligned}
\bar{u}(x,y,z) &= \bar{u}^{SV}(x,y,z) + \bar{u}^{R}(x,y,z) = \underbrace{u(x) + \theta_Y(x)Z - \theta_Z(x)Y}_{\textit{rigid body movement}} + \underbrace{\sum_{i=1}^{m} \alpha_i(x) W_i(y,z)}_{\textbf{out-of-plane warping}} \\
\bar{v}(x,y,z) &= \bar{v}^{SV}(x,y,z) + \bar{v}^{R}(x,y,z) = \underbrace{v(x) - z\theta_x(x)}_{\textit{rigid body movement}} + \underbrace{\sum_{i=1}^{m} \alpha_i(x)_{,x} DY_i(y,z)}_{\textbf{distortion in Y direction}} \qquad (1) \\
\bar{w}(x,y,z) &= \bar{w}^{SV}(x,y,z) + \bar{w}^{R}(x,y,z) = \underbrace{w(x) + y\theta_x(x)}_{\textit{rigid body movement}} + \underbrace{\sum_{i=1}^{m} \alpha_i(x)_{,x} DZ_i(y,z)}_{\textbf{distortion in Z direction}}
\end{aligned}$$

where $(\,)_{,j}$ is for differentiation with respect to j, i is the number of higher order cross sectional functions considered, $\bar{u}$, $\bar{v}$, $\bar{w}$ are the axial, transverse and radial beam displacement components with respect to the $Sxyz$ system of axes, respectively, $W(y,z)$ is the warping function, $DY(y,z)$ and $DZ(y,z)$ are the distortional functions of the in-plane deformation mode $D(y,z)$ while $\alpha(x)$ is a function describing the decay of deformation along beam length. Moreover, $v(x)$ and $w(x)$ describe the deflection of the centre of twist $S$, while $u(x)$ denotes the "average" axial displacement of the cross section. $\theta_x(x)$ is the angle of twist due to torsion, while $\theta_Y(x)$ and $\theta_Z(x)$ are the angles of rotation due to

bending about the centroidal $Y$ , $Z$ axes, respectively.The derivation of rigid body motions is in more detail explained in the work of Kang and Yoo [18], while $\sin\theta_x \approx \theta_x, \cos\theta_x \approx 1$ assumption is adopted and higher order terms are neglected in this study. Considering the fact that end-effects decay exponentially away from the support, $\alpha(x) = e^{-cx}$ where $c$ is a constant to be specified. However, different expressions of this parameter have also been adopted in other research efforts (i.e. polynomials of various degrees).

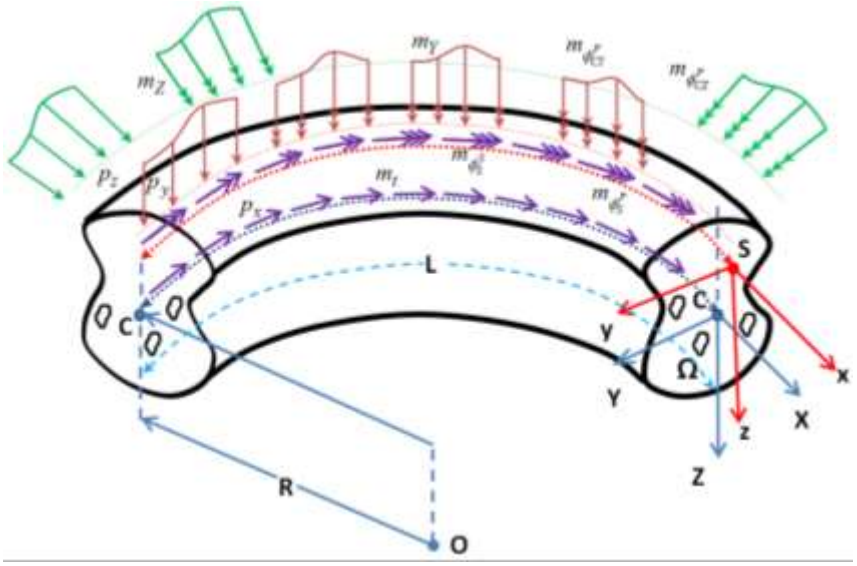


Figure 1: Prismatic curved beam under axial-flexural-torsional loading of an arbitrary homogenous cross section.

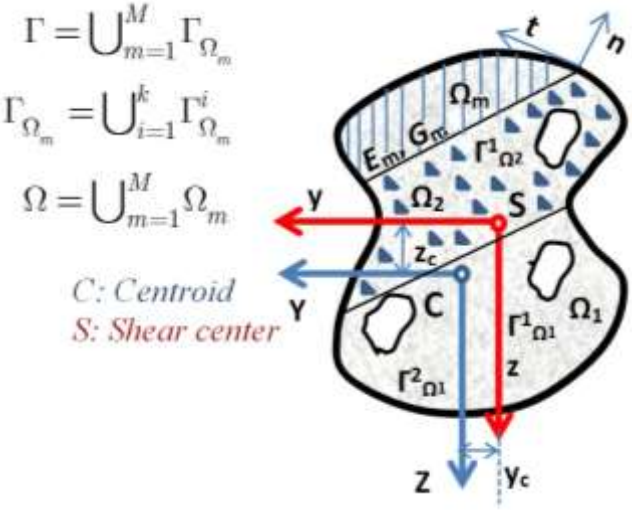


Figure 2: Arbitrary composite cross section of m homogenous materials occupying the two dimensional region $\Omega$.

After establishing the displacement field, the strain components for *m*th material due to end-effects can be computed as

$$
\begin{aligned}
&\left(\varepsilon_{xx}\right)_m = \left(\bar{u}^R\left(x,y,z\right)_{,x}\right)_m = \alpha_{,x}\left(W\right)_m \\
&\left(\varepsilon_{yy}\right)_m = \left(\bar{v}^R\left(x,y,z\right)_{,y}\right)_m = \alpha_{,x}\left(DY_{,y}\right)_m \\
&\left(\varepsilon_{zz}\right)_m = \left(\bar{w}^R\left(x,y,z\right)_{,z}\right)_m = \alpha_{,x}\left(DZ_{,z}\right)_m \\
&\left(\gamma_{xy}\right)_m = \left(\gamma_{yx}\right)_m = \left(\bar{v}^R\left(x,y,z\right)_{,x}\right)_m + \left(\bar{u}^R\left(x,y,z\right)_{,y}\right)_m = \alpha_{,xx}\left(DY\right)_m + \alpha\left(W_{,y}\right)_m \\
&\left(\gamma_{xz}\right)_m = \left(\gamma_{zx}\right)_m = \left(\bar{w}^R\left(x,y,z\right)_{,x}\right)_m + \left(\bar{u}^R\left(x,y,z\right)_{,z}\right)_m = \alpha_{,xx}\left(DZ\right)_m + \alpha\left(W_{,z}\right)_m \\
&\left(\gamma_{yz}\right)_m = \left(\gamma_{zy}\right)_m = \left(\bar{w}^R\left(x,y,z\right)_{,y}\right)_m + \left(\bar{v}^R\left(x,y,z\right)_{,z}\right)_m = \alpha_{,x}\left[\left(DZ_{,y}\right)_m + \left(DY_{,z}\right)_m\right]
\end{aligned}
\tag{2}
$$

Employing the well-known stress-strain constitutive relationship for elastic media and isotropic solid, the stress components of the *m*th material can be derived. Afterwards, employing local equilibrium equations of three-dimensional elasticity considering body forces to be absent, substituting stress components and the exponential function $\alpha(x)$, the system of partial differential equations for the *m*th material is stated together with the boundary conditions and, finally, employing the relation $\nu_m = \lambda_m / \left[2\left(\lambda_m + \mu_m\right)\right]$ and expanding the stresses in the boundary conditions, a boundary value problem together with the boundary conditions is formulated in eqs. (3a), (3b) and (3c) for the warping and two distortional functions, respectively.

$$
\begin{aligned}
&\left(\nabla^2 W\right)_m = c^2\left[-\frac{2}{1-\nu_m^e}\left(W\right)_m - \frac{1+\nu_m^e}{1-\nu_m^e}\left(\nabla D\right)_m\right] \\
&\begin{cases}
\left(W_{,n}\right)_m = c^2\left[-\left(DY\right)_m n_y - \left(DZ\right)_m n_z\right] & \text{on free surface} \\
g_m\left(W_{,n}\right)_m + g_n\left(W_{,n}\right)_n = c^2\left(g_m - g_n\right)\left[-\left(DY\right)_m n_y - \left(DZ\right)_m n_z\right] & \text{on Interfaces}
\end{cases}
\end{aligned}
\tag{3a}
$$

$$
\begin{aligned}
&\left(\nabla^2 DY\right)_m + \frac{1+\nu_m^e}{1-\nu_m^e}\left[\left(\nabla D\right)_{m,y} + \left(W_{,y}\right)_m\right] = c^2\left[-\left(DY\right)_m\right] \\
&\begin{cases}
g_m\left\{\left(DY_{,n}\right)_m + \left[\left(DY_{,y}\right)_m n_y + \left(DZ_{,y}\right)_m n_z\right]\right\} + g_m^*\left[\left(DY_{,y}\right)_m + \left(DZ_{,z}\right)_m\right] n_y \\
= -g_m^*\left(W\right)_m n_y \qquad \text{on free surface} \\
g_m\left\{\left(DY_{,n}\right)_m + \left[\left(DY_{,y}\right)_m n_y + \left(DZ_{,y}\right)_m n_z\right]\right\} + g_m^*\left[\left(DY_{,y}\right)_m + \left(DZ_{,z}\right)_m\right] n_y + \\
g_n\left\{\left(DY_{,n}\right)_n + \left[\left(DY_{,y}\right)_n n_y + \left(DZ_{,y}\right)_n n_z\right]\right\} + g_n^*\left[\left(DY_{,y}\right)_n + \left(DZ_{,z}\right)_n\right] n_y \\
= -\left(g_m^* - g_n^*\right)\left(W\right)_m n_y \qquad \text{on Interfaces}
\end{cases}
\end{aligned}
\tag{3b}
$$

Where $\nu_m^e = \nu_m / \left(1-\nu_m\right)$ is the effective Poisson ratio while $g_m = \mu_m / \mu_{ref}$, $g_m^* = \lambda_m / \mu_{ref}$ are weighted elastic constants with respect to $\mu_{ref}$ which is the shear modulus of reference

$$\left(\nabla^2 DZ\right)_m + \frac{1+\nu_m^e}{1-\nu_m^e}\left[\left(\nabla D\right)_{m,z} + \left(W_{,z}\right)_m\right] = c^2\left[-\left(DZ\right)_m\right]$$

$$\begin{cases} g_m\left\{\left(DZ_{,n}\right)_m + \left[\left(DY_{,z}\right)_m n_y + \left(DZ_{,z}\right)_m n_z\right]\right\} + g_m^*\left[\left(DY_{,y}\right)_m + \left(DZ_{,z}\right)_m\right] n_z \\ = -g_m^*\left(W\right)_m n_z \qquad \textit{on free surface} \\ g_m\left\{\left(DZ_{,n}\right)_m + \left[\left(DY_{,z}\right)_m n_y + \left(DZ_{,z}\right)_m n_z\right]\right\} + g_m^*\left[\left(DY_{,y}\right)_m + \left(DZ_{,z}\right)_m\right] n_z + \\ g_n\left\{\left(DZ_{,n}\right)_n + \left[\left(DY_{,z}\right)_n n_y + \left(DZ_{,z}\right)_n n_z\right]\right\} + g_n^*\left[\left(DY_{,y}\right)_n + \left(DZ_{,z}\right)_n\right] n_z \\ = -\left(g_m^* - g_n^*\right)\left(W\right)_m n_z \qquad \textit{on Interfaces} \end{cases} \tag{3c}$$

material. If a plane stress assumption is employed, $\nu_m^e$ is substituted by $\nu_m$. When $\nu_m = 0$ it holds that $g_m = E_m / E_{ref}$ , $g_m^* = 0$, with $E_{ref}$ being the elastic modulus of reference material, and the aforementioned boundary value problem is simplified. Therefore, employing a proper discretization for the cross section, the above coupled boundary value problem (eqs. (3)) will lead to the formulation of a generalized eigenvalue problem of the form $AF = c^2 BF$ where $A, B$ are known coefficient matrices, $c$ is the eigenvalue and $F = \left[W \quad DY \quad DZ\right]^T$ is the eigenvector of the problem. The solution of eigenvalue problem yields a set of eigenvalues together with the corresponding eigenvectors which constitute a basis of cross sectional deformation modes suitable for distortional analysis of beams.

As mentioned earlier, the iterative equilibrium scheme described by Ferradi, Cespedes and Arquier [1] as well as Dikaros and Sapountzakis [32] is employed here until a sufficient number of modes is obtained to represent accurately the non-uniform warping effects and the corresponding distortional ones. In order to initialize the above stated boundary value problem, the rigid body movements of the cross section are employed. These correspond to SV flexural and torsional warping modes. Afterwards, in order to restore equilibrium the secondary warping modes are determined together with their corresponding distortional ones. Following this concept, the iterative procedure is formulated converging to the exact shape of the warping in a section. Each functional vector $F_{i+1}$ has to fulfil the orthogonality condition with respect to the functions $F_i$ corresponding to the previous set of modes.

Within the context of the above considerations and considering up to secondary warping as well as distortional displacements, the enriched kinematics of an arbitrary point of the beam for *m*th material at any time instant is given as

$$\begin{aligned} \bar{u}\left(x,y,z,t\right) &= \bar{u}^P\left(x,y,z,t\right) + \bar{u}^S\left(x,y,z,t\right) = \\ &\underbrace{u\left(x\right) + \theta_Y\left(x\right)Z - \theta_Z\left(x\right)Y + \eta_x\left(x\right)\phi_S^P\left(y,z\right)}_{\text{primary}} \\ &+ \underbrace{\eta_Y\left(x\right)\phi_{CY}^P\left(y,z\right) + \eta_Z\left(x\right)\phi_{CZ}^P\left(y,z\right) + \xi_x\left(x\right)\phi_S^S\left(y,z\right)}_{\text{secondary}} \end{aligned} \tag{4a}$$

$$\begin{aligned}\bar{v}(x,y,z,t) &= v(x) - z\theta_x(x) \\ &+ \underbrace{\zeta_x(x)v_S^P(y,z) + \zeta_Y(x)v_{CY}^P(y,z) + \zeta_Z(x)v_{CZ}^P(y,z)}_{\text{primary}} \\ &+ \underbrace{\chi_x(x)v_S^S(y,z) + \chi_Y(x)v_{CY}^S(y,z) + \chi_Z(x)v_{CZ}^S(y,z)}_{\text{secondary}}\end{aligned} \tag{4b}$$

$$\begin{aligned}\bar{w}(x,y,z,t) &= w(x) + y\theta_x(x) \\ &+ \underbrace{\zeta_x(x)w_S^P(y,z) + \zeta_Y(x)w_{CY}^P(y,z) + \zeta_Z(x)w_{CZ}^P(y,z)}_{\text{primary}} \\ &+ \underbrace{\chi_x(x)w_S^S(y,z) + \chi_Y(x)w_{CY}^S(y,z) + \chi_Z(x)w_{CZ}^S(y,z)}_{\text{secondary}}\end{aligned} \tag{4c}$$

where $\bar{u}^P$, $\bar{u}^S$, denote the primary and secondary longitudinal displacements, respectively. $\eta_x(x)$, $\xi_x(x)$ are the independent warping parameters introduced to describe the nonuniform distribution of primary and secondary torsional warping, while $\eta_Y(x)$, $\eta_Z(x)$ are the independent warping parameters introduced to describe the nonuniform distribution of primary warping due to shear. Similarly, $\zeta_x(x)$, $\chi_x(x)$ are the independent distortional parameters introduced to describe the nonuniform distribution of primary and secondary distortion due to torsion, while $\zeta_Y(x)$, $\zeta_Z(x)$, $\chi_Y(x)$, $\chi_Z(x)$ are the independent distortional parameters introduced to describe the nonuniform distribution of primary and secondary distortion due to flexure. All these parameters are multiplied by the corresponding warping and distortional functions which are components of the $W(y,z)$ and $D(y,z)$ vectors derived by the solution of the coupled boundary value problem stated in eqs. (3). In eqs. (4), 16 degrees of freedom have been employed in 3D space. These activate 12 cross sectional deformation modes, namely rigid (4), primary (4) and secondary motions (4), including extension.

If tertiary displacements have to be employed for accuracy reasons, the beam's kinematics is enriched further. In this case 22 degrees of freedom have been employed in order to describe the beam's behavior. The additional 6 degrees, namely $\xi_Y(x)$, $\xi_Z(x)$, $\omega_x(x)$, $\psi_x(x)$, $\psi_Y(x)$ and $\psi_Z(x)$, account for 3 tertiary warping and 3 tertiary distortional effects, respectively. These activate 4 additional cross sectional deformation modes including extension. The enrichment of the beam's kinematics can be done automatically by increasing the number of modes, which are an input value for the boundary value problem to be solved. This results in the evaluation of additional cross sectional operators which will be employed in the analysis of the beam model, after establishing the strain components as it will be described in the following.

After establishing the displacement field, the linear strain-displacement relations in the system $(x,y,z)$ can be written. Employing the expressions of the displacement components (eqs. (4)), the strains and stresses can be computed. Applying the principle of virtual work or any other variational principle following standard arguments in the calculus of variations, the governing differential equations for the beam in terms of the kinematical components can be

derived. Thus, the local stiffness matrix $[k_l]$ of the spatial curved beam can be evaluated after solving a system of linear equations. Finally, the matrix form of stiffness matrix is derived as follows

$$[Aux1]=\begin{bmatrix} 1 & 0 & 0 & 0 & Z & -Y & \phi_S^P & \phi_{CY}^P & \phi_{CZ}^P & \phi_S^S & 0 & 0 & 0 & 0 & 0 & 0 \\ 0 & 0 & 0 & 0 & 0 & 0 & 0 & 0 & 0 & 0 & 0 & 0 & 0 & 0 & 0 & 0 \\ 0 & 0 & 0 & 0 & 0 & 0 & 0 & 0 & 0 & 0 & 0 & 0 & 0 & 0 & 0 & 0 \\ 0 & 1 & 0 & -z & 0 & 0 & 0 & 0 & 0 & 0 & v_S^P & v_{CY}^P & v_{CZ}^P & v_S^S & v_{CY}^S & v_{CZ}^S \\ 0 & 0 & 1 & y & 0 & 0 & 0 & 0 & 0 & 0 & w_S^P & w_{CY}^P & w_{CZ}^P & w_S^S & w_{CY}^S & w_{CZ}^S \\ 0 & 0 & 0 & 0 & 0 & 0 & 0 & 0 & 0 & 0 & 0 & 0 & 0 & 0 & 0 & 0 \end{bmatrix} e(R) \tag{5a}$$

$$[Aux2]=\begin{bmatrix} 0 & -\frac{1}{R}e(R) & 0 & \frac{z}{R}e(R) & 0 & 0 & 0 & 0 & 0 & 0 \\ 0 & 0 & 0 & 0 & 0 & 0 & 0 & 0 & 0 & 0 \\ 0 & 0 & 0 & 0 & 0 & 0 & 0 & 0 & 0 & 0 \\ \frac{1}{R}e(R) & 0 & 0 & 0 & \frac{Z}{R}e(R) & -1-\frac{Y}{R}e(R) & \frac{\phi_S^P}{R}e(R)+\phi_{S,y}^P & \frac{\phi_{CY}^P}{R}e(R)+\phi_{CY,y}^P & \frac{\phi_{CZ}^P}{R}e(R)+\phi_{CZ,y}^P & \frac{\phi_S^S}{R}e(R)+\phi_{S,y}^S \\ 0 & 0 & 0 & 0 & 1 & 0 & \phi_{S,z}^P & \phi_{CY,z}^P & \phi_{CZ,z}^P & \phi_{S,z}^S \\ 0 & 0 & 0 & 0 & 0 & 0 & 0 & 0 & 0 & 0 \end{bmatrix} \cdots$$

$$\cdots \begin{bmatrix} \frac{v_S^P}{R}e(R) & \frac{v_{CY}^P}{R}e(R) & \frac{v_{CZ}^P}{R}e(R) & \frac{v_S^S}{R}e(R) & \frac{v_{CY}^S}{R}e(R) & \frac{v_{CZ}^S}{R}e(R) \\ v_{S,y}^P & v_{CY,y}^P & v_{CZ,y}^P & v_{S,y}^S & v_{CY,y}^S & v_{CZ,y}^S \\ w_{S,z}^P & w_{CY,z}^P & w_{CZ,z}^P & w_{S,z}^S & w_{CY,z}^S & w_{CZ,z}^S \\ 0 & 0 & 0 & 0 & 0 & 0 \\ 0 & 0 & 0 & 0 & 0 & 0 \\ w_{S,y}^P+v_{S,z}^P & w_{CY,y}^P+v_{CY,z}^P & w_{CZ,y}^P+v_{CZ,z}^P & w_{S,y}^S+v_{S,z}^S & w_{CY,y}^S+v_{CY,z}^S & w_{CZ,y}^S+v_{CZ,z}^S \end{bmatrix} \tag{5b}$$

$$\varepsilon=[Aux1]u_{,x}+[Aux2]u \tag{5c}$$

$$\sigma=[C][Aux1]u_{,x}+[C][Aux2]u \tag{5d}$$

$$\delta U=\int_0^L\int_\Omega\left(\delta u_{,x}^T[Aux1]^T+\delta u^T[Aux2]^T\right)\left([C][Aux1]u_{,x}+[C][Aux2]u\right)\frac{1}{e(R)}d\Omega dx \Rightarrow$$

$$\Rightarrow \delta U=\int_0^L\left(\delta u_{,x}^T k_{22}u_{,x}+\delta u^T k_{12}u_{,x}+\delta u_{,x}^T k_{21}u+\delta u^T k_{11}u\right)dx \Rightarrow \text{by parts integration} \tag{5e}$$

$$\Rightarrow \delta U=\int_0^L\left(\delta u^T\left\{-k_{22}u_{,xx}+[k_{12}-k_{21}]u_{,x}+k_{11}u\right\}\right)dx+\left[\delta u^T\left\{k_{22}u_{,x}+k_{21}u\right\}\right]_0^L$$

$$[k_l]=\begin{bmatrix} k_{11} & k_{12} \\ k_{21} & k_{22} \end{bmatrix} \tag{5f}$$

where [*Aux1*], [*Aux2*] are auxiliary matrices to express strains $\varepsilon$ in matrix form, [*C*] is the

elasticity matrix employed to derive stresses $\sigma$, $\frac{R}{R-Y}=e(R)$ , $\frac{1}{e(R)}d\Omega dx=dV$ is the differential volume of the curved beam for constant radius of curvature, $\delta U$ is the virtual strain energy and $k_{11}$, $k_{12}$, $k_{21}$ and $k_{22}$ are 16X16 coefficient matrices containing the geometric properties of the cross section. These are calculated as follows

$$\begin{aligned} k_{11}&=\int_{\Omega_m}\left[Aux1\right]^T\left[C\right]\left[Aux1\right]\frac{1}{e(R)}d\Omega, \qquad k_{12}=\int_{\Omega_m}\left[Aux1\right]^T\left[C\right]\left[Aux2\right]\frac{1}{e(R)}d\Omega \\ k_{21}&=\int_{\Omega_m}\left[Aux2\right]^T\left[C\right]\left[Aux1\right]\frac{1}{e(R)}d\Omega, \qquad k_{22}=\int_{\Omega_m}\left[Aux2\right]^T\left[C\right]\left[Aux2\right]\frac{1}{e(R)}d\Omega \end{aligned} \tag{6}$$

Moreover, the external work can be derived as follows

$$\left[Aux\right]=\begin{bmatrix} 1 & 0 & 0 & 0 & Z & -Y & \phi_S^P & \phi_{CY}^P & \phi_{CZ}^P & \phi_S^S & 0 & 0 & 0 & 0 & 0 & 0 \\ 0 & 1 & 0 & -z & 0 & 0 & 0 & 0 & 0 & 0 & v_S^P & v_{CY}^P & v_{CZ}^P & v_S^S & v_{CY}^S & v_{CZ}^S \\ 0 & 0 & 1 & y & 0 & 0 & 0 & 0 & 0 & 0 & w_S^P & w_{CY}^P & w_{CZ}^P & w_S^S & w_{CY}^S & w_{CZ}^S \end{bmatrix} \tag{7}$$

$$\delta W=\underbrace{\int_0^L\left(\delta u^T\left[Aux\right]^T t\right)dx}_{\delta u^T p}+\left[\int_\Omega\left(\delta u^T\left[Aux\right]^T t\right)d\Omega\right]_0^L \tag{8}$$

where $t$ is the traction vector applied on the lateral surface of the beam including the end cross sections and $p$ is the external load vector of the beam.

Employing the expressions of the displacement components, the cross sectional operators (eqs. (6)) and the governing differential equations of the curved beam can be obtained in a similar way when tertiary or higher warping and distortional effects are considered.

In order to derive the differential equations of motion with respect to the kinematical components, the terms of inertia contributions $\delta W_{\text{mass}}=\int_V\rho\left(\bar{u}_{,tt}\delta\bar{u}+\bar{v}_{,tt}\delta\bar{v}+\bar{w}_{,tt}\delta\bar{w}\right)\text{d}V$ (with $dV=\frac{1}{e(R)}d\Omega dx$) have to be added in the previous (eqns. (5e) and (8)) and constitutive equations should be employed. $\rho$ is the density of the material and $\bar{u},\bar{v},\bar{w}$ are the generalized displacements as previously described. Thus, the local spatial mass coefficient matrix $\left[m_l\right]$ can finally be derived. This can be extracted in matrix form from the following expression

$$\delta W_{\text{mass}}=\int_0^L\int_\Omega\rho\left(\delta u^T\left[Aux\right]^T\left[Aux\right]u_{,tt}\right)\frac{1}{e(R)}d\Omega dx\Rightarrow\delta U=\int_0^L\left(\delta u^T\left[m_l\right]u_{,tt}\right)dx \tag{9}$$

with [*Aux*] given in eqn. (7), $u$ representing the total displacement and $\left[m_l\right]$ being a 16X16 coefficient matrix when displacements of eqns. (4) are employed.

Except for the boundary conditions there are also the initial conditions at $x \in (0, L)$ for each kinematical component. After establishing the stiffness and mass matrices of the spatial curved beam element the equation of motion in matrix form can be stated.

The natural frequencies and modes in which the beam vibrates for the different motions (including also distortional ones) can be obtained by separation of variables and $u_i(x,t)$ is assumed as $u_i(x,t) = u_i(x)e^{i\omega t}$ . Finally, the typical generalized eigenvalue problem $\left([k_t] - \omega^2 [m_t]\right) u_i = \{0\}$ is formulated and solved.

## 3 NUMERICAL SOLUTIONS

The evaluation of the warping and distortional functions is accomplished by solving the problems described by eqns. (3). Warping functions $W$ and their derivatives are at first computed by solving eqns. (3a). Afterwards, these values are inserted as generalized body forces in eqns. (3b,c) which are solved as a 2D elasticity problem in order to obtain distortional functions $D$. The solution of the problem is accomplished employing BEM within the context of the method of subdomains and BEM for Navier operator [33, 38]. Afterwards, the values are normalized and the procedure is repeated for the desired number of modes. Finally, the functions calculated are employed in order to obtain the cross sectional operation factors given in eqns. (6) as well as mass operation factors derived by eqn. (9). These are used as input values together with the elasticity and function matrices to solve the curved beam model with the methods described below.

According to the precedent analysis, the analysis of curved beams of arbitrary cross section including generalized warping and distortional effects reduces in establishing the components the kinematical components $u_i$ having continuous derivatives up to the second order with respect to $x$ at the interval $(0, L)$, up to the first order at $x = 0, L$, and for the dynamic problem up to the second order with respect to time $t$, satisfying the initial-boundary value problem described by the coupled governing differential equations of equilibrium along the beam and the boundary conditions at the beam ends, at $x = 0, L$ as well as the initial conditions [37]. The problem is solved using the Analog Equation Method in a similar way as the one described in detail [37]. However, some differences arise here due to the nature of the problem stated. The number of the kinematical components depends on the number of modes employed.

## 4 NUMERICAL EXAMPLES

### 4.1 Doubly Symmetric box-shaped cross section

A cantilever beam model is studied. This has a rectangular box-shaped cross section 5.0X3.5 $m$ with plate thickness 0.30 $m$ ( $E = 3E7\, kN/m^2$ , $G = 1.5E7\, kN/m^2$ , $\nu = 0$ , $t/d = 0.085$, $d/L = 0.087$ ). Its cross section is shown in Fig. 3. This beam is examined as curved with $R = 25.465m$ and an arc length $L$ of 40 $m$. The displacement field considered is the one described in eqns. (4).

Finally, in Table 1 the first eight eigenfrequencies are compiled for the curved ( $\rho = 2.5kN\, sec^2/m^4$ ) rectangular box-shaped cross section when employing FEM solid

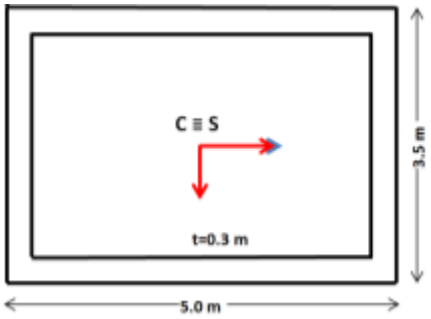


Figure 3: Rectangular box-shaped cross section (t=0.3m and d=3.5m).

| *Mode Number* | FEMsolid 2880 NO Diaph. | FEMsolid 2880 8 Diaphs. | FEMsolid 2880 NO Diaph. (straight) | 10 cubic B-splines in AEM | Type of mode (Only for NO Diaph.) |
|---|---|---|---|---|---|
| *1* | 1.605 | 1.726 | 1.630 | 1.611 | 1st mode of Vertical displacement (insignificant distortion) |
| *2* | 2.221 | 2.261 | 2.168 | 2.155 | 1st mode of Lateral displacement (insignificant distortion) |
| *3* | 7.038 | 7.329 | 9.167 | 7.063 | 2nd mode of Vertical displacement (significant distortion) |
| *4* | 9.440 | 9.626 | 12.099 | 9.296 | 2nd mode of Lateral displacement (significant distortion) |
| *5* | 14.455 | 16.108 | 12.791 | 14.795 | 1st mode of Torsion (significant distortion) |
| *6* | 19.131 | 22.770 | 21.591 | 20.552 | 3rd mode of Vertical displacement (excessive distortion) |
| *7* | 23.306 | 32.479 | 29.194 | 22.961 | 3rd mode of Lateral displacement (excessive distortion) |
| *8* | 23.478 | 41.895 | 22.848 | 25.312 | 2nd mode of Torsion (excessive distortion) |

Table 1: Eigenfrequencies for the doubly symmetric box-shaped cross section curved or straight beam.

models with 8 or without diaphragms (NO Diaph.) and the proposed beam formulation with cubic B-splines in AEM as well as for the corresponding straight beam element (forth column of the Table 1) with FEM solid elements without the use of any diaphragms. It is obvious that the values obtained by the proposed beam formulation are in well coincidence with those of the FEM solid solution without any diaphragms. The placement of diaphragms

results in a slight increase of the eigenfrequencies of the first four modes and a significant increase for the rest four modes due to the fact that distortion becomes more important as indicated from the description of the modes (last column of the Table 1). In addition to these, comparing to the straight beam formulation, the behavior of the beam is different. The first two modes exhibit similar eigenfrequencies for both the curved and straight model. Regarding the rest of the modes, significant discrepancies can be noticed either in the values of the eigenfrequencies or in the order of modes' significance. Particularly, it seems that torsional modes ($5^{th}$ and $7^{th}$ for the straight beam) are more of importance in the straight beam model comparing to bending modes due to the lower value of the $5^{th}$ eigenfrequency and the altered order of significance between the $7^{th}$ and $8^{th}$ modes.

### 4.2 Monosymmetric open-shaped cross sections

A cantilever beam of a monosymmetric C-shaped cross section ( $E = 73000\, kN/m^2$ , $G = 28000\, kN/m^2$ , $\nu = 0.3$ , $t/d = 0.049$ , $d/L = 0.055$ ), as this is shown in Fig. 4, is examined. The beam is analysed as curved with $R = 0.636m$ and an arc length $L$ of 1 $m$.

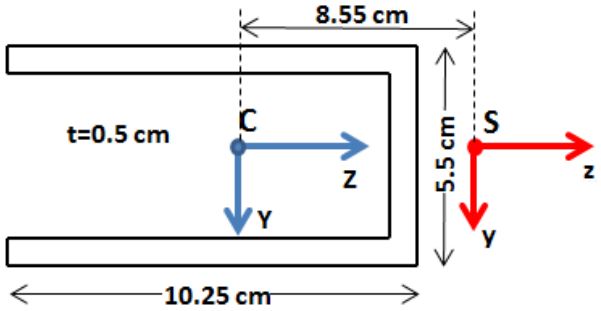


Figure 4: C-shaped cross section (t=0.5cm and d=5.5cm).

In Table 2 the first five eigenfrequencies are compiled for the curved ( $\rho = 0.785 N\, sec^2/m^4$ ) C-shaped cross section when employing a FEM solid model without

| *Mode Number* | FEMsolid NO Diaph. | FEMsolid NO Diaph. (straight) | 10 cubic NURBS | Type of mode |
|---|---|---|---|---|
| *1* | 0.341 | 0.630 | 0.355 | $1^{st}$ mode of Vertical displacement |
| *2* | 1.843 | 1.749 | 1.849 | $1^{st}$ mode of Lateral displacement |
| *3* | 2.506 | 2.712 | 2.581 | $2^{nd}$ mode of Vertical displacement (excessive Torsion) |
| *4* | 7.244 | 3.288 | 6.626 | $1^{st}$ mode of Torsion |
| *5* | 7.908 | 5.990 | 8.376 | $2^{nd}$ mode of Torsion |

Table 2: Eigenfrequencies for the C-shaped cross section curved or straight beam.

diaphragms (NO Diaph.) and the proposed beam formulation with cubic NURBS as well as for the corresponding straight beam element (second column of the Table 2) with FEM solid elements without the use of any diaphragms. It is obvious that the values obtained by the proposed beam formulation are in well coincidence with those of the FEM solid solution without any diaphragms. Comparing to the straight beam formulation, the behavior of the beam is different. The first mode exhibits a much lower eigenfrequency for the curved beam model. In general, modes of vertical displacement in curved arrangement are coupled with torsional modes. Particularly, the 4$^{th}$ mode of the straight beam is pure torsional, while all of the vertical modes of the curved beam exhibit torsional displacements, too. It should also be noted that after the 3$^{rd}$ mode, the eigenfrequencies of the straight beam are lower than those of the curved model, which seems to be stiffer.

### 4.3 Monosymmetric box-shaped cross sections

The last case studied is a box-shaped cross section curved beam ( $E = 3.25E7\, kN/m^2$, $G = 1.39E7\, kN/m^2$, $R = 100\, m$, $\nu = 0.1667$, $t/d = 0.1$, $d/L = 0.065$ ) with an arc length $L$ of 33 *m*. Its cross section is shown in Fig. 5.

In Table 3 the first eight eigenfrequencies are compiled for the curved ( $\rho = 2.5kN\, sec^2/m^4$ ) monosymmetric box-shaped cross section when employing FEM solid models with 1 or without diaphragms (NO Diaph.) and the proposed beam formulation with cubic NURBS. Both clamped and cantilever beam models have been studied for the FEM solid model without diaphragms (NO Diaph.). It is obvious that the values obtained by the proposed beam formulation are in well coincidence with those of the FEM solid solution without any diaphragms and the accuracy is improved comparing to the corresponding values compiled in Table 4.19 (where distortional effects had not been considered). The placement of the diaphragm at the midpoint of the curved length (forth column of the Table 5.13) results in a slight increase of the eigenfrequencies of the first four modes and a significant increase for the 5$^{th}$ and 6$^{th}$ modes. In addition to these, comparing to the cantilevered model, the behavior of the beam is much different. All of the eigenfrequencies are decreased while the order of significance is altered for the 6$^{th}$ and7$^{th}$ modes. In general distortional effects are of more importance for most of the modes (3$^{rd}$ to 8$^{th}$) and torsional modes become more significant comparing to the clamped beam model. It should also be noted here that the procedure of finding the modes of the cantilever beam corresponding to the same ones of the clamped beam is quite cumbersome due to the fact that many local vibrational modes arise in the FEM solid model.

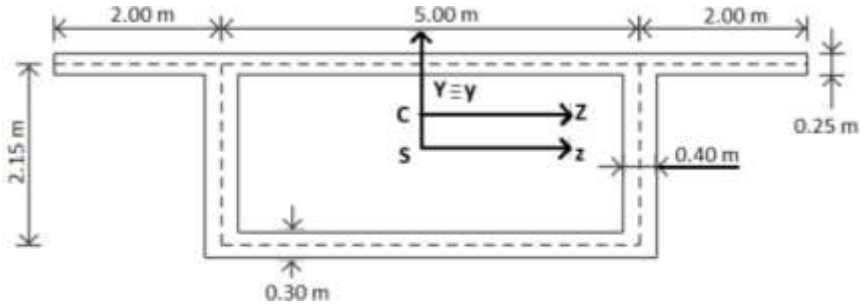


Figure 5: Box-shaped monosymmetric cross section (t=0.25m and d=2.15m).

| *Mode Number* | FEMsolid 6600 NO Diaph. (cantilever) | FEMsolid 6600 NO Diaph. (clamped) | FEMsolid 6600 1 Diaph. (clamped) | 10 cubic NURBS (clamped) | Type of mode |
|---|---|---|---|---|---|
| *1* | 1.725 | 9.328 | 9.414 | 9.470 | 1st mode of Vertical displacement |
| *2* | 4.065 | 17.099 | 19.230 | 16.887 | 1st mode of Lateral displacement |
| *3* | 9.084 | 20.495 | 21.160 | 21.154 | 1st mode of Torsion |
| *4* | 10.183 | 21.174 | 22.126 | 21.949 | 2nd mode of Vertical displacement |
| *5* | 19.191 | 27.898 | 35.428 | 26.003 | 2nd mode of Lateral displacement |
| *6* | 22.321 | 31.948 | 36.230 | 32.789 | 3rd mode of Vertical displacement |
| *7* | 21.649 | 43.247 | 42.768 | 44.500 | 2nd mode of Torsion |
| *8* | 29.165 | 47.490 | 47.013 | 49.602 | 3rd mode of Torsion |

Table 3: Eigenfrequencies for the monosymmetric box-shaped cross section cantilever or clamped beam.

## 5 CONCLUSIONS

The importance of the proposed formulation is highlighted when considering the advantages of beam models compared to solid ones for the free vibrational case, as it is mentioned in the introduction. Therefore, the main purpose of this beam formulation is to remain simple and with the least number of degrees of freedom needed to describe its behavior accurately. In addition to this, creation of coarse curved models with quadrilateral solid elements and diaphragms is very time-consuming. The main conclusions that can be drawn from this investigation are:

- Highly accurate results can be obtained using B-splines in the AEM technique as well as NURBS in FE beam formulations for the analysis of the proposed beam elements. Computational cost and post-processing of the results is significantly reduced by the use of NURBS comparing to FEM solid models.
- The distortion of thin-walled box-shaped beams contributes significantly to lowering the natural frequency of torsional and bending vibration modes. Therefore, distortional effects must be considered in order to predict the dynamic behavior of beams accurately.
- Curved geometry alters the dynamic behavior of beam models with open or closed-shaped cross section and not necessarily in the same way.

**ACKNOWLEDGEMENTS** This work has been supported by IKY Fellowships of Excellence for Postgraduate Studies in Greece-Siemens Program.

## REFERENCES

[1] M.K. Ferradi, X. Cespedes, M. Arquier, A higher Order Beam Finite Element with Warping Eigenmodes. *Engineering Structures*, **46**, 748-762, 2013.

[2] M.K. Ferradi, X. Cespedes, A New Beam Element with Transversal and Warping Eigenmodes. *Computers and Structures*, **131**, 12-33, 2014.

[3] R. El Fatmi, N. Ghazouani, Higher Order Composite Beam Theory built on Saint-Venant's Solution. Part-I: Theoretical Developments. *Composite Structures*, **93**, 557-566, 2011.

[4] E.J. Sapountzakis, I.N. Tsiptsis, Generalized warping analysis of curved beams by BEM. *Engineering Structures*, 100, 535-549, 2015.

[5] R. Schardt, *Verallgemeinerte Technische Biegetheorie*. Springer-Verlag, 1989.

[6] R. Schardt, Generalized Beam Theory – An adequate method for coupled stability problems. *Thin-walled Structures*, **19**, 161-180, 1994.

[7] G. Ranzi, A. Luongo, A New Approach for Thin-Walled Member Analysis in the Framework of GBT. *Thin-Walled Structures*, **49**, 1404-1414, 2011.

[8] J. Jönsson, Distortional theory of thin-walled beams. *Thin-Walled Structures*, **33**(4), 269-303, 1999.

[9] J. Jönsson, M.J. Andreassen, Distortional Eigenmodes and Homogeneous Solutions for Semi-Discretized Thin-Walled Beams. *Thin-Walled Structures*, **49**, 691-707, 2011.

[10] M.J. Andreassen, J. Jönsson, Distortional Solutions for Loaded Semi-Discretized Thin-Walled Beams. *Thin-Walled Structures*, **50**, 116-127, 2012a.

[11] M.J. Andreassen, J. Jönsson, Distortional Buckling Modes of Semi-Discretized Thin-Walled Columns. *Thin-Walled Structures*, **51**, 53-63, 2012b.

[12] M.J. Andreassen, J. Jönsson, A Distortional Semi-Discretized Thin-Walled Beam Element. *Thin-Walled Structures*, **62**, 142-157, 2013.

[13] I.C. Dikaros, E.J. Sapountzakis, Distorsional Analysis of Beams of Arbitrary Cross Section by BEM. *11th HSTAM International Congress on Mechanics*, Athens, Greece, May 27-30, 2016.

[14] E. Petrov, M. Géradin, Finite Element Theory for Curved and Twisted Beams Based on Exact Solutions for Three-Dimensional Solids, Part 1: Beam Concept and Geometrically Exact Nonlinear Formulation. *Computational Methods in Applied Mechanics and Engineering*, **165**, 43-92, 1998.

[15] Y.Y Kim, Y. Kim, A one-dimensional theory of thin-walled curved rectangular box beams under torsion and out-of-plane bending. *International Journal for Numerical Methods in Engineering*, **53**, 1675-1693, 2002.

[16] N.H. Park, Y. Choi, Y. Kang, Spacing of intermediate diaphragms in horizontally curved steel box girder bridges. *Finite Elements in Analysis and Design*, **41**(9-10), 925-43, 2005a.

[17] N.H. Park, S. Choi, Y.J. Kang, Exact Distortional Behavior and Practical Distortional Analysis of Multicell Box Girders Using an Expanded Method. *Computers and Structures*, **83**, 1607-1626, 2005b.

[18] Y.J. Kang, C.H. Yoo, Thin-walled curved beams, I: formulation of nonlinear equations. *Journal of Engineering Mechanics*, **120**(10), 2072-2101, 1994.

[19] N.H. Park, N.H. Lim, Y.J. Kang, A Consideration on Intermediate Diaphragm Spacing in Steel Box Girder Bridges with a Doubly Symmetric Section. *Engineering Structures*, **25**, 1665-1674, 2003.

[20] C.H. Yoo, J. Kang, K. Kim, Stresses due to distortion on horizontally curved tub-girders. *Engineering Structures*, **87**, 70-85, 2015.

[21] M. Arici, M.F. Granata, Unified theory for analysis of curved thin-walled girders with open and closed cross section through HSA method. *Engineering Structures*, **113**, 299-314, 2016.

[22] Y.Y. Kim, J.H. Kim, Thin-Walled Closed Box Beam Element for Static and Dynamic Analysis. *International Journal for Numerical Methods in Engineering*, **45**, 473-490, 1999a.

[23] J. H. Kim, Y.Y. Kim, Analysis of thin-walled closed beams with general quadrilateral cross-sections. *Journal of Applied Mechanics*, **66**(4), 904-912, 1999b.

[24] J. H. Kim, Y.Y. Kim, One-dimensional analysis of thin-walled closed beams having general cross-sections. *International Journal for Numerical Methods in Engineering*, **49**(5), 653-668, 2000.

[25] G.-W. Jang, Y.Y Kim, Vibration analysis of piecewise straight thin-walled box beams without using artificial joint springs. *Journal of Sound and Vibration*, **326**, 647-670, 2009.

[26] M. Petrolo, E. Zappino, E. Carrera, Refined free vibration analysis of one-dimensional structures with compact and bridge-like cross-sections. *Thin-Walled Structures*, **56**, 49-61, 2012.

[27] E. Carrera, A. Varello, Dynamic response of thin-walled structures by variable kinematic one-dimensional models. *Journal of Sound and Vibration*, **331**, 5268-5282, 2012.

[28] G.-W. Jang, M.-J. Kim, Y.Y. Kim, Analysis of Thin-Walled Straight Beams with Generally Shaped Closed Sections Using Numerically Determined Sectional Deformation Functions. *Journal of Structural Engineering*, **138**(12), 1427-1435, 2012.

[29] R. Bebiano, D. Camotim, N. Silvestre, Dynamic analysis of thin-walled members using Generalised Beam Theory (GBT). *Thin-Walled Structures*, **72**, 188-205, 2013.

[30] Z. Zhu, L. Zhanga, D. Zhenga, G. Cao, Free vibration of horizontally curved thin-walled beams with rectangular hollow sections considering two compatible displacement fields. *Mechanics Based Design of Structures and Machines*, **44**(4), 354-371, 2016. DOI: 10.1080/15397734.2015.1075410

[31] E. Hamed, Y. Frosting, Free vibrations of multi-girder and multi-cell box bridges with transverse deformations effects. *Journal of Sound and Vibration*, **279**, 699-722, 2005.

[32] I.C. Dikaros, E.J. Sapountzakis, Generalized Warping Analysis of Composite Beams of an Arbitrary Cross Section by BEM. I: Theoretical Considerations and Numerical Implementation. *Journal of Engineering Mechanics*, **140**(9), 04014062, 2014.

[33] J.T. Katsikadelis, *Boundary Elements: Theory and Applications*. Elsevier, Amsterdam-London, 2002a.

[34] T. Hughes, J. Cottrell, Y. Bazilevs, *Isogeometric analysis: Toward Integration of CAD and FEA*. Wiley, 2009.

[35] J.T. Katsikadelis, The Analog Equation Method. A Boundary – only Integral Equation Method for Nonlinear Static and Dynamic Problems in General Bodies. *Theoretical and Applied Mechanics*, **27**, 13-38, 2002b.

[36] E.J. Sapountzakis, I.N. Tsiptsis, Quadratic B-splines in the analog equation method for the nonuniform torsional problem of bars, *Acta Mechanica*, **225**(12), 3511-3534, 2014.

[37] I.N. Tsiptsis, E.J. Sapountzakis, Isogeometric analysis for the dynamic problem of curved structures including warping effects. *Mechanics Based Design of Structures and Machines*, 2017. DOI: 10.1080/15397734.2016.1275974.

[38] G. Beer, I. Smith, Ch. Duenser, *The Boundary Element Method with Programming – For Engineers and Scientists*. Springer, Wien, New York, 2008.

COMPDYN 2017
6th ECCOMAS Thematic Conference on
Computational Methods in Structural Dynamics and Earthquake Engineering
M. Papadrakakis, M. Fragiadakis (eds.)
Rhodes Island, Greece, 15–17 June, 2017

# ACCURATE NUMERICAL METHODS FOR STUDYING THE NONLINEAR WAVE-DYNAMICS OF TENSEGRITY METAMATERIALS

**Francesco Fabbrocino[1], Gerardo Carpentieri[2], Ada Amendola[2], Rosa Penna[2], Fernando Fraternali[2]**

[1]Department of Engineering, Pegaso University
Piazza Trieste e Trento, 48- 80132- Naples, Italy
e-mail: francesco.fabbrocino@unipegaso.it

[2]Department of Civil Engineering, University of Salerno
84084 Fisciano (Salerno), Italy
e-mail: gerardo_carpentieri@unisa.it, adaamendola1@unisa.it, rpenna@unisa.it, f.fraternali@unisa.it

**Keywords:** lattice metamaterials, tensegrity structures, wave dynamics.

**Abstract.** *This paper presents presents an effective numerical approach to the nonlinear dynamics of columns of tensegrity prisms subject to impulsive compressive loading. The equations of motions of the analyzed structures are formulated in vector form, by modeling the cables as deformable members and the bars as rigid bodies. The given numerical results investigate the wave dynamics of tensegrity columns, with focus on the propagation of compression solitary waves with variable size and amplitude throughout the system, as a function of the applied impact velocity and the state of prestress of the structure. The engineering potential of the examined structures as tunable acoustic actuators is discussed.*

## 1 INTRODUCTION

Recent studies have shown that tensegrity lattices exhibit a tunable geometrically nonlinear response, which switches from stiffening to softening by playing with a number of mechanical, geometrical, and prestress variables [1, 2, 3, 4]. Tensegrity lattices consists of networks of prestressable truss structures, obtained by connecting compressive members (bars or struts) through pre-stretched tensile elements (cables or strings). Special attention is receiving the formulation of analytical and numerical procedures for the optimal design of such structures, due to both their easy control (geometry, size, topology and prestress control) [5, 6], and the fact that such structures provide minimum mass systems under different loading conditions [5, 7, 8, 9, 10, 11, 12].

The importance of protecting materials and buildings against impacts with external objects is well known (cf., e.g., [13, 14]). Equally, there is growing interest in research into noninvasive tools to target defects in materials, and for monitoring structural health in materials and structures [16, 17, 18, 19]. Highly efficient and unconventional mechanisms for protecting materials and focusing mechanical waves through the use of rarefaction and compression solitary waves have recently been discovered by [4, 15]. It is worth noting that arrays of tensegrity lattices with elastically hardening response can be employed to fabricate tunable focus acoustic lenses that support extremely compact solitary waves [4, 15].

Three-dimensional finite element (FE) models of lattice structures usually make use of tetrahedral elements with a large number of degrees of freedom [20]. Such models are hardly applicable to dynamic simulations, even for lattices constituted by a small number of cells. A key goal of the present work is to develop efficient and accurate models of tensegrity lattices that make use of 3D assemblies of one-dimensional models for bars and strings. By describing the bars as rigid members and the cables as elastically deformable elements, we develop the dynamics of an arbitrary tensegrity network in vector form. Sucha formulation proves to be useful in order to coupling the proposed model with standard FE models that may interact with tensegrity networks. The time-integration of the equations of motion is conducted through a Runge-Kutta algorithm that accounts for a rigidity constraint of the bars [21].

IWe apply the proposed numerical model to investigate the nonlinear wave dynamics of tensegrity columns under impact loading, by establishing comparisons with the alternative model proposed in Ref. [22]. We show that our 3D modeling of tensegrity columns allows us to detect different strain wave profiles, as a function of the applied prestress, and a rigidity parameter describing the kinematics of the terminal bases. Such tunable response can be profitably used to build tensegrity actuators, which can subjected to different levels of prestress, so as to generate solitary waves with different phases that coalesce at a focal point in an adjacent host medium [16, 17].

## 2 VECTOR FORM OF THE DYNAMICS OF TENSEGRITY NETWORKS

Let us consider a tensegrity network made up of $n_n$ nodes (or joints), $n_b$ bars and $n_s$ cables. The joints are frictionless hinges, and each member carries only axial forces. The bars (i.e., the compressed members) are assumed to behave as straight rigid bodies (rods) with uniform mass density, constant cross-section, and negligible rotational inertia about the longitudinal axis. The cables are instead modeled as straight elastic springs that can carry only tensile forces.

The generic node $i$, with $i \in [1, ..., n_n]$, is located by the vector $\mathbf{n}_i \in \mathbb{R}^3$ in the three-dimensional Euclidean space, and is loaded with an external force vector $\mathbf{w}_i \in \mathbb{R}^3$. By suitably collecting the vectors $\mathbf{n}_i$ and $\mathbf{w}_i$, we introduce the following nodal and force matrices:

$$\mathbf{N} = \begin{bmatrix} \mathbf{n}_1 & \mathbf{n}_2 & ... & \mathbf{n}_i & ... & \mathbf{n}_{n_n} \end{bmatrix} \in \mathbb{R}^{3 \times n_n} \tag{1}$$

$$\mathbf{W} = \begin{bmatrix} \mathbf{w}_1 & \mathbf{w}_2 & ... & \mathbf{w}_i & ... & \mathbf{w}_{n_n} \end{bmatrix} \in \mathbb{R}^{3 \times n_n} \tag{2}$$

The $k$-th bar (or cable) $k$ of the network, with $k \in [1, ..., n_b]$ (or $k \in [1, ..., n_s]$), is located by the vector $\mathbf{b}_k \in \mathbb{R}^3$ (or $\mathbf{s}_k \in \mathbb{R}^3$). For example, if the $k$-th bar connects nodes $i$ and $j$, then $\mathbf{b}_k = \mathbf{n}_j - \mathbf{n}_i$. By stacking up the bar and string vectors, we obtain the following matrices describing the geometry of all bars and cables:

$$\mathbf{B} = \begin{bmatrix} \mathbf{b}_1 & \mathbf{b}_2 & ... & \mathbf{b}_k & ... & \mathbf{b}_{n_b} \end{bmatrix} \in \mathbb{R}^{3 \times n_b}, \tag{3}$$

$$\mathbf{S} = \begin{bmatrix} \mathbf{s}_1 & \mathbf{s}_2 & ... & \mathbf{s}_k & ... & \mathbf{s}_{n_s} \end{bmatrix} \in \mathbb{R}^{3 \times n_s} \tag{4}$$

The center of mass of the $k$-th bar between nodes $i$ and $j$ is located by the vector $\mathbf{r}_k = (\mathbf{n}_i + \mathbf{n}_j)/2$. Collecting all the $\mathbf{r}_k$ vectors, we get the matrix:

$$\mathbf{R} = \begin{bmatrix} \mathbf{r}_1 & \mathbf{r}_2 & ... & \mathbf{r}_k & ... & \mathbf{r}_{n_b} \end{bmatrix} \in \mathbb{R}^{3 \times n_b} \tag{5}$$

It is useful to rewrite the above matrices as follows:

$$\mathbf{B} = \mathbf{N}\mathbf{C}_\mathbf{B}^\mathbf{T}, \quad \mathbf{S} = \mathbf{N}\mathbf{C}_\mathbf{S}^\mathbf{T}, \quad \mathbf{R} = \mathbf{N}\mathbf{C}_\mathbf{R}^\mathbf{T} \tag{6}$$

where $\mathbf{C_B} \in \mathbb{R}^{n_b \times n_n}$ and $\mathbf{C_S} \in \mathbb{R}^{n_s \times n_n}$ are *connectivity* matrices of bars and cables, respectively. The general $i^{th}$ row of $\mathbf{C_B}$ (or $\mathbf{C_S}$) corresponds to the $i^{th}$ bar (or cable), and the element $\mathbf{C_B}_{ij}$ (or $\mathbf{C_S}_{ij}$) is equal to: $-1$ if vector $\mathbf{b}_i$ (or $\mathbf{s}_i$) is directed away from node $j^{th}$, $1$ if vector $\mathbf{b}_i$ (or $\mathbf{s}_i$) is directed toward node $j^{th}$, and $0$ if vector $\mathbf{b}_i$ (or $\mathbf{s}_i$) does not touch node $j$. Similarly, the $i^{th}$ row of $\mathbf{C_R} \in \mathbb{R}^{n_b \times n_n}$ corresponds to the bar $\mathbf{b}_i$, and the element $\mathbf{C_R}_{ij}$ is equal to: $1$ if vector $\mathbf{b}_i$ is touching node $j$, or $0$ if vector $\mathbf{b}_i$ does not touch node $j$. Following Ref. [5], we say that a tensegrity network is of *class n*, if the maximum number of bars concurring in each node is equal to $n$.

Let us consider now the generic cable (say the $k$-th one) with Young modulus of the material $E_{sk}$, cross-section area $A_{sk}$, rest length $L_k$, and stretched length $s_k$ (i.e. $s_k = \|\mathbf{s}_k\|$, and $s_k \geq L_k$). We define the stiffness $k_{sk}$ and the prestrain $p_k$ through the following equations:

$$k_{sk} = \frac{E_{sk} A_{sk}}{L_k}, \tag{7}$$

$$p_k = \frac{s_k - L_k}{L_k} \tag{8}$$

The force density carried by the current cable is given by the following (unilateral) constituve equation (*elastic, no-compression response*):

$$\gamma_k = \max \left[ k_{sk} \left( 1 - \frac{L_k}{s_k} \right), 0 \right], \qquad if: s_k \geq L_k, \tag{9}$$

$$\gamma_k = 0, \qquad if: s_k < L_k \tag{10}$$

As we shall see in the sequel, it is convenient to collect all the quantities $\gamma_k$ into the diagonal matrix: $\hat{\boldsymbol{\gamma}} = diag\begin{pmatrix}\gamma_1 & \gamma_2 & \dots & \gamma_{n_s}\end{pmatrix} \in \mathbb{R}^{n_s \times n_s}$.
On adopting the matrix from of the tensegrity dynamics presented in Ref. [24], we write the equations of motion of a class 1 tensegrity network as follows:

$$\ddot{\mathbf{N}}\mathbf{M} + \mathbf{N}\mathbf{K} = \mathbf{W} \tag{11}$$

where:

$$\mathbf{M} = \mathbf{C}_{\mathbf{B}}^{\mathbf{T}} \hat{\boldsymbol{m}} \mathbf{C}_{\mathbf{B}} \frac{1}{12} + \mathbf{C}_{\mathbf{R}}^{\mathbf{T}} \hat{\boldsymbol{m}} \mathbf{C}_{\mathbf{R}} \in \mathbb{R}^{n_n \times n_n} \tag{12}$$

$$\mathbf{K} = \mathbf{C}_{\mathbf{S}}^{\mathbf{T}} \hat{\boldsymbol{\gamma}} \mathbf{C}_{\mathbf{S}} - \mathbf{C}_{\mathbf{B}}^{\mathbf{T}} \hat{\boldsymbol{\lambda}} \mathbf{C}_{\mathbf{B}} \in \mathbb{R}^{n_n \times n_n} \tag{13}$$

and:

$$\hat{\boldsymbol{m}} = diag\left(m_1, m_2, \dots, m_{n_b}\right) \in \mathbb{R}^{n_b \times n_b} \tag{14}$$

$$-\hat{\boldsymbol{\lambda}} = \left\lfloor \dot{\mathbf{B}}^{\mathbf{T}} \dot{\mathbf{B}} \right\rfloor \hat{\boldsymbol{m}} \hat{\ell}^{-2} \frac{1}{12} + \left\lfloor \mathbf{B}^{\mathbf{T}} \left(\mathbf{W} - \mathbf{S}\hat{\boldsymbol{\gamma}}\mathbf{C}_{\mathbf{S}}\right) \mathbf{C}_{\mathbf{B}}^{\mathbf{T}} \right\rfloor \hat{\ell}^{-2} \frac{1}{2} \in \mathbb{R}^{n_b \times n_b} \tag{15}$$

$$\hat{\ell}^{-2} = diag\left(\|\mathbf{b}_1\|^{-2}, \|\mathbf{b}_2\|^{-2}, \dots, \|\mathbf{b}_{n_b}\|^{-2}\right) \in \mathbb{R}^{n_b \times n_b} \tag{16}$$

The generalization of the above equations to the case of a class $k$ system is straightforward, by making recourse to the *Lagrange multipliers* technique illustrated in [25].

The vector form of the equations of motions (11) is as follows:

$$\mathbf{M}_n \ddot{\mathbf{n}} + \mathbf{K}_n \mathbf{n} = \mathbf{w} \in \mathbb{R}^{3n_n} \tag{17}$$

where: $\mathbf{n} = vec\left(\mathbf{N}\right)$, $\mathbf{M}_n = \mathbf{M} \otimes \mathbf{I}_3$, and $\mathbf{K}_n = \mathbf{K} \otimes \mathbf{I}_3$. On applying the vectorizing operator to (11), we obtain:

$$vec\left(\ddot{\mathbf{N}}\mathbf{M}\right) + vec\left(\mathbf{N}\mathbf{K}\right) = vec\left(\mathbf{W}\right) \in \mathbb{R}^{3n_n} \tag{18}$$

which implies, after some calculations:

$$\left(\mathbf{M}^T \otimes \mathbf{I}_3\right) \ddot{\mathbf{n}} + \left(\mathbf{K}^T \otimes \mathbf{I}_3\right) \mathbf{n} = \mathbf{w} \in \mathbb{R}^{3n_n} \tag{19}$$

Since $\mathbf{M}$ and $\mathbf{K}$ are symmetric, upon defining $\mathbf{M}_n = \mathbf{M} \otimes \mathbf{I}_3$ and $\mathbf{K}_n = \mathbf{K} \otimes \mathbf{I}_3$, we can finally reduce Eqn. (19) to the vector form (17). We employ the Runge-Kutta integration algorithm described in Ref. [21] to perform the time-integration of Eqn. (17). Such an algorithm prevents numerical violations of the rigidity constraint of the bars, ensuring that the bar vectors $\mathbf{b}_k$ remain constant at each time step.

## 3 WAVE DYNAMICS OF TENSEGRITY COLUMNS

Let us examine the wave dynamics of tensegrity columns which may feature either flexible (Fig. 1(a-b)) or rigid bases (Fig. 1(c-d)) in each prism, and are equipped with $n_p = 50$ right-handed prisms and cables featuring Young modulus $E_s = 5.48x10^6\ N/m^2$, and cross-section

radius $r_s = 0.14mm$. The lattice constant $a$ of the anlyzed columns is set equal to 5 mm, while the reference height of each prism is equal to $h_0 = 6.2mm$, giving a total height of the column of $0.31m$. The bases of the prisms forming the coulmn are endowed with lumped masses and the total mass of each unit is equal to $0.0249kg$. We characterize the state of prestrain/prestress of the column through the cross-string prestrain $p$. We refer to the quantity $\epsilon = (h - h_0)/h$ as the *axial strain* of the prism (positive when the prism is stretched from the reference configuration), $h$ denoting the current (deformed) height of the generic prism. The wave dynamics of the analyzed systems is studied through the numerical model given in Sect. 2, by applying different initial velocities $v_0$ to the nodes of the free end (right-end), which are directed along the axis of the column, so as to generate a compressive impulsive loading (impact velocites).

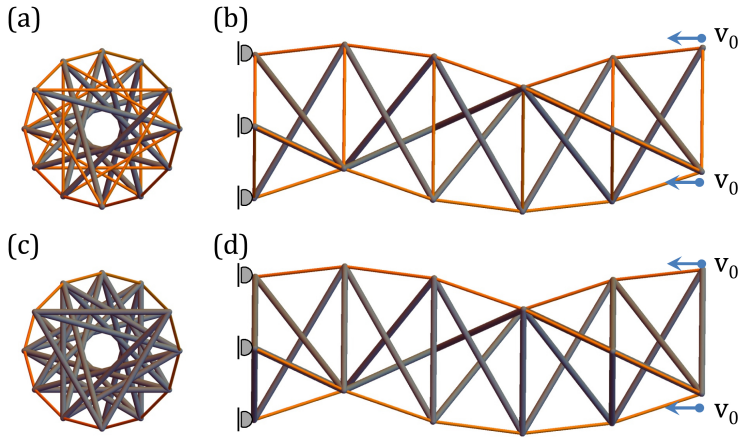


Figure 1: Top views and front views of tensegrity columns of right handed prisms with flexible bases (a-b: FB columns), and rigid bases (c-d: RB colums).

We compare the dynamics of columns composed of prisms with flexible bases (hereafter referred to as FB-columns) with that of columns composed of prisms equipped with rigid bases (RB-columns). The analyzed columns have the same geometric and mass data of those analized in [22]. We consider tensegrity columns subject to a state of prestress in the reference configuration, which is obtained by applying a prestrain $p = 0.002$ to the cross cables. The compression wave dynamics of prestressed FB columns is illustrated in Fig. 2, for impact velocities ranging between $v_0 = 0.1m/s$, and $v_0 = 0.15m/s$. We apply larger impact velocities to the prestressed column, as compared to the column under zero prestress, to account for the prestress-induced increse in the acoustic impedence of the system. We note the propagation of leading compression pulses with oscillatory tails, which span approximatively 4 prisms at $t = 0.5s$, and exhibit speed varying from $0.248m/s$ for $v_0 = 0.1m/s$ to $0.372m/s$ for $v_0 = 0.15m/s$ (Fig. 2). The leading strain pulses illustrated in Fig. 2 have amplitudes of: $\epsilon = 5.4 \times 10^{-2}$ for $v_0 = 0.1m/s$; $\epsilon = 6.97 \times 10^{-2}$ for $v_0 = 0.125m/s$; and $\epsilon = 8.5 \times 10^{-2}$ for $v_0 = 0.15m/s$.

The response of prestressed RB columns to impact velocities ranging between $v_0 = 0.1m/s$, and $v_0 = 0.15m/s$ is illustrated in Fig. 3. One observes the propagation of compact solitary pulses spanning about 3 units and featuring the following amplitudes: $\epsilon = 8.93 \times 10^{-2}$ for $v_0 = 0.1m/s$; $\epsilon = 0.106$ for $v_0 = 0.125 \div 0.15m/s$. The mean speeds of the compression pulses are: $0.186m/s$ for $v_0 = 0.1m/s$, and $0.248m/s$ for $v_0 = 0.125 \div 0.15m/s$.

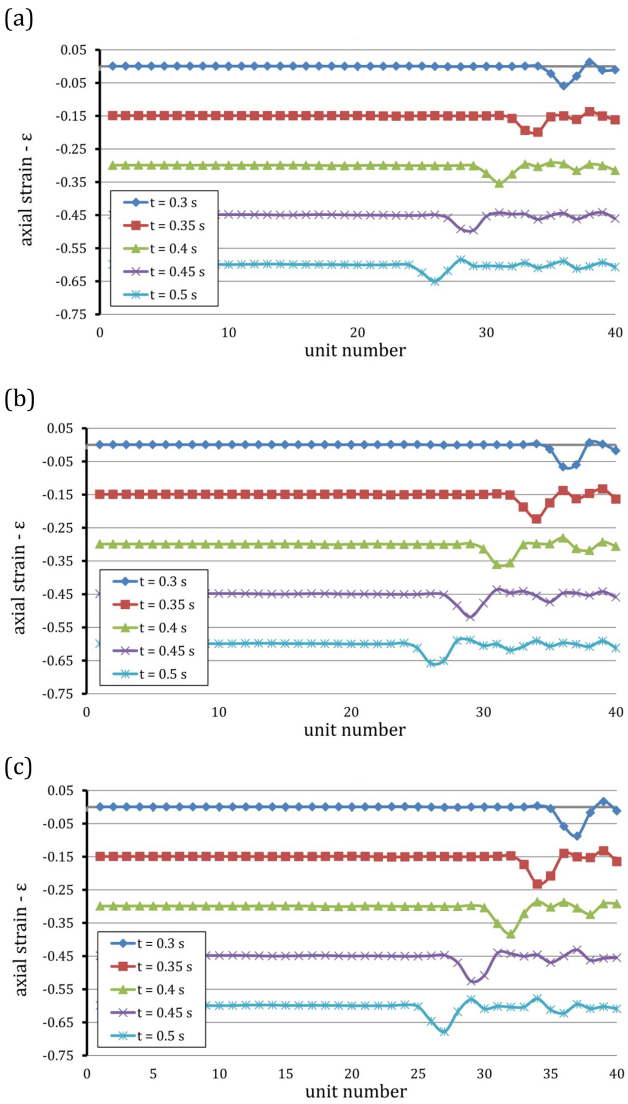


Figure 2: Axial strain wave profiles in a FB chain of 50 prisms under cross string prestrain $p = 0.002$, for various initial velocities: (a) $v_0 = 0.1m/s$, (b) $v_0 = 0.125m/s$, (c) $v_0 = 0.15m/s$.

## 4 CONCLUSIONS

We have presented a three-dimensional numerical model for the dynamics of arbitrary tensegrity networks that accounts for a rigidity constraint of the compressed members, elastic response of cable elements, and vector form of the equations of motions. Such a model can be easily coupled with standard FE models of bodies and structures interacting with tensegrity networks, and proves to be useful for studying the highly nonlinear dynamics of tensegrity metamaterials. It has been applied to investigate the wave dynamics of tensegrity columns traversed by propagating compressive strains waves under impulsive impact loading.

The numerical results presented in Sect. 3 allow us to conclude that the more rigid is the response of the bases of the units, the more compact is the nature of the compressive solitary pulses that traverse tensegrity columns, under initial compressive disturbances. We are led to conclude that it is possible to exploit the use of highly nonlinear dynamic response in tensegrity units to create novel metamaterials that will enable unconventional wavefocusing methodologies. Arrays of tensegrity columns may indeed be employed to fabricate tunable focus acoustic

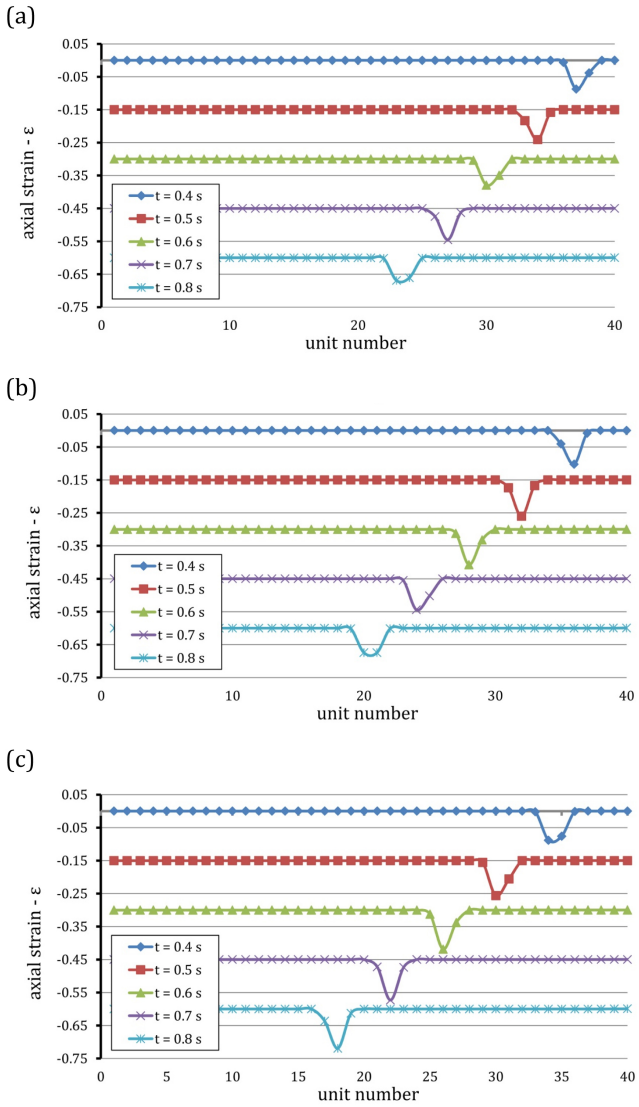


Figure 3: Axial strain wave profiles in a RB chain of 50 prisms under cross string prestrain $p = 0.002$, for various initial velocities: (a) $v_0 = 0.1m/s$, (b) $v_0 = 0.125m/s$, (c) $v_0 = 0.15m/s$.

lenses supporting extremely compact solitary waves. Such lattices can be subjected to different levels of prestress, so as to generate compact solitary waves with different phases within the lens, which will coalesce at a focal point [16, 17] in an adjacent host medium (i.e., a material defect to be targeted). The 3D modeling presented in this work offers a very useful tool to simulate the mechanical response of such spatial arrays of tensegrity columns, and can also be used to deal with their design by computation. As compared to acoustic lenses based on arrays of granular metamaterials [16, 17], tensegrity acoustic lenses will profit from the adjustable width of compression solitary waves in such metamaterials (cf. Sect. 3). While compression solitary waves in uniform granular chains have a constant width, which is independent of the amplitude [29], the width of similar waves in tensegrity metamaterials changes with amplitude and speed, and the solitary wave tends to concentrate on a single lattice spacing in the high energy regime [15, 4].

We address specific studies about engineering applications of tensegrity networks to future work. A key goal of such a research will regard the design of 3D innovative devices for monitoring structural health and damage detection in materials and structures. Combined tensegrity

actuators and sensors will be tested to detect the mechanical properties and/or the presence of damage in materials and structures through closed-loop identification procedures [26, 18, 19]. A second goal will regard the design, manufacture and testing of effective impact mitigation systems based on tensegrity metamaterials with softening-type response. Such nonlinear metamaterials will be able to transform compressive disturbances into solitary rarefaction waves with progressively vanishing oscillatory tail, and/or rarefaction shock-like waves [4]. Finally, we address to future studies the employment of tensegrity concepts in a variety of mechanical problems involving innvovative materials and structures [61]-[65].

## REFERENCES

[1] A. Amendola, G. Carpentieri, M. De Oliveira, R.E. Skelton, F. Fraternali, Experimental investigation of the softening-stiffening response of tensegrity prisms under compressive loading. *Compos. Struct.*, **117**, 234–243, 2014.

[2] A. Amendola, E. Hernndez-Nava, R. Goodall, I. Todd, R.E. Skelton, F. Fraternali, On the additive manufacturing, post-tensioning and testing of bi-material tensegrity structures. *Compos. Struct.*, **131**, 66–71, 2015, ISSN 0263-8223, http://dx.doi.org/10.1016/j.compstruct.2015.04.038.

[3] F. Fraternali, G. Carpentieri, A. Amendola, On the mechanical modeling of the extreme softening/stiffening response of axially loaded tensegrity prisms. *J. Mech. Phys. Solids*, **74**, 136–157, 2014.

[4] F. Fraternali, G. Carpentieri, A. Amendola, R.E. Skelton, V.F. Nesterenko, Multiscale tunability of solitary wave dynamics in tensegrity metamaterials. *Appl. Phys. Lett.*, **105**, 201903, 2014.

[5] R.E. Skelton, M.C. de Oliveira, Tensegrity Systems. *Springer*, 2010.

[6] A.G. Tilbert, S. Pellegrino, Review of form-finding methods for tensegritystructures. *Int. J. Space Struct.*, **18**, 209–223, 2011.

[7] K. Nagase, R.E. Skelton, Double-helix tensegrity structures. *AIAA J.*, DOI: 10.2514/1.J053264, 2014.

[8] R.E. Skelton, M.C. de Oliveira, Optimal complexity of deployable compressive structures. *J. Franklin I.*, **347**, 228–256, 2010.

[9] R.E. Skelton, M.C. de Oliveira, Optimal tensegrity structures in bending: the discrete Michell truss. *J. Franklin I.*, **347**, 257–283, 2010.

[10] R.E. Skelton, K. Nagase, Tensile tensegrity structures. *Int. J. Space Struct.*, **27**, 131–137, 2012.

[11] R.E. Skelton, F. Fraternali, G. Carpentieri, A. Micheletti, Minimum mass design of tensegrity bridges with parametric architecture and multiscale complexity. *Mech Res. Commun.*, **58**, 124–132, 2014.

[12] G. Carpentieri, R.E. Skelton, F. Fraternali, Parametric design of minimal mass tensegrity bridges under yielding and buckling constraints. Eprint: arXiv:1411.7966 [cond-mat.mtrl-sci]. DOI: 10.13140/2.1.3224.2248, 2014.

[13] F. Fraternali, M. Porter, C. Daraio, Optimal design of composite granular protectors. *Mech. Adv. Mat. Struct.*, **17**, 1-19, 2010.

[14] S.J. Mitchell, A. Pandolfi, M. Ortiz, Metaconcrete: designed aggregates to enhance dynamic performance. *J. Mech. Phys. Solids*, **65**, 69–81, 2014.

[15] F. Fraternali, L. Senatore, C. Daraio, Solitary waves on tensegrity lattices. *J.Mech. Phys. Solids*, **60**, 1137–1144, 2012.

[16] A. Spadoni, C. Daraio, Generation and control of sound bullets with a nonlinear acoustic lens. *Proc. Natl. Acad. Sci. U.S.A.*, **107**, 16, 7230–7234, 2010.

[17] C. Donahue, P. Anzel, L. Bonanomi, T. Keller, C. Daraio, Experimental realization of a nonlinear acoustic lens with a tunable focus. *Appl. Phys. Lett.*, **104**, 014103, 2014.

[18] X. Ni, Nondestructive Evaluation And Structural Health Monitoring Based On Highly Nonlinear Solitary Waves, Phd Dissertation, University of Pittsburgh, USA, 2011.

[19] P. Rizzo, X. Ni, S. Nassiri, J. Vandenbossche, A solitary wave-based sensor to monitor the setting of fresh concrete. *Sensors*, **14**, 7, 12568–12584, 2014.

[20] R. Schittny, T. Bckmann, M. Kadic, M. Wegener, Elastic measurements on macroscopic three-dimensional pentamode metamaterials. *Appl. Phys. Lett.*, **103**, 23, 231905, 2013.

[21] K. Nagase, Skelton RE, Network and vector forms of tensegrity system dynamics. *Mech. Res. Commun.*, **59**, 14–25, 2014.

[22] C. Davini, A. Micheletti, P. Podio-Guidugli, On the impulsive dynamics of T3 tensegrity chains. *Meccanica*, **51**, 11, 2763–2776, 2016.

[23] I. Oppenheim,W. Williams, Geometric effects in an elastic tensegrity structure. *J. Elast.*, **59**, 51–65, 2000.

[24] R.E. Skelton, Dynamics and control of tensegrity systems. In: IUTAM Symposium on Vibration Control of Nonlinear Mechanisms and Structures. *Springer Netherlands*, 309–318, 2005.

[25] J. Cheong, R.E. Skelton, Nonminimal Dynamics of General Class k Tensegrity Systems. *International Journal of Structural Stability and Dynamics*, **15**,2, 1450042, 2015.

[26] C. Daraio, F. Fraternali, Method and Apparatus for Wave Generation and Detection Using Tensegrity Structures. US Patent No. 8,616,328, granted on December 31, 2013.

[27] C. Daraio, D. Ngo, V.F. Nesterenko, F. Fraternali, Highly Nonlinear Pulse Splitting and Recombination in a Two Dimensional Granular Network. *Phys Rev. E*, **82**, 036603, 2010.

[28] A. Leonard, F. Fraternali, C. Daraio, Directional wave propagation in a highly nonlinear square packing of spheres. *Exp. Mech.*, **53**,3, 327–337, 2013.

[29] V.F. Nesterenko Dynamics of Heterogeneous Materials. *Springer-Verlag*, New York, 2001.

[30] D. Ngo, F. Fraternali, C. Daraio, Highly Nonlinear Solitary Wave Propagation in Y-Shaped Granular Crystals with Variable Branch Angles. *Phys Rev. E*, **85**, 036602, 1–10, 2012.

[31] B. Schmidt, F. Fraternali, Universal formulae for the limiting elastic energy of membrane networks. *Journal of the Mechanics and Physics of Solids*, **60**, 172-180, 2012.

[32] L. Ascione, F. Fraternali, A penalty model for the analysis of composite curved beams. *Computers & Structures*, **45**, 985-999, 1992.

[33] F. Fraternali, J.N. Reddy, A penalty model for the analysis of laminated composite shells. *International Journal of Solids and Structures*, **30**,3337-3355, 1993.

[34] F. Fraternali, Free Discontinuity Finite element models in two-dimensions for in-plane crack problems. *Theoretical and Applied Fracture Mechanics*, **47**,274-282, 2007.

[35] F. Fraternali, C.D Lorenz, G. Marcelli, On the estimation of the curvatures and bending rigidity of membrane networks via a local maximum-entropy approach. *Journal of Computational Physics*, **231**,528-540, 2012.

[36] A. Amendola, G. Carpentieri, M. De Oliveira, R.E. Skelton, F. Fraternali, Experimental investigation of the softening-stiffening response of tensegrity prisms under compressive loading. *Composite Structures*, **117**, 234-243, 2014.

[37] F. Fraternali, G. Bilotti, Non-Linear Elastic Stress Analysis in Curved Composite Beams. *Computers & Structures*, **62**, 837-869, 1997.

[38] F. Fraternali, G. Carpentieri, A. Amendola, On the mechanical modeling of the extreme softening/stiffening response of axially loaded tensegrity prisms. *Journal of the Mechanics and Physics of Solids*, **74**, 136-157, 2015.

[39] A. Amendola, E.H. Nava, R. Goodall, I. Todd, R.E. Skelton, F. Fraternali, On the additive manufacturing, post-tensioning and testing of bi-material tensegrity structures. *Composite Structures*, **131**, 66-71, 2015.

[40] A. Amendola, E.H. Nava, R. Goodall, I. Todd, R.E. Skelton, F. Fraternali, On the additive manufacturing, post-tensioning and testing of bi-material tensegrity structures. *Composite Structures*, **131**, 66-71, 2015.

[41] D. Ngo, F. Fraternali, C. Daraio, Highly Nonlinear Solitary Wave Propagation in Y-Shaped Granular Crystals with Variable Branch Angles. *Physical Review E*, **85**,036602-1-10, 2012.

[42] R.E. Skelton, F. Fraternali, G. Carpentieri, A. Micheletti, Minimum mass design of tensegrity bridges with parametric architecture and multiscale complexity. *Mechanics Research Communications*, **58**,124-132, 2014.

[43] A. Leonard, F. Fraternali, C. Daraio, Directional wave propagation in a highly nonlinear square packing of spheres. *Experimental Mechanics*, **53**(3), 327-337, 2013.

[44] F. Fraternali, G. Carpentieri, A. Amendola, R.E. Skelton, V. F. Nesterenko, Multiscale tunability of solitary wave dynamics in tensegrity metamaterials. *Applied Physics Letters*, **105**, 201903, 2014.

[45] F. Fraternali, I. Farina, C. Polzone, E. Pagliuca, L. Feo, On the use of R-PET strips for the reinforcement of cement mortars. *Composites. Part B*, **46**, 207-210, 2013.

[46] J.R. Raney, F. Fraternali, A. Amendola, C. Daraio, Modeling and In Situ Identification of Material Parameters for Layered Structures based on Carbon Nanotube Arrays. *Composite Structures*, **93**, 30133018, 2011.

[47] C. Daraio, D . Ngo, V. F. Nesterenko, F. Fraternali, Highly Nonlinear Pulse Splitting and Recombination in a Two Dimensional Granular Network. *Physical Review E*, **82**, 036603, 2010.

[48] F. Fraternali, A. Marino, T. Elsayed, A. Della Cioppa, On the structural shape optimization via variational methods and evolutionary algorithms. *Mechanics of Advanced Materials and Structures*, **18**,225-243, 2011.

[49] F. Fraternali, S. Spadea, V.P. Berardi, Effects of recycled PET fibers on the mechanical properties and seawater curing of Portland cement-based concretes. *Construction and Building Materials*, **61**, 293-302, 2014.

[50] I. Farina, F. Fabbrocino, G. Carpentieri, M. Modano, A. Amendola, R. Goodall, L. Feo, F. Fraternali, On the reinforcement of cement mortars through 3D printed polymeric and metallic fibers. *Composites Part B: Engineering*, **90**, 76-85, 2016.

[51] T. Blesgen, F. Fraternali, J.R. Raney, A. Amendola, C. Daraio, Continuum Limits of Bistable Spring Models of Carbon Nanotube Arrays accounting for Material Damage. *Mechanics Research Communications*, **45**, 58-63, 2012.

[52] F. Fraternali, A Mixed Lumped Stress  Displacement Approach to the Elastic Problem of Masonry Walls. *Mechanics Research Communications*, **38**, 176-180, 2011.

[53] F. Fraternali, M. Negri, M. Ortiz, On the Convergence of 3D Free Discontinuity Models in Variational Fracture. *International Journal of Fracture*, **166**(1-2), 3-11, 2010.

[54] G. Lomiento , N. Bonessio, G. Benzoni, Friction Model for Sliding Bearings under Seismic Excitation, *Journal of Earthquake Engineering*, **17** (8), 1162-1191, 2013.

[55] Hae-Bum Yun, Sami F. Masri, Raymond W. Wolfe, Gianmario Benzoni , Data-driven methodologies for change detection in large-scale nonlinear dampers with noisy measurements, *Journal of Sound and Vibration*, **322**(12), 336357, 2009.

[56] D. D'Ayala, G. Benzoni, Historic and Traditional Structures during the 2010 Chile Earthquake: Observations, Codes, and Conservation Strategies. Earthquake Spectra, **28** (S1), S425-S451, 2012.

[57] N. Bonessio, G. Lomiento, G. Benzoni, Damage identification procedure for seismically isolated bridges, *Structural Control Health Monitoring*, **19**(5), 565578, 2012.

[58] G. Benzoni, C. Casarotti , Effects of Vertical Load, Strain Rate and Cycling on the Response of Lead-Rubber Seismic Isolators, *Journal of Earthquake Engineering*, **13**, 2009.

[59] A. Budek-Schmeisser, G. Benzoni, Rational seismic design of precast, prestressed concrete piles, *PCI Journal*,**53**(5), 40-53, 2008.

[60] G. Benzoni, M. J. N. Priestley, Seismic response of linked marginal wharf segments, *Journal of Earthquake Engineering*, **74**, 513-539, 2003.

[61] F. Fraternali, S. Spadea, L. Ascione, Buckling behavior of curved composite beams with different elastic response in tension and compression. *Composite Structures*, **100**, 280-289, 2013.

[62] M. Budek, M. J. N. Priestley, G. Benzoni, The Effect of External Confinement on Flexural Hinging in Drilled Pile Shafts, *Earthquake Spectra*, **20**(1), 1-24, 2004.

[63] A. Amendola, G. Benzoni, F. Fraternali, Non-linear elastic response of layered structures, alternating pentamode lattices and confinement plates. *Composite Part B, Engineering*, Online First, DOI: 10.1016/j.compositesb.2016.10.027, 2016.

[64] A. Amendola, C.J. Smith, R. Goodall, F. Auricchio, L. Feo, G. Benzoni, F. Fraternali, Experimental response of additively manufactured metallic pentamode materials confined between stiffening plates. *Composite Structures*, **142**, 254-262, 2016.

[65] F. Fraternali, G. Carpentieri, R. Montuori, A. Amendola, G. Benzoni, On the use of mechanical metamaterials for innovative seismic isolation systems, COMPDYN 2015 - 5th ECCOMAS Thematic Conference on Computational Methods in Structural Dynamics and Earthquake Engineering, 349-358.

COMPDYN 2017
6th ECCOMAS Thematic Conference on
Computational Methods in Structural Dynamics and Earthquake Engineering
M. Papadrakakis, M. Fragiadakis (eds.)
Rhodes Island, Greece, 15–17 June 2017

# ANALYSES OF THE SEISMIC ACTIONS RECORDED DURING THE 2016 CENTRAL ITALY SEISMIC SEQUENCE: OBSERVED VS CODE PROVISION VALUES

**F.C. Ponzo[1], R. Ditommaso[1], A. Nigro[1], C. Iacovino[1]**

[1] School of Engineering, University of Basilicata, Italy
felice.ponzo@unibas.it
r.ditommaso@unibas.it
antonella.nigro@unibas.it
chiara.iacovino@unibas.it

**Keywords:** Central Italy Earthquake, Seismic Parameters, NTC 2008.

**Abstract.** *On August 24, 2016 at 03.36 a.m. (Italian time), a Mw 6.0 earthquake struck an extensive portion of the Central Italy. The epicentre was located among the municipalities of Accumoli (province of Rieti), Amatrice (province of Rieti) and Arquata del Tronto (province of Ascoli Piceno). After this first seismic event, from the academic point of view, several technical and scientific activities started with the aim to carry out preliminary evaluations on the characteristics of the seismic sequence, in order to interpret the possible effects of soil amplification in the areas affected by the earthquake and the damages observed on structures. The activities are continuing after the Mw 5.9 earthquake on October 26, 2016 and the Mw 6.5 earthquake on October 30, 2016. The strong motion recorded signals have been analysed in terms of peaks (PGA, PGV and PGD) and integral seismic parameters starting from data recorded by the closest stations to the epicentres. Several comparisons between the elastic response spectra retrieved from accelerometric recordings and the elastic demand spectra provided by the Italian seismic code (NTC 2008) have also been performed.*

## 1 INTRODUCTION

The earthquake occurred on October 30, 2016 at 06:40:17 UTC, (07:40:17, Italian time) was the Italian strongest event after the 1980 Irpinia earthquake ($M_W$ 6.9). The local magnitude evaluated by the INGV is equal to 6.1 $M_L$ while the moment magnitude is equal to 6.5 $M_W$. The earthquake affected the provinces of Perugia, Rieti and Macerata and was strongly felt in central Italy; the epicenter is located 5 km far from Norcia, 7 km far from Castelsantangelo sul Nera and Preci, 10 km far from Visso. Up to this moment the 30$^{th}$ of October earthquake is the strongest event of the sequence which began with the earthquake of August 24 ($M_W$ 6.0), followed by a quake of magnitude $M_W$ equal to 5.9 of October 26, 2016 [1].

The main events of the ongoing Monti della Laga-Valnerina seismic sequence occurred in a territory that was affected by relevant earthquakes in the past. Some of these historical earthquakes occurred within sequences, none of which comparable with the current one.

In the Amatrice area, where the major effects of the August 24 earthquake took place, the most distinctive feature is a cluster of four earthquakes occurred in: 1627 (Accumoli, $M_W$ 5.3); 1639 (Amatrice, $M_W$ 6.2); 1646 (Monti della Laga, $M_W$ 5.9) and 1672 (Amatrice, $M_W$ 5.3). In Valnerina, the earthquakes located closest to the epicentre of the October 30 main event are those of 1328 (Valnerina, $M_W$ 6.5); 1719 (Valnerina, M 5.6); 1730 (Valnerina, $M_W$ 6) and 1859 (Valnerina, $M_W$ 5.7). In the Visso-Ussita-Castelsantangelo sul Nera area, the intensity degrees now being assessed for the October 26 events appear very likely to be the historical maximum for this sector, at the current state of knowledge [1].

The area struck by the earthquake sequence is characterised by active fault systems already described in the geological literature published since the 90s of the past century. Particularly, the Apennine sector between Campotosto (south) and Colfiorito (north) presents normal fault systems trending NW-SE to NNW-SSE, with surface expression longer about 20-30 km, made of minor fault sections about 5-10 km long. The fault systems and the related fault sections are supposed to represent the superficial expression of seismogenic sources potentially responsible for earthquakes with M ranging between 5.5 and 7.0 [1].

After the Mw 6.0 mainshock of August 24, 2016 several activities were started in order to perform some preliminary evaluations on the seismic parameters of the recent seismic sequence that affected central Italy and to evaluate possible effects of local soil amplification in the areas affected by the earthquake [2].

Ambient vibration acquisitions have been performed using two three-directional velocimetric synchronized stations, with a natural frequency equal to 0.5Hz and a digitizer resolution of equal to 24bit.

This paper shows preliminary results of the experimental campaign carried out on 13$^{th}$ and 14$^{th}$ of September 2016 in the town of Amatrice. The activities are continuing after the events of the seismic sequence of 26 October and 30 October, 2016. Particularly, starting from the accelerometric time-histories acquired the RAN (Italian Accelerometric Network), peak (PGA) and integral parameters (Housner Intensity) have been evaluated and compared with Italian Seismic Code provisions.

## 2 PRELIMINARY ANALYSIS OF THE ONGOING SEISMIC SEQUENCE

The preliminary results described in this section are related to the Mw 6.0 mainshock of August 24, 2016 acquired by the accelerometric AMT station and to the seismic sequence of October 26 and October 30, 2016 acquired by the accelerometric CNE and NRC stations, respectively.

The three different earthquakes analysed in this work have been acquired using a sampling frequency equal to 200 Hz (data ITACA INGV).

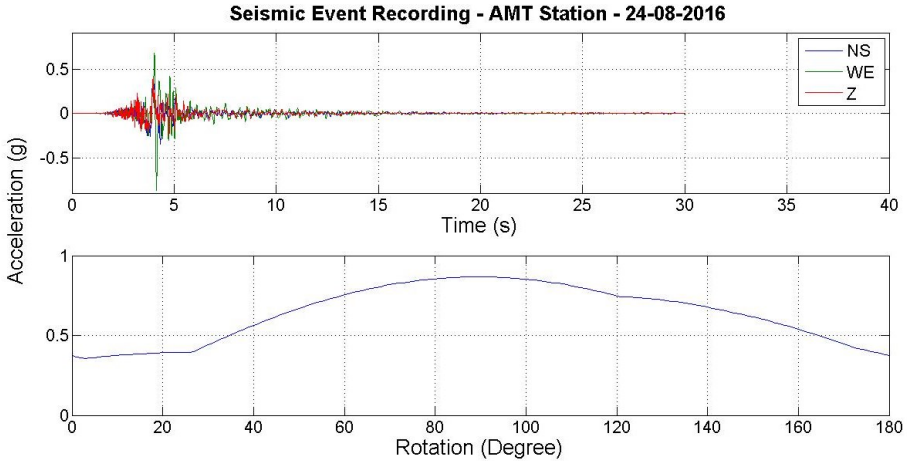


Figure 1: Earthquake on August 24, 2016 - accelerometric recordings and rotational analysis.

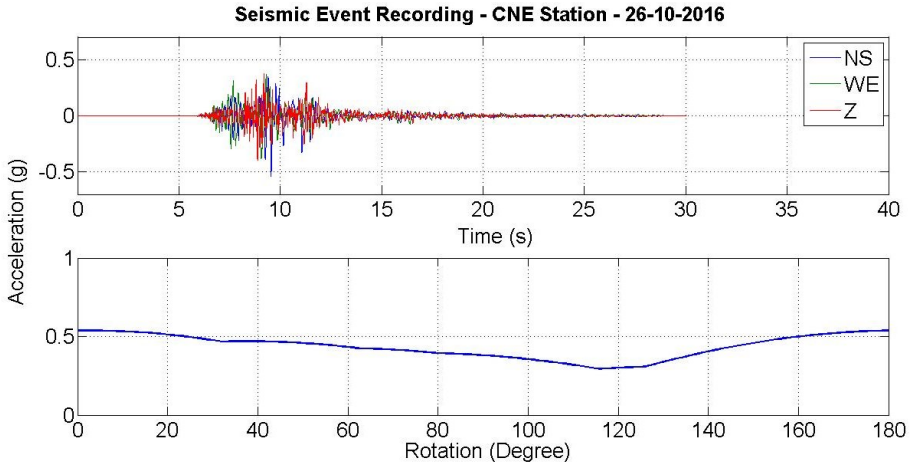


Figure 2: Earthquake on October 26, 2016 - accelerometric recordings and rotational analysis.

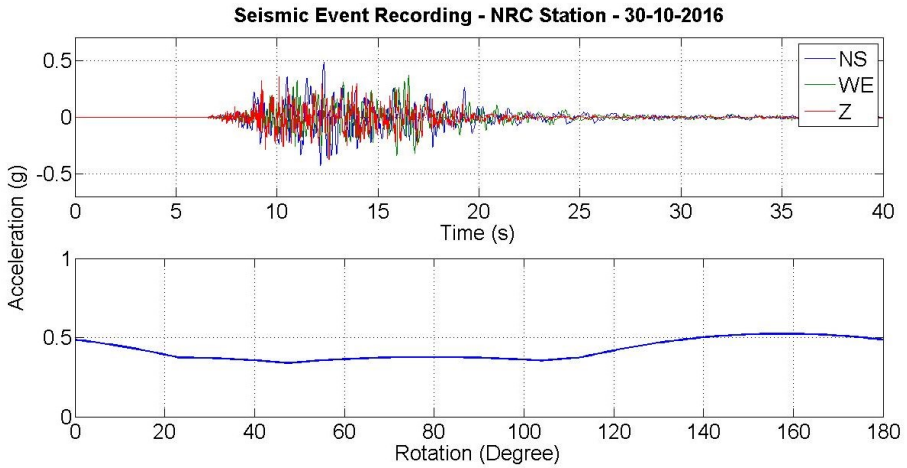


Figure 3: Earthquake on October 30, 2016 - accelerometric recordings and rotational analysis.

The mainshock recorded by the AMT station is characterized by a Peak Ground Acceleration (PGA) value equal to 0.85g (Figure 1). PGA values of the 26$^{th}$ and 30$^{th}$ of October seismic events are 0.53g and 0.51g, respectively.

Figures 4, 5, 6 show the rotational acceleration response spectra related to the above mentioned seismic events.

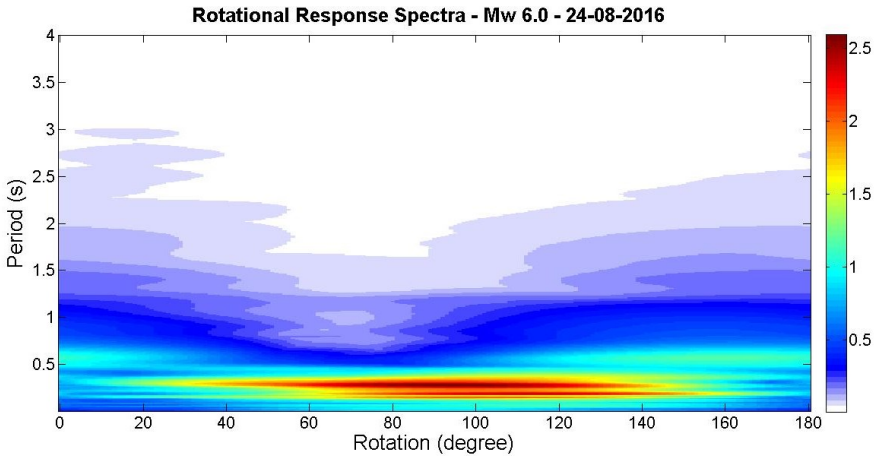


Figure 4: Rotational acceleration response spectra of the 24th of August 2016 seismic event.

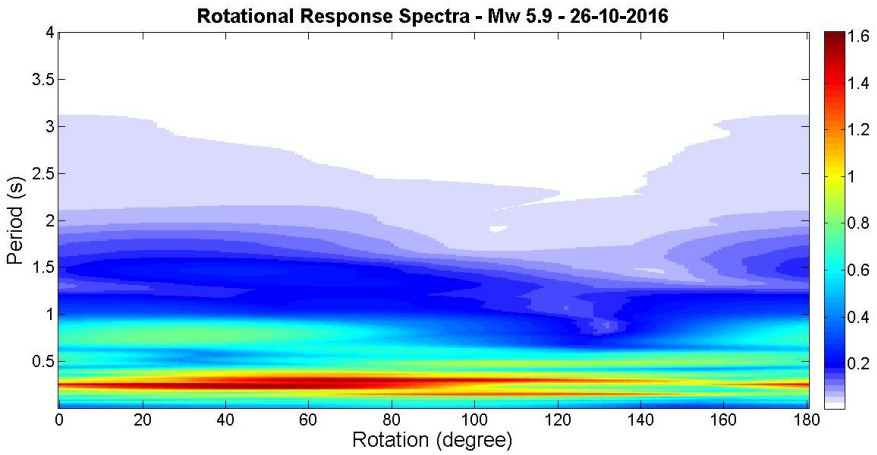


Figure 5: Rotational acceleration response spectra of the 26th of October 2016 seismic event.

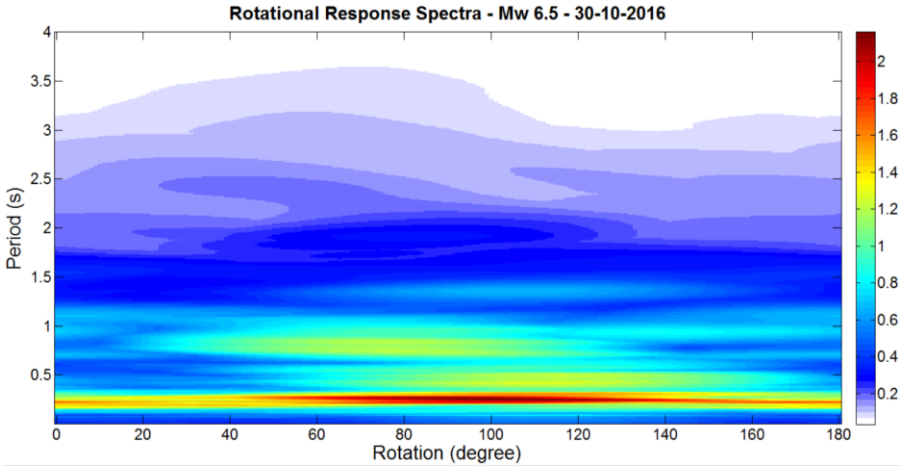


Figure 6: Rotational acceleration response spectra of the 30th of October 2016 seismic event.

For the mainshock of August 24, 2016 it can be observed that the maximum acceleration has been recorded along the WE direction while the maximum acceleration is less than 0.5g along the NS direction [2]. The preliminary analyses showed that the maximum spectral acceleration, equal to 2.586g, occurred along a direction at 90° from the NS direction in correspondence of a period equal to 0.28s. For the 26$^{th}$ of October seismic event, the maximum spectral acceleration, equal to 1.6g, occurred along a direction at 45° from the NS direction in correspondence of a period equal to 0.26s, while, for the 30$^{th}$ of October seismic event, the maximum spectral acceleration, equal to 2.16g, occurred along a direction at 89° from the NS direction in correspondence of a period equal to 0.27s. Figures 7, 8, 9 show the results of the time-frequency analysis of the three earthquakes.

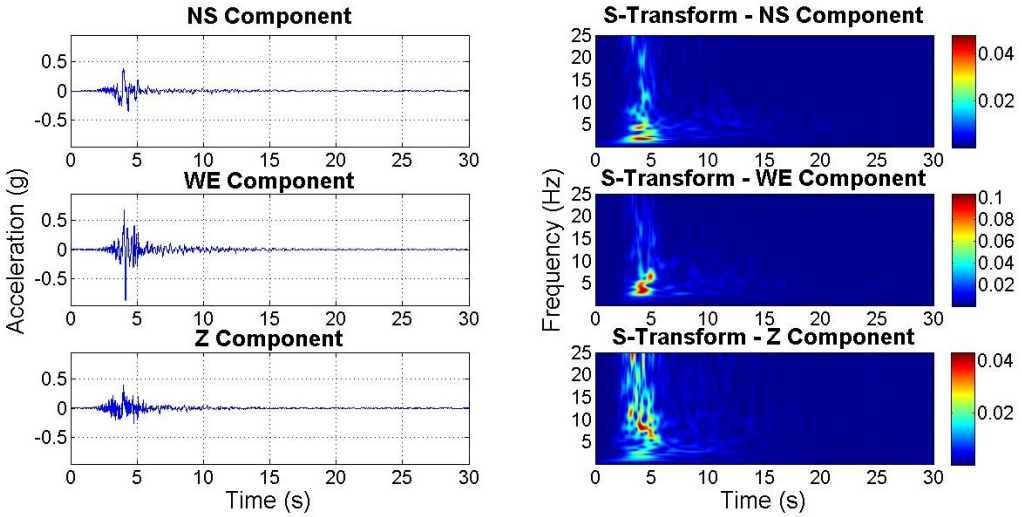


Figure 7: Stockwell Transform of the 24th of August 2016 seismic event.

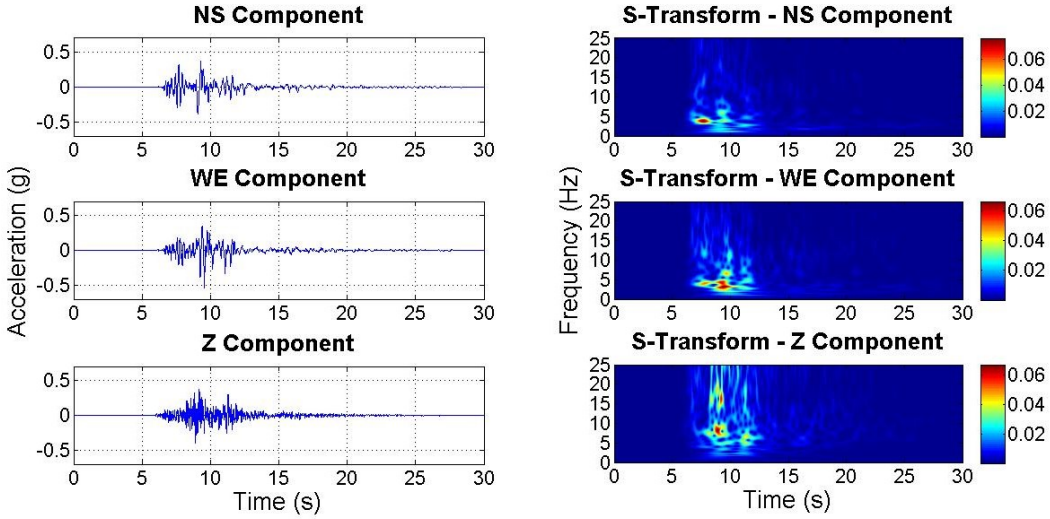


Figure 8: Stockwell Transform of the 26th of October 2016 seismic event.

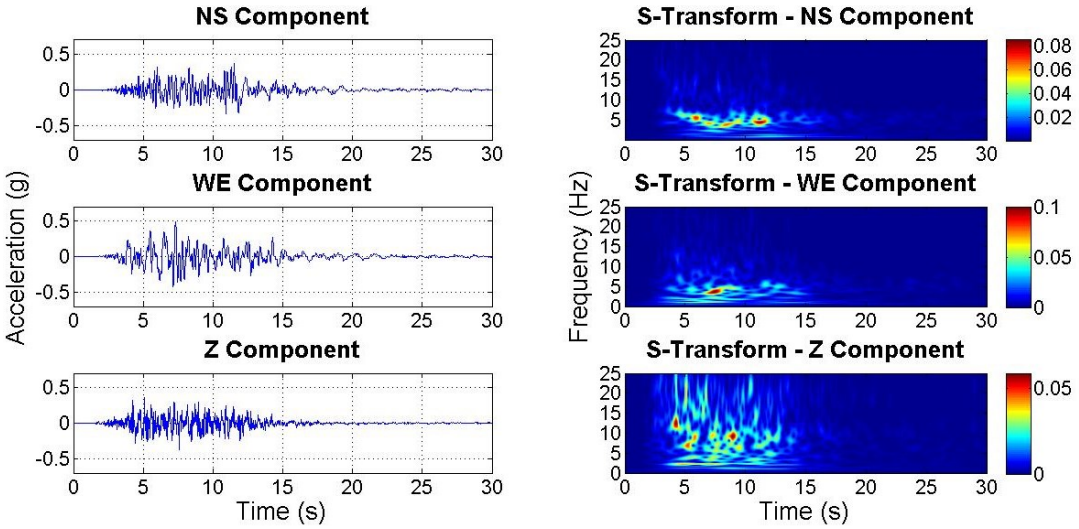


Figure 9: Stockwell Transform of the 30th of October 2016 seismic event (mainshock).

The analyses performed by the Stockwell Transform show an higher energy of the WE component for the mainshock August 24, 2016. Furthermore, the maximum energy was released in a range of frequencies close to 2Hz (NS direction) and between 2Hz and 6Hz (WE direction). For the vertical component, a peak value can be observed in a range of frequencies between 7.5Hz and 9Hz. For the 26$^{th}$ of October event, the maximum energy was released in a range of frequencies close to 4Hz (NS direction) and between 3Hz and 5Hz (WE direction). For the 30$^{th}$ of October event, the maximum energy was released in a range of frequencies between 4Hz and 5Hz (NS direction) and between 3Hz and 5Hz (WE direction).

## 3 AMBIENT VIBRATION MEASUREMENTS PERFORMED IN THE TOWN OF AMATRICE

In order to characterize the dynamic behaviour of the soil in the most damaged area of Amatrice, several ambient vibration measurements have been performed on September 14, 2016 (Figure 10a). Figure 10 shows the preliminary results of the experimental campaign in terms of HVSR (Horizontal to Vertical Spectral Ratio) in three different locations [2].

a)

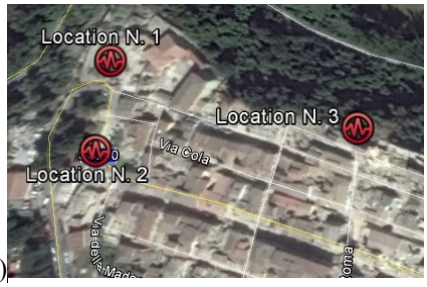


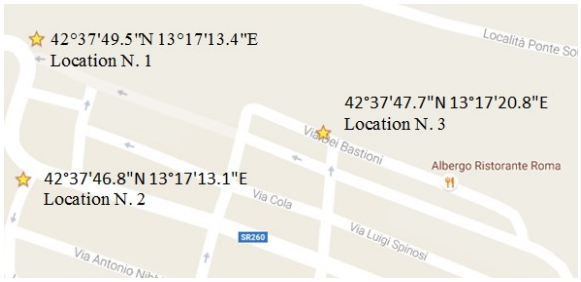

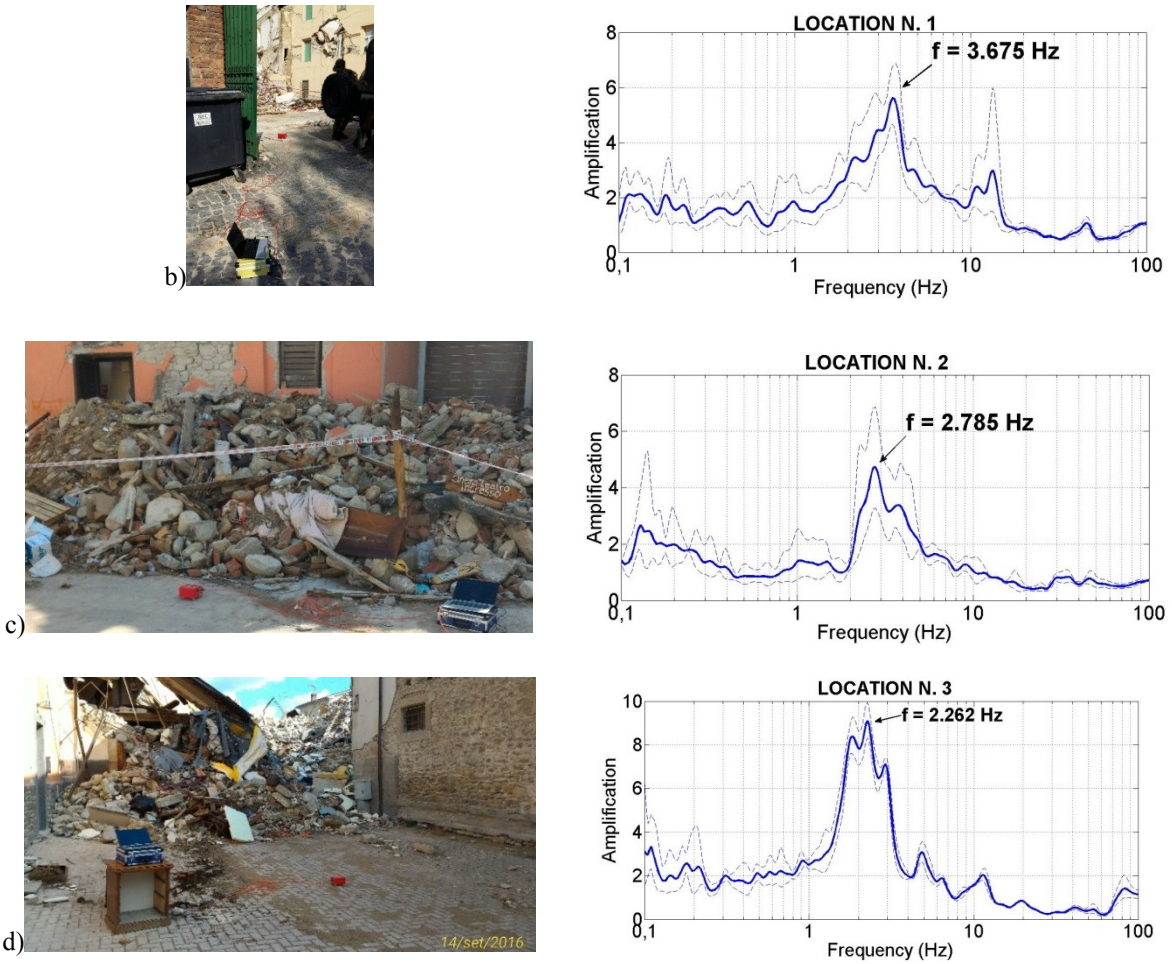


Figure 10: a) Map and GPS coordinates of the sites of ambient vibration measurements carried out in the town of Amatrice – b) Analysis HVSR – Location n. 1 ; c) Analysis HVSR - Location n. 2; d) Analysis HVSR - Location n. 3.

Analysing preliminary results, the resonance frequencies are next to the frequency at which the earthquake has exhibited the maximum value of spectral acceleration (Period=0.28s => Frequency=3.57Hz) (Figure 4). Furthermore, it can be observed that the investigated sites exhibit a significant amplification peak that could affect structures characterised by a range of frequencies between 2 and 5Hz.

## 4 ANALYSIS OF ACCELEROMETRIC RECORDED DATA

Starting from the Mw 6.0 mainshock of August 24, 2016 some activities are continuing after the events of the seismic sequence of October 26 and October 30, 2016. Particularly, the strong motion recorded signals in terms of peak (PGA, PGV and PGD) and integral (Housner Intensity) seismic parameters have been analysed starting from data recorded by the closest stations to the epicentres [3].

The National Accelerometric Network (RAN) managed by the Italian Department of Civil Protection recorded a great deal of accelerometric data of the ongoing Monti della Laga-Valnerina seismic sequence. Three different stations have been selected: AMT – Amatrice for the 24$^{th}$ of August main shock, CNE – Castelsantangelo sul Nera for the 26$^{th}$ of October earthquake, NRC – Norcia for the 30$^{th}$ of October earthquake. Table 1 shows the selected

strong motion stations with their site coordinates, EC8 [4] soil type classification, epicentral ($R_{EP}$) and Joyner-Boore distance ($R_{JB}$) [5] and magnitude.

| Date (YYYY-MM-DD) | Station Code | Name RAN Station | Latitude | Longitude | EC8 Soil Type | $R_{EP}$ (km) | $R_{JB}$ (km) | $M_W$ | $M_L$ |
|---|---|---|---|---|---|---|---|---|---|
| 2016-08-24 | AMT | AMATRICE | 42.6325 | 13.2862 | B* | 8.5 | - | 6.0 | 6.0 |
| 2016-10-26 | CNE | CASTELSANTANGELO SUL NERA | 42.8944 | 13.1528 | C* | 2.5 | 0 | 5.9 | 5.9 |
| 2016-10-30 | NRC | NORCIA | 42.7925 | 13.0965 | B | 5.4 | 2.17 | 6.5 | 6.1 |

Table 1: Near-field accelerometric stations with site coordinates, EC8 soil type classification, epicentral distance (REP), fault distance (RJB) and magnitude.

* indicates that site classification is not based on a direct Vs 30 measurement

### 4.1 Peak parameters: PGA, PGV and PGD

Peak Ground Acceleration (PGA), Velocity (PGV) and Displacement (PGD) values for the three components (horizontal: NS and WE; vertical: UP) at each station are reported in Table 2. With regard to the values of the PGA horizontal components, the maximum value (850 cm/s$^2$) was recorded for the WE component at the AMT station. High values have also been recorded at the other stations, particularly 527 cm/s$^2$ for CNE and 476 cm/s$^2$ for NRC. Also for the vertical component, high values of PGA have been observed, respectively 391, 389, 376 cm/s$^2$ for AMT, CNE and NRC.

In terms of PGV values on the horizontal plane, NRC and AMT stations show the maximum values (48.29 and 43.55 cm/s, WE direction), while smaller but still remarkable value has been found at the station CNE, equal to 23.08 cm/s. As for the PGV values, the maximum value of PGD (17.98 cm, WE direction) has been recorded by the NRC station. Lower values of PGD have been found at the other stations.

| Date (YYYY-MM-DD) | Station Code | Direction | PGA_RAN (cm/s$^2$) | PGV_RAN (cm/s) | PGD_RAN (cm) |
|---|---|---|---|---|---|
| 2016-08-24 | AMT | WE | -850.804 | 43.549 | -3.265 |
| | | NS | 368.387 | -41.501 | 8.544 |
| | | UD | 391.368 | -33.695 | -8.871 |
| 2016-10-26 | CNE | WE | -527.006 | 23.076 | 2.728 |
| | | NS | -373.134 | -36.542 | 5.274 |
| | | UD | -389.218 | -19.579 | -3.008 |
| 2016-10-30 | NRC | WE | 476.428 | -48.293 | -17.978 |
| | | NS | 365.051 | 41.446 | 8.138 |
| | | UD | -376.529 | 25.597 | 6.414 |

Table 2: Peak ground acceleration (PGA), Velocity (PGV) and Displacement (PGD) values at the recording stations (AMT, CNE and NRC) for horizontal (NS and WE) and vertical (UP) components.

### 4.2 Housner Intensity

As an alternative to PGA or other seismic peak parameters, some studies [6, 7] have demonstrated that Housner Intensity [8] can be an effective parameter to correlate the severity of seismic motions to structural damage, particularly, in cases of existing non-ductile Reinforced Concrete (RC) buildings [9]. The $I_H$ values for the recorded data three different

main shocks have been computed. $I_H$ is calculated as the area under the pseudo-velocity response spectrum (*S*v), as shown in Eq. (1):

$$I_H = \int_{T\ inf}^{T_{sup}} S_v(T,\xi)dT \quad (1)$$

where T is the fundamental period of the structure under examination, ξ is the damping ratio (equal to 5% in the analyses developed in this work), $T_{inf}$ and $T_{sup}$ define the interval of period values where ordinary buildings can be mostly placed. In the present work the period range [0.2–2s] has been used, in accordance with the choice adopted in the studies carried out for the previous seismic classification of the Italian territory proposed by the GNDT Working Group [10].

| Date (YYYY-MM-DD) | Station Code | Direction | $I_{H_NTC08}$ ($T_R$=475) (m) | $I_{H_NTC08}$ ($T_R$=975) (m) | $I_{H_NTC08}$ ($T_R$=2475) (m) | $I_{H_RAN}$ (m) |
|---|---|---|---|---|---|---|
| 2016-08-24 | AMT | WE | 0.902 | 1.204 | 1.531 | 0.654 |
| | | NS | 0.902 | 1.204 | 1.531 | 0.929 |
| | | ROT | 0.902 | 1.204 | 1.531 | 0.654 |
| 2016-10-26 | CNE | WE | 1.125 | 1.381 | 1.603 | 0.692 |
| | | NS | 1.125 | 1.381 | 1.603 | 0.840 |
| | | ROT | 1.125 | 1.381 | 1.603 | 0.692 |
| 2016-10-30 | NRC | WE | 0.878 | 1.172 | 1.488 | 1.746 |
| | | NS | 0.878 | 1.172 | 1.488 | 1.252 |
| | | ROT | 0.878 | 1.172 | 1.488 | 1.651 |

Table 3: Housner intensity for each recording station (AMT, CNE, NRC) for horizontal (NS and WE) and rotational (ROT) components and NTC08 Italian Code values for return periods (475, 975, 2475 years).

## 5 COMPARISON BETWEEN RECORDED AND CODE PROVISION VALUES

### 5.1 Comparison in terms of PGA

Table 4 shows Peak Ground Acceleration (PGA) values for the three components (horizontal: NS and WE and rotational: ROT) at each station and NTC08 Italian Code [11] PGA values for the three different return periods considered in this work. Furthermore, comparisons between code (NTC08) and recorded (RAN) PGA values has been performed in terms of differences according to Eq. (2):

$$\Delta_{PGA,T_R} = \left(100 \cdot \frac{PGA_{NTC08} - PGA_{RAN}}{PGA_{NTC08}}\right)_{T_R} \quad (2)$$

| Station Code | Direction | PGA_ NTC08 ($T_R$=475) (g) | PGA_ NTC08 ($T_R$=975) (g) | PGA_ NTC08 ($T_R$=2475) (g) | $PGA_{_RAN}$ (g) | $\Delta_{PGA}$ ($T_R$=475) (%) | $\Delta_{PGA}$ ($T_R$=975) (%) | $\Delta_{PGA}$ ($T_R$=2475) (%) |
|---|---|---|---|---|---|---|---|---|
| AMT | WE | 0.2988 | 0.3588 | 0.450 | 0.8508 | -184.7 | -137.1 | -88.9 |
| | NS | 0.2988 | 0.3588 | 0.450 | 0.3684 | -23.3 | -2.07 | 18.2 |
| | ROT | 0.2988 | 0.3588 | 0.450 | 0.8508 | -184.7 | -137.1 | -88.9 |
| CNE | WE | 0.3334 | 0.3936 | 0.461 | 0.5270 | -58.0 | -33.9 | -14.3 |
| | NS | 0.3334 | 0.3936 | 0.461 | 0.3731 | -11.9 | 5.2 | 19.1 |
| | ROT | 0.3334 | 0.3936 | 0.461 | 0.5270 | -58.0 | -33.9 | -14.3 |

| | | | | | | | | |
|---|---|---|---|---|---|---|---|---|
| NRC | WE | 0.2953 | 0.3551 | 0.447 | 0.4764 | -61.4 | -34.2 | -6.7 |
| | NS | 0.2953 | 0.3551 | 0.447 | 0.3651 | -23.6 | -2.8 | 18.3 |
| | ROT | 0.2953 | 0.3551 | 0.447 | 0.5137 | -74.0 | -44.6 | -15.0 |

Table 4: Peak Ground Acceleration (PGA) values of the recording stations (AMT, CNE, NRC) and NTC08 Italian Code values for return periods equal to 475, 975 and 2475 years and variations ΔPGA.

Code values are always lower than recorded data for $T_R$= 475, $T_R$= 975 and $T_R$=2475 years. The maximum difference between observed and code values are -184.7% (WE and ROT direction), -137.1% (WE and ROT direction) and -88.9% (WE and ROT direction) at the AMT station, -58% (WE and ROT direction), -33.9% (WE and ROT direction) and 19.1% (NS direction) at the CNE station, -74% (ROT direction ), -44.6% (ROT direction ) and 18.3% (NS direction) at the NRC station, for the different return periods as showed in Table 4.

### 5.2 Comparison in terms of Housner Intensity

As described in the previous section, recorded and the Italian seismic code values have also been compared in terms of $I_H$. The differences between code (NTC08) and recorded (RAN) values have been reported in Table 5 for $T_R$ equal to 475, 975 and 2475 years, computed according to Eq. (3).

| Station Code | Direction | $I_{H_NTC08}$ ($T_R$=475) (m) | $I_{H_NTC08}$ ($T_R$=975) (m) | $I_{H_NTC08}$ ($T_R$=2475) (m) | $I_{H_RAN}$ (m) | $\Delta I_H$ ($T_R$=475) (%) | $\Delta I_H$ ($T_R$=975) (%) | $\Delta I_H$ ($T_R$=2475) (%) |
|---|---|---|---|---|---|---|---|---|
| AMT | WE | 0.902 | 1.204 | 1.531 | 0.654 | 27.5 | 45.7 | 57.3 |
| | NS | 0.902 | 1.204 | 1.531 | 0.929 | -3.0 | 22.8 | 39.3 |
| | ROT | 0.902 | 1.204 | 1.531 | 0.654 | 27.5 | 45.7 | 57.3 |
| CNE | WE | 1.125 | 1.381 | 1.603 | 0.692 | 38.4 | 49.9 | 56.8 |
| | NS | 1.125 | 1.381 | 1.603 | 0.840 | 25.3 | 39.2 | 47.6 |
| | ROT | 1.125 | 1.381 | 1.603 | 0.692 | 38.4 | 49.9 | 56.8 |
| NRC | WE | 0.878 | 1.172 | 1.488 | 1.746 | -98.8 | -49.0 | -17.3 |
| | NS | 0.878 | 1.172 | 1.488 | 1.252 | -42.5 | -6.8 | 15.9 |
| | ROT | 0.878 | 1.172 | 1.488 | 1.651 | -87.9 | -40.9 | -10.9 |

Table 5: Housner intensity (IH) values of the recording stations (AMT, CNE, NRC) and NTC08 Italian Code values for return periods equal to 475, 975 and 2475 years and variations ΔIH.

$$_{I_H,T_R} = \left(100 \cdot \frac{I_{H,NTC08} - I_{H,RAN}}{I_{H,NTC08}}\right)_{T_R} \quad (3)$$

Comparisons in terms of $I_H$ show that code values are generally higher than recorded values at the AMT station for the three different return periods. The values computed using code spectra are generally comparable with those from recorded data for $T_R$= 475 years at the CNE station. The minimum variation $\Delta I_H$ between code and recorded data are exhibited for $T_R$= 2475 years at the NRC station.

### 5.3 Comparison in terms of elastic response spectra

Analyses and comparisons in terms of peak values provide a clear reading of earthquake ground motion through parameters usually used in seismic design. Therefore, in this section,

in order to give a description of the potential ground motion severity, elastic response spectra have been evaluated for the seismic time histories recorded at the three stations. As for PGA and $I_H$, the estimated elastic response spectra have been compared with the ones provided by NTC08 Italian Code considering the return periods of 475, 975 and 2475 years and the different soil type conditions of the accelerometric stations.

Computed and code response spectra are displayed in the figures 11, 12 and 13 in terms of pseudo-acceleration (*S*a), considering the horizontal components (NS and WE) of recorded signals.

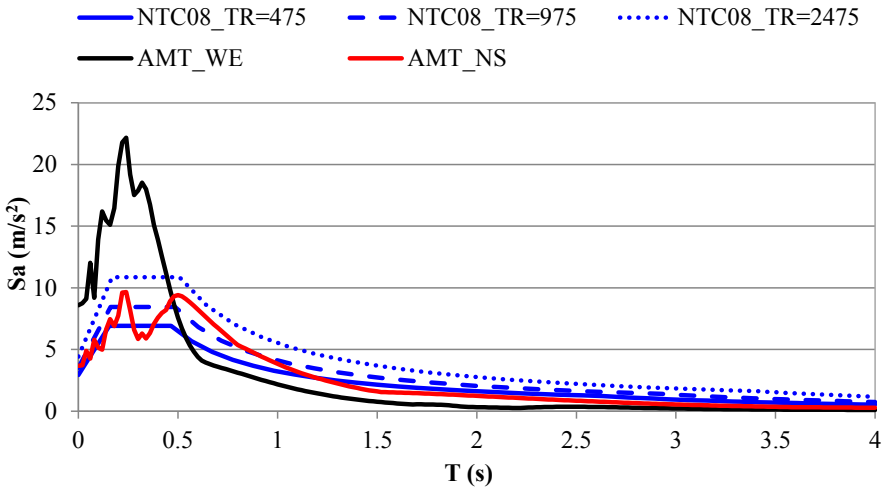


Figure 11: Comparison of the pseudoacceleration response spectra S(T,ξ = 5%) of the Amatrice recording station and of the NTC08 Italian Code for the return period of 475, 975 and 2475 years.

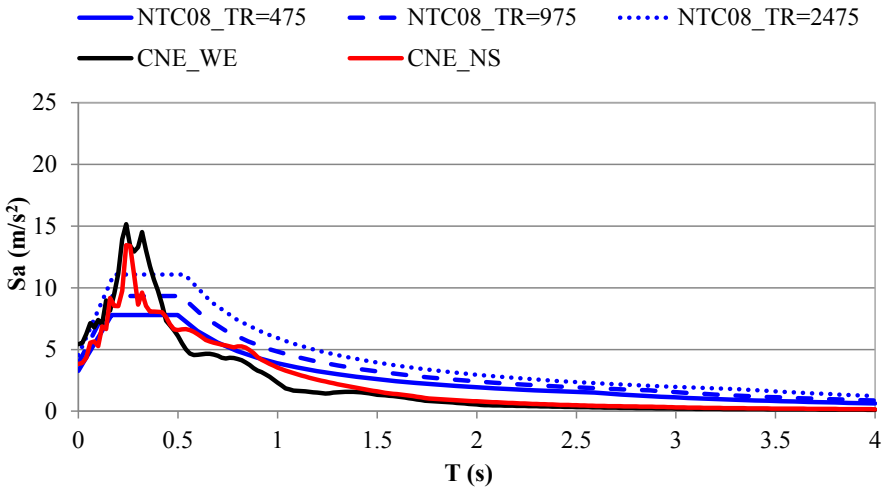


Figure 12: Comparison of the pseudoacceleration response spectra S(T,ξ = 5%) of the Castelsantangelo sul Nera recording station and of the NTC08 Italian Code for the return period of 475, 975 and 2475 years.

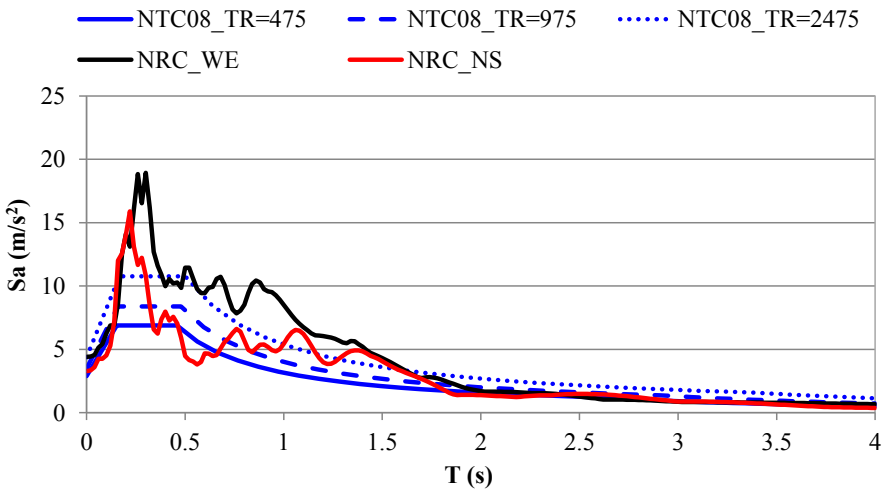


Figure 13: Comparison of the pseudoacceleration response spectra S(T,ξ = 5%) of the Norcia recording station and of the NTC08 Italian Code for the return period of 475, 975 and 2475 years.

Comparison in terms of pseudo-acceleration response spectra *Sa* showed in figure 11 shows that the spectral values from NTC08 are by far lower than those from the recorded signals for WE direction, while, the recorded response spectrum is comparable with the code spectrum for $T_R$= 975 years for NS direction.

Figure 12 shows that the recorded response spectra (NS and WE direction) are higher than the spectral values from NTC08 for the three different return periods considered in this work, particularly in the range of periods between 0.15 and 0.4s. Response spectra obtained from recorded data of the event of October 30$^{th}$ (NRC station), as for the Castelsantangelo sul Nera recording station, are higher than the spectral values from NTC08 for the three different return periods ($T_R$= 475, $T_R$=975, $T_R$=2475 years) (Figure 13). Particularly in the WE direction, pseudo-acceleration (*Sa*) are about twice the spectral values from NTC08 for $T_R$=2475 years, in the range of periods between 0.15 and 0.35s.

Figure 14 shows the probabilities in 50 years at towns of Amatrice, Castelsantangelo sul Nera and Norcia returned by NTC08 code for their respective soil class (the class of the recording stations reported in Table 1) as a function of PGA (Figure 14a) and $I_H$ (Figure 14b). The maximum value of PGA and $I_H$ for each recording stations has been depicted.

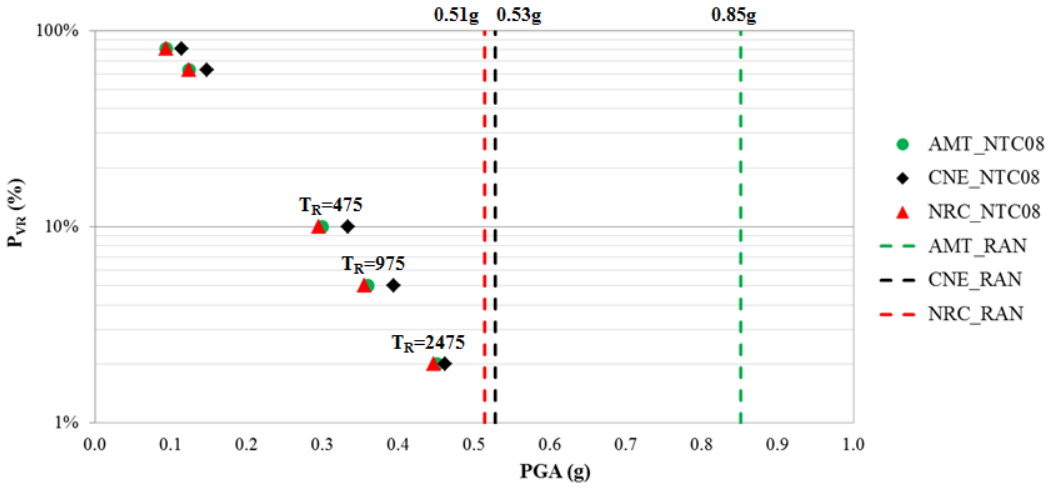


(a)

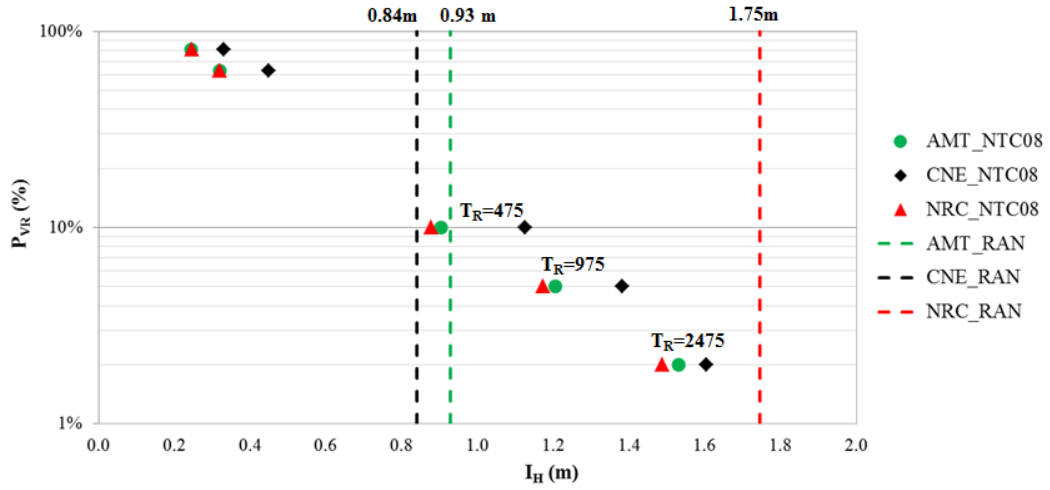


(b)

Figure 14: Exceedance probability in 50 years at three considered towns provided by the NTC2008 code in terms of PGA (a) and Housner Intensity (b).

The maximum PGA of the earthquakes recorded on October 26, 2016(CNE station) and October 30, 2016 (NRC station) would correspond to a return period of 2475 years, while the maximum PGA of the earthquake recorded on August 24, 2016 (AMT station) is about twice the value corresponding to $T_R$=2475 years. In terms of $I_H$, recorded data from AMT and CNE stations shows that maximum $I_H$ are close to the values corresponding to a return period of 475 years. Maximum value for NRC station would correspond to a return period larger than 2475 years.

## 6 DISCUSSION AND FINAL REMARKS

The earthquake occurred on October 30, 2016 at 06:40:17 UTC, (07:40:17, local time) is the Italian strongest event after the 1980 Irpinia earthquake ($M_W$ 6.9). The local magnitude evaluated by the INGV is equal to 6.1 $M_L$ while the moment magnitude is equal to 6.5 $M_W$. In order to compare recorded and code provision values in terms of peak, spectral and integral parameters, several preliminary analyses have been performed on accelerometric time-histories acquired by three near fault station of the RAN network: Amatrice station (station code AMT), Norcia station (station code NRC) and Castelsantangelo sul Nera station (station code CNE).

As expected, results retrieved from these preliminary analyses highlights several apparent difference between experimental data and conventional code provision. Taking into account the results retrieved in terms of PGA, experimental data showed peaks higher than those provided by the NTC 2008 code when a return period equal to 475 years is considered. On the contrary, considering a return period equal to 2475, recordings and NTC 2008 code provide comparable peaks values for the earthquakes recorded on October 26, 2016(CNE station) and October 30, 2016 (NRC station).The PGA of the earthquake recorded on August 24, 2016 (AMT station) is about twice the value corresponding to $T_R$=2475 years. Then, the ongoing seismic sequence appears compatible with the historical seismicity in terms of integral parameters, but not in terms of peak and spectral values. It seems appropriate to reconsider the necessity to revise the simplified design approach based on the conventional spectral values.

Last, but not least, a significant soil amplification has been documented in the historical centre of Amatrice town in the frequency range 2-5Hz.

In order to complete this preliminary work more measurements and analyses on soil and buildings are necessary for better understand a possible role played by soil-structure interaction effects on the damage observed within the city located into the area interested by the ongoing seismic sequence in Central Italy.

## 7 ACKNOWLEDGEMENTS

This study was partially funded by the Italian Civil Protection Department within the project DPC-RELUIS 2016 - RS4 ‘‘Seismic observatory of structures and health monitoring’’ and by the “Centre of Integrated Geomorphology for the Mediterranean Area - CGIAM” within the Framework Agreement with the University of Basilicata for the “Study, Research and Experimentation in the Field of Analysis and Monitoring of Seismic Vulnerability of Strategic and Relevant Buildings for the purposes of Civil Protection and Development of Innovative Strategies of Seismic Reinforcement”.

## REFERENCES

[1] INGV, Summary report on the 30 October, 2016 Earthquake in central Italy MW 6.5, 2016.

[2] F.C. Ponzo, R. Ditommaso, A. Nigro, D. Spina, Valutazioni preliminari su possibili fenomeni di interazione terreno-struttura rilevate nelle aree colpite dal sisma del 24/08/2016. *35° edizione del Convegno GNGTS,* Lecce, 22-24 novembre 2016.

[3] ITACA, 2008 http://itaca.mi.ingv.it.

[4] CEN Eurocode 8. *Design of structures for earthquake resistance - Part 1: General rules, seismic actions and rules for buildings*. EN 1998-1, Brussels, 2004.

[5] W.B. Joyner, D.M. Boore, Peak horizontal acceleration and velocity from strong-motion records including records from the 1979 Imperial Valley, California, earthquake. *Bull Seismol Soc Am* **71**:2011–2038, 1981.

[6] L. Decanini, F. Mollaioli, G. Oliveto, Structural and seismological implications of the 1997 seismic sequence in Umbria and Marche, Italy. *Innovative approaches to earthquake engineering*. In: Oliveto G (ed) WIT Press, Southampton, pp 229–323, 2002.

[7] A. Masi, M. Vona, M. Mucciarelli, Selection of natural and synthetic accelerograms for seismic vulnerability studies on RC frames. *J Struct Eng*. doi:10.1061/(ASCE)ST.1943-541X.209, 2010.

[8] G.W. Housner, Intensity of ground motion during strong earthquakes. *Second technical report*. August 1952, California Institute of Technology, Pasedena, California, 1952.

[9] A. Masi, L. Chiauzzi, F. Braga, M. Mucciarelli, M. Vona, R. Ditommaso, Peak and integral seismic parameters of L’Aquila 2009 ground motions: observed versus code provision values. *Bull Earthquake Eng*. **9**:139–156, 2011.

[10] GNDT Working Group, Proposta di riclassificazione sismica del territorio nazionale (in Italian). *Ingegneria Sismica*. XVI N.1, gennaio—aprile 1999.

[11] Nuove norme tecniche per le costruzioni. D.M. Infrastrutture 14 Gennaio 2008.

COMPDYN 2017
6th ECCOMAS Thematic Conference on
Computational Methods in Structural Dynamics and Earthquake Engineering
M. Papadrakakis, M. Fragiadakis (eds.)
Rhodes Island, Greece, 15–17 June, 2017

# ANALYTICAL MODEL OF THE DYNAMICS OF RAILWAY SLEEPER

**L-H. Tran[1], T. Hoang[1], G. Foret[1], D. Duhamel[1], S. Messad[2] and A. Loaec[2]**

[1]Laboratoire Navier, UMR 8205, Ecole des Ponts, IFSTTAR, CNRS,
6-8 Avenue Blaise Pascal, Cité Descartes,
Champs-sur-Marne, 77455 Marne-la-Vallée Cedex 2, France
e-mail: {le-hung.tran, gilles.foret, denis.duhamel, tien.hoang}@enpc.fr

[2] SATEBA, 33 places des Corolles, 92400 Courbevoie, Courbevoie, France
e-mail: s.messad@sateba.com, arnaud.loaec@consolis.com

**Keywords:** Railway, analytical method, periodically supported beam, Fourier transform, Green function.

**Abstract.** *The periodically supported beam is an analytical model of the dynamics of a railway track, where each rail together with its supports (sleepers) is independent of the other one. However, the sleepers connect the two rails and their behaviour could influence the response. This study develops an analytical model for this type of track by considering the sleepers as Euler-Bernoulli beams resting on a visco-elastic foundation. By using a relation between the reaction forces and displacement of the periodically supported beam [1], we can obtain a dynamic equation of a sleeper based on Dirac delta distribution. Then, the response of the sleepers can be obtained by using the Green function. This model is a fast method to calculate the dynamic responses of railway sleepers and track.*

## 1 Introduction

Currently, there are many kinds of railway tracks constructed using different technologies. Among many choices of sleeper types, the concrete monoblock sleeper remains popular. In addition, the sleeper dynamic response is important because it affects the stability of the railway track and the maximum speed of the train. Substantial researches using analytic methods for rail track have been carried out, for example : the effect of wheel-rail contact forces [17, 18] or the vibration of the railway track (by considering the model of a ballasted track with discrete supports [8, 9, 13, 14, 1] or the model of the infinite beam placed on a continuous foundation [10, 7, 6, 11]). The studies of each component of the rail track were performed on the rail [19, 16, 15], or on the ballast [20, 22].

An other important component of the railay track is the sleeper which has been investigated by using several different methods. The main objective is to analyse the sleeper behaviour and model it in the case of different moving charge values. The dynamic lateral resistance of the sleeper has been studied to better understand the interaction zones between the sleeper and the ballast layer [5]. Kaewunruen S. [23] researched the influence of the rail pad on the free vibration of the concrete sleeper by using finite element analysis. By using experimental and numerical methods, Laryea et al. [4] compared the sleeper's perfomance when made out of different materials. Some works focus on the pre-stressed concrete sleeper using FEM in 2D and in 3D [24, 21].

In this paper, an analytical model is presented based on the theory of a beam resting on visco-elastic foundation. Indeed, the ratio between the length and the height of the sleeper ($L/h$) is greater than 10 and we can consider the sleeper as an Euler-Bernoulli beam. The dynamic equation of the beam in the frequency domain by using the Fourier transform. Then by using the relation between the reaction forces and displacement of the beam [1] in the frequency domain and the Dirac delta distribution, the dynamic equation for the beam (sleeper) together with the rails and foundation is written and solved by using Green functions. The method of Green function to obtain the response of a beam structure to a moving mass has been successfully applied previously [25, 26]. The use of Green function not only leads to exact results but also involves less cumbersome manipulations. Finally, the inverse Fourier transform gives the time responses of the beam.

The dynamic response of the sleeper has been investigated in two cases of moving charges. The numerical computations shows the displacements and reaction forces in the time domain. The model can be used for parametric analyses to study the influence of sleeper on the dynamic response. This simple model shows an efficient and fast way to estimate the responses of railway sleepers and can be further developed for the analysis of more complex cases.

## 2 Formulations

Let us consider a periodically supported beam subjected to moving forces as shown in Figure (1). In the steady-state, we suppose that all sleepers have the same response but with a delay which is equal to the time for the moving forces to cover the distance between two sleepers. By using this condition, Hoang et al. [1] have shown a relation between the beam displacement ($w_r$) and reaction force ($R$) at the sleeper position as follows :

$$\hat{R}(\omega) = \mathcal{K}(\omega)\hat{w}_r(\omega) + \mathcal{Q}(\omega) \tag{1}$$

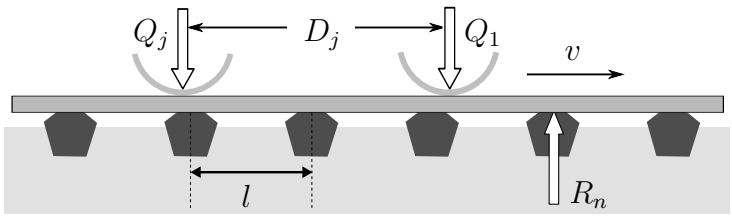


Figure 1: Periodically supported beam subjected to moving loads

where $\mathcal{K}(\omega)$ and $\mathcal{Q}(\omega)$ are so-called equivalent stiffness and pre-force of the periodically supported beam, calculated by :

$$\begin{aligned}\mathcal{K}(\omega) &= 4\lambda_r^3 E_r I_r \left[\frac{\sin l\lambda_r}{\cos l\lambda_r - \cos\frac{\omega l}{v}} - \frac{\sinh l\lambda_r}{\cosh l\lambda_r - \cos\frac{\omega l}{v}}\right]^{-1} \\ \mathcal{Q}(\omega) &= \frac{\mathcal{K}(\omega)}{vE_r I_r\left[\left(\frac{\omega}{v}\right)^4 - \lambda_r^4\right]} \sum_{j=1}^{K} Q_j \mathrm{e}^{-\mathrm{i}\omega\frac{D_j}{v}}\end{aligned} \tag{2}$$

where $\lambda_r = \sqrt[4]{\frac{\rho_r S_r \omega^2}{E_r I_r}}$, $\rho_r, E_r, S_r$ and $I_r$ are the density, Young's modulus, section and the longitudinal inertia of the rail respectively.

We now develop an analytical model for the dynamics of sleepers based on this equivalent system. Let us consider a railway track as shown in Figure 2. This track contains:

- Two rails: modelled by two periodically supported beams
- Rail pads: modelled by spring-damper systems
- Sleepers: modelled by Euler-Bernoulli's beams
- Ballast and foundation: modelled by a Kevin-Voight foundation
- Loads of train: concentrated moving loads

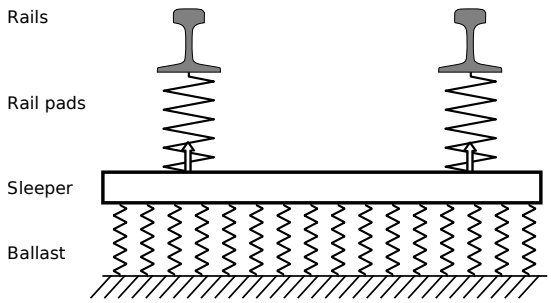


Figure 2: Dynamic model of a sleeper

The vertical displacement $w(x,t)$ of the sleeper under a force $F(x,t)$ is driven by the dynamic equation :

$$E_s I_s \frac{\partial^4 w(x,t)}{\partial x^4} + \rho_s S_s \frac{\partial^2 w(x,t)}{\partial t^2} + kw(x,t) + \zeta\frac{\partial w(x,t)}{\partial t} = F(x,t) \tag{3}$$

where $\rho_s, E_s, S_s$ and $I_s$ are the density, the Young's modulus, the section and the longitudinal inertia of the sleeper respectively; $k$ and $\zeta$ are the stiffness and the damping coefficient of the ballast layer.

The total force of two rails applied on the sleeper can be written with the help of Dirac functions as follows :

$$F(x,t) = -R_1(t)\delta(x-a) - R_2(t)\delta(x+a) \tag{4}$$

where $2a$ is a distance between two rails, and $R_1, R_2$ are the reaction forces of the sleeper applied on two rails. These forces are driven by the equivalent systems of the two rails (equation (2)) as follows:

$$\begin{aligned} \hat{R}_1 &= \mathcal{K}\hat{w}_1(\omega) + \mathcal{Q}_1 \\ \hat{R}_2 &= \mathcal{K}\hat{w}_2(\omega) + \mathcal{Q}_2 \end{aligned} \tag{5}$$

In addition, the reaction forces $\hat{R}_1, \hat{R}_2$ can be expressed by the constitutive law of the two rail pads :

$$\begin{aligned} \hat{R}_1 &= -k_p(\hat{w}_1(\omega) - \hat{w}(a,\omega)) \\ \hat{R}_2 &= -k_p(\hat{w}_2(\omega) - \hat{w}(-a,\omega)) \end{aligned} \tag{6}$$

where $k_p = k_{rp} + \mathrm{i}\omega\zeta_{rp}$ are the dynamic stiffness of the rail pad ($k_{rp}$, $\zeta_{rp}$ is the stiffness and damping coefficient of the rail pads) and $2a$ is the track gauges. By substituting the aforementioned equation (5) into equation (6), we obtain

$$\begin{aligned} \hat{R}_1 &= \frac{k_p\mathcal{K}}{k_p+\mathcal{K}}\hat{w}(a,\omega) + \frac{k_p}{k_p+\mathcal{K}}\mathcal{Q}_1 \\ \hat{R}_2 &= \frac{k_p\mathcal{K}}{k_p+\mathcal{K}}\hat{w}(-a,\omega) + \frac{k_p}{k_p+\mathcal{K}}\mathcal{Q}_2 \end{aligned} \tag{7}$$

By combining equations (3) and (7), then by performing the Fourier transform, we obtain :

$$E_sI_s\frac{\partial^4\hat{w}(x,\omega)}{\partial x^4} - \left(\rho S\omega^2 - k_b\right)\hat{w}(x,\omega) = -\hat{R}_1(\omega)\delta(x-a) - \hat{R}_2(\omega)\delta(x+a) \tag{8}$$

where $k_b = k + \mathrm{i}\zeta\omega$ is dynamic stiffness of the ballast.

Equation (8) describes the dynamics of the sleeper on the ballast. In order to solve these equations, we will use Green function for the dynamics of the beam defined by:

$$\frac{\partial^4\mathrm{G}(x,a)}{\partial x^4} - \lambda_s^4\mathrm{G}(x,a) = \delta(x-a) \tag{9}$$

where $\lambda_s = \sqrt[4]{\dfrac{\rho S\omega^2 - k_b}{E_sI_s}}$. The general form of the Green function is :

$$\mathrm{G}(x,a) = \begin{cases} A_1\cos\lambda_s x + A_2\sin\lambda_s x + A_3\cosh\lambda_s x + A_4\sinh\lambda_s x & \text{for } x\in[-L,a] \\ B_1\cos\lambda_s x + B_2\sin\lambda_s x + B_3\cosh\lambda_s x + B_4\sinh\lambda_s x & \text{for } x\in[a,L] \end{cases} \tag{10}$$

where $2L$ is the sleeper length. The boundary conditions of the Green function are :

$$\begin{aligned}
&\mathrm{G}''(-L,a) = \mathrm{G}''(L,a) = \mathrm{G}'''(-L,a) = \mathrm{G}'''(L,a) = 0\\
&\mathrm{G}(a^+,a) - \mathrm{G}(a^-,a) = 0\\
&\mathrm{G}'(a^+,a) - \mathrm{G}'(a^-,a) = 0\\
&\mathrm{G}''(a^+,a) - \mathrm{G}''(a^-,a) = 0\\
&\mathrm{G}'''(a^+,a) - \mathrm{G}'''(a^-,a) = 1
\end{aligned} \tag{11}$$

where the prime ($'$) stands for the derivation with regard to $x$. By using this boundary condtion, we can obtain the expressions of $A_i$, $B_i$ ($i$ = 1, 2, 3, 4) as shown in Appendix A.

The solution of equation (8) can be written with the help of the Green function as follows:

$$\hat{w}(x,\omega) = \frac{-\hat{R}_1}{E_s I_s}\mathrm{G}(x,a) + \frac{-\hat{R}_2}{E_s I_s}\mathrm{G}(x,-a) \tag{12}$$

In order to calculate $\hat{R}_1$ and $\hat{R}_2$, we substitute $x = a$ and $x = -a$ in the aforementioned equation and obtain:

$$\begin{cases}
\hat{w}(a,\omega) = \dfrac{-\hat{R}_1}{E_s I_s}\mathrm{G}(a,a) + \dfrac{-\hat{R}_2}{E_s I_s}\mathrm{G}(a,-a)\\
\hat{w}(-a,\omega) = \dfrac{-\hat{R}_1}{E_s I_s}\mathrm{G}(-a,a) + \dfrac{-\hat{R}_2}{E_s I_s}\mathrm{G}(-a,-a)
\end{cases} \tag{13}$$

By combining equations (7) and (13), we obtain

$$\begin{cases}
\hat{R}_1 = \kappa\dfrac{\mathcal{Q}_1\left[\mathrm{G}(-a,-a)+\chi\right] - \mathcal{Q}_2\mathrm{G}(a,-a)}{\left[\chi+\mathrm{G}(a,a)\right]\left[\chi+\mathrm{G}(-a,-a)\right] - \mathrm{G}(-a,a)\mathrm{G}(a,-a)}\\
\hat{R}_2 = \kappa\dfrac{\mathcal{Q}_2\left[\mathrm{G}(a,a)+\chi\right] - \mathcal{Q}_1\mathrm{G}(-a,a)}{\left[\chi+\mathrm{G}(a,a)\right]\left[\chi+\mathrm{G}(-a,-a)\right] - \mathrm{G}(-a,a)\mathrm{G}(a,-a)}
\end{cases} \tag{14}$$

where $\kappa = \dfrac{E_s I_s}{\mathcal{K}}$ and $\chi = E_s I_s \dfrac{k_p + \mathcal{K}}{k_p \mathcal{K}}$. Equation (14) defines the reaction force of the sleeper on the two rail. Then, the response of the sleeper can be obtained by using (12)

## 3 Applications

The dynamic response of the sleepers is calculated by using the formulae established in previous section for two cases : the same charges in both rails ($Q_1 = Q_2$) and the different charges in two rails ($Q_1 \neq Q_2$).

As the charge applied to the rail is periodic and moreover to simplify the comparison of results, the calculations are carried out in case of a point force. Some of the results in the case of a series of charges are shown in Appendix B. We consider a railway track parameters in Table 1.

Figure 3 shows the displacement of the sleeper in two cases: $Q_1 = Q_2 = 100$ kN and $Q_1 = 100$ kN, $Q_2 = 75$ kN. The figures are obtained through the inverse Fourier transform of equation (12). The two rails positions are presented by two dash lines. The sleeper displacement in the two cases is minimum in the interval between two rails. In the first case, the minimum displacement is at the sleeper center ($x = 0$) and in the second case, it is 0.39 mm and this point is not the center.

| Content | Unit | Notation | Value |
|---|---|---|---|
| Young's modulus of the rail | GPa | $E_r$ | 210 |
| Moment of inertia of the rail | $m^4$ | $I_r$ | 3.055E-5 |
| Density of the rail | $kgm^{-3}$ | $\rho_r$ | 7850 |
| Section of the rail | $m^2$ | $s_r$ | 7.69E-3 |
| Young's modulus of the sleeper | GPa | $E_s$ | 35 |
| Density of the sleeper | $kgm^{-3}$ | $\rho_s$ | 2350 |
| Height of the sleeper | m | $h_s$ | 0.22 |
| Width of the sleeper | m | $w_s$ | 0.29 |
| Length of the sleeper | m | $2L$ | 2.2245 |
| Track gauge | m | $2a$ | 1.435 |
| Stiffness of the ballast | $MNm^{-1}$ | $k$ | 158.11 |
| Damping coefficient of the ballast | $kNms^{-1}$ | $\zeta$ | 41.30 |
| Stiffness of the rail pad | $MNm^{-1}$ | $k_{rp}$ | 60 |
| Damping coefficient of rail pad | $kNms^{-1}$ | $\zeta_{rp}$ | 77.76 |
| Train speed | $ms^{-1}$ | $v$ | 44.4 |
| Charge on the first rail seat | kN | $Q_2$ | 75 |
| Charge on the second rail seat | kN | $Q_1$ | 100 |
| Sleeper distance | m | $l$ | 0.6 |

Table 1: Parameters of the analytical model

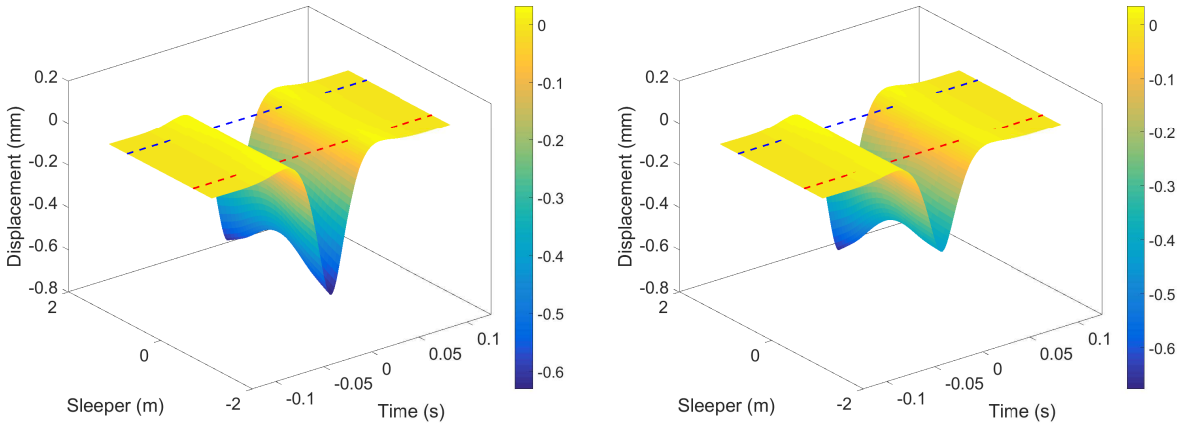


(a) $Q_1 = Q_2 = 100$ kN (b) $Q_1 = 100$ kN, $Q_2 = 75$ kN

Figure 3: Displacement of sleeper for the same loads and different loads on two rails

We observed this phenomenon because the displacement of the beam is not symmetric resulted by the different charges values. The sleeper displacements at the middle point and at the two rail seats are given by the Figure 4.

Figure 4a shows that the sleeper displacement at the rail seats are the same. The maximum value of the displacement at the rail seat is 0.57077 mm. However, the displacements at the rail seats in Figure 4b are not the same. Precisely, the first rail moves 0.41495 mm and the displacement of the second rail is 0.58390 mm (the red and blue curve). Moreover, Figure 5 shows the sleeper displacement in the two loading cases.

Under the action of the same forces, the deformation of the sleeper is symmetric and the

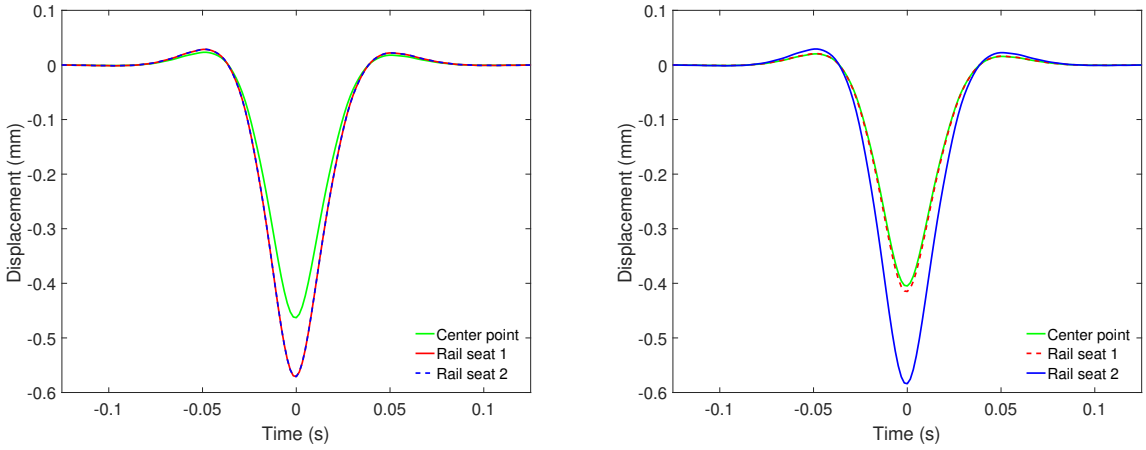


(a) $Q_1 = Q_2 = 100$ kN (b) $Q_1 = 100$ kN, $Q_2 = 75$ kN

Figure 4: Sleeper displacement under the moving charge at 3 positions : middle point (green curve), the first rail seat (red curve) and second rail seat (blue curve)

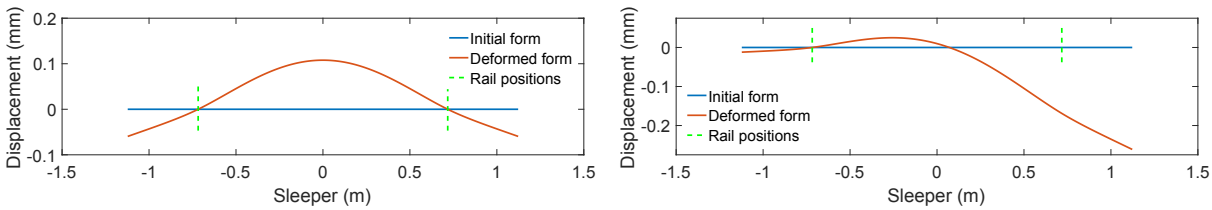


(a) $Q_1 = Q_2 = 100$ kN (b) $Q_1 = 100$ kN, $Q_2 = 75$ kN

Figure 5: Deformation form of the sleeper under the moving charge

displacements at the positions of two rail seats are at the same level. But in the second case, the displacements are different. The difference between two positions is referred to as the levelling of 0.17 mm. This phenomenon shows that the sleeper is not only deformed but also tilted. When there is a signfication difference between the moving charges, the levelling will change the distance between two rails and influence the risk of derailment.

The reactions forces $\hat{R}_1$ and $\hat{R}_2$ are calculated by the equation (14). Obviously, the reaction forces at the rail seat $\hat{R}_1$ and $\hat{R}_2$ are equal when $Q_1 = Q_2$. The reaction force is 42 kN in this case.

When the two moving charges are different, the reaction force is bigger when the rail is subjected to the bigger charge (42 kN and 31 kN respectively). The damage of the wheels, rails etc., can lead to significantly different charges on the two rails.

## 4 Conclusions

In this study, an analytical model of the dynamics of railway sleeper has been investigated using the relation between the reaction force and the displacement in the frequency domain. The time responses are obtained by the inverse Fourier transform. The displacement at the critical sections (rail seats and center) has been evaluated for various moving charges. In the case of the imperfection of the moving charges, the phenomenon of levelling on the railway track occurs and it could influence the railway track stability. In future research, this model will be developed by using the Timoshenko beam in order to take in account of the sleeper rotation. Moreover, this

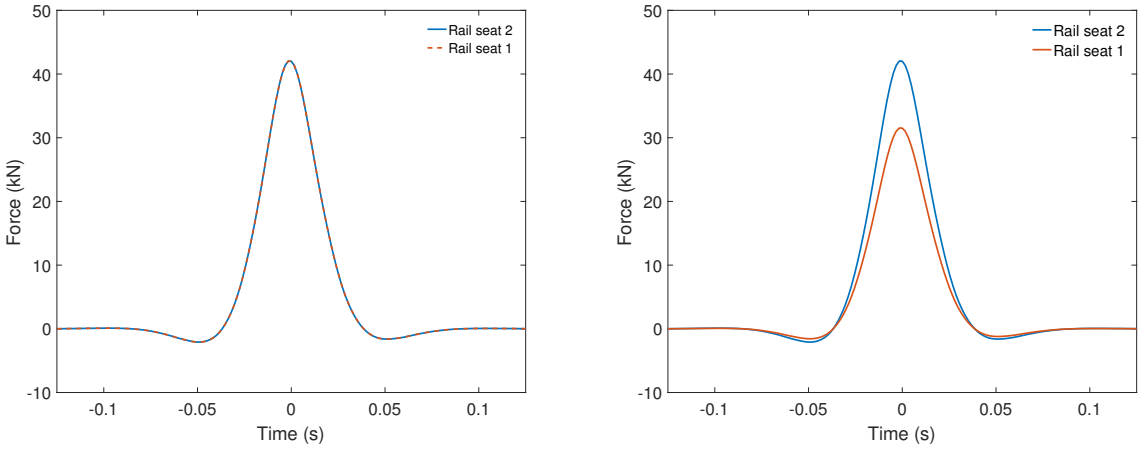


(a) $Q_1 = Q_2 = 100$ kN (b) $Q_1 = 100$ kN, $Q_2 = 75$ kN

Figure 6: Reaction force

model can be developed with other foundation behaviours such as a multi-layered foundation of ballast.

## A Calculation of Green function

By substituting into equation (10), the first condition of the boundary condition in equation (11), we obtain can be rewritten as follows:

$$\begin{aligned}
-A_1 \cos\lambda_s L + A_2 \sin\lambda_s L + A_3 \cosh\lambda_s L - A_4 \sinh\lambda_s L = 0 \\
-A_1 \sin\lambda_s L - A_2 \cos\lambda_s L - A_3 \sinh\lambda_s L + A_4 \cosh\lambda_s L = 0 \\
-B_1 \cos(\lambda_s L) - B_2 \sin(\lambda_s L) + B_3 \cosh(\lambda_s L) + B_4 \sinh\lambda_s L = 0 \\
B_1 \sin(\lambda_s L) - B_2 \cos(\lambda_s L) + B_3 \sinh(\lambda_s L) + B_4 \cosh\lambda_s L = 0
\end{aligned} \tag{15}$$

We can also rewrite the four last conditions of equation (11) as follows:

$$\begin{aligned}
(B_1 - A_1)\cos\lambda_s a + (B_2 - A_2)\sin\lambda_s a + (B_3 - A_3)\cosh\lambda_s a + (B_4 - A_4)\sinh\lambda_s a = 0 \\
-(B_1 - A_1)\sin\lambda_s a + (B_2 - A_2)\cos\lambda_s a + (B_3 - A_3)\sinh\lambda_s a + (B_4 - A_4)\cosh\lambda_s a = 0 \\
-(B_1 - A_1)\cos\lambda_s a - (B_2 - A_2)\sin\lambda_s a + (B_3 - A_3)\cosh\lambda_s a + (B_4 - A_4)\sinh\lambda_s a = 0 \\
(B_1 - A_1)\sin\lambda_s a - (B_2 - A_2)\cos\lambda_s a + (B_3 - A_3)\sinh\lambda_s a + (B_4 - A_4)\cosh\lambda_s a = \lambda_s^{-3}
\end{aligned}$$

The aforementioned equation leads to the following result:

$$\begin{aligned}
B_1 - A_1 &= \frac{\sin\lambda_s a}{2\lambda_s^3} \quad \text{and} \quad B_2 - A_2 = -\frac{\cos\lambda_s a}{2\lambda_s^3} \\
B_3 - A_3 &= -\frac{\sinh\lambda_s a}{2\lambda_s^3} \quad \text{and} \quad B_4 - A_4 = \frac{\cosh\lambda_s a}{2\lambda_s^3}
\end{aligned} \tag{16}$$

By substituting equation (16) into equation (15), we obtain

$$
\begin{aligned}
A_1 &= \frac{1}{4\lambda_s^3}\frac{-\cosh\lambda_s L\cos\lambda_s(L-a)+\sinh\lambda_s L\sin\lambda_s(L-a)+\cosh\lambda_s a}{\cos\lambda_s L\sinh\lambda_s L+\sin\lambda_s L\cosh\lambda_s L}\\
A_2 &= \frac{1}{4\lambda_s^3}\frac{-\cosh\lambda_s L\sin\lambda_s(L-a)+\sinh\lambda_s L\cos\lambda_s(L-a)+\sinh\lambda_s a}{\cos\lambda_s L\sinh\lambda_s L-\sin\lambda_s L\cosh\lambda_s L}\\
A_3 &= \frac{1}{4\lambda_s^3}\frac{-\cos\lambda_s L\cosh\lambda_s(L-a)-\sin\lambda_s L\sinh\lambda_s(L-a)-\cos\lambda_s a}{\cos\lambda_s L\sinh\lambda_s L+\sin\lambda_s L\cosh\lambda_s L}\\
A_4 &= \frac{1}{4\lambda_s^3}\frac{\sin\lambda_s a+\sin\lambda_s L\cosh\lambda_s(L-a)-\cos\lambda_s L\sinh\lambda_s(L-a)}{\cos\lambda_s L\sinh\lambda_s L-\sin\lambda_s L\cosh\lambda_s L}\\
B_1 &= \frac{1}{4\lambda_s^3}\frac{-\cosh\lambda_s a+\sinh\lambda_s L\sin\lambda_s(L+a)-\cosh\lambda_s L\cos\lambda_s(L+a)}{\cos\lambda_s L\sinh\lambda_s L+\sin\lambda_s L\cosh\lambda_s L}\\
B_2 &= \frac{1}{4\lambda_s^3}\frac{\cosh\lambda_s L\sin\lambda_s(L+a)-\sinh\lambda_s L\cos\lambda_s(L+a)+\sinh\lambda_s a}{\cos\lambda_s L\sinh\lambda_s L-\sin\lambda_s L\cosh\lambda_s L}\\
B_3 &= \frac{1}{4\lambda_s^3}\frac{-\cos\lambda_s a-\sin\lambda_s L\sinh\lambda_s(L+a)-\cos\lambda_s L\cosh\lambda_s(L+a)}{\cos\lambda_s L\sinh\lambda_s L+\sin\lambda_s L\cosh\lambda_s L}\\
B_4 &= \frac{1}{4\lambda_s^3}\frac{-\sin\lambda_s a-\cos\lambda_s L\sinh\lambda_s(L+a)+\sin\lambda_s L\cosh\lambda_s(L+a)}{\cosh\lambda_s L\sin\lambda_s L-\sinh\lambda_s L\cos\lambda_s L}
\end{aligned}
\tag{17}
$$

## B Example in the case of series of charges

Here, we present an example with the series of charges on two rails. The distance between two wheels is $D$ = 3 (m) and the length of the wagon is $H$ = 18m. In this example, we have one imperfection at the wheel number 2 on the first rail with $\mathcal{Q}$ = 75kN and the other moving charges $\mathcal{Q}$ = 100kN.

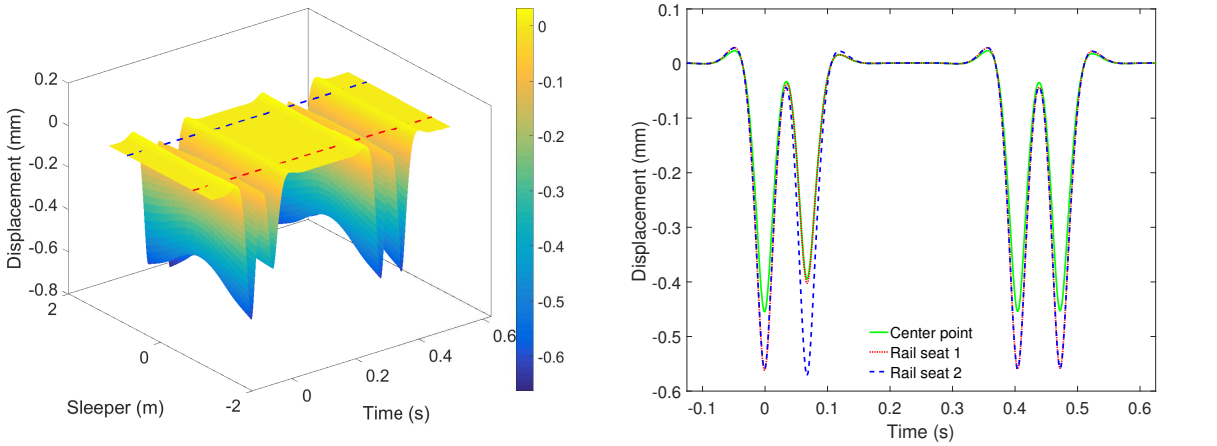


(a) Sleeper displacement (b) Sleeper displacement at middle and two rail seats

Figure 7: Sleeper displacement

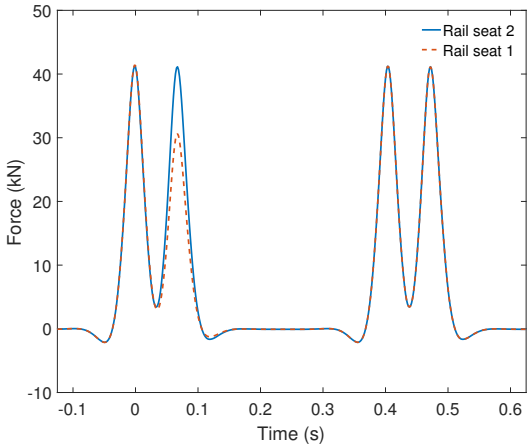


Figure 8: Reaction forces at two rail seats

## REFERENCES

[1] T. Hoang, D. Duhamel, G. Foret, H.P. Yin, P. Joyez, R. Caby, Calculation of force distribution for a periodically supported beam subjected to moving loads. *Journal of Sound and Vibration*, **388**, 327–338, 2017.

[2] S.L. Grassie, Dynamic modelling of concrete railway sleepers *Journal of Sound and Vibration*, **187**, 799–813, 1995.

[3] C. Guigou-Carter, M. Villot, B. Guillerme, C. Petit, Analytical and experimental study of sleeper SAT S 312 in slab track Sateba system *Journal of Sound and Vibration*, **293**, 878–887, 2006.

[4] S. Laryea, M. Safari-Baghsorkhi, J-F. Ferellec, G.R. McDowell, C. Chen, Comparison of performance of concrete and steel sleepers using experimental and discrete element methods *Transportation Geotechnics*, **1** 225-240, 2014.

[5] M. Esmaeili, S.A.S. Hosseini, M. Sharavi, Experimental assessment of dynamic lateral resistance of railway concrete sleeper *Soil Dynamics and Earthquake Engineering*, **82** 40–54, 2016.

[6] V.H. Nguyen, D. Duhamel, Finite element procedures for nonlinear structures in moving coordinates. Part II: Infinite beam under moving harmonic loads *Computers & Structures*, **86** 2056–2063, 2008.

[7] V.H. Nguyen, D. Duhamel, Finite element procedures for nonlinear structures in moving coordinates. Part 1: Infinite bar under moving axial loads *Computers & Structures*, **84** 1368–1380, 2006. pages = 1368–1380,

[8] D.J. Mead, Y. Yaman, The response of infinite periodic beams to point harmonic forces: A flexural wave analysis *Journal of Sound and Vibration*, **144**, 507–529, 1991.

[9] D.M. Mead, Wave propagation in continuous periodic structures : Research contributions from southamton, 1964-1995 *Journal of Sound and Vibration*, **190**, 495–524, 1996.

[10] L. Fryba *Vibration of solids and structures under moving load*. Thomas Telford, 1972.

[11] H. Ding, L-Q. Chen, S-P. Yang, Convergence of Galerkin truncation for dynamic response of finite beams on nonlinear foundations under a moving load *Journal of Sound and Vibration*, **331**, 2426–2442, 2012.

[12] X. Sheng, C.J.C Jones, M. Petyt, Ground vibration generated by a harmonic load acting on a railway track *Journal of Sound and Vibration*, **225**, 3–28, 1999.

[13] X. Sheng, C.J.C Jones, D.J. Thompson, Responses of infinite periodic structures to moving or stationary harmonic loads *Journal of Sound and Vibration*, **282**, 125–149, 2005.

[14] X. Sheng, M. Li, C.J.C Jones, D.J. Thompson, Using the Fourier-series approach to study interactions between moving wheels and a periodically supported rail *Journal of Sound and Vibration*, **303**, 873–894, 2007.

[15] D. Kostovasilis, D.J. Thompson, M.F.M. Hussein, A semi-analytical beam model for the vibration of railway tracks *Journal of Sound and Vibration*, **393**, 312–337, 2017.

[16] D.J. Thompson, Experimental analysis of wave propagation in railway track *Journal of Sound and Vibration*, **203**, 867–888, 1997.

[17] A. Matsumoto, Y. Sato, H. Ohno, M. Tomeoka, K. Matsumoto, J. Kurihara, T. Ogino, M. Tanimoto, Y. Kishimoto, Y. Sato, T. Nakai, A new measuring method of wheelrail contact forces and related considerations *Wear*, **265**, 1518–1525, 2008.

[18] R. Bogacz, K. Frischmuth, On dynamic effects of wheelrail interaction in the case of Polygonalisation *Mechanical Systems and Signal Processing*, **79**, 166–173, 2016.

[19] L. Gavrić, Computation of propagative waves in free rail using a finite element technique *Journal of Sound and Vibration*, **185**, 531–543, 1995.

[20] G. Di Mino, M. Di Liberto, C. Maggiore, S. Noto, A Dynamic Model of Ballasted Rail Track with Bituminous Sub-Ballast Layer *Procedia - Social and Behavioral Sciences*, **53** 366–378, 2012.

[21] A.A. Arab, S.S. Badie, M.T. Manzari, A methodological approach for finite element modeling of pretensioned concrete members at the release of pretensioning *Engineering Structures*, **33**, 1918–1929, 2011.

[22] A. Aikawa, Dynamic characterisation of a ballast layer subject to traffic impact loads using three-dimensional sensing stones and a special sensing sleeper *Construction and Building Materials*, **92** 23–30, 2015.

[23] S. Kaewunruen, A.M. Remennikov, Sensitivity analysis of free vibration characteristics of an in situ railway concrete sleeper to variations of rail pad parameters *Journal of Sound and Vibration*, **298**, 453–461, 2006.

[24] G. Kumaran, D. Menon, K. Krishnan Nair, Dynamic studies of railtrack sleepers in a track structure system *Journal of Sound and Vibration*, **268**, 485–501, 2003.

[25] A.S. Mohamad, Tables of Green's functions for the theory of beam vibrations with general intermediate appendages *International Journal of Solids and Structures*, **31**, 257–268, 1994.

[26] M.A. Foda, Z. Abduljabbar, A dynamic Green function formulation for the response of a beam structure to a moving mass *Journal of Sound and Vibration*, **210**, 295–306, 1998.

COMPDYN 2017
6th ECCOMAS Thematic Conference on
Computational Methods in Structural Dynamics and Earthquake Engineering
M. Papadrakakis, M. Fragiadakis (eds.)
Rhodes Island, Greece, 15–17 June 2017

# THE USE OF ARTIFICIAL NEURAL NETWORKS (ANN) FOR PRELIMINARY DESIGN OF HIGH-RISE BUILDINGS

**Aadhish Man Rajbhandari[1], Naveed Anwar[2], and Fawad Najam[3]**

[1] Asian Institute of Technology (AIT)
Bangkok, Thailand
e-mail: aaadhish@gmail.com

[2] Asian Institute of Technology (AIT)
Bangkok, Thailand
e-mail: nanwar@ait.ac.th

[3] Asian Institute of Technology (AIT)
Bangkok, Thailand
e-mail: fawad.ahmed.najam@ait.ac.th

K**eywords:** ANN, preliminary design, MLP-BP, ELM, OS-ELM, high-rise buildings

**Abstract.** *The need for high-rise buildings is increasing in order to meet the challenges posed by rapid urbanization and the exponential growth in population. With recent advancements in computing technologies, innovative materials and new structural systems, the need of prior knowledge about proportioning the geometry and configuration of structural members is also increasing. A relatively quicker and reliable estimation of approximate sizes of members can greatly facilitate the preliminary design and feasibility of the project. This study uses an Artificial Neural Network (ANN) based approach to directly determine some key design parameters based on experience gained from previously designed buildings. It uses a heuristic tool using ANN that can provide fast and reliable results based on two algorithms (i.e. Multi-layer Perceptron with Back Propagation using Levenberg-Marquardt algorithm MLP-BP, and PCA-Sparse-Extreme Learning Machine with online Sequential learning). The ANN models are trained to determine structural design indicators from architectural parameters. The proposed approach can not only provide means for quick estimation of design output, but can also for crosschecking of code based & performance based design very quickly. The objective is to provide means of assisting the design team and clients to make key design decisions based on cumulative experience rather than relying on judgment of individual designers. The approach is demonstrated through the sample networks trained on various case study high-rise buildings for which the required architectural and structural design results have been generated through detailed design.*

## 1. INTRODUCTION

A rapid increase in urbanization, limited land for increasing population and the developments in field of construction technology are some of the factors resulting in improved popularity of tall buildings. The convenience of having all of the services in a single building is now becoming a reality with tall buildings even known as mixed-use buildings; some of these buildings may also bring the prospect of being able to live and work without leaving the building [1]. The construction of taller structures becomes more challenging with increasing height [2]. Serviceability, strength and sustainability of a tall building are most important parameters to be considered during building construction which can be obtained by detailed Analysis and design processes. These processes are divided into many phases such as the conceptual designing, preliminary designing, modelling, analysis, final design and detail designing.

The preliminary design of tall buildings involves detailed mathematical justifications and expert knowledge. It is a tedious and time consuming work. Hence to overcome such issues, and to utilize experience obtained from available data, we introduce heuristic tools of Machine Learning. Machine learning is solely focused on developing an algorithm that can learn from past experiences. Artificial Neural Network (ANN), Support Vector Machines (SVM), Genetic algorithm, Decision tree, Fuzzy Logic are few popular Machine learning techniques used for the regression and classification problems. Artificial Neural Network (ANN) is a type of Machine learning tool which consists of massive parallel computational model that imitates the function of a brain. It uses learning algorithm to model and save the knowledge in weighted connections [3]. ANN have been used in many structural engineering related works in past such as Structure Control using Neural Network [4], Predicting drying shrinkage of concrete using Neural Network [5], Neural Network approach for cost estimation of structural systems of building [6]. Trained network can be used to simulate structural data as output for set of new architectural data.

In this study, we use ANN to perform preliminary design of tall buildings by obtaining structural data of buildings as output while feeding in the architectural data as input. The algorithms used are Multi-Layer Perceptron with Back propagation which is the most commonly used procedure and Online Sequential Extreme Learning Machine which is one of the fastest and accurate algorithm. Among various computational tools, Neural Networks have gained lot of popularity due to their ability to identify and learn highly complex and non-linear relationships by employing a black box approach [7]. After years of works and research in ANN, MLP Neural network with back propagation as training algorithm have been the most used and successful computational tool. It consists of number of hidden layers with various number of neurons that traces non-linear relationship between input and output data. Gradient decent is considered to be the most popular back propagation learning method but second order method such as Levenberg-Marquardt algorithm prove to be more accurate. The general concept of Back Propagation in training of network is to find a value of weights to minimize the error between obtained output and target output. ELM are simple learning algorithm for single layer Feed Forward Networks whose learning speed can be thousands of times faster than traditional algorithms such as MLP-ANN, SVM etc. with comparable prediction capability [8]. The basic concept of an ELM is to generate a fixed set of random input weight matrix and compute the best output weight matrix such that the error between target and obtained output is zero. The number of neurons in hidden layer of ELM plays vital role in its performance.

Principal Component Analysis (PCA) are linear dimensionality reduction tools used to shrink multi-dimensional correlated data set into smaller dimensional set of uncorrelated variables. PCA is used for dimensional reduction of data set as well as determining the number of neuron in hidden layer as proposed in [9]. The computed hidden layer architecture is cross validated using concept of Sparse-ELM as proposed in [10]. The network is then regularized using regularization tools and further extended to online sequential learning.

## 2. METHODOLOGY

Figure 1 below shows the overall methodology adopted in this study. Each part of this methodology will be discussed separately.

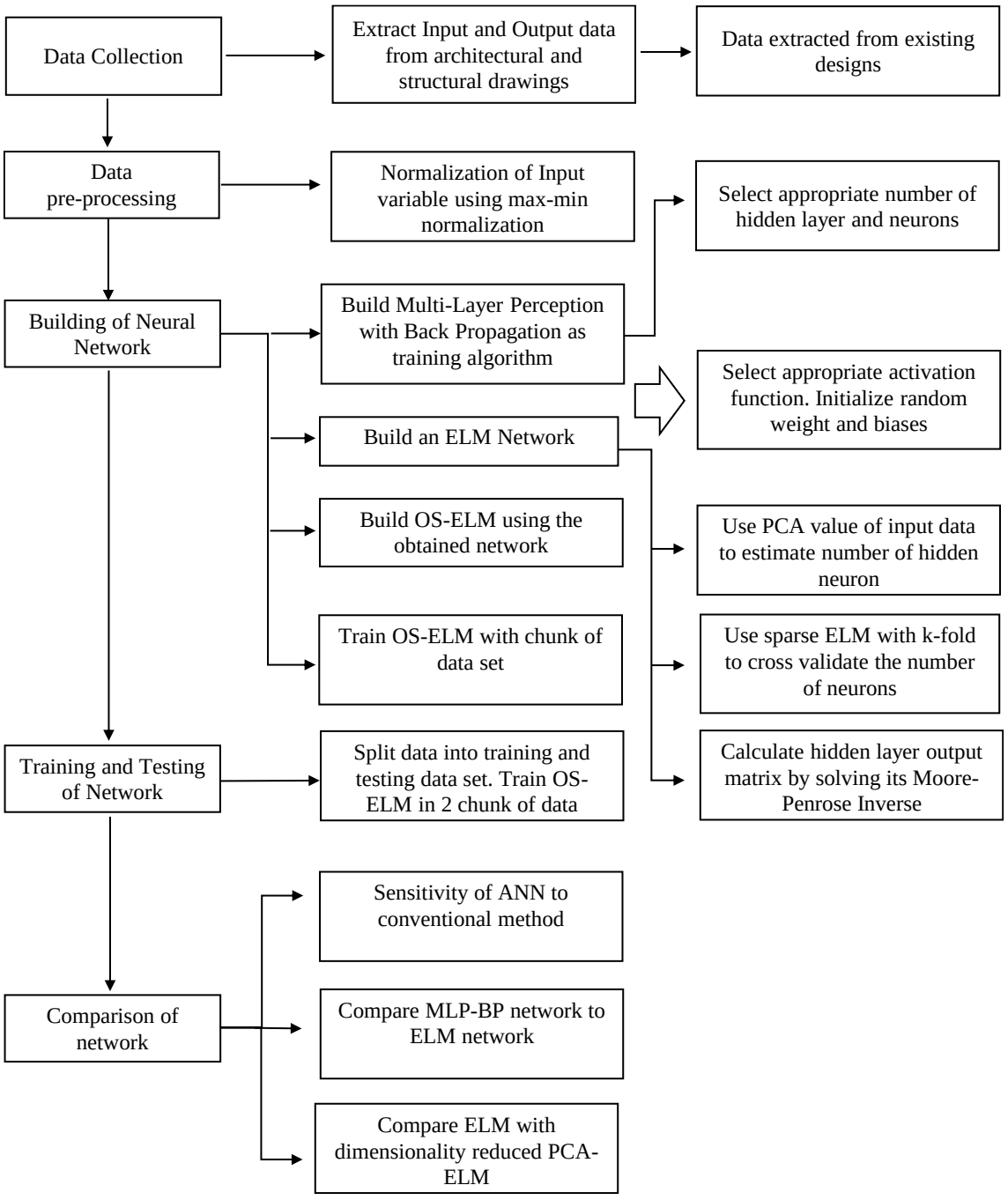


Figure 1: The overall methodology

## 2.1 Input-output parameters selection

Set of architectural data and structural data were used as input and output data respectively. 14 input parameters such as Number of story, Height of building, cumulative floor area of tower, Floor area of tower, Length of building in X and Y direction, Height per Length in X and Y directions, ratio of length of building in X directions to total length, Height to Length ratio in X and Y directions were provided from the architectural data. Fundamental structural data such as Natural period, Ratio of area of column to total area of tower, Ratio of core Area to Area of tower, Ratio of Weight of building to Floor Area Ratio and Volume of tower, Shear wall thickness, Maximum percentage story drift ratio and Ratio of maximum base shear to total weight of building were taken as output parameters. The data were normalized in range of [0 to 1] using max min normalization. Convergence of network output is usually faster if the average of each training set of data is close to zero [11]. The final output obtained from the models were DE normalized back to the initial scale.

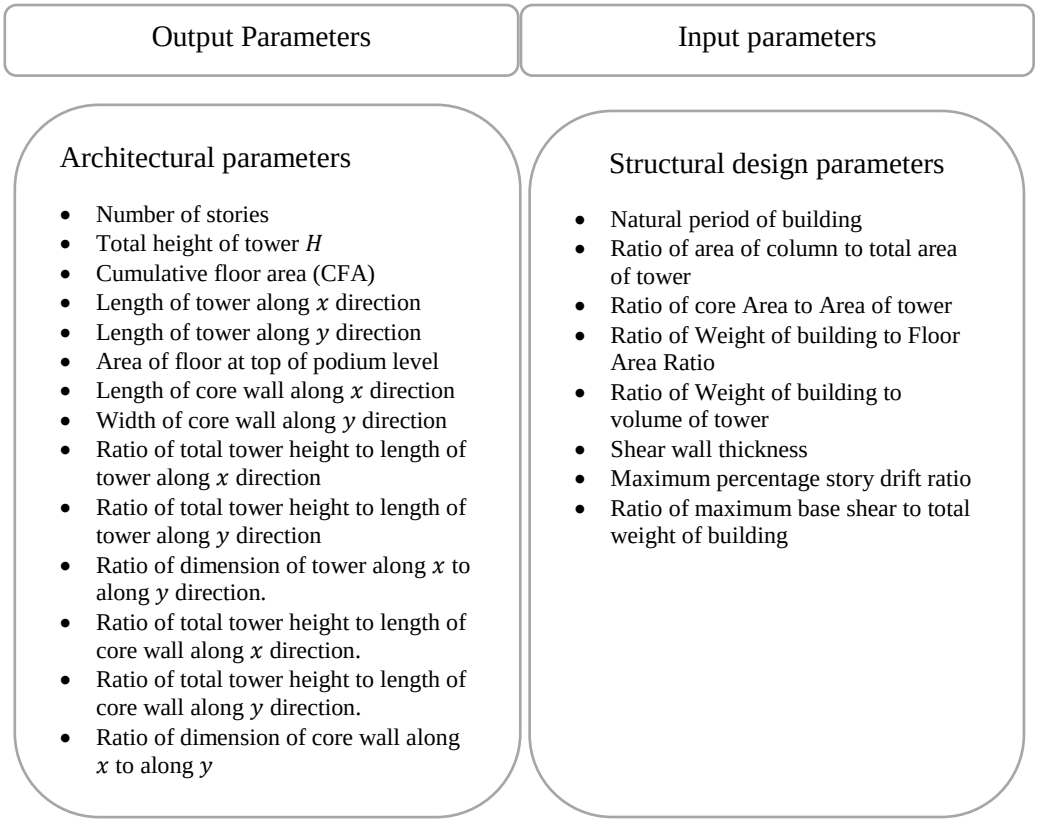


Figure 2: Input and Output parameters Extracted from Architectural drawings and Structural drawings respectively

## 2.2 Data processing

The total input-output data set of 38 buildings were divided into 30 training data and 8 testing data sets. 14 input parameters were taken as input from the architectural data and 8 output parameters were taken as output from the structural data. Same data sets were trained and tested using both the MLP-BP and OS-ELM models respectively and compared in terms of speed and accuracy. In MLP-BP algorithm, all input parameters were used to predict each output parameter individually. Each model was designed with different architecture, i.e. the number of hidden layers and their neurons for prediction of different set of outputs. There is no direct

difference in the ultimate separation capabilities of networks with various number of layers; they might, however, differ in other aspects like the separation performance with a limited number of neurons, or the generalization made or training speed [12]. The OS-ELM model were first tested for general ELM algorithm and then Online Sequential (OS) process was added later onto the model. The OS refers to sequential learning procedure where the network is trained using chunk by chunk of data [13]. 14 input parameters were used to map single outputs and multiple set of outputs. Several important parameters that control the network model include the max-min data normalization, nonlinear transfer function (Sigmoid), bias and weights, hidden layers and their neurons, learning rate, and the number of epochs in MLP and Moore Penrose inverse in ELM.

In MLP-BP network, the weight parameters and biases between all the layers were randomly generated. The output of previous layer acts as input for next layer. The weights, bias and input were calculated and passed through the activation function. The output of last layer was compared to the target output and error was calculated. The error was back propagated using second order Levenberg-Marquardt algorithm and weights were updated at each epoch. The weights were updated with a learning rate which improves the convergence capacity of the model [14]. The architecture of network depends upon nature of data set, learning parameter, number of iterations, transfer function and the characteristics of the data used [15]. Different networks with various architecture were tried and the best performing networks were selected. Stopping criteria was introduced to stop the training process once the error tend to zero. The final updated weights were saved for the training purpose. Although the MLP-BP shows good generalization, it has few drawbacks such as the local minima, overfitting of data, difficulties in defining the structure, and repetitive iteration or Epoch. The overfitting of model cause network to lose its generalization ability [16].

In OS-ELM network, the single hidden layer (with neurons equal to or less than the number of sample) is initialized and the input weights and bias are generated in random [17]. The ELM uses non-differentiable or even discontinuous functions as an activation functions. For example, the Sigmoid, hyperbolic tan, and Gaussian functions can be used to map the non-linear relations [18]. The output weights are calculated using Least Mean Square Error equation such that the error between target and obtained output is zero. Basically, the ELM trains a Single Layer Feed Forward in two main stages: (1) random feature mapping and (2) linear parameter solving [19]. The output weights were saved and used for testing of data. The ELM shows extremely fast training speed, good generalization, and universal approximation capability [20]. The data was reduced to 2 dimensional set from 14 using PCA.

The network architecture of ELM was specified using PCA method in which 98% of variance was taken into consideration. The obtained number of hidden neuron were cross validated using the concept of Sparse-ELM. The input data were divided into cross validation data set using the k-fold, where the input data were divided into equal number of data sets. The networks with specific hidden node were trained using three-fourth of data set and tested on remaining one-fourth. The best network architecture was selected based on its mean accuracy. The OS ELM was introduced on selected networks. In OS-ELM, the network is added using chunk by chunk of data. The weights connecting hidden layer to output weight is updated with addition of each chunk of data. The weight between input layer to hidden layer and its bias are again randomly generated and lumped below the existing weight matrix array for initial data

set. The process is carried out in two stages, (a) the initialization phase where the initial set of data is trained, and (b) the sequential learning phase where the network is updated for additional chunk of data.

The simulated output values of network were reported and compared with the actual values obtained from the results of detailed analysis and structural design. The model with least error was saved in each case. The accuracy of developed networks was evaluated with a view to use them in future as a helpful tool to perform the preliminary design of tall buildings.

### 2.3 Computer Software

The Python based IDE called PyCharm was used for modelling of both MLP and ELM. Software selection was based on ability of the software to perform the computation required, its availability and most importantly the platform it provides to develop a user interface package. Neural Network requires solving of various mathematical calculations which can be performed using tool such as 'numpy' in Python. It is one of the most used programing languages for solving various classification, regression, pattern recognition, curve fitting problems as it contains one of the best toolboxes for construction of a Neural network.

### 2.4 Improvement of generalization capability of network

The performance of networks with different architecture was checked. The performance of networks were evaluated in terms of mean square error between actual output and target of data set. Errors may be calculated using other measure such as the sum square error, the root of mean square error, correlation coefficient between actual and simulated value. The least value of mean square error for train and test set shows the actual performance of the network. The data were divided into training and testing set. Generally network works well with training data set but its prediction capability to the test data may be poor due to overfitting. Hence, early stopping criteria comes in handy to overcome overfitting problems [21]. Random weight generation can affect the generalization capability of network as well [8]. Nguyen & Widrow method was introduced such that the random initialized weights were controlled and it improved the generalization of the network. The selection of learning rate affects the network hence, momentum can be added to improve the prediction ability of the network [11]. Bias and its weight added to the network aligns the irregularities in the transfer function. All these functions were added to the network as to improve its performance.

### 2.5 Implementation of network

The Neural network developed in this research work can be used by structural engineers to perform preliminary design of buildings in a non-conventional fashion. They can feed in set of input and output data, train the network and then use it to predict output for further unknown input data set. The input parameters can be taken from the architectural data of the building to predict the structural design of the building. The designer can select data set from either performance based design or code based design to predict building design of new buildings. This research moreover helps in evaluation of the appropriate network out of the two algorithms used i.e. MLP-BP and OSELM.

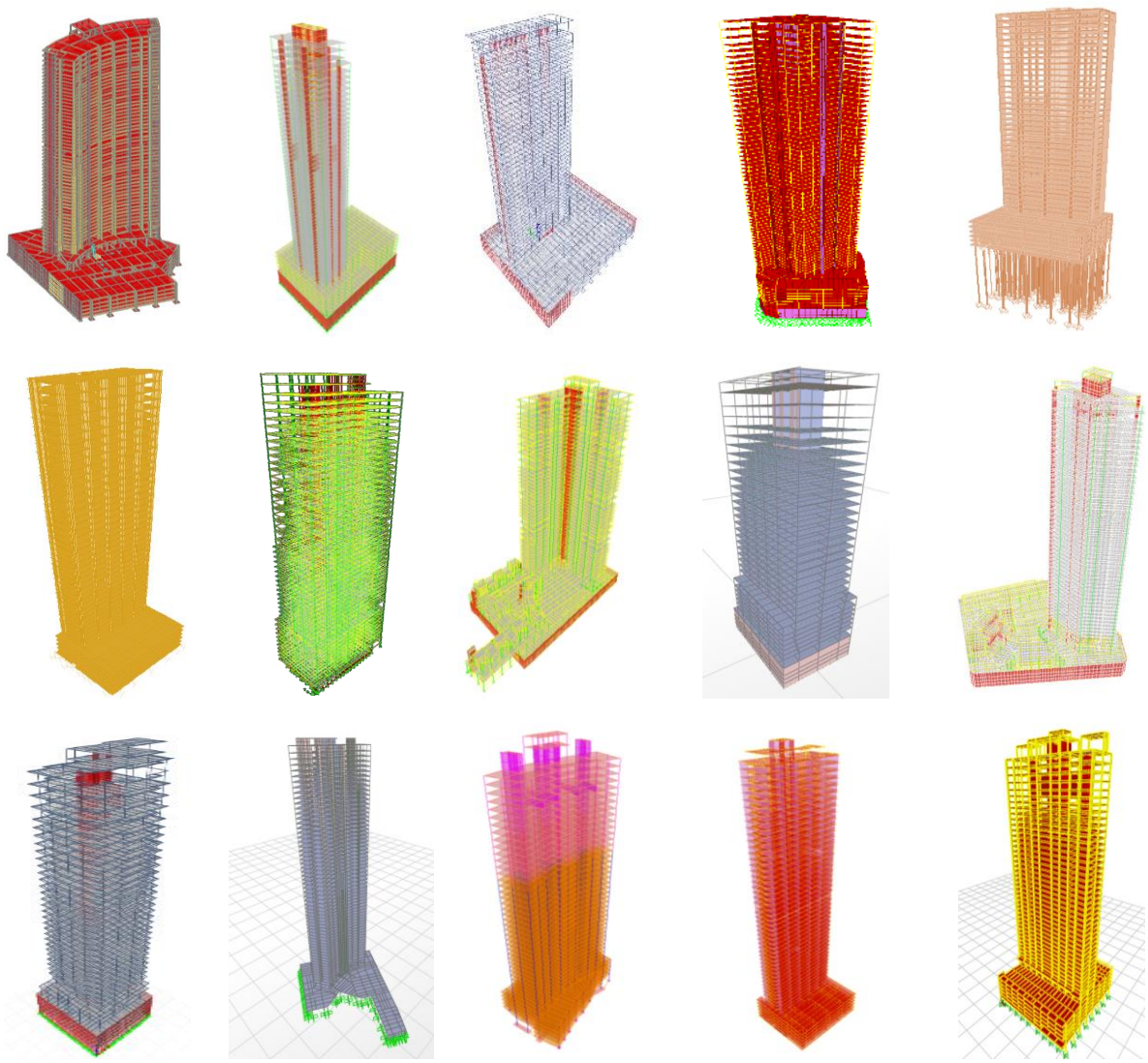

Figure 3: Full 3D nonlinear models of some of the tall buildings used in this study

## 3. ANALYSIS, RESULTS AND DISCUSSION

*Model I: Model for prediction of natural period of building (sec) using MLP-BP*

The architecture of network was changed and the network with least MSE was selected as best network. The network was selected for minimum MSE between computed output and actual output of natural period of the building. For Model I, The architecture was selected in 14:20:1 ratio as it showed least MSE in training. The network was used to test the test data set. Its performance for test data set is as per Figure 4.

*Model II: Model assessment for prediction of natural period of building (sec) using ELM*

The model trained can be used to predict the natural period of building response using 14 architectural parameters. The model was trained using fix set of input weights generated using Nguyen method. The network architecture consisted of 2 neurons in hidden layer. The network showed fast training speed with good generalization capability comparable to MLP-BP network. The network was tested for the training set and its prediction capability is shown in Figure 4.

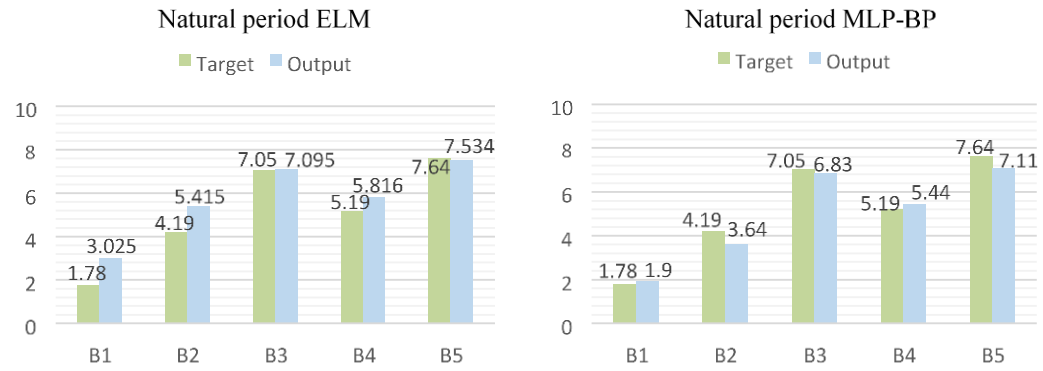


Figure 4: Comparison of natural period of test buildings with simulated natural periods from artificial neural network using ELM and MLP-BP.

*Model III: Model assessment for ratio of weight per unit floor area of tower (KN/m$^2$) using MLP-BP*

ANN model III was trained to predict weight of building per unit floor area of tower. The data set were taken from code based design of buildings. The network architecture was changed and network with least MSE between obtained output and target output was selected as the best network. For Network model II, network architecture of (14:15:1) showed higher correlation to training and testing set. The prediction ability of network is shown in Figure 5.

*Model IV: Models assessment for ratio of weight of building per unit area of tower (KN/m$^2$) Using ELM*

ELM was used to train a network that predicts ratio of weight of building per unit area of tower using architectural data set. The input output parameters were passed through the network and best fit output weight is generated. Hidden layer with 2 neurons showed the best prediction performance. The weights were saved and used for testing. The training speed of network was really fast with good generalization capability. The prediction capability on testing data set is shown in Figure 5.

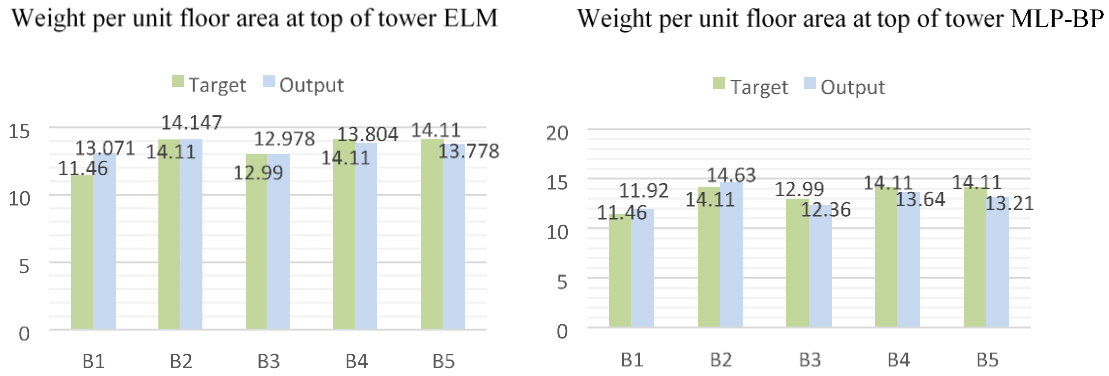


Figure 5: Comparison of weight per unit area of tower of test buildings with simulated weight per unit area of tower from artificial neural network using ELM and MLP-BP.

*Model V: Models assessment for ratio of weight of building per unit volume of tower (KN/m$^3$) Using MLP-BP*

The minimum mean square error for training set was found with an architecture of ratio 14:10:5:1. The network contained two hidden layers with 10 and 5 neurons. The model can be

used for calculation of ratio of weight of building per unit volume from architectural data set. The performance of the selected network to test data set is shown in Figure 6.

*Model VI: Models assessment for ratio of weight of building per unit volume of tower (KN/m$^3$) using ELM*

The best fit output for training and testing set was found with an architecture of ratio 14:12:1. The network contained hidden layer with 9 neurons. The model can be used for calculation of ratio of weight of building per unit volume from architectural data set. The performance of the selected network to test data set is shown in Figure 6.

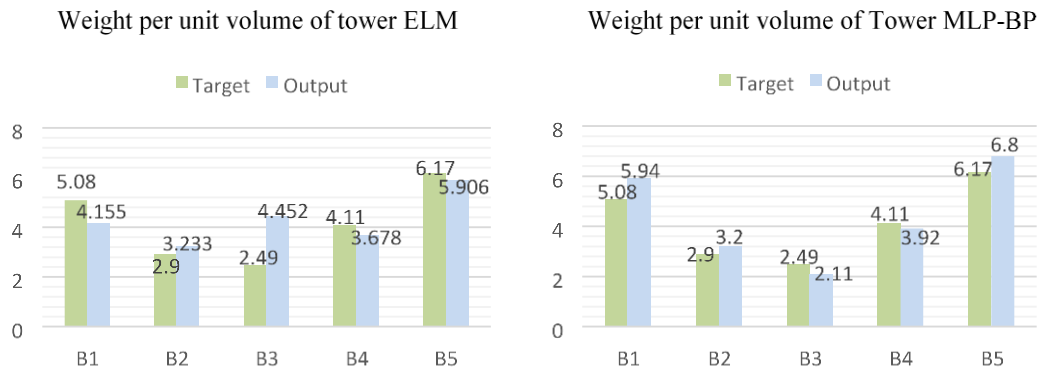


Figure 6: Comparison of weight per unit volume of test buildings with simulated weight per unit volume from artificial neural network using ELM and MLP-BP

*Model VII: Models assessment for maximum story drift ratio using MLP-BP*

Network model VII is used to predict maximum story drift of the building from given set of architectural data. The network with architecture 14:10:1 was selected as best network due to its low mean square error for the training set. The network was used to test the testing set of data and its ability is shown in Figure 7.

*Model VIII: Models assessment for maximum story drift ratio using ELM*

This network model is used to predict maximum story drift of the building from given set of architectural data. The network with architecture 14:9:1 was selected as it showed best fit on training and testing data. The network was used to test the testing set of data and its ability is shown in Figure 7. The training time of network was 0.14 sec and testing time was 0.034 sec.

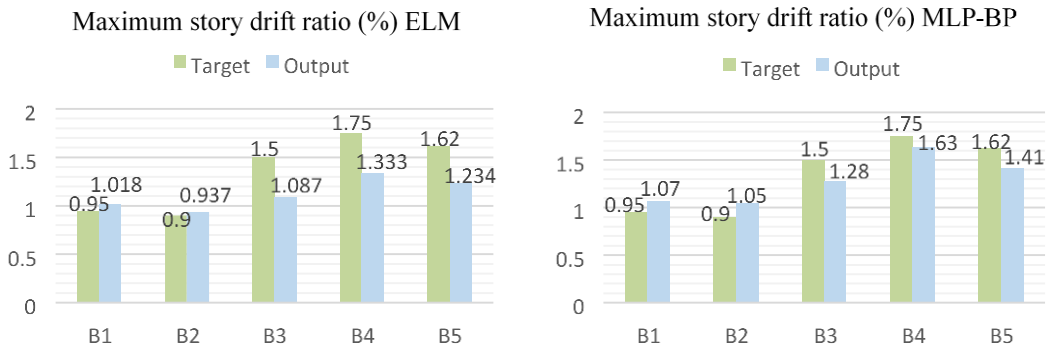


Figure 7: Comparison of Maximum story drift of test buildings with simulated Maximum story drift from artificial neural network using ELM and MLP-BP

*Model IX: Model assessment for prediction of 2 output i.e. natural period of building (s) and Maximum story drift using ELM*

Two output data were tested using same set of architectural data set. The network showed good generalization capability with two output as well. The Training speed was as fast as 0.084 sec and testing time was 0.015 sec with good accuracy. The network was trained using set of 14 input parameters and 2 output parameters with hidden layer consisting 2 neurons. Its performance is shown in Figure 8.




Figure 8: Comparison between Actual output and simulated output of two output data predicted at once from architectural data using ELM.

*Model X: Model assessment for prediction of 3 output i.e. natural period of building (s), ratio of weight of building per unit volume of tower (KN/m$^3$) and Maximum story drift*

The network was trained to predict 3 output at once using the architectural data. The training speed was 0.099 sec and testing time was 0.031 sec. The performance of the network on testing data is shown in Figure 9.

*Model XI: Model assessment for estimation of best network*

The network model were selected on basis of its accuracy using k-fold ELM. In this model, we display the accuracy to predict natural period of 5 building using architectural data of model with different number of neurons. The number of neurons is obtained using PCA and numbers near that value is tested for better options.

*Model XII: Model assessment on network with reduced dimensionality on input data set using PCA*

The network model were selected on basis of its accuracy using k-fold ELM. In this model, we display the accuracy to predict natural period of 5 building using architectural data of model with different number of neurons. The number of neurons is obtained using PCA and numbers near that value is tested for better options. The dimension of input data is reduced using PCA. For 98% variance, the PCA value was 2 on our input set. Hence the data with 14 parameters were reduced to 2 parameters. The accuracy of each network model is presented in Figure 11. Figure 12 shows that ELM performs better than PCA-ELM, i.e. higher dimensional data set shows better prediction capability compared to smaller dimension. But PCA-ELM have almost comparable accuracy compared to normal ELM. With increasing data set, dimensionality reduction helps in larger data handling with robustness in prediction ability.

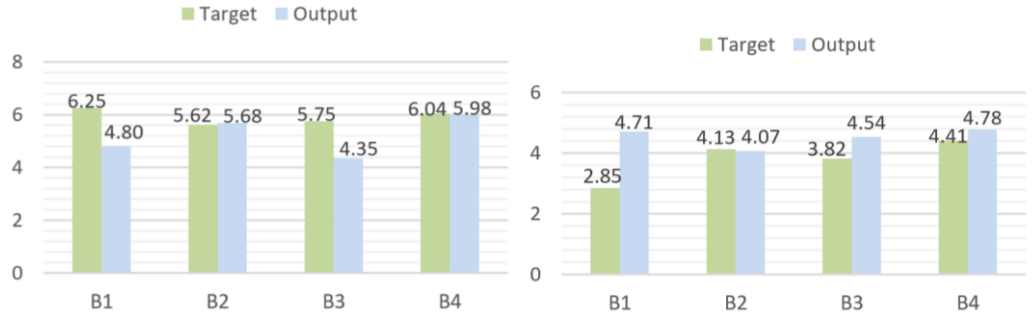


(a) Natural period (b) Weight of building per unit volume of tower

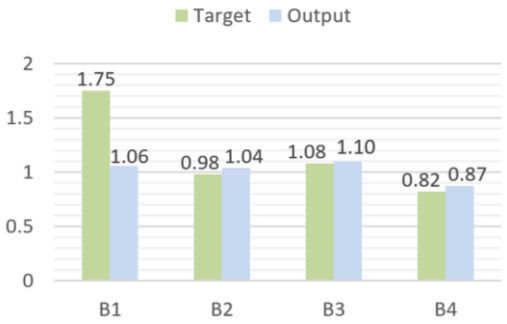


(c) Maximum story drift

Figure 9: Comparison between actual output and simulated output of three output data predicted at once from architectural data using ELM.

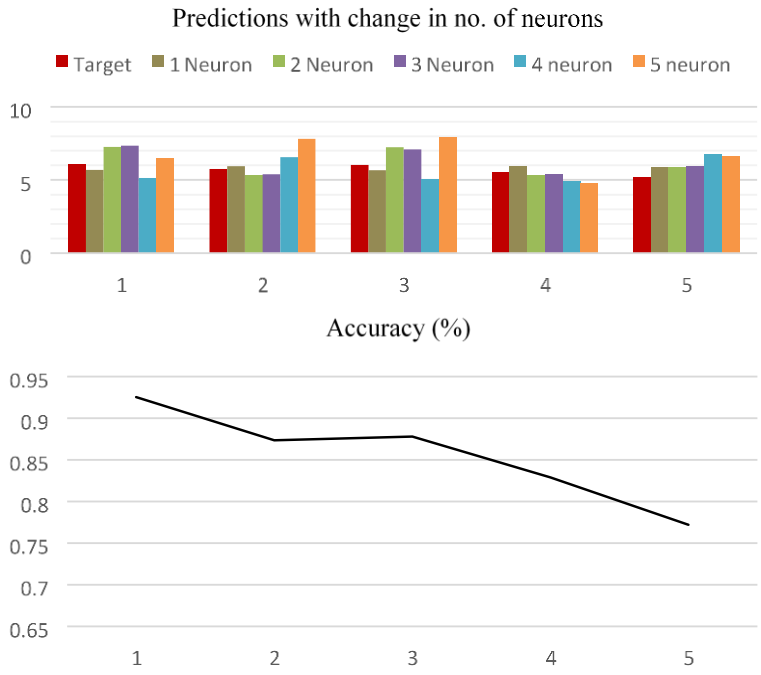


Figure 10: Prediction capability of network with different number of hidden layer neurons on natural period of building using architectural data.

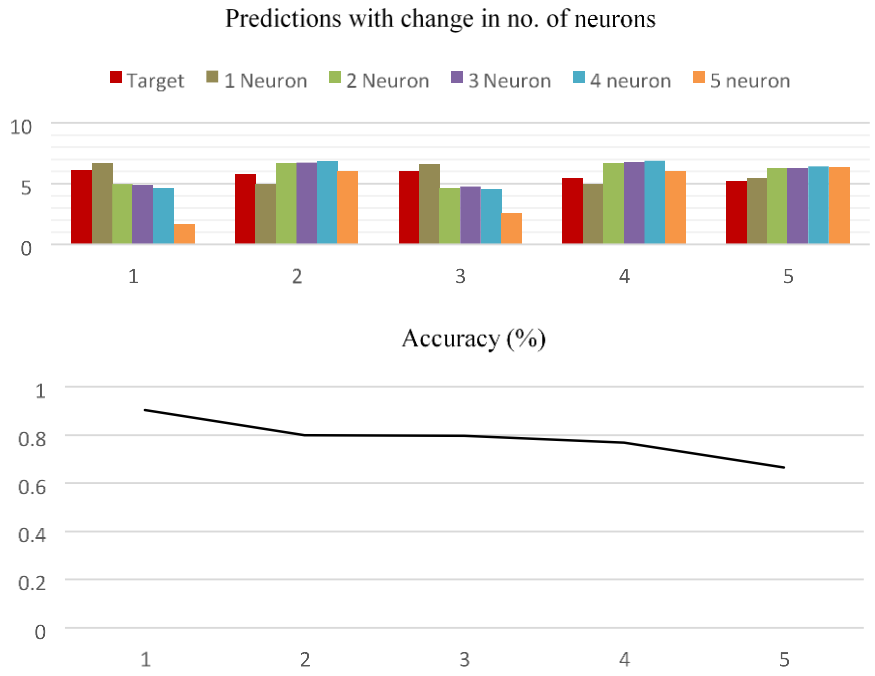


Figure 11: Prediction capability of network with different number of hidden layer neurons on natural period of building using dimensional reduced architectural data.

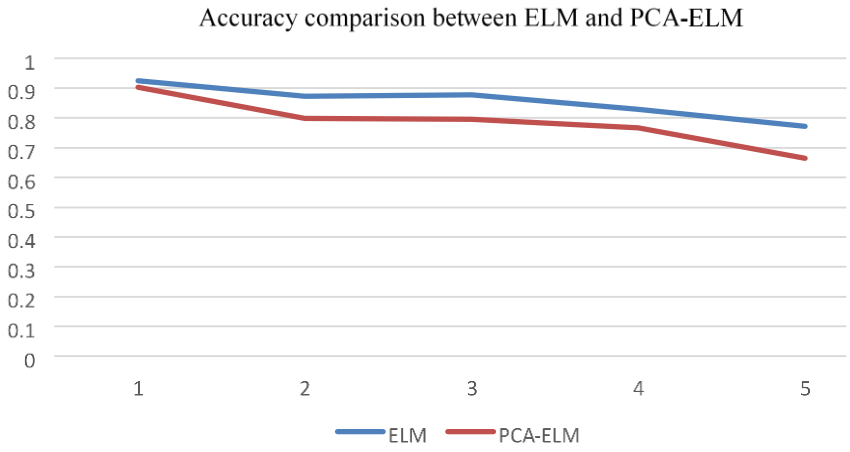


Figure 12: comparison of accuracy of ELM and PCA-ELM in prediction of natural period of building using architectural data.

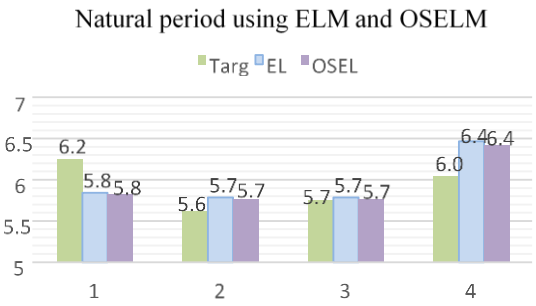


Figure 13: Comparison between target natural period and simulated natural period using ELM and OSELM network

*Model XIII: Model assessment for prediction of target natural period of test building to simulated natural period using ELM and OSELM*

Natural period was computed using extreme learning machine where set of 20 data were trained. The network was tested for 4 building. Online sequential algorithm was implemented and 2 data set were trained again. Then the network was tested for same set of test data. The result is shown in Figure 13. The network architecture used was hidden layer with 2 neurons. The OSELM network i.e. network with additional training data added shows slightly better predicting capability.

## 4. CONCLUSION

- Various key structural parameters can be determined from architectural data using the ANN approach. The selected models can be used in preliminary design of tall buildings. Well-trained ANNs can reliably predict the key structural parameters from architectural drawings. These networks map the nonlinear relationship between input and output.
- The MLP with Back Propagation as learning algorithm have good generalization capability but requires large training time. For new building set, the Pearson correlation coefficient was found to be over 80% for MLP-BP.
- The ELM algorithm shows fast training speed with comparable generalization capability. The training and testing time of network was less than a second for each model. Online sequential learning in ELM helps the model to be used in online platform where additional training data can be used to fine tune the network.
- The accuracy obtained using ELM is up to 93% for the best fit network. The network is selected using PCA value and cross validation concept of Sparse-ELM.
- The dimensionality reduction of input data using PCA shows comparable generalization capability and its concept can be brought in use when the parameter and sample of data increases.
- The performance of networks can be improved by adding more data and using regularization functions or bootstrapping. The network performance of MLP-BP can be improved by using optimization tools such as genetic algorithm.
- Wind design parameters can be added for higher accuracy and wider applicability in future studies.

## REFERENCES

[1] H. Herath, P. Mendis, T. Ngo, N. Haritos, Seismic performance of super tall buildings, *International Conference on Sustainable Built Environment (ICSBE)*, Kandy, 160-168, 2010.

[2] L. Halder, S. C. Dutta, Wind effects on multi-storied buildings: a critical review of Indian codal provisions with special reference to American standard, *Asian Journal of Civil Engineering*, 2010.

[3] M. Zare, H. R. Pourghasemi, M. Vafakhah, and B. Pradhan, Landslide susceptibility mapping at Vaz Watershed (Iran) using an artificial neural network model: a comparison between multilayer perceptron (MLP) and radial basic function (RBF) algorithms, *Arabian Journal of Geosciences*, 6(8), 2876-2888, 2013.

[4] H. M. Chen, K. H. Tsai, G. Z. Qi, J. C. S. Yang, and F. Amini, Neural network for structure control, *Journal of computing in civil Engineering*, 9(2), 168-176, 1995.

[5] L. Bal, and B. François, Artificial neural network for predicting drying shrinkage of concrete. *Construction and Building Materials*, 38, 248-254, 2013.

[6] H. M. Günaydın and S. Z. Doğan, A neural network approach for early cost estimation of structural systems of buildings, *International Journal of Project Management*, 22(7), pp.595-602, 2004.

[7] A. Alexandridis, Evolving RBF neural networks for adaptive soft-sensor design, *International Journal of Neural Systems*, 23(06), 2013.
[8] L. D. Tavares, R. R. Saldanha, & D. A. Vieira, Extreme learning machine with initialized hidden weight, *12th IEEE International Conference on Industrial Informatics* (pp. 43-47). IEEE, 2014.
[9] A. Castaño, F. Fernández-Navarro, and C. Hervás-Martínez, PCA-ELM: a robust and pruned extreme learning machine approach based on principal component analysis, *Neural processing letters*, 37(3), pp.377-392, 2013.
[10] S. Suresh, S. Saraswathi and N. Sundararajan, Performance enhancement of extreme learning machine for multi-category sparse data classification problems, *Engineering Applications of Artificial Intelligence*, 23(7), 2010.
[11] J. Tompson, R. Goroshin, A. Jain, Y. LeCun, Y. and C. Bregler, Efficient object localization using convolutional networks. In Proceedings of the *IEEE Conference on Computer Vision and Pattern Recognition* (pp. 648-656), 2015.
[12] G. B. Huang, Q. Y. Zhu, and C. K. Siew, Extreme learning machine: a new learning scheme of feedforward neural networks. *IEEE International Joint Conference on Neural Networks* (Vol. 2, pp. 985-990), 2004.
[13] Y. Jun, and M. J. Er, An enhanced online sequential extreme learning machine algorithm. In *Control and Decision Conference*, 2008. CCDC 2008. Chinese (pp. 2902-2907). IEEE.
[14] J. De Villiers, and E. Barnard, Backpropagation neural nets with one and two hidden layers. *IEEE Transactions on Neural Networks*, 4(1), pp.136-141, 1993.
[15] T. Kavzoglu, Determining optimum structure for artificial neural networks. In Proceedings of the *25th Annual Technical Conference and Exhibition of the Remote Sensing Society* (pp. 675-682). Nottingham, UK: Remote Sensing Society, 1999.
[16] N. Rotich, *Forecasting of wind speeds and directions with artificial neural network*, Masters Thesis, Lappeenranta University of Technology, 2014.
[17] G. B. Huang, Q. Y. Zhu and C. K. Siew, Extreme learning machine: theory and applications. *Neurocomputing*, 70(1), pp.489-501, 2006.
[18] S. Suresh, S. Saraswathi and N. Sundararajan, Performance enhancement of extreme learning machine for multi-category sparse data classification problems. *Engineering Applications of Artificial Intelligence*, 23(7), pp.1149-1157, 2010.
[19] G. Huang, G. B. Huang, S. Song, and K. You, Trends in extreme learning machines: A review. *Neural Networks*, 61, pp.32-48, 2015.
[20] J. Tang, C. Deng, and G. B. Huang, Extreme learning machine for multilayer perceptron. *IEEE transactions on neural networks and learning systems*, 27(4), pp.809-821, 2016.
[21] G. A. Calin, C. D. Dumitru, M. Shimizu, R. Bichi, S. Zupo, E. Noch, H. Aldler, S. Rattan, M. Keating, K. Rai and L. Rassenti, Frequent deletions and down-regulation of micro-RNA genes miR15 and miR16 at 13q14 in chronic lymphocytic leukemia. *Proceedings of the National Academy of Sciences*, 99(24), pp.15524-15529, 2002.

COMPDYN 2017
6th ECCOMAS Thematic Conference on
Computational Methods in Structural Dynamics and Earthquake Engineering
M. Papadrakakis, M. Fragiadakis (eds.)
Rhodes Island, Greece, 15–17 June 2017

# OPTIMAL FRICTION COEFFICIENTS FOR ISOLATED STRUCTURES DEPENDING ON THE SOIL CONDITION

**P. Castaldo**[1] **and M. Ripani**[2]

[1]Department of Structural, Geotechnical and Building Engineering (DISEG), Politecnico di Torino,
Corso Duca degli Abruzzi, 24, Turin, Italy (corresponding author);
e-mail: paolo.castaldo@polito.it; pcastaldo@unisa.it

[2]CONICET-National Scientific and Technical Research Council, Materials and Structures Laboratory,
University of Buenos Aires, Argentina;
e-mail: mripani@fi.uba.ar

**Keywords:** seismic isolation; friction pendulum isolators; performance-based engineering; non-dimensional form; optimal isolator properties; power spectral density method; soil condition.

**Abstract.** *This study aims at evaluating the optimal properties of friction pendulum bearings to be employed for the seismic protection of elastic isolated structural systems under earthquake excitations with different characteristics in terms of frequency content. A two-degree-of-freedom model is considered to describe the isolated system behavior while accounting for the superstructure flexibility and a non-dimensional formulation of the governing equations of motion is employed to relate the characteristic parameters describing the isolator and structure properties to the response parameters of interest for the performance assessment. Seismic excitations are modelled as time-modulated filtered Gaussian white noise random processes of different intensity within the power spectral density method. The filter parameters control the frequency content of the random excitations and are calibrated to describe stiff, medium and soft soil conditions, respectively. Finally, multi-variate regression expressions are obtained for the optimum values of the friction coefficient that minimize the superstructure displacements relative to the base mass as a function of the structural system properties, of the seismic input intensity and of the soil condition.*

## 1 INTRODUCTION

Over the years, within the issue of the passive control of structures, many works have developed new design strategies and methodologies [1]-[4]. Isolation systems have emerged as a very effective technique for seismic protection of building frames [5]. Friction pendulum system (FPS) bearings are often preferred to other types of bearings due to their capability of providing an isolation period independent of the mass of the supported structure, their high dissipation and recentering capacity, and their longevity and durability characteristics [6]-[7]. Many experimental and numerical studies have been carried out to investigate the behavior of these devices and to define reliable models for describing it [8]-[13]. Other studies have focused on the seismic response of structures isolated with FPS bearings by accounting for the variability of the seismic input characteristics [14]-[16]. In [17] the influence of friction pendulum system (FPS) isolator properties on the seismic performance of base-isolated building frames was investigated by employing a two-degree-of-freedom model accounting for the superstructure flexibility with a velocity-dependent model for the FPS isolator behaviour. The variation of the statistics of the response parameters relevant to the seismic performance has been investigated through the nondimensionalization of the motion equation considering different isolator and system properties.

Other works (e.g. [18]-[25]) have been more oriented to develop design approaches for the isolators and to identify the optimal isolator properties. In this context, Castaldo et al. [18]-[19] proposed a seismic reliability-based design (SRBD) criterion to define the isolator dimensions in plan based on the evaluation of performance curves for the isolator and the superstructure. Bucher [25] proposed a reliability-based design approach for the bearings accounting for the probabilistic performance properties in terms of maximum and residual isolator displacements, and the maximum interstorey structural displacement. Jangid [21]-[22], considering a stochastic model of the earthquake ground motion, evaluated the seismic performance of a single shear type building isolated by FPS bearings whose behavior was described by a Coulomb model showing that there exists an optimal value of the friction coefficient for which the top floor absolute acceleration of the building is minimized. This value is influenced by the building properties and the isolation period, and it increases with the increase of the earthquake intensity. The minimization of the absolute accelerations of the isolated superstructure was employed as optimization criterion also in other works [23]-[24]. In [26], considering a ten-story shear type building as case study, a multi-objective optimization for the optimal design of sliding isolation systems for suppression of seismic responses of building structures is presented applying a genetic algorithm to minimize the building's top story displacement, its acceleration and also the base raft's displacement.

As for the effect of the frequency characteristics and its influence on the seismic response of base-isolated systems and on the optimal isolator properties, other studies (e.g., [27]-[29]), concerning isolated buildings and bridges, demonstrated that soft soil condition leads to a great alteration of the variances with large increment of the peak ratios, in terms of displacements and shear forces, by negatively affecting the isolated systems. Similarly, Kulkarni and Jangid [30] analyzed the effects of superstructure flexibility on the response of base-isolated structures subjected to non-stationary random processes by comparing the stochastic response of a base-isolated structure with superstructure modelled as flexible and rigid and highlighting that the seismic isolation is more effective for firm or rock type soil than the soft soils.

This work aims to investigate the influence of soil characteristics in terms of frequency content on the seismic performance of elastic building frames isolated with FPS isolators and the optimal isolator friction properties. The two-degree-of-freedom model, already employed in [17], is used for this purpose, as it was shown to provide a reliable representation of the

structural response of more complex systems, especially in the case of low values of the friction coefficient and high isolation degrees such that the effects of the higher modes are negligible. It is also useful because it leads to a condensed description of the problem in terms of few characteristic parameters representing the isolator and structural system properties. A parametric study of the system is performed for different values of these characteristic parameters by considering three different sets of artificial ground motion records, modelled as non-stationary stochastic processes and generated through the power spectral density method [31], with different frequency content corresponding to stiff, medium and soft soil conditions [32], respectively. The nondimensionalization of the governing equations of motions permits to investigate wide ranges of seismic intensities while limiting the required nonlinear response history analyses. For each set of random excitations, numerical simulations are first carried out to evaluate the relation between the characteristic system and isolator parameters and the structural performance. Successively, multi-variate regression expressions are derived for the optimal values of the friction coefficient that minimize the superstructure displacements relative to the base, as a function of the system characteristic parameters, of the seismic input intensity and of the soil condition. More details may be found in [33].

## 2 NON-DIMENSIONAL EQUATION OF MOTION

The equations of motion governing the response of a 2dof model representing an elastic system on single concave FPS isolation bearings (Fig. 1) subjected to the seismic input $\ddot{u}_g(t)$, in the hypothesis of considering the horizontal component of the bearings displacement, is:

$$\begin{aligned} &m_s\ddot{u}_s(t)+c_s\dot{u}_s(t)+k_s u_s(t)=-m_s\left[\ddot{u}_g(t)+\ddot{u}_b(t)\right] \\ &m_b\ddot{u}_b(t)+f_b(t)+c_b\dot{u}_b(t)-c_s\dot{u}_s(t)-k_s u_s(t)=-m_b\ddot{u}_g(t) \end{aligned} \tag{1}$$

where $u_s$ denotes the displacement of the superstructure relative to isolation bearing, $u_b$ the isolator displacement relative to the ground, $m_s$ and $m_b$ respectively the mass of the superstructure and of the base floor above the isolation system, $k_s$ and $c_s$ respectively the superstructure stiffness and inherent viscous damping constant, $c_b$ the bearing viscous damping constant, $t$ the time instant, the dot differentiation over time, and $f_b(t)$ denotes the FPS bearing resisting force. This latter can be expressed as:

$$f_b(t)=k_b u_b(t)+\mu(\dot{u}_b)(m+m_b)gZ(t) \tag{2}$$

where $k_b=W/R=(m_s+m_b)g/R$, $g$ is the gravity constant, $R$ is the radius of curvature of the FPS, $\mu(\dot{u}_b(t))$ the coefficient of sliding friction, which depends on the bearing slip velocity $\dot{u}_b(t)$, and $Z(t)=\mathrm{sgn}(\dot{u}_b)$, with $sgn(\cdot)$ denoting the sign function. The fundamental period of vibration of a base-isolated system, $T_b=2\pi\sqrt{R/g}$, corresponding to the pendulum component, is independent of the superstructure mass and related only to the radius of curvature $R$ [17].

Experimental results [9]-[11] suggest that the coefficient of sliding friction of Teflon-steel interfaces obeys to the following equation:

$$\mu(\dot{u}_b)=f_{\max}-Df\cdot\exp\left(-\alpha|\dot{u}_b|\right) \tag{3}$$

in which $f_{\max}$ represents the maximum value of friction coefficient attained at large velocities of sliding, and $f_{\min} = f_{\max} - Df$ represents the value at zero velocity. In this study, to further simplify the problem, it is assumed that $f_{\max} = 3 f_{\min}$ with the exponent $\alpha$ equal to 30 [17].

Moreover, note that, in the hypothesis of considering the maximum value of the sliding friction coefficient, it is possible to evaluate the effective stiffness of the isolation level $k_{eff} = W\left(1/R + f_{\max}/u_b\right)$ depending on the bearings displacement (Fig. 1) which leads to an effective isolated period $T_{b,eff}$ [34],[35].

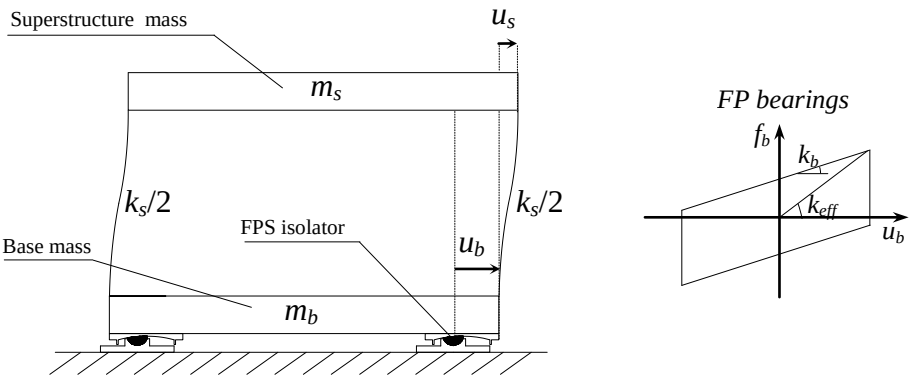


Fig. 1. 2dof model of elastic system isolated with FPS in the deformed configuration.

The non-dimensional form of the equations of motion can be derived by introducing the time scale $\tau = t\omega_b$, where $\omega_b = \sqrt{k_b/\left(m_s + m_b\right)}$ denotes the fundamental circular frequency of the isolated system with infinitely rigid superstructure, and the seismic intensity scale $a_0$, which has the dimension of an acceleration and it is such that $\ddot{u}_g(t) = a_0\lambda(\tau)$, where $\lambda(\tau)$ is a non-dimensional function of time describing the seismic input time-history. In [17], the following non-dimensional equations are obtained:

$$\begin{aligned}
&\ddot{\psi}_s(\tau) + 2\xi_s\frac{\omega_s}{\omega_b}\dot{\psi}_s(\tau) + \frac{\omega_s^2}{\omega_b^2}\psi_s(\tau) = -\left[\lambda(\tau) + \ddot{\psi}_b(\tau)\right] \\
&\ddot{\psi}_b(\tau) + \frac{1}{1-\gamma}\left[2\xi_b\dot{\psi}_b(\tau) + \psi_b(\tau) + \frac{\mu(\dot{u}_b)g}{a_0}\operatorname{sgn}\left(\dot{\psi}_b\right)\right] - 2\xi_s\frac{\omega_s}{\omega_b}\frac{\gamma}{1-\gamma}\dot{\psi}_s(\tau) - \frac{\omega_s^2}{\omega_b^2}\frac{\gamma}{1-\gamma}\psi_s(\tau) = -\lambda(\tau)
\end{aligned} \tag{4}$$

where $\omega_s = \sqrt{k_s/m_s}$ and $\xi_s = c_s/2m_s\omega_s$ denote respectively the circular frequency and damping factor of the superstructure; $\xi_b = c_b/2m_b\omega_b$ the isolator damping factor; $\gamma = m_s/\left(m_s + m_b\right)$ [34] the mass ratio. The non-dimensional parameters $\psi_s = u_s\omega_b^2/a_0$ and $\psi_b = u_b\omega_b^2/a_0$ describe the dynamic response of the superstructure and the isolators respectively. Eqn.(4) also reveals that the non-dimensional parameters ($\Pi$ terms) [36]-[37] that control the system non-dimensional response to the seismic input $\lambda(\tau)$ are:

$$\Pi_\omega = \frac{\omega_s}{\omega_b}, \Pi_\gamma = \gamma, \Pi_\mu\left(\dot{\psi}_b\right) = \frac{\mu(\dot{u}_b)g}{a_0}, \Pi_{\xi_b} = \xi_b, \Pi_{\xi_s} = \xi_s \tag{5}$$

Parameter $\Pi_\omega$ measures the isolation degree [34],[38], $\Pi_\gamma$ is the previously defined mass ratio, $\Pi_{\xi_b}$ and $\Pi_{\xi_s}$ describe the viscous damping inherent respectively to the system and the isolator. The non-dimensional parameter $\Pi_\mu$ measures the isolator strength, provided by the friction coefficient $\mu(\dot{u}_b)$, relative to the seismic intensity. Since this parameter depends on the response through the velocity $\dot{u}_b$, the following parameter is used in its stead:

$$\Pi_\mu^* = \frac{f_{\max} g}{a_0} \tag{6}$$

It is noteworthy that the non-dimensional seismic response of the system does not depend on the seismic intensity level $a_0$, but it depends only on $\Pi_{\xi_b}, \Pi_{\xi_s}, \Pi_\omega, \Pi_\gamma$, $\Pi_\mu^*$, and on the function $\lambda(\tau)$, describing the frequency content and time-modulation of the seismic input. Moreover, having assumed $1/\omega_b$ as time scale, it follows that also $\omega_b$ influences the non-dimensional seismic response of the system [17].

## 3 PARAMETRIC STUDY

This section presents the results of the parametric study carried out on the system of Fig. 1 to evaluate the performance of elastic buildings isolated with FPS bearings for different structural properties and soil conditions. The first two subsections describe respectively the stochastic model employed to generate the random excitations and the response parameters used to monitor the seismic performance, whereas the final subsection shows the parametric study results.

### 3.1 Random excitations and intensity measure (*IM*)

In Eqn.(4), the seismic input is described by the intensity scale factor, $a_0$, which is commonly denoted to as seismic intensity measure (*IM)* in the context of the performance-based earthquake engineering (PBEE) [39],[40], and through the non-dimensional function $\lambda(\tau)$, which describes the time-history of the ground motions.

The "record-to-record" variability of the characteristics of the seismic inputs is herein described by defining three wide sets of artificial record time histories with different frequency content corresponding to stiff, medium and soft soil conditions, respectively. These artificial records are modelled as time-modulated filtered Gaussian white noise random processes [30],[31],[41]. The power spectral density (PSD) function [42] of the embedded stationary process is described by the widely-used Kanai-Tajimi model [43]-[44], as modified by Clough and Penzien [45],[29],[46]-[50], i.e.:

$$S_f(\omega) = \frac{\omega_g^4 + 4\xi_g^2\omega_g^2\omega^2}{(\omega_g^2 - \omega^2) + 4\xi_g^2\omega_g^2\omega^2} \cdot \frac{\omega^4}{(\omega_f^2 - \omega^2) + 4\xi_f^2\omega_f^2\omega^2} S_0 \tag{7}$$

where $S_0$ = amplitude of the bedrock excitation spectrum, modeled as a white noise process; $\omega_g$ and $\xi_g$ = fundamental circular frequency and damping factor of the soil, respectively; $\omega_f$ and $\xi_f$ = parameters describing the Clough-Penzien filter; and $\omega$ = the circular frequency ranging between 0 and 50 rad/s. The parameters $\omega_g$ and $\xi_g$ are assumed as uniformly distributed independent random variables, with the following ranges of variation [32],[51]:

$\omega_g$ =5π-9π (high frequency/short period) and $\xi_g$ =0.6-1 for stiff soil condition, $\omega_g$ =3π-5π (intermediate frequency/ period) and $\xi_g$ =0.4-0.6 for medium soil condition, $\omega_g$ =π-3π (low frequency/high period) and $\xi_g$ =0.2-0.4 for soft soil condition. The values of the Clough-Penzien filter parameters are assumed as deterministic and equal to $\omega_f = 1.6$ (rad/s) and $\xi_f = 0.6$.

The Shinozuka-Sato function [52] is used to modulate in time the embedded stationary processes, Eqn.(8):

$$I(t) = c \cdot (e^{-b_1 \cdot t} - e^{-b_2 \cdot t}) \tag{8}$$

where $b_1$= 0.045π s$^{-1}$, $b_2$= 0.050π s$^{-1}$ and $c$=25.302. A duration equal to 31.25 s, longer than 25s according to [53], is considered. The same duration has been assumed for all the artificial record time histories since the duration of the random excitations has not a strong influence when a peak response quantity is of interest, like the maximum response displacement, velocity or acceleration [54],[55].

An ensemble of 100 artificial ground motions, generated through the Spectral Representation Method [31], is considered for each soil condition. By this way, each set of artificial records reflects the wide uncertainty in terms of frequency content related to each soil condition [32],[51] and is composed of a high number of random excitations in order to strongly reduce the standard errors [16] of the statistics of the response parameters evaluated in the following subsections.

Fig. 2(a) shows the PSD functions for the different soil conditions corresponding to $S_0$=1 m$^2$/s$^3$ and to the sample values of the filter parameters, illustrating the energy associated with the frequency contents for each soil condition [56], whereas, Fig. 2(b) shows the elastic pseudo-acceleration response spectra of the 100 artificial ground motions for each soil condition, scaled to the common *IM* value $S_A(T)$ = 0.1 g, for $T$ = 4 s, which is a typical isolated system period.

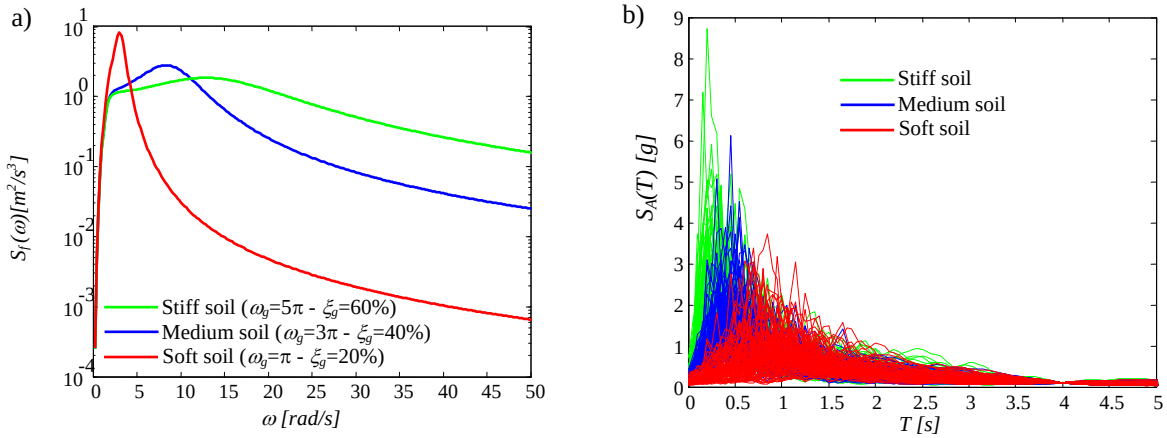


Fig. 2. PSD functions corresponding to stiff, medium and soft soil conditions (a); Pseudo-acceleration response spectra for the 300 records scaled to the common seismic intensity measure $S_A(T)$ = 0.1 g, for $T$=4s (b).

Regarding the intensity measure, it is worth to note that although the non-dimensional response to a single ground motion input does not depend on the *IM* level $a_0$, the response dispersion, and thus the accuracy of the estimate, is affected by the *IM* choice [17]. In this study, the spectral pseudo-acceleration, $S_A(T_b, \xi_b)$, at the isolated period of the system, $T_b = 2\pi / \omega_b$, and for the damping ratio $\Pi_{\xi_b} = \xi_b$, is assumed as *IM*. This *IM* is related to the spectral displacement $S_d$ by the relation $S_A(T_b, \xi_b) = \omega_b^2 S_d(T_b, \xi_b)$. It is also worth to observe that if all

the records for each soil type are normalized to $S_A\left(T_b,\xi_b\right)$, then the normalized displacement response of a system with period $T_b$, damping ratio $\xi_b$, rigid superstructure (i.e., high $\Pi_\omega$) and mounted on a frictionless isolator, equals to 1 for each record and soil condition and it is not affected by the record-to-record variability. Thus, this system can be assumed as reference case for evaluating the influence of the isolator friction $\Pi_\mu$ and of the period ratio $\Pi_\omega$ on the response statistics [17]. In the analyses carried out in this study, the damping ratio $\xi_b$ is taken equal to zero, consistently with other works which assume that friction is the only source of damping in the isolators [17],[22],[57]. The corresponding *IM* is hereinafter denoted to as $S_A\left(T_b\right)$.

### 3.2 Seismic response parameters

This study considers the following set of response parameters relevant to the performance of the isolated system: the peak isolator displacement $u_{b,\max}$ (important for the design of the FPS isolator and of the seismic gap around the building), the peak superstructure displacement relative to the isolator $u_{s,\max}$ (related to internal forces in the structure and to the performance of displacement-sensitive non-structural components). These response parameters can be expressed in non-dimensional form, according to Eqn. (4), as:

$$\psi_{u_b}=\frac{u_{b,\max}\omega_b^2}{S_A\left(T_b\right)}=\frac{u_{b,\max}}{S_d\left(T_b\right)} \quad , \quad \psi_{u_s}=\frac{u_{s,\max}\omega_b^2}{S_A\left(T_b\right)}=\frac{u_{s,\max}}{S_d\left(T_b\right)} \tag{9a,b}$$

where the normalized displacement response $\psi_{u_b}$ can be interpreted as the reduction factor of the response spectrum at the isolation period $T_b$ with damping ratio $\xi_b$=0.

By repeatedly solving Eqn. (4) for each set of the 100 ground motion records, a set of samples is obtained for the output variables used to monitor the performance. In this paper, the response parameters are assumed to follow a lognormal distribution [17]-[18],[39],[57]-[58]. The lognormality assumption permits to estimate, with a limited number of samples, the response at different percentile levels, which is very useful for system reliability assessment. It also permits to obtain a closed-form analytical estimate of the seismic risk [59].

A lognormal distribution can be fitted to the generic response parameter *D* (i.e., the extreme values $\psi_{u_b},\psi_{u_s}$ of Eq. (4)) by estimating the sample geometric mean, $GM\left(D\right)$, and the sample lognormal standard deviation $\sigma_{\ln}\left(D\right)$, or dispersion $\beta\left(D\right)$, defined, respectively, as follows:

$$GM\left(D\right)=\sqrt[N]{d_1\cdot\ldots\cdot d_N} \tag{10}$$

$$\beta\left(D\right)=\sigma_{\ln}\left(D\right)=\sqrt{\frac{\left(\ln d_1-\ln\left[GM\left(D\right)\right]\right)^2+\ldots\ldots+\left(\ln d_N-\ln\left[GM\left(D\right)\right]\right)^2}{N-1}} \tag{11}$$

where $d_i$ denotes the *i*-th sample value of *D*, and *N* is the total number of samples. The sample geometric mean is an estimator of the median of the response and its logarithm coincides with the lognormal sample mean $\mu_{\ln}\left(D\right)$. Under the lognormality assumption, the relation between the geometric mean $GM\left(D\right)$, the dispersion $\beta\left(D\right)$, and the *k*th percentile of the generic response parameter *D* can be expressed as:

$$d_k = GM(D)\exp[f(k)\beta(D)] \tag{12}$$

where $f(k)$ is a function assuming the values $f(50)=0$, $f(84)=1$ and $f(16)=-1$ [60].

### 3.3 Parametric study results

This section shows the results of the parametric study carried out to evaluate the relation between the isolation and structure properties and the system performance, for each set of 100 ground motion records corresponding to different soil conditions. The parameters $\Pi_{\xi_b}=\xi_b$ and $\Pi_{\xi_s}=\xi_s$ are assumed respectively equal to 0% and 2%, the base-isolated system period $T_b$ is varied in the range between 2s and 5s, the parameter $\Pi_\omega$ in the range between 3 (flexible superstructure) and 12 (rigid superstructure), $\Pi_\gamma=\gamma$ in the range between 0.6 and 0.9, $\Pi_\mu^*$ in the range between 0 (no friction) and 2 (very high friction). Indeed, a high value for the upper bound of $\Pi_\mu^*$ is also considered due to the very low values of the *IM* at high isolated periods (i.e., $T_b$=5s) depending on the seismic hazard [53]. For each value of the parameters varied in the parametric study, the differential equation of motion, i.e., Eqn.(4), has been repeatedly solved for the different random excitation. The Bogacki-Shampine integration algorithm available in Matlab-Simulink [61] has been employed. The probabilistic properties of the normalized response have been evaluated by estimating the geometric mean, *GM*, and the dispersion, $\beta$, of the parameters of interest through Eqns. (10) and (11).

Figs. 3-8 show the statistics (*GM* and $\beta$ values) of the response parameters considered, obtained for different values of the system parameters varying in the range of interest and for each soil type. Each figure contains several surface plots, corresponding to different values of $\Pi_\gamma$. Only the results corresponding to $\Pi_\omega$ = 6 and $\Pi_\omega$ = 9 are reported.

Fig.s 3 and 4 plot the results concerning the normalized bearing displacement $\psi_{u_b}$, related to cases $\Pi_\omega$=6 and $\Pi_\omega$=9 respectively. The trend of $GM\left(\psi_{u_b}\right)$ is similar to that discussed in [17], where natural records were considered without taking into account soil types.

This is the consequence of the non-dimensionalization and of the efficient intensity measure employed for the study. In fact, $GM\left(\psi_{u_b}\right)$ is equal to unit for $\Pi_\mu^*=0$ and higher $\Pi_\omega$ and increases slightly for increasing $T_b$ because of period elongation and of the influence of the second mode of vibration on the response. Obviously, $GM\left(\psi_{u_b}\right)$ decreases significantly as $\Pi_\mu^*$ increases and is also slightly influenced by $\Pi_\gamma$, especially, for low $\Pi_\omega$ values. For soft soil condition and low $\Pi_\omega$ values, the influence of $\Pi_\gamma$ is higher as well as the decrease of $GM\left(\psi_{u_b}\right)$ for increasing $\Pi_\mu^*$ is more gradual. The dispersion $\beta\left(\psi_{u_b}\right)$ for high $T_b$ increases for increasing values of $\Pi_\mu^*$, as a result of the reduction of the efficiency of the *IM* employed in the study for each soil condition. Moreover, with reference to soft soils, the values of $\beta\left(\psi_{u_b}\right)$ also result to be higher for low values of both the isolated periods $T_b$ and $\Pi_\mu^*$. Obviously, in the case of $\Pi_\mu^*=0$ and higher $\Pi_\omega$, the dispersion is zero for all the values of $T_b$ and of $\Pi_\gamma$ considered and for all the soil conditions.

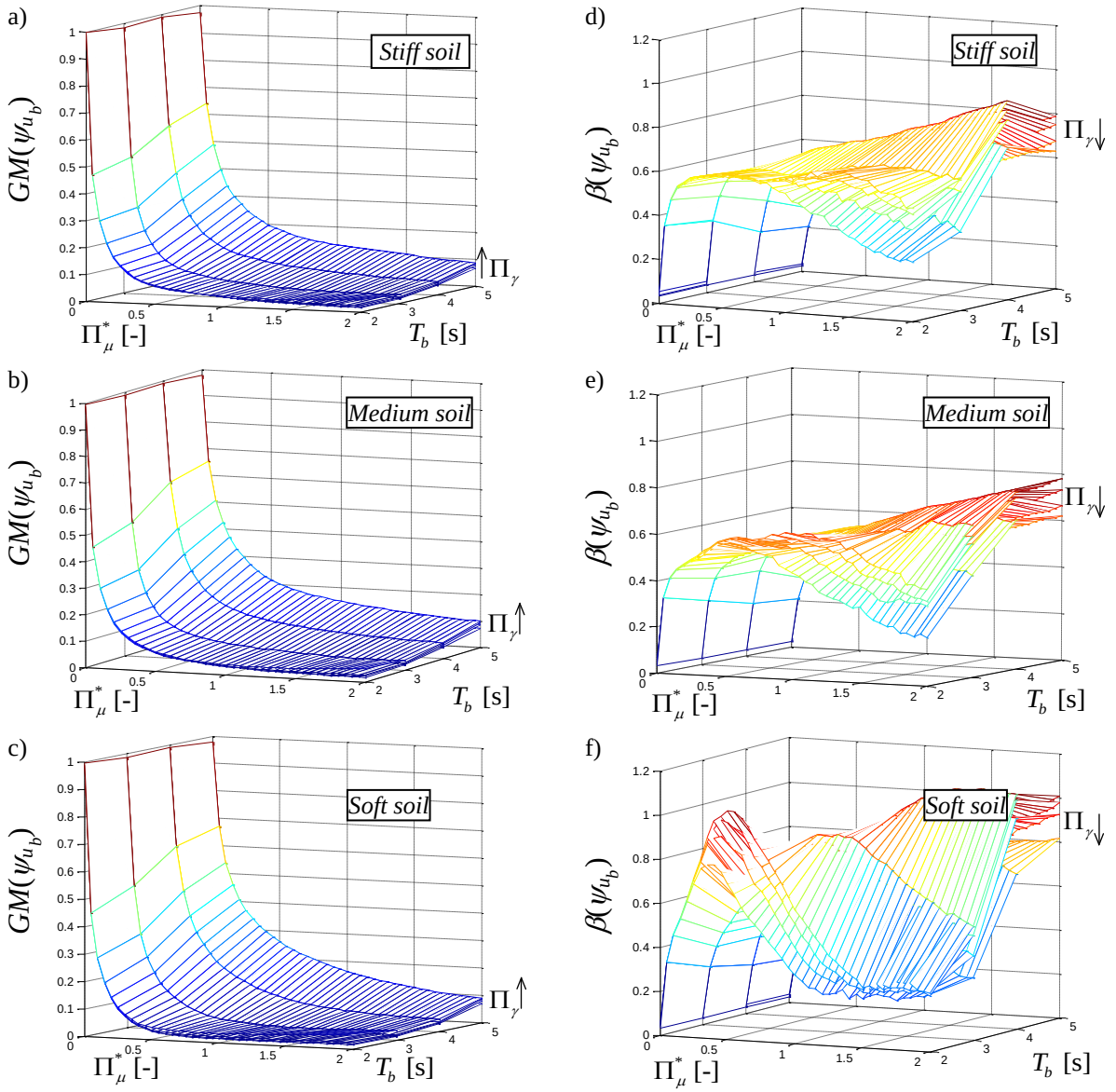


Fig. 3. Normalized bearing displacement vs. $\Pi^*_\mu$ and $T_b$ for $\Pi_\omega$=6 and each soil condition: median value (a,b,c) and dispersion (d,e,f) for different values of $\Pi_\gamma$. The arrow denotes the increasing direction of $\Pi_\gamma$.

The mass ratio $\Pi_\gamma$ does not affect significantly the response dispersion, especially in the case of high $\Pi_\omega$ values. The above described peak values of both $GM\left(\psi_{u_b}\right)$ and $\beta\left(\psi_{u_b}\right)$ in the case of soft soil condition are due to resonance effects which mainly affect the effective frequency charactering the dynamic behaviour of the frictional bearings and the dominant frequency of the corresponding random excitations.

Fig.s 5 and 6 show the response statistics of the normalized superstructure displacements relative to the base mass $\psi_{u_s}$. Also the trend of $GM\left(\psi_{u_s}\right)$ is quite similar to that discussed in [17]: $GM\left(\psi_{u_s}\right)$ increases for increasing values of $T_b$ as well as for decreasing values of $\Pi_\gamma$ and of $\Pi_\omega$, whereas it first decreases and then increases for increasing values of $\Pi^*_\mu$. Thus, there exists an optimal value of $\Pi^*_\mu$ such that the superstructure displacement is minimized

for each soil condition. This optimal value is in the range between 0 and 0.3 depending on the values of $\Pi_\omega$, $T_b$, $\Pi_\gamma$ and soil condition. In particular, increasing values of the optimal friction coefficient are required from stiff to soft soil condition.

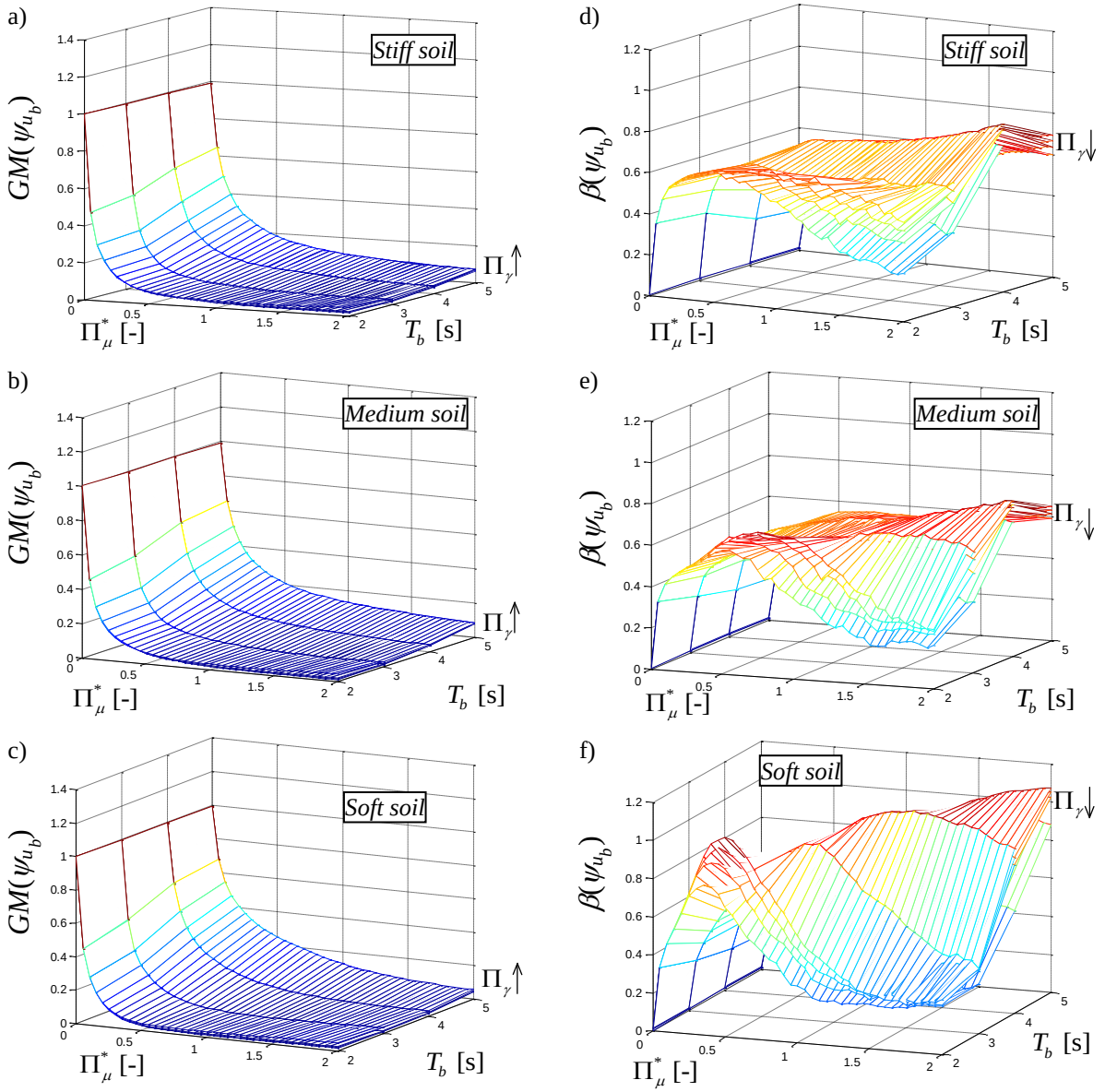


Fig. 4. Normalized bearing displacement vs. $\Pi^*_\mu$ and $T_b$ for $\Pi_\omega$=9 and each soil type: median value (a,b,c) and dispersion (d,e,f) for different values of $\Pi_\gamma$. The arrow denotes the increasing direction of $\Pi_\gamma$.

The values of the dispersion $\beta(\psi_{u_s})$, are very low for low $\Pi^*_\mu$ values due to the high efficiency of the *IM* employed in the study, and attain their peak for values of $\Pi^*_\mu$ close to the optimal ones. The other system parameters have a reduced influence on $\beta(\psi_{u_s})$ compared to the influence of $\Pi^*_\mu$. In the case of soft soil condition, the dispersion $\beta(\psi_{u_s})$ strongly increases for increasing values of $\Pi^*_\mu$ for both lower isolation degrees and isolated periods because of the resonance effects which mainly affect the effective frequency of the frictional bearings and the dominant frequency of the corresponding random excitations. The different

influence of the three soil conditions and, in particular, the increase of the statistics values of the response parameters from stiff to soft soil condition results to be consistent with the results described in [28]-[30].

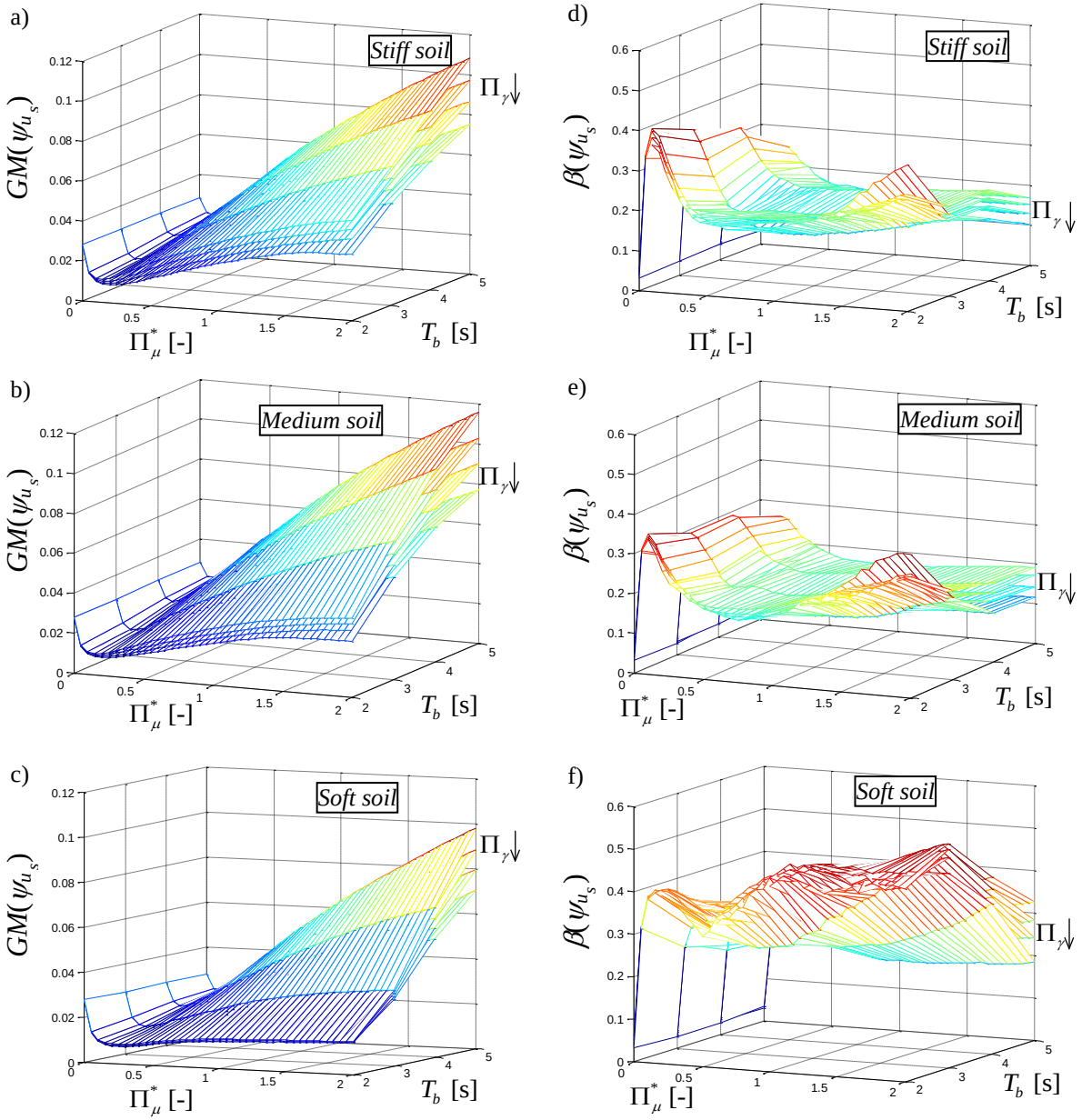


Fig. 5. Normalized superstructure displacement vs. $\Pi^*_\mu$ and $T_b$ for $\Pi_\omega$=6 and each soil condition: median value (a,b,c) and dispersion (d,e,f) for different values of $\Pi_\gamma$. The arrow denotes the increasing direction of $\Pi_\gamma$.

The existence of an optimal value of the friction coefficient has been pointed out in many studies on systems isolated by FPS bearings [17],[21]-[24],[26] and it depends on some effects that follow an increase of the friction coefficient. In fact, an increase of the friction coefficient leads to an increase of the isolator strength (and thus of the equivalent stiffness, with a reduction of the corresponding effective fundamental vibration period (Fig.1)) and the increase of participation of higher vibration modes as well as transfer of forces towards the superstructure. However, the forces transmitted to the superstructure also depend on the bearings displacements which decrease as the friction coefficient increases. An increase of the forces transmitted to the superstructure generally increases the superstructure displacements.

Another effect is an increase of energy dissipation (equivalent damping), which reduces the superstructure displacements. The equilibrium between these effects is strongly influenced by the characteristic structural parameters as well as the frequency content of the random excitations related to each soil condition. In fact, for soft soil condition, higher optimal values of the normalised friction coefficient are required due to the resonance effects as well as to increase the equivalent damping. The dependency on these parameters is discussed in more detail in the next section.

For all the statistics of the response parameters within the parametric analysis, the standard errors [16] result to be lower than 5% for low values of $\Pi_{\mu}^{*}$ and lower than 10% for increasing values of $\Pi_{\mu}^{*}$ due to the high number of the random excitations employed.

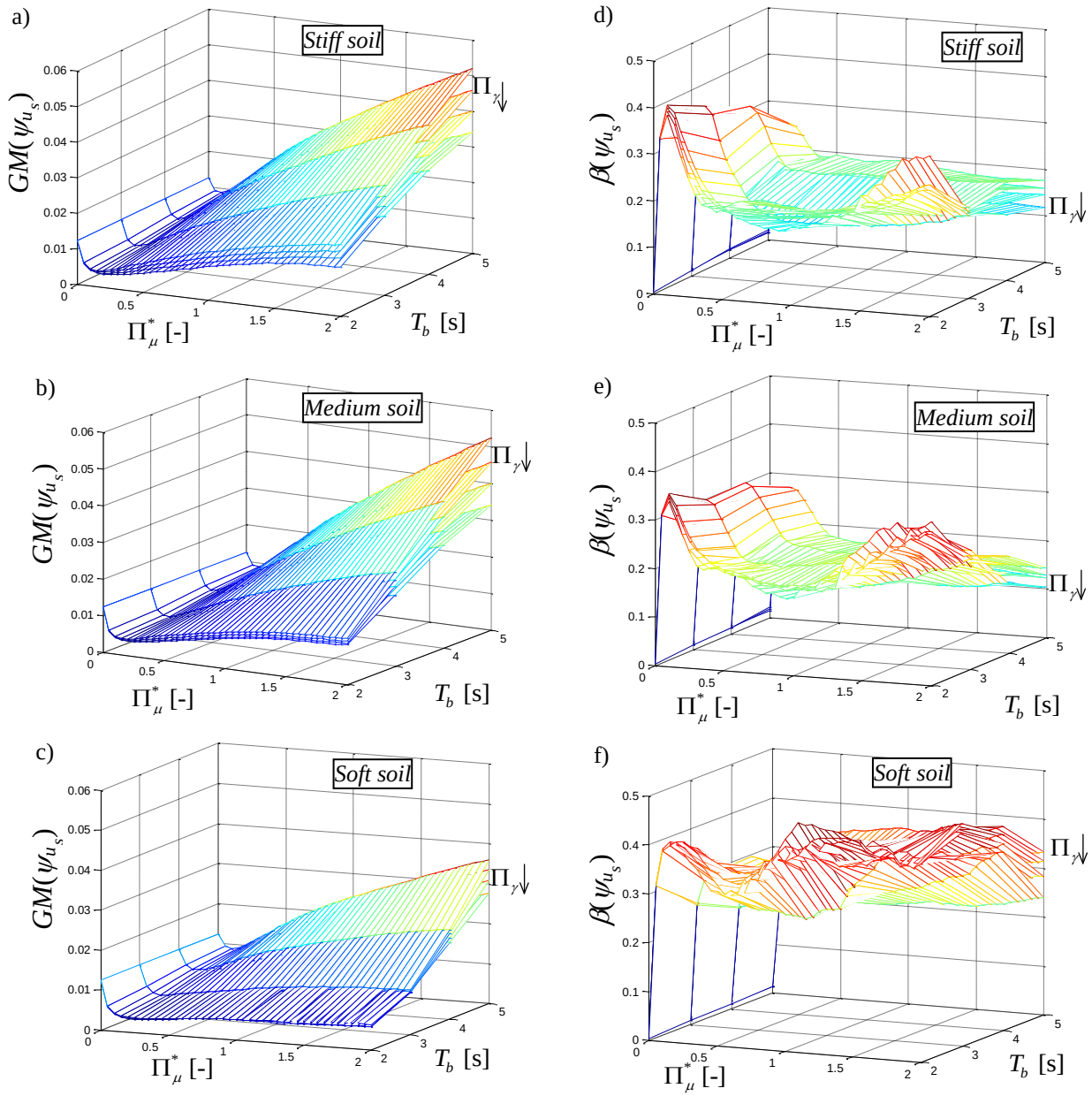


Fig. 6. Normalized superstructure displacement vs. $\Pi^{*}_{\mu}$ and $T_b$ for $\Pi_{\omega}$=9 and each soil condition: median value (a,b,c) and dispersion (d,e,f) for different values of $\Pi_{\gamma}$. The arrow denotes the increasing direction of $\Pi_{\gamma}$.

## 4 OPTIMAL SLIDING FRICTION COEFFICIENT DEPENDING ON THE SOIL CONDITION

The results previously described show that for each combination of the system properties (i.e., of $\Pi_\gamma$, $T_b$ and $\Pi_\omega$) there exists an optimal value of the normalized sliding friction coefficient, $\Pi^*_{\mu,\text{opt}}$, depending on the soil condition such that the median normalized superstructure displacements are minimized according to Fig.s 5-6.

Minimizing the superstructure displacements relative to the base mass can be an important design requirement for base isolated systems to avoid inelastic response of the superstructure, which can lead to very high displacement ductility demand [62]. In fact, an inelastic response of the superstructure can lead to a disproportionately large displacement ductility demand that could also be amplified in the case of soft soil condition due to the resonance effects, considering structural systems in ordinary conditions and neglecting aging effects [63]-[72].

From a design point of view, it may be of interest to evaluate the values of $\Pi^*_{\mu,\text{opt}}$ that minimize response percentile others than the 50$^{\text{th}}$, corresponding to different exceedance probabilities [57]. Therefore, for each soil type, through a multivariate nonlinear regression analysis, a regression expression is obtained for $\Pi^*_{\mu,\text{opt}}$ as a function of the parameters $\Pi_\gamma$, $T_b$ and $\Pi_\omega$ and of three percentile levels (i.e., 50$^{\text{th}}$, 16$^{\text{th}}$ and 84$^{\text{th}}$ percentiles). In particular, the expressions for $\Pi^*_{\mu,opt}$ is derived by fitting in Matlab [61] the following second-order polynomial expression:

$$\Pi^*_{\mu,\text{opt}} = c_1 + c_2 \cdot T_b + c_3 \cdot \Pi_\omega + c_4 \cdot \Pi_\gamma + c_5 \cdot T_b \cdot \Pi_\omega + c_6 \cdot T_b \cdot \Pi_\gamma + \\ + c_7 \cdot \Pi_\gamma \cdot \Pi_\omega + c_8 \cdot {T_b}^2 + c_9 \cdot {\Pi_\omega}^2 + c_{10} \cdot {\Pi_\gamma}^2 \tag{13}$$

where $c_i$, $i$=1,…,10, are the regression coefficients, whose values are reported in Tables 1-3 as a function of the different percentile levels and soil condition. It is noteworthy that the order of the polynomials is kept as small as possible to balance the contrasting requirements of accuracy and simplicity, thus providing a polynomial expression easy to be applied for the preliminary designing of FPS characteristics.

| | $c_1$ | $c_2$ | $c_3$ | $c_4$ | $c_5$ | $c_6$ | $c_7$ | $c_8$ | $c_9$ | $c_{10}$ |
|---|---|---|---|---|---|---|---|---|---|---|
| 50$^{\text{th}}$ percentile | 0.2657 | -0.0380 | -0.0083 | -0.2022 | -0.0012 | -0.0028 | 0.0071 | 0.0045 | 0.0005 | 0.2187 |
| 84$^{\text{th}}$ percentile | 0.2643 | -0.0249 | -0.0034 | -0.2641 | -0.0016 | -0.0126 | 0.0044 | 0.0020 | 0.0005 | 0.3359 |
| 16$^{\text{th}}$ percentile | 0.3038 | -0.0392 | -0.0083 | -0.3230 | -0.0010 | 0.0181 | 0.0034 | 0.0037 | 0.0005 | 0.2422 |

Table 1. Coefficients of multi-variate non-linear regression for stiff soil.

| | $c_1$ | $c_2$ | $c_3$ | $c_4$ | $c_5$ | $c_6$ | $c_7$ | $c_8$ | $c_9$ | $c_{10}$ |
|---|---|---|---|---|---|---|---|---|---|---|
| 50$^{\text{th}}$ percentile | 0.2248 | -0.0327 | -0.0034 | -0.1122 | -0.0007 | 0.0162 | 0.0059 | 0.0008 | 0.0002 | 0.1094 |
| 84$^{\text{th}}$ percentile | 0.1973 | 0.0055 | -0.0064 | -0.1456 | -0.0011 | 0.0090 | 0.0080 | -0.0055 | 0.0005 | 0.1719 |
| 16$^{\text{th}}$ percentile | 0.2483 | -0.0376 | -0.0058 | -0.1906 | -0.0011 | 0.0301 | 0.0049 | 0.0020 | 0.0005 | 0.1172 |

Table 2. Coefficients of multi-variate non-linear regression for medium soil.

The regression R-squared values are higher than 0.92 for all the cases considered, indicating that the fitted model describes well the variation of $\Pi^*_{\mu,opt}$ with the parameters considered. Only the regressions, related to the 16$^{th}$ percentile for stiff and medium soil conditions, present slightly lower values of R-squared. Eqn. (13) can be used to design the optimum FPS properties for the isolated system, provided that a seismic intensity level $S_A(T_b)$ is assigned. In fact, according to Eqn. (6), the optimum friction coefficient (at high velocity) can be easily calculated as $f_{\max,\text{opt}} = \dfrac{\Pi^*_{\mu,\text{opt}} \cdot S_A(T_b)}{g}$. This implies that the optimum friction coefficient increases linearly with the *IM* level. Furthermore, friction pendulum properties that are "optimal" for a given seismic intensity, are not "optimal" for the other intensities. It follows that the optimal friction coefficient can be defined considering the seismic intensity corresponding to the collapse limit state [53] in order to ensure an adequate response of the isolated superstructure under strong earthquake events. More details may be found in [33].

| | $c_1$ | $c_2$ | $c_3$ | $c_4$ | $c_5$ | $c_6$ | $c_7$ | $c_8$ | $c_9$ | $c_{10}$ |
|---|---|---|---|---|---|---|---|---|---|---|
| 50$^{th}$ percentile | 0.5689 | -0.1603 | 0.0113 | -0.4345 | -0.0005 | 0.0632 | 0.0007 | 0.0108 | -0.0003 | 0.2187 |
| 84$^{th}$ percentile | 0.3726 | -0.0629 | 0.0204 | -0.4317 | -0.0018 | 0.0292 | -0.0038 | 0.0008 | -0.0004 | 0.3437 |
| 16$^{th}$ percentile | 0.5751 | -0.1607 | 0.0022 | -0.3256 | 0.0002 | 0.0665 | 0.0079 | 0.0103 | -0.0004 | 0.0781 |

Table 3. Coefficients of multi-variate non-linear regression for soft soil.

## 5 CONCLUSIONS

This paper investigates the influence of the soil characteristics in terms of frequency content, related to stiff, medium and soft soils, on the seismic performance of elastic buildings isolated with friction pendulum system (FPS) bearings and the optimal isolator friction properties. In particular, the results of an extensive parametric study, encompassing a wide range of isolator and building properties, different seismic intensity levels, different soil conditions and various response parameters that are of interest for monitoring the seismic behavior, are described. The behavior of these systems is analyzed by employing a two-degree-of-freedom model accounting for the superstructure flexibility, whereas the FPS isolator behaviour is described by adopting a widespread model which considers the variation of the friction coefficient with the velocity.

The uncertainty in the seismic inputs is taken into account by considering for each (stiff, medium and soft) soil condition a set of 100 artificial records, obtained through the power spectral density method, with different frequency content and scaled to increasing intensity levels. A nondimensionalization of the equation of motion is carried out to unveil the parameters controlling the problem and also allows to explore a wide range of situations while limiting the required nonlinear response history analyses. The estimates of the response statistics obtained for each combination of the parameters reflect the effect of the variability of the frequency characteristics of the seismic input at different intensity levels and can be used for deriving approximate fragility curves and for simplified seismic risk analyses.

For each set of random excitations, the influence of superstructure and FPS system properties are evaluated by considering the geometric mean (*GM*) and dispersion of each normalised response parameter, assumed to follow a lognormal distribution. With reference to both isolation device and superstructures response, it is possible to conclude that low-frequency random excitations related to soft soil condition negatively influences the statistics of the response pa-

rameters of the whole isolated systems due to resonance effects which affect seismic inputs dominant frequencies and the effective frequency of the frictional bearings.

Finally, multi-variate regression expressions are derived for the optimal values of the normalized friction coefficient minimizing the $50^{th}$, $16^{th}$ and $84^{th}$ percentile values of the superstructure displacements relative to the base mass, as function of the identified system characteristic parameters and soil type. Thus the performance of both the structural and non-structural components of the superstructure can be controlled. Higher values of the optimum friction coefficient are required, especially for low isolated periods, in the case of soft soil condition in order to reduce the bearing displacements and, consequently, the forces transmitted to the superstructure as well as to increase the energy dissipation (equivalent damping).

## REFERENCES


[1] De Iuliis M., Castaldo P., Palazzo B., Analisi della domanda sismica inelastica del terremoto de L'Aquila su sistemi dimensionati secondo le NTC2008. *Ingegneria Sismica*, Patron Editore **XXVII**(3), 55–68, 2010.

[2] Castaldo, P., Palazzo, B., Perri F. FEM simulations of a new hysteretic damper: the dissipative column, *Ingegneria Sismica - International Journal of Earthquake Engineering*, Anno XXXIII – Speciale CTA- 2015- Num. 1-2:34-45.

[3] Castaldo P., *Integrated Seismic Design of Structure and Control Systems*. Springer International Publishing: New York, 2014 . DOI 10.1007/978-3-319-02615-2.

[4] De Iuliis M., Castaldo P., An energy-based approach to the seismic control of one-way asymmetrical structural systems using semi-active devices, *Ingegneria Sismica - International Journal of Earthquake Engineering* **XXIX**(4):31-42, 2012.

[5] Christopoulos C, Filiatrault A. *Principles of Passive Supplemental Damping and Seismic Isolation*. IUSS Press: Pavia, Italy, 2006.

[6] Su L, Ahmadi G, Tadjbakhsh IG. Comparative study of base isolation systems. *Journal of Engineering Mechanic* 1989; **115**(9):1976–92.

[7] Zayas VA, Low SS, Mahin SA. A simple pendulum technique for achieving seismic isolation. *Earthquake Spectra* 1990; **6**(2):317–33.

[8] Mosqueda G, Whittaker AS, Fenves GL. Characterization and modeling of Friction Pendulum bearings subjected to multiple components of excitation. *Journal of Structural Engineering* 2004; **130**(3):433-442.

[9] Mokha A, Constantinou MC, Reinhorn AM. Teflon Bearings in Base Isolation. I: Testing. *Journal of Structural Engineering* 1990; **116**(2):438-454.

[10] Constantinou MC, Mokha A, Reinhorn AM. Teflon Bearings in Base Isolation. II: Modeling. *Journal of Structural Engineering* 1990; **116**(2):455-474.

[11] Constantinou MC, Whittaker AS, Kalpakidis Y, Fenz DM, Warn GP. Performance of Seismic Isolation Hardware Under Service and Seismic Loading. *Technical Report* MCEER-07-0012, 2007.

[12] Almazàn JL, De la Llera JC. Physical model for dynamic analysis of structures with FPS isolators. *Earthquake Engineering and Structural Dynamics* 2003;**32**(8):1157–1184.

[13] Landi, L, Grazi G, and Diotallevi P P. Comparison of different models for friction pendulum isolators in structures subjected to horizontal and vertical ground motions, *Soil Dynamics and Earthquake Engineering* 2016;**81**:75-83.

[14] Ryan KL, Chopra AK. Estimating the seismic displacement of friction pendulum isolators based on non-linear response history analysis. *Earthquake Engineering and Structural Dynamics* 2004;**33**(3):359–373.

[15] Barroso LR. Performance evaluation of vibration controlled steel structures under seismic loads. PhD thesis, Stanford University, California, US, 1999.

[16] Barroso LR, Winterstein S. Probabilistic seismic demand analysis of controlled steel moment-resisting frame structures. *Earthquake Engineering and Structural Dynamics* 2002;**31**(12):2049–2066.

[17] Castaldo, P, Tubaldi, E. Influence of FPS bearing properties on the seismic performance of base-isolated structures. *Earthquake Engineering and Structural Dynamics* 2015;**44**(15):2817–2836.

[18] Castaldo P., Amendola G., Palazzo B., Seismic fragility and reliability of structures isolated by friction pendulum devices: seismic reliability-based design (SRBD), *Earthquake Engineering and Structural Dynamics*, **46**(3); 425–446, 2017, DOI: 10.1002/eqe.2798.

[19] Castaldo P., Palazzo B. and Ferrentino T. Seismic reliability-based ductility demand evaluation for inelastic base-isolated structures with friction pendulum devices, Earthquake Engineering and Structural Dynamics 2017; 46:1245–1266, DOI: 10.1002/eqe.2854.

[20] Castaldo, P., Amendola, G., Palazzo, B. Effetcs of class B site on the seismic reliability of base-isolated steel systems, Ingegneria Sismica, **33**(3), 29-41, 2015.

[21] Jangid RS. Optimum frictional elements in sliding isolation systems. *Computers and Structures* 2000;**76**(5):651–661.

[22] Jangid RS. Optimum friction pendulum system for near-fault motions. *Engineering Structures* 2005;**27**(3):349-359.

[23] Chung LL, Kao PS, Yang CY, Wu LY, Chen HM. Optimal frictional coefficient of structural isolation system. *Journal of Vibration and Control* 2013, Early view. DOI: 10.1177/1077546313487938.

[24] Iemura H, Taghikhany T, Jain S. Optimum design of resilient sliding isolation system for seismic protection of equipments. *Bulletin of Earthquake Engineering* 2007;**5**(1):85-103.

[25] Bucher C. Probability-based optimization of friction-based seismic isolation devices. *Structural Safety* 2009;**31**(6):500-507.

[26] Fallah, N., Zamiri G. Multi-objective optimal design of sliding base isolation using genetic algorithm. *Scientia Iranica A*, 2013;**20**(1):87–96.

[27] Dicleli, M., & Buddaram, S. Effect of isolator and ground motion characteristics on the performance of seismic-isolated bridges. *Earthquake Engineering and Structural Dynamics* 2006;**35**(2):233-250.

[28] Safak, E., Frankel, A. Effects of ground motion characteristics on the response of base-isolated structures. *11th World Conference on Earthquake Engineering 1996* (paper no. 1430).

[29] Saritaş, F, Hasgür Z. Dynamic Behavior of an Isolated Bridge Pier under Earthquake Effects for Different Soil layers and Support Conditions, *Digest* 2014, 1733-1756.

[30] Kulkarni JA, Jangid RS. Effects of superstructure flexibility on the response of base-isolated structures. Shock and Vibration 2003;26:1-13.

[31] Shinozuka M., Deodatis G. Simulation of stochastic processes by spectral representation. *Applied Mechanics Reviews* 1991;**44**(4):191-203.

[32] Pinto P, Giannini R, Franchin P. Seismic Reliability Analysis of Structures. *Iuss Press* 2004.

[33] Castaldo P., Ripani M. Optimal design of friction pendulum system properties for isolated structures considering different soil conditions. *Soil Dynamics and Earthquake Engineering*; 90:74 – 87, 2016. DOI:10.1016/j.soildyn.2016.08.025.

[34] Kelly JM. *Earthquake-Resistant Design with Rubber*. 2nd ed. Berlin and New York: Springer-Verlag; 1997.

[35] Building Seismic Safety Council. NEHRP Recommended Provisions: Design Examples FEMA 451 - Washington, D.C., August 2006.

[36] Karavasilis TL, Seo CY, Makris N. Dimensional Response Analysis of Bilinear Systems Subjected to Non-pulse like Earthquake Ground Motions. *Journal of Structural Engineering* 2011;**137**(5):600-606.

[37] Barbato M, and Tubaldi E. A probabilistic performance-based approach for mitigating the seismic pounding risk between adjacent buildings. *Earthquake Engineering & Structural Dynamics* 2013;**42**(8):1203-1219.

[38] Palazzo B. Seismic Behavior of base-isolated Buildings. Proceedings of the International Meeting on earthquake Protection of Buildings, Ancona, 1991.

[39] Aslani H, Miranda E. Probability-based seismic response analysis. *Engineering Structures* 2005;**27**(8):1151-1163.

[40] Porter KA. An overview of PEER's performance-based earthquake engineering methodology. Proceedings, *Proceedings of the 9th International Conference on Application of Statistics and Probability in Civil Engineering* (*ICASP9*), San Francisco, California, 2003.

[41] Pradlwarter H. J., SchuiRler G. I., Dorka U. Reliability of MDOF-systems with hysteretic devices. *Engineering Structures*, 1998;**20**(8):685-691.

[42] Tung ATY, Wang JN, Kiremidjian A, Kavazanjian E. Statistical parameters of AM and PSD functions for the generation of site-specific strong ground motions. Proceedings *of the 10th World Conference on Earthquake Engineering*, Madrid, Spain, 1992;**2**:867-872.

[43] Kanai K. Semiempirical formula for the seismic characteristics of the ground. *Bulletin of earthquake research institute* 1957;**35**:309-325.

[44] Tajimi H. A statistical method of determining the maximum response of a building structure during an earthquake. *Proc., 2nd World Conf. on earthquake Engineering* 1960;**II**:781-798.

[45] Clough R.W., Penzien J.: Dynamics of Structures, 2nd edn. McGraw-Hill, New York; 1993.

[46] Zentner I., Allain F., Humbert N., Caudron M. Generation of spectrum compatible ground motion and its use in regulatory and performance-based seismic analysis. *Proceedings of the 9th Internat. Conf. on Str. Dyn.s*, EURODYN 2014 Porto, Portugal, 30 June - 2 July 2014.

[47] Peng Y., Chen J., Li J. Nonlinear Response of Structures Subjected to Stochastic Excitations via Probability Density Evolution Method. *Advances in Structural Engineering*, 2014;**17**(6):801-816.

[48] Li, C., Liu, Y. Ground Motion Dominant Frequency Effect On The Design Of Multiple Tuned Mass Dampers. *Journal of Earthquake Engineering*, 2004;**8**(1):89-105.

[49] Lopez-Garcia, D., Soong T.T. Assessment of the separation necessary to prevent seismic pounding between linear structural systems. *Prob. Engineering Mechanics*, 2009;**24**:210-223.

[50] Tubaldi, E., Barbato, M., Ghazizadeh S. A probabilistic performance-based risk assessment approach for seismic pounding with efficient application to linear systems. *Structural Safety* 2012;36-37:14–22.

[51] Talaslidis D.G., Manolis G.D., Paraskevopoulos E.A., Panagiotopoulos C.G. Risk analysis of industrial structures with hazardous materials under seismic input, 13th World Conference on Earthquake Engineering, Vancouver, B.C., Canada, August 1-6, 2004.

[52] Shinozuka M, Sato Y. Simulation of nonstationary random process. *J. Engrg. Mech. Div.* 1967;**93**(1):11-40.

[53] NTC08. Norme tecniche per le costruzioni. Gazzetta Ufficiale del 04.02.08, DM 14.01.08, Ministero delle Infrastrutture.

[54] Hancock J, Bommer JJ. A state-of-knowledge review of the influence of strong- motion duration on structural damage. *Earthquake Spectra* 2006;**22**(3):827-845.

[55] Hancock J, Bommer JJ. Using spectral matched records to explore the influence of strong-motion duration on inelastic structural response. *Soil Dynamics and Earthquake Engineering* 2007;**27**:291-299.

[56] Armouti, N.S. Response of structures to synthetic earthquakes. *Emerging Technologies in Structural Engineering. Proc. of the 9th Arab Structural Engineering Conf.*, Nov. 29 – Dec. 1, 2003, Abu Dhabi, UAE, 331-340.

[57] Ryan K, Chopra A. Estimation of Seismic Demands on Isolators Based on Nonlinear Analysis. *Journal of Structural Engineering* 2004;**130**(3):392-402.

[58] Karavasilis T, Seo C. Seismic structural and non-structural performance evaluation of highly damped self-centering and conventional systems. *Eng. Structures* 2011,**33**(8):2248-2258.

[59] Cornell C, Jalayer F, Hamburger R, Foutch D. Probabilistic Basis for 2000 SAC Federal Emergency Management Agency Steel Moment Frame Guidelines. *Journal of Structural Engineering* 2002;**128**(4):526-533.

[60] Ang AHS, Tang WH. Probability Concepts in Engineering-Emphasis on Applications to Civil and Environmental Engineering. John Wiley & Sons, New York, USA; 2007.

[61] Math Works Inc. MATLAB-High Performance Numeric Computation and Visualization Software. User's Guide. Natick: MA, USA; 1997.

[62] Vassiliou F M, Tsiavos A, Stojadinović B. Dynamics of inelastic base-isolated structures subjected to analytical pulse ground motions. *Earth.Eng.& Str. Dyn.*, 2013;**42**(14):2043-2060.

[63] Castaldo, P., Palazzo, B., Mariniello, A.. Effects of the axial force eccentricity on the time-variant structural reliability of aging r.c. cross-sections subjected to chloride-induced corrosion Engineering Structures, **130**: 261-274, 2017.

[64] Palazzo, B., Castaldo, P., Mariniello, A. Time-variant structural reliability of R.C. structures affected by chloride-induced deterioration, American Concrete Institute, ACI Special Publication 2015-January (SP 305), pp. 19.1-19.10

[65] Etse, G.J., Ripani, M., Vrech, S.M. "Fracture energy-based thermodynamically consistent gradient model for concrete under high temperature," Proceedings of the 8th International Conference on Fracture Mechanics of Concrete and Concrete Structures, FraMCoS 2013, 1506-1515.

[66] Etse, G., Ripani, M., Caggiano, A. & Schicchi, D.S. "Strength and durability of concrete subjected to high temperature: continuous and discrete constitutive approaches," American Concrete Institute, ACI Special Publication 2015-January (SP 305), 9.1-9.18.

[67] Etse, G., Ripani, M. & Mroginski, J.L. "Computational failure analysis of concrete under high temperature," Computational Modelling of Concrete Structures - Proceedings of EURO-C 2014, 2:715-722.

[68] Etse, G., Vrech, S.M. & Ripani, M. "Constitutive theory for Recycled Aggregate Concretes subjected to high temperature," Construction and Building Materials; **111**: 43-53, 2016.

[69] Mroginski, J.L., Etse, G., Ripani, M. "A non-isothermal consolidation model for gradient-based poroplasticity," PANACM 2015 - 1st Pan-American Congress on Computational Mechanics, in conjunction with the 11th Argentine Congress on Computational Mechanics, MECOM 2015, pp. 75-88.

[70] Ripani, M., Etse, G., Vrech, S. & Mroginski, J.L. "Thermodynamic gradient-based poroplastic theory for concrete under high temperature," International Journal of Plasticity; **61**: 157-177, 2014.

[71] Ripani, M., Etse, G., Vrech, S. "Recycled aggregate concrete: localized failure assessment in thermodynamically consistent non-local plasticity framework", Computers and Structures, **178**: 47–57, 2017, doi: 10.1016/j.compstruc.2016.08.007.

[72] Vrech, S.M., Ripani, M. & Etse, G. "Localized versus diffused failure modes in concrete subjected to high temperature," PANACM 2015 - 1st Pan-American Congress on Computational Mechanics, in conjunction with the 11th Argentine Congress on Computational Mechanics, MECOM 2015, pp. 225-236.

COMPDYN 2017
6th ECCOMAS Thematic Conference on
Computational Methods in Structural Dynamics and Earthquake Engineering
M. Papadrakakis, M. Fragiadakis (eds.)
Rhodes Island, Greece, 15–17 June 2017

# STUDY ON THE SHEAR WALL STRUCTURE WITH COMBINED FORM OF REPLACEABLE COMPONENTS

**Cong Chen**[1], **Xilin Lu** [2], **and Renjie Xiao**[2]

[1] Chinese-German Insititute of Engineering, Zhejiang University of Science and Technology
Zhejiang 310023, China
e-mail: 1989chencong@tongji.edu.cn

[2] State Key Laboratory of Disaster Reduction in Civil Engineering, Tongji University
Shanghai 200092, China
lxlst@tongji.edu.cn
xiaorenjie2015@163.com

**Keywords:** Replaceable, Coupling Beam, Wall Foot, Shear Wall, Reinforced Concrete.

**Abstract.** *Earthquake resilient structure is an innovative type of structure developed for the purpose to restore the structure immediately after strong earthquakes. The structures with replaceable components is a kind of earthquake resilient structure. Based on the previous studies, combined form of the replaceable devices were applied in the coupled shear wall in this paper. Replaceable coupling beam and replaceable wall foot were used to concentrate the possible damage in the coupled shear wall. The numerical simulation models were verified by the test results of shear walls with each type of the replaceable devices. Then the shear wall model with the replaceable coupling beam and the replaceable wall foot together was studied in detail through parameter analysis. The results show that the influence of the shear wall capacity is small, and the variable parameters have some influence on the stiffness.*

## 1 INTRODUCTION

The structure design method to prevent the structural collapse under earthquakes is necessary. However, the damage after earthquakes is hard to repair or the repair time would be so long that to disturb the normal operation of the building. Earthquake resilient structure [1] is an innovative type of structure developed for the purpose to restore the structure immediately after strong earthquakes, in a way that little repair is needed and the repair time is very short. The earthquake resilient structural system includes the self-centering structures, rocking structures, the structures with replaceable components and so on. Previous research proved the structure with replaceable components could achieve the goal of quick repair. When parts of the structural component are replaced by replaceable devices, the structural component will act as a structural "fuse". The damage concentrates in the replaceable device during an earthquake, and the damaged part could be replaced conveniently after the earthquake, which could have less repair time than the traditional structure.

The structure with replaceable components was first introduced for steel structures. A replaceable "fuse" device in steel coupling beam was proposed by Fortney [2]. Cyclic tests of the specimens that consisted of two wall piers and connected by a single coupling beam were carried out. An excellent energy dissipation capacity and reduced damage was found in the steel coupling beam with central fuse [3,4]. A type of replaceable link was bolted to the tower shafts of east span of the new San Francisco-Oakland Bay Bridge [5]. Cyclic tests of the replaceable links excellent plastic deformation capabilities with easy replacement after the test [6]. Christopoulos developed two types of nonlinear replaceable links for steel moment resisting frames [7] and eccentrically braced steel frames [8]. Full-scale cyclic tests of steel beam-to-column subassemblies with replaceable links and the steel eccentric braced frame with replaceable links were carried out. The test results showed that the replaceable links exhibited great energy dissipation and higher rotation.

As for the reinforced concrete (RC) shear wall structures, the structure with replaceable coupling beams and the structure with replaceable wall foots were proposed by the authors[1, 9,10]. The replaceable coupling beam consists of the central replaceable device and the non-yield connecting beams at the two ends. The replaceable wall foot is a compression-tension rubber bearing replacing the RC wall foot. The replaceable device is allowed to undergo plastic deformation and the end-plate bolt connection is used to implement replacement of the damaged device after strong earthquakes. Three coupled shear walls with replaceable coupling beams and one shear wall with conventional coupling beams were tested under static cyclic loading .The results showed that the conventional RC coupling beams experienced failure at beam ends whereas the plastic deformation of the replaceable coupling beam mainly concentrated on the replaceable device. Four innovative shear walls with replaceable wall foots and one conventional shear wall were also tested under cyclic loads. The severe damage at the conventional shear wall foots was observed whereas the damage was concentrated in the replaceable foots of the innovative shear walls. The replacement could be easily implemented owing to the bolt connection between the replaceable part and the remaining part.

It is noted that previous research focused on the structure with one type of the replaceable devices. To further investigate the combined form of the replaceable coupling beam and the replaceable wall foot, the numerical study was conducted in this paper. First, the numerical simulations of the shear walls with one type of the replaceable devices were carried out by comparison with the tested results. Then the shear wall with the replaceable coupling beam and the replaceable wall foot together was studied in detail.

## 2 FINETE ELEMENT STUDY

The object-oriented, open source software OpenSees is used to develop nonlinear finite element model of the shear walls. Cyclic Softened Membrane Model (CSMM) is used to simulate the RC wall panel. The boundary zone is modeled by displacement-based beam-column element with fiber sections. The numerical models of the replaceable devices are discussed as follows.

### 2.1 Replaceable coupling beam modeling

Figure 1 shows the replaceable coupling beam proposed by authors. It consists of the non-yield parts at the two sides and the yield part at the center. It is expected that the yield part undergoes shear yielding and the non-yield parts remain elastic under strong earthquakes. The non-yield part was conventional SRC beam, the RC beam embedded with the shape steel. The yield part was the replaceable device made of low yielding point steel. The end-plate bolt connection was used to implement the replacement of the yield part easily after strong earthquakes.

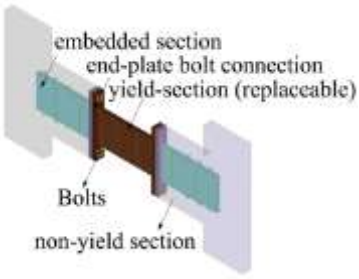


Figure 1. Overview of the replaceable coupling beam

To simulate the shear force-displacement relationship of the replaceable device, a truss element with the Hysteretic material was used. The SRC beam was modeled by beam-column element with fiber section. Parallel truss elements were used to transfer the axial force of the replaceable device. The numerical model is shown in Figure 2.

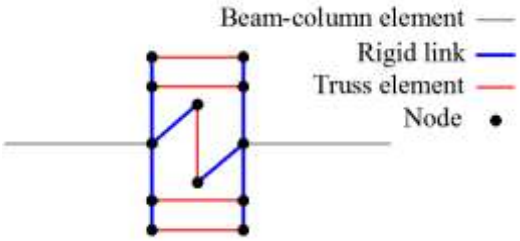


Figure 2. Numerical model of the replaceable coupling beam

### 2.2 Replaceable wall foot modeling

The proposed replaceable wall foot is illustrated in Figure 3. The central part was the laminated rubber with steel shims in-between. On each side of the rubber layers, a steel plate made of low yielding point steel was settled. The laminated rubber is supposed to resist most of the compression force and the tension force is mainly resisted by the steel plates. A strong connection plate was used to make the rubber layers and steel plates work together. Replacement was also achieved by the end-plate bolts.

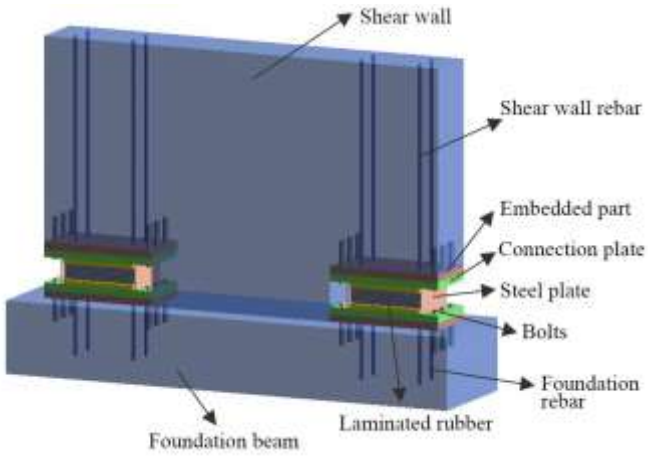


Figure 3. Overview of the replaceable wall foot

To simplify the behavior of the replaceable wall foot, beam-column element with fiber section was used, as shown in Figure 4. Hysterical material was adopted to simulate the behavior of the steel plate and the laminated rubber layers was represented by Elastic-No tension material. Previous research [1] suggests a calculation method of the key points of the skeleton curve for the proposed replaceable wall foot. As for the simulation, the tension strength of the laminated rubber layer was considered in the hysterical material, so no tension strength was included in Elastic-No tension material.

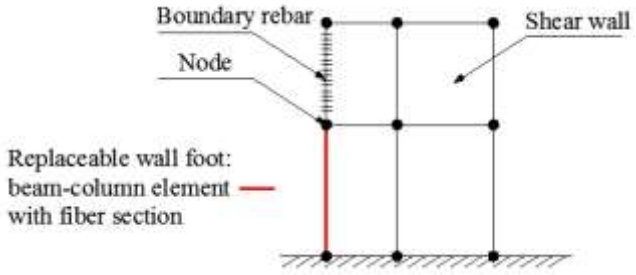


Figure 4. Numerical model of the replaceable wall foot

## 2.3 Model verification

The finite model results are compared with the test results to verify the modeling approach discussed above. Specimen CSW and F1SW tested by Chen[9] were modeled to validate the simulation of replaceable coupling beam. Specimen SW-0 and NSW1-2[1] were created to verify the modeling of replaceable wall foot. The axial force was applied to the model as nodal force and a multi-point constraint was placed at the top nodes to apply the horizontal displacement loads. Figure 5 compares the top displacement-base shear hysteretic curves of the experimental and numerical results. The model properly predicted the behavior of the conventional shear wall and the shear wall with replaceable devices. Figure 6(a) is the numerical hysterical behavior of the replaceable device in coupling beam, and the comparison of the test and simulation behavior of the replaceable wall foot is shown in Figure 6(b). The simulation results agree well with the experimental results, which proves a proper simulation method of the replaceable devices.

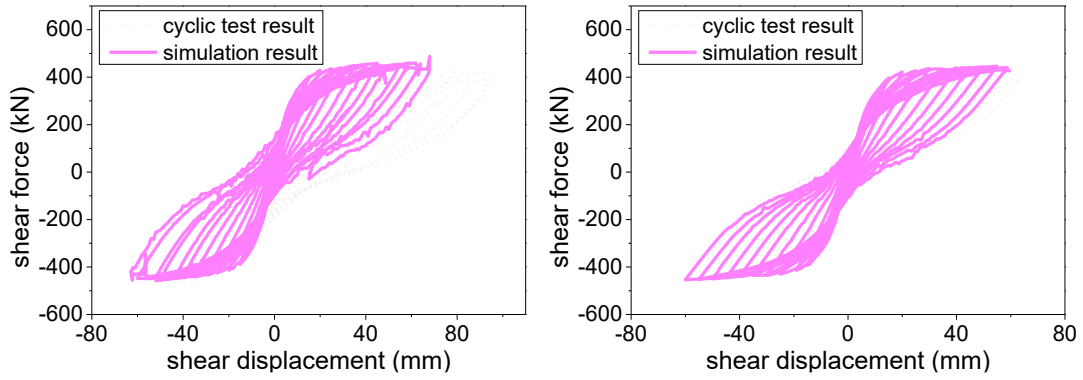


(a) CSW (b) F1SW

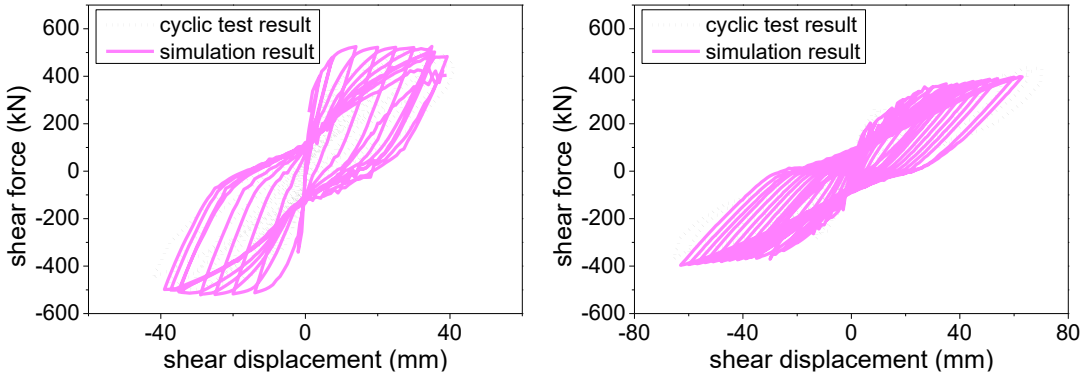


(c) SW-0 (d) NSW1-2

Figure 5. Top displacement-base shear hysteretic curves

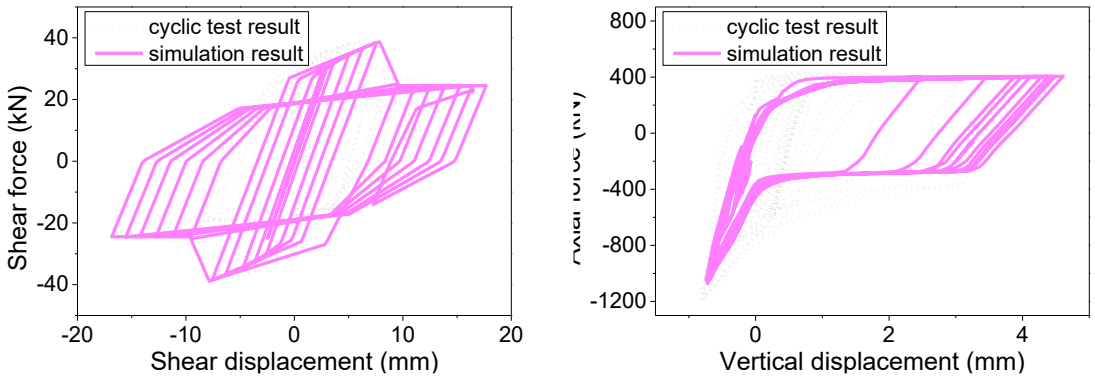


(a) Replaceable device in F1SW (b) Replaceable wall foot in NSW1-2

Figure 6. Numerical hysterical behavior of the replaceable devices

## 3 SHEAR WALL WITH COMBINED FORM OF REPLACABLE DEVICES

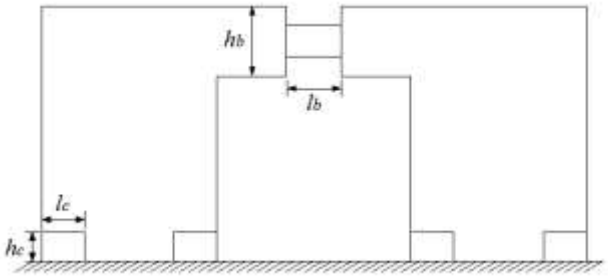


Figure 7. Dimension mark of the combined replaceable devices in shear wall

According to the design method proposed by the authors [9,11], shear wall with combined form of the replaceable coupling beam and the replaceable wall foot was created. As shown in Figure 7, the height of the non-yield connection beam $h_b$ and the span of the replaceable device $l_b$ are defined according to the strength and stiffness equivalence of the replaceable coupling beam to the conventional coupling beam [12]. To concentrate the plastic damage, the height of the replaceable wall foot $h_c$ should be larger than the length of the plastic hinges [13].The width of the replaceable wall foot $l_c$ was determined by the region where the compression strain of the concrete exceeds $\varepsilon_x$, in order to avoid the concrete crush. The minimal height and width of the replaceable foot are calculated as follows:

$$h_c \geq 0.2h_w + 0.044H \tag{1}$$

$$l_c \geq 1.5(1-\frac{\varepsilon_x}{\varepsilon_{c,\max}})\xi h_0 = 1.5(1-\frac{\varepsilon_x h_p}{\theta_u \xi h_0})\xi h_0 \tag{2}$$

where $h_w$, $H$ are the cross-section depth and effective height of the shear wall respectively [14], $\varepsilon_{c,\max}$ is the maximum compressive strain at the extreme compression edge, which equals the ultimate curvature plus the equivalent compression zone height $\xi h_0$ of the bottom section of the shear wall. The ultimate curvature of the section is defined as the ratio of the maximum story drift $\theta_u$ to the height of the plastic hinge $h_p$.

In order to further study the parameter influence to the performance of shear wall with replaceable devices, a parameter study was conducted. A base model for the parameter analysis was chosen as shown in Figure 8. The influence of four parameters was analyzed by changing one parameter and keeping the other three unchanged at a time.

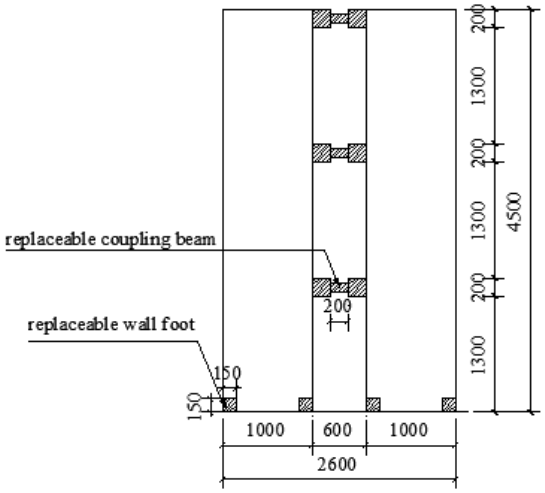


Figure 8. The base model for parameter analysis

### 3.1 Height of the replaceable wall foot

To investigate the influence of height of the replaceable wall foot $h_c$, several numerical models with different height ratio were analyzed. The height ratio $R_h$ was defined as Equation (3):

$$R_h = h_c / H \tag{3}$$

where $h_c$, $H$ are height of the replaceable wall foot and the effective height of the shear wall respectively. Figure 9 shows the comparison of load capacity and stiffness of the numerical models with different height ratio. The shear wall capacities are almost the same with different wall foot height. With the increasing of the wall foot height, the initial stiffness increases first and then decrease, which indicates a proper height ratio range is 0.05~0.10.

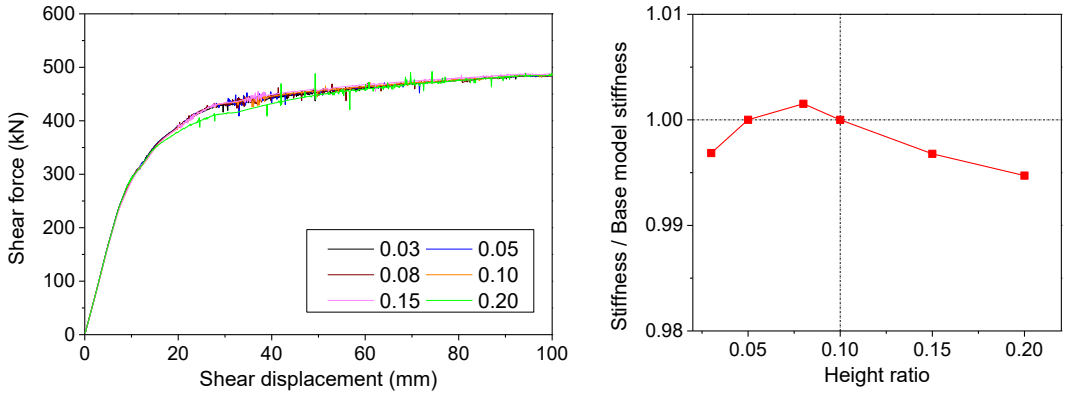


(a) Load-displacement curves (b) Comparison of initial stiffness

Figure 9. Influence of the wall foot height

### 3.2 Width of the replaceable wall foot

The width ratio $R_w$ was defined by Equation (4) and several numerical models with different width ratio $R_w$ were used to investigate the influence of width of the replaceable wall foot:

$$R_w = l_c / h_w \tag{4}$$

where $l_c$, $h_w$ are the width of the replaceable wall foot and the cross-section depth of the shear wall respectively. As shown in Figure 10, the shear wall capacities are almost the same but the initial stiffness decreases with the increase of wall foot width.

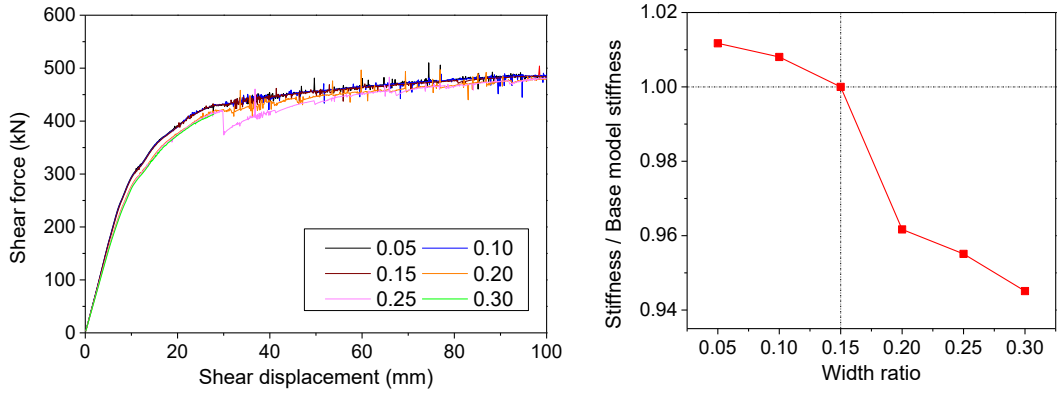


(a) Load-displacement curves (b) Comparison of initial stiffness

Figure 10. Influence of the wall foot width

### 3.3 Height of the non-yield connection beam

Figure 11 shows load-displacement curves with different height of non-yield connection beams and the comparison of initial stiffness. The influence to the shear wall capacity is small because the capacity is determined by the shear capacity of the replaceable device, not the connection beam. The initial stiffness results show that the stiffness increases with the larger connection beam height, but the difference is not so obvious because the coupling beam height is not so deep and the stiffness contribution to the shear wall is small. Supposing a much deep coupling, the stiffness deviation due to connection height change would be larger.

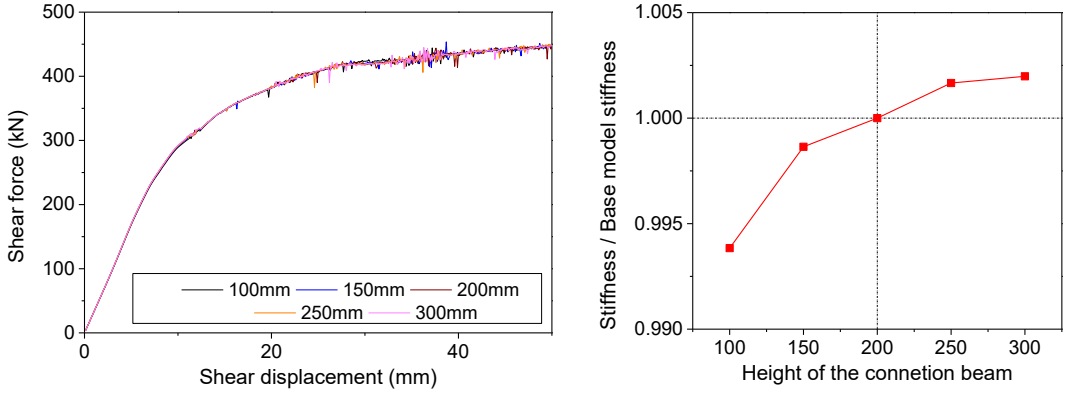


(a) Load-displacement curves (b) Comparison of initial stiffness

Figure 11. Influence of the connection beam height

### 3.4 Span of the replaceable device

The influence of the replaceable device span is shown in Figure 12. The shear wall capacities are similar but the difference is larger than that of the connection beam height. The initial stiffness gets larger when the span of the replaceable device gets smaller, and the increase becomes higher with the small span.

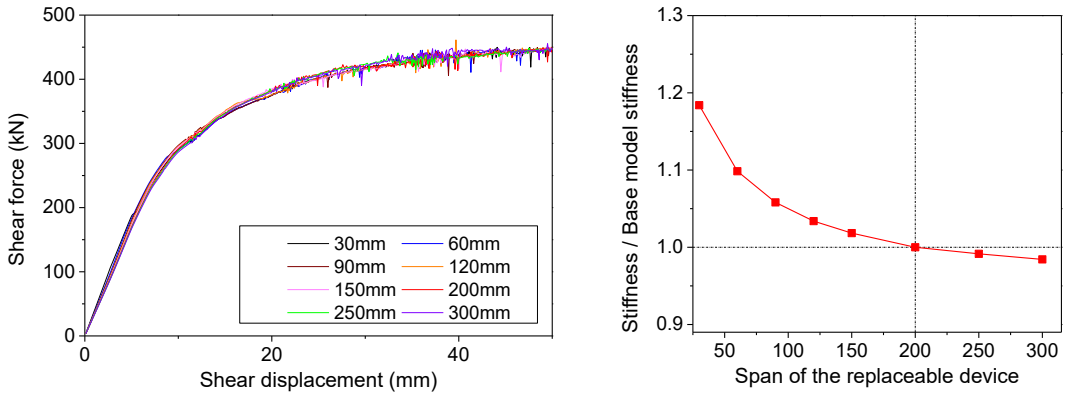


(a) Load-displacement curves (b) Comparison of initial stiffness

Figure 12. Influence of the replaceable device span

## 4 CONCLUSIONS

- To make the damage replaceable and the structure earthquake resilient, replaceable devices should be located in all area which could be easily damaged. For coupled shear wall, coupling beam and wall foot are parts which are easy to be damaged. So based on the previous study, combined form of the replaceable devices were applied in the coupled shear wall in this paper. Numerical simulation was carried out in OpenSees and parameter analysis was conducted based on the verified finite element models.
- Truss element with the hysteretic material could be used to simulate the replaceable device in coupling beam and the behavior of the replaceable wall foot could be modelled by beam-column element with fiber section. Simulation results of the replaceable devices and the shear wall agree well with the experimental results, which proves a proper simulation method.
- The height of the non-yield connection beam, the span of the replaceable device, the height and width of the replaceable wall foot are variable parameters for the coupled shear wall with combined form of replaceable components. The parameter study shows that the shear wall capacity is little influenced by the variable parameters of each replaceable devices but the stiffness are different. With the increasing of the wall foot height, the initial stiffness increases first and then decrease, and a proper wall foot height ratio range of 0.05~0.10 is proposed. The initial stiffness decreases with the increase of wall foot width and the decrease of connection beam height. When the span of the replaceable device gets smaller, the initial stiffness increases, and the increase gets faster in the small range.

## REFERENCES

[1] X.L. Lu, Y.J. Mao, Y. Chen, et al, New structural system for earthquake resilient design. *Journal of Earthquake and Tsunami*, **7**(3), 26-38, 2013.

[2] P.J. Fortney, B.M.Shahrooz, G.A.Rassati, The next generation of coupling beams. *Proceedings of the Composite Construction in Steel and Concrete V-Asce* 2006, pp: 619-630.

[3] P.J. Fortney, B.M.Shahrooz, G.A.Rassati, Large-scale testing of a replaceable "fuse" steel coupling beam. *Journal of Structural Engineering,* **133**(12), 1801-1807, 2007.

[4] P.J. Fortney, The next generation of coupling beams. *College of Engineering and Applied Science, University of Cincinnati, Cincinnati*, 2005.

[5] M.C. Tang and R. Manzanarez, San francisco-oakland bay bridge design concepts and alternatives. *The 2001 Structures Congress and Exposition*, Washington, D.C., United States, 2001, pp: 1-7.

[6] C.C. Mcdaniel, C.M. Uang, F. Seible, Cyclic testing of built-up steel shear links for the new bay bridge. *Journal of Structural Engineering-Asce,* **129**(6), 801-809, 2003. DOI: 10.1061/(ASCE)0733-9445 (2003)129:6(801).

[7] Y. Shen, C. Christopoulos, N. Mansour, et al. Seismic design and performance of steel moment-resisting frames with nonlinear replaceable links. *Journal of Structural Engineering-Asce*, **137**(10), 1107-1117, 2011. DOI: 10.1061/(ASCE)ST.1943-541X.0000359.

[8] N. Mansour, C. Christopoulos, R. Tremblay. Experimental validation of replaceable shear links for eccentrically braced steel frames. *Journal of Structural Engineering-Asce,* **137**(10): 1141-1152, 2011. DOI: 10.1061/(ASCE)ST.1943-541X.0000350.

[9] X.L. Lu, Y.J. Mao, Y. Chen, et al, Earthquake resilience of tall buildings using replaceable energy dissipation members. *10th U.S. National Conference on Earthquake Engineering (10NCEE)*, Anchorage, Alaska, USA, July 21-25, 2014.

[10] X.L. Lu, Y.J. Mao, Y. Chen, Test and analysis on shear walls with replaceable devices under cyclic loading for earthquake resilient structures. *9th International Conference on Urban Earthquake Engineering /4th Asia Conference on Earthquake Engineering*, Tokyo Institute of Technology, Tokyo, Japan, March 6-8, 2012.

[11] Y. Chen, X. L. Lu. New replaceable coupling beams for shear wall structures. *15th world conference on earthquake engineering*, Lisbon, Portugal, 2012: paper ID 2254.

[12] C. Chen, X. L. Lu. Experimental analysis of steel panel dampers in replaceable coupling beams. *IABSE Conference, Geneva 2015: Structural Engineering: Providing Solutions to Global Challenges*, Geneva, Switzerland, September 23-25, 2015.

[13] H.J. Jiang, Q.Z. Liu. Study of a new type of RC shear wall with replaceable corner components. *13th International Symposium on Structural Engineering (ISSE-13)*, Hefei, China, October 24-27, 2014.

[14] T. Paulay, M. J. Priestley, *Seismic design of reinforced concrete and masonry buildings*. New York: John Wiley & Sons, 1992.

COMPDYN 2017
6th ECCOMAS Thematic Conference on
Computational Methods in Structural Dynamics and Earthquake Engineering
M. Papadrakakis, M. Fragiadakis (eds.)
Rhodes Island, Greece, 15–17 June 2017

# FINITE ELEMENT ANALYSIS OF EXTERNAL RC WIDE BEAM-COLUMN JOINTS PROVIDED WITH DIFFERENT DETAILING SOLUTIONS

**Giuseppe Santarsiero**[1] **and Angelo Masi**[1]

[1] University of Basilicata
via dell'Ateneo Lucano, 10, Potenza, Italy
{giuseppe.santarsiero, angelo.masi}@unibas.it

**Keywords:** wide beam-column joints, cracking, seismic performance, nonlinear analysis, finite element models.

**Abstract.** *Wide beams are part of the residential buildings' construction habits in Italy as well as in other Mediterranean countries. In fact, undoubted advantages are provided by this type of beams with respect to architectural functionality and time-saving in formwork installation. However, in the design process of new RC buildings, some penalties in terms of ductility are prescribed in seismic codes when this type of beam is used. Previous studies demonstrated that the detailing of beam reinforcement can influence the response of external wide beam-column connections, especially for what concern the reinforcing bars bent outside the column width. In order to investigate the influence of this aspect on the global performance of external wide beam-column joints, the authors calibrated detailed finite element models based on the experimental results of cyclic tests carried out on two full-scale specimens. Beyond the detection of the main phenomena characterizing the subassemblages' behavior, a parametric analysis has been performed to evaluate the influence of reinforcement amounts placed inside and outside the column core. Particularly, three values of the beam reinforcement area have been considered either placed inside or outside the column core, and the corresponding global lateral response curves of the beam-column joint have been obtained. It has been observed that in the cases where the additional amount of longitudinal reinforcement in the beam was placed inside the column core, both a more ductile behavior and a higher strength of the connection were obtained. This finding suggests that slip phenomena and torsion cracking occurred in the non-confined zone outside the column core, accounted for by the numerical model, can heavily influence the seismic behavior of this kind of beam-column joints even though they are seismically designed.*

# 1 INTRODUCTION

The capacity to reduce emergency impact on communities due to seismic events [1] is strongly based on the prevention of collapse of both private and public buildings. This requires careful seismic assessments of the existing buildings as well by enhancing the seismic design of the new ones. The present study is aimed at characterizing the seismic behavior of beam-column connections equipped with wide beams (wide beam-column joints). This kind of beam is frequently used in the Italian and Mediterranean building stock both for older and newly designed buildings, especially for the residential ones.

This study is based on a remarkable experimental campaign carried out at the laboratory of structures of the University of Basilicata, where a set of wide beam-column joint specimens were tested under reversed cyclic lateral loads to study their seismic behavior [2, 3] and possible strengthening techniques [4]. Beam-column joints equipped with deep beams were part of the same research program [5, 6, 7]. Based on the results of the experimental tests on wide beam-column joints, the authors calibrated a detailed finite element model in order to perform a parametric analysis to evaluate the influence of some detailing solutions on the seismic behavior of joints. A software package able to appropriately account for the nonlinear properties of concrete, like cracking and crushing, as well as the reduction of shear and compressive strength after cracking, has been used in setting up the models [8, 9, 10]. Moreover, appropriate bond laws have been considered at the interface between concrete and steel to account for possible slippage phenomena [11]. The model, properly calibrated, allowed to understand the main damage mechanisms influencing the seismic performance of wide beam-column joints. In fact, bond slips of beam longitudinal reinforcement outside the column width is responsible for the limited contribution of these bars to the flexural capacity of the beam and, in turn, of the whole beam-column connection. Indeed, the beam bars bent outside the column core are not able to achieve the yielding stress. Contrarily, the internal ones reach the yielding stress and, additionally, are subjected to hardening better exploiting their tensile strength. Another key mechanism occurring in wide beam-column joints under cyclic loading is the cracking due to torsion in the beam width exceeding the column dimension. This is due to the pull-push effect of the beam bars outside the column and to the absence of confining reinforcement in that zone. As shown by the experimental results, this can lead to extensive damage and to the concrete cover spalling further decreasing the strength contribution of the beam external bars.

In order to obtain indications on the design of this kind of structural elements, a parametric analysis has been performed essentially by changing the amount of beam longitudinal reinforcement placed inside and outside the column core. It has been found that slip phenomena and torsion cracking occurred in the non-confined zone outside the column core, accounted for by the numerical model, are able to heavily influence the seismic behavior of this kind of beam-column joints even though they are seismically designed. The structural ductility is significantly influenced while minor changes are found for the maximum load value. This points out that the beam reinforcement in wide beams should not be evenly distributed along the width of the beam, but it should be placed prevailingly in the column core, where a better confinement condition is generally present, contrarily to the outer zones of the beam-column intersection.

## 1.1 EXPERIMENTAL CAMPAIGN

The experimental program related to this study is reported in detail in [3]. However, for sake of clarity, a short summary is reported in the following. Cyclic quasi-static tests on deep and wide beam-column connections considered to belong to a four-storey residential RC building were included in the experimental program. Out of a total of 26 full-scale specimens, 12 were wide beam-column joints. They have different detailing but identical geometry. The reinforcement detailing was related to three different seismic design levels that is: i) no seismic design, ii) seismic design with respect to a design ground acceleration $a_g$ for the Life Safety limit state equal to 0.25g, iii) seismic design with respect to a design ground acceleration $a_g$ for the Life Safety limit state equal to 0.05g. The subject of this study is a beam-column specimen having the latter seismic design level, i.e. with a low Earthquake Resistant Design level matching the seismic zone 4, being the less hazardous in Italy.

The details of the beam-column specimen under study and the test set-up are displayed in Fig. 1 and 2, respectively.

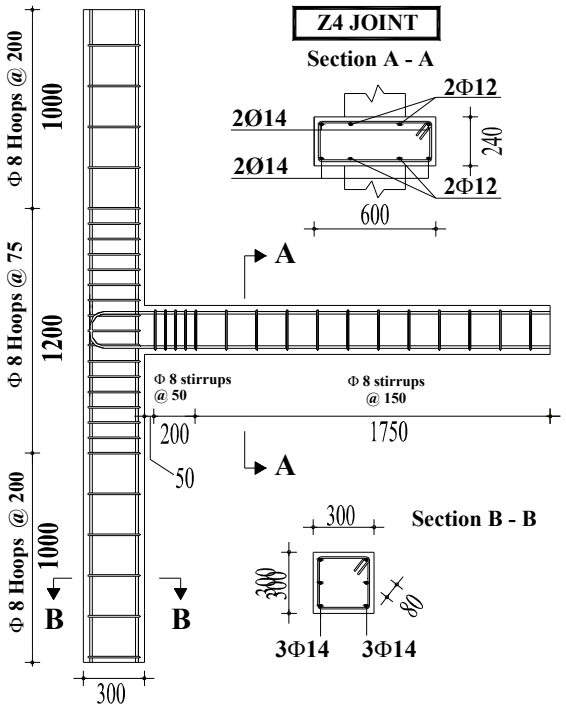


Figure 1: Geometry and detailing of the wide beam-column specimen under study.

The column in placed in vertical position so that an axial load can be applied to the column to simulate the upper storeys' dead load effect. A horizontal actuator is able to apply a lateral load to simulate the seismic effects in a cyclic quasi-static manner. The loading history was displacement controlled with 4 mm/s. A constant vertical load equal to 290 kN was applied for the entire duration of the test. The specimen was equipped with several devices to measure both deformations and forces applied during the tests. Load cells were placed at the top of the column to record the horizontal force applied by the actuator as well as at the beam end to measure the reaction of the restraint made-up of steel strut. The top column displacement was acquired by means of a wire transducer, while the deformations at the beam-column intersection were acquired through Linear Variable Displacement Transducers (LVDT). More details on the instrumentation and test apparatus can be found in [3].



Figure 2: Test set-up.

## 2 EXPERIMENTAL RESULTS

The experimental behavior of a structural assemblage or member under cyclic loading is usually analyzed by plotting the envelope of all load-displacement curves obtained from the different tests carried out at increasing amplitude. In this case, the displacement has been normalized to the storey height *h* of the building to which the specimen is supposed to belong. The interstorey height is h=3200mm so that the drift values are computed as the ratio between the top column displacement and *h*.

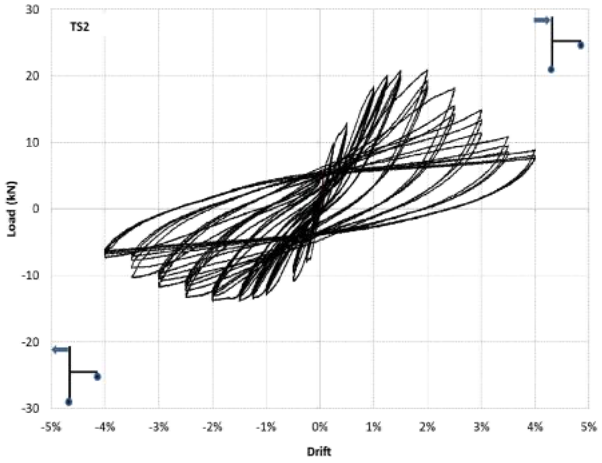


Figure 3: Load-drift envelopes.

As can be seen in Fig. 3 the maximum drift value attained during the test is 4%. The maximum load is achieved at about 1.5% of drift both for positive and negative loading, attaining values of 20.96 kN and 14.00 kN, respectively. Around 2% drift the load starts to decrease due to degrading phenomena. Making reference to the approach proposed by Panagiotakos

and Fardis [12], the ultimate drift can be assumed as the value where a strength drop of 20% with respect to the maximum is observed. In this way, ultimate drift values equal to 2.7% and 3.2% have been computed for positive and negative loading, respectively.

This significant degrading effect is quite peculiar to this joint specimens and is related to the damage which develops near the intersection of beam and column, precisely at beam sides (see Fig. 4).

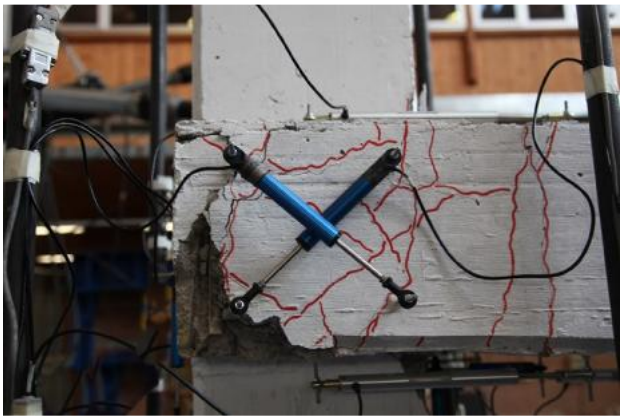

Figure 4: Cracking pattern at 4% drift.

Firstly, vertical cracks appeared at the beam-column intersection due to flexure. In the following stages of the test, inclined cracks developed at beam sides as can be seen in Fig. 4. This is due to torsion stresses generated by the flexure transfer from the beam to the column. Moreover, the cracked zones at beam sides are not confined by stirrups as can be seen from Fig. 1. Indeed, column hoops confine only the column core, while the beam zones outside the column width are not confined despite some of the beam rebars are bonded there. Although the specimen under study is seismically designed, its cyclic behavior is not fully satisfactory. To better understand this behavior, a detailed finite element model using ATENA 3D software [8] is built and calibrated on the basis of the experimental results. Afterward, the model is used to perform a parametric analysis mainly aimed at evaluating the effect of different beam rebar arrangements on the whole subassemblage behavior.

## 3 FEM MODELING

Exploiting the experimental test results, a nonlinear finite element model developed with ATENA 3D software package [8] was developed. The software is based on the nonlinear fracture mechanics and, among its capabilities, there is the possibility to take into account the softening in compression as well as the tensile cracking of concrete. Moreover, the software incorporates different bond laws which can be applied to the steel reinforcement bars to take into account in a realistic way the bond slips between concrete and steel.

For the concrete, the robust smeared crack model was used. The main mechanical properties of the concrete, are as follows: $f_t$ = 2.89 MPa, $f_c$ = 37MPa, $\nu$ = 0.2, and $E_c$ = 32.5 GPa, being respectively the tensile strength, compressive strength, Poisson ratio and elastic modulus. Experimental tests on concrete cubes allowed to evaluate the compressive strength $f_c$ to which all other mechanical properties are related.

Compression stresses of concrete were simulated using a fictitious uniaxial model proposed by Chen & Saleb [13] with a softening based on displacements.

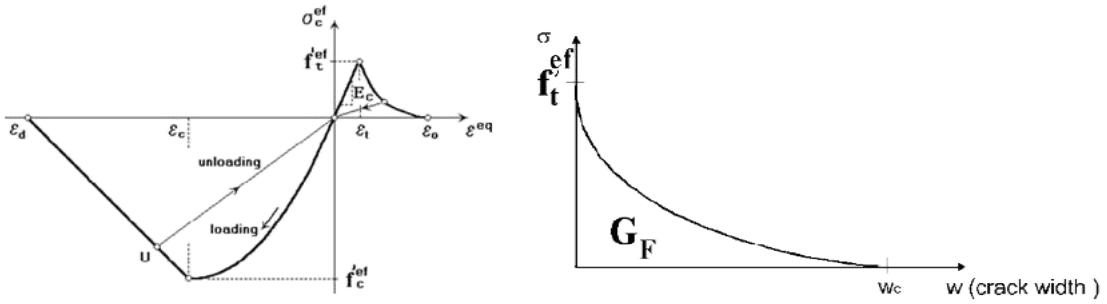


a) b)

Figure 5: a) Uniaxial compressive stress-strain law and b) crack opening law for tensile stresses for concrete.

The tensile behavior of concrete is ruled by the crack opening law (tensile stress vs crack opening displacement, see Fig. 5b) whose underlying area is the fracture energy ($G_F$). The tensile strength drops with an exponential softening law. One of the most important parameters governing the tensile behavior is the fracture energy, that is the energy amount required to produce a crack of unit area. The fracture energy was computed by means of the Remmel's law [14]. Also, the tension stiffening effect was considered as related to the apparently stiffer tensile behavior of concrete due to the presence of steel reinforcement. A tension stiffening coefficient $C_{ts}$ equal to 0.3 has been assumed, meaning that even when a crack is open a residual 30% tensile strength is considered.

An elastoplastic law with hardening was chosen for the reinforcing steel stress-strain relationship, with yielding stress $f_y$=480 MPa and failure stress $f_t$=590 MPa. These values were based on experimental tests carried out on rebars belonging to the same steel supply used for the specimens' construction.

Regarding the simulation of the bond slip between concrete and steel, it has to say that, whereas in some cases a perfect connection could be considered, the experimental evidence drawn from the test under study shows that bond slip could contribute to the observed degrading phenomena. For this reason, the CEB-FIP Model Code (1990) bond law was adopted to account for the bond-slip behavior. Different laws were used depending on the bond and confining conditions of the beam rebars.

In particular, the bond law adopted for the bottom beam rebars outside the column width assumes unconfined concrete (no stirrups) and poor bond conditions (concrete cover size equal to 20mm). The resulting bond-slip law is depicted in Fig. 6, where the peak bond stress is $\tau_{\max} = 5.38MPa$ and the residual one is $\tau_f = 0.80MPa$. Critical slip values are $s_1$=$s_2$=0.6mm and $s_3$=2.5mm, as reported in Tab. 3.1.1 of Model Code (1990) for splitting type bond failure.

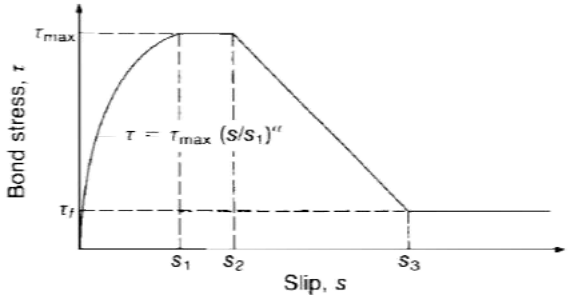


Figure 6: Bond-slip relationship.

Due to the presence of a concrete cover equal to 80mm, good bond conditions can be assumed for the upper beam bars placed outside the column core, with still unconfined concrete. This determines different values of bond stresses and bond slips, that is $\tau_{\max} = 10.76MPa$,

$\tau_f = 1.6MPa$, $s_1$=$s_2$=0.6mm and $s_3$=1.0mm (see Tab. 3.1.1 Model Code 1990, good bond conditions and splitting type bond failure). For all the other longitudinal rebars of the beam (placed within the column width), as well as for the column reinforcement bars, a perfect bond condition was assumed.

The global finite element model (see Fig. 7) is made-up of 5470 3D 8-node hexahedral volume elements with a size of 5.0cm simulating the concrete volumes and the reinforcement bars were modeled through truss elements (i.e. capable of carrying only axial loads). The bars are embedded in the concrete, and the software is able to automatically create nodes shared by the truss elements and the hexahedral elements, thus contributing to adequately model the collaboration between steel and concrete. The finite element model was also provided with so-called monitoring points which give the model response at selected locations. Two monitoring points, located at the top of the column, where the displacement is applied, provide the column top displacement and the applied horizontal load values.

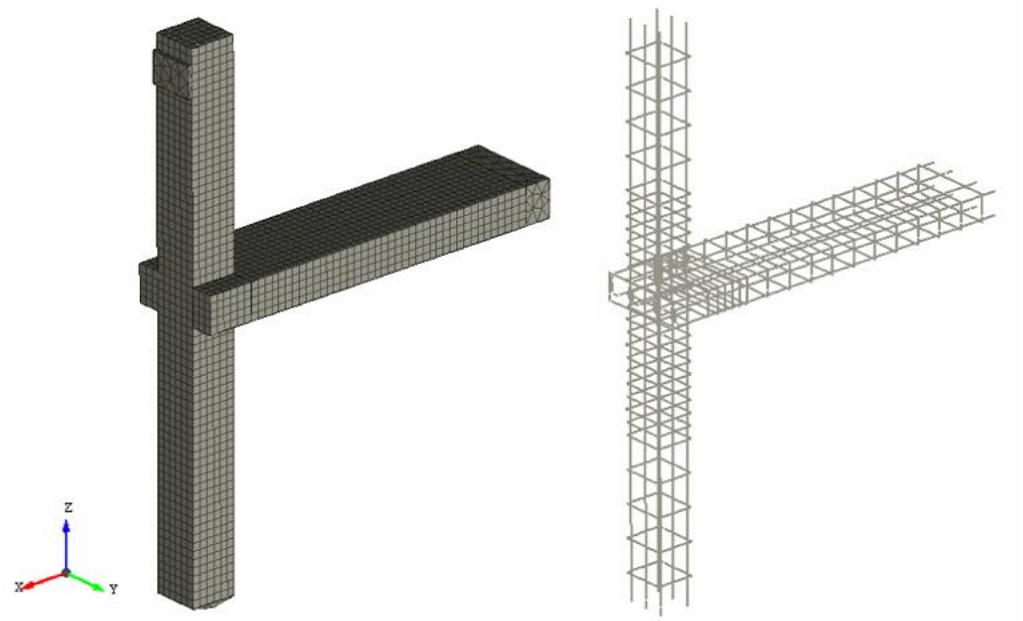


Figure 7: The concrete mesh of hexahedral elements and truss elements simulating the reinforcement.

### 3.1 Comparison of numerical and experimental results

The calibration of a nonlinear finite element model aims at reproducing the load-displacement curve, as good as possible, so evaluating whether the numerical simulations account for the main phenomena that characterize the experimental behavior and properly predict them [15].

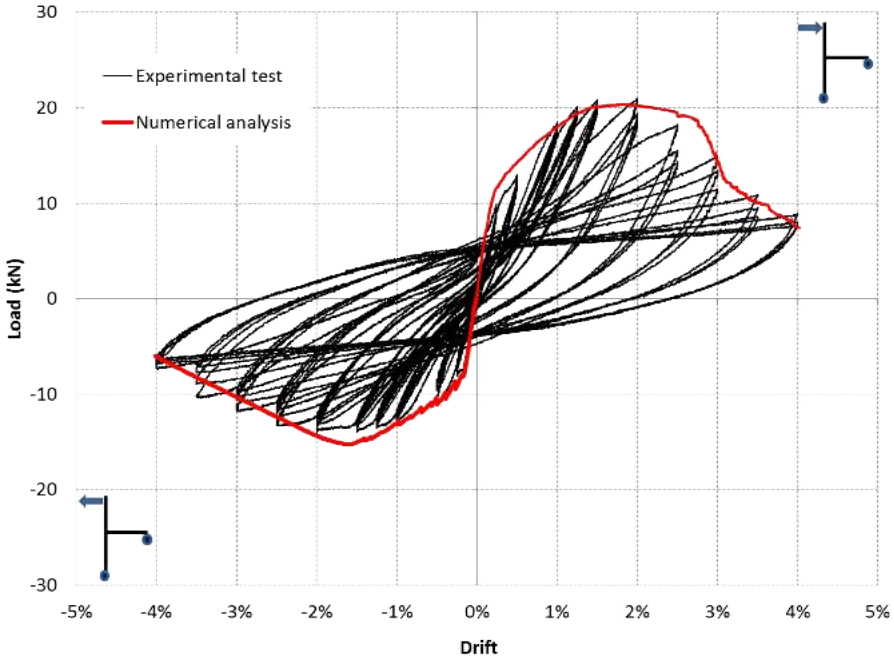


Figure 8: Comparison between numerical and experimental behavior.

First, it is worth noting that the performed numerical analyses were monotonic and not cyclic like in the test. For this reason, two separate steps of numerical analysis were necessary with respect to positive and negative loading. As can be seen in Fig. 8, the performed calibration process led to a numerical load-drift curve very close to the peak load values of the experimental envelope. This is observed through the entire drift range even when severe strength degradation effects occur. Fig. 9 depicts the experimental crack pattern at the end of the test and the related crack patterns obtained from the simulations under positive and negative loading. The comparison is satisfactory even though the monotonic numerical loading of the specimens yields necessarily different damage, at least in terms of crack sizes. However, from a qualitative point of view, numerical patterns show the presence of inclined cracks in the joint panel as well as vertical cracks at the beam-column intersection. The spalling effects at the end of the beam are not captured by the numerical model since is mainly due to the cyclic loading, not simulated by the numerical analysis.

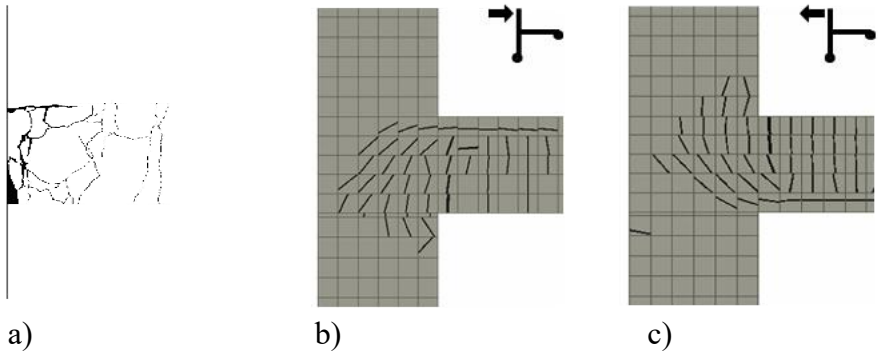


Figure 9: a) Experimental crack pattern, b) numerical crack pattern for positive loading and c) numerical crack pattern for negative loading.

Results of the experimental-numerical comparison confirm that the 3D nonlinear finite element model is able to adequately capture the experimental behavior of the specimen and, then, can be used for further numerical analysis devoted to investigating different detailing conditions as, for example, different amounts and positions of rebars in the beam.

## 4 PARAMETRIC ANALYSIS

A parametric analysis referred to the joint specimen numerically and experimentally analyzed before is carried out, by varying the longitudinal reinforcement area in the beam. Additional rebars have been considered and located in two different zones of the beam section, that is either externally to (E) or inside (I) the column core. For each position, two different amount of reinforcement have been considered. Referring to Fig. 10, the number associated with the letter E and I indicates the number of couples of 14mm diameter bars added to the as-built arrangement. For example, solution E1 has one additional couple of 14mm diameter bars for both the upper and lower reinforcement layers. Note that in all the three configurations, a symmetric reinforcement arrangement is considered.

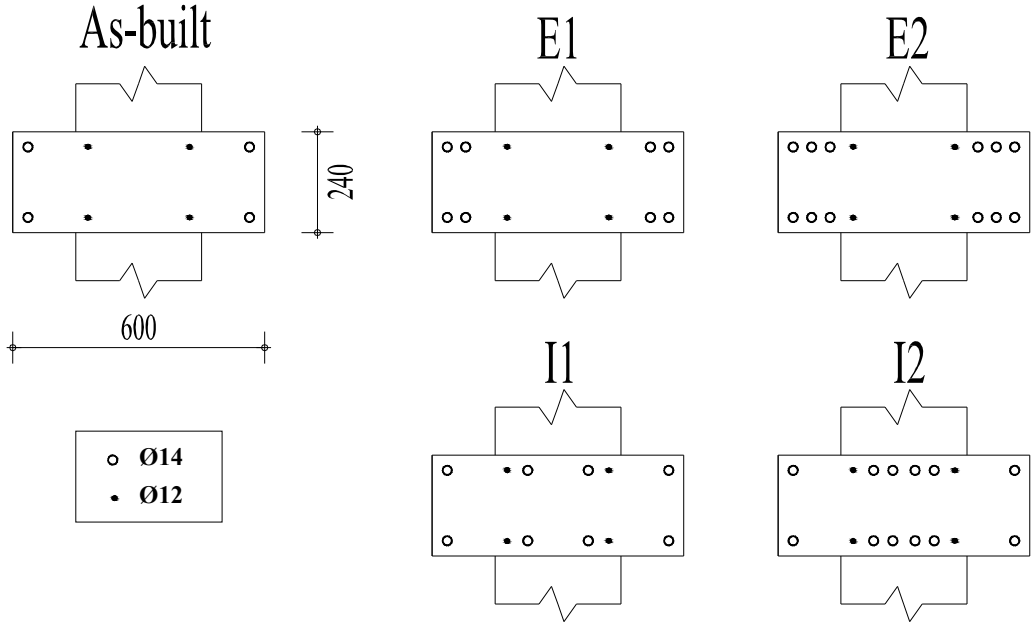


Figure 10: Different beam rebars arrangements for the parametric analysis.

The resulting reinforcement areas are reported in Tab. 1.

Starting from the 3D nonlinear FEM model of the as-built specimen, four additional FEM models were created by modifying the amount of steel longitudinal bars in the beam according to Fig. 10 and Tab. 1.

In order to evaluate the influence of the different bars' positions and amount on the post-elastic behavior of the beam-column connections, nonlinear numerical simulations were carried out on the specimens E1, E2, I1 and I2. The numerical simulations provided the load-drift behavior and the damage mechanisms considering only positive loading in order to keep the computational effort under acceptable limits.

| Specimen | Bottom/Top area ($mm^2$) | Bottom/Top area (%) | Bottom/Top area External (%) | Bottom/Top area Internal (%) |
|---|---|---|---|---|
| As-built | 532 | 0.37 | 0.21 | 0.16 |
| E1 | 838 | 0.58 | 0.43 | 0.16 |
| E2 | 1144 | 0.79 | 0.64 | 0.16 |
| I1 | 838 | 0.58 | 0.21 | 0.37 |
| I2 | 1144 | 0.79 | 0.21 | 0.58 |

Table 1: Reinforcement amounts for the parametric analysis.

As can be seen from Fig. 11 the addition of reinforcement generally improves the performance in terms of maximum load but not always in terms of ductility. In Tab. 2, the main results from the numerical simulations are summarized.

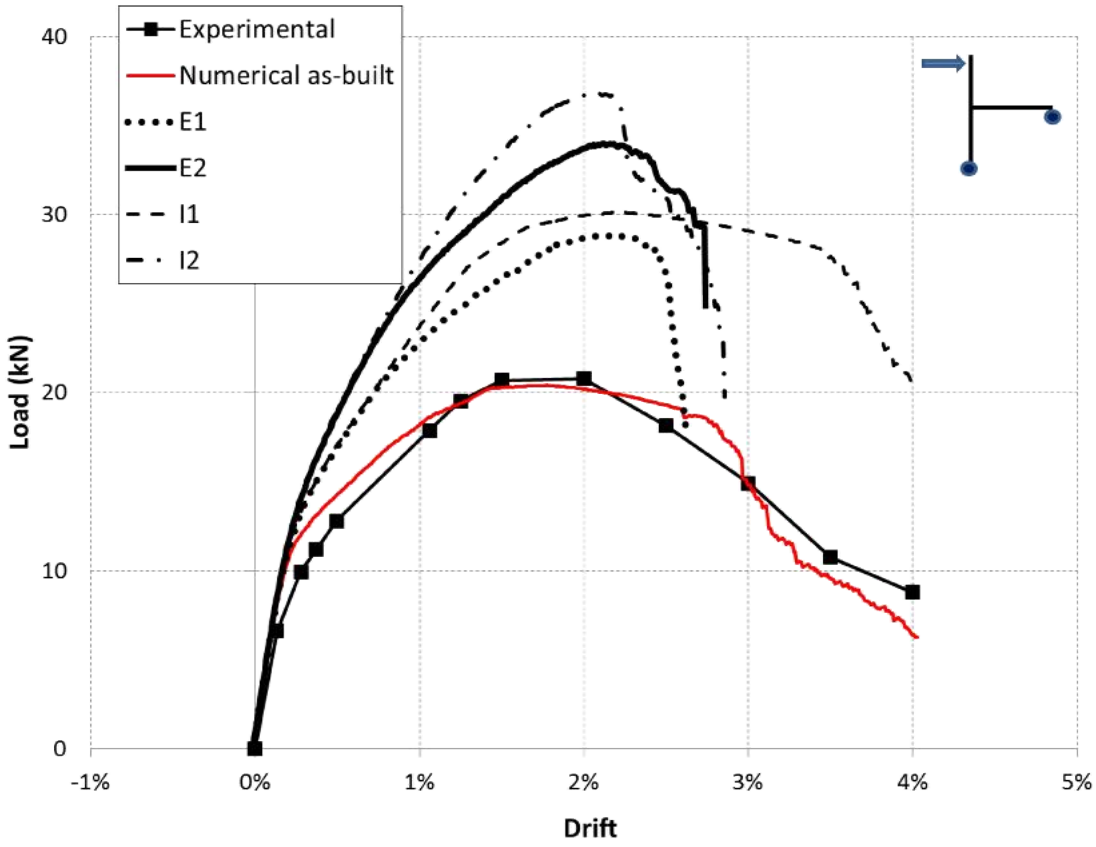


Figure 11: Load-drift curves from parametric analysis.

Note that the yielding points of the different cases have been derived directly from the FEM models by reading the drift values where the reinforcement stress attains values equal to the yielding strength $f_y$. For each of the models with increased amount of reinforcement, also the percentage increase with respect to the as-built model is reported ($\Delta$%).

The results show that comparing models with equal reinforcement amount, higher load values are found when the additional bars are placed inside the column core. In this case, lower slip phenomena occur, thus permitting a better exploitation of the rebars' strength. Indeed,

41.2 and 66.5% increases are provided by E1 and E2 models while 46.9 and 80% increases are provided by I1 and I2 models respectively.

Similar values of the deformation capacity values are found among the different models (giving a slight decrease with respect to the as-built model), with the exception of model I1 whose ultimate drift and ductility values are significantly higher than in the other models. Therefore, the configuration I1 appears preferable with respect to the other ones, determining a significant increase in terms of both maximum strength (80% with respect to the as-built model) and, above all, ductility value (more than 90% increase).

| | **Model** | | | | | | | | |
|---|---|---|---|---|---|---|---|---|---|
| | **As-built (numerical)** | **E1** | | **E2** | | **I1** | | **I2** | |
| | **Value** | **Value** | **Δ%** | **Value** | **Δ%** | **Value** | **Δ%** | **Value** | **Δ%** |
| $F_{max}$ [kN] | 20.42 | 28.84 | 41.2 | 34.00 | 66.5 | 30.00 | 46.9 | 36.76 | 80.0 |
| $d_u$ [%] | 2.9 | 2.54 | -12.4 | 2.70 | -6.9 | 3.75 | 29.3 | 2.62 | -9.7 |
| $d_y$ [%] | 1.97 | 1.52 | -22.8 | 1.40 | -28.9 | 1.33 | -32.5 | 1.77 | -10.2 |
| $\mu$ [-] | 1.47 | 1.67 | 13.6 | 1.93 | 31.3 | 2.82 | 91.8 | 1.48 | 0.7 |

Table 2: Main results from parametric analysis

In order to better understand the resisting mechanism of the parametric models E and I, the crack width plots are reported in Fig. 12.

It is worth noting that these plots are set with a color scale able to properly highlight the crack width value over the whole beam-column intersection. To this end, the highest values are out of the scale and are represented by cyan color. The cyan areas reach a crack width higher than the maximum scale value (0.7mm), being of the order of magnitude of 2mm.

The plots are relevant to the side views (exterior appearance of the crack pattern) and are taken at a drift value equal to 4%, whereas achieved by the model, or to the maximum achieved value in case the analysis ended before 4% due to convergence problems. As can be seen, moving from the as-built model to E1 and I1 models and then to E2 and I2, a larger damage to the column can be observed. In fact, the higher flexural strength of the beam in E2 and I2 models shifts the collapse mechanism from a weak beam-strong column nearer to a balanced mechanism where the column is subjected to a higher flexural demand. However, only in the model I2 the column reinforcement attains the yielding stress almost simultaneously to the beam rebars.

As a result, the models with higher steel amount (E2 and I2) show lower crack width values in the beam near the beam-column interface. Looking at the large difference in terms of ductility between the two models with additional rebars inside the column core (I1 and I2), the worst performance of I2 model can be related to the heavier damage suffered by the column attributable to the higher flexural demand to the column.

This conclusion is supported by the colormaps in Fig. 13 where the residual tensile strength is depicted at the load step corresponding to the peak loads observed for I1 and I2 models (the colormaps are relevant to a vertical section plane passing from the mid-side of the column). As already said, the tensile behavior of concrete has been simulated through a crack opening law (see Fig. 5b), where the residual tensile strength is dependent on the crack opening displacement. This means that the larger are the cracking opening displacements (crack sizes and, consequently, damage), the lower is the residual tensile strength.

As can be seen, in model I1 the area with the lower residual tensile strength values (most damaged area) is essentially around the beam rebars partially affecting the column core. In model I2 (with larger beam reinforcement), this area has a larger extent due to the yielding of column longitudinal rebars.

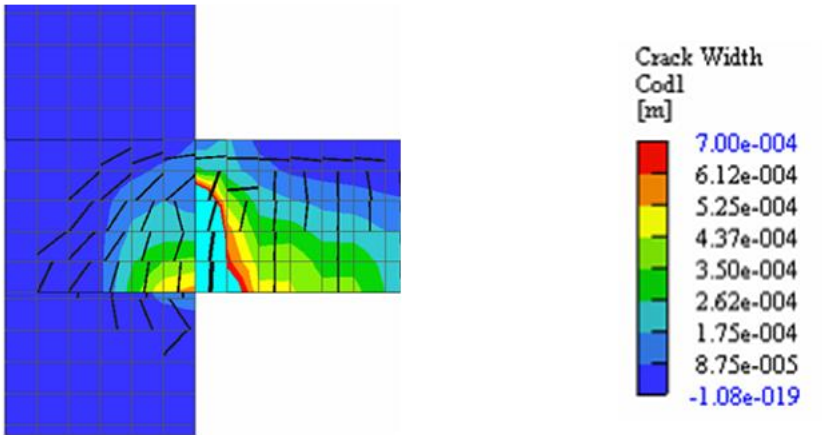


**As-built (@ 4.00% drift)**

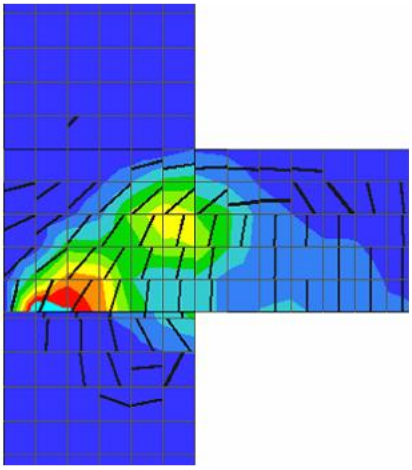

**E1 (@ 2.62% drift)**

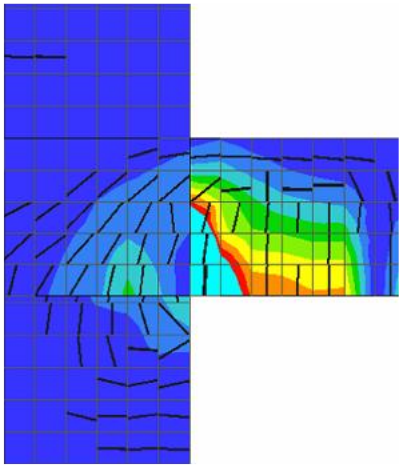

**I1 (@ 4.00% drift)**

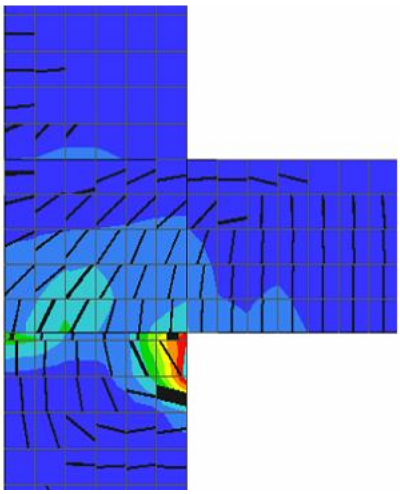

**E2 (@ 2.78% drift)**

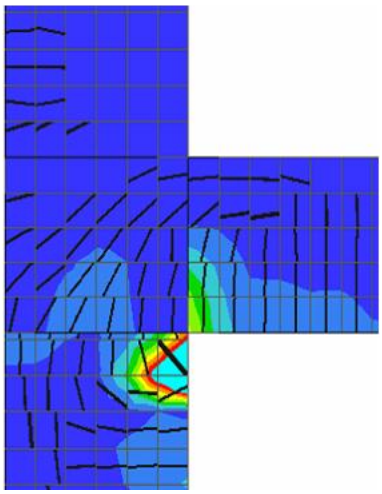

**I2 (@ 2.85% drift)**

Figure 12: Crack width plots in the four different models (side views).

The heavier damage to the beam-column intersection of model I2 (especially in the rear part of the column, where the beam rebars are bent) causes a reduction of the tensile stress of beam and column rebars causing, in turn, a whole strength drop of the specimen and less favorable ductile performances.

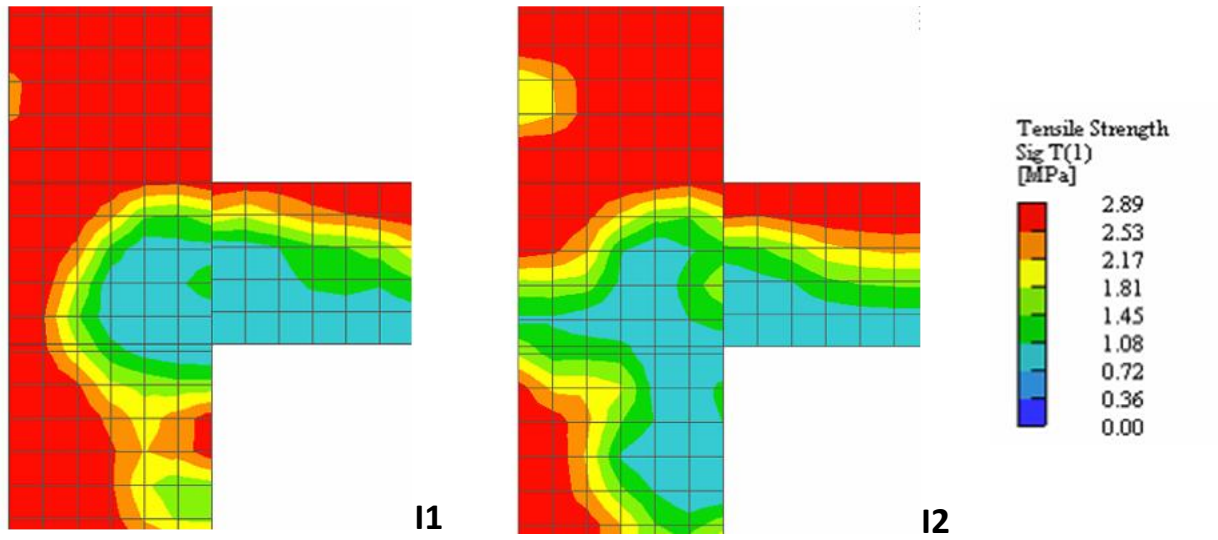


Figure. 13: Tensile strength field inside the column core at peak load.

## 5 CONCLUDING REMARKS

This study is focused on investigating the effect of the distribution of the beam rebars in wide beam-column joints. To this end, a parametric study based on nonlinear FEM analysis has been carried out. A detailed 3D nonlinear finite element model set-up with ATENA 3D software was built and calibrated aiming at reproducing the experimental results of a cyclic quasi-static test on a full-scale wide beam-column specimen.

The model was able to fully predict the nonlinear behavior of the specimen as well as to permit the execution of a parametric analysis in which other different models were created by modifying the number and the position of longitudinal reinforcement in the beam. Particularly, two different kinds of rebar positions were assumed. In the "E" models the additional rebars were placed outside the column core, in unconfined concrete while in the "I" models they were placed inside the column core, where some confinement due to the action of the hoops is present. Two levels of additional reinforcement area were assumed giving a total of four different models.

New numerical analyses on these four models revealed that, making a comparison for equal amount of beam reinforcement, E models have lower strength performance due to higher slip phenomena. In fact, most of the beam reinforcement bars are bonded in non-confined concrete causing a low bond strength. However, these models have also low ductility ratio due to the sudden deterioration and cracking at the beam sides. I models show better performance in terms of both strength and ductility. Indeed, the model with the lower amount of reinforcement offers the best solution because it provides 50% increment of the strength as well as an almost doubled value of the ductility ratio with respect the as-built specimen. This latter, be-

cause the additional rebars are able to increase the beam flexure strength without triggering significant damage to the column and to the beam-column joint, which, in the I2 model (provided with a larger amount of reinforcement) suffer a heavier cracking near the beam intersection.

It can be concluded that whenever is possible, longitudinal beam rebars in wide beam-column joints have to be placed mostly inside the column core. The amount needs to be determined in such a way to avoid excessive flexural demand in the framing column, possibly leading to the failure of the joint panel. Further study is needed to identify these limits also taking into account the shape factor of the beam-column intersection.

## ACKNOWLEDGEMENTS

The work reported in this article was carried out within the framework of the DPC-ReLUIS 2014-2016 Project, Research Line "Reinforced Concrete Structures", WP1.3 "Capacity of Joints".

## REFERENCES

[1] Masi, A., Mucciarelli, M., Chiauzzi, L., De Costanzo, G., & Loperte, G. (2014). Emergency preparedness activities during an ongoing seismic swarm: the experience of the 2011-2012 Pollino (Southern Italy) sequence. *Bollettino di Geofisica Teorica ed Applicata.* Volume 55, Issue 3, 1 December 2014, Pages 665-682

[2] Masi, A., Santarsiero, G., Mossucca, A., Nigro, D., (2014). Influence of axial load on the seismic behavior of RC beam-column joints with wide beam. 2014 *2nd International Conference on Energy Material, Chemical Engineering and Mining Engineering, EMCEM 2014.* Wuhan. https://doi.org/10.4028/www.scientific.net/AMM.508.208

[3] Masi A., Santarsiero, G. (2013). Seismic Tests on RC Building Exterior Joints with Wide Beams. *Advanced Materials Research* Vol. 787 (2013) pp 771-777.

[4] Masi A., Santarsiero G., Mossucca A., and Nigro D. (2016) Viable seismic strengthening solutions for RC wide beam-column joints. *Applied Engineering, Materials and Mechanics*: pp. 229-237.

[5] Masi, A., Santarsiero, G., & Nigro, D. (2013). Cyclic Tests on External RC Beam-Column Joints: Role of Seismic Design Level and Axial Load Value on the Ultimate Capacity. *Journal of Earthquake Engineering*, 17(1), 110–136. https://doi.org/10.1080/13632469.2012.707345

[6] Masi, A., Santarsiero, G., Lignola, G. P., & Verderame, G. M. (2013). Study of the seismic behavior of external RC beam-column joints through experimental tests and numerical simulations. *Engineering Structures*, 52, 207–219. https://doi.org/10.1016/j.engstruct.2013.02.023

[7] Santarsiero, G., & Masi, A. (2015). Seismic performance of RC beam-column joints retrofitted with steel dissipation jackets. *Engineering Structures*, 85, 95–106. https://doi.org/10.1016/j.engstruct.2014.12.013

[8] Cervenka Consulting, 2000-2014. ATENA Program Documentation, Part 1, ATENA Theory Manual. Praha.

[9] Pukl, R.a, Jansta, M.a, Červenka, J.a, Vořechovský, M.b, Novák, D.b, Rusina, R.b (2006) Spatial variability of material properties in nonlinear computer simulation. *Computational Modelling of Concrete Structures* - Proceedings of EURO-C 2006 2006, Pages 891-896 EURO-C 2006 Conference; Mayrhofen, Tyrol; Austria; 27 March 2006 through 30 March 2006; Code 88426.

[10] Pryl, D., Pukl, R., Cervenka, J. (2012) Modelling high-cycle fatigue of concrete specimens in three point bending. Proceedings of the 3rd International Symposium on Life-Cycle Civil Engineering, IALCCE 2012 Life-Cycle and Sustainability of Civil Infrastructure Systems - Pages 1303-1306. Vienna; Austria; 3 October 2012 through 6 October 2012; Code 93181

[11] MC90. CEB-FIP Model Code 1990. Comité Euro-International du Béton; 1993.

[12] Panagiotakos T.B., Fardis M.N.: Deformation of reinforced concrete members at yielding and ultimate. *ACI Structural Journal*, 2001. 98(2), 135-148.

[13] Chen, W.F, Saleeb, A.F. (1982) - *Constitutive Equations For Engineering Materials*, John Willey \& Sons, ISBN 0-471-09149-9.

[14] Remmel G. Zum Zug- und Schubtragverhalten von Bauteilen aus hochfestem Beton. DAfStb, Heft 444. *Beuth Verlag*, Berlin; 1994.

[15] Santarsiero G., Masi A., Seismic behavior of external RC wide beam–column joints through experimental tests and numerical simulations. Submitted to *Engineering Structures.*

[16] Masi, A., Digrisolo, A., & Santarsiero, G. (2014). Concrete Strength Variability in Italian RC Buildings: Analysis of a Large DataBase of Core Tests. *Applied Mechanics and Materials*, 597, 283–290. https://doi.org/10.4028/www.scientific.net/AMM.597.283

COMPDYN 2017
6th ECCOMAS Thematic Conference on
Computational Methods in Structural Dynamics and Earthquake Engineering
M. Papadrakakis, M. Fragiadakis (eds.)
Rhodes Island, Greece, 15–17 June 2017

# INNOVATIVE STRUCTURES FOR DYNAMIC SOLAR FAÇADES

**R. Miranda[1], F. Fabbrocino[2], E.Sicignano[1], R. E. Skelton[3], F. Fraternali[1]**

[1]Department of Civil Engineering, University of Salerno,
84084 Fisciano (Salerno), Italy
ramiranda@unisa.it (R. Miranda), e.sicignano@unisa.it (E. Sicignano), fraternali@unisa.it (F. Fraternali),

[2]Pegaso University, Department of Engineering
80132 Naples, Italy
francesco.fabbrocino@unipegaso.it (F. Fabbrocino)

[3]Department of Aerospace Engineering, Texas A&M University,
3141 TAMU, College Station, TX 77843-3141, USA
bobskelton@tamu.edu (R. E. Skelton)

**Keywords:** Renewable Energy, Tensegrity Structures, Dynamic Solar Façades.

**Abstract.**

*Recent studies have investigated the use of tensegrity structures for the construction of active solar façades of Energy Efficient Buildings (EEBs). The present work moves along such lines by proposing a methodology that supports the development of the design and construction process of new façade components with tensegrity architecture. The activation motion of the examined tensegrity façade system mimics the dynamics a blinking sail. The use of the proposed façade system as a dynamic sun-screen or a wind-energy harvesting device is presented, with the aim of illustrating the application of tensegrity architectures to the design of next-generation dynamic solar façades of EEBs.*

## 1. INTRODUCTION

A civil structural system is composed of the design of: structures; HVAC (heating, ventilating and air conditioning) system; electrical system; sighting design; etc. Such systems have traditionally been designed in the order listed, in sequence. Modern building technology must be more efficient and sustainable, both in construction and in operation [1]-[5].

Recent studies have investigated the use of tensegrity structures for the construction of active solar façades of Energy Efficient Buildings (EEB), by profiting of the special ability of tensegrity structures in serving as controllable, deployable, and smart systems [6]-[12].

The present work moves along the lines of the research presented in Refs. [6]-[7], by proposing a methodology that supports the development of the design and construction process of new façade components with tensegrity architecture. The uses of the proposed tensegrity façade system as a dynamic sun-screen or a wind-energy harvesting device are discussed through mechanical and technological arguments. We close by outlining directions of future research devoted to exploit the use of tensegrity concepts within innovative façades of energy efficient buildings.

## 2. DESIGN AND OPERATION OF A DYNAMIC SOLAR FAÇADE WITH TENSEGRITY ARCHITECTURE

Adaptive architecture must be considered the future of contemporary architectural research because it can decrease the energy balance of buildings by controlling thermal energy, light energy and sound waves [13]. This research aimed to identify design principles and operative tools for the design and production of innovative building envelopes that could integrate renewable energy, in form of photovoltaic and solar thermal panels.

Sunscreens absorb and reflect incident solar radiation but cannot transfer solar heat gain directly into the building. When sun screens transform incident sunlight into electricity for immediate use or transmit thermal energy into the building by use of electrical or mechanical equipment, they are called opaque sunscreens and form part of an active solar façade. In this research, we designed two innovative prototypes according to the fundamentals of the tensegrity structural system [8].

The façade system that we study in this work is designed like a set of *blinking sails*, which is inspired by the wave-powered station-keeping buoy with tensegrity architecture illustrated in Chapter 1 of reference [8], and a recent US patent on a blinking sail windmill [14]. The module of this structure is composed of six bars (compressive members), two cables (tensile members) and five nodes. Node 1 is fixed on the sub-structure, nodes 2 and 4 are constrained to move in the x-y plane (parallel to the building façade), node 5 is constrained to move along the z-axis (perpendicular to the building façade) and node 3 is free to move within the space. The design of the elementary module depends on two angular aspect variables $\alpha$ and $\beta$, which define the node coordinates as shown in Fig. 1. Our next developments assume $\alpha = 0$ and $\beta = 45°$ in the undeformed (planar) configuration of the blinking sail module.

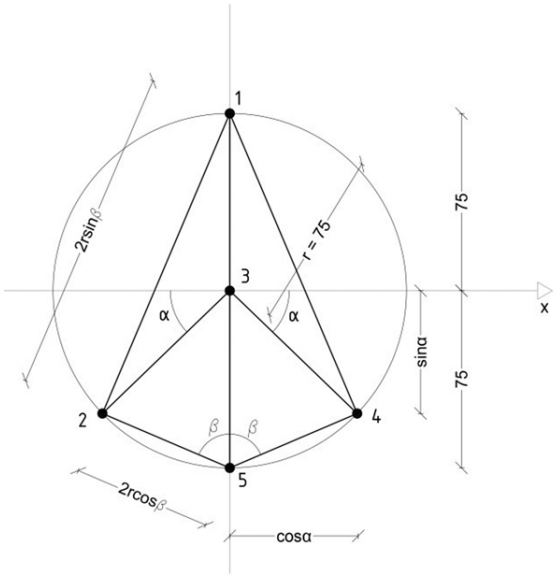


| | | | |
|---|---|---|---|
| node 1 | 0 | r | 0 |
| node 2 | -rcosα | -rsinα | 0 |
| node 3 | 0 | 0 | 0 |
| node 4 | rcosα | -rsinα | 0 |
| node 5 | 0 | -r | 0 |

$0<\alpha<|\pi|$

Figure 1. Blinking sail façade system – Geometry of the elementary module

We will see later on that the blinking sail structure illustrated in Figs. 1-2 can operate as an adaptive solar screen or a wind harvester device. In both cases, such a structure is equipped with bendable, composite photovoltaic modules and/or fiber-membrane sails. Each elementary module of such a façade system is shaped like a rhombus (Fig. 2) and is actuated by controlling the elongations of selected cables, in such a way that the motion of the structure mimics a blinking sail.

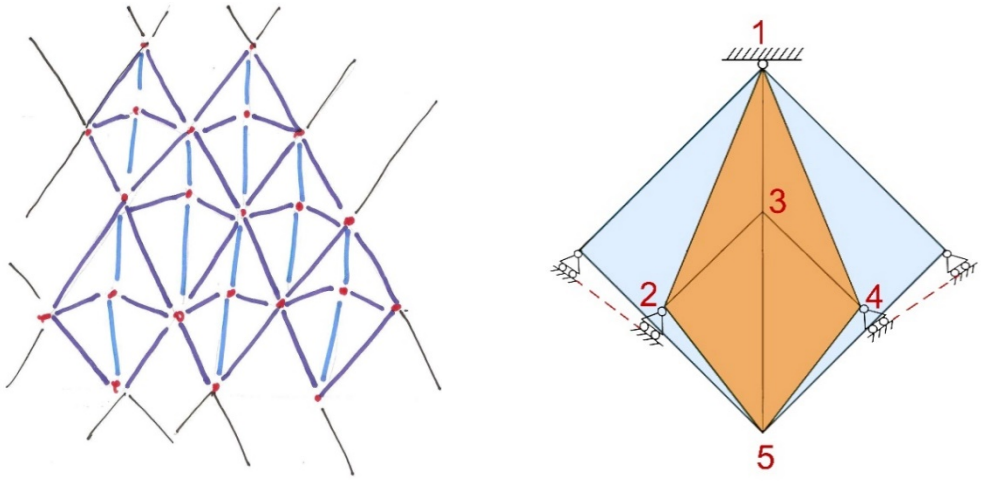


Figure 2. Conceptual (left) and mechanical (right) models of the blinking sail façade system.

Let us examine the motion of the blinking sail elementary module described in Fig. 2, which is produced by applying suitable elongations to the cables 1-3 and 3-5. At the current time $t$, the elongation rate of the $m$-th element connecting nodes $i$ and $j$ is given by the *compatibility equation*

$$\dot{e}_m = (\dot{u}_j - \dot{u}_i) \cdot a_m \tag{1}$$

where $\dot{u}_i$ and $\dot{u}_j$ denote the velocity vectors of the nodes *i* and *j*, respectively; $a_m$ is the unit vector parallel to segment connecting such nodes (pointing towards node *j*); and $\ell_m$ is the current length of the element.

Upon assembling the free (i.e., unconstrained) Cartesian components of the velocities of all the nodes into a global velocity vector $\dot{q}$, and the elongation rates in all the bars and cables into a vector of control variables $\dot{e}$, we can rewrite the compatibility equations of the overall structure into the following matrix form

$$\mathbf{B}\,\dot{q} = \dot{e} \tag{2}$$

where $\mathbf{B}$ denotes the instantaneous *kinematic* (or *compatibility*) *matrix* [6].

Let us now consider a prescribed time history $\dot{e} = \dot{\bar{e}}(t)$ of the control variables. The motion generated by such an actuation strategy of the structure is computed from the integral equation

$$q = \int_0^t \dot{q}\,dt = \int_0^t \mathbf{B}^{-1}\,\dot{\bar{e}}\,dt \tag{3}$$

where $\mathbf{B}^{-1}$ is the inverse of the kinematic matrix $\mathbf{B}$ in correspondence with the current configuration of the structure, which it is assumed exist.

The examined actuation mechanism of the blinking sail module is illustrated in Figure 3. It is generated by actuating the cables 1-3 and 3-5, through the application of the elongation histories indicated in correspondence with the different panels of Figure 3. The remaining members of the module remain unstretched during the motion of the structure illustrated in Figure 3. By suitably changing the tension in the cables 1-3 and 3-5, it is seen from such a Figure that the nodes 3 and 5 moves outward along the z-axis (with respect to the building surface), while nodes 2 and 4 move in the x-y plane by producing the folding of the module, whose deformation resembles that of a sail inflated by the wind. The aspect angles of the module initially assume the values $\alpha = 0$ and $\beta = 45°$ (top-left configuration in Fig. 3), as we already noticed, and assume the values $\alpha = 45°$ and $\beta = 38°$ in the fully folded configuration.

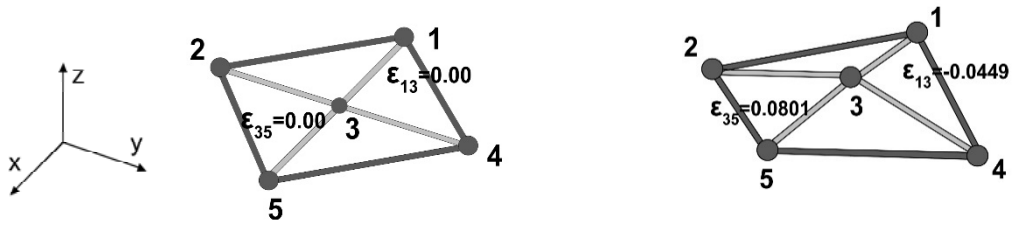

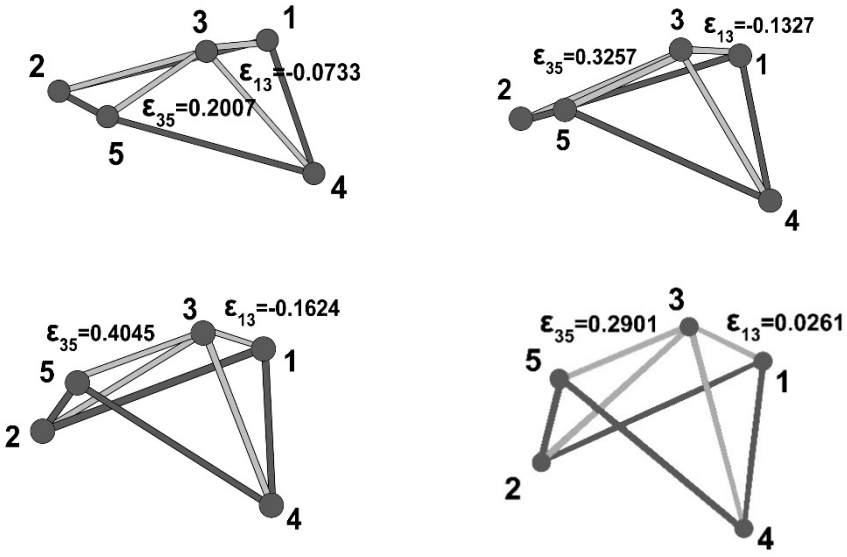


Figure 3. Activation mechanism of the Blinking sail module.

## 3. ENGINEERING APPLICATIONS

The activation mechanism illustrated in Figure 3 is at the basis of the solar façade system illustrated in Fig. 4. Such a smart skin of an EEB consists of several rhombus-shaped elementary modules assembled together. The modules are dynamic and can change configuration according to the actuation mechanism in Fig. 3, by modifying the shading properties of the envelope.




Figure 4. Blinking sail solar façade

A blinking sail wind energy harvester can also be designed in order to convert wind-induced motion of a membrane attached to the generic module into electrical energy. The blinking sail module is formed in this case by all stretchable elements (strings) attached to a rigid truss protruding from the served building (cf. Fig. 5). Such cables are connected to a fiber-reinforced membrane sail that is inflated by the wind. Additional cables attached to the module wrap around a generator rotor (Fig. 5). The wind-flow induced elongations of such cables rotate the generator, creating power for immediate use of the served building, operate solar façades, etc. In addition, the aeroelastic flutter of the wind-excited membrane, eventually equipped piezoelectric or electromagnetic actuators, can be employed to harvest supplementary energy from wind. Fig. 5 shows the functional diagram of the elementary module of the wind-energy harvesting façade, which is inspired by the wave-powered station-keeping illustrated in Chapter 1 of reference [8].

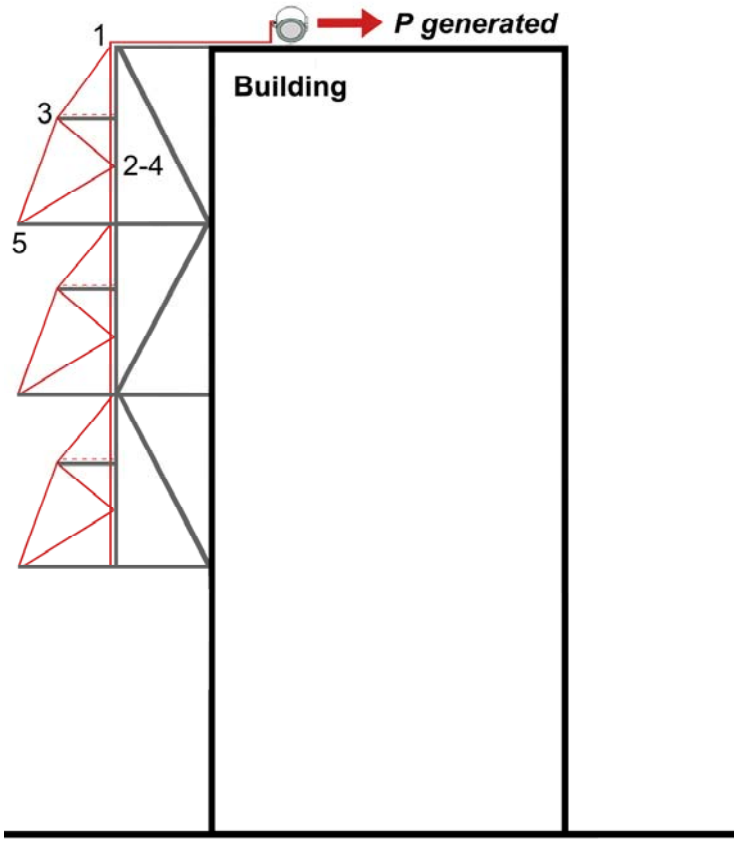


Figure 5. Functional diagram of the wind-energy harvester module

## 4. CONCLUDING REMARKS

We have formulates tensegrity solutions for the design of active façades that are able to harvest wind and solar energy through on-site wind power generator, and offer portable applications for small spans and in the case of large spans can be easily assembled using prefabricated components.

Future research lines include the design of different deployment schemes and the optimal design of sustainable kinetic membranes and panels for energy efficient buildings, to be

carried out by combining parametric design approaches, energy optimization techniques, sustainable materials and additive manufacturing techniques [48]-[53].

## REFERENCES


[1] Lombard LP, Ortiz J, Pout C. A review on buildings energy consumption information. Energ Buildings 2010; 40:394-398.

[2] European Commission, HORIZON 2020 Work Programme 2014-2015, PART 5.ii, p. 98, 2014.

[3] Directive 2012/27/EU of the European Parliament and of the Council of 25 October 2012 on energy efficiency, amending Directives 2009/125/EC and 2010/30/EU and repealing Directives 2004/8/EC and 2006/32/EC

[4] Schittich C. In Detail: Solar Architecture. Birkhäuser: Edition Detail, 2003.

[5] Raji B, Tenpierik MJ, van den Dobbelsteen A. A comparative study: Design strategies for energy-efficiency of high-rise office buildings. J Green Build 2016; 11:134-158.

[6] Fraternali F, De Chiara E, Skelton RE. On the use of morphing and wind stable tensegrity structures for shading facades of smart buildings. Smart Mater Struct 2015; 24, 105032 (10pp).

[7] Cimmino MC, Miranda R, Sicignano E, Ferreira AJM, Skelton RE, Fraternali F. Composite solar façades and wind generators with tensegrity architecture. Compos Part B-Eng 2016; Online first, DOI: 10.1016/j.compositesb.2016.09.077

[8] Skelton RE, de Oliveira MC. Tensegrity Systems. New York: Springer Science+Business Media, 2009.

[9] Skelton RE, Fraternali F, Carpentieri G, Micheletti A. Minimum mass design of tensegrity bridges with parametric architecture and multiscale complexity. Mech Res Commun 2014; 58: 124-132.

[10] Carpentieri G, Skelton RE, Fraternali F. Minimum mass and optimal complexity of planar tensegrity bridges. International Journal Space Structure 2015; 30(3–4):221–244.

[11] Carpentieri G, Skelton RE, Fraternali F. A minimal mass deployable structure for solar energy harvesting on water canals. Struct Multidiscip O, Online First: DOI:10.1017/s00158-016-1503-5.

[12] Skelton RE. Structural systems: a marriage of structural engineering and system science. J Struct Contr 2002; 9:113-133.

[13] Pizzi E, Iannaccone G, Ruttico P. Innovative strategies for adaptive buildings in large cities. Int J Housing Sci 2012; 36:99-107.

[14] Al-Azzawi, J.S, Blinking sail windmill, Google Patents, 2010, https://www.google.com/patents/US7780416.

[15] I. Farina, F. Fabbrocino, G. Carpentieri, M. Modano, A. Amendola, R. Goodall, L. Feo, F. Fraternali, *On the reinforcement of cement mortars through 3D printed polymeric and metallic fibers,* Composites Part B: Engineering, **90**, 76-85, 2016.

[16] F. Fraternali, Free Discontinuity Finite element models in two-dimensions for in-plane crack problems*, Theoretical and Applied Fracture Mechanics*, **47**, 274-282, 2007.

[17] F. Fraternali, C.D Lorenz, G. Marcelli, On the estimation of the curvatures and bending rigidity of membrane networks via a local maximum-entropy approach, *Journal of Computational Physics*, **231**, 528-540, 2012.

[18] L. Ascione, F. Fraternali, A penalty model for the analysis of composite curved beams, *Computers & Structures*, **45**, 985-999, 1992.

[19] F. Fraternali, J.N. Reddy, A penalty model for the analysis of laminated composite shells, *International Journal of Solids and Structures*, **30**, 3337-3355, 1993.

[20] F. Fraternali, G. Bilotti, Non-Linear Elastic Stress Analysis in Curved Composite Beams. *Computers & Structures*, **62**, 837-869, 1997.

[21] F. Fraternali, G. Carpentieri, A. Amendola, On the mechanical modeling of the extreme softening/stiffening response of axially loaded tensegrity prisms. *Journal of the Mechanics and Physics of Solids*, **74**, 136-157, 2015.

[22] D. Ngo, F. Fraternali, C. Daraio, Highly Nonlinear Solitary Wave Propagation in Y-Shaped Granular Crystals with Variable Branch Angles. Physical Review E, **85**, 036602-1-10, 2012.

[23] R.E. Skelton, F. Fraternali, G. Carpentieri, A. Micheletti, Minimum mass design of tensegrity bridges with parametric architecture and multiscale complexity. *Mechanics Research Communications*, 58, 124-132, 2014.

[24] A. Leonard, F. Fraternali, C. Daraio, Directional wave propagation in a highly nonlinear square packing of spheres. *Experimental Mechanics*, **53**(3), 327-337, 2013.

[25] F. Fraternali, G. Carpentieri, A. Amendola, R.E. Skelton, V. F. Nesterenko, Multiscale tunability of solitary wave dynamics in tensegrity metamaterials. *Applied Physics Letters*, **105**, 201903, 2014.

[26] F. Fraternali, I. Farina, C. Polzone, E. Pagliuca, L. Feo, On the use of R-PET strips for the reinforcement of cement mortars. *Composites. Part B*, **46**, 207-210, 2013.

[27] J.R. Raney, F. Fraternali, A. Amendola, C. Daraio, Modeling and In Situ Identification of Material Parameters for Layered Structures based on Carbon Nanotube Arrays. *Composite Structures*, **93**, 3013–3018, 2011.

[28] T. Blesgen, F. Fraternali, J.R. Raney, A. Amendola, C. Daraio, Continuum Limits of Bistable Spring Models of Carbon Nanotube Arrays accounting for Material Damage. *Mechanics Research Communications*, **45**, 58-63, 2012.

[29] F. Fraternali. A Mixed Lumped Stress – Displacement Approach to the Elastic Problem of Masonry Walls. Mechanics Research Communications, **38**, 176-180, 2011.

[30] F. Fraternali, M. Negri, M. Ortiz, On the Convergence of 3D Free Discontinuity Models in Variational Fracture. *International Journal of Fracture*, **166**(1-2), 3-11, 2010.

[31] C. Daraio, D . Ngo, V. F. Nesterenko, F. Fraternali, Highly Nonlinear Pulse Splitting and Recombination in a Two Dimensional Granular Network. *Physical Review E*, **82**, 036603, 2010. G. Lomiento , N. Bonessio, G. Benzoni, Friction Model for Sliding Bearings under Seismic Excitation, Journal of Earthquake Engineering, **17**(8):1162-1191, 2013..

[32] M. Budek, M. J. N. Priestley, G. Benzoni, The Effect of External Confinement on Flexural Hinging in Drilled Pile Shafts, *Earthquake Spectra*, **20** (1), 1-24, 2004.

[33] Hae-Bum Yun, Sami F. Masri, Raymond W. Wolfe, Gianmario Benzoni , Data-driven methodologies for change detection in large-scale nonlinear dampers with noisy measurements, *Journal of Sound and Vibration*, **322**, Issues 1–2, 24 April 2009, Pages 336–357.

[34] D. D'Ayala, G. Benzoni, Historic and Traditional Structures during the 2010 Chile Earthquake: Observations, Codes, and Conservation Strategies. *Earthquake Spectra*, **28** (S1), S425-S451, 2012.

[35] N. Bonessio, G. Lomiento, G. Benzoni, Damage identification procedure for seismically isolated bridges, *Structural Control Health Monitoring*, **19**(5), 565–578, 2012.

[36] G. Benzoni, C. Casarotti , Effects of Vertical Load, Strain Rate and Cycling on the Response of Lead-Rubber Seismic Isolators, *Journal of Earthquake Engineering* ,**13**, 2009.

[37] A. Budek-Schmeisser, G. Benzoni, Rational seismic design of precast, prestressed concrete piles, *PCI Journal*, **53**(5), 40-53, 2008.

[38] G. Benzoni, M. J. N. Priestley, Seismic response of linked marginal wharf segments, *Journal of Earthquake Engineering* **74**, 513-539, 2003.

[39] A. Amendola, G. Benzoni, F. Fraternali, Non-linear elastic response of layered structures, alternating pentamode lattices and confinement plates. *Composite Part B, Engineering*, Online first, DOI: 10.1016/j.compositesb.2016.10.027, 2016.

[40] F. Fraternali, G. Carpentieri, R. Montuori, A. Amendola, G. Benzoni, On the use of mechanical metamaterials for innovative seismic isolation systems, COMPDYN 2015 - 5th ECCOMAS Thematic Conference on Computational Methods in Structural Dynamics and Earthquake Engineering, 349-358.

[41] F. Fraternali, S. Spadea, L. Ascione, Buckling behavior of curved composite beams with different elastic response in tension and compression. *Composite Structures*, **100**, 280-289, 2013.

[42] F. Fraternali, S. Spadea, V.P. Berardi, Effects of recycled PET fibers on the mechanical properties and seawater curing of Portland cement-based concretes. *Construction and Building Materials*, **61**, 293-302, 2014.

[43] Singh R, Singh S, Fraternali F. Development of in-house composite wire based feed stock filaments of fused deposition modelling for wear-resistant materials and structures. Compos Part B-Eng 2016; 98: 244-249.

[44] Farina I, Fabbrocino F, Colangelo F, Feo L, Fraternali F, Surface roughness effects on the reinforcement of cement mortars through 3D printed metallic fibers. Compos Part B-Eng 2016; 99: 305-311.

[45] Singh R, Kumar R, Feo L, Fraternali F. Friction welding of dissimilar plastic/polymer materials with metal powder reinforcement. Compos Part B-Eng 2016; 101: 77-86.

[46] Boparai KS, Singh R, Fabbrocino F, Fraternali F. Thermal characterization of recycled polymer for additive manufacturing applications. Compos Part B-Eng, Online first (2016): DOI: 10.1016/j.compositesb.2016.09.009.

[47] Amendola, C.J. Smith, R. Goodall, F. Auricchio, L. Feo, G. Benzoni, F. Fraternali, Experimental response of additively manufactured metallic pentamode materials confined between stiffening plates. *Composite Structures*, **142**, 254–262, 2016.

[48] F. Fraternali, A. Marino, T. Elsayed, A. Della Cioppa, On the structural shape optimization via variational methods and evolutionary algorithms. Mechanics of Advanced Materials and Structures, **18**, 225-243, 2011.

[49] A. Amendola, E.H. Nava, R. Goodall, I. Todd, R.E. Skelton, F. Fraternali, On the additive manufacturing, post-tensioning and testing of bi-material tensegrity structures, *Composite Structures*, **131**, 66-71, 2015.

[50] A. Amendola, G. Carpentieri, M. De Oliveira, R.E. Skelton, F. Fraternali, Experimental investigation of the softening-stiffening response of tensegrity prisms under compressive loading. *Composite Structures*, **117**, 234-243, 2014.

[51] F. Fraternali, G. Carpentieri, A. Amendola, On the mechanical modeling of the extreme softening/stiffening response of axially loaded tensegrity prisms. *Journal of the Mechanics and Physics of Solids*, **74**, 136-157, 2015.

[52] Singh R, Singh N, Fabbrocino F, Fraternali F, Ahuja I. Waste management by recycling of polymers with reinforcement of metal powder. Compos Part B-Eng 2016:105: 23-29.

[53] B. Schmidt, F. Fraternali, Universal formulae for the limiting elastic energy of membrane networks, *Journal of the Mechanics and Physics of Solids*, **60**, 172-180, 2012.

COMPDYN 2017
6th ECCOMAS Thematic Conference on
Computational Methods in Structural Dynamics and Earthquake Engineering
M. Papadrakakis, M. Fragiadakis (eds.)
Rhodes Island, Greece, 15–17 June 2017

# ADAPTIVE NEURO FUZZY CONTROL FOR VIBRATION SUPPRESSION OF A SMART BUILT-IN PLATE WITH EMBEDED PIEZOELECTRIC SENSORS AND ACTUATORS

**Georgios Tairidis**[1] **and Georgios E. Stavroulakis**[1]

[1] Technical University of Crete
School of Production Engineering and Management
GR-73100 Chania, Greece
e-mail: tairidis@gmail.com, gestavr@dpem.tuc.gr

**Keywords:** Smart structures, Control, Neuro fuzzy control, piezoelectricity.

**Abstract.** *One of the most important problems in engineering is, among others, the vibration suppression of smart composite structures, i.e. the reduction of the oscillations, which in turn are caused by external dynamic loadings. Embedded sensors and actuators, made of piezoelectric materials, along with a suitable control system provide intelligent behavior to the smart structures. Vibration suppression can be achieved using fuzzy controllers. Fine-tuning of the involved parameters may become necessary and can be achieved either by using the trial and error method, or via global optimization, such as genetic algorithms (GAs), particle swarm optimization (PSO), differential evolution (DE) etc. In this case the results are usually very satisfactory, however, the computational cost increases. On the other hand, adaptive, optimized neuro fuzzy controllers, like the ones which are presented here, can be even more effective in the design and application of smooth robust controllers. These smart controllers are able to follow a training procedure, and thus to increase their robustness, i.e. their adaptivity under several -and some times completely different- conditions. The modeling of neuro fuzzy controllers is quite similar to other system identification techniques. The first step is the construction of the control system and subsequently a set of training data is necessary for configuration. These data will be used for the tuning of the control parameters until an error criterion is met. In other words, the controllers are first designed, based on the dynamic characteristics of the modeled structures, and then an optimization process, which is based on adaptive neural fuzzy techniques, i.e. on neural networks, is applied. Some good results in this direction have already been presented in previous investigations of the authors [1, 2, 3]. An important feature of these controllers lies to the fact that they can achieve significant suppression of the oscillations without knowledge of the full state-space (measurements) of the problem and without the application of any classical optimization method. Recent developments and applications mostly on linear smart structures are presented here. More specifically, several plate models with different support scenarios and loadings are modeled and studied, in order to prove the robustness and the efficiency of the control.*

## 1 INTRODUCTION

One of the most important problems in engineering is the suppression of the vibrations of structures due to external excitation factors, i.e. wind or seismic loadings. Moreover, in smart structures, a significant degree of uncertainty is always present, due to potential imperfections and errors of both the control mechanisms and the model itself. Especially in multilayer structures, several failures, such as delamination between the different layers, fatigue or other damages, may appear. In laminated materials, such as the ones used in laminated structures, the repeated applied stresses, impact the layers of the structures and can lead them to separate. This phenomenon can form a less tough structure. Prediction of failure in composite laminates can be accomplished using computational methods based on material strength and fracture toughness, as it is presented in [4].

Classic monitoring tools and control techniques often encounter several limitations to the study of such problems. For this reason, the use of intelligent fuzzy and neuro-fuzzy control techniques is suggested. An introductory survey of fuzzy control has been conducted in [5]. Indeed, to maximize the efficiency of the proposed controllers, their characteristics can be subjected to a fine-tuning process either using global optimization algorithms [6, 7] or artificial neural networks [2, 3]. Artificial neural networks provide better solutions to some problems due to their capability of parallelism and learning. More specifically, the use of neural networks in control is considered as a natural step in the evolution of control methodology. A short review on neural networks for control systems is done in [8].

A well-established implementation of the adaptive neuro-fuzzy system is the adaptive neuro fuzzy inference system (ANFIS) of MATLAB®, as presented in [9]. The procedure followed, may be summarized in several steps as follows. Firstly, a detailed mechanical model of the total system is constructed. Subsequently, the dynamics of the system are calculated and saved. These data are used for the optimization and training of the neuro-fuzzy controller by using the ANFIS procedure. The resulting controller can be used for the control of the total system. The numerical results indicate the efficiency of the proposed control scheme for the vibration suppression on a cantilever beam under sinusoidal and ramp-type excitations. The control is not only efficient, but smooth as well.

The objective is the development of an intelligent, reliable and robust control system, as well as the establishment of a proper connection with numerical integration algorithms for the study of dynamic systems. For the development of such controllers at the present investigation, fuzzy inference tools, as well as artificial neural networks techniques are used. More specifically, the controllers are first designed and subsequently they are subjected to an optimization process, by using either adaptive neural fuzzy techniques. The proposed methods for control and optimization are proved to be very efficient and robust as well.

## 2 STRUCTURAL MODEL OF THE BUILT-IN PLATE

The structural model of the present investigation consists of a smart laminated plate with integrated piezoelectric sensors and actuators, which is based on the First-order Shear Deformation Theory for laminated composite plates (FSDT) or Mindlin theory. This is an extension to the widely used Mindlin-Reissner theory. The FSDT which was proposed by Reissner and Mindlin, takes into consideration shear deformation effects by the way of linear variation of in-plane displacements through the thickness.

In the model considered here, two piezoelectric layers are symmetrically bonded perfectly on the top and bottom surface of the host composite plate. The top layer acts like an actuator, while the bottom one is used as a sensor. The poling direction of the piezoelectric actuator is assumed to be along the *z*-axis.

## 2.1 Structural dynamics

To derive the equations of motion for the laminated composite plate with surface bonded sensor and actuator layers, Hamilton's principle is used:

$$\int_0^T \left(\delta T - \delta U + \delta W\right) dt = 0 \tag{1}$$

The kinetic energy $T$, the potential energy $U$ and the total work done due to virtual displacements $\delta u$ are given as follows:

$$\begin{aligned} \delta T &= -\int_V \rho \{\ddot{u}\}^T \{\delta u\}\, dV \qquad \delta U = \int_V \left(\{\sigma\}^T \{\delta\varepsilon\} - \{D\}^T \{\delta E\}\right) dV \\ \delta W &= \{\delta u\}^T \{F_c\} + \int_S \{\delta u\}^T \{f_S\}\, dS + \int_V \{\delta u\}^T \{f_V\}\, dV - \int_{S_p} \{\delta E\}^T \{q\}\, dS \end{aligned} \tag{2}$$

where $\{F_c\}$ is the concentrated force vector, $\{f_S\}$ is the surface force vector, $\{f_V\}$ is the body force vector, $\{q\}$ is the surface charge vector, $S$ is the surface area where external force is acting, and $S_p$ is the surface area of piezoelectric layer where applied electric charge is acting.

Substituting relations (2) in Hamilton's principle (1), we obtain:

$$\begin{aligned} \int_0^T \Bigg\{ &\int_V \left(\{\ddot{u}\}^T \{\delta u\} + \{\sigma\}^T \{\delta\varepsilon\} - \{D\}^T \{\delta E\} - \{\delta u\}^T \{f_V\}\right) dV \\ &- \{\delta u\}^T \{F_c\} - \int_S \{\delta u\}^T \{f_S\}\, dS + \int_{S_p} \{\delta E\}^T \{q\}\, dS \Bigg\} dt = 0 \end{aligned} \tag{3}$$

Equation (3) is a good starting point for finite element approximations using independent variables $\{u\}$ and $\phi^p$.

## 2.2 Finite element formulation

For the discretization of the composite plate the finite element method is used. Namely, four-node rectangular bilinear isoparametric elements with five degrees of freedom per node, i.e. $\{u_0, v_0, w_0, \theta_x, \theta_y\}$, are used. The first three degrees of freedom of each node correspond to the displacements in directions x, y and z respectively, while the last two the rotations around the axes x and y.

The governing equations of an element can be written as:

$$\begin{aligned} [M]_e \{\ddot{d}_e\} + [K_{uu}]_e \{d_e\} + [K_{u\phi}]_e \{\phi\}_e &= \{F_{(m)}\}_e \\ [K_{\phi u}]_e^T \{d_e\} - [K_{\phi\phi}]_e \{\phi\}_e &= \{F_{(q)}\}_e \end{aligned} \tag{4}$$

where the element mass matrix $[M]_e$, the element elastic stiffness matrix $[K_{uu}]_e$ and the element mechanical load vector $\{F_m\}_e$ are given by:

$$[M]_e = \sum_{k=1}^{nplies} \int_{-1}^{1}\int_{-1}^{1} \rho_k [N]^T \left[\int_{z_k}^{z_{k+1}} [L_Z]^T [L_Z] dz\right][N]|J| d\xi d\eta$$

$$[K_{uu}]_e = \sum_{k=1}^{nplies} \int_{-1}^{1}\int_{-1}^{1} \left[\int_{z_k}^{z_{k+1}} [B]^T [\bar{Q}]_k [B] dz\right]|J| d\xi d\eta$$

$$\{F_m\}_e = \int_{V_e} [N]^T \{f_V\}_e dV + \int_{S_e} [N]^T \{f_S\}_e dS + [N]^T \{F_c\}_e$$

At the $p^{\text{th}}$ piezoelectric layer, the electromechanical coupling matrix and the permittivity matrix are given by:

$$[K_{u\phi}]_e = \int_{V_p} [B]^T [\bar{e}] [B_\phi] dV = [K_{\phi u}]_e^T$$

$$[K_{\phi\phi}]_e = \int_{V_p} [B_\phi]^T [\bar{\xi}]_k [B_\phi] dV$$

The global equations can be obtained by assembling the elemental equations (4) as:

$$\begin{aligned} [M]\{\ddot{d}\} + [K_{uu}]\{d\} + [K_{u\phi}]\{\phi\} &= \{F_m\} \\ [K_{\phi u}]\{d\} + [K_{\phi\phi}]\{\phi\} &= \{F_q\} \end{aligned} \tag{5}$$

where $\{d\}$ and $\{\phi\}$ are the global mechanical and electrical DoFs vectors, $[M]$ is the global mass matrix, $[K_{uu}]$, $[K_{u\phi}] = [K_{u\phi}]^T$ and $[K_{\phi\phi}]$ are the global mechanical stiffness, mechanical–electrical coupling stiffness and dielectric stiffness matrices respectively. $\{F_m\}$ and $\{F_q\}$ are the respective global mechanical and electrical loads vectors.

Next we assume that the electrical DoFs vector in Equation (5) can be divided into the actuating and sensing DoFs, $\{\phi\}_e = \{\phi_a, \phi_s\}^T$, where the subscripts ‘a’ and ‘s’ denote the actuating and sensing capabilities. Hence, considering open-circuit electrodes, and in that case $\{F_q\} = \{0\}$, the non-specified potential differences in Equation (5) can be statically condensed and the equations of motion and charge equilibrium become:

$$\begin{aligned} [M]\{\ddot{d}\} + [K_{uu}]\{d\} &= \{F_m\} - [K_{u\phi}]_a \{\phi\}_a \\ \{\phi\}_s &= -[K_{\phi\phi}]_s^{-1} [K_{\phi u}]_s \{d\} \end{aligned} \tag{6}$$

where $[K_{uu}^*] = [K_{uu}] - [K_{u\phi}]_s [K_{\phi\phi}]_s^{-1} [K_{\phi u}]_s$.

Equations

(6**)** are the final equations of motion and can be used in smart structures applications such as vibration control.

## 3 NEURO FUZZY CONTROL

The adaptive neuro-fuzzy control scheme which is used at the present investigation is based on Sugeno inference, thus it is a Sugeno-type controller, which is capable of training via neural networks, and namely, the back-propagation method. The control system takes two

inputs (the displacement and the velocity) and returns a single output (control force), thus is a multiple input – single output (MISO) controller.

The inputs of the controller are described by Gaussian membership functions, while the output take constant values, due to the limitations of Sugeno inference. Optimization is achieved via a training process. Namely, the characteristics of the fuzzy system of this controller are tuned using artificial neural networks, and more specifically, a well-chosen set of training data, which is used in order to adjust the system parameters. For the compilation of these data, the model is first simulated without any control mechanism attached, in order to collect the necessary vibration data. Subsequently, these data are used for the training of the Sugeno controller. It is worth mentioning that the training of this controller has been performed based on data provided by a simpler beam model as it was presented in [3]. The fact that the same controller functions well also in other models proves its robustness.

The resulting form of the membership functions (clusters) of the inputs i.e. the displacement (in1) and the velocity (out2), after the initialization process are shown in Figure 1 and Figure 2 respectively. Namely, four clusters of Gaussian form for each input occurred from the subtractive clustering process.

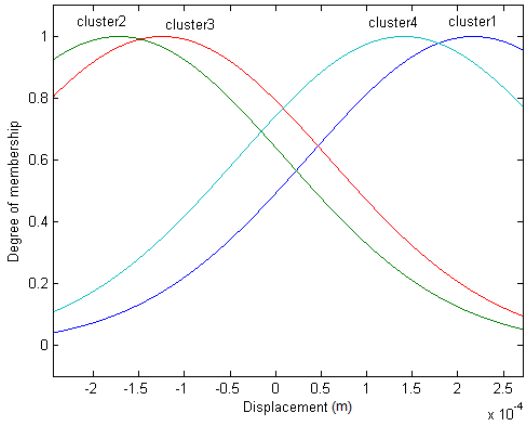


Figure 1: Membership function of the displacement

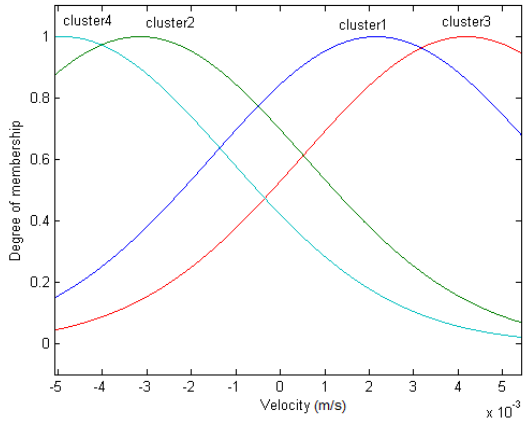


Figure 2: Membership function of the velocity

The output variable, i.e. the control force (out1), can take either constant values or linear functions taking values within the range [-1 1].

The if-then verbal rules which describe the emerging system are given in detail in Table 1. For example: if Displacement is in cluster 1 and velocity is in cluster 1 then the control force is out1.

| | Displ. Cluster 1 | Displ. Cluster 2 | Displ. Cluster 3 | Displ. Cluster 4 |
|---|---|---|---|---|
| Vel. Cluster 1 | Out1 | - | - | - |
| Vel. Cluster 2 | - | Out2 | - | - |
| Vel. Cluster 3 | - | - | Out3 | - |
| Vel. Cluster 4 | - | - | - | Out4 |

Table 1: Fuzzy rules of the ANFIS controller (Displ=displacement, Vel=velocity)

For the structure of rules in ANFIS see Figure 3. The visualization of the rules is shown in Figure 4.

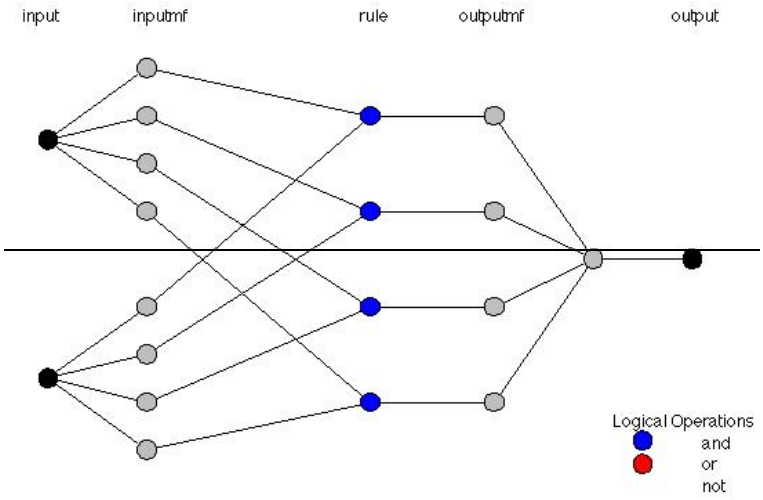


Figure 3: The structure of rules in ANFIS

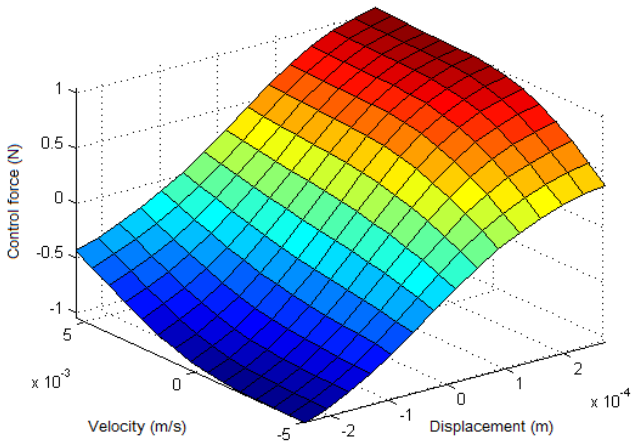


Figure 4: Graphic representation of the fuzzy rules of controller 3

The “and” method has been set to prod (product), while the “or” method has been set to probor (probabilistic or). The implication and the aggregation method have been set to min and max respectively. As defuzzification method the weighted average (wtaver) method is chosen.

It is worth mentioning that the characteristics of this controller (membership functions, rules, etc.) came through a training process, unlike the ones of fuzzy controllers which have been set based on experience.

## 4 NUMERICAL RESULTS

### 4.1 Plate model

The plate model which is considered in this investigation consists of a quadratic built-in plate fixed at two opposite edges. The dimensions of the host structure measure 0.8 m × 0.8 m, while thet material properties are given in detail in Table 2 [10].

| Property | T300/976 graphite-epoxy composite | G1195N PZT |
|---|---|---|
| $E_1$ (GPa) | 150 | 63 |
| $E_2 = E_3$ (GPa) | 9.0 | 63 |
| $G_{12}$ (GPa) | 7.1 | 24.2 |
| $G_{23} = G_{13}$ (GPa) | 2.5 | 24.2 |
| $\nu_{12} = \nu_{13} = \nu_{23}$ | 0.3 | 0.3 |
| $\rho$ (kg/m$^3$) | 1600 | 7600 |
| $d_{13} = d_{23}$ (m/V) | - | $254 \cdot 10^{-12}$ |
| $d_{42} = d_{51}$ (m/V) | - | $584 \cdot 10^{-12}$ |
| Ply thickness (mm) | 0.25 | 0.1 |

Table 2: Material properties

The plate is discretized in 144 quadratic finite elements, which yield to a system with 169 nodes with 5 degrees of freedom per node. The first three degrees indicate the displacement at the x, y and z axes respectively, while the other two denote the rotation around the x and y axes respectively. In the present paper, we consider the vertical displacement at the z axis. The plate is fixed at two opposite edges as shown in Figure 5.

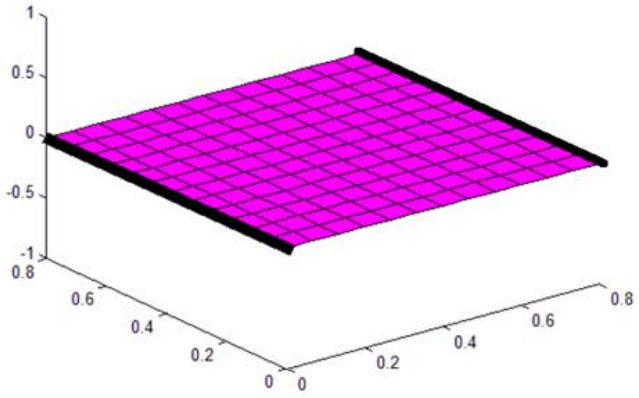


Figure 5: The built-in plate

The counting of the nodes and of the elements of the structure are shown in Figure 6 and Figure 7 respectively.

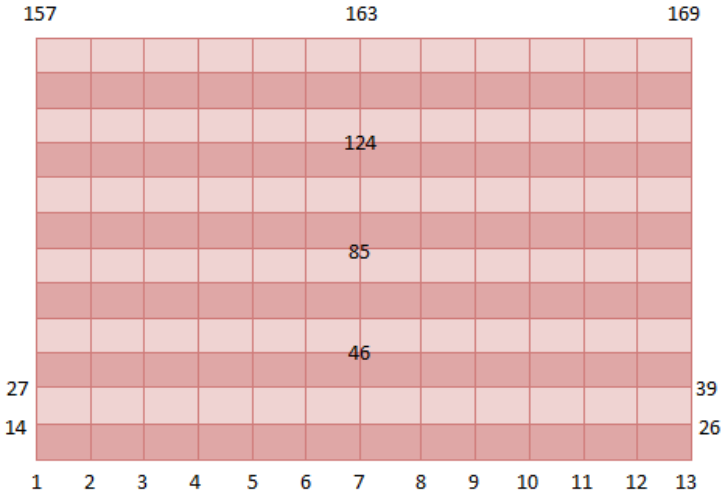


Figure 6: Counting of nodes

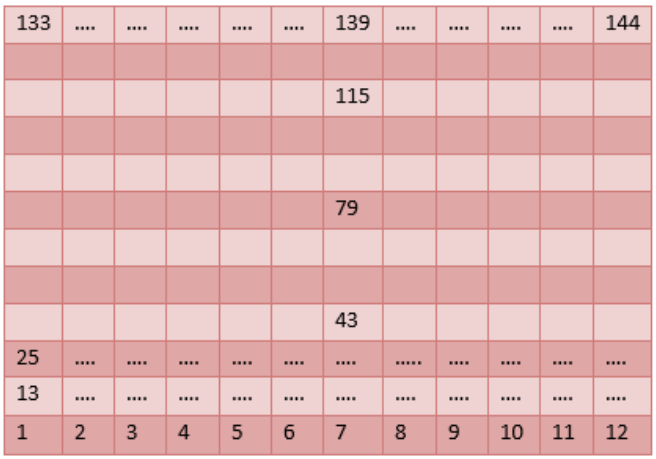


Figure 7: Counting of elements

## 4.2 Numerical results

The plate is excited through an external loading of sinusoidal form. We consider two different loading scenarios. In the first scenario, the external loading is applied to three different points at node 7, 85 and 163, while the control force is applied at node 85. The loading which is applied to each node is given as:

$$P = \frac{1}{3} sin(20t) \ \ (\mathrm{N}) \tag{7}$$

For the second scenario, the loading is applied at five different nodes, namely at node 7, 46, 85, 124 and 163. The control force is again applied at node 85. The loading which is applied to each node in this case is given as:

$$P = \frac{1}{5} sin(20t) \ (\mathrm{N}) \tag{8}$$

The results regarding the suppression which is achieved from the use of the neuro-fuzzy controller regarding the displacement, the velocity and the acceleration, along with the forces for the two different scenarios are presented in Figure 8 and in Figure 9 respectively.

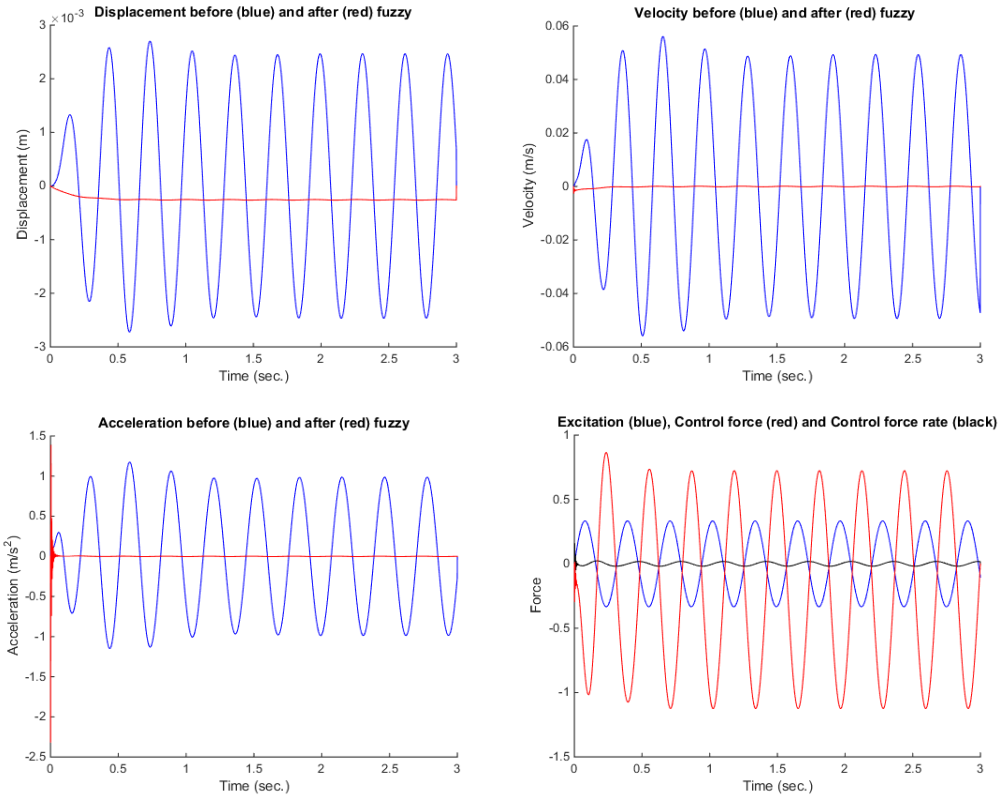


Figure 8: Displacement, velocity, acceleration and forces at node 85 for three point loading

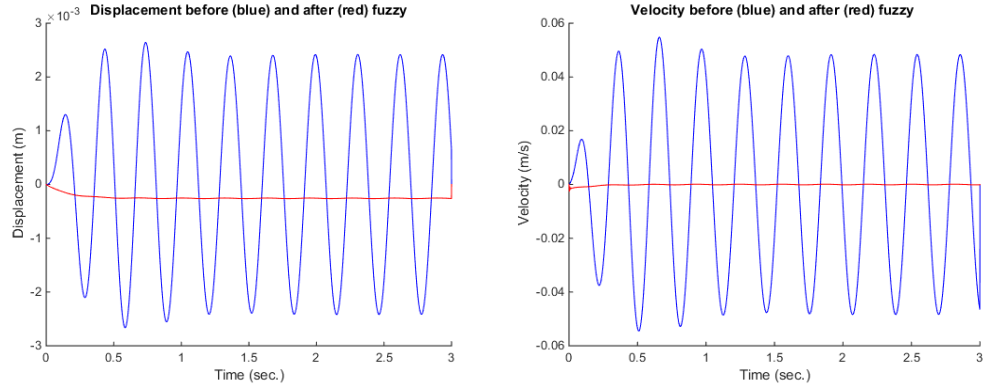

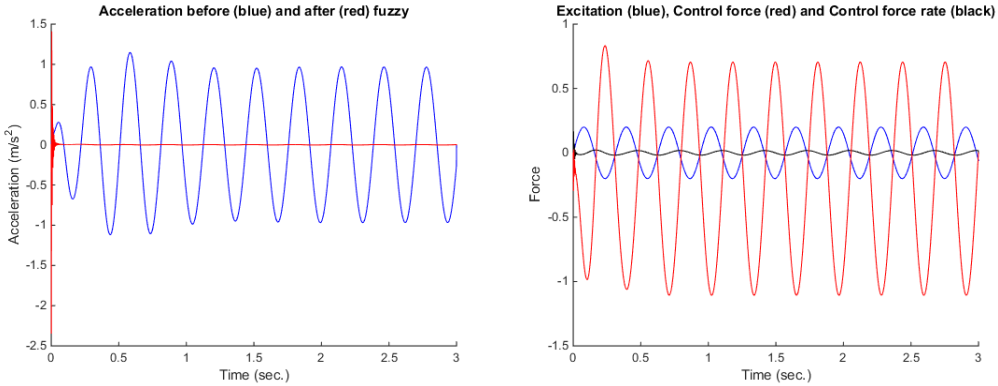


Figure 9: Displacement, velocity, acceleration and forces at node 85 for five point loading

In the first three diagrams of each figure with blue color is denoted each measure before the application of the control, while with red color is shown the corresponding measure after control. As for the forces, with blue color is shown the external loading, with red color is denoted the control force which came out of the neuro-fuzzy system and with black color is given the control force rate.

The numerical results for the two different loading scenarios are presented in Table 3 and Table 4 respectively.

| | Maximum displacement (m) | Maximum velocity (m/s) | Maximum acceleration ($m/s^2$) | Maximum acceleration after t=0.3 sec. |
|---|---|---|---|---|
| Without control | 0.0054 | 0.1119 | 2.3213 | 2.3213 |
| With control | $2.6355\times10^{-4}$ | 0.0027 | 3.7102 | 0.0198 |
| Fluctuation percentage | -95.14% | -97.55% | +59.83% | -99.15% |

Table 3: Numerical results at node 85 for the case of the three-point external loading

| | Maximum displacement (m) | Maximum velocity (m/s) | Maximum acceleration ($m/s^2$) | Maximum acceleration after t=0.3 sec. |
|---|---|---|---|---|
| Without control | 0.0053 | 0.1093 | 2.2643 | 2.2643 |
| With control | $2.6343\times10^{-4}$ | 0.0028 | 3.7592 | 0.0200 |
| Fluctuation percentage | -95.03% | -97.47% | +66.00% | -99.11% |

Table 4: Numerical results at node 85 for the case of the three-point external loading

The results for the suppression of the displacement and the velocity are very satisfactory. Regarding the acceleration one may observe that there is an increase of the vibrations, which could be a burden for the material and/or the sensors and the actuators. However, this problem occurs at the beginning of the simulation and it is vanished after less than half a second.

## 5 CONCLUSIONS

Taking into account the numerical results, as well as the results of other investigations of our team [2, 3, 9], one can observe that the intelligent neuro-fuzzy control scheme which is

proposed and tested here is not only very efficient, but and very robust as well. This conclusion comes out from the proved ability of the proposed controller to function perfectly not only for different models, but also under several conditions. This may include different support scenarios, application of different external loadings, etc.

It is also shown that the proposed control system has the ability to handle non-linearities, and to function well, even if it was not trained for the specific model which was studied in the present paper, i.e. the built-in plate, but instead for a simpler one, i.e. a cantilever beam.

## REFERENCES


[1] G.K. Tairidis, G.E. Stavroulakis, D. Marinova, E. Zacharenakis, Classical and soft robust active control of smart beams. M. Papadrakaikis, D.C. Charmpis, Y. Tsompanakis, N. D. Lagaros eds. *Computational Structural Dynamics and Earthquake Engineering*, CRC Press - Taylor & Francis Group, London, UK, Chapter 11, 165-178, 2009

[2] G.E. Stavroulakis, I. Papachristou, S. Salonikidis, I. Papalaios, G.K. Tairidis, Neurofuzzy Control for Smart Structures. Y. Tsompanakis, B.H.V. Topping eds. *Soft Computing Methods for Civil and Structural Engineering*, Saxe-Coburg Publications, Stirlingshire, UK, Chapter 7, 149-172, 2011

[3] G.K. Tairidis, I. Papachristou, M. Katagas and G.E. Stavroulakis, Neuro - fuzzy control of smart structures, *10th HSTAM International Congress on Mechanics*, Chania, Crete, Greece, May 25-27, 2013

[4] C.G. Dávila, P.P. Camanho, C.A. Rose, Failure criteria for FRP laminates. *J Compos Mater,* 39, 323-345, 2005

[5] M. Sugeno, An Introductory Survey of Fuzzy Control, *Inform Sciences,* 36, 59-83, 1985

[6] G.K. Tairidis, G. Foutsitzi, P. Koutsianitis, G.E. Stavroulakis, Fine tuning of a Fuzzy Controller for Vibration Suppression of Smart Plates using Genetic Algorithms. *Adv Eng Softw,* 101, C, 123-135, 2016

[7] G.K. Tairidis, G. Foutsitzi, P. Koutsianitis, G.E. Stavroulakis, Fine tuning of Fuzzy Controllers for Vibration Suppression of Smart Plates using Particle Swarm Optimization, *8th GRACM International Congress on Computational Mechanics*, Volos, Greece, July 12-15, 2015

[8] P. Antsaklis, Neural Networks for Control Systems, *IEEE T Neural Networ,* 1(2), 242-244, 1990

[9] G.E. Stavroulakis, I. Papachristou, S. Salonikidis, I. Papalaios, G.K. Tairidis, Neurofuzzy Control for Smart Structures. Y. Tsompanakis, B. Topping eds. *Soft Computing Methods for Civil and Structural Engineering.* Stirlingshire: Saxe-Coburg Publications, 149-172, 2011

[10] K.Y. Lam, X.Q. Peng,G.R. Liu, J.N. Reddy, A finite-element model for piezoelectric composite laminates, *Smart Mater Struct*, 6, 583-591, 1997

COMPDYN 2017
6th ECCOMAS Thematic Conference on
Computational Methods in Structural Dynamics and Earthquake Engineering
M. Papadrakakis, M. Fragiadakis (eds.)
Rhodes Island, Greece, 15–17 June 2017

# TORSIONAL BALANCE OF TWO-WAY ASYMMETRIC PLANS WITH OPTIMAL DISTRIBUTION OF VISCOUS DAMPERS

**Amir Shahmohammadian**[1], **Mohammad Reza Mansoori**[2], **Mir Hamid Hosseini**[2]

[1] M.Sc. Student of Earthquake Engineering, Department of Civil Engineering, Science and Research branch, Islamic Azad University
a.shahmohammadian@srbiau.ac.ir

[2] Assistant Professor, Department of Civil Engineering, Science and Research branch, Islamic Azad University
{m.mansoori,mirhamid.hosseini}@srbiau.ac.ir

**Keywords:** Asymmetric buildings, Torsional balance, Viscous dampers, Particle Swarm Optimization Algorithm

**Abstract**. *Lateral-torsional coupling in asymmetric-plan buildings results in an increase of lateral displacement in the end-points of the building plan and therefore the production of disorderly deformation demand in seismically resistant frames. The demand for deformation in resistant frames depends on the relative magnitude of the plan translation and rotation and also the correlation between these two signals. Therefore, great correlation of small rotations with lateral displacement may result in considerably different deformations in the resistant frames of the structure's two-edges. With regard to the inability to eliminate the asymmetric state due to various reasons such as architectural issues, in this study an attempt has been made to use supplemental dampers to decrease the lateral-torsional correlation of the plan displacement. This can result in a nearly uniform demand of deformation in seismically resistant frames. On this basis, using the concept of "torsional balance", the optimized distribution of viscous dampers is determined for the decrease of this correlation by moving the "Empirical Center of Balance" (ECB) to the geometrical center of the structure. Which results in an equal mean-square-values of displacement in the edges of the plan. One-way and two-way mass asymmetry has been considered for torsional stiff and flexible structures and the optimal layout of dampers has been determined using the particle swarm optimization algorithm. The results show that the optimum center of viscous dampers depends on size of the mass eccentricity, uncoupled torsional-to-lateral frequency ratio and the amount of supplemental damping considered.*

## 1 INTRODUCTION

The previous studies on recent earthquakes showed that sometimes, asymmetry of structures was one of the reasons for building's collapse in earthquake [1]. The main factors of structure asymmetry are including mass asymmetry, stiffness asymmetry, and strength asymmetry in plan and structure height which plays an important role in increasing the structural response in earthquake. For this reason, many studies have been carried out in order to control the seismic response in asymmetric structures. In line with such investigations, one of the proposed methods for controlling the structure's torsion is using energy dissipation devices such as fluid viscous dampers (FVD) regarding to its advantages including structure's high level of performance.

Fluid viscous dampers are effective specifically in controlling structure's seismic response by increasing the ratio of damping of total system. To this end, it is needed to establish appropriate distribution of dampers in plan and height of the structure to decrease structural response in earthquake and minimize the response raised by structure asymmetry.

Goel (1998) has analyzed the effect of supplemental fluid viscous damping devices on the response of asymmetric structures. The results showed that supplemental fluid viscous damping devices can decrease the structure drift in comparison with the systems without damping system. Moreover, when the center of damping is on the opposite side of stiffness center, respect to mass center and in a distance equal to stiffness eccentricity, the displacement of stiff and flexible edges decreases in an optimized manner. On the other hand, if damping radius of gyration is increased more, the response in each edges will decrease [2].

During investigating the plan asymmetric structures in earthquake, Goel (2000) referred to this subject that the amount of damping of first mode increases with the increase of damping eccentricity in opposite side of stiffness center and whereas the flexible edge displacement is controlled by first mode, such a distribution of dampers causes to high decrease in deformation of flexible edge [3].

De La Llera et al (2004) submitted an investigation into the concept of "torsional balance". Torsional balance is a status of dampers distribution in plan (including fluid viscous, viscoelastic, and frictional dampers) which causes to equality of mean square value (MSV) of building response (such as acceleration, velocity and displacement) during earthquake in diaphragm points which have the same distance from the center of diaphragm[4].

Figure 1 shows a typical plan of a one-way asymmetric, single-story structural model with its mass center (CM), stiffness center (CS), strength center (CR) and the center of supplemental damping (CSD) as well as its flexible and stiff edges considered by De La Llera et al. (2005). The Parameters of $C_{xi}$ and $C_{yi}$ is related to damping constants which is the *i*th supplemental dampers along the X and Y directions, respectively. Moreover, $S_{xi}$, $R_{xi}$, $S_{yi}$ & $R_{yi}$ are stiff nesses and strengths of the resistant frames elements in the X and Y directions, respectively. The Stiffness, strength and damping eccentricities are defined as $e_s=\frac{E_s}{L_x}$, $e_R=\frac{E_R}{L_x}$ and $e_d=\frac{E_d}{L_x}$ which each one of $E_s$, $E_R$ & $E_d$ are the distance of CS, CR & CD from CM, respectively.

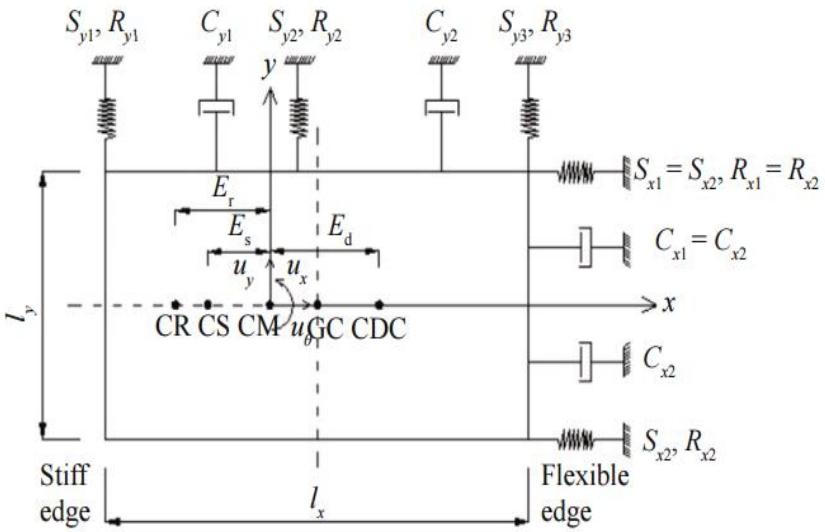


Fig. 1: Single-story structural model considered with one-way stiffness, strength and damping constant eccentricities [5]

In order to investigate the torsional balance, diaphragm of a single story structure, in which CM is placed in a desired point and is only asymmetric in X direction, is considered. Degrees of freedom in CM include uncoupled degree of freedom in in X direction ($u_x$), coupled degree of freedom of lateral displacement in Y direction ($u_y$) and rotation ($u_\theta$). Omitting uncoupled displacement of $u_x$:

$$u(t)=[u_y(t,e_d)\ ,\ L_x u_\theta(t,e_d)] \tag{1}$$

Consequently by considering a rigid diaphragm, displacement vector in a point which have a distance of P from Cm is equal to:

$$u_y^{(p)}(t,e_d)=u_y(t,e_d)+Pu_\theta(t,e_d) \tag{2}$$

The MSV of displacement at a distance of P from CM is equal to:

$$E[u_y^{(p)}(t,e_d)^2] = E[\ u_y(t,e_d)^2] + 2\ PE[u_y(t,e_d)u_\theta(t,e_d)] + P^2\ E[u_\theta(t,e_d)^2] \tag{3}$$

In a point, at a distance of $P^*$, which placed from CM, the minimum square of expected response that is similar to a point which the coefficient correlation between two lateral and rotational movement is zero, is happened.

The amount of $P^*$ is equal to:

$$P^* = -\frac{E[u_y\, u_\theta]}{E[u_\theta^2]} = -\rho_{y\theta}\frac{\sigma_y}{\sigma_\theta} \tag{4}$$

Where $\rho_{y\theta}$ is linear correlation coefficient between lateral and rotational motions at the CM and $\sigma_y$ & $\sigma_\theta$ are lateral and rotational displacement standard deviation, respectively. The $P^*$ point is known as "Empirical Center of Balance" or ECB. The MSV of the expected lateral displacement in a point with distance of d from ECB is in a form of parabola which its value is minimum in ECB.

$$E[u_y^{\tilde{}(d)}(t,e_d)^2]= E[u_y^{\tilde{}*2}] + d^2\ E[u_\theta^{*2}] \tag{5}$$

Therefore, if ECB is located in the diaphragm middle point (surface geometrical center in the form of rectangular diaphragm), for resistant elements with the same distance form surface center, the amount of lateral displacement MSV, became equal. Even though, this is not meant to zero rotation of asymmetric structure, but due to the existence of equal expected maximum displacement of two edges of structure, it shows the optimized mode of performance of resistant elements [6].

Mansoori and Sarvghad Moghadam (2009) assessed the possibility of simultaneous control of irregular structure's acceleration and displacement by using viscous damper. They used single-story systems with moment-resistant steel frames and one-way strength and stiffness eccentricity. They came to the conclusion that damping distribution can put a significant effect on modal properties and structure seismic response [7].

De La Llera and Almazan (2009) presented more complete concept of torsional balance in one-way single-story asymmetric structure considering the elastic behavior of structure. The effects of structure period, uncoupled torsional-to-lateral frequency ratio, static eccentricity and damping radius of gyration are studied too. Moreover, they submitted some criteria for torsional balance [8].

Almazan et al (2013) submitted an optimization method for control of seismic response of structures with one-way plan asymmetry considering linear and non-linear behavior relying on the concept of torsional balance. They decreased not only the two-edged displacement around the structure, but also they leveled the amount of displacements. They came to the conclusion that the location of damping eccentricity was not considerably affected by structure non-linear behavior and the results of two linear and non-linear models were the same [9].

Rahimzadeh Rofoie et al (2016) investigated the improvement of torsional responses of asymmetric structures with moment-resisting concrete frames and equipped with viscous dampers. They assessed a single-story model with one-way stiffness eccentricity with various arrangements of dampers and came to conclusion that dampers' appropriate distribution has a considerable effect on the torsional response of asymmetric concrete structures [5].

## 2 DAMPING PARAMETERS

The inherent damping matrix of a structure is defined as follows:

$$C_o=\alpha M + \beta K \tag{6}$$

Where M & K are mass and stiffness matrix and the amounts of $\alpha$ & $\beta$ is calculated based on dominant vibrating modes. Total damping matrix of structure including inherent damping and supplemental damping is measured as below:

$$C_t=C_o+C_{sd} \tag{7}$$

$C_{sd}$ is damping matrix resulted from FVDs. According to single-story structure by stiffness eccentricity, the strength and damping of figure 1, $C_{sd}$ can be calculated as below:

$$C_x=\sum_i C_{xi} \quad , \quad C_y=\sum_i C_{yi} \quad , \quad C_\theta=\sum_i C_{xi}\, y_i^2+\sum_i C_{yi}\, x_i^2 \tag{8}$$

Where $C_{xi}$ and $C_{yi}$ are damping factor of *i*th damper in X,Y direction and $x_i$,$y_i$, are distance of *i*th damper from CM in X and Y direction, respectively. Also, damping eccentricities in X, Y directions and normalized damping eccentricity is expressed as follows:

$$E_{sdx}=\frac{1}{C_y}\sum x_i\ C_{yi} \quad , \quad e_{sdx}=\frac{E_{sdx}}{L_x}=\frac{1}{L_x\, C_y}\sum x_i\ C_{yi} \tag{9}$$

$$E_{sdy} = \frac{1}{C_x} \sum y_i \, C_{xi} \quad , \quad e_{sdy} = \frac{E_{sdy}}{L_y} = \frac{1}{L_y \, C_x} \sum y_i \, C_{xi} \tag{10}$$

Supplemental damping matrix [$C_{sd}$] is:

$$[C_{sd}] = \begin{bmatrix} C_x & 0 & -E_{sdy} \, C_x \\ 0 & C_y & E_{sdx} \, C_y \\ -E_{sdy} \, C_x & E_{sdx} \, C_y & C_\theta \end{bmatrix} \tag{11}$$

One of the most important parameters in the response for systems containing torsional radius of gyration supplemental viscous damper. For calculating the amount of this parameter, it is needed that the amount of torsional damping ratio is calculated in proportion to center of damping.

$$C_{\theta csd} = C_\theta - E_{sdx}^2 \, C_y - E_{sdy}^2 \, C_x \tag{12}$$

By such a definition, the amount of damping radius of gyration in X and Y directions is equal to:

$$\rho_{sd,x} = \sqrt{\frac{C_{\theta csd}}{C_x}} \tag{13}$$

$$\rho_{sd,y} = \sqrt{\frac{C_{\theta csd}}{C_y}} \tag{14}$$

## 3 MODELING

The considered model of this study is including a symmetric single-story steel structure of 3×3 bays. The bay dimensions are 6 and 5 meters in X and Y direction respectively and the height of the structure is 3.3 meters. The mass, stiffness and strength properties are assumed in a symmetric form in X and Y directions. Therefore, centers of mass, stiffness and strength are coincident with the geometrical center of the rigid diaphragm. Figure 2 shows a three-dimensional view of the basic model. Two models of torsional stiff and torsional flexible structure is extracted from the basic model. The parameters of these two models are shown in Table 1. Furthermore, for accounting the effect of uncoupled torsional-to-lateral frequency ratio ($\Omega_s$), two flexible and stiff torsional structures with $\Omega_s$=1.2 and $\Omega_s$=0.89 are modeled according to table 1.

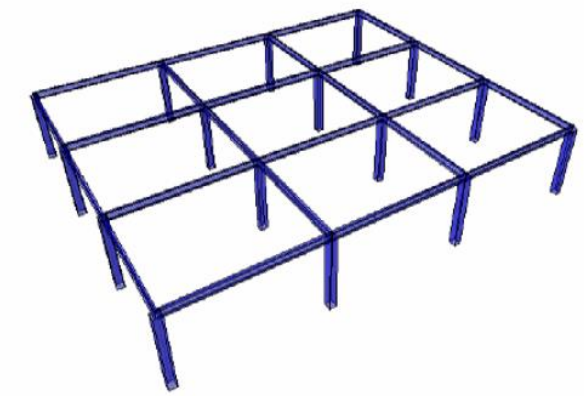

Fig.2: 3D view of the basic model [7]

| Model No. | $\%e_s$ | $\%e_R$ | $\%e_m$ | $T_x$(sec) (Uncoupled) | $T_y$(sec) (Uncoupled) | $T_\theta$(sec) (Uncoupled) | $\Omega_{sx}$ | $\Omega_{sy}$ |
|---|---|---|---|---|---|---|---|---|
| 1 | 0.0 | 0.0 | 0.0 | 0.3633 | 0.3529 | 0.3052 | 1.16 | 1.19 |
| 2 | 0.0 | 0.0 | 0.0 | 0.3365 | 0.3277 | 0.3728 | 0.88 | 0.90 |

Table 1: Static and dynamic parameters of models 1&2

Asymmetry in structure is considered as a mass eccentricity. In order to create the mass eccentricity it is needed the mass center to move to a distance of $e_m$ from the geometric center of the plan. It is worth mentioning to the change in structure mass moment of inertia which should be considered in calculations In order to create one-way mass eccentricity, Method applied by Mansoori et.al (2014) [10] is considered in this study.

### 3.1 Creating two-way mass eccentricity

In order to create two-way mass eccentricity, CM has been moved in plan diameter length. To this end, the plan has been divided into four sections and it is supposed firstly that, structure mass is uniformly distributed with surface density σ and then the surface density is increased in a tape with determined width in right side above the structure plan (location 1 in Fig.3) and the counterpart density of tape (Locations 2, 3&4 Fig 3) is decrease the same in a way that the total mass of plan remains constant.

Structure plan with the dimension of a & b is considered in X & Y directions according to figure 3 having mass density of σ where $\sigma=\frac{m}{a\,b}$ .The center of the surface is considered as the origin of coordinate and it is supposed that in a tape with the width of λa (λ=0.5) in right side of structure, the amount of surface density is equal to σ(1+η) and in counterpart tape, surface density is equal to σ(1-η). Moreover, in a tape with the width of λb at the top of plan, the amount of surface density is equal to σ(1+η) and in counterpart tape, surface density is equal to σ(1-η). In this equation, $\eta$ ($-1 < \eta < 1$), indicates density variation ratio. Here, the amount of normalized eccentricity is as follows:

$$e_{mx} = \frac{1}{a}\left(\frac{\sigma(1+\eta)\lambda ab\left(\frac{a}{2}-\frac{\lambda a}{2}\right)+\sigma(1-\eta)\lambda ab\left(-\frac{a}{2}+\frac{\lambda a}{2}\right)}{\sigma ab}\right) = \eta\lambda(1-\lambda) \qquad (15)$$

Also, with refer to diagonal form of mass eccentricity, it can be observed that:

$$e_{mx}=e_{my} \qquad (16)$$

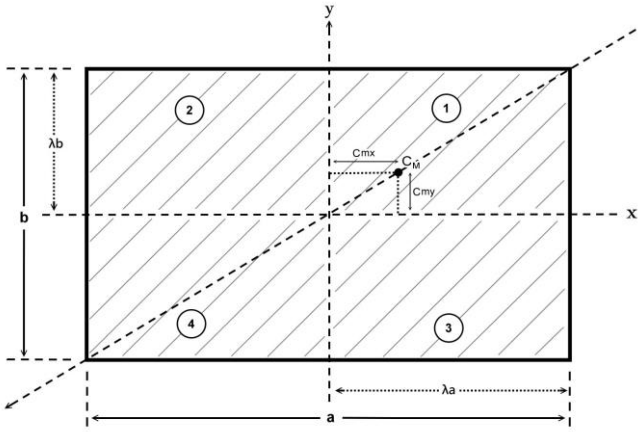


Fig. 3: Method of creating two-way mass eccentricity

In the case of uniform mass distribution, mass moment of Inertia is measured to $I_o=\frac{m(a^2+b^2)}{12}$. In order to calculate plan mass moment of inertia around second mass center, it is needed that each tape inertia calculated separately and added together. Therefore, in can be observed that:

$$\begin{aligned} m_1 &= m\,(1+\eta)\,(1+\eta)\,/4 \\ m_2 &= m_3 = m\,(1+\eta)\,(1-\eta)\,/4 \\ m_4 &= m\,(1-\eta)\,(1-\eta)\,/4 \end{aligned} \tag{17}$$

The amount of plan mass moment of inertia around second mass center is as follows:

$$I_{CM}=I_{CM1}+I_{CM2}+I_{CM3}+I_{CM4} \tag{18}$$

$I_{CM1}$, $I_{CM2}$, $I_{CM3}$ and $I_{CM4}$ are mass inertia moment for section 1, 2, 3 and 4 (Fig.3) and is determined as follows:

$$I_{CM1} = m_1\left[\frac{(\lambda^2a^2+\lambda^2b^2)}{12}+\left(\frac{a}{2}-\frac{\lambda a}{2}-ae_{mx}\right)^2+\left(\frac{b}{2}-\frac{\lambda b}{2}-be_{my}\right)^2\right] \tag{19}$$

$$I_{CM2} = m_2\left[\frac{(\lambda^2a^2+\lambda^2b^2)}{12}+\left(\frac{a}{2}-\frac{\lambda a}{2}+ae_{mx}\right)^2+\left(\frac{b}{2}-\frac{\lambda b}{2}-be_{my}\right)^2\right] \tag{20}$$

$$I_{CM3} = m_3\left[\frac{(\lambda^2a^2+\lambda^2b^2)}{12}+\left(\frac{a}{2}-\frac{\lambda a}{2}-ae_{mx}\right)^2+\left(\frac{b}{2}-\frac{\lambda b}{2}+be_{my}\right)^2\right] \tag{21}$$

$$I_{CM4} = m_4\left[\frac{(\lambda^2a^2+\lambda^2b^2)}{12}+\left(\frac{a}{2}-\frac{\lambda a}{2}+ae_{mx}\right)^2+\left(\frac{b}{2}-\frac{\lambda b}{2}+be_{my}\right)^2\right] \tag{22}$$

The numerical models are created in OpenSees software [11] and several non-linear analysis are performed. In order to consider the non-linear effects for beams and columns, fiber elements with strength hardening behavior is used for steel. The dampers are modeled as linear viscous zero length elements in both structure's edges. The models are analyzed under two synthetic records compatible with design spectrum of European code (EC8) with soil type B.

According to figure 4, one component record (Y direction, figure 4-b) is used for structure with one-way eccentricities and two component record (X and Y direction, figure 4-a and 4-b) is employed for structures with two-way eccentricities.

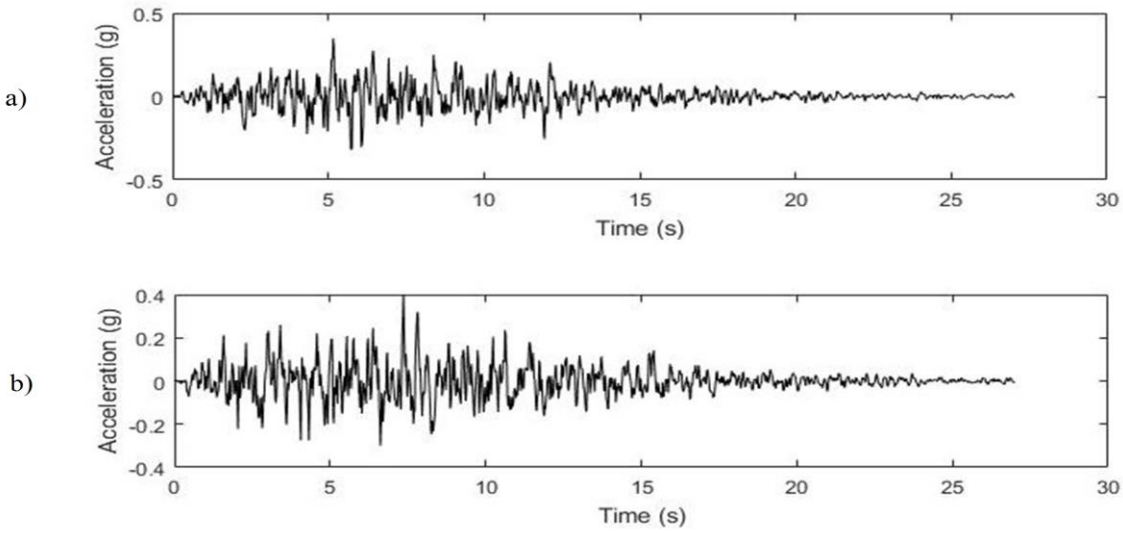


Fig.4: Synthetic records. a) Ground motion in X direction b) Ground motion in Y direction

Also, particle swarm optimization algorithm is used to minimize torsional response and reaching to torsional balance conditions. Objective function of PSO algorithm is defined as below:

$$\text{Objective Function} = ( E[u_{yfe}^2] - E[u_{yse}^2] ) + ( E[u_{xfe}^2] - E[u_{xse}^2] ) \quad (23)$$

$u_{yfe}$ and $u_{yse}$ are structure's flexible and stiff displacement in Y direction and $u_{xfe}$ and $u_{xse}$ are structure's flexible and stiff displacement in X direction Linking of Matlab and OpenSees softwares are used for implementation of the PSO algorithm.

## 4 ANALYSIS RESULTS:

The results of time history analyses for the lateral displacement by using torsional balance concept are shown in figures to. For simplicity the expected values are only shown in flexible and stiff edges of diaphragm.

For example, figure 5 shows the displacement of flexible and stiff edges of structure with normalized one-way eccentricity equal to 0.1, with uncoupled torsional-to-lateral frequency ratio of 1.2 in two modes without damping (figure 5-a) and with optimum damper distribution using torsional balance conditions (figure 5-b).

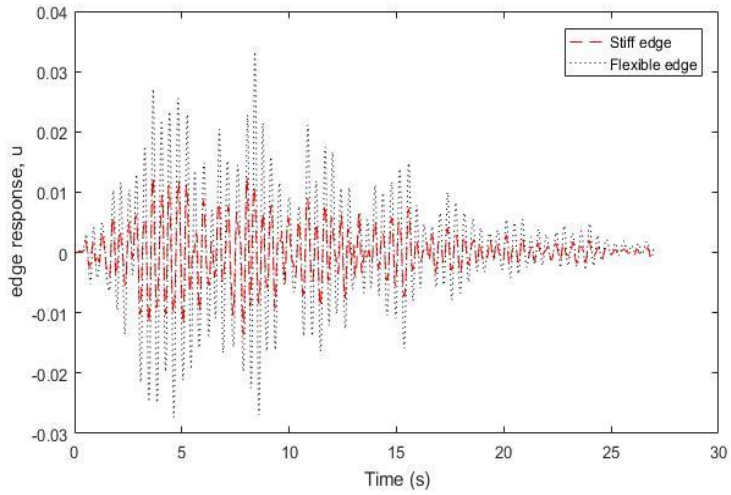


Fig.5-a: Typical response of a torsionally stiff asymmetric structure without FVDs

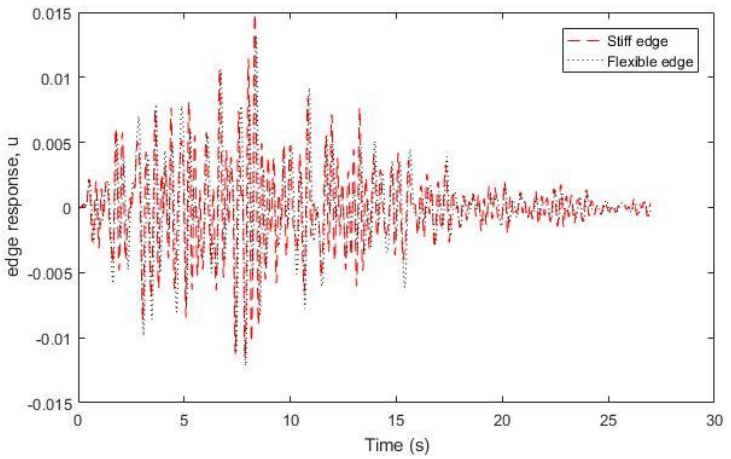


Fig.5-b: Typical response of a torsionally stiff asymmetric structure with optimum distribution of FVDs

It can be observed that in torsional balance condition, not only responses of two edges are decreased significantly, but also the responses are almost equal and improved in comparison with the case that no damper is used in the structures.

Figure 6 indicates the standard deviation of normalized displacement of structure plan having normalized one-way eccentricity 0.1 and $\Omega_s$=1.2 in two modes without supplemental damping and with supplemental damping considering torsional balance concept.

It can be seen that in a torsional condition, the standard deviation of plan displacement is parabola and two points with the same distance from geometrical center of structure plan have the same standard deviation of displacement according to equation 5.

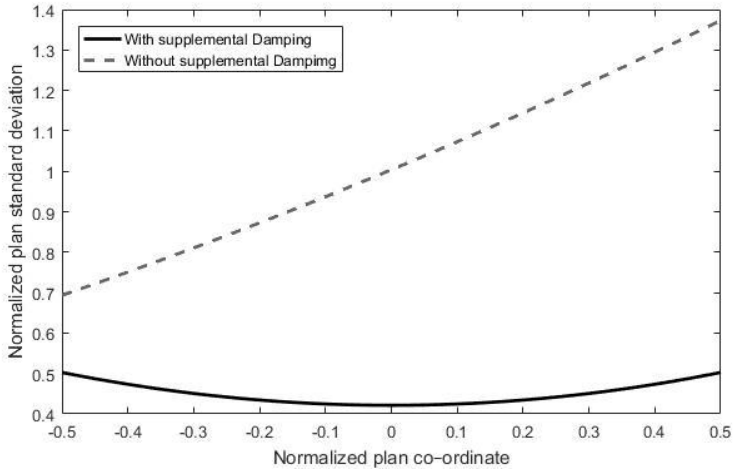


Fig.6: Standard deviation profiles of plan displacement for asymmetric-plan structures

figure 7 shows the optimized values of normalized damping eccentricity versus normalized one-way mass eccentricity for two torsional stiff and flexible structures with $\Omega_s$=1.2 (Fig. 7-a) and $\Omega_s$=0.89 (Fig.7-b) and supplemental damping of 15 percent by using torsional balance concept. In figure 7-a, it can be seen that in order to achieving torsional balance condition, damping center should be in same side with CM and bigger than CM distance to geometric center. Moreover, by increasing the structure asymmetry and consequently, increase of mass eccentricity, it is needed to have more damping eccentricities to achieve torsional balance.

It can be seen that for a normalized mass eccentricity bigger than 0.125 ($e_m$>0.125), and damping ratio of 15% is not be a response to torsional balance conditions. Figure 7-b show the optimized normalized mass damping eccentricity versus normalized eccentricity for torsional flexible structure.

The results gained from two torsional flexible and stiff models are the same, but with a difference that in torsional flexible structure it is needed to have less mass damping eccentricity in order to achieve optimized distribution of viscous dampers in comparison with torsional stiff structure. As can be seen, for mass eccentricity bigger than 0.175 ($e_m$>0.175) supplemental damping ratio of 15% is not be a respond to achieve the optimized condition.

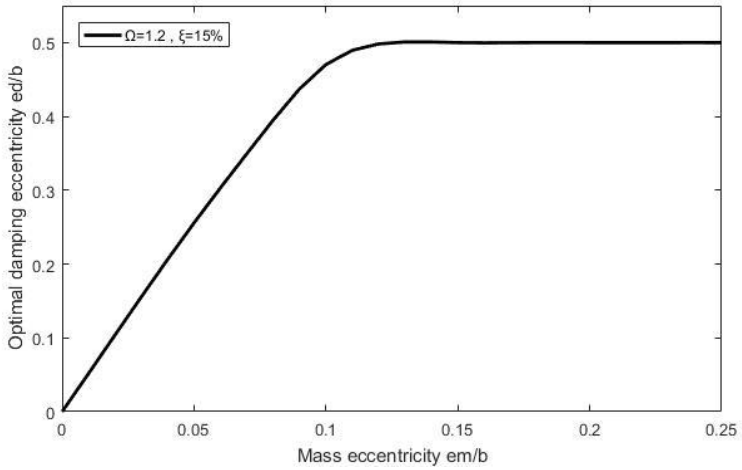


Fig.7-a: Optimal eccentricity curve $e_d$ for asymmetric-plan structure. ($\Omega_s$=1.2, $\xi$=15%)

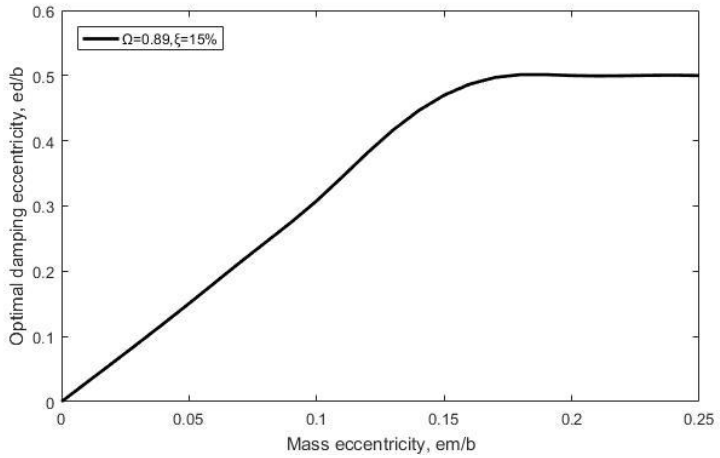


Fig.7-b: Optimal eccentricity curve $e_d$ for asymmetric-plan structure. ($\Omega_s$=0.89, $\xi$15%)

Figure 8 shows the changes of normalized damping center in terms of normalized one way mass eccentricity of torsional stiff structure for 15, 20 & 25 percent of supplemental damping. It can be concluded that it is needed less damping eccentricity in order to achieving torsional balance condition by increasing the damping percent.

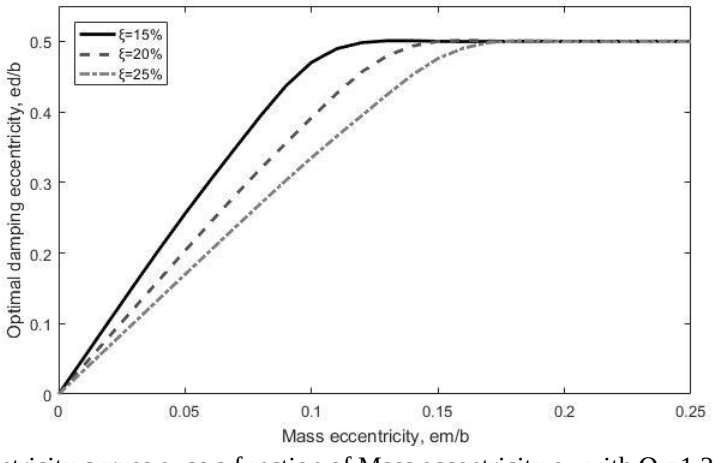


Fig.8: Optimal eccentricity curves $e_d$ as a function of Mass eccentricity $e_m$ with $\Omega_s$=1.2 and $\xi$=15, 20&25%

Figure 9 presents normalized optimized changes of damping center in X and Y directions versus of normalized two-ways mass eccentricity for two torsional stiff structures of 9-a and torsional flexible structure of 9-b and $\xi$=15%. The diaphragm center has been changed in order to considering two-ways asymmetry in structure. The results show that in order to achieve optimized design, dampers in two directions of X and Y should be distributed in a way that damping eccentricity be in a same side with CM and more than the distance of CM to geometric center.

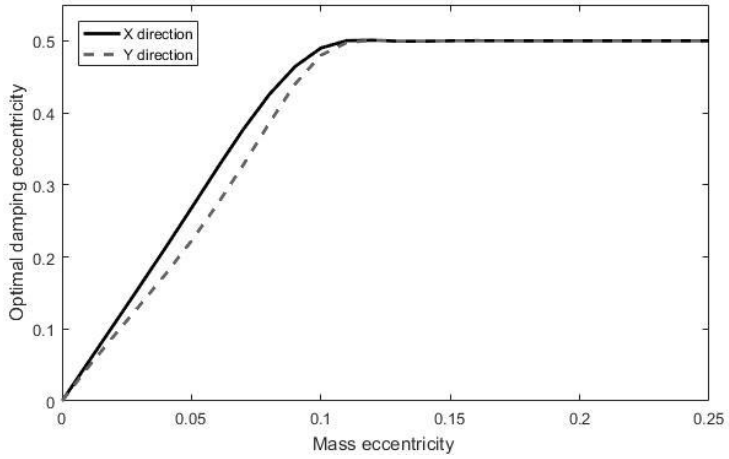


Fig.9-a: Optimal eccentricity curves $e_d$ as a function of Mass eccentricity $e_m$ with $\Omega_s$=1.2 and $\xi$=15%

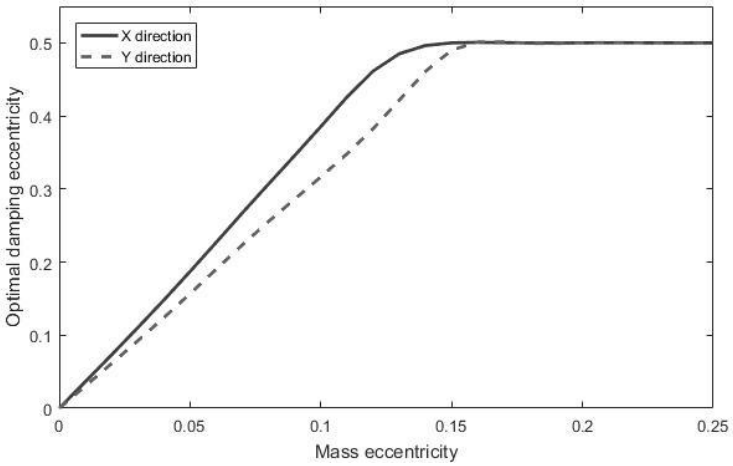


Fig.9-b: Optimal eccentricity curves $e_d$ as a function of Mass eccentricity $e_m$ with $\Omega_s$=0.89 and $\xi$=15%

Moreover, similar to one-way mass asymmetric model, with increasing of mass eccentricity, higher values of damping eccentricities is needed to achieve torsional balance condition. It can be seen that; in comparison with torsional stiff structures, it is needed to have less damping eccentricity in torsional flexible structure for achieving torsional balance in two directions.

Besides, by comparing figure 9-a and 10 , it can be observed that less damping eccentricity is needed in order to achieve optimized design by increasing damping ratio in torsional stiff structure and the structure can reach to torsional balance against more two-ways asymmetry by increasing damping ratio.

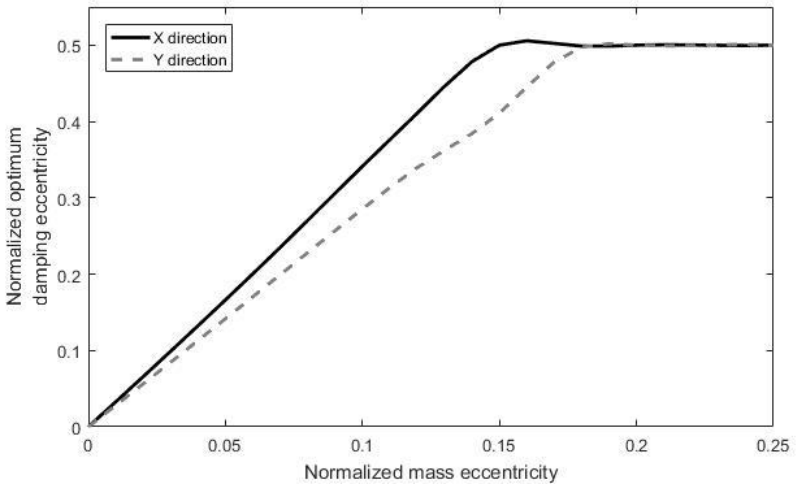


Fig.10: Optimal eccentricity curves $e_d$ as a function of Mass eccentricity $e_m$ with $\Omega_s$=1.20 and $\xi$=25%

## 5 CONCLUSIONS:

In this research several parametric analysis has been carried out on a single-story torsional stiff and flexible structure with one-way and two-ways mass asymmetry .The lateral strength and stiffness in all models are constant for comparing the results in different items.

By using the theory of torsional balance, the MSV of lateral displacement of two edges of diaphragm is measured and the amount of optimized damping eccentricity is determined using PSO optimizing algorithm in terms of different values of mass eccentricity, damping ratio and uncoupled torsional-to-lateral frequency ratio.

The summaries of results are as follows:

1- It can be seen that using of viscous damper not only caused to decrease responses of structural lateral displacement, but also it makes displacement of two asymmetric edges of structure close together by appropriate distribution of dampers in structure plan.
2- Damping optimized eccentricity for controlling the displacement, mostly have the same direction of mass eccentricity and bigger than the distance of stiff center to geometric center.
3- By increasing the asymmetry of structure resulted from increasing mass eccentricity, it is needed to have more damping eccentricity or more damping ratio for controlling the displacement of two asymmetric edges of structure.
4- It seems that it is needed less damping eccentricity in order to achieving torsional balance by increasing damping ratio.
5- Torsional stiff structures need more damping eccentricity in order to achieving the control of displacement of two stiff and flexible edges of structure in comparison with torsional flexible structures.
6- The results gained from two-ways mass eccentricity with the results gained from one-way mass eccentricity are conformed and it is seen that the result of these two comparisons is almost the same.

## REFERENCES

[1]De la Llera, J. C., Chopra, A. K. and Almazan, J. L. "Three- dimensional inelastic response of an RC building during the Northridge earthquake." Journal of Structural Engineering (ASCE), Vol. 127, No. 5, PP. 482-489, 2001.

[2]Goel, R. K. "Effects of supplemental viscous damping on seismic response of asymmetric-plan systems." Earthquake Engineering and Structural Dynamics, Vol. 27, No. 2, PP. 125-141, 1998.

[3]Goel, R. K. "Passive control of earthquake-induced vibration in asymmetric buildings." Proceeding of 12th world conference on earthquake engineering, 2000.

[4]De La Llera, J. C., Almazan, J. L., Vial, I. J., Ceballos, V. and Garcia, M. "Analytical and experimental response of asymmetric structures with friction and viscoelastic dampers." Proceeding of 13th World Conference on Earthquake Engineering, Vancouver, B.C., Canada, paper No. 531, 2004.

[5]Rofooei Fr, Mohammadzadeh S, Improving the seismic torsional behavior of plan-asymmetric, single-storey, concrete moment resisting buildings with fluid viscous dampers. Earthquake Engineering and Engineering Vibration; 15: 61- 78, 2016.

[6]De La Llera, J. C., Almazan, J. L. and Vial, I. J. "Torsional balance of plan-asymmetric structures with frictional dampers: Analytical results." Earthquake Engineering and Structural Dynamics, Vol. 34, No. 9, PP. 1089-1108, 2005.

[7]Mansoori MR and Moghadam AS, "Using Viscous Damper Distribution to Reduce Multiple Seismic Response of Asymmetric Structures," Journal of Constructional Steel Research, 65(12): 2176−2185, 2009.

[8]Almazán JL, De la Llera JC. Torsional balance as new design criterion for asymmetric structures with energy dissipation devices. Earthquake Engineering and Structural Dynamics; 38:1421–1440, 2009.

[9]Aguirre JJ, Almazán JL and Paul CJ. Optimal control of linear and nonlinear asymmetric structures by means of passive energy dampers. Earthquake Engineering and Structural Dynamics. 42: 377-395, 2013.

[10]Mansoori MR, Moghadam AS. "Controlling Torsional Responses of Structures Under One and Two Directional Excitation Using Dampers", Second European conference on earthquake engineering and seismology, Aug 25-29, 2014

[11]McKenna F, Fenves GL, Scott MH, Jeremic B. Open system for earthquake engineering simulation (2000). Web page. http://OpenSees.berkeley.edu.

COMPDYN 2017
6th ECCOMAS Thematic Conference on
Computational Methods in Structural Dynamics and Earthquake Engineering
M. Papadrakakis, M. Fragiadakis (eds.)
Rhodes Island, Greece, 15–17 June 2017

# A SEMI-ANALYTICAL MODEL FOR DISSIPATIVE SHEAR LINKS: EXPERIMENTAL TESTS AND NUMERICAL ANALYSES

Silvia Caprili[a], Nicola Mussini[a,*] and Walter Salvatore[a]

[a] *Università di Pisa, Dipartimento di Ingegneria Civile ed Industriale*

[*] Author for contact. Tel.: 050 2218248; E-mail: nicola.mussini@ing.unipi.it

**Keywords:** shear links, eccentrically braced frames (EBF), cyclic behavior, experimental tests, numerical simulation.

**Abstract.** *Eccentrically braced frames (EBF) represent an optimal structural solution for seismic prone areas, being characterized by a high dissipative capacity, able to withstand strong seismic events, and by a relevant elastic stiffness, able to avoid (or limit) the damage of non-structural elements during low-to-moderate seismic events. The knowledge of the cyclic behaviour of the dissipative link elements is required to perform reliable and accurate nonlinear analyses and, in particular, to finally optimize the design of EBFs and their structural performance. Notwithstanding such aspects, in the current scientific literature few models are proposed for the modelling of EBFs equipped with short/shear links, mainly adopting simple bilinear springs with kinematic hardening constitutive laws that are not always able to correctly represent the real experimental behaviour of EBFs, especially for what concerns the influence of the hardening phenomena. In the present work, a semi-analytical model for short/shear link is proposed and calibrated basing on the results of experimental tests on real-scale one store/one bay EBFs equipped with horizontal and vertical dissipative elements. The main aim of the proposed model consists in the ability to represent the cyclic/seismic behaviour of EBFs with more accuracy with respect to what actually used in the current scientific works and, at the same, with a low computational burden with respect to solid models, becoming then an optimal solution for the implementation in design models and for the representation of multi-storey buildings' behaviour.*

## 1 INTRODUCTION

The seismic events of the 1980s-1990s caused severe damages to steel buildings highlighting critical features of structural details and components [1-3]; most of the observed damages were related to the initiation and propagation of cracks in correspondence of connections and to local buckling phenomena of dissipative elements. This situation evidenced the inadequacy of the current technical guidelines and, at the same time, the need to provide indications able to guarantee the human safety together with the reduction of the economic losses.

Technical codes were then improved through the introduction of the *Performance Based Design* [4, 5], foreseeing the reaching of specific seismic performances in relation to different hazard levels, described as a function of the seismic action return period ($T_R$). In this context, among steel structural typologies, Eccentrically Braced Frames (EBF) systems, joining together the ductility of Moment Resisting Frames (MRF) and the stiffness of Concentrically Braced Frames (CBF) [6-9] and whose dissipative performance are fully devoted to the hysteretic behaviour of 'link' elements, became then the most promising structural solution for earthquake prone areas.

The possibility to optimize the design of EBF structures fully exploiting link performance, is related to the correct representation of their actual behaviour towards horizontal/seismic events; this, otherwise, evidences the need to perform reliable nonlinear analyses through the exact modelling of the dissipative elements (links) including, in particular, their flexural and shear behaviour. Nonlinear modelling approaches, spreading from simple concentrated plasticity models [10] to distributed fibre elements and, finally, to complex continuum models [11], shall be properly defined depending on the purpose of the analysis, being their accuracy strongly dependent on the computational burden.

While the dissipative behaviour of long/bending link, whose plastic deformation is governed by flexural stresses, can be represented adopting the common reliable constitutive models used for steel beams [12], in the case of short/shear links the same cannot be stated and further investigations are needed.

In the present paper, a new semi-analytical model able to take into consideration the two different contributions of hardening phenomena, both kinematic and isotropic – strongly influencing the cyclic/seismic behaviour, is presented. The proposed formulation allows to reduce the computational effort related, for example, to solid models and can be simply applied to multi-storey buildings, being more accurate respect to simplified models commonly adopted in the current scientific literature [13-15]. The calibration of the proposed model, based on the results of experimental tests on real-scale prototypes, is also presented.

The work has been developed in the framework of the European research project *'MATCH: material choice for seismic resistant structures'*, funded by the Research Fund for Coal and Steel and aiming at defining the influence of material variability on the structural performance of steel structures.

## 2 METHODOLOGY

The methodology adopted for the achievement of the above mentioned objective can be organized in the following steps.

**Step 1.** *Elaboration of a semi-analytical model.* A semi-analytical model has been elaborated to represent the monotonic and cyclic behaviour of link elements and to include the two contribution of kinematic and isotropic hardening.

**Step 2.** *Execution of the experimental tests.* Experimental tests on real scale EBF systems

have been performed to characterize the cyclic/seismic behaviour of links till the collapse achievement.

**Step 3.** *Calibration of the semi analytical model.* The semi-analytical model is calibrated basing on the experimental tests' results on real scale specimens.

## 3 ELABORATION OF SEMI-ANALYTICAL MODEL FOR LINK ELEMENTS

The proposed semi-analytical model, simply represented in Figure 1, consists of two nonlinear springs working in parallel, respectively representing the shear/displacement and the bending/rotation behaviour.

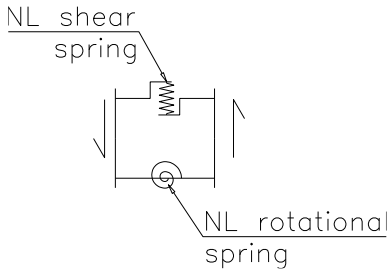


Figure 1: Schematic overview of the two in parallel springs for shear and flexural behaviour.

Since the axial stress is usually negligible in the dissipative links of EBF systems, only the bending behaviour was introduced in the model through a nonlinear spring characterized by kinematic behaviour. The shear behaviour was, otherwise, reproduced through the adoption of an additional spring whose V-γ (shear/distortion) relationship was calibrated basing on the results of experimental tests. Flexural and shear nonlinear springs were then linked to work in parallel.

The model was firstly elaborated using OpenSees software and the available relationships. Two different constitutive laws were adopted for the preliminary model of the V-γ relation of the link: the linear (LKH) and nonlinear (NLKH) kinematic hardening relationships; the last one, accounting for the nonlinear kinematic hardening, based on the Menegotto-Pinto model [16], and for the isotropic hardening, was directly represented using the *Steel4* material model.

The definition of the LKH law requires only 3 parameters: the initial stiffness, the yielding force and the tangent modulus of the plastic range. The first two parameters are directly determined by means of analytical considerations, while the third parameter is tuned considering two different conditions, corresponding to what foreseen according to Eurocode 8 (i.e. ultimate strength $V_u=1.5V_y$ reached in correspondence of an angular distortion equal to 80 mrad - LKH1) or, in alternative, considering the real ultimate strength and maximum shear deformation, estimated, for example, on the base of experimental tests (LKH2).

Besides the three aforementioned parameters, the definition of the NLKH law requires three additional parameters for the kinematic hardening, five parameters for the isotropic hardening, and information about the ultimate strength limit at which the isotropic behaviour is saturated (that is when only the kinematic hardening with yield plateau continues). Such parameters need to be calibrated on the basis of the results of the experimental tests.

### 3.1 Design of EBF prototypes

Experimental tests have been executed on real-scale one storey/one bay EBF frames with horizontal and vertical links. The prototypes are characterized by a span length equal to 5.0 and a storey height up to 3.0 m and by the adoption of short shear links. Steel grade S355 was

used for all the elements. The design of the frames was executed in compliance with actual seismic design regulations [17, 18], optimizing as much as possible dissipative elements' sections and pursuing easiness in joints and connections.

The EBF systems have been designed considering a 'limit' angular rotation of links equal to 110 mrad: this value, in agreement with FEMA 356, is higher than what actually foreseen by Eurocode 8 (i.e. 80 mrad) but reliable in relation to what observed during experimental tests revealing a higher rotational capacity and, besides, higher over-strength factors ([19]-[20]-[21]). A safety/confidence factor equal to 1.30 has been also applied during the design. Basing on above mentioned assumptions and considerations, a HEA100 profile with length equal to 300 mm for the horizontal link and a HEB120 profile of length equal to 150 mm for the vertical link have been selected. Table 1 summarizes the maximum expected horizontal forces ($F_{h,max}$) and displacements ($d_{max,110mrad}$) for links in horizontal and vertical configurations.

| Link profile | e [mm] | $F_y$ [kN] | $F_{h,max}$ [kN] | $d_y$[mm] | $d_{max(110mrad)}$ [mm] |
|---|---|---|---|---|---|
| HEA100 (hor.) | 300 | 90.1 | 162.3 | 0.8 | 24 |
| HEB120 (vert. | 150 | 145.2 | 217.8 | 0.4 | 19.5 |

Table 1: Summarizing characteristics and maximum expected forces and displacements for links.

The non-dissipative elements (i.e. beams, columns and braces) were then designed to remain elastic until the links reached the ultimate shear $V_{u,link}$. To this aim, according to EN 1998-1:2005, being $F_{h,y}$ the horizontal force needed to yield the link, Equation (1) can be adopted:

$$F_{h,y} \cdot 1.1 \cdot \gamma_{ov} \cdot \Omega \tag{1}$$

being $\Omega = 1.5 \cdot V_{y,link} / V_{Ed}$ the design over-strength factor of the dissipative element and $\gamma_{ov}$ the material overstrength factor, equal to 1.25.

Since during the experimental test is expected the complete plastic deformation of the link, the ratio $V_{y,link} / V_{Ed}$ was assumed unitary in the design; to account for eventual higher over-strength ratio of links, the $\Omega$ factor was assumed equal to 2.0. Figure 2 shows the final configuration of the EBFs systems with vertical and horizontal links. For both the configurations, columns and beams were realized using HEB180 sections, while for braces 2UPN160, coupled with 3 bolted connections equally spaced, were employed.

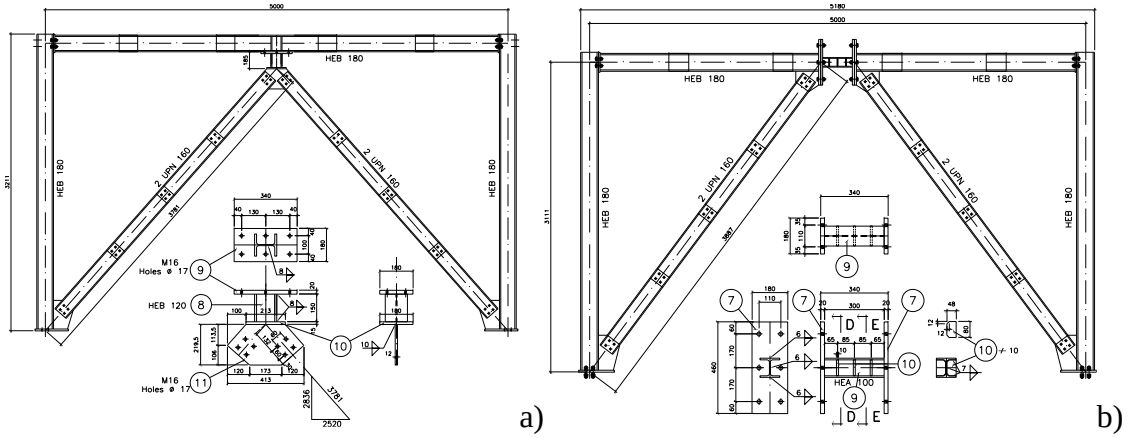


Figure 2: EBFs with a) vertical links and b) horizontal links.

## 3.2 Experimental test set – up and organization

Real-scale prototypes were realized according to what described in the previous paragraph. In order to avoid possible out-of-plane and buckling phenomena (i.e. global instability of the tested frames, buckling of the top beam), additional components were necessary to safely connect the EBFs systems to the bidirectional concrete slab of the Laboratory of Pisa University. To this aim, four additional structures/substructures were opportunely designed and adopted, being:

*(i).* A rigid basement connecting the testing prototypes to the slab of the Laboratory (Figure 3).
*(ii).* A stabilizing frame avoiding the warping of the columns (Figure 3).
*(iii).* A loading transfer frame (Figure 3). This last, in particular, connects the EBF system to the hydraulic jackets and, at the same time, restrains both the top beam and the whole frame from buckling phenomena.
*(iv).* A contrast frame, to which the actuator are fixed to (Figure 3).

The load was applied at the height of the top beam (~3000 mm) with two hydraulic jackets with maximum stroke equal to ± 150 mm and maximum load capacity equal to ± 200 kN each one, able to apply a cyclic loading history. For both the two configurations - with vertical and horizontal link - the applied load was recorded using two load cells placed between the hydraulic jackets and the loading transfer frame. The sensors were placed in order to monitor the shear force-displacement behaviour of the links (or, that is the same, the shear - angular deformation one). LVDTs were organized to account for the possible slip due to hole-to-bolt clearances. With reference to Figure 4 and Figure 5 respectively for the vertical and horizontal links, the effective displacement of the link due to shear deformation, depurated from all the slip to which the total displacement of the hydraulic actuators can be affected by, was evaluated monitoring directly the transversal deformation and the displacement of the diagonals.

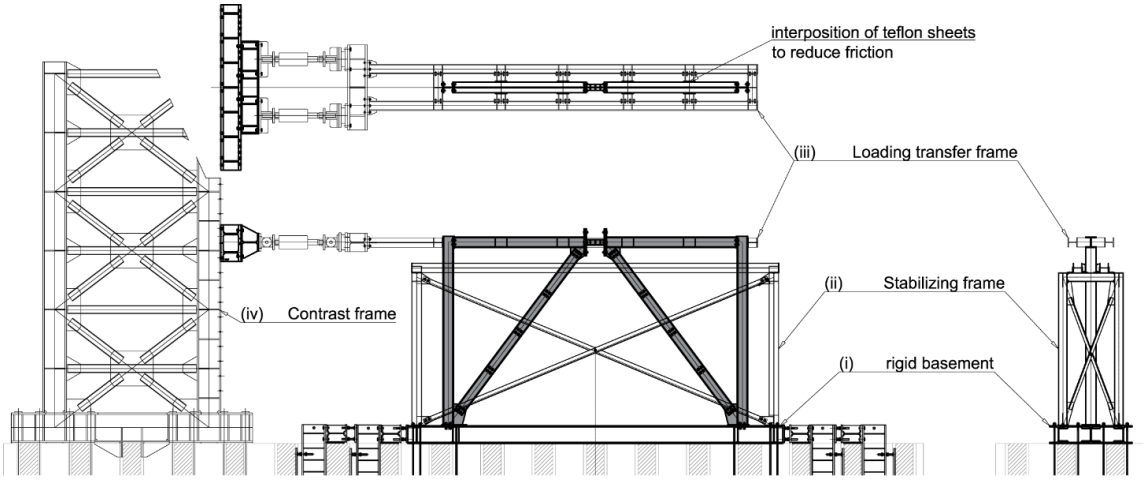


Figure 3: General set up of the test.




Figure 4: LVDTs on the vertical link EBF



Figure 5: LVDTs on the horizontal link EBF

The cyclic tests have been performed following the ECCS45 protocol [19]; the value of $e_y$ (i.e. displacement corresponding to the yielding) was selected to achieve an angular distortion equal to 130 mrad within 16 steps of 3 cycles each, without considering the first elastic part and allowing to reduce the duration of the whole test. After the detection of the crack initiation in the specimen, the test was prosecuted without increasing the displacement amplitude until the total loss of shear capacity.

### 3.3 Experimental tests' results

Experimental tests evidenced a stable hysteretic behaviour of the EBF frames during all the steps of the cyclic loading application (Figure 6). The cyclic behaviour was characterized by a strong isotropic and nonlinear kinematic hardening, this last one presenting, in the plastic branch, a variable tangent modulus decreasing with the increase of the plastic strain. The isotropic hardening showed a variable yielding surface that can increase from one cycle to the next one. All the specimens experienced a crack within the web, that propagated parallel to the flanges, as represented in Figure 7 and Figure 8, respectively in the case of vertical and horizontal links. A rather steep loss of shear capacity was observed in the case of specimens tested using the ECCS protocol.

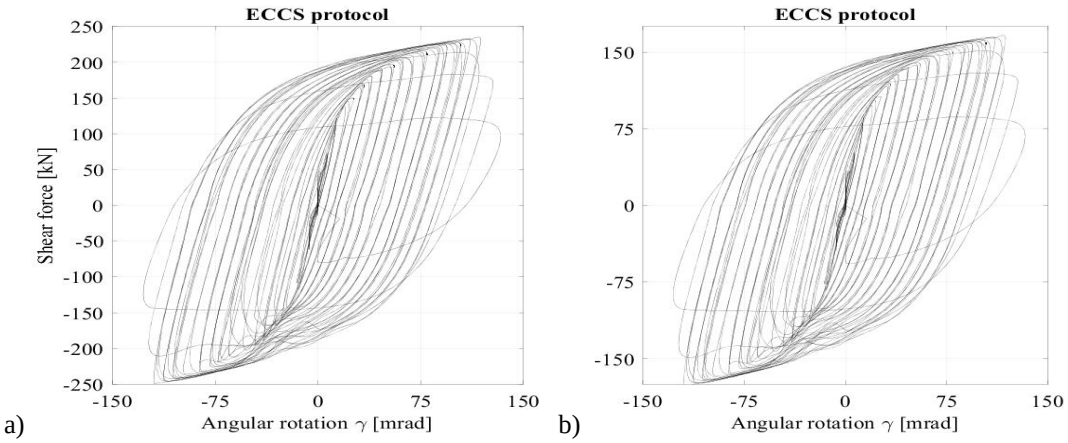


Figure 6: Force/angular distortion diagrams (F-γ) for a) the vertical link and b) the horizontal link.

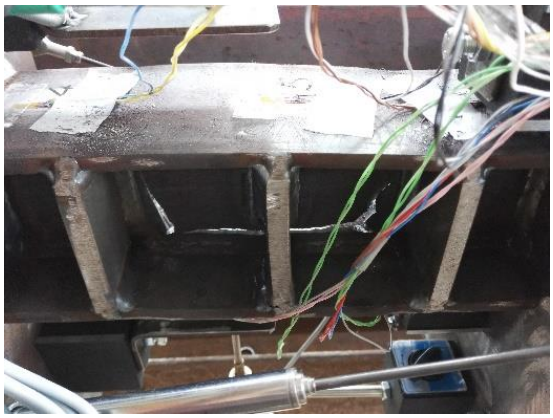

Figure 7: Collapse mechanism of the horizontal link.

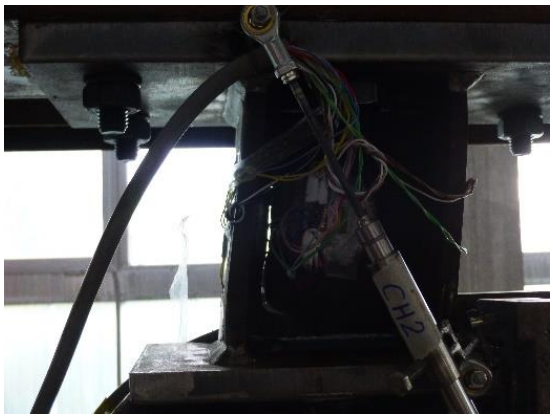


Figure 8: Collapse mechanism of the vertical link.

In the case of EBF prototypes with horizontal links, the presence of equally spaced stiffeners within the web hindered the propagation of the crack, slowing the loss of shear capacity. All the specimens reached an average angular rotation $\gamma$ close to 125 mrad (**Errore. L'origine riferimento non è stata trovata.**), higher than the imposed collapse limitation defined by EN1998-1:2005 and FEMA 356, respectively equal to 80 and 110 mrad.

What above presented highlighted the general oversizing of dissipative structural elements of EBFs designed according to the capacity design approach imposed by EN1998-1:2005 [18], that is, otherwise, more relevant in the case of frames equipped with horizontal links.

| Vertical link | Test 1 ECCS | Test 2 ECCS |
|---|---|---|
| Angular rotation at collapse | 125 | 119 |
| Maximum applied force | 244.03 | 248.73 |
| Horizontal link | Test 1 ECCS | Test 2 ECCS |
| Angular rotation at collapse | 128 | 123 |
| Maximum applied force | 172.62 | 175.95 |

Table 2: Results of the experimental tests.

## 4 CALIBRATION OF THE PROPOSED MODEL

In order to calibrate the proposed model, the experimental tests were modelled in OpenSees [22, 23]. To assess the limitations of each model, a two level comparison has been performed, including a first *'graphical'* assessment of the results in terms of cyclic behaviour (i.e. shape of the cycle and degradation of the hysteretic capacity) and, secondly, evaluating the differences in terms of cumulated energy (global and per cycle). The erroneous characterization of the hysteretic energy of the EBF system might strongly affect the assessment of its seismic capacity. The above mentioned comparison procedure was performed considering the two LKH and NLKH constitutive laws. A graphical interpretation of the results is provided in

Figure **9** and

Figure **10**.

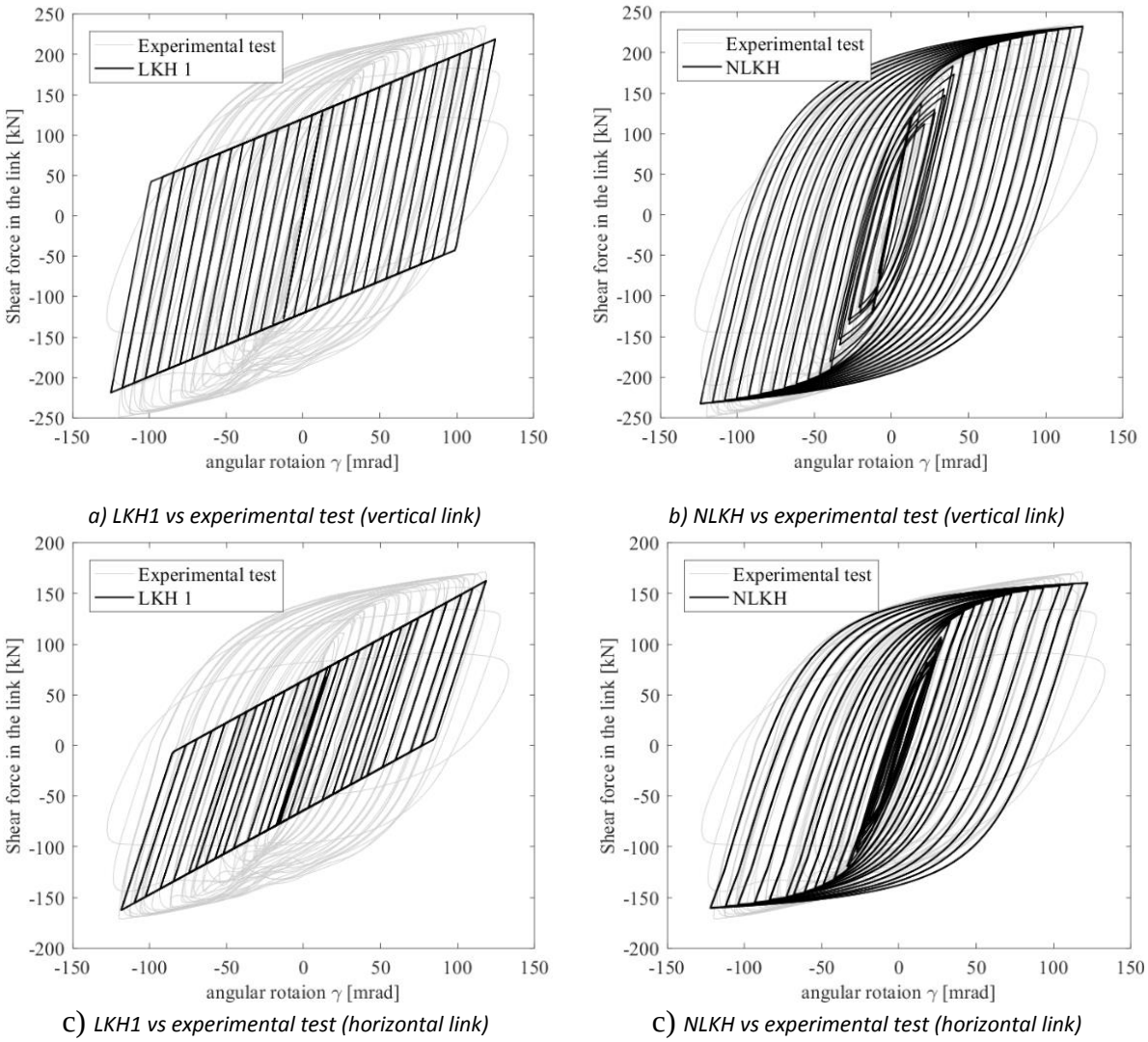


*a) LKH1 vs experimental test (vertical link)*

*b) NLKH vs experimental test (vertical link)*

c) *LKH1 vs experimental test (horizontal link)*

c) *NLKH vs experimental test (horizontal link)*

Figure 9: Experimental vs numerical cyclic behaviour ( ECCS protocol).

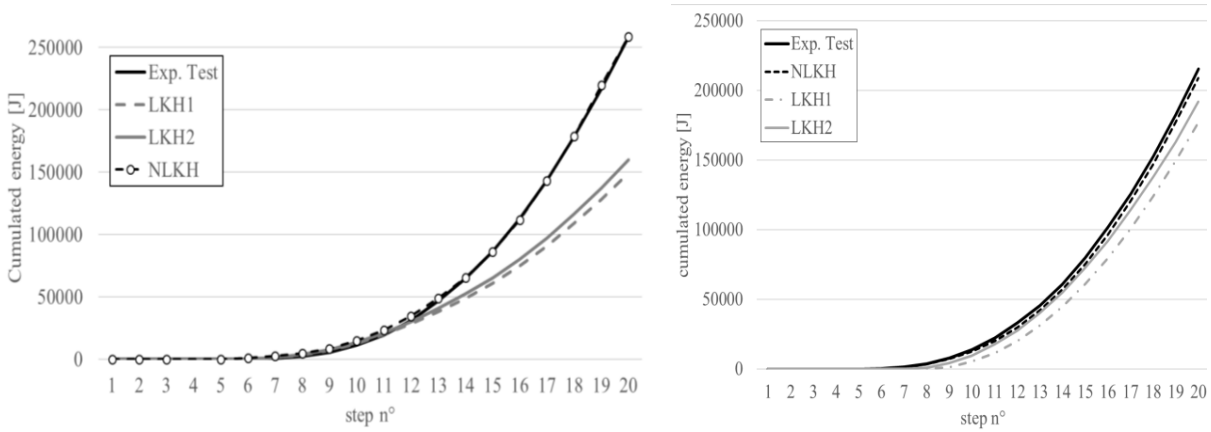


*a) horizontal link* *b) vertical link*

Figure 10: Comparison in terms of cumulated energy (ECCS protocol)

The LKH models underestimates the plastic branch. Although the LKH2 is calibrated on the basis of the experimental results, the underestimation of the plastic branch strongly reflects on the reduction of the hysteretic energy. For the vertical link, considering the ECCS protocol, the difference in terms of hysteretic energy, evaluated at the collapse, is -22% for the LKH1 and -10% for the LKH2 (note that the negative value means an underestimation of the cumulated energy). Regarding the horizontal link, the difference increases to -42% for the LKH1 and -38% for the LKH2. It should be noted that such difference is reduced to half, if the hysteretic energy is computed at 80mrad of angular deformation. The NLKH model, on the contrary, is able to correctly represent the cyclic behaviour and also to correctly estimate the absorbed hysteretic energy.

## 5 CONCLUSIONS

A modelling approach for short/shear links, based on the adoption of two springs working in parallel, respectively representing the shear/displacement and the bending/rotation behaviour, has been proposed. The model has the capability to reproduce the cyclic/seismic behaviour of the dissipative element of EBF structures with a reduced computational burden respect to what actually proposed in the current scientific literature and is able to simulate the two contribution of hardening, i.e. isotropic and kinematic.

To calibrate the model and to validate the assumptions used for the semi-analytical formulation, a set of experimental tests have been carried out on real-scale one storey/one bay EBF system, equipped with vertical and horizontal links. Several studies are actually ongoing aiming to effectively prove the impact of the adoption of the proposed model on multi-storey EBF structures.

## ACKNOWLEDGMENTS

The present work was developed inside the European Research Project *"MATCH: Material choice for Seismic resistant structure"*. The authors would like to thank all the partners involved in the project for their contributions. The authors would like also to thank Michele Di Ruscio, Mirko Donati and Simone Cavallini of the Official Laboratory of the University of Pisa for their important and strong help in the organization and execution of tests on real scale prototypes.

## REFERENCES


[1] Nakashima, M., *Classification of damage to steel buildings observed in the 1995 Hyogoken-Nanbu earthquake.* Engineering Structures, 1998. **20**(4-6): p. 271-281.

[2] Nakashima, M. and M. Bruneau, *Preliminary Reconnaissance Report of the 1995 Hyogoken-Nanbu Earthquake* ed. T.A.I.o. Japan. 1995.

[3] Bertero, V.V., J.C. Anderson, and H. Krawinkler, *Performance of steel building structures during the Northridge Earthquake*. University of California, ed. E.E.R. Center. 1994.

[4] Applied Technology Council, *Seismic Evaluation and Retrofit of Concrete Buildings. Redwood*. 1996: California.

[5] American Society of Civil Engineers, *Commentary for the seismic rehabilitation of buildings*. 2000: Washington D.C.

[6] Roeder C. W. and E.P. Popov, *Eccentrically Braced Steel Frames for Earthquakes.* Journal of the Structural Division, 1978. **104**: p. 391-412.

[7] Popov, E.P., *Recent research on eccentrically braced frames.* Engineering Structures, 1983. **5**(1): p. 3-9.

[8] Engelhardt, M.D. and E.P. Popov, *On Design of Eccentrically Braced Frames.* Earthquake Spectra, 1989. **5**: p. 495-511.

[9] Hjelmstad, K.D. and S.G. Lee, *Lateral buckling of beams in eccentrically-braced frames.* Journal of Constructional Steel Research, 1989. **14**: p. 251-272.

[10] Bosco, M. and P.P. Rossi, *Seismic behaviour of eccentrically braced frames.* Engineering Structures, 2009. **31**(3): p. 664-674.

[11] D'Aniello, M., R. Landolfo, and G. della Corte, *Overstrength of Shear Links in Eccentric Braces* in *15th World Conference on Earthquake Engineering*. 2012: Lisbon (PT).

[12] Dimakogianni, D., G. Dougka, and I. Vayas, *Seismic behavior of frames with innovative energy dissipation systems (FUSEIS1-2).* Engineering Structures, 2015. **90**: p. 83-95.

[13] Badalassi, M., et al., *Influence of variability of material mechanical properties on seismic performance of steel and steel–concrete composite structures.* Bulletin of Earthquake Engineering, 2017. **15**(4): p. 1559-1607.

[14] Braconi, A., et al., *Efficiency of Eurocode 8 design rules for steel and steel-concrete composite structures.* Journal of Constructional Steel Research, 2015. **112**: p. 108-129.

[15] Badalassi, M., et al., *Influence of steel mechanical properties on EBF seismic behaviour* Bulletin of Earthquake Engineering, 2013. **11**(6): p. 2249-2285.

[16] Menegotto, M. and P.E. Pinto, *Method of analysis of cyclically loaded RC plane frames including changes in geometry and non-elastic behavior of elements under normal force and bending*, P.R. IABSE, Editor. 1973.

[17] D.M 14/01/2008, *D.M 14/01/2008: Norme Tecniche sulle Costruzioni*. 2008.

[18] EN 1998-1:2005, *UNI-EN 1998-1:2005. Eurocode 8: design of structures for earthquake resistance. Part 1: general rules, seismic action and rules for buildings*. 2005: Brussels.

[19] Keith, D.H. and P.P. Egor, *Cyclic Behavior and Design of Link Beams.* Journal of Structural Engineering, 1983. **109**(10): p. 2387-2403.

[20] Peter, D., M.I. Ahmad, and G.B. Ian, *Cyclic Behavior of Shear Links of Various Grades of Plate Steel.* Journal of Structural Engineering, 2010. **136**(4): p. 370-378.
[21] Mazzolani, F.M., G.D. Corte, and M. D'Aniello, *Experimental analysis of steel dissipative bracing systems for seismic upgrading.* Journal of Civil Engineering and Management, 2009. **15**(1): p. 7-19.
[22] Mazzoni, S., et al., *OpenSees command language manual.* Pacific Earthquake Engineering Research (PEER) Center, 2006.
[23] McKenna, F., G.L. Fenves, and M.H. Scott, *Open System for Earthquake Engineering Simulation.* PACIFIC EARTHQUAKE ENGINEERING RESEARCH CENTER, 2000.

COMPDYN 2017
6th ECCOMAS Thematic Conference on
Computational Methods in Structural Dynamics and Earthquake Engineering
M. Papadrakakis, M. Fragiadakis (eds.)
Rhodes Island, Greece, 15–17 June 2017

# DUAL-PHASE STEEL REINFORCING BARS FOR MRFS STRUCTURES IN SEISMIC PRONE AREAS

**R. Aiuti[1], C. Ascanio[2], S. Caprili[1], M. Dolšek[3], W. Salvatore[1], R. Valentini[1] and J. Žižmond[3]**

[1] Dept. of Civil and Industrial Engineering, University of Pisa
Largo L. Lazzarino 1, 56122 Pisa - Italy
e-mail: silvia.caprili@ing.unipi.it, walter@ing.unipi.it, riccardo.aiuti@gmail.com, renzo.valentini@ing.unipi.it

[2] FERRIERE NORD S.p.A.
Zona Industriale Rivoli – 33010 Osoppo - Italy
e-mail: cascaio@pittini.it

[3] Faculty of Civil Engineering and Geodesy, University of Ljubljana
Jamova cesta 2, 1000 Ljubljana - Slovenia
e-mail: Jure.Zizmond@fgg.uni-lj.si, Matjaz.Dolsek@fgg.uni-lj.si

**Keywords:** Steel reinforcing bars, Dual-Phase steel, ductility, corrosion, reinforced concrete structures.

**Abstract.** *Reinforced concrete structures in seismic areas are designed according to the capacity design approach, aiming to achieve ductile global collapse mechanisms dissipating the seismic energy through high deformations in correspondence of the ends of beams and columns. The global dissipative capacity of the building is related to the rotational capacity of sections and to the ductile properties of reinforcing bars. TempCore steel is used for RC constructions, due to its optimal strength and ductility properties and to the satisfaction of Eurocode 8 requirements concerning $A_{gt}$ and $R_m/R_e$. Several studies in the current scientific literature anyway highlighted durability problems of TempCore bars exposed to corrosion conditions, with loss of ductility and strength even below the standards requirements. Dual-Phase (DP) steels, characterized by excellent mechanical and durability properties due to their Ferrite-Martensite microstructure and commonly adopted in the automotive sector, can be a possible solution to the problem. The possibility to produce DP rebars for RC structures is deeply analyzed in the European research project NEWREBAR "New Dual-Phase steel reinforcing bars for enhancing capacity and durability of anti-seismic moment resisting frames", actually ongoing. The elaboration of new technical models for the design of RC elements, to be implemented in design guidelines and standards, is needed. In the present paper, preliminary results are presented concerning the selection of DP steel bars and the definition of technical models for RC elements with DP reinforcements.*

## 1 INTRODUCTION

Reinforced Concrete (RC) buildings in seismic areas are designed following the *capacity design* approach ([1]-[2]-[3]): structures shall satisfy the deformation requirements due to seismic action without the exhibition of significant losses of strength and stiffness and dissipating the stored energy through high inelastic deformations in selected dissipative regions, located, in the case of Moment Resisting Frames (MRF), at the end of beams and columns and known as 'plastic hinges'.

The dissipative capacity of the building (i.e. structural ductility $\mu_d$) is directly related to the element ductility (in terms of rotation $\mu_\theta=\theta_u/\theta_y$), to the section ductility (in terms of curvature $\mu_\chi=\chi_u/\chi_y$) and to the material ductility (in terms of deformation $\mu_\varepsilon=\varepsilon_u/\varepsilon_y$): the ductile capacity of steel reinforcing bars is then needed for the global ductile behaviour of RC buildings.

In this context, actual technical codes prescribe the adoption of bars with minimum requirements of the mechanical parameters, in terms of yielding and tensile strength ($R_e$ and $R_m$), elongation at maximum load ($A_{gt}$) and hardening ratio ($R_m/R_e$): Annex C of EN1992-1-1:2005 [4] defines three different ductility classes for bars (A, B and C), characterized by increasing levels of minimum $A_{gt}$ and $R_m/R_e$, while Eurocode 8 [1] limits the employment of class B to buildings realized in Medium Ductility Class (MDC). The *design* prescriptions imposed by Eurocodes and National technical standards reflect into a large variety of steel grades – with different levels of yielding strength, ductility and hardening ratio – whose *production* is governed by several standards, valid at Country level, that highlight the pressing need to harmonize strength/ductility classes and testing procedures .

Nowadays, the most diffused typology of steel reinforcements in Europe, satisfying the mechanical requirements imposed by design standards, is TempCore steel. The TempCore production process, characterized by two following phases of quenching and tempering, provides optimal mechanical characteristics without the addition of chemical elements, consequently keeping the production costs acceptable if compared, for example, to Micro-Alloyed steels. These two aspects allowed, during the last decades, the wide spread of TempCore bars for the realization of RC buildings in seismic prone areas.

Recent works in the current literature ([6]-[7]-[8]-[9]) evidenced durability problems of TempCore rebars, with relevant drops of ductility and dissipative capacity, respectively expressed in terms of $A_{gt}$ and dissipated energy (total and per cycle) in the case of monotonic and cyclic/seismic behaviour. The decrease of the strength, as widely described in [10], was otherwise, less significant. The analysis of the results of experimental data on a representative sample of corroded bars allowed the correlation between Performance Indicators (i.e. mechanical performances) and Corrosion Damage Indicators (i.e. mainly mass loss) and the following estimation of the reduction of mechanical properties after the exposure, for a certain period, to aggressive environmental conditions such as the ones defined according to Eurocode 2 [4]. The effects of corrosion phenomena, as presented in the current scientific literature [11], are translated on a global reduced structural performance of RC buildings, related to the decrease of the mechanical properties of materials (both steel reinforcing bars and concrete [9]-[10]-[12]), to the reduction of the cross section of steel rebars and to the cracking and spalling of the concrete cover, with the following loss of bond between concrete and steel bars, as widely reported in [13].

Despite the possible overcoming of such problems through the adoption of, for example, higher concrete classes, thicker concrete covers, reinforcements with higher uncorroded properties and/or higher diameters as suggested in [10] and [14], actual trends in the current scientific literature are directed to avoid of the corrosion initiation and propagation and, at the same time, to select materials less exposed to durability problems.

Basing on the these considerations, taking into account the need to exploit sufficient ductility in RC elements through reinforcing steels characterized by high mechanical performance and, at the same time, the significant decrease of the mechanical properties of corroded TempCore rebars, during the last years the scientific interest in the possibility to adopt Dual-Phase (DP) steels for reinforcement strongly increased ([15]-[16]).

DP steel, widely used in the automotive industry, are characterized by excellent ductile properties (high hardening ratio and values of ultimate deformation) and improved durability properties towards aggressive environmental conditions respect to traditional reinforcing steel embedded in concrete [17], due to their specific microstructural configuration showing the co-existence of a Ferrite matrix in which Martensite is directly embedded.

Preliminary investigations dealing with the use of DP steels in RC structures [16] showed the improved performance of sections in terms of moment-curvature relationship, with curvatures higher and less localized than in the case of reinforcement with TempCore rebars.

Despite the high potential of DP steels, actually two main aspects limit their possible application in the field of civil engineering: the first one is related to the production process, nowadays foreseeing the realization of DP steels mainly into sheets or plate products, the second one concerns the need to modify/improve actual design codes with technical models and guidelines able to allow the adoption of steels characterized by a different behaviour respect to the one basing on which codes are developed. DP steel present, in fact, a higher hardening ratio and strength/ductility properties that are not aligned with the limitations imposed by Eurocodes ([1]-[4])

Basing on what herein stated, a deep investigations of the behaviour of DP steel reinforcing bars for their potential application to RC constructions is needed and is going to be developed in the main context of the European research project NEWREBAR *"New Dual-Phase steel reinforcing bars for enhancing capacity and durability of anti-seismic moment resisting frames"* (2015-2019), funded by the Research Fund for Coal and Steel (RFCS) of European Commission. In the present paper, first, absolutely preliminary, results obtained in the project are presented.

## 2 SELECTION OF DP STEEL REINFORCING BARS

DP steels present a composite microstructure, made up of a ductile Ferrite matrix, providing high ductility, in which a second hard Martensite phase, responsible for the strengthening effect, is embedded. The difference from usual composite materials is that in DP steels there is no clear interface between the matrix and the reinforcing structure, such as, for example, in the case of TempCore steel.

DP microstructure can be produced as-rolled or by intercritical annealing (in alpha-gamma $\alpha$-$\gamma$ field) after cold-rolling. Actual literature data are related to DP rebars produced in batch process, by means of intercritical quench of hot rolled bars, with a first heating step within the intercritical region (where nucleation occurs in the Ferrite matrix of Austenite with a carbon content higher than the nominal one) and a following rapid cooling phase, allowing the transformation of the Austenite into Martensite ([15]-[18]). The intercritical quenching process generates a harder phase into the Ferrite matrix, which causes (partly due to the considerable volume differences) high residual stresses and the increase in the density of the mobile dislocations in correspondence to the Ferrite–Martensite interface. The particular mechanical behaviour of the DP steel generates from the formation of a two-phase Ferrite–Martensite structure.

In the worldwide scenario anyway, DP rebars (and, in general, DP long products) are not yet produced through a continuous process: although the batch process is able to obtain the desired microstructure, this is actually not economically advantageous.

Stating the above mentioned considerations, NEWREBAR research project foresee two main objectives: the first, that can be considered as a '*short-term*' objective, aims at producing DP steels fulfilling actual European design standards' requirements but improved towards seismic performance and structural durability, consequently directly usable as reinforcing elements for RC buildings. The second, a '*medium-term*' objective, aims at characterizing DP steels with optimal mechanical and durability properties also not fulfilling Eurocodes' indications and for which, consequently, specific guidelines need to be elaborated.

To these aims, the procedure briefly summarized in the following pages has been adopted.

## 2.1 Selection of chemical compositions

The analysis of the steel bars actually produced at European level (executed thanks to the direct participation of steel producers to the research project) allowed to determine the different combinations of the main elements (C, Mn and Si) to obtain DP microstructures suitable to achieve the desired objectives. Specific thermal cycles were, moreover, detected to obtain different Martensite amounts and morphologies, directly influencing the mechanical properties.

Numerical simulations using *ThermoCalc*® software were executed to evaluate the influence of the intercritical austenitization treatment temperature (i.e. 'intercritical temperature') on low carbon DP steels. Various chemical compositions (maximum, medium and minimum values of range) were simulated getting the relative state diagram and consequently estimating the volume fraction and Carbon content of the two phases, when the steel is subjected to intercritical austenitization treatment in a temperature range 740÷840 °C (i.e. in the α-γ field). The different intercritical austenitization temperatures allowed to obtain microstructures with different phase fractions and mechanical properties.

The two most influencing chemical components, as known, were Manganese (Mn) and Silicon (Si). Manganese (Mn) is the fundamental element in DP, added to increase Austenite fraction promoting adequate hardenability, necessary for Martensite formation during the rapid cooling stage (i.e. quenching). Silicon (Si), on the other hand, is useful to increase the strength of solid solution and the ductility of Ferrite phase, inhibiting the precipitation of cementite at the Ferrite–Martensite interface during the water cooling stage. The chemical compositions considered for the simulations are presented in Table 1.

Table 1: Chemical composition used for ThermoCalc simulations.

| | | C (%) | Mn (%) | Si (%) | P (%) | S (%) | Cu (%) | N (%) |
|---|---|---|---|---|---|---|---|---|
| Type A | Min | 0.08 | 0.35 | 0.12 | - | - | - | - |
| | Max | 0.12 | 0.55 | 0.20 | 0.035 | 0.045 | 0.50 | 0.012 |
| Type B | Min | 0.16 | 0.60 | 0.12 | - | - | - | - |
| | Max | 0.20 | 0.70 | 0.20 | 0.035 | 0.045 | 0.50 | 0.012 |
| Type C | Min | 0.18 | 0.95 | 0.15 | - | - | - | - |
| | Max | 0.22 | 1.05 | 0.25 | 0.045 | 0.045 | 0.60 | 0.012 |
| Type D | Min | 0.18 | 1.20 | 0.20 | - | - | - | - |
| | Max | 0.22 | 1.30 | 0.30 | 0.045 | 0.045 | 0.60 | 0.012 |
| Type E | Min | 0.06 | 1.40 | 0.80 | - | - | - | - |
| | Max | 0.08 | 1.50 | 0.90 | 0.020 | 0.020 | 0.10 | 0.009 |

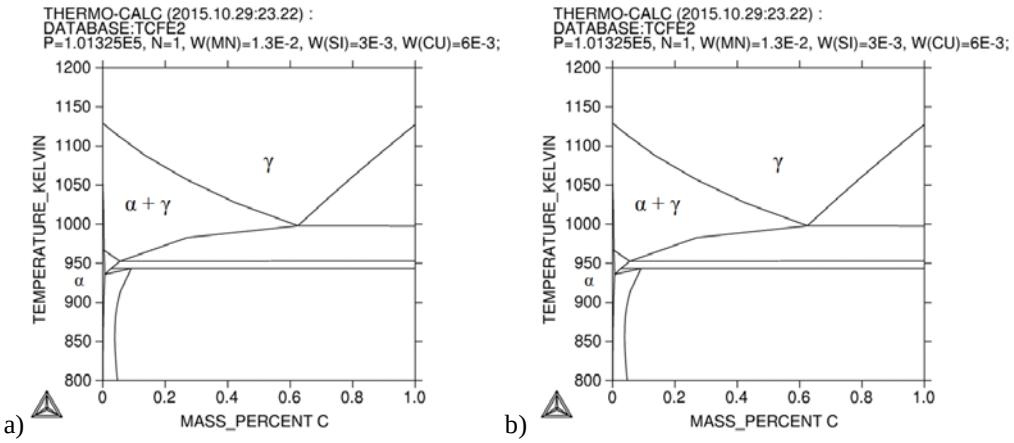


Figure 1: State diagrams from ThermoCalc simulations: a) effect of Mn on state diagram for steel type D - Mn = 1.20 ÷ 1.30 %, b) effect of Si on state diagram for steel type D - Si = 0.20 ÷ 0.30 %.

The carbon content ($C_\gamma$) formed in the Austenite following heating in the intercritical field, responsible for the hardenability of the phase in the following cooling stage of quenching, was evaluated through the lever rule as presented by Equation (1):

$$C_{base} = C_\gamma \cdot \gamma\% + C_\alpha \cdot \alpha\% \qquad (1)$$

Being $C_{base}$ the Carbon content in the base steel, $C_\alpha$ the weight percentage of Carbon in the α phase, $\gamma\%$ the Austenite content and $\alpha\%$ that of the Ferrite in the intercritical field.

Due to the absence of diffusion processes during the phase transformation, the chemical composition of the Martensite is identical to that of the Austenite from which it is formed. The Carbon content of Martensite, determining its hardness and shape, depends on the nominal content of the base steel and the intercritical quenching temperature.

Basing on the results of simulations on DP chemical compositions presented in Table 1, three intercritical temperatures, respectively equal to 740, 760 and 780°C, were selected to achieve different Martensite volume fractions ranging from about 5 % to 30 %.

## 2.2 Determination of the optimal thermal cycle

The main aim of this first part of the research consists in the 'transformation' of TempCore steel bars into DP ones: this operation can potentially allow the direct re-use of actual industrial plants for the realization of specimens with optimized mechanical performances and slight modifications of the production sequence.

A preliminary thermal cycle, in the following named A1, was selected for the production of DP steel reinforcing bars starting from the typical TempCore process and aiming to achieve the '*short-term*' objective, that means to realize steel bars following the actual standards' requirements but with improved mechanical properties – especially concerning ductility and durability. Beside the chemical compositions listed in Table 1, after preliminary mechanical and metallurgical tests, an additional one (type F) was introduced for the production of the specimens, as summarized in Table 2.

Table 2: Chemical compositions of produced casts for transformation into DP steels.

| Cast | ID | C % | Mn % | Si % | P % | S % | Cr % | Ni % | Mo % | Cu % | V % | N % | $C_{eq}$ % |
|---|---|---|---|---|---|---|---|---|---|---|---|---|---|
| 9076/15 | A | 0.09 | 0.5 | 0.17 | 0.015 | 0.012 | 0.1 | 0.13 | 0.03 | 0.35 | 0 | 0.009 | 0.23 |
| 8929/15 | B | 0.17 | 0.78 | 0.16 | 0.014 | 0.013 | 0.07 | 0.22 | 0.05 | 0.28 | 0 | 0.012 | 0.36 |

| | | | | | | | | | | | | | |
|---|---|---|---|---|---|---|---|---|---|---|---|---|---|
| 8254/15 | C | 0.18 | 1.01 | 0.21 | 0.035 | 0.017 | 0.1 | 0.12 | 0.02 | 0.35 | 0 | 0.011 | 0.4 |
| 8977/15 | D | 0.21 | 1.27 | 0.29 | 0.025 | 0.021 | 0.08 | 0.12 | 0.02 | 0.31 | 0 | 0.009 | 0.47 |
| 1760/16 | E | 0.1 | 1.14 | 0.12 | 0.015 | 0.01 | 0.04 | 0.05 | 0.01 | 0.14 | 0 | 0.011 | 0.31 |
| 2048/16 | F | 0.15 | 1.01 | 0.2 | 0.019 | 0.031 | 0.07 | 0.13 | 0.03 | 0.35 | 0 | 0.012 | 0.37 |

Thermal cycle A1 is represented in Figure 2a: after the industrial *Thermex* process (austenitization + quenching) the specimens are introduced and maintained in the laboratory furnace at the prescribed intercritical temperature (i.e. 740°C, 760°C or 780°C) for one hour. After this, the intercritical quenching is applied, introducing the specimens in a container with water kept at controlled temperature (between 10 and 35°C); samples are then removed after about 10 minutes.

The application of A1 process highlighted several problems: in some cases specimens provided low values of the yielding strength (i.e. steels A and B, with $R_e$ around 300 MPa and $R_m/R_e$ higher than Eurocode 8 prescriptions) or low values of the $A_{gt}$ (i.e. steels C and F, with values around 6%). Several mechanical transformations were then adopted to increase $R_e$ and $A_{gt}$, respectively applying a *stretching process* with deformation between 1% and 2% (i.e. producing the increase of $R_e$ and the decrease of $R_m/R_e$) or a *tempering process* with temperatures between 400 and 600°C (i.e. producing the decrease of the $R_m$ and the increase of $A_{gt}$). The mechanical properties, after such treatments, allowed the achievement of the short-term objective, presenting a traditional stress-strain behaviour with values of Agt and hardening ratios aligned with actual Eurocodes' requirements. Anyway, the microstructural analyses still evidenced the presence of an external layer of Martensite, with internal DP microstructure: this negatively affects the corrosion performance of bars with the following need to determine of a different thermal cycle, as presented in Figure 2b.

In this cycle, named A2, the original specimens (coming from Thermex process) are firstly kept in the furnace at 900 °C for 1.0 hour and then immediately put in water tank at room temperature until the reaching of the total cooling. An intercritical quenching (temperature 750°C) is finally applied. The annealing process with high temperatures allows to completely destroy the TempCore effects and to finally obtain a traditional DP microstructure associated to a not-defined yielding stress-strain curve.

Obtained specimens can be also finally tempered (600°C for 1h), achieving high values of the mechanical properties and keeping, moreover, a defined yielding stress-strain curve. This last thermal cycle (Figure 2c) will be called, in the following, cycle A3.

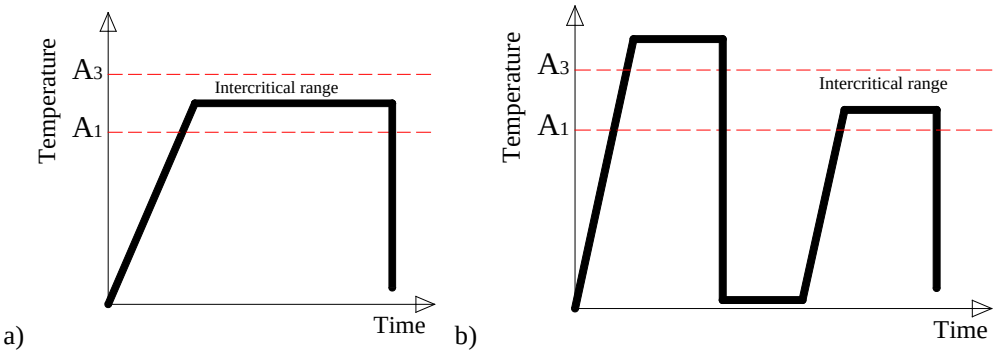

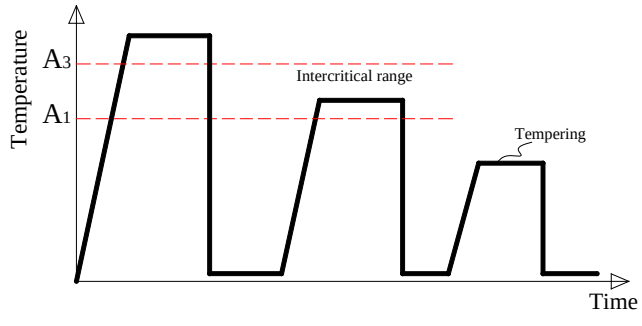


c)

Figure 2: Thermal cycles selected: a) preliminary A1 cycle and b) thermal cycle A2 (note that intercritical quenching temperature has different values for cycle A1 and A2) and c) application of tempering after intercritical quenching (cycle A3).

## 2.3 Production and treatment of DP specimens

Dual-Phase steel reinforcing bars were then produced starting from TempCore specimens ϕ16 mm following the thermal cycles depicted in Figure 2b and Figure 2c (being the only difference among cycles A2 and A3 the final application of the tempering process). It's necessary to underline that consistent differences were revealed producing specimens in *laboratory*, where the production and the thermal cycles can be controlled step by step with high accuracy concerning temperatures and exposure times, and specimens directly produced in an *industrial plant*, where, despite the slavish reproduction of the different stages, the outcomes cannot be so deeply controlled. DP specimens produced both in laboratory and in a real industrial plant were then subjected to mechanical test aiming at determining the ductility and strength properties of obtained reinforcing steels.

## 2.4 Mechanical tests on produced DP specimens

Experimental tests, including monotonic tensile and Low-Cycle Fatigue (LCF) tests were executed on produced specimens following the prescriptions of EN15630-1:2010 [19] and the protocol elaborated in a previous research project [14] and already used as presented in [9] and [10]. The results of monotonic tensile tests are summarized in Figure 3 and in Table 3, comparing obtained data with the behaviour of TempCore reinforcing steels B500B and B450C; Figure 4 and Table 4 briefly summarize the results of LCF tests (executed, until now, only on specimens produced following cycle A3).

Results presented are related to 'DPF' specimens (i.e. rebars produced following thermal cycle A3 through an industrial process) and to 'DPlab' specimens (i.e. rebars with chemical composition type C produced in laboratory following thermal process A2).

The thermal processes previously illustrated, allow the achievement of optimal values of mechanical properties. In particular, DPF can be used to satisfy the '*short-term*' objective while DPlab can be adopted to satisfy the '*medium-term*' objective.

DPF shows excellent ductile performance in terms of $A_{gt}$, with values around 16% respect to the average value of 10% of TempCore and a stable cyclic behaviour. In this sense, it is necessary to underline that, as visible from Figure 4, the values of the yielding and ultimate strengths are lower than the one of TempCore bars, consequently resulting in a lower amount of total dissipated energy, anyway not associated to a more brittle behaviour of the specimens.

DPF, moreover, is directly able to satisfy the ductility requirements of actual European design standards concerning minimum values of $A_{gt}$ and, in particular, hardening ratio $R_m/R_e$, being than able to pursue the '*short-term*' objective of NEWREBAR research project.

Similar considerations can be executed also in the case of DPlab steel reinforcing bars, characterized by the 'traditional' not-defined yielding stress-strain curve with values of $A_{gt}$ around 18% and, otherwise, an hardening ratio $R_m/R_e$ equal to 2.04 and consequently higher than the one actually foreseen by European standards.

| Specimen | $R_e$ [MPa] | $R_m$ [MPa] | $R_m/R_e$ [-] | $A_{gt}$ [%] | $A_5$ [%] |
|---|---|---|---|---|---|
| DPF | 449.4 | 564.8 | 1.26 | 16.3 | 30.5 |
| DPlab | 391.8 | 799.4 | 2.04 | 18,6 | 24.0 |
| B500B | 560.7 | 653.6 | 1.17 | 11.7 | 23.6 |
| B450C | 517.1 | 613.2 | 1.19 | 13.6 | 27.6 |

Table 3: Average values of the mechanical properties of reinforcing steels DP and TempCore from tensile tests.

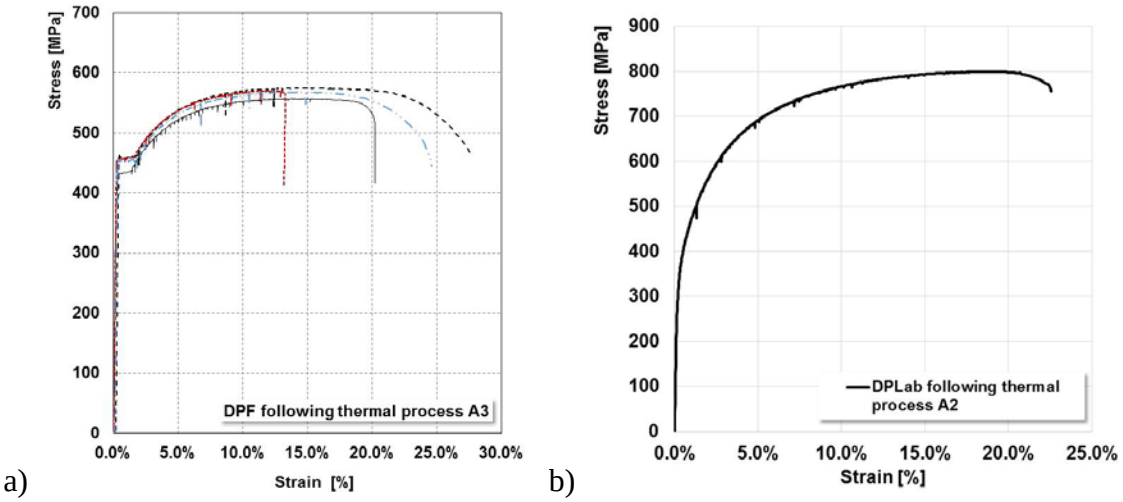


Figure 3: Experimental stress-strain diagrams for: a) DPF specimens (thermal process A3 – short term objective) and b) DPLab specimens (thermal process A2 – long term objective).

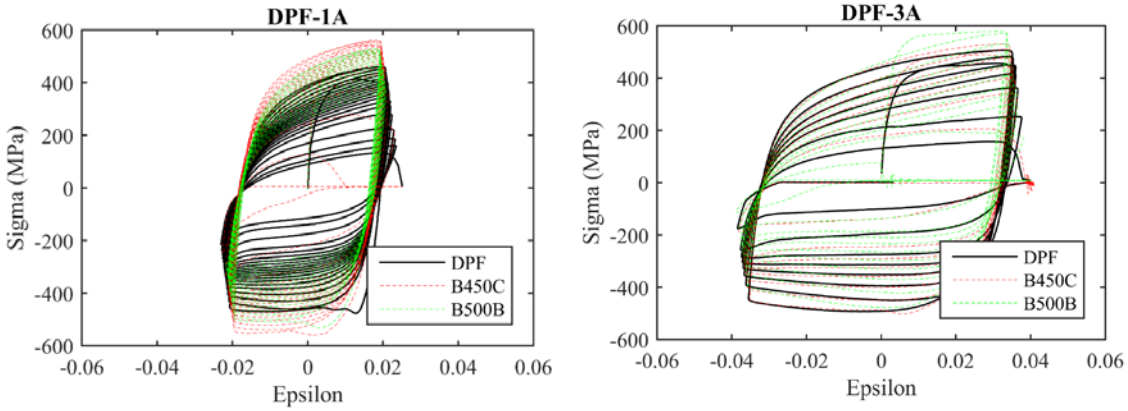


Figure 4: Results of LCF tests on DP steel type F with testing frequency equal to 0.5 Hz, imposed deformation equal to ±2.5% and ±4.0% and free length of the specimen equal to 6 diameters, compared with TempCore bars.

| Steel grade | Δε | $L_0$ | Energy [MPa] | $N_{cycles}$ |
|---|---|---|---|---|
| DPF | | | 360 | 21 |
| B450C | 2.50% | 6ϕ | 545 | 19 |
| B500B | | | 530 | 19 |

| Steel grade | Δε | $L_0$ | Energy [MPa] | $N_{cycles}$ |
|---|---|---|---|---|
| DPF | | | 325 | 9 |
| B450C | 4.00% | 6ϕ | 639 | 16 |
| B500B | | | 373 | 9 |

Table 4: LCF tests on DPF in terms of dissipated energy and $N_{cycles}$ to failure compared to TempCore bars.

## 3 INFLUENCE OF DP STEEL ON THE STRUCTURAL PERFORMANCE

In order to evaluate the influence of the adoption of DP steels on the structural performance of RC elements, a preliminary investigation of the moment-curvature (M-χ) and moment-rotation (M-θ) behaviour of typical RC sections was executed through a parametric analysis varying size and geometry of sections and elements, type, disposition and amount of longitudinal and transversal reinforcements, percentage of reinforcements (ρ and $\rho_{st}$) and axial load acting on the element.

A typical cantilever column, as designed following actual Eurocode 8 prescriptions for RC buildings, has been selected and subjected to pushover analyses. The two previously identified types of DP steels (DPF and DPLab) were considered for reinforcing bars; the comparison with TempCore steel grade (B500B) was also executed.

The cantilever element is a half column 1.80 meters height, with square section 50x50 $cm^2$, a total longitudinal reinforcement ratio ρ=2% and a total transversal reinforcement ratio $\rho_{st}$=0.7%. The ratio between the height of the element (H) and the depth of its section (h) is equal to 3.6.

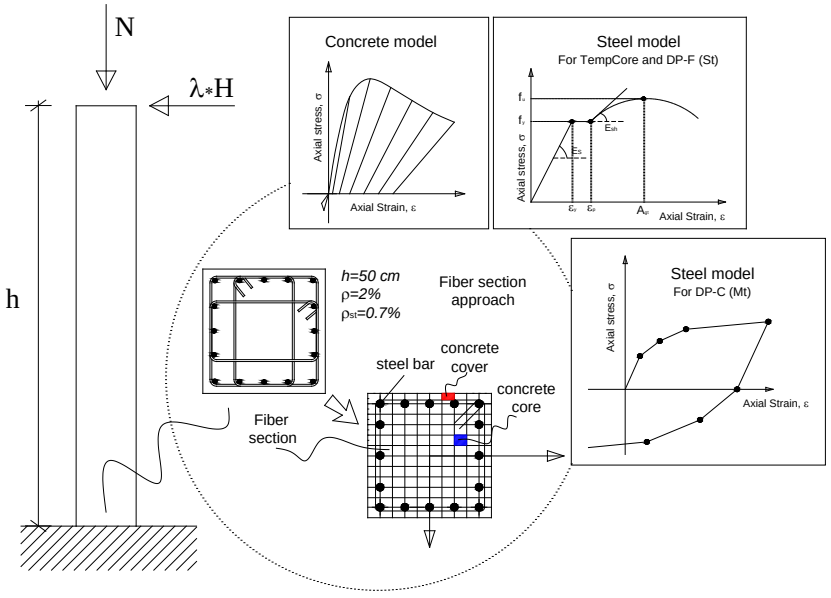


Figure 5: Scheme of the cantilever column considered in the analysis and of material models adopted.

Numerical models were realized using OpenSees software adopting a fiber approach for sections. The Popovics material model [20] was used for concrete with values of strength and deformation defined according to [21]; TempCore and *DPF* steel bars – with defined yielding plateau - were modeled using a elasto-plastic with hardening law with mechanical parameters defined according to average values coming from experimental tests. For *DPLab*, characterized by a not-defined yielding stress-strain curve, as presented in Figure 5, a

multilinear law was adopted. A simple schematization of the considered element and materials is presented in Figure 5.

Sections and elements were analyzed considering, as ultimate conditions for the determination of the M-$\chi$ and/or M-$\theta$ curves, the failure of the concrete core, or, otherwise the achievement of the ultimate tensile deformation in correspondence of the steel reinforcing bars, as simply presented in Figure 6. Figure 7 and Figure 8 show the M-$\chi$ diagrams obtained for a base square section 50x50 cm with $\rho$=2% and $\rho_{st}$=0.7% with, respectively, no axial load acting on the column and axial load equal to the 30% of the ultimate strength.

Obviously, there is a strong difference in the behaviour of sections/elements with or without axial force: in the first case (Figure 8) the failure is associated to the achievement of the maximum deformation in correspondence of the concrete core, for all the typologies of steel reinforcing bars considered; in the second case (Figure 7) the failure is associated to the achievement of the ultimate deformation of rebar in tension and, in particular, in the case of DPLab, it is possible to observe a quite 'balanced' failure mechanism associated to a balanced exploitation of concrete and steel ductile properties.

As visible from figures presented below, low values of the axial force and relatively small amount of longitudinal reinforcement ($\rho$=2%) are related to ductility, both in terms of curvature and rotation, higher in the case of DP steels than in the case of TempCore bars.

In particular, in the case of axial force equal to zero (N=0) – that is very close to the case of beam elements – the curvature ductility ($\mu_\chi$) obtained from DPLab and DPF was the 20% higher than the one directly obtained from the adoption of TempCore B500B, with increasing improvement of the ductility in terms of rotation ($\mu_\theta$).

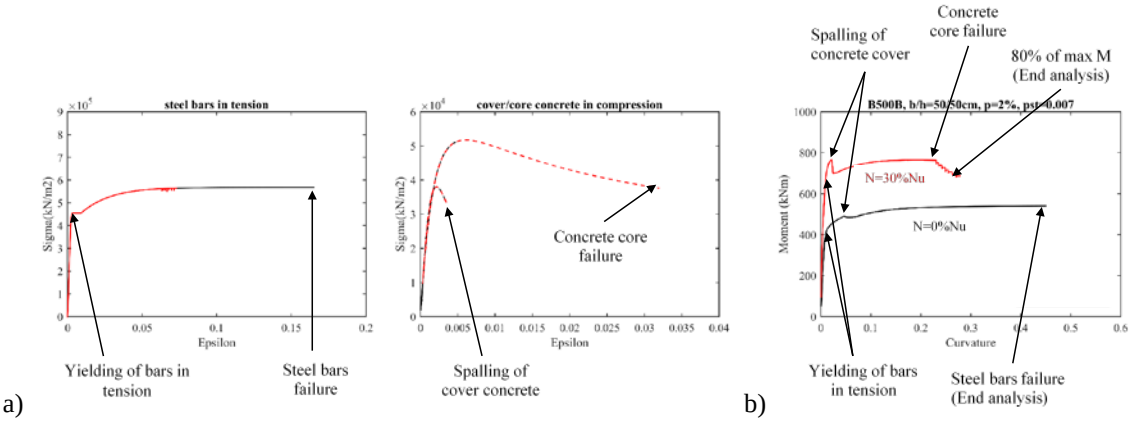


Figure 6: Criteria adopted for the analysis of the M-$\chi$ relationships for the considered section: a) stress-strain adopted for steel reinforcing bars and concrete and b) example of M-$\chi$ for different levels of the axial force.

When the axial force is equal zero (i.e. beam condition) column sections failure is led by steel bars in tension, which achieve their ultimate strain (Figure 7b). The unconfined concrete is expelled, while the confined concrete experiences high stresses, without reaching its ultimate strain (Figure 7c). Sections present large curvatures (Figure 7a), allowing higher spread of plastic deformations along the element. This phenomenon produces remarkable plastic hinge lengths, which lead to large displacements and rotations (Figure 9a), especially in the case of DPLab reinforcements, with the highest ultimate strain and tensile strength.

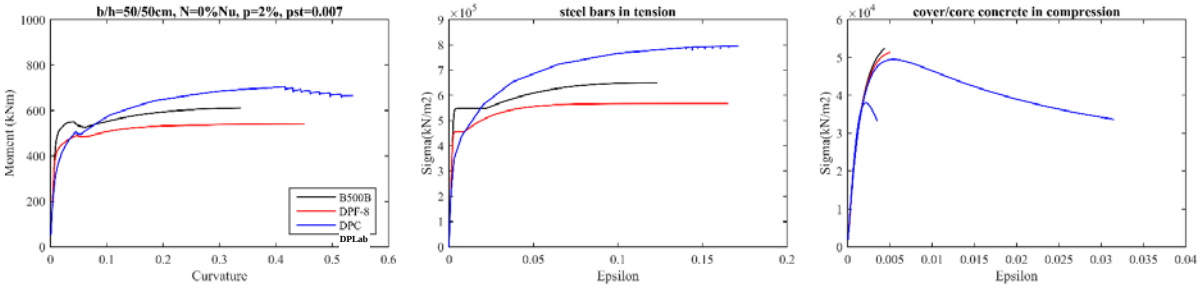


a) b) c)

Figure 7: Pushover analysis for zero axial force: a) M-χ of column bottom section; b) stress-strain relationship of steel bars in tension; c) stress-strain relationship of unconfined and confined concrete in compression.

When axial force is applied (e.g. *30%$N_u$*), column sections failure is led by confined concrete, which manage to achieve its ultimate strain (Figure 8c). Before that, there is spalling of unconfined concrete and yielding of steel bars in tension (Figure 8b), which however don't achieve their ultimate strain. Section presents low curvatures (Figure 8a) and the spread of plastic deformation is contained. Element displacements and rotations are lower than in the previous case (Figure 9b). Among the different steel grades, DPLab is the one with the highest tensile stress, after a certain level of deformation, and ultimate strain. Because of that the element reinforced with this type of steel grade presents the largest bending capacity and ultimate rotation.

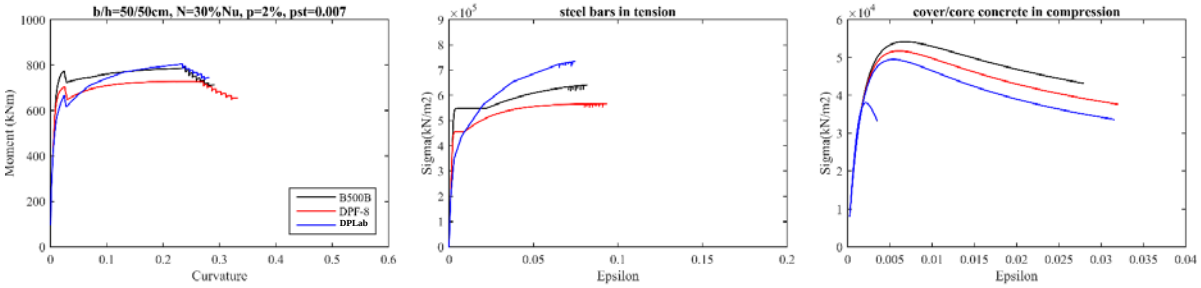


a) b) c)

Figure 8: Pushover analysis for compression force 30%$N_u$: a) M-χ of column bottom section; b) stress-strain law of bars in tension; c) stress-strain law of unconfined/confined concrete in compression.

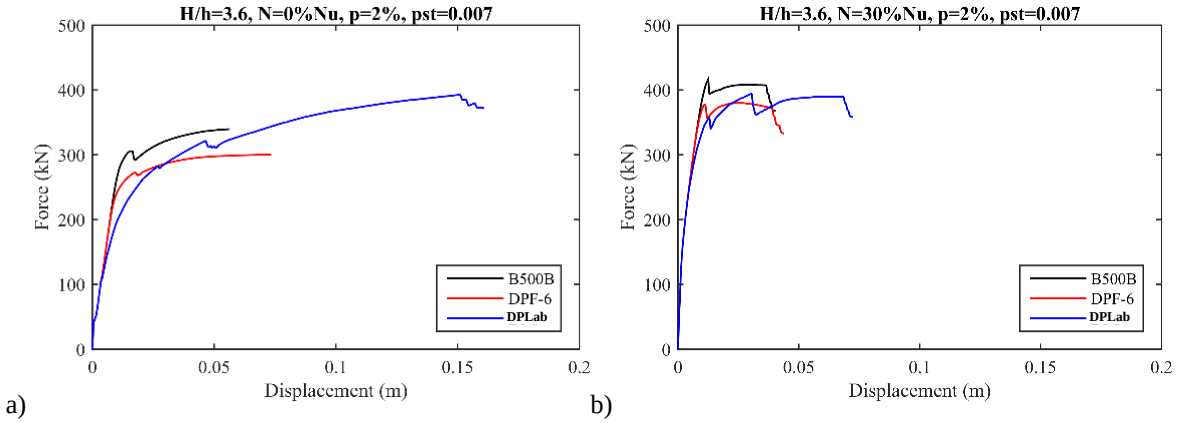


a) b)

Figure 9: M-θ relationships square section 50x50 a) without and b) with axial force.

## 4 CONCLUSIONS AND FUTURE WORKS

In the present paper the preliminary results of the beneficial effects of adopting Dual-Phase reinforcing steel for RC elements, in terms of curvature and rotational capacity, are presented.

DP steels, actually adopted for the automotive sector, are provided by optimal performances in terms of ductility, strength and, in particular, durability, becoming a valid alternative to traditional TempCore steels, whose degradation in presence of aggressive environmental conditions has been widely presented in the current scientific literature, with resulting loss of bearing capacity, bond and mechanical properties.

The main aim of the research project in whose framework the actual paper has been developed consists in the possibility to produce DP reinforcing steels starting from original TempCore, selecting opportune chemical compositions and thermal cycles able to improve mechanical and durability properties.

The results of numerical pushover simulations on a simple cantilever column highlighted the higher ductile performance of DP respect to TempCore; anyway, such results can be improved taking into account the effects of relative slip between steel reinforcing bars and surrounding concrete, actually neglected but strongly influencing the structural performance of RC elements.

**Acknowledgements** The present work was developed inside the European Research Project NEWREBAR (RFSR-CT-2015-00023), funded by the Research Fund for Coal and Steel (RFCS). The authors would like to thank all the partners involved in the project for their contributions.

## REFERENCES

[1] EN 1998–1: Eurocode 8: Design of structures for earthquake resistance - Part 1: General rules, seismic actions and rules for buildings, *CEN - European Committee for Standardization*.

[2] FEMA 356 (2000). Pre-standard and Commentary for the Seismic Rehabilitation of Buildings, Federal Emergency Management Agency, Washington DC.

[3] NTC (2008) Norme tecniche per le Costruzioni. Gazzetta Ufficiale n. 29, February 4, 2008, Suppl. Ordinario n.30, Italy. (in Italian).

[4] UNI EN 1992-1-1:2005, Eurocode 2 (Annex C) - Design of concrete structures - Part 1-1: General rules and rules for buildings, 2005.

[5] prEN 10080:2012, rev. 19/01/2012 - Steel for the reinforcement of concrete - Weldable reinforcing steel – General, ECISS/TC-104/WG1, 2012.

[6] C.A. Apostolopoulos, V.G. Papadakis V.G.. Consequences of steel corrosion on the ductility properties of reinforcement bar. *Construction and Building Materials*, **22**, 2316–2324, 2008.

[7] C.A. Apostolopoulos, M.P. Papadopoulos. Tensile and low cycle fatigue behavior of corroded reinforcing steel bars S400. Construction and Building Materials, **21**, 855–864, 2007.

[8] M. Al Hashemi, M. De Sanctis, W. Salvatore, R. Valentini. Effects of corrosion induced damages on the tensile and fatigue properties of concrete reinforcing bars. *XII Convegno ANIDIS L'Ingegneria Sismica in Italia*, Pisa, Italy, June 10-14, 2007.

[9] S. Caprili, W. Salvatore. Cyclic behaviour of uncorroded and corroded steel reinforcing bars. *Constructions and Building Materials*, **76**, 168–186, 2015.

[10] S. Caprili, J. Moersch, W. Salvatore. Mechanical Performance vs. Corrosion Damage Indicators for corroded steel reinforcing bars. *Advances in Materials Science and Engineering.* Article ID 739625, 2015.

[11] L. Berto, P. Simioni, A. Saetta Structural risk assessment of corroding RC structures under seismic excitation. *Construction and Building Materials*, **30**, 803–813, 2012.

[12] A. Saetta, R. Scotta, R. Vitaliani. Mechanical behavior of concrete under physical-chemical attacks. *Journal of Engineering Mechanics*, 124(10), 1100-1109, 1998.

[13] L. Berto, P. Simioni, A. Saetta. Numerical modelling of bond behaviour in RC structures affected by reinforcement corrosion. *Engineering Structures* **30**, 1375–1385, 2008.

[14] W. Salvatore, S. Caprili, A. Braconi, M. Finetto, L. Bianco, C. Ascanio, J. Moersch, C.A. Apostolopoulos, G. Ferreira Pimenta Effects of corrosion on low-cycle fatigue (seismic) behaviour of high-strength steel reinforcing bars (Rusteel) - RFSR-CT-2009-00023 - Technical Steel Research Series, European Commission - Directorate General for Research, Bruxelles, 2015.

[15] B. Maffei, W. Salvatore, R. Valentini. Dual-phase steel rebars for high-ductile r.c. structures, Part 1: Microstructural and mechanical characterization of steel rebars. *Engineering Structures*, **29**, 3323-3332, 2007.

[16] W. Salvatore, G. Buratti, B. Maffei, R. Valentini. Dual-phase steel rebars for high-ductile r.c. structures, Part 2: Rotational capacity of beams. *Engineering Structures*, **29**, 3333-3341, 2007.

[17] O. Keleştemur, S. Yıldız. Effect of various dual-phase heat treatments on the corrosion behavior of reinforcing steel used in the reinforced concrete structures. *Construction and Building Materials*, **23**, 78 – 84, 2009.

[18] J.L. Dossett, G.E.Totten. ASM Handbook, Volume 04 - Steel heat Treating Fundamentals and Processes. ASM International, 2013.

[19] EN ISO 15630-1:2010. Steel for the reinforcement and prestressing of concrete – test methods – part 1: reinforcing bars, wire rod and wire, 2010.

[20] S. Popovics. A numerical approach to the complete stress strain curve for concrete. *Cement and concrete research*, 3(5), 583-599, 1973.

[21] J.B. Mander, M.J.N. Priestley, R. Park. Theoretical stress-strain model for confined concrete. *Journal of Structural Engineering ASCE*, 114(8), 1804-1825, 1988.

COMPDYN 2017
6th ECCOMAS Thematic Conference on
Computational Methods in Structural Dynamics and Earthquake Engineering
M. Papadrakakis, M. Fragiadakis (eds.)
Rhodes Island, Greece, 15–17 June 2017

# Collapse capacity prediction of SDOF systems Equipped with Fluid Viscous Dampers

**Zeynab Gharyanpoor, Benyamin Mohebi*, Mansoor Yakhchalian**

Imam Khomeini International University (IKIU)
Department of Civil Engineering, Faculty of Engineering and Technology, Imam Khomeini International University, PO Box 34149-16818, Qazvin, Iran
gharyanpoor@gmail.com, mohebi@eng.ikiu.ac.ir, yakhchalian@eng.ikiu.ac.ir

**Keywords:** Collapse capacity, Single-Degree-of-Freedom system, Viscous damper, Incremental dynamic analysis

## ABSTRACT

There are various types of passive energy dissipation systems that are used in the seismic design of new structures and the seismic rehabilitation of existing structures. One of the most important kinds of passive energy dissipation systems, which reduce both displacements and accelerations simultaneously, are fluid viscous dampers (FVDs). Using FVDs can reduce the seismic response and improve the performance of structures during earthquake excitations and has a significant effect on the damping of structure. In this paper, Single-Degree-of-Freedom (SDOF) systems with different periods and ductility values, equipped with FVDs, are considered. In order to evaluate the collapse capacity of structures with higher precision, P-Δ effects and strength degradation are taken into account in modeling. Incremental dynamic analysis (IDA) is applied to obtain the collapse capacity of the SDOF systems under far-field ground motion records, and finally the results are investigated. It should be mentioned that the results of this study can be extended to Multi-Degree-of-Freedom (MDOF) structures.

# 1 INTRODUCTION

Life safety and collapse prevention have always been the most important goals in seismic design. Advances in computing power and the development of models that can more accurately simulate the behavior of structural components at the time of collapse have made probabilistic assessment of seismic collapse possible. Seismic collapse is the final limit at which dynamic instability occurs. Preventing the collapse of structures with a good margin of safety, is one of most important goals of seismic design. Vamvatsikos and Cornell [1], introduced a method called Incremental Dynamic Analysis (IDA) to evaluate the seismic performance of structures. The IDA method is a tool for investigating the performance a structures form elastic range to collapse under the set of ground motion records.

Conventional lateral force resisting systems (e.g., moment resisting frames) dissipate the energy due to seismic excitations by inelastic deformations in the components of the system and resist destructive forces such as earthquake by using ductility. But the amount of damping in these structures is not so much. After 1989 Loma Prieta and 1994 Northridge earthquakes, using passive energy dissipation systems for seismic design of structures was developed increasingly [2]. The principle role of a passive energy dissipation system is to reduce the inelastic deformation demands on the framing system of a structure [3]. These systems absorb a significant amount of the input energy from earthquake to the structure. Nowadays, there are various types of passive energy dissipation systems, such as Fluid Viscous Dampers (FVDs), hysteretic dampers, viscoelastic dampers and friction dampers [4, 5]. These dampers improve seismic performance by absorbing earthquake force and reducing structural response. Among these passive energy dissipation systems, FVDs are nowadays extensively used for the seismic design of new structures and seismic rehabilitation of existing structures [3, 6]. They can enhance the viscous damping of structures to more than 20-30% of critical damping (in addition to the inherent damping of structures) and decrease stresses and strains caused by the earthquake. Therefore, a number of procedures have been developed for the design of structures with FVDs [7-10]. These dampers can behave as linear or nonlinear elements. The velocity-dependent force developed by FVDs is as follows:

$$F_d = C \times |v|^{\alpha} \times \mathrm{sgn}(v) \tag{1}$$

where $C$ is the damping coefficient, $v$ is the relative velocity between the two ends of the damper, $\alpha$ is the velocity exponent, and sgn is the signum function. The velocity exponent $\alpha$ indicates the degree of nonlinearity of FVD. $\alpha$=1 corresponds to a linear FVD and the values of α lower than one correspond to nonlinear FVDs. It should be mentioned that the value of $\alpha$, can vary in the range of 0.2 to 1.0 [11].

Due to the existence of the IDA method as a powerful tool for analysis, seismic collapse of structures, has been studied by many researchers [12, 13]. As a result, documents such as FEMA P695 [13] and FEMA P-58 [14] have been published, which present guides for assessing seismic collapse of structures. Collapse capacity is defined as the maximum earthquake intensity level at which the structure still keeps its dynamic stability [15]. Ibarra and Krawinkler [16] investigated the uncertainty in the deterioration parameters of SDOF systems on the variance of collapse capacity. In their study, dynamic analyses were performed on deteriorating hysteretic models. The results of the analyses indicated that uncertainties in the displacement at the peak strength and the post-capping stiffness significantly contribute to the variance of collapse capacity. Several researchers evaluated the collapse capacity of structures by use of simplified SDOF models, because of their efficacy in terms of calculation time. Certainly, the results can be extended to the Multi-

Degree-of-Freedom (MDOF) structures [17,18]. The P-Δ effects are moments that are created in the structure by gravity loads due to displacement by the lateral force. Although hysteretic models have been considered in studies have positive post-yield stiffness, but considering P-Δ effects creates negative post-yield stiffness and finally leads to the collapse of structure. Adam et al. [17] investigated the P-Δ effects on collapse mechanism of non-deteriorating MDOF structures by use of equivalent SDOF systems and pushover analysis. They showed that the collapse capacities obtained from simplified SDOF models were very close, with good accuracy, to the results obtained from the corresponding actual MDOF structures by use of IDAs. Sun et al. [19] investigated the effect of gravity on the dynamic behavior of SDOF systems and its impacts on the change of periods of systems. They showed that the maximum displacement, the system can bear without collapse is directly related to the stability coefficients and yield displacement. Jennings and Husid. [20] evaluated the time required to occur collapse in SDOF systems. The systems had positive post-yield stiffness but because of assuming P-Δ effects, negative post-yield stiffness had been created in structures. The results showed that the time to collapse was related to the yield strength, and the post-yield stiffness. Adam and Jäger [21] investigated the effect of both near-field ground motions and a finite ductility on the collapse capacity of inelastic non-deteriorating SDOF systems by use IDAs. The P-Δ effect was taken into account in modeling. The results showed that for short period structures the median "instability collapse capacity" based on a near-field ground motion set is smaller compared to a corresponding one based on a far-field ground motion set; however, for structures with a period larger than 1.5 s the opposite was true. Miranda and Akkar [22] investigated the effects of the negative post-yield stiffness and structural vibration period of bilinear SDOF systems on lateral resistance required to avoid dynamic instability. They proposed an empirical equation to estimate the minimum lateral resistance to prevent the collapse of SDOF systems with P-Δ. The results showed that the lateral strength required to prevent collapse increased as the post-yield descending branch of the force-deformation relationship was steeper. Many researchers investigated the seismic behavior of structures equipped with FVDs [23-27]. Hamidia et al. [28] proposed a simplified procedure to assess the seismic collapse of steel moment resisting frames equipped with linear and nonlinear FVDs. The proposed procedure is based on the seismic response of nonlinear equivalent SDOF systems equipped with FVDs, and using pushover analysis without the need for nonlinear time history dynamic analysis. However, this method is only a fast approximate procedure for assessing the collapse capacity with acceptable accuracy, and cannot completely replace very detailed nonlinear time history dynamic analyses. Due to the increasing use of FVDs to improve the seismic performance of structures, in this study the collapse capacity of SDOF systems equipped with FVDs is investigated. For this aim, 21 SDOF systems without supplemental viscous damping and 420 SDOF systems with FVDs, having different values of ductility, damping ratio and velocity exponent, are considered. The collapse capacities of these SDOF systems are obtained by use of IDAs.

## 2 STRUCTURAL MODELING AND ANALYSIS

In this study, the seismic collapse capacity of SDOF systems equipped with FVDs was investigated. OpenSees software [29] was used to create the structural models of the SDOF systems. The elastic periods of the considered SDOF systems ($T_{el}$) are 0.4, 0.6, 0.8, 1, 1.5, 2 and 3 s. For each period, three ductility, $\mu=\delta_c/\delta_y$, values of 2, 4 and 8, which correspond respectively to brittle, moderately-ductile and ductile structures were assumed. To model the

inherent damping of the SDOF systems, a mass proportional damping ratio of 0.05 was considered. To improve the seismic performance of the systems, in addition to the inherent damping, linear and nonlinear FVDs were added to the SDOF systems. Five values for velocity exponent of FVD (i.e., $\alpha$=0.2, 0.4, 0.6, 0.8 and 1) and four values for supplemental viscous damping ratio (i.e., $\xi_{sup}$=0.05, 0.1, 0.15 and 0.2) corresponding to each value of $\alpha$ were selected. Thus, a total number of 420 SDOF systems with FVDs having different values of $\xi_{sup}$ and $\alpha$, and 21 SDOF systems without FVDs were considered. The IDA method was used to compute the collapse capacity of SDOF systems under the 44 far-field ground motion records in FEMA P695 [13]. The P-Δ effect was taken into account in modeling and cyclic deterioration was neglected. The modified Ibarra-Medina-Krawinkler model (Bilin) [30] was applied to model the nonlinear behavior of the systems. Figure 1 illustrates the moment-rotation relationship of the structural models.

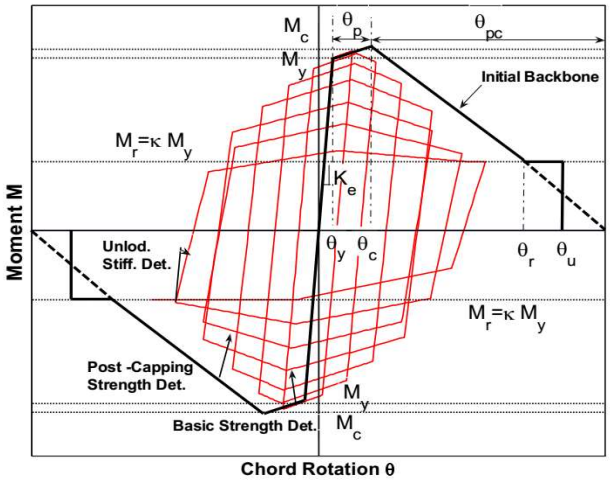


Figure 1: Modified Ibarra-Medina-Krawinkler model [30]

Concentrated plasticity approach was used to model the nonlinear behavior of the systems. Each system was modeled by an elastic beam-column element, and a zero-length rotational spring at its end. To model FVD, a horizontal two-node-link element connected to the mass of SDOF system was used, and a ViscousDamper material [31] was assigned to it. This material uses the Maxwell model [32], which consists of a dashpot and an elastic spring element in series. The input parameters for the ViscousDamper material are the damping coefficient *C*, velocity exponent, $\alpha$, and an equivalent damper stiffness. In this study, a very large value was used as the damper stiffness. It should be mentioned that residual strength was assumed equal to zero in this study (i.e., $\kappa$=0). It was assumed that the collapse occurs when the drift ratio of the system reaches the collapse drift limit, which corresponds to the point of zero strength at the end of the softening branch of the back-bone curve. Figures 2(a) and 2(b) respectively illustrate SDOF systems without and with supplemental viscous damping.

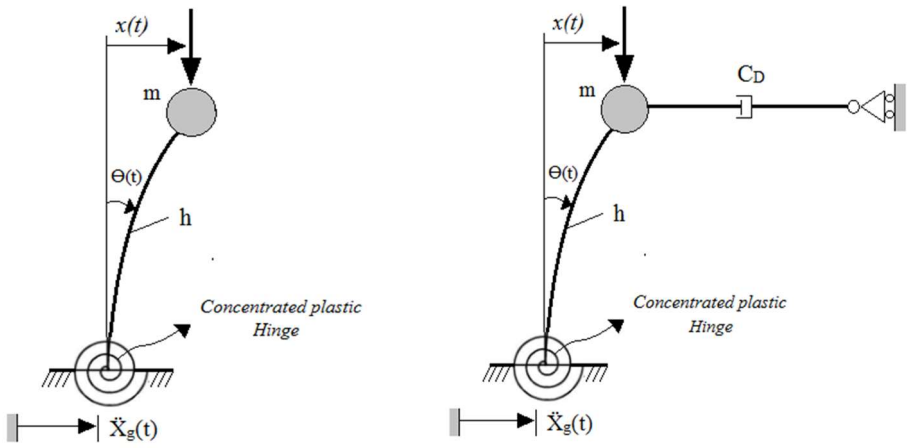


Figure 2: a) SDOF system without FVD and b) SDOF system with FVD

The supplemental viscous damping ratio for a SDOF system equipped with FVD can be obtained as:

$$\xi_{\text{sup}} = \frac{\lambda}{\pi} \frac{1}{2m\omega} \frac{C}{(\Omega u_0)^{1-\alpha}} \tag{2}$$

where $u_0$ is the displacement of the SDOF system, λ is a constant that is a function of the velocity exponent $\alpha$, $C$ is the damping coefficient of the SDOF system, $m$ is the mass of the SDOF system, and Ω is the excitation frequency, which is assumed equal to the natural frequency of the SDOF system, ω. Given a supplemental viscous damping ratio, the damping coefficient of the SDOF system can be obtained as follows:

$$C = \frac{2\pi m \xi_{\text{sup}} \omega^{2-\alpha}}{\lambda u_0^{\alpha-1}} \tag{3}$$

To determine the damping coefficient of a SDOF system with nonlinear FVD, $u_0$ was assumed equal to the yield displacement of the system, δy. The yield displacement of the SDOF system was obtained by using pushover analysis. Five percent damped pseudo-spectral acceleration at the elastic period of each system, $Sa(T_{el})$, was used as the IM for performing IDAs. Ground motion records were scaled to several intensity levels until the collapse occurs for each SDOF system. Therefore, the intensities of ground motion records corresponding to the collapse, (i.e., 44 $Sa_{col}$ values) were computed for each of the SDOF systems. Figure 3 indicates the IDA curves of the SDOF system with T=0.8, μ=4 and α=0.6 having a supplemental viscous damping ratio of 0.2.

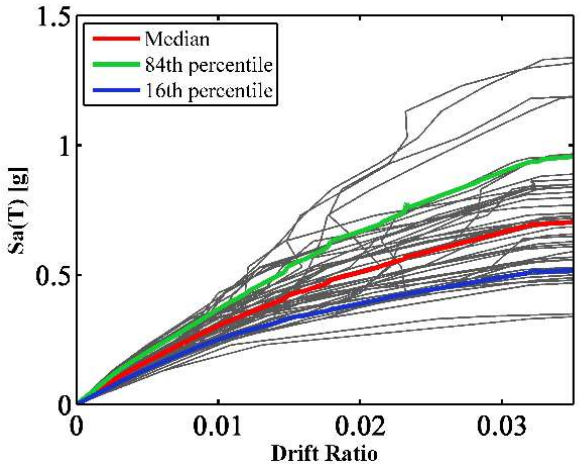


Figure 3: IDA curves of the SDOF system with T=0.8, μ=4 and α=0.6 having a supplemental viscous damping ratio of 0.2

## 3 INVESTIGATING THE EFFECT OF DUCTILITY AND SUPPLEMENTAL VISCOUS DAMPING RATIO ON THE COLLAPSE CAPACITY

In this section, the median collapse capacities of SDOF systems for different values of ductility and supplemental viscous damping ratio with respect to the elastic periods of the considered SDOF systems are presented. Each chart in Figure 4 corresponds to a specified supplemental viscous damping ratio and α=1. Ductility, $\mu=\delta_c/\delta_y$, varies between three values of 2, 4 and 8 in each chart, which corresponds to brittle, moderately-ductile and ductile structures, respectively. For a better comparison between the charts, the median collapse capacity of each SDOF system equipped with FVD was normalized to the median collapse capacity of its corresponding SDOF system without supplemental viscous damping, with only the 5% inherent viscous damping. It can be seen that, for a specified supplemental viscous damping ratio, the median collapse capacity of the system equipped with FVD normalized to the median collapse capacity of its corresponding SDOF system without supplemental viscous damping is not a function of ductility as the elastic period of SDOF system increases. Because the P-Δ effects control the collapse capacity of long period structures with and without supplemental viscous damping. According to the charts, by increasing the supplemental viscous damping ratio in structures, the median collapse capacities of SDOF systems increase.

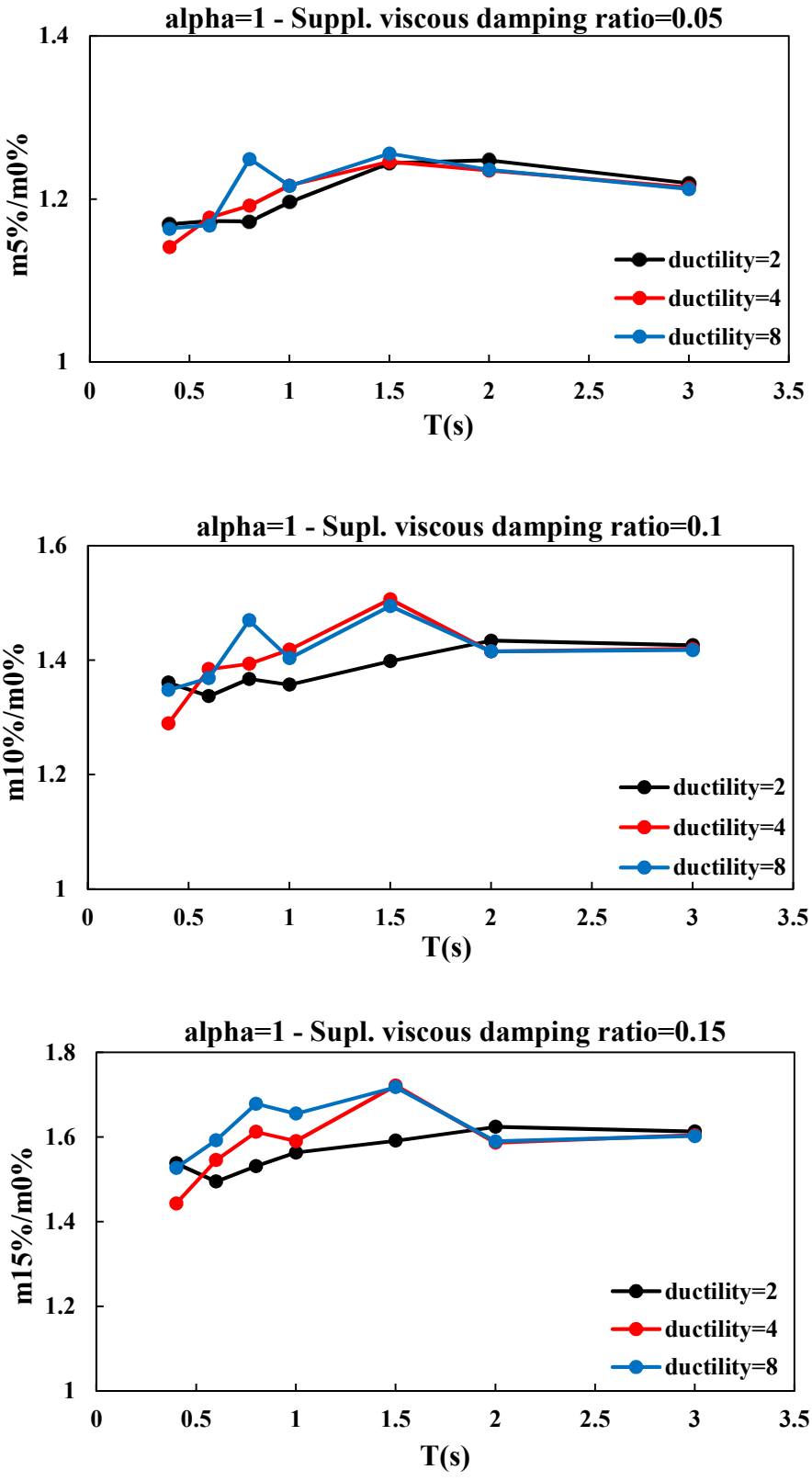


Figure 4. Median collapse capacity of SDOF systems equipped with FVDs normalized to the median collapse capacity of their corresponding SDOF systems without supplemental viscous damping, considering different ductility values, $\alpha = 1$

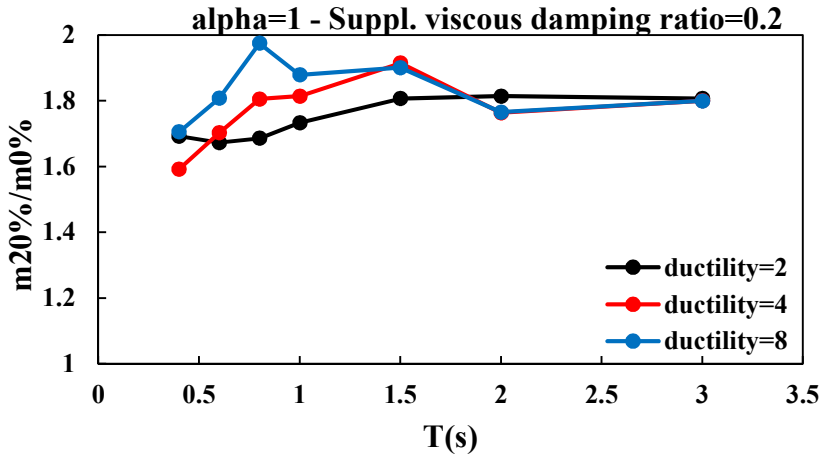


Figure 4. continued

## 4 CONCLUSIONS

In this study, the collapse capacity of SDOF systems equipped with FVDs under 44 far-field ground motion records were investigated. The results indicate that for a given level of supplemental viscous damping ratio and velocity exponent, by increasing the elastic period of SDOF system the median collapse capacity of the system equipped with FVD normalized to the median collapse capacity of its corresponding SDOF system without supplemental viscous damping is not a function of ductility. This is because of the fact that the P-Δ effects control the collapse capacity of long period structures with and without supplemental viscous damping.

## References

[1] Vamvatsikos, D. and Cornell, C.A. (2002) "Incremental dynamic analysis. *Earthquake*" *Engineering & Structural Dynamics*, *31*(3), pp.491-514.

[2] Ramirez, O.M., et al. ( 2000) "Development and Evaluation of Simplified Procedures for Analysis and Design of Buildings with Passive Energy Dissipation Systems", MCEER Report 00-0010, Revision, 1, Multidisciplinary Center for Earthquake Engineering Research, University at Buffalo, State University of New York, Buffalo, NY, 470 pp. Multidisciplinary Center for Earthquake Engineering Research, University at Buffalo, State University of New York, Buffalo, NY.

[3] Symans, M.D. Charney, F.A. Whittaker, A.S. Constantinou, M.C. Kircher, C.A. Johnson, M.W. and McNamara, R.J. (2008) "Energy dissipation systems for seismic applications: current practice and recent developments",*Journal of Structural Engineering* 2008; 134(1): 3–21. DOI: 10.1061/ (ASCE) 0733-9445, 134:1(3).

[4] Soong, T.T. and Dargush, G.F. (1997) "Passive Energy Dissipation Systems in Structural Engineering", John Wiley & Sons: Chichester.

[5] Constantinou, M.C., Soong, T.T. and Dargush, G.F. (1998) "Passive energy dissipation systems for structural design and retrofit", Monograph Series, MCEER, University of Buffalo, NY.

[6] Dargush, G.F. and Sant, R.S. (2005) "Evolutionary aseismic design and retrofit of structures with passive energy dissipation", *Earthquake Engineering and Structural Dynamics* 2005; 34(13): 1601–1626. DOI: 10.1002/eqe.497.

[7] Hwang, J.S., Huang, Y.N., Yi, S.L. and Ho, S.Y. (2008) "Design formulations for supplemental viscous dampers to building structures", *Journal of Structural Engineering* 2008; 134(1): 22–31. DOI: 10.1061/ (ASCE) 0733-9445, 134:1(22).

[8] Silvestri, S., Gasparini, G. and Trombetti, T. (2010) "A five-step procedure for the dimensioning of viscous dampers to be inserted in building structures", *Journal of Earthquake Engineering* 2010; 14(3): 417–447. DOI: 10.1080/13632460903093891.
[9] ASCE (2010). *Minimum design loads for buildings and other structures (ASCE/SEI 7-10)*, American Society of Civil Engineers (ASCE), Reston, VA.
[10] Guo, J.W.W., and Christopoulos, C. (2013) "Performance spectra based method for the seismic design of structures equipped with passive supplemental damping systems", *Earthquake Engineering and Structural Dynamics* 2013; 42(6): 935–952. DOI:10.1002/eqe.2261.
[11] Christopoulos, C. and Filiatrault, A. (2006) "Principles of Passive Supplemental Damping and Seismic Isolation", IUSS Press: Pavia, Italy, 2006.
[12] Haselton, C.B.(2006) "Assessing collapse safety of modern reinforced concrete moment frame buidlings", *Ph.D. Thesis*, Department of Civil and Environmental Engineering, Stanford University, 2006.
[13] ATC. Quantification of building seismic performance factors, FEMA P-695.(2009) *Technical Report*, Applied Technology Council: Redwood City, California.
[14] FEMA. (2012) "FEMA P-58-1: Seismic Performance Assessment of Buildings. Volume 1– Methodology."
[15] Krawinkler, H., Zareian, F., Lignos, D.G. and Ibarra, L.F. (2009) "Prediction of collapse of structures underearthquake excitations", 2nd International Conference on Computational Methods in Structural Dynamics and Earthquake Engineering. (Papadrakakis M, Lagaros ND, Fragiadakis M. eds). June 22-24, 2009, Rhodes, Greece, CD-ROM paper, paper no. CD449.
[16] Ibarra, L. and Krawinkler, H. (2011) "Variance of collapse capacity of SDOF systems under earthquake excitations", *Earthquake Engineering and Structural Dynamics* 40:12, 1299-1314.
[17] Adam, C., Ibarra, L. F., and Krawinkler H. (2004) "Evaluation of P-Delta Effects in Nondeteriorating MDOF Structures from Equivalent SDOF Systems", *Proceedings of 13th World Conference on Earthquake Engineering,* Vancouver, B.C., Canada.
[18] Vamvatsikos, D., and Cornell, C. A. (2005) "Direct Estimation of Seismic Demand and Capacity of Multidegree-of-Freedom Systems Through Incremental Dynamic Analysis of Single Degree of Freedom Approximation", *Journal of Structural Engineering,* 131(4), 589–599.
[19] Sun, C.K. Berg, G.V. and Hanson, R.D. (1973) "Gravity effect on single-degree inelastic systems", *Journal of Engineering Mechanics, ASCE,* 99, 1, pages 183-200.
[20] Jennings, P. and Husid, R. (1968) "Collapse of yielding structures during earthquakes," *Journal of the Engineering Mechanics Division, ASCE,* 94, EM5, pages 1045-1065,Oct. 1968.
[21] Jäger, C. and Adam, C. (2013) "Influence of collapse definition and near-field effects on collapse capacity spectra", *Journal of Earthquake Engineering* 17.6: 859-878.
[22] Miranda, E.and Akkar, S.D. (2003) "Dynamic instability of simple structural systems.", Journal of Structural Engineering; 129:1722–1726.
[23] Constantinou MC, Symans MD. Experimental and analytical investigation of seismic response of structures with supplemental fluid viscous dampers. *Report No. NCEER-92-0032*, National Center for Earthquake Engineering Research, Buffalo, NY.
[24] Dong, B., Sause, R. and Ricles, J.M. (2016) "Seismic response and performance of a steel MRF building with nonlinear viscous dampers under DBE and MCE", *Journal of Structural Engineering* 2016; 142(6). DOI: 10.1061/ (ASCE) ST.1943-541X.0001482, 04016023.
[25]Syman, M.D. and Constatinou, M.C. (1998) "Passive fluid viscous passive systems for seismic energy dissipation", ISET J. Earthq. Technol. 35 (4), 185–206, Paper No. 382.
[26] Lee, D. and Taylor, D.P. (2001) "Viscous damper development and future trends", The Structural Design of Tall Buildings 2001; 10(5): 311-320
[27] Hwang, J., Tsai, C., Wang, S. and Huang, Y. (2006) "Experimental study of RC building structures with supplemental viscous dampers and lightly reinforced walls", Engineering Structures 2006; 28(13):1816–1824.
[28] Hamidia, M., Filiatrault, A. and Aref, A. (2014) "Simplified seismic collapse capacity-based evaluation and design of frame buildings with and without supplemental damping systems", *MCEER-14-0001*, Multidisciplinary Center for Earthquake Engineering Research, Buffalo, NY.

[29] Mazzoni, Silvia, et al. "OpenSees command language manual." *Pacific Earthquake Engineering Research (PEER) Center* (2006).

[30] Lignos, D. G., H. Krawinkler, and A. S. Whittaker. (2011) "Prediction and validation of sidesway collapse of two scale models of a 4-story steel moment frame", *Earthquake Engineering & Structural Dynamics* 40, 807-825.

[31] Akcelyan, S. et al. (2016) "Evaluation of Simplified and State-of-the-Art Analysis Procedures for Steel Frame Buildings Equipped with Supplemental Damping Devices Based on E-Defense Full-Scale Shake Table Tests."*Journal of Structural Engineering* 142.6, 04016024

[32] Makris, N. and Constantinou, M.C. (1991) "Fractional-derivative Maxwell model for viscous dampers", *Journal of Structural Engineering*, *117*(9), pp.2708-2724.

COMPDYN 2017
6th ECCOMAS Thematic Conference on
Computational Methods in Structural Dynamics and Earthquake Engineering
M. Papadrakakis, M. Fragiadakis (eds.)
Rhodes Island, Greece, 15–17 June 2017

# ON THE USE OF GENETIC ALGORITHMS TO ASSESS THE SEISMIC RESISTANCE OF PLANAR FRAME STRUCTURES

**A. Greco[1], F. Cannizzaro[1], and A. Pluchino[2]**

[1] Department of Civil Engineering and Architecture, University of Catania
Via Santa Sofia, 64 - 95125 Catania, Italy
e-mail: {agreco,francesco.cannizzaro}@dica.unict.it

[2] Department of Physics and Astronomy
Via Santa Sofia, 64 - 95125 Catania, Italy
e-mail: alessandro@pluchino.it

**Keywords:** Limit analysis, Seismic behaviour, Elementary mechanisms method, Genetic algorithms, NetLogo.

**Abstract.** *Limit analysis represents a widely adopted strategy for the assessment of the bearing capacity and collapse mechanism of frame structures. Within this framework, in this paper an original strategy for the effective evaluation of the ultimate resistance and the corresponding failure mechanism of planar frame structures subjected to lateral loads is presented. The methodology is based on the generation of the elementary collapse mechanisms to be combined following a collapse load factor minimization criterion. When a large number of possible combinations has to be investigated a prompt procedure able to quickly converge to the actual collapse load factor and to jump out of local minima is needed. For this reason a procedure based on genetic algorithms is here adopted and a dedicated user-friendly software was developed in the NetLogo programming environment. Validations of the proposed procedure with respect to nonlinear static analysis are reported together with some significant sensitivity analyses with respect to load distribution parameters. The results demonstrate the reliability of the procedure and can provide useful information also in view of seismic design optimization strategies.*

## 1 INTRODUCTION

The plastic analysis of frame structures has been studied in the relevant literature mainly by means of two different approaches. The first of these is the structural analysis based on the finite element method in which, by means of iterative algorithms, the nonlinear static analysis is conducted on structures till the structural collapse [1]. Since the structural response is computed at each step of the loading history, the analysis can be very time-consuming.

On the other hand, limit analysis provides information on the carrying capacity and collapse mechanism of structures. It is a reliable strategy, faster than nonlinear static and dynamic analyses, thus making this method widely employed by practitioners. The conventional strategy is based on the fundamental kinematic theorem which analyses all the possible collapse mechanisms of a structure and the related collapse loads. The theorem states that the absolute lowest value among the considered mechanisms corresponds to the actual failure mode and the associated load to the actual collapse load. This method therefore does not require the direct computation of stiffness matrix and it is not necessary to apply the complete history of loading. Within the framework of limit analysis many proposals have been presented, mainly by means of linear programming [2]-[4].

Among those approaches a clever and frequently used method is that firstly developed by Neal and Symonds [5],[6] which is based on the analysis of a small number of independent collapse mechanisms (the so called elementary mechanisms), and on the subsequent search of the combination of those mechanisms which guarantees the lowest load factor. The mechanism associated to the lowest load factor represents the actual failure mechanism of the structure. However, this method requires a tedious work of combining the elementary mechanisms aiming at finding the combination associated to the lowest load multiplier. The latter aspect induced some authors to automate both steps of generating the elementary mechanisms and combining them; in particular, heuristic algorithms based on natural computation [7],[8] and genetic algorithms have been often employed [9] for a fast computerization of this methodology. Nevertheless in the existing literature only the case in which all the loads increase proportionally is taken into account.

In this paper the method proposed in [5],[6] is extended to account for a seismic load condition in which there is the contemporary presence of permanent vertical loads on the beams and incremental horizontal forces at each floor. In the described seismic load scenario the plastic hinges may occur at the two ends of the columns and also in any section along the beam. In the paper the exact location of the plastic hinges along the beam is calculated by means of the strategy proposed in [10].

The proposed methodology is able to provide fast and reliable information on the resistance and collapse mechanisms of frame structures subjected to seismic load.

A second novelty of the paper is the development of an original software code in the agent-based programming language NetLogo [11]. The developed code allows, without performing any analytical resolution of equations or matrices, to build into a virtual metrical space and to visualize in the user interface, every single mechanism and the correspondent collapse load by means of a user-friendly approach.

Then, the elementary mechanisms are combined and the minimum collapse load is obtained by means of an optimization procedure based on genetic algorithms which guarantees a fast convergence.

Several applications have been performed both with reference to the classical plastic analysis approach (all the loads increase proportionally), and with a seismic point of view considering a system of horizontal forces whose magnitude increases while the vertical loads are assumed to be constant. The values of the collapse load and the plastic hinge distribution at

collapse, obtained by means of the proposed method for seismic applications, have been compared to the correspondent results provided by nonlinear push over analysis showing a very good correspondence. In addition, a parametric study to assess the influence of the magnitude of the permanent loads acting on beams is showed.

## 2 COMBINATION OF ELEMENTARY COLLAPSE MECHANISMS

A generic planar regular frame, characterized by the number of floors $N_f$ and the number of columns $N_c$, is here considered. The frame is clamped at its base, therefore the degree of hyperstaticity of the structure, denoted by $h$, is given by

$$h = 3\left[ N_c - 1 + \left( N_f - 1 \right)\left( N_c - 1 \right) \right] \tag{1}$$

The plastic moments are assumed to be $M_{b,ij}$ for beams and $M_{c,ij}$ for columns, being $i$ and $j$ the generic floor and column of the frame, respectively. The loads acting on the frame are, at each floor, $F_{h,i}$ the concentrated horizontal forces and either by vertical incremental forces $F_{v,ij}$, applied in the mid span, or by permanent vertical distributed loads $q_{ij}$. Plastic hinges in can be located in $s$ "critical sections" correspondent to each joint and to a certain section of each beam which can coincide with its middle, in case of concentrated forces, or it can vary along the span in case of distributed loading. Floor heights and bays are indicated with $L_j$ and $H_i$, respectively. The layout of a generic frame is showed in Figure 1.

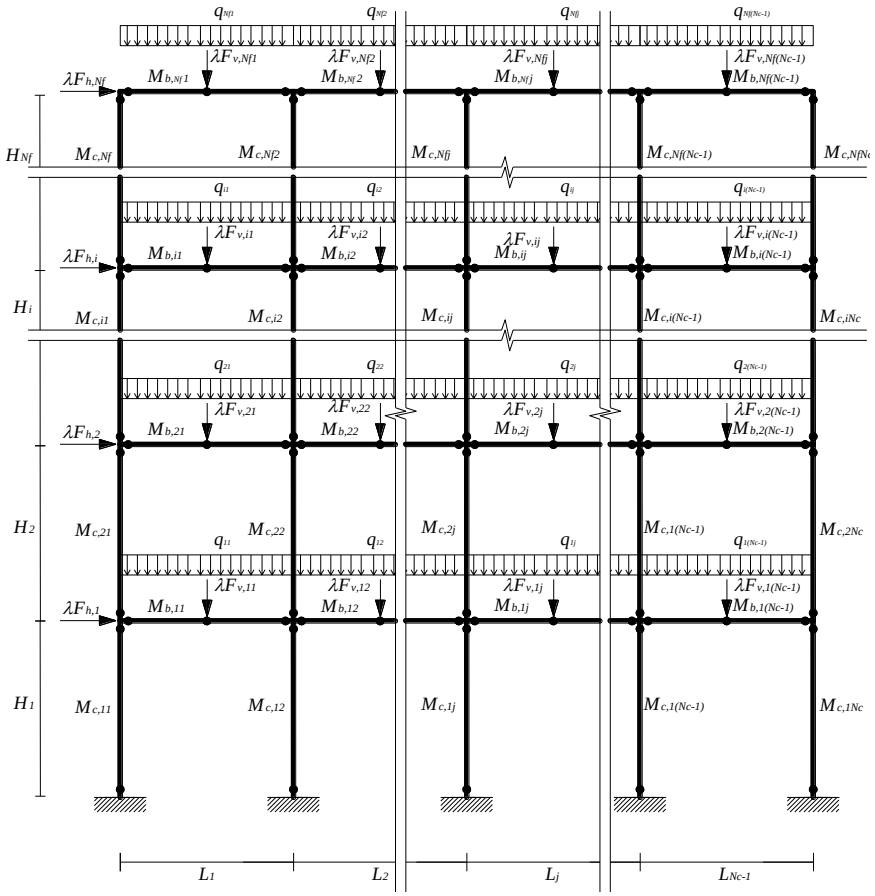


Figure 1: Layout of a generic planar frame.

As introduced by Neal and Symonds [5],[6] a small number $e=s-h$ of independent elementary collapse mechanisms can be taken into account and these may be classified in three different types: floor, beam and node mechanisms. In Figure 2 the three independent elementary collapse mechanisms for a generic frame are reported for clarity.

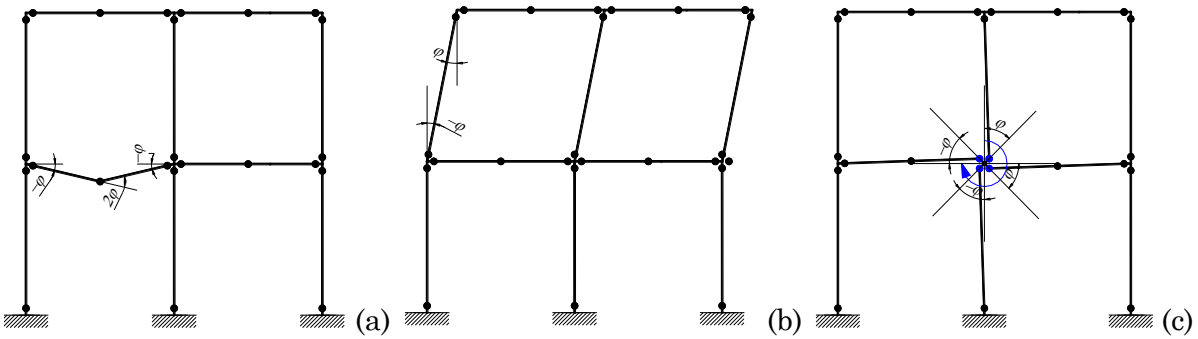


Figure 2: Elementary collapse mechanisms: (a) beam, (b) floor and (c) node mechanisms.

In the following two subsections the classical approach of the method of combination of elementary mechanisms applied to proportional loads is briefly recalled first, then the extension to account permanent loads is presented.

## 2.1 Proportional loads

When all the applied loads increase proportionally for each collapse mechanism the external work $W_{ext}$ is associated to all the vertical and horizontal concentrated forces $F_{h,i}$ and $F_{v,ij}$ for the correspondent displacements $d_{h,i}$ and $d_{v,ij}$, while the internal work (plastic dissipation) is referred to the plastic hinges and is the product of the plastic moments of beams and columns for the related rotations.

The elementary mechanisms are successively combined by adding the rotations related to each critical section and then multiplying each total rotation for the plastic moment of the related element, while the external work is the sum of the elementary ones. Therefore the collapse load multiplier $\lambda_c$ is the minimum ratio

$$\lambda_c = \frac{W_{\text{int}}}{W_{ext}} \tag{2}$$

## 2.2 Seismic load

In seismic conditions the vertical loads are assumed to be distributed and of constant value therefore for each collapse mechanism the collapse load multiplier $\lambda_c$ can be calculated as:

$$\lambda_c = \frac{W_{\text{int}} - W_{extV}}{W_{extH}} \tag{3}$$

where $W_{extH}$ and $W_{extV}$ represent respectively the work associated to the amplified horizontal forces and to permanent vertical load. In this case either the external or the internal work for each beam mechanism must be calculated considering that, as shown in Figure 3, a plastic hinge can be opened at a position $x_{ij}$ from the left end of the beam dependent on the magnitude of the uniform load acting on the beam. The superimposition of the uniformly distributed vertical loads and of the horizontal forces implies that, by increasing the horizontal forces the first plastic hinge opens at the right end of the beam, while the second hinge occurs at the left end when the distributed load is equal to the limit value [10]:

$$q_{\lim,ij} = \frac{4M_{b,ij}}{L_j^2} \tag{4}$$

When the vertical load $q_{ij}$ exceeds such a limit value the abscissa of the potential along-span plastic hinge is given by

$$x_{ij} = L_j - 2\sqrt{\frac{M_{b,ij}}{q_{ij}}} \tag{5}$$

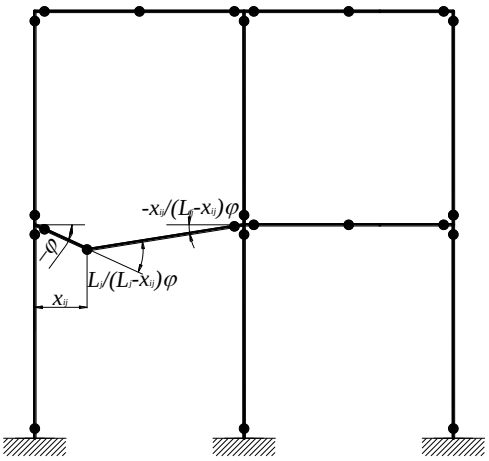


Figure 3: Beam mechanism in case of permanent loads.

For the evaluation of the external and internal work in a combined mechanism, the considerations described in the case of proportional load hold.

Analysing all the possible combinations of elementary mechanisms, the minimum value of $\lambda_c$ must be sought in order to obtain the real collapse load.

## 3 OPTIMIZATION PROCEDURE BASED ON GENETIC ALGORITHM

In this paper a genetic algorithm strategy for the optimization procedure which seeks the minimum value of $\lambda_c$ is employed.

A “genetic algorithm” is an adaptive stochastic method based on an opportune combination of random mutations and natural selection of chromosomes, that is arrays of integer values which correspond to a specific configuration of the problem under study, aiming at numerical-

ly finding optimal values of some specific function. The algorithm acts over a population of $P$ potential solutions by applying, iteratively, the "survival of the fittest" principle: in such a way it produces a sequence of new generations of individuals that evolves towards a stationary population where the large majority of surviving solutions approach the real solution of a practical problem.

Within the specific problem here treated, each number of a chromosome (called gene) represents how many times a given elementary mechanism enters in the combination. Therefore, if a total amount $N = N_{fm} + N_{bm} + N_{nm}$ of elementary mechanisms (being $N_{fm}$, $N_{bm}$ and $N_{nm}$ the number of floor beam and node mechanisms respectively), a generic chromosome $C_i$ of the population represents a weighted combination of those mechanisms and can be coded in the string $C_i$ $(c_1, c_2, c_3, \ldots c_k, \ldots, c_N)$ with $c_k \in [0, c_{\max}]$, being $c_{max}$ the maximum number of times the $k$-th mechanism is involved in the combination ($c_k = 0$ means that the mechanism is not involved at all). The load factor $\lambda_i$ of the corresponding combination (chromosome) can be consistently computed. The overall number of possible different chromosomes is thus $P_{max} = (c_{max} + 1)^N$, a quantity which rapidly increases with $N$ even for small values of $c_{max}$. Aiming at the minimization of $\lambda_i$ an opportune "fitness function" to be maximized is here defined as follows

$$f(\lambda_i) = K - \lambda_i \tag{6}$$

where K is an arbitrary constant great enough to have $f_i > 0$. Starting from the initial population of P chromosomes (typically P = 100), a new generation is created from the old one, where chromosomes that have a higher fitness score are more likely to be chosen as "parent" than those that have low fitness scores. The selection method adopted in this paper is called "tournament selection", with a tournament size of three. Either one or two parents (depending on the crossover-rate variable, see later) are chosen to create children: with one parent, the child is simply a clone of the parent; with two parents, the process is the digital analogue of sexual recombination (crossing-over). Once the new generation is created, there is also a chance that random mutations will occur at level of the single genes $c_k$ of the child chromosomes, and some of them will be changed into new ones (always chosen in the interval $[0, c_{max}]$). By iteratively repeating this process several times, chromosomes with the highest fitness will be progressively selected in the space of all the possible combinations and will quickly spread among the population reducing the diversity of the individuals.

One of the main goals of this paper is to develop an original code for both the calculation of all the elementary collapse mechanisms of a given planar frame and the implementation of the genetic algorithm described above for the determination of the combination of elementary mechanisms with the minimum collapse load factor for the structure considered. For this purpose, a very powerful software has been adopted, that is NetLogo, which is a freeware multiplatform environment with an owner high level programming language and with a very ductile and versatile user interface. The idea is to harness the power of the NetLogo graphical user interface and the versatility of its agent-oriented programming language in order to write an original code for the complete and automatic analysis of the limit behaviour of structures under earthquake excitations. In Figure 4 the layout of the user interface in NetLogo is reported. The interface is visually organized in two parts: (i) the *central-left* part, dedicated to the input parameters, to the setup of the frame and to the calculation of its elementary mechanisms; the chosen frame is then visualized in the World of NetLogo; (ii) the *right* part, dedicated to the plastic analysis of the frame through the genetic algorithm.

All the options of the genetic algorithm can be set. In particular, the *crossover-rate* slider controls the percentage of each new generation that has to be created through recombination

of the genes of two parents' chromosomes and the percentage (*100 – crossover-rate*) to be created through cloning of one parent's chromosome, while the mutation-rate slider controls the percentage probability of mutation, which applies to each genes of all the chromosomes in the new generation. Typical values of these two quantities are about 80% for the crossover rate and about 1% for the mutation rate. On the other hand, typical values for the population size are between 25 and 100 chromosomes, while usually $c_{max}$ is not greater than 3. At the end of the simulation it is also possible to visualize the combination of elementary mechanisms corresponding to the winning chromosome (that is the actual collapse mechanism). However, it is preferable to launch the multi-event version of the algorithm, which runs the same genetic routines several times with different random initial populations, in order to escape from local minima of the collapse load and to have more chances to reach a global one.

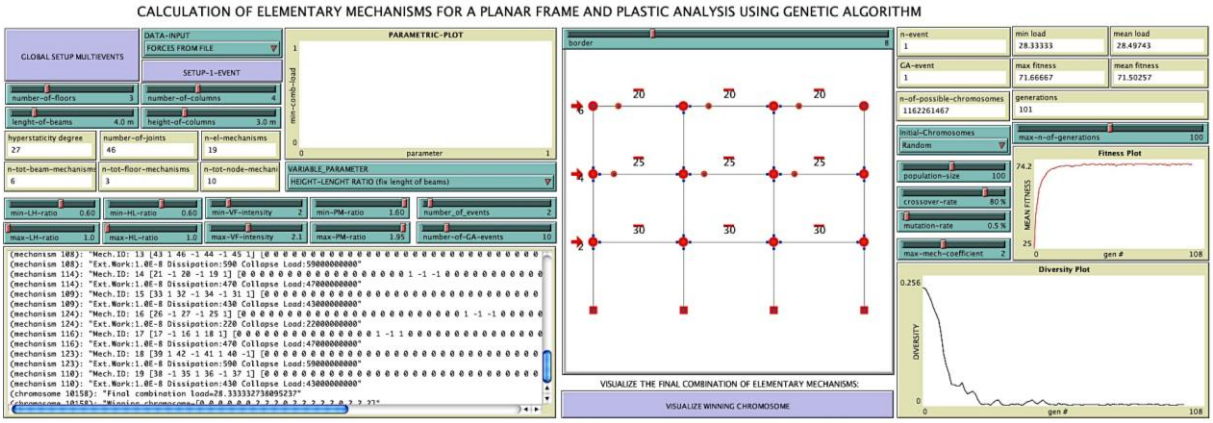


Figure 4: Layout of the NetLogo user interface.

## 4 NUMERICAL APPLICATIONS

In this section several applications will be presented, aiming at validating the proposed approach and performing a parametric study in order to assess how the magnitude of the permanent loads can affect the collapse load and mechanisms of frame structures under seismic conditions

In the first sub-section the case of frames subjected to a proportionally increasing load distribution is treated to validate the proposed approach on two frames already studied in the literature.

In the second sub-section the case of seismic collapse load is faced with. In this second case, a distribution of increasing horizontal loads (seismic contribution) is considered together with a constant vertical load distribution (gravitational loads) and the results are compared with a classic pushover analysis by means of a FEM software [12]. In addition a parametric study is performed to assess the sensitivity of the ultimate load with respect to the magnitude of the gravitational loads. In all the considered cases, the relevant collapse mechanisms are reported and discussed.

### 4.1 Proportionally increasing loads

The applications reported in this subsection can be found in [13] where the ant colony algorithm is employed as optimization procedure, and represent a validation of the proposed approach. The two analyzed frames are reported in Figure 5, which are in the following addressed as Frame A and Frame B respectively.

The previously described NetLogo code provided for Frame A the load multiplier of $\lambda_c$=2.1538 (vs 2.15 reported in [13]), which is the minimum value over 10 runs. The setup for the main parameters of the genetic algorithm was the following: a population size of 100 chromosomes (with $c_{max}$ = 2) was considered, a time range of 100 generations with 80% of crossover rate and 1% of mutation rate. These values will be adopted for almost all the simulations in the paper. Figure 6a shows the corresponding collapse mechanism of the NetLogo code which is the same one obtained in [13].

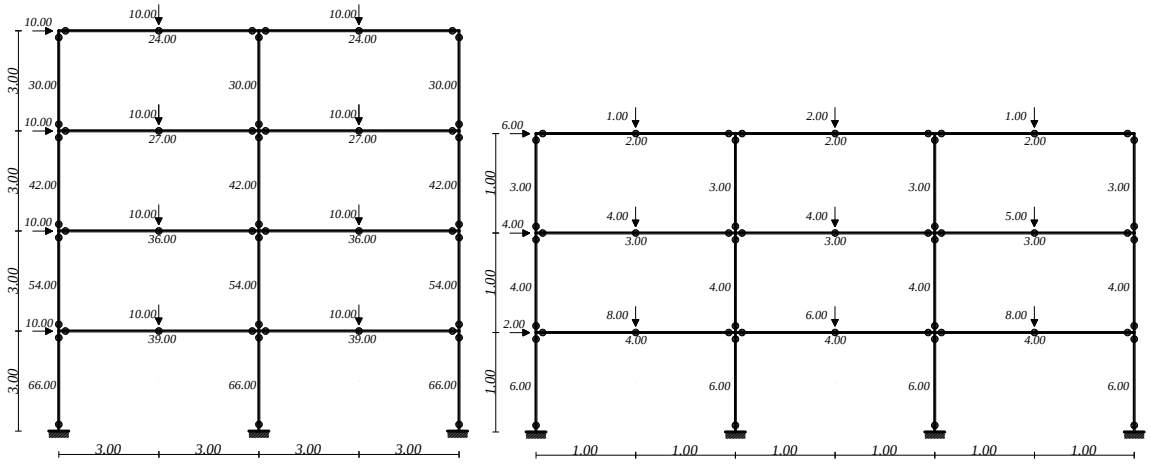

Figure 5: Layout of the two analyzed frames.

It is worth to point out that potential along span plastic hinges are reported with an orange circle irrespectively of the actual participation of the hinge to the overall collapse mechanism. Only in presence of relative rotation in correspondence of its location, the plastic hinge can be considered participating to the failure mechanism.

For the Frame B the load multiplier of 1.8734 (vs 1.873 reported in [13]) over 10 runs was obtained with the proposed approach while the collapse mechanism is reported in Figure 6b. Again, the collapse mechanism and the ultimate load factor are in good agreement with those available in the literature.

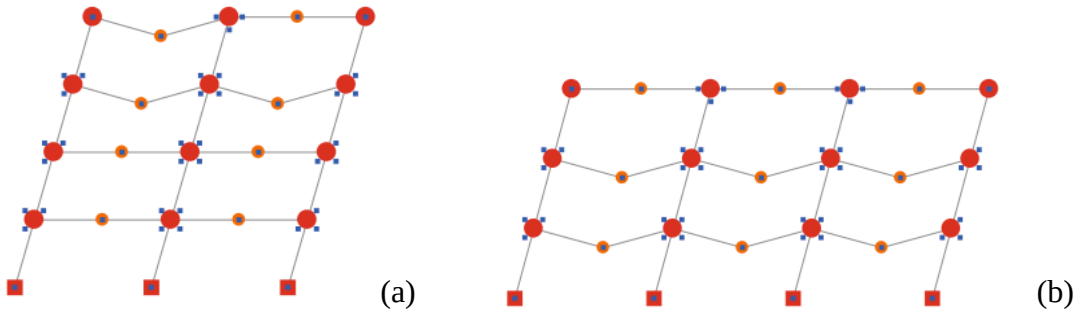

(a) (b)

Figure 6: Collapse mechanisms obtained for th oach.

## 4.2 Seismic loads

In this section the case of a frame subjected to permanent distributed vertical loads acting on the beams and increasing horizontal floor forces is treated. The considered frame is a three storey and three bay one whose geometry is reported in Figure 7. In the same figure the plastic moments are reported next to each beam and column and the values of the horizontal and vertical forces are also indicated.

As already described, the location of this potential along span plastic hinge depends on the length and on the plastic moment of the beam, as well as on the intensity of the permanent

vertical load acting on it. In particular, when the acting load is lower than a limit value, no along span plastic hinge can occur (i.e. plastic hinges can occur only at the two ends of the beam), while when the acting load is higher than the limit load the along span plastic hinge can occur at a specific section. These potential plastic hinges may anyway not be involved in the failure mechanism. In order to show all the possible scenarios, in the reported applications the cases of permanent vertical loads lower and higher than the limit values are considered as well as the case in which the acting load is exactly equal to the limit value. In particular, in the following reported applications the vertical load acting on the beams of the first floor has been chosen to be equal to the limit value ($q_{\lim,1} = 30$) while for the second and third floors it is assumed to be greater ($q_{\lim,2} = 22.5$, $q_{\lim,3} = 15$). Correspondingly, in terms of possible along span plastic hinges, none can occur at the beams of the first floor, while at the second and the third floors the along plastic hinges can occur at the abscissae 0.205 and 0.536 from the left ends of the beam, respectively.

In this case the comparison with the proposed procedure has been performed with a classic pushover approach in terms of ultimate load. A numerical model was implemented in the well known FEM software SAP2000 [12]. The considered model employs lumped nonlinearities, simulated by means of perfectly plastic hinges. Since in a pushover analysis the location of plastic hinges has to be set 'a priori', in the beams the critical sections have been set every 10 cm.

For the considered frame, the FEM approach leads to a collapse multiplier of the horizontal loads equal to $\lambda_{c,SAP} = 28.1645$, while with the proposed approach the collapse multiplier is equal to $l_c = 28.28$. It is worth to notice that, since the forces are gradually incremented in a pushover analysis, the actual collapse multiplier $\lambda_u$ of a structure represents an upper bound for such an approach. Furthermore, due to the kinematic theorem of plastic analysis $\lambda_u$ represents a lower bound for a limit analysis approach. Therefore it has to be $\lambda_{c,SAP} \le \lambda_u \le \lambda_c$.

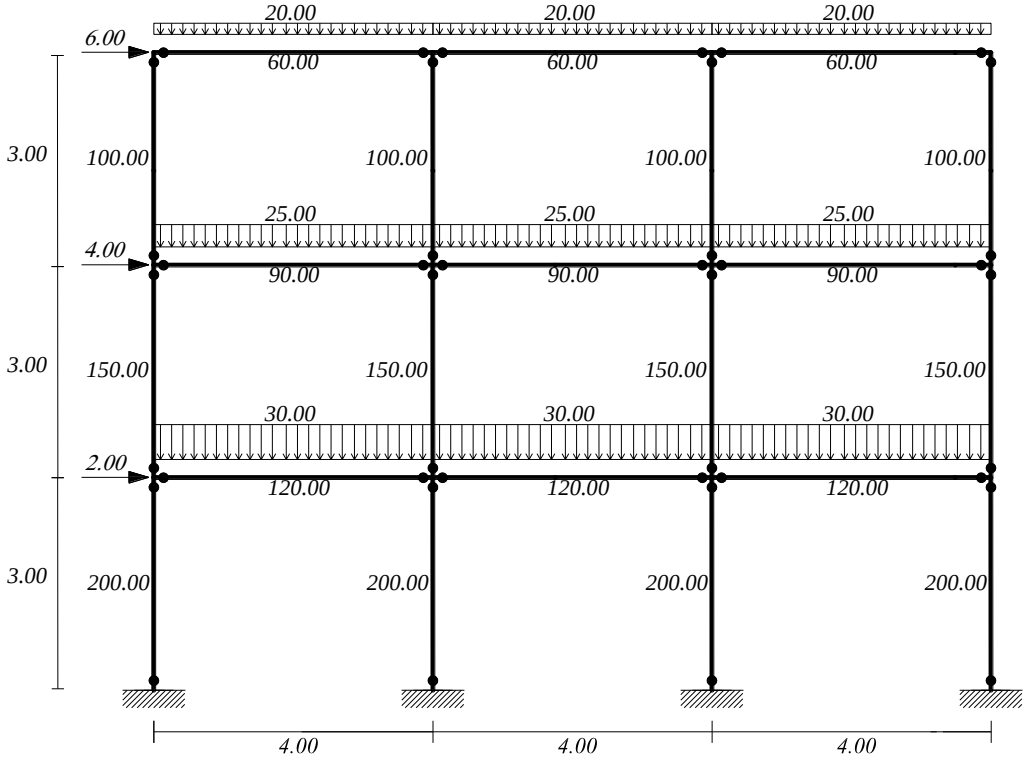


Figure 7: Geometrical and mechanical layout of the frame studied in seismic conditions.

Figure 8 reports a comparison of the collapse mechanisms for the considered frame obtained with the proposed approach (Figure 8a) and with a classic pushover approach (Figure 8b) and shows that some of the potential plastic hinges along the span of the beams on the third floor do not rotate in the total collapse mechanism. The collapse mechanisms again are almost coincident.

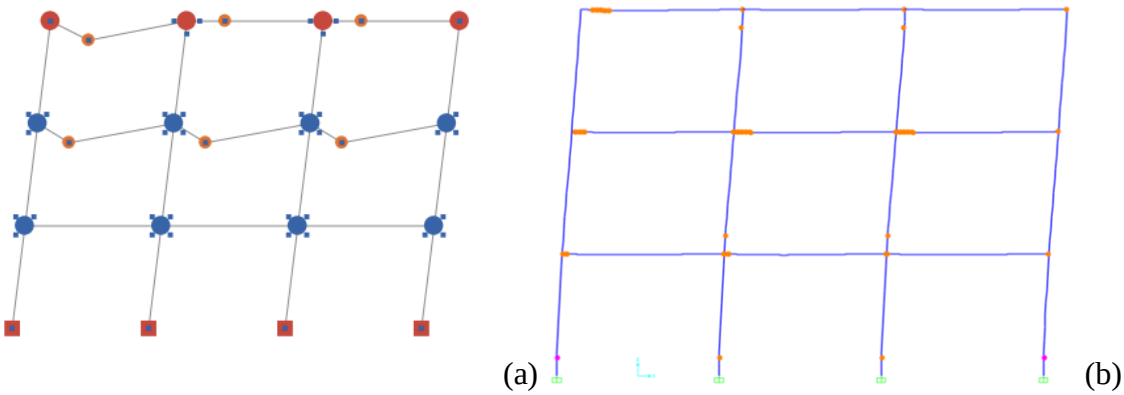


Figure 8: Collapse mechanisms of the frame under seismic conditions: (a) proposed model (b) pushover analysis.

In Figure 9 the multiplier $\alpha$ of the permanent loads is considered variable in the range [0-3]. In particular the conditions $\alpha = 0$ and $\alpha = 1$ represent, respectively, the cases of no permanent loads acting on beams and permanent load of the benchmark case (Figure 7). In the top left panel, the locations of the plastic hinges at each floor versus $\alpha$ are reported, in terms of their normalized abscissae $x_{ij}/L$, showing that above a certain threshold (different for each floor), increasing the value of $\alpha$ the hinges progressively move towards the right end of the beam. On the top right panel of Figure 9 the trend of the obtained ultimate load versus $\alpha$ is shown in comparison with the correspondent values provided by pushover analysis. The results show a good agreement between the FEM and the proposed approach. It is worth to notice that as the multiplier $\alpha$ is lower than a transition value equal to 1.06, the permanent load acting on all beams does not imply any plastic rotation located at the hinges along the axis of the beams and the collapse mechanism does not change, therefore the ultimate load is constant in this range. Then, when $\alpha$ increases the ultimate load decreases progressively and plastic hinges also open along the beams producing relative rotations. It can be easily seen, from the collapse mechanisms reported in the same figure, that increasing the value of $\alpha$ the positions of the plastic hinges in the beams move towards the right end.

## 5 CONCLUSIONS

An automatic approach for the evaluation of plastic loads and failure modes of planar frames, based on the generation of elementary collapse mechanisms and on their linear combination, has been presented.

The proposed approach, representing an extension of the method of combination of elementary mechanisms, accounts for permanent distributed vertical loads in addition to horizontal concentrated increasing forces and makes use of an original software developed in the agent-based programming language NetLogo, which is here applied for the first time to structural engineering. The code is able to automatically determine and visualize all the elementary mechanisms in planar frames and, by means of an optimization procedure based on genetic algorithms, to calculate, with great accuracy and in a very short computing time, the collapse load and the related mechanism.

Several applications have been performed either with reference to the classical plastic analysis approach, in which all the loads increase proportionally, or with a seismic point of view considering a system of horizontal forces whose magnitude increases while the vertical loads are assumed to be constant.

The performed applications have been compared either to some of the available results provided in the literature, in the case of proportional loads, or to the results provided by non linear pushover analysis in the seismic approach.

The seismic applications represent an original contribution towards the limit behaviour of structures under earthquake excitations, since general trends of seismic behaviour of planar frames can be deduced from the obtained results.

To this purpose, a parametric study has been performed aiming at evaluating the influence of the intensity of permanent vertical weights on the ultimate collapse load of planar frames. In particular it has been shown that the collapse load decreases, and the location of the plastic hinges on the beams involved in the collapse mechanism move towards the right end of the beam, for increasing values of the permanent vertical loads. The achieved results, with reference to the parametric studies, not only may provide significant information on the seismic performance of frame structures but also represent a useful tool in their optimal design.

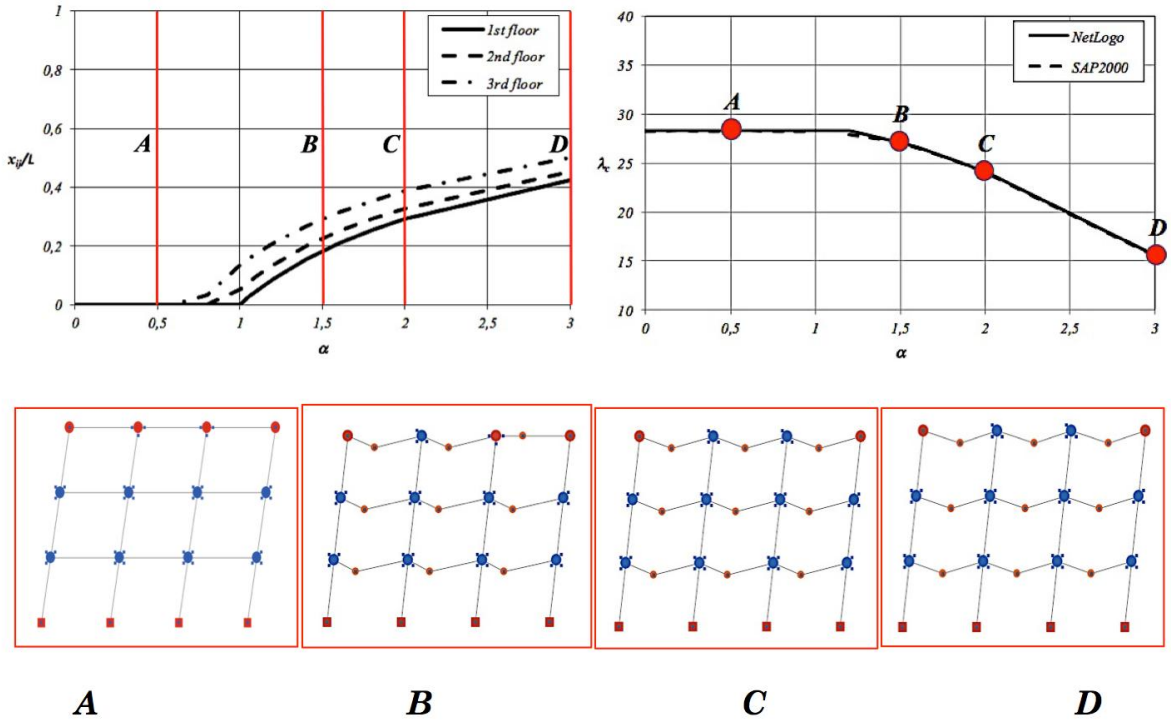


Figure 9: Location of plastic hinges on the beams (top left panel) and collapse load multiplier (top right panel) vs intensity of the permanent vertical loads; Bottom panels: selected collapse mechanisms.

## REFERENCES

[1] Bergan P.J, Søreide T. A comparative study of different numerical solution techniques as applied to a nonlinear structural problem. Comput Methods Appl Mech Eng 1973; 2(2):185–201. J.T. Oden, T. Belytschko, I. Babuska, T.J.R. Hughes, Research directions in computational mechanics. *Computer Methods in Applied Mechanics and Engineering*, **192**, 913-922, 2003.

[2] Charnes A, Greenberg HJ. Plastic collapse and linear programming, *Summer Meeting of the American Mathematical Society*; 1959.

[3] Livesley RK. Linear programming in structural analysis and design. In: Gallagher RH et al., editors. Optimum structural design. New York: Wiley; 1977 [Chapter 6].

[4] Cohen MZ, Maier G, editors. Engineering plasticity by mathematical programming. Proceedings of the NATO Advanced Study Institute, University of Waterloo, Waterloo, Canada, 2–12 August 1977. Pergamon Press Ltd; 1979.

[5] Neal BG, Symonds PS. The rapid calculation of plastic collapse loads for a framed structure. In: Proceedings of the institution of civil engineers London, vol. 1, part 3; 1952. p. 58–100.

[6] Neal BG, Symonds PS. The calculations of collapse loads for framed structures. J Inst Civil Eng 1951; 35:21–40.

[7] Goldberg DE. Genetic algorithms in search, optimization and machine learning. Addison-Wesley, USA; 1989.

[8] Holland JH. Adaptation in natural and artificial systems. MIT Press, USA; 1992.

[9] Kaveh A, Khanlari K. Collapse load factor of planar frames using a modified genetic algorithm. *Commun Numer Methods Eng* 2004; 20:911–25.

[10] Mazzolani F, Piluso V. Plastic design of seismic resistant steel frames. *Earthquake Engineering and Structural Dynamics.* 1997; 26:167-191.

[11] U. Wilensky NetLogo, http://ccl.northwestern.edu/netlogo, Center for Connected Learning and Computer-Based Modeling. Northwestern University, Evanston, IL 1999.

[12] CSI Analysis Reference Manual for SAP2000, Computers and Structures Inc., 2007.

[13] M. Jahanshahi, M. Pouraghajana, M. Pouraghajanb, Enhanced ACS algorithms for plastic analysis of planar frames, *Comp. Meth. Civil Eng.*, Vol.4 No.1 (2013) 65 - 82

COMPDYN 2017
6th ECCOMAS Thematic Conference on
Computational Methods in Structural Dynamics and Earthquake Engineering
M. Papadrakakis, M. Fragiadakis (eds.)
Rhodes Island, Greece, 15–17 June 2017

# SEISMIC PROGRESSIVE COLLAPSE OF MRF-EBF DUAL STEEL SYSTEMS

**Alireza Faroughi**[1], **Abdolreza S.Moghadam**[2], **Mahmood Hosseini**[3]

1 Assistant Professor
Department of Civil Engineering, College of Engineering, East Tehran Branch, Islamic Azad University, Tehran, Iran
e-mail: faroughi@iauet.ac.ir
2 Associate Professor
International Institute of Earthquake Engineering and Seismology (IIEES), Tehran, Iran
e-mail: moghadam@iiees.ac.ir
3 Associate Professor
International Institute of Earthquake Engineering and Seismology (IIEES), Tehran, Iran
e-mail: hosseini@iiees.ac.ir

**Keywords:** Columns' Failure, Progressive Collapse, Eccentric Steel Bracing, Seismic.

**Abstract.***In structural engineering, it is always attempted to predict a set of events which greatly contribute to lifecycle of the structure. These factors must be considered by design engineer and ensure resistance of the structure against those events. Seismic progressive collapse is one of the causes of serious damages and losses which may happen in events such as earthquakes. In this paper, it is intended to introduce more appropriate brace configuration based on an upper-bound estimation of the probability of seismic progressive collapse in MRF-EBF dual systems designed based on the 3rd edition of Iranian Seismic Code. In fact, in that standard there are only provisions for capacity of moment frames and no detail is given for bracings elements. The study has been concentrated on low to mid-rise buildings with residential and office usage. Results show that for 5-story buildings the best number of bracing bays is as many as 10-20% of the number of building's circumferential bays, and for 8-story buildings best number of bracing bays is as many as 20-30% of the number of building's circumferential bays. Results also show that regular bracing in internal bays are more appropriate for more resistance of the structure against progressive collapse.*

## 1. INTRODUCTION

Advances in methods of analysis and design of structures and development of performance-based concepts together with the observation of collapse in many structures as a result of natural and non-natural events, directed researchers toward investigation of structures in conditions far beyond the service conditions which is considered in conventional designs. In recent years, natural disasters such as Northridge earthquake (1994) and Kobe (1995), as well as non-natural events such as explosion of Mora federal building (1995), collapse of the Ronan famous building (1996) and terrorist attacks to buildings of world trade center (2001) resulted in structural failure of members progressively and finally, progressive collapse of the structure whose consequence was a major life loss and considerable economic losses. For this reason, progressive collapse has been taken into consideration during past decade. Progressive collapse is the failure of overall structure or an extensive part of it as a result of local events such as failure of one or more load bearing members and failure of adjacent members to redistribute the excessive loads through a path which can maintain the resistance and overall integrity. According to the definition of ASCE-7, progressive collapse is diffusion of the initial failure from one element into another whose consequence is the overall collapse of the whole structure or a large portion of it. More recently some researchers have worked on progressive collapse of steel frames using pushdown analysis [1].

Braced frames with the ability of eccentricity were introduced first in 1978 by Popov et.al. This system was initially designed for confronting lateral loading and its effect on large deformation and relative displacement particularly in high-rise buildings. Therefore, these researches presented eccentric bracing frame in regulations as a new system resisting against earthquake. According to extensive researches performed in this regard, systems of eccentric bracing have the capacity to combine high stiffness in inelastic range. Eccentric systems are in fact combined systems and the purpose of making eccentric bracing frames is to direct shear yield in a small portion of the main beam which is referred to as linking beam [2 , 3, 4, 5].

Although several researchers have worked on Seismic design of MRF-EBF dual systems [6], very few studies have been conducted with regard to their progressive collapse. This paper tries to suggest a rational approach for identifying the columns that should be removed for “seismic progressive collapse” studies in MRF-EBF dual systems, and then tries to suggest the most appropriate placement of the eccentrically braced bays to achieve the minimum potential of seismic progressive collapse. The columns have been selected to represent the most vulnerable columns to seismic damage, as identified by pushover analysis. Thus, instead of removing certain preset and predefined columns, the potential of progressive collapse at the end of earthquake is evaluated by removing the seismically damaged column. Details of the study are presented in the following sections.

## 2. PROBABILITY OF SEISMIC PROGRESSIVE COLLAPSE

Investigation of the progressive collapse is performed with elimination of some columns due to extensive loads such as explosion and then assessing the probability of progressive failure of other main structural elements caused by the intensification of gravity load of floors. However, in this paper, the issue of progressive collapse has been looked at from a different viewpoint. In this viewpoint it is assumed that the primary members which lose their load bearing capability (have passed point E in the performance curve) due to earthquake are removed from the structure, and then the structure is analyzed under the amplified effect of gravity loads (to account for the dynamic effect of gravity loads due to the sudden elimination of vertical load bearing elements). In this way an upper-bound estimation of the progressive collapse probability of the building’s structure is obtained.

For this purpose, first, structure is analyzed under the gravity and lateral loads using pushover analysis method and in this stage, hinges with different levels of performance will be created, which can represent the probability of initiation of the seismic progressive collapse in the structure. On this basis some columns are selected for removal and stating the progressive collapse analysis. These are often at the lowest floor and connected to a braced and moment frame. Finally, it is investigated whether structure is able to bear gravity loads resulted from removal of the column and transfer loads to its other members.

This is a new trend in the field of progressive collapse in which removal of column occurs as a result of earthquake and analysis is performed on a structure which is damaged by earthquake which is known as 'seismic progressive collapse'. This issue is studied in models which have most hinges in performance level near collapse. Therefore, two models of low-rise five floor buildings with distribution of damage in columns adjacent to the bracing bay (models 7 and 9 in Figure 1) and four models of mid-rise buildings with distribution of damage in bays of moment frame as well as bracing bays (models 20, 22, 23 and 24 in Figure 1) will be provided.

## 3. PROCESS OF DESIGN RESISTANT AGAINST PROGRESSIVE COLLAPSE

### 3.1. Instructions of the US department of defense (DoD)

US Department of Defense published a document entitled "unified facilities criteria (UFC)" [7] which must take the progressive collapse for new buildings which have three floors or more. DoD instruction can be applied for reinforced concrete, steel, wooden and cold-rolled steel buildings.

#### 3.1.1. Alternative logical method

In this method, structure must be able to bridge damaged portions. Analyses must be applied for linear and nonlinear statistical analyses by taking into account the appropriate portion for removal of columns and load bearing walls according to UFC4-023, 2009 [7] and ASCE7, 2010 [8] as well as maximum emergency load with load multipliers. These criteria must be applicable in alternative logical analysis.

## 4. MAIN CHALLENGES

Many challenges facing the system of bracing in dual systems for this research is conceivable and number and location of braces and its effect on seismic capacity and probability of the progressive collapse will be determined as a main challenge of selection.

## 5. RESEARCH METHODOLOGY

To start, the first step is to select the models and their characteristics for investigation and performing intended analyses of this work. For this end and understanding the requirements of the model, the method and recommendations of FEMA P 695 – 2009 [9] will be used.

### 5.1. Statistical population and volume of the sample

a. Statistical population: common residential and official buildings
b. Method of sampling: using professional software
c. Volume of sample: investigation, analysis and design of 28 different plans of the structure with afore mentioned characteristics

d. Method of calculation: based on regulation ASCE 41-13 [10] and instruction of seismic improvement 360 [12] and design using allowable stress and nonlinear analysis (pushover).

### 5.2. Design considerations

For the purposes of this research, in this stage, certain structural models were selected. At the beginning, with a test pattern of design, number of required bracing bays of the structure was assumed as 10-30% of the building's circumferential bays. Regarding the number of structural models, due to importance of the models, 28 models were considered. Sections used for software modeling were all box section with the size varying from 8-40 according to their function. Beams are mainly I-shaped (From No. 16 to 27). The material used in all cases is steel ST37. (The following models were analyzed as numerated from 1-28 from left to right).

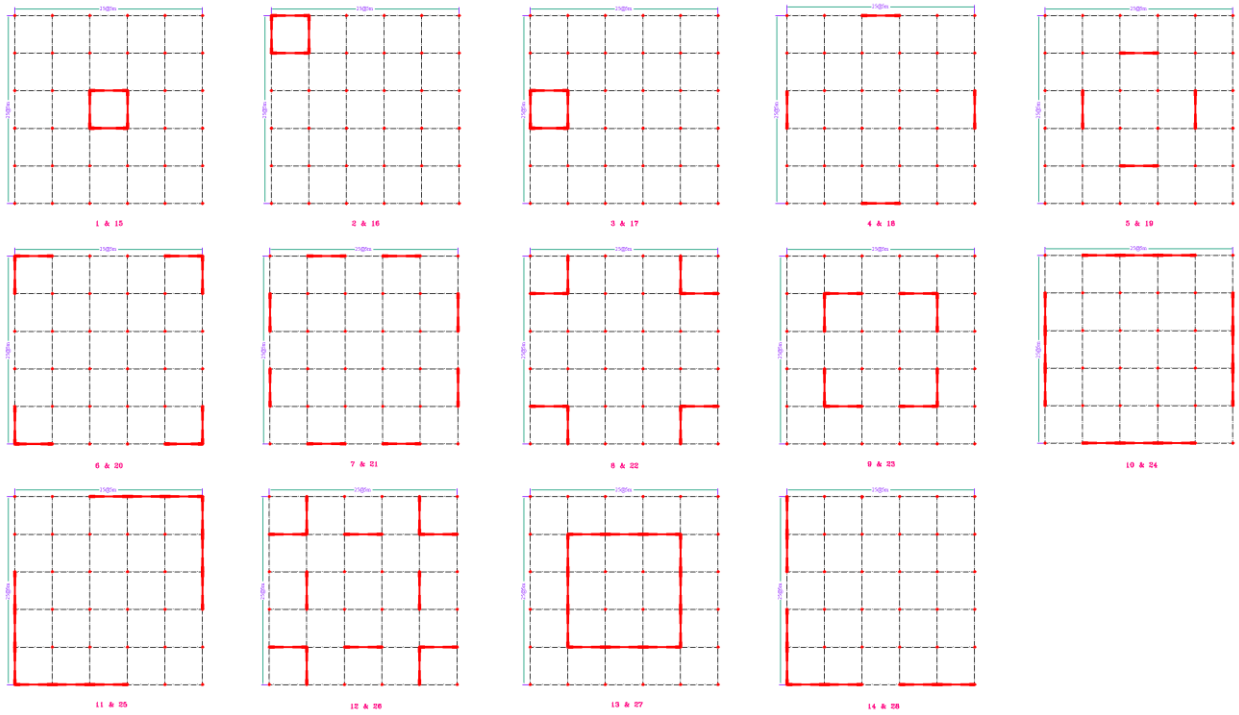

Fig. 1: Bracing patterns considered in the study for two sets of 5- and 8-story buildings

To meet the criteria listed in the AISC 341-10 [11] Section F3, as the length of all link beams are shorter than 1.6Mp/Vp therefore shear mode governs their behavior.

## 6. MODELS OF DESIGN AND ANALYSIS

### 6.1. Design of structure

Structural design was performed according to design regulations and 3rd edition of the Iranian Standard No. 2800 [13] of earthquake as linear and elastic with allowable stress method.

### 6.2. Analysis method: Pushover nonlinear static

Nonlinear models are defined for models which have the highest probability of the nonlinear – inelastic behavior. In this method in order to evaluate a structure, it has been

analyzed under the effect of constant loading pattern (statistic) and this analysis carries on till displacement of point of structure (displacement of control point) .This displacement which is evaluated with a specific improvement goal is called target displacement and will be the basis of investigation of structural components so that deformation, rotation and forces of the members will be investigated if they approach such limit (calculation of the required displacement of members is impossible, [14]).

## 7. ANALYSIS OF RESEARCH FINDINGS

In this section, results of models will be analyzed and divergence of analytical models and loading pattern using redistribution of the secondary stiffness is used.

Here, results will be analyzed and models are classified into two parts; low-rise with 5 floors and mid-rise with 8 floors.

### 7.1. Classification and analysis of data

| Model | No. of floors | No. of CP hinges in braces | | No. of CP hinges in beams | | No. of CP hinges in columns connected to MR bays | | No. of CP hinges in columns connected to BF bays | |
|---|---|---|---|---|---|---|---|---|---|
| | | Push Y | Push X | Push Y | Push X | Push Y | Push X | Push Y | Push X |
| 1 | 5 | 0 | 0 | 8 | 8 | 0 | 0 | 0 | 0 |
| 2 | 5 | 0 | 0 | 10 | 6 | 0 | 3 | 0 | 0 |
| 3 | 5 | 0 | 0 | 10 | 10 | 0 | 0 | 0 | 0 |
| 4 | 5 | 0 | 0 | 10 | 10 | 0 | 0 | 0 | 0 |
| 5 | 5 | 0 | 0 | 8 | 8 | 0 | 0 | 0 | 0 |
| 6 | 5 | 0 | 0 | 12 | 12 | 0 | 0 | 4 | 2 |
| 7 | 5 | 0 | 0 | 12 | 12 | 0 | 0 | 4 | 4 |
| 8 | 5 | 0 | 0 | 12 | 12 | 0 | 0 | 4 | 3 |
| 9 | 5 | 0 | 0 | 12 | 12 | 0 | 0 | 4 | 4 |
| 10 | 5 | 0 | 0 | 12 | 12 | 0 | 0 | 0 | 0 |
| 11 | 5 | 0 | 0 | 12 | 12 | 0 | 0 | 0 | 0 |
| 12 | 5 | 0 | 0 | 12 | 12 | 0 | 0 | 0 | 0 |
| 13 | 5 | 0 | 0 | 12 | 12 | 0 | 0 | 0 | 0 |
| 14 | 5 | 0 | 0 | 20 | 20 | 0 | 3 | 0 | 0 |
| 15 | 8 | 0 | 0 | 16 | 16 | 2 | 0 | 0 | 0 |
| 16 | 8 | 0 | 0 | 16 | 22 | 12 | 43 | 0 | 4 |
| 17 | 8 | 1 | 0 | 10 | 14 | 1 | 0 | 0 | 0 |
| 18 | 8 | 0 | 0 | 16 | 14 | 1 | 2 | 0 | 0 |
| 19 | 8 | 0 | 0 | 14 | 14 | 0 | 0 | 0 | 0 |
| 20 | 8 | 0 | 0 | 28 | 28 | 2 | 6 | 0 | 0 |
| 21 | 8 | 0 | 0 | 24 | 24 | 1 | 0 | 0 | 4 |
| 22 | 8 | 0 | 0 | 24 | 24 | 8 | 4 | 0 | 0 |
| 23 | 8 | 0 | 0 | 24 | 24 | 0 | 0 | 2 | 2 |
| 24 | 8 | 0 | 0 | 36 | 36 | 2 | 0 | 3 | 2 |
| 25 | 8 | 0 | 0 | 30 | 30 | 1 | 1 | 1 | 0 |
| 26 | 8 | 0 | 0 | 36 | 36 | 0 | 0 | 0 | 0 |
| 27 | 8 | 0 | 0 | 30 | 30 | 2 | 2 | 0 | 2 |
| 28 | 8 | 0 | 0 | 32 | 32 | 8 | 3 | 0 | 0 |

Table 1: Characteristics of hinges in collapse of the different structural members

## 8. ANALYSIS OF THE RESULTS OF PROBABILITY OF PROGRESSIVE COLLAPSE

### 8.1. Probability of progressive collapse in mid-rise and low-rise models

Model 7: in this model, number of hinges passing from the threshold of collapse as a result of pushover analysis in X-direction and in braced frames will be studied.

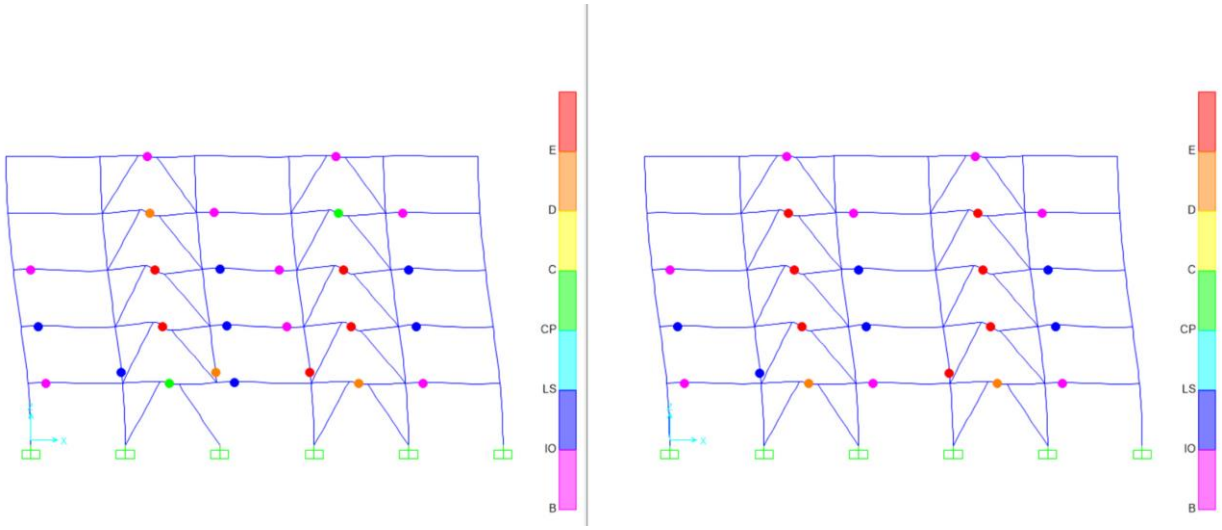


Fig. 2: hinges of pushover analysis (left), removal of column in progressive collapse (right)

After pushover analysis, it is observed that in linking beams connected to bracing bays, shear hinges are formed. Moreover, in other bracings, bending hinges are formed in beams and columns with LS and IO performance levels which can be seen in Fig. 2. After the pushover analysis and removal of column according to Fig. 2, it is observed that the number of hinges formed in linking beams remained constant while some of them pass the CP performance level and in beams bear the bracing span in which no hinge was formed before, two hinges are formed now with IO performance level in 2nd and 3rd floors and bending hinges are formed with LS performance level in 1st floor.

Model 9: in this model, number of hinges passing from the threshold of collapse in pushover analysis in X direction is bracing frame is studied.

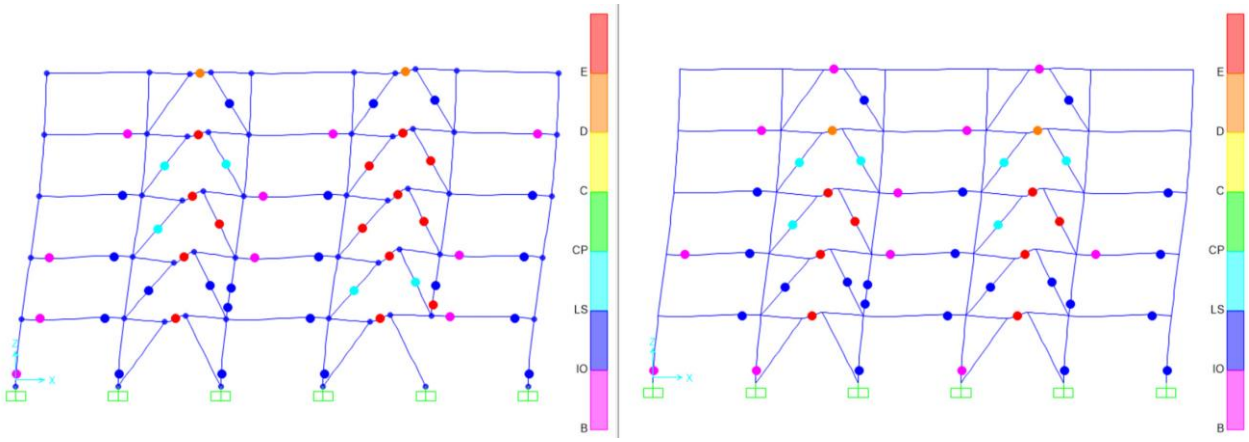


Fig. 3: hinges of pushover analysis (left), removal of column in progressive collapse (right)

After pushover analysis and removal of the intended column (Fig. 3), a number of shear hinges are formed in all floors of the structure and in D-E range. In first stage, hinges are formed only in four floors. Furthermore, some of the bracing members in which CP hinges are formed pass now the CP level and are in critical limit. In what follows, it can be seen that column of the top floor which had a bending hinge with CP level before, now passes this performance level. In addition, the beam connected to the top floor is removed in which no column was formed before, has now a bending hinge with IO performance level.

Model 20: in this model, number of hinges passing the threshold of collapse as a result of pushover analysis in X direction and in moment frame is studies.

In this model, probability of progressive collapse of columns of moment frame is investigated. In first stage of the pushover analysis, it is observed that in linking beams shearing hinges with CP performance level are formed. Furthermore, in the column of the second floor of a moment frame, a bending hinge is formed in the range of passing the point E and beams connected to this column in higher floors have mostly bending hinges with LS performance level. This issue can be seen in Fig. 4 and after removal of aforesaid column according to Fig. 4, following results were obtained:

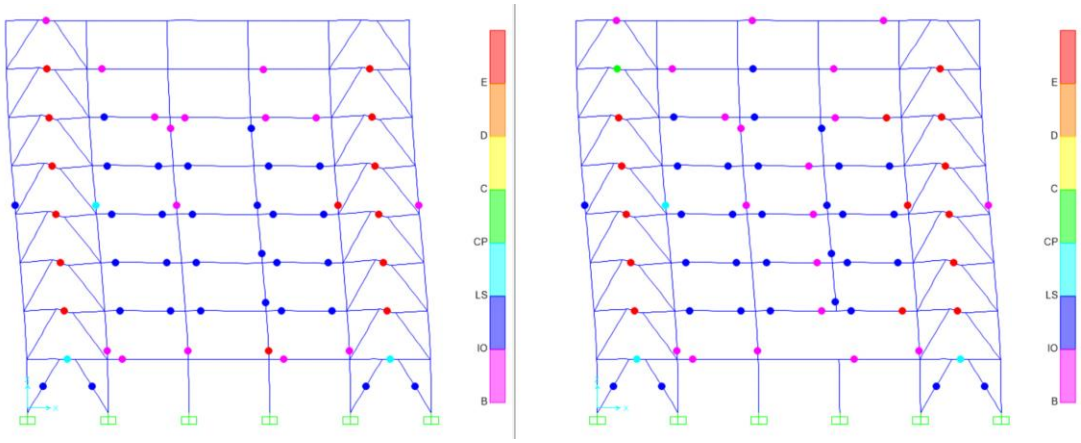


Fig. 4: hinges of pushover analysis (left), removal of column in progressive collapse (right)

Beams connected to this column from 2nd to 5th floor in which no hinge was formed before, have now bending hinges with IO performance level. In addition, in beams near to the bracing bays which had bending hinges with IO and LS performance levels before removal of the column, pass these performance levels at this stage and are now in the range of point E. Of course, other bending hinges are formed in other floors and frames now which are not important from changes in performance level point of view and don't contribute to the probability of progressive collapse.

Model 22: in this model, number of hinges passing the threshold of collapse as a result of pushover analysis in Y direction in moment frame is studied.

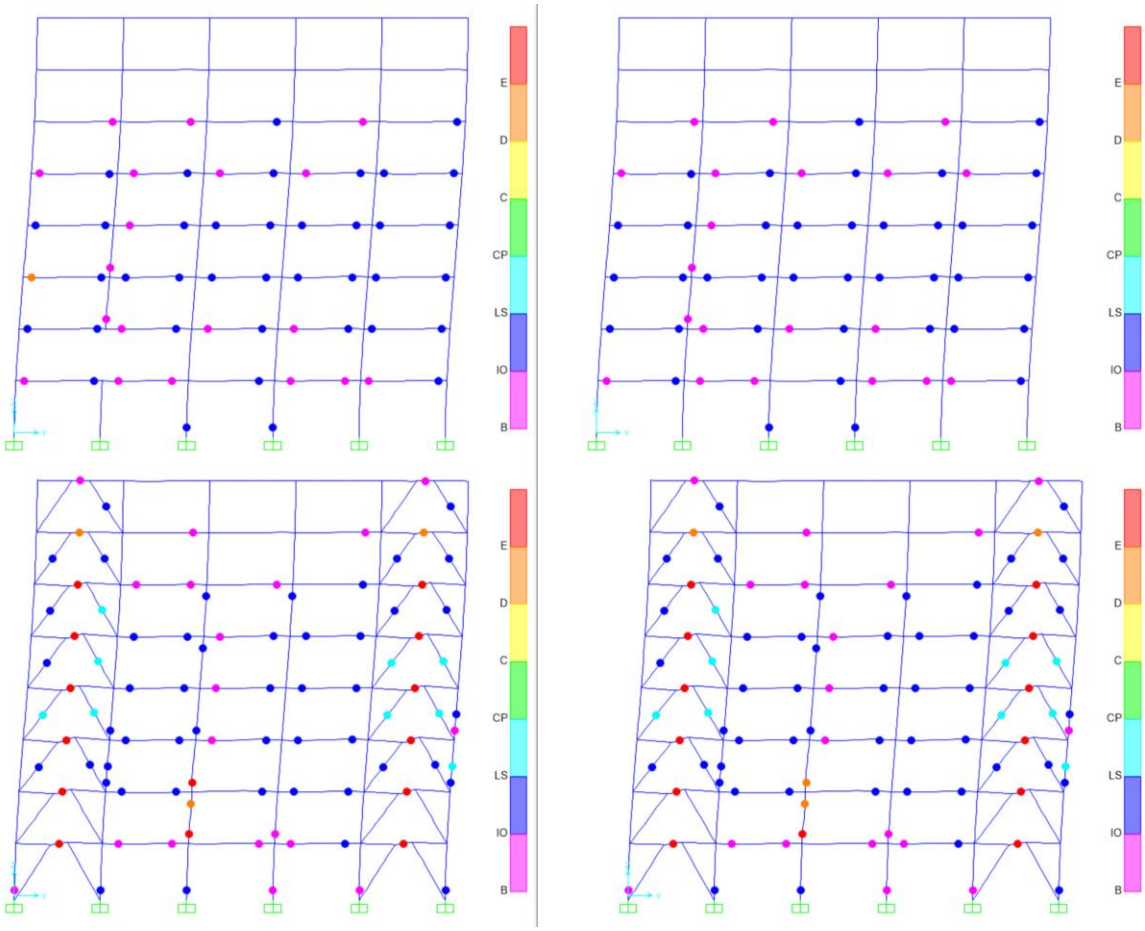


Fig. 5: hinges of pushover analysis (left), removal of column in progressive collapse (right)

In this model, column of the moment frame bays is investigated again. In first step and according to Fig. 5, after the pushover analysis in bracing frames of this model, linking beams have all shear hinges in D-E range and in some columns, bending hinges are formed in the same region. Bracing members have axial force hinges with CP performance level in worst conditions and regarding the moment frames which are the main topic of this model, as can be seen in Fig. 5, bending hinges are formed in beams and columns with IO and LS performance levels. Now, according to Fig. 5, after removal of the column, a lot of bending hinges which were in IO and LS levels before remains unchanged now and only a bending hinge is formed in one of the beams of the third floor in E level which has no considerable importance for change in performance level and no contribution to the probability of seismic progressive collapse.

In addition, as shown in Fig. 5, no change is observed in bracing bays as a result of removal of a column in a moment frame and only one of the columns of the third floor which had bending hinge with LS performance level before, passes now the point E.

Model 23: in this model, number of hinges passing the threshold of collapse as a result of pushover analysis in X direction in moment frame is studied.

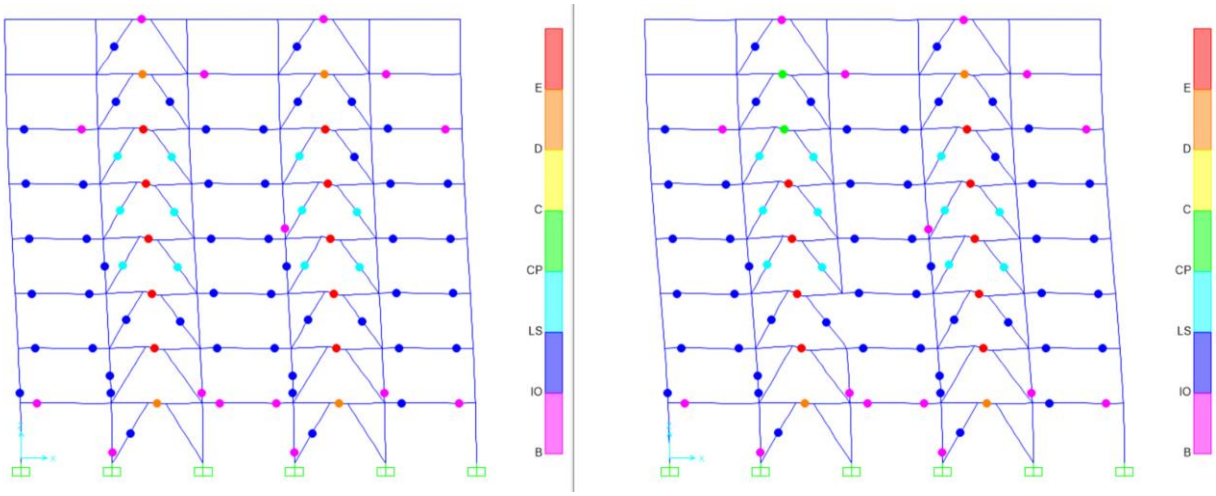


Fig. 6: hinges of pushover analysis (left), removal of column in progressive collapse (right)

In this model, column of the moment frame bays is investigated again. In first step and according to Fig. 6, after the pushover analysis in bracing frames of this model, linking beams have all shear hinges in D-E range and in some columns, bending hinges are formed in the same region. In addition, as shown in Fig. 6, no change is observed in bracing bays as a result of removal of a column in a moment frame and only one of the columns of the third floor which had bending hinge with LS performance level before, passes now the point E.

Model 24: in this model, number of hinges passing the threshold of collapse as a result of pushover analysis in Y direction in moment frame is studied.

The last model in which progressive collapse is studied is model 24. This model has 30% bracing span with respect to perimeter. According to Fig. 7, in the next stage after the pushover analysis, in linking beams, shearing hinges which pass the point E are formed. Moreover, bracing members have mainly the hinges of axial forces with LS performance level or passing point E. now, after removal of column of the fourth floor of one of the bracing bays shown in Fig. 7, linking beams remained in the same state and only a number of linking beams of the last floor in which no hinge was formed before now have hinges with IO performance level and many hinges which pass the point E. in addition, bracing members which are close to the removed column and had hinges with LS performance level before, approach the CP performance level now.

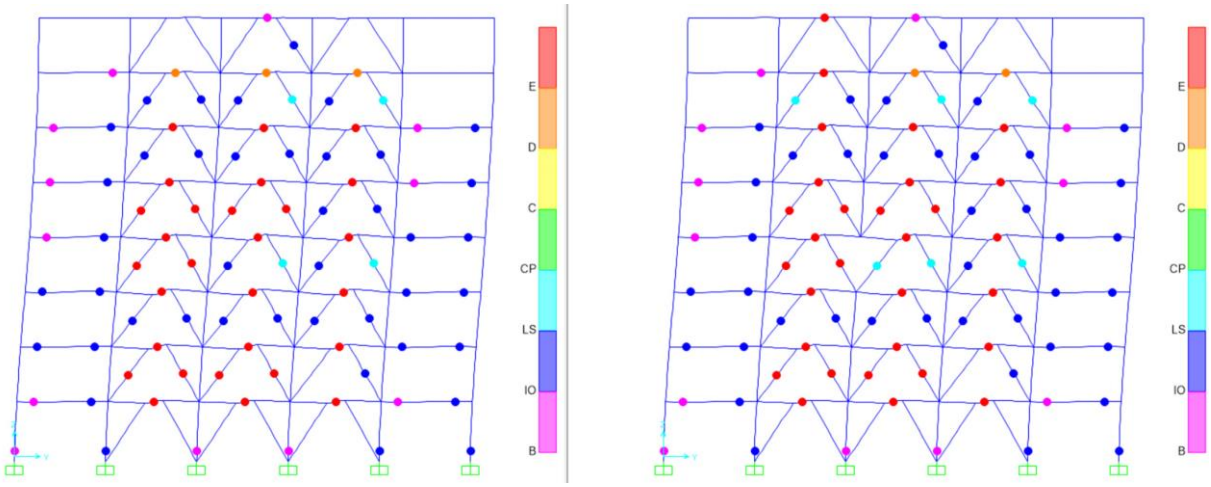


Fig. 7: hinges of pushover analysis (left), removal of column in progressive collapse (right)

## 9. CONCLUSIONS

- For 5 story buildings, configuration of the model 6 has a low level of risk of progressive collapse. Furthermore, except models 2 and 14, other models are not considerably different and it can be inferred that for 5-soty buildings with conditions of the models, with respect to the number of bracing bays, 10-20% of the building perimeter is an acceptable level and in these models, regular position of bracings has no considerable effect on the probability of progressive collapse. In 5-story models, it was proved that structures with 1-2 bracing bays will be appropriate models and more bays have no contribution to the reduction of weight and probability of the progressive collapse.
- For 8-story buildings models; 23 and 25 are the best. In these models, location of bracing are more effective than their number. With respect to the number of bracing bays, 20-30% of the building's perimeter is an acceptable level. Moreover, irregular models such as 16 and 28 are not appropriate because of contribution of the moment frame, secondary torsional effects and consequently, more hinges in threshold of collapse. In 8–story models, it was proved that structures with 2-3 bracing bays will be suitable models.
- As it can be seen, in low-rise 5-story structures, such as models 3-5 and 10-13, no hinge is formed in moment frames with exceeding collapse prevention performance level and it means that number and location of bracing bays in these models is more appropriate.
- Comparing models 7 and 9, it can be said that in model 9 since columns are connected to braces from both directions and seismic force is applied from both directions to the column, number of failure hinges and effect of progressive collapse increases more than model 7.
- Regarding mid-rise 8-storystructures, it can be observed that as number of floors increases, the structure needs more bracing bays since in model 24, despite of the sufficient number of columns, enough number of bracing bays leads to preventing collapse of the roof and adjacent beams and consequently preventing the seismic progressive collapse in the structure performance level changes significantly. Now, according to conclusion 2, 20-30% of the building's perimeter is of great importance and will be a good factor for maintaining stability of the structure and transfer of force to all of the structure.
- In models such as model 23 in which braces are inside the structure and in middle bays, if the column connected to the bracing bay is removed, no considerable change occurs in efficiency and performance level of other hinges since gravitational loads are transferred to braces and distribution of forces to other members takes place well and it seems that removal of the column connected to the bracing bay has no significant effect on other structural frames and the seismic progressive collapse. Model 23 is considered as the ideal model.
- In general, in structural systems which have bracings, probability of progressive collapse is not high since braces contribute to bearing gravitational loads and if hinges passing from the collapse threshold are not formed in vertical or diagonal bracing members, they can greatly resist against seismic progressive collapse.

## REFERENCES

[1] Ferraioli, M., Avossa, A.M., Mandara, A. ,(2014) "Assessment of progressive collapse capacity of earthquake-resistant steel moment frames using pushdown analysis", Open Construction and Building Technology Journal 8(1): 324-336.

[2] Merovich, A.T., Nicoletti, J.P. and Hartle, E. (1982). "Eccentric Bracing in Tall Buildings," ASCE Journal of the Structural Division, 108(ST9):2066-2079

[3] Roeder, C.W. and Popov, E.P. (1978). "Eccentrically Braced Steel Frames for Earthquakes," ASCE Journal of the Structural Division 104(ST3): 391-411

[4] Libby, J.R. (1981). "Eccentric Braced Frame Construction—A Case History," AISC Engineering Journal, 4th Quarter:149-153

[5] Engelhardt, M.D. and Ricles, J.M. (1989). "Eccentrically Braced Frames: U.S. Practice," AISC Engineering Journal, 26(2): 66-80.

[6] Montuori R., Nastri E., Piluso V. (2015) "Seismic design of MRF-EBF dual systems with vertical links: EC8 vs plastic design", Journal of Earthquake Engineering 19(3): 480-504.

[7] DOD (Department of Defense) (2009), UFC (Unified Facilities Criteria), UFC 4-023-03: Design of buildings to resist progressive collapse, Washington ,USA

[8] ASCE (American Society of Civil Engineers) (2010), ASCE7-10: Minimum Design Loads for Buildings and Other Structures , Virginia, USA

[9] FEMA (Federal Emergency Management Agency) (2009), FEMA P695-2009: Quantification of Building Seismic Performance Factors, USA

[10] ASCE (American Society of Civil Engineers) (2013), ASCE41-13: Seismic Evaluation and Retrofit of Existing Buildings , Virginia ,USA

[11] AISC (American Institute of Steel Construction (2010),AISC341-10 Seismic Provisions for Structural Steel Buildings, Chicago, Illinois, USA

[12] Permanent committee of revision, (2013), instruction of seismic optimization of the available buildings, no. 360, deputy of planning and strategic monitoring of the president.

[13] Permanent committee of revision, (2005), third edition of the earthquake standard 2800, regulation of the building design, center of housing and building researches.

[14] Richards, Paul.W. (2010). "Estimating the stiffness of eccentrically braced frames (EBFs)." ASCE Practice Periodical on Structural Design and Construction 15(1): 91-95.

COMPDYN 2017
6th ECCOMAS Thematic Conference on
Computational Methods in Structural Dynamics and Earthquake Engineering
M. Papadrakakis, M. Fragiadakis (eds.)
Rhodes Island, Greece, 15–17 June 2017

# REDUCING VIBRATIONS IN A FOOTBRIDGE USING A SEMI-ACTIVE TUNED MASS DAMPER

**C. Moutinho**[1], **A. Cunha**[1], **and E. Caetano**[1]

[1] CONSTRUCT-Vibest, Faculty of Engineering (FEUP), University of Porto
R. Dr. Roberto Frias S/N, 4200-465 Porto
e-mail: moutinho@fe.up.pt; acunha@fe.up.pt; ecaetano@fe.up.pt

**Keywords:** Footbridges, Vibration problems, Tuned Mass Damper, Semi-Active control.

**Abstract.** *The stress-ribbon footbridge located at the campus of the Faculty of Engineering of University of Porto (FEUP) is a slender structure that connects the main buildings of the university to the students' canteen. Its dynamic behaviour has been studied over the last few years in several areas of the system dynamics. First, the modal parameters in terms of natural frequencies, damping ratios and modal shapes were identified, and a complex non-linear numerical model of the structure that takes into account the various construction phases was calibrated. Then, a comprehensive study of the analysis of the vibration levels of the footbridge involving either regular and vandal loads was developed. Given the perceptible levels of vibration that often affect that structure, an active vibration control system was implemented for research purposes. Since 2009, a dynamic monitoring system composed of 4 accelerometers and 4 thermal sensors collets time series, enabling the Operational Modal Analysis and the Vibration-based Structural Health Monitoring of the footbridge. In 2013, a Tuned Mass Damper was installed in the context of a research project related to Smart Inertial Vibration Control Systems. At a first stage, this device worked passively, tuned close to the critical natural frequency in terms of proneness to resonant pedestrian loads. More recently, the control system was updated to a semi-active functioning with the objective of increasing the system efficiency. This was done because the footbridge has several critical vibration modes around 2 Hz and only one control device was installed. Using the Phase Control law, it is possible to adjust, in real-time, the vibrating frequency of the inertial mass to the structure frequency, enabling not only the correct tuning of the device but also the possibility of performing multimodal control. After a description about how Phase Control works, this paper describes the laboratory tests of the semi-active device, which showed that the system behaved as numerically expected. Then, the implementation of the device in the footbridge is described and all equipment and instrumentation are listed. Finally, the effect of the control system in reducing the vibration levels of the footbridge over the last few years is analysed. This was done by observing the data from the continuous dynamic monitoring system from 2010 until 2016. It was noted a tendency in the reduction of the peak accelerations of some sections of the deck after the installation of the passive TMD, which were even more attenuated after the activation of the semi-active device.*

## 1 INTRODUCTION

Many Civil Engineering structures have vibration problems in terms of serviceability limit states due to several transient or periodic dynamic loads, e.g., footbridges subjected to pedestrian actions, road and railway bridges excited by traffic loads and tall buildings exposed to wind forces.

In these situations, the implementation of control systems can improve the structural performance by reducing the vibration levels to acceptable values, which are established for each case. To achieve this, several passive, active, semi-active or hybrid control schemes can be adopted. The most popular techniques are those that involve passive systems because, compared to other cases, they are more reliable, more robust, relatively more economical and require low maintenance. When controlling harmonic vibrations, one of the most interesting devices is the vibration absorber, also known as Tuned Mass Damper (TMD). However, these devices may have some functioning problems common to passive systems. In fact, because they are purely passive, they don't have the possibility of adapting themselves to the actual characteristics of the external actions or to the identified structural properties. In case of external harmonic excitations, to work properly TMDs must be accurately tuned to the system's vibration frequency, otherwise they will lose a significant portion of their efficiency. One possible way is to solve this problem is to use active TMDs, which are not so sensitive to the vibrating frequency of the structure [1]. However, active systems are not so attractive because of their cost, particularly dealing with large structures. Indeed, they require sophisticated technology as well as powerful actuators and energy supply, which also calls for a lot of maintenance. For these reasons, in last few years, special attention has been given to semi-active systems which are still based on feedback control schemes, but require much simpler technology and actuators. Besides, they can work with a small amount of energy, including the possibility of operating with batteries [2].

In this context, this paper presents the research work involving the application of a semi-active system in the functioning of a TMD installed in a slender footbridge. At a first stage, the device that was installed in February of 2013 worked in passive mode until September 2014. The objective was to experimentally check the effect of a passive TMD in reducing structure vibrations. This part of the work is extensively described in reference [3]. It was concluded that the control device produced a slight reduction in the number of occurrences of high levels of acceleration in certain sections of the deck. As explained in that document, this is in part due to the fact that the TMD is not perfectly tuned to any of the natural frequencies of the footbridge.

To correct this problem, the semi-active functioning of the TMD was activated by the end of September of 2014. In this case, the control action was based on the imposing of a correct phase angle between the motion of the structure and the inertial mass of the TMD, which can be achieved by introducing blocking actions at certain positions of the device. The specific version of the Phase Control law used in this work is described in reference [4] and summarized in a further section of this paper. This control law requires the continuous measurement of the structure acceleration and the velocity of the TMD, being different from other proposals that demand the measurement of displacements. The blocking of the inertial mass was implemented by using a solution based on a Magneto-Rheological (MR) damper, which seems to be a very interesting device and recently gained a certain popularity in the Structural Control area [2]. This paper gives particular attention to the experimental tests of the semi-active system performed before being installed in the footbridge, as well as to the control system implementation and the analysis of the vibration levels of the structure over last few years, including the period without control, with the passive TMD and with the semi-active TMD.

## 2 CHARACTERIZATION OF THE FOOTBRIDGE

### 2.1 General description

The footbridge under analysis provides a pedestrian link between the main buildings of FEUP and the student's canteen and parking areas (Figure 1). This structure is characterized as a stress-ribbon footbridge formed by two spans of 28m and 30m. The deck comprises four prestressing cables embedded in reinforced concrete and it takes on a catenary shape over the two spans with a circular curve over the intermediate support. The deck is a rectangular cross-section of external design dimensions of 3.80m×0.15m.

### 2.2 Identified and calculated modal parameters

The natural frequencies of the structure were identified through ambient vibrations tests using four seismographs including force-balance accelerometers, duly synchronized via GPS [5]. The ambient response of the system was recorded according to several setups, using two fixed reference stations and eighteen other measurement stations distributed over the total length of the deck. Using the conventional peak peaking method applied to the set of FRFs, it was possible to identify the natural frequencies (listed in Table 1) as well as the corresponding vibration mode shapes, some of which are represented in Figure 2. The numerical model developed to represent the dynamic characteristics of the system was obtained by considering the experimental results, by taking into account the geometrical nonlinearity of the structure and given the different phases of the construction process [5]. Table 1 and Figure 2 also include a comparison between analytical and experimental results in terms of natural frequencies and modal shapes.



Figure 1: General view of the footbridge.

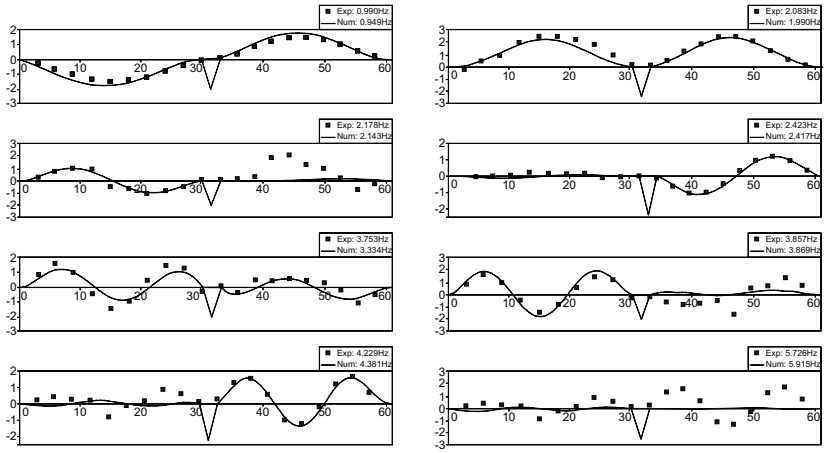


Figure 2: Identified and calculated vibration modes.

## 2.3 Location of the Tuned Mass Damper

By consulting Table 1, it can be stated that the structure has 3 natural frequencies in the range of 2 – 2.5Hz, which is considered critical in terms of the possibility of occurring resonance phenomena with the pedestrians' step frequency. From this point of view, 1st vibration mode with a frequency close to 1Hz is not critical, and the same can be concluded for the vibrations modes higher than the 4th order.

To considerer the problem of where to install the TMD and which vibration modes are to be controlled, Figure 3 represents a superposition of the system's numerical main vibration modes. The small dots define equal modal amplitudes of the vibration modes in the critical range inside each span. In the first span, section 13 has equal modal amplitudes of the 2nd and 3rd vibration modes with natural frequencies of 1.99 and 2.14Hz, respectively. In the second one, section 49 equalizes modal amplitudes of the 2nd and 4th vibrations modes with natural frequencies of 1.99 and 2.42Hz, respectively. Because only one TMD is available for installation, it was decided to implement the TMD in the second span, mainly because it is more accessible and has vibration modes with more separate frequencies. In this case it would be possible to reduce the dynamics of the 2nd (global) vibration mode and the 4th (local) one.

However, it is necessary to consider that one TMD cannot be optimally tuned to both vibration modes. Given the proximity of mean step frequency of pedestrians around 2 Hz, the 2nd vibration mode of 1.99 Hz frequency is more critical than the other of 2.42 Hz, which means that preferably the TMD should be tuned to this lower frequency. However, the existing TMD for this project has a minimum vibrating frequency of 2.06 Hz, meaning that the TMD cannot be optimally tuned to this vibration mode. Even so, this corresponds to an intermediate tuning between the two critical vibration modes, which still leads to a level of reduction of vibrations associated with these modes. The effect of implementing the TMD with this frequency evaluated over several years is described in reference [3].

| Order | Measured frequency (Hz) | Calculated frequency (Hz) | Type of mode |
|---|---|---|---|
| 1 | 0.99 | 0.949 | First antisymmetric (two spans, opposite phase) |
| 2 | 2.083 | 1.99 | First symmetric (two spans, in-phase) |
| 3 | 2.178 | 2.143 | Second antisymmetric (L=30m) |
| 4 | 2.423 | 2.417 | Second antisymmetric (L=28m) |
| 5 | 3.753 | 3.334 | Second symmetric (two spans, opposite phase) |
| 6 | 3.857 | 3.869 | Second symmetric (L=30m) |
| 7 | 4.229 | 4.381 | Second symmetric (L=28m) |
| 8 | 5.726 | 5.915 | Third antisymmetric (L=30m) |
| 9 | 6.517 | 6.82 | Third antisymmetric (L=28m) |
| 10 | 8.262 | 8.271 | Fourth symmetric (two spans, opposite phase) |

Table 1: Identified and calculated natural frequencies.

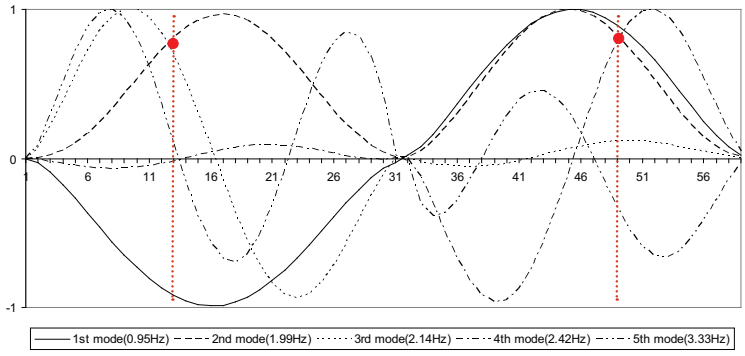


Figure 3: Superposition of the first vibration modes shapes.

# 3 CONTROL STRATEGY

## 3.1 Phase Control

The problem of detuning present in the installed TMD may be attenuated by implementing a semi-active mechanism in the functioning of the control device, in such a way that it automatically tunes the TMD to the actual vibrating frequency of the system. This means that the existing TMD may be able to control simultaneously the two critical vibration modes of the second span without the need of two control devices.

This objective may be achieved by using a control law designated by Phase Control. In the context of this research, a simplified version of the classical formula was derived [4]. The goal was to improve the functioning of semi-active TMDs by simplifying the measurement process and reducing the number of variables involved, making the control system more feasible and reliable. Because the control law is of ON/OFF type, combined with appropriate trigger conditions, the activity of the actuation system may be significantly reduced, which may be of a few seconds a day in many practical cases, increasing the durability of the device and reducing its maintenance. Moreover, due to the ability of the control system to command the motion of the inertial mass, the semi-active TMD is relatively insensitive to its initial tuning, resulting in the capability of self-tuning and in the possibility of controlling several vibration modes of a structure over a significant broadband frequency [4]. The proposed control law is defined as follows:

$$\begin{cases} \ddot{x}_1 \cdot \dot{x}_2 \leq 0 \Rightarrow c_2 = c_{\min} \\ \ddot{x}_1 \cdot \dot{x}_2 \cdot \alpha > 0 \Rightarrow c_2 = c_{\max} \end{cases} \quad (1)$$

In this case, $x_1$ is the displacement of structure where the TMD is attached, with the second derivate as the respective acceleration, and $x_2$ is the displacement of the TMD mass, with the first derivate as the respective velocity. $c_{\min}$ and $c_{\max}$ are damping constants imposed on the control device, assumed to be an MR damper, as a means of applying control actions by imposing a correct phase angle between the motion of the TMD mass relative to the structure. On the other hand, $\alpha$ is defined as $\alpha = \alpha_1 \,.\, \alpha_2 \,.\, \alpha_3$, which is a variable that only assumes binary values, 0 or 1, which, in turn, depends on other $\alpha_i$ variables ($i$=1, 2, 3), also binary valued. Each $\alpha_i$ is associated with a specific condition.

The first condition is related to evaluation of the actual levels of vibration of the structure and the need for the existence of a control action. If the vibrations levels are considered excessive according to some design criteria, the control should be activated, i.e., $\alpha_1$=1. By contrast, if the vibration levels are low, the structure does not need to be controlled, which leads to $\alpha_1$=0. This is an important condition because, in many practical situations, structures have excessive vibrations for short periods of time, which greatly decreases the activity and saves the control system.

The second condition is related to the fact that the blocking of the motion of the TMD's inertial mass does not need to occur twice in a cycle. As indicated in reference [4], the application of the control law expressed in equation (1) corrects the phase of the motion of the mass in both its extreme positions. A possible simplification is to correct the phase once in a cycle, which would be sufficient and desirable in most cases. This decision to correct the motion once or twice in a cycle can be implemented by observing the acceleration signal of the TMD mass because it has opposite signs at each extreme position. For instance, if it is intended to correct the motion once in a cycle when the mass is in positive acceleration extreme, $\alpha_2$=1 for positive acceleration and $\alpha_2$=0 for negative acceleration. If the option is to correct to motion twice in a cycle, $\alpha_2$ will always be set to 1.

The third condition is about the error (ε) allowed in the evaluation of the condition expressed in equation (1). In other words, it is not be necessary for the phase angle of acceleration of the structure and the velocity of the TMD mass to be exactly in the opposite phase. In practical cases, it would be enough to have a very close opposite phase instead of an exact one. Therefore, the control signal should be only activated, i.e., $\alpha_3=1$, if the product of the second equation of inequality (2) is greater than the error ε, being null in the opposite case.

### 3.2 Expected control effect

The effect of the application of this law in controlling a structure modelled as an equivalent single degree-of-freedom (1-DOF) can be observed by analysing the system dynamic amplification curves of Figure 4a), where an example of an undamped 1-DOF of 1 t mass and 2 Hz natural frequency have an attached TMD characterized by a mass ratio of 1%. If the semi-active (SA) TMD has the same tuning as the optimal TMD, it exhibits a higher efficiency than the passive device. However, the great advantage of the semi-active solution lies in its ability to adjust its vibration frequency in the presence of detuning as shown in that figure, where the case of a detuning of the natural frequency of the semi-active TMD of 5% is represented. The interest in using semi-active TMDs increases when extending their use in controlling vibration modes with frequencies away from their initial tuning. This can be seen in Figure 4b), where a single semi-active TMD is used to control a 3-DOF system, by contrast to the use of 3 independent passive TMDs tuned to each natural frequency. Knowing that the semi-active TMD is passively tuned to the 2nd system frequency, its ability in reducing the dynamics of vibrations modes out of its tuning is truly remarkable.

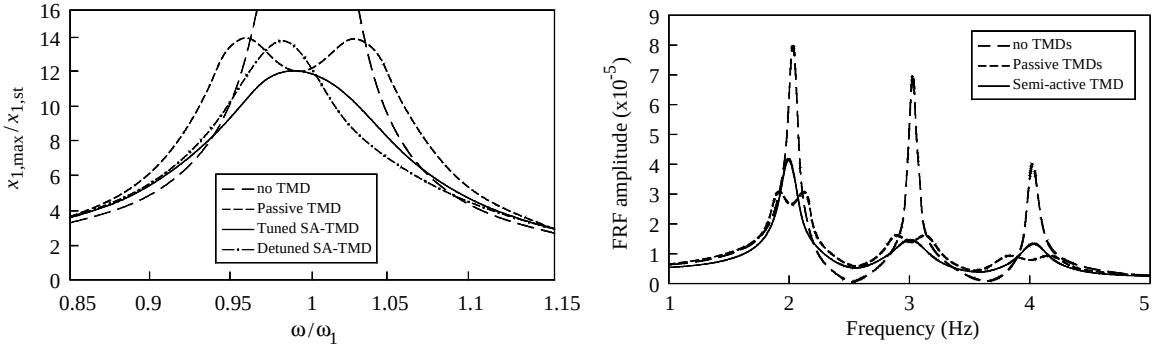


Figure 4: Dynamic amplification curves comparing the effect of passive and semi-active TMDs: a) 1-DOF system; b) multi-DOF system.

## 4 LABORATORY TESTS

### 4.1 Description of models and equipment

Prior to installing the TMD in the footbridge, the device was subject to several laboratory tests in order to characterize its dynamic properties and mechanical functioning. Reference [3] describes several aspects of the passive functioning of the device and reference [6] briefly describes other aspects related to the semi-active operation. In this paper, more detailed results of the tests of the semi-active component are included. The objective of these tests was to verify experimentally that the system works as predicted in the previous section, which encouraged its actual implementation in the footbridge. The developed semi-active TMD is depicted in Figure 5a), which is composed of several layers of individual masses that are connected to each other and can be added or subtracted in order to achieve a desired level of total mass with a maximum of 550 kg. The mass is guided by means of shafts and has 4 compression springs connecting it to the structure. The damper used in this device is of MR type which can

work passively if no electrical current is applied, or can work in semi-active mode which is the ultimate purpose of its use. The TMD was installed under a concrete slab which, in turn, is supported in steel frame by means of helical springs. This structure can be excited either manually or by means of a shaker installed at the top of the slab (Figure 5b)).

In order to measure all variables involved in the control problem, several sensors were installed. The TMD is instrumented with an LVDT to measure relative displacements between the mass and the structure, and the damper force is measured by means of a load cell installed between the MR damper and the structure (see Figure 5c)). The vertical motion of the slab and the TMD mass is measured by 2 accelerometers. All these sensors and equipment are controlled by a National Instruments PXI platform, taking advantage of the real-time operating system adequate to guarantee determinism in control loops.

### 4.2 Dynamic properties of the laboratory model and TMD

The concrete slab of dimensions 1.5 × 2.5 $m^2$ area and 0.2 m thickness that is used to suspend the TMD has a mass of approximately 2 ton and functions as a primary structure. Its natural frequency was measured and evaluated at 3.5 Hz. Because it is supported on helical springs, a free decay test revealed a rather low associated damping ratio, such that, after several minutes, the slab was still vibrating.

Similarly, the TMD was subjected to dynamic tests which are described in reference [3]. It was concluded that its springs have a non-linear behaviour depending on the compression ratio associated with several TMD masses. Considering the total mass of 550 kg, the natural frequency was estimated at 2.06 Hz. Given the MR damper type used with this device, the estimated equivalent viscous damping ratio was estimated as varying from 6 to 8%.

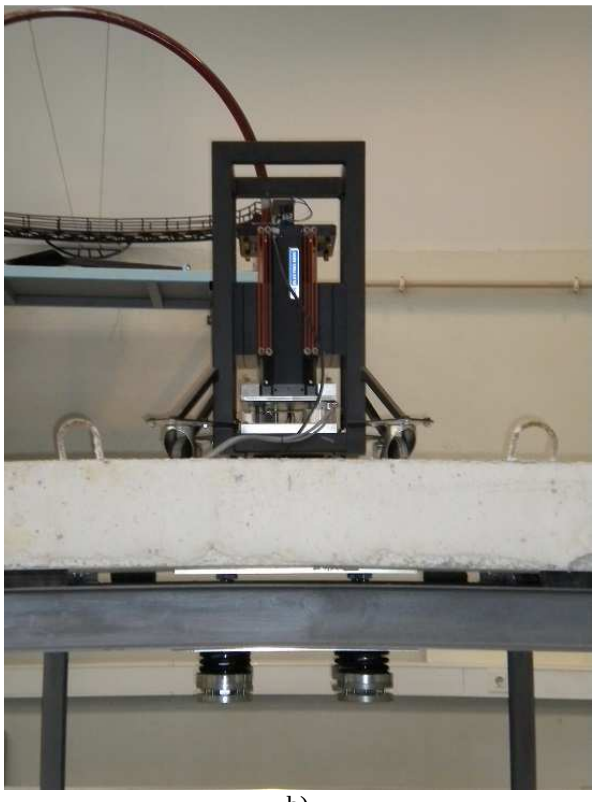

b)



a)



c)

Figure 5: Laboratory setup: a) Semi-active TMD; b) Shaker on the slab; c) Detail of the LVDT and force sensor.

### 4.3 Experimental verification of the semi-active system

The objective of the laboratory tests was to validate the functioning of the semi-active TMD comparing the numerical predictions with the experimental results, as well as to verify the effectiveness of the control device in reducing the slab vibrations. In this case, given the natural frequency of the structure to be controlled of 3.5 Hz, the use of an out-of-tuning semi-active TMD of frequency 2.06 Hz is a challenge.

At a first stage, a numerical model of the coupled system slab plus semi-active TMD was developed. Figure 6a) includes a representation of the FRF of the slab response where a first peak can be seen associated with the functioning of the TMD and the second one representing the large amplitude motion of the slab. If the TMD was properly tuned to the natural frequency of the primary structure, two low picks with same amplitude would characterize the system response. However, the TMD is not tuned and the peak of the structural response is not damped. To correct this problem, the semi-active system was switched on guided by the control law indicated in equation (1). In this case, $\alpha_1$ was permanently set to $\alpha_1=1$, $\alpha_2$ assumes values in order to enable the semi-active system to correct the motion of the TMD mass once in a cycle, and $\alpha_3$ follows the procedure indicated in section 5.2. $c_{min}$ corresponds to the passive functioning of the TMD and $c_{max}$ was imposed by applying an electric current of 0.5 A to the MR damper. As a result, Figure 6a) also includes the numerical prediction of the effect of this control system, as well as the respective experimental evaluation at specific vibration frequencies. It can be observed that the semi-active TMD is able to attenuate vibrations in a frequency away from its passive tuning. In addition, the remarkable approximation between numerical predictions and experimental results can be noted, leading to the conclusion that the proposed control system may be effectively used in practical cases of actual structures.

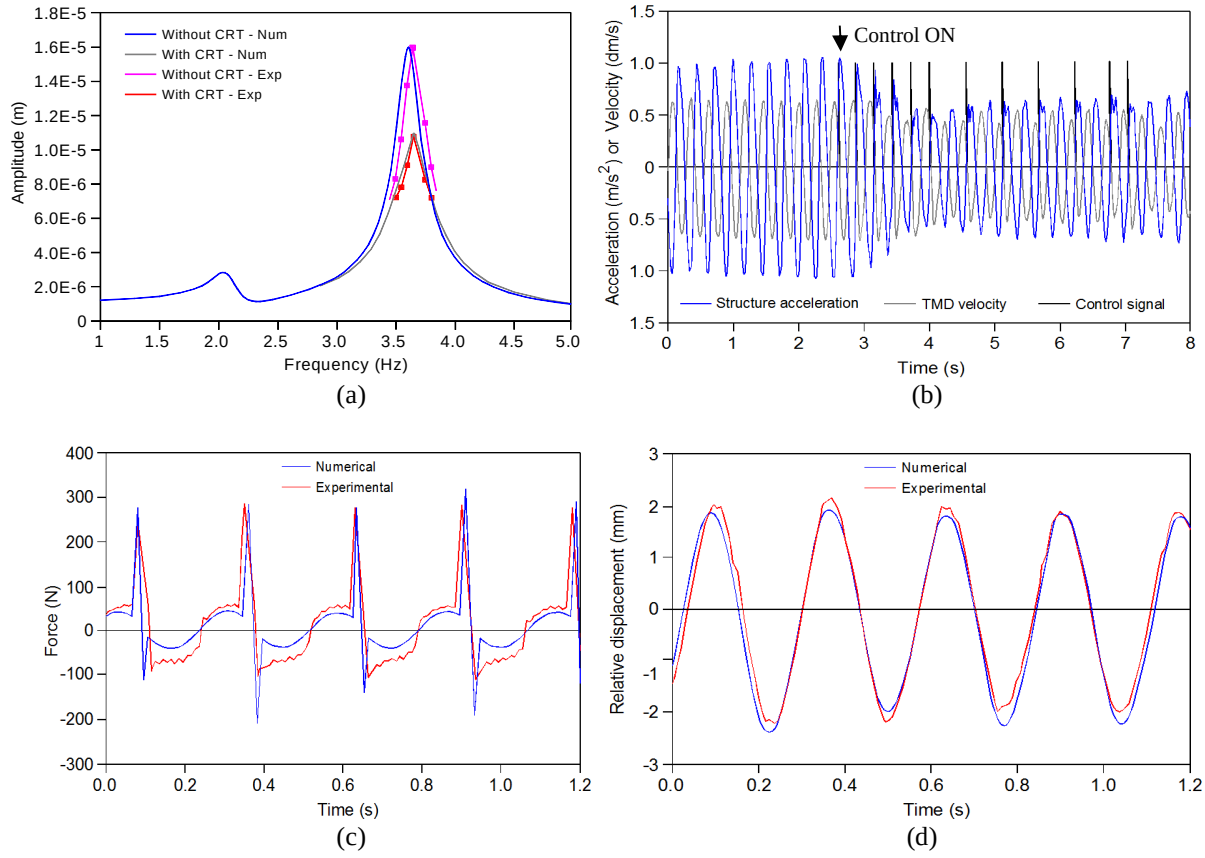


Figure 6: System with and without semi-active control: a) FRFs curves; b) Time signals; c) Force measured at the damper; d) Measured relative displacement.

To show the effect of the control action, Figure 6b) represents the time signals of the acceleration of the structure and the velocity of the TMD mass. In this case, a resonant excitation frequency of 3.6 Hz was applied, as the control was switched on at a certain time. Before the control, the two signals are not in opposite phase, and, after switching the control on, they are compelled to have opposite phase angles corresponding to an adequate functioning of a damping system [4]. To achieve this, impulsive control forces correct the motion of the TMD at specific moments in certain maximum relative positions. Figure 6c) depicts a sample of the time signal of the control force applied by the MR damper, where the peaks of the force may ascend, in this case, to around 300 N. On the other hand, Figure 6d) represents the corresponding relative displacement between the structure and the TMD mass, where it can be seen that the control action is produced when the relative displacement is maximum as required by the control law [4]. Again, in both previous figures there is a good approximation between the experimental measurements and numerical predictions, which allowed gaining confidence in the function of the control system and its further implementation in the footbridge.

### 4.4 Evaluation of time delay

Time delay is an undesirable effect in control systems which may arise from several stages of the control process, particularly during system measurement, control force computing and mechanical actuation. Time delay may be compensated by introducing some anticipation capability to the control system in such a way that the control inputs are calculated taking into account the predicted time needed for the effective implementation of the control action. However, this process usually introduces some complexity to the control algorithm which was avoided in this application. Besides, Civil Structures are characterized as having low vibrating frequencies in the range of interest (typically below 10Hz), which reduces the time delay effects.

In order to evaluate this parameter in the actual semi-active control system, a test consisting of measuring the electrical current that feeds the MR damper and the corresponding developed force when the control signal is switched on was performed. Figure 7 shows a normalized representation of these signals in order to be possible to compare them in one graph. The control signal represents the control order given by the controller, which takes some time to be implemented. At least, one control loop is always necessary to see the control effect. However in this case, the system took longer to react. The current amplifier takes some time to respond to the control input, and takes some time to reach full power. On the other hand, the MR damper seems to respond quite fast to the electrical signal.

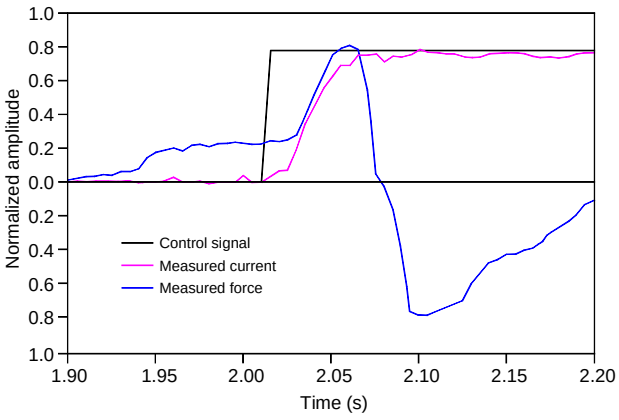


Figure 7: Evaluation of time delay.

When observing Figure 7, it is not possible to identify the exact value of the time delay. Instead, it can be said that the damper takes about 10 ms to respond to the control order, it needs about 20 ms to implement 50% of the total force, 30 ms to implement 75% of the total force and takes about 40 ms to reach the total control force. As explained in reference [4], taking into account that the control action does not need to be a complete blocking of the TMD mass, the time delay in this case may be estimated between 20 and 30 ms. In the previous comparisons between experimental measurements and numerical simulations, time delay was set at 20 ms, which led to good approximations between them.

Regarding the expected loss of efficiency of the semi-active system in controlling vibrations in the footbridge due to time delay, and taking into account that the critical frequencies are in the range of 2 – 2.4 Hz, the corresponding delay angle ranges from 14 to 17 degrees. According to reference [7], in structures with 1% damping ratio, delay angles of that order lead to a loss of efficiency of the semi-active control system less than 6% when comparing the amplitude of the controlled response with the uncontrolled one. Because this loss of efficiency is relatively low, it was decided to assume it and keep a simple control law instead of trying to compensate time delay.

## 5 INSTALLATION OF THE SEMI-ACTIVE SYSTEM IN FEUP FOOTBRIDGE

### 5.1 Implementation of the controller using NI hardware and software

The implementation of the semi-active system in the footbridge requires the installation of a local controller able to command the MR damper according to the selected control law. As a first option, it was decided to use National Instruments hardware and Labview software to manage all control process. Figure 8 shows a layout of how data flows. The control algorithm is running in a computer inside the building close to the bridge, which, in turn, is connected to an Ethernet cDAQ chassis located in a small box at the abutment of the structure. That connection uses a powerline device to establish communication between both pieces of equipment by means of the power grid, given that it was not possible to install a direct Ethernet cable between them. The MR device is then controlled from the NI chassis by inducing electrical power to the damper. Although somewhat complex, the control loop takes less than 10 ms to complete a turn, which has conducted to the establishment of a fixed-rate loop of 100 Hz.

The control algorithm only needs to receive feedback of the structure acceleration and TMD velocity to generate the ON/OFF control signal. For this purpose, 2 MEM accelerometers were used to measure the system response, as the velocity of the TMD was obtained by integrating the acceleration signal. In addition, several other variables are measured and recorded by a parallel application intended to monitor the control process. In this case, files containing periods of 10 minutes make a complete record of the bridge response and control actions, including the TMD velocity, the control order (1 or 0), the force in the MR damper, the temperature of the external surface of the damper, the relative displacement between the structure and the TMD, and the electrical current applied to the MR damper. This last variable is measured by a non-contact LEM sensor which is also connected to a safety circuit to prevent MR damper damage in case of system failure. If the system blocks or the electrical current is excessive according to the manufacturer recommendations, a relay turns off the damper and the TMD switches to passive mode.

### 5.2 Implementation of the controller using a microcontroller

The previous described control system operated during September 2014 and January 2015. Since then, given the potentialities and popularity of microcontrollers, the control system was substituted by a device of this type. The main advantage of this is the simplicity of the controller compared to the previous solution. In addition, there is a significant saving of power consumption. The controller may also be located very close to the TMD, reducing the length of the cables and the noise in sensors. This way, the controller receives the signals from the MEMs installed in the structure and the TMD, integrates the acceleration of the TMD to obtain velocity and generates the control signal according to the control law indicated in section 3.1.

The National Instruments hardware and software was also used in the recording of all previously indicated control variables. Therefore, it is possible to verify all steps in the control process and to monitor the control system itself.

## 6 EVALUATION OF THE CONTROL SYSTEM PERFORMANCE

### 6.1 Evaluation of the reduction of vibration levels over last few years

The effect of the control system in reducing vibration of the footbridge may be evaluated by several methods. One possible way is to obtain the FRF curve of the structure with and without control, as done in laboratory tests described in section 4.3. However, the 2$^{nd}$ and 4$^{th}$ vibration modes under control have 55 and 36 ton of modal mass, respectively, which cannot be excited with the existing means at the laboratory due to the amplitude of required dynamic force. Another possibility involves turning to tests with pedestrians or groups of pedestrians. In this case, the amplitude of the structure response is not the same for several tests of the same type, due to the variability of the excitation applied by the pedestrians. Therefore, the effect of the control system cannot be accurately quantified this way.

On the other hand, the dynamic monitoring system of the FEUP footbridge was installed in 2009 and, since then, has been measuring the accelerations at 4 critical sections, which may be used to evaluate the vibration levels over the last 7 years. This analysis may include the period when no control system was installed in the footbridge, as well as in the period that the TMD worked in passive mode, and in the period when the TMD worked in semi-active mode.



Figure 8: Layout of control system using National Instruments hardware and software.

The 4 critical sections that are being monitored by the dynamic monitoring system are located approximately at the anti-nodes of the structure's main vibration modes. Section S1 is where the TMD was positioned, which is close to the 1/3$^{rd}$ span of the FEUP side, and S2 is at mid-span on the same side. Sections S3 and S4 are located at mid-span and 1/3$^{rd}$ span of the canteen side, respectively. The location of all instrumented sections is schematically depicted in Figure 9.

The evaluation of the structure's vibration levels during last few years may be achieved by analysing Figure 10. This figure represents the measured maximum accelerations at the 4 sections of the deck from 2010 to 2016. Each dot on the graphs corresponds to an occurrence of a vibration caused by the crossing of pedestrians. It is important to mention that each occurrence was selected taking into account several criteria: *i*) time signals are filtered to remove frequency contributions above 5Hz, ensuring that only harmonic vibrations of the first vibration modes are considered; *ii*) the signal should be clearly dominated by a single frequency, in order to facilitate the construction of graphs of this type; *iii*) each occurrence should have a signal that has a first phase where the amplitude increases as pedestrians excite the structure, and then the signal reaches a maximum amplitude before it starts to decrease; *iv*) the maximum amplitude is identified by the maximum acceleration of the signal just described; *v*) the frequency is calculated taking into account the average of the periods occurring between consecutive local peaks (if the period is not constant unless a small error the signal is rejected); *vi*) only amplitudes higher than 0.2m/s$^2$ were considered, which are deemed to be representative of the higher levels of vibration.

Taking into account the timing of the implementation of control system in the footbridge, it is noted that the passive TMD was installed in early 2013, meaning that in 2010, 2011 and 2012 the structure is considered uncontrolled (first 3 columns of graphs in Figure 10). Then, the semi-active TMD was activated in September 2014, meaning that in 2013 and in a significant part of 2014 the footbridge may be considered passively controlled by that device (4$^{th}$ and 5$^{th}$ columns of graphs). After that, the footbridge is controlled by the semi-active TMD (last 2 columns of graphs). The organization of the graphs in 4 lines of figures aims to depict the vibrations in the 4 critical sections of the deck (S1 to S4).

From the analysis of Figure 10, even though a drastic reduction of the vibration levels has not been observed after the implementation of control systems, a progressive reduction of the vibrations can be noted over time, especially with regard to section S1 to S3. This is because of the influence of the 2$^{nd}$ and 4$^{th}$ vibration modes in these sections, which are attenuated by the control devices. In the opposite situation is S4, where no significant reduction is observed. This is because S4 is dominated by the contribution of a local vibration mode (3$^{rd}$ mode) of 2.28Hz frequency, which has a very limited modal component in the location of the TMD.

One possible way to quantify the effect of the control system on the structure is to calculate the number of occurrences of maximum vibration levels above a certain limit, relative to the total number of occurrences observed in each section of the deck from 2010 to 2016. Graphs of this type allow estimating the concentration of occurrences in higher vibration levels, which is an indicator of how often high accelerations occur in the structure.

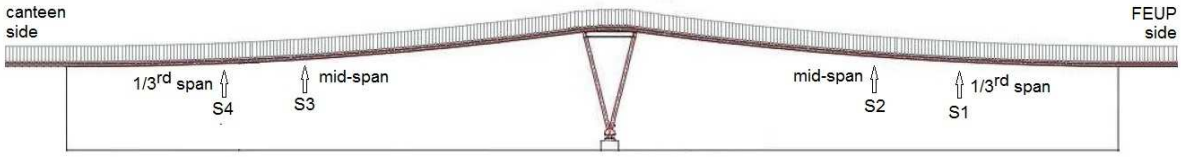


Figure 9: Location of measurement sections (S1 to S4).

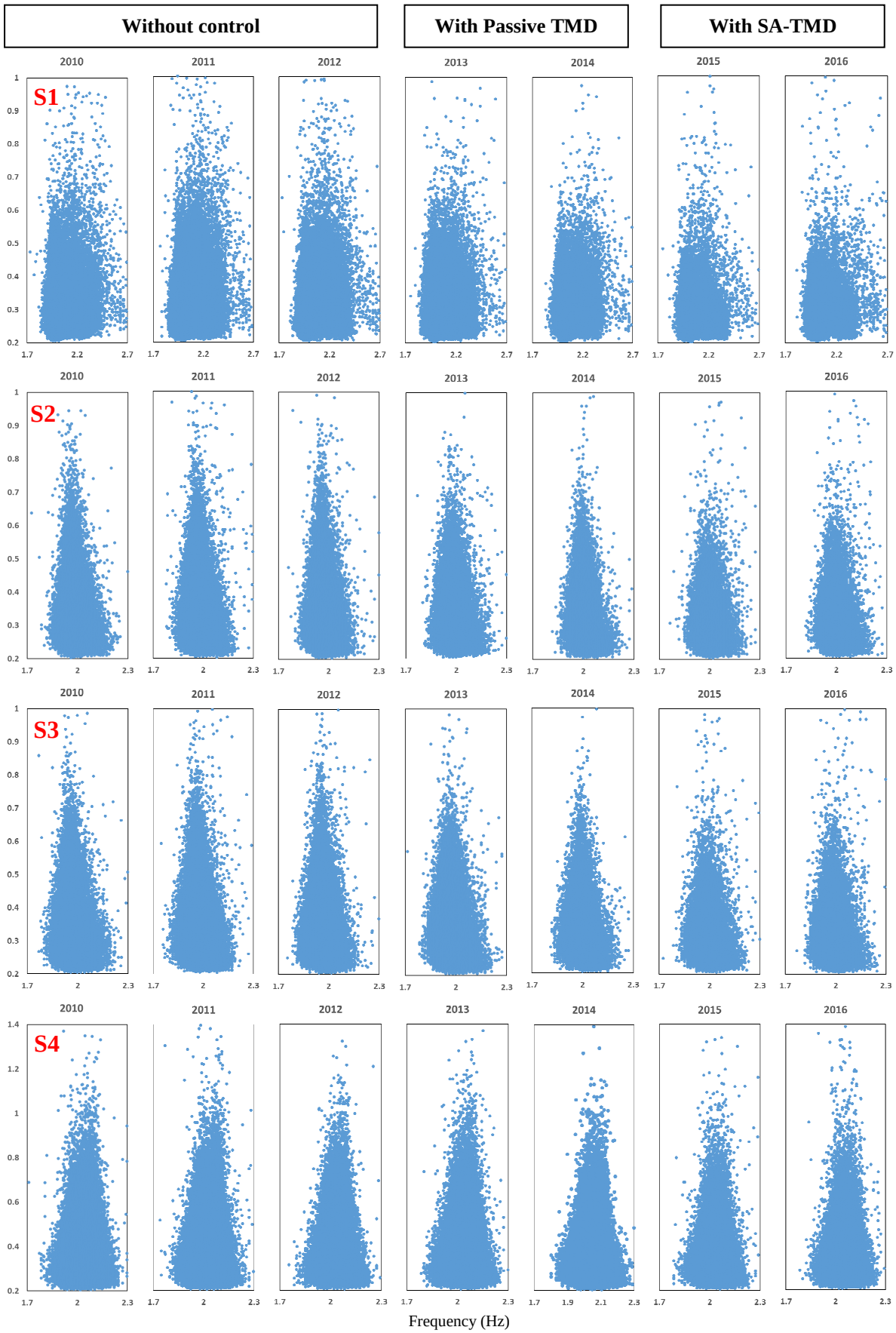


Figure 10: Maximum vibration levels (in m/s$^2$) at sections S1 to S4 of the footbridge from 2010 until 2016.

For this purpose, Figure 11 represents this parameter obtained by considering vibration levels above 0.4 m/s$^2$ and Figure 12 above 0.5 m/s$^2$. The limit of 0.4 m/s$^2$ was defined according to reference [3] where the TMD shows clear functioning above this threshold after unblocking. On other hand, the limit of 0.5 m/s$^2$ defines a vibration level above which vibrations are considered in many guidelines, such as Sétra [8], as not providing maximum comfort to pedestrians, thus being the main target of the control systems.

The analysis of both Figures 11 and 12 allows establishing a tendency in the maximum amplitude of the vibrations over past years. From 2010 to 2012, the footbridge was not controlled. Therefore, this period is characterized by higher levels of vibration. The implementation of the TMD clearly led to a reduction of vibrations during its functioning in 2013 and 2014. It should be emphasized that the passive device was not optimally tuned to any natural frequency. Even in this situation, it was able to produce an attenuation of vibrations by conditioning the contribution of the structural natural frequencies close to the TMD frequency, as studied in reference [3]. Figures 11 and 12 also suggest that, after implementing the semi-active system, during 2015 and 2016, the footbridge's vibration levels were further attenuated, fulfilling the objective of the semi-active system in correcting tuning problems in the passive system.

The observed reduction of vibrations over time could not be caused by any other external situation because of the following facts: *i*) the number of students during the considered period remained practically the same (about 7000 registered students); *ii*) the vibration levels of section S4, which is not significantly affected by the control system, also remained practically the same. If the reduction of vibrations was a global phenomenon, S4 would also reflect that, which is not the case. A small reduction of the vibrations in S4 during the last couple of years may even be attributed the ability of the semi-active to perform multimodal control, despite considering a limited modal contribution of the 3$^{rd}$ vibration mode in the section where the TMD is installed.

Despite the effect of the control system in reducing the vibration in the footbridge, it must be mentioned that the higher vibration levels occur at section S4, where the TMD has quite a limited effect. To reduce these vibrations, it would be necessary to install another local TMD in the other span, which is hampered by the difficult access to section S4 caused by the intense car traffic existing in the main street just below that place. However, the objective of installing the TMD was not to reduce the structure's overall behaviour, but, rather, to observe the effect of the installation of a passive and then a semi-active system on a structure, which was widely achieved.

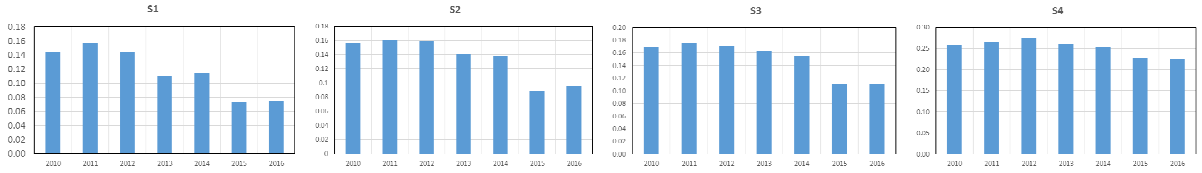


Figure 11: Percentage of occurrences of maximum vibration levels above 0.4 m/s2 relative to the total number of occurrences

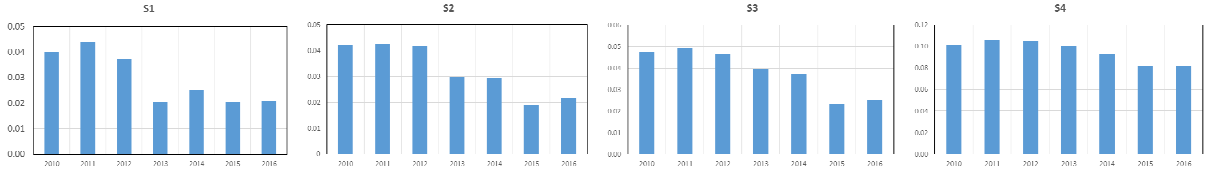


Figure 12: Percentage of occurrences of maximum vibration levels above 0.5 m/s2 relative to the total number of occurrences.

### 6.2 Power consumption

One of the most important features of semi-active systems is related to power consumption. Compared to active systems, they require much less power and much less sophisticated actuation systems, so much so that semi-active systems are indicated as being able to run on batteries. In order to evaluate this aspect in the semi-active control system of FEUP footbridge, this section exposes detailed information about the implementation of the control forces. For this purpose, one complete month was analysed. In this case, October 2016 was considered as corresponding to a period of classes for all students, who cross the footbridge particularly at lunch time.

The semi-active system commanded by Phase Control law applies a daily average of 232 impulses of electric current to the MR damper with a mean duration time of 41.9 ms, meaning that the actuation system is activated, on average, 9.72 s per day. Each impulse applied to the MR damper requires 0.8 Amps of electric current with a voltage of 12 V, that is, 9.6 W of power. Considering 6 months (180 days) of the operation of the actuation system in the described conditions, it would require a 12 V battery with a capacity of 0.39 Ah or 4.66 Wh, which is really a very low power. It is noted that this is the power needed only for the MR damper. The power required for the entire control system, including structure measurement by accelerometers and the functioning of the microcontroller is not included.

## 7 CONCLUSIONS

This paper describes the implementation of a semi-active control system used to reduce vibrations in a slender footbridge located at the FEUP campus. For this purpose, a semi-active Tuned Mass Damper including an MR damper was developed, which is controlled by Phase Control law. At a first stage, the TMD was installed in the footbridge working in passive mode. However, due to the existence of several critical frequencies around 2 Hz, the TMD could not be tuned to all these frequencies, which reduced the control efficiency. To solve this problem, the semi-active mode of the TMD was activated in order to correct the tuning of the device to the structure's vibrating frequency, enabling the possibility of performing multimodal control.

Before being installed in the footbridge, the semi-active TMD was tested in the laboratory, enabling the identification of its main dynamic characteristics, including time delay. These tests allowed concluding that the control device was working as numerically predicted, which has encouraged the implementation of the device in the actual structure. Two types of controllers were implemented. At a first stage, the system was controlled using National Instruments hardware and software, and, secondly, it was replaced with a microcontroller specially designed for this application, which is much simpler than the former.

The effect of the control system in reducing vibrations was evaluated over the past 7 years, using the data provided by the dynamic monitoring system installed in 2009. The analysis of the vibration levels of the structure allowed observing a tendency in the reduction of the peak accelerations of some sections of the deck after the installation of the passive TMD, which were even more attenuated after the activation of the semi-active device. This fact demonstrates the potentialities of a semi-active system of this type, which increased the control efficiency and enabled the performing of multimodal control without introducing an excessive complexity in the control system. In addition, the power requirements of such a control system were evaluated. It was concluded that a battery of 12 V voltage with a capacity of 0.39 Ah or 4.66 Wh was sufficient to supply power to the MR damper during 180 consecutive days, given the actual usage of the footbridge during classes.

## ACKNOWLEDGMENTS

This work was financially supported by Project POCI-01-0145-FEDER-007457 - CONSTRUCT - Institute of R&D In Structures and Construction funded by FEDER funds through COMPETE2020 - Programa Operacional Competitividade e Internacionalização (POCI) – and by national funds through FCT - Fundação para a Ciência e a Tecnologia – in the context of the research project PTDC/ECM-EST/0535/2012 - Development of a smart damping system to reduce vibrations in Civil Engineering structures.

## REFERENCES

[1] A. Preumont, Vibration Control of Active Structures – An introduction, *Kluwer Academic Publishers*, 1997.

[2] F. Casciati, G. Magonette and F. Marazzi, Technology of Semiactive Devices and Applications in Vibration Mitigation, *John Wiley & Sons, Ltd*, 2006.

[3] C. Moutinho, A. Cunha, W. Hu and E. Caetano, Analysis of the behaviour of a Tuned Mass Damper installed in a stress-ribbon footbridge, *9th International Conference on Structural Dynamics (Eurodyn 2014)*, Porto, 2014.

[4] C. Moutinho, Testing a simple control law to reduce broadband frequency harmonic vibrations using semi-active Tuned Mass Dampers, *Smart Materials and Structures*, vol.24, nr5, 2015.

[5] E. Caetano and A. Cunha, Experimental and Numerical Assessment of the Dynamic Behaviour of a Stress-ribbon Footbridge, *Structural Concrete, Journal of FIB*, 5, No 1, pp.29-38, 2004.

[6] C. Moutinho, A. Cunha and J. Martins de Carvalho, Implementation of a semi-active tuned mass damper to reduce vibrations in a slender footbridge, *7th ECCOMAS Thematic Conference on Smart Structures and Materials (Smart 2015)*, Azores, 2015.

[7] F. Ferreira, Semi-active control of Civil Engineering Structures, *PhD dissertation*, FEUP, 2015.

[8] SÉTRA, Guide méthodologique – Passerelles piétonnes – Évaluation du comportement vibratoire sous l'action des piétons, 2006.

COMPDYN 2017
6th ECCOMAS Thematic Conference on
Computational Methods in Structural Dynamics and Earthquake Engineering
M. Papadrakakis, M. Fragiadakis (eds.)
Rhodes Island, Greece, 15–17 June 2017

# AN APPROACH TO THE DYNAMIC CONTROL OF VIBRATIONS IN STRUCTURAL SYSTEMS SUBJECT TO EARTHQUAKES

**Ileana Corbi[1], Ottavia Corbi[2], and Francesca Tropeano[3]**

[1] Department of Structural Engineering and Architecture, University of Naples "Federico II", Italy
e-mail: ileana.corbi@unina.it

[2] Department of Structural Engineering and Architecture, University of Naples "Federico II", Italy
e-mail: ottavia.corbi@unina.it

[3] Department of Structural Engineering and Architecture, University of Naples "Federico II", Italy
e-mail: francesca.tropeano@unina.it

**Keywords:** Structural Dynamics, Dynamic Control, Algorithm, Response Mitigation.

**Abstract.** *The mitigation of the structural response under seismic action can be achieved , as well known, by introducing proper variations to the mechanical parameters of the structural system through the recourse to dynamic control strategies. In order to pursue some optimality in the setup of the problem, sometimes it is necessary to tune the coefficients of the motion equation in a measure that might result not compatible with the characteristics of current structural materials, thus pushing towards active control techniques, where the proper selection of the algorithm is of fundamental importance.*

*As concerns the performance of base-isolation (BI) devices in mitigating inertia forces due to intense earthquakes, it strongly depends on the proper calibration of the own frequency of the BI system, that should be designed on the basis of the dynamic characteristics of both the structural system and the expected disturbance. Nevertheless the passive mode may fail, without guaranteeing the real effectiveness of the device.*

*The best improvement would, thus, require a resettlement of the problem and, possibly, the transformation into a more complex coupled system where some active component is allowed in order to refit the system to its optimality when required.*

*In the paper the design of such system is then proposed in order to respond to major requirements about the performance of the control action, with an active component selected in way to yield a powerful and simple approach, which appears particularly effective for mitigation of dynamic earthquake-induced motion.*

## 1 INTRODUCTION

The research interest in the field of structural control of dynamic vibrations mainly relies upon the need of protecting the existing constructions or the new ones from damages caused by earthquakes, which might result even in the global collapse of the structure or give rise to local crises of parts of the structure.

Minor damages refer to decrease or loss of serviceability of the structure after the event, and disease/malfunctions during the occurring of the event because of significant displacements/accelerations, exceeding some thresholds.

The problem is deeply felt because of the wide seismic areas characterized by high earthquake hazard, spread all over the world. Additionally, the significant seismic risk in some geographic regions often superposes to an high vulnerability of the structures in the area to seismic events.

The last decades witness a large effort both from the scientists and from the factory, for developing a variety of systems, devices, technologies, reinforcement techniques devoted to increase the degree of prevention of structural damages against strong motions in civil structures. Also infra-structural systems and constructions with monumental/artistic/historical value, besides other class of special objects requiring preservation against dynamic motion, such as artistic objects in museums, statues, ancient columns, electrical equipment and so on have been attracting special attention for preserving their integrity.

Approaches to the problem of attenuation of the structural response vary from the setup of control devices for reducing the structural vibrations [1]-[10] to the development of reinforcement techniques, also involving new composite materials [11]-[14], for increasing the dynamic strength of the structure, even in masonry constructions [15]-[19].

Under the theoretical profile, they include the setup of analytic methods for the development of control algorithms and the compensation of errors and noises possibly occurring in active control systems, as well as the design of control systems, actuating and sensing devices also with reference to semi-active systems founded on the adoption of special smart materials, and coupling of passive or semi-active systems with active systems in integrated hybrid systems.

With reference to composite reinforcements, mainly preferred in existing or ancient constructions, theoretical and numerical tools have been developed for the setup and analysis of the mechanical model of the composite material and body, and its coupling with the structural material, as well as for the analysis and forecast of the unreinforced and reinforced structure, and the design of the reinforcement provision and the identification of the areas needing the adoption of the reinforcement.

On the other side, experimental investigations have been widely developed on structures scaled from the small dimension up to full/real scale case, setting up laboratory facilities and machines, such as shaking tables, as well as instruments for the real scale tests to be used in situ. In the following one presents some researches in course of execution in the field of structural control of seismic vibrations.

## 2 MAIN ISSUES AND GENERAL SETTLEMENT OF THE PROBLEM

Many researches and real-scale applications do refer to the mitigation of structural vibrations through the recourse to Base Isolation (BI) devices.

The design of BI systems is usually aimed at two primary objectives: on one side, to move far from the main frequency range of the expected ground motion the dominant frequencies of the isolated structure; on the other side, to reduce the energetic transmission of the dynamic

input, by realizing a damping filter and interrupting the continuity between the surface layers of the soils and the foundation of the structure.

The performance of base-isolation devices in mitigating inertia forces due to intense earthquakes thus strongly depends on the proper calibration of the isolation devices own frequency, that should take into account both the dynamical characteristics of the superstructure and the frequency content of the expected disturbance.

In the paper a BI design approach has been developed for optimally tuning the parameters of a seismic isolation device accounting for either the structure dynamic characters or the ground input expected macro-properties. In the approach one introduces a measure of the energy transmitted to the superstructure, compared to the energy filtered by the isolator, which is given a closed-form. An optimization procedure is then set up by searching for the optimal tuning of the BI in order to minimize the structural response and, in the meanwhile, to keep bounded the BI energy absorption.

Further improvement of the performance of the base-isolation system may be obtained by turning the passive isolator into an hybrid one. This is accomplished by coupling the passive isolator with an actuation device introducing an active force aimed at counteracting the incoming excitation. A new constrained optimization strategy is formulated to this purpose, where the active device is re-tuned in order to get the best performance of the hybrid combined system. The proposed control algorithm basically acts in the frequency environment managing the analytic expressions of the passively and actively controlled response gain functions, and achieving a proper distribution of the control effort over the frequency ranges where it is needed.

## 3 HYBRID STRATEGY BASED ON AN EQUIVALENT-MODEL SETUP

### 3.1 The BI structural system

As concerns to the overall formulation mentioned in the previous Sect.2, with reference to a mdof structural shear frame, in order to improve the overall performance of the control system and effectively counteracting the incoming dynamic excitation at the base of the building, one introduces in the dynamic equilibrium equation the active term $\mathbf{w}(t)$ in such a way to increase the reliability of the overall BI system

$$\begin{cases} \mathbf{M}\ddot{\mathbf{y}}(t)+\mathbf{C}\dot{\mathbf{y}}(t)+\mathbf{K}\mathbf{y}(t)+\mathbf{w}(t)=\mathbf{C}\dot{\mathbf{u}}_g(t)+\mathbf{K}\mathbf{u}_g(t)=\mathbf{f}^*(t) \\ \mathbf{y}(0)=\mathbf{0} \\ \dot{\mathbf{y}}(0)=\mathbf{0} \end{cases} \tag{1}$$

where $\mathbf{M}$ denotes the n×n mass diagonal matrix of the structural system, $\mathbf{C}$ and $\mathbf{K}$ denote the n×n symmetric positive-definite matrixes of damping and stiffness respectively.

Moreover $\mathbf{y}(t)$, with its first and second time derivatives marked by the superimposed dots, $\dot{\mathbf{y}}(t)$, $\ddot{\mathbf{y}}(t)$, denote respectively the n×1 vectors of the storey drift, velocity and acceleration. The vector of base acceleration $\ddot{\mathbf{u}}_g(t)$, with the related base velocity $\dot{\mathbf{u}}_g(t)$ and displacement $\mathbf{u}_g(t)$, is given in the form

$$\begin{cases} \mathbf{u}_g(t) = u_g(t)\mathbf{1} \\ \dot{\mathbf{u}}_g(t) = \dot{u}_g(t)\mathbf{1} \\ \ddot{\mathbf{u}}_g(t) = \ddot{u}_g(t)\mathbf{1} \end{cases} \tag{2}$$

with **1** the unit n×1 vector.

After denoting by $(\cdot)_1$ the quantities relevant to the isolation storey, let consider the active control force $w_1(\omega,t)$ acting at the isolation level, with the related control vector

$$\mathbf{w}(\omega,t) = q(\omega)\mathbf{B}\dot{\mathbf{y}}(t) \tag{3}$$

where $q(\omega)$ denotes the control coefficient to be suitably designed and depending on the frequency variable $\omega$, and **B** is a suitable matrix governing the distribution of the control action and the dependence on the response variables.

### 3.2 Selection of the active component

With reference to the control expression in Eq. (3) and by referring to an equivalent-based-model strategy allowing some simplification of the mdof problem, the control parameter $q(\omega)$ is to be selected according to some optimization criterion in order to pursue a predefined set of objectives.

In the specific case, as specified in the above, the primary objective consists of improving the performance of the BI system in terms of mitigation of structural vibrations, while containing the active component at its minimum. The choice of a suitable control strategy designed in the frequency domain can successfully lead to an effective device, since one may employ all the response data monitored up to the instant of control application and control the single harmonics, also keeping contained the active control component.

The definition of $q(\omega)$ is then pursued by solving an optimum problem where one aims at minimizing the employed control force, while keeping the isolator absolute acceleration under a prefixed percentage (defined through the function $\alpha(\omega)\in[0,1]$) of the uncontrolled isolator acceleration $\ddot{y}_{o,1}(\omega|0)$.

Therefore, after introducing the excitation and response frequency functions, in the frequency domain one has

$$w_1(\omega,t) = w_{o,1}(\omega|q)e^{j\omega t} = q(\omega)\dot{y}_{o,1}(\omega|q)e^{j\omega t} \tag{4}$$

with

$$w_{o,1}(\omega|q) = -jq(\omega)H_{is}(\omega|q)\ddot{u}_{go,eq}(\omega|q) \tag{5}$$

where $H_{is}(\omega|q)$ is the BI gain in the equivalent model and $\ddot{u}_{go,eq}(\omega|q)$ the relevant excitation .

The final problem is then set in the form

$$\begin{cases} \text{Find} & w_{o,1}(\omega \mid q) = \min \\ \text{Sub} & \ddot{y}_{o,1}(\omega \mid q) \le \alpha(\omega)\ddot{y}_{o,1}(\omega \mid 0) \end{cases} \tag{6}$$

After a number of further developments, one may get the expression of the optimal control parameter in the form

$$q(\omega) = -c_1 + \frac{1}{\omega}\sqrt{\frac{k_1^2 + \omega^2 c_1^2}{\alpha^2(\omega)\ddot{H}_{is}^2(\omega|0)}\frac{\ddot{u}_{go,eq}^2(\omega \mid q)}{\ddot{u}_{go}^2(\omega)} - \left(k_1 - m_1\omega^2\right)^2} \tag{7}$$

which represents the optimally tuned shape at the considered frequency, which is then reassembled in order to fit the forcing function.

### 3.3 Performance of the control system

A numerical investigation is developed on a 5-storey shear-frame structure subject to a white noise base acceleration with zero mean and unitary variance, which is scaled in such a manner to have a peak acceleration of 0.4g, with the first floor coinciding with the BI-level, shows the effectiveness of the hybrid system with comparison to the passive one.

In Figure 1, as an example concerning the performance of the control system, one reports a sample drift diagram vs the time variable referred to the BI floor, showing the significant response reduction for the coupled optimized control system.

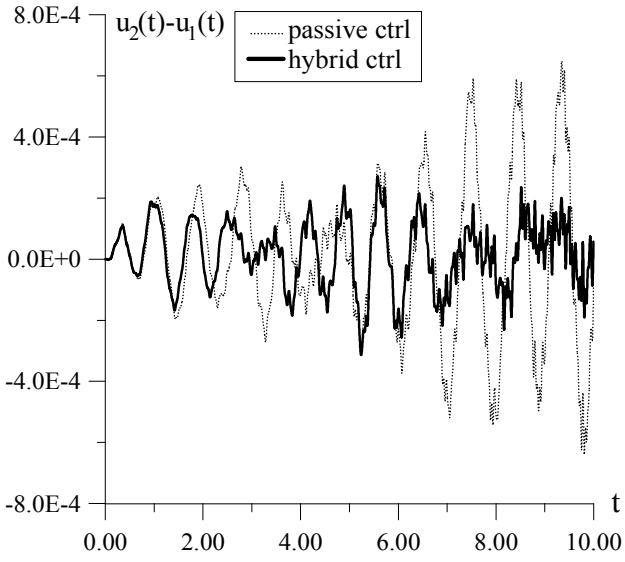


Figure 1: Inter-storey drifts of the structural frame equipped with the passive or hybrid BI device.

## 4 CONCLUSIONS

Passively controlled structural systems may exhibit a rare capability in resisting dynamic actions under adverse special or unexpected conditions. In the paper improvements of the overall performance of a passive BI system are obtained by introducing some additional control device, coupling different technological solutions and moving to mixed systems. In the specific case, the performance of a base isolation system is increased by embedding in the control layout an active device, controlled by a properly designed control algorithm.

## 5 ACKNOWLEDGEMENT

The present research has been supported by the Dept of Civil Protection of the Italian Government through the ReLuis Pool (DCP/ReLUIS 2017).

## REFERENCES

[1] Baratta, A., Corbi, I., Corbi, O., Algorithm design of an hybrid system embedding influence of soil for dynamic vibration control, *J. Soil Dynamics and Earthquake Engineering*, 74, 79-88 (2015).

[2] Baratta, A., Corbi, I., Corbi, O., Mastorakis, N., Strategies for the protection from structural failures under seismic events, *International Journal of Mechanics*, 9, 69-75 (2015).

[3] Corbi, I., Corbi, O., Macro-mechanical modelling of pseudo-elasticity in shape memory alloys for structural applications, *J. Acta Mechanica*, 1-9, DOI: 10.1007/s00707-016-1624-3 (2016).

[4] Baratta, A., Corbi, O., Dynamic Response and Control of Hysteretic Structures, Intern. *Journal of Simulation Modeling Practice and Theory*, 11, 371-385 (2003).

[5] Constantinou, M.C., Whittaker, A.S., Kalpakidis, Y., Fenz, D.M., Warn, G.P., Performance of Seismic Isolation Hardware under Service and Seismic Loading; Technical Report MCEER-07-0012; *Multidisciplinary Center for Earthquake Engineering Research*, State University of New York at Buffalo: Buffalo, NY, USA (2008).

[6] Corbi, I., Rakicevic, Z.T., Shaking table testing for structural analysis, *International Journal of Mechanics*, 7(4), 459-466 (2013).

[7] Corbi, O., de Barros, R.C., Seismic protection of civil buildings by visco-elastic magneto-rheological fluids, *International Journal of Mechanics*, 7(4), 518-525 (2013).

[8] Corbi, O., Zaghw, A.H., Properties and design of dissipative viscorecentring SMA members for civil structures, *International Journal of Mechanics*, 7(3), 285-292 (2013).

[9] Corbi, O., Zaghw, A.H., Elattar, A., Saleh, A., Preservation provisions for the environmental protection of egyptian monuments subject to structural vibrations, *International Journal of Mechanics*, 7(3), 172-179 (2013).

[10] Sang-Hoon O., Sang-Hoon S., Sang-Ho L., Hyung- Joon K., Seismic Response of Base Isolating Systems with U-Shaped Hysteretic Dampers, *Int J Steel and Structures*, 12(2), 285-298 (2012).

[11] Baratta, A., Corbi, I., Topology optimization for reinforcement of no-tension structures, *J. Acta Mechanica*, 225 (3), 663-678 (2014).

[12] Baratta, A., Corbi, O., An approach to the positioning of FRP provisions in vaulted masonry structures, *J. Composites Part B: Engineering*, 53, 334-341 (2013).

[13] Corbi, I., FRP reinforcement of masonry panels by means of c-fiber strips, *Journal Composites Part B*, DOI: 10.1016/j.compositesb.2012.11.005 (2012).

[14] Corbi, I., FRP Composites Retrofitting for Protection of Monumental and Ancient Constructions, *Open Construction and Building Technology Journal*, 6, 361-367 (2012).

[15] Corbi, I., Corbi, O., Analysis of bi-dimensional solids with internal unilateral constraint coupled to structural elements with different degree of connection, *J. Acta Mechanica*, 228(2), 607-616 (2017).

[16] Corbi, I., Corbi, O., Theorems for masonry solids with brittle time-decaying tensile limit strength, *J. Acta Mechanica*, 228(3), 837-849 (2017).

[17] Corbi, I., Corbi, O., F. Tropeano, Stability assessment of an historical masonry bridge through the LA kinematic theorem for NT structures, *Int. J. Mechanics*, 10, 305-311 (2016).

[18] Baratta, A., Corbi I., Corbi, O. , Stability of evolutionary brittle-tension 2D solids with heterogeneous resistance, *J. Computers and Structures*, 174, 133-138 (2016).

[19] Baratta, A., Corbi, I., Corbi, O., Analytical Formulation of Generalized Incremental Theorems for 2D No-Tension Solids, *J. Acta Mechanica*, 226 (9), 2849-2859 (2105).

COMPDYN 2017
6th ECCOMAS Thematic Conference on
Computational Methods in Structural Dynamics and Earthquake Engineering
M. Papadrakakis, M. Fragiadakis (eds.)
Rhodes Island, Greece, 15–17 June 2017

# DYNAMIC CONTROL OF RIGID-FAILURES MODES IN MASONRY STRUCTURES SUBJECT TO GROUND MOTION

**Ileana Corbi[1], Ottavia Corbi[2], and Francesca Tropeano[3]**

[1] Department of Structural Engineering and Architecture, University of Naples "Federico II", Italy
e-mail: ileana.corbi@unina.it

[2] Department of Structural Engineering and Architecture, University of Naples "Federico II", Italy
e-mail: ottavia.corbi@unina.it

[3] Department of Structural Engineering and Architecture, University of Naples "Federico II", Italy
e-mail: francesca.tropeano@unina.it

**Keywords:** Structural Dynamics, Dynamic Control, Rigid-mode failure.

**Abstract.** *In the paper one presents some research developed at the University of Naples in the field of structural dynamic control. The research is mainly focused on the possibility of applying control systems to the protection of existing and masonry constructions through the setup of ad-hoc strategies and devices, which are suitably conceived and designed in order to fit the main characteristics, behavior and collapse modes of the structural components. Rigid-failure modes are referred to, with the articulated model consisting of macro-elements whose motion is activated during the dynamic event.*

*The final task consists of achieving an adequate mitigation of the dynamic effects due to the possible occurrence of earthquakes. The researches involve both theoretical, numerical and experimental features on the topic, including some design issues.*

# 1 INTRODUCTION

Approaches to the problem of attenuation of the structural response vary from the setup of control devices for reducing the structural vibrations [1]-[10] to the development of reinforcement techniques, also involving new composite materials [11]-[14], for increasing the dynamic strength of the structure, even in masonry constructions [15]-[19].

In the paper one presents some research developed in the field of protection of new and existing structures subject to dynamic events. The described researches involve both theoretical, numerical and experimental features on the topic.

One essentially refers to the mitigations of the effects relevant to the activation of rigid modes under dynamic ground shaking, which do often occur in a variety of existing structures and structural components subject to earthquake and may be responsible of the achievement of the collapse condition.

In more details, when referring to monumental constructions such as masonry vaulted structures subject to dynamic ground motion, the structural model is usually assumed to activate some rigid-failure schemed behaviour due to the formation of the cracks, which allow the formation of kind of macro-elements with the development of relative rotations constrained in their sign.

The whole dynamic analysis would require to remove the small displacement hypothesis , and to account for the response of rigid-plastic structures subjected to impulsive or pseudo-impulsive dynamic loads through the search of approximate solutions. Some studies are reported aimed at controlling the articulated motion by the proper design of a chain cable.

In the second part of the paper, one refers to studies concerning models that may be assimilated to rigid blocks, and where pure rocking motion is analyzed; in this case, the response attenuation is accomplished by means of dampers that introduce additional dissipative liquid masses.

# 2 TIE-ROD DEVICE FOR VAULTED STRUCTURES UNDER DYNAMIC SHAKING

## 2.1 The model and the control approach

In order to control the dynamic articulated motion of masonry vaulted structures occurring during earthquakes, some possible modification of classical retrofit provisions may be considered in order to realize more effective control strategies.

In particular a control strategy may consist of designing a device based on the regulation of a chain cable and of setting up an ad-hoc control algorithm for the proper tuning of the chain in order to get an overall stress reduction in the masonry.

By referring to articulated modes of masonry portal arches, based on the coupling of the single modes which may be referred to for the two cases of the unchained and chained model, one may perform dynamic analyses through modal approximation methods. The arch model, interpreted by a rigid-failure scheme in masonry material, is assumed to be equipped with a tie-rod, whose length may be ruled through the selected control algorithm.

This condition is considered to constitute an intermediate situation between the two single-mode cases of the arch without tie or with non-stretch (inextensible), as shown in Figure 1. a) and b), respectively. The coupled behaviour is inferred from a suitable combination of the modal contributions representing the two considered cases.

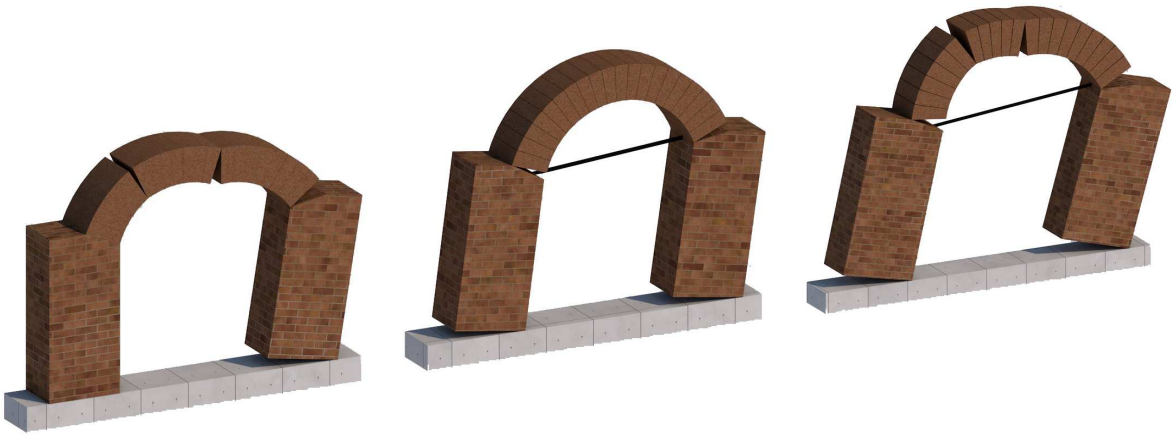

a) b) c)

Figure 1: The not retrofitted model a); the model with the inextensible chain cable b), and with the extensible chain cable c).

The dynamic equilibrium of the combined modal behaviour is then handled by introducing a first order approximation and linearization in order to subsequently formulate the algorithm, which is aimed at controlling the length of the tie and at mitigating the dynamic effects on the structural response. The final behaviour referred to the arch equipped with an extensible tie, is shown in Figure 1.c).

## 2.2 Design of the control algorithm

The control strategy is aimed at suitably calibrating the length variation of the rod cable in order to mitigate the dynamic effects induced in the vaulted structure by the ground motion.

With reference to the second order differential dynamic equilibrium system, the problem is essentially set up in such a way to push the coupled behaviour of the masonry portal towards an uncoupled rigid one; a linear feedback governing the dependence of the tie elongation on the response variables is introduced through the control parameter $\psi$ in the controlled motion equation .

The search of the optimal control coefficient can be turned into the problem of the search of the constrained minimum of a properly defined operator of the impulsive response function, mainly inferred in energetic terms.

In synthesis, in order to realize an effective and energetically economic control, the problem may be formulated in such a way that the maximum value of the tie length $\Delta\ell_{max}$ attained during the motion duration $T_o$ is kept contained within a certain predefined threshold. After some further developments, the problem is then set up in energetic terms, by introducing some operators accounting for the maximum attained response $\Re(T_o|\Psi)$ during the motion and the maximum rod elongation $\Im(T_o|\Psi)$ and performing the constrained minimization, such that $\Im(T_o|\Psi)$ is kept bounded by the threshold value $\Im^*$

$$\begin{cases} \text{Find} \quad \underset{\Psi}{\text{Min}}\ \Re(T_o|\Psi) \\ \text{Sub} \quad \Im(T_o|\Psi) \le \Im^* \end{cases} \tag{1}$$

### 2.3 Control performance

As concerns the performance of the proposed control system one may refer to the diagram reported in Figure 2, where the operator representing the maximum attained response (to be quantified according to the scale on the left side of the diagram) and the operator representing the maximum chain elongation (to be referred to the right side scale) are plotted versus the control coefficient $\psi$. One may notice that the response operator attains its minimum values under negative values of the parameter.

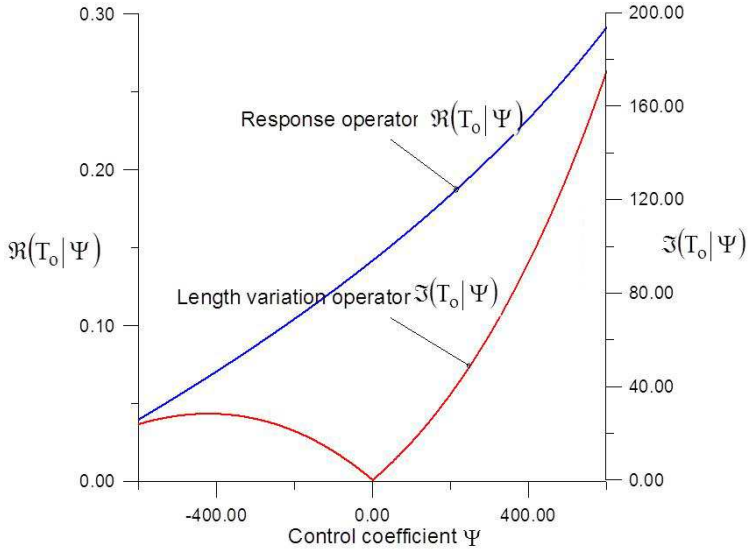


Figure 2: Diagram of the response and tie length operators versus the control coefficient $\psi$.

The comparison with the uncontrolled case of the tie (achieved under a null value of $\psi$) allows to observe that a further improvement in the response mitigation may be attained by controlling the elongation of the chain cable. Good results may be still obtained when choosing a more binding value of the control operator, namely by giving more weight to the energetic economy. Actually, by selecting large negative values of the control coefficient one may then achieve, at the same time, the double effect of minimizing costs while maximizing control effectiveness; in this case particular attention has to be paid to prevent compression in the tie.

## 3 TLD DEVICES FOR RIGID-FAILURES UNDER DYNAMIC SHAKING

### 3.1 Overall framework

The attachment of additional masses to the main structure with the objective of dissipating the energy supplied by the dynamic event and counteracting the incoming dynamic forces is a well-known control approach. Even in its passive mode it may give appreciable results in terms of attenuation of the structural vibration with a null control energy supply, once properly tuned the properties of the mass with reference to the characteristics of the structure.

When adopting sloshing masses, based on the energy dissipation through the liquid mass motion in suitably shaped tanks, high damping capacity may be conferred to the structure. This strategy may be applied in order to reduce vibrations occurring also in special structures, monolithically rocking under ground motion. This kind of failures often occurs in existing

building elements and structures, which may behave according to rigid failure modes in many cases.

At the University of Naples "Federico II" some experimental tests have been executed on structural models assimilated to rigid blocks equipped or not with some liquid sloshing devices, demonstrating that the adoption of the Tuned Liquid Dampers (TLD), and their proper tuning, may lead to satisfactory results, in terms of mitigation of dynamics effects as regards to such type of failure.

Actually the need of predicting and preventing failures associated to rocking and overturning of rigid structures undergoing strong ground shaking have motivated a consistent number of studies on rocking response. Therefore the possibility of coupling some sloshing devices to rigid blocks for attenuating their response to dynamic excitations appears of main interest.

### 3.2 Experimental activity and results

In the following, one refers to some tests executed on some models acting as rigid blocks by means of a unidirectional shaking table moving in the horizontal direction for simulating the dynamic motion. The shaking table is an MTS system and is automatically connected to a system which both gives the input signal to the table and records the output signal.

The dynamic experiments have been executed on block models moving under pure rocking. The rocking motion is affected by very complex dynamics, that push towards the adoption of worst scenario approaches for vulnerability assessment that increase the robustness of forecasts.

The experiments were executed by keeping a fixed span and varying the frequency of the harmonic base-excitation inferred by the shaking table, and using different span values.

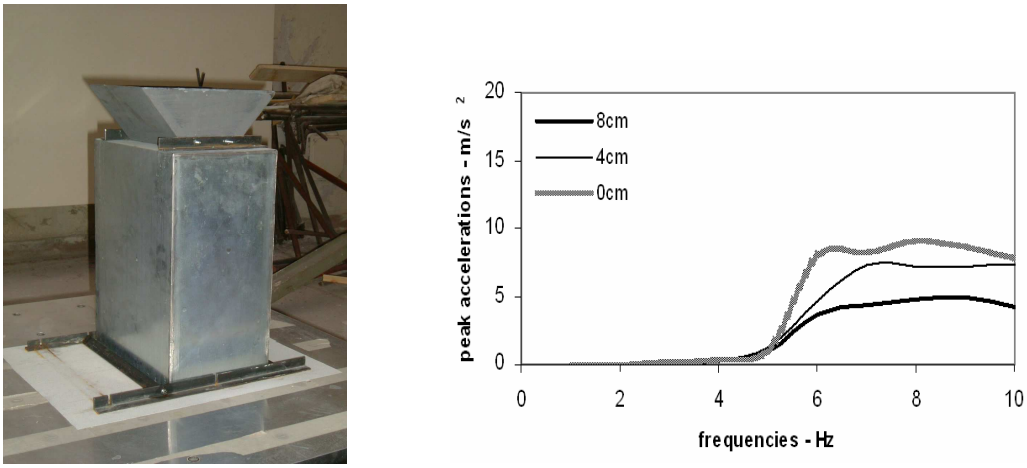


a) b)

Figure 3: Sample of dynamic tests on rocking blocks with TLD: a) experimental test; b) comparison of data for the empty tank and the tank with 4 or 8 cm of liquid.

The first experimental campaign was developed on blocks, both having various sizes and geometric dimensions' ratios (thickness/height), made of thin aluminum plates of the type shown in Figure 3.a), and subject to pure rocking motion around its base edges.

At the second stage, an experimental investigation on the blocks coupled with a number of tuned liquid dampers (TLDs) with different geometries, shapes and liquid ratios was developed. Collected data from tests allow to show the potential of the strategy even in this case

and to relate the response reduction to the liquid amount in the tanks and tank shape, as clear from the sample test whose results are reported in Figure 3.b).

The overall benefit by the liquid damper does not appear to be homogeneous on the frequency range, it is much higher in some frequency range which also depends of the geometrical/inertial properties of the structure under observation. As regards to the dynamic test execution, one should emphasize that shaking tables are usually adopted in order to reproduce/simulate the incoming dynamic excitation and to record the response data for the structural model under examination.

Actually, due to shaking table complexity, that includes a variety of mechanical, hydraulic and electronic components, there are many potential highly interdependent sources of distortion that alter the total effect of the system, so that a given command does not produce the expected response. It must be required for any case a specific setting of the systems which considers all the components of the problem. Anyway, although forecasts about the seismic motion are not easy to be obtained, such facilities allow to understand the behavior of different typologies of structures and materials, as well as to evaluate the effects of protection strategies.

## 4 CONCLUSIONS

In the paper, some possible approaches to the control of structures activating under ground shaking rigid failure modes are presented. In this class, typical examples are represented by masonry constructions which usually obey articulated rigid mode behaviours. As regards to vaulted structures a possible variation to classical retrofit methods is presented in order to improve their performance, resulting in a good balance between performance and energy costs; on the other side, when referring to constructions or single structural components such as walls behaving according to the rigid block model, the mitigation of the dynamic response is successfully achieved through the adoption of special oscillating masses.

## 5 ACKNOWLEDGEMENT

The present research has been supported by the Dept of Civil Protection of the Italian Government through the ReLuis Pool (DCP/ReLUIS 2017).

## REFERENCES

[1] Baratta, A., Corbi, I., Corbi, O., Algorithm design of an hybrid system embedding influence of soil for dynamic vibration control, *J. Soil Dynamics and Earthquake Engineering*, 74, 79-88 (2015).

[2] Baratta, A., Corbi, I., Corbi, O., Mastorakis, N., Strategies for the protection from structural failures under seismic events, *International Journal of Mechanics*, 9, 69-75 (2015).

[3] Corbi, I., Corbi, O., Macro-mechanical modelling of pseudo-elasticity in shape memory alloys for structural applications, *J. Acta Mechanica*, 1-9, DOI: 10.1007/s00707-016-1624-3 (2016).

[4] Baratta, A., Corbi, O., Dynamic Response and Control of Hysteretic Structures, Intern. *Journal of Simulation Modeling Practice and Theory*, 11, 371-385 (2003).

[5] Constantinou, M.C., Whittaker, A.S., Kalpakidis, Y., Fenz, D.M., Warn, G.P., Performance of Seismic Isolation Hardware under Service and Seismic Loading; Technical

Report MCEER-07-0012; *Multidisciplinary Center for Earthquake Engineering Research*, State University of New York at Buffalo: Buffalo, NY, USA (2008).

[6] Corbi, I., Rakicevic, Z.T., Shaking table testing for structural analysis, *International Journal of Mechanics*, 7(4), 459-466 (2013).

[7] Corbi, O., de Barros, R.C., Seismic protection of civil buildings by visco-elastic magneto-rheological fluids, *International Journal of Mechanics*, 7(4), 518-525 (2013).

[8] Corbi, O., Zaghw, A.H., Properties and design of dissipative visco-recentring SMA members for civil structures, *International Journal of Mechanics*, 7(3), 285-292 (2013).

[9] Corbi, O., Zaghw, A.H., Elattar, A., Saleh, A., Preservation provisions for the environmental protection of egyptian monuments subject to structural vibrations, *International Journal of Mechanics*, 7(3), 172-179 (2013).

[10] Sang-Hoon O., Sang-Hoon S., Sang-Ho L., Hyung- Joon K., Seismic Response of Base Isolating Systems with U-Shaped Hysteretic Dampers, *Int J Steel and Structures*, 12(2), 285-298 (2012).

[11] Baratta, A., Corbi, I., Topology optimization for reinforcement of no-tension structures, *J. Acta Mechanica*, 225 (3), 663-678 (2014).

[12] Baratta, A., Corbi, O., An approach to the positioning of FRP provisions in vaulted masonry structures, *J. Composites Part B: Engineering*, 53, 334-341 (2013).

[13] Corbi, I., FRP reinforcement of masonry panels by means of c-fiber strips, *Journal Composites Part B*, DOI: 10.1016/j.compositesb.2012.11.005 (2012).

[14] Corbi, I., FRP Composites Retrofitting for Protection of Monumental and Ancient Constructions, *Open Construction and Building Technology Journal*, 6, 361-367 (2012).

[15] Corbi, I., Corbi, O., Analysis of bi-dimensional solids with internal unilateral constraint coupled to structural elements with different degree of connection, *J. Acta Mechanica*, 228(2), 607-616 (2017).

[16] Corbi, I., Corbi, O., Theorems for masonry solids with brittle time-decaying tensile limit strength, *J. Acta Mechanica*, 228(3), 837-849 (2017).

[17] Corbi, I., Corbi, O., F. Tropeano, Stability assessment of an historical masonry bridge through the LA kinematic theorem for NT structures, *Int. J. Mechanics*, 10, 305-311 (2016).

[18] Baratta, A., Corbi I., Corbi, O. , Stability of evolutionary brittle-tension 2D solids with heterogeneous resistance, *J. Computers and Structures*, 174, 133-138 (2016).

[19] Baratta, A., Corbi, I., Corbi, O., Analytical Formulation of Generalized Incremental Theorems for 2D No-Tension Solids, *J. Acta Mechanica*, 226 (9), 2849-2859 (2105).

COMPDYN 2017
6th ECCOMAS Thematic Conference on
Computational Methods in Structural Dynamics and Earthquake Engineering
M. Papadrakakis, M. Fragiadakis (eds.)
Rhodes Island, Greece, 15–17 June 2017

# SEISMIC RELIABILITY-BASED DESIGN OF PERFECTLY ELASTOPLASTIC STRUCTURES ISOLATED BY FPS

**P. Castaldo[1], B. Palazzo[2] and T. Ferrentino[3]**

[1]Department of Structural, Geotechnical and Building Engineering (DISEG), Politecnico di Torino,
Corso Duca degli Abruzzi, 24, Turin, Italy (corresponding author);
e-mail: paolo.castaldo@polito.it; pcastaldo@unisa.it

[2]Department of Civil Engineering, University of Salerno,
Via Giovanni Paolo II (SA), Italy;
e-mail: palazzo@unisa.it

[3]Department of Civil Engineering, University of Salerno,
Via Giovanni Paolo II (SA), Italy;
e-mail tatianaferrentino@gmail.com

**Keywords:** seismic isolation; friction coefficient; seismic reliability; displacement ductility demand; strength reduction factor.

**Abstract.** *This paper deals with seismic reliability of nonlinear structural systems equipped with friction pendulum isolators (FPS). The isolated structures are described by employing an equivalent 2dof model characterized by a perfectly elastoplastic rule to account for the inelastic response of the superstructure, whereas, the FPS behavior is described by a velocity dependent model. An extensive parametric study is carried out encompassing a wide range of elastic and inelastic building properties, different seismic intensity levels and considering the friction coefficient as a random variable. Employing a set of natural seismic records and scaled to the seismic intensity corresponding to life safety limit state for L'Aquila site (Italy) according to NTC08, the inelastic characteristics of the superstructures are designed as the ratio between the average elastic responses and increasing strength reduction factors. Incremental dynamic analyses (IDA) are developed to evaluate the seismic fragility curves of both the inelastic superstructure and the isolation level assuming different values of the corresponding limit states. Integrating the fragility curves with the seismic hazard curves related to L'Aquila site (Italy), the reliability curves of the equivalent inelastic base-isolated structural systems, with a design life of 50 years, are derived proposing seismic reliability-based design (SRBD) abacuses useful to define the FPS properties and superstructure properties.*

## 1 INTRODUCTION

In the last decades, friction pendulum system (FPS) has emerged as a very effective technique for the seismic isolation [1] of building frames due to its advantages, mainly related to the capability of providing an isolation period independent of the mass of the supported structure, its high dissipation and recentering capacity [2]-[3]. Over the years, within the issue of the passive control of structures, many works have developed new design strategies and methodologies [4]-[19] as well as probabilistic analyses in structural dynamics, structural reliability methods, and reliability-based analysis have been presented [20]-[30]. The influence of the friction pendulum system (FPS) isolator properties on the seismic performance of base-isolated building frames by employing 3D systems as well as two-degree-of-freedom (2dof) model accounting for the superstructure flexibility with a velocity-dependent model for the FPS isolator behaviour has been analyzed by Castaldo et al. [31]-[34]. In particular, seismic reliability analyses of a 3D r.c. elastic system isolated by FPS bearings have been carried out in [31]-[32] by accounting for the randomness of both the isolator properties (i.e., coefficient of friction) and of the earthquake main characteristics. The seismic reliability-based design approach has been proposed in [33]-[34] for elastic and inelastic systems isolated by friction pendulum devices.

With reference to the inelastic behavior of base-isolated systems under strong seismic events, seismic codes [35]-[38] provide design response spectra, defined by the ratio of elastic response spectrum ordinates to a parameter, called strength reduction factor [35],[39] or behaviour factor [36]-[37], usually defined, within a force-based design approach of new structures, as the product between two terms: ductility-dependent component and overstrength factor [39]. In particular, the Italian seismic code, NTC08 [37], the European seismic code Eurocode 8 [36] and the Japanese building code [38] provide a maximum behavior factor value of 1.5 for base-isolated structures, without explicitly distinguishing the different terms (i.e., ductility and overstrength factors). The US seismic design codes, ASCE 7 [35], prescribes the strength reduction factor for a seismically isolated structure to be 0.375 times the one for a corresponding fixed-base structure and no larger than 2.

The aim of this work is to propose reliability-based formulae for the preliminary design of base-isolated regular frames, located in an area characterized by a seismic hazard similar to the local seismic hazard of L'Aquila site (Italy). The results of the reliability analyses demonstrate that within the investigated parameter combinations the values of the strength reduction factor for base-isolated systems with FPS should be lower than 1.5.

## 2 INELASTIC MODEL OF A BASE-ISOLATED STRUCTURE WITH FPS

In this study the 2dof (degree-of-freedom) model proposed by Kelly [40], modified to account for inelastic responses of both the isolation level and the superstructure (Fig. 1), is adopted. The bearing response is modelled using a bilinear hysteretic response envelope, while the superstructure behaviour is described using a perfectly elastoplastic model. With reference to the symbols in Fig. 1, the equations of motion are:

$$\begin{aligned} &\left(m_b + m_s\right)\ddot{u}_b + m_s\ddot{u}_s + c_b\dot{u}_b + \frac{W}{R}u_b + \mu_d W \operatorname{sgn}\dot{u}_b = -\left(m_b + m_s\right)\ddot{u}_g \\ &m_s\ddot{u}_b + m_s\ddot{u}_s + c_s\dot{u}_s + f_s\left(u_s, \operatorname{sgn}\dot{u}_s\right) = -m_s\ddot{u}_g \end{aligned} \tag{1}$$

where $W=(m_b+m_s)g$ is the weight on the bearing, $R$ is the radius of curvature of the FPS, $\mu_d$ is the bearing friction coefficient, that varies with the velocity according to Mokha et el. and Constantinou et el. [4]-[6]:

$$\mu_d = f_{\max} - (f_{\max} - f_{\min})\exp(-\alpha \dot{u}_b) \tag{2}$$

where $f_{max}$ and $f_{min}$ are the friction coefficient attained at high and at very low velocities of sliding respectively, $\alpha$ is a constant for a given pressure, temperature and condition of FPS interfaces. In this study, this constant equal to 30 and the ratio $f_{max}/f_{min}$ equal to 3, based on regression of the experimental results [4]-[6], are assumed.

The superstructure is in the elastic phases if (3) is satisfied and the corresponding restoring force is given by (4).

$$\left|u_{s,i} - u_{0,i-1}\right| < u_y \text{ or } (f_{s,i-1} = f_y \,\&\, \dot{u}_{s,i}\dot{u}_{s,i-1} < 0) \tag{3}$$

$$f_{s,i}(u_s, \operatorname{sgn}\dot{u}_s) = k_s(u_{s,i} - u_{0,i-1}) \tag{4}$$

Otherwise, the superstructure is in the plastic phases if

$$\left|u_{s,i} - u_{0,i-1}\right| \geq u_y \tag{5}$$

$$f_{s,i}(u_s, \operatorname{sgn}\dot{u}_s) = f_y \operatorname{sgn}(u_{s,i} - u_{0,i-1}) \tag{6}$$

where *i* and *(i-1)* indicate the time instants. The seismic isolation degree [41] is an indicator of the isolation system efficiency for elastic structures and results to be the ratio between the isolation $T_b=2\pi\sqrt{(m_b+m_s)/k_b}$ and superstructure $T_s=2\pi\sqrt{m_s/k_s}$ period of vibration: $I_d=T_b/T_s$. Regarding the inelastic response of a yielding superstructure (Fig. 1), characterized by a single degree of freedom with a perfectly elastoplastic behavior and assumed as the equivalent model representative of multi-story building frames [42]-[44], the corresponding strength reduction factor is defined as $q=f_{s,el}/f_y=u_{s,el}/u_y$, where $f_{s,el}$ and $u_{s,el}$ are, respectively, the minimum yield strength and yield deformation required for the superstructure to remain elastic during a ground motion, or the peak response values for the corresponding linear system. Note that $q$ is different from the one provided by [35]-[39] because it does not explicitly consider the overstrength factor since the overstrength capacities are taken into account in the perfectly elastoplastic system assumed as equivalent model of the inelastic behavior of real multi-story building frames [39]; so $q$ is related only to the ductility-dependent component [42]-[44].The displacement ductility, $\mu$, of the superstructure is the ratio between the peak displacement of the inelastic system, $u_{s,max}$, and the yield displacement $u_y$. According to [40], the mass ratio $\gamma=m_s/(m_b+m_s)$, isolation $\xi_b=c_bT_b/[2(m_b+m_s)]$ and superstructure $\xi_s=c_sT_s/(2m_s)$ damping ratio are defined.

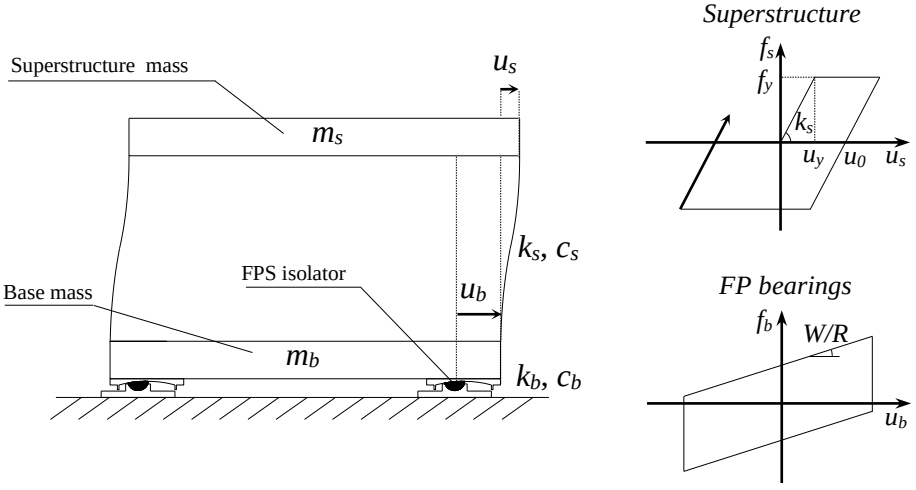


Figure 1: 2dof model of a building isolated with FPS.

## 3 UNCERTAINTIES CONSIDERED

Seismic reliability assessment of a building structure, according to the structural performance (SP) evaluation method [45]-[47], is based on the coupling between structural performance levels [48] and associated exceeding probabilities during its design life [49]-[50]. According to [51]-[53], the uncertainties related to the seismic input intensity are separated from those related to the characteristics of the record (record-to-record variability) by introducing a scale factor, called intensity measure (*IM*).

| # | Year | Earthquake Name | Recording Station Name | $Vs_{30}$ [m/s] | Fault Type | M [-] | $R_s$[km] | PGA [g] |
|---|---|---|---|---|---|---|---|---|
| 1 | 1994 | Northridge | Beverly Hills - Mulhol | 356 | Thrust | 6.7 | 13.3 | 0.52 |
| 2 | 1994 | Northridge | Canyon Country-WLC | 309 | Thrust | 6.7 | 26.5 | 0.48 |
| 3 | 1994 | Northridge | LA-Hollywood Stor | 316 | Thrust | 6.7 | 22.9 | 0.36 |
| 4 | 1999 | Duzce, Turkey | Bolu | 326 | Strike-slip | 7.1 | 41.3 | 0.82 |
| 5 | 1999 | Hector Mine | Hector | 685 | Strike-slip | 7.1 | 26.5 | 0.34 |
| 6 | 1979 | Imperial Valley | Delta | 275 | Strike-slip | 6.5 | 33.7 | 0.35 |
| 7 | 1979 | Imperial Valley | El Centro Array #11 | 196 | Strike-slip | 6.5 | 29.4 | 0.38 |
| 8 | 1995 | Kobe, Japan | Nishi-Akashi | 609 | Strike-slip | 6.9 | 8.7 | 0.51 |
| 9 | 1995 | Kobe, Japan | Shin-Osaka | 256 | Strike-slip | 6.9 | 46.0 | 0.24 |
| 10 | 1999 | Kocaeli, Turkey | Duzce | 276 | Strike-slip | 7.5 | 98.2 | 0.36 |
| 11 | 1999 | Kocaeli, Turkey | Arcelik | 523 | Strike-slip | 7.5 | 53.7 | 0.22 |
| 12 | 1992 | Landers | Yermo Fire Station | 354 | Strike-slip | 7.3 | 86.0 | 0.24 |
| 13 | 1992 | Landers | Coolwater | 271 | Strike-slip | 7.3 | 82.1 | 0.42 |
| 14 | 1989 | Loma Prieta | Capitola | 289 | Strike-slip | 6.9 | 9.8 | 0.53 |
| 15 | 1989 | Loma Prieta | Gilroy Array #3 | 350 | Strike-slip | 6.9 | 31.4 | 0.56 |
| 16 | 1990 | Manjil, Iran | Abbar | 724 | Strike-slip | 7.4 | 40.4 | 0.51 |
| 17 | 1987 | Superstition Hills | El Centro Imp. Co. | 192 | Strike-slip | 6.5 | 35.8 | 0.36 |
| 18 | 1987 | Superstition Hills | Poe Road (temp) | 208 | Strike-slip | 6.5 | 11.2 | 0.45 |
| 19 | 1987 | Superstition Hills | Westmorland Fire Stat. | 194 | Strike Slip | 6.5 | 15.1 | 0.21 |
| 20 | 1992 | Cape Mendocino | Rio Dell Overpass | 312 | Thrust | 7.0 | 22.7 | 0.55 |
| 21 | 1999 | Chi-Chi, Taiwan | CHY101 | 259 | Thrust | 7.6 | 32 | 0.44 |
| 22 | 1999 | Chi-Chi, Taiwan | TCU045 | 705 | Thrust | 7.6 | 77.5 | 0.51 |
| 23 | 1971 | San Fernando | LA - Hollywood Stor | 316 | Thrust | 6.6 | 39.5 | 0.21 |
| 24 | 1976 | Friuli, Italy | Tolmezzo | 425 | Thrust | 6.5 | 20.2 | 0.35 |
| 25 | 1980 | Irpinia | Bisaccia | 496 |  | 6.9 | 21.3 | 0.94 |
| 26 | 1979 | Montenegro | ST64 | 1083 | Thrust | 6.9 | 21.0 | 0.18 |
| 27 | 1997 | Umbria Marche | ST238 | n/a | Normal | 6.0 | 21.5 | 0.19 |
| 28 | 2000 | South Iceland | ST2487 | n/a | Strike Slip | 6.5 | 13 | 0.16 |
| 29 | 2000 | South Iceland (a.s.) | ST2557 | n/a | Strike Slip | 6.4 | 15.0 | 0.13 |
| 30 | 2003 | Bingol | ST539 | 806 | Strike Slip | 6.3 | 14.0 | 0.30 |

Table 1: Selected ground motions for the time history analyses.

The approach is based on calculating the probabilities of exceeding different limit state thresholds, properly defined, given different values of the intensity measure with the aim to define the fragility curves of the system. Afterward, the abovementioned fragility curves integrated with a seismic hazard curve, expressed in terms of the same *IM*, related to a reference site, lead to the mean annual rates of exceeding the limit states. Using a Poisson distribution, it is possible to transform the mean annual rates of exceeding the limit states into probabilities of exceedance in the time frame of interest (e.g., 50 years).

The aim of this work consists of evaluating the seismic reliability of inelastic structural systems equipped with friction pendulum isolators (FPS) considering both the friction coefficient and earthquake characteristics as random variables within the uncertainties relevant to the problem.

The spectral displacement, $S_D(\xi_b, T_b)$, at the isolated period of the system, $T_b$, and for the damping ratio, $\xi_b$, is assumed as intensity measure, *IM*. In the analyses carried out in this study, the damping ratio $\xi_b$ is taken equal to zero, consistently with other works which assume that friction is the only source of damping in the isolators [54]. The corresponding *IM* is hereinafter denoted to as $S_D(T_b)$ and it is assumed ranging from 0.1 m to 0.45 m. The record-to-record variability is described through a set of 30 ground motion records, selected within the ground motion databases of PEER (Pacific Earthquake Engineering Research Center) [55], of ITACA (Italian Accelerometric Archive) [56] and of ISESD (Internet-Site for European Strong-Motion Data) [57]. The characteristics of the selected ground motion records are reported in Tab. 1. Their source-to-site distance, $R_s$, is greater than 8.7 km, and their moment magnitude, M, is in the range between 6 and 7.6.

As discussed in [4]-[6], the friction is a complex phenomenon and several mechanisms contribute to its variability. It follows that a Gaussian probability density function (PDF), interrupted from 0.5% to 5.5% with a mean value equal to 3%, is employed to model the friction coefficient at large velocity as random variable $f_{max}$. For the generation of 15 sampled values of $f_{max}$ the stratified sampling technique the Latin Hypercube Sampling (LHS) method [31],[58]-[60] is adopted.

## 4 RELIABILITY ANALYSIS OF INELASTIC BASE-ISOLATED STRUCTURES WITH FPS

### 4.1 Parametric study

The first step to determinate the seismic reliability of the inelastic base-isolated equivalent systems consists of developing incremental dynamic analyses (IDAs) [61]. For this reason, an extensive parametric study is carried out encompassing a wide range of the parameter combinations related to isolation level and superstructure, according to Eqn. (1).

The deterministic parameters are: the isolation degree $I_d$, assumed equal to 6, the isolation period of vibration, $T_b$, varying between 3 s and 6 s, the mass ratio $\gamma$ assumed equal to 0.6 and 0.8 and the (ductility-dependent) strength reduction factor $q$ ranging from 1.1 to 2, corresponding to the values provided by the codes [35]-[38] for the behavior factor, in the case of unitary overstrength factor. Furthermore, the analyzed inelastic 2DOF systems have the isolation $\xi_b$ and superstructure $\xi_s$ damping ratio respectively equal to 0% and 2% and the seismic isolation degree $I_d$ equal to 6.

In order to define the inelastic characteristics of each equivalent structural system, dynamic analysis of the base-isolated systems (defined for different values of $T_b$, $\gamma$ and $q$ ), with a friction coefficient equal to 3%, have been subjected to the set of 30 seismic records, scaled to the *IM* value related to the life safety limit state (NTC08 [37]) for L'Aquila site (Italy): the *IM* is equal to 0.311 m for $T_b$=3, 4, 5 s (Fig. 2b) and equal to 0.26 m for $T_b$=6 s. The superstructure dynamic responses, expressed in terms of displacements relative to the base $u_{s,el}$, have allowed to evaluate the average yield displacement for each value of $q$. In this way, the inelastic characteristics of the equivalent structural systems have been defined.

## 4.2 Incremental dynamic analysis (IDA)

The above-mentioned equivalent structural systems, with the different structural parameters ($T_b$, $\gamma$, $q$) and combined for each value of the sampled friction coefficient, are subjected to the 30 ground motions, scaled to eight intensity levels values within the incremental dynamic analysis. The response parameters $\mu$ and $u_{b,max}=|u_b(t)|_{max}$, are adopted as the engineering demand parameters (EDPs) and assumed to follow a lognormal distribution. A lognormal distribution can be fitted to the both response parameters by estimating the sample lognormal mean, $\mu_{ln}(EDP)$, and the sample lognormal standard deviation $\sigma_{ln}(EDP)$, through the maximum likelihood estimation method.

The IDA results of the isolation level and the superstructure are plotted in Fig.s 2-3, in the form of meshes versus the intensity measure *IM* and the (ductility-dependent) strength reduction factor $q$. Each figure contains several surface plots, corresponding to the different values of the percentile and to both values of the mass ratio.

Fig. 2 shows the IDA results regarding the isolation level. The statistics of the EDP $u_{b,max}$ are influenced by $T_b$: the lognormal mean slightly decreases by increasing $T_b$, while the dispersion increases for higher $T_b$. Both the statistical values are also influenced by $\gamma$: the isolation displacement decreases by increasing $\gamma$. In fact, the mass ratio controls the contribution of the second mode of vibration to the response. This mode induces significant deformations in the superstructure only. On the other hand, the increase of $q$ leads to a slight decrease of the displacement $u_{b,max}$.

Fig. 3 show the IDA curves regarding the superstructure. The increase of strength reduction factor $q$ leads to a very high increase of the displacement ductility demand $\mu$. The response parameter $\mu$ increases for increasing $\gamma$ and for decreasing $T_b$.

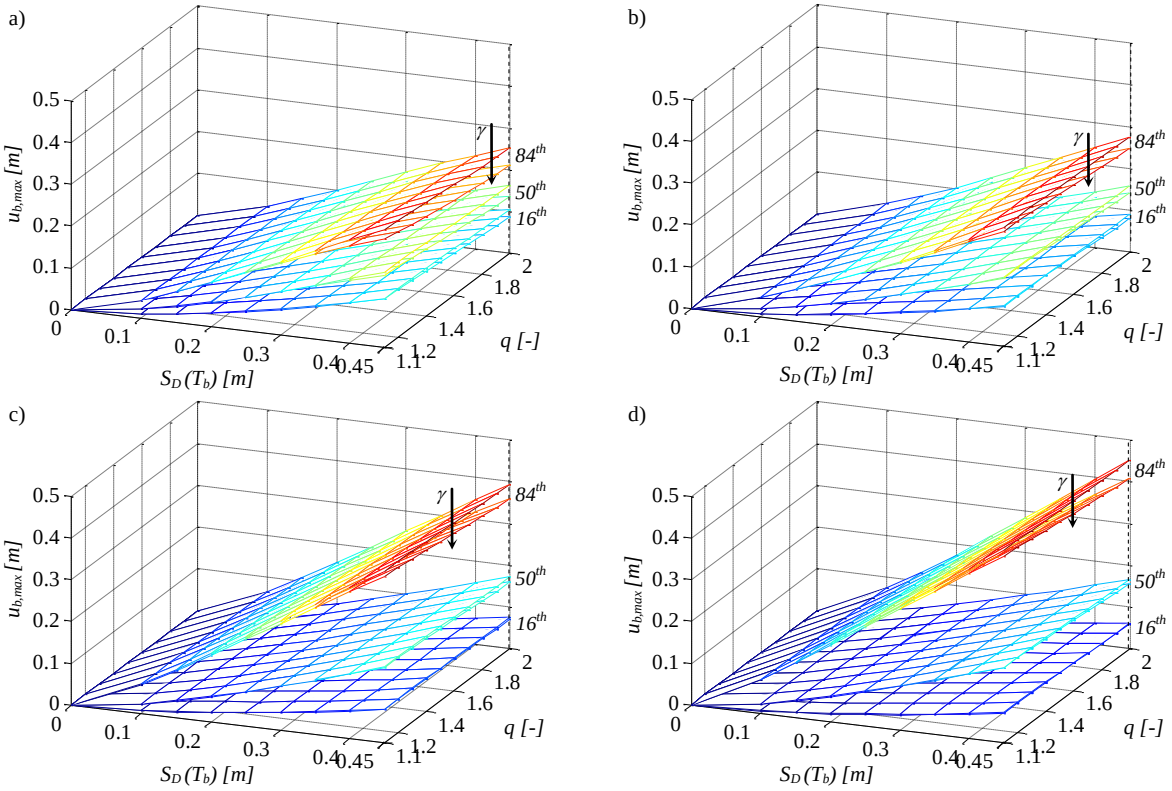


Figure 2: IDA curves of the isolation level with $I_d$=6 and $T_b$=3 s (a), $T_b$=4 s (b), $T_b$=5 s (c), $T_b$=6 s (d). The arrow denotes the increasing direction of $\gamma$ = 0.6-0.8.

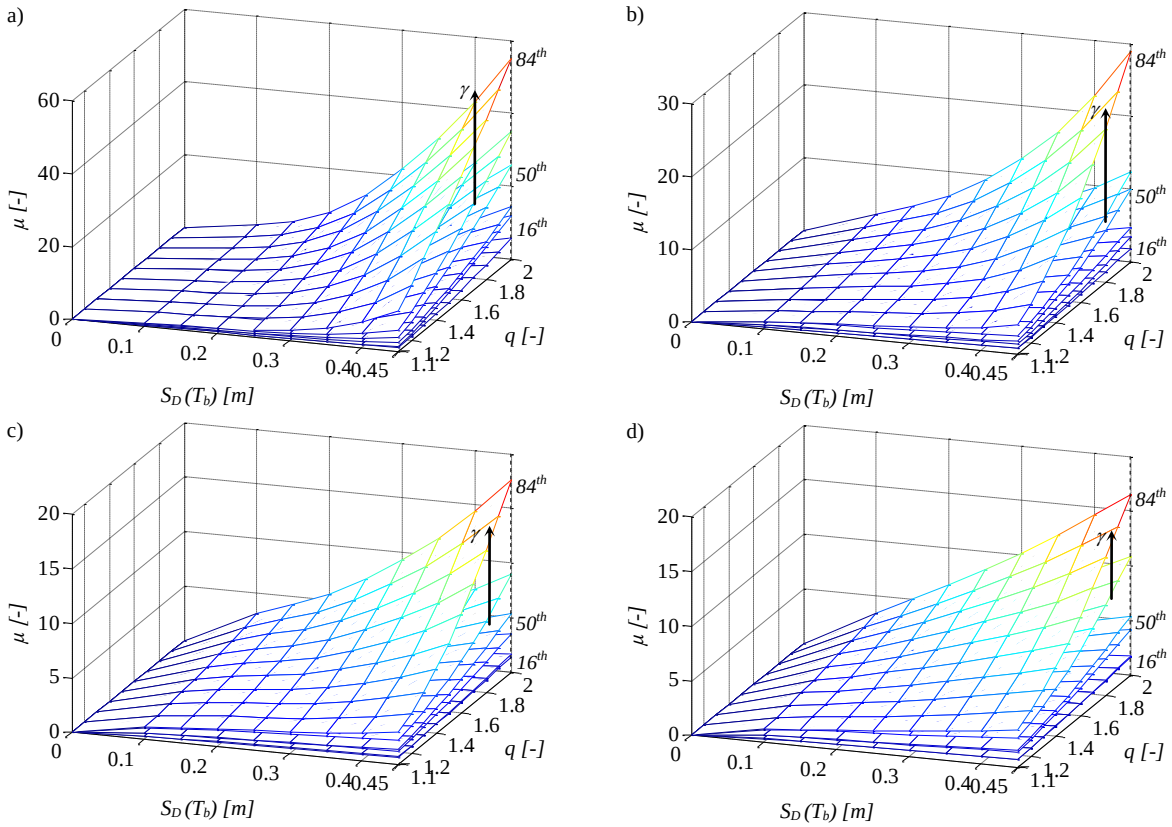


Figure 3: IDA curves of superstructure with $I_d$=6 and $T_b$=3 s (a), $T_b$=4 s (b), $T_b$=5 s (c), $T_b$=6 s (d). The arrow denotes the increasing direction of $\gamma$ = 0.6-0.8.

## 4.3 Seismic fragility analysis

The following step for the seismic reliability assessment of inelastic buildings isolated by FPS, is the evaluation of the seismic fragility. The seismic fragility can be defined as the probabilities $P_f$ exceeding different limit states at each level of the intensity measure *IM*. For this reason the limit state thresholds need to be defined. In particular, the performance levels of the isolation system are assumed in terms of radius in plan of the concave surface, $r$ [m] (Tab. 2); while, the performance levels of the equivalent system superstructure are defined in terms of available ductility, $\mu$ [-] (Tab. 3) considering structural systems in ordinary conditions and neglecting aging effects [62]-[71].

| | $LS_{b,1}$ | $LS_{b,2}$ | $LS_{b,3}$ | $LS_{b,4}$ | $LS_{b,5}$ | $LS_{b,6}$ | $LS_{b,7}$ | $LS_{b,8}$ | $LS_{b,9}$ | $LS_{b,10}$ |
|---|---|---|---|---|---|---|---|---|---|---|
| ***r* [m]** | 0.05 | 0.1 | 0.15 | 0.2 | 0.25 | 0.3 | 0.35 | 0.4 | 0.45 | 0.5 |
| $p_f$ (50 years)=$1.5\cdot10^{-3}$ | | | | | | | | | | |

Table 2: Limit state thresholds for the isolation level.

| | $LS_{\mu,1}$ | $LS_{\mu,2}$ | $LS_{\mu,3}$ | $LS_{\mu,4}$ | $LS_{\mu,5}$ | $LS_{\mu,6}$ | $LS_{\mu,7}$ | $LS_{\mu,8}$ | $LS_{\mu,9}$ | $LS_{\mu,10}$ |
|---|---|---|---|---|---|---|---|---|---|---|
| **$\mu$ [-]** | 1 | 2 | 3 | 4 | 5 | 6 | 7 | 8 | 9 | 10 |
| $p_f$ (50 years)=$2.2\cdot10^{-2}$ | | | | | | | | | | |

Table 3: Limit state thresholds for the superstructure.

Fig.s 4-5 show the fragility curves regarding the isolation level and the superstructure. Each figure contains several curves corresponding to the different values of the mass ratio and strength reduction factors $q$, considered in this study. Only the results corresponding to some limit state thresholds and to $T_b$=3, 6 s are reported because of space constraints. Generally, the seismic fragility decreases for increasing the limit state thresholds. The curves reflect the same trend of the IDA curves.

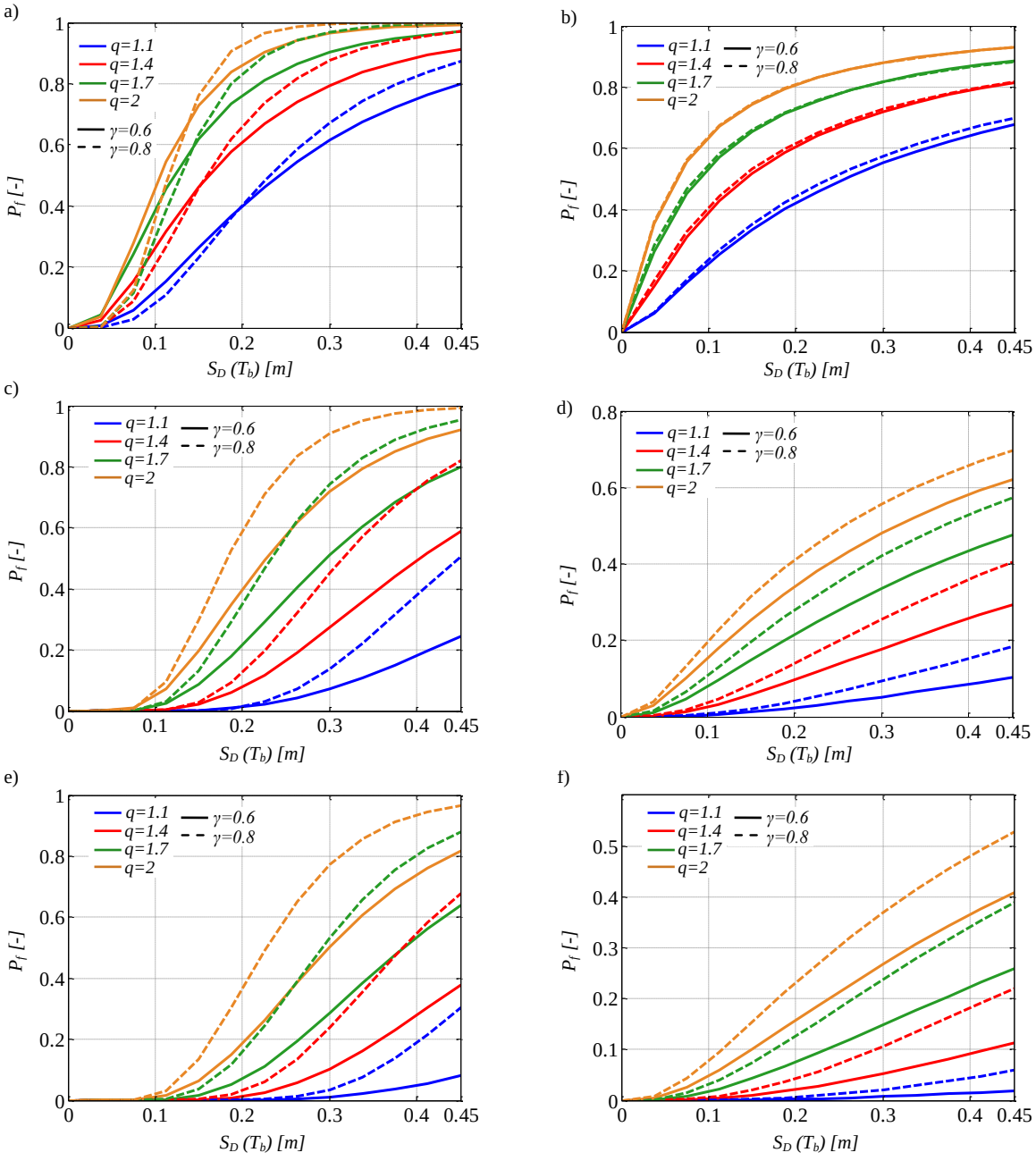


Figure 4: Seismic fragility curves of the superstructure related to $I_d$=6 for $L_{\mu,1}$=1 and $T_b$ =3 s (a), $L_{\mu,1}$=1 and $T_b$ =6 s (b), $L_{\mu,3}$=3 and $T_b$ =3 s (c), $L_{\mu,3}$=3 and $T_b$ =6 s (d), $L_{\mu,5}$=5 and $T_b$ =3 s (e), $L_{\mu,5}$=5 and $T_b$ =6 s (f).

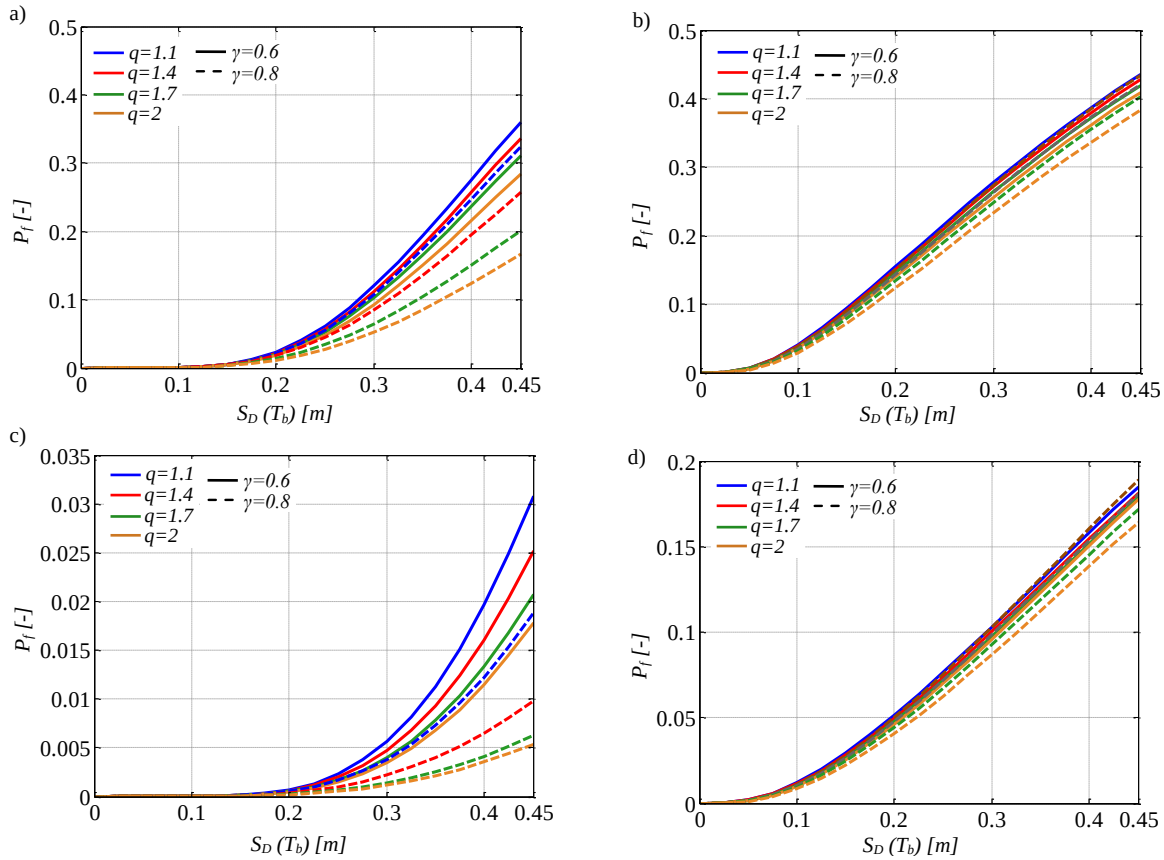


Figure 5: Seismic fragility curves of the isolation level related to $I_d$=6 for $L_{Sb,4}$=0.2 m and $T_b$ =3 s (a), $L_{Sb,4}$=0.2 m and $T_b$ =6 s (b), $L_{Sb,8}$=0.4 m and $T_b$ =3 s (c), $L_{Sb,8}$=0.4 m and $T_b$ =6 s (d).

## 4.4 Site seismic hazard

The local seismic hazard of L'Aquila site (Italy), soil class B, with geographic coordinates 42°38'49''N and 13°42'25''E, has been considered. The seismic hazard curves (Fig. 6), expressed in terms of $IM = S_D(T_b)$ and related to the four values of the isolated periods analysed in the parametric study, have been realized according to NTC08 [37]. Each curve represents the average values of the annual rate $\lambda_s$ of exceeding the *IM* level.

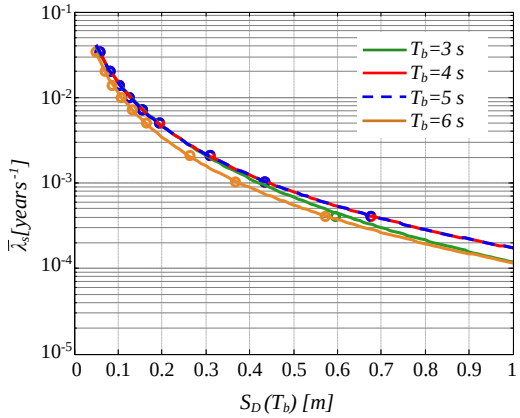


Figure 6: Seismic hazard curves related to the different isolated periods $T_b$ for L'Aquila site (Italy).

### 4.5 Seismic reliability analysis

Integrating the previously defined fragility curves with the seismic hazard curve, expressed in terms of the same *IM*, related to the reference site, allows to calculate the mean annual rates of exceeding the limit states. These latter ones have to be transformed into probabilities of exceedance in the time frame of interest (e.g., 50 years) by using a Poisson distribution in order to evaluate the seismic reliability of the base-isolated structures equipped with FP devices.

In Fig. 7-8, the linear regressions of the curves representing the seismic reliability (structural performance (SP) curves) of the isolation level and of the superstructure are plotted in logarithmic scale for the different limit state thresholds in terms of radius in plan $r$ and the displacement ductility $\mu$, respectively, and for different values of mass ratio and (ductility-dependent) strength reduction factor.

Fig. 7 shows the seismic reliability curves of the isolation level. It is possible to observe that, in most of cases, the increase of the (ductility-dependent) strength reduction factor and of the mass ratio leads to a slight increase of the seismic reliability, while an increase of $T_b$ lead to a decrease of the seismic reliability. From these seismic reliability-based design (SRBD) abacuses, it is possible to design the plan dimension of the isolator (i.e., radius in plan $r$ of the concave surface) in order to respect the expected reliability level. In particular, an exceeding probability of $P_f = 1.5 \cdot 10^{-3}$ (related to the collapse limit state, reliability index $\beta = 3$ in 50 years) [46]-[49] is achieved through a radius in plan $r$ ranging from about 0.35 m to about 0.8 m depending on the values of the structural properties.

Fig. 8 represent the seismic reliability (structural performance (SP)) curves of the inelastic superstructure. From these abacuses, it is possible to evaluate the displacement ductility demand as function of $q$ for each parameter combination corresponding to the exceeding probability in 50 years, equal to $2.2 \cdot 10^{-2}$ [46].

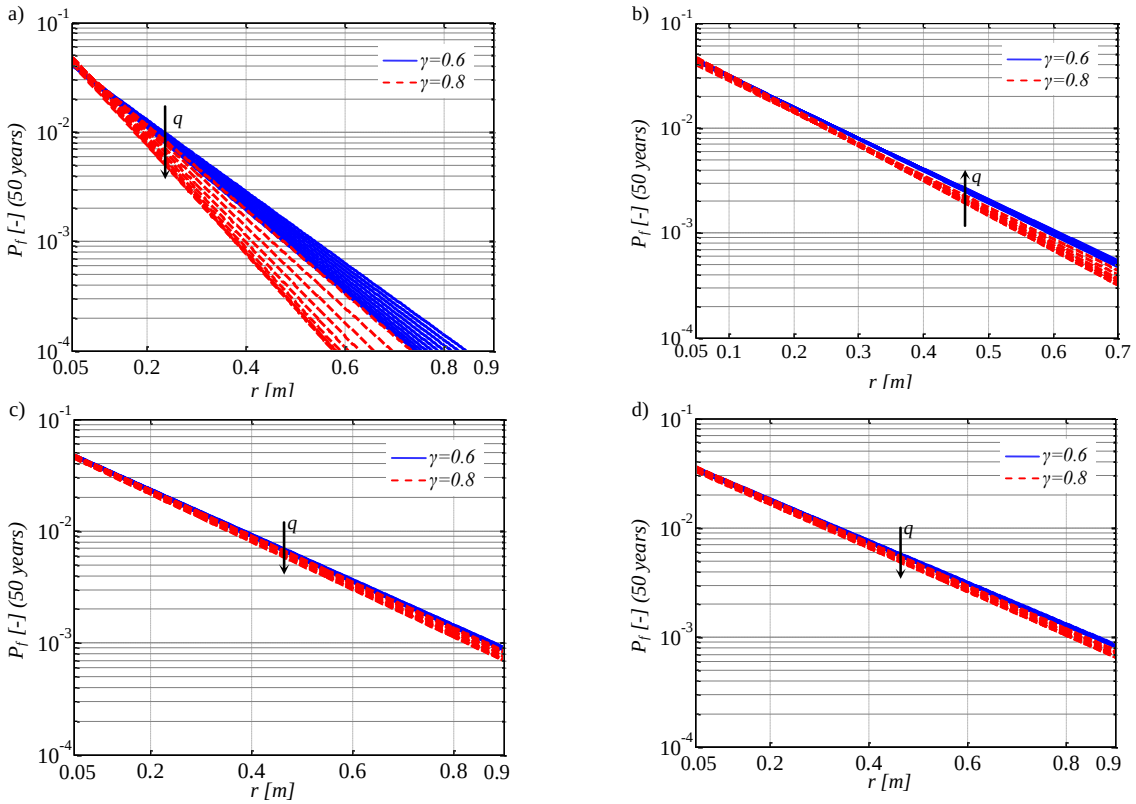


Figure 7: Seismic reliability curves of the isolation level related to $I_d$=6, for $T_b$ =3 s (a), $T_b$ =4 s (b), $T_b$ =5 s (c), $T_b$ =6 s (d).

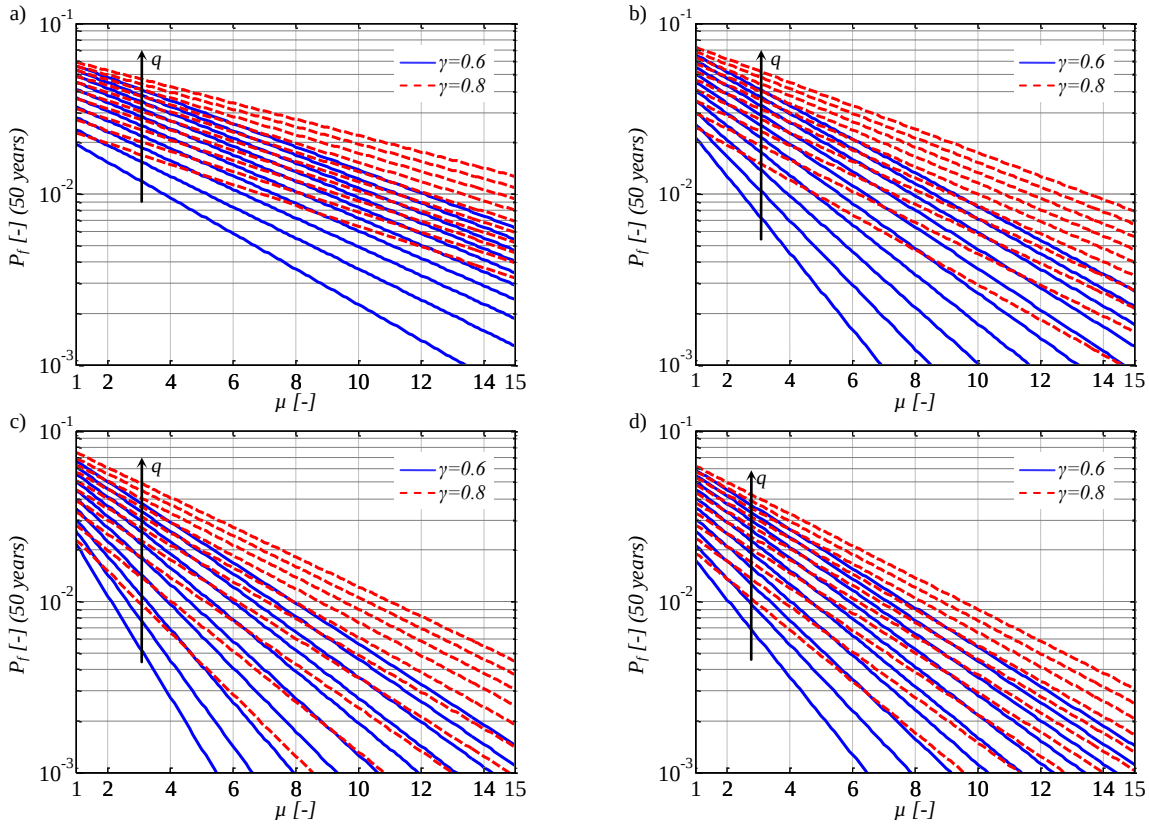


Figure 8: Seismic reliability curves of the isolation level related to $I_d$=6, for $T_b$ =3 s (a), $T_b$ =4 s (b), $T_b$ =5 s (c), $T_b$ =6 s (d).

In fact, this value of failure probability is related to the life safety limit state , adopted as reference limit state in order to define the seismic intensity of the reference site (L'Aquila, Italy) and design the inelastic characteristics of the several base-isolated structural systems analyzed, as provided by [37] and previously described. The results show that the seismic reliability of the superstructure decreases for higher values of $\gamma$, $q$ and $T_b$. Therefore, it is possible to declare that for some parameter combinations the values of the (ductility-dependent) strength reduction factor $q$ can lead to very high values of the ductility demand for base-isolated systems with FPS also due to the uncertainty on the sliding friction coefficient. Indeed, especially for high mass ratio with low isolated periods, the upper limit value of $q$ should be lower than 1.5. In the hypothesis of regular building frames, these proposed reliability-based design (SRBD) abacuses can be used for the preliminary design of the dimensions in plan of the friction pendulum devices and for the evaluation of the ductility demand of the superstructure depending on structural properties in an area with a seismic hazard similar to that considered. Within the force-based approach for designing new base-isolated systems, the codes [35]-[39] provide behaviour factors which consider both the ductility-dependent and overstrength factors depending on the properties of the superstructure. The results of the seismic reliability analysis in this study, related to both superstructure and isolation devices, represent the corresponding behaviour of the equivalent perfectly elastoplastic models and, therefore, are influenced only by the ductility-dependent term of the behaviour factor recommended by [35]-[39]. Therefore, considering a reduced value of the behaviour factor provided by the provisions [35]-[39], obtained from the ratio with respect to the corresponding overstrength factor recommended by [35]-[39], it is possible to design the FPS properties in compliance with the codes.

## 5 CONCLUSIONS

This paper deals with the seismic reliability of inelastic structural systems equipped with FPS. The isolated structures are described by employing an equivalent 2dof model characterized by a perfectly elastoplastic rule to account for the inelastic response of the yielding superstructure, whereas, the FPS behavior is described by a velocity-dependent model. Then, incremental dynamic analyses are developed to evaluate the response statistics related to both superstructure and isolation level for different mass ratios and (ductility-dependent) strength reduction factors. The estimates of the response statistics, then, are used for deriving seismic fragility curves for the yielding superstructure and the isolation level assuming different values of the corresponding limit state thresholds. In the final part of the work, considering the seismic hazard curves related to L'Aquila site (Italy), as provided by NTC08, regarding systems with a design life of 50 years, seismic reliability-based (SRBD) abacuses are proposed with the aim to define the radius in plan of the FP isolators and the ductility demand in function of the structural properties and the reliability level expected. From the results of reliability analysis of the superstructure, it is possible to declare that the values of the strength reduction factor for base-isolated systems with FPS should be lower than 1.5.

## REFERENCES

[1] C. Christopoulos, A. Filiatrault, *Principles of Passive Supplemental Damping and Seismic Isolation*. IUSS Press: Pavia, Italy, 2006.

[2] Zayas VA, Low SS, Mahin SA. A simple pendulum technique for achieving seismic isolation. *Earthquake Spectra*; **6**:317–33, 1990.

[3] Su L, Ahmadi G, Tadjbakhsh IG. Comparative study of base isolation systems. *Journal of Engineering Mechanic*; **115**:1976–92, 1989.

[4] Mokha A, Constantinou MC, Reinhorn AM. Teflon Bearings in Base Isolation. I: Testing. *J. Struct. Eng.*; **116**(2): 438-454, 1990.

[5] Constantinou MC, Mokha A, Reinhorn AM. Teflon Bearings in Base Isolation. II: Modeling. *J. Struct. Eng.*; **116**(2):455-474, 1990.

[6] Constantinou MC, Whittaker AS, Kalpakidis Y, Fenz DM, Warn GP. Performance of Seismic Isolation Hardware Under Service and Seismic Loading. Tech. Report, 2007.

[7] De Iuliis M., Castaldo P., Palazzo B., Analisi della domanda sismica inelastica del terremoto de L'Aquila su sistemi dimensionati secondo le NTC2008. *Ingegneria Sismica*, Patron Editore **XXVII**(3), 55–68, 2010.

[8] Palazzo B., Castaldo P., Marino I., The Dissipative Column: A New Hysteretic Damper," *Buildings* **5**(1), 163-178, 2015, doi:10.3390/buildings5010163.

[9] Castaldo, P., Palazzo, B., Perri F. FEM simulations of a new hysteretic damper: the dissipative column, *Ingegneria Sismica - International Journal of Earthquake Engineering*, Anno XXXIII – Speciale CTA- 2015- Num. 1-2:34-45.

[10] Castaldo P., *Integrated Seismic Design of Structure and Control Systems*. Springer International Publishing: New York, 2014 . DOI 10.1007/978-3-319-02615-2.

[11] Giugliano M.T., Longo A., Montuori R., Piluso V., Plastic design of CB-frames with reduced section solution for bracing members. *Journal of Constructional Steel Research.* Vol. 66 pp 611-621. 2010.

[12] Montuori R., Nastri E., Piluso V. Theory of plastic mechanism control for the seismic design of braced frames equipped with friction dampers - *Mechanics Research Communications* – Vol. 58. pp. 112-123 2014.

[13] Montuori R., Piluso V., Troisi M. Innovative structural details in MR-frames for free from damage structures *Mechanics Research Communications* –58, 146-156, 2014.

[14] Longo A., Montuori R., Piluso V., Theory of Plastic Mechanism Control of Dissipative Truss Moment Frames, *Engineering Structures*, Vol. 37, pp. 63-75, 2012.

[15] A. Longo, R. Montuori, V. Piluso, Failure mode control and seismic response of dissipative truss moment frames, *Journal of Structural Eng.*, **138**(11), 1388-1397, 2012.

[16] Asteris, P.G., Tsaris, A.K., Cavaleri, L., Repapis, C., Papalou, A., Di Trapani, F., Karypidis, D.F. (2015). Prediction of the Fundamental Period of Infilled RC Frame Structures Using Artificial Neural Networks, Computational Intelligence and Neuroscience, Article ID 474106, http://dx.doi.org/10.1155/2016/5104907.

[17] Asteris PG, Cavaleri L, Di Trapani F, Sarhosis V. A macro-modelling approach for the analysis of infilled frame structures considering the effects of openings and vertical loads. Structure and Infrastructure Engineering 2016 12(5): 551-566.

[18] Almazàn JL, De la Llera JC. Physical model for dynamic analysis of structures with FPS isolators. *Earthquake Engineering and Structural Dynamics*; **32**:1157–1184, 2003.

[19] Ayyub BM, McCuen RH. Probability, statistics, and reliability for engineers. 2nd ed. NY: CRC Press; 2002.

[20] Lin YK, Cai GQ. Probabilistic structural dynamics—advanced theory and applications. NY: McGraw-Hill; 1995.

[21] Cavaleri, L., Di Trapani, F., Ferrotto, M.F. A new hybrid procedure for the definition of seismic vulnerability in Mediterranean cross-border urban areas, Natural Hazards, 1-25, 2016.

[22] Asteris, P.G., Cavaleri, L., di Trapani, F., Macaluso, G., Scaduto, G. Definition of seismic vulnerability maps for civil protection systems: The case of lampedusa Island., Open Construction and Building Technology Journal 10 (Suppl 1: M5), 87-105, 2016.

[23] Chen J, Liu W, Peng Y, Li J. Stochastic seismic response and reliability analysis of base-isolated structures. *J Earthquake Eng*; **11**:903 – 24, 2007.

[24] Alhan C, Gavin HP. Reliability of base isolation for the protection of critical equipment from earthquake hazards. *Eng Struct*; **27**:1435 – 49, 2005.

[25] Zou XK, Wang Q, Li G, Chan CM. Integrated reliability-based seismic drift design optimization of base-isolated concrete buildings. *J Struct Eng*; **136**:1282 – 95, 2010.

[26] Mishra SK, Roy BK, Chakraborty S. Reliability-based-design-optimization of base isolated buildings considering stochastic system parameters subjected to random earthquakes. *Int J Mech Sci*; **75**:123 – 33, 2013.

[27] M.T. Giugliano, A. Longo, R. Montuori, V.Piluso, Influence of homoschedasticity hypothesis of structural response parameters on seismic reliability of CB-frames, *Georisk*, **5**(2), 120-131, 2011.

[28] M.T. Giugliano, A. Longo, R. Montuori, V. Piluso, Seismic reliability of traditional and innovative concentrically braced frames, *Earthquake Engineering and Structural Dynamics*, **40**(13), 1455–1474, 2011.

[29] A. Longo, R. Montuori, V. Piluso, Seismic reliability of V-braced frames: Influence of design methodologies, *Earthquake Engineering and Structural Dynamics*, **38**(14), 1587–1608, 2009.

[30] Zhao C, Chen J. Numerical simulation and investigation of the base isolated NPPC building under three-directional seisemic loading. *Nucl Eng Des*; **265**:484 – 96, 2013.

[31] Castaldo P, Palazzo B, Della Vecchia P. Seismic reliability of base-isolated structures with friction pendulum bearings. *Engineering Structures*; **95**:80-93, 2015.

[32] Castaldo P., Palazzo B., Della Vecchia P. Life-cycle cost and seismic reliability analysis of 3D systems equipped with FPS for different isolation degrees, *Engineering Structures*; 125:349–363, 2016. DOI:10.1016/j.engstruct.2016.06.056.

[33] Castaldo P., Amendola G., Palazzo B., Seismic fragility and reliability of structures isolated by friction pendulum devices: seismic reliability-based design (SRBD), *Earthquake Engineering and Structural Dynamics*, **46**(3); 425–446, 2017, DOI: 10.1002/eqe.2798.

[34] Castaldo, P., Palazzo, B., Ferrentino, T., Petrone, G.. Influence of the strength reduction factor on the seismic reliability of structures with FPS considering intermediate PGA/PGV ratios. Composites Part B: Engineering, 2016, http://dx.doi.org/10.1016/j.compositesb.2016.09.072.

[35] Structural Engineering Institute. Minimum design loads for buildings and other structures (Vol. 7, No. 5). Amer Society of Civil Engineers, 2010.

[36] European Committee for Standardization. Eurocode 8-Design of Structures for Earthquake Resistance. Part 1: General Rules, Seismic Actions and Rules for Buildings, Brussels, 2004.

[37] NTC08. Norme tecniche per le costruzioni. Gazzetta Ufficiale del 04.02.08, DM 14.01.08, Ministero delle Infrastrutture.

[38] Japanese Ministry of Land, Infrastructure and Transport, Notification No. 2009–2000, Technical Standard for Structural Specifications and Calculation of Seismically Isolated Buildings 2000.

[39] Quantification of Building Seismic Performance Factors, FEMA P695 / June 2009.

[40] Naeim F, Kelly JM. Design of Seismic Isolated Structures: From Theory to Practice. John Wiley & Sons, Inc.; 1999.

[41] Palazzo B. Seismic Behavior of base-isolated Buildings. Proc. International Meeting on earthquake Protection of Buildings, Ancona, 1991.

[42] Fanaiea N. and Afsar Dizaj E. Response modification factor of the frames braced with reduced yielding segment BRB *Structural Engin. and Mechanics*; **50**(1):1-17, 2014.

[43] Abdollahzadeh, Gh., Banihashemi, M.R. Response modification factor of dual moment-resistant frame with buckling restrained brace (BRB), *Steel Com. Str.*,**14**(6),621-636, 2013.

[44] Niroomandi A., Maheri A. Upgrading the ductility and seismic behavior factor of ordinary rc frames using fiber composite sheets, *Conference: 3rd International Conference on Concrete & Development*, 2009, Tehran, Iran, 587-598.

[45] Collins KR, Stojadinovic B. Limit states for performance-based design. 12WCEE, 2000.

[46] Bertero RD, Bertero VV. Performance-based seismic engineering: the need for a reliable conceptual comprehensive approach. *Earthquake Engineering and Structural Dynamics*; **31**:627–652, 2002 (DOI: 10.1002/eqe.146).

[47] Aoki Y, Ohashi Y, Fujitani H, Saito T, Kanda J, Emoto T, Kohno M. Target seismic performance levels in structural design for buildings. 12WCEE, 2000.

[48] SEAOC Vision 2000 Committee. Performance-based seismic engineering. Report prepared by Structural Engineers Association of California, Sacramento, CA., 1995.

[49] CEN – European Committee for Standardization. Eurocode 0: Basis of Structural Design. Final draft. Brussels, 2006.

[50] Saito T, Kanda J, Kani N. Seismic reliability estimate of building structures designed according to the current Japanese design code. Proc.s of the Str. Eng.s World Congress, 1998.

[51] Cornell CA, Krawinkler H. Progress and challenges in seismic performance assessment. PEER Center News 2000;4(1):1-3

[52] Aslani H, Miranda E. Probability-based seismic response analysis. *Engineering Structures*; **27**(8): 1151-1163, 2005.

[53] Porter KA. An overview of PEER's performance-based earthquake engineering methodology. Proceedings, *Proceedings of the 9th Internat. Conf. on Application of Statistics and Probability in Civil Engin.* (*ICASP9*), San Francisco, California, 2003; 973-980.

[54] Ryan KL, Chopra AK. Estimation of Seismic Demands on Isolators Based on Nonlinear Analysis. J. Struct. Eng., 130(3), 392–402, 2004.

[55] PEER, *Pacific Earthquake Engineering Research Center* http://peer.berkeley.edu/

[56] ITACA, *Italian Accelerometric Archive* http://itaca.mi.ingv.it/ItacaNet/itaca10_links.htm

[57] ISESD, *Internet-Site for European Strong-Motion Data* http://www.isesd.hi.is/ESD_Local/frameset.htm

[58] Mckey MD, Conover WJ, Beckman RJ. A comparison of three methods for selecting values of input variables in the analysis from a computer code. Tec..s; **21**:239-45, 1979.

[59] Vořechovský M, Novák D. Correlation control in small-sample Monte Carlo type simulations I: a simulated annealing approach. *Probabilistic Engineering Mechanics*; **24**(3):452 – 62, 2009.

[60] Celarec D, Dolšek M. The impact of modelling uncertainties on the seismic performance assessment of reinforced concrete frame buildings. *Eng. Str.*; **52**:340 – 354, 2013.

[61] Vamvatsikos D, Cornell CA. Incremental dynamic analysis. *Earthquake Engineering and Structural Dynamics*; **31**(3): 491–514, 2002.

[62] Castaldo, P., Palazzo, B., Mariniello, A.. Effects of the axial force eccentricity on the time-variant structural reliability of aging r.c. cross-sections subjected to chloride-induced corrosion Engineering Structures, **130**: 261-274, 2017.

[63] Etse, G.J., Ripani, M., Vrech, S.M. "Fracture energy-based thermodynamically consistent gradient model for concrete under high temperature," Proceedings of the 8th International Conference on Fracture Mechanics of Concrete and Concrete Structures, FraMCoS 2013, 1506-1515.

[64] Etse, G., Ripani, M., Caggiano, A. & Schicchi, D.S. "Strength and durability of concrete subjected to high temperature: continuous and discrete constitutive approaches," American Concrete Institute, ACI Special Publication 2015-January (SP 305), 9.1-9.18.

[65] Etse, G., Ripani, M. & Mroginski, J.L. "Computational failure analysis of concrete under high temperature," Computational Modelling of Concrete Structures - Proceedings of EURO-C 2014, 2:715-722.

[66] Etse, G., Vrech, S.M. & Ripani, M. "Constitutive theory for Recycled Aggregate Concretes subjected to high temperature," Construction and Building Materials; **111**: 43-53, 2016.

[67] Mroginski, J.L., Etse, G., Ripani, M. "A non-isothermal consolidation model for gradient-based poroplasticity," PANACM 2015 - 1st Pan-American Congress on Computational Mechanics, in conjunction with the 11th Argentine Congress on Computational Mechanics, MECOM 2015, pp. 75-88.

[68] Ripani, M., Etse, G., Vrech, S. & Mroginski, J.L. "Thermodynamic gradient-based poroplastic theory for concrete under high temperature," International Journal of Plasticity; **61**: 157-177, 2014.

[69] Ripani, M., Etse, G., Vrech, S. "Recycled aggregate concrete: localized failure assessment in thermodynamically consistent non-local plasticity framework", Computers and Structures, **178**: 47–57, 2017, doi: 10.1016/j.compstruc.2016.08.007.

[70] Vrech, S.M., Ripani, M. & Etse, G. "Localized versus diffused failure modes in concrete subjected to high temperature," PANACM 2015 - 1st Pan-American Congress on Computational Mechanics, in conjunction with the 11th Argentine Congress on Computational Mechanics, MECOM 2015, pp. 225-236.

[71] Campione, G., Cavaleri, L., Di Trapani, F., Macaluso, G., Scaduto, G. Biaxial deformation and ductility domains for engineered rectangular RC cross-sections: A parametric study highlighting the positive roles of axial load, geometry and materials, Engineering Structures **107**, 116-134, 2016.

COMPDYN 2017
6th ECCOMAS Thematic Conference on
Computational Methods in Structural Dynamics and Earthquake Engineering
M. Papadrakakis, M. Fragiadakis (eds.)
Rhodes Island, Greece, 15–17 June 2017

# SEISMIC RELIABILITY-BASED DESIGN OF INELASTIC STRUCTURES WITH DIFFERENT VALUES OF THE POST-YIELDING STIFFNESS ISOLATED BY FPS

**P. Castaldo[1], B. Palazzo[2], G. Alfano[2] and M. F. Palumbo[2]**

[1]Department of Structural, Geotechnical and Building Engineering (DISEG), Politecnico di Torino,
Corso Duca degli Abruzzi, 24, Turin, Italy (corresponding author);
e-mail: paolo.castaldo@polito.it; pcastaldo@unisa.it

[2]Department of Civil Engineering, University of Salerno,
Via Giovanni Paolo II (SA), Italy;
e-mail: palazzo@unisa.it; gae.alfano@gmail.com; mfr.plm@gmail.com

**Keywords:** seismic isolation; friction coefficient; seismic reliability; ductility demand; behaviour factor; post-yield stiffness..

**Abstract.** *This work aims to evaluate the seismic reliability of nonlinear systems, considering both a hardening and softening post-yielding behavior, isolated by friction pendulum devices (FPS) for different values of the strength reduction factor. The isolated structure is described through an equivalent 2dof model, whereas, the FPS behavior is described by a velocity dependent model. An extensive parametric study is carried out encompassing a wide range of inelastic building properties considering different values of the post-yielding stiffness, different seismic intensity levels and considering the friction coefficient as a random variable. Defined a set of natural seismic records and scaled to the seismic intensity corresponding to life safety limit state for L'Aquila site (Italy) according to NTC08, the yielding characteristics of the superstructures are consequently designed according to NTC08 for different values of the strength reduction factor. Incremental dynamic analyses (IDA) are developed to evaluate the seismic fragility curves of both the inelastic superstructure and the isolation level assuming different values of the corresponding limit states. Integrating the fragility curves with the seismic hazard curves related to L'Aquila site (Italy), the reliability curves of the inelastic base-isolated structural systems, with a design life of 50 years, are derived and proposed in order to provide useful design recommendations depending on both the strength reduction factors and post-yielding behavior.*

## 1 INTRODUCTION

Friction pendulum system (FPS) represents an effective technique for the seismic isolation [1] of building frames [2]-[3]. The modeling aspects of the FPS isolation technique (e.g., [4]-[7]) and the effects of the variation of both systems and FP devices as well the influence of the seismic input have been object of many works. Over the years, within the issue of the passive control of structures, many works have developed new design strategies and methodologies [8]-[14]. Reliability analysis and reliability-based optimization of base-isolated systems including uncertainties of both the isolation devices properties and ground motion characteristics have been evaluated by [15]-[18].

In [19], the life-cycle cost analysis of the abovementioned r.c. 3D system isolated by FPS bearings has been evaluated for increasing values of the isolation degree. The seismic reliability-based design (SRBD) approach for elastic systems has been proposed by Castaldo et al. [20]. Optimal friction coefficient values have been defined in [21] depending on the soil condition.

Seismic codes [22]-[26] aim to keeping the response of base-isolated structures, under strong earthquake events, elastic in order to avoid non linear amplification phenomenon [27] by means of low values of the strength reduction factor [22],[26] or behaviour factor [23]-[24]. In particular, the Italian seismic code, NTC08 [24], the European seismic code Eurocode 8 [23] and the Japanese building code [25] provide a maximum behavior factor value of 1.5 for base-isolated structures, without explicitly distinguishing the different terms (i.e., ductility and overstrength factors). The US seismic design codes, ASCE 7 [22], prescribes the strength reduction factor for a seismically isolated structure to be 0.375 times the one for a corresponding fixed-base structure and no larger than 2. Indeed, Vassiliou et al. [28], proved that if the base-isolated structures are designed to respond inelastically, the displacement ductility demand of the inelastic base-isolated structure is 3 times the strength reduction factor. Furthermore, [29] and [30] proved that the equal displacement rule and the equal energy rule cannot be used for isolated systems. Reliability-based relationship between the ductility-dependent strength reduction factors and the displacement ductility demand are proposed by [31] for a perfectly elastoplastic structural system equipped with FPS and located in L'Aquila site (Italy) for different structural system properties.

The aim of this work is to further advance the study of Castaldo et al. [31] evaluating the seismic reliability of non linear base-isolated systems with hardening and softening post-yield stiffness and for increasing strength reduction factors.

## 2 NON-LINEAR SOFTENING MODEL OF A BASE-ISOLATED STRUCTURE WITH FPS

The model used in this study is the 2dof system proposed by Kelly [35], modified to account for the non-linear responses of both the isolation level and the superstructure (Fig. 1). The bearing response is modelled using a bilinear hysteretic response envelope, a typical model used for FPS system in the hypothesis to consider the horizontal component of the FP displacements [2].Therefore, the bearing restoring force is:

$$f_b = \frac{W}{R} u_b + \mu_d W \operatorname{sgn}\left(\dot{u}_b\right) \tag{1}$$

where $W = \left(m_b + m_s\right)g$ is the weight on the bearing, $g$ is the gravity constant, $R$ is the radius of curvature of the FPS, $u_b$ is the displacement of the isolation level with respect to the

ground, $\mu_d$ is the bearing friction coefficient, sgn is the signum function of the sliding velocity, $\dot{u}_b$.

The friction coefficient at sliding velocity $\dot{u}_b$, according to Mokha et el. and Constantinou et al. [4]-[6], can be approximated by the following equation:

$$\mu_d = f_{\max} - (f_{\max} - f_{\min})\exp(-\alpha \dot{u}_b) \tag{2}$$

where $f_{\max}$ and $f_{\min}$ are the friction coefficient attained at high and at very low velocities of sliding respectively, $\alpha$ is a constant for a given pressure, temperature and condition of FPS interfaces, assumed equal to 30 and the ratio $f_{\max} / f_{\min}$ equal to 3 [21],[31].

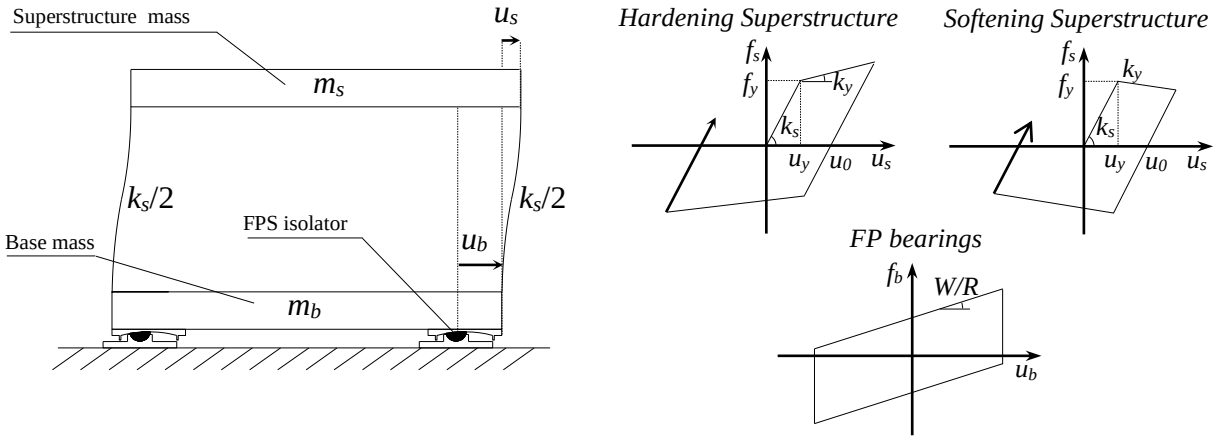


Figure 1: 2dof model of a building isolated with FPS.

Regarding the inelastic response of the superstructure, the behaviour is described using a non-linear constitutive law, for which the restoring force varies if the superstructure is in the elastic or in plastic phases. The superstructure is in the elastic phases if Eqn.(3) is satisfied and the corresponding restoring force is given by Eqn.(4).

$$\left|u_{s,i} - u_{0,i-1}\right| < y\left(u_{s,i}\right) \tag{3}$$

$$f_{s,i}\left(u_{s,i}\right) = k_s\left(u_{s,i} - u_{0,i-1}\right) \tag{4}$$

In the equations (3) and (4), $f_{s,i}$ is the superstructure restoring force at time instant $i$, $u_{s,i}$ is the deformation of the superstructure with respect to the base at time instant $i$, $u_{0,i-1}$ is the maximum plastic excursion at time instant $(i-1)$, $k_s$ is the elastic stiffness of the superstructure. The function $y(u_{s,i})$ is the yielding condition that is not univocally defined because the elastic domain translates, so the yielding limits are different in function of the direction of the displacement. The yielding condition can assume the following values:

$$y(u_{s,i}) = u_y + S\left(u_{s,i} - u_y\right) \text{ for } (u_{0,i-1} \geq 0 \ \&\ u_{s,i} > u_{0,i-1}) \text{ and } (u_{0,i-1} < 0 \ \&\ u_{s,i} < u_{0,i-1})$$

$$y(u_{s,i}) = u_y - S\left(u_{s,i} - u_y\right) \text{ for } (u_{0,i-1} \leq 0 \ \&\ u_{s,i} > u_{0,i-1}) \text{ and } (u_{0,i-1} > 0 \ \&\ u_{s,i} < u_{0,i-1}) \tag{5a,b}$$

where $u_y$ is the yield displacement, whose yield force is $f_y$, $S$ is the ratio between the post-yield and the elastic stiffness [36],[37]:

$$S = \frac{k_y}{k_s} \tag{6}$$

The superstructure is in the plastic phases if:

$$\left|u_{s,i}-u_{0,i-1}\right| \geq y(u_{s,i}) \tag{7}$$

the restoring force applies:

$$f_{s,i}\left(u_s\right)=k_s(u_{s,i}-y)\operatorname{sgn}(u_{s,i}-u_{0,i-1}) \tag{8}$$

It follows that the response of an inelastic 2dof system isolated with FPS devices (Fig. 1) to the seismic input $\ddot{u}_g\left(t\right)$ is governed by Eqn. (9):

$$\begin{aligned}&\left(m_b+m_s\right)\ddot{u}_b+m_s\ddot{u}_s+c_b\dot{u}_b+\frac{W}{R}u_b+\mu_d W\operatorname{sgn}\dot{u}_b=-\left(m_b+m_s\right)\ddot{u}_g\\&m_s\ddot{u}_b+m_s\ddot{u}_s+c_s\dot{u}_s+f_s\left(u_s\right)=-m_s\ddot{u}_g\end{aligned} \tag{9a,b}$$

where $m_s$ and $m_b$ are respectively the mass of the superstructure and of the basement, $c_s$ is the superstructure viscous damping constant, $c_b$ is the bearing viscous damping constant. By introducing the mass ratio $\gamma=\dfrac{m_s}{\left(m_s+m_b\right)}$ [35], the isolation $\omega_b=\sqrt{\dfrac{k_b}{\left(m_s+m_b\right)}}=\sqrt{\dfrac{g}{R}}$ and structural $\omega_s=\sqrt{k_s/m_s}$ circular frequency, the isolation $\xi_b=c_b/2\left(m_b+m_s\right)\omega_b$ and structural $\xi_s=c_s/2m_s\omega_s$ damping ratio, and dividing Eqn.(9a) by $m_b+m_s$ and Eqn.(9b) by $m_s$, the equations of motion can be reduced to a non-dimensional form:

$$\begin{aligned}&\ddot{u}_b+\gamma\ddot{u}_s+2\xi_b\omega_b\dot{u}_b+\frac{g}{R}u_b+\mu_d g\operatorname{sgn}\dot{u}_b=-\ddot{u}_g\\&\ddot{u}_b+\ddot{u}_s+2\xi_s\omega_s\dot{u}_s+a_s\left(u_s\right)=-\ddot{u}_g\end{aligned} \tag{10a,b}$$

where $a_s\left(u_s\right)=f_s\left(u_s\right)/m_s$ is the dimensionless force of the superstructure that changes if the superstructure is in an elastic or plastic phase. The seismic isolation degree [40] is an indicator of isolation system efficiency for elastic structures and results to be the ratio between the isolation $T_b=2\pi/\omega_b$ and structural $T_s=2\pi/\omega_s$ period of vibration: $I_d=T_b/T_s$ [40].

### 2.1 Behavior factor and displacement ductility of the non-linear superstructure

Regarding the inelastic response of a superstructure ([40]), characterized by a single degree of freedom with an hardening or softening behavior the strength reduction factor is defined as:

$$q=\frac{f_{s,el}}{f_y}=\frac{u_{s,el}}{u_y} \tag{11}$$

where $f_{s,el}$ and $u_{s,el}$ are, respectively, the minimum yield strength and yield deformation required for the superstructure to remain elastic during a ground motion, or the peak response values for the corresponding linear system. Note that in the case of softening systems, assumed as the equivalent model representative of multistory frame taking count of the $P-\Delta$ effect [38],[39] the abovementioned behaviour factor $q$ represents only the ductility-dependent term strength reduction factor because overstrength capacities, assumed with the equivalent model, are completely absent. Therefore, the reduction factor or behavior factor, hereinafter denoted as $q$, is consistent with the code provisions [22]-[26] in the case of a unitary overstrength factor and with the one discussed by [31] for the case of softening systems.

The displacement ductility, $\mu$, of the superstructure is defined as:

$$\mu=\frac{u_{\mathrm{s,max}}}{u_y} \tag{12}$$

where $u_{s,\max} = \left| u_s(t) \right|_{\max}$ is the peak displacement of the inelastic system

## 3 UNCERTAINTIES WITHIN THE SEISMIC RELIABILITY OF NON-LINEAR SUPERSTRUCTURES EQUIPPED WITH FPS

According to the structural performance (SP) evaluation method [41]-[43], the seismic reliability assessment of buildings is based on the coupling between SP levels [44] and associated exceeding probabilities during its design life [45]-[46]. Coherently with the PEER-like modular approach [47] and performance-based earthquake engineering (PBEE) approach [48]-[49], the uncertainties related to the seismic input intensity are separated from those related to the characteristics of the record (record-to-record variability) by introducing an intensity measure (*IM*). The approach, as also discussed in [20],[31], is based on calculating the convolution integral between the fragility curves and a seismic hazard curve, expressed in terms of the same *IM*, related to a reference site, in order to define the mean annual rates exceeding the limit states and, next, using a Poisson distribution, evaluate the exceeding probabilities in the time frame of interest (e.g., 50 years). Superstructure properties are not included as random variables as discussed in [31],[50]. Regarding the uncertainty of the sliding friction coefficient at large velocity of the FP devices, an appropriate Gaussian probability density function (PDF) is employed and the Latin Hypercube Sampling (LHS) method [31]-[34] is adopted as random sampling technique in order to define the input data set, as also described in [31] in order to compare the results. In particular, the friction coefficient at large velocity is modelled through a Gaussian probability density function (PDF), defined from 0.5% to 5.5% with a mean value equal to 3% [51] and a standard deviation equal to the dispersion of a corresponding uniform PDF truncated on both sides to 0.5% and 5.5%. As widely discussed in [31], 15 values of the random variable $f_{\max}$ are sampled through the LHS method.

### 3.1 Seismic input and intensity measure (IM) description

In this study, the spectral displacement, $S_D(\xi_b, T_b)$, at the isolated period of the system, $T_b = 2\pi / \omega_b$ and for the damping ratio $\xi_b$, is assumed as intensity measure. The spectral displacement is related to the spectral acceleration $S_D(\xi_b, T_b) = S_{pa}(\xi_b, T_b) / \omega_b^2$. In the analyses carried out in this study, the damping ratio $\xi_b$ is taken equal to zero, consistently with other works which assume that friction is the only source of damping in the isolators [31],[52]. The corresponding *IM* is hereinafter denoted as $S_D(T_b)$ and it is assumed ranging from 0 m to 0.45 m according to the seismic hazard of L'Aquila site (Italy) [24]. A set of 30 natural ground motion records, selected within the ground motion databases [53]-[55]. The details and characteristics of the selected ground motion records may be found in [31].

## 4 PARAMETRIC STUDY: INCREMENTAL DINAMIC ANALYSIS RESULT

The first step to determinate the seismic reliability of the inelastic softening base-isolated equivalent systems, located in L'Aquila site (Italy), consists in developing incremental dynamic analyses (IDAs) [56]. An extensive parametric study is carried out encompassing a wide range of the parameter combinations related to isolation level and superstructure, according to Eqn.(10).

### 4.1 Parametric study

The parametric study encompasses several values related to elastic and inelastic building properties combined with the 15 input values of the friction coefficient random variable, the 30 ground motion records scaled to the different levels of the $IM = S_D(T_b)$, ranging from 0 m to 0.45 m. The deterministic parameters are: the seismic isolation degree $I_d$ equal to 4, the isolation period of vibration $T_b$ equal to 6 s, the mass ratio $\gamma$ assumed equal to 0.6 and 0.8, the behavior factor *q* ranging from 1.1 to 2 according to the codes [22]-[25] and the post-yield stiffness *S* assumed equal to $\pm 0.03$ [36]-[39]. It follows that several equivalent 2dof structural systems, with isolation damping ratio $\xi_b$ and superstructure damping ratio $\xi_s$ respectively equal to 0% and 2%, are defined. In order to develop the incremental non-linear dynamic analyses, the yielding characteristics of each equivalent structural system have to be designed. Therefore, the elastic equivalent 2dof system with a design friction coefficient equal to 3% has been subjected to the set of 30 seismic records, scaled to the $IM = S_D(T_b)$ value related to the life safety limit state (NTC08 [24]) for L'Aquila site (Italy): the $IM = S_D(T_b)$ is equal to 0.26 m for $T_b$ =6 s [31]. The dynamic analyses, carried out in Matlab-Simulink [68], of the 32 base-isolated systems equipped with velocity-dependent FPS and with a superstructure linear behaviour have allowed to evaluate the average values of both the yield strength $f_{y,\text{average}}$ and displacement $u_{y,\text{average}}$ of the superstructure for each value of *q*, according to Eqn.(13) and as developed in [31]. In this way, all the yielding characteristics of the seveal equivalent non-linear structural systems have been defined according to the codes [22]-[25] in order to compare the results with the outcomes described in [31] and evaluate the influence of the post-yield stiffness.

$$u_{y,average} = \frac{f_{y,average}}{k_s} = \frac{f_{s,el,average}}{k_s q} = \frac{u_{s,el,average}}{q} \tag{11}$$

### 4.2 Incremental dynamic analysis (IDA) result for different structural parameters

The above-mentioned equivalent non-linear structural systems, with the different structural parameters (*q* and *S*) and combined for each value of the sampled friction coefficient, are subjected to the 30 ground motions, scaled to the several intensity levels values within the IDA. The isolated non-linear systems are modelled in Matlab-Simulink [68] to solve the coupled equations (Eqn.(10)) and determine the isolation and superstructure responses. In particular, the Runge-Kutta-Fehlberg integration algorithm available in Matlab-Simulink has been employed. A total number of 450 simulations has been carried out for each IM and parameters combination. Note that for a structure with a softening behaviour the maximum available ductility capacity, assumed herein as the collapse condition, is reached when the reduction in the strength is complete. This assumption represents the failure condition assumed within the numerical analyses. The results of the incremental non-linear dynamic analyses (IDAs), taking into account the collapsed systems, have allowed to estimate the superstructure and isolation response parameters, expressed in terms of displacement ductility demand $\mu$ and of maximum displacement of the isolation level with respect to the ground $u_{b,\max} = |u_b(t)|_{\max}$, respectively, adopted as the engineering demand parameters (EDPs) and assumed to follow a lognormal distribution [21],[31],[48],[52]. Knowing the sample lognormal mean $\mu_{\ln}(EDP)$ and the dispersion $\beta(EDP)$, it is possible to determine the 50$^{\text{th}}$, 84$^{\text{th}}$ and 16$^{\text{th}}$ percentile of

each lognormal distribution [20]. The IDA results of the isolation level and the superstructure are respectively illustrated in Fig.s 2-3 depending on the intensity measure *IM* and on the behavior factor *q*.

Note that the 50$^{th}$, 84$^{th}$ and 16$^{th}$ percentiles, related to both isolation level and superstructure shown in the figures of this section, have been evaluated only from the results without considering the failures. The presence of the data characterized by the dynamic collapses has been taken into account within the seismic fragility assessment as discussed later. This means that, for the case of softening systems, some results from the IDA curves do not represent the real response of these systems. In particular, all IDA curves, related to softening systems, illustrate that for quite all parameter combinations and *IM* levels, the number of dynamic collapses is very high.

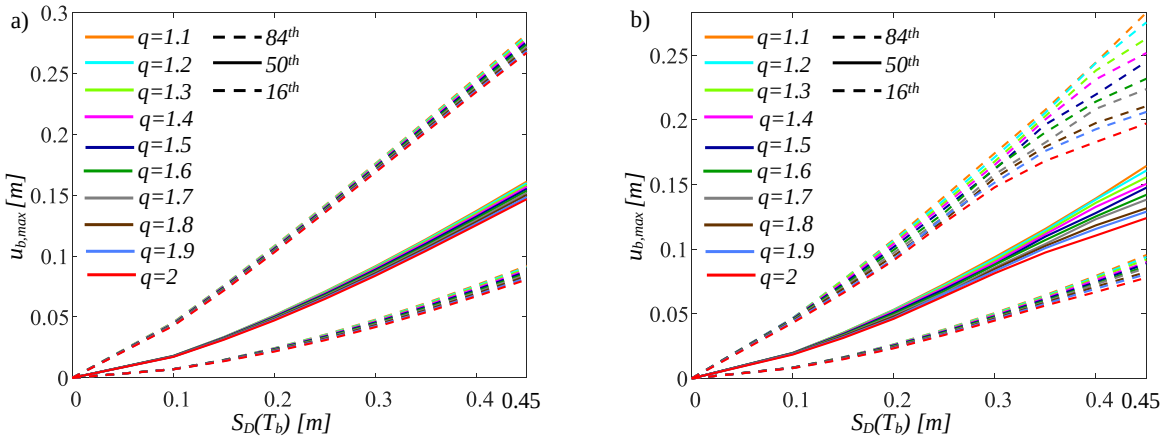


Fig. 2. IDA curves of the isolation level with $\gamma$ =0.6, $I_d$=4, and $T_b$=6 s for $S$=+0.03 (a), $S$=-0.03 (b)

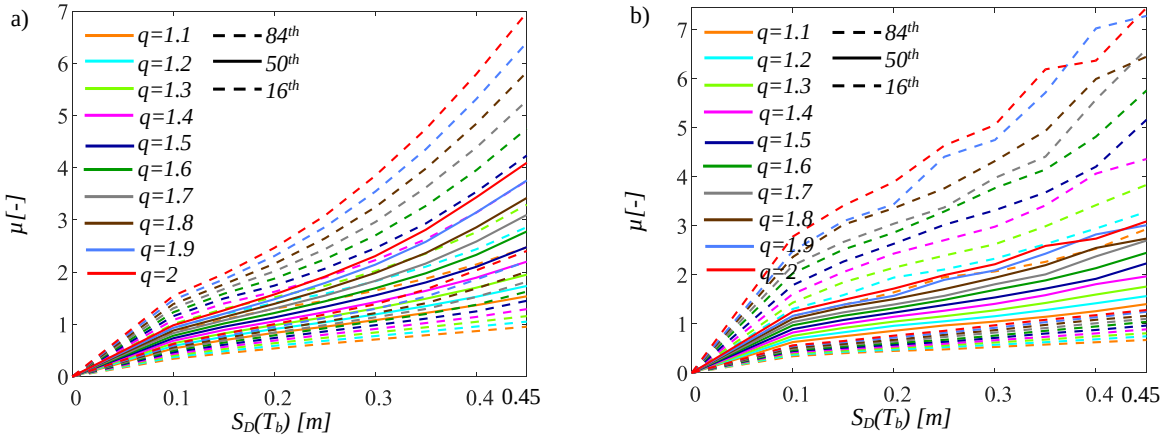


Fig. 3. IDA curves of the superstructure with $\gamma$ =0.6, $I_d$=4, and $T_b$=6 s for $S$=+0.03 (a), $S$=-0.03 (b).

Fig. 2 shows the IDA results regarding the isolation level response parameter $u_{b,\max}$, whereas Fig. 3 shows the IDA curves regarding the superstructure EDP $\mu$. The statistics of the EDP $\mu$ are strongly influenced by *q*: the increase of the strength reduction factor *q* leads to a very high increase of the displacement ductility demand $\mu$.

## 5 SEISMIC FRAGILITY OF INELASTIC SOFTENING STRUCTURES WITH FPS

In order to evaluate the seismic fragility, defined as the probabilities $P_f$ exceeding different limit states (*LSs*) at each level of the *IM*, of the isolation level and of the superstructure, the limit state *LS* thresholds have to be defined. In particular, the performance levels of the isolation system are assumed in terms of radius in plan of the concave surface, $r$ [m]; while, the performance levels of the superstructure are defined in terms of available displacement ductility, $\mu$ [-]. Tables 1-2 show the *LS* for the isolation level and the superstructure related to the collapse and the safety limit state respectively considering structural systems in ordinary conditions and neglecting aging effects [57]-[67]. For both collapse and life safety *LSs*, characterized by appropriate failure probabilities in 50 years [19],[42],[43], several thresholds are analyzed because the scope of the study is to define the *LS* thresholds to be employed for a reliable design or verification of base-isolated non linear systems analyzing the response of the equivalent inelastic 2dof model, as discussed in the following sections.

| | $LS_{b,1}$ | $LS_{b,2}$ | $LS_{b,3}$ | $LS_{b,4}$ | $LS_{b,5}$ | $LS_{b,6}$ | $LS_{b,7}$ | $LS_{b,8}$ | $LS_{b,9}$ | $LS_{b,10}$ |
|---|---|---|---|---|---|---|---|---|---|---|
| ***r [m]*** | *0.05* | *0.1* | *0.15* | *0.2* | *0.25* | *0.3* | *0.35* | *0.4* | *0.45* | *0.5* |
| $p_f(50\ years)=1.5\cdot10^{-3}$ | | | | | | | | | | |

Table 1: Limit state thresholds for the isolation level.

| | $LS_{\mu,1}$ | $LS_{\mu,2}$ | $LS_{\mu,3}$ | $LS_{\mu,4}$ | $LS_{\mu,5}$ | $LS_{\mu,6}$ | $LS_{\mu,7}$ | $LS_{\mu,8}$ | $LS_{\mu,9}$ | $LS_{\mu,10}$ |
|---|---|---|---|---|---|---|---|---|---|---|
| ***μ [-]*** | *1* | *2* | *3* | *4* | *5* | *6* | *7* | *8* | *9* | *10* |
| $p_f(50\ years)=2.2\cdot10^{-2}$ | | | | | | | | | | |

Table 2: Limit state thresholds for the superstructure.

The probabilities $P_f$ exceeding different *LSs* at each level of the *IM*, are numerically computed for each combination of the structural properties (1280 equivalent structural systems) and then fitted through lognormal distributions [20]. In this phase, as for the softening systems and with the aim to consider both the collapse and not-collapse cases for each parameter combination at each *IM* level, the total probability theorem allows to estimate the probability exceeding a limit state at each intensity measure level considering the collapse number [69] as follows:

$$P_{SL}(IM = im) = (1 - F_{EDP|IM=im}(LS_{EDP})) \cdot \frac{N_{not-collapse}}{N} + 1 \cdot \left(1 - \frac{N_{not-collapse}}{N}\right) \qquad (12)$$

where $N$ is the total number of analyses for the structural system at each *IM* level, and $N_{not-collapse}$ is the number of numerical simulations without any collapse. The first term of Eq.(12) defines the probability exceeding a *LS* corresponding to not-collapsing structural models [69]. The fragility curves are plotted in Fig.s 4-7 showing the exceedance probabilities $P_f$ versus the ground motion intensity. Each figure contains several curves corresponding to the different values of the mass ratio and strength reduction factors $q$ considered. Only the results corresponding to some limit state thresholds and to $I_d$=4 and $T_b$=6 s are reported because of space constraints.

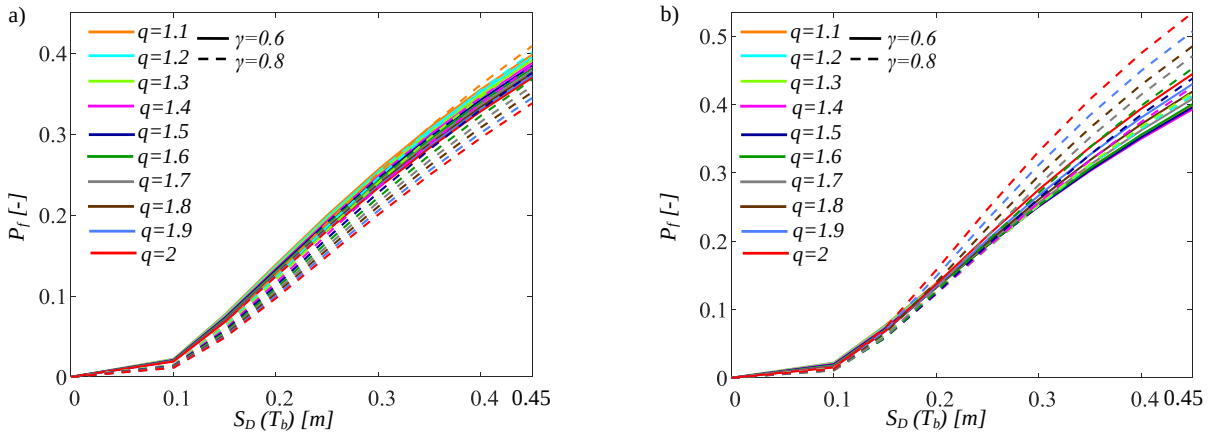


Fig. 4. Seismic fragility curves of the isolation level related to $LS_{b,4}$=0.2 m, for $I_d$=4 and $T_b$=6 s, $S$=+0.03 (a), $I_d$=4 and $T_b$=6 s, $S$=-0.03 (b).

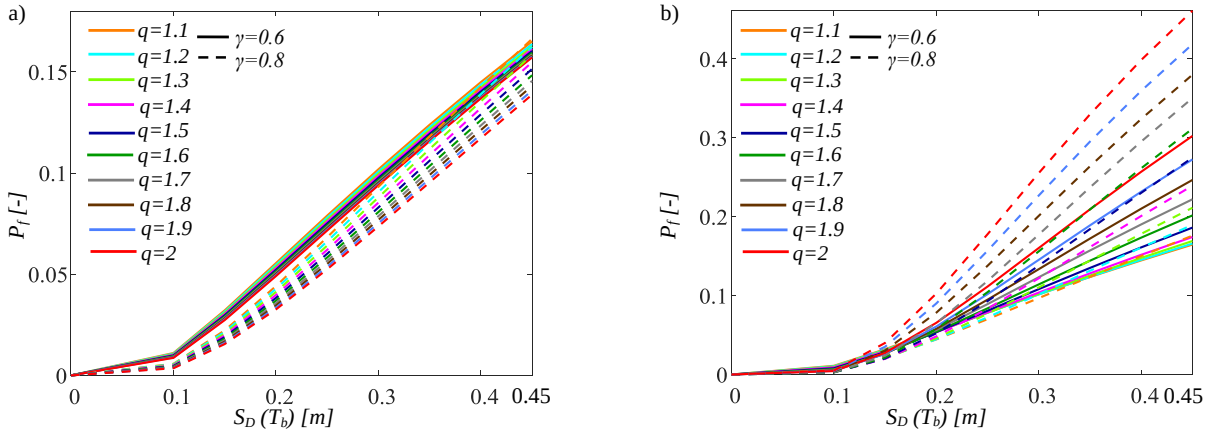


Fig. 5. Seismic fragility curves of the isolation level related to $LS_{b,8}$=0.4 m, for $I_d$=4 and $T_b$=6 s, $S$=+0.03 (a), $I_d$=4 and $T_b$=6 s, $S$=-0.03 (b).

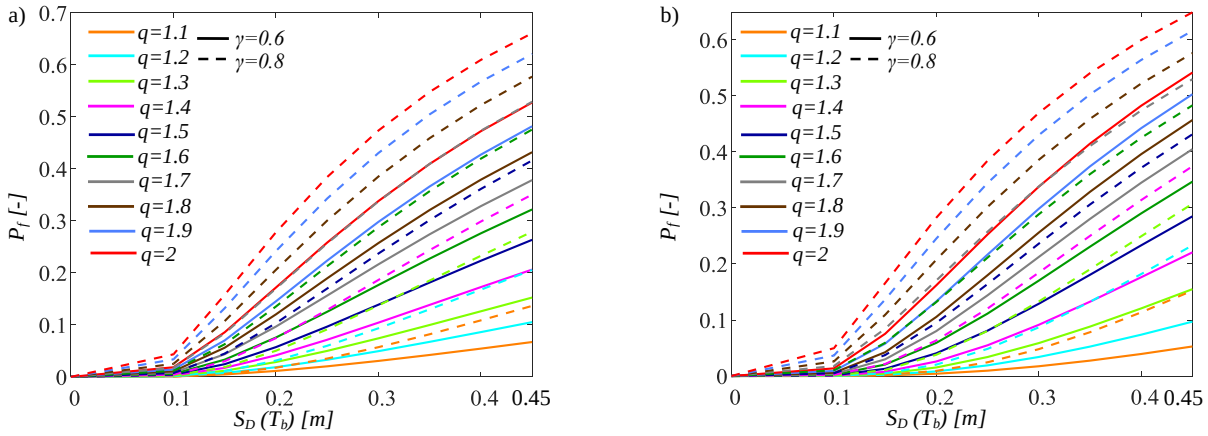


Fig. 6. Seismic fragility curves of the superstructure related to $LS_{\mu,3}$=3, for $I_d$=4 and $T_b$=6 s, $S$=+0.03 (a), $I_d$=4 and $T_b$=6 s, $S$=-0.03 (b).

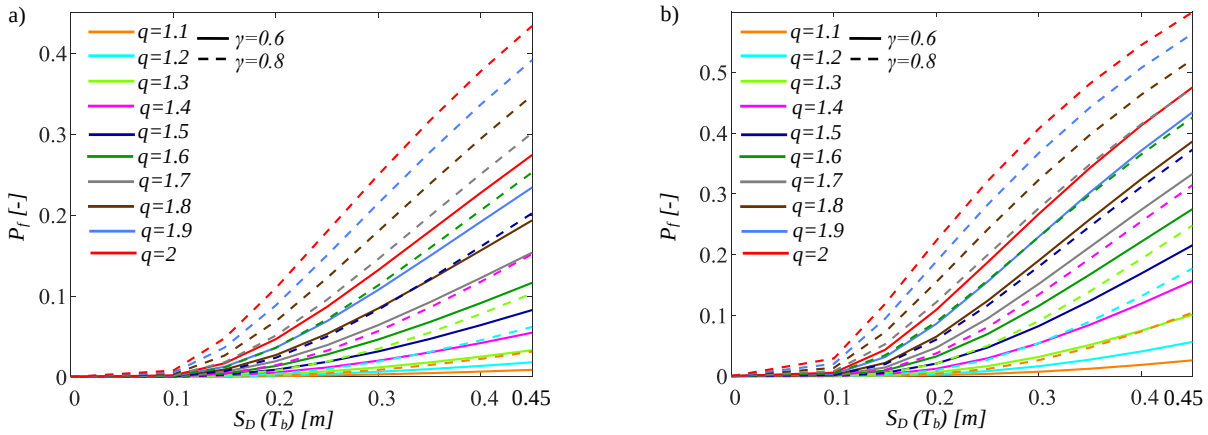


Fig. 7. Seismic fragility curves of the superstructure related to $LS_{\mu,5}$=5, for $I_d$=4 and $T_b$=6 s, $S$=+0.03 (a), $I_d$=4 and $T_b$=6 s, $S$=-0.03 (b).

Fig.s 4-5 show the fragility curves regarding the isolation level. Generally, the seismic fragility decreases for increasing the limit state thresholds. For all limit states, the exceeding probabilities slightly decrease for higher values of $\gamma$. The influence of $\gamma$ is amplified also due to the uncertainty of the friction coefficient. Especially, in the case of high values of limit state thresholds, the exceeding probabilities $P_f$ increase by increasing $q$. Furthermore, a decrease of the post-yield stiffness ratio $S$ also leads to higher probability of exceedance.

Fig.s 6-7 show the fragility curves regarding the superstructure. Similarly to the isolation seismic fragility curves, the exceeding probabilities decrease by increasing the limit state thresholds. Higher values of $\gamma$ lead to slightly higher values of the exceeding probabilities as well as higher values of $q$ lead to strongly higher values of seismic fragility. Moreover, the post-yield stiffness ratio $S$ strongly influences leading to a higher displacement ductility demand for lower values of $S$.

## 6 SEISMIC RELIABILITY OF INELASTIC BASE-ISOLATED STRUCTURES WITH FPS

Integrating the previously defined seismic fragility curves with the seismic hazard curves, expressed in terms of the same $IM$, $S_D(T_b)$, related to the reference site (L'Aquila (Italy)), allows to calculate the mean annual rates exceeding the limit states in the time frame of interest. These latter ones have to be transformed into exceeding probabilities in the time frame of interest (e.g., 50 years) by using a Poisson distribution in order to evaluate the seismic reliability of the non-linear structures isolated by FPS. In this work, the local seismic hazard of L'Aquila site (Italy), soil class B, with geographic coordinates 42°38'49''N and 13°42'25''E, has been considered according to [31]. The seismic hazard curves have been defined in terms of $IM = S_D(T_b)$ and related to the isolated period analysed in the parametric study, according to NTC08 [24]. The seismic hazard curve represents the average values of the annual rate exceeding the $IM = S_D(T_b)$ level, as widely discussed in [31].

The linear regression curves, for the isolation level, defined in the range between $10^{-1}$-$10^{-4}$ in the semi-logarithmic space, representative of the seismic reliability of the friction devices, are plotted for different displacement thresholds, varying from 0.05 m to 1 m, in Fig. 8. The lowest value of R-square is higher than to 0.8 confirming a quite good effectiveness of the regressions. It is possible to observe that the seismic reliability of the isolation level is slightly influenced by $\gamma$ as previously described for the fragility curves. The increase of the strength

reduction factor leads a decrease of the seismic reliability. These performance curves, ($SP_{isolator}$), (Fig. 8), can be used for the preliminary design of the dimensions in plan of the FP devices, depending on the elastic and inelastic structural properties in an area with a seismic hazard similar to that considered, in order to respect the expected reliability level. In particular, an exceeding probability of $P_f$ = 1.5·10-3 (related to the collapse limit state, reliability index $\beta$=3 in 50 years) [42]-[45] can be respected through a radius in plan $r$ having a dimension lower than 1m, in the case of very low values of the behaviour factor.

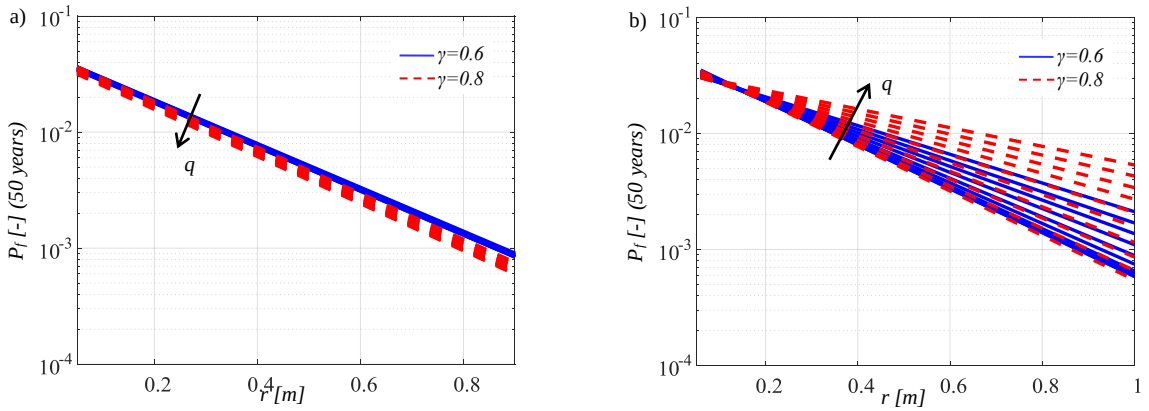


Fig. 8. Seismic reliability curves of the isolation level related to $I_d$=4, for $T_b$=6 s, $S$=+0.03 (a), $T_b$=6 s, $S$=-0.03 (b). The arrow denotes the increasing direction of $q$.

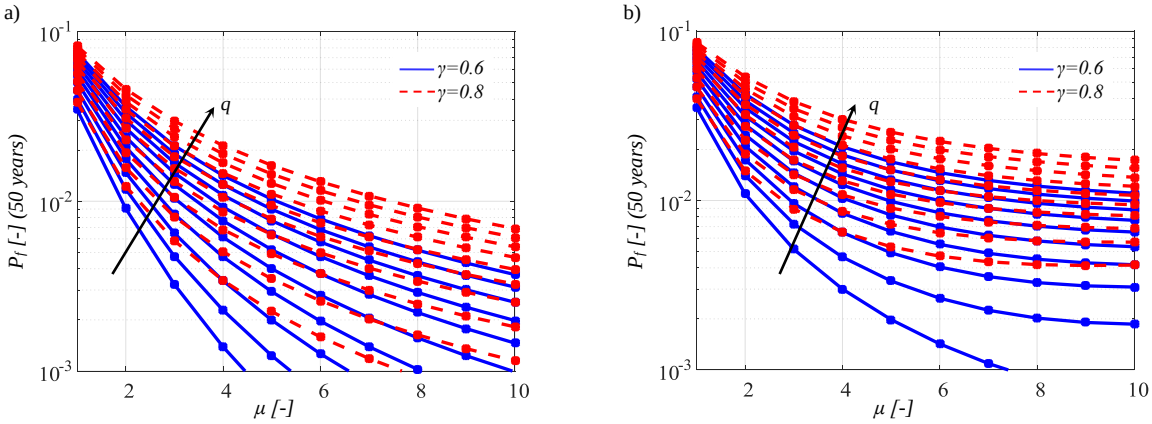


Fig. 9. Seismic reliability curves of the superstructure related to $I_d$=4, for $T_b$=6 s, $S$=+0.03 (a), $T_b$=6 s, $S$=-0.03 (b). The arrow denotes the increasing direction of $q$.

In Fig. 9, the results, evaluated for $\mu \geq 1$, representing the seismic reliability (SP curves) of the inelastic superstructure, that is, the exceeding probabilities (Complementary CDFs) in the time frame of interest (50 years), are plotted in logarithmic scale for the different *LS* thresholds in terms of the displacement ductility and for different values of the superstructure properties. The seismic reliability of the superstructure decreases for higher values of $\gamma$, $q$ and decreasing values of $S$ (from hardening to softening systems).

## 7 CONCLUSIONS

This paper describes the seismic reliability of inelastic softening structural systems, equipped with friction pendulum isolators (FPS) through an extensive parametric study encompassing a wide range of elastic and inelastic building properties, different seismic intensity levels and considering the friction coefficient and the uncertainties related to the seismic

input intensity and to the characteristics of the records as random variables within the uncertainties relevant to the problem. The isolated system is described by a 2dof system in order to take account of the hardening and softening superstructure response, and the FPS behavior is described by employing a velocity dependent model. Considering a set of seismic records, the inelastic characteristics of the structural systems are designed according to the life safety limit state for L'Aquila site (Italy), as provided by NTC08 provisions, for increasing strength reduction factors. Then, incremental dynamic analyses are developed to evaluate the response statistics related to both superstructure and isolation level for different structural properties, strength reduction factors and post-yield hardening and softening stiffness ratios. The estimates of the response statistics, then, are used for deriving seismic fragility curves for the superstructure and the isolation level assuming different values of the corresponding limit state thresholds. In the final part of the work, considering the seismic hazard curves related to L'Aquila site (Italy), as provided by NTC08 provisions, regarding systems isolated by FP bearings with a design life of 50 years, seismic reliability-based design (SRBD) abacuses are proposed with the aim to design the radius in plan of the FP isolators, highlighting the effects of the post-yield hardening and softening stiffness. In particular, an exceeding probability related to the collapse limit state can be achieved through a radius in plan *r* having a dimension lower than 1m, in the case of very low values of the behaviour factor for softening systems.

As for the superstructure, the seismic reliability assessment demonstrates the negative effects due to the post-yield softening stiffness able to strongly amplify the displacement ductility demand for isolated structure designed to yield under the expected seismic base shear and may lead to collapse. The proposed SRBD formulae can be used for the preliminary design of hardening structures and verification of base-isolated hardening or softening regular frames, located in an area characterized by a seismic hazard similar to that considered.

## 8 REFERENCES

[1] Christopoulos C, Filiatrault A. *Principles of Passive Supplemental Damping and Seismic Isolation*. IUSS Press: Pavia, Italy, 2006.

[2] Zayas VA, Low SS, Mahin SA. A simple pendulum technique for achieving seismic isolation. *Earthquake Spectra* 1990; 6:317–33.

[3] Su L, Ahmadi G, Tadjbakhsh IG. Comparative study of base isolation systems. *Journal of Engineering Mechanic* 1989; 115:1976–92.

[4] Mokha A, Constantinou MC, Reinhorn AM. Teflon Bearings in Base Isolation. I: Testing. *J. Struct. Eng.* 1990; 116(2): 438-454.

[5] Constantinou MC, Mokha A, Reinhorn AM. Teflon Bearings in Base Isolation. II: Modeling. *J. Struct. Eng*. 1990; 116(2):455-474.

[6] Constantinou MC, Whittaker AS, Kalpakidis Y, Fenz DM, Warn GP. Performance of Seismic Isolation Hardware Under Service and Seismic Loading. Technical Report, 2007.

[7] Almazàn JL, De la Llera JC. Physical model for dynamic analysis of structures with FPS isolators. *Earthquake Engineering and Structural Dynamics* 2003; 32:1157–1184.

[8] Palazzo B., Castaldo P., Marino I., The Dissipative Column: A New Hysteretic Damper," Buildings 5(1), 163-178, 2015, doi:10.3390/buildings5010163.

[9] Castaldo P., Integrated Seismic Design of Structure and Control Systems. Springer International Publishing: New York, 2014 . DOI 10.1007/978-3-319-02615-2.

[10] De Iuliis M., Castaldo P., An energy-based approach to the seismic control of one-way asymmetrical structural systems using semi-active devices, Ingegneria Sismica - Inter-

national Journal of Earthquake Engineering XXIX(4):31-42, 2012.

[11] M.T. Giugliano, A. Longo, R. Montuori, V.Piluso, Influence of homoschedasticity hypothesis of structural response parameters on seismic reliability of CB-frames, *Georisk*, **5**(2), 120-131, 2011.

[12] M.T. Giugliano, A. Longo, R. Montuori, V. Piluso, Seismic reliability of traditional and innovative concentrically braced frames, *Earthquake Engineering and Structural Dynamics*, **40**(13), 1455–1474, 2011.

[13] A. Longo, R. Montuori, V. Piluso, Seismic reliability of V-braced frames: Influence of design methodologies, *Earthquake Engineering and Structural Dynamics*, **38**(14), 1587–1608, 2009.

[14] Ayyub BM, McCuen RH. Probability, statistics, and reliability for engineers. 2nd ed. NY: CRC Press; 2002.

[15] Chen J, Liu W, Peng Y, Li J. Stochastic seismic response and reliability analysis of base-isolated structures. *J Earthquake Eng* 2007;11:903‑24.

[16] Alhan C, Gavin HP. Reliability of base isolation for the protection of critical equipment from earthquake hazards. *Eng Struct* 2005;27:1435‑49.

[17] Zou XK, Wang Q, Li G, Chan CM. Integrated reliability-based seismic drift design optimization of base-isolated concrete buildings. *J Struct Eng* 2010;136:1282‑95.

[18] Mishra SK, Roy BK, Chakraborty S. Reliability-based-design-optimization of base isolated buildings considering stochastic system parameters subjected to random earthquakes. *Int J Mech Sci* 2013;75:123‑33.

[19] Castaldo P., Palazzo B., Della Vecchia P., (2016) "Life-cycle cost and seismic reliability analysis of 3D systems equipped with FPS for different isolation degrees", Engineering Structures, 125;349–363, http://dx.doi.org/10.1016/j.engstruct.2016.06.056.

[20] Castaldo P., Amendola G., Palazzo B., (2017) "Seismic fragility and reliability of structures isolated by friction pendulum devices: Seismic reliability-based design (SRBD)", Earthquake Engineering and Structural Dynamics, 46(3); 425–446, DOI: 10.1002/eqe.2798.

[21] Castaldo P., Ripani M., "Optimal design of friction pendulum system properties for isolated structures considering different soil conditions", Soil Dynamics and Earthquake Engineering, 2016, 90:74–87, DOI: 10.1016/j.soildyn.2016.08.025.

[22] Structural Engineering Institute. Minimum design loads for buildings and other structures (Vol. 7, No. 5). Amer Society of Civil Engineers, 2010.

[23] European Committee for Standardization. Eurocode 8-Design of Structures for Earthquake Resistance. Part 1: General Rules, Seismic Actions and Rules for Buildings, Brussels, 2004.

[24] NTC08. Norme tecniche per le costruzioni. Gazzetta Ufficiale del 04.02.08, DM 14.01.08, Ministero delle Infrastrutture.

[25] Japanese Ministry of Land, Infrastructure and Transport, Notification No. 2009–2000, Technical Standard for Structural Specifications and Calculation of Seismically Isolated Buildings 2000.

[26] Quantification of Building Seismic Performance Factors, FEMA P695 / June 2009.

[27] Occhiuzzi, A, Veneziano, D.and Van Dyck, J. (1994) Seismic design of base isolated structures, Savidis (Ed.), Balkema, Rotterdam, NL.

[28] Vassiliou M.F., Tsiavos A., Stojadinović B. Dynamics of inelastic base-isolated structures subjected to analytical pulse ground motions. *Eart. Eng. and Str. Dyn.* 2013; 42:2043–2060.

[29] Newmark NM, Hall WJ. Seismic design criteria for nuclear reactor facilities, Report 46, Building Practices for Disaster Mitigation, National Bureau of Standards, 1973.

[30] Miranda E, Bertero VV. Evaluation of strength reduction factors for earthquake-resistant design. Earthquake Spectra 1994; 10:357–379.

[31] Castaldo P., Palazzo B. and Ferrentino T. Seismic reliability-based ductility demand evaluation for inelastic base-isolated structures with friction pendulum devices, Earthquake Engineering and Structural Dynamics 2017; 46:1245–1266, DOI: 10.1002/eqe.2854.

[32] Mckey MD, Conover WJ, Beckman RJ. A comparison of three methods for selecting values of input variables in the analysis from a computer code. Technometrics 1979;21:239-45.

[33] Vořechovský M, Novák D. Correlation control in small-sample Monte Carlo type simulations I: a simulated annealing approach. *Probabilistic Engineering Mechanics* 2009;24(3):452‑62.

[34] Celarec D, Dolšek M. The impact of modelling uncertainties on the seismic performance assessment of reinforced concrete frame buildings. *Engineering Structures* 2013;52:340‑354.

[35] Naeim F, Kelly JM. Design of Seismic Isolated Structures: From Theory to Practice. John Wiley & Sons, Inc.; 1999.

[36] Hatzigeorgiou GD. Ductility demand spectra for multiple near- and far-fault earthquakes. *Soil Dynamics and Earthquake Engineering* 2010;30 170-183.

[37] Hatzigeorgiou GD, Papagiannopoulos GA, Beskos DE. Evaluation of maximum seismic displacements of SDOF systems form their residual deformation. *Engineering Structures* 2011;33 3422-3431.

[38] Gupta A, Krawinkler H. Seismic demands for performance evaluation of steel moment resisting frame structures. The John A. Blume Earth. Eng. Center report No. 132, June 1999.

[39] Adam C, Ibarra LF, Krawinkler H. Evaluation of P-Delta effects in non-deteriorating MDOF structures from equivalent SDOF systems. *13th Word Conference on Earthquake Engineering*, Vancouver, B.C., Canada 2004, Paper No. 3407.

[40] Palazzo B. Seismic Behavior of base-isolated Buildings. Proc. International Meeting on earthquake Protection of Buildings, Ancona, 1991.

[41] Collins KR, Stojadinovic B. Limit states for performance-based design. 12WCEE, 2000.

[42] Bertero RD, Bertero VV. Performance-based seismic engineering: the need for a reliable conceptual comprehensive approach. *Earthquake Engineering and Structural Dynamics* 2002;31:627–652 (DOI: 10.1002/eqe.146).

[43] Aoki Y, Ohashi Y, Fujitani H, Saito T, Kanda J, Emoto T, Kohno M. Target seismic performance levels in structural design for buildings. 12WCEE, 2000.

[44] SEAOC Vision 2000 Committee. Performance-based seismic engineering. Report prepared by Structural Engineers Association of California, Sacramento, CA., 1995.

[45] CEN – European Committee for Standardization. Eurocode 0: Basis of Structural De-

sign. Final draft. Brussels, 2006.

[46] Saito T, Kanda J, Kani N. Seismic reliability estimate of building structures designed according to the current Japanese design code. Proc.s of the Str. Eng.s World Congress, 1998.

[47] Cornell CA, Krawinkler H. Progress and challenges in seismic performance assessment. PEER Center News 2000;4(1):1-3

[48] Aslani H, Miranda E. Probability-based seismic response analysis. *Engineering Structures* 2005; **27**(8): 1151-1163.

[49] Porter KA. An overview of PEER's performance-based earthquake engineering methodology. Proceedings, *Proceedings of the 9th International Conference on Application of Statistics and Probability in Civil Engineering* (*ICASP9*), San Francisco, California, 2003; 973-980.

[50] Kulkarni JA, Jangid RS. Effects of superstructure flexibility on the response of base-isolated structures. Shock and Vibration 2003;26:1-13.

[51] http://www.fipindustriale.it/

[52] Ryan KL, Chopra AK (2004). Estimation of Seismic Demands on Isolators Based on Nonlinear Analysis. J. Struct. Eng., 130(3), 392–402.

[53] PEER, *Pacific Earthquake Engineering Research Center* http://peer.berkeley.edu/

[54] ITACA, *Italian Accelerometric Archive* http://itaca.mi.ingv.it/ItacaNet/itaca10_links.htm

[55] ISESD, *Internet-Site for European Strong-Motion Data* http://www.isesd.hi.is/ESD_Local/frameset.htm

[56] Vamvatsikos D, Cornell CA. Incremental dynamic analysis. *Earthquake Engineering and Structural Dynamics* 2002; 31(3): 491–514.

[57] Palazzo, B., Castaldo, P., Mariniello, A. Time-variant structural reliability of R.C. structures affected by chloride-induced deterioration, American Concrete Institute, ACI Special Publication 2015-January (SP 305), pp. 19.1-19.10.

[58] Faleschini F., Hofer L., Zanini M.A., Dalla Benetta M., Pellegrino C. Experimental behavior of beam-column joints made with EAF concrete under cyclic loading. Engineering Structures 139, 81-95, 2017.

[59] Faleschini F., Zanini M.A., Pellegrino C., Pasinato S. Sustainable management and supply of natural and recycled aggregates in a medium-size integrated plant. Waste Management 49, 146-155, 2016.

[60] Etse, G.J., Ripani, M., Vrech, S.M. "Fracture energy-based thermodynamically consistent gradient model for concrete under high temperature," Proceedings of the 8th International Conference on Fracture Mechanics of Concrete and Concrete Structures, FraMCoS 2013, 1506-1515.

[61] Etse, G., Ripani, M., Caggiano, A. & Schicchi, D.S. "Strength and durability of concrete subjected to high temperature: continuous and discrete constitutive approaches," American Concrete Institute, ACI Special Publication 2015-January (SP 305), 9.1-9.18.

[62] Etse, G., Ripani, M. & Mroginski, J.L. "Computational failure analysis of concrete under high temperature," Computational Modelling of Concrete Structures - Proceedings of EURO-C 2014, 2:715-722.

[63] Etse, G., Vrech, S.M. & Ripani, M. "Constitutive theory for Recycled Aggregate Concretes subjected to high temperature," Construction and Building Materials; 111: 43-53,

2016.

[64] Mroginski, J.L., Etse, G., Ripani, M. "A non-isothermal consolidation model for gradient-based poroplasticity," PANACM 2015 - 1st Pan-American Congress on Computational Mechanics, in conjunction with the 11th Argentine Congress on Computational Mechanics, MECOM 2015, pp. 75-88.

[65] Ripani, M., Etse, G., Vrech, S. & Mroginski, J.L. "Thermodynamic gradient-based poroplastic theory for concrete under high temperature," International Journal of Plasticity; 61: 157-177, 2014.

[66] Ripani, M., Etse, G., Vrech, S. "Recycled aggregate concrete: localized failure assessment in thermodynamically consistent non-local plasticity framework", Computers and Structures, 178: 47–57, 2017, doi: 10.1016/j.compstruc.2016.08.007.

[67] Vrech, S.M., Ripani, M. & Etse, G. "Localized versus diffused failure modes in concrete subjected to high temperature," PANACM 2015 - 1st Pan-American Congress on Computational Mechanics, in conjunction with the 11th Argentine Congress on Computational Mechanics, MECOM 2015, pp. 225-236.

[68] Math Works Inc. MATLAB-High Performance Numeric Computation and Visualization Software. User's Guide. Natick: MA, USA, 1997.

[69] Bazzurro P, Cornell CA, Shome N, Carballo JE (1998): Three proposals for characterizing MDOF nonlinear seismic response. Journal of Structural Engineering, 124(11), 1281-1289.

[70] Peter Fajfar, M.EERI. A Nonlinear Analysis Method for Performance Based Seismic Design. Earthquake Spectra, Vol.16, No.3, pp.573-592, August 2000.

[71] Paulay T., Priestley M. J. N.: Seismic design of reinforced concrete and masonry buildings, John Wiley & Sons, 1992.

COMPDYN 2017
6th ECCOMAS Thematic Conference on
Computational Methods in Structural Dynamics and Earthquake Engineering
M. Papadrakakis, M. Fragiadakis (eds.)
Rhodes Island, Greece, 15–17 June 2017

# INFLUENCE FACTORS FOR THE ASSESSMENT OF MAXIMUM LATERAL SEISMIC DEFORMATIONS IN ITALIAN MULTISTOREY RC BUILDINGS

**Marco Gaetani d'Aragona**[1], **Maria Polese**[1] **and Andrea Prota**[1]

[1] Department of Structures for Engineering and Architecture, University of Naples Federico II
via Claudio 21, 80125 Naples, Italy
{marco.gaetanidaragona, maria.polese, andrea.prota}@unina.it

**Keywords:** Interstorey Drift Ratio, Infills, lateral stiffness, Reinforced Concrete

**Abstract.** *In the aftermath of low-to-moderate earthquakes, simplified methods allowing fast estimate of maximum lateral deformations experienced in multistory building are particularly useful when estimating nonstructural damage on a large building inventory. In particular, Miranda [1] introduced a simplified method that adopts an equivalent continuum elastic structure to estimate both maximum roof displacement and maximum interstorey drift ratio for a given response spectrum. Based on a closed-form solution, this method was further extended [2] to account for higher vibration modes, different distributions of lateral forces and non-uniform stiffness along the height. However, the method assumes that building properties will continuously vary along the height, assumption that is not generally valid for the Italian building stock due to the presence of knee beams and infill panels. This paper investigates on the effect of variation of infill properties on the elastic lateral response of infilled RC buildings, assessing the influence of different characteristics, such as geometric and material properties or the opening percentage, on $IDR_{max}$. Plane Multi-degree-of-freedom elastic models including explicit modeling of infill panels are adopted and the effect of local discontinuities is included, while linear time-history analyses are performed considering several input ground motions. The effect on the interstorey drift ratio of different opening percentages and infill arrangements, both at the same storey and along the height, are considered to account for discontinuities caused by the presence of infills. Further, the influence of different types and thicknesses of the infill panels, level connection to the surrounding frame is analyzed.*

## 1 INTRODUCTION

The inter-story drift ratio, IDR, defined as the difference in lateral displacements between two consecutive floors normalized by the inter-story height, has proven to be one of the best correlated parameters to damage in buildings ([3]-[8]), and this applies especially also for those part of the nonstructural system that are rigidly connected to the structure, such as masonry infill walls. There exist a number of proposals in literature for the simplified evaluation of lateral demands in multistory buildings ([9]-[12]). Among them, the approach by Miranda [1], successively corrected to account for the stiffness variation in elevation [2], allows a simplified estimation of maximum roof displacement and inter-story drift $IDR_{max}$ that has proven to yield reliable results for multistory buildings in the USA, designed according to modern seismic standards. However, existing buildings that were not designed according to modern seismic design codes may be characterized by a non-uniform stiffness variation along the height and as a consequence these simplified methods may loose their effectiveness [13]. This may happen also for infilled RC buildings, whose lateral stiffness is largely influenced by the infill characteristics and on the efficacy of their casting with the surrounding frame.
This paper investigates on the effect of variation of infill properties on the elastic lateral response of infilled RC buildings, assessing the influence of different characteristics, such as geometric and material properties or the opening percentage, on $IDR_{max}$.
Adopting a single RC frame as the "reference" structure the consequence of variation of single parameters on $IDR_{max}$ is studied, and their joint effect evaluated through the story level stiffness. The latter, that can be even computed in a simplified manner according to the proposal in [14], is used as a synthetic representative parameter for building elastic characteristics at the story level. Also, the story level stiffness variation (at the lower or upper stories of a building) is used to investigate on its influence on the elastic response, also in comparison with the results of simplified approaches.

## 2 ELASTIC MODEL OF UNIFORMLY INFILLED RC FRAME

*Reference structure*
The reference structure is a six-story gravity load designed RC frame with three bays, with length equal to 6.0m and an interstorey height equal to 3.0m. The analyzed planar frame is the perimeter longitudinal frame extracted from a 3D structure symmetric in plane, in both longitudinal and transverse directions, with three bays in both the longitudinal and the transverse direction and with a floor area equal to 216 $m^2$. The slab way is parallel to the transverse direction, as typical for existing gravity load designed GLD buildings [15]-[16]; the dead load is equal to 5.95 $kN/m^2$ for all stories and the live load is equal to 2 $kN/m^2$. The element dimensions of the analyzed frame were obtained via a simulated design procedure applied for a GLD building [17], assuming a mean concrete strength equal to 20MPa. Beams are 25cm wide and 55cm high; columns are 25cm wide and 25cm high except for interior columns from first to third story that are 40cm-35cm-30cm high, respectively. The model geometry for the reference frame is sketched in Fig. 1. In the reference frame, infill panels are realized with hollow clay brick panels and are uniformly distributed along the height. Panel thickness is assumed equal to $t_w$=20 cm (corresponding to a double layer brick infill -12+8) and elastic shear modulus $G_w$= 1350 MPa. Height $h_w$ and length $l_w$ of infill panels take into account the beam and column dimensions, i.e. are clear dimensions.

*Analytical model*

The building model is a two-dimensional finite element multi-degree of freedom system developed using OpenSees [18]. The response of beams and columns is represented by axially rigid elastic elements. Both beams and columns are assumed cracked and the element stiffness is evaluated according to [19]. Rigid beam-columns joints of finite size are adopted in the model.

The presence of infill panels is simulated through a simplified macro-model adopting equivalent struts acting only in compression, as sketched in Figure 1. The numerical model of the infill panels adopts the relationship proposed in [20]). In particular, the parameters defining the force-displacement relationship depend on mechanical and geometric properties of the masonry panel and of the surrounding frame. Referring to the infill behavior, only the first (elastic) branch, which corresponds to initial shear behavior of the un-cracked panel, is employed. The parameter defining first branch of the force-displacement curve is the initial stiffness of the un-cracked initial tract $K_w$:

$$K_w = \frac{G_w t_w l_w}{h_w} \tag{1}$$

Where $G_w$ is the elastic shear modulus of the infill material; $l_w$ and $h_w$ are the clear length and height of the infill panel, respectively; and $t_w$ is the thickness of the infill panel.

The compression strut is modeled as a truss element employing a uniaxial elastic-no tension material.

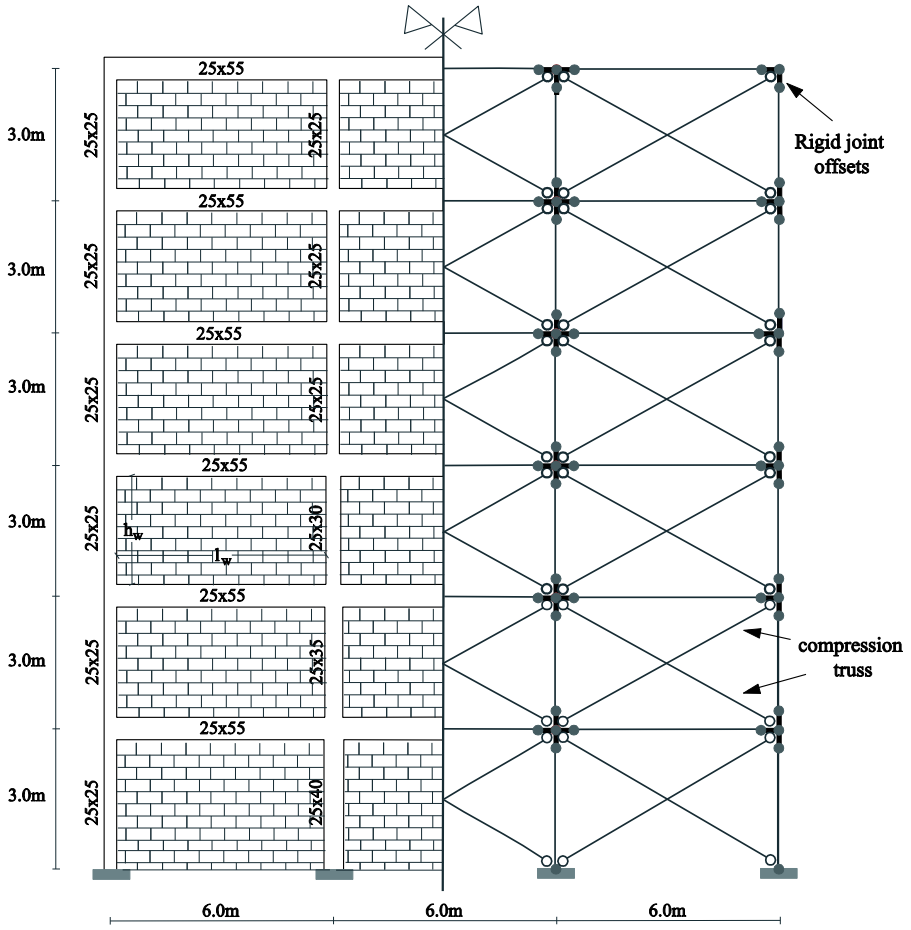


Figure 1: "Reference" structure geometry and analytical model.

Noticeably, when openings are present in the infill panel, a reduction of lateral stiffness has to be expected. In order to take into account the effect of infill openings, a reduction of the envelope forces in the load-displacement relationship of the panel is obtained by multiplying it by $\lambda_{openings}$ , as suggested in [21]:

$$\lambda_{openings} = \max\left(0;1-1.8\cdot\frac{A_{openings}}{A_{panel}}\right) \quad (2)$$

where $A_{openings}$ and $A_{panel}$ represents the area of the openings and of the infill panel, respectively.
Finally, both structural and nonstructural masses are considered as acting only in the horizontal direction. In order to include the influence of infill walls on structural damping, a 10% Rayleigh damping is assumed according to [22].

## 2.1 Influence of infill characteristics on elastic periods and modes

In this study, we refer to infill panels realised with clay-holed bricks disposed in double arrays. The definition of mechanical characteristics of the panels is affected by high uncertainties. With the aim of considering the possible variability of such characteristics and to investigate its effect, the minimum and maximum values of the elastic tangential modulus $G_w$ suggested for masonry formed by clay bricks, with hole percentage less than 45% in the actual Italian seismic code [23], are considered, namely 1080 and 1620 MPa; the "reference" value $G_w$= 1350 MPa corresponds to the mean. For what concerns the geometric characteristics, three possible values for the infill thickness are assumed, $t_{w1}$= 16 cm and $t_{w2}$=20 cm and $t_{w3}$=24 cm, first case corresponding to double layer brick infill 8+8, second one to 12+8 and third to 12+12. Moreover, the effect of opening is considered; in particular, the ratio $\alpha_{openings}=A_{openings}/A_{panel}$ is varied from 0% (the reference case) to 20% and 40%.

A parameter that that could be used to synthetically represent the effect of variation of the aforementioned parameters on the structural model and response is the story lateral stiffness. A simplified approach for its evaluation was proposed in [14]; it defines the storey lateral stiffness of MRFs through equivalent simple systems that consists of sub-modules of one-bay/one-story frames. The method allows to account for the influence on lateral stiffness of both columns and beams and infill panels (considered as an equivalent concentrically braced frame).

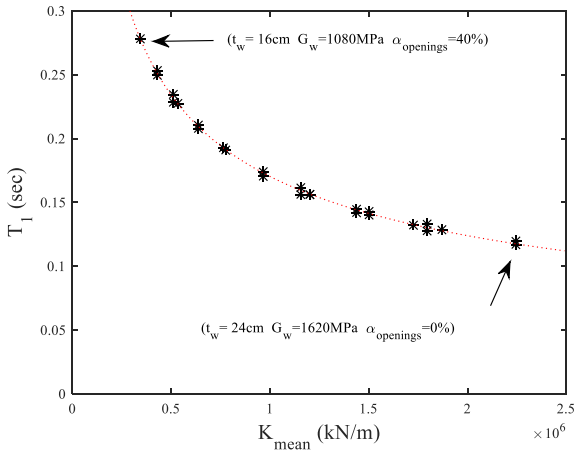


Figure 2: Variation of $T_1$ as a function of mean story lateral stiffness $K_{mean}$.

Fig. 2 synthetically shows the effect of the three parameters $G_w$, $t_w$ and $\alpha_{openings}$ on the mean story lateral stiffness ($K_{mean}$) and the associated fundamental period of the frame ($T_1$). $K_{mean}$ is here defined as the mean lateral stiffness of the all the frame stories, with storey stiffness evaluated according to [14]. In particular, combining the possible variations for the three considered parameters ($G_w$, $t_w$ and $\alpha_{openings}$) a total number of 27 configurations is obtained. The $K_{mean}$-$T_1$ points representing the different configurations are shown in figure. It can be noted that $T_1$ varies proportionally to 1 versus the square root of $K_{mean}$, with slight deviations due to the variation of seismic masses among the different configurations (depending on the the variation of $t_w$ and $\alpha_{openings}$). In the figure, it is also evidenced that the lower and the upper bounds for $K_{mean}$ are represented by the case in which the triplet ($G_w$, $t_w$, $\alpha_{openings}$) assumes minimum and maximum values, respectively.

## 3 ELASTIC ANALYSIS OF THE INFILLED FRAME

The elastic response of the RC infilled frames is studied using the set of accelerograms (two components from 21 earthquakes of the far field record set) included in ATC 63 [24]. All the accelerograms are scaled to the same intensity level and elastic analysis is performed. Adopting the peak ground acceleration $a_g$ as Intensity Measure IM, and scaling all accelerograms to $a_g$=0.1 g, the IDR profiles shown in Figure 3 (a) are obtained. Black profile represents median results while red profiles represent the results obtained for each accelerogram. As it can be noted a high dispersion of maximum IDR at the various stories is obtained; this dispersion is mainly due to the variation of displacement spectrum value $S_d(T_1)$ for the different accelerograms when scaled to the same $a_g$; notably, the logarithmic dispersion is not constant along the height and varies between 0.23 and 0.27.

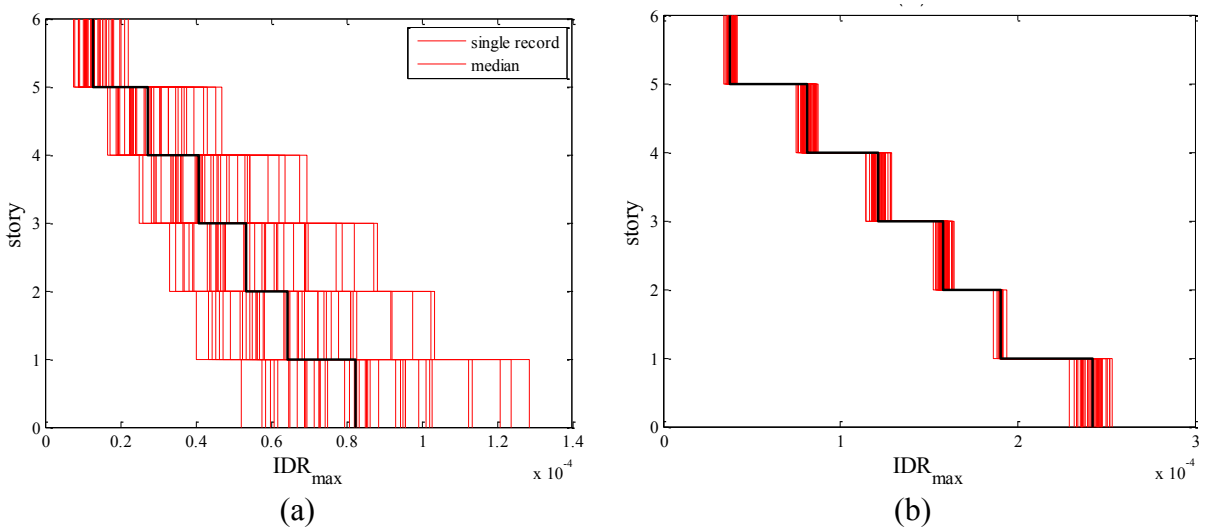


Figure 3: IDR profiles obtained for the "reference" structure after scaling the accelerograms to $a_g$=0.1 g (a) or to $S_d(T_1)$ =0.02 m (b).

Adopting $S_d(T_1)$ as IM and scaling all the accelerograms to $S_d(T_1)$=0.02m a lower dispersion is obtained, as shown in Figure 3 (b). The latter dispersion is due to the variation of displacement spectrum ordinates, with respect to period higher than the first, for the different accelerograms. In particular, the logarithmic dispersion decreases from a mean of 0.26 to 0.03.
Although the use of $S_d(T_1)$ as IM is appealing for the significant reduction of dispersion, in the following analyses it is chosen to scale accelerograms with respect to $a_g$ in order to allow comparison of results among RC frames characterized by a different period $T_1$. Indeed, as

shown in § 2.1, the variation of infills characteristics determines the variation of $K_{mean}$ and of the period $T_1$.

### 3.1 Variation of $IDR_{max}$ depending on infill characteristics

Figure 4 (a)-(c) show the influence of the different parameters on the expected lateral IDR profiles for the 27 configurations obtained varying $G_w$, $t_w$ and $\alpha_{openings}$. In particular, Figure 4 (a) shows the effect of variation of infills thickness $t_w$, Figure 4 (b) the effect of variation of $G_w$ while Figure 4 (c) the effect of variation of $\alpha_{openings}$. As it could be expected, the increase (lowering) of thickness $t_w$ and infill stiffness $G_w$, shown in Figure 4 (a) and (b), leads to an increase (decrease) in the system lateral stiffness and to the consequent lowering (increasing) of the expected lateral IDR with respect to the reference structure of about 22% and 29% (24% and 30%), respectively.

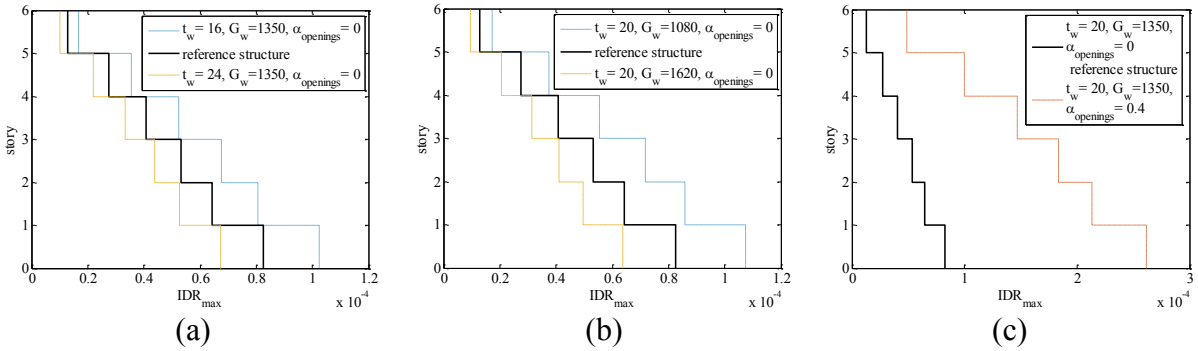


Figure 4: IDR profiles along building height considering the variation of $t_w$ (a), $G_W$ (b) and $\alpha_{openings}$ (c).

Opposite effect is observed for $\alpha_{openings}$; its higher value corresponding to more flexible structures and therefore to higher IDR (320% higher than that for the reference structure).

Figure 5 (a)-(c) show the variation of $IDR_{max}$ for the different configurations as a function of $\alpha_{openings}$ (Figure 5 (a)), $t_w$ (Figure 5 (b)) and $G_w$ (Figure 5 (c)). Comparing results with respect to the ones obtained for the reference structure it can be observed that a maximum decrease of $IDR_{max}$ of about 40% can be expected for the case of the stiffer structures considered ($G_W$=1620 MPa and $t_W$=24 cm), while maximum expected increase of $IDR_{max}$ is nearly 500% for the case of more deformable structures ($G_W$=1080 MPa, $t_W$=16 cm and $\alpha_{openings}$=0.4).

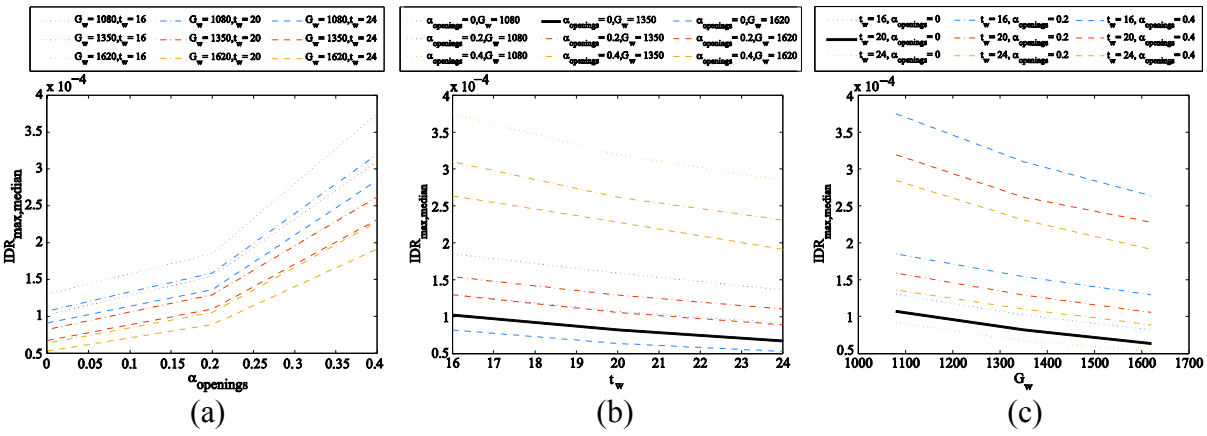


Figure 5: $IDR_{max}$ variation as a function of $\alpha_{openings}$ (a), $t_w$ (b) and $G_W$ (c)

As evidenced in section 2.1 the variation of infill properties has a direct influence on system's lateral stiffness and consequently on the elastic period and modes. The period is clearly connected to maximum system's elastic displacement response through $S_d(T_1)$ and modal participation factor, while also mode shapes influence the inter-storey drift profile. Figure 6 shows the variation of $IDR_{max}$ as a function of $T_1$ (median values among the 42 records scaled to $a_g$=0.1 g). In figure, square markers of different colors refer to the case of frames with different infill characteristics, namely black squares ($t_w$=16 cm, $\alpha_{openings}$=0); magenta squares ($t_w$=20 cm, $\alpha_{openings}$=0); cyan squares ($t_w$=24 cm, $\alpha_{openings}$=0); red squares ($t_w$=16 cm, $\alpha_{openings}\neq0$); green squares ($t_w$=20 cm, $\alpha_{openings}\neq0$); blue squares ($t_w$=24 cm, $\alpha_{openings}\neq0$).

For comparison, also the $IDR_{max}$ obtained with the approach proposed in [1] are considered. In [1] a multistory building is modeled as equivalent continuum structure consisting of a combination of a flexural cantilever beam and a shear cantilever beam. The response of this equivalent system depends on a dimensionless parameter $\alpha$, that controls the degree of participation of overall flexural and shear deformations in the simplified model of multistory buildings, on the period $T_1$ of the fundamental mode and on the damping. A value of $\alpha$ approximately equal to zero represents a pure flexural model while for $\alpha \rightarrow \infty$ a pure shear model is obtained. Generally, larger $\alpha$ (e.g. 30) correspond to shear-type buildings, while intermediate values correspond to a multistory building that combines shear and flexural deformations. In [1] a simplified formulation for estimation of $IDR_{max}$ is proposed:

$$IDR_{max} = \beta_1 \beta_2 \frac{S_d(T)_1}{H} \tag{3}$$

In Eq. (3) $\beta_1$ can be considered as an amplification factor acting on the spectral displacement in order to obtain an estimate of the maximum roof displacement (similar to first mode participation factor) while $\beta_2$ as an amplification factor acting on roof drift ratio in order to obtain the maximum IDR for a building of height H. $\beta_2$ takes into account that usually the distribution of interstory drifts along the height of the building is not uniform. The authors have studied the relationship of $\beta_1$ and $\beta_2$ with $\alpha$, number of storeys and the shape of the vector of horizontal loads applied to the equivalent system in the simplified formulation (a=0.01 triangular loads; a=2000 uniform loads). $\beta_2$ is significantly larger for buildings where shear deformations dominate over flexural deformations ($\alpha > 20$) with respect to the one obtained for flexure dominated buildings ($\alpha \approx 0$); this evidences that shear-type buildings have larger concentrations of interstory drifts than flexural-type ones.

In Figure 6 the $IDR_{max}$ calculated with Eq. (3) for each configuration obtained varying infill parameters are also shown (circle markers of the same color as previously explained). The $\alpha$ of these buildings ranges between 18 and 22 when considering a=2000, and it is constant and equal to 710 when considering a=0.1.

In Figure 6 it is also reported $IDR_{max}$ calculated with Eq. (3) when considering an approximate formulation for the fundamental period $T_1$ (triangles) and adopting $\alpha$=20 as suggested in [11] for RC frames (diamond markers of the same color as previously explained). In particular, the expression for $T_1$ proposed in [25] is employed. It accounts for the effect of infill panels on the fundamental period and relays on the infill area in each story, normalized with respect to the story area, the building height and the presence of openings, while not accounting explicitly for the effect of $G_w$ and the opening percentage on $T_1$. In this case, the difference in the estimate of $IDR_{max}$ can be significant, mainly due to the variation of $S_d(T_1)$. For instance, for the reference frame the difference between $T_1$ from analysis and simplified for-

mula is about 35%, that entail a difference in $S_d$ (thus, in $IDR_{max}$ according to eq. (3)) of about 60%.

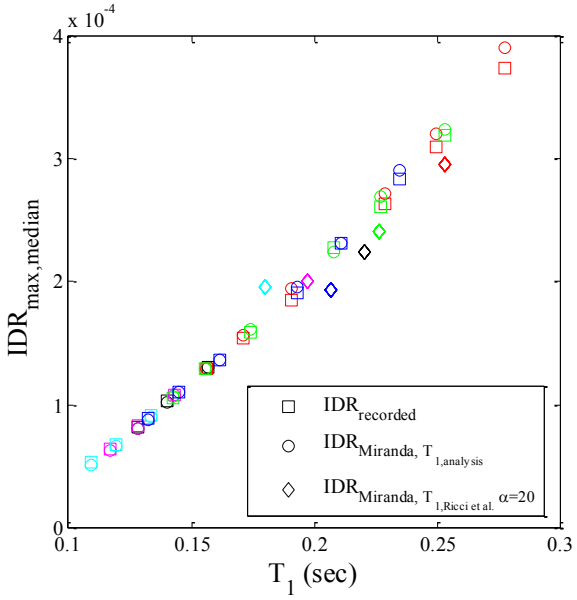


Figure 6: $IDR_{max}$ variation as a function of $T_1$ (squares). $IDR_{max}$ from Eq. (3) are also shown: (circles) uniform load distribution (a=2000) for calibration of $\alpha$ and $T_1$ from analyses; (diamonds) $\alpha$ =20 and $T_1$ from [25].

## 3.2 Preliminary evaluation of the influence of stiffness variation in elevation on $IDR_{max}$

In addition to uniform lateral stiffness variation along the height due to the variability of material properties ($G_w$) as well as the infill geometry ($t_w$, $\alpha_{openings}$), non-uniform stiffness variations along the height may occur in one or more stories due to the lacking of efficacy of the infill casting with the surrounding frame (i.e. participation to the lateral stiffness of the frame), to the presence of large openings (i.e., $\lambda_{openings}$=0) or even to the lacking infills in one or more spans at the same story.

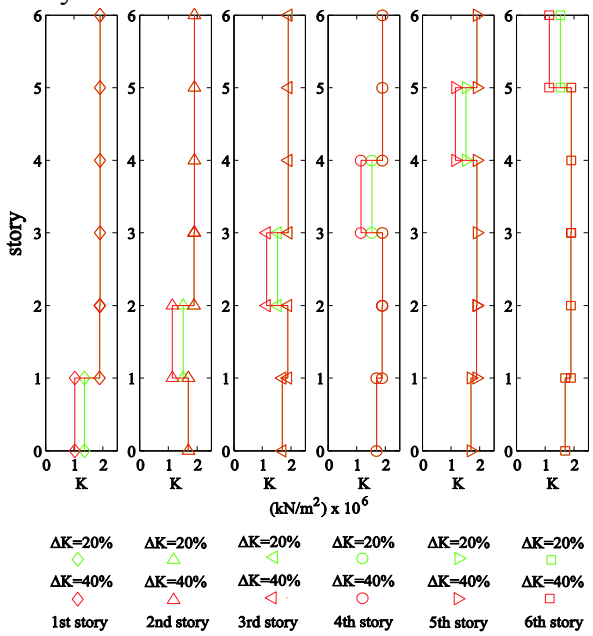


Figure 7: Local story lateral stiffness variation (K) of 20% (green) and 40% (red) applied to different storeys

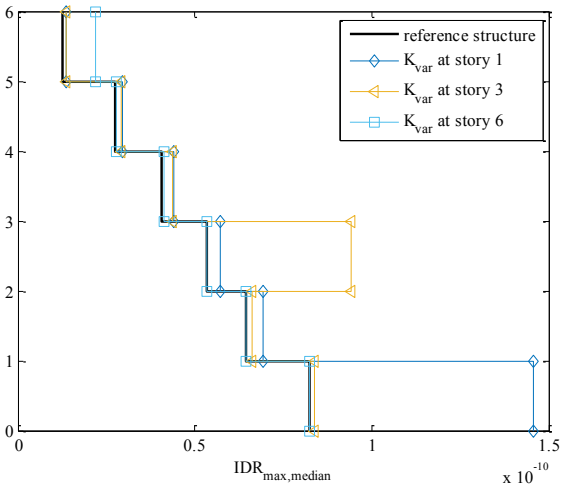


Figure 8: Median $IDR_{max}$ profile for 40% reduction of story lateral stiffness considered at 1st, 3rd,6th story and for reference structure.

In order to investigate the effect of local variations in story lateral stiffness, in this paragraph two different values of stiffness reduction, namely 20% and 40%, are in each different story, see Figure 7.

Figure 8 shows the effect on $IDR_{max}$ of the 40%-reduction of lateral stiffness in 1st, 3rd and 6th story with respect to the reference structure. It is possible to note that in the story in which the reduction of lateral stiffness is considered lateral deformation is generally 70-80% higher than the one recorded in the reference structure at the same story.

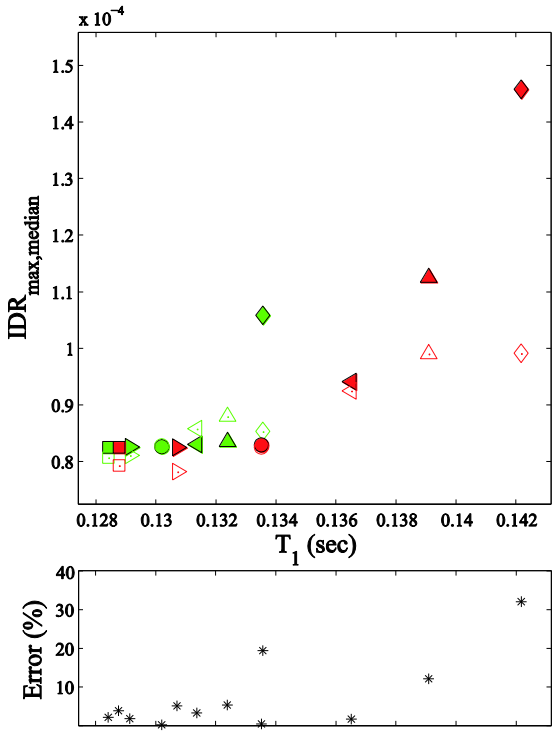


Figure 9: $IDR_{max}$ (median) as a function of $T_1$, for 20% and 40% of reduction in lateral stiffness considered in different storeys (see Figure 7 for Markers). Filled markers represent IDR as recorded, empty markers are obtained adopting Eq. (3). For each period also the error between predicted and calculated $IDR_{max}$ are reported.

In particular, when the reduction is applied to 1st story, deformation concentrates in that story determining an increase of $IDR_{max}$, while the deformation demand slightly increases in upper stories with respect to the one of the reference structure and the increase is almost constant along the height. Instead, the influence of lateral stiffness variation on other stories reduces when it is considered in upper stories. In fact, when 40% variation of stiffness is considered in 3rd story, the deviation in other stories with respect to the IDR profile for the reference structure decreases, and when the variation is considered in the 6th story the effect in other stories in terms of lateral deformations is negligible.

In Figure 9 the median $IDR_{max}$ from analyses of the configurations obtained varying story lateral stiffness are shown; green is adopted for 20% and red for 40%. Also, $IDR_{max}$ calculated with Eq. (3), considering uniform load pattern, are represented with hollow markers. The $\alpha$ of these buildings show a significant scatter being equal to 710 when stiffness variations it is applied to 1st story, 34 to 2nd, 14 to 3rd and 6th story, and 10 to 4th and 5th. In Figure 9, filled markers represent the median results obtained from analyses, while hollow markers are obtained adopting Eq. (3) (for application of Eq. (3) $T_1$ from eigen analysis and $\alpha$ calibrated on the analytical models were adopted).

From Figure 9 it is possible to note that when lateral stiffness reductions are considered in first two storeys a larger error in the prediction of $IDR_{max}$ with the method proposed in [1] is obtained (about 30% and 10% error when considering 40% of variation of stiffness in 1st and 2nd story, respectively). Despite $T_1$ and $\alpha$ are explicitly calibrated on the analytical model significantly reducing the error between predicted and calculated values, the high error in these cases is mainly ascribable to the basic hypothesis of the model that assumes continuous systems (i.e., no local variation in system properties such as lateral stiffness). When the reduction in lateral stiffness is considered in upper stories, the prediction error is generally lower than 10% since, as evidenced above for the 40% reduction in upper three stories, the maximum IDR still occurs at the 1st story and it is quite similar to the one calculated for the reference structure.

## 4 CONCLUSIONS AND FUTURE STUDIES

The study presented in this paper investigates on the influence of relevant factors for the assessment of maximum elastic lateral deformations in typical Italian RC multistory buildings and on the effect of their variation along building height.

The response of a six-story gravity load designed RC frame with three bays, obtained via a simulated design procedure, was simulated by means of a 2D nonlinear multi-degree-of freedom finite element model that properly simulates the effect of infill panels on the seismic behavior of the frames in the elastic range.

The analytical model of building was subjected to multiple records scaled to the same intensity measure to account for record-to-record variability.

A sensitivity analysis was carried out to evidence the influence of different parameters on the expected lateral deformations. In particular, the effect of uncertainties in the definition of mechanical characteristics of the panels ($G_w$, $t_w$) and the effect of different openings percentages ($\alpha_{openings}$) is considered.

The results show that, assuming boundary values of $G_w$ and $t_w$, the variation of maximum lateral deformations with respect to a reference structure with "mean" properties of infill panel properties, are of about 23% and 30%, respectively. When the effect of infill openings is accounted for, a variation of 320% of lateral deformation with respect to the reference structure may occur.

Further, comparing results with respect to those obtained for the reference structure it can be observed that a maximum decrease of maximum lateral deformations of about 40% can be expected for the case of the stiffer structures ($G_w$=1620 MPa and $t_w$=24 cm), while maximum expected increase is nearly 500% for the case of more deformable structures ($G_w$=1080 MPa, $t_w$=16 cm and $\alpha_{openings}$=0.4).

For comparison, also the maximum Interstorey drift ratio ($IDR_{max}$) obtained with a simplified approach proposed in [1] is calculated. The method efficiently predicts $IDR_{max}$ when the main parameters ($T_1$, $\alpha$) are calibrated on the analytical model, while it may lead to substantial error (nearly to 60% with respect to a reference structure with mean values of the considered parameters) when simplified expression are adopted to calculate $T_1$ and $\alpha$.

The effect of non-uniform stiffness variations along the height is also considered. In particular, two values of stiffness reduction, namely 20% and 40%, were considered in different stories. The results show that, for a storey lateral stiffness reduction of 40%, a lateral deformation about 70-80% higher with respect to the one of the reference structure is obtained at the story in which the reduction of lateral stiffness is considered. The stiffness variation also slightly increases the deformation demand in other stories with respect to that of the reference structure, while this increase is almost constant along the height.

It is possible to note that when the simplified method proposed in [1] is applied, even considering $T_1$ and $\alpha$ calibrated on the analytical model, it fails to predict $IDR_{max}$ when lateral stiffness reductions are considered in first two stories. In particular, the error is about 30% and 10% when considering a stiffness variation of 40% in 1st and 2nd story, respectively. The high error is mainly ascribable to the basic hypothesis of the model that assumes continuous systems. When the reduction in lateral stiffness is considered in upper stories, the prediction error is generally lower than 10%; this happens because, in spite of an increasing of IDR at the upper stories, the maximum IDR still occurs at the 1st story and it is quite similar to that recorded for the reference structure.

In this study, the effect of aspect ratio of infill panels and number of spans on maximum lateral deformations was not investigated. Further studies are required to address this topic.

Based on previous observations, further studies are required to extend the validity of simplified methods to the assessment of RC frame structures considering infills with both uniform and non-uniform stiffness along the height.

## ACKNOWLEDGEMENTS

This study was performed within the framework of the joint program DPC-Reluis 2017 – RC constructions - WP1: Vulnerability of RC constructions at the territorial scale. It also benefited from the results of the concluded joint program DPC-Reluis 2016 – special project RS4: Seismic observatory of structures and monitoring.

## REFERENCES

[1] E. Miranda. Approximate seismic lateral deformation demands in multistory buildings, *Journal of Structural Engineering*, 125(4), 417-425, 1999.

[2] E. Miranda, and C.J. Reyes. Approximate lateral deformation demands in multistory buildings with nonuniform stiffness, *Journal of Structural Engineering*, 128(7), 840-849, 2002.

[3] Y. Bozorgnia, and V.V. Bertero. Improved shaking and damage parameters for post-earthquake applications, *Proc., SMIP01 Seminar on Utilization of Strong-Motion Data*, California Division of Mines and Geology, Los Angeles, 1–22, 2001

[4] A. Ghobarah. On drift limits associated with different damage levels. In Performance-Based Seismic Design Concepts and Implementation: *Proceedings of the International Workshop*, *Bled, Slovenia* (Vol. 28, pp. 321-332), 2004

[5] C. Michel, P. Gueguen, & M. Causse. Seismic vulnerability assessment to slight damage based on experimental modal parameters. *Earthquake engineering & structural dynamics*, 41(1), 81-98, 2012

[6] M. Polese, M. Gaetani d'Aragona, A. Prota, & G. Manfredi. Seismic behavior of damaged buildings: a comparison of static and dynamic nonlinear approach. In *4th ECCOMAS Thematic Conference on Computational Methods in Structural Dynamics and Earthquake Engineering*, Kos Island, Greece, 12–14 June, paper 1134 (pp. 608-625), 2013.

[7] M. Gaetani d'Aragona, M. Polese, & A. Prota. Relationship between the variation of seismic capacity after damaging earthquakes, collapse probability and repair costs: detailed evaluation for a non-ductile building. In *5th ECCOMAS Thematic Conference on Computational Methods in Structural Dynamics and Earthquake Engineering,* Crete Island, Greece, 25–27 May, (pp. 1478-1495), *2015*.

[8] M. Gaetani d'Aragona, M. Polese, & M. Di Ludovico. Building Retrofit Prior to Damaging Earthquakes: Reduction of Residual Capacity and Repair Costs. In *16th World Conference on Earthquake Engineering*, Santiago Chile, January 9th-13th, Paper N° 2490, 2017.

[9] A. Gupta, & H. Krawinkler. Estimation of seismic drift demands for frame structures, *Earthquake Engineering and Structural Dynamics*, 29, 1287-1305, 2000

[10] T. Eroğlu, & S. Akkar. Lateral stiffness estimation in frames and its implementation to continuum models for linear and nonlinear static analysis. *Bulletin of Earthquake Engineering*, 9(4), 1097-1114, 2011

[11] E. Miranda, & S.D. Akkar. Generalized interstory drift spectrum. *Journal of Structural Engineering*, 132(6), 840-852, 2006

[12] N. Caterino, E. Cosenza, B.M Azmoodeh. Approximate methods to evaluate storey stiffness and interstory drift of RC buildings in seismic area, *Structural Engineering and Mechanics*, 46 (2), pp. 245-267, 2013

[13] M Polese, E. Cosenza, M. Varriale. Analisi del database di edifici monitorati dall'osservatorio sismico delle strutture e prima proposta di formulazione semplificata per la stima di $IDR_{max}$, *XVI Convegno Anidis*, L'Aquila, 13-17 settembre 2015

[14] M. Hosseini, M.R. Imagh-e-Naiini. A quick method for estimating the lateral stiffness of building systems. *Struct Design Tall Build* 8:247–260, 1999

[15] G.M. Verderame, M. Polese, E. Cosenza. Vulnerability of existing R.C. buildings under gravity loads: A simplified approach for non sway structures, *Engineering Structures* 31 (9) 2141-2151, 2009. ISSN 0141-0296

[16] M. Polese, G.M. Verderame, G. Manfredi. Static vulnerability of existing R.C. buildings in Italy: a case study, *Structural Engineering and Mechanics,* Techno-Press, 39 (4), 599-620, 2011. ISSN 1225-4568

[17] G.M. Verderame, M. Polese, C. Mariniello, G. Manfredi. A simulated design procedure for the assessment of seismic capacity of existing reinforced concrete buildings, *Advances in Engineering Software*, 41 (2) 323-335, ISSN 0965-9978, 2010

[18] OpenSees. Open system for earthquake engineering simulation OpenSees framework-Version 2.5.0. Univ. of California, Berkeley, 2016.

[19] K. J. Elwood, A.B. Matamoros, J.W. Wallace, D.E. Lehman, J.A. Heintz, A. D. Mitchell, , ... & J.P. Moehle. Update to ASCE/SEI 41 concrete provisions. Earthquake Spectra, 23(3), 493-523, 2007.

[20] T.B. Panagiotakos, M.N. Fardis. Seismic response of infilled RC frames structures. In *11th World Conference on Earthquake Engineering*, Acapulco, México, June 23-28. Paper No. 225, 1996.

[21] D.J. Kakaletsis, K.N. David, C.G. Karayannis. Analytical modeling of masonry infills with openings, *Structural Engineering and Mechanics*, vol 31, N.4, 2009.

[22] H. Ozkaynak, E. Yuksel, C. Yalcin, A.A. Dindar, & O. Buyukozturk. Masonry infill walls in reinforced concrete frames as a source of structural damping. Earthquake Engineering & Structural Dynamics, 43(7), 949-968, 2014.

[23] Circolare n. 617 del 2 Febbraio 2009, Guidelines for the application of the "New technical code for constructions D.M. 14 gennaio 2008", (in italian), 2009.

[24] Applied Technology Council. Quantification of building seismic performance factors. ATC 63. Redwood city, California, 2008.

[25] P. Ricci, G.M. Verderame, & G. Manfredi. Analytical investigation of elastic period of infilled RC MRF buildings. *Engineering Structures*, 33(2), 308-319, 2011.

COMPDYN 2017
6th ECCOMAS Thematic Conference on
Computational Methods in Structural Dynamics and Earthquake Engineering
M. Papadrakakis, M. Fragiadakis (eds.)
Rhodes Island, Greece, 15ï 17 June 2017

# PROCESSING OF 3D OPTICAL MOTION DATA OF SHAKING TABLE TESTS: FILTERING OPTIMIZATION AND MODAL ANALYSIS

**I. Roselli[1], D. Paolini[2], M. Mongelli[1], G. De Canio[1], and G. de Felice[2]**

[1] Enea, Casaccia Research Center
Via Anguillarese 301, 00123 ï Rome, Italy
e-mail: ivan.roselli@enea.it, marialuisa.mongelli@enea.it, gerardo.decanio@enea.it

[2] Department of Engineering, Roma Tre University
Via Vito Volterra 62, 00146 ï Rome, Italy
daniela.paolini87@gmail.com, gianmarco.defelice@uniroma3.it

**Keywords:** 3D Motion Capture, Shaking Table, Displacement Signal Filtering, Modal Analysis.

**Abstract.** *The use of 3D optical motion data for structural dynamics is both promising and challenging. Further developments for on-the-filed applications are still needed, but, at the present stage, such techniques are already feasible for laboratory dynamic tests. A measurement system of this kind was installed for the first time for shaking table testing at the ENEA Casaccia Research Center. This 3D motion capture system is capable of acquiring the positions of more than a hundred passive markers with a constellation of 10 near-infrared cameras. In particular, this paper focuses on filtering and processing the markers displacements. A methodology is proposed for optimizing the displacement data processing to obtain an estimation of markers accelerations. Such methodology implies the optimal choice of the Savitzky-Golay-filter parameters for the implementation of a filtered numerical derivative of displacement data. The optimal parameters are calculated minimizing the error in the estimation of the peak acceleration of a reference marker compared to a conventional accelerometer located at the same measurement point. The accuracy of markers accelerations was estimated in the range of 0.01-0.02 g, which is appropriate for providing interesting indications for studied structures subjected to most shaking table testing. For example, markers displacements data and related estimated accelerations can be combined to obtain the hysteretic behavior of the structure or of portions of it. Markers data were also used for Experimental and Operational Modal Analysis (EMA/OMA) in order to extract the modal parameters and to calibrate/validate the Finite Element Models (FEM) of the structure. In particular, the combined used of OMA by markers data and numerical modal analysis by FEM permits to compare the resulting modal shapes for a more precise dynamic identification. An example of practical application is illustrated on a shaking table experimentation conducted on a two-story tuff-masonry prototype, which reproduces a typical ancient buildings of Central Italy.*

## 1 INTRODUCTION

In shaking table experiments the measurement of motion parameters is typically carried out by means of accelerometers and displacement sensors. This is due to the well-known difficulty of obtaining the complete motion of measurement points through a single device with appropriate accuracy. In the past decades a vast literature has been published over the correction and the processing of accelerometric signals in order to estimate the displacement by numerical algorithms [1]. Nonetheless, results are not always satisfactory, especially when baseline correction is manifestly ineffective [2]. Theoretically, the complete motion of a point can be calculated starting from its trajectory, which means, in practical, to measure its absolute displacement. Subsequently, velocity and acceleration can be estimated through successive operations of numerical derivation. In such a direction, an interesting prospective is provided by the recent developments of displacement sensors based on opto-electronic technologies applied to laser or digital vision systems. Such kind of systems are increasingly utilized as motion measurement devices also for shaking table tests [3, 4].

In the frame of an increasing interest for the measurement of the absolute displacement in seismic tests, in order to provide experimental validation for the application of the increasingly relevant displacement based approach to the seismic design, ENEA is engaged in exploring all its 3D motion capture potentialities. In fact, among the earliest shaking table facilities in Italy to install a 3D motion capture system was the ENEA Casaccia Research Center [5]. This specific system, named 3DVision, offers advantages in terms of instrumentation flexibility, large number of measurement points, easy and low-encumbrance marker installation [6]. Besides, 3D computer graphic potentialities and friendly visualization of real-time data and movies are particularly suitable for experiment remote sharing via the internet, like in the DYSCO virtual lab implemented by ENEA [7].

Particularly interesting is the possibility of measuring even more than a hundred 3D points through passive cheap markers to obtain information also on the acceleration in destructive shaking table tests, as an alternative to installing numerous conventional expensive accelerometers. The accelerations estimated from markers can provide valuable indications for studying structures subjected to shaking table testing, even if accuracy cannot be as accurate as conventional accelerometers. In fact, accuracy in the order of 0.01-0.02 g is still appropriate for providing interesting information for seismic tests with input peak accelerations that typically fall in the range 0.1-1.0 g. The present paper illustrates a methodology for processing 3DVision data in order to obtain an optimal estimation of acceleration for shaking table tests. To such aim, the problems related to error propagation and numerical derivative of data were explored in order to make a proper choice of digital filter and processing algorithm.

The methodology was applied to experimental data acquired in shaking table tests on a two-story tuff-masonry prototype, representing a traditional building typology of Central Italy. In particular, the results in terms of estimation of accelerations and hysteretic behavior of portions of the structure are illustrated.

Another interesting application of markers data is to perform the Experimental and Operational Modal Analysis (EMA/OMA). The great number of 3D measurement points available permits to improve the accuracy in the identification of modal shapes and frequencies [8], as well as to distinguish global and local modes, on the basis of the specific markers selected for the analysis. EMA and OMA techniques, such as FRF-MIMO and FDD, were calculated to extract the modal parameters of the tested tuff-masonry prototype allowing to calibrate and finally validate the Finite Element Model (FEM) of the structure.

## 2 DATA FILTERING

Digital filters are used to attenuate the measurement error from the acquired signals, once that all hardware sources of noise are avoided or limited as much as possible. In the proposed DDP the main objective is to reduce the measurement noise through digital filtering of acquired data in order to optimize the estimation of velocity and, especially, acceleration. In this optic it is relevant to premise how displacement noise propagation to velocity and acceleration was modelled. Moreover, as well known in digital signal processing, even the numerical operation of derivation itself adds another source of noise [9]. Consequently, a proper DDP must include filtering algorithms that should provide good performance also in terms of attenuation the error amplification caused by numerical derivative.

### 2.1 Displacement error propagation to acceleration error

Let us consider a pure sine vibration of amplitude *A* and frequency *f*. Then the displacement *s(t)* can be expressed with the following equation with time *t*:

$$s(t) = A \cdot \cos(\omega \cdot t) \tag{1}$$

where $\omega = 2\pi f$. Besides, be the measurement error dependent only on the vibration amplitude *A*, which is true for substantially white noise. According to the general formulation of the error propagation theory, the displacement error can be expressed as follows [10]:

$$\Delta s(t) = \Delta A \cdot \cos(\omega \cdot t) \tag{2}$$

Similarly, for velocity *v* and acceleration *a* the error can be written:

$$\Delta v(t) = -\Delta A \omega \cdot \sin(\omega \cdot t) \tag{3}$$

$$\Delta a(t) = -\Delta A \omega^2 \cdot \cos(\omega \cdot t) \tag{4}$$

The Eq.s (3) and (4) show that the error in displacement amplitude $\varphi A$ propagates to *v* and *a* increasing with $\omega$. In particular, acceleration error is characterized by quadratic growth with the frequency for a white displacement noise (Figure 1).

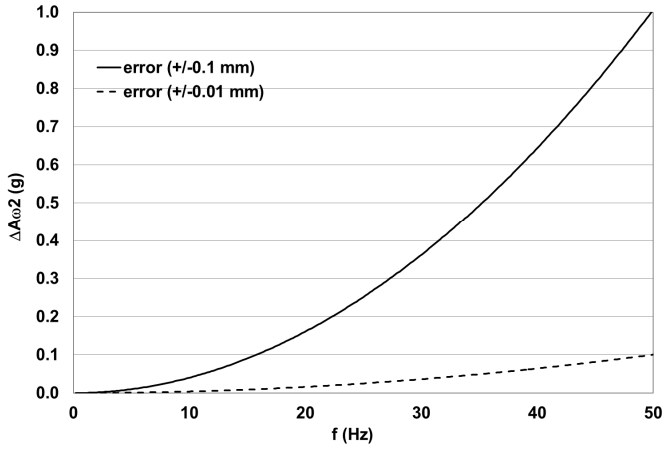


Figure 1. Error propagation effect on the acceleration amplitude ($\varphi A\omega^2$) vs. signal frequency f (Hz).

## 2.2 Filtering technique

Several filtering approaches can be considered for measurement noise reduction, whose performances mainly depend on the noise and the signal properties in both the time and the frequency domain.

One very common approach is represented by the band-pass family. As a first step, signals are analyzed in the frequency domain. When the frequency content of the signal is clearly different from that of the noise, than band-pass filters performance is optimal. In seismic applications typical cut-off frequencies are between 0.1-0.5 Hz and 25-30 Hz, since natural spectra generally have most of their energetic content within this range [11]. Many band-pass filters are available in literature.

Instead of a band-pass filter, in the present paper the Savitzkyï Golay smoothing filter was considered, as it is one of the most effective algorithms in removing random noise from experimental data without excluding completely the contribution of frequencies higher than an upper cut-off limit [12]. It essentially performs a local polynomial regression on a series of equally spaced data points (windowing), to determine smoothed values [13]. This filter is characterized by two parameters: the fitting polynomial degree ($n$) and the windowing width ($m$ points). Furthermore, the Savitzkyï Golay can be implemented to perform differentiation operations, which is particularly useful in case successive derivatives of raw data must be calculated, like in the present case for obtaining velocity and acceleration from displacement data.

In fact, various techniques of numerical differentiation can be implemented. Classical methods based on higher-order central finite differences provide a somewhat low-pass effect [8]. According to such methods a general expression of the first derivative $f\hat{o}$ can be written as:

$$f' = \frac{1}{\Delta t}\sum_{k=1}^{M} c_k \left( f_k - f_{-k} \right) \tag{5}$$

where $M = (N\text{-}1)/2$ with $N$ number of data within the moving window, $\Delta t$ is the time step and $c_k$ are called convolution coefficients. Several methods descending from such approach, also known as convolution methods, combine the derivative estimation with the filtering effect by choosing the appropriate $c_k$ coefficients in Eq. 5. The Savitzkyï Golay filter can be considered a specific case of this general method.

## 2.3 Filtering optimization methodology

The used filtering strategy was based on the assumption that filter parameters $n$ and $m$ values can be optimized through the minimization of the difference $\Delta f$ between results by filtered markers and by reference measurements at the same points on the structure (objective function). In the present study, the reference measurements were carried out through a limited number of conventional accelerometers (capacitive devices with sensitivity of 1 V/g and broadband resolution of 0.03 mg in terms of RMS error). The optimization problem can be expressed mathematically as follows [14]:

$$\begin{cases} \min \Delta F(n,m) \\ n,m \in R \end{cases} \tag{6}$$

Generally speaking, $F$ can be whatever function or physical quantity we are interested in and, more specifically in the present application, whatever motion parameter we want to use to optimize markers data. The simplest choice for $F$ is the peak acceleration $a_p$ of the recorded time-history, but also more sophisticated ground motion parameters (Arias Intensity, Housner Intensity, etc.) can be considered.

Assessing the performance of filtering algorithms is a quite elusive issue and depends on the specific result they are design to or intended for. In the proposed methodology, the focus is to optimize noise reduction from displacement data in order to have an estimate of the acceleration good enough for structural analysis. Consequently, the filtering performance was assessed by comparing the final result with signals acquired by control points equipped with accelerometers. In practice, this can be done using only a part of the installed accelerometers as reference for the optimization process and the other ones for checking the filtering performance.

## 3 EXPERIMENTAL APPLICATION TO SHAKING TABLE TESTS

### 3.1 Tested specimen

A 2/3-scaled two-story tuff-masonry prototype was subjected to shaking table test (Figure 2). The specimen dimensions were 3.50 m × 3.00 m and the inter-story height was 2.30 m. The walls thickness was 0.25 m. The overall weight was 193.00 kN.

### 3.2 3D optical acquisition setup

The equipment installed at ENEA Casaccia Research Center is able to acquire the trajectory of a large number of retro-reflecting markers located within the measurement volume by triangulating data from a constellation of 10 high-frequency Near Infra-Red (NIR) cameras, based on VICON technology. The NIR cameras are equipped with a 4-Mpixel high-frequency CMOS digital sensor. Data were acquired at 100 fps (which as saying the sampling frequency in Hz).

The total number of markers located on the specimen was 141. Two triaxial accelerometers were located at positions depicted in Figure 2.

Measurement error calculated for each marker resulted in the range 0.014-0.035 mm in terms of RMS error of markers displacement and was approximately considered as white noise, as confirmed by its FFT in Figure 3a. FFT of the acceleration error calculated by 2nd numerical derivative of 3DVision displacement data, depicted in Figure 3b, show a quasi-quadratic growth, in substantial accordance to the proposed model of error propagation.

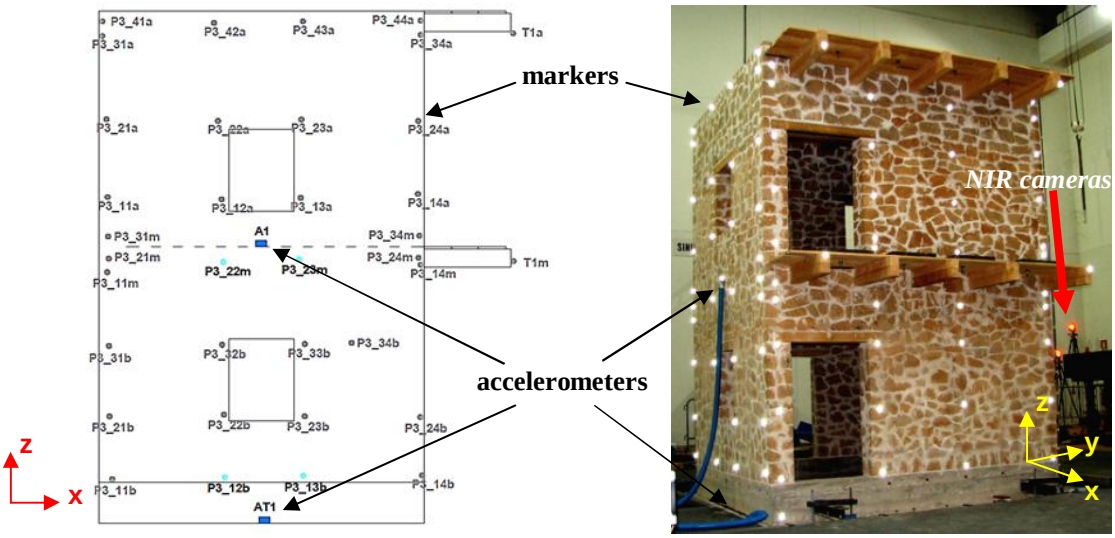


Figure 2. Markers and accelerometers positioned on the specimen. Retro-reflecting markers appear lighted in photos taken by common camera using a flash (right).

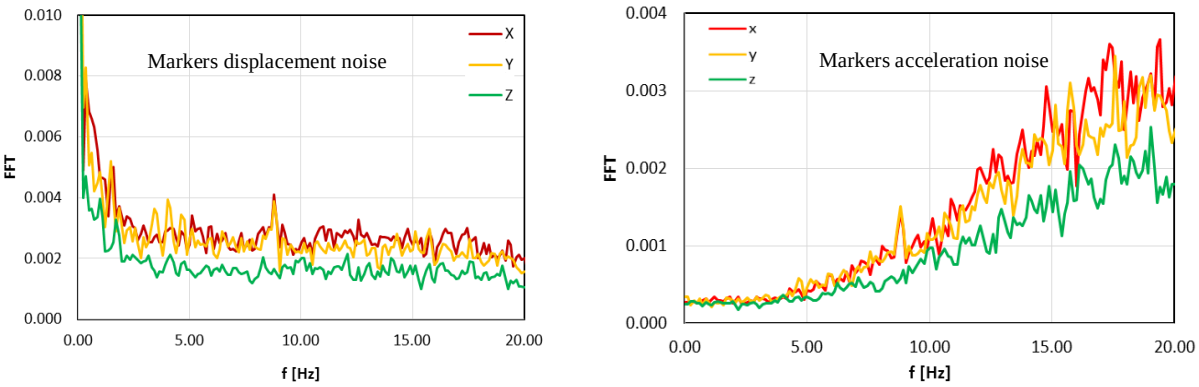


Figure 3. FFT of markers noise in static condition (left) and error propagation to unfiltered acceleration (right).

### 3.3 Experimental campaign

The experimental tests were carried out on the largest of the two shake tables available at ENEA Casaccia laboratory (System 1 in Table 1). A natural input based on the time-history recorded at Colfiorito station during Umbria-Marche earthquake, 1997, was considered for the tests sequence. The above triaxial seismic signal was submitted to the shaking table, increasing gradually the input Peak Ground Acceleration (PGA) at each trial by 0.05 g. Before the test sequence and after each trial a random test (white noise input) at 0.05 g was performed for the dynamic identification of the structure. The specimen showed some initial damage at 0.15 g (nominal PGA) and final collapse occurred at 0.40 g.

| | System 1 | System 2 |
|---|---|---|
| Table size | 4 x 4 [m] | 2 x 2 [m] |
| Degrees of Freedom | 6 | 6 |
| Frequency range | 0-50 [Hz] | 0-100 [Hz] |
| Acceleration | 3g peak | 5g peak |
| Velocity | 0.5 m/s (0-peak) | 1 m/s (0-peak) |
| Displacement | 0.125 m (0-peak) | 0.15 m (0- peak) |
| Specimen Mass | 30 [t] | 5 [t] |

Table 1. ENEA Casaccia shake tables technical specifications.

### 3.4 Filtering optimization application

The filtering optimization methodology was applied considering the accelerometer AT1 as reference point for calculating the objective function of *F*. Synthetically, the optimization problem was formulated as follows:

$$\begin{cases} \min \Delta a(n,m) \\ \Delta a = \left| a_{p(AT1)} - a_p^{SG} \right| \\ n,m \in R \end{cases} \tag{7}$$

where $a^{SG}$ indicates the acceleration calculated by double differentiation according to Eq. 5 implemented with Savitzkyï Golay filtering of the marker located near AT1.

The accelerometer located at first floor (A1) was taken as control point to assess the performance of the filtered double differentiation methodology.

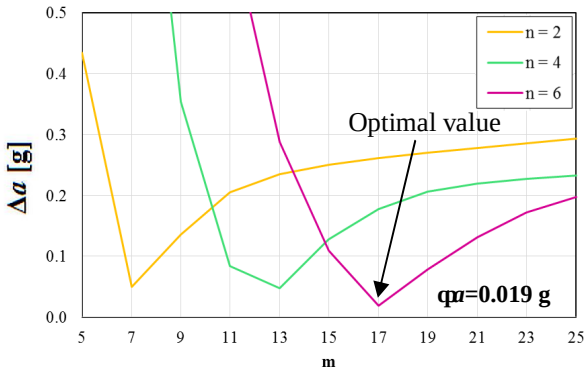


Figure 4. Identification of optimal filter parameters *n* and *m* by minimizing the acceleration error q*pa* with respect to the reference accelerometer AT1.

## 4 RESULTS

### 4.1 Optimal acceleration estimation

The results of the optimization problem of Eq. 6 are shown in Figure 4. The optimal values of the Savitzkyï Golay parameters were $n = 6$ and $m = 17$ (corresponding to a windowing half-width of 0.08 s at a sampling frequency of 100 Hz).

The optimal acceleration error at control point A1 obtained in shaking table tests at initial damage and at final collapse of specimen (0.15 g and 0.40 g of PGA, respectively) is depicted in Table 2, showing that in both x and y directions the acceleration error remained in the order of 0.01-0.02 g. The estimated acceleration of markers was utilized to calculate the hysteretic behavior. On the one hand, the hysteretic behavior can be obtained for any portion of the specimen that is described by a given amount of markers. On the other hand, seismic tests are not cyclic, thus hysteretic cycles calculated in shaking table tests are very noisy.

| Test input PGA | Acceleration error [g] | |
|---|---|---|
| | x | y |
| 0.15 g | 0.006 | 0.024 |
| 0.40 g | 0.018 | 0.024 |

Table 2. Acceleration error at the control point A1 at the first floor in x and y direction in shaking table tests with input Peak Ground Acceleration (PGA) of 0.15 g and 0.40 g.

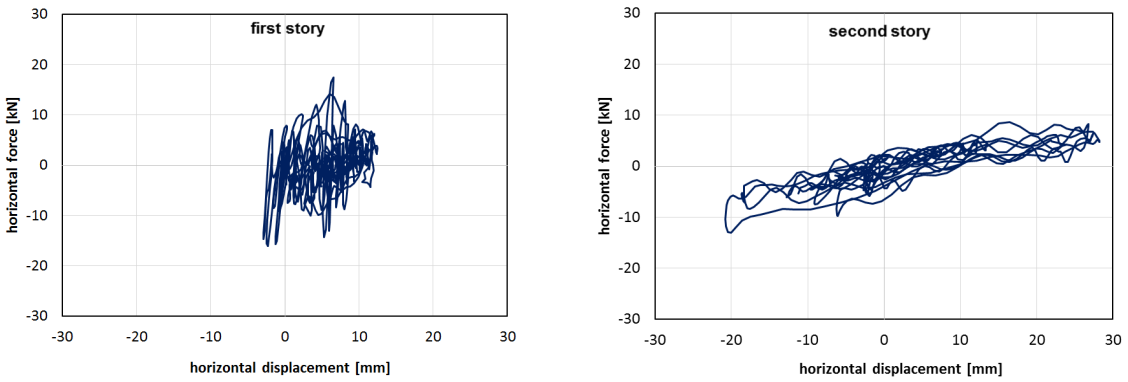


Figure 5. Hysteretic behavior of specimen façade wall of first story (left) and second story (right).

Nonetheless, they can give interesting indications on the walls behavior under dynamic conditions. As an example, in Figure 5 the hysteretic behavior during the trial at 0.40 g was calculated for the façade wall at the first and the second story. It is evident the loss of stiffness at the second story with respect to the first one.

### 4.2 Modal analysis

The availability of a large number of measurement points allowed the application of Frequency Response Function Multi-Input Multi-Output (FRF-MIMO) technique. In particular, the transmissibility function H was considered to calculate the FRF. The markers at the specimen base were taken as input signals. In Figure 6 the FRF of markers at first story (MIMO 1) and at second story (MIMO 2) are compared with the FRF of the theoretical Single Degree Of Freedom (SDOF). It is evident that the markers located at the second story are characterized by higher amplification, providing a clearer identification of the first mode. This is confirmed by Figure 7 that compares the modal shape and frequency $f_n$ of the first mode obtained by Frequency Domain Decomposition (FDD) with the same by FEM, indicating clearly a bending mode in x direction.

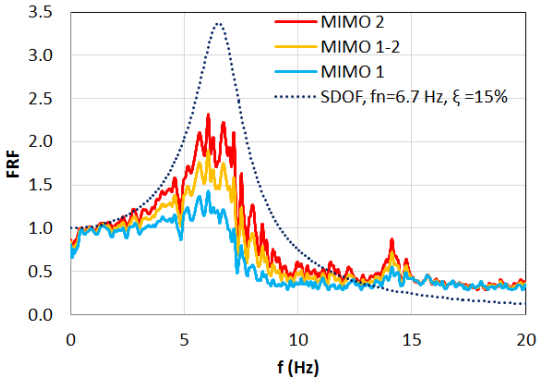


Figure 6. Frequency Response Function (FRF) of markers at first story (MIMO 1), at second story (MIMO 2), and at both stories (MIMO 1-2) with respect to markers at the specimen base compared with FRF of theoretical Single Degree Of Freedom (SDOF).

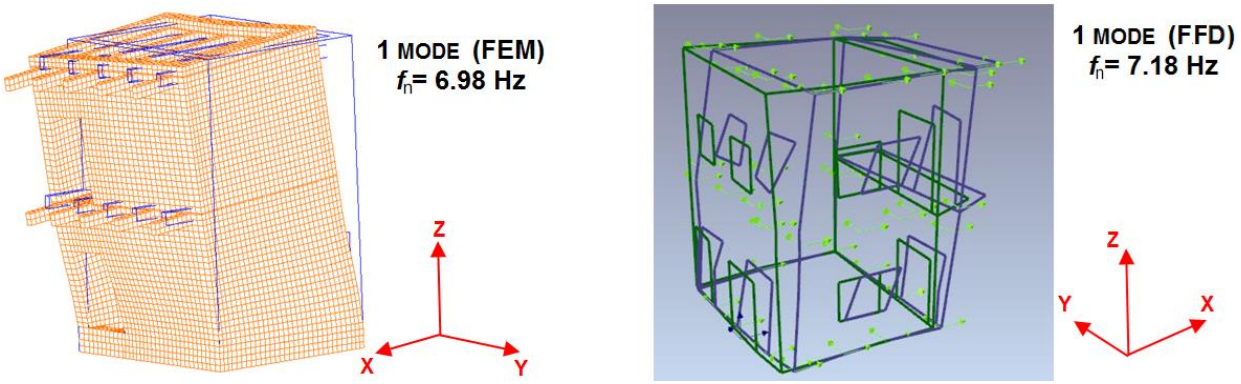


Figure 7. Modal shape and frequency $f_n$ of the first mode by FEM (left) and by Frequency Domain Decomposition (FDD) with markers data (right).

## 5 CONCLUSIONS

A methodology was proposed for the optimal choice of the filter parameters to process 3D displacement data, such as 3D motion capture markers data, in order to obtain an estimation of the peak acceleration of a large number of measurement points of structures subjected to

laboratory dynamic testing. The above methodology was described and a practical application to shaking table tests on a two-story tuff-masonry specimen was illustrated. The accuracy achieved in the estimation of the peak acceleration resulted in order 0.01-0.02 g. The filtered acceleration was then utilized for calculating the hysteretic behavior of the specimen walls during the seismic tests providing valuable indications on the loss of stiffness of the masonry.

Markers data were also processed for the dynamic identification of the specimen through modal analysis techniques. In particular, FRF-MIMO and FDD were used to extract the modal parameters of the tested prototype. The great number of 3D measurement points available (141) permitted to provide an accurate identification of modal shapes and frequencies. This allowed to calibrate and finally validate a FEM of the specimen for subsequent structural analysis.

## REFERENCES


[1] G.V. Berg, G.W. Housner, Integrated velocity and displacement of strong earthquake ground motion. *Bull. Seismol. Soc. Amer.*, **51**(2), 175-189, 1961.

[2] D.M. Boore, Effect of Baseline Corrections on Displacements and Response Spectra for Several Recordings of the 1999 Chi-Chi, Taiwan. *Earthquake Bull. Seismol. Soc. Amer.*, **91**(5), 1199ï 1211, 2001.

[3] J.A Beraldin, C. Latouche, S.F. El-Hakim, A. Filiatrault, Applications Of Photogrammetric And Computer Vision Techniques In Shake Table Testing. *13th World Conference on Earthquake Engineering*, Vancouver, Ca, USA, August 1-6, 2004.

[4] F. Lunghi, A. Pavese, Computer Vision System for Monitoring in Dynamic Structural Testing. *Geotechnical, Geological, and Earthquake Engineering*, **22**, 159-176, 2012.

[5] M. Mongelli, G. De Canio, I. Roselli, A. Colucci, A. Tatì,. 3D motion capture and FEM Analysis for Shaking Table Tests at ENEA Casaccia Research Center. *14th European Conference On Earthquake Engineering*, Ohrid, Republic of Macedonia August 30-September 3, 2010.

[6] G. De Canio, M. Mongelli, I. Roselli, 3D Motion Capture Application to Seismic Tests at ENEA Casaccia Research Center: 3DVision System and DySCo Virtual Lab. *WIT Transactions on The Built Environment*, **134**, 803-814, 2013.

[7] I. Roselli, G. Mencuccini, M. Mongelli, F. Beone, G. De Canio, F. Di Biagio, A.Rocchi, The DySCo virtual lab for Seismic and Vibration Tests at the ENEA Casaccia Research Center. *14th European Conference On Earthquake Engineering*, Ohrid, Republic of Macedonia August 30-September 3, 2010.

[8] G. De Canio, P. Andersen, I. Roselli, M. Mongelli, E. Esposito,. Displacement Based Approach for a Ro-bust Operational Modal Analysis. *Conference & Exposition on Structural dynamics Advanced Aerospace Applications (IMAC XXIX),* Jacksonville, Florida, USA, January 31 - February 3, 2011.

[9] J.N. Lyness, C.B. Moler, Numerical Differentiation of Analytic Functions. *SIAM Journal on Numerical Analysis*, **4**(2), 202-210, 1967.

[10] P.R. Bevington, *Data Reduction and Error Analysis for the Physical Sciences.* McGraw-Hill, 1969.

[11] D. Rinaldis, Acquisition and processing of analogue and digital accelerometric records: ENEA methodology and experience from Italian earthquakes, *COSMOS Invited Workshop on Strong-Motion Record Processing*, Richmond, Ca, USA, May 26-27, 2004.

[12] G. De Canio, G. de Felice, S. De Santis, A. Giocoli, M. Mongelli, F. Paolacci, I. Roselli, Passive 3D motion optical data in shaking table tests of a SRG-reinforced masonry wall, *Earthquakes and Structures*, **40**(1), 53-71, 2016.

[13] A. Savitzky, M.J.E. Golay, Smoothing and Differentiation of Data by Simplified Least Squares Procedures, *Analytical Chemistry*, **36**(8), 1627-1639, 1964.

[14] S.P. Boyd, L. Vandenberghe, *Convex Optimization*. Cambridge University Press, 2004.

COMPDYN 2017
6th ECCOMAS Thematic Conference on
Computational Methods in Structural Dynamics and Earthquake Engineering
M. Papadrakakis, M. Fragiadakis (eds.)
Rhodes Island, Greece, 15ï 17 June 2017

# PERFORMANCE BASED EARTHQUAKE ASSESSMENT OF AN INDUSTRIAL GAS FILTER STRUCTURE

**Raffaele Laguardia[1], Andrea Piscini[2], Marco Faggella[1], Rosario Gigliotti[1], Francesco Morelli[2], Franco Braga[1] and Walter Salvatore[2]**

[1]Sapienza University of Rome
Via Eudossiana 18
{marco.faggella, raffaele.laguardia, rosario.gigliotti, franco.braga}@uniroma1.it

[2]University of Pisa
Largo Lucio Lazzarino 2, 56126 Pisa, Italy
{andrea.piscini@ing, francesco.morelli@dic, walter@ing}.unipi.it

**Keywords:** Nonlinear Response History Analysis (NL RHA), Performance Based Earthquake Engineering (PBEE), Incremental Dynamic Analysis (IDA), Ground Motions (GM), Uniform Hazard Spectrum (UHS), Conditional Mean Spectrum (CMS).

***Abstract.***
Industrial facilities often store a large amount of hazardous material and, in case of seismic event, there is a high probability that accidental scenarios as fire, explosion, toxic or radioactive dispersion may occur. Moreover, the structural configuration of industrial facilities are often the fruit of plants and functionality requirements, that lead to strong irregularities and different load resisting systems within the same structure. This paper presents a performance-based earthquake assessment of an industrial gas filter structure, characterized by the presence of important masses placed at significant height and of different horizontal resisting systems, such as moment resisting frames, inverted V bracings and diagonal bracings. Within the framework of the PROINDUSTRY research project critical failure mechanisms of industrial structures and relevant limit states are analyzed and discussed. The structural response is computed via nonlinear finite elements analyses of the static pushover (PO) and dynamic response history type (RHA). The seismic input is defined through Probabilistic Seismic Hazard Analysis (PSHA) and a set of natural Ground Motions (GM) which are selected and scaled with different criteria with respect to the Uniform Hazard Spectrum (UHS) and the Conditional Mean Spectrum (CMS). An overview of significant aspects of the structural performance assessment is presented with respect to input definition and choice of Intensity Measures (IM), irregular structural behaviour and probabilistic treatment of key Engineering Demand Parameters (EDP) for this type of industrial structure.

## 1 INTRODUCTION

Recent earthquakes have pointed out the high vulnerability of industrial facilities[1][2][3][4][5][6]. The risk associated to the failure of the plant, or a part of it, is very high since the consequences may be disastrous, in terms of human lives, environmental contamination and economic losses. These aspects make the risk assessment of industrial buildings particularly complex requiring different approach with respect to risk assessment of residential and commercial buildings [7][8]. Such buildings are characterized by structures often designed according to old codes, which were not performance oriented or did not consider anti-seismic design. Some efforts were carried out in the past to address evaluation and upgrading of seismic performances of non-structural elements [9][10][11][12].

Seismic design provisions for industrial plants can be found in ASCE/SEI 7-10 [13], ASCE-SEI 43-05 [14], FERC 2007 (Liquified Natural Gas facilities) [15], API Standard 620 and 650 (Storage Tanks) [16][17], UNI EN 1998-4 (Silos, tanks and pipelines)[18], UNI EN 1998-6 (Towers, piles and chimneys) [19]. Such international codes define rules for performance assessment at the component level, checking/comparing member demand with capacity through a traditional Performance Based Earthquake Engineering (PBEE) approach. These codes prescribe also methods of nonlinear analysis, both static and dynamic, and rules for Response History Analysis (RHA) and Ground Motions (GMs) selection. A comprehensive review of Non-Linear Response History Analysis (NL RHA) code procedures for different types of structures is carried out in the NIST GCR 11-917-15 document [20]. Despite the high number of references in literature and international codes, to date, there is not a unique and recognized method for selecting and scaling GMs.

In this paper, an industrial structure from the PROINDUSTRY project is selected as case study, and NL RHA are performed adopting two different GMs sets, respectively coherent with UHS and CMS. The results obtained in terms of different EDPs are investigated and discussed, focusing on the influence of the different GMs selection and scaling techniques.

## 2 CASE STUDY DESCRIPTION

The building analyzed in this paper is characterized by a mass placed at a significant height and different typologies of horizontal forces resisting systems, as it is shown in Figure 1. The same building was already adopted in [21] for the evaluation of the seismic behavior of steel structures equipped with self-centering devices [21].

The building has a regular plan with dimensions 37.80 m x 16.94 m and total height 29.64 m. The supporting structure, with a total height of about 10.80 m, has six bays in the longitudinal direction and three in the transversal one. The horizontal loads resisting systems comprises moment resisting frames (X direction - ground floor), inverted V bracings (Y direction - ground floor) and diagonal bracings (X and Y directions - first floors). The total mass of the silo (23700 kN), considering the structural elements and the infill material, represents the 86% of the total mass (27650 kN).

A 3D model was created in OpenSEES [22] adopting the simplified geometry shown in Figure 1. The nonlinear analyses carried out through a more geometrically accurate model in [21] and the linear modal analysis, showed that the building behavior is governed by the deformation of the supporting structure and the silo and roof behave as a rigid body. Steel elements are modeled through Fiber sections, each fiber is assigned the “Steel02” material property, second order effects are modeled through a “corotational transformation” for braces and through a “P-Delta transformation” for columns.

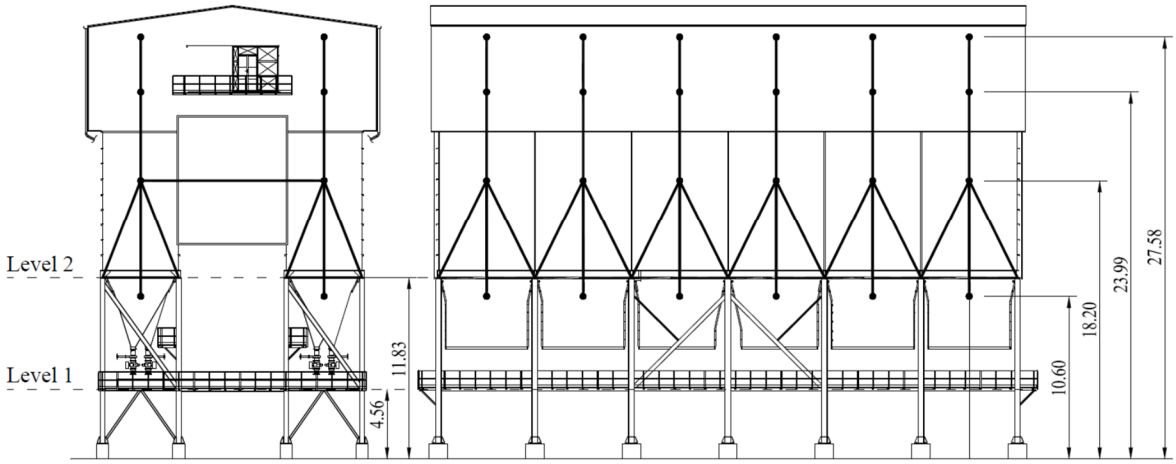


Figure 1. Case study nonlinear model geometry [21].

## 3 SEISMIC INPUT DEFINITION

Two sets of GMs are selected for an Italian high seismicity zone corresponding to the site of Reggio Calabria (Italy). One set is coherent with the spectral shape of UHS and the other is coherent with CMS. The spectrum coherence rules used is consistent with the requirements of Eurocode 8 (§3.2.3.1) [32][32]. The target spectrum is matched with the Geomean spectrum of the two orthogonal GM components. Coherence is sought in the period range between 0 sec and 2 sec. The reference spectrum chosen is the Italian code NTC08 [31] Design Spectrum computed for Reggio Calabria (Lat 38.1, Long 15.65), with Soil C, reference period $V_R$ =100 years and a probability of exceedance PoE=10%, which corresponds to a return period of 949 years. GMs have been selected in accordance with Magnitude-distance (M-R) hazard deaggregation in the range of $6<M_w<8$ and $0<R[km]<40$. The selected UHS coherent GMs, are those used also in [21] [29] [33] [34] [35] [36] and [37], for the seismic evaluation of different industrial structures. The seismic action associated to the Damage Limitation Limit State (DLS), characterized by a probability of exceedance PoE=50% in the reference period (100 years), is evaluated scaling the reference spectrum by a factor of 0.433. The CMS refers to a scenario event for a given Hazard Level (HL) and conditioning period $T^*$ based on disaggregation data (M, R); the spectral ordinate at this period is maximized (through the parameter ε) and should reach the value given by the UHS for the HL selected. The spectral ordinates at other periods are then related to the $S_a(T^*)$ through conditional probability and correlation factors, and their values are lower than those on the UHS. The conditioning period T* has been chosen as the average period of the two first vibration modes $T_{1x}$=1.08sec and $T_{1y}$=0.57sec.
Starting from the deaggregation analysis of the chosen site, the scenario event which mainly influences the hazard is computed based on the hazard data of INGV [23] and through the Ground Motion Prediction Equations (GMPE) proposed by Ambraseys et al. [24]. Through this procedure the average values of M,R and ε are respectively 6.9, 12.62Km and 0.61.
The CMS is then computed as described by Baker [25] and is shown in Figure 2.

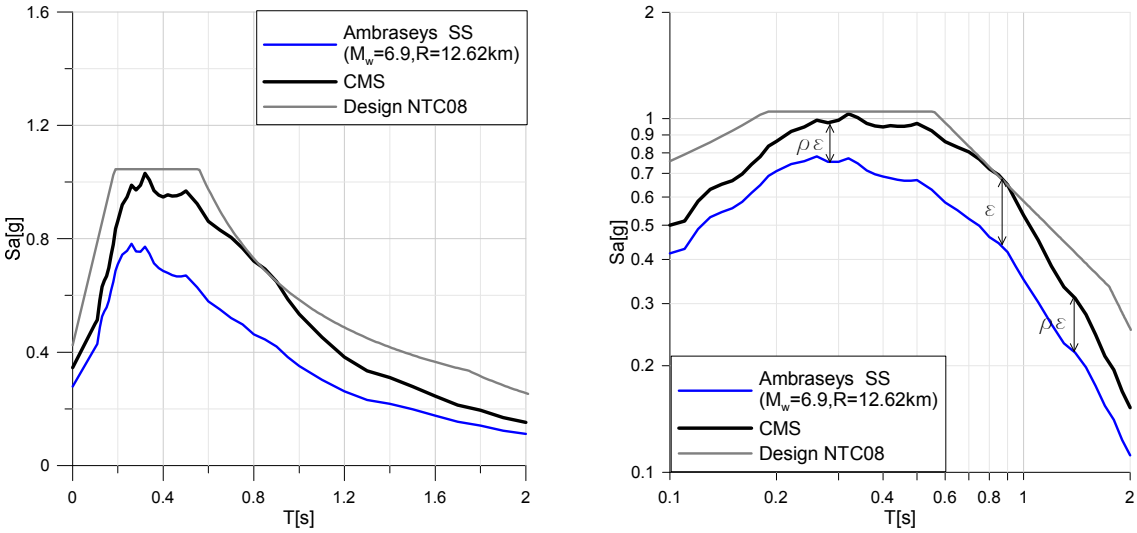


Figure 2. CMS for the Reggio Calabria site. Decimal scale (left). Logarithmic scale (right).

Once the CMS is defined a corresponding set of GMs is selected based on coherence rules and deaggregation data. The selected records are shown in Figure 3 (right).

In order to investigate the effects of the dispersion of some IMs that most influence the response, the UHS coherent set has been scaled to the spectral acceleration of the first mode of vibration in the X direction ($S_a(T_{1X})$) and in the y direction ($S_a(T_{1Y})$), as it is shown in Figure 4 and Figure 5.

## 4 NONLINEAR ANALYSIS

The seismic performance is evaluated through both non linear static (pushover) and Non linear Response History Analysis (NL RHA). Table 1 summarizes the total number of NL RHA performed using the different GMs sets described above at hazard levels with PoE =10% and PoE=50%. The NL RHAs were performed applying to the building the three concurrent components, two horizontals and one vertical, of each GM.

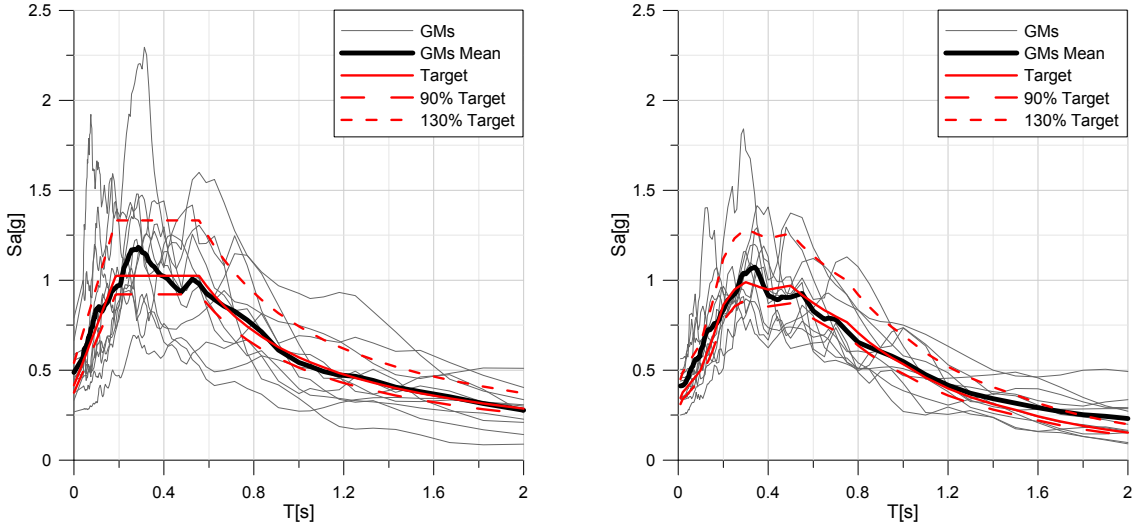


Figure 3. Set UHS coherent (left), set CMS coherent (Right).Unscaled GeoMean components

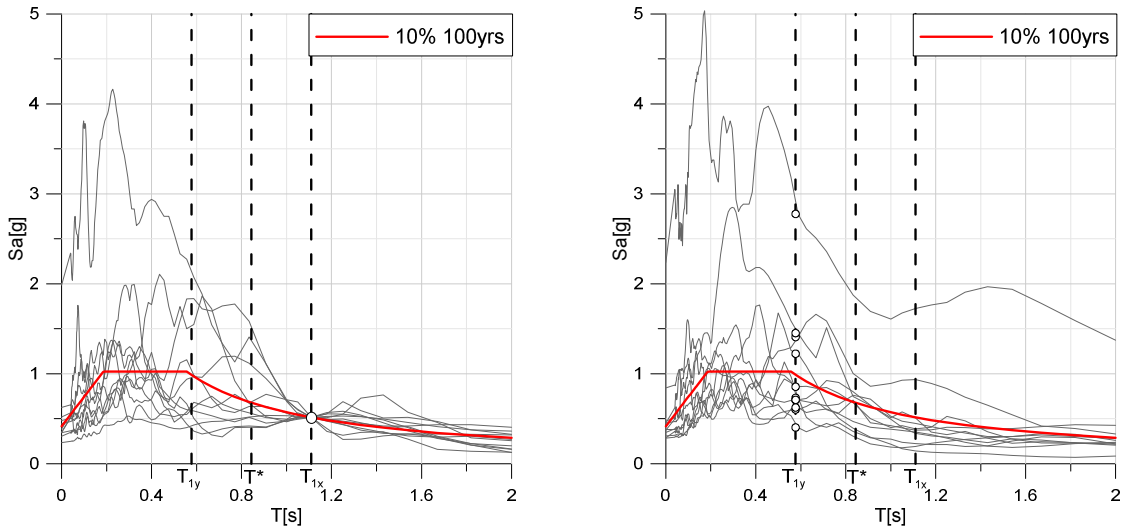


Figure 4. Set UHS scaled to Sa(T1x). Long.-component (left). 2Trasv.-component (right)

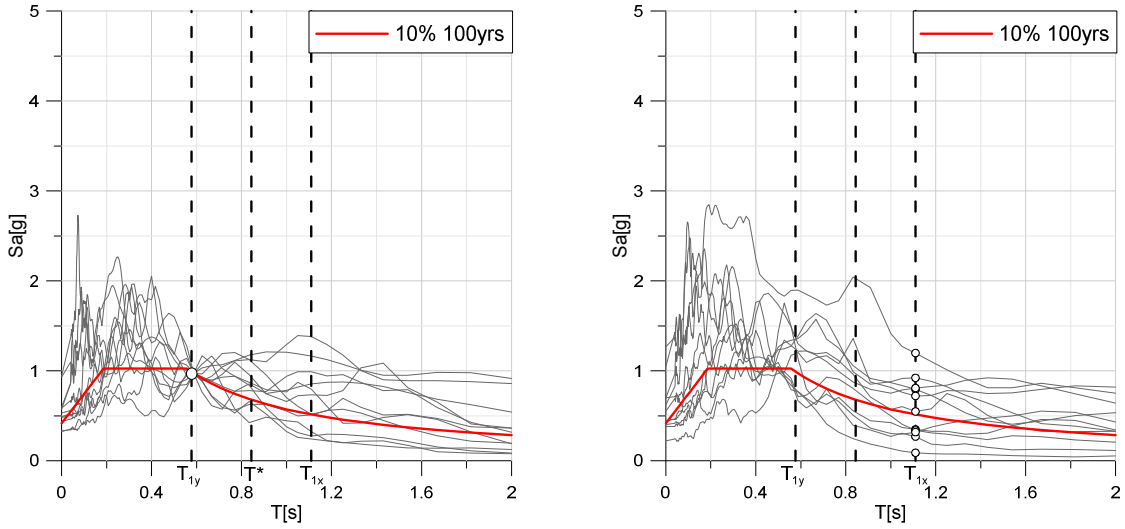


Figure 5. Set UHS scaled to Sa(T1y). Long.-component (left). Trasv.-component (right)

Table 1. NL RHA executed for HL 10%.

| GM selection | Scaling technique | Total number of analyses | Directional combination |
|---|---|---|---|
| UHS | Unscaled | 22 | 11 analyses. GM long. comp. - building X dir.<br>GM trans. comp. - building Y dir. |
| | Scaled on $S_a(T_{1X})$ | 11 | 11 analyses. GM long. comp. - building X dir.<br>GM trans. comp. - building Y dir. |
| | Scaled on $S_a(T_{1Y})$ | 11 | 11 analyses. GM long. comp. - building Y dir.<br>GM trans. comp. - building X dir. |
| CMS | Unscaled | 22 | 11 analyses. GM long. comp. - building X dir.<br>GM trans. comp. - building Y dir.<br>11 analyses. GM long. comp. - building Y dir.<br>GM trans. comp. - building X dir. |

## 4.1 Results of NL RHA

The pushover curve and NL RHA for all the GMs sets adopted in terms of $V_{max}$ - $d_{max}$ for the X direction and $V_{max}$ – $V(d_{max})$ for the Y-direction are shown in Figure 6 and **Figure 7**,

respectively. Each plot reports also the performance points evaluated based on the N2 method for NL static analysis and the performance points evaluated as mean values of the maximum base shear and maximum displacement obtained through the NL RHA. It should be noted that in the X direction the structure is more flexible than the Y direction and post-yielding behavior is governed mainly by the flexural deformations of the moment resisting frames at ground and first floor. In the Y direction, the behavior is completely different and the displacement ductility is limited due to the buckling of the inverted V diagonal bracings causing a fast drop of the global resistance. The structure is stiffer due to the presence of several bracings. The collapse mechanism is thus characterized by the formation of a soft-storey mechanism at the ground level, while the first floor remains substantially elastic.

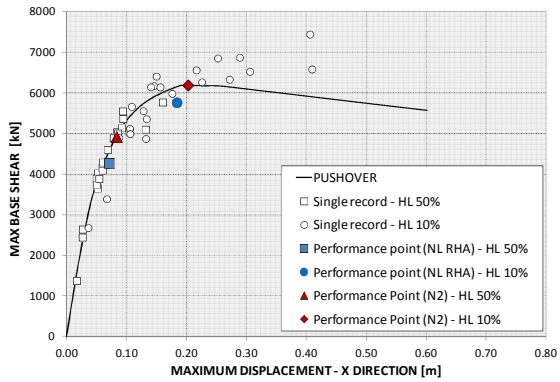


a) GM set: UHS unscaled

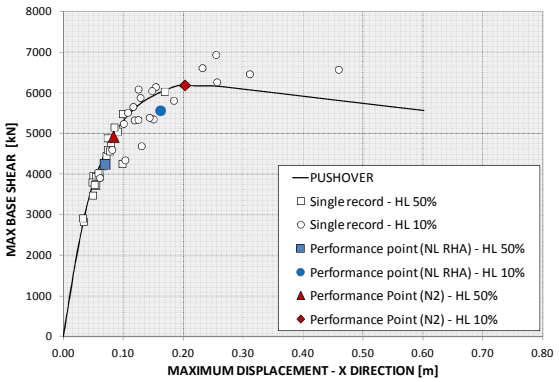


e) GM set: CMS unscaled

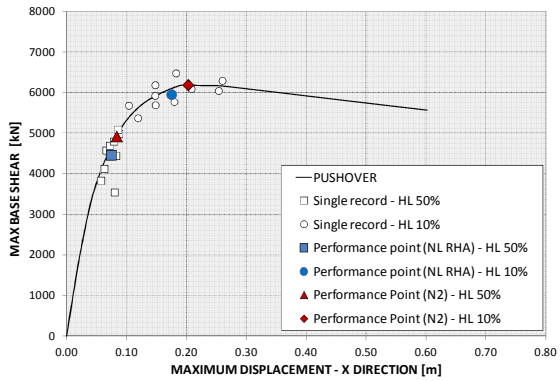


c) GM set: UHS scaled on $Sa(T_{1X})$

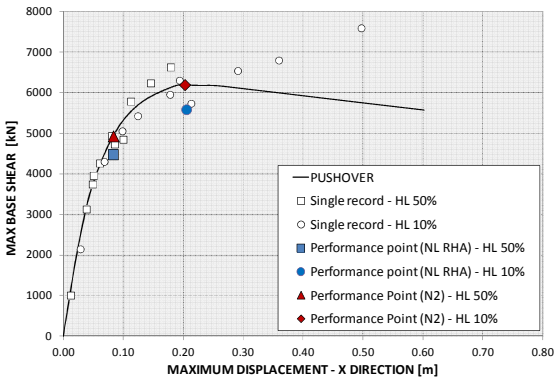


d) GM set: UHS scaled on $Sa(T_{1Y})$

Figure 6. Pushover curve and NL RHA results, in terms of maximum base shear - maximum displacement, in the X direction.

Analyzing the structural response in the X-direction, in all the cases, dynamic analyses yield lower values of EDPs with respect to static analysis. Considering first the "Unscaled set", it should be noted that for PoE=50% the results obtained based on the CMS and on the UHS sets are very similar, while for PoE=10% the CMS set produces lower values of EDPs (about 12% for displacements and IDR) due to the elongation of the period and lower spectral accelerations for $T>T_{1x}$ of the CMS compared to UHS. The coefficients of variation are very similar between the two Unscaled sets and there is only a slight increase of this parameter for seismic action with PoE=10%, as it was expected. The set scaled on $S_a(T_{1x})$ provides less scattered response for both the hazard levels considered, however, when the set is scaled on the spectral ordinates of the spectrum of the orthogonal direction (i.e. $S_a(T_{1y})$ when X-direction is investigated) the dispersion of results due to input uncertainty increase significantly, consistent with observations made by [26] [27] and [28].

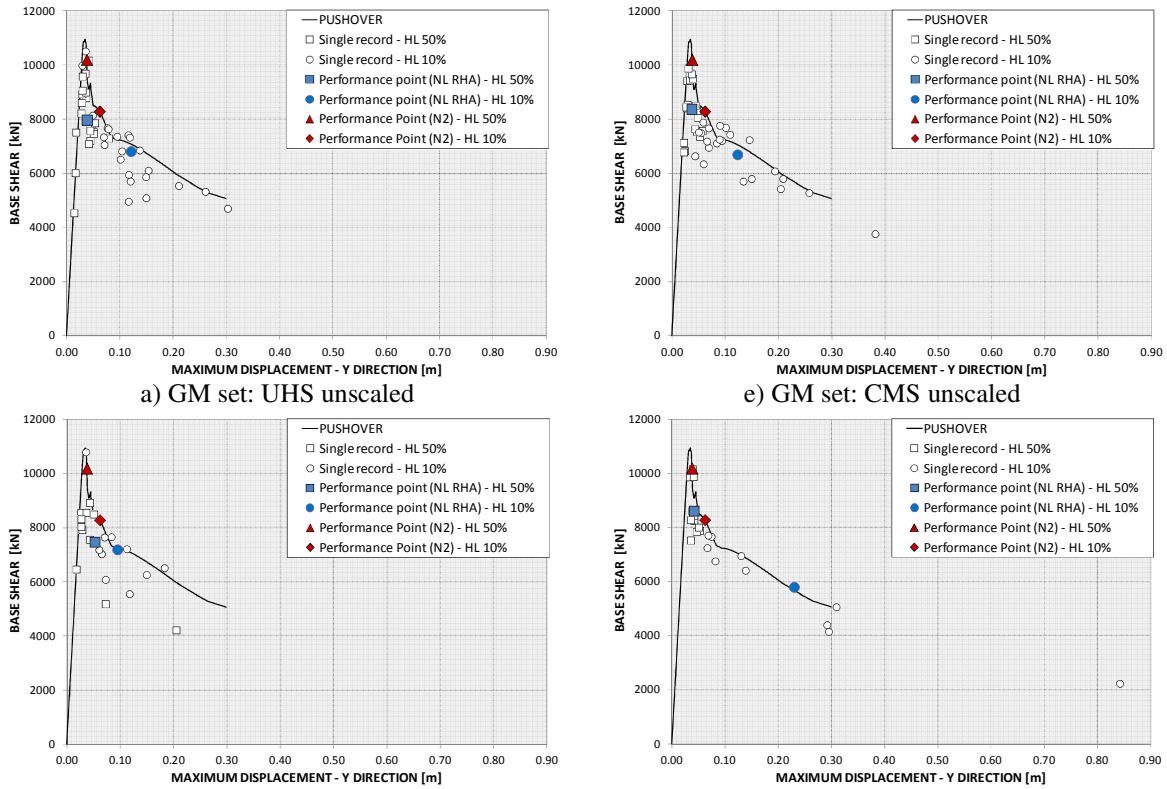


a) GM set: UHS unscaled

e) GM set: CMS unscaled

c) GM set: UHS scaled on $Sa(T_{1X})$

d) GM set: UHS scaled on $Sa(T_{1Y})$

Figure 7. Pushover curve and NL RHA results, in terms of base shear associated to the maximum displacement - maximum displacement, in the Y direction.

For the Y-direction, when the hazard level with PoE=50% is investigated, the results of static and dynamic analysis are comparable in terms of mean values and the set "Scaled on $S_a(T_{1y})$" gives the lower dispersion, as expected. Results for the hazard level with PoE=10% show how the static analysis underestimates significantly drift and displacements but, more significantly, the dispersion of results is very high for all the investigated cases. Furthermore, scaling on $S_a(T_{1y})$ does not give the expected advantages in terms of coefficients of variation and mean values. These values are considerably higher compared to the other case, also due to a few analyses with very high displacement demand which affect the final estimate.

## 5 CONCLUSIONS

The industrial structure investigated herein exhibits very different behavior in the two principal directions, and this behavior leads to very different observations regarding the effectiveness of the different GMs sets and scaling techniques.

In the X direction, the CMS provides less conservative results when the structure exhibits an inelastic behavior, due to the reduced values of spectral accelerations for periods longer than the first elastic mode period $T_{1x}$. Scaling GMs to $Sa(T_{1x})$ and $Sa(T_{1y})$ we observed that, for all the action levels investigated, the dispersion is highly reduced in the principal direction but, on the contrary, it becomes significant in the perpendicular direction. In the Y-direction, none of the GMs sets investigated herein led to significant advantages in the prediction of the response, due to the soft story mechanism and buckling of V bracings.

For this particular industrial structure, it is complex to define an IM that governs entirely the response, especially when the structure exhibits inelastic behavior and when 3D response is

investigated. The use of CMS and the proposed scaling techniques may be not conservative or unsuitable for 3D analysis of industrial facilities and, in general, for structures which exhibit very different behavior in the two principal directions.

**ACKNOWLEDGEMENTS**

The authors acknowledge the support of the European Union's Research Fund for Coal and Steel (RFCS) research programme through the project PROINDUSTRY, "Seismic PROtection of INDUSTRial plants by enhanced steel based sYstems", grant agreement n° [RFSR-CT-2013-00019]. The content of this paper reflects the opinions of the authors and do not necessarily represent the opinions of the funding agency.

## REFERENCES

[1] M.K. Lindell, R.W. Perry, Identifying and managing conjoint threats: earthquake-induced hazardous materials releases in the US, J. Hazard. Mater. 50 (1996) 31.

[2] S.Young, L. Balluz, J. Malilay, Natural and technologic hazardous material releases during and after natural disasters: a review, Sci. Total Environ. 322 (2004) 3.

[3] G. Antonioni, S. Bonvicini, G.Spadoni, and V. Cozzani. 2009, Development of a Framework for the Risk Assessment of Na-Tech Accidental Events. Reliability Engineering & System Safety 94 (9): 1442–50. doi:10.1016/j.ress.2009.02.026.

[4] ARIA, Overview of the Industrial Accidents caused by the Great Tohoku Earthquake and Tsunami, 2011.

[5] H.Sezen, and A. S. Whittaker. 2006, Seismic Performance of Industrial Facilities Affected by the 1999 Turkey Earthquake. Journal of Performance of Constructed Facilities 20 (1): 28–36. doi: 10.1061/(ASCE)0887-3828(2006)20:1(28).

[6] A. Belleri, E. Brunesi, R. Nascimbene, M. Pagani, P. Riva, Seismic performance of precast industrial facilities following major earthquakes in the Italian territory. J Perform Constr Facil 2014:04014135.

[7] F. Braga, R. Gigliotti, G. Monti, F. Morelli, C. Nuti, W. Salvatore, I. Vanzi, Speedup of post earthquake community recovery: the case of precast industrial buildings after the Emilia 2012 earthquake. Bulletin of Earthquake Engineering, 12(5), 2405-2418, 2014.

[8] F. Braga, R. Gigliotti, G. Monti, F. Morelli, C.Nuti, I. Vanzi, W. Salvatore, Post-seismic assessment of existing constructions: evaluation of the shakemaps for identifying exclusion zones in Emilia. Earthquakes and Structures, Vol. 8, No. 1 (2014) DOI: http://dx.doi.org/10.12989/eas.2015.8.1.895.

[9] J. Moehle and G. Deierlein, A Framework Methodology for Performance-Based Earthquake Engineering, Proceedings, 13th World Conference on Earthquake Engineering, Vancouver, British Columbia, Paper No. 679, 2004.

[10] R.O. Hamburger, C. Rojahn, J.A. Heintz, M.G. Mahoney, FEMA P58: Next-Generation Building Seismic Performance Assessment Methodology,15th World Conference on Earthquake Engineering, Lisbon, 2012.

[11] A. Kanyilmaz, G. Brambilla, G. Chiarelli, C.A. Castiglioni, Assessment of the seismic behavior of braced steel storage racking systems by mean of full scale push over tests, Thin- Walled Structures, 107(2016) 138–155.

[12] A. Kanyilmaz, C.A. Castiglioni, G. Brambilla, G. Chiarelli, Experimental assessment of the seismic behavior of unbraced steel storage pallet racks (2016) Thin-Walled Structures, 108, pp. 391-405

[13] ASCE/SEI 7-10, Minimum Design Loads for Buildings and Other Structures. American Society of Civil Engineers, Reston, 2010.

[14] ASCE/SEI 43-05, Seismic Design Criteria for Structures, Systems, and Components in Nuclear Facilities. American Society of Civil Engineers.

[15] FERC 2007, Seismic Design Guidelines and Data submittal Requirements for LNG facilities. Federal Energy Regulatory Commision. 2007.

[16] API Standard 620: "Design and Construction of Large, Welded, Low-pressure Storage Tanks", 11th Edition, American petroleum Institute, Washington D.C., 2009.

[17] API Standard 650: "Welded Steel Tanks for Oil Storage", 11th Edition, American petroleum Institute, Washington D.C., 2007.

[18] EN 1998-4:2007-07. Design of structures for earthquake resistance – Part 4: Silos, tanks and pipelines. European Committee for Standardization, Brussels, 2007.

[19] EN 1998-4:2007-07. Design of structures for earthquake resistance – Part 6: Towers,piles and chimneys. European Committee for Standardization, Brussels, 2007.

[20] NIST, 2011, Selecting and Scaling Earthquake Ground Motions for Performing Response-History Analyses, GCR 11-917-15.

[21] F. Morelli, A. Piscini, W. Salvatore, Seismic retrofit of an industrial structure through an innovative self-centering hysteretic damper: modelling, analysis and optimization, Proceedings of the VII European Congress on Computational Methods in Applied Sciences and Engineering, M. Papadrakakis, V. Papadopoulos, G. Stefanou, V. Plevris (Editors), Crete Island, Greece, 5–10 June 2016.

[22] S. Mazzoni, F. McKenna, M. H. Scott, G. L. Fenves, et al. Open System for Earthquake Engineering Simulation (OpenSEES), OpenSEES Command Language Manual, Pacific Earthquake Engineering Research (PEER) Center, 2007.

[23] V. Montaldo, C. Meletti, F. Martinelli, M. Stucchi, M. Locati M, On-line seismic hazard data for the new italian building code. J EarthqEng 11(S1):119–132, 2007.

[24] N. Ambraseys, A. Simpson, J.J. Bommer (1996). Prediction of horizontal response spectra. Earthquake Engineering & Structural Dynamics, 25(June 1995), 371–400.

[25] J. Baker, Conditional Mean Spectrum: Tool for Ground-Motion Selection. J. Struct. Eng. 137, SPECIAL ISSUE: Earthquake Ground Motion Selection and Modification for Nonlinear Dynamic Analysis of Structures, 322–331, 2011.

[26] M. Faggella, A. Barbosa, J.P. Conte, E. Spacone, J.I. Restrepo., 2013. Probabilistic seismic response analysis of a 3-D reinforced concrete building. Structural Safety 44, 11-27.

[27] M. Faggella, A.R. Barbosa, J.P. Conte, E. Spacone, J.I. Restrepo, Seismic Assessment of R/C Building Structure through Nonlinear Probabilistic Analysis with High performance Computing. In AIP Conference Proceedings, (Vol. 1020, p. 930), 2008.

[28] M. Faggella, A.R. Barbosa, J.P. Conte, E. Spacone, J.I. Restrepo, Use of High Performance Computing for Probabilistic Seismic Response Sensitivity Analyses of a Building Structure, in B.H.V. Topping, P. Iványi, (Editors), Proceedings of the First International

Conference on Parallel, Distributed and Grid Computing for Engineering, Civil-Comp Press, Stirlingshire, UK, Paper 28, 2009.

[29] E. Rossi, M. Ventrella, M. Faggella, R. Gigliotti, F. Braga, Performance-based Earthquake Assessment of an Industrial Silos Structure and Retrofit with Sliding Isolators. In ECCOMAS Congress 2016 VII European Congress on Computational Methods in Applied Sciences and Engineering, Crete Island, Greece, 5–10 June, 2016.

[30] F. Romano, M. Faggella, R. Gigliotti, F. Braga, Components Fragility Functions and Comparative Seismic Risk Analysis of an older R/C Building based on FEMA P-58, XVI Convegno ANIDIS Ingegneria Sismica in Italia, L'Aquila, Italy, September 13-17, 2015.

[31] Ministero delle Infrastrutture (2008) NormeTecniche per le Costruzioni, D.Min. Inf. 14 gennaio 2008, Gazzetta Ufficiale n. 29 of february 4th 2008 - Suppl. Ordinario n. 30. In Italian.

[32] European Committee for Standardization, Eurocode 8: Design of structures for earthquake resistance - Part 1: General rules, seismic actions and rules for buildings. EN 1998-1, December 2004.

[33] M. Faggella, R. Laguardia, R. Gigliotti, F. Morelli, F. Braga, W. Salvatore, (2016), "Performance-based nonlinear response history analysis framework for the "PROINDUSTRY" project case studies", Proceedings of the VII European Congress on Computational Methods in Applied Sciences and Engineering, M. Papadrakakis, V. Papadopoulos, G. Stefanou, V. Plevris (Editors), Crete Island, Greece, 5–10 June 2016.

[34] J. Henriques, F. Morelli, B. Vandoren, W. Salvtore and H. Degée (2016), Efficiency of seismic isolation on industrial plants - case study of a gas tank, Proceedings of the VII European Congress on Computational Methods in Applied Sciences and Engineering, M. Papadrakakis, V. Papadopoulos, G. Stefanou, V. Plevris (Editors), Crete Island, Greece, 5–10 June 2016.

[35] M. Pinkawa, B. Hoffmeister, M. Feldmann (2016) Performance Assessment Of Seismic Retrofitting Measures On Silo Structures Using Innovative Seismic Protection Systems, Proceedings of the VII European Congress on Computational Methods in Applied Sciences and Engineering, M. Papadrakakis, V. Papadopoulos, G. Stefanou, V. Plevris (Editors), Crete Island, Greece, 5–10 June 2016.

[36] A. Kanyilmaz, C. A. Castiglioni, J. Georgi (2016) Seismic Retrofit Of Industrial Silos By Means Of Base Isolation Devices, Proceedings of the VII European Congress on Computational Methods in Applied Sciences and Engineering, M. Papadrakakis, V. Papadopoulos, G. Stefanou, V. Plevris (Editors), Crete Island, Greece, 5–10 June 2016.

[37] N. Bakas, J. Bellos, A. Kanyilmaz, S. Makridakis (2016), Regression Analysis Vs Genetic Algorithms: Computational Efficiency Assesment On The Design Of Proindustry Project SSCD Isolators Under Incremental Dynamic Loading, Proceedings of the VII European Congress on Computational Methods in Applied Sciences and Engineering, M. Papadrakakis, V. Papadopoulos, G. Stefanou, V. Plevris (Editors), Crete Island, Greece, 5–10 June 2016.

COMPDYN 2017
6th ECCOMAS Thematic Conference on
Computational Methods in Structural Dynamics and Earthquake Engineering
M. Papadrakakis, M. Fragiadakis (eds.)
Rhodes Island, Greece, 15–17 June 2017

# RATIONAL SEISMIC RETROFITTING OF RC STRUCTURES BASED ON GENETIC ALGORITHMS

**R. Falcone[1], C. Faella[2], C. Lima[3], E. Martinelli[4]**

[1] PhD student, DiCiv – Dept. of Civil Eng., University of Salerno, rfalcone@unisa.it

[2] Full Professor, DiCiv – Dept. of Civil Eng., University of Salerno, c.faella@unisa.it

[3] Research Assistant, PhD, DiCiv – Dept. of Civil Eng., University of Salerno, clima@unisa.it

[4] Associate Professor, PhD, DiCiv – Dept. of Civil Eng., University of Salerno, e.martinelli@unisa.it

**Keywords:** RC frames, Seismic Retrofitting, Optimal Strategy, Soft-Computing.

**Abstract.** *This paper presents a rational strategy developed for optimizing seismic retrofitting of Reinforced Concrete (RC) frames. It is based on combing member- and structure-level techniques in order to achieve optimal design objectives within a multi-level Performance-Based approach. On the one hand, in principle, confinement with composite materials, steel and/or concrete jacketing might be considered as a member-level technique capable to enhance the capacity of under-designed members and, consequently, of the structure as a whole. On the other hand, introducing steel bracing systems or shear walls might be taken into account as structure-level techniques. Generally, member- and structure-level techniques are not employed together in seismic retrofitting or, in the cases in which they are combined, no well-established rules are available for choosing their optimal combination. However, a synergistic use of such techniques by means of well-defined procedures could help designers obtain optimal seismic retrofitting performance. The latest progresses about a procedure developed by the authors for selecting the optimal retrofitting solution among the technically feasible ones, obtained by combining alternative configurations of steel bracing systems and FRP-confinement of critical members, are presented herein. Specifically, the main aspects about formulating a genetic algorithm capable to select the "fittest" retrofitting solution is implemented and summarised. The main assumptions about the representations of "individuals" as part of this genetic algorithm and the main information about the generic operations (i.e. selection, crossover and mutation) are outlined. Finally, the procedure is applied to a 3D frame with the aim to demonstrate its potential.*

## 1 INTRODUCTION

Seismic retrofitting is generally requested by the significant number of Reinforced Concrete (RC) buildings existing in earthquake prone areas, as they were built according to past design codes and standards. In fact, existing RC frames are often found vulnerable to seismic actions due to inadequate structural detailing, material deterioration and underestimated earthquake loads, without any considerations of Capacity Design rules introduced by modern seismic codes [1]. The high cost of new construction and historical importance of older buildings has led owners to renovate rather than demolish and rebuild their properties. This has caused governmental institutions to implement mandatory seismic strengthening regulations. Therefore, seismic retrofitting is nowadays a technical challenge for engineers and a societal priority [2]. Plenty of researches have been conducted in the last two decades on seismic assessment and retrofitting of RC frames: they have been mainly aimed at developing both effective methodologies for quantifying seismic vulnerability and consistent technical solutions for seismic retrofitting [3]-[5]. A retrofit scheme can be said to be successful if it results in modifying capacity and demand, making the latter smaller than the former with respect to all the performance objectives of relevance for the structure under consideration.

As a matter of principle, retrofitting solutions can be grouped into two broad classes: on the one hand, the so-called "Member-level" (or so called "local") techniques and, on the other hand, the "Structure-level" (also referred to as "global") techniques [2]. Confining existing members with composite materials [6], steel and/or concrete jacketing can be classified in the first group, as they are capable to enhance capacity (in terms of ductility and/or strength) in under-designed members [7] and, hence, improving the capacity of the structure as a whole in order to meet the requested seismic demand. Conversely, the second group collects all those techniques capable to reducing seismic demand on the existing structure, whose single members' capacity is fairly unchanged [8]. Connecting RC shear walls or steel bracing systems with the existing members or realizing a seismic isolation system are relevant examples of structure-level techniques.

That said, it is clear that member- and structure-level techniques, considered on their own, represent two somehow "extreme" solutions for retrofitting existing structures and generally they are not employed together in seismic retrofitting. Moreover, in that few cases in which they are combined, no well-established rules are currently available for choosing their optimal combination. However, the aforementioned techniques may suitably be combined with the aim to obtain a synergy in increasing seismic capacity of under-designed members and reducing demand on the structure as a whole. In this light, choosing the "fittest" solution among the potentially infinite combinations of member- and structure-level techniques is a task that can be regarded as a constrained optimisation problem [9]. In fact, each one of the combinations leads to different direct costs, life-cycle costs, reliability levels and other quantitative/qualitative parameters describing their "fitness" to be considered as a retrofitting solution. Several researches have been carried out for selecting the most structurally efficient and cost-effective seismic retrofitting solution: the possibility of combining member- and structure-level techniques for minimizing the initial cost of retrofitting is only conceptually explored in previous papers [8]. However, no well-established and completely accepted procedures are available for obtaining the optimal retrofitting solution. Therefore, the definition of a rational strategy for seismic retrofitting is still an open issue. In the Authors' best knowledge, no relevant study is currently available for approaching seismic retrofitting of existing RC frames as an optimisation problem, as recent scientific contributions on optimisation algorithms are restricted to seismic design of new structures [10]-[12]]. Conversely, in the current practice, as well as in most relevant scientific contributions on this topic [3]-[5], [7], [13], [15], seismic

retrofitting of RC frames is addressed as a solely technical problem. Considerations about optimisation (often restricted to the "economic" standpoint) are left to the engineering judgement and, hence, they are not part of a systematic analysis. This is partly due to the complexity of the constrained optimisation problem under consideration, which cannot be duly approached by means of analytical techniques commonly employed in structural engineering, as it can only be solved by means of meta-heuristic techniques [16] that are not in the background of common structural engineers.
Therefore, this paper proposes a genetic algorithm capable of selecting the "fittest" solution (in terms of initial costs) obtained by combining structure-level interventions, based on steel bracing systems, and FRP-based member-level techniques. More specifically, the paper outlines a Genetic Algorithm (GAs) inspired to the well-known Darwin's "evolution of species" and the assumption of the "survival of the fittest" rule [17]. Although some pioneering applications of these techniques are already available in the field of structural engineering, they are mainly restricted to the design of new structures [18]-[21]]. The following sections summarize the main aspects of the proposed genetic algorithm and its application in the rational design of retrofitting interventions. Finally, as an example, the last section presents an application of the proposed procedure.

## 2 THE GENETIC ALGORITHM

### 2.1 Problem statement and formulation

The problem of defining seismic retrofitting interventions on existing RC structures can be conceptually described by the following Limit State (LS) function $g_{LS}$:

$$g_{LS,i} = C_{LS,i} - D_{LS,i} \geq 0 \tag{1}$$

where $C_{LS,i}$ is the capacity of the strengthened structure at the Limit State (LS) or Performance Level under consideration and $D_{LS,i}$ the corresponding demand at the same Limit State. The LS of Damage Limitation (SLD), related to a seismic event whose Probability of Exceedance (PoE) equal to 63% in 50 years, and the Limit State of Life Safety (SLV), corresponding to an event with 10% PoE in 50 years, are taken into account herein [22]. Capacity and demand mentioned in Eq. (1) can be intended in terms of both displacement (for ductile mechanisms) and forces (for brittle failure mechanisms). As a matter of principle, the above inequality, that should be checked at all the relevant LSs, is not met by the structure in its "as built" condition and, more specifically, the capacity is lower than demand in seismically vulnerable structures. Hence, retrofitting intervention aims to enhance their "as built" condition at the i-th relevant LS under consideration and raise the values of $g_{LS,i}$ towards positive values. Then, two opposite "extreme" approaches can be followed to get the inequality (1) valid for the structures under strengthening:

- the capacity of all members could be increased by means of member-level-techniques (i.e., confinement of deficient sections, concrete or steel jacketing of columns, etc.) aimed at obtaining an enhanced global capacity $C_{LS}$ which is not lower than the corresponding seismic demand $D_{LS}$ (which, on the contrary, is almost unaffected by the above mentioned local intervention);
- the exceeding demand on the existing members can be reduced by acting at the structure-level by either introducing a structural sub-system, aimed at working in parallel with the structure and absorbing a significant part of the seismic excitation, or modify-

ing the vibration period of the structure as a whole to reduce the input seismic excitation on the super-structure.

However, as a matter of principle, the retrofitting objective can be achieved by acting on both capacity and demand and, hence, implementing a combination of strengthening techniques belonging to the above mentioned general classes [8]. The choice of the "best" possible combination of such intervention techniques clearly defines an optimisation problem which can be based on the assumption of different types of objective functions. The easiest (and more simplistic) choice is represented by assuming the actual cost of the intervention as the objective function whose minimization represents the optimal solution for the problem of seismic retrofitting under consideration [9]. The optimal retrofitting solution can be found by solving the following constrained optimisation problem stated as follows:

$$\begin{gathered} \overline{x}_{opt} = \arg\min_{x} \left[ f(\mathbf{x}) \right] \\ \text{subjected to} \\ g_{LS,i} \geq 0 \quad \forall i = 1...n_{LS} \end{gathered} \tag{2}$$

where f(●) is the selected objective function and **x** is the vector of design variables defining the interventions consisting of both FRP confinement of single RC members and concentric steel bracings installed in parallel with the existing structure. The total direct cost is defined by adding the terms in Eq. (3):

$$C_{tot}(\mathbf{x}) = C_{loc}(\mathbf{x}) + C_{glob}(\mathbf{x}) + C_{found}(\mathbf{x}) \tag{3}$$

where $C_{loc}(x)$ and $C_{glob}(x)$, respectively referred to member- and structure-level techniques. It is worth highlighting that the two cost functions take into account both demolition and reconstruction operations needed for realizing FRP confinement and installing steel bracings. Moreover, $C_{found}(x)$ is the cost of possible interventions on the existing foundations, often needed to respond to the possible increase in vertical and horizontal reactions at the base of the retrofitted structure. Specifically, with the simplified assumption that the intervention is made with micro-piles, whose bearing capacity $q_{lim}$ is known, the cost $C_{found}(x)$ might stem out from a relationship conceptually defined as follows:

$$C_{found}(\mathbf{x}) = C_{found}\left[ \sum_{i=1}^{n_{col}} \frac{\Delta N_i(\mathbf{x})}{q_{lim}} \right] \tag{4}$$

where $\Delta N_i$ is the increase of axial force (with respect to the gravitational loads only) due to the seismic actions on the retrofitted structure. Finally, the objective function shown in Eq. (5) include a penalty function $\Phi(\bullet)$:

$$f(x) = C_{tot}(x) + \Phi\left\{ \max\left( \frac{D_{LS,i}}{C_{LS,i}} \right) \right\} \tag{5}$$

which effectively transform the constrained problem into an unconstrained one by augmenting the objective function with a penalty term whose value determines the amount of constraint violation present in a particular retrofitting solution. The complex nature of the multi-objective optimisation problem addressed here cannot be duly approached by means of analytical techniques commonly employed in structural engineering. Conversely, it can only be solved by means of meta-heuristic techniques. Therefore, the authors propose a rational procedure based on a Genetic Algorithm (GA) for finding the optimal retrofitting solution of the

constrained problem described by Eq. (2). The conceptual flow-chart shown in Figure 1 depicts the main steps of the procedure.

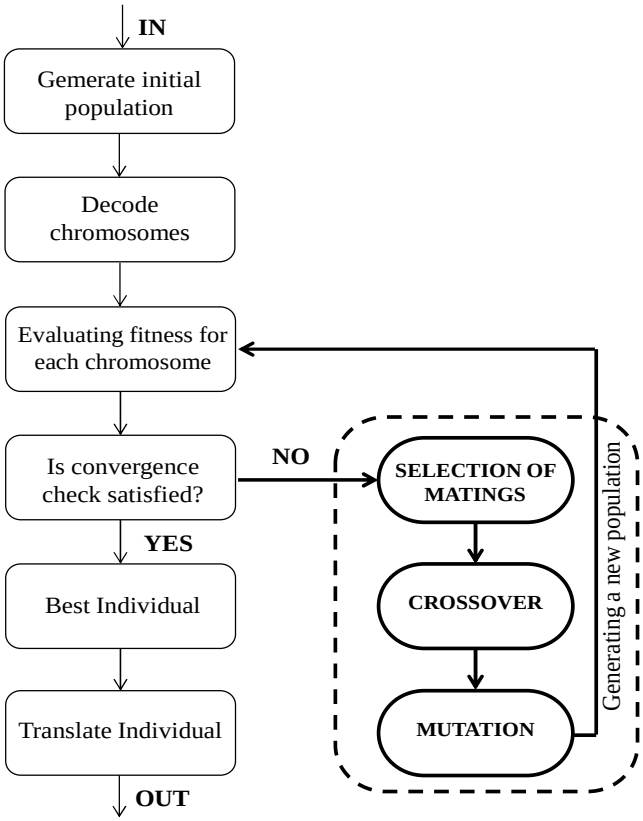


Figure 1: Flow-chart of the optimisation procedure

Goldberg [24] discussed how genetic algorithms have several fundamental advantages over other soft computing tool that allow them to be more robust than other optimisation methods:

1. GAs work with a coding of the parameter set, not the parameters themselves. This is advantageous because often times the parameters are in different units or measurement scales and can be very difficult to model. It is also beneficial when the number of parameters in the multi-objective optimisation problem is very large;
2. GAs search parallel from a population of points, not a single point. This is beneficial when there are multiple local optima because the GA will avoid premature convergence to local optimal solutions or false-peaks;
3. GAs use objective function information, not derivatives or other auxiliary information. This is beneficial if the objective function is not smooth, or is nonlinear, or if there are a large number of parameters to which the gradient information is not known;
4. GAs use probabilistic transition rules, not deterministic ones making them quite robust and able to solve most optimisation problems.

## 2.2 Generation of initial population

The procedure starts with randomly generating a group of $N_{ind}$ individuals known as the population, whose number typically ranges between 50 and 100. Since it is important to have highly diverse composition of the initial population, this step is achieved by generating the required number of individuals by using a random number generator that uniformly distributes numbers in the desired range. The individuale are encoded as strings

(chromosomes) composed over some alphabet(s), so that the genotypes (chromosome values) are uniquely mapped onto the decision variable (phenotypic) domain [25]. Several coding methods are currently available, such as binary, gray, non-binary, etc. [26]-[28]]. The binary alphabet {0, 1} is actually adopted in coding for the present work: hence, each individual "x" of such a population is, herein represented through a simple "chromosome-like" array of bits. Hence, in the first step of the proposed procedure a population of 100 individuals is generated by the following random generator (6):

$$\text{pop} = \text{round}\left[\text{rand}\left(N_{\text{ind}}, N_{\text{bits}}\right)\right] \tag{6}$$

where the function rand generates a $N_{ind}$ x $N_{bits}$ matrix (Figure 2) of uniform random numbers between 0 and 1. The function round, instead, rounds the numbers to the closest integer which in this case is either 0 or 1.

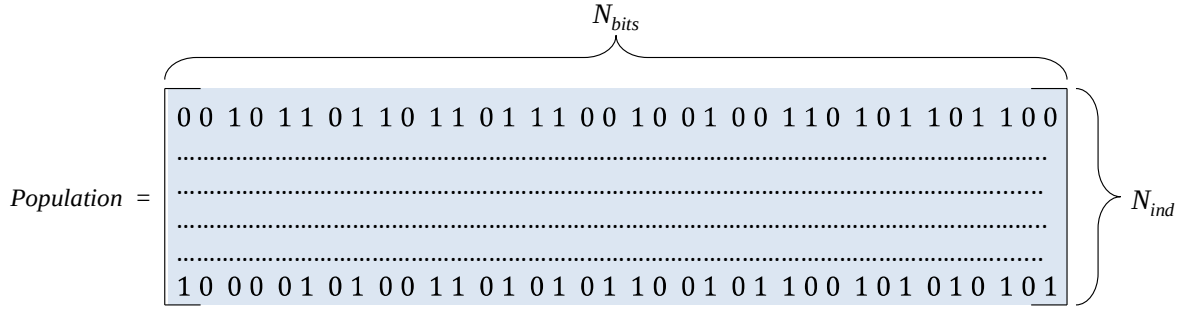


Figure 2: Example of initial population randomly generated

According to Hajela [29] a β-digit binary number representation of a variable allows for $2^{\beta}$ distinct variations of that design variable to be considered. The length of the coded representation of the design variables, i.e. the number of bits, corresponds to their range and precision. The length of the sub-string varies with the desired precision of the results: the longer the string length, the higher the accuracy. The relationship between string length β and precision α is expressed as follows:

$$\left(X_U - X_L\right) \cdot 10^{\alpha} \leq \left(2^{\beta} - 1\right) \tag{7}$$

where $X_U$ and $X_L$ are the upper and the lower bound of the variable, respectively. As described below, the search process operate on this encoding of the decision variables, rather than the decision variables themselves.

## 2.3 Decoding of individual

To proceed with the genetic analogy, the individuals of the population are assumed as chromosomes and the variables corresponds to genes. Thus, a chromosome, i.e. each row of the generated matrix, represent a possible retrofitting solution and is composed of several genes (variables). Examining the chromosome string in isolation yields no information about the problem under consideration. It is only with the decoding of the chromosome into its phenotypic values that any meaning can be found to the representation. Within the present algorithm, the vector **x** is composed of variables describing both member- and structure-level techniques: the string representing the binary coding of one individual [25] is structured by concatenating the set of variables that represent it. Figure 3 depicts an example of the binary genotype adopted in the present algorithm for representing a simple three-storey structure with four beams at each floor (one-bay for each direction in plan): the first part of the string describes

the member-level techniques considered in the aforementioned individual, whereas the second part is dedicated to describing the structure-level ones. The variables are not encoded in equal sub-string lengths.

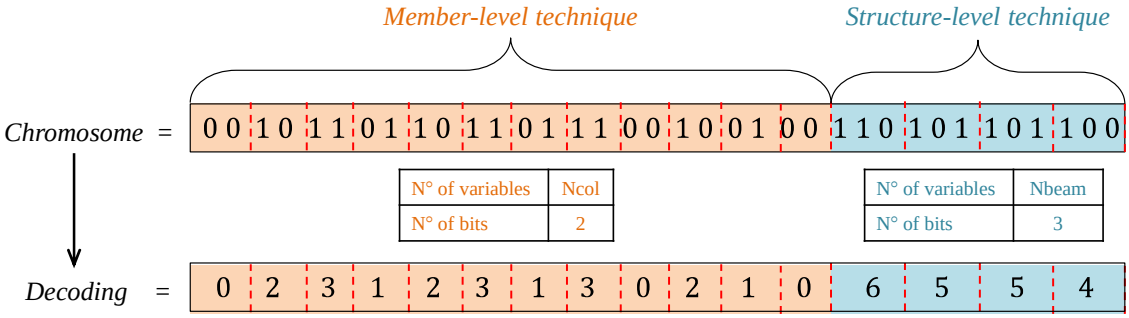


Figure 3: Example of binary genotype for coding a retrofitting intervention

In fact, in the first part of the individual, each couple of bits contains a code related to the number of FRP layers possibly employed for confining the corresponding column of the structure under consideration: hence, a total of $2N_{col}$ bits is contained, $N_{col}$ being the number of column elements in the structural model of the existing frame. The accuracy that can be obtained through two-bit coding is only approximately $1/4^{th}$ of the search space, but as this string length is increased by 1, the obtainable accuracy increases exponentially to $1/8^{th}$ of the search space. In the current implementation, the confinement ranges between zero (as-built configuration denoted by the value “00” assumed in the binary code of the corresponding column) and three layers of FRP (denoted by the value “11” of the binary code representing the i-th column). The information collected in this part of the codified **x** vector are employed for modifying the original (unconfined) mechanical values of the Kent and Park model [30] available in OpenSEES [31] for simulating the behavior of concrete in columns. Particularly, based on various parameters, such as the number of layers, the shape of section transverse section and the type of FRP considered for this application, the original (unconfined) stress-strain relationship describing the material behavior for each column is duly modified are schematically described in Figure 4. As is well-known, the resulting relationship for confined concrete depends on several parameters, such as the number of FRP layers, the shape of transverse section and the type of FRP considered for this application.

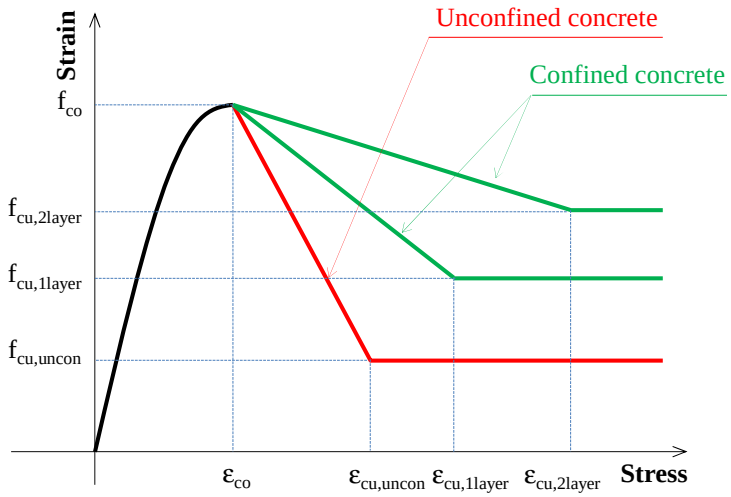


Figure 4: Model by Kent & Park [30] for confined concrete

On the other hand, the following assumption are considered for describing the steel bracings system representing the global intervention codified in the second part of the genotype:

1. the transverse section of each couple of diagonals is identified by means of a label corresponding to a commercial steel profile;
2. only the profiles of the first storey level are reported in the codified "x" vector, whereas those adopted for the upper levels stem out of a consistent design criterion;
3. steel bracings are supposed to be possibly realised between each couple of columns connected by a beam: therefore, the maximum number of bracings is equal to the number of beam $N_{beam}$ at the first floor.

The aforementioned assumptions are intended at keeping the set of design variables as small as possible. Therefore, the current implementation of the proposed procedure employs three bits for each variable related to steel diagonal bracings and, hence, only $2^3 = 8$ codes are available to describe the section of diagonals possibly installed at the first storey level, in correspondence of a generic beam (see assumption n. 3). They can range from 0 (absence of bracing) to 7: each code included between "001" and "111" points to a position in a commercial steel profile table (assumption n. 1) and, hence, the relevant properties of bracing diagonals are available therein (Figure 5).

| **LABEL** | HEB | b [mm] | h [mm] | a [mm] | e [mm] | r [mm] | $A_1$ [cm$^2$] |
|---|---|---|---|---|---|---|---|
| **1** | 100 | 100 | 100 | 6,0 | 10,0 | 12 | 26,04 |
| **2** | 120 | 120 | 120 | 6,5 | 11,0 | 12 | 34,01 |
| **3** | 140 | 140 | 140 | 7,0 | 12,0 | 12 | 42,96 |
| **4** | 160 | 160 | 160 | 8,0 | 13,0 | 15 | 54,25 |
| **5** | 180 | 180 | 180 | 8,5 | 14,0 | 15 | 65,25 |
| **6** | 200 | 200 | 200 | 9,0 | 15,0 | 18 | 78,08 |
| **7** | 220 | 220 | 220 | 9,5 | 16,0 | 18 | 91,04 |

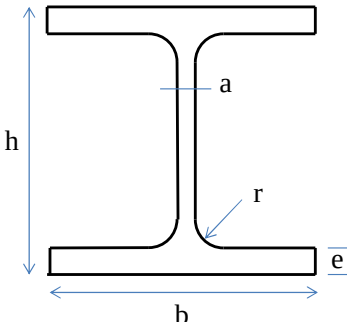


Figure 5: Set of commercial steel profile and corresponding labels

The relationship between the section of steel members at the first level and the section of steel bracings at upper floors is defined according the Eq. (8):

$$A_{k,des} = \frac{\sum_{j=k}^{n} h_j \cdot W_j}{\sum_{i=1}^{n} h_i \cdot W_i} \cdot A_1 \tag{8}$$

where $h_j$ represents the position in height of the floor with respect to the foundation level, n is the total number of floors, $W_j$ is the seismic mass of the j-th floor. Moreover, $A_1$ is the area of the cross section of the bracing at the first level and $A_{k,des}$ is the theoretical area of the bracing cross section required at the k-th floor. It is worth highlighting that any other consistent design criteria, defining the upper level sections depending on the first level ones, might be possibly adopted in lieu of Eq. (8). Finally, the knowledge of theoretical areas allows to select the steel commercial section whose area must be greater than $A_{k,des}$.

## 2.4 Evaluating of fitness

The optimisation target can be measured both in terms of objective f(**x**) and fitness F(**x**) functions, but the latter has a closer association with biology than the former. In fact, fitness in biological sense is a quality value which is a measure of the reproductive efficiency of chromosomes. In the proposed genetic algorithm, fitness is used to allocate reproductive traits to the individuals in the population and thus act as some measure of goodness to be maximized. On the other hand, the objective function is used to provide a measure of how individuals have performed in the problem domain. As already seen, the search of the optimal solution is affected both by the actual cost $C_{tot}$ of the retrofitting solution and the additional information related to the seismic check on Limit State function $g_{LS,i}$. With regards to the latter, Static Non Linear (Pushover) Static Analysis (Figure 6) is considered for determining capacity curves through an incremental static analysis on a nonlinear model of the structure subjected to a triangular distribution of lateral forces, both in x and y directions (further distributions might be easily taken into account for performing the seismic analysis) [22] [32]. A capacity fiber model with plasticity spread along the non-linear elements is taken into account.

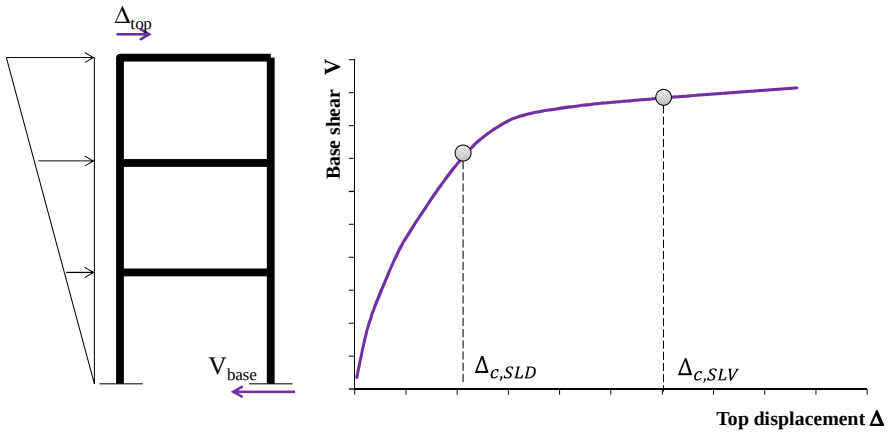


Figure 6: Static Non Linear Analysis and capacity curve

The deformation capacity $C_{LS,i}$ of frame elements, to be verified in accordance with Eq. (1) at Limit State of Damage Limitation (SLD) and Limit State of Life Safety (SLV), is defined in terms of chord rotation θ at yielding and collapse conditions, respectively. The chord rotation is the angle between the tangent to the axis at the yielding end and the chord connecting that end with the end of the shear span ($L_V$ = M/V = moment/shear at the end section). It is also equal to the element drift ratio, i.e., the deflection at the end of the shear span with respect to the tangent to the axis at the yielding end, divided by the shear span. With regard to collapse conditions, the capacity rotation $\theta_{um}$ is herein assessed by the following empirical formulations **Errore. L'origine riferimento non è stata trovata.**:

$$\theta_{um} = \theta_{C,SLV} = \frac{1}{\gamma_{el}} \cdot 0{,}016 \cdot \left(0{,}3^{\nu}\right) \cdot \left[\frac{\max\left(0{,}01;\omega'\right)}{\max\left(0{,}01;\omega\right)} \cdot f_c\right]^{0{,}225} \cdot \left(\frac{L_v}{h}\right)^{0{,}35} \cdot 25^{\left(\alpha\rho_{sx}\frac{f_{yw}}{f_c}\right)} \cdot \left(1{,}25^{100\cdot\rho_d}\right) \qquad (9)$$

Similarly, the chord rotation at yielding $\theta_y$ is determined in accordance with the empirical relationship (10):

$$\theta_y = \left(\theta_{um} - \theta_{um}^{pl}\right) = \theta_{C,SLD}$$

$$\theta_{um}^{pl} = \frac{1}{\gamma_{el}} \cdot 0{,}0145 \cdot \left(0{,}25^{\nu}\right) \cdot \left[\frac{\max(0{,}01;\omega')}{\max(0{,}01;\omega)} \cdot f_c\right]^{0{,}35} \cdot f_c^{0{,}25} \cdot \left(\frac{L_v}{h}\right)^{0{,}35} \cdot 25^{\left(\alpha\rho_{sx}\frac{f_{yw}}{f_c}\right)} \cdot \left(1{,}275^{100\cdot\rho_d}\right) \quad (10)$$

where h is the depth of cross-section, $L_v$ is the ratio moment/shear at the end section, α is the confinement effectiveness factor, ω/ω' is the mechanical reinforcement ratio of the tension and compression, respectively, longitudinal reinforcement, ν is the dimensionless axial force, $\rho_d$ is the steel ratio of diagonal reinforcement, $f_c$ and $f_{wc}$ are the concrete compressive strength and the stirrup yield strength, respectively. On the one hand, the seismic demand is determined according to the well-known N2-Method [33]: Figure 7 depicts the main operations requested to calculate the "performance-point", whose abscissa is the displacement demand $D_{LS,i}$.

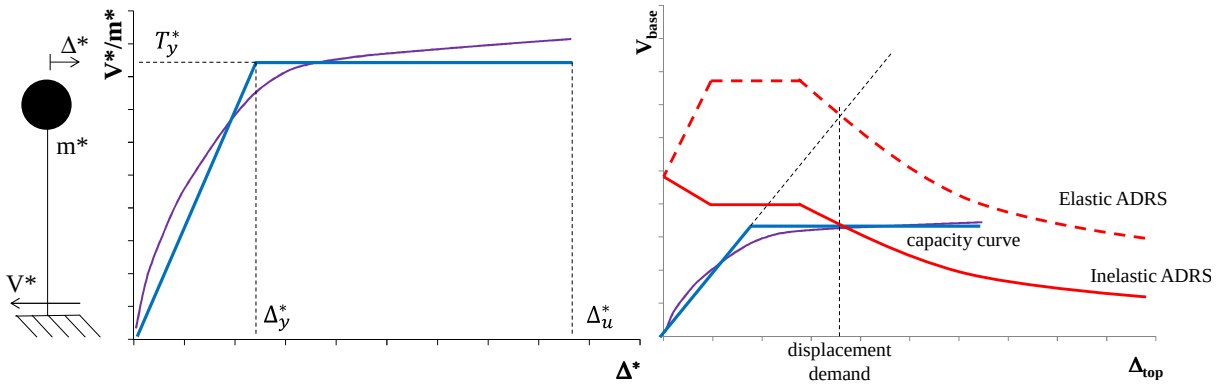


Figure 7: Evaluating seismic displacement demand via N2 Method

Moreover, the proposed heuristic strategy use the penalty function Φ in Eq. (5) with the aim to penalize unsuccessful solutions characterized by seismic demand higher than capacity. The penalty function depends on the maximum value of the capacity to demand ratio. The latter is evaluated through four Non Linear Static Analysis carried out for simulating the seismic response of the structure under consideration both in x and y direction (Table 1).

| | **X+** | **X-** | **Y+** | **Y-** | |
|---|---|---|---|---|---|
| **SLD** | $(D/C)_{SLD,x+}$ | $(D/C)_{SLD,x-}$ | $(D/C)_{SLD,y+}$ | $(D/C)_{SLD,y-}$ | $\max_i \left(\frac{D_{LS,i}}{C_{LS,i}}\right)$ |
| **SLV** | $(D/C)_{SLV,x+}$ | $(D/C)_{SLV,x-}$ | $(D/C)_{SLV,y+}$ | $(D/C)_{SLV,y-}$ | |

Table 1: Evaluating maximum value of limit state function

One of the major challenges in any application of penalty function concerns achieving an appropriate balance of the penalty value. Large penalty values discourage algorithm from exploring infeasible regions and the search is quickly moved inside the feasible region. On the other hand, low penalty values do not prohibit algorithm from searching infeasible regions most of the time. As a result of these findings, the authors propose a "death penalty functions" which immediately reject infeasible solutions [35]. The feasible region is shown graphically in Figure 8. In the domain of technically successful solutions, where no violation is found, a low penalty belonging to the linear branch is imposed on the objective function: it grows monotonically until the threshold value 1 above which the term Φ reaches an almost vertical asymptote.

On the contrary, if the maximum demand to capacity ratio is greater than unit, then the penalty cost becomes very high.

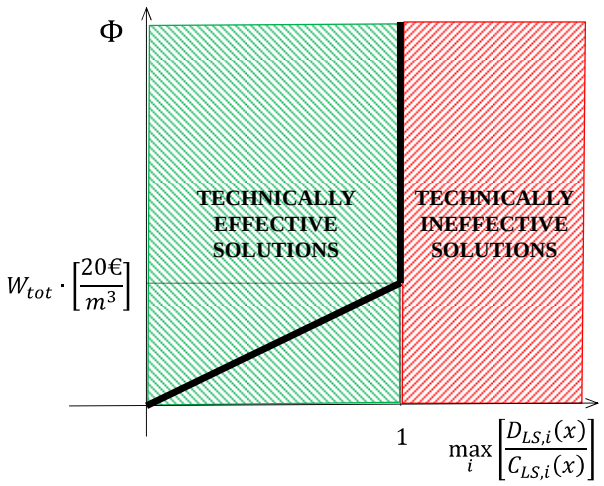


Figure 8: Penalty function

Based on typical retrofitting costs and their possible correlation with the demand to capacity ratio [36], the penalties solution is defined as represented in Figure 8, in which a unit cost of 20 €/m$^3$ is assumed for retrofitting [37]. This definition of penalty function aims at increasing the nominal cost for those solutions that do not meet the constraint condition in Eq. (2). Once the total cost and the limit state function $g_{LS,i}$ are evaluated for all $N_{ind}$ individuals of the population, for the minimization problem under consideration, it is necessary to map the objective function to fitness function form. Within the present work, the authors employ a proportional fitness assignment as transformation. The fitness $F(x_i)$ assigned to each solution "measures" the capability of the i-th individual to "compete" with the other ones of the same generation in achieving the objective of the optimisation problem under consideration. It is computed as the individual's raw performance, $f(x_i)$, relative to the whole population, according to the Eq. (11):

$$F(x_i) = \frac{\min_{i=1..N_{ind}} \left[f(x_i)\right]}{f(x_i)} \tag{11}$$

As can be easily understood from Eq. (11) it is always lower than the unit, which is determined for the individual characterised by the lower value of the objective function. In other words, the fitness function value corresponds to the number of offspring that an individual can expect to produce in the following generation.

## 2.5 Convergence test

Because GA is a stochastic search method, it is difficult to formally specify convergence criteria. As the fitness of a population may remain unchanged for a number of generations before a superior individual is found, the application of conventional termination criteria becomes problematic. A common practice is to terminate the GA after a predefined number of generations. In the present work, starting from the randomly generated initial population, the genetic algorithm evolves through three operators described below until the counter of population reaches a maximum number fixed to 150.

## 2.6 Selection

The selection operator selects individuals on the bases of their fitness with the aim of realising the "survival of the fittest" principle, which is the basis of the evolution theory [17]. This principle translates into discarding the chromosomes with the highest cost and into the exclusion of the solutions that don't comply with the seismic check. The essential idea is that individuals are picked out of the current population and, based on probabilistic assumptions, they are included in a mating pool. First, the $N_{ind}$ costs $f(x_i)$ and associated chromosomes are ranked from lowest cost to highest cost. Then, only the best are selected to continue, while the rest are deleted. The selection rate, $X_{rate}$, is the fraction of $N_{ind}$ that survives for the next step of mating. The number of chromosomes that are kept each generation is:

$$N_{keep} = X_{rate} \cdot N_{ind} \tag{12}$$

Of the $N_{ind}$ chromosomes in a generation, only the top $N_{keep}$ survive for mating, and the bottom $N_{ind}$ - $N_{keep}$ are discarded to make room for the new "offspring" solutions. Deciding how many chromosomes to keep is somewhat arbitrary. Keeping too many chromosomes allows bad performers a chance to contribute their traits to the next generation. For this reason, the authors keep 10% ($X_{rate}$ = 0.1) in the selection process. In the present example, $N_{ind}$ = 100. With a 10% selection rate, $N_{keep}$ = 10. Then, 10 individuals with the lowest cost f(x) survive to the next generation and become potential parents. The fitness $F(x_i)$ of each individual is employed in determining the "probability of survival" $p(x_i)$ of the i-th solution as follows:

$$p(x_i) = \frac{F(x_i)}{\sum_{i=1}^{N_{ind}} F(x_i)} \tag{13}$$

It is evident that, by definition, the values of $p(x_i)$ range between 0 and 1 and the sum of probabilities for each individual is equal to the unity. Under the algorithmic standpoint, $p(x_i)$ is the probability that the i-th individual is "selected" within the current generation to be part of the mating pool and, hence, "reproduce" itself into the following generation. The individuals featuring higher values of $p(x_i)$ have the higher probability to be selected as "parents" for generating "offsprings" in the following generation. In the present work, the selection procedure is implemented through the so-called "roulette-wheel" rule [38]. The circular sections within the roulette wheel are marked proportionally to the probability of survival of each individual (Figure 9): in the example, the individual #3 is the fittest individual and, hence, it corresponds to the wider circular sector, whereas individuals #2 is the least fit and, correspondingly, it has a smaller area.

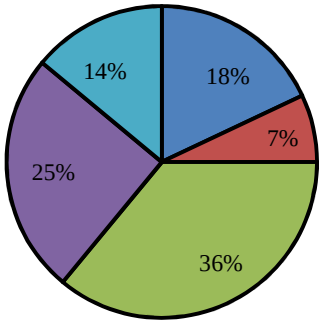


| Individual | Chromosome | Probability | Cumulative P. |
|---|---|---|---|
| 1 | 00101011101011101011010 | 0.18 | 0.18 |
| 2 | 10101010101010101010011 | 0.07 | 0.25 |
| 3 | 00001011001001101001010 | 0.36 | 0.61 |
| 4 | 11101011001011101011111 | 0.25 | 0.86 |
| 5 | 11001011101010101111110 | 0.14 | 1.00 |

Figure 9: Roulette wheel rule in the selection operator

If $N_{ind}$ - $N_{keep}$ individuals have to be selected, $N_{ind}$ - $N_{keep}$ random numbers are generated in the [0,1] range and the individual whose circular segment includes the random number is actually selected for reproduction.

## 2.7 Crossover

The crossover operator aims at creating different individuals in the following generations by combining material extracted from individuals of the previous generation. It is worth highlighting that, in order to preserve some of the fitter individuals, not all the strings in the mating pool are used in crossover. Hence, a threshold combination probability $p_c$ is defined: only $N_{ind}*p_c$ individuals of the population are used in the crossover operation, whereas $N_{ind}*(1-p_c)$ remain unchanged and preserve themselves for following population. Typically, the probability for crossover ranges from 0.6 to 0.95. Because the selection rate $X_{rate}$ is equals to 0.1, the employed probability $p_c = 1- X_{rate}$ results 0.9. Once $0.5*N_{ind}*p_c$ pairs of individuals are selected according to their fitness $F(x_i)$, crossover operator "mixes" the segments of each pair and the information contained between these segments is exchanged. As well as its ideal counterpart in nature, the two genotype strings of the individual participating in the crossover are selected as "parents" and the resulting strings are defined as "children". Figure 10 shows the working principle of the crossover operator: the method used in the present GA is the "multipoint" crossover.

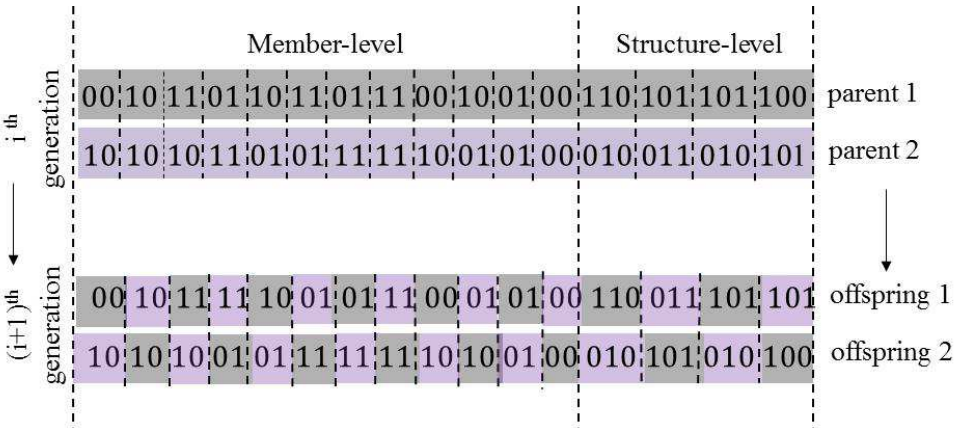


Figure 10: Crossover operator applied to couples of "parent" individuals

In the example shown in Figure 10 the segments are delimited with dashed lines and crossover operator is applied column-by column and bay-by-bay, respectively in the first and second part of the genotype. The influence of the number of crossover points on the resulting efficiency is a key aspect, whose discussion is outside the scope of this paper. Readers may refer to Spears [39]-[40] for further details.

## 2.8 Mutation

In natural evolution, mutation is a random process through which one allele of a gene is replaced by another to produce a new genetic structure. Mutation is the second way a GA explores the solution space. This operator provides a guarantee that the probability of searching any given string will never be zero and acting as a safety net to recover good genetic material that may be lost through the action of selection and crossover [41]. Under the operational standpoint, it introduces diversity not in the original population whenever the population tends to become homogeneous due to repeated use of reproduction and crossover operators. It also tends to distract the GA from converging too fast at local optima before sampling the entire solution space. The need for mutation is in fact to create a point in the neighborhood of

the current point, thereby achieving a local search around the current solution. Even though better strings are not guaranteed and/or tested while creating them, it is expected that if weak (or bad) strings are created they will be eliminated by the reproduction operator in the next generation and if good strings are created, they will be increasingly emphasized. Mutation operates at the bit level of the genotype code. To this end, the so-called "mutation probability" $p_m$ is defined as the probability of a single bit to be "inverted" in each offspring individual when the bits are being copied from the current string to the new string. As well as in nature, this probability is usually assumed as a small value, typically in the range 0.001 and 0.01. In the current implementation this parameter is set equal to 0.01. A high value is selected in order to enhance the so-called "ergodicity" of the algorithm, namely its capability to explore the parametric field of the problem under consideration. A coin toss mechanism is employed: if random number between zero and one is less than the mutation probability, then the bit is inverted, so zero becomes one and vice versa (Figure 11). If $N_{bits}$ is the number of bits totally allocated in each string, mutation points are randomly selected from the $(N_{ind}- N_{keep})*N_{bits}$ total number of bits in the population matrix. It is possible that a given binary string may be mutated at more than one point. Figure 11 shows an example of mutation occurring in a generic individual.

Mutation point

| | | | | | | | | | |
|---|---|---|---|---|---|---|---|---|---|
| Original string | 0 | 1 | 1 | 0 | **0** | 1 | **1** | 0 | 1 |
| Random number | 0.234 | 0.703 | 0.167 | 0.345 | **0.008** | 0.806 | **0.005** | 0.624 | 0.411 |
| Mutated string | 0 | 1 | 1 | 0 | **1** | 1 | **0** | 0 | 1 |

Figure 11: Examples of mutation points

Finally, the application of selection, crossover and mutation operators on the current population creates a new population. This new population is used to generate subsequent populations and so on, yielding solutions that are closer to the optimum solution. The values of the objective function of the individuals of the new population are again determined by decoding the strings. This completes one cycle of genetic algorithm called a generation. In each generation if the solution is improved, it is stored as the best solution. The process described is repeated till convergence.

## 3 PROPOSED APPLICATION

The working detail and the potential of the presented optimisation procedure are shown in an application: Figure 12 depicts the in-plane configuration of the simple stucture considered herein.

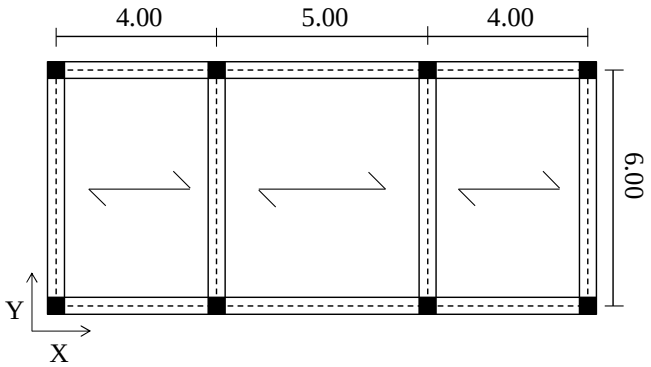


Figure 12: In-plain configuration of the considered structure

A simple 3D three-storey RC frame with three bays in x-direction and one bay along y axis, considered in a construction site caracterized by higl level of seismicity ($PGA_{LD}$ = 0.12g; $PGA_{LV}$ = 0.35g) is taken as preliminary case for applying the proposed retrofitting strategy. The cross sectional area of beams and columns is 30x40 $cm^2$ and 30x30 $cm^2$, respectively. Foundation is not simulated and fixed supports are considered. Rigid joints are used for simulating beam-to-column connections. The total number of design variables considered in the test example (Figure 13) is 34: 3 x 8 member-level variables (8 columns for each floor), plus 10 structure-level variables (6 bays in x-direction and 4 along the y axes).

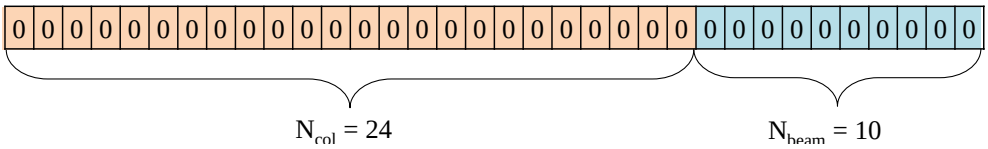


Figure 13: As-built genotype of the considered structure

Each generation includes 100 individuals and the genetic algorithm stops either 150 after generations or if the objective function keeps unchanged for 20 consecutive generations. Both the LS of Life Safety (SLV) and Damage Limitation (SLD) are considered and, hence, demand and capacity are evaluated in both LSs. A bilinear stress-strain curve with Young modulus equal to 210 GPa and yield stress $F_y$= 220 MPa is adopted for describing the elasto-plastic behaviour of steel. The Kent-Scott-Park model [30] with degraded linear unloading/reloading stiffness and no tensile strength is used in order to describe the constitutive law of existing concrete. The effects of FRP confinement result in increasing the ductility of concrete (Figure 4), according to the afore mentioned model. The live load is taken as Q=2.00 kN/$m^2$ and the permanent load is G=5.00 kN/$m^2$. The gravity loads are contributed from an effective area of 78 $m^2$. A Finite Element model is built in OpenSEES [31] for simulating the seismic response of the structure under consideration. The well-known fiber approach is used to account for material non-linearity by means of the so-called “nonlinear beam-column elements”. Five integration sections, located at the Gauss-Lobatto quadrature points, are considered for each beam-column element. Each section is divided into a number of fibers. Similar elements are also employed for modelling the concentric steel bracings in structure-level intervention. An accidental eccentricity is assigned in the middle point according to EN 1993-1-1 [32] in order to obtain the buckling of the bracing in compression. Figure 14 depicts the outcome of the proposed algorithm.

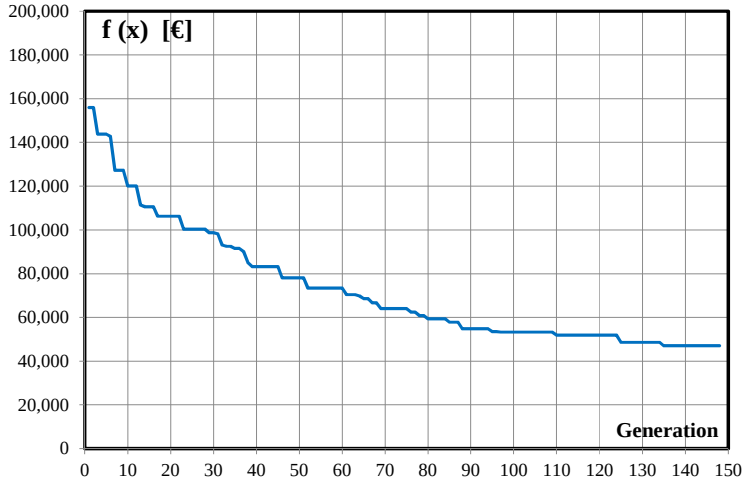


Figure 14: Convergence history: objective function vs generation

The objective function starts from a cost of 156’481 € and decreases progressively. As expected, the curve shows a very steep slope over the first generations and a slower and slower reduction, often characterised by a staircase shape, towards the final convergence, which is supposed to be achieved after 150 generations, as no further relevant improvement is observed in f(x) over the last 15 iterations. Finally, the optimal phenotype in the 150th population (Figure 15) has a cost of 43’703 €, the lowest of all previously processed solutions. In the example proposed herein, the optimal solution came up to consist of a concentric steel bracing (realised in the two plain frame along the y-direction and one in the x direction) and no local FRP interventions are actually required. The optimal section of steel members for the first bracing level is a HE 100 A.

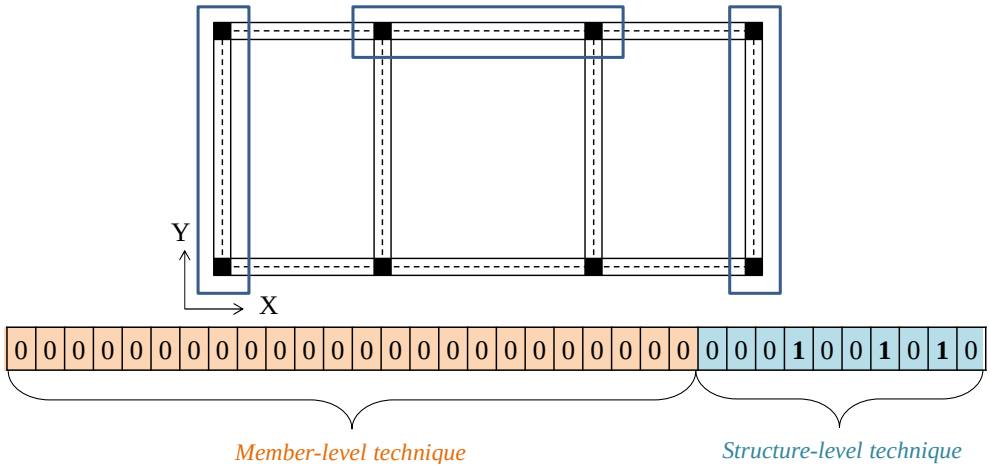


Figure 15: Optimal phenotype and corresponding technical solution

## 4 CONCLUSIONS

This paper outlined the formulation of a rational procedure intended at optimising seismic retrofitting of existing structures by combining member- and structure-level techniques. The proposed genetic algorithm has the potential to support engineering judgement (being far from the ambition to rule it out) in determining the “fittest” seismic retrofitting solution for RC frames. The proposed procedure demonstrates its potential in formally. In fact, the considered application demonstrates that the implemented genetic algorithm is capable of finding a solution characterised by a cost significantly lower than the initially assumed trial solution. Nevertheless, the implementation of this numerical model is still under development: the work ahead should be primarily intended at including the aspects that are not taken into account yet (i.e. multi-criteria objective function, among the others). Moreover, it should also aim at enhancing the computational efficiency of the computer procedure, whose computational cost is one of the main critical issues to be duly addressed for the proposed method be actually feasible in real applications.

## REFERENCES


[1] European Standard EN (Eurocode 8) 1998-1:2005, Design of structures for earthquake resistance, Part 1: General rules, seismic actions and rules for buildings. European Committee for Standardization (CEN), Bruxelles, 2005.

[2] fib 2003. Seismic assessment and retrofit of reinforced concrete buildings. Bulletin No. 24, 138, ISBN: 978-2-88394-054-3.

[3] G.E. Thermou, A.S. Elnashai, Seismic retrofit schemes for RC structures and local–global consequences. *Progress in Structural Engineering and Materials*, 8: 1–15, 2006.

[4] M.G. Ireland, S. Pampanin, D.K. Bull, Experimental Investigations of a Selective Weakening Approach for the Seismic Retrofit of R.C. Walls. Palmerston North (New Zealand), 30 March- 1 April, 2007.

[5] H. Kaplan, S. Yilmaz, N.Cetinkaya, E. Atimtay, Seismic strengthening of RC structures with exterior shear walls, Sadhana, Indian Academy of Sciences, 36 (1): 17–34, 2011.

[6] fib 2006. Retrofitting of concrete structures by externally bonded FRPs, with emphasis on seismic applications, Bulletin No. 35, 220, ISBN: 978-2-88394-075-8.

[7] M. Rodriguez, R. Park, Repair and Strengthening of Reinforced Concrete Buildings for Seismic Resistance. *Earthquake Spectra*, 7(3): 817-841, 1991.

[8] E. Martinelli, C. Lima, C. Faella, Towards a rational strategy for seismic retrofitting of RC frames by combining member- and structure-level techniques. SMAR2015 – *Third Conference on Smart Monitoring, Assessment and Rehabilitation of Civil Structures*, Antalya (Turkey), 6-9 September, 2015.

[9] FEMA 156, Typical Costs for Seismic Rehabilitation of Existing Buildings. Vol 1: Summary (Second Edition), 1994.

[10] G. Quan, M. Barbato, J.P. Conte, P.E. Gill, F. McKenna, OpenSees-SNOP Framework for Finite-Element-Based Optimisation of Structural and Geotechnical Systems. *Journal of Structural Engineering*, 138(6): 822-834, 2012.

[11] S. Gharehbaghia, M.J. Fadaee, Design Optimisation of RC Frames under Earthquake Loads, Int. J. Optim. Civil Eng, vol. 2 n. 4, , pp. 459 – 477, 2012.

[12] A. Guerra, D.P. Kiousis, Design optimisation of reinforced concrete structures, *Computers and Concrete*, 3(5), 313-334, 2006.

[13] A. Kunisue, N. Koshika, Y. Kurokawa, N. Suzuki, J. Agami, M. Sakamoto,. Retrofitting method of existing rein-forced concrete buildings using elastoplastic steel dampers. *Proceedings of the twelfth World Conference on Earth-quake Engineering (12WCEE)*, Paper 0648, 2000.

[14] G.E. Thermou, A.S. Elnashai, Seismic retrofit schemes for RC structures and local–global consequences, *Progress in Structural Engineering and Materials*, 8:1–15, 2006.

[15] S. Bordea, D. Dubina, Retrofitting/upgrading of reinforced concrete elements with buckling restrained bracing elements. *Proceedings of the 11th WSEAS International Conference on Sustainability in Science Engineering*, Timisoara (Romania), 27-29 May 2009, 407-402, 2009.

[16] N. Caterino, I. Iervolino, G. Manfredi, E. Cosenza, Comparative Analysis of Multi-Criteria Decision-Making Methods for Seismic Structural Retrofitting, *Computer-Aided Civil and Infrastructure Engineering*, 24(6): 432–445, 2009.

[17] C. Darwin, *On the Origin of Species by means of Natural Selection or the Preservation of Favored Races in the Struggle for Life* (The Origin of Species), London: Murray, 1859.

[18] M. Papadrakakis, N.D. Lagaros, Soft computing methodologies for structural optimisation. *Applied Soft Computing*, 3: 283-300, 2002.

[19] M. Fragiadakis, N.D. Lagaros, M. Papadrakakis, Performance-based multi-objective optimum design of steel structures considering life-cycle cost. *Structural and Multidisciplinary Optimisation*, 32: 1–11, 2006

[20] N.D. Lagaros, Y. Tsompanakis, M. Fragiadakis, M. Papadrakakis, Soft Computing Techniques in Probabilistic Seismic Analysis of Structures. *Intelligent Computational Paradigms in Earthquake Engineering* edited by N. Lagaros and Y. Tsompanakis, Idea Group Publishing ltd, Hershey, PA (USA), 2007.

[21] M. Fragiadakis, M. Papadrakakis, Performance-based optimum seismic design of Reinforced Concrete Structures. *Earthquake Engineering and Structural Dynamics*, 37(6): 825–844, 2008.

[22] M.II.TT. 2008, Norme tecniche per le costruzioni - D.M. 14 gennaio 2008 (in Italian).

[23] C.A. Coello, Theoretical and numerical constraint-handling techniques used with evolutionary algorithms: a survey of the state of the art. *Computer Methods in Applied Mechanics and Engineering*, 191, 1245-1287, 2002.

[24] D.E. Goldberg, B. Korb, K. Deb, Messy genetic algorithms: motivation, analysis, and first results. *Complex Systems*, 3(5), 493-530, 1989.

[25] F. Biondini, Optimal limit states design of concrete structures using genetic algorithms. *Studies & Researches* 20, 1999.

[26] W.M. Jenkins, Towards Structural Optimisation via the Genetic Algorithm. *Computers & Structures*, 40(5): 1321–1327, 1991.

[27] W.M. Jenkins, Structural Optimisation with the Genetic Algorithm. *The Structural Engineer*, 69(24): 418-422, December, 1991.

[28] G.R. Reeves, Modern Heuristic Techniques for Combinatorial Problems. *John Wiley & Sons*, Inc. 1993.

[29] P. Hajela, Stochastic Search in Structural Optimisation: Genetic Algorithms and Simulated Annealing. Chapter 22: 611-635, 1992.

[30] D. C. Kent, R. Park, Flexural members with confined concrete. *Journal of the Structural Division*, 97(7): 1969-1990, 1971.

[31] S. Mazzoni, F. McKenna, M.H. Scott, G.L. Fenves, OpenSEES command language manual. *Pacific Earthquake Engineering Research* (PEER), 2006.

[32] European Standard EN (Eurocode 3) 1993-1-1:2005, Design of steel structures, Part 1-1: General rules and rules for buildings. European Committee for Standardization (CEN), Bruxelles, 2005.

[33] European Standard EN (Eurocode 8) 1998-3-2005, Design of structures for earthquake resistance, Part 3: Assessment and retrofitting of Buildings, European Committee for Standardization (CEN), Bruxelles, 2005.

[34] P. Fajfar, Capacity spectrum method based on inelastic demand spectra. *Earthquake Engineering & Structural Dynamics*, 28(9): 979-993, 1999.

[35] H.P. Schwefel, Numerical optimisation of computer models. *John Wiley & Sons*, Chichester, UK, 1981.

[36] Ordinanza P.C.M. n° 3362 del 08/07/2004 (in Italian) "Modalità di attivazione del Fondo per interventi straordinari della presidenza del Consiglio dei Ministri, istituito ai sensi dell'Art. 32 bis del decreto legge 30 settembre 2003, n° 269, convertito con modificazioni dalla legge 24 novembre 2003, n° 326".

[37] J.T. Richardson, M.R. Palmer, G.E. Liepins, M.R. Hilliard, Some guidelines for genetic algorithms with penalty functions. In J. D. Schaffer (Ed.), *Proceedings of the Third International Conference on Genetic Algorithms* (ICGA'89), Fairfax, VA, USA, 191-197, 1989.

[38] A. Lipowski, D. Lipowska, Roulette-wheel selection via stochastic acceptance. *Physica A: Statistical Mechanics and its Applications*, 6: 2193–2196, 2012.

[39] W.M. Spears, Crossover or mutation? *Proceedings of the Foundations of Genetic Algorithms Workshop*, Vail, Colorado: Morgan Kaufmann, 1992.

[40] W.M. Spears, Adapting crossover in a genetic algorithm. *Naval Research Laboratory AI Center Report* AIC-92-025. Washington, DC 20375 USA, 1992.

[41] D.E. Goldberg, Genetic Algorithms in Search, Optimisation and Machine Learning, *Addison Wesley Publishing Company*, January 1989.

COMPDYN 2017
6th ECCOMAS Thematic Conference on
Computational Methods in Structural Dynamics and Earthquake Engineering
M. Papadrakakis, M. Fragiadakis (eds.)
Rhodes Island, Greece, 15–17 June, 2017

# EXPERIMENTAL ASSESSMENT OF CARBON FIBER JACKETING OF STEEL PLATES

**Salvatore Sessa**[1], **Ferdinando Toraldo**[1],
**Francesco Marmo**[1], **Daniele Masi**[1] **and Luciano Rosati**[1]

[1]University of Naples Federico II
Department of Structures for Engineering and Architecture
Via Claudio 21, 80125, Napoli, Italy
e-mail: salvatore.sessa2@unina.it

**Keywords:** Jacket steel, Inverse identification, Fiber reinforced, Cohesive fracture

**Abstract.** *It is presented a numerical assessment of experimental data concerning Mode–II delamination tests of steel plates jacketed with Carbon fiber textile sheets. In particular, an inverse identification procedure, based on finite element analysis, has been performed in order to estimate the constitutive parameters of the interface bonding steel and textile. Such a procedure proved to be capable of characterizing a constitutive model which reproduces with sufficient accuracy the peak load and the fracture triggering propagation of the bonding interface. The identified finite element model is accurate enough to be employed in force–based design or in structural analysis where a suitable displacement–ultimate limit state is considered.*

*The contribution analyzes the physical interpretation of the Mode–II delamination process with particular focus on its representation by means of finite element models. In particular, a discussion about the delamination process will show the consistency of the finite element model with the physical behavior of the specimen observed during the experimental tests. Such considerations, although encouraging, introduced further issues which outlines future research directions in order to improve the identification strategy.*

## 1 INTRODUCTION

Use of Fiber–Reinforced Polymers (FRP) composites for reinforcing structural elements is a widely diffused technology particularly suitable for the structural retrofit of concrete and masonry structures. More recently, some peculiar FRP features made the scientific community explore possible applications in reinforcing steel elements [1, 2].

The fast installation of FRP devices, accompanied by the high strength–to–weight rate, results in a minor disturbance of structural functionality. Further advantages concern their mechanical properties and lay-up protocols; in particular, FRP textiles are capable of following curved or irregular surfaces of a structural element where steel plates require a preliminary grinding. In addition, the most appealing feature concerns the use of polymeric adhesives instead of welded and bolted joints [3] what allows one to avoid residual stress and steel weakening due to high temperatures [4].

The chance of using FRP in conjunction with steel elements introduces the necessity to properly account for the mechanical characterization of jacketing–substrate adhesion. In particular, the high strength of metallic adherends characterizes the interface as a well–identified region establishing a force/displacement relationship where the damage is likely to be concentrated. For this reason, it is usual to focus on *fracture* rather than adhesion. Nevertheless, these are two aspects of the same physical phenomenon: similarly to adhesion, fracture is a progressive process in which adhesion forces, acting on an extended region, contrasts the separation of two bonded interfaces.

To properly model fracture propagation several models, based on both theoretical and experimental research, have been developed. While microscale approaches [5] are capable of reproducing the interface behavior, their application in design practices is arduous; on the contrary, Cohesive–Zone Models (CZMs), originated from the original proposal by Barenblatt [6] and Dugdale [7], characterize the stress state in bonding interfaces near to crack regions.

The constitutive model of the cohesive–zone is usually defined by means of physical parameters, such as interface strength and fracture energy (thoughness), whose experimental calibration is based on testing standardized specimens. In order to characterize the constitutive parameters, several approaches are available.

A first methodology consists in the definition of theoretical models establishing closed–form relations between constitutive parameters and experimental response, as in the case of beam–theory [8, 9], compliance [10] and elasto–plastic [11] approaches.

Despite of their easy–to–use attitude, the applicability of the previous methods is conditioned to a stable propagation of the fracture during the experimental test [12]. In this sense, whenever underlying hypothesis of the theoretical model are not satisfied, the experimental test cannot define any reliable parameter.

On the contrary, recently developed inverse–identification procedures based on Finite Element (FE) analysis [13] avoid the above mentioned drawbacks. They reproduce the monitored quantities of the experimental test by means of a finite element model that adopt the quantities to be identified as parameters; an objective function measures the residual between the FEM and the experimental response [12, 14, 15]. Subsequently, numerical optimization strategies can be performed in order to identify the parameters' values that minimize the residual norm.

The significant versatility of finite elements, as well as the chance of selecting the minimization algorithm depending on the peculiar features of the experimental records [16], make inverse identification a very powerful tool.

In particular this research aims to identify the constitutive parameters of a specimen typol-

ogy consisting of steel plates reinforced with Carbon–FRP textiles, tested in a round–robin experimental campaign.

Record datasets of experimental tests, presented in Section 2, monitor the behavior of the tested specimens by means of overall load–displacement and local strain responses. Although not exhaustive of fracture propagation, the datasets are sufficiently detailed to describe the non-linear interaction between steel and FRP.

Test responses are then reproduced by a finite element model in order to define objective functions as the least–square difference between estimated and experimental responses. The FEM model is used in an optimization procedure, described in Section 3, in order to identify the parameters of the interface constitutive model.

Numerical results are discussed in Section 4 where a physical interpretation and considerations about the acceptability of the identified parameters are discussed.

Finally, conclusions provided in Section 5 discuss the open issues of the proposed strategy introducing future research directions.

## 2 MODEL SPECIFICATIONS AND MODE-II EXPERIMENTAL TEST

Experimental tests were carried out on symmetric specimens constituted by two $S355J0$ steel plates bonded to uniaxial Fiber reinforced textile. Steel plates, designed in order to remain elastic during the fracture tests, are cured by mechanical brushing.

The two steel plates are therefore bonded by four layers of the uniaxial Carbon–fiber textile *FiberFIP CARBON T-UNI 390*, crafted by the *FIP Chemicals S.r.l.*, applied by room–temperature impregnation with bi–component epoxy resin type *FiberFIP ADESIVO 800*, produced by the same manufacturer.

Characteristic mechanical parameters of CFRP textile and epoxy adhesive are reported in Table 1 while the adopted geometrical scheme is shown in Figure 1 where only half specimen is represented due to its symmetry. It is worth being emphasized that, although inducing flexure, the bonding is applied only on the bottom surfaces of the plates in order to detect the strain both in the CFRP and in the steel.

| CFRP textile | | |
|---|---|---|
| Parameter | Units | Value |
| Tensile Stress $f_{tk} = f_m - 3\delta$ | $MPa$ | $\geq 2400$ |
| Avg Ult. strain | $\%$ | $\geq 0.6$ |
| Elastic Moduli | $GPa$ | 390 |
| Textile Weight | $g/m^2$ | 450 |
| Fiber Eq. thick. | $mm$ | 0.247 |

| Epoxy adhesive | | |
|---|---|---|
| Parameter | Units | Value |
| Weight Ratio $(A : B)$ | | $3.3 : 1$ |
| Weight $(A + B)$ | $kg/dm^3$ | $1.10 + 0.05$ |
| Compr. stress (23°C) | $MPa$ | $\geq 90$ |
| Flex. stress (23°C) | $MPa$ | $\geq 36$ |
| Flex.-Trac. stress | $MPa$ | $\geq 50$ |
| Adhesion to steel for direct traction | $MPa$ | $\geq 14$ |

Table 1: Characteristic Values of Mechanical parameters of the CFRP textile and of the bi–components epoxy adhesive

A set of five symmetrically located measurement devices has been used in order to record the strain evolution during the delamination test: strain gauges of type *HBM Hottinger Baldwin Masstechnil GmbH* – $6\,mm$, *k-factor* $2.16 \pm 1.0\%$ have been applied on the external surfaces of both the steel and the CFRP, as shown in Figure 1. Specifically, strain gauges $SG1$ and $SG5$ are applied on the top surface of the steel plates simmetrically with respect to the midspan.

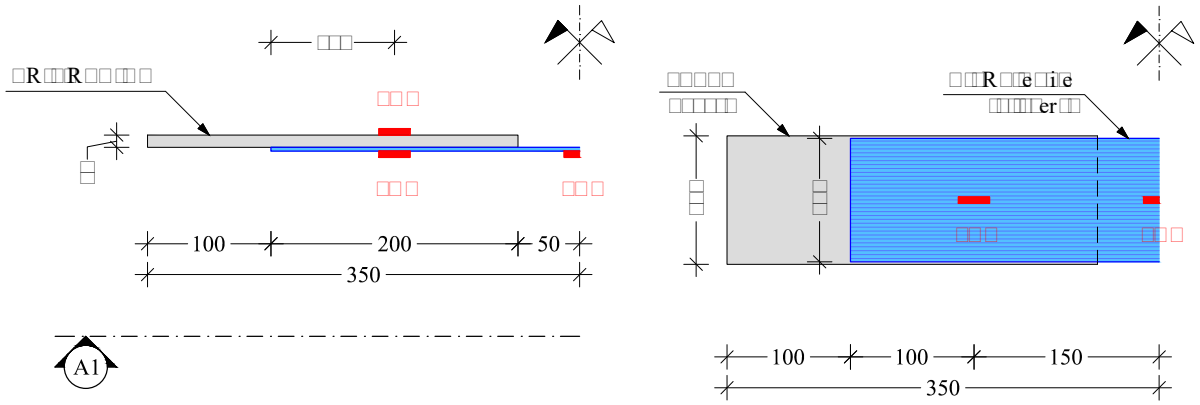


(a) Frontal view of half specimen. (b) Plan view of half specimen.

Figure 1: Geometric layout of the tested Specimen (lengths in $mm$).



(a) Specimen $S1$ before the test. (b) Specimen $S1$ after delamination.

Figure 2: Pure Mode–II delamination test $S1$.

Moreover, $SG2$ and $SG4$ have been fixed on the external surface of the CFRP textile. Gauge $SG3$, applied on the CFRP textile, is located at the middle point of the specimen and its record is inconsequential for the purposes of the present identification.

Experimental data illustrated in this contribution are referred to two Mode–II delamination tests carried out by a load–control electromechanical testing system type *MST810*, as shown in Figure 2(a). Loading, displacements and strains were recorded by the internal toolkit of the testing machine.

Both tests were carried out by monotonically increasing a quasi–static tensile load until complete delamination of the specimens, shown in Figure 2(b), was attained. Records of both experimental tests are reported in Figure 3. Specifically, load–displacement curves are plotted in Fig. 3(a) while Fig. 3(b) reports the loading plotted vs. the strain values recorded by strain–gauges $S4$ and $S5$ on the horizontal axis. It should be emphasized that both tests provided consistent experimental dataset since the differences between load–displacement curves and strains are negligible, as expected considering the natural dispersion of mechanical parameters. For

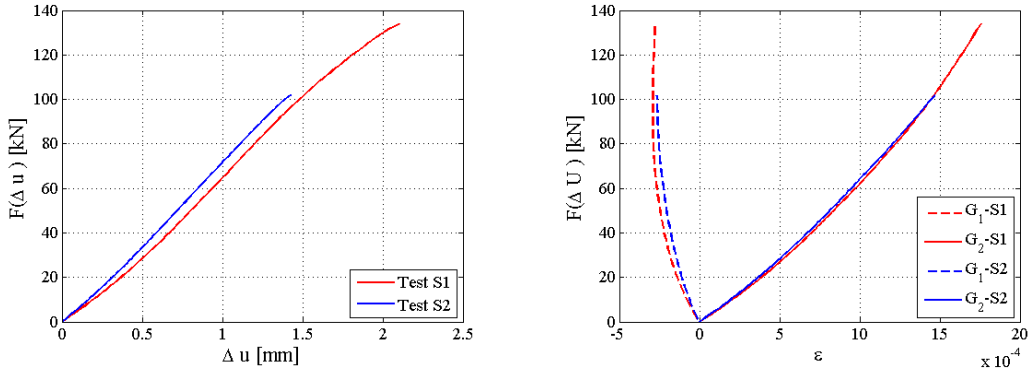


(a) Load–displacement curves. (b) Strain gauges record.

Figure 3: Mode–II delamination experimental test dataset.

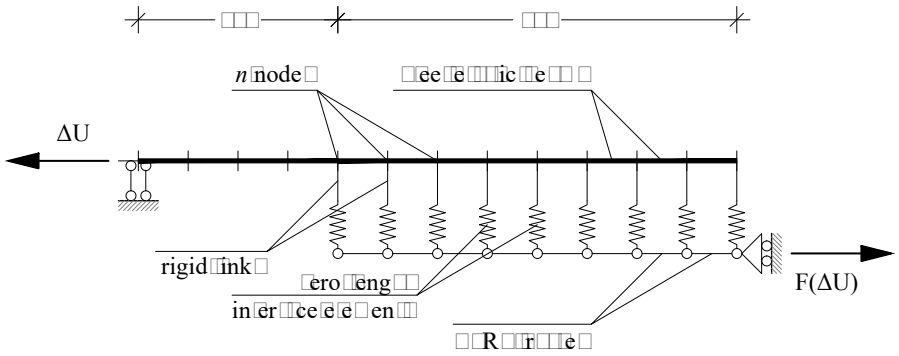


Figure 4: Scheme of the Finite Element model of the delamination test (lengths in $mm$).

this reason, the experimental dataset can be reasonably employed in inverse identification of adhesion constitutive parameters, an issue pursued in the following subsection.

## 3 INVERSE IDENTIFICATION PROCEDURE

In order to perform inverse identification of the adhesion parameters, the response of the pure Mode–II delamination test is reproduced by a Finite Element (FE) model analyzed in OpenSees [17], an object–oriented framework for structural analysis.

Figure 4 reports a simple scheme of the model which takes advantage of the specimen symmetry. Steel plates have been modeled by means of 30 elastic frames characterized by Young modulus $E_s = 210.0\,GPa$ and geometrical properties deduced from Fig. 1.

CFRP textiles have been modeled by elastic trusses with area $A_c = 0.247 \times 4 \times 104 = 102.752\,mm^2$, connected to the steel frames by rigid links with eccentricity $e = 6.5\,mm$; their Young's modulus has been experimentally characterized by preliminary tests and turn out to be $E_c = 424.0\,GPa$.

Interface between steel and CFRP is modeled by zero–lengths elements located at the end of rigid links and characterized by two independent constitutive models. Specifically, relationship between vertical forces and displacements is linearly elastic adopting the steel Young's modulus while the corresponding behavior in the horizontal direction is reported in Figure 5.

Such a constitutive model, proposed in [18], proved to be suitable for modeling Mode–II delamination and has become a consolidated standard in common practice [3]. It is characterized

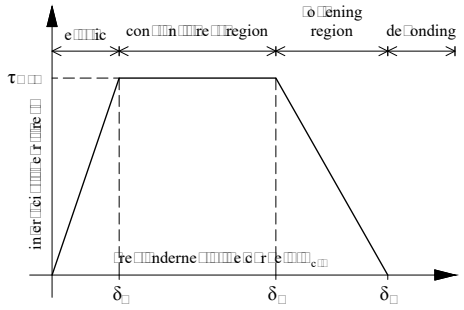

Figure 5: Typical constitutive model of the bonding interface for Mode–II delamination.

by a horizontal peak stress $\tau_{max}$ and strains $\delta_1$, $\delta_2$ and $\delta_f$ which have to be identified.

Fixed a trial value of the parameters, the FE estimate of the delamination test is computed that a displacement-control algorithm that applies the experimental displacements to the steel frame. In order to perform the inverse identification, it is necessary to define structural responses and an objective function $\Theta$. In particular, for each trial value of the identifying parameters array $\boldsymbol{\beta}$, the objective function $\Theta(\boldsymbol{\beta})$ evaluates the *distance* between the FE–estimated and experimental responses.

An effective approach introduced in [14] defines $\Theta(\boldsymbol{\beta})$ as the standard deviation of the difference between recorded and estimated responses; nevertheless, it has been shown in [12] how their selection is a critical issue that can significantly influence the parameters identification.

In particular, if a structural response has low sensitivity with respect to the identifying parameters, this adds noise to the objective function what could compromise its effectiveness. In the present application, load–displacement curves shown in Fig. 3(a) present almost–linear trend with fragile collapse. This can be expected since, in case of load–control, pure Mode–II delamination presents an instantaneous propagation of the fracture. Therefore, the load–displacement relationship can characterize the initial stiffness of the system but will add very few information about the fracture propagation phase.

For this reason, an exhaustive characterization of the whole test should consider experimental records able to capture the progressive collapse of interface elements.

It has been shown in [19] that, in order to detect shear delamination, it is necessary to provide a gradual drive of the strain. For the presented tests, this progressive strain increment can be observed locally by the strain gauges. For this reason, their record has to be taken into account in the identification procedure.

In order define the objective function, the displacement governing the experimental test is discretized in $m$ steps and is denoted as $\Delta u_i$. The experimental dataset consists of the recorded load $F^{exp}(\Delta u_i)$ and strains $\varepsilon_1^{exp}(\Delta u_i)$ and $\varepsilon_2^{exp}(\Delta u_i)$, referring to the SG1 and SG2 strain gauges, respectively.

Moreover, arranging the identifying parameters in the array $\boldsymbol{\beta} = \begin{bmatrix} \tau_{max} & \delta_1 & \delta_2 & \delta_f \end{bmatrix}$, a finite element analysis is performed adopting $\Delta u_i$ as controlled displacement; it computes the parametrized responses $F^{fem}(\Delta u_i, \boldsymbol{\beta})$, $\varepsilon_1^{fem}(\Delta u_i, \boldsymbol{\beta})$ and $\varepsilon_2^{fem}(\Delta u_i, \boldsymbol{\beta})$ corresponding to the components of the experimental dataset. Denoting as $R_{ld}$ the residual of the load and as $R_{gj}$ with $j = 1, 2$ the residuals of the $j$-th strain gauge, they can be computed as:

$$R_{ld}(\Delta u_i, \boldsymbol{\beta}) = \frac{1}{m} \sum_{i=1}^{m} \left[ \frac{F^{fem}(\Delta u_i, \boldsymbol{\beta}) - F^{exp}(\Delta u_i)}{F^{exp}(\Delta u_i)} \right]^2 \tag{1}$$

$$R_{gj}\left(\Delta u_i, \boldsymbol{\beta}\right) = \frac{1}{m}\sum_{i=1}^{m}\left[\frac{\varepsilon_j^{fem}\left(\Delta u_i, \boldsymbol{\beta}\right) - \varepsilon_j^{exp}\left(\Delta u_i\right)}{\varepsilon_j^{exp}\left(\Delta u_i\right)}\right]^2 \tag{2}$$

Eventually, the objective function is defined as:

$$\Theta\left(\boldsymbol{\beta}\right) = \frac{1}{3}\left[w_{ld}R_{ld}\left(\Delta u_i, \boldsymbol{\beta}\right) + w_{G1}R_{g1}\left(\Delta u_i, \boldsymbol{\beta}\right) + w_{G2}R_{g2}\left(\Delta u_i, \boldsymbol{\beta}\right)\right] \tag{3}$$

where $w_{ld}$, $w_{G1}$ and $w_{G2}$ are combination weights. Identification of the interface parameters is finally performed by the optimization problem:

$$\boldsymbol{\beta}^{\star} = \arg\min\left[\Theta\left(\boldsymbol{\beta}\right)|\boldsymbol{\beta}\right] \tag{4}$$

where $\boldsymbol{\beta}^{\star}$ is the occurrence of the parameter array which minimizes $\Theta\left(\boldsymbol{\beta}\right)$.

It is worth being emphasized that the objective function defined by Equations (1)-(3) can be physically interpreted as the mean–square of the structural response percentage residual.

## 4 NUMERICAL RESULTS

The procedure described in the previous section has been performed for both the introduced experimental datasets and results of the parameters identification are hereby presented.

Numerical computations have been performed by a constrained–symplex optimization algorithm available in the Matlab Optimization Toolbox v.R2013b [20] with tolerance $10^{-8}$, while finite element models have been analyzed by OpenSees v. 2.2.0 [17].

Identified parameters values for both the test S1 and S2 are reported in Table 2 and corresponds to the area underneath the identified constitutive curves shown in Figure 6.

A first consideration concerns peak stress $\tau_{max}$. In particular, let us denote as $\tau_{avg}$ the average shear stress at the specimen failure, computed as the ratio between the maximum load and the interface area and reported in the right column of Table 2. For both tests the identified values of $\tau_{max}$ are consistent with the corresponding $\tau_{avg}$. Moreover, area underneath the constitutive curve of test S1, which is related to the Mode–II fracture energy, is consistent with the integral of experimental load displacement curve shown in Fig. 3(a). On the contrary, Test S2 presents high values of $\delta_2$ and $\delta_f$ resulting in an over-estimation of fracture energy. For this reason, further considerations about the acceptability of the results is required.

| Test | $\tau_{max}\ (MPa)$ | $\delta_1$ | $\delta_2$ | $\delta_f$ | $\tau_{avg}\ (MPa)$ |
|---|---|---|---|---|---|
| S1 | 4.1248 | 0.0462 | 0.3941 | 0.8421 | 6.4413 |
| S2 | 3.6406 | 0.0355 | 1.6748 | 3.4138 | 4.8952 |

Table 2: Results of the parameter inverse identification

In order to qualitatively investigate if the identified parameters are significant and can be used in structural analyses, finite element responses computed at convergence have been compared with the experimental dataset.

Figures 7(a) and 8(a) present the FE and experimental load–displacement curves for the S1 and S2 test, respectively. In both cases the finite–element estimate of the load presents a good matching if initial stiffness while load at collapse turns out to be conservative with respect to the experimental curve although finite element curves present a plastic plateau.

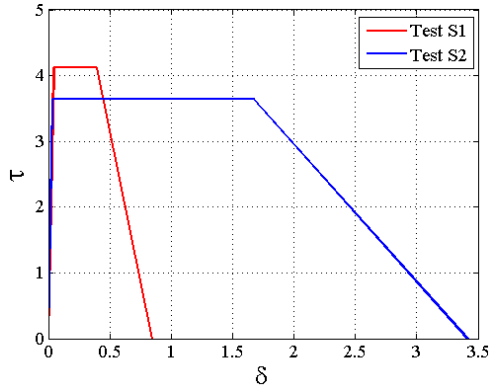


Figure 6: Identified Mode–II constitutive relationships of the interface (stress in $MPa$).

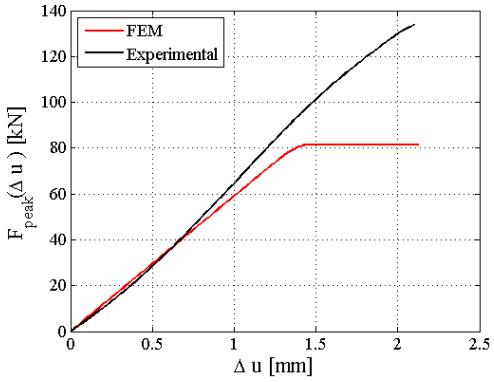


(a) Load–displacement curve.

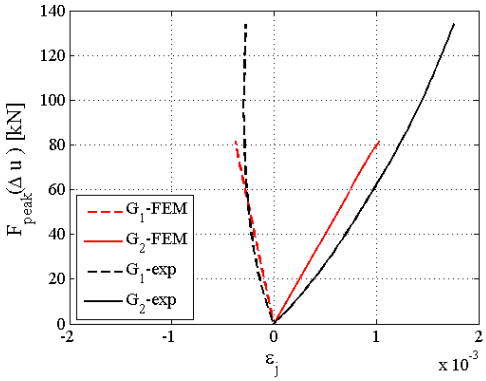


(b) Strain gauges curves.

Figure 7: Pure Mode–II delamination test $S1$. Experimental vs. identified responses.

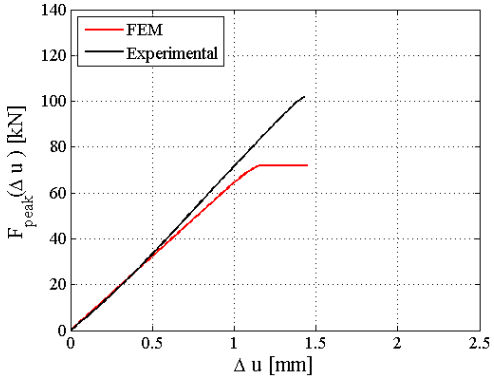


(a) Load–displacement curve.

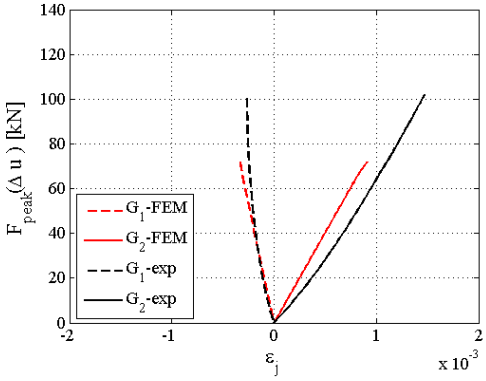


(b) Strain gauges curves.

Figure 8: Pure Mode–II delamination test $S2$. Experimental vs. identified responses.

Moreover strain responses, computed at the strain gauges application points and reported in Figures 7(b) and 8(b), show a less accurate matching with the experimental dataset, as proved by the values of the objective function computed at convergence. Recalling that the objective function $\Theta$ is defined in terms of the residual mean–square, it turns out to be $\sqrt{\Theta} = 28.11\%$ and $\sqrt{\Theta} = 23.61\%$ for test S1 and S2, respectively.

In particular such identification, obtained by adopting equal weights $w_{ld} = w_{G1} = w_{G2} = 1/3$ for all responses, is the best compromise for estimating constitutive parameters in such a way to provide acceptable matchings. Further tests with different weights, omitted for brevity, although matching the strains, fail to estimate the load.

Nevertheless, the identified parameters are capable of computing the interface responses with sufficient approximation although the plastic behavior of the load-displacement curve, as well as the over estimation of $\delta_2$ and $ultdisp$ for test S2, require a further discussion.

Recalling the constitutive relationship reported in Figure 5, $\delta_1$ denotes the strain value for which the fracture process is triggered while collapse of interface elements is ruled by $\delta_2$ and $\delta_f$. Fracture triggering and collapse do not necessarily propagate proportionally while specimens are loaded. In particular, in presence of the constitutive horizontal branch, triggering propagation is smooth since, as the interface elements reach the maximum stress, they preserve their integrity for a significant increment of strain. On the contrary, collapse propagation is expected to be fragile.

For this reason, fracture triggering results in nonlinear structural responses while collapse propagation corresponds to the sudden and complete failure of the specimen. This implies that, while nonlinearities are well recorded and can be reproduced by the finite element model, peak load represent the only information concerning the collapse. Thus, identification of $\tau_{max}$ and $\delta_1$ is reasonably reliable while $\delta_2$ and $\delta_f$ require further investigations.

In conclusion, the use of the identified parameters is capable to match with sufficient approximation the behavior of the bonding interface in terms of strains and maximum load while, to account for collapse, a suitable ultimate limit state should be introduced.

A final remark concerns the convergence trend of the minimization algorithm. In general, optimizations have shown good convergence as long as the parameters' starting estimates are set to physically reasonable values. On the contrary, the algorithm is not robust if its starting point does not belong to a suitable neighborhood of the solution.

This issue should be addressed by analyzing the response sensitivity with respect to the interface parameters and by defining a rule for choosing a suitable starting point of the algorithm.

## 5 CONCLUSIONS

Experimental and numerical assessments of Mode-II delamination tests performed on steel plates jacketed by uniaxial carbon-FRP textile sheets have been presented. In particular, the presented procedure estimates the parameters of the bonding interface constitutive model.

Experimental data have been deduced by a test protocol concerning two specimens, each one constituted by two steel plates axially jacketed by a carbon fiber textile sheet applied by means of an epoxy adhesive. The experimental dataset has been obtained driving the specimens through complete delamination and recording imposed external loads, displacements and local strains on both the steel and CFRP textile. Experimental curves present fragile collapses; nevertheless, transient nonlinear behaviors describe the propagation of the fracture triggering along the interface.

The experimental dataset has been numerically assessed in order to get the interface constitutive parameters by finite-element-based inverse identification. To this end, test responses

have been reproduced by a finite element model parameterized with respect to the identifying parameters. Subsequently, the identification procedure minimizes an objective function defined as the mean square of the difference between experimental and finite-element responses.

The values of the identified parameters proved to be capable of estimating the behavior of the bonding interface in terms of stress and strain magnitudes; moreover, the computed peak force conservatively approximates the experimental values. Nevertheless, because of the fragile failure of the tested specimens, the identified parameters are not capable of predicting the interface collapse propagation. Yet, the results can be applied in force–based structural design approaches.

Although the presented results should be considered as a preliminary stage of further investigations, they are encouraging and mark future research directions revealing some unresolved issues that should be addressed.

In particular, more refined finite element model, accounting for large displacements and local behaviors, should be used for defining the objective function and a suitable rule for fixing the starting point of the identification algorithm since this can significantly improve the accuracy of the identification. Both issues will be the topic of a future publication where constitutive behavior at collapse will be addressed by including the interface failure in the objective function.

As a final remark, some numerical results, which have been omitted for brevity, revealed a significant sensitivity of the identification procedure with respect to the constitutive parameters of the underlying (steel) adherends. Further investigations will therefore investigate such aspects by combining experimental datasets of different test typologies.

## REFERENCES

[1] L. C. Hollaway, J. Cadei, *Progress in the technique of upgrading metallic structures with advanced polymer composites*, Progress in Structural Engineering and Materials 4 (2) (2002) 131–148.

[2] M. Batikha, J. Chen, J. Rotter, J. Teng, *Strengthening metallic cylindrical shells against elephant's foot buckling with FRP*, Thin-Walled Structures 47 (10) (2009) 1078 – 1091.

[3] J. Teng, T. Yu, D. Fernando, *Strengthening of steel structures with fiber-reinforced polymer composites*, Journal of Constructional Steel Research 78 (2012) 131–143.

[4] H. Jiao, X.-L. Zhao, *CFRP strengthened butt-welded very high strength (VHS) circular steel tubes* , Thin-Walled Structures 42 (7) (2004) 963 – 978.

[5] S. M. Lee, *Mode II delamination failure mechanisms of polymer matrix composites*, Journal of Materials Science 32 (5) (1997) 1287–1295.

[6] G. Barenblatt, *The Mathematical Theory of Equilibrium Cracks in Brittle Fracture*, Vol. 7 of Advances in Applied Mechanics, Elsevier, 1962, pp. 55 – 129.

[7] D. Dugdale, *Yielding of steel sheets containing slits*, Journal of the Mechanics and Physics of Solids 8 (2) (1960) 100 – 104.

[8] S. Hashemi, A. J. Kinloch, J. G. Williams, *The Analysis of Interlaminar Fracture in Uniaxial Fibre-Polymer Composites*, Proceedings of the Royal Society of London A: Mathematical, Physical and Engineering Sciences 427 (1872) (1990) 173–199.

[9] B. Blackman, J. P. Dear, A. J. Kinloch, S. Osiyemi, *The calculation of adhesive fracture energies from double-cantilever beam test specimens*, Journal of Materials Science Letters 10 (5) (1991) 253–256.

[10] J. Berry, *Some kinetic considerations of the Griffith criterion for fracture–II*, Journal of the Mechanics and Physics of Solids 8 (3) (1960) 207 – 216.

[11] M. Bocciarelli, P. Colombi, *Elasto-plastic debonding strength of tensile steel/CFRP joints*, Engineering Fracture Mechanics 85 (2012) 59–72.

[12] N. Valoroso, S. Sessa, M. Lepore, G. Cricrí, *Identification of Mode-I cohesive parameters for bonded interfaces based on DCB test* , Engineering Fracture Mechanics 104 (2013) 56 – 79.

[13] F. Ceroni, M. Ianniciello, M. Pecce, *Bond behavior of FRP carbon plates externally bonded over steel and concrete elements: Experimental outcomes and numerical investigations*, Composites Part B: Engineering 92 (2016) 434–446.

[14] R. Fedele, S. Sessa, N. Valoroso, *Image correlation–based identification of fracture parameters for structural adhesives*, Technische Mechanik 32 (2) (2012) 195 – 204.

[15] R. Sun, E. Sevillano, R. Perera, *Identification of intermediate debonding damage in FRP-strengthened RC beams based on a multi-objective updating approach and PZT sensors*, Composites Part B: Engineering 109 (2017) 248 – 258.

[16] S. Sessa, N. Valoroso, *Use of kriging to surrogate finite element models of bonded double cantilever beams*, 2015.

[17] S. Mazzoni, F. McKenna, M. H. Scott, G. L. Fenves, et al., *OpenSees command language manual*, Pacific Earthquake Engineering Research (PEER) Center.

[18] X. Lu, J. Teng, L. Ye, J. Jiang, *Bond-slip models for FRP sheets/plates bonded to concrete* , Engineering Structures 27 (6) (2005) 920 – 937.

[19] G. Cricrí, M. Perrella, S. Sessa, N. Valoroso, *A novel fixture for measuring mode III toughness of bonded assemblies* , Engineering Fracture Mechanics 138 (2015) 1 – 18.

[20] The MathWorks Inc., *Matlab R2013b user manual*, Natick, MA, USA (2013).

6th ECCOMAS Thematic Conference on
Computational Methods in Structural Dynamics and Earthquake Engineering
M. Papadrakakis, M. Fragiadakis (eds.)
Rhodes Island, Greece, 15–17 June 2017

# COMPARING EN1998-3 AND KAN.EPE. MODELS FOR RETROFITTING REINFORCED CONCRETE COLUMNS WITH INADEQUATE DUCTILITY

**Nefeli V. Peponi[1], Stephanos E. Dritsos[2], and Sotiria N. Athanasopoulou[3]**

[1] Civil Engineer
Department of Civil Engineering, University of Patras, Greece
e-mail: nef_pep@yahoo.gr

[2] Professor
Department of Civil Engineering, University of Patras, Greece
email: dritsos@upatras.gr

[3] Civil Engineer
Department of Civil Engineering, University of Patras, Greece
email: sotiria90@gmail.com

**Keywords:** Column, EC8-3, KAN.EPE, Fiber Reinforced Polymers, Ductility, Reinforcement Corrosion.

**Abstract.** *Many existing structures which are designed according to older anti-seismic regulations appear to have insufficient seismic behavior. One of the most critical factors that contributes to the vulnerability of those structures is either insufficient ductility or significant corrosion of the reinforcement. This article investigates through experimental results the use of composite materials (fiber reinforced polymers) for strengthening columns of reinforced concrete with corroded and non-corroded reinforcement and the influence of the strengthening on the local ductility of the elements. Then, a presentation and comparison between the two available regulations of KAN.EPE. and Eurocode 8, part 3 is performed as far as the strengthening of linear elements to increase their ductility is concerned. In a second phase, a comparison between the resulting ductility of experimental results and the results of the above two regulations is carried out in order to highlight any ambiguities in the regulations.*

## 1 INTRODUCTION

Many existing reinforced concrete structures have been designed and constructed according to old regulations or even in the absence of regulations. As a consequence, they suffer from reduced seismic capacity. One of the most critical factors that contribute to the seismic vulnerability of these structures is inadequate ductility, i.e. an insufficient capacity of the elements to develop residual deformations after reaching their maximum strength resulting in sudden brittle failure. In addition, many of these structures have developed significant corrosion in their reinforcement because of their age or due to the extremely close placement of the transverse reinforcement to the outer surface of the concrete. Notably, the rusting problem is intensified by the widespread use of S500 steel, which is more susceptible to corrosion.

The increase in local ductility of linear elements can be achieved by imposing external confinement (in the form of collars, jackets or external connectors), or by the application of a reinforced concrete jacket. The material which is most extensively used for external confinement is either steel or composite materials (fiber reinforced polymers (FRP)). Confronting the vulnerability of corroded elements can also be carried out by the assistance of external confinement, with the most common method of confinement being that of FRPs. This article investigates the strengthening of damaged reinforced concrete columns with materials and detailing emulating older construction, insufficient ductility, and reinforcement corrosion using FRP jackets.

Both the Greek Code of Structural Interventions, (KAN.EPE.) [1] and Eurocode 8, part 3 (EC8-3) [2] propose models to determine the local ductility of reinforced concrete columns unstrengthened or strengthened using composite layers. Moreover, models of experimental data have emerged as an alternative procedure to that proposed by EC8-3 [2] according to researchers such as Fardis [3]. This article extensively presents these models, which are then applied to experimental data, compared with each other and evaluated. Finally, ambiguities and weaknesses in the relationships of the above models are clarified.

## 2 SIMULATION MODELS OF INTERVENTION AIMED AT INCREASING LOCAL DUCTILITY

The calculation of the local ductility of linear elements unstrengthened or strengthened with FRPs is determined in terms of chord rotation, $\mu_\theta$. Approximate formulas are presented in KAN.EPE. [1], analytical types are included in EC8-3 [2] and alternative methods according to Fardis [3] can be used to calculate the curvature ductility index. These models are presented in detail below.

### 2.1 KAN.EPE model

According to KAN.EPE. [1], the total displacement ductility index equals the chord rotation ductility index ($\mu_\delta = \mu_\theta$). The total displacement ductility index can be calculated from one of the following equations:

$$\mu_\delta = \mu_\theta = \frac{\mu_\varphi + 2}{3} \tag{1}$$

$$\mu_\delta = \mu_\theta = \frac{\mu_\varphi + 1}{2} \tag{2}$$

where $\mu_\varphi$ is the curvature ductility index, which can be approximately determined from:

$$\mu_\varphi = \frac{\varepsilon_{cu,c}}{2.2\ \varepsilon_{sy} v} \tag{3}$$

where $\varepsilon_{cu,c}$ is the reduced deflection of the concrete, which is given by the equations:

$$\varepsilon_{cu,c} = 0.004 + 0.4\frac{\alpha\ \rho_{sx}\ f_{yw}}{f_{cc}} \quad (4)$$

for unstrengthened columns, or

$$\varepsilon_{cu,c} = \gamma_{IOII}\ 0.0035(f_{cc}/f_c)^2 \quad (5)$$

for strengthened columns. $\varepsilon_{sy}$ is the average yield deformation of the longitudinal reinforcement of the element, $\upsilon$ is the normalized axial force (positive for compression), $\alpha$ is the confinement efficiency index, $\rho_{sx}=\frac{A_{sx}}{b_w s_h}$ is the percentage of the transverse reinforcement parallel to the direction $x$ of the loading, $f_{yw}$ is the average yield strength of the stirrups, $f_{cc}$ can be determined from:

$$f_{cc} = f_c(1 + 3.5(\frac{a_f\ \rho_f\ f_u}{f_c})^{\frac{3}{4}} \quad (6)$$

$\gamma_{IOII}$ = 1.0 or 2.0 for carbon fiber reinforced polymer (CFRP) or glass fiber reinforced polymer (GFRP), respectively, $f_c$ is the concrete compressive strength, $A_{sx}$ is the area of the steel, $b_w$ is the section width, $s_h$ is the stirrup spacing, $a_f$ is the confinement effectiveness index of the CFRP or the GFRP, $\rho_f = \frac{2t_f}{b_w}$ is the percentage of FRP parallel to the direction of the load, $f_u$ is the ultimate strength of the stirrups, and $t_f$ is the nominal thickness of the FRP.

## 2.2 Eurocode model

The rotation chord ductility index is the ratio of the limit value of total capacity of the chord rotation ($\theta_u$) to the chord rotation of the element at yielding ($\theta_y$), i.e. $\mu_\theta = \theta_u/\theta_y$. The limit value of the total chord rotation capacity of a non-confined element can be calculated from the following equation:

$$\theta_{um} = 0.0016(0.3^{\nu})[\frac{\max(0,01;\omega')}{\max(0,01;\omega)}f_c]^{0,225}\min\left(9;\frac{L_v}{h}\right)^{0,35}25^{(\alpha_s\rho_{sx}\frac{f_{yw}}{f_c})}(1.25^{100\rho_d}) \quad (7)$$

where $\omega$ and $\omega$' are the mechanical reinforcement ratio and the compressive longitudinal reinforcement ratio, respectively, $L_v$ is the ratio of the moment to the shear strength in the outer section, $h$ the height of the section, $\rho_d$ is the diagonal reinforcement ratio, and $\alpha_s$ is a transverse reinforcement confinement effectiveness factor, which can be calculated from the following equation:

$$\alpha_s = 1 - \frac{b_o^2 + h_o^2}{3b_o h_o} \quad (8)$$

where $b_o$ and $h_o$ are the dimensions of the concrete core based on the axes of the longitudinal reinforcement.

The total capacity of the chord rotation of the section confined with FRPs can be calculated from the following relationship:

$$\theta_{um} = 0.0016\cdot(0.3^{\nu})[\frac{\max(0.01;\omega')}{\max(0.01;\omega)}f_c]^{0,225}\min\left(9;\frac{L_v}{h}\right)^{0.35}25^{(\alpha_s\rho_{sx}\frac{f_{yw}}{f_c}+\alpha_f\rho_f\frac{f_{f,e}}{f_c})}(1.25^{100\rho_d}) \quad (9)$$

where $\alpha_f$ is the confinement efficiency index of the FRP which can be calculated from the relationship:

$$\alpha_f = 1 - \frac{(b-2R)^2 + (h-2R)^2}{3bh} \quad (10)$$

where $b$ and $h$ are the full dimensions of the cross section, $R$ is the radius of the rounded corners of the section, $\rho_f = 2t_f/b$ is the ratio of FRP parallel to the direction of the loading, $f_{f,e}$ is

the active stress of the material retrofitting the section and is given by the following relationship:

$$f_{f,e} = \min(f_{uf}, \varepsilon_{uf}, E_f)\,(1 - 0.7\,\min(f_{uf}, \varepsilon_{uf}, E_f)\frac{\rho_f}{f_c}) \quad (11)$$

where $f_{uf}$ and $E_f$ are the strength and modulus of elasticity of the FRP, respectively, and $\varepsilon_{uf}$ is a marginally reduced deflection which, when not given a different value, can be taken as 0.015 for CFRP and 0.02 for GFRP.

The product $a_f \rho_f \frac{f_{f,e}}{f_c}$ from equation (9) can also be written as:

$$a_f \rho_f \frac{f_{f,e}}{f_c} = a_f \frac{\omega_w}{2}(1 - 0.35\,\omega_w) \quad (12)$$

where $\omega_w = \frac{4\,t_f\,f_u}{b f_c}$ is the volumetric confinement rate for a square section.

The chord rotation at yielding is determined by the following relationship:

$$\theta_y = \varphi_y \frac{L_V + a_v z}{3} + 0.0014(1 + 1.5\frac{h}{L_v}) + 0.125\varphi_y \frac{d_{bL} f_y}{\sqrt{f_c}} \quad (13)$$

where, $\varphi_y$ is the curvature of the cross section at yielding, $a_v z$ is a term which expresses the influence of the "displacement length" of the bending moment, with $\alpha_v = 1$ if the shear cracking capacity, $V_{R1}$, is less than the shear force $V_{Mu} = M_y/L_v$, or else it equals 0, z is the length of the internal lever arm, which is equal to $d' - d$ in columns, $d_{bL}$ is the diameter of the longitudinal reinforcement**,** $f_y$ the average yield strength of the stirrups, *My* is the moment at yeild, *d'* is the depth to the compression reinforcement, and *d* is the effective depth of the section.

### 2.3 Alternative Eurocode model

According to Fardis [3], the final rotation at failure for non-retrofitted elements with a rectangular compression zone and reinforcement detailing for earthquake resistance (including the use of reinforcing bars with ribs) can be calculated from the following relationship:

$$\theta_u = \alpha_{st}(1 - 0.43\alpha_{cy})\,(1 + \frac{a_{sl}}{2})\,(1 - 0.4\alpha_{w,r})\,(1 - \frac{2}{7}\alpha_{w,nr})\,(0.3^{\nu})\,[\frac{\max(0.01;\omega')}{\max(0.01;\omega)} f_c]\,0.225[\min(9; \frac{L_v}{h})]$$
$$0.35\,25^{\alpha\,\rho_s \frac{f_{yw}}{f_c}}\,(1.25^{100\rho_d}) \quad (14)$$

where $\alpha_{st} = 0.0185$ for hot rolled steel and 0.0115 for cold rolled steel, $\alpha_{cy} = 0$ for monotonic loading and $\alpha_{cy} = 1$ for cyclic loading, $\alpha_{sl} = 1$ if there is slippage in the longitudinal reinforcement and 0 if not, $\alpha_{w,r} = 1$ for rectangular walls, otherwise $\alpha_{w,r} = 0$, and $\alpha_{w,nr} = 1$ for T, H or U shaped section walls or hollow rectangular sections, otherwise it equals 0.

For columns confined with FRP, the target chord rotation at failure is determined by the above type of equation with the exponent of the term 25 increased by the factor $a_f \rho_f \frac{f_u}{f_c}$, which addresses the confinement material, as follows:

$$\theta_u = \alpha_{st}\,(1 - 0.43\alpha_{cy})\,(1 + \frac{a_{sl}}{2})\,(1 - 0.4\,\alpha_{w,r})\,(1 - \frac{2}{7}\alpha_{w,nr})\,(0.3\nu)\,[\frac{\max(0.01;\omega_2)}{\max(0.01;\omega_1)} f_c]0.225[\min(9;$$
$$\frac{L_v}{h})]0.35\,25^{\alpha\,\rho_s \frac{f_{yw}}{f_c} + a_f \rho_f \frac{f_u}{f_c}}\,(1.25^{100\rho_d}) \quad (15)$$

The term $a_f \rho_f \frac{f_u}{f_c}$ can be estimated by noting that:

$$f_u = f_{fe} = \min(f_{u,nom}; \varepsilon_{uf} E_f)\,(1 - \min[0.5; 0.7\,\min(f_{u,nom}; \varepsilon_{uf} E_f)\frac{\rho_f}{f_c}) \quad (16)$$

where $f_{u,nom}$ is the nominal capacity of the strengthening material, or by using one of the following equations:

$$(a_f \rho_f \frac{f_u}{f_c}) = \alpha_f \min[1.0; \min(f_{u,nom}; \varepsilon_{uf1} E_f) \frac{\rho_f}{f_c}) (1 - 0.4 \min[1.0; \min(f_{u,nom}; \varepsilon_{uf1} E_f) \frac{\rho_f}{f_c}]) \quad (17)$$

where $\varepsilon_{uf1} = 0.015$, or

$$(a_f \rho_f \frac{f_u}{f_c}) = a_f c_f \min[0.4; \frac{\rho_f f_{uf,L\&T}}{f_c}] (1 - 0.5\min [0.4; \frac{\rho_f f_{uf,L\&T}}{f_c}]) \quad (18)$$

where $f_{uf,L\&T} = E_f \varepsilon_{uf2}$, with $\varepsilon_{uf2}$ approximately equal to 60% of the nominal value of the deformation failure, and $c_f = 1.80$ for CFRP or 0.80 for GFRP.

## 3 RESULTS AND COMPARISONS

For the comparison of the aforementioned models amongst themselves and with actual data, the results from a previous experimental study were used. The experimental study was conducted by Bousias et al. [4], where 6 reinforced concrete specimens were constructed and tested in their strong direction. Those specimens had the same steel reinforcement and detailing as structures constructed before 1980 and the steel reinforcement was corroded. In other words, the experimental study concerned simulating non-seismically designed and reinforced elements exposed to cyclic loading. The force-displacement diagrams of the specimens were idealized as bilinear and, thereby, the values of shear force and displacement of the tested specimens were determined at yield and failure. With the data obtained, the experimental ductility index, $\mu_\delta$, could be easily calculated.

### 3.1 Experimental data

The columns investigated were the half of the height of a standard floor height (1.60 m) with rectangular dimensions of 250x500 mm as shown in figure 1. The longitudinal reinforcement was 4Φ18 ribbed bars while the transverse steel was smooth bars of Φ8/200 mm. Ready-mixed concrete class C12/15 was used for the specimens. The longitudinal reinforcement had a yield stress of 595.5 MPa. For every column, a 50 mm radius of the rounded corner of the section and a 20 mm concrete cover were assumed. The materials used for the strengthened specimens were either 2 layers of CFRP with $t_f = 0.13$ mm, $E_f = 230$ GPa, $f_u = 3450$ Mpa and $\varepsilon_{ju} = 0.015$ or 5 layers of CFRP with $t_f = 0.17$ mm, $E_f = 70$ GPa, $f_u = 2170$ MPa and $\varepsilon_{ju} = 0.031$. The reinforcement of the columns were considered to be hot rolled and continuous without lap splices. Finally, the ratio $L/h$ of columns was 3.2. Table 1 lists the characteristics of the columns.

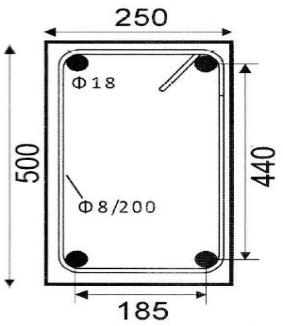


Figure 1. Cross Section of the Experimental Columns

| Specimen | U_0S | C_0S | C_C2Sin | C_C2S | C_C5S | C_G5S |
|---|---|---|---|---|---|---|
| $f_c$ (MPa) | 18.3 | 18.3 | 18.1 | 18.1 | 20.4 | 18.7 |
| $N$ (kN) | 190 | 182 | 167 | 190 | 182 | 182 |
| $\nu$ | 0.38 | 0.38 | 0.37 | 0.38 | 0.34 | 0.37 |
| Retrofitting Material | - | - | CFRP | CFRP | CFRP | GFRP |
| Retrofitting Layers | 0 | 0 | 2 | 2 | 5 | 5 |
| Loading Axis | strong | strong | strong | strong | strong | strong |
| Preloading | no | no | yes | no | no | no |
| $\delta_u$ (mm) | 40.41 | 45.76 | 72.75 | 80.16 | 61.48 | 69.39 |
| $\delta_y$ (mm) | 14.66 | 11.50 | 23.25 | 12.70 | 9.29 | 8.40 |

Table 1. Compressive strength, maximum axial force and normalized axial force of the specimens

In the above table, the first letter of each specimen indicates whether the steel was corroded (C) or not corroded (U), the second and third letters indicate the retrofit material of the jacket (C for CFRP and G for GFRP) and the number of layers, respectively, S indicates that the specimens were tested through their strong axis, while the term "in" indicates that the specimen had been damaged through previous cyclic loading. $N$ is the axial load, $\delta_u$ is the ultimate displacement, and $\delta_y$ is the displacement at yield.

### 3.2 Results and comparisons with the experimental data

The data referred to in the above section was applied to calculate the chord rotation ductility index. The results are shown in detail in Tables 2 and 3.

| Specimen | Experimental | Approx. KAN.EPE. eq. (1) | Approx. KAN.EPE. eq. (2) | EC8-3 eq. (7) | Alternative EC8-3 eq. (14) |
|---|---|---|---|---|---|
| U_0S | 2.76 | 1.63 | 1.96 | 3.56 | 2.35 |
| C_0S | 3.98 | 1.63 | 1.95 | 4.06 | 2.68 |

Table 2. Chord rotation ductility index of the unstrengthened specimens

| Specimen | Experimental | Approx. KAN.-EPE. eq. (1) | Approx. KAN.-EPE. eq. (2) | EC8-3 eq. (7) | Alterative EC8-3 eq. (16) | Alterative EC8-3 eq. (17) | Alterative EC8-3 eq. (18) |
|---|---|---|---|---|---|---|---|
| C_C2Sin | 3.13 | 1.90 | 2.35 | 3.55 | 3.10 | 5.67 | 4.74 |
| C_C2S | 3.13 | 1.87 | 2.30 | 5.65 | 3.35 | 5.60 | 4.68 |
| C_C5S | 6.62 | 2.88 | 3.82 | 6.84 | 4.24 | 5.77 | 4.53 |
| C_G5S | 8.26 | 7.97 | 11.5 | 6.24 | 3.78 | 5.80 | 4.47 |

Table 3. Chord rotation ductility index of the strengthened specimens

From the above results, it is evident that divergences exist between the experimental results and those of the models. The approximate equations of KAN.EPE. [1] give more conservative results, with the exception of the GFRP retrofitted column where equation (1) closely approaches the index $\mu_\theta$ of the experimental result, whereas equation (2) exceeds it. On the other

hand, the values from equation (7) of EC8-3 [2] are in excess of the experimental value for the GFRP 5 layer specimen. Concerning the alternative equations to EC8-3 [2] presented by Fardis [3], equation (16), (17), and (18) give more conservative results to those of equation (7). Equation (16) gives similar results to the experimental for the 2 layer specimens. Equation (16) is the most conservative, while equation (17) is the least conservative. Note that for the specimens with corroded steel, increasing the FRP layer thickness increases the ductility, which indicates retrofitting with FRP can offset the detrimental effect of corroded steel.

### 3.3 Comparison between the models

For better understanding of the models, a comparison was made between different values of normalized axial force and nominal thickness of the FRP as well as between a constant value normalized axial force and increasing thickness of CFRP and GFRP.

Figure 2 compares the various models when determining the chord rotation ductility index for different values of normalized axial force. For this comparison, 5 layers of CFRP were used with $t_f$ = 0.13 mm, $E_f$ = 230 GPa, $f_u$ = 3450 MPa and $\varepsilon_{ju}$ = 0.015.

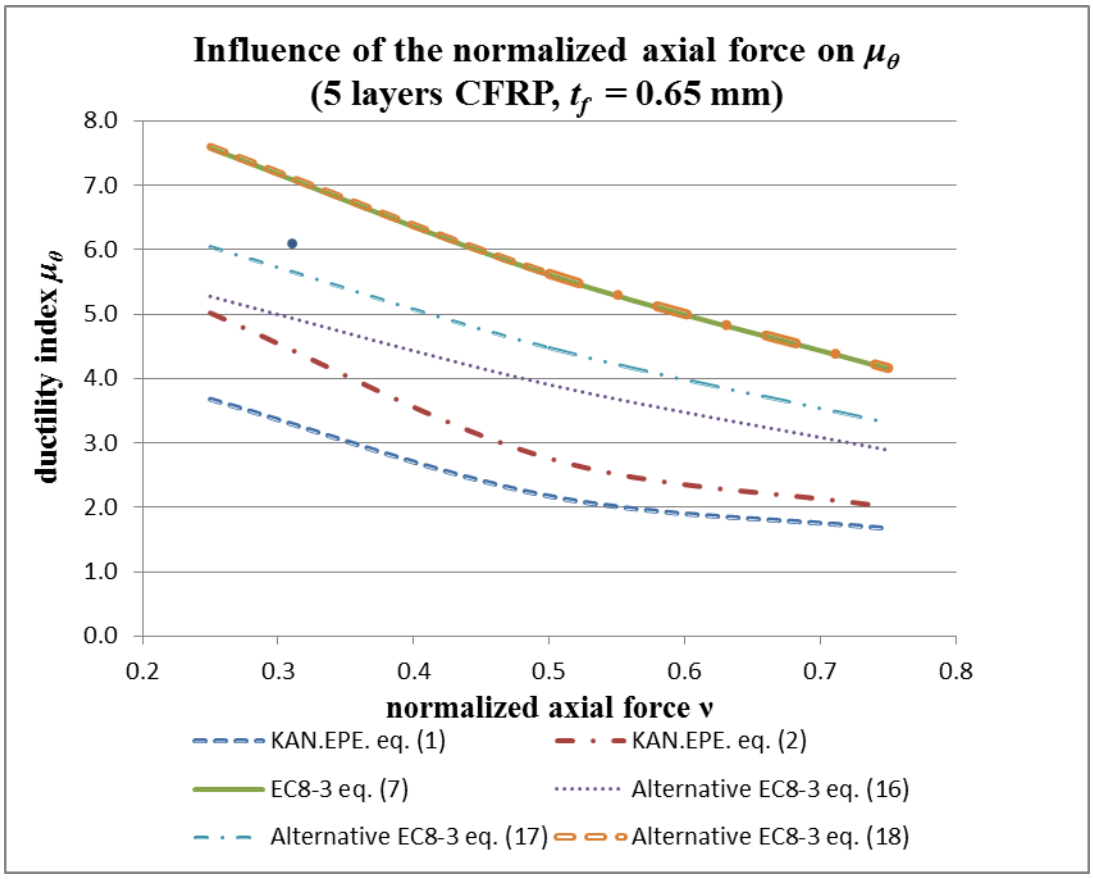


Figure 2. Influence of Normalized Axial Force on $\mu_\theta$

Figure 2 shows that all models are affected by changing the normalized axial force. The influence of the reduced axial force to the approximate models of KAN.EPE. [1] was expected, as the curvature ductility index is inversely proportional to the normalized axial force. The influence of the normalized axial force on the other models can be attributed to the term $0.3^{\nu}$ that is in the equation for all EC8-3 [2] and Fardis [3] models. Indeed, for a range of normalized axial force from 0.25 to 0.80, this term gives values from 0.74 to 0.38, which causes the divergence in the results as the CFRP layer thickness is constant. This is unrealistic as the

models should only be affected by the change in the thickness of the FRP layers and not by the term $v$.

The convergence of the results between EC8-3 equation (7) model and the alternative model of Fardis [3] equation (18) is worth noting, as the results of the ductility index of those two models differ only in the second decimal place.

Finally, the dot in figure 2 represents the ductility index derived from the experimental data for specimen C_C5S and it can be seen that the best convergence between the experimental result and the analytical models is given by equation (17) of Fadis [3].

Figure 3 presents the effect of changing the CFRP layer thickness on the chord rotation ductility index for a constant value of normalized axial force equal to 0.5. For this comparison, $E_f$ = 230 GPa, $f_u$ = 3450 MPa, and $\varepsilon_{ju}$ = 0.015.

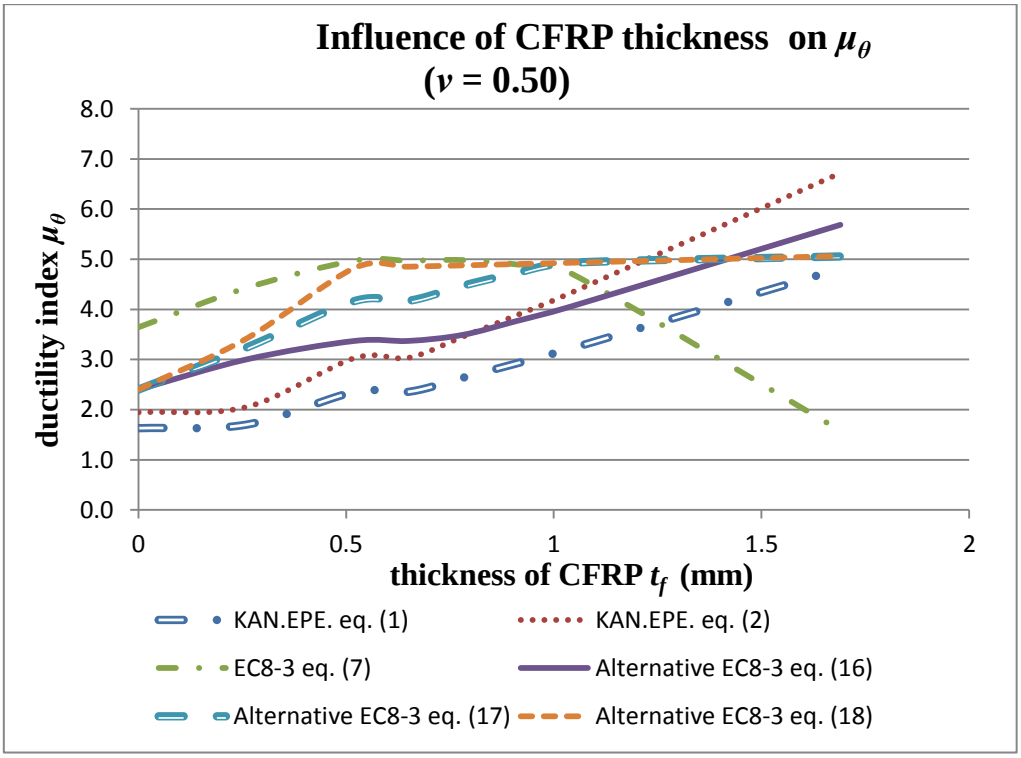


Figure 3. Influence on Ductility Index of Increasing CFRP Layer Thickness with Constant Normalized Axial Force

Figure 3 clearly shows that equation (7) of EC8-3 [2] initially has an upward trend, then stabilizes and finally trends downwards at 1 mm thickness of CFRP, which is illogical. The alternative models of EC8-3 [2] of Fardis [3] (equations (16), (17) and (18)) give markedly improved ductility index values in comparison to the basic model (equation (7)). It can be seen that equations (17) and (18) reach a certain thickness value and then give constant values for increased thicknesses. This indicates a limit to the increase in the ductility as the CFRP layers increase.

### 3.4 Influence of the different types of strengthening material on ductility

Figure 4 presents a comparison of the influence of the type of strengthening material on the calculation of the chord rotation ductility index. For CFRP, $t_f$ = 0.13 mm, $E_f$ = 230 GPa, $f_u$ = 3450 MPa, and $\varepsilon_{ju}$ = 0.015, while for GFRP, $t_f$ = 0.17 mm, $E_f$ = 70 GPa, $f_u$ = 2170 MPa, and $\varepsilon_{ju}$ = 0.031. The normalized axial force was constant and equal to 0.5.

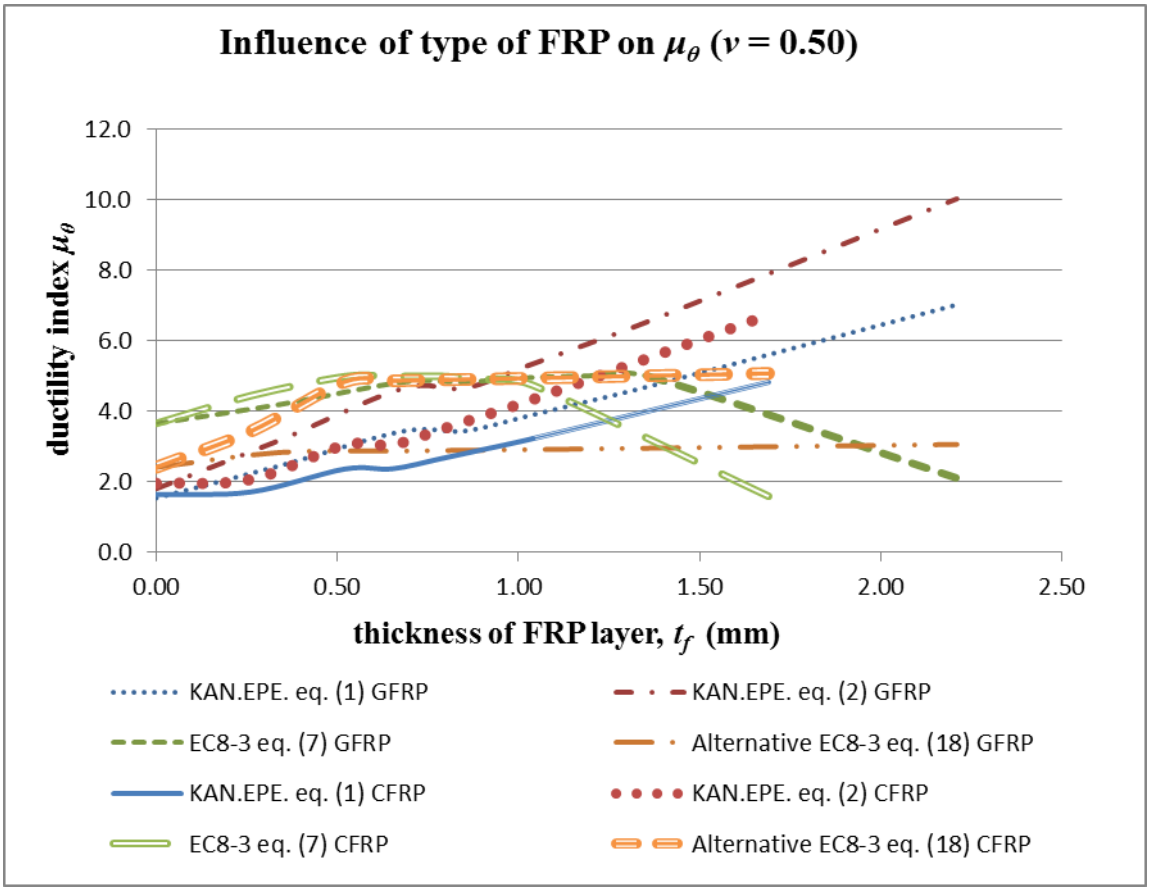


Figure 4. Influence of FRP Type on the Ductility Index for a Constant Normalized Axial Force

Figure 4 clearly shows that the type of FRP material affects the ductility index values. The basic model of EC8-3 [2] is an exception to this, as it is not particularly affected by the type FRP. The approximate models of KAN.EPE. [1] present a slight deviation of the ductility index between them for the same material layer thickness, with the values for GFRP being greater than those for CFRP. It is to be noted the deviation of the $\mu_\theta$ values that derive from the alternative model of EC8-3 [2] of Fardis [3] (equation (18)). This deviation is due to the factor $c_f$ , which was 1.8 for CFRP and 0.8 for GFRP. In fact, it is the only model in which the values of $\mu_\theta$ for CFRP are greater than those of GFRP.

## 4 CONCLUSIONS

- The increase in the ductility index is feasible in columns with corroded reinforcement. This fact is attributed to the increase in deformability of the confined concrete inhibiting the buckling of longitudinal reinforcement and limiting shear.
- All ductility index calculation models were affected by a change in the normalized axial force. The influence of the normalized axial force on the approximate models of KAN.EPE. [1] was due to the curvature ductility index being inversely proportional to the normalized axial force. The influence of the normalized axial force on the basic Eurocode 8-3 [2] model and the Fardis [3] alternative models was attributed to the term $0.3^{v}$, where $v$ is the normalized axial force. Further research into this term would be wise, as the models should only be affected by the change in the thickness of the retrofitting layers and not by the term normalized axial force.

- The basic Eurocode 8-3 [2] model used to calculate the chord rotation ductility index acquires unrealistic values for large thicknesses of fiber reinforced polymer. The alternative models proposed by Fardis [3] improve this situation. However, two of the alternative models gave an upper limit to the increase of chord rotation ductility for increased fiber reinforced polymer layer thickness.
- All the models used to calculate the chord rotation ductility index show a slight influence depending on the type of reinforcement material used (carbon fiber reinforced polymer or glass fiber reinforced polymer) with the exception of the basic model of Eurocode 8-3 [2].
- Finally, the term $c_f$ in one of the alternative Eurocode 8-3 [2] models proposed by Fardis [3], should be further investigated as it greatly affects the chord rotation ductility index depending on the type of fiber reinforced polymer used.

## REFERENCES

[1] KAN.EPE., *Greek code for structural interventions*. Earthquake Planning and Protection Organization, Greek Ministry for Environmental Planning and Public Works, Athens, Greece, 2013 and draft 2017.

[2] EC8-3, *Eurocode 8 part 3, Design of structures for earthquake resistance: Assessment and retrofitting of buildings*. EN 1998-3: European Committee for Standardization, CEN/TC250, Brussels, 2005.

[3] M.N. Fardis, *Seismic design, assessment and retrofitting of concrete buildings based on EN-Eurocode 8,* Dordrecht, Springer Science+Business Media B.V., 2009.

[4] S.N. Bousias, T.C. Triantafillou, M.N. Fardis, L. Spathis, and B.A. O'Regan, Fiber-reinforced polymer retrofitting of rectangular reinforced concrete columns with or without corrosion. *ACI Structural Journal*, **101(4)**, 512-520, 2004.

COMPDYN 2017
6th ECCOMAS Thematic Conference on
Computational Methods in Structural Dynamics and Earthquake Engineering
M. Papadrakakis, M. Fragiadakis (eds.)
Rhodes Island, Greece, 15–17 June 2017

# PREFABRICATED RESPONSIVE DIAGRIDS FOR HOLISTIC RENOVATION OF EXISTING MID-RISE RC BUILDINGS

**S. Labò[1], C. Passoni[1], A. Marini[1], A. Belleri[1], G. Camata[2], P. Riva[1], E. Spacone[2]**

[1] University of Bergamo
via Marconi 5, 24044, Dalmine, Bergamo, Italy
{simone.labo, chiara.passoni, alessandra.marini, andrea.belleri, paolo.riva}@unibg.it

[2] University G. D'Annunzio of Chieti-Pescara
Via dei Vestini, 31, 66100 Chieti, Italy,
{g.camata, espacone}@unich.it

**Keywords:** Holistic renovation, Existing RC buildings, Sustainability, Diagrid, Responsive structures, non-linear supports.

**Abstract.** *The holistic renovation of existing buildings is nowadays acknowledged as an essential and urgent action to reduce the environmental impact and increase the resilience of the existing building stock. Such holistic interventions envision the adoption of an exoskeleton, entirely built from outside. In this paper, the exoskeleton is designed as an external diagrid, consisting in a lattice structure. Among possible structural typologies, diagrids are particularly interesting for their remarkable architectural potential and for the possible standardization of the components, which highly increases replicability of the retrofit solution. Furthermore, prefabrication of components speeds up the assembly process and reduces the construction time. In the paper, focus is made on the dynamic behaviour of a retrofitted building featuring a responsive diagrid. The responsive behaviour is attained by changing boundary conditions at the diagrid's base supports as a function of the earthquake intensity, while the diagrid lattice structure remains elastic. At the Operational Limit State, the diagrid is designed as hinged at the base, whereas at Life Safety Limit State, beyond a target base shear, hinges are conceived to downgrade into non-linear supports allowing for the controlled sliding of the diagrid's base. Non-linear restraints limit the maximum base shear force, while avoiding excessive horizontal displacements and second order effects. Non-linear time history analyses are carried out to study the responsive behaviour of a reference 3 storey building strengthened with an external responsive diagrid. Results show that responsive diagrids require preliminary interventions at the existing building ground floor to reduce the damage following the onset of the diagrid sliding. Such interventions are for instance the disengagement of the infills from the RC frame and the local increase of the column ends ductility.*

## 1 INTRODUCTION

Nowadays, the refurbishment of existing buildings has become a priority to meet international targets of energy saving and emission control and to foster safety amongst European communities. The existing building stock accounts for 40% of the total EU energy consumption while emitting 36% of the $CO_2$ [1], mainly as the result of obsolete envelopes and technologies. These buildings show remarkable signs of decay, leading to poor housing conditions with thermal and living discomfort. From a structural point of view, 40% of European buildings have already exhausted their nominal structural service life (50 years). Moreover, having been built before 1970s, such buildings were often built without any seismic regulation. This scenario refers also to industrial facilities [2], where the majority of these structures have shown inadequate seismic performance [3]. Besides being a safety hazard, damage to buildings or their collapse following natural disasters have a great impact on the environment in terms of waste production and $CO_2$ emissions, greatly affecting the energy savings obtained with a sole energy retrofit intervention [4]. These considerations contributed to move towards a holistic and sustainable renovation approach [5] [6] [7] [8], where the intervention is aimed at improving seismic resilience as well as energy consumption and architectural renovation. Such multidisciplinary aspects are accounted for during each step of the design process.

To this aim, an additional exoskeleton is proposed, which integrates the structural elements for the seismic upgrading, the insulation layer, and the new architectural layer. The intervention is built entirely from the outside, thus avoiding the relocation of the building inhabitants and the inhibition of the building functions [9]. Moreover, prefabricated components, recyclable materials, and easily demountable, repairable, and adaptable technologies are adopted to increase the sustainability of the intervention and to reduce the $CO_2$ emission throughout the building life cycle.

In this paper, the exoskeleton is designed as an external diagrid, consisting of a lattice structure which can change boundary conditions according to the earthquake intensity; such behaviour is referred to as “responsive diagrid” hereinafter. The dynamic behaviour of a responsive diagrid is analysed in the paper, showing how this type of solution controls the seismic response of the existing building by dissipating energy into localized devices or elements.

## 2 DIAGRID

Traditionally, the seismic upgrading of existing buildings is pursued by adopting local or global strengthening. In general, global interventions are based on the construction of a new seismic-resistant structure. Such interventions are most effective and reliable from the structural point of view and do not necessarily require the demolition of the architectural finishings. Some traditional global solutions integrate the existing frames with RC shear walls or steel bracing systems [10] [11] [12] [13] [14] [15]; as an alternative, the seismic resistant structure can be obtained by reinforcing the existing concrete walls with high performance jackets [16], or by transforming a single bay of the frame into a seismic resistant shear wall by strengthening the infill wall.

When working from the outside, structural performance design targets can be attained by complementing the encasing exoskeleton with shear walls or, more innovatively, by conceiving and exploiting the shell behaviour of the new façade [9].

In the case of shear walls, the additional structural stiffness and strength are concentrated into few elements. Shear walls can either adhere to or be perpendicular to the existing structure, thus enabling maximum flexibility in the architectural restyling and in energy upgrading solutions.

Shear wall solution is the more traditional intervention; however, in areas of high seismicity, it may not be a viable solution due to the excessive length or to the significant number of walls. With the shell solution, the shape and extension are exploited to reduce the cross-section area of each single structural component [6] [7]. The envelope can be innovatively designed to enable both energy efficiency upgrade and structural safety. Structural shells may be continuous or discrete (gridshells). When gridshells constitute the exoskeleton of new high-rise buildings, they are referred to as diagrids [17]. In this paper, the concept of diagrid and exoskeleton is extended. In particular, a diagrid exoskeleton is here conceived as a new envelope designed for the seismic upgrading of an existing building. Moreover, the solution is designed to be adaptive and responsive.

## 3 ADAPTIVE-RESPONSIVE DIAGRIDS

Traditionally, seismic retrofit solutions can be designed as dissipative or non-dissipative over-resistant. Focusing on post-WWII RC constructions clustered in urban outskirts, non-dissipative solutions may be considered the most viable option. In fact, the presence of stiff masonry infill walls and stairwells leads to very stiff and brittle structures, which may collapse prior to the activation of a damping system [7]. However, when over-resistant, stiff façades are added on existing structures, the building stiffness increase may lead to a substantial increment of seismic actions, resulting in a remarkable overload of floor diaphragms and foundations. In this scenario, 'passive-responsive' structures are here proposed.

Responsive structures may be designed to act as stiff systems for the Damage Limit State, and as dissipative systems for the Life Safety Limit State, therefore avoiding the damage for low-intensity earthquakes and reducing the loads transferred to the floor diaphragms and to the foundations in case of strong earthquakes.

In order to exhibit such a behaviour, the responsive structures are conceived to change their boundary conditions as a function of the earthquake intensity. For low intensity earthquakes, the diagrid is designed as hinged at the base; for high intensity earthquakes, beyond a target base shear, the boundary conditions will downgrade into special non-linear supports allowing for the controlled sliding of the diagrid base. Activation of these supports significantly reduces the stiffness of the structure, thus increasing its fundamental period; as a result, seismic loads decrease and building displacements increase. An excessive horizontal displacement and second order effects are avoided by limiting the maximum displacement of the supports with a bumper at the end of the gap. A sketch of the retrofitted building is shown in Figure 1 along with a scheme of the sliding support.

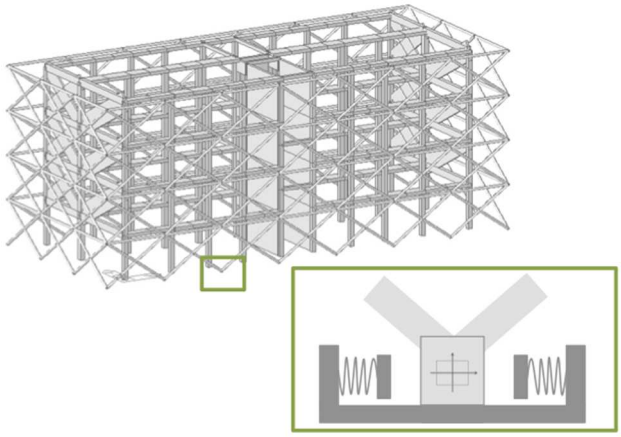

Figure1 –Sketch of the retrofitted building equipped with special sliding supports

The mechanism requires large displacement ductility of the first floor columns, which can be attained by deliberately creating and controlling a soft storey configuration (weakening the first level infills) and by increasing the columns rotational capacity (providing confinement, as for instance by means of fiber reinforced polymer wrapping or HPFRC Jacketing). The retrofitted building behaves as an isolated structure with the isolation concentrated at the ground floor to avoid an extensive damage of the existing structure.
This preliminary intervention allows to accommodate the displacements induced by the sliding system and to overcome all the uncertainties related to infills modelling and other details of the existing building, to the little knowledge of existing buildings, and to the correctness of the structural model [7]. Indeed, the controlled soft story behaviour will dominate the deformed shape of the building during the earthquake.
Thanks to the preliminary interventions, the maximum allowable inter-story drift at the first level represents the main design parameter considered in the retrofit.

## 4 APPLICATION TO A REFERENCE BUILDING

The reference building is a four-storey rectangular structure featuring three one-way longitudinal frames and two infilled lateral frames. The geometry of the main frame is reported in Figure 2.

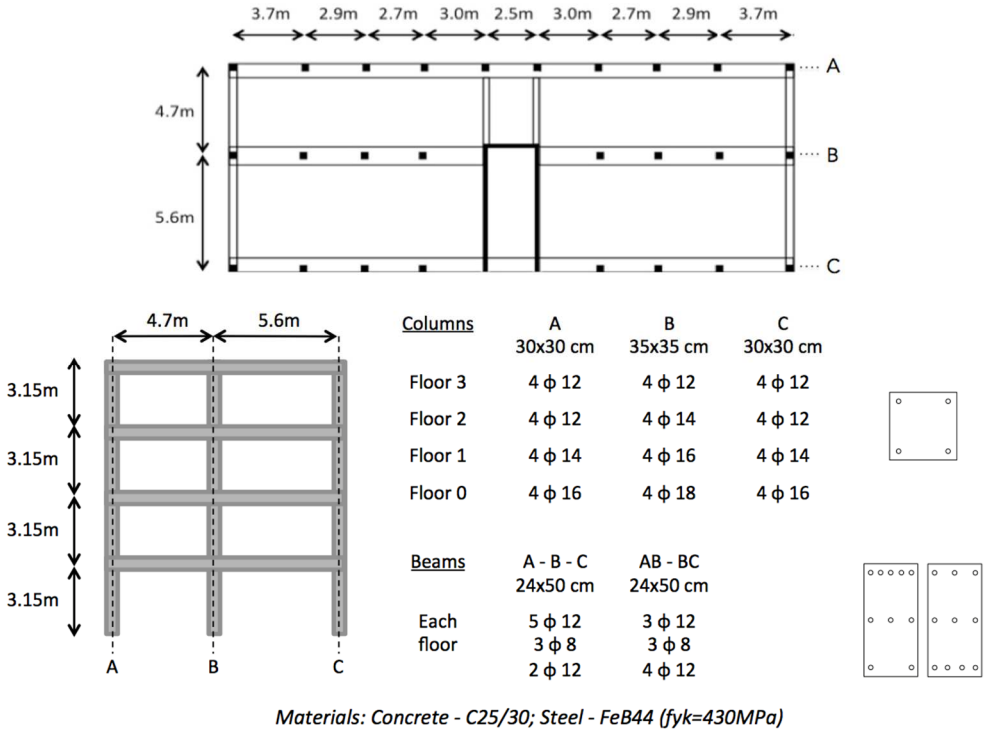


Figure 2 – Reference Italian building built in 1972, selected as representative of the European post-WWII RC building stock: plan view (top) and external transverse frame (bottom) of the 3D finite element model

The building is modelled as a tridimensional structure with the software MidasGEN v.2015 [18] (Fig.3a). The frame components are modelled as beam elements and the inelastic behaviour is accounted for by means of lumped plastic hinges. The flexural and shear resistance of the columns are both modelled with a degrading Takeda constitutive law [19]. The flexural plastic hinge is a trilinear curve followed by a degrading branch, and the shear plastic hinge has a linear

behaviour until the ultimate capacity; beyond that limit the curve decays very quickly thus exhibiting a sudden brittle mechanism. The ultimate shear resistance is also estimated according to the Italian [120] and European building codes [21]. In the beam, only the flexural plastic hinge is considered since the shear failure of these elements is very rare for the considered structural typology. The columns are fixed to the ground. The floors are modelled as rigid diaphragms [7] and the infill panels are modelled by means of two compression-only diagonal struts [22] converging in the beam-column joints. The hysteretic law describing the adaptive sliding support response in shown in Figure 3b where k is the stiffness, $F_y$ the yield strength, r is the post yield stiffness ratio, s the yielding exponent and o is the opening of the gap.
It is worth noting that the staircase core is not designed to withstand seismic loads; therefore, the staircase walls cannot be considered as RC seismic walls, but should be considered as stiff walls with low ductility. In the finite element model the staircase walls are modelled with beam elements whose non-linear behaviour is considered by lumped plastic hinge at each floor. The staircase foundation does not guarantee a fixed support and it is therefore modelled with rotational spring supports to account for the flexibility of the soil [5].

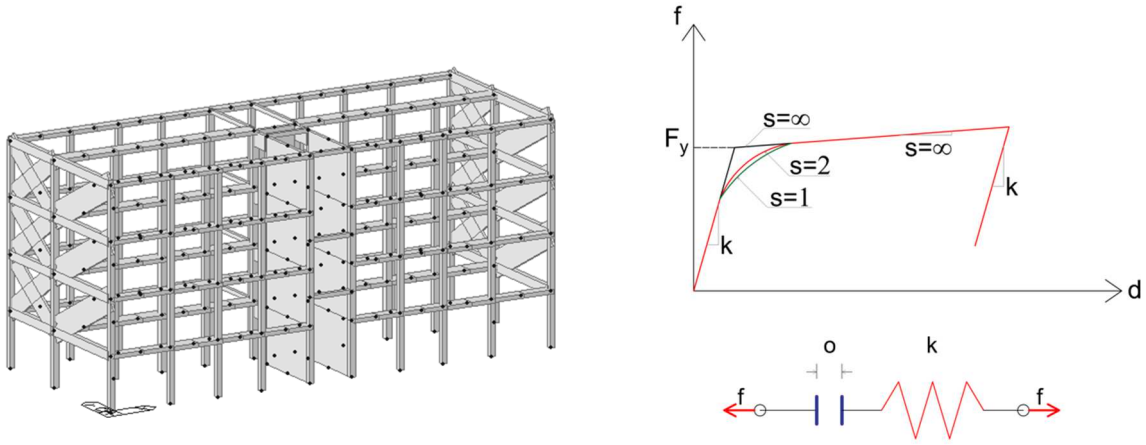


a) b)

Figure 3 – a) Finite element model (MidasGEN v.2015); b) Hysteretic cycle of the sliding support as sum of an elasto-plastic support (top) and a gap system (bottom)

The Life-safety Limit State (LLS) is selected to define the performance level and the seismic input. In this case, due to the presence of the infills and staircase, a target drift of 0.1% is imposed to maintain the structure into the elastic range. Eventually a maximum shear flow at the foundation up to 150 kN/m is considered acceptable.

### 4.1 Design of innovative passive adaptive solution

The building is supposed to be located in a high seismicity zone (L'Aquila, Italy). According to the roof drift target (0.1%) associated to LLS, a commercial tubular profile with D=219.1mm and s=16mm is selected supposing a one-floor high grid module. An angle of about 35° is taken for the diagrid module, as it is considered the optimal angle for low-medium rise buildings according to Moon [23].

Regarding the new supports, they are designed as to be initially rigid and to behave as an elastoplastic system beyond a base shear flow of 60kN/m. In addition, an elastic bumper is provided

to limit the diagrid displacements at the ground level; the bumper is activated for base displacements greater than 20mm. The hysteresis shape of the diagrid base restraints is shown in Figure 4.

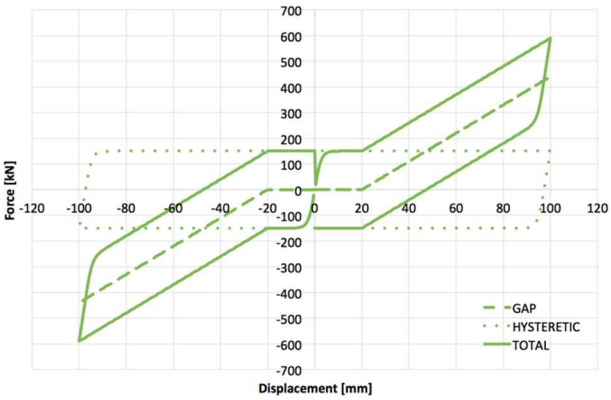


Figure 4 – Hysteretic cycle of the sliding support as sum of an elasto-plastic support (dashed line) and a gap system (dotted line)

As a preliminary intervention, the stiff elements are disconnected from the existing RC frame at the ground floor to avoid interference with the lateral displacements. In particular, vertical sliding joints are inserted in the masonry infills and in the RC walls of the staircase wells with a technique similar to what proposed by Preti et al. (2012) [24]. Moreover, in order to ensure the required ductility, the shear capacity and the end rotation ductility capacity of the columns are increased by means of fiber reinforced polymer wrapping. A maximum target drift of the ground floor equal to 1.5% is here considered, which corresponds to a 0.36% total roof drift.
Seven nonlinear time history analyses are performed on the retrofitted structure. Supposing the building is located in L'Aquila – with site class C and topology T1 –, a set of seven natural records compatible with NTC and EC8 spectrums are selected [25]. To evaluate the performance of the structure at the Damage Limit State (DLS), another set of accelerograms is adopted [25].
Results obtained for the adaptive diagrid solution are plotted in terms of total roof displacement and base shear in Figure 5a and 5b respectively, with reference to a single accelerogram for representation purpose. Figure 5a shows that the behaviour changes as soon as the target displacement is reached, with a consequent shift of fundamental period and change of the amount of displacement of the building. In the first part, the solution is stiff, the period is very short, and the displacements are very small. In Figure 5b, the base shear time histories of the bare frame and of the retrofitted building at the LLS and at the DLS are compared. It may be noted that the maximum value of the base shear is very close for both the considered limit states, thus the activation of the base sliders results in a significant reduction of the seismic action on the structure.
The hinge distribution resulting from the time history analyses (Fig.6) shows that there is no damage in columns at DLS. However, non-linear behaviour of the plastic hinges at the first level columns occurs at the LLS, in accordance with the activation of the non-linear supports. In both cases, there is no damage to the infills.
The average and maximum results of the seven accelerograms in terms of roof displacement and total base shear are shown in Figure 7.

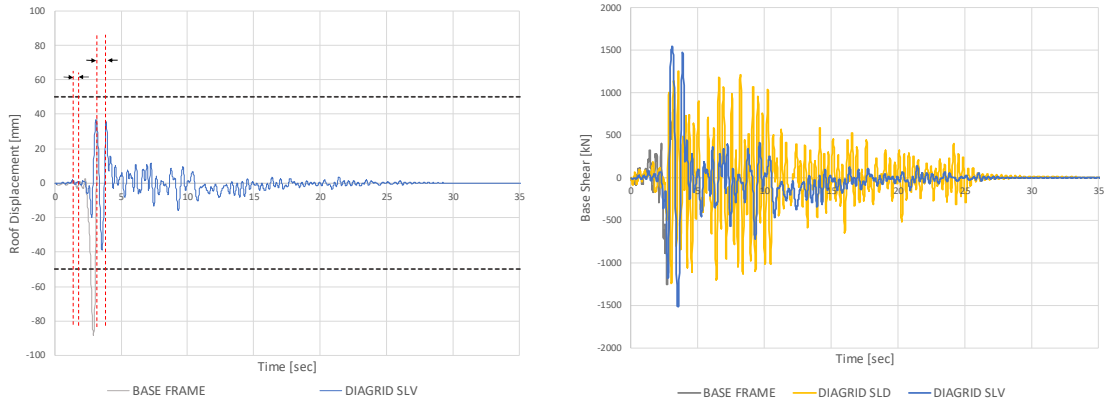


a) b)

Figure 5 –Roof displacement at the Life Safety Limit State (a) and base shear (b) of the frame with the sliding diagrid solution at the Life Safety Limit state in comparison with the shear at the Damage Limit State

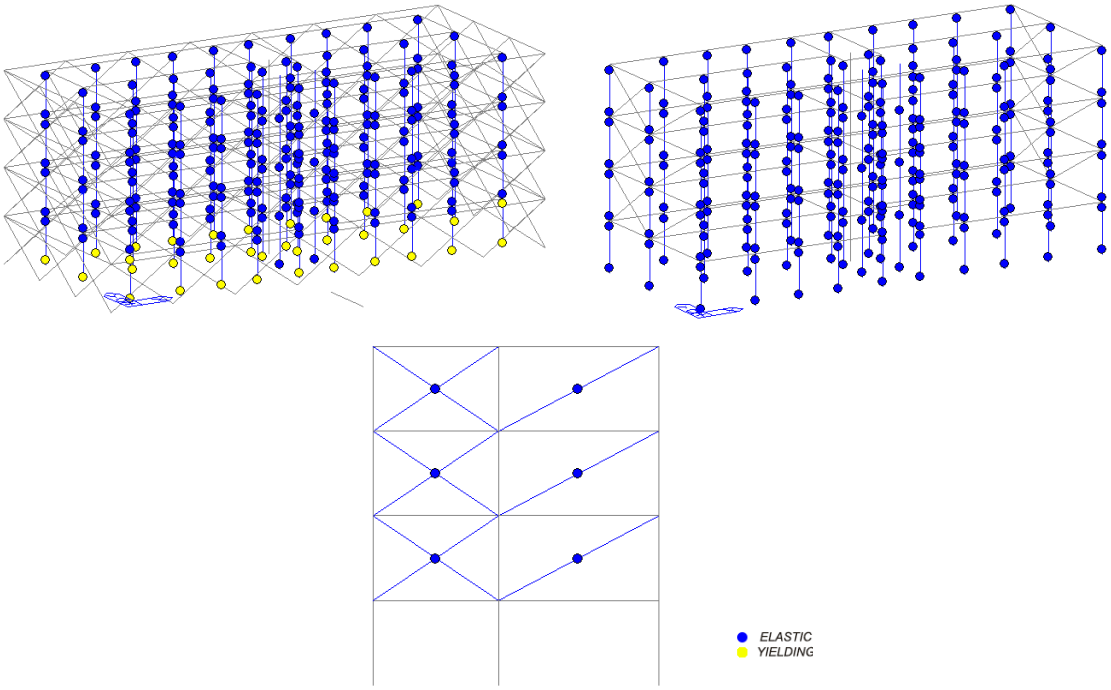


Fig. 6 Damage in the reinforced building at the end of the time history analyses: a) Columns plastic hinges at SLV, b) Columns plastic hinges at SLV, c) Infills plastic hinges in both cases.

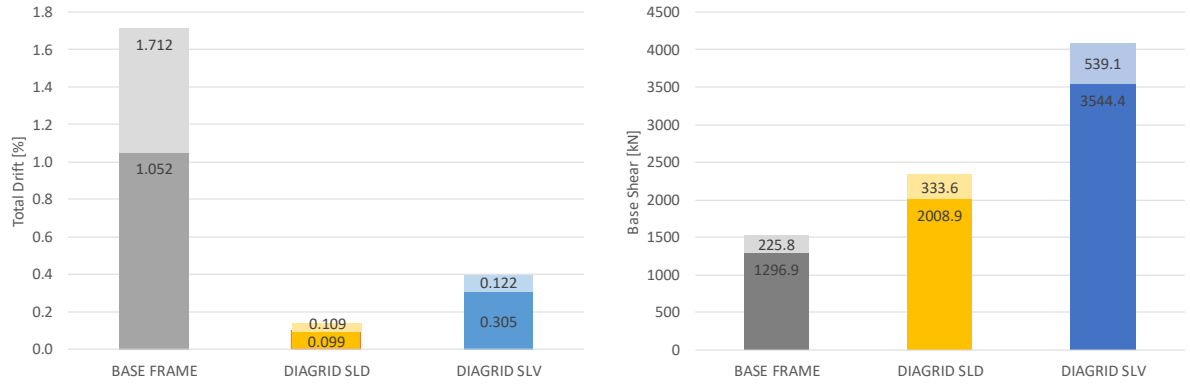


Figure 7 –Life Safety Limit State. Average and maximum roof displacement (left) and total base shear for the base frame SLV (grey), SLD (orange), SLV (blue)

Finally, the floor drift and floor shear are reported in Figure 8. The drift distribution shows how the building shifts to a soft storey mechanism in the adaptive sliding solution at the Life Safety Limit.

As for the floor shear loads, the capacity of existing floors to transfer the seismic action from the floor diaphragms to the vertical resisting structure should be verified. Recent research has shown that even the heterogeneous beam and block floor systems (UNI EN 15037) may resist low-medium seismic loads by developing a tied-arch resistant mechanism [5] [7]. Considering the reference case study after retrofit, the shear capacity of the floors is about 625 kN. Although the floor loads are reduced with the sliding diagrid solution with respect to a traditional stiff solution, the retrofit of the existing floor diaphragms is still required.

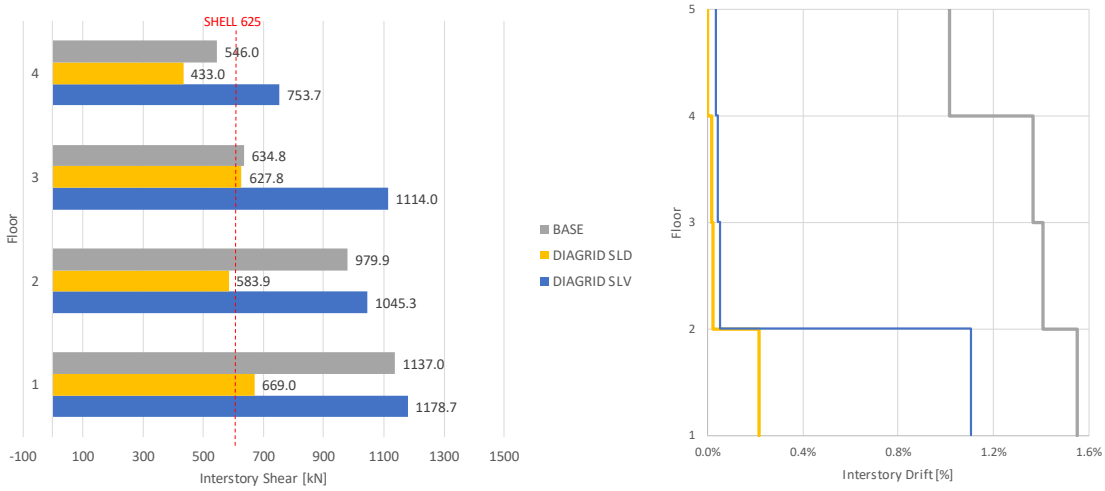


Figure 8 – Average inter-storey drift and floor shear along the building height for different solutions

## 5 CONCLUSION

The present work is part of an ongoing research focusing on the holistic renovation of existing buildings. In this study the feasibility of structural retrofit from outside is currently being evaluated considering European RC buildings. Preliminary results of the analyses highlighted that there are some aspects that may represent an obstacle for the seismic retrofit from outside, as for instance extremely high seismic actions and the need of special foundation system [7]. In

this context the performance of passive-adaptive diagrid has been presented herein. In general, diagrids present great flexibility in construction geometry, and may be easily coupled with the energy and architectural retrofit. Diagrid elements are conceived as totally demountable, modular and provided with standardized connections.

The "responsive diagrid" retrofit technique presented herein consists in a lattice structure conceived to change its ground boundary conditions from hinges to sliders depending on the earthquake intensity, allowing a controlled soft-story mechanism of the existing structure. The existing structure requires preliminary interventions at the ground floor, such as the increase of the deformation capacity of the first level columns and infills.

It is important to note that the performance evaluation of a retrofit solution is affected by the non-structural elements modelling. The proposed retrofit scheme overcomes all the uncertainties related to the infill models thanks to the controlled soft-story behaviour that will dominate the inelastic deformed shape of the structure.

A reference building located in a high-seismicity Italian city has been selected, and a diagrid system has been designed to meet specific performance targets. The diagrid behaves as hinged at the base at the Damage Limit State; conversely, beyond a target base shear, the boundaries downgrade into special non-linear supports. By means of nonlinear time history analyses the behaviour of adaptive diagrid solution has been examined. The comparison of the structural response of the retrofitted frame at the Damage Limit State and at the Life Safety Limit State has been evaluated.

The results show that the responsive-diagrid avoids damage at the Damage Limit State. After exceeding the design target, the activation of the non-linear support limits the maximum base shear and the damage above the first level while avoiding excessive horizontal displacement at the ground floor. This also allows to meet specific performance targets in terms of damage distribution, inter-storey drift and base shear. The seismic inertia loads in the floors need to be transferred to the diagrid system. The in-plane shear transfer capacity of existing floors needs to be evaluated. Indeed, in the case demand exceeds capacity, specific floor strengthening interventions need to be implemented.

## REFERENCES

[1] A. Marini, C. Passoni, P. Riva, P. Negro, E. Romano, F. Taucer, Technology options for earthquake resistant, eco-efficient buildings in Europe: Research needs. Report EUR 26497 EN. JRC87425. ISBN 978-92-79-35424-3. doi:10.2788/68902. Publications Office of the European Union, 2014.

[2] A. Belleri, E. Brunesi, R. Nascimbene, M. Pagani, P. Riva, Seismic performance of precast industrial facilities following major earthquakes in the Italian territory. *Journal of Performance of Constructed Facilities*, 29 (5), art. no. 04014135, 2015.

[3] G. Magliulo, M. Ercolino, C. Petrone, O. Coppola, G. Manfredi, The Emilia earthquake: Seismic performance of precast reinforced concrete buildings. *Earthquake Spectra,* 30 (2), pp. 891-912, 2014.

[4] A. Belleri, A. Marini, Does seismic risk affect the environmental impact of existing buildings? *Energy and Buildings,* 110, 149-158. doi:10.1016/j.enbuild.2015.10.048.

[5] F. Feroldi, Sustainable renewal of the post WWII building stock through engineered double skin, allowing for structural retrofit, energy efficiency upgrade, architectural restyling and urban regeneration. Ph.D. thesis, University of Brescia (in Italian), 2014.

[6] A. Marini, A. Belleri, F. Feroldi, C. Passoni, M. Pret, P. Riva, E. Giuriani, G. Plizzari, Coupling energy refurbishment with structural strengthening in retrofit interventions. *SAFESUST Workshop, 26-27 November 2015*, Ispra, Italy, 2015.

[7] C. Passoni, Holistic renovation of existing RC buildings: a framework for possible integrated structural interventions. Ph.D. thesis, University of Brescia, 2016.

[8] A. Marini, A. Belleri, C. Passoni, F. Feroldi, M. Preti, G. Metelli, E. Giuriani, P. Riva, G. Plizzari, Integrated architectural, energy and seismic renovation of the reinforced concrete building stock targeting sustainability and resilience. *Submitted for publication to European Journal of Environmental and Civil Engineering*, 2016.

[9] B. Angi, (editor), *Eutopia Urbanscape – The combined redevelopment of social housing*, edited by Barbara Angi, ISBN: 978-88-6242-190-4, 2016.

[10] P. Riva, E. Perani, A. Belleri, External R.C. Structural Walls for the Repair of Earthquake Damaged Buildings. *Sustainable Development Strategies for Constructions in Europe and China*, Rome 19-20 April, 2010.

[11] T. Görgülü, Y. S. Tama, S. Yilmaz, H. Kaplan and Z. Ay., Strengthening of reinforced concrete structures with external steel shear walls. *Journal of Constructional Steel Research* 70: 226–235, 2012.

[12] M. Baran, D. Okuyucu, M. Susoy and T. Tankut., Seismic strengthening of reinforced concrete frames by precast concrete panels. *Magazine of Concrete Research* 63(5): 321-332, 2011.

[13] Z. Qu., A. Wada, S. Motoyui, H. Sakata and S. Kishiki, Pin-supported walls for enhancing the seismic performance of building structures. *Earthquake Engineering and Structural Dynamics* 41(14): 2075-2091, 2012.

[14] E. Strepelias, X. Palios, S. N. Bousias and M.N. Fardis, Experimental investigation of concrete frames infilled with RC for seismic rehabilitation. *ASCE Journal of Structural Engineering* 140(1), 2013.

[15] H. Varum, F. Teixeira-Dias, P. Marques, A. V. Pinto and A.Q. Bhatti, Performance evaluation of retrofitting strategies for non-seismically designed RC buildings using steel braces. *Bulletin of Earthquake Engineering* 11(4): 1129-1156, 2013.

[16] A. Marini, A. Meda, Retrofitting of R/C shear walls by means of high performance jackets, *Engineering Structures*, 31 (12), pp. 3059-3064, 2009.

[17] T. M. Boake, The emergence of Diagrid - It's all about the nodes, *International Journal of High-Rise Buildings*, December 2016, Vol 5, No 4, 293-304, doi:10.21022/IJHRB.2016.5.4.293, 2016.

[18] Midas GEN, "Analysis Manual for Midas GEN".

[19] S. Otani, SAKE: A Computer Program for Inelastic Response of R/C Frames to Earthquakes. *Civil Engineering Studies, University of Illinois at Urbana, Champaign, Report* SRS-413, 1974.

[20] D.M. 14/01/2008, "Norme Tecniche per le Costruzioni (NTC 2008)", Gazzetta Ufficiale, n. 29 del 14/02/2008, Supplemento ordinario n.30. (in Italian)

[21] [EC2] European Committee for Standardization, "Eurocode 2: Design of concrete structures (EN 1992-1:2004)", Brussels, 2004

[22] LD. Decanini, C. Gavarini, SH. Bertoldi, Telai tamponati soggetti ad azioni sismiche, un modello semplificato: confronto sperimentale e numerico. *Acts of the VI Convegno Nazionale di Ingegneria Sismica in Italia*, Perugia, 1993. (in Italian), 1993.

[23] KS. Moon, JJ. Connor, JE. Fernandez, Diagrid Structural Systems for Tall Buildings: Characteristics and Methodology for Preliminary Design. *The Structural Design of Tall and Special Buildings*, 16, pp. 205-230, 2007.

[24] M. Preti, N. Bettini, GA. Plizzari, Infill walls with sliding joints to limit infill- frame seismic interaction: large-scale experimental test. *Journal of Earthquake Engineering*, 16, pp. 125-141, 2012.

[25] I. Iervolino, C. Galasso, E. Cosenza, REXEL, computer aided record selection for code-based seismic structural analysis. *Bulletin of Earthquake Engineering*, 8, pp. 339-362 , 2010.

COMPDYN 2017
6th ECCOMAS Thematic Conference on
Computational Methods in Structural Dynamics and Earthquake Engineering
M. Papadrakakis, M. Fragiadakis (eds.)
Rhodes Island, Greece, 15–17 June 2017

# REINFORCED CONCRETE FRAMES STRENGTHENED BY TENSION-TIE ELEMENTS UNDER CYCLIC LOADING: A COMPUTATIONAL APPROACH

**Angelos A. Liolios**[1] **and Constantin E. Chalioris**[2]

[1] PhD Candidate
Democritus University of Thrace, Department of Civil Engineering,
Division of Structural Engineering, Xanthi 67100, GREECE
e-mail: aliolios@civil.duth.gr

[2] Associate Professor
Democritus University of Thrace, Department of Civil Engineering,
Division of Structural Engineering, Xanthi 67100, GREECE
e-mail: chaliori@civil.duth.gr

**Keywords:** Seismic Strengthening of RC Structures, X-braced Systems, Cable Elements, Tension-Ties, Shear-critical Frames, Computational Calibration Procedures.

**Abstract.** *An efficient numerical simulation of the seismic response of single-story single-span Reinforced Concrete (RC) frames strengthened using diagonal tension-tie elements is presented. The developed analysis is based, calibrated and verified on test results of bare and X-braced RC frames subjected to cyclic imposed lateral deformations described in a companion paper. The dimensional and the reinforcement configurations of the frames represent earlier RC frame structures that have been designed using old Code provisions without consideration of seismic design criteria and. The columns of the RC frames have shear-critical character due to the inadequate amount of stirrups provided and their low height-to-depth ratio (short columns). Therefore, an easy-to-apply strengthening technique using a pair of two steel crossed tension-ties (X-type bracing) is applied and examined. For the numerical simulation, the unilateral behavior of the cable elements that undertake only tension stresses is strictly taken into account. Comparisons between the analytical curves derived from the numerical simulation and the experimental ones from the cyclic tests showed a very good agreement.*

## 1 INTRODUCTION

It is well known that many existing Reinforced Concrete (RC) frame buildings in seismically active countries have been designed and built according to past seismic Code standards. The provisions for reinforcement details of such old Codes are often not adequate for proper ductile seismic structural response with regards to modern Codes and structures. This holds especially for the shear-flexure behavior of existing RC members or/and structures under seismic excitations. A typical example of problematic local behavior is the case of the beam-column connections [1-6]. Concerning the global seismic response, a necessity for extensive strengthening often arises for such deficient RC frames and some of the well-known rehabilitation and upgrading techniques are widely applied [7-9].

A rather simple, low cost and efficient method for the global strengthening of RC frame structures against lateral induced earthquake loading is the use of steel cross X-bracings [10, 11]. An alternative technique that uses cable-like members as tension-ties instead of the common steel bracing has been proposed for seismic strengthening of RC frames [12, 13]. Cable restrainers have also been used for concrete and steel superstructure movement joints in bridges [14]. These cable elements can undertake severe tensional loads but when subjected to a compressive force they buckle and become slack and structurally ineffective under compression. Thus, the governing conditions take an equality form, as well as an inequality one, and the problem becomes nonlinear [15]. The mathematical solution of this problem can be achieved by the concept of variational and/or hemivariational inequalities [15, 16]. First approach of a computational procedure for single-story, single-span RC frame specimens has recently been developed by the authors [17].

Concerning the shear-flexure behavior of old RC structures under seismic actions a numerical procedure for shear-critical RC frames using layer-fiber micro-modeling in the sectional analysis has been presented [18]. Such micro-modeling methodologies are suitable for simulating simple laboratory RC frames of single-span and one or two stories [18, 19]. However, as emphasized by Fardis et al. [20], these methods seem to be very time-consuming and prohibiting for multi-story, multi-span RC frames, as is the case of the most common practical applications. On the other hand, special provisions for the shear-flexure behavior of existing RC members are included in recent intervention Code specifications that should be taken into account for assessment and retrofitting of older RC structures when their shear-dominated response has to be numerically estimated [21, 22,26-28].

This study presents a computational approach for the cyclic analysis under shear effects of existing RC frame structures strengthened by tension-tie elements. Two typical single-story single-span RC frames, one bare and one X-braced, are considered. The lateral cyclic behavior of these reference RC frames has been experimentally investigated and reported in a companion paper [23]. The dimensional and the reinforcement configurations of the examined frames represent typical RC frame structures that have been designed and constructed using old Code provisions without consideration of seismic design criteria and their columns have shear-critical character (inadequate amount of stirrups and low height-to-depth ratio). The shear effects are taken into account in the presented numerical procedure using the Ruaumoko code [24]. This computational procedure is verified by comparisons between the available test data and the herein computed results in terms of full cyclic lateral load versus displacement curves.

## 2 COMPUTATIONAL APPROACH

### 2.1 General principles of the numerical simulation

A double discretization in space and time is usually applied in Structural Dynamics [25]. First, the structural system is discretized in space by usual Finite Elements (FE). The macro-elements approach [8-10, 24] is preferable to the micro-elements one [18] for practical applications that concern multi-story multi-span RC frames. The most complex FE models are appropriate mainly for studying details and the simulation of tests on individual members or sub-assemblies due to their severe computational requirements and numerous input parameters [26]. Even fiber- models for distributed plasticity can be prohibitively complex for the simulation of entire realistic RC structures. Thus, a simple frame FE model that implements one-component model with concentrated plasticity at member ends is used herein as the best option for the practical non-linear seismic response analysis [24].

As concerns the cable-type steel elements modelling, pin-jointed bar elements are used. The unilateral behavior of these elements can in general include loosening, elastoplastic or/and elastoplastic-softening-fracturing and unloading-reloading effects. Concerning the full constitutive law of these steel elements and the usual general non-linearities concentrated at the two end critical regions (e.g. plasticity) of the RC structural members, these characteristics can be expressed mathematically by using concepts of convex and non-convex analysis [15, 16]. Thus, for the cable-elements behavior, the following relation holds:

$$s_i\ (d_i)\ \in\ \hat{\partial}\, SP_i(d_i) \tag{1}$$

where $s_i$ and $d_i$ are the (tensile) force (in [kN]) and the deformation (elongation) (in [m]), respectively, of the i cable element, $\hat{\partial}$ is the generalized gradient and $SP_i$ is the super-potential function.

Incremental dynamic equilibrium for the assembled structural system with cables is expressed by the matrix relation:

$$M\,\Delta\ddot{\boldsymbol{u}} + C\,\Delta\dot{\boldsymbol{u}} + K_T\,\Delta u = -M\,\Delta\ddot{\boldsymbol{u}}_g + A\,\Delta s + \Delta p \tag{2}$$

where u(t) and p(t) are the displacement and the load time dependent vectors, respectively; $C(\dot{\boldsymbol{u}})$ and $K_T$ (u) are the damping and the tangent stiffness matrix, respectively; A is a transformation matrix and $u_g$ the ground seismic excitation. Dots over symbols denote derivatives with respect to time. By s(t) is denoted the cable stress vector satisfying the relation (1).

The above relations combined with the initial conditions consist the problem formulation, where, for given p and/or $\ddot{\boldsymbol{u}}_g$, the vectors u(t) and s(t) have to be computed.

### 2.2 Consideration of effects due to shear and to concrete cracking and confinement

Considering the shear effects, the RC structural elements are classified according to their shear span-to-depth ratio:

$$a_S = \frac{L_S}{d} = \frac{M}{Vd} \tag{3}$$

where $L_s = M/V$ is the shear length, $M$ is the bending moment, $V$ is the shear force and $d$ is the section depth (height) of the examined member. In the case of RC frame columns or beams, the shear length $L_s$ is equal to the half of the net height or span, respectively of the examined structural element [5, 20, 21].

Due to shear effects, the RC structural elements appear one of the following three behaviors depending on the shear span-to-depth ratio [9]:

1. Bending prevails and bending failure occurs before any shear failure, no matter if shear reinforcement exists or not if:

$$a_s = \frac{L_s}{d} = \frac{M}{Vd} \geq 7.0 \tag{4b}$$

2. Final flexural or shear failure mode depends on the provided shear reinforcement if:

$$2.0 \leq a_s = \frac{L_s}{d} = \frac{M}{Vd} \leq 7.0 \tag{4b}$$

3. Shear-critical short RC member is considered and special design procedure must be followed so that an explosive cleavage failure of the short column to be avoided if:

$$a_s = \frac{L_s}{d} = \frac{M}{Vd} \leq 2.0 \tag{4c}$$

Shear effects reduce the available plastic curvature $\varphi_p$ of the critical sections of a RC member, as shown in Figure 1 of a typical moment versus curvature *(M - φ)* diagram [14]. So, the flexural ductile behavior is modified to a brittle one. The *M - φ* diagram of Figure 1 can be transformed to the shear force versus ductility diagram shown in Fig. 2 using $V = M / L_s$. According to the relation between the available shear strength capacity $V_R$ and the required shear demand due to the flexural state, one of the three cases shown in Figure 2 can be realized. Thus, a shear failure and a so-caused reduction of the curvature ductility $\mu_\varphi = \varphi_u / \varphi_y$ can be eventually appeared or not.

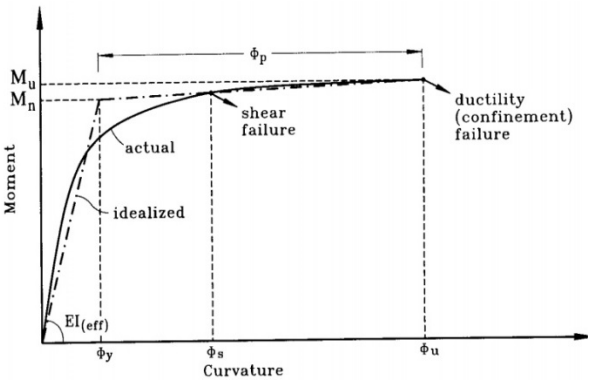


Fig.1. Reduction of the curvature and flexural ductility due to the shear failure [14]

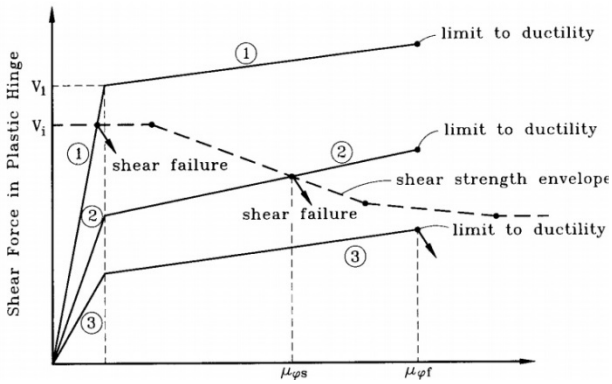


Fig.2. Available ductility under shear effects [14]

### 2.2.1. Effective flexural stiffness

During a seismic excitation the RC structural elements have a linear-elastic behavior until one or two of their critical end-regions enter to the yielding state, after concrete cracking, and therefore, plastic hinges are appeared [8,9, 20, 26]. The cracking effects on columns and beams are estimated by applying the guidelines of Eurocode 8, part 3 [21] and Greek Code of Interventions [22]. So, the effective flexural stiffness $E_c I_{eff}$ is given by the formula:

$$E_c I_{eff} = \frac{M_y \cdot L_s}{3 \cdot \theta_y} \tag{5}$$

where $M_y$ and $\theta_y$ are the flexural moment and the chord rotation at yield, respectively, and $L_s$ is the shear length corresponding to the member end.

### 2.2.2. Available cyclic shear strength

The available cyclic shear strength $V_R$ of the examined member end is decreased with the incremental demand plastic chord rotation $\theta_{p,d}$ according to the following semi-empirical experimental expression [8, 21, 22, 26]:

$$V_R = \frac{1}{\gamma_{el}} \cdot \left[ \frac{(h-x)\lambda_1}{2L_s} + (1-0.05\lambda_2) \cdot \left[ 0.16\lambda_3 (1-0.16\lambda_4) A_c \sqrt{f_{cm}/CF} + V_w \right] \right] \quad (6)$$

where $\gamma_{el}$ is a safety factor that is taken equal to 1.15 for primary seismic structural elements (due to scattering of the experimental values) and is taken 1.00 for secondary seismic members; x is the compression zone depth (in m) known by the sectional analysis, CF is the Confidence Factor according to EC8-3 [21]; $V_w$ is the contribution of the transverse reinforcement to the shear strength, taken as $V_w = \rho_w\, b_w\, z\, f_{yw,m}/CF$ for cross-section with web width $b_w$; $\rho_w$ is the transverse reinforcement ratio: $\rho_w = (A_{sw}\, l_w)/(h_c\, b_c\, s_h)$; $l_w$ is the total length of the stirrups, $A_{sw}$ is the steel section area of the stirrup, $h_c$ and $b_c$ the dimensions of the confined core of the section and $s_h$ is the centerline spacing of stirrups.

The λ parameters in Eq. (6) are considered as follows:

$$\lambda_1 = \min\left(N,\ 0.55A_c\, f_{cm}/CF\right) \quad (7a)$$

where $N$ is the axial force (in MN), positive for compression and taken equal to zero when the axial force is tensional; $A_c = b_w\, d$; $b_w$ is the width of compression zone and $d$ is the depth of the tension reinforcement (in m); $f_{cm}$ is the mean concrete compressive strength (in MPa).

$$\lambda_2 = \min\left(5,\ \mu_\Delta^p\right) \quad (7b)$$

where $\mu_\Delta^p = \theta_p/\theta_y$ .

$$\lambda_3 = \max\left(0.5,\ 100\rho_{tot}\right) \quad (7c)$$

where $\rho_{tot}$ is the total longitudinal reinforcement ratio (tensional, compression and intermediate bars).

$$\lambda_4 = \min\left(5,\ a_s\right) \quad (7d)$$

where $a_s$ is the contemporary shear ratio.

### 2.2.3. Moment versus chord rotation diagram for the critical sections

In order to define the final elastic-plastic diagram of the Moment versus Chord Rotation ($M$ - $\theta$) of the critical section at the considered member end, it must be checked which type of failure precedes, the flexural or the shear failure [26-29]. Thus, using the calculated value of the shear strength $V_R$ from Eq.(6), the moment $M_{u,v}$ at the critical section due to the $V_R$ is estimated as

$$M_{u,v} = L_s \cdot V_R \quad (8)$$

When $M_{u,v} > M_y$ , ($M_y$ is the flexural yielding moment) then the flexural failure precedes the shear one and the final elastic-plastic of $M$ - $\theta$ diagram of the examined member end is given by Figure 3(a). On the contrary, when $M_{u,v} < M_y$ then the shear failure precedes the flexural one and the final elastic-plastic $M$ - $\theta$ diagram is given as the curve OABCD of Figure 3(b) [22, 26]. After the above check the final (corrected) values of $M_y$ and $\theta_y$ are used in Eq. (5).

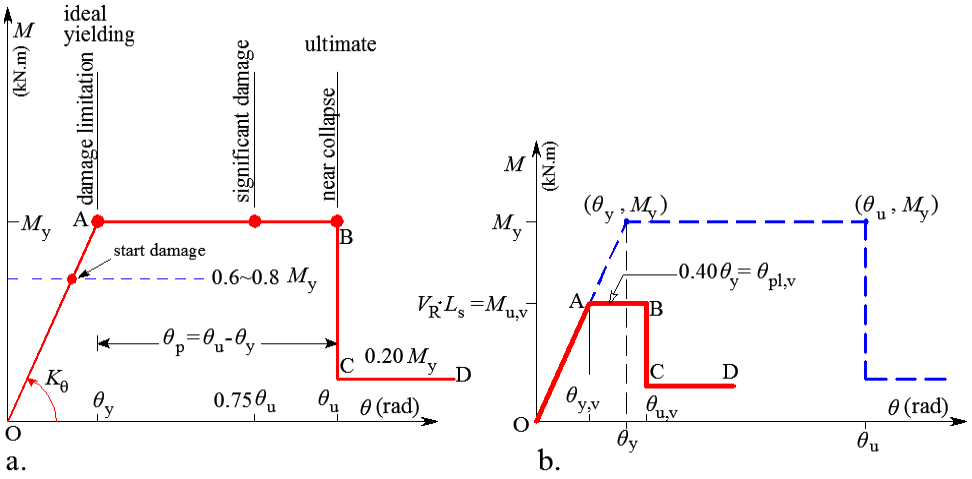


Fig.3. Moment versus chord rotation diagram for (a) ductile failure and (b) shear failure [26].

### 2.2.4. Effects of the concrete confinement for the critical sections

The ductility of RC structural elements is strongly influenced by the concrete confinement [5, 8, 9]. The stress versus strain diagram (σ - ε) of the confined concrete core can be calculated using a proper confined concrete model [21, 26]. Ductility also dependents on the ultimate strain $\varepsilon_{cu,c}$ of the extreme fiber in the compressive zone of the confined section and can be estimated by [9]:

$$\varepsilon_{cu,c} = \varepsilon_{cu} + 0.10 \cdot \alpha . \omega_{wd} \tag{9}$$

where $\varepsilon_{cu}$ is the ultimate strain of unconfined concrete, $\omega_{wd}$ is the mechanical volumetric ratio of confining closed stirrups within the critical region and α is the confinement effectiveness factor of the core of the section, that is given as:

$$\alpha = \left(1 - \frac{s_h}{2b_c}\right) \cdot \left(1 - \frac{s_h}{2h_c}\right) \cdot \left(1 - \frac{\sum b_i^2}{6 \cdot b_c \cdot h_c}\right) \tag{10}$$

where $s_h$ is the pure spacing of the provided transverse shear reinforcement (stirrups), $b_1$ is the centerline spacing of longitudinal bars laterally restrained by a stirrup corner along the perimeter of the cross-section, $h_c$ and $b_c$ is the dimension of confined core to the internal line of the external stirrup.

### 2.3 The software for the numerical simulation

For the numerical treatment of the problem, the structural analysis software Ruaumoko [24] is used. Ruaumoko is based on the FE method and can provide results for the RC buildings analysis [30] which concern, among others, the following critical parameters: Local or global structural damage, maximum displacements, inter-story drift ratios, development of plastic hinges and various response quantities, which allow the use of the incremental dynamic analysis (IDA) method [29] and the analysis of RC structures under multiple earthquakes [17]. For the consideration of inelastic shear behavior the SINA hysteresis model is implemented in Ruaumoko although it requires numerous input parameters. Generally, many additional input parameters for shear-effects are also required in such analyses for treating shear hinges.

Because of the aforementioned remarks and the reasons reported in the beginning of subsection 2.1, the software Ruaumoko is used. Moreover, in order to take into account shear and

other failure effects, the strength degradation model implemented in Ruaumoko and depicted in Figure 4 is used. “DUCT1”, “DUCT2” and “DUCT3” denote the ductility at which degradation begins, stops and at 0.01 initial strength, respectively. “RDUCT” is the residual strength as a fraction of the initial yield strength.

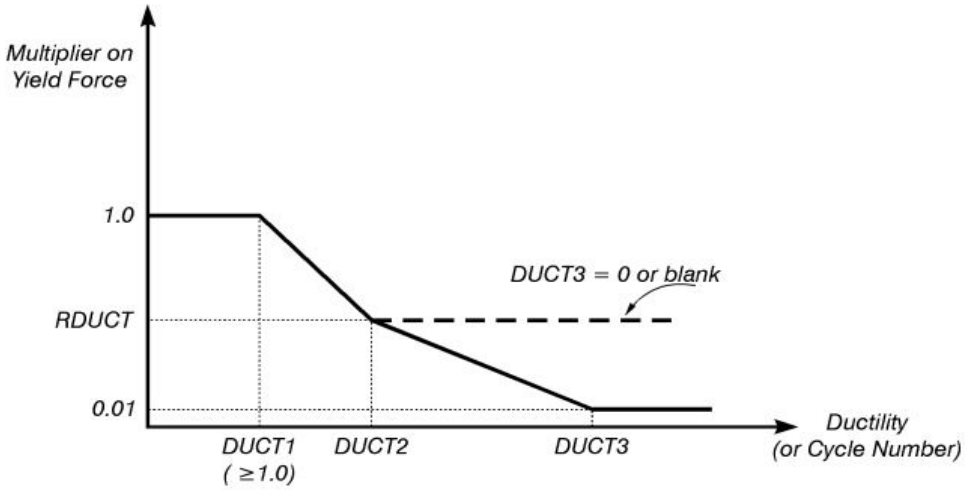


Fig.4. Strength degradation model implemented in Ruaumoko [24].

## 3 EXPERIMENTAL RESULTS FOR THE CALIBRATION OF THE COMPUTATIONAL APPROACH

The proposed numerical approach has already been used for the case of flexure-critical RC frames [17] using the available experimental results of typical flexural one-bay one-story RC moment-resistant frames, bare and strengthened with steel cross X-bracing [11]. Comparisons between the analytical curves derived from the numerical simulation and the experimental ones from these cyclic tests showed a very good agreement.

Here, for the calibration and verification of the presented numerical approach for the case of shear-critical RC frame structures the test results of relevant experiments reported in the companion paper [23] are used. Two models of RC frames have been investigated; the first is a bare frame without bracing (reference specimen), whereas the second one is strengthened with steel X-bracing of non-compression type (ties). The X-type bracing system consists of two steel rods installed as cable elements, connected to the RC frame through steel brackets. Dimensions and reinforcements of the examined frames represent typical RC frame of an old existing RC frame structure designed in accordance with past Code Standards in Greece.

A lateral additive cyclic quasi-static load was applied to the story beam in a displacement-controlled mode. The displacement history applied to both RC frames includes five different increasing loading steps at ± 1.0, ± 3.5, ± 12.0, ± 22.5 and ± 45.5 mm with two equal imposed cycles at each step. Details of the characteristics of the RC frame specimens, the X-bracing system, the experimental procedure and the test results can be found in [23].

The overall behavior of both specimens is presented in Figure 5 and compared in terms of load versus displacement hysteretic response. The X-braced RC frame (red dashed line) demonstrated increased load capacity and enhanced hysteretic performance with respect to the bare frame (blue continuous line). The bare RC frame failed due to the sudden shear diagonal cracking of the column, whereas in the X-braced one the shear failure has been prevented and two distinctive flexural plastic hinges have been formed in the beam. However, the X-braced frame

exhibited a rather sudden failure at both crossed tension-ties when the steel rods reached their ultimate strain limits.

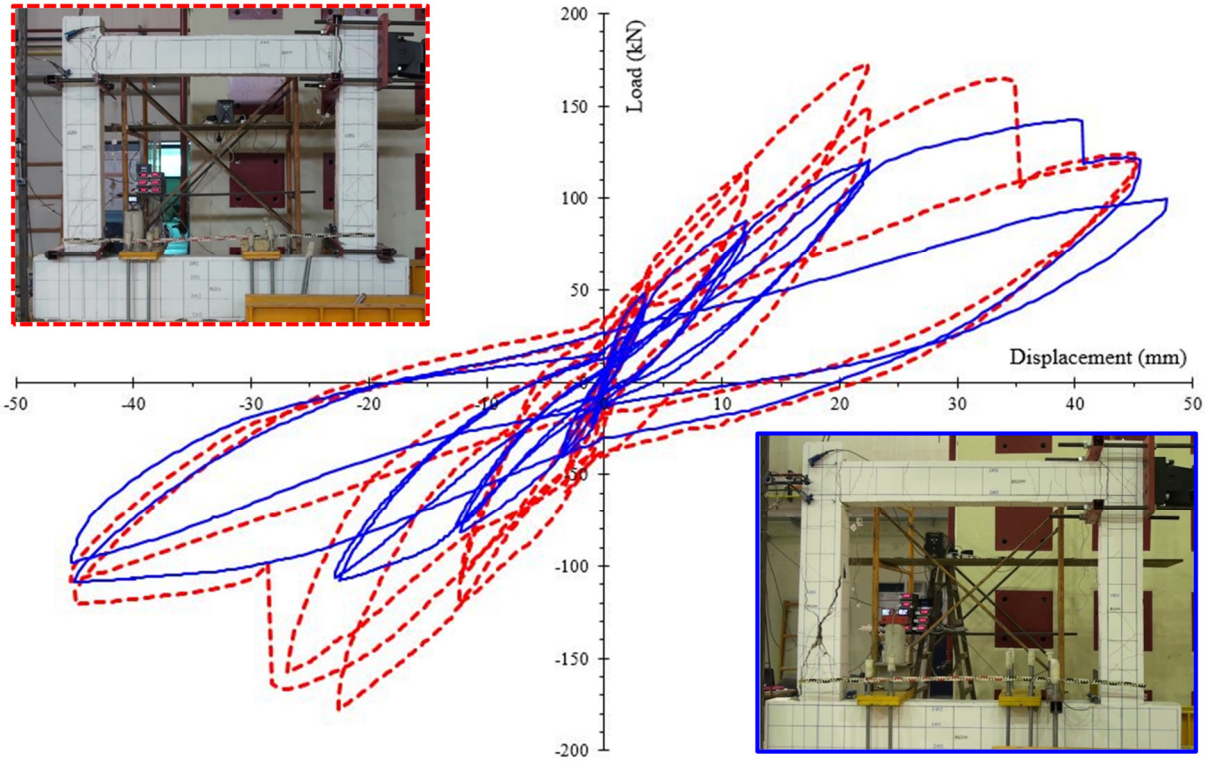


Fig.5. Comparative load versus displacement hysteretic diagram and failure modes of the X-braced frame (red dashed line) and the bare one (blue continuous line) [23]

## 4 COMPUTATIONAL SIMULATION OF THE TEST PROCEDURE

### 4.1 The Finite Element (FE) discretization of the RC frames

The FE models of the unbraced and braced RC frames are based on the test data. The columns and the beam are modeled using prismatic frame elements (Fig. 6). The imposed loading history has been simulated as displacement-controlled multiple earthquake excitation imposed on the top left node 3 of the frame (Fig. 6).

Nonlinearity at the two ends of RC members is idealized using one-component plastic hinge models, following the Takeda hysteresis rule. In order to check for shear-effects, the shear span-to-depth ratios of the RC members are computed according to Eq. (4) resulting to $a_s = 3.167$ for the beam and $a_s = 2.417$ for the columns. Thus, Eq. (4b) holds for each RC member since $2.0 \leq a_s \leq 7.0$ and the failure mode depends on the shear reinforcement of the member. The amount of the provided stirrups is rather low (∅6/200 mm) and their efficiency should be checked.

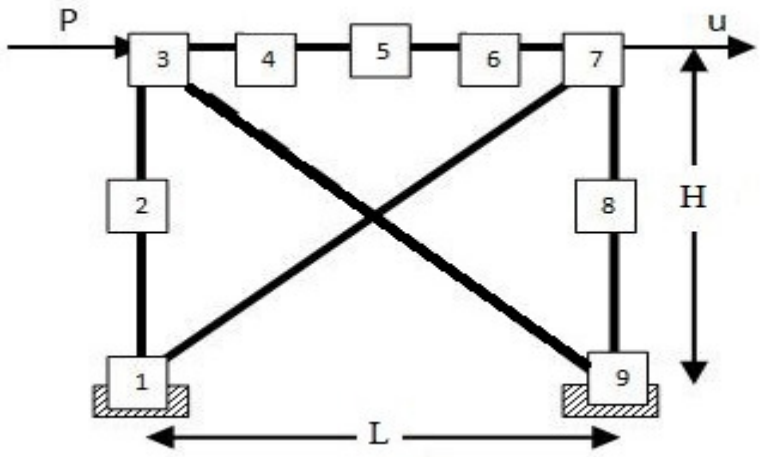


Fig.6. Finite element discretization of the simulated frame.

The absence of significant vertical gravity loads on the columns has as result the appearance of alternative axial forces (positive and negative, not only negative ones) as is the case of only compressive axial forces reported in the literature [11, 13, 19]. A preliminary simulation has given for these alternative axial forces the order results of the about values from -48 kN to +37 kN for the columns and from -67 kN to +55kN for the beam. Modelling of the two columns as well as of the beam is made by using the column-beam FE model of Ruaumoko [24]. The corresponding moment versus axial load (M - N) interaction curves computed by the section-analysis software RESPONSE-2000 [31] are shown in Fig. 7.

Based on the analysis of the critical sections insufficient confinement of the concrete core has first been detected. The spacing of the closed two-legged steel stirrups is 200 mm and therefore the confinement effectiveness factor α of the core of the sections is very low for the columns (α = 0.0495). Further, the mechanical volumetric ratio of the confining stirrups of the columns is $\omega_{wd} = 0.077 < 0.10$. Thus, Eq.(9) gives $\varepsilon_{cu,c} = \varepsilon_{cu}$ and the influence of the concrete - confinement to improve the RC member's ductility is minor and can be neglected.

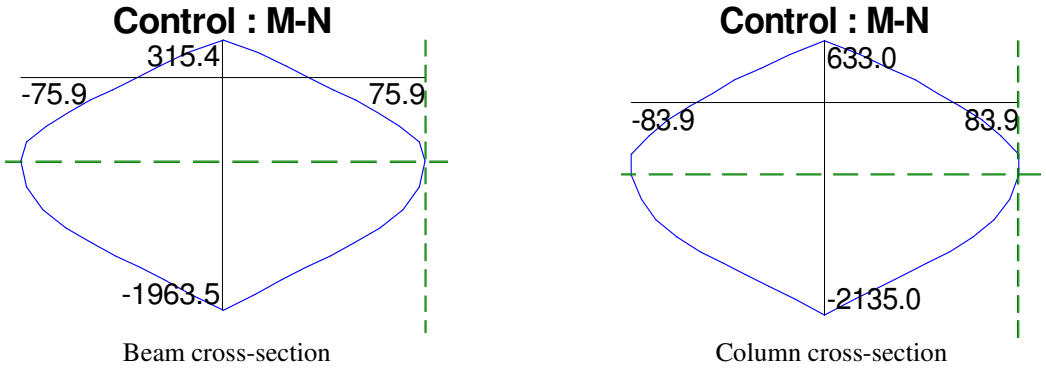


Fig.7. M - N interaction curves (in kNm and kN units) of the cross-sections of the members of the examined RC frames.

Concerning the available cyclic shear strength, $V_R$, computed by Eq.(6), it is about 5% lower than the developed required shear strength demand due to the flexure from -63 kN to +57 kN for the columns. So, shear effects according to Fig. 3(b) have been taken into account and slightly reduced values are used. The effective stiffness of the RC members is calculated by Eq.

(5) taking into account the shear effects. Moreover, the yield and the available ultimate ductility in plastic hinges are estimated for using the strength degradation model of Fig. 4.

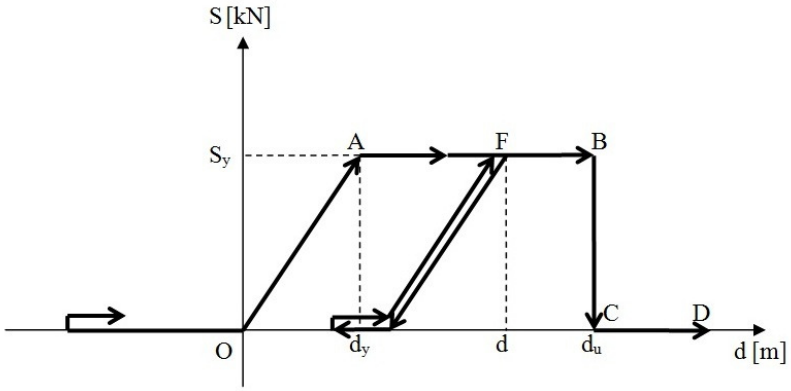


Fig.8. Constitutive law of the tension-tie elements.

For the X-bracing simulation spring-elements are used by applying the bilinear with slackness hysteresis rule of Ruaumoko [24]. These elements have cross-sectional area 1.0 $cm^2$ (corresponding to diameter ∅16 mm of the applied steel rods as tension-ties) and steel elasticity modulus 200 GPa. The cable constitutive law concerning the unilateral (slackness), hysteretic, fracturing, unloading-reloading behavior, has the simplified diagram *S-d* depicted in Fig. 8, where the ductility index is $\mu = d/d_y$. In the experimental procedure the failure strain of the crossed steel tension-ties has been measured for the ascending tie (member 1-7 in Fig. 6) and for the descending tie (member 3-9 in Fig. 6). Taking into account these failure limits the corresponding available ultimate ductility for each tie are computed and used for the strength degradation model of Fig. 4.

### 4.2 Representative results of the numerical simulation

The computationally derived diagrams of the load, P, versus top displacement, u, hysteretic behavioral curves for the unbraced (bare) frame and the X-braced frame are shown in Fig. 9 and Fig.10, respectively, in comparison with the experimentally obtained ones. From these comparisons it is indicated that the computed results are in very good agreement with the experimental data curves.

## 5 CONCLUDING REMARKS

A computational approach for the lateral cyclic inelastic behavior of single-story single-span RC frames under shear effects, which are strengthened using X-type steel tension-ties has been presented. Emphasis is given to the dimensional and reinforcement configuration of old RC frame structures that have been designed and constructed using past Code provisions without proper seismic requirements and appear shear character problems due to the lack of adequate stirrups and the short shear length in the columns, and therefore a shear-dominated behavior is expected.

The developed approach has been calibrated and verified by simulating available experimental results presented in a companion paper. Comparisons between experimental and computed results show that the presented computational approach could effectively be used for the seismic assessment and the strengthening of existing shear-critical RC frame structures by X-type tension-tie or cable elements.

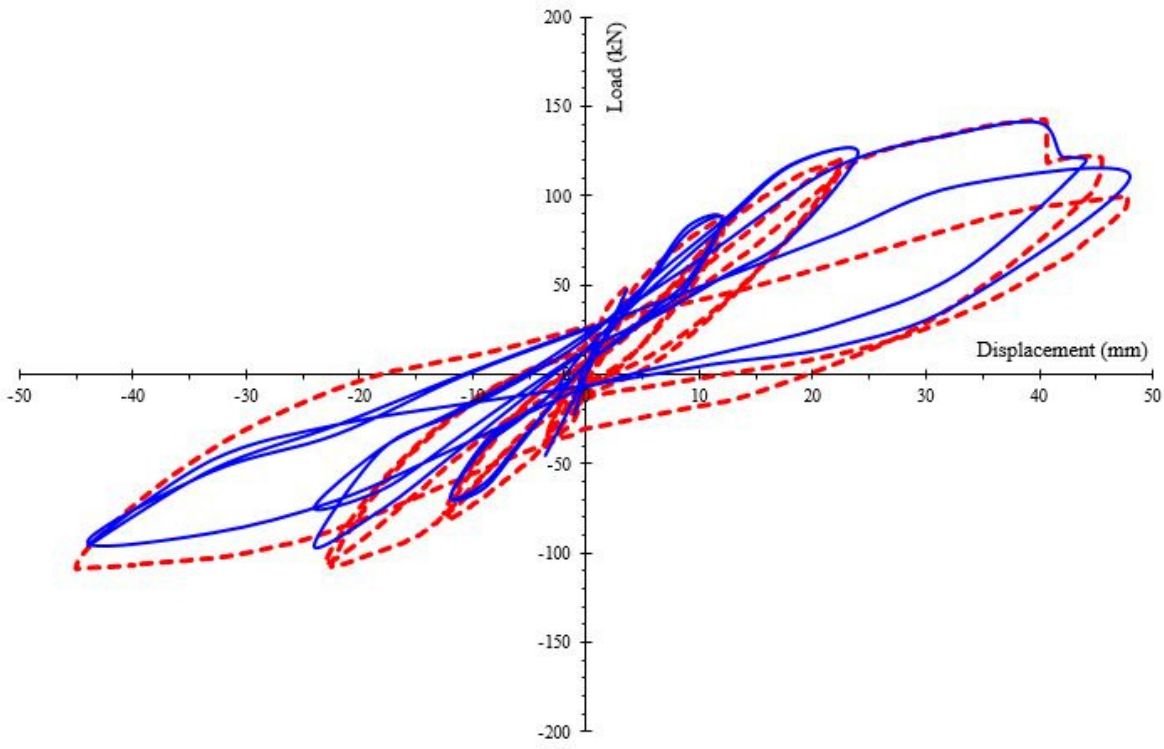


Fig.9. Unbraced (bare) RC frame: Computational (*continuous blue lines*) versus experimental (*dashed red lines*) hysteretic response.

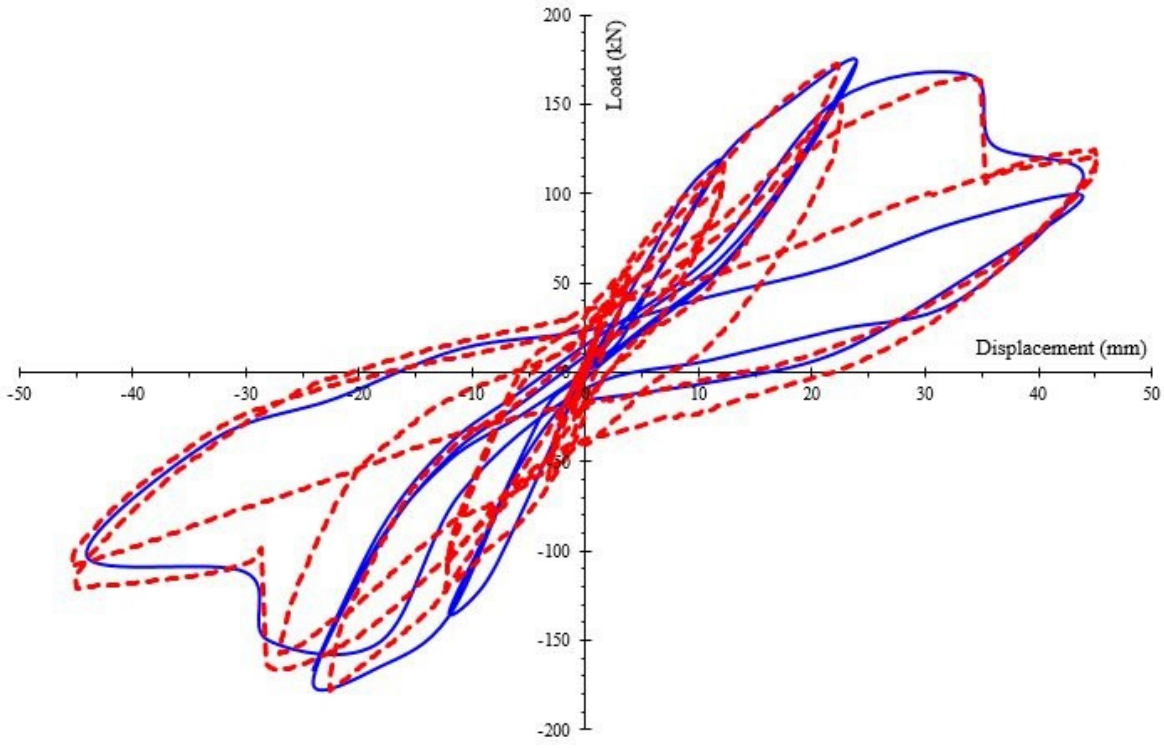


Fig.10. Braced (X-strengthened) RC frame: Computational (*continuous blue lines*) versus experimental (*dashed red lines*) hysteretic response.

## REFERENCES


[1] Tsonos, A.-D.G. (2007). *Cyclic load behavior of RC beam-column subassemblages of modern structures*. ACI Structural Journal, 104(4), 468-478.

[2] Chalioris, C.E., Favvata, M.J. and Karayannis, C.G. (2008). *Reinforced concrete beam–column joints with crossed inclined bars under cyclic deformations*. Earthquake Engineering & Structural Dynamics, 37(6), 881-897.

[3] Favvata, M.J., Izzuddin, B.A. and Karayannis, C.G. (2008). *Modelling exterior beam-column joints for seismic analysis of RC frame structures*. Earthquake Engineering & Structural Dynamics, 37(13), 1527-1548.

[4] Karayannis, C.G. Favvata, M.J. and Kakaletsis, D.J. (2011). *Seismic behaviour of infilled and pilotis RC frame structures with beam–column joint degradation effect*. Engineering Structures, 33(10), 2821-2831.

[5] Karayannis, C. G. (2014), *Seismic design of reinforced concrete structures*. (in greek). Sofia Publications, Thessaloniki, Greece.

[6] Kalogeropoulos, G.I., Tsonos, A.-D.G., Konstandinidis, D. and Tsetines, S. (2016). *Pre-earthquake and post-earthquake retrofitting of poorly detailed exterior RC beam-to-column joints*. Engineering Structures, 109, 1-15.

[7] Dritsos, S.E., (2001). *Repair and strengthening of reinforced concrete structures* (in greek). University of Patras, Greece.

[8] Fardis, M.N., (2009). *Seismic design, assessment and retrofitting of concrete buildings: based on EN-Eurocode 8*. Springer, Berlin.

[9] Penelis, G. and Penelis, Greg. (2014). *Concrete buildings in seismic regions*. CRC Press, Taylor & Francis Ltd.

[10] Antonopoulos, T.A. and Anagnostopoulos, S.A. (2013). *Improving the seismic performance of existing old pilotis type buildings by strengthening only the ground story*, In: M. Papadrakakis, V. Papadopoulos & V. Plevris (eds.), *COMPDYN 2013, ECCOMAS: Thematic Conference on Computational Methods in Structural Dynamics and Earthquake Engineering*, Kos Island, Greece, 12–14 June 2013.

[11] Massumi, A. and Absalan, M. (2013). *Interaction between bracing system and moment resisting frame in braced RC frames.* Archives of Civil and Mechanical Engineering, 13(2), 260-268.

[12] Markogiannaki, O. and Tegos, I. (2011). *Strengthening of a multistory R/C building under lateral loading by utilizing ties.* Applied Mechanics and Materials, 82, 559-564.

[13] Lee, K. S. (2015). *An experimental study on non-compression X-bracing systems using carbon fiber composite cable for seismic strengthening of RC buildings*. Polymers, 7(9), 1716-1731.

[14] Priestley, M.J.N., Seible, F.C. and Calvi, G.G.M. (1996). *Seismic design and retrofit of bridges*. John Wiley & Sons, Inc.

[15] Panagiotopoulos, P.D. (1993). *Hemivariational inequalities. Applications in mechanics and engineering*. Springer-Verlag, Berlin, New York, (1993).

[16] Mistakidis, E.S. and Stavroulakis, G.E. (1998). *Nonconvex optimization in mechanics. Smooth and nonsmooth algorithmes, heuristic and engineering applications*. Kluwer, London.

[17] Liolios, A. and Chalioris, C.E. (2015). *Reinforced concrete frames strengthened by cable elements under multiple earthquakes: A computational approach simulating experimental results*. In: *Proceedings of 8th GRACM International Congress on Computational Mechanics,* pp. 12-15, *Volos, Greece*.

[18] Güner, S. and Vecchio, F.J. (2010). *Analysis of shear-critical reinforced concrete plane frame elements under cyclic loading*. Journal of Structural Engineering, 137(8), 834-843.

[19] Karalis, A. A., Georgiadi-Stefanidi, K. A., Salonikios, T. N., Stylianidis, K. C., & Mistakidis, E. S. (2011). *Experimental and numerical study of the behaviour of high dissipation metallic devices for the strengthening of existing structures*. In: M. Papadrakakis et al, (eds.), *Proceedings of COMPDYN 2011, ECCOMAS: Thematic Conference on Computational Methods in Structural Dynamics and Earthquake Engineering,* Corfu, Greece, 26–28 May 2011.

[20] Fardis, M. N., Carvalho, E. C., Fajfar, P. and Pecker, A. (2015). *Seismic design of concrete buildings to Eurocode 8.* CRC Press, Taylor and Francis Group, New York.

[21] EC8-3, Eurocode 8 (CEN 2004). *Design of structures for earthquake resistance, Part 3: Assessment and retrofitting of buildings*, (EC8-part3), EN 1998-3, Brussels.

[22] KAN.EPE (2013). *Greek Code of Interventions*. Team for development of code of interventions on reinforced concrete buildings, Harmonization team of code of interventions to Eurocodes: Council of Europe, European Centre on Prevention and Forecasting of Earthquakes (E.C.P.F.E.), Earthquake Planning and Protection Organization (E.P.P.O.), Athens.

[23] Liolios A., Efthymiopoulos P., Mergoupis T., Rizavas V. and Chalioris C. E. (2017). *Reinforced concrete frames strengthened by tension-tie elements under cyclic loading: Experimental investigation*. In: Papadrakakis, M. et al (eds.), Proceedings of COMPDYN 2017: *Computational Methods in Structural Dynamics and Earthquake Engineering, paper C18197*, 15-17 June 2017, Rhodes Island, Greece

[24] Carr, A.J. (2008). *RUAUMOKO - Inelastic Dynamic Analysis Program*. Department of Civil Engineering, University of Canterbury, Christchurch, New Zealand.

[25] Chopra, A.K., (2007). *Dynamics of Structures: Theory and Applications to Earthquake Engineering*, Pearson Prentice Hall, New York.

[26] Makarios T. (2013), "*Modelling of characteristics of inelastic members of reinforced concrete structures in seismic nonlinear analysis*", Ch. 1, pp. 1-41, In: G. Padovani and M. Occhino (Editors): *Focus on Nonlinear Analysis Research*, Nova Publishers, New York.

[27] Psycharis, I. N. (2015), *Antiseismic Design with Performance Levels*. Postgrad. Lecture Notes (in greek), National Technical University of Athens, Dept. Civil Engineering.

[28] Mergos, P.E. & Kappos, A. J. (2013). *Damage Analysis of Reinforced Concrete Structures with Substandard Detailing.* In: M. Papadrakakis, M. Fragiadakis & V. Plevris (Eds.), *Computational methods in earthquake engineering: Volume 2.* Computational Methods in Applied Sciences, 30. (pp. 149-176). Springer. ISBN 978-94-007-6572-6.

[29] Vamvatsikos, D. and Cornell, C.A., (2002). *Incremental dynamic analysis*. Earthquake Engineering and Structural Dynamics, vol. 31, 491–514.

[30] Paulay T. and Priestley, M.J.N. (1992), "*Seismic design of reinforced concrete and masonry buildings*". Wiley, New York.

[31] Bentz, E. C. (2000). *Sectional analysis of reinforced concrete members, (RESPONSE-2000).* PhD thesis, Dept. Civil Engineering, University of Toronto.

COMPDYN 2017
6th ECCOMAS Thematic Conference on
Computational Methods in Structural Dynamics and Earthquake Engineering
M. Papadrakakis, M. Fragiadakis (eds.)
Rhodes Island, Greece, 15–17 June 2017

# REINFORCED CONCRETE FRAMES STRENGTHENED BY TENSION-TIE ELEMENTS UNDER CYCLIC LOADING: EXPERIMENTAL INVESTIGATION

**Angelos A. Liolios[1], Panagiotis N. Efthymiopoulos [2], Theofilos A. Mergoupis [2], Vaios D. Rizavas [3], and Constantin E. Chalioris[4]**

[1] PhD Candidate
Democritus University of Thrace, Department of Civil Engineering,
Division of Structural Engineering, Xanthi 67100, GREECE
e-mail: aliolios@civil.duth.gr

[2] MSc students
Democritus University of Thrace, Department of Civil Engineering,
Division of Structural Engineering, Xanthi 67100, GREECE

[3] Graduate student
Democritus University of Thrace, Department of Civil Engineering,
Division of Structural Engineering, Xanthi 67100, GREECE

[4] Associate Professor
Democritus University of Thrace, Department of Civil Engineering,
Division of Structural Engineering, Xanthi 67100, GREECE
e-mail: chaliori@civil.duth.gr

**Keywords:** Seismic Strengthening of RC Structures, X-braced Systems, Cable Elements, Tension-Ties, Experimental Investigation.

**Abstract.** *The cyclic response of existing Reinforced Concrete (RC) frames upgraded using diagonal X-type steel elements as tension-ties is experimentally investigated. Test results of two single-story single-span RC frames subjected to cyclic imposed lateral deformations are presented. The dimensional and the reinforcement configurations of the examined frames are the same and represent typical RC frame structures that have been designed and constructed using old Code provisions without consideration of seismic design criteria. The columns of the tested frames have shear-critical character due to the inadequate amount of stirrups provided and their low height-to-depth ratio (short columns). The experimental program includes a bare frame and a strengthened one using a pair of two steel crossed tension-ties (X-type bracing). Emphasis is given to the unilateral behavior of the steel bracing elements that undertake only tension stresses. In a companion paper, the herein experimental results are simulated and used as a comparative basis for the calibration of a numerical approach concerning a typical example problem.*

# 1 INTRODUCTION

Strengthening of seismically deficient Reinforced Concrete (RC) buildings is a current necessity in earthquake prone areas. It is known that the majority of the existing buildings in Greece were designed and built according to older Codes with inadequate seismic requirements regarding the provisions of modern Codes such as Eurocode 8. Many of these structures have insufficient transverse and longitudinal reinforcement, morphological problems such as soft story, short columns, lack of strong RC walls, weak column strong beam frames, etc., and low quality of building materials. Apparently, these RC buildings present weaknesses concerning their strength, ductility and stiffness in lateral seismic excitations. Thus, seismic upgrading in this type of structures is essential in order to avoid sudden total or local collapses, excessive damages or even loss of life from earthquakes [1-4].

Strengthening of existing RC buildings can be local and applied to specific RC members, or global in order to upgrade the structure as a whole. The response of beam-column connections in old RC frame structures is often characterized by the lack of ductility, sudden decrease of strength and low energy dissipation capacity due to the inadequate shear reinforcement provided. Examples of different local strengthening techniques have successfully been applied is typical cases of beam-column joints [5-9]. Further, global upgrading of RC structures can be achieved using various and well-known methods [10-13].

Concerning the strengthening of RC frames, tests of rehabilitated bare and infilled single-story single-bay RC frames using conventional retrofitting techniques under cyclic loading have been performed [14, 15]. Similar RC frames have also been strengthened in laboratory tests using an advanced steel bracing system that utilizes a small steel link element having an I-shaped cross-section connected to the RC frame through bracing elements [16]. The use of steel braces has proven to be an effective system in resisting lateral loads and became a popular method for the local or global strengthening of RC frames and structures. Several studies demonstrated that through the use of steel braces enhances the seismic performance of the strengthened frame improving strength, stiffness and energy dissipation capacity. A specific category in the brace strengthening technique of existing RC frames concerns the use of X-type cable elements [17-20].

In the present study, the efficiency of an easy-to-apply X-type bracing system that consists of two steel rods installed as tension-tie or cable elements, connected to the RC frame through steel brackets is experimentally investigated. Two RC frame specimens are tested under imposed lateral cyclic deformations, a bare frame and a strengthened one. The examined RC frames have dimensional and reinforcement configuration of typical earlier RC frame structures in Greece that have been designed and constructed using past Code provisions without proper seismic requirements. Such structures usually appear typical shear character problems due to the lack of adequate transverse reinforcement (stirrups) and the short shear length in the columns.

# 2 EXPERIMENTAL PROGRAM

## 2.1 Characteristics of the RC frame specimens

The experimental program consists of two single-story, one-bay and half-scale RC frame specimens subjected to lateral cyclic loading. The first RC frame is bare (Fig. 1) and the second has been strengthened using a X-type bracing system with diagonal tension-ties (Figs. 2 and 3). Both frames have the same dimensions and reinforcement configuration.

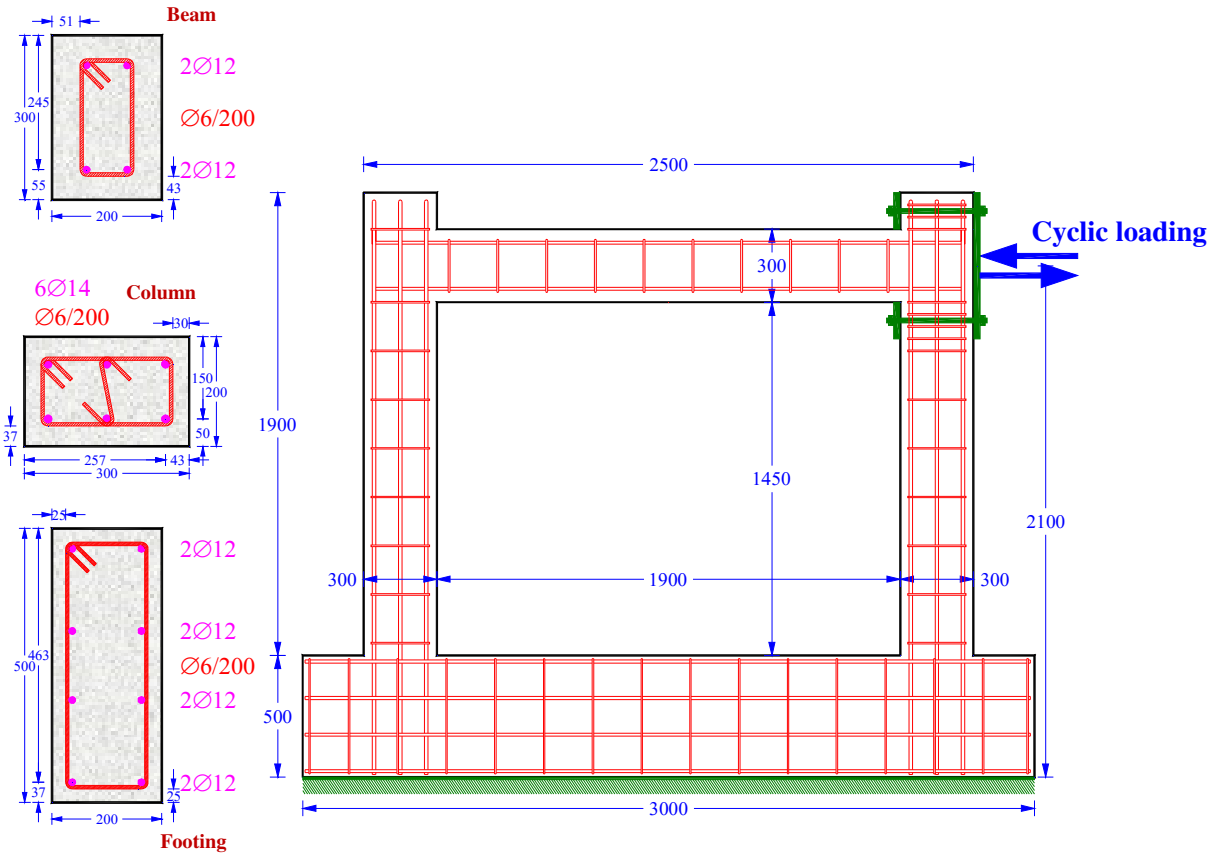


Fig.1. Dimensions and reinforcement configuration of the bare RC frame specimen

The cross-sectional dimensions of the beam and the columns of both RC frames are 200 x 300 mm. The longitudinal reinforcing bars of the beam and the columns have diameter ∅12 and ∅14 (deformed steel bars in mm), respectively. The transverse reinforcement of all structural members of the RC frames consists of mild steel closed stirrups of 6 mm diameter uniformly distributed throughout their length with 200mm spacing (∅6/200 mm). The dimensional and reinforcement configuration of the examined RC frames represents a typical RC frame of an old existing RC frame structure designed in accordance with past Code Standards in Greece.

It is noted that the shear ratio of the RC columns is low and equal to $\alpha_s = M_{Ed}/(V_{Ed}\, h) = L_s/h = 0.925/0.30 = 3.1$ (> 2.5). Also, the ratio of the column net height to the maximum sectional dimension is 1.45 / 0.30 = 4.8 (> 3). Therefore, the columns of the RC frames could be considered as shear-critical elements due to the inadequate stirrups provided [21- 23].

The first, bare RC frame is the reference specimen, whereas the second one has been strengthened using two rods of St46 structural steel with diameter of 16 mm that have placed diagonally inside the RC frame in X-type arrangement (steel X-bracing). These rods have been connected to the columns of the RC frame very close to the upper and lower joints of the frame using steel brackets. Each steel rod has been installed in order to operate only in tension as a cable element (see also Figs. 2 and 3).

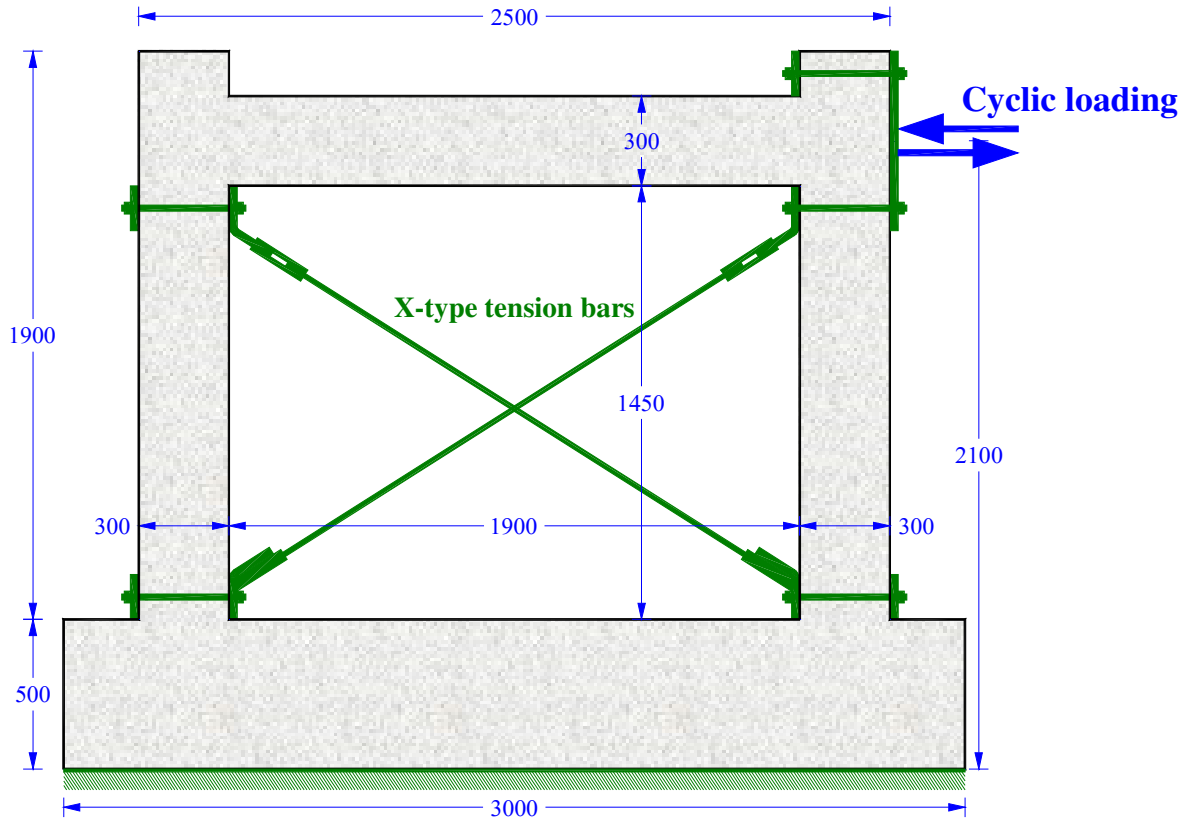


Fig.2. Dimensions and strengthening system of the steel X-braced RC frame specimen

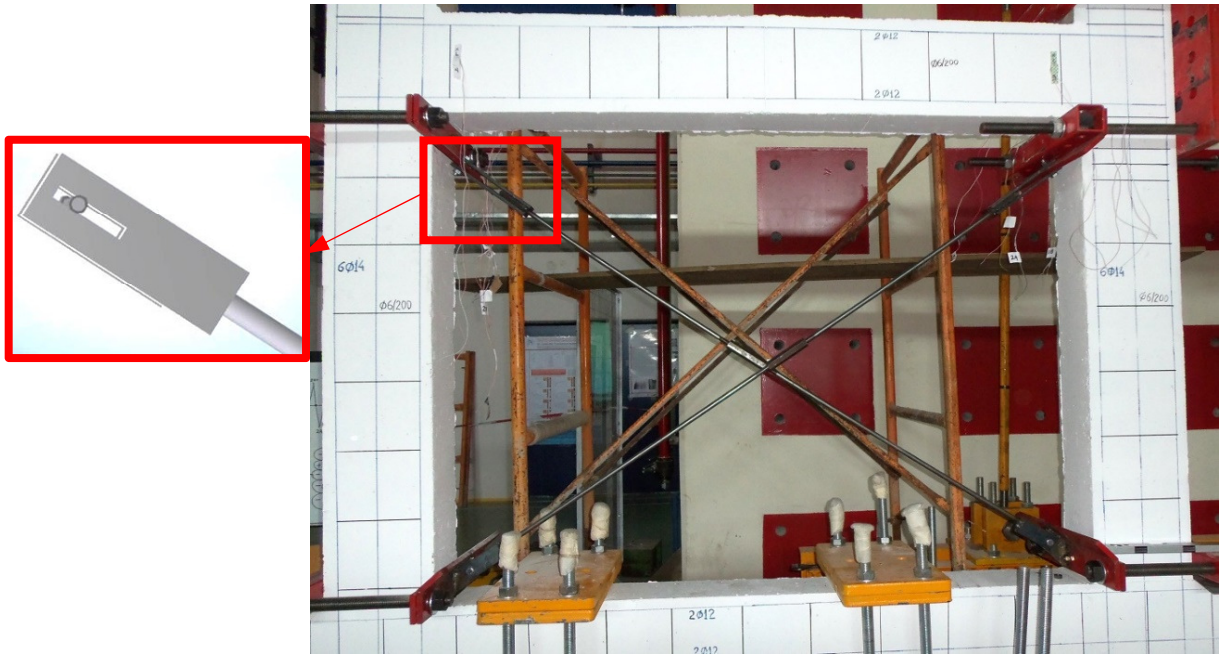

Fig.3. Details of the strengthened RC frame using X-type rods that operate only in tension as cable elements

## 2.2 Experimental setup

The examined RC frames have been tested under lateral cyclic in-plane displacement-control loading in the rigid RC floor - wall testing area of the Laboratory of Reinforced Concrete of Democritus University of Thrace (Fig. 4). The specimens were fixed to the rigid floor by bolts and nuts in order to prevent them from possible displacements. The load was imposed to the top corner of the RC frame using a double acting servo-hydraulic actuator fixed to the rigid wall of the laboratory with maximum capacity of 500 kN and 500 mm total stroke connected to an intermediate hydraulic control unit to ensure its smooth operation.

Displacements were measured via a number of digital strain gauges, positioned at different locations on the frame. Linear Variable Differential Transformers (LVDTs) and String Displacement Transducers (SDTs) were used (Figs. 4, 5 and 6). LVDTs were positioned on the top and bottom corners of the frame to measure the in-plane horizontal displacements of the frame and on the opposite faces to measure any possible twisting or out-of-plane deformation of the frame. SDTs were positioned on the internal diagonals of the frame to measure the diagonal displacements. SDTs were also diagonally positioned on the upper beam-column connection of the frame to measure the shear deformations of the joint area. All measuring devices were placed in appropriate locations and connected to data logger for digital recording.

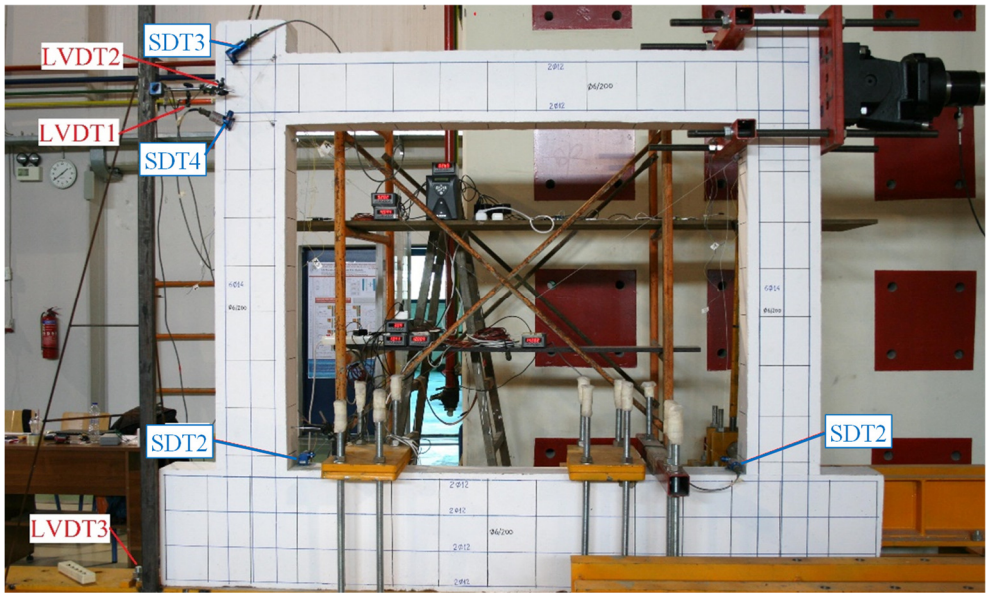


Fig.4. Test rig and instrumentation

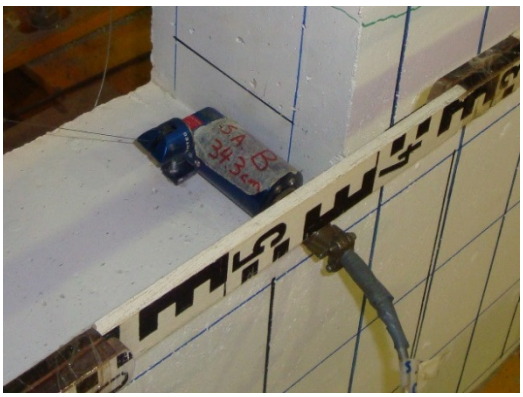

Fig. 5. SDT1

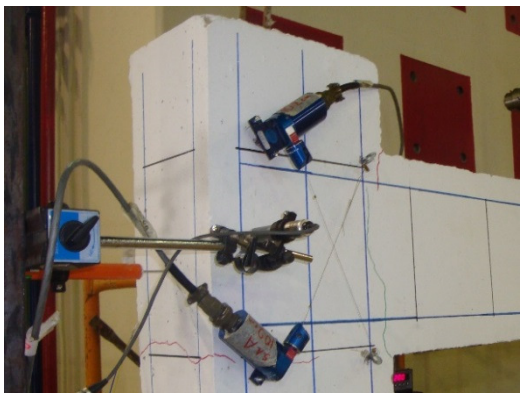

Fig.6. LVDT1, LVDT2, SDT3 and SDT4

### 2.3 Loading

The horizontal loading was imposed in a displacement control mode with a rate of 0.2 mm/sec. The displacement history applied to both RC frames includes five different increasing loading steps at ± 1.0, ± 3.5, ± 12.0, ± 22.5 and ± 45.5 mm with two equal imposed cycles at each step (Fig. 7).

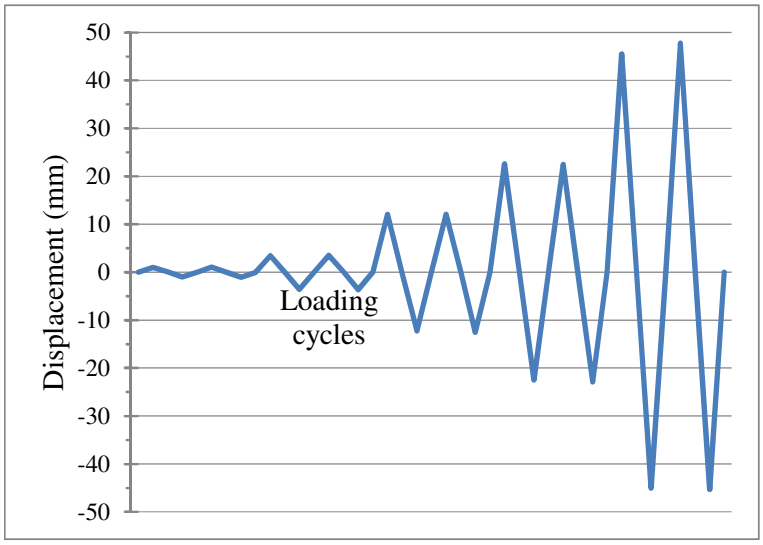


Fig.7. Imposed displacement history

## 3 TEST RESULTS

### 3.1 Bare RC frame (reference specimen)

The lateral hysteretic response of the bare RC frame specimen is presented in Figure 8 in terms of load versus horizontal displacement. The failure of the frame obtained at displacement equal to approximately 40 mm of the first positive cycle of the fifth loading step due to the sudden shear diagonal crack of the left column (Fig. 9). This failure caused a rapid and significant reduction of the load bearing capacity of the bare frame. It is obvious that this failure occurred due to the combination of the low length to depth ratio of the column that corresponds to a rather short element and the insufficient shear reinforcement, which results to low shear resistance, insufficient confinement and low ductility.

### 3.2 Strengthened RC frame (X-braced specimen)

The lateral hysteretic response of the steel X-braced RC frame is presented in Figure 10 in terms of load versus horizontal displacement. The first failure of the specimen obtained at displacement equal to approximately 35 mm of the first positive cycle of the fifth loading step due to the sudden rupture of the first steel diagonal rod, Right afterwards, the second failure obtained at displacement equal to approximately 30 mm of the forthcoming first negative cycle of the fifth loading step due to the sudden rupture of the second steel diagonal rod. Nevertheless, the cracking pattern of the strengthened frame presented in Figure 11 indicates that critical shear failure of the column has been prevented, whereas two distinctive flexural plastic hinges have been formed in the beam extremities while both beam-column joints of the frame remained undamaged and practically elastic.

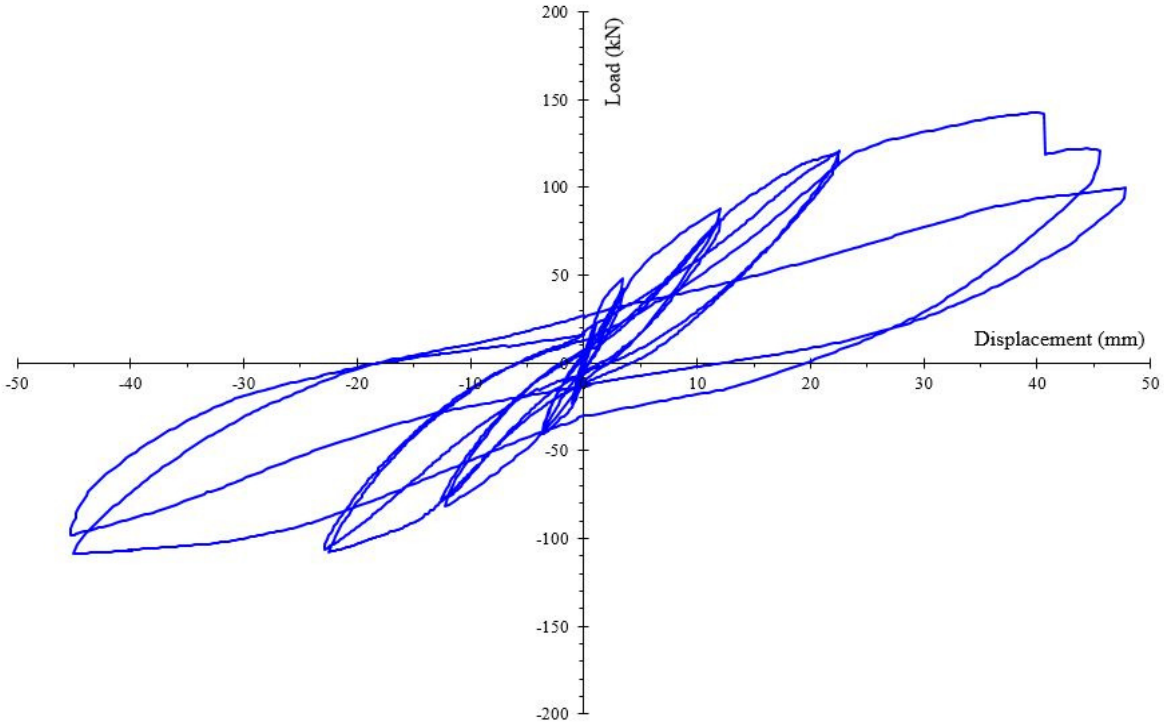


Fig.8. Load versus displacement hysteretic response for the bare RC frame specimen

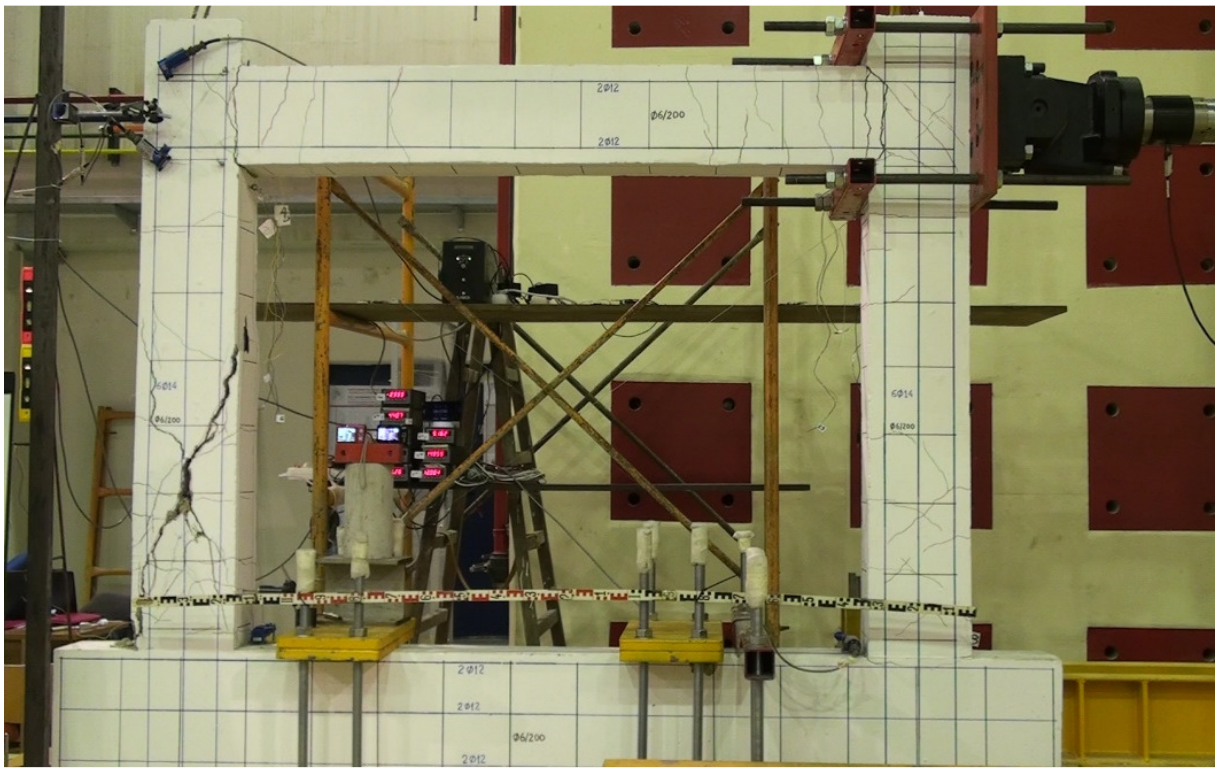

Fig.9. Shear failure occurred at the column of the bare RC frame

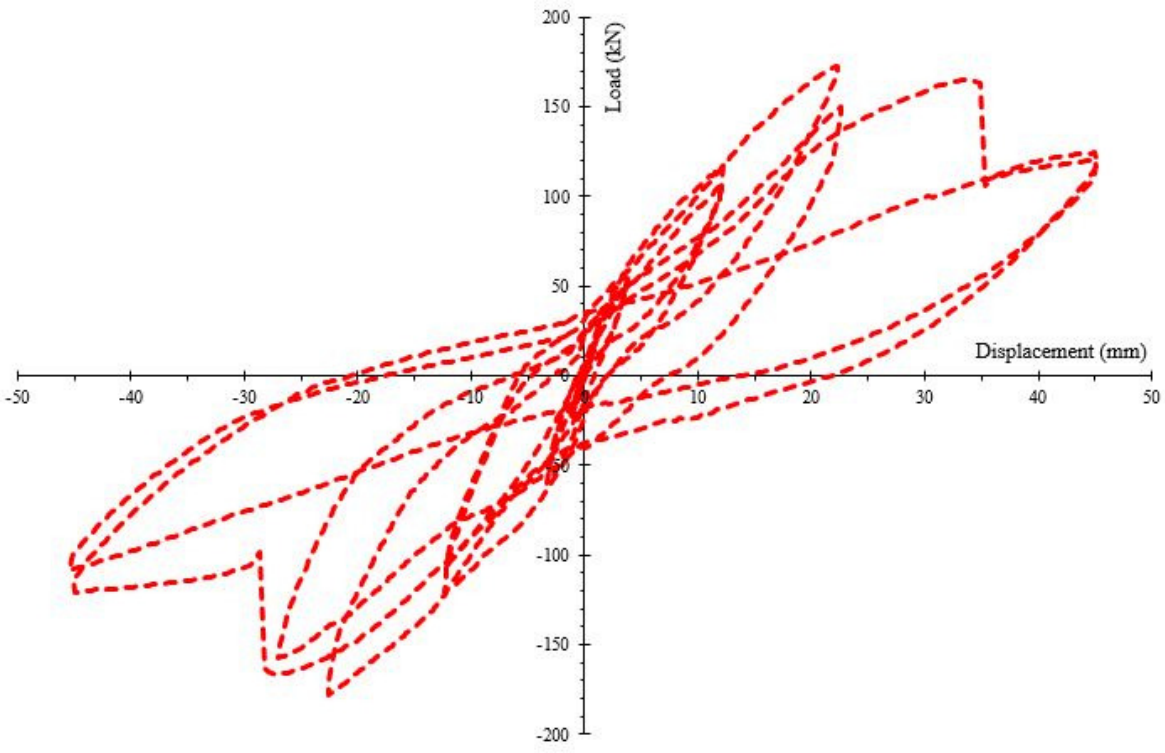


Fig.10. Load versus displacement hysteretic response for the X-braced RC frame specimen

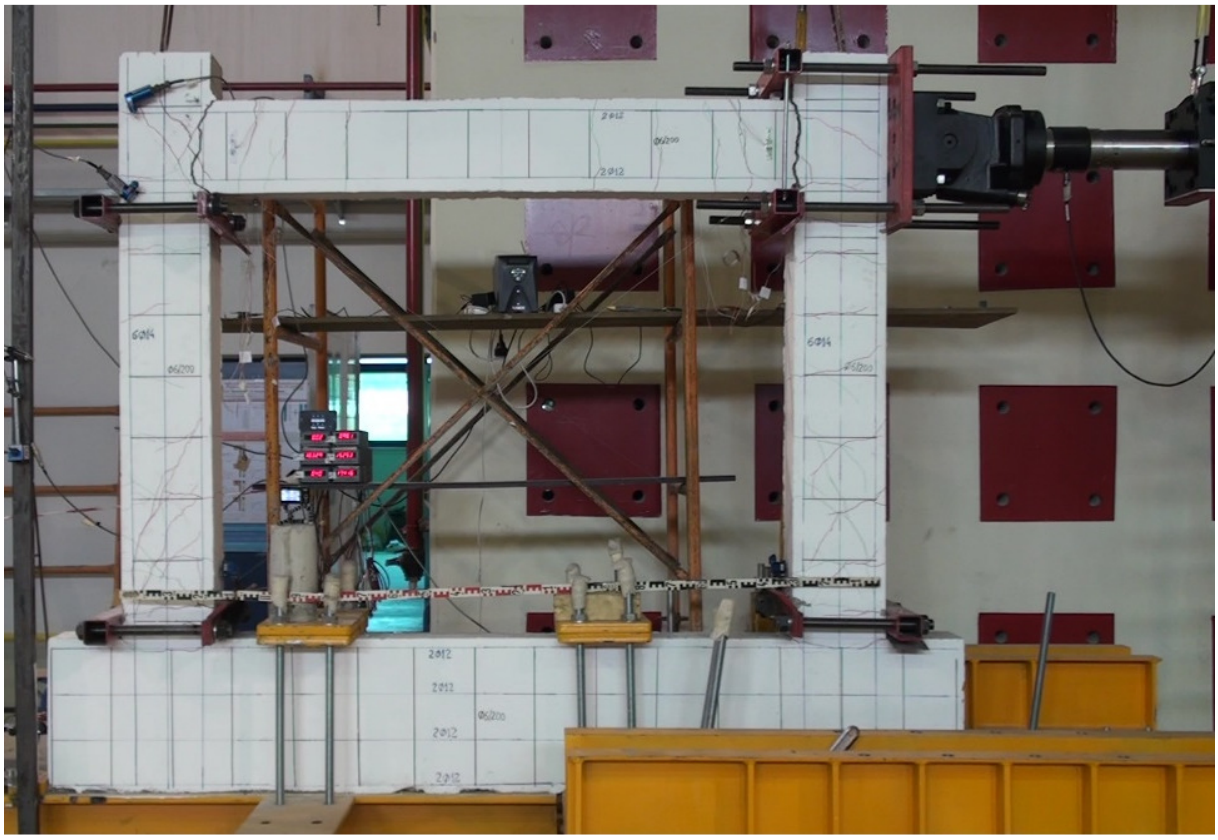

Fig.11. Cracking pattern of the steel X-braced RC frame at the end of the test (after the removal of the ruptured rods)

### 3.3 Increase of the frame load capacity due to steel X-bracing

Figure 12 shows the comparison of the hysteretic responses of the examined RC frames. Comparing the maximum values of load capacities it is concluded that the load capacity of the RC frame has been increased from 141 kN to 178 kN due to the application of the steel X-bracing. Thus, an increase for load capacity of about 26% has been obtained due to the applied strengthening.

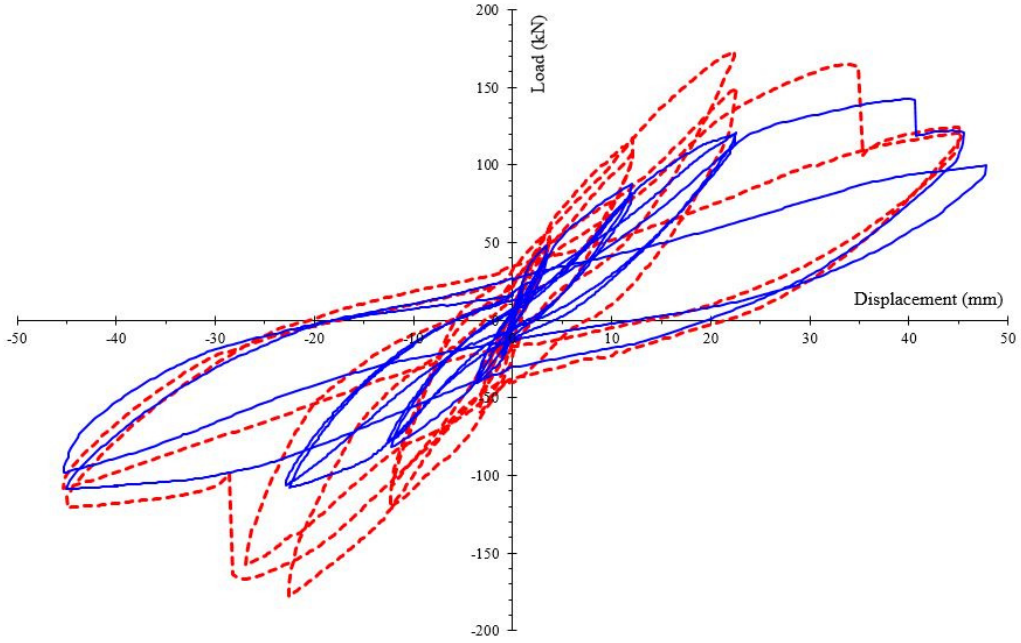


Fig.12. Comparative load versus displacement hysteretic diagram of the X-braced frame (red dashed line) and the bare one (blue continuous line)

## 4 CONCLUDING REMARKS

An experimental investigation concerning the lateral response of two single-story single-span RC frames under cyclic loading has been presented. Dimensions and reinforcement of the frame specimens are the same and represent typical old RC frame structures with insufficient shear reinforcement and short columns. The X-bracing system includes two steel rods placed diagonally inside the RC frame. These rods have been connected to the columns of the RC frame very close to the upper and lower joints of the frame using steel brackets. Each steel rod has been installed in order to operate only in tension as a cable element.

Results of the tests reported indicate the effectiveness of the applied internal steel X-bracing as a shear resisting system and a strengthening method against lateral loading. The strengthened frame demonstrated increased load capacity and enhanced hysteretic performance. The bare RC frame failed due to the sudden shear diagonal cracking of the column, whereas in the X-braced one the shear failure has been prevented and two distinctive flexural plastic hinges have been formed in the beam.

The herein obtained experimental results are used in a companion paper [24] for the calibration of a numerical approach concerning the hysteretic response of RC frame structures strengthened by tension-tie elements.

## REFERENCES


[1] Karayannis, C.G. (2014), *Seismic design of reinforced concrete structures*. Sofia Publ., Thessaloniki (in Greek).

[2] Karabinis, A.I. and Baltzopoulou, A.D. (2006). *Correlation of damage factor and repair cost in structures damaged after the 7th-9-1999 Athens earthquake*. In: Proceedings of 15th Greek Concrete Conference, Vol B3, 294-304 (in Greek).

[3] Kappos, A.J., Lekidis, V., Panagopoulos, G., Sous, I., Theodulidis, N., Karakostas, Ch., Anastasiadis, T., Salonikios, T. and Margaris, B. (2007). *Analytical estimation of economic loss for buildings in the area struck by the 1999 Athens earthquake and comparison with statistical repair costs*. Earthquake Spectra, 23(2), 333-355.

[4] EC8, Eurocode 8 (CEN 2004). *Design of structures for earthquake resistance, Part 3: Assessment and retrofitting of buildings*, (EC8-part3), EN 1998-3, Brussels.

[5] Karayannis, C.G., Chalioris, C.E. and Sideris, K.K. (1998). *Effectiveness of RC beam-column connection repairing using epoxy resin injections*. Journal of Earthquake Engineering, 2(2), 217-240.

[6] Karayannis, C.G., Chalioris, C.E. and Sirkelis, G.M. (2008). *Local retrofit of exterior RC beam–column joints using thin RC jackets - An experimental study*. Earthquake Engineering & Structural Dynamics, 37(5), 727-746.

[7] Karayannis, C.G. and Sirkelis, G.M. (2008). *Strengthening and rehabilitation of RC beam–column joints using carbon-FRP jacketing and epoxy resin injection*. Earthquake Engineering & Structural Dynamics, 37(5), 769-790.

[8] Tsonos, A.-D.G. (2008). *Effectiveness of CFRP-jackets and RC-jackets in post-earthquake and pre-earthquake retrofitting of beam-column subassemblages*. Engineering Structures, 30(3), 777-793.

[9] Tsonos, A.-D.G. (2014). *A new method for earthquake strengthening of old R/C structures without the use of conventional reinforcement*. Structural Engineering and Mechanics, 52(2), 391-403.

[10] Penelis, G.G. and Kappos, A.J. (1997), *Earthquake-resistant concrete structures*, E&FN Spon (Chapman & Hall), London.

[11] Penelis, G. and Penelis, Greg. (2014), "*Concrete buildings in seismic regions*", CRC Press, Taylor & Francis Ltd.

[12] Dritsos, S.E., (2001). *Repair and strengthening of reinforced concrete structures* (in greek). University of Patras, Greece.

[13] Fardis, M.N., (2009). *Seismic design, assessment and retrofitting of concrete buildings: based on EN-Eurocode 8.* Springer, Berlin.

[14] Kakaletsis, D.J. David, K.N. and Karayannis, C.G., (2011). *Effectiveness of some conventional seismic retrofitting techniques for bare and infilled R/C frames.* Structural Engineering and Mechanics, 39 (4), 499-520.

[15] Kakaletsis, D.J. and Karayannis, C.G., (2009). *Experimental investigation of infilled reinforced concrete frames with openings.* ACI Structural Journal, 106(2), 132-141.

[16] Karalis, A. A., Georgiadi-Stefanidi, K. A., Salonikios, T. N., Stylianidis, K. C., & Mistakidis, E. S. (2011). *Experimental and numerical study of the behaviour of high dissipation metallic devices for the strengthening of existing structures*. In: M. Papadrakakis et al, (eds.), Proceedings of COMPDYN 2011, ECCOMAS: Thematic Conference on Computational Methods in Structural Dynamics and Earthquake Engineering, Corfu, Greece, 26-28 May 2011.

[17] Markogiannaki, O. and Tegos, I., (2011). *Strengthening of a multistory R/C building under lateral loading by utilizing ties.* Applied Mechanics and Materials, 82, 559-564.

[18] Massumi, A. and Absalan, M. (2013). *"Interaction between bracing system and moment resisting frame in braced RC frames"*. Archives of Civil and Mechanical Engineering, 13(2), 260-268.

[19] Lee, K. S. (2015). *An experimental study on non-compression X-bracing systems using carbon fiber composite cable for seismic strengthening of RC buildings.* Polymers, 7(9), 1716-1731.

[20] Liolios, A., & Chalioris, C. (2015). *Reinforced concrete frames strengthened by cable elements under multiple earthquakes: A computational approach simulating experimental results*. In: Proceedings of 8th GRACM International Congress on Computational Mechanics, pp. 12-15, Volos, Greece.

[21] Paulay T. and Priestley, M.J.N. (1992), "*Seismic design of reinforced concrete and masonry buildings*". Wiley, New York.

[22] Salonikios, T.N., Kappos, A.J., Tegos, I.A. and Penelis, G.G. (2000), "*Cyclic load behavior of low-slenderness reinforced concrete walls: Failure modes, strength and deformation analysis, and design implications*", ACI Structural Journal, Vol. 97, No. 1, pp. 132-142.

[23] Fardis, M. N., Carvalho, E. C., Fajfar, P., and Pecker, A. (2015). *Seismic design of concrete buildings to Eurocode 8.* CRC Press, Taylor and Francis Group, New York.

[24] Liolios A. and Chalioris C. E. (2017). *Reinforced concrete frames strengthened by tensionties elements under cyclic loading: A computational approach.* In: Papadrakakis, M. et al (eds.) Proceedings of COMPDYN 2017: Computational Methods in Structural Dynamics and Earthquake Engineering, paper C18195.

COMPDYN 2017
6th ECCOMAS Thematic Conference on
Computational Methods in Structural Dynamics and Earthquake Engineering
M. Papadrakakis, M. Fragiadakis (eds.)
Rhodes Island, Greece, 15–17 June 2017

# RESPONSE OF REPAIRED FUSE BEAMS TO DYNAMIC TESTING

**Emmanouil Vougioukas[1], Stella Avgerinou[1], and Konstantinos Theocharis[2]**

[1] School of Civil Engineering/ NTUA
Iroon Polytechniou 5-13, GR 157 73, Zografou
e-mail: manolis@central.ntua.gr, avgerinoustella@gmail.com

[2] ACSE/ ASPETE
GR 141 21, Iraklio Attikis
kostheocharis@gmail.com

**Keywords:** Concrete Filled Composite Beams (CFCBs), Fuse Beams (FBs), Seismic Energy Absorption.

***Abstract.*** *Controlled energy distribution is desirable for structures subjected to severe earthquakes. EC8[1] prescribes (for steel structures) that reduced beam sections may behave like a fuse that protects beam-to-column connections against early fracture (cl. B.S.3.), provided that they can develop the minimum rotations specified. Unlike common steel structures, innovative types of seismic resistant steel frames have been proposed, with dissipative fuses, where only damage will occur. Fuses are designed to be easily replaced. They usually consist of steel hollow sections. In the present paper, used hollow beams, that had suffered strength degradation of more than 50% were filled with cement based repair mortar ($f_{cd}$ =35 MPa), forming concrete filled composite beams (CFCBs) and were retested, without any other kind of repair. CFCBs are reported to have demonstrated higher axial load capacity, better ductility performance, larger energy absorption capacity and lower strength degradation than conventional reinforced concrete and steel hollow section columns. This became apparent by the results or the tests achieved by the experiments; bearing capacity of fuse beam was practically restored to its initial value when the damaged side of the initial beam was subjected to tension, while it increased to about 2.5 times its initial value, when the damaged side is subjected to compression. Increase of energy dissipation per loading cycle was also remarkable (increase about 150%). Calculation of the stiffness of the fuse beam is performed, as it varies with the imposed displacement. Its effect on the eigenperiod of the main structure is discussed. The deformation limits that the cement based repair mortar has reached are calculated. Ideas for further research on the subject are proposed.*

## 1 INTRODUCTION

Design against earthquakes combines sufficient strength, stiffness and ductility for structures to be built. Ductility is connected to inelastic deformation of members [1].

Instead of potentially permitting such deformation to all members, effective structural design could exclude primary members of damage, by leading it to secondary members or, even better, to disposable special members. The late ones can act as “fuses”, in case of extreme loading; damage will occur to them only and can be easily replaced after the incident.

Usually, fuses are hollow steel members, welded with plates at both ends. They are connected to other structural members via bolts, so that they can be easily (and immediately) replaced after earthquakes. Bolts and plates are overdesigned, in order to assure that damage will occur at the hollow member only.

Relevant full scale tests have been performed at the Laboratory of Steel Structures of the National Technical University of Athens in the context of the "MATCH" research program, in addition to the tests that were performed in the previous "FUSEIS" research program [2-4].

Used specimens, that had suffered strength degradation of more than 50% were filled with cement based repair mortar (fc =35 MPa), forming concrete filled composite beams (CFCBs) and were retested, without any other kind of repair.

CFCBs are reported to have demonstrated higher axial load capacity, better ductility performance, larger energy absorption capacity and lower strength degradation than conventional reinforced concrete and steel hollow section columns[6]. This became apparent by the results or the tests achieved by the experiments, as reported below.

## 2 DESCRIPTION OF TESTS

The experimental setup is the same with the one used for the tests of the initial specimens. It consists of a rigid frame test rig, an actuator and the test frame. The test frame has height 3.40 m and two strong columns in a distance of 1.50m. The specimens are rigidly connected to the columns (Figure 1) via bolts. In order to assure that plastic hinges would form prior to the demounting of the plates, the specimens had small holes near their ends. The general properties of the fuses beams are presented in Table 1. The steel grade of specimens is S700.



Photo 1 Specimens during retrofit.

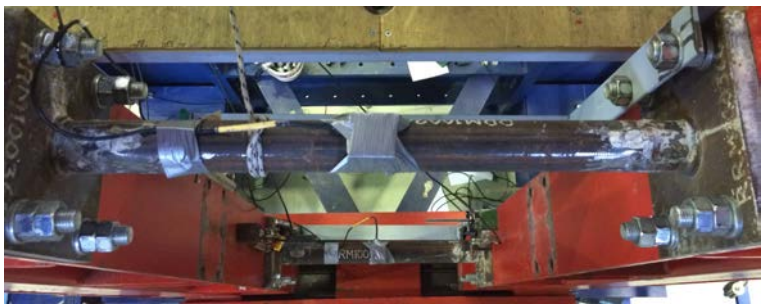

Photo 2 Experimental setup (top view).

Two specimens, initially tested till failure, were filled with cement based repair mortar (fcd =35 MPa), forming concrete filled composite beams (CFCBs) and were retested, without any other kind of repair. The specimens are presented during retrofit (photo 1) and during testing (photo 2).

The initial behaviour of these 2 specimens is analytically reported elsewhere [4], together with another 3 specimens (totally 5), tested simultaneously.

| Cross section | Grade | Length (mm) | Yield Stress (MPa) |
|---|---|---|---|
| CHS 76.1*3.2 | S700 | 722 | 790 |
| CHS 60.3*4.0 | S700 | 722 | 790 |

Table 1: Properties of the tested specimens

The specimens were mounted to the test frame, and were subjected to horizontal displacement (δ), that was recorded in accordance to the corresponding force F. (Figure 1).

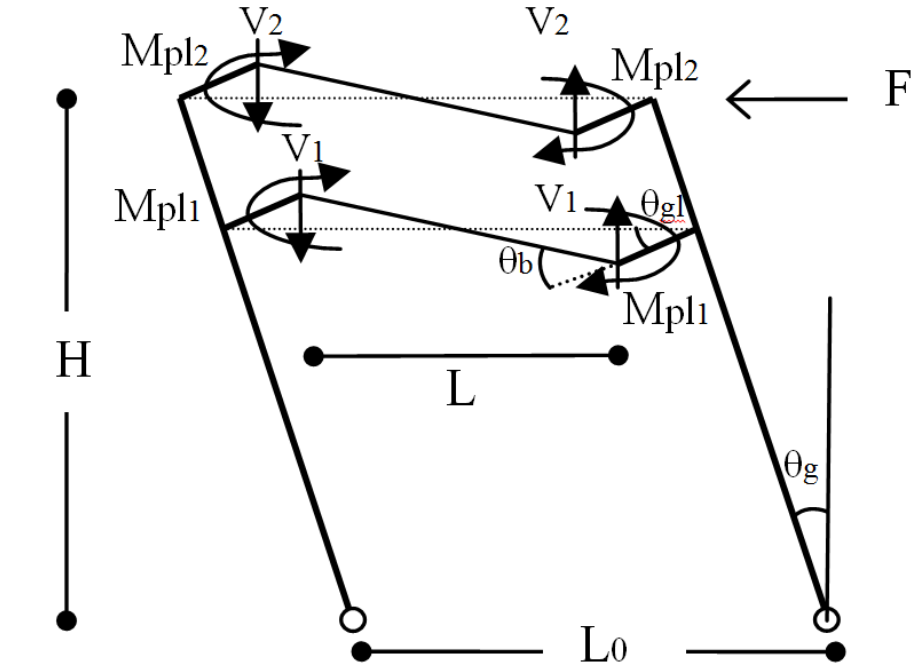


Figure 1: Test layout

## 3 ANALYTICAL MODEL

Two simple elasto-plastic models of the steel and of the composite beam were used for comparison to the experimental results. These models consist of a simple steel hollow beam for the one and the composition of the same hollow beam with a concrete core that fills the hollow part of the second. The two materials are assumed to be in full contact without interface phenomena (Figure 2(a)). The two existing holes were also modeled (Figure 2(b)). These holes assure that the specimen yields in this section, which is desirable, compared to support damage. Typical stress distribution is calculated; concrete is considered inactive in the case of tension.

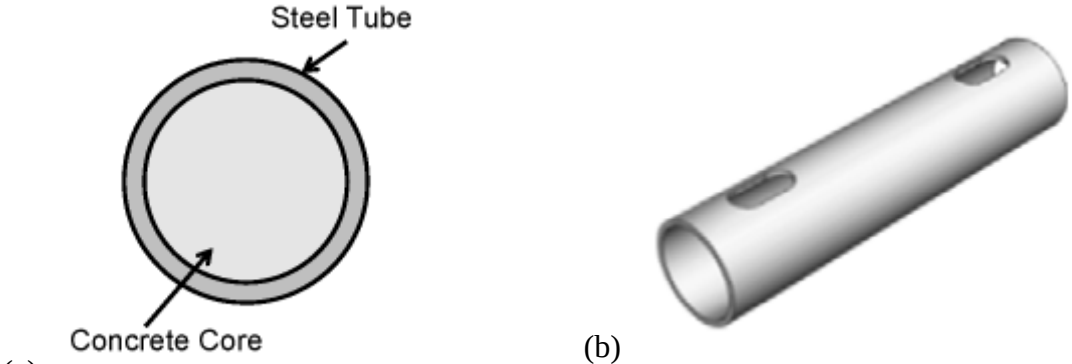


(a) (b)

Figure 2: (a) Steel hollow beam section filled with concrete (b) general view

These simplified models are analyzed in monotonic loading. In order to find the stress diagram, the section is divided to stripes parallel to neutral axis. For each stripe the geometrical properties, the bearing capacity and the effective stiffness are calculated via analytical method. The maximum compressive strain of concrete has been estimated to achieve double its nominal value (0.70 %) due to the confinement effectiveness. Axial strain is applied to the model and the forces are subsequently calculated. The moment capacity of the section is calculated under zero axial load. The curvature of the section is:

$$\frac{1}{R} = v'' = \frac{|\varepsilon_{down}| + |\varepsilon_{up}|}{L},$$

where L is the length of the beam and ε are the limit strains.

The displacement of the beams as an integral of the product of the unit and the maximum moment to the flexural rigidity, for different values of strains, is calculated. For each beam and section that was used in the laboratory, a function between force and displacement has been determined. For each tested specimen. The relevant force-displacement diagram according to the analytical model has been produced and is presented in Figure 3(a) both for the 2 repaired specimens and the five initial specimens [4].

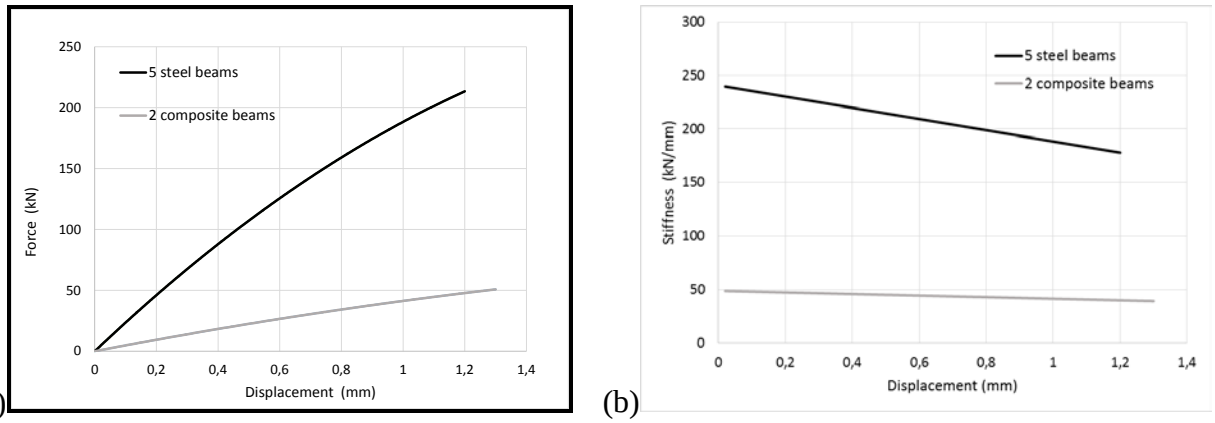


(a) (b)

Figure 3: Force displacement diagram and Stiffness Displacement diagram for the 5 steel beams and the 2 composite beams

The difference between the two lines is obvious and is primarily due to the number of the beams. Besides it, there is a difference in stiffness produced in the two cases. The stiffness in Figure 3(b) is calculated as the tangential “Force/Displacement” rate and clearly shows the

difference for the two situations. For the initial 5 steel beams this stiffness is higher at the beginning and decreases rapidly until its final value, while for the 2 composite beams the initial stiffness is lower and decreases slightly. The final value of the 2 composite beams stiffness over the value of the 5 steel beams is 0.22 and is used to normalize make the results of the two cases comparative.

## 4 ANALYSIS OF EXPERIMENTAL RESULTS

The loading, in terms of displacement, applied for the experiments used for the 5 steel beams and with the 2 composite beams described in the prequel, is presented in Figure 4(a). The two loading histories are practically identical; notice that the cyclic displacement loading for the 2 composite beams stopped at 4352sec due to failure while for the simple steel beams reached 5803sec and has not yet failed.

Measured forces for the two different sections, presented in Figure 4(b), are remarkable. For the case of the simple steel hollow section, the forces are symmetrical in tension and compression and they follow the increase in the intensity of the displacements. The forces measured on the composite beam present a totally different response. The response forces are asymmetrical and drastically favor the compression; obviously the concrete fill of the hollow steel section actively participate in the development of this force and is the reason for this asymmetry. The development of the forces with time follow the increase of the displacement intensity until approximately 2500 sec when they start to decrease; this decrease is clear in the case of the composite beam while it seems more subtle in the case of the steel beam. Notice that the force diagram is normalized, i.e. the forces are measured for the combined response of the beams and not each one individually, but a normalization, e.g. with the value 0.22.

This normalization is used also in Figure 4, where the response is presented in terms of force - displacement loops. To be able to compare the two cases, the forces measured for the steel hollow beams are multiplied with 0.22, the coefficient calculated from the stiffness. The final results present vividly the difference due to the initial damage (local buckling) at the region of the holes. It seems this local buckling reduces dramatically the confinement effect.

For the other direction, where concrete remains fully confined, its performance is impressive (Fig.5).

Finally, an equivalent mean stiffness for the first ten loading cycles has been calculated, based on the analytical mode, and was compared to the experiment results. The corresponding values are 48 kN/mm and 16 kN/mm respectively. These values are compatible and, partially, their difference would have been reduced if flexibility of fixation was included in the calculations.

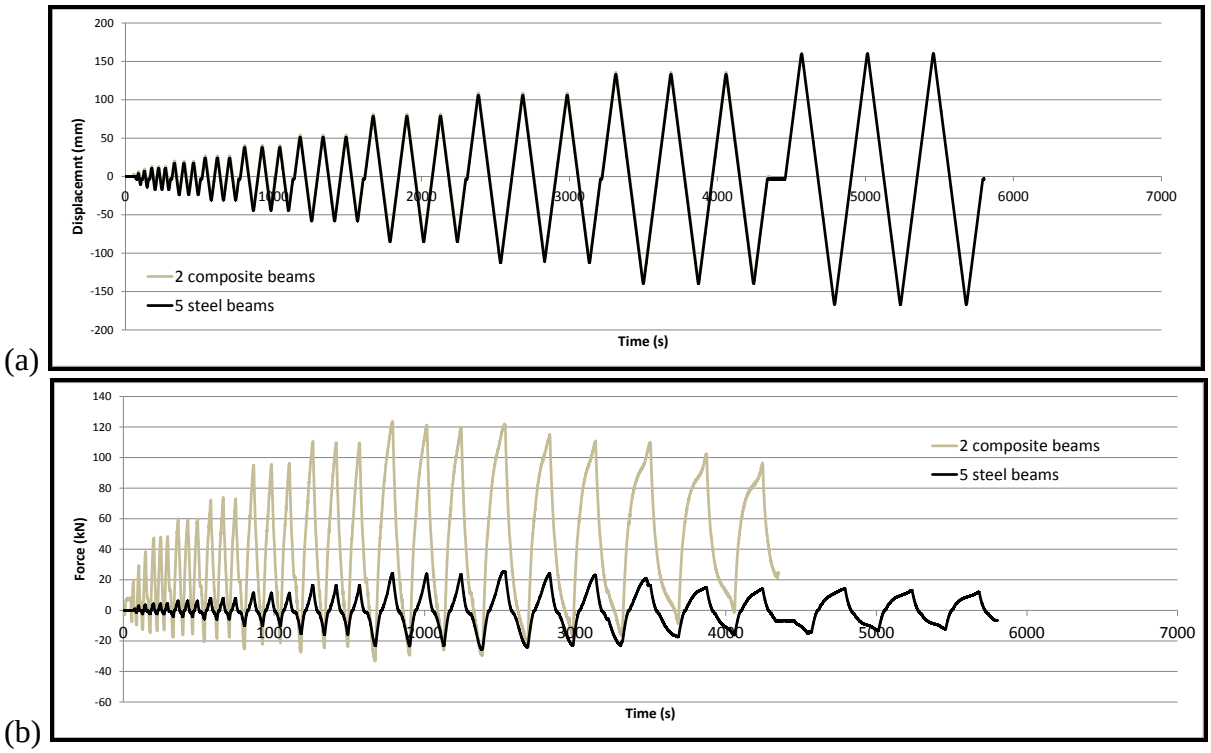


Figure 5: Time histories for the measured (a) displacement and (b) force for the two experiments

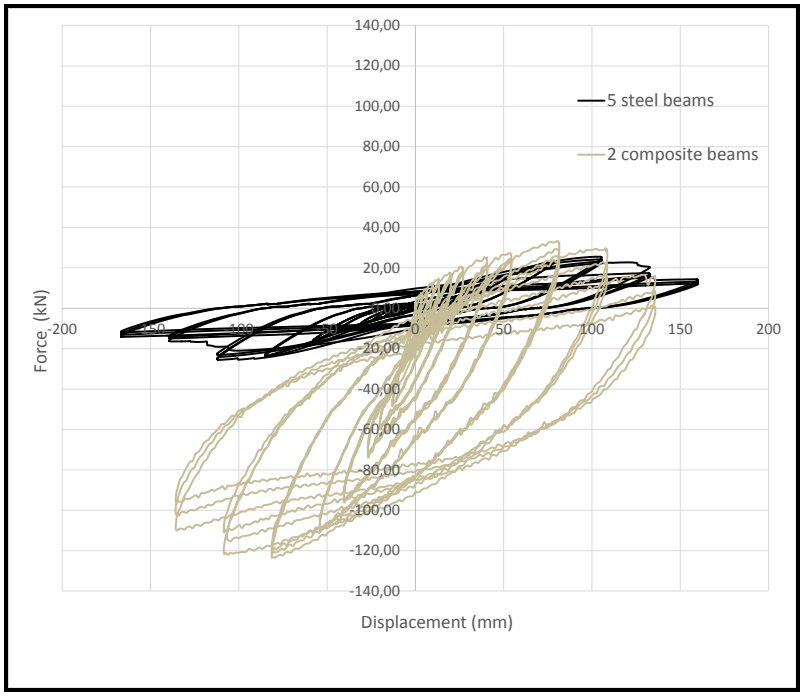


Figure 6: Force displacement loops for the 5 steel beams and the 2 composite beams

## 3 CONCLUSIONS

- Steel hollow sections, used and damaged as fuses, may retain or increase significantly their initial stiffness and bearing capacity, if they are filled with concrete, and reused.
- Concrete, confined in the tube, can retain extremely high deformations without rupture, due to triaxial behavior.
- Triaxial behavior of conrete is very sensitive to loss of confinement, even locally; this may lead to abrupt reduction of the bearing capacity.
- Steel hollow sections, filled with concrete, appeared to exhibit ductility of the order of $\mu$=10, in terms of displacement.
- Bearing capacity of fuse beam was practically restored to its initial value when the damaged side of the initial specimen was subjected to tension, while it increased to about 5 times its initial value, when the damaged side is subjected to compression.
- Increase of energy dissipation per loading cycle was also remarkable (about 150%).
- The deformation limits that the cement based repair mortar has reached are larger enough than the initially assumed (0,7%).
- It's evident that further research on the subject is needed.


## AKNOWLEDGEMENT

The help of Dr. X. Lignos at the performance of the tests is acknowledged.


## REFERENCES


[1] EN1998-3, Eurocode 8: design of structures for earthquake resistance — part 3: assessment and retrofitting of buildings. Brussels: *Comitee Europeen de Normalisation (CEN)*, 2005.

[2] C.A. Castiglioni, A. Kanyilmaz, A. Drei, L. Calado, I. Vayas, T. Rauert, R.M. Gonçalves. Dissipative devices for seismic resistant steel frames, *EUROSTEEL 2011*, August 31 - September 2, 2011, Budapest, Hungary.

[3] I. Vayas, Ph. Karydakis, D. Dimakogianni, G. Dougka, C.A. Castiglioni, A. Kanyilmaz A, et al. Dissipative devices for seismic resistant steel frames. The FUSEIS project, final report. *Research Programme of the Research Fund for Coal and Steel*, 2012.

[4] G. Dougka, D. Dimakogianni, I. Vayas, Innovative energy dissipation systems (FUSEIS 1-1) - Experimental analysis, *Journal of Constructional Steel Research*, **96,** 69–80, 2014.

[5] S. Avgerinou, I. Vayas, Behaviour of high strength steel FUSEIS seismic resistant systems, COMPDYN, 5th ECCOMAS Thematic Conference on Computational Methods in Structural Dynamics and Earthquake Engineering, 2015.

[6] Z.-T. Zhong, L.-H Lin, D.-Y. Wang. Strength and ductility of stiffened thin-walled hollow steel structural stub columns filled with concrete, *Thin Wall Struct*ures, **46**, 1113–1128, 2008.

COMPDYN 2017
6th ECCOMAS Thematic Conference on
Computational Methods in Structural Dynamics and Earthquake Engineering
M. Papadrakakis, M. Fragiadakis (eds.)
Rhodes Island, Greece, 15–17 June 2017

# DESIGN OF GROUTS FOR STRENGTHENING THREE OR TWO LEAF MASONRY WITH MUD MORTARS.

**Nikolopoulou Vasiliki**[1], **Adami Chryssi- Elpida**[2], **Vintzileou Elizabeth**[3], **Palieraki Vasiliki**[4]

[1] Civil Engineer, PhD Candidate, National Technical University of Athens, Faculty of Civil Engineering, villynik@central.ntua.gr

[2] Dr. Civil Engineer, National Technical University of Athens, Faculty of Civil Engineering, adamis@central.ntua.gr

[3] Professor, National Technical University of Athens, Faculty of Civil Engineering, elvintz@central.ntua.gr

[4] Dr. Civil Engineer, National Technical University of Athens, Faculty of Civil Engineering, vaspal@central.ntua.gr

**Keywords:** Masonry, Mud mortar, grout, reinforcement.

**Abstract.** *This paper presents the experimental procedure that has been followed, with main goal to develop various grout compositions adequate for strengthening stone masonry constructed with poor quality mortars. Two or three-leaf masonry frequently met in historic masonry structures is very vulnerable to environmental and seismic actions, especially when made with mud (very low strength) mortar. Although significant research effort is devoted to the development of grouts adequate for strengthening masonries made with lime or lime-pozzolan mortar, the respective studies on masonries made with mud mortar are scarce and inconclusive. Within the present work, a comprehensive investigation on mud mortars was conducted on samples that have been selected and sampled from three different buildings and sites, in order to identify their physicochemical and mineralogical properties, as well as their grain size distribution. Based on the studied samples of the aforementioned historical buildings with mud mortars, six wallettes were constructed, in order to study the mechanical properties of the two and three stone masonry before and after grouting. After the construction, non- destructive techniques (radar and boroscopy) were applied for the calibration of the methods and the comparison of the results before and after grouting, with main goal to develop various grout compositions according to the parameters which determine the efficiency of the intervention. Based on the characterization results, various grout mixes will be produced and will be examined in terms of compatibility between the mortar and the grout, as well as*

*injectability, fluidity, stability and penetrability. This research will lead to a number of suitable mixes that satisfy the performance criteria set for their design. The suitability of those mixes will then be checked by injecting them to the constructed wallettes.*

# 1 INTRODUCTION

Mud is one of the oldest building material, which has been used for thousands of years. It has been used on its own or in combination with other materials, such as lime, timber or stone, for the construction of various structures [1,2,3]. Mud-mortars, dated back to 8000BC, were found in structures in Mesopotamia and Babylonia. In Greece, the first examples of mud mortars were identified in the Neolithic settlements of Dimini and Sesklo. Nowadays, there are still buildings with this type of mortar, in several regions of Greece (i.e. Cyclades, Athens, Crete and Prespes Lake) [4].

Despite the long usage of this structure material over centuries, the respective studies on masonries made with mud mortar are scarce and inconclusive and include mainly studies on adobe and earthen structures. As mud mortars have different properties, depending on the parent ground and the climate conditions, a comprehensive investigation has to be conducted, to identify their physical and mineralogical properties, as well as their grain size distribution. These data are a prerequisite for the development of adequate strengthening techniques.

Based on the fact that mud mortars were used to several historic two or three- leaf masonry structures, there is the need to maintain and strengthen them. These masonries are vulnerable to environmental and seismic actions. For this reason, this study aims to (a) determine the physicochemical properties of historic mud mortars, (b) construct wallettes according to the traditional way and subject them to compression, (c) apply non- destructive techniques (radar and boroscopy) to the constructed wallettes for the calibration of the methods and the comparison of the results before and after grouting, with main goal to develop various grout compositions according to the parameters which determine the efficiency of the intervention.

# 2 EXPERIMENTAL WORK

## 2.1 Material characterization from samples on historical mud mortars

The sampling and characterization of historical mud mortars aims to determine the type of construction and use similar traditional materials for the reinforcement of this type of structures, based on the principle of the compatibility (repair materials should have similar properties with the authentic ones). At a first step, authentic mud mortars were carefully selected and sampled from three different buildings and sites (Saint Dimitrios, Marousi, Historic Building in Plaka, Rural house in Lasithi, Crete) dated back 19$^{th}$ century. The characterization findings of these indicative mud mortar samples did contribute to the final design of the wallettes that were constructed within this paper.



(a) (b) (c)

Figure 1: Buildings with mud mortars: (a) Saint Dimitrios, Marousi, (b) Building in Plaka, (c) Rural Building in Lasithi

The samples were subjected to chemical analysis with X-RAY fluorescence technique (XRF) (Table 1) and mineralogical analysis with X-RAY diffraction (XRD) (Figure 2).

Chemical analysis with XRF of the samples (Table 1) indicates that the main elements present are SiO2 and CaO, along with Al2O3, Fe2O3 MgO, K2O and Na2O having variable concentration. From XRD analysis (Figure 2), it can be concluded that all samples are composed mainly of Quartz. Particularly in Marousi sample calcite and albite minerals were present whereas kaolinite mineral was also identified in Plaka sample. Additionally, Crete sample is composed mainly of quartz and dolomite minerals.

| **Chemical elements** | **Concentration (%)** | | |
|---|---|---|---|
| | Sample I (Marousi) | Sample II (Plaka) | Sample III (Crete) |
| $Na_2O$ | 0.31% | 2.23% | 0.95% |
| MgO | 1.08% | 2.80% | 7.04% |
| $Al_2O_3$ | 3.20% | 5.07% | 10.41% |
| $SiO_2$ | 18.07% | 21.13% | 32.02% |
| $P_2O_5$ | 0.015% | 0.45% | 0.20% |
| $SO_3$ | 0.08% | 0.59% | 0.18% |
| Cl | 0.01% | 1.12% | 0.09% |
| $TiO_2$ | 0.22% | 0.33% | 0.66% |
| $K_2O$ | 0.95% | 3.25% | 2.95% |
| CaO | 37.89% | 26.92% | 13.12% |
| $Fe_2O_3$ | 2.09% | 3.51% | 4.75% |
| $ZrO_2$ | 0.82% | 0.80% | 0.75% |

Table 1: XRF results for the three samples of mud mortars.

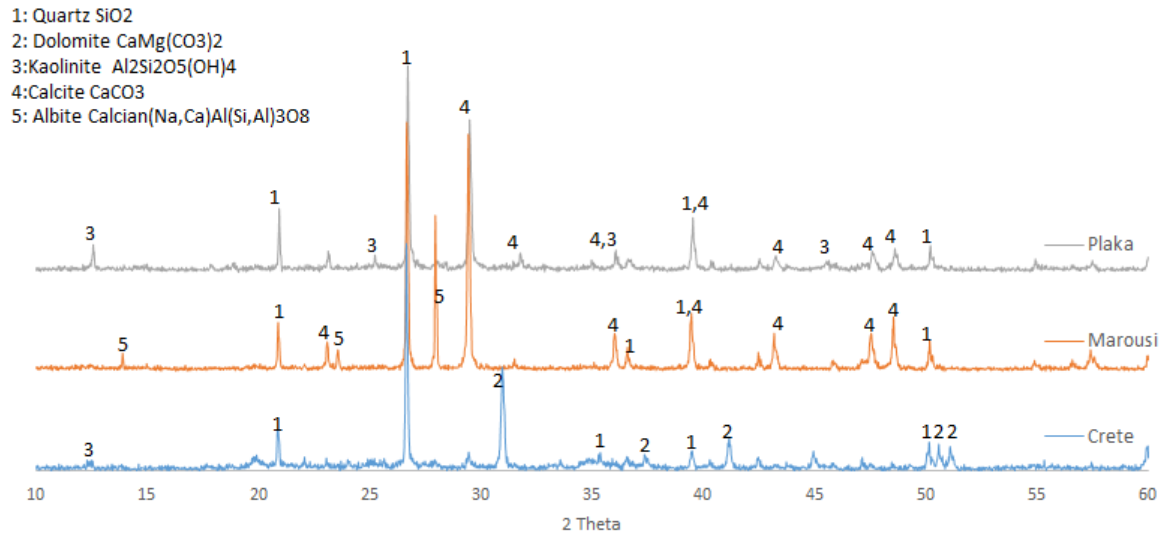


Figure 2: XRD results for the three samples of mud mortars.

Grain size distribution was conducted with combination of sieves for coarse particles and laser particle analysis for finer (<400μm) particles size (Figure 3, Figure 4). The particle mean

size value $D_{0.5\mu m}$ was found to be almost similar to all studied samples ($D_{0.5,Sample\ I}$ =67.16μm, $D_{0.5,Sample\ II}$ =78.21μm, $D_{0.5,Sample\ III}$ =70.28μm).

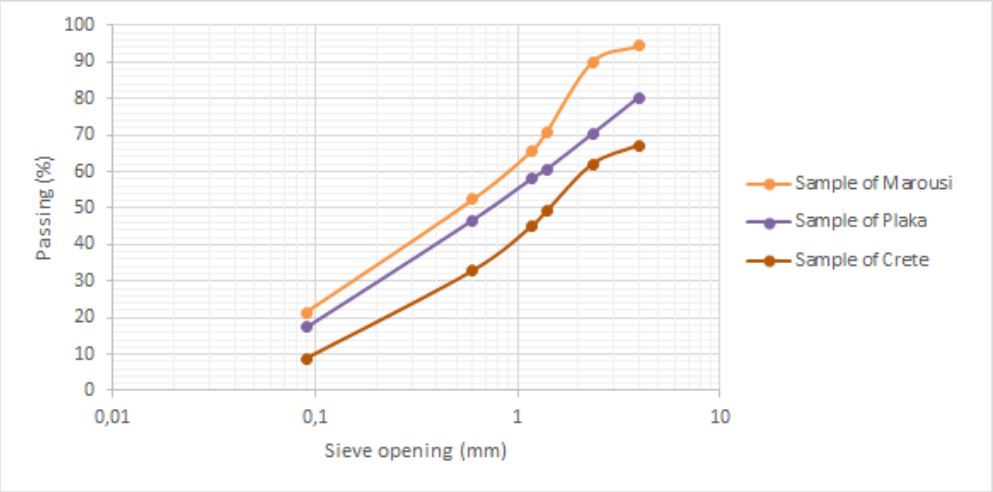


Figure 3 : Grain size distribution with the use of sieves for the three samples of mud mortars.

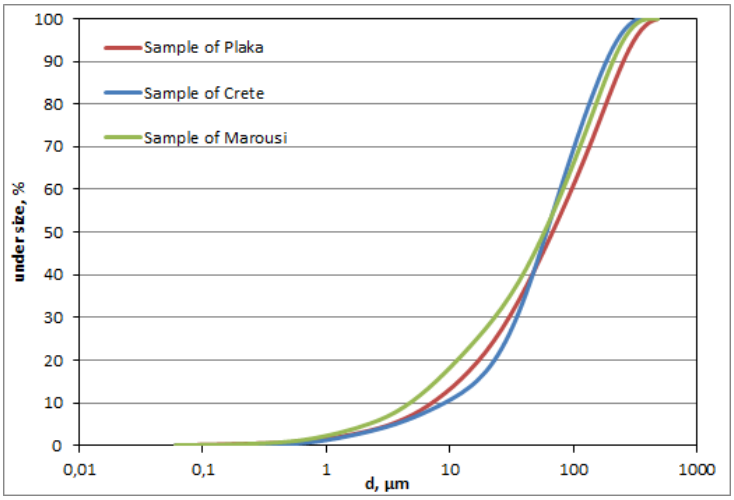


Figure 4: Grain size distribution of fine particles (<400μm) for the three samples of mud mortars.

## 2.2 Construction of two and three leaf wallettes

In order to study the mechanical properties of the two and three stone masonry before and after grouting, six wallettes were constructed.

### *2.2.1 Materials*

Based on the study of the aforementioned historical buildings with mud mortars, a stone from Sparta (Greece) was used for the construction of the stone masonry wallettes. Its compressive strength is approximately 70 MPa. Two compositions of mortar were used for the external leaves and the infill material of the wallettes. These compositions were selected on the basis of the research of the historic mortars and the relevant literature [5]. The soil used for the mortars was obtained from an Industry at Giannitsa that produces byzantine bricks. The river sand is from Aliartos river.

The proportions of the mortar components are given in Table 2, whereas the compressive and flexural strength of the two mortars at the age of 28 days are presented in Table 3.

From compressive and flexural tests that applied on mud mortars, it was found that the compressive strength of composition I is 35% higher compare to composition II. Additionally, for composition I, the flexural strength is almost half of its compressive one, whereas for composition II, the flexural strength greatly reduces.

| Compositions (%) | | | | | |
|---|---|---|---|---|---|
| | Soil | Sand (0-2.5 mm) | Gravel (0.5-3.5 mm) | Lime putty (with 40% water) | Water/soil (% w/w) |
| Composition I | 80 | 16 | 4 | - | 34.15 |
| Composition II | 75 | 16 | 4 | 5 | 41.09 |

Table 2: Proportions of the components of the mortars.

| | $f_{m,c}$ (MPa) | $f_{m,fl}$ (MPa) |
|---|---|---|
| Composition I | 4.55 | 2.76 |
| Composition II | 2.92 | 0.66 |

Table 3: Compressive and flexular strength of mortars.

### *2.2.2 Wallettes*

Six specimens were constructed. Three specimen with mud mortar (two with two-leaf masonry and one with three-leaf masonry) and other three specimens with mud mortar mixed with lime putty (two of them were made of two-leaf masonry and one of three-leaf masonry, as well). The dimensions of the masonry wallettes were selected to be comparable with other prior studies [6,7]: length=1.00m, height= 1.20m. The wallettes thickness was 0.45m and 0.30m for the three and two leaf masonry respectively. The two external leaves were constructed of stone masonry, with a thickness of 0.15m. Especially for the three leaf masonry the intermediate leaf is made of rubble materials (mortars and small stones) and no connection between the external leaves was considered. On the contrary in two leaf masonry there are connecting stones present. The walls specimens (Figure 5 and Figure 6) left to be curried for three months for future testing.

Upon construction, the wallettes were stepwise built by 30cm layers to avoid slump occuring from the mortar softness. Furthermore several cracks appeared on the exterior of the wallettes due to drying shrinkage of the mud mortar.



(a) (b) (c) (d)

Figure 5: Two-leaf masonries with mud mortar (a,b) and mud mortar with lime (c,d).



(a) (b) (c) (d)

Figure 6: Three-leaf masonries with mud mortar (a,b) and mud mortar with lime adding (c,d).

*2.2.3 Non-destructive techniques*

In-situ investigations were conducted on the six stone masonry wallettes, using non-destructive techniques, particularly radar technique and boroscopy. The main aim of the investigations was (a) to calibrate the two techniques on mud mortar stone masonry, (b) to check clay interferences on the measurements (clay affects the accuracy of the emitted and received signal of radar, due to the attenuation of the signal [8]) and (c) to gain data for comparison after grouting of wallettes.

**Radar technique** is a non-destructive technique, therefore suitable for historic structures. The technique is based on the theory of electromagnetic signals. Using a radar system, consisting of a central unit and an antenna of 1600MHz, electromagnetic signals are emitted-through the material under investigation. When the signal meets an interface (be it a void or a discontinuity within the material or a different material), part of the emitted radiation is reflected and recorded by the central unit and part of it travels deeper into the material. Prior to the application, calibration of the measurements has taken place in converting the time units into length units.

According to the calibration of the method, the dielectic constant of each type of masonry differs, as it depends on the materials, the thickness and the voids in the interior of the examined element. The dielectic constant of the three-leaf masonry with mud mortar mixed with lime was estimated equal to 8.7, whereas for the three-leaf masonry with mud mortar was equal to 10 (Figure 7). The dielectic constant of the two-leaf masonry with mud mortar and lime is approximately equal to 8.5, while for the one with mud mortar, it is equal to 9.0. The value of dielectric constant of two-leaf masonry is smaller, due to the fact that this type of masonry is more compact (smaller voids in the interior of masonry), compared to the three-leaf masonry.

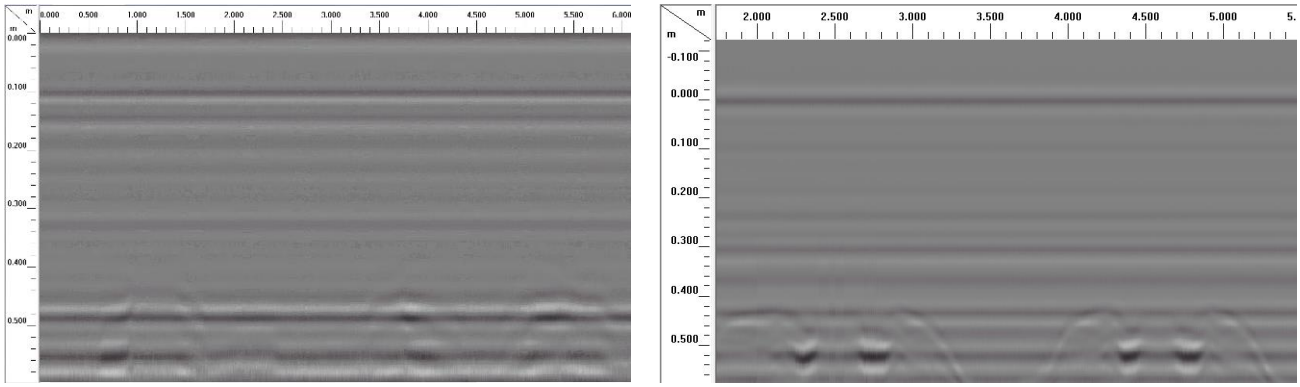

(a) (b)

Figure 7: Static test for calibration on three-leaf masonries: (a) Composition I, (b) Composition II

Despite the fact that clay affects the clarity of the measurements, no significant interactions observed in all the measurements (horizontal and vertical) that were carried out. Clear indications of the stones of the examined leaf were found (Figure 8).

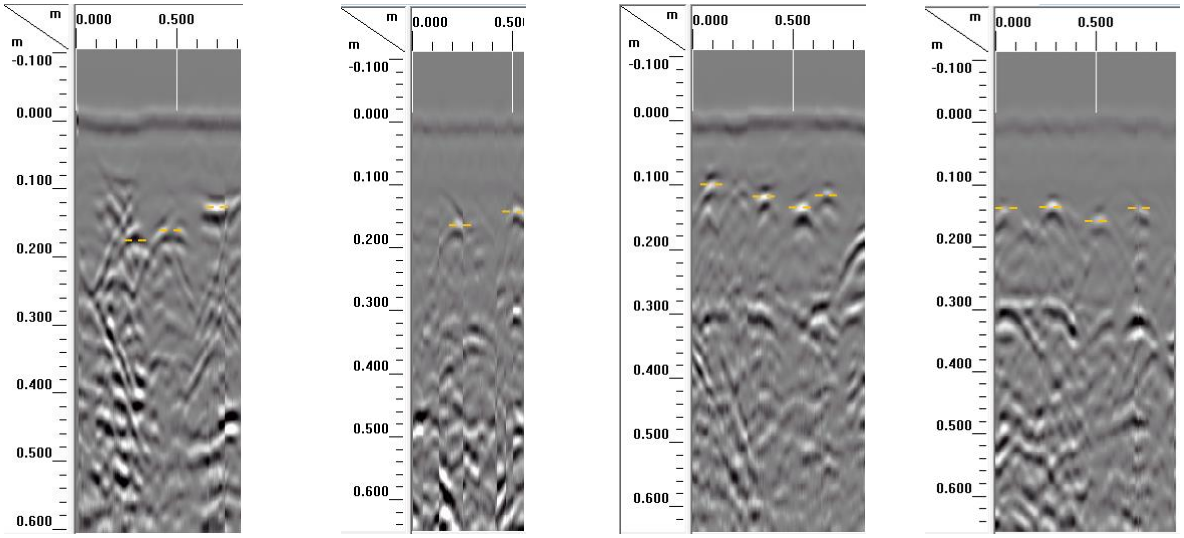

(a) (b) (c) (d)

Figure 8: Radar measurements: (a) Three- leaf masonry with Composition I, (b) Three leaf masonry with Composition II, (c) Two- leaf masonry with Composition I, (d) Two-leaf masonry with Composition II.

Boroscopy is one of the techniques often applied in combination with the radar technique. It is usually applied to historic (two or three leaf) stone masonries, in order to investigate their construction type within the thickness of the wallette. Small diameter holes (25mm or smaller) are drilled in masonry or already formed holes are used. After meticulous cleaning of the hole from dust and loose material, the boroscope is introduced into the hole. The core of the boroscope, consisting of optical fibres, allows for direct observation of the interior of the walls. In addition, pictures can be taken at various depths.

By the use of the boroscope, the voids between the stones, in the interior leaf of the three leaf stone masonry, can be seen in Figure 9.

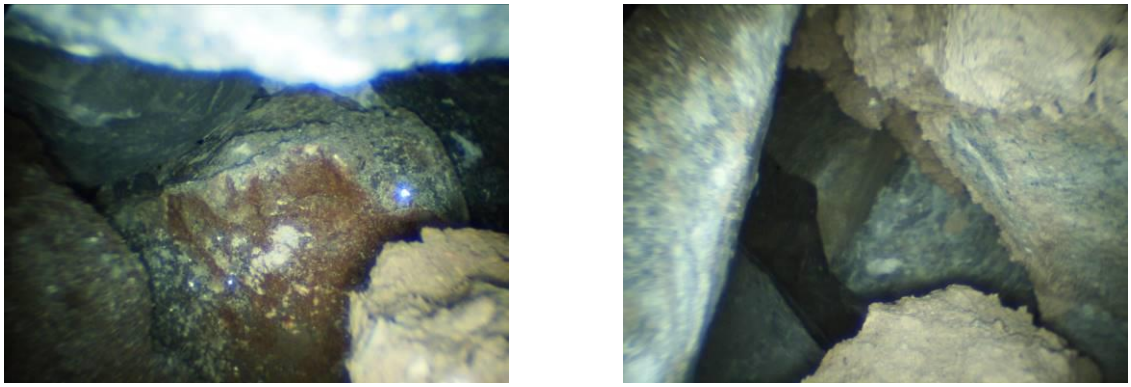

(a) (b)

Figure 9: Voids in the three-leaf wallettes: (a) Composition I, (b) Composition II.

Furthermore, from the application of the method in the two-leaf stone masonries, the different color of the mortars is observed, as it was expected from the construction. There is also voids and discontinuities within the mortar (Figure 10).

The presence of voids in the interior of the masonries indicates that the grouting as a repair technique may be applicable and efficient for the strengthening of two and three leaf masonry having poor mortar quality.

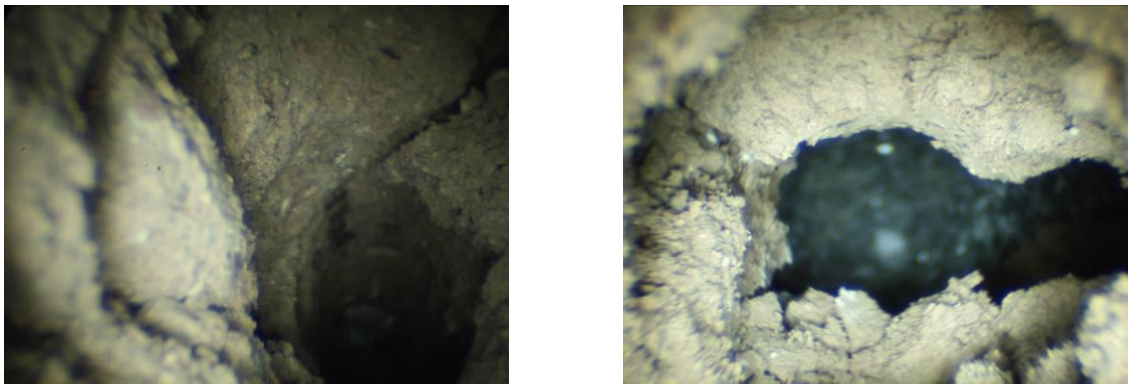

(a) (b)

Figure 10: Voids in the two-leaf wallettes: (a) Composition I, (b) Composition II.

## 2.3 Grout mixes for strengthening masonry with mud mortars

One of the most frequently applied strengthening techniques for stone masonry is grouting. Two or three-leaf masonry quite common in historic masonry structures tend to loss the bond between the two leaves, especially when made with poor quality mortar [12]. Although significant research effort was devoted to the development of grouts adequate for strengthening masonries made with lime or lime-pozzolan mortar, the respective studies on masonries made with mud mortar are scarce and inconclusive. Investigations determine the properties of earthen structures can be found in [9,10,11]. Within the present work, a comprehensive investigation on mud mortars was conducted on samples, to identify their psychical and mineralogical properties, as well as their grain size distribution. Based on this study, a series of experiments have been designed for the development of grouts adequate for strengthening stone masonry constructed with mud mortars. Compatibility between the mortar and the grout, injectability, fluidity, stability and penetrability are the basic criteria for the selection of the most suitable mixes. For this reason, a thorough research investigation take place to determine the physical, rheological, chemical and mechanical characteristics of the designed mixes. This research will

lead to a number of suitable mixes that satisfy the performance criteria set for their design. The suitability of those mixes will then be checked by injecting them to the six masonry specimens that have been constructed. The efficiency of the grouting will be checked by the use of non- destructive techniques.

## 3 CONCLUSIONS

- The investigation of the physicochemical properties (chemical (XRF) analysis, mineralogical analysis (XRD) and grain size distribution analysis) of authentic mud mortars gives useful information about the components of them for the production of similar mortars, compatible with the authentic ones.
- Non-destructive techniques such as radar technique and boroscopy, were applied to six stone masonry wallettes before grouting, giving valuable information about the voids and the discontinuities in the interior of the wallettes. The results will be used in comparison with the ones after grouting.
- The observation of the interior of the wallettes and the cracks on the exterior leaves promotes the use of grouts for strengthening stone masonry constructed with mud mortars.

## ACKNOWLEDGEMENTS

This work has been financed by the State Scholarships Foundation (IKY), through the program “Research Projects for Excellence IKY/SIEMENS.

## REFERENCES

[1] R. Curtis, *Clay Mortars for Masonry Buildings, Historic Scotland*, INFORM, July 2015.

[2] Olivier M, El Gharbi Z., Mechanical behavior of earthwall panels: Experimental Investigations, *3rd International Masonry Conference*.

[3] Houben H., Guillaud H., Earth Construction: A comprehensive guide, *CRATerre-EAG, ITDG Publications*, 2003.

[4] V. Pachta, M. Stefanidou, S. Konopisi, I. Papayianni, Technological Evolution of Historic Structural Mortars, *Journal of Civil Engineering and Architecture*, Vol. 8, No7, pp. 846-854, July 2014.

[5] G. Bei, I. Papayianni, Compressive strength of compressed earth block masonry, *Transactions on the Built Environment, Structural Studies, Repairs and Maintenance of Heritage Architecture VIII*, Vol. 66,pp. 367-375, 2003.

[6] Adami C.E., Vintzileou E., Mouzakis Ch., Badogiannis E., Kalagri A., The effect of hydraulic lime pozzolanic grouts on the mechanical properties of three-leaf stone masonry in compression, *Structural Analysis of Historical Constructions*, 2012.

[7] Vintzileou E., Mechanics of three-leaf masonry before and after grouting, *International Journal of Architectural Heritage*, 2010.

[8] Daniels, D.J. (1996). Surface-penetrating radar. The Institution of Electrical Engineers, Radar, Sonar, *Navigation and Avionics Series*, London.

[9] Chaudry C., Evaluation of Grouting as a Strengthening Technique for Earthen Structures in Seismic Areas: Case Study Chiripa, *Master Thesis, University of Pennsylvania*, 2007.

[10] Papayianni I., Pachta V., Experimental study on the performance of lime-based grouts used in consolidating historic masonries, *Materials and Structures*, 2015.

[11] Papayianni I., Pachta V., Constructional characteristics and Restoration aspects of Historic Earth Block Structures, *Engineering Structures and Materials*, 2015.

[12] Toumbakari E., Lime-pozzolan-cement grouts and their structural effects on composite masonry walls, *Doctor Thesis, Katholieke Univ. Leuven*, 2002.

COMPDYN 2017
6th ECCOMAS Thematic Conference on
Computational Methods in Structural Dynamics and Earthquake Engineering
M. Papadrakakis, M. Fragiadakis (eds.)
Rhodes Island, Greece, 15–17 June, 2017

# NUMERICAL ASSESSMENT OF CONCAVE SLIDING ISOLATOR'S MECHANICAL BEHAVIOR UNDER BI-DIRECTIONAL MOTION

**Dario De Domenico**[1], **Giuseppe Ricciardi**[1], **and Gianmario Benzoni**[2]

[1]Department of Engineering, University of Messina
Contrada Di Dio, 98166 Sant'Agata, Messina, Italy
e-mail: dario.dedomenico@unirc.it, gricciardi@unime.it

[2]Department of Structural Engineering, University of California San Diego, La Jolla, California, 92093-0085, USA
e-mail: gbenzoni@ucsd.edu

**Keywords:** Friction pendulum system (FPS), seismic isolation, multi-directional excitation, friction coefficient degradation, finite element model, coupled thermo-mechanical analysis.

**Abstract.** *In this contribution, some aspects of the mechanical behavior of friction pendulum (FP) isolators are investigated from a numerical point of view. Attention is focused on the distinctive features observed in FP bearings when subjected to multi-directional excitations like those occurring in a real earthquake scenario. Due to the peculiarities related to the kinematics of the device and the curvature of the sliding surface, neglecting the bi-directional interaction and considering a uni-directional idealization would lead to underestimate the displacements expected during seismic events and to overestimate the dissipative capacity of the isolator accordingly. Furthermore, the resultant horizontal force of the FP bearing may differ markedly from what expected (and predicted by most numerical models) in the uni-directional case. This deviation is mainly ascribed to the geometrical features of the device itself. Additionally, the force-displacement behaviour of the FP bearing depends upon the coefficient of sliding friction, which is not constant as postulated by the simplified Coulomb model but varies during the course of an earthquake with sliding velocity, vertical load and, above all, repetition of cycles and consequent heating phenomena arising at the sliding interface. Among these effects, frictional heating has been recognized as the most important factor that affects the FP maximum displacement because it may induce significant friction degradation, consequently it should be properly considered in a truthful model of the FP bearing via a sophisticated coupled thermo-mechanical analysis.*

*The aim of this paper is to scrutinize the above physical phenomena by means of a 3D finite element model. The developed model allows us to closely analyze the kinematics of the device, to assess the contact force distribution between the sliding surfaces and to examine certain nonlinear phenomena that become manifest especially during bi-directional excitations.*

## 1 INTRODUCTION

In the last decades, the Curved Surface Slider (CSS), also known as the Friction Pendulum System™(FPS) [20, 18, 9], has been extensively and increasingly adopted as base-isolation strategy of buildings, bridges and industrial facilities. The worldwide popularity of the FPS is mainly due to the attractive features of FP bearings as compared to other isolators (e.g. elastomeric bearings) having similar characteristics. Among others, it is worth recalling the following factors that have contributed to the success of this technology: *i*) inherently low vibration frequency even when the mass pertaining to each isolator is not particularly high since the natural period primarily depends on the radius of curvature of the concave sliding surface rather than on the supported mass; *ii*) large displacement capability, limited only by the in-plane geometric dimensions of the device; *iii*) compact shape with considerably lower thickness than the elastomeric devices, a feature that makes them appealing for seismic retrofitting of existing structures; *iv*) theoretically zero residual displacements owing to the self-centering action induced by the pendulum operating principle; *v*) quite stable energy dissipation mainly controlled by the tribological properties of the sliding interfaces, a field on which material science has made significant progress in developing high performance materials with enhanced durability, mechanical and physical characteristics, see e.g. [12, 15, 19].

Besides these advantages, experimental investigations on FP bearings have shed light on their highly complex, nonlinear mechanical behavior, especially when tested under multi-directional paths like in a real earthquake scenario [5, 13, 14, 10, 16]. Nevertheless, some aspects recorded in experiments are not properly addressed in existing codes and typically neglected in structural models, based on extreme simplification of the device behavior. A few sources of this nonlinearity and the causes for such a complex mechanical behavior of FP bearings are discussed and analyzed in this paper.

In its single concave configuration, cf. Fig. 1, the FP bearing is composed of a primary, lower sliding surface made of polished stainless steel and having a concave profile with curvature radius $R$, which determines the natural period of vibration and allows the horizontal movement according to the pendulum operating principle, and an upper steel plate featuring a secondary concave sliding surface via an internal semi-spherical articulation of radius $r$, the latter permitting the rotation and assuring the kinematic compatibility of the overall motion. In between these two opposed surfaces a lentil-shaped articulated steel slider is placed, whose upper and lower external surfaces are both convex-shaped so as to match the two concave profiles described above. These two external surfaces of the slider are coated with a pad of material having specific frictional properties, typically high-bearing-capacity polymer composites like polytetrafluoroethylene (PTFE, Teflon®), PTFE-based composites with fillers or other enhanced variants of thermoplastic, self-lubricating polymers such as ultra-high-molecular-weight polyethylene (UHMWPE). It is worth noting that the coefficient of friction plays a key role in dissipating seismic energy and limiting accelerations and displacements induced in the isolated structure. As will be shown in this paper, special care should be taken to the technological design and manufacturing aspects not only of the primary sliding surface, but also of the secondary rotation surface, indeed also the latter surface affects, to some extent, the overall energy dissipated by the device. Recent progress achieved in the development and improvement of materials along with sophisticated lubrication techniques have permitted manufacturing FP bearings with very small dynamic friction coefficients, down to the order of $\approx 1 \div 5\%$ [5, 14]. The FPS is sometimes presented in an upside-down configuration as compared to Fig. 1, i.e., with the primary sliding surface on the top rather than on the bottom, however this different geometric

layout does not affect the mechanical behavior of the device as a whole. Regardless of the geometric variants, the single CSS and the more recent advancements in double [9] and triple [19] CSS alike are highly flexible devices in the horizontal direction and stiff in the vertical one.

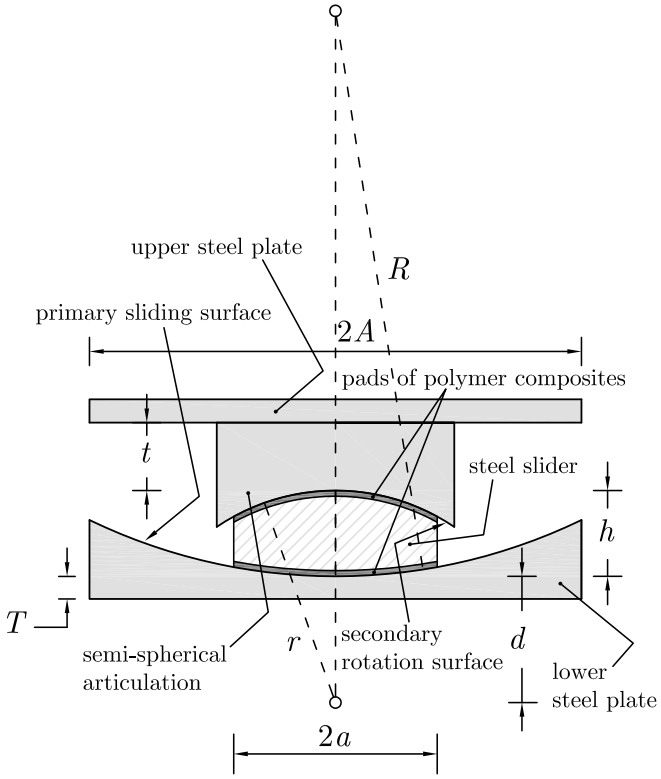


Figure 1: Section through a FP bearing (single concave configuration) with constituting elements and materials

The goal of this paper is to examine, from a numerical point of view, some aspects of the mechanical behavior of FP bearings. Attention is focused on the distinctive features observed in FP bearings when subjected to multi-directional paths like in a real earthquake scenario. First, we overview the simplest mechanical model based on the unidirectional idealization in conjunction with the Coulomb-type friction model (i.e., a constant value of the friction coefficient is assumed). Then, we critically identify the reasons why the above simplistic idealization fails to capture the actual hysteretic behavior of the FPS as recorded experimentally. To this aim, a 3D finite element (FE) model is set up in order to simulate the mechanical behavior of a real FP bearing. The examined isolator was tested at the Caltrans SRMD testing facility at the University of California San Diego (UCSD) [13, 14]. Reference experiments concern cloverleaf bi-directional tests under three different vertical loads. Also monodirectional tests with the single cloverleaf components were performed, and simulated in the FE model accordingly, in an attempt to highlight the salient differences in comparison with the bi-directional counterpart. Some interesting remarks arise from the critical analysis of the numerical results: the developed FE model allows us to closely analyze the kinematics of the FP isolator, to assess the contact force distribution between the sliding surfaces and to compare the force-displacement hysteretic loops under bi-directional and mono-directional excitations.

## 2 UNIDIRECTIONAL MODEL WITH COULOMB FRICTION

The simplest model describing the mechanical behavior of FP bearings is based on the assumption of constant value of vertical load and constant value of the coefficient of sliding friction (Coulomb simplified theory). According to what summarized in the previous section, the FPS incorporates in a single device both the re-centering action, which is due to the curvature of the sliding surface, and the energy dissipation by friction: indeed, as the slider displaces over the concave primary surface, a continuous re-centering force is provided by the gravity load of the supported mass based on the pendulum operating principle and, simultaneously, the frictional force opposes the motion of the slider thus dissipating hysteretic energy.

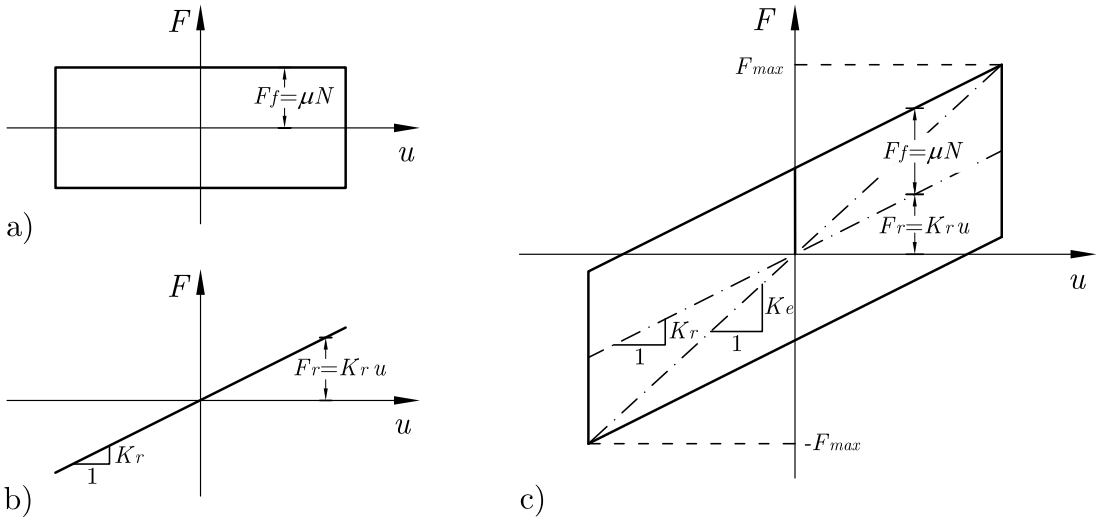


Figure 2: Force-displacement behavior contributions: a) frictional $F_f$; b) pendulum (restoring) $F_r$; c) total $F$

Therefore, the mathematical model describing such mechanical behavior is the simple bilinear force-displacement curve depicted in Fig. 2. More specifically, the pendulum mechanism would make the natural period (and the stiffness alike) of the FPS uniquely dependent on the sliding surface radius. The restoring (re-centering) force, directed towards the geometric centre of the concave sliding surface throughout the isolator motion, is expressed as follows, cf. Fig. 2b)

$$F_r = K_r\, u \qquad \text{with} \quad K_r = \frac{N}{R_{\text{eff}} \cos\theta}\,, \tag{1}$$

where, with reference to the schematic kinematic analysis sketched in Fig. 3, $R_{\text{eff}} = R + d$ is the so-called effective radius of the pendulum that accounts for the dimensions of the slider ($d = r - h$) [9, 13], $N$ is the vertical load acting on the FPS and $\theta$ is the rotation angle associated with the horizontal (radial in 3D) displacement $u$, which identifies the position of the slider. From Eq. (1) it is found that the lateral stiffness $K_r$ associated with the restoring force is a function of the vertical load and the isolator geometrical characteristics. Under some simplified hypotheses (frictionless contact, zero deformation of the slider and negligible rotations of the top and bottom plates as compared to the angle $\theta$), the horizontal and vertical displacements can be expressed through the following closed-form relations, respectively [13]

$$u = R_{\text{eff}} \sin\theta\,, \qquad w = R_{\text{eff}}\,(1 - \cos\theta). \tag{2}$$

The upper plate of the FPS (together with below semi-spherical articulation) moves along a circular (spherical in 3D) surface of radius $R_{\text{eff}}$. For the usual dimensions of the slider in commercially available FPS the effective radius is $R_{\text{eff}} \simeq 1.08 \div 1.10R$, which implies that neglecting the dimensions of the slider in computing the curvature radius of the sliding surface would lead to an overestimation of the restoring stiffness of approximately $10\%$ [13] (the expected displacements of the device would be underestimated accordingly).

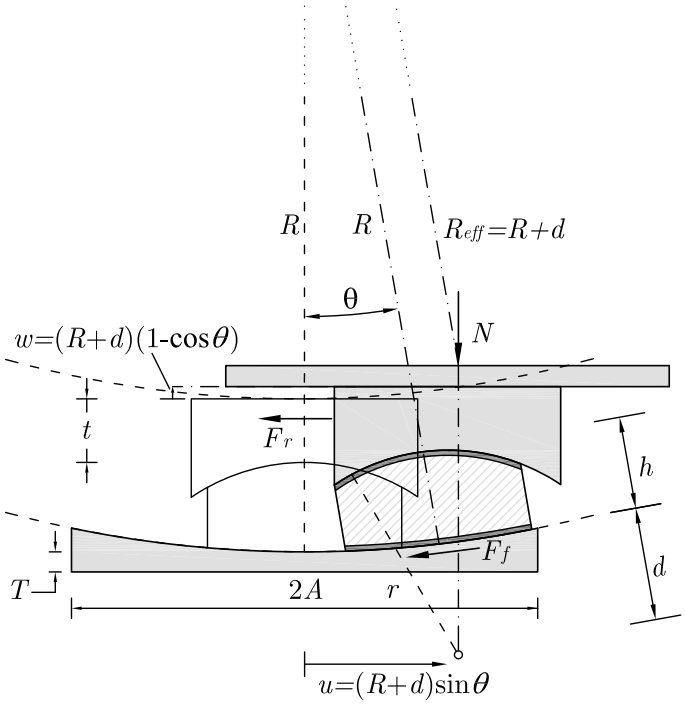


Figure 3: Schematic kinematic analysis of a FP bearing

In reality, the frictional contribution slightly modifies the simple pendulum mechanism described by Eq. (1). According to the simplified Coulomb theory for sliding bodies, the friction force opposes the sliding motion and is expressed by the product of the friction coefficient $\mu$ and the vertical load acting on the isolator, cf. Fig. 2a)

$$F_f = \mu N \text{sgn}(\dot{u}) \tag{3}$$

where $\dot{u}$ represents the sliding velocity and $\text{sgn}(\cdot)$ is the signum function so that $F_f = \pm\mu N$ depending on whether $\dot{u}$ is positive or negative, respectively. The combination of the restoring contribution (1) and the frictional contribution (3) yields the following unidirectional rigid-plastic hysteretic model for the total horizontal force [20], cf. Fig. 2c)

$$F = F_r + F_f = \frac{N}{R_{\text{eff}} \cos\theta}\, u + \mu N \text{sgn}(\dot{u}). \tag{4}$$

If some specific geometric and mechanical conditions regarding the isolation system are met, an equivalent linear visco-elastic model can be assumed [1, 7]. The nonlinear behavior shown in Fig. 2c) is thus converted into an equivalent linear one as if a simpler spring-damper system could reflect the FPS hysteretic behavior. The equivalent linearized behavior is characterized

by a so-called effective stiffness and an effective damping[1] expressed as, respectively

$$K_{\text{eff}} = \frac{N_d}{R_{\text{eff}} \cos\theta} + \mu \frac{N_d}{u_d}, \qquad \xi_{\text{eff}} = \frac{2\mu R_{\text{eff}} \cos\theta}{\pi(\mu R_{\text{eff}} \cos\theta + u_d)} \tag{5}$$

and the effective natural period of vibration may easily be calculated from (5) as follows

$$T_{\text{eff}} = 2\pi\sqrt{\frac{M}{K_{\text{eff}}}} = 2\pi\sqrt{\frac{N_d}{\text{g}\, K_{\text{eff}}}} = 2\pi\sqrt{\frac{u_d\, R_{\text{eff}} \cos\theta}{\text{g}\,(u_d + \mu R_{\text{eff}} \cos\theta)}} \tag{6}$$

where $N_d$ and $u_d$ are the "design" vertical load (mass of the superstructure multiplied by the acceleration of gravity g) and displacement, respectively. Typical values of the effective damping range from $10\%$ up to $30 - 40\%$, mainly depending on the friction coefficient of the lining material, the curvature radius and the design displacement. By inspection of Eqs. (5) and (6), the following four remarks arise:

1. both the parameters $K_{\text{eff}}$ and $\xi_{\text{eff}}$ depend on the displacement, consequently an iterative procedure should be applied in which a design displacement, say $u_1$, is assumed as first-attempt value, the relevant stiffness (and corresponding natural period) and damping values are computed through Eqs. (5) and (6), then a new spectral ordinate in terms of displacement, say $u_2$, is identified from the response spectrum for the maximum considered earthquake, with $u_2 \neq u_1$ in a general case, hence the procedure is carried on iteratively by adjusting $K_{\text{eff}}$ and $\xi_{\text{eff}}$ with the new displacement $u_2$ until convergence is achieved;

2. the effective stiffness linearly depends on the vertical load: this makes the stiffness centre and mass centre of the isolation system coincident, thus nullifying the torsional effects about the vertical axis, moreover the natural period imposed to the superstructure is not affected by the supported mass as emphasized by Eq. (6);

3. the linear visco-elastic idealization implicitly assumes, in the expression of $K_{\text{eff}}$ and $\xi_{\text{eff}}$, that the friction coefficient remains constant throughout the seismic event, which is not true as better clarified in the following subsection;

4. the $K_{\text{eff}}$ and $\xi_{\text{eff}}$ parameters arise from a simple unidirectional idealization of the FPS behavior, whereas multi-directional excitations actually occur in a real earthquake scenario.

The last two aspects may induce significant numerical errors and may lead to wrong outcomes in terms of forces, displacements and energy dissipation prediction as better clarified in the following subsection.

### 2.1 Critical remarks on the unidirectional model with Coulomb friction

The simplified rigid-plastic idealization given in Eq. (4) is based on the assumptions that: 1) $N$ is constant; 2) $\mu$ is constant; 3) the device motion is unidirectional or, equivalently, the horizontal response is uncoupled in two orthogonal directions. Unfortunately, such idealization is not appropriate in most cases and the underlying assumptions cannot reflect the actual hysteretic behavior of FP bearings measured in experimental tests. In this regards, a few observations and critical remarks are made in this subsection to justify this statement.

[1] Adopting a common terminology of most building codes [1, 7], the adjective *effective* denotes the linearized counterpart of an intrinsically nonlinear variable.

First of all, it is worth noting that the vertical load acting on a FP bearing in an isolation system evolves during an earthquake due to the feedback (dynamic interaction) exerted by the superstructure when subjected to the vertical and horizontal shaking. This leads to a rocking behavior, normal force fluctuations and consequent continuous changes in both $F_f$ and $K_r$ (implying changes in the restoring force $F_r$ as well). Therefore, both the terms in Eq. (4) vary over the course of an earthquake, which is not considered in the effective parameters introduced in Eqs. (5) and (6) and adopted in most building codes and seismic standards (see e.g. [1, 7]).

Second, in principle the lining material coating the upper and lower surface of the slider, cf. again Fig. 1, should be selected such that guarantees stable and reliable frictional behavior under a range of contact pressures, sliding velocities and temperatures typically arising in seismic service conditions. Additionally, it should be able to provide adequate load bearing capacity, minimum wear and degradation due to ageing, travel and accumulated movements, and should be characterized by a melting temperature well above the maximum temperature experienced in seismic conditions. Unfortunately, friction degradation and wear in thermoplastic materials are rather complex phenomena that are actually affected by operating conditions. This is why it is widely recognized that the friction coefficient evolves over the course of an earthquake. More specifically, a plethora of studies have been presented in the literature addressing the dependence of the friction coefficient upon contact pressure, sliding velocity and repetition of cycles that induces temperature rise at the sliding interfaces, see e.g. [3, 5, 9, 10, 11, 13, 14, 17] just to quote a few. The common backbone of these studies is to alert the structural designer against oversimplification of the FPS behavior at the modeling stage. A concise yet effective overview of the variability of $\mu$ with the operating conditions occurring during an earthquake is provided in [8]. For instance, the sliding velocity affects the friction coefficient as a result of the viscous nature of the PTFE-type composite used for the liner. A simple and widely recognized expression, incorporated in a few software codes like SAP 2000 [4], is that proposed by Constantinou *et al.* [5]

$$\mu = \mu_{\text{max}} - (\mu_{\text{max}} - \mu_{\text{min}}) \exp(-\alpha|\dot{u}|) \tag{7}$$

where $\mu_{\text{max}}$ and $\mu_{\text{min}}$ are the coefficients of friction at large and very low sliding velocity, respectively, and $\alpha$ is a constant (for given bearing pressure) determining the shape of the relationship. According to (7) the coefficient of friction increases with increasing sliding velocity up to a constant value reached at a specific velocity threshold (approximately $130$ mm/s in [5], a bit lower namely about $25$ mm/s in [16]). Quite similar exponential relationships to Eq. (7) have been developed by researchers to describe the dependence of $\mu$ upon contact pressure [11, 14] as well as upon heating of the sliding interface [11, 17] or, equivalently, some related parameter quantifying the energy dissipated over the repetition of cycles [10, 14]. In particular, the coefficient of friction decreases with increasing pressure and approaches a constant value at high pressure values and, similarly, progressively reduces with the distance traveled due to frictional heating. Therefore, the friction force reported in (3) and (4) should be corrected as follows

$$F_f = \mu N \qquad \text{with} \quad \mu = \mu(N, v, T) \tag{8}$$

where it is emphasized that the friction coefficient to be implemented in FPS models is a function of the vertical load (or contact pressure), sliding velocity and temperature.

Third, earthquake excitations are generally multidirectional but the model described in (4) assumes the FPS response is uncoupled in two orthogonal directions. On the contrary, experimental investigations [10, 13, 16] have demonstrated that there exists significant coupling

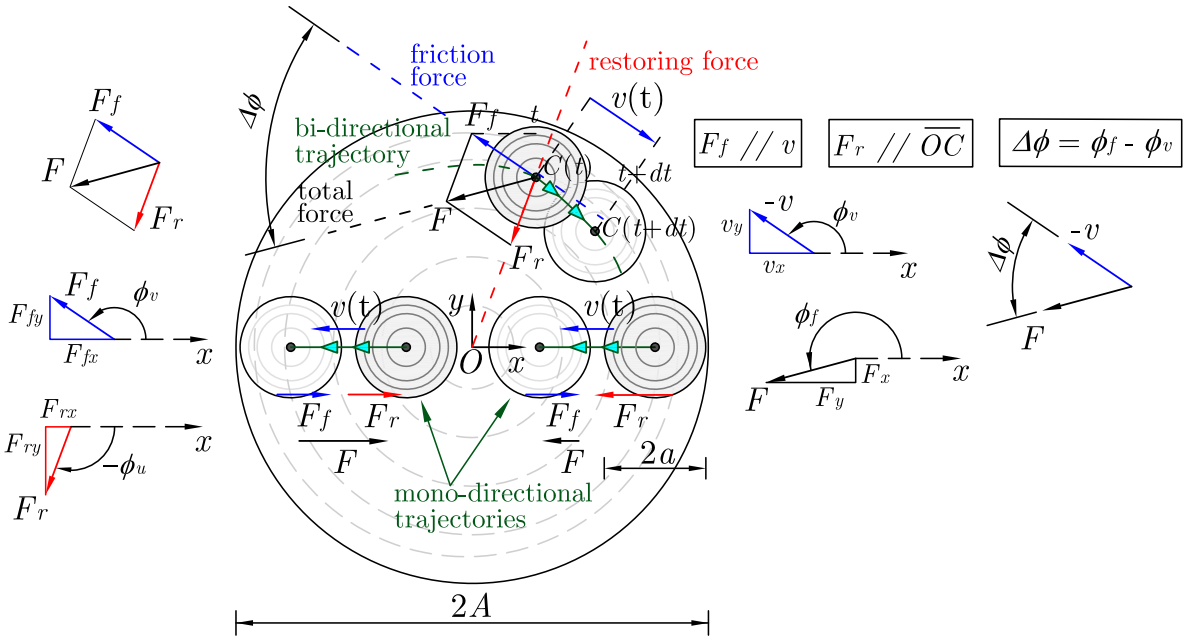


Figure 4: Photograph at two time instants of in-plane motion of the slider with the resulting forces highlighted

between the orthogonal components of the FPS response (bi-directional interaction). Indeed, for bi-directional motion the displacements and forces across the isolator are expressed by vectors, i.e. $\mathbf{u} = [u_x, u_y]^T$, $\mathbf{F} = [F_x, F_y]^T$, and the force-displacement relationship is expressed as

$$\begin{bmatrix} F_x \\ F_y \end{bmatrix} = \begin{bmatrix} F_{rx} \\ F_{ry} \end{bmatrix} + \begin{bmatrix} F_{fx} \\ F_{fy} \end{bmatrix} = \frac{N}{R_{\text{eff}}} \begin{bmatrix} u_x \\ u_y \end{bmatrix} + \mu N \frac{1}{\|\dot{\mathbf{u}}\|} \begin{bmatrix} \dot{u}_x \\ \dot{u}_y \end{bmatrix} \tag{9}$$

from which Eq. (4) is retrieved for the special case of a uni-directional excitation. The in-plane motion of the slider is sketched in Fig. 4 along with the force components entering Eq. (9). At any instant of time, the slider interface undergoes a displacement increment in the direction specified by the angle $\phi_v$ with respect to the $x$-axis, with $\phi_v = \arctan(\dot{u}_y/\dot{u}_x)$. The direction of frictional forces is the same as that of the displacement increment defined by $\phi_v$ (and depends on the magnitude of the instantaneous velocity $\|\dot{\mathbf{u}}\| = \sqrt{\dot{u}_x^2 + \dot{u}_y^2}$), whereas the line of action of the restoring (re-centering) force is radial, i.e., is parallel to the vector $\overline{OC}$ at any time instant, with $O$ being the center of the isolator and $C$ the center of the lower interface of the slider. For a reference axis system with origin at the center of the isolator as that shown in Fig 4, the direction $\overline{OC}$ can be represented by the angle $\phi_u = \arctan(u_y/u_x)$. Finally, the direction of the total force is identified by the angle $\phi_f = \arctan(F_y/F_x)$. From Fig. 4 it emerges that an angular shift exists between the directions of the velocity vector and the force vector, namely $\Delta\phi = \phi_v - \phi_f$. Indeed, the restoring force component gives rive to deviations of the total resisting force with respect to the active seismic force that is directed along the traveled trajectory (or instantaneous velocity). We notice that these deviations would be zero both under uni-directional excitations (because in this case the restoring force would be parallel to the traveled trajectory) and under general multi-directional excitations but flat (not concave) sliding surface (because in this case the restoring force would cancel out as $R_{\text{eff}} \to \infty$ in Eq. (9)). Moreover, by comparing Eq. (9) with Eq. (4) it is found that neglecting the orthogonal coupling in bi-directional excitations leads to an underestimation of displacements and an overestimation of forces (and dissipation of energy), thus implying that the design of the overlying isolated

Table 1: Geometrical data of the analyzed FPS (after Lomiento *et al.* [13])

| geometric dimension | length [mm] |
|---|---|
| $A$ | 435 |
| $a$ | 180 |
| $R$ | 2235 |
| $r$ | 375 |
| $T$ | 40 |
| $t$ | 120 |
| $h$ | 160 |
| $d$ | 215 |

structure would be carried out in a nonconservative (unsafe) manner. It is concluded that in the majority of cases uni-directional analyses are not capable of capturing the actual seismic response of the FPS.

## 3 NUMERICAL FINITE ELEMENT MODEL

Among the research contributions in the field of finite element modeling of FP bearings, one of the pioneering work is that of Tsai *et al.* [18], who successfully developed a general 3D FE formulation including local bending moments at the bottom of the isolator and vertical force variation, the latter aspect being of significant importance for a correct friction force calculation. From this research work on, later contributions in the relevant literature have been focused on the development of predictive models for the determination of the dynamic friction coefficient as well as for the identification and description of the physical phenomena connected to friction degradation (or friction evolution) under seismic events.

Along this research line, this contribution aims at investigating the mechanical behavior of FP bearings through a 3D finite element model. A real, full-scale (single concave) FPS is addressed in this paper that was tested at the Caltrans SRMD laboratory at the UCSD [13]. With reference to the symbols defined in the sketch of Fig. 1, the analyzed FPS is characterized by the geometric dimensions reported in the following Table 1.

### 3.1 Simulated testing protocol

The testing protocol performed in [13] and simulated in the FE model of this paper concerns bi-directional tests following a cloverleaf path (sometimes abbreviated as CL in the sequel). The test specifications are reported in Table 2: the first three tests, namely CL$\#01$, CL$\#02$ and CL$\#03$, involve a bi-directional motion of the FPS, whereas tests labelled as CL$\#04$ and CL$\#05$ regard mono-directional excitations consisting in the single cloverleaf longitudinal and lateral components, respectively. This allows a consistent comparison between the bi-directional and mono-directional response of the FPS.

The cloverleaf displacement pattern is depicted in Fig. 5 together with the individual longitudinal (along the $x$-axis) and lateral (along the $y$-axis) components. A starting and an ending branch of limited amplitude were also applied to the FPS during the experimental campaign [13]: these branches, introduced to avoid the impulse effects due to high accelerations induced at the beginning and at the end of the tests, are here neglected as they are of no practical importance for a numerical investigation. Three different vertical loads are investigated, corresponding to contact pressures equal to 15, 30, and 60 MPa.

Table 2: Testing protocol examined in the FE analyses (after Lomiento *et al.* [13])

| Test # | Test type | Vertical load $N$ [kN] | Contact pressure $p_c$ [MPa] | Peak long. disp. $u_{xP}$ [mm] | Peak lat. disp. $u_{yP}$ [mm] |
|---|---|---|---|---|---|
| 01 | CL | 3263 | 15 | 200 | 100 |
| 02 | CL | 6525 | 30 | 200 | 100 |
| 03 | CL | 13050 | 60 | 200 | 100 |
| 04 | CL long. comp. | 6525 | 30 | 200 | – |
| 05 | CL lat. comp. | 6525 | 30 | – | 100 |

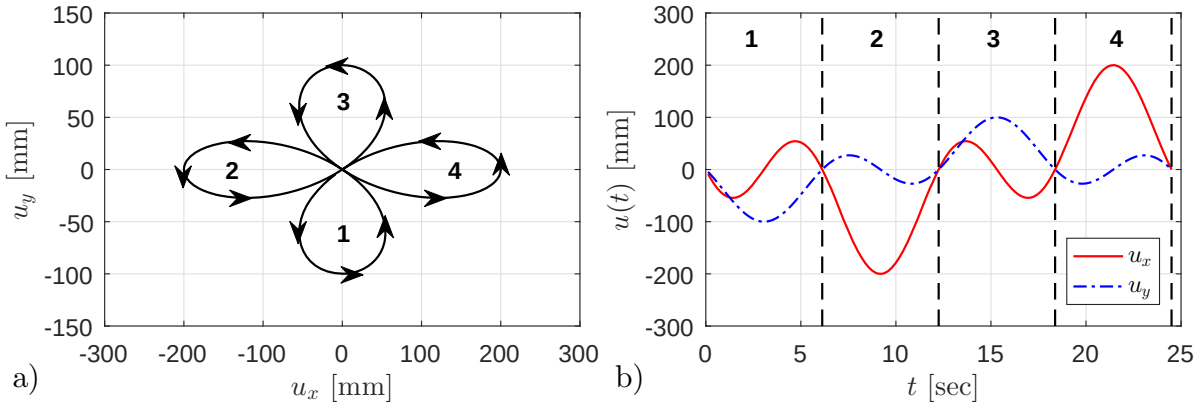


Figure 5: Cloverleaf test: a) in-plane trajectory; b) longitudinal ($u_x$) and lateral ($u_y$) components of motion

### 3.2 Finite element model and assumptions

The FPS analyzed in this paper has been modeled through the FE code ADINA [2], employing 3D-solid (hexahedral) elements equipped with 20 nodes per element (i.e., quadratic shape functions are adopted throughout to better describe the kinematics and the contact conditions of the model). The number of FEs has been chosen after a preliminary mesh sensitivity study to assure an accurate FE solution. The total number of FEs and the final mesh is illustrated in Fig. 6a) and is composed of 8820 elements and corresponding 42325 nodes, each node having three degrees of freedom (DOFs), namely the three translations with respect to the Cartesian axis system shown in the figure. Note that the upper steel plate rigidly connected to the semi-spherical articulation (cf. Fig. 1) is not included in the FE model as it is does not affect the results. Large displacement formulation is assumed; additionally, the (very small) deformability of the plate components has been accounted for by including the elastic properties of steel ($E = 200$ GPa, $\nu = 0.3$), whereas PTFE pads have been assumed with elastic isotropic material having $E = 1.5$ GPa, $\nu = 0.46$. Contact conditions between interfaces have been implemented through the *constraint function method* [2]. For each contact pair that may come into contact during the solution, so-called target and contactor surfaces are defined as reported in Fig. 6b): at each time instant, the constraint equations are imposed such that the nodes belonging to the contactor surface cannot penetrate the corresponding nodes lying on the target surface (the prevented motion is that along the direction specified by the normal vector to the target surface). The FPS is fixed on the lower face of the lower steel plate, and the loading condition is applied by means of a constant vertical load (in the $z$-direction) in conjunction with a history of horizontal displacements, i.e., the bi-directional path shown Fig. 5b) and applied to the $x$- and

$y$-direction. The duration of the experimental test (purged of the starting and ending branches) was approximately $25$ s, which corresponds to peak velocities equal to $90$ mm/s and $45$ mm/s in the longitudinal and lateral direction, respectively. In the FE model, the time is discretized in $200$ equally spaced time steps.

Preliminary results may be obtained by implementing a constant friction coefficient according to the simplified Coulomb theory. To highlight some interesting aspects observed in the FPS response under bi-directional excitation, a constant friction coefficient is first assumed. More refined results will be presented next by incorporating the variability of $\mu$ with the sliding velocity and temperature according to Eq. (8) via a specifically developed subroutine. Following the experimental findings reported in [13], the friction coefficient has been set equal to $\mu = 0.11$, $0.06$ and $0.03$ for the three contact pressures of $p_c = 15, 30, 60$ MPa, respectively.

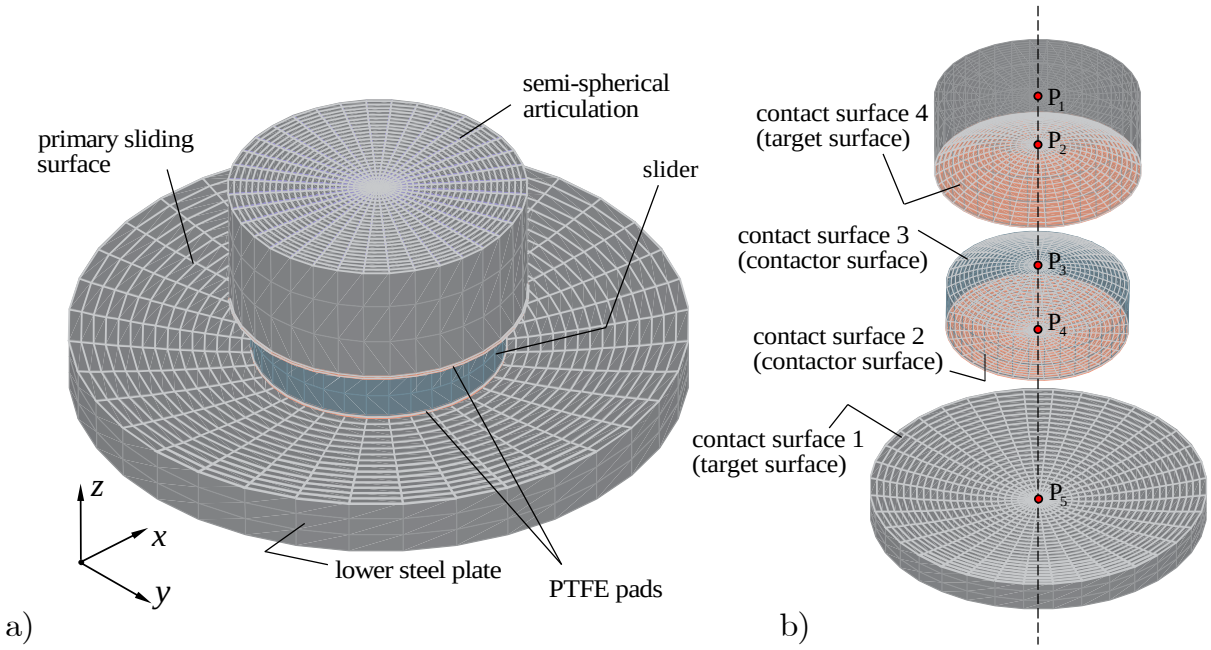


Figure 6: Finite element model of the FPS: a) isometric view; b) exploded drawing with contact surface labels

### 3.3 Results obtained by the simplified Coulomb friction model

The main results of the FE analysis are here presented and discussed. Due to the rotation of the slider occurring concurrently with the translation induced by the semi-spherical articulation, the displacement of the centre of contact surface 2, i.e., the point $P_4$ on the lower face of the slider in Fig. 6b), is lower than the displacement imposed on the top of the isolator, point $P_1$. The relevant trajectories computed for the test CL#02 are compared in Fig. 7: more specifically, the maximum displacement of the point $P_4$ is approximately $10\%$ lower than that of the point $P_1$, i.e., $u_{x4} \cong 182$ mm and $u_{y4} \cong 91$ mm in comparison with $u_{x1} \cong 200$ mm and $u_{y1} \cong 100$ mm. By closely analyzing the trajectories we note that, if the vertical component of motion is neglected, most of the energy introduced into the system is expended to make the slider translate up to the maximum values $u_{x4}$ and $u_{y4}$, however a small remaining part is spent to guarantee that such translation is compatible with the curvature of the above semi-spherical articulation having radius $r$. To this aim, a relative displacement occurs between contact surface 3 (belonging to the slider) and contact surface 4 (of the semi-spherical articulation), with the former moving relative to the latter in a direction opposed to the overall isolator translation. This

relative displacement can be quantified by computing the relative displacement $\Delta P_{23}$ between points $P_2$ and $P_3$. For the analyzed isolator the displacement of the point $P_3$, $u_{x3} \cong 169\,\text{mm}$ and $u_{y3} \cong 85\,\text{mm}$, is nearly $15\%$ lower than that of point $P_2$, which in turn coincides with the displacement imposed on the top of the isolator (point $P_1$). The relative displacement $\Delta P_{23}$ generates contact force transmission between the two sliding surfaces, thus dissipating further energy. As a result, the energy introduced into the system is dissipated via a twofold mechanism, consisting in the slider translation along the primary sliding surface and the slider rotation along the secondary surface. Therefore, in the manufacturing process it is important to pay attention to the lubrication and tribological properties of both the sliding interfaces.

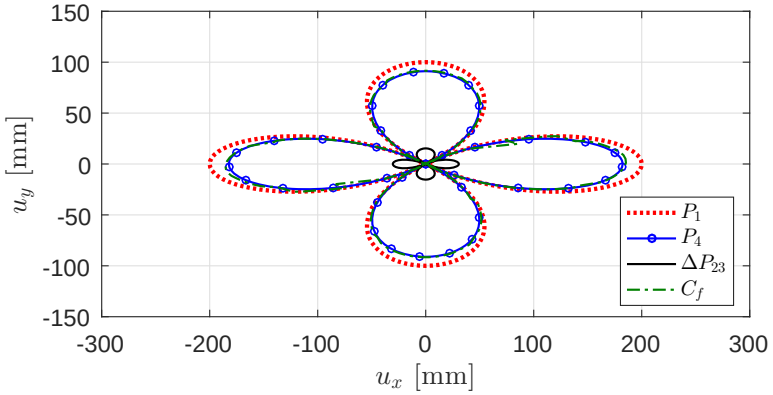


Figure 7: Comparative analysis of the trajectories traveled by the FPS during the test

In Fig. 7 we also report the trajectory of the centroid $C_f$ of the total contact force $\mathbf{F}$ whose $x$- and $y$-components are given in (9). The coordinates of such point $C_f$ at each time instant are computed based on the distribution of the nodal forces $\mathbf{f}_i$

$$x_{C_f} = \frac{\sum_i f_{yi}\, x_i}{\sum_i f_{yi}} = \frac{S_y}{F_y}\,; \qquad y_{C_f} = \frac{\sum_i f_{xi}\, y_i}{\sum_i f_{xi}} = \frac{S_x}{F_x} \tag{10}$$

whose vector plot at a generic time step is depicted in Fig.8. The $C_f$ trajectory slightly deviates from that of the slider (point $P_4$) with differences mainly observed near the points of motion reversal. It is worth noting that if the sliding surface were flat (not concave), a uniform distribution of the contact forces would be found and the centroid $C_f$ would coincide with the centre of the slider $P_4$ throughout the system motion.

In addition to the trajectory of $C_f$, it is interesting to evaluate the angle $\phi_f = \arctan_2(F_y, F_x)$ formed by the total force vector with respect to the $x$-axis, and compare it to the angle $\phi_v = \arctan_2(v_y, v_x)$ formed by the velocity vector (tangent to the traveled cloverleaf trajectory at each time instant), where $\arctan_2$ is the two-arguments arctangent function taking into account which quadrant the solution is in. In so doing, we can identify and quantify the angular shift $\Delta\phi = \phi_v - \phi_f$ formed by the force and velocity vectors, which has already been discussed in Section 2.1 and depicted in Fig. 4. The relevant results are illustrated in Fig. 9 with reference to the test CL#02. It can be seen that the velocity vector is parallel to the force vector (i.e., $\Delta\phi = 0$) only when the slider centre (point $P_4$ in Fig. 6) is going through the centroid of the primary sliding surface, point $P_5$, a situation that is identified by the condition $u_x = u_y = 0$, compare Fig. 9a) and b). In all the other kinematic configurations, the restoring force $F_r$, characterized by a radial re-centering direction, generates deviations of the total resisting force opposed to the active seismic force (the latter being parallel to the trajectory traveled during

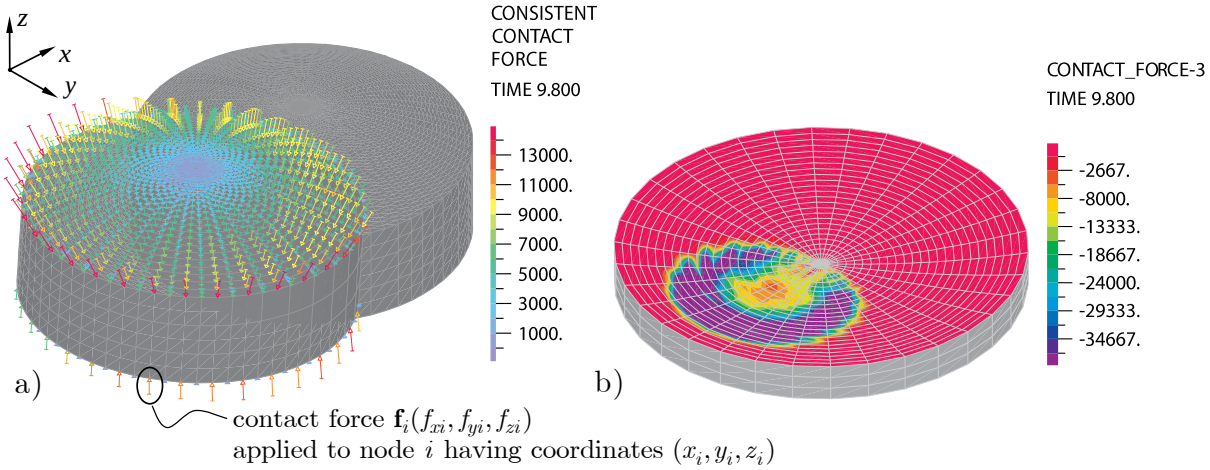


Figure 8: Contact force distribution: a) vector plot of $\mathbf{f}_i$ on the slider; b) band plot of $f_{zi}$ on the sliding surface

the isolator motion). On the other hand, the friction force keeps the same direction as the velocity vector throughout the duration of the test. As a result, the maximum angular shift occurs concurrently with the maximum radial displacement as illustrated by analyzing Fig. 9a) and b) simultaneously, with $\Delta\phi$ even higher than $90°$ and a mean value over the entire duration of the test equal to $23°$, cf. Fig. 9c). Once again, we emphasize that these deviations would cancel out in a uni-directional loading condition (because in this case the restoring force would be parallel to the traveled trajectory) as well as under general multi-directional excitations but flat (not concave) sliding surface (because in this case the restoring force would be zero as $R_{\text{eff}} \to \infty$ in Eq. (9)). Furthermore, by inspection of the time histories reported in Fig. 9b) we note that the angle of the velocity vector $\phi_v$ anticipates that of the force vector $\phi_f$, which is physically reasonable: the velocity is the cause that produces the reactive force, i.e., the direction of the force vector arises as a consequence of the trajectory traveled during the test. Mean values of the angular shifts measured for tests CL#01 and CL#03 are $11°$ and $44°$, respectively, thus indicating a dependence on the friction coefficient or, equivalently, on the vertical load acting on the FPS. Indeed, for higher contact pressures the friction coefficient (and the friction force accordingly) reduces, therefore the restoring force, which is responsible for the angular shift, contributes to a larger extent to the overall resisting force.

According to the testing protocol reported in Table 2, mono-directional excitations consisting in the single cloverleaf longitudinal and lateral component have also been analyzed in order to highlight the salient differences in comparison with the bi-directional counterpart. In Fig. 10 the force-displacement loops obtained for the longitudinal and lateral directions are compared for the bi-directional and mono-directional case. It is observed that the hysteretic loops in the bi-directional case are narrower than the corresponding loops in the mono-directional case. This is due to the contemporaneous sliding motion occurring in two directions as compared to the uni-directional test. No abrupt inversions of motion occur in the bi-directional case since the magnitude of the velocity vector is always non-zero although in certain time instants the single components $v_x$ and $v_y$ are zero (more specifically, in the four points having horizontal and vertical tangent in the cloverleaf trajectory shown in Fig. 7). This concept is clarified in Fig. 11 where the time-histories of the longitudinal and lateral reaction forces are depicted. The displacement components under bi-directional excitations may be significantly higher than the corresponding components in the mono-directional case. Consequently, neglecting the bi-directional interaction could lead to considerably overestimate the dissipative capacity of the

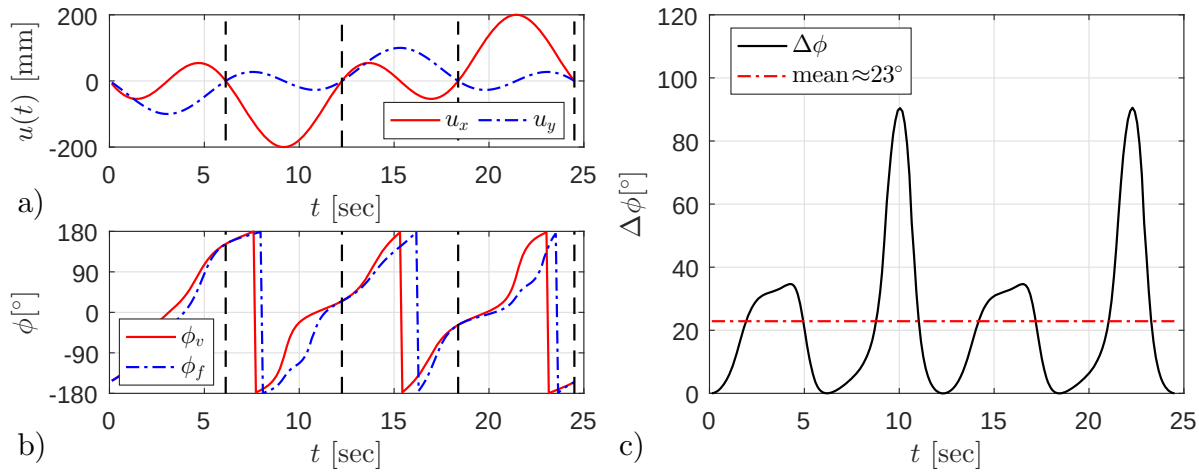


Figure 9: Angular shift $\Delta\phi$ between the force vector and velocity vector for test CL#02

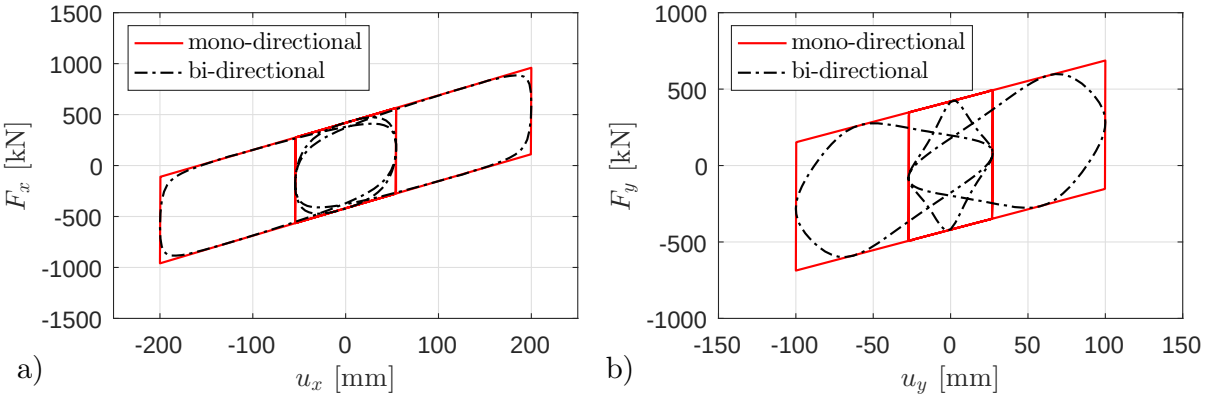


Figure 10: Force-displacement loops for mono-directional and bi-directional excitation: a) longitudinal; b) lateral

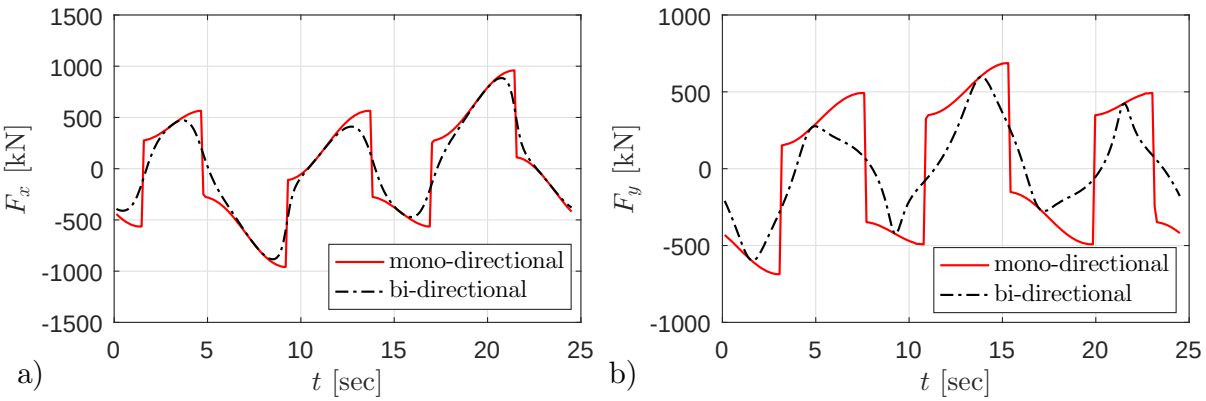


Figure 11: Time-history of the reaction force for mono- and bi-directional excitation: a) longitudinal; b) lateral

isolator or, equivalently, underestimate the maximum displacements expected during seismic events. For the examined case, the energy dissipated in bi-directional conditions is reduced in comparison with the uni-directional case of 10% in the longitudinal direction (changing from 514 kN m to 462 kN m) and of 37% in the lateral direction (reducing from 256 kN m to 162 kN m). These results are consistent with the experimental findings [13], in which reduction

of the dissipated energy of $23\%$ and $41\%$ are observed in the longitudinal and lateral direction, respectively. The slight differences between numerical predictions and corresponding experimental results are ascribed to other aspects that so far have been neglected in the FE model, above all the thermal effects and the influence of heating phenomena arising at the sliding interface, which increases friction reduction in the bi-directional case due to the coexistence of sliding motion components in two directions.

### 3.4 Variable friction coefficient: thermo-mechanical coupling analysis

The dependence of the friction coefficient upon sliding velocity (taking into account also the breakaway effects at motion reversals) and above all the temperature rise at the sliding interfaces should be properly accounted for in the numerical model. To this aim, according to the remarks outlined in Section 2.1 and the general formula reported in (8), a new customized Fortran subroutine governing the friction coefficient has been implemented in the FE code [6]. This thermo-mechanical coupling (TMC) subroutine generates a variability of $\mu$ (from node to node) with sliding velocity and temperature according to the following conditional expressions

$$\mu = \mu(v,T) = \mu_v\,\mu_T \quad \text{where} \tag{11a}$$

$$\mu_v = \begin{cases} \mu_{\text{st}} + (\mu_{\text{min}} - \mu_{\text{st}})\,\|\dot{\mathbf{u}}\|/\dot{u}_0 & \text{if } \|\dot{\mathbf{u}}\| \le \dot{u}_0 \\ \mu_{\text{max}} - (\mu_{\text{max}} - \mu_{\text{min}})\exp\left(-\alpha\left(\|\dot{\mathbf{u}}\| - \dot{u}_0\right)\right) & \text{if } \|\dot{\mathbf{u}}\| > \dot{u}_0 \end{cases} \tag{11b}$$

$$\mu_T = \begin{cases} 1 & \text{if } T \le T_0 \\ \exp\left(-\beta\left(T - T_0\right)\right) & \text{if } T > T_0 \end{cases} \tag{11c}$$

The meaning of the coefficients entering the developed TMC subroutine is the following: $\mu_{\text{st}}$ is the static friction coefficient; $\mu_{\text{min}}$ and $\mu_{\text{max}}$ are the dynamic friction coefficients in the low- and high-velocity range, respectively; $\dot{u}_0$ is a small (positive) velocity threshold identifying the transition between the stick and slip phase; the $\alpha$ parameter controls the rate of change of $\mu$ with sliding velocity; $T_0$ is the initial (environmental) temperature that is also the temperature threshold for identification of friction degradation due to heating phenomena; the $\beta$ parameter governs the rate of change of $\mu$ with temperature. It is worth noting that a linear interpolation between $\mu_{\text{st}}$ and $\mu_{\text{min}}$ is assumed in the range $\|\dot{\mathbf{u}}\| = [0 - \dot{u}_0]$, whereas an exponential trend is adopted for $\|\dot{\mathbf{u}}\| > \dot{u}_0$ in line with the expressions (7) proposed by Constantinou *et al.* [5].

A *fully coupled thermo-mechanical problem* is therefore addressed in which the thermal solution affects the structural solution (since $\mu$ depends on the local temperature) and, in turn, the structural solution affects the thermal solution (since heat generation is produced by contact friction at the interfaces). Details of all the thermal parameters involved in the fully coupled thermo-mechanical analysis are here omitted for the sake of brevity. We limit ourselves to point out that the introduction of the PTFE pads above and below the slider (cf. Fig. 6) is necessary to account for the low thermal conductivity of the PTFE as compared to the stainless steel so as to properly reproduce the thermal solution in the FE TMC model.

The main results in terms of hysteretic loops are reported in Figs. 12 and 13. It can be seen that the developed subroutine is capable of capturing the breakaway effects at motion reversals occurring in the mono-directional tests. On the contrary, the bi-directional tests does not imply any abrupt inversion of motion as the magnitude of the velocity vector is always non-zero; as a result, no sudden increase of the friction coefficient is predicted except for that at the start of sliding motion, which does involve a momentary sticking of the interfaces [14] not only in the mono-directional but also in the bi-directional test. The variability of $\mu$ with the sliding velocity

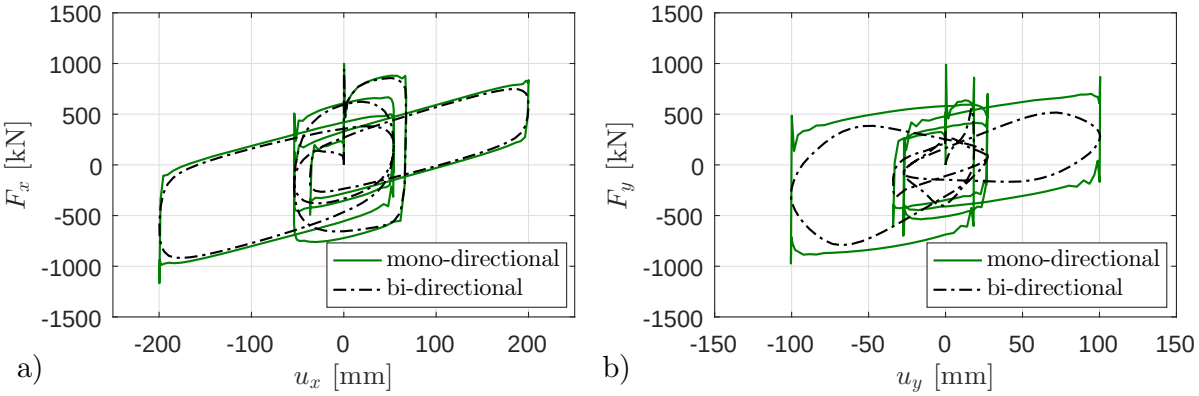


Figure 12: Force-displacement loops from the TMC analysis with friction subroutine: a) longitudinal; b) lateral

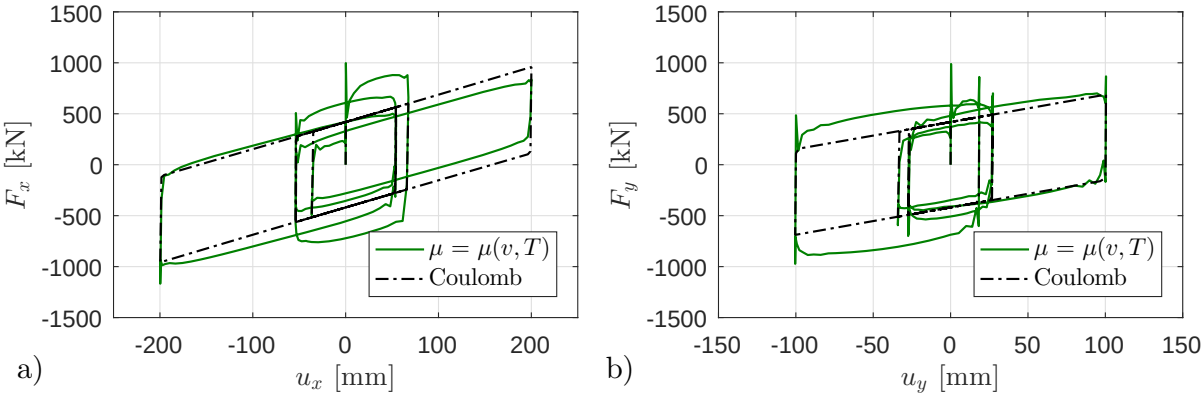


Figure 13: Mono-directional loops with the TMC subroutine and with the constant Coulomb friction

is highlighted in the vicinity of the motion reversals, where the sliding velocity reduces (and tends to zero in the mono-directional test) as can be inferred by inspection of Fig. 5b). Finally, the friction coefficient evolves over the course of the test since heating phenomena arise at the sliding interfaces that contribute to a significant friction degradation: this is evidenced by the subsequent loops appearing narrower than the first loop in Figs. 12 and 13.

When comparing bi-directional and mono-directional results in Fig. 12, more pronounced reductions of hysteretic loops are found as compared to the Coulomb friction hypothesis (constant $\mu$) previously analyzed in Fig. 10. Reduction of the energy dissipated from the bi-directional to the mono-directional case increases from $10\%$ (constant $\mu$) to $13\%$ ($\mu = \mu(v,T)$) in the longitudinal direction, and from $37\%$ (constant $\mu$) to $47\%$ ($\mu = \mu(v,T)$) in the lateral direction. This enhanced reduction is due to an augmented and more widely distributed temperature increase in the bi-directional case as compared to the mono-directional path (caused by higher heat fluxes spread over a broader area). Obviously, the simplified Coulomb friction model cannot capture this phenomenon because the temperature field has no effect on the friction coefficient that remains constant both in the bi-directional and in the mono-directional tests.

Strictly speaking, the thermo-mechanical coupling parameters entering the developed subroutine (11) should be tuned so as to fit the friction degradation observed experimentally [13]. In this contribution, we have not carried out sophisticated curve-fitting procedures to accurately calibrate the best-fit TMC parameters based on the experimental data. Only qualitative plots using preliminary estimates of the TMC parameters are here reported to show the overall ef-

fects of the modeling assumptions on the expected results. Further considerations about the most appropriate TMC parameters as well as on the temperature profiles in the bi-directional and mono-directional loading paths will be discussed in a forthcoming study.

## 4 Concluding remarks and future developments

A numerical investigation has been carried out to scrutinize the mechanical behavior of FP isolators when subjected to bi-directional motion. First, a few considerations concerning the kinematics of the device and the distribution of the contact forces at the sliding interfaces have been discussed. These considerations justify the different behavior of the FPS under bi-directional and mono-directional excitations, with the latter representing the single longitudinal and lateral components of the bi-directional path. The numerical investigation has been supported by the development of a three-dimensional FE model of a full-scale FP bearing. A customized friction law has been specifically formulated via a Fortran subroutine and implemented into the FE-code in order to incorporate the main physical phenomena occurring in real experimental tests. These phenomena include the breakaway effects that become manifest at the beginning of the sliding motion or at each motion reversal, the dependence of the friction coefficient upon sliding velocity, and the friction degradation over the repetition of cycles which is induced by frictional heating arising at the sliding interface. To properly account for the latter effect, a sophisticated thermo-mechanical coupling analysis has been performed in which the thermal solution and the structural solution affect each other, thereby implying that an iterative scheme must be adopted to identify the correct solution for both problems.

The majority of these aspects are not appropriately accounted for by the structural engineers that, when designing a base-isolated building, often rely upon a simpler 1D schematic idealization of the base isolation system, which may lead to a significant to underestimation of the displacements and overestimation of the dissipative capacity of the isolator, with errors up to $50\%$. Moreover, the technical standards [1, 7] allow the isolation system be modelled with equivalent linear viscoelastic behavior or simple bilinear elastic-plastic constitutive law with constant friction coefficient, which are both simplistic idealizations of the actual hysteretic behavior recorded experimentally. These simplifications may induce additional numerical errors in terms of forces, displacements and energy dissipation prediction.

Although restricted to single pendulum devices, most of the above considerations also apply to the double pendulum devices and, apart from the required geometric modifications, the developed TMC FE-model can easily be extended to deal with the increasingly popular FPS with double concave configuration. The numerical investigation carried out in this study represents the basis of a more extensive numerical assessment of the FPS thermo-mechanical behavior under bi-directional excitations. The generalization of these results to a variety of multi-directional paths and more detailed analyses of the temperature profiles is the object of an ongoing research.

## REFERENCES

[1] American Association of State Highway and Transportation Officials. *Guide Specifications for Seismic Isolation Design* (AASHTO 14). Washington DC, USA, 2014.

[2] ADINA R & D, Inc. Theory and Modeling Guide Volume I: ADINA. Report ARD 11-8. Watertown (MA,USA), 2011.

[3] G. Bondonet, A. Filiatrault, Frictional response of PTFE sliding bearings at higher frequencies. *Journal of Bridge Engineering*, **2:4**, 139–148, 1997.

[4] Computers and Structures Incorporated (CSI). SAP2000 v. 15. Berkeley, California, 2013.

[5] M. Constantinou, A. Mokha, A.R. Reinhorn, Teflon bearings in base isolation II: Modeling. *Journal of Structural Engineering*, **116**(2), 455–474, 1990.

[6] D. De Domenico, RC members strengthened with externally bonded FRP plates: A FE-based limit analysis approach. *Composites Part B: Engineering*, **71**, 159–174, 2015.

[7] European Committee for standardization. *Eurocode 8: Design of structures for earthquake resistance* - Part 1 (Final draft prEN 1998-1). Brussels, 2003.

[8] M. Eröz, *Advanced models for sliding seismic isolation and applications for typical multi-span highway bridges*. PhD thesis, Georgia Institute of Technology, December 2007.

[9] D.M. Fenz, M.C. Constantinou, Behaviour of the double concave Friction Pendulum bearing. *Earthq Eng Struct Dyn*, **35**, 1403–1424, 2006.

[10] M. Furinghetti, C. Casarotti, A. Pavese, Bi-directional experimental response of full scale DCSS devices. *Second European Conference on Earthquake Engineering and Seismology*, Istanbul, Turkey, August 25-29, 2014.

[11] M. Kumar, A.S. Whittaker, M.C. Constantinou, Characterizing friction in sliding isolation bearings. *Earthq Eng Struct Dyn*, **44**, 1409–1425, 2015.

[12] S. Lissia, C. Casarotti, A. Pavese, F. Dacarro, Experimental response of full scale curved surface sliders equipped with high dissipation sliding material. $15^{th}$ *World Conference on Earthquake Engineering*, Lisbon, Portugal, September 24-28, 2012.

[13] G. Lomiento, N. Bonessio, G. Benzoni, Concave sliding isolators performance under multi-directional excitation. *Ingegneria Sismica*, Anno XXX (3), Luglio-Settembre 2013.

[14] G. Lomiento, N. Bonessio, G. Benzoni, Friction model for sliding bearings under seismic excitation. *Journal of Earthquake Engineering*, **17**, 1162–1191, 2013.

[15] A. Mokha, M. Constantinou, A.R. Reinhorn, Teflon bearings in base isolation I: Testing. *Journal of Structural Engineering*, **116**(2), 438–454, 1990.

[16] G. Mosqueda, A.S. Whittaker, G.L. Fenves, Characterization and modeling of friction pendulum bearings subjected to multiple components of excitation. *Journal of Structural Engineering*, **130**(3), 433–442, 2004.

[17] V. Quaglini, M. Bocciarelli, E. Gandelli, P. Dubini, Numerical assessment of frictional heating in sliding bearings for seismic isolation. *Journal of Earthquake Engineering*, **18**, 1198–1216, 2014.

[18] C.S. Tsai, Finite element formulations for friction pendulum seismic isolation bearings. *Int J Numer Methods Eng*, **40**, 29–49, 1997.

[19] C.S. Tsai, W.S. Chen, T.C. Chiang, B.J. Chen, Component and shaking table tests for full-scale multiple friction pendulum system. *Earthq Eng Struct Dyn*, **35**, 1653–1675, 2006.

[20] V. Zayas, S. Low, S. Mahin, *The FPS earthquake resisting system*. Report No. CB/EERC-87/01, Earthquake Engineering Research Center, University of California, Berkeley, 1987.

COMPDYN 2017
6th ECCOMAS Thematic Conference on
Computational Methods in Structural Dynamics and Earthquake Engineering
M. Papadrakakis, M. Fragiadakis (eds.)
Rhodes Island, Greece, 15–17 June 2017

# CALIBRATION OF CONSTITUTIVE MACRO MODEL FOR A LEAD-CORE BEARING DEVICE: IDENTIFICATION BASED ON RESULTS OBTAINED BY FINITE ELEMENT ANALYSIS

**Todor Zhelyazov[1], Rajesh Rupakhety[2] and Símon Ólafsson[2]**

[1] Technical University of Sofia, Sofia, Bulgaria
Sofia, 1000, 8 Kl. Ohridski Blvd
e-mail: todor.zhelyazov@tu-sofia.bg

[2] Earthquake Engineering Research Centre, University of Iceland
Austurvegur 2a, 800 Selfoss, Iceland
rajesh@hi.is
rajesh@hi.is

**Keywords:** Lead-Core Bearing, Model Parameter identification, Multicriteria Design, Genetic algorithm.

**Abstract.** *An identification procedure based on genetic algorithm is discussed in this paper. The procedure is aimed to calibrate a single-degree-of freedom (SDOF) model capable to simulate the mechanical response of lead-core bearing device for passive seismic isolation.*
*The identification is based on data obtained by finite element simulation. An accurate finite element model is built. All components of the bearing device: lead-core, rubber layers and steel shims are discretely modeled. The lead-core bearing device is seen as a multiple component system. Constitutive laws are defined on the meso-scale for all materials: lead (-core), rubber, steel. Furthermore a typical identification test is simulated to obtain the shear stress-shear strain relationship which characterizes the response of the lead-core bearing device.*
*In the SDOF model describing the response of the bearing device on the macro-scale, a damage variable is introduced to account for mechanical damage accumulated in the lead-core.*

## 1 INTRODUCTION

Single-degree-of- freedom (SDOF) models capable of simulating the mechanical response of lead-core bearing device for passive seismic isolation are discussed in this contribution. SDOF models have evolved to differential equations models which involve variables design to account for degradation effects.
Model parameters are in general identified through comparison with reference data. Reference data is commonly obtained by experimental testing- e.g. identification test.
Alternatively reference set of data can be obtained by finite element analysis.
Details of the identification procedure are discussed.

## 2 SDOF MODELS

The widely used Bouc-Wen model ([1], [2], [3], [4], [5]) is described by the following set of equations:

$$Q = \alpha \frac{Q_y}{d_y} u + (1-\alpha)\frac{Q_y}{d_y} Z \tag{1}$$

$$\frac{dZ}{dt} = -\gamma \left|\frac{du}{dt}\right| Z|Z|^{(\eta-1)} - \beta \frac{du}{dt}|Z|^{\eta} + A\frac{du}{dt} \tag{2}$$

The first equation defines the constitutive relation $Q=Q(u)$ which characterizes the bearing device. $Q$ stands for the shear force generated in the bearing device and $u$ is the lateral displacement (see **Грешка! Източникът на препратката не е намерен.**). $Q_y$ denotes the shear force in the lead-core bearing device at the moment of yielding of the lead-core; $d_y$ denotes displacement at yielding.

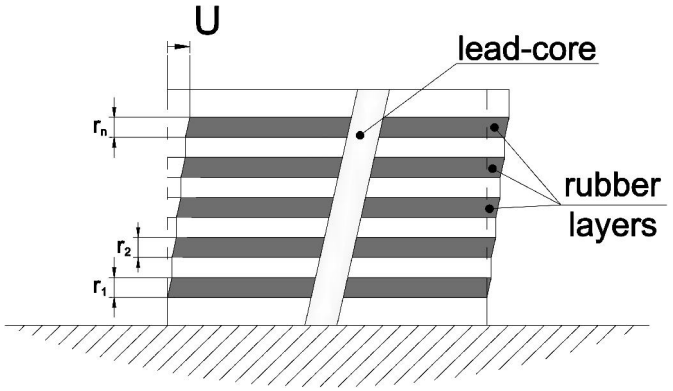


Figure 1**:** lead-core bearing; neutral position is depicted with dashed line

In equation (1) $\alpha$ is the ratio between the post- yield to pre-yield stiffness and $Z$ is a hysteresis parameter. The evolution of $Z$ is defined by the differential equation (2). In this equation $\gamma$, $\eta$, $\beta$ and $A$ are model parameters which are to be calibrated.
It should be noted that constitutive relation describing a lead-core bearing device is typically defined by postulating the relation $Q=Q[\gamma(t)]$ where $\gamma$ is referred to as shear strain e.g. the ratio between the shear displacement u and the total high of the rubber layers ( $\sum_{i=1}^{n} r_i$ ) in the lead-core bearing device (Figure 1):

$$\gamma = \frac{u}{\sum_{i=1}^{n} r_i} \tag{3}$$

As an alternative, a model in which a variable associated with material degradation is considered. This model, as already stated postulates a relation between shear stress and shear displacement:

$$\tau = f(\gamma) \tag{4}$$

Shear stress is conventionally split into three components:

$$\tau = \tau_e + \tau_1 + \tau_2 \tag{5}$$

The first term- $\tau_e$ denotes an elastic contribution, and the two others- overstresses relaxing with time. A variable accounting for damage accumulation is incorporated in the second term- $\tau_1$. The evolution of the damage variable $q_e$ is defined as a function of the shear strain and of a model parameter $p_e$ [6]:

$$\frac{dq_e}{dt} = \begin{cases} \zeta_e \left|\frac{d\gamma}{dt}\right| \left(0{,}5|\gamma| - q_e\right) & if \quad q_e \le 0.5|\gamma| \\ 0 & if \quad 0.5|\gamma| \le q_e \le 1 \end{cases} \tag{6}$$

As it can be seen, in the above formulation it is presumed that material degradation depends on the shear strain and on the shear strain rate.
There exist also constitutive relations in which damage variable is introduced in the stress-strain relationship of the material [7]:

$$\sigma = E(D)\varepsilon \tag{7}$$

The above equation describes

All material parameters should be identified through curve fitting.

## 3 REFERENCE DATA

Material parameters occurring in the constitutive laws are commonly identified through comparison with experimental data. Authors support the idea that identification of the material constants in the SDOF models can be done on the basis of data obtained by finite element analysis ([8], [9]).

An explicit and accurate finite element model of the bearing device is set up. Geometry is reproduced in high level of detail.

Material models are defined for each component of the bearing device: lead-core, rubber, steel shims.

SDOF constitutive models are commonly calibrated on the basis of experimental data obtained by identification test (see for example [10]). Therefore an identification test is simulated in an implicit transient dynamic analysis.

## 4 CURVE FITTING

In this section stochastic algorithms which can be implemented in a numerical procedure for identification of model constants are discussed. The focus is on the genetic algorithms [11]. The input of the procedure is formed by a lot of 'chromosomes': sets (or vectors) of model parameters.

A test function (*TF*) is defined to assess the proximity of a Stress-strain (or Shear force- shear displacement relationship) to a chosen reference curve.
TF supplies a criterion whether a set of points $\{P_i^{(t)}=(u_i^{(t)},Q_i^{(t)})\}$ in the criterion space is close to the reference set $\{P_i^{(r)}=(u_i^{(r)},Q_i^{(r)})\}$.
For each iteration an optimal set is chosen by using TF. In the context of the 'genetic' algorithm other sets are manipulated, e.g. subjected to cross-over and mutations.
Pairs of arbitrary sets of model constants are compared. Pairs should be randomly chosen. This can be achieved by using one of the following schemes: a roulette wheel, a stochastic remainder, ranking tournament selection etc. ([13], [15]. Another strategy for generating random numbers, specifically a quasi-random sequence is discussed in the next section.
Thus for two compared sets $S_1$ and $S_2$ the set which is less convergent to the reference curve

$$TF_i^{(out)} > TF_j^{(out)} \tag{8}$$

is modified as follows:

$$S_j^* = fS_i + (1-f)S_j \tag{9}$$

where $f$ is a random number ($f \in [0,1]$).

Test function is defined on the basis of the error estimation (following [12]):

$$e_i = \frac{1}{n}\sum_{i=1}^{n}\left(\frac{Q_i^{(m)} - Q_i^{(FEM)}}{\Delta Q}\right)^2 \tag{10}$$

In equation (10) superscripts *m* and *FEM* denote data points of the curve obtained by using the SDOF model and the curve obtained by finite element analysis respectively; *n* is the number of data points in the compared curves and ΔQ is the difference between maximum and minimum values of the shear force generated in the lead-core bearing:

$$\Delta Q = Q_{\max} - Q_{\min} \tag{11}$$

Test functions corresponding to each set of model parameters is evaluated by using the following set of equations:

$$PPTF_i = 1 - \frac{e_i}{\max(e_j)} \qquad j = 1..n \tag{12}$$

$$PTF_i = PPTF_i - \min\{PPTF_j\} \qquad j = 1..n \tag{13}$$

$$TF_i = \frac{PTF_i}{\max\{PTF_j\}} \qquad j = 1..n \tag{14}$$

In the following iteration the set $S_i$ is kept as it stands whereas the set $S_j$ is replaced by the set $S_j$* as defined above.

## 5 QUASI RANDOM SEQUENCE

A quasi random sequence can be constructed in the following way [15]:

$$q_{i,j} = e_1 V_j^{(1)} * e_2 V_j^{(2)} * \ldots * e_m V_j^{(m)} \quad i = 1 \ldots n \tag{15}$$

In equation (15) $q_{ij}$ are coordinates of a point $Q_i$. The reference number of a given point $Q_i=(q_{i,1}, q_{i,2} \ldots q_{i,n})$ must be presented in binary format:

$$i = e_m \ldots e_2 e_1 \tag{16}$$

The quasi random sequence can be constructed by using the following arithmetic algorithm [15]:

$$m = 1 + \left[ \frac{\ln(i)}{\ln(2)} \right] \tag{17}$$

$$q_{i,j} = \sum_{k=1}^{m} 2^{1-k} \left\{ \frac{1}{2} \cdot \sum_{l=k}^{m} \left[ 2. \left\{ i 2^{-l} \right\} \right] \left[ 2. \left\{ r_j^{(i)} 2^{k-1-l} \right\} \right] \right\} \quad j = 1 \ldots n \tag{18}$$

In equation (17) $i$ stands for the number of a given point of the quasi random sequence. In equation (18) $[q]$ denotes the integer part of a given quantity $q$ whereas $\{q\}$- the fractional part of $q$.

## 6 CURVE FITTING

Reference “shear displacement- shear force” curve obtained by finite element analysis as outlined in paragraph 3 is depicted in Figure 2.

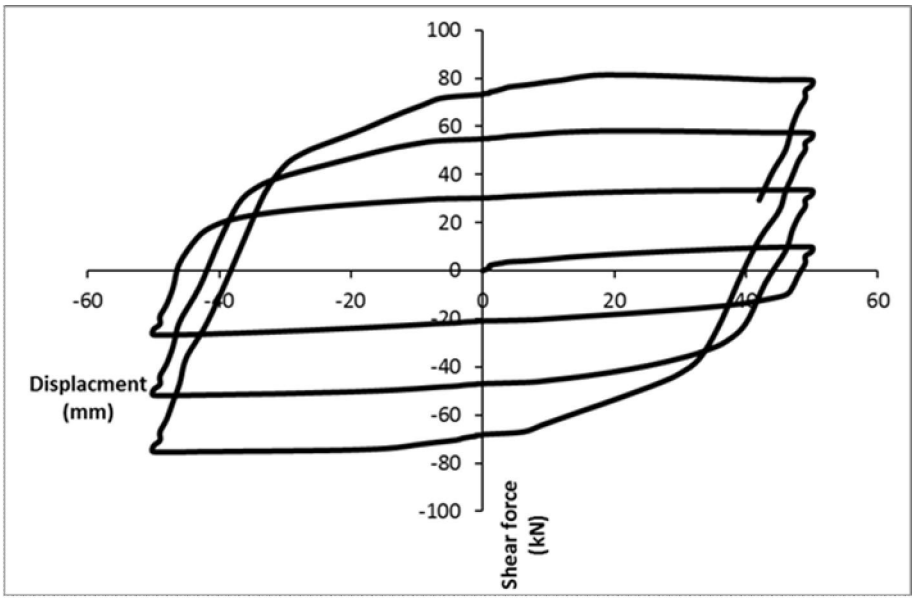


Figure 2: Reference Load- shear displacement curve obtained by finite element analysis

After defining initial data sets containing model parameters

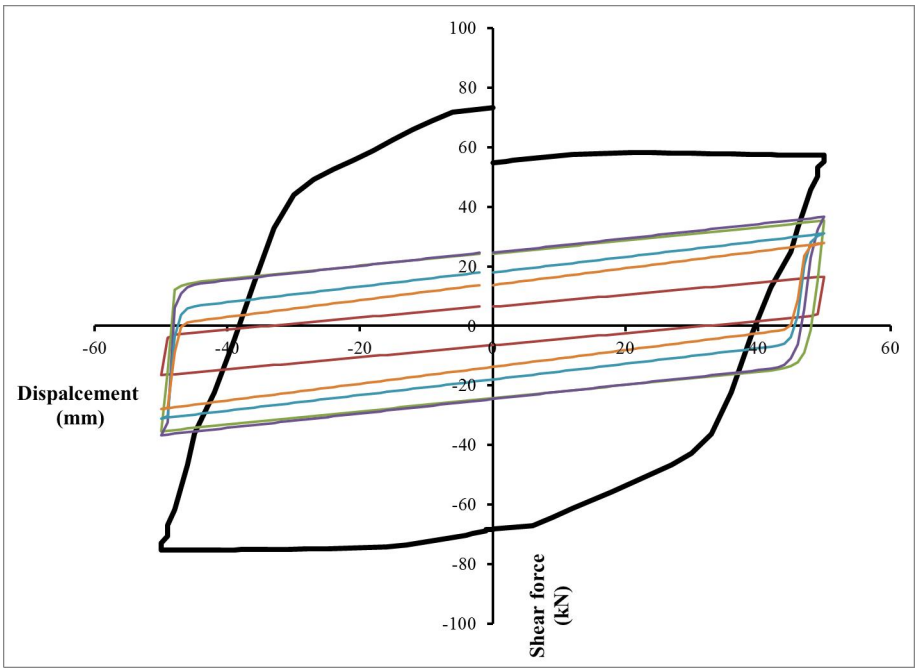


Figure 3 : Reference hysteresis curve (in black) obtained by finite element analysis and SDOF produced curves corresponding to different initial data sets: first iteration

the proximity of each set of model parameters (Figure 3) to the reference data is evaluated by using a test function as outlined in paragraph 4.

In further iterations sets of model constants which are estimated as less convergent are manipulated to search a better fit with the reference hysteresis curve (Figure 4)

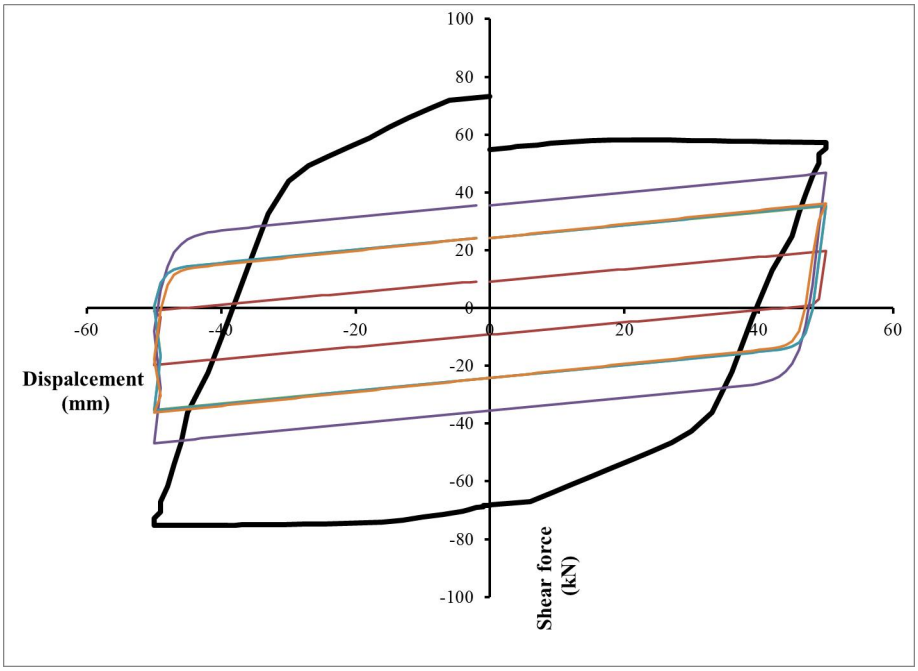


Figure 4: Reference hysteresis curve (in black) obtained by finite element analysis and SDOF produced curves corresponding to different initial data sets: further iterations

and to choose eventually a set giving maximum possible approximation of the reference shear force- displacement curve (Figure 5).

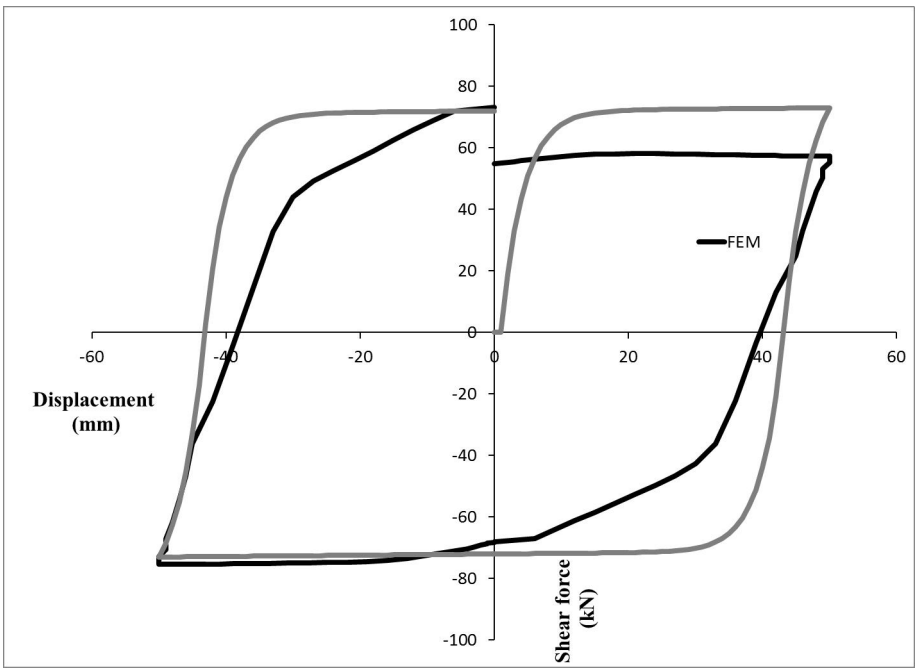


Figure 5: Shear force- displacement relationships obtained by finite element modeling (I black) and by Single-Degree-of-Freedom (Bouc-Wen) model (in grey).

## 7 CONCLUDING REMARKS

In this contribution steps of a numerical procedure designed to calibrate the parameters of single-degree of freedom models aimed to simulate the mechanical response of lead-core bearing devices for passive seismic isolation have been discussed.

It should be noted that authors support the idea for parameter identification partially or gully based on results obtained by finite element analysis instead of using experimentally obtained reference data.

The identification procedure is based on a genetic algorithm. It starts by defining a number of initial set of model parameters. The output from the single-degree-of-freedom model produced by each is compared to the reference hysteresis curve obtained by finite element analysis. A test function based on error estimation is used to compare output curves produced by different data sets. Before the next iteration of the identification process datasets are manipulated in order to assure a better fit with reference hysteresis curve in subsequent iterations. The manipulation rule accounts for test functions associated to each data set.

Further work is related to the "automation" of the identification algorithm as well as to the identification of mechanical parameters of a single-degree-of-freedom model accounting for material degradation.

This contribution appears in the framework of collaboration between the first author and the Earthquake Engineering Research Center of the University of Iceland (affiliation of the other authors) started in 2014.

## REFERENCES

[1] R. Bouc, Forced vibration of mechanical systems with hysteresis In Proceedings of the Fourth Conference on Nonlinear Oscillation, Prague, Czechoslovakia p. 315, 1967.

[2] R. Bouc, Modèle mathématique d'hystérésis: application aux systèmes à un degré de liberté. *Acoustica* (in French) **24**:16–25, 1971.

[3] Y. K. Wen, Method of Random Vibration of hysteretic system. *J Engineering Mechanics Division, ASCE*, **102**(2):249-263, 1976.

[4] M. C. Constantinou, M. Tadjbakhsh, Hysteretic Dampers in Base Isolation: Rando Approach. *Journal of structural Engineering* **111**(4):705-721, 1985.

[5] J. Song and A. Der Kiureghian, Generalized Bouc–Wen model for highly asymmetric hysteresis. *Journal Engineering Mechanics ASCE*, **132**(6):610-618, 2006

[6] Dall'Astra A., Ragni L., Experimental tests and Analytical Model of high Damping Rubber Dissipating Devices, *Engineering Structures*, **28**(13), 1874-1884, 2006

[7] J. Lemaitre, *A Course on Damage Mechanics*, Springer, 1996.

[8] T. Zhelyazov, E. Thorhallsson, S. Olafsson, J.T. Snaebjornsson and R. Sigbjornsson, Seismic Isolation: assessment of the damping capacity**,** Second European conference on earthquake engineering and seismology, Istanbul, august 25-29, 2014.

[9] T. Zhelyazov R Rupakhety and S. Ólafsson, Modeling the mechanical response of a lead- core bearing device: damage mechanics approach, ECCOMAS Congress 2016,

VII European Congress on Computational Methods in Applied Sciences and Engineering, M. Papadrakakis, V. Papadopoulos, G. Stefanou, V. Plevris (eds.), Crete Island, Greece, June, 5–10 2016.

[10] G. Benzoni and C. Casarotti, Performance of lead- Rubber and Sliding Bearings under Different Axial Load and Velocity Conditions, Technical Report/SRMD-2006/05-rev3, 2008.

[11] D.E. Goldberg, *Genetic algorithms in search, optimization and machine learning. Reading* (MA): Addison-Wesley, 1989.

[12] N.M. Kwok, Q.P. Ha, M. T. Nguyen, J. Li, B. Samali, Bouc- Wen model parameter identification for a MR fluid damper using computationally efficient GA, ISA Trans. Apr, **46**(2), 167-79. Epub 2007.

[13] D. E. Goldberg, K. Deb, A comparative analysis of selection schemes used in genetic algorithms, Rawlins GJE, editor, *Foundations of genetic algorithms. San Mateo (CA): Morgan aufmann*, p. 69–93, 1991.

[14] J.E. Baker, Reducing bias and inefficiency in the selection algorithm, *Proc. 2nd intl. conf. on genetic algorithms*. Cambridge (MA), pp: 14–21, 1987.

[15] I.M. Sobol, R.B. Statnikov, *Multicriteria Design: Optimization and Identification* (in Russian), Moscow, 2006.

COMPDYN 2017
6th ECCOMAS Thematic Conference on
Computational Methods in Structural Dynamics and Earthquake Engineering
M. Papadrakakis, M. Fragiadakis (eds.)
Rhodes Island, Greece, 15–17 June 2017

# EFFECTS OF EQUIVALENT RADIAL ACCELEROGRAMS FOR BIDIRECTIONAL SEISMIC EVENTS ON BASE-ISOLATED STRUCTURES

**M. Furinghetti[1], A. Pavese[2], and A. Foti[1]**

[1] EUCENTRE - Pavia
via Ferrata 1, 27100 Pavia - Italy
e-mail: marco.furinghetti@eucentre.it

[2] University of Pavia
via Ferrata 3, 27100 Pavia - Italy
e-mail: a.pavese@unipv.it

**Keywords:** Equivalent Uniaxial Accelerogram, Bidirectional motion, base-isolation, Concave Surface Slider, bi-axial interaction, frictional force.

**Abstract.** *A general seismic event can be considered as the superposition of two individual time histories of ground acceleration, acting simultaneously at the base of a structural system, along the main directions of a given reference system. Response spectra can be computed either for each component, or for the global seismic event, by considering a Single Degree of Freedom with different values of self-period, subjected to both the x and y accelerograms. Such a bi-directional response spectrum has higher spectral coordinates with respect to the individual ones, because of the instantaneous contributions of both directions of ground motion in the structural response. Nonetheless, an earthquake is expected to release most of the total energy of the event along an actual radial direction, mainly due to the propagation direction of seismic waves from the hypocenter toward the ground surface, even though the ground motion develops according to a random trajectory. A recent research work proposed an analytical procedure for the computation of an "equivalent uniaxial accelerogram" for a bidirectional earthquake: the proposed theory allows to compute a single ground acceleration time-history, related to a proper direction angle, able to reproduce the same effects of a two-components seismic event on a base-isolated structural system: results showed a good agreement between the equivalent radial and the bidirectional structural responses, even if non-negligible differences were observed. In this work a more refined procedure is proposed for the definition of the equivalent unidirectional accelerogram for a base-isolated structure. A wide validation study is reported, by analyzing 100 bidirectional seismic events: two different ranges for vibration period have been assumed, in order to evaluate the accuracy of the overall procedure, by considering a large rather than a small portion of the reference response spectrum. Finally, a case study structure has been modeled, to underline effects of the equivalent radial response, in comparison to the reference bidirectional case.*

## INTRODUCTION

The non-linear time history analysis represents the most realistic structural analysis typology which can be considered: a structural F.E.M. can be subjected to real recordings of ground accelerations along the main directions of motion, and so internal actions of each structural element can be stepwise computed and checked. Generally, seismic events can be considered as three individual translational ground motions, simultaneously acting at the base of a structural system, since ground rotational degrees of freedom can be neglected [1]. In most of cases, also the vertical component is not modeled, since its effects on the main response parameters are not comparable to the ones induced by horizontal seismic motions. On the other hand, unidirectional approaches are much more common among practitioners, given the higher level of simplicity. Standard codes provide prescriptions for directional combinations of radial response results, whereas some guidelines for selection of real and spectrum-matched single component accelerograms can be found in the literature [9]. When bidirectional earthquakes are considered, the response spectrum should be able to represent a two component seismic event as a single response parameter. Different combinations of the single-component response spectra can be found, such as the geometric mean, rather than the arithmetic mean or the Square Root of the Sum of Squares (SRSS), although the geometric mean seems to be the most commonly used, also for Ground Motion Prediction Equations. Also for base-isolated structures, it is important to reproduce the ground shaking conditions in the best and most realistic way possible. Concerning friction-based isolators, it is well known that the hysteretic behavior is affected by the shape of the trajectory of the devices, due to the stepwise projection of the friction force along the main directions of motion [5, 10, 11, 12]. However, especially in the design phase, unidirectional approaches are assumed, and bilinearized hysteretic constitutive laws are considered to design/check the implemented isolators [2, 4]. Moreover, it is possible to compute an equivalent damping ratio of the isolation system by considering a symmetric unidirectional hysteretic loop at the maximum displacement, which is actually an unknown at the beginning, so that an iterative procedure has to be solved. In addition, standard codes for testing isolation friction-based devices provide expressions for an average friction coefficient per cycle, under unidirectional sinusoidal motion [3], and no prescriptions for bidirectional tests are given.

In the present endeavor a refined procedure for the computation of an equivalent ground acceleration time series is presented, for bidirectional seismic events: precisely, an optimum orientation angle is computed, by minimizing the Mean Square Error between a bidirectional reference response spectrum and a radial one, related to the projection of both the planar components along the considered direction. Two different period ranges for the computation of the MSE value have been analyzed, in order to highlight the effect of a smaller rather than a larger period range. The presented procedure has been applied to a selection of 100 individual bidirectional earthquakes, and results have been statistically studied. Finally, a case study base-isolated structure has been modeled, and bidirectional Non Linear Time History Analyses have been performed: results have been compared to the effects of equivalent radial motions, in terms of peak vectorial response parameters, for both the isolation system (displacement and force demands) and the building structure (displacement, absolute acceleration and interstorey shear profiles).

Results have shown that the structural response returned by the equivalent unidirectional ground motions provides a very good estimate of the seismic behavior of the system, when subjected to bidirectional motions.

## 1. DEFINITION OF THE EQUIVALENT RADIAL EVENT

In this section a refined procedure for the evaluation of an equivalent radial accelerogram for bidirectional earthquakes is proposed, as a subsequent development of a previous study on the seismic response of base isolated structures under general seismic motions [6]. According to the aforementioned theory, it is possible to determine an actual horizontal direction for a radial motion, which can reproduce approximately same effects of a bidirectional seismic event on a structural system, even though a preferential direction of motion can not be recognized, by considering the ground acceleration diagram (Figure 1, left).

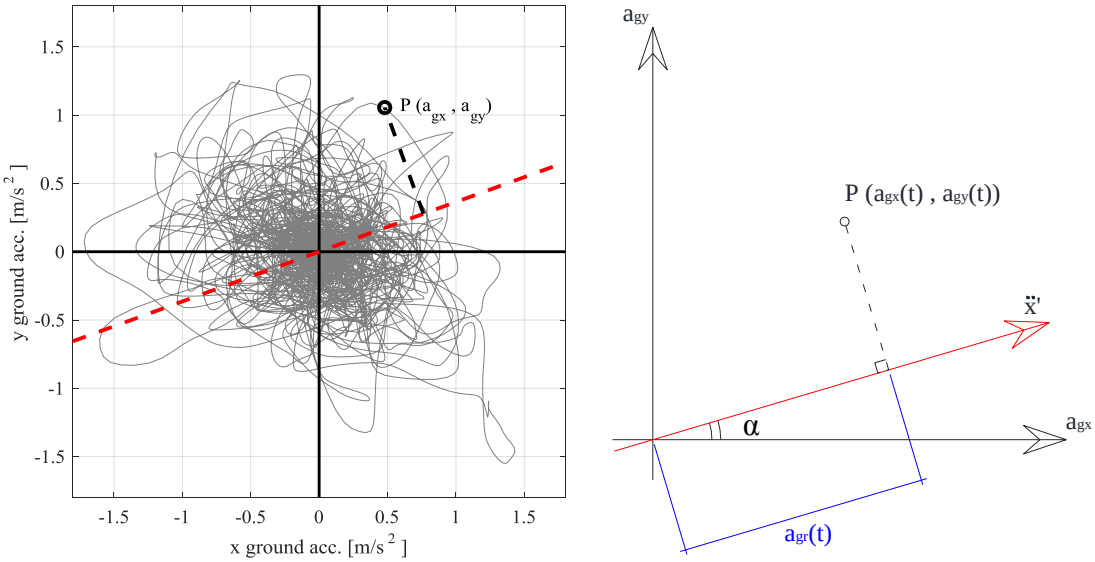


Figure 1: Acceleration points projection scheme – Irpinia earthquake 1980.

Effects of the reference bidirectional earthquake for each case is considered in terms of bidirectional response spectra: since a general planar seismic event can be represented by a couple of ground acceleration signals along two orthogonal horizontal directions, reference displacement and acceleration spectra are computed by considering for every period values a Single Degree of Freedom system, subjected to both x and y components simultaneously. Thus, for a given damping ratio $\xi$, the following equations of motion can be defined and time-integrated:

$$\begin{aligned} \ddot{x} + 2\xi\omega\dot{x} + \omega^2 x &= -\ddot{x}_g \\ \ddot{y} + 2\xi\omega\dot{y} + \omega^2 y &= -\ddot{y}_g \end{aligned} \tag{1}$$

Hence, Spectral coordinates can be computed, by collecting maximum vectorial displacement and absolute acceleration.

$$\begin{aligned} S_d^{2D}(\xi,T) &= \max\left(\sqrt{x^2+y^2}\right) \\ S_a^{2D}(\xi,T) &= \max\left(\sqrt{\left(\ddot{x}+\ddot{x}_g\right)^2+\left(\ddot{y}+\ddot{y}_g\right)^2}\right) \end{aligned} \tag{2}$$

In Figure 1 (right) the projection procedure is shown: for a given orientation angle all the acceleration points are projected along the considered direction. Therefore, the radial projection of the bidirectional earthquake $a_{gr}(t)$ is defined as follows:

$$a_{gr}(t) = a_{gx}(t)\cdot\cos(\alpha) + a_{gy}(t)\cdot\sin(\alpha) \tag{3}$$

The optimum value for the orientation angle is computed, by minimizing the square root of the Mean Square Error (MSE) between the reference bidirectional and the equivalent radial spectra, both displacement and absolute acceleration, for a given period range.

$$E^{S_d}(\xi,\alpha) = \sqrt{MSE^{S_d}} = \sqrt{\frac{1}{n_T}\sum_{i=1}^{n_T}\left(S_d^{2D}(\xi,T_i) - S_d^{1D}(\xi,\alpha,T_i)\right)^2}$$
$$E^{S_a}(\xi,\alpha) = \sqrt{MSE^{S_a}} = \sqrt{\frac{1}{n_T}\sum_{i=1}^{n_T}\left(S_a^{2D}(\xi,T_i) - S_a^{1D}(\xi,\alpha,T_i)\right)^2} \quad (4)$$

Where $n_T$ is the total number of structural periods, contained in the considered period range. A previous study has reported results related to a full range of periods, that is from 0.0 sec to 4.0 sec (Furinghetti and Pavese, 2017); generally, given the high variability of spectral coordinates in the acceleration plateau, better results are expected, if a smaller period range is assumed. Thus, in the present endeavor the period range has been defined, according to prescriptions of the Italian Building Code (I.B.C.) for spectrum-compatibility: period range for base-isolated structures is assumed bounded between 0.15sec and $1.2T_{is}$, where $T_{is}$ is the secant period of the base-isolated structure. In Figure 2 different period ranges are shown for Irpinia earthquake 1980, by assuming an isolated secant period of 2,5 sec.

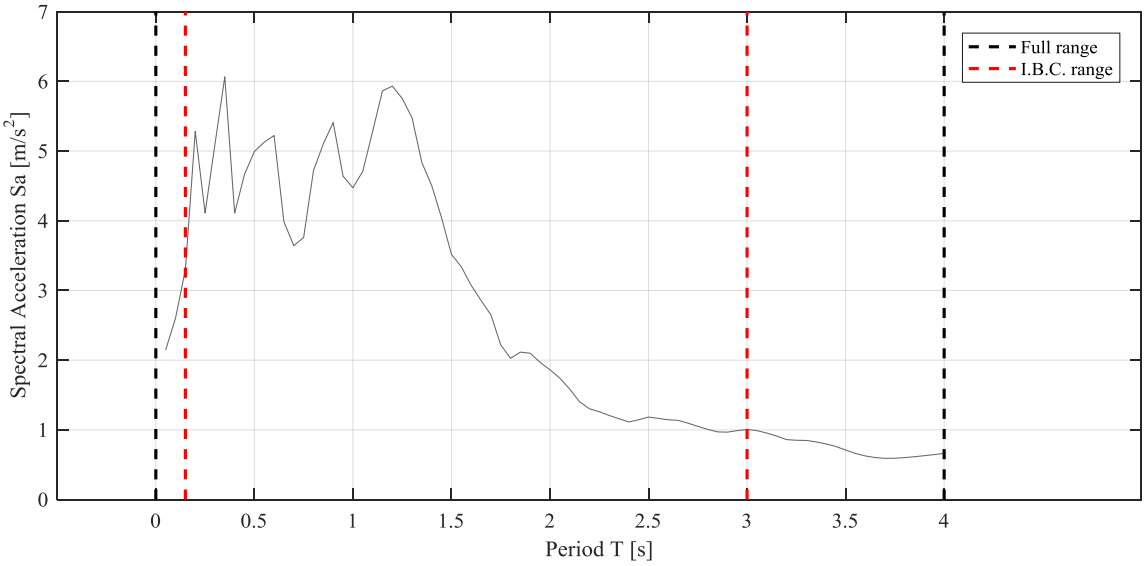


Figure 2: Period ranges for 5% damping response spectrum – Irpinia earthquake 1980.

Thus, equivalent radial accelerograms can be also adopted, when non-linear time history analyses are performed, by checking spectrum compatibility of 7 equivalent signals with respect to the target spectrum.

## 2. STATISTICAL ANALYSIS OF BIDIRECTIONAL EVENTS

In this section the comparison of the previously defined period range definitions is reported, by considering 100 bidirectional seismic events, which have been selected from databases of the program REXEL [9]:

- ESD: European Strong-motion Database;
- ITACA: Italian Accelerometric Archive;

- SIMBAD v3.0: Selected Input Motions for displacement-Based Assessment and Design.

A selection and scaling procedure has been applied in order to consider a high displacement demand, since base-isolated structure are considered: precisely, the vectorial displacement demand of a Single Degree Of Freedom system (SDOF) has been computed for each seismic event, by considering the actual non-linear constitutive law of a bidirectional isolation system of Curved Surface Slider (CSS) devices [7]:

$$\begin{aligned} \ddot{x} + g\left\{\frac{x}{R_{eq}} + \mu \cdot \tanh\left(\frac{\sqrt{\dot{x}^2+\dot{y}^2}}{v_s}\right)\cdot\frac{\dot{x}}{\sqrt{\dot{x}^2+\dot{y}^2}}\right\} = -\ddot{x}_g \\ \ddot{y} + g\left\{\frac{y}{R_{eq}} + \mu \cdot \tanh\left(\frac{\sqrt{\dot{x}^2+\dot{y}^2}}{v_s}\right)\cdot\frac{\dot{y}}{\sqrt{\dot{x}^2+\dot{y}^2}}\right\} = -\ddot{y}_g \end{aligned} \tag{5}$$

With such a hysteretic model, it is possible to account for the actual biaxial interaction of the directions of motion, for the stepwise projection of the main frictional force, which is assumed to be parallel to the trajectory of the isolation system. Then, records have been scaled in order to achieve a displacement demand bounded between ±20% of the design displacement of the considered device (200,0 mm); a constant friction coefficient μ equal to 7% and an equivalent radius of curvature $R_{eq}$ equal to 3,0m have been assumed. A small variation range for scale factors has been considered, in order not to obtained unrealistic ground acceleration signals: all scale factors have been bounded between 0,5 and 2,0.

In Figure 3 results of the selected records are reported, in terms of peak displacements and scale factors. Thus, for the selected events, the optimum orientation angle has been computed, by considering both acceleration and displacement approaches, for several damping ratio values; furthermore, results related to full-range of period and I.B.C. range have been compared.

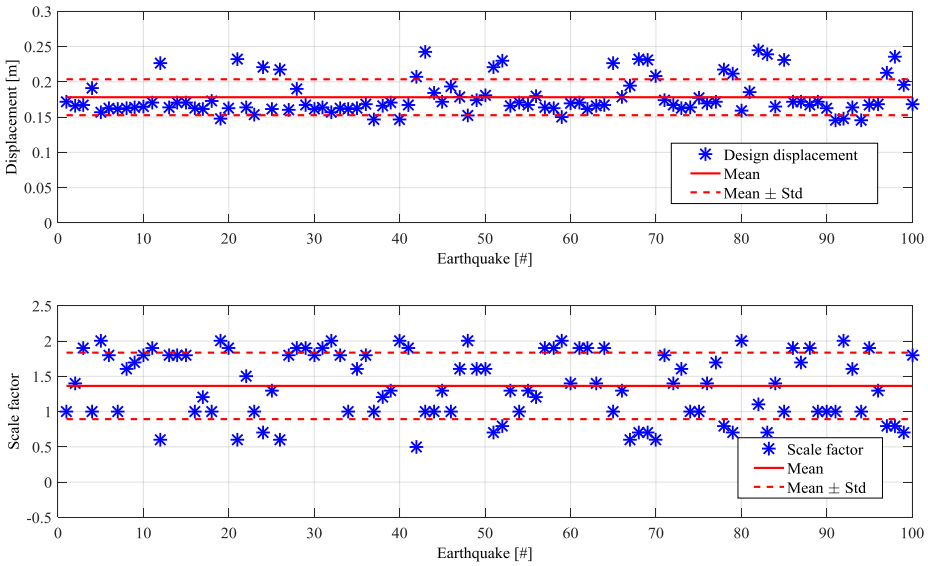


Figure 3: Selection of bidirectional events for statistical study.

In Figure 4 results in terms of variation of the optimum orientation angle are shown for acceleration (top) and displacement (bottom) approaches, by considering full-range (left) and

Italian Building Code I.B.C. (right), as a function of increasing damping ratio, with respect to the reference value at 5% damping.

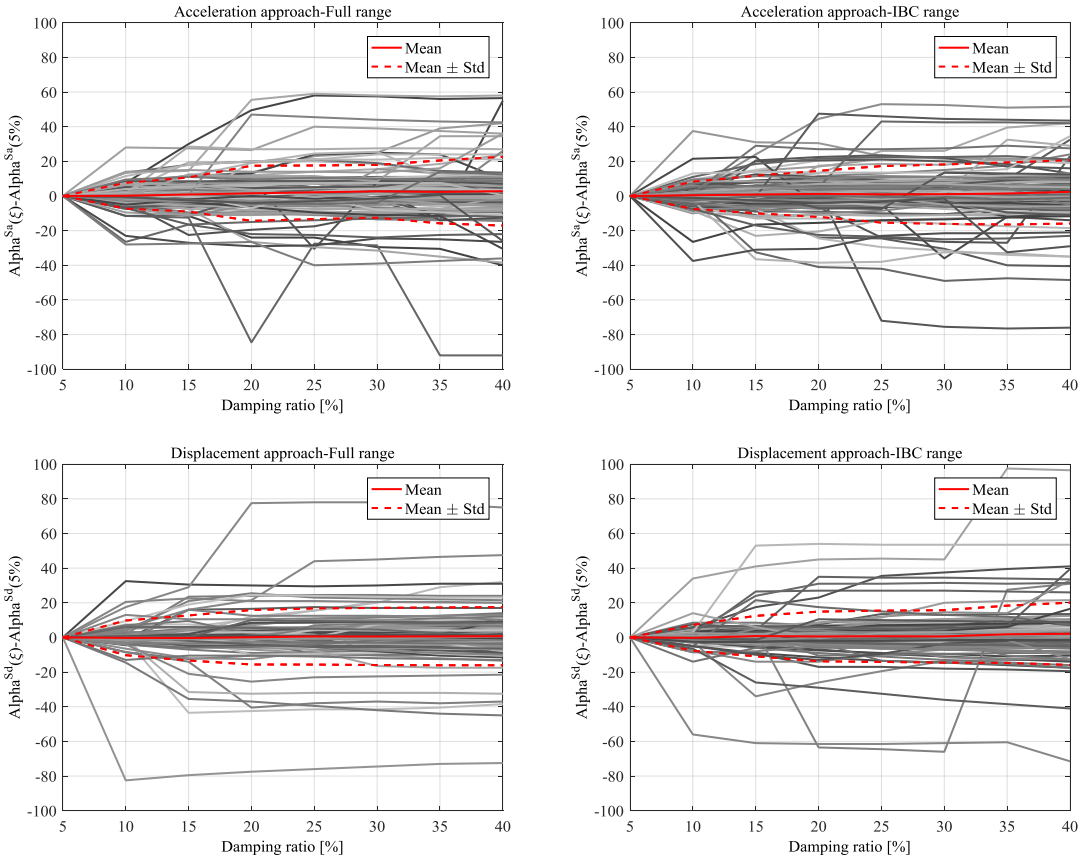


Figure 4: Variation of the orientation angle vs damping ratio: full range (left) and I.B.C. (right) results.

Statistical results show that for damping ratios higher than 5% the optimum orientation angle is averagely constant, with an increasing variability, up to an asymptotic range of variation (±20°): this aspect allows to compute the equivalent radial seismic input, by assuming 5% damping, as for spectrum-compatibility check of a records set, without any more refined evaluation of the damping ratio, which is not a priori known for highly non-linear behaviors. Approximately same variability is noticed for both acceleration and displacement approaches. Nonetheless, in some case a higher damping ratio leads to non-negligible changes in the optimum orientation angle.

In Figure 5 error variation values of the optimum orientation angle are shown for acceleration (top) and displacement (bottom) approaches, by considering full-range (left) and Italian Building Code I.B.C. (right), as a function of increasing damping ratio, with respect to the reference value at 5% damping. Results returned by I.B.C. assumptions have been multiplied by $\gamma$, which represents the ratio between the average values at 5% damping for I.B.C. and full range respectively, aiming at comparing the accuracy level of the considered period ranges.

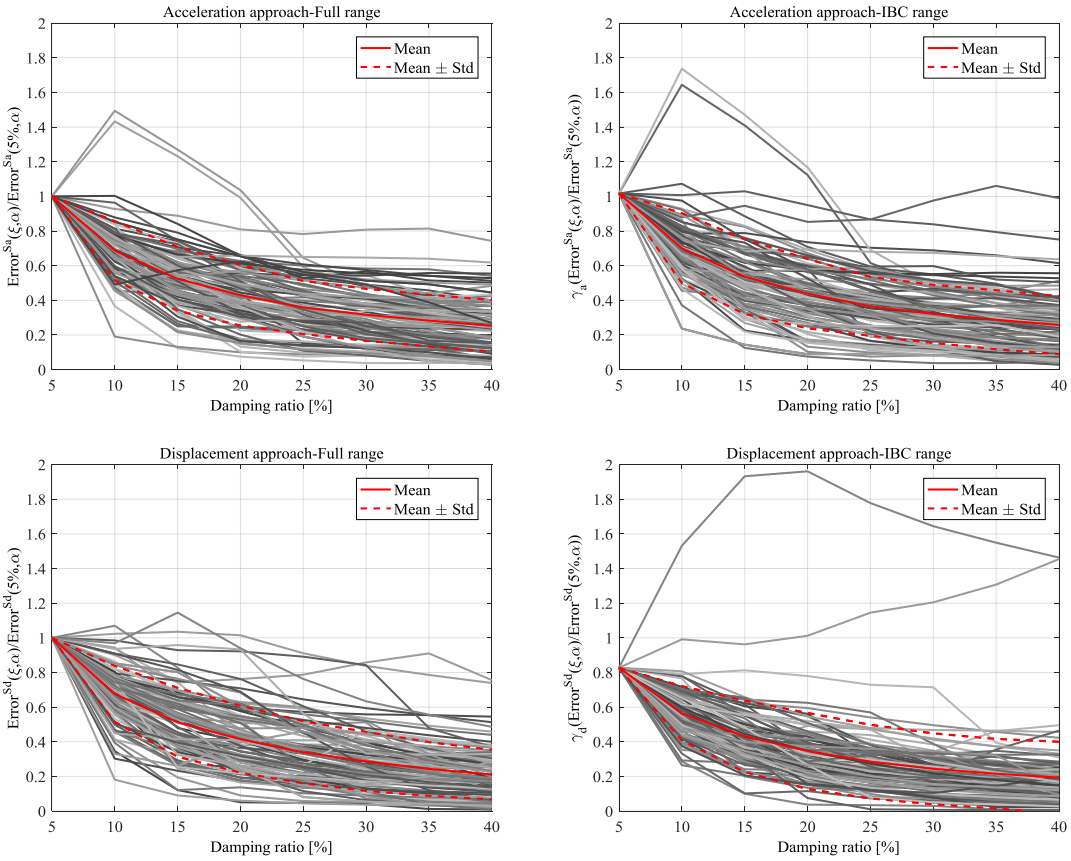


Figure 5: Error variation vs damping ratio: full range (left) and I.B.C. (right) results.

As expected, the Mean Square Error (MSE) between the reference bidirectional and the equivalent radial response spectra decreases as the damping ratio increases: for both the considered period ranges, the MSE at 5% of damping is reduced of 50% if a damping ratio of approximately 15% is assumed: thus, if base-isolated structures are analyzed, a damping ratio higher than 5% would surely return more accurate results. Furthermore, it can be assessed that a smaller period range leads to lower MSE values, if the displacement approach is applied.

Finally, mean curves of full-range results are compared to the ones related to the I.B.C. period range, in order to investigate if a smaller period range produces the same variability of the full range case (Figure 6).

Results show that the considered period ranges lead to approximately the same variability of the optimum orientation angle for both the approaches: averagely, the orientation angle does not change for higher values of damping ratio, in comparison to 5% case, with maximum variation range bounded between ±20°.

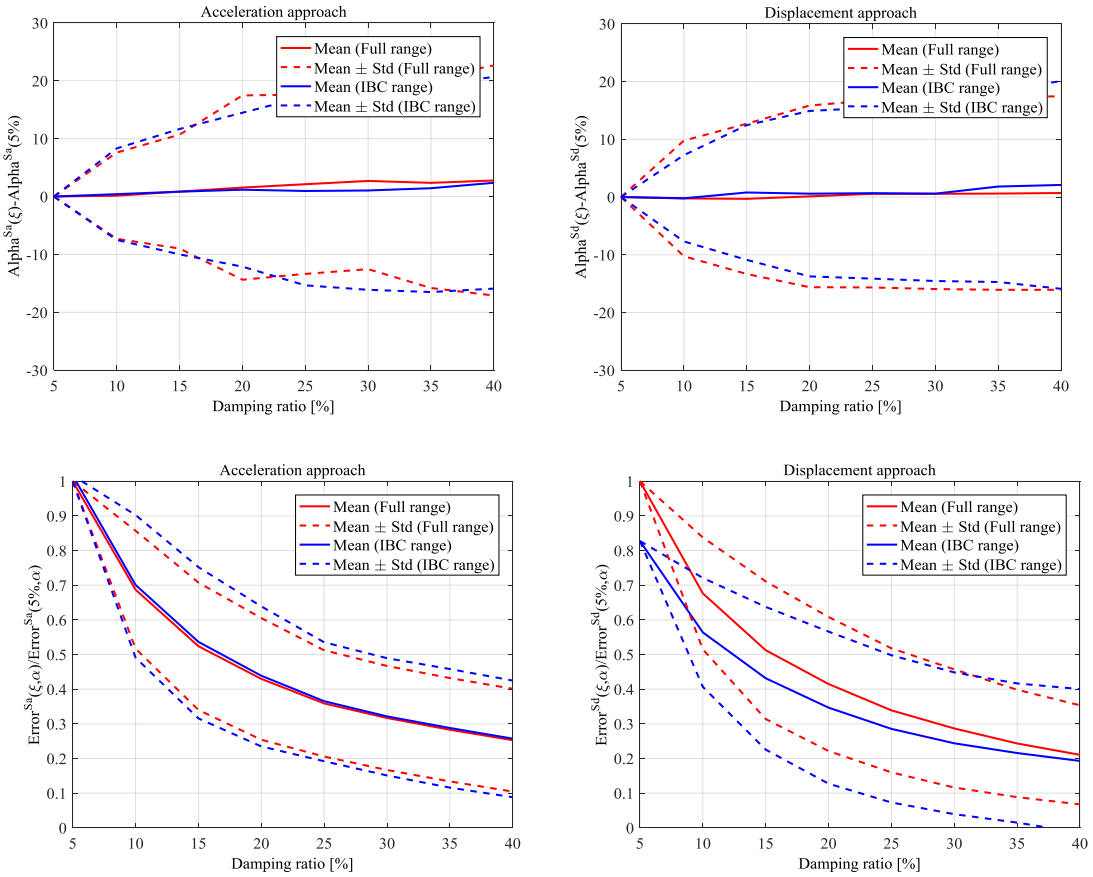


Figure 6: Period ranges comparison for orientation angle (top) and error (bottom): acceleration (left) and displacement (right) approaches.

MSE results show that the acceleration approach leads to the same mean curve, with comparable variability; on the other hand, the displacement approach with I.B.C. period range returns lower MSE values at all damping ratio values, even though a slightly larger variability can be noticed.

## 3. CASE STUDY STRUCTURE

In this work a case study structure has been analyzed, by considering bidirectional rather than equivalent radial seismic events, according to both acceleration and displacement approaches. The structural system consists of a three stories reinforced concrete frame structure, base isolated by means of Concave Surface Slider devices; the structure has been implemented in a F.E.M. software, by considering a linear-elastic model for all the structural elements, and the actual constitutive law of CSS isolators for the non-linear links, which represent the isolation devices: such a link does account for the biaxial interaction of the directions of motion, so the main frictional force for all the isolators is stepwise projected along the main directions of motion, when bidirectional earthquakes are applied. In Figure 7 the structural F.E.M. is shown.

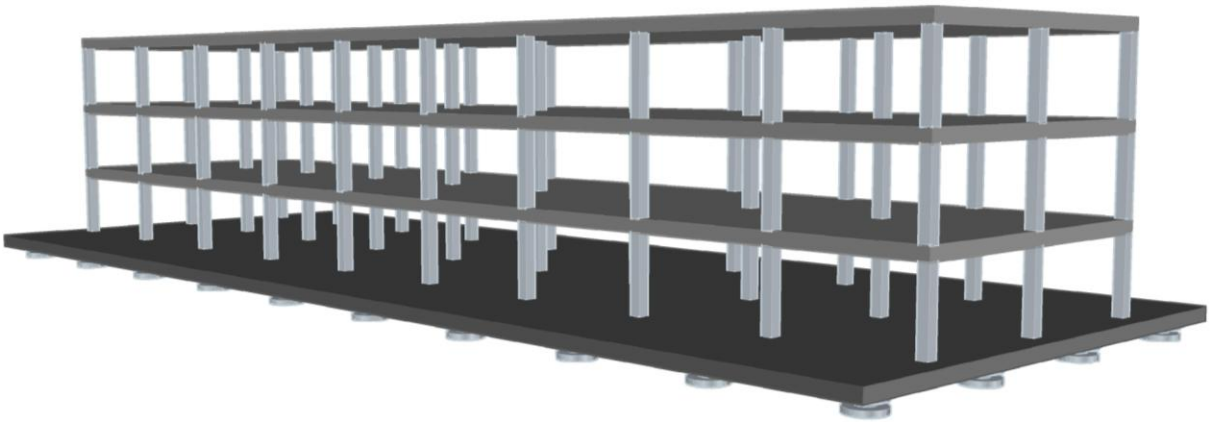

Figure 7: Case study structure

The building is located on a reinforced concrete slab, which has been implemented by using shell-thin elements, 0.5m thick, in order to model both the in-plane and out-of-plane behavior.

In Table 1 main characteristics of the analyzed structural systems are listed, in terms of building mass, isolated plate mass, "fixed-base" fundamental periods and behavior factor.

| $M_s$ [t] | $M_p$ [t] | $T_{FB,x}$ [s] | $T_{FB,y}$ [s] | q |
|---|---|---|---|---|
| 1800 | 1200 | 0.42 | 0.56 | 3.45 |

Table 1: Characteristics of the structural system.

Beneath the R.C. slab, all the isolators have been placed. For all the simulations Double Concave Surface Slider devices have been considered (Figure 8).



Figure 8: Double Concave Surface Slider device.

Both the sliding surfaces have the same radius of curvature (1.6m), and the height of the inner non-articulated slider is equal to 120,0mm. Thus, the equivalent radius of curvature of a single device results 3,08m. For all the analyses the friction coefficient has been assumed to be constant with respect to both sliding velocity and contact pressure; furthermore, no cyclic decay has been considered, due to heating phenomena at the sliding interfaces [7, 14]. Hence, the friction coefficient is constantly equal to 7%, according to the outcomes of a testing campaign, carried out at the EUCENTRE TREES-Lab (Pavia) [13] on a full scale device, and given dimensions of the sliding materials and vertical reactions of the isolators [7].

Six bidirectional events have been applied, and equivalent radial accelerograms as well, computed with both acceleration and displacement approaches. An initial value of 5% damping has been considered, for the computation of the optimum orientation angle of the radial events: results have shown that the optimum orientation angle can be considered averagely constant, for increasing values of damping ratio; moreover, for a damping ratio higher than 15% the error between the radial and the bidirectional response spectra is reduced by 50%, in comparison to the 5% damping case. Since the damping ratio is not a priori known, when friction-based isolators are considered, a reference damping ratio of 5% has been assumed. In Table 2 the applied seismic events have been summarized.

| Event # | Location | Year | Mw | $PGA_X$ [g] | $PGA_Y$ [g] | $\alpha_{acc}$ ($\xi$=5%) | $\alpha_{disp}$ ($\xi$=5%) |
|---|---|---|---|---|---|---|---|
| 1 | L'Aquila | 2009 | 6.3 | 0.31 | 0.33 | 40 | 40 |
| 2 | Friuli | 1976 | 5.9 | 0.30 | 0.48 | 112 | 117.5 |
| 3 | Irpinia | 1980 | 6.9 | 0.21 | 0.32 | 61.5 | 74.5 |
| 4 | Emilia | 2012 | 6 | 0.23 | 0.29 | 95 | 74.5 |
| 5 | Loma Prieta | 1989 | 6.9 | 0.32 | 0.28 | 42 | 32.5 |
| 6 | Tirana | 1988 | 5,9 | 0.22 | 0.36 | 65 | 62.5 |

Table 2: Characteristics of applied seismic events.

## 4. ANALYSES RESULTS

In what follows results are shown, in terms of trajectories of the isolation system, and vectorial displacement, absolute acceleration and shear profiles of the whole structural system, by considering bidirectional rather than equivalent radial events, with both acceleration (Sa) and displacement (Sd) approaches. In Figure 9 trajectories of the isolation system are reported.

It can be noted that radial motions develop along the largest size of the bidirectional trajectories in all the considered seismic events. The maximum displacement at the isolation level looks to be fairly estimated by radial signals, for both acceleration and displacement approaches, even though orientation angles at 5% damping have been assumed: this is mainly due to the constant trend of the average orientation angle of the equivalent radial event, with respect to the damping ratio, as underlined in the statistical study (Figure 4); moreover, the error decreases as higher damping ratios are considered, so that the displacement demand of the isolation system is well approximated. In addition, radial trajectories are not perfectly linear: as can be noticed, small displacements occur orthogonally with respect to the main direction of motion, for both acceleration and displacement approaches. Precisely, the non-linear time history analyses have been performed by applying the equivalent radial accelerogram according to the optimum variation angle at 5% of damping ratio: thus, transverse displacements are induced by the actual bi-axial interaction of the directions of motion, modeled by the non-linear links which represent all the isolators.

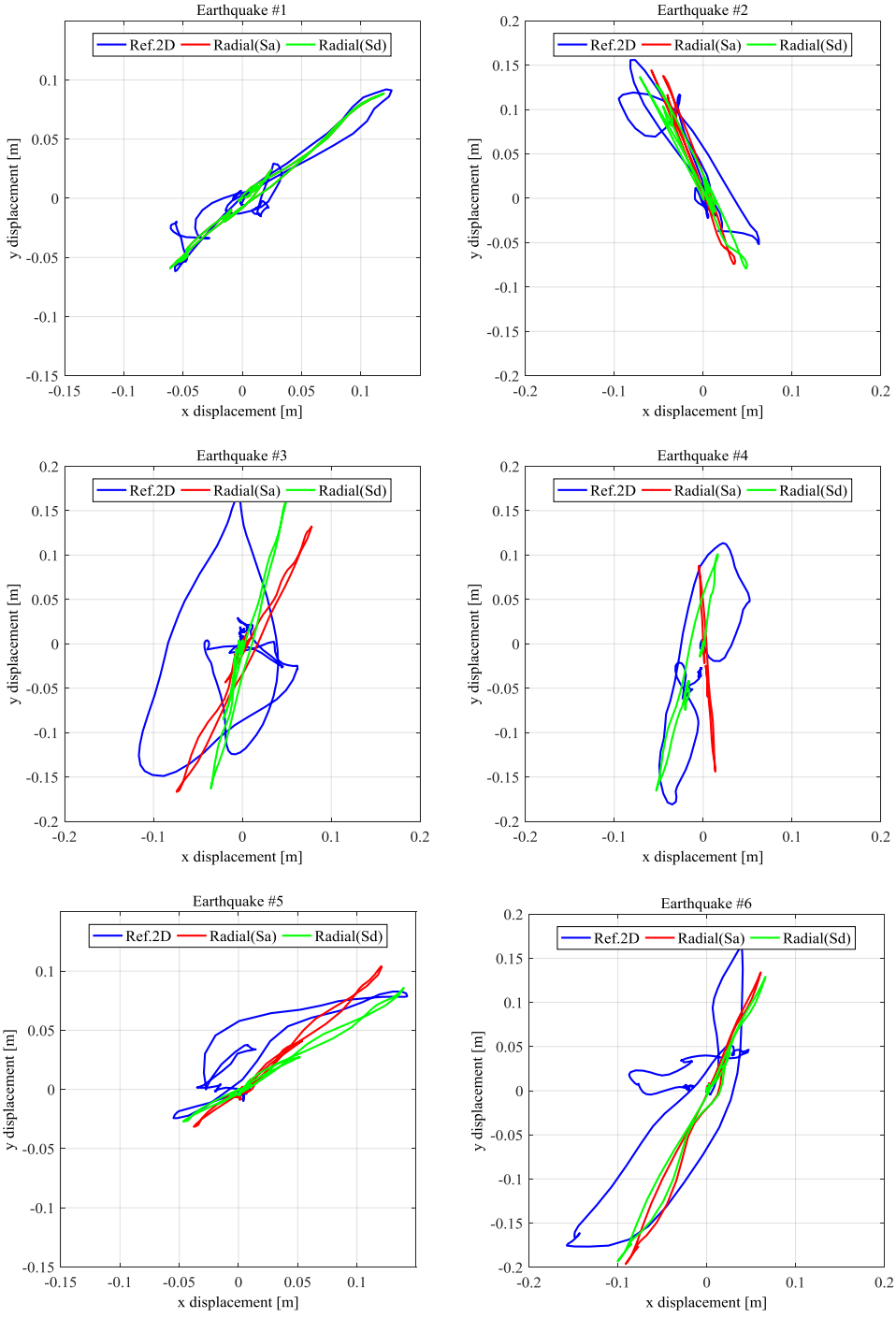


Figure 9: Analyses results: Trajectories of the isolation system.

Nonetheless, the structural system can be considered as subjected to radial motion for all the seismic events, when equivalent accelerograms are applied.

In Figure 10 results are shown in terms of vectorial displacement profiles for all the considered seismic events.

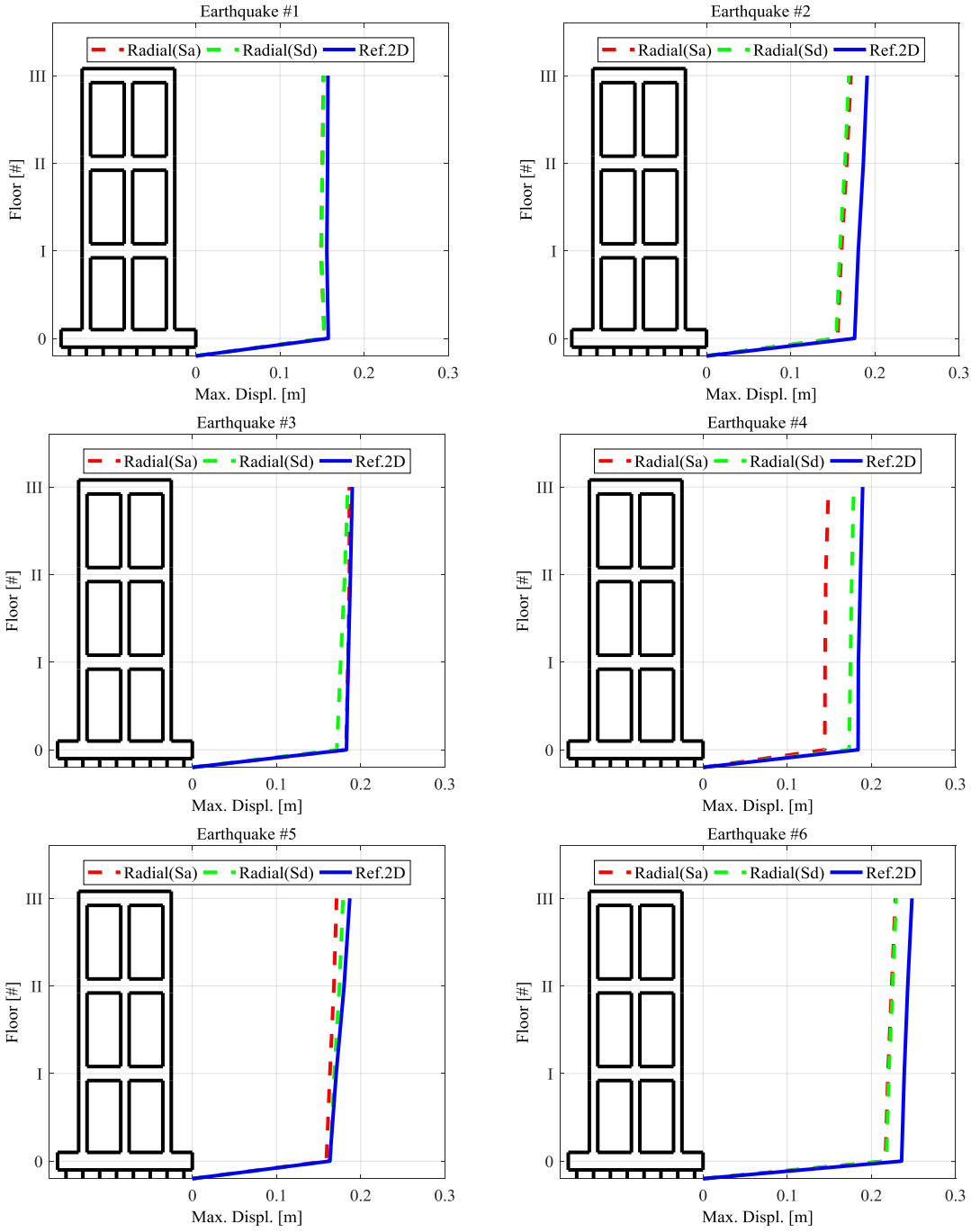


Figure 10: Analyses results: displacement profiles.

For all the considered seismic events, equivalent radial accelerograms lead to a good estimate of the displacement demand at all levels, for both acceleration and displacement approaches. In some cases, both the considered unidirectional motions return overlapped displacement profiles, due to the similar values of optimum orientation angles. Generally, a reference bidirectional event seems to lead to the highest displacement demand at all levels, whereas lower displacement values are returned by equivalent radial ground signals.

In Figure 11 vectorial absolute acceleration values are shown at all levels of the structural system.

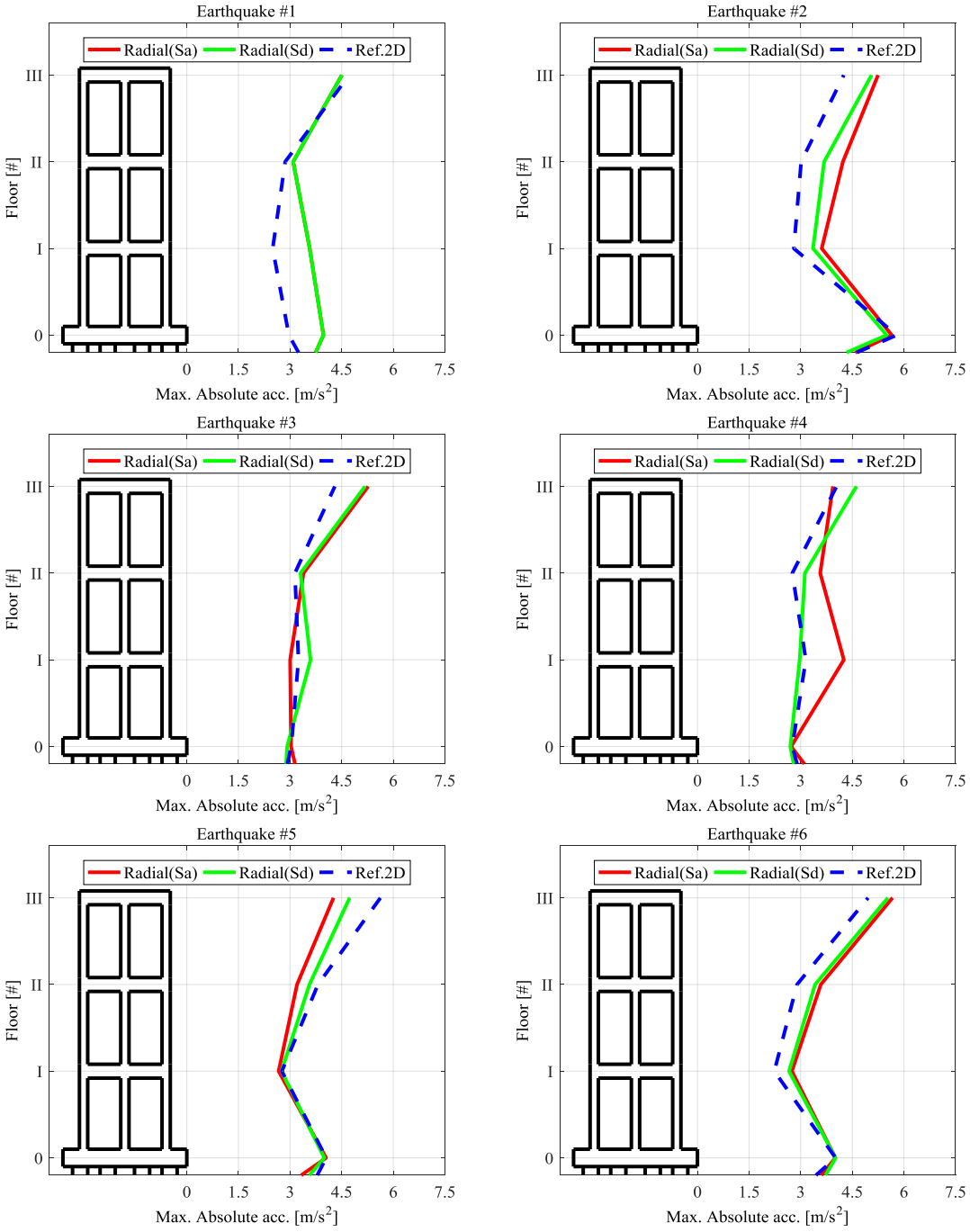


Figure 11: Analyses results: Absolute Acceleration profiles.

As for the displacement response, the acceleration response under equivalent unidirectional seismic motion well capture the reference bidirectional one for all the considered events. On the other hand, equivalent radial motions can lead to both higher and lower acceleration values, especially for the building floors levels. Furthermore, acceleration profiles in most of the cases can be considered approximately constant along the height of the structural system.

Finally, results have been analyzed, in terms of vectorial interstorey shear values for all the structural levels (Figure 12): values have been normalized with respect to the total weight of the structural system.

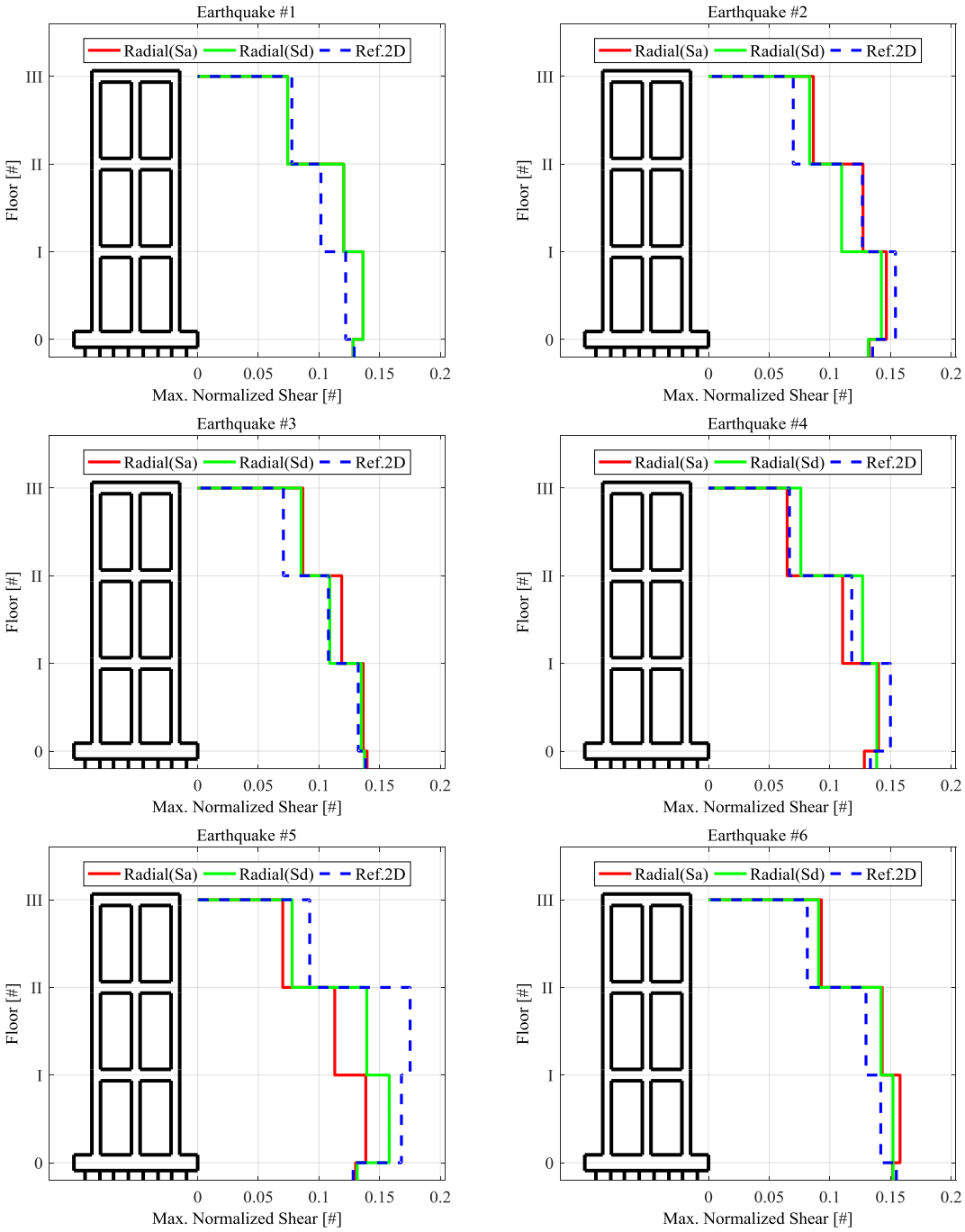


Figure 12: Analyses results: Shear profiles.

Also interstorey shear responses are properly estimated by equivalent radial events, in comparison to the bidirectional reference case. However, in some cases non-negligible variations have been found. The maximum force at the isolation level is well approximated by equivalent radial accelerograms, and the best simulation is generally returned by the displacement approach, as well as for both displacement and absolute acceleration responses.

Thus, for base-isolated structures the displacement approach seems to be the best procedure for the computation of the equivalent unidirectional signal.

## 5. CONCLUSIONS

In the present work a more refined procedure for the computation of an equivalent radial accelerogram for bidirectional seismic events is presented. Precisely, given the reference response spectrum of a biaxial earthquake, which is represented by two individual ground acceleration time series, an optimum orientation angle is detected, by minimizing the Mean Square Error between the reference 2D and the equivalent 1D response spectra. Two different period ranges have been considered, for the computation of the MSE value, for a given damping ratio, according to the full-range, rather than the period range for spectrum compatibility ruled by the Italian Building Code (I.B.C.). Such a procedure has been applied to 100 bidirectional seismic events, in order to highlight the effect of the damping ratio on both the optimum orientation angle and the MSE. Since the presented procedure has been defined for base-isolated structure, generally represented by a variable damping ratio, as a function of the displacement demand, results have been reported in comparison to the 5% damping ratio, which can be considered as a reference case. The optimum orientation angle is averagely independent with respect to the damping ratio, even though a non-negligible variability is found, asymptotically bounded between ±20°. On the other hand, the Mean Square Error (MSE) decreases, if high damping ratio values are assumed, and the error at 5% damping is reduced of 50%, if damping values higher than 15% are considered. Furthermore, a smaller period range for the computation of the MSE leads to comparable variability to the full-range case, for what concerns the optimum orientation angle; however, smaller MSE values are can be found, with the I.B.C. period range.

Finally, a case study structure has been modeled by means of a F.E.M. commercial software, and bidirectional and equivalent radial seismic inputs have been applied. Six different earthquakes have been considered, by applying both the x and y components simultaneously, and computing an equivalent radial accelerogram with acceleration and displacement approaches, by assuming 5% damping ratio. Results have been analyzed in terms of trajectory of the isolation system, vectorial displacement, absolute acceleration and interstorey shear profiles. The displacement demand of the bidirectional trajectory of the isolation system seems to be well captured by the equivalent radial events, for both acceleration and displacement approaches, and small variabilities are found. Concerning displacement profiles, the reference bidirectional case returns the highest displacement demand at all levels and for all the considered seismic events, and better results are achieved if the displacement approach is applied. Regarding both absolute acceleration and interstorey shear responses, the equivalent radial accelerograms lead to good estimates of the bidirectional profiles, at all levels; on the other hand, the bidirectional response is no longer the upper bound of the equivalent unidirectional ones, as for the displacement profiles. Also the maximum force at the isolation level is well approximated by the equivalent single component events: thus, the proposed procedure allows to reproduce approximately the same effects of a general bidirectional seismic event, by applying a single component ground motion, which is computed by assuming 5% damping ratio for the optimum orientation angle; if base-isolated structures are modeled, higher damping ratio values will be found during Non Linear Time History Analysis (NLTHA), so that smaller MSE values will be averagely experienced, with no significant changes in the optimum orientation angle. Further research is needed on the topic, especially for what concerns isolation devices with smaller damping levels, rather than common fixed-base structures.

## REFERENCES


[1] Beyer K, Bommer J (2007), Selection and Scaling of Real Accelerograms for Bi-Directional Loading: A review of current practice and code provisions. Journal of Earthquake Engineering, 11, 13-45, DOI: 10.1080/13632460701280013.

[2] Casarotti C, Furinghetti M, Pavese A, Evaluation of response of an isolated system based on Double Curved Surface Slider. *Computational method in Earthquake Engineering*, **30**, pp 397-416, 2013, DOI: 10.1007/978-94-007-6573-3_19.

[3] CEN, Comité Européen de Normalisation TC 340, *European Code UNI EN 15129:2009 Anti-seismic devices*. Brussels, 2009.

[4] Fenz D, Constantinou MC, Behaviour of the double concave friction pendulum bearing. *Earthquake Engineering And Structural Dynamics*, **35**,1403–1424, 2006.

[5] Furinghetti M, Casarotti C, Pavese A, Investigation of the consequences of mounting laying defects for curved surface slider devices under general seismic input. *Journal of Earthquake Engineering*, Under review.

[6] Furinghetti M, Pavese A (2017) Equivalent Uniaxial Accelerogram for Css-Based Isolation Systems Assessment under Two-Components Seismic Events. Mechanics Based Design of Structures and Machines, DOI: 10.1080/15397734.2017.1281145.

[7] Furinghetti M, Pavese A (2015), Numerical Assessment on the Seismic Response of a Base-Isolated Building under Bi-Directional Motion. *5th ECCOMAS Thematic Conference on Computational Methods in Structural Dynamics and Earthquake Engineering*, Crete Island, Greece, May 25-27, 2015.

[8] Grant D, Diaferia R (2012), Assessing adequacy of spectrum-matched ground motions for response history analysis. Earthquake Engineering and Structural Dynamics, 42, 1265-1280, DOI: 10.1002/eqe.2270.

[9] Iervolino I, Galasso C, Cosenza E (2009), REXEL: computer aided record selsction for code-based seismic structural analysis. Bulletin of Earthquake Engineering, DOI: 10.1007/s10518-009-9146-1.

[10] Khoshnoudian F, Hagdoust VR, Response of pure-friction sliding structures to three components of earthquake excitation considering variations in the coefficient of friction. *Scientia Iranica*, **16**, 429-442, 2009.

[11] Lomiento G, Bonessio N, Benzoni G, Concave sliding isolator's performance under multi-directional excitation. *Ingegneria Sismica*, **30:3**,17-32, 2013.

[12] Mosqueda G, Whittaker AS, Fenves GL, Characterization and modeling of friction pendulum bearings subjected to multiple components of excitation. *Journal of Structural Engineering*, **130**, 433-442, 2004.

[13] Peloso S, Pavese A, Casarotti C (2012), EUCENTRE TREES lab: Laboratory for training and research in earthquake engineering and seismology, Geotechnical, Geological and Earthquake Engineering, 20, 65-81, DOI: 10.1007/978-94-007-1977-4_4.

[14] Quaglini V, Bocciarelli M, Gandelli E, Dubini P (2014), Numerical Assessment of Frictional Heating in Sliding Bearings for Seismic Isolation. Journal of Earthquake Engineering, 18(8), 1198-1216, DOI: 10.1080/13632469.2014.924890.

COMPDYN 2017
6th ECCOMAS Thematic Conference on
Computational Methods in Structural Dynamics and Earthquake Engineering
M. Papadrakakis, M. Fragiadakis (eds.)
Rhodes Island, Greece, 15–17 June 2017

# DOWNSIZING OF MEMBERS THROUGH NUMERICAL ANALYSIS OF STEEL MULTI-STORIED FRAME WITH PASSIVE FRICTION DAMPERS AT BASE

**Jingye LIU[1], and Minoru YAMANARI[2]**

[1] Graduate School of Science and Technology, Kumamoto University
2-39-1 Kurokami, Chuo-ku, 860-8555 Kumamoto, JAPAN
e-mail: 153d8931@st.kumamoto-u.ac.jp

[2] Faculty of Advanced Science and Technology, Division of Material Science, Building Structure and Disaster Prevention, Kumamoto University
2-39-1 Kurokami, Chuo-ku, 860-8555 Kumamoto, JAPAN
yamanari@kumamoto-u.ac.jp

**Keywords:** Vibration Control, Passive Friction Damper, Steel Frame, Energy Dissipation, Weight Reduction.

**Abstract.** *In this paper, the vibration control systems using passive dampers settled at the base of steel buildings with the effect of reducing the total steel weight of multi-storied frames with sliding bearings is investigated. The passive friction is one of the vibration control device that is important to use the technology to prevent or minimize damage to buildings[1], and the device can dissipate the seismic energy by sliding during an earthquake excitation. This research address vibration control system permits the downsizing of members of the steel super-structure, which reduces the total steel weight. The first story of the building could contribute to base-isolation because of the passive friction dampers at the bottoms of some columns. Two steel frames were simulated for the research by using OpenSees. The first consisted of large-sized columns and beams while the other utilized smaller member sizes. Both steel frames used columns in the first story equipped with passive friction dampers, which were connected at the base with side-by-side columns. A series of numerical simulations was conducted and the results were compared regarding the inter-story drift angle, slide deviation and seismic energy under earthquake excitations. Finally, results from the numerical analyses of the effect of the base-isolation on the total weight reduction of the multi-storied steel frame were summarized.*

# 1 INTRODUCTION

Friction dampers are generally used as a member of vibration control in architectural buildings. In recent, study on friction dampers is making steady progress because the device performance is not only highly controlled and maintained, but also the mechanical property of the device is rather simple. Although there are many experimental analyses[2] and numerical analyses[3] of friction dampers and application for equipment into structures, the study on the flexible use of the friction damper is sparse. Therefore, the objective of this research is to investigate the practical properties of weight reduction of steel frame, which equipped with friction dampers at the base of a building. For designing the weight reduced frame the seismic response of frame equipped with friction dampers has been investigated for determine the coefficient of friction dampers equipped into weight reduced frame.

In this research, friction dampers settled at the bottom of a building frame without connection at the column bases can act as vibration controls for the building. These passive friction dampers can decrease the seismic energy absorbed by the building by sliding motions, thus decreasing the maximum inter-story drift angle of the building. A base-isolation system can be realized by incorporating friction dampers at all column bases in a frame[4]. In order to distribute the slip load uniformly across all dampers, each column base in the building framework can be connected with tying beams. Therefore, all bases of the frame with friction dampers can be restored for spring-back[5]. This permits the flexible use of the reduction of the total steel weight, achieved by downsizing the members of the steel frame equipped with passive dampers[6]. The indices describing the seismic responses of the frameworks and friction dampers are the inter-story drift angle and slide deviation, which must be characterized prior to implementing the described base-isolation system. In this study, the seismic response of the frames and friction dampers are examined by means of analytical simulations.

In this paper, friction dampers are modeled and analyzed by means of OpenSees that is one of multi-purpose structural analysis program. Friction elements are settled at the bottom of a frame. Incorporating friction dampers into the steel frame influences the seismic response of the steel frame. Indexes for the grasp of seismic responses of the frame and friction elements are inter-story drift angle and slide deviation of friction elements, and they were examined by comparing with respect to the indexes by means of analytical parameters.

# 2 ANALYTICAL MODEL

Analytical model in numerical analysis of this research is described in this chapter.

## 2.1 Analytical Frame

In this chapter, the outline of the analysis frame shown in Fig. 1. The two-bay three-story steel frame, designed based on Japanese building codes, was prepared for a series of numerical analyses. The original frame that the base is fixed on a foundation is depicted in Fig. 1(a). The original frame equipped with friction dampers is shown in Fig. 1(b).

The columns and beams of the original frame both with and without friction dampers are steel hollow sections and steel side-flange sections, respectively, while the friction dampers are represented as special mechanical elements. The hysteretic behavior of the columns and beams include isotropic and kinematic hardening. The size of the cross-sections of the beams and columns of the original frame and steel weight of every story of original frame are shown in Table 1. The size of a cross section of the tying beam is same with the first story. The material property of each member is summarized in Table 2.

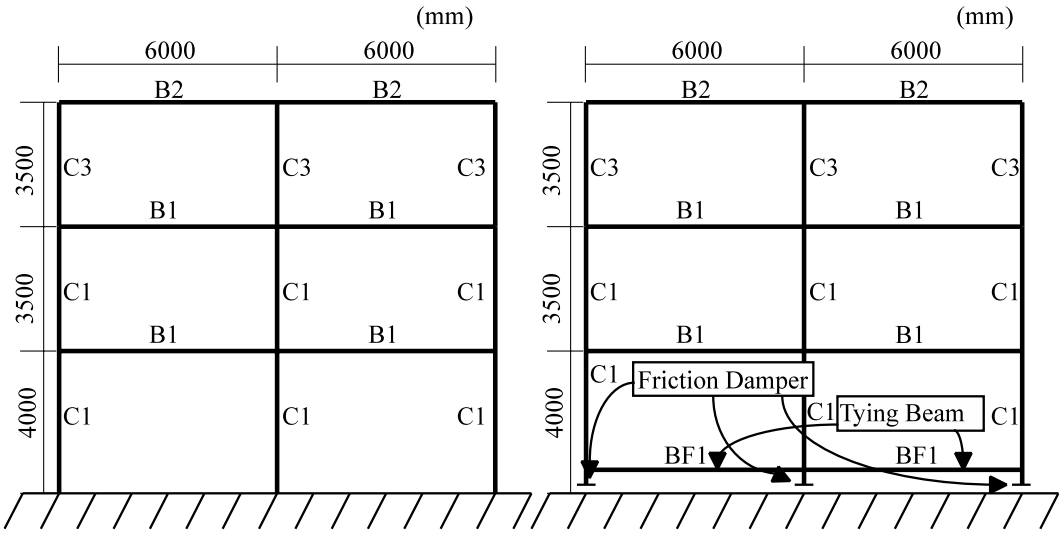


(a) Without fiction damper (b) With friction damper

Figure 1: Original frame models.

| Story | Column (mm) | Beam (mm) | Steel Weight (t) |
|---|---|---|---|
| 1 | RHS - 300 x 300 x 16 | H - 400 x 200 x 8 x 13 | 6.06 |
| 2 | RHS - 300 x 300 x 16 | H - 400 x 200 x 8 x 13 | 5.64 |
| 3 | RHS - 300 x 300 x 12 | H - 350 x 175 x 7 x 11 | 4.30 |

Table 1: Cross sections of members and steel weight of original frame.

| Young's modulus | Poisson's ratio | Strain hardening factor | Yield stress |
|---|---|---|---|
| 205000N/mm$^2$ | 0.3 | 0.006 | 258.72 N/mm$^2$ |

Table 2: Material property.

## 2.2 Friction Damper

The analytical model and corresponding mechanical system describing the friction dampers under sliding conditions are shown in Fig. 2.

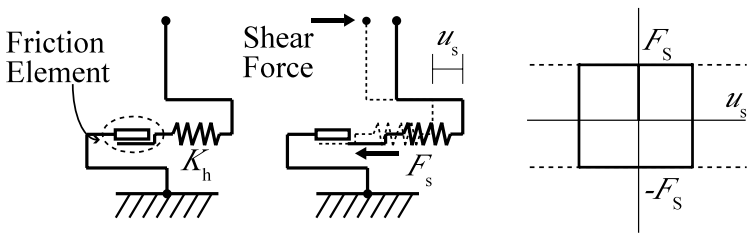


(a) Friction damper (b) Hysteretic behavior

Figure 2: Analytical and mechanical models of friction damper.

$K_h$ is the stiffness of the friction dampers has infinity values. The hysteretic behavior of the friction dampers is based on the Coulomb model of friction as expressed in Equation (1):

$$F_s = \mu \cdot W \tag{1}$$

where

$F_s$: slip load

$\mu$: coefficient of friction

$W$: contact force on the friction damper

The value of $F_s$ is determined by $\mu$ and $W$. When the frictional force approaches the slip load value, the friction damper starts to slide. The characteristics of the sliding of the friction dampers and its deterioration under dynamic loading must be closely related. However, it is assumed that the surface of the friction damper experiences on deterioration throughout the analyses in this research.

## 3 PARAMETER AND METHOD OF ANALYSIS

This chapter describes analytical parameter of sliding coefficient and analytical method.

### 3.1 Coefficient of Friction

The contact force of the friction damper that is considered a vertical load, keeps constant value through the analysis as the above mention. The slip load changes with sliding coefficient. Therefore, the numerical works were conducted with the sliding coefficient as the analytical parameters. When the coefficient of friction takes large value, the friction damper does not slide, the effect of energy dissipation can not give play to energy dissipation. As this reason, the sliding coefficient varied from 0.1 to 0.5.

### 3.2 Method of analysis

OpenSees (the Open System for Earthquake Engineering Simulation) is an object-oriented open-source software framework incorporating the finite element method (FEM). The numerical analyses of the building schematics here were performed using this framework. In this research, the dynamic analyses were conducted. In the dynamic analyses, ground motion was applied to the frames in the lateral direction. The ground motion followed the vibration data are shown in Table 2. Eventually, the maximum velocity of the ground motion was set to 0.50 [m/s], representing an unexpected major earthquake. The numerical work was performed using the Newmark-$\beta$ method in which $\beta$ takes the value of 1/4. The Rayleigh damping model was used with both the first and the second damping constants take the value of 0.02.

| Ground motion | Acceleration [m/s$^2$] | Velocity [m/s] | Duration time [s] |
|---|---|---|---|
| El Centro NS 1940 | 5.11 | 0.50 | 20.0 |
| JMA Kobe NS 1995 | 4.92 | | 20.0 |
| NTT Kobe NS 1995 | 1.90 | | 20.0 |
| Taft EW 1952 | 4.97 | | 20.0 |

Table 3: Input earthquake wave.

# 4 DYNAMIC ANALYSIS OF ORIGINAL FRAME

## 4.1 Sliding coefficient

The contact force on the friction damper, defined as the total weight of the frame, is approximately constant throughout the analysis. The slip load changes with the coefficient of friction. Therefore, numerical simulations were conducted using the coefficient of friction as the analytical parameter varied from 0.1 to 0.5. Equal horizontal ground motion was applied to the frame for all analyses, using data from the wave of Table 2. Because the various possible magnitudes of earthquakes can cause very different results, the maximum velocity of ground motion was set to 0.50 [m/s], representing an earthquake of medium intensity. The step time of the numerical integration of the seismic response analysis was 0.002 [s], and the duration of the analysis was 20.0 [s].

## 4.2 Maximum inter-story drift angle

The maximum inter-story drift angle $R_{i\ \max}$ for each story in the original frame and the original frame with damper are shown in Fig. 3. When the coefficient of friction takes the value smaller than 0.3, the values of $R_{i\ \max}$ for the original frame with friction dampers are smaller than that of the original frame for all stories. However, larger coefficients of friction decrease the effect of vibration control, which is why the sliding displacement of the friction damper is decreased for large coefficient of friction.

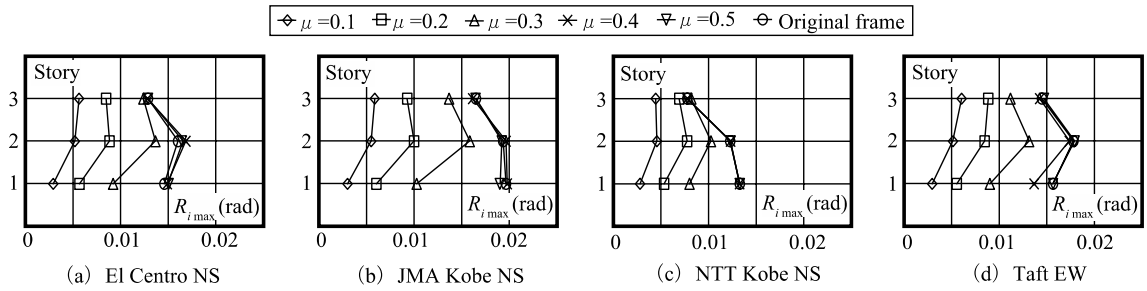


Figure 3: Maximum drift response

## 4.3 Slide deviation

The relationship between the absolute value of the maximum slide deviation ($u_{s\ \max}$) and the coefficient of friction for the original frame and the original frame with damper are shown in Fig. 4 (a). The maximum slide deviations are similar when the coefficient of friction is set between 0.1 and 0.3. However, the slide deviation is almost zero when the coefficient of friction is set to 0.4 or 0.5, because the friction damper does not slide when the coefficient of friction is enough large.

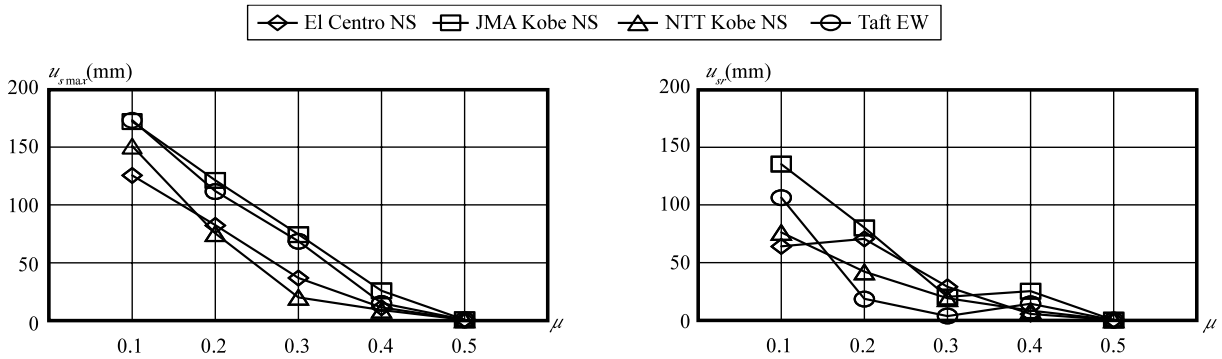


(a) Maximum Slide Deviation (b) Residual Slide Deviation

Figure 4: Maximum slide deviation

Therefore, the residual slide deviation is also important. Because of the friction damper that is related to the weight of the frame at the base of all first column of the frame, the restoring force of the damper cannot work for sliding back to the original position. According to this reason, a decrease in residual slide deviation by elastically returning it of the frame after ground motion disappeared cannot be expected. The relationship of the residual slide deviation ($u_{Sr}$) and the coefficient of friction is shown in Fig. 4 (b). According to this graph, the residual slide deviation decreases with the coefficient of friction increase. The prediction of the residual slide coefficient of friction is difficult, although the residual slide deviation can be greatly restrained by a suitable coefficient of friction when design the weight reduced frame.

### 4.4 Energy calculation

The energy dissipation is the amount of dynamic energy absorbed by sliding of the friction elements. Variations in the amount of energy dissipation influence the hysteric behaviour of the frame. When subjected to lateral force, the frame and friction elements absorb dynamic energy. To evaluate this energy, the amount of energy dissipation by friction elements ($E_p$) and the amount of strain energy absorbed by the frame ($E_c$) are compared. The amount of the accumulated strain energy that is obtained with the inter-story drift angle and the story shear, is expressed by Equation (2):

$$E_c = \sum_{i=1}^{N} E_{ci} = \sum_i \sum_j \{\frac{1}{2} \cdot (Q_{i,j+1} + Q_{i,j}) \cdot (R_{i,j+1} - R_{i,j}) \cdot h_i\} \tag{2}$$

where

$i$: story number
$j$: step number in calculation
$N$: number of stories
$E_{ci}$: $i$th story's strain energy
$Q_i$: $i$th story's shear
$R_i$: $i$th story's drift angle
$h_i$: $i$th story's height

The amount of the energy dissipation is obtained using the frictional force and thesliding displacement as expressed by Equation (3):

$$E_p = \int F(u_s) du_s \tag{3}$$

where

$F$: friction force of friction damper
$u_s$: slide deviation

The relationship between the energies of the original frame with damper and the coefficient of friction is shown in Fig. 5. In the graphs, the horizontal lines are the accumulate strain energy of the original frame in four earthquake waves.

By changing the coefficient of friction, the value of energy dissipation is reduced and the value of strain energy is enhanced. However, the value of energy dissipation increases when the coefficient of friction changed from 0.1 to 0.3. Through the dynamic analysis, when the coefficient of friction is set between 0.1 and 0.5, the sliding bearing accommodates energy absorption by sliding. When the coefficient of friction takes the value between 0.1 and 0.3, the effect of energy dissipation is the most efficient.

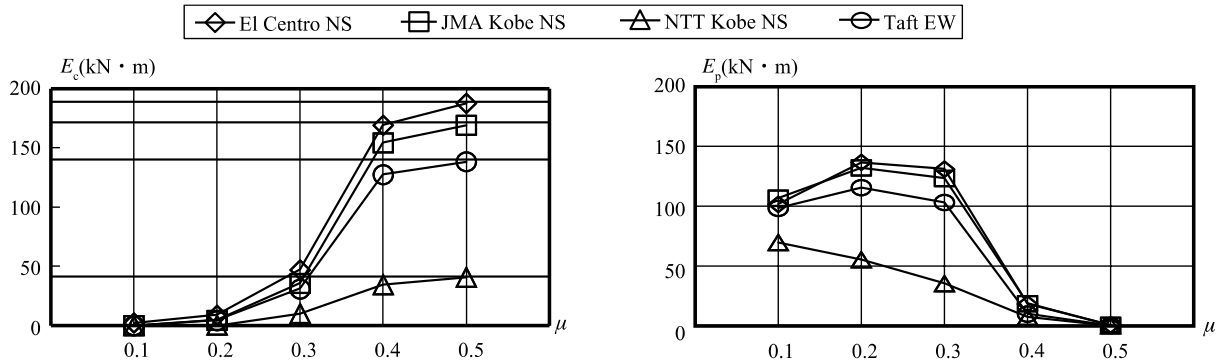

(a) Strain Energy (b) Energy Dissipation

Figure 5: Relationship between coefficient of friction and energy

## 5 DESIGN OF WEIGHT REDUCED FRAME

According to Figs. 3 and 4, when the coefficient of friction exceeds 0.3, the maximum inter-story drift angle approximately are same as that of the original frame, because the larger coefficient of friction leads the sliding displacement decreased, the effect of vibration control also decreased. In addition, according to Fig. 5, when the coefficient of friction takes larger values, the strain energy rapidly increases. On the other hand, the energy dissipation was reduced. Because of these reasons, and the base on the experimental analysis[2], the design goal of the weight reduced frame is the maximum inter-story drift angle of each story falls within 0.02 rad when the coefficient friction takes the value of varying from 0.2 to 0.3.

The weight reduced frame that consisted of smaller member sizes is shown in Fig. 6. The columns and beams of the weight-reduced frame are also the steel hollow sections and the steel wide-flange sections. The summary of the size of the cross-sections of the beams and the columns in the weight-reduced frame, the steel weight of each story and the ratio of the weight reduction of the weight-reduced frame are shown in Table 4.

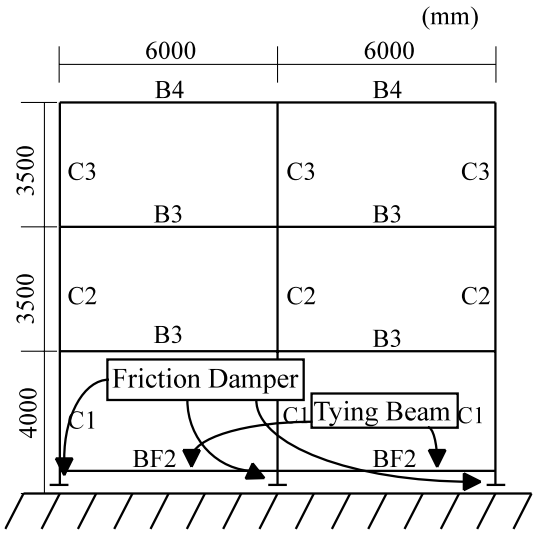


Figure 6: Model of weight reduced frame.

| Coefficient of friction | Story | Steel weight (t) | Column (mm) | Beam (mm) | Ratio of weight reduction (%) |
|---|---|---|---|---|---|
| 0.20 | 1 | 9.83 | RHS - 300 x 300 x 12 | H - 350 x 175 x 7 x 11 | 20.41 |
| | 2 | 9.19 | RHS - 300 x 300 x 12 | H - 350 x 175 x 7 x 11 | |
| | 3 | 7.17 | RHS - 250 x 250 x 12 | H - 300 x 150 x 6.5 x 9 | |
| 0.22 | 1 | 9.83 | RHS - 300 x 300 x 12 | H - 350 x 175 x 7 x 11 | 16.71 |
| | 2 | 9.19 | RHS - 300 x 300 x 12 | H - 350 x 175 x 7 x 11 | |
| | 3 | 8.39 | RHS - 250 x 250 x 12 | H - 350 x 175 x 7 x 11 | |
| 0.24 | 1 | 11.37 | RHS - 300 x 300 x 12 | H - 354 x 176 x 8 x 13 | 12.04 |
| | 2 | 9.19 | RHS - 300 x 300 x 12 | H - 350 x 175 x 7 x 11 | |
| | 3 | 8.39 | RHS - 250 x 250 x 12 | H - 350 x 175 x 7 x 11 | |
| 0.26 | 1 | 11.37 | RHS - 300 x 300 x 12 | H - 354 x 176 x 8 x 13 | 7.37 |
| | 2 | 10.73 | RHS - 300 x 300 x 12 | H - 354 x 176 x 8 x 13 | |
| | 3 | 8.39 | RHS - 250 x 250 x 12 | H - 350 x 175 x 7 x 11 | |
| 0.28 | 1 | 11.37 | RHS - 300 x 300 x 12 | H - 354 x 176 x 8 x 13 | 4.92 |
| | 2 | 10.73 | RHS - 300 x 300 x 12 | H - 354 x 176 x 8 x 13 | |
| | 3 | 9.19 | RHS - 300 x 300 x 12 | H - 350 x 175 x 7 x 11 | |
| 0.30 | 1 | 12.23 | RHS - 300 x 300 x 12 | H - 350 x 175 x 7 x 11 | 2.30 |
| | 2 | 10.37 | RHS - 300 x 300 x 12 | H - 354 x 176 x 8 x 11 | |
| | 3 | 9.19 | RHS - 350 x 350 x 12 | H - 354 x 176 x 8 x 13 | |

Table 4: Cross section of members of weight reduced frame.

## 6 EFFECT OF WEIGHT REDUCTION

### 6.1 Maximum inter-story drift angle

The comparisons of the maximum inter-story drift angle distribution of the original frame, the original frame with damper and the weight-reduced frame are shown in Fig. 7. According to Fig. 7, in dynamic analysis, the maximum inter-story drift angle of the weight-reduced frame is approximately 0.02 rad, and is almost the same as the result of the original frame.

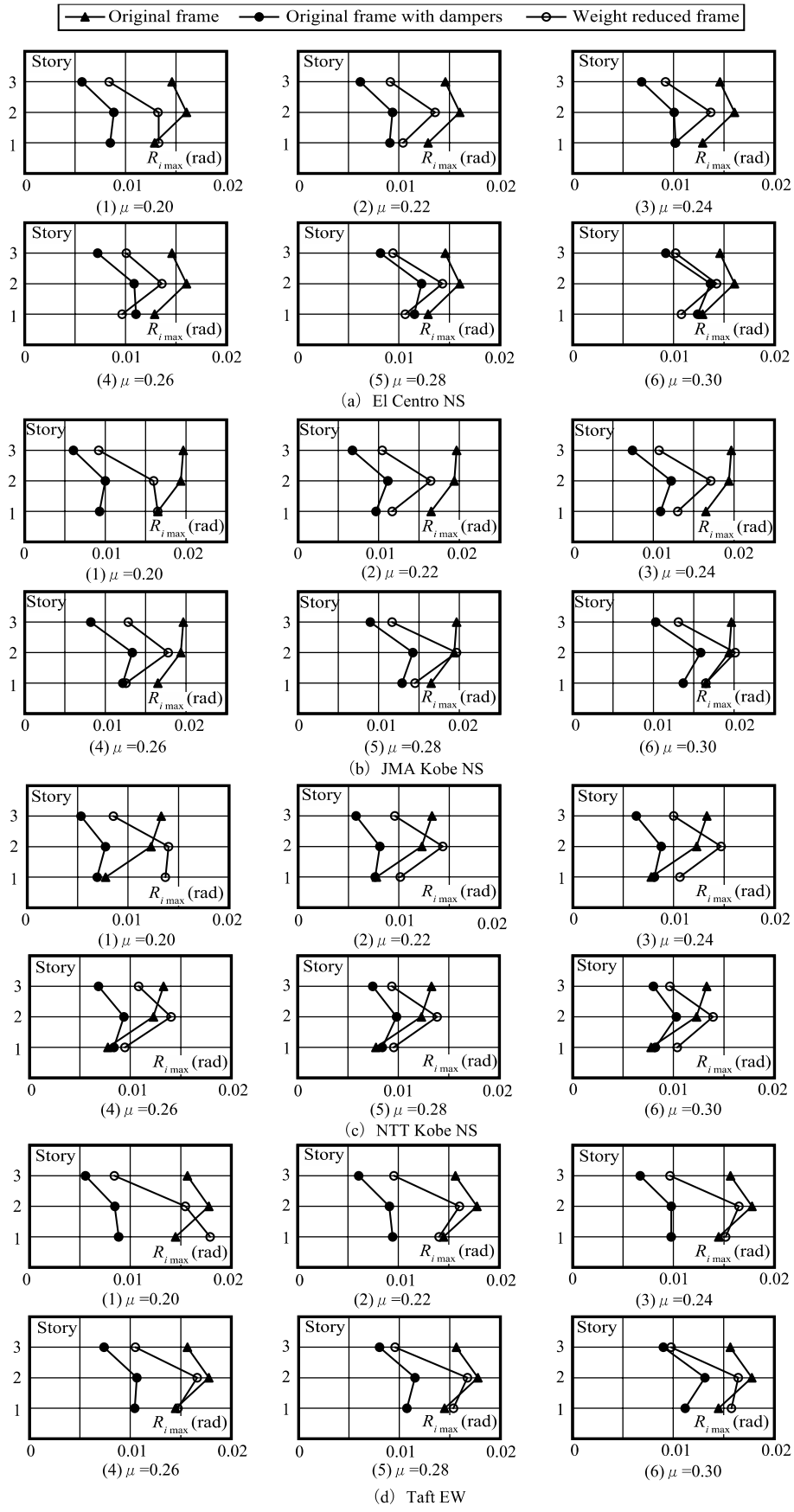


Figure 7: Comparison of maximum inter-story drift angle.

## 6.2 Strain energy and energy dissipation

The weight reduction effect of the strain energy and energy dissipation are shown in Figs. 8 and 9. According to Fig. 8, the accumulated strain energy of the weight-reduced frame increased more than that of the original frame. Instead, It reduced almost 70% that of the original frame. It is thought the most effect of the frame equipped with friction damper at the base of column. According to Fig. 9, the energy dissipation also decreased almost 50% of the original frame with damper except for earthquakes NTT and Kobe NS. It is thought that the f force decreased by reduction of the contact force, because the weight of the frame reduced.

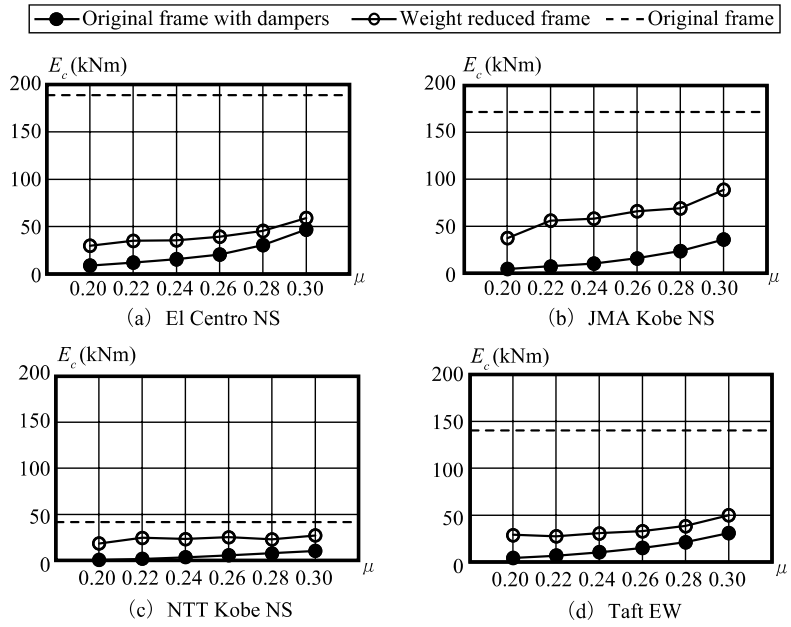


Figure 8: Weight reduction effect of strain energy.

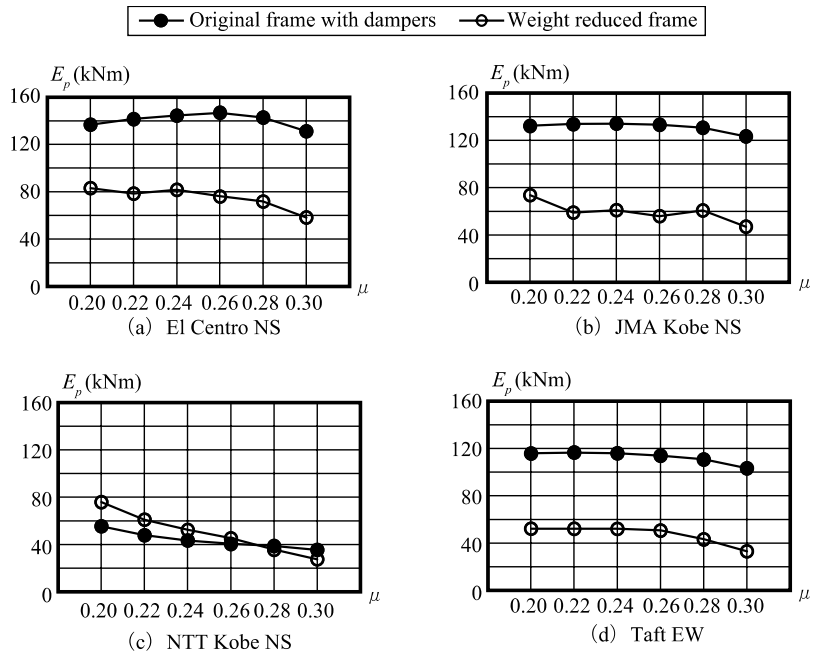


Figure 9: Weight reduction effect of energy dissipation.

## 7 CONCLUSIONS

This is a basic study on the weight reduction effect of steel multi-storied frame with friction damper. The maximum inter-story drift angle and the slide deviation of a building frame with sliding bearings were investigated regarding the weight reduction of the frame through numerical analyses. The vibration control system was confirmed to have an advantage in reducing the total weight of the steel super-structure by permitting the downsizing of steel structure members. Some trends were observed by the numerical analyses for the frame equipped with the friction dampers, when the friction coefficient varied from 0.2 to 0.3:

1) The weight of the frame can reduced approximately 20% when the maximum drift angle is set to less than 0.02 rad.

2) The energy dissipation of weight reduced frame decreased around 50% than the original frame with friction damper.

3) The strain energy of the weight-reduced frame reduced 70% of the original frame.

4) The passive friction dampers have an advantage of reducing the size of the cross section of members of the steel frame.

## REFERENCES

[1] Prof.R.B.Ghodke, Dr. S.V.Admane, Effect Of Base-Isolation For Building Structures, International Journal of Science, Engineering and Technology Research Volume 4, Issue 4, pp. 971-974, April 2015.

[2] Ryuta ENOKIDA, Takuya NAGAE, Masahiro IKENAGA, Michitaka INAMI, and Masayoshi NAKASHIMA, “APPLICATION OF GRAPHITE LUBRICATION FOR COLUMN BASE IN FREE STANDING STEEL STRUCTURE”, J. Struct. Constr, Eng., AIJ, Vol, 78 NO.685, 435-444, Mar., 2013

[3] M. Jabbareh Asl, M. M. Rahman, A. Karbakhsh, “Numerical Analysis of Seismic Elastomeric Isolation Bearing in the Base-Isolated Buildings” Open Journal of Earthquake Research, 2014, 3, 1-4

[4] Masahiko OZAKI, Yousuke MURAKAMI, Naohiko TSUNASHIMA, Tomio NAKANO, Ryota MASEKI, Takeshi UGATA, “FREQUENCY CHARACTERISTICS OF SEISMIC ISOLATION SYSTEM USING SLIDING BEARINGS AND MULTI-RUBBER BEARINGS”, AIJ J. Technol. Des. No. 17, 159-164, Jun., 2003

[5] Ryota NAKAMURA, Minoru YAMANARI, “NUMERICAL STUDY ON BASE-ISOLATION EFFECT OF FRICTION DAMPER TO DYNAMIC BEHAVIOR OF STEEL STRUCTURE”, JSSC STEEL CONSTRUCTION ENGINEERGING, Vol. 21, No. 83, 19-29, September, 2014

[6] Jingye LIU, Ryota KOYAMA, Takuya NISHIMURA and Minoru YAMANARI : Weight Reduction of Multi-storied Steel Frame by Using of Base-isolation System with Passive Friction Bearings, Proc. of International Symposium of Temporal Design, 2015.11.

COMPDYN 2017
6th ECCOMAS Thematic Conference on
Computational Methods in Structural Dynamics and Earthquake Engineering
M. Papadrakakis, M. Fragiadakis (eds.)
Rhodes Island, Greece, 15–17 June 2017

# RESIDUAL LOAD CAPACITY OF FIRE-DAMAGED RUBBER BEARINGS FOR R.C. BASE-ISOLATED BUILDINGS SUBJECTED TO NEAR-FAULT EARTHQUAKES

**F. Mazza**[1] **and F. Alesina**[2]

[1] Dipartimento di Ingegneria Civile, Università della Calabria
Via P. Bucci, 87036 Rende (CS), Italy
e-mail: fabio.mazza@unical.it

[2] Dipartimento di Ingegneria Civile, Università della Calabria
Via P. Bucci, 87036 Rende (CS), Italy
fabio.alesina@unical.it

**Keywords:** R.C. Base-isolated Framed Structure; Fire-Damaged Rubber and Lead-Rubber Bearings; Nonlinear Incremental Dynamic Analysis; Near- and Far-Fault earthquakes.

**Abstract.** *A base-isolation system of framed buildings frequently involves elastomeric materials (e.g. High-Damping-Laminated-Rubber Bearings, HDLRBs, and Lead-Rubber Bearings, LRBs), which are susceptible to deterioration when fire occurs. On the other hand, fire-damaged HDLRBs and LRBs may elongate the fundamental vibration period of a base-isolated building, shifting it into the resonant region under the long-duration horizontal pulses of near-fault ground motions. To study the nonlinear seismic response following fire in HDLRBs and LRBs, a numerical investigation is carried out on six-storey r.c. base-isolated buildings comprising a basement and five storeys above ground. Three fire scenarios are considered, with the fire compartment confined to the area of the base-isolated level (i.e. F0), first level of the superstructure (i.e. F1) and both levels (i.e. F0/1). Base-isolated structures in a no fire situation are compared with those in the event of fire, at different durations of fire resistance for the basement (i.e. R30) and the superstructure (i.e. R60). Different values of the opening factor are assumed in the basement so as to obtain the R30 fire resistance with different fire temperatures for HDLRBs and LRBs. To this end, transient analysis corresponding to the EC1 time-temperature curves in the basement is carried out by means of a finite element modelling of HDLRBs and LRBs. A reduction of the mechanical properties of the fire-damaged isolators is evaluated in line with a 200°C isotherm method. Reduced mechanical properties of r.c. cross-sections are considered by means of a thermal-mechanical mapping analysis, in line with the 500°C isotherm method proposed by Eurocode 2. A nonlinear incremental dynamic analysis of the base-isolated structures is carried out considering near- and far-fault earthquakes. The nonlinear seismic analysis uses a lumped plasticity model to describe the inelastic behaviour of the r.c. frame members; the response of an HDLRB is simulated with a viscoelastic model, with variable stiffness properties in the horizontal and vertical directions, while a bilinear model is considered for an LRB.*

## 1 INTRODUCTION

Thanks to major improvements of seismic codes and guidelines, considerable advances in the application of base-isolation technique have been accomplished in recent years in the area of seismic protection of structures. Thus, fire in a base-isolated structure following a seismic event is not uncommon making the structure more vulnerable to aftershocks, because it will experience an earthquake without any retrofit. Given the extensive use of reinforced concrete (r.c.) for the superstructure and elastomeric materials (e.g. High-Damping-Laminated-Rubber Bearings, HDLRBs, and Lead-Rubber Bearings, LRBs) for the bearings, it is necessary to fully understand the effect of fire on their seismic resistance. Under high temperatures, r.c. frame members undergo degradation of material properties [1], weakening steel reinforcement and concrete, stiffness [2, 3], produced by spalling of concrete on the sides exposed to fire, and ultimate ductility [4, 5], with a reduction in the frame members exposed to fire on three and four sides and an increase on the bottom side of beams due to fire-reduced yield strength of the longitudinal bars in tension. Moreover, mechanical and geometrical properties of HDLRBs and LRBs are reduced when temperatures exceed the point at which vulcanization between layers of rubber and steel plates occurs [6]. However, there is a high degree of uncertainty about the residual seismic load capacity of fire-damaged isolators and r.c. frame members, so a lack of in-depth knowledge to decide whether strengthening of the superstructure and replacement of the base-isolation system are necessary. This paper contributes toward a solution of this problem, by providing outcomes on how a base-isolated building damaged by fire would perform during near- and far-fault seismic aftershocks.

A numerical study is presented to investigate the nonlinear seismic response following fire of a six-storey r.c. base-isolated building, composed of a basement and five storeys above ground, designed in a high-risk seismic zone in accordance with the current Italian code [7]. The base-isolation system consists of HDLRBs and LRBs, inserted at the top of the columns of the basement, designed on the basis of different values of the fundamental vibration periods and equivalent viscous damping ratios in order to obtain the same value of the spectral acceleration. Three fire scenarios are considered, with the fire compartment confined to the area of the base-isolated level (i.e. F0), first level of the superstructure (i.e. F1) and both levels (i.e. F0/1). For each scenario, parametric temperature-time curves are evaluated in accordance with Eurocode 1 [8], with different values of the opening factor representing the amount of ventilation. Specifically, R30 fire resistance is obtained in the basement when assuming two fire temperatures for HDLRBs (i.e. T=300°C and 400°C) and LRBs (i.e. 250°C and 300°C) while R60 fire resistance in the superstructure is related to T=800°C. Reduction factors of the horizontal and vertical stiffnesses of the HDLRBs and LRBs, due to the fire-damaged cross-section, are considered in line with a proposed 200°C isotherm method. To this end, transient response, obtained by means of a finite element modelling of the bearings implemented in the computer program ABAQUS [9]. Reduced mechanical properties of r.c. cross-sections of beams and columns are also assumed in accordance with the 500°C isotherm provided by Eurocode 2 [10]. Nonlinear incremental dynamic analysis of the test structures is carried out by considering two sets of records scaled on the design hypotheses: i.e. NFE set, consisting of seven near-fault earthquakes, with significant horizontal pulses, selected from the Pacific Earthquake Engineering Research center database [11]; FFE set, consisting of seven far-fault records derived from the European Strong Motion database [12].

## 2 BASE-ISOLATED TEST STRUCTURES

A six-storey r.c. base-isolated (BI) office building with symmetric plan (Figure 1a), composed of a basement and five storeys above ground (Figure 1b), is the test structure chosen for the numerical investigation. Specifically, two base-isolation systems are considered, consisting of fifteen identical HDLRBs and LRBs inserted on the top of the columns of the basement. A grid of rigid beams is placed at the base of the superstructure on the isolators, while rigid columns are placed in the basement below the isolators. Dead and live gravity loads used in the design are assumed equal to: 6.1 kN/m$^2$ and 3 kN/m$^2$, for the isolated floor; 4.4 kN/m$^2$ and 3 kN/m$^2$, for the top floor; 5.7 kN/m$^2$ and 3 kN/m$^2$, for the other floors. Then, perimeter masonry infills are taken into account considering a gravity load of 2.7 kN/m$^2$ along the perimeter. A cylindrical compressive strength of 25 N/mm$^2$ for the concrete and a yield strength of 450 N/mm$^2$ for the steel are assumed for the r.c. frame members. Seismic loads are evaluated in line with the Italian code (NTC08, [7]), assuming: high-risk seismic zone (peak ground acceleration in the horizontal direction, $PGA_H$=0.283g and 0.345g, at the life-safety (LS) and collapse-prevention (CP) limit states, respectively); elastic response of the superstructure (behaviour factor, $q_H$=1.0); medium-dense subsoil type (class C, with subsoil parameter $S_H$=1.41 and 1.31 at the LS and CP limit states, respectively).

Base-isolated structures are designed for the same value of spectral acceleration at the LS limit state (i.e. $S_a$=0.09g) and nominal stiffness ratio of the isolation system (i.e. $\alpha_{K0}=K_{V0}/K_{H0}$ =1770, being $K_{V0}$ and $K_{H0}$ the vertical and horizontal nominal stiffnesses). To this end, different values of the fundamental vibration period (i.e. $T_{I,H}$=2.84s and 2.5s) and equivalent viscous damping ratio (i.e. $\xi_{I,H}$=10% and 20%) are assumed in the horizontal direction for the HDLRBs and LRBs, respectively. Moreover, the vibration periods with prevailing component in the vertical direction (i.e. $T_{I,V}$=0.067s, for HDLRBs, and 0.059s, for LRBs) correspond to the same value of the equivalent viscous damping ratio in the same direction (i.e. $\xi_{I,V}$=5%).

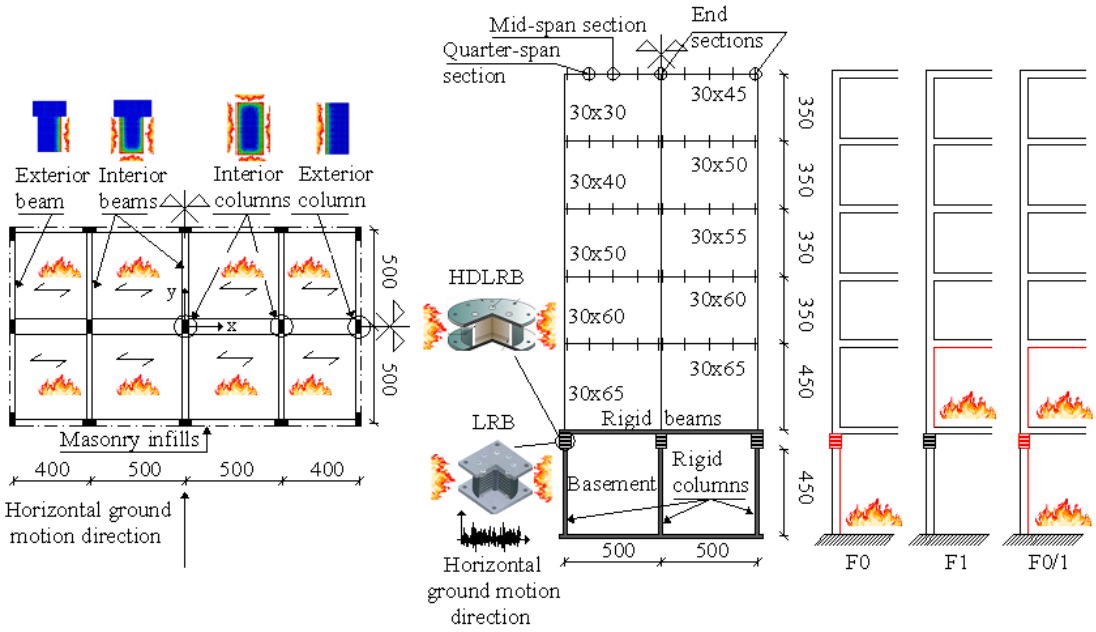


(a) In-plan fire scenario and fire-damaged r.c. frame members.

(b) In-elevation fire scenarios and fire-damaged HDLRBs and LRBs.

Figure 1: Base-isolated test structure (unit in cm).

Different values of the isolation ratio $\alpha_I$, defined as the ratio between the fundamental vibration period of base-isolated structure ($T_{I,H}$) and fixed-base structure above the isolation

system ($T_{F,x}$ and $T_{F,y}$), are obtained for HDLRBs, $\alpha_{I,x}$=3.69 and $\alpha_{I,y}$=4.0, and LRBs, $\alpha_{I,x}$=3.25 and $\alpha_{I,y}\cong$3.52, along the principal in-plan directions. The design of the superstructure complies with the LS limit state, satisfying minimum conditions for the longitudinal bars of the r.c. frame members according to the provisions for low ductility class imposed by NTC08 [7]. The length and cross-sections of the r.c. frame members are also shown in Figure 1. Further details can be found in previous works by the author [13, 14].

The design of the HDLRBs and LRBs fulfill the CP limit state checks: i.e. $\gamma_{tot}=\gamma_s+\gamma_c+\gamma_\alpha\leq 5$ and $\gamma_s\leq 2$, where $\gamma_{tot}$ represents the total design shear strain, while $\gamma_s$, $\gamma_c$ and $\gamma_\alpha$ represent the shear strains of the elastomer due to seismic displacement, axial compression and angular rotation, respectively; $(P_{cr}/P)_{min}\geq 2$, where P and $P_{cr}$ represent the maximum compression axial load and the corresponding critical buckling load; $|\sigma_t/\sigma_{tu}|_{max}\leq\min(2G,1MPa)$, $\sigma_t$ being the minimum tensile stress and $\sigma_{tu}$ the corresponding ultimate value. The following mechanical properties of the HDLRB and LRB are reported in Table 1: G and $E_b$, shear and volumetric compression moduli of the elastomer; $G_p$ and $E_p$, shear and elastic moduli of the lead; $\tau_{py}$, yield stress of the lead. It should be noted that the lead core is neglected in the calculation of the critical buckling load for LRBs [15]; design values of $P_{cr}$ and displacement at the collapse prevention limit state ($d_{dC}$) are also reported in Table 1.

| *Type* | *G* | $E_b$ | $G_p$ | $E_p$ | $\tau_{py}$ | $P_{cr}$ | $d_{dC}$ |
|---|---|---|---|---|---|---|---|
| *HDLRB* | 0.35 | 2000 | - | - | - | 3359 | 0.289 |
| *LRB* | 0.43 | 2000 | 130 | 16000 | 10.5 | 3008 | 0.220 |

Table 1: Mechanical and design parameters of the base-isolation systems (units in MPa, kN and m).

In Table 2 initial stiffnesses (i.e. $K_{H0}$ and $K_{V0}$) and corresponding equivalent damping coefficients (i.e. $C_H$ and $C_V$) of the HDLRBs and LRBs are reported together with the following geometrical properties: the diameter of the elastomer ($D_e$) and that of the lead core ($D_l$); the total thickness of elastomer ($t_e$); primary ($S_1$) and secondary ($S_2$) shape factors. Usually, the lead plug has a diameter about 1/7 times that of the outer diameter of the rubber. Note that the design of the isolators depends on the condition imposed on the maximum value of the total shear strain ($\gamma_{tot}$), while no tensile forces are found in the isolators.

| *Type* | $K_{H0}$ | $K_{V0}$ | $C_H$ | $C_V$ | $D_e$ | $D_l$ | $t_e$ | $S_1$ | $S_2$ |
|---|---|---|---|---|---|---|---|---|---|
| *HDLRB* | 6360 | 11263000 | 574 | 12070 | 0.538 | - | 0.187 | 22.4 | 2.9 |
| *LRB* | 8190 | 14487500 | 1303 | 13685 | 0.428 | 0.064 | 0.153 | 26.1 | 2.8 |

Table 2: Geometrical and design parameters of the base-isolation systems (units in kN, m and s).

## 3 FIRE-DAMAGE IN THE SUPERSTRUCTURE AND ISOLATORS

Three fire scenarios with uniform temperature within the fire compartment are considered, assuming fire confined to the whole area (Figure 1a) of the lower levels in the base-isolated test structures (Figure 1b): i.e. base-isolated level (i.e. F0), first level of the superstructure (i.e. F1) and both levels (i.e. F0/1). On ther hand, HDLRBs and LRBs of the basement, in the F0 and F0/1 scenarios, are exposed to fire on all lateral surfaces (Figure 1b), hypothesizing a seismic gap around the building which allows the base-isolation horizontal movement during an earthquake. To simulate the time-temperature evolution, during the heating and cooling phases of an actual fire, the EC1 natural fire curves [8] are considered

$$\theta_g = 20+1325\left(1-0.324e^{-0.2t^*}-0.204e^{-1.7t^*}-0.472e^{-19t^*}\right) \quad (1a)$$

$$\theta_g = \theta_{\max}-250\left(3-t^*_{\max}\right)\left(t^*-t^*_{\max}\right) \quad (1b)$$

where $t^*$ is a fictitious time obtained considering the time $t$ (in hours) multiplied by a dimensionless parameter equal to

$$\Gamma = \left(O/b\right)^2 \Big/ \left(0.04/1160\right)^2 \tag{1}$$

function of the opening factor (O) and thermal absorptivity (b) of surrounding surfaces of the compartment. Moreover, $t^*_{max}$ corresponds to the maximum temperature $\theta_{max}$ in the heating phase which lasts

$$t^*_{max} = \left(0.2 \cdot 10^{-3} q_{t,d} / O\right) \Gamma \tag{3}$$

being the total design fire load density

$$q_{t,d} = q_{f,d} \, A_f / A_t \tag{4}$$

related to the total area of the compartment ($A_t$) and the floor value ($q_{f,d}$) corresponding to the surface area of the floor ($A_f$). Table 3 reports the aforementioned design parameters of fire load in the case of the F1 (i.e. superstructure) and F0 (i.e. basement) fire scenarios assuming 60 min (i.e. R60) and 30 min (i.e. R30) of exposure, respectively. Note that a temperature of about 800°C corresponds to R60 fire resistance in the superstructure. Different values of the opening factor are considered in the basement so as to obtain the same fire resistance (i.e. R30) when assuming two fire temperatures for HDLRBs (i.e. T=300°C and 400°C) and LRBs (i.e. 250°C and 300°C). Finally, the F0/1 fire scenario is derived from F0 and F1, which occur simultaneously. Further details on fire modelling can be found in [14].

| *Fire resistance (min)* | *Fire scenario* | *T (°C)* | $q_{f,d}$ ($MJ/m^2$) | $A_f$ ($m^2$) | $A_t$ ($m^2$) | $O$ ($m^{1/2}$) | $b$ ($J/m^2s^{1/2}K$) |
|---|---|---|---|---|---|---|---|
| R30 | F0 (HDLRB) | 300 | 445 | 180 | 612 | 0.0094 | 1100 |
| | | 400 | | | | 0.0114 | |
| | F0 (LRB) | 250 | | | | 0.0083 | |
| | | 300 | | | | 0.0094 | |
| R60 | F1 | 800 | 612 | | | 0.0480 | 1127 |

Table 3: Fire parameters in the EC1 time-temperature curve [8].

The corresponding EC1 time-temperature curves are shown in Figure 2, with reference to the F1 (Figure 2a) and F0 (Figure 2b) fire scenarios.

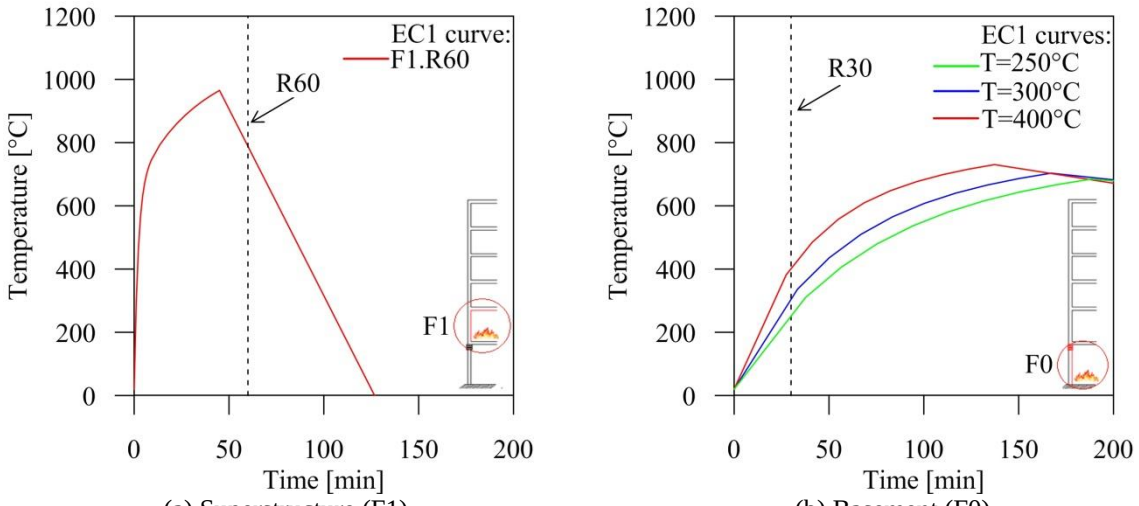


(a) Superstructure (F1). (b) Basement (F0).

Figure 2: Natural (EC1) fire curves for different fire scenarios [8].

As can be observed, temperatures corresponding to R30 in the basement are always placed in the heating branch of the time-temperature curves, unlike R60 in the superstructure characterized by a temperature in the cooling branch.

Once the time-temperature curve of the fire compartment is determined with the EC1 model, it becomes possible to evaluate the temperature distribution in the r.c. frame members and isolators, by means of the ABAQUS structural program [9]. Mean values of thermal parameters adopted for the structural materials in the finite element analysis are reported in Table 4: i.e. thermal conductivity, k; specific heat, $c_p$; density, ρ. On the assumption that the temperature does not change along the longitudinal axis, two-dimensional thermal mappings of cross-sections of the interior and perimeter r.c. frame members are shown in Figure 3, with reference to the first level of the superstructure (i.e. F1 and F0/1 fire scenarios) with R60 fire resistance. By contrast, three-dimensional plots need to be considered for the non-isotropic isolators, where mainly longitudinal (i.e. through steel shims) and much lower transversal (i.e. through layers of rubber) conduction takes place. To this end, isolators in the basement (i.e. F0 and F0/1 fire scenarios) with R30 fire resistance are represented in Figure 4, distinguishing HDLRB (see Figures 4a,b corresponding to T=300°C and 400°C, respectively) and LRB (see Figures 4c,d corresponding to T=250°C and 300°C, respectively).

| *Material* | *k [W/mK]* | *$c_p$ [J/kgK]* | *ρ [kg/m$^3$]* |
|---|---|---|---|
| *Concrete* | 2 | 1000 | 2400 |
| *Rubber* | 0.17 | 1400 | 1200 |
| *Steel* | 50 | 450 | 7800 |
| *Lead* | 35 | 130 | 11300 |

Table 4: Thermal properties of the structural materials.

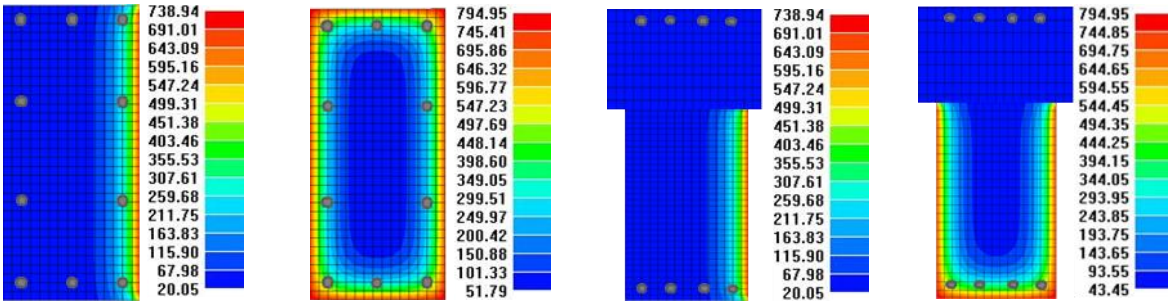


(a) Exterior column: $t_{dc}$=0.025m, corner bar, $f_{y,ds}$=445MPa, perimeter bar, $f_{y,ds}$ =438MPa

(b) Interior column: $t_{dc}$=0.035m, corner bar, $f_{y,ds}$=240MPa, perimeter bar, $f_{y,ds}$=434MPa

(c) Exterior beam: $t_{dc}$=0.025m, corner bar, $f_{y,ds}$=445MPa

(d) Interior beam: $t_{dc}$=0.035m, corner bar, $f_{y,ds}$=240MPa, perimeter bar, $f_{y,ds}$=428MPa

Figure 3: Two-dimensional thermal mappings for r.c. frame members (F1 and F0/1 fire scenarios, R60).

Thermal mapping of the r.c. cross-sections combined with the 500°C isotherm method proposed by Eurocode 2 [10] ignore concrete with temperatures exceeding 500°C. More specifically, on the fire-exposed sides of the cross-sections, the thickness of the damaged concrete ($t_{dc}$) and the reduced (damaged) yield strength ($f_{y,ds}$) of each corner and perimeter steel reinforcement, evaluated with respect to the temperature in the centre of the bar, are also reported in Figure 3. It is worth noting that some of the reinforcing bars may fall outside the reduced cross-section, but they are still included in the calculation of the ultimate values of strength and curvature ductility. Fire effects in the basement consist in a reduction of the seismic load capacity of HDLRBs and LRBs, which are subjected to irreversible degradation when exposed to high temperatures. However, vulcanization between layers of rubber and steel plates makes rubber more resistant to changes in temperature. Thus, a 200°C isotherm method is adopted [16], where rubber with temperatures exceeding the vulcanization

threshold is not considered, while the residual cross-section retains its initial values of strength and stiffness. In detail, the radial thickness of the damaged rubber ($t_{dr}$) on the fire-exposed cross-sections of HDLRBs and LRBs is also reported in Figures 4a,b and 4c,d, respectively.

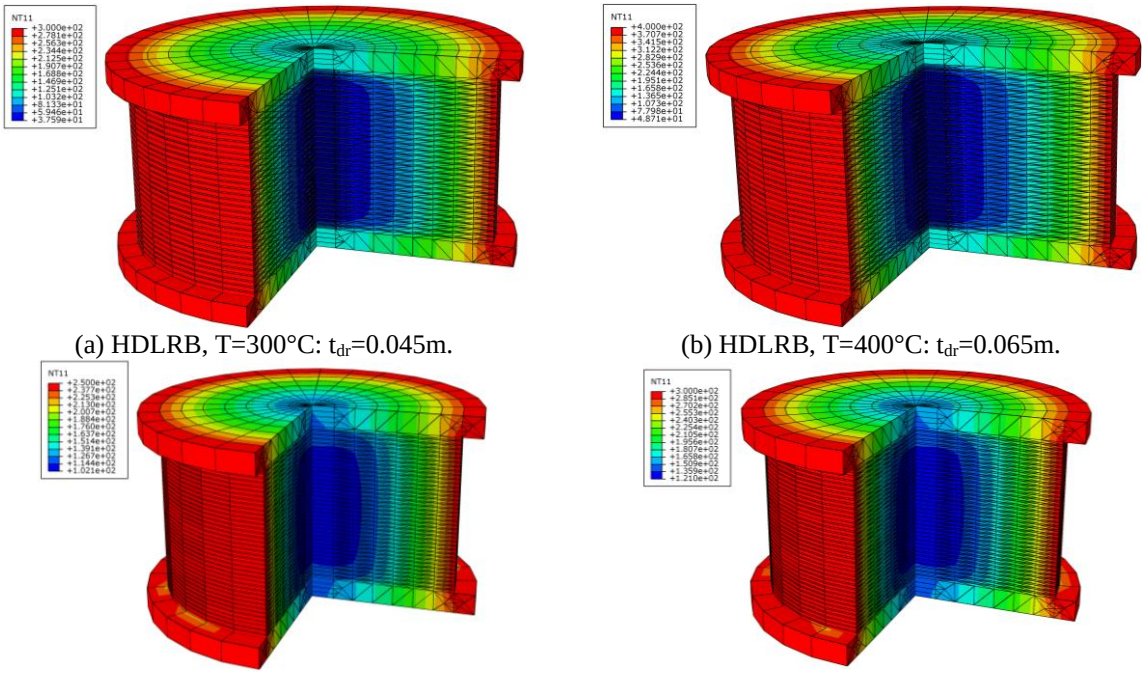

(a) HDLRB, T=300°C: $t_{dr}$=0.045m. (b) HDLRB, T=400°C: $t_{dr}$=0.065m.

(c) LRB, T=250°C: $t_{dr}$=0.034m. (d) LRB, T=300°C: $t_{dr}$=0.061m.

Figure 4: Three-dimensional thermal mappings for isolators (F0 and F0/1 fire scenarios, R30).

In Figure 5, reduction factors of the flexural stiffness $\alpha_{KF,T}(=K_{F,T}/K_{F,0})$ are plotted as function of the time of fire exposure for columns (Figure 5a) and beams (Figure 5b) in the first level, assuming a direct correspondence between the examined level and the fire compartment. As expected, interior columns and beams exposed to fire on four and three sides, respectively, highlight $\alpha_{KF,T}$ lower values than those obtained for exterior columns and beams exposed to fire on one side only.

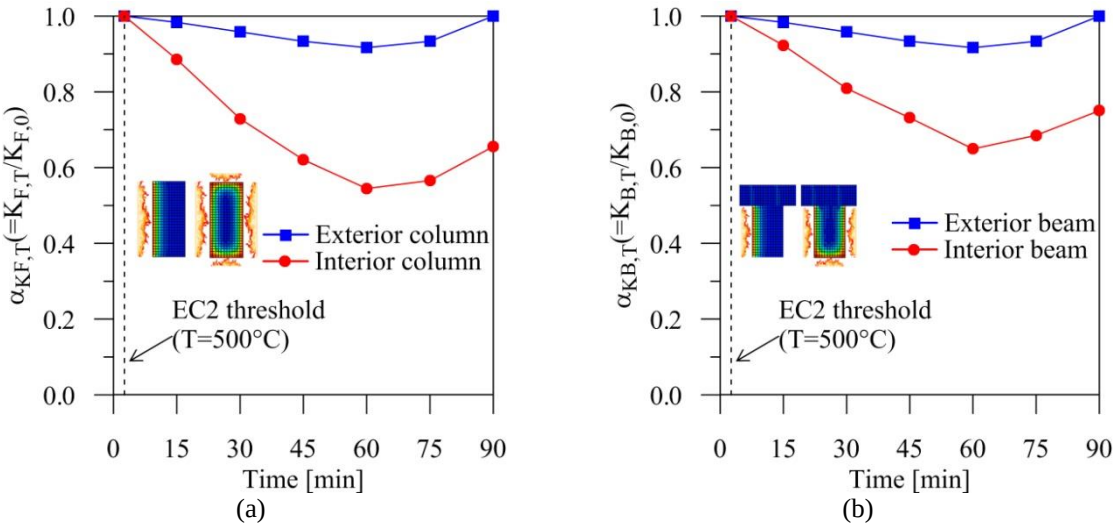


Figure 5: Reduction factors of flexural stiffness for r.c. frame member exposed to fire.

The time threshold corresponding to T=500°C is also plotted in Figure 5 as a reference value. Moreover, for all the examined cases, it is interesting to note that the minimum value of $\alpha_{KF,T}$ corresponds to R60 although, in accordance with EC1 natural fire curve shown in Figure 2a, the temperature profile shows a decrease during the cooling phase.

Next, reduction factors of the effective shear $\alpha_{KS,T}(=K_{S,T}/K_{S,0})$ and axial $\alpha_{KA,T}(=K_{A,T}/K_{A,0})$ stiffnesses and primary and secondary $\alpha_{S,T}(=S_T/S_0)$ shape factors are shown in Figure 6, as function of the fire temperature for HDLRBs (Figure 6a) and LRBs (Figure 6b) in the basement. The proposed temperature threshold (i.e. T=200°C) is also plotted as a reference value. As can be observed, reduction factors for LRBs are always higher than for HDLRBs, due to their lesser diameter. Moreover, the highest reduction factors are obtained for $\alpha_{KA,T}$ where the compression modulus also decreases for increasing values of fire temperature.

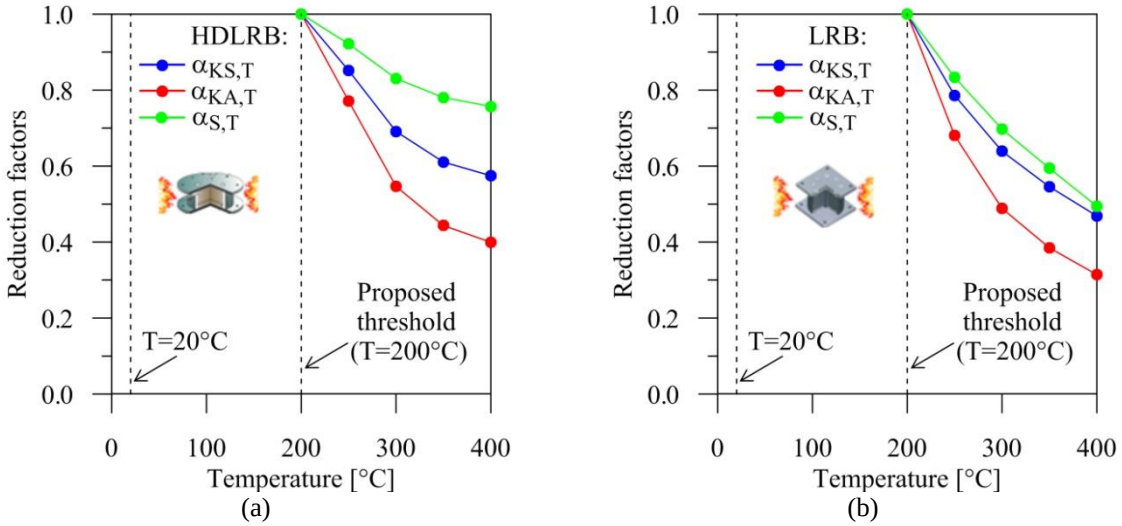


Figure 6: Reduction factors of mechanical and geometrical properties for isolators exposed to fire.

## 4 NEAR- AND FAR-FAULT EARTHQUAKES

To study the residual seismic load capacity of fire-damaged r.c. base-isolated buildings, the horizontal components of real near- and far-fault ground motions are considered in line with the design hypotheses adopted for the test structures: i.e. high-risk seismic zone and medium-dense subsoil type. In detail, seven near-fault earthquakes (NFE set), exhibiting high-amplitude and long-period velocity pulses [17], are selected from the Pacific Earthquake Engineering Research center database [11]. Next, seven far-fault earthquakes (FFE set), reflecting the provisions of the Italian seismic code [7, 18] for the geographical coordinates (longitude 17.08° and latitude 39.11°) at the site where the building is hypothesized, are derived by the European Strong Motion database [12]. In Tables 5 and 6, the main data of the NFE and FFE sets are reported, respectively: i.e. country, date, recording station, component, magnitude, peak ground acceleration. The corresponding elastic response spectra of velocity ($S_{v,H}$) are plotted in Figure 7, assuming an equivalent viscous damping ratio in the horizontal direction, $\xi_H$, equal to 5%. The response spectra are compared with the corresponding target NTC08 response spectra at the serviceability (i.e. operational, $PGA_{OP}$=0.108g) and ultimate (i.e. life-safety, $PGA_{LS}$=0.283g, and collapse prevention, $PGA_{CP}$=0.345g) limit states. As can be observed, spectral values of the selected near-fault (Figure 7a) and far-fault (Figure 7b) earthquakes are quite different from those corresponding to the NTC08 spectra, in the range of rather long vibration periods which are more significant for the base-isolated test structures, hence requiring evaluation of suitable scale factors. The selection of an intensity measure to

predict structural demand of base-isolated buildings is a difficult task, because ground motions characterized by similar spectral values at specific vibration periods can produce different structural responses due to the lengthening of vibration periods as the structure enters the inelastic range. In the present work, the *Modified Velocity Spectrum Intensity* (MVSI), obtained from integration of the velocity (elastic) response spectra over a defined range of vibration periods (T), is adopted [19-21]:

$$MVSI = \int_{0.5T}^{1.25T} S_{v,H}(T,\xi) \cdot dT \tag{5}$$

Then, the selected real accelerograms are normalized with respect to the NTC08 ones by scaling their $PGA_H$ values

$$PGA_{H,S}^{NFE} = PGA_H^{NFE} \cdot SF_{NFE};\ PGA_{H,S}^{FFE} = PGA_H^{FFE} \cdot SF_{FFE} \tag{6a,b}$$

through the scale factors for NFE and FFE sets

$$SF_{NFE} = MVSI_{NTC08} / MVSI_{NFE};\ SF_{FFE} = MVSI_{NTC08} / MVSI_{FFE} \tag{7a,b}$$

| *Country* | *Earthquake* | *Date* | *Station* | *Component* | $M_w$ | $PGA_H$ |
|---|---|---|---|---|---|---|
| Taiwan | Chi-Chi | 20/09/1999 | TCU068 | EW | 7.3 | 0.566 g |
| USA | Northridge | 17/01/1994 | Rinaldi | 228 | 6.6 | 0.837 g |
| USA | Superstition Hills | 24/11/1987 | Parachute | 225 | 6.4 | 0.455 g |
| USA | Cape Mendocino | 25/04/1992 | Petrolia | 090 | 7.1 | 0.662 g |
| Japan | Kobe | 16/01/1995 | Takatori | 090 | 6.9 | 0.616 g |
| Iran | Tabas | 16/09/1978 | Tabas | TR | 7.7 | 0.852 g |
| Turkey | Erzincan | 13/03/1992 | Erzincan | NS | 6.7 | 0.515 g |

Table 5: Main data of the selected near-fault ground motions.

| *Country* | *Earthquake* | *Date* | *Station* | *Component* | $M_w$ | $PGA_H$ |
|---|---|---|---|---|---|---|
| Greece | Alkion | 24/02/1981 | Korinthos-OTE Building | 000333xa | 6.6 | 0.230g |
| Turkey | Adana | 27/06/1998 | Ceyhan-Tarim Ilce | 001726ya | 6.3 | 0.270g |
| Italy | Friuli | 15/09/1976 | Buia | 000151xa | 6.0 | 0.083g |
| Italy | Umbria-Marche | 26/09/1997 | Castelnuovo-Assisi | 000600ya | 6.0 | 0.106g |
| Turkey | Izmit | 13/09/1999 | Adapazari Bayindirlik | 006978ya | 5.8 | 0.071g |
| Turkey | Ishakli | 03/02/2002 | Afyon-Bayindirlik | 007104ya | 5.8 | 0.052g |
| Turkey | Dinar | 01/10/1995 | Dinar-Meteoroloji | 000879ya | 6.4 | 0.319g |

Table 6: Main data of the selected far-fault ground motions.

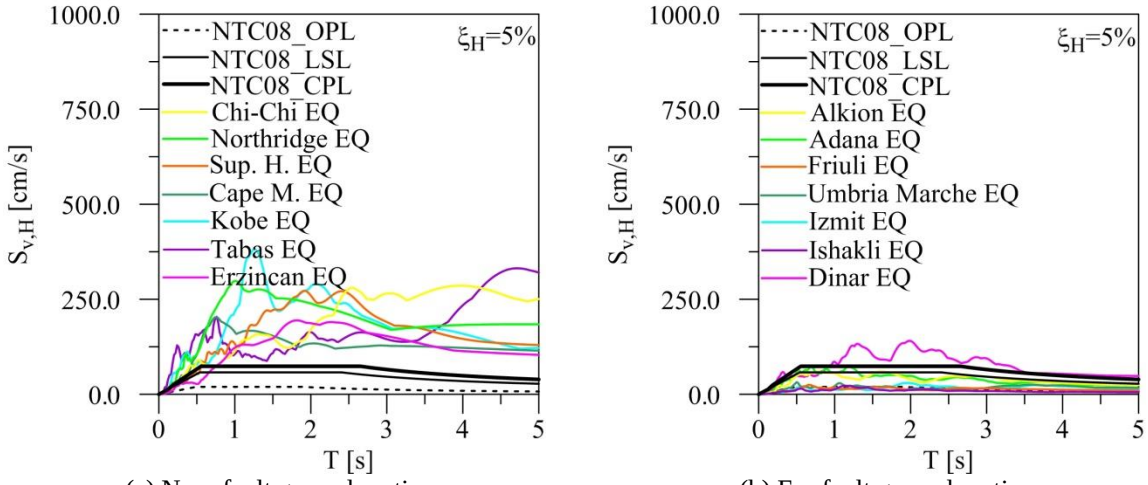


(a) Near-fault ground motions. (b) Far-fault ground motions.

Figure 7: Velocity (elastic) response spectra.

## 5 NUMERICAL RESULTS

A multi-record incremental dynamic analysis (IDA) of the base-isolated structures is carried out in a series of nonlinear dynamic analyses under the above mentioned NFE and FFE sets of seven near-fault and far-fault earthquakes, respectively. It should be noted that each earthquake is scaled to several intensity levels ($a_g$) of the corresponding PGA value, but all earthquakes are preliminarily normalized by scaling their PGA value with reference to the *Modified Velocity Spectrum Intensity* provided by NTC08 at the CP limit state. Afterwards, a mean of the results separately obtained for ground motions of the NFE and FFE sets is calculated. Specifically, the mean IDAs are interrupted once the ultimate state on the base-isolation systems and superstructure are reached. The ultimate values of the total shear strain ($\gamma_{tot,u}$) and the corresponding shear strain due to seismic displacement ($\gamma_{s,u}$) of the HDLRBs and LRBs are assumed equal to 1.5 times the corresponding design values. Moreover, the compressive and tensile axial loads of the HDLRBs and LRBs are limited to the critical buckling load and the ultimate tensile load, respectively. On the other hand, the local damage suffered by the r.c. frame members is evaluated by considering the ultimate ductility demand calculated in terms of curvature at the potential critical sections of the beams (i.e. end, quarter-span and mid-span sections) and columns (i.e. end sections). A two-spring-two-dashpot model is adopted for modelling the coupling of horizontal and vertical responses for HDLRBs [22]. Moreover, LRBs are idealized by means of a two-component model, comprising an elastic-perfectly-plastic component and an elastic component, based on a bilinear force-displacement law. Finally, a lumped plasticity model based on the Haar-Kàrmàn principle describes the elastic-plastic response of the r.c. frame members, assuming a bilinear moment-curvature law with hardening ratio equal to 3% [23]. In the present work, viscous damping in the isolation system is avoided by using the hysteretic models of the HDLRBs and LRBs, while the damping matrix of the superstructure is calculated on the basis of the Rayleigh damping, assuming constant values of the damping coefficients evaluated from the modal analysis of the base-isolated structure with the initial stiffness of the isolation system [24]. Specifically, a viscous damping ratio equal to 2% is considered with reference to the two vibration periods corresponding to high-participation modes with components prevailing in the horizontal ($T_{IH}$) or vertical ($T_{IV}$) direction, respectively.

To represent seismic effects in the fire-damaged basement, mean values of maximum total shear strain ($\gamma_{tot}$) and dimensionless axial load ($P/P_{cr}$) are plotted in Figure 8 for the HDLRBs (Figs. 8a,c) and LRBs (Figs. 8b,d), referring to base-isolated structures subjected to NFE and FFE sets of ground motions. The no fire condition is compared with the fire compartment in the basement at the end of 30 (i.e. R30) minutes of fire exposure. In particular, the F0A (i.e. T=300°C) and F0B (i.e. T=400°C) fire scenarios are considered for HDLRBs, while the F0C (i.e. T=250°C) and F0D (i.e. T=300°C) are examined for LRBs. Additionally, serviceability (i.e. operational limit, OPL) and ultimate (i.e. life-safety and collapse prevention limits, LSL and CPL) limit states are represented to highlight the probability of exceeding a specified limit-state given the $a_g$/PGA level. As can be observed, an amplification in the structural response of fire-exposed base-isolated structures is obtained for increasing values of fire temperature (T) and dimensionless acceleration ratio $\alpha_a$(=$a_g$/PGA). This result is more pronounced for the NFE set (solid lines) than for the FFE set (dashed lines), confirming the detrimental effects of pulse-like near-fault ground motions on base-isolated structures. Moreover, the F0A and F0C scenarios correspond to fire temperatures generally reaching the CPL state for HDLRBs and LRBs, respectively. Under the NFE set of ground motions, the F0B scenario corresponds to collapse of the HDLRBs before reaching the LSL state (Figure 8a), while the F0D scenario is border-line for the LRBs (Figures 8b,d). However, the residual seismic load capacity of the

HDLRBs is greater than that observed for the LRBs, because the F0A and F0B scenarios correspond to a higher temperature than that obtained for the F0C and F0D scenarios, respectively. This result can be interpreted by observing that for a same value of fire temperature (e.g. T=300°C in the F0A and F0D scenarios) the percentage of the damaged rubber increases for decreasing values of the initial diameter of the isolator (see Table 2). Finally, maximum global ductility demand of the superstructure is plotted in Figures 8e and 8f referring to base-isolated structures with HDLRBs and LRBs, respectively. It is interesting to note that the no fire condition corresponds to the highest values of ductility demand for both NFE and FFE sets of ground motions, highlighting the fact that the elongation of the fundamental vibration period due to fire damage in the base-isolation system prevents high ductility demand in the superstructure.

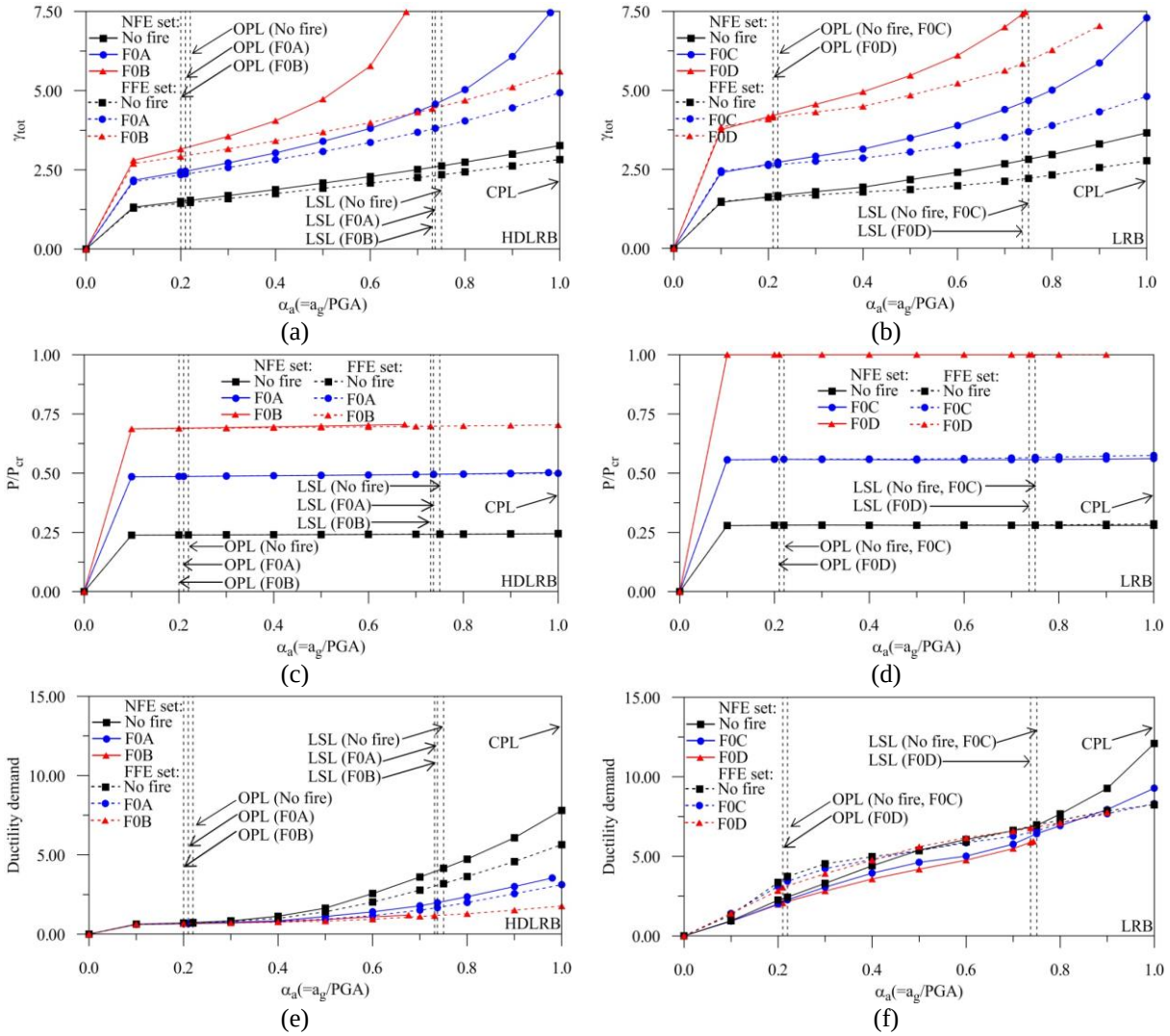


Figure 8: Nonlinear incremental dynamic analysis under near-fault (NFE set) and far-fault (FFE set) earthquakes: comparison of base-isolated structures in the no fire and fire scenarios.

Plots similar to the previous ones are reported in Figure 9 to illustrate seismic effects in the basement (Figures 9a-9d) and superstructure (Figures 9e,f), on the assumption that the fire compartment is only confined to the area of the first level (i.e. F1 scenario with fire resistance R60) or also occurs simultaneously in the basement (i.e. F0A/1 and F0C/1 scenarios). Specifically, the F0A/1 (Figures 9a,c,e) and F0C/1 (Figures 9b,d,f) scenarios are considered for the

HDLRBs and LRBs subjected to T=300°C and T=250°C fire temperatures, respectively. As can be observed, all base-isolated structures are able to reach the dimensionless acceleration ratios $\alpha_a$ related to the LSL and CPL states, for both the NFE and FFE sets of ground motions, the F0A/1 scenario being the only exception with $\gamma_{tot}$ ultimate value for the HLDRBs corresponding to $\alpha_a$=0.98 (Figure 9a). Similar responses of the base-isolation systems are obtained for the no fire and F1 scenario, for both HDLRBs (Figures 9a,c) and LRBs (Figures 9b,d), because the residual seismic load capacity of the base-isolated structures depends on fire damaged r.c. frame members in the first level of the superstructure. As expected, the post-fire seismic performance of the superstructure (Figures 9e,f) for the F1 fire scenario is worse than that of the base-isolated structure in the no fire condition and F0/1 fire scenarios. It is worth noting that the ductility demand of base-isolated structures equipped with LRBs mainly depends on the FFE set for low-intensity earthquakes (i.e. $a_g$/PGA<0.5) while it is more influenced by the NFE set for increasing values of $a_g$/PGA (Figure 9f). This behaviour can be interpreted by observing that the horizontal stiffness of the LRBs significantly increases at the small amplitude deformations, shortening the fundamental vibration period and consequently shifting the response towards the resonant region in the acceleration response spectrum of the FFE set.

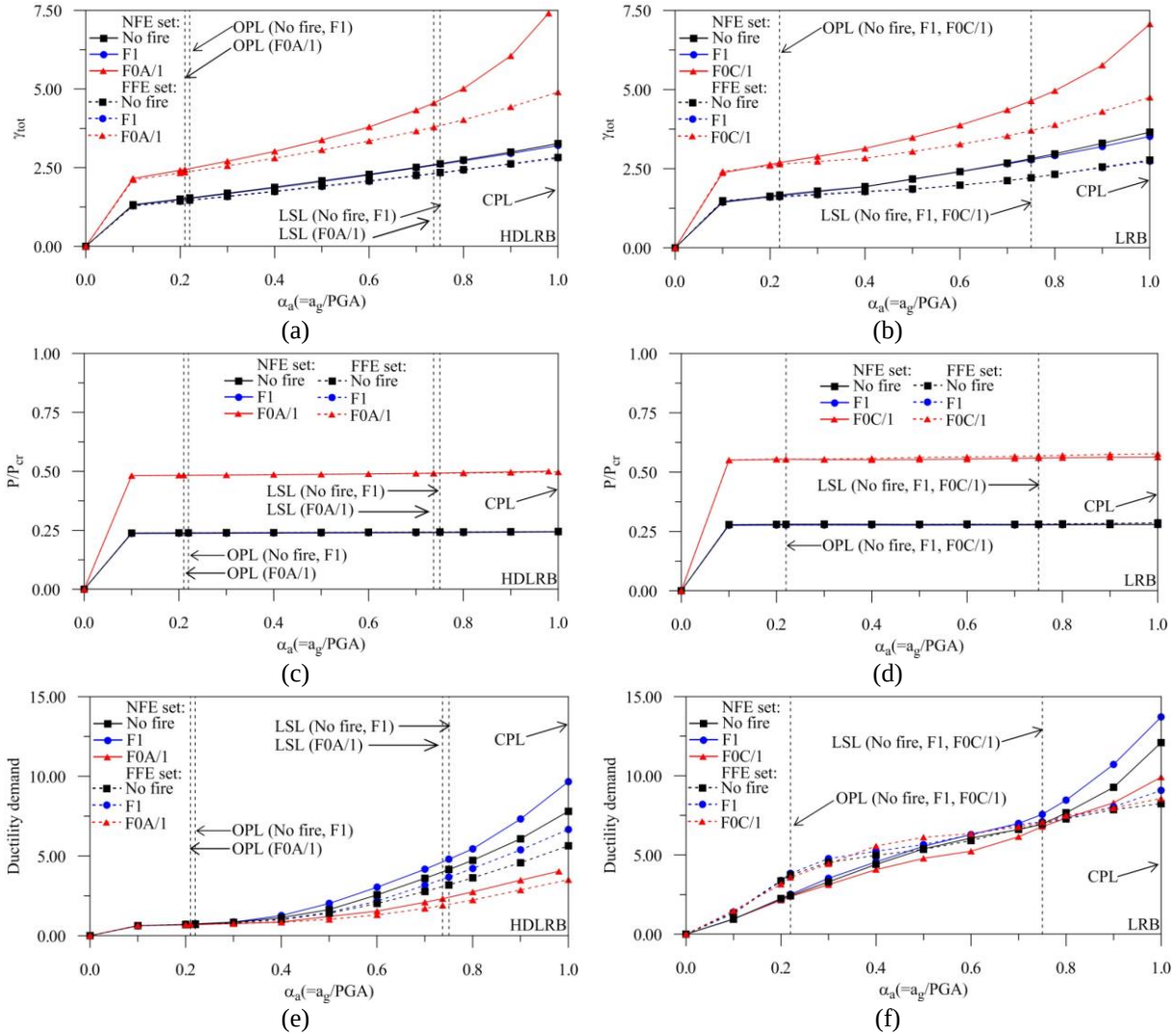


Figure 9: Nonlinear incremental dynamic analysis under near-fault (NFE set) and far-fault (FFE set) earthquakes: comparison of base-isolated structures in the no fire and fire scenarios.

To investigate the distribution of local damage along the building height, mean ductility demand at end sections of interior beams is plotted in Figure 10, considering base-isolated structures with HDLRBs (Figures 10a,c) and LRBs (Figures 10b,d) subjected to the NFE and FFE sets of earthquakes. A picture of the residual load capacity at the CPL state is generally represented, assuming the minimum value of the dimensionless acceleration ratio $\alpha_a$ for both NFE and FFE sets when the IDAs are early interrupted. In detail, this happens in the case of the F0A, F0B, F0D and F0A/1 scenarios, due to the attainment of the ultimate value imposed on the total shear strain of the isolators under the NFE set. The effects of the NFE set on the ductility demand are found to be more marked at the lower floors when the F1 fire scenario is considered (Figures 10c,d), while the no fire condition always prevails over the cases of fire occurring in the basement (i.e. F0 scenarios) and simultaneously in the first level of the super-structure (i.e. F0A/1 and F0C/1 scenarios). Moreover, the effects of the FFE set are generally more significant than those of the NFE set at the higher floor levels of base-isolated structures with LRBs (Figures 10b,d). Further results, omitted for the sake of brevity, confirm similar findings for the quarter-span sections of the interior beams while mid-span sections of beams together with end-sections of the columns exhibit negligible ductility demand.

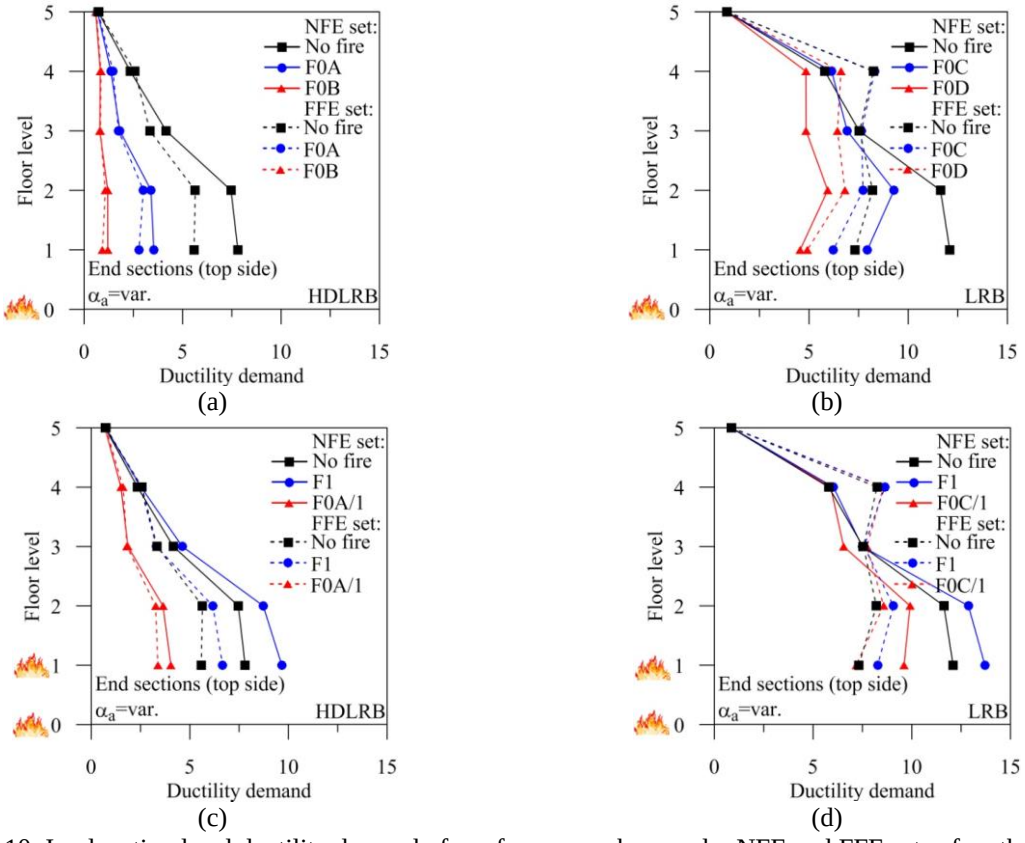


Figure 10: In-elevation local ductility demand of r.c. frame members under NFE and FFE sets of earthquakes: base-isolated structures with HDLRBs and LRBs.

Finally, the local in-plan damage distribution of the isolators is plotted in Figure 11, with reference to HDLRBs (Figures 11a,c) and LRBs (Figure 11b,d) of the base-isolated structures subjected to NFE and FFE sets of earthquakes. Only the fire scenarios in the basement are compared for the HDLRBs (i.e. F0A and F0B) and LRBs (i.e. F0C and F0D). Specifically, total shear strain ($\gamma_{tot}$) and dimensionless axial load ($P/P_{cr}$) are contemporaneously examined, by considering only half of the symmetric building plan. In all the examined cases, maximum values of $\gamma_{tot}$ and $P/P_{cr}$ under the NFE set are obtained for the central isolator followed by the

interior one. As expected, local response parameters of the isolators under the FFE set of earthquakes are generally lower than under the NFE set. Moreover, the effectiveness of the LRBs to retain a residual seismic load capacity is limited in comparison with the HDLRBs, also taking into account the lower temperatures (i.e. T=250°C and 300°C) characterizing the F0C and F0D fire scenarios with respect to F0A and F0B ones (i.e. T=300°C and 400°C).

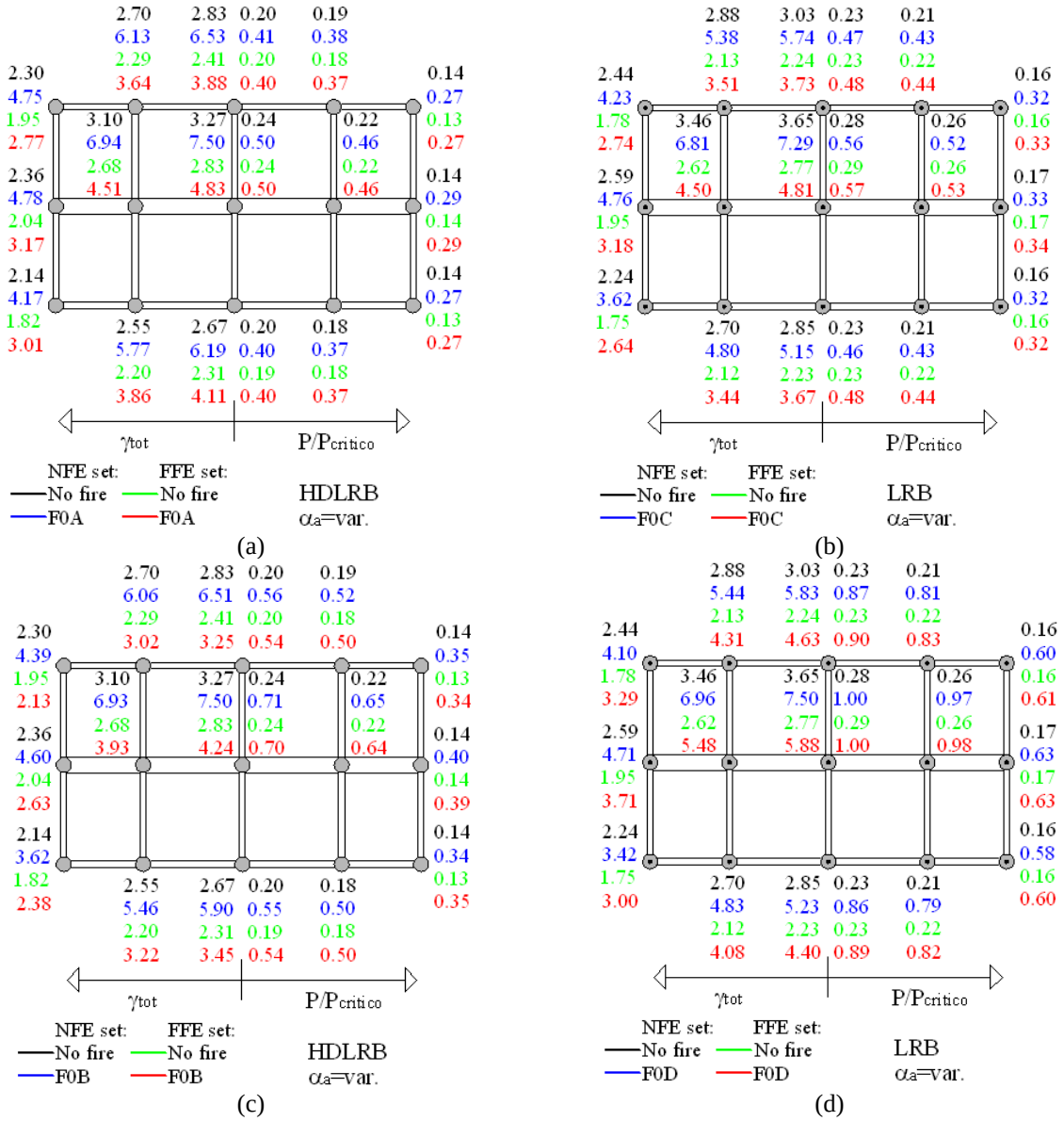


Figure 11: In-plan local response parameters of the isolators under NFE and FFE sets of earthquakes: base-isolated structures with HDLRBs and LRBs.

## 6 CONCLUSIONS

A multi-record nonlinear incremental dynamic analysis of base-isolated framed structures, damaged by fire and then subjected to near- and far-fault earthquakes, is carried out in order to evaluate their residual seismic load capacity. To this end, different scenarios are considered, involving fire in the first level of the superstructure and/or in the base-isolation system made with rubber bearings (i.e. HDLRBs and LRBs). To evaluate the temperature distribution in the r.c. frame members and isolators, bi- and three-dimensional thermal mappings are evaluated by means of the ABAQUS computer code. Similarly to the 500°C isotherm method proposed

by Eurocode 2 to evaluate residual properties of fire-damaged r.c. cross-sections, a 200°C isotherm method is proposed for the residual cross-section of HDLRBs and LRBs, neglecting rubber with temperatures exceeding the vulcanization threshold with steel shims. Fire loading before earthquake confirms reduction factors of the flexural stiffness for interior columns and beams exposed to fire on four and three sides, respectively, lower than those obtained for exterior columns and beams exposed to fire on one side only. Next, reduction factors of the effective shear and axial stiffnesses and primary and secondary shape factors for LRBs exhibit values higher than for HDLRBs, due to their lesser initial diameter.

Seismic aftershocks after fire highlight amplification in the structural response of fire-exposed base-isolated structures for the NFE set rather than FFE set of earthquakes, confirming the detrimental effects of pulse-like near-fault ground motions on base-isolated structures. Under the NFE set, the F0B fire scenario corresponds to collapse of the HDLRBs before the attainment of the LSL state, while the F0D fire scenario is border-line for the LRBs. However, the residual seismic load capacity of the HDLRBs is greater than that observed for the LRBs, because the F0A and F0B scenarios are characterized by higher temperatures than for the F0C and F0D scenarios, respectively. The post-fire seismic performance of the superstructure for the F1 fire scenario is worse than that observed in the no fire condition and F0/1 scenarios. Note that maximum ductility demand of base isolated structures equipped with LRBs mainly depends on the FFE set for low-intensity earthquakes, while it is more influenced by the NFE set for increasing values of the acceleration ratio. Finally, the effects of the NFE set on the ductility demand are found to be more marked at the lower floor levels when the F1 fire scenario is considered, while the effects of the FFE set are generally more significant than those of the NFE set at the higher floor levels of base-isolated structures with LRBs.

## ACKNOWLEDGEMENTS

The present work was financed by Re.L.U.I.S. (Italian network of university laboratories of earthquake engineering), in accordance with “Convenzione D.P.C.–Re.L.U.I.S. 2017, PR6 line, Isolation and Dissipation”.

## REFERENCES

[1] V.K.R. Kodur, M. Garlock, N. Iwankiw. Structures in fire: state-of-the-art, research and training needs, *Fire Technology*, **48**, 825-839, 2012.

[2] B. Behnam, H. Ronagh. Performance of reinforced concrete structures subjected to fire following earthquake. *European Journal of Environmental and Civil Engineering*, **17**(4), 270-292, 2013.

[3] V.K.R. Kodur, N.K. Raut, X.Y. Mao, W. Khaliq. Simplified approach for evaluating residual strength of fire-exposed reinforced concrete columns. *Materials and Structures* **46**, 2059-2075, 2013.

[4] F. Mazza. Seismic vulnerability and retrofitting by damped braces of fire-damaged r.c. framed buildings. *Engineering Structures*, **101**, 179-192, 2015.

[5] F. Mazza. Effects of near-fault vertical earthquakes on the nonlinear incremental response of r.c. base-isolated structures exposed to fire. *Bulletin of Earthquake Engineering* **14**, 433-454, 2016.

[6] A.K. Bhowmick, R. Mukhopadhyah, S.K. De. High temperature vulcanization of elastomers. *Rubber Chemistry and Technology*, **52**(4), 725-734, 1979.

[7] NTC08. Technical Regulations for the Constructions. Italian Ministry of the Infrastructures, 2008.

[8] Eurocode 1. Actions on structures – Part 1-2: General actions, actions on structures exposed to fire. *C.E.N., European Committee for Standardization*, October 2004.

[9] ABAQUS. Computer software, Dassault Systems, version 6.12. Users and Theory Manual Version 6.12. Hibbitt, Karlsonn and Sorensen.

[10] Eurocode 2. Design of concrete structures – Part 1-2: General rules, structural fire design. *C.E.N., European Committee for Standardization*, December 2004.

[11] PEER. Pacific Earthquake Engineering Research Center database. http://peer.berkeley.edu/smcat/search.html, 2014.

[12] ESD. European Strong Motion database. http://esm.mi.ingv.it/, 2015.

[13] F. Mazza. Torsional response of fire-damaged base-isolated buildings with elastomeric bearings subjected to near-fault earthquakes. *Bulletin of Earthquake Engineering*, DOI 10.1007/s10518-017-0103-0, 2017.

[14] F. Mazza. Nonlinear incremental analysis of fire-damaged r.c. base-isolated structures subjected to near-fault ground motions. *Soil Dynamics and Earthquake Engineering*, **77**, 192-202, 2015.

[15] J. Weisman, G.P. Warn. Stability of elastomeric and lead-rubber seismic isolation bearings. *Journal of Structural Engineering*, **138**(2), 215-223, 2012.

[16] F. Mazza. Behaviour during seismic aftershocks of r.c. base-isolated framed structure with fire-induced damage. *Engineering Structures*, DOI10.1016/j.engstruct.2017.03.008.

[17] E. Chioccarelli, I. Iervolino. Near-source seismic demand and pulse-like records: A discussion for L'Aquila earthquake. *Earthquake Engineering and Structural Dynamics*, **39**(9), 1039-1062, 2010.

[18] I. Iervolino, C. Galasso, E. Cosenza. REXEL: computer aided record selection for code-based seismic structural analysis. *Bulletin of Earthquake Engineering*, **8**(2), 339-362, 2010.

[19] F. Mollaioli, A. Lucchini, Y. Cheng, G. Monti. Intensity measures for the seismic response prediction of base-isolated buildings. *Bulletin of Earthquake Engineering*, **11**: 1841-1866, 2013.

[20] F. Mazza, F. Alesina. Effects of site condition in near-fault area on the nonlinear response of fire-damaged base-isolated structures. *Engineering Structures*, **111**(3), 297-311, 2016.

[21] F. Mazza, R. Labernarda. Structural and non-structural intensity measures for the assessment of base-isolated structures subjected to pulse-like near-fault earthquakes. Soil Dynamics and Earthquake Engineering, **96**, 115-127, 2017.

[22] F. Mazza, A. Vulcano, Effects of the near-fault ground motions on the nonlinear dynamic response of base-isolated r.c. framed buildings. *Earthquake Engineering and Structural Dynamics*, **41**, 211-232, 2012.

[23] F. Mazza, M. Mazza, Nonlinear analysis of spatial framed structures by a lumped plasticity model based on the Haar-Kàrmàn principle. *Computational Mechanics*, **45**, 647-664, 2010.

[24] D.R. Pant, A.C. Wijeyewickrema, M.A. ElGawady. Appropriate viscous damping for nonlinear time-history analysis of base-isolated reinforced concrete buildings. *Earthquake Engineering and Structural Dynamics*, **42**, 2321-2339, 2013.

COMPDYN 2017
6th ECCOMAS Thematic Conference on
Computational Methods in Structural Dynamics and Earthquake Engineering
M. Papadrakakis, M. Fragiadakis (eds.)
Rhodes Island, Greece, 15–17 June 2017

# COMPARISON OF FRICTION MODELS FOR THE CURVED SURFACE SLIDING SYSTEM IN THE NONLINEAR SEISMIC ANALYSIS OF BASE-ISOLATED BUILDINGS

**F. Mazza**[1] **and M. Loprete**[2]

[1] Dipartimento di Ingegneria Civile, Università della Calabria
Via P. Bucci, 87036 Rende (CS), Italy
e-mail: fabio.mazza@unical.it

[2] Dipartimento di Ingegneria Civile, Università della Calabria
Via P. Bucci, 87036 Rende (CS), Italy
mattia_loprete@outlook.com

**Keywords:** R.C. Base-isolated Structure; Curved Surface Sliding System; Sliding Velocity; Axial Pressure; Stick-Slip Effect; Axial Load; Temperature; Nonlinear Dynamic Analysis.

**Abstract.** *Current seismic codes allow for the use of simple bilinear curves to describe the nonlinear response of the curved surface sliding (CSS) bearings. However, the CSS bearings show a complex nonlinear behavior with variations in the friction coefficient, depending on the sliding velocity, axial pressure, heating at the sliding surface and stick-slip phases at the initial motion and motion reversals. Moreover, the friction force and lateral stiffness during the sliding phase are proportional to the axial load. The main object of this study is to investigate the influence that different modelling assumptions of the CSS bearings may have on the lateral-torsional response of irregular base-isolated structures located in near-fault area, characterized by ground motions with large amplitudes and long period horizontal velocity pulses. To this end, a six-storey base-isolated reinforced concrete (r.c.) framed building, with an L-shaped plan and setbacks in elevation, is designed assuming low- and medium-type friction properties, both with two in-plan distributions of the dynamic-fast friction coefficient, corresponding to: (i) the same value for all isolators; (ii) a different value for each isolator. Four additional cases are compared reducing the friction coefficient in accordance with a temperature increase up to 250°C during ground motions. A computer code for the nonlinear dynamic analysis, with a lumped plasticity model to describe the inelastic behaviour of the superstructure, is developed in order to compare eight structural solutions through five models of the CSS bearings that consider: i) constant axial load and constant friction coefficient; ii) constant axial load and variable friction coefficient with velocity; iii) variable axial load and variable friction coefficient with velocity; iv) variable axial load and variable friction coefficient with velocity and pressure; v) variable axial load and variable friction coefficient with velocity, pressure and stick-slip effect. To this end, near-fault ground motions are selected from the Pacific Earthquake Engineering Research center database.*

## 1 INTRODUCTION

Curved surface sliding (CSS) bearings are generally recommended for irregular framed structures because, in comparison with other base-isolation systems, allow the minimization of torsional effects and residual displacements [1]. More specifically, mass irregularities of the superstructure are balanced by spatial variation in the horizontal stiffness and friction force of the CSS bearings, proportional to the axial load during the sliding phase. However, theoretical and experimental studies have uncovered the complex nonlinear behaviour of the CSS bearings, highlighting the presence of many parameters affecting their friction coefficient at the sliding surface. More specifically, the friction force changes with: (a) the sliding velocity, whose increasing values produce a friction coefficient which increases by an exponential law [2]; (b) the axial pressure, with a high-velocity (dynamic-fast) value of the friction coefficient significantly reducing with the axial pressure and a low-velocity (dynamic-low) value which is relatively unaffected [3, 4]; (c) the temperature when the slider is in motion, influencing the friction coefficient which decreases rapidly as the temperature at the sliding interface increases from -40 °C to 20°C and trends to a constant value for temperatures greater than 250 °C [5]; (d) the stick-slip phases, producing a transition between static and kinetic friction coefficients, whose ratio varies between 1.5 and 4.5 depending on the friction material adopted to coat the slider [6]. On the other hand, the axial load changes continuously during an earthquake and high values of the sliding velocity are expected under the horizontal components of near-fault ground motions, thus inducing torsional effects and residual displacements of the CSS system [7-9]. These considerations show the need for a suitable numerical model to describe the nonlinear behaviour of a CSS bearing, contrary to current international seismic codes [10] and guidelines [11] which allow for the use of simple bilinear curves to reduce the computational effort for the nonlinear dynamic analyses.

To this end, a computer code for the nonlinear dynamic analysis is developed, in order to compare five models of the CSS bearings that consider: i) constant axial load and constant friction coefficient (CALCFC model); ii) constant axial load and variable friction coefficient with velocity (CALVFC1 model); iii) variable axial load and variable friction coefficient with velocity (VALVFC1 model); iv) variable axial load and variable friction coefficient with velocity and pressure (VALVFC2 model); v) variable axial load and variable friction coefficient with velocity, pressure and stick-slip effect (VALVFC3 model). A numerical investigation is carried out considering a six-storey reinforced concrete (r.c.) office building, with an L-shaped plan and setbacks at different heights along the in-plan X (i.e. one setback, at the third-storey) and Y (i.e. two setbacks, at the second- and fourth-storey) principal directions, designed in line with the Italian seismic code [12]. Eight structural solutions are compared, assuming: i) low- and medium-type friction properties; ii) two in-plan distributions of the dynamic-fast friction coefficient (i.e. the same value for all isolators and a different value for each isolator); iii) a reduction of the friction coefficient in accordance with a temperature increase up to 250°C during ground motions. A lumped plasticity model describes the inelastic behaviour of the superstructure, including a 26-flat surface modelling of the axial load-biaxial bending moment elastic domain at the end sections of r.c. frame members. Seven near-fault ground motions are selected from the *Pacific Earthquake Engineering Research center database* [13] and normalized in accordance with the design hypotheses adopted for the test structure (i.e. high-risk seismic region and soil-site).

## 2 MODELLING OF THE CURVED SURFACE SLIDING BEARING

The CSS bearing consists of a spherical concave sliding surface, with a radius of curvature $R$, and an articulated slider, with contact surface $S$ and friction coefficient $\mu$. For bidirectional

motion, the restoring force during the sliding phase contains pendular ($\boldsymbol{F}_p$) and friction ($\boldsymbol{F}_f$) components that can be evaluated by considering the rotational equilibrium equation around the centre of curvature [14]

$$\boldsymbol{F}_H = \boldsymbol{F}_p + \boldsymbol{F}_f = \begin{Bmatrix} F_{H,x} \\ F_{H,y} \end{Bmatrix} \cong \frac{N}{R} \begin{Bmatrix} u_{H,x} \\ u_{H,y} \end{Bmatrix} + \mu N \frac{1}{\|\dot{u}_H\|} \begin{Bmatrix} \dot{u}_{H,x} \\ \dot{u}_{H,y} \end{Bmatrix} \tag{1}$$

where $N$ is the axial load on the CSS bearing corresponding to the axial pressure $p=N/S$. Moreover, a circular interaction domain can be used to represent the biaxial interaction, where the direction of the hysteretic force is controlled by the incremental plastic displacements [15].

## 2.1 CALCFC model: constant axial load and constant friction coefficient

The response of the CSS bearing in the horizontal direction can be idealized by means of a two-component model (Figure 1a), constituted of an elastic component with restoring stiffness $K_r=N/R$ and an elastic-plastic component with elastic stiffness $K_i$-$K_r$ and yield force $\mu W$. A bilinear force-displacement ($\boldsymbol{F}_H$-$\boldsymbol{u}_H$) law (Figure 2b) can be assumed for constant values of the axial load (i.e. $N=W$, $W$ being the weight of the superstructure) and friction coefficient $\mu$. It should be noted that the initial stiffness $K_i$ takes into account the slight deformation (i.e. $\boldsymbol{u}_{Hi}\cong 0.5$ mm) at the sliding surface during the stick phase [16].

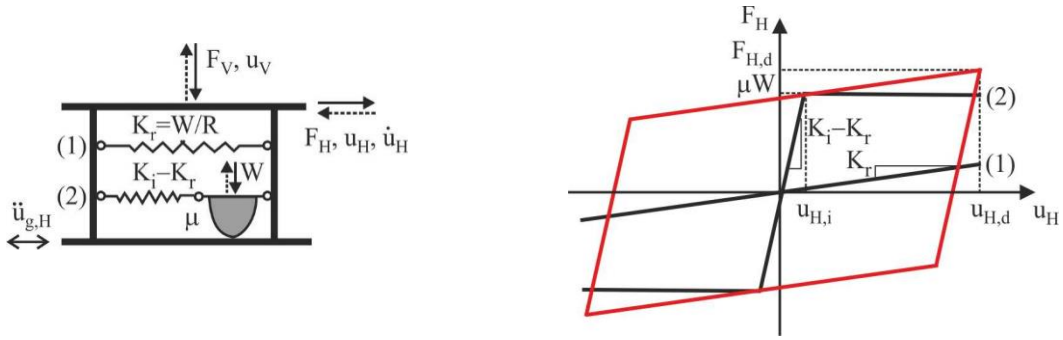


(a) (b)

Figure 1: CALCFC model for a CSS bearing.

## 2.2 CALVFC1 model: constant axial load and variable friction coefficient with velocity

The instantaneous sliding velocity affects the friction force of a CSS bearing (Figure 2), with a monotonic increase with the sliding velocity up to a constant value [2].

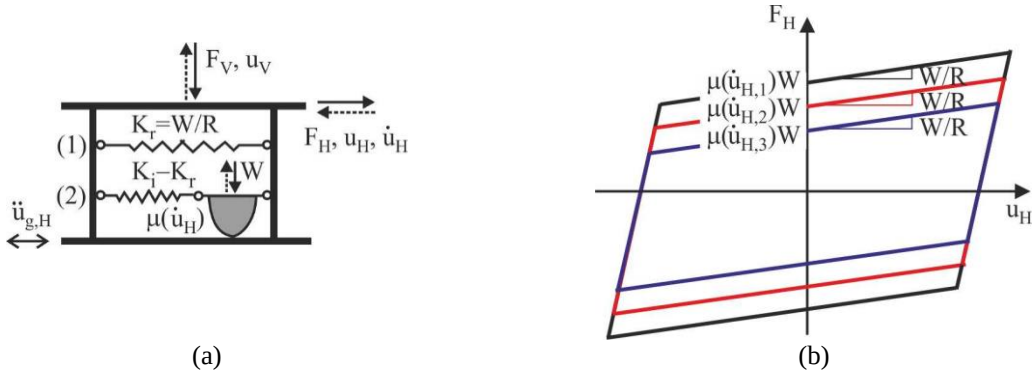


(a) (b)

Figure 2: CALVFC1 model for a CSS bearing.

An exponential law can describe the velocity dependence of the friction coefficient [2]:

$$\mu(\dot{u}_H) = \mu_{fast} - (\mu_{fast} - \mu_{slow}) e^{-\alpha \dot{u}_H} \tag{2}$$

where $\mu_{slow}$ and $\mu_{fast}$ are the friction coefficients at low and fast sliding velocities, respectively, and $\alpha$ is a rate parameter which depends on the axial load and condition of the interface. In particular, experimental results indicate that the dynamic-slow friction coefficient can be assumed 2.5 times lower than $\mu_{fast}$ [17], while parameter $\alpha$ can be considered equal to approximately 0.1 s/mm [5].

### 2.3 VALVFC1 model: variable axial load and variable friction coefficient with velocity

At any given moment during an earthquake, the fluctuation in the bearing axial load produces changes in $\boldsymbol{F}_f$ and $K_r$ (Figure 3). The axial load acting on a CSS bearing can be modified in accordance with the following expression which also accounts for the vertical-horizontal coupling [18]

$$N = W\left(1 + \frac{N_{OM}}{W}\right) \tag{3}$$

where $N_{OM}$ is the additional axial load, positive when compressive, due to the overturning moment produced by the horizontal ground acceleration $\ddot{u}_{g,H}$ (Figure 3a).

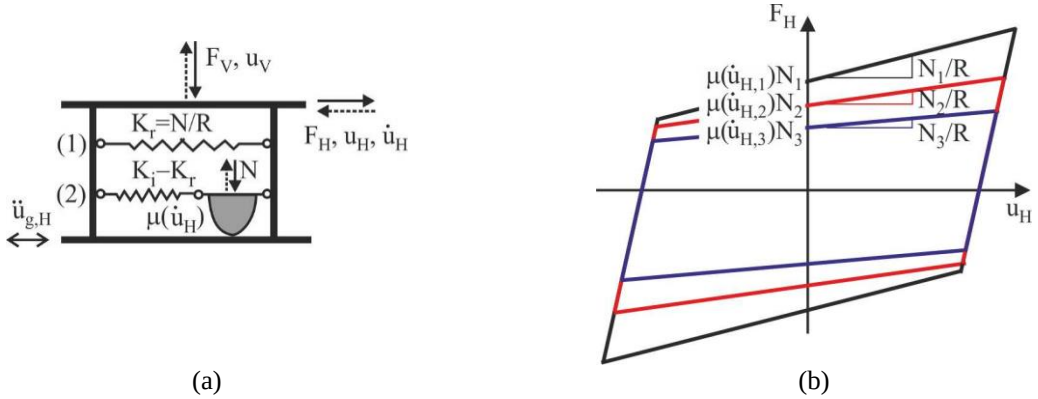


(a) (b)

Figure 3: VALVFC1 model for a CSS bearing.

Furthermore, the CSS bearing does not resist tensile axial loads and it is thus free to uplift. A gap element with infinitely rigid behaviour in compression is assumed in the vertical direction, to consider the fact that the reversal of the axial load from compression to tension is possible

$$F_V = N \quad \text{for } u_V \geq 0 \text{ and } F_V = 0 \quad \text{for } u_V < 0 \tag{4}$$

where the equivalent viscous damping in the vertical direction is neglected.

### 2.4 VALVFC2 model: variable axial load and variable friction coefficient with velocity and pressure

The instantaneous pressure due to the axial load affects the friction coefficient of a CSS bearing (Figure 4), with a reduction of $\mu_{fast}$ for increasing values of axial load, while the dependence of $\mu_{slow}$ and $\alpha$ on the axial load can be neglected [3]. Experimental laws can be assumed to take into account the variability of the dynamic-fast friction coefficient with the axial pressure [4], assuming low-

$$\mu_{fast,LF}(\%) = 2.5\left(\frac{p_{Sd}}{p_{Ed}}\right)^{-0.834} \text{ for } \left(\frac{p_{Sd}}{p_{Ed}}\right) > 0.1;\ \mu_{fast,LF}(\%) = 17 \text{ for } \left(\frac{p_{Sd}}{p_{Ed}}\right) \le 0.1 \quad (5a,b)$$

and medium-type

$$\mu_{fast,MF}(\%) = 5.5\left(\frac{p_{Sd}}{p_{Ed}}\right)^{-0.563} \text{ for } \left(\frac{p_{Sd}}{p_{Ed}}\right) > 0.135;\ \mu_{fast,MF}(\%) = 17 \text{ for } \left(\frac{p_{Sd}}{p_{Ed}}\right) \le 0.135 \quad (6a,b)$$

friction properties, where $p_{Ed}$ and $p_{Sd}$ represent, respectively, the maximum axial pressure capacity and the quasi-permanent gravity pressure ($p_{Sd}=p_v$) evaluated in the CSS system.

Then, a modified expression of the friction law can be formulated:

$$\mu(\dot{u}_H, p) = k_p\left[\mu_{fast} - \left(\mu_{fast} - \mu_{slow}\right)e^{-\alpha\dot{u}_H}\right] \quad (7)$$

where the modification factor

$$k_p = \mu_{fast}(p)/\mu_{fast}(p_v) \quad (8)$$

is defined as ratio between the dynamic-fast friction coefficient during the motion and corresponding value at the reference axial pressure under gravity loads ($p_v$).

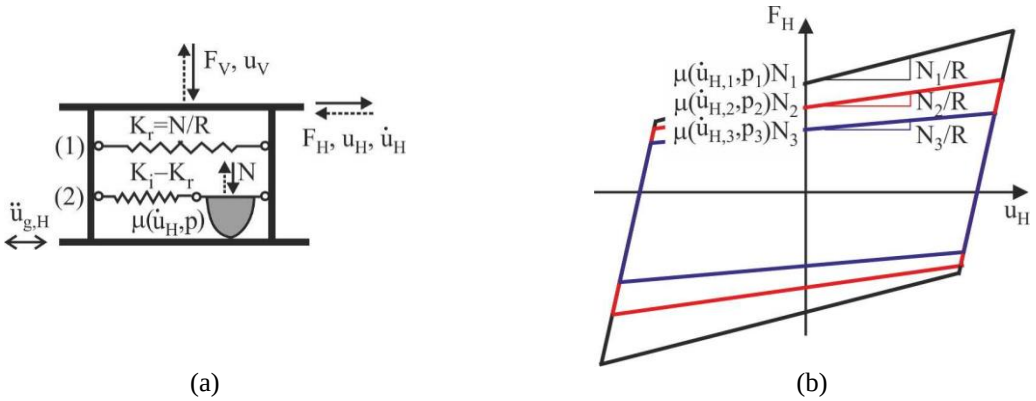


Figure 4: VALVFC2 model for a CSS bearing.

## 2.5 VALVFC3 model: variable axial load and variable friction coefficient with velocity, pressure and stick-slip effect

At initial motion and motion reversals, the response of the CSS bearing shifts between sticking and sliding phases highlighting a static friction coefficient greater than the dynamic one (Figure 5).

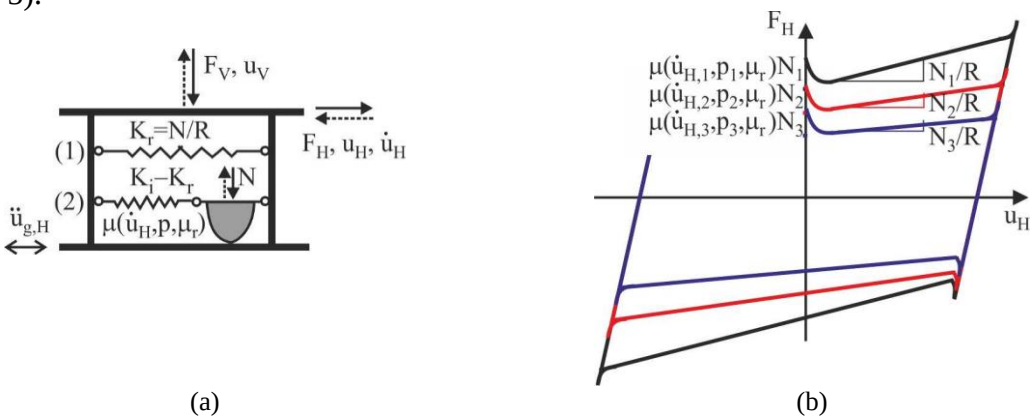


Figure 5: VALVFC3 model for a CSS bearing.

In particular, initial sliding occurs when the frictional force, depending on the breakaway friction coefficient ($\mu_b$), is overcome. Moreover, an increase of the lateral force can be observed when the maximum displacement is reached, corresponding to the friction coefficient at motion reversal ($\mu_r$). In order to take into account the transition between the sliding and sticking phase, the following simplified expression can be used

$$\mu\left(\dot{u}_H, p, \mu_b, \mu_r\right) \cong \mu\left(\dot{u}_H, p, \mu_r\right) = k_p\left[\mu_{fast} - \left(\mu_{fast} - \mu_r\right)e^{-c\dot{u}_H}\right] \tag{9}$$

where the dynamic-slow friction coefficient ($\mu_{min}$) is replaced with the static value at motion reversal ($\mu_r$) and $\mu_r \cong \mu_b$ is assumed, so observing that the breakaway friction coefficient disappears after one cycle of loading [6]. A ratio $\mu_r/\mu_{max} \cong 2$ and a parameter $c \cong \alpha$ are also assumed [6].

## 3 TEST STRUCTURES AND SELECTED EARTHQUAKES

Eight six-storey base-isolated r.c. framed office buildings, irregular in plan (Figure 6a) and elevation (Figures 6b,c), are designed in line with the Italian seismic code (NTC08, [12]). The following assumptions are considered to evaluate the horizontal seismic loads: elastic response of the superstructure (i.e. behaviour factor $q_H$=1); soil site (i.e. subsoil class D); high risk seismic region (i.e. peak ground accelerations: $PGA_{LS}$=0.27gx1.416=0.382g, at the life-safety limit state for the superstructure; $PGA_{CP}$=0.36gx1.061=0.382g, at the collapse prevention limit state for the base-isolation system). The gravity loads used in the design are represented by a dead load of 6.7 kN/m$^2$ and a live load of 2.0 kN/m$^2$, on all floors. Masonry infill walls of 2.7 kN/m$^2$ are considered as nonstructural elements regularly distributed along the perimeter and in elevation. The design of the superstructure is carried out in compliance with the life-safety limit state. Detailing for local ductility is also imposed to satisfy minimum conditions for the longitudinal bars of the r.c. frame members. A cylindrical compressive strength of 25 N/mm$^2$ for the concrete and a yield strength of 450 N/mm$^2$ for the steel are assumed for the r.c. frame members. Cross sections of columns and beams along the in-plan X and Y directions are reported in Tables 1 and 2, respectively. Further details can be found in a previous work [19].

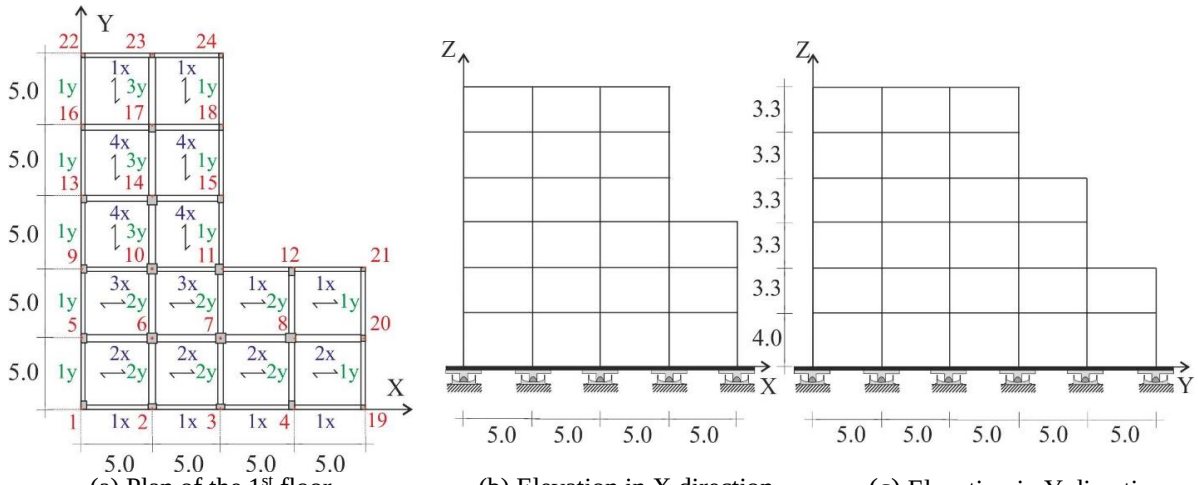


(a) Plan of the 1st floor (b) Elevation in X direction (c) Elevation in Y direction

Figure 6: Base-isolated r.c. test structure (units in m).

A grid of rigid beams is placed at the base of the framed structure on the single CSS system. The FP system is designed at the CP limit state, requiring the fulfilment of the provisions

imposed by NTC08: i.e. maximum compression axial load of the FP bearing less than its capacity; maximum horizontal displacements less than the spectral value; absence of tensile axial loads at the level of the FP system.

| | Storey | | | | | |
|---|---|---|---|---|---|---|
| Column | 1 | 2 | 3 | 4 | 5 | 6 |
| 1 | 40×60 | 35×55 | 30×50 | 30×45 | 30×40 | 30×35 |
| 2 | 60×40 | 50×35 | 50×30 | 40×30 | 30×30 | 30×30 |
| 3 | 60×40 | 50×35 | 50×30 | 40×30 | 30×30 | 30×30 |
| 4 | 40×60 | 35×55 | 30×50 | 30×45 | 30×40 | 30×35 |
| 5 | 40×60 | 35×50 | 35×40 | 30×40 | 30×30 | 30×30 |
| 6 | 70×70 | 65×65 | 60×60 | 50×50 | 40×40 | 30×30 |
| 7 | 70×70 | 65×65 | 60×60 | 50×50 | 40×40 | 30×30 |
| 8 | 60×60 | 55×55 | 50×50 | 45×40 | 40×30 | 35×30 |
| 9 | 40×60 | 35×50 | 30×50 | 30×40 | 30×30 | 30×30 |
| 10 | 70×70 | 65×65 | 60×60 | 50×50 | 40×40 | 30×30 |
| 11 | 55×70 | 50×65 | 45×60 | 40×50 | 35×40 | 30×30 |
| 12 | 40×60 | 35×55 | 30×50 | 30×45 | 30×40 | 30×35 |
| 13 | 40×50 | 35×50 | 30×40 | 30×35 | 30×30 | 30×30 |
| 14 | 65×65 | 60×60 | 50×50 | 45×45 | 35×40 | 30×35 |
| 15 | 40×50 | 35×45 | 30×40 | 30×35 | 30×30 | 30×30 |
| 16 | 30×40 | 30×35 | 30×30 | 30×30 | - | - |
| 17 | 50×50 | 45×45 | 35×40 | 30×35 | - | - |
| 18 | 30×40 | 30×35 | 30×30 | 30×30 | - | - |
| 19 | 30×30 | 30×30 | 30×30 | - | - | - |
| 20 | 30×40 | 30×35 | 30×30 | - | - | - |
| 21 | 30×30 | 30×30 | 30×30 | - | - | - |
| 22 | 30×30 | 30×30 | - | - | - | - |
| 23 | 35×30 | 30×30 | - | - | - | - |
| 24 | 30×30 | 30×30 | - | - | - | - |

Table 1: Cross-sections of r.c. columns (units in cm).

| | Floor | | | | | |
|---|---|---|---|---|---|---|
| Beam | 1 | 2 | 3 | 4 | 5 | 6 |
| 1x | 30×60 | 30×60 | 30×60 | 30×60 | 30×60 | 30×60 |
| 2x | 50×21 | 50×21 | 50×21 | 50×21 | 50×21 | 50×21 |
| 3x | 30×55 | 30×55 | 30×55 | 30×55 | 30×55 | 30×55 |
| 4x | 40×65 | 40×65 | 40×65 | 40×65 | - | - |
| 1y | 30×60 | 30×60 | 30×60 | 30×60 | 30×60 | 30×60 |
| 2y | 40×65 | 40×65 | 40×65 | 40×65 | 40×65 | 40×65 |
| 3y | 50×21 | 50×21 | 50×21 | 50×21 | 50×21 | 50×21 |

Table 2: Cross-sections of r.c. beams (units in cm).

Starting from the fundamental vibration period and equivalent viscous damping

$$T_{e,I} = 2\pi \sqrt{\left[ g\left( \frac{1}{R} + \frac{\mu_{fast}}{u_{H,d}} \right) \right]^{-1}} \quad ; \quad \xi_{e,I} = \frac{2}{\pi} \frac{1}{1 + \dfrac{u_{H,d}}{\mu_{fast} R}} \tag{10a,b}$$

with effective values equal to 3s and 15%, respectively, the values of the radius of curvature ($R$=2.93 m) and dynamic-fast friction coefficient ($\mu_{fast}$= 4.2%) of the CSS system are evaluated in relation to the spectral displacement $u_{H,d}$= 0.394 m at the collapse prevention limit state. In the case of low friction, the maximum axial load capacity of the CSS bearings

($N_{Ed}$) is evaluated by Equations (5a,b), as function of the assigned value of the quasi-permanent gravity loads ($N_{Sd}$) transmitted from the superstructure. Then, in the case of medium friction, the friction coefficient corresponding to the same ratio $N_{Sd}/N_{Ed}$ is obtained by Equations (6a,b). Moreover, two in-plan distributions of $N_{Ed}$ are assumed for the base-isolated structures: BIA.LF and BIA.MF structures in Figure 7a, with fifteen types of friction pendulum (FP) bearings (i.e. having the same $\mu_{fast}$ value for all isolators); BIB.LF and BIB.MF structures in Figure 7b, with only three types of FP bearings (i.e. exhibiting different $\mu_{fast}$ value for each isolator), which are selected with reference to the maximum value of $N_{Ed}$ from those of the isolators corresponding to three ranges of $\beta=N_{Sd}/N_{Sd,max}$ (i.e. $\beta\leq0.4$; $0.4<\beta\leq0.7$; $\beta>0.7$).

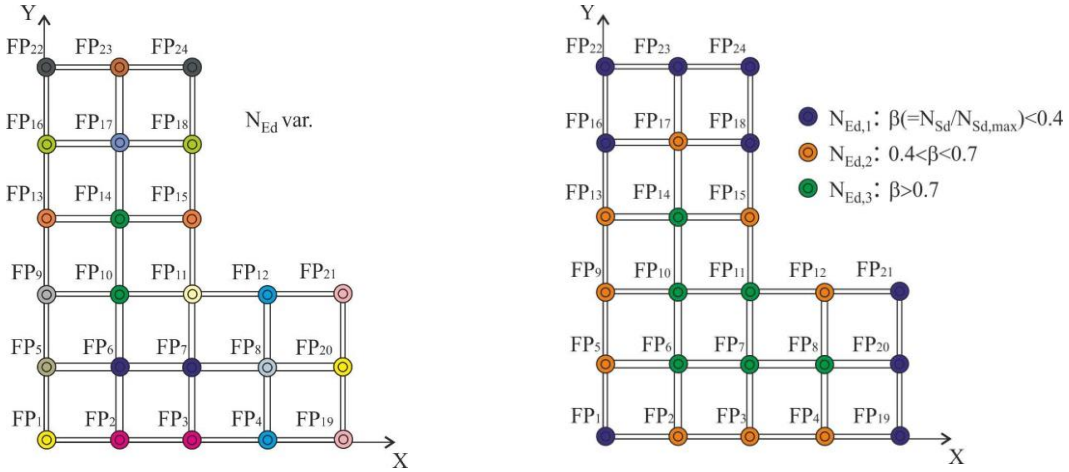


(a) BI.AL and BI.AM structures: n.15 FP. (b) BI.BL and BI.BM structures: n.3 FP.

Figure 7: In-plan distributions of axial load capacity for the Friction Pendulum (FP) bearings.

Thereafter, four additional structures are designed for low- (i.e. BIA.LFT and BIB.LFT) and medium-type (i.e. BIA.MFT and BIB.MFT) friction properties by taking into account the dependence of the dynamic-fast friction coefficient on the heating at the sliding surface when the slider is in motion. To this end, a reduction factor $k_T$ of the friction coefficient [5]

$$k_{Tf} = \frac{\mu_{fast,T_f}}{\mu_{fast}} = 0.79\left(0.7^{0.02T_f} + 0.4\right) \tag{11}$$

is applied to the Equations (5a,b) and (6a,b). It is worth noting that the reduction in the friction coefficient is sudden for increasing temperature from $T_f$=–40 °C to $T_f$=20 °C and trends to a constant value for temperatures greater than $T_f$=250 °C, where a reduction factor equal to 0.45 is obtained. Design parameters of the CSS systems are reported in Table 3.

| | BIA.LF | BIB.LF | BIA.MF | BIB.MF | BIA.LFT | BIB.LFT | BIA.MFT | BIB.MFT |
|---|---|---|---|---|---|---|---|---|
| $T_{eI}$ | 2.96 | 2.89 | 2.45 | 2.41 | 3.08 | 3.04 | 3.07 | 3.02 |
| $\xi_{eI}$ (%) | 16 | 18 | 31 | 32 | 12 | 13 | 13 | 14 |
| $u_{H,d}$ | 0.376 | 0.352 | 0.252 | 0.246 | 0.429 | 0.416 | 0.423 | 0.404 |
| $T_f$ | 20 | 20 | 20 | 20 | 250 | 250 | 250 | 250 |
| *FP types* | 15 | 3 | 15 | 3 | 15 | 3 | 15 | 3 |

Table 3: Design parameters of the CSS systems (units in s, m and °C).

Horizontal components of seven near-fault earthquakes characterized by long-duration velocity pulses are selected from the *Pacific Earthquake Engineering Research center database* [13], on the basis of the design hypotheses adopted for the test structures (i.e. soil site and

high risk seismic region). In Table 4 the main data of the selected near-fault ground motions are shown: i.e. year; recording station; magnitude ($M_w$); distance from the fault ($\Delta$); pulse period ($T_P$); peak ground acceleration for the two horizontal components (i.e. $PGA_{H1}$ and $PGA_{H2}$). The elastic response spectra of velocity ($S_{v,H}$) for the two horizontal components of each ground motion are plotted in Figure 8, assuming an equivalent viscous damping ratio in the horizontal direction ($\xi_H$) of 15%. These response spectra are compared with the corresponding NTC08 response spectra for a high-risk seismic region and subsoil class D (i.e. soil site), considering the collapse prevention limit state.

| Earthquake | Recording station | $M_w$ | $\Delta$ [km] | $T_p$ [s] | $PGA_{H1}$ | $PGA_{H2}$ |
|---|---|---|---|---|---|---|
| Chi-Chi, 1999 | TCU068 | 7.6 | 0.3 | 12.29 | 0.566 g | 0.462 g |
| Imperial Valley, 1979 | El Centro D.A. | 6.5 | 5.1 | 6.27 | 0.353 g | 0.481 g |
| Kobe,1995 | Takatori | 6.9 | 1.5 | 1.55 | 0.618 g | 0.671 g |
| Loma Prieta, 1989 | Gilroy #3 | 6.9 | 12.8 | 2.64 | 0.559 g | 0.368 g |
| Northridge, 1994 | Rinaldi R.S. | 6.7 | 6.5 | 1.25 | 0.874 g | 0.472 g |
| Parkfield, 2004 | Fault Zone 1 | 6.0 | 2.5 | 1.19 | 0.605 g | 0.833 g |
| Superstition H., 1987 | Parachute T.S. | 6.5 | 1.0 | 2.39 | 0.432 g | 0.384 g |

Table 4: Main data of the selected near-fault ground motions.

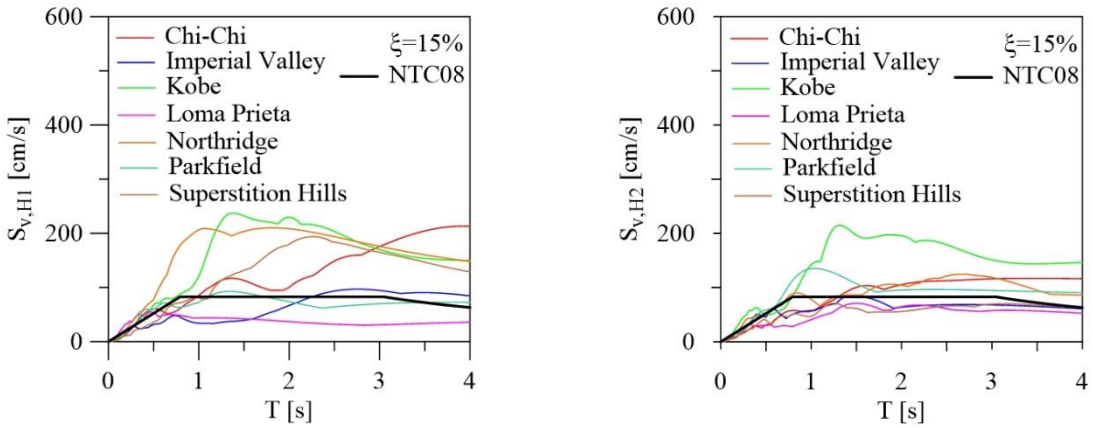


Figure 8: Velocity (elastic) response spectra for the horizontal components of the selected earthquakes.

Note that within the range of quite long horizontal vibration periods (i.e. $T_I \geq 2.4$s), corresponding to the base-isolated test structures, $S_{v,H}$ values for the selected motions are considerably different from those of the corresponding NTC08 design spectrum. Thus, the choice of the *Modified Velocity Spectrum Intensity* (*MVSI*) for scaling real motions [20]

$$MVSI = \int_{0.5T}^{1.25T} S_v(T,\xi)\cdot dT \tag{12}$$

being $T$ the fundamental vibration period of the base-isolated structure. Then, the scale factor (*SF*), whereby the horizontal components of the selected real accelerograms are normalized with respect to the NTC08 ones, is calculated as

$$SF_{MVSI} = \int_{0.5T}^{1.25T} S_{v,NTC08}(T,\eta)\cdot dT \Bigg/ \left[ 0.5 \left( \int_{0.5T}^{1.25T} S_{v1,NF}(T,\xi)\cdot dT + \int_{0.5T}^{1.25T} S_{v2,NF}(T,\xi)\cdot dT \right) \right] \tag{13}$$

Scale factors of the selected near-fault earthquakes are reported in Table 5.

| Structure | TCU068 | El Centro | Takatori | Gilroy #3 | Rinaldi R.S. | Fault Zone 1 | Parachute T.S. |
|---|---|---|---|---|---|---|---|
| BIA.LF | 0.58 | 1.00 | 0.49 | 1.70 | 0.59 | 1.05 | 0.71 |
| BIB.LF | 0.58 | 0.99 | 0.48 | 1.67 | 0.59 | 1.03 | 0.70 |
| BIA.MF | 0.63 | 0.97 | 0.46 | 1.45 | 0.55 | 0.90 | 0.69 |
| BIB.MF | 0.64 | 0.97 | 0.45 | 1.43 | 0.54 | 0.89 | 0.70 |
| BIA.LFT | 0.57 | 1.04 | 0.50 | 1.77 | 0.61 | 1.09 | 0.72 |
| BIB.LFT | 0.58 | 1.03 | 0.49 | 1.75 | 0.61 | 1.08 | 0.72 |
| BIA.MFT | 0.57 | 1.03 | 0.49 | 1.76 | 0.61 | 1.08 | 0.72 |
| BIB.MFT | 0.57 | 1.02 | 0.49 | 1.74 | 0.60 | 1.07 | 0.72 |

Table 5: Scale factors of the selected near-fault ground motions.

## 4 NUMERICAL RESULTS

Nonlinear dynamic analyses of eight structural solutions are carried out to evaluate the effects of different modelling and design assumptions of CSS bearings on the seismic response of irregular r.c. base-isolated structures subjected to strong near-fault ground motions. For this purpose, five models of CSS bearings, that consider constant and variable axial load combined with constant and variable friction coefficient, are compared for the CSS base-isolation system. A lumped plasticity model comprising two parallel elements, one linearly elastic and the other elastic-perfectly plastic, is used to describe the inelastic behaviour of r.c. frame members of the superstructure [21]. A piecewise linearization of the axial load-biaxial bending moment ultimate domain is considered for r.c. cross-sections [22]. Moreover, a stiffness-proportional damping matrix of the superstructure is considered, by applying a viscous damping ratio $\xi_S$=1% to the fundamental vibration period of the base-isolated structures [8]. The results discussed below are evaluated as an average of those separately obtained for each set of seven near-fault earthquakes scaled in accordance to MVSI [20].

First, three demand parameters are evaluated at the level of the CSS system: i) maximum bearing displacement ($u_{BI,max}$), representing a measure of the damage at the isolation level; residual bearing displacement ($u_{BI,res}$), related to the re-centring capability of the CSS bearings; iii) in-plan drift ratio $(tg\theta)_{BI,max}$ evaluated as the in-plan relative displacement of the CSS system divided by the length of the building plan, which is an indicator of the displacement due to torsion. In particular, five nonlinear models of the CSS bearings are compared at an ambient temperature $T$=20 °C (i.e. CALCFC, CALVFC1, VALVFC1, VALVFC2 and VALVFC3). Moreover, two in-plan distributions of dynamic-fast friction coefficient for the CSS system (i.e. BIA and BIB structures) are examined in Figures 9-11, considering low- (i.e. BIA.LF and BIB.LF) and medium-type (i.e. BIA.MF and BIB.MF) friction properties of the CSS bearings.

As shown in Figure 9, similar values of maximum bearing displacement are obtained in all the examined cases where constant (i.e. CAL) and variable (i.e. VAL) axial load in the modelling of CSS bearings are combined with friction coefficient constant (i.e. CFC) and variable depending on sliding velocity (i.e. VFC1) and axial pressure (i.e. VFC2).

On the other hand, notable underestimation of residual displacement in the CSS bearings is obtained with the CALCFC and CALVFC1 models of the base-isolation system, especially when low-type friction properties are considered in the BIA.LF (Figure 10a) and BIB.LF (Figure 10c) structures. Variable friction coefficient with velocity (i.e. CALVFC1 model) corresponds to a decrease of residual displacement in the CSS system, in comparison with results assuming constant values of axial load and friction coefficient (i.e. CALCFC model). Moreover, a significant increase of the residual displacement is reached when variable axial load (i.e. VALCFC1 model) is taken into account, while negligible effects of friction coefficient variability with the axial pressure (i.e. VALCFC2 model) are highlighted. Finally, the inclusion of the stick-slip phases in the modelling assumptions of the CSS bearings (i.e. VALVFC3 model) can be significant, as they always induce an increase of the residual displacement.

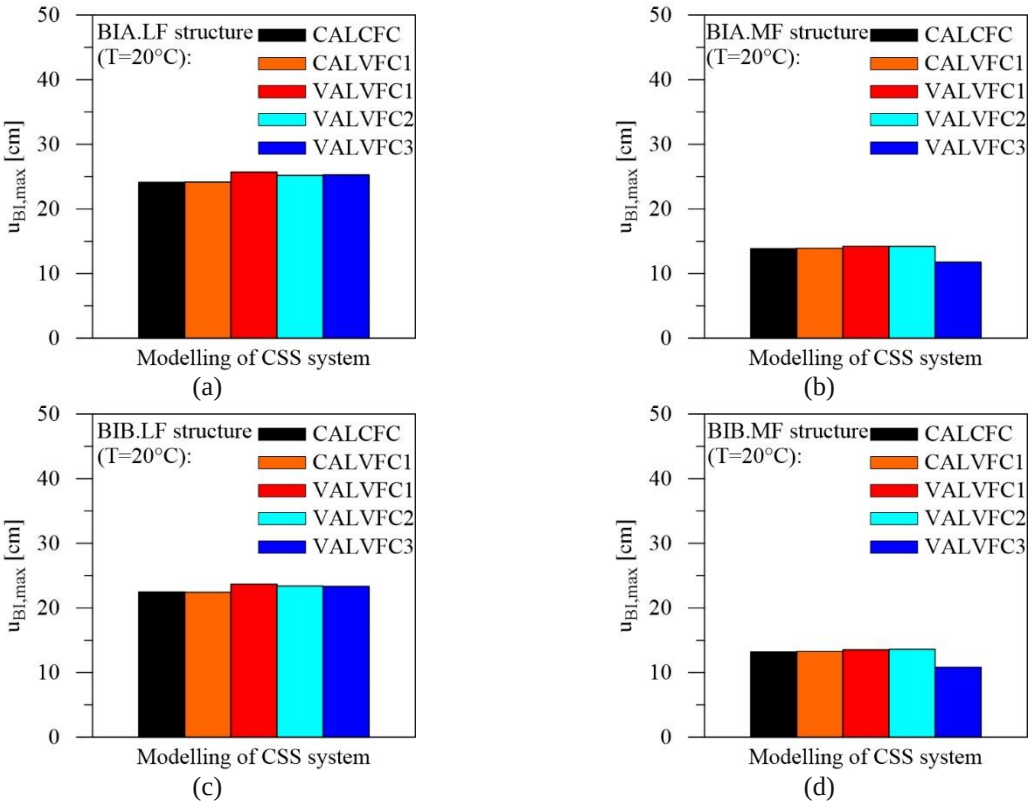


Figure 9: Effects of modelling assumptions of the CSS system on the bearing displacement.

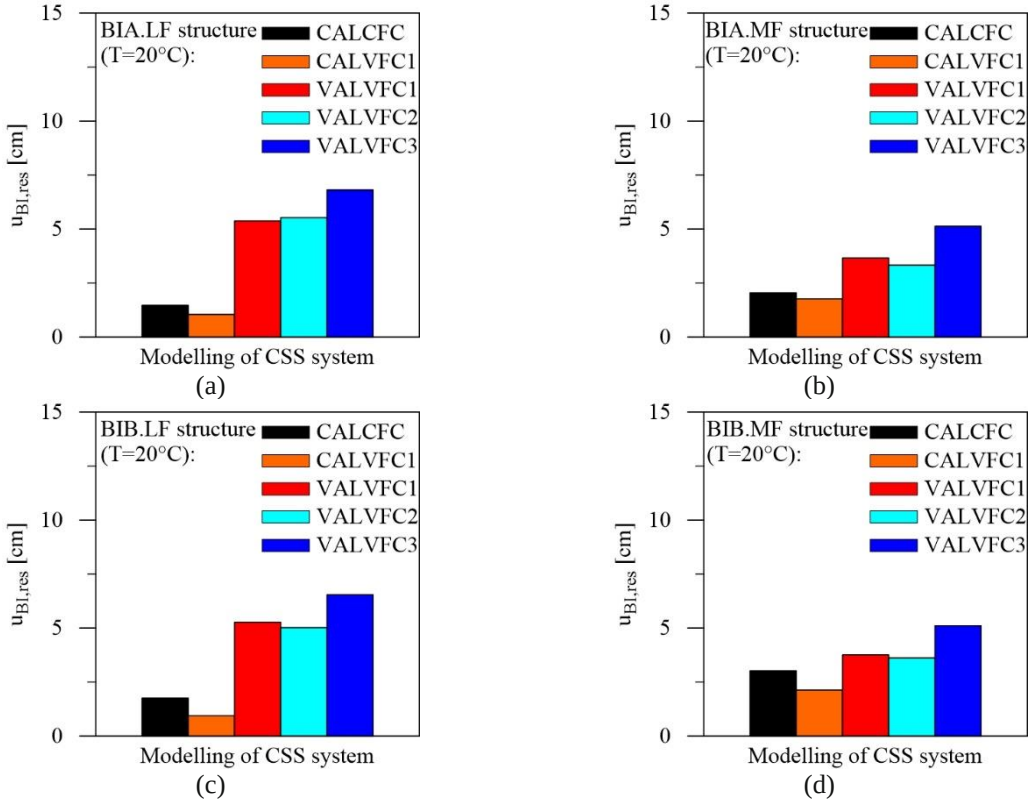


Figure 10: Effects of modelling assumptions of the CSS system on the residual bearing displacement.

Subsequently, maximum values of floor rotation at the level of the CSS system (Figure 11) highlight minor torsional effect induced by sliding velocity (i.e. CALVFC1 model) and axial pressure (i.e. VALVFC2 model), in comparison with the corresponding CSS models related

to constant values (i.e. CALCFC and VALVFC1 models). Moreover, a considerable reduction of $(tg\theta)_{BI,max}$ is found for medium-type friction properties (Figures 11b,d) when the nonlinear modelling of the CSS bearings also takes into account the sticking and sliding phases (i.e. VALVFC3 model).

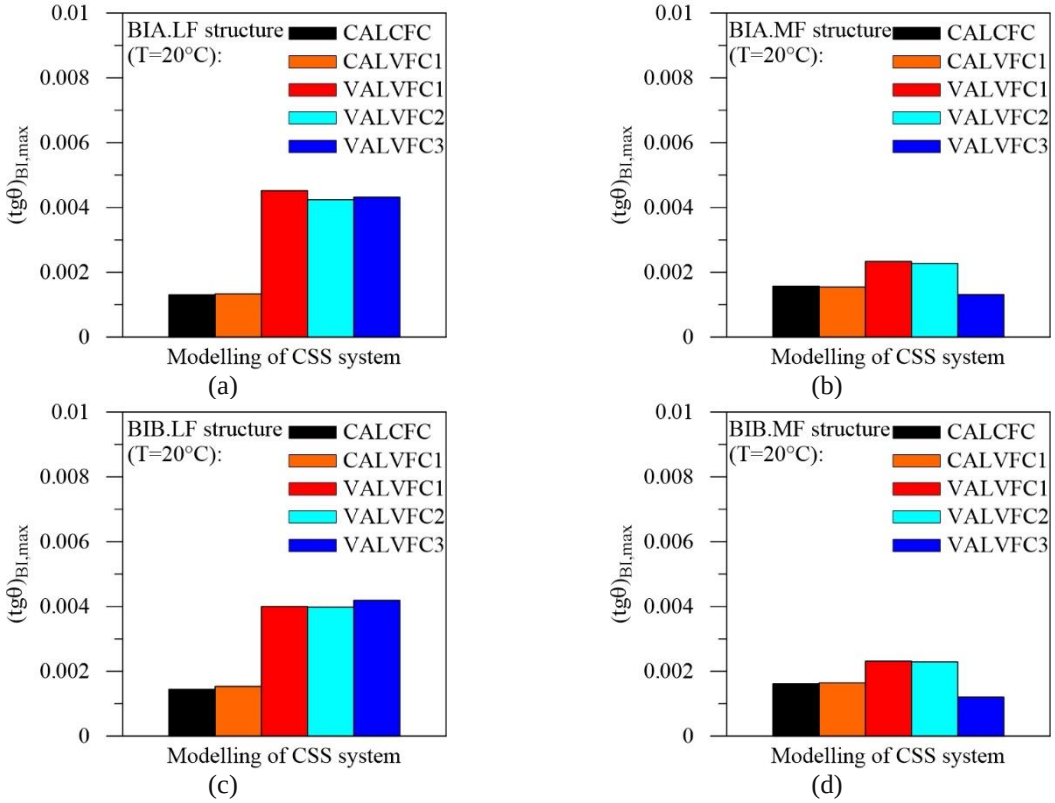


Figure 11: Effects of modelling assumptions of the CSS system on the in-plan drift ratio.

Next, in Figure 12 the sensitivity of the nonlinear seismic response parameters at the level of the CSS system is evaluated for different design and modelling assumptions of base-isolated r.c. framed buildings. To this aim, eight structural solutions are compared by considering two in-plan distributions of the dynamic-fast friction coefficient, which correspond to the same value for all isolators (i.e. the BIA structure) and a different value for each isolator (i.e. the BIB structure), and two types of friction properties (i.e. low, L, and medium, M) both evaluated in accordance with an ambient temperature $T$=20 °C and an increased temperature during ground motions up to $T$=250 °C. Moreover, the most simplified (i.e. CALCFC) and refined (i.e. VALVFC3) models of the CSS bearings are compared in Figures 12a,c,e and Figures 12b,d,f, respectively. As expected, the maximum horizontal displacement of the CSS system decreases with the change from low to medium friction properties (Figures 12a,b), but this difference becomes negligible when the heating of the CSS bearings is considered. The high temperature of the CSS bearings produces an increase of displacement which is roughly inversely proportional to the reduction factor of the friction coefficient (i.e. $k_{Tf}$=0.45) when medium-type friction is considered (Figure 12b). A slight increase of the horizontal displacement of the CSS system is obtained assuming the VALVFC3 model (Figure 12b) instead of the CALCFC one (Figure 12a) for both in-plan distributions of the friction coefficient. On the other hand, the residual displacement of the CSS system is affected by the modelling of the CSS system, with a marked underestimation of its value when the CALCFC model is adopted (Figure 12c). Moreover, the in-plan distribution of the friction coefficient does not produce significant changes of the residual displacement (Figures 12c,d), instead it highlights sensitiv-

ity to friction properties of the CSS bearings and reference temperature. As can be observed in Figure 12d, the highest values are those corresponding to low friction and $T$=250 °C (i.e. BIA.LFT and BIB.LFT structures) while the lowest ones are recorded for medium friction and $T$=20 °C (i.e. BIA.LF and BIB.LF structures). Note, however, that medium-type friction of the CSS bearings corresponds to less re-centring capabilities than the low-type, when expressed as a percentage of the corresponding maximum horizontal displacements.

Maximum floor rotation at the level of the CSS system proves to be sensitive to the design assumptions related to frictional heating of the CSS bearings. Specifically, the torsional effects are amplified in the case of $T$=250 °C and VALVFC3 model, for both low (i.e. BIA.LFT and BIB.LFT structures) and medium (i.e. BIA.MFT and BIB.MFT structures) friction-type. Moreover, the selection of medium-type friction properties produces a significant reduction of torsional effects only if the warming of the CSS bearings is ignored (i.e. assuming $T$=20 °C). Negligible differences among different design solutions of the CSS system are observed for the CALCFC model.

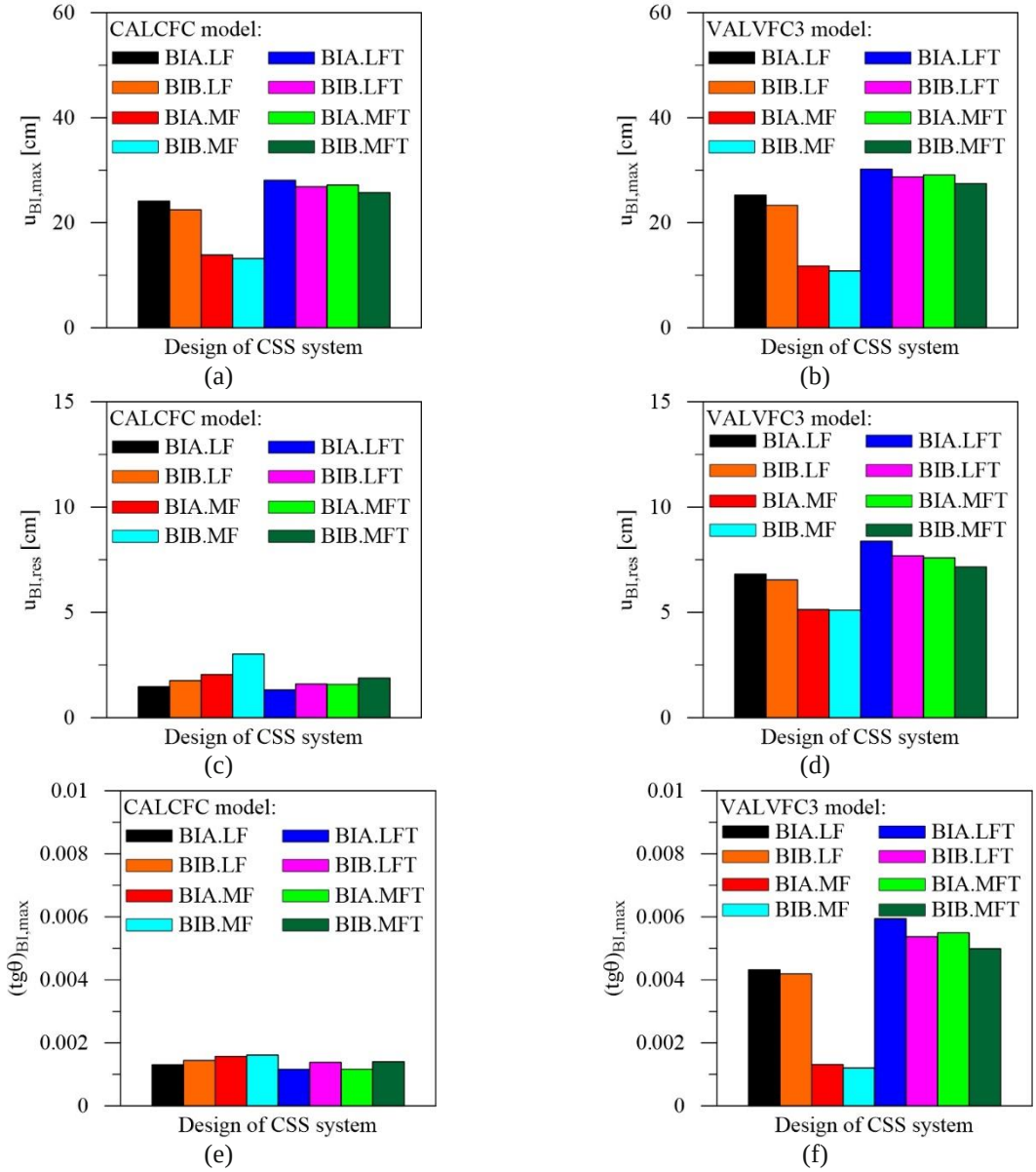


Figure 12: Effects of design assumptions of the CSS system on the response parameters.

Finally, in Figure 13 attention is focused on the sensitivity of the nonlinear seismic response of the superstructure to modelling and design assumptions of the CSS system. To this end, eight structural solutions of the CSS system are compared through the CALCFC and VALVFC3 models of the CSS bearings, while a lumped plasticity model is considered for the r.c. frame members. Maximum interstorey drift ratio $(\Delta/h)_{max}$, defined as drift normalized by storey height, is considered to represent storey damage of the superstructure. As expected, severe damage with highly irregular vertical distribution of the interstorey drift ratio is found in the case of medium friction of the CSS bearings combined with $T$=20 °C (i.e. BIA.MF and BIB.MF structures), especially when the VALVFC3 model is considered (Figure 13b). This behaviour can be explained by observing that for rather high values of friction the response in the horizontal direction is like that of a fixed-base structure until the friction threshold of the CSS system is not exceeded. Moreover, the other six structural solutions show light to moderate repairable damage at the storey levels and comparable results are obtained for both the CALCFC (Figure 13a) and VALVFC3 (Figure 13b) models.

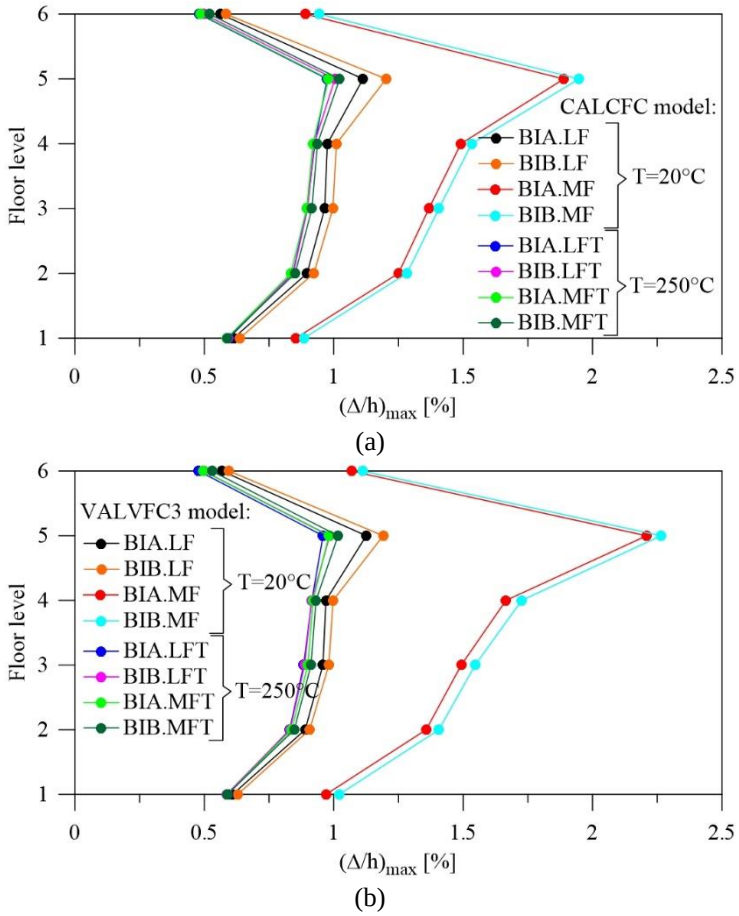


Figure 13: Effects of the modelling and design assumptions of the CSS system on the interstorey drift ratio.

## 5 CONCLUSIONS

The nonlinear dynamic analysis of irregular base-isolated r.c. framed structures subjected to the horizontal components of near-fault earthquakes is carried out to evaluate the effect of nonlinear modelling and seismic design of CSS bearings. Five nonlinear force-displacement laws for the CSS bearings, as function of axial load and sliding friction, are considered. Friction coefficient dependences on sliding velocity, axial pressure and stick-slip phases are also investigated. Finally, eight design solutions for the CSS system are compared to evaluate the

influence of: i) low- and medium-type friction properties; ii) two in-plan distributions of the dynamic-fast friction coefficient; iii) frictional heating at the sliding surface.

As regards the nonlinear modelling of the CSS bearings, residual displacement and floor rotation at the level of the CSS system are found to depend on the selected model, while similar values of maximum bearing displacement are obtained for all five models of CSS bearings. A significant increase in the residual displacement is reached when variable axial load (VALVFC1) and stick-slip phases (VALVFC3) are taken into account, while a considerable reduction of torsional effects occurs for medium-type friction properties when adopting the VALVFC3 model. On the other hand, maximum drift ratio of the superstructure highlights limited effects related to modelling assumptions of the CSS bearings with the only exception of medium friction of the CSS bearings combined with $T$=20 °C.

As regards the seismic design of the CSS system, the in-plan distribution of the friction coefficient does not produce significant changes in the demand parameters evaluated at the level of the base-isolation system. Yet, maximum horizontal displacement of the CSS system decreases with the change from low to medium friction properties, while the high temperature of the CSS bearings increases displacement. However, note that medium-type friction of the CSS bearings corresponds to less re-centring capabilities than the low-type. Finally, maximum floor rotation at the level of the CSS system proves to be sensitive to frictional heating of the CSS bearings. On the other hand, severe damage of the superstructure with highly irregular vertical distribution of the interstorey drift ratio is found in the case of medium friction of the CSS bearings and $T$=20 °C, while the other six structural solutions show light to moderate repairable damage. Finally, the in-plan distribution of the friction coefficient of the CSS system does not produce significant effects on the response of the superstructure.

## ACKNOWLEDGEMENTS

The present work was financed by Re.L.U.I.S. (Italian network of university laboratories of earthquake engineering), in accordance with “Convenzione D.P.C.–Re.L.U.I.S. 2017, PR6 line, Isolation and Dissipation”.

## REFERENCES

[1] V.A. Zayas, S.S. Low, S.A. Mahin. A simple pendulum technique for achieving seismic isolation. *Earthquake Spectra*, **6**, 317-333, 1990.

[2] M.C. Constantinou, A. Mokha, A.M. Reinhorn. Teflon bearings in base isolation. II: modeling. *Journal of Structural Engineering*, **116**(2), 455-474, 1990.

[3] P.C. Tsopelas, M.C. Constantinou, A.M. Reinhorn. 3D-BASIS-ME: computer program for nonlinear dynamic analysis of seismically isolated single and multiple structures and liquid storage tanks. *Multidisciplinary Center for Earthquake Engineering Research*, Buffalo, NY, Technical Report MCEER-94-0010, 1994.

[4] FIP Industriale S.p.A. Catalogue S04: Curved Surface Sliders. Padova, Italy. http://www.fipindustriale.it, 2013.

[5] M. Kumar, A.S. Whittaker, M.C. Constantinou. Characterizing friction in sliding isolation bearings. *Earthquake Engineering and Structural Dynamics*, **44**(9), 1409-1425, 2015.

[6] E. Fagà, P. Ceresa, R. Nascimbene, M. Moratti, A. Pavese. Modelling curved surface sliding bearings with bilinear constitutive law: effects on the response of seismically isolated buildings. *Materials and Structures*, **49**(6), 2179-2196, 2016.

[7] S. Nagarajaiah, A.M. Reinhorn, M.C. Constantinou. Torsional coupling in base isolated structures: sliding isolated systems. *ASCE/Journal of Structural Engineering*, **119**(1): 130-149, 1993.

[8] F. Mazza. Nonlinear incremental analysis of fire-damaged r.c. base-isolated structures subjected to near-fault ground motions. *Soil Dynamics and Earthquake Engineering*, **77**, 192-202, 2015.

[9] F. Mazza. Lateral-torsional response of base-isolated buildings with curved surface sliding system subjected to near-fault earthquakes. *Mechanical Systems and Signal Processing*, **92**, 64-85, 2017.

[10] Eurocode 8. Design of structures for earthquake resistance, Part1: General rules, seismic actions and rules for buildings. CEN, European Committee for Standardization, 2004.

[11] FEMA, Federal Emergency Management Agency P-751. NEHRP Recommended Seismic Provisions: Design Examples. National Earthquake Hazards Reduction Program, 2009.

[12] NTC08. Technical Regulations for the Constructions. Italian Ministry of the Infrastructures, 2008.

[13] PEER. Pacific Earthquake Engineering Research Center database. http://ngawest2.berkeley.edu, 2008.

[14] J.L. Almazan, J.C. De la Llera. Analytical model of structures with frictional pendulum isolators. *Earthquake Engineering and Structural Dynamics*, **31**, 305-332, 2002.

[15] G. Mosqueda, A.S. Whittaker, G.L. Fenves. Characterization and modeling of friction pendulum bearings subjected to multiple components of excitation. *Journal of Structural Engineering (ASCE)*, **130**(3), 433-442, 2004.

[16] J. Scheller, M.C. Constantinou. Response history analysis of structures with seismic isolation and energy dissipation systems: verification examples for program SAP2000. *Multidisciplinary Center for Earthquake Engineering Research*, State Univ. of New York at Buffalo, Buffalo, N.Y., Report No. MCEER-99-0002, 1999.

[17] M. Dolce, D. Cardone, F. Croatto. Frictional behavior of steel-PTFE interfaces for seismic isolation. *Bulletin of Earthquake Engineering*, **3**, 75-99, 2005.

[18] P.C. Roussis, M.C. Constantinou. Uplift-restraining friction pendulum seismic isolation system. *Earthquake Engineering and Structural Dynamics*, **35**, 577-593, 2006.

[19] F. Mazza, M. Mazza. Nonlinear seismic analysis of irregular r.c. framed buildings base-isolated with friction pendulum system under near-fault excitations. *Soil Dynamics and Earthquake Engineering*, **90**, 299-312, 2016.

[20] F. Mollaioli, A. Lucchini, Y. Cheng, G. Monti. Intensity measures for the seismic response prediction of base-isolated buildings. *Bulletin of Earthquake Engineering*, **11**(5), 1841-1866, 2013.

[21] F. Mazza, M. Mazza. Nonlinear analysis of spatial framed structures by a lumped plasticity model based on the Haar–Kàrmàn principle. *Computational Mechanichs*, **45,** 647-664, 2010.

[22] F. Mazza. A distributed plasticity model to simulate the biaxial behaviour in the nonlinear analysis of spatial framed. *Computers and Structures*, **135**, 141-154, 2014.

COMPDYN 2017
6th ECCOMAS Thematic Conference on
Computational Methods in Structural Dynamics and Earthquake Engineering
M. Papadrakakis, M. Fragiadakis (eds.)
Rhodes Island, Greece, 15–17 June 2017

# SEISMIC ASSESSMENT OF AN UNCONVENTIONAL STRUCTURE: THE CRYOSTAT OF "CUORE" EXPERIMENT

**Raffaele Ardito**[1], **Oliviero Cremonesi**[2], **and Federico Perotti**[1]

[1] Department of Civil and Environmental Engineering, Politecnico di Milano
Piazza Leonardo da Vinci 32, 20154 Milan, Italy
{raffaele.ardito, federico.perotti}@polimi.it

[2] Istituto Nazionale di Fisica Nucleare INFN – Sez. di Milano-Bicocca
Piazza della Scienza 3, 20126 Milan, Italy
oliviero.cremonesi@mib.infn.it

**Keywords:** Structural Dynamics, Earthquake Engineering, Contact Mechanics, Explicit Algorithms, Seismic Isolation.

**Abstract.** *This paper deals with the seismic assessment of a complex structure supporting the CUORE experiment (Cryogenic Underground Observatory for Rare Events). The main issues, that require a special computational treatment, are: (i) non-linear geometric behavior of the suspended vessels; (ii) multiple contacts between the nested vessels and between the cryostat and the external shields; (iii) non-linear constitutive law of the HDR bearings. The problem has been tackled by building a 3D detailed finite element model, that has been used for simulating, via an explicit step-by-step algorithm, the dynamic response to artificial spectrum-compatible accelerograms. The results of the analyses have been used for introducing some specific structural improvements.*

## 1 INTRODUCTION

The CUORE experiment (Cryogenic Underground Observatory for Rare Events, see [1, 2]) is a nuclear physics experiment funded by several agencies, among which the National Italian Institute of Nuclear Physics (INFN), the US Department of Energy (DOE) and the National Science Foundation (NSF, USA). The experiment is set up in the Gran Sasso National (Italian) Laboratory (LNGS), an underground facility in a highly seismic zone. In fact, the laboratory is located in a gallery beneath the Gran Sasso mountain, not far from the city of L'Aquila: that zone has been hit by a destructive earthquake in 2009 (MMS 6.3) and is currently involved in the earthquake swarm that follows the Amatrice earthquake (August 2016, MMS 6.2). In spite of the fact that the underground gallery seems to mitigate the seismic effects [3, 4], there is a major concern on the structural safety of all the experiments hosted by LNGS. The complexity of the structures, along with the strict requirements from the point of view of experimental physics, calls for the application of computational tools at the cutting-edge of technology.

The main purpose of the CUORE experiment is the search for neutrinoless double beta decay, with many important consequences on particle physics and astrophysics. The heart of the experiment is a detector (i.e. a large mass of $TeO_2$ crystals) that is contained in a cryostat of exceptional performance [5, 6]: indeed, the detector is cooled down until absolute temperatures lower than 10 mK. A base temperature lower than 8 mK has actually been reached on January 30, 2017. The thermal shield system is represented by a set of nested vessels, whose structural behavior resembles to that of pendulums. Moreover, the protection from physical interferences (cosmic rays and environmental radioactivity) requires the presence of a set of lead shields and of a borated polyethylene cap. The cryostat hangs from a steel frame, that is based on a r.c. structure supported by a base isolation system. The r.c. structure, that is clearly visible in Figure 1, is composed of two parallel walls, connected by three horizontal beams. The walls are supported by four elastomeric bearings (High Damping Rubber Bearings, HDRB).

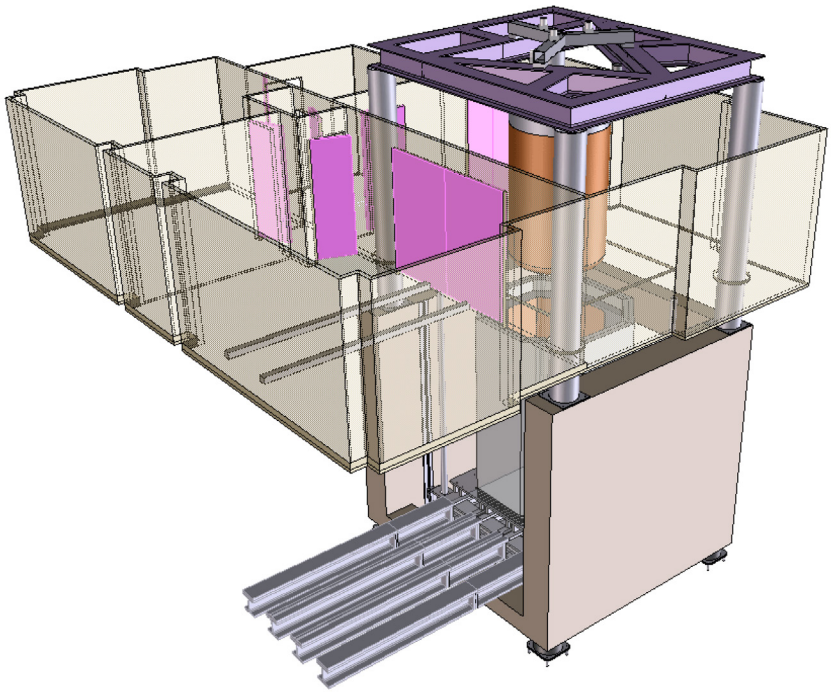

Figure 1: Rendering of the structure that contains the CUORE experiment. The external vessel of the cryostat is visible since the lead shield is completely lowered.

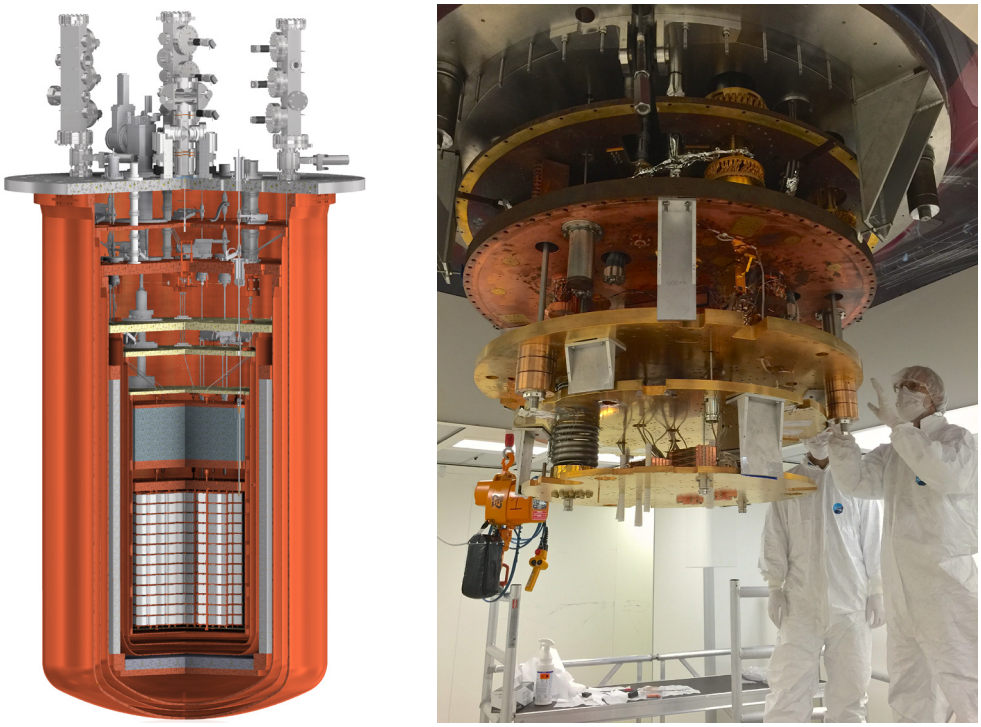

Figure 2: On the left, cut-out of the CUORE cryostat, with the inner detector constituted of about 1000 $TeO_2$ crystals. On the right, actual view of some of the cryostat's flanges.

In the operative configuration, the external lead shield is raised so that it covers completely the cryostat. The shield, that is placed on a very stiff steel plate raised and lowered by four threaded bars (jacks), is connected to the four steel columns by means of eight steel ties. The cryostat, that is depicted in Figure 2, is attached, by means of steel ropes, to the horizontal framed structure that is visible on the top of the columns in Figure 1. The flanges of each vessel are connected to one another by means of copper rods. The gap between two consecutive vessels is around one centimeter so that the mutual contact is likely to occur during seismic excitation. The total mass of the cryostat (with the detector) is about 18 t. The mass of the external lead shield is 75 t, and the mass of the steel and r.c. members is 85 t.

## 2 COMPUTATIONAL MODEL

The analyses have been carried out by means of the Finite Element method, building a 3D detailed model, that has been used for carrying out step-by-step dynamic analyses of the response to artificial accelerograms. A schematic view of the model is depicted in Figure 3. The concrete walls have been modeled by means of shell elements (constant strain triangles), whereas the steel columns and the other steel members have been discretized by Timoshenko beam elements. In order to ease the computational burden, the various vessels of the cryostat, the detector and the external shields have been modeled as rigid parts. Conversely, the suspensions of the cryostat's elements have been introduced as Timoshenko beams or truss elements, according to the specific constraints. Finally, the HDR bearings have been represented by means of non-linear springs with different behavior in the vertical and the horizontal directions.

The mechanical response is intrinsically non-linear for several reasons: (i) the rubber of the isolator is a non-linear elastic material; (ii) the cryostat is basically constituted of several nested pendulums, whose dynamic behavior is properly caught only by analyses with non-linear geometry; (iii) ideally hard and frictionless contacts should be envisaged between the vessels.

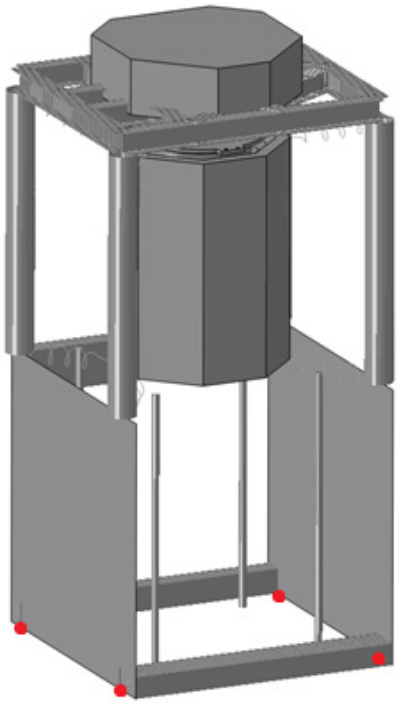

Figure 3: Schematic view of the model that has been adopted for the analyses.

For the above reasons, the explicit scheme of integration has been chosen. Such an algorithm, though conditionally stable [7], is perfectly suited to handle the occurrence of severe internal and external contacts. The stable time increment has been evaluated on the basis of the wave propagation modes in the smallest finite element; in the present case, the mass scaling procedure does not entail significant benefits.

The mechanical behavior of the elastomeric bearings has been simulated by means of the Fujino model [8, 9]. In this way, it was possible to capture the hysteretic behavior of rubber, represented in Figure 4. It is worth noting that the preliminary analyses have been carried out by considering a linearized version of the constitutive model: the secant stiffness has been obtained by means of an iterative procedure, that usually converges in no more than 6 iterations.

## 3 MAIN RESULTS OF THE ANALYSES

The step-by-step analyses have been preceded by a set of spectrum response analysis, with the purpose of obtaining some general information on the mechanical behavior. The eigenvalue extraction included the linearized geometric effects, so that the correct “small oscillation” frequency of each pendulums has been achieved. The base isolators have been linearized by means of the abovementioned iterative procedure. The contact between vessels cannot be reproduced by means of linear analyses. An approximate solution can be obtained if one assumes that, in view of the close proximity of the nested vessels, the cryostat behaves as a unique rigid body. Such a procedure has yielded acceptable results for seismic intensity corresponding to the ultimate limit state. The first natural frequencies for the isolated structure are equal to 1.1138 Hz and 1.2305 Hz, in the direction orthogonal and parallel to the concrete walls, respectively. The earthquake response spectrum has been selected according to the Italian seismic code: the peak ground acceleration is 0.261 g and the maximum spectral acceleration is 0.616 g, in the case of 5% damping. The natural frequencies fall in the constant velocity branch of the response spectrum, as it is desirable for an isolated structure. The max-

imum displacement of the isolators is about 38 mm, which means that the working point corresponds to an overall angular strain about 30%. The strain level is rather low: indeed, the original structural design, which was executed by an independent professional engineer, introduced largely oversized isolators.

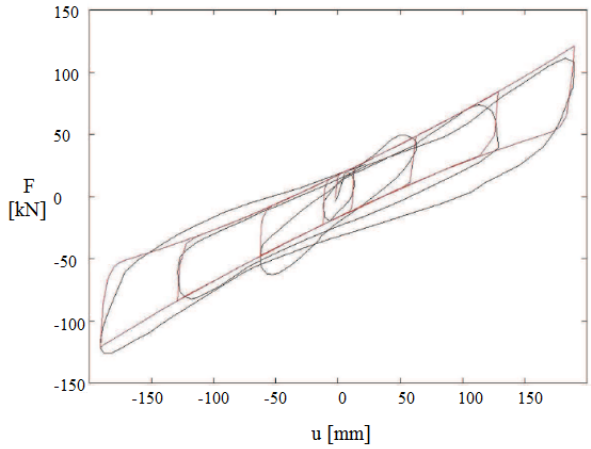


Figure 4: Hysteretic behavior of the HDRB: experimental results (black) vs. Fujino model (red).

As an example of the results achieved by the response spectrum analyses, Figure 5 shows the contour plot of horizontal displacements in the support structure. The maximum displacement is about 55 mm.

The time-marching analyses have been based on artificial accelerograms, generated on the basis of the same response spectrum that has been used for the linearized model. An example of the artificial accelerogram is reported in Figure 6. The analyses included the non-linear behavior both for geometric effects and for material behavior of the isolator. Moreover, hard and frictionless contact has been established between the cryostat's vessels and between the cryostat and the external lead shield. The complexity of the analysis is very high, as well as the computational burden.

A typical feature of the non-linear step-by-step analyses was the occurrence of extremely high acceleration peaks: that was due to the occurrence of pounding between rigid parts. On the other hand, the displacement pattern was in satisfactory agreement with the preliminary linearized analyses. Figure 7 shows that the maximum horizontal displacements is about 35 mm. The displacement for linearized analyses was slightly larger, but this is an expected outcome for systems having intermediate-to-low natural frequencies. Moreover, the linearized analyses were based on the hypothesis of rigidity of the whole cryostat, that is clearly surpassed by the non-linear analyses. The effect of internal contacts is clearly visible if one examines the absolute displacement and the acceleration of the vessels: the impacts correspond to acceleration peaks and to abrupt change of the displacement pattern.

## 4 CONCLUSIONS

The paper has presented the computational details for the seismic analysis of a complex structure, used for an experiment in nuclear physics. The strongly non-linear behavior has been dealt with through explicit step-by-step analyses, whose results have been critically compared to the outcomes of a simplified linearized model.

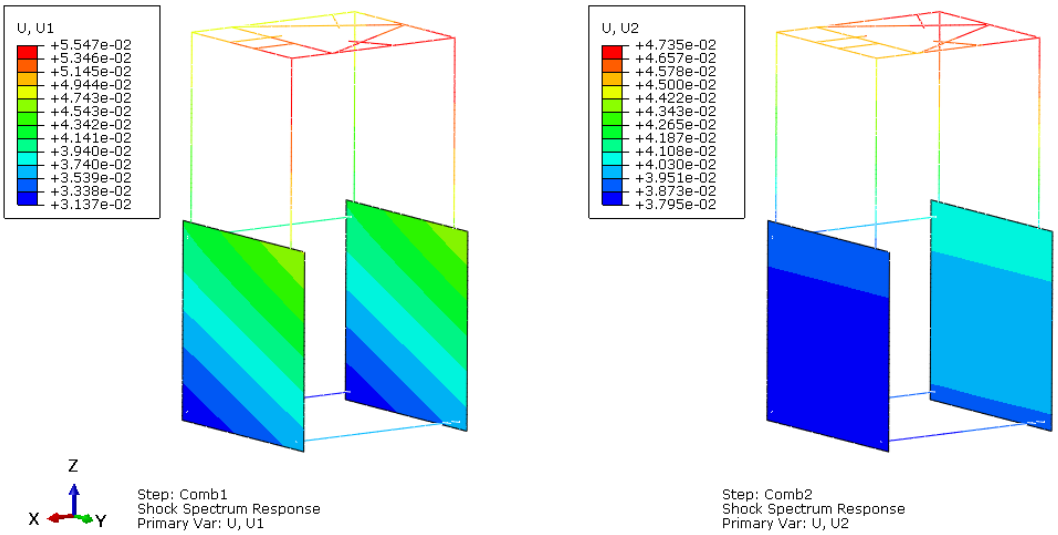


Figure 5: Results of the response spectrum analyses: horizontal displacement in the orthogonal (left) and parallel (right) direction with respect to the concrete walls.

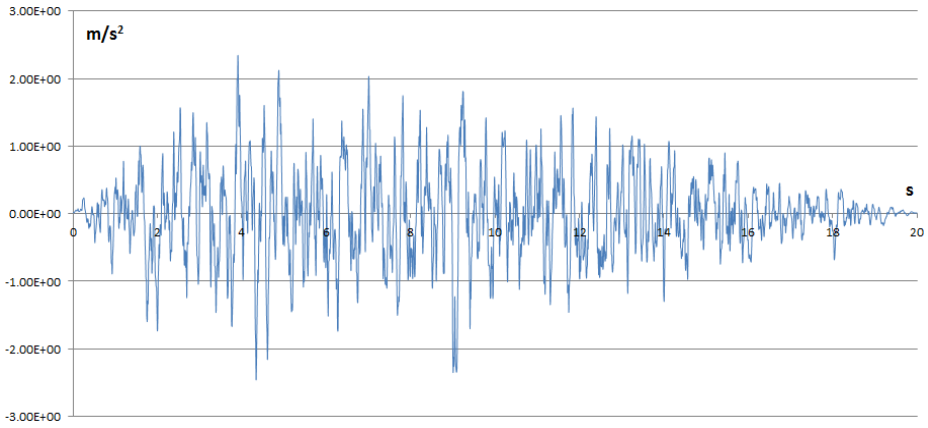


Figure 6: Typical accelerogram used for the time-marching analysis. The accelerogram has been artificially generated on the basis of the elastic response spectrum provided by the Italian seismic regulation.

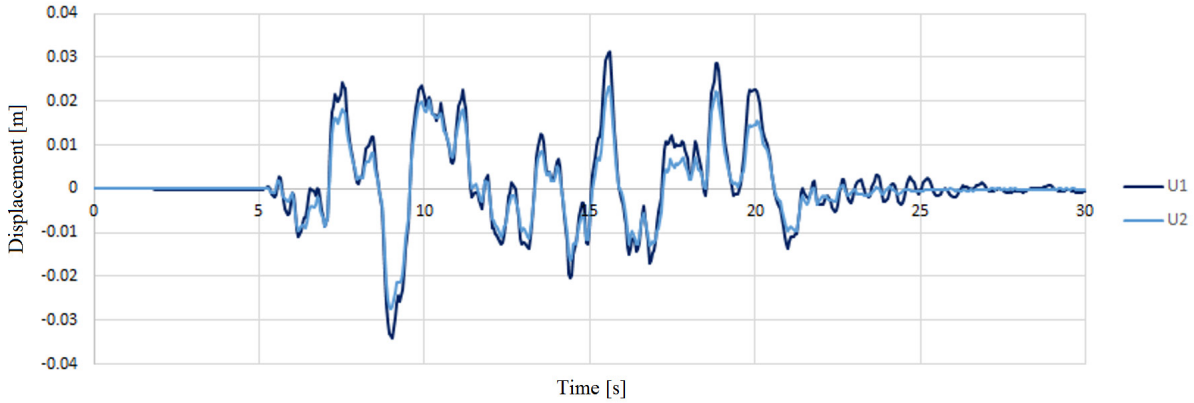


Figure 7: Time history of the horizontal displacement for the non-linear analyses.

The complete set of results, which have not been reported herein for the sake of brevity, have been thoroughly examined in order to assess the seismic safety of the structure. It is worth noting that, on one hand, the structural layout should guarantee the typical decoupling of isolated structures under seismic actions. On the other hand, in service conditions, a full connection to ground should ensure the correct irradiation of internal vibrational energy due to the pumping systems and to the cryocoolers. For the ultimate limit state, the analyses have shown a critical behavior in correspondence of the r.c. beam which connects the two concrete walls. The as-built reinforcement does not seem to match the ductility and strength requirements, so that a specific seismic retrofitting is required. After several attempts, the best solution seems to be represented by the introduction of a K-shaped or X-shaped bracing system, that provides the suitable resistant mechanism in the orthogonal direction with respect to the concrete walls. The linear and non-linear analyses confirm that such a provision is able to establish the correct seismic behavior.

## REFERENCES

[1] R. Ardito et al., The CUORICINO and CUORE double beta decay experiments, *Progress in Particle and Nuclear Physics*, **57**, 203-216, 2006.

[2] F. Alessandria et al., CUORE crystal validation runs: Results on radioactive contamination and extrapolation to CUORE background, *Astroparticle Physics*, **35**, 839-849, 2012.

[3] D. Kolymbas, *Tunneling and Tunnel Mechanics*, Springer, 2008.

[4] A. Castellani, G. Canetta, S. Pace, R. Guidotti The vaults of the Gran Sasso National Laboratory Halls, during the 2009 L'Aquila earthquake. Design of a monitoring system against earthquakes (in Italian), *Gallerie e Grandi Opere Sotterranee,* **103**, 25-39, 2012.

[5] A. Nucciotti et al., Design of the cryogen-free cryogenic system for the CUORE experiment, *Journal of Low Temperature Physics*, **151**, 662-668, 2008.

[6] F. Alessandria et al., The 4 K outer cryostat for the CUORE experiment: Construction and quality control, *Nuclear Instruments and Methods in Physics Research Section A*, **727**, 65-72, 2013.

[7] K.-J. Bathe, *Finite Element Procedures,* Prentice-Hall, 1996.

[8] M. Abe, J. Yoshida, Y. Fujino, Multiaxial behaviors of laminated rubber bearings and their modeling. I: Experimental study, *Journal of Structural Engineering*, **130**, 1119-1132, 2004.

[9] M. Abe, J. Yoshida, Y. Fujino, Multiaxial behaviors of laminated rubber bearings and their modeling. II: Modeling, *Journal of Structural Engineering*, **130**, 1133-1144, 2004.

COMPDYN 2017
6th ECCOMAS Thematic Conference on
Computational Methods in Structural Dynamics and Earthquake Engineering
M. Papadrakakis, M. Fragiadakis (eds.)
Rhodes Island, Greece, 15–17 June 2017

# ON THE DESIGN OF PERFORMANCE-BASED PENTAMODE BEARINGS

**A. Amendola[1], M. Titirtla[1], R. Penna[1], F. Fabbrocino[2]**

[1]Department of Civil Engineering, University of Salerno,
84084 Fisciano (Salerno), Italy
adaamendola1@unisa.it (A. Amendola), titirlamagdalini@gmail.com (M. Tititrla)
rpenna@unisa.it (R. Penna),

[2]Pegaso University, Department of Engineering
80132 Naples, Italy
francesco.fabbrocino@unipegaso.it (F. Fabbrocino)

**Keywords:** Pentamode Lattices, Seismic Isolation, Hardening, Tension-Capacity

**Abstract.**

*Pentamode lattices are particular metamaterials belonging to the class of extremal materials, which feature a primitive unit cell equipped with four rods meeting at a point. The potential of confined pentamode lattices in different engineering fields, such as, e.g., structural engineering, has not been largely explored yet. In this area, what is particularly interesting is the confinement of pentamode structural "crystals" between stiffening plates for the design of novel impact or seismic protection devices. Such a research line has recently appeared in the literature, with the aim of developing performance-based, vibration-isolation devices. The present study makes use of discrete-to-continuum approaches to the elastic moduli of pentamode lattices, and investigates the feasibility of pentamode structures as innovative anti-seismic devices. Experimental results and analytic formulae are employed to understand the mechanics of pentamode structures equipped with rigid and hinged connections, and the role played by design variables characterizing the aspect ratio of the structure and the response of the junctions. The final part of the work deals with the design of pentamode bearings that feature stiffness and strength properties similar to those of a commercial rubber bearing available on the market for the seismic isolation of buildings and bridges.*

## 1. INTRODUCTION

Pentamode lattices are mechanical metamaterials that exhibit the minimal coordination number required to achieve a fully positive definite elasticity tensor in three dimensions [1]-[11]. The peculiar mechanical behavior of pentamode lattices motivates researchers to investigate their use in transformation acoustics and elasto-mechanical cloak [6]. Their potential in different engineering fields, such as, e.g., structural engineering, has not been largely explored yet. In this area, what is particularly interesting is the use of pentamode structural "crystals" for the design of novel impact or seismic protection devices. Such a research line has recently appeared in the literature, with the aim of developing performance-based, vibration-isolation devices [8]-[11]. The results obtained so far in this field have shown several analogies between the mechanics of confined pentamode lattices [8]-[11] and that of elastomeric and triple friction pendulum bearings [12]- [25].

The present study aims at developing discrete-to-continuum approaches to the elastic moduli of pentamode lattices, and investigating the feasibility of pentamode structures as innovative anti-seismic devices. Our approach combines experimental results and analytic formulae to understand the mechanics of pentamode structures equipped with rigid connections, and the role played by design variables characterizing the aspect ratio of the structure and the response of the junctions. We begin with an experimental of the mechanical theory presented in [3] by comparing the theoretical previsions of such a theory with experimental results examining the mechanical response of additively manufactured, physical models of confined pentamode lattices [8]. We then pass to examine the response of computational models of pentamode bearings in the small strain regime, on comparing such a response with that of a commercial rubber bearing. We end by reviewing of the main results of the present study and drawing directions of future research.

## 2. COMPARISON BETWEEN THEORETICAL AND EXPERIMENTAL MODULI OF CONFINED PENTAMODE LATTICES

We present an experimental validation of the theoretical predictions of the pentamode elastic moduli given in Ref. [3] against experimental values obtained through quasi-static laboratory tests on physical samples of pentamode structures. The latter were additively manufactured through Electron Beam Melting (EBM), as described in Ref. [8]. Such samples are made of a Ti-6Al-4V titanium alloy featuring mass density $\rho_0$ = 4.42 g/cm$^3$; yield strength $\sigma_{y_0}$ = 910 MPa; Young's modulus $E_0$ = 120 GPa; and Poisson's ratio $\upsilon_0$ = 0.342. Let $n_x, n_y$ and $n_z$ respectively denote the number of unit cells placed along the $x, y$ and $z$ axes in the generic layer, with the $z$-axis placed in the vertical direction.

The experimental validation presented in the current section relates experimental and numerical values of vertical and horizontal stiffness properties of single-layer pentamode lattices featuring thick and slender macroscopic aspect ratios. The analyzed lattices are composed of two fcc unit cells in the horizontal plane ($n_a = n_x = n_y = 2$) and varying number of unit cells along quasi the $z$-axis. Following the notation given in Ref. [8], we hereafter name TPM the systems featuring $n_v = n_z = 2$ (*"thick pentamode materials")*, and SPM systems featuring $n_z = 4$ (*"slender pentamode materials"*). For each of such systems, we analyze physical samples featuring different values of $d$ ($d_1, d_2, d_3$) and fixed values of $a$

and $D$, as shown in Table 1. We use the label $i$ to denote the SPM /TMP sample featuring $d = d_i$.

| | $a$ [mm] | $D$ [mm] | $d_1$ [mm] | $d_2$ [mm] | $d_3$ [mm] |
|---|---|---|---|---|---|
| Built size (CAD size) | 30 (30) | 2.72 (2.71) | 0.49 (0.45) | 1.04 (0.90) | 1.43 (1.35) |

Table 1. Geometrical properties of physical samples of confined fcc pentamode lattices.

Table 2 shows the mean values and standard deviations of the experimental values of the secant horizontal stiffness $K_{h,eff}$, which were obtained for the above specimens under the analyzed values of the vertical load $F_v$. Such a quantity was defined as follows

$$K_{h,eff} = \frac{\left|F_h^{+}\right| + \left|F_h^{-}\right|}{\left|\delta_l^{+}\right| + \left|\delta_l^{-}\right|} \tag{1}$$

where the symbols + and – denote the maximum and minimum values, respectively, of the lateral force and the lateral displacement recorded during the shear tests presented in [8]. The results in Table 3 include the effective shear modulus defined as follows

$$G_{eff} = K_{h,eff} \cdot \frac{H}{A} \tag{2}$$

where $H$ denotes the height of the specimen, and $A = 2a \times 2a$ denotes the lattice covered area of the terminal plates. The effective modulus $G_{eff}$ is compared with the theoretical shear modulus $G_{th}$ obtained through the scale-bridgeing theory presented in Ref. [3]. The results in Figure 2 and Table 2 highlight a marked increase of $K_{h,eff}$ with increasing values of $d/a$, which follows by the increase in the bending rigidity of the lattice for growing sizes of the nodal junctions. Table 2 also shows a small dispersion of $K_{h,eff}$ with the vertical load $F_v$ in the small displacement regime. We observe that $G_{eff}$ is always larger than $G_{th}$, which is explained by the stiffening effect of the terminal plates in the physical models of pentamode lattices. Concerning SPM systems, the difference between $G_{eff}$ and $G_{th}$ is equal to 35.62% in SPM1, 26.91% in SPM2 and 27.02% in SPM3. For what instead concerns TPM systems, the difference between $G_{eff}$ and $G_{th}$ is equal to 6.18% in TPM1, 389.7% in TPM2 and 226.67% in TPM3.

The experimental results given in Ref. [8] include vertical force ( $F_v$ ) vs. vertical displacement ( $\delta_v$ ) tests, on considering one specimen for each examined $d/a$ ratio, and applying incremental weights on top of the specimens in quasi-static conditions (no lateral displacements were applied during such tests). We let $K_{v,eff}$ denote the effective stiffness defined as follows

$$K_{v,eff} = \frac{F_v^{\max}}{\delta_v^{\max}} \tag{3}$$

where $F_v^{\max}$ denotes the maximum applied vertical load and $\delta_v^{\max}$ denotes the corresponding vertical displacement. Table 2 shows the experimental values of the secant stiffness $K_{v,eff}$ obtained for SPM and TPM specimens, and the values of the effective Young's modulus defined as follows

$$E_{eff} = K_{v,eff} \cdot \frac{h}{A} \tag{4}$$

The experimental moduli (4) are compared in Table 2 with the theoretical moduli $E_{th}$ obtained through the mechanical theory presented in in Ref. [3]. Comparing results in Table 2 for SPM systems we observe that $E_{th}$ assumes values very similar to $G_{th}$ and that $E_{eff}$ is markedly greater than $E_{th}$, especially in presence of low $d/a$ ratios. The difference between $E_{eff}$ and $E_{th}$ is indeed equal to 85.82% in SPM1, 37.67% in SPM2 and 1.72% in SPM3, and is again explained by the presence of the terminal plates (as in the case of the increase of $G_{eff}/G_{th}$). It is interesting to note that both the $G_{eff}/G_{th}$ and $E_{eff}/E_{th}$ ratios decrease with increasing values of the $d/a$ ratio. Concerning TPM systems, we note that the difference between $E_{eff}$ and $E_{th}$ is indeed equal to 1.75% in TPM1, 1505.93% in TPM2 and 810.18% in TPM3. Overall, we are led to conclude that the elastic response of confined pentamode lattices is rather different from that of the unconfined pentamode lattices analyzed in Ref. [3], due to the marked confinement effect played by the stiffening plates against the deformation of the structure.

| | | SPM1 | SPM2 | SPM3 | TPM1 | TPM2 | TPM3 |
|---|---|---|---|---|---|---|---|
| $K_{h,eff}$ | mean (std Dev) | 2.02 (0.20) | 13.23 (0.24) | 30.73 (0.60) | 13.1 (-0.12) | 62.67 (-0.27) | 115.54 (-0.66) |
| $G_{eff}$ | | 70.43 | 444.77 | 1033.01 | 222.03 | 1061.89 | 1957.76 |
| $G_{th}$ | | 45.34 | 325.07 | 972.84 | 45.34 | 325.07 | 972.84 |
| $K_{v,eff}$ | | 15.55 | 95.22 | 295.81 | 43 | 175.03 | 470.5 |
| $E_{eff}$ | | 320,04 | 522,65 | 994,25 | 728.61 | 2965.27 | 7963.88 |
| $E_{th}$ | | 45.37 | 325.79 | 977.14 | 45.37 | 325.79 | 977.14 |

Table 2. Experimental values of the effective values of the horizontal stiffness $K_{h,eff}$ (N/mm); the shear modulus $G_{eff}$ (kPa); the vertical stiffness $K_{v,eff}$ (N/mm), and the Young modulus $E_{eff}$ (kPa) of SPM and TPM specimens. $G_{th}$ and $E_{th}$ denote the theoretical values of the shear modulus and Young modulus obtained through the mechanical model presented in Ref. [3].

## 3. ENGINEERING APPLICATIONS OF PENTAMODE BEARINGS

The present section aims at investigating the use of pentamode lattices as next-generation seismic isolators. According to the European Standard EN 15129 [21], a seismic isolator is a "*device possessing the characteristics needed for seismic isolation, namely, the ability to support a gravity load of superstructure, and the ability to accommodate lateral displacements*". Our current goal is to compare the mechanical response of computational models of pentamode lattices with that of a commercial rubber bearing with diameter $\varnothing 33.5"\,(0.8509\,m)$ and height $13.85"\,(0.3518\,m)$, which is composed of 29 rubber layers of $7\,mm$ each; 28 steel shims (spacers) of $3.04\,mm$ each; two terminal rubber layers of $31.8\,mm$ each and covers, without lead plug (isolator Type E [RB-800] produced by Dynamic Isolation Systems, Inc, McCarran, NV, USA).

As we have already observed, the multiscale approach to the elastic moduli of pentamode lattices presented in Ref. [3] is not accurate in predicting the elastic response of confined pentamode lattices, since it ignores the confinement effect played by the stiffening plates. In consideration of this, we now make use of the theory presented in Ref. [10] to design pentamode bearings that are equipped with hinged (stretching-dominated regime), and are obtained by repeating in the 3D space a sub-lattice of the fcc unit cell characterizing ordinary pentamode lattices. The latter is formed by two primitive cells, in place of the four primitive unite cells forming the fcc cell (sfcc pentamode lattices, cf. Fig. 1 of Ref. [10]).

We aim at showing that it is possible to design sfcc pentamode bearings equipped with hinged connections that feature the same vertical stiffness $K_v$ of the commercial rubber bearing under consideration. We focus our attention on a square multi-layer pentamode bearing with edge length $L$, which is formed by $n_a \times n_a$ sfcc unit cells in the horizontal plane and $n_z$ layers, denoting the solid volume fraction of the sfcc unit cell by $\phi$. Making use of the design formula given in Sect. 5 of Ref. [10], we obtain

$$\frac{2}{9} E_0 L \frac{n_a}{n_z} \phi = K_v \tag{5}$$

where $E_0$ denotes the Young modulus of the rods. In order to avoid material yielding under vertical loading, we also make use Eqn. (30) of Ref. [10] to predict the incremental axial stress induced by an incremental vertical displacement $\dot{w}$ of the device from the reference configuration, which corresponds to an incremental vertical displacement of the generic layer equal to $\dot{w}/n_z$. By setting such an incremental stress equal to $f_y \alpha$, where $f_y$ denotes the yielding stress of the material and $\alpha$ denotes a safety factor, we obtain the second design formula that follows

$$\frac{2}{3} E_0 n_a \frac{\dot{w}}{n_z L} = f_y \alpha \tag{6}$$

Upon solving the above design formulae (5) and (6) for $n_a$ and $\phi$, we obtain

$$n_a = \frac{3 \alpha f_y n_z L}{2 E_0 \dot{w}} \quad , \quad \phi = \frac{3 K_v \dot{w}}{\alpha f_y L^2} \tag{7}$$

Let us now employ steel bars grade S335JH, with Young modulus $E_o = 210$ GPa and yield strength $f_y = 355$ MPa [27][28], and let us assume $L = 600$ mm, $\dot{w} = 1.00$ mm, $\alpha = 0.5$, and and $K_v = 733$ kN/mm. Table 5 and Figure 5 illustrate different designs of sfcc pentamode bearings that correspond to such a set of design parameters, and exhibit different numbers of layers $n_z$. It is seen that the bilayer pentamode bearing of design (c) exhibits horizontal and vertical dimensions rather similar to those of the commercial bearing under consideration.

| | $n_z$ | $n_a$ | $a$ [mm] | $H$ [mm] |
|---|---|---|---|---|
| (a) | 3 | 2 | 300 | 450 |
| (b) | 4 | 3 | 200 | 400 |
| (c) | 2 | 2 | 300 | 300 |

Table 3. Geometrical properties of square sfcc pentamode bearings replicating a commercial rubber bearing.

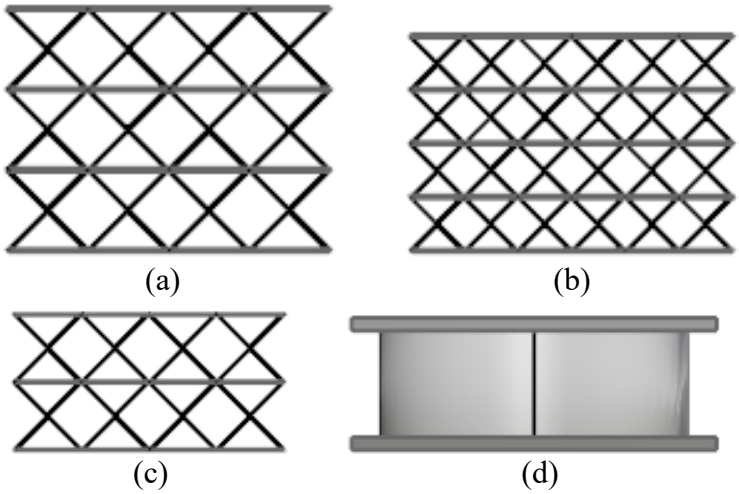


Figure 1. Designs of sfcc pentamode bearings (a, b, c) that exhibit equal vertical stiffness and load-carrying capacity of a commercial rubber-bearing (d).

## 4. CONCLUDING REMARKS

We have presented novel versions of pentamode materials: artificial structural crystals showing shear moduli markedly smaller than the bulk modulus [3]-[5]. On examining fcc pentamode bearings equipped with rigid connections of variable size and geometry, we have observed that the bulk modulus of such systems is always larger than the shear modulus. The validation of theoretical predictions of the elastic moduli of such systems against the experimental data presented in Sect. 3 highlighted that the elastic response of confined pentamode lattices is rather different from that of the unconfined pentamode lattices analyzed in Ref. [3], due to the marked confinement effect played by the stiffening plates against the deformation of the structure.

As we already noticed, the ability of pentamode lattices to show very soft and very stiff deformation modes, which has been recognized both in the bending- [9] and in the strecthing-dominated [10] regimes of such structures, suggests they are potentially suitable for use as seismic isolators [8][9][29][30]. The major analogy between the mechanics of confined pentamode lattices and that of seismic isolation devices alternating rubber layers and

stiffening plates [8][11][15] consists of the fact that, in both cases, the plates forming such laminated structures stiffen the compressive deformation mode of the system, and, at the same time, keep its compliance against shear actions sufficiently large.

Unlike most other seismic isolators, where the response depends entirely on the properties of the materials used, we wish to remark the response of pentamode lattices depends mostly on their geometry. This is advantageous, as their response can be easily tuned by altering the geometry to control the vertical and horizontal stiffness for each application [8]. As a matter of fact, by simulating the mechanical response of physical models of sfcc systems in the large elastic strain regime, it has been observed a stiffening effect in terms of the lateral force vs. lateral displacement response with increasing amplitude of lateral displacements (cf. Ref. [11]). It is worth noting that a similar hardening response is a desirable performance for seismic isolators potentially experiencing large displacements, like, e.g., triple pendulum bearings [18][19]. In addition, pentamode bearings are tension-capable, i.e., can bear both compression and tension vertical loads during seismic excitations, due to the nonzero tensile strength of the rods forming the pentamode lattices (refer, e.g., to the recent paper [17], and references therein, for the technical relevance of tension-capable bearings).

In Sect. 3 we have designed innovative seismic isolators based on either fcc or sfcc pentamode lattices confined between stiffening plates. The soft modes of such materials have been controlled by tuning of the mechanical properties and the geometry of members and junctions. We have shown that such novel isolators can exhibit mechanical response similar to that of conventional rubber bearings, provided that the material and the geometry of the lattice are suitably designed.

We may conclude that pentamode bearings offer several potential advantages over traditional structural bearings [16]-[18], which essentially follow from the fact that the mechanical properties of such systems are driven by the geometry of the lattice microstructure, more than the chemical composition of the material (i.e, such systems behave as mechanical metamaterials). It is worth noting that it is possible to play with the lattice microstructure in order to achieve the desired combination of shear and compression moduli. Additionally, the choice of the material offers additional design opportunities, both in terms of the elastic response, and for what concerns the energy dissipation properties of the system (cf. Ref.[8]). We have also observed that it is possible to design laminated structures that feature multiple pentamode layers equipped with different materials and properties, while in laminated rubber the only lamination variable relative to the soft layers consists of the use of natural or synthetic rubber (Sect. 3) [31]-[33]. Finally, pentamode bearings can be manufactured on employing rapid prototyping techniques that make use of single or multiple materials (metals, polymers, etc.) [31]-[36].

Future extension of the present research will regard experimental testing of real-scale physical models of pentamode bearings [38]; the modeling of facture damage in the rods of pentamode bearings under stress [39]; discrete-to-continuum approaches to the mechanics of multilayered structures [67]-[69]; and the use of pentamode lattices within innovative materials and structures [70]-[71].

## REFERENCES

[1] G.W. Milton, A.V. Cherkaev, "*Which Elasticity Tensors are Realizable?*" J Eng Mater-T 1995; 117(4), 483-493.

[2] G. Gurtner, M. Durand, 2014. Stiffest elastic networks, Proc. R. Soc. A 470, 20130611.

[3] A.N. Norris, 2014. Mechanics of elastic networks. Proc. R. Soc. A 470, 20140522.

[4] M. Schittny, T. Bückmann, M. Kadic, M. Wegener, "*Elastic measurements on macroscopic three-dimensional pentamode metamaterials*". Appl Phys Lett 2013; 103.

[5] M. Kadic, T. Bückmann, N. Stenger, M. Thiel, M. Wegener, "*On the practicability of pentamode mechanical metamaterials*". Appl Phys Lett 2012; 100.

[6] T. Bückmann, M. Thiel, M. Kadic, R. Schittny, M. Wegener, "*An elastomechanical unfeelability cloak made of pentamode metamaterials*". Nat Common 2014; 5, 4130.

[7] M. Kadic, T. Bückmann, R. Schittny, Wegener M., 2013. On anisotropic versions of three-dimensional pentamode metamaterials. New J. Phys. 15, 023029.

[8] A. Amendola, C.J. Smith, R. Goodall, F. Auricchio, L. Feo, G. Benzoni, F. Fraternali, Experimental response of additively manufactured metallic pentamode materials confined between stiffening plates. *Composite Structures*, **142**, 254-262, 2016.

[9] A. Amendola, G. Carpentieri, L. Feo, F. Fraternali, 2016. Bending dominated response of layered mechanical metamaterials alternating pentamode lattices and confinement plates. Compos. Struct. 151,71-77.

[10] F. Fraternali, A. Amendola, 2017. Mechanical modeling of innovative metamaterials alternating pentamode lattices and confinement plates. J. Mech. Phys. Solids, 99, 259-271.

[11] A. Amendola, G. Benzoni, F. Fraternali, 2016. Non-linear elastic response of layered structures, alternating pentamode lattices and confinement plates. Compos Part B-Eng 2016, http://dx.doi.org/10.1016/j.compositesb.2016.10.027.

[12] R.I. Skinner, W.H. Robinson, G.H. Mcverry, 1993. An introduction to seismic isolation. Wiley.

[13] J.M. Kelly, 1993. Earthquake-resistant design with rubber. London: Springer-Verlag.

[14] G. Benzoni, C. Casarotti, 2009. Effects of Vertical Load, strain rate and cycling on the response of lead-rubber seismic isolators. J. Earthquake Eng. 13(3), 293-312.

[15] M. Higashino, H. Hamaguchi, S. Minewaki, S. Aizawa, 2003. Basic characteristics and durability of low-friction sliding bearings for base isolation. Earthquake Eng. Eng. Seismolog. 4(1), 95-105.

[16] G. P. Warn, A. S. Whittaker, M.C. Constantinou, 2007. Vertical stiffness of elastomeric and lead- rubber seismic isolation bearings. J. Struct. Eng.-ASCE 133 (9), 1227-1236.

[17] Z. Zhou, J. Wong, S. Mahin, 2016. Potentiality of using vertical and three-dimensional isolation systems in nuclear structures, Nucl. Eng. Technol, 48 (5), 1237-1251.

[18] T.C. Becker, S.A. Mahin, 2012. Experimental and analytical study of the bi-directional behavior of the triple friction pendulum isolator. Earthquake Eng. Struct. Dyn. 41, 355–373.

[19] D.M. Fenz, M.C. Constantinou, 2008. Modeling triple friction pendulum bearings for response-history analysis. Earthq. Spectra 24, 1011-1028.

[20] D. R. Pant, A. C. Wijeyewickrema, M. A. ElGawady, 2013. Appropriate viscous damping for nonlinear time-history analysis of base-isolated reinforced concrete buildings. Earthquake Engng Struct. Dyn. 42(4), 2321-2339.

[21] European Committee for Standardization. Anti-seismic devices, EN 15129. Brussels, Belgium, 2009.

[22] M. Higashino, H. Hamaguchi, S. Minewaki, S. Aizawa. "*Basic characteristics and durability of low-friction sliding bearings for base isolation*". Earthquake Engineering and Engineering Seismology 2003; 4(1), 95-105.

[23] Toopchi-Nezhad H, Tait MJ, Drysdale RG. Bonded versus unbonded strip fiber reinforced elastomeric isolators: finite element analysis. Compos Struct 2014;93(2):850-9.

[24] Osgooei PM, Tait MJ, Konstantinidis D. Three-dimensional finite element analysis of circular fiber-reinforced elastomeric bearings under compression. Compos Struct 2014;108(1):191-204.

[25] Osgooei PM, Tait MJ, Konstantinidis D. Finite element analysis of unbonded square fiber-reinforced elastomeric isolators (FREIs) under lateral loading in different directions. Compos Struct 2014;113(1):164-73.

[26] J.M. Kelly, J.-W Lai, "*The use of tests on high-shape-factor bearings to estimate the bulk modulus of natural rubber*". Seismic Isolation and Protective Systems 2011; 2(1), 21-33.

[27] EN 10210-2:2006, Hot finished structural hollow sections of non-alloy and fine grain steels - Part 2: Tolerances, dimensions and sectional properties.

[28] European Commission, 2014. HORIZON 2020 Work Programme 2014-2015, PART 5.ii, 98.

[29] Fraternali F., Carpentieri G., Montuori R., Amendola A., Benzoni G., 2015.On the use of mechanical metamaterials for innovative seismic isolation systems, COMPDYN 2015 - 5th ECCOMAS Thematic Conference on Computational Methods in Structural Dynamics and Earthquake Engineering, 349-358.

[30] Fabbrocino, F., Amendola, A., Benzoni, G., Fraternali, F., Seismic application of pentamode lattices. Ingegneria Sismica/International Journal of Earthquake Engineering 2016; 1-2, 62-71.

[31] A. Amendola, E.H. Nava, R. Goodall, I. Todd, R.E. Skelton, F. Fraternali, On the additive manufacturing, post-tensioning and testing of bi-material tensegrity structures, *Composite Structures*, **131**, 66-71, 2015.

[32] A. Amendola, G. Carpentieri, L. Feo, F. Fraternali, "*Bending dominated response of layered mechanical metamaterials alternating pentamode lattices and confinement plates*". Compos Struct 2016, 71-77.

[33] A. Amendola, F. Fabbrocino, L. Feo, F. Fraternali, "*Dependence of the mechanical properties of pentamode materials on the lattice microstructure*", (2016) ECCOMAS Congress 2016 - Proceedings of the 7th European Congress on Computational Methods in Applied Sciences and Engineering, 1, pp. 2134-2150.

[34] I. Farina, F. Fabbrocino, G. Carpentieri, M. Modano, A. Amendola, R. Goodall, L. Feo, F. Fraternali, *On the reinforcement of cement mortars through 3D printed polymeric and metallic fibers,* Composites Part B: Engineering, **90**, 76-85, 2016.

[35] R. Singh, S. Singh, F. Fraternali, "*Development of in-house composite wire based feed stock filaments of fused deposition modelling for wear-resistant materials and structures*". Compos Part B-Eng 2016; 98, 244-249.

[36] I. Farina, F. Fabbrocino, F. Colangelo, L. Feo, F. Fraternali, "*Surface roughness effects on the reinforcement of cement mortars through 3D printed metallic fibers*". Compos Part B-Eng 2016; 99, 305-311.

[37] R. Singh, R. Kumar, L. Feo, F. Fraternali; "*Friction welding of dissimilar plastic/polymer materials with metal powder reinforcement*". Compos Part B-Eng, 2016; 101, 77-86.

[38] M. Modano, F. Fabbrocino, A. Gesualdo, G. Matrone, I. Farina, F. Fraternali, "*On the forced vibration test by vibrodyne*" COMPDYN 2015 - 5th ECCOMAS Thematic Conference on Computational Methods in Structural Dynamics and Earthquake Engineering, 209-217.

[39] F. Fraternali, Free Discontinuity Finite element models in two-dimensions for in-plane crack problems*, Theoretical and Applied Fracture Mechanics*, **47**, 274-282, 2007.

[40] F. Fraternali, S. Spadea, L. Ascione, Buckling behavior of curved composite beams with different elastic response in tension and compression. *Composite Structures*, **100**, 280-289, 2013.

[41] G. Lomiento , N. Bonessio, G. Benzoni, Friction Model for Sliding Bearings under Seismic Excitation, *Journal of Earthquake Engineering*, **17**(8):1162-1191, 2013.

[42] M. Budek, M. J. N. Priestley, G. Benzoni, The Effect of External Confinement on Flexural Hinging in Drilled Pile Shafts, *Earthquake Spectra*, **20** (1), 1-24, 2004.

[43] Hae-Bum Yun, Sami F. Masri, Raymond W. Wolfe, Gianmario Benzoni , Data-driven methodologies for change detection in large-scale nonlinear dampers with noisy measurements, *Journal of Sound and Vibration*, **322**, Issues 1–2, 24 April 2009, Pages 336–357.

[44] D. D'Ayala, G. Benzoni, Historic and Traditional Structures during the 2010 Chile Earthquake: Observations, Codes, and Conservation Strategies. *Earthquake Spectra*, **28** (S1), S425-S451, 2012.

[45] N. Bonessio, G. Lomiento, G. Benzoni, Damage identification procedure for seismically isolated bridges, *Structural Control Health Monitoring*, **19**(5), 565–578, 2012.

[46] G. Benzoni, C. Casarotti , Effects of Vertical Load, Strain Rate and Cycling on the Response of Lead-Rubber Seismic Isolators, *Journal of Earthquake Engineering* ,**13**, 2009.

[47] A. Budek-Schmeisser, G. Benzoni, Rational seismic design of precast, prestressed concrete piles, *PCI Journal*, **53**(5), 40-53, 2008.

[48] G. Benzoni, M. J. N. Priestley, Seismic response of linked marginal wharf segments, *Journal of Earthquake Engineering* **74**, 513-539, 2003.

[49] F. Fraternali, I. Farina, G. Carpentieri, A discrete-to-continuum approach to the curvatures of membrane networks and parametric surfaces, *Mechanics Research Communications*, **56**, 18-15, 2014.

[50] L. Ascione, F. Fraternali, A penalty model for the analysis of composite curved beams, *Computers & Structures*, **45**, 985-999, 1992.

[51] F. Fraternali, J.N. Reddy, A penalty model for the analysis of laminated composite shells, *International Journal of Solids and Structures*, **30**, 3337-3355, 1993.

[52] A. Amendola, G. Carpentieri, M. De Oliveira, R.E. Skelton, F. Fraternali, Experimental investigation of the softening-stiffening response of tensegrity prisms under compressive loading. *Composite Structures*, **117**, 234-243, 2014.

[53] F. Fraternali, G. Bilotti, Non-Linear Elastic Stress Analysis in Curved Composite Beams. *Computers & Structures*, **62**, 837-869, 1997.

[54] F. Fraternali, G. Carpentieri, A. Amendola, On the mechanical modeling of the extreme softening/stiffening response of axially loaded tensegrity prisms. *Journal of the Mechanics and Physics of Solids*, **74**, 136-157, 2015.

[55] D. Ngo, F. Fraternali, C. Daraio, Highly Nonlinear Solitary Wave Propagation in Y-Shaped Granular Crystals with Variable Branch Angles. Physical Review E, **85**, 036602-1-10, 2012.

[56] R.E. Skelton, F. Fraternali, G. Carpentieri, A. Micheletti, Minimum mass design of tensegrity bridges with parametric architecture and multiscale complexity. *Mechanics Research Communications*, 58, 124-132, 2014.

[57] A. Leonard, F. Fraternali, C. Daraio, Directional wave propagation in a highly nonlinear square packing of spheres. *Experimental Mechanics*, **53**(3), 327-337, 2013.

[58] F. Fraternali, G. Carpentieri, A. Amendola, R.E. Skelton, V. F. Nesterenko, Multiscale tunability of solitary wave dynamics in tensegrity metamaterials. *Applied Physics Letters*, **105**, 201903, 2014.

[59] F. Fraternali, I. Farina, C. Polzone, E. Pagliuca, L. Feo, On the use of R-PET strips for the reinforcement of cement mortars. *Composites. Part B*, **46**, 207-210, 2013.

[60] J.R. Raney, F. Fraternali, A. Amendola, C. Daraio, Modeling and In Situ Identification of Material Parameters for Layered Structures based on Carbon Nanotube Arrays. *Composite Structures*, **93**, 3013–3018, 2011.

[61] C. Daraio, D . Ngo, V. F. Nesterenko, F. Fraternali, Highly Nonlinear Pulse Splitting and Recombination in a Two Dimensional Granular Network. *Physical Review E*, **82**, 036603, 2010.

[62] F. Fraternali, A. Marino, T. Elsayed, A. Della Cioppa, On the structural shape optimization via variational methods and evolutionary algorithms. Mechanics of Advanced Materials and Structures, **18**, 225-243, 2011.

[63] F. Fraternali, S. Spadea, V.P. Berardi, Effects of recycled PET fibers on the mechanical properties and seawater curing of Portland cement-based concretes. *Construction and Building Materials*, **61**, 293-302, 2014.

[64] T. Blesgen, F. Fraternali, J.R. Raney, A. Amendola, C. Daraio, Continuum Limits of Bistable Spring Models of Carbon Nanotube Arrays accounting for Material Damage. *Mechanics Research Communications*, **45**, 58-63, 2012.

[65] F. Fraternali. A Mixed Lumped Stress – Displacement Approach to the Elastic Problem of Masonry Walls. Mechanics Research Communications, **38**, 176-180, 2011.

[66] F. Fraternali, M. Negri, M. Ortiz, On the Convergence of 3D Free Discontinuity Models in Variational Fracture. *International Journal of Fracture*, **166**(1-2), 3-11, 2010.

[67] F. Fraternali, C.D Lorenz, G. Marcelli, On the estimation of the curvatures and bending rigidity of membrane networks via a local maximum-entropy approach, *Journal of Computational Physics*, **231**, 528-540, 2012.

[68] F. Fraternali, G. Marcelli, "*A multiscale approach to the elastic moduli of biomembrane networks*". Biomech Model Mechan 2012: 11(7), 1097-1108.

[69] B. Schmidt, F. Fraternali, Universal formulae for the limiting elastic energy of membrane networks, *Journal of the Mechanics and Physics of Solids*, **60**, 172-180, 2012.

[70] A. Amendola, G. Benzoni, F. Fraternali, Non-linear elastic response of layered structures, alternating pentamode lattices and confinement plates. *Composite Part B, Engineering*, Online first, DOI: 10.1016/j.compositesb.2016.10.027, 2016

[71] F. Fraternali, G. Carpentieri, R. Montuori, A. Amendola, G. Benzoni, On the use of mechanical metamaterials for innovative seismic isolation systems, COMPDYN 2015 - 5th ECCOMAS Thematic Conference on Computational Methods in Structural Dynamics and Earthquake Engineering, 349-358.

COMPDYN 2017
6th ECCOMAS Thematic Conference on
Computational Methods in Structural Dynamics and Earthquake Engineering
M. Papadrakakis, M. Fragiadakis (eds.)
Rhodes Island, Greece, 15–17 June 2017

# INNOVATIVE DEVICES FOR THE BASE ISOLATION OF EXISTING BUILDINGS

**F. Fabbrocino[1], M. Titirla[2], A. Amendola[2], G.Benzoni[3], F. Fraternali[2]**

[1]Pegaso University, Department of Engineering, 80132 Naples, Italy
francesco.fabbrocino@unipegaso.it (F. Fabbrocino)

[2] Department of Civil Engineering, University of Salerno, 84084 Fisciano (SA), Italy
titirlamagdalini@gmail.com (M. Titirla), adaamendola1@unisa.it (A. Amendola),
f.fraternali@unisa.it (F. Fraternali),

[3]Department of Structural Engineering, University of California San Diego, San Diego, CA 92161, USA. gbenzoni@ucsd.edu (G. Benzoni)

**Keywords:** Seismic Isolation; Historical buildings; Pentamode Lattices

## Abstract

*It is well known that pre-existing buildings are often inadequate to resist strong ground motions, and that their seismic rehabilitation is not an easy task. Several studies available in the to-date literature have shown that seismic isolation is a cost-effective and efficient method that can be employed to protect existing structures from earthquakes. A new class of performance-based seismic isolators has been proposed in recent studies, making use of pentamode lattices confined between stiffening plates. The present work illustrates experimental results concerned with shear and compression tests on physical (reduced-scale) models of pentamode bearings, and discusses the use of such systems for the base isolation of existing buildings. Given results highlight the special ability of such systems to behave as tension-capable and performance-based systems, whose mechanical properties are driven largely by the geometry of the lattice microstructure (i.e, such systems behave as mechanical metamaterials), and can be finely adjusted to the properties of the structure to be protected.*

## 1. INTRODUCTION

Extremal materials that are receiving increasing interest are the so-called pentamode lattices, which consist of diamond-like lattices featuring five soft modes of deformation (unit cell with four rods meeting at a point) [1]. Such lattices exhibit very low shear moduli (theoretically equal to zero) [1], and may be able to stop or dramatically attenuate shear waves [2]. Physical models of pentamode materials have been fabricated through additive manufacturing (AM) techniques over the last few years, both at the macro- [3] and at the micro-scale [3]. Schittny et al. [3] have studied the experimental behavior of macroscopic, polymeric samples of pentamode lattices in the elastic regime: the results obtained by such authors prove that the elastic moduli of pentamode materials are strongly related to the geometry of the lattice micro-structure, being markedly affected by the dimensions of the rods forming the lattice, and particularly sensitive to the ratio between the diameter $d$ of the connections between the rods and the lattice constant $a$. The experimental Young's modulus $E$ of the lattice has been found approximately three times stiffer than the experimental shear modulus $G$. The results presented in [3] also show that the ratio between the bulk modulus $B$ and the shear modulus $G$ strongly increases by reducing the contact area between the rods. Similar results have been found at the microscale by Kadic et al. [3]. Polymeric samples of pentamode lattices have been fabricated by such authors using dip-in direct-laser-writing (DLW) optical lithography, a technique well suited to build three-dimensional structures across a range of scales from micro to small [5]. Experimental and numerical results given in [3] and [3] demonstrate that the mechanical behavior of pentamode lattices replicates that of fluids in the limit of $d \to 0$, when the shear modulus $G$ tends to zero. For finite, nonzero values of $d$, it has been found that the $B/G$ ratio is extremely high, even if $G$ is positive and nonzero [3][3]. Because of their unusual mechanical features, pentamode materials have been proposed for transformation acoustics and elasto-mechanical cloak (refer, e.g., to the recent paper [6] and the references therein), but their potential in different engineering fields is still only partially explored.

The present study investigates the elastic and post-elastic responses of additively manufactured pentamode lattices confined between stiffening plates. We analyze metallic samples obtained through additive manufacturing by Electron Beam Melting (EBM) of a powder of the titanium alloy Ti-6Al-4V [7][8][9], for different aspect ratios of the unit-cell, and two macroscale aspect ratios (slender and thick samples). We find that the confinement of pentamode lattices between stiffening plates greatly affects the elastic response of the overall structure, compared with the case of unconfined, infinite pentamode lattices [10]. The obtained results highlight several similarities between the elastic response of confined pentamode materials and the analogous response of elastomeric bearings composed of rigid steel or fiber-reinforced composite layers and soft layers of natural or synthetic rubber [11]-[17]. Concerning the post-elastic response, we observe that the examined pentamode materials feature acceptable energy dissipation capacity, and ranges of supplemental damping in line with values of common isolation devices. Their use for the base isolation of existing buildings is discussed.

## 2. MATERIALS AND METHODS

### 2.1 Physical models of confined pentamode materials

We manufactured pentamode lattices confined by stiffening plates and made by the titanium alloy Ti-6Al-4V (hereafter simply denoted by Ti6Al4V) through the Arcam S12 EBM facility at the Department of Materials Science and Engineering, University of Sheffield. Such an additive manufacturing (AM) technology allows the manufacture of features with size down to 0.4 mm by progressively depositing, heating and melting layers of Ti6Al4V powder, with the

melted regions in each layer defined according to a CAD model of the specimen to be manufactured [7][8]. It is worth noting that the size of the specimen designed by CAD does not correspond perfectly to the built object. The beam scan strategies and the surface roughness will result in larger (in diameter) printed members [9]. The main properties of the employed titanium alloy, when in the fully dense state, are given in Table 1 [18].

| | |
|---|---|
| mass density [g/cm$^3$] | 4.42 |
| yield strength [MPa] | 910.00 |
| Young's modulus [GPa] | 120.00 |
| Poisson's ratio | 0.342 |

Table 1. Main physical and mechanical properties of the fully dense isotropic polycrystalline Ti6Al4V titanium alloy [18].

Figure 1 shows the extended face-centered-cubic (fcc) unit cell of a pentamode lattice formed by sixteen rods that are composed of two truncated bi-cones featuring large diameter $D$ at the mid-span and small diameter $d$ at the extremities [2][3][3][5][6]. Upon selecting the lattice constant $a = 30$ mm and $D = 2.72$ mm ($D/a \approx 9\%$), we manufactured pentamode specimens with the unit cell shown in Figure 1, using three different values of $d$: $d_1 = 0.49$ mm ($d_1/a = 1.6\%$); $d_2 = 1.04$ mm ($d_2/a = 3.5\%$); and $d_3 = 1.43$ mm ($d_3/a = 4.8\%$, cf. Table 2). It is worth remarking that the limit $d/a \to 0$ corresponds to a perfectly pin-jointed lattice (stretching-dominated response), while the case with $d/a > 0$ corresponds to a lattice featuring nonzero bending rigidities of nodal junctions and rods, which deforms through both stretching of rods and bending of rods and nodes [10].

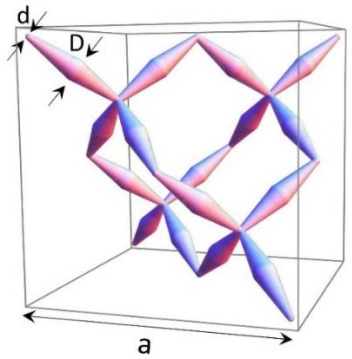


Figure 1. Extended fcc unit cell of the pentamode lattices analyzed in the present study.

| | a [mm] | D [mm] | $d_1$ [mm] | $d_2$ [mm] | $d_3$ [mm] |
|---|---|---|---|---|---|
| Built size | 30 | 2.72 | 0.49 | 1.04 | 1.43 |
| (CAD size) | (30) | (2.71) | (0.45) | (0.90) | (1.35) |

Table 2. Geometrical parameters of the EBM built pentamode materials (CAD sizes in brackets).

We additively manufactured two different sets of pentamode specimens:

(a) *"Slender Pentamode Materials"* (SPM): obtained by replicating the extended fcc unit cell of Figure 1 $2x2$ times in the horizontal plane, 4 times along the vertical axis, and confining the $2x2x4$ lattice between Ti6Al4V plates with 80 mm edge and $t_p = 1$ mm thickness (see Figure 2);

(b) *"Thick Pentamode Materials"* (TPM): obtained by replicating the extended fcc unit cell of Figure 1 $2x2$ times in the horizontal plane, 2 times along the vertical axis, and confining the $2x2x2$ lattice between the above mentioned plates (see Figure 3).

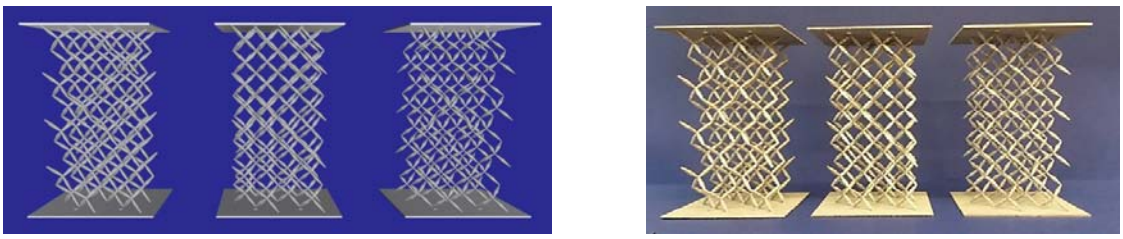

(a) (b)

Figure 2. CAD (a) and EBM (b) models of slender (SPM) specimens ( $2x2x4$ extended unit cells).

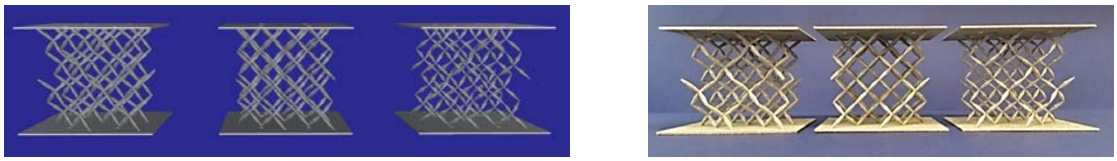

(a) (b)

Figure 3. CAD (a) and EBM (b) models of thick (TPM) specimens ( $2x2x2$ extended unit cells).

Hereafter, we name SPM1, SPM2 and SPM3 the SPM-specimens with $d = d_1$, $d = d_2$, and $d = d_3$, respectively. Similarly, TPM1, TPM2 and TPM3 $d = d_1$, $d = d_2$, and $d = d_3$, respectively. We built three different SPM specimens and one TPM specimen for each analyzed $d/a$ ratio. It is well known that the EBM manufacturing process creates solid material with some level of porosity (typically below 0.2% if suitable parameters for the alloy are used in the machine) instead of fully dense materials for both solid structures [9] and those intended to contain free space [8]. Based on a recent, detailed study of porosity in EBM titanium made with the same conditions used for the current material [9], we hereafter assume the internal porosity of such a material is of the order of 0.2%, and its Young modulus $E_m$ is therefore approximately equal to that of the fully dense Ti6Al4V alloy (Table 1).

### 2.2 Experimental setup

An in-house experimental setup was assembled to apply lateral force-displacement histories under constant vertical load on the pentamode specimens described in the previous section (Figure 4).

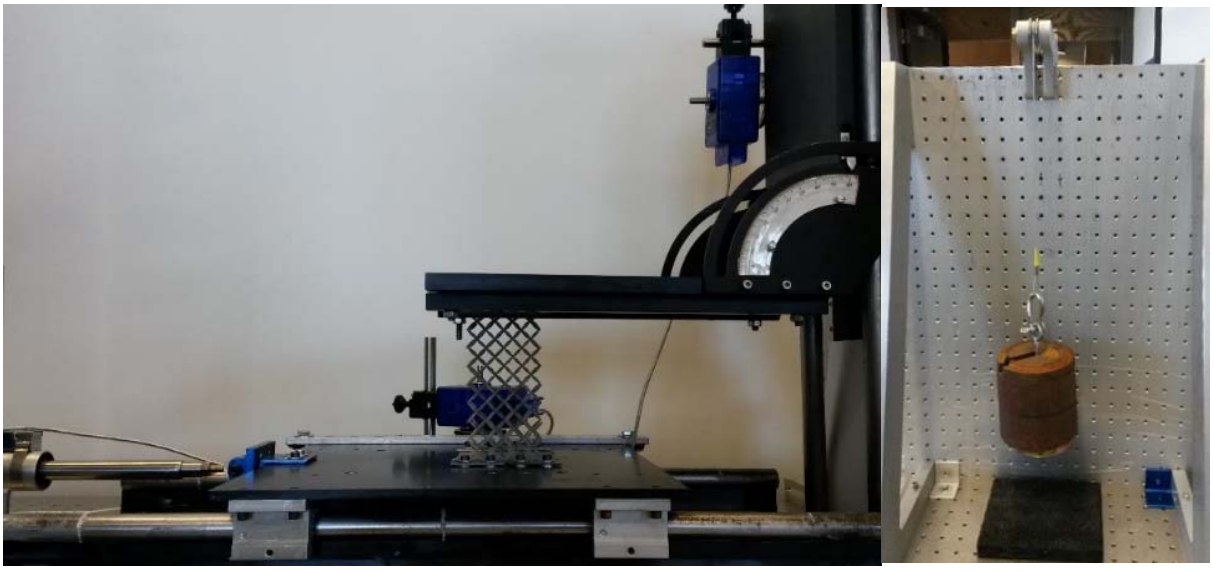

Figure 4. Left: overall view of the experimental setup. Right: counter balancing system introduced to remove platen self-weight.

An L-shaped plate, sliding vertically over linear bearings, allows the application of the vertical load through calibrated weights. The selfweight of the plate is removed with a counter balancing system of pulley and weights (Figure 4). The top base of the specimen is firmly connected to the plate by clamping strips located all around the base edges. The same clamping mechanism is applied to the bottom base of the specimen that is connected to the horizontally sliding table (Figure 5). Horizontal displacements are applied through an actuator connected to the sliding table and reacting against a solid metal block. The force rating of the actuator is 300 lb (1.3 kN), with a displacement range of +/-100 mm. Forces are acquired by a load cell installed between the back of the actuator and the reaction block. Vertical and lateral displacements are measured with rotary motion sensors.

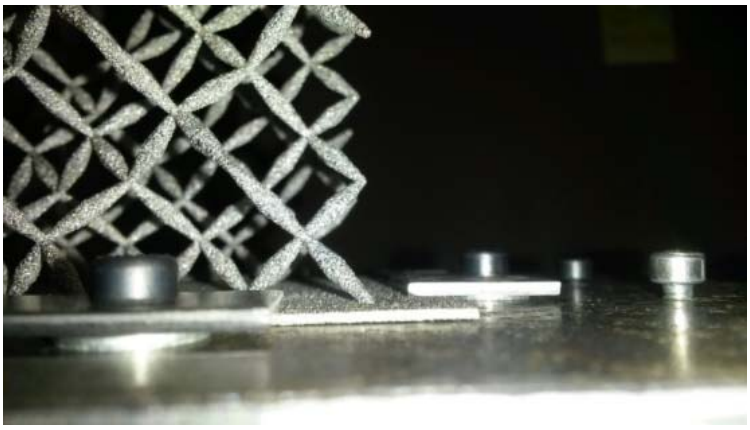

Figure 5. Connection of the specimen to the sliding table.

The same setup allows the application of the vertical load through calibrated weights while no horizontal motion is applied. With this procedure compression tests were completed by manual application of weights and automatic recording of vertical displacements of the plate. Preliminary to any actual test, the setup was subjected to a shakedown phase to assess the frictional force components and to verify alignments and parallelisms. The test data were consistently processed with the removal of friction from the testing equipment.

## 3. EXPERIMENTAL RESULTS

The present section illustrates the results of the laboratory tests that we conducted to characterize the mechanical response of the pentamode materials illustrated in Sect. 2.1. We begin by estimating the elastic moduli of slender and thick pentamode materials through cyclic lateral force-displacement tests at constant vertical loading, and monotonic vertical force-displacement tests under zero horizontal force. Next, we investigate the inelastic response of the analyzed materials via (cyclic and monotonic) lateral force-displacement tests conducted up to specimen's failure. Figure 6 illustrates pictures of selected slender and thick specimens extracted from in-situ videos of lateral force-displacement tests.

We investigated the post-elastic response of SPM and TPM specimens by conducting cyclic lateral force - displacement tests in displacement control up to specimen's failure (under the vertical load $F_v = 44.45$N, and the strain rate $\dot{\delta}_h = 0.8$ mm/sec, cf. Figure 7-Figure 8). In the case of SPM specimens, we also performed monotonic lateral force-displacement tests up to specimen's failure (Figure 7). All such tests were carried out starting from the virgin state, for a single specimen of each microstructure aspect ratio $d/a$ (cf. Sect. 2.1). Figure 7 shows the measured envelope force– displacement $F_h$-$\delta_h$ curves, where the labels a,b and c indicate the final point of the initial linear branch, the peak of horizontal force and the failure point, respectively. For these specimens, point c corresponds to the ultimate vertical bearing capacity. The actual $F_h$-$\delta_h$ curves of the monotonic tests on SPM specimens showed marked oscillations in the unstable phase characterized by a decrease of $F_h$ for increasing values of $\delta_h$, due to progressive joint failure. The final collapse of the specimen occurred due to the rupture of several terminal nodes placed along the stretched diagonals (Figure 9).

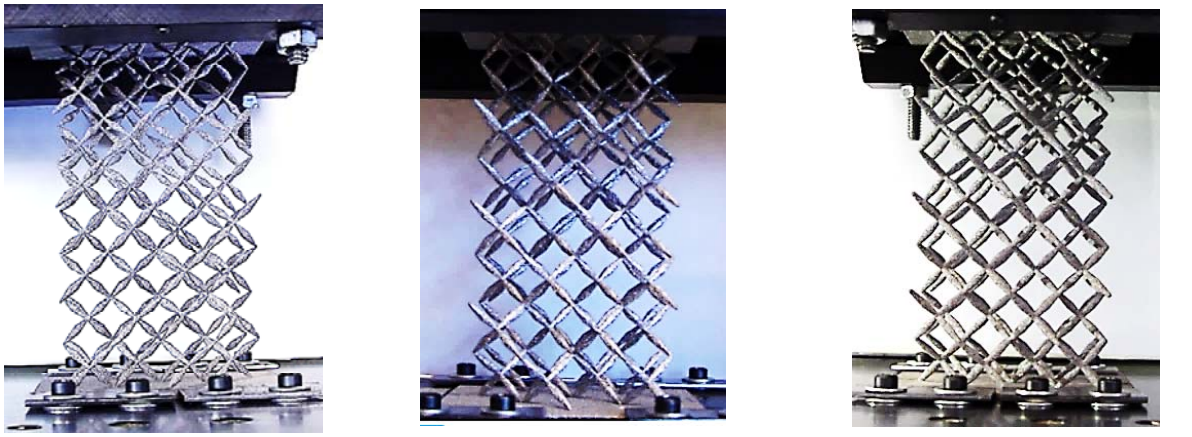

(a): SPM1 (b): SPM2 (c): SPM3

(d): TPM1 (e): TPM2 (f): TPM3

Figure 6. Frames from in-situ videos of lateral displacement tests on SPM and TPM specimens.

The results in Figure 7 highlight an initial hardening branch of the post-elastic response of each examined specimen. Such a branch is followed by a second post-elastic branch with negative tangent stiffness, which progressively leads the specimen to collapse. The coordinates of the above *a-b-c* points are provided in Table 3, together with the ductility values computed as follows

$$\mu = \frac{\delta_h - \delta_{h,el}}{\delta_{h,el}} \tag{6}$$

where $\delta_h$ is the current value of the lateral displacement, and $\delta_{h,el}$ is the lateral displacement in correspondence to point *a*.

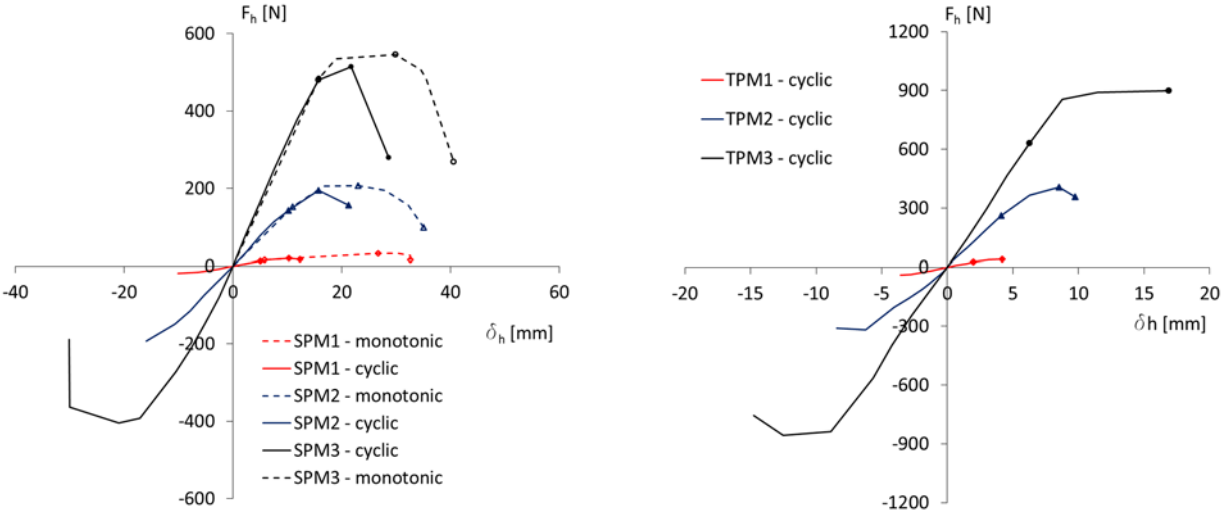


Figure 7. Measured envelops of cyclic (solid lines) and monotonic (dashed lines) lateral force-displacement tests.

| | | $F_a$ | $\delta_a$ | $\mu_a$ | $F_b$ | $\delta_b$ | $\mu_b$ | $F_c$ | $\delta_c$ | $\mu_c$ |
|---|---|---|---|---|---|---|---|---|---|---|
| | | [N] | [mm] | | [N] | [mm] | | [N] | [mm] | |
| SPM1 | monotonic | 15.92 | 5.85 | 1.00 | 32.93 | 26.74 | 4.57 | 16.20 | 32.67 | 5.58 |
| | cyclic | 12.70 | 5.02 | 1.00 | 20.19 | 10.29 | 2.06 | 17.67 | 12.35 | 2.47 |
| SPM2 | monotonic | 152.38 | 10.98 | 1.00 | 206.83 | 22.97 | 2.09 | 100.01 | 35.03 | 3.19 |
| | cyclic | 143.10 | 10.23 | 1.00 | 195.12 | 15.75 | 1.54 | 157.03 | 21.26 | 2.07 |
| SPM3 | monotonic | 485.01 | 15.79 | 1.00 | 545.56 | 29.92 | 1.89 | 268.5 | 40.64 | 2.57 |
| | cyclic | 480.12 | 15.70 | 1.00 | 514.00 | 21.70 | 1.38 | 280.00 | 28.65 | 1.82 |
| TPM1 | cyclic | 25.22 | 2.00 | 1.00 | 40.20 | 4.17 | 2.08 | 40.20 | 4.17 | 2.08 |
| TPM2 | cyclic | 262.18 | 4.11 | 1.00 | 407.34 | 8.53 | 2.07 | 357.45 | 9.76 | 2.37 |
| TPM3 | cyclic | 467.93 | 4.55 | 1.00 | 899.02 | 16.88 | 2.70 | 899.02 | 16.88 | 2.70 |

Table 3. Coordinates and ductility values of noticeable points of the curves in Figure 7.

The cyclic tests in Figure 8 where performed at controlled ductility on a SPM1 and a TPM3 specimen, by letting the maximum lateral displacement to grow progressively in such a way that it results $\mu = 0.25$ in the first cycle; $\mu$ grows with step 0.25 in the next cycles up to $\mu = 1.00$; and, finally, $\mu$ grows with step 0.50 in the post-elastic cycles up to specimen's failure. Figure 7-left shows a comparison between the measured envelopes of cyclic tests and monotonic tests on SPM specimens, which highlights the fact that the envelopes of the monotonic tests always lie above those of the cyclic tests in the post-elastic range, due to (low-cycle) fatigue-damage [13].

Post-yield stiffness degradation is a common observation in a range of different tests and lattice designs of EBM manufactured Ti6Al4V porous structures (e.g [8][9]), due to progressive brittle fracture of individual struts of the lattice from the point of first macroscopic yield [7].

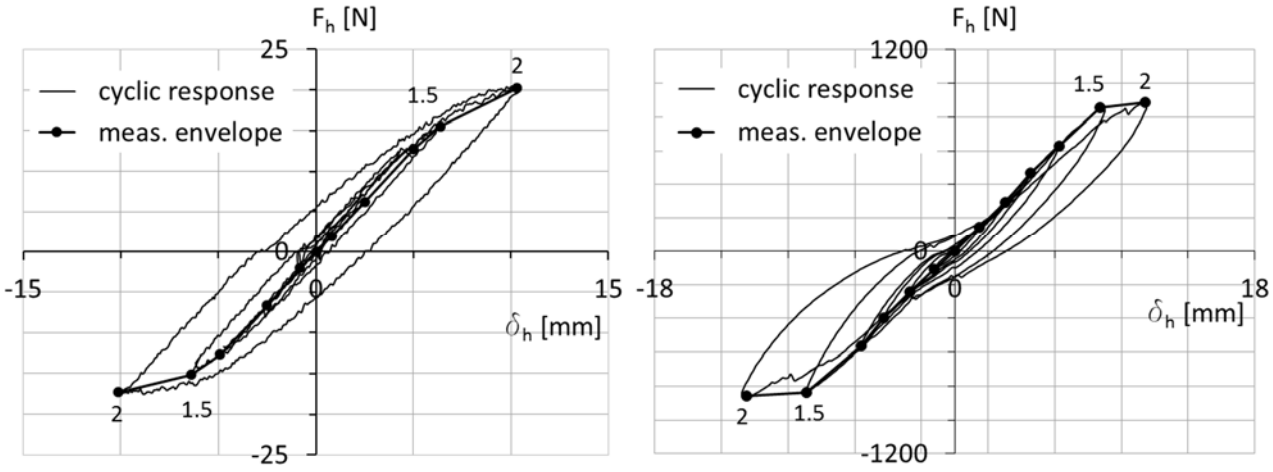


(a) (b)

Figure 8. Lateral force - displacement responses of a SPM1 (a) and a TPM3 (b) specimen under cyclic tests at constant vertical load $F_v = 45.34$ N (solid curves: measured envelope curves; numbers indicate ductility).

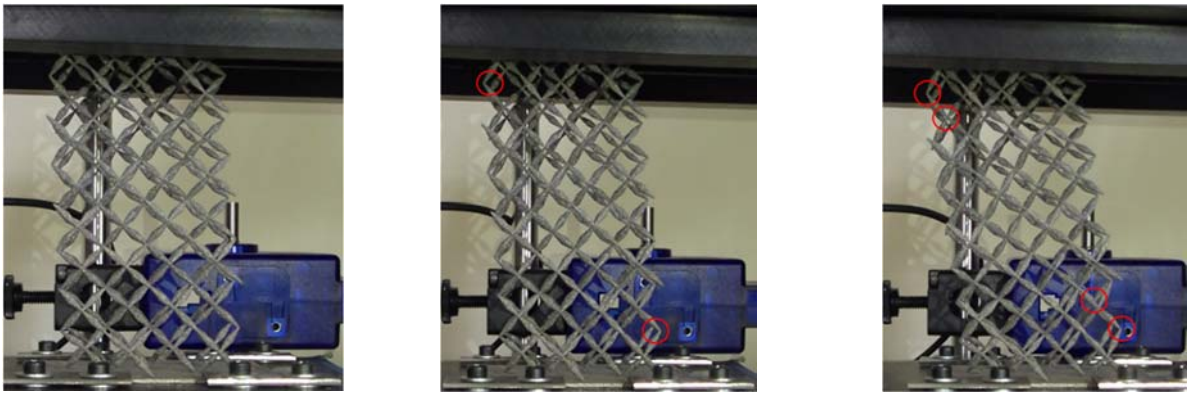

(a) SPM1 – *3rd elastic cycle* $\delta_h = 5.12$ mm, $\mu = 1.0$

(b) SPM1 - *1st inelastic cycle* $\delta_h = 6.40$ mm, $\mu = 1.5$

(c) SPM1 - *2nd inelastic cycle* $\delta_h = 10.29$, $\mu = 2.0$

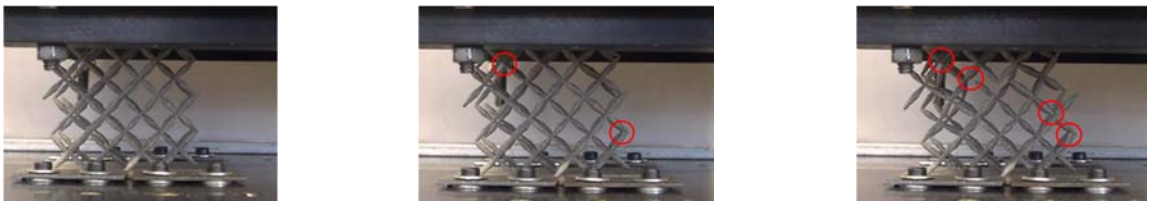

(d) TPM3 - *4th elastic cycle* $\delta_h = 6.25$ mm, $\mu = 1.0$

(e) TPM3 - *1st inelastic cycle* $\delta_h = 8.74$ mm, $\mu = 1.5$

(f) TPM3 - *2nd inelastic cycle* $\delta_h = 11.45$ mm, $\mu = 2.0$

Figure 9. Frames from in-situ videos of lateral displacement tests on a SPM1 (a-b-c) and a TPM3 (d-e-f) specimen. The circled struts are affected by fracture damage.

Table 7 shows the Energy Dissipated per Cycle $EDC$ the effective viscous damping $\xi_{eff}$; the post-yield ($K_d$) vs. elastic ($K_e$) stiffness ratio $|K_d - K_e|/K_e$; and characteristic strength $Q_d$ defined as force at zero horizontal displacement (cf. point 8.2.1.2.2 of [24]).

| | | $EDC$ $(10^3\, kN \cdot mm)$ | $\xi_{eff}$ (%) | $\lvert K_d - K_e \rvert / K_e$ (%) | $Q_d$ (N) |
|---|---|---|---|---|---|
| SPM1 | $\mu_{\max} = 1.5$ | 191.44 | 25.11 | 25.73 | 1.52 |
| | $\mu_{\max} = 2.0$ | 406.27 | 31.12 | 57.44 | 5.27 |
| TPM3 | $\mu_{\max} = 1.5$ | $12.97 \cdot 10^3$ | 28.02 | 10.07 | 93.12 |
| | $\mu_{\max} = 2.0$ | $18.86 \cdot 10^3$ | 30.12 | 88.73 | 95.01 |

Table 4. Energy dissipation per cycle ( $E_{diss}$ ); effective viscous damping ( $\xi_{eff}$ ); post-yield vs. elastic stiffness ratio ( $\lvert K_d - K_e \rvert / K_e$ ); and characteristic strength ( $Q_d$ ) at different post-elastic cycles of lateral force – displacement test on SPM1 and TPM3 specimens.

The effective damping in Table 7 is defined in line with the European standard on anti-seismic devices EN 15129:2009 [24], and corresponds to the energy dissipated $E_{diss}$ through the following formula

$$\xi_{eff} = \frac{E_{diss}}{2\pi K_{h,eff}\, \delta_{h,\max}^2} \tag{5}$$

where $K_{h,eff}$ is the effective secant stiffness, and $\delta_{h,\max}$ is the maximum lateral displacement of the current cycle (see point 3.1.10 of [24]). The results in Table 7 highlight progressive increases of $\xi_{eff}$, $\lvert K_d - K_e \rvert / K_e$, and $Q_d$ with the amplitude of the maximum lateral displacement (i.e., with $\mu_{\max}$), due to progressive fracture of lattice struts [8] (cf. Figure 9). The results in terms of energy dissipated per cycle (and effective damping) while indicating a progressive increase with displacement show also values of supplemental damping (25% to 30%) that are suitable for seismic isolation applications. The failure mechanisms in Figure 9 indicate a quite symmetric pattern of broken elements between top and bottom of the specimen. It was also observed that during the tests the failure of struts happened in a rather smooth progression and in expected locations. This performance new configurations that can significantly increase the required structural ductility to be forseen.

## 3 CONCLUDING REMARKS

We have experimentally investigated the response of EBM printed Ti6Al4V specimens of pentamode materials confined between stiffening plates, under lateral and vertical force-displacement tests. The examined tests were aimed at researching the effective shear and compression properties of such systems, and their inelastic response under cyclic and monotonic loading histories. We have examined a collection of specimens that differ in microstructural and macrostructural aspect ratios, which are related to the size of the nodal junctions (microstructure aspect ratio) and the ratio between the number of unit cells placed in the vertical and horizontal directions (macrostructure aspect ratio).

Several results of the present study highlight analogies between the mechanical response of the analyzed systems and that of elastomeric bearings consisting of alternating layers of synthetic or natural rubber and stiffening layers made of steel plates or fiber-reinforced composites, which are commonly used as bridge support devices or seismic or vibration isolators for buildings [11]-[17]. We have observed that the ratio between the effective compression

modulus $E_{eff}$ and the effective shear modulus $G_{eff}$ of the analyzed pentamode materials is markedly affected by the presence of the stiffening plates, as compared to available theoretical predictions of the $E/G$ ratio of unconfined pentamode lattices [10] ($E/G \approx 1.0$). Such a stiffening effect is larger in the case of slender specimens and large-size nodal junctions, since the $E_{eff}/G_{eff}$ ratio varies between 7.93, in case of the SPM3 specimen, and 2.96, in case of the TPM1 specimen. It replicates the stiffening role played by steel layers in elastomeric bearings. It is worth noting, however, that the absolute vertical and lateral stiffness coefficients of the examined pentamode materials increase when passing from slender to thick specimens.

Despite the very preliminary nature of this study on feasibility for base isolation applications, some observations support the potential of pentamode structures for use in anti-seismic system development and/or as shear-wave band gap systems [2], with special attention to the isolation of existing buildings. The strict dependency of the response by the geometry of the lattice allows the design of structures of controlled performance. The ranges of supplemental damping observed for the specimens are well in line with values of common isolation devices. The levels of energy dissipated is acceptable and could be significantly improved by reducing material porosity, using different construction techniques, materials, and/or through the insertion of dissipative lead-cores within the pentamode isolator [11][14]. Additional horizontal ductility and vertical stiffness is expected to be developed also using different configurations that will provide more confinement to the single layers of the pentamode structure.

We address the design and modeling of highly dissipative pentamode bearings and impact mitigation devices to future work, on employing either manual assembling procedures [26], layered structures showing different materials and/or lattice geometries in different layers, and additive manufacturing techniques in polymeric and metallic materials [3][3][7]. We also address researches on the use of pentamode lattices within a large variety of materials and structures to future studies [58]-[60].

## REFERENCES


[1] G.W. Milton, A.V. Cherkaev, Which Elasticity Tensors are Realizable?, *Journal of Engineering Materials and Technology*, **117**(4), 483-493, 1995.

[2] Martin A., Kadic M., Schittny M., Bückmann T., Wegener M., Phonon band structures of three-dimensional pentamode metamaterials, *Physical Review B*, **86**, 155116, 2010.

[3] M. Schittny, T. Bückmann, M. Kadic, M. Wegener, Elastic measurements on macroscopic three-dimensional pentamode metamaterials. *Applied Physics Letters*, **103**, 231905, 2013.

[4] M. Kadic, T. Bückmann, N. Stenger, M. Thiel, M. Wegener, On the practicability of pentamode mechanical metamaterials, *Applied Physics Letters*, **100**:191901, 2012.

[5] T. Buckmann, N. Stenger, M. Kadic, J. Kaschke, A. Frölich, T. Kennerknecht, C. Eberl, M. Thiel, M. Wegener, Tailored 3D Mechanical Metamaterials Made by Dip-in Direct-Laser-Writing Optical Lithography. *Advanced Materials*, **24**(20):2710-4, 2012.

[6] T. Bückmann, M. Thiel, M. Kadic, R. Schittny, M. Wegener, An elastomechanical unfeelability cloak made of pentamode metamaterials. *Nature Communications*, **5**:4130, 2014.

[7] A. Amendola, E.H. Nava, R. Goodall, I. Todd, R.E. Skelton, F. Fraternali, On the additive manufacturing and testing of tensegrity structures. *Composite Structures*, **131**, 66-71, 2015.

[8] E. Hernandez-Nava, C.J. Smith, F. Derguti, S. Tammas-Williams, F. Leonard, P.J. Withers, I. Todd, R. Goodall, The effect of density and feature size on mechanical properties of isostructural metallic foams produced by additive manufacturing. Acta Materialia, **85**, 387-395, 2015.

[9] S. Tammas-Williams, H. Zhao, F. Léonard, F. Derguti, I. Todd, PB. Prangnell, XCT analysis of the influence of melt strategies on defect population in Ti–6Al–4V components manufactured by Selective Electron Beam Melting. Materials Characterization, **102**, 47-61, 2015.

[10] W. van Grunsven, E. Hernandez-Nava, G.C. Reilly, R. Goodall, Fabrication and mechanical characterisation of titanium lattices with graded porosity. Metals, **4**(3), 401-9, 2014.

[11] A.N. Norris, Mechanics of elastic networks. Proceedings of the Royal Society of London A, **470**(522):1-18, 2014.

[12] M.C. Constantinou, A.S. Whittaker, Y. Kalpakidis, D.M. Fenz, G.P. Warn, Performance of seismic isolation hardware under service and seismic loading, Technical Report MCEER-07-0012, 2007.

[13] R.I. Skinner, W.H. Robinson, G.H. McVerry, An introduction to seismic isolation. Wiley, 1993.

[14] J.M. Kelly, Earthquake-resistant design with rubber. London: Springer-Verlag, 1993.

[15] G. Benzoni, C. Casarotti, Effects of vertical load, strain rate and cycling on the response of lead-rubber seismic isolators. *Journal of Earthquake Engineering*, **13**(3), 293-312, 2009.

[16] H. Toopchi-Nezhad, M.J. Tait, R.G., Drysdale Bonded versus unbonded strip fiber reinforced elastomeric isolators: Finite element analysis. *Composite Structures*, **93**(2), 850-859, 2014.

[17] P.M. Osgooei, M.J. Tait, D. Konstantinidis, Three-dimensional finite element analysis of circular fiber- reinforced elastomeric bearings under compression. *Composite Structures* **108**(1), 191-204, 2014.

[18] P.M. Osgooei, M.J. Tait, D. Konstantinidis, Finite element analysis of unbonded square fiber-reinforced elastomeric isolators (FREIs) under lateral loading in different directions. *Composite Structures* **113**(1):164-173, 2014.

[19] Metals Handbook, (2) Properties and selection: nonferrous alloys and special-purpose materials. ASM International, Metals Park, OH, 1990.

[20] L.R. Meza, S. Das, J.R. Greer, Strong, light weight, and recoverable three-dimensional ceramic nanolattices. *Science* **6202**(345):1322-1326, 2014.

[21] VS Deshpande, NA Fleck, MF.Ashby, Effective properties of the octet-truss lattice material. *Journal of the Mechanics and Physics of Solids*, **22**, 409-428, 2001.

[22] T.A. Schaedler, A.J. Jacobsen, A. Torrents, A.E. Sorensen, J. Lian, J.R. Greer, L. Valdevit, W.B. Carter. Ultralight Metallic Microlattices. *Science* **6058**(334), 962-965, 2011.

[23] R.K. Steele, A.J. McEvily, The high-cycle fatigue behavior of Ti-6Al-4V alloy. *Engineering Fracture Mechanics*, **8**, 31-37, 1976.

[24] I. Szachogluchowicz, L. Sniezek, V. Hutsaylyuk, Low cycle fatigue properties laminate AA2519-TI6AL4V. *Procedia Engineering*, **114**, 26-33, 2015.

[25] European Committee for Standardization. Anti-seismic devices, EN 15129. Brussels, Belgium, 2009.

[26] Atlas of stress-strain curves, 2nd Edition, ASM International, Materials Park, OH, 2002.

[27] A. Amendola, G. Carpentieri, M. de Oliveira, R.E. Skelton, F. Fraternali, Experimental investigation of the softening stiffening response of tensegrity prisms under compressive loading. *Composite Structures*, **117,** 234-243, 2014.

[28] B. Schmidt, F. Fraternali, Universal formulae for the limiting elastic energy of membrane networks, *Journal of the Mechanics and Physics of Solids*, **60**, 172-180, 2012.

[29] L. Ascione, F. Fraternali, A penalty model for the analysis of composite curved beams, *Computers & Structures*, **45**, 985-999, 1992.

[30] F. Fraternali, J.N. Reddy, A penalty model for the analysis of laminated composite shells, *International Journal of Solids and Structures*, **30**, 3337-3355, 1993.

[31] F. Fraternali, Free Discontinuity Finite element models in two-dimensions for in-plane crack problems, *Theoretical and Applied Fracture Mechanics*, **47**, 274-282, 2007.

[32] F. Fraternali, C.D Lorenz, G. Marcelli, On the estimation of the curvatures and bending rigidity of membrane networks via a local maximum-entropy approach, *Journal of Computational Physics*, **231**, 528-540, 2012.

[33] F. Fraternali, G. Bilotti, Non-Linear Elastic Stress Analysis in Curved Composite Beams. *Computers & Structures*, **62**, 837-869, 1997.

[34] F. Fraternali, G. Carpentieri, A. Amendola, On the mechanical modeling of the extreme softening/stiffening response of axially loaded tensegrity prisms. *Journal of the Mechanics and Physics of Solids*, **74**, 136-157, 2015.

[35] A. Amendola, E.H. Nava, R. Goodall, I. Todd, R.E. Skelton, F. Fraternali, On the additive manufacturing, post-tensioning and testing of bi-material tensegrity structures, *Composite Structures*, **131**, 66-71, 2015.

[36] D. Ngo, F. Fraternali, C. Daraio, Highly Nonlinear Solitary Wave Propagation in Y-Shaped Granular Crystals with Variable Branch Angles. Physical Review E, **85**, 036602-1-10, 2012.

[37] R.E. Skelton, F. Fraternali, G. Carpentieri, A. Micheletti, Minimum mass design of tensegrity bridges with parametric architecture and multiscale complexity. *Mechanics Research Communications*, 58, 124-132, 2014.

[38] A. Leonard, F. Fraternali, C. Daraio, Directional wave propagation in a highly nonlinear square packing of spheres. *Experimental Mechanics*, **53**(3), 327-337, 2013.

[39] F. Fraternali, G. Carpentieri, A. Amendola, R.E. Skelton, V. F. Nesterenko, Multiscale tunability of solitary wave dynamics in tensegrity metamaterials. *Applied Physics Letters*, **105**, 201903, 2014.

[40] F. Fraternali, I. Farina, C. Polzone, E. Pagliuca, L. Feo, On the use of R-PET strips for the reinforcement of cement mortars. *Composites. Part B*, **46**, 207-210, 2013.

[41] J.R. Raney, F. Fraternali, A. Amendola, C. Daraio, Modeling and In Situ Identification of Material Parameters for Layered Structures based on Carbon Nanotube Arrays. *Composite Structures*, **93**, 3013–3018, 2011.

[42] G. Lomiento , N. Bonessio, G. Benzoni, Friction Model for Sliding Bearings under Seismic Excitation, Journal of Earthquake Engineering, **17**(8):1162-1191, 2013.

[43] M. Budek, M. J. N. Priestley, G. Benzoni, The Effect of External Confinement on Flexural Hinging in Drilled Pile Shafts, *Earthquake Spectra*, **20** (1), 1-24, 2004.

[44] Hae-Bum Yun, Sami F. Masri, Raymond W. Wolfe, Gianmario Benzoni , Data-driven methodologies for change detection in large-scale nonlinear dampers with noisy measurements, *Journal of Sound and Vibration*, **322**, Issues 1–2, 24 April 2009, Pages 336–357.

[45] D. D'Ayala, G. Benzoni, Historic and Traditional Structures during the 2010 Chile Earthquake: Observations, Codes, and Conservation Strategies. *Earthquake Spectra*, **28** (S1), S425-S451, 2012.

[46] N. Bonessio, G. Lomiento, G. Benzoni, Damage identification procedure for seismically isolated bridges, *Structural Control Health Monitoring*, **19**(5), 565–578, 2012.

[47] G. Benzoni, C. Casarotti , Effects of Vertical Load, Strain Rate and Cycling on the Response of Lead-Rubber Seismic Isolators, *Journal of Earthquake Engineering* ,**13**, 2009.

[48] A. Budek-Schmeisser, G. Benzoni, Rational seismic design of precast, prestressed concrete piles, *PCI Journal*, **53**(5), 40-53, 2008.

[49] G. Benzoni, M. J. N. Priestley, Seismic response of linked marginal wharf segments, *Journal of Earthquake Engineering* **74**, 513-539, 2003.

[50] F. Fraternali, S. Spadea, V.P. Berardi, Effects of recycled PET fibers on the mechanical properties and seawater curing of Portland cement-based concretes. *Construction and Building Materials*, **61**, 293-302, 2014.

[51] I. Farina, F. Fabbrocino, G. Carpentieri, M. Modano, A. Amendola, R. Goodall, L. Feo, F. Fraternali, *On the reinforcement of cement mortars through 3D printed polymeric and metallic fibers,* Composites Part B: Engineering, **90**, 76-85, 2016

[52] T. Blesgen, F. Fraternali, J.R. Raney, A. Amendola, C. Daraio, Continuum Limits of Bistable Spring Models of Carbon Nanotube Arrays accounting for Material Damage. *Mechanics Research Communications*, **45**, 58-63, 2012.

[53] F. Fraternali. A Mixed Lumped Stress – Displacement Approach to the Elastic Problem of Masonry Walls. Mechanics Research Communications, **38**, 176-180, 2011.

[54] F. Fraternali, M. Negri, M. Ortiz, On the Convergence of 3D Free Discontinuity Models in Variational Fracture. *International Journal of Fracture*, **166**(1-2), 3-11, 2010.

[55] F. Fraternali, S. Spadea, L. Ascione, Buckling behavior of curved composite beams with different elastic response in tension and compression. *Composite Structures*, **100**, 280-289, 2013.

[56] C. Daraio, D . Ngo, V. F. Nesterenko, F. Fraternali, Highly Nonlinear Pulse Splitting and Recombination in a Two Dimensional Granular Network. *Physical Review E*, **82**, 036603, 2010.

[57] F. Fraternali, A. Marino, T. Elsayed, A. Della Cioppa, On the structural shape optimization via variational methods and evolutionary algorithms. Mechanics of Advanced Materials and Structures, **18**, 225-243, 2011.

[58] A. Amendola, G. Benzoni, F. Fraternali, Non-linear elastic response of layered structures, alternating pentamode lattices and confinement plates. *Composite Part B, Engineering*, Online first, DOI: 10.1016/j.compositesb.2016.10.027, 2016.

[59] F. Fraternali, G. Carpentieri, R. Montuori, A. Amendola, G. Benzoni, On the use of mechanical metamaterials for innovative seismic isolation systems, COMPDYN 2015 - 5th ECCOMAS Thematic Conference on Computational Methods in Structural Dynamics and Earthquake Engineering, 349-358.

[60] A. Amendola, C.J. Smith, R. Goodall, F. Auricchio, L. Feo, G. Benzoni, F. Fraternali, Experimental response of additively manufactured metallic pentamode materials confined between stiffening plates. *Composite Structures*, **142**, 254-262, 2016.

COMPDYN 2017
6th ECCOMAS Thematic Conference on
Computational Methods in Structural Dynamics and Earthquake Engineering
M. Papadrakakis, M. Fragiadakis (eds.)
Rhodes Island, Greece, 15–17 June 2017

# FINITE ELEMENT MODELING OF SINGLE AND MULTI-SPHERICAL FRICTION PENDULUM BEARINGS

**Ioannis E. Kavvadias**[1], **Henrick F. Bibo**[1], **and Lazaros K. Vasiliadis**[1]

[1] Democritus University of Thrace, Department of Civil Engineering
Campus of Kimmeria, 67100 Xanthi, Greece
{ikavvadi, ebimpo, lvasilia}@civil.duth.gr

**Keywords:** Finite Element Modeling, Base Isolation, Single Friction Pendulum Bearings, Multi-Spherical Friction Pendulum Bearings, Earthquake Engineering.

**Abstract.** *Base isolation is a modern strategy to decrease the effects of earthquakes on buildings of high significance. The general principle is that the structure is decoupled from the horizontal components of the earthquake ground motion by interposing a layer with low lateral stiffness between the structure and the foundation. One of the major devices to apply seismic isolation is Friction Pendulum Systems, which use the characteristics of a pendulum to lengthen the natural period of the isolated structure. These systems consist of an upper and a lower spherical plate with sliding surface applied with special coating, and an articulated slider. The aim of this paper is to simulate Friction Pendulum Isolation Systems, using the finite element method. All models are constructed using full three dimensional continuum modeling in ABAQUS software. Particularly, this study includes single, and multi-spherical Friction Pendulum Bearings simulation. Dynamic time history analyses are performed and results in terms of hysteretic loops are presented. The analyses results of the proposed models are verified with the analytical solution of the friction pendulums response and with those obtained by analyses in other commercial software which contains Friction Pendulum Bearing model.*

## 1 INTRODUCTION

Base isolation consist an intervention technique which aims to relieve the structure from the ground motion excitations. Introducing isolation devices in a certain level, a base with low lateral stiffness is generated. Due to this fact the superstructure is decoupled from the ground, and as a result the seismic forces are significantly reduced [1]. Two main categories of base isolation devices are in use, the rubber bearings [2] and the friction ones [3]. The main devices based on the friction mechanism are the friction pendulum (FP) bearings. Their application in buildings [4] are growing the current year.

The single friction pendulum (SFP) bearings have been studied since 1990 [3, 5, 6]. A FP is composed by an articulated slider that moves on a concave spherical surface. The surfaces in which sliding occurs, are coated to a low friction material. Based on the pendulum function, the superstructures period depends on the curvature R of the FP bearing.

Due to the concave surface, re-centering forces are introduced, which are proportional of the superstructure weight. During the last decade sliding bearings with adaptive seismic behavior are presented [7-9]. The adaptive response is achieved by using multi-spherical sliding devices. Based on this, double friction pendulum (DFP) triple friction pendulum (TFP) and even quintuple friction pendulum (QFP) bearings are developed [10-13]. The DFP are consist of two concave surfaces, the TFP of four surfaces and the QFP of six sliding surfaces.

Modeling principles of these systems are discussed by, Morgan and Mahin [8], Tsai et al. [9], Fenz and Constantinou [11], Sarlis and Constantinou [12], Becker and Mahin [14] among others. A simulation model of a sliding bearing have to obey some basic principles. First, it is required to have the capability of simulating the overall force-deformation behavior. Moreover, it has to track the sliding of the individual interfaces and simulates when the restrainer is hit. A secondary but very interesting attribute of a simulation model is to take into account the uplift of the individual parts.

## 2 EXAMINING FRICTION PENDULUM BEARINGS

In this study a finite element modeling approach for the simulation of friction pendulum bearings is presented. Single friction pendulum (SFP), double friction pendulum (DFP) and triple friction pendulum (TFP) bearings are simulated and their models are validated. In Figure 1 the main characteristics of single and multi-spherical isolators are depicted. These characteristics are, each surfaces curvature (R) and coefficient of friction (μ), the displacement capacity of each surface that sliding occurs (d) and finally the radial distance between the spherical surface and the pivot point of the articulated slider (h) by which the effective curvature is calculated ($R_{eff,\,i} = R_i - h_i$).

Regarding the DFP it was selected for the concave surfaces to have the same curvatures $R_1 = R_2$ and the same coefficients of friction $\mu_1 = \mu_2$. By this, it model could be easily verified with the response of a SFP bearing with $R_{eff} = R_{eff,\,1} + R_{eff,\,2}$. The examined TFP bearing was considered with the same curvature and coefficient of friction for the two inner and the two outer surfaces ($R_1 = R_4$, $\mu_1 = \mu_4$ and $R_2 = R_3$, $\mu_2 = \mu_3$). In Table 1 the main properties of the FP bearing considered in this study are listed.

| Model | $R_1$ (m) | $R_2$ (m) | $R_{eff,1}$ (m) | $R_{eff,2}$ (m) | $\mu_1$ | $\mu_2$ | $T_1$ (s) | $T_2$ (s) |
|---|---|---|---|---|---|---|---|---|
| SFP | 1080 | - | 1 | - | 0.1 | - | 2 | - |
| DFP | 650 | 650 | 0.5 | 0.5 | 0.1 | 0.1 | 2 | - |
| TFP | 2050 | 530 | 2 | 0.5 | 0.1 | 0.03 | 4.65 | 2 |

Table 1. Simulated friction pendulums characteristics.

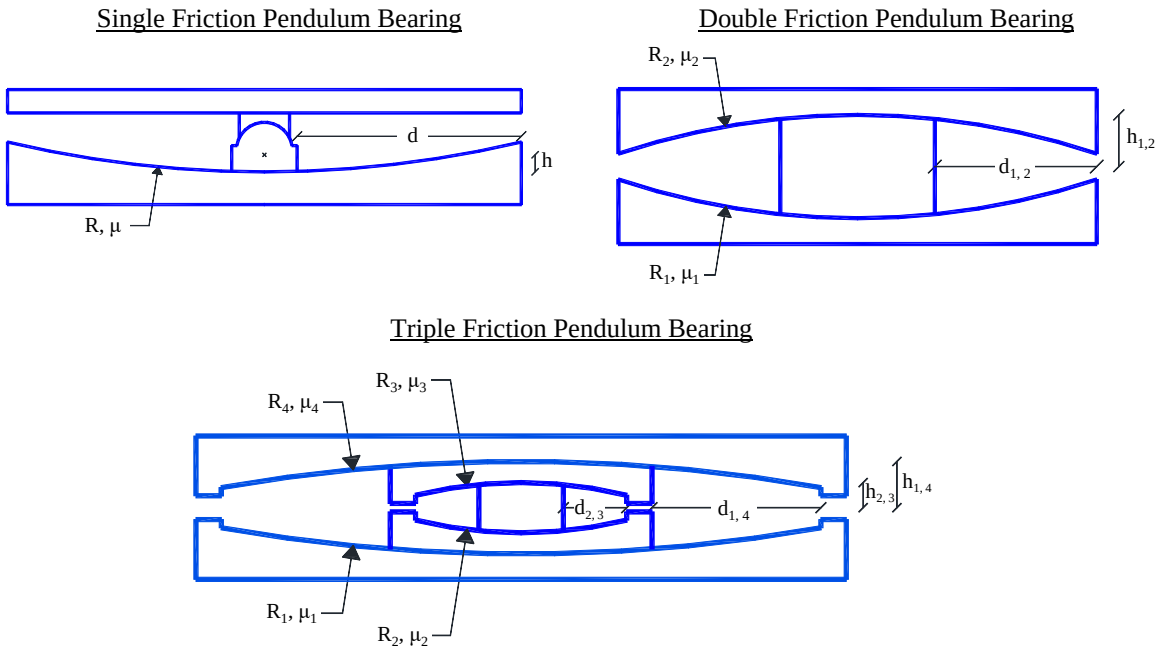


Figure 1. Cross sections of friction pendulum bearing.

A first task is to define the force-displacement relations in order to construct the hysteretic loops of the bearings (Figure 2). The force-displacement relationship that governs the SFP and the DFP as it configured above is given by the following equation:

$$F = \frac{W}{2R_{eff}} u + \mu W \tag{1}$$

where W is the axial force of the bearing, $R_{eff} = R_{eff,\,1} + R_{eff,\,2}$ for the DFP and u is the displacement that the device develops.

The TFP with the same properties in the outer and inner surfaces operates with three different schemes, which activation depends on the level of the seismic excitation following the attributes: (a) high damping and stiffness at low level forces; (b) low stiffness at moderate level earthquakes; and (c) high damping and high stiffness at severe level earthquakes. That adaptive response is achieved through a progressive activation of different sliding surfaces.

When sliding occurs to the inner surfaces (Region I) the force displacement is calculated by the following equation:

$$F_1 = \frac{W}{2R_{eff\,2}} u + \mu_2 W \tag{2}$$

When the outer surfaces are activated (Region II) the lateral forces are calculated by Eq (3)

$$F_2 = \frac{W}{2R_{eff\,1}} u + \left[ \mu_1 - (\mu_1 - \mu_2) \frac{R_{eff\,2}}{R_{eff\,1}} \right] W \tag{3}$$

While when the displacement capacity of the outer surfaces are reached, the inner ones are activated again (Region III) and the forces are given as follows.

$$F_3 = \frac{W}{2R_{eff\,2}} (u - u^{**}) + \frac{W}{R_{eff\,1}} d_1^{*} + \mu_1 W \tag{4}$$

where $d_1^{*} = d_1 (R_{eff\,1} / R_{eff})$ and $u^{**} = 2(\mu_1 - \mu_2) R_{eff\,1} + 2d_1^{*}$

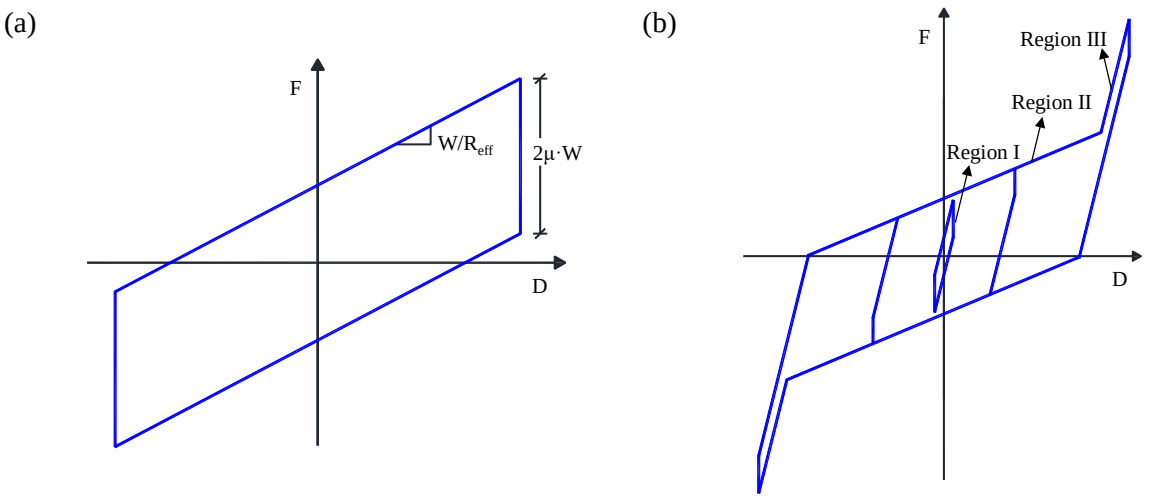


Figure 2. Force-displacement relations for (a) a SFP and a DFP and (b) for a TFP.

## 3 FINITE ELEMENT MODELING

The FP bearings are simulated with full three dimensional continuum modelling by using solid element in ABAQUS software [15]. The FP components material are considered as homogenous isotropic, with Young's Modulus equal to E = 210 GPa a Poisson ratio v = 0.3. All the parts are meshed using 8 node linear brick elements C3D8R. Hourglass control was adopted to minimize the effects of spurious/hourglass modes effects that may be initialized by the reduced integration elements that are used. Mesh size was moderate considering acceptable and reliable results as well as the computational time. The detailed model of the FP bearings geometry (Figure 3) allows a complete description of it kinematic behavior, accounting the restoring forces, variation of contact pressure as a consequence of overturning moments, and uplift [16].

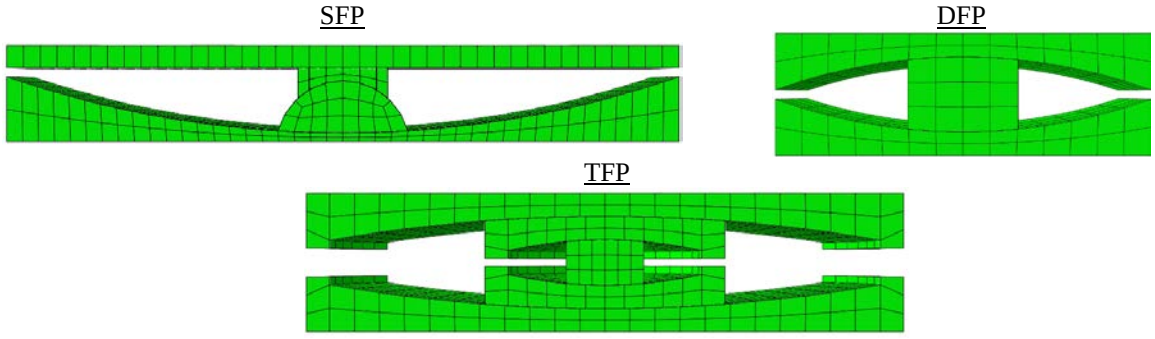


Figure 3. Finite element models of the examined FP bearings

Regarding the friction which is the most important characteristic for the operation of the FP bearing, rigid contact is used to model the interfaces between the isolators' parts. In literature [17] it has been thoroughly investigated the influence of the friction models adopted for the analyses. Comparing Coulomb friction model with other more sophisticated which took into account the sliding velocity [6], the pressure or the temperature, have been concluded that the Coulomb friction is adequate to simulate the friction of the sliding surfaces of a FP bearing. Thus, a Coulomb model is adopted to describe the tangential behavior between the sliding surfaces. For the normal direction of the contact element, the stiffness is assumed as infinite.

A simplified analysis model are selected to verify the finite element models of the isolation bearing (Figure 4). That model consist of two identical bearings connected with a rigid and massless beam. The gravity loads W are considered at the top of the isolators, while the ground motion excitation are applied at the base in terms of seismic acceleration. Four ground motion records are used for the validation of the models (Table 2).

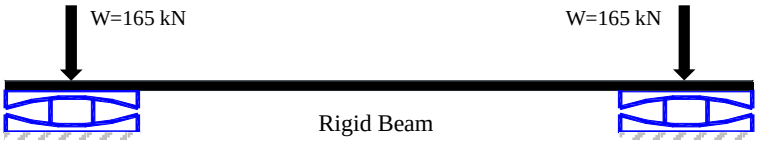


Figure 4. Analysis model.

| Earthquake | Station | Date | $M_s$ | R (km) |
|---|---|---|---|---|
| Kobe | Nishi -Akashi | 16/1/1995 | 6.9 | 7.08 |
| Chuetsuoki | Nakanoshima Nagaoka | 16/7/2007 | 6.8 | 19.89 |
| El Mayor Cucapah | Chihuahua | 4/4/2010 | 7.2 | 19.47 |
| Chi-Chi | CHY101 | 20/9/1999 | 7.62 | 9.94 |

Table 2. Ground motion records list.

## 4 RESULTS

The validation of the models are performs by comparing two individual results. First, the Force–Displacement which consist the most representative result that indicates the appropriate operation of the bearing. In more detail, it highlights the correctly sliding movement between the FP parts. Moreover, another feature that point out the effectiveness of the FP bearings in the superstructure are the accelerations at the level of the isolated base. Results obtained by the similar analysis problem, performed in SAP2000 software, in which the bearing are simulated with link elements, are used in order to validate the results of the proposed model.

### 4.1 Single Friction Pendulum

In Figure 5 the hysteretic loops of the proposed model are compared with the loops of the analyses in the SAP200 software. The ground motion records induce to the bearings maximum displacements ranged from 0.044 m to 0.165 m. Thus, the performance of the isolators to different operation levels are examined. As observed in Figure 5, the proposed model is in great agreement with the results of the commercial program. FP features like the stiffness and the hysteretic loops' width are the same with the analytical ones. Regarding the developed displacements minor alteration are displayed between the models. Moreover, due the type of the proposed model any variation of contact pressure can be captured in the results.

In Figure 6 the acceleration of the isolated base is demonstrated. The amplitude results from both models are alike. Furthermore, the time histories of the accelerations are identical. The only difference is that the proposed model results are sharper than the results of the model with link elements.

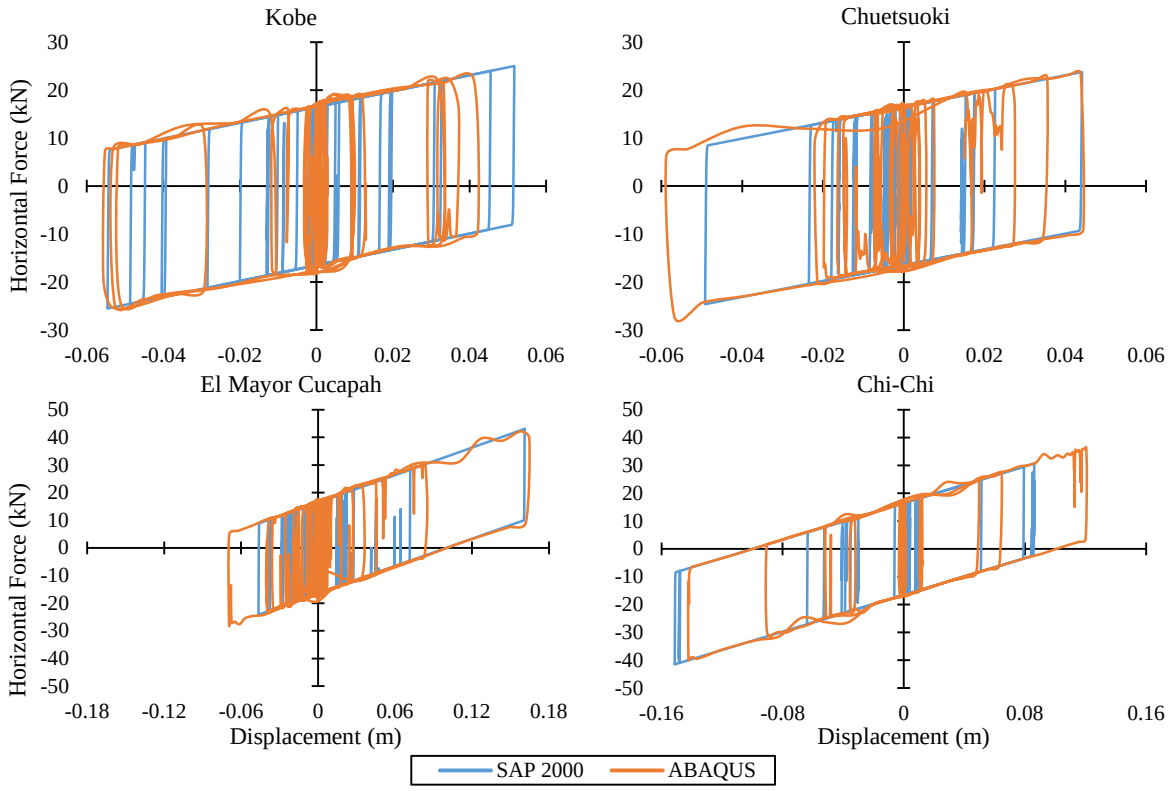


Figure 5. Comparison of SAP2000 and ABAQUS models Force-Displacement loops.

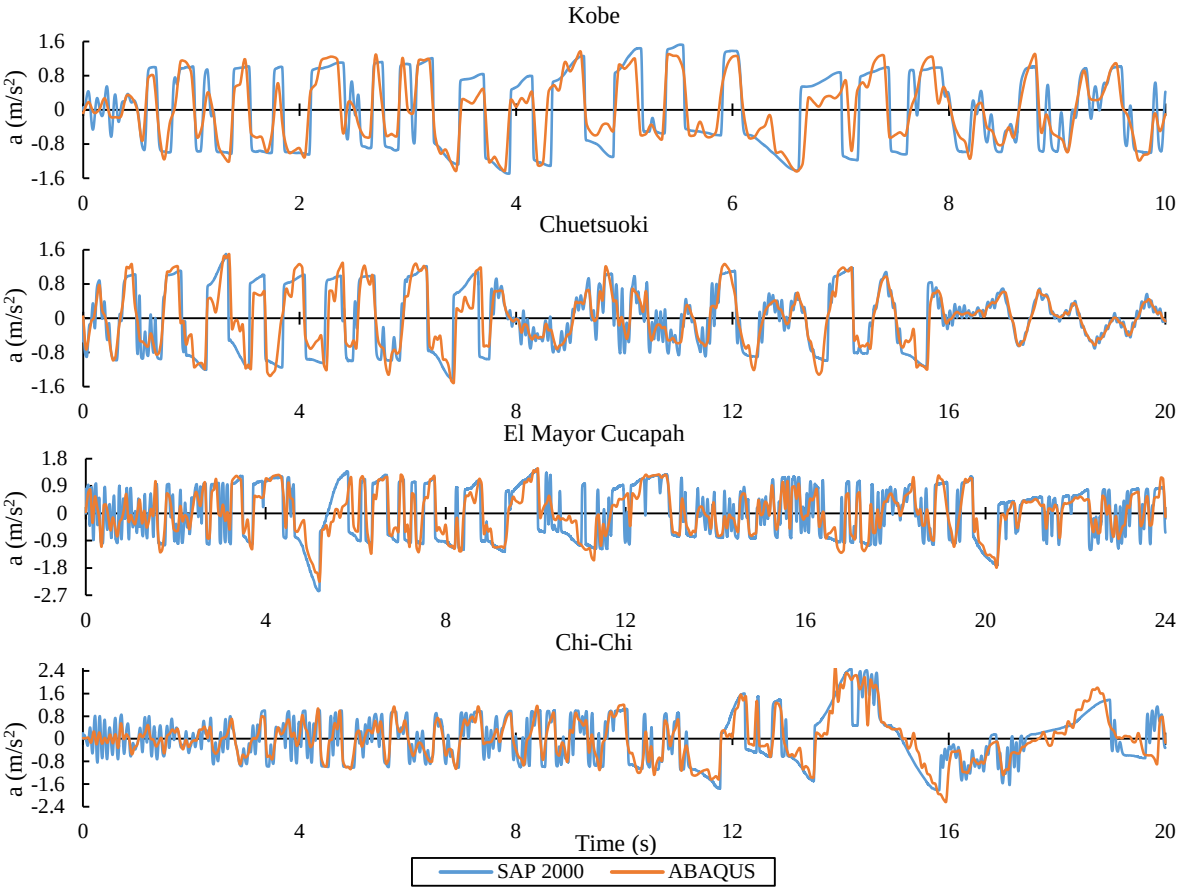


Figure 6. Comparison of SAP2000 and ABAQUS models accelerations.

## 4.2 Double Friction Pendulum

The DFP bearings with curvatures $R_1 = R_2$ and coefficient of friction $\mu_1 = \mu_2$, performs similar to a SFP bearing with curvature $R = R_1+R_2$ and $\mu = \mu_1 = \mu_2$. Therefore, the results of the DFP are compared with those of the equivalent SFP. In Figures 7 and 8, are presented the hysteretic loops and the accelerations of the analysis model respectively. Considering the force displacement loops the results have similar characteristics, as it should be. It can be observed that the DFP results are even closer to those obtained by SAP2000 (Figure 6). Regarding the acceleration of the isolated base, the values are equivalent between teach other. As remarked for the hysteretic loops, the acceleration of the DFP are smother and identical with those of the modeling with link elements results.

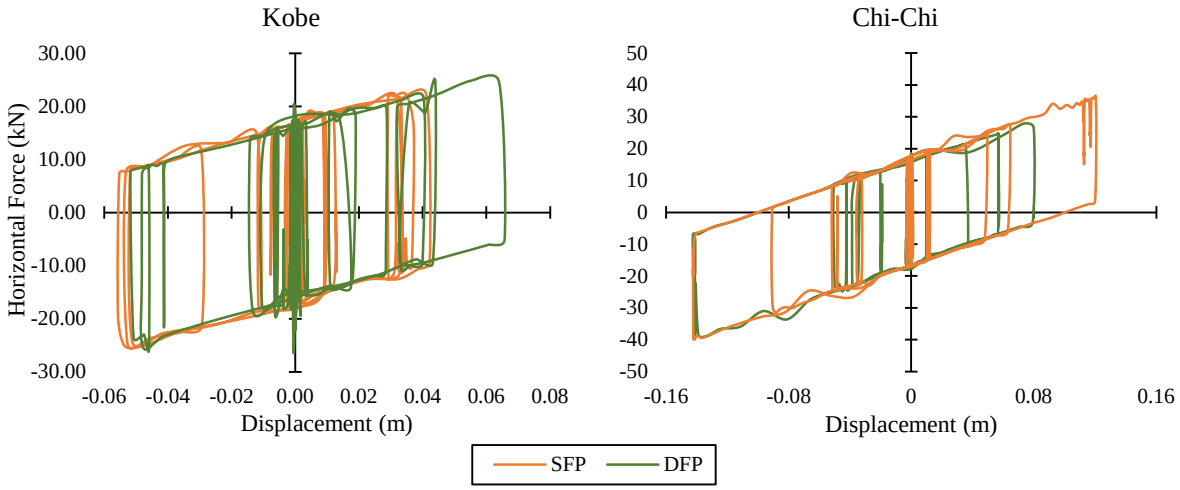


Figure 7. Comparison of SFP and DFP Force-Displacement loops.

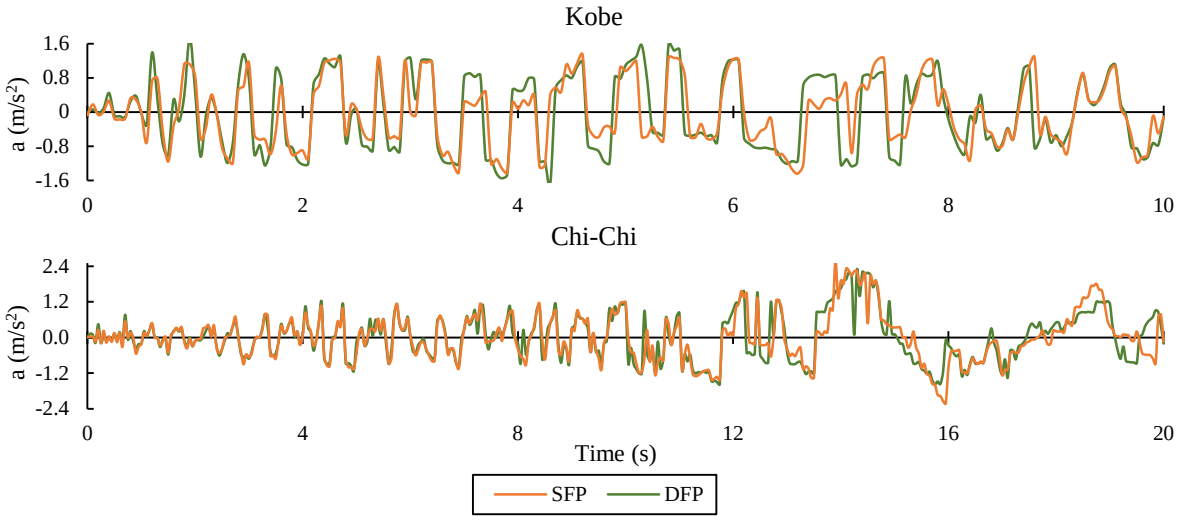


Figure 8. Comparison of SFP and DFP accelerations.

## 4.3 Triple Friction Pendulum

The examined TFP bearing has such curvatures that correspond to isolated period $T_2$ =2 s when the inner surfaces are activated and to $T_1$ =4.65 s, when sliding occurs on the outer surfaces. Results in terms of acceleration time histories are presented. In Figure 9 the accelerations of the isolated base supported to the DFP and the TFP are displayed. Two interesting

fact are arose throughout this comparison. First the TFP devices reduce the acceleration values more than the DFP ones and especially of the Kobe excitation, which has a higher frequency content. Second, due to the actuation of the outer surfaces, it lengthens even more the acceleration signal.

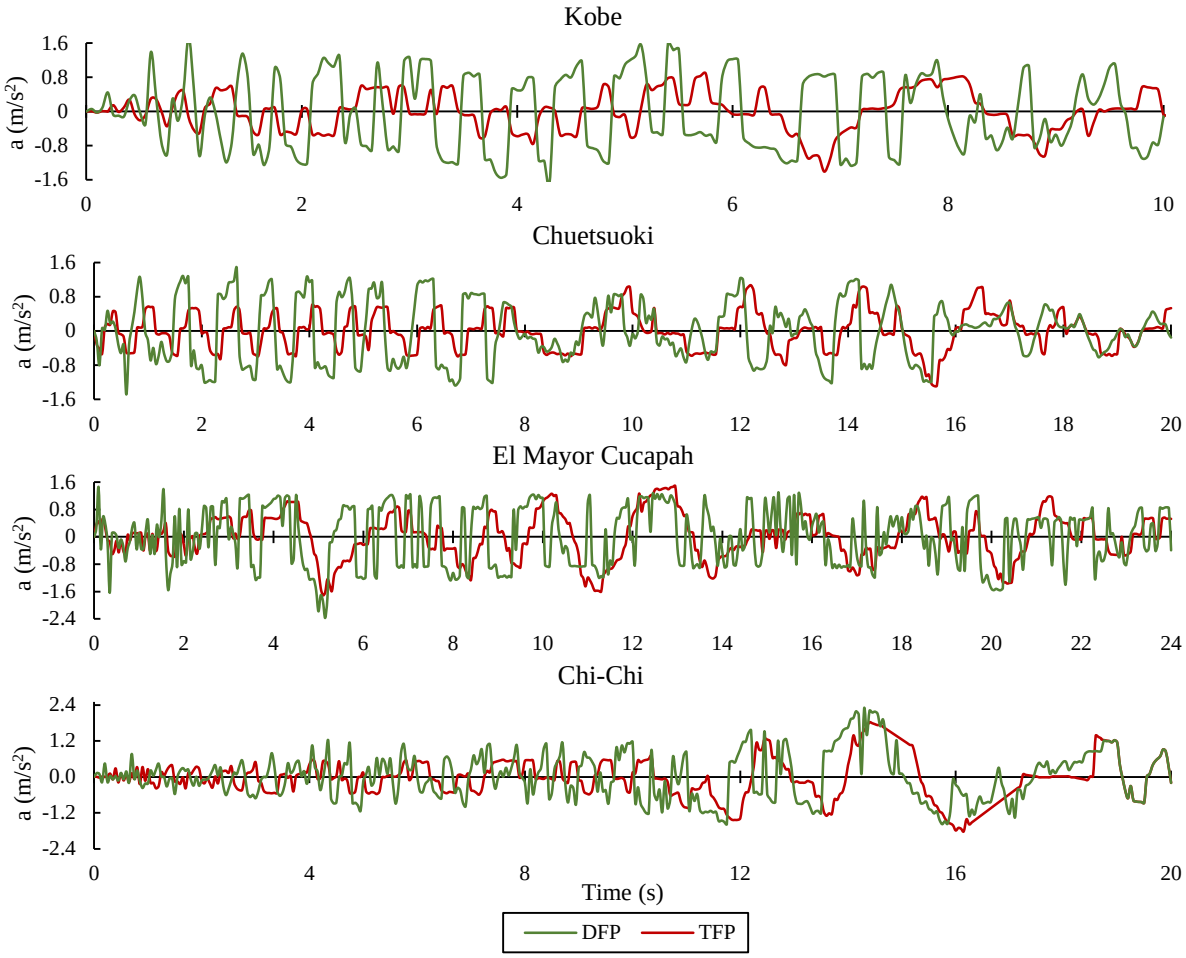


Figure 9. Comparison of DFP and TFP accelerations.

## 5 CONCLUSIONS

A proposed finite element simulation of single and multi-spherical friction pendulum bearings is examined in the present study. Single, double and triple friction pendulum isolation devices are simulated in ABAQUS software. A simple analysis model is adopted and time history analyses using four ground motion records are performed to verify the results of the FP finite element models. The analyses results are contrasted with those obtained by link isolator modeling in the commercial program SAP2000.

The results are satisfactory as the proposed models could estimate with great accuracy the seismic response of the FP bearings. Moreover, due to the type of the simulation it took into account the restoring forces and the variation of contact pressure due to overturning moments and uplift. Firstly, by the hysteretic loops, the characteristic values such as the stiffness and it width are correctly given. The force-displacement results are much similar for both SFP and DFP bearings. Furthermore, the acceleration transmitted through the isolation devices are acceptable as they are identical between the models. Finally, comparing the acceleration results of the TFP with those of the DFP, the superior performance of the former are highlighted.

## REFERENCES


[1] F. Naeim, J.M. Kelly, *Design of seismic isolated structures. Wiley, New* York, USA, 1999.

[2] J.M. Kelly, *Earthquake-Resistant Design with Rubber, 2nd Edition.* Springer-Verlag, London, UK, 1997

[3] V. Zayas, S.S. Low, S.A. Mahin. A simple pendulum technique for achieving seismic isolation. *Earthquake Spectra*, **6**, 317–333, 1990

[4] L.K. Vasiliadis, Seismic evaluation and retrofitting of reinforced concrete buildings with base isolation systems. *Earthquakes and Structures*, **10**, 293-311, 2016.

[5] M. Constantinou, A. Mokha, A. Reinhorn, Teflon bearings in base isolation I: testing. *Journal of Structural Engineering*, **116**, 438-454, 1990

[6] M. Constantinou, A. Mokha, A. Reinhorn, Teflon bearings in base isolation II: modeling. *Journal of Structural Engineering*, **116**, 455-474, 1990

[7] D.M. Fenz, M.C. Constantinou. Spherical sliding isolation bearings with adaptive behavior: theory. *Earthquake Engineering and Structural Dynamics*, **37**, 163–183, 2008.

[8] T.A. Morgan, S.A. Mahin, Achieving reliable seismic performance enhancement usingmulti-stage friction pendulum isolators. *Earthquake Engineering and Structural Dynamic*, **39**, 1443–1461, 2010.

[9] C.S. Tsai, Y.C. Lin, H.C. Su, Characterization and modeling of multiple friction pendulum isolation system with numerous sliding interfaces. *Earthquake Engineering and Structural Dynamics*, **39**, 1463–1491, 2010.

[10] D.M. Fenz, M.C. Constantinou, Behavior of the double concave Friction Pendulum bearing. *Earthquake Engineering and Structural Dynamics*, **35**, 1403–1424., 2006.

[11] D.M. Fenz, M.C. Constantinou, Modeling triple friction pendulum bearings for response-history analysis. *Earthquake Spectra*, **24**, 1011–1028, 2008.

[12] A.A Sarlis, M.C. Constantinou, A model of triple friction pendulum bearing for general geometric and frictional parameters. *Earthquake Engineering and Structural Dynamic*, **45**, 1837–1853, 2016.

[13] D. Lee, M.C. Constantinou, Quintuple Friction Pendulum Isolator: Behavior, Modeling, and Validation. *Earthquake Spectra*, **32**, 1607-1626, 2016.

[14] T.C Becker, S.A Mahin, Correct treatment of rotation of sliding surfaces in a kinematic model of the triple friction pendulum bearing. *Earthquake Engineering & Structural Dynamics*, **42**, 311–317, 2012.

[15] Dassault Systems Simulia Corp. *ABAQUS Analysis user's manual Version 6.10*, 2012.

[16] P.C. Tsopelas, P.C. Roussis, M.C. Constantinou, Nonlinear dynamic analysis of multibase seismically isolated structures with uplift potential I: formulation. *Earthquake Engineering and Engineering Vibration*, **8**, 421-431, 2009.

[17] M. Kumar, A.S. Whittaker, M.C. Constantinou, Characterizing friction in sliding isolation bearings. *Earthquake Engineering & Structural Dynamics*, **44,** 1409-1425, 2015.

COMPDYN 2017
6th ECCOMAS Thematic Conference on
Computational Methods in Structural Dynamics and Earthquake Engineering
M. Papadrakakis, M. Fragiadakis (eds.)
Rhodes Island, Greece, 15–17 June 2017

# SENSITIVITY OF THE SEISMIC PERFORMANCE OF LIQUID STORAGE TANKS WITH NONLIEAR ISOLATION SYTEMS TO DEVIATIONS IN MECHANICAL CHARACTERISTICS OF THE SEISMIC ISOLATORS

**Elif Güler[1], Hatice Gazi[1], and Cenk Alhan[1]**

[1] Department of Civil Engineering
Istanbul University, Turkey
e-mail: guler.elif@gmail.com, hgazi@istanbul.edu.tr, cenkalhan@istanbul.edu.tr

**Keywords:** Seismic Isolation, Liquid Storage Tanks, Nonlinear Isolation System, Sensitivity Analysis, Seismic Performance.

**Abstract.** *Liquid storage tanks, one of the important components of industrial production, may be out of service for a temporary period of time or become completely unserviceable when subjected to large earthquake ground motions that may cause severe damages. Many studies in literature suggest seismic base isolation technique in protecting liquid storage tanks from the harmful effects of strong ground motions. And, the dynamic behaviors of these structural systems, which are composed of the sloshing of the fluid inside and the dynamic response of the tank itself, are directly dependent on the isolation system design. While seismic base isolation is an emerging successful earthquake resistant design method for liquid storage tanks, seismic performances of such structures may be affected negatively from potential deviations that may occur in the mechanical properties of the isolators from the nominal design values. Deviations may come into scene due to a variety of reasons such as the errors and/or uncertainties in the properties of the materials, dimensions of the elements, manufacturing methods, quality control and installation steps. In this paper, the effects of subject deviations in the mechanical characteristics of the seismic isolators on the seismic performances of liquid storage tanks equipped with nonlinear isolation systems are investigated under different historical earthquake records. To this end, sensitivity analyses are carried out by first conducting nonlinear time history analyses of a benchmark liquid storage tank mounted on a nonlinear isolation system in 3DBASIS-ME and then comparing its seismic responses including bearing displacements and sloshing displacements, which are obtained separately for nominal and deviated cases. In the context of this study, the characteristic isolator parameters including the yield force and the post-yield to pre-yield stiffness ratio are considered as the mechanical properties which may deviate from their nominal design values.*

## 1 INTRODUCTION

Liquid storage tanks are one of the important industrial-type structural systems which are generally used for storing water, chemicals, petroleum products, toxic and flammable fluids etc. [1]. These tanks play an extremely important role in production for many industries. In addition, these structures have to suffer no damage to be able to serve right after an external factor such as flood, landslide, and particularly earthquakes which may cause huge economic losses. For this reason, protecting these structures from the harmful effects of the abovementioned external factors may be of vital importance in a country's economy.

As is the case for building type of structural systems, the desired seismic performance level can be effectively provided using base-isolation, which is an effective alternative earthquake resistant design method based on the concept of seismic performance by lengthening the fundamental period of the structural system [2]. However, seismic performances of base-isolated structures may be affected negatively from potential deviations that may occur in the mechanical properties of the isolators with respect to their nominal design values due to a variety of reasons such as the errors and/or uncertainties in the properties of the materials, dimensions of the elements, manufacturing methods, quality control and installation steps. There are a number of research studies investigating the effects of such deviations in the mechanical isolator properties of the base-isolated buildings [3, 4]. And, the subject deviations are also important for the seismic performance of base-isolated liquid storage tanks, since the dynamic behaviors of the base-isolated liquid storage tanks, which are composed of the sloshing of the fluid inside and the dynamic response of the tank itself, are directly dependent on the isolation system design. However, limited number of studies [5, 6] investigate the effects of subject deviations on the seismic performances of base-isolated liquid storage tanks.

In order to shed light to this issue, in this study the effects of the deviations in the mechanical characteristics of the seismic isolators, including yield force and the post-yield to pre-yield stiffness ratio, on the structural response parameters of base-isolated liquid storage tanks, including bearing displacements and sloshing displacements, are investigated under two different historical earthquake records via sensitivity analyses that compare the subject seismic responses which are obtained for nominal and deviated cases.

## 2 BASE-ISOLATED LIQUID STORAGE TANK

A benchmark base-isolated liquid storage tank whose superstructure and overall geometrical properties are obtained from Tsopelas et al., 1994 [7] is used in this study. The superstructure and the isolation system are described in this section.

### 2.1 Superstructure

The circular tank, assumed to be used for water storage within the scope of this study, consists of a steel wall and a concave-down steel roof, and is mounted on a circular rigid concrete basemat which is placed on a nonlinear isolation system consisting of 52 identical rubber based isolators. The radius ($R$) and the total height of the subject tank are 18.29 m and 12.80 m, respectively while the steel thickness ($h$) for both the tank wall and its concave-down roof is 2.54 cm. The height ($H$) of the water inside the tank is 12.19 m, which results in a height to radius ratio ($H/R$) of 0.67. The weights for the steel tank (including the wall and the roof), the concrete basemat, and the stored water inside the tank are equal to 4998.91 kN, 11697.93 kN, and 126273.45 kN, respectively.

Numerical modelling and time history analyses of the subject storage tank are carried out in 3D-BASIS-ME [7] which is a computer program that can conduct nonlinear dynamic analyses of seismically isolated liquid storage tanks following the mechanical analog developed

for this type of structural systems by Haroun and Housner, 1981 [8]. The details of the subject mechanical analog which takes into account the deformability of the tank wall and sloshing of the fluid can be found in [8]. As for the details of the numerical modelling of the tank, which is based on that analog, they can be found in [7] and also in [9] who used the tank superstructure and overall geometry presented by Tsopelas et al., 1994 [7] but introduced their own elastomeric isolation system properties.

## 2.2 Substructure

The circular rigid concrete basemat of the benchmark liquid storage tank sits on a nonlinear isolation system consisting of 52 identical rubber based isolators which are placed symmetrically in two horizontal orthogonal directions with a typical center-to-center distance of 5.18 m. In this study, the force-displacement relationship of all these isolators, exhibiting nonlinear material behavior as well as hysteretic energy dissipation, is modelled by a smooth bilinear hysteretic curve which is based on the Bouc-Wen [10] hysteretic model. One of the main mechanical parameters of the isolation system consisting of the subject isolators is the post-yield stiffness ($K_2$), which can be determined using its relationship with the isolation period ($T_0$) and the effective weight of the tank ($W_{eff}$) given in Equation 1 [11] where $g$ is the gravitational acceleration. In this study, $T_0$ is assumed to be 4 s for the benchmark base-isolated liquid storage tank, while $W_{eff}$ is obtained as 70388.66 kN for the subject tank by extracting the sloshing mode weight of 72581.63 kN from the total physical weight of 142970.29 kN. So, the total isolation system post-yield stiffness is obtained as $K_2$=17710.13 kN. As for the rest of the main mechanical parameters of the isolation system, i.e. the total isolation system pre-yield stiffness ($K_1$), the yield force ($F_y$), and the post-yield to pre-yield stiffness ratio (α), they are obtained as 487405.90 kN/m, 7304.27 kN, and 0.036, respectively using the relationships given in Equations 2-4 [12], assuming characteristic strength ratio ($Q/W_{eff}$), and yield displacement ($D_y$) as 10% and 1.5 cm, respectively.

$$T_0 = 2\pi\sqrt{W_{eff}/(K_2 \times g)} \tag{1}$$

$$Q = (K_1 - K_2) \times D_y \tag{2}$$

$$F_y = K_1 \times D_y \tag{3}$$

$$\alpha = K_2/K_1 \tag{4}$$

The values obtained above are considered as the nominal design values of the mechanical parameters of the isolators. And the deviated cases are generated by assuming $F_y$ and α to be the mechanical properties which may deviate from their nominal values. The deviations from the nominal design values are considered as ±5%, ±15%, and ±25% for both of $F_y$ and α (Table 1). As seen in Table 1, the deviated cases generated in the context of this study are divided into two main cases. And, each of the main deviated cases consists of six deviated subcases denoted with A, B, C, D, E, and F corresponding to to +5%, +15%, +25%, -5%, -15%, and -25% deviations, respectively. For the first main case, $F_y$ is the deviated parameter while α keeps its nominal design value for the subcases of the first main deviated case and for the second main case α is the deviated parameter while $F_y$ keeps its nominal design value for the subcases of the second main deviated case.

| Main Case | Mechanical Parameter | Nominal Value | Subcases | | | | | |
|---|---|---|---|---|---|---|---|---|
| | | | Parameters | A (+5%) | B (+15%) | C (+25%) | D (-5%) | E (-15%) | F (-25%) |
| 1st | $F_y$ (kN) | 7304.27 | $F_y$ (kN) | 7669.48 | 8399.91 | 9130.34 | 6939.06 | 6208.63 | 5478.20 |
| | | | α (-) | 0.0360 | 0.0360 | 0.0360 | 0.0360 | 0.0360 | 0.0360 |
| 2nd | α (-) | 0.0360 | $F_y$ (kN) | 7304.27 | 7304.27 | 7304.27 | 7304.27 | 7304.27 | 7304.27 |
| | | | α (-) | 0.0378 | 0.0414 | 0.0450 | 0.0342 | 0.0306 | 0.0270 |

Table 1: Nominal and deviated case values of isolation system yield force ($F_y$) and isolation system post-yield to pre-yield stiffness ratio (α)

## 3 GROUND MOTION DATA

Two historical earthquake records used in this study are obtained from PEER Ground Motion Database [13]. The benchmark liquid storage tank with the nominal case isolation system and the tanks with the isolation systems of the deviated subcases are unidirectionally subjected to the earthquake records of I-ELC180 and SYL360, which are recorded during the 1940 Imperial Valley Earthquake and the 1994 Northridge Earthquake, respectively. Necessary information about these records are presented in Table 2. In this table, $M_s$ is the earthquake magnitude, *PGA* is the peak ground acceleration, *PGV* is the peak ground velocity and *PGD* is the peak ground displacement. The response spectra (ζ=5%, 10%, and 15% damped) of the subject ground motions are presented in Figure 1.

| Component name | Record station | Record date | $M_s$ | *PGA* (g) | *PGV* (cm/s) | *PGD* (cm) |
|---|---|---|---|---|---|---|
| I-ELC180 | El Centro | 05/19/1940 | 7.2 | 0.313 | 29.8 | 13.32 |
| SYL360 | Sylmar | 01/17/1994 | 6.7 | 0.843 | 129.6 | 32.68 |

Table 2: Characteristics of earthquake records.

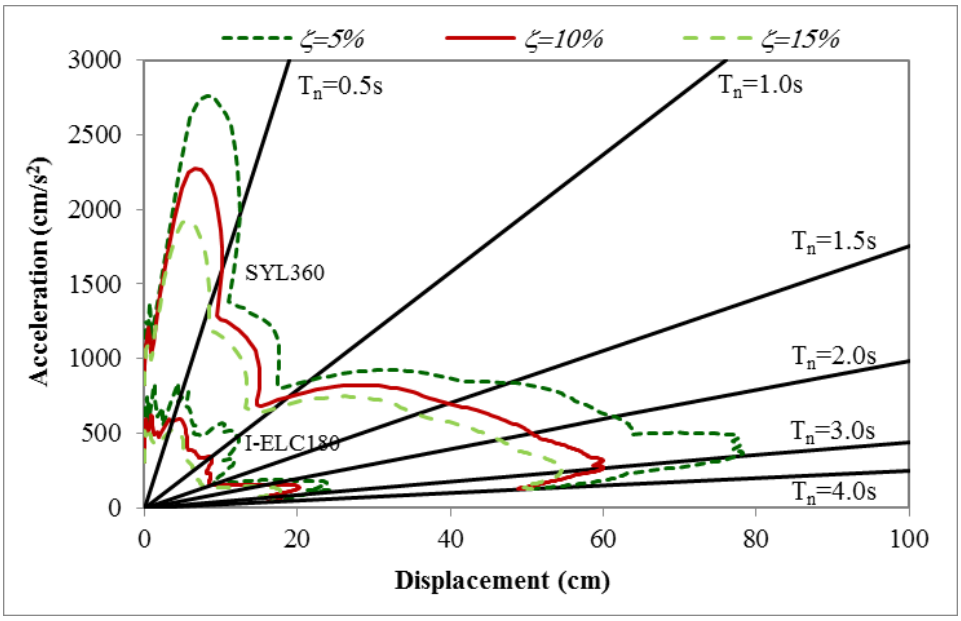


Figure 1: Response spectra (ζ=5%, 10%, and 15% damped) for I-ELC180 and SYL360 records.

## 4 SENSITIVITY ANALYSES

In this section, the results of the sensitivity analyses, which are carried out for investigating the effects of the deviations in the mechanical characteristics of the seismic isolators on the seismic performances of liquid storage tanks equipped with nonlinear isolation systems under historical earthquake records, are presented. In the context of the sensitivity analyses, unidirectional nonlinear time history analyses of the benchmark liquid storage tank equipped with the nominal case isolation system and the tanks equipped with the deviated subcase isolation systems (Table 1) are conducted under I-ELC180 and SYL360 ground motion records in order to obtain the seismic responses including the bearing displacements and the sloshing displacements corresponding to both nominal and deviated cases. Then, these responses are compared to each other.

As mentioned in Sec. 2, when $F_y$ is the deviated parameter, α keeps its nominal design value for the subcases of the first main deviated case (i.e., 1A, 1B, 1C, 1D, 1E, and 1F) whereas, when α is the deviated parameter, $F_y$ keeps its nominal design value for the subcases of the second main deviated case (i.e., 2A, 2B, 2C, 2D, 2E, and 2F). This approach makes it possible to determine the sensitivity of seismic performance of the subject structural systems to only the deviated isolator parameter.

The bearing and the sloshing displacement time history plots obtained under I-ELC180 and SYL360 records for the nominal case and the deviated subcases 1C and 1F (where $F_y$ deviates from its nominal value (7304.27 kN) by +25% and -25% respectively), are presented in Figure 2. It is seen from the comparison of the time history plots given in Figure 2 that, the bearing displacements (Figures 2a and 2c) are more sensitive to the deviations in $F_y$ than the sloshing displacements (Figures 2b and 2d). It is also seen that the deviations in the bearing and the sloshing displacements vary with respect to the ground motion record.

As for the bearing displacement and the sloshing displacement time history plots obtained under the I-ELC180 and SYL 360 records for the nominal case and the deviated subcases 2C and 2F (where α deviates from its nominal value (0.0360) by +25% and -25% respectively), they are presented in Figure 3. The comparison of the time history of plots given in Figure 3 shows that, both of the structural response parameters shows little sensitivity to the deviations in α and the comparison of the plots given in Figure 2 and Figure 3 indicate that both of the structural response parameters in question are more sensitive to the deviations in $F_y$ than to the deviations in α, under the ground motion records used in this study.

In addition to the time history plots presented, positive and negative percent deviations in the peak response parameters are also calculated via Equations 5 and 6 which are named here as "error ratios" ($e_{bd}$ and $e_{sd}$) using the peak values of the bearing displacements (*bd*) and sloshing displacements (*sd*). In these equations, the subscripts "*n*" and "*d*" refer to the nominal and the deviated cases, respectively.

$$e_{bd} = \frac{bd_d - bd_n}{bd_n} \times 100 \tag{5}$$

$$e_{sd} = \frac{sd_d - sd_n}{sd_n} \times 100 \tag{6}$$

The error ratios calculated for all of the deviated cases (Table 1) under the I-ELC180 and SYL360 records are presented in Table 3. Actual peak values of the subject response parameters (*bd* and *sd*) obtained for the nominal and deviated cases under both records are also provided in this table.

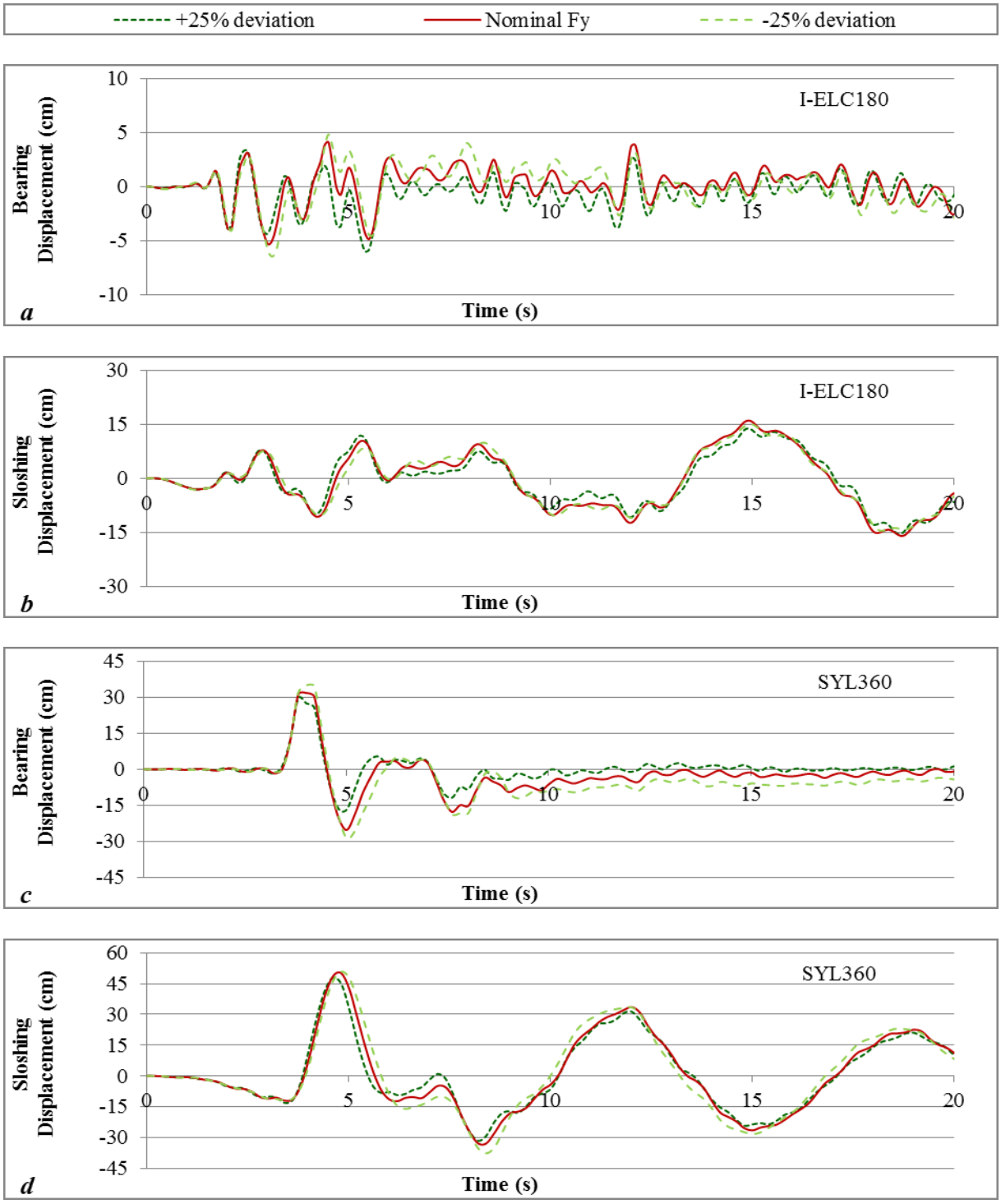


Figure 2: Sensitivity of the bearing and the sloshing displacements to the yield force - subcases 1C and 1F under I-ELC180 and SYL360 earthquake records.

It is seen from Table 3 that, the absolute values of the error ratios calculated for both of the response parameters under both of the records generally increase with the increasing deviation in the subject isolator parameter. Therefore, the largest (positive or negative) error ratios are obtained for C or F subcases corresponding to +25% and -25% deviations are in the isolator parameters, respectively. It is also seen from this table that, the peak error ratio for the bearing displacements is obtained as $e_{bd}$ = 20.60% in subcase 1F, where $F_y$ deviates by -25% from its

nominal value, under the IELC-180 record. The peak error ratio for the sloshing displacements is obtained as $e_{sd}$ = -5.85% in subcase 1C, where $F_y$ deviates by +25% from its nominal value, under the IELC-180 record. On the other hand, the largest (positive or negative) error ratios for the 2nd main case (deviated α) are obtained for case 2F under SYL360 record. That is, a -25% deviation in α causes peak error ratios of 2.35% and -3.51% in the bearing displacements and the sloshing displacements, respectively as seen from Table3.

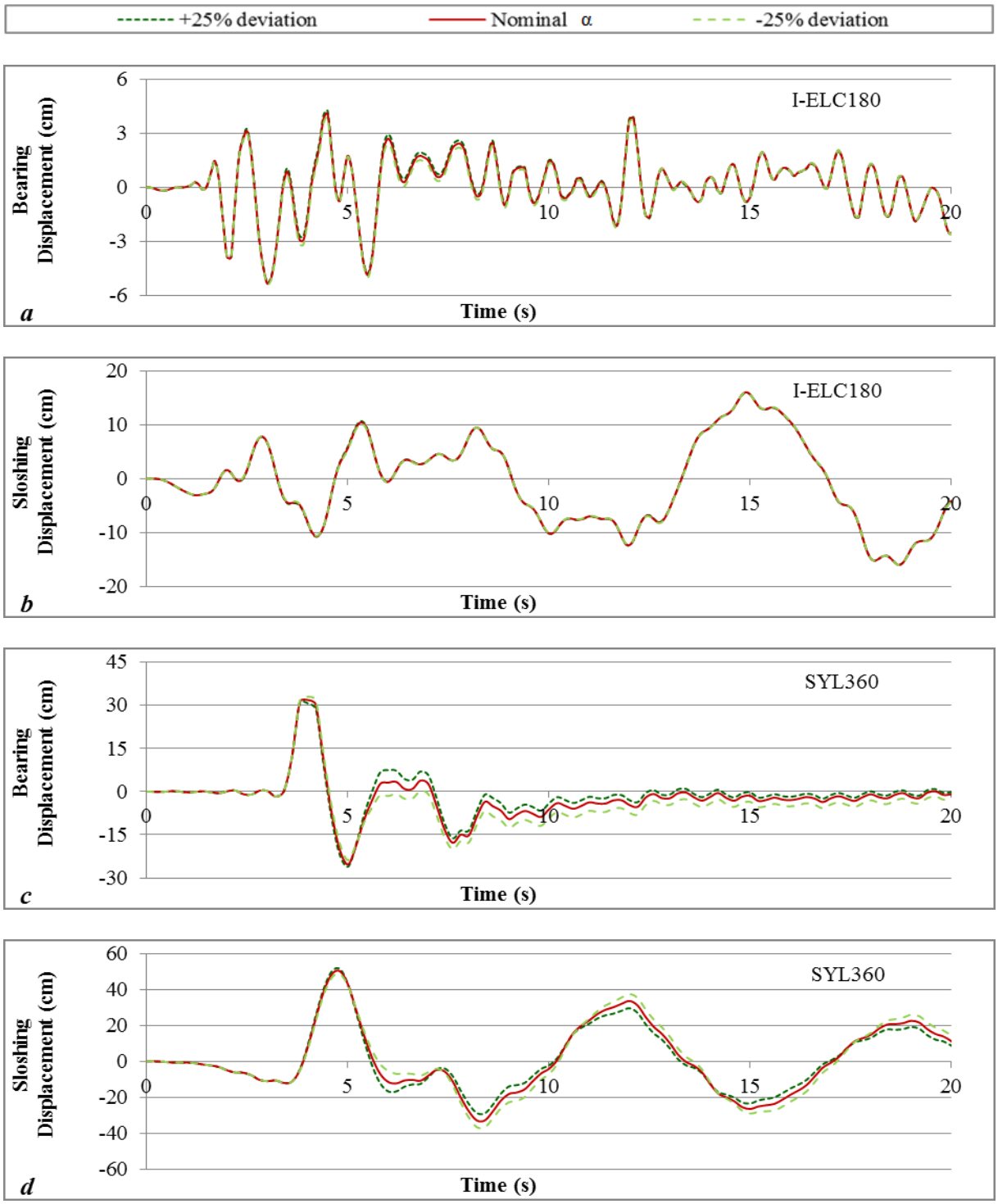


Figure 3: Sensitivity of the bearing and the sloshing displacements to the post-yield to pre-yield stiffness ratio - subcases 2C and 2F under I-ELC180 and SYL360 earthquake records.

| Case | Subcase | Earthquake Records | | | | | | | |
|---|---|---|---|---|---|---|---|---|---|
| | | I-ELC180 | | | | SYL360 | | | |
| | | *bd* (cm) | $e_{bd}$ (%) | *sd* (cm) | $e_{sd}$ (%) | *bd* (cm) | $e_{bd}$ (%) | *sd* (cm) | $e_{sd}$ (%) |
| Nominal | - | 5.39 | 0 | 19.00 | 0 | 33.45 | 0 | 50.65 | 0 |
| 1st main case (Deviated parameter: $F_y$) | 1A (+5%) | 5.18 | -3.77 | 18.94 | -0.33 | 33.12 | -0.99 | 49.81 | -1.65 |
| | 1B (+15%) | 5.73 | 6.27 | 18.51 | -2.59 | 32.36 | -3.26 | 48.56 | -4.11 |
| | 1C (+25%) | 6.17 | 14.57 | 17.89 | **-5.85** | 30.94 | -7.52 | 48.08 | **-5.07** |
| | 1D (-5%) | 5.58 | 3.54 | 19.07 | 0.33 | 33.73 | 0.84 | 51.31 | 1.30 |
| | 1E (-15%) | 6.01 | 11.55 | 18.61 | -2.05 | 34.87 | 4.25 | 51.99 | 2.66 |
| | 1F (-25%) | 6.50 | **20.60** | 18.22 | -4.09 | 36.83 | **10.10** | 50.90 | 0.50 |
| 2nd main case (Deviated parameter: α) | 2A (+5%) | 5.37 | -0.24 | 19.00 | -0.03 | 33.30 | -0.46 | 50.93 | 0.55 |
| | 2B (+15%) | 5.36 | -0.57 | 18.98 | -0.11 | 33.07 | -1.14 | 51.44 | 1.55 |
| | 2C (+25%) | 5.34 | -0.90 | 18.96 | **-0.21** | 32.87 | -1.75 | 52.07 | 2.81 |
| | 2D (-5%) | 5.40 | 0.19 | 19.01 | 0.03 | 33.58 | 0.38 | 50.37 | -0.55 |
| | 2E (-15%) | 5.42 | 0.66 | 19.01 | 0.04 | 33.83 | 1.14 | 49.71 | -1.86 |
| | 2F (-25%) | 5.45 | **1.13** | 19.01 | 0.07 | 34.24 | **2.35** | 48.87 | **-3.51** |

Table 3: Error ratios in peak values of bearing displacement (*bd*) and sloshing displacement (*sd*) responses under I-ELC180 and SYL360 earthquake records.

## 5 CONCLUSIONS

In this study, the sensitivity of the seismic performance of liquid storage tanks equipped with nonlinear isolation systems to the deviations in the mechanical properties of the seismic isolators are investigated under two historical earthquake records. Bearing displacements and sloshing displacements are considered as the seismic performance criteria while yield force and post-yield to pre-yield stiffness ratio are assumed as the deviated mechanical parameters. Based on the limited parametric analyses conducted here, the following conclusions are reached:

- Both bearing and sloshing displacements are more sensitive to the deviations in the yield force than to the deviations in the post-yield to pre-yield stiffness ratio.
- Bearing displacements seem to be more sensitive to the deviations in the mechanical properties of the seismic isolators compared to sloshing displacements.
- The level of the sensitivity of the seismic performance of liquid storage tanks with nonlinear isolation systems to deviations in mechanical characteristics of the seismic isolators depends on the mechanical property of the seismic isolator in question and the characteristics of the subject earthquake record.

In order to reach more comprehensive and generalizable conclusions, more subcases representing deviations of wider spectrum and more earthquake data should be used. Such a comprehensive parametric investigation considering other mechanical properties of the seismic isolators and different seismic responses under different earthquake records is currently being conducted by the authors of this paper.

## ACKNOWLEDGMENTS

We would like to acknowledge The Scientific Research Projects Coordination Unit of Istanbul University (IU BAP) for providing financial support under Project No: BEK-24000.

## REFERENCES


[1] O.R. Jaiswal, D.C. Rai, S.K. Jain, 2007, Review of seismic codes on liquid-containing tanks. *Earthquake Spectra*, **23(1)**, 239-260, 2007.

[2] C. Alhan, E. Güler, H. Gazi, Behavior of base-isolated liquid storage tanks under synthetic near-fault earthquake pulses. *Fifth International Symposium on Life-Cycle Civil Engineering (IALCCE'16)*, Delft, Holland, October 16-19, 2016.

[3] H. Gazi, C. Alhan, Sismik izolasyon sistemi parametrelerindeki rastgele değişimlerin etkisinin monte carlo simülasyon metoduyla incelenmesi, *2. Türkiye Deprem Mühendisliği ve Sismoloji Konferansı*, Hatay, Turkey, September, 25-27, 2013.

[4] C. Alhan, K. Hışman, Seismic isolation performance sensitivity to potential deviations from design values. *Smart Structures and Systems*, **8**, 293-315, 2016.

[5] S.K. Saha, K. Sepahvand, V.A. Matsagar, A.K. Jain, S. Marburg, Stochastic analysis of base-isolated liquid storage tanks with uncertain isolator parameters under random excitation. *Engineering Structures*, **57**, 465-474, 2013.

[6] O. Curadelli, Equivalent linear stochastic seismic analysis of cylindrical base-isolated liquid storage tanks. *Journal of Constructional Steel Research*, **83**, 166-176, 2013.

[7] P.C. Tsopelas, M.C. Constantinou, A.M. Reinhorn, *3D-BASIS-ME: Computer program for nonlinear dynamic analysis of seismically isolated single and multiple structures and liquid storage tanks, Technical report NCEER-94-0010*. National Center for Earthquake Engineering Research, 1994.

[8] M.A. Haroun, G.W. Housner, Seismic design of liquid storage tanks. *Journal of the Technical Councils of ASCE*, **107**, 191-207, 1981.

[9] H. Gazi, C.M. Kazezyılmaz-Alhan, C. Alhan, Behavior of seismically isolated liquid storage tanks equipped with nonlinear viscous dampers in seismic environment, *10th Pacific Conference on Earthquake Engineering (PCEE 2015)*, Sydney, Australia, November 6-8, 2015.

[10] Y.K. Wen, Method for random vibration of hysteretic systems. *Journal of the Engineering Mechanics Division (ASCE)*, **102**, 249–263, 1976.

[11] S. Nagarajaiah, A.M. Reinhorn, M.C. Constantinou, *Nonlinear dynamic analysis of three-dimensional base isolated structures (3D-BASIS), Technical Report NCEER-89-0019*. National Center for Earthquake Engineering Research, 1989.

[12] F. Naeim, J.M. Kelly, *Design of seismic isolated structures: from theory to practice, mechanical characteristics and modeling of isolators*, Wiley, 1999.

[13] Pacific Earthquake Engineering Resource Center (PEER), *NGA database (http://peer.berkeley.edu/nga/).* University of California, January 2017.

COMPDYN 2017
6th ECCOMAS Thematic Conference on
Computational Methods in Structural Dynamics and Earthquake Engineering
M. Papadrakakis, M. Fragiadakis (eds.)
Rhodes Island, Greece, 15–17 June 2017

# EARTHQUAKE DAMAGE ESTIMATION OF FOUR PALACE BUILDINGS AND MEASUREMENTS OF VIBRATION DECREASING FOR CULTURAL RELICS CABINET IN BEIJING FORBIDDEN CITY

**Junwu DAI[1,2], Lulu ZHANG[1,2] and Yongqiang YANG[1,2]**

[1] Key Laboratory of Earthquake Engineering and Engineering Mechanics
[2] Institute of Engineering Mechanics, China Earthquake Administration
Xuefu road no.29, Harbin city, Heilongjiang Province
email: jwdai@iem.cn.

[1] Key Laboratory of Earthquake Engineering and Engineering Mechanics
[2] Institute of Engineering Mechanics, China Earthquake Administration
Xuefu road no.29, Harbin city, Heilongjiang Province
email: 18845090562@163.com ;yangiem@foxmail.com

**Keywords:** Seismic Damage Estimation, Palace, Wooden Structure, Storage Cabinets, Damper

**Abstract.** *In order to research the seismic performance of Taihe, Zhonghe, Baohe and Wenhua Palace, nonlinear dynamic time response analyses under different earthquakes and PGA levels are carried out. ANSYS/LS-DYNA is used to conduct the finite element analysis. Moreover, in order to select more effective seismic protection measurements for the storage cabinets of cultural relics in the existing underground storehouse of the Palace Museum, seismic responses of storage cabinets with different spring-dampers connected between each other are calculated. Corresponding acceleration and displacement responses are compared. Suggestions on parameter settings of spring dampers which maximum the damping efficiency are finally given.*

## 1 INTRODUCTION

Beijing is located in 8-degree seismic fortification district, it's beneficial to research the seismic performance of some typical structures in The Forbidden City. Four typical buildings, Taihe Palace, Zhonghe Palace, Baohe Palace and Wenhua Palace are chosen and relevant nonlinear dynamic time response analyses are conducted. Based on the existing research, selecting 1999 Chi-Chi earthquake and 1976 Tangshan earthquake respectively those durations are 40 seconds from four PGA levels, i.e. 0.05g, 0.1g, 0.2g and 0.4g, corresponding to the local seismic risk level of Beijing area. Peak acceleration ratio among the three directions is $a_{PGx}:a_{PGy}:a_{PGz}=1:0.85:0.65$, x and z is horizontal, y for vertical. The finite elements used are as follows, BEAM161 for beams and columns, SHELL163 for roofs and walls and COMNI165 for mortise-tenon joints.

Consulting the documents and reference [2], wooden beam itself has little energy dissipation capacity, energy dissipation is mainly relied on the mortise-tenon joint. The mortise-tenon joint energy dissipation is generated through extrusion and rotation. According to the results of related experiments[1] bending moment and corner restoring force curve chart of mortis-tenon joint is plotted in figure 1, for the value of relevant parameters: $k_1=3.602kN\cdot m/rad$ when $\theta$=0~0.005$rad$, $k_2=5.755kN\cdot m/rad$ when $\theta$=0.005~0.07$rad$, $k_3=1.781kN\cdot m/rad$ when $\theta$=0.070~0.100$rad$.

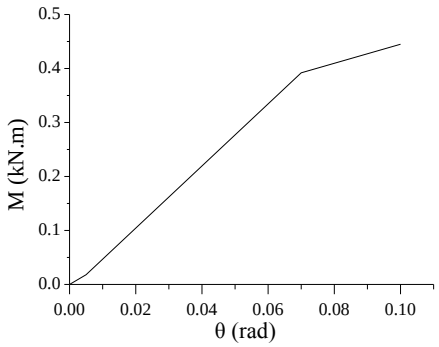


Figure 1:Bending moment and corner restoring force curve of mortis-tenon joint

Acceleration histories of ground motion records used in this paper are plotted in figure 2 and figure 3.

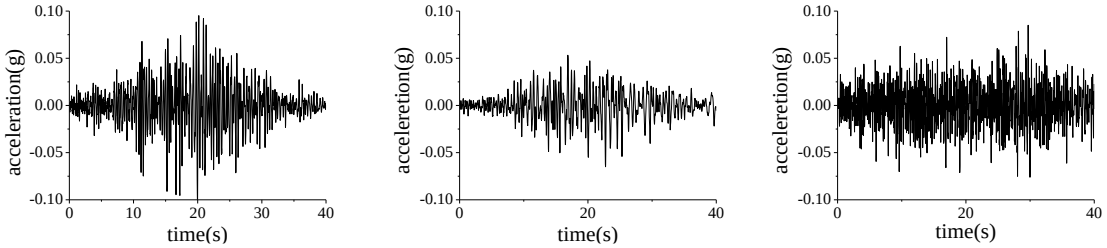


Figure 2:Three direction time history of Tangshan earthquake

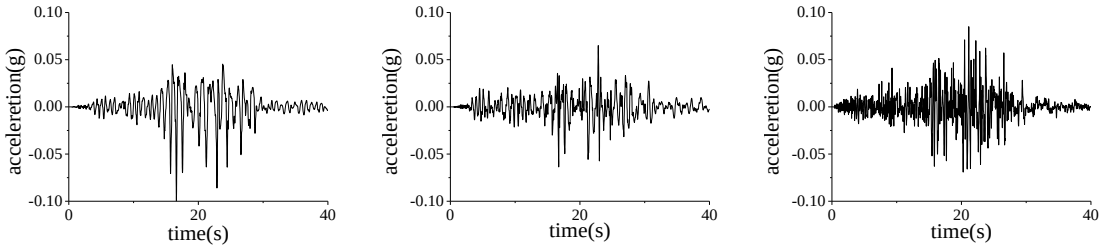


Figure 3: Three direction time history of Chichi earthquake

Simplified measures as follows are used in the process of establishing the finite element models: (1) Low walls, doors and windows are not considered. (2) Roof weight is set as $4.1kN/m^2$ according to the reference[3]. (3) The weight of building ridge beast is not considered. (4) The details of tiles are not established. (5) The influence of the steps is not involved.

## 2 SEISMIC PERFORMANCE OF CULTURAL RELIC BUILDINGS

### 2.1 The seismic performance of Taihe palace

Taihe Palace is located in the central axis of the Forbidden City. It is the largest existing wood structure of Chinese timberwork temple and commonly known as the essence of the ancient Chinese palace buildings. It is 64m long, 37m wide and 26.92m high. Two nodes of the numerical model at the center of the roof (Node 40026) and outer pillars point (Node802) is selected to study its acceleration and displacement responses. Realistic picture and finite element model of Taihe palace are shown in figure 4.




Figure 4: Realistic picture and finite element model of Taihe palace

Based on the numerical simulation result, the acceleration amplification factors and maximum displacements under different earthquakes (Chichi and Tangshan) and different PGA levels (0.05g, 0.10g, 0.02g and 0.40g) are plotted in figure 5 and 6. Acceleration amplification factors represent the ratio between the maximum acceleration response of selected node and corresponding PGA.

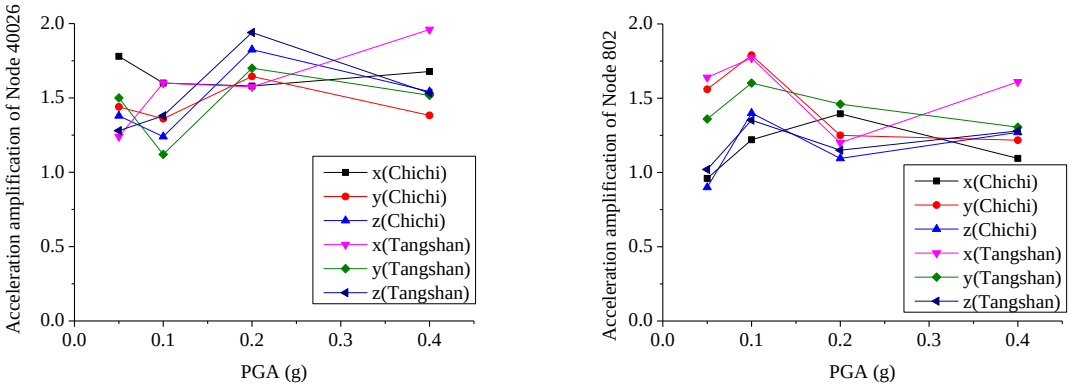


Figure 5:Acceleration amplification of Node 40026 node and Node 802

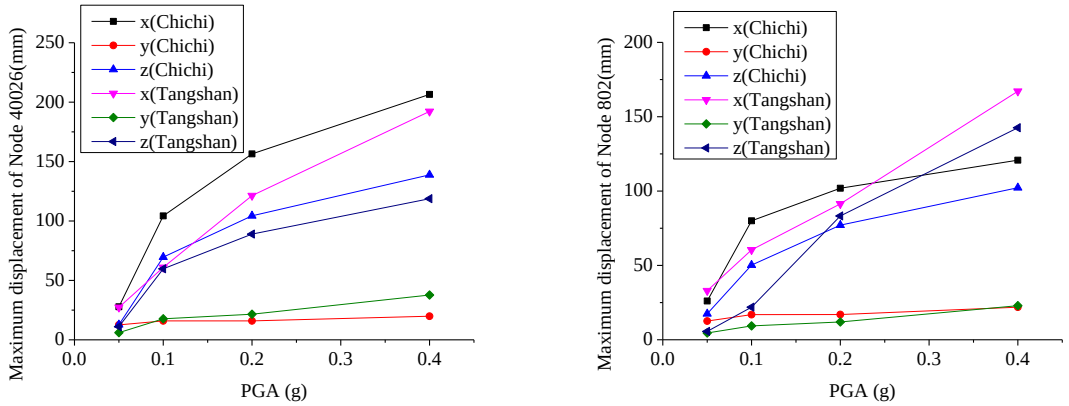


Figure 6: displacement response of Node 40026 node and Node 802

## 2.2 The seismic performance of Zhonghe Palace

Zhonghe Palace is one of the three main halls in The Forbidden City. It is 22m long, 22m wide and 19m high. Two nodes of the numerical model at roof top (Node 6517) and outer pillars point (Node 328) are selected to study its acceleration and displacement responses. Realistic picture and finite element model of Zhonghe Palace are shown at figure 7. In the peak of 0.05g, 0.1g, 0.2 g ,0.4 g Chichi and Tangshan ground motion, the acceleration amplification and displacement reaction of Node 6517, Node 328 is shown at figure 8 to figure 9.




Figure 7: Realistic picture and finite element model of Zhonghe palace

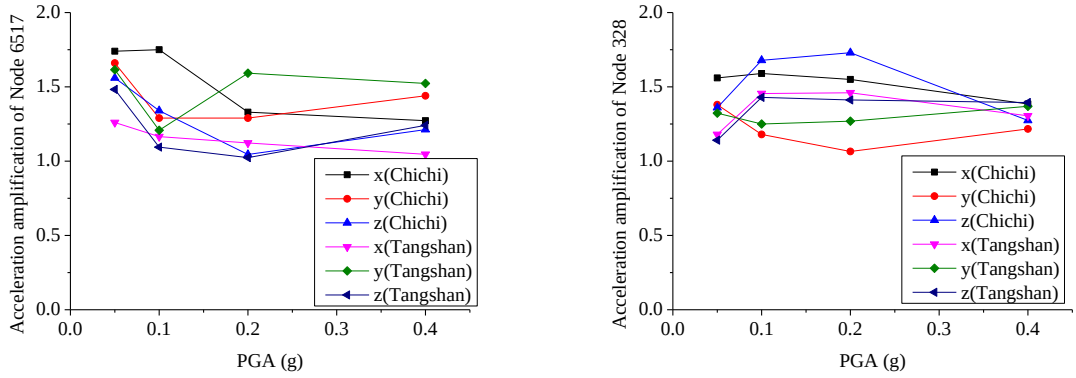


Figure 8:Acceleration amplification of Node 6517, Node 328

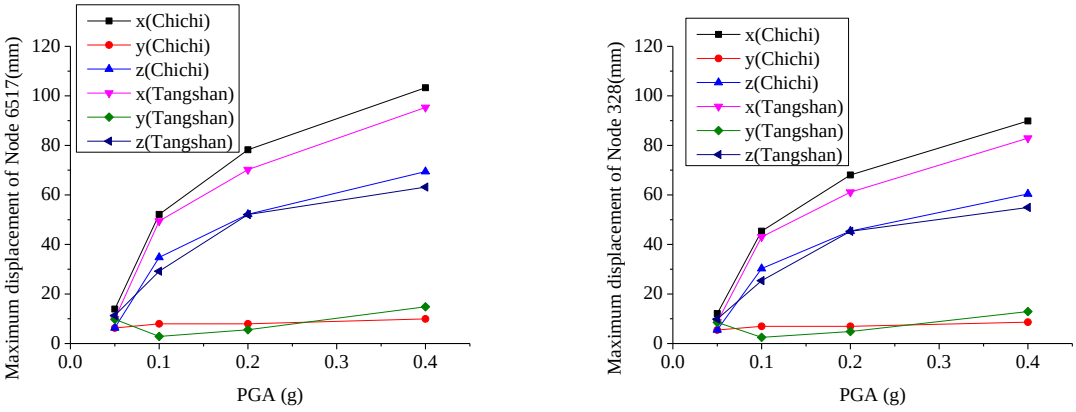


Figure 9:Displacement response of Node 6517, Node 328

## 2.3 The seismic performance of Baohe Palace

Baohe Palace is one of the three main halls in The Forbidden City. It is 42m long, 21.66m wide and 29.50m high. Two nodes of the numerical model at the center of the roof (Node 2602) and outer pillars point (Node 107) is selected to study its acceleration and displacement responses. Finite element model of Baohe Palace is shown in figure10.

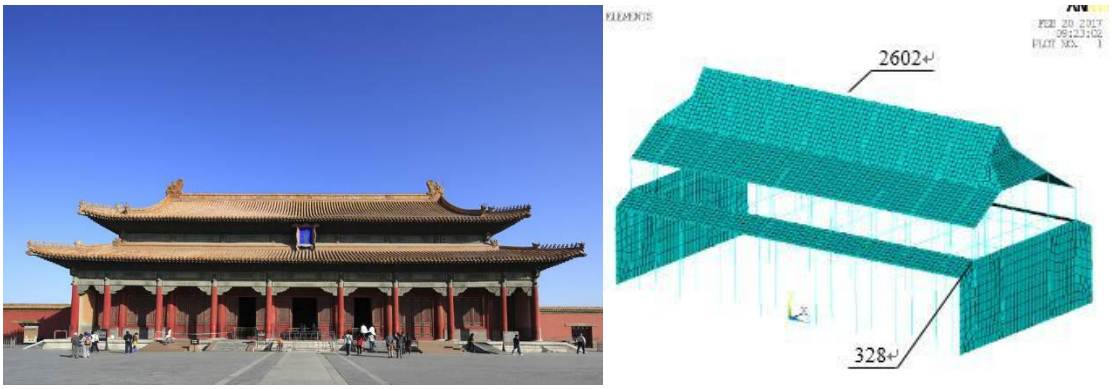


Figure 10: Realistic picture and finite element model of Baohe palace

The acceleration amplification factors and maximum displacements under Chichi and Tangshan earthquakes at 4 PGA levels are plotted in figure 11 and 12.

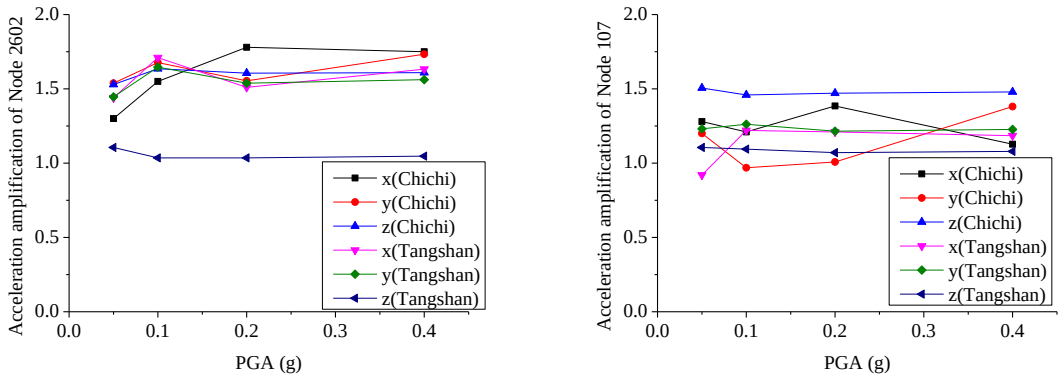


Figure 11:Acceleration amplification of Node 2602 and Node107

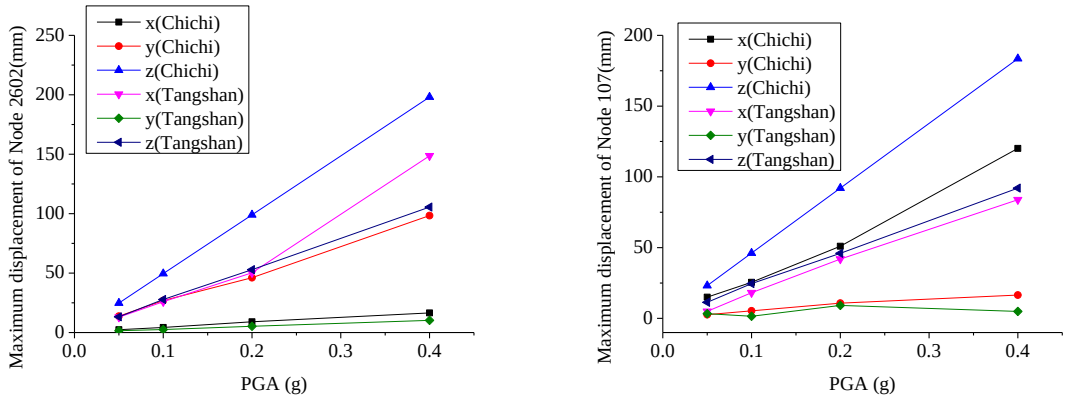


Figure 12: displacement response of Node 2602 and Node107

## 2.4 The seismic performance of Wenhua Palace

The horizontal shape of the Main Palace is I-section. As shown in figure 13. The Front Hall is similar as the Rear Hall but a little shallower. The two halls are connected by corridor. select 4 nodes at the center of the roof (Node 11240, Node 1140) and outer pillars point (Node 601, Node 5737) are selected to study the palace's acceleration and displacement response. Finite element model of Wenhua Palace is shown in figure 13. In the peak of 0.05g ,0.1g, 0.2g ,0.4 g Chichi and Tangshan ground motion, the maximum acceleration and displacement reaction of Node 11240, Node 601, Node 11140 and Node 5737 is shown at figure 14 to figure15.




Figure 13: Realistic picture and finite element model of Wenhua palace

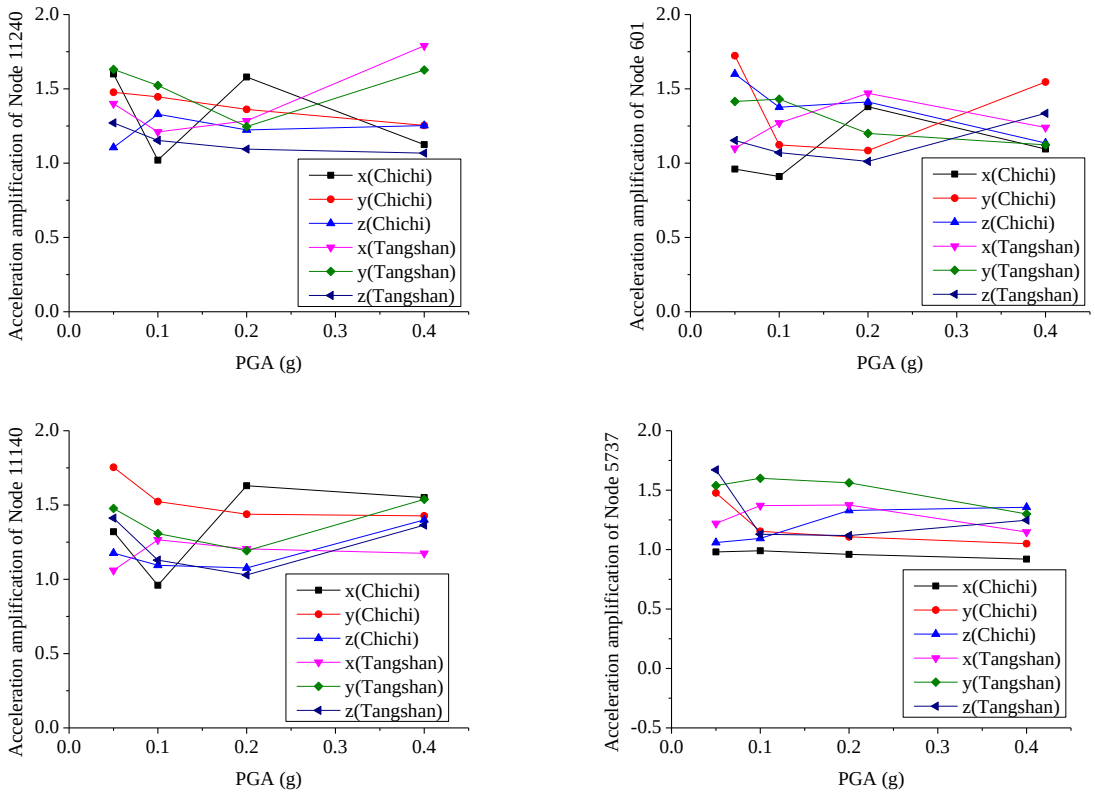


Figure 14:Acceleration amplification of Node 11240, Node 601, Node 11140 and Node 5737

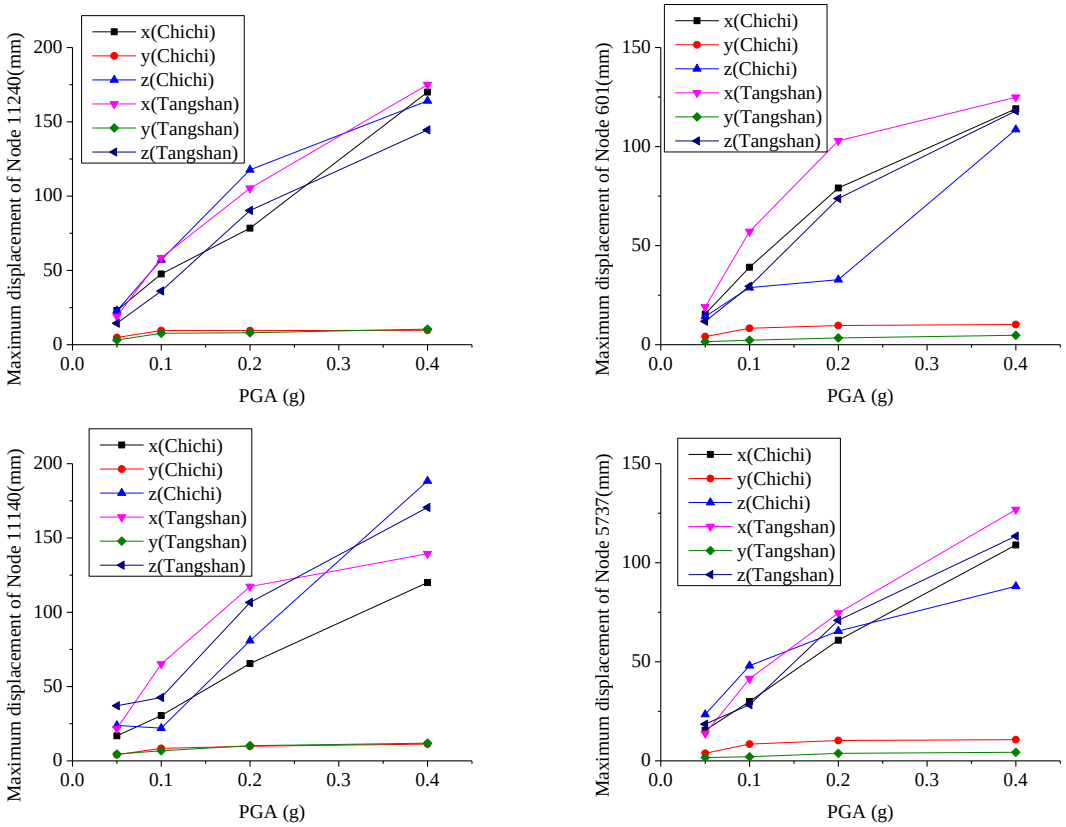


Figure 15: displacement responses of Node 11240, Node 601, Node 11140 and Node 5737

## 3 SEISMIC PROTECTION MEASUREMENTS FOR THE STORAGE CABINETS

All cultural relics cabinets are made by metal materials. According to the actual circumstance of cultural relics tank placed in the storehouse, the following three cases, listed as below, are numerically simulated to show damping effect:

Case 1: a set of cultural relics are placed against the wall while another group of cultural relics cabinet floated on the ground, no isolation or damping measures are used. The space between cultural relics tank is 1000 mm.

Case 2: a set of cultural relics placed against the wall, another group of cultural relics cabinet floated on the ground, two groups of cultural relics are linked together by damper, cultural relics tank spacing is 1000 mm.

Case 3: Two groups of cultural relics were floating on the ground, a set of cultural relics are connected to the wall by dampers, also two groups of cultural relics are linked together by damper

Air dampers are recommended, the maximum stroke of the damper used in this paper is 130 mm, the load range is from 500 to 1500 N, the weight is 2.2 kg and the length is 460 mm. Air damper is connected by rod and connecting rod is fixed with cultural relics ark by the bolt. All 6 degrees at the connected node are coupled.

The shell element is adopted to establish the numerical FEA model of the standard storage cabinets. All models have the same size, W1000mm* T600mm* H1800mm. No anchorage is used between the cabinets and the floor. Solid elements are used to establish the floor and walls. The static friction coefficient between storage cabinets and ground is set as 0.2 while the dynamic friction coefficient is 0.34. The damping coefficient of the damper is $60N \cdot s/mm$ and the damping unit length is 460 mm according to the actual length and is connected with storage cabinets by beam unit. The three translational degrees of freedom and three rotational degrees of freedom are coupled in connected nodes, the finite element models of all the three groups cultural relics cabinets are shown in figure 17 to figure 19.

Spring-damping unit COMBI165 is used to simulate air damper. COMBI165 can be used for simple spring and damping system modeling, also can be used in some more complex system, this unit provides a series of discrete element method, thus can simulate complex force-displacement relationship. COMBI165 have two nodes of a one-dimensional units and support all the nonlinear characteristics of the software. Characteristics of the unit are shown in figure 16, it has 9 translational degree of freedom (UX, UY, UZ, VX, VY, VZ, AX, AY, AZ) and three rotary degrees of freedom (ROTX, ROTY, ROTZ).

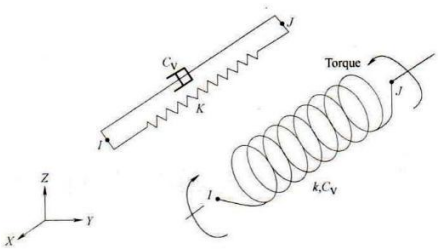


Figure 16 : Characteristics of the unit COMBI165

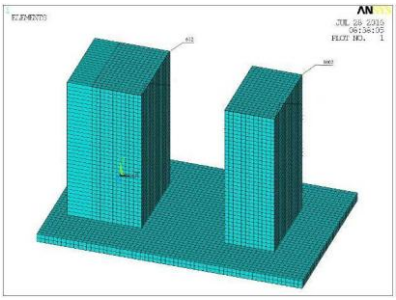

Figure 17 :First mode figure

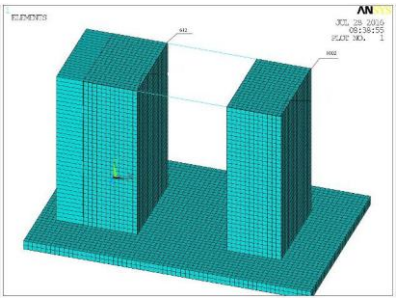

Figure 18:Second mode figure

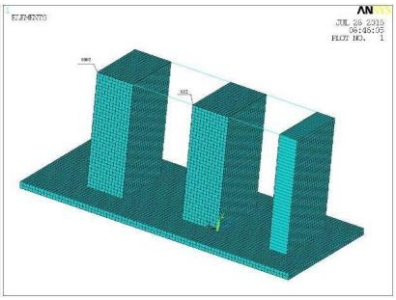

Figure 19:Third mode figure

From the case of Tangshan earthquake under PGA 0.40g, the displacement and acceleration responses of the two perpendicular horizontal direction at Node 612 and Node 1002 are extracted and shown in figure 20 to figure 23.

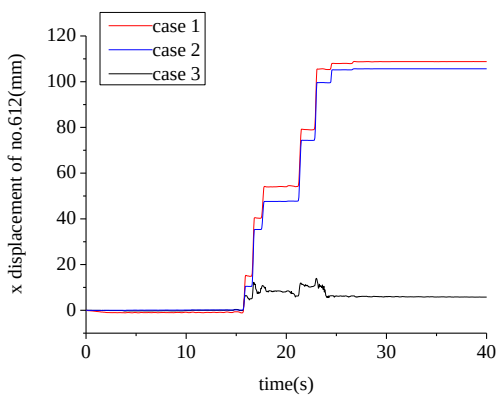


Figure 20: displacement response of Node 612

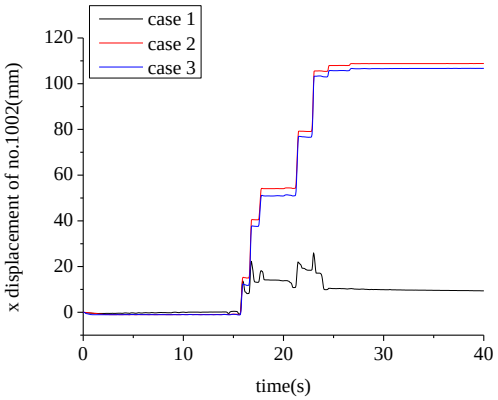


Figure 21: displacement response of Node 1002

According to the time history curves, it can be found that the maximum x and z acceleration of Node 612 and Node 1002 under 0.4 g ground motion in figure 22 to figure 23.

| | Maximum x acceleration of Node 612 (g) | Maximum x acceleration of Node 1002 (g) |
|---|---|---|
| Case 1 | 1.03 | 0.97 |
| Case 2 | 0.95 | 1.10 |
| Case 3 | 0.74 | 0.88 |

Figure 22: Maximum x acceleration of Node 612 and Node 1002

| | Maximum z acceleration of Node 612 (g) | Maximum z acceleration of Node 1002 (g) |
|---|---|---|
| Case 1 | 0.96 | 0.92 |
| Case 2 | 0.90 | 0.93 |
| Case 3 | 0.78 | 0.78 |

Figure 23: Maximum z acceleration of Node 612 and Node 1002

The maximum displacement response and acceleration of case 1 and case 2 are basically identical. When the cabinet close to the wall vibrate under the earthquake, the constraint of the cabinet disappear. For two cabinets floating on the ground, their seismic responses are the same and the relative speed between the two cultural relics is 0, so damper does not have any effect. We connect the cultural relics ark and the wall in case 3, maximum displacement of the cultural relics is 26 mm, but maximum displacement of the cultural relics is 107 mm in case 1. The maximum acceleration of the cultural relics is 0.88g in case 3, but maximum acceleration of the cultural relics is 0.97g in case 1.The simulation results show that the maximum displacement is reduced by 76% and the maximum acceleration is reduced by 10%.

## 4 CONCLUSION

1. Seismic hazards of The Forbidden City under different earthquake intensity are listed as follows:

(1) Under the influence of earthquakes at PGA 0.05 g (corresponding to the seismic intensity is 6 degree), few walls surface will spall, few slip tile may happen on roof.

(2) In the face of earthquake ground motion peak of 0.1 g (corresponding to the seismic intensity is 7 degree), walls crack slightly, a little slip tile may happen on roof.

(3) In the face of earthquake ground motion peak of 0.2 g (corresponding to the seismic intensity is 8 degree), the wall cracks seriously, the roof will collapse.

(4) In the face of earthquake ground motion peak of 0.4 g (corresponding to the seismic intensity is 9 degree), the wall roofs are totally damaged, some mortise-tenon joints will be pulled out.

2. It is recommended to use connection mode adopted by the working case 3. Two groups of cultural relics were floating on the ground, a set of cultural relics are connected to the wall by dampers, also two groups of cultural relics are linked together by damper. In these kind of cases, both acceleration and displacement responses are reduced effectively.

## ACKNOWLEDGEMENT

The authors appreciate the financial support from the Earthquake Scientific Research Funds Program (No. 201508023), the National Science and Technology Supporting Program (2015BAK17B02) and Program for Innovative Research Team in China Earthquake Administration

## REFERENCES

[1] ZHOU Qian, YAN Weiming, GUAN Hongzhi, JI Jinbao, *Seismic performance of Tai-he Palace in the Forbidden City under rear earthquake*. Journal of Building Structures, 1000-6869(2014) S1-0025-08.

[2] Zhao Shoujiang, *Seismic Performance Analysis of Ancient Wooden Structure and inner Culture Relics on display*. Institute of Engineering Mechanics, China Earthquake Administration, Harbin, China, May,2012

[3] Zhang Chenxiao, *Study on The Seismic Performance and Numerical Simulation Methods of Ancient Beam-lifted Timber Structure*. Institute of Engineering Mechanics, China Earthquake Administration, Harbin, China, May,2013

COMPDYN 2017
6th ECCOMAS Thematic Conference on
Computational Methods in Structural Dynamics and Earthquake Engineering
M. Papadrakakis, M. Fragiadakis (eds.)
Rhodes Island, Greece, 15–17 June 2017

# VULNERABILITY DATA COLLECTION AND DEFINITION OF SEISMIC RISK FOR CITIES IN PALESTINE

**Antonella Di Meo[1], Barbara Borzi[2], Marta Faravelli[2], Diego Polli[2], Marco Pagano[2] and Alessio Cantoni[2]**

[1] European Centre for Training and Research in Earthquake Engineering (EUCENTRE)
Via Ferrata, 1, 27100 Pavia, Italy
antonella.dimeo@eucentre.it

[2] European Centre for Training and Research in Earthquake Engineering (EUCENTRE)
Via Ferrata, 1, 27100 Pavia, Italy
{barbara.borzi, marta.faravelli, diego.polli, marco.pagano, alessio cantoni}@ eucentre.it

**Keywords:** Residential Buildings, Data Collection, Vulnerability, Seismic Risk, WebGIS.

**Abstract.** *This paper investigates the web with GIS functionality (WebGIS) realized by Eucentre (EUropean CENtre for Training and Research in Earthquake engineering) for SASPARM 2.0 (Support Action for Strengthening PAlestine capabilities for seismic Risk Mitigation) project [1]. The end users of the WebGIS are citizens, students, practitioners, governmental and non-governmental institutions. The platform represents a very useful and intuitive tool to load and manage data collected during the survey of residential buildings. Both practitioners and citizens can collect structural data for residential buildings by using two forms, different from each other only in terms of detail. The forms are organized into sections and they allow to identify the main geometrical and structural features of the surveyed buildings. The forms can be compiled directly on WebGIS or through two apps specifically created for Android operating system 4.0 and following. The apps enable the compilation of the fields also when internet connection is not available: data are stored on smartphone or tablet and then sent to the Web portal once internet connection is available. Starting from collected data, the seismic risk of each building is evaluated. In particular, the seismic demand to which each building is subjected to is defined from the hazard curve. In the specific case study of Nablus, the hazard curve is obtained by referring to the "West Bank and Gaza Strip: Seismic Hazard Distribution Map". For what concern the structural vulnerability, it is quantified through fragility curves. Fragility curves are defined for five damage levels [2] by using the mechanical method SP-BELA (Simplified Pushover-Based Earthquake Loss Assessment) modified in order to represent the building environment in Nablus. By combining the hazard and the vulnerability of each building, it is possible to calculate the seismic risk.*

## 1 INTRODUCTION

Earthquakes are one of the most catastrophic natural events, both in terms of casualties and economic losses. Nevertheless, the mitigation of seismic risk, which comes from the convolution of hazard (i.e. the measure of the shaking severity), exposure (i.e. the scale of the impact of the damage) and vulnerability (i.e. the measure of how a structure is prone to be damaged by the ground shaking), is possible. Since hazard and exposure cannot be reduced, the vulnerability is the only element on which it is conceivable to mitigate the seismic risk. This awareness highlighted the need to identify a process that estimates the seismic vulnerability of Palestinian residential buildings in Nablus, the city taken as a case study in the SASPARM 2.0 project [1]. The final product of SASPARM 2.0 is a WebGIS with multiple functions.

Collecting geometrical and structural data of residential buildings is one of the main WebGIS functions. Data are collected by using two forms defined according to the building environment of Nablus. The forms are different from each other only in terms of detail: practitioners compile the form with more details and citizens an easier one. The users can decide to fill in the forms directly on the WebGIS, at the tab dedicated to them (i.e. tab *Building Form – Practitioners* and tab *Building Form – Citizens*), or through two apps downloadable from the tab *Downloads* of the WebGIS. Once selected the building at the tab *Map* (see Figure 1), the WebGIS allows to check corresponding data.

Another function of the WebGIS is to determine the seismic vulnerability of buildings (i.e. tab *Fragility*). In particular, the seismic vulnerability is defined by fragility curves calculated through the mechanical method SP-BELA (Simplified Pushover-Based Earthquake Loss Assessment) ([3] and [4]). SP-BELA is an analytical procedure implemented initially to assess the seismic vulnerability of Italian building stock. In the specific case of Palestine, SP-BELA has been modified to best perform the building environment of those territories. The fragility curves are determined for five damage levels (i.e. *DL1…DL5*) according to EMS98 (European Macroseismic Scale) scale [2] and associated to each building in relation to its structural type and its number of storeys.

Then, the hazard is defined as the probability of occurrence of an earthquake exceeding a certain threshold of intensity magnitude (i.e. PGA) in a given area and in a certain time window (i.e. tab *Hazard*).

Once defined both the vulnerability and the hazard, the WebGIS calculates the seismic risk of the selected building (i.e. tab *Risk*) for three different time windows, and suggests a series of retrofit measures (i.e. tab *Retrofit*) to reduce its seismic vulnerability and consequently the risk ([5] and [6]).

The above is described in detail in the next paragraphs where also a brief description of the building environment present in Nablus is proposed.

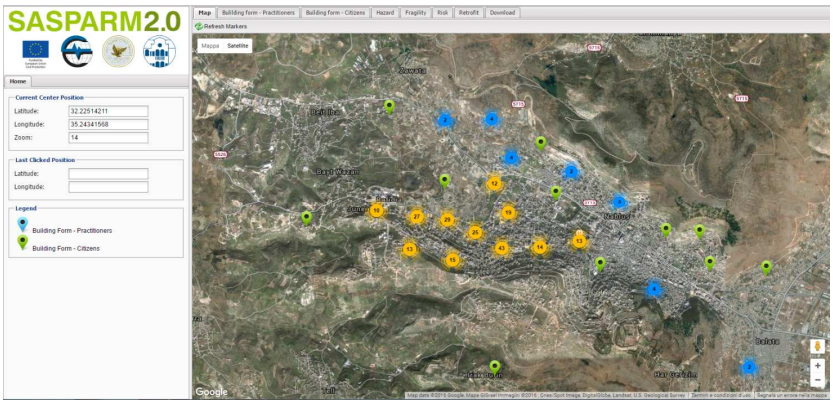


Figure 1**:** Tab *Map* - Screenshot of the initial view of the WebGIS that allows to select surveyed buildings.

## 2 BUILDING ENVIROMENT IN PALESTINE

In order to define survey forms adequate to assess the vulnerability of buildings, it has been necessary to identify the main structural types in the city of Nablus. Here the buildings are mainly new construction (see Figure 2) but seismically vulnerable as designed according to pre-code seismic standards. The latter, in fact, has been introduced only nowadays, when Palestine adopted the Jordan Code [7] which is very similar to Eurocode [8]. Figure 2 shows the buildings distribution in Nablus in relation to their year of construction: it has been obtained on the basis of data collected through the forms for practitioners filled in during the project that ended the 31st of December 2016 [1].

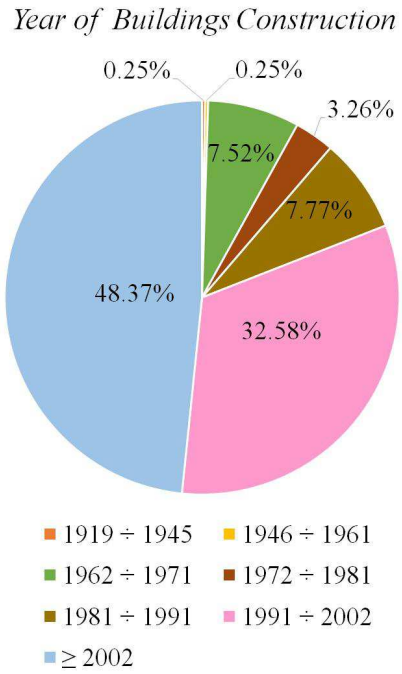


Figure 2: Distribution of buildings in Nablus in relation to their year of construction.

Nablus residential buildings can be grouped in four main structural classes:

- masonry buildings;
- reinforced concrete frame (RC) buildings;
- RC soft storey buildings (*pilotis*);
- RC shear wall buildings.

Masonry buildings are more regular both in plan and in elevation than RC ones. They have generally not more than 4 storeys and 1 or 2 bays in X-Y directions. Generally, masonry walls can be of two types:

a. the concrete is sandwiches between two surface layers of masonry stones, thus resulting in a wall thickness around 400-500 mm;

b. the masonry stones are installed row-by-row and then concrete is cast behind them via suitable framework, thus resulting in a wall with one-side masonry stones and the other side concrete surface. In recent days, concrete hollow blocks are generally used in lieu of framework so as to provide permanent support for the masonry walls. Such

method generates a wall with concrete blocks on one side and masonry stones on the other side with filling concrete in between. This type of walls can have a thickness up to 350 mm.

For what concerns slabs, two types of slab construction are used. The first is a two-way solid slab with typical thickness around 200-250 mm. The second, instead, is a composite steel-concrete construction made of steel joists as supporting beams for the solid slabs. The result is a slab with typical thickness around 100-120 mm with simple reinforcement. While in the first type slab spans might range 4-5 meters, in the second type spans may range 5-7 m in both directions. Figure 3 shows some examples of masonry buildings in Nablus.



Figure 3: Masonry buildings in Nablus.

RC buildings can reach 15 storeys and have generally 2 or 3 bays in both directions. The resistant structural system can be either frames or shear walls, with consequent variation on the vulnerability level. The structural vulnerability, in fact, is higher for frame buildings than for shear walls ones, especially if frame buildings misses cladding partially or totally at one or more floors (i.e. soft storey buildings). Outer infill walls can be made of either three layers (i.e. hollow concrete blocks of 100 mm thickness, weak concrete layer of about 130 mm thickness, and stone layer of about 70 mm thickness) or only one layer thick from 150 to 200 mm, composed of hollow concrete blocks. Finally, slabs can have a one or two way ribbed slab system according to the plan dimensions of the building. Figure 4 shows some examples of the different types of RC buildings in Nablus.



(a) (b) (c)

Figure 4: RC buildings in Nablus – (a) RC frame building, (b) RC soft storey building, and (c) RC shear wall building.

Figure 5 and Figure 6 document data collected by practitioners until now. In particular, pie-charts show that RC frame buildings are most common in Nablus (see Figure 5(a)) and that a large part of them has partial or total absence of infill walls (outer/inner) at one or more

floors (i.e. soft storey buildings) (see Figure 5(b)). This causes a higher level of structural vulnerability, especially in case of irregularity of the building both in plan and in elevation. The irregularity, in fact, is a really common characteristic of Palestinian buildings, as shown in Figure 6. The latter, in fact, indicates the number of surveyed buildings in Nablus that are irregular respectively in plan (see Figure 6(a)) and in elevation (see Figure 6(b)).

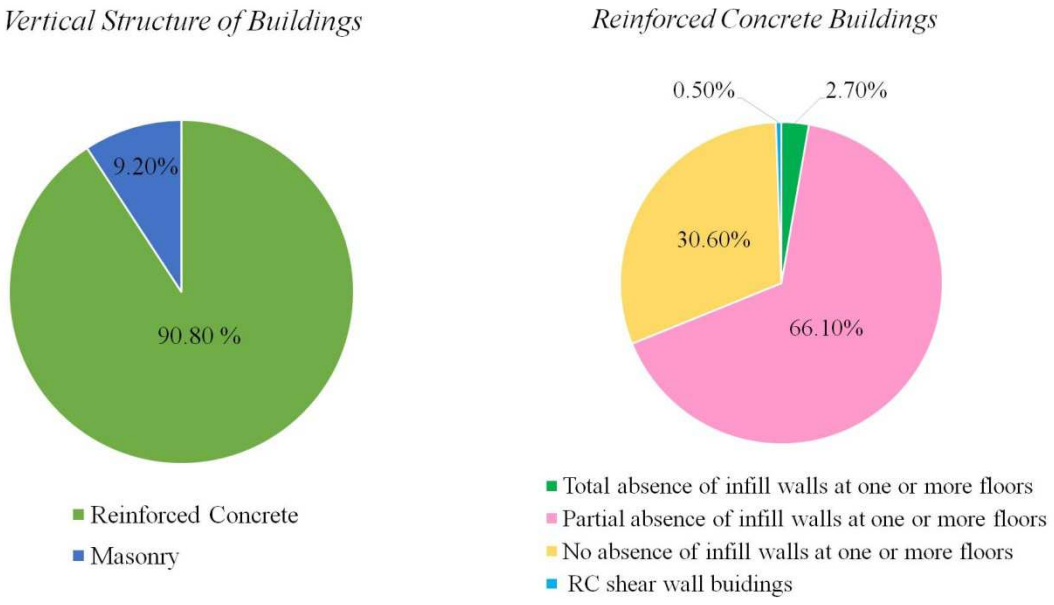


(a) (b)

Figure 5: Distribution of structural types in Nablus - (a) Vertical structure of buildings, and (b) RC buildings.

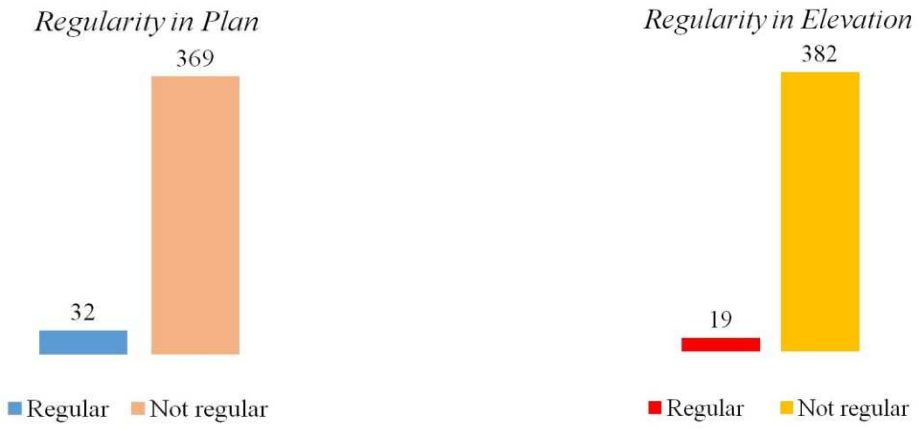


(a) (b)

Figure 6: Distribution of buildings - (a) Regular/not regular in plan, and (b) Regular/not regular in elevation.

## 3 DATA COLLECTION

According to the different structural types in the city of Nablus, survey forms were created to collect geometrical and structural data to calculate the seismic vulnerability of residential buildings. In particular, the redacted forms are two and targeted to:

- citizens;
- practitioners.

The forms are different only in level of detail and allow to make a quick assessment of seismic performance of the building. Herein, buildings are considered as structural units of ordinary construction type (such as masonry, RC frames or walls) used for housing and/or services. Therefore, the forms are not suitable for monumental or specialized types (such as industrial depots, sport constructions, theaters, churches, etc.).

The forms can be compiled directly on the WebGIS platform at the tab *Building Form – Practitioners* and tab *Building Form – Citizens.*

Both forms start with a section devoted to information on the compiler, followed by the section named *Identification of the building*. Both sections are displayed in Figure 7.

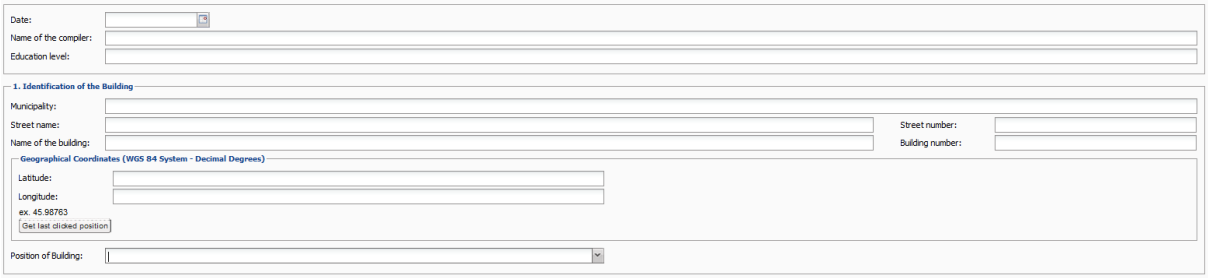


Figure 7: Sections for compiler information (from tab *Building Form – Practitioners*) and for the identification of the building.

The section *Identification of the building* allows to locate the building across the street name and number, and geographic coordinates expressed in terms of WGS84 (World Geodetic System 1984) system. Since the behavior of a building depends also on its position towards others buildings (i.e. structural aggregates), the compiler shall specify whether the structure is an *isolated building*, *internal building*, *end building* or *corner building*, as shown in Figure 8.

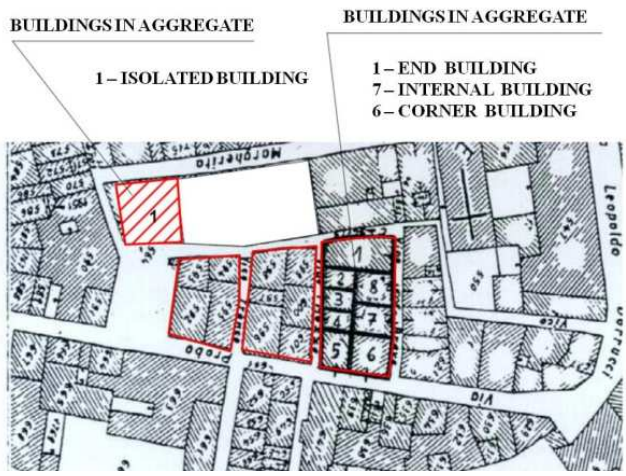


Figure 8: Buildings in aggregate and different types of location.

The section *Description of the building* allows to describe the building in terms of numbers of storeys, year of construction and year of eventual structural upgrade, exposure (i.e. number of units, percentage of use and occupants), and type of property (i.e. public or private). In the same section, in addition to the previous information, practitioners shall indicate the average of floor height and average of floor area to get more precise geometrical measure to use in case of structural modeling. The section *Description of the building* is reported in Figure 9.

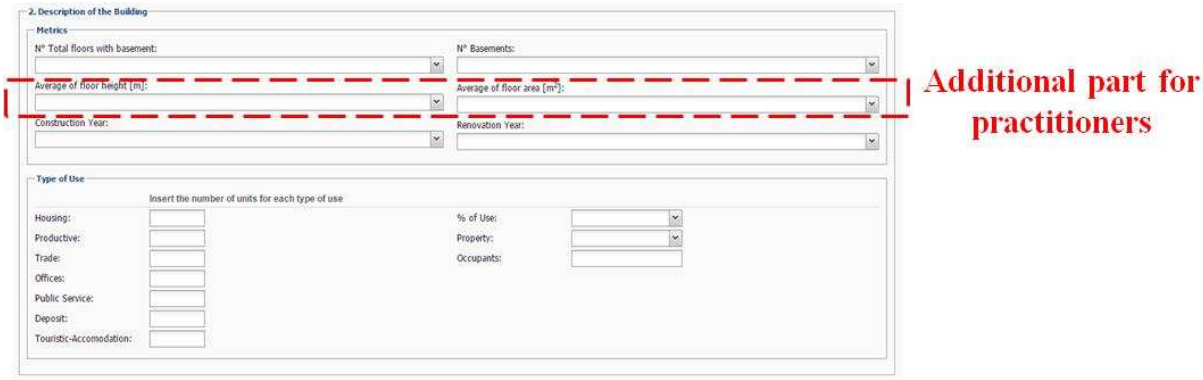


Figure 9: *Description of the Building*.

After defining the building from a geometrical point of view, the next step regards the identification of structural properties. This can be done in the section *Structural data* where citizens and practitioners have to compile different parts. As illustrated in Figure 10, practitioners have to define both the vertical and horizontal structure of the building (including the eventual presence of RC shear walls). Citizens, instead, have to focus only on the vertical structure. Finally, both citizens and practitioners have to indicate if the building misses inner/outer infill walls, partially or totally, at one or more floors. The lack of cladding, in fact, drives to the occurrence of the weak story mechanism in case of medium or high intensity ground shaking.

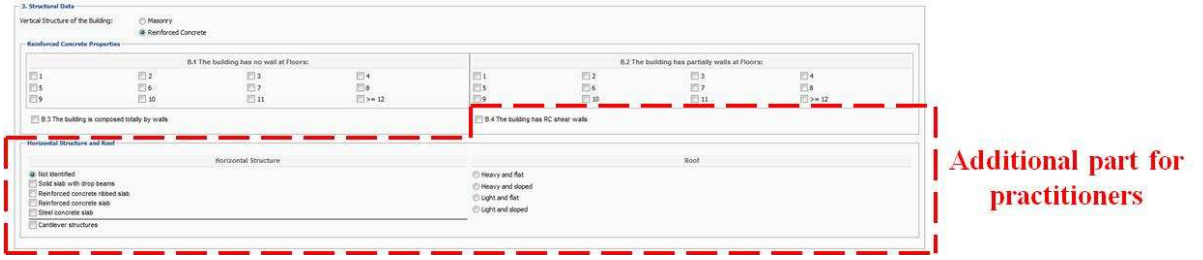


Figure 10: *Structural Data*.

The sections *Regularity* and *Geomorphological Data* can be found only in the tab *Building Form – Practitioners*. They regard respectively the regularity of the building (both in plan and in elevation), the morphology of the site and the category of the soil foundation on which the building was constructed. The criteria for the definition of the structural regularity and the type of soil foundation are described in Eurocode 8 [8]. Figure 11 shows sections *Regularity* and *Geomorphological Data*.

Finally, for both practitioners and citizens, the form ends with the sections *Notes* and *Photos*, to record more detailed information on the surveyed building that cannot be caught from the sections described above.

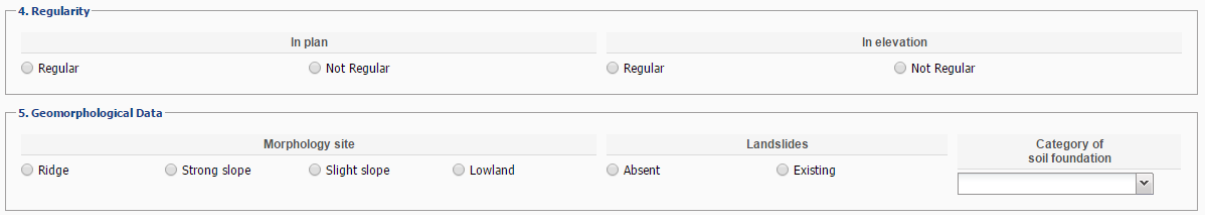


Figure 11: *Regularity* and *Geomorphological Data*.

As well as on the WebGIS, citizens and practitioners can fill in the forms also by using two apps for smartphones and tablet with Android system, downloadable from the tab *Downloads* in the WebGIS platform. The apps reflect exactly the forms for practitioners and citizens implemented in the WebGIS, and allow a quick and easy data entry, even without internet connection. Once internet is available again, the apps will send the loaded data to the WebGIS platform. Figure 12 shows the home page of the apps for citizens (see Figure 12(a)) and practitioners (see Figure 12(b)).

The user has to fill in all the sections of the form as the ones reported in Figure 13(a). The compiler can save, upload or delete the form at any time only by clicking the button in the upper right, as showed in Figure 13(b). In the same list shown in Figure 13(b), the button *Send* can be selected once completed the form.

After having sent the form, in relation to the compiler, the form will be available on the WebGIS platform at the tab *Building Form – Citizens* or *Building Form – Practitioners.*

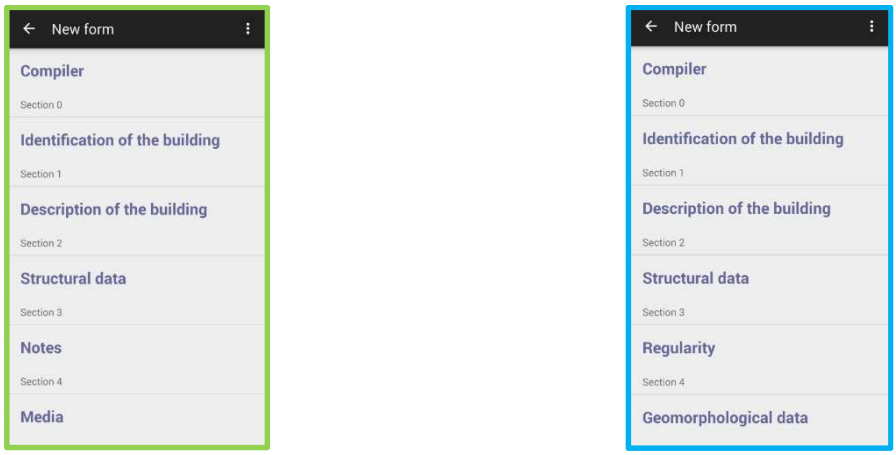


(a) (b)

Figure 12**:** Home Page of the SASPARM 2.0 app for: (a) citizens and (b) practitioners.

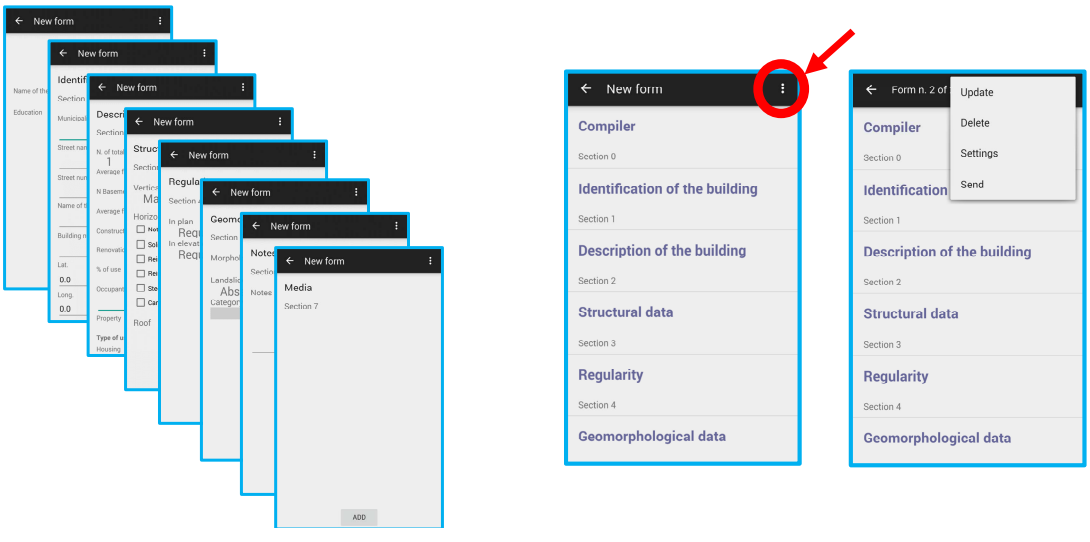


(a) (b)

Figure 13: (a) Sections to insert data in the SASPARM 2.0 app for practitioners and (b) Operations on the apps.

## 4 ESTIMATION OF SEISMIC RISK

The seismic risk quantifies the probability of reaching or exceeding a damage level for a building subjected to an earthquake of a certain intensity. As well as the importance of the structure and the number of people who occupy it (i.e. exposure), the seismic risk is mainly related to the vulnerability of buildings and to the hazard of the area where the building is located. Since the hazard is an intrinsic property of the site, the seismic risk can be reduced only acting on the structural vulnerability. In case of new buildings, the level of vulnerability can be reduced by using standards which provides appropriate design criteria to limit the building propensity to be damaged by seismic event. For existing buildings, instead, the limitation of the damage can be obtained through retrofit measures that depend on the structural type and the level of vulnerability of the building itself.

As already reported in the §2, the seismic code has been introduced in Palestine only recently. The awareness on seismic risk, and hence on the necessity of adopting a seismic code, increased thanks to SASPARM FP7-Project [9] which was undertaken by the same partnership that carried out SASPARM 2.0 [1]. As a consequence of the very recent adoption of a seismic code, most of Palestinian buildings has a high level of vulnerability from which it follows a high seismic risk. The seismic risk of a selected building is reported in the tab *Risk* of the WebGIS. In particular, as it is shown in Figure 14, the risk is expressed in probability and calculated for three time windows (i.e. 1, 10, and 50 years). The following paragraphs describe the procedure and the assumptions used to determine the local hazard and the structural vulnerability, whose combination defines the seismic risk.

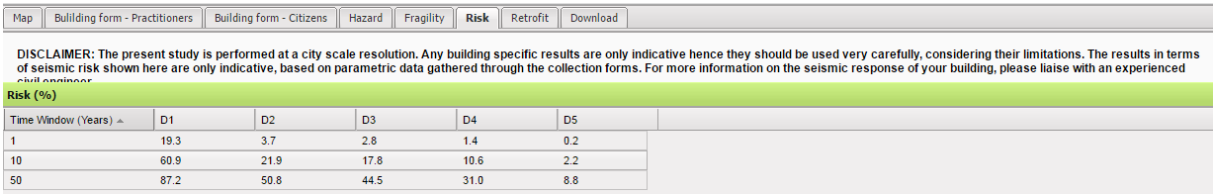


Figure 14: Tab *Risk* - Risk values related to a selected 8-storeys RC frame building, not regular both in plan and in elevation and recently built.

## 5 HAZARD MODEL FOR NABLUS CITY

The hazard is a parameter that depends exclusively on seismicity of the area. Precisely, the hazard represents the estimation of the expected level of seismic intensity in a certain area and for a given observation period. The definition of seismic hazard occurs through the hazard curve. In particular, the curve relates the severity of shaking, in this case defined by the *PGA* (peak ground acceleration), with the *AFE* (Annual Frequency of Exceedance), which correspond to the inverse of the $T_r$ (return period).

The logarithm of a ground-motion parameter and the logarithm of the corresponding annual frequency of exceedance can be assumed to be linearly-related, at least for return periods of engineering interest, and represents the hazard curve. The negative gradient of the log–log hazard curve is referred to as *k* in this paper, following the definition in Part 1 of Eurocode 8 [8]. Thanks to the approximation of linear trend, to define the hazard curve it is sufficient to determine the *PGA* value, corresponding to a return period $T_r$, and the negative gradient of the log–log hazard curve *k* that passes through the reference point. The point on the curve here considered corresponds to $T_r$ of 475 years. The hazard curve is then defined by the relation (1):

$$AFE = AFE_{475}\left(\frac{S \cdot PGA_{475}}{PGA}\right)^{k} \quad (1)$$

where $AFE_{475}$ e $PGA_{475}$ are the annual frequency of exceedance and the *PGA* corresponding to the return period $T_r$ of 475 years while *S* is the soil factor. Once defined the hazard curve, it is possible to calculate the seismic demand related to *PGA* for any return period $T_r$.

For the case study of Nablus, the "West Bank and Gaza Strip: Seismic Hazard Distribution Map" shown in Figure 15 is considered: it displays the *PGA* corresponding to a return period $T_r$ of 475 years. Since the gradient *k* of hazard curve is unknown, the value of *k* is assumed equal to 3 as suggested in the Eurocode 8 [8]. In summary, the parameters that allow to calculate the hazard curve in the equation (1) are:

- $AFE_{475}$=1/475;
- $PGA_{475}$=0.24g;
- *k*=3;
- *S*=1 (soil A), 1.2 (soil B or C), 1.4 (soil D o E).

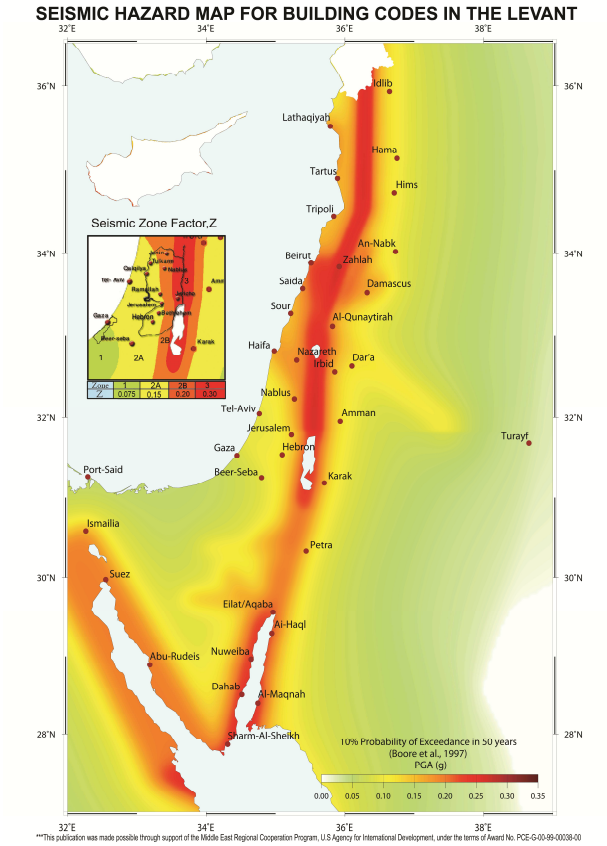


Figure 15: Seismic hazard map for building codes in the Levant [9].

Figure 16 shows tab *Hazard* of the WebGIS corresponding to the selected building and it displays the hazard curve for a soil "C". Since the type of the soil can be specified only in the form filled in by practitioners, the hazard curve related to the forms compiled by citizens is determined by considering the soil type "B".




Figure 16: Tab *Hazard* – Hazard curve for soil "C".

## 6 DEVELOPMENT OF ANALYTICAL FRAGILITY CURVES FOR DIFFERENT BUILDING TYPES

From survey data collected as described in the §3, fragility curves can be calculated by using SP-BELA (Simplified Pushover-Based Earthquake Loss Assessment) method ([3] and [4]). The curves are determined as functions of each structural type and then associated to each building in relation to the number of storeys. SP-BELA was implemented to investigate the seismic behavior of masonry buildings [3], RC frame buildings [4], and precast buildings [10] on the Italian territory. Since it is really versatile, SP-BELA can be modified to represent any building environment, as done for the city of Nablus.

Initially, the procedure took into account three different limit states: *LS1* (light damage), *LS2* (significant damage) and *LS3* (collapse). Recently, according to EMS98 scale [2], the fragility curves are instead calculated for five damage levels: *DL1* (slight damage), *DL2* (moderate damage), *DL3* (extensive damage), *DL4* (complete damage), and *DL5* (collapse). To do that, it was necessary to find a relationship between the previous three limit states, which can be numerically identified, and the five damage levels. To this purpose, observed damage data available for Italy have been used, since damage data for Palestine are not available.

SP-BELA allows to define fragility curves by comparing the displacement capacity of representative building classes with the displacement demand for the considered damage levels. The first step of the procedure is to generate a sample of buildings that is representative of the analyzed structural type by using Monte Carlo method. Afterwards, a non linear static analysis is carried out on each building of the sample to determine the structural behavior under seismic action. The final product is a pushover curve on which limit conditions (i.e. *LS1*, *LS2* and *LS3*) are identified in terms of the displacement of a pre-selected control point. The pushover curve refers to a MDOF (Multi-Degree of Freedom) system from which it is possible to define the properties of an equivalent SDOF (Single-Degree of Freedom), thus obtaining the capacity curve. The latter describes the behavior of a SDOF that is equivalent to the original MDOF in terms of period of vibration, displacement capacity and dissipation capacity. Through the equivalent SDOF system the displacement capacity is obtained. The displacement spectrum, corresponding to the various ground shaking intensity (i.e. PGA), is then used to define the displacement demand. By comparing the displacement demand with the displacement capacity, it is available to define the proportion of buildings, belonging to the sample, that survive the considered limit conditions. By varying the ground shaking intensity, it is finally possible to build all the points of the fragility curve for each limit state.

By using the survey data and the procedure described above, fragility curves can be determined for masonry buildings [11], RC frame buildings ([11] and [12]), and RC soft storey buildings ([11] and [12]).

For RC shear wall buildings, the lack of information to best represent this structural type didn't allow to calculate fragility curves directly through SP-BELA method. In fact, the fragility curves of RC shear wall buildings are defined from the ones of RC frame buildings with the same number of storeys [11]. Precisely, a correction factor has been identified and applied to the average value of the fragility curves of RC frame buildings while the coefficient of variation remains constant. The considered correction factor is equal to 1.3 and it has been evaluated by comparing the fragility proposed by HAZUS [13] for concrete frame with unreinforced masonry infill walls buildings and for concrete shear wall ones.

Figure 17 displays respectively the fragility curves of: (a) 3-storeys masonry buildings, (b) 7-storeys RC frame buildings, and (c) 10-storeys RC shear wall buildings, all located in the city of Nablus.

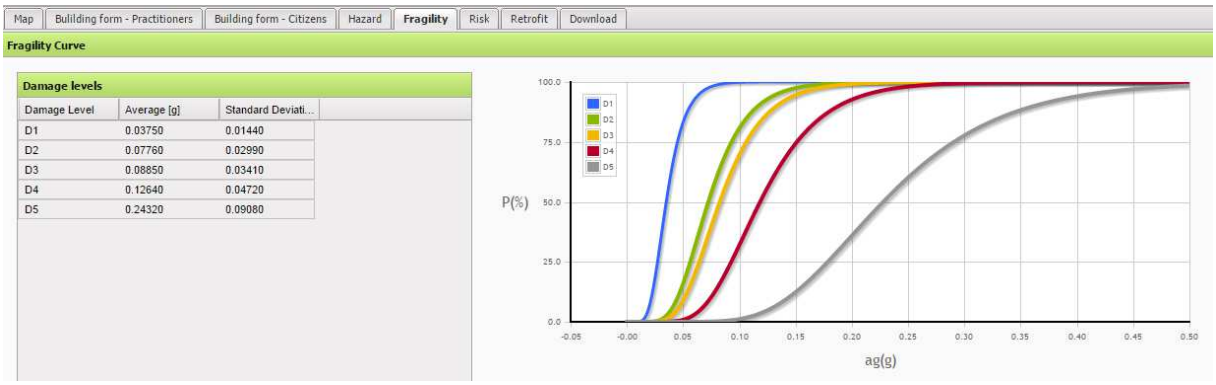


(a)

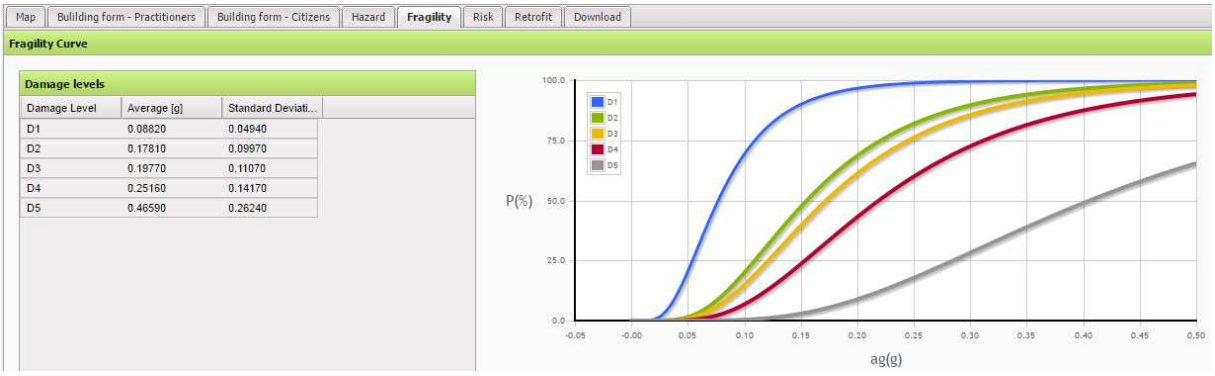


(b)

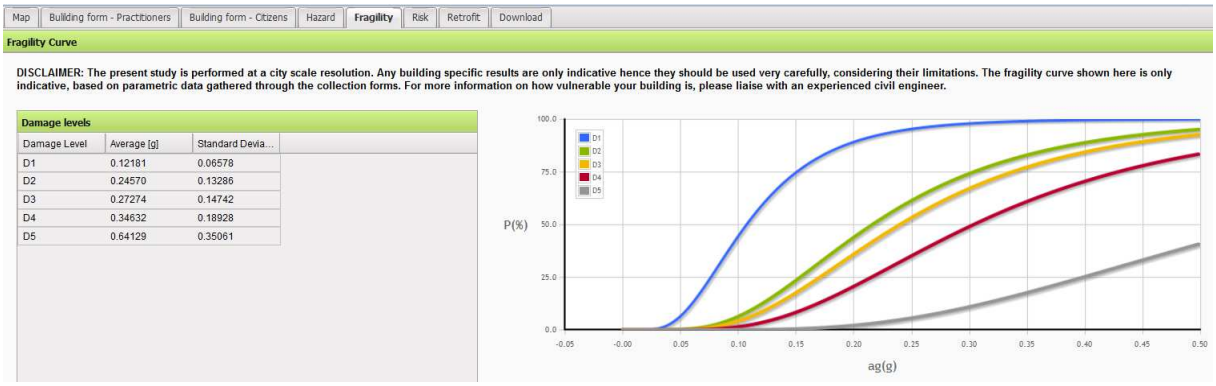


(c)

Figure 17: Tab *Fragility* – Fragility curves for: (a) 3-storeys masonry buildings, (b) 7-storeys RC frame buildings, and (c) 10-storeys RC shear wall buildings.

## 7 RETROFIT MEASURES

Palestinian buildings, herein represented by the ones of Nablus, present a high level of vulnerability.

To improve the structural behavior of buildings even in case of low or medium intensity ground shaking, the WebGIS suggests possible structural rehabilitations ([5] and [6]) at the tab *Retrofit* on the basis of vulnerability conditions detected through data compiled in the forms.

The tab *Retrofit*, as shown in Figure 18, is organized to identify in a simple way all possible retrofit measures towards any structural deficiency (e.g., soft storey mechanism, irregularity both in plan and in elevation, etc.).

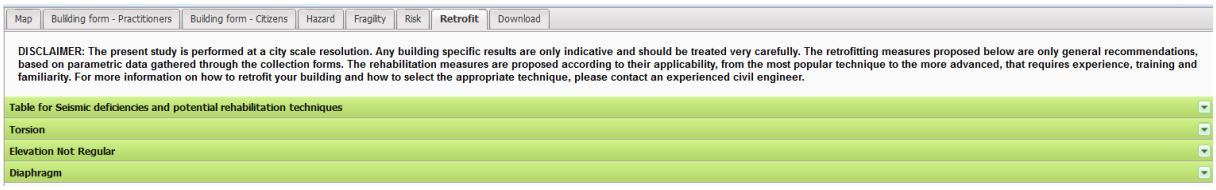


Figure 18: Tab *Retrofit* – Retrofit measures suggested for any structural deficiency.

## 8 CONCLUSIONS

This paper describes the WebGIS developed for SASPARM 2.0 project [1]. The WebGIS allows to estimate the seismic risk of residential buildings in the city of Nablus by combining the structural vulnerability with local hazard. The data required to define the seismic vulnerability of buildings are collected by citizens and/or practitioners who shall fill in two survey forms. The forms can be compiled directly on the WebGIS or through two apps developed for smartphones or tablet. According to collected data, the WebGIS calculates the seismic vulnerability of each building with the analytical method SP-BELA. The structural vulnerability is then combined to the local hazard, thus obtaining the seismic risk for three observation time windows. In relation to the structural deficiencies, the WebGIS proposes also different retrofit measures with the aim of reducing the seismic vulnerability of the selected building and consequently its seismic risk.

The SASPARM 2.0 WebGIS is a simple and intuitive tool, open to all and suitable to any type of user. Through the site, a massive amount of data on vulnerability of the building stock can be gathered with no cost. Although it started as an instrument to be used on the Palestin-

ian territory, the SASPARM 2.0 WebGIS could be modified to extend its use also to others realities.

## ACKNOWLEDGMENTS

This research has been conducted within the project "ECHO / SUB / 2014/694399 SASPARM 2.0 Support Action for Strengthening Palestine capabilities for seismic risk mitigation", a project co-financed by DG-ECHO - Humanitarian Aid and Civil Protection.

We thank R. Monteiro, P. Ceresa, V. Cerchiello and I. Grigoratos (IUSS, Pavia) who provided guidelines for the WebGIS section dedicated to retrofit. We are also grateful to Prof. J. Dabbeek and his staff (An-Najah National University, Nablus) who carried on the building surveys and offer their valuable expertise in the definition of building taxonomy in Nablus.

## REFERENCES

[1] SASPARM 2.0 project. Support Action for Strengthening Palestine's capabilities for seismic Risk Mitigation, DG-ECHO 2014, ECHO/SUB/2014/694399; www.sasparm2.com.

[2] Grünthal, G. (editor). "Cahiers du Centre Européen de Géodynamique et de Séismologie: Volume 15 – European Macroseismic Scale 1998". *European Center for Geodynamics and Seismology* 1998; Luxembourg.

[3] Borzi B, Crowley H, Pinho R. Simplified Pushover-Based Earthquake Loss Assessment (SP-BELA) Method for Masonry Buildings. *International Journal of Architectural Heritage*, 2008, 2(4): 353-376.

[4] Borzi B, Pinho R, Crowley H. Simplified Pushover-Based Vulnerability Analysis for Large Scale Assessment of RC Buildings. *Engineering Structures*, 2008, 30(3): 804-820.

[5] FEMA 547. Techniques for the Seismic Rehabilitation of Existing Buildings. *Federal Emergency Management Agency* 2006; Washington D.C.

[6] Deliverable D.C.1. Report on the Identification of Retrofit Measures. *SASPARM 2.0 project* 2016, DG-ECHO 2014, ECHO/SUB/2014/694399.

[7] Jordanian National Building Council; 2005: Jordanian Code for Earthquake-Resistant Buildings. 236 pp.

[8] Eurocode 8, prEN 1998-1. Design of Structures for Earthquake Resistance – Part 1: General Rules, Seismic Actions and Rules for Buildings. *European Committee for Standardization (CEN)* 2004; Brussels, Belgium.

[9] SASPARM project. Support Action for Strengthening Palestinian-administrated Areas capabilities for Seismic Risk Mitigation, FP7-INCO, ID. 295122; www.sasparm.ps/en/.

[10] Bolognini D, Borzi B, Pinho R. Simplified Pushover-Based Vulnerability Analysis of Traditional Italian RC Precast Structures. *14th World Conference on Earthquake Engineering* 2008; Beijing, China.

[11] Deliverable D.F.1. Fragility curves for each structural typology that sub-classifies the building stock. *SASPARM 2.0 project* 2016, DG-ECHO 2014, ECHO/SUB/2014/694399.

[12] Borzi B, Di Meo A, Faravelli M, Ceresa P, Monteiro R, and Dabbeek J. Definition of Fragility Curves for Frame Buildings in Palestine. *1st International Conference on Natural Hazards and Infrastructure* 2016; Chania, Greece.

[13] FEMA HAZUS 99. Earthquake Loss Estimation Methodology. Technical Manual. *Federal Emergency Management Agency* 1999; Washington D.C.

COMPDYN 2017
6th ECCOMAS Thematic Conference on
Computational Methods in Structural Dynamics and Earthquake Engineering
M. Papadrakakis, M. Fragiadakis (eds.)
Rhodes Island, Greece, 15–17 June 2017

# SEISMIC VULNERABILITY MODELS OF PIERS UNDER NEAR-FAULT GROUND MOTIONS

**CHEN Li-bo[1], WANG Hua-he[2], GU Yin[2]**

[1] Civil Engineering College, Fuzhou University
Xueyuan Road No.2 ,University Town, Fuzhou City, Fujian Province, China
e-mail: { lbchen }@fzu.edu.cn

[2] Civil Engineering College, Fuzhou University
Xueyuan Road No.2 ,University Town, Fuzhou City, Fujian Province, China
e-mail: { n140520074, cinoa }@fzu.edu.cn

**Keywords:** Near-fault Ground Motions, Seismic Vulnerability, Residual Deformation, Incremental Dynamic Analysis, Orthogonal Design.

**Abstract.** *Seismic vulnerability models of typical highway piers under the near-fault ground motions were developed based on the incremental dynamic analysis (IDA) method. On the selection criteria of ground motions determined by the authors, totally 30 near-fault or far-field earthquake records were selected. Totally 36 piers were designed as samples by using the orthogonal experimental design method. Each sample was matched by all of the selected ground motions. The numerical models of the piers were established by using OpenSees, in which the nonlinear time history analyses were carried out by the incremental dynamic analysis method. For estimation of the seismic fragility parameters, three different methods were adopted, including the estimation method based on the multiple-stripe analysis idea, the frequency point regression methods from the Monte Carlo sampling and the two-dimensional probability density function integration. The fragility curves were then built up accordingly. The following results can be obtained from the analysis: I) the probability of collapse is higher under near-fault ground motions whereas lower under the far-field motions, i.e., the other three damage states are more likely to happen, when given the same intensity of ground motions; II) by considering two damage indexes, the median values of the fragility curves decrease sharply compared to those with single damage index, which means the pier damage probability increased. Based on the results, it is found that the use of two damage indexes yields more accurate evaluation for the seismic risks of the pier damage and decision making of the seismic retrofit prioritization.*

## 1 INTRODUCTION

Near-fault ground motions have been a hot research topic in the field of earthquake engineering for their special characteristics in recent years. In particular, the pulse-like near-fault ground motions caused by the forward effect and slip effect have a significant dynamic effect on structures, which lead to severe structural damage [1,2,3]. The seismic responses of bridge piers such as strain, curvature and drift ratio can be further amplified, the residual displacements of piers are also very significant for piers under the near-fault ground motions [4,5,6,7]. Therefore, the damage of piers and its probabilities of occurrence should be studied further to investigate the seismic risk of the bridge system. Seismic vulnerability analysis is an important step in the procedure of seismic risk assessment. The fragility function and the incremental dynamic analysis (IDA) are commonly adopted when researchers analyses the seismic risk [8,9]. Nevertheless, the study of seismic vulnerability models of piers under near-fault ground motions is still in its beginning [10,11]. Besides, previous studies have mostly been conducted for ordinary ground motions by using unique bridge sample in the process of seismic fragility analysis. It's necessary to analyze the seismic vulnerability of piers under near-fault ground motions with respect to the special characteristics of near-fault ground motions and by considering severe damage of piers.

## 2 SEISMIC FRAGILITY MODELS' THEORY OF PIERS

The research object of this paper is to set up the vulnerability models of piers which refer to the probability of exceeding a certain damage state when they are under certain level of ground motions. The vulnerability model is assumed to follow the lognormal distribution in this paper, which is expressed as follows:

$$\text{Fragility}=P\left[D \geq C \middle| IM\right]=\Phi\left[\frac{\ln(IM)-\ln(m)}{\beta}\right] \tag{1}$$

where, $C$ is the capacity of piers, $D$ is seismic responses of piers, $IM$ is the intensity of ground motions, $m$ and $\beta$ are the median and logarithmic standard deviations of the seismic fragility models.

### 2.1 Seismic Fragility Models Based on IDA method

The seismic vulnerability analysis of piers is carried out by IDA method in this paper. The specific processes are described as below: the values of the ground motion intensity measure are scaled and the seismic responses are obtained by performing nonlinear time-history, then the damage measures and their limit values are selected and determined respectively, finally different methods are adopted to analyze and obtain the fragility parameters, and these models are included in the estimation method such as that based on the multiple-stripe analysis idea, the frequency point regression methods from the Monte Carlo sampling or the two-dimensional probability density function integration method [12,13,14].

### 2.2 The Definition of Piers' Limit States

According to the literature review, the performance levels and damage states of piers are divided into five types[15].The displacement ductility coefficient $\mu_\Delta$ and residual displacement drift ratio $DR$ are commonly selected as the damage indexes and their limit values of damage states are identified respectively[16,17,18]. The specific quantifications of the damage states of piers are listed in the table 1.

| Performance level | Damage States | Displacement Ductility Coefficient | Residual Displacement Drift Ratio |
|---|---|---|---|
| Level-I | Non-damage | $\mu_\Delta$<1.0 | $DR$<0.1% |
| Level-II | Minor damage | 1.0≤$\mu_\Delta$<1.2 | 0.1%≤$DR$<1% |
| Level-III | Moderate damage | 1.2≤$\mu_\Delta$<1.76 | 1%≤$DR$<1.5% |
| Level-IV | Major damage | 1.76≤$\mu_\Delta$<4.76 | 1.5%≤$DR$<1.75% |
| Level-V | Collapse | $\mu_\Delta$≥4.76 | $DR$≥1.75% |

Table 1: Limit states of piers

## 3 PIER SAMPLES AND NONLINEAR FINITE ELEMENT ANALYSIS

### 3.1 Design of Pier Samples

With reference to the existing design codes of China and the literature material, pier samples are designed by orthogonal test method in this paper[19,20]. The specific information of pier samples is listed in the table 2.

| Number of Level | Designed Parameters | The Value of Designed Parameters | | |
|---|---|---|---|---|
| 3 | Slenderness Ratio | 4 | 7 | 10 |
| | Axial Load Ratio | 6% | 12% | 18% |
| | Reinforcement Ratio | 1.0% | 1.6% | 2.2% |
| | Stirrup Ratio | 0.4% | 0.8% | 1.2% |
| | Pier's Diameter(m) | 1.2 | 1.6 | 2.0 |
| 2 | Strength Grades of Concrete | C30 | | C35 |
| | Strength Grades of Longitudinal | HRB400 | | HRB335 |
| | Strength Grades of Stirrup | HRB335 | | HPB300 |

Table 2: Selected parameters and its values of piers

According to the level of the designed parameters as well as the mixed level orthogonal design test table, the mixed level design test table $L_{36}(2^3\times3^5)$ is selected and 36 pier samples are obtained in this paper.

### 3.2 Nonlinear Finite Element Pier Models

Finite element analytical models of piers are built by using the OpenSees software[21]. The specific modeling details are shown as below: Force-based beam-column element is adopted to simulate piers. Piers are considered to be made up of fiber element. Concrete01 WithSITC material is selected as the concrete constitutive model of pier and consequently the residual displacement could be captured more accurately [22]. Steel02 material is elected as piers' steel constitutive model. Rayleigh damping mode is chosen and the adopted damping ratio is 3%[23]. The connection between the pier and foundation is rigid linked directly.

### 3.3 The Input of Ground Motions

The input of ground motions are selected from PEER Strong Motion Database. According to the relevant literature, the selection criteria of earthquakes are determined and listed in the table 3[24].

| The Type of Earthquakes | Type | Distance to Fault | Magnitude | PGV/PGA |
|---|---|---|---|---|
| Near-fault Ground Motions | Pluse-like | 0~20km | 6~8 | >0.15s |
| Far-field Ground Motions | Ordinary | 20~100km | 6~8 | ≤0.15s |

Table 3: Selected criteria of ground motions

Totally 30 near-fault or far-field ground motions are selected based on the aforementioned criteria. In order to simulate the seismic response of piers more accurately, three-directional ground motion input is taken in this paper. Simultaneously, PGV is selected to be the intensity measure[25]. Moreover, the selected ground motions are truncated because the original durations are too long.

## 4 SEISMIC FRAGILITY ANALYSIS OF PIERS

Thirty-six pier samples are matched by all of the selected ground motions in this section. The seismic responses of piers are obtained by IDA method and analyzed by different methods, the seismic fragility models and their parameters are got by different mathematical statistics method.

### 4.1 The Estimation Method Based on the Multiple-Stripe Analysis Idea

Multiple-stripe analysis is an alternative nonlinear dynamic analysis method. It is mainly for performing the nonlinear time history analysis by a series of ground motions scaled to specific levels. The principle of the method is used as reference in this paper and the concrete steps are as follows. The pier damage states are calculated based on the seismic responses of piers that are obtained from the IDA method. Then, the likelihood function is assumed to follow the binomial distribution. Finally, the fragility parameters and corresponding curves are acquired by the maximum likelihood method [12].

In the process of fragility analysis, the likelihood function is assumed to follow the binomial distribution which is expressed as follows:

$$\text{Likelihood} = \mathrm{C}_n^j p^j \left(1-p\right)^{n-j} \tag{2}$$

where, $n$ is the number of pier samples, $j$ is the number of piers that are in a certain damage state, $p$ is the probability of damage that can be calculated from equation (1).

The specific calculated equation of the likelihood function can be got by equation (1) and equation (2), which is shown as below:

$$\text{Likelihood} = \prod_{i=1}^{m} \mathrm{C}_n^j \Phi\left(\frac{\ln\left(IM_i\right)-\ln\left(\theta\right)}{\beta}\right)^j \times\left(1-\Phi\left(\frac{\ln\left(IM_i\right)-\ln\left(\theta\right)}{\beta}\right)\right)^{n-j} \tag{3}$$

According to the maximum likelihood method, the parameters of seismic fragility models can be estimated, based on the following equation.

$$\left\{\hat{\theta},\hat{\beta}\right\} = \arg\max_{\theta,\beta} \sum_{i=1}^{m}\left\{\ln \mathrm{C}_n^j + j\ln\Phi\left(\frac{\ln\left(IM_i/\theta\right)}{\beta}\right)+\left(n-j\right)\ln\left(1-\Phi\left(\frac{\ln\left(IM_i/\theta\right)}{\beta}\right)\right)\right\} \tag{4}$$

The seismic vulnerability curves obtained by this method are listed in Figure 1.

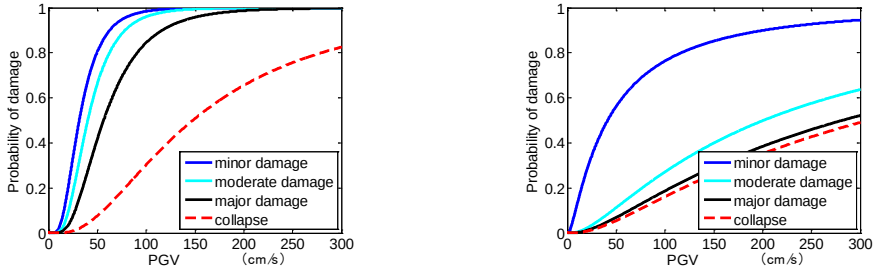


(a) Displacement Ductility Coefficient (b) Residual Displacement Drift Ratio

Figure 1: Seismic fragility curves of piers (Near-fault)

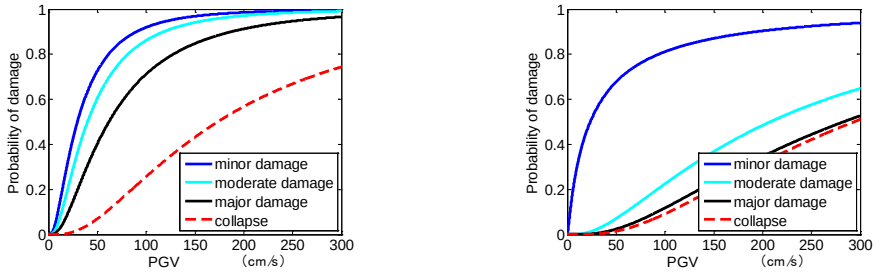


(a) Displacement Ductility Coefficient (b) Residual Displacement Drift Ratio

Figure 2: Seismic fragility curves of piers (Far-field)

### 4.2 The Frequency Point Regression Methods from the Monte Carlo Sampling

The seismic responses of piers under the selected ground motions are firstly recorded in this method and the damage states of piers are evaluated by the responses. Then the number of piers in four types of damage states is counted and divided by the total number of piers to get the corresponding damage probability. The Fragility curves and their parameters are got by using the method of the least squares method [13].

The damage probability in this method can be illustrated as follows:

$$p_j = \frac{\left(\sum_{i=1}^{\mathrm{k}\times N} F_i\right)_j}{\mathrm{k}\times N} \tag{5}$$

where, $N$ is the number of pier samples, k is the number of selected ground motions and k is equal to 30, $F_i$ is the limit state function of piers and its values are below:

$$F_i = \begin{cases} 0, & D^i < C^i \\ 1, & D^i \geq C^i \end{cases} \tag{6}$$

According to equation (1) and equation (5), the deviation between the two equations can be illustrated by,

$$\sum_{j=1}^{M} \delta_j^2 = \sum_{j=1}^{M} \left[ \frac{\left(\sum_{i=1}^{k\times N} F_i\right)_j}{\mathrm{k}\times N} - \Phi\left[\frac{\ln(IM_j) - \ln(m)}{\beta}\right] \right]^2 \tag{7}$$

In order to obtain the parameters of the fragility models, the least squares method is adopted to minimize the deviation, the values are as below:

$$\left\{\hat{\theta},\hat{\beta}\right\}=\arg\min_{\theta,\beta}\sum_{j=1}^{M}\left[\frac{\left(\sum_{i=1}^{k\times N}F_i\right)_j}{\mathrm{k}\times N}-\Phi\left[\frac{\ln(IM_j)-\ln(m)}{\beta}\right]\right]^2 \tag{8}$$

The seismic fragility curves obtained by this method are listed in the following figure.

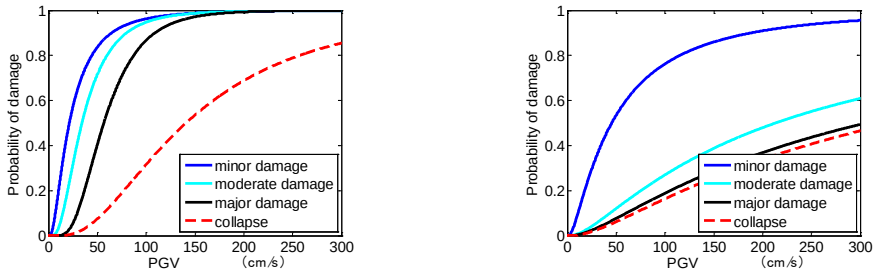


(a) Displacement Ductility Coefficient (b) Residual Displacement Drift Ratio

Figure 3: Seismic fragility curves of piers (Near-fault)

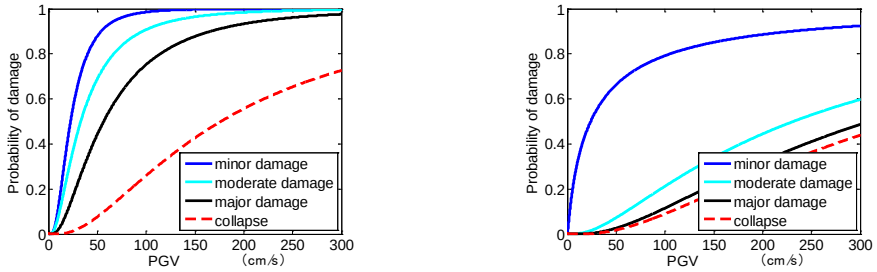


(a) Displacement Ductility Coefficient (b) Residual Displacement Drift Ratio

Figure 4: Seismic fragility curves of piers (Far-field)

### 4.3 The Frequency Point Regression Methods from the Monte Carlo Sampling

The damage index of piers is assumed to yield a certain distribution function in this method, which is assumed to follow the logarithmic normal distribution function in this paper. Given the defined performance level of piers as well as their damage limit states, the damage probability of exceedance can be obtained by integrating the region that is made up of the damage limit states. Furtherly the fragility curves and their parameters are obtained by the least squares method[14]. This method mentioned in this section is mainly under the condition of two damage indexes.

The logarithmic normal distribution function in this method is shown as follows:

$$f(x,y)=\frac{1}{2\pi xy\xi_x\xi_y\sqrt{1-\rho^2}}\exp(-\frac{q}{2})$$
$$q=\frac{1}{1-\rho^2}\left[\left(\frac{\ln x-\lambda_x}{\xi_x}\right)^2-\frac{2\rho(\ln x-\lambda_x)(\ln y-\lambda_y)}{\xi_x\xi_y}+\left(\frac{\ln y-\lambda_y}{\xi_y}\right)^2\right] \tag{9}$$

Where, $\lambda_x$, $\lambda_y$, $\xi_x$ and $\xi_y$ are the location and scale parameters of the marginal PDF of $X$ and $Y$ , respectively. $X$ and $Y$ are the selected damage indexes. The parameter $\rho$ forms a linear correlation coefficient between the two variables.

Each integrated region is composed of the displacement ductility coefficient and the residual displacement drift ratio, the probability is illustrated as follows:

$$PL(x_i,\ y_i)=\iint_S f(x,y)dS \tag{10}$$

The probability of exceeding a certain damage state can be got by the equation (10), which is shown in equation (11):

$$P=\int_0^{y_i}\int_{x_i}^{\infty} f(x,y)dxdy+\int_0^{x_i}\int_{y_i}^{\infty} f(x,y)dxdy+\int_{x_i}^{\infty}\int_{y_i}^{\infty} f(x,y)dxdy \tag{11}$$

Furtherly, the equation (11) can be thought to be composed of three parts, which are illustrated below.

$$A=\int_0^{y_i}\int_{x_i}^{\infty} f(x,y)dxdy\,,\ B=\int_0^{x_i}\int_{y_i}^{\infty} f(x,y)dxdy\,,\ C=\int_{x_i}^{\infty}\int_{y_i}^{\infty} f(x,y)dxdy \tag{12}$$

Where region A is mainly controlled by the displacement ductility coefficient, region B is controlled by the residual displacement drift ratio and region C is controlled by the two damage indexes. The probability density surface and its corresponding integrated region are listed for better illustration of each damaged region, which are shown in the following figure.

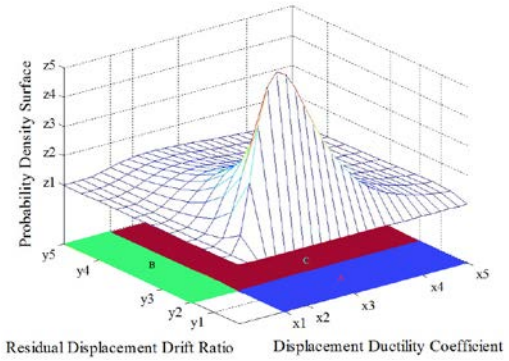


Figure 5: Probability density surface and its integrated range

The contribution of different regions to each damage state of piers is shown in the form of histogram. As the trend that the pier under the near-fault ground motions and far-field ground motions is almost the same, piers under the near-fault ground motions are taken as an example in this paper, which are illustrated in Figure 6.

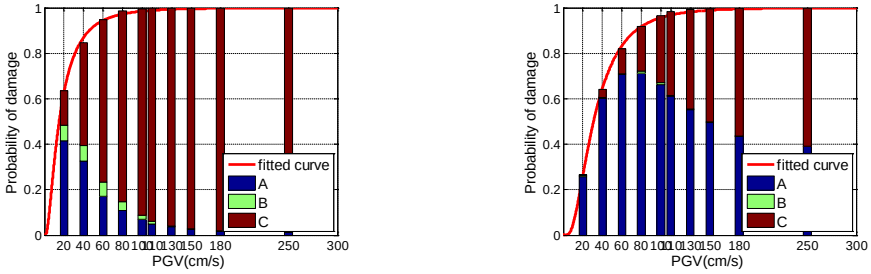


(a) Minor damage (b) Moderate damage

(c) Major damage (d) Collapse

Figure 6: Seismic fragility curves and proportion of each part (near-fault ground motions)

The following results can be obtained from the above figure. The displacement ductility coefficient and the residual displacement drift ratio both play a major role in the condition that piers are in in the case of minor damage state. The displacement ductility coefficient is important in the circumstance where piers are in the other three damage states. However, the importance of residual displacement drift ratio doesn't stand out when piers are in the Minor damage state and Moderate damage as well as Major damage, yet when piers are in the Collapsed damage state, its significance improves greatly. Therefore, when piers are under the near-fault ground motions, the residual displacement of piers isn't negligible and it is necessary to consider both the ductility coefficient and the residual displacement in the analysis of seismic risk.

Similarly, the deviations between equation (1) and the equation (11) can be acquired and according to the east squares method, the parameters can be obtained and be illustrated in the equation (13).

$$\left\{\hat{\theta},\hat{\beta}\right\}=\arg\min_{\theta,\beta}\sum_{j=1}^{N}\left[\left(1-\iint_{S}f(x,y)dS\right)_{j}-\Phi\left[\frac{\ln(IM_{j})-\ln(m)}{\beta}\right]\right]^{2} \tag{13}$$

The seismic vulnerability curves of piers are acquired under the circumstances with both the displacement ductility coefficient and the residual displacement drift ratio, which are shown as follows.

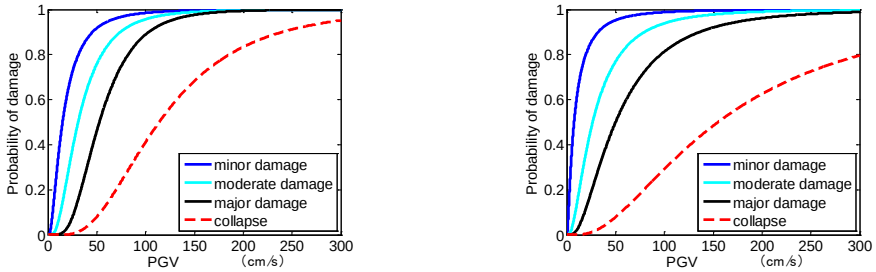

(a) Near-fault (b) Far-field

Figure 7: Seismic fragility curves of piers

The seismic vulnerability analysis of piers is carried out according to the three methods previously presented in this paper and the corresponding seismic fragility parameters are obtained. In order to facilitate the analysis, the three analysis methods are denoted Method 1 Method 2 and Method 3, respectively. The specific summary is presented in the following table 4 and table 5.

| Method | Damage | Minor damage | | Moderate damage | | Major damage | | Collapsed | |
|---|---|---|---|---|---|---|---|---|---|
| | Index | $m$ | $\beta$ | $m$ | $\beta$ | $m$ | $\beta$ | $m$ | $\beta$ |
| 1 | $\mu_\Delta$ | 31.51 | 0.54 | 40.24 | 0.52 | 56.41 | 0.57 | 145.05 | 0.76 |
| | $DR$ | 41.26 | 1.24 | 201.09 | 1.14 | 281.69 | 1.16 | 308.10 | 1.13 |
| 2 | $\mu_\Delta$ | 27.25 | 0.50 | 37.22 | 0.48 | 56.72 | 0.51 | 151.24 | 0.71 |
| | $DR$ | 45.43 | 1.11 | 213.47 | 1.23 | 306.01 | 1.26 | 334.15 | 1.23 |
| 3 | $\mu_\Delta$+ $DR$ | 15.00 | 0.87 | 31.01 | 0.68 | 52.74 | 0.53 | 113.89 | 0.58 |

Table 4 Fragility parameters of piers (near-fault ground motions)

| Method | Damage | Minor damage | | Moderate damage | | Major damage | | Collapsed | |
|---|---|---|---|---|---|---|---|---|---|
| | Index | $m$ | $\beta$ | $m$ | $\beta$ | $m$ | $\beta$ | $m$ | $\beta$ |
| 1 | $\mu_\Delta$ | 29.61 | 0.87 | 39.97 | 0.85 | 61.84 | 0.86 | 173.53 | 0.84 |
| | $DR$ | 23.51 | 1.64 | 207.99 | 0.96 | 283.10 | 0.87 | 293.85 | 0.81 |
| 2 | $\mu_\Delta$ | 22.88 | 0.89 | 33.09 | 0.84 | 56.41 | 0.84 | 176.75 | 0.88 |
| | $DR$ | 23.89 | 1.76 | 231.74 | 1.05 | 309.57 | 0.94 | 345.72 | 0.92 |
| 3 | $\mu_\Delta$+ $DR$ | 7.51 | 1.14 | 26.58 | 0.86 | 49.98 | 0.78 | 155.19 | 0.79 |

Table 5 Fragility parameters of piers (far-fault ground motions)

The following results can be obtained from Table 4 and Table 5:

1) Given the same intensity and the analyzed method 3, the probability of collapse is higher under near-fault ground motions, whereas the probability of damage is lower when piers are in the other three damage states. When it comes to the far-field ground motions, damage states of piers are just of the contrary tendency.

2) Considering the single damage index, the fragility parameters acquired by method 1 and method 2 approximates and they deviate slightly. The main reason for the deviation is due to their own limitations of the mathematical statistics methods used in the analysis. The deviations of the parameters decrease when the number of the considered ground motions and pier samples increase.

3) The median values of the seismic vulnerability curves obtained by Method 3 are lower than those obtained by Method 1 and Method 2. The reason for the decrease is due to the effect of residual displacements. The decrease of the median value also indicates that the damage probability of piers under the same ground motion can further increase.

## 5 CONCLUSIONS

The piers which serve as the main components of bridges usually suffer more serious damage than other components under the near-fault ground motions. Therefore, it is of great importance theoretically and practically to analyze the seismic vulnerability of the piers under near-fault ground motions. Based on the results, the suggestions on the seismic evaluation and seismic retrofit prioritization can be furtherly provided. The seismic vulnerability models of piers under near-fault ground motions are studied in this paper, the main research conclusions are as follows:

- From analyzing the effect of near-fault or far-field ground motions on the seismic vulnerability of piers, the following results can be obtained: when the double damage indexes are considered, the probability of collapse is higher under near-fault ground motions whereas the probability of the other three damage states is higher under the far-field motions when given the same intensity of ground motions. Therefore, the effect of near-fault ground motions should be taken into account in the subsequent analysis of the seismic risk assessment of the structure.

- With respect to the proportion of probability of piers under each damage state, the following conclusions can be drawn: (1) The contribution of the displacement ductility coefficient to the damaged probability that piers under near-fault ground motions are in four damage states is prominent. (2)The contribution of the residual displacement of the pier is mirror in the case of the condition that piers are in the first three damage states whereas its contribution increases sharply when piers are collapsed. Therefore, the residual displacement of the pier under the near-fault ground motions can't be ignored in the process of vulnerability assessment

- By comparison on the seismic fragility models acquired by different methods, it is indicated that: Considering the two damage indexes, the median values of seismic vulnerability models obtained by the two-dimensional probability density function integration method decreasecompared to that of considering a single damage index. With the decrease of median value, the damage probability of pier increases correspondingly. Therefore, the seismic risk of the pier can be more accurately assessed under the consideration of two damage indexes.

## REFERENCES

[1] Abrahamson N A, Somerville P G. Effects of rupture directivity on probabilistic seismic hazard analysis [C]. Proceedings of the 6th International Conference on Seismic Zonation, Earthquake Engineering Research Institute, Palm Spring, 2000.

[2] Bray J D, Marek R A. Characterization of forward-directivity ground motions in the near-fault region [J]. Soil Dynamics and Earthquake Engineering, 2004, 24(11):815-828.

[3] Somerville P G, Smith N F, Graves R W. Modification of empirical strong ground attenuation relations to include the amplitude and duration effects of rupture directivity [J]. Seismological Research Letters, 1997, 68(10):199-222.

[4] Phan V, Saiidi M S, Anderson J, Ghasemi H. Near-fault ground motion effects on reinforced concrete bridge columns [J]. Journal of Structural Engineering, 2007, 133(7): 982-989.

[5] Kunnath S K, Erduran E, Chai Y, Yashinsky M. Effect of near-fault vertical ground motions on seismic response of highway overcrossings [J].Journal of Bridge Engineering, 2008, 13(3): 282-290.

[6] Brown A, Saiidi M S. Investigation of effect of near-fault motions on substandard bridge structures [J]. Earthquake Engineering and Engineering Vibration, 2011, 10(1): 1-11.

[7] Choi H H, Saiidi M S. An Exploratory Experimental Study of Near-fault Ground Motion Effects on Reinforced Concrete Bridge Columns [J].American Concrete Institute Structural Journal, 2010, 107(1):3-12.

[8] Shinozuka M, Feng M Q, Kim H, Kim S. Nonlinear Static Procedure for Fragility curve Development [J]. Journal of Engineering Mechanics, 2000, 126(12): 1287–1295.

[9] Nielson B G, DesRoches R. Analytical seismic fragility curves for typical bridges in the central and southeastern United States [J]. Earthquake Spectra, 2007, 23(3): 615-633.

[10] Psycharis I N, Fragiadakis M, Stefanou I. Seismic reliability assessment of classical columns subjected to near-fault ground motions. [J]. Earthquake engineering & structural dynamics, 2013, 42(14): 2061-2079.

[11] Billah A M, Alam S. Seismic performance evaluation of multi-column bridge bents retrofitted with different alternatives using incremental dynamic analysis [J].Engineering Structures, 2014,s 62–63(3):105-117.

[12] Baker J W. Efficient Analytical Fragility Function Fitting Using Dynamic Structural Analysis [J]. Earthquake Spectra, 2015, 31(1):579-599.

[13] Chen Libo, Wang Jiajia, Shangguan Ping. Research of seismic vulnerability model for skew highway girder bridges. Engineering Mechanics. (in Chinese, accepted)

[14] Uma S R, Stefano Pampanin, Constantin Christopoulos. Development of Probabilistic Framework for Performance-Based Seismic Assessment of Structures Considering Residual Deformations [J]. Earthquake Engineering, 2010, 14(7):1092-1111.

[15] HAZUS-MH. Earthquake model technical manual [M]. Washington, D C: Federal Emergency Management Agency. 2003.

[16] Hwang H, Liu J, Chiu Y. Seismic fragility analysis of highway bridges [R]. Memphis, T N. Center for Earthquake Research and Information, the University of Memphi, 2001.

[17] Japan Road Association. Design specifications of highway bridges. Part V:Seismic design [S]. Tokyo, Japan, 2012.

[18] Li Yu. Research on Performance-based Seismic Design and Evaluation for Bridge Structures Considering Residual Displacement and Soil-structure Interaction Effects [D]. Beijing Jiaotong University,2010.

[19] JTG/T B02-01-2008. Guideline for seismic design for highway bridges [S]. Beijing: China Communications Press, 2008.

[20] Li Gui-qian. Experimental Study and Numerical Analysis on Seismic Performance of Reinforced Concrete Bridge Columns [D].Chong Qing Jiaotong University ,2010.

[21] Mazzoni S, Mckenna F, Fenves G L. OpenSees command language manual [M]. Pacific Earthquake Engineering Research Center. Berkeley, CA. 2005.

[22] Won K L. Simulation and Performance-based Earthquake Engineering Assessment of Self-centering Posttensioned Concrete Bridge Systems [D]. Stanford University, 2007.

[23] Hsu K T, Cheng C C, Yu C P, et al. Evaluation of the Dynamic Characteristics of an Extradosed Bridge Using Microwave Interferometer[J]. Advanced Materials Research, 2011,374(377):2426-2429.

[24] Qiao Min-yuan. Research on Bridge Seismic Responses Under the Excitation of Near-fault Ground Motions [D]. Beijing Jiaotong University ,2013.

[25] Akkar S, Özen Ö. Effect of peak ground velocity on deformation demands for SDOF systems [J]. Earthquake Engineering & Structural Dynamics, 2005, 34(13):1551–1571.

COMPDYN 2017
6th ECCOMAS Thematic Conference on
Computational Methods in Structural Dynamics and Earthquake Engineering
M. Papadrakakis, M. Fragiadakis (eds.)
Rhodes Island, Greece, 15–17 June 2017

# A CLASS-ORIENTED LARGE SCALE COMPARISON WITH POSTEARTHQUAKE DAMAGE FOR ABRUZZI REGION

**Carlo Del Gaudio**[1], **Paolo Ricci**[1], **Gerardo Mario Verderame**[1]

[1] Department of Structures for Engineering and Architecture, University of Naples Federico II
via Claudio 21, 80125 Naples - Italy
carlo.delgaudio@unina.it, paolo.ricci@unina.it, verderam@unina.it

**Keywords:** RC buildings; Mechanical; Seismic fragility; Damage States; Post-earthquake

**Abstract.** *The need to quickly and accurately estimate the number of involved people, dead and the injured, missing people and homeless represent a topic issue in the emergency management and disaster planning. Obviously, such an estimation is closely related to the evaluation of building damage scenario for the area of interest. To this aim, it may be used different methodological approaches for the evaluation of seismic vulnerability at large-scale, consisting of empirical or mechanical methodologies, more or less simplified and that require a different level of detail in input parameters.*

*In present work, a simplified mechanical method – PushOver on Shear Type models (POST) – for seismic vulnerability assessment of infilled RC building is briefly recalled [1, 2, 3]. The methodology allows the definition of building structural characteristic through a simulated design procedure in compliance with design code prescriptions, professional practice and seismic classification of the area of interest at the time of construction. The evaluation of non-linear static response is performed through a simplified model, considering the contribution of both RC columns and infill panels to lateral resistance, based on Shear Type assumption. Seismic capacity assessment is made in the SPO2IDA framework [4] for different performance levels, defined according to the damage classification proposed by [5]. Finally, the use of a Monte Carlo simulation approach allows the derivation of fragility curves for different damage states (DSs).*

*Therefore, predicted damage scenario is derived from POST methodology for a database consisting of 7597Moment Resisting Frame (MRF) residential RC buildings located in the Abruzzi region, which after the 2009 catastrophic earthquake have been charged to post-earthquake usability assessment procedure [6]. Due to the use of spatially extended and massive amount of data, the reference unit is the class of building. The choice of key parameters for the identification of classes is carried out evaluating their impact on the observed damage collected through post-earthquake survey. Then, within each class, the remaining parameters are assumed as random variables chosen in appropriate distributions evaluated from data collected during the post-earthquake survey. Correlation values among the variable of each class are evaluated. Predicted damage scenario is then compared with damage scenario based on post-earthquake data.*

## 1 INTRODUCTION

Italian earthquakes of the last three decades have highlighted the high seismic vulnerability of the existing building stock, as demonstrated by the significant human, financial and functionality losses due to the severe damage suffered by structural and non-structural components observed after moderate-to-high magnitude events. Therefore, there is a growing interest in seismic fragility assessment of buildings at regional and urban scale.

Generally speaking, a seismic fragility assessment can be carried out by means of analytical or empirical methods.

Analytical methods are based on the use of numerical models providing the expected damage (typically corresponding to a fixed displacement threshold) as a function of the seismic intensity. Several approaches have been developed in literature, different from each other both in structural (usually simplified) modelling and in seismic capacity assessment procedure. Among them, methods based on simplified mechanics-based procedures (e.g. Cosenza et al. [7]; Borzi et al. [8]), Capacity Spectrum Methods (e.g. Iervolino et al. [9]; Del Gaudio et al.[1,2,3]), and Displacement-Based methods (e.g. Calvi, [10]; Crowley et al. [11]; Borzi et al. [12]).

In empirical methods the assessment of the expected damage to a building is based on the observation of damage suffered during past seismic events (e.g. Braga et al. [13]; Sabetta et al. [14]; Lagomarsino and Giovinazzi [15]; Rota et al. [15]; Zuccaro and Cacace [17]). Empirical vulnerability methods have the advantage of providing a realistic damage estimation since they are derived from observed post-earthquake damage data. Hence, their reliability is related to the quality and amount of data they are based on. For instance, depending on the available building dataset, it may be necessary to convert and homogenize damage data collected in different surveys into a unique damage scale.

In present work, a simplified mechanical method – PushOver on Shear Type models (POST) – is used in order to derive seismic damage scenario for a database consisting of 7597 Moment Resisting Frame (MRF) residential RC buildings located in the Abruzzi region.

## 2 DATABASE DESCRIPTION

The empirical data collected during L'Aquila post-earthquake surveys are presented in this section. The 2009 L'Aquila (Abruzzi Region) earthquake hit 130 municipalities (Dolce and Goretti [18]) and caused extensive damage to public and private structures, to artistic and cultural heritage of L'Aquila and provinces.

Few days after the earthquake, the damage and usability assessment of the buildings started to determine whether they could be safely used in the case of aftershocks.

The damage and usability assessment of ordinary buildings was performed by means of the first level survey form, the AeDES form (Baggio et al. [19]).

The field inspections carried out after L'Aquila earthquake allowed to collect a database containing first-level data, on 74254 buildings (Dolce and Goretti [18]), out of which, 8750 is constituted by Moment Resisting Frame (MRF) RC buildings characterized by a residential use and located in Municipalities classified with macroseismic intensity in the Mercalli-Cancani-Sieberg (MCS) scale (Sieberg 1930) ($I_{MCS}$) higher than VI.

Furthermore, in order to avoid bias in the results, only buildings located in a Municipalities with a predetermined “threshold of completeness” on the survey activities are herein considered (for further details see Del Gaudio et al.[1,2,3]). According to such assumptions, the final subset consists of 7597 MRF residential RC buildings.

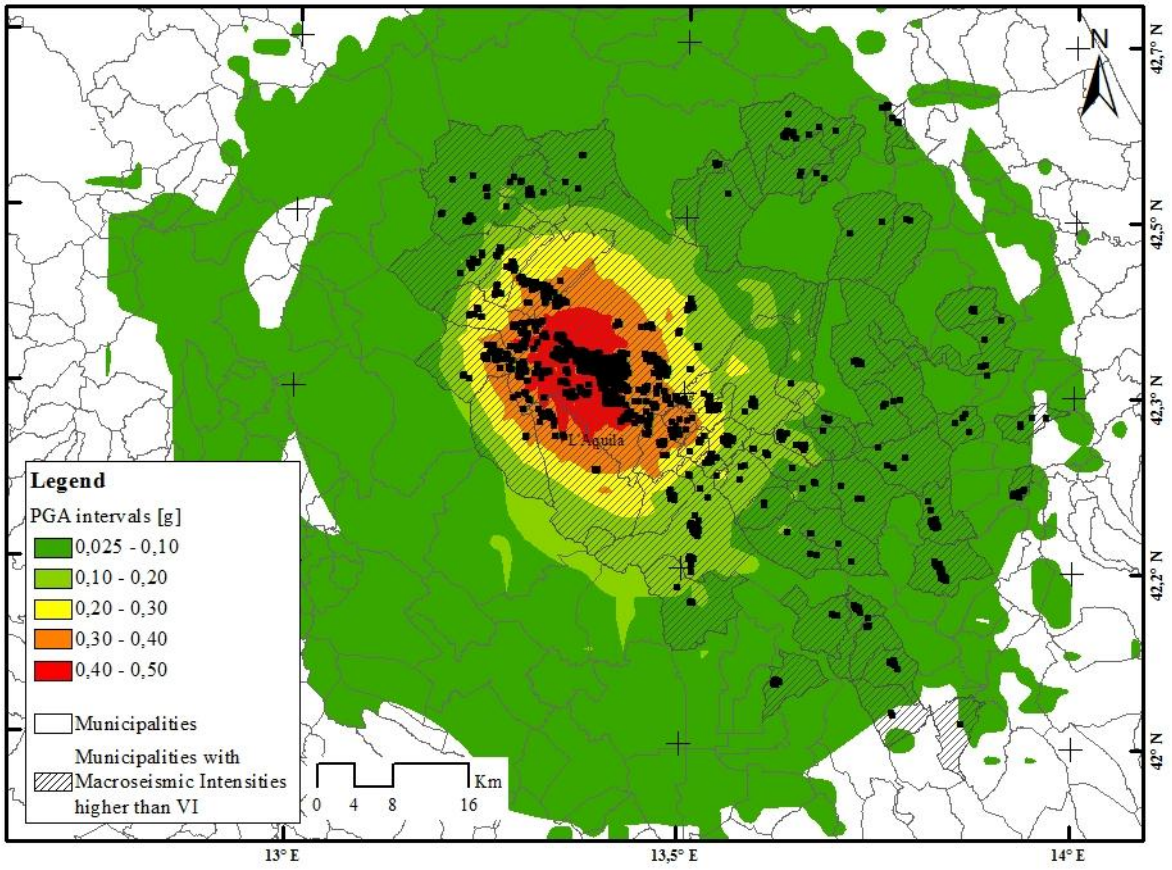


Figure 1: Isoseismic areas corresponding to the assumed PGA bins form 0.025g to 0.50g and Municipalities classified with MCS Intensity higher than VI

Figure 1 also reports the ShakeMap of the event published soon after the earthquake by the Italian National Institute of Geophysics and Volcanology (Istituto Nazionale di Geofisica e Vulcanologia, INGV), generated through the software package ShakeMap® developed by the U. S. Geological Survey Earthquake Hazards Program (Wald et al., 2006) specifically designed to obtain maps of the peak ground motion parameters (Michelini et al. [20]).

Figure 2 reports information about construction age, number of storeys and average storey surface collected during the field inspections. The construction age is classified according to eight periods (i.e. before 1919, between 1919 and 1945, 1946-1961, 1962-1971, 1972-1981, 1982-1991, 1991-2001, after 2001) as commonly adopted in the census data collections (and in the AeDES form). Figure 3 (a) shows that 87% of the building dataset (corresponding to 6616 buildings) was built after 1972; the graphs in Figure 3 (b), (c) show that 85% of the building dataset (corresponding to 6482 buildings) had a number of storeys between 2 and 4, while 67% of the building dataset (corresponding to 5131 buildings) had an average storey surface between 70m$^2$ and 230m$^2$.

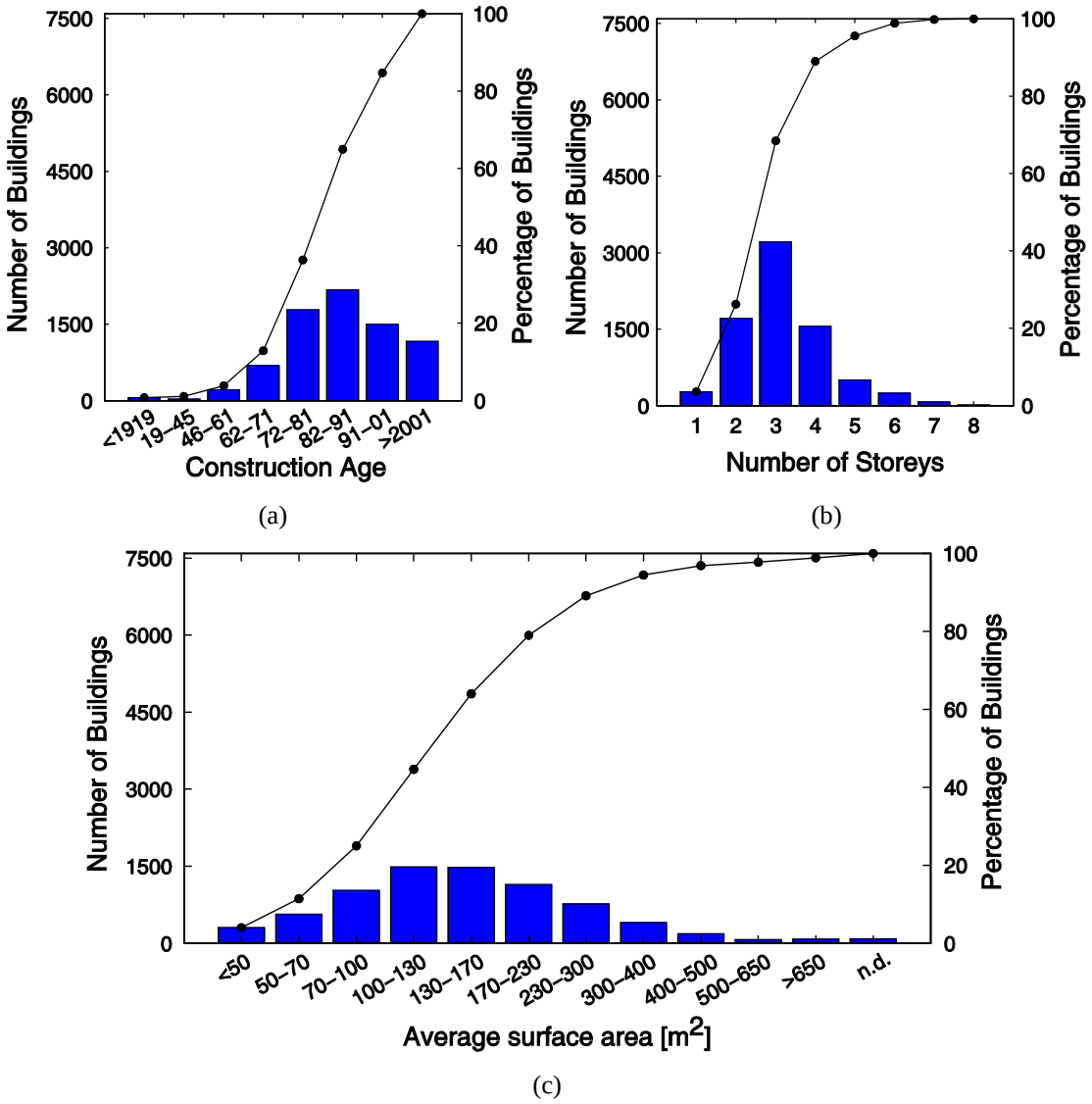


Figure 2: Distribution and cumulative percentage of buildings as a function of construction age (a), number of storeys (b) and average storey surface (c)

Furthermore, AeDES survey form gives information on damage (Ds) detected on structural components: vertical structures, floors, stairs, roofs and infills-partitions. The definition of the observed damage grades is based on the European Macroseismic Scale EMS98 (Grünthal [5]).

AeDES survey form provides only three Ds, combining level D2 with D3 and D4 with D5 of EMS98.

On the other hand, observed damage scenario is herein derived considering 5 damage grades (DGs) according to the EMS98 damage classification (from D0-no damage to D5-destruction). Only damage to vertical structures and infills-partitions will be used to derive observed damage scenario obtained in present work.

The equivalence between 5 (EMS98) DGs and 3 (AeDES) Ds is performed according to the scheme reported in Dolce et al [21] and Rota et al [16] for vertical structure and to the scheme reported in Del Gaudio et al [2] for infill-partitions.

Figure 3 reports the observed damage scenario for the whole building stock. It is to noted that 34% of the building stock has a “Negligible damage” (DG0), 36% ,15% and 10% belong to “Slight damage” (DG1), “Moderate damage” (DG2) and “Substantial to heavy damage”

(DG3) respectively, and only the 4% and 1% by "Very heavy damage" (DG4) and "Destruction" (DG5), respectively.

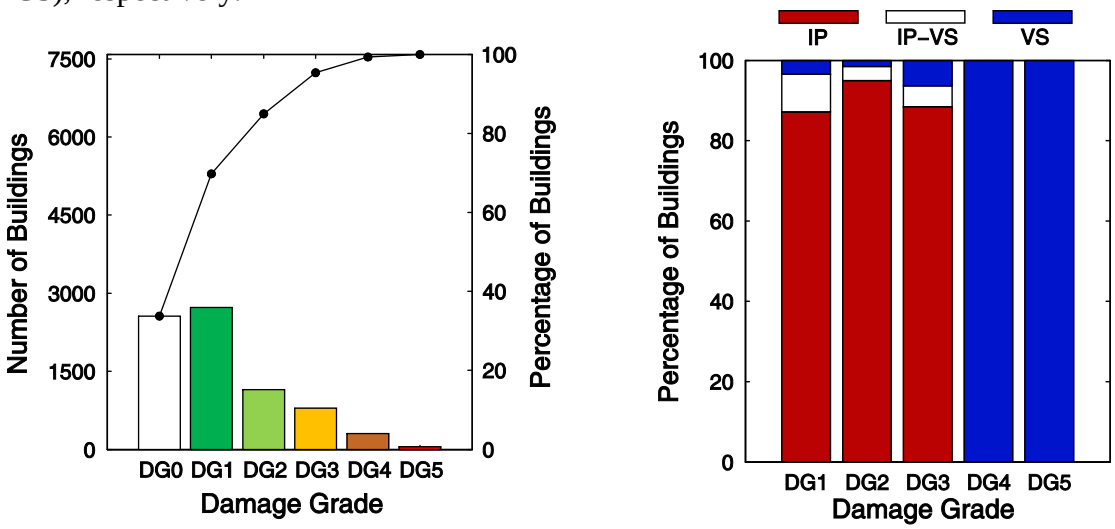


(a) (b)

Figure 3: Distribution and cumulative percentage of buildings as a function of damage grades (DGs) (a); Percentage ratio of buildings belonging to a given DG due to the maximum damage detected on VS, IP or VS-IP (b).

Figure 3b reports the percentage ratio of buildings in which the maximum damage to a given DG is detected on vertical structures (VS), infill-partitions (IP) or both (VS-IP). It is to be noted that on average, in 87% of the cases the damage to IP governs the lighter DGs of the building (DS1, DG2, DG3), highlighting the very significant role of the non-structural damage affecting infill components; vice-versa, DG4 and DG5 are related exclusively to damage to Vertical Structures (VS).

## 3 POST DESCRIPTION

In this section, the simplified mechanical method POST (PushOver on Shear Type models) for seismic vulnerability assessment of RC buildings is presented and briefly described; for further details, the reader is referred to (Del Gaudio et al. [1,2,3]).

The methodology is based on the following steps:

I. Definition of building model: the structural model of the building is constructed through a simulated design procedure in compliance with design code prescriptions, professional practice and the seismic classification of the area of interest at the time of construction. For further details, the reader is referred to Verderame et al [22].

II. Non-linear static response: the evaluation of the non-linear static response of the building is performed through a simplified model based on Shear Type assumption; the latter allows to consider RC columns and infill elements acting in parallel, considering a tri-linear envelope for RC columns and a multi-linear model for infill panels according to Panagiotakos and Fardis [23]. The pushover curve is obtained in closed-form through a force-controlled procedure up to the peak and through a displacement-controlled procedure thereafter. Hence the storey characterized by the maximum value of the ratio between interstorey shear demand and interstorey shear strength will be the only one to reach its maximum resistance and to experience its softening post-peak behavior, giving to the pushover curve the corresponding degrading trend.

III. Definition of DSs: DSs adopted in the proposed method are defined according to the damage scale proposed by EMS-98;

IV. Seismic capacity assessment: the SPO2IDA (Vamvatsikos and Cornell [4]) framework is applied to evaluate the seismic capacity at the performance levels of interest in terms of spectral intensity measures;

V. Evaluation of fragility curves: depending on the level of knowledge achieved, certain random variables have to be introduced. Then, a Monte Carlo simulation approach is used, generating a population of buildings. For each run of the procedure, an n-vector with the realization of each random variable, where n is the total number, is extracted from the corresponding distribution. Hence for each run the building model and the corresponding non-linear static response is determined. DSs and corresponding displacement values are determined on the building response and seismic capacity assessment is performed in terms of spectral ordinates and PGA values. Therefore, if the PGA capacity at a given DS is calculated for all the generated buildings, the corresponding cumulative frequency distributions provide the corresponding fragility curves.

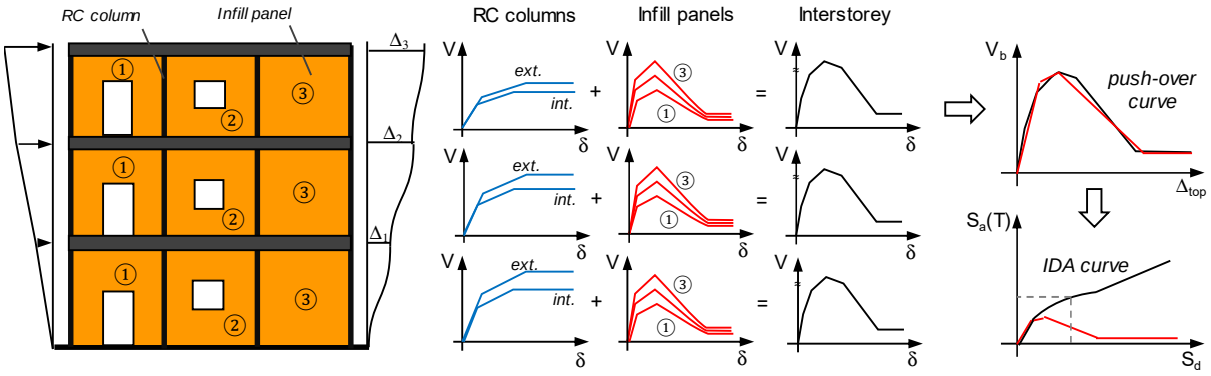


Figure 4: POST methodology: building model, non-linear static response and seismic capacity assessment

It is to worth noting that the expected failure mode is determined for each column through the comparison between the flexural plastic shear ($V_y=M_y/0.5\ h$) and the shear strength ($V_n$ according to Sezen and Moehle [24]). Hence, columns with $(V_y/V_n)<k$ are expected to fail in flexure, while columns with $(V_y/V_n)\geq k$ are expected to fail in shear or flexure-shear, where the coefficient k related to the maximum ductility-related shear strength decrease, is assumed to be equal to 0.7.

In addition, different configurations for infill panels have been considered: (i) solid-, (ii) with window opening- and (iii) with door opening-panels. Openings in infill panels are considered to modify the non-linear behaviour of the infill panels according to the model presented in Kakaletsis and Karayannis [25] by means of control parameters depending on the window and door opening sizes.

A fundamental issue is represented by the definition of DSs. As a matter of fact the qualitative description of observational DSs reported by EMS-98 damage classification is translated into numerical mechanical-based displacement thresholds in the building structural model (such as the Interstorey Drift Ratio (IDR) capacity).

Capacity for infill panel ($IDR_{IP,DS1}$, $IDR_{IP,DS2}$, $IDR_{IP,DS3}$) is set according to IDR values reported in Cardone and Perrone [26].

On the other hand, the IDR capacity for RC columns is evaluated in correspondence of physical condition related to the qualitative description of EMS-98 DSs, namely to the first attainment of:

- **DS1**: the cracking moment ($IDR_{RC,cr}$);
- **DS2**: the yielding moment ($IDR_{RC,y}$);
- **DS3**: the IDR value corresponding to the concrete cover spalling and the longitudinal reinforcement buckling, ($IDR_{RC,s}$, $IDR_{RC,b}$) or the IDR value corresponding to the Shear failure according to Aslani and Miranda [27] model ($IDR_{RC,SF}$);
- **DS4**: the IDR value corresponding to the zero resistance point ($IDR_{RC,pc}$) of the degrading backbone curve provided by the model by Haselton et al. [28] or the IDR value corresponding to the loss of vertical load carrying capacity ($IDR_{RC,A-SF}$) of the first (previously shear-damaged) RC column provided by Aslani and Miranda [27];
- **DS5**: the IDR value corresponding to the zero resistance point ($IDR_{RC,pc}$) of the backbone curve provided by the model by Haselton et al. [28] for all the columns of a floor or the IDR value at which all the shear-controlled columns of a floor reach the $IDR_{RC,A-SF}$ (if both flexure- and shear-controlled columns are present in the same floor, IDR at DS5 corresponds to the attainment of zero resistance point and loss of vertical load carrying capacity in all the former and latter columns, respectively).

The numerical values of such an IDR capacity are reported in Table 2.

| **EMS-98 Damage State** | | **Infill panels** | | **RC columns** | | |
|---|---|---|---|---|---|---|
| | | **EMS-98 descriptions** | **POST thresholds** | **EMS-98 descriptions** | **POST thresholds** | |
| | | | | | F-Type* | S-Type* |
| **DS1** | Negligible to slight damage | *Fine cracks in partitions and infills* | $IDR_{IP,DS1}$ | *Fine cracks in plaster over frame members* | $IDR_{RC,cr}$ | |
| **DS2** | Moderate damage | *Cracks in partition and infill walls.* | $IDR_{IP,DS2}$ | *Cracks in columns* | $IDR_{RC,y}$ | |
| **DS3** | Substantial to heavy damage | *Large cracks in partition and infill walls, failure of individual infill panels* | $IDR_{IP,DS3}$ | *Spalling of concrete cover, buckling of reinforced rods* | $\min(IDR_{RC,s}; IDR_{RC,b})$ | $IDR_{RC,SF}$ |
| **DS4** | Very heavy damage | | | *Large cracks in structural elements (...) Collapse of a few columns or of a single upper floor* | First attainment of $IDR_{RC,pc}$ | First attainment of $IDR_{RC,A-SF}$ |
| **DS5** | Destruction | | | *Collapse of ground floor or parts of buildings* | Last attainment of $IDR_{RC,pc}$ | Last attainment of $IDR_{RC,A-SF}$ |

**: F-Type: columns failing in Flexure; S-Type: columns failing in Shear or Flexure-Shear*

Table 1: Displacement thresholds at the assumed DSs, based on the mechanical interpretation of the DSs described by EMS-98.

The resulting displacement thresholds at each DS are summarized in Table 1. Note that, due to the assumed Shear-Type behaviour, the IDR leading to the attainment of each DS is the minimum between the values reported in Table 1 for infill panels and RC columns.

The capacity in terms of spectral ordinate $S_a(T)$ is calculated through the use of an approximate IDA curve, evaluated according to the SPO2IDA framework (Vamvatsikos and Cornell, [4]) in correspondence of IDR value for the assumed DS. The corresponding PGA capacity is evaluated as a function of the adopted elastic pseudo-acceleration response spectrum.

## 4 DERIVATION OF CLASS-SPECIFIC ANALYTICAL FRAGILITY CURVES

POST methodology has been applied at single building level in (Del Gaudio et al. [1,2,3]).

In the present work, POST methodology will be applied at building class level. The definition of homogeneous classes of buildings will be carried out identifying the parameters that greatly influence their seismic fragility. In Del Gaudio et al. [29], two classes of buildings have been defined as a function of the *number of storeys* ($N_s$): "L", Low rise ($1 \leq N_s \leq 3$) buildings, and "MH", Medium-High rise ($N_s \geq 4$) buildings.

Generally speaking, some of the input parameters of the POST procedure can be modeled as random variables to reflect their expected variability. The definition of these random variables also depends on the type of analysis that is carried out. For instance, the methodology can be applied to single buildings for which the number of storeys, the plan dimensions and the age of construction can be considered as deterministically known, and other parameters are assumed as random variables, in order to account for aleatoric (e.g., the record-to-record variability, which can be taken into account, although in a simplified way, also within a spectral assessment framework as in the present study, see Section 4.1.4) or epistemic uncertainties (for parameters whose deterministic knowledge would require an excessive cost or, however, could not be easily and quickly obtained, see Section 4.1.2). If, instead, the methodology is applied to classes of buildings, i.e. in order to derive the seismic fragility of groups of buildings characterized by common values of some parameters – assumed as "distinguishing" parameters between one class and the other due to their prominent influence on seismic fragility – such as, in the present study, the number of storeys (within a given interval), further parameters have to be modeled as random variables in order to reflect their variability between one building and the other (inter-building) within the class (intra-class), such as, for instance, the number of storeys itself (within the given interval), the plan dimensions and the age of construction, see Section 4.1.1.

In this study, on the whole, $N=24$ parameters are modeled as random variables (see Table 2), each one characterized by a marginal distribution chosen to define its variability. $N = k+s+m$, with $k=1$ parameter (number of storeys) chosen to define the buildings classes, $s=3$ parameters (construction age, average storey surface and plan ratio) defining the inter-building variability within the class, and $m=20$ parameters defining the uncertainties in geometry, materials, capacity models, damage thresholds, spectral shape and record-to-record variability.

### 4.1 Uncertainties characterization

Below, the random variables assumed in the present work will be introduced and specialized, reporting the parameters of the distributions required for their definition (see Table 2).

#### 4.1.1. (Intra-class) Inter-building variability

As seen previously, two classes of buildings will be introduced as a function of the *number of storeys* ($N_s$): *L*-class and *MH*-class of buildings.

The statistics of construction age, number of storeys and average storey surface collected during the field inspections (Figure 2) will be analyzed in order to determine the correlation matrix.

In the Monte Carlo simulation technique in the $i^{th}$-run, the value of construction age, number of storeys and average storey surface will be extracted so that at the end of the simulated procedure the correlation matrix between the parameters is equal to that obtained from data collected during the field inspections. The algorithm proposed by (Vorechovský and Novák, [30]) is used, which attempt to minimize the difference between the target correlation matrix and the actual correlation matrix by means of an optimal sample ordering through the so-called Simulated Annealing method.

Plan ratio is assumed as a uniform random variable between [1-2,5] according to statistics reported in (Del Gaudio et al. [1, 29]).

#### 4.1.2. Uncertainties in geometry, materials, capacity models, damage thresholds

The selected variables are the compressive strength of concrete ($f_c$), steel yield strength ($f_y$), and infill material characteristics. The corresponding probability distributions are selected from statistical analyses provided by the technical literature to be representative of the existing Italian building stock (Del Gaudio et al. [1,2,3]).

- Compressive strength of concrete ($f_c$). A distribution with a mean value of 25 MPa, and a coefficient of variation (CoV) of 31% for pre-1981 buildings and of 25% thereafter, reflecting the higher reliability in the preparation of the concrete for recent construction, have been assumed.
- Steel yield strength ($f_y$). Distributions according to statistics reported by STIL software (Verderame et al., [31]) have been considered, with the variable as a function of the age of construction and the type of reinforcement. The latter is assumed to change with the age of construction: for buildings constructed before 1971, plain bars have been considered as reinforcement and deformed bars thereafter.
- Infill mechanical characteristics ($E_w$). Reference has been made to the proposal of the Italian code (Circolare 617, 2009) for hollow clay brick panels. A full correlation between the dependent variables (shear modulus $G_w$, shear strength $\tau_{cr}$) and the independent variable (Young Modulus $E_w$) has been adopted. Hence, the elastic modulus is assumed in the following as a random variable with a lognormal distribution, a mean value equal to 4500 MPa and a CoV of 30%. $G_w$ is evaluated as 3/10 of $E_w$. $\tau_{cr}$ is assumed as linearly dependent on $G_w$, with values of 0.3 MPa and 0.4 MPa corresponding to $G_w$ values of 1080 MPa and 1620 MPa. The same material characteristics are assumed for external and internal infill panels.

Uncertainties in modelling are taken into account for the non-linear behaviour of both RC columns and infill panels. They are taken into consideration through a twofold contribution. On the one hand, the lateral force-displacement relationship would indirectly change through random variables related to geometrical characteristics and material properties.

On the other hand, uncertainty in modelling is explicitly considered assuming the secant stiffness at yielding ($EI_y$) as a random variable, determined according to model of Haselton et al. [28], for what concerning RC columns.

For infill panel, elastic and secant stiffness to peak resistance, cracking and peak resistance are considered as random variable. In the $i^{th}$-run of Monte Carlo simulation technique, the values will be extracted so that to minimize the difference between the actual and the target correlation matrix, the latter evaluated from the ratio between the model predictions and test result values used by the authors to derive their response model.

Furthermore, due to lack of specific information about the amount and openings in external infills, the following assumptions have been made based on expert judgement:

- Thickness of external infill panels ($s_w$). A discrete random variable in the interval {200; 220; 240} mm with a uniform probability distribution. In fact, the photographic documentation collected after the last 30 years earthquake has shown a thickness of infill panels equal to approximately 200-240 mm, typical of a double layer of hollow clay bricks, commonly employed in construction in Italy and in the Mediterranean area.
- The type of opening. The distribution of type of opening among the bays of a generic storey represents a critical issue that varies strongly depending on architectural aspects and professional practice. Hence, a discrete random variable is assumed with a uniform probability distribution as a function of three typologies: (i) solid-, (ii) with window opening- and (iii) with door opening-panel. The opening width is assumed to be equal to 25% of the corresponding infill length, for both window and door openings.

The distributions associated with IDR thresholds for infill panels have been identified according to the prediction model of Cardone and Perrone [26].

The distribution of IDR thresholds for RC columns (concrete cover spalling and longitudinal reinforcement buckling, post-capping IDR capacity, see Table 2) have been set according to the empirical capacity models of Haselton et al. [28] and Berry and Eberhard [32].

#### 4.1.3. Spectral shape from ShakeMap

The spectral shape can also be modelled as a random variable.

INGV ShakeMaps provide spectral pseudo-acceleration values at T = {0; 0.3; 1.0; 3.0} s for the sites where each building is located. Hence, a Newmark-Hall elastic pseudo-acceleration spectrum can be determined, with a plateau passing through the 0.3 s acceleration, a curve passing through the 1.0 s acceleration with a 1/T decay, and another curve passing through the 3.0 s acceleration with 1/T2 decay, according to Del Gaudio et al. [3].

In such a way, 7597 elastic spectra can be evaluated from the ShakeMaps for each building site.

Hence, for each run of the Monte Carlo simulation procedure, a realization out of 7597 elastic spectra is obtained through data mining procedure previously shown.

#### 4.1.4. Record-to-record variability (SPO2IDA relationship)

Uncertainties related to seismic ground motion are taken into account considering a lognormal distribution, whose median value is the spectral ordinate evaluated on the approximate IDA curve as function of displacement capacity. Further, logarithmic standard deviation is evaluated depending on 84%- and 16%-IDA curves. The latter is taken as equal to:

$$\beta = \frac{1}{2}\left(\ln S_a^{84\%} - \ln S_a^{16\%}\right) \tag{1}$$

where $S_a^{i^{th}\%}$ represents the ith%-fractile of spectral ordinate provided by the corresponding IDA curves provided by Vamvatsikos and Cornell (2006).

| Type of R.V. | R.V. | Reference | Distribution | Median value | CoV [-] |
|---|---|---|---|---|---|
| Material properties | $f_c$ | Verderame et al. (2001); Masi and Vona (2009) | lognormal | 25 MPa | 31% or 25% |
| | $f_y$ | STIL Verderame et al. (2012) | lognormal | Calculated | Calculated |
| | $E_w$ | Circolare 617 (2009) | lognormal | 4500 MPa | 30% |
| Geometrical characteristics | $s_w$ | - | uniform | [200; 220; 240] | - |
| | Type of opening | - | uniform | [solid; window opening; door opening] | - |
| | Plan ratio | | uniform | [1-2.5] | |
| | Number of storeys | | uniform | Simulated annealing | |
| | Average surface | | uniform | Simulated annealing | |
| | Construction age | | uniform | Simulated annealing | |
| Modelling parameters | $EI_y$ | Haselton et al. (2008) | lognormal | 0.95*Calculated | 28% |
| | $k_{1,infill}$ | | uniform | Simulated annealing | |
| | $k_{2,infill}$ | | uniform | Simulated annealing | |
| | $F_{cr}$ | | uniform | Simulated annealing | |
| | $F_{max}$ | | uniform | Simulated annealing | |
| Displacement thresholds | $IDR_{RC,b}$ | Berry and Eberhard (2003) | lognormal | Calculated | 26.2% |
| | $IDR_{RC,s}$ | Berry and Eberhard (2003). | lognormal | Calculated | 35.6% |
| | $IDR_{RC,cap,pl}$ | Haselton et al. (2008 | lognormal | 1.02*Calculated | 54% |
| | $IDR_{RC,SF}$ | Aslani and Miranda (2005) | lognormal | 1.05*Calculated | 55% |
| | $IDR_{RC,A-SF}$ | Aslani and Miranda (2005) | lognormal | 1.03*Calculated | 33% |
| | $IDR_{IP,DS1}$ | Cardone and Perrone (2015) | normal | 0.03% | 59.9% |
| | $IDR_{IP,DS2}$ | Cardone and Perrone (2015) | normal | 0.35% | 96.5% |
| | $IDR_{IP,DS3}$ | Cardone and Perrone (2015) | normal | 1.62% | 23.7% |
| Spectral Shape | Spectral shape from ShakeMap | http://shakemap.rm.ingv.it | uniform | From data collected | |
| Record-to-record variability | Record-to-record variability | Vamvatsikos and Cornell, (2006) | lognormal | Calculated | Eq.1 |

Table 2: Summary of median and CoV values for the selected random variables.

## 5 COMPARISON IN TERMS OF FRAGILITY CURVES AND DAMAGE SCENARIO

The damage scenario is evaluated based on the PGA value obtained for each building from the ShakeMap of the event.

The information about number of storeys allows to define the class of building, which the single building belongs to, and hence the corresponding fragility curves. Therefore, the latter, together with the information about the ground motion to which each building has been subjected during the 6th April 2009 seismic event (PGA value), allows to determine the probabilities of being in each assumed DS ($Pr[ds = DS_i | PGA]$) for each single building.

Summing up all the corresponding probabilities of being in each DS for a N-number of buildings, the damage distribution of the considered dataset is evaluated.

The above procedure is herein applied starting from fragility curves derived with POST methodology for L-class of buildings ($1 \leq Ns \leq 3$) and the MH-class of buildings ($Ns \geq 4$) is shown.

Hence, the distribution and cumulative distribution of damage, reporting, respectively, the number of buildings in each DSi, i=0:5, ($N[ds = DS_i]$) and the number of buildings with a damage at least equal to DSi, ($N[ds \geq DS_i]$), are shown in Figures 5, 6 and 7.

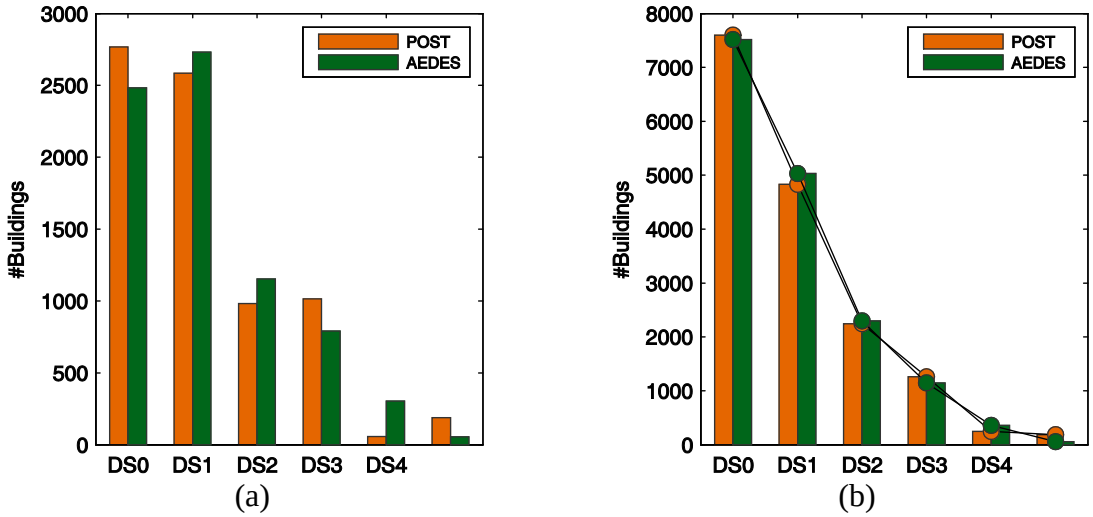


Figure 5: Distribution (a) and cumulative distribution (b) of damage predicted by POST methodology

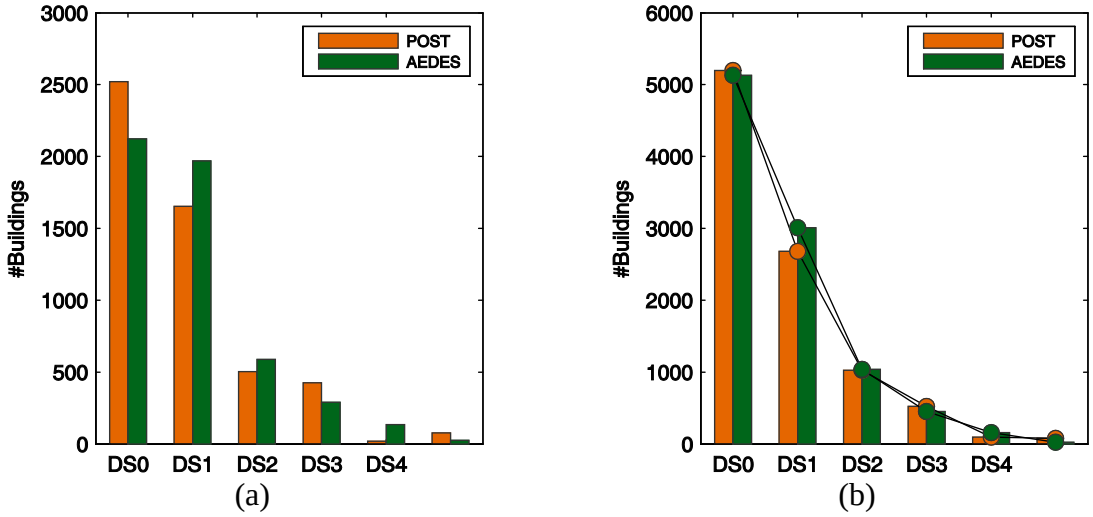


Figure 6: Cumulative distribution of damage predicted by POST methodology for L-class of buildings

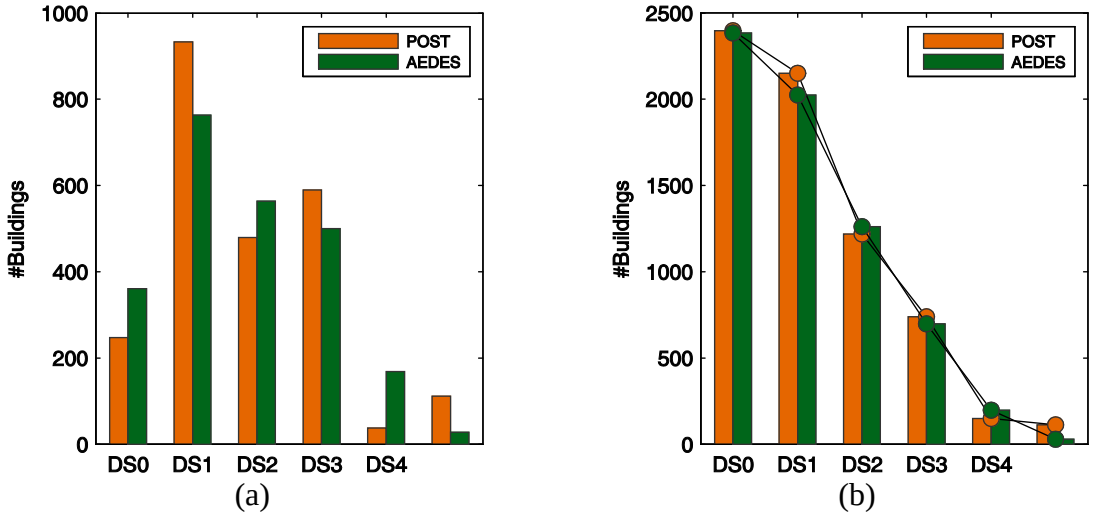


Figure 7: Cumulative distribution of damage predicted by POST methodology for MH-class of buildings

A very good agreement from the comparison between POST-predicted and observed damage scenario can be observed. The latter derived according to section 2 from the interpretation of AeDES survey forms and already reported in figure 3a.

Furthermore, figure 6 and 7 report the same comparison for the homogenous building class above defined: L-class buildings ($1 \leq N_s \leq 3$), and MH-class buildings ($N_s \geq 4$). The good agreement between the observed and predicted results is confirmed for both building classes.

Finally, figure 8 reports the comparison between the fragility curves above discussed, derived according to POST methodology for the 7597 MRF residential RC buildings considered in the present study, with the empirical fragility curves derived on the same building dataset obtained in Del Gaudio et al., [29]. A very good agreement is observed except for DG1, where empirical curve shows a lower fragility respect to analytical POST-derived fragility curve.

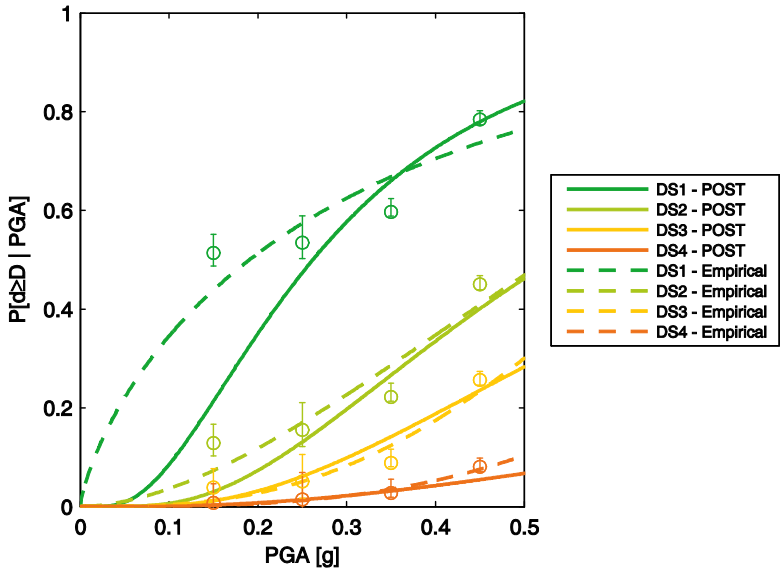


Figure 8: Comparison between empirical fragility curves for RC buildings (dashed lines) and by POST methodology (solid lines).

## 6 CONCLUSIONS

In present work, damage scenario is derived according to POST (PushOver on Shear Type models) methodology (Del Gaudio et al., [1, 2, 3]) for a database consisting of 7597 Moment Resisting Frame (MRF) residential RC buildings located in the Abruzzi region. Each buildings have been charged to post-earthquake usability assessment procedure after the 2009 catastrophic earthquake, leading to the definition of an observed damage scenario according to the EMS98 (Grünthal [5]) damage classification.

Due to the use of spatially extended and massive amount of data, the reference unit is the class of building, which definition of has been carried out as a function of the parameters that greatly influence seismic fragility In Del Gaudio et al. [29] two classes of buildings have been defined as a function of number of storeys ($N_s$): L-class buildings ($1 \leq N_s \leq 3$) and MH-class buildings ($N_s \geq 4$).

Random variables for the derivation of fragility curves are chosen in appropriate distributions, evaluated from data collected during post-earthquake survey, considering also the correlation values among the variables within each class.

In this study, on the whole, $N=24$ parameters have been modeled as random variables, each one characterized by a marginal distribution chosen to define its variability. $N = k+s+m$, with

*k=1* parameter (number of storeys) chosen to define the buildings classes, *s=3* parameters (construction age, average storey surface and plan ratio) defining the inter-building variability within the class, and *m=20* parameters defining the uncertainties in geometry, materials, capacity models, damage thresholds, spectral shape and record-to-record variability.

The comparison between observed and predicted damage scenario for the 7597 MRF residential RC buildings considered in the present study, shows a very good agreement between the results, also confirmed for both predefined building classes (L rise and MH rise classes).

Fragility curves derived according to POST methodology, are then compared with the empirical fragility curves derived on the same dataset (7597 MRF residential RC buildings) obtained in Del Gaudio et al., [29], showing a very good agreement for all DGs, except for DG1, where empirical curve shows a lower fragility respect to analytical POST-derived fragility curve.

## 7 AKNOLEDGEMENTS

This work was developed under the financial support of METROPOLIS ("Metodologie e tecnologie integrate e sostenibili per l'adattamento e la sicurezza di sistemi urbani" - Programma Operativo Nazionale - Ricerca e Competitività 2007-2013) and "ReLUIS-DPC 2014-2018 PR 2- Linea Strutture in cemento armato", funded by the Italian Department of Civil Protection (DPC). These supports are gratefully acknowledged.

## 8 REFERENCES

[1] Del Gaudio C., Ricci P., Verderame G.M., Manfredi G., 2015. Development and urban-scale application of a simplified method for seismic fragility assessment of RC buildings. Engineering Structures, 91, 40-57.

[2] Del Gaudio C., Ricci P., Verderame G.M., Manfredi G., 2016. Observed and predicted earthquake damage scenarios: the case study of Pettino (L'Aquila) after the 6th April 2009 event. Bulletin of Earthquake Engineering.

[3] Del Gaudio C., Ricci P., Verderame G.M., Manfredi G., 2017. Urban-scale seismic fragility assessment of RC buildings subjected to L'Aquila earthquake. Soil Dynamics and Earthquake Engineering. 96, 49–63.

[4] Vamvatsikos D., Cornell C.A., 2006. Direct estimation of the seismic demand and capacity of oscillators with multi-linear static pushovers through IDA. Earthquake Engineering and Structural Dynamics, 35(9), 1097-1117.

[5] Grünthal G. (1998). Cahiers du Centre Européen de Géodynamique et de Séismologie: Volume 15 – European Macroseismic Scale 1998. European Center for Geodynamics and Seismology, Luxembourg.

[6] Del Gaudio C., De Martino G., Di Ludovico M., Manfredi G., Prota A., Ricci P., Verderame G.M., 2016. Empirical fragility curves from damage data on RC buildings after the 2009 L'Aquila earthquake. 14, 1–26.

[7] Cosenza E., Manfredi G., Polese M., Verderame G.M. (2005). A multi-level approach to the capacity assessment of existing RC buildings. Journal of Earthquake Engineering, 9(1), 1-22.

[8] Borzi B., Pinho R., Crowley H. (2008). Simplified pushover-based vulnerability analysis for large scale assessment of RC buildings, Engineering Structures, 30(3), 804-820.

[9] Iervolino, I., Manfredi, G., Polese, M., Verderame, G. M., & Fabbrocino, G. (2007). Seismic risk of RC building classes. Engineering Structures, 29(5), 813-820.

[10] Calvi G.M. (1999). A displacement-based approach for vulnerability evaluation of classes of buildings. Journal of Earthquake Engineering, 3(3), 411-438.

[11] Crowley H., Pinho R., Bommer J.J. (2004). A probabilistic displacement-based vulnerability assessment procedure for earthquake loss estimation. Bulletin of Earthquake Engineering, 2(2), 173-219.

[12] Borzi B., Pinho R., Crowley H. (2008). Simplified pushover-based vulnerability analysis for large scale assessment of RC buildings, Engineering Structures, 30(3), 804-820.

[13] Braga F., Dolce M., Liberatore D. (1982). A statistical study on damaged buildings and an ensuing review of the MSK-76 scale. Proceedings of the 7th European Conference on Earthquake Engineering, Athens, Greece. Pp.431-450.

[14] Sabetta F., Goretti A., Lucantoni A. (1998). Empirical fragility curves from damage surveys and estimated strong ground motion. Proceedings of the 11th European Conference on earthquake Engineering, Paris, France, September 6-11.

[15] Lagomarsino G. and Giovinazzi S. (2006). Macroseismic and mechanical models for the vulnerability and damage assessment of current buildings. Bulletin of Earthquake Engineering, 4:415–443

[16] Rota M., Penna A., and Strobbia C.L. (2008). Processing Italian damage data to derive typological fragility curves. Soil Dynamics and Earthquake Engineering, 28.10: 933-947.

[17] Zuccaro, G., Cacace, F. (2009). Revisione dell'inventario a scala nazionale delle classi tipologiche di vulnerabilità ed aggiornamento delle mappe nazionali di rischio sismico. Atti del XIII Convegno ANIDIS "L'ingegneria sismica in Italia", June 28-July 2, Bologna, Italy. Paper S14.39. (in Italian)

[18] Dolce M., Goretti A. (2015). "Building damage assessment after the 2009 Abruzzi earthquake." Bulletin of Earthquake Engineering, 1-24.

[19] Baggio C., Bernardini A., Colozza R., Coppari S., Corazza L., Della Bella M., Di Pasquale G., Dolce M., Goretti A., Martinelli A., Orsini G., Papa F., Zuccaro G. (2007). Field manual for post-earthquake damage and safety assessment and short term countermeasures (Pinto A, Taucer F eds), Translation from Italian: Goretti A, Rota M, JRC Scientific and Technical Reports, EUR 22868 EN-2007.

[20] Michelini, A., L. Faenza, V. Lauciani, and L. Malagnini (2008). ShakeMap implementation in Italy. Seismological Research Letters 79.5: 688-697.

[21] Dolce M., Masi A., Goretti A. (1999). Damage to buildings due to 1997 Umbria-Marche earthquake. In: Bernardini, editor. Seismic damage to masonry buildings. Rotterdam: Balkema.

[22] Verderame G.M., Polese M., Mariniello C., Manfredi G., 2010. A simulated design procedure for the assessment of seismic capacity of existing reinforced concrete buildings. Advances in Engineering Software, 41(2), 323-335.

[23] Panagiotakos T.B., Fardis M.N., 1996. Seismic response of infilled RC frames structures. Proceedings of the 11th World Conference on Earthquake Engineering, Acapulco, México. Paper No. 225.

[24] Sezen, H., and Moehle, J. P., 2004. Shear strength model for lightly reinforced concrete columns. J. Struct. Eng., 130 (11), 1692–1703.

[25] Kakaletsis D.J., Karayannis C.G., 2009. Experimental investigation of infilled reinforced concrete frames with openings. ACI Structural Journal, 106(2), 132-141.

[26] Cardone D. and Perrone G. Developing fragility curves and loss functions for masonry infill walls. Earthquakes and Structures, 9.1, 257-279, 2015.

[27] Aslani H., and Miranda E., 2005. Probabilistic earthquake loss estimation and loss disaggregation in buildings. Diss. Stanford University.

[28] Haselton C.B., Liel A.B., Taylor-Lange S., Deierlein G.G., 2008. Beam-column element model calibrated for predicting flexural response leading to global collapse of RC frame buildings. PEER Report 2007/03, Pacific Engineering Research Center, University of California, Berkeley, CA, USA.

[29] Del Gaudio C., De Martino G., Di Ludovico M., Manfredi G., Prota A., Ricci P., Verderame G.M., 2016b. Empirical fragility curves from damage data on RC buildings after the 2009 L'Aquila earthquake. Bulletin of Earthquake Engineering. doi: 10.1007/s10518-016-0026-1

[30] Vorechovsky M., Novak D., 2009. Correlation control in small-sample Monte Carlo type simulations I: A simulated annealing approach. Probabilistic Engineering Mechanics, 24(3), 452-462.

[31] Verderame G.M., Ricci P., Esposito M., Manfredi G., 2012. STIL v1.0 - Software per la caratterizzazione delle proprietà meccaniche degli acciai da c.a. tra il 1950 e il 2000. Re-LUIS, http://www.reluis.it/

[32] Berry M., Eberhard M.O., 2003. Performance models for flexural damage in reinforced concrete columns. PEER Report 2003/18, Pacific Engineering Research Center, University of California, Berkeley, CA, USA.

COMPDYN 2017
6th ECCOMAS Thematic Conference on
Computational Methods in Structural Dynamics and Earthquake Engineering
M. Papadrakakis, M. Fragiadakis (eds.)
Rhodes Island, Greece, 15–17 June 2017

# SEISMIC HAZARD ANALYSIS BASED ON FUZZY-PROBABILISTIC APPROACH

**Jelena M. Andrić[1] and Dagang Lu[2]**

[1, 2] Harbin Institute of Technology
School of Civil Engineering
Huanghe Road 73, 150090 Harbin, China
e-mail: jln.andric@gmail.com[1], ludagang@hit.edu.cn[2]

**Keywords:** Seismic Hazard Analysis, Earthquakes, Ground Motion, Peak Ground Acceleration, Fuzzy sets, Fuzzy-probability, Yunnan Province.

**Abstract.** *China is a country prone to frequent earthquakes due to geography and climate complexity. The task of seismic hazard analysis is to estimate the potential level of ground motion parameters that would be produced by future earthquakes. In this paper, a novel method for seismic hazard analysis is proposed based on the fuzzy probabilistic approach. The earthquake magnitude and source-to-site distance are defined as fuzzy-random variables. Further, Cornell model is applied to evaluate the ground motion and the fuzzy-probability of exceedance of the peak ground acceleration level. The advantage of the fuzzy probabilistic seismic hazard analysis model over the traditional deterministic and probabilistic seismic hazard models is that it considers two types of uncertainties, aleatory and epistemic. The proposed model investigates the seismic hazard of Kunming, the capital of Yunnan province in China.*

## 1 INTRODUCTION

Earthquakes are one of the most frequent natural disasters. Seismic hazard analysis estimates the level of ground-motion intensity parameters such as peak ground acceleration PGA, peak ground velocity PGV that would be produced by future earthquakes[1]. The purpose of seismic hazard analysis is to ensure that the civil structures and infrastructure systems withstand an earthquake of the specific return period, perform a desired level of functionality and enable fast recovery to full capacity.

In the current literature, two approaches have been used for evaluating seismic hazard. The Deterministic Seismic Hazard Analysis (DSHA) is applied in the case when the single earthquake scenario for the particular site is considered. This method assumes deterministic information about the earthquake size and source-to-site distance [2]. Also, the single earthquake scenario which is chosen for analyzing represents the "worst-case" scenario. However, the disadvantage of this method is the lack of information about the likelihood of the occurrence of controlling earthquake and the effects of uncertainties involved such as uncertainties in the earthquake size, source location, source-to-site distances and resulting shaking caused by earthquakes [3]. Furthermore, the "worse-case" scenario is not enough for its use of the mean motion when field evidence has pointed out the observed motion exceeding two standard deviations above the mean [4]. The socio-economic impacts of earthquakes for relatively small regions which are bordering specific seismic sources could be estimated by DSHA since this method is useful for the particular case. However, it is impossible to predict the exact future earthquakes and earthquake randomness is of high aleatory uncertainties [5]. In order to account these uncertainties, the Probabilistic Seismic Hazard Analysis (PSHA) is used. It analyzes different earthquake scenarios which vary in the earthquake size, source-to-site distance, and ground motion models in order to predict the most probable value of future ground shaking. The aleatory uncertainties of the earthquake magnitude, the source-to-site distance and wave attenuation have been taken into account by this method [6]. Further, this method has been prescribed as part of site-specific earthquake resistant design [7]. On the other hand, the PSHA is potentially critical when it comes to the epistemic uncertainty [8]. Besides aleatory uncertainty, the epistemic uncertainty arises due to the lack of information about the earthquake size and location. The characteristic of epistemic uncertainty is fuzziness [9].

The aim of this paper is to bridge the gap in the existing analysis methods and to propose the fuzzy probabilistic seismic hazard analysis (FPSHA) approach. A novel seismic hazard analysis method is based on the fuzzy-probabilistic approach. The proposed method represents the upgrade of the existing methods, in which the concepts from the fuzzy sets and probabilistic theory have been applied to estimate the potential seismic hazard. The aim of the fuzzy set theory is to solve high uncertainty problems, represent vague, ambiguous, conflicting and chaotic information, handle imprecise data and information possessing non-statistical uncertainties[10-12]. The motivation to apply fuzzy set theory has its origin in its effectiveness and reliability. Fuzzy-probability approach has verified as the efficient tool in risk assessment in construction industry [13], seismic resilience assessment [14, 15], safety assessment of structures [16], flood risk assessment [17], risk assessment for oil and gas [18], design of water distribution network [19], human health risk assessment [20] and others.

The paper is organized as follows: Chapter 2 reviews the existing methods for the seismic hazard analysis, the deterministic and the probabilistic seismic hazard analysis. Further, Chapter 3 introduces the proposed method for fuzzy-probabilistic seismic hazard analysis. The case study about the seismic hazard in Yunnan Province in China is investigated in Chapter 4. The Chapter 5 provides the conclusions and further research.

## 2 LITERATURE REVIEW

The DSHA investigates one or more critical earthquake scenarios for which a ground motion hazard evaluation is based. The earthquake scenario is determined by the occurrence of an earthquake of a specified size at a specified location. To estimate the site ground motions, the magnitude, the source-to-site distance and site characteristics are included [21]. The DSHA is a simple straight-forward procedure which is usually used for evaluation of worst-case scenario of ground motions.

The DSHA is a four-step process:

- Identification and characterization of seismic sources which produce significant ground motion on the site;
- Source-to-site distance for each source zone which can be distance from hypocenter-to-site or distance from epicenter-to-site;
- Levels of shaking produced by earthquakes;
- Definition of hazard in terms of the ground motion parameters (PGA, PGV and response spectrum) obtained from attenuation relationships.

The PSHA approach estimates the annual frequency of exceedance as a function of a ground measures, such as spectral acceleration or peak ground acceleration based on seismological and geological data [22]. The uncertainties about the size of earthquakes, location and recurrence rate of earthquakes are identified, quantified and combined in the procedure of the PSHA. The PSHA is similar to DSHA since it consists of four steps which are similar. Compared to DSHA, all possible earthquakes scenarios of each source are characterized and described by probability distribution.

The PSHA procedure includes steps as follows [23]:

- All earthquake sources are identified and the probability distributions of potential rupture locations are characterized. Earthquakes are equally likely to occur at any point within the source zone, so uniform probability distribution is assigned to each zone. Further, the probability distribution of source-to-site distance is determined.
- Seismicity of the source zones are characterized by recurrence relationship which provide the average rate of earthquake of a particular magnitude will be exceeded.
- Attenuation relationships are used to determine the ground motion produced at the site of interest considering earthquakes of any possible magnitudes in any possible point of the source zone.
- The uncertainties about the earthquake size, location and ground motion parameters are combined to obtain the total probability or exceedance rate of the ground motion parameter.

## 3 FUZZY-PROBABILISTIC SEISMIC HAZARD ANALYSIS (FPSHA)

Generally, the proposed procedure for FPSHA is the extension of the PSHA method, in which the concepts from the fuzzy sets theory are applied to treat the epistemic uncertainty. Fuzzy set theory is introduced by Zadeh [24]. According to him, fuzzy set theory is "***a theory in which everything is matter of degree or everything has elasticity***"[25]. Fuzzy sets is defined as the class with a continuum of membership grades [26]. Membership function is defined as the function which ties a number to each element of the universe. This number indicates the degree of the element belonging to a fuzzy set.

The magnitudes of earthquakes that have been occurred at the fault can be extracted from historical geological data or measured by instruments. This information is used for predicting the size of future earthquakes. Since there is a variety of data about the earthquakes which already occurred, the dominant uncertainty for predicting earthquake magnitudes is randomness.

In the following model, randomness is extracted from the previous earthquake occurrence which delivers an estimated probability *M*. Additionally, the estimated probability could be accompanied by some measures of uncertainty such as imprecise probabilities in the form of interval [3]. Beside randomness, also fuzziness is included in the model for predicting earthquake magnitude. To include fuzziness of magnitudes, the point probability of magnitude is modeled in form of fuzzy number. Further, the epistemic uncertainty rises due to the lack-of-knowledge of the seismic source location. The lack-of-knowledge of the source-to-site distance is modeled in terms of fuzzy sets and for each fuzzy set, corresponding probability is attributed. In conclusion, the fuzzy-randomness in the process of seismic hazard analysis is handled by ascribing fuzzy probability density functions to earthquake magnitudes and source-to-site distances.

The fuzzy probabilistic seismic hazard analysis (FPSHA) is established and the flowchart is depicted in Figure 1. In the given flowchart, the first step is to identify all possible locations of the sources on the fault which are capable producing earthquakes to the site of interest. Once when the earthquake sources are recognized, the seismic occurrence probability is estimated using the historical seismicity data.

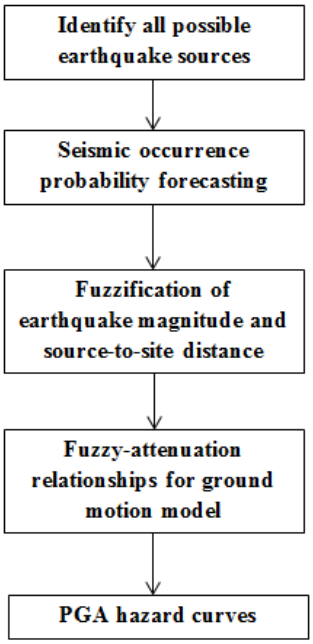


Figure 1 Flowchart of fuzzy-probabilistic seismic hazard analysis

Further, fuzzification the probability distribution of the earthquake magnitudes that are estimated by observed data for the particular site or using fuzzify G-R recurrence law for predicting the fuzzy probability of exceedance:

- fuzzify the probability distribution of the source-to-site distance;
- predict the resulting fuzzy distribution of ground motion intensity as a function of earthquake magnitude and location distance;
- combine all uncertainties including fuzziness in earthquake size, location and ground motion using a theorem known as total fuzzy probability theorem in order to estimate fuzzy hazard curves;
- estimate the fuzzy probability of exceeding certain levels of PGA.

### 3.1 Earthquake sources and seismic occurrence probability forecasting

This step is similar to the first step in the PSHA which task is to identify all possible sources that contribute to producing ground motions at the particular site. These sources are faults which can be determined from the past earthquake locations and geology data. If the faults could not be identified than the earthquake sources are described by areal regions. The earthquake sources are described as point sources which distance from the site could be model as fuzzy distance. The fuzzy-distance takes the range of values since earthquakes are equally likely to occur at any point within the source zone.

After the earthquake sources are determined, the next step in flowchart is to evaluate the probability of earthquake occurrence. The probability of occurrence of earthquakes with specific magnitude is based on the analysis of historical seismicity records. The future time series will have the similar distribution to the observed one if it is assumed that the past and future data sets are stationary.

The seismic occurrence probability forecasting model is estimated based on the historical earthquakes data. The historical earthquakes data can be found in different earthquakes catalogs. The catalog of seismic events is required in order to calculate the seismicity parameters for region of interest. In earthquake catalog, the historical data of seismicity, global and local earthquake records are collected and stored. Earthquake catalog is a list that provides the information of recorded earthquakes: time of occurrence (year, day, time), longitude and latitude of location, focal depth, earthquake size – magnitudes [27]. From the catalog, it could be derived recurrence relations for predicting annual rate of earthquakes of different magnitudes within a source zone. Further, the obtained information is used in the procedure of FPSHA. The data for the earthquake catalogs could be obtained from the US Geological Survey (USGS) [28], National Centers for Environmental Information - National Oceanic and Atmospheric Administration (NOAA)[29] and etc.

### 3.2 Fuzzification of Magnitude and Source-to-site Distance

Fuzzification is the process of converting crisp magnitude values from into the fuzzy triangular numbers. The pointed value of the magnitude is extended to the range of value so the confidence interval is obtained for any level. For a given point value of magnitude, the fuzzy value is modeled in form of a symmetric triangular fuzzy number, in which the center is the point value of magnitude $\overline{M}$ and left and right bound of supports are given in the form [$\overline{M}$ - s, $\overline{M}$ + s], where s is the uncertainty factor. The uncertainty factor s is constant estimated by the experts' opinion which takes value between 0 and 1, and usually equal to 0.5.

Earthquake magnitudes are defined as fuzzy triangular numbers which are expressed by the following formula:

$$\tilde{M} = (M - 0.5, M, M + 0.5) \tag{1}$$

The membership function for the fuzzy triangular magnitude is given as:

$$\tilde{M} = \begin{cases} 0, & m < M - 0.5 \\ \dfrac{m - (M - 0.5)}{(M + 0.5) - (M - 0.5)} = \dfrac{m + 0.5 - M}{1} = m + 0.5 - M, & M - 0.5 < m < M \\ 1, & m = M \\ \dfrac{(M + 0.5) - m}{(M + 0.5) - (M - 0.5)} = M + 0.5 - m, & M < m < M + 0.5 \\ 0, & m = M + 0.5 \end{cases} \tag{2}$$

To estimate ground shaking at a particular site, it is necessary to model the distribution of distances from earthquake fault to the site of interest. When it comes to modeling source-to-site distance, it is assumed that earthquakes occur with the same probability at any location on the fault [23]. This assumption is taken from the PSHA. Furthermore, Satriano, et al. [30] have showed that uncertainties associated with the source-to-site distance can be negligible compared to those associated to magnitude.

In the FPSHA method, the source-to-site distances are fuzzified and modeled as fuzzy sets with a triangular shape of membership function. Further, a probability to each fuzzy set has been prescribed based on studies of seismic zones in the area. According to the engineering judgment, it is customarily used the source-to-site distance threshold of 200 km [31]. All seismic zones with 200 km range have been considered in the source model. Further, the linguistic scale for distances classification is developed as highlighted in Figure 2. In this paper, we propose 11 different fuzzy sets to describe the distance between the potential source and site. For each fuzzy set, the membership function is prescribed as follows:

$$\tilde{R} = \begin{cases} 0, & r < R_1 \\ \dfrac{r - R_1}{R_2 - R_1}, & R_1 < r < R_2 \\ 1, & r = R_2 \\ \dfrac{R_3 - r}{R_3 - R_2}, & R_2 < r < R_3 \\ 0, & r > R_3 \end{cases} \tag{3}$$

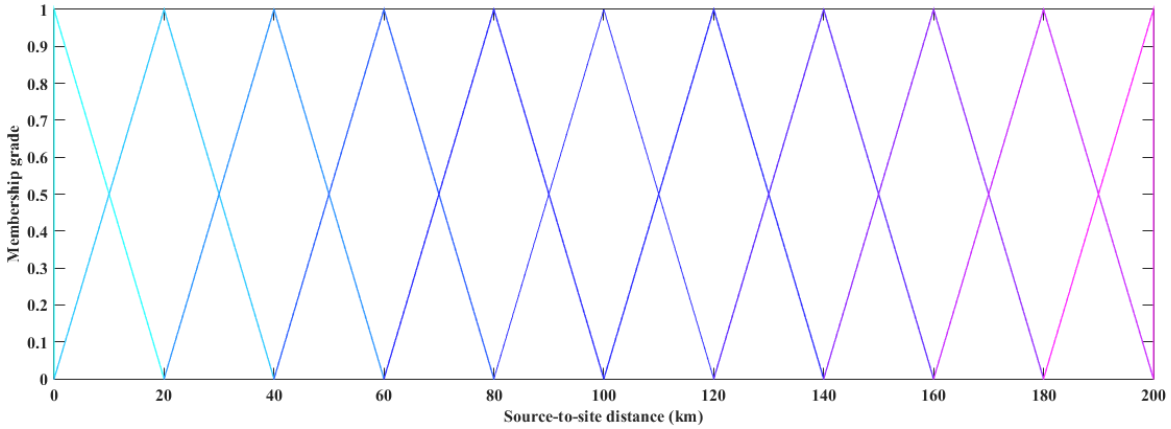


Figure 2 Fuzzification of the source-to-site distances

### 3.3 Fuzzy Recurrence law

The likelihood of the magnitudes that could occur at the particular site is determined by the Gutenberg-Richter (G-R) recurrence law. Since the magnitudes are given as fuzzy sets, the G-R recurrence law should be extended in order to operate with fuzzy numbers. The extension of the recurrence law for fuzzy magnitudes gives fuzzy recurrence law:

$$\log \tilde{\lambda}_m = \tilde{a} - b\tilde{m} \tag{4}$$

where, $\tilde{m}$- fuzzy magnitudes; $\tilde{\lambda}_m$ -the fuzzy rate of earthquake occurrence with magnitudes greater than *m*, constant *'$\tilde{a}$'* – the fuzzy rate of earthquakes in region; and constant *'b'* - the relative ratio of small and large magnitudes. The '$\tilde{a}$' and '*b*' constants are estimated using statistical analysis of historical observations. The value of '*b*' depends on the continent plate.

The proposed equation is used to estimate the fuzzy probability ratio of the earthquake occurrence. Further, fuzzy probability distribution function is derived from the fuzzy recurrence law in order to describe the membership degree of earthquake magnitude (the value of belonging the of earthquake magnitude to the fuzzy set) to certain level of probability of exceedance for that magnitude value.

Recalling the fuzzy probability theory, the fuzzy probability cumulative distribution function of magnitudes can be calculated by following equation:

$$\tilde{F}_M(\tilde{m}) = \frac{1-10^{-b(\tilde{m}-\tilde{m}_{min})}}{1-10^{-b(\tilde{m}_{max}-\tilde{m}_{min})}} \tag{5}$$

where, $\tilde{m}_{min}$ - minimum fuzzy magnitude value; $\tilde{m}_{max}$ - maximum fuzzy magnitude value; $\tilde{F}_M(\tilde{m})$ - fuzzy probability cumulative distribution function.

Further, the continuous distribution of magnitudes is transformed to a discrete fuzzy set of magnitudes. The first step in order to estimate the fuzzy probabilities of the exceedance is to fuzzify earthquake magnitudes. The earthquake magnitudes are converted into fuzzy values according to the formula (1). After fuzzification, the earthquake magnitudes are given in Figure 3.

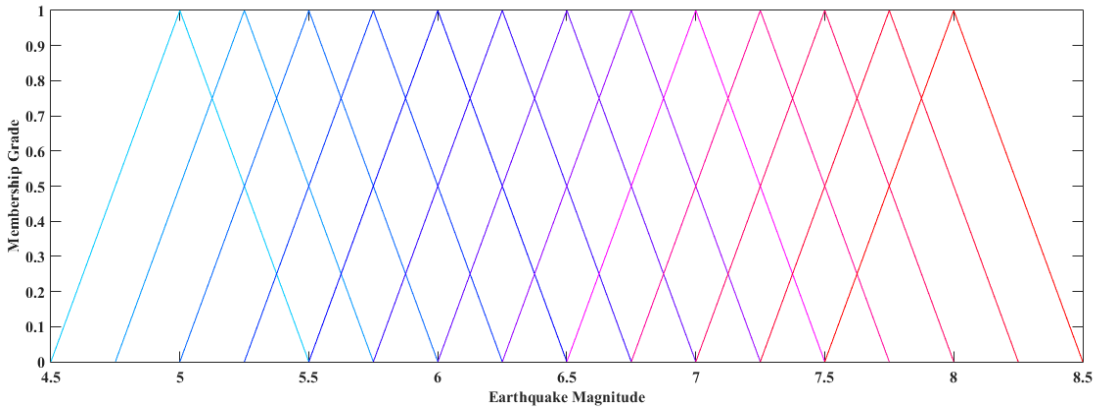


Figure 3 Linguistic scale of earthquake magnitudes

The magnitude threshold of $5.0M_w$ is adopted due to the fact that earthquakes with magnitude smaller than 5.0 could cause small damages to structures [6]. Applying the formula (1), the threshold for fuzzy magnitude is equal to (4.5, 5.0, 5.5). Further, for the magnitude increment, ten bins is used as in a benchmark PSHA example [2]. The magnitude increment is estimated by expression:

$$m_{inc} = \frac{m_{max}-m_0}{10} \tag{6}$$

The maximum magnitude is selected from the earthquake catalog. The probabilities of occurrence of fuzzy sets of magnitudes are computed by the following equation:

$$\tilde{\mathrm{P}}(\tilde{M} = \tilde{m}) = \tilde{F}_M(\tilde{m}_{j+1}) - \tilde{F}_M(\tilde{m}_j) \tag{7}$$

### 3.4 Ground motion models

Ground motion prediction models have been used to estimate ground motion intensity and to develop PGA hazard curves. A total three attenuation relationships models have been considered and used to develop the PGA hazard curves. These models have been adopted to predict a fuzzy probability distribution of the ground motion intensity as a function of variables

such as magnitudes, the source-to-site distances and fault mechanisms. In the models, magnitudes and source-to-site distances are calculated through fuzzy probability distribution and given by fuzzy triangular numbers.

The predictive model for the mean of log peak ground acceleration proposed by Cornell, et al. [32] is adopted for the case of fuzzy triangular values of magnitudes and source-to-site distances. The model is extended in order to predict the fuzzy probabilities of the peak ground motions. The proposed fuzzy probabilistic predictive model of log peak ground acceleration is:

$$ln\widetilde{PGA} = -0.152 + 0.859\tilde{M} - 1.803\ \ln(\tilde{R} + 25) \tag{8}$$

where, $\tilde{M}$ and $\tilde{R}$ - fuzzy random variable presenting the earthquake magnitude and distance from earthquake fault, $\widetilde{PGA}$ – fuzzy random peak ground acceleration.

The standard deviation of *lnPGA* was 0.57 in the Cornell, et al. [32] model and it was constant for all magnitudes and distances. Also, the standard deviation of $\ln\widetilde{PGA}$ for every membership degree of belonging for all magnitudes and distance will be also constant.

The second model which is used for predicting ground motions is proposed by Cheng, et al. [33]:

$$ln\widetilde{PGA} = -3.25 + 1.075\tilde{M} - 1.723\ \ln(\tilde{R} + 0.156\ e^{0.62391\ \tilde{M}}) \tag{9}$$

The standard deviation for this model is 0.577.

Another model for predicting ground motions is given by Wu, et al. [34]:

$$ln\widetilde{PGA} = 2.303 * 0.00215 + 0.581\tilde{M} - \log\left(\tilde{R} + 0.00871\ * 10^{0.5\,\tilde{M}}\right) - 0.00414\,\tilde{R} \tag{10}$$

For this model, the standard deviation is equal to 0.79.

Further, models are utilized to generate seismic hazard curve [2] which represent the relationship between annual exceedance rate and ground motion level.

Since the natural logarithm of PGA was normally distributed and the fuzzy probability of exceeding any PGA level is estimated by using fuzzy mean and standard deviation:

$$\tilde{P}(PGA > x|m,r) = 1 - \Phi\left(\frac{\ln x - ln\widetilde{PGA}}{\sigma_{\ln PGA}}\right) \tag{11}$$

## 4 A CASE STUDY IN YUNNAN PROVINCE, CHINA

### 4.1 Historical earthquake data for Yunnan Province, China

Due to the specific geographic location and climate complexity, China has been affected by different catastrophic events [35]. Some of the major disasters in China are floods [36-39], droughts [40-42], earthquakes [43, 44], typhoons [45-47], landslides [48-51] and others. The center of droughts, floods, typhoons and landslides is identified in central, southern, southwest and southeast areas of China [50].

China is prone to earthquakes [52] and it has the most severe seismic disasters in the world since it is located between the two large seismic zones, the Circum-Pacific and the Himalaya-Mediterranean seismic zones [53]. The frequency of occurrence of severe earthquakes is about 1/3 and the loss of lives is about 1/2 of the whole world [53].

Yunnan province is situated in the far southwest of China, its land covers area of approximately 394,000 square kilometers and it has a population about 45.7 millions. It is a mountainous area with high elevations in the northwest and low elevations in the southeast. The Province borders provinces Sichuan to the north, Guizhou to the northeast, Guangxi to the east, and countries, Vietnam to the southeast, Laos to the south, and Myanmar to the west (Figure 4). Kunming is the capital and the largest city in Yunnan Province.

Yunnan province is known for high seismicity (Figure 5). The Yunnan-Burma active block region is located south and east of the Himalayan syntax. It includes western Yunnan province [52]. It is an earthquake-prone region. The block region consists of the West Yunnan and the South Yunnan blocks. The Langcang River-Nu River fault zone shows very strong seismic activity.

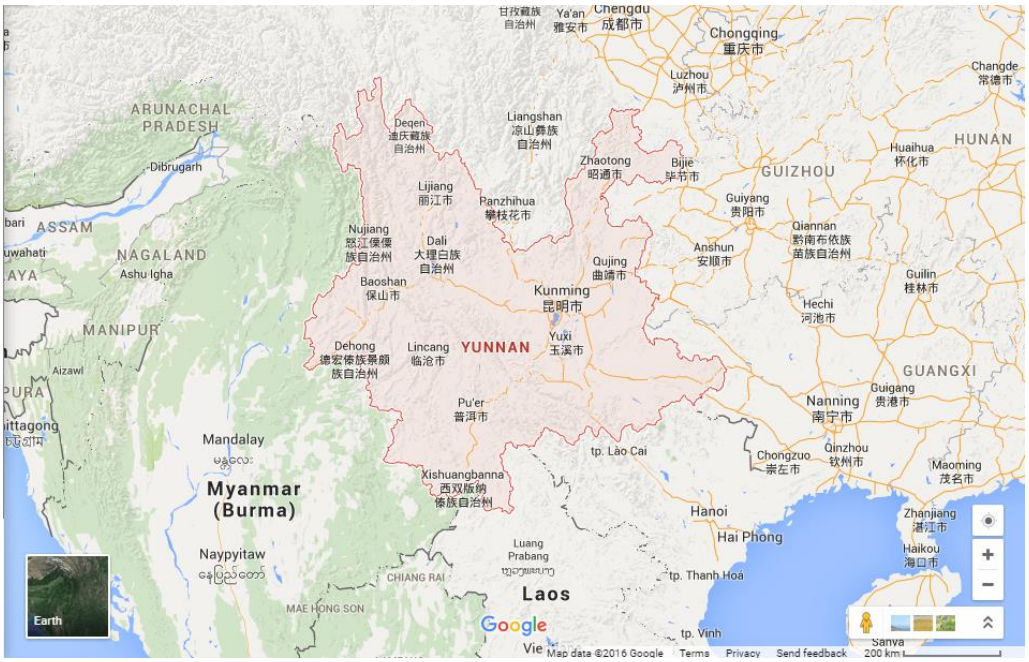


Figure 4 Location of Yunnan Province and neighboring Provinces and countries

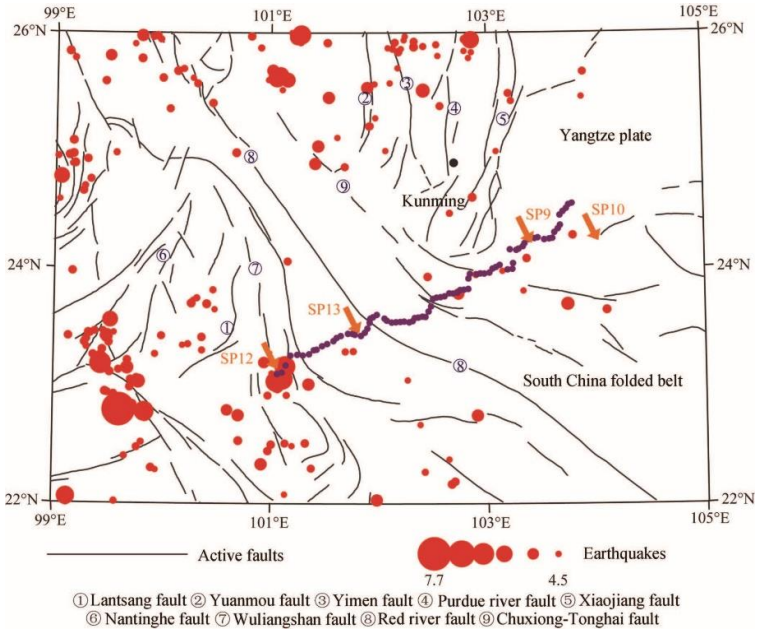


Figure 5 Active seismic faults in the Yunnan Province [54]

The PGA is estimated from using actual seismicity and ground motion models. The catalog includes 93 events, which are listed in Table 1 (Appendix A). The records are taken for the period of 100 years, between 1916 and 2015.

The estimated mean value and standard deviation are estimated from the probabilistic paper which is shown in Figure 6. The mean value of earthquake magnitude is 5.8 and the standard deviation is 0.8.

For this study, thresholds in this study are based on engineering judgment. A magnitude threshold ($m_0$) of 5.0 is selected. and a distance threshold ($d_0$) of 200 km are selected for this case study [31].

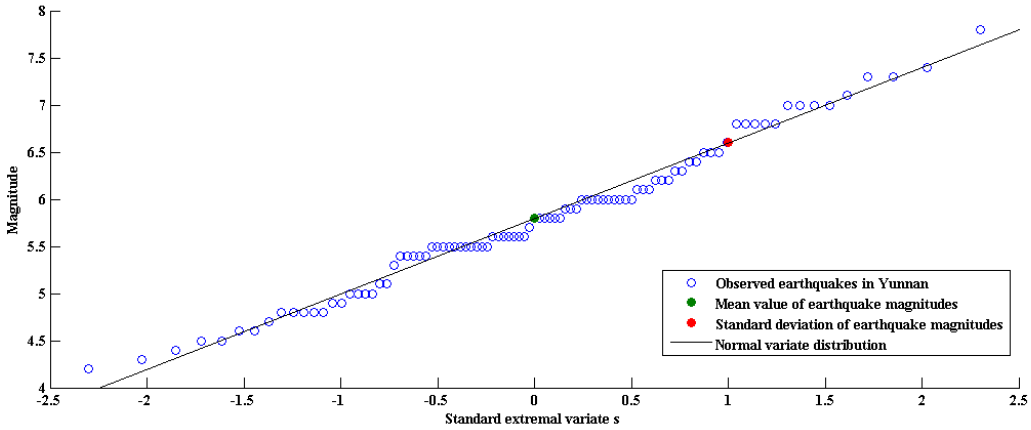


Figure 6 The probability paper for observed earthquakes in China, Yunnan Province

## 4.2 Results

The fuzzy-probability of exceedance of PGA level is determined for 10,000 earthquake scenarios. Earthquake scenarios have been simulated for earthquake magnitude which follows fuzzy-probabilistic distribution and the fault-distance prescribed in the Chapter 3. The earthquake magnitude follows normal distribution, which is determined in Chapter 3.2 for Yunnan Province. Further, the earthquake magnitude has been fuzzified according to the equation (9). The hazard curves are depicted in Figure 7. On this graph, the x-axis illustrates the level of PGA which takes values from 0 to 1.5 g. On the y-axis, the probability of exceedance the certain level of PGA for each hazard curve is denoted with the membership degree.

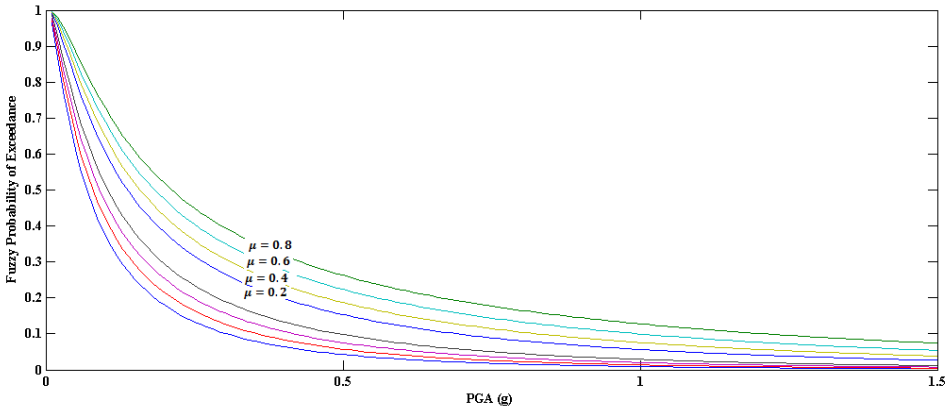


Figure 7 Hazard curve in terms of fuzzy probability for Yunnan Province, China

## 5 CONCLUSION

This paper introduces the model for the seismic hazard analysis based on the fuzzy-probabilistic approach. In this model, the earthquake magnitude and the source-to-site dis-

tance are defined as fuzzy sets. In comparison with other models, fuzzy triangular numbers are more suitable to represent the parameters of the seismic hazard since they include epistemic uncertainty in the seismic risk assessment. Further, FPSHA enables to evaluate the seismic risk more precisely and to assign the corresponding membership functions to each curve of the seismic hazard. In this paper, it is shown that fuzzy sets could help to integrate all the uncertainties which occur in the process of seismic hazard analysis.

## ACKNOWLEDGMENT

The financial support received from the National Science Foundation of China (Grant Nos. 51378162, 51178150, 50978080, 90715021), the Research fund from Ministry of Science and Technology of China (2013BAJ08B01), the Open Research Fund of State Key Laboratory for Disaster Reduction in Civil Engineering (SLDRCE12-MB-04), and the Specialized Research fund for the doctoral program of higher education (20112302110005) is gratefully appreciated.

## Appendix A: The historical earthquake data for Yunnan Province, China

| Year | Earthquake magnitude |
|---|---|
| 1917 | 6.8 |
| 1918 | 5.5 |
| 1925 | 7 |
| 1925 | 5.8 |
| 1926 | 5.5 |
| 1927 | 6 |
| 1927 | 5 |
| 1927 | 5.5 |
| 1930 | 6 |
| 1930 | 6.5 |
| 1934 | 6 |
| 1936 | 5.5 |
| 1938 | 6 |
| 1939 | 5.5 |
| 1940 | 6 |
| 1940 | 5.5 |
| 1941 | 7 |
| 1941 | 7 |
| 1942 | 6.8 |
| 1947 | 5.5 |
| 1948 | 6.8 |
| 1950 | 7 |
| 1950 | 5.8 |
| 1951 | 6.3 |
| 1952 | 6.5 |
| 1952 | 5.8 |

| | |
|---|---|
| 1953 | 5 |
| 1955 | 6 |
| 1955 | 6.8 |
| 1961 | 5.8 |
| 1961 | 6 |
| 1962 | 5.5 |
| 1962 | 6.2 |
| 1963 | 6 |
| 1964 | 5.4 |
| 1965 | 6.1 |
| 1966 | 5.1 |
| 1966 | 6.5 |
| 1966 | 6.2 |
| 1966 | 5.4 |
| 1966 | 6.4 |
| 1970 | 7.8 |
| 1974 | 7.1 |
| 1976 | 7.3 |
| 1976 | 7.4 |
| 1985 | 5.8 |
| 1988 | 7.3 |
| 1988 | 6.4 |
| 1989 | 5.6 |
| 1993 | 5.6 |
| 1995 | 6.8 |
| 1995 | 6.2 |
| 1996 | 6.6 |
| 1998 | 4.5 |
| 1999 | 4.6 |
| 2000 | 5.9 |
| 2000 | 6.3 |
| 2000 | 4.2 |
| 2001 | 5.5 |
| 2001 | 4.3 |
| 2001 | 5.6 |
| 2003 | 5.9 |
| 2003 | 5.6 |
| 2003 | 5.6 |
| 2003 | 4.7 |
| 2004 | 5.4 |
| 2004 | 4.4 |
| 2005 | 4.8 |
| 2005 | 4.8 |

| | |
|---|---|
| 2005 | 4.5 |
| 2007 | 6.1 |
| 2008 | 5 |
| 2008 | 6 |
| 2008 | 4.8 |
| 2009 | 5.7 |
| 2009 | 4.9 |
| 2010 | 4.8 |
| 2011 | 4.8 |
| 2011 | 5.5 |
| 2011 | 5.3 |
| 2011 | 5 |
| 2012 | 5.5 |
| 2012 | 5.6 |
| 2013 | 4.9 |
| 2013 | 5.4 |
| 2013 | 5.8 |
| 2014 | 5.4 |
| 2014 | 5.9 |
| 2014 | 6.1 |
| 2014 | 5.1 |
| 2014 | 6 |
| 2014 | 5.6 |
| 2015 | 4.6 |

Table 1 Historical earthquake data (1916-2015) for Yunnan Province in China

## REFERENCES


[1] H. Sucuoğlu and S. Akkar, *Basic Earthquake Engineering: From Seismology to Analysis and Design*: Springer, 2014.

[2] S. L. Kramer, *Geotechnical earthquake engineering*: Pearson Education India, 1996.

[3] I. Karimi and K. Meskouris, "Risk management of natural disasters: a fuzzy-probabilistic methodology and its application to seismic hazard," Fakultät für Bauingenieurwesen2006.

[4] J. J. Bommer, "Uncertainty about the uncertainty in seismic hazard analysis," *Engineering Geology*, vol. 70, pp. 165-168, 2003.

[5] R. J. Geller, D. D. Jackson, Y. Y. Kagan, and F. Mulargia, "Earthquakes cannot be predicted," *Science*, vol. 275, p. 1616, 1997.

[6] J.-P. Wang, D. Huang, C.-T. Cheng, K.-S. Shao, Y.-C. Wu, and C.-W. Chang, "Seismic hazard analyses for Taipei city including deaggregation, design spectra, and time history with excel applications," *Computers & Geosciences*, vol. 52, pp. 146-154, 2013.

[7] N. R. Commission, "A performance-based approach to define the site-specific earthquake ground motion," *Regulatory Guide*, vol. 1, 2007.

[8] E. L. Krinitzsky, "How to combine deterministic and probabilistic methods for assessing earthquake hazards," *Engineering Geology*, vol. 70, pp. 157-163, 2003.

[9] B. Möller and M. Beer, *Fuzzy randomness: uncertainty in civil engineering and computational mechanics*: Springer Science & Business Media, 2013.
[10] J. Quelch and I. T. Cameron, "Uncertainty representation and propagation in quantified risk assessment using fuzzy sets," *Journal of loss prevention in the process industries*, vol. 7, pp. 463-473, 1994.
[11] S. Bonvicini, P. Leonelli, and G. Spadoni, "Risk analysis of hazardous materials transportation: evaluating uncertainty by means of fuzzy logic," *Journal of Hazardous Materials*, vol. 62, pp. 59-74, 1998.
[12] V. J. Davidson, J. Ryks, and A. Fazil, "Fuzzy risk assessment tool for microbial hazards in food systems," *Fuzzy Sets and Systems*, vol. 157, pp. 1201-1210, 2006.
[13] M. Amiri, A. Ardeshir, and M. H. F. Zarandi, "Fuzzy probabilistic expert system for occupational hazard assessment in construction," *Safety Science*, vol. 93, pp. 16-28, 2017.
[14] J. M. Andrić and D.-G. Lu, "Fuzzy methods for prediction of seismic resilience of bridges," *International Journal of Disaster Risk Reduction*, 2017.
[15] M. Papadrakakis, V. Papadopoulos, and V. Plevris, "SEISMIC RESILIENCE OF A BRIDGE BASED ON FUZZY-PROBABILISTIC APPROACH."
[16] B. Möller, W. Graf, and M. Beer, "Safety assessment of structures in view of fuzzy randomness," *Computers & Structures*, vol. 81, pp. 1567-1582, 2003.
[17] J. Yazdi and S. S. Neyshabouri, "Identifying low impact development strategies for flood mitigation using a fuzzy-probabilistic approach," *Environmental Modelling & Software*, vol. 60, pp. 31-44, 2014.
[18] M. Singh and T. Markeset, "Fuzzy Reliability Analysis of Corroded Oil and Gas Pipes," *Evaluation of the Structural Integrity of Corroding Oil and Gas Pipes*, p. 77, 2009.
[19] G. Fu and Z. Kapelan, "Fuzzy probabilistic design of water distribution networks," *Water Resources Research*, vol. 47, 2011.
[20] P. Dutta, "Modeling of variability and uncertainty in human health risk assessment," *MethodsX*, vol. 4, pp. 76-85, 2017.
[21] L. Reiter, *Earthquake hazard analysis: issues and insights*: Columbia University Press, 1991.
[22] R. K. McGuire, *Seismic hazard and risk analysis*: Earthquake engineering research institute, 2004.
[23] J. W. Baker, "An introduction to probabilistic seismic hazard analysis (PSHA)," *White paper, version*, vol. 1, p. 72, 2008.
[24] L. A. Zadeh, "Fuzzy sets," *Information and control*, vol. 8, pp. 338-353, 1965.
[25] L. A. Zadeh, "Outline of a new approach to the analysis of complex systems and decision processes," *Systems, Man and Cybernetics, IEEE Transactions on*, pp. 28-44, 1973.
[26] B. Barnabas, "Mathematics of Fuzzy Sets and Fuzzy Logic," ed: Springer, 2013.
[27] A. F. Ares and A. Fatehi, "Development of probabilistic seismic hazard analysis for international sites, challenges and guidelines," *Nuclear Engineering and Design*, vol. 259, pp. 222-229, 2013.
[28] R. Garbarino and C. G. Groat, "US Geological Survey," 2002.
[29] N. C. f. E. Information. *NOAA*. Available: http://www.ngdc.noaa.gov/
[30] C. Satriano, A. Lomax, and A. Zollo, "Optimal, real-time earthquake location for early warning," in *Earthquake Early Warning Systems*, ed: Springer, 2007, pp. 85-96.
[31] J. Wang, L. Brant, Y.-M. Wu, and H. Taheri, "Probability-based PGA estimations using the double-lognormal distribution: including site-specific seismic hazard

analysis for four sites in Taiwan," *Soil Dynamics and Earthquake Engineering,* vol. 42, pp. 177-183, 2012.
[32] C. A. Cornell, H. Banon, and A. F. Shakal, "Seismic motion and response prediction alternatives," *Earthquake Engineering & Structural Dynamics,* vol. 7, pp. 295-315, 1979.
[33] C.-T. Cheng, S.-J. Chiou, C.-T. Lee, and Y.-B. Tsai, "Study on probabilistic seismic hazard maps of Taiwan after Chi-Chi earthquake," *Journal of GeoEngineering,* vol. 2, pp. 19-28, 2007.
[34] Y.-M. Wu, T.-C. Shin, and C.-H. Chang, "Near real-time mapping of peak ground acceleration and peak ground velocity following a strong earthquake," *Bulletin of the Seismological Society of America,* vol. 91, pp. 1218-1228, 2001.
[35] S. Chen, Z. Luo, and X. Pan, "Natural disasters in China: 1900–2011," *Natural hazards,* vol. 69, pp. 1597-1605, 2013.
[36] D. Huang, R. Zhang, Z. Huo, F. Mao, E. Youhao, and W. Zheng, "An assessment of multidimensional flood vulnerability at the provincial scale in China based on the DEA method," *Natural hazards,* vol. 64, pp. 1575-1586, 2012.
[37] L. Hong, M. Ouyang, S. Peeta, X. He, and Y. Yan, "Vulnerability assessment and mitigation for the Chinese railway system under floods," *Reliability Engineering & System Safety,* vol. 137, pp. 58-68, 2015.
[38] J. Du, F. Kong, S. Du, N. Li, Y. Li, and P. Shi, "Floods in China," in *Natural Disasters in China*, ed: Springer, 2016, pp. 133-159.
[39] C. Li, G. Wang, and R. Li, "Maximum observed floods in China," *Hydrological Sciences Journal,* vol. 58, pp. 728-735, 2013.
[40] S.-w. Wang and Z.-c. Zhao, "Droughts and floods in China, 1470–1979," *Climate and history,* pp. 271-288, 1981.
[41] T. Ye, H. Jia, Y. Lei, and P. Shi, "Droughts in China," in *Natural Disasters in China*, ed: Springer, 2016, pp. 161-186.
[42] Z. X. Z. Qiang, "Preliminary studies on variations in droughts over China During past 50 Years [J]," *Journal of Applied Meteorological Science,* vol. 6, p. 006, 2008.
[43] J. Yang, J. Chen, H. Liu, and J. Zheng, "Comparison of two large earthquakes in China: the 2008 Sichuan Wenchuan Earthquake and the 2013 Sichuan Lushan Earthquake," *Natural Hazards,* vol. 73, pp. 1127-1136, 2014.
[44] H. Wang, H. Li, J. Si, Z. Sun, X. Fu, D. Liu, *et al.*, "Progress in the study of the Wenchuan Earthquake Faulting," *Acta Geosci Sci,* vol. 36, pp. 257-269, 2015.
[45] Z. Gong, C. Chai, C. Tu, J. Lin, Y. Gao, and Y. Qiu, "Injuries after a Typhoon in China," *New England journal of medicine,* vol. 356, pp. 196-197, 2007.
[46] Y.-h. Yang and X.-t. Lei, "Statistics of strong wind distribution caused by landfall typhoon in China," *Journal of Tropical Meteorology,* vol. 6, p. 002, 2004.
[47] H. Shi, X. Cao, X. Wen, M. Shi, D. Zhao, and P. Guo, "The research on typhoon wave spectrum in northwestern South China Sea," *Journal of Ocean University of China,* vol. 16, pp. 8-14, 2017.
[48] R. Huang and W. Li, "Formation, distribution and risk control of landslides in China," *Journal of Rock Mechanics and Geotechnical Engineering,* vol. 3, pp. 97-116, 2011.
[49] H. Chai, H. Liu, Z. Zhang, and Z. Xu, "The distribution, causes and effects of damming landslides in China," *Journal of the Chengdu Institute of Technology,* vol. 27, pp. 302-307, 2000.
[50] W. Han, C. Liang, B. Jiang, W. Ma, and Y. Zhang, "Major Natural Disasters in China, 1985–2014: Occurrence and Damages," *International journal of environmental research and public health,* vol. 13, p. 1118, 2016.

[51] M. Chang, C. Tang, C. Xia, and Q. Fang, "Spatial distribution analysis of landslides triggered by the 2013-04-20 Lushan earthquake, China," *Earthquake engineering and engineering vibration*, vol. 15, pp. 163-171, 2016.

[52] P. Zhang, Q. Deng, G. Zhang, J. Ma, W. Gan, W. Min, *et al.*, "Active tectonic blocks and strong earthquakes in the continent of China," *Science in China Series D: Earth Sciences*, vol. 46, pp. 13-24, 2003.

[53] A. Tang and A. Wen, "An intelligent simulation system for earthquake disaster assessment," *Computers & Geosciences*, vol. 35, pp. 871-879, 2009.

[54] Z. En‐Hui, L. Hai, J. Shi‐Xu, and L. Yong‐Hua, "Characteristics of deep crust structure beneath Western Yunnan," *Chinese Journal of Geophysics*, vol. 56, pp. 252-264, 2013.

COMPDYN 2017
6th ECCOMAS Thematic Conference on
Computational Methods in Structural Dynamics and Earthquake Engineering
M. Papadrakakis, M. Fragiadakis (eds.)
Rhodes Island, Greece, 15–17 June 2017

# PREDICTION OF DUCTILE DAMAGE IN CASE OF SEISMIC ACTION USING INNOVATIVE DAMAGE MECHANICS

**Simon Schaffrath[1], Helen Bartsch[*1], Benno Hoffmeister[1], Markus Feldmann[1]**

[1] Institute of Steel Construction, RWTH Aachen University

Mies-van-der-Rohe-Str. 1

D-52074 Aachen

{schaffrath, h.bartsch, hoff, feldmann}@stb.rwth-aachen.de

**Keywords:** Moment-resisting frames, beam-column connections, cyclic loading, ultra-low-cycle fatigue, damage mechanics, ductile crack initiation, toughness.

***Abstract.*** *An approach to investigate the true behaviour of dissipative elements utilising numerical simulations is presented. By way of example dissipative members in terms of beam-column connections of moment-resisting frames are considered. Material failure in terms of crack formation is taken into account by incorporating a damage mechanics model into the numerical analyses. By means of a phenomenological damage mechanics model, which is based on critical strains depending on the stress state, an efficient simulation of large scale components is enabled. To validate this approach, an extensive testing program has been performed. Subsequently, numerical simulations of the experimental investigations have been conducted.*

## 1 INTRODUCTION

Severe seismic activity can cause as well tragic loss of human lives as disastrous economic damages. Therefore, buildings and engineering works have to sustain these actions beyond dispute. Steel structures in earthquake-prone areas are designed according to EUROCODE 3 [1] and EUROCODE 8 [2]. Some design procedures of these codes are simplified and based on phenomenological approaches. The actual seismic loading, for instance, is only considered in a simple way by the seismic base shear force in the context of EUROCODE 8 [2] and the proper impact of the earthquake is vague. Hence, common design rules proved to be insufficient in case of strong seismic events, as for instance the severe earthquakes 1994 in NORTHRIDGE and 1995 in KOBE. Devastating damages during such strong earthquakes are on one side caused by inappropriate connections and their realisation. Inadequate toughness properties can on the other side also be responsible for structural failures during powerful earthquakes of this type. Mostly a combination of the above named reasons for structural failure occurs. A detailed knowledge about the actual behaviour of the dissipative members in a structure is crucial.

Investigations on failure estimation methods using traditional fatigue formulas have already been made on innovative dissipative FUSEIS-elements [3, 4].

Furthermore, a more innovative approach using damage mechanics to ensure a sufficient ductile behaviour related to toughness demands has been developed during previous researches [5]. However, this concept exhibits deficiencies in case of shear-stress induced plastic strains. The investigations presented in this paper aim to establish a more general application to analyse the true behaviour of dissipative elements utilising numerical simulations.

First, an innovative damage mechanics approach, applicable to cyclic loading scenarios in case of stress states with both nominal and shear stresses is described. An extensive testing program presented hereinafter serves to validate the new approach. Simulations of the experimental investigations have been conducted subsequently applying the damage model, which is able to predict ductile crack initiation in numerical analyses. These simulations are realised in terms of detailed 3D finite element models.

## 2 DAMAGE MECHANICS APPROACH

Damage mechanics models provide a wide field of application, where the prediction of ductile crack initiation is one main focus. However, common damage concepts [7] are only applicable to monotone loading scenarios. Hence, the EFFECTIVE DAMAGE CONCEPT [8] by OHATA and TOYODA which is applicable in case of ultra-low-cycle fatigue (ULCF) during earthquakes is highly relevant. An innovative damage concept proposed by BAI and WIERZBICKI [6] who designed a spatial fracture locus characterising material resistance by means of critical plastic strains depending on stress triaxiality and on the LODE angle provides extension. In comparison to conventional two parameter criterions, a higher accuracy of evaluating stress states with nominal and shear stresses is achieved by additionally considering the third invariant of the deviatoric stress tensor. [6]

For the purpose of a realistic prediction of material damage behaviour and component failure a hybrid plasticity and damage model is applied.

### 2.1 Plasticity model

To describe the plastic material behaviour as realistic as possible a sophisticated plasticity model is required. In the course of this paper, a modification of the ARMSTRONG-FREDERICK non-linear kinematic plasticity model [9] is utilised to characterise isotropic and kinematic material hardening, considering the BAUSCHINGER effect.

One disadvantage of the original ARMSTRONG-FREDERICK model [9] is the assumption of the yield surface's size to be constant. Therefore, in the modified model the yield surface is able to change, depending on the amount of the equivalent plastic strain. Moreover, the original model is not able to describe the yield plateau region after initial yielding. For this reason, the modification of the ARMSTRONG-FREDERICK model by UCAK and TSOPELAS [10] is additionally adopted.

## 2.2 Damage mechanics model

Concerning the damage mechanics approach, not only a damage initiation but also the damage development is described by a damage evolution law according to LIAN et al. [11]. The softening as a result of damage initiation is taken into account. Final failure occurs if a critical damage value is obtained.

The evolution of the effective plastic strain is described by a modification of the EFFECTIVE DAMAGE CONCEPT of OHATA and TOYODA [8], which leads to the possibility of using the combined damage concept not only for monotonic but also for cyclic loading situations. According to the EFFECTIVE DAMAGE CONCEPT only a part of the equivalent plastic strain named effective equivalent plastic strain contributes to the damage, as seen in Figure 1.

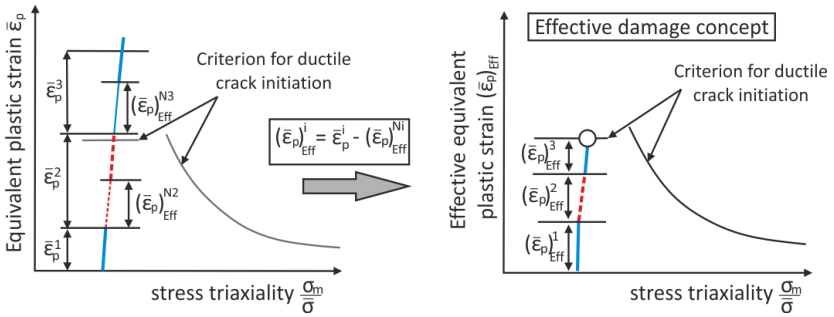


Figure 1: Effective damage concept [8]

In accordance with OHATA and TOYODA the determination of the effective equivalent plastic strain depends on the equivalent back stress. Applied plastic strain where the back stress remains below the maximum back stress of the previous loading cycle is not counted as effective, confer grey coloured ranges in Figure 2. [8]

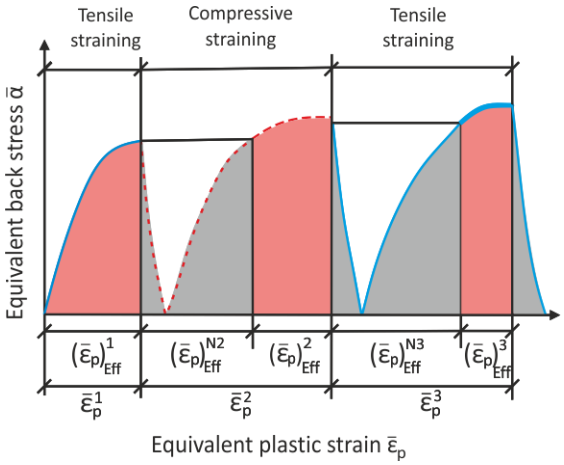


Figure 2: Effective equivalent plastic strain depending on the evolution of equivalent back stress [8]

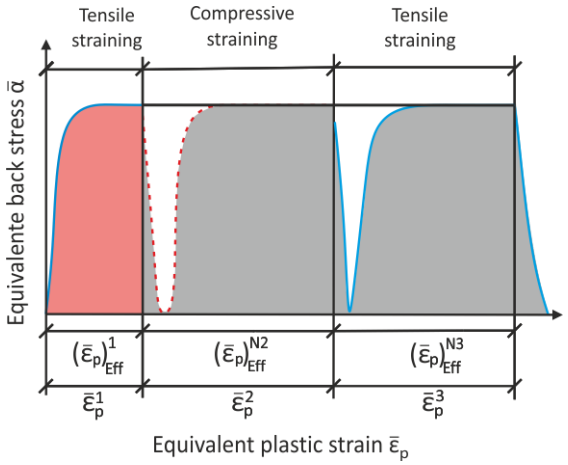


Figure 3: Effective equivalent plastic strain depending on the evolution of saturated equivalent back stress

The plastic strain where the back stress however exceeds the maximum of the previous back stress depicts the effective plastic strain increment $\Delta(\bar{\varepsilon}_p)_{eff}$, which affects the material damage, as illustrated in Figure 1 and Figure 2, confer orange coloured ranges.

However, Figure 3 indicates the effective strain evolution in case of an early saturation of the equivalent back stress. The EFFECTIVE DAMAGE CONCEPT is ineffectual if the equivalent back stress only exceeds the maximum equivalent back stress in the first tension process, as seen in Figure 3. In this instance no effective equivalent plastic strain is accumulated after the first tensile loading cycle.

In the course of the present investigations, the plastic strain arising when the equivalent back stress is saturated is partly counted as effective equivalent plastic strain, see equation (1).

$$\Delta(\bar{\varepsilon}_p)_{eff} = \left(1 - e^{-m\cdot(\bar{\varepsilon}_p)_{eff}}\right) \cdot \Delta(\bar{\varepsilon}_p) \tag{1}$$

The equivalent plastic strain increment $\Delta(\bar{\varepsilon}_p)$ is degenerated by a factor, depending on the accumulated effective equivalent plastic strain $(\bar{\varepsilon}_p)_{eff}$ and a coefficient m, which has to be calibrated to large scale test results.

Additionally to the new effective strain evolution, no damage is accumulated in case of negative stress triaxiality values, as another modification.

In the present model, the influence of the third invariant of the deviatoric stress tensor is taken into account by the damage concept of BAI and WIERZBICKI [6], which is described by equation (2).

$$\bar{\varepsilon}_i = (C_1 e^{-C_2\eta} - C_3 e^{-C_4\eta})\bar{\theta}^2 + C_3 e^{-C_4\eta} \tag{2}$$

The parameters $C_1$, $C_2$, $C_3$ and $C_4$ are material parameters calibrated from small scale tests. By incorporating the Lode angle into the damage concept, BAI and WIERZBICKI enhanced common two-parameter criterions in terms of 2D damage curve to a 3D damage initiation locus. [6]

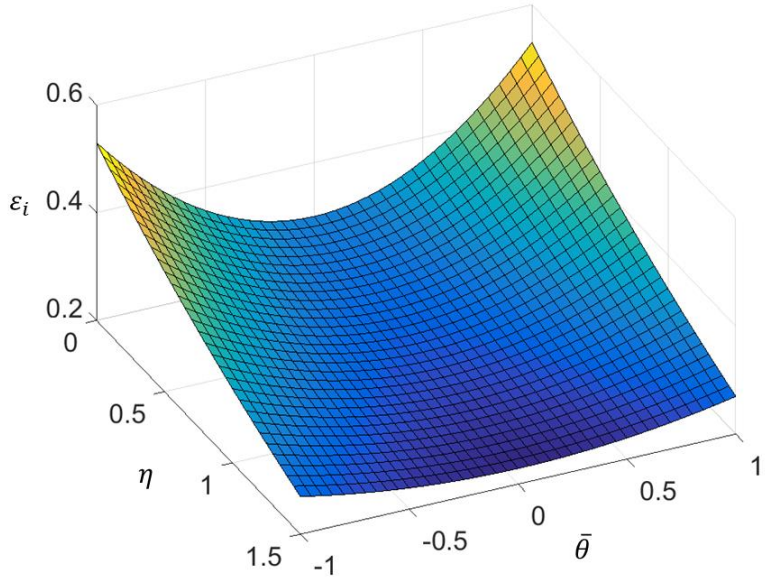


Figure 4: Applied damage initiation locus

Figure 4 depicts the damage initiation locus applied for the simulations decribed in section 4. The material parameters describing the damage initiation locus have been determined by small scale tests.

# 3 EXPERIMENTAL INVESTIGATIONS

## 3.1 Specimens and test set-ups

In total, 14 cyclic test have been conducted on four different specimens, illustrated in Figure 5 to Figure 8. To define the location of failure and to prevent cracks in welds or heat affected zones, the specimens have been provided with reduced beam sections (RBS according to [12]).



Figure 5: 3D illustration of specimen type D1

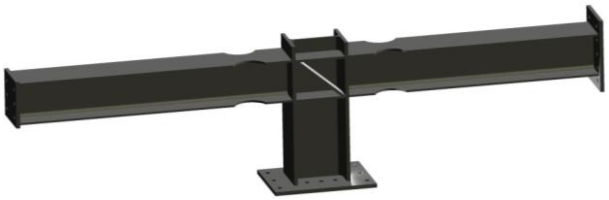

Figure 6: 3D illustration of specimen type D3



Figure 7: 3D illustration of specimen type D2

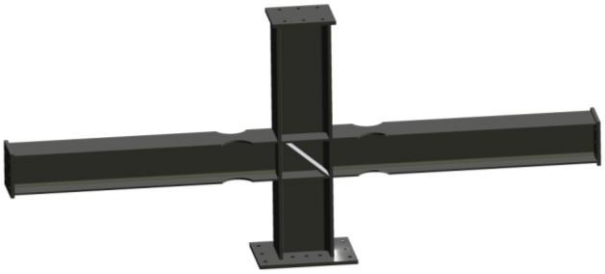

Figure 8: 3D illustration of specimen type D4

All specimens constitute of steel grade S355J2 with beam section HEA280 and column section HEB360.

The tests can be subdivided into four test series D1 to D4. The first type of specimen D1 is a beam, which is clamped at one end, as illustrated in Figure 5. The design of this detail is based on the experimental tests of Ballio and Castiglioni ([13][14][15]) and the five tested specimens are used for a first calibration of numerical and damage model because of the easy statical system and boundary conditions.

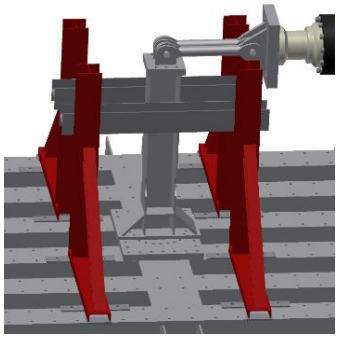

Figure 9: Test rig of D1

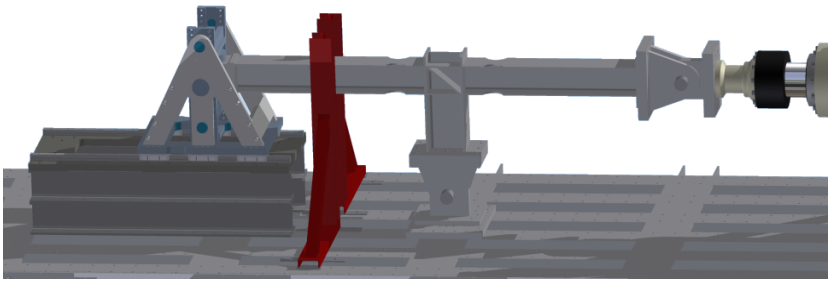

Figure 10: Test rig of D3

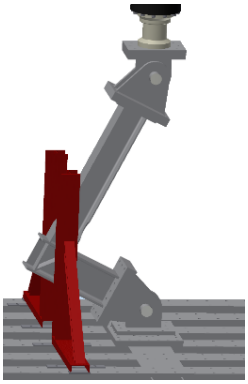

Figure 11: Test rig of D2

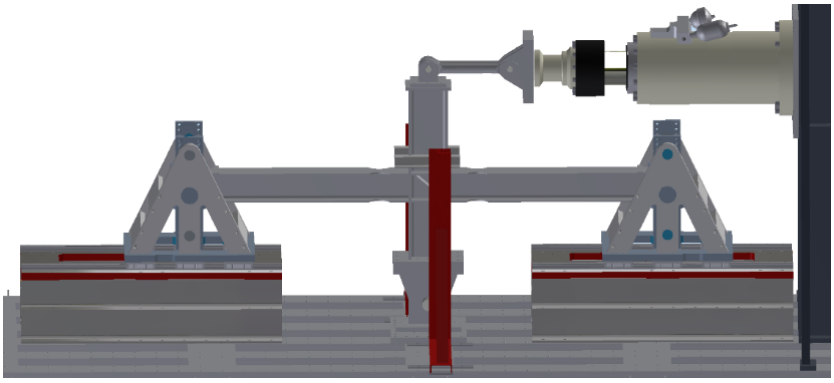

Figure 12: Test rig of D4

The second type D2, depicted in Figure 7, is an ordinary beam-column connection in an outer node of a roof and has been tested in terms of three specimens. In order to prevent harmful shear forces on the hydraulic cylinder specimen type D2 has been rotated, as illustrated in Figure 11. Furthermore, a connection in a middle node of a roof is investigated by three specimens of the type D3, seen in Figure 6. The remaining three specimens depict a middle node in a lower floor and belong to the type D4, as depicted in Figure 8. Figure 9 to Figure 12 depict the test rigs of the four specimen types.

### 3.2 Loading and measurement instrumentation

To attain the ability to compare different tests a load protocol has been taken into account. Increasing amplitudes according to ECCS recommendations [16] have been applied to the specimens in a modified, refined version (mECCS). Moreover, additionally constant amplitudes have also been utilised as loading scenario.

In order to obtain meaningful results adequate measurement instrumentation has been used during the investigations. Firstly, the stroke displacement of the hydraulic cylinder and the resulting reaction force, measured by the cylinder itself or a load cell have been recorded. Moreover, wire displacement transducers have been utilised to measure the actual displacement in an accurate manner. Furthermore, strain gauges have been applied to all specimens on both flanges at one reduced beam section. As large plastic deformations are expected, high strain gauges, which are designed to measure strains up to 15%, have been applied. Besides, strain gauge rosettes have been placed on the web of the reduced beam sections to measure strains in three directions. Finally, inclinometers are placed in a distance of 100 mm away from the beams' or column's ends. An inclinometer measures rotations up to 30° each side.

### 3.3 Results and evaluation

A distinctive ductile behaviour with cracks in the base material and a slow crack propagation could be observed during the tests of all specimens. During all tests the cracks occurred on different positions in the reduced beam section area. The occurrence of buckles was mainly dependent on the amplitude of the displacement. Furthermore, the location where the first cracks occur is in general depending on these buckles.

Table 1 gives an overview of loading scheme, maximum amplitude as well as specific cycle and corresponding location of the first visible surface cracks. Since the amplitudes in the elastic range do not vary between the single tests they are not included into the overview. For the numerical recalculations of the experimental tests presented in section 4 the effective applied amplitudes (neglecting slippage etc.) measured by the wire displacement transducers have been integrated into the numerical models.

| Test | Designation | Loading | Maximal amplitude | Plastic cycles | Location of failure |
|---|---|---|---|---|---|
| 1 | D1_S1 | mECCS | 9 $e_y$ - 133.2 mm | 22 | |
| 2 | D1_S2[1)] | mECCS | 9 $e_y$ - 133.2 mm | 22 | |
| 3 | D1_S3 | constant amplitude - 7 $e_y$ | 7 $e_y$ - 103.6 mm | 10 | |
| 4 | D1_S4 | constant amplitude - 6 $e_y$ | 6 $e_y$ - 88.8 mm | 18/19 | |
| 5 | D1_S5 | constant amplitude - 7 $e_y$ | 7 $e_y$ - 103.6 mm | 11 | |
| 6 | D2_S1 | mECCS | 6 $e_y$ - 76.8 mm | 12 | |
| 7 | D2_S2 | constant amplitude - 4 $e_y$ | 4 $e_y$ - 51.2 mm | 7 | reduced beam section area |
| 8 | D2_S3 | constant amplitude - 3.5 $e_y$ | 3.5 $e_y$ - 44.8 mm | 10 | |
| 9 | D3_S1 | mECCS | 6 $e_y$ - 88.8 mm | 15 | |
| 10 | D3_S2 | constant amplitude - 5 $e_y$ | 5 $e_y$ - 74 mm | 8 | |
| 11 | D3_S3 | constant amplitude – 4.5 $e_y$ | 4.5 $e_y$ – 66.6 mm | 10 | |
| 12 | D4_S1 | mECCS | 6 $e_y$ – 156 mm | 18 | |
| 13 | D4_S2 | constant amplitude | 4 $e_y$ – 104 mm | 18 | |
| 14 | D4_S3 | constant amplitude | 4.5 $e_y$ – 117 mm | 9 | |

[1)] Trial specimen

Table 1: Overview of loading scheme, maximal amplitude and location of failure

Figure 13 and Figure 14 show exemplary test results in terms of cyclic load-displacement curves referring to the wire displacement transducer and exemplary pictures of buckles and cracks at the end of the loading history.

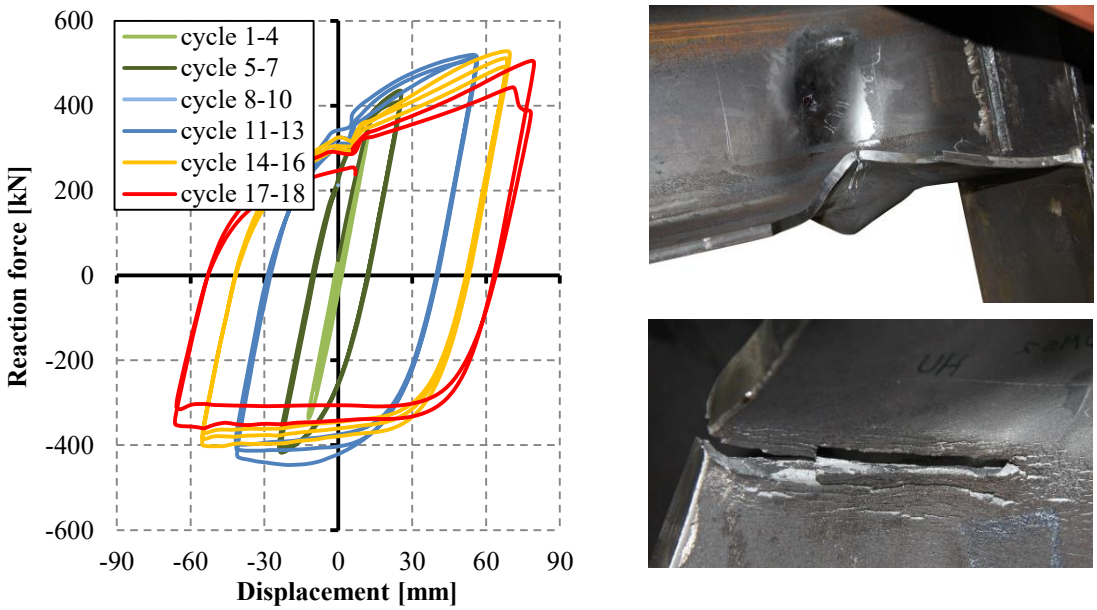


Figure 13: Cyclic load-displacement curve and pictures of D2_S1

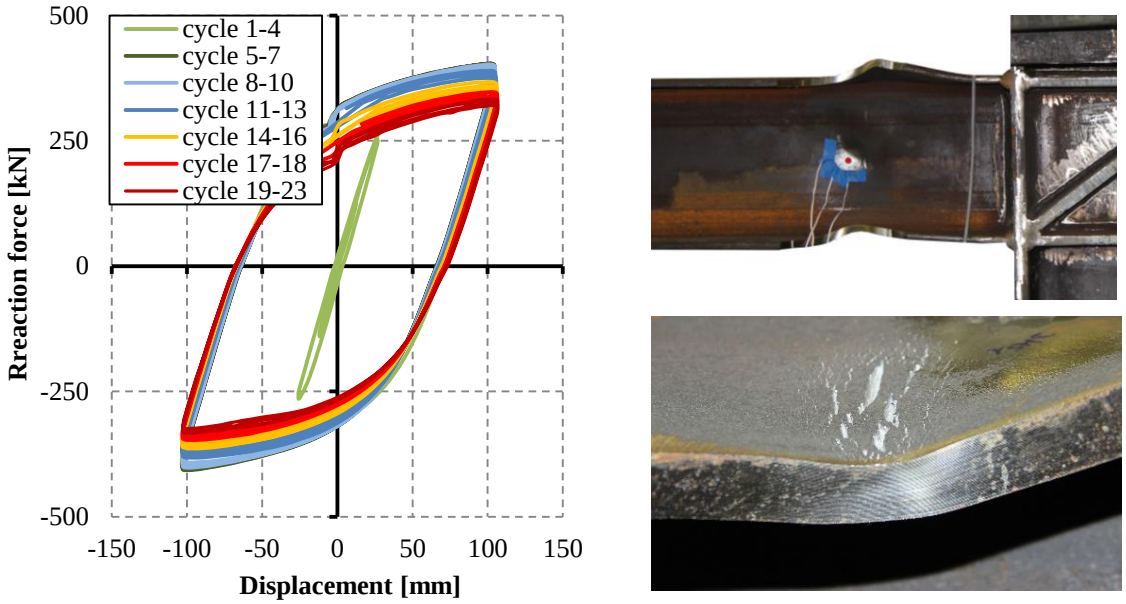


Figure 14: Cyclic load-displacement curve and pictures of D4_S2

## 4 NUMERICAL SIMULATIONS

For the recalculation of the experimental investigations 3D finite element (FE) models have been created using ABAQUS CAE.

### 4.1 Finite element models

In order to create realistic finite element models actually measured geometric values of the specimens have been considered. Moreover, only the relevant parts of the test rigs (cf. section 3.1) influencing the simulation results have been modelled. The bolted connections of the different test-rigs have been taken into account by incorporating extension springs, as indicated in Figure 15 to Figure 18. Furthermore, also the lateral support of the test rigs has been considered by extension springs.

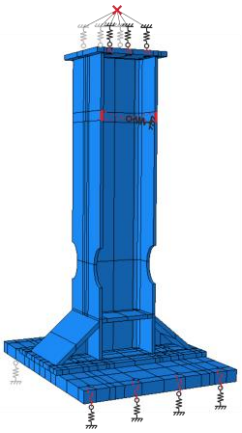

Figure 15: D1 FE model

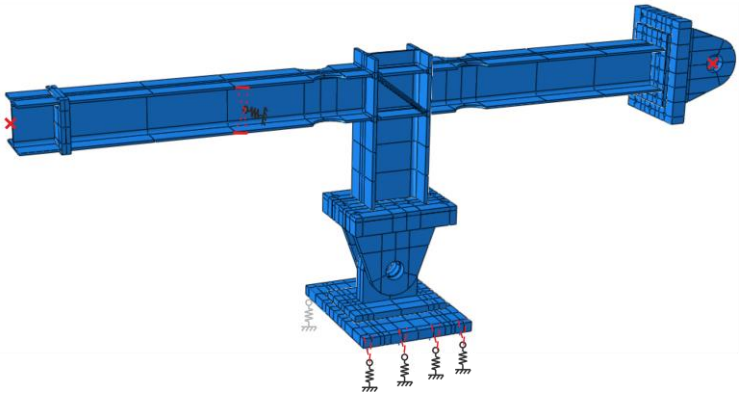

Figure 16: D3 FE model

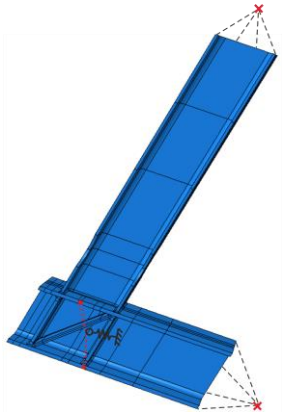

Figure 17: D2 FE model

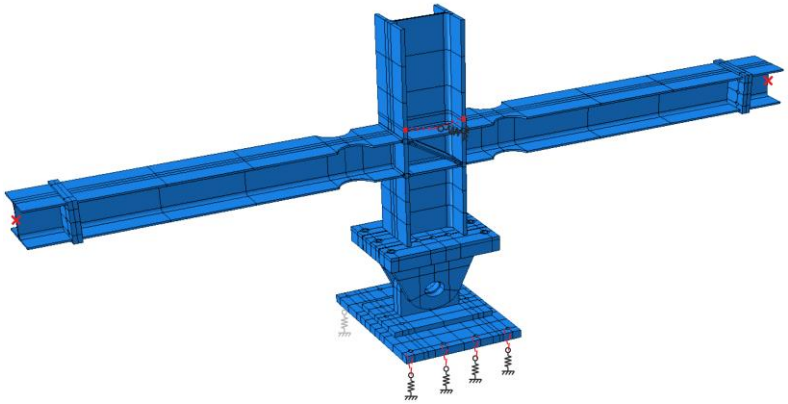

Figure 18: D4 FE model

The material characteristics of the models have been defined by parameters of the hybrid plasticity and damage model explained in section 2. The utilised parameter set has firstly been calibrated on the basis of small scale tests and furthermore slightly fitted to the full scale test results presented in chapter 3. Linear three-dimensional continuum stress/displacement elements (C3D8) with a global mesh size of 20 mm have been utilised. However a smaller mesh size has been applied to the models of D4 in order to realistically simulate the occurrence of buckles. The mesh of relevant parts of the models, for instance the reduced beam section area where the cracks occurred, has additionally been refined. One single set of plasticity and damage parameters and equal model adjustments have been utilised for the four models. Moreover, physical and geometrical non-linearities have been taken into account.

## 4.2 Validation of plasticity approach

To verify the applied plasticity approach, experimental and numerical hystereses have been compared to each other as a first step. Additionally the deformations of specimen and FE model have been regarded.

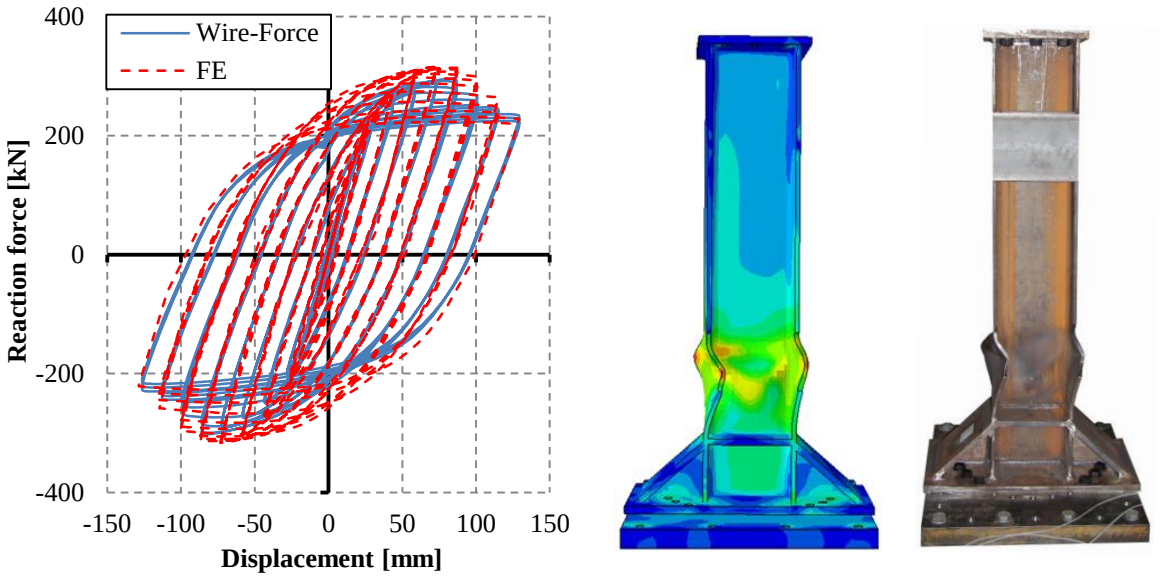


Figure 19: Comparison of test and simulation of D1_S2

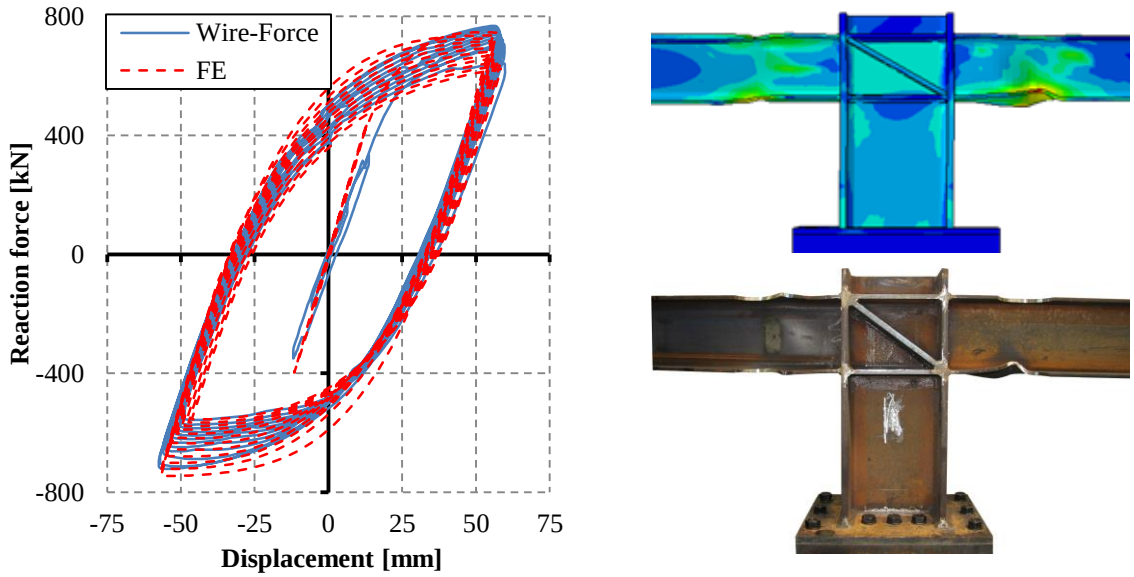


Figure 20: Comparison of test and simulation of D3_S3

As exemplary seen in Figure 19 and Figure 20 the finite element models depict the specimens' experimental behaviour in a distinguished and realistic manner. Remaining deviations can be ascribed to the difficult modelling of the boundary conditions containing bolted connections.

Moreover, the comparison of local strains serves as additional verification method. The strains obtained from numerical simulations fit the experimental data of the strain gauges qualitatively. Minor deviations of experiment and simulation are ascribed to the precarious attachment of the strain gauges, which distort if expiring plastic deformations. Figure 21 depicts the comparison of experimentally and numerically measured strains recorded by high strain gauges. Additionally, the verification in terms of inclination proves to provide good accordance between experimental and numerical analysis, as exemplary illustrated in Figure 22.

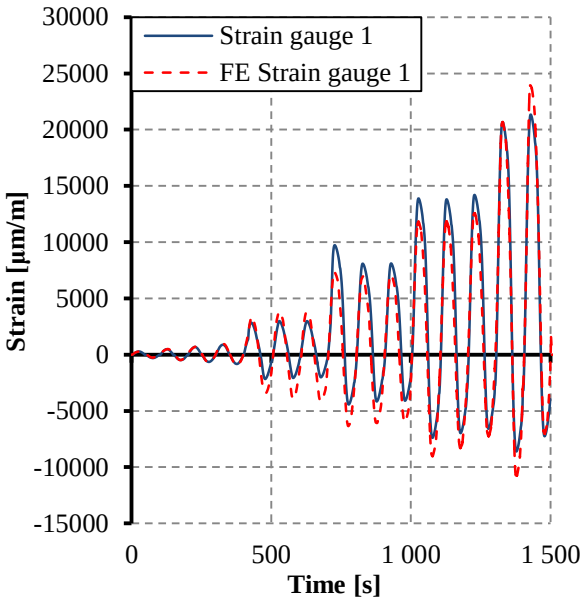


Figure 21: Strains of test and simulation of D1_S1

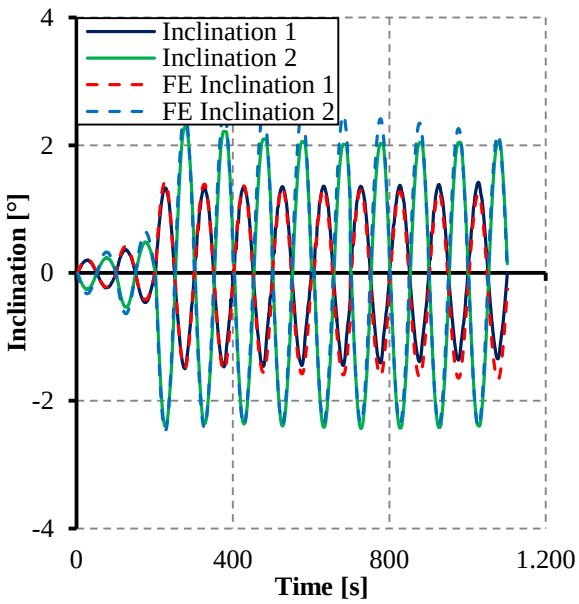


Figure 22: Inclination of test and simulation of D2_S2

### 4.3 Validation of damage mechanics approach

In order to validate the damage mechanics approach the experimental and numerical damage initiation has been compared, as presented in Table 2. The trial specimen D1_S2 has not been taken into account.

| Specimen | Loading | Experimental damage | | Numerical damage | |
|---|---|---|---|---|---|
| | | Cycle | Location | Cycle | Location |
| D1_S1 | mECCS | 26 | RBS R - outside | 25 | RBS R - inside |
| D1_S3 | const. amp. | 12 | fillet L + RBS L outside | 7 | RBS L - inside |
| D1_S4 | const. amp. | 21 | RBS R + L outside | 9 | RBS L - outside |
| D1_S5 | const. amp. | 13 | RBS L - outside | 7 | RBS L - inside |
| D2_S1 | mECCS | 16 | RBS R - inside + outside | 16 | RBS R - outside |
| D2_S2 | const. amp. | 9 | RBS R - outside | 8 | RBS R - outside |
| D2_S3 | const. amp. | 12 | RBS R - outside | 10 | RBS R - outside |
| D3_S1 | mECCS | 19 | RSB R - outside | 17 | RBS R - outside |
| D3_S2 | const. amp. | 10 | RSB R - outside | 7 | RBS R - outside |
| D3_S3 | const. amp. | 12 | RSB R - outside | 8 | RBS R - outside |
| D4_S1 | mECCS | 22 | RBS L - outside | 18 | RBS L - outside |
| D4_S2 | const. amp. | 20 | RBS L - outside | 15 | RBS R - outside |
| D4_S3 | const. amp. | 11 | RBS L - outside | 11 | RBS L - outside |

Table 2: Comparison of experimental and numerical damage initiation of all specimens

First, the forecast of the number of cycles to failure is evaluated. According to Table 2 and Figure 23, the prediction of the cycle at which damage occurs for the first time is hugely satisfying regarding specimens subjected to the mECCS loading scheme. During simulations of some models subjected to constant amplitudes, damage is announced too early.

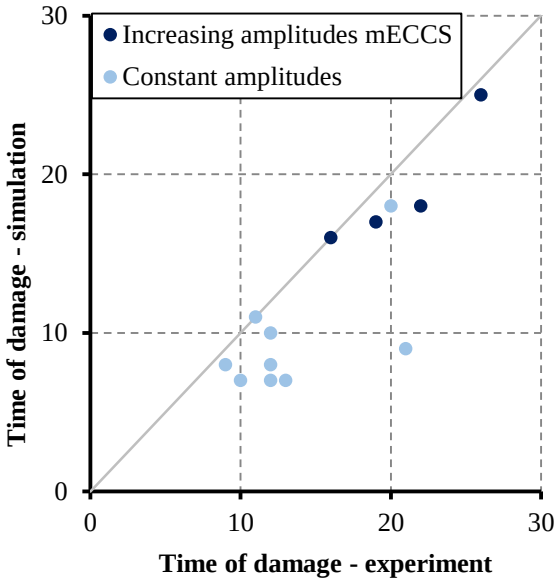


Figure 23: Comparison of experimental und numerical damage initiation of all specimens

Furthermore, the forecast of the damage location is evaluated. Table 2 contains the damage initiation locations of the different models. RBS L denotes the left, RBS R the right reduced beam section, seen from front view of Figure 5 to Figure 8. Moreover, 'outside' designates the outer surfaces of the flanges, whereas 'inside' denotes the inner surfaces of the flanges. The damage location is mostly predicted satisfactorily, as shown in Table 2.

Figure 24 exemplary depicts the comparison of experimental and numerical damage location of specimen D2_S3. It can be observed that the presented damage mechanics approach leads to a precise prediction of the first damage location.

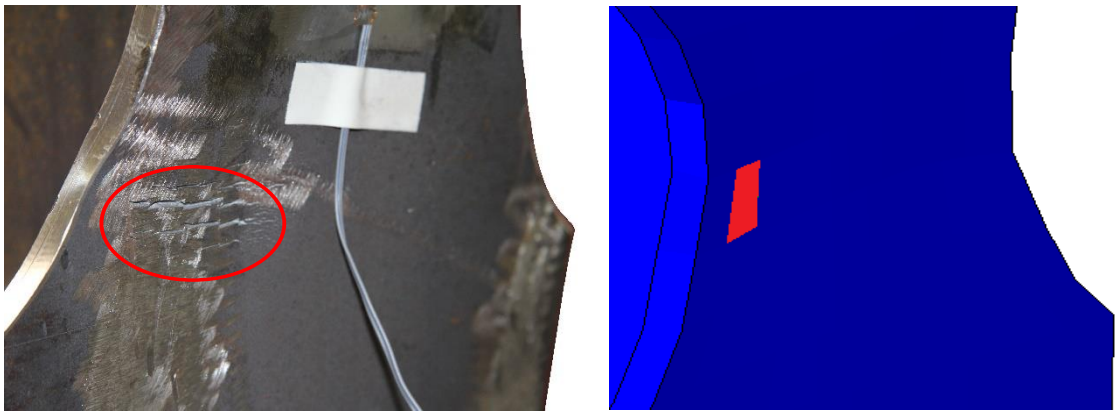

Figure 24: Comparison of experimental and numerical damage location of D2_S3

## 5 CONCLUSIONS

The ductile damage of dissipative elements has been predicted by using innovative damage mechanics. In the majority of the simulations the number of cycles to failure has been predicted exactly or with minimal deviation. Six simulations resulted in a notably early damage prediction. This behaviour has mostly been observed in simulations of specimens subjected to constant instead of increasing amplitudes. However, the results are conservative. A correct location of failure has been forecasted for all specimens, except one. It has to be noted, that the first damage location is strongly dependent on the instant of time, at which damage is announced for the first time.

The applied damage mechanics approach could be validated for increasing loads, but still needs enhancement to accomplish a successful damage prediction in case of constant amplitudes or random loadings.

## 6 ACKNOWLEDGEMENTS

The presented investigations have been conducted in the framework of the European Research Project "Material Choice for Seismic Resistant Structures (MATCH)" [4]. The financial contribution of the Research Fund for Coal and Steel of the European Community is greatly acknowledged.

## REFERENCES

[1] Eurocode 3: Design of steel structures - Part 1-1: General rules and rules for buildings; EN 1993-1-1:2005 + AC: 2009.

[2] Eurocode 8: Design of structures for earthquake resistance – Part 1: General rules, seismic actions and rules for buildings; EN 1998-1:2004 + AC: 2009.

[3] Valkonen I., "Ultimate Limit Load Capacity of FUSEIS-element made of Cold Formed Sections with a Yield Strength of 700 MPa", IIW Document XV-1489-15, 2015.

[4] MATCH: Material Choice for Seismic Resistant Structures, Research Fund for Coal and Steel, Final Report (in preparation), 2017.

[5] PLASTOTOUGH: Modern Plastic Design of Steel Structures. Research Fund for Coal and Steel, Final Report, 2010.

[6] Bai, Y., Wierzbicki, T., "A new model of metal plasticity and fracture with pressure and Lode dependence", International Journal of Plasticity, Vol. 24, pp. 1071-1096, 2008.

[7] Johnson, G. R., Cook W. H., "Fracture characteristics of three metals subjected to various strains, strain rates, temperatures and pressures," 1985.

[8] Ohata M., Toyoda, M., "Damage concept for evaluating ductile cracking of steel structure subjected to large-scale cyclic straining", Science and Technology of Advanced Materials, Vol. 5, pp. 241-249, 2004.

[9] Armstrong, P.J., Frederick, C.O., "A mathematical representation of the multiaxial Bauschinger effect", CEGB Report No. RD/B/N 731, 1966.

[10] Ucak, A., Tsopelas, P., "Constitutive Model for Cyclic Response of Structural Steels with Yield Plateau", Journal of the Structural Engineering, Vol. 137, No.2, pp.195-206, 2001.

[11] Lian, J., Sharaf, M., Archie, F., Münstermann, S., "A hybrid approach for modelling of plasticity and failure behaviour of advanced high-strength steel sheets", International Journal of Damage Mechanics, Vol. 22(2), pp. 188-218, 2012.

[12] Eurocode 8: Design of structures for earthquake resistance - Part 3: Assessment and Retrofitting of buildings; EN 1998-3:2004.

[13] Ballio, G. and Castiglioni, C. A.: "Seismic Behaviour of Steel Sections", Journal of Constructional Steel Research 29, pp. 21-54, 1994.

[14] Ballio, G. and Castiglioni, C. A.: "An Approach to the Seismic Design of Steel Structures", Earthquake Engineering and Structural Dynamics 23, pp. 969-986, 1994.

[15] Ballio, G. and Castiglioni, C. A.: "Unified Approach for the Design of Steel Structures under Low and/or High Cycle Fatigue", Journal of Constructional Steel Research 34, pp. 75-101, 1995.

[16] ECCS: Recommended testing procedure for assessing the behaviour of structural steel elements under cyclic loads. Technical committee 1: structural safety and loadings, technical working group 1.3: seismic design, 1986.

COMPDYN 2017
6th ECCOMAS Thematic Conference on
Computational Methods in Structural Dynamics and Earthquake Engineering
M. Papadrakakis, M. Fragiadakis (eds.)
Rhodes Island, Greece, 15–17 June 2017

# EFFECT OF MAJOR SEISMOLOGICAL PARAMETERS ON DIRECTIVITY DOMINANT SPECTRAL AMPLIFICATION (COMPDYN 2017)

**Saed Moghimi**[1], **Sinan Akkar**[2]

[1] Department of Civil Engineering, Middle East Technical University
06800 Ankara, Turkey
e-mail: Saaed_m@yahoo.com

[2] Department of Earthquake Engineering, Bogazici University
34684 Istanbul, Turkey
sinan.akkar@boun.edu.tr

**Keywords:** Directivity, Narrow-band model, Pulse period, Pulse type ground motion, Response spectrum

**Abstract.** *One of the most important features of directivity-dominant near-fault ground motions is the existence of impulsive signals in the beginning of ground velocity. Directivity is observed when rupture propagates toward a site at a velocity close to particle shear-wave velocity. Such ground motions with large-amplitude and long-period velocity pulses amplify the response spectrum in medium to long period ranges. As such, they have the potential to impose severe inelastic demands on the medium to high-rise buildings.*

*In this study we discuss the differences between the directivity models proposed in NGA-WEST2 [i.e., Shahi and Baker and Chiou and Spudich presented in Spudich et al. (2013)] and Shahi and Baker (2011). Deterministic and probabilistic seismic hazard analyses are done with and without considering directivity effects for different earthquake scenarios as well as 475-year and 2475-year return periods. The response spectrum amplification due to directivity is extracted from these hazard analyses and the effects of major seismological parameters on the computed spectral amplifications are investigated. The observed results suggest some differences in the investigated directivity models for deterministic and probabilistic earthquake scenarios. The characteristic magnitude and fault-site geometry play an important role in all models within probabilistic hazard framework. The Shahi and Baker directivity models also bring forward the significance of slip rate and return period in spectral amplifications. The slip rate and return period do not prominently affect the spectral amplifications in Chiou and Spudich directivity model. The observations suggest a need for the consideration of forward directivity on code-based design spectrum via some practical rules.*

## 1 INTRODUCTION

One of the important features of near fault ground motions is directivity effect. In near fault earthquakes when rupture propagates toward a site a pulse is formed in the beginning of the velocity wave form. These pulses are mostly seen in the fault normal direction. This kind of records which have higher amplitude with shorter duration are known as ground motions with forward directivity effect. On the other hand when rupture propagates away from the site the ground motion will have lower amplitude with longer duration. This case is called backward directivity.

Housner and Trifunac (1967) were the first that observed ground motions with long period, strong velocity and displacement pulses in 1966 Parkfield earthquake. The second earthquake with impulsive signal in fault normal component was reported in 1971 San Fernando earthquake (Boore & Zoback 1974; Niazy 1975). Bertero et al. (1978) have studied destructive effect of pulse type ground motions on medium to high-rise buildings for the first time. However, 1994 Northridge earthquake was the first that revealed vulnerability of high-rise buildings against pulse type ground motions. Later on the observations from 1995 Kobe, 1999 Izmit and 2009 L'Aquila Earthquakes confirmed the previously seen destructive potential of the near-fault impulsive ground motions (Alavi & Krawinkler 2001; Chioccarelli & Iervolino 2010).

Some of design codes incorporated the effects of near fault ground motions after the destructive potential of these ground motions were identified. Uniform Building Code (UBC, 1997) applies a uniform scaling on the design spectrum with 475-year return period for the near fault effects of ground motions. Near source effects are defined with Na (for short period range of design spectrum) and Nv (for long period range of design spectrum) factors in UBC, 1997. These factors are applied on the seismic coefficients Ca and Cv for the sites located in high seismicity regions (seismic zone 4).

In order to better estimate the effects of near fault impulsive ground motions the directivity effect is needed to be incorporated in ground motion models. Traditional ground-motion models do not account for the effect of pulse-like ground motions and hence, they may under predict the spectral acceleration for impulsive ground motions in medium to high period ranges depending on earthquake magnitude. Several researchers have proposed different directivity models to be implemented on ground motion equations.

One of the first important directivity models was proposed by Somerville et al. (1997). This model basically uses two geometric parameters to assemble the directivity effect on ground motion equations. First, the angle between the direction of rupture propagation and the direction of waves traveling from the fault to the site, second, the fraction of the fault rupture surface that lies between the hypocenter and the site. Somerville et al. (1997) modifies ground motion average horizontal response spectral acceleration, and duration of acceleration time history in order to incorporate directivity effect in ground motion equations. The model also proposes a ratio for strike normal to strike parallel component of ground motions with directivity effect. This model was modified by Abrahamson (2000) in order to incorporate the magnitude and distance saturation in directivity model.

Shahi and Baker (2011) (hereafter SHB-11) used together with Boore and Atkinson (2008) (hereafter BA-08) have calibrated a new framework on the PSHA in order to incorporate directivity effect. The method first has been proposed with Tothong et al. (2007) which considers the probability of pulse occurrence and pulse period in hazard analysis. Iervolino and Cornell (2008) have used the source to site geometrical parameters used in this model in order to quantify the probability of pulse occurrence.

Although some primary models have been proposed for directivity in NGAWEST1 (2008) project but they did not include directivity and guidance for its application in their equations explicitly. The most recent and comprehensive directivity models have been proposed by NGA-WEST2 Directivity Working Group (Spudich et al. 2013). This report include five directivity models. The models proposed by Roshandel, Shahi & Baker (hereafter SHB-13), Spudich & Chiou (models proposed in chapter 3, 4 and 5 in Spudich et al. 2013) are explicitly narrow-band in which the spectral acceleration is amplified in a narrow range of periods close to pulse period. Bayless & Somerville (the model proposed in chapter 2 in Spudich et al. 2013) have updated Somerville et al. (1997) directivity model which is a broad-band model and amplifies the response spectrum uniformly in medium to high spectral period ranges. Chiou & Spudich (hereafter CHS-13) (the model proposed in chapter 6 in Spudich et al. 2013) uses Directivity Predictor Parameter (DPP) as the predictor of directivity together with ground motion equation proposed by Chiou and Young (2014) (hereafter CHY-14).

In this study we have discussed the theoretical and mathematical differences between SHB-11, SHB-13 and CHS-13 directivity models. The results will be discussed in terms of deterministic and probabilistic hazard analysis. In deterministic analysis the variation of amplification factor for three cases has been studied and discussed. The comparisons and discussions are done on the basis of deterministic hazard analysis. In addition Probabilistic Seismic Hazard Analysis has been done in order to investigate the effect of earthquake scenarios and source to site geometric parameters on the level of amplification due to directivity. In PSHA SHB-11and CHS-13 directivity models have been assembled in a Matlab code that has been written for this purpose. Uniform hazard spectrum has been extracted for each site with and without considering directivity effect for two return periods (475 and 2475-Year). SH-11 and CHS-13 models have been used for calculation of response spectrum with directivity effect. Response spectrum without directivity effect is calculated with conventional probabilistic seismic hazard analysis. The amplification is calculated from the normalization of spectral acceleration with directivity effect to spectral acceleration of conventional PSHA.

In the next section general framework of SHB-11, SHB-13 and CHS-13 directivity models have been described. The geometric illustrations and the differences among these models will be illustrated and explained. Selection of input parameters for the seismic hazard analysis and the effect of these parameters on the level of amplification will be discussed in the next sections of this study.

## 2 INTRODUCTION OF DIRECTIVITY MODELS

### 2.1 General Framework of Shahi and Baker 2011 (SHB-11)

The general framework of this method is to some extend different from the conventional PSHA methods. This model considers the probability of pulse occurrence and pulse period distribution in hazard analysis. Equation (1) shows the annual exceedance rate of spectral acceleration with directivity effect:

$$\nu_{Sa}(x) = \sum_{i=1}^{\#\,faults} \nu_i \iiint P^*\left(S_a > x \mid m,r,z,t_p\right).f_i(m,r,z).dm.dr.dz.dt_p \qquad (1)$$

where m, r, z and $t_p$ represent magnitude, distance, source to site geometry and pulse period parameters respectively. The PSHA model proposed in Equation 1 can be practically evaluated by splitting $P^*\left(S_a > x \mid m,r,z,t_p\right)$ into two cases, depending on whether or not pulse-like ground motion is observed. These two cases are shown in Equation 2.

$$P^*(S_a > x \mid m,r,z) = P(pulse \mid m,r,z).P(S_a > x \mid m,r,z,pulse) + [1 - P(pulse \mid m,r,z)].P(S_a > x \mid m,r,no\ pulse) \quad (2)$$

Regarding this model the spectral acceleration is amplified for pulse like ground motions and de-amplified for non-pulse like cases. In this method the probability of pulse occurrence depends on source to site geometric parameters.

## 2.2 Chiou and Spudich-2013 (CHS-13) Directivity Model

Chiou and Young (2014) have adapted a directivity model ($f_{DPP}$) on their Ground Motion Equation (CHY-14) in order to incorporate effect of near fault impulsive ground motions in response spectrum estimation. This model uses Direct Point Parameter (DPP) as the predictor of directivity effect. The functional form of $f_{DPP}$ is shown in Equation 3 in which $f_R$ and $f_M$ are distance and magnitude taper functions represented in Equations 4 and 5 respectively.

$$f_{DPP} = c_8 . f_R . f_M . e^{-c_{8a}(M - c_{8b})^2} . \Delta DPP \quad (3)$$

$$f_R = \max[0, 1 - \frac{\max(R_{rup} - 40)}{30}] \quad (4)$$

$$f_M = \max[1, \frac{\max(M - 5.5, 0))}{0.8}] \quad (5)$$

In Equation 3, $c_8$ and $c_{8b}$ are period dependent coefficients and $c_{8a}$ is period independent coefficient given in Chiou and Young (2014). The distance taper function reduces $f_{DPP}$ effect to zero starting from 40 to 70km. The magnitude taper also has the same function for the magnitude range 6.3 to 5.5. This is due to the fact that directivity effect is not seen in larger distances and smaller magnitude ranges. ΔDPP in Equation 3 is centered value of direct point parameter. Since conventional ground motion equations take some account of rupture directivity effects in the average sense due to existence of pulse type ground motions in the dataset used to develop these equations the directivity models cannot be used directly as an add-on directivity correction in these equations. Therefore a centering value of directivity parameter is used in directivity model. The centered value of DPP has been defined in CHS-13 model and it is calculated from Equation 6 for a specific site in which $\overline{DPP}$ is the average value of DPP for the sites with a constant distance from the fault rupture.

$$\Delta DPP_i = DPP_i - \overline{DPP} \quad (6)$$

DPP has three factors, a measure of isochrone velocity ($\hat{c}'$); a measure of rupture propagation distance (E); and a radiation pattern term ($\overline{FS}$). DPP is calculated from Equation 7 for a single planar rupture surface.

$$DPP = ln(\hat{c}'.max(E, 0.1f).max(\overline{FS}, 0.2)) \quad (7)$$

In this equation E is the distance between hypocenter ($P_H$) and direct point ($P_D$), f is the larger of fault length and width, $\overline{FS}$ is the average S-wave radiation pattern over E-Path and $\hat{c}'$ is the isochrone velocity which is calculated from Equation 8.

$$\hat{c}' = \frac{1}{(\frac{1}{0.8} - \frac{R_{HYP} - R_D}{E})} \quad \text{for E>0}$$
$$\hat{c}' = 0.8 \quad \text{for E=0} \quad (8)$$

where $R_{HYP}$ is hypocenter to site distance ($P_HP_S$) and $R_D$ is the direct point to site distance ($P_DP_S$).

## 2.3 Chiou and Spudich-2013 (CHS-13) Directivity Model

This model extends the approach of SHB-11 in order to incorporate directivity effect in Ground Motion Equations. The model is composed of two parts as can be seen in Equation 9. The first term is the base Ground Motion Equation which predicts the natural logarithm of spectral acceleration in spectral period of T seconds.

$$lnSa_{ij} = f\left(M_i, R_j, T, Vs30_j, \theta, \dots\right) + I_{directivity}.\ln amp\left(T, T_p\right) + \eta_i + \varepsilon_{ij} \qquad (9)$$

The first term is a function of magnitude, distance, period and shear wave velocity of the site. The coefficients in the base ground motion model (θ) are refitted without considering directivity effect. In this way the directivity effect which is implicitly included in the original Ground Motion Equation due to existence of pulse type ground motions in the dataset is removed. The second term amplifies the base ground motion model due to existence of impulsive period which is the function of spectral period and pulse period ratio as can be seen in Equation 10. $I_{Directivity}$ is a binary value which takes one when the ground motion contains a pulse and takes zero otherwise.

$$\ln amp\left(T, T_p\right) = b_0.\exp\left(b_1(\ln\left(\frac{T}{T_p}\right) - b_2)^2\right) \qquad (10)$$

the coefficients have been determined from refitting the ground motion model to the NGA-WEST2 data set. Finally $\eta_i$ and $\varepsilon_{ij}$ in Equation 9 are between-event and within-event errors respectively.

## 2.4 COMPARISION OF SHB-11, SHB-13 AND CHS-13 DIRECTIVITY MODELS

As stated before SHB-13 is extended version of SHB-11 and therefore the general framework and utilized geometric parameters in the both models are similar to each other. Both models are narrow-band which amplify the ground motion spectral acceleration at periods close to pulse period. These two models also have differences in terms of mathematical form and development procedure. SHB-11 de-amplifies the spectral acceleration for non-pulse cases while SHB-13 uses the spectral acceleration of base ground motion equation without applying any de-amplification for these cases. Both of the models use the same source to site geometric models which are illustrated in Figure 1.

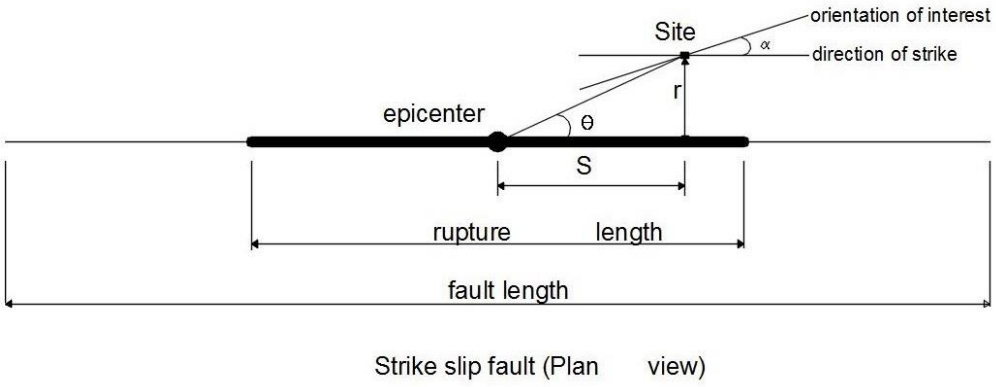


**Figure 1 Source to site geometric parameters of SHB-11 and SHB-13 models for Strike Slip Faults**

In this figure "r" is the closest distance of the site to the rupture and "s" is the rupture length that lays between the hypocenter and closest distance of the site to the fault in the fault strike direction and θ is the angle between fault strike direction and the line that joins epicenter and the site. These parameters (r, s and θ) are used to calculate probability of pulse occurrence distribution pattern around the fault in SHB-11 and SHB-13 directivity models.

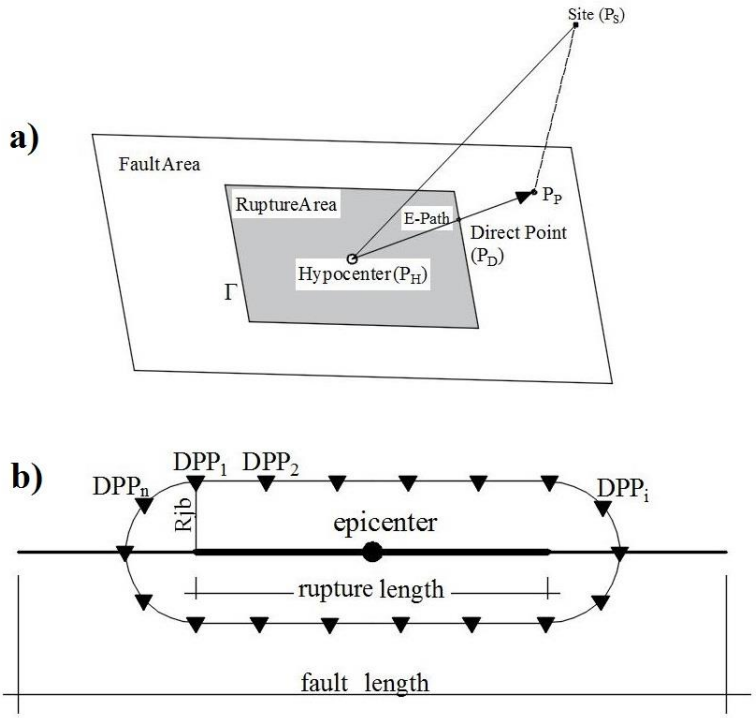


**Figure 2 CHS-13 model a) Source to site geometric parameters b) Direct Point Parameter distribution around the rupture**

As stated in section 2.2 CHS-13 model uses Direct Point Parameter (DPP) as the predictor of directivity effect. In this model the direct point concept (DP) is the intersecting point of the fault-projected direct ray ($P_H P_P$) with the slipped-area boundary, where $P_H$ is the hypocenter and $P_P$ is the projection of the site onto the plane containing the slipped area (Figure 2a). When a site is normal to the slipped area (i.e., $P_P$ is inside slipped area), the direct point is the same as Pp ($P_D$ and $P_P$ will coincide on each other). Direct point concept (DP) in CHS-13 is used to define centered value of Direct Point Parameter (ΔDPP) as shown in Figure 2b.

The other difference between these models is the component that they predict for ground motion spectral acceleration. SHB-11 model is used together with Boore and Atkinson (2008) (BA-08) Ground Motion Equation in order to investigate the directivity effect. BA-08 predicts RotI50 component of ground motion and SHB-11 modifies RotI50 component to predict spectral acceleration in a desired orientation with respect to fault strike direction for pulse type ground motions. SHB-13 uses Refitted Campbell and Bozorgnia (2008) (CBR) Ground Motion Equation in order to predict the spectral acceleration with directivity effect. Therefore this model modifies RotD50 component of the ground motion model in a desired orientation in order to predict spectral acceleration with directivity effect. On the other hand, CHS-13 directivity model is adapted on Chiou and Youngs (2014) (CHY-14) Ground Motion Equation which estimates RotD50 component. Therefore CHS-13 modifies RotD50 component to estimate RotD50 component with directivity effect ($RotD50_{Directivity}$).

## 3 SELECTION OF INPUT PARAMETERS FOR HAZARD ANALYSIS

This study aims to investigate the effect of seismological and geometrical parameters on the level of amplification for considered directivity models. For this purpose we have run both Deterministic and Probabilistic Seismic Hazard Analysis for different earthquake scenarios with these directivity models. Gridded mesh of 42 sites spatially distributed around the fault have been selected for the analysis in order to investigate the effect of source to site geometry on the amplification of response spectrum. The distances in fault strike direction (X direction) are normalized to the fault length and this normalized distance is measured from the center of the fault projection on the ground. The fault length is taken as "L" and the sites are extended 0.3×L beyond the fault edge in X direction. In addition, the sites are placed every 5km in the fault normal direction (Y direction) from 0 to 30km. Due to symmetry sites are scattered just in upper right quarter of the fault (Figure 3).

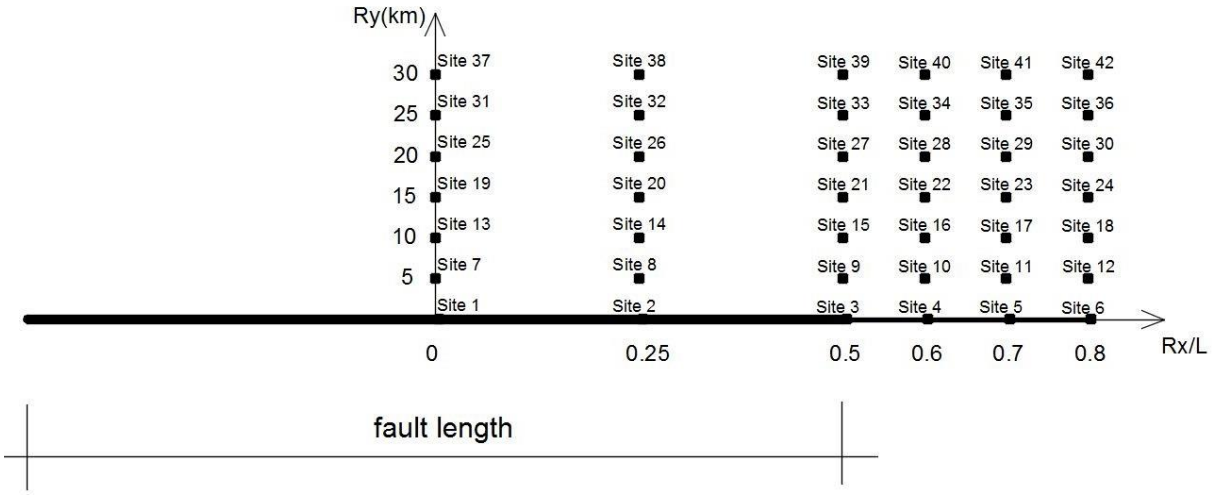


**Figure 3 Gridded sites around the fault for investigation of Source to site geometry effect**

The other parameter that can play important role on the amplification of response spectrum due to directivity effect is the earthquake magnitude. Five different faults with different characteristic magnitudes have been selected for the hazard analysis in order to investigate the effect of this parameter on the amplification. As mentioned before pulse-type ground motions with directivity effect are mostly seen in earthquakes with medium to large magnitude. Therefore the faults are selected in a way that their characteristic magnitude represent this magnitude range. The faults are selected with 20, 50, 100, 150 and 300km length and 10km width for all cases with characteristic magnitudes equal to 6.25, 6.7, 7.0, 7.2 and 7.5 respectively. Characteristic earthquake reccurence model (Youngs & Coppersmith 1985) has been used in all the hazard analysis. The earthquake magnitudes greater than 5 have been considered in probabilistic hazard analysis.

The other important parameter than can be effective on the level of amplification is the slip rate of the fault. Three slip rate values have been assigned to the faults (SR=0.5, 1.0 and 2.0 cm/year) for the analysis indicating low, medium and high seismicity levels.

## 4 DISCUSSIONS ON DETERMINISTIC HAZARD ANALYSIS

In deterministic hazard analysis the spectral acceleration is calculated for a single earthquake scenario. In our case we have calculated the amplification of spectral acceleration with

three directivity models discussed in the last sections. The amplification has been calculated for a fault with 100km length, slip rate 1.0 cm/year and for the sites 8, 9 and 10 (illustrated in Figure 3) which are located 5km away from the fault in Y direction. Figure 4 illustrates the median of spectral acceleration calculated for site 9 with and without considering directivity effect for SHB-11, SHB-13 and CHS-13 directivity models. As can be seen from this figure the SHB-11 has the largest amplification in a narrow period range. But the point that should be considered here is that SHB-11 combines amplification and de-amplification cases in a full probabilistic analysis. The de-amplification case is shown with **SHB 11-NoDirectivity** dotted line in this figure. In order to better see the difference between these models we have plotted the spectral amplification of three directivity models for sites 8, 9 and 10 in Figure 5.

In SHB-11 and SHB-13 the amplification is the same for all three sites (8, 9 and 10) since the amplification is just a function of T/Tp parameter which is the same for all of these three sites. In SHB-11 the Deamplification is the same for site 8 and 9 because the deamplification term is a function of magnitude and distance. For the site 8 and 9 the magnitude and distance parameters are equal ($M_{ch}$= and Rjb=5km). In Site 10 we do not observe any deamplification because there is a distance cap for the deamplification factor which makes it equal to 1 for the distances greater that 10km (note that Rjb of site 10 is 11.18km). The overall amplification in SHB-11 is calculated from the combination of pulse and no pulse cases for the full probabilistic seismic hazard analysis.

In CHS-13 we observe an increasing trend for the Amplification while we are moving from site 8 toward site 10. This is due to the fact that the directivity effect is a function of ΔDPP (Chiou and Youngs 2014). Since ΔDPP has an increasing trend while moving from site 8 toward site 10 the amplification also shows the same trend.

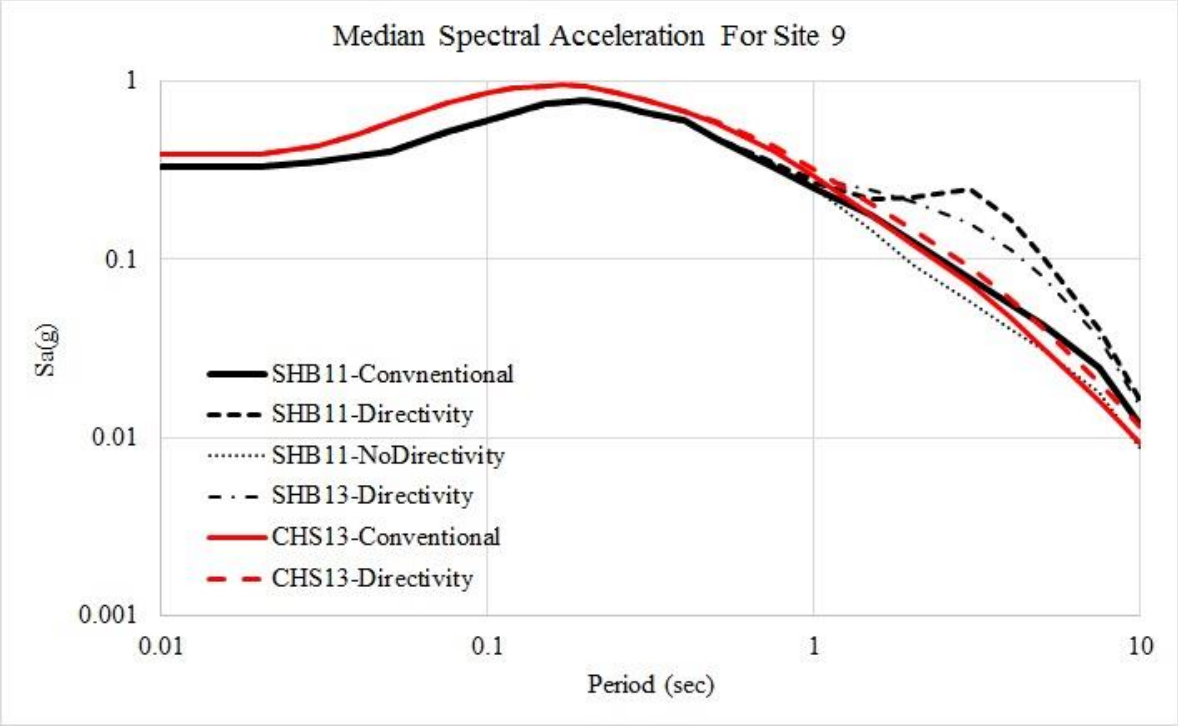


**Figure 4 Median of spectral acceleration for Site 9 and earthquake scenario with FL=100 and SR=1cm/year calculated by DSHA**

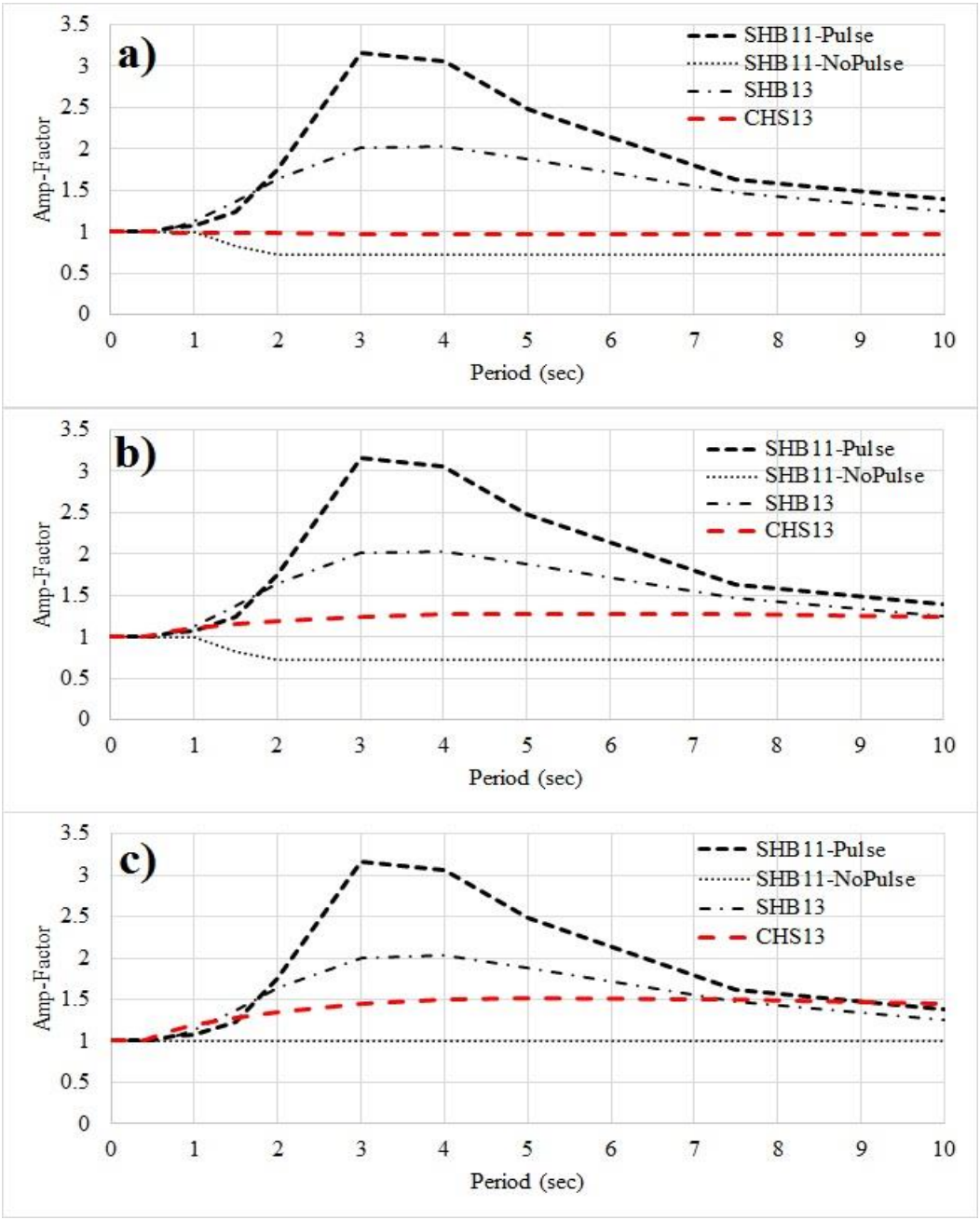


**Figure 5 Amplification factor calculated with three directivity models**
**a) FL=100km, SR=1.0cm/year, Site 8 b) FL=100km, SR=1.0cm/year, Site 9**
**c) FL=100km, SR=1.0cm/year, Site 10**

## 5 AMPLIFICATION INVESTIGATION FOR PSHA

In this section we have investigated the effect of source to site geometry, slip rate, fault magnitude and the hazard level (return period of response spectrum) on the level of amplification when PSHA is applied on the directivity models. All the considered faults are planar with the strike slip mechanism. The amplification factor is the ratio of uniform hazard spectrum calculated with SHB-11, and CHS-13 directivity models to conventional response spectrum (Equation 11).

$$AMP(T) = \frac{Sa(T)_{directivity}}{Sa(T)_{conventional}} \tag{11}$$

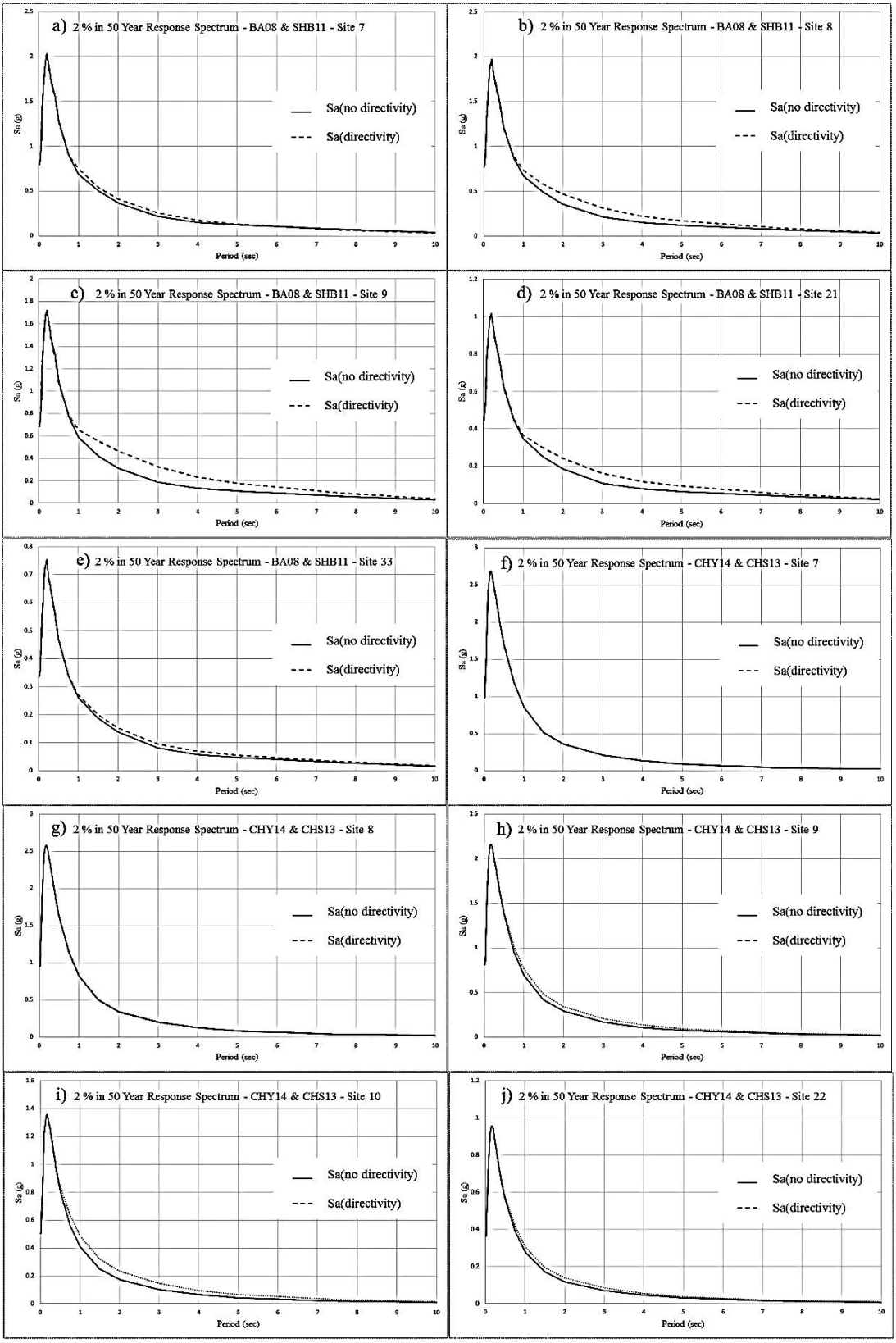


**Figure 6 Effect of site location on the amplification due to directivity for SHB-11 and CH-13 models**

### 5.1 Source to site geometry effect on the amplification factor

In order to better understand how source to site geometry affect on the level of amplification the hazard analysis have been done for different sites scattered spatially around the fault. Response spectrum has been extracted for each site with and without considering directivity effect. The distribution pattern of the sites around the fault has been shown in Figure 3.

In Figure 6a, to 6e we have compared the response spectrum from conventional PSHA with response spectrum calculated from SHB-11 model for different source to site locations around the fault. The site which is located on the Rx/L=0 and Ry=5km (Site 7 shown in Figure 6a) is amplified very slightly and the amplification is almost close to 1. The amplification increases when we move from site 7 (Rx/L=0 and Ry=5km) toward the edge of the fault in X direction. The maximum amplification is reached for the site located on Rx/L=0.5 and Ry=5km (Site 9 in Figure 6c). On the other hand when we move away from the fault in Y-direction (from Site 9 toward Site 33 shown in Figure 6c, 6d and 6e) the amplification has a descending trend. This amplification pattern for different source to site geometries is due to the source to site geometric parameters used to calculate probability of pulse occurrence in SHB-11.

In Figure 6f to 6j the response spectrum calculated with CHS-13 model is compared with conventional response spectrum for different source to site locations. In this model also we don't observe any amplification for site 7 (Figure 6f) like SHB-11 model. Unlike SHB-11 model the ascending trend of amplification in X direction for CHS-13 model starts from site 8 (Rx/L=0.25 and Ry=5km) and reaches its maximum in Site 10 (Rx/L=0.6 and Ry=5km). This is due to the effect of centered value of DPP (Direct Point Parameter) in this model. As stated before E-path parameter is used to calculate the DPP for each site. This parameter (E-path which is distance between hypocenter and direct point) reaches its maximum values for the sites located along the Rx/L=0.6 line. Therefore the ΔDPP and subsequently the amplification will be maximum for these sites.

In Y direction the amplification of CHS-13 model also has descending trend like SHB-11 model. This can be seen if we compare the amplification level of site 10 (shown in Figure 6i with Rx=0.6 and Ry=5km) with site 22 (shown in Figure 6j with Rx/L=0.5 and Ry=15km). In site 22 the response spectrum extracted with CHS-13 model is slightly larger than conventional response spectrum meaning that amplification level is slightly larger than 1.

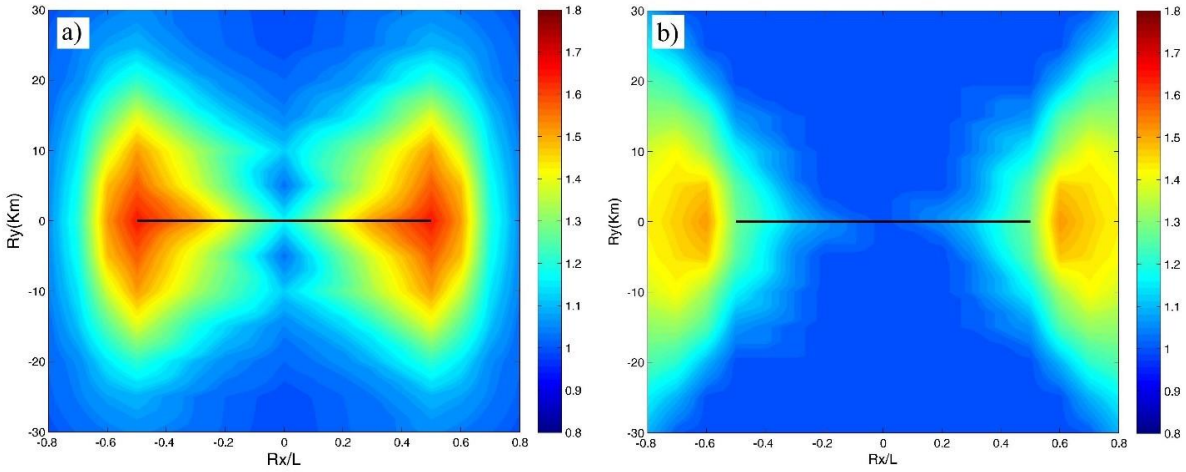


**Figure 7 Amplification factor contour map for 100km length fault, Slip rate=2cm/year and 475 year return period spectrum, T=4sec. a) Shahi and Baker 2011, b) Chiou Spudich 2013**

In order to better see the amplification distribution pattern around the fault, the contour maps of amplification have been plotted for a fault with 100km length, slip rate 2cm/year and 475 year return period at spectral period T=4sec. The Figure 7a shows the amplification contour map for SHB-11 model and Figure 7b is the counter map of amplification for CHS-13 model. The location of the sites which experience maximum amplification, the variation of the amplification pattern along X and Y directions and the differences between these two models which were discussed in previous paragraphs can be seen in this figure very clearly.

### 5.2 Effect of Hazard Level and Slip Rate on the Amplification Factor

As stated before three slip rate values (SR=0.5, 1, 2 cm/year) have been considered in the probabilistic hazard analysis for low medium and high seismicity levels. The amplification factor has been calculated for all the sites around the fault (42 sites) and two hazard levels (2% and 10% probability of exceedance in 50 year). These amplification factors have been plotted for all 42 sites together with their median values for SHB-11 model in Figure 8. As can be seen from this figure all the amplification curves reach their maximum value at spectral period T=4 sec for the fault with 100km length. The general shape of the amplification curves are similar to each other in all figures with just one exception in Figure 8a.

In this figure (Figure 8a) we see a bump for the amplification curves in small period ranges. This is due to the fact that SHB-11 model does not apply deamplification for the magnitudes less than 6, Rjb larger than 10km and spectral periods smaller than 1sec for non-pulse type cases. On the other hand large magnitude earthquakes do not contribute effectively in hazard analysis for this case. Therefore the larger period ranges are not amplified as much as small magnitude ranges for 475 year return period case.

The results of the analysis from SHB-11 model (Figure 8) show that both slip rate and return period are determining parameters on the level of amplification factor. For both 2% and 10% in 50 year exceedance hazard levels the amplification factor increases with slip rate increment. This increment can be seen in both median and maximum amplification factor curves. The important point here is that the rate of increment for the sites which are more exposed to directivity effect (the sites that experience larger amplification values) is more than the other sites when slip rate increases from 0.5 to 2 cm/year. This can be seen more clearly if we compare the maximum values of amplification for 10% in 50 year exceedance cases. Table 1 shows the maximum and median amplification values at T=4sec for two hazard levels. The maximum amplification of the fault with SR=0.5 cm/year at spectral period T=4sec is 1.19 (Figure 8a) while this maximum value for the case of SR=1.0 cm/year reaches 1.38 (Figure 8c) and for the SR=2.0cm/year it reaches to 1.65 (Figure 8e). This is equivalent to 16% and 38% increase for the maximum amplification of SR=1.0 and 2.0 cm/year from maximum amplification of SR=0.5 cm/year. For the median values at the same spectral period the amplification increases from 1.04 for SR=0.5 cm/year to 1.10 and 1.16 for SR= 1.0 and 2.0 cm/year respectively which is equivalent to 5.7% and 11.5% increment. As can be seen the rate of amplification increment for the maximum and the median values are not the same.

The difference between the maximum and median amplification indicates the importance of source to site geometry because the median amplification is the mean of lnAMP of all 42 sites amplification factor. On the other hand the rate of amplification increment is different for maximum and median amplification. This means that slip rate and source to site geometry are correlated to each other and the amplification level cannot be estimated for each of these parameters independently.

We can also see the same trend for the case of 2475 year return period (2% in 50 year exceedance) amplification factor. First, the maximum and median amplification factors are not the same for a given slip rate value. Second, the amplification increases with the slip rate in-

crement for both median and maximum amplification curves but the rate of this increment for maximum and median values are not the same.

The last thing that can be seen in this model is that the amplification of 2475 year return period (2% in 50 year exceedance) has larger values comparing to the amplifications of 475 year return period (10% in 50 year exceedance). The maximum amplification shows a 43% increment for the case of SR=0.5cm/year and 13.3% for the fault with SR=2.0cm/year when return period changes from 475 to 2475 year.

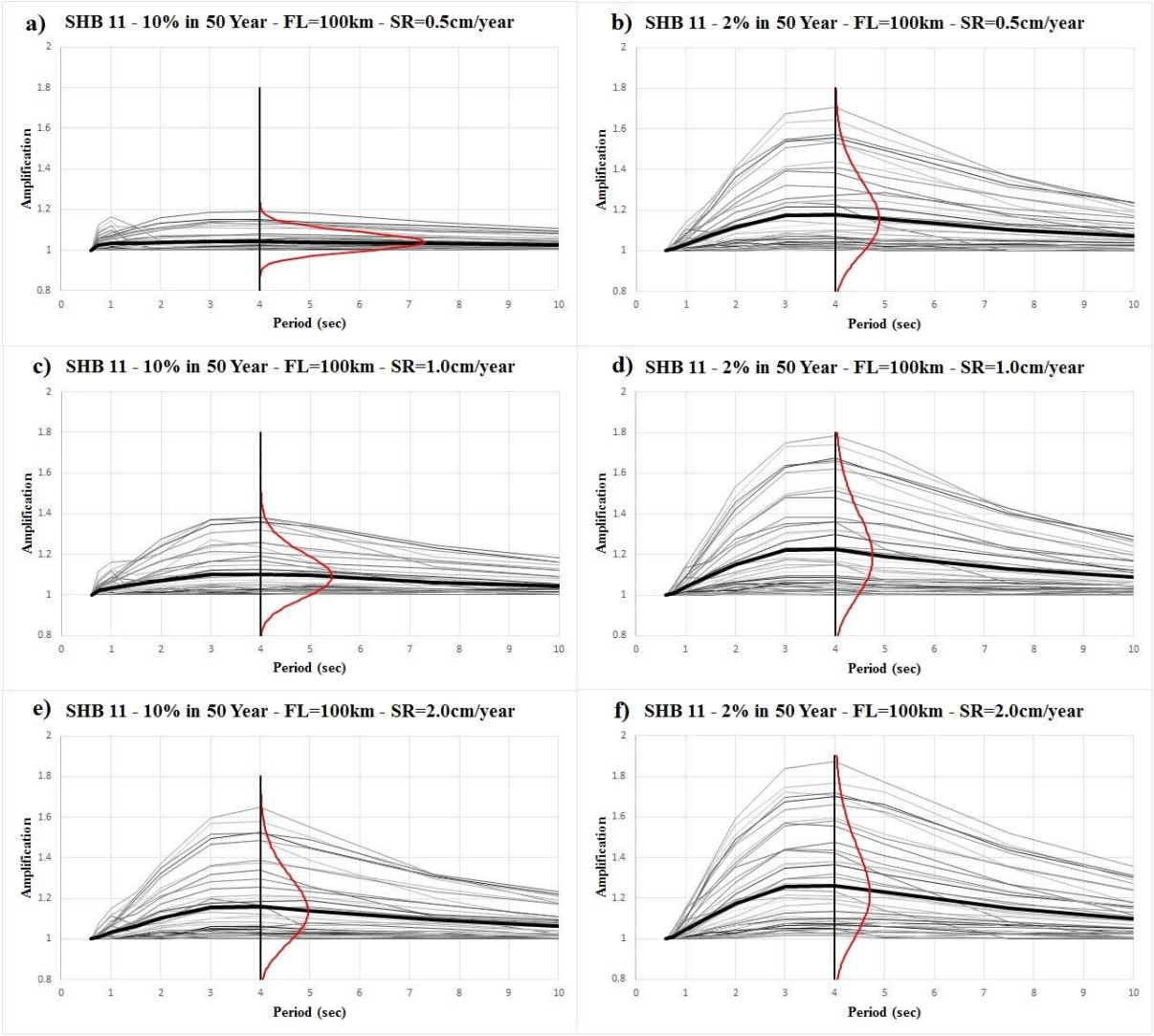


**Figure 8 Effect of slip rate and return period on the amplification in SHB-11 model**

| | 10% in 50 year exceedance (475 year RP) | | 2% in 50 year exceedance (2475 year RP) | |
|---|---|---|---|---|
| | $AMP_{max}$(T=4sec) | $AMP_{median}$(T=4sec) | $AMP_{max}$(T=4sec) | $AMP_{median}$(T=4sec) |
| SR=0.5 | 1.19 | 1.04 | 1.71 | 1.18 |
| SR=1.0 | 1.38 | 1.10 | 1.79 | 1.22 |
| SR=2.0 | 1.65 | 1.16 | 1.87 | 1.26 |

**Table 1 Maximum and median amplification at T=4sec for the faults with SR=0.5, 1 and 2cm/year-SHB-11 model**

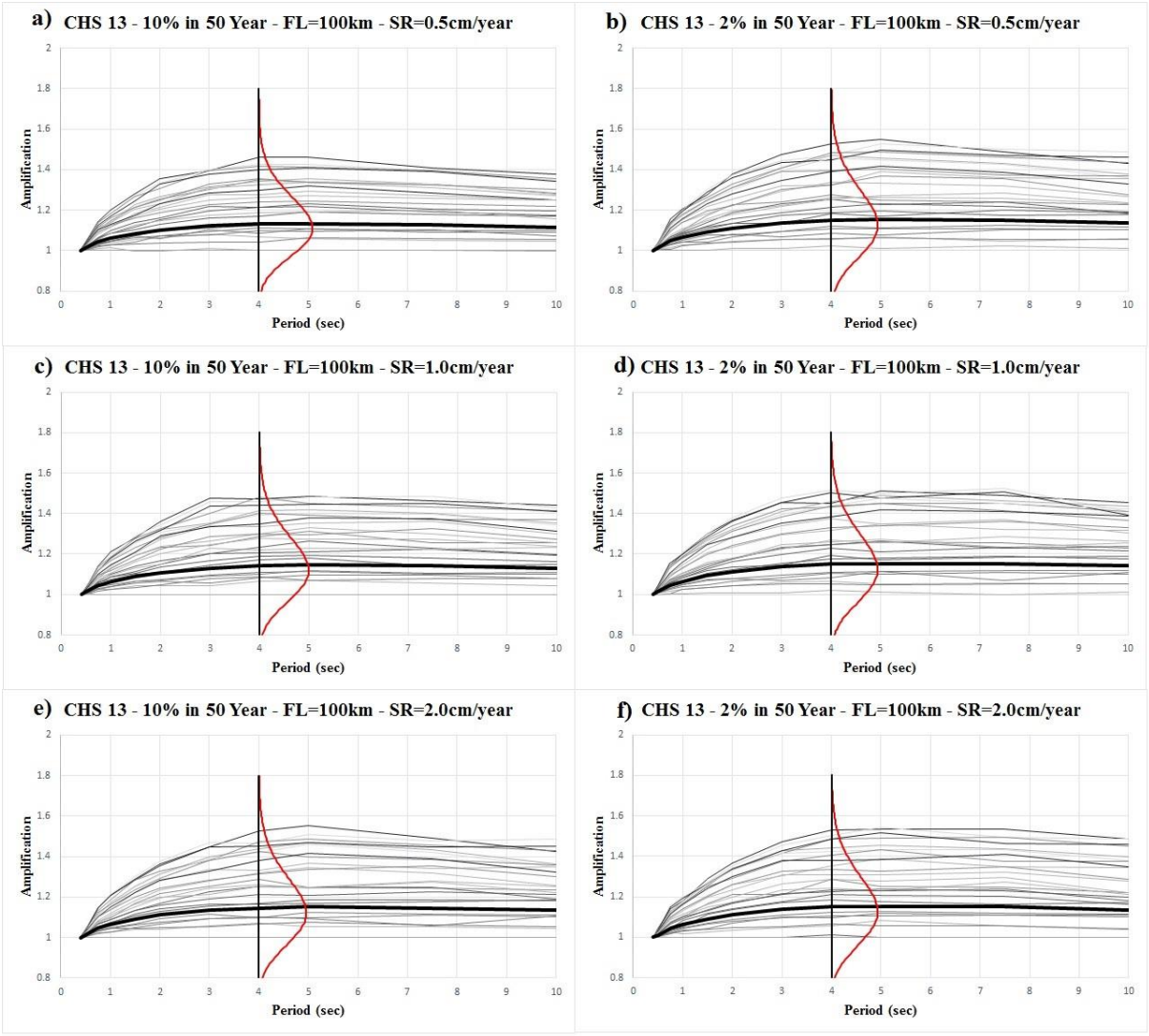


**Figure 9 Effect of slip rate and return period on the amplification in CHS-13 model**

| | 10% in 50 year exceedance (475 year RP) | | 2% in 50 year exceedance (2475 year RP) | |
|---|---|---|---|---|
| | $AMP_{max}$(T=4sec) | $AMP_{median}$(T=4sec) | $AMP_{max}$(T=4sec) | $AMP_{median}$(T=4sec) |
| SR=0.5 | 1.45 | 1.13 | 1.52 | 1.15 |
| SR=1.0 | 1.47 | 1.14 | 1.5 | 1.15 |
| SR=2.0 | 1.52 | 1.15 | 1.53 | 1.15 |

**Table 2 Maximum and median amplification level at T=4 sec for the faults with SR=0.5, 1 and 2cm/year-CHS-13 model**

Figure 9 shows the amplification curves of CHS-13 model for a fault with 100km length, slip rate=0.5, 1.0 and 2cm/year and 2 hazard levels (10% and 2% exceedance rate). The maximum and median of amplification factor for 42 sites are shown in Table 2 for 3 slip rate values and 2 hazard levels at spectral period T=4sec.

The results of the analysis for this model also shows several observations. First, the amplification level is not affected by slip rate values. As can be seen from Figure 9 and the results given in Table 2, the maximum amplification do not change considerably when slip rate increases from 0.5cm/year to 2.0cm/year for both 475 and 2475 year return period cases. Fur-

thermore the median amplification value is almost the same for all slip rate values and hazard levels.

The other important point is the difference between maximum and median amplification for a given slip rate and hazard level. As stated before since all source to site geometries contribute on the amount of median amplification it shows that that source to site geometry is still determining parameter on the level of amplification.

The last point here is the effect of return period on the level of amplification. As can be seen from Table 2 the maximum and median amplification factor do not change considerably for these two hazard levels. The amplification of 2475 year is slightly larger than amplification of 475 year but this difference is less than 4% in the worst case. Therefore it can be concluded that CHS-13 model is not affected by slip rate and hazard level considerably but source to site geometry still has important effect on the level of amplification.

### 5.3 Effect of Fault Characteristic Magnitude on the Amplification Factor

The last parameter that has been investigated in this study is the effect of fault characteristic magnitude on the level of amplification. Figure 10 shows the amplification factor for two faults with different characteristic magnitudes for both SHB-11 and CHS-13 models. Several features can be seen in this figure. Both SHB-11 and CHS-13 models have a bilinear trend for the amplification factor. The difference between these two models is that SHB-11 model tends to amplify the response spectrum in a narrow range of period while CHS-13 model amplifies the spectrum in a wider range of periods. This is due to the fact that SHB-11 model tries to amplify the $Sa$ at periods close to the period of the directivity pulse ($T$p). The amplification factor in SHB-11 reaches the maximum value at a spectral period ($T_{max}$) followed by a descending trend for larger periods. The amplification factor in CHS-13 has an ascending trend up to spectral period called as $T_{corner}$. For the periods greater than $T_{corner}$ the amplification has plateau form and is almost constant.

In SHB-11 model the amplification amplitude starts from 1.0 at spectral period T=0.6sec and reaches the maximum amplitude at $T_{max}$=3.0sec for the fault with 50km length and characteristic magnitude equal to 6.7. For the fault with 150km length and characteristic magnitude 7.2 the amplification amplitude starts from 1.0 at spectral period T=0.6sec and reaches the maximum amplitude at spectral period $T_{max}$=4 sec. In CHS-13 the amplification amplitude starts from 1.0 at spectral period T=0.5sec and reaches the maximum amplitude at $T_{corner}$=3.0sec for the fault with 50km length and $T_{corner}$=4.0sec for the fault with 150km length. As can be seen, the spectral period that maximum amplification occur in both SHB-11 and CHS-13 models depend on characteristic magnitude of the fault, meaning that the larger is the characteristic magnitude, the greater is the spectral period that maximum amplification occur.

Fault magnitude can also affect on the amplitude of amplification. As can be seen from Figure 10 the amplitude of amplification increases with fault magnitude for both SHB-11 and CHS-13 models. Faults with greater magnitude have greater amplification amplitude especially in the period range that the maximum amplification occur.

The results of analysis have also shown that increment of amplification amplitude due to characteristic magnitude increase, show a saturation for the faults with characteristic magnitude greater than 7.5. The results confirms that the maximum amplification for the fault with characteristic magnitude 7.75 is slightly larger than the maximum amplification of the fault with characteristic magnitude 7.5 for both SHB-11 and CHS-13 models. This is due to the effect of distance taper functions used in the directivity models, because the sites located in one

edge of fault which experience the maximum amplifications, are too far from the ruptures that occur on the other edge of the fault.

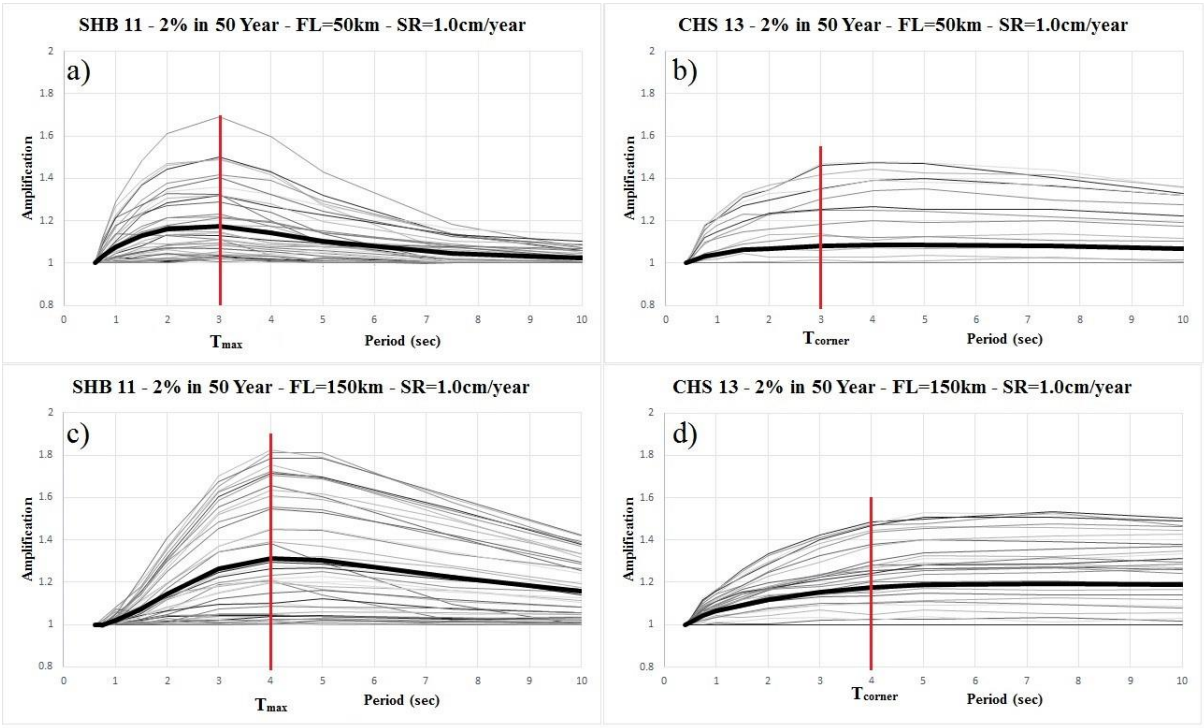


**Figure 10 Effect of characteristic magnitude of the fault on the amplification factor in SHB-11 and CHS-13 models**

## 6 CONCLUSIONS

- The results of Deterministic Hazard Analysis have shown that the general trend of amplification pattern is the same for SHB-11 and SHB-13 directivity models. Both of these models amplify the response spectrum proportional with T/Tp ratio. The probability of pulse occurrence also contribute on the level of amplification in these models in terms of source to site geometric parameters.
- In CHS-13 the amplification is a function of DPP which is directivity indicator parameter in this model.
- According to PSHA results the maximum amplification occur on the sites located near the fault edges in SHB-11 model while the maximum amplification occur on the sites located beyond the fault edges in CHS-13.
- PSHA results shows that the amplification factor in SHB-11 model is a coupled function of slip rate, fault magnitude, source to site geometry and hazard level all together. But it has been shown that amplification factor in CHS-13 model is not affected by slip rate and hazard level and it is a function of fault characteristic magnitude and source to site geometry.

## REFERENCES


[1] Abrahamson, N. A. (2000). Effects of rupture directivity on probabilistic seismic hazard analysis. In *Proceedings of the Sixth International Conference on Seismic Zonation: Managing Earthquake Risk in the 21st Century, Palm Springs, CA, 12-15 November 2000*. Retrieved from http://nisee.berkeley.edu/elibrary/Text/200803124

[2] Alavi, B., & Krawinkler, H. (2001). *Effects of Near Fault Ground Motions on Frame Structures. Blume Earthquake Engineering Center, Report No. 138, Department of Civil and Environmental Engineering, Stanford University, CA*. Retrieved from http://blume.stanford.edu/

[3] Bertero, V., Mahn, S., & Herrera, R. (1978). Aseismic design implications of near-fault San Fernando earthquake records. *Earthquake Engineering & Structural Dynamics*, *6*(July 1976), 31–42. http://doi.org/10.1002/eqe.4290060105

[4] Boore, D. M. (2010). Orientation-Independent, Nongeometric-Mean Measures of Seismic Intensity from Two Horizontal Components of Motion. *Bulletin of the Seismological Society of America*, *100*(4), 1830–1835. http://doi.org/10.1785/0120090400

[5] Boore, D. M., & Atkinson, G. M. (2008). Ground-motion prediction equations for the average horizontal component of PGA, PGV, and 5%-damped PSA at spectral periods between 0.01 s and 10.0 s. *Earthquake Spectra*, *24*(1), 99–138. http://doi.org/10.1193/1.2830434

[6] Boore, D. M., Watson-Lamprey, J., & Abrahamson, N. A. (2006). Orientation-Independent Measures of Ground Motion. *Bulletin of the Seismological Society of America*, *96*(4A), 1502–1511. http://doi.org/10.1785/0120050209

[7] Boore, D. M., & Zoback, M. D. (1974). Two-dimensional kinematic fault modeling of the Pacoima Dam strong-motion recordings of the February 9, 1971, San Fernando earthquake. *Bulletin of the Seismological Society of America*, *64*(3–1), 555–570. Retrieved from http://bssa.geoscienceworld.org/content/64/3-1/555%5Cnfiles/772/Boore_Zoback_1974_Two-dimensional kinematic fault modeling of the Pacoima Dam strong-motion.pdf%5Cnfiles/808/555.html

[8] Chioccarelli, E., & Iervolino, I. (2010). Near-source seismic demand and pulse-like records: A discussion for L'Aquila earthquake. *Earthquake Engineering and Structural Dynamics*, *39*(9), 1039–1062. http://doi.org/10.1002/eqe.987

[9] Chiou, B. S. J., & Youngs, R. R. (2014). Update of the Chiou and Youngs NGA model for the average horizontal component of peak ground motion and response spectra. *Earthquake Spectra*, *30*(3), 1117–1153. http://doi.org/10.1193/072813EQS219M

[10] Housner, G. W., & Trifunac, M. D. (1967). Analysis of accelerograms--Parkfield earthquake. *Bulletin of the Seismological Society of America*, *57*(6), 1193–1220. Retrieved from http://www.bssaonline.org/cgi/content/abstract/57/6/1193

[11] Iervolino, I., & Cornell, C. A. (2008). Probability of occurrence of velocity pulses in near-source ground motions. *Bulletin of the Seismological Society of America*, *98*(5), 2262–2277. http://doi.org/10.1785/0120080033

[12] Kramer, Steven L., (1996). Geotechnical Earthquake Engineering, Publ. Prentice Hall.

[13] McGuire, R. K. (2004). *Seismic Hazard and Risk Analysis*. *Book*. Earthquake Engineering Research Institute.

[14] Niazy, A. (1975). An exact solution for a finite, two-dimensional moving dislocation in an elastic half-space with application to the San Fernando earthquake of 1971. *Bulletin of the Seismological Society of America*, *65*(6), 1797–1826.

[15] Rowshandel, B. (2010). Directivity correction for the next generation attenuation (NGA) relations. *Earthquake Spectra*, *26*(2), 525–559. http://doi.org/10.1193/1.3381043

[16] Shahi, S. K. (2013). *A probabilistic framework to include the effects of near-fault directivity in seismic hazard assessment*. Stanford University, Stanford, CA.

[17] Shahi, S. K., & Baker, J. W. (2011). An empirically calibrated framework for including the effects of near-fault directivity in probabilistic seismic hazard analysis. *Bulletin of the Seismological Society of America*, *101*(2), 742–755. http://doi.org/10.1785/0120100090

[18] Somerville, P. G., Smith, N. F., Graves, R. W., & Abrahamson, N. A. (1997). Empirical strong ground motion attenuation relations to include the amplitude and duration effects of rupture directivity. *Seismological Research Letters*, *68*(1), 199–222. http://doi.org/10.1785/gssrl.68.1.199

[19] Spudich, P., Bayless, J. R., Baker, J., Chiou, B. S. J., Rowshandel, B., Shahi, S., & Somerville, P. (2013). *Final Report of the NGA-West2 Directivity Working Group*. *Pacific Engineering Research Center Report PEER Report 2013/09. NGA west 2 Database*.

[20] Spudich, P., & Chiou, B. S. J. (2008). Directivity in NGA earthquake ground motions: Analysis using isochrone theory. *Earthquake Spectra*, *24*(1), 279–298. http://doi.org/10.1193/1.2928225

[21] Tothong, P., Cornell, C. A., & Baker, J. W. (2007). Explicit directivity-pulse inclusion in probabilistic seismic hazard analysis. *Earthquake Spectra*, *23*(4), 867–891. http://doi.org/10.1193/1.2790487

[22] Wells, D. L., & Coppersmith, K. J. (1994). New Empirical Relationships among Magnitude, Rupture Length, Rupture Width, Rupture Area, and Surface Displacement. *Bulletin of the Seismological Society of America*, *84*(4), 974–1002. http://doi.org/

[23] Youngs, R. R., & Coppersmith, K. J. (1985). Implications of fault slip rates and earthquake recurrence models to probabilisic seismic hazrad estimates. *Bulletin of the Seismological Society of America*, *75*(4), 939–964.

COMPDYN 2017
6th ECCOMAS Thematic Conference on
Computational Methods in Structural Dynamics and Earthquake Engineering
M. Papadrakakis, M. Fragiadakis (eds.)
Rhodes Island, Greece, 15–17 June 2017

# SINGLE STATION SIGMA FOR TURKISH STRONG MOTION STATIONS

**Zehra Çağnan[1], and Sinan Akkar[2]**
[1] Civil Engineering Department, TED University
Ziya Gökalp Caddesi, No:48, Kolej, 06420 Çankaya, Ankara, Turkey.
e-mail: zehra.cagnan@tedu.edu.tr

[2] Earthquake Engineering Department, Kandilli Observatory and Earthquake Research Institute,
Boğaziçi University
34684 Çengelköy, Istanbul, Turkey
sinan.akkar@boun.edu.tr

**Keywords:** Single station sigma, probabilistic seismic hazard assessment, ergodic assumption.

**Abstract.** *As ground motion observations over long enough time periods are unavailable for majority of sites, most of the ground motion prediction equations have been derived using observed data from multiple stations and seismic sources, and standard deviations (sigmas) of these equations are related to the statistics of the spatial variability of ground motion instead of temporal variability at a single site (ergodic assumption). This is one of the major shortcomings of carrying out site specific seismic hazard assessment with currently available ground motion prediction equations. In this study, we explore the variability at single sites within Turkey, decomposing sigma into different components so that the various contributions to the variability can be identified. The period and magnitude dependent standard deviation values obtained for Turkey using the ergodic assumption is changing between 0.56-0.82 ln units [1]. When single stations are considered instead, standard deviation estimates are reduced by 20%. Through the restriction of the analysis to a particular seismic source (i.e. North Anatolian Fault zone), the standard deviation values obtained for Turkey by [1] are further shown to reduce by about 10-20% depending on the spectral period under consideration. Implications of these findings for the seismic hazard of Istanbul district are further discussed within the scope of this study.*

## 1 INTRODUCTION

Ground motion prediction equations (GMPE) are based on datasets of ground motion parameters recorded at multiple stations, the source of which are different earthquakes generated by various tectonic sources. These equations that are utilized to predict ground motion at a specific site, describe its distribution (log-normal distribution) in terms of a median and a logarithmic standard deviation. [2] explained aleatory variability as that "inherent to the unpredictable nature of future events and cannot be reduced by collection of additional information". Whereas they described epistemic variability as that "is due to incomplete knowledge and data about the physics of the earthquake process and can be reduced to zero with sufficient knowledge (at least theoretically)". Although it is usually envisioned that through standard deviation of ground motion prediction equations, only aleatory variability of ground motion is represented that is not the case in reality.

When ground motion prediction equations are utilized as part of seismic hazard assessment studies, an inherent assumption is made: the ground motion variability obtained based on a global (or regional) dataset is the same as the variability of ground motion caused by a single source at a single site. This assumption has been referred to as the ergodic assumption (i.e. [3-5]. Over the last decade, the availability of recorded ground motions at single sites caused by multiple earthquakes originating from the same tectonic sources has allowed researchers to estimate what is referred to as nonergodic standard deviation (also referred to as single station standard deviation or single station sigma) of ground motion [6-13]. These studies illustrated in general that average nonergodic standard deviations are lower than their ergodic equivalents. Quantification of nonergodic standard deviation enables elimination of epistemic site to site, path to path and source to source variability from the ground motion prediction equation standard deviation hence is a step forward towards quantification of true aleatory variability of ground motion at a specific site. For an ideal probabilistic seismic hazard assessment study, standard deviation of ground motion prediction equation should only represent aleatory variability of ground motion and epistemic uncertainty should be captured through following the logic tree approach.

Ground motion standard deviation exerts a strong influence on the results of the probabilistic seismic hazard analysis, even small variations causing considerable differences on hazard results particularly at long return periods [14]. Hence computing nonergodic standard deviation, that offers more realistic quantification of ground motion variability at a specific site has become particularly important in the evaluation of ground motions utilized for the design of critical facilities especially such as nuclear power plants [11, 15-16]. The focus of this study is to compute nonergodic standard deviation based on the Turkish strong motion database and determine the effect of using it instead of ergodic standard deviation on seismic hazard estimates for the Fatih-Kadikoy districts of Istanbul.

## 2 THEORETICAL BACKGROUND

Following the notation of [17] in this study, total residuals ($\Delta_{es}$) are defined as the difference between recorded ground motions and the values predicted by a ground motion prediction equation in log units. Two main terms: between-event ($\delta B_e$) and within-event ($\delta W_{es}$) terms can be thought of contributing to these total residuals:

$$\Delta_{es} = \delta B_e + \delta W_{es} \tag{1}$$

in which the subscripts denote an observed ground motion parameter corresponding to an event e at station s. Between-event term represents the average shift, corresponding to an in-

dividual earthquake - e, of the observed ground motions from corresponding median estimates of ground motion prediction equation. Within-event term on the other hand represents the difference between an individual observation at station s from the earthquake-specific median prediction. The between-event and within-event residuals are independent normally distributed random variables with zero means and standard deviations τ and φ, respectively. The between-event standard deviation, τ, represents the earthquake to earthquake variability reflecting influence of factors such as stress drop and variation of slip in space and time that are not captured by ground motion prediction equations through inclusion of parameters such as magnitude, style of faulting and source depth. The within-event standard deviation, φ, represents the record to record variability reflecting influence of factors such as crustal heterogeneities, deeper geological structures, near-surface layering that are not captured by ground motion prediction equations through inclusion of parameters such as distance, site classification.

The within-event residuals can be further divided into two terms:

$$\delta W_{es} = \delta S2S_s + \delta WS_{es} \tag{2}$$

$\delta S2S_s$, site term, represents the average within-event residual at each station, and $\delta WS_{es}$ is the site- and event-corrected residual. $\delta S2S_s$ and $\delta WS_{es}$ are zero mean normally distributed random variables as well with standard deviations $\varphi_{S2S}$ and $\varphi_{SS}$, respectively. The uncertainty in the site term can be reduced with additional information (i.e. ground motion observations, analytical site specific response models). The site term represents the systematic deviation of the observed amplification at a station site from the median amplification predicted by the site amplification model of the ground motion prediction equation. The site- and event-corrected residual on the other hand represents unexplained path and radiation pattern effects. The site term can be computed as:

$$\delta S2S_s = \frac{1}{NE_s}\sum_{e=1}^{NE_s} \delta W_{es} \tag{3}$$

where $NE_s$ stands for the number of earthquakes, e, recorded by station s and the event-corrected single station standard deviation can be computed as:

$$\varphi_{ss} = \sqrt{\frac{\sum_{s=1}^{NS}\sum_{e=1}^{NE_s}(\delta W_{es} - \delta S2S_s)^2}{(\sum_{s=1}^{NS} NE_s - 1)}} \tag{4}$$

where NS represents the total number of stations or sites considered in the computation of event corrected single station standard deviation. As the site term is unique for a specific site, the event corrected single station standard deviation is unique as well. For a specific site, it is possible to compute an estimate of event corrected single station ($\varphi_{ss,s}$) by letting NS of equation 4 above to be equal to 1. Average of $\varphi_{ss,s}$ estimates for a number of stations approximately equals to $\varphi_{ss}$ for a region containing these stations.

The between-event residuals can also be divided into two terms:

$$\delta B_e = \delta L2L_l + \delta B_{el} \tag{5}$$

$\delta L2L_l$, source term, represents the average between-event residual for each source region, l, and $\delta B_{el}$ is the source-corrected between-event residual. $\delta L2L_l$ and $\delta B_{el}$ are zero mean normally distributed random variables as well with standard deviations $\tau_{L2L}$ and $\tau_{SS}$, respectively. The source term represents the systematic deviation of the ground motion for an earthquake in a single region from the median predicted by the ground motion prediction equation. The source-corrected between-event residual on the other hand represents unexplained source and slip pattern effects. The source term can be determined as:

$$\delta L2L_l = \frac{1}{NE_l}\sum_{e=1}^{NE_l}\delta B_e \tag{6}$$

where $NE_l$ stands for the number of earthquakes, e, associated with the source region l and the source-corrected between-event standard deviation can be computed as:

$$\tau_{ss} = \sqrt{\frac{\sum_{e=1}^{NE_l}(\delta B_e - \delta L2L_l)^2}{(NE_l - 1)}} \tag{7}$$

Finally, the single source single station standard deviation can be computed by combining event corrected single station standard deviations with source corrected between-event standard deviations through:

$$\sigma_{ss} = \sqrt{{\varphi_{ss}}^2 + {\tau_{SS}}^2} \tag{8}$$

In the process of computation of single source single station standard deviation only two components (i.e. source and site effects) of the total ground motion variability that are not representative of the variability of future ground motion observations at a specific site are removed from the ground motion prediction equation standard deviation (total standard deviation). Hence it can be said that single source single station standard deviation is only partially nonergodic. To get a fully nonergodic standard deviation, all of the components (i.e. path effects in addition to site and source effects) of the total ground motion variability that are not representative of the variability of future observations of ground motion at a single site must be removed. Within the scope of this study, we did not make an effort towards removing the path effects from site- and event-corrected residuals, $\delta WS_{es}$, as currently the stations of the Turkish strong motion network do not possess the necessary level of density that would enable such an analysis.

| Components of Variability | Definition |
|---|---|
| Total standard deviation | $\sigma=\text{std}(\Delta_{es})=\sqrt{\tau^2+\varphi^2}$ |
| Single source single station standard deviation | $\sigma_{ss}=\sqrt{\tau_{ss}^2+{\varphi_{ss}}^2}$ |
| Between-event standard deviation | $\tau=\text{std}(\delta B_e)$ |
| Within-event standard deviation | $\varphi=\text{std}(\delta W_{es})$ |
| Site to site variability | $\varphi_{S2S}=\text{std}(\delta S2S_s)$ |
| Event corrected single station standard deviation | $\varphi_{SS}=\text{std}(\delta WS_{es})$ |

| | |
|---|---|
| Source to source variability | $\tau_{L2L}$=std($\delta L2L_l$) |
| Source corrected between-event standard deviation | $\tau_{SS}$=std($\delta B_{el}$) |

Table 1: Components of the Variability of Ground Motion Prediction Equations (std below stands for the standard deviation operator)

## 3 DATABASE

In order to constrain event corrected single station standard deviation and source corrected between-event standard deviation values for Turkey, the Turkish strong motion database developed within the scope of the EMME project was utilized [18]. This database includes 1190 strong motion records from 203 earthquakes. The accelerograms are recorded at 304 strong-motion stations.

All accelerograms belonging to this database are uniformly processed following the procedure outlined in [19]. The maximum spectral period values below which each accelerogram can be utilized were also determined from the empirical formulations given in [19]. However, after carrying out a preliminary study in order to obtain more stable results towards the higher end of the considered period range it was decided to increase these maximum spectral period values by 25% and to utilize the following empirical relations instead: $1.0T_c$ for rock, $1.125T_c$ for stiff soil and $1.213T_c$ for soft soil sites in the case of digital records; $0.813T_c$ for rock, $0.813T_c$ for stiff soil and $0.875T_c$ for soft soil sites in the case of analogue records where $T_c$ represents long period cut off filter periods used when processing the records. The moment magnitude ($M_w$) information available in the database was obtained from double couple fault plane solutions for some events and from magnitude conversion equations for others. The ruptured fault geometry information from the literature or its estimates from empirical relationships of [20] were utilized to compute the Joyner and Boore distances ($R_{JB}$) included in the database. All the record entries of this database have corresponding measured average shear wave velocity for the upper 30m of soil profile, $V_{s30,}$ values [21]. An upper limit for depth in accordance with the study of [22] was selected for this database so that it only includes shallow event data. The magnitude, distance, site class and style of faulting based distributions of the strong motion data used in this study are given in the figures below.

In order to obtain stable event corrected single station sigma values, initially only data recorded by stations with at least 5 records were utilized. This is referred to as the main database and consists of 736 records from 174 earthquakes that are recorded by 84 different stations. The choice of employing this minimum number of records per station limitation depends on a detailed parametric study. In this parametric study, various least number of records per station limitations (i.e. none, 5, 10, 15, 20 records) were adopted and effects of this parameter on $\varphi$ (or $\varphi_{ss}$) vs. spectral period relationships, distributions of $\varphi_{ss,s}$ values at various spectral periods, variability of $\varphi_{ss}$/ $\varphi_{ss,s}$ ratios were studied. Details of this parametric study will not be shared as part of this manuscript due to space limitations; however we will utilize its aforementioned conclusion in the rest of this work. Further to be able to compute a stable single source between-event standard deviation value for the North Anatolian Fault (NAF), records of events that are associated with NAF were selected from the main database. This new database will be referred to as the NAF database in the rest of this manuscript. It consists of 370 records from 26 earthquakes that are recorded by 68 unique stations.

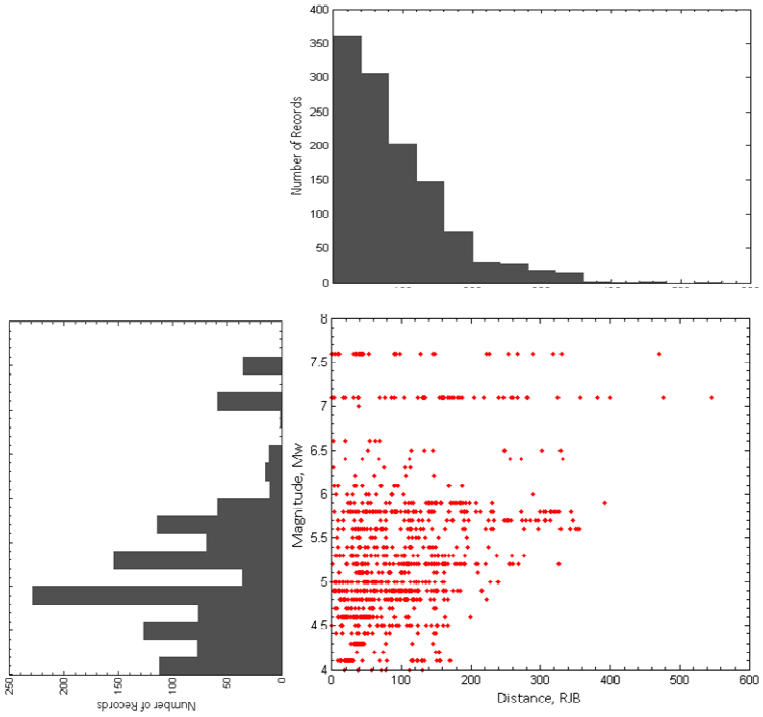


Figure 1: Distribution of records in the Turkish strong motion database with respect to the moment magnitude, $M_w$ and Joyner and Boore distance, $R_{JB}$ parameters. Majority of records in the database have corresponding moment magnitude, $M_w$ values in the range 4.0-6.0 with a median value of 5.0 and corresponding Joyner and Boore distance, $R_{JB}$ values in the range 0-100 km with a median value of 65 km. Distributions of records in the database with respect to site class and style of faulting parameters are not uniform either. Majority of records having corresponding NEHRP C or D site classes and strike-slip or normal styles of faulting.

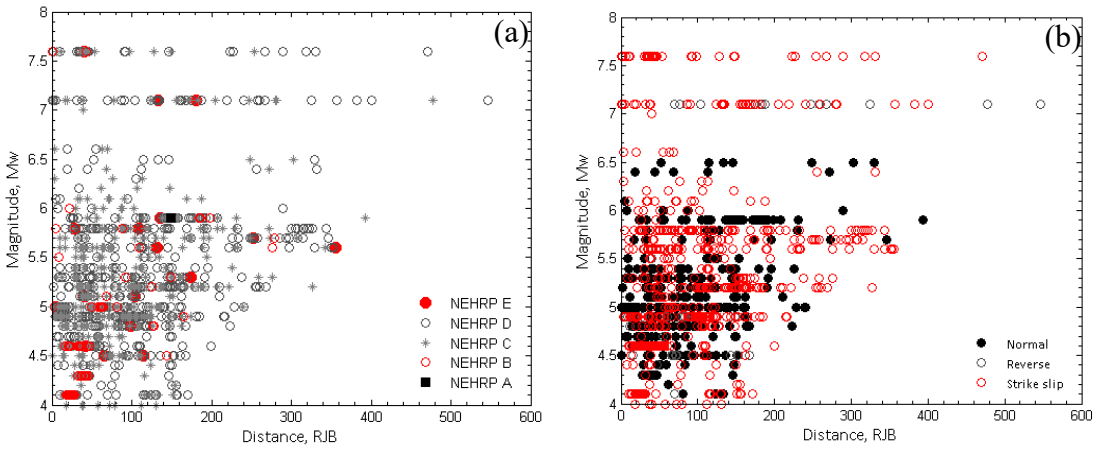


Figure 2: Distribution of records in the Turkish strong motion database with respect to (a) site class and (b) style of faulting parameters. National Earthquake Hazards Reduction Program site classification scheme is adopted in this study [23]: NEHRP Class E – $V_{s30}$ <180 m/s, NEHRP Class D – 180 m/s< $V_{s30}$ <360 m/s, NEHRP Class C – 360 m/s< $V_{s30}$ <760 m/s, NEHRP Class B – 760 m/s< $V_{s30}$ <1500 m/s, NEHRP Class A – 1500 m/s< $V_{s30}$.

## 4 EVENT CORRECTED SINGLE STATION STANDARD DEVIATION ($\phi_{SS}$)

Towards computation of $\varphi_{ss}$ values, firstly horizontal ground-motion estimates of [1] GMPE corresponding to each entry of the Turkish strong motion database was obtained. By subtracting these median estimates from the ground motion observations of the Turkish strong motion database, total residuals were computed. Total residuals were then separated into between-event and within-event residuals through following [24]. And as the final step, by following the definitions of within-event standard deviation ($\varphi$), event corrected single station standard deviation ($\varphi_{ss}$), event corrected single station standard deviation for a specific station/site ($\varphi_{ss,s}$) as given in the theoretical background part of this manuscript, these standard deviation values were computed. Distributions of within-event residuals computed based on the main strong motion database with $R_{JB}$ and $V_{S30}$ are shown in figures 3 and 4 respectively for peak ground acceleration (PGA), peak ground velocity (PGV) and pseudo spectral acceleration (PSA) at spectral periods of 0.1 and 2s. Expectedly no trends are observable with the parameters $R_{JB}$ and $V_{S30}$.

[1] suggests $M_w$ dependent equations for the estimation of within-event standard deviation. However within the scope of our study, a weak magnitude dependency was observed for event corrected single station standard deviations corresponding to spectral period values not exceeding 0.75s and for source corrected between-event standard deviations corresponding to all spectral periods. As a result magnitude independent event corrected single station standard deviations and source corrected between-event standard deviations are suggested (table 2). In order to preserve the [1] suggested within-event standard deviation-spectral period model for the event corrected single station standard deviations, the maximum likelihood approach was adopted. In figure 5, variation of within-event standard deviation and event corrected single station standard deviation values with spectral period is given for $M_w$<6.0 and $M_w$>6.5 events. Figure 5 suggests at least 50% reduction in within-event standard deviation values as a result of excluding the site to site variability.

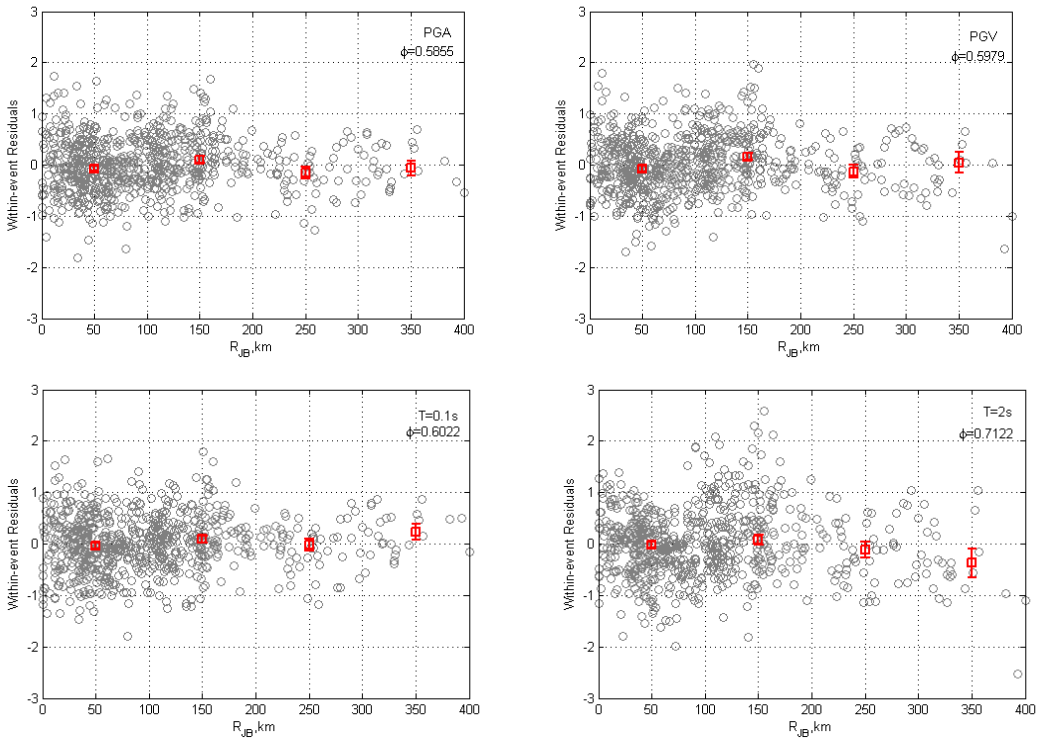

Figure 3: Distribution of within-event residuals with Joyner and Boore distance for PGA, PGV and PSA at spectral periods of 0.1 and 2s. Error bars represent the mean and 95$^{th}$-percentile confidence limits of the mean binned residuals.

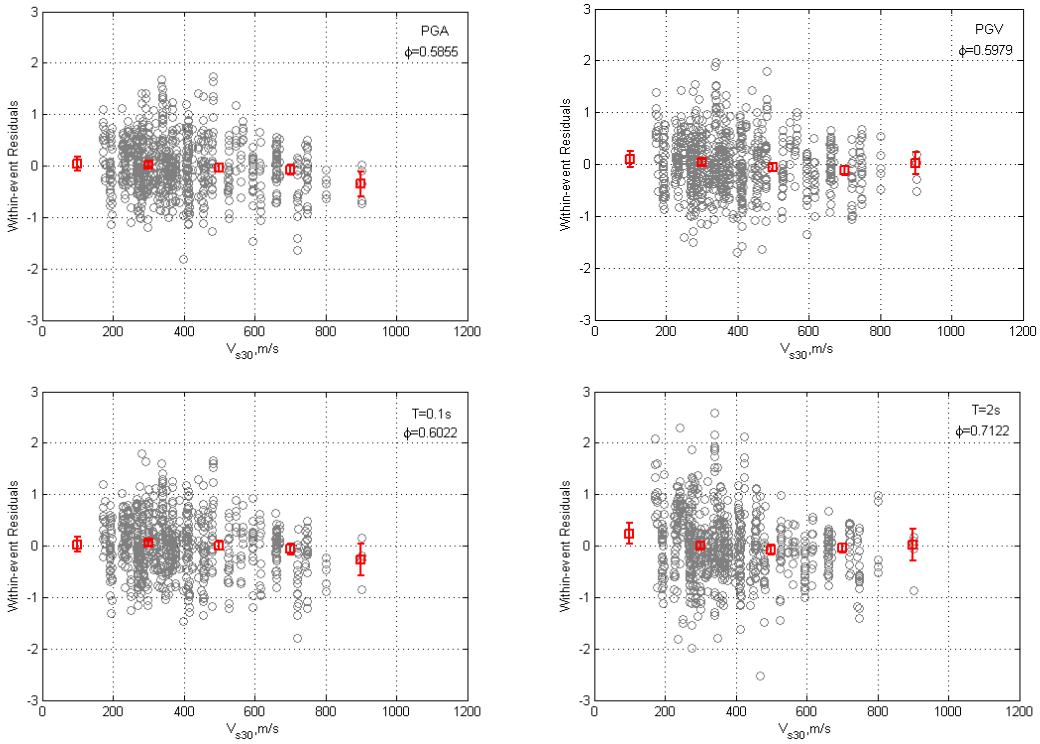


Figure 4: Distribution of within-event residuals with $V_{s30}$ for PGA, PGV and PSA at spectral periods of 0.1 and 2s. Error bars represent the mean and 95$^{th}$-percentile confidence limits of the mean binned residuals.

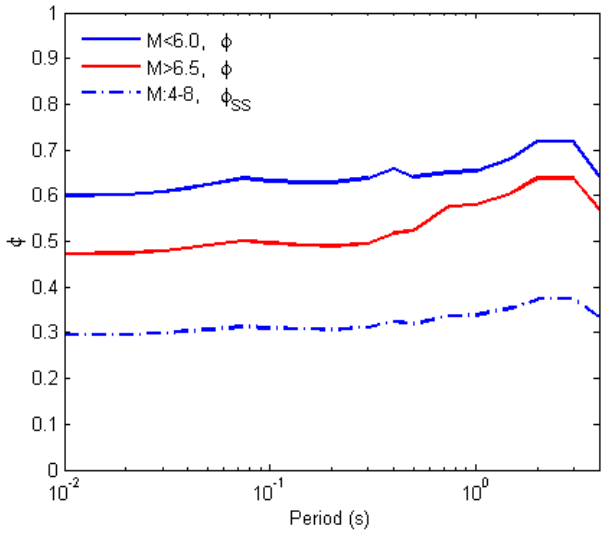


Figure 5: Variation of within-event standard deviation (φ) and event corrected single station standard deviation ($\varphi_{SS}$) with spectral period for $M_w$<6.0 and $M_w$>6.5 events.

Finally, the epistemic uncertainty estimate of this study associated with $\varphi_{ss}$ values is 0.10 that is in close agreement with those suggested by [6-9, 11 and 13]. The same epistemic uncertainty value was adopted for $\tau_{ss}$ in this study.

| Period | $b_1$ | $\varphi_{SS}$ | $\tau_{SS}$ |
|---|---|---|---|
| PGA | 2.02431 | 0.295 | 0.191 |
| 0.01 | 2.03625 | 0.295 | 0.191 |
| 0.02 | 2.06791 | 0.296 | 0.192 |
| 0.03 | 2.16509 | 0.299 | 0.192 |
| 0.04 | 2.31478 | 0.303 | 0.194 |
| 0.05 | 2.4642 | 0.307 | 0.196 |
| 0.075 | 2.98459 | 0.313 | 0.213 |
| 0.1 | 3.09176 | 0.31 | 0.217 |
| 0.15 | 3.26922 | 0.308 | 0.215 |
| 0.2 | 3.19846 | 0.307 | 0.214 |
| 0.3 | 2.62229 | 0.311 | 0.205 |
| 0.4 | 2.11359 | 0.324 | 0.208 |
| 0.5 | 1.60036 | 0.32 | 0.207 |
| 0.75 | 0.76360 | 0.337 | 0.200 |
| 1 | 0.39277 | 0.339 | 0.193 |
| 1.5 | -0.01037 | 0.354 | 0.188 |
| 2 | 0.00454 | 0.373 | 0.174 |
| 3 | -0.07912 | 0.373 | 0.190 |
| 4 | 0.03525 | 0.334 | 0.165 |
| PGV | 5.72860 | 0.293 | 0.171 |

Table 2: Period dependent coefficients for event corrected single station standard deviation, source (NAF) corrected between-event standard deviation and $b_1$ values for the [1] GMPE in the case of $M_w$<6.5 events.

## 5 SOURCE CORRECTED BETWEEN-EVENT STANDARD DEVIATION ($\tau_{SS}$)

By utilizing the NAF database together with equations 6 and 7, the source term corresponding to the North Anatolian Fault and the source corrected between-event standard deviation ($\tau_{SS}$) are estimated in this part of the study. Distributions of between-event residuals with magnitude obtained by utilizing the main database are given for PGA, PGV and PSA at spectral periods of 0.1 and 0.2s in figure 6. Expectedly, no trend is observable in these distributions when positions of the error bars with respect to the zero residual line are considered. In figure 7, distributions of between-event residuals with magnitude obtained by utilizing the NAF database only are given instead for the same spectral periods of above. The shift of mean between-event residuals for $M_w$<6.5 events towards positive values is apparent in the case of PGA, PGV and 0.1s PSA plots. This is an indication that when NAF originated events considered only, there is a none zero source term. The mean between-event residuals for the two $M_w$>6.5 events of the database on the other hand have negative values for all spectral periods considered. These two correspond to the 1999 Kocaeli and Duzce earthquakes that are characterized with lower than expected peak acceleration values as thoroughly discussed in the literature until now. We are therefore suggesting application of the estimated source term only to $M_w$<6.5 events until magnitude saturation effects are better understood for the NAF source by capturing more records of large magnitude events in the future. In order to obtain source corrected between-event residuals, the estimated source term for NAF is subtracted from the between-event residuals of $M_w$<6.5 events as suggested by equation 5. The source corrected between-event residuals and their distribution with magnitude for PGA, PGV and PSA at spectral periods of 0.1 and 0.2s are given in figure 8. By subtracting the source term, error bars approached to the zero residual line once again. It is further possible to reflect the esti-

mated source term to the [1] suggested GMPE and by doing so it would be possible to convert it from a regional GMPE to a local GMPE specifically suitable for the Marmara region. This modification can be achieved by suggesting updated $b_1$ coefficients for the [1] GMPE (listed in table 2); only to be used in the case of $M_w$<6.5 events. For $M_w$>6.5 events, use of original $b_1$ coefficients as proposed by [1] is recommended.

With source corrected between-event residuals, $\tau_{SS}$ values were further computed corresponding to different spectral periods. As magnitude dependency for $\tau_{SS}$ values was not observed in this study, they are suggested in table 2 as constants although between-event standard deviations, $\tau$, of [1] have magnitude dependency. In figure 9, variation of between-event standard deviation and source corrected between-event standard deviation values with spectral period is given for $M_w$<6.0 and $M_w$>6.5 events. In order to preserve the [1] suggested between-event standard deviation-spectral period model for the source corrected between-event standard deviation; the maximum likelihood approach was adopted once again. Figure 9 suggests 10-55% reduction in between-event standard deviation values resulting from excluding the source effect.

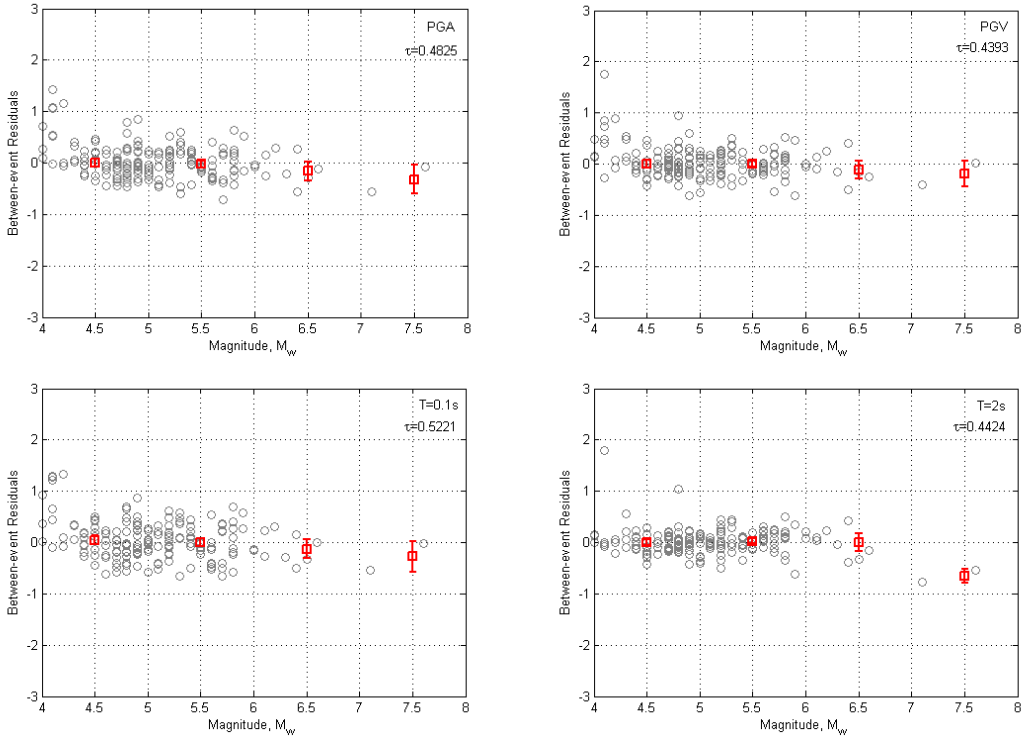


Figure 6: Distribution of between-event residuals obtained based on the main database with moment magnitude, $M_w$ for PGA, PGV and PSA at spectral periods of 0.1 and 2s. Error bars represent the mean and 95$^{th}$-percentile confidence limits of the mean binned residuals.

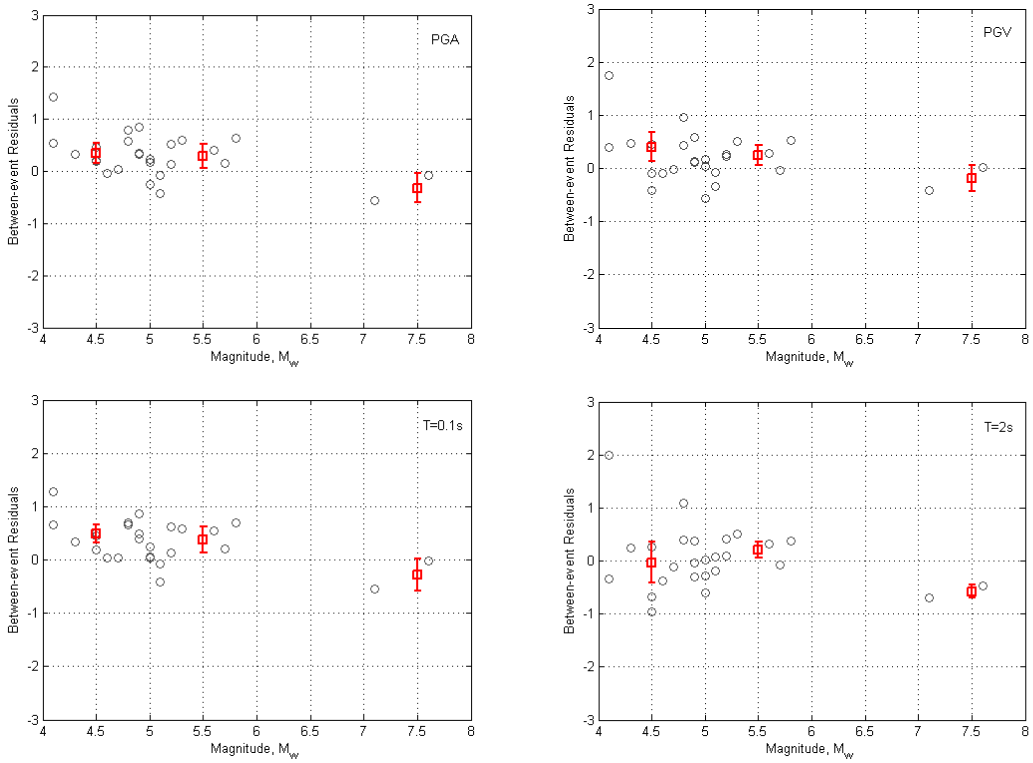


Figure 7: Distribution of between-event residuals obtained based on the NAF database with moment magnitude, $M_w$ for PGA, PGV and PSA at spectral periods of 0.1 and 2s. Error bars represent the mean and 95$^{th}$-percentile confidence limits of the mean binned residuals.

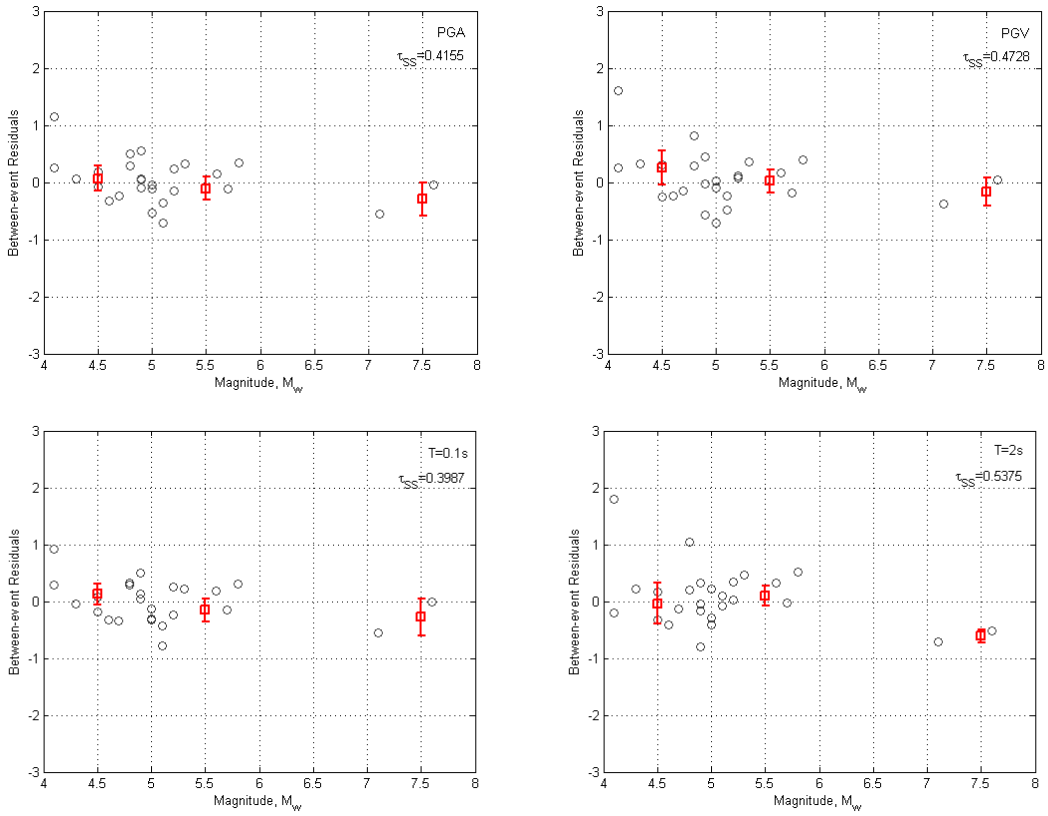

Figure 8: Distribution of source corrected between-event residuals obtained based on the NAF database with moment magnitude, $M_w$ for PGA, PGV and PSA at spectral periods of 0.1 and 2s. Error bars represent the mean and 95$^{th}$-percentile confidence limits of the mean binned residuals.

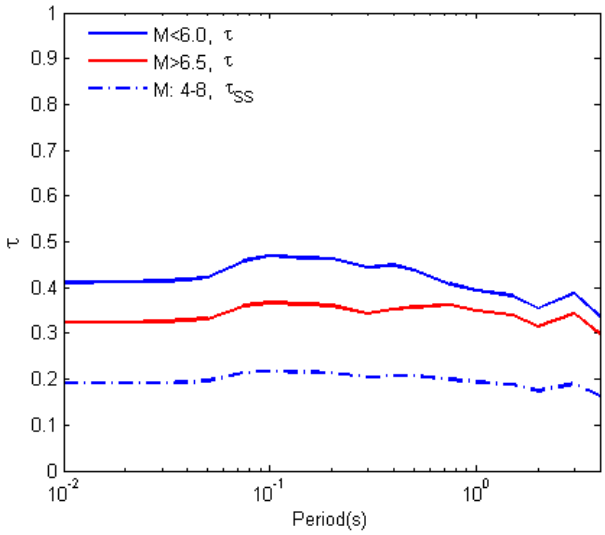


Figure 9. Variation of between-event standard deviation ($\tau$) and source corrected between-event standard deviation ($\tau_{SS}$) with period for Mw<6.0 and Mw>6.5 events.

## 6 EFFECT OF SINGLE SOURCE SINGLE STATION STANDARD DEVIATION ($\sigma_{SS}$) ON SEISMIC HAZARD CURVE

In order to observe the effect on seismic hazard estimates of utilizing $\sigma_{SS}$ rather than $\sigma$, the probabilistic seismic hazard assessment software developed by [25] that is based on the Monte Carlo simulation approach was used. Following the suggestions of [26], the Princes Islands and Marmara segments of the North Anatolian Fault beneath the Marmara Sea were considered as the major source of seismicity for Istanbul (figure 10). Within the scope of this study, seismic hazard for the Fatih and Kadikoy districts of Istanbul was assessed (figure 10). A slip rate of 20mm/yr producing characteristic earthquakes of $M_w$ 6.9-7.3 was assumed for both segments. The probability density function on event magnitude was assumed to follow the maximum magnitude model and the rate of event occurrence was modeled with Poisson process [27]. Within the scope of this study, we used a 100 year catalogue period and ran 10,000 simulations that resulted in a total catalogue interval of 1 million years. [25]'s probabilistic seismic hazard assessment software is capable of taking into account the effects of spatial correlation as well as near fault directivity for ground motion simulations however spatial correlation and near fault directivity were not incorporated into the current study. A cell size of $0.005^o$x$0.005^o$ was used (figures 11 and 15). In the first part of the study, a fixed soil condition with a $V_{S30}$ value of 760m/s (corresponding to NEHRP B-C boundary) for the whole region of interest was used. In the second part, however, actual soil conditions deducted from the previously completed microzonation studies were used: a unique $V_{S30}$ value was assigned for each cell [28].

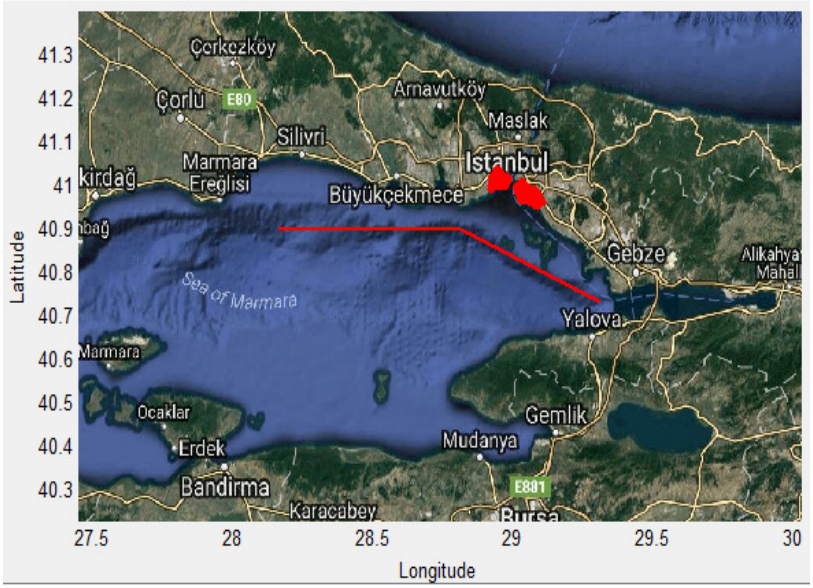


Figure 10: Segments of the North Anatolian Fault (red line) rupture of which considered and Fatih-Kadikoy districts of Istanbul (red shaded regions) for which seismic hazard was assessed within the scope of this study.

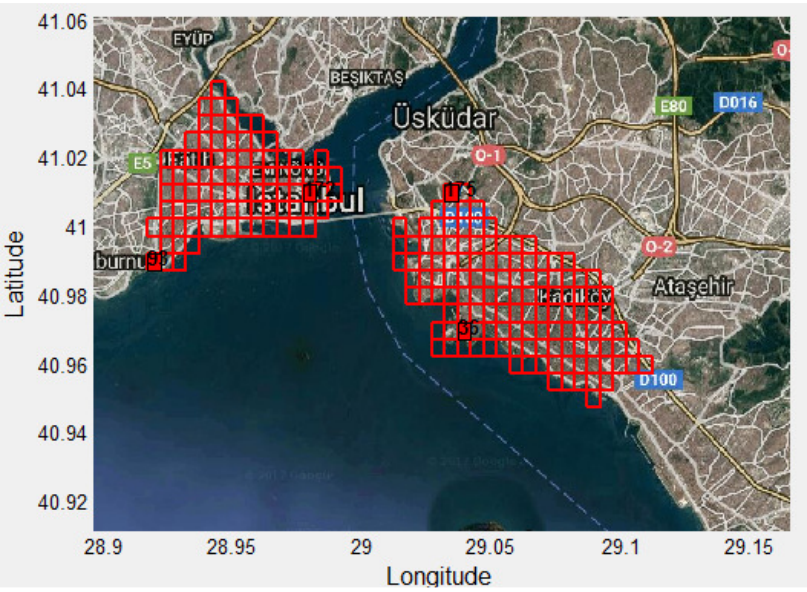


Figure 11: 0.005° by 0.005° grid covering Fatih-Kadikoy districts of Istanbul. Seismic hazard curves were developed specifically for 36, 93, 172 and 175 numbered grids (red shaded grids).

In the first part of the study, the site effect, δS2S, in addition to the epistemic uncertainty associated with it, $\delta\varphi_{S2S,}$ were ignored. Single source single station standard deviation, $\sigma_{SS}$, was computed based on single station standard deviation, $\phi_{SS}$, epistemic uncertainty associated with it, $\delta\phi_{SS}$, and single source between-event standard deviation, $\tau_{SS}$ together with its epistemic uncertainty $\delta\tau_{SS}$. The epistemic uncertainties of $\phi_{SS}$ and $\tau_{SS}$ were assumed to be normally distributed and were modeled using three-point distributions (discrete distribution with values of mean-1.6 standard deviation, mean and mean+1.6 standard deviation and weights of 0.2, 0.6, and 0.2, respectively) that maintain the mean and standard deviation values of the original distribution (continuous distribution). This sigma model is illustrated in figure 12 below schematically. The epistemic uncertainty associated with the source term was taken into account through the median logic tree model.

The seismic hazard curves developed by utilizing total standard deviation, σ, as well as single source single station standard deviation, $\sigma_{SS}$, for 4 separate sites are given in figure 13. These sites were selected such that they represent high, moderate and low seismic hazard levels for the region of interest (figure 11 and figure 14a). At an annual exceedance rate level of $10^{-4}$, up to 20% overestimations in seismic hazard estimates by utilizing total standard deviation, σ, instead of single source single station standard deviation, $\sigma_{SS}$, were detected when PGA is the intensity measure utilized.

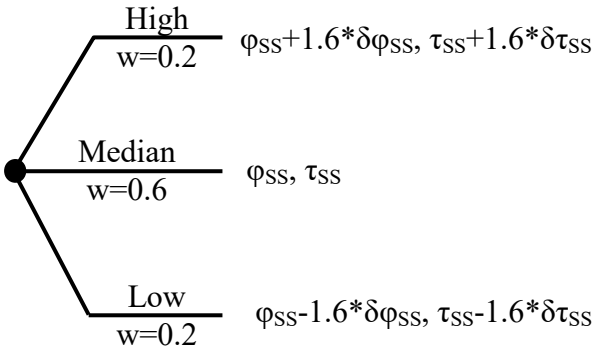


Figure 12: Schematic representation of the sigma model of this study.

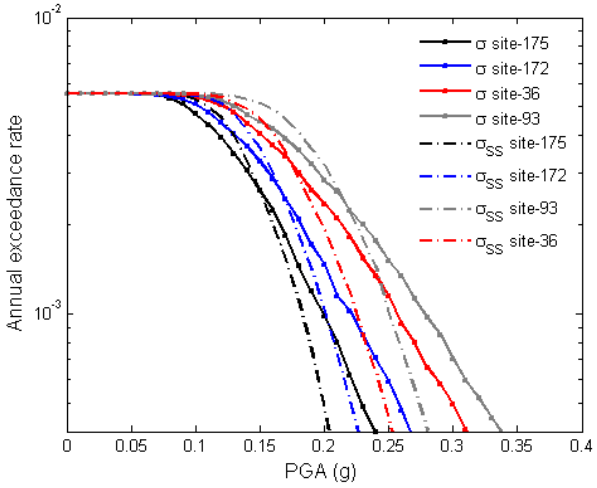


Figure 13: Effect of using σ vs $\sigma_{SS}$ on seismic hazard curves for grids 36, 93, 172 and 175 (exact locations indicated in figure 11).

In the second part of the study in order to reflect the effect of site term on the results as well, site of a strong motion station was selected and seismic hazard estimates corresponding to actual site conditions were obtained. The selected strong motion station site is shown in figure 15. Data recorded (10 records) by this station is part of the main and NAF strong motion databases of this study. According to these databases, the measured $V_{S30}$ value corresponding to this station site is 338.6 m/s, which corresponds to NEHRP D type soil condition. Based on these 10 records belonging to the station site, corresponding site term, δS2S, was estimated to be 0.5094 and epistemic uncertainty associated with the site term, $\delta\phi_{S2S,}$ to be 0.12 when PGA is used as the intensity measure.

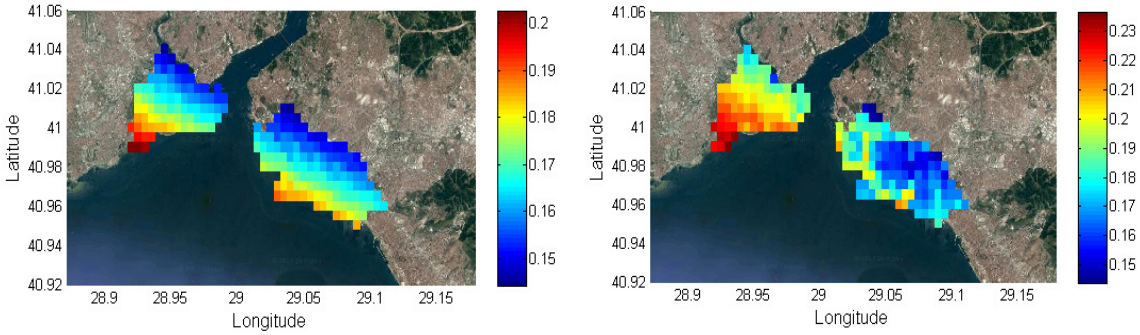


Figure 14. Median PGA (g) distributions for the Fatih-Kadikoy districts of Istanbul when (a) $V_{s30}$:760m/s site condition for all grids, (b) actual site condition for all grids and total standard deviation, σ, parameters were utilized in seismic hazard computations.

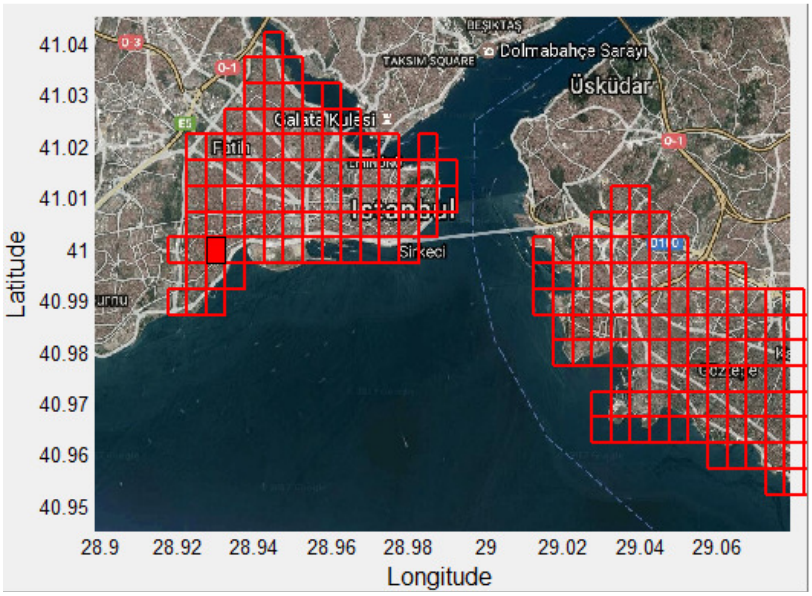


Figure 15: 0.005° by 0.005° grid covering Fatih-Kadikoy districts of Istanbul. Seismic hazard curve with site effect reflected fully was developed specifically for the 126 numbered grid which corresponds to a strong motion site (red shaded grids).

In figure 17, the seismic hazard curve obtained for the station site by utilizing the total standard deviation, σ, as well as the site amplification model of [1] is given. Figure 17 also includes the seismic hazard curve obtained for the station site when single source single station standard deviation, $\sigma_{SS}$, (figure 12) was utilized together with the site amplification model of [1] and estimated site term, δS2S, as given above. The epistemic uncertainties associated with the site and source terms were taken into account through the median logic tree model (figure 16). Figure 17 indicates that for the specific site considered, at an annual exceedance rate of $10^{-4}$ up to 20% underestimation in seismic hazard estimates can be obtained by utilizing total standard deviation, σ, instead of single source single station standard deviation, $\sigma_{SS}$, when PGA is the intensity measure used.

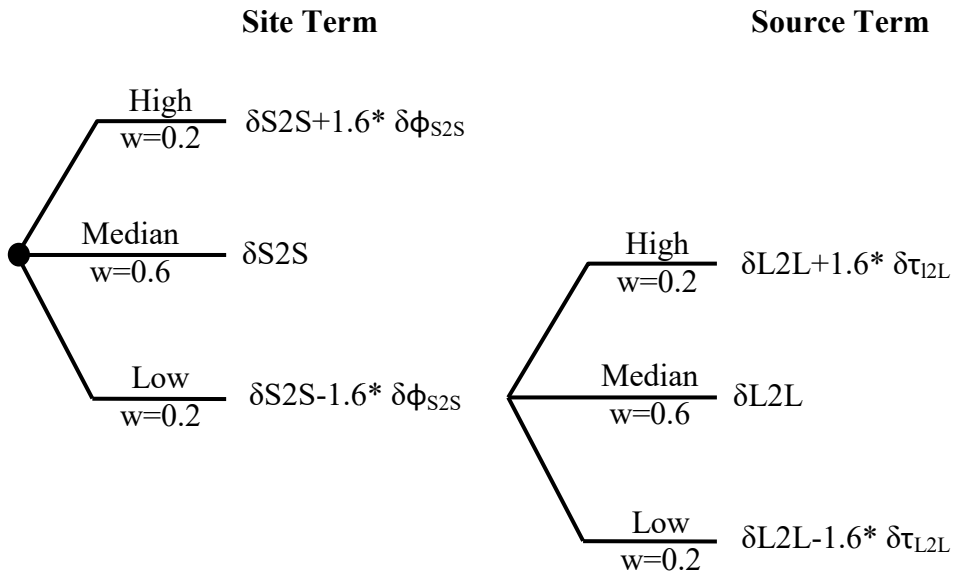


Figure 16: Schematic representation of the median logic tree model of this study.

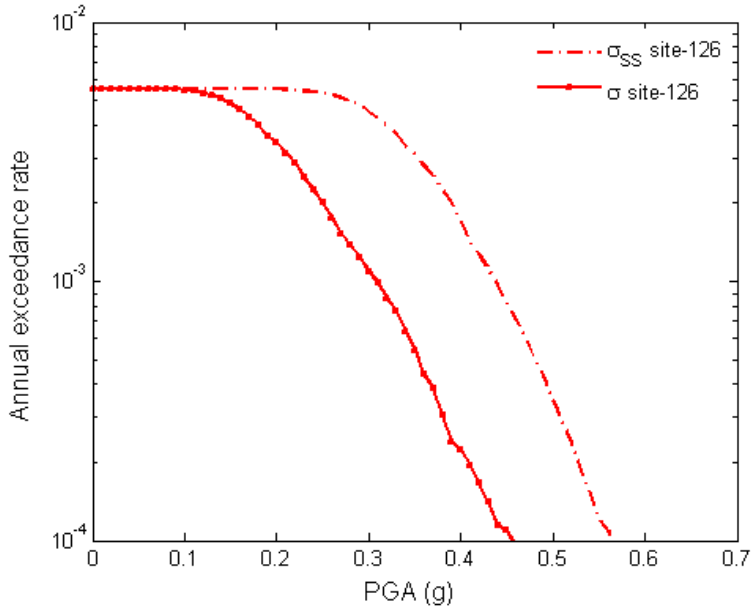


Figure 17: Effect of using σ vs $\sigma_{SS}$ on the seismic hazard curve of investigated strong motion site (exact location indicated in figure 15).

## 7 CONCLUSIONS

Main conclusions of this study are the following:

- The spectral period and magnitude dependent standard deviation obtained for Turkey using the ergodic assumption is changing between 0.56-0.82 ln units [1]. This range reduces to about 0.42-0.56 ln units when single station standard deviation is considered (minimum of 20% reduction).
- When results of this study are compared with results of other single station sigma studies (i.e. [6, 8 and 9]), we observe that standard deviation values with and without

the ergodic assumption computed based on the Turkish strong motion database are larger than the corresponding standard deviation values computed based on other databases. This suggests that by improving event and station metadata of the Turkish strong motion database as well as the number of records per station parameter, standard deviation values can further be reduced in the future.

- Restricting the analysis to the North Anatolian Fault seismic source only, enabled reducing (single source) single station standard deviation values to a range of 0.34-0.42 ln units. This result is significant as it suggests that standard deviation values at a particular site due to a specific source may be reduced by about 40-50% depending on the spectral period under consideration in comparison to the total standard deviation values of 0.56-0.82 ln units for Turkey.
- As utilizing single source single station standard deviation values instead of total standard deviation values as part of the seismic hazard assessment exercises carried out also lead to encouraging results, new efforts in strong motion data collection are strongly suggested for Turkey in addition to revision of currently available event and station metadata.

## REFERENCES

[1] Kale Ö, Akkar S, Ansari A, Hamzehloo H. A ground-motion predictive model for Iran and Turkey for horizontal PGA, PGV and 5%-damped response spectrum: Investigation of possible regional effects. *Bull. Seismol. Soc. Am.* 103, no. 2A, 963-980, 2015.

[2] Toro G, Abrahamson N, Schneider J. Letter to the editor, *Seismological Research Letters* 68, 3, 481-482,1997.

[3] Anderson J G and Brune J N. Probabilistic seismic hazard assessment without the ergodic assumption, *Seismological Research Letters* 70, 19–28, 1999.

[4] Douglas J. Earthquake ground motion estimation using strong motion records: A review of equations for the estimation of peak ground acceleration and response spectral ordinates. *Earth Sci. Rev.* 61, 43–104, 2003.

[5] Strasser F O, Abrahamson N A and Bommer J J. Sigma: Issues, insights and challenges. *Seismological Research Letters* 80, 40–54, 2009.

[6] Atkinson G M. Single-station sigma. *Bulletin of Seismological Society of America* 96, 446–455, 2006.

[7] Morikawa N, T Kanno, A Narita, H Fujiwara, T Okumura, Y Fukushima and A Gurpinar. Strong motion uncertainty determined from observed records by dense network in Japan. *Journal of Seismology* 12, 529–546, 2008.

[8] Lin P, N Abrahamson, M Walling, C-T Lee, B Chiou and C Cheng. Repeatable path effects on the standard deviation for empirical ground-motion models. *Bulletin of Seismological Society of America* 101, 2281–2295, 2011.

[9] Rodriguez-Marek A, G A Montalva, F Cotton and F Bonilla. Analysis of single-station standard deviation using the KiK-net data. *Bulletin of Seismological Society of America* 101, 1242–1258, 2011.

[10] Rodriguez-Marek A, F Cotton, NA Abrahamson, S Akkar, L Al Atik, B Edwards, G A Montalva and H M Dawood. A model for single station standard deviation using data from various tectonic regions. *Bulletin of Seismological Society of America* 103, 6, 3149–3163, 2013.

[11] Rodriguez-Marek A, E M Rathje, J J Bommer, F Scherbaum and P J Stafford. Application of single station sigma and site response characterization in a probabilistic seismic hazard analysis for a new nuclear site. *Bulletin of Seismological Society of America* 104, 4, 1601–1619, 2014.

[12] Edwards B and D Fäh. A stochastic ground-motion model for Switzerland. *Bulletin of Seismological Society of America*, 103, 1, 2013.

[13] Luzi L, D Bindi, R Puglia, F Pacor and A Oth. Single station sigma for Italian strong motion stations. *Bulletin of Seismological Society of America* 104, 1, 467-483, 2014.

[14] Bommer J J and N A Abrahamson. Why do modern probabilistic seismic-hazard analyses often lead to increased hazard estimates? *Bulletin of Seismological Society of America* 96, 1967–1977, 2006.

[15] Abrahamson N A and Hollenback J C. Application of single station sigma ground motion prediction equations in practice. Proceedings of the 15th world Conference on Earthquake Engineering, Lisboa, Portugal, 2012.

[16] Bommer J, Coppersmith JK, Coppersmith RT, Hanson KL, Mangongolo A, Neveling J, Rathje EM, Rodriguez-Marek A, Scherbaum F, Shelembe R, Stafford P, Strasser FO. A SSHAC Level 3 probabilistic seismic hazard analysis for a new building nuclear site in South Africa. *Earthquake Spectra* 31, no. 2, 661-698, 2015.

[17] Al Atik L, N Abrahamson, F Cotton, F Scherbaum J Bommer and N Kuehn. The variability of ground-motion prediction models and its components, *Seismological Research Letters* 81, 794–801, 2010.

[18] Akkar S, Kale Ö, Ansari A, Durgaryan R, Askan Gündoğan A, Hamzehloo H, Harmandar E, Tsereteli N, Waseem M, Yazjeen T, Yılmaz MT. EMME Strong-Motion Database Serving for Predictive Model Selection to EMME Ground-Motion Logic-Tree Applications, Second European Conference on Earthquake Engineering and Seismology, İstanbul, Turkey, Paper No. 3220, 2014.

[19] Akkar S and Bommer JJ. Influence of long-period filter cut-off on elastic spectral displacements. *Earthq. Eng. Struct. Dynam.* 35, no. 9, 1145-1165, 2006.

[20] Wells DL and Coppersmith KJ. New empirical relationships among magnitude, rupture length, rupture width, rupture area, and surface displacement. *Bull. Seismol. Soc. Am*. 84, 974-1002, 1994.

[21] Sandıkkaya MA, Yılmaz MT, Bakır BS, Yılmaz Ö. Site classification of Turkish national strong-motion stations. *Journal of Seismology* 14, 543-563, 2010.

[22] Türkelli N, E Sandvol, E Zor, R Gok, T Bekler, A Al-Lazki, H Karabulut, S Kuleli, T Eken, C Gurbuz et al.. Seismogenic zones in eastern Turkey. *Geophysical Research Letters* 30, 1–4, 2013.

[23] Building Seismic Safety Council (BSSC). 2009 NEHRP Recommended Seismic Provisions For New Buildings and Other Structures: Part 1, Provisions, Federal Emergency Management Agency (P-750), Washington, D.C, 2009.

[24] Abrahamson, N.A., and Youngs, R.R. A stable algorithm for regression analyses using the randım effects model, *Bulletin of the Seismological Society of America*, 82, 505-510, 1992.

[25] Akkar,S. and Cheng, Y. Application of a Monte-Carlo simulation approach for the probabilistic assessment of seismic hazard for geographically distributed portfolio, *Earthquake Engineering and Structural Dynamics*, 45,525-541, 2016.

[26] Bohnhoff, M., Bulur, F., Dresen, G., Malin, P., Eken, T. and M. Aktar. An earthquake gap south of Istanbul, *Nature Communications*, 1-6, 2003.

[27] Steward, J., Chiou, S.J., Bray, J.D., Graves, R.W., Somerville, P.G. and N.A. Abrahamson. Ground motion evaluation procedures for performance-based design. *Pacific Earthquake Engineering Research Center Report PEER 2001/09*, 226p, 2001.

[28] OYO International Corporation. Updating estimations of the probable earthquake in Istanbul final report. *Production of Microzonation Report and Maps for Asian Side Project*. 251p, 2009.

COMPDYN 2017
6th ECCOMAS Thematic Conference on
Computational Methods in Structural Dynamics and Earthquake Engineering
M. Papadrakakis, M. Fragiadakis (eds.)
Rhodes Island, Greece, 15–17 June 2017

# A NEW DECISION MAKING METHOD TO SELECT PRIORITY INTERVENTIONS AFTER EXTREME EVENTS

**Glen Dervishaj**[1], **Gian Paolo Cimellaro**[1], **Anil Agrawal**[2]

[1] Department of Structural, Building and Geotechnical Engineering, Politecnico di Torino,
address
glen.dervishaj@outlook.com , gianpaolo.cimellaro@polito.it

[2] Department of Civil Engineering, The City College of New York
address
agrawal@ccny.cuny.edu

**Keywords:** Resilience, Hyogo Framework for Action, Decision Making, SMART model.

**Abstract.** *This study proposes the implementation of decision making tools in quantifying and ranking resilience initiatives. The objective of this study was to build a flexible model capable of assessing and ranking any resilience dimension, like initiatives, projects and indices. The model used is in the study is called Simple Multi-Attribute Technique (SMART), the simplest form of Multi-Attribute Utility Theory. SMART offers a simplified and easy to use approach. The benefit of the SMART model lies on how simple the scoring criteria of alternatives and weights of these criteria are established. They can be defined by the decision maker by building a hierarchy and then assign scores to each of them. Otherwise, a set of formulas exist to compare or help the decision maker asses these weights based on the same hierarchy (importance) he previously built. Three criteria were used in the SMART model: Time (the amount of months required or planned to complete a project), Cost (budget for each intervention) and Phase (if the project is either completed or still in planning, design or construction). After evaluating these projects with the SMART model, a comparison was made by assessing the same projects through their functionality curve, which is described by the drop in functionality (the cost of projects was used to describe this value) and the time required to complete a specific project. The study highlights the difference between these two seemingly similar models and their different results to then add a third component of calculation, the Social Impact of these projects. This dimension was added because it was recognized that the output of the previous models only took into consideration their performance, and not their impact in the quality of the urban space they are surrounded by. The case study for this approach was New York City and its ongoing recovery projects post Hurricane Sandy. The projects are part of four main Initiatives: Infrastructure, Buildings, Coastal Defense and Neighborhoods.*

## 1 INTRODUCTION

Many studies have found that resilience was first used in the field of ecological studies, and it was introduced by Holling in 1973 **[1]**. The definition given by Holling is the following: "Resilience determines the persistence of relationships within a system and is a measure of the ability of these systems to absorb change of state variable, driving variables, and parameters, and still persist". In other words, ecological resilience is defined as a "characteristic of ecosystems to maintain themselves in the face of disturbance" as said by Adger **[2]**. One aspect of resilience is the speed of recovery from a disturbance, which is different from what we perceive as a "response" that generally describes the direct reaction to impacts **[3]**.

Following what has been stated by Folke **[4]**, resilience of social systems is closely connected to ecological resilience, significantly in cases of communities where the livelihoods of the individuals rely greatly on natural resources. The capability of social systems to adapt and to develop is extremely reliant on the support capability of the encompassing network. Reducing this capability might cause an increase in vulnerability within the social organization. Similarly, the performance of an ecosystem is closely related to the actions of the interlinked social systems, resulting in high and dynamic reciprocity between the two. At the center of these disturbances lies human activity which can have great repercussion in both ecological and social system resilience.

An increased number of Natural and man-made disasters and their respective damage has resulted in the introduction and emerging topic of Resilience. A new dimension that is being attributed now to regions inhabited by humans, specifically dense ones. Cities welcome more than 50% of the current global population and by 2050 that number is expected to increase to 70%. As the population increases, more people will live in large cities. Many people will live in the growing number of cities with over 10 million inhabitants, known as megacities. These large conglomerations suffer an immense number of losses during a catastrophic event.

The most important asset of cities is us, the people living in them. A high concentration of people means bigger cities, complicated infrastructure and infinite number of buildings and public spaces. How is this all related to the risk cities face from disasters? Simply because we can look at cities or areas the same way as we look at our own self. A person being prepared for an unexpected event is the same as a system being prepared for one. There are 4 main drivers that make a person/city resilient:

1. Knowledge/ Awareness (misinformation can cause a great deal of harm in cases of emergency)
2. Training / Experience
3. Resources / Redundancy (how to use these resources and how to manage them appropriately)
4. Plan of Action / Mitigation

These four drivers were chosen based on the generalization between low risk and impact event and the high risk and impact ones. Then we can have a short example on how these drivers are related to each other, the human behavior and the risks we face every day as similar little disturbances like cutting a finger to having an accident or getting an illness. In case we cut a finger, we can just clean the wound, sterilize it and put a bandage. In the next scenario, depending on what kind of accident and impact it has, there would be different measures to take. One might not have suffered an injury or the situation might be critical. In the latter, the help of exterior agents is needed. This is the case for most natural disasters ranging from none to some warning before the impact and with varying damage.

What does this mean for urban resilience? The examples help understand the main factor of these events: their magnitude. Based on the level of impact, different measures can be taken, and the "*treatment*" for the area differs in time.

It is important to understand the risk, exposure, sensitivity and vulnerability of a country in order to be prepared. In the worst case scenario of a catastrophic event taking place, the damage would be extraordinarily big for areas that have no mitigation plans and are not aware of the risk they face. That is why it is of great importance to implement policies and laws regarding disaster mitigation. This will increase awareness and knowledge will be shared between experts and communities to be informed and educated on how to behave during these events. This will also increase the work willing to be put on early warning systems, which play an enormous part in saving precious lives before the event occurs. Take New York for example and the Rockaway community. The New York State issued a warning before Superstorm Sandy for areas like the Rockaway to evacuate their homes since they were the most at risk. What happened is that people felt safe in their homes after they had gone through Hurricane Irene without major damages. A warning had been issued for Hurricane Irene as well and it was said to have a great impact (and it had in general, most destructive hurricane in the US) but this community did not suffer losses. That is why they chose not to evacuate and Sandy hit hard. The damage Sandy caused to the transportation system was considerable everywhere but was extremely unforgiving for the Rockaway community and its only connecting bridge to the land. The people living, in what is defined as a Barrier Island, were stuck for several days after the storm. The only way of moving people from the island and exchanging supplies was by starting a ferry service. The Bloomberg administration started the ferry Nov. 12. 2012 less than a month after the superstorm knocked out A line service to the Rockaways. Subway service was not restored until May 2013.

New York serves as an example not only for its stark particularity but also for its immediate response in terms of actions and policies. It is one of the cities that partnered with ARUP and the Rockefeller foundation for implementing resilient measures in their urban fabric. The US are also part of the nations which have agreed upon and implemented the Hyogo Framework for Action, a blueprint for nearly 173 nations worldwide in disaster mitigation and early warning systems.

The research focuses on the resilience and rebuilding initiatives of the city of New York. The study was conducted partly at the Politecnico di Torino, Italy under the supervision of Professor Gian Paolo Cimellaro and in collaboration with The City College of New York, USA with the supervision of Professor Anil Kumar Agrawal.

The study is based on the work done by the New York City government. Extensive research was put into decision making models and resilience evaluating models. Moreover, previous literature sources related to Hurricane Sandy and the emerging topic of resilience were considered.

One objective of the study is to bring attention regarding the impacts of climate change and on the recovery of communities living in the affected area and describe possible and most "profitable" rebuilding strategies from this perspective.

## 2 LITERATURE REVIEW

A lot of studies have been made on this topic by experts in different fields. An interesting approach is the one taken by the Rockefeller Foundation and ARUP which define "Urban Resilience as the capacity of individuals, communities, institutions, businesses, and systems within a city to survive, adapt, and grow no matter what kinds of chronic stresses and acute shocks they experience" **[5].** Their work extends to a great number of cities around the world who face natural or man-made events.

The UN have also done an immensely good job in the interesting topic of preparedness and hazard mitigation. Their definition for resilience goes as followed: "The ability of a system, community or society exposed to hazards to resist, absorb, accommodate to and recover from the effects of a hazard in a timely and efficient manner, including through the preservation

and restoration of its essential basic structures and functions" **[6]**. Found in the UNISDR Terminology in English document. The work done by the UN, specifically the Hyogo Framework for Action plays a key part in an analysis done in this study. It was decided to use the data from the HFA to build a model with which to quantify the progress in resilience of countries around the world. This part will be expanded upon on a separate chapter below.

In summary, Resilience can be defined as "the ability of a system to cope with change" **[7]**. Walker highlights the importance of including a great number of different stakeholders, especially the common and ordinary people, very early in the phases of assessment in order to get a realistic view of the local conditions **[8]**.

Nowadays assessing resilience, at different levels, can be done using a number of different tools. Many methods focus on the capacity to adapt, or bounce back which in itself is a difficult task. In order to learn and adapt, a look back at the history of hardships a community has been through is required. By doing so, we can acquire a better idea on what the response and level of adaptability of that specific community is. It is however apparent that certain problems and difficulties are predominant in different parts of the world simply because communities (areas) are not affected by similar events or problems. This aspect can be analysed and expressed in different methods. One of these is by looking at migration.

Mobility can be considered as a significant sign of the resilience of a community. If this shift is done at a bigger scale, then mobility can mark vulnerability which can then translate to negative effects on both areas. In some rare cases, this phenomenon can be positive or improve resilience only if it is generated by positive pull factors of the receiving area.

As it can be observed, the complexity of resilient systems and mobility highlights the need for increased basic resilience of any place.

A system should be resilient at any times, before the migration in order to withstand change. An important factor at play here is diversity, in terms of economic options and social opportunities since it encourages learning and adaptation.

Diversity, in many aspects, affects the community, its properties as well as its level of resilience. Folke presents another key aspect which is local knowledge and community participation in studying a certain case **[4]**. This can be accomplished simply by taking advantage of the previous experiences of the local communities regarding natural resource management. This will then play a key role in this work as the framework proposed at the city level strongly endorses the participation of various stakeholders. Although the above are related to economic and social resilience, quite a few concepts can be applied to any type of **resilience, like awareness, preparedness, resourcefulness, robustness, adaptability** and the ability to learn.

Public institutions on the other hand have the ability to empower an environment and practices that improve resilience. They have a major contribution in developing an equitable distribution of resources among populations, economic growth (coupled with stability), all these factors can possibly have a big impact on augmenting local resilience. Managing the social-ecological systems is if truth be told a very important part in increasing their resilience as long as the various stakeholders within the system are included as well. It is so established that the role of institutions in increasing social resilience is vital, as they incorporate all social systems and control the distribution of asset

An interesting aspect brought up is that short-term management efforts, could lead to a loss in the long-term plan and development of a systems resilience **[4]**. Additionally, they also emphasize that not measuring the impacts on the ecological system, could have a negative outcome and weaken the resilience of the whole system, if it is combined with efforts that do not take the interdependence of both the social and ecological systems adequately into consideration. This is predominantly true in cases where the system is considerably fragile. Another key characteristic to keep in mind when considering the management of these systems, regarding resilience obviously, is focusing more on long-term actions and development.

Since achieving resilience is so complex, future plans should aim to increase resilience of the entire system and not only of individual components. One of the biggest challenges and important factor is uncertainty. The effect that humans will have, climate change and other unpredictable factors, pose a big problem in predicting what will happen **[8]**. It should be noted that the social resilience of a system is not equal to its individual components. Increasing resilience does not mean that vulnerability decreases, at least not for all stakeholders.

## 3 APPLYING DECISION MAKING METHOD CONCENPTS IN RESILIENCE

This chapter describes the methodological approach of this work. It details the specific technique used and concludes with a comparison of the results.

The city of New York took immediate action following Hurricane Sandys landfall. A great number of initiatives and strategies were devised in order to mitigate and rebuild from the storms rubble. The aim of this study is to propose a simple methodology that would help understand the advancement of this process. This study will be helpful for stakeholders, decision makers, and communities alike.

The decision maker's aim is to improve the services associated with the preferences and habits of the users. Therefore, the need for a tool that can describe which action would benefit more a certain region is required. In this study, the tool that has been chosen to accomplish this feat is the SMART model. The reason for using this model lies in a few reasons. Firstly, it was an objective of the study to find a way of processing, describing and evaluating projects in a weighted and reasonable manner. During the literature review and state of the art on resilience, quite a lot of assessment methodologies were found by different authors. There is actually a very long list of techniques. Considering the difficult and lengthy process of assessing resilience, as well as the fact that most of these techniques are not flexible to various situations, it was decided to find, adapt or build an easy to use and understand methodology. Its aim is to be able to evaluate and describe a number of parameters, projects or any form of resilience indicators. A research on decision making methods with the above intentions in mind led to consider the multi criteria methods. Afterwards, the SMART technique was chosen as the most appropriate and interesting method to try and put into use in the context of resilience.

The SMART technique presented itself as precisely an easy to use, adaptable and flexible method, capable of evaluating different criteria, in this case various projects, in which weights could also be attributed to the measuring criteria. Some background on these tools and on how the SMART model was used for the purpose of this study is given below.

The tools and techniques are used for selecting or proposing the "best" or more convenient choice. Decision making tools are used and find applications in many different fields. A topic which could benefit from the aforementioned tools is Resilience.

Baker et al., provide some context on some aspects of decision making that include goals, criteria, requirement and problem definition **[9]**. In order to reduce the possible disagreement of the above elements it is suggested that the first steps of decision making should be deciding who the decision makers and stakeholders are. A step by step overview regarding a general decision making process is: 1) Define the issue, 2) Determine requirements, 3) Establish objectives, 4) Identify the possibilities, 5) Define the evaluating criteria, 6) Choose a decision making tool, 7) Assess the alternatives based on the established criteria, 8) Check that the chosen alternative is actually a solution to the issue established at first.

It is vital to form distinction between the cases whether or not we've one or multiple criteria (Fülöp 2005) **[10]**. In some cases, there might be one criterion, either kilometers per hour, cost, color, time or whatever the criteria of that case is set to be. Then the choice is easily done by choosing the highest value for that criterion.

When it so happens that we have a determined number of criteria and the number of alternatives is theoretically infinite then the decision is made with what is called multiple criteria optimization.

In summary: "Decision making is the study of identifying and choosing alternatives based on the values and preferences of the decision maker. Making a decision implies that there are alternative choices to be considered, and in such a case we want not only to identify as many of these alternatives as possible but to choose the one that best fits with our goals, objectives, desires, values, and so on." **[11]**.

A problem of multi-attribute decision making has two main elements, the criteria and alternatives that have been chosen to be scored. As we will see below and also in the SMART model further, a common feature of these methods is the so called *decision table*. On the rows of the table there can be found the criteria and on the columns the score of for each alternative is listed. Scores represent the performance of that alternative in a given criterion.

Firstly, weights are assigned to each criterion based on their importance. There are different methods to develop these weights, some easier than others. More importantly weight distribution is a key aspect of these methods as it has a big influence on the results. These weights can be calculated with formulas or they can be agreed upon between the decision makers, the decision makers and stakeholders or as part of the personal sensibility.

Then the final scores for each alternative is calculated as a product of the performance of each alternative on the criterions and their associated weights. Usually, higher ranking value means a better performance of the alternative, so the alternative with the highest ranking value is the best of the alternatives which is also the one that should be picked at the end unless further considerations are made.

These methods have the ability to partly or entirely rank alternatives. In one case, the best and preferred alternative can be chosen. In other cases, it can be opted to choose from a list of the best performing alternatives.

### 3.1 SMART model

This section introduces the Simple multi-attribute rating technique (SMART), developed by Edwards **[1]**. The objective is to help decision makers understand the advancement and benefits of certain initiatives, strategies or activities in the field of Urban Resilience. The model allows various stakeholders to take into consideration which policy or action is most appropriate in each case, as well as providing information on the budget, timeframe and state of operations. Assigning weights to each criteria is also achieved through an easy process that reflects the relative importance of each criteria. A hierarchy of importance is established by the decision maker. Generally, 10 points are assigned to the least important criterion. Afterwards, the next criterion is assigned more points and this operation is repeated for each criterion. The final weights are obtained by dividing the total by the sum of the points and normalize it to one.

The SMART model is part of the Multi-Attribute Utility Theory (MAUT). It describes the simplest form of the MAUT technique. The model is used when evaluating the performance of various attributes by assigning multiple criteria. The values associated to the criteria can be both qualitative and quantitative. Once the objectives and criteria have been identified then it is required to give weights to each criteria. The utility $U_j$ (final score) of the alternatives is computed as the total sum of the criteria (dimension) score multiplied with the weight of the same criteria. The values for each dimension can usually be expressed in a linear function by setting minimum and maximum rules. Edwards supposedly proposed a ten step technique. An overview of these steps has been already given by These steps are very similar to the steps of a general decision making tool with the presence of weights as the main difference and the way the scores are assigned. Adopted by Olson **[12]** these ten steps are: 1) Identify the deci-

sion-maker(s), 2) Identify the issue of issues, 3) Identify the alternatives, 4) Identify the criteria, 5) Assign values for each criterion, 6) Determine the weight of each of the criteria, 7) Calculate a weighted average of the values assigned to each alternative, 8) Make a provisional decision, 9) Perform sensitivity analysis 10) Decide. Depending on the desired result, the alternative with the highest final (utility) $U_j$ score should be selected.

SMART is the simplest form of the MAUT methods. There are a few ways of giving ratings to alternatives in SMART, considering the ordinary scale of a given criteria. In SMART rating criteria scales are converted to a general inner scale. This is done for the sole purpose of differentiating between the alternative rating and the criteria weighting. This is primarily done by using a Value Function. As a simple and quick rating method, SMART uses the easiest and most common of a value function: The additive model which is applied using a linear. Usually ratings are set going from 0 to 100 and then normalizing where appropriate or desired **[13]**.

### 3.2 Applying the SMART model to the resilience projects in New York City

In the case of New York and the advancement of the strategies for resilience, the goal is to put into perspective and show the relation between different initiatives, as well as ranking them. Using the SMART model gives us the opportunity to get a better understanding of how the city has done so far. Our objective are the initiatives. The measuring criteria identified in the study are: the cost of each project, the timeframe required to complete these projects and finally, the current state operations (phase).

The benefit of the SMART technique is that it possesses great flexibility. For example, the weights of each criterion are easily determined by the decision maker and can also be easily changed in further stages based on the sensibility of other users, may that be a government, a mayor or another person interested in the particular development of his area. After assigning weights, the next step is using the data available to evaluate the initiatives and their performance in the present moment.

In order to give values to the initiatives it is required to develop an attribute scoring rule used to set system utility values. To establish the values, some rules or preferences need to be created. For example, it was decided to give scores from 0 to 1. Regarding Cost, the higher the investment, the higher the score achieved. For the criterion Time, the less time it took for a project to be completed, the higher the score achieved, whereas an extended duration of the operations would assign that initiative a lower score. Phase, the last dimension (criterion), was set in a way to describe and ground furthermore the final results.

Specifically, in this case study the data was obtained by the OneNYC Report provided by the state of New York. The dimensions and scoring rules mentioned above were tailored to the data found in this report. However, the bulk of the data was extracted online by the interactive and up to date map at https://maps.nyc.gov/resiliency/. Firstly, an overview of the data was required. Analyzing the minimum, maximum, average and other various patterns found in the data. This step was crucial for setting the rules of the scoring technique.

The resiliency projects started around New York City are established as the alternatives. The next step in building the SMART model is identifying the dimensions by which to evaluate these alternatives. As already mentioned the dimensions (criterions) are: Budget (Cost), Time and State of Operations (Phase). Afterwards, the weight of each of the dimensions should be established. There are a couple variations on how to properly weight our criterions.

However, in this study, it was chosen to rank the dimensions first, and subsequently assign "importance" to them. The hierarchy for evaluating the project is as follows:

Time > Cost > Phase

This ranking puts the criterion of Time as the most significant. Once this priority ranking is set, the least important criterion is assigned a rating of 10. The other ratings are decided start-

ing from this base value. Cost and Time were assigned a rating of respectively 20 and 35. The weight associated to each of them is each rating divided by the total. This allows the normalization of weights so their sum amounts to 1. After performing the divisions, the weights ($W_i$) for Time = 0.54, Cost = 0.31 and Phase = 0.15 are obtained.

The next step in completing the model is giving scores for each project. The scoring values were decided by analyzing the data available in order to reflect a fair final score. Rules for all criterions were set. Each different from the other. A simple calculation that normalizes the time each project was completed (or expected to be completed) was chosen for the Time criterion, on the other hand for scoring projects related to their Cost and Phase criterion, it was decided to build scoring tables respectively (Table 1 and Table 2).

It was observed that the longest project planned to date has a duration of nearly nine years. Based on this observation, it was decided that a value of 0 would be given for periods equal or longer than ten years. The available data is provided in four quarters, yearly three-month periods denoted as Q1, Q2, Q3 and Q4. For the purpose of this study, the completion date corresponds to the last month of the quarter. Rebuilding and recovering is considered to have started right after Hurricane Sandy made landfall October 28th, 2012. For example, the project *"World Trade Center Command Repairs"* was completed the first quarter of 2013 (Q1 2013) so the project had a lifespan of roughly 3 months until its completion. Projects finished in the same quarter as the disaster, specifically the last quarter of 2012 are assigned a value of 1. The scores are obtained with the following equation:

$$S_{jt} = 1 - \frac{t_j}{t} \tag{1}$$

Where $Sj_t$ is the score of the time criterion of each project, $t_j$ is the time the project is completed or is expected to be completed and $t$ is the longest period considered for calculation (in this case ten years).

| Score | Investment in millions of USD |
|---|---|
| 0.1 | 0 - 1 |
| 0.2 | 1 - 5 |
| 0.3 | 5 - 10 |
| 0.4 | 10 - 15 |
| 0.5 | 15 - 20 |
| 0.6 | 20 - 30 |
| 0.7 | 30 - 42 |
| 0.8 | 42 - 55 |
| 0.9 | 55 - 70 |
| 1 | 70+ |

Table.1 Scoring table used for evaluating the Cost criterion

The next criteria is budget. The scoring method related to cost is approximately the same as the above but with a few variations. For example, an investment is given a score of 1 if the cost is equal or higher than $70 million. The rules for the values were decided based on a couple observations. The average investment per project resulted to be near $15 million, that is why the breaking point between a score of 0.4 and 0.5 is at $15 million. Afterwards, the difference between the score and the amount invested increases slightly until it reaches $70 million. It was also decided to give a score of 1 for projects with investments upwards of $70 million, which are limited in number.

Finally, a simple scoring technique was attributed to the last dimension of Phase (State of Operations). The projects are divided into four categories: currently *Completed*, still in *Con-*

*struction*, in the *Design* phase and lastly, still in the early *Planning* phase. The scores ($S_{ip}$) for each are shown in the table below.

| Phase | Score |
|---|---|
| Completed | 1 |
| Construction | 0.75 |
| Design | 0.5 |
| Planning | 0.25 |

Table 2 Scoring table for the State of Operations (Phase)

The rules for scoring each alternative are now established. The next step is filling out the table of all the projects in Manhattan.

After an overview of the data, the scores for each projects were compiled with the method described above. A comprehensive table with the weighted scores of each criterion and the results of the top ten scoring projects can be found below in Table 3. The equation with which the final scores are attained is the following:

$$U_i = \sum W_i S_{ij} \tag{2}$$

Where $U_i$ is the final score of the projects, $W_j$ is the weight of the $j$ criterion and $S_{ij}$ is the score obtained by project $i$ in criterion $j$.

The last step would be to analyze the result and draw conclusions from the weighted scores. The demanding part of this stage is the critical thinking and brainstorming process so that decision makers take actions accordingly. With these results there is room to rank the projects by their effectiveness. The same method can be used in various case studies, depending on the desired result.

| Project N. | Category | Time | Budget | Phase | Score |
|---|---|---|---|---|---|
| Project 7 | Buildings | 0.54 | 0.21 | 0.15 | 0.91 |
| Project 6 | Buildings | 0.54 | 0.09 | 0.15 | 0.78 |
| Project 9 | Buildings | 0.51 | 0.09 | 0.15 | 0.76 |
| Project 6 | Infrastructure | 0.40 | 0.18 | 0.15 | 0.74 |
| Project 3 | Infrastructure | 0.54 | 0.03 | 0.15 | 0.72 |
| Project 10 | Infrastructure | 0.54 | 0.03 | 0.15 | 0.72 |
| Project 5 | Buildings | 0.54 | 0.03 | 0.15 | 0.72 |
| Project 8 | Buildings | 0.54 | 0.03 | 0.15 | 0.72 |
| Project 12 | Buildings | 0.54 | 0.03 | 0.15 | 0.72 |
| Project 4 | Infrastructure | 0.52 | 0.03 | 0.15 | 0.71 |
| Project 2 | Coastal Defense | 0.52 | 0.03 | 0.15 | 0.71 |
| Project 4 | Buildings | 0.52 | 0.03 | 0.15 | 0.71 |
| Project 7 | Infrastructure | 0.51 | 0.03 | 0.15 | 0.69 |
| Project 4 | Coastal Defense | 0.51 | 0.03 | 0.15 | 0.69 |

Table 3 Final scores and ranking

It is apparent from the table above that the highest ranking projects are the ones that have already been completed. The completed phase itself doesn't play a big role in the end result as it is only weighed at about 15% of importance in relation to the other three dimensions. Most importantly, the pattern at which the top projects are distributed is related to obviously *Time*. The amount of time it takes for a project to be completed was the most important factor in the

calculations and bears a great importance in the final ranking. This can be easily demonstrated by the vast difference projects have in relation to their budget. The amount of money invested differs greatly between the highest ranking projects. Specifically, the recovery of 110 William Street (Project 7) in the Buildings category is ranked number one. The reason behind this is the very quick period of completion as well as a gigantic budget. The project was completed in the last quarter of 2012. The same quarter Hurricane Sandy hit the city of New York. Also, the comprehensive budget of the project was of nearly $37 million. Situated in the Financial District of Manhattan the building is of great importance for the New York City Economic Development Corporation. Currently restored, the building is being rented at the present moment. It is interesting to note that a great number of financial buildings of this district were planned to be upgraded and transformed into residential buildings or hotels. The reason for this change was primarily the flooding risk and problem these types of constructions have. A very similar phenomenon has happened once before in Downtown Manhattan after the 9/11 attack. Regardless, the work detailed in the report for this project was described as *"re-energizing all electrical systems after weekend emergency shutdown"*

Project 7 is directly followed by Projects 6 and 9. Both of these projects have similar properties to their competitor since they were also completed in the last quarter of 2012. The biggest difference between these three projects is their budget. While projects 6 and 9 had investments of $5 million and $6 million dollars respectively, project 7 had the enormous amount of $37 million. There is a clear pattern that is observed in every subsequent project. The results show that the final score and ranking is primarily based on the response time. These results agree with our premise, which valued the necessary time of operations as the top priority. Then, the rankings vary slightly here and there based on the budget.

### 3.3 Comparison with the Functionality Index

This section describes and compares the results from above (Smart Index) through the use of the functionality curve of resilience. It was decided to build the "functionality" curves of resilience for selected projects (specifically only projects that are part of the Infrastructure initiative) considering only two parameters, respectively Time and Cost. The data has been interpreted as Cost being the drop or "damage" sustained by the system at the start of the event (Y axis). On the X axis there is Time, or the period required to finish a project from the time Sandy hit New York. Based on the results from the SMART model it was established a Time of control - $T_c$ which expresses the worst case scenario, the project that is planned to take most time to finish. In this work it was chosen to use only projects of the Infrastructure initiative because this sector is regarded as the most important for the City of New York.

Project 21 is the one expected to finish last after nearly 9 years of work (2021). Alternatively, Project 3 is recorded as the fastest to completion. Same as Project 10, they both finished in the fourth quarter of 2012, right after the storm had hit. Instead, Project 6 was the best performing project as calculated by the SMART model. Results vary but are similar to the SMART technique which proves the efficiency of the methodology. The main difference between the two methods is that when using the decision making tool and its weighting factors, then the projects with the highest score in the most important criteria would float to the top of the list. Also, we can notice that even though two of the criterions are the same in both calculations, the difference in ranks comes from SMARTs weights, which play a big role in the final score.

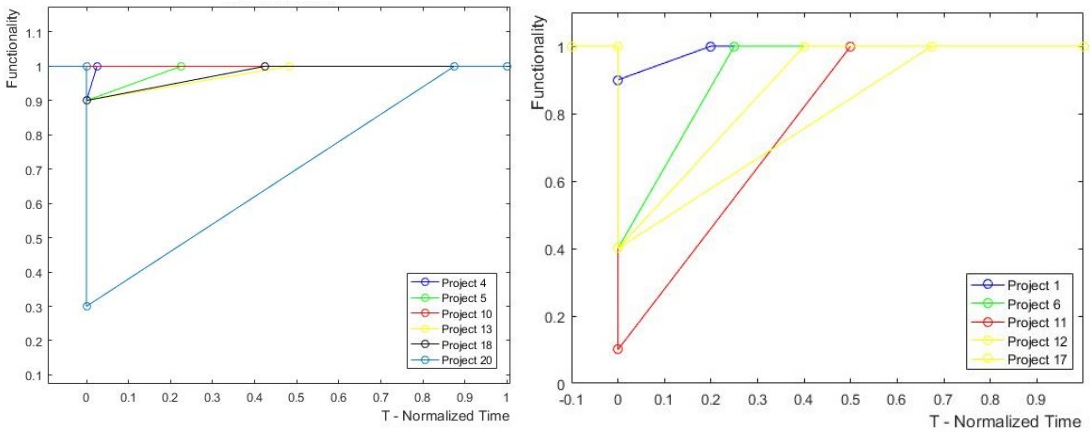


Figure 1: Functionality curves for some projects. Curves for "facilities" (left), citywide infrastructure projects (right).

Curves were calculated for all the remaining infrastructure projects and a new rank was obtained by measuring resilience as the area under the curve. These results are illustrated in the next section alongside the SMART results and the combination with the Social Impact.

### 3.4 Urban quality of spaces

The value of spaces is always defined by the location, history, peoples cultural background of the place, function, size and purpose. Therefore, the quality assessment of Urban open areas cannot and should not be generalized. A simple example of the concept is found between the difference of noisy and quiet places. Both of them are enjoyable if they are situated in the right context. People expect tranquility and peace from a remote park, so the park needs to be a quiet, private place. It depends what mood it was made for and what the community is looking for. The key part of understanding what the goal must be is to interact with the community. These differences can be observed in most cities when you travel near a university or school, where the services and environment around those areas is much different from other places. Also, a small and well curated private park inside a neighborhood doesn't have the same impression as a big public park. Landscape Architects certainly play a key role in planning and analyzing urban spaces.

Open spaces like commercial centers have a different distribution and services compared to a space within the city or an office complex. Architects and planners play a big role in giving environments they build the appropriate character. If public spaces are so important to our existence, then it means that humans and/or whole communities receive an even bigger hit when disasters occur. They could be stripped of their homes and at the same time of their favorite place to either work, play or just spend some hours of the day. This consideration was in fact made after the results achieved by the decision making tools. It seemed apparent that none of the methods took into consideration what social impact each of the projects would have on the community. It comes from an easy concept that a resident will "mentally heal" faster and be more resilient if public spaces of importance where restored and improved upon after an event like Hurricane Sandy.

There is a considerable amount of sustainability indicators nowadays. Nonetheless, for the purpose of this study, attention was turned towards qualitative aspects of the urban fabric. That implies that the main focus was finding attributes that attracted people to places. With those attributes, a new Social Impact Index will be introduced. The purpose of this new Index is to create a new rank of the Infrastructure projects. This ranking would now be influenced

by attributes that express a community's interest. Contrary to the previous methods where only the performance of the projects themselves was taken into consideration.

An interesting study related to an urban quality like walkability was used for supporting this new index. The study tries to implement a scoring sheet of various qualities connected to walkability.

New York City is one of the most populous cities in the world with a population of more than 8 million people in its five boroughs (as of 2014, recorded by city-data.com). Not only, but an extremely large amount of tourists visits the city every day. This makes it difficult to actually measure which places should be prioritized either in finishing first or which projects would have the most impact.

The study on walkability was particularly interesting because it makes possible evaluating places by their intrinsic property and not by the actual flow of people. An area with high walkability attracts a higher number of people. Improvements on these places would affect a great number of people in a more meaningful way.

The five attributes that will be used to assess walkability and be combined into forming the Social Index (SI) are adopted from Ewing **[14]**:

- Imageability: Imageability is the quality of a place that makes it distinct, recognizable, and memorable. A place has high imageability when specific physical elements and their arrangement capture attention, evoke feelings, and create a lasting impression.
- Enclosure: Enclosure refers to the degree to which streets and other public spaces are visually defined by buildings, walls, trees, and other elements. Spaces where the height of vertical elements is proportionally related to the width of the space between them have a room-like quality.
- Human scale: Human scale refers to the size, texture, and articulation of physical elements that match the size and proportions of humans and, equally important, correspond to the speed at which humans walk. Building details, pavement texture, street trees, and street furniture are all physical elements contributing to human scale.
- Transparency: Transparency refers to the degree to which people can see or perceive what lies beyond the edge of a street or other public space and, more specifically, the degree to which people can see or perceive human activity beyond the edge of a street or other public space. Physical elements that influence transparency include walls, windows, doors, fences, landscaping, and openings into midblock spaces.
- Complexity: Complexity refers to the visual richness of a place. The complexity of a place depends on the variety of the physical environment, specifically the numbers and kinds of buildings, architectural diversity and ornamentation, landscape elements, street furniture, signage, and human activity.

Based on the above assumptions a measurement of all five properties was conducted. The scoring criteria is divided by levels. It was decided to have the following levels: Maximum, (highest attainable score in that particular quality) assigned a value of 1, High, assigned a value of 0.75, Medium, assigned a value of 0.5, Low, assigned a value of to 0.25.

Imageability is estimated by taking into consideration a few aspects of the area. In general, places with no character have no imageability. On the other hand, places with high imageability are recognizable and memorable. This can be achieved with the presence of architecture that suggests importance, presence of historical buildings and landmarks. This quality of urban spaces is not limited to these rigid forms, in fact, places with distinct views that make it memorable are also considered. Lastly, the main component of imageability is the answer to the question: "is the place unique?"

Enclosure can be seen as how well defined a space is and it is altered by different building heights and levels. Continuous edges provide enclosure. A busy street with old trees with large canopies can make otherwise low enclosed places more enclosed. These elements contribute to the room-like feeling of the space.

Human Scale is the presence of people and activity, presence of street furniture, protection from traffic, focus on street level. Cafes on both sides of sidewalk increase human scale as well as the presence of stores and activities that invite you in.

Transparency is the sense of what's going on inside the buildings that surround you. This is influenced if buildings are so far back from street edge that you cannot have a clear view. Like Human Scale, continuous exposure to uses that are clear and accessible also plays a role.

Complexity is hard to measure but there are a few indicators of a complex space. For example, a block with one building is less complex than a block made of several buildings. Having many people on the street/plaza add to complexity. Overly controlled design makes a place less complex; you lose complexity with predictability. Like previous qualities, complexity is higher in places where human activity with various uses is higher.

I – Imageability, E – Enclosure, HS - Human Scale, T – Transparency, C – Complexity

| | I | E | HS | T | C | Total | Normalized |
|---|---|---|---|---|---|---|---|
| Project 1 | 0.50 | 0.50 | 0.50 | 0.50 | 0.50 | 2.50 | 0.50 |
| Project 2 | 0.50 | 0.25 | 0.25 | 0.25 | 0.25 | 1.50 | 0.30 |
| Project 3 | 0.75 | 0.25 | 0.25 | 0.25 | 0.25 | 1.75 | 0.35 |
| Project 4 | 1.00 | 0.75 | 0.50 | 0.25 | 0.75 | 3.25 | 0.65 |
| Project 5 | 0.25 | 0.25 | 0.25 | 0.25 | 0.25 | 1.25 | 0.25 |
| Project 6 | 0.50 | 0.50 | 0.50 | 0.50 | 0.50 | 2.50 | 0.50 |
| Project 7 | 0.50 | 0.75 | 0.25 | 0.25 | 0.50 | 2.25 | 0.45 |
| Project 8 | 0.50 | 0.25 | 0.25 | 0.25 | 0.25 | 1.50 | 0.30 |
| Project 10 | 0.25 | 0.50 | 0.50 | 0.25 | 0.50 | 2.00 | 0.40 |
| Project 11 | 0.25 | 0.25 | 0.25 | 0.25 | 0.25 | 1.25 | 0.25 |
| Project 12 | 0.25 | 0.50 | 0.25 | 0.25 | 0.50 | 1.75 | 0.35 |
| Project 13 | 0.25 | 0.75 | 0.50 | 0.50 | 0.50 | 2.50 | 0.50 |
| Project 15 | 0.50 | 0.50 | 0.50 | 0.50 | 0.50 | 2.50 | 0.50 |
| Project 16 | 0.25 | 0.25 | 0.25 | 0.25 | 0.25 | 1.25 | 0.25 |
| Project 17 | 0.50 | 0.50 | 0.25 | 0.25 | 0.50 | 2.00 | 0.40 |
| Project 18 | 0.50 | 0.50 | 0.25 | 0.25 | 0.50 | 2.00 | 0.40 |
| Project 19 | 0.50 | 0.50 | 0.75 | 0.50 | 0.50 | 2.75 | 0.55 |
| Project 20 | 0.25 | 0.25 | 0.25 | 0.25 | 0.25 | 1.25 | 0.25 |
| Project 21 | 0.25 | 0.25 | 0.25 | 0.25 | 0.25 | 1.25 | 0.25 |

Table 4 Summary of values attributed to each urban quality per project

Both the combinations of the SMART and Functionality Index with the new index proved to give yet again a new insight on the results. Obviously, the highest ranking project in the latest table is an area with an enormous amount of people walking by every day. The difference in ranks and the final results proves that it is very hard to express resilience as a whole with only one technique. That is why during this study, a comparison with the Functionality curves was needed and at the end a combination with the social impact (importance) of projects.

| Project N. | SMART Index | Functionality Index | SI | SMART x SI | Fun x SI |
|---|---|---|---|---|---|
| Project 4 | 0.708 | 0.869 | 0.65 | 0.46 | 0.56 |
| Project 6 | 0.741 | 0.795 | 0.50 | 0.37 | 0.40 |
| Project 7 | 0.694 | 0.868 | 0.45 | 0.31 | 0.39 |
| Project 1 | 0.613 | 0.860 | 0.50 | 0.31 | 0.43 |
| Project 10 | 0.721 | 0.870 | 0.40 | 0.29 | 0.35 |
| Project 3 | 0.721 | 0.870 | 0.35 | 0.25 | 0.30 |
| Project 19 | 0.402 | 0.745 | 0.55 | 0.22 | 0.41 |
| Project 12 | 0.623 | 0.750 | 0.35 | 0.22 | 0.26 |
| Project 15 | 0.429 | 0.755 | 0.50 | 0.21 | 0.38 |
| Project 13 | 0.423 | 0.846 | 0.50 | 0.21 | 0.42 |
| Project 2 | 0.644 | 0.850 | 0.30 | 0.19 | 0.26 |
| Project 8 | 0.613 | 0.860 | 0.30 | 0.18 | 0.26 |
| Project 17 | 0.437 | 0.668 | 0.40 | 0.17 | 0.27 |
| Project 18 | 0.417 | 0.849 | 0.40 | 0.17 | 0.34 |
| Project 11 | 0.662 | 0.645 | 0.25 | 0.17 | 0.16 |
| Project 5 | 0.600 | 0.859 | 0.25 | 0.15 | 0.21 |
| Project 20 | 0.360 | 0.566 | 0.25 | 0.09 | 0.14 |
| Project 16 | 0.326 | 0.805 | 0.25 | 0.08 | 0.20 |
| Project 21 | 0.205 | 0.783 | 0.25 | 0.05 | 0.20 |

Table 5 Combination of the SMART Index and Functionality Index with the Social Index (Rank by SMART x SI)

## 4 CONCLUSIONS

The objective of this research was to build and express progress made by different entities regarding resilience. Firstly, the importance and meaning of resilience nowadays in the urban context was established. Afterwards, the study explored a new methodology on how to quantify resilience at different levels.

As per the objective of this research, attention was turned to the level of a single city. The chosen case study was New York City, a thriving economic and cultural conglomerate. The results of the methodology, accompanied by a comparison with another model, proved to be very descriptive of the priorities of stakeholders.

The last part of the work was focused on the development of a framework capable of measuring and ranking the actions that were taken by the City of New York after Hurricane Sandy. The selection and attainability of good data created a problem in the first phase of the framework. After a review of various methodologies, it was decided to use the SMART model, a decision making technique, as the quantifying methodology.

A few considerations should be made about the choice and value of this model. It was mainly chosen for its adaptability, a key component of resilience as well, since it is believed that it can be the foundation for an easy to use tool by everyone. In evaluating resilience and the impact that spaces have, it is of great importance to try and involve a considerable amount of diverse stakeholders. In doing so, a larger amount of information is available which then contributes towards building a more precise model around each different case.

The possibility to add or remove criteria freely, assign scoring criteria based on the objectives of the study, area or sensibility of the decision maker and the capability to develop weights either by formula or by preference of the decision maker, it allows the SMART model to be flexible to a great number of applications. Contrary to what it might be expected, another positive aspect of the model is the fact that it is sometimes more precise and descriptive

than MAUT methods which are complicated to use and cannot be applied by everyone. This in turn, is a big plus for an easy to use technique such as the SMART model.

The justification of the SMART model lies on how simple the scoring criteria and weights of these criteria are established. They can be defined by the decision maker by building a hierarchy and then assign scores to each of them. Otherwise, a set of formulas exist to compare or help the decision maker assess these weights based on the same hierarchy (importance) he previously built. Three criteria were used in the SMART model: Time (the amount of months required or planned to complete a project), Cost (budget for each intervention) and Phase (if the project is either completed or still in planning, design or construction).

The last aspect that the study approaches is the importance at the urban, social dimension of the projects. It was noted that in a busy city like New York, different aspects come to play when quantifying the importance of public spaces. This new dimension, Social Impact, was implemented to be combined with the results from SMART and Functionality Index.

This last step proved as difficult to achieve as it is interesting. Measuring the quality of urban spaces was as demanding as measuring resilience. Nonetheless, the process and considerations made in order to assess this dimension proved to be more interesting and/or important than the final rankings as it also brought to light a couple inconsistencies regarding the procedure of work in New York such as the delayed completion of the update and repair of the Hospital.

The study at the end offers an understanding of how long-term resiliency can be measured and optimized through planning and easy to use models of decision making through the participation of various stakeholders. In most developed countries there is a certain level of emergency response that takes place strictly after a disruptive event. In most cases though, rebuilding and adapting is a long process especially after a powerfully impacting event. That is why this kind of approach puts into perspective not only future projects but also preventive measures for existing structures.

The research highlights the difference between these two seemingly similar models and their different results to then add a third component of calculation, the Social Impact of these projects. This dimension was added because it was recognized that the output of the previous models only took into consideration their performance, and not their impact in the quality of the urban space they are surrounded by.

The case study for this approach was New York City and its ongoing recovery projects post Hurricane Sandy. The projects that were used in this work are part of four main Initiatives: Infrastructure, Buildings, Coastal Defense and Neighborhoods.

## ACKNOWLEDGEMENTS

The research leading to these results has received funding from the European Research Council under the Grant Agreement n° ERC_IDEal reSCUE_637842 of the project IDEAL RESCUE— Integrated DEsign and control of Sustainable CommUnities during Emergencies.

## REFERENCES

[1] Holling, C S. (1973). Resilience and Stability of Ecological Systems. Annual Review of Ecology and Systematics, 4(1), 1-23. doi: doi:10.1146/annurev.es.04.110173.000245

[2] Adger, W Neil. (2000). Social and ecological resilience: are they related? Progress in human geography, 24(3), 347-364.

[3] Marschke, Melissa J, & Berkes, Fikret. (2006). Exploring strategies that build livelihood resilience: a case from Cambodia. Ecology and Society, 11(1), 42.

[4] Folke, Carl, Carpenter, Steve, Elmqvist, Thomas, Gunderson, Lance, Holling, Crawford S, & Walker, Brian. (2002). Resilience and sustainable development: building adaptive capacity in a world of transformations. AMBIO: A journal of the human environment, 31(5), 437-440.

[5] 100 Resilient Cities.

[6] UNISDR. (2009). UNISDR Terminology on Disaster Risk Reduction.

[7] Walkera, Brian, Carpenter, Stephen, Anderies1b, John, Abel1b, Nick, Cumming, Graeme, Janssen, Marco, . . . Pritchard, Rusty. (2002). Resilience management in social-ecological systems: a working hypothesis for a participatory approach. Conservation ecology, 6(1), 14.

[8] Wieland, Andreas, & Marcus Wallenburg, Carl. (2013). The influence of relational competencies on supply chain resilience: a relational view. International Journal of Physical Distribution & Logistics Management, 43(4), 300-320. doi: doi:10.1108/IJPDLM-08-2012-0243

[9] Baker, Dennis, Bridges, Donald, Hunter, Regina, Johnson, Gregory, Krupa, Joseph, Murphy, James, & Sorenson, Ken. (2002). Guidebook to decision-making methods. Retrieved from Department of Energy, USA: http://emiweb. inel. gov/Nissmg/Guidebook_2002. pdf.

[10] Fülöp, János. (2005). Introduction to decision making methods. Paper presented at the BDEI-3 workshop, Washington.

[11] Harris, R. (1998). Introduction to Decision Making, VirtualSalt. Online http://www. virtualsalt. com/crebook5. htm (accessed on 09/10/2011).

[12] Olson, David L. Decision aids for selection problems. Springer Science & Business Media, 1996.

[13] Barfod, Michael Bruhn, & Leleur, M. (2014). Multi-criteria decision analysis for use in transport decision making. Technical University of Denmark: Transport Compendium Series Part, 2.

[14] Ewing, Reid, Handy, Susan, Brownson, Ross C, Clemente, Otto, & Winston, Emily. (2006). Identifying and measuring urban design qualities related to walkability. Journal of Physical Activity & Health, 3, S223.

COMPDYN 2017
6th ECCOMAS Thematic Conference on
Computational Methods in Structural Dynamics and Earthquake Engineering
M. Papadrakakis, M. Fragiadakis (eds.)
Rhodes Island, Greece, 15–17 June 2017

# SIMULATED DESIGN PROCEDURE FOR AN IMPROVED SEISMIC VULNERABILITY ASSESSEMENT OF EXISTING RC BRIDGES

**P. Ceresa**[1]**, and L. Marziali**[2]

[1] Institute for Advanced Studies, IUSS Pavia
Piazza della Vittoria 15, 27100 Pavia, Italy
e-mail: paola.ceresa@iusspavia.it

[2] UME School, Institute for Advanced Studies, IUSS Pavia
Piazza della Vittoria 15, 27100 Pavia, Italy
e-mail: marziali.lorenzo@gmail.com

**Keywords:** simulated design, existing bridges, RC bents, seismic response

**Abstract.** *This research work proposes the development of a simplified method for simulated design of existing reinforced concrete (RC) motor-way bridges. Given the fragmentary availability of data, the simulated design procedure should provide information about the reinforcement of bent members in order to proceed with the seismic response assessment of the whole bridge. The developed methodology should be as simple as possible in order to be suitable for large scale seismic vulnerability assessment of the Italian roadway bridge stock. Nevertheless, the methodology should be general in order to take into account the evolution of both construction technologies and regulations within a time window of 50 years, from 1940 to 1990, the most productive period concerning the construction of Italian roadway bridge stock. The validation of the method has been carried out through the comparison of the available executive design documentation of several existing bridges with the corresponding simulated design results, quantifying the discrepancy. Finally, the seismic response of both the existing structure and the "simulated" one have been analyzed by means of non-linear static and dynamic analyses, in order to estimate the influence of such discrepancy on the assessment of the bridge response and, mainly, to evaluate its influence on the large scale seismic vulnerability assessment.*

## 1 BACKGROUND AND MOTIVATION

The assessment of the seismic response of existing structures requires an adequate level of information concerning the geometry of structural members and connections as well as their material properties. Collecting a sufficient level of knowledge of the structure is indeed a preliminary and fundamental step in the seismic response analysis [1] [2]. The required information should be gathered through the review of the executive design documentation, when available, in combination with in-situ surveys and material tests. Given that the aforementioned procedure is likely to be quite expensive in terms of resources and time (especially for those structures whose executive design documentation is not available), the simulated design should be considered as an alternative solution. The simulated design is particularly suitable for large scale seismic risk assessment, with the aim of providing a preliminary estimation of the seismic vulnerability and an order of priority for further analysis and retrofit interventions, when a large sample of structures has to be assessed.

This research work focuses on the development of a simple but general procedure for the simulated design of existing reinforced concrete (RC) bridges designed in Italy from 1940 to 1990. The target of the proposed procedure for simulated design is the estimation of the amount and the configuration of longitudinal and transversal steel reinforcement in RC bent members, knowing the member geometry and the material properties as input data. The procedure should be as simple and general as possible in order to be suitable for large-scale assessment, without neglecting the evolution of both construction technologies and regulations within the period of interest. The development of the procedure is based upon the contemporary regulatory framework concerning bridge design and seismic design, which provide information about the external actions to be considered for the design. A review of several contemporary academic manuals about bridge design ([3]÷[12]) have been also considered as a fundamental reference on this matter. The contemporary regulation concerning the design of RC bridges and buildings has been considered for material classification and for steel bar detailing.

## 2 EVOLUTION OF THE ITALIAN REGULATIONS IN THE 20TH CENTURY

The design of RC motorway-bridges has been subjected to regulations dedicated to bridges, but also to prescriptions which are not specifically related to bridges. From a comprehensive literature review carried out in this work, it can be stated that the Italian regulatory framework consists of three main areas:

a. Prescriptions for structural design of bridges ([13]÷[19]);
b. Prescriptions for structural design of buildings located in seismic areas ([20]÷[22]);
c. Prescriptions for structural design of RC buildings ([23]÷[26])**.**

The above mentioned regulations provide information on both the external loads and actions, and the detailing prescriptions the designer should have considered in the project. A detailed description of the most important aspects of the evolution of the Italian regulations is provided in [27].

## 3 SIMPLIFIED METHOD FOR THE SIMULATED DESIGN OF BRIDGES

The target of the simulated design of existing structures is to provide information about those characteristics not directly obtainable from in-situ surveys, such as member reinforcement or joints detailing, in the cases when the design documentation is not available. Simulated design should be preferred to surveys or documentation review when the seismic response assessment has to be carried out for a large number of homogeneous structures and the effort of the surveys is not affordable. Design output should be as closer as possible to the

actual configuration of the existing structure in order to proceed with an effective assessment of its seismic response. The proposed method focuses on substructure details (steel reinforcement configuration) for motorway-bridges with continuous or discontinuous deck, designed between 1940 and 1990. The methodology is based on the elaboration of data such as age, location and geometry of the structure and mechanical properties of materials, according to the appropriate design prescriptions inferred from the contemporary regulation, the technical literature and the design reports on the available cases of study.

### 3.1 Main assumptions

For the sake of simplicity, the design procedure relays upon assumptions about structure geometry, distribution of forces among structural members and nodal degrees of freedom. Such assumptions are considered to have negligible impact on design results. Furthermore, given that most of the data about material properties is usually missing, the latter need to be derived from the review of the contemporary regulatory framework, technical literature and available design reports. This review represents also a reference for several assumptions and simplifications concerning the design procedure, which allows the method to be as general as required for large scale application but consistent with contemporary construction practice and technologies.

One of the most important simplifications adopted in the proposed method is to consider each pier as if it was not connected to the rest of the structure. An ideal superstructure portion including half of each tributary span length gives the load on the piers. This implies neglecting the eventual stiffness irregularity along the structure, due to differences in bent heights and to abutments stiffness. In case of regular and irregular bridges with discontinuous superstructure, in which relative rotation between adjacent girders is weakly inhibited, this assumption is fairly consistent with the actual transversal behaviour of the structure. Also the transversal behaviour of regular bridges with continuous superstructure is compatible with such assumption. On the other hand, the longitudinal behaviour of irregular bridges with continuous or discontinuous superstructure is captured with limited accuracy, since in this case all the bents are constrained to the same top displacement. However, it should be pointed out that discontinuous superstructure is the main representative among existing motorway bridges.

Then the bearing devices between the super- and sub-structure are assumed to transfer the entire lateral load to the substructure, including the case of merely frictional bearing capacity [2] [28]. This is considered to be consistent with the requirement for structure serviceability prescribed for the design level of loads.

Furthermore, it is assumed that the foundations do not suffer any stiffness loss for the design level of loads and thus the substructure base is assigned to be fully fixed.

Superstructure torsional and flexural stiffness is assumed to be negligible with respect to substructure flexural stiffness, implying bent top is assigned free-end boundary conditions in both longitudinal and transverse direction. Once more, this ensures a better fit to discontinuous superstructure bridges behaviour than to continuous ones. Nevertheless, as continuous superstructure is usually associated to large span lengths, the assumption is considered to be acceptable for both bridges categories.

The method refers to contemporary regulations for what concerns external loads, particularly for horizontal actions (wind, braking vehicles and earthquake) combined with permanent and moving gravity loads. Additionally, multiple configurations of moving loads are considered in order to determine the more unfavourable set of actions (in terms of vertical and horizontal forces and flexural moments) transmitted from superstructure to bent top. Vertical loads are thus assigned a longitudinal and a transversal eccentricity, standing respectively for

the eventual non-symmetric distribution of moving loads across the deck width and the bearing device eccentricity (in case of bridges with discontinuous superstructure).

Seismic actions are included in the design procedure within the equivalent static analysis framework. The modal analysis framework, included in national provisions from 1975, is not included in the design procedure, because it is considered to be incompatible with the desirable level of simplicity. Moreover, the modal analysis is unlikely to have found widespread application for bridge seismic design within the period of interest due to limited available computational tools.

According to the framework of provisions for bridges, the design method considers two conventional loading directions: longitudinal and transversal with respect to the bridge deck. A set of actions is assigned to each conventional direction, including the corresponding vertical and horizontal forces and bending moment, to be applied at bent top. When the local reference system of the bent does not coincide with the one of the deck, the sets of actions are provided referring to the former one. Deformations and forces distribution among the pier members is estimated by means of bi-dimensional elastic frame models, one for each conventional loading direction. It should be pointed out that the axial deformability of the members is neglected. This leads to a loss of accuracy in the estimation of axial actions within the members, in particular for framed substructures. In these structures, assuming no member axial deformability implies that no vertical displacement is captured at the frame nodes and, thus, the axial actions induced in vertical members by the external moment applied to bent-top cannot be properly estimated.

Section detailing design and verification are performed by means of the allowable stress method, independently from the year of design of the bridge, since this method was used in the time window of reference. The section is not verified for the bi-axial bending condition, but only for the two corresponding uniaxial components.

Lateral instability verifications are considered only for bridges designed after 1972 and the member effective length is related to the boundary conditions and the height of the piers.

### 3.2 Proposed methodology

The simulated design method is organized into four main steps, namely:

- Input;
- Estimation of external actions transmitted to bent top;
- Estimation of internal actions in bent members;
- Design and verification of steel reinforcement.

Each step is described in the next subsections.

***Input***

The year when the executive design of the bridge was redacted is one of the fundamental input information, as it allows the design process to be related to the corresponding regulatory, scientific and technological context. Also the location, in terms of municipality, distance from the coast and altitude, is an important input information, for an adequate estimation of seismic and wind actions, in accordance with the specific regulation.

Sufficiently detailed information about the geometrical characteristic of the structure is also needed. The width and the span-lengths of the deck are the minimum required information about the superstructure; all the other parameters, if not available, could be obtained by a combination of those basic data with the road traffic class (i.e. motorway or not). In particular, superstructure height and weight could be related to its span-length; while the eventual presence of pedestrians sidewalks is easily inferable from the traffic class of the road. The geo-

metrical configuration of the bearing devices, both in terms of their height above the bent cap-beam and eccentricity, is required for an accurate estimation of the external actions transmitted to the bent top. Information about the bearing height, if unavailable, could be related to the year of the executive design: the employment of polymeric bearings with reinforcing steel plates can be excluded for bridges designed before 1971 (because of the lack of regulations on the subject) and friction supports employing relatively thin rubber layers are considered to be quite widespread for those bridges. Information about the longitudinal eccentricity of bearings, if not available, could be related to the longitudinal dimension of the bent cap-beam.

The geometrical characteristics of the bents should be as detailed as possible. Fundamental information are the sectional typology and the dimensions of both columns and beams. A standard input format have been adopted for bent geometry, according to which the former must be defined as an assembly of segments. The data assigned to each segment can be summarised as follows: height, sectional geometry and sectional multiplicity both in longitudinal and transversal direction. The sectional geometry is represented by means of the minimum required number of parameters in order to describe it accurately. The sectional multiplicity parameter allows multi-column bents or spatial-frame bents to be taken into account by the input format.

Information on the material properties, such as characteristic concrete cubic strength and the steel yielding stress, should be also provided for a more accurate simulation of the design of the section detailing. It has to be noted that concrete quality results to have a great influence on detailing simulation, especially for massive bents containing the minimum prescribed steel percentage and designed before 1972, when that percentage was related to the sole member sectional area necessary to resist purely axial loads.

For bridges designed before 1960, if there are no information on the mechanical properties of materials, the simulated design procedure refers to the acceptability criteria for concrete and steel provided in R.D. n.2229 [23]. For bridges designed between 1960 and 1970, if the information is not available, the procedure assigns conventional mechanical properties according to the statistical mean values provided in [29] [30] for concrete and steel bars employed for RC structures during that time window of reference. For bridges designed after 1970, in absence of detailed information, the simulated design procedure refers to the acceptability criteria for steel provided in D.M. 1972 and D.M. 1974 [31] [32]. If the class of steel is unknown, the procedure employs the steel class FeB 38 with the corresponding minimum mechanical properties. Concrete characteristic compressive strength is assumed to be $R_{ck}$ = 25 MPa, if no different information is provided, in order to be conservative with respect to the available statistical data provided in [29].

***Estimation of external actions transmitted to bent top***

The actions transmitted to the top of each pier are grouped in a vector, named $A_{ext,k}$, containing five elements, for each considered load combination k: the vertical force N, two horizontal forces $V_L$ and $V_T$, acting in longitudinal and transversal direction respectively, and two flexural moments $M_L$ and $M_T$ acting around transversal and longitudinal axis, respectively.

According to code provisions, the following sources of external actions on the top of the pier have been included in the procedure: i) structural self-weight and permanent loads; ii) moving loads and their dynamic effects; iii) wind; iv) earthquake (EQ); v) deformations (e.g. shrinkage, pre-compression, thermal excursions). The prescribed combinations, with very small differences between different regulations, are:

1. Structural and permanent loads + wind + deformations;
2. Structural and permanent loads + moving loads + wind (reduced) + deformations;
3. Structural and permanent loads + moving loads (reduced) + EQ + deformations.

Each set of external forces, $A_{ext,k}$, is then rearranged in two independent vectors, $A_{ext,dir,k}$, defined for each direction *dir* (dir = 1, 2 where 1 stays for the longitudinal direction and 2 for the transversal direction) and load combination *k* (Figure 1).

### *Estimation of internal actions in bent members*

The target of the current design step is to provide different sets of vectors $A_{int}$, collecting internal member actions at the sections of interest, for each set of external forces $A_{ext,dir,k}$. Such a vector can be expressed, for each direction *dir*, load combination *k* and member section *m*. The internal actions, for each member section of interest, are estimated by means of elastic analysis of planar frames. The analysis takes into account external actions $A_{ext,dir,k}$, together with pier members self weight (Figure 1). Each set of member internal forces obtained for pier columns, expressed as vector $A_{int,dir,k,m}$, is rearranged in two independent vectors: $A^{+}_{int,dir,k,m}$ and $A^{-}_{int,\ dir,k,m}$, in order to take into account for both axial load conditions of tension and compression induced by reversal lateral loading. These vectors collect all possible configurations of the internal actions for each considered loading combination and direction and are thus appropriate for section reinforcement design and verification.

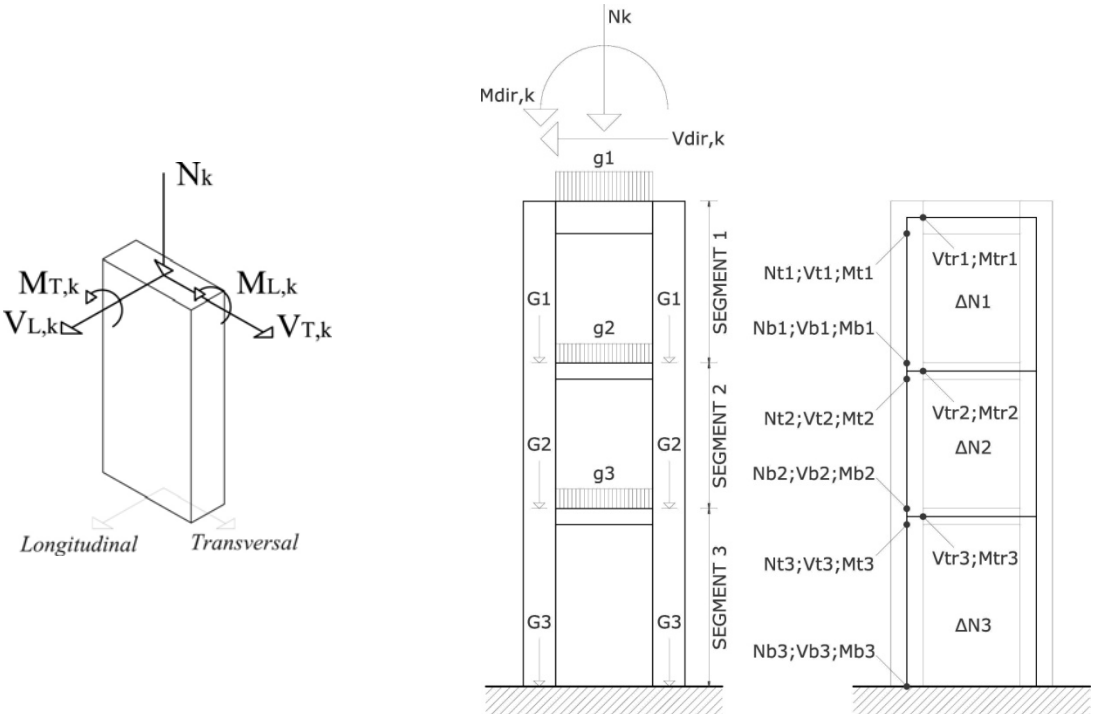


Figure 1: External actions transmitted to a generic bent (left) and internal actions for a generic bent (right)

### *Design and verification of steel reinforcement*

Knowing the internal actions, the longitudinal and transversal reinforcement bars are designed with the allowable stress method according to the design prescriptions of the time and being compatible with the geometrical dimensions of the section of reference.

The design of longitudinal reinforcement configuration takes into account the executive prescriptions provided by the contemporary regulation for RC design. In particular, the minimum and maximum acceptable bar diameter as well as the minimum bar spacing and concrete cover are some of the restrictions to be observed for section rebar detailing.

According to the regulation, a minimum standard configuration of transversal reinforcement should be assigned to all column and beam members. For what concerns the bar diameter, a minimum of 6 mm is to be adopted and no restrictions are specified as an upper limit.

The simulated design starts assuming the minimum amount of reinforcement prescribed in the code of reference. When the minimum prescribed reinforcement is not sufficient for the verification of the section, it is progressively increased until the material stresses remain below the acceptable limits.

## 4 VALIDATION

In order to estimate the accuracy of the proposed method, the simulated design procedure has been applied to several existing bridges. For such bridges, sufficient information had been collected to check whether the results of simulated procedure are accurate. Section details, such as the amount and spacing of longitudinal and transversal reinforcements, have been regarded as the main terms of comparison for accuracy estimation. The internal actions, if available in the documentation, have been also compared.

Within the considered case-studies, ten bridges, grouped according to their sub-structural type, are the focus of the validation (Figure 2):

- Bridges with wall-type substructure;
- Bridges with framed substructure;
- Bridges with single-pier substructure.

Considering the group of the bridges with wall-type substructure, five bridges over the River Adige, located in Trento District and designed between 1961 and 1981, are considered (Avio, 1961; Faedo, 1962; Trento, 1963; Nomi, 1976; Rovereto, 1981). All these bridges present the same structural typology, consisting of a constant span-length discontinuous deck simply supported on a regular substructure. The latter is fixed at the base by means of pile foundations. The only exception is the bridge located in Rovereto (Trento) in which the first wall is fixed to a pile-supported foundation; the other walls have drilled shaft foundations reaching different depths. This group of bridges allowed to investigate the accuracy of the simulated design procedure for structures designed in different periods and, thus, according to different provisions.

Two are the bridges belonging to the group of bridges with framed substructure. They were designed before 1950. Even if they have the same substructure typology and member sectional geometry, the two structures are very dissimilar to each other because of the traffic level and the bents height. The first bridge over the Adige river in Trento was designed in 1943 and is supported on single-level frames being 5.3 m height. The second is the viaduct Rio Torto in Castiglione dei Pepoli (Bologna) which is supported on multi-level frames of variable heights ranging between 13.8 m and 41.35 m. This allows the accuracy of the simulated design procedure to be investigated for the same sectional geometry for two different conditions.

Three viaducts, located in Southern Italy and designed between 1965 and 1988, belongs to the third group considered for the validation - the bridge “Vose” in Picerno (Potenza), designed in 1965; the viaduct “La Rossa” in Vietri di Potenza (Potenza), 1971; the viaduct “Egolo” in Caltagirone (Catania), 1988. All these bridges present the same structural typology, consisting of a constant span-length discontinuous deck simply supported on an irregular substructure. A minor variation of this scheme is represented by the viaduct “Vose” in Picerno (Potenza), which has a slightly curved deck, and by viaduct “Egolo” whose span-length is not constant. The section geometry of the pier is hollow rectangular in the first two cases and hollow circular in the third case. This group of bridges allowed the accuracy of simulated design procedure to be investigated for structures with different sectional geometry and designed according to different provisions.

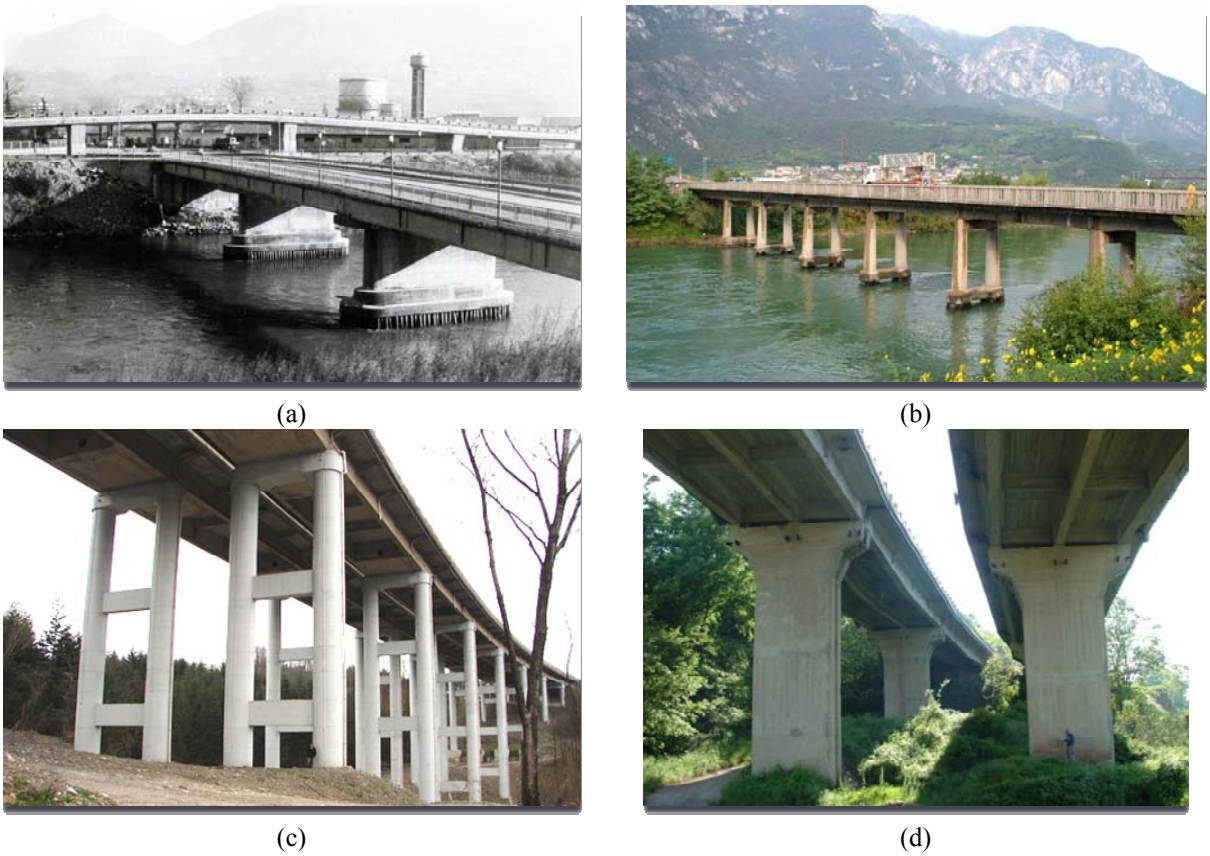

Figure 2: Some of the RC bridges considered in the validation process. Bridges over the Adige river, Trento, 1962 (a) and 1943 (b). Viaduct over the river Rio Torto, Roncobilaccio (Bologna), 1950 c). Viaduct "Vose", Picerno (Potenza), 1965 d).

The focus of the validation is the evaluation of the discrepancy of the results in terms of computed reinforcing bars with respect to the actual reinforcement configuration in the existing structures, as reported in the available executive design documentation. A discrepancy of 30% has been considered as an acceptability criterion for the validation, taking into account that the proposed methodology should be applied in large-scale assessment evaluations.

The procedure demonstrated to have a significant variability with the substructure typology for what concerns the level of accuracy in the estimation of both longitudinal and transversal reinforcement, although for most of the considered case studies, a better level of accuracy is achieved for the longitudinal reinforcement with respect to the transversal one. On the other hand, it has been derived that the level of accuracy appears to be independent from the year of redaction of the executive design.

In case of single pier bents with wall-type section the median discrepancy affecting the estimation of longitudinal reinforcement ranges between an underestimation of 12% and an overestimation of 20%, which can be considered a fairly good grade of accuracy. On the other hand, the average discrepancy affecting transversal reinforcement ranges between an underestimation of 20% and an overestimation of 120%, which is extremely far from the assumed acceptability limit. On this issue, it should be recalled that the majority of the considered case studies seem to be in contrast with the contemporary regulations about the maximum allowable spacing of the transversal reinforcement bars.

The two considered cases of bridges with framed bents cannot be regarded to be part of the same category, because of incomparable bent heights which lead to very different level of accuracy. The bridge over the Adige river is characterised by piers with constant height of 5.3

meters; the piers of the viaduct over the Rio Torto river have very different heights ranging from 13.8 to 41.35 meters. Nevertheless, it can be generally observed that the simulated design method achieve a fairly good grade of accuracy (overestimation not exceeding 30%) for those part of the structure where the required reinforcement is determined by the magnitude of the applied actions (i.e. lower part of tall columns or beams), while less satisfactory results (underestimation up to 50%) are achieved for the parts where the minimum prescribed reinforcement results to be adequate (i.e. upper parts of tall columns or short columns). This could be related to the fact that construction requirements or other design choices could have lead designers to adopt a higher quantity of reinforcement independently from contemporary prescriptions and from the level of design actions.

For what concerns the single pier bents with hollow rectangular or circular sections the longitudinal reinforcement results to be generally underestimated. The median discrepancy is 35%, which exceeds the adopted acceptability limit. The discrepancy affecting the estimation of transversal reinforcement for this type of substructures also results not to be always satisfactory, with peaks of 33% overestimation and of 40% underestimation.

## 5 SEISMIC RESPONSE ASSESSEMENT OF THE BRIDGES

The simplified method for simulated design determines a discrepancy in the estimation of steel reinforcement of member sections. In order to investigate the influence of such discrepancy on the seismic response assessment of the whole structure, both nonlinear static and dynamic analyses have been performed. Each bridge has been analysed considering the outputs of the simulated design and the data derived from the executive design drawings. The results have been compared evaluating the discrepancy in terms of base shear, deck displacement and section hysteresis. The results of two structures among those considered for the validation of the simulated design method will be discussed in this Section: the viaduct “Egolo” in Caltagirone (Catania) and the bridge over the Rio Torto river in Castiglione dei Pepoli (Bologna). The analyses have been performed by means of the commercial software Midas Civil. The finite element model of each bridge is characterised by masses lumped in the joints and by fibre beam-column elements with distributed inelasticity able to catch the nonlinear response of the piers. The fibre beam element is a standard Euler-Bernoulli force-based beam element since, to the authors’ knowledge, the axial-flexure-shear interaction is not yet implemented in a commercial software ([33]÷[38]). The Kent-Park constitutive model is adopted for modelling the behaviour of concrete, the Menegotto-Pinto constitutive relationship is used for steel.

Before analysing the bridges, a comprehensive review of the state-of-the-art and code provisions about nonlinear static analysis methods has been required in order to determine the most appropriate one for the above mentioned purpose. It should be recalled that nonlinear static analysis procedures have been developed for seismic assessment and design of regular buildings, whose seismic response is mainly dominated by the fundamental mode of vibration.

The basic conceptual procedure consists of the following steps:

- Estimation of the push-over curve by means of bi-dimensional incremental nonlinear analysis. The curve relates the total base shear $V_b$ to the lateral displacement $u_R$ of a reference degree of freedom (DOF), usually a node of the roof level is chosen in case of building analysis.
- Derivation of the equivalent SDOF system capacity curve from push-over curve; the former relates the applied lateral force $V^*$ to the corresponding lateral displacement $D^*$.
- Estimation of displacement demand of the SDOF system by means of either over damped or reduced elastic spectrum.

- Derivation of seismic response parameters by means of the incremental nonlinear analysis database for the step corresponding to the SDOF target displacement.

Within the above described conceptual framework, several variations of this method have been proposed in order to improve its accuracy ([39]÷[41]). Attempts have also been made by Chopra and Goel [42] and by Casarotti and Pinho [43] in order to take higher mode effects into account, despite the methods are based on equivalent SDOF systems for seismic demand estimation. The current state-of-the-art on nonlinear static method for bridge assessment is represented by the following commonly employed push-over-based methods: i) Capacity Spectrum Method (CSM), ii) N2 Method, iii) Modal Pushover Analysis (MPA) and iv) Adaptive Capacity Spectrum Method (ACSM). The application of these procedures to bridges required an ad-hoc selection of the reference joint, with the exception of the ACSM method.

According to the prescriptions of the Italian building code [44] and on the basis of the review of the state-of-the-art concerning non-linear static analysis of bridges, the modal push-over analysis (MPA) method and N2 method have been employed respectively for the transversal and longitudinal seismic response assessment of the continuous-deck bridge over the Rio Torto rived in Castiglione dei Pepoli. The latter method has also been employed for the transversal and longitudinal seismic response assessment of the Viaduct "Egolo" in Caltagirone.

The non-linear dynamic analysis consists in the direct integration of the system of equations of motion referred to the analysed structure. The forcing function is a ground acceleration time history, assigned at the base nodes of the finite element model. The implicit method of Newmark is adopted for the integration, performing Newton-Raphson iterations until convergence is obtained for each step increment of the considered ground acceleration time history. For the aims of this work, suites of natural accelerograms compatible with the considered elastic acceleration response spectrum for the collapse limit state, have been obtained by means of the software REXEL [45], which provides suites of 7 spectrum-compatible ground motions (each including up to three components) chosen within the European Strong Motion Database. In this work, single component ground motions have been selected within a limited group of events matching the magnitude and distance characteristics obtained through the de-aggregation of the uniform hazard spectrum. The elastic damping has been modelled by means of Rayleigh's approach with a percentage of 2% damping in correspondence of the first two periods of the structure (the fundamental period has been adopted for SDOF systems).

### 5.1 Nonlinear static analysis of the bridge "Egolo"

This RC bridge (Figure 3) consists of a 24-span discontinuous deck resting on single-pier bents of different heights. Since no translational constraint is provided between adjacent spans, each pier can be analyzed separately from the rest of the structure for what concerns both the transversal and longitudinal response, in agreement with the nonlinear static approach proposed in the Italian Building Code [44]. In order to investigate the influence of the discrepancy in member reinforcement due to the simulated design procedure, the response of two representative piers has been analyzed. The latter are the shortest (7.3 m) and the tallest (14.7 m) pier of the bridge and they have hollow circular cross-section (Figure 3). The seismic hazard of the site where the bridge is located has been determined according to the Italian Building Code[44]. The seismic hazard parameters have been inferred from the Italian hazard map in correspondence of the geographical coordinates of the bridge. Two limit states are considered in the analysis – SLC and SLV according to D.M. 2008 [44].

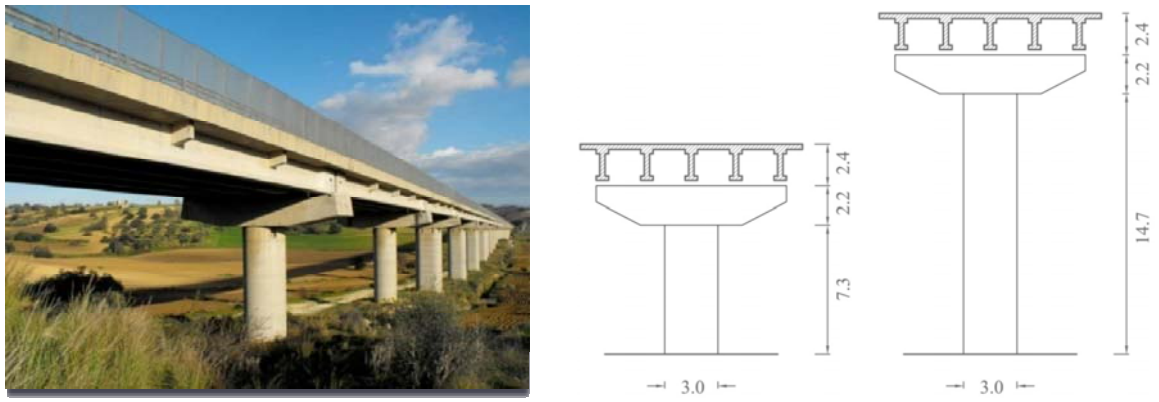


(a) (b)

Figure 3: Viaduct "Egolo" (Caltagirone, 1988): general view (a) and its shortest and tallest piers (b)

Each pier is considered as a SDOF system with a mass M lumped at the deck centre of mass. The mass M has been assumed to include the mass of the tributary deck length, that of the cap beam and 1/3 of that of the pier. A force-based and displacement controlled pushover analysis has been performed for each pier.

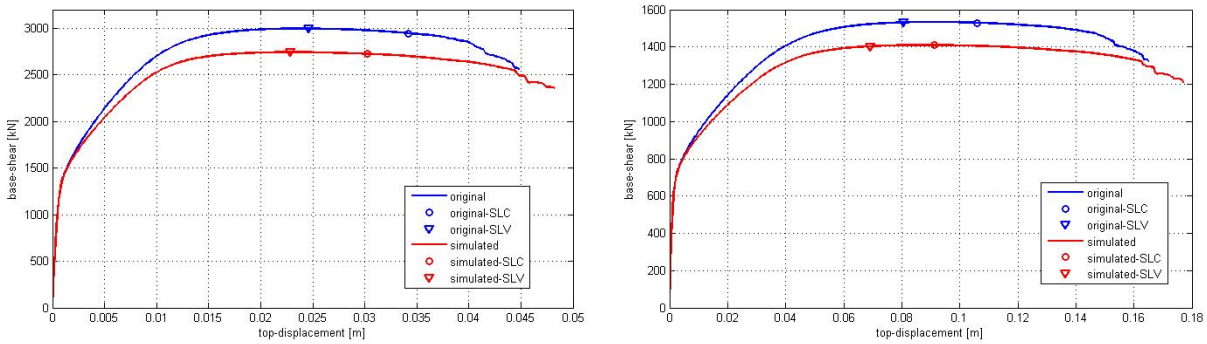


(a) (b)

Figure 4: Pushover curves and performance points for the damage and collapse limit states for the shortest (a) and the tallest pier (b)

| Pier | | $V_{SLC}$ (kN) | $V_{SLV}$ (kN) |
|---|---|---|---|
| Smallest pier | Executive drawings | 2947 | 2995 |
| | Simulated design | 2725 | 2743 |
| | Difference (%) | -7.5 | -8.4 |
| Tallest pier | Executive drawings | 1530 | 1530 |
| | Simulated design | 1410 | 1403 |
| | Difference (%) | -7.8 | -8.3 |

Table 1: Influence of the reinforcement discrepancy on the base shear considering two limit states (where SLC and SLV are two limit states defined as in D.M. 2008 [44]

As result of the simulated design, an underestimation of longitudinal reinforcement of about 15% was obtained. Such discrepancy directly affects the pushover curve of both piers, as shown in Figure 4. The base-shear capacity results to be underestimated of about 10% and 7% for shortest and tallest pier, respectively. Anyway the assessment of the general behaviour of the piers is not affected by the reinforcement discrepancy. A lower maximum capacity of the system implies a higher elastic stiffness, provided that the elastic branch of the curve is coincident. This overestimation of the ideal elastic stiffness produces an underestimation of

about 15% in the estimation of the displacement demand (i.e. performance point) for both the considered piers.

The reinforcing discrepancy results to have a very low influence on the estimation of the base shear and bending moment demands, which is slightly (below 10%) underestimated for both the considered piers, as reported in Table 1. Nevertheless, it should be noticed that the seismic demand for the bridge location is not adequate to bring the piers widely into the inelastic branch of the response, as can be observed in Figure 4.

### 5.2 Nonlinear dynamic analysis of the bridge "Egolo"

In order to further investigate the influence of the discrepancy in member reinforcement on the seismic response, nonlinear dynamic analysis has been performed for the above mentioned representative piers of the bridge. Since the piers have a circular section and are analyzed separately from the rest of the bridge, there is no difference in transversal and longitudinal response. Therefore, the selected ground motions have been arbitrarily applied in transversal direction. The analysis employs the same distributed plasticity FE model of the nonlinear static analysis. The results of the analyses of the bridge with the reinforcement derived from the simulated design are compared with the results of the bridge with reinforcement obtained from the executive drawings. The deck displacements (i.e. the displacement of the top of the pier) and the base shear of the piers have been compared (Table 2).

The influence of member reinforcement discrepancy on top-displacement response is quite significant for the shortest pier. The FE model with simulated design reinforcement, which is affected by a 15% underestimation, generally experiences a higher top-displacement than the one with the original reinforcement (Table 2) . On the other hand, the top-displacement of the tallest pier does not appear to be significantly affected by the discrepancy of reinforcement. This could be due to its higher deformation capacity within the elastic range.

The base shear response is not significantly affected by the discrepancy in member reinforcement and is generally affected by an underestimation of about 10% (Table 2). This is consistent with the 15% underestimation of the longitudinal reinforcement obtained from the simulated design procedure.

It can be concluded that the discrepancy in the estimation of the member reinforcement has a small influence on the assessment of the seismic response of the considered piers, in particular when the tallest and more flexible pier are considered.

| Pier | Maximum deck displacement | | Maximum base shear | |
|---|---|---|---|---|
| | Average difference (+) [%] | Average difference (-) [%] | Average difference (+) [%] | Average difference (-) [%] |
| Smallest pier | + 6.5 | +39.2 | -10.5 | -4.3 |
| Tallest pier | -10.0 | -7.7 | -10.0 | -7.7 |

Table 2: Influence of simulated design on the maximum deck displacement and the maximum base shear

### 5.3 Nonlinear static analysis of the bridge over the Rio Torto river

Since the bridge presents a continuous deck, it is not possible to analyze each bent as if it was an independent single degree of freedom (SDOF). Nevertheless, the dilatation gaps located between the spans are assumed not to transmit transversal actions between one deck segment to the other. This allows the transversal seismic response of each segment to be analyzed separately from the rest of the structure. Moreover, since the deck consists of two independent girders, the structure can be simplified as if it consisted of two identical bridges next to each other and analyzed separately. The analyses presented herein are limited to the transversal and longitudinal response of the portion of the bridge shown in Figure 5.

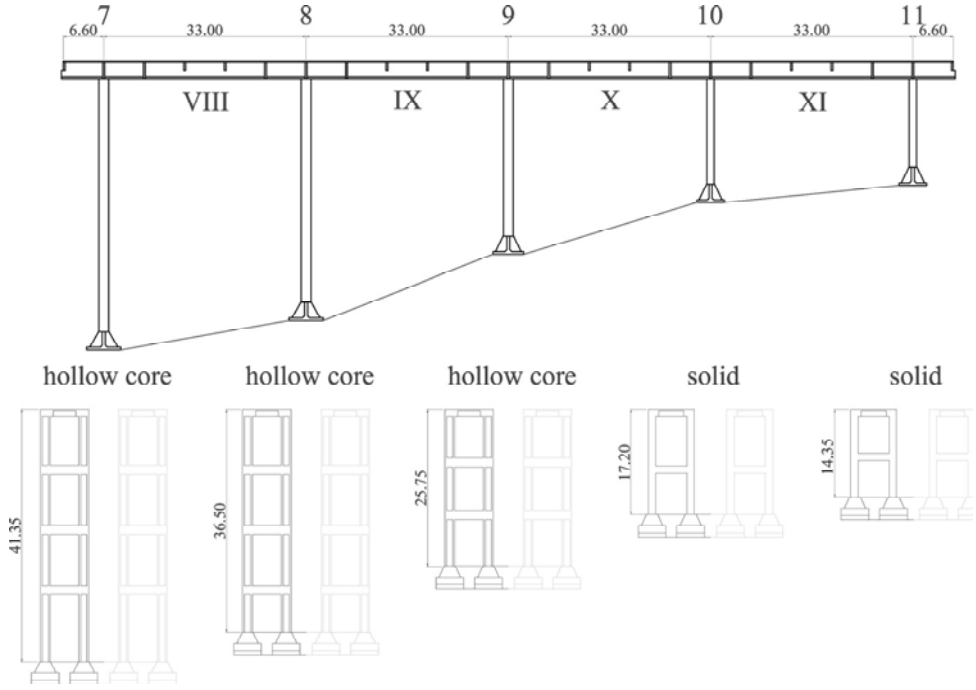


Figure 5: Analysed portion of the viaduct over the Rio Torto river (1950, Roncobilaccio)

The numerical model consists of a lumped-mass and distributed plasticity model and employs mono-dimensional frame elements both for the bridge deck and the bent columns and beams (Figure 6) . Each span of the bridge deck has been divided in three elastic elements of 11 m each; the two cantilever portions of the deck are not included in the model, but the corresponding mass is lumped at the deck end joints. The former elements are located at a distance from the cap-beam axis consistent with the position of the centre of mass of the deck section and are assigned a generic sectional shape with the same geometrical properties of the actual deck section. The connection between deck elements and the bents is such that all the translational displacements are constrained and that the torsion and the transversal bending of the deck are transmitted to the bents by means of vertical and horizontal forces, respectively. This is achieved by means of two additional joints, with the spatial coordinates equal to the nodes of the top of the columns, constraint to behave as a rigid body with the deck centre of mass in all directions except from the transversal one. Those nodes are hinged to the column top nodes by means of spring elements with high translational stiffness and negligible rotational stiffness. The afore described ideal connection is sketched in Figure 6, where K [kN/m] and Kr [kNm/rad] stand respectively for the axial and flexural stiffness, while D and R stand respectively for translational and rotational degrees of freedom (1 standing for constrained DOF). No restrains are applied to the deck end nodes, due to the presence of the dilatation gaps.

As mentioned before, the selected method for the non-linear static analysis is the Modal Pushover Method (MPA), since it represents a satisfactory trade-off between computational simplicity and analytical accuracy and is also recommended by the current Italian Building Code [44] for seismic assessment of existing bridges with continuous deck.

In order to proceed with the modal pushover analysis, the significant modes of vibration for the transversal seismic response of the bridge have been identified by means of modal analysis. The deck mass has been lumped at the elements nodes. The actual distribution of mass within the bents has been considered by means of the consistent mass approach. The uncracked gross section of the members has been considered for the analysis, since a reduction

of member stiffness would only affect the estimation of modal forces, which have no relevance within the MPA approach. Stiffness reduction is expected to have a negligible effect on the modal shapes and participant mass factors, which are of primary importance for MPA.

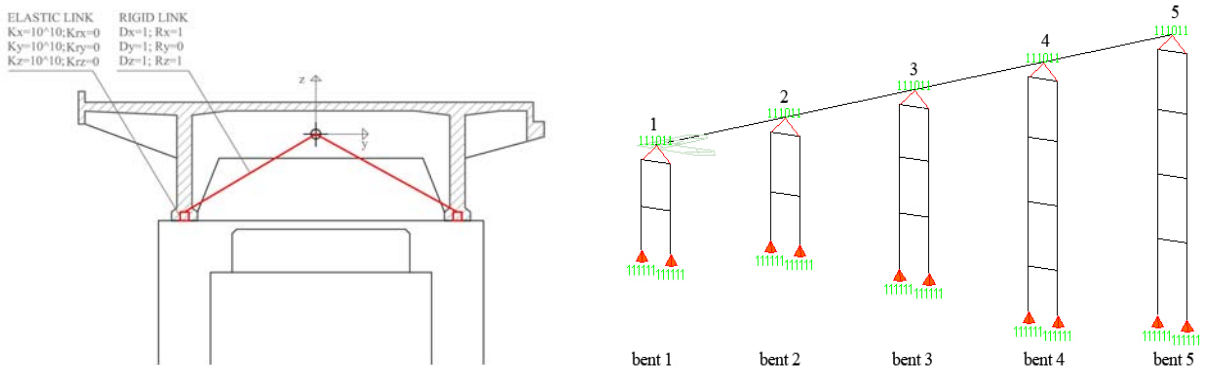


Figure 6: FE model of the analysed portion of the viaduct over the Rio Torto river

The first two transversal modes of vibration sum up a participant mass of 87.3% and, thus, have been considered to be adequate for the assessment of the transversal seismic response of the bridge through MPA. The modal parameters of interest within the presented analysis procedure are M.P.M. which stands for the modal participant mass and Γ which stands for the modal participation factor. The results of the modal analysis are not affected by the discrepancy in steel reinforcement evaluation highlighted, since the reinforcement configuration and quantity are not involved.

Two non-adaptive force-based and displacement-controlled push-over analysis have been carried out, one for each of the above mentioned mode of vibration. The load pattern for each analysis have been defined according to modal shapes. The node expected to experience the maximum lateral displacement has been chosen as reference point for the pushover curve.

Since the structure is symmetric with respect to its longitudinal axis, the transversal response is not changing with the sign of the loading pattern (i.e. positive or negative direction). Therefore, only the positive direction has been adopted for the analysis. It should be also pointed out that geometrical non-linearity is not taken into account since this kind of analysis is not supported by the software Midas Civil in combination with the distributed plasticity approach. The procedure has been repeated for two different models, one being assigned the reinforcement configuration and quantity reported in the available executive drawings and the other being assigned the reinforcement configuration and quantity estimated by means of the simulated design procedure. A total of four push-over curves is obtained for the bridge.

The discrepancy in member reinforcement has a limited impact on the transversal push-over curves for both the load patterns. A first observation is that the load pattern (a) proportional to mode 2 results in a far more flexible response of the bridge than load pattern (b) proportional to mode 3. The elastic stiffness is much lower for pattern (a) with respect to pattern (b). This is due to the fact that the former is much more demanding for the flexible side of the sub-structure (i.e. bents 3-4-5), which is able to experience larger elastic deformations, than for the stiff side (i.e. bents 1-2). The latter, instead, allocates the forces more uniformly along the deck and particularly involves the stiff side of the substructure.

Moreover, the bridge displays a higher shear capacity and a hardening behaviour for pattern (a) and a softening behaviour for pattern (b). Also this difference is related to the distribution of forces between the flexible and stiff side of the substructure. Due to limited elastic flexibility of bents 1 and 2, plastic hinges are rapidly developed at column base sections for pattern (b) and manifest a relatively brittle behaviour because of low confinement and severe

compressive loading. The aforementioned observations on the structure behaviour are confirmed by the comparison of the individual push-over curves for each bent and each load pattern. Bents 1-2 experience very low displacement levels with respect to bents 4-5 for pattern (a), while the opposite can be observed for pattern (b). Combining this with the fact that the curvature demand at column base section is sensibly lower for flexible bents 3-4-5, a further explanation of the different behaviour of the structure for load pattern (a) and (b) is provided. The influence of the member reinforcement discrepancy, due to simulated design, on the pushover curves is observed to be fairly low and not to affect the global behaviour of the structure. Nevertheless, a noticeable influence can be observed on the base-shear capacity of the bridge for both load patterns (a) and (b), which results to be lower for the model with simulated reinforcement. For what concerns pattern (a), it should be noted that in the model with simulated reinforcement the flexural capacity of column members of bents 3-4-5, which practically govern the response, is overestimated at the base sections and underestimated at the intermediate sections. This is consistent with the results of simulated design, which provide a 12% overestimation and a 50% underestimation of longitudinal reinforcement for base and top sections, respectively. The combination of the two aforementioned opposite effects leads to a slight underestimation of the base-shear capacity, specially for high displacement levels at which the concrete cracking interests also the upper part of the columns and allow the reinforcement underestimation to affect the capacity. On the other hand, the base shear capacity for low displacement levels appears not to be affected by the reinforcement underestimation at the upper part of the columns, where concrete cracking has not yet occurred, and therefore results to be slightly overestimated, consistently with the overestimation of reinforcement at column base-sections obtained in simulated design.

For what concerns pattern (b), it should be noted that, in the model with simulated reinforcement, the flexural capacity of column members of bents 1-2, which practically governs the response, is underestimated at the base sections. This can be related to an even more brittle behaviour of the section with simulated design reinforcement with respect to the original one, due to a longitudinal reinforcement overestimation of 28%. The effect of such reinforcement discrepancy directly reflects on the response of the whole bents 1-2, since no cracking of the sections is achieved at the upper part of the columns.

In order to investigate the influence of reinforcement discrepancy on the assessment of the transversal seismic response of the structure the performance point has been computed for each load pattern and the corresponding response parameters (deck-displacement and base shear) have been combined according to SRSS rule. The determination of the performance point, i.e. the seismic demand on the structure, associated to each of the two load patterns require each pushover curve to be transformed in the idealized capacity curve $V_n^*$-$D_n^*$ of the corresponding equivalent SDOF system.

As it can be observed in Figure 7, there is a significant difference for the elastic stiffness of the equivalent SDOF systems for both modal push-over cases. In particular, the load pattern (a) results in an overestimation of 17%, which is consistent with the aforementioned observations related to the structural response. On this subject, it should also be noted that the elastic stiffness estimation by means of the code based approach is affected by the discrepancy in the maximum base-shear capacity; in fact, a lower maximum capacity of the system implies a higher stiffness, provided that the elastic branch of the curve is coincident. The load pattern (b) results in an elastic stiffness overestimation of about 9%, which is only due to the difference in the maximum base-shear capacity of the system. The error in the estimation of the elastic stiffness of the equivalent SDOF system results in a low discrepancy in the estimation of the displacement demand for both the modal pushover cases. Therefore, there is no significant influence on the computation of the performance point for both cases, as shown in Figure 8.

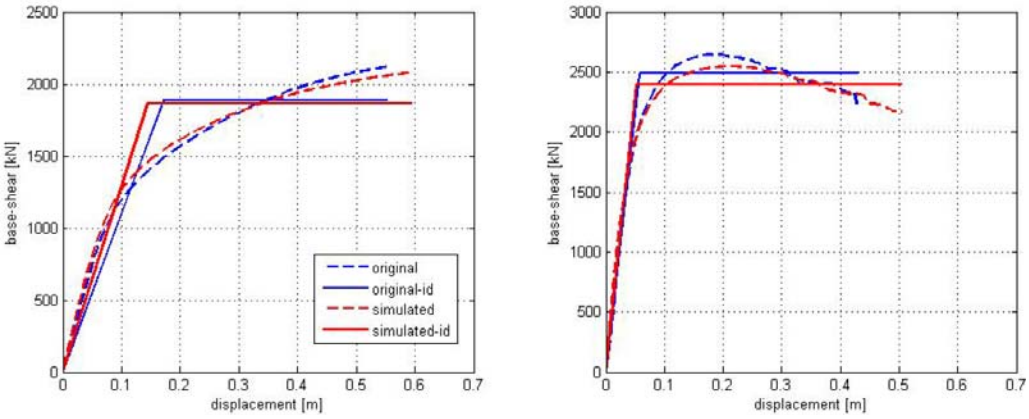


Figure 7: MPA – Capacity curves of the equivalent SDOF systems for mode 2 (left) and mode 3 (right)

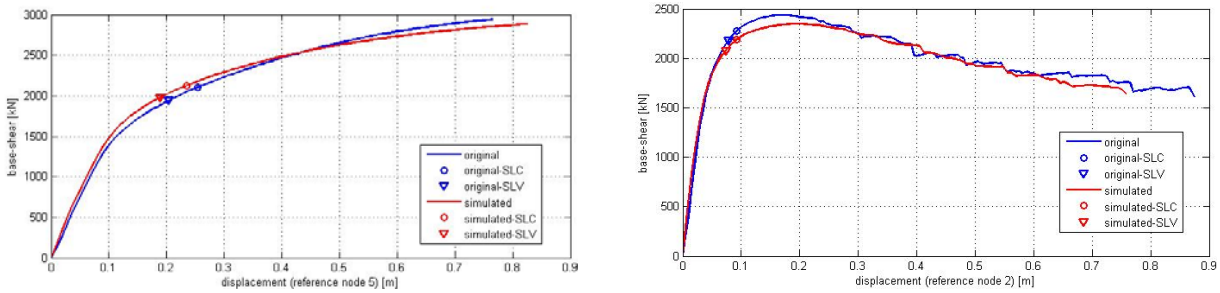


(a) (b)

Figure 8: MPA – Performance points for SLC and SLV limit states for load patterns (a) and (b)

For what concerns the assessment of the transversal response of the bridge it can be concluded that the influence of the discrepancy in steel reinforcement is negligible. The difference in the estimation of the deck-displacement for SLC limit state is well below the 10% (Table 3), the response of the structure being generally underestimated due to the overestimation of elastic stiffness. The difference in the estimation of the base shear at each bent for the same limit state is well below the 5% (Table 3), the action being slightly underestimated and overestimated respectively for the stiff side and the flexible side of the substructure.

| Node | | 1 | 2 | 3 | 4 | 5 |
|---|---|---|---|---|---|---|
| Deck displacement [cm] | Executive drawings | 11.2 | 8.7 | 9.1 | 15.2 | 24.5 |
| | Simulated design | 11.0 | 8.4 | 8.5 | 14.5 | 23.8 |
| | Difference (%) | -1.8 | -3.5 | -6.6 | -4.6 | -2.9 |
| Bent | | 1 | 2 | 3 | 4 | 5 |
| Base shear [kN] | Executive drawings | 1075 | 853 | 1130 | 732 | 742 |
| | Simulated design | 1040 | 840 | 1145 | 753 | 754 |
| | Difference (%) | -3.3 | -1.5 | +1.3 | +2.9 | +1.6 |

Table 3: MPA – Influence of reinforcement discrepancy on bridge deformed shape and base-shear for SLC limit state

It can be concluded that the discrepancy in steel reinforcement estimation of members has a low influence on the assessment of the transversal bridge response, but it should also be pointed out that the level of seismic demand is relatively low. A more sever seismic hazard would eventually have resulted in a more relevant influence because of a larger excursion in the nonlinear branch of the response. The former is no doubt more affected by the discrepancy, in particular for the load pattern (b) proportional to mode 3.

In order to investigate the influence of the reinforcement discrepancy on the assessment of the longitudinal response of the bridge a non-adaptive force-based and displacement controlled pushover has been performed. According to the Italian Building Code approach for continuous deck bridges, the structure has been considered as a SDOF system and the displacement at the deck level has been adopted for the push-over analysis. Since the longitudinal response is not changing with the sign of the loading pattern (i.e. positive or negative direction), only the positive direction has been adopted for the analysis. The procedure has been repeated for two different models, one being assigned the reinforcement configuration and quantity reported in the available executive drawings and the other being assigned the reinforcement configuration and quantity estimated by means of the simulated design procedure. A total of two push-over curves is obtained for the bridge.

As shown on the left of Figure 9, the discrepancy in member reinforcement has a limited impact on the longitudinal pushover curve for what concerns the maximum base shear capacity and the global behaviour of the structure within the elastic and yielding branch of the response. On the other hand, the global behaviour of the structure is significantly affected for what concerns the inelastic branch, where the original structure suffers a more severe softening than the one with simulated design reinforcement. This is due to the influence of the reinforcement discrepancy on the column sectional response, which generate a difference in the softening branch of the response in the columns of bents 1-2 and a slightly higher post-yielding flexural capacity in the columns of bents 3-4-5.

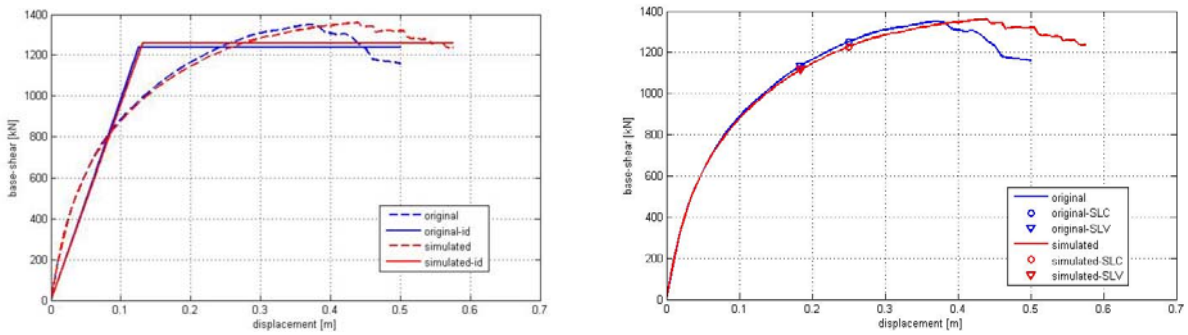


(a) (b)

Figure 9: Capacity curve of the SDOF system – longitudinal direction (a). Performance points for SLC and SLV limit states (b)

The local behaviour of the members seems to be more significantly affected by the reinforcement discrepancy in longitudinal direction than it is in transversal one, in particular for taller hollow core columns. In the original structure, the nonlinearity is concentrated at the base of the columns, since their longitudinal reinforcement is almost constant along the height. In the structure with simulated design reinforcement, on the other hand, the nonlinearity is not concentrated at the base of the columns, which are affected by an overestimation of 12% and an underestimation of 50% for the longitudinal reinforcement of the bottom and top parts, respectively. This effect is particularly evident for the columns of bent n°3, which is subjected to a higher level of moment due to its higher stiffness with respect to the other two hollow core bents.

In order to investigate the influence of reinforcement discrepancy on the assessment of the longitudinal seismic response of the structure the performance point has been computed according and the corresponding response parameters (deck-displacement and base-shear) have been derived from pushover analysis. As shown on the right of Figure 9, there is no influence of reinforcement discrepancy on the estimation of the displacement demand for SLC and SLV limit state, since the equivalent period $T^*$ corresponds to the displacement plateau for both

models. The difference in the estimation of the base shear at each bent for the SLC limit state is well below the 5%, the action being slightly underestimated and overestimated respectively for the stiff side and the flexible side of the substructure.

It can be concluded that the discrepancy in the estimation of member steel reinforcement has a low influence on the assessment of the longitudinal bridge response, at least for seismic requirements in Italy, where there is a low probability of large non-linear excursions of the piers.

### 5.4 Nonlinear dynamic analysis of the bridge over the Rio Torto river

The nonlinear analysis is focused on the portion of the bridge shown in Figure 5. Each considered acceleration time history has been applied independently in transversal and longitudinal direction. This simplification is considered to be adequate for the purpose of this research work. Moreover, the decoupling of the two orthogonal responses seems to be consistent with the geometry of the bridge, which consists of a straight deck supported on a symmetric substructure with respect to the longitudinal axis. The analysis employs the same distributed plasticity FE model as the non linear static one.

The comparison between the transversal response of the original structure and the simulated one to each considered time history is carried out in terms of the displacement envelope of the deck. It can be stated that, in general, the simulated structure experiences sensibly lower displacements in the stiffer side of the substructure (i.e. bents 1-2) and slightly higher displacement of the more flexible side of the substructure (i.e. bents 4-5). This seems to be consistent with the difference in member reinforcement between the executive drawings and the simulated design, where a sensible overestimation of longitudinal and transversal reinforcements affects the columns of the stiffer side. However, the effect of the estimation in member reinforcement seems to have a low influence on the displacement response, with an average percent difference in the displacement profile not exceeding 12.5%.

The same can be concluded considering the base shear envelope, for which the influence of reinforcement discrepancy does not exceed the 11.5%. The action results to be slightly overestimated for the bents at the end-segments of the bridge and underestimated for the others.

The influence of reinforcement discrepancy on the interstory drift of the bents results to be quite significant for the shorter ones (1-2) and almost negligible for the taller ones (3-4-5), as reported in Table 4. This could be related to the fact that the shorter and stiffer bents suffer more relevant excursions in the inelastic branch of sectional response and therefore their deformation is more affected by the reinforcement discrepancy than the taller ones. As expected, some variability of the influence is registered among the different accelerograms, related to their different frequency contents. However, it should be noted that the influence of the reinforcement discrepancy does not exceed 10% and 25% for tall and short bents, respectively.

The aforementioned average percent differences concerning the considered response parameters (i.e. deck displacement envelope, base shear envelope and interstory drift) can be regarded as an acceptable grade of accuracy in the assessment of the bridge seismic response. Nevertheless, it is important to point out that the response of the bent members remains almost entirely within the elastic field for the considered level of seismic actions and that the influence would have been more relevant for a higher seismicity level.

The influence of the discrepancy in steel reinforcement on the analysis of the longitudinal response is evaluated in terms of deck displacement and base shear. From the comparison of the results, it can be stated that the longitudinal response is no significantly affected by the discrepancy in member reinforcement estimation. This is due to the fact that the piers do not experience any significant excursion into the inelastic branch of their response. Therefore, the

discrepancy in reinforcement amount does not play any significant role in the assessment of the bridge response in longitudinal direction.

| Bent | | 1 | 2 | 3 | 4 | 5 |
|---|---|---|---|---|---|---|
| Segment 1 | Difference (+) [%] | -22.9 | -11.7 | -10.0 | -5.3 | +0.5 |
| | Difference (-) [%] | -25.6 | -9.4 | -8.9 | -0.6 | +0.5 |
| Segment 2 | Difference (+) [%] | 4.1 | -6.9 | -5.9 | -0.6 | +6.0 |
| | Difference (-) [%] | 14.3 | -4.9 | -5.2 | +4.6 | +6.0 |
| Segment 3 | Difference (+) [%] | - | - | -4.8 | -0.3 | +6.5 |
| | Difference (-) [%] | - | - | -3.7 | +5.8 | +7.1 |
| Segment 4 | Difference (+) [%] | - | - | - | -0.6 | +5.6 |
| | Difference (-) [%] | - | - | - | +4.2 | +6.1 |

Table 4: THA – Influence of simulated design on the interstory drift – average of the considered accelerograms

A scarcely appreciable influence of the reinforcement discrepancy is obtained in the estimation of base shear envelope for the shorter bents (1-2), which suffer higher excursions into the inelastic branch of sectional response than the taller ones (3-4-5). Anyway, the influence is well below the 5%, and it can be concluded that no influence affects the response assessment.

## 6 CONCLUSIONS

The present work aimed to provide a simple procedure for simulated design of longitudinal and transversal reinforcement of existing RC bridge bents. The simulated design is a helpful tool within the seismic response assessment of existing structures whose reinforcement configuration is not available or in those cases when a large scale vulnerability assessment has to be performed on a large number of homogeneous structures. According to the obtained results, it can be concluded that the simulated design procedure is suitable to the seismic response assessment of existing RC bridges, when no detailed information is available on member reinforcement, since it does not significantly affect the results. Nevertheless, the proposed procedure could be further elaborated and developed in order to obtain an estimation of reinforcement detailing closer to the real structure subjected to seismic assessment.

First of all, a review of a wider set of original executive design documentation would allow to include in the procedure eventual tendencies in the practice of design and construction which are not inferable from the review of the contemporary design regulations. The same can be said for what concerns the choice of bar diameter and concrete cover. Moreover, such review could provide a wider documentation about the tendency in the choice of concrete and steel types for bridge bents, together with their mechanical properties; this would improve the correspondence of the input data to the contemporary technologies.

Secondly, limit states verifications such as cover concrete cracking and steel reinforcement fatigue could be included in the procedure in addition to allowable stress verifications, in order to take into account the possibility of more demanding conditions on reinforcement detailing.

Finally, the procedure could be elaborated in order to include a wider range of sectional geometries and bent typologies in order to obtain a more general methodology and avoid several simplifications which could affect its accuracy. This is the case of walls with smoothed extremities or hollow core elliptical piers, which are simplified as solid rectangular and hollow core rectangular section in the current procedure. This is also the case of tapered members and irregular framed bents, which are simplified respectively as non-tapered members

with the average dimension expanded throughout the entire member length and as regular frames with constant inter-axis of bays and constant height of columns within the same level.

Further investigation could address the influence of the reinforcement discrepancy, due to simulated design, on the verification of local behaviour in terms of usage ratio of the chord rotation capacity and shear capacity of the bent members. The chord rotation capacity calculation according to the Italian Building Code [44] depends both on the reinforcement configuration and the seismic demand (in terms of bending moment distribution along the element) and, therefore, the evaluation of the influence of reinforcement discrepancy on this response parameter could be of interest. The same can be said for the shear capacity usage ratio, which is strongly affected by the reinforcement configuration and could be more sensitive to the discrepancy due to simulated design than the shear demand on the member itself.

## ACKNOWLEDGMENTS

Thanks are given to the "Provincia Autonoma of Trento" and Dr Daniele Zonta (University of Trento) as well as the company ANAS s.p.a., for having kindly provided the executive design documentation about many of the bridges analysed in this work. The authors would like to thank Prof. Paolo Pinto and Dr Alessio Lupoi (University of Rome "La Sapienza"), who kindly provided the graphical documentation about the bridge over the River Rio Torto.

Thanks are given to Dr Barbara Borzi (Eucentre) for her supervision during the development of the Master thesis of the second author, and to Dr Ricardo Monteiro (IUSS) for the fruitful discussion about FE modeling of bridges. The authors are grateful to Ms Lucia Cecere (Library of "Ministero delle Infrastrutture e dei Trasporti") and to Ms Roberta Lucentini (formerly, Documentation Centre of Eucentre) for their effective assistance in the collection of the contemporary design regulatory framework.

## REFERENCES

[1] B. Borzi, P. Ceresa, M. Faravelli, E. Fiorini, M. Onida, Seismic Risk Assessment of Italian School Buildings. *Computational methods in applied sciences*, 30, 317-344, 2013.

[2] B. Borzi, P. Ceresa, P. Franchin, F. Noto, G.M. Calvi, P.E. Pinto, Seismic Vulnerability of the Italian Roadway Bridge Stock, *Earthquake Spectra*, **31**(4), 2137-2161, 2015.

[3] G. Albenga, *I Ponti. L'esperienza,* U.T.E.T., Torino, Italy 1985a.

[4] G. Albenga, *I Ponti. La teoria,* U.T.E.T., Torino, Italy, 1985b.

[5] G. Albenga, *I Ponti. La pratica,* U.T.E.T., Torino, Italy, 1985c.

[6] M. Greco, *Costruzioni di ponti, lezioni di,* Arti Grafiche Castiglia, Palermo, Italy, 1928.

[7] A.F. Jorini, *Costruzione dei ponti – Teoria e pratica,* Hoepli, Milano, Italy, 1927.

[8] A. Raithel, *Costruzioni di ponti,* Liguori, Napoli, Italy, 1964.

[9] A. Raithel, *Costruzioni di ponti,* Liguori, Napoli, Italy, 1970.

[10] A. Raithel, *Costruzioni di ponti,* Liguori, Napoli, Italy, 1977.

[11] L. Santarella, *Ponti in muratura ed in cemento armato,* Edizioni del gruppo universitario fascista, Milano, Italy, 1930.

[12] L. Stabilini, *Ponti,* Libreria Editrice Tecnica Cesare Tamburini, Milano, Italy, 1954.

[13] Circolare n.7100, *Carichi da considerare nella progettazione delle strade militari,* Ministero della Guerra, (11 aprile) 1930.

[14] Normale n.8, *Carichi da considerare nel calcolo dei ponti per strade ordinarie*, Ministero dei Lavori Pubblici, G.U. 21/10/1933 n.30, 1933.

[15] Normale n.1, *Carichi da considerare nel calcolo dei ponti per strade ordinarie,*Ministero dei Lavori Pubblici, (9 giugno) 1945.

[16] Circolare n.820, *Carichi per la progettazione delle strade,* Ispettorato Tecnico A.N.A.S., (15 marzo) 1952.

[17] Circolare n.384, *Norme relative ai carichi per il calcolo dei ponti stradali*, Ministero dei Lavori Pubblici, (14 febbraio) 1962.

[18] D.M. 1980a, *Norme tecniche per la disciplina di opere in cemento armato normale e precompresso ed a struttura metallica,* G.U.R.I. 28/6/1980 n.176, 1980a.

[19] D.M. 1980b, *Criteri generali e prescrizioni tecniche per la progettazione, esecuzione e collaudo dei ponti stradali,* G.U.R.I. 10/11/1980 n.308, 1980b.

[20] R.D.L. n.2105, *Norme tecniche di edilizia per tutti i comuni del Regno e speciali norme tecniche di edilizia asismica per i paesi colpiti da terremoti,* G.U. 27/12/1937 n.298, 1937.

[21] L. n.1684, *Norme tecniche di edilizia con particolari prescrizioni per le località colpite dai terremoti,* G.U.R.I. 22/12/1962 n.326, 1962.

[22] L. n.64, *Provvedimenti per le costruzioni con particolari prescrizioni per le zone sismiche,* G.U.R.I. 21/3/1974 n.76, 1974.

[23] R.D. n.2229, *Norme per la esecuzione delle opere in conglomerato cementizio semplice od armato,* G.U. 18/4/1940 n.92, 1939.

[24] Circolare n.1472, *Le armature delle strutture in cemento armato*, Ministero dei Lavori Pubblici, (23 maggio) 1957.

[25] Circolare n.1547, *Caratteristiche e modalità di impiego nel cemento armato degli acciai ad aderenza migliorata*, Ministero dei Lavori Pubblici, (17 maggio) 1965.

[26] L. n.1086, *Norme tecniche per la disciplina di opere in cemento armato normale e precompresso ed a struttura metallica,* G.U.R.I. 21/12/1971 n.321, 1971.

[27] L. Marziali, Seismic response assessment of RC bridges, *Master Dissertation*, UME Graduate School (ROSE Programme), IUSS Pavia, 2011.

[28] E. Fagà, P. Ceresa, R. Nascimbene, M. Moratti, A. Pavese, Modelling curved surface sliding bearings with bilinear constitutive law: effects on the response of seismically isolated buildings, *Materials and Structures*, **49**(6), 2179-2196, 2016.

[29] G.M. Verderame, G. Manfredi, G. Frunzio, Le proprietà meccaniche dei calcestruzzi impiegati nelle strutture in cemento armato degli anni '60, *10th ANIDIS National Conference on Earthquake Engineering in Italy,* Potenza-Matera, Italy, 2001a.

[30] G.M. Verderame, A. Stella, E. Cosenza, Le proprietà meccaniche degli acciai impiegati nelle strutture in cemento armato degli anni '60, *10th ANIDIS National Conference on Earthquake Engineering in Italy,* Potenza-Matera, Italy, 2001b.

[31] D.M. 1972, *Norme tecniche per la disciplina di opere in cemento armato normale e precompresso ed a struttura metallica,* G.U.R.I. 22/7/1972 n.190, 1972.

[32] D.M. 1974, *Norme tecniche per la disciplina di opere in cemento armato normale e precompresso ed a struttura metallica,* G.U.R.I. 29/7/1974 n.198, 1974.

[33] P. Ceresa, L. Petrini, R. Pinho, Flexure-Shear Fiber Beam-Column Elements for Modeling Frame Structures Under Seismic Loading — State of the Art. *Journal of Earthquake Engineering*, **11**(1), 46-88, 2007.

[34] P. Ceresa, L. Petrini, R. Pinho, R. Sousa, A fibre flexure–shear model for seismic analysis of RC-framed structures. *Earthquake Engineering and Structural Dynamics*, **38**, 565-586, 2009.

[35] A. Kagermanov, P. Ceresa, Physically-based cyclic tensile model for RC membrane elements. *Journal of Structural Engineering ASCE*, **142**(12) DOI:10.1061/(ASCE)ST.1943-541X.0001590, 04016118, 2016.

[36] A. Kagermanov, P. Ceresa, Fiber-section model with an exact shear strain profile for two-dimensional RC frame structures. *Journal of Structural Engineering ASCE* (in press).

[37] P. Ceresa P, A. González Víquez, Nonlinear analysis of shear critical RC members using current FE software, *6th ECCOMAS Thematic Conference, Computational Methods in Structural Dynamics and Earthquake Engineering, COMPDYN 2017*, 15-17 June, 2017.

[38] P. Ceresa, G. Negrisoli, Hysteretic models considering axial-shear-flexure interaction, *Procedia Engineering, World Multidisciplinary Civil-Engineering-Architecture-Urban Planning Symposium - WMCUAS*, Prague, 12-16 June, 2017.

[39] S.A. Freeman, J.P. Nicoletti, J.V. Tyrell, Evaluation of existing buildings for seismic risk – A case study of Puget Sound Naval Shipyard, Bremerton, Washington, *U.S. National Conference on Earthquake Engineering,* Berkeley, California, 1975.

[40] S.A. Freeman, Development and use of capacity spectrum method, *6th U.S. National Conference on Earthquake Engineering,* Seattle, Washington, 1998.

[41] P. Fajfar, P. Gašperšič, The N2 method for the seismic damage analysis of RC buildings, *Earthquake Engineering and Structural Dynamics,* **25**, 31-46, 1996.

[42] A.K. Chopra, R.K. Goel, A modal pushover analysis procedure for estimating seismic demands for buildings, *Earthquake Engineering and Structural Dynamics,* **31**, 561-582, 2002.

[43] C. Casarotti, R. Pinho, An Adaptive Capacity Spectrum Method for assessment of bridges subjected to earthquake action, *Bulletin of Earthquake Engineering,* **5**, 377-390, 2007.

[44] D.M. 2008, *Norme tecniche per le costruzioni,* G.U.R.I. 4/2/2008 n.29, 2008.

[45] I. Iervolino, C. Galasso, E. Cosenza, REXEL: computer aided record selection for code based seismic structural analysis, *Bulletin of Earthquake Engineering*, **8**, 339-362, 2010.

COMPDYN 2017
6th ECCOMAS Thematic Conference on
Computational Methods in Structural Dynamics and Earthquake Engineering
M. Papadrakakis, M. Fragiadakis (eds.)
Rhodes Island, Greece, 15–17 June 2017

# SMALL-STRAIN STIFFNESS AND DAMPING OF LOESS IN CHINA

**Binghui. Song[1,2], Angelos. Tsinaris[2], Anastasios. Anastasiadis[2], Kyriazis. Pitilakis[2], and Wenwu. Chen[1]**

[1] Key Laboratory of Mechanics on Disaster and Environment in Western China, the Ministry of Education of China and College of Civil Engineering and Mechanics, Lanzhou University, Lanzhou, 730000 P.R. China
e-mail: songbh09@gmail.address, sungp@lzu.edu.cn

[2] Department of Civil Engineering, Aristotle University of Thessaloniki, P.O.B. 424, Thessaloniki, 54124 Greece
e-mail: tsinaris@civil.auth.gr, anas@civil.auth.gr, kpitilak@civil.auth.gr

**Keywords:** Loess, Small-Strain Stiffness, Damping, Resonant Column Test, Down-hole Test.

**Abstract.** *Loess Plateau of China is one of the most representative geomorphologic regions for loess around the world due to the deep covering layer and wide distribution area. Many catastrophic disasters induced by earthquake had been identified in this area. This study examined systematically the small-strain stiffness and damping of loess in Lanzhou, Northwest of China, through the laboratory resonant column (RC) test method and the field down-hole test method. On the basis of the analyses of test results, it was found that the small-strain shear modulus $G_0$ of loess was more sensitive to water content than the small-strain damping $D_{min}$. A linear relationship between log($G_0$) and log($\sigma'_m$) was observed for loess, while the corresponding slope in log-log coordinates decreased with water content increasing. Similarly, log($D_{min}$) decreased linearly with log($\sigma'_m$) as well. $G_0$ of undisturbed loess was much higher than reconstituted ones at low water content and this difference could be negligible for saturated loess. The similar phenomenon was observed for $D_{min}$ too. The pattern of correlation between $G_0$ and $\sigma'_m$ for loess accorded well with the findings in literature but in the present study, higher values of $G_0$ could be expected, which may be ascribed to the different device used. In comparison with the down-hole test results, there was a good agreement between RC results and laboratory results for $G_0$ of loess. Finally, the correlations between $G/G_0$ and $\gamma/\gamma_{0.85}$ could be normalized perfectly for Lanzhou loess, irrespective of water content and confining pressure.*

## 1 INTRODUCTION

China loess is a kind of aeolian deposited loess, covering more than 6.3% of the country's land area (named loess plateau) distributed mainly at the northwest regions of China as overlaying soil [1, 2]. The thickest loess profile reported in Lanzhou is more than 400m [3], which is one of the most representative loess profiles in the world.

Loess Plateau was an earthquake-prone area where tectonic movements were very active and throughout history several catastrophic disasters caused by earthquakes had been identified and documented fully [4, 5]. Studies on the dynamic properties of loess were very essential and significant to the mission of earthquake protection and mitigation in this region. Several recent researches on the stress-strain properties during cyclic loading of loess were conducted in the laboratory by using conventional cyclic triaxial testing [6, 7, 8], while the cyclic strains investigated in these studies were large ($>10^{-2}$%) due to the lack of sensitive LVDT with high precision. Actually, studies on the stress-strain properties of loess during cyclic loading at small strain levels, especially considering the effect of various factors, e.g. water content, confining pressure and soil structure, are rather limited [9, 10]. In this research work, a comprehensive set of resonant column tests were conducted to evaluate the stress-strain properties of loess under relatively fast cyclic loading conditions from small to medium shear strains ($10^{-5}$%$<\gamma<10^{-2}$%), in order to improve the research level of the dynamic properties of loess.

## 2 TEST PROGRAM

### 2.1 Testing material

The studied loess specimens were collected from a geotechnical borehole in the National New Area of Lanzhou, Northwest of China. The representative soil profile of the studied site is shown in Figure 1 with the corresponding SPT blows and the shear wave velocity $V_s$ obtained from down-hole measurements included as well.

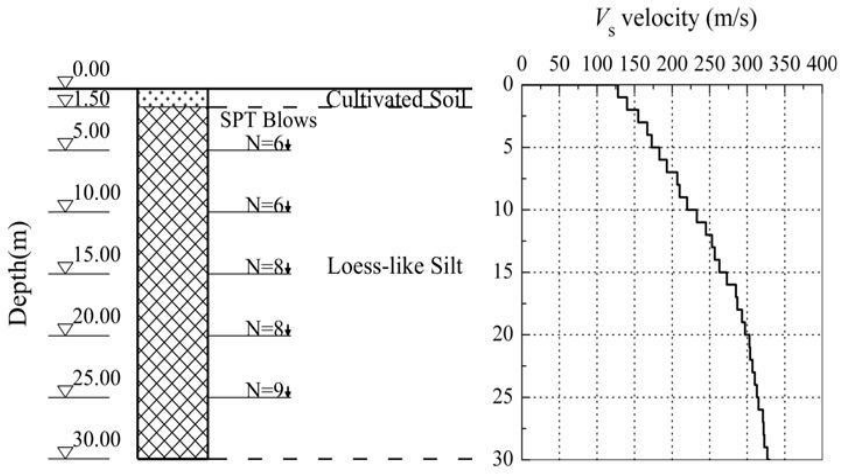


Figure 1: Loess profile with in situ test results.

As shown in Figure 1, apart from limited thickness of the top cultivated soil layer (about 1.5m), loess-like silt which is commonly designated as $Q_4$ loess [11] in China based on the age of deposition, comprises the major part of the investigated soil strata. The variation of SPT blows for loess ranges from 6 to 9 within the top 25m thickness, which can be attributed

to the metastable structure of loess with high void ratio. In addition, shear wave velocity of loess obtained from down-hole measurements increases monotonically with depth indicating relatively homogeneous soil strata with depth. A series of undisturbed loess specimens with different burial depth were collected from the borehole and shipped carefully to the laboratory for subsequent tests. Table 1 presents the basic physical properties of loess.

Table 1: Physical properties of loess in natural condition.

| Sample | Depth (m) | Water content W (%) | Total density $\rho_t$ (g/cm$^3$) | Void ratio e | Specific Gravity $\gamma_s$ | LL (%) | PL (%) |
|---|---|---|---|---|---|---|---|
| LZL-4 | 4 | 14.33 | 1.50 | 1.058 | 2.70 | 24.31 | 16.62 |
| LZL-6 | 6 | 13.42 | 1.53 | 1.002 | 2.70 | 24.80 | 16.71 |
| LZL-8 | 8 | 11.54 | 1.49 | 1.029 | 2.71 | 24.72 | 16.63 |
| LZL-10 | 10 | 14.21 | 1.55 | 0.997 | 2.71 | 24.52 | 17.12 |
| LZL-12 | 12 | 16.93 | 1.54 | 1.058 | 2.71 | 25.41 | 17.82 |
| LZL-13 | 13 | 16.11 | 1.56 | 1.017 | 2.71 | 25.72 | 18.40 |

Based on the physical properties (Table 1) and the particle size distribution of loess shown in Figure 2, Lanzhou loess is classified as CL silt loam according to the unified soil classification system (USCS).

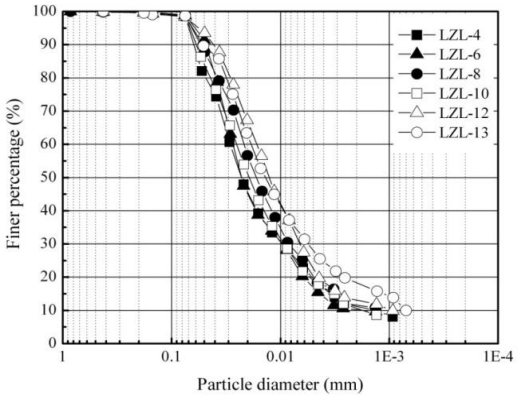


Figure 2: Particle composition characteristics of loess.

In order to investigate the effect of water content on the dynamic properties of loess, wetting and drying method [12, 13] were adopted to prepare loess specimens with various water contents. Saturated specimens were prepared under the standard procedure of saturation by using the back-pressure method. Following the same principles, reconstituted specimens having the same water content and dry density with undisturbed specimen were prepared following the standard compaction method [14]. In total, eight groups of loess specimens were prepared for RC test with their characteristics shown in Table 2.

Table 2: Physical properties of loess in natural condition.

| Sample | Depth (m) | Current moisture (%) | Current saturation (%) |
|---|---|---|---|
| LZL-4-U(1) | 4 | 24.41 | 59.95 |
| LZL-6-U | 6 | 6.83 | 18.90 |
| LZL-6-R(2) | 6 | 6.52 | 18.15 |
| LZL-8-U | 8 | 22.52 | 56.08 |
| LZL-10-U | 10 | 13.69 | 37.56 |
| LZL-12-U | 12 | 17.11 | 43.71 |
| LZL-13-U | 13 | 33.41 | 84.00 |
| LZL-13-R | 13 | 34.58 | 86.44 |

Note: (1) U means undisturbed specimen; (2) R represents reconstituted specimen; Current moisture (%) is the water content of loess measured after wetting or drying process

A resonant column device of free-fixed end designed by Drenvich [15] and manufactured by Soil Dynamics Instruments (Soil Dynamics Instruments, Inc), capable of longitudinal and torsional dynamic loading was used. The dimension of loess specimen was 140mm in height and 70mm in diameter. The whole experimental procedure and the analysis of the RC test results were performed according to the ASTM 4015-92 specification [16].

## 3 EXPERIMENTAL RESULTS AND DISCUSSION

### 3.1 Small-strain shear modulus $G_o$

(a) Effect of water content

Figure 3 presents the influence of water content against small-strain shear modulus $G_0$ for undisturbed Lanzhou loess obtained from the present testing program together with results stemming from literature [17].

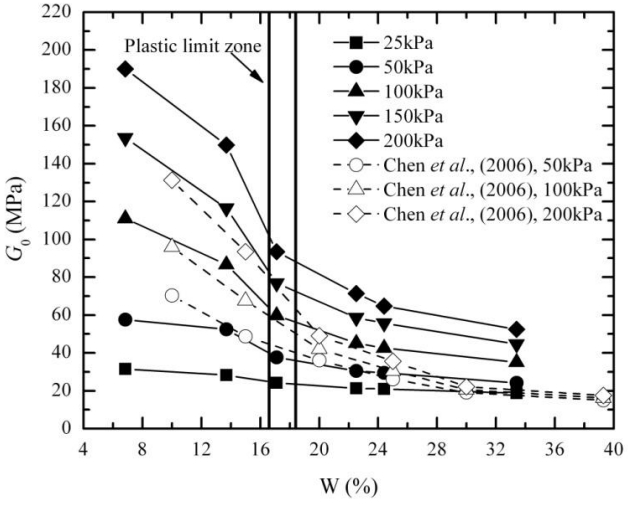


Figure 3: Relationships between $G_0$ and W for loess.

As shown in Figure 3, under the same confining pressure, the initial shear modulus $G_0$ of loess decreases continuously with water content. It is interesting to notice that when water content approaches the plastic limit, there is a dramatic decrease of $G_0$, especially for the cases of high confining pressure (≥100kPa). According to [17], the correlations between $G_0$

and water content for loess measured in cyclic triaxial test, coincides well with the trends of $G_0$ with water content in the present study. However, due to the limitations of the apparatus, the values of $G_0$ reported in [17] under the same confining pressure, are a bit lower than the corresponding ones of our study, especially for high confining pressures and water contents.

(b) Effect of confining pressure

A power function initially proposed in [18] has been widely used to describe the quantitative relationship between the small-strain shear modulus $G_0$ and effective mean confining stress $\sigma'_m$:

$$\frac{G_o}{P_r} = \frac{A}{F(e)} * \left(\frac{\sigma_m^{'}}{P_r}\right)^m \tag{1}$$

where, $P_r$ is reference pressure and can be set as 1kPa; $A$ is a dimensionless material constant with respect to soil types; $F(e)$ is a function of void ratio $e$ and commonly $F(e)=(1+e)/(2.973-e)^2$ for most kinds of soil; $m$ is the exponent representing the effect of effective mean confining stress $\sigma'_m$ on $G_0$.

Figure 4 shows the effect of the mean effective confining pressure $\sigma'_m$ on the small-strain shear modulus $G_0$ of the tested undisturbed Lanzhou loess specimens in this work. The correlations between $G_0$ and $\sigma'_m$ are fitted by using Equation (1) and the corresponding fitting results are shown in Figure 4 and Table 3.

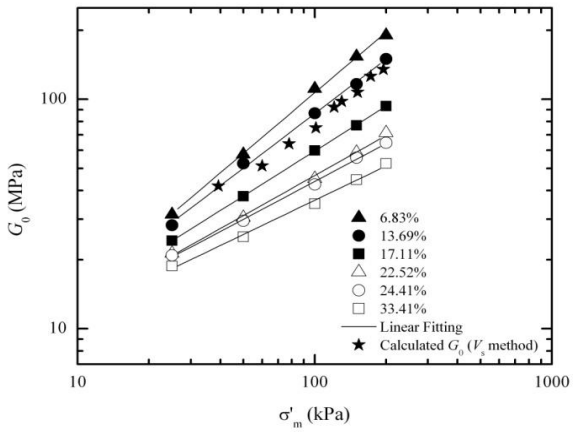


Figure 4: Relationships between $G_0$ and $\sigma'_m$ for loess.

Table 3: Fitting parameters of Hardin equation for Lanzhou loess.

| Water content (%) | $A$ | $m$ | Correlation coefficient $R^2$ | Shear strain amplitude (%) |
|---|---|---|---|---|
| 6.83 | 973.48 | 0.876 | 0.999 | $3.9\times10^{-5}$-$1.2\times10^{-4}$ |
| 13.69 | 1183.96 | 0.788 | 0.999 | $5.6\times10^{-5}$-$2.2\times10^{-4}$ |
| 17.11 | 1535.60 | 0.650 | 0.999 | $9.9\times10^{-5}$-$3.0\times10^{-4}$ |
| 22.52 | 1662.83 | 0.579 | 0.998 | $1.3\times10^{-4}$-$3.0\times10^{-4}$ |
| 24.41 | 1816.97 | 0.547 | 0.999 | $1.3\times10^{-4}$-$3.0\times10^{-4}$ |
| 33.41 | 1911.43 | 0.495 | 0.998 | $1.2\times10^{-4}$-$3.0\times10^{-4}$ |

Note: Shear strain amplitude (%) where $G_0$ and $D_{min}$ are defined in this study and lower values correspond to higher confinement stress.

As shown in Figure 4, it is observed that there is a clear linear increase of $G_0$ with $\sigma'_m$ in double logarithm coordinates, and the inclination decreases with the water content. The values of the $G_0$ calculated using the shear wave velocity $V_s$ (Figure 1) which is measured through down-hole method are also presented in Figure 4. The comparisons with our laboratory results are quite good for natural water content W around 14%.

The variations of the exponent $m$ and dimensionless constant $A$ with water content are shown in Figure 5. The relevant empirical correlations are formulated as follows:

$$m = 1.813 * W^{-0.361} \tag{2}$$

$$A = 398.553 * W^{0.457} \tag{3}$$

where, W is the water content of loess.

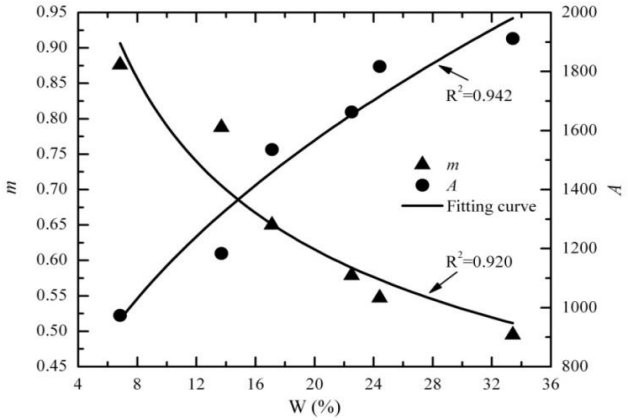


Figure 5: Correlations between fitting parameters ($m$ and $A$) and water content.

(c) Effect of structure strength

The results of small-strain stiffness $G_0$ for undisturbed and reconstituted loess are compared in Figure 6. As illustrated, when loess is a little dry, e.g. LZL-6-U/R specimens, the difference of $G_0$ between undisturbed and reconstituted specimens is big, while the values of $G_0$ between the undisturbed and reconstituted specimen are very close in saturated state.

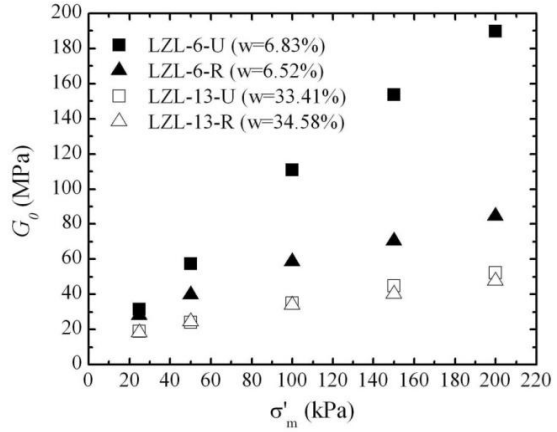


Figure 6: Comparison of $G_0$ values between undisturbed and reconstituted loess.

### 3.2 Small-strain damping $D_{min}$

(a) Effect of water content

Figure 7 depicts the variations of $D_{min}$ of loess with water content under different confining pressures. As shown, with the increase of water content, $D_{min}$ of loess decreases firstly and then tends to increase when loess is fully saturated. Regarding the limited range of $D_{min}$, it can be concluded that the effect of water content on $D_{min}$ of loess is insignificant.

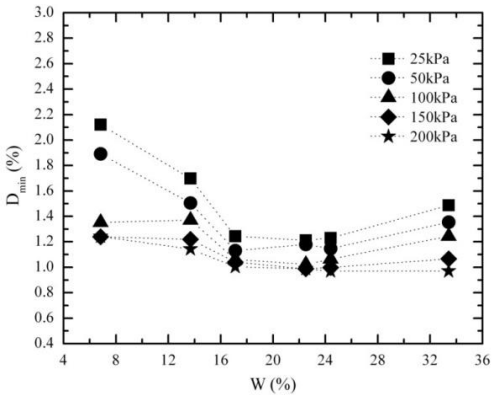


Figure 7: Effect of water content on the small-strain damping ratio $D_{min}$.

(b) Effect of confining pressure

The general trends of the effect of the mean effective confining stress $\sigma'_m$ on the small-strain damping ratio $D_{min}$ of Lanzhou loess are illustrated in Figure 8, where the representative experimental results of $D_{min}$ for sand and cohesive soils [19, 20, 21] are included in the same figure as well. Table 5 summarizes the fitting results of the relationships between $D_{min}$ and $\sigma'_m$.

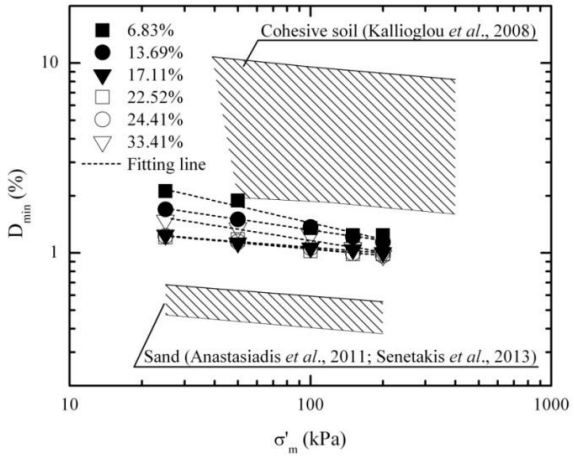


Figure 8: Effect of mean effective confining stress $\sigma'_m$ on the small-strain damping ratio $D_{min}$.

As shown in Figure 8, it can be observed that $D_{min}$ of loess decreases linearly as confining stress increases in double logarithm coordinates. In comparison to the data of $D_{min}$ of sand published in [20, 21], loess possesses higher values of $D_{min}$ under the same confining pressure. However, the data of $D_{min}$ of loess are much lower than that of cohesive soils with

higher PI published in [19]. From a qualitative point of view, it appears that the small-strain damping ratio $D_{min}$ of soil has the trend to increase with plasticity index, which is consistent with the findings presented in [22].

(c) Effect of structure strength

The effect of structure strength on $D_{min}$ of loess is illustrated in Figure 9. It can be seen from Figure 9 that $D_{min}$ of undisturbed loess is higher than for remolded loess under the same confining pressure, which may result from the alternation of soil fabric [23]. However, the effect of structure strength of loess on $D_{min}$ is limited in view of the small variation of $D_{min}$ in Figure 9.

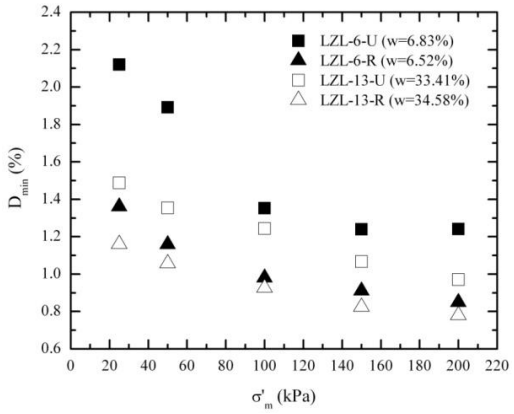


Figure 9: The small-strain damping ratio $D_{min}$ of undisturbed and reconstituted loess specimens.

### 3.3 $G/G_0$-γ curves

The relationship between normalized shear modulus $G/G_0$ and shear strain γ characterized the behavior of soil stiffness degradation [24]. Figure 10 depicts the variation of $G/G_0$ with γ determined for intact loess under different confining pressures. As shown, the normalized shear modulus $G/G_0$ degrades continuously with the increment of shear strain, and the degradation curves tend to move up and to the right as confining pressure increases. Although the data points of $G/G_0$ vs. γ curves between different confining pressures are scattered, most of them fall into a relative narrow band corresponding to the curves with plasticity indexes of 0 and 30, respectively [25].

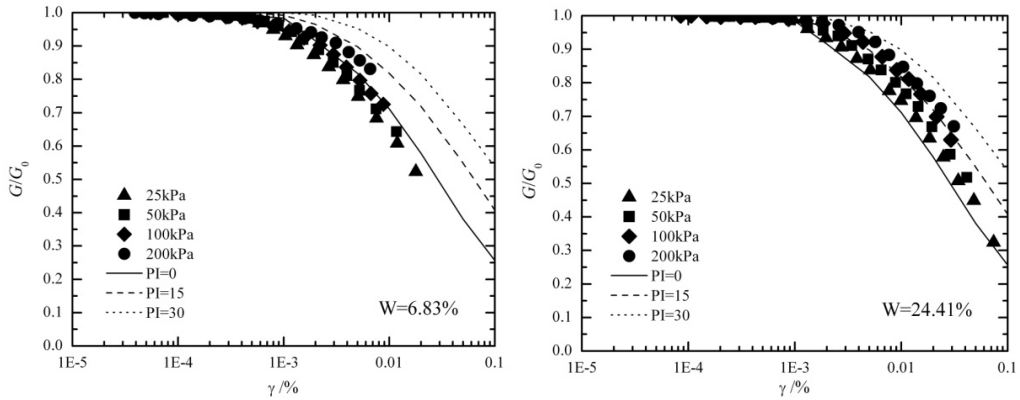


Figure 10: Effect of shear strain amplitude (γ) and confinement on the normalized shear modulus ($G/G_0$) of loess specimens with different water content (in the same figure the empirical curves for cohesive soil are also shown [25]).

On the basis of a summarization of previous researches, volumetric threshold shear strain, $\gamma_v$, was proposed to define significant changes in the cyclic soil behaviour [26]. After that, $\gamma_v$ was adopted as a reference shear strain to depict the normalization characteristics of $G/G_0$ vs. $\gamma$ curves [27, 28] based on the conventional stress-strain hyperbolic model given in [24] shown as Equation (4):

$$\frac{G}{G_o} = \frac{1}{\left[1+(\frac{\gamma}{\gamma_v})^a\right]} \tag{4}$$

where, $G$ is the secant shear modulus of soil; $G_0$ is the initial shear modulus; $a$ is a fitting parameter; $\gamma$ is shear strain; $\gamma_v$ is reference shear strain.

Considering the structure strength of undisturbed loess, $\gamma_{0.85}$ was adopted in this study to investigate the normalization characteristics of relationships between $G/G_0$ and $\gamma$ for Lanzhou loess. The modified relationships between $G/G_0$ and $\gamma/\gamma_{0.85}$ were presented in Figure 11 with the corresponding fitting curve included in the same figure as well. As indicated in Figure 11, there is almost a perfect coincidence for all the curves of $G/G_0$ vs. $\gamma/\gamma_{0.85}$ for Lanzhou loess, irrespective of water content and confining pressure. The fitting results shown in Figure 11 verified the feasibility of the empirical model (Equation (4)) to describe the normalized relationship between $G/G_0$ and $\gamma/\gamma_{0.85}$ for Lanzhou loess.

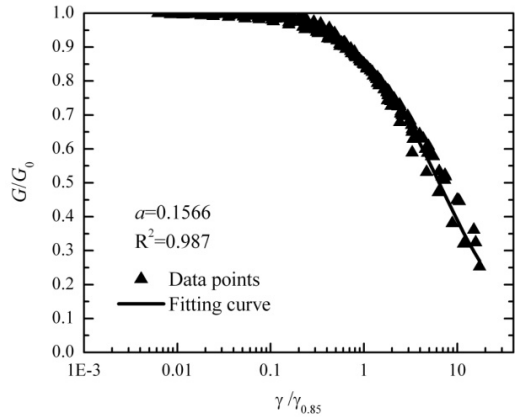


Figure 11: Normalized relationship between $G/G_0$ and $\gamma/\gamma_{0.85}$ for Lanzhou loess.

## 4 CONCLUSIONS

- Small-strain shear modulus $G_0$ of loess was more sensitive to water content than the small-strain damping $D_{min}$.
- $\log(G_0)$ increased and $\log(D_{min})$ decreased linearly with $\log(\sigma'_m)$.
- Small-strain shear modulus $G_0$ of undisturbed loess was much higher than reconstituted ones at low water content, and this difference could be negligible for saturated loess. The similar case was observed for $D_{min}$ as well.
- The correlations between $G/G_0$ and $\gamma/\gamma_{0.85}$ could be normalized perfectly for Lanzhou loess, irrespective of water content and confining pressure.

## REFERENCES


[1] Lin Z.G, Liang W.M, Distribution and engineering properties of loess and loesslike soils in China. Schematic map of engineering geological zoning. *Bulletin of the International Association of Engineering Geology*, **21**: 112-117, 1980.

[2] Lin Z.G, Liang W.M, Engineering properties and zoning of loess and loess-like soils in China. *Canadian Geotechnical Journal*, **19**(1): 76-91, 1982.

[3] Chen F.H, Li J.J, Zhang W.X, Loess stratigraphy of the Lanzhou profile and its comparison with deep-sea sediment and ice core record. *GeoJournal*, **24**(2): 201-209, 1991.

[4] Luo W.B, Seismic problems of cave dwellings on China's loess Plateau. *Tunnelling and Underground Space Technology*, **2**(2): 203-208, 1987.

[5] Zhang Z, Wang L, Geological Disasters in loess areas during the 1920 Haiyuan earthquake, China. *GeoJournal*, **36**(2): 269-274, 1995.

[6] Wang J, Yuan Z.X, Li L, Study on liquefaction of loess site. *Proceedings of the 4th international conference on earthquake geotechnical engineering*, Thessaloniki, Greece, 2007.

[7] Yuan Z.X, Wang L.M, Collapsibility and seismic settlement of loess. *Engineering Geology*, **105**: 119-123, 2009.

[8] Wang L.M, Wu Z.J, Xia K, Study on the effect of loess sites on seismic ground motion and its application in seismic design. *Proceedings of the 6th International Conference on Earthquake Geotechnical Engineering*, Christchurch, New Zealand, 2015.

[9] Wang Q, Sun J, Wang L.M, Chen X,. Review and discussion on seismic subsidence of loess. *Earthquake Research in China*, **27**(4): 479-489, 2013.

[10] Tian W, Wang L, Sun J, Xu S, Liu K, Sun Y, Progress and possible breakthroughs in research into the dynamic deformation of loess. *Journal of Lanzhou University (Natural Sciences)*, **50**(5): 645-652, 2014. (In Chinese with English Abstract)

[11] Liu D.S, Zhang Z.H, Chinese loess. *Acta Geologica Sinica*, **42**(1): 1-14, 1962. (In Chinese with English Abstract)

[12] Haeri S.M, Zamani A, Garakani A.A, Collapse potential and permeability of undisturbed and remolded loessial soil samples. *Unsaturated soils: Research and applications*, Springer, New York: 301-308, 2012.

[13] Wen B.P, Yan Y.J, Influence of structure on shear characteristics of the unsaturated loess in Lanzhou, China. *Engineering Geology*, **168**: 46-58, 2014.

[14] Ladd R.S, Preparing test specimens using undercompaction. *Geotechnical Testing Journal*, **1**(1): 16-23, 1978.

[15] Drnevich V.P, Hardin B.O, Shippy D.J, Modulus and damping of soils by the resonant-column method. *Dynamic Geotechnical Testing, ASTM STP 654, American Society for Testing and Materials*: 91-125, 1978.

[16] ASTM, Standard test methods for modulus and damping of soils by the resonant column method: D4015-92. Annual Book of ASTM Standards, ASTM International, 1992.

[17] Chen C, He J, Gao P, Dynamic deformation characteristics of intact loess under different water content. *Journal of Xi'an University of Technology*, **22**(4): 390-394, 2006. (In Chinese with English Abstract)

[18] Hardin B.O, Richart F.E, Elastic wave velocities in granular soils. *Journal of Soil Mechanics and Foundations Division*, **89**(SM1): 33-65, 1963.

[19] Kallioglou P, Tika T, Pitilakis K, Shear modulus and damping ratio of cohesive soils. *Journal of Earthquake Engineering*, **12**(6): 879-913, 2008.

[20] Anastasiadis A, Senetakis K, and Pitilakis K, Small-strain shear modulus and damping ratio of sand-rubber and gravel-rubber mixtures. *Geotechnical and Geological Engineering*, **30**(2): 363-382, 2011.

[21] Senetakis K, Anastasiadis A, Pitilakis K, Coop M.R, The dynamics of a pumice granular soil in dry state under isotropic resonant column testing. *Soil Dynamics and Earthquake Engineering*, **45**: 70-79, 2013.

[22] Lanzo G, Vucetic M, Effect of soil plasticity on damping ratio at small cyclic strains. *Soils and Foundations*, **39**(4): 131-141, 1999.

[23] Ashmawy A.K, Salgado R, Guha S, Drnevich V.P, Soil damping and its use in dynamic analyses. *International Conferences on Recent Advances in Geotechnical Earthquake Engineering and Soil Dynamics*, Paper 9, 1995.

[24] Hardin B.O, Drnevich, V.P, Shear modulus and damping in soil: design equations and curves. *Journal of the Soil mechanics and Foundation Engineering Division*, **98**(7): 667-692, 1972.

[25] Vucetic M, Dobry R, Effect of Soil Plasticity on Cyclic Response. *Journal of Geotechnical Engineering*, **117**(1): 89-107, 1991.

[26] Vucetic M, Cyclic threshold shear strain in soils. *Journal of Geotechnical Engineering*, **120**(12): 2208-2228, 1994.

[27] Santos J.A, Correia A.G, Shear modulus of soils under cyclic loading at small and medium strain level. *12th World Conference on Earthquake Engineering*, paper ID 0530. Auckland, New Zealand, 2000.

[28] Correia A.G, Santos J.A, Barros J.M.C, Niyama S, An Approach to Predict Shear Modulus of Soils in the Range of $10^{-6}$ to $10^{-2}$ Strain Levels. *International Conference on Recent Advances in Geotechnical Earthquake Engineering and Soil Dynamics*. San Diego, California, Missouri University of Science and Technology. Paper 18, 2001.

COMPDYN 2017
6th ECCOMAS Thematic Conference on
Computational Methods in Structural Dynamics and Earthquake Engineering
M. Papadrakakis, M. Fragiadakis (eds.)
Rhodes Island, Greece, 15–17 June 2017

# COMPARATIVE STUDY ON THE INFLUENCE OF DIFFERENT DAMPING VALUES IN SEISMIC SITE RESPONSE ANALYSIS

**H.P. Ding [1], J.L. Ma [1], J.Liao[1]**

[1] Suzhou University of Science and Technology, Suzhou 215011, China
e-mail: hpding@126.com

**Keywords:** Hysteretic Damping, Equivalent Linear, Rayleigh Damping, Target Frequency, Soil Seismic Response.

**Abstract.** *The methods of damping selection are different, therefore there will be a great difference in the results of time domain analysis and frequency domain analysis. The results of time domain analysis and frequency domain equivalent linear analysis are compared by single-layered soil columns with different thicknesses and multi-layered soil column under different input ground motions. How to evaluate Rayleigh damping coefficient is also discussed. The results show that the selection of different target frequency influencing viscous damping coefficient is the main reason leading to different results in time domain analysis. Hysteretic damping can be used more exactly in time domain site response analysis. To reduce the differences of the results of time domain analysis and frequency domain analysis, the full Rayleigh damping formulation and the first and third natural frequency can be employed.*

## 1 INTRODUCTION

Seismic site response analysis is an important part to determine the ground motion parameters. The equivalent linear frequency domain analysis method based on one-dimensional site elastic response analysis is commonly performed to account for local site effects on ground motion propagation under an earthquake [1]. Horizontal soil layers represent site stratigraphy, and vertically propagating horizontal shear waves (i.e., SH waves) approximate the ground motion. The damping force is assumed to be proportional to displacement amplitude and in phase with velocity, and the damping is frequency independent. In time domain analysis, it is generally used the Rayleigh damping formulation (i.e., $\boldsymbol{C} = \alpha\boldsymbol{M} + \beta\boldsymbol{K}$) which results in frequency dependent damping. The only difference between time domain analysis and frequency domain analysis is the selection of damping. The fundamental reason of damping difference is the frequency selected to calculate Rayleigh damping coefficient (i.e., target frequency in this paper). Many scholars have done research on the selection of target frequency [2-13]. In this paper, according to different selection of target frequency, two single-layered soil columns and one multi-layered soil column are calculated under Ninghe wave, Taft wave and El-Centro wave respectively. The results of seismic site response analysis with different damping coefficients are compared, which can provide reference for the selection of target frequency in practical engineering application.

## 2 EQUATION OF MOTION

For one-dimensional soil model, the equation of nodal motion in frequency domain analysis is expressed as:

$$[(1+2\zeta i)\boldsymbol{K} - \omega^2\boldsymbol{M}]\boldsymbol{U} = \boldsymbol{P} \tag{1}$$

where $\zeta$ = hysteretic damping ratio, $\omega$= natural circular frequency, $\boldsymbol{M}$ = mass matrix, $\boldsymbol{K}$ =stiffness matrix, $\boldsymbol{U}$ =vector of nodal relative displacements, and $\boldsymbol{P}$ = vector of nodal equivalent seismic load.

The following dynamic equation of motion in time domain analysis is solved:

$$\boldsymbol{M}\ddot{\boldsymbol{u}} + \boldsymbol{C}\dot{\boldsymbol{u}} + \boldsymbol{K}\boldsymbol{u} = -\boldsymbol{M}\boldsymbol{I}\ddot{\boldsymbol{u}}_g \tag{2}$$

where $\boldsymbol{M}$ = mass matrix, $\boldsymbol{C}$ = viscous damping matrix, $\boldsymbol{K}$ = stiffness matrix, $\ddot{\boldsymbol{u}}$ = vector of nodal relative acceleration, $\dot{\boldsymbol{u}}$ = vector of nodal relative velocities, $\boldsymbol{u}$ = vector of nodal relative displacements, $\ddot{\boldsymbol{u}}_g$ is the acceleration at the base of the soil column and $I$ is the unit vector.

## 3 DETERMINATION OF RAYLEIGH DAMPING COEFFICIENT

For Rayleigh damping is simple and convenient to use, it is widely performed in time domain analysis. The damping matrix $\boldsymbol{C}$ is derived from a linear combination of the mass matrix $\boldsymbol{M}$ and the stiffness matrix $\boldsymbol{K}$:

$$\boldsymbol{C} = \alpha\boldsymbol{M} + \beta\boldsymbol{K} \tag{3}$$

where $\boldsymbol{C}$ , $\boldsymbol{M}$ and $\boldsymbol{K}$ are viscous damping matrix, mass matrix and stiffness matrix respectively, and $\alpha$, $\beta$ are the Rayleigh damping coefficients.

In frequency domain analysis, damping ratio is a frequency independent constant. In time domain analysis, the same assumption as in structural dynamic calculation is often used, and it is written as:

$$\begin{Bmatrix} \alpha \\ \beta \end{Bmatrix} = \frac{2\omega_i \omega_j}{\omega_j^2 - \omega_i^2} \begin{bmatrix} \omega_j & -\omega_i \\ -\dfrac{1}{\omega_j} & \dfrac{1}{\omega_i} \end{bmatrix} \begin{Bmatrix} \zeta_i \\ \zeta_j \end{Bmatrix} \tag{4}$$

where $\zeta_i$ and $\zeta_j$ are the damping ratio of soil for mode *i* and *j*. Viscous damping ratio is often used in seismic site response analysis. Damping ratio $\zeta_n$ can be expressed by $\alpha$, $\beta$ and corresponding natural circular frequency:

$$\zeta_n = \frac{\alpha}{2\omega_{\mathrm{n}}} + \frac{\beta\omega_{\mathrm{n}}}{2} \tag{5}$$

As can be seen from above, damping ratio in time domain analysis is frequency dependent. The relationship between hysteretic damping of frequency domain and Rayleigh damping of time domain can be seen in Fig.1. In general, it is assumed that $\zeta_i = \zeta_i = \zeta$ . By Eq. (4), it can be obtained:

$$\begin{Bmatrix} \alpha \\ \beta \end{Bmatrix} = \frac{2\zeta}{\omega_i + \omega_j} \begin{Bmatrix} \omega_i \omega_j \\ 1 \end{Bmatrix} \tag{6}$$

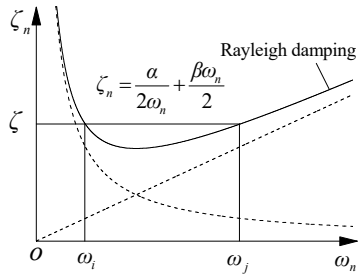


Fig.1: The relationship between hysteretic damping and Rayleigh damping.

Different methods are proposed on the value of Rayleigh damping. The damping matrix is assumed in early formulations to be only stiffness proportional since the value of $\alpha\boldsymbol{M}$ is small compared to $\beta\boldsymbol{K}$. The Eq. (3) can be further simplified to $\boldsymbol{C} = \beta\boldsymbol{K}$ , which is called simplified Rayleigh damping formulation. It can be obtained $\beta = 2\zeta / \omega = \zeta / \pi f$ by Eq. (5), defining *f* as

target frequency, and the damping coefficient $\beta$ will be controlled by the target frequency $f$. Main methods of selecting the target frequency $f$ are as follows:

(1) The first natural frequency of soil, $f_1$ (Ref. [2])

(2) The predominant frequency of Fourier spectrum of input ground motion, $f_p$ (Ref. [3])

(3) The centroid frequency of Fourier spectrum of input ground motion, $f_c$ (Ref. [4])

(4) A suitable frequency is obtained by fitting formulation (Ref. [5])

If the full Rayleigh damping formulation $\boldsymbol{C} = \alpha\boldsymbol{M} + \beta\boldsymbol{K}$ is performed, main methods of selecting the target frequency $f$ are as follows:

(1) $\alpha = \zeta\omega$ , $\beta = \zeta / \omega$ , generally, $\omega = \omega_1$ (the first natural circular frequency), $\omega_1 = 2\pi f_1$ (Ref. [6])

(2) $\alpha_i = \beta_i = \zeta_i\omega_i$, $\zeta = 0.05$, $\omega_i = \dfrac{\pi v_{si}}{2h_i}$, where $v_{si}$ = shear wave velocity (Ref. [7])

(3) $\alpha = 2\zeta(\dfrac{\omega_m\omega_n}{\omega_m + \omega_n})$, $\beta = 2\zeta(\dfrac{1}{\omega_m + \omega_n})$

Two natural frequencies within a significant frequency range of the input ground motion are defined as $\omega_m$ and $\omega_n$ respectively in Ref. [8]. In Ref. [9], $\omega_m$ is the first natural circular frequency, $\omega_n = N\omega_m$, where N is an odd number greater than $\omega_e / \omega_1$ ($\omega_e$ is the dominant frequency of input ground motion). The first and third natural frequency of soil are defined as $\omega_m$ and $\omega_n$ respectively in Ref. [10], that is, $\omega_1 = 2\pi f_1$ and $\omega_3 = 2\pi f_3$.

(4) $\alpha = 2\zeta(\dfrac{\omega_a\omega_b}{\omega_a + \omega_b})$, $\beta = 2\zeta(\dfrac{1}{\omega_a + \omega_b})$

where $\omega_a$ and $\omega_b$ are selected target frequencies. In Ref. [11], if $\dfrac{d\zeta}{d\omega} = -\dfrac{\alpha}{2\omega^2} + \dfrac{\beta}{2} = 0$ , it is obtained $\omega = \sqrt{\alpha / \beta}$ , and by Eq. (5) the minimum damping ratio can be obtained as follows:

$$\zeta_{\min} = \sqrt{\alpha\beta} \tag{7}$$

The damping ratio at the selected frequency range boundary is:

$$\begin{aligned} \zeta_{\max} &= \frac{\alpha}{2\omega_a} + \frac{\beta\omega_a}{2} \\ \zeta_{\max} &= \frac{\alpha}{2\omega_b} + \frac{\beta\omega_b}{2} \end{aligned} \tag{8}$$

$$\zeta_0 = (\zeta_{\max} + \zeta_{\min})/2 \tag{9}$$

Jean-Francois semblat et al. [12] used the method in Ref. [11] to determine damping coefficient. Degao Zou et al. [13] selected appropriate target frequency to determine damping coefficient based on the Ref. [9] and Ref. [11].

For single-layered soil,

$$f_n = \frac{V_s}{4H}(2n-1) \tag{10}$$

where $n$ is the mode number, $f_n$ is the natural frequency of the corresponding mode, $V_s$ = shear wave velocity, and $H$ = the thickness of soil column.

For multi-layered soil,

$$V_{seq} = \frac{H}{\sum_i (h_i / v_{si})} \tag{11}$$

$$f_n = \frac{V_{seq}}{4H}(2n-1) \tag{12}$$

where $H = \sum_i h_i$, $v_{si} = \sqrt{\frac{G_i}{\rho_i}}$ ($v_{si}$ = shear wave velocity for layer $i$), $h_i$, $G_i$ and $\rho_i$ are thickness, shear modulus and density for layer $i$ respectively.

## 4 INPUT GROUND MOTION AND CALCULATION MODEL

### 4.1 Input ground motion

Vertically propagating horizontal shear waves approximate the ground motion. Taking processed Ninghe wave, Taft wave and El-Centro wave as input ground motions, acceleration time history, Fourier amplitude spectrum and 5% damped elastic response spectra are shown in Fig. 2.

### 4.2 Calculation model

30 m single-layered soil column, 50 m single-layered soil column and 50 m multi-layered soil column are calculated respectively. In this paper, the results of the last iteration of the equivalent linear frequency domain analysis method in Ref. [1] are used to define the soil parameters in time domain analysis. The soil parameters are shown in Table 1 to Table 3 (the shear modulus and damping ratio in Table 1 to Table 3 are the final iteration results).

### 4.3 Target frequency *f*

When determining the Rayleigh damping coefficient, the key is to select the target frequency. The target frequencies obtained using the methods in related references are shown in Table 4.

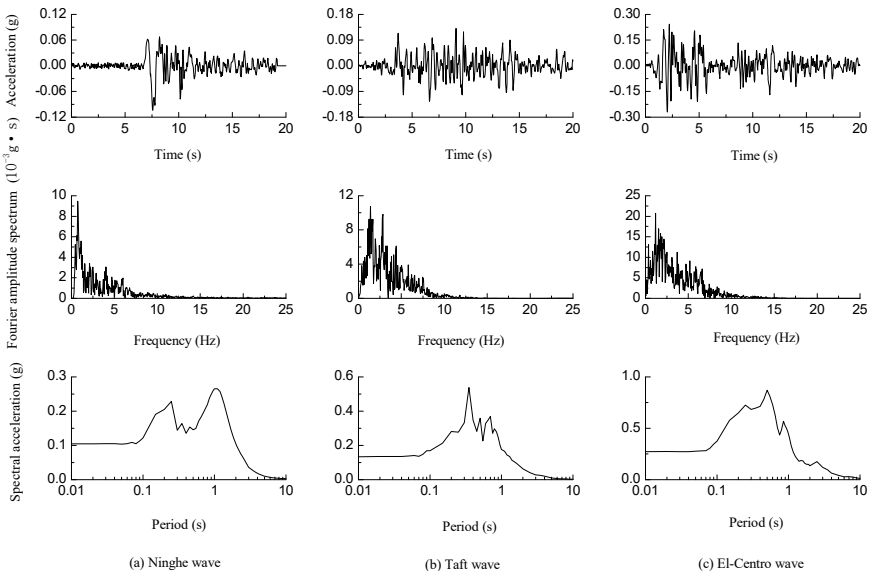


Fig.2: From top to bottom, respectively, acceleration time history, Fourier amplitude spectrum and 5% damped elastic response spectra.

| Layer Type | Thickness h/m | Density $\rho/(t\cdot m^{-3})$ | Poisson's Ratio υ | Shear Modulus G / ($10^7$ Pa) | | | Damping Ratio ζ | | |
|---|---|---|---|---|---|---|---|---|---|
| | | | | Ninghe wave | Taft wave | El-Centro wave | Ninghe wave | Taft wave | El-Centro wave |
| Clay | 10 | 1.9 | 0.3 | 5.26 | 6.23 | 3.06 | 0.097 | 0.082 | 0.149 |
| Clay | 10 | 1.9 | 0.3 | 1.34 | 1.92 | 0.87 | 0.185 | 0.174 | 0.201 |
| Clay | 10 | 1.9 | 0.3 | 0.76 | 1.44 | 0.59 | 0.202 | 0.182 | 0.205 |
| Bedrock | | 2.2 | 0.2 | 58.3 | 56.1 | 64.3 | 0 | 0 | 0 |

Table 1: Properties of 30 m single-layered soil column.

| Layer Type | Thickness h/m | Density $\rho/(t\cdot m^{-3})$ | Poisson's Ratio υ | Shear Modulus G / ($10^7$ Pa) | | | Damping Ratio ζ | | |
|---|---|---|---|---|---|---|---|---|---|
| | | | | Ninghe wave | Taft wave | El-Centro wave | Ninghe wave | Taft wave | El-Centro wave |
| Clay | 10 | 1.9 | 0.3 | 7.83 | 8.14 | 5.17 | 0.066 | 0.064 | 0.099 |
| Clay | 10 | 1.9 | 0.3 | 2.20 | 2.47 | 1.26 | 0.172 | 0.166 | 0.187 |
| Clay | 10 | 1.9 | 0.3 | 1.40 | 1.92 | 0.66 | 0.183 | 0.174 | 0.204 |
| Clay | 10 | 1.9 | 0.3 | 1.08 | 1.75 | 0.59 | 0.194 | 0.177 | 0.205 |
| Clay | 10 | 1.9 | 0.3 | 0.99 | 1.57 | 0.59 | 0.198 | 0.180 | 0.205 |
| Bedrock | | 2.2 | 0.2 | 55.6 | 56.1 | 66.0 | 0 | 0 | 0 |

Table 2: Properties of 50 m single-layered soil column.

| Layer Type | Thick-ness h/m | Density ρ/(t·$m^{-3}$) | Poisson's Ratio υ | Shear Modulus G / ($10^7$ Pa) | | | Damping Ratio ζ | | |
|---|---|---|---|---|---|---|---|---|---|
| | | | | Ninghe wave | Taft wave | El-Centro wave | Ninghe wave | Taft wave | El-Centro wave |
| Clay | 3 | 1.99 | 0.35 | 1.62 | 1.74 | 0.52 | 0.074 | 0.069 | 0.172 |
| Clay | 2 | 1.89 | 0.35 | 1.75 | 1.97 | 0.56 | 0.120 | 0.106 | 0.184 |
| Silty clay | 8 | 1.99 | 0.30 | 3.47 | 4.16 | 0.33 | 0.092 | 0.072 | 0.159 |
| Sandy clay | 4 | 2.00 | 0.30 | 1.94 | 1.95 | 1.23 | 0.138 | 0.135 | 0.167 |
| Sandy clay | 4 | 2.00 | 0.30 | 1.82 | 1.96 | 1.09 | 0.142 | 0.137 | 0.176 |
| Silt | 4 | 2.07 | 0.30 | 0.19 | 9.23 | 0.19 | 0.156 | 0.089 | 0.156 |
| Sandy clay | 5 | 2.01 | 0.30 | 4.60 | 5.46 | 3.54 | 0.131 | 0.126 | 0.147 |
| Sandy clay | 2 | 1.96 | 0.30 | 20.1 | 21.1 | 10.8 | 0.085 | 0.081 | 0.130 |
| Sandy clay | 5 | 2.10 | 0.30 | 3.07 | 3.07 | 1.73 | 0.136 | 0.136 | 0.175 |
| Silt | 2 | 2.04 | 0.30 | 0.16 | 0.16 | 0.16 | 0.156 | 0.156 | 0.156 |
| Sandy clay | 6 | 2.00 | 0.30 | 3.48 | 3.47 | 2.11 | 0.136 | 0.135 | 0.169 |
| Sandy clay | 5 | 2.00 | 0.30 | 3.48 | 3.47 | 1.95 | 0.136 | 0.137 | 0.175 |
| Bedrock | | 2.20 | 0.20 | 56.1 | 55.8 | 69.6 | 0 | 0 | 0 |

Table 3: Properties of 50 m multi-layered soil column.

## 5 CALCULATION RESULTS

It is used the form $\boldsymbol{C} = \beta \boldsymbol{K}$ , $\beta = 2\zeta / \omega = \zeta / \pi f$ in Ref. [5]. The ratio between the arithmetic mean of the target frequency $f$ and the first natural frequency $f_1$ of soil, and the ratio between the arithmetic mean of the target frequency $f$ of soil and the centroid frequency of Fourier spectrum of the input ground motion $f_c$ are calculated under input ground motions, thereby the relationship of $f$, $f_1$ and $f_c$ is fitted. It can provide reference for determining damping coefficient in time domain analysis, but it is more trouble in application. In Ref. [8, 9, 12, 13], based on appropriate target frequency, Rayleigh damping is determined for given soil column and input ground motion, but a regular and universal conclusion is not given for selection of target frequency. An averaged damping ratio is used in Ref.[11], while the damping ratio is extracted from the equivalent linear frequency domain analysis procedure in this paper, and therefore, the results using the method in Ref. [11] are not compared with that of the equivalent linear frequency domain analysis method in Ref. [1].

In this paper, the results using the methods in Ref. [2-4, 6, 7, 10] are compared with that of Ref. [1] respectively. Taking the results of equivalent linear frequency domain analysis in Ref. [1] as standard, the relative error of the result of time domain analysis and frequency domain analysis is expressed as:

$$e = \frac{|a_{\max}| - |a^*_{\max}|}{|a^*_{\max}|} \times 100\% \tag{13}$$

where $a_{\max}$ = peak ground acceleration in time domain analysis, and $a^*_{\max}$ = peak ground acceleration in frequency domain analysis.

The absolute value of peak ground acceleration is:

$$A_{\max} = |a_{\max}| \; or \; |a^*_{\max}| \tag{14}$$

The absolute values of the peak ground accelerations and the relative errors are shown in Table 5 to Table 7, and the 5% damped elastic response spectrum are shown in Fig. 3.

| $f$/Hz | | Ninghe wave | Taft wave | El-Centro wave | References |
|---|---|---|---|---|---|
| $f_p$ | | 0.73 | 1.42 | 1.17 | [3] |
| $f_c$ | | 4.03 | 3.61 | 3.71 | [4] |
| 30 m single-layered | $f_1$ | 0.74 | 0.93 | 0.62 | [2,6,10] |
| soil column | $f_3$ | 3.71 | 4.64 | 3.08 | [10] |
| 50 m single-layered | $f_1$ | 0.47 | 0.56 | 0.35 | [2,6,10] |
| soil column | $f_3$ | 2.36 | 2.78 | 1.76 | [10] |
| 50 m multi-layered | $f_1$ | 0.44 | 0.57 | 0.31 | [2,6,10] |
| soil column | $f_3$ | 2.21 | 2.84 | 1.54 | [10] |

Table 4: Target frequencies to calculate Rayleigh damping coefficient under different ground motions.

Note: $f$ = target frequency, $f_p$ = the predominant frequency of Fourier spectrum of the input ground motion, $f_c$ = the centroid frequency of Fourier spectrum of the input ground motion, $f_1$ = the first natural frequency, $f_3$ = the third natural frequency.

| Methods in references | Ninghe wave | | Taft wave | | El-Centro wave | |
|---|---|---|---|---|---|---|
| | $A_{\max}$/g | e (%) | $A_{\max}$/g | e (%) | $A_{\max}$/g | e (%) |
| Input | 0.104 | — | 0.132 | — | 0.271 | — |
| [1] | 0.231 | 0 | 0.223 | 0 | 0.278 | 0 |
| [2] | 0.246 | 6.5 | 0.211 | -5.4 | 0.223 | -19.8 |
| [3] | 0.246 | 6.2 | 0.236 | 5.8 | 0.249 | -10.5 |
| [4] | 0.324 | 40.2 | 0.287 | 28.6 | 0.377 | 35.2 |
| [6] | 0.239 | 3.4 | 0.215 | -3.7 | 0.219 | -21.4 |
| [7] | 0.158 | -31.8 | 0.148 | -33.6 | 0.169 | -39.2 |
| [10] | 0.243 | 5.0 | 0.238 | 6.6 | 0.268 | -3.7 |

Table 5: The absolute values of peak ground acceleration and relative errors of 30 m single-layered soil column.

| Methods in references | Ninghe wave | | Taft wave | | El-Centro wave | |
|---|---|---|---|---|---|---|
| | $A_{max}$ /g | e (%) | $A_{max}$ /g | e (%) | $A_{max}$ /g | e (%) |
| Input | 0.104 | — | 0.132 | — | 0.271 | — |
| [1] | 0.151 | 0 | 0.155 | 0 | 0.200 | 0 |
| [2] | 0.131 | -13.4 | 0.121 | -22.5 | 0.155. | -22.4 |
| [3] | 0.149 | -1.3 | 0.157 | 1.3 | 0.267 | 33.7 |
| [4] | 0.201 | 33.2 | 0.200 | 28.8 | 0.420 | 110.2 |
| [6] | 0.141 | -6.6 | 0.130 | -16.1 | 0.162 | -18.7 |
| [7] | 0.106 | -30.0 | 0.097 | -37.3 | 0.094 | -53.1 |
| [10] | 0.161 | 6.6 | 0.159 | 2.4 | 0.214 | 7.0 |

Table 6: The absolute values of peak ground acceleration and relative errors of 50 m single-layered soil column.

| Methods in references | Ninghe wave | | Taft wave | | El-Centro wave | |
|---|---|---|---|---|---|---|
| | $A_{max}$ /g | e (%) | $A_{max}$ /g | e (%) | $A_{max}$ /g | e (%) |
| Input | 0.104 | — | 0.132 | — | 0.271 | — |
| [1] | 0.155 | 0 | 0.130 | 0 | 0.269 | 0 |
| [2] | 0.118 | -23.8 | 0.095 | -26.7 | 0.195 | -27.4 |
| [3] | 0.141 | -9.1 | 0.114 | -12.7 | 0.345 | 28.2 |
| [4] | 0.208 | 34.0 | 0.147 | 12.9 | 0.503 | 86.8 |
| [6] | 0.133 | -14.2 | 0.101 | -22.6 | 0.209 | -22.2 |
| [7] | 0.086 | -44.7 | 0.089 | -32.1 | 0.102 | -62.1 |
| [10] | 0.159 | 2.6 | 0.135 | 3.4 | 0.268 | -0.3 |

Table 7: The absolute values of peak ground acceleration and relative errors of 50 m multi-layered soil column.

## 6 CONCLUSIONS

In this paper, two single-layered soil columns and one multi-layered soil column are calculated under different input ground motions, and the results of different Rayleigh damping coefficients in time domain analysis are compared with that of frequency domain analysis respectively. Conclusions are obtained as follows:

(1) As can be seen from Fig.1, the damping ratio in the Rayleigh damping formulation is frequency dependent, in contrast to experimental results showing that the damping of soil is mostly frequency independent. The damping coefficients $\alpha$ and $\beta$ are controlled by the target frequency $f$. Based on different selection of target frequency $f$, the damping ratio calculated by the formulation $\boldsymbol{C} = \alpha\boldsymbol{M}$ or $\boldsymbol{C} = \beta\boldsymbol{K}$ and the frequency domain hysteretic damping ratio are quite different.

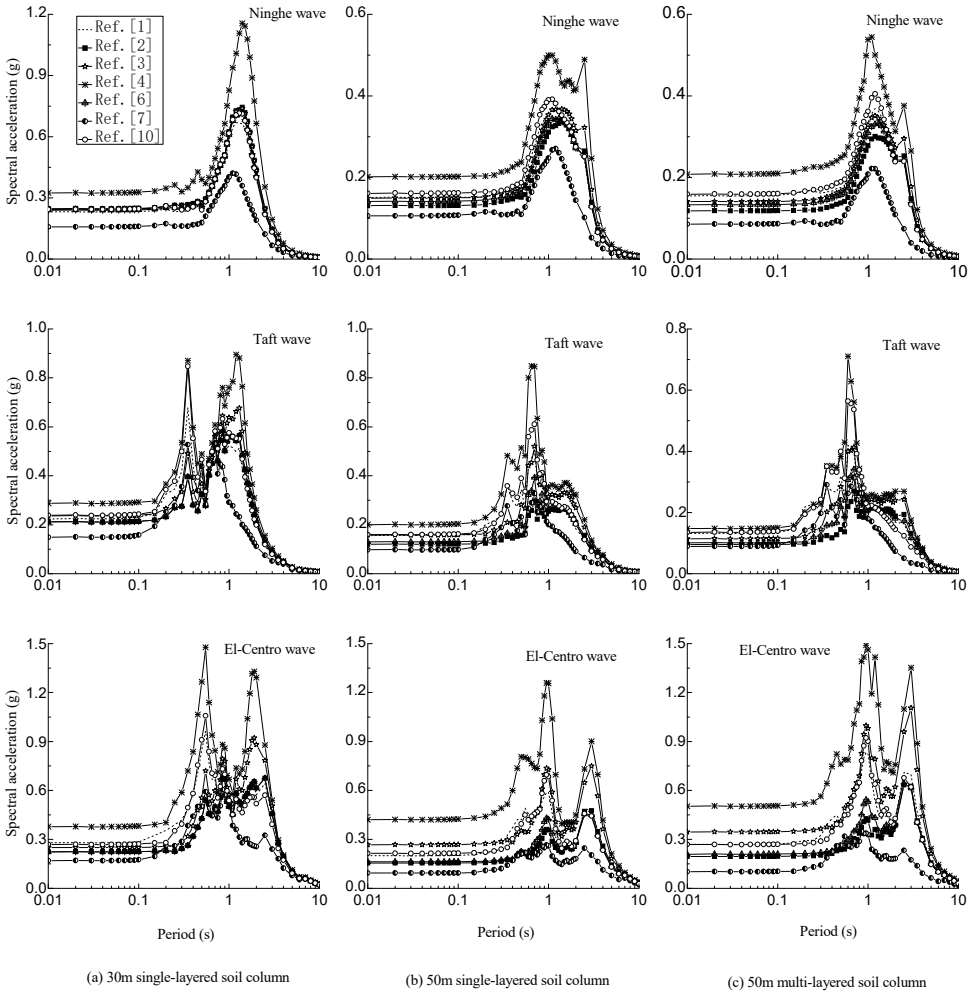


Fig.3: 5% damped elastic response spectra.

(2) From Table 5 to Table 7, conclusions can be obtained as follows. In contrast with the absolute values of the peak ground accelerations calculated using the method in Ref. [1], the errors of the calculation results using the methods in Ref. [2-4, 6, 7] are large, and they are more sensitive to the thickness of soil and the input ground motion, that is, the errors have large discrete with different thicknesses of soil and different input ground motions. To the contrary of the absolute values of the peak ground accelerations calculated using the method in Ref. [1], the errors of the calculation results using the method in Ref. [10] are small, generally less than 10%, and they are insensitive to the thickness of soil and the input ground motion, that is, the errors have small discrete with different thicknesses of soil and different input ground motions. As presented in Fig. 3, the calculation results using the method in Ref. [4] are obviously large, while the calculation results using the method in Ref. [7] are obviously small, which are different from the elastic response spectrum calculated using the method in

Ref. [1]. The errors of the calculation results using the methods in Ref. [2, 3, 6] are relatively large. The calculation results using the method in Ref. [10] agree well with that of Ref. [1].

(3) According to the elastic response spectrum in Fig. 3, unlike the calculation results using the method in Ref. [1], the results using the method in Ref. [10] are large in the corresponding period of the selected target frequency, while the results using the method in Ref. [10] are small in other periods. It can be observed from Fig.1, in the corresponding period of the selected target frequency, the damping ratio calculated using the method in Ref. [10] is smaller than the frequency domain hysteretic damping ratio, so the calculated results are large. In other periods, the damping ratio calculated by the method in Ref. [10] is larger than the frequency domain hysteretic damping ratio, so the calculation results are small.

(4) The determination of Rayleigh damping coefficient in time domain analysis has great influence on the calculation results. When using the method in Ref. [10], that is, using the full Rayleigh damping formulation and selecting the first and second natural frequency as two target frequencies, the results obtained agree well with that of frequency domain analysis. At present, the method in Ref. [10] is an effective approach for selecting damping in time domain analysis, but a better method needs to be studied further.

## ACKNOWLEDGEMENTS

This research is supported by the National Natural Science Foundation of China under Grant No. 51278323.

## REFERENCES

[1] Liao Z P, *Theory and practice for seismic microzonation*, *1th Edition.* Seismological Press, 1989. (in Chinese)

[2] Youssef M.A.Hashash, Duhee Park, Viscous damping formulation and high frequency motion propagation in non-linear site response analysis. *Soil Dynamics and Earthquake Engineering*, **22**, 611–624, 2002.

[3] Liao Z P, Introduction to wave motion theories for engineering, 2th Edition. Science Press, 2002. (in Chinese)

[4] Ding H P, Zhou Z H, Numerical simulation of seismic response of soil layers. *World Earthquake Engineering*, **14**, 26-31, 1998. (in Chinese)

[5] Lou M L, Pan D G, Hysteretic damping application in time domain analysis of soil layer. *Journal of Tongji University*, **3**, 281-285, 2004. (in Chinese)

[6] Zhang K X, Xie J F, *Soil Dynamics, 1th Edition*. Seismological Press, 1989. (in Chinese)

[7] Wang S T, Cao Z, *Modern Seismic Design Method, 1th Edition*. China Building Industry Press, 1997. (in Chinese)

[8] Duhee Park, Youssef M.A.Hashash, Soil damping formulation in nonlinear time domain site response anlysis. *Journal of Earthquake Engineering*, **8**, 249–274, 2004.

[9] HUDSON M, IDRlSS I M, BEIKAE M, *User manual for QUAD4M: A computer program to evaluate the seismic response of soil structures using finite element procedures and incorporating a compliant base, 1th Edition*. Berkeley:University of California, 52-80, 1994.

[10] Annie O.L.Kwok, Jonathan P.Stewart, Youssef M.A.Hashash, et al, Use of exact solutions of wave propagation problems to guide implementation of nonlinear seismic ground response analysis procedures. *Journal of Geotechnical and Geoenvironmental Engineering*, **133**, 1385-1398, 2007.

[11] Nozomu Yoshida, Satoshi Kobayashi, Iwao Suetomi, et a1, Equivalent linear method considering frequency dependent characteristics of stiffness and damping. *Soil Dynamics and Earthquake Engineering*, **22**, 205-222, 2002.

[12] Jean-Francois Semblat, Ali Gandomzadeh,Luca Lenti, A simple numerical absorbing layer method in elastodynamics. *Comptes Rendus Mecanique*, **338**, 24–32, 2010.

[13] Zou D G, XU B, Kong X J, Study of influence of different methods for calculating Rayleigh damping coefficient on high earth-rock dam seismic response. *Rock and Soil Mechanics*, **32**, 797-803, 2011. (in Chinese)

COMPDYN 2017
6th ECCOMAS Thematic Conference on
Computational Methods in Structural Dynamics and Earthquake Engineering
M. Papadrakakis, M. Fragiadakis (eds.)
Rhodes Island, Greece, 15–17 June, 2017

# SIMPLIFIED NUMERICAL MODELING STRATEGIES OF DEEP VIBRATORY COMPACTION

**Maximilian Schmitter**[1], **Christoph Adam**[2]

[1] Unit of Applied Mechanics
University of Innsbruck, Innsbruck, Austria
e-mail: maximilian.schmitter@uibk.ac.at

[2] Unit of Applied Mechanics
University of Innsbruck, Innsbruck, Austria
e-mail: christoph.adam@uibk.ac.at

**Keywords:** Soil Dynamics, Deep Vibratory Compaction, Current State Simulation, Parameter Identification, Numerical Modeling

**Abstract.** *In this paper different simplified approaches for numerical simulation of deep vibratory compaction are presented. In the first approach, modal analysis yields the mode shapes and natural frequencies of a planar soil model, with the objective of reducing the degrees of freedom of the soil continuum in a subsequent response history analysis considering only the most dominate modes. Based on the maximum elastic strain energy per mode criterion, the most dominant modes excited by a rotating force are identified, revealing that the most dominant natural frequencies are clustered around multiples of the excitation frequency. It is also shown that* $1.4\,\%$ *of the modes contribute to* $80\,\%$ *of the total strain energy. The second study addresses modeling of vibro-soil interaction, approximating the soil as three-dimensional planar circular section and the vibratory as rigid cylinder rotating in the hole at the soil center. To the surfaces of the two bodies potentially in contact, a contact formulation is assigned. The outcomes of the numerical simulations on this finite element model serve as input for system identification of the soil parameters varying with time due to the compaction process. The underlying lumped parameter model is composed of two discrete spring-dashpot systems and a lumped mass subjected to a rotating force. The contact force can be reasonably identified, however, the utilized mapping algorithm for identification of the time varying soil parameter needs further investigation.*

## 1 INTRODUCTION

Since more than five decades *deep vibratory compaction* has been used to compact non-cohesive granular soil media of considerable depth [14]. The deep vibratory compaction device consists of the vibrator, which is attached to a crane. Inside the vibrator an eccentric rotating mass generates horizontal dynamic forces. As depicted in Fig. 1, *deep vibratory compaction* is

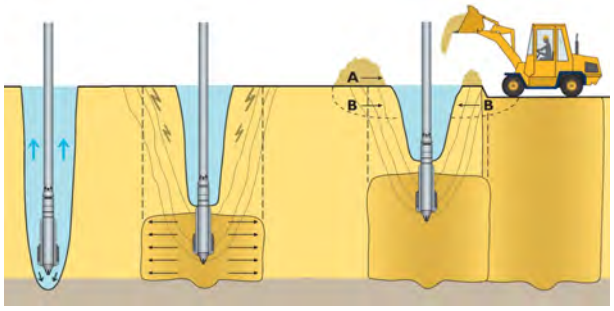


Figure 1: Sketch of soil densification by means of *deep vibratory compaction* [11].

conducted in two stages. In the first stage, the vibrator with rotating mass and high volume water jets at the tip penetrates the soil, taking advantage of the vibrator self-weight, up to the desired depth of compaction. Depending on the utilized crane, additional downward and upward forces accelerate the penetration. From the point of view of mechanical science, the processes at this stage can be explained by means of cavity expansion theories, see e.g. [20]. In the subsequent prescribed stepwise periodical upward motion of the vibratory with simultaneously prescribed mass flow rate of water at the vibrator tip, the adjacent soil media is stepwise compacted. At each step the compaction process is completed when an a priori defined limit value of the power consumption (measured in ampere) is reached. With this kind of intuitive compaction control, in general, reliable soil densification is achieved.

However, there is a demand on a more objective compaction control procedure based on physically quantifiable parameters, such as the dynamic response of the compaction device or of the adjacent soil surface, which would facilitate a fully automated compaction process yielding to more homogeneously compacted subsoil. This procedure should be based on data continuously recorded during compaction, and thus, simultaneous adjustment of operational parameters such as the excitation frequency of the vibratory would be possible. For near-surface compaction by means of vibratory rollers, such a method, i.e. the continuous compaction control (CCC) method, is available [1]. Since launching more than two decades ago, it has become the state of the art control method for roller compaction application. In an attempt to close the gap, Wehr [18] proposed a method for optimal compaction control of deep vibratory compaction.

More recently, a research consortium with members from industry (Keller Grundbau GmbH, Vienna Consulting Engineers ZT GmbH) and academia (TU Wien - Institute of Geotechnics, University of Innsbruck - Unit of Applied Mechanics) was founded, aiming at developing a physically based and reliable compaction control method for deep vibratory compaction. In a project [7] funded by the Austrian Research Promotion Agency (FFG) this research consortium pursues this goal based on in-situ experimental and numerical investigations of deep vibratory compaction.

This papers reports on both simplified and more elaborate, however, feasible numerical modeling efforts of deep vibratory compaction, conducted within the aforementioned research project. The overall goal is to quantify the dynamic behavior of the vibrator-soil interaction system

and the evolution of the compacted soil domain.

In the literature, for *vibro replacement stone columns*, a method similar deep vibratory compaction, several simplified analytical and numerical models have been developed in an effort to estimate the ultimate bearing capacity respectively the magnitude of consolidation settlement of the improved soil. An overview on these studies is found in [13]. Vibratory displacement and vibratory compaction methods used in different soil types rely on a similar rotating vibrator. Both methods have in common that a detailed numerical simulation of the compaction process is extremely demanding in terms of modeling and computational costs, because of three-dimensional dynamic excitation, nonlinear interaction between vibrator and soil, soil liquefaction, soil fluidization and subsequent soil compaction, etc. To reduce the computational effort, for instance, Kessler et al. [12] simulated numerically vibratory compaction using an axial-symmetric thin planar soil section, and compared the outcomes with the ones of a full three-dimensional numerical model. In this approach, due to the axial-symmetric setup, the vibrator model performs a pulsating motion, and therefore, shear distortion of the soil cannot be reproduced although this effect contributes significantly to soil compaction [10]. Cudmani et al. [3] used a hypoplastic infinite cylindrical cavity soil model with a prescribed radial stress component to evaluate the cone penetration resistance after compaction. Based on a planar soil section similar the one used in [12], in [2] elastic strain paths were derived that served as input for a strain excited single element simulation with assigned hypoplastic constitutive law. In [2] the compaction distribution in radial direction was predicted in agreement to the common soil densification hypothesis (e.g. [6, 17]). In the work of Qiu and Hamann [16, 9], a full three-dimensional model of the vibrator-soil interaction system was created to simulate the vibrator penetration (pile installation), using an elaborate coupled Lagrangian and Eulerian displacement field formulation and hypoplastic soil properties. The effect of different excitation frequency and vibrator displacement amplitudes on the void ratio in the subsoil was also investigated.

In the past in-situ experiments have been conducted to reveal the underlying dynamic processes of *deep vibratory compaction*. For instance, in an in-situ test series Wehr [18] varied the excitation frequency of the vibrator to identify optimal conditions for deep vibratory compaction. From his studies Wehr concluded that at a certain frequency the vibrator is in a state of resonance. However, it is still controversially discussed if vibrator resonance is related to soil response amplification and consequently to optimal soil compaction, due to complex interaction and nonlinear material behavior. Small scaled tests were conducted in [15], emphasizing optimal compaction control as proposed in [18]. Fellin et al. [5] estimated the increase of soil compaction based on a hybrid approach of experimental and numerical simulations. They identified parameters for a simple lumped parameter model of the vibrator-soil interaction system from in-situ data of vibratory displacement and phase delay between excitation and vibratory response.

In the present contribution, two different numerical approaches of different elaboration are used to study different aspects of this demanding problem. In the first study a simplified two-dimensional planar model of the vibrator-soil system is subjected to modal analysis, aiming at synthesizing dominant modes vulnerable to specific excitation of the vibrator. Since the soil is assumed to behave linear elastic, this simulation represents a current state description of the system at specific time instants during the compaction process. The second study addresses online time-variant evaluation of soil properties based on recorded response data and a simplified inverse lumped parameter model, similar to [5]. An algorithm based on *Wolf's cone model* [19] is used to map lumped parameter data to feasible soil parameters.

## 2 DOMINANT MODES OF A PLANAR SOIL SECTION

Numerical analysis of wave propagation in the infinite three-dimensional halfspace is prohibitively computationally expensive, even for a linear time-invariant system. One possibility to reduce the computational effort is the application of modal analysis, considering only modes that contribute significantly to the dynamic response. In the present problem, this approach can be utilized for current state simulations of the dynamic soil behavior, i.e., it is assumed that at the considered discrete time instant the increase of the soil stiffness due to compaction is negligible, and thus, in the simulation the soil properties are assumed to be linear elastic. The dominant modes of the soil, which is an infinite continuum, depend heavily on the specific vibratory excitation frequency, and they are a priori unknown. Thus, in a first step modal analysis is conducted to derive all modes of the continuum in a certain frequency range. Subsequently, from the entire mode set the modes that dominate the dynamic steady state response to a specific periodic excitation are identified, utilizing the maximum elastic strain energy per mode $U_i$ in the steady state. The strain energy of the $i$-th mode, $U_i$, is defined as

$$U_i = \frac{1}{2} k_i q_i^2 \tag{1}$$

where $k_i$ is the $i$-th modal stiffness, and $q_i$ the $i$-th modal coordinate.

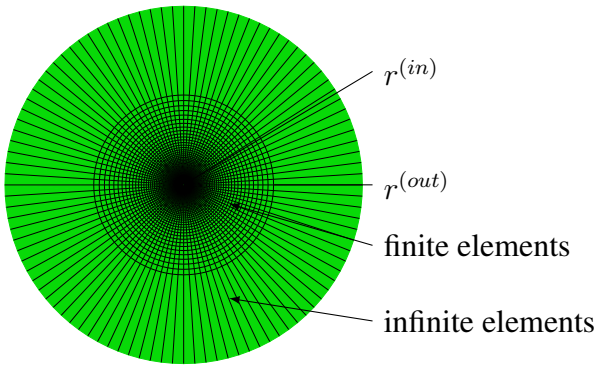


Figure 2: Spatial domain for the modal analysis.

In the present study, this approach is adopted upon a simple two-dimensional representation of the vibro-soil system, see Fig. 2. The soil is modeled as an annular planar plate of radius $r^{(out)} = 12\,\mathrm{m}$ with an circular hole of radius $r^{(in)} = 0.15\,\mathrm{m}$. A linear elastic homogeneous material with Young's modulus of $20\,\mathrm{MPa}$, Poisson ratio of $1/3$, void ratio of $0.735$ and a dry skeleton density of $2650\,\mathrm{kg\,m^{-3}}$ is assigned to the plate. This material represents loose granular soil. Material damping according to Rayleigh with a ratio of critical damping $\zeta = 0.05$ at frequencies of $40\,\mathrm{Hz}$ and $72\,\mathrm{Hz}$ is used. The vibro excitation is simplified as a concentrated force rotating with a frequency of $60\,\mathrm{Hz}$ along the inner boundary of the soil plate in radial direction. The plate is spatially discretized by means of finite elements (FE) with a structured mesh of $100$ four-nodes-full-integrated bilinear elements (CPE4) distributed along the circumference, as shown in Fig. 2. For the infinite continuum outside of the plate domain infinite elements (CINPE4) are used. Plane strain condition perpendicular to the excitation direction is assumed. The numerical model exhibits in total $13\,800$ degrees of freedom. The analysis is conducted by the FE software Abaqus 6.13-2 and it represents a linear perturbation step, also referred to as current state simulation.

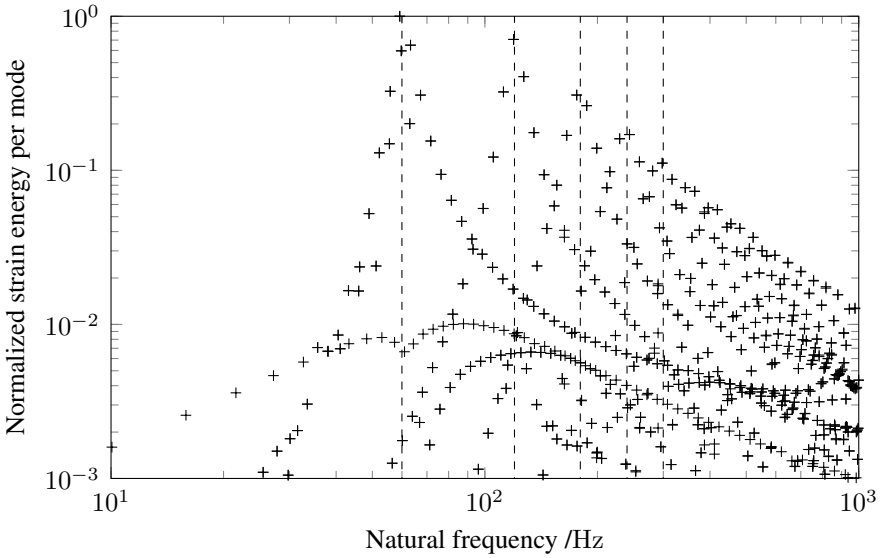


Figure 3: Normalized maximum elastic strain energy per mode for 13600 modes (detail).

As a result of the analysis, Fig. 3 displays for $13\,600\,\mathrm{modes}$ the maximum elastic strain energy per mode of the discretized planar soil continuum subjected to harmonic vibratory excitation as a function of the corresponding natural frequency up to $4230\,\mathrm{Hz}$. The vertical dashed lines indicate the excitation frequency of $60\,\mathrm{Hz}$ and multiples of it, i.e. $120\,\mathrm{Hz}$ and $180\,\mathrm{Hz}$. It is readily observed that there is no single isolated dominant mode, and modes clustered around $60$, $120$ and $180\,\mathrm{Hz}$ contribute the most to the dominant modes. This behavior is a result of the specific excitation, as subsequently outlined. At fixed location $(r^{(in)}, \phi)$ (with $r^{(in)}$ denoting the radius of the inner hole and $\phi$ the angel in cylindrical coordinates), the inner surface is subjected to a force excitation according to a Dirac comb $\delta$ ,

$$f_i\left(r^{(in)}, \phi, t\right) = \sum_{n=0}^{\infty} \delta\left(t - nT - t_0\right)\delta_{ir} \tag{2}$$

with phase time delay $t_0 = \phi T/2\pi$ ($T$ denotes the excitation period) at the boundary to realize a spatial continuous force distribution. Symbol $\delta_{ir}$ denotes the Kronecker symbol. Fourier transformation of this expression,

$$F_i\left(r^{(in)}, \phi, \omega\right) = 1/T \sum_{n=0}^{\infty} \delta\left(\omega - n/T\right) e^{-j\omega t_0}\delta_{ir} \tag{3}$$

with $j = \sqrt{-1}$ reveals that spectral lines at multiples of the excitation frequency, $n/T$, occur. This is even true for an arbitrary force distribution $g\left(\tilde{t}\right)$ with $0 \leq \tilde{t} \leq a\,(\leq T)$, as exemplary shown in Fig. 4, where $g\left(\tilde{t}\right)$ is depicted at two fixed locations of the inner surface of the hole. For such arbitrary distributed force, the force excitation in the time reads as

$$f_i\left(r^{(in)}, \phi, t\right) = g\left(\tilde{t}\right) * \sum_{n=0}^{\infty} \delta\left(t - nT - t_0\right)\delta_{ir} \tag{4}$$

with the corresponding Fourier transformation

$$F_i\left(r^{(in)}, \phi, \omega\right) = G\left(\omega\right) 1/T \sum_{n=0}^{\infty} \delta\left(\omega - n/T\right) e^{-j\omega t_0}\delta_{ir}\ . \tag{5}$$

Symbol $*$ denotes the convolution. These relations not only hold true for continuous signals but also for discrete ones. The periodization of the signal with period $T$ in the time domain by means of the discrete Fourier transformation is reflected in the frequency domain by spectral lines equally spaced with $1/T$. Thus, in Fig. 3 the maximum modal strain energies are clustered around these spectral lines.

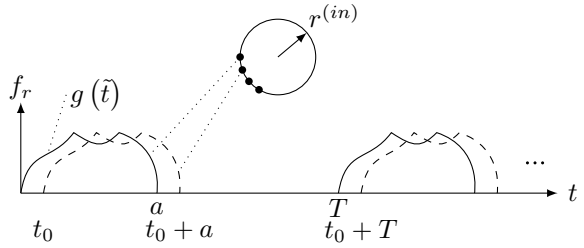


Figure 4: Rotating force excitation according to an arbitrary force distribution along the inner radius of the planar soil section.

In Fig. 5 the first to forth and the 15th and 16th most dominant mode shape are shown. The modes depicted in Figs 5(a) and (b) describe a translational motion of the inner boundary, and thus, the soil is subjected to a dominant shear distortion. This behavior is in agreement with the observation that the most effective compaction is related to shear distortion [10]. Due to the symmetric geometry of the numerical model, the eigenvalues come in pairs, and the corresponding mode shapes are rotated to each other but are otherwise identical. According to Figs 5(c) and (d), the hole of the planar soil section is elliptically deformed. In comparison between Fig. 5(c), (d) the mode shapes shown in Figs 5(e) and (f) represent higher modes compared to the previously discussed ones, and thus, the shape of the hole deflection is also of higher order.

Figure 6 shows the cumulative maximum elastic strain energy $S\,(n) = \sum_{i=1}^{n} U_i$ as a function of $n$, with $i = 1$ denoting the mode representing the largest strain energy, $i = 2$ the mode with the second largest strain energy, and so on. This figure shows that the increase of the modal strain energy becomes gradually smaller with increasing $i$. The first $200\,\mathrm{most}$ dominating modes (i.e. $1.4\,\%$) contribute to $80\,\%$ of the strain energy of all $13\,600\,\mathrm{modes}$. Thus, approximation of the system response using a modal analysis technique based on the most dominant modes identified from this figure significantly reduces the number of degrees of freedom without significant loss of accuracy.

## 3 DYNAMIC RESPONSE SIMULATION OF THE VIBRO-SOIL SYSTEM BASED ON A PLANAR MODEL

In the previous section, a two-dimensional planar soil section model subjected to a rotating force along the inner boundary has been used to describe vibrator-soil interaction. This modeling strategy cannot capture the physical processes at the vibro-soil interface. Thus, in a more elaborate approach according to [12], subsequently the soil is modeled as a three-dimensional planar annular soil section and the vibrator as a rigid cylinder body, as shown schematically in Fig. 7.

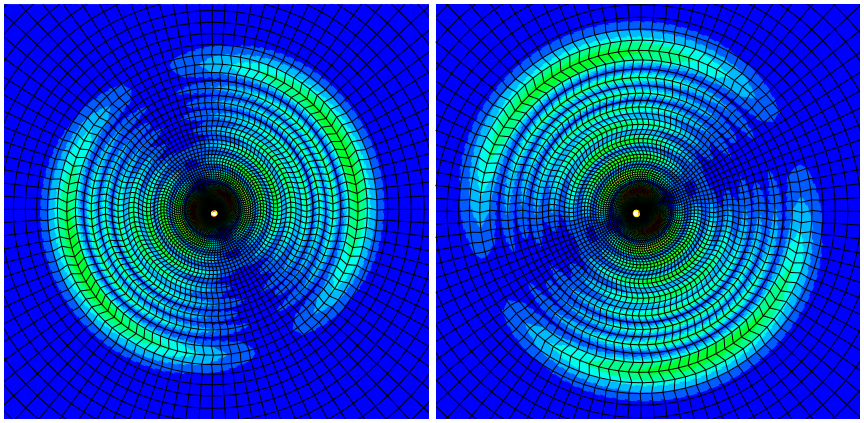

(a) First dominant mode shape with natural frequency of $59.20\,\mathrm{Hz}$.

(b) Second dominant mode shape with natural frequency of $59.20\,\mathrm{Hz}$.

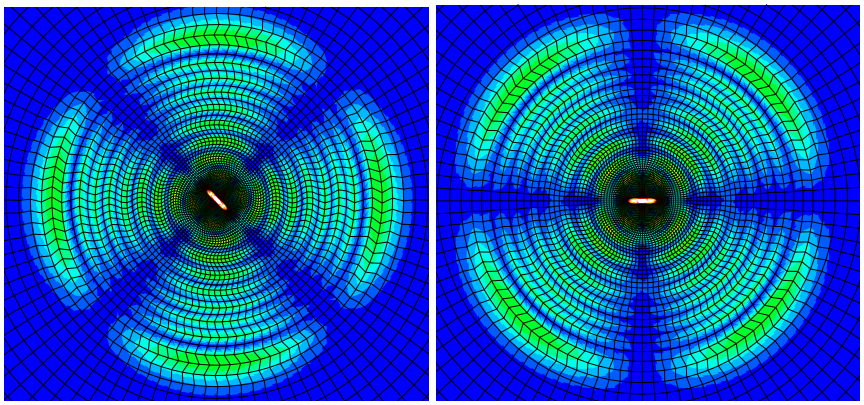

(c) Third dominant mode shape with natural frequency of $119.36\,\mathrm{Hz}$.

(d) Fourth dominant mode shape with natural frequency of $119.36\,\mathrm{Hz}$.

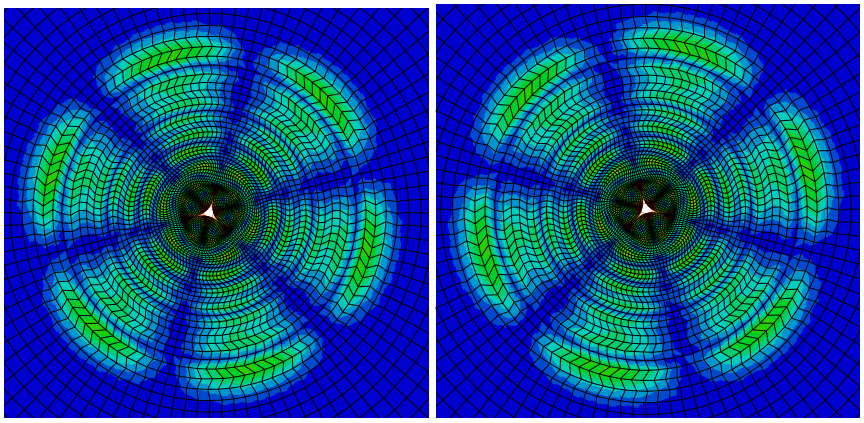

(e) $15^{\mathrm{th}}$ dominant mode shape with natural frequency of $176.05\,\mathrm{Hz}$.

(f) $16^{\mathrm{th}}$ dominant mode shape with natural frequency of $176.05\,\mathrm{Hz}$.

Figure 5: Selection of dominant mode shapes, sorted by the maximum of elastic strain energy per mode criterion in steady state. The contour indicates the norm of the corresponding eigenvalues.

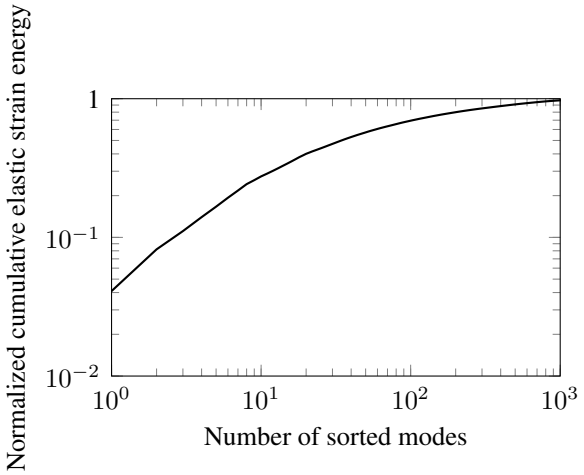


Figure 6: Normalized cumulative elastic strain energy.

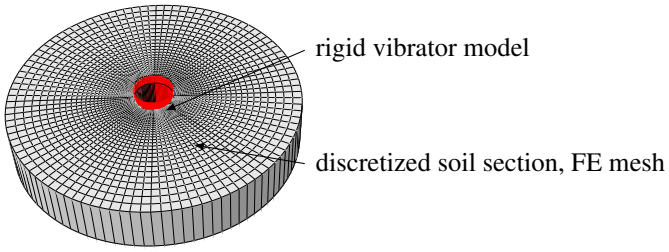


Figure 7: Model of the vibro-soil interaction system (detail).

The model of the annular soil continuum has the same dimensions and material properties as the one of the previous section, however, a thickness of $0.5\,\mathrm{m}$ is assigned. The upper and lower horizontal surface of the soil section is subjected to the vertical geostatic pressure at a depth of $15\,\mathrm{m}$, and at the outer radius the displacements are fixed. The rigid vibrator model has a lumped mass $m$ of $2592\,\mathrm{kg}$ and a mass moment of inertia of $1662\,\mathrm{kg\,m^2}$ (with respect to the centroid). The adjacent surfaces of this rigid body and of the soil stay in full or partial contact, depending on the excitation frequency. In the simulation of the motion, for this "contact pair" the "surface to surface" algorithm implemented in the FE analysis software Abaqus is applied. The soil domain is discretized by means of $7102$ eight-nodes-full-integrated elements (C3D8) from the Abaqus element library, arranged in a structured mesh, see Fig. 7. The maximum number of degrees of freedom of this model is $42\,006$ , depending on the actual contact state between soil surface and vibrator. In reality, the motion of the vibrator is induced by an eccentric mass rotating with prescribed angular velocity of frequency $\nu$. In the present simulations, the effect of this rotating eccentric mass is captured by a rotating in-plane centrifugal (radial) force $\mathbf{F}$, applied at the centroid of the rigid vibrator model. Force $|\mathbf{F}| = m_u e \nu^2$ is composed of the squared angular velocity $\nu^2$ times eccentric mass $m_u$ times eccentricity $e$, with $m_u e = 1.59\,\mathrm{kg\,m}$ for the considered vibrator. The tangential force component (Coriolis force), which is proportional to the angular acceleration, is neglected, because for slightly varying excitation frequency it is negligible small compared to the centrifugal force, and for steady state motion it

vanishes.

The results of the parametric study with a series of different excitation frequencies $\nu/2\pi$ ranging from $30$ to $60\,\mathrm{Hz}$, spaced with $3\,\mathrm{Hz}$, are presented in Figs 8 to 12. As first outcome, the phase delay between the excitation force and the vibro-displacement shown in Fig. 8 is discussed. In this figure each graph represents the phase angle for a discrete excitation frequency specified at the right hand side of the figure in ascending order from the bottom of the circular marker. The horizontal axis represents time $t$ normalized with respect to excitation period $T = 2\pi/\nu$. It is readily observed that after application of the force the phase angle increases sharply. Subsequently, the steady state solution is obtained after 10 to 20 (excitation) periods, depending on the excitation frequency. However, for excitation frequencies of $30$, $33$, $36$ and $39\,\mathrm{Hz}$ the steady state is not reached during the predefined simulation time. For the lowest excitation frequency of $30\,\mathrm{Hz}$, at the end of the observation time the phase angle is about $60°$. With increasing excitation frequency this value gradually increases, and finally for the largest frequency $\nu/2\pi = 60\,\mathrm{Hz}$ it is already about $160°$. According to Fig. 9 resonance is attained between $\nu/2\pi = 30$ and $33\,\mathrm{Hz}$.

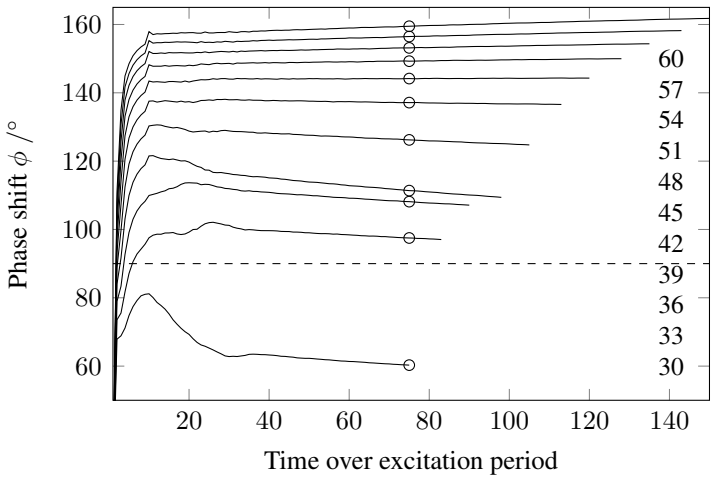


Figure 8: Phase shift between the centrifugal force and vibrator displacement.

The vibro-displacement is non-proportional to the excitation force (which is itself proportional to the square of the excitation frequency), as revealed by the displacement amplitudes depicted in Fig. 9. The largest amplitudes are related to an excitation frequency of $\nu/2\pi = 42\,\mathrm{Hz}$, and the lowest to $\nu/2\pi = 30\,\mathrm{Hz}$. The contact area normalized with respect the full area of the circular hole (i.e. full contact) shown in Fig. 10 is less sensitive to the excitation frequency sensitivity than expected. At the end of the observation time, the normalized contact area is between $0.38$ (for the lowest considered frequency) and $0.28$ (for the largest frequency).

As a further result, Fig. 11 shows the so-called eccentricity of ellipse of an arbitrary selected soil node at the contact surface in steady state condition. The eccentricity of ellipse is a criterion of the rotational motion of the soil, and it is calculated according to $\sqrt{a^2 - b^2}/a^2$, with $a$ and $b$ denoting the semi-major axis respectively the semi-minor axis of the elliptic soil node displacement. If the eccentricity is zero, the soil describes a circular motion. As expected, the eccentricity of the ellipse increases with increasing excitation frequency. However, the eccentricity values for frequencies $30$, $33$, $36$ and $39\,\mathrm{Hz}$ are not representative because in these cases the outcomes are based on non-stationary transient response, as discussed before (see, for instance,

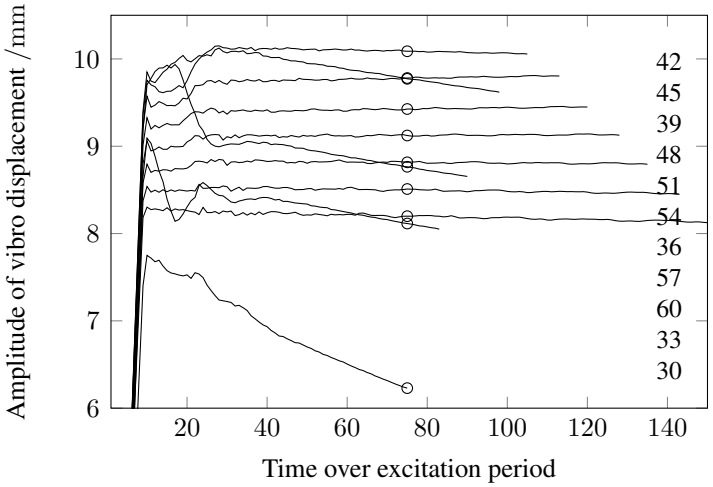


Figure 9: Amplitude of vibro displacement.

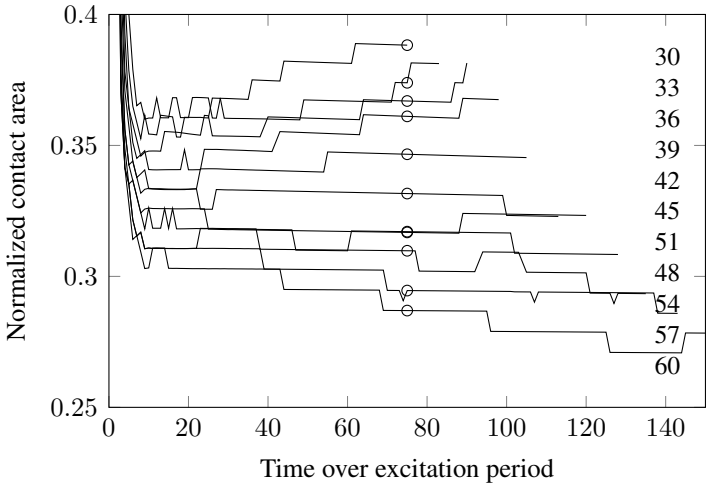


Figure 10: Normalized contact area.

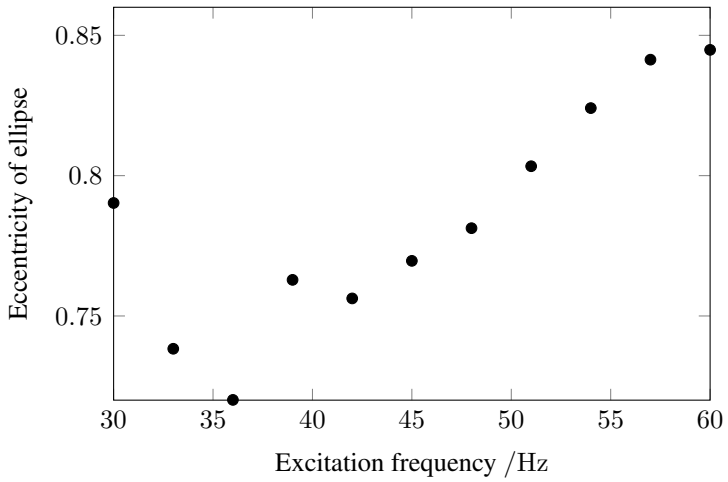


Figure 11: Eccentricity of ellipse of a soil node on the contact surface due to different excitation frequencies.

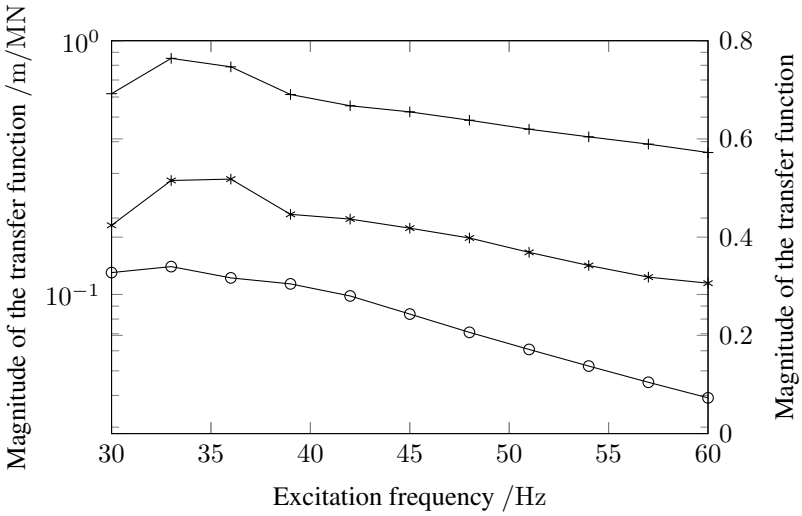


Figure 12: Magnitude of the transferfunction between centrifugal force and vibro displacement (circled markers) between vibro displacement and semi-major, respectively semi-minor axis (plus and asterisk markers).

Fig. 9).

The transfer function representing the ratio of force excitation and vibro-displacement in the frequency domain is shown in Fig. 12 by circular markers (dimension $\mathrm{m\,MN^{-1}}$). The vertical axis is logarithmic scaled. According to this function, the vibrator is at resonance between frequencies of $30\,\mathrm{Hz}$ and $33\,\mathrm{Hz}$. This is in agreement with the outcomes of Fig. 8 showing the phase delay between excitation and displacement.

The remaining graphs of this plot represent the transfer functions based on the ratio of vibro-displacement and the semi-major and semi-minor axis displacement components $a$ respectively $b$ of the considered soil node (none dimensional). An amplification in soil displacement due to the vibrator motion around $33\,\mathrm{Hz}$ is not as clear as in the before mentioned case. These transfer functions are almost affine.

## 4 IDENTIFACTION OF SOIL PROPERTIES BASED ON AN INVERSE MODEL

When appropriately equipped with sensors, the motion of the vibrator and its force exerted to the soil during deep vibratory compaction can be recorded. It is, however, difficult or even impossible to directly record the corresponding soil behavior and its densification. Thus, it would be desirable to deduce (respectively identify) from the vibrator response the evolution of the soil properties, applying a procedure referred to as inverse problem. For the solution of an inverse problem a simple mechanical model must be established, implying that this model responds in the same manner as the real system, which is in the present study the vibrator-soil interaction system. In contrast to a direct response simulation, the response of the real system, and thus, also of the mechanical model, is a priori known, and the parameters of the corresponding mechanical model are unknown. System identification aims at analyzing these model parameters based on the a priori known response.

In the subsequent study, the lumped parameter model shown in Fig. 13 [5] is assumed to describe appropriately the considered vibrator-soil interaction system. The given vibrator mass $m$ is lumped, and the perpendicular arranged spring-dashpot systems with a priori unknown stiffness $k$ and damper parameter $c$ model the soil. The influence of the soil mass on the dynamic near field response is usually small, and thus, neglected. In general, the depicted system has two degrees of freedom, represented by the orthogonal displacement components in $x$- and $y$-direction. Since, however, the stiffness and damping are the same in both direction, and only the steady state response due to a force rotating with constant angular velocity is considered, the displacement of mass $m$ is circular. Therefore, the orthogonal displacement components are the same with a phase shift of $\pi/2$, and consequently, the system has only one degree of freedom.

In a similar investigation, Fellin et al. [5] used the same model for identification of soil parameters based on the vibrator response recorded during *in-situ* vibratory compaction. In contrast, the present study uses *numerically* generated response data, derived by the simulations described in the previous section. This approach allows a validation of this system identification procedure, because the underlying data are based on a more elaborate model with well defined geometry and material properties.

Assuming harmonic excitation and steady state response, identification of time depending parameters $k$ and $c$ (respectively critical damping ratio $\zeta = c/(2\omega m)$ with $\omega = \sqrt{k/m}$) of the model shown Fig. 13 requires that the displacement amplitude $A$ of the mass, excitation force $F = |\mathbf{F}|$, phase shift $\phi$ between excitation force $\mathbf{F}$ and displacement $\mathbf{u}$, and angular excitation frequency $\nu$ are known. In such steady state condition, stiffness $k$ and damping parameter $c$ can

be expressed in closed form as a function of $A$, $F$, $\nu$, and $\phi$ [5],

$$k = \frac{F}{A}\sin\phi \quad , \quad c = \frac{F}{\nu A}\cos\phi \tag{6}$$

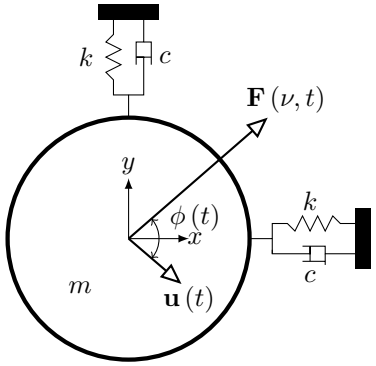


Figure 13: Simplified mechanical vibrator-soil interaction model used for system identification.

After identification of $k$ and $c$, the relationship of the cone model of Wolf [19] is used to map the lumped stiffness $k$ into Young's moduli $E$ of the soil, Poisson $\mu$ ratio is assume to be known,

$$k = \frac{E r^{(in)}}{2\left(1-\mu^2\right)}\left(3.1\left(\frac{2d}{r^{(in)}}\right)^{0.75} + 1.6\right) \tag{7}$$

assuming rectangular contact between soil and vibratory, i.e. thickness $d$ of the planar soil section times the radius of the vibratory $r^{(in)}$, as described in [4]. This assumption is, however, not supported by the results of the numerical simulation in the previous section, where the contact area according to Fig. 10 is less than $50\,\%$ of the total area.

Equation 6 is fed with the outcomes of the numerical simulations presented in the previous section, and subsequently Eq. 7 solved for Young's modulus $E$ of the soil. In Fig. 14(a) the ratio of predicted modulus to actual modulus of the underlying numerical model is depicted with respect to normalized time (time $t$ over excitation period $T$) for various excitation frequencies. It is observed that the predicted Young's modulus is about $60\,\%$ less than the actual one. However, the results indicate that at excitation frequencies close to resonance, i.e. $30$, $33$, $36$ and $39\,\mathrm{Hz}$, Young's modulus can be predicted more accurately. Since for these frequencies the steady state response was not reached, additional studies are required to support this statement. The identified critical damping ratio $\zeta$ is between 0.22 ($60\,\mathrm{Hz}$ excitation frequency) and 0.4 ($33\,\mathrm{Hz}$ excitation frequency), and depends more on the excitation frequency than the predicted Young's modulus, see Fig. 14(b). The observed "fluctuations" in parameters $E$ and $\zeta$ possibly arise from numerical instabilities of an ill-posed problem [8].

The absolute value $|\mathbf{R}|$ of the resulting model contact force $\mathbf{R}$ between the vibrator and the soil surface in steady state,

$$\mathbf{R} = k\mathbf{u} + c\dot{\mathbf{u}} \tag{8}$$

with the steady state displacement vector

$$\mathbf{u} = A\begin{pmatrix} \sin(\nu t + \phi) \\ -\cos(\nu t + \phi) \end{pmatrix} \tag{9}$$

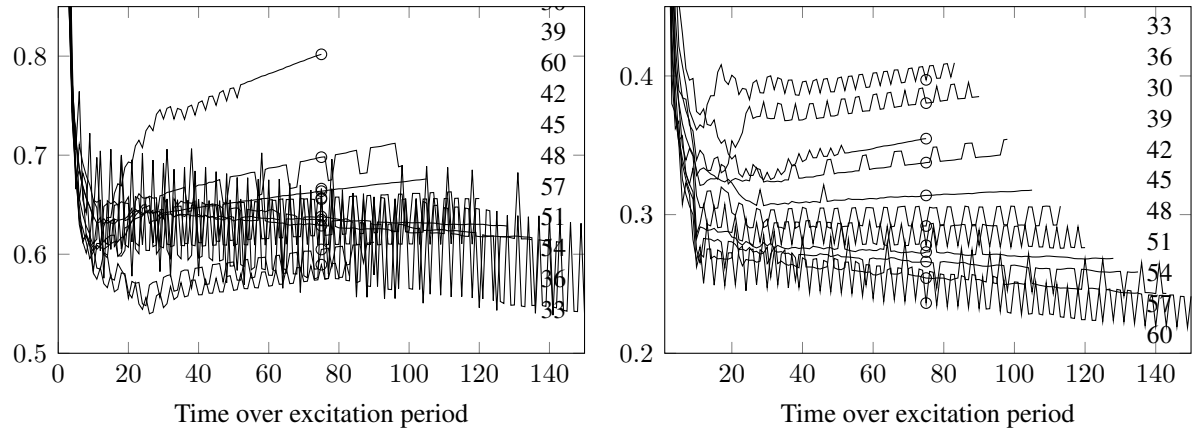


(a) Normalized Young's moduli (b) Ratio of critical damping

Figure 14: Results of the inverse model to reproduce (a) the Young's moduli and (b) the ratios of critical damping. The Young's moduli were normalized by this target value.

can be expressed as [4]

$$|\mathbf{R}| = A\sqrt{k^2 + (c\nu)^2} \tag{10}$$

Substituting the identified parameters $k$ and $c$ into this expression yields the contact force based on the lumped parameter model. Figure 15 shows for three excitation frequencies specified in the figure caption the identified contact force normalized with respect to its peak value. The dashed lines refer to the normalized forces as outcome of FE simulations, and the continuous graph refer to the normalized forces of the lumped parameter model according to Eq. 10. It is observed that both normalized forces are in the entire observation time both quantitatively and qualitatively in close agreement.

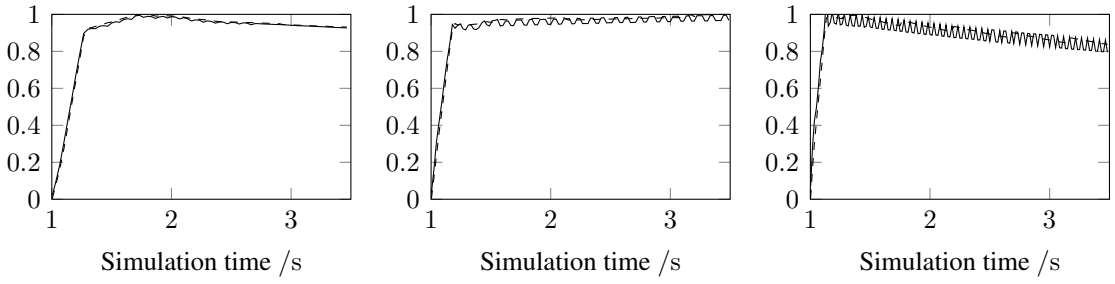


(a) 30 Hz of excitation frequency. (b) 45 Hz of excitation frequency. (c) 60 Hz of excitation frequency.

Figure 15: Normalized contact force as outcome of FE analysis (dashed line) and based on the fitted lumped parameter model according to Eq. 10 (continuous line).

## 5 SUMMARY, CONCLUSIONS, AND OUTLOOK

In this paper numerical modeling of deep vibratory compaction has been addressed. In the first study modal analysis delivered the natural frequencies and mode shapes of a crude annular

two-dimensional finite element (FE) model of the compacted soil. The most dominant modes excited by a rotating concentrated force were determined, based on the peak elastic strain energy per mode criterion in steady state condition. It was shown that the corresponding mode shapes are subjected to significant shear distortion, an observation that is in agreement with effective soil compaction. When taking into account only the most dominant modes, modal decomposition reduces significantly the computation costs of numerical response prediction of the interacting vibrator-soil system in a current state simulation. In such approach to be solved in future research, soil compaction can be modeled by changing the natural frequencies and mode shapes at discrete time instants during a transient modal analysis.

The second part of this paper aims at describing vibrator-soil interaction by means of a simplified FE model in terms of a three-dimensional elastic planar circular soil section subjected to a rigid rotating cylinder. Contact between soil and rigid cylinder has been simulated using an appropriate contact formulation.

In the third part the outcomes of the latter numerical study serve as input for system identification of soil parameters and contact force based on a simple lumped parameter model.

Despite the modeling efforts described in the literature and in this paper, simulation of deep vibratory compaction is still a challenging and in many aspects unsolved problem. Further research should take into account the influence of pore water and fluid flow injection, vertical cyclic vibrator motion and nonlinear constitutive behavior to reveal the most relevant physical processes during deep vibratory compaction. Based on such studies, it should be possible to create physically more meaningful and more reliable simplified models describing the compaction process.

## 6 ACKNOWLEDGEMENT

The research described in this paper has been partially funded by the Austrian Research Promotion Agency (FFG) through the project GeoGlueStrengthening within the framework of the FFG Program EraSME (846136). This support is gratefully acknowledged.

## REFERENCES

[1] D. Adam, *Continuous compaction control with vibratory rollers* (in German). Dissertation. TU Wien, Vienna, 1996.

[2] M. Arnold, I. Herle, Comparison of vibrocompaction methods by numerical simulations. *International Journal for Numerical and Analytical Methods in Geomechanics*, **33**(16), 1823–1838, 2009.

[3] R. Cudmani, T. Meier, V Osiney, Development of a numerical model for the prediction of densification of cohesionless soils during deep vibratory compaction. In H. Gonin, Holeyman A., F. Rocher-Lacoste eds. *Symposium International sur le Vibrofoncage et la Vibrocompaction (TRANSVIB 2006)*, pp. 131–140, Paris, France, September 21-22, 2006.

[4] W. Fellin, *Rütteldruckverdichtung als plastodynamisches Problem* (in German). A.A. Balkema, 2000.

[5] W. Fellin, G. Hochenwarter, A. Geiß, On-line Verdichtungskontrolle bei der Rütteldruckverdichtung (in German). *Bauingenieur*, **75**(9), 607–612, 2000.

[6] D.A. Greenwood, Vibrational loading used in the construction process, In M.P. OReilly, S.F. Brown eds. *Cyclic loading of soils: from theory to design*, chapter 10, pp. 434–475, Blackie and Son Ltd., 1991.

[7] FFG Program EraSME, *GeoGlueStrengthening*, project no. 846136, 2014–2017.

[8] J. Hadamard, *Lectures on Cauchy's problem in linear partial differential equations.* Courier Corporation, 2014.

[9] T. Hamann, S. Henke, J. Grabe, Numerische Modellierung der Verdichtung rolliger Boeden mittels Impulsverdichter, Rütteldruckverfahren und Rüttelbohle (in German). In D. Adam, R. Herrmann eds. *Baugrundverbesserung in der Geotechnik*, Institut für Geotechnik der Universität Siegen, Germany, September 14-15, 2010.

[10] I. Herle, Influence of pressure level and stress amplitude on the compaction of granular soils. In D. Kolymbas, W. Fellin, eds. *Compaction of Soils, Granulates and Powders*, Vol. 3 of Advances in Geotechnical Engineering and Tunneling, pp. 285–295, 2000. A.A.Balkema.

[11] Keller Grundbau GmbH, *Die Tiefenrüttelverfahren* (in German), Brochure, 10-02D.

[12] S. Kessler, G. Heibrock, T. Triantafyllidis, On prediction of vibrocompaction performance using numerical models. In H. Gonin, Holeyman A., F. Rocher-Lacoste eds. *Symposium International sur le Vibrofoncage et la Vibrocompaction (TRANSVIB 2006)*, pp. 233–242, Paris, France, September 21-22, 2006.

[13] M. Killeen, *Numerical modelling of small groups of stone columns*. Dissertation, National University of Ireland, Galway, 2012.

[14] K. Kirsch, K. Kirsch, *Ground improvement by deep vibratory methods.* CRC Press, 2016.

[15] M. Nendza, *Untersuchungen zu den Mechanismen der dynamischen Bodenverdichtung bei Anwendung des Rütteldruckverfahrens* (in German). Dissertation, Technische Universität Braunschweig, 2007.

[16] G. Qiu, S. Henke, J. Grabe, Application of a Coupled EulerianLagrangian approach on geomechanical problems involving large deformations. *Computers and Geotechnics*, **38**(1), 30–39, 2011.

[17] A.A. Rodger, Vibrocompaction of cohesionless soils. *Cementation Research Limited*, Internal Report, R.7/79, 1979.

[18] J. Wehr, Variation der Frequenz von Tiefenrüttlern zur Otimierung der Rütteldruckverdichtung (in German). *Mitteilungen des Fachgebiets Grundbau und Bodenmechanik*, Vol. 38, pp. 67–77, 2005.

[19] J.P. Wolf, *Foundation vibration analysis using simple physical models*. Pearson Education, 1994.

[20] H. Yu, *Cavity Expansion Methods in Geomechanics.* Springer Science+Business Media, 2000.

COMPDYN 2017
6th ECCOMAS Thematic Conference on
Computational Methods in Structural Dynamics and Earthquake Engineering
M. Papadrakakis, M. Fragiadakis (eds.)
Rhodes Island, Greece, 15–17 June 2017

# DYNAMIC MODULUS AND DAMPING RATIO OF EPS COMPOSITE SOIL UNDER SMALL STRAIN CONDITION

**Hu Ying[1,2], Gao Hongmei[1,2], Wang Zhihua[1,2], and Wang Xudong[1,2]**

[1]Urban Underground Space Research Center, Nanjing Tech University
[2] Institute of Geotechnical Engineering, Nanjing Tech University
200 North Zhongshan Road, Nanjing 210009, China
email: huying4682@163.com; hongmei54@163.com; wzhnjut@163.com; cewxd@163.com

**Key words:** EPS composite soil, Resonant column tests, Small strain, Dynamic shear modulus, Damping ratio.

**Abstract:** *Dynamic shear modulus and damping ratio are important parameters to evaluate mechanical properties of soils. Expanded polystyrene (EPS) composite soil is mixed with EPS beads, cement, soil and water, which is usually used as a filling material in Road Engineering, Civil Engineering and so on. A series of resonant column tests were carried out to study the effect of EPS beads content, cement content and confining pressure on the dynamic modulus and damping ratio of EPS composite soil under small strain condition. Testing results show that the effect of cement content on the dynamic shear modulus is the most significant followed by EPS beads content, while the confining pressure has a slight effect. The initial shear modulus of EPS composite soil increases linearly with the confining pressure, while EPS beads impact on the initial shear modulus associated with cement content. The normalized shear modulus of EPS composite soil is less affect by EPS beads, while it is significantly influenced by cement content and confining pressure. The attenuation characteristic of normalized shear modulus for EPS composite soil can be well fitted by Davidenkov model. The damping ratio of EPS composite soil increases with cement content, while confining pressure has a slight effect on the damping ratio. The influence of EPS beads content on the damping ratio is more complicated due to the uncertainty of weak interface between EPS beads and soil particle. This study can provide references for the design and application of EPS composite soil in practical engineering.*

## 1 INTRODUCTION

EPS composite soil is a mixture that is usually mixed with EPS (expanded polystyrene) beads, soil, cement and water. Since it was proposed in the 1960s, EPS composite soil has attracted more attention. Owing to its high-strength, light-weight, and controllable deformation, EPS composite soil has been widely used in practice such as soft soil treatment, embankments and bridge abutments, expressways, and underground pipelines [1-3]. Over the past twenty years, numerous tests have been conducted on EPS composite soil to study its physical and mechanical characteristics including unconfined compression tests, uniaxial compression tests, direct shear tests, and triaxial compression tests [4-7]. The mixing ratio and its influence on the strength, deformation and failure modes for EPS composite soil were investigated and discussed [8, 9].

When used on land, in the coast, or underwater, EPS composite soil is likely to undertake dynamic loadings such as seismic loading, traffic loading, and wave loading. Therefore, the dynamic characteristics of EPS composite soil are also a concern for engineering. Some experimental studies have been conducted to study dynamic characteristics of EPS composite soil like dynamic stress–strain relationship and dynamic strength. Cyclic triaxial shear tests are the most commonly used methods. Minegishi et al. concluded that the deformation and strength of EPS composite soil under cyclic loadings are mainly determined by the confining pressure [10]. Li and Miao conducted cyclic triaxial tests on EPS composite soil and discovered that the resilient modulus increased with an increase in the confining pressure and cement content, while the damping ratio slightly changed [11]. However, numerous engineering and experimental studies show that soils are mostly in a small strain condition [12]. Few experiments have been conducted to study the dynamic deformation and strength of EPS composite soil under small strain condition.

In this paper, a series of resonant column tests were carried out to study the effect of EPS bead content, cement content and confining pressure on the dynamic modulus and damping ratio of EPS composite soil under small strain condition.

## 2 EXPERIMENTAL PROGRAM

### 2.1 Experimental materials

EPS composite soil was mixed by EPS beads, soil, cement and water with different mixing ratios. The soil used in this study was muddy and silty clay which was taken from Yangzi Jiang River. Physical and mechanical properties of the mucky and silty clay are shown in Table 1. The round EPS beads are 2-3 mm in diameter. The unit weight and the bulk unit weight for EPS composite soil were 0.237 kN/m$^3$ and 0.159 kN/m$^3$, respectively. Portland cement (P.O 32.5) was used as a binding material.

| Water content (%) | Wet unit weight (kN/m$^3$) | Dry unit weight (kN/m$^3$) | Saturation degree (%) | Void ratio | Relative density | Liquid limit (%) | Plastic limit (%) |
|---|---|---|---|---|---|---|---|
| 48.1 | 16.8 | 1.13 | 96 | 1.373 | 2.74 | 39.2 | 22.6 |

Table1: Physical and mechanical properties of mucky silty clay

### 2.2 Specimen preparation

The cylindrical specimen of EPS composite soil used in this study is 50 mm in diameter and 100 mm in height.

The specimen preparation process mainly includes the followings: 1) The soil was oven-dried and crushed into powder with a rubber hammer; 2) According to the mixing ratio, the dried soil, Portland cement and water were weighed and stirred to form a slurry; 3) The desired amount of EPS beads were added into the slurry and fully stirred again until a uniform mixture was formed; 4) The mixture was placed into a three-section mould with a inner diameter of 50 mm and height of 100 mm; and 5) The specimen was cured for 7 days with a constant temperature of 20±2 ℃ and relative humidity at 100%.

### 2.3 Test scheme and procedure

This experiment mainly discusses two factors, which affect dynamic characteristics of EPS composite soil, that is, mixing ratio and confining pressure. The mixing ratios include cement content and EPS beads content. Cement content ($m_c/m_s$) that is the mass ratio of cement to dried soil considered 6%, 8% and 10%. EPS beads content ($V_E/V_S$) that is the volume ratio of EPS beads to the mixture considered 0, 20%, 50%, 70% and 100%. The confining pressures considered 20kPa, 50kPa, 70kPa and 100kPa. The water content for all specimens was 60%, which was denoted as the mass ratio of water to dried soil. Experiments were carried out on the resonant column apparatus, TSH-100, manufactured by GCTS.

## 3 EXPERIMENTAL RESULTS AND ANALYSIS

### 3.1 Characteristics of dynamic shear modulus

Sixty sets of data were obtained from the resonant column test for EPS composite soil with various mixing ratios and confining pressures. The relationship between dynamic shear modulus and shear strain amplitude of EPS composite soil is shown in Figure 1. It can be demonstrated that under small strain condition (smaller than $10^{-3}$) the effect of cement content on the dynamic shear modulus is the most significant followed by EPS beads content, and the confining pressure is the least.

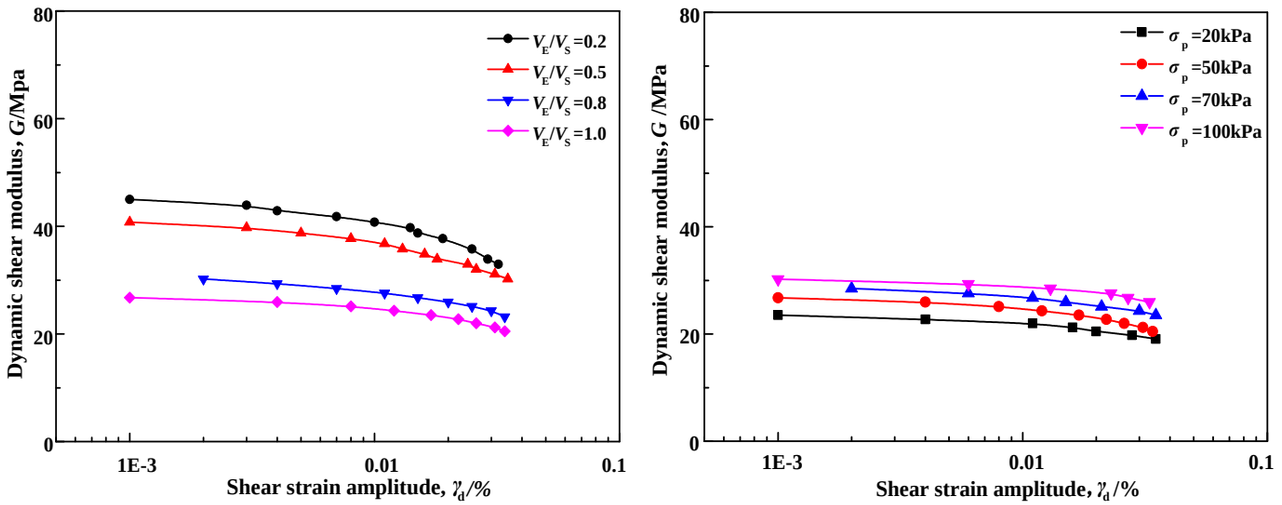


(a) $m_c/m_s$=8%, $\sigma_p$=50kPa (b) $m_c/m_s$=8%, $V_E/V_S$=1.0

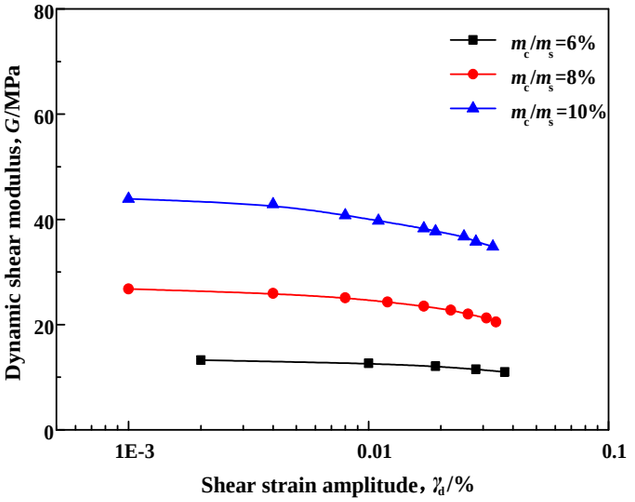


(c) $\sigma_p$=50kPa ,$V_E/V_S$ =1.0

Figure 1: Relation between dynamic shear modulus and shear strain amplitude for EPS composite soil

### 3.1.1 Initial shear modulus

A hyperbolic model proposed by Hardin-Drnevich [13] can be used to describe the dynamic stress-strain skeleton curves of soils, which is expressed as follows:

$$\tau_d = \frac{\gamma_d}{a_t + b_t \gamma_d} \tag{1}$$

$$a_t = 1/G_0 \qquad b_t = G_0/\gamma_r \tag{2}$$

where $\tau_d$ is dynamic shear stress, $\gamma_d$ is shear strain, $G_0$ is initial dynamic shear modulus, $\gamma_r$ is reference shear strain, and $a_t$ , $b_t$ are fitting parameters.

The initial shear modulus of EPS composite soil can be calculated through Eq.s (1) and (2). Figure 2 shows the effect of EPS beads on the initial dynamic shear modulus of EPS composite soil under small strain condition. $V_E/V_S$=0 indicates that EPS bead is not included in composite soil, namely cemented soil. It can be seen from the figure that the initial dynamic shear modulus decreases gradually with the increase of EPS beads content when the confining pressure and cement content are constant. However, when cement content is smaller, the change of the initial dynamic shear modulus of EPS composite soil is not obvious with the increase of EPS beads content. The reason is that the product of hydration wrapped around the soil skeleton to form a cemented medium, which has a quite greater strength than the soil skeleton. More cemented medium produced with the increase of cement content contributed more strength to EPS composite soil. As the cement content was reduced, the hydration reaction was inadequate and the strength of composite soil was controlled by EPS beads. So the strength of composite soil was smaller since the strength of EPS beads in the elastic stage was much smaller than that of cemented medium. When the confining pressure and cement content were constant, more EPS beads resulted in smaller initial shear modulus which was induced by the lower strength of EPS beads.

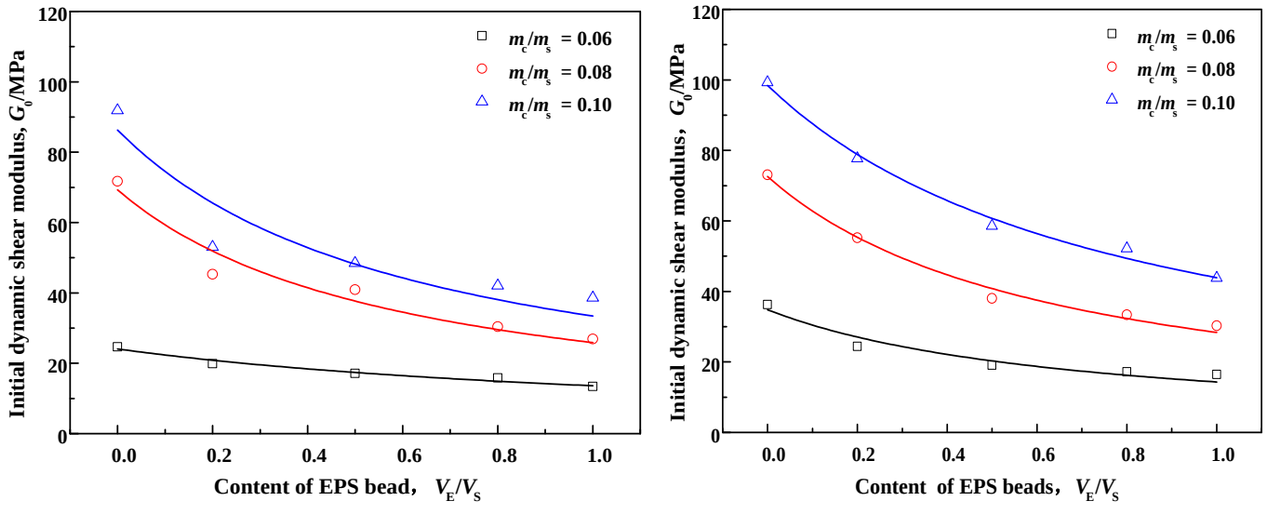


(a) $\sigma_p$=50kPa (b) $\sigma_p$=100kPa

Figure 2: Effect of EPS beads content on the initial dynamic shear modulus for EPS composite soil

Figure 3 shows the relationship between confining pressure and initial shear modulus in the case that EPS beads content are 50% and 100%. It can be obtained that the initial dynamic shear modulus of EPS composite soil is increased approximately linearly with the confining pressure.

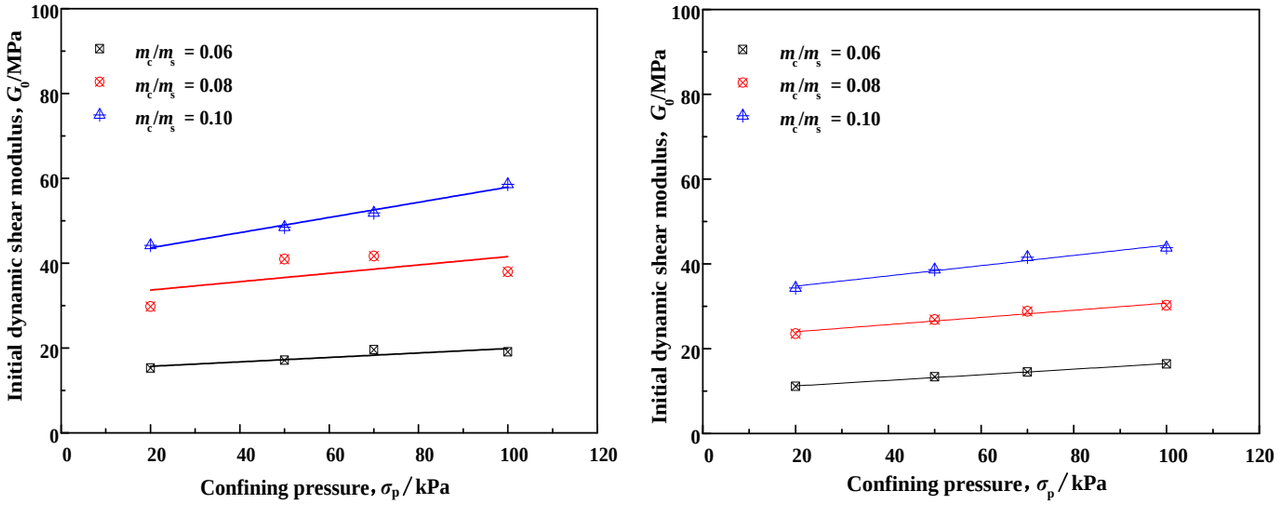


(a) $V_E/V_S$=50% (b) $V_E/V_S$=100%

Figure 3: Effect of confining pressure on the initial dynamic shear modulus for EPS composite soil

The influence of cement content on the initial shear modulus is shown in Figure 4. It is apparent from the figure that the initial shear modulus of EPS composite soil increased with the increase of cement content, which is approximately a linear change when other conditions keep the same. The cementation action ensures a higher stability of the soil skeleton. By comparing the effect of cement content and confining pressure, we can draw a conclusion that the effect of cement content on the shear modulus of EPS composite soil is greater than that of confining pressure.

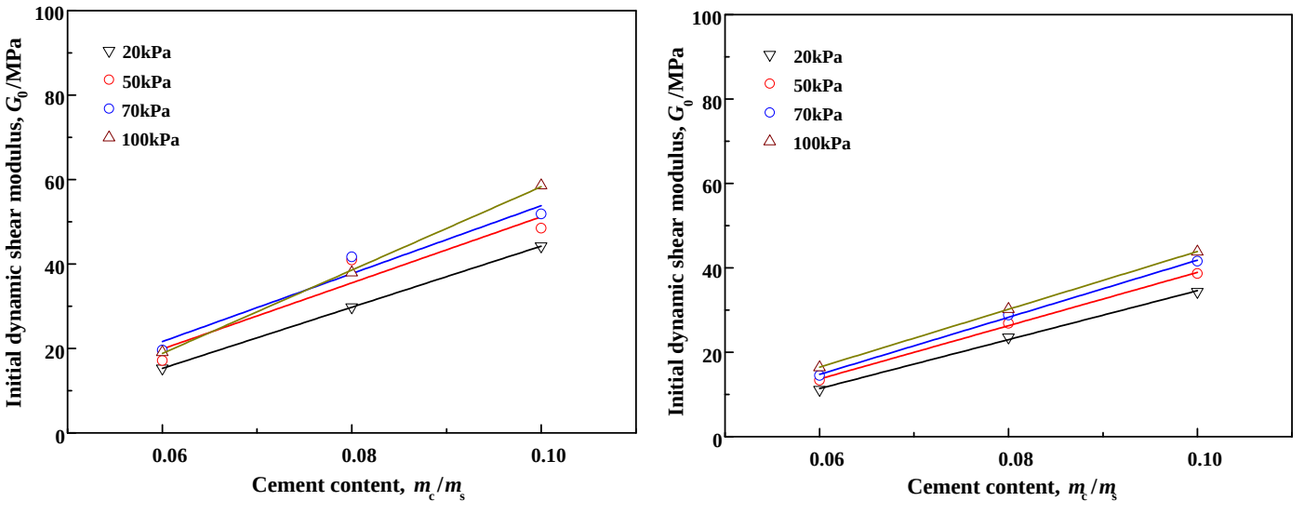


(a) $V_E/V_S$=0.5 (b) $V_E/V_S$=1.0

Figure 4: The influence of cement content on initial dynamic shear modulus

### 3.1.2 Attenuation characteristics of normalized dynamic shear modulus

Combined the existing attenuation formula with the experimental data, Martin-Davidenkov model [14] is used to fit the normalized curve of dynamic shear modulus. Martin-Davidenkov model is expressed as follows:

$$\frac{G}{G_0}=1-\left[\frac{\left(\gamma/\gamma_0\right)^{2B}}{1+\left(\gamma/\gamma_0\right)^{2B}}\right]^{A} \tag{3}$$

where $G$ is dynamic shear modulus; $G_0$ is initial shear modulus; $\gamma$ is shear strain; $A$, $B$ and $\gamma_0$ are fitting parameters related with soil properties. The value of parameter $A$ ranged from 0.85 to 1.20, and $B$ ranged from 0.38 to 0.53. It will be demonstrated that Martin-Davidenkov model can well fit the attenuation characteristics of normalized shear modulus for EPS composite soil.

Figure 5 shows the normalized dynamic shear modulus of EPS composite soil changing with EPS beads under the confining pressure of 50 kPa. When the cement content is lower, the normalized curve with different EPS beads contents (excluding $V_E/V_s$=0) concentrated in a narrow range. However, there is a large difference in the normalized curve between cemented soil ($V_E/V_s$=0) and EPS composite soil. This is because when $V_E/V_s$=0 the strength of composite soil originated from the cemented medium formed by the cement around the soil particle. When the cement content was smaller, the cemented strength was easily to be destroyed as the shear strain increased, thus leading to a quick attenuation in the shear modulus. When adding the EPS beads, the cement would be wrapped around EPS beads and soil particle. Owing to their good elastic performance, EPS beads could delay the damage of the cemented strength. With lower cement content, the surface of EPS beads could not be fully wrapped by the cement resulting in that the variation of dynamic shear modulus was not obvious.

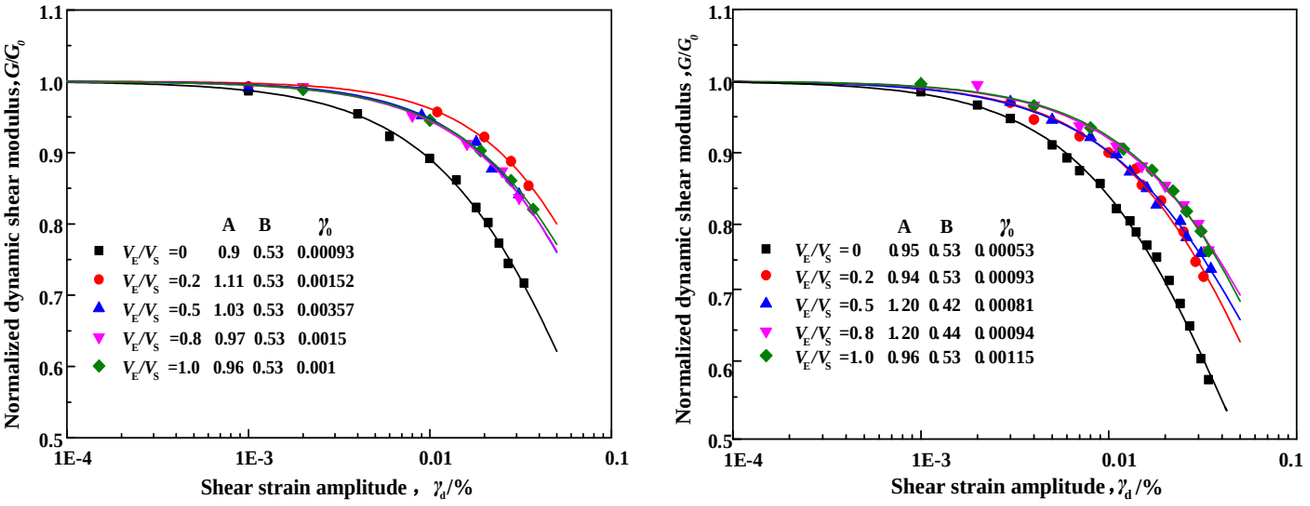


(a) $m_c/m_s$=6% (b) $m_c/m_s$=8%

Figure 5: Effect of EPS beads content on normalized dynamic shear modulus ($\sigma_p$=50kPa)

The attenuation curve of normalized dynamic shear modulus for EPS composite soil with different cement contents is shown in Figure 6. What can be seen is that the larger cement content leads to a sharper attenuation.

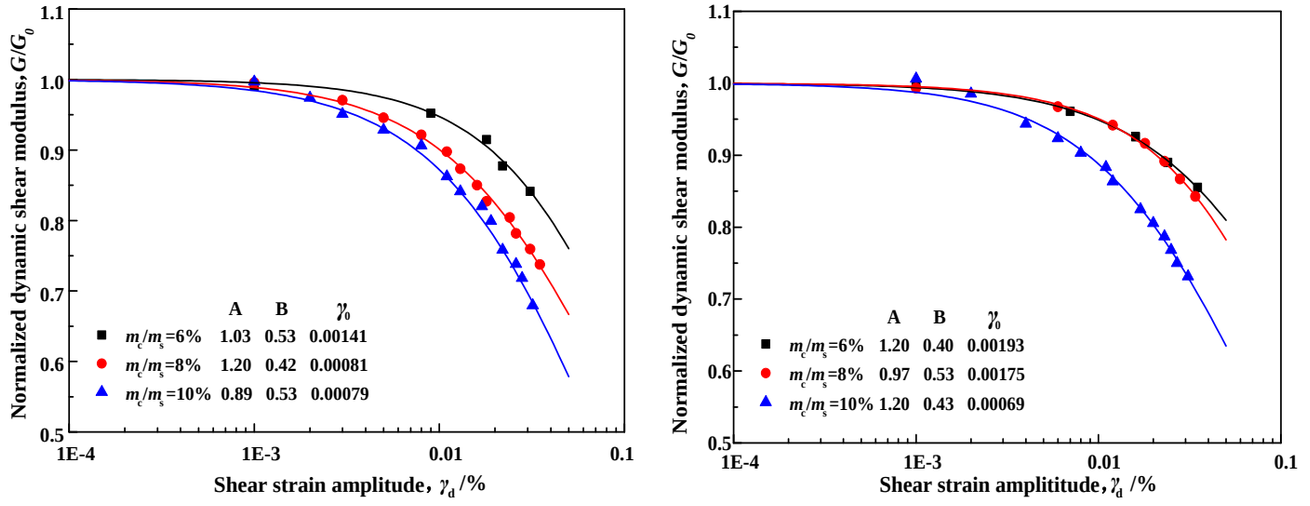


(a) $\sigma_p$=50kPa (b) $\sigma_p$=100kPa

Figure6: The influence of cement content on normalized dynamic shear modulus ($V_E/V_s$=50%)

Figure 7 shows the fitting curve of normalized dynamic shear modulus for EPS composite soil under different confining pressures when EPS beads content is 50%. The figure demonstrates that the normalized curve varies more gently with the increase of confining pressure. The larger friction resistance among EPS composite soil induced by the increasing confining pressure slows down the sliding of soil particle. So the attenuation of dynamic shear modulus tends to slow down. It also can be found that the normalized curves have a certain difference under different confining pressures, which indicates the confining pressure has some impact on the normalized shear modulus of EPS composite soil.

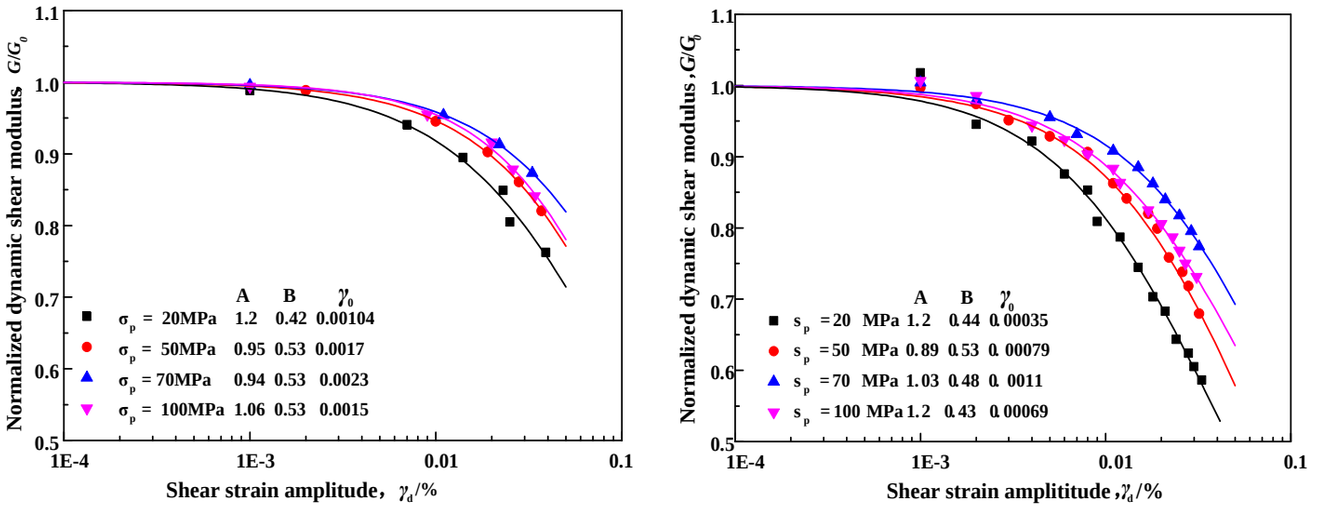


（a）$m_c/m_s$=6%　　（b）$m_c/m_s$=10%

Figure7: Effect of confining pressure on normalized dynamic shear modulus ($V_E/V_S$=50%) for EPS composite soil

## 3.2 Characteristics of damping ratio

The damping ratio reflects the loss of energy caused by the internal resistance of soils under dynamic loads [15]. The damping ratio of EPS composite soil increases with shear strain under dynamic loads. The influences of EPS beads content, cement content and confining pressure on damping ratio are discussed in small strain stage.

The influences of EPS beads content and cement content on damping ratio under small strain condition are shown in Figure 8 and Figure 9, respectively. Limited by the accuracy of testing instrument, the confining pressure at the lower level is difficult to keep stable, which results in the discreteness of testing data. It is found that the influence of EPS beads on damping ratio is more complex. Due to the interface between soil particle and EPS beads belongs to weak plane of cementation under small strain, while the damping ratio is related to the strength of cement and the number of weak cementation surface. Soil particle and EPS beads are connected by the weak cementation action and the damping ratio is related to the cementation strength and the number of weak cementation interface.

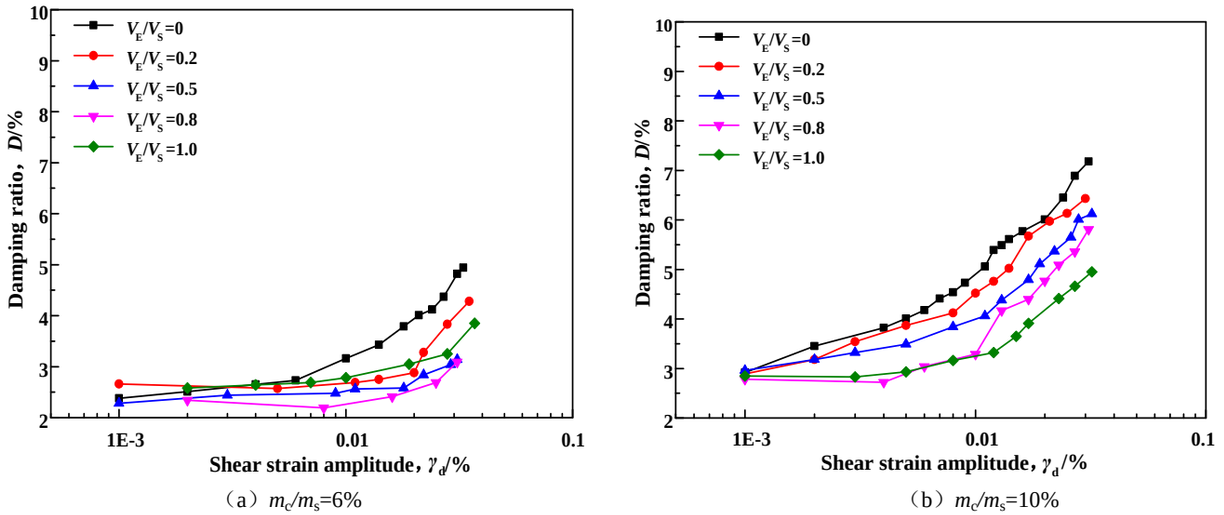


（a）$m_c/m_s$=6%　　（b）$m_c/m_s$=10%

Figure 8: Influence of EPS content on damping ratio ($\sigma_p$=50kPa)

It is worth noting that the increase of cement content led to the increase of damping ratio under small strain condition. This conclusion is inconsistent with that from general understanding. In small strain stage, soil skeleton was not damaged and structural damping played a significant role. Large cement content results in great cementation strength. It is necessary to overcome the large hysteretic damping force when the same shear strain occurs, which led to large damping ratio.

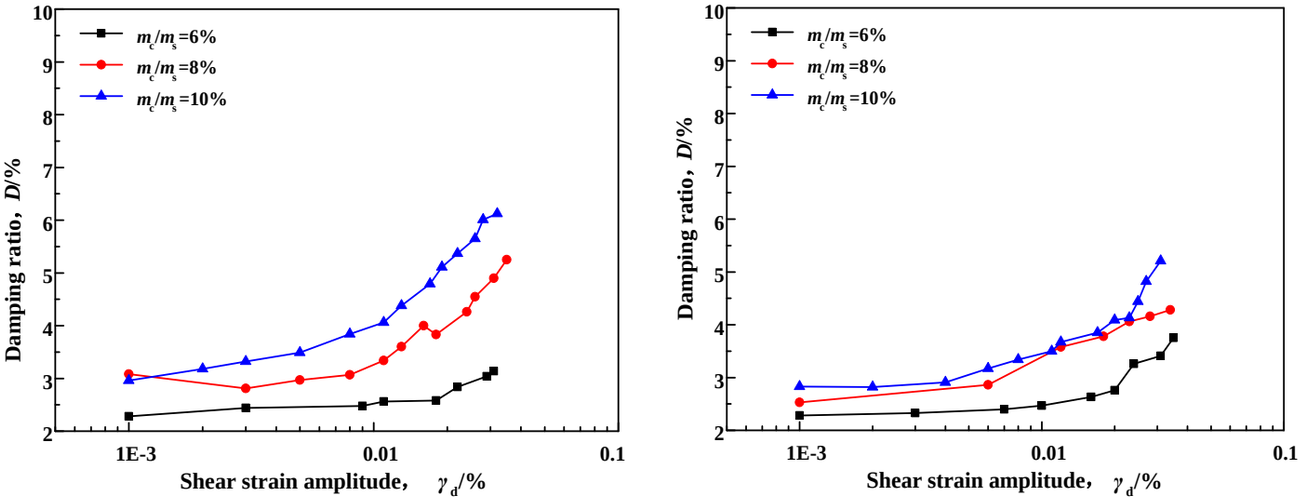


（a）$\sigma_p$=50kPa　　（b）$\sigma_p$=100kPa

Figure 9: Influence of cement content on damping ratio ($V_E/V_S$=50%)

Figure 10 shows the effect of the confining pressure on damping ratio of EPS composite soil under small strain condition. As shown in the figure, the damping ratio roughly increases with the decrease of confining pressure. The reason is the contact between EPS beads and soil particle becomes denser with the increase of confining pressure. This leads to a decrease in the energy dissipation for EPS composite soil.

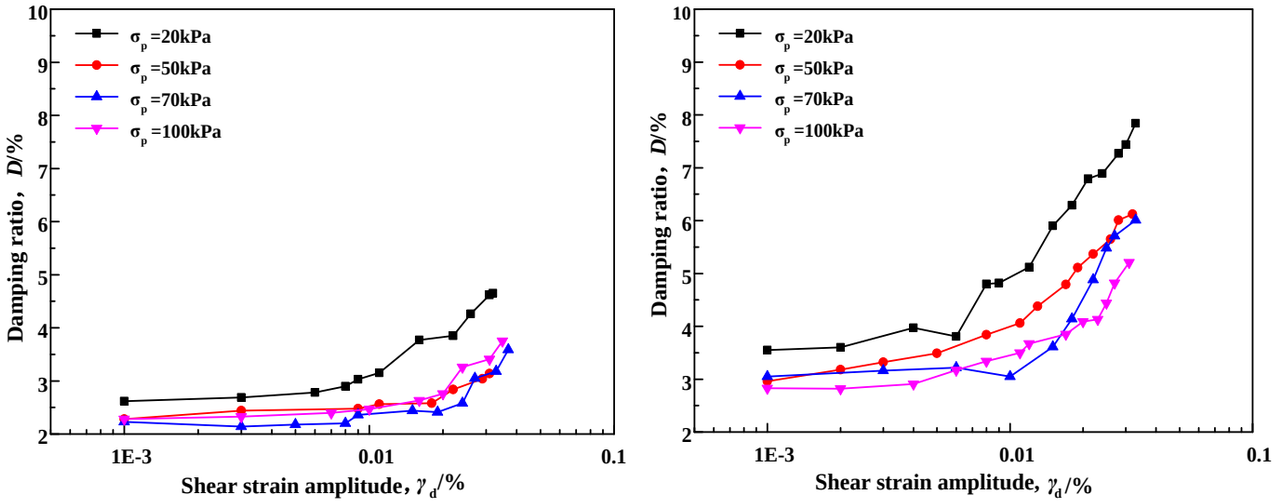


（a）$m_c/m_s$=6%　　（c）$m_c/m_s$=10%

Figure 10: Influence of confining pressure on damping ratio ($V_E/V_S$=50%)

## 4 CONCLUSIONS

- The effect of cement content on the dynamic shear modulus is the most significant followed by EPS beads content, while the confining pressure has a slight effect.
- When cement content is smaller, the change of the initial dynamic shear modulus is not obvious with the increase of EPS beads content. Initial shear modulus of EPS composite soil increased approximately linearly with the confining pressure and cement content.
- Confining pressure and cement content have a certain influence on the normalized shear modulus. The normalized curve varies more gently with the increase of EPS beads content. Martin-Davidenkov model can well fit the change of normalized dynamic shear modulus.
- The influence of EPS beads on damping ratio is more complex under small strain condition. The damping ratio of EPS composite soil increases gradually with the increase of cement content and the decrease of confining pressure.

## ACKNOWLEDGEMENT

This work was supported by the National Natural Science Foundation of China (grant number 51578286) and China Postdoctoral Science Foundation (grant number 2013T60529). The contributions of anonymous reviewers and editors are also acknowledged.

## REFERENCES

[1] L.C Miao, F. Miao, J. Han, W. Lv, J. Li, Properties and applications of cement-treated sand-expanded polystyrene bead lightweight fill. *Journal of Materials in Civil Engineering*, 25(1), 86-93, 2013.

[2] H.K. Illuri, Development of soil-EPS mixes for geotechnical applications [dissertation]. *Queensland University of Technology*, 2007.

[3] L.C. Miao, F. Wang, A proposed lightweight fill for embankments using cement-treated Yangzi River sand and expanded polystyrene (EPS) beads. *Bulletin of engineering geology and the environment*, 68(4), 517-524, 2009.

[4] G.L. Yoonz, S.S. Jeon, B.T. Kim, Mechanical characteristics of light-weighted soils using dredged materials. *Marine Georesources & Geotechnology*, 22(4), 215-229, 2004.

[5] H.M. Gao, J.Y. Liu, H.L. Liu, Geotechnical properties of EPS composite soil. *International Journal of Geotechnical Engineering*, 5(1), 69-77, 2011.

[6] H.M. Gao, Y.M. Chen, H.L. Liu, J.Y. Liu, J. Chu, Creep behavior of EPS composite soil. *Science China-Technological Sciences*, 55(11), 3070-3080, 2012.

[7] Y.T. Kim, J. Ahn, W.J. Han, M.A. Gabr, Experimental evaluation of strength characteristics of stabilized dredged soil. *Journal of Materials in Civil Engineering*, 22(5), 539-544, 2010.

[8] H.L. Liu, A. Deng, J. Chu, Effect of different mixing ratios of polystyrene pre-puff beads and cement on the mechanical behaviour of lightweight fill. *Journal of Materials in Civil Engineering*, 24(6), 331-338, 2006.

[9] A. Deng, Y. Xiao, Shear behavior of sand-expanded polystyrene beads lightweight fills. *Journal of Central*

*South University of Technology*, 15 (s1), 174-179, 2008.

[10] K. Minegishi, K. Makiuchi, R. Takahashi, Strength-deformation characteristics of EPS beads-mixed lightweight geomaterial subjected to cyclic loadings. *Proceedings of the International Workshop on Lightweight Geo-Materials*, Tokyo, Japan. 119-125, 2002.

[11] J. Li, L.C. Miao, J.C. Zhong, Z.X. Feng, Deformation and damping characteristics of EPS beads-mixed lightweight soil under repeated load-unloading. *Rock and Soil Mechanics*, 31(6), 1769-1775, 2010.

[12] J.B. Burland, Ninth laurits bjerrum memorial lecture. 'Small is beautiful'—the stiffness of soils at small strains. *Canadian Geotechnical Journal*, 26, 499-516, 1989.

[13] B.O. Hardin, V.P. Drnevich, Shear modulus and damping in soils: measurement and parameter effect. *Journal of Soil Mechanics and Foundations Division*, 98 (SM6), 603-624, 1972.

[14] P.P. Martin, H.B. Seed, One dimensional dynamic ground response analysis. *Journal of geotechnical engineering*, 108(7), 935-952, 1982.

[15] D.Y. Xie, Soil Dynamics, 1th Edition. Higher Education Press Beijing, 2011.

COMPDYN 2017
6th ECCOMAS Thematic Conference on
Computational Methods in Structural Dynamics and Earthquake Engineering
M. Papadrakakis, M. Fragiadakis (eds.)
Rhodes Island, Greece, 15–17 June 2017

# SENSITIVITY OF STRUCTURES AND GEOLOGICAL DATA

**V.A. Barvashov**[1], **G.G.Boldyrev**[2]

[1] NITs "Stroytelstvo" Inc., NIIOSP
barvash@mail.ru

[2] Penza state university architecture and construction
g-boldyrev@geoteck.ru

**Keywords:** Subgrade-structure sensitivity, Geological data, In situ tests, Subsoil stiffness factor, Numerical simulation, Soil data uncertainties.

**Abstract.** *The paper discusses the subgrade-structure sensitivity to uncertainties, ambiguities and scarcity of geological data, obtained and processed in the course of geological surveys. These aspects have mostly been neglected: two special in situ tests, staged in USA and in Russia, showed considerable soil data uncertainties and scatter even at nearby points. On the other hand, most structures are insensitive to many (not all) these uncertainties. So, a compromise between structure sensitivity and soil data uncertainties is an issue. Numerical simulation with the help of specially developed software showed some sensitivity evaluation results.*

## 1 INTRODUCTION

The Conference guidelines are in tune with coincide the issues of geotechnical engineering: i.e. uncertainty, ambiguity and scarcity of on-site geological survey data along with multiple and diverse subsoil-structure system (SSS) interaction theories and analytical methods. Theoretical models and assumptions for solving geotechnical problems are too many. Finite elements method (FEM) enables detailed numerical simulations of SSS behavior; however, the input soil data and their scatter are insufficient and often dubious. E.g., the subsoil test holes are spaced at least 25 m from each other, and they are very few. Why do the built structures stay healthy for centuries despite of such input soil data scarcity? There is only one realistic explanation to this: the real SSSs are very insensitive to the errors and scarcity of input soil data and to the diversities of many analytical assumptions and theories. The paper presents examples of soil data uncertainties and SSS analysis deficiencies, based on in situ and small-scale model test data and some numerical simulations.

## 2 SPECIFIC FEATURES OF SSS GEOTECHNICAL ANALYSES

Any SSS project design involves only one numeric analysis. Multiple numeric simulations are very rare. This is not so in other sectors. E.g., automobiles, aircraft, spacecraft and their components, etc. are subjected to physical and numerical tests and simulations. The material strength, deformations, ageing, etc. are thoroughly tested, and the test data is stored in databases along with many numeric and real scenarios for handling possible contingencies. These research and development involves multiple numeric and physical simulations on real models, including full-scale ones, the data is stored in databases along with various numeric and real scenarios of future contingencies and respective countermeasures.

It is not so in the building construction sector. Monitoring the settlements of existing structures just prove their existence, which is evident anyway, while stresses in structural elements can only be measured at a very limited number of accessible points. The real contingencies and failures are extremely rare and are mostly due to human error and/or contingencies.

The soil data, investigated for any project design is scarce: the total tested soil volume on any site is literally infinitesimal: only millionth parts ($10^{-6}$, ppm) of the total volume of subsoil are tested and sampled in just a few test holes, located more than 20 m and farther apart from each other. Soil properties between test holes remain practically uncertain even if investigated with a geo radar. After in situ tests are over, the geologists produce several vertical subsoil cross sections with subjectively "inflated" soil stratification between widely spaced test holes. The geologists also subjectively (i.e. ambiguously, creatively) delineate stratigraphic geotechnical elements (GEs) in several cross sections wrongly assigning identical properties to soils in each GE. Then design engineers creatively inflate the soil properties in-between these cross sections. Therefore, there is always a rather large space for doubt as how realistic these subjective results could be. There is no other choice, however, because geological investigations (GI) costs are traditionally low: just 0,05-0,1% of the total construction cost. A question arises: how effective are these low costs at the global scale in comparison to safety?

Soil mechanics and SSS geotechnical analyses appeared long ago based on very simplified assumptions and analyses. E.g., homogeneous elastic solutions prevailed in soil mechanics for many decades. Then dozens of non-linear soil continuum models appeared and some of them entered Finite Elements Method (FEM) computer codes (PLAXIS and MIDAS prevail in Russia now). However, due to uncertainties of soil data the reality of such FEM analytical results remains uncertain. The scarce soil data from several GI test holes is insufficient for input in FEM computer codes. Therefore, GI data is inflated in the form of virtual strata and geotechnical elements to sort of "make up" for the soil data scarcity. These procedures look very

realistic, as the relative contingency rate due to subsoil failures is very small ($\approx 0{,}01\%$). Just compare it with more than 2% failure rate of spacecraft launches.

Geotechnical engineers do not practically investigate how realistic, unambiguous and sufficient GI data are, obtained in situ or in laboratory tests for SSS project designs. The authors are aware of just two following experiments, specially staged to investigate the uncertainty of soil data measurements.

### 2.1 Experiment 1

The Louisiana State University (USA) performed experimental CPTs (Cone Penetration Tests) on an ordinary site, following the request from USA Federal Highway Administration [1]. The tests were performed at 16 points, located along two concentric circles, having 0.9 and 1.8 m radii, with one test point in the center. There were measured cone resistance $q_c$ and soil unit weight $\gamma$ values versus depth. The obtained data showed that the soils were very non-homogeneous both vertically and horizontally, therefore the homogeneous strata that all geologists so creatively delineate on geological cross sections are subjective, i.e. and non-realistic.

### 2.2 Experiment 2

A similar experiment was done in Russia (NPP Geotek, Russia) with the help of the famous Marchetti dilatometer (Fig. 1).

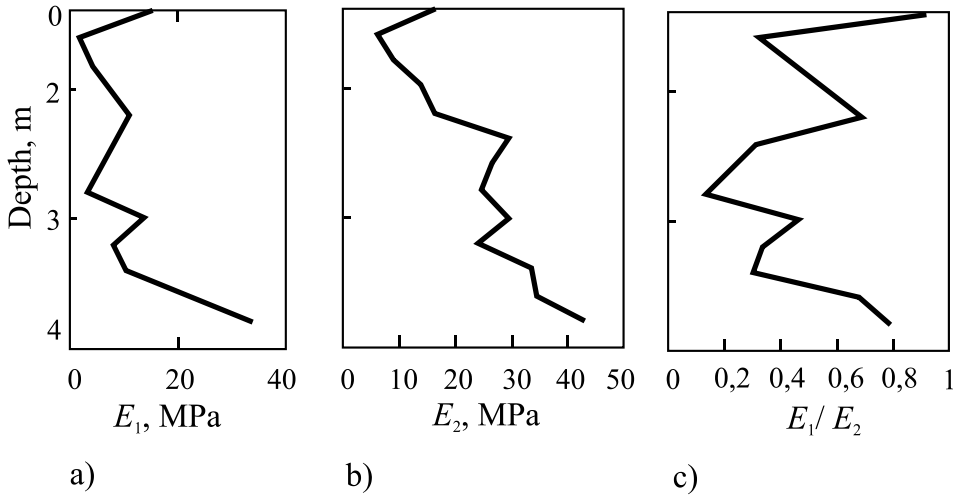


Figure 1: Soil moduli $E_1$ and $E_2$ profiles, measured with Marchetti dilatometer in test holes a) $E_1$ and b) $E_2$, spaced at 2 m from each other and c) $E_1/E_2$ ratio.

Fig. 1 shows the measured deformation modules $E_1$ and $E_2$ profiles (Figs. 1a, b) and their ratio $E_1/E_2$ variations versus depth (Fig. 1c) in two test holes, located 2 m apart from each other. Evidently, $E_1/E_2$ values are far from being equal to 1.

A question arises, is it worthwhile to complicate geotechnical analyses if the detailed and consistent GI soil data for such analysis is never available? If data scatter is such then simplified SSS analyses could successfully compete with sophisticated and highly expensive FEM software capabilities.

Geological investigations include other test types beside CPT and dilatometer: plate tests, SPT, dynamic penetration tests, boring penetration tests etc. The obtained results are processed with the help known correlation equations to obtain data for project design analysis. However, despite of inevitable data scatter and ambiguities: only one test is done at each point.

The authors do not have information of any other similar soil tests at close distances except for the ones presented on Figs. 1.

There is one optimistic aspect, worth mentioning. In a SSS settlement analysis soil deformations (always positive) are summed up/integrated versus depth. This integration transformans forms rough deformations profiles into rather smooth settlements-versus-depth curve, as is shown on Fig. 2, where such transformation. a strongly oscillating function $s = s(x) \geq 0$ (red) is integrated to obtain function $S(x)$ as per Eq. (1). This integration produces a rather smoothly growing function $S(x)$ (blue curve)

$$S(x) = \int_0^x s(x)dx\,. \tag{1}$$

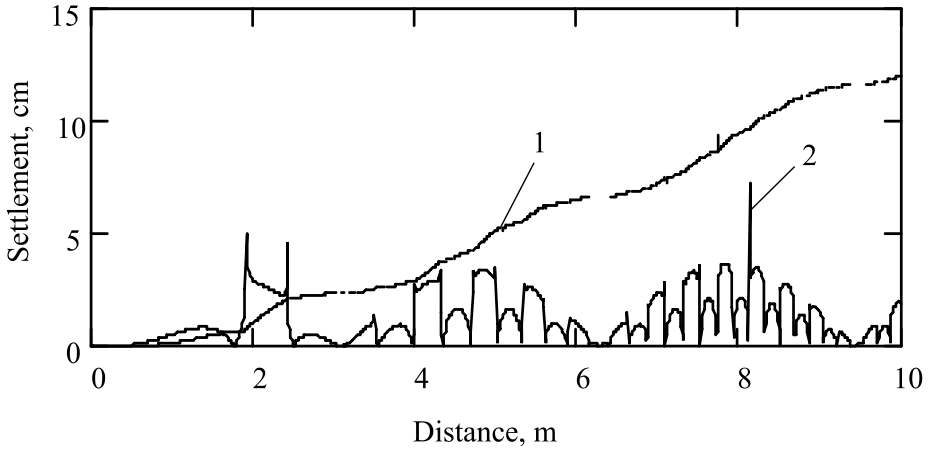


Figure 2: An example of smoothing a strongly oscillating function by integration:
1 – smoothing; 2 – oscillation.

## 3 CONTACT MODELS OF SUBSOIL

Thanks to "smoothing", shown on Fig.6, it is possible to apply linearly deforming subsoil contact models (CM) to subsoil analysis. Many authors proposed different CMs, each of which features unique properties, defined by its Green function, some of them coincide with each other despite of their different physical representation. The Green function gives the respective subsoil surface settlement at a point, caused by a unit vertical force, applied at distance $r$ from that point. Surface settlements under distributed load $q(x, y)$ are determined by evident integration. Green functions are defined for many CMs, including Winkler (delta function) and Pasternak CMs, elastic space, elastic layer, etc.

Hundreds of publications, including doctorate theses, books and conference proceedings, are dedicated to to CMs' applications in the subsoil settlements analysis. CMs are included in Russian Geotechnical Codes of Practice for subsoil and footing design.

CMs are applied to settlement analysis of non-uniform subsoils with just one assumption that vertical normal stresses $\sigma_z$ from any vertical load, distributed over the subgrade surface, coincide versus depth for uniform and layered subgrades. However not well proved, this assumption is globally applied to CM-based settlement analyses with defined Green functions.

Green functions application have their own paradoxes in exact analytical solutions, e.g. infinite contact pressures under a stiff footing edges on elastic half-space. A layer of Winkler springs on top of such CM corrects the situation

## 4 FINITE ELEMENTS METHOD

FEM gives numerical solutions for the problems of non-linear continuum mechanics with complicated configurations, any boundary conditions and heterogeneities, etc. However, these possibilities are often excessive when applied to practical problems, whose solutions depend on GI ever scarce and uncertain soil data. But there is a good chance that numerical FEM simulation modelling could replace difficult material experiments, especially qualitative ones.

There is also on more issue: PLAXIS and MIDAS do not account for discontinuities of soil media, caused by shear stresses, that results in ambiguity of analytical results, because they depend on the FEM grid density, i.e. on the dimensions of finite elements (see below).

## 5 SUBSOIL DEFORMATIONS AND STRENGTH

The problems of subsoil bearing capacity (strength) have been solved with the help of limit equilibrium theory Terzaghi [2] and Sokolovsky [3] have been solved since 1940s. This theory assumes that subsoil failure process is static, i.e. occurs simultaneously at all points of the limit equilibrium zone. These solutions were developed for homogeneous subsoils.

In fact, after the load is applied the soil first reaches limit state at points under the footing edges. If the load keeps on increasing, then downward cracks appear and grow downwards with rupture points at their lowermost ends that result in excessive tilts of the structure. This subsoil kinematic condition is reached at much lower external load than the abstract limit load that causes the simultaneous abstract static subsoil failure at all points of the limit equilibrium zone as per Terzaghi [2] and Sokolovsky [3]. It is more justified to view the load, creating "inadmissible" structure tilts well before the total subsoil failure.

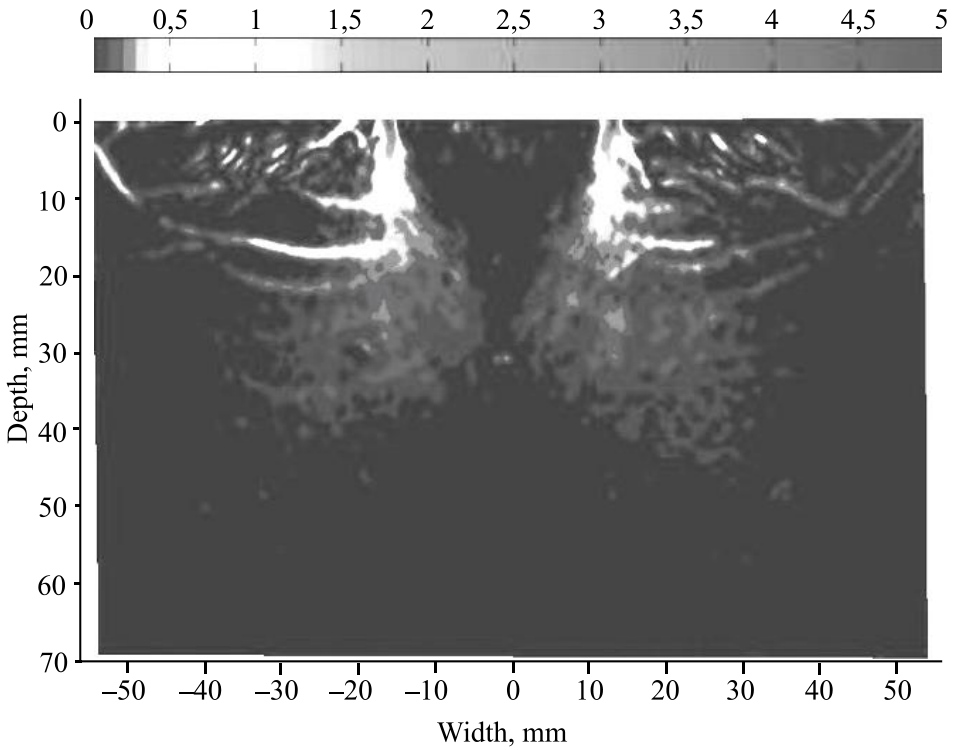


Figure 3: Formation of "cuts" (against the light) under the model footing edges. The scale indicates the intensity of shear strain, %. White color is tension cracks

Fig. 3 shows soil tension cracks ("cuts") under the edges of a vertically loaded small footing model on clay in a test box. Tests were carried out by the method of digital processing of images. These "cuts" result from a typical progressive (kinematic) failure. It is principally different from instantaneous (static) failure, i.e. collapse, assumed in solutions by Terzaghi [2] and Sokolovsky [3], which occurs simultaneously within the abstract limit equilibrium zones. This photo shows that "cuts" rather than limit equilibrium zones form up under footings before the footing failure.

The same "cuts" appear under footing edges as result of footing-subsoil FEM analysis with FEM simulated shear cuts due to shear modulus degradation and tension cracks, without it analytical values of tilts and bending moments in footings are distorted

### 5.1 Subsoil heterogeneity as per GI data by Shepard approximation

As was indicated above, geologists believe that they can manually restore (inflate) subsoil stratification, although two geologists would produce different pictures. It can be done in even greater detail with the help of Shepard approximation. But whatever is the inflation it is always ambiguous and fictitious.

### 5.2 Qualitative analysis of SSS virtual behavior

Physical simulations of contingencies and failures of full-size structures is practically impossible. Numerical computer simulations are much more effective and yield ample data to identify and to assess qualitative effects. Below are given two such cases, linked up with "cut" formation.

1. Concentration of contact stresses under footing edges (Fig. 4) in the cases of "cut" absence (unlimited) contact stresses under edges and "cut" formation under the edges (limited contact stresses).

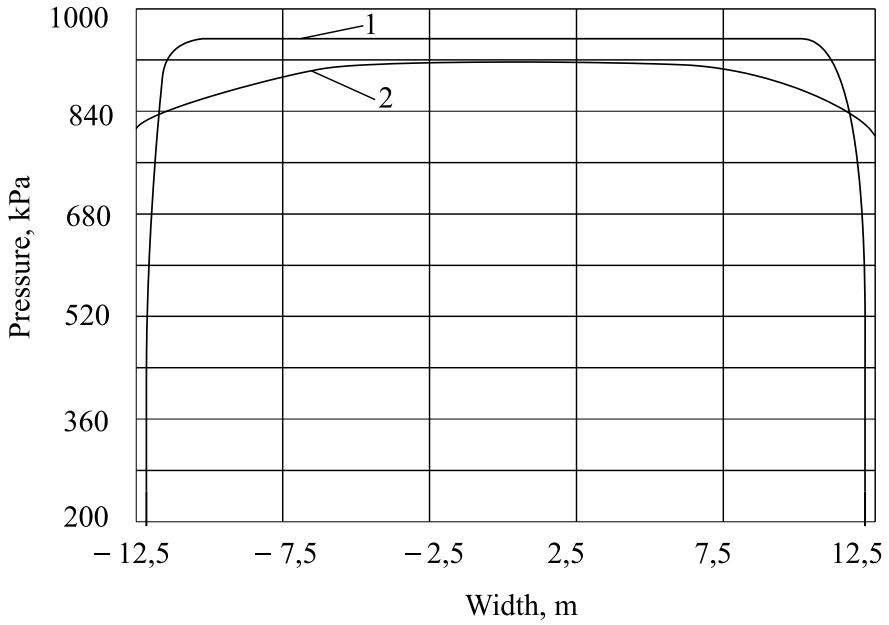


Figure 4: Side contact stresses without and with "cut" taken into account under footing edges: 1 – unlimited contact stresses; 2 – limited contact stresses

"Cut" formation under footing edges is inevitable, because otherwise theoretical solutions give infinite contact pressures under footing edges. A "cut" straightens the stresses under the footing and transforms their distribution to practically uniform. These transformations change the distribution of bending moments.

2. Growth and tilts of a symmetrically loaded structure if soil strength ($c$ and $\varphi$ values) is different under footing edges.

Numeric simulations showed that a structure can "rock" in the process of erection if the load is symmetric and the soil strength parameters under opposite edges are different. The tilts may firstly grow and then change directions in the process of the building erection (Fig. 5). It is a sort of "rocking" from side to side.

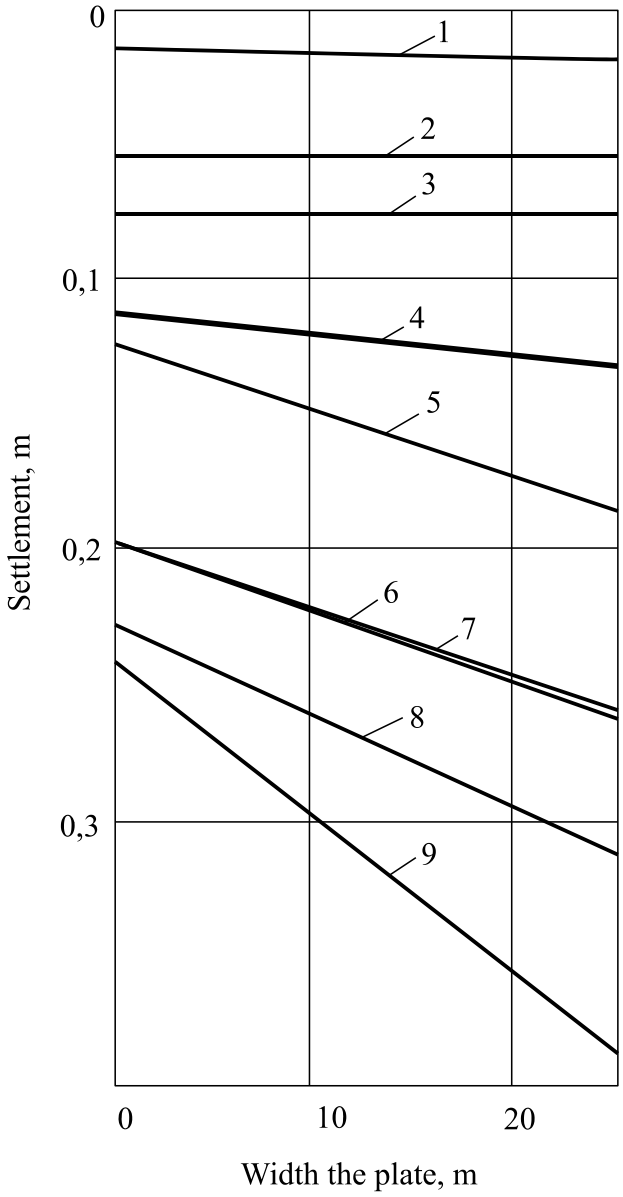


Figure 5: Growth of tilts erected buildings 25 m width:
1 – 9 – settlement left and right edges of the plate at different loads
(in ascending order of load from 0 to 0.5 MPa).

The tilts "straighten" at the last stage although the structure rocks from side to side during erection. But such "rocking" can be progressive: it is a critical state as per Eurocode 7.

The above numeric examples show that random inflation of GI data and ignorance of various factors (e.g. different soil strength under footing edges) can result in unpredictable situations and contingencies.

## 6 SETTLEMENT ANALYSIS WITHOUT "INFLATING" GI DATA

During GI the most reliable soil data are measured in the test holes, and this very data (no more) shall be applied in the analysis without any subjective "inflation" over the whole volume of subsoil. Two commonly applied assumptions shall be used to carry out settlement analysis.

*1st assumption*

Distribution of vertical normal stresses $\sigma_z = \sigma_z(x, y, z)$ under any footing along any vertical line under it does not depend on the subsoil inhomogeneity.

In the case of shallow rock $\sigma_z = q = \text{const}$, wih $q$ as mean structure-subsoil pressure.

*2nd assumption*

Within the "cut" depth under footing vertical normal stresses $\sigma_z$ in soil under footing are constant. This assumption is both realistic and necessary because otherwise infinite footing-soil contact stresses would appear that would make the analysis impossible.

Apply a uniformly distributed load q, equal to the mean structure-subsoil contact pressure. Subsoil settlement $s_i = s(x_i, y_i)$ at the location of the $i$-th test hole with $x_i, y_i$ coordinates is computed by integrating vertical deformations $\varepsilon_{zi} = \varepsilon_z(x_i, y_i, z)$, caused by stresses $\sigma_{zi} = \sigma_z(x_i, y_i, z)$ along the depth of compressible layer $H_i$:

$$s_i = \int_0^H \varepsilon_i \, dx = \int_0^{H_i} \frac{\sigma_{zi} dz}{E(x_i, y_{i,} z_i)} \tag{2}$$

with $i = 1.....N$, and $N$ as test holes number on the site.

Then subsoil stiffness factor ($K$) at $i$-th point $(x_{i,} y_i)$:

$$K_i = K(x_i, y_i) = \frac{q}{s_i}. \tag{3}$$

$K$ – values for points under the footing edges should involve formation of the "cut" to avoid non-existent singularities. Many existing methods of footing-structure analysis do not "see" this singularity, e.g. Boussinesq [4] and Schleicher [5] exact mathematical solutions for stiff plate on elastic half-space or half-plane.

The obtained values of all $K_i$ could be extrapolated over the whole surface of the subsoil under the structure. E.g., it can be done with the help of Shepard [6] technique:

$$W(x, y, n, N) = \frac{\sum_{i=0}^{N} \frac{K_i}{\left[(x - XY_{i,1})^2 + (y - XY_{i,2})^2\right]^n + 0,001}}{\sum_{i=1}^{N} \frac{1}{\left[(x - XY_{i,1})^2 + (y - XY_{i,2})^2\right]^n + 0,001}}, \tag{4}$$

with $n$ as free approximation surface shape parameter to simulate uncertainty of soil data from test holes, $N$ as number of test holes, $X,Y$ as $(x,y)$ coordinates array: $XY_{i,0} = x_i$, $XY_{i,1} = y_i$.

The value 0,001 is introduced to smooth removable discontinuities in Eq. (4) at locations of test holes.

Then the system three equations of static equilibrium can be compiled:

$$Gs = F, \tag{5}$$

with $G(I_{i,j})$ as square 3rd order matrix of the system linear equations (5) with:

$$I_{i,j} = \int_0^L \int_0^B W(x, y, n, N) x^i y^i dy dx, \tag{6}$$

$$F = \begin{pmatrix} Q \cdot \frac{L}{2} \\ Q \cdot \frac{B}{2} \\ Q \\ \end{pmatrix}. \tag{7}$$

with $Q$ as resultant of vertical loads, applied to the structure, including its proper weight; $L$ as length and $B$ as width of the structure.

Hence:

$$s = G^{-1} F, \tag{8}$$

with $G^{-1}$ as inverse matrix. Wherefrom:

$$s = \begin{pmatrix} \alpha \\ \beta \\ S \end{pmatrix}. \tag{9}$$

with α, β as tilts versus *Oy*,*Ox* axes respectively; $S$ as their structure settlement at point $(0{,}5L,\ 0{,}5B)$. Or $s(x, y) = \alpha x + \beta y + S$, with coordinate $x$ and $y$ versus geometrical SSS center $S$ as settlement of SSS geometrical center.

### 6.1 Settlement analysis of a 40x20 m SSS

Two virtual cases have been analyzed: with 5 test holes (located at the corners and in the center of a would-be rectangular structure) and 9 test holes (5 + 4 holes at the centers of rectangle side). The mean (uniform) pressure from the structure on subsoil $q$ =0,3 МПа. $E, c, \varphi$ values of the soil parameters with vertical distributions in test holes were assigned randomly with the help of random numbers generator.

The obtained results are presented below as columns with three values each as per (9): two tilts α, β and one mean settlement $S_{mean}$ values. The uncertainty of these results between boreholes was simulated by parameter *n*.

| | *n*=1 | *n*=2 | *n*=3 | *n*=4 |
|---|---|---|---|---|
| α | –0,00191 | –0,00244 | –0,00255 | –0,00258 |
| β | –0,00365 | –0,00552 | –0,00604 | –0,00620 |
| $S_{mean}$, cm | 0,18752 | 0,22895 | 0,23946 | 0,24288 |

Table 1: Results by number boreholes $N = 9$

| | $n$=1 | $n$=2 | $n$=3 | $n$=4 |
|---|---|---|---|---|
| α | –0,00322 | –0,00375 | –0,00384 | –0,00388 |
| β | –0,00079 | –0,00113 | –0,00122 | –0,00124 |
| $S_{mean}$, cm | 0,22406 | 0,23376 | 0,23457 | 0,23481 |

Table 2: Results by number boreholes $N$=5

In order to evaluate possible output scatter four cases with $n$=1,2,3,4 were computed, $n=1$is least realistic, calculated for comparison with the more "realistic" values. In both cases ($N$=5 and $N$=9) the settlements are almost identical with ≈ 1% accuracy except $n$=1. The calculated tilts for $N$=9 are ≈ 4-5 times greater than for $N$=5 and changed the sign from plus to minus. So whatever are $N$=9 the representative value.

This the brief description of the new GI approach that is being developed in NPP Geotek (Russia, Penza) now. It will enable on-line GI data processing during GI to identify the representative number of test holes is and to be chosen correct values of analytical settlements and tilts. It will also yield E, c and φ values distribution for further SSS computer analysis.

With α, β, $S$ values known it is possible to calculate subsoil (Winkler) $K(x,y)$ distribution under SSS. The map of $K(x,y)$ isolines is shown below (Fig. 6).

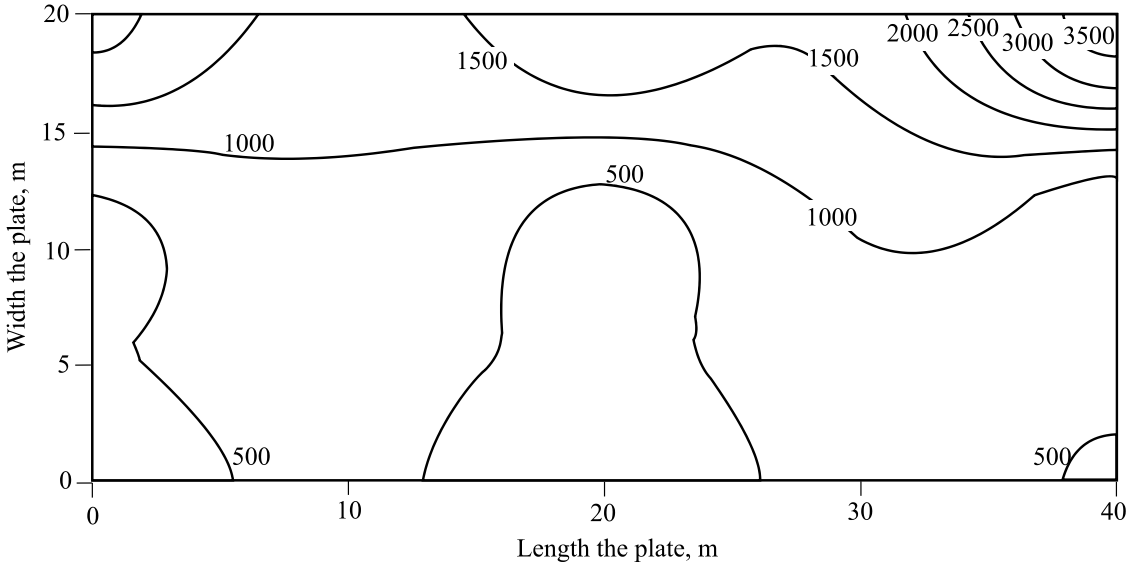


Figure 6: The map $K(x,y)$ isolines under SSS

## 7 CONCLUSIONS

SSS settlements analysis, based on a subsoil ratio concept, dates back to XVIII century and was firstly proposed by the great Swiss scientist Leonard Euler, then a Member of Russian Academy of Sciences in St. Petersburg. Later this subsoil ratio was renamed into Winkler parameter K=const. (Karl Winkler was also a Member Russian Academy of Sciences later in XIX century).

Ever since this method has been broadly applied thanks to its clarity and simplicity. It can also be applied to simulate any other subsoil models (elastic half-space, elastic layer, Pasternak model, etc.), non-homogeneous ones included, with the help of a method, proposed long ago (in 1869) by a German mathematician H.W. Schwartz [7]. It is an iterative procedure

for solving the problem of two contacting elastic bodies, having different elastic parameters $E_1$, $E_2$ and $\nu_1$, $\nu_2$ respectively. Schwarz method is broadly applied in Russian for SSS interaction analysis. The Winkler (subgrade) model is broadly applied with $K \neq const$.

SSS simulation analysis can help assess the SSS sensitivity to various input data scatter and to multiple analytical hypotheses by numeric simulations (virtual monitoring) that will yield more data than any in situ (very costly and low informative) monitoring. It means that it is possible to solve geotechnical problems of soil-structure interaction with the help of simple methods right on the site during geotechnical survey with high accuracy and reliability.

## REFERENCES


[1] K. Alshibi K., A.M. Okeil A.M., B. Alramahi. Update of correlations between cone penetration and boring log data. LTRC Report 439, 2008.

[2] K. Terzaghi, K. *Theoretical Soil Mechanics*, John Wiley & Sons, New York., 1943.

[3] V.V. Sokolovsky. *The statics of the granular medium*, 1965.

[4] J. Boussinesq, J. Application des Potentiels á L'Étude de L'Équilibreet due Mouvement des Solides Élastiques, Gauthier-Villars, Paris, 1885.

[5] F. Schleicher. Zur Theorie des Baugrundes, Der Bauingenieur, **48**, 1926.

[6] D.A. Shepard. A two-dimensional interpolation function for irregularly space data. Proceedings of the 23-th National conference of the Association for Computing Machinery (ACM). New York: ACM Press, 1968, 517-528.

[7] H.A. Schwartz. Uber einige Abbildungsaufgaben, Ges. Math. Abh., 1869,65-83.

COMPDYN 2017
6th ECCOMAS Thematic Conference on
Computational Methods in Structural Dynamics and Earthquake Engineering
M. Papadrakakis, M. Fragiadakis (eds.)
Rhodes Island, Greece, 15–17 June 2017

# IMPACT ASSESSMENT OF EPICENTRAL DISTANCES AND ENERGIES OF MINING SHOCKS ON THE TRANSMISSION OF FREE-FIELD VIBRATIONS TO THE BUILDING FOUNDATIONS

**Krystyna Kuzniar**[1] **and Tadeusz Tatara**[2]

[1] Pedagogical University of Cracow
ul. Podchorazych 2, 30-084 Krakow, Poland
e-mail: kkuzniar@up.krakow.pl

[2] Cracow University of Technology
ul. Warszawska 24, 31-155 Krakow, Poland
e-mail: ttatara@pk.edu.pl

**Keywords:** Mining Shocks, Epicentral Distance, Mining Energy, Free-field Vibrations, Foundation Vibrations, Response Spectra, Transmission of Vibrations.

**Abstract.** *The study analyses the results of measurements of mining related surface vibrations in the Legnica-Glogow Copper Region (LGCR) to assess the impact of mining tremor epicentral distances as well as mining tremors energies on a curve relationship (ratio) of response spectra (RRS) from simultaneously measured free-field vibrations and building foundations vibrations. The sources of considered vibrations were mine-induced rockbursts resulting from underground exploitation of copper ore. Only records induced by rockbursts with energy higher than $10^6$ J and horizontal components of peak ground accelerations larger than 10cm/s$^2$ are analysed. Epicentral distances of considered mining shocks are in the range re = 270 – 5839 m and energies are in the range En = $1 \cdot 10^6 – 2 \cdot 10^9$ J. Dimensionless acceleration response spectra (β) as well as dimensional acceleration response spectra ($S_a$) from the horizontal vibrations were taken into account. The focus is on residential buildings – medium-rise building and high-rise building. The results of analyses show that the epicentral distance of mining shock can have a significant impact on the transmission of response spectra from the free-field to the residential building foundations (medium-rise building and high-rise building). This effect is more visible in the case of curves RRS(β) determined using dimensionless acceleration response spectra β than curves RRS($S_a$) calculated for corresponding pairs for dimensional spectra $S_a$. The appropriate conclusions regarding the influence of mining tremors energies also have been achieved.*

## 1 INTRODUCTION

Soil-structure interaction problems are extensively studied with respect to earthquake excitations. However the ground motion can be induced not only by earthquakes, but also by so-called paraseismic sources resulted from human activity. Surface vibrations originating from mining rockbursts belong to the most intensive such vibrations. Although the intensity of mining tremors is smaller than in the case of natural earthquakes, mining-induced ground motion also can result in damage of surface structures.

During the transition of vibrations from the free-field to the building there is the phenomenon so-called dynamic soil-structure interaction. A comparison of a huge number of records of accelerations of vibrations induced by mining tremors measured at the same time on the ground near the building and on the building foundation level leads to conclusion that they can differ significantly [1].

The paper analyses the results of measurements *in-situ* of mine-induced surface vibrations in the most seismically active mining area in Poland – Legnica-Glogow Copper Region (LGCR), to assess the impact of mining rockbursts parameters (epicentral distances as well as mining tremors energies) on a curve relationship (ratio) of response spectra (*RRS – Ratio of Response Spectra*) from simultaneously measured free-field vibrations and building foundations vibrations in the cases of typical actual apartment medium-rise and high-rise buildings.

## 2 SCOPE OF THE STUDIES OF EXPERIMENTAL DATA

Mine-induced rockbursts resulting from underground exploitation of copper ore in Legnica-Glogow Copper Region in Poland were the sources of considered vibrations. Only records induced by rockbursts with energy higher than $10^6$ J and horizontal components of peak ground accelerations larger than 10cm/s$^2$ are analysed. Epicentral distances of considered mining shocks are in the range $re$=270–5839 m and energies are in the range $En$=$1\cdot10^6$–$2\cdot10^9$ J.

The focus is on actual residential buildings – medium-rise (5-storey) building denoted as building M, and high-rise (12-storey) building denoted as H building. The M and H buildings are wall-bearing walls, prefabricated objects. They have basements, continuous footings as foundations and they are located close to each other in one housing estate.

Fundamental frequencies of natural vibrations ($f_1$) experimentally determined in horizontal directions of the buildings are equal respectively: 2.9–3.3 Hz in a direction parallel to the transverse axis ($x$) and 2.9–3.1 Hz in a direction parallel to the longitudinal axis ($y$) in the case of building M, as well as 1.44–1.50 Hz in a direction parallel to the transverse axis ($x$) and 2.06–2.17 Hz in a direction parallel to the longitudinal axis ($y$) in the case of building H [1].

Simultaneously measured pairs of records of horizontal vibration accelerations of the free-field vibrations next to the building and the building foundation vibrations (parallel to the $x$ and $y$ axis of the building respectively) were taken into account in the case of each of the considered mining rockbursts. Next, dimensionless acceleration response spectra ($\beta$) as well as dimensional acceleration response spectra ($S_a$) from the horizontal vibrations were calculated. According to the results of experimental analysis relating to damping of considered types of buildings [2], the fraction of critical damping $\xi$ was adopted equal to 3%.

The number of analysed pairs (free-field – building foundation) of acceleration response spectra $\beta$ and $S_a$ in the successive ranges of epicentral distances are listed in Table 1, whereas the number of analysed pairs of these spectra for the successive orders of magnitude of rockbursts energies are shown in Table 2. The orders of magnitude of rockbursts energies $10^6$J, $10^7$J, $10^8$J, $10^9$J are denoted as E6, E7, E8, and E9 respectively. It is worth mentioning that the numbers included in Table 1 and Table 2 refer to the data with precisely verified values of epicentral distance or mining tremor energy and only such data were taken into analysis.

| *re* [m] | Response spectra $\beta$ | | Response spectra $S_a$ | |
|---|---|---|---|---|
| | Building M | Building H | Building M | Building H |
| to 500 | 2 | 3 | 2 | 3 |
| 501 – 800 | 29 | 12 | 26 | 11 |
| 801 – 1100 | 28 | 51 | 22 | 44 |
| 1101 – 1700 | 27 | 23 | 25 | 17 |
| 1701 – 2500 | 44 | 41 | 34 | 24 |
| over 2501 | 60 | 47 | 44 | 25 |
| whole range | 190 | 177 | 153 | 124 |

Table 1: Summary of the number of analysed pairs (free-field – building foundation) of response spectra ($\beta$ and $S_a$) in the successive ranges of epicentral distances.

| *En* [J] – order of magnitude | Response spectra $\beta$ | | Response spectra $S_a$ | |
|---|---|---|---|---|
| | Building M | Building H | Building M | Building H |
| E6 | 41 | 37 | 40 | 24 |
| E7 | 84 | 97 | 67 | 64 |
| E8 | 42 | 41 | 30 | 34 |
| E9 | 8 | 2 | 6 | 2 |
| whole range | 175 | 177 | 143 | 124 |

Table 2: Summary of the number of analysed pairs (free-field – building foundation) of response spectra ($\beta$ and $S_a$) for the successive orders of magnitude of rockbursts energies.

## 3 THE IMPACT OF ROCKBURSTS PARAMETERS ON THE TRANSMISSION OF GROUND MOTIONS TO THE BUILDINGS

### 3.1 Relationship between building foundation input and free-field ground motions

The response spectrum enables the evaluation of the maximum response of a given structure to seismic-type ground motion. The application of response spectra is well known in earthquake engineering, for instance, in the design process of buildings [3 – 5].

Comparison of the response spectra curves obtained on the basis of mining origin vibrations simultaneously recorded on free-field near the buildings and on building foundations allows for analysis of the one of the soil structure interaction effects – vibration transmission from the ground to the building foundations [1, 6, 7].

Modification of this method involves the calculation of the Ratio of Response Spectra (*RRS*) with respect to free-field and building foundation vibrations [8 – 11].

For each pair of response spectra (free-field – building foundation) corresponding ratios *RRS*($\beta$) for the dimensionless acceleration response spectra ($\beta$) as well as *RRS*($S_a$) for dimensional acceleration response spectra ($S_a$) are calculated according to formulae (1) and (2) respectively:

$$RRS(\beta) = \frac{\beta_f}{\beta_g} \tag{1}$$

$$RRS(S_a) = \frac{S_{af}}{S_{ag}} \tag{2}$$

where:

*RRS*($\beta$), *RRS*($S_a$) – relationship (ratio) describing the transition of response spectra from the free-field to the building foundation in the case of dimensionless and dimensional acceleration response spectra respectively,
$\beta_f$, $S_{af}$ – respectively dimensionless and dimensional acceleration response spectrum originating from the building foundation vibrations,
$\beta_g$, $S_{ag}$ – respectively dimensionless and dimensional acceleration response spectrum obtained on the basis of free-field vibrations next to the building.

### 3.2 The influence of epicentral distances of mine-induced tremors on the ratio of response spectra

Ratios *RRS*($\beta$) for the dimensionless acceleration response spectra ($\beta$) as well as *RRS*($S_a$) for dimensional acceleration response spectra ($S_a$) were used to try to assess the impact of epicentral distances of mining tremors on the transition of free-field vibrations to the building foundations.

Separately, for the building M and the building H, each of the relationship *RRS*($\beta$), and the relationship *RRS*($S_a$) defined for each of the considered mining shock, is placed into one of six groups. The criterion for assigning *RRS* relation to the group was the epicentral distance of the mining shock. Successive ranges of epicentral distances which correspond to the established relationship groups *RRS* are presented in Table 1.

a)

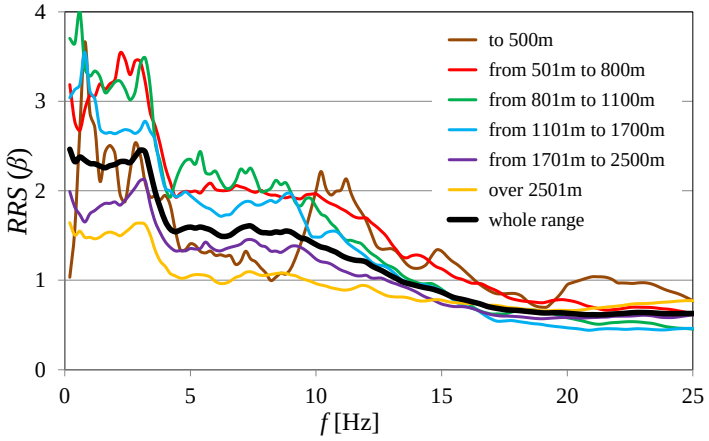


b)

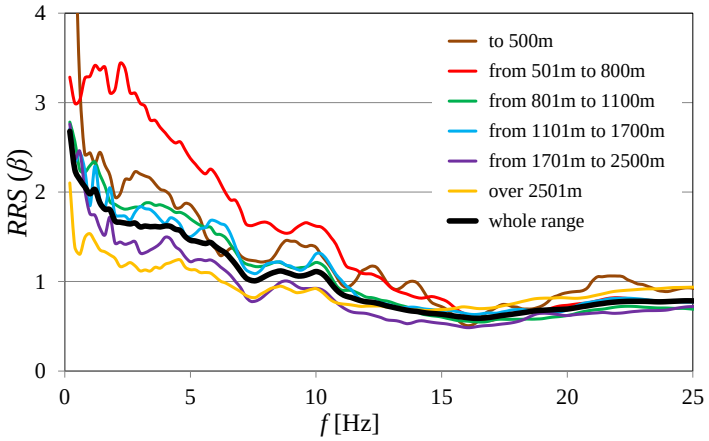


Figure 1: Relations *RRS*($\beta$) averaged in the ranges of mining tremors epicentral distances: a) building M; b) building H.

a)

b)

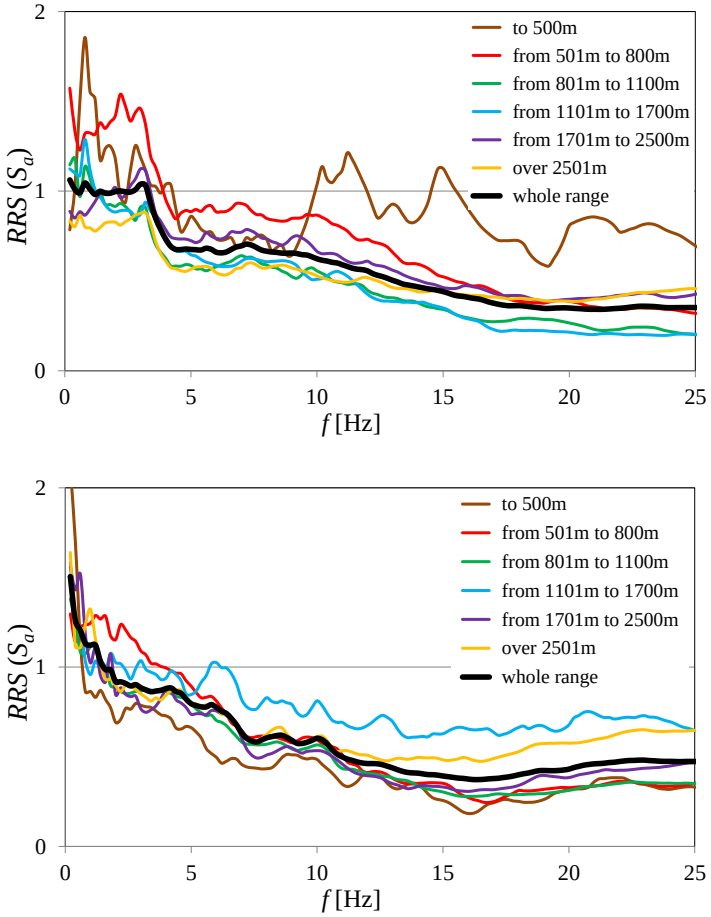


Figure 2: Relations $RRS(S_a)$ averaged in the ranges of mining tremors epicentral distances: a) building M; b) building H.

Averaged relationships were determined in each set of relationship $RRS(\beta)$ and $RRS(S_a)$. They corresponded to the range of epicentre distances. Furthermore, averaged relationships $RRS(\beta)$ and $RRS(S_a)$ were also calculated in the whole range of epicentral distances of the considered mining shocks, both in the case of the building M and the building H.

Fig. 1 shows relationships $RRS(\beta)$ averaged in the considered ranges of epicentral distances of mining tremors, for the building M and the building H. Analogous curves prepared for the ratios $RRS(S_a)$ are presented in Fig. 2.

Significant differences in the curves $RRS(\beta)$ and $RRS(S_a)$ which were obtained by averaging of the collections referring to individual ranges of epicentral distances, are visible (cf. Fig. 1 and Fig. 2) for both of the building cases: the building M as well as the building H, especially for the ratios $RRS(\beta)$.

Moreover the graphs of $RRS$ made for the individual epicentral distance ranges clearly distinguish from curves averaged in all over the range of distances.

These differences are especially evident at frequencies important from a practical point of view, namely in the relatively low frequency range (to approx. 10 Hz).

Additionally, Table 3 contains the values of ratios of $RRS(\beta)$ and $RRS(S_a)$ averaged within the adopted ranges of epicentral distances, which correspond to the appropriate mean values of the fundamental frequency of natural vibrations $f_1$ in the $x$ and $y$ directions of the building M as well as the building H.

| *re* [m] | Building M – $f_1$ = 3 Hz | | Building H – $f_1$ = 1.8 Hz | |
|---|---|---|---|---|
| | *RRS*($\beta$) | *RRS*($S_a$) | *RRS*($\beta$) | *RRS*($S_a$) |
| to 500 | 2.41 | 1.19 | 2.18 | 0.77 |
| 501 – 800 | 3.45 | 1.46 | 3.11 | 1.17 |
| 801 – 1100 | 3.41 | 0.91 | 1.89 | 0.90 |
| 1101 – 1700 | 2.68 | 0.87 | 2.05 | 1.08 |
| 1701 – 2500 | 2.11 | 1.12 | 1.72 | 1.07 |
| over 2501 | 1.64 | 0.88 | 1.30 | 0.93 |
| whole range | 2.45 | 1.04 | 1.80 | 0.98 |

Table 3: Values of *RRS*($\beta$) and *RRS*($S_a$) corresponding to the frequencies of natural vibrations $f_1$ of M and H buildings, averaged in the successive ranges of epicentral distances.

It is visible that substantial differences may occur in the values (ordinates) *RRS*($\beta$) and *RRS*($S_a$) corresponding to the natural fundamental frequencies of building vibrations, calculated in the individual ranges of epicentral distances (cf. Table 3). For example, both in the case of the building M and the building H, value *RRS*($\beta$) in the range of epicentral distances within 501 – 800 m is approximately twice greater than calculated for epicentral distances within the range over 2,501 meters. However, the differences in the values *RRS* corresponding to the natural fundamental frequencies of the buildings from the individual intervals of epicentral distances, in relation to the values *RRS* averaged in all over the range of epicentral distances, reach tens percent.

### 3.3 The influence of energies of mine-induced tremors on the ratio of response spectra

Ratios *RRS*($\beta$) as well as *RRS*($S_a$) were also used to estimate the impact of the order of magnitude of rockbursts energy on the transition of free-field vibrations to the building M and the building H foundations.

Analogously as it was for the case of analysis of the influence of the rockburst's epicentral distance on the ratios of response spectra, the curves of relations *RRS*($\beta$) as well as relations *RRS*($S_a$) averaged for the successive orders of magnitude of rockbursts energies were prepared for the buildings M and H. These graphs are shown in Fig. 3 and Fig. 4, respectively.

Furthermore, in Table 4, the values of *RRS*($\beta$) and *RRS*($S_a$) corresponding to the fundamental frequencies of natural vibrations $f_1$ of M and H buildings, averaged for the successive orders of magnitude of rockbursts energies are collected.

It is visible that just as it can be observed in the case of epicentral distance impact, the value of mining tremor energy also plays important role in the transmission of free-field vibrations to the building foundations, in the case of medium-rise building as well as in the case of high-rise building.

Also similar, clear differences between the graphs of *RRS* performed for the individual orders of magnitude of rockbursts energies, and the curves averaged in all over the range of energies, are visible.

Both in the case of the building M, and the building H, in ordinates of relationship *RRS* referring to the dimensionless acceleration response spectra ($\beta$) prepared in the individual successive orders of magnitude of rockbursts energies, there are bigger differences than in the analogous relationship *RRS* based on dimensional acceleration response spectra ($S_a$).

An interesting, very clear trend can be observed in Fig. 3 which concerns the ratio *RRS*($\beta$): the smaller values of mining tremors energies the greater ordinates of *RRS*($\beta$), both in the cases of the M and H buildings.

a)

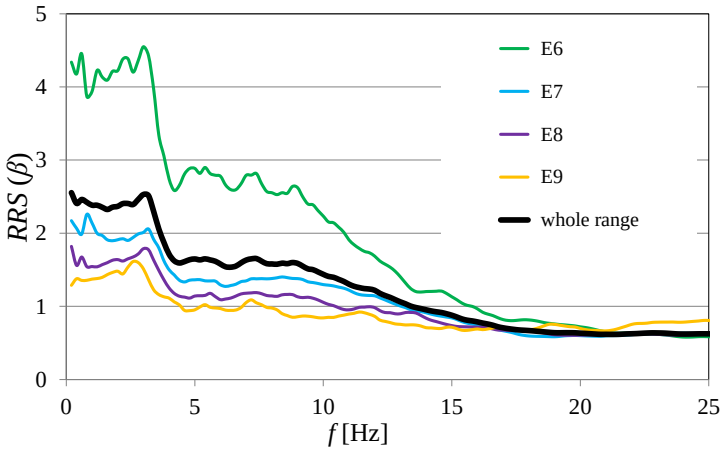


b)

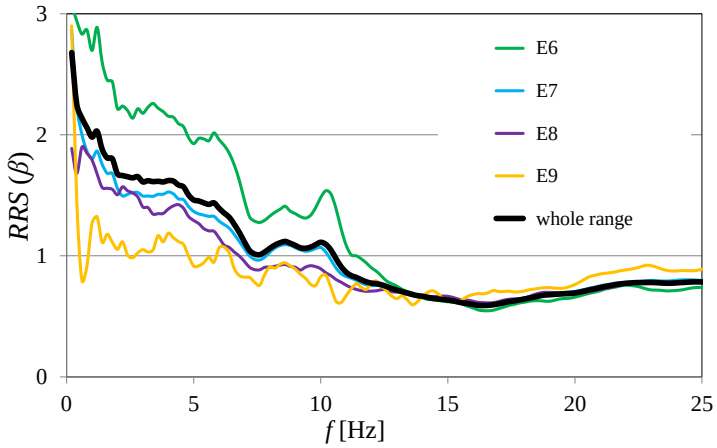


Figure 3: Relations *RRS*($\beta$) averaged for the successive orders of magnitude of rockbursts energies: a) building M; b) building H.

Similarly as in the case of the influence of epicentral distances on the features of *RRS* graphs, practically, in all of the individual successive orders of magnitude of rockbursts energies is not seen significant dependence of differences in the relationship *RRS*($\beta$) referring different building construction of buildings M and H versus values of mining tremor energy.

However, much greater differences than in the previous results of analysis regarding to epicentral distances, may concern the values of *RRS*($\beta$) and *RRS*($S_a$) corresponding to the fundamental frequencies of natural vibrations of the buildings averaged in the individual ranges of energies (cf. Table 4).

For instance, in the case the building M, value of *RRS*($\beta$) averaged for the order of magnitude of mining tremor energy equal $10^6$ (E6) is three times greater than the corresponding value obtained for the energy with the order of magnitude equal $10^9$ (E9). In the analogous proportion for the building H, the value of *RRS*($\beta$) for the energy E9 is approximately twice smaller than the value for the energy E6.

Besides, the differences in the values of *RRS* corresponding to the fundamental natural frequencies of building vibrations, calculated for the individual intervals of energies, in relation to the values *RRS* averaged in all over the range of energies, respectively reach: the building M, *RRS*($\beta$) – approx. 80%, *RRS*($S_a$) – approx. 17%; the building H, *RRS*($\beta$) – approx. 36%, *RRS*($S_a$) – approx. 3%.

a)

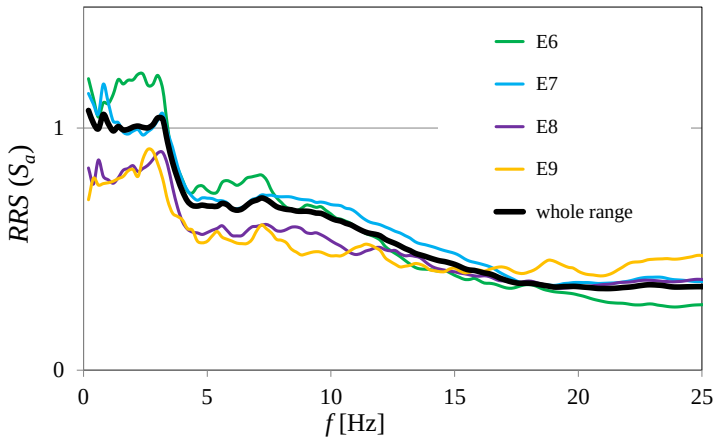


b)

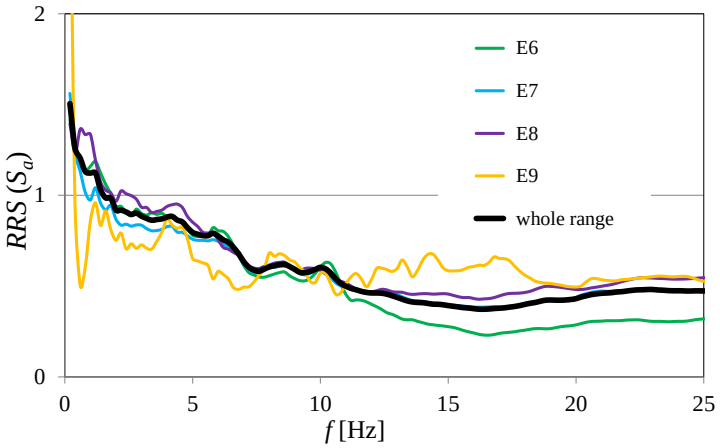


Figure 4: Relations $RRS(S_a)$ averaged for the successive orders of magnitude of rockbursts energies: a) building M; b) building H.

| *En* [J] – order of magnitude | Building M – $f_1$ = 3 Hz | | Building H – $f_1$ = 1.8 Hz | |
|---|---|---|---|---|
| | $RRS(\beta)$ | $RRS(S_a)$ | $RRS(\beta)$ | $RRS(S_a)$ |
| E6 | 4.45 | 1.22 | 2.44 | 1.01 |
| E7 | 2.01 | 1.03 | 1.68 | 0.94 |
| E8 | 1.79 | 0.90 | 1.55 | 1.01 |
| E9 | 1.51 | 0.85 | 1.11 | 0.81 |
| whole range | 2.53 | 1.04 | 1.80 | 0.98 |

Table 4: Values of $RRS(\beta)$ and $RRS(S_a)$ corresponding to the frequencies of natural vibrations $f_1$ of M and H buildings, averaged for the successive orders of magnitude of rockbursts energies.

## 4 CONCLUSIONS

From the results of analyses it can be stated that the epicentral distance of mining rockburst as well as the order of magnitude of the value of mining tremor energy, can have a significant impact on the transmission of response spectra from the free-field to the apartment medium-rise building and high-rise building foundations. This effect is clearer visible in the case of curves $RRS(\beta)$ determined using dimensionless acceleration response spectra $\beta$ than in the case of curves $RRS(S_a)$ calculated for analogous pairs of dimensional response spectra $S_a$.

## REFERENCES


[1] E. Maciag, K. Kuzniar, T. Tatara, Response spectra of ground motions and building foundation vibrations excited by rockbursts in the LGC region. *Earthquake Spectra*, **32**, 3, 1769–1791, 2016.

[2] R. Ciesielski, K. Kuzniar, E. Maciag, T. Tatara, Damping of vibration in precast buildings with bearing concrete walls. *Archives of Civil Engineering*, **41**, 3, 329-341, 1995.

[3] EN 1998-1 Eurocode 8, 1998. Design of structures for earthquake resistance – Part 1: General rules, seismic actions and rules for buildings (European standard EN 1998, December 2004).

[4] O.A. Lopez, J.J. Hernandez, R. Bonilla, A. Fernandez, Response Spectra for Multicomponent Structural Analysis. *Earthquake Spectra*, **22**, 1, 85-113, 2006.

[5] M.D. Trifunac, Earthquake response spectra for performance design – A critical review. *Soil Dynamics and Earthquake Engineering*, **37**, 73-83, 2012.

[6] K. Kuzniar, *Analysis of vibrations of medium-height buildings with load bearing walls subjected to mining tremors using neural networks (in Polish),* Monografia 310, seria: Inzynieria Ladowa, Wydawnictwo PK, Krakow, 2004.

[7] T. Tatara, *Dynamic resistance of buildings in mining tremors conditions in Polish)*, Wydawnictwo PK, Krakow, 2012.

[8] FEMA 440, Improvement of Nonlinear Static Seismic Analysis Procedures, ATC-55 Project, 2005.

[9] S. Kim, J.P. Stewart, Kinematic soil-structure interaction from strong motion recordings. *Journal Geotechnical and Geoenvironmental Engineering*, **129,** 4, 323-335, 2003.

[10] G. Mylonakis, S. Nikolaou, G. Gazetas, Footings under seismic loading: Analysis and design issues with emphasis on bridge foundations. *Soil Dynamics and Earthquake Engineering*, **48**, 26, 824-853, 2006.

[11] NIST GCR 12-917-21, Soil-Structure Interaction for Building Structures, prepared by NEHRP Consultants Joint Venture (a partnership of the Applied Technology Council and the Consortium of Universities for Research in Earthquake Engineering), 2012.

COMPDYN 2017
6th ECCOMAS Thematic Conference on
Computational Methods in Structural Dynamics and Earthquake Engineering
M. Papadrakakis, M. Fragiadakis (eds.)
Rhodes Island, Greece, 15–17 June 2017

# IMPEDANCE FUNCTIONS OF ADJACENT STRIP FOUNDATIONS

**Vasiliki G. Terzi**[1]

[1] Laboratory teaching staff
Laboratory for Statics and Dynamics, Civil Engineering Department, Aristotle University, Greece
e-mail: terziv@civil.auth.gr

**Keywords:** Soil-structure interaction, Strip footings, Finite Element Method.

**Abstract.** *The interaction between two adjacent strip footings resting on an elastic isotropic half-space is studied. The finite element method is used in order to investigate the response of the footings under vertical, lateral and rocking loading. The accuracy of the finite element model is verified by a comparison study with the rigorous results from the boundary element method concerning a single strip footing. Impedance functions are presented over a wide range of frequencies for typical values of the distance ratio S/L, where S is the distance between the footings and L is the width of each footing. The condition under which the interaction between adjacent strip footings should be taken into consideration is further discussed.*

## 1 INTRODUCTION

The assumption of a fixed based structure can be considered appropriate only in limited cases of a hard substratum site. Therefore, the soil-structure interaction (SSI) phenomenon must be taken into account during dynamic structural analysis. However, in practical situations, due to space limitations, structures are usually placed closed to each. Hence, in order to evaluate their dynamic characteristics, it is necessary to investigate not only the interaction between the foundation and the soil medium, but also the interaction between adjacent foundations through the soil [1]. The presence of adjacent foundations may affect the others further in a way such that each foundation which diffracts the incident wave field can be regarded as a disturbance producing a secondary wave field affecting the adjacent ones [2]. The aforementioned phenomenon is known as dynamic cross interaction (DCI) problem [1], structure-soil-structure interaction (SSSI) [3] or foundation-soil-foundation interaction (FSFI) [4].

The present paper investigates the dynamic behavior of an isolated, rigid, massless strip foundation bonded to an elastic half-space as well as the dynamic cross interaction between two strip foundations with the aforementioned characteristics.

Many researchers investigated the dynamic characteristics of the strip foundation-soil interaction. Luco and Westmann (1972) studied the coupled horizontal rocking response of a surface strip foundation under the assumption of welded soil contact. Such response arises when the superstructure is subjected to lateral forces (e.g. wind), when the foundation is exposed to earthquake condition or when it is subjected to machine vibrations [6]. Wang et al. (2015) verified their boundary element model using the results of the aforementioned study [1, 7]. Karasudhi et al. (1968) studied the coupled and uncoupled horizontal rocking response of a surface strip foundation under the assumption of relaxed and welded boundary conditions as well. Hryniewicz (1981) investigated the dynamic response of a strip foundation without taking into account the coupled horizontal-rocking response. Wickham's study (1977) referred to a rigid strip foundation in smooth contact with a semi-infinite elastic solid. Gazetas and Roesset (1976) applied a semi-analytical technique to estimate the dynamic compliances of a rigid strip foundation resting on an elastic, linearly hysteretic, layered half-space. Von Estorff and Schmid (1984) analyzed the dynamic behavior of a strip foundation resting on a soil layer using the BEM. A frequency domain BEM formulation has been used by Dominguez and Abascal (1989) in a 2-D analysis of a strip footing on zoned viscoelastic soils. Ahmad and Bharadwaj (1991) studied the horizontal impedance of embedded strip footing in layered soil. Jendoubi et al. (2008) studied the response of a strip footing resting on a half-space with constant or variable shear wave velocity.

The primary studies on structure-soil-structure interaction referred to the two-dimensional space. A frequency domain BEM formulation was applied by Cruze and Rizzo (1968) in order to study two and three dimensional elastodynamic problems between two rigid surface foundations. The through the soil coupling between adjacent infinitely long shear walls supported on semi-cylindrical foundations under the prism of two-dimensional anti-plane shear problem was studied by Luco and Contesse (1973) for the case of two structures, by Wong (1975) and Wong and Trifunac (1975) for several structures and by Murakami and Luco (1977) for an infinite number of equally spaced structures. Two-dimensional plane-strain models have been studied by Lysmer et al. (1974, 1975), Liang (1974) and Aydinoglu and Cakiroglu (1977) by use of the finite element approach and by Nakai and Fukuwa (1982), Antes and v. Estorff (1986) and Kokkinos and Spyrakos (1991) by a boundary integral equation approach.

The main target of the present study is the estimation of the impedance matrix referring to a system of two strip foundations. The influence of the distance between the two foundations on the impedance values is further investigated.

## 2 PROBLEM AND MODEL DESCRIPTION

The problem under study is depicted in Fig.1. Two rigid, massless, strip foundations are perfectly bonded to the free surface of an elastic half-space. Perfect bond is defined to be the type of attachment between the foundation and the underlying half-space which is characterized by the complete continuity of displacements in the area of contact. This type of attachment is also referred to as welded contact [9]. The two foundations have the same length (L) and their separation distance is denoted by S. Each foundation is excited by a vertical force (V), a horizontal force (H) and a moment (M). Each external load varies harmonically in time. Subscript 1 refers to the left and subscript 2 refers to the right foundation. The letter w refers to the vertical displacement, u to the horizontal displacement and φ to the rocking angle. The positive directions of external loads and the corresponding positive displacements as well are depicted in Fig. 1.

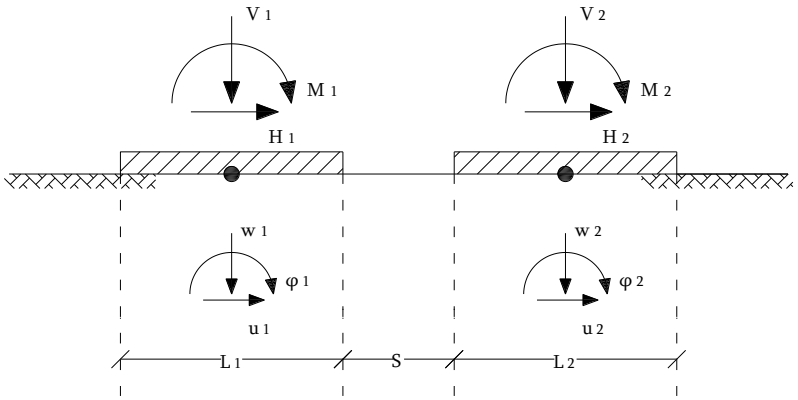


Figure 1: Adjacent strip foundations bonded to an elastic half-space.

The relationship between the external forces and the corresponding displacements of the two foundations is expressed by the following equation.

$$\begin{Bmatrix} V_1 \\ H_1 \\ M_1 \\ V_2 \\ H_2 \\ M_2 \end{Bmatrix} = \begin{bmatrix} K_{11} & K_{12} & K_{13} & K_{14} & K_{15} & K_{16} \\ & K_{22} & K_{23} & K_{24} & K_{25} & K_{26} \\ & & K_{33} & K_{34} & K_{35} & K_{36} \\ & & & K_{44} & K_{45} & K_{46} \\ & \text{symm.} & & & K_{55} & K_{56} \\ & & & & & K_{66} \end{bmatrix} \cdot \begin{Bmatrix} w_1 \\ u_1 \\ \varphi_1 \\ w_2 \\ u_2 \\ \varphi_2 \end{Bmatrix} \tag{1}$$

Each foundation has three degrees of freedom. Therefore, matrix [K] is a 6x6 matrix. Furthermore, matrix [K] is characterized as the impedance matrix. Each matrix term is frequency-dependent and complex. In a simplified model, the real parts represent the springs which are related to the restraining action of the supporting soil or the true stiffness, whereas the imaginary parts represent the dashpots or the out-of-phase components which are related to the effect of energy dissipation by radiation [3,4]. The impedance matrix is symmetrical. During the analyses, it was observed that the impedance matrix is simplified in the following form:

$$\begin{Bmatrix} V_1 \\ H_1 \\ M_1 \\ V_2 \\ H_2 \\ M_2 \end{Bmatrix} = \begin{bmatrix} K_{11} & K_{12} & K_{13} & K_{14} & K_{15} & K_{16} \\ & K_{22} & K_{23} & -K_{15} & K_{25} & K_{26} \\ & & K_{33} & -K_{16} & K_{26} & K_{36} \\ & & & K_{11} & -K_{12} & -K_{13} \\ & \text{symm.} & & & K_{22} & K_{23} \\ & & & & & K_{33} \end{bmatrix} \cdot \begin{Bmatrix} w_1 \\ u_1 \\ \varphi_1 \\ w_2 \\ u_2 \\ \varphi_2 \end{Bmatrix} \tag{2}$$

Therefore, the calculation of the complete impedance matrix can be achieved by imposing the appropriate loading (vertical force, horizontal force, moment) in only one of the two foundations. In particular, the following displacements are considered to be necessary: (i) vertical loading – complete displacement field of the two foundations, (ii) horizontal loading – horizontal displacements and rocking angles of both foundations and (iii) moment loading - rocking angles of both foundations.

The soil is assumed to be an elastic half-space. The shear modulus (G) equals to 132MPa, the Poisson's ratio (v) equals to 0.25 and the density (ρ) equals to 1.75t/m$^3$. In the case of a strip foundation, referring to a track, dam or building foundation with a high ratio of length to width, plane strain conditions is reasonable to be assumed [1]. Therefore, the finite element model is created in 2D space by using 9-node quadrilateral 2-D solid elements [27].

The wave propagation problem that takes place in a half-space cannot be simulated perfectly by the finite element method due to the restriction imposed by the model length and the finite elements size [28]. In particular, the model must be large enough in order to reduce any reflected waves at its boundaries [29] and the finite elements size must be as small as possible in order to accurately describe a wavelength. Therefore, in order to avoid any wave reflections, quiet boundaries suggested by Lysmer and Kuhlemeyer (1969) were used. Furthermore, the minimum finite element size for each frequency was equal to $\lambda_R/10$, where $\lambda_R$ is the wavelength of Rayleigh waves.

## 3 FINITE ELEMENT RESULTS

### 3.1 Validation study

In order to validate the finite element model, the impedance functions of an isolated, rigid, massless strip foundation bonded to an elastic half-space were compared with the results of the studies by Luco and Westmann (1972), Hryniewicz (1981) and Wang et al. (2015). The calculated impedance matrix was transformed into the flexibility matrix by $[K]^{-1}=[F]$. In Fig. 2 the comparison charts are depicted.

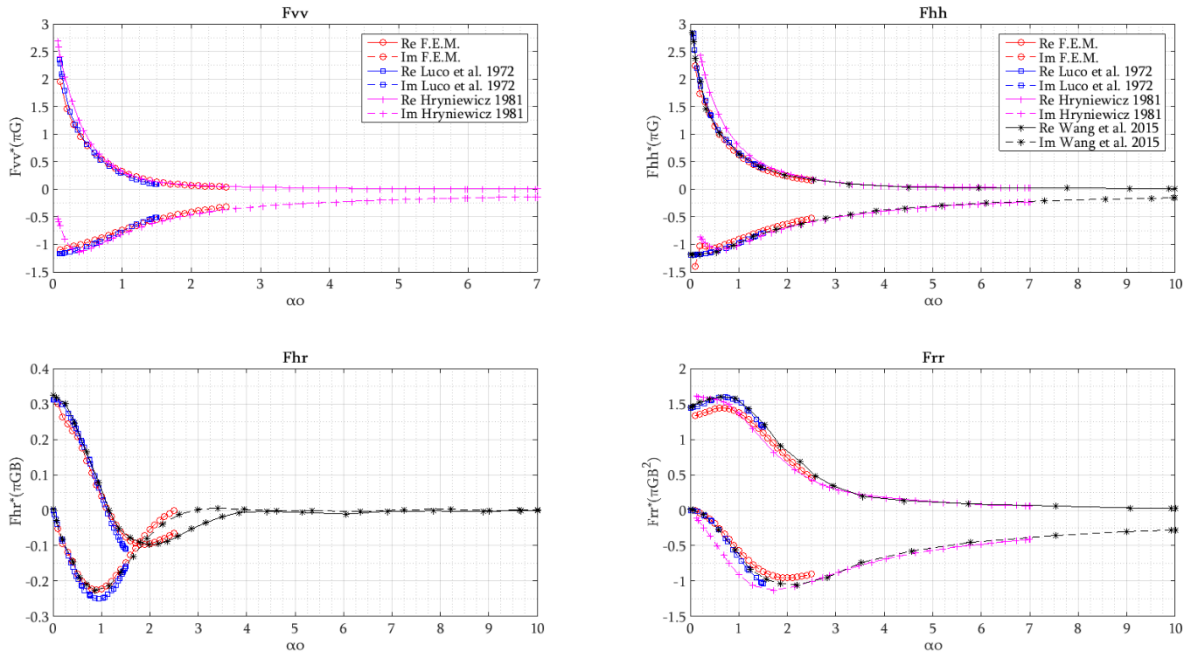


Figure 2. Validation study results for the case of an isolated, rigid, massless strip foundation bonded to an elastic half-space.

The charts refer to the vertical, the horizontal, the rocking and the coupled horizontal-rocking degree of freedom. The vertical loading of the strip foundation does not produce any horizontal or rocking movement. Therefore, there are no coupling terms for the vertical degree of freedom. It can be seen that the finite element results are in good agreement with the results of the other researchers. It must be taken into account that the comparison results were produced by the use of the boundary element method, which treats accurately the wave propagation problem in half-space.

### 3.2 Coupling of two foundations study

The main part of this study refers to the estimation of the dynamic cross interaction between two rigid, massless, strip foundations bonded to an elastic half-space. Therefore, the question that must be answered is the following: How much an external loading imposed on a foundation affects the dynamic behavior of its adjacent one? In order to answer the above question the necessary terms of the impedance matrix, based on equation (2), were estimated for the following ratios of S/L: 0.125, 0.5, 3 and 5.

In order to establish the accuracy of the finite element analyses, a comparative study was performed with the results available from Wang et al. (2015). Therefore, the real and imaginary parts of K22 and K33 are depicted for the various S/L ratios in Fig.3. The term K22 is related to the horizontal and the term K33 to the rocking movement of foundation 1. The vertical axis of the charts is normalized by the parameters π, G and B, which corresponds to foundation's half-width and the horizontal axis represents the normalized frequency αo, $\alpha_o = (\omega \cdot B)/V_s$, where $V_s$ is the shear wave velocity. It can be seen that the F.E.M. overestimates the real parts of the impedances for low values S/L (0.125, 0.5). On the contrary, the agreement between the real parts of the impedances for high values of S/L (3, 5) and the imaginary parts for all the values of S/L, is considered to be very good. In general, taking into account the limitations of the F.E.M. on wave propagation in half-space, the finite element model can be considered to be accurate in a satisfactory manner.

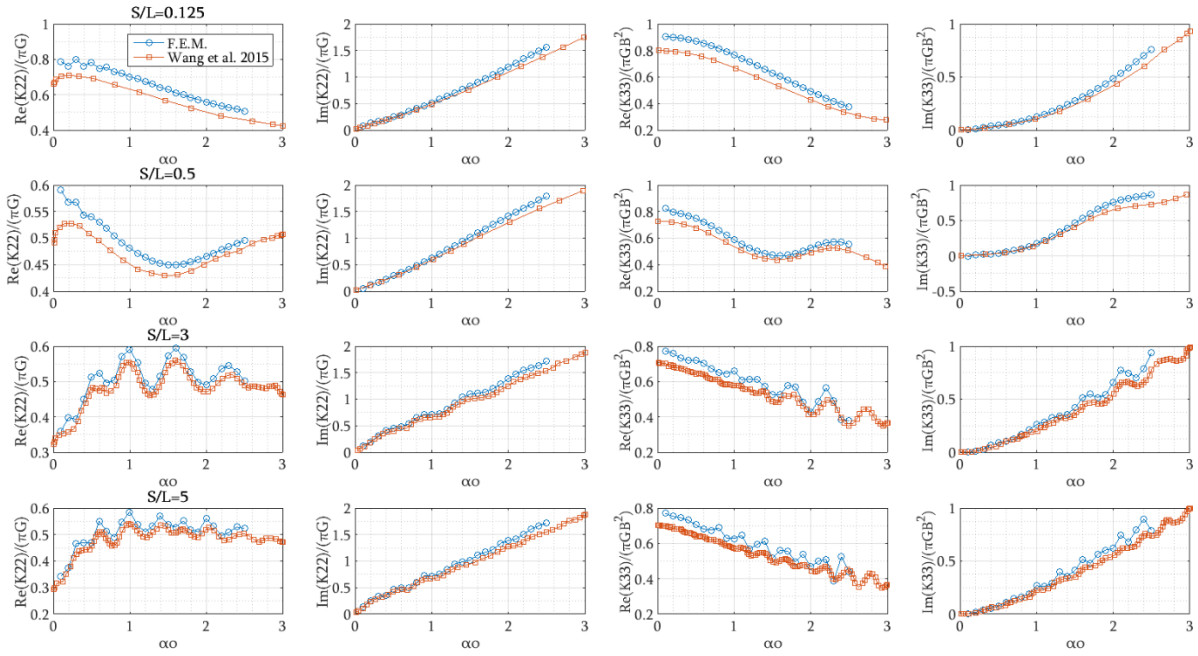


Figure 3: Validation study results for the case of two rigid, massless strip foundations bonded to an elastic half-space.

The following part of the finite element analyses refers to the investigation of the through-soil-coupling of two strip foundations. Based on the analyses results, it was found that the displacement field of each foundation is attributed not only on its external loading but on the adjacent foundation's loading as well. The smaller the ratio S/L is the bigger the effects of the foundation-soil-foundation interaction phenomenon are. Therefore, not only there are coupling terms between the horizontal and rocking movement of the foundation itself but coupling terms also appear between the two foundations even for the vertical excitation. In particular, Fig. 4 depicts the foundations movement at a random time frame for the case of S/L=0.5. It can be observed that even the vertical excitation causes a rocking movement not only on the foundation itself but on the adjacent foundation as well. The blue color depicts the initial position of the foundations while the cyan the deformed one.

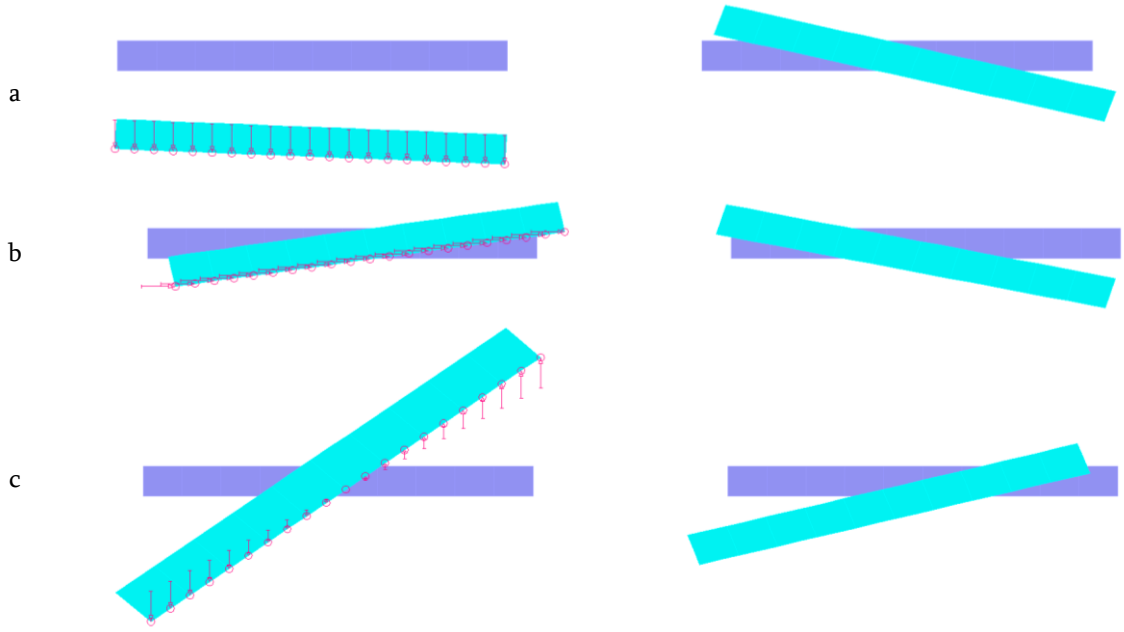


Figure 4. Foundations response at a random time frame for the case of S/L=0.5: a) vertical loading, b) horizontal loading, c) moment loading.

The foundation-soil-foundation interaction is expressed by the impedance matrix which connects the external loads imposed on the foundations to foundations displacements. The following figure, Fig.5, depicts the real and parts of the necessary terms for the definition of the impedance matrix, based on equation (2) while the next one, Fig. 6, depicts the imaginary parts.

Some of the most important observations regarding the real parts are the following:

- At low values of ratio S/L the real parts can be represented by a smooth line, while at high values of ratio S/L they present spikes at various frequencies.
- The higher the value of S/L, e.g. S/L=0.5, the smaller the differences with an isolated strip foundation.
- Vertical excitation. Regarding the loaded foundation (terms K11, K12 and K13): the coupling vertical-rocking (K13) is stronger than vertical-horizontal (K12) for low values of S/L while it fades for high values of S/L.
- Vertical excitation. Regarding the adjacent foundation (terms K14, K15 and K16): a) the vertical-vertical coupling (K14) cannot be ignored for low values of S/L; b) the vertical-vertical coupling (K14) receives negative values at the low range of ao for low

values S/L, while for high values of S/L, negative spikes are noticed through the whole range of ao; c) the coupling between the two foundations cannot be ignored at high frequencies, αo, even for high values of S/L; d) the vertical-horizontal (K15) and vertical-rocking (K16) coupling is strong for all values of S/L.

- Horizontal excitation. Regarding the loaded foundation (terms K22, K23): the horizontal-rocking coupling (K23) receives extremely small values in comparison to term K22 for all values of S/L.
- Horizontal excitation. Regarding the adjacent foundation (terms K25, K26): a) the horizontal-horizontal coupling (K25) cannot be ignored for low values of S/L; b) the horizontal-horizontal coupling (K25) receives negative values at the low range of ao for low values S/L; c) the horizontal-rocking coupling (K26) receives extremely small values in comparison to term K22 but equal range values in comparison to term K25 for all values of S/L.
- Rocking excitation. The foundation coupling cannot be ignored at high frequencies, αo, for all values of S/L.

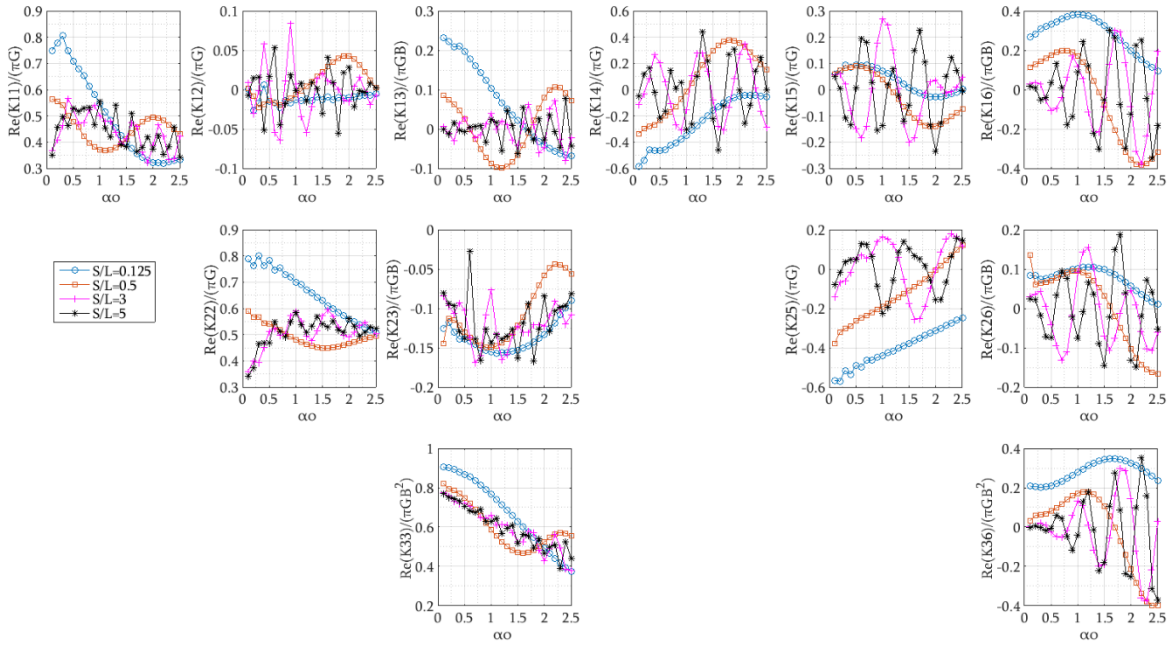


Figure 5. Real parts of the necessary terms for the definition of the impedance matrix.

Some of the most important observations regarding the imaginary parts are the following:

- At low values of ratio S/L the real parts can be represented by a smooth line, while at high values of ratio S/L they present spikes at various frequencies.
- Vertical excitation. The values of all coupling terms (K12-K16) are much smaller in comparison to K11 for all values of S/L.
- Horizontal excitation. The values of all coupling terms (K23-K26) are much smaller in comparison to K22 for all values of S/L.
- Rocking excitation. The values of K36 cannot be ignored for high values of frequency, αo, for all values of S/L.

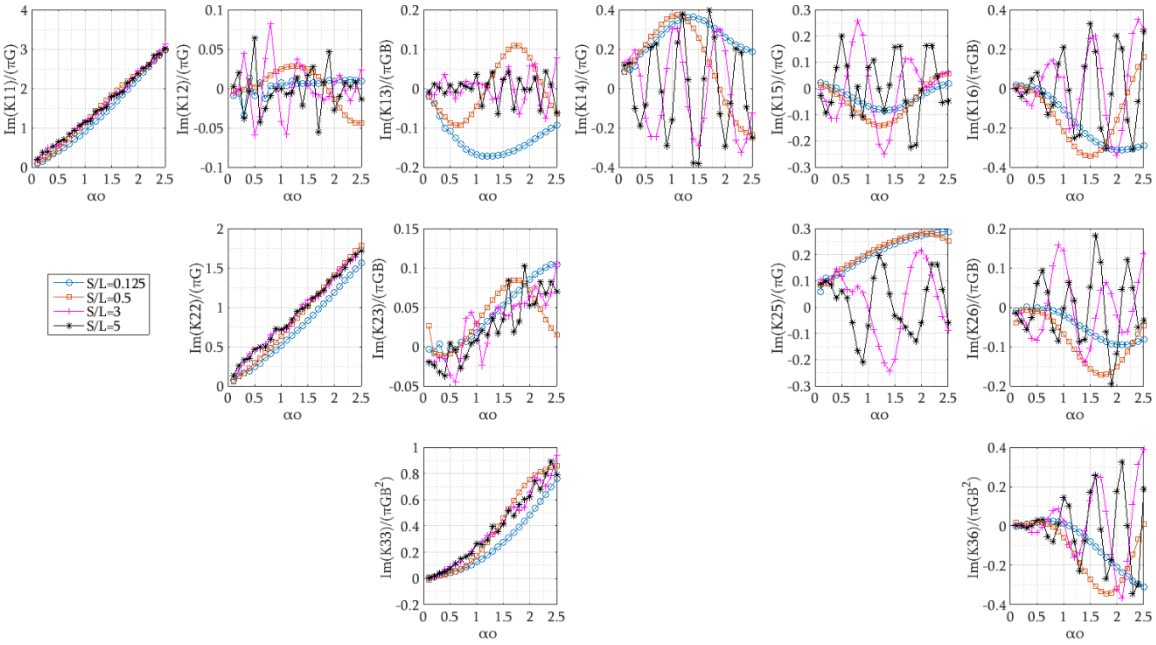


Figure 6. Imaginary parts of the necessary terms for the definition of the impedance matrix.

In the following figure, the impedance matrix terms are depicted in the complex number space. In particular, the horizontal axis represents the real part while the vertical axis represents the imaginary part of each impedance term. Each point in every chart follows a frequency, αo, step of 0.1, starting from 0.1.

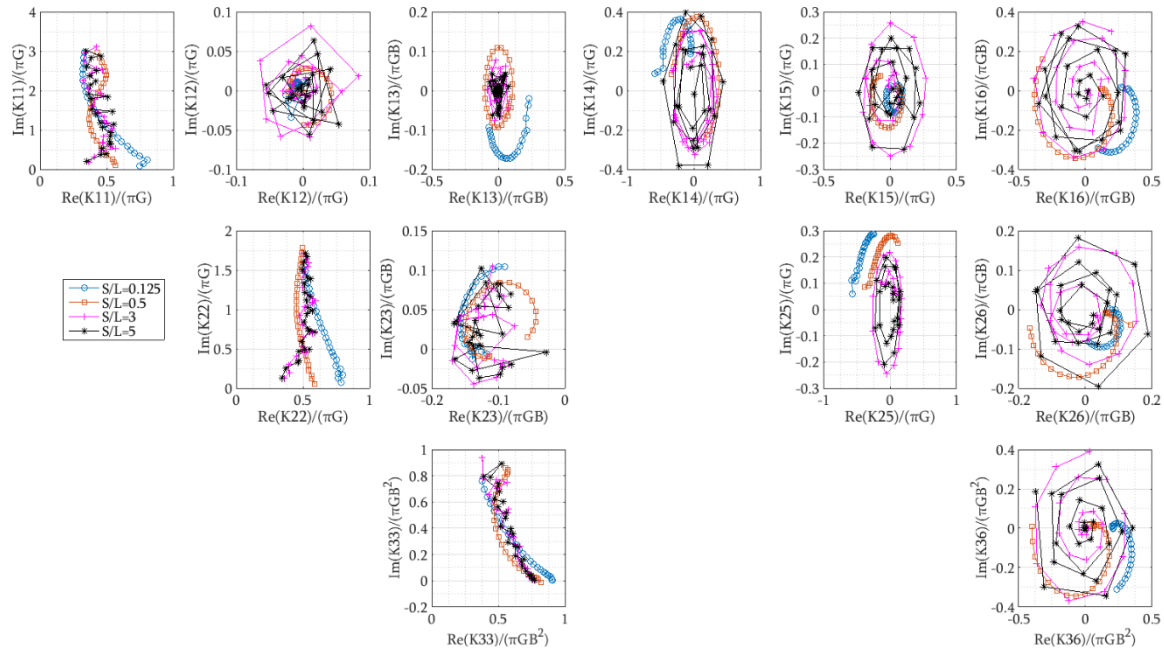


Figure 7. Representation of impedance terms on complex number space.

It can be seen that the representation of the diagonal terms (K11, K22, K33) corresponds to a line, almost smooth for low values of S/L and with spikes for high values of S/L. Whereas, the representation of the off diagonal terms corresponds to a spiral line for low values of S/L and a polygon for high values of S/L.

## 4 CONCLUSIONS

The through-the soil coupling of two rigid, massless strip foundations bonded to an elastic half-space has been studied by the use of the finite element method. The accuracy of the model has been verified by the comparison studies referring to an isolated strip foundation and a system of two. The foundation-soil-foundation is expressed by the impedance matrix. For low values of S/L, the coupled response cannot be ignored even for the vertical excitation. The charts of real and imaginary parts can be used in a simplified model of springs and dashpots.

## RFERENCES


[1] J. Wang, D. Zhou and W. Liu, Simplified model for coupled vibration of adjacent strip footings. M. Papadrakakis, V. Papadopoulos, V. Plevris eds. *5th ECCOMAS Thematic Conference on Computational Methods in Structural Dynamic and Earthquake Engineering (COMPDYN 2015)*, Crete Island, Greece, May 25-27, 2015.

[2] L.G. Tham, J. Qian and Y.K. Cheung, Dynamic response of a group of flexible foundations to incident seismic waves. *Soil Dynamic and Earthquake Engineering*, 17, 127-137, 1998.

[3] A. Bharadwaj and S. Ahmad, Rocking impedance of embedded strip foundations in layered soil. *Journal of Geotechnical Engineering*, 118(5), 796-813, 1992.

[4] D.L. Karabalsi and M. Mohammadi, 3-D dynamic foundation-soil-foundation interaction on layered soil. *Soil Dynamics and Earthquake Engineering*, 17, 139-152, 1998.

[5] J.E. Luco and R.A. Westmann, Dynamic response of a rigid footing bonded to an elastic half-space. *Journal of Engineering Mechanics Division ASME*, 39(2), 527-534, 1972.

[6] B. Suhol and L.C. Hong, Coupled horizontal-rocking impedance functions for embedded square foundations at high frequency factors. *Journal of Earthquake Engineering*, 3(4), 561-587, 1999.

[7] J. Wang, S.H. Lo, D. Zhou and B. O. Xu, Frequency-dependent impedance of a strip foundation group and its representation in time domain. *Applied Mathematical Modelling*, 39, 2861-2881, 2015.

[8] P. Karasudhi, L.M. Keer and S.L. Lee, Vibratory motion of a body on an elastic half plane, *Journal of Applied Mechanics ASME*, 35(4), 697-705, 1968.

[9] Z. Hryniewicz, Dynamic response of a rigid strip on an elastic half-space. *Computer methods in applied and mechanical engineering*, 25, 355-364, 1981.

[10] G.M. Wickham, The forced two dimensional oscillations of a rigid strip in smooth contact with a semi-infinite elastic solid. Mathematical Proceedings of Cambridge Philosophical Society, 81 (2), 291-311, 1977.

[11] G. Gazetas and J.M. Roesset, Forced vibrations of strip footing on layered soils. *Proceedings of Methods in Structural Analysis ASCE*, 1, 115-131, 1976.

[12] O. Von Estorff and G. Schmid, Application of the boundary element method to the analysis of the vibration behavior of strip foundations on a soil layer. *Proceedings of the International Symposium on Dynamic Soil-structure interaction*, A.A. Balkema, Minneapolis, Minn., 11-17, 1984.

[13] J. Dominguez and R. Abascal, Seismic response of strip footings on zoned viscoelastic soils. *Journal of Engineering Mechanics*, 115, 913-934, 1989.

[14] S. Ahmad and A. Bharadwaj, Horizontal impedance of embedded strip foundations in layered soil. *Journal of Geotechnical Engineering*, 117(7), 1021-1041, 1991.

[15] A. Jendoubi, F. Legeron and M. Karray, Numerical simulation of displacement functions of strip footings. *Geotechnical Earthquake Engineering and Soil Dynamics IV Congress*, 1-10, 2008.
[16] T.A. Cruze and F.J. Rizzo, A direct formulation and numerical solution of the general transient elastodynamic problem. *International Journal of Mathematical Analysis and Applications*, 22, 244-259, 1968.
[17] J.E. Luco and L. Contesse, Dynamic structure-soil-structure interaction. *Bulletin of the Seismological Society of America*, 63(4), 1289-1303, 1973.
[18] H.L. Wong, Dynamic soil-structure interaction. *Report EERL-75-01*, Earthquake Engineering Research Lab., California Institute of Technology, Pasadena, California, 1975.
[19] H.L. Wong and M.D. Trifunac, Two dimensional, antiplane, building-soil-building interaction for two or more buildings and for incident plane SH-waves. *Bulleting of the Seismological Society of America*, 65(6), 1863-1885, 1975.
[20] M. Murakami and J.E. Luco, Seismic response of a periodic array of structures, *Journal of the Engineering Mechanics Division ASCE*, 103 (EM5), 967-977, 1977.
[21] J.T. Lysmer, T. Udaka, H.B. Seed and R. Hwang, A computer program for complex response analysis of soil-structure interaction. *Report EERC 74-4*, Earthquake Engineering Research Center, University of California, Berkeley, CA, 1975.
[22] V.C. Liang, Dynamic response of structures in layered soils. *Report 1274-10*, Department of Civil Engineering, Massachusetts Institute of Technology, Cambridge, 1974.
[23] M.N. Aydinoglu and A. Cakiroglu, Dynamic interaction between soil and a group of buildings. *Proceeding of the 6th World Conference on Earthquake Engineering*, New Delhi, India, 2, 1596-1601, 1977.
[24] S. Nakai and N. Fukuwa, Boundary element analysis of approximate three-dimensional soil-structure interaction. *Proceedings of the 6th Japan Earthquake Engineering Symposium*, Tokyo, Japan, 1633-1640, 1982.
[25] H. Antes and V. O. Estorff, Dynamic soil-structure interaction by BEM in the time and frequency domain. *8th European Conference on Earthquake Engineering*, Lisbon, Portugal, 1986.
[26] F.T. Kokkinos and C.C. Spyrakos, Dynamic analysis of flexible strip-foundations in the frequency domain. *Computers and Structures*, 39 (5), 473-482, 1991.
[27] ADINA, Theory and Modeling Guide, Volume I: ADINA. *Report ARD 11-8*, ADINA R & D, Inc., 2011.
[28] W. Smith, A non-reflecting plane boundary for wave propagation problem. *Journal of Computer Physics*, 15, 492-503, 1974.
[29] J.M. Roesset and M.M. Ettouney, Transmitting boundaries: comparison. *Journal of numerical and analytical methods in geomechanics*, 1(2), 151-176, 1977.
[30] J. Lysmer and R.L. Kuhlemeyr, Finite dynamic model for infinite media. *Journal of the Engineering Mechanics Division ASCE*, 95, 859-878, 1969.

COMPDYN 2017
6th ECCOMAS Thematic Conference on
Computational Methods in Structural Dynamics and Earthquake Engineering
M. Papadrakakis, M. Fragiadakis (eds.)
Rhodes Island, Greece, 15–17 June 2017

# LANDSLIDE-PILE-TUNNEL INTERACTION BY 2D AND 3D FINITE ELEMENT MODELLING

**Mayank Mishra[1], Roberto Vassallo[1], Giuseppe Santarsiero[1], and Angelo Masi[1]**

[1] Scuola di Ingegneria, Università degli Studi della Basilicata
Via dell'Ateneo Lucano 10, 85100 Potenza, Italy
e-mail: meister.mayank@gmail.com
{roberto.vassallo,giuseppe.santarsiero,angelo.masi}@unibas.it

**Keywords:** Landslide, Tunnel, Earth thrust, Slope stability, Soil-structure interaction.

**Abstract.** *This paper is focused on the interaction of a railway tunnel with a slow-moving landslide in clay soil. The tunnel, built as a reinforced concrete box structure protected by sheet-piled walls, crosses the accumulation of an earthflow situated at the eastern suburbs of Potenza city, in southern Italy. The landslide develops in the formation of Varicoloured Clays and, due to its very slow but continuous displacements, induces progressive damage to structures and infrastructures built on it. As for the tunnel, there are signs suggesting an evolution of its state of stress and deformation over the last 30 years. The study of the landslide-pile-tunnel interaction required sophisticated FEM analyses to adequately take into account all the involved elements and the real 3D nature of the problem. Analyses were carried out by FEM geotechnical and structural software. Some results selected from a comprehensive numerical study are hereby reported and discussed. A geotechnical software was used in its 2D and 3D versions to obtain the spatial distribution of earth pressure on the tunnel owing to soil movements. The interaction was confirmed to be strongly 3-dimensional, with more evident displacements and bending of the tunnel box concentrated at one end. As a matter of fact, the movements of the landslide seem to make the structure open in horizontal, like a fan. The structural analysis made by applying the above mentioned pressure values confirmed which are the most stressed sections of the tunnel, giving a useful information toward the provision of possible interventions aimed to lengthen the life span of the tunnel.*

## 1 INTRODUCTION

Landslides can be responsible for a considerable damage to constructions arising on them such as buildings and infrastructure facilities. The safety of existing tunnels in landslide zones is always a matter of concern, although rarely addressed by a comprehensive understanding of the soil-structure phenomenon taking place. In the case of slow-moving landslides, the time variable plays an important role, and the key question becomes how long a structure can live with the landslide, interacting with it until a level of acceptable damage, and if appropriate building strategies can make this lifespan increase. This is important also in the case of transportation infrastructures crossing the accumulation of a landslide. Some authors (e.g. [1]) have tried to identify some thresholds for displacements by analysing a number of case histories, showing that the vulnerability of linear infrastructures like tunnels is linked to the level of differential displacements that can compromise their performance. The decision of crossing an accumulation area by a tunnel could be justified by the fact that, in some stages of a landslide life, such area can appear as the more stable part, so that the existence of a landslide phenomenon could even not be recognised. On the other hand, acting as a buttress hindering the movements of the upslope material, the accumulation can receive a thrust progressively increasing with time. Current research lacks accurate recommendations on how to study and numerically simulate this interaction, whose effects are frequently predicted by engineering judgement and experience only. Literature is not very rich in examples of slow-moving landslides interacting with tunnels. Unfortunately, in many cases, the collected data are not brought to the attention of the scientific community for several reasons, including the difficulty of interpreting phenomena that sometimes do not seem to have a clear explanation [2].

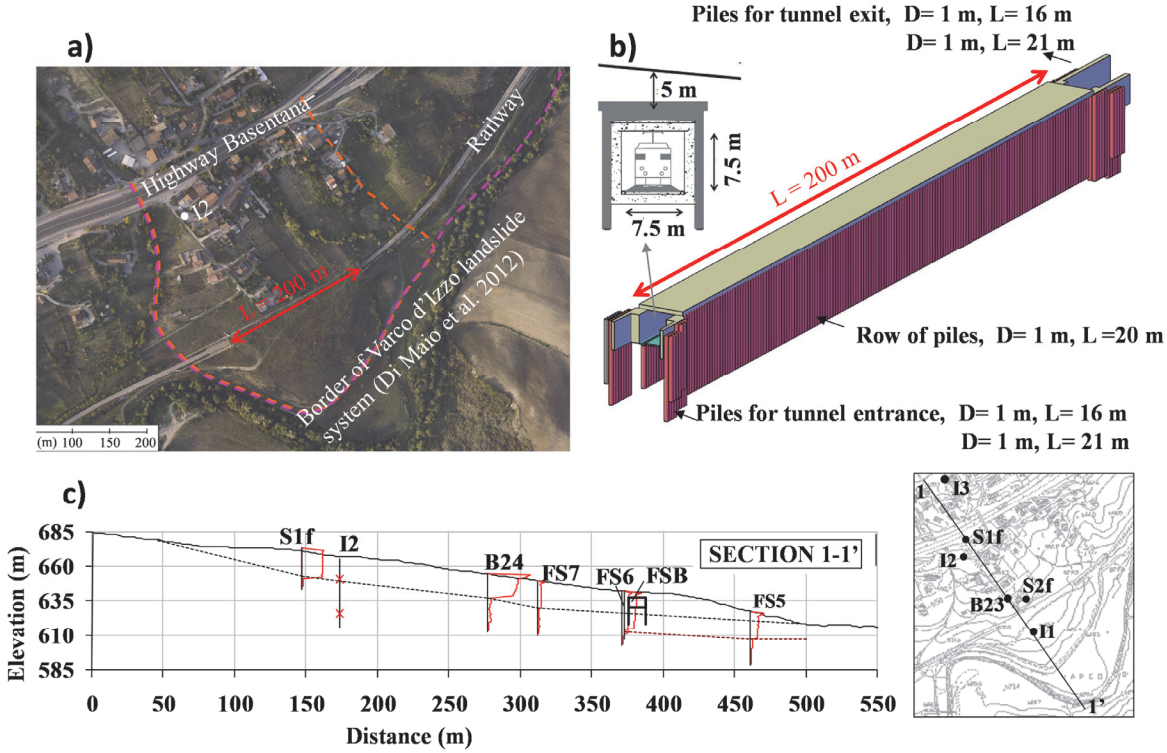


Figure 1: a) Varco d'Izzo landslide view with location of railway tunnel; b) 3D representation of tunnel 'Calabrese' (in grey) with the sheet-pile wall (in purple); c) Vertical section across the landslide with inclinometer profiles (modified from [3]).

The earthflow under study, situated in the eastern suburbs of the city of Potenza in a zone called Varco d'Izzo (Fig. 1a), develops in the Varicoloured Clays formation and is an extremely slow-moving landslide according to the classification by Cruden and Varnes [4]. The tunnel of the National Railway (Fig. 1a-b), which crosses the landslide accumulation, is the focus of this paper. A number of geotechnical investigations, including displacement monitoring, have been carried out in the area in the last 30 years. The geotechnical research group at University of Basilicata has been studying many aspects of several landslide phenomena occurring in the same slope, facing the valley of Basento river [5, 6, 7]. As for the landslide system of Varco d'Izzo [3, 8] all the available monitoring data are relative to the period after the reconstruction of the railway tunnel. Landslide movements were slow but continuous till nowadays, in the order of one to several cm/year. They have caused the unusability of a residential building, the dismantling of a pedestrian bridge overpassing the local highway, and damage to roads and other constructions. In the period 2005-2011, available inclinometer and GPS data have shown no significant changes in displacement rates [3, 9], which have been of about 1 cm/year in the zone of inclinometer I2 (see Fig. 1c). Note that the cross section of the landslide body through I2 will be the control section for displacements in the numerical model. The inclinometer profiles allow reconstructing the geometry of possible slip surfaces or, at least, of parts of them as shown in Fig. 1c. The upper slip surface, which outcrops at the river floodplain, reaches a depth of about 20 m and directly interacts with the sheet-pile wall protecting the tunnel. A second slip surface, or at least a zone with concentrated deformations, seems to be located at about 40 m depth, below the pile-tunnel system.

## 2 DESCRIPTION OF THE TUNNEL GEOMETRY AND CURRENT CONDITIONS

Tunnel "Calabrese" was re-built in 1992, after the previous one had suffered severe damage due to landslide movements, by the 'cut and cover' method, in which a trench is excavated, the tunnel lining is put in place, and then the whole is covered up to the ground level. The concrete box structure has internal dimensions 7.5 x 7.5 m and an average soil overburden of about 5 m, as shown in Fig. 1b. Along its length of about 200 m, it is made up of eight sectors separated by construction joints at an average length of 25 m. The interaction with the landslide is thus characterised by the fact that the main structural elements (piled walls and box structure) were constructed in sequence and also interact with one another. The piles, in a single row at both sides of the tunnel, are 20 m in length and 1 m in diameter. A double row of piles is present at the tunnel entry and exit (Fig. 1b). The pile-tunnel system, with its low deformability, represents an obstacle to the slow landslide movements, with a possible increase of earth thrust acting from upslope. This justifies the need for accurate soil-structure interaction, along with continuous monitoring of the structure deformation.

In the very last years, an evolution of deformation could be observed and measured [8, 10], thanks to the collaboration with the Italian Rail Infrastructure Manager (RFI). Relative displacements along tunnel joints and a number of vertical fissures have been observed, the more open ones located along the upslope wall facing the landslide, at the western side. Furthermore, Vassallo et al. [8] report, as a result of a 3D laser scan survey carried out in the tunnel in 2015, maximum horizontal displacements of about 5 cm between tunnel roof and base. Deformed shapes at several locations are those expected as the result of unbalanced actions on the upslope and downslope side.

## 3 NUMERICAL ANALYSES

The earth thrust distribution, the state of stress in the lining and their evolution with landslide displacements have been analysed by a geotechnical FEM software, Plaxis 2D/3D [11], and a structural FEM software, SAP2000 [12]. The former allowed an accurate description of the landslide behaviour and a simplified description of tunnel behaviour, the latter a more detailed description of the tunnel behaviour. To better understand the tunnel behaviour, also a number of structural models with different degrees of interaction between tunnel sectors were implemented.

Mishra [10] considered two mechanisms to numerically activate the landslide displacements in Plaxis: 1) by applying prescribed displacements at a control section chosen far from the tunnel (as in [13]), and 2) by increasing phreatic level (as in [14, 15]). Both of these effects lead to soil movements, hence inducing additional stresses on the tunnel lining. For the scope of this paper, only results of mechanism 1 are illustrated.

In Plaxis 2D/3D, the landslide body was simulated by a linear elastic-perfectly plastic material satisfying Mohr-Coulomb's yield criterion. Although other more advanced constitutive models were available in the software, this simple model was considered adequate to tackle the problem, also given the limited amount of available laboratory results on undisturbed specimens [3]. Peak shear strength and stiffness parameters estimated from such results were used in the analysis. As for slip surface modelling, interface elements with frictional shear strength and zero cohesion were considered. Nil cohesion is consistent with the observation that this active landslide underwent large displacements, so that the residual strength is now available. Stable soil was considered elastic. Being the model described here a total stress model, without explicit consideration of pore water pressures, the equivalent friction angle $\varphi_{eq}$ assigned to the slip surface is lower than the laboratory determined residual friction angle $\varphi'_r$. Such parameter was set so as to obtain a global safety factor of the landslide as close to one as numerically possible before the tunnel construction. Properties of structural materials were inferred from design documents and corroborated by some preliminary in-situ non-destructive tests. Table 1 summarises the used soil and structure parameters.

Plaxis 2D was used to analyse, in plain strain conditions, the median longitudinal section of the landslide. The mesh is made of triangular elements (see Fig. 2) more refined close to the tunnel to carefully evaluate the evolution of stress and strain at critical locations. For the simulation of two concrete members placed next to each other, the software does not allow to use two adjacent plate elements. To overcome this limitation they were placed with a physical gap in between and the nodes in the two concrete members were connected by struts to make the contact transfer only compressive, i.e. without any shear transferred by the piles to the box structure (Fig. 2), accordingly to how the structure was constructed, that is without any specific reinforcement linking the piles to the box.

The model in Plaxis 3D, shown in Fig. 3, was implemented to better analyse the spatial distribution of landslide thrust along the tunnel length. The model geometry was derived from a digital terrain model (DTM) of the landslide area, geomorphological and inclinometer data for the landslide, and from design documents and in-situ survey for the structure. The sheet-piled walls were simulated as two separate equivalent volumes of concrete, crossing the slip surface and embedded for some meters in the stable soil, and were assumed as fully connected to the tunnel box structure.

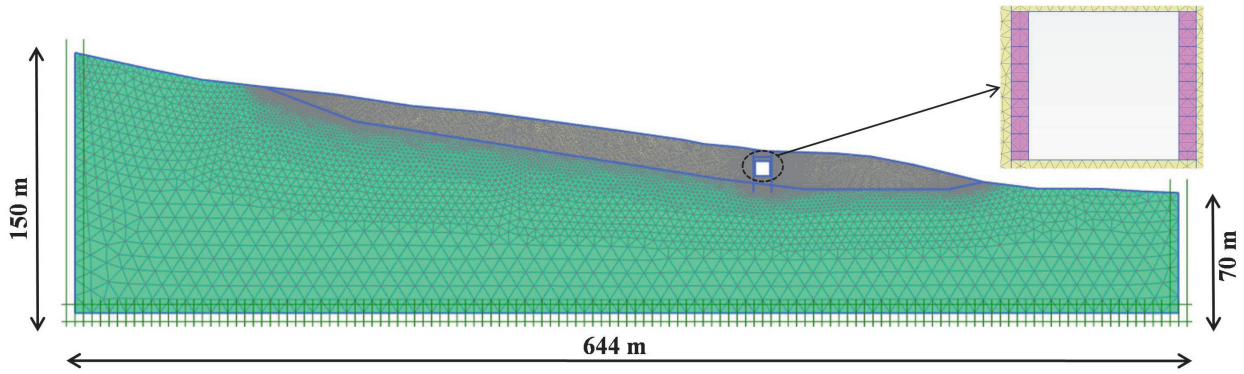


Figure 2: Finite element mesh in Plaxis 2D showing local refinement near tunnel.

| Material | Properties |
|---|---|
| Stable material | Elastic (E = 1000 MPa, ν=0.4) |
| Slip surface | Rigid perfectly plastic, residual shear strength ($\varphi_{eq}$=6.5° for 2D and $\varphi_{eq}$ = 8.5° for 3D) |
| Landslide body | Mohr Coulomb (E = 50 MPa, ν=0.4), peak shear strength (c = 50 kPa, φ=14°) |
| Pile/tunnel lining | Elastic (E = 32,900 MPa, ν=0.2) |
| Strut | Elastoplastic (compression only, EA=16.4·10$^6$ kN/m, spacing = 5 m) |
| Flexural rigidity (EI) | Per unit width in the out of plane direction EI (kN m$^2$/m) 1.6·10$^6$ |
| Axial stiffness (EA) | Per unit width in the out of plane direction EA (kN /m) 25·10$^6$ |

Table 1: Material models used in Plaxis.

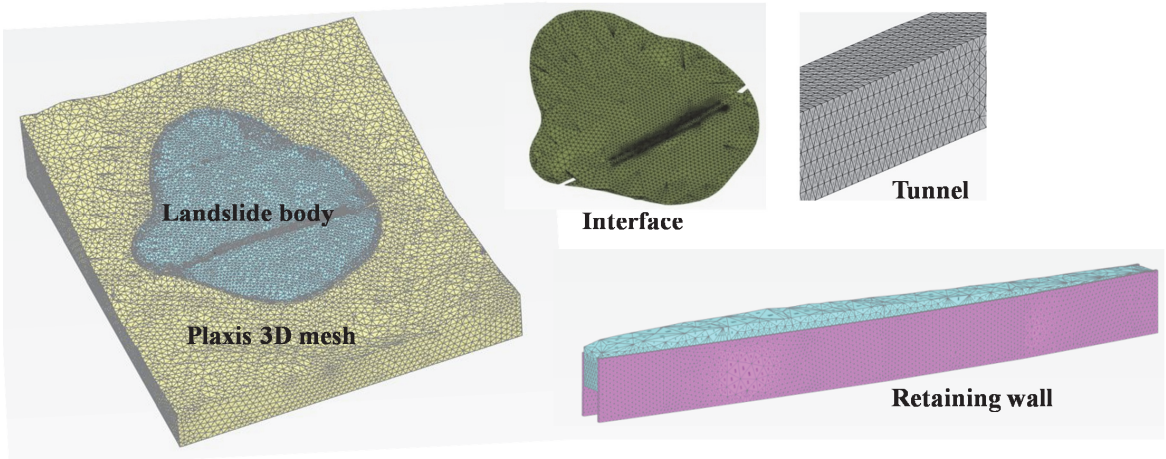


Figure 3: Model in Plaxis 3D: Finite element mesh, the landslide body, view of the slip surface simulated by interface elements, tunnel using plate elements and retaining wall.

This was accepted as a useful compromise to study the effect of the tunnel presence on earth thrust, leaving to the successive structural analysis the detailed study of stress transmission among structural elements. In fact, the geometrical complexity of the 3D geotechnical model did not allow to simulate just a compressive force transfer as in the 2D simulations.

The model is 1200 m x 800 m x 150 m in size, with a total number of 650,000 10 noded tetrahedral elements. The tunnel was modelled as a continuous structure by plate elements.

Structural models in SAP2000 were implemented to deal with the influence of the uneven distribution of earth pressure along tunnel length on the deformation profile of the tunnel. The analyses carried out permitted to evaluate the global response of the tunnel with and without joints. The piles were simulated as single elements, and a number of rigid link elements were used to connect them to the tunnel (Fig. 4a), allowing only compression transfer. The Plaxis 3D output has been used as input data for the SAP2000 model in terms of earth pressures acting from upslope and reactions of the landslide accumulation acting from downslope, simulated by equivalent springs. The model is shown in Fig. 4b, it uses shell elements and has 12,000 nodes and 5473 frame elements.

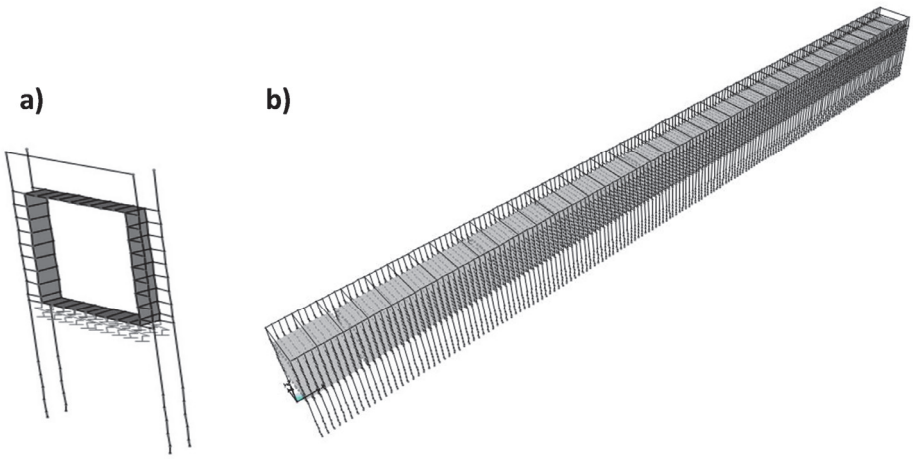


Figure 4: Tunnel model in SAP2000: a) portion of the model with shells and 10 links connection b) 3D view.

## 4 ANALYSIS OF RESULTS

Distribution of landslide thrust along the length of the tunnel and its comparison with 2D results is one of the main output results of the calculations performed. Fig. 5a shows the evolution of relative shear $\tau_{rel}$ (i.e., ratio of acting shear stress to available shear strength) along the slip surface with application of increasing prescribed displacements u*. Based on the landslide activity in the monitoring period, u* = 10 cm can be assumed as approximately representative of a decade of displacements. As written above, shear strength of the landslide slip surface was set so as to obtain a global safety factor approximately equal to one after tunnel construction. Nevertheless, some portions start with local safety factor slightly higher than one, and thus relative shear $\tau_{rel}$ lower than 1. As can be seen, as landslide displacements increase such shear strength surplus is utilised first at the entry of the tunnel (west side) and then at the exit (east side). With the increasing value of u*, almost all the force increment acting from upslope becomes an increasing thrust on the tunnel, as more and more portions of the slip surface reach $\tau_{rel}$ = 1. Fig. 5b shows contour plots of horizontal earth pressure in the direction orthogonal to the tunnel (i.e., $\sigma_y$). A non-uniform distribution of stresses along the tunnel length is observed, with higher values at the western side. Such distribution can be attributed to the local topography and to the assumed geometry of the slip surface, based on the data of a significant number of inclinometers, although not all pertaining to the same monitoring period and prevailingly concentrated on the western half of the earthflow [10]. The scheduled new geological and new geotechnical investigations of the area will hopefully clarify this

aspect. A non-uniform earth thrust distribution is the presumable cause of the observed in-situ style of tunnel relative displacements, mainly concentrated at the structural joints and with higher values at the western end of the tunnel, and also of the cracks observed on the tunnel walls.

Fig. 6 shows the increment in earth pressures $\sigma_y$ acting on the tunnel from upslope as a consequence of prescribed displacements. Results are plotted for three values of prescribed displacements u*. At the mid-height of the tunnel, for u*= 40 cm, $\Delta\sigma_h$ varies from 150 kPa at the entrance to 40 kPa at the exit. The same figure also reports values obtained in 2D conditions. For the sake of completeness, 2D calculations were carried out with two friction angle values available on the slip surface. In fact, we used: a) the friction angle leading, before tunnel construction, to a global safety factor of the landslide SF=1 in 2D; b) the friction angle leading to the same condition in 3D. Irrespective of such differentiation, calculated pressures in 3D have values even half of those estimated in 2D, due to the possibility of sideways movement and the less effective lateral confinement arising in 3D conditions. In the 2D model, in fact, the tunnel acts as a barrier which extends infinitely in the transversal direction providing maximum resistance and hence inducing higher earth pressures.

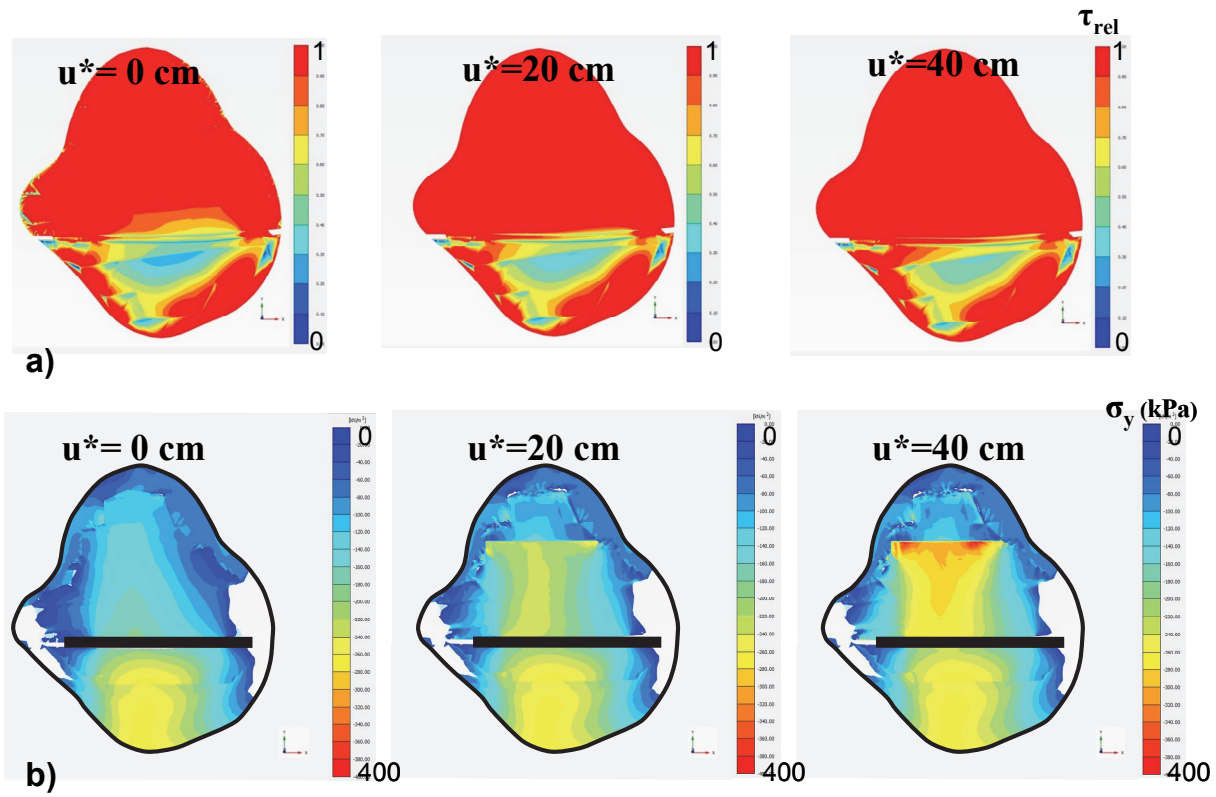


Figure 5: Evolution with prescribed displacement u* applied at the landslide control section of a) relative shear ($\tau_{rel}$) along the slip surface; b) horizontal earth pressure $\sigma_y$ in a plane at about 10 m depth from the ground surface. Values of u* of 0, 20 cm and 40 cm are considered.

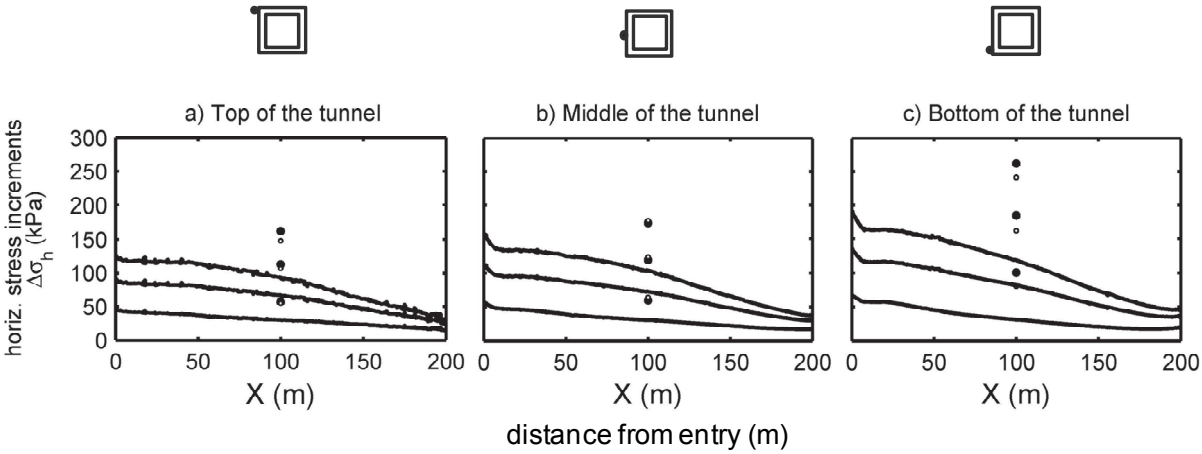


Figure 6: Horizontal earth pressure increment induced by prescribed displacements at the level of a) top; b) middle; c) bottom of tunnel. Plaxis 2D results are also reported for comparison, either as full dots (●) for calculations carried out by assuming the same friction angle along the slip surface as in 3D calculations, or as empty dots (o) for calculations carried out with the friction angle reported for 2D in Table 1.

The effect of the earth thrust on tunnel displacements, also analysed by the structural software SAP2000, is shown in Fig. 7. It is worth noting that the tunnel bears a small percentage of the initial earth thrust due to the presence of the sheet pile walls retaining the excavation, which deform before tunnel construction. To study the effect of collaboration between different sectors, different models were constructed. Case 1 in Fig. 7 is a continuous tunnel having maximum collaboration while case 3 is a tunnel whose joints are considered also extended to the capping beam. Case 2 has just the 7 tunnel joints present in the real situation. The effect of joints in the studied structure does not seem very significant, globally, on displacements. The similar overall trend of displacements in cases 1 and 2 is justified by the fact that the rows of piles well confine all the sectors. Nevertheless, the non-negligible contribution of relative displacements calculated at joint locations in case 2 seems in qualitative agreement with the out of plane separation of tunnel segments observed in-situ. The presence of joints in a tunnel crossing a landslide might be useful even though it can increase displacements because it can help to accommodate the shear deformations throughout the tunnel length. In cases of a local instability of some landslide portion, joints can help to isolate the effects mainly to the affected tunnel segment rather than "dragging" the whole structure with it.

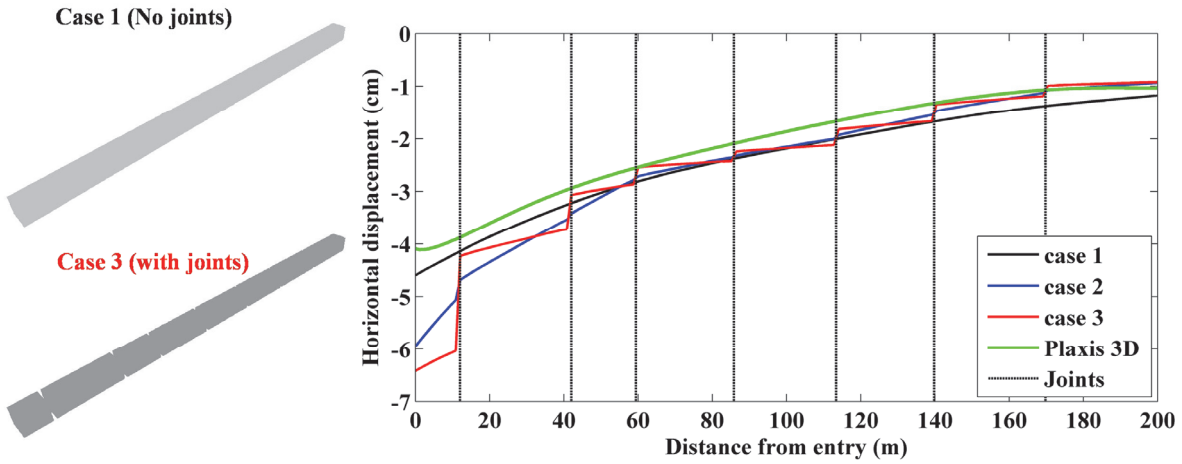


Figure 7: Deformed shape of the tunnel obtained by using different models in Plaxis 3D (Prescribed displacements u*=40 cm) and SAP2000. Displacements are relative to the mid-height of the box structure.

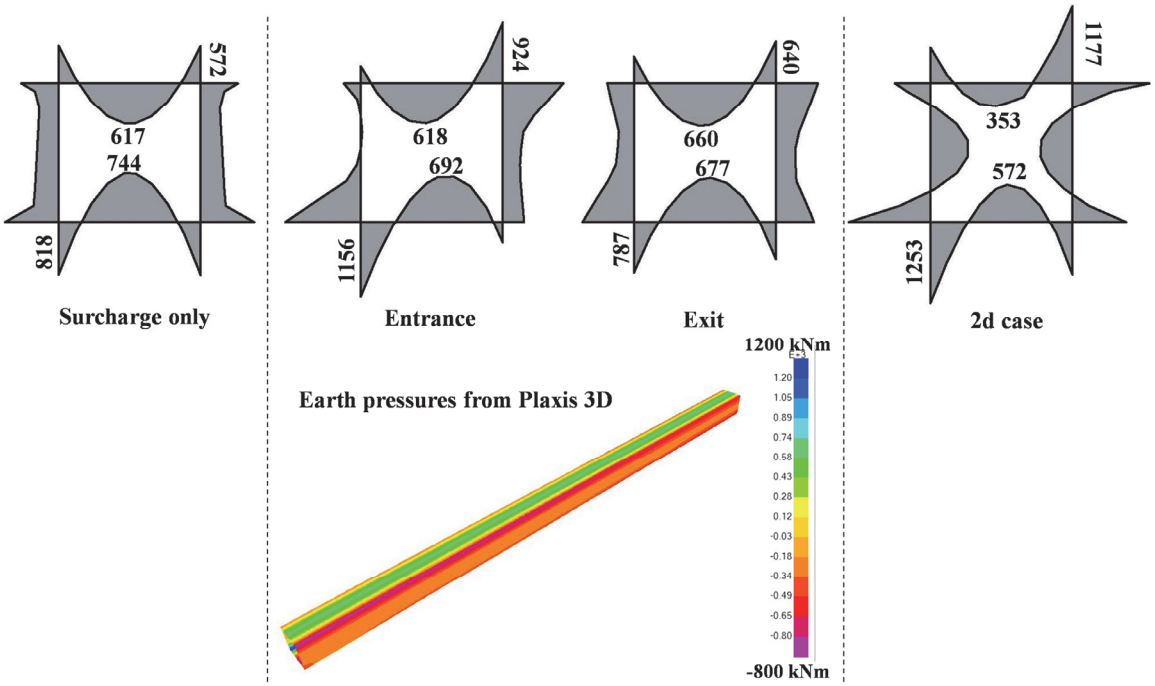


**Figure 8:** SAP2000 models results: bending moments in tunnel lining in 3D conditions (effect of surcharge only in the middle section, effect of surcharge and landslide thrust at entrance and exit sections) and 2D conditions. Earth pressures due to the landslide were derived from Plaxis models with prescribed displacement u* = 40 cm.

The significant 3D effect in the soil-structure interaction has not negligible consequences also on tunnel's stress state. Fig. 8 reports the comparison of bending moments acting on the tunnel for the cases of a 3D model and a 2D model, both linear. As can be seen, the 2D model shows higher bending moments than the 3D model. Values in the most stressed tunnel section in 3D conditions are 1.3 times lower than those evaluated in 2D conditions. As for the section with the lower bending moment value, the ratio is 1:1.8. Apart from linear analyses, Vassallo et al. [8] performed non-linear 2D analyses to evaluate the stress-strain condition of the structure. The tunnel deformations estimated by such calculations agree satisfactorily with those measured in-situ.

## 5 CONCLUSIONS

This paper presents a case study of the interaction between a slow-moving landslide with a railway tunnel supplemented by data from in-situ inspections. Earth thrust distribution on the tunnel and its evolution with landslide displacements, and tunnel response, were analyzed by different models, each aimed at studying in detail a certain aspect of soil-structure interaction, but all taking into simultaneous consideration soil and structural behaviour. 2D models gave conservative results on earth pressure values when compared with 3D models. The tunnel behaviour analysed, in this case, is similar to that of a beam which is loaded with a non-uniform pressure distribution and develops vertical cracks due to it.

Less computationally demanding models in SAP2000 allowed to understand the role of joints in the distribution of displacements and stresses in the tunnel lining. The results showed the presence of large differences between stress values at the entrance and at the exit of the

tunnel, identifying the most affected areas in terms of possible damage and, thus, to which more attention should be paid in designing retrofit intervention.

Although not generalisable, the discussed results suggest that the realisation of joints, say every 20-30 m, should be considered in the design of tunnels crossing slow landslides to accommodate shear deformations due to landslide thrust. With respect to joint spacing, lower values on the one hand could better accommodate shear deformations but, on the other hand, would have negative consequences regarding the railway maintenance.

## ACKNOWLEDGEMENTS

The authors would like to gratefully thank Prof. C. Di Maio for contributing to this work by stimulating discussions. The Italian Rail Infrastructure Manager (RFI) is acknowledged for granting permission to access the tunnel for surveys and for providing useful information.

## REFERENCES

[1] M.F. Mansour, N.R. Morgenstern, C.D. Martin, Expected damage from displacement of slow-moving slides. **8**(1), 117–131, 2011.

[2] L. Picarelli, S. Petrazzuoli, C. Warren, Interazione tra gallerie e versanti, Le opere in sotterraneo in rapporto con l'ambiente. *Proc. IX cycle of conferences on rock mechanics and engineering*, Torino, Italy, 219-248, 2002.

[3] C. Di Maio, M. Vallario, R. Vassallo, Displacements of a large landslide in structurally complex clays, *Proceedings of XI International Symposium on Landslides and Engineered Slopes*, Banff, Alberta, Canada, 607–613, 2012.

[4] D.M. Cruden, D.J. Varnes, Landslide types and processes. *Special Report - National Research Council, Transportation Research Board* , **247**, 36–75, 1996.

[5] C. Di Maio, R. Vassallo, M. Vallario, S. Pascale, F. Sdao, Structure and kinematics of a landslide in a complex clayey formation of the Italian southern Apennines, *Engineering Geology*, **116**, 311-322, 2010.

[6] R. Vassallo, G.M. Grimaldi, C. Di Maio, Pore water pressures induced by historical rain series in a clayey landslide: 3D modeling, *Landslides*, **12**, 731–744, 2015.

[7] C. Di Maio, R. Vassallo, G. Scaringi, J. De Rosa, D.M. Pontolillo, Monitoring and analysis of an earthflow in tectonized clay shales and study of a remedial intervention by KCl wells, accepted for publication on *Italian Geotechnical Journa*l, 2017.

[8] R. Vassallo, M. Mishra, G. Santarsiero, A. Masi, Interaction of a railway tunnel with a deep slow landslide in clay shales. *Procedia Earth and Planetary Science,* **16**, 15–24, 2016.

[9] C. Di Maio, R. Vassallo, M. Vallario, S. Calcaterra, P. Gambino, Surface and deep displacements evaluated by GPS and inclinometers in a clayey slope. *Proceedings of II World Landslide Forum*, Rome, 3-9 October, vol. **2**, pp. 265-271, 2011.

[10] M. Mishra, Interaction between a slow active landslide in consistent clay and a railway tunnel. Ph.D. thesis, University of Basilicata, Potenza, Italy, 2017.

[11] R. Brinkgreve, Plaxis introductory: student pack and tutorial manual. CRC Press Inc., Boca Raton, FL, USA, 2014.

[12] CSI Computers and Structures Inc, SAP2000 integrated finite element analysis and design of structures : concrete design manual; steel design manual. Berkeley, CA, 2013.

[13] S. Scandale, Effetti dei movimenti di versante sui rivestimenti di una galleria (In Italian). Ph.D. thesis, Università di Roma la Sapienza, Roma, Italy, 2015.

[14] A. Galli, C. Di Prisco, Displacement-based design procedure for slope-stabilizing piles, *Canadian Geotechnical Journal,* **50(1)**, 41–53, 2012.

[15] C. Zhou, W. Shao, C.J. Van Westen, Comparing two methods to estimate lateral force acting on stabilizing piles for a landslide in the Three Gorges Reservoir, China. *Engineering Geology,* **173**, 41–53, 2014.

COMPDYN 2017
6th ECCOMAS Thematic Conference on
Computational Methods in Structural Dynamics and Earthquake Engineering
M. Papadrakakis, M. Fragiadakis (eds.)
Rhodes Island, Greece, 15–17 June 2017

# STATIC AND DYNAMIC BEHAVIOUR OF PILE FOUNDATIONS IN HOMOGENEOUS AND INHOMOGENEOUS SOILS

**Lutz Auersch**[1], **Greta Markfort**[1]

[1] Federal Institute of Materials Research and Testing (BAM),
D 12200 Berlin, Germany
e-mail: lutz.auersch-saworski@bam.de

**Keywords:** pile foundation, finite-element boundary-element method, pile bending stiffness, soil stiffness, continuously inhomogeneous soils, layered soils, wind energy tower.

**Abstract.** *Offshore wind energy towers are dynamically loaded by waves and wind. Pile foundations provide stiffness and damping and should be properly calculated. A combined finite-element boundary-element method for the dynamic interaction of flexible structures and the soil has been developed. The flexible structures such as single piles or complete wind energy towers are modeled by the finite element method whereas the homogeneous or layered soil is modeled by the boundary element method which uses the Green's functions for interior loads in the layered half-space to establish the dynamic stiffness matrix of the soil. Soils with a stiffness that is continuously increasing with depth can be modeled as multi-layer soils with step-wise increasing stiffness. The effects of different parameters such as the stiffness of the soil, the axial and bending stiffness of the pile, and the radius of the cylindrical contact area will be analysed for the different components of excitation (vertical, horizontal, rotation and coupling). The results can be determined as specific power laws which are different for the different load cases and for the different soil models (Winkler support, homogeneous continuum, continuum with increasing stiffness). The dynamic effect of radiation damping will be analysed by the frequency-dependent compliance functions. A clear layering of the soil can cause noticeable changes in the dynamic compliances as reductions of the stiffness and the damping in certain frequency ranges (below and around layer resonance frequencies). The distribution of the displacements along the pile help to explain the observed laws. An example of an offshore wind energy tower has been modeled and calculated for wind, wave and weight loads. The resonances of the tower are usually limited by the radiation damping which is strongest for a soft soil.*

## 1 INTRODUCTION

The problem of the foundation of wind energy towers is outlined in Figure 1. The high (offshore) wind energy towers are founded on thick monopiles or on jackets which stand on four thinner piles. This contribution presents a method to calculate the dynamics of piles in a continuum soil (section 2), performs a parametric study for a single jacket pile in a homogeneous soil (section 4) or different inhomogeneous soils (section 5) and demonstrates the consequences for a wind energy tower on a monopile (section 6).

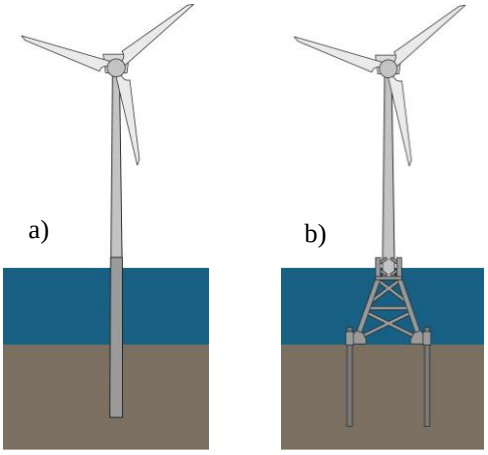


Figure 1: Offshore wind energy towers with a) monopile foundation and b) jacket-pile foundation.

## 2 COMBINED FINITE-ELEMENT BOUNDARY-ELEMENT METHOD

The dynamic soil-structure interaction is analysed by a combined finite-element boundary-element method [1]. Flexible structures such as beams, plates, walls, box-type buildings, railway tracks, single piles and pile groups are modeled by the finite element method whereas the homogeneous or layered soil is modeled by the boundary element method. A point load, a wheel-set load or and a wave field have been used as excitation. In this contribution, single piles and wind energy towers are presented.

The basis is the point-load solution (Green's function) for a layered soil. The Green's functions are calculated by the following procedure. For each layer, a 4x4 symmetric stiffness matrix is calculated in wave number domain [2]. All layer matrices and the matrix of the underlying half-space are assembled in a stiffness matrix $\mathbf{K}_S$ of the whole soil body, which is inverted to a compliance matrix **N**. The appropriate elements of this compliance matrix, for example $N_{zz}(k,z_1,z_2)$ for an interior source at $z_1$ and an interior response at $z_2$, are integrated over the wave number $k$ to get the displacement at a distance $r$ of the source

$$F_{zz}(r,z_1,z_2)=\frac{1}{2\pi}\int_0^\infty N_{zz}(k,z_1,z_2)\mathrm{J}_0(kr)k\,dk \tag{1}$$

Similar formulas hold for the other four components of the Green's function $F$. These Green's functions are used in the combined finite-element boundary-element method to establish a boundary stiffness matrix of the soil (in frequency domain, for $n$ discrete points). A displacement matrix is compiled directly by using the point-load solutions

$$\mathbf{u}(\mathbf{x}_\beta)=\mathbf{F}(\mathbf{x}_\beta-\mathbf{x}_\alpha)\,\mathbf{p}(\mathbf{x}_\alpha) \qquad \mathbf{u}_\beta=\mathbf{F}_{\beta\alpha}\,\mathbf{p}_\alpha \tag{2}$$

At the loading point, this would yield infinite values. Therefore, mean values on the cylindrical (in case of a pile) or circular surface (in case of a surface foundation) are calculated as the diagonal elements of the displacement matrix

$$\mathbf{u}_\alpha=\frac{1}{A_\alpha}\int_{A_\alpha}\mathbf{F}(\mathbf{x}-\mathbf{x}_\alpha)\mathbf{p}(\mathbf{x}_\alpha)\,dA \qquad \mathbf{u}_\alpha=\mathbf{F}_{\alpha\alpha}\,\mathbf{p}_\alpha \tag{3}$$

The force matrix of the soil is the identity matrix, as 1) the Green's function has no stresses at the soil surface and 2) the stresses in the interior do not yield forces at another pile element (as far as the dimension is small compared to the distance and wavelength). Thus, the inverse of the displacement matrix $\mathbf{U}=[\mathbf{F}_{\alpha\beta}]_{\alpha,\beta=1,n}$ is the boundary stiffness matrix $\mathbf{K}_S$ of the soil

which is added to the finite-element stiffness matrix $\mathbf{K}_P$ of the structure to yield the global dynamic stiffness matrix $\mathbf{K}_S+\mathbf{K}_P$ of the combined structure-soil system, and the FEBE method is complete.

## 3 PILE AND SOIL PARAMETERS AND THEIR VARIATION

A typical tubular steel pile of a jacket foundation of an offshore wind energy tower is analysed with the following standard parameters [3]: The mass density $\rho_P = 7.8\ 10^3$ kg/m$^3$, and the elasticity modulus $E_P = 2.1\ 10^{11}$ N/m$^2$ of steel, a circular cross section of radius $R = 1$ m, a wall thickness of $t = 0.03$ m, yielding a longitudinal stiffness of $EA = 0.4\ 10^{11}$ N, a bending stiffness of $EI = 1.9\ 10^{10}$ Nm$^2$, and a mass per length $m' = 1.48\ 10^3$ kg/m. The length of the pile is $L = 30$ m, the material damping is defined as $D_P = 0$.

The standard soil is homogeneous with the following parameters: The shear modulus is $G = 8\ 10^7$ N/m$^2$, the mass density $\rho = 2\ 10^3$ kg/m$^3$, the material damping $D = 2.5\%$, and the Poisson's ratio $\nu = 0.33$, which yield the shear wave velocity $v_S = 200$ m/s, and the compressional wave velocity $v_P = 400$ m/s.

The stiffness of the homogeneous soil is varied as $G = 2, 4.5, 8, 18\ 10^7$ N/m$^2$. Three other soil models are analysed: layered soils and two soils with a continuous variation. The continuous variations are defined as a function of $z$

$G(z) = G'z$ linear variation and

$G(z) = G^*\sqrt{z}$ parabolic variation.

The new soil parameters are varied as $G' = 2, 4.5, 8, 18\ 10^7$ N/m$^3$, and $G^* = 2, 4.5, 8, 18\ 10^7$ N/m$^{2.5}$. By this definition all soil models have the same stiffness at 1 m depth. The layered soil has a soft top layer of $G_1 = 2\ 10^7$ N/m$^2$ and a stiff underlying half-space of $G_2 = 5\ 10^8$ N/m$^2$, and the layer height is varied as $H = 2.5, 5, 10, 20, 30$ m.

The results are presented as four frequency-dependent complex compliance functions for the horizontal, the vertical, the rocking and the horizontal-rocking coupling mode. The static deformations of all pile foundations are given in the appendix for a better interpretation.

## 4 COMPLIANCE FUNCTIONS OF PILES IN HOMOGENEOUS SOILS

The compliance functions of the pile foundations are presented as amplitude and phase in the frequency range between 0 to 16 Hz. The principle behavior can be discussed with the horizontal component in Figure 2a. The amplitudes show only little variations with frequency, whereas the phase is continuously decreasing with frequency. The horizontal component has the most regular phase behavior, the phase delay increases almost linearly with frequency.

The corresponding horizontal deformation is shown in the Appendix, Fig. 8a. The displacement has its maximum at the top of the pile. The displacements decrease rapidly with the depth and reaches almost zero at 10 m. Therefore, it can be concluded that the standard pile of 30 m length behaves like an infinitely long pile for the horizontal vibration modes.

The vertical vibration component is completely different (Fig. 8b). The vertical displacements change only a little along the pile length of 30 m. At the pile end, there are still considerable amplitudes, and that means that the pile behaves like an almost rigid pile in the vertical direction. The rocking and coupling components display at least one change of sign before the displacements vanish at 15 or 20 m depth. The decrease is as strong as for the horizontal component, the first minimum can be found at 5 to 7 m depth.

The rocking and coupling compliances in Figure 2c and 2d can therefore be read as the compliances of infinitely long piles. They have also nearly constant amplitudes and decreasing phases. The phase delay has one difference compared to the horizontal one. It starts not at zero frequency but at a later frequency of 4 to 8 Hz (rocking) or 2 to 4 Hz (coupling). The

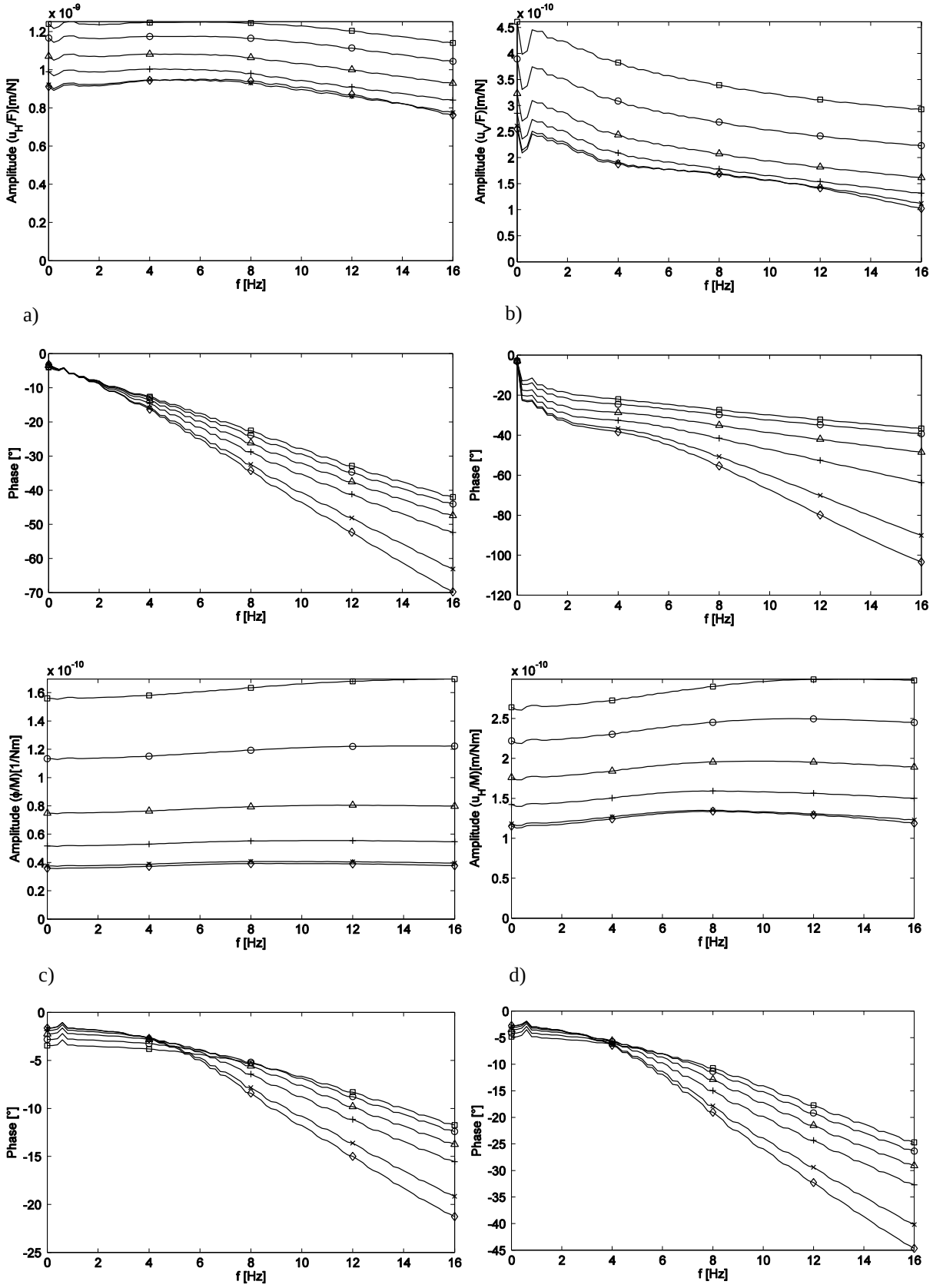


Figure 2: Amplitude and phase of the a) horizontal, b) vertical, c) rocking, and d) coupling compliance of the standard pile foundation. Variation of the wall thickness $t$ = □ 0.03, ○0.05, △ 0.1, + 0.2, ×0.5, ◇ 1 m.

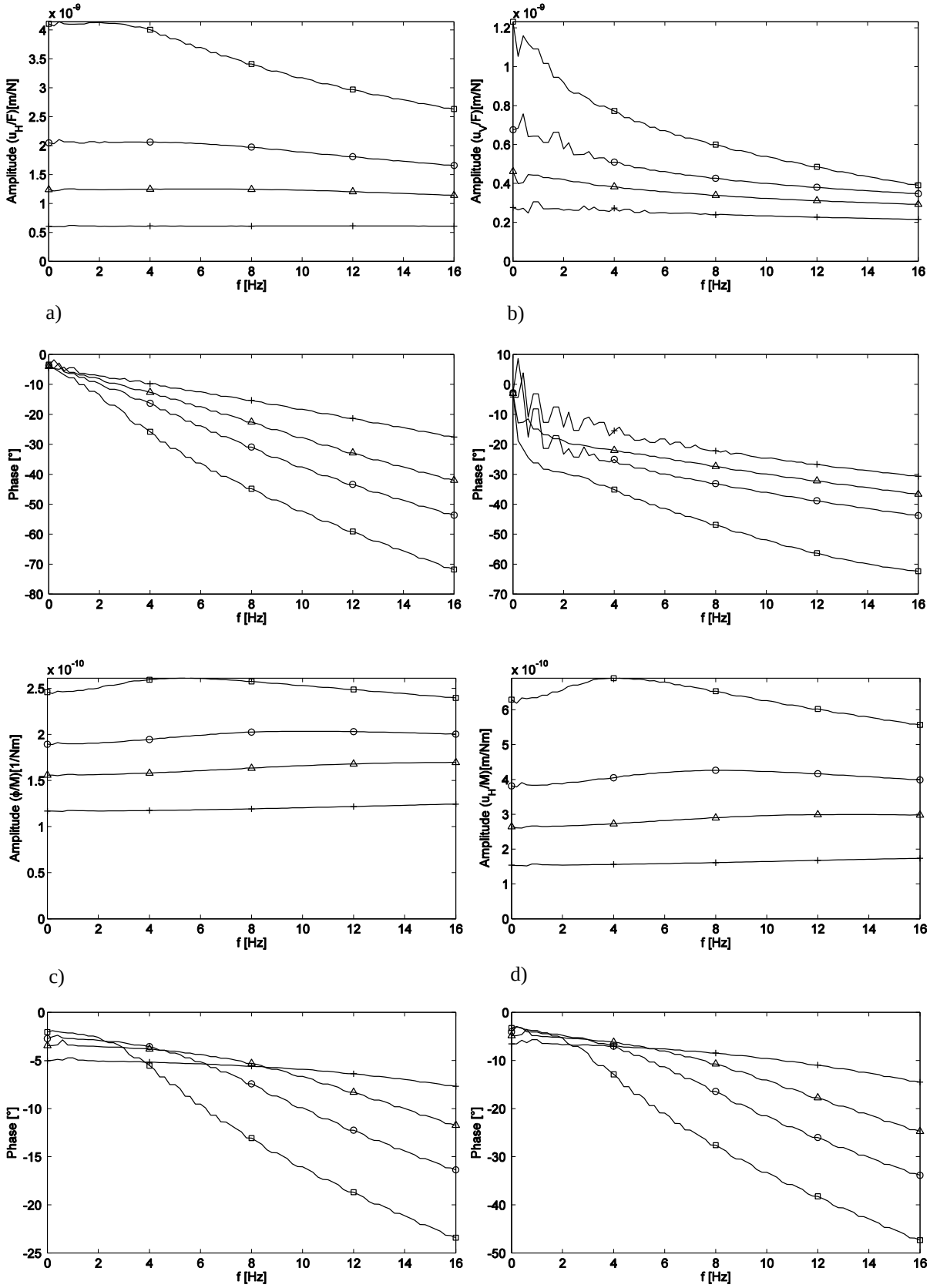


Figure 3: Amplitude and phase of the a) horizontal, b) vertical, c) rocking, and d) coupling compliance of the standard pile foundation. Variation of the soil stiffness $G$ = □ 2, ○ 4.5, △ 8, + 18 $10^7$ N/m$^2$.

maximum phase delay at 16 Hz is only 12 to 22° for the rocking and 25 to 45° for the coupling component. This is small compared to 41 to 70° for the horizontal component. This sequence horizontal, coupling, rocking will be found also for other characteristics.

The influence of the pile bending stiffness on the compliances is strongest for the rocking, mid-strong for the coupling, and weakest for the horizontal component. The highest factor between the softest and the stiffest pile is $A_1/A_2 = 1.6/0.4 = 4$ (rocking), the lowest factor is $A_1/A_2 = 1.25/0.9 = 1.4$ (horizontal), whereas the ratio of the bending stiffness is $EI_2/EI_1 = 0.79/0.09 = 8.8$.

While Figure 2 shows the influence of the pile bending stiffness, Figure 3 demonstrates the influence of the soil stiffness which is varied in the range of $G_2/G_1 = 18/2 = 9$. The horizontal response varies quite strong between 0.6 and 4.1 $10^{-9}$ m/N, a factor of 7 close to the variation of the soil stiffness. Quite contrary, the rocking amplitude displays the weakest influence of the soil stiffness. The phases of the compliance, which correlate well with the damping of the pile foundation, are strongly influenced by the soil stiffness for all components. The maximum phase delay at 16 Hz is 28 to 71° (horizontal), 14 to 48° (coupling) and 7.5 to 23° (rocking). (This is approximately $\varphi \sim G^{-0.5}$, whereas the influence of the pile stiffness is only $\varphi \sim EI^{-0.25}$.) The damping by the radiation into the soil starts at higher frequencies for the stiffer soils, at about 12 Hz for the rocking and at about 8 Hz for the coupling component. The damping of the horizontal component starts at zero frequency.

When looking at the deformations in Fig. 9, the influence of the soil is clearly stronger than the influence of the pile (Fig. 8) although the variations of $G_2/G_1 \approx EI_2/EI_1 \approx 9$ are almost the same. A soft soil yields a much deeper horizontal deformation (up to $z = 15$ m) than a stiff soil ($z = 5$ m).

## 5 THE PILES IN INHOMOGENEOUS SOILS

### 5.1 Soil with parabolic increase of stiffness with depth (“parabolic soil”)

A soil body is loaded by its own weight. The static pressure is linearly increasing with depth and yields a stiffening of the soil. The influence of the static pre-stress is in that way that the stiffness of the soil increases with the square root of the depth. This natural soil model has the smoothest variation of $G$ and is presented in Figure 4 (compliance functions) and Figures 10 (deformation).

The deformation of the “parabolic soil” (Fig. 10) is more restricted to the near-surface soil compared to the homogeneous half-space (Fig. 9). This holds for all compliance components. The amplitudes of the compliances seem to follow the same rules as for the homogeneous soil: The influence of the soil is increasing in the order rocking, coupling, and horizontal component. The main difference to the homogeneous soil can be found for the phase functions (the damping). The damping values are considerably reduced, see Table 1. The starting point of the radiation damping is shifted to higher frequencies, for example from 2 to 4 Hz for the softest soil and the rocking component (Figs. 3c and 4c). Moreover, the damping of the horizontal component does no longer start at zero frequency, but has its own starting frequency between 2 and 5 Hz (Fig. 4a).

### 5.2 Soil with linear increase of stiffness with depth (“linear soil”)

The soil model with a linearly increasing stiffness is a more theoretical model which has a stronger variation $G(z)$. The shear modulus at 1 m depth is the same for the homogeneous, the parabolic and the linear soil model. The stiffness of shallower depths is lowest for the linear and highest for the homogeneous soil model, and the stiffness at greater depths is highest for

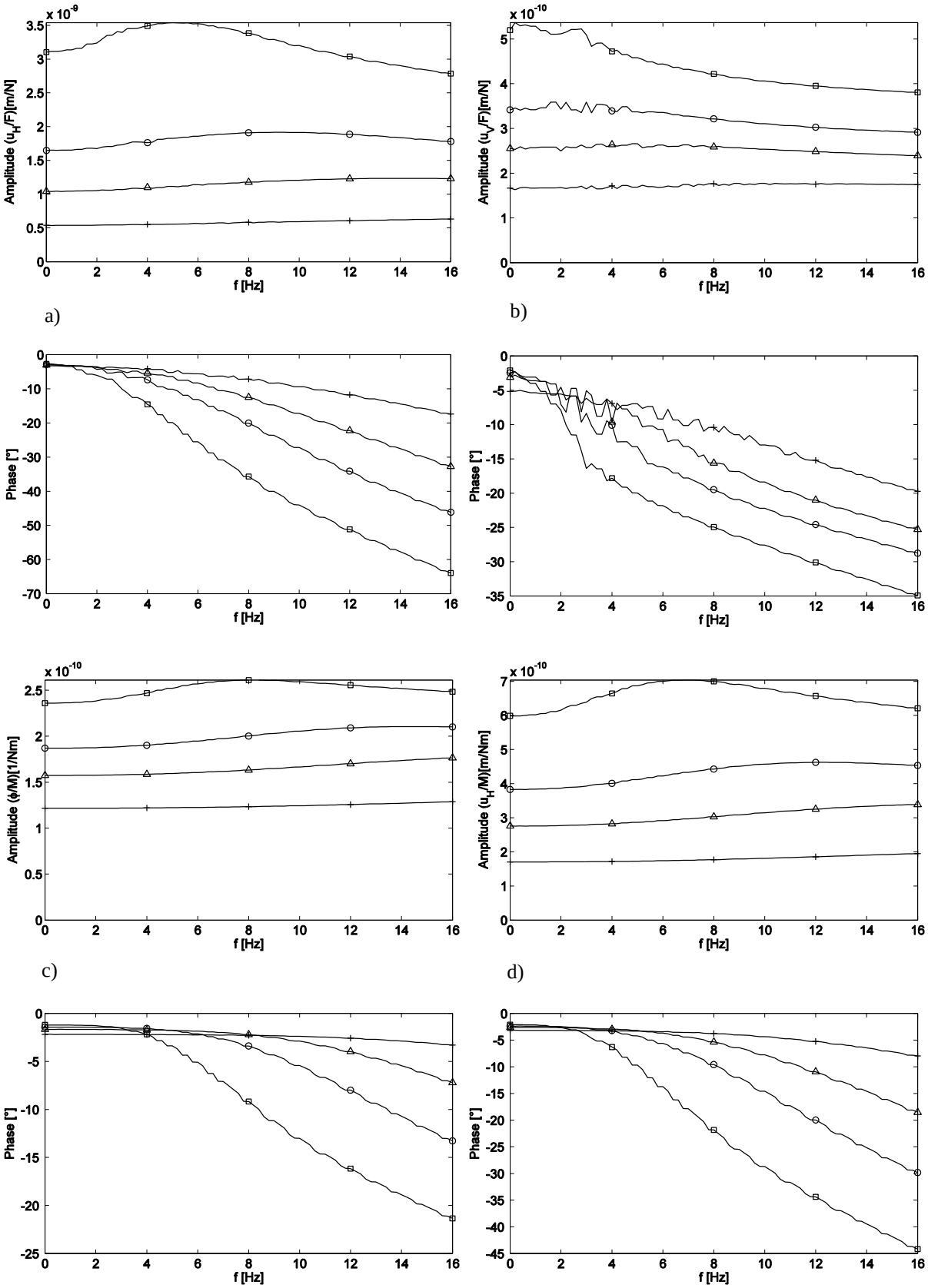


Figure 4: Amplitude and phase of the a) horizontal, b) vertical, c) rocking, and c) coupling compliance of the standard pile in parabolic soil. Variation of the soil stiffness $G^*$ = □ 2, ○ 4.5, △ 8, + 18 $10^7$ N/m$^{2.5}$.

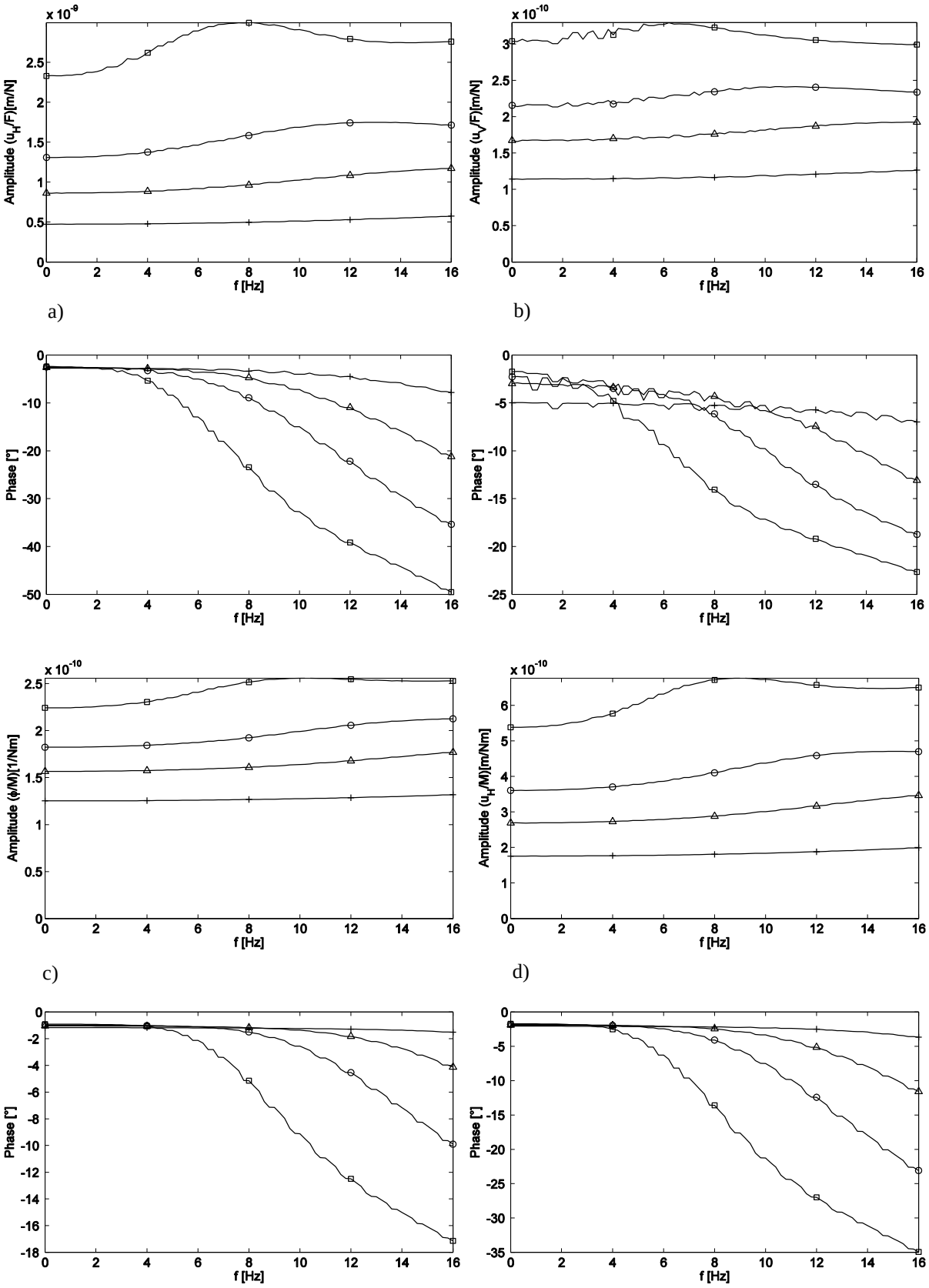


Figure 5: Amplitude and phase of the a) horizontal, b) vertical, c) rocking, and c) coupling compliance of the standard pile in linearly varying soil. Variation of the soil stiffness $G'$ = □ 2, ○ 4.5, △ 8, + 18 $10^7$ N/m$^3$.

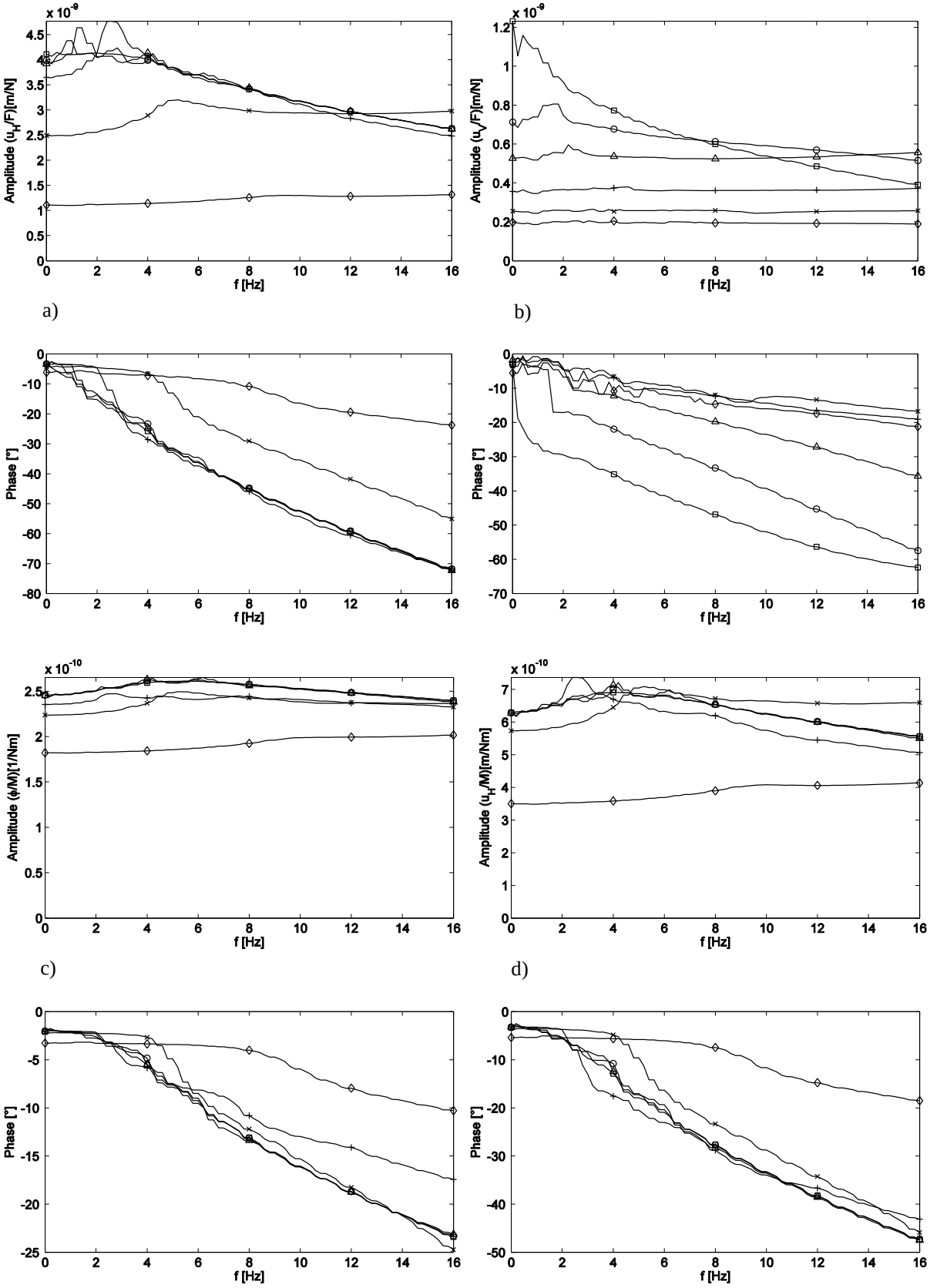


Figure 6: Amplitude and phase of the a) horizontal, b) vertical, c) rocking, and c) coupling compliance of the pile in layered soils ($G_1/G_2$ = 2/50), variation of the layer height $H$ = □ ∞, ○ 30, △ 20, ＋10, × 5, ◇ 2.5 m.

the linear and lowest for the homogeneous soil. The linear soil model shows the same characteristics as the parabolic soil, but all in a stronger realization. The deformation is concentrated on shallower depths (Fig. 11), the damping (the phase delay) starts at higher frequencies and reaches lower maximum values, see Figure 5 and Table 1.

| variation | Figure | horizontal | coupling | rocking |
|---|---|---|---|---|
| pile stiffness | 2 | 40°-70° | 25°-45° | 12°-22° |
| homogeneous soil | 3 | 28°-71° | 14°-48° | 7.5°-24° |
| parabolic soil | 4 | 18°-63° | 8°-45° | 3°-22° |
| linear soil | 5 | 8°-50° | 3°-35° | 1.5°-17° |
| layered soil | 6 | 22°-72° | 18°-48° | 10°-23° |

Table 1: Damping expressed as the phase delay of the different compliance components for the parameter variations in Figures 2 to 6.

### 5.3 Layered soils with different layer heights

The layered soils have some similarities to the continuously varying soil models, but also some additional characteristics. Similarly, the displacements approach faster the zero (Fig. 12 compared to Fig. 9). Similarly, the phase delays are smaller (Fig. 6). In addition, small peaks can be found in the compliances, for example at $f$ = 0.7, 1.3, 2.6, 4.8, 8.5 Hz for the horizontal component (Fig. 6a). At the same frequencies, the phase delay (the radiation damping) starts. These frequencies are the resonant frequencies of the layer $f_L = v_S/4H$ (= 0.8, 1.25, 2.5, 5, 10 Hz). Deep layers have a low layer frequency so that only the low frequencies are concerned. On the other hand, the shallow layers affect a wider frequency range, but it should be stated that the damping is not zero below the layer frequency. The low frequency damping follows the damping of the stiff underlying half-space. Another special point is that a layering deeper than 10 m has little effect on the results. The results are almost the same as for the soft half-space (curve □ in Fig. 6) because the deformation for a soft half-space does not reach beyond 10 m (Fig. 9). In case of shallow layers, the compliances are reduced by the stiff underlying half-space, most strongly for the horizontal component where $A_L/A_H = 1/4$ for $H$ = 2.5 m and $A_L/A_H = 2.5/4 = 0.6$ for $H$ = 5 m.

## 6 EVALUATION OF STATIC RULES

The influence of the bending stiffness $EI$ of the pile and the stiffness $G$ of the soil on the compliances of the pile foundation can be analysed in more detail. It is convenient to use the ratio of the pile and soil stiffness as the elastic length

$$l = \sqrt[4]{\frac{EI}{G}} \quad . \tag{4}$$

The static compliances of an infinitely long pile can then be presented as

$$\frac{u}{F} = \frac{1}{Gl} f_1\left(\frac{R}{l}\right) \qquad \frac{u}{M} = \frac{1}{Gl^2} f_2\left(\frac{R}{l}\right) \qquad \frac{\varphi}{M} = \frac{1}{Gl^3} f_3\left(\frac{R}{l}\right) \tag{5}$$

with the n-th power ($n$ = 1, 2, 3) of the elastic length. The numerical results of section 4 (homogeneous soils) are evaluated for the functions $f_i(R/l)$ which are power functions with the power $q$

$$\frac{u}{F} \sim \frac{1}{Gl}\left(\frac{R}{l}\right)^{-q} \quad \text{or} \quad \frac{F}{u} \sim Gl\left(\frac{R}{l}\right)^{q} = R^q EI^{\frac{1}{4}-\frac{q}{4}} G^{\frac{3}{4}-\frac{q}{4}} = R^q EI^{0.13} G^{0.87} \tag{6}$$

with the power $q = 0.49$ for the horizontal compliance in a homogeneous soil. The equation expresses the strong influence of the soil on the horizontal compliance and, at the same time, the weak influence of the pile. The exponents of the power laws for all compliance or stiffness components are compiled in Table 2.

In case of the continuously inhomogeneous soils, the stiffness of the soil is expressed by different moduli which yield different elastic lengths

$$G^* = \frac{G}{\sqrt{z}} \quad \text{and} \quad l^* = \sqrt[4.5]{\frac{EI}{G^*}} \qquad\qquad G' = \frac{G}{z} \quad \text{and} \quad l' = \sqrt[5]{\frac{EI}{G'}} \tag{7}$$

where the fourth root is replaced by a higher root with 4+p, p = 0.5 or 1.0. Finally, the stiffnesses of different components and different soil models can be calculated as

$$K \sim R^q EI^{\frac{n+p-q}{4+p}} G^{1-\frac{n+p-q}{4+p}} \tag{8}$$

The exponents of all power laws follow from the corresponding exponent $q$, which has been derived from the FEBEM calculations, and are given in Table 2.

| parameter | component | homogeneous | parabolic | linear |
|---|---|---|---|---|
| radius R | horizontal | 0.49 | 0.59 | 0.62 |
| | coupling | 0.57 | 0.58 | 0.56 |
| | rocking | 0.36 | 0.33 | 0.36 |
| pile stiffnesss EI | horizontal | 0.13 | 0.20 | 0.28 |
| | coupling | 0.36 | 0.43 | 0.49 |
| | rocking | 0.66 | 0.70 | 0.73 |
| soil stiffness G, G*, G’ | horizontal | 0.87 | 0.80 | 0.72 |
| | coupling | 0.64 | 0.57 | 0.51 |
| | rocking | 0.34 | 0.30 | 0.27 |

Table 2: Exponents of the power laws for the static stiffnesses of pile foundations

The strong influence of the soil for horizontal excitation can be found for all soil models as well as the reduced soil influence for the coupling and especially for the rocking excitation. The more inhomogeneous the soil is, the weaker is its influence on the foundation stiffness components. While a homogenous soil has a much stronger influence than a Winkler support, the linearly inhomogeneous soil has nearly the lower powers of the Winkler soil (0.75, 0.5 0.25 for the influence of the homogeneous bedding modulus on the horizontal, coupling and rocking component). The influence of the pile radius as parameter of the pile-soil contact has been found similarly strong for the three continuous soil models.

## 7 WIND ENERGY TOWER

An offshore wind energy tower of total length $L = L_T+L_W+L_P$ = 70+20+30 m = 120 m has been modelled in detail. The tower is founded on a monopile foundation with a pile radius of $R$ = 3 m and a wall thickness of $t$ = 0.06 m. The tower has a thinner wall above the water level where the thickness is in the range of $t$ = 0.034 to 0.016 m decreasing with height. The tower

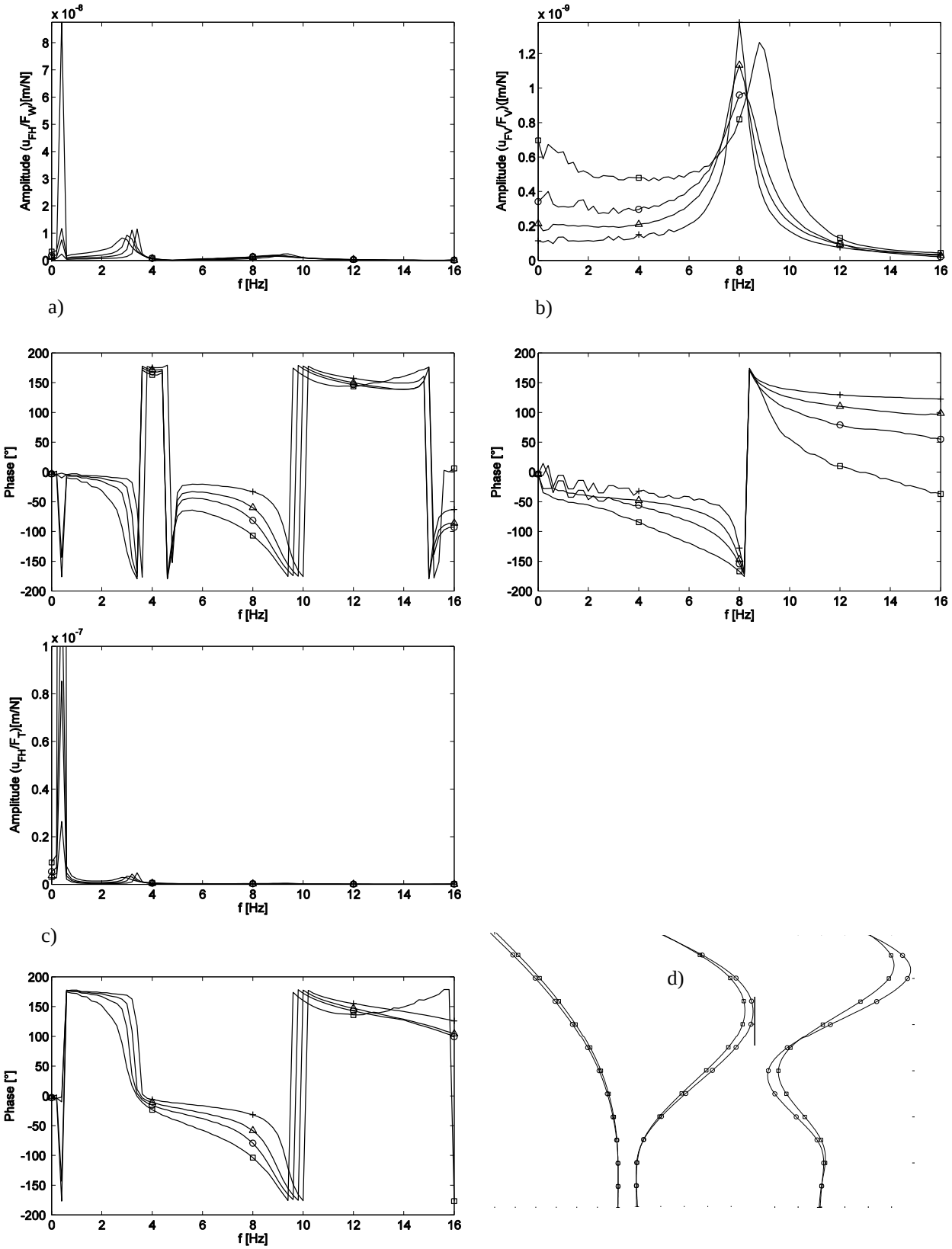


Figure 7: Amplitude and phase of the transfer functions of a wind energy tower, a) horizontal wave load, b) vertical top load, c) horizontal wind load, response at the top of the pile, variation of the soil stiffness $G$ = □ 2, ○ 4.5, △ 8, + 18 $10^7$ N/m$^2$. d) 1$^{st}$, 2$^{nd}$, 3$^{rd}$ horizontal mode

radius becomes smaller with increasing height from $R$ = 3 m to 2 m on the top 35 meters. On the top of the tower, a concentrated mass of 300.000 kg is assumed to represent the rotor and the nacelle. The wind energy tower is excited by horizontal wind loads $F_T$ at the top of the tower, by horizontal wave loads $F_W$ at the sea level, and by vertical loads $F_V$ at the top of the tower (machine loads, weight). The corresponding horizontal and vertical responses are analysed at the top of the pile foundation.

Figure 7 shows the transfer functions of the pile foundations for all three excitations and for four different homogeneous soils. The vertical load yields a vertical resonance at 8 Hz (Fig. 7b). The horizontal loads yield three resonances up to 16 Hz (Fig. 7a,c). The vibration modes at 0.4, 3.6, and 8.4 Hz in Figure 7d can be characterized as 1) a dominant tower top motion, 2) a dominant mid-tower vibration with one maximum, and 3) a tower vibration with two opposite maxima. The heavy top mass has reduced amplitudes for the 3rd and especially for the 2nd vibration mode.

The 2nd and 3rd horizontal resonance frequencies are increased with a stiffer soil. The resonance amplitudes also increase with increasing soil stiffness. Thus, a soft soil is advantageous because of its higher radiation damping. On the other hand, the soft soil causes a higher static response which can yield a higher resonance amplitude as in Figure 7b. If the material damping is dominant over the small radiation damping at very low frequencies, the order of the amplitudes can be even reverse (Fig. 7a). Obviously, the correct behavior of the pile foundation is important for the response of wind energy towers to dynamic loads.

## 8 CONCLUSION

The soil has a strong influence on the dynamic compliance, the stiffness and damping, of pile foundations. This influence has been quantified for homogeneous, continuously inhomogeneous, and layered soil models. The influence of the soil increases from the rocking to the coupling to the horizontal foundation stiffness. The influence also increases from the most inhomogeneous soil with linearly increasing modulus to the less inhomogeneous parabolic soil to the homogeneous soil. The same rules hold for the damping which is strongest for a homogeneous soil and the horizontal component. The damping of all inhomogeneous soils and the damping of the rocking and coupling component have almost zero damping at low frequencies. The results for the dynamic pile compliances are used to calculate the response of an example wind energy tower demonstrating the damping effects of different homogeneous soils.

## ACKNOWLEDGEMENT

G. Markfort has performed the calculations and evaluations at BAM as her bachelor thesis for the University of Applied Sciences Kiel, Prof. C. Keindorf. L. Auersch has developed the FEBEM-software, has been the adviser, and has written the article.

## REFERENCES

[1] L. Auersch, *Wechselwirkung starrer und flexibler Strukturen mit dem Baugrund insbesondere bei Anregung durch Bodenerschütterungen*. BAM-Research Report 151/Thesis, Berlin, 1988.

[2] L. Auersch, Wave propagation in the elastic half-space due to an interior load and its application to ground vibration problems and buildings on pile foundations. *Soil Dynamics and Earthquake Engineering* **30**, 925-936, 2010.

[3] G. Markfort, *Dynamische Steifigkeiten in Abhängigkeit von Boden- und Pfahlparametern bei Tiefgründungen von Offshore-Windenergieanlagen*. Bachelor Thesis, University of Applied Sciences, Kiel, 2017.

## APPENDIX: PILE DEFORMATIONS

The following Figures 8 to 12 present the static deformations of all pile foundations of the parameter variation. Sub-figures a show the horizontal displacements due to the horizontal load which are usually smoothly approaching zero. The vertical displacements due to the vertical load in sub-figures b have only a weak reduction along the pile length. The response to a moment is given in sub-figures c and d (the rotation and the displacement) which both show one or more changes of sign before they approach zero. The approach to zero is faster for stiffer and for more inhomogeneous soils. A softer soil or a stiffer pile yield a deeper deformation or in other words a longer elastic length means a longer or deeper deformation.

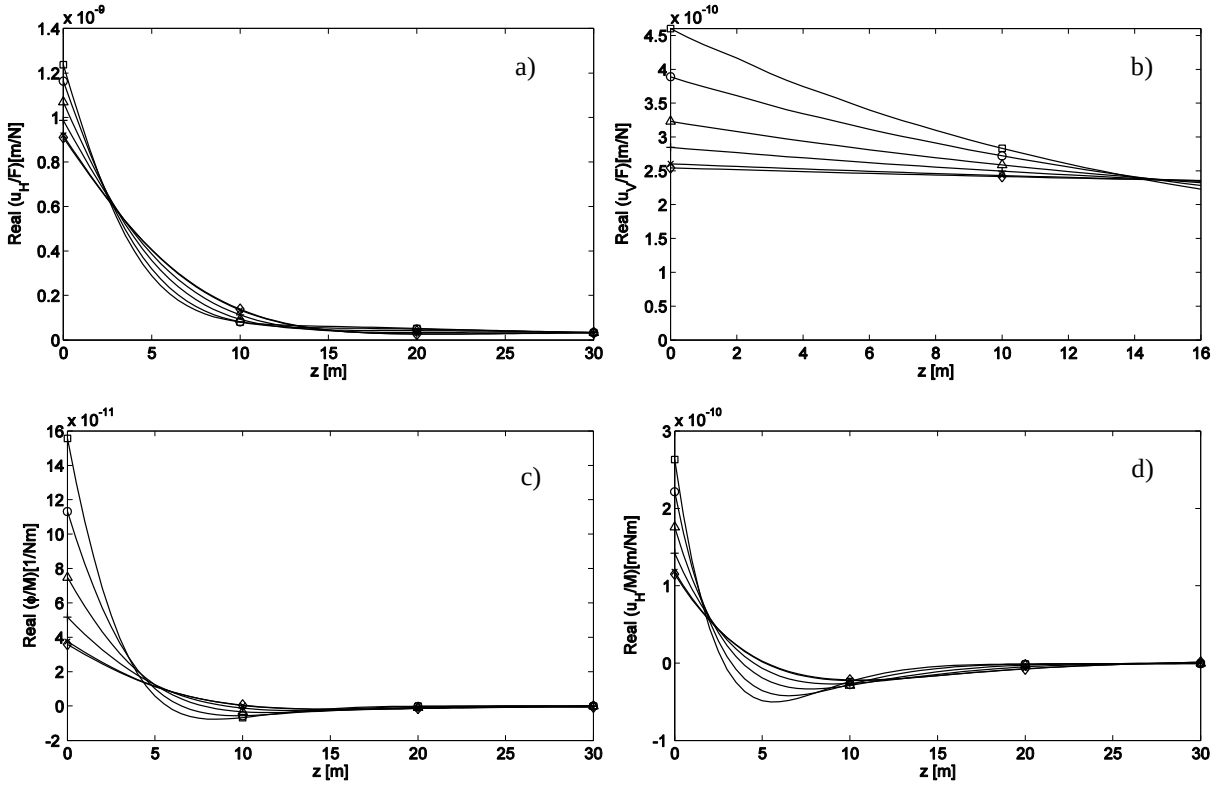


Figure 8: Static deformation of the standard pile foundation, the a) horizontal, b) vertical, c) rocking, and d) coupling component. Variation of the wall thickness $t$ = □ 0.03, ○ 0.05, △ 0.1, + 0.2, × 0.5, ◇ 1 m.

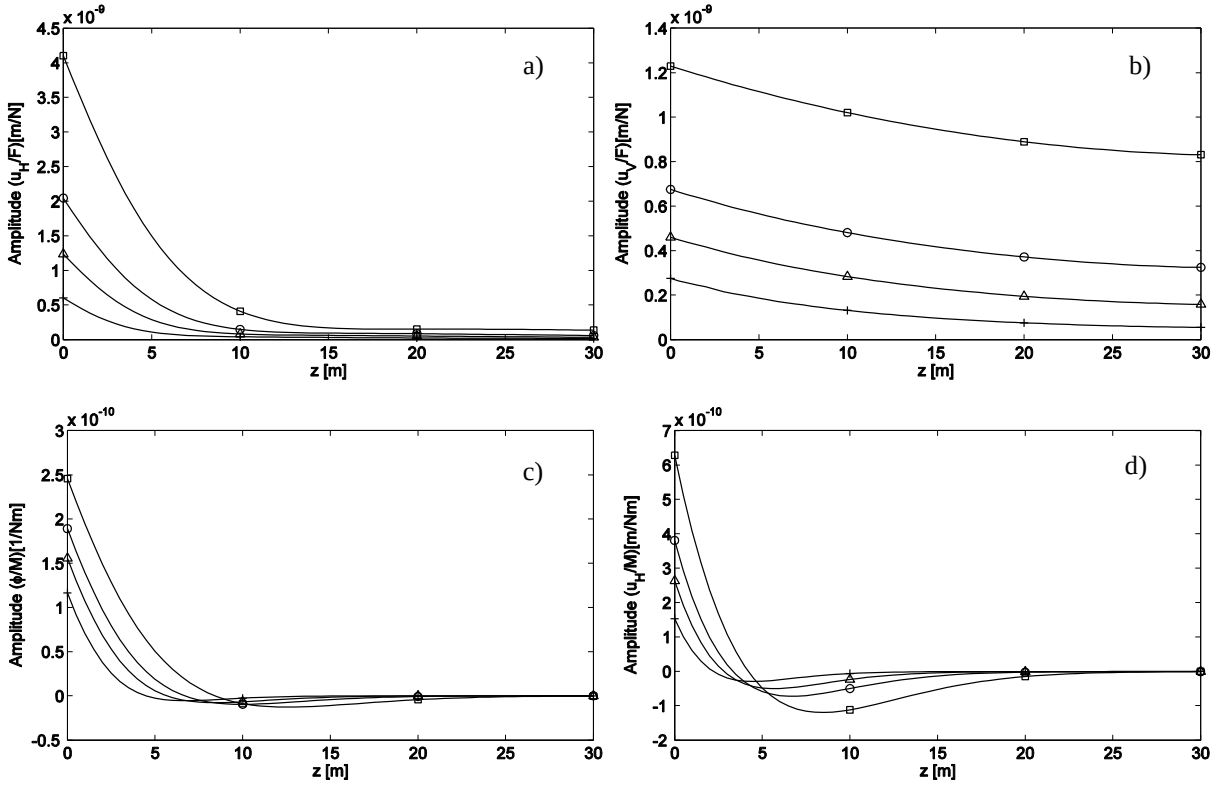


Figure 9: Static deformation of the standard pile foundation, the a) horizontal, b) vertical, c) rocking, and d) coupling component. Variation of the soil stiffness $G$ = □ 2, ○ 4.5, △ 8, + 18 $10^7$ N/m$^2$.

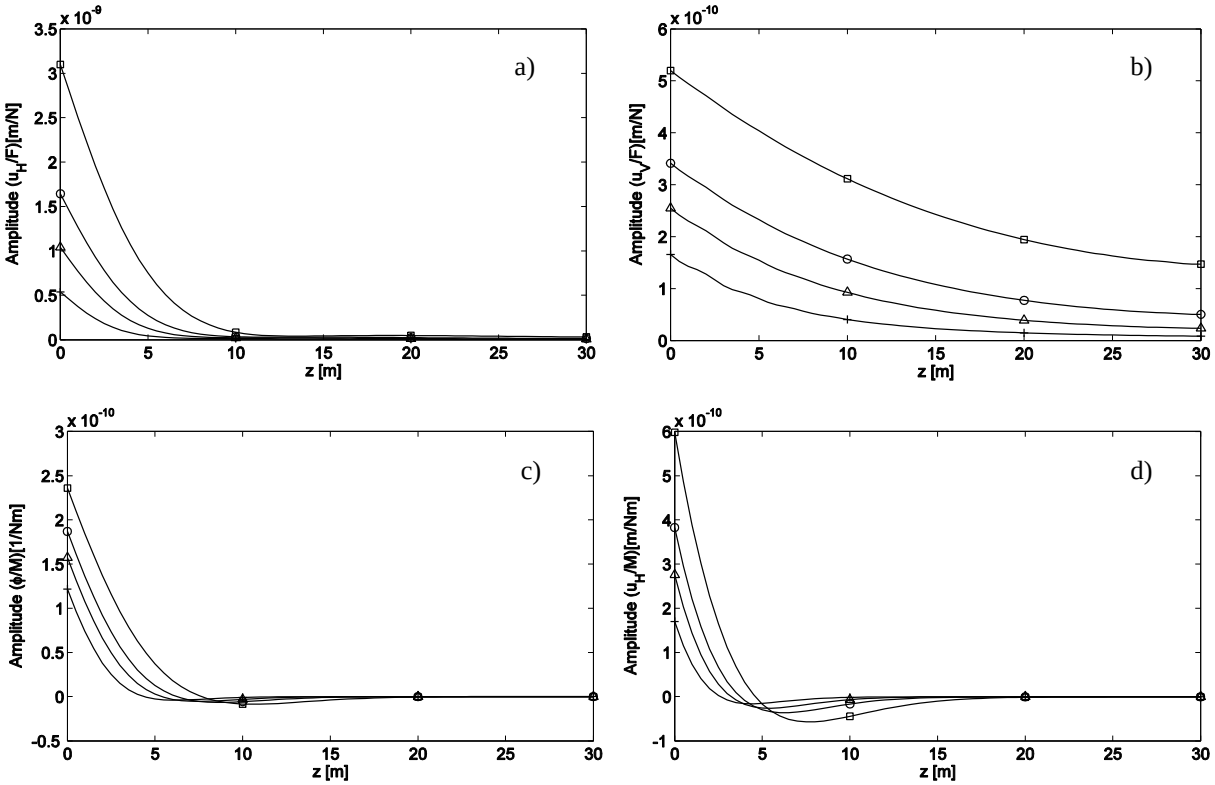


Figure 10: Static deformation of the standard pile in parabolic soil, the a) horizontal, b) vertical, c) rocking, and d) coupling component. Variation of the soil stiffness $G^*$ = □ 2, ○ 4.5, △ 8, + 18 $10^7$ N/m$^{2.5}$.

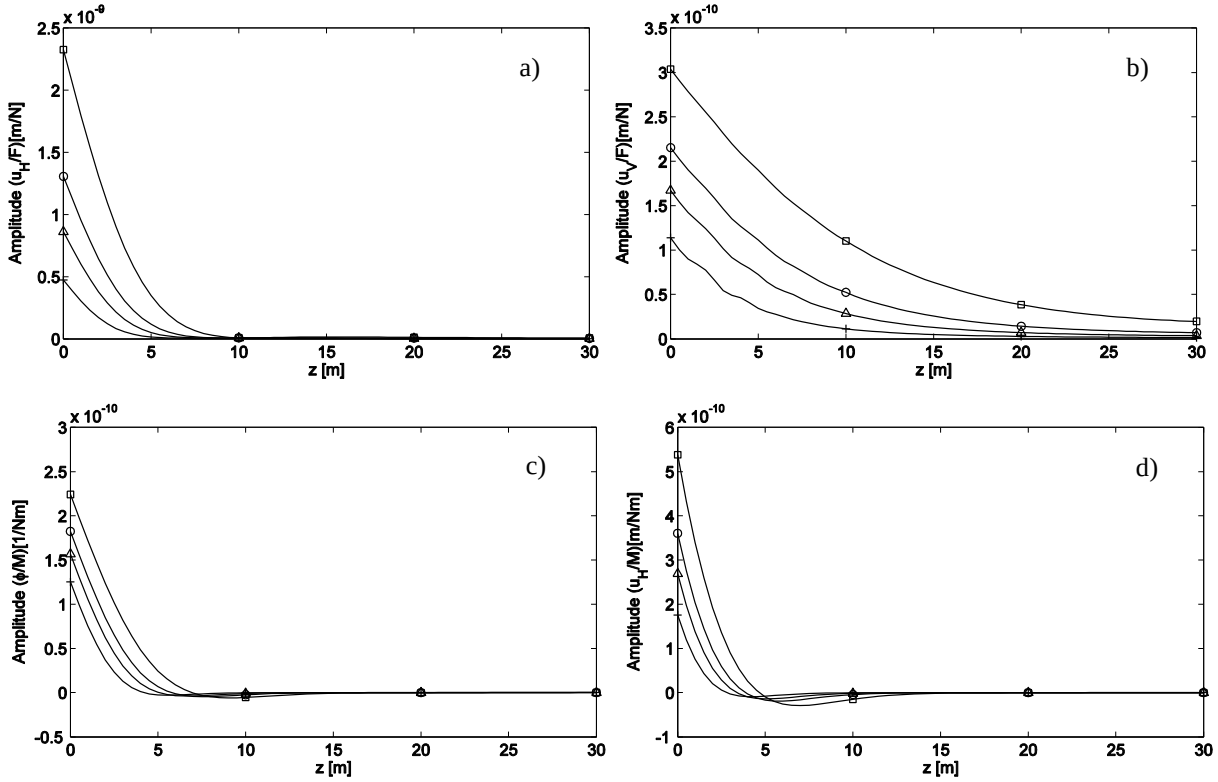


Figure 11: Static deformation of the standard pile in linearly varying soil, the a) horizontal, b) vertical, c) rocking, and d) coupling component. Variation of the soil stiffness $G'$ = □ 2, ○ 4.5, △ 8, + 18 $10^7$ N/m$^3$.

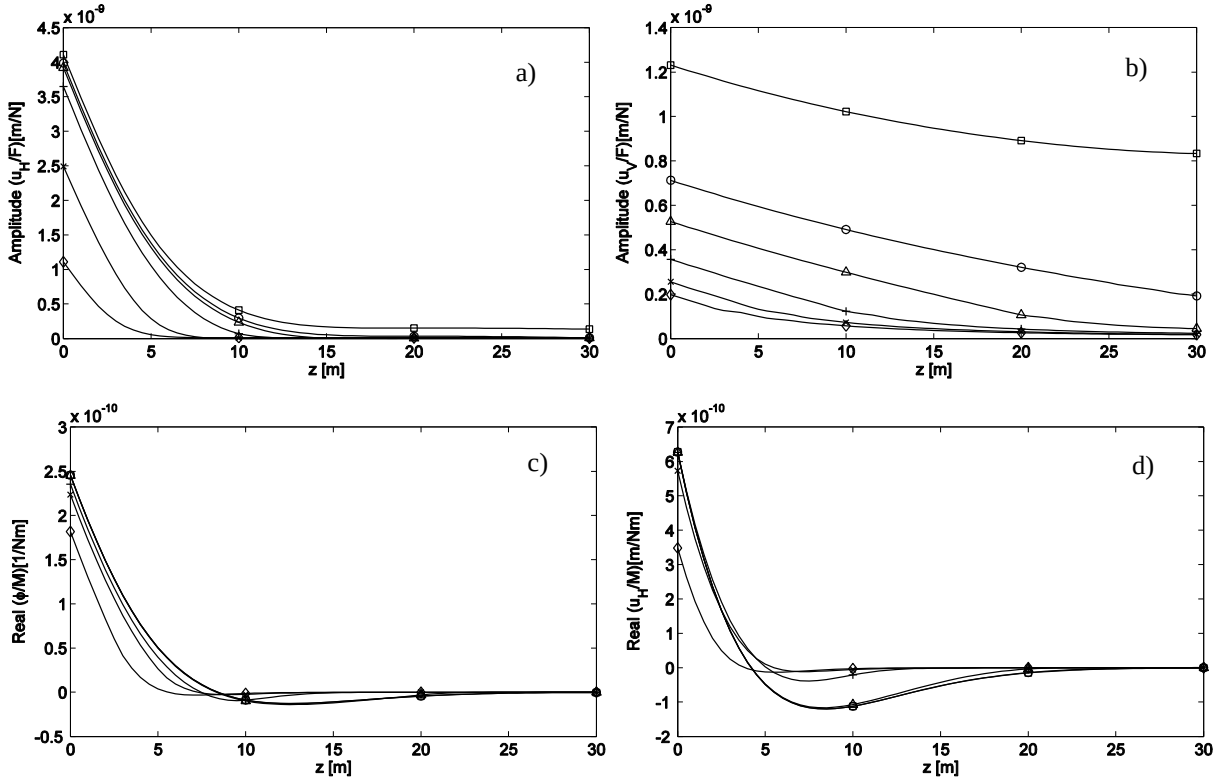


Figure 12: Static deformation of the pile in layered soils ($G_1/G_2$ = 2/50), the a) horizontal, b) vertical, c) rocking, and d) coupling component. Variation of the layer height $H$ = □ ∞, ○ 30, △ 20, +10, × 5, ◇ 2.5 m.

COMPDYN 2017
6th ECCOMAS Thematic Conference on
Computational Methods in Structural Dynamics and Earthquake Engineering
M. Papadrakakis, M. Fragiadakis (eds.)
Rhodes Island, Greece, 15–17 June 2017

# KINEMATIC STRESS RESULTANTS IN INCLINED SINGLE PILES SUBJECTED TO PRAPAGATING SEISMIC WAVES: AN ANALYTICAL FORMULATION

**S. Carbonari[1], M. Morici[2], F. Dezi[3] and G. Leoni[2]**

[1] Università Politecnica delle Marche - DICEA
via Brecce Bianche, Ancona, 60131, Italy
e-mail: s.carbonari@univpm.it

[2] University of Camerino - SAAD
viale della Rimembranza, Ascoli Piceno, 63100, Italy
e-mail: {michele.morici,graziano.leoni}@unicam.it

[3] University of San Marino - DESD
via Salita alla Rocca, San Marino, 47890, San Marino
e-mail: francsca.dezi@unirsm.sm

**Keywords:** Instructions, ECCOMAS Thematic Conference, Structural Dynamics, Earthquake Engineering, Proceedings.

**Abstract.** *This paper presents an analytical model, based on the beam-on-dynamic Winkler foundation approach, for the evaluation of the kinematic stress resultants in single inclined piles subjected to the propagation of seismic waves. The Euler-Bernoulli beam model is adopted for the pile whereas analytical solutions available in literature for viscoelastic layers undergoing harmonic vibrations of a rigid disk are used for the soil. The coupled flexural and axial behaviour of the pile is governed by a system of partial differential equations, with the relevant boundary conditions, that is solved analytically in terms of exponential matrices. The solution for piles embedded in a homogeneous soil deposit is presented. Some applications, including comparisons of results with those obtained from rigorous boundary element formulations, demonstrate that the model, characterised by a very low computational effort, is able to accurately predict stress resultants in inclined piles subjected to seismic loading.*

## 1 INTRODUCTION

The Beam-on-Dynamic Winkler Foundation approach (BDWF) has been largely used in the literature to study the problem of a single pile subjected to seismic loading. According to this approach, the soil-pile interaction is captured through the definition of Winkler's coefficients (spring and dashpot coefficients) that may be characterised by a linear or nonlinear behaviour. Despite the nonlinear approach is more suited to model soil-pile interaction phenomena under severe earthquakes, linear approaches are very often preferred for different reasons, the most important of which is the possibility to solve the problem in the frequency domain, where the frequency dependent nature of the soil-pile interaction phenomena can be directly included and convergence problems can be avoided. In this framework, the definition of Winkler's coefficients, able to capture the dynamic stiffness of the soil-pile system and the frequency dependent radiation damping phenomena, constitutes an important task, since they strongly affect both the kinematic and the inertial response of the soil-foundation system [1].

The linear BDWF approach has been used extensively to study the response of vertical piles subjected to dynamic loading for which closed-form solutions, as well as simplified expressions for the prediction of the dynamic stiffness, the kinematic pile response and the maximum bending moments along the pile, have been derived. On the contrary, applications of such approaches to inclined piles are not so popular in the literature and more sophisticated finite element or boundary element models are preferred [2-7].

In this paper an analytical model for the analysis of kinematic stress resultants arising in inclined single piles subjected to the propagation of seismic waves is presented. The model is based on the BDWF approach and an analytical solution of the problem is derived by assuming a linear behaviour of both the pile and soil. In particular, the pile is modelled as a Euler-Bernoulli beam having a generic inclination and the soil-pile interaction is captured by defining soil impedances according to expressions available in the literature for viscoelastic layers undergoing harmonic vibrations of a rigid disk. The coupled flexural and axial behaviour of the pile is described by a system of partial differential equations, with the relevant boundary conditions, that is solved analytically exploiting exponential matrices. Some applications are performed to demonstrate the model efficiency, comparing results, in terms of stress resultants along piles, with those available in the literature, resulting from rigorous boundary element formulations.

## 2 ANALYTICAL MODEL

The analytical formulation of the dynamic problem of a single pile embedded in a homogenous soil deposit and subjected to the free-field seismic displacements is presented in this section. The problem is formulated in the frequency domain by assuming a linear viscoelastic behaviour for the pile and soil.

### 2.1 Kinematics

A single circular pile of diameter $\phi$ and length $L$, embedded with a generic inclination in a homogeneous soil deposit and subjected to a free field motion, is considered and a global orthonormal reference system frame $\{0, x, y, z\}$ is defined with the origin at the top plane of the stratum and the $z$ axis directed downward (Figure 1a). A local reference system $\{0, \xi, \eta, \zeta\}$ of the pile, having the $\zeta$ axis passing through centroids of the circular cross sections, is also introduced.

With reference to points lying on the pile axis, if $\omega$ is the circular frequency, the soil displacements at depth $z$ are described by the complex valued vector

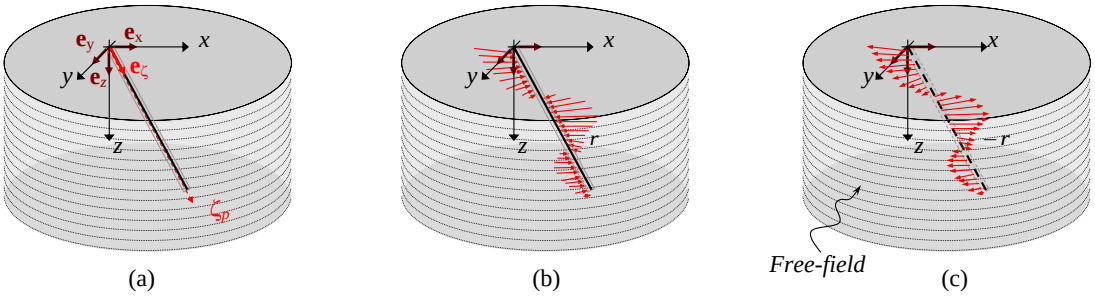


Figure 1: (a): Pile section in the homogeneous stratum; (b) pile section subjected to interaction forces and (c) soil stratum subjected to propagating seismic waves and interaction forces.

$$\mathbf{u}_g(\omega;z)=\begin{bmatrix}\mathbf{u}_h(\omega;z)\\ u_z(\omega;z)\end{bmatrix}_{3\times1} \tag{1}$$

in which sub-vector $\mathbf{u}_h$ groups horizontal components in $x$ and $y$ directions. Similarly, the free-field motion at the pile location $\mathbf{u}_{ff}$ is partitioned by grouping horizontal components in sub-vector $\mathbf{u}_{ff,h}$

$$\mathbf{u}_{ff}(\omega;z)=\begin{bmatrix}\mathbf{u}_{ff,h}(\omega;z)\\ u_{ff,z}(\omega;z)\end{bmatrix}_{3\times1} \tag{2}$$

Under the assumption that no gap between the pile and the soil arises during the motion, pile displacements are conveniently expressed as

$$\mathbf{u}_l(\omega;\zeta)=\mathbf{R}\mathbf{u}_g(\omega;z) \tag{3}$$

where $\mathbf{R}$ is a rotation matrix that allow expressing pile displacements with respect to the local reference system, starting from displacements expressed with respect to the global one. According to the Euler-Bernoulli model, the displacement field of the generic point of the pile cross-section can be obtained from

$$\mathbf{s}_l^T(\omega;\xi,\eta,\zeta)=\begin{bmatrix}\mathbf{u}_t(\omega;\zeta)\\ u_\zeta(\omega;\zeta)-\mathbf{u}_t'(\omega;\zeta)\cdot\mathbf{a}(\xi,\eta)\end{bmatrix}_{3\times1} \tag{4}$$

where prime denotes derivatives with respect to $\zeta$ and $\mathbf{a}(\xi,\eta)=[\xi,\eta]^T$ is the vector of local coordinates $\xi$ and $\eta$ of the cross section generic point. The pile undergoes only the longitudinal normal strain

$$\varepsilon_\zeta(\omega;\xi,\eta,\zeta)=u_\zeta'(\omega;\zeta)-\mathbf{u}_t''(\omega;\zeta)\cdot\mathbf{a}(\xi,\eta) \tag{5}$$

## 2.2 Viscoelastic linear problem

The pile is constituted by a linear viscoelastic material, characterized by Young's modulus $E_p$ and material damping $\delta_p$, taken into account according to the correspondence principle [8]. During the motion, the pile interacts with the surrounding soil and resultants of the soil reactions are assumed to be constituted by forces distributed along the pile.

By grouping the horizontal components of the soil reaction resultants in sub-vector $\mathbf{r}_h$, and denoting by $r_z$ the vertical component, vector of the line reaction forces is (Figure 1b)

$$\mathbf{r}(\omega;z)=\begin{bmatrix}\mathbf{r}_h(\omega;z)\\ r_z(\omega;z)\end{bmatrix}_{3\times 1} \tag{6}$$

By considering the soil stratum constituted by infinite horizontal independent layers with linear viscoelastic behaviour, reaction forces are given by (Figure 1c)

$$\mathbf{r}(\omega;z)=\mathfrak{I}(\omega)\left[\mathbf{u}_{ff}(\omega;z)-\mathbf{u}_g(\omega;z)\right] \tag{7}$$

where $\mathfrak{I}$ is the 3x3 impedance matrix of the unbounded soil layers. Matrix $\mathfrak{I}$ can be populated considering results of studies by Dobry et al. [9], Makris and Gazetas [10] and Gazetas and Dobry [11]. Components of matrix $\mathfrak{I}$ represent forces necessary to induce unitary harmonic vibrations of a rigid disk at depth *z*. The equilibrium condition of the pile may be expressed by the Lagrange-D'Alembert principle that, suitably integrated by parts, furnishes

$$\begin{aligned}
&E_p^*\left(\mathbf{J}\int_0^L \mathbf{u}_t''''\cdot\hat{\mathbf{u}}_t d\zeta - A\int_0^L u_\zeta''\hat{u}_\zeta d\zeta\right)-\omega^2\rho_p\left(A\int_0^L \mathbf{u}_t\cdot\hat{\mathbf{u}}_t\mathrm{d}\zeta + A\int_0^L u_\zeta\hat{u}_\zeta\mathrm{d}\zeta - \mathbf{J}\int_0^L \mathbf{u}_t''\cdot\hat{\mathbf{u}}_t\mathrm{d}\zeta\right)\\
&+\int_0^L\left(\mathbf{R}\mathfrak{I}\mathbf{R}^T\mathbf{u}_l\cdot\hat{\mathbf{u}}_l\right)c_{z\zeta}\mathrm{d}\zeta-\int_0^L\left(\mathbf{R}\mathfrak{I}\mathbf{u}_{ff}\cdot\hat{\mathbf{u}}_l\right)c_{z\zeta}\mathrm{d}\zeta+E_p^*\left(Au_\zeta'\hat{u}_\zeta+\mathbf{J}\mathbf{u}_t''\cdot\hat{\mathbf{u}}_t'-\mathbf{J}\mathbf{u}_t'''\cdot\hat{\mathbf{u}}_t\right)\Big|_0^L\\
&-\omega^2\rho_p\left(\mathbf{J}\mathbf{u}_t'\cdot\hat{\mathbf{u}}_t\right)\Big|_0^L-\left(\mathbf{F}_t\cdot\hat{\mathbf{u}}_t+F_\zeta\hat{u}_\zeta+\mathbf{M}_t\cdot\hat{\mathbf{u}}_t'\right)\Big|_0-\left(\mathbf{F}_t\cdot\hat{\mathbf{u}}_t+F_\zeta\hat{u}_\zeta+\mathbf{M}_t\cdot\hat{\mathbf{u}}_t'\right)\Big|_L=0\qquad\forall\hat{\mathbf{u}}_l\neq\mathbf{0}
\end{aligned} \tag{8}$$

where **J** is the inertia matrix and *A* is the area of the pile cross section, respectively, while $E_p^*=E_p(1+2i\delta_p)$ is the complex elastic modulus of the pile material [8]. From Equation (8), according to the fundamental theorem of variational calculus, the local balance conditions

$$\begin{aligned}
&E_p^*\mathbf{J}\mathbf{u}_t''''+\omega^2\rho_p\mathbf{J}\mathbf{u}_t''-\omega^2\rho_pA\mathbf{u}_t+c_{z\zeta}\sum_{1,2}^{1,2}\left(\mathbf{R}\mathfrak{I}\mathbf{R}^T\right)\mathbf{u}_t+c_{z\zeta}\sum_{1,2}^{3}\left(\mathbf{R}\mathfrak{I}\mathbf{R}^T\right)u_\zeta\\
&\qquad=c_{z\zeta}\sum_{1,2}^{1,2}\left(\mathbf{R}\mathfrak{I}\right)\mathbf{u}_{ff,h}+c_{z\zeta}\sum_{1,2}^{3}\left(\mathbf{R}\mathfrak{I}\right)u_{ff,z}\\
&-E_p^*Au_\zeta''-\omega^2\rho_pAu_\zeta+c_{z\zeta}\sum_{3}^{1,2}\left(\mathbf{R}\mathfrak{I}\mathbf{R}^T\right)\mathbf{u}_t+c_{z\zeta}\sum_{3}^{3}\left(\mathbf{R}\mathfrak{I}\mathbf{R}^T\right)u_\zeta\\
&\qquad=c_{z\zeta}\sum_{3}^{1,2}\left(\mathbf{R}\mathfrak{I}\right)\mathbf{u}_{ff,h}+c_{z\zeta}\sum_{3}^{3}\left(\mathbf{R}\mathfrak{I}\right)u_{ff,z}
\end{aligned} \tag{9}$$

as well as the relevant boundary conditions

$$\begin{aligned}
&\left(E_p^*Au_\zeta'+F_\zeta\right)\hat{u}_\zeta\Big|_0=0\quad\forall\hat{u}_\zeta && \left(E_p^*Au_\zeta'-F_\zeta\right)\hat{u}_\zeta\Big|_L=0\quad\forall\hat{u}_\zeta\\
&\left(E_p^*\mathbf{J}\mathbf{u}_t'''+\omega^2\rho_p\mathbf{J}\mathbf{u}_t'-\mathbf{F}_t\right)\cdot\hat{\mathbf{u}}_t\Big|_0=0\quad\forall\hat{\mathbf{u}}_t && \left(E_p^*\mathbf{J}\mathbf{u}_t'''+\omega^2\rho_p\mathbf{J}\mathbf{u}_t'+\mathbf{F}_t\right)\cdot\hat{\mathbf{u}}_t\Big|_L=0\quad\forall\hat{\mathbf{u}}_t\\
&\left(E_p^*\mathbf{J}\mathbf{u}_t''+\mathbf{M}_t\right)\cdot\hat{\mathbf{u}}_t'\Big|_0=0\quad\forall\hat{\mathbf{u}}_t' && \left(E_p^*\mathbf{J}\mathbf{u}_t''-\mathbf{M}_t\right)\cdot\hat{\mathbf{u}}_t'\Big|_L=0\quad\forall\hat{\mathbf{u}}_t'
\end{aligned} \tag{10}$$

are derived. In equations (9), $\sum_{i,j}^{l,m}\mathbf{A}$ indicates segments of a generic matrix **A** constituted by the subset of rows comprised between *i* and *j* and the subset of columns comprised between *l* and *m*. Equations (9) is a system of ordinary differential equations with constant coefficients whose unknowns are the complex valued function $\mathbf{u}_l(\zeta)$ fulfilling the boundary conditions (10) that encompass both kinematic and static conditions.

$$\mathbf{x}(\omega;\zeta)=\begin{bmatrix}\mathbf{u}_t\\ u_\zeta\\ \mathbf{u}_t'\\ u_\zeta'\\ \mathbf{u}_t''\\ \mathbf{u}_t'''\end{bmatrix}_{10\times 1} \tag{11}$$

System (9), with the boundary conditions (10), can be thus rewritten in the canonical form

$$\mathbf{x}'-\mathbf{B}(\omega)\mathbf{x}=\mathbf{c}(\omega;\zeta) \tag{12}$$

$$\begin{aligned}&\left[\mathbf{D}(\omega)\mathbf{x}+\mathbf{P}(\omega)\right]\cdot\overset{1}{\underset{1,5}{\mathbf{S}}}\hat{\mathbf{x}}\Big|_0=\mathbf{0}\qquad\forall\hat{\mathbf{x}}\\ &\left[\mathbf{D}(\omega)\mathbf{x}-\mathbf{P}(\omega)\right]\cdot\overset{1}{\underset{1,5}{\mathbf{S}}}\hat{\mathbf{x}}\Big|_L=\mathbf{0}\qquad\forall\hat{\mathbf{x}}\end{aligned} \tag{13}$$

where

$$\mathbf{B}=\begin{bmatrix}\mathbf{0} & \mathbf{0} & \mathbf{I}_2 & \mathbf{0} & \mathbf{0} & \mathbf{0}\\ \mathbf{0} & 0 & \mathbf{0} & 1 & \mathbf{0} & \mathbf{0}\\ \mathbf{0} & \mathbf{0} & \mathbf{0} & \mathbf{0} & \mathbf{I}_2 & \mathbf{0}\\ \frac{c_{z\zeta}}{E_p^*A}\overset{1,2}{\underset{3}{\mathbf{S}}}\left(\mathbf{R}\mathfrak{I}\mathbf{R}^T\right) & \frac{c_{z\zeta}}{E_p^*A}\overset{3}{\underset{3}{\mathbf{S}}}\left(\mathbf{R}\mathfrak{I}\mathbf{R}^T\right)-\frac{\omega^2\rho_p}{E_p^*} & \mathbf{0} & 0 & \mathbf{0} & \mathbf{0}\\ \mathbf{0} & \mathbf{0} & \mathbf{0} & \mathbf{0} & \mathbf{0} & \mathbf{I}_2\\ \frac{\omega^2\rho_p}{E_p^*}A\mathbf{J}^{-1}-\frac{c_{z\zeta}}{E_p^*}\mathbf{J}^{-1}\overset{1,2}{\underset{1,2}{\mathbf{S}}}\left(\mathbf{R}\mathfrak{I}\mathbf{R}^T\right) & -\frac{c_{z\zeta}}{E_p^*}\mathbf{J}^{-1}\overset{3}{\underset{1,2}{\mathbf{S}}}\left(\mathbf{R}\mathfrak{I}\mathbf{R}^T\right) & \mathbf{0} & \mathbf{0} & -\frac{\omega^2\rho_p}{E_p^*}\mathbf{I}_2 & \mathbf{0}\end{bmatrix} \tag{14}$$

$$\mathbf{D}=\begin{bmatrix}\mathbf{0} & 0 & -\omega^2\rho_p\mathbf{J} & 0 & \mathbf{0} & -E_p^*\mathbf{J}\\ \mathbf{0} & 0 & \mathbf{0} & E_p^*A & \mathbf{0} & \mathbf{0}\\ \mathbf{0} & 0 & \mathbf{0} & 0 & E_p^*\mathbf{J} & \mathbf{0}\end{bmatrix} \tag{15}$$

are complex valued matrices, depending on the stiffness of the pile cross section and on the impedance of the soil layers, while

$$\mathbf{c}=\begin{bmatrix}\mathbf{0}\\ 0\\ \mathbf{0}\\ -\frac{1}{E_p^*A}\left(c_{z\zeta}\overset{1,2}{\underset{3}{\mathbf{S}}}(\mathbf{R}\mathfrak{I})\mathbf{u}_{ff,h}+c_{z\zeta}\overset{3}{\underset{3}{\mathbf{S}}}(\mathbf{R}\mathfrak{I})u_{ff,z}\right)\\ \mathbf{0}\\ \frac{1}{E_p^*}\mathbf{J}^{-1}\left(c_{z\zeta}\overset{1,2}{\underset{1,2}{\mathbf{S}}}(\mathbf{R}\mathfrak{I})\mathbf{u}_{ff,h}+c_{z\zeta}\overset{3}{\underset{1,2}{\mathbf{S}}}(\mathbf{R}\mathfrak{I})u_{ff,z}\right)\end{bmatrix} \tag{16}$$

$$\mathbf{P}=\begin{bmatrix}\mathbf{F}_t\\ F_\zeta\\ \mathbf{M}_t\end{bmatrix} \tag{17}$$

are vectors depending on distributed soil-pile reaction forces and loads concentrated at the pile ends, respectively.

Equation (12) is a linear system of ordinary differential equations with constant coefficients whose general solution is obtained by summing the complementary solution (solution of the associate homogeneous equation) to a particular solution depending on the external loads. It can be demonstrated that such a solution may be written as

$$\mathbf{x} = \mathbf{E}(\omega;\zeta)\mathbf{g}(\omega) + \mathbf{E}(\omega;\zeta)\int \mathbf{E}^{-1}(\omega;\zeta)\mathbf{c}\,\mathrm{d}\zeta \tag{18}$$

where **E** is the exponential matrix defined through a series expansion by

$$\mathbf{E}(\omega;\zeta) = \sum_{k=0}^{\infty} \frac{1}{k!}\mathbf{B}^k(\omega)\zeta^k \tag{19}$$

and **g** is the vector of the integration constants that has to be calculated from the boundary conditions (13). Equation (18) is of general validity and the evaluation of the particular solution requires to know the expression of the free field motion; in this paper the case of one-dimensional propagation of shear and pressure waves in the vertical direction is considered. These are governed by expressions

$$\mathbf{u}_{ff,h}(\omega;z) = \mathbf{q}_h(\omega)e^{ik_h z} + \mathbf{t}_h(\omega)e^{-ik_h z} \tag{20}$$

$$u_{ff,z}(\omega;z) = q_z(\omega)e^{ik_z z} + t_z(\omega)e^{-ik_z z} \tag{21}$$

where

$$k_h = \sqrt{\frac{\omega^2}{V_s^2(1+2i\delta_s)}} \qquad k_z = \sqrt{\frac{\omega^2}{V_{La}^2(1+2i\delta_s)}} \tag{22}$$

are the complex wavenumbers associated to the propagation of shear and pressure waves, respectively, and $\mathbf{q}_h$, $\mathbf{t}_h$, $q_z$ and $t_z$ are integration constants depending on the boundary conditions (i.e. at the ground surface and at the bedrock level) [12]. Taking into account equation (16)

$$\mathbf{c} = \mathbf{Q}_h(\omega)e^{ik_h c_{z\zeta}\zeta} + \mathbf{T}_h(\omega)e^{-ik_h c_{z\zeta}\zeta} + \mathbf{Q}_z(\omega)e^{ik_z c_{z\zeta}\zeta} + \mathbf{T}_z(\omega)e^{-ik_z c_{z\zeta}\zeta} \tag{23}$$

where

$$\mathbf{Q}_h(\omega) = \begin{bmatrix} \mathbf{0} \\ 0 \\ \mathbf{0} \\ -\dfrac{c_{z\zeta}}{E_p^* A}\displaystyle\sum_{3}^{1,2}(\mathbf{R}\Im)\mathbf{q}_h \\ \mathbf{0} \\ \dfrac{c_{z\zeta}}{E_p^*}\mathbf{J}^{-1}\displaystyle\sum_{1,2}^{1,2}(\mathbf{R}\Im)\mathbf{q}_h \end{bmatrix} \qquad \mathbf{T}_h(\omega) = \begin{bmatrix} \mathbf{0} \\ 0 \\ \mathbf{0} \\ -\dfrac{c_{z\zeta}}{E_p^* A}\displaystyle\sum_{3}^{1,2}(\mathbf{R}\Im)\mathbf{t}_h \\ \mathbf{0} \\ \dfrac{c_{z\zeta}}{E_p^*}\mathbf{J}^{-1}\displaystyle\sum_{1,2}^{1,2}(\mathbf{R}\Im)\mathbf{t}_h \end{bmatrix} \tag{24}$$

$$\mathbf{Q}_z(\omega)=\begin{bmatrix}\mathbf{0}\\0\\\mathbf{0}\\-\dfrac{c_{z\zeta}}{E_p^*A}\sum\limits_{3}^{3}(\mathbf{R}\Im)q_z\\\mathbf{0}\\\dfrac{c_{z\zeta}}{E_p^*}\mathbf{J}^{-1}\sum\limits_{1,2}^{3}(\mathbf{R}\Im)q_z\end{bmatrix}\qquad \mathbf{T}_z(\omega)=\begin{bmatrix}\mathbf{0}\\0\\\mathbf{0}\\-\dfrac{c_{z\zeta}}{E_p^*A}\sum\limits_{3}^{3}(\mathbf{R}\Im)t_z\\\mathbf{0}\\\dfrac{c_{z\zeta}}{E_p^*}\mathbf{J}^{-1}\sum\limits_{1,2}^{3}(\mathbf{R}\Im)t_z\end{bmatrix} \tag{25}$$

By substituting (23) in (18) yields

$$\mathbf{x}=\mathbf{E}\mathbf{g}_f+\mathbf{E}\int\mathbf{E}^{-1}\left(\mathbf{Q}_h e^{ik_h c_{z\zeta}\zeta}+\mathbf{T}_h e^{-ik_h c_{z\zeta}\zeta}+\mathbf{Q}_z e^{ik_z c_{z\zeta}\zeta}+\mathbf{T}_z e^{-ik_z c_{z\zeta}\zeta}\right)d\zeta \tag{26}$$

which, for properties of exponential matrix, can be rewritten as

$$\mathbf{x}=\mathbf{E}\mathbf{g}_f+\tilde{\mathbf{x}}_h+\tilde{\mathbf{x}}_z \tag{27}$$

where

$$\tilde{\mathbf{x}}_h=\mathbf{E}\left[\left(ik_h c_{z\zeta}\mathbf{I}-\mathbf{B}\right)^{-1}\mathbf{E}^{-1}\mathbf{Q}_h e^{ik_h c_{z\zeta}\zeta}-\left(ik_h c_{z\zeta}\mathbf{I}+\mathbf{B}\right)^{-1}\mathbf{E}^{-1}\mathbf{T}_h e^{-ik_h c_{z\zeta}\zeta}\right] \tag{28}$$

$$\tilde{\mathbf{x}}_z=\mathbf{E}\left[\left(ik_z c_{z\zeta}\mathbf{I}-\mathbf{B}\right)^{-1}\mathbf{E}^{-1}\mathbf{Q}_z e^{ik_z c_{z\zeta}\zeta}-\left(ik_z c_{z\zeta}\mathbf{I}+\mathbf{B}\right)^{-1}\mathbf{E}^{-1}\mathbf{T}_z e^{-ik_z c_{z\zeta}\zeta}\right] \tag{29}$$

are the particular solutions for shear and pressure waves propagating in the vertical direction, respectively. Differently from classical numerical methods (e.g finite element method and finite difference method), this approach allows expressing the problem solution analytically; in the case of homogeneous soil deposit the discretization of the pile axis is not needed to achieve an accurate numerical solution.

Once the solution is determined, stress resultants in the pile can be obtained with

$$\begin{bmatrix}N(\omega;\zeta)\\M_\eta(\omega;\zeta)\\M_\xi(\omega;\zeta)\\V_\xi(\omega;\zeta)\\V_\eta(\omega;\zeta)\end{bmatrix}=E_p^*\frac{\pi\phi^4}{64}\begin{bmatrix}0&0&\dfrac{16}{\phi^2}&0&0&0&0\\0&0&0&1&0&0&0\\0&0&0&0&-1&0&0\\-\omega^2\dfrac{\rho_p}{E_p^*}&0&0&0&0&-1&0\\0&-\omega^2\dfrac{\rho_p}{E_p^*}&0&0&0&0&-1\end{bmatrix}\sum_{4,10}^{1}\mathbf{x}(\omega;\zeta) \tag{30}$$

## 3 APPLICATIONS

In this section, some applications are presented in order to show the model potential in capturing the kinematic stress resultants in inclined piles subjected to propagating seismic waves. For this proposes, results of some applications available in Padron et al. [5], performed with a boundary element model, are considered as benchmarks. The adopted geometrical and mechanical parameters are reported in Figure 2; applications are performed considering 12 m long piles with different inclination (θ = 0°, 10°, 20°, 30°) embedded in a homogeneous soil deposit characterised by two different shear wave velocites ($V_s$ = 250 and 110 m/s). The pile Young's modulus and density are $E_p$ = 30000 MPa and $\rho_p$ = 2.5 t/m$^3$, respectively. The seis-

mic input at the ground surface is constituted by an artificial accelerogram with a peak ground acceleration $a_g$ = 0.375g, individually matching the elastic response spectrum for ground type C and 5% damping. This has been obtained according to the Gasparini & Vanmarcke spectrum-compatible nonstationary ground motion model [13]. The seismic action is applied in the *x* direction. For this applications the pile is not subdivided and the Lysmer's analogue velocity is assumed for the compression waves within the whole pile.

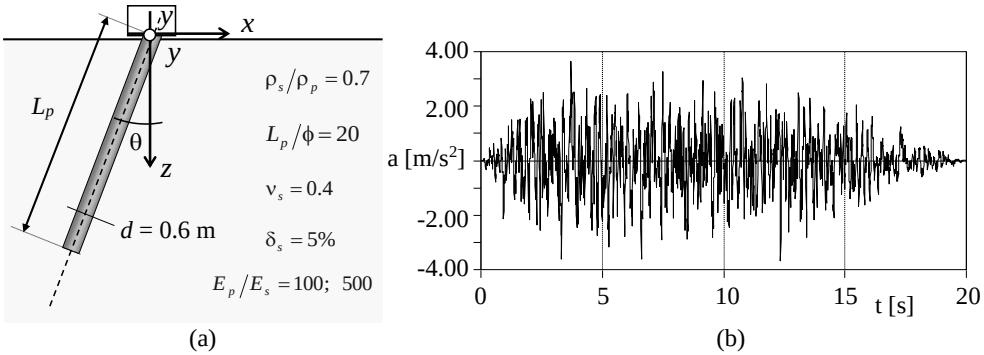


(a) (b)

Figure 1: (a) Pile geometry and (b) seismic input.

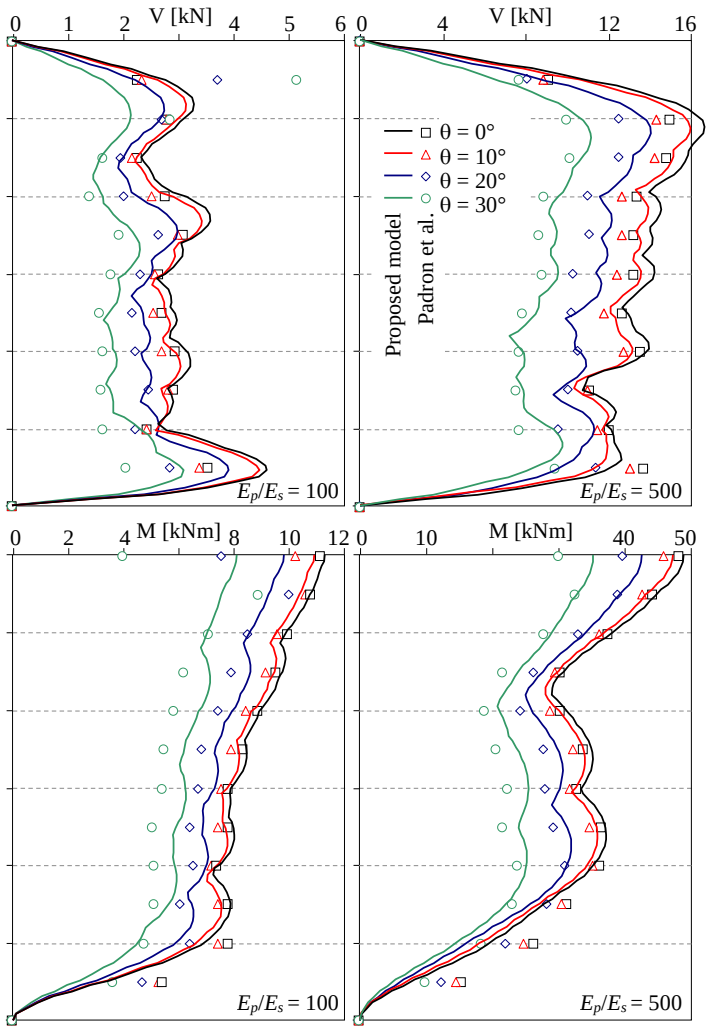


Figure 2: (a) Envelops of absolute kinematic shear force and bending moments along the pile.

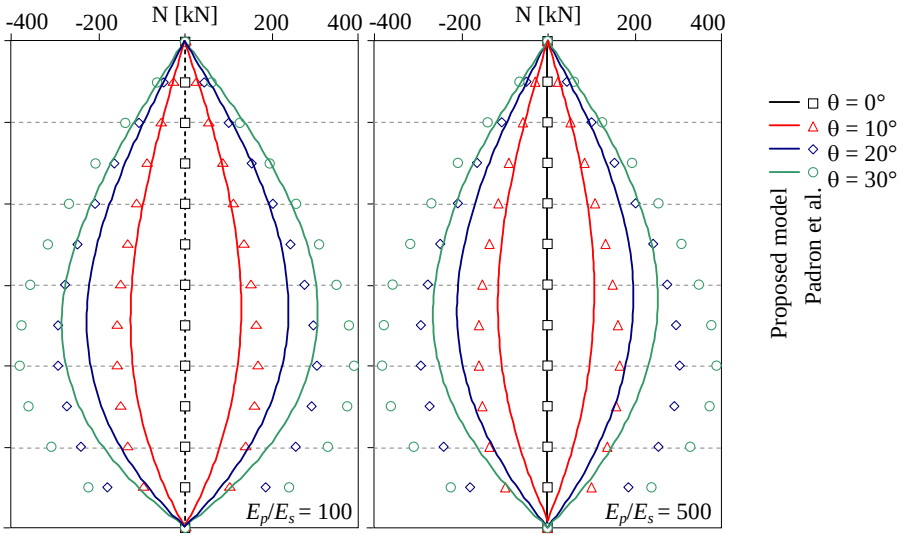


Figure 3: Envelops of maximum and minimum axial force along the pile.

Figure 3 shows the envelopes of absolute values of shear forces and bending moments arising along the pile as a consequence of the kinematic interaction. Results obtained by considering different pile inclinations are reported with curves of different colours for both the investigated soil deposits, characterised by pile-soil modulus ratios $E_p/E_s$ = 100 ($V_s$ = 250 m/s) and $E_p/E_s$ = 500 ($V_s$ = 110 m/s). Furthermore, benchmarks are reported with marks while continuous lines are used for results of the proposed formulation. For both pile-soil modulus ratios benchmark shear forces are overall well reproduced, independently on the pile rake angle. However, with reference to $E_p/E_s$ = 100 significant differences are evident in proximity of the pile head and also nearby the pile base; in particular, benchmark shear forces are higher than those evaluated with the proposed approach at the pile head and slightly lower at the pile base. Local inconsistency at the pile head is probably due to the adopted local soil-pile impedances, based on the plane-strain assumption, which are not able to capture the dynamics of soil layers near the ground surface, characterised by a reduced degree of confinement and by the propagation of surface waves. Previous observation is confirmed by results of $E_p/E_s$ = 500, namely of a softer soil, for which shear forces arising in proximity of the pile head are better captured. As for bending moments, the benchmarks are well reproduced for both soil conditions ($E_p/E_s$ = 100, 500) expect for the local inconsistencies in proximity of the pile head where bending moments resulting from the BE approach tend to reduce, probably as a consequence of the minor degree of confinement exerted by the superficial soil. As explained above, this effect cannot be captured by the proposed model unless different local soil-pile impedances, suitably calibrated to capture these phenomena, are implemented. As expected, discrepancies between benchmarks and the present results at the pile head reduce in the case of softer soils ($E_p/E_s$ = 500). Anyway, bending moments at the head appear to be consistent as they are characterised by a vertical tangent, according to the null value of shear force.

Figure 4 shows the envelopes of maximum and minimum axial forces along the pile obtained from the applications. Maximum discrepancies of about 25÷30% between benchmarks and the proposed solution are observed for both soil conditions ($E_p/E_s$ = 100, 500), mainly concentrated in the lower half-length of the pile.

From an overall standpoint, kinematic shear forces and bending moments induced by the seismic wave propagation reduce by increasing the pile rake angle, independently on the soil stiffness, while, as expected, axial forces increase.

## 4 CONCLUSIONS

An analytical model, based on the BDWF approach, for the evaluation of kinematic stress resultants arising in inclined single piles subjected to the propagation of seismic waves in the soil has been presented. The pile is modelled as a Euler-Bernoulli beam having a generic inclined configuration and the soil-pile interaction is captured exploiting elastodynamic solutions available in the literature. The coupled flexural and axial problem is solved analytically exploiting exponential matrices and analytical expressions of kinematic stress resultants are provided. The model is characterised by a computational effort much lower than that associated with numerical solutions formulated with the finite element or boundary element methods.

Some applications are performed comparing results with those available in the literature, derived from rigorous boundary element solutions. Results demonstrate that shear forces and bending moments along the pile resulting from more rigorous approaches, are well reproduced, independently on the pile rake angle and soil conditions (overall errors of about 10% are obtained). However, local inconsistencies at the pile head are observed; these may be due to the adopted elastodynamic solutions to model the soil-pile interaction. As for axial forces, greater discrepancies with benchmarks (ranging between 25÷30%) are evident for both soil conditions, mainly concentrated in the lower half-length of the pile.

## REFERENCES

[1] G. Mylonakis, A. Nikolaou, G. Gazetas, Soil–pile–bridge interaction: kinematic and inertial effects. Part I: soft soil. *Earthquake Engng Struct. Dynamics*, **26**(3), 337–359, 1997.

[2] N. Gerolymos, A. Giannakou, I. Anastasopoulos, G. Gazetas, Evidence of beneficial role of inclined piles: observations and summary of numerical analyses. *Bulletin of Earthquake Engineering*, **6**(4), 705–722, 2008.

[3] A. Giannakou, N. Gerolymos, G. Gazetas, T. Tazoh, I. Anastasopoulos, Seismic Behavior of Batter Piles: Elastic Response. *Journal of Geotechnical and Geoenvironmental Engineering*, **136**, 1187–1199, 2010.

[4] L.A. Padrón, J.J. Aznárez, O. Maeso, A. Santana, Dynamic stiffness of deep foundations with inclined piles. *Earthquake Engng Struct. Dynamics*, **39**(12), 1343–1367, 2010.

[5] L.A. Padrón, A. Suárez, J.J. Aznárez, O. Maeso, Kinematic internal forces in deep foundations with inclined piles. *Earthquake Engng. Struct. Dynamics*, **44**(12), 2129–2135, 2015.

[6] C. Medina, L.A. Padrón, J.J. Aznárez, A. Santana, O. Maeso, Kinematic interaction factors of deep foundations with inclined piles. *Earthquake Engng. Struct. Dynamics*, **43**(13), 2035–2050, 2014.

[7] F. Dezi, S. Carbonari, M. Morici, A Numerical Model for the Dynamic Analysis of Inclined Pile Groups. *Earthquake Engng Struct. Dynamics*, **45**(1), 45–68, 2016.

[8] N. Makris, Causal hysteretic element. *Journal of Engineering Mechanics, ASCE*, **123**(11): 1209–1214, 1997.

[9] R. Dobry, E. Vicente, M.J. O'Rourke, J.M. Roesset, Horizontal Stiffness and Damping of Single Piles. *Journal of Geotechnical Engineering Division, ASCE*, **108**(GT3), 439–459, 1982.

[10] N. Makris, G. Gazetas, Displacement phase differences in a harmonically oscillating pile. *Geotechnique*, **43**(1), 135–150, 1993.

[11] G. Gazetas, R. Dobry, Single radiation damping model for piles and footings. *J. Engng. Mech., ASCE*, **110**(6), 937–956, 1984.

[12] S.L. Kramer, *Geotechnical Earthquake Engineering*. Prentice Hall, Upper Saddle River, RJ, 1996

[13] D.A. Gasparini, E.H. Vanmarcke, Evaluation of Seismic Safety of Buildings – Simulated Earthquake Motions with Prescribed Response Spectra. Massachusetts Institute of Technology, Report No.2, 1976.

COMPDYN 2017
6th ECCOMAS Thematic Conference on
Computational Methods in Structural Dynamics and Earthquake Engineering
M. Papadrakakis, m. Fragiadakis (eds.)
Rhodes Island, Greece, 15–17 June 2017

# EXCITATION OF STRUCTURES NEAR RAILWAY TRACKS—ANALYSIS OF THE WAVE PROPAGATION PATH

**Paulius Bucinskas**[1] **and Lars V. Andersen**[1]

[1] Department of Civil Engineering, Aalborg University
Thomas Manns Vej 23, Aalborg 9220, Denmark
{pbu, la}@civil.aau.dk

**Keywords:** Soil vibration, wave propagation path, structure-soil interaction, railway vibrations.

**Abstract.** *High-speed rails are an attractive alternative to other forms of intercity transportation. It is a fast, cost-efficient and environmentally friendly solution, which is being developed in various countries across the world. However, in order to be successful, high-speed rails need to transport the passengers as close as possible to the city centres. Therefore, railway tracks have to go through densely populated urban areas, which causes a number of issues. One of the biggest complaints from the inhabitants living near such infrastructures is the high vibration and noise levels caused by the passing trains.*

*Unfortunately, the prediction of vibrations in nearby structures is difficult, as wave propagation from the vibration source to the structure is a complex phenomenon. The behaviour of the structure is highly dependent on the path along which the vibrations travel between their source and the building itself. Especially in the densely built urban environment, the wave propagation path can have different features, such as underground infrastructure, roads, pavements or even other nearby buildings. Such features might have a significant effect on the final excitation of the structure in question.*

*This work aims to analyse how different features in the wave propagation path affect the excitation of a structure. A numerical model is constructed to account for the track structure and the underlying soil. The model utilizes a finite-element model for the structures together with a semi-analytical model of the underlying soil. Different features in the wave-propagation path are introduced, and their effects are compared regarding the behaviour of the structure and the free-field.*

# 1 INTRODUCTION

Continued development of railway infrastructure causes some issues related to vibrations in nearby structures. To make the railways an effective form of passenger transportation the railway stations need to be as close as possible to urban centres. This means that railway tracks need to go through densely built urban environments, causing unwanted vibrations in nearby structures. However, in situ testing of these cases is an expensive and time-consuming task which is sometimes even impossible to carry out. Therefore, computational prediction tools are needed to evaluate the effect on nearby structures. It is not an easy job as wave propagation through soil is a complex phenomenon that depends on a large number of unknowns. The ground between the source of vibrations and receiver point might often contain various obstructions. These obstructions might be on the ground surface or embedded inside the soil body, for example roads, footpaths, demolished building foundations, or sewer lines. This is especially true in a tightly built urban environment.

One of the most commonly used approaches to model the soil body is the finite-element (FE) method. Using this method it is possible to model both the structures interacting with the ground and the ground itself. However, to avoid reflections from the boundaries, absorbing boundary conditions must be used, as in the work by Connolly et al. [1], or the FE model must be coupled to a boundary-element formulation, as in the work by Andersen and Nielsen [2], Nielsen et al. [3] or Andersen [4]. Hence, a semi-analytical soil model can be beneficial to use, especially if the modelled geometry is not very complicated. The semi-analytical approach requires less computational resources and is faster to compute, and infinite boundaries are already included in the formulation. The method is based on analytical evaluation of the Green's function in frequency–wavenumber domain. The original layer-transfer matrix, used in the model, was developed by Thomson [5] and Haskell [6]. Further, the semi-analytical model is commonly used for problems involving wave propagation through soil. For example, Sheng et al. [7] used this method to analyse the vibrations from a simplified railway track placed on the soil surface.

This work also uses the semi-analytical model to model the ground, which is later coupled to structures modelled using an FE approach. The aim is to analyse the effects of various obstructions in the wave propagation path. The effects of these obstructions in the wave path might be an important factor to consider when analysing the ground-borne vibrations, and often they are completely dismissed in this type of analysis. For this, a computational model was constructed that considers a railway track coupled to the underlying ground as described in Section 2. Further, the analysed cases and parameters used are introduced in Section 3. Finally, the obtained results are presented in Section 4, and Section 5 contains the main conclusions.

# 2 COMPUTATIONAL MODEL

Problems regarding wave propagation through soil can be split into three main components: the vibration source, the propagation path and the receiver. Each of these elements has an effect on the overall system behaviour. In this paper, the vibration source is a railway track, which is introduced in Subsection 2.2. Further, the vibrations propagate through a layered soil for which a semi-analytical model is used as explained in Subsection 2.1. To reduce the number of variables, the receiver is only modelled as a rigid footing on the soil surface.

## 2.1 Soil model and coupling to finite elements

A semi-analytical approach is used to model the ground. In this case it is more advantageous compared to FE-based approaches due to lower computation times, which allows testing a wider variety of cases. The method is based on an analytical expression for the Green's function in horizontal wavenumber–frequency domain:

$$\mathbf{U}_2(k_x, k_y, z_2, \omega) = \mathbf{G}_{12}(k_x, k_y, z_1, z_2, \omega)\mathbf{P}_1(k_x, k_y, z_1, \omega). \quad (1)$$

Equation (1) provides a relation between a load $\mathbf{P}_1$ applied at point 1 and the corresponding displacements $\mathbf{U}_2$ at point 2. The Green's function $\mathbf{G}_{12}$ is dependent on the horizontal wave-numbers $k_x, k_y$ the vertical coordinates $z_1, z_2$ of both points, and the circular frequency $\omega$.

After establishing the solution, a numerical inverse Fourier transform is performed to obtain a solution in space–frequency domain. The method assumes that the soil is linear viscoelastic, composed of layers with perfectly horizontal interfaces and with a horizontal ground surface.

To couple the semi-analytical model to the FE formulation of other parts, soil–structure-interaction (SSI) nodes are used. By establishing Green's function relations between these nodes, a flexibility matrix for the soil is obtained. Inverting the flexibility matrix provides the dynamic stiffness matrix for the soil, $\mathbf{D}_{\text{soil}}$, which can then be added to the dynamic stiffness matrix of the FE-based parts, $\mathbf{D}_{\text{FE}}$, to obtain an expression for the whole system:

$$\mathbf{D}_{\text{full}} = \mathbf{D}_{\text{FE}} + \mathbf{D}_{\text{soil}}, \quad \mathbf{D}_{\text{FE}} = \mathbf{K}_{\text{FE}} + \mathrm{i}\omega\mathbf{C}_{\text{FE}} - \omega^2\mathbf{M}_{\text{FE}}, \quad (2)$$

where $\mathbf{K}_{\text{FE}}$ is the stiffness matrix, $\mathbf{C}_{\text{FE}}$ is the damping matrix, $\mathbf{M}_{\text{FE}}$ is the mass matrix, and i is the imaginary unit: $\mathrm{i} = \sqrt{-1}$. The calculations are then performed for the fully coupled system in frequency domain. A more detailed description of the soil model is available in the work by Andersen and Clausen [8], and coupling of multiple structures via the soil was discussed by Andersen [9] and Bucinskas et al. [10].

## 2.2 Railway track and embankment model

The structure of the railway track has a great impact on how the vibrations are transferred to the soil body. Further, the presence of the track introduces secondary effects to the system such as waves travelling through the embankment and back coupling to the surrounding structures. Therefore, proper modelling of the track structure is important.

To reduce the computational requirements of the model and decrease the computation time, shell elements were used to model the railway track and embankment. A cross-section of an embankment can be seen in Figure 1. A single plate was constructed to model the whole embankment. Mindlin-Reissner shell finite elements were used with four nodes and linear Lagrangian interpolation of the displacements and bending rotations. Two types of elements were used: an element type with three layers to model the three-layered embankment, and an element type with four layers to model the sleepers together with the embankment. Using these element types, the embankment plate is assembled to model the sleepers and all layers of the embankment.

Two rails are connected separately to the embankment. The rails are modelled as Euler-Bernoulli beam elements with two nodes and cubic displacement interpolation. The rails and sleepers are connected through rail pads, which are modelled as a spring and damper system. Thus, the rails are discretely supported only at the positions where the sleepers are located.

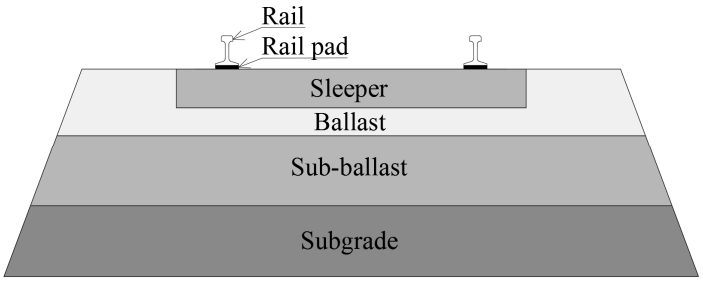


Figure 1: Railway track and embankment cross-section.

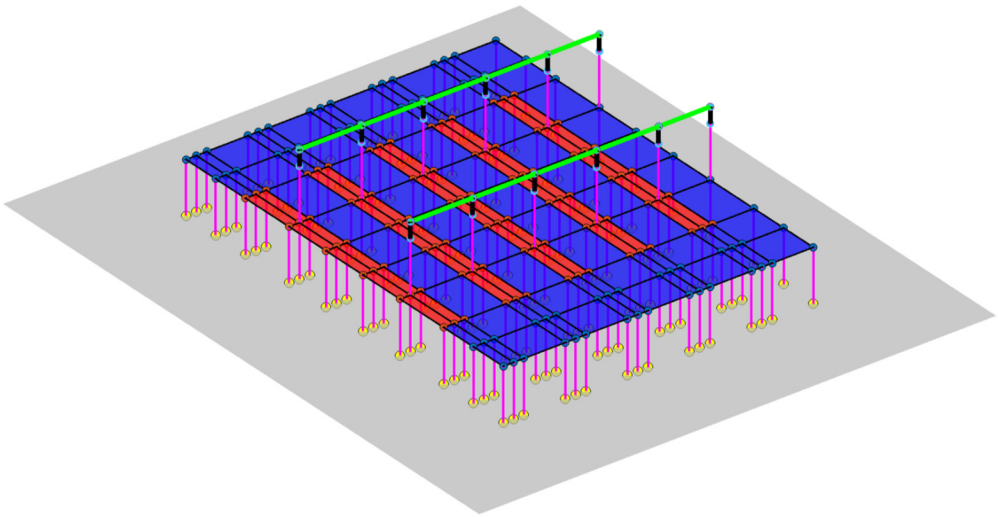

Figure 2: Parts of the track structure. In blue: three layered embankment shell elements; in red: four layered (including sleepers) embankment shell elements; in green: rail beam elements; in grey: soil surface; in yellow: SSI nodes; in magenta: rigid links between soil–embankment and embankment–rail.

The railway embankment is a three-dimensional structure with a considerable thickness. Therefore, modelling the whole embankment as a single flat plate might not be sufficient. To obtain a more realistic model, the plate was placed at the mid-plane of the embankment and then connected to the soil through rigid links. The rigid link length is equal half of the thickness of the embankment. This way the lateral displacements and rotations of the embankment nodes were coupled to lateral displacements of the SSI nodes. The same approach was then used to connect the embankment and the rail pads. The rigid links were introduced into the FE matrices using Lagrange multipliers. This approach was not difficult to implement, as the FE matrix structure stayed unchanged. An example of the FE model of the track can be seen in Figure 2.

Introducing rigid links to the system better represents the real structure, but this kind of formulation also has some disadvantages. The plate representing the embankment does not share nodes with the soil, and thus the number of degrees of freedom in the system increases significantly. Further, Lagrange multipliers also introduce additional constraints to the system, which leads to further increase of FE matrix sizes.

## 3 ANALYSED CASE

A rail track of 30.0 m length was modelled as described in the previous section. The embankment has a width of 4.0 m and is composed of three layers: a 0.5 m thick subgrade layer, a 0.2 m thick sub-ballast layer, and a 0.3 m thick ballast layer. The material properties for these and other materials used are given in Table 1. The sleepers are embedded in the ballast layer, and they are placed at 0.6 m intervals along the track. The sleepers are constructed from concrete with dimensions $0.2\times0.2\times2.5$ m$^3$. The rails are made from steel and modelled with a rectangular $0.15\times0.08$ m cross-section, and the gauge is 1.4 m. The rails are connected to the sleepers via rail pads with stiffness $1.2\cdot10^8$ N/m and damping $1.24\cdot10^5$ Ns/m.

Vibrations are measured on a rigid surface footing placed 20.0 m from the track structure. The rigid footing has a square shape with a side length of 3.0 m. The footing is assumed to be 0.8 m thick and made from concrete. Therefore, the mass density of concrete is used to calculate the mass and mass moments of inertia, which are then added to the corresponding degrees of freedom of the rigid footing.

| Material | Young's modulus (MPa) | Poisson's ration (-) | Mass density (kg/m$^3$) | Damping ratio (-) |
|---|---|---|---|---|
| Concrete | 30000 | 0.15 | 2400 | 0.040 |
| Steel | 210000 | 0.25 | 7900 | 0.040 |
| Ballast | 100 | 0.35 | 1800 | 0.040 |
| Sub-ballast | 300 | 0.35 | 2200 | 0.040 |
| Subgrade | 120 | 0.35 | 2100 | 0.040 |
| Clay | 80 | 0.48 | 2000 | 0.045 |
| Sand | 250 | 0.30 | 2000 | 0.050 |

Table 1: Materials and their properties used in the analysis

The whole rail track structure and the receiver footing are placed on a 4.0 m thick layer of clay which lies on top of a half-space of sand. This stratification was chosen because the relatively soft layer of clay over the stiffer material (sand) "traps" the propagating vibrations in the upper soil layer, leading to higher excitation at the receiver position.

The system is excited by placing a vertical unit load on one of the rails. It is placed in three different positions along the rail: Position 1—at the centre of the track in the longitudinal direction; Position 2—6.0 m along the track from the centre; Position 3—12.0 m from the centre. In all of the positions, the load is acting on a node that is also connected to a sleeper through the rail pad. Using different positions allows analysis of the system response for cases in which the obstructions in the soil are not in the direct path of the propagating waves.

Four different cases were investigated:

- Free-field conditions. Nothing is placed between the rail track and the receiver footing. This case is used for comparison with other cases.
- A rigid box is embedded between the track and the footing, 10.0 m from the track. The box dimensions are 3.0×3.0×3.0 m$^3$. The top of the box is embedded 1.0 m from the ground surface. It is assumed that the box is filled with soil and that the density of the walls is close to the density of the surrounding soil. Therefore, the additional mass is not considered.
- A single-lane road is placed on the ground surface between the source and the receiver, 10.0 m from the track. The road is placed alongside the track and has the same length (30.0 m) as the rail track. It is constructed from concrete. The dimensions are: width 4.0 m and thickness 0.3 m. The road structure is modelled using Mindlin-Reissner shell finite elements coupled to soil through SSI nodes.
- A concrete pipe is placed alongside the rail track, 10.0 m from the track and embedded 1.5 m into the soil. As in the previous case, the pipe runs alongside the track and has the same length. The pipe is modelled as a cylindrical tube with an outer diameter of 1.0 m and an inner diameter of 0.75 m. It is modelled as a finite Euler-Bernoulli beam coupled to the soil through SSI nodes.
- Same as previous case, just this time the pipe is oriented at 45° angle to the rail track. The pipe centre is 10 m from the track.
- Once again the same embedded pipe is used. In this case, the pipe is at 90° angle to the track, that is the pipe goes under the rail track and extends towards the receiver footing.

## 4 THE EFFECT OF OBSTRUCTIONS IN THE WAVE PROPAGATION PATH

The wave propagation path was analysed for the previously described six cases. The analysis was performed from 1 Hz up to 50 Hz, with 1 Hz intervals. The results are presented in Figures 3 and 4.

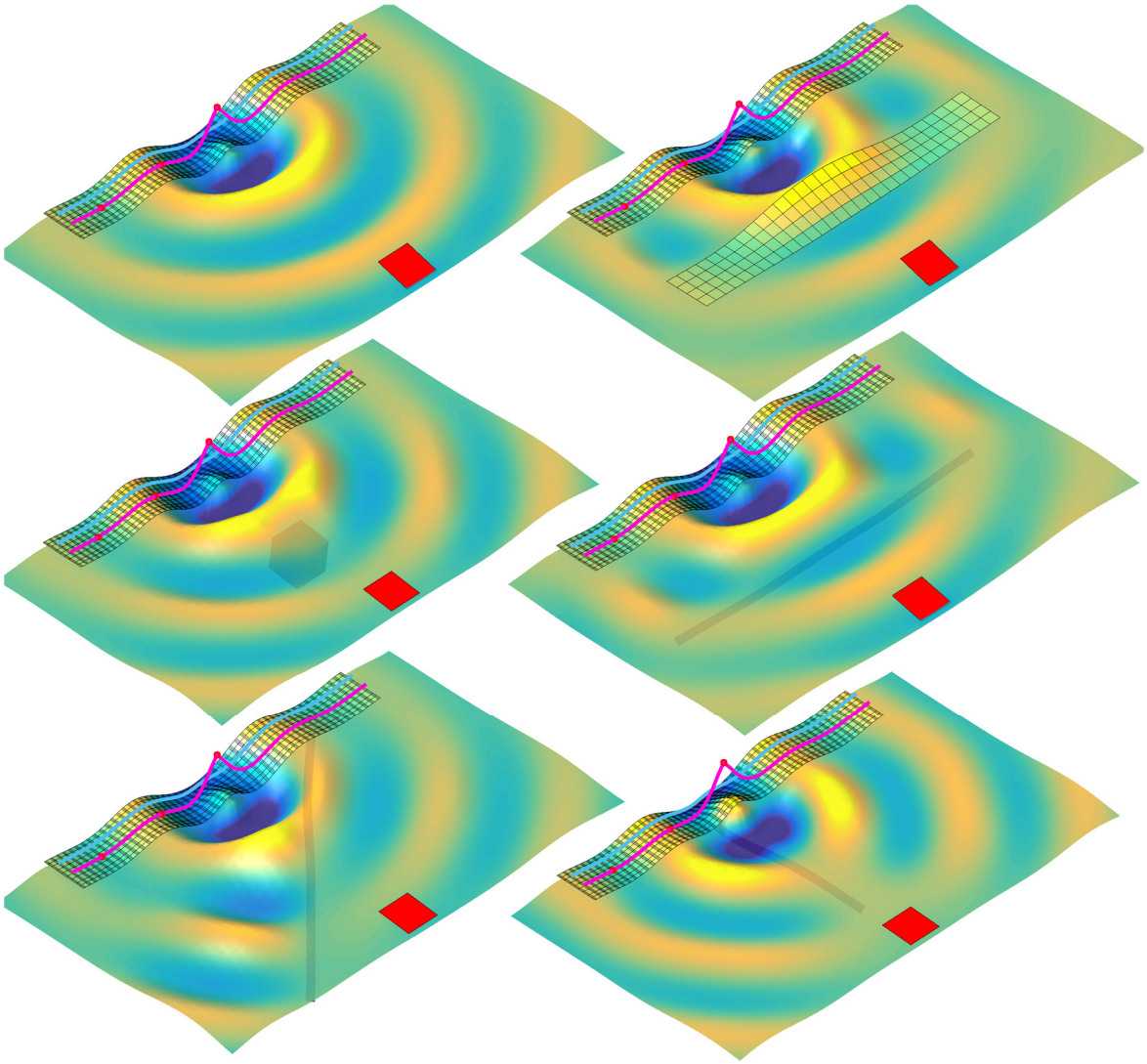

Figure 3: Steady state soil surface response for a load applied on the rail at the centre of the track, excited at 25 Hz. Blue/yellow shades indicate positive/negative displacement in vertical direction. The red dots on the rail show the three positions in which the load is applied within the analysis. In this case, the load is only applied in the first point. Top left: free-field; top right: road placed between the track and receiver; middle left: embedded rigid box; middle right: embedded pipe along the track; bottom left: embedded pipe at 45° angle to the track; bottom right: embedded pipe at orthogonal to the track.

Figure 3 shows the response of the soil surface excited at 15 Hz. All cases are shown for the load placed on the rail at Position 1. It is evident that the displacements of the soil are effected significantly by obstructions in the wave propagation path. The road surface forms a wave-impeding barrier for the propagating surface waves, thus decreasing the displacement field over a large area. However, the effect at the receiver footing is rather small. Further, the embedded rigid box has a larger effect for the receiver footing, however it is localized to a small shadow area behind the box. The overall effect to the displacement is much smaller when compared to the road case. Further, all three cases of embedded pipes cause very different behaviour of the system. For the pipe laid along the track, the effects are very similar to the road case—the displacement field is reduced in a large area, but the effects at the receiver footing are small. It can be seen that obstructions have less impact when the obstructions are laid orthogonally to the propagating waves. This is illustrated in the next case—embedded pipe at 45° angle. In this

case there is a significant reduction of displacements at the receiver footing, while the displacements are increased directly in front of the embedded pipe. Finally, the last case, the embedded pipe orthogonal to the track, provides the most significant reduction of displacements for the receiver footing. However, similar to the embedded box, the effects are localized to a smaller area and the surrounding displacement field is largely unaffected.

Further, Figure 4 shows the absolute velocities at the receiver position for all cases. Overall it can be seen that introducing obstructions in the wave propagation field have the highest effect in frequency ranges between 7–40 Hz, while frequencies up to 7 Hz are almost unaffected. In the 7–30 Hz range, the obstructions tend to reduce the velocities at the receiver position when compared to the free-field case. However, in the 30–40 Hz range the effects are not as evident. In this range, some cases—especially the road—tend to increase the velocities significantly.

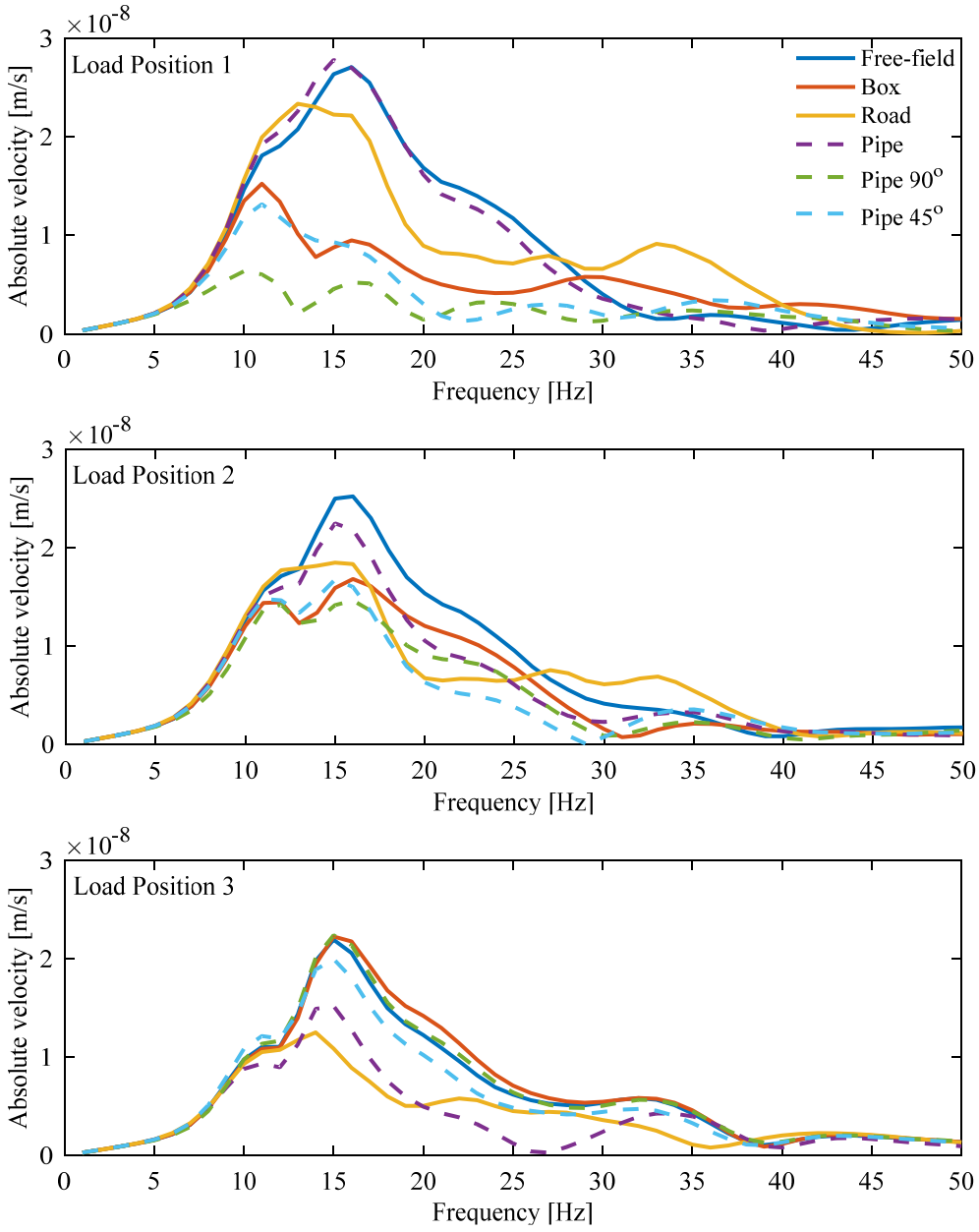


Figure 4: Response at the receiver for obstructions in the wave propagation path: a) load Position 1, applied on a rail at the centre of track; b) load Position 2, applied on a rail 6.0 m from the centre of the track; c) load Position 3, applied on a rail 12.0 m from the centre of the track.

Further, Figure 4 shows that pipe running along the rail track has a very small effect when the load is placed at Position 1. However, this effect increases when the load is placed further from the track centre. A completely opposite behaviour is observed with the pipe placed orthogonally to the track—the effects become smaller when the centre the load is placed further away from the track. This shows that the angle at which the waves reach the obstruction is a very important factor in the analysed system. The road case has a similar effect as the pipe placed along the track, but the overall effects across all loading positions are higher. This is due to larger stiffness and mass introduced to the system by the road, when compared to an embedded pipe. However, in the 30–40 Hz frequency range, the changes in absolute velocity relative to the reference case become positive, that is the velocities at the receiver increase when compared to the free-field case. Finally, the rigid box has a more localized effect. For loading in Positions 1 and 2, the effects are positive and rather large, but as soon as the box is not in the direct wave path between source and receiver (loading at Position 3) these effects disappear almost completely.

## 5 CONCLUSIONS

A presentation has been given of ground vibration due to harmonic excitation. Analysis was performed to investigate the effects of obstacles placed inside the soil body or on the ground surface between the source and the receiver. The load was applied on a railway track and the response was checked on a surface footing. Five different cases were tested: an embedded rigid box (simulating an infilled tank or former cellar), a segment of a single-lane road (or a large footpath) running parallel to the rail track on the soil surface, and three different orientations of an embedded pipe in the wave propagation path. The cases were compared to the free-field response with no obstacles in or on the ground. A computational model was created using an FE formulation to model the rail track structure and the obstructions, while the soil was modelled using a semi-analytical approach.

The results show that obstruction in the wave propagation field does cause significant changes in the overall system behaviour. In most cases, the obstacles have a mitigation effect, thus reducing the absolute velocities, especially within the 7–30 Hz frequency range. However, in some cases, the response increases within the 30–40 Hz frequency range. The effects of the structures considered in this paper are mostly seen at higher frequencies. This can be explained by the relatively small size of the considered structures, where at lower frequencies the wavelength in the soil body is much longer than the dimensions of the structures. Therefore, the effects at low frequencies are very small.

Future work could investigate these effects for a wider frequency range together with different soil-stratification cases. Further, analysis could be performed for different obstructions to the propagating waves that are commonly present, such as: tree roots, large boulders, underground cables, etc. Also more in-depth analysis of different orientations of the structures considered might reveal different effects caused to the system.

## ACKNOWLEDGMENTS

The research was carried out in the framework of the project “Urban Tranquility” under the Interreg V programme. The authors of this work gratefully acknowledge the European Regional Development Fund for the financial support.

## REFERENCES


[1] D. Connolly, A. Giannopoulos, and M. C. Forde. Numerical modelling of ground borne vibrations from high speed rail lines on embankments. *Soil Dynamics and Earthquake Engineering* **46**: 13–19, 2013.

[2] L. Andersen and S. R. K. Nielsen, Reduction of ground vibration by means of barriers or soil improvement along a railway track, *Soil Dyn. Earthq. Eng.*, **25**(7–10), 701–716, 2005.

[3] J.C.O. Nielsen, G. Lombaert, and S. François. A hybrid model for prediction of ground-borne vibration due to discrete wheel/rail irregularities. *Journal of Sound and Vibration* **345**: 103–120, 2015.

[4] L.V. Andersen, Influence of dynamic soil-structure interaction on building response to ground vibration, in Numerical Methods in Geotechnical Engineering—Proceedings of the 8th European Conference on Numerical Methods in Geotechnical Engineering, NUMGE 2014, 2014, vol. 2.

[5] W.T. Thomson, Transmission of elastic waves through a stratified solid medium, Journal of applied Physics **21.2:** 89–93, 1950.

[6] N.A. Haskell, The dispersion of surface waves on multilayered media, *Bulletin of the seismological Society of America* **43.1:** 17–34. 1953.

[7] X. Sheng, C. J. C. Jones, and M. Petyt, Ground vibration generated by a harmonic load acting on a railway track, *Journal of sound and vibration* **225.1**: 3–28, 1999.

[8] L. Andersen and J. Clausen, Impedance of surface footings on layered ground, *Computers & structures* **86.1**: 72–87, 2008.

[9] L. V. Andersen, "Dynamic soil–structure interaction of monopod and polypod foundations," in *Insights and Innovations in Structural Engineering, Mechanics and Computation, Proceedings of the Sixth International Conference on Structural Engineering, Mechanics and Computation, 5–7 September 2016, Cape Town, South Africa*, 2016, pp. 2036–2041.

[10] P. Bucinskas, L. V. Andersen, and K. Persson, "Numerical modelling of ground vibration caused by elevated high-speed railway lines considering structure-soil-structure interaction," in *Proceedings of the INTER-NOISE 2016 - 45th International Congress and Exposition on Noise Control Engineering: Towards a Quieter Future*, 2016.

COMPDYN 2017
6th ECCOMAS Thematic Conference on
Computational Methods in Structural Dynamics and Earthquake Engineering
M. Papadrakakis, M. Fragiadakis (eds.)
Rhodes Island, Greece, 15–17 June, 2017

# THE INFLUENCE OF IMPERFECTLY KNOWN LOCAL SUBSOIL CONDITIONS ON THE PREDICTION OF GROUND-BORNE VIBRATION IN BUILDINGS

**Manthos Papadopoulos, Stijn François, Geert Degrande and Geert Lombaert**

KU Leuven, Department of Civil Engineering, Structural Mechanics Section
Kasteelpark Arenberg 40, 3001 Leuven, Belgium
e-mail: {manthos.papadopoulos, stijn.francois, geert.degrande, geert.lombaert}@kuleuven.be

**Keywords:** ground-borne vibrations, dynamic soil-structure interaction, elastic wave propagation, stochastic elastic media, perfectly matched layers; Monte-Carlo simulation.

**Abstract.** *This paper examines the influence of imperfectly known local subsoil conditions on the response prediction of buildings to ground-borne environmental vibration. A probabilistic finite element-perfectly matched layers model is developed for the analysis of the dynamic soil-structure interaction problem where the shear modulus of the soil is modeled as a conditional random field. An incident wave field is propagated through the finite element-perfectly matched layers model by decomposing the displacement field of the soil in accordance with the subdomain formulation developed for the dynamic soil-structure interaction problem. Monte Carlo simulation is used to propagate the uncertainty on the subsoil properties to the response of a building. A parametric study is performed with respect to the spatial correlation length of the random field representing the shear modulus of the subsoil, and the foundation type of the building. The uncertain subsoil properties affect both the incident wave field exciting the building and the dynamic stiffness of the coupled soil-building system. The uncertainty of the building response varies over frequency bands but as a general trend increases with frequency.*

## 1 INTRODUCTION

Ground-borne vibration in the built environment are induced by environmental sources like road and railway traffic or construction and industrial activities. The passage of vehicles over uneven roads or tracks and the operation of heavy machinery generate elastodynamic waves that propagate through the soil and impinge on the foundation of nearby structures leading to structural vibrations. These vibrations may lead to malfunctioning of sensitive equipment, discomfort of people and structural damage. Furthermore, noise can be re-radiated from floors and walls.

Dynamic soil-structure interaction plays a crucial role in the prediction of the response of structures due to ground-borne vibration. Studies on dynamic soil-structure interaction initiated in the field of earthquake engineering for the design and construction of structures of high importance [1]. More recently, the growing traffic volume, the development of high-speed railway lines and the expansion of underground transportation networks in densely populated urban areas have lead to an interest in the problem for environmental vibration where building on the prior developments computational models have been developed for both the prediction of the induced incident wave field and the structural response [2].

In these models, the soil is commonly idealized as a horizontally stratified visco-elastic half-space composed by homogeneous layers. However, geotechnical investigations suggest that the soil properties exhibit considerable spatial variability even within apparently homogeneous soil deposits [3]. This variability is mainly attributed to the physical processes involved in the formation of the soil layers but also to man-made activities that may perturb the properties of virgin land. Since the soil directly beneath a building can have a predominant role in its response [4], the aim of this paper is to assess the influence of imperfectly known local subsoil conditions on the response predictions of buildings to ground-borne induced vibrations.

The paper starts with introduction of the dynamic soil-structure interaction model and the particularities of incorporating an incident wave field in the analysis. Next, the modeling of the stochastic subsoil is discussed. Finally, the results of a parametric study involving investigation with respect to the spatial correlation length of the random field representing the shear modulus of the subsoil, and the foundation type of the building are presented.

## 2 METHOD OF ANALYSIS

In dynamic soil-structure interaction computational models, the semi-infinite extent of the soil needs to be taken into account by allowing the radiation of elastodynamic waves to infinity. This is achieved by using either coupled finite element (FE)-boundary element (BE) formulations [5] or finite element formulations in conjunction with absorbing boundary conditions (ABC) [6, 7] or perfectly matched layers (PML) [8]. Both the coupled FE-BE formulations and the FE formulations with ABC or PML have advantages and disadvantages that make them preferable for different problem settings. For the applications of this paper, a FE-PML formulation is used as it proved computationally more efficient.

### 2.1 The dynamic soil-structure interaction model

Figure 1a depicts the dynamic soil-structure interaction problem considered in this work. The building $\Omega_{\mathrm{b}}$ is surrounded by a bounded volume of subsoil $\Omega_{\mathrm{s}}^{\mathrm{i}}$ with imperfectly known properties whereas the rest of the subsoil $\Omega_{\mathrm{s}}^{\mathrm{e}}$ is considered well known. The building is excited by an incident wave field $\hat{\mathbf{u}}_{\mathrm{inc}}$, where the hat above the variable denotes its representation in the frequency domain. Figure 1b shows how this problem is modeled by means of finite elements

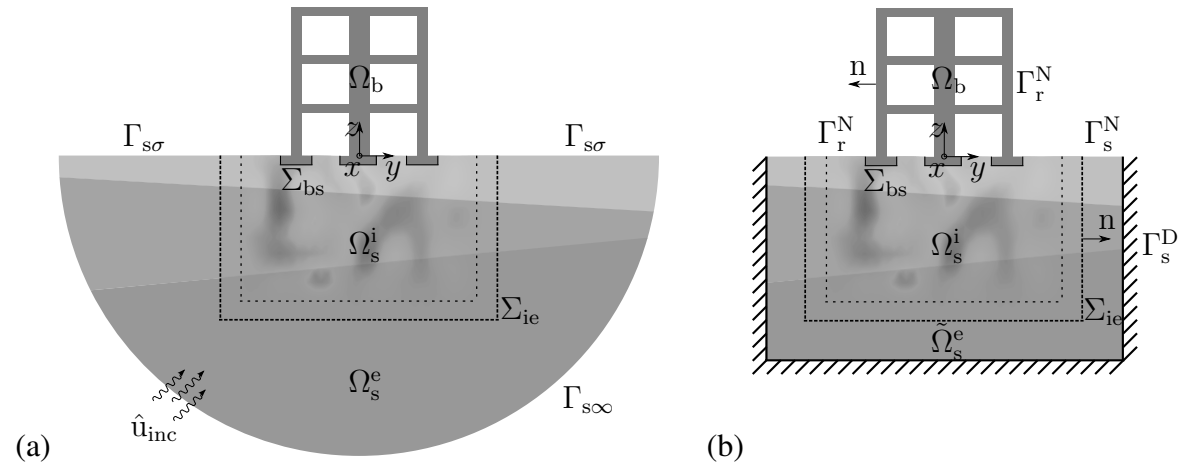


Figure 1: (a) Dynamic soil-structure interaction problem and (b) FE-PML model.

and perfectly matched layers. The computational domain $\Omega$ is divided into the regular domain $\Omega_r = \Omega_b \cup \Omega_s^i$ and the PML buffer zone $\tilde{\Omega}_s^e$ surrounding this domain. The regular domain $\Omega_r$ is modeled with FE where the material properties of $\Omega_s^i$ are modeled as conditional random fields (section 2.3) with a small zone close to the boundaries of this domain having deterministic properties. The PML buffer zone $\tilde{\Omega}_s^e$ aims to simulate the truncated unbounded soil $\Omega_s^e$ at the limits of the regular domain $\Sigma_{ie}$. The soil-foundation interface is denoted as $\Sigma_{bs}$. The FE-PML model is developed based on the three-dimensional elastodynamic equations in the frequency domain.

In order to artificially attenuate the elastodynamic waves that enter into the PML buffer zone, complex coordinate stretching is applied in $\tilde{\Omega}_s^e$. For a coordinate $s$, representing the $x$, $y$ or $z$ coordinate, the stretched coordinate $\tilde{s}$ is defined as [8]:

$$\tilde{s} = \int_0^s \hat{\lambda}_s(s)\,\mathrm{d}s = s_o + \int_{s_o}^{s_t} \hat{\lambda}_s(s)\,\mathrm{d}s \tag{1}$$

The stretch function $\hat{\lambda}_s$ is defined as:

$$\hat{\lambda}_s(s) = \alpha_{0s}(s) + \frac{\alpha_{1s}(s)}{i\omega} \tag{2}$$

where $\alpha_{0s}$ and $\alpha_{1s}$ are polynomial functions that control the amplitude attenuation of the evanescent and propagating waves inside the PML buffer zone, and $\omega \in R$ is the frequency of analysis. The FE system of equations is written in the frequency domain as:

$$\hat{\mathbf{K}}\underline{\hat{\mathbf{u}}} = \underline{\hat{\mathbf{f}}} \tag{3}$$

where $\hat{\mathbf{K}} = \mathbf{K} + (i\omega)^2\,\mathbf{M}$ is the dynamic stiffness matrix of the system with $\mathbf{K} \in \mathrm{C}^{n\times n}$ and $\mathbf{M} \in \mathrm{C}^{n\times n}$ the stiffness and mass matrix with $n$ the number of degrees of freedom in the model. The vector $\underline{\hat{\mathbf{u}}} \in \mathrm{C}^{n\times 1}$ collects the nodal displacements while $\underline{\hat{\mathbf{f}}} \in \mathrm{C}^{n\times 1}$ collects the equivalent nodal loads. Equation (3) can be rewritten in an expanded form according to the subdomain definitions of figure 1:

$$\begin{bmatrix} \hat{\mathbf{K}}_{bb} & \hat{\mathbf{K}}_{b\Sigma_{bs}} & \mathbf{0} \\ \hat{\mathbf{K}}_{\Sigma_{bs}b} & \hat{\mathbf{K}}_{\Sigma_{bs}\Sigma_{bs}}(\theta) & \hat{\mathbf{K}}_{\Sigma_{bs}s}(\theta) \\ \mathbf{0} & \hat{\mathbf{K}}_{s\Sigma_{bs}}(\theta) & \hat{\mathbf{K}}_{ss}(\theta) \end{bmatrix} \begin{Bmatrix} \underline{\hat{\mathbf{u}}}_b \\ \underline{\hat{\mathbf{u}}}_{\Sigma_{bs}} \\ \underline{\hat{\mathbf{u}}}_s \end{Bmatrix} = \begin{Bmatrix} \underline{\hat{\mathbf{f}}}_b \\ \underline{\hat{\mathbf{f}}}_{\Sigma_{bs}} \\ \underline{\hat{\mathbf{f}}}_s \end{Bmatrix} \tag{4}$$

where $\theta$ denotes an elementary event of the event space $\Theta$. Since the material properties in $\Omega_{\mathrm{s}}^{\mathrm{i}}$ are modeled as random fields, the corresponding dynamic stiffness block matrices in equation (4) are also stochastic. The mapping of the stochastic material properties of $\Omega_{\mathrm{s}}^{\mathrm{i}}$ onto the finite element model is briefly discussed in section 2.3.

To facilitate the subsequent discussion, it is useful to rewrite equation (4) by dynamically condensing the degrees of freedom of the soil $\underline{\hat{\mathbf{u}}}_{\mathrm{s}}$ on the degrees of freedom $\underline{\hat{\mathbf{u}}}_{\Sigma_{\mathrm{bs}}}$ of the soil-foundation interface $\Sigma_{\mathrm{bs}}$:

$$\begin{bmatrix} \hat{\mathbf{K}}_{\mathrm{bb}} & \hat{\mathbf{K}}_{\mathrm{b}\Sigma_{\mathrm{bs}}} \\ \hat{\mathbf{K}}_{\Sigma_{\mathrm{bs}}\mathrm{b}} & \hat{\tilde{\mathbf{K}}}_{\Sigma_{\mathrm{bs}}\Sigma_{\mathrm{bs}}}(\theta) \end{bmatrix} \begin{Bmatrix} \underline{\hat{\mathbf{u}}}_{\mathrm{b}} \\ \underline{\hat{\mathbf{u}}}_{\Sigma_{\mathrm{bs}}} \end{Bmatrix} = \begin{Bmatrix} \underline{\hat{\mathbf{f}}}_{\mathrm{b}} \\ \underline{\hat{\tilde{\mathbf{f}}}}_{\Sigma_{\mathrm{bs}}}(\theta) \end{Bmatrix} \tag{5}$$

with $\underline{\hat{\tilde{\mathbf{f}}}}_{\Sigma_{\mathrm{bs}}} = \underline{\hat{\mathbf{f}}}_{\Sigma_{\mathrm{bs}}} - \hat{\mathbf{K}}_{\Sigma_{\mathrm{bs}}\mathrm{s}}\hat{\mathbf{K}}_{\mathrm{ss}}^{-1}\underline{\hat{\mathbf{f}}}_{\mathrm{s}}$ and $\hat{\tilde{\mathbf{K}}}_{\Sigma_{\mathrm{bs}}\Sigma_{\mathrm{bs}}}$ the Schur complement of $\hat{\mathbf{K}}_{\mathrm{ss}}$ on $\hat{\mathbf{K}}_{\Sigma_{\mathrm{bs}}\Sigma_{\mathrm{bs}}}$:

$$\hat{\tilde{\mathbf{K}}}_{\Sigma_{\mathrm{bs}}\Sigma_{\mathrm{bs}}} = \hat{\mathbf{K}}_{\Sigma_{\mathrm{bs}}\Sigma_{\mathrm{bs}}} - \hat{\mathbf{K}}_{\Sigma_{\mathrm{bs}}\mathrm{s}}\hat{\mathbf{K}}_{\mathrm{ss}}^{-1}\hat{\mathbf{K}}_{\mathrm{s}\Sigma_{\mathrm{bs}}} \tag{6}$$

## 2.2 Incorporation of an incident wave field

In order to propagate an incident wave field $\hat{\mathbf{u}}_{\mathrm{inc}}$ generated by a remote excitation source in $\Omega_{\mathrm{s}}^{\mathrm{e}}$ through the FE-PML model, an equivalent traction field $\hat{\mathbf{t}}^{\mathbf{n}}$ on the interface $\Sigma_{\mathrm{ie}}$ needs first to be determined. This traction field is defined based on a methodology where the displacement field of the soil in $\Omega_{\mathrm{s}}^{\mathrm{e}}$ is decomposed in accordance with the subdomain formulation of the soil-structure interaction problem as was originally conceived for FE-BE formulations [9]. The displacement field $\hat{\mathbf{u}}_{\mathrm{s}}^{\mathrm{e}}$ in the exterior soil $\Omega_{\mathrm{s}}^{\mathrm{e}}$ is decomposed as (figure 2):

$$\hat{\mathbf{u}}_{\mathrm{s}}^{\mathrm{e}} = \hat{\mathbf{u}}_{\mathrm{inc}} + \hat{\mathbf{u}}_{\mathrm{d0}} + \hat{\mathbf{u}}_{\mathrm{sc}} \tag{7}$$

In this expression, $\hat{\mathbf{u}}_{\mathrm{inc}}$ is the displacement field of the globally deterministic soil $\Omega_{\mathrm{s}} = \Omega_{\mathrm{s}}^{\mathrm{e}} \cup \Omega_{\mathrm{s}}^{\mathrm{i,det}}$ due to a remote excitation source (figure 2b), $\hat{\mathbf{u}}_{\mathrm{d0}}$ is the locally diffracted displacement field radiated in the exterior soil $\Omega_{\mathrm{s}}^{\mathrm{e}}$ with excavated the interior soil $\Omega_{\mathrm{s}}^{\mathrm{i}}$ for which applies $\hat{\mathbf{u}}_{\mathrm{d0}|\Sigma_{\mathrm{ie}}} = -\hat{\mathbf{u}}_{\mathrm{inc}|\Sigma_{\mathrm{ie}}}$ on the interface $\Sigma_{\mathrm{ie}}$ (figure 2c), and $\hat{\mathbf{u}}_{\mathrm{sc}}$ is the stochastic diffracted displacement field radiated in the exterior soil $\Omega_{\mathrm{s}}^{\mathrm{e}}$ due to the displacements of the stochastic interior soil $\Omega_{\mathrm{s}}^{\mathrm{i}}$ on the interface $\Sigma_{\mathrm{ie}}$ (figure 2d).

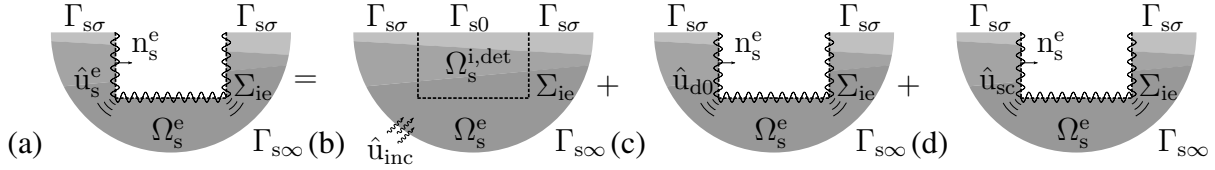


Figure 2: Decomposition of (a) the displacement field $\hat{\mathbf{u}}_{\mathrm{s}}^{\mathrm{e}}$ of the exterior soil $\Omega_{\mathrm{s}}^{\mathrm{e}}$ into (b) the incident wave field $\hat{\mathbf{u}}_{\mathrm{inc}}$ of the globally deterministic soil $\Omega_{\mathrm{s}} = \Omega_{\mathrm{s}}^{\mathrm{e}} \cup \Omega_{\mathrm{s}}^{\mathrm{i,det}}$, (c) the locally diffracted displacement field $\hat{\mathbf{u}}_{\mathrm{d0}}$ and (d) the diffracted displacement field $\hat{\mathbf{u}}_{\mathrm{sc}}$.

On the interface $\Sigma_{\mathrm{ie}}$, the compatibility condition $\hat{\mathbf{u}}_{\mathrm{s}}^{\mathrm{i}} = \hat{\mathbf{u}}_{\mathrm{s}}^{\mathrm{e}}$ applies and the equilibrium equation reads as:

$$\hat{\mathbf{t}}^{\mathbf{n}}\left(\hat{\mathbf{u}}_{\mathrm{s}}^{\mathrm{i}}\right) + \hat{\mathbf{t}}^{\mathbf{n_s^e}}\left(\hat{\mathbf{u}}_{\mathrm{s}}^{\mathrm{e}}\right) = \mathbf{0} \quad \text{on } \Sigma_{\mathrm{ie}} \tag{8}$$

where $\hat{\mathbf{t}}^{\mathbf{n}}\left(\hat{\mathbf{u}}_{\mathrm{s}}^{\mathrm{i}}\right)$ and $\hat{\mathbf{t}}^{\mathbf{n_s^e}}\left(\hat{\mathbf{u}}_{\mathrm{s}}^{\mathrm{e}}\right)$ are the traction fields imposed on the interface $\Sigma_{\mathrm{ie}}$ by the stochastic interior soil $\Omega_{\mathrm{s}}^{\mathrm{i}}$ and the deterministic exterior soil $\Omega_{\mathrm{s}}^{\mathrm{e}}$, respectively. Subsequently, the decomposition of equation (7) is introduced in equation (8):

$$\hat{\mathbf{t}}^{\mathbf{n}}\left(\hat{\mathbf{u}}_{\mathrm{s}}^{\mathrm{i}}\right)+\hat{\mathbf{t}}^{\mathbf{n_s^e}}\left(\hat{\mathbf{u}}_{\mathrm{sc}}\right)=\underbrace{-\hat{\mathbf{t}}^{\mathbf{n_s^e}}\left(\hat{\mathbf{u}}_{\mathrm{inc}}\right)-\hat{\mathbf{t}}^{\mathbf{n_s^e}}\left(\hat{\mathbf{u}}_{\mathrm{d0}}\right)}_{\hat{\hat{\mathbf{t}}}^{\mathrm{n}}}\quad\text{on }\Sigma_{\mathrm{ie}} \tag{9}$$

The resultant tractions on the left hand side of equation (9) are the stochastic tractions imposed on the interface $\Sigma_{\mathrm{ie}}$ by $\Omega_{\mathrm{s}}=\Omega_{\mathrm{s}}^{\mathrm{e}}\cup\Omega_{\mathrm{s}}^{\mathrm{i}}$, whereas the resultant tractions on the right hand side of the equation are the required deterministic tractions $\hat{\hat{\mathbf{t}}}^{\mathrm{n}}$ on the interface $\Sigma_{\mathrm{ie}}$ to propagate the exterior incident wave field $\hat{\mathbf{u}}_{\mathrm{inc}}$ through the stochastic interior soil $\Omega_{\mathrm{s}}^{\mathrm{i}}$.

The weak form of equation (9) is obtained by considering a virtual displacement field $\hat{\mathbf{v}}$ over the interface $\Sigma_{\mathrm{ie}}$ where after using the same shape functions as for the FE-PML model discretization, the following set of equations is obtained:

$$\int_{\Sigma_{\mathrm{ie}}}\mathbf{N}^{\mathrm{T}}\hat{\mathbf{t}}^{\mathbf{n}}\left(\hat{\mathbf{u}}_{\mathrm{s}}^{\mathrm{i}}\right)\mathrm{d}\Gamma+\int_{\Sigma_{\mathrm{ie}}}\mathbf{N}^{\mathrm{T}}\hat{\mathbf{t}}^{\mathbf{n_s^e}}\left(\hat{\mathbf{u}}_{\mathrm{sc}}\right)\mathrm{d}\Gamma= \underbrace{-\int_{\Sigma_{\mathrm{ie}}}\mathbf{N}^{\mathrm{T}}\hat{\mathbf{t}}^{\mathbf{n_s^e}}\left(\hat{\mathbf{u}}_{\mathrm{inc}}\right)\mathrm{d}\Gamma-\int_{\Sigma_{\mathrm{ie}}}\mathbf{N}^{\mathrm{T}}\hat{\mathbf{t}}^{\mathbf{n_s^e}}\left(\hat{\mathbf{u}}_{\mathrm{d0}}\right)\mathrm{d}\Gamma}_{\left\{\mathbf{0},\,\mathbf{0},\,\underline{\hat{\mathbf{f}}}_{\mathrm{s}}\right\}^{\mathrm{T}}} \tag{10}$$

The left hand side of equation (10) corresponds now to the dynamic impedance of the FE-PML model on interface $\Sigma_{\mathrm{ie}}$, while the right hand side contains the required equivalent nodal forces on the interface $\Sigma_{\mathrm{ie}}$ that represent the exterior incident wave field $\hat{\mathbf{u}}_{\mathrm{inc}}$.

The deterministic displacement field $\hat{\mathbf{u}}_{\mathrm{inc}}$ and traction field $\hat{\mathbf{t}}_{\mathrm{inc}}=\hat{\mathbf{t}}^{\mathbf{n_s^e}}\left(\hat{\mathbf{u}}_{\mathrm{inc}}\right)$ of the globally deterministic soil $\Omega_{\mathrm{s}}=\Omega_{\mathrm{s}}^{\mathrm{e}}\cup\Omega_{\mathrm{s}}^{\mathrm{i,det}}$ are computed using a source model, generally assuming that the coupling between the subproblems of the source and the receiver can be disregarded [10]. In the present work, the direct stiffness method is used for this purpose [11].

The second integral on the right-hand side of equation (10) is not computed directly as the traction field $\hat{\mathbf{t}}_{\mathrm{d0}}=\hat{\mathbf{t}}^{\mathbf{n_s^e}}\left(\hat{\mathbf{u}}_{\mathrm{d0}}\right)$ is not known a priori. Instead, the integral is implicitly evaluated through the displacement field $\hat{\mathbf{u}}_{\mathrm{inc}}$ on the interface $\Sigma_{\mathrm{ie}}$. According to the definition of the locally diffracted displacement field $\hat{\mathbf{u}}_{\mathrm{d0}}$, this problem boils down to computing the reaction forces $\underline{\hat{\mathbf{r}}}_{\Sigma_{\mathrm{ie}}}^{\mathrm{e}}=\underline{\hat{\mathbf{r}}}_{\Sigma_{\mathrm{ie}}}^{\mathrm{e}}\left(\hat{\mathbf{u}}_{\mathrm{d0}|\Sigma_{\mathrm{ie}}}\right)$ on the interface $\Sigma_{\mathrm{ie}}$ of the FE-PML model with excavated the interior soil $\Omega_{\mathrm{s}}^{\mathrm{i}}$ due to imposed displacements $\hat{\mathbf{u}}_{\mathrm{d0}|\Sigma_{\mathrm{ie}}}=-\hat{\mathbf{u}}_{\mathrm{inc}|\Sigma_{\mathrm{ie}}}$ on the interface $\Sigma_{\mathrm{ie}}$ (figure 3). The FE-PML system of equations of the truncated exterior soil $\tilde{\Omega}_{\mathrm{s}}^{\mathrm{e}}$ due to imposed displacements $\underline{\hat{\mathbf{u}}}_{\Sigma_{\mathrm{ie}}}^{\mathrm{e}}$ on the interface $\Sigma_{\mathrm{ie}}$ is:

$$\begin{bmatrix}\hat{\mathbf{K}}_{\Sigma_{\mathrm{ie}}\Sigma_{\mathrm{ie}}}^{\mathrm{e}} & \hat{\mathbf{K}}_{\Sigma_{\mathrm{ie}}\mathrm{s}}^{\mathrm{e}}\\ \hat{\mathbf{K}}_{\mathrm{s}\Sigma_{\mathrm{ie}}}^{\mathrm{e}} & \hat{\mathbf{K}}_{\mathrm{ss}}^{\mathrm{e}}\end{bmatrix}\begin{Bmatrix}\underline{\hat{\mathbf{u}}}_{\Sigma_{\mathrm{ie}}}^{\mathrm{e}}\\ \underline{\hat{\mathbf{u}}}_{\mathrm{s}}^{\mathrm{e}}\end{Bmatrix}=\begin{Bmatrix}\underline{\hat{\mathbf{r}}}_{\Sigma_{\mathrm{ie}}}^{\mathrm{e}}\\ \mathbf{0}\end{Bmatrix} \tag{11}$$

with $\underline{\hat{\mathbf{u}}}_{\Sigma_{\mathrm{ie}}}^{\mathrm{e}}=\hat{\mathbf{u}}_{\mathrm{d0}|\Sigma_{\mathrm{ie}}}=-\hat{\mathbf{u}}_{\mathrm{inc}|\Sigma_{\mathrm{ie}}}$. Rearranging and solving this system with respect to $\underline{\hat{\mathbf{r}}}_{\Sigma_{\mathrm{ie}}}^{\mathrm{e}}$ yields:

$$\underline{\hat{\mathbf{r}}}_{\Sigma_{\mathrm{ie}}}^{\mathrm{e}}\left(-\hat{\mathbf{u}}_{\mathrm{inc}|\Sigma_{\mathrm{ie}}}\right)=\left(\hat{\mathbf{K}}_{\mathrm{s}\Sigma_{\mathrm{ie}}}^{\mathrm{e}}\hat{\mathbf{K}}_{\mathrm{ss}}^{\mathrm{e}-1}\hat{\mathbf{K}}_{\mathrm{s}\Sigma_{\mathrm{ie}}}^{\mathrm{e}}-\hat{\mathbf{K}}_{\Sigma_{\mathrm{ie}}\Sigma_{\mathrm{ie}}}^{\mathrm{e}}\right)\hat{\mathbf{u}}_{\mathrm{inc}|\Sigma_{\mathrm{ie}}} \tag{12}$$

The required nodal loads $\underline{\hat{\mathbf{f}}}_{\mathrm{s}}$ due to an incident wave field are finally obtained as:

$$\begin{Bmatrix}\mathbf{0}\\ \mathbf{0}\\ \underline{\hat{\mathbf{f}}}_{\mathrm{s}}\end{Bmatrix}\simeq-\int_{\Sigma_{\mathrm{ie}}}\mathbf{N}^{\mathrm{T}}\hat{\mathbf{t}}^{\mathbf{n_s^e}}\left(\hat{\mathbf{u}}_{\mathrm{inc}}\right)\mathrm{d}\Gamma-\begin{Bmatrix}\mathbf{0}\\ \mathbf{0}\\ \underline{\hat{\mathbf{r}}}^{\mathrm{e}}\end{Bmatrix} \tag{13}$$

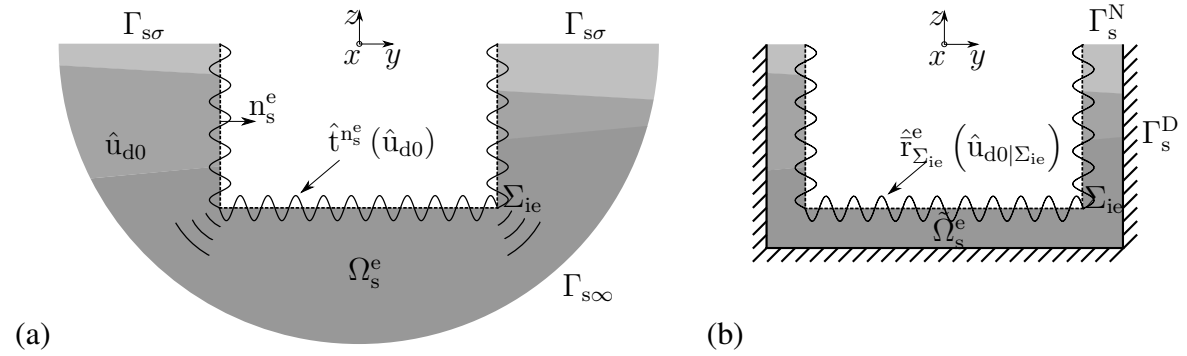


Figure 3: (a) Locally diffracted displacement field $\hat{\mathbf{u}}_{\mathrm{d0}}$ and (b) FE-PML model of the truncated exterior soil $\tilde{\Omega}_{\mathrm{s}}^{\mathrm{e}}$.

where $\hat{\underline{\mathbf{r}}}^{\mathrm{e}} = \left\{\hat{\underline{\mathbf{r}}}^{\mathrm{e}}_{\Sigma_{\mathrm{ie}}},\, \mathbf{0}\right\}^{\mathrm{T}}$ according to equation (11).

### 2.3 Stochastic subsoil modeling

The subsoil in $\Omega_{\mathrm{s}}^{\mathrm{i}}$ is modeled as a heterogeneous isotropic elastic medium with imperfectly known material properties. In the present paper, the characterization of the elastic properties of the subsoil is based on its shear modulus $G$ and Poisson's ratio $\nu$. The shear modulus is selected as an elastic parameter to characterize the subsoil because some of its statistical properties can be implicitly elicited from cone penetration test (CPT) data for which a large database is available [12]. Because the variation of the Poisson's ratio $\nu$ and the material density $\rho$ within soil deposits is rather small, their values are fairly considered as deterministic. Hence, the investigation focuses only on the shear modulus $G$ of the subsoil in the following.

The shear modulus $G$ of the subsoil in $\Omega_{\mathrm{s}}^{\mathrm{i}}$ is modeled as a random field $G(\boldsymbol{x}, \theta)$ defined over the parameter space $\boldsymbol{x} \in \Omega_{\mathrm{s}}^{\mathrm{i}}$ [13]. Since the complete probabilistic characterization of the shear modulus $G(\boldsymbol{x}, \theta)$ is infeasible, its description relies only on its second order statistics. Thus, the information on the shear modulus $G(\boldsymbol{x}, \theta)$ limited to its marginal probability distribution function (PDF) $p_{\mathrm{G}}(\theta)$, mean $\mu_{\mathrm{G}}(\boldsymbol{x})$, variance $\sigma_{\mathrm{G}}^2(\boldsymbol{x})$ and auto-correlation coefficient $\rho_{\mathrm{GG}}(\boldsymbol{x}, \boldsymbol{x'})$. Because the shear modulus $G(\boldsymbol{x}, \theta)$ should take strictly positive values, the Gamma distribution is opted as its marginal PDF. The covariance function $C_{\mathrm{GG}}(\boldsymbol{x}, \boldsymbol{x'})$ is defined as:

$$C_{\mathrm{GG}}(\boldsymbol{x}, \boldsymbol{x'}) = \sigma_{\mathrm{G}}(\boldsymbol{x})\, \sigma_{\mathrm{G}}(\boldsymbol{x'})\, \rho_{\mathrm{GG}}(\boldsymbol{x}, \boldsymbol{x'}) \tag{14}$$

The stochastic shear modulus $G(\boldsymbol{x}, \theta)$ is simulated through a translation process based on the Nataf multivariate distribution [14]. The non-Gaussian shear modulus $G(\boldsymbol{x}, \theta)$ is defined as a non-linear function of an underlying Gaussian random field $\mathcal{G}(\boldsymbol{x}, \theta)$ as:

$$G(\boldsymbol{x}, \theta) = P_{\Gamma}^{-1}\left(P_{\mathrm{N}}\left(\frac{\mathcal{G}(\boldsymbol{x}, \theta) - \mu_{\mathcal{G}}(\boldsymbol{x})}{\sigma_{\mathcal{G}}(\boldsymbol{x})}\right)\right) \tag{15}$$

where $P_{\Gamma}^{-1}$ is the inverse of the target Gamma marginal cumulative distribution (CDF), $P_{\mathrm{N}}$ is the standard normal CDF function, and $\mu_{\mathcal{G}}(\boldsymbol{x}) = \mu_{\mathrm{G}}(\boldsymbol{x})$ and $\sigma_{\mathcal{G}}(\boldsymbol{x}) = \sigma_{\mathrm{G}}(\boldsymbol{x})$ are respectively the mean and variance of $\mathcal{G}(\boldsymbol{x}, \theta)$. Furthermore, because matching material properties at the interface between $\Omega_{\mathrm{s}}^{\mathrm{i}}$ and $\Omega_{\mathrm{s}}^{\mathrm{e}}$ are desirable, the shear modulus $G(\boldsymbol{x}, \theta)$ is modeled as a conditional random field $\bar{G}(\boldsymbol{x}, \theta)$ with prescribed deterministic values at the interface $\Sigma_{\mathrm{ie}}$ [13].

In order to generate realizations of the shear modulus $\bar{G}(\boldsymbol{x}, \theta)$, it is necessary to reduce its infinite dimensionality into a finite set of random variables. In this work, this is achieved by

discretizing the continuous parameter space $\boldsymbol{x} \in \Omega_{\mathrm{s}}^{\mathrm{i}}$ into a finite set of control points $\boldsymbol{x}_k \in \Omega_{\mathrm{s}}^{\mathrm{i}}$ with $k \in \{1, ..., n_{\mathrm{k}}\}$ [15]. After discretization, the random field $\bar{G}(\boldsymbol{x}, \theta)$ is represented by a random vector $\bar{\mathbf{G}}(\theta)$ corresponding to the evaluation of the random field at the set of control points $\boldsymbol{x}_k$. Realizations of the random vector $\bar{\boldsymbol{\mathcal{G}}}(\theta)$ can be then generated as:

$$\bar{\boldsymbol{\mathcal{G}}}(\theta) \approx \boldsymbol{\mu}_{\boldsymbol{\mathcal{G}}} + \sum_{k=1}^{n_{\mathrm{m}}} \xi_k(\theta) \sqrt{\lambda_k} \boldsymbol{\phi}_k \tag{16}$$

where $\lambda_k$ and $\boldsymbol{\phi}_k$ are the $k$-th eigenvalue and eigenvector of the covariance matrix $\bar{\mathbf{C}}_{\boldsymbol{\mathcal{G}}\boldsymbol{\mathcal{G}}}$ respectively, and $\xi_k(\theta)$ are random variables sampled from the standard Gaussian distribution $\mathcal{N}(0, 1)$. In order to improve the representativeness of the sampled pool of realizations, Latin hypercube sampling with artificial correlation reduction is used in the present paper [16]. This sampling scheme explores the event space more uniformly avoiding the formation of clusters of realizations that might stall convergence in a Monte Carlo simulation. The number $n_{\mathrm{m}} \leq n_{\mathrm{k}}$ of eigenpairs ($\lambda_k$, $\boldsymbol{\phi}_k$) included in the expansion of equation (16) can be decided based on a maximum acceptable relative truncation error:

$$\epsilon(n_{\mathrm{m}}) = 1 - \frac{1}{\mathrm{Tr}\left(\bar{\mathbf{C}}_{\boldsymbol{\mathcal{G}}\boldsymbol{\mathcal{G}}}\right)} \sum_{k=1}^{n_{\mathrm{m}}} \lambda_k \leq \epsilon_{\max} \tag{17}$$

where $\mathrm{Tr}(\cdot)$ denotes the trace of a matrix.

In equation (4), the dynamic stiffness block matrices are formulated by taking into account the continuous variation of the shear modulus $\bar{G}(\boldsymbol{x}, \theta)$ in $\Omega_{\mathrm{s}}^{\mathrm{i}}$. The stochastic shear modulus $\bar{\mathbf{G}}(\theta)$ is first evaluated at the finite element nodes and subsequently interpolated at any point of domain $\Omega_{\mathrm{s}}^{\mathrm{i}}$ by using the same FE shape functions as for the interpolation of the displacements [17].

## 3 PARAMETRIC STUDY

The influence of the imperfectly known local subsoil conditions on the response predictions of buildings to ground-borne vibration is assessed in a parametric study. To this end, a three story reinforced concrete office building is considered with the dimensions shown in table 1. The Young's modulus of the building is $E_{\mathrm{s}} = 30\,\mathrm{GPa}$ while its material density is $\rho_{\mathrm{s}} = 2500\,\mathrm{kg/m^3}$. Figure 4 shows the $i$-th floor layout of the building. Two different cases are

| $h_{\mathrm{s}}$ [m] | $t_{\mathrm{s}}$ [m] | $C$ [m × m] | $B$ [m × m] | $W_x$ [m × m] | $W_y$ [m × m] |
|---|---|---|---|---|---|
| 3 | 0.15 | 0.35 × 0.35 | 0.20 × 0.50 | 1.50 × 0.20 | 0.20 × 1.50 |

Table 1: R/C building characteristics.

examined for the building's foundation: a) a uniform raft foundation with thickness $t_{\mathrm{f}} = 0.60$ m, and b) individual footings for each column and wall with a thickness of $t_{\mathrm{f}} = 0.40$ m. The soil underneath the building is modeled as a visco-elastic half-space with the mean properties shown in table 2. The building response is investigated by computing transfer functions which relate its displacements to a point load applied at the surface of the soil at the point $\boldsymbol{S}(-34\,\mathrm{m}, -26\,\mathrm{m}, 0\,\mathrm{m})$ with respect to the origin of the reference system. The analysis is performed in the frequency range between 1 Hz and 80 Hz which is of interest for problems of environmental ground vibration.

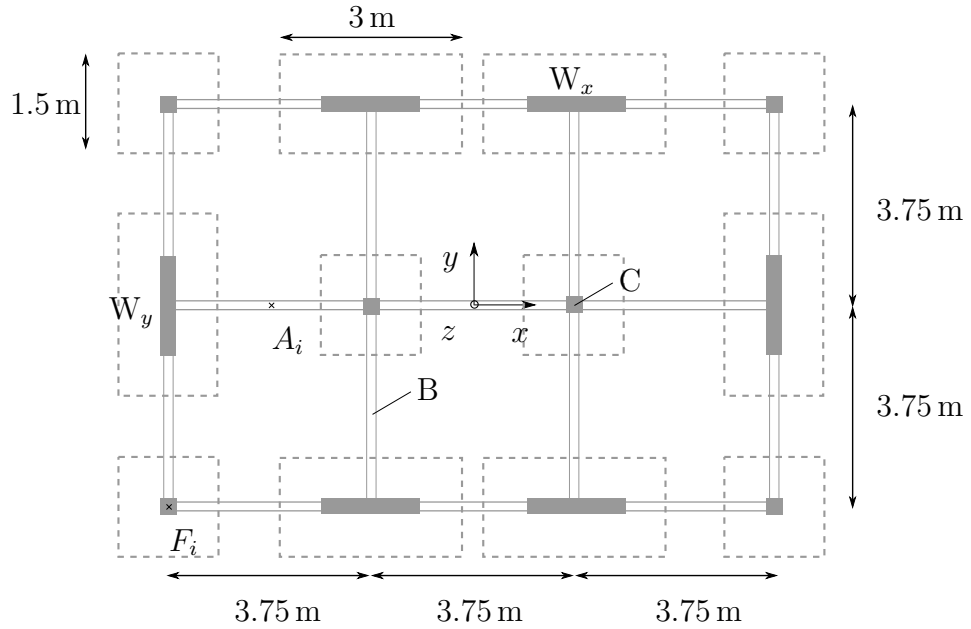


Figure 4: Building layout at the $i$-th floor where $\mathrm{W}_x$ and $\mathrm{W}_y$ stands for the walls in the $x$ and the $y$ direction, C stands for the columns and B for the beams. The outline of the foundation footings is also shown with dashed lines. The receiver locations $A_i$ and $F_i$ at the $i$-th floor are indicated with $\times$.

| $h$ [m] | $C_\mathrm{s}$ [m/s] | $C_\mathrm{p}$ [m/s] | $G$ [MPa] | $\nu$ [$-$] | $\rho$ [kg/m$^3$] | $\beta$ [$-$] |
|---|---|---|---|---|---|---|
| $\infty$ | 300 | 600 | 162 | 1/3 | 1800 | 0.01 |

Table 2: Subsoil mean properties.

Figure 5 shows the FE-PML model. The subsoil is discretized with three-dimensional twenty-node finite elements. A maximum element size $l_\mathrm{e} = 0.75$ m is used for the mesh, corresponding to 5 quadratic finite elements per shear wavelength $\lambda_\mathrm{s}$ at a frequency of 80 Hz. The building is modeled with frame and eight-node shell elements. Hysteretic damping is assumed for the building with $\eta = 2\xi = 0.05$.

The shear modulus of the soil in $\Omega_\mathrm{s}^\mathrm{i}$ (figure 5) is modeled as a conditional random field $\bar{G}\left(\boldsymbol{x}, \theta\right)$ with a Gamma marginal PDF and a coefficient of variation $\mathrm{CoV} = 0.25$ according to the methodology outlined in section 2.3. An isotropic squared exponential correlation coefficient function is assumed for the covariance of the unconditional random field $G\left(\boldsymbol{x}, \theta\right)$ which ensures continuous field realizations:

$$C_\mathrm{GG}(\boldsymbol{x}, \boldsymbol{x'}) = \sigma_\mathrm{G}^2 \exp\left(-\frac{|\boldsymbol{x} - \boldsymbol{x'}|^2}{l_\mathrm{c}^2}\right) \tag{18}$$

In general, the variation of the material properties in soil deposits is anisotropic as the correlation length in the vertical and horizontal directions are not the same. However, in order to develop a general understanding of how the spatial variability of the subsoil properties influences the response predictions of buildings, a single isotropic correlation length is considered in the present paper. The correlation length $l_\mathrm{c}$ of the shear modulus $\bar{G}\left(\boldsymbol{x}, \theta\right)$ is chosen to lie within the upper range of typical correlation lengths of CPT data [12]. Thus, two correlation lengths are examined: $l_\mathrm{c} = 1$ m and $l_\mathrm{c} = 1.50$ m. The generation of the stochastic shear modulus realizations is performed for a relative truncation error $\epsilon_\mathrm{max} = 0.05$. Figure 6 shows two

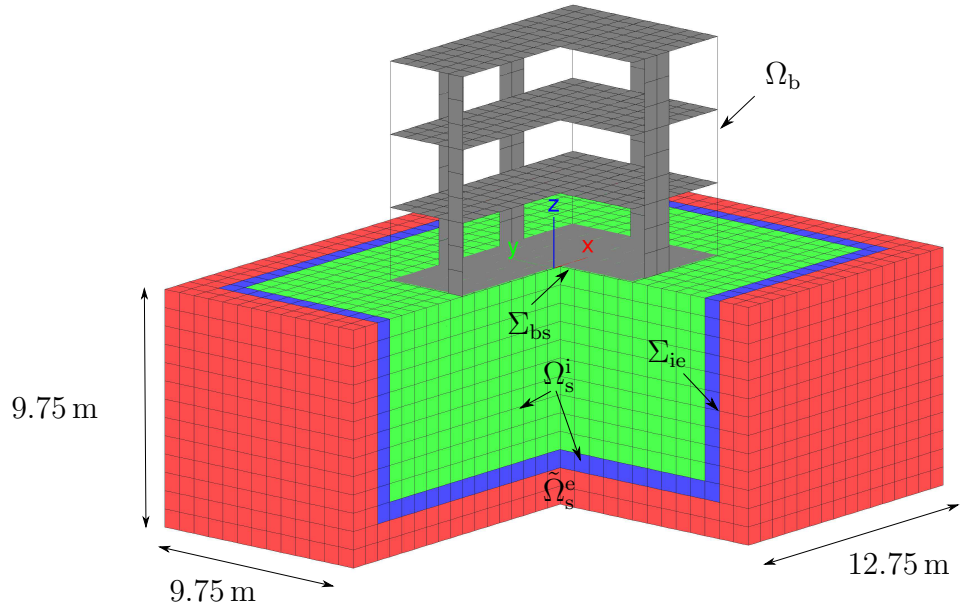


Figure 5: FE-PML model. The shear modulus in the green part of $\Omega_s^i$ is modeled as a conditional random field whereas in the blue part it is deterministic. The subdomain definitions are in accordance with figure 1.

realizations of the stochastic shear modulus of the soil mapped onto the finite element mesh for the two correlation lengths considered.

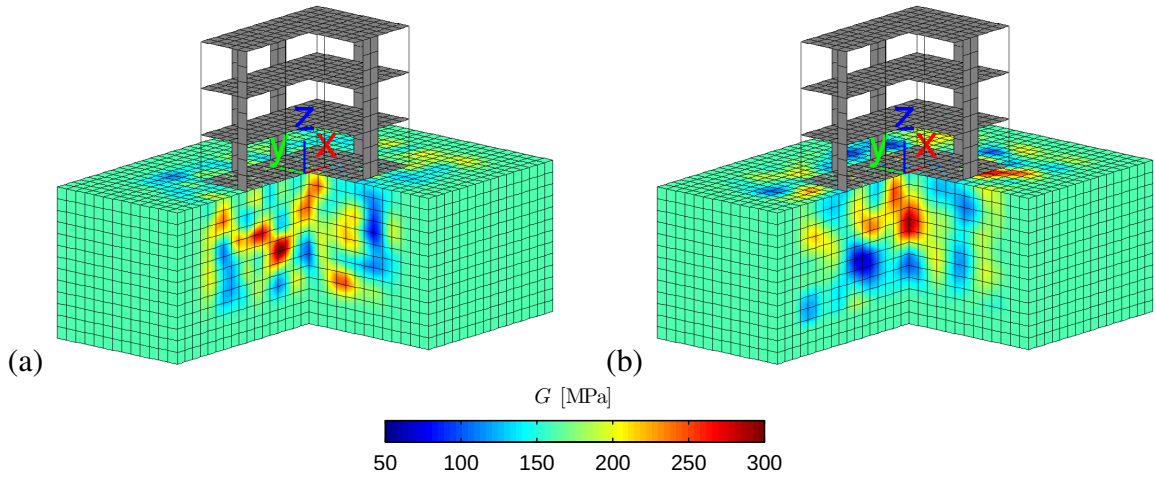


Figure 6: Realizations of the stochastic shear modulus of the soil mapped onto the finite element mesh. Shear modulus with correlation length (a) $l_c = 1$ m and (b) $l_c = 1.50$ m.

In order to understand how the uncertain local subsoil conditions affect the response of buildings to ground-borne vibration, two loading cases are considered, an actual and an artificial. The actual loading case (LC1) is the solution of the problem where the incident wave field propagates through $\Omega_s^i$ before it impinges the foundation of the building. This loading case allows to assess the overall influence of the uncertain local subsoil conditions on the response of the building. In this case, the nodal forces $\hat{\underline{f}}_s$ of equation (4) are used to propagate the incident wave field through the FE-PML model. In the artificial loading case (LC2), the incident wave field is applied as nodal forces $\hat{\hat{\underline{f}}}_{\Sigma_{bs}}$ directly on the soil-foundation interface $\Sigma_{bs}$ according to equation

(5) and assuming it has propagated through the subsoil with the deterministic properties of table 2. The main difference between the two loading cases is that the incident wave field which finally impinges the foundation of the building in LC1 is perturbed by the (stochastic) heterogeneity of $\Omega_{\mathrm{s}}^{\mathrm{i}}$ (figure 7b) whereas in LC2 it is not. The artificial loading case is considered as it provides additional insight by allowing to examine solely how the uncertain subsoil conditions affect the dynamic stiffness matrix of the coupled soil-building system and, equivalently, its modal characteristics.

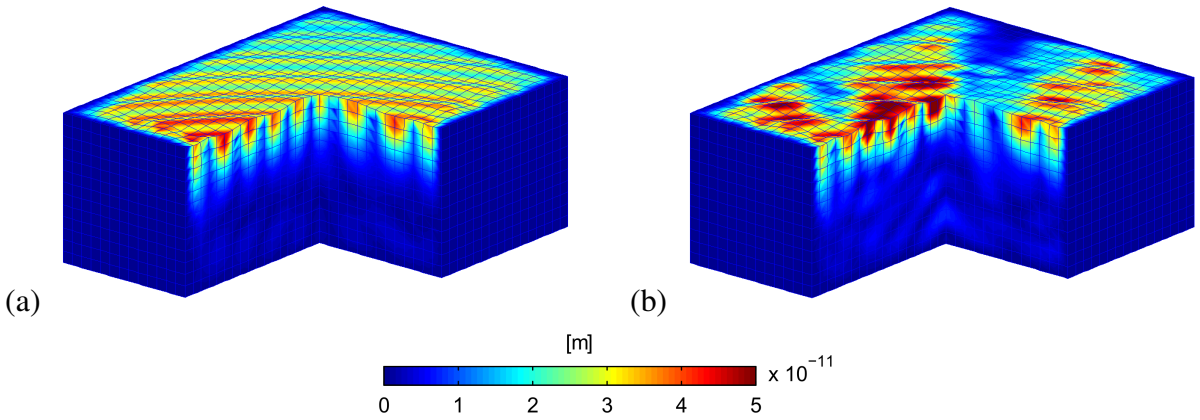


Figure 7: Snapshot of the free field response $\underline{\mathbf{u}}(t) = \mathrm{Re}\left(|\underline{\hat{\mathbf{u}}}|\exp\left(i\omega t + i\angle\underline{\hat{\mathbf{u}}}\right)\right)$ at 80 Hz and $t = 0$. (a) Homogeneous subsoil with the mean properties of table (2) and (b) subsoil with the shear modulus realization of figure 6b.

The uncertainty is propagated from the subsoil properties to the response of the building by means of Monte-Carlo simulation. In total, $n_{\mathrm{R}} = 1000$ realizations are used to estimate the uncertainty on the building response. This uncertainty is quantified by computing the coefficient of variation and by constructing confidence regions for the building response. The former is defined as:

$$\mathrm{CoV}_{|\underline{\hat{u}}_j|} = \frac{\sigma_{|\underline{\hat{u}}_j|}}{\mu_{|\underline{\hat{u}}_j|}} \tag{19}$$

where $\sigma_{|\underline{\hat{u}}_j|}$ and $\mu_{|\underline{\hat{u}}_j|}$ are the standard deviation and the mean value of the response $|\underline{\hat{u}}_j|$ of the $j$-th degree of freedom. Alternatively, a confidence region with a confidence level of $p_c = 90\%$ for the response $|\underline{\hat{u}}_j|$ can be defined such that:

$$P(|\underline{\bar{u}}_j^l| \leq |\underline{\hat{u}}_j| \hat{\leq} |\underline{\hat{u}}_j^u|) \geq p_c \tag{20}$$

where the lower $|\underline{\hat{u}}_j^l|$ and the upper $|\underline{\hat{u}}_j^u|$ bounds are obtained as the $5\%$ and $95\%$ percentiles of $|\underline{\hat{u}}_j|$ respectively. By utilizing the bootstrap method [18], confidence regions can be also estimated for $\mathrm{CoV}_{|\underline{\hat{u}}_j|}$.

### 3.1 Free field and foundation response transfer functions

Figure 8 shows the transfer function of receiver $F_0$ (figure 4) in the $z$ direction for the case where the correlation length of the random field representing the shear modulus of the subsoil is $l_{\mathrm{c}} = 1$ m. The response is presented for the free field without the presence of the building and the cases of the building with raft foundation and the building with individual foundation footings.

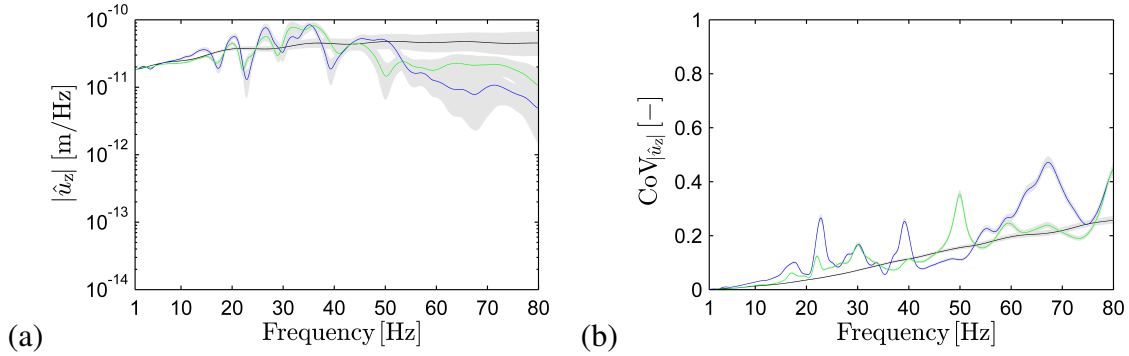


Figure 8: (a) Mean and (b) coefficient of variation of the transfer function of receiver $F_0$ (figure 4) in the $z$ direction for $l_c = 1$ m. Free field response (black), building with raft foundation (blue) and building with individual foundation footings (green). The 90% confidence regions are shaded grey.

The uncertainty of the free field response of $F_0$ increases almost linearly with the frequency. After the construction of the building the response of $F_0$ generally follows a similar trend but with some major difference as the stiffness of the building and especially the foundation affect the response of $F_0$ in two ways. First, the response near the resonance and antiresonance frequencies of the coupled building-soil system gets amplified and decreased respectively when compared to the free field response [19]. Second, the response at higher frequencies is lower than the free field response for increasing stiffness of the foundation.

### 3.2 Building response transfer functions

Figures 9 and 10 show the response of receiver $\mathrm{A}_1$ (figure 4) of the building with raft foundation for the two considered correlation lengths $l_c$ of the random field representing the shear modulus of the subsoil. The uncertainty of the response is larger in LC1 than in LC2 as the former includes both the influence of the stochastically perturbed incident wave field and the impact of the stochastic subsoil on the modal characteristics of the coupled soil-building system. In LC1 the uncertainty increases almost linearly with respect to the frequency for the vertical response (figure 9d) while for the horizontal response there are certain frequency bands where the response of the coupled soil-structure system is found to be more sensitive to the subsoil properties (figures 9b and 9b). These frequency bands can be associated with the eigenmodes of the coupled soil-building system that get particularly activated by the induced excitation. As for each realization of the shear modulus of the subsoil the modal characteristics of the coupled system are slightly different and since the response close to resonance frequencies is extremely sensitive to the damping present in the system, frequency bands of increased uncertainty emerge. Similarly, there are other frequency bands in which the structural response is less sensitive. These frequency bands can be associated with eigenmodes of the system that are not sensitive to the subsoil properties. Furthermore, the uncertainty bounds of the response decrease when the stochastic shear modulus of the subsoil has a shorter correlation length. In this case, the wavelength of the elastodynamic waves in the soil is much larger compared to the length scale of spatial fluctuations of the material properties and consequently any local scale variation of the subsoil properties is not resolved in the response.

Figure 11 compares the response of receiver $\mathrm{A}_1$ between the building with raft foundation and the building with individual footings. The correlation length of the random field representing the shear modulus of the subsoil is $l_c = 1$ m. The general trends of the response are in

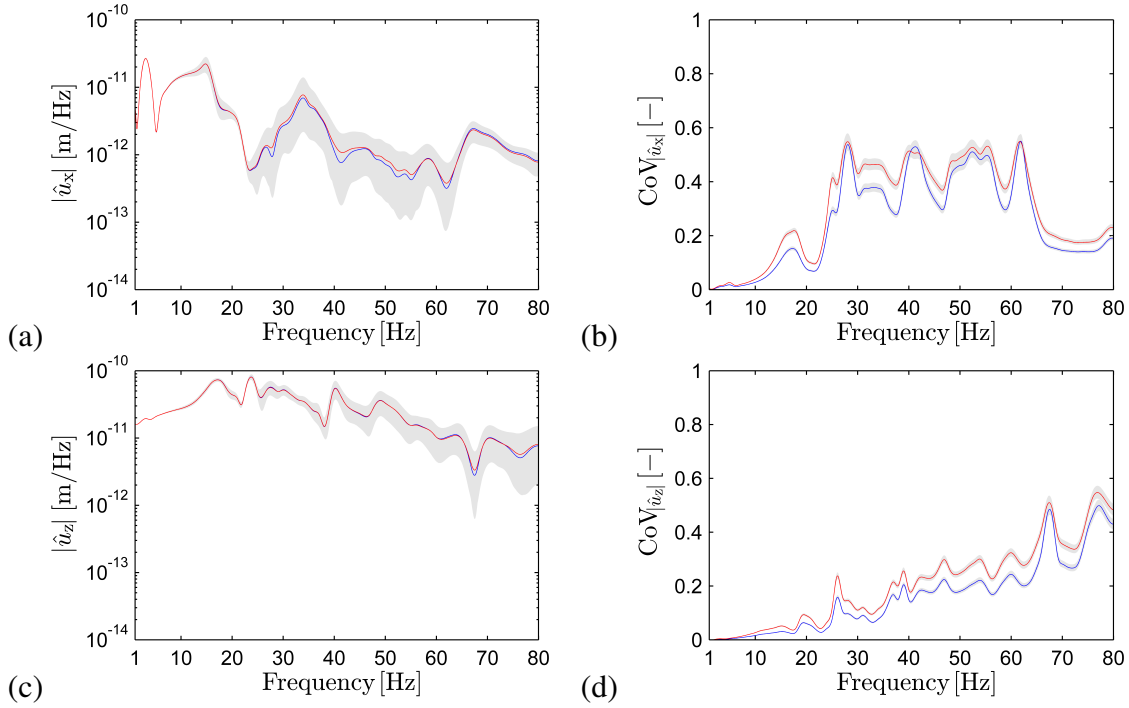


Figure 9: Transfer functions of receiver $R_1$ (figure 4) for the building with raft foundation and the LC1 with $l_c = 1$ m (blue line) and $l_c = 1.5$ m (red line). (a) Mean and (b) coefficient of variation of the response in the $x$ direction, (c) mean and (d) coefficient of variation of the response in the $z$ direction. The 90% confidence regions are shaded grey.

accordance with the previously stated observations. Nevertheless, the building with individual footings is more sensitive to the subsoil properties, exhibiting higher uncertainty to its response. Because the size of the individual footings is small compared to the scale of variation of the subsoil material properties, each footing rests on top of a soil with different material properties. As a result, the spatial variation of the material properties of the soil cannot be averaged out in the response of the building.

## 4 CONCLUSIONS

In this paper the influence of the imperfectly known local subsoil conditions on the response predictions of buildings to environmental ground vibration is examined. A parametric analysis is performed with respect to the statistical characterization of the shear modulus of the soil and the foundation type of the building.

The uncertainty of the response of the building is traced on the stochastically perturbed incident wave field that excites the building and the impact of the stochastic subsoil on the modal characteristics of the coupled soil-building system. The correlation length of the stochastic subsoil properties affects the uncertainty bounds of the response of the building. Furthermore, it is demonstrated that the foundation type of the building is a crucial factor determining its response and the associated uncertainty bounds. Generally, the structural response uncertainty increases at higher frequencies. The sensitivity of the structural response to the subsoil properties varies considerably over frequency bands, however.

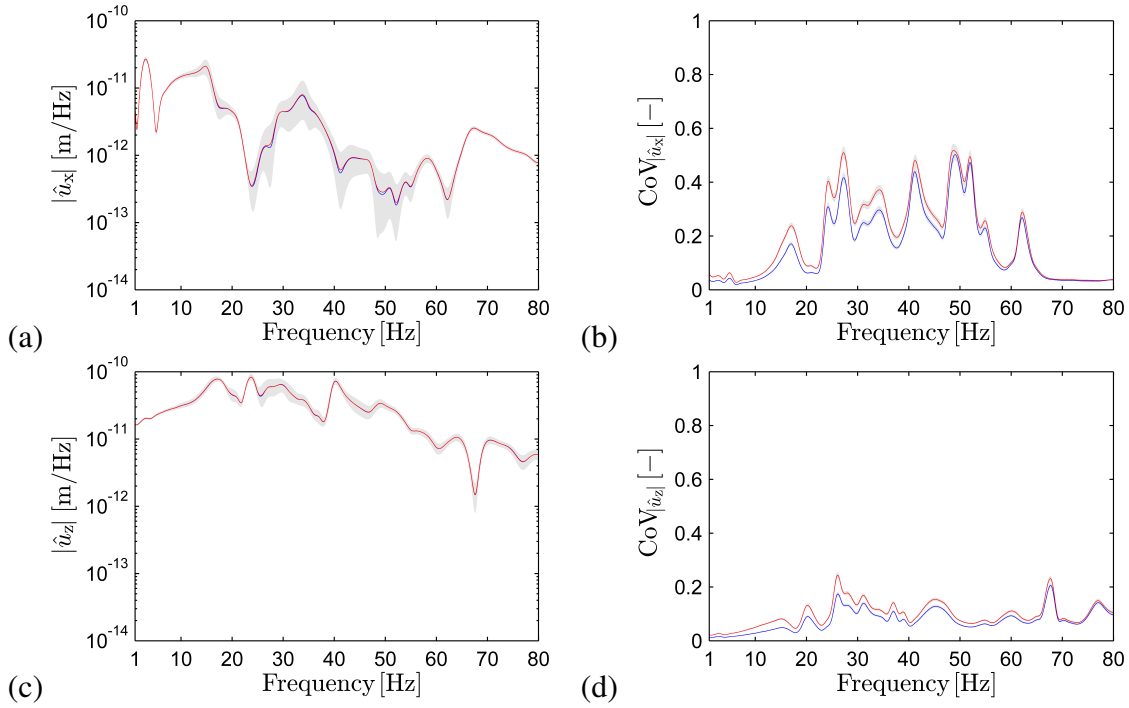


Figure 10: Transfer functions of receiver $R_1$ (figure 4) for the building with raft foundation and the LC2 with $l_c = 1$ m (blue line) and $l_c = 1.5$ m (red line). (a) Mean and (b) coefficient of variation of the response in the $x$ direction, and (c) mean and (d) coefficient of variation of the response in the $z$ direction. The 90% confidence regions are shaded grey.

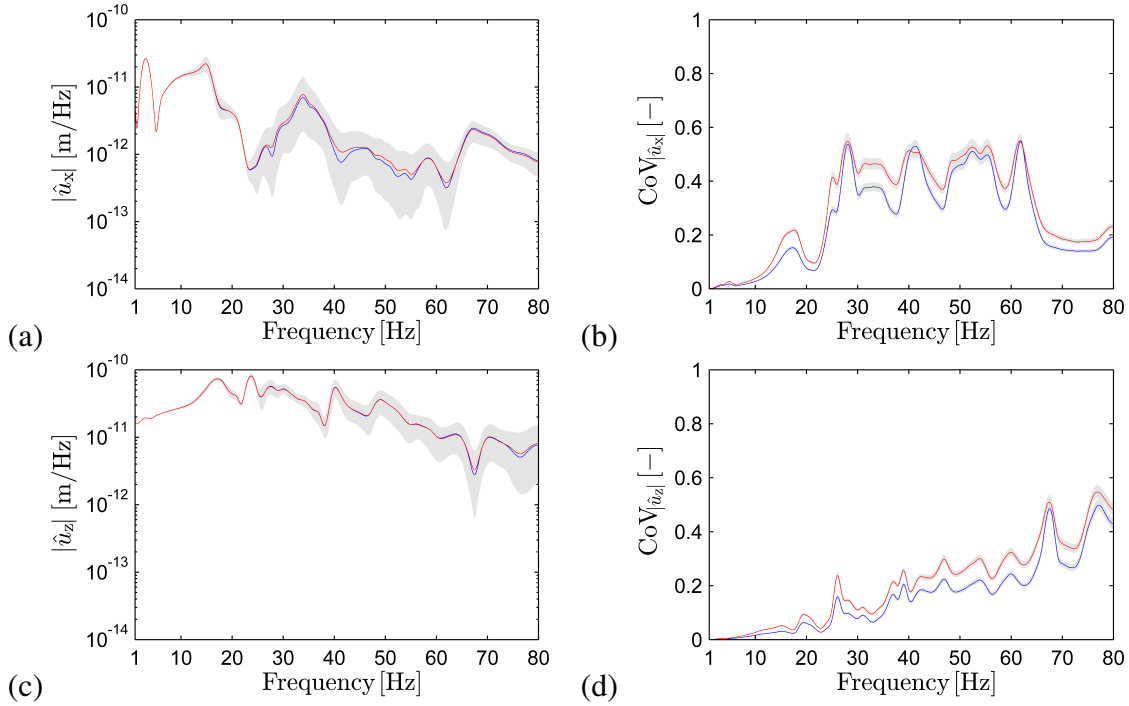


Figure 11: Transfer functions of receiver $R_1$ (figure 4) for the building with raft foundation (blue line) and the building with individual foundation footings (red line) for the LC1 with $l_c = 1$ m. (a) Mean and (b) coefficient of variation of the response in the $x$ direction, and (c) mean and (d) coefficient of variation of the response in the $z$ direction. The 90% confidence regions are shaded grey.

## ACKNOWLEDGMENTS

The research presented in this paper has been performed within the frame of the project OT/13/59 "Quantifying and reducing uncertainty in structural dynamics" funded by the Research Council of KU Leuven. The financial support is gratefully acknowledged.

## REFERENCES

[1] J.P. Wolf, *Dynamic soil-structure interaction*, Prentice-Hall, 1985.

[2] D. Clouteau, Degrande G., Lombaert G., Numerical modeling off traffic induced vibrations, *Meccanica*,**36**(4), 401-420, 2001.

[3] G.B. Baecher, J.T.Christian, *Reliability and Statistics in Geotechnical Engineering*, Wiley & Sons, 2003.

[4] E. Savin, D. Clouteau, Elastic wave propagation in a 3D unbounded random heterogeneous medium coupled with a bounded medium. Application to seismic soil-structure interaction (SSSI), *International Journal for Numerical Methods in Engineering*,**54**, 607-630, 2002.

[5] O. Vonestorff, E. Kausel. Coupling of boundary and finite-elements for soil-structure interaction problems. *Earthquake Engineering and Structural Dynamics*, **18**(7), 1065–1075, 1989.

[6] J. Lysmer, R. Kuhlemeyer. Finite dynamic model for infinite media. *Journal of the Engineering Mechanics Division*, **95**(EM4), 859–877, 1969.

[7] F. Medina, J. Penzien. Infinite elements for elastodynamics. *Earthquake Engineering and Structural Dynamics*, **10**(5), 699–709, 1982.

[8] U. Basu, A.K. Chopra, Perfectly matched layers for time-harmonic elastodynamics of unbounded domains: theory and finite-element implementation, *Computer Methods in Applied Mechanics and Engineering*,**192**(11-12), 1337-1375, 2003.

[9] D. Aubry, D. Clouteau, A subdomain approach to dynamic soil-structure interaction, *Recent advances in earthquake engineering and structural dynamics*, V. Davidovici, R.W. Clough eds., Ouest Editions/AFPS, Nantes 251-272, 1992.

[10] P. Coulier, S. François, G. Degrande, G. Lombaert. The influence of source-receiver interaction on the numerical prediction of traffic induced vibrations. *Journal of Sound and Vibration*, **333**(12), 81–86, 2014.

[11] M. Schevenels, S. François, G. Degrande, EDT: An ElastoDynamics Toolbox for MATLAB, *Computers & Geosciences*,**35**(8), 1752-1754, 2009.

[12] M. Huber, Soil variability and its consequences in geotechnical engineering, PhD thesis, Institut für Geotechnik der Universität Stuttgart, 2013.

[13] E. Vanmarcke, *Random Fields: Analysis and Synthesis*, MIT Press Classics, 1983.

[14] P. Liu, A. Der Kiureghian, Multivariate distribution models with prescribed marginals and covariances, *Probabilistic Engineering Mechanics*,**1**(2), 105-112, 1986.

[15] C. Li, A. Der Kiureghian, Optimal discretization of random fields, *Journal of Engineering Mechanics*,**119**(6), 1136-1154, 1993.

[16] A.M. Olsson, G.E. Sandberg, Latin hypercube sampling for stochastic finite element analysis, *Journal of Engineering Mechanics*,**128**(1), 121-125, 2002.

[17] M.H. Santare, Thamburaj P., G.A. Gazonas, The use of graded finite elements in the study of elastic wave propagation in continuously nonhomogeneous materials, *International Journal of Solids and Structures*,**40**, 5621-5634, 2003.

[18] B. Efron, R.J. Tibshirani, *An Introduction to the Bootstrap*, Chapman & Hall, 1993.

[19] S. François, L. Pyl, H.R. Masoumi, G. Degrande. The influence of dynamic soil-structure interaction on traffic induced vibrations in buildings. *Soil Dynamics and Earthquake Engineering*, **27**, 655–674, 2007.

COMPDYN 2017
6th ECCOMAS Thematic Conference on
Computational Methods in Structural Dynamics and Earthquake Engineering
M. Papadrakakis, M. Fragiadakis (eds.)
Rhodes Island, Greece, 15–17 June, 2017

# STOCHASTIC RESPONSE OF NONLINEAR BASE ISOLATION SYSTEMS

**Athanasios A. Markou**[1], **George Stefanou**[2] **and George D. Manolis**[3]

[1]Postdoctoral Researcher, Norwegian Geotechnical Institute
Sognsveien 72, 0806 Oslo
e-mail: athanasios.markou@ngi.no

[2] Assistant Professor, Aristotle University of Thessaloniki
Panepistimioupolis, Thessaloniki 54124, Greece
e-mail: gstefanou@civil.auth.gr

[3] Professor, Aristotle University of Thessaloniki
Panepistimioupolis, Thessaloniki 54124, Greece
e-mail: gdm@civil.auth.gr

**Keywords:** Stochastic Response, Hybrid Base Isolation System, Trilinear Hysteretic Model, Monte-Carlo Simulations.

**Abstract.** *A hybrid base isolation system was used to retrofit two residential buildings in Solarino, Sicily. Subsequently, five free vibration tests were carried out in one of these buildings to assess its functionality. The hybrid base isolation system combined high damping rubber bearings with low friction sliders. In terms of numerical modeling, a single-degree-of-freedom system is used here with a new five-parameter trilinear hysteretic model for the simulation of the high damping rubber bearing, coupled with a Coulomb friction model for the simulation of the low friction sliders. Next, experimentally obtained data from the five free vibration tests were used for the calibration of this six parameter model. Following up on the model development, the present study employs Monte-Carlo simulations in order to investigate the effect of the unavoidable variation in the values of the six-parameter model on the response of the base isolation system. The calibrated parameters values from all the experiments are used as mean values, while the standard deviation for each parameter is deduced from the identification tests employing best-fit optimization for each experiment separately. The results show that variation in the material parameters of the base isolation system produce a nonstationary effect in the response. In addition, there is a magnification effect, since the coefficient of variation of the response, for most of the parameters, is larger than the coefficient of variation in the parameter values.*



Figure 1: The Solarino building in Via Baden Powell 25, Solarino, Sicily.

## 1 INTRODUCTION

Base isolation has been extensively used over the last decades for the protection of structures against earthquakes. The concept behind base isolation is the idea of introducing a flexible layer between the superstructure and its foundation [1], so to simply reduce the transmission of energy from the ground to the superstructure [2]. To this end, the mechanics behind an isolation system are: (i) a flexible support in order to elongate the natural period of the structure, (ii) energy dissipation in order to control the relative displacements and (iii) sufficient rigidity under service loads to avoid unnecessary motion [3]. The first mode of an isolated structure involves only deformations in the superstructure, while the higher modes do not contribute to the response due to orthogonality conditions [4].

The first efforts for Italian buildings to be retrofitted with base isolation started in 2004, [5]. Among those buildings were two four-story R/C residential buildings in Via Baden Powell 23-25, Solarino, Eastern Sicily, [6]. The retrofit included a hybrid base isolation system (HBIS), which combined 12 high damping rubber bearings (HDRB) with 13 low friction sliding bearings (LFSB), [6]. In July 2004, static and dynamic tests were performed on one of the two Solarino buildings, [7], see Fig. 1. The static tests were used for the identification of the static friction force, while the dynamic ones were in the form of free vibration tests following application and instantaneous release of a displacement close to the design value.

In the years following these experiments, research efforts were made towards dynamic identification of the Solarino HBIS by using several mechanical models and various identification techniques [8, 9, 10, 11, 12]. In the present study, a five-parameter trilinear hysteretic model (THM) developed in [10, 11] will be used for the HDRB response, while a single-parameter constant Coulomb friction model (CCFM) will be used for the LFSB response.

Uncertainties inherently exist in the loading as well as in the material and geometric parameters of engineering systems. Within the framework of safe engineering design, papers in the literature primarily deal with the effect of stochastic earthquake excitation on the structural response. For instance, Ref. [13] studies the stochastic response of secondary systems attached to a BI structure undergoing random ground motions described by a filtered white noise model. In Ref. [14], the randomness of earthquake loads is considered, but a parametric investigation with regard to deterministic structural - isolator parameters is also conducted. In [15], only the properties of the superstructure are treated as random variables in an optimization procedure. The effect of uncertain near-field excitations on the reliability-based performance and design of

Table 1: List of abbreviations.

| | |
|---|---|
| BHM | bilinear hysteretic model |
| CCFM | constant Coulomb friction model |
| CMA-ES | covariance matrix adaptation - evolution strategy |
| HBIS | hybrid base isolation system |
| HDRB | high damping rubber bearing |
| LCFM | linear Coulomb friction model |
| LFSB | low friction sliding bearing |
| MCS | Monte Carlo simulation |
| SDOF | single-degree-of-freedom |
| THM | trilinear hysteretic model |

base-isolated systems is explored in [16]. In fact, very few publications consider uncertainty in the base isolator parameters. For instance, the stochastic response of base isolated liquid storage tanks is computed in [17] using a polynomial chaos expansion to represent the uncertainty in the characteristic parameters of a laminated rubber bearing isolator. Finally Ref. [18], [19] perform robust optimum design of BI systems taking into account the uncertainty in the isolator parameters.

In the above work, assumptions were made regarding the statistical characteristics of the isolator parameters. In the present paper, the parameters of the adopted HBIS are calibrated by using experimental evidence [20]. Specifically, the aforementioned five free vibration tests performed in Solarino will be used to define the mean value and standard deviation of the six-parameter mechanical model. The effect of parameter variation on the response of the HBIS will be investigated in the framework of Monte Carlo simulation (MCS), leading to useful conclusions about the probabilistic characteristics of the response. Finally, for a list of abbreviations used throughout the paper, the reader is referred to Table 1.

## 2 MECHANICAL MODELS

Two possible THMs based on different mechanical representations exist, but as it was shown in [11] only one is able to describe the HDRB response satisfactorily. This THM comprises three elements, a linear elastic spring of stiffness $k_e$ (element 1) in series with a parallel system, namely a plastic slider of characteristic force $f_s$ (element 2) connected in parallel with a trilinear elastic spring with stiffnesses $k_{h1}, k_{h2}$ and characteristic displacement $u_c$ (element 3), see Fig. 2. The compatibility, equilibrium and constitutive equations of the THM are presented in Table 2. As shown in Fig. 2(e) the THM has three plastic phases (1-3) and one elastic phase. Plastic phase 1 has stiffness $k_2$ (shown in yellow), plastic phase 2 has stiffness $k_1$ (shown in green), plastic phase 3 has stiffness $k_2$ (shown in blue) and the elastic phase has stiffness $k_0$ (shown in red), Fig. 2(e). The two characteristic displacements are also shown, namely the first yield displacement $u_y$ and the second yield displacement $u_3$. The force at zero displacement after yielding ($F_2$) and the force at second yield displacement $u_3$ in the loading phase with positive displacement, ($F_3$) are defined as follows:

$$F_2 = (k_0 - k_1)u_y; \quad F_3 = k_0 u_y + k_1(u_3 - u_y) \tag{1}$$

The resulting THM is a five-parameter system and the relationships between the mechanical parameters ($k_e, k_{h1}, k_{h2}, f_s, u_c$) shown in Fig. 2(a) and the mathematical ones ($k_0, k_1, k_2, u_y, u_3$) shown in Fig. 2(e) are listed in Table 3.

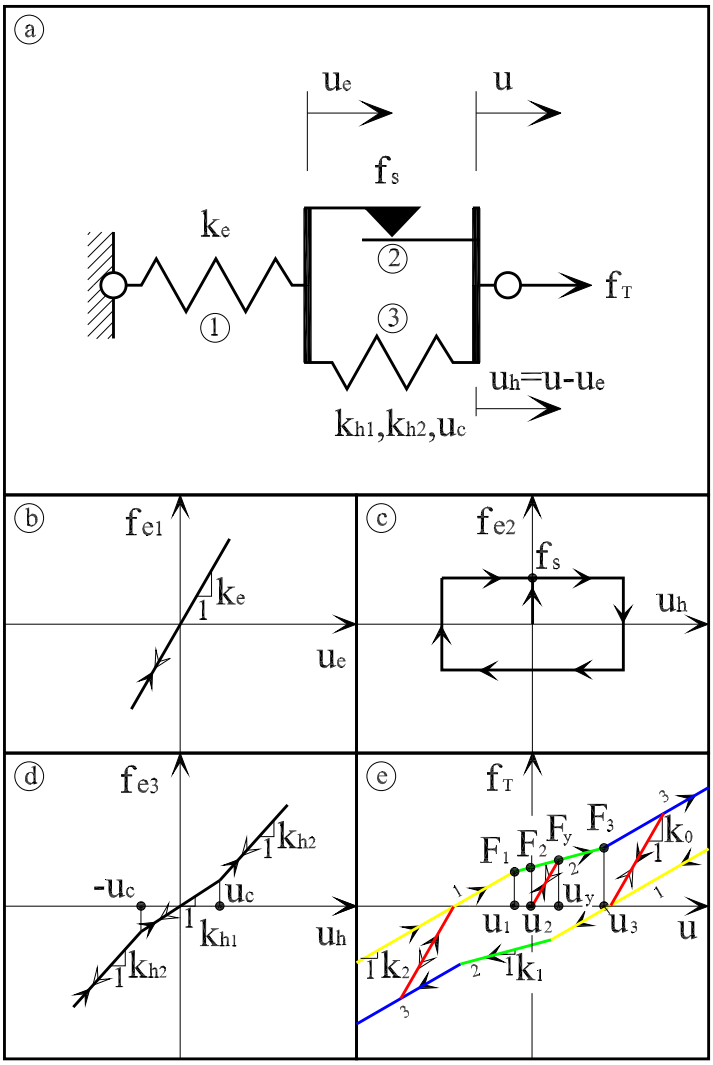


Figure 2: Trilinear hysteretic model (THM): (a) mechanical model (b) $f_{e1} - u_e$ for element 1 (c) $f_{e2} - u_h$ for element 2 (d) $f_{e3} - u_h$ for element 3 and (e) overall $f_T - u$ graph.

Table 2: Compatibility, equilibrium and constitutive equations of the THM.

| | |
|---|---|
| Compatibility | $u = u_e + u_h$ |
| Equilibrium | $f_T = f_{e1} = f_{e2} + f_{e3}$ |
| Constitutive law | $f_{e1} = k_e u_e$<br>$f_{e2}(\dot{u}_h \neq 0) = f_s sgn(\dot{u}_h)$<br>$f_{e2}(\dot{u}_h = 0) = f_{e1} - f_{e3}$<br>$f_{e3}(\lvert u_h \rvert \leq u_c) = k_{h1} u_h$<br>$f_{e3}(\lvert u_h \rvert > u_c) = (k_{h1} u_c + k_{h2}(\lvert u_h \rvert - u_c)) sgn(u_h)$ |

Table 3: Relationships between mechanical and mathematical parameters of the THM, see Figs. 2(a),(e).

| | | | | |
|---|---|---|---|---|
| $k_e = k_0;$ | $k_{h1} = k_1 \frac{k_0}{k_0 - k_1};$ | $k_{h2} = k_2 \frac{k_0}{k_0 - k_2};$ | $f_s = k_0 u_y;$ | $u_c = (u_3 - u_y) \frac{k_0 - k_1}{k_0}$ |

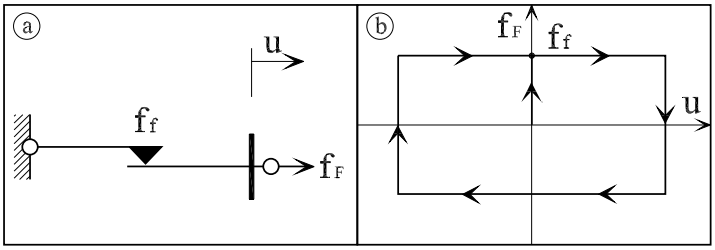


Figure 3: Constant Coulomb friction model (CCFM): (a) mechanical model (b) overall $f_F - u$ graph.

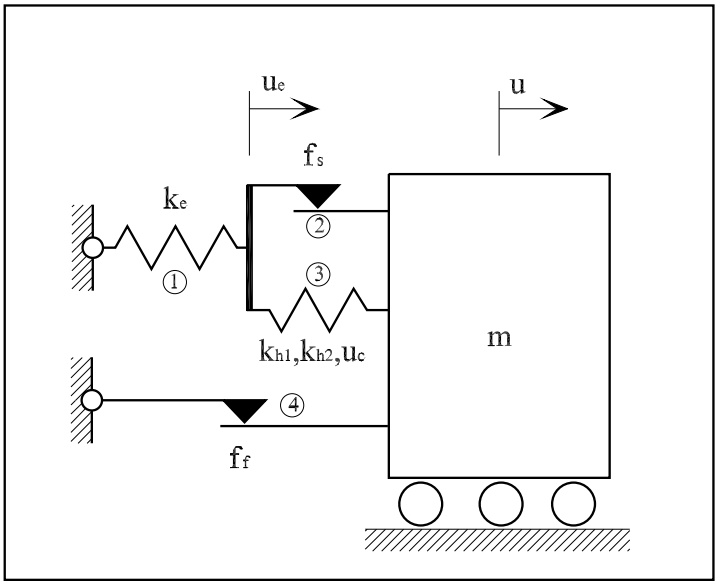


Figure 4: Single-degree-of-freedom (SDOF) system representing a base-isolated building.

The constant Coulomb friction model is used for the description of the behavior of the LFSB component, Fig. 3. This model is defined by the characteristic force $f_f$ and its constitutive equation after initiation of motion ($\dot{u} \neq 0$) as follows:

$$f_F = f_f sgn(\dot{u}) \tag{2}$$

When motion stops ($\dot{u} = 0$) the friction force $f_F$ can take any value between $-f_f < f_F < f_f$.

## 3 EQUATION OF MOTION UNDER FREE VIBRATIONS

In terms of numerical modeling, a single-degree-of-freedom (SDOF) system is used, see Fig. 4. The equation of motion of the SDOF system under free vibration excitation is given by:

$$m\ddot{u} + f_T + f_F = 0 \tag{3}$$

where $f_T$ denotes the force in the trilinear model of the HDRB component and $f_F$ denotes the force in the friction model of the LFSB component.

### 3.1 Constitutive equations for the THM

The restoring force in the THM, $f_T(u, \dot{u})$ assumes different forms according to whether the system experiences an elastic phase or a plastic phase of motion. The force-displacement

relationship for the elastic phases is given by the following expression:

$$f_T(u, \dot{u}) = F_I^e(\dot{u}) + k_0(u - u_I^e) \tag{4}$$

where $(F_I^e, u_I^e)$ is the starting point of the elastic phase. The three plastic phases are governed by the following equations:

$$f_T(u, \dot{u}) = F_J sgn(\dot{u}) + h_J(u - u_J sgn(\dot{u})), \quad (J = 1, 2, 3) \tag{5}$$

where $(F_J, u_J)$ are characteristic points of the upper plastic phases. As it may be seen from Fig. 2(e), $u_2 = 0$, $h_1 = h_3 = k_2$ and $h_2 = k_1$.

### 3.2 Constitutive equation for the CCFM

Independently of the phase of motion, the resisting force in the slider, $f_F(u, \dot{u})$, is always given by Eq. 2. At times when the system stops, the friction force must satisfy the following inequality:

$$|\tilde{f}_F(u_R, 0)| \leq f_f \tag{6}$$

where $u_R$ is the residual displacement.

### 3.3 Rest conditions

The system will come to rest if the following conditions are satisfied:

$$sgn(\ddot{u}_{_}) = -sgn(\dot{u}_{_}) \tag{7}$$

$$|\ddot{u}_{_}| \leq 2\frac{f_F}{m} \tag{8}$$

where $\ddot{u}_{_}$ and $\dot{u}_{_}$ denote the acceleration and the velocity just before the stoppage. When the system stops ($\dot{u} = 0$), it can reach a position of static equilibrium different from the original unstrained one, as long as the following equation is satisfied:

$$f_T(u_R, 0) + \tilde{f}_F(u_R, 0) = 0 \tag{9}$$

### 3.4 Analytical solution

The above expressions for the restoring force in the THM, and for the friction force in the slider, show that each phase of motion, whether elastic or plastic, is governed by linear equations. The differential equation of motion can then solved analytically, see [20].

## 4 IDENTIFICATION PROCEDURE

As previously mentioned a static test and six free vibration tests were performed on one of the two Solarino buildings in 2004. Test numbers 1 and 2 were the static test and a trial test for the push-and-release device, respectively. The following six tests, numbered from 3 to 8, were dynamic free vibration tests under imposed initial displacements. The identification procedure was applied to five of the six dynamic tests, namely tests 3, 5, 6, 7 and 8. Test number 4 was not considered, since it was performed under a nominal initial displacement of only $4.06cm$.

The parameters defining the dynamic system described by the models shown in Fig. 2(e) and Fig. 3(a) are listed in the following system parameter vector: $[m, k_0, k_1, k_2, u_y, u_3, f_f]$. Consider first the following relationships:

$$\omega_i = \sqrt{\frac{k_i}{m}}; \quad f_i = \frac{\omega_i}{2\pi}; \quad u_f = \frac{f_f}{k_0}; \quad (i = 0, 1, 2) \tag{10}$$

Next, if we include the imposed initial displacement $u_0$, the system parameter vector to be optimized becomes:

$$S = [u_0, u_y, u_f, f_0, f_1, f_2, u_3] \tag{11}$$

where $f_0$ the elastic frequency, $f_1$ the first post-yield frequency, $f_2$ the second post-yield frequency.

The identification procedure is based on fitting the acceleration response predicted by the model to that measured during the experiments. Accelerations are used because they can be measured reliably. Let $A_0$ and $t_0$ be the experimental acceleration and time vectors, while $A$ and $t$ are the acceleration and time vectors of a candidate solution. Then the error, or fitness function, of the identification procedure, can be defined as:

$$e^2 = \frac{(A_0 - A, A_0 - A)}{(A_0, A_0)} + \frac{(t_0 - t, t_0 - t)}{(t_0, t_0)} \tag{12}$$

where

$$(A, B) = \sum_{i=1}^{N} A_i B_i \tag{13}$$

is the standard inner product and $N$ is the length of the vectors considered. The Covariance Matrix Adaptation-Evolution Strategy (CMA-ES) was used to minimize the error defined by Equation 12, [21].

Finally, the mass of the system was evaluated as

$$m = \frac{F_0 - F_{fS}}{\omega_0^2 u_y + \omega_1^2 (u_3 - u_y) + \omega_2^2 (u_0 - u_3)} \tag{14}$$

when using the THM. In the above equation, $F_0$ is the magnitude of the force applied to impose the initial displacement $u_0$, and $F_{fS}$ is the static friction force measured in the first static test.

## 5 NUMERICAL RESULTS

The effect of parameter variation on the response of the HBIS is examined here in the framework of MCS. The set of parameters derived by the identification procedure from the previous section will constitute the mean parameter set for all the experimental tests to be used in the MCS (see Table 4). The identified mass for each test is presented in Table 5 along with the static friction force in the first static test $F_{fS}$ and the magnitude of the force applied to generate the initial displacement $u_0$, $F_0$. The standard deviation (std), for each parameter is deduced from the identification tests employing best-fit optimization for each experiment separately, see Table 6, [10].

From Tables 4 and 6 it can be observed that the second yield displacement $u_3$ is the parameter with the largest coefficient of variation ($cov = \frac{std}{mean}$), which is equal to $15.4\%$. A normal distribution is assumed for all parameters since there is inadequate amount of data to validate a (more realistic) non-Gaussian assumption. The monitored response quantity is the acceleration of the HBIS, whose recorded and identified values are plotted in Fig. 5 for each test.

Next, one thousand MCS were performed considering the variation of each parameter separately. Fig. 6 shows that statistical convergence is achieved in all cases with this number of samples. In the same figure, it can be observed that the std of the acceleration at three different time instants is substantially different, particularly when $u_f$, $u_y$ and $f_0$ are varying, which means that the response is non-stationary. This is reflected in Fig. 7, where the acceleration versus time

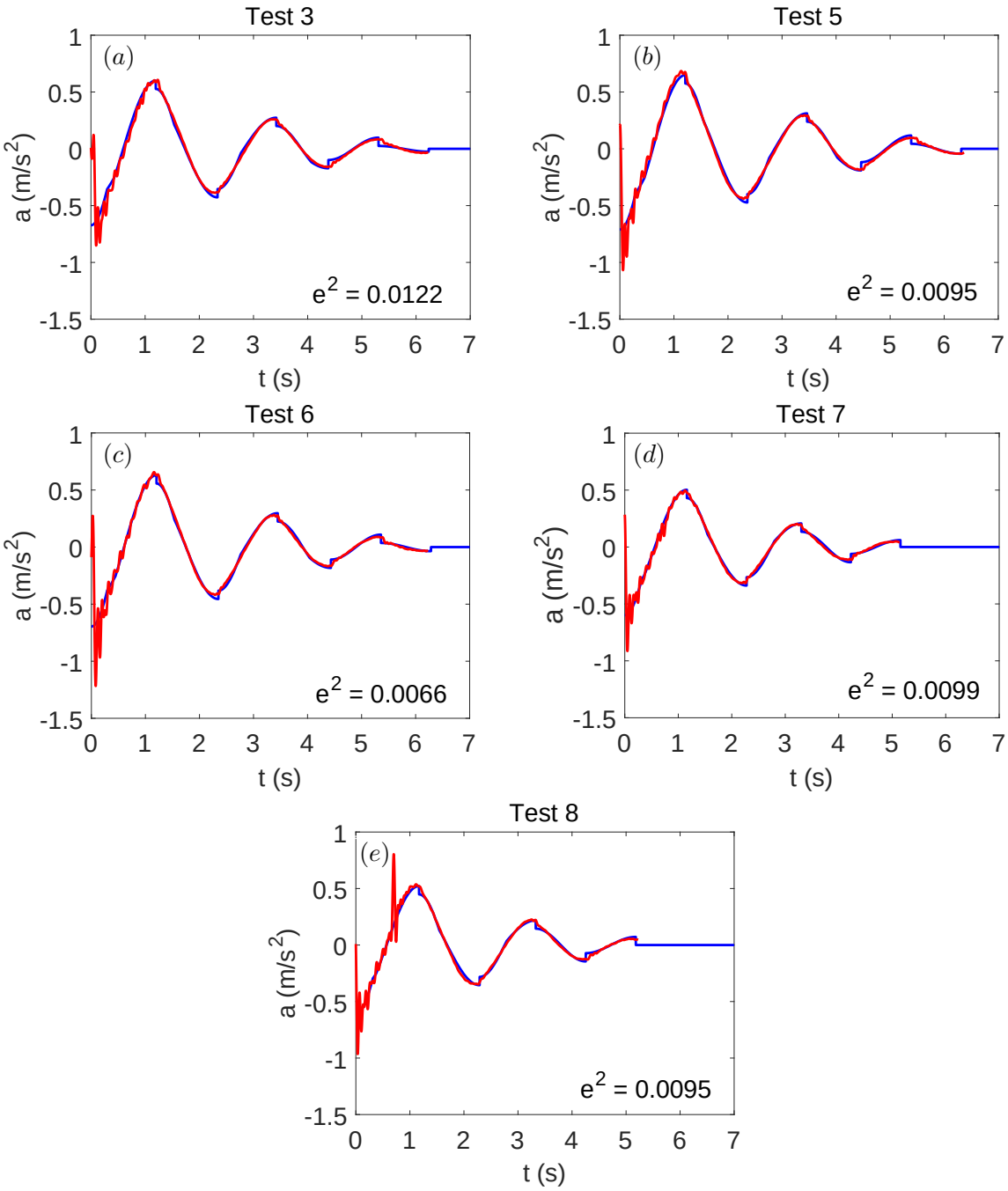


Figure 5: Identified and recorded accelerations (a) Test 3, (b) Test 5, (c) Test 6, (d) Test 7, (e) Test 8 (the red line denotes the recorded signal and the blue line the identified one).

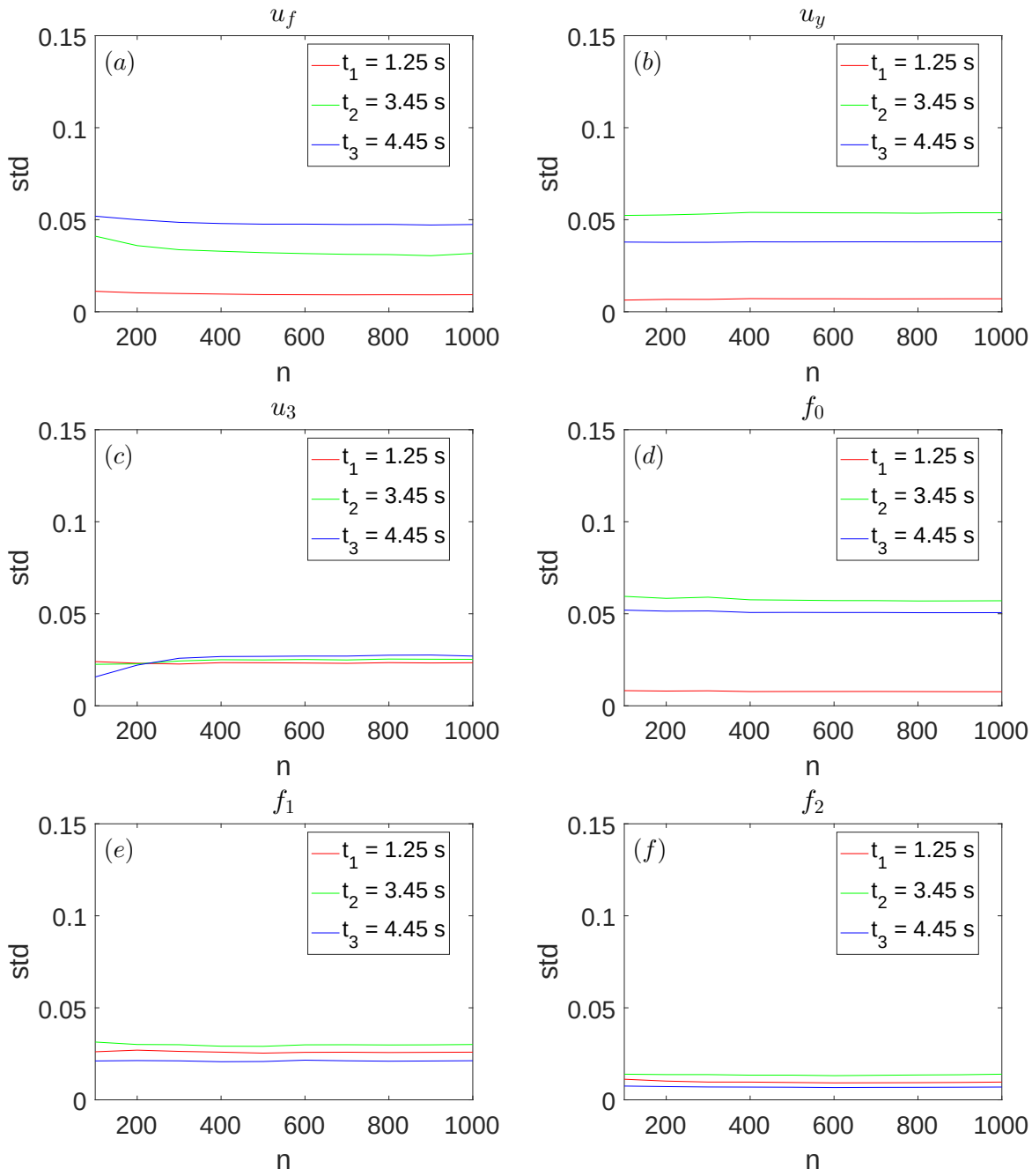


Figure 6: Convergence of the acceleration standard deviation vs Monte-Carlo simulations at three different time intervals for test 5 with varying parameters: (a) $u_f$, (b) $u_y$, (c) $u_3$, (d) $f_0$, (e) $f_1$, (f) $f_2$.

Table 4: Set of identified parameters for all tests.

| | | |
|---|---|---|
| Test 3 | | 0.1041 |
| Test 5 | | 0.1132 |
| Test 6 | $u_0(m)$ | 0.1097 |
| Test 7 | | 0.0859 |
| Test 8 | | 0.0893 |
| LFSB | $u_f(m)$ | 0.0032 |
| HDRB | $u_y(m)$ | 0.0138 |
| | $u_3(m)$ | 0.0799 |
| | $f_0(Hz)$ | 0.5400 |
| | $f_1(Hz)$ | 0.4159 |
| | $f_2(Hz)$ | 0.3227 |
| Error | $\sum_{i=1}^{5} e_i^2(\%)$ | 4.77 |

Table 5: Identified mass, $F_0$ and $F_{fS}$ measures.

| Test | 3 | 5 | 6 | 7 | 8 |
|---|---|---|---|---|---|
| $F_0(kN)$ | 1027 | 1140 | 1177 | 828 | 927 |
| $m(\frac{kNs^2}{m})$ | 1306 | 1392 | 1470 | 1147 | 1274 |
| $F_{fS}(kN)$ | | | 100 | | |

graphs are given for a separate variation of the six model parameters. Based on this figure, it is concluded that $u_y$, $u_3$ and $f_1$ are the most critical parameters in terms of response variability. The non-stationary effect is verified in Fig. 8, where the complete temporal evolution of the std is shown. The above effects can be attributed to the high level of nonlinearity in the base isolation system for large initial displacements.

## 6 CONCLUSIONS

MCS have been employed here in order to investigate the effect of the uncertainty in the values of a six-parameter mechanical model used to simulate the response of base isolation systems. The parameters of the hybrid base isolation system examined herein was used in practice in the Solarino 2004 retrofit project, and were calibrated from experimental data. The results have shown that variation in the material parameters of the isolation system produce a non-stationary effect in the response, which can be traced by the time evolution of the standard deviation computed from the response at different time intervals. The first and second yield displacements and the first post-yield frequency have been identified as the most critical parameters in terms of response variability. In addition, there was a magnification effect, due to the fact that the coefficient of variation of the response was larger than the coefficient of variation

Table 6: Standard deviation (std) of the six system parameters.

| Parameter | $u_f(m)$ | $u_y(m)$ | $u_3(m)$ | $f_0(Hz)$ | $f_1(Hz)$ | $f_2(Hz)$ |
|---|---|---|---|---|---|---|
| std | 0.00025 | 0.00174 | 0.01233 | 0.00935 | 0.01319 | 0.04094 |

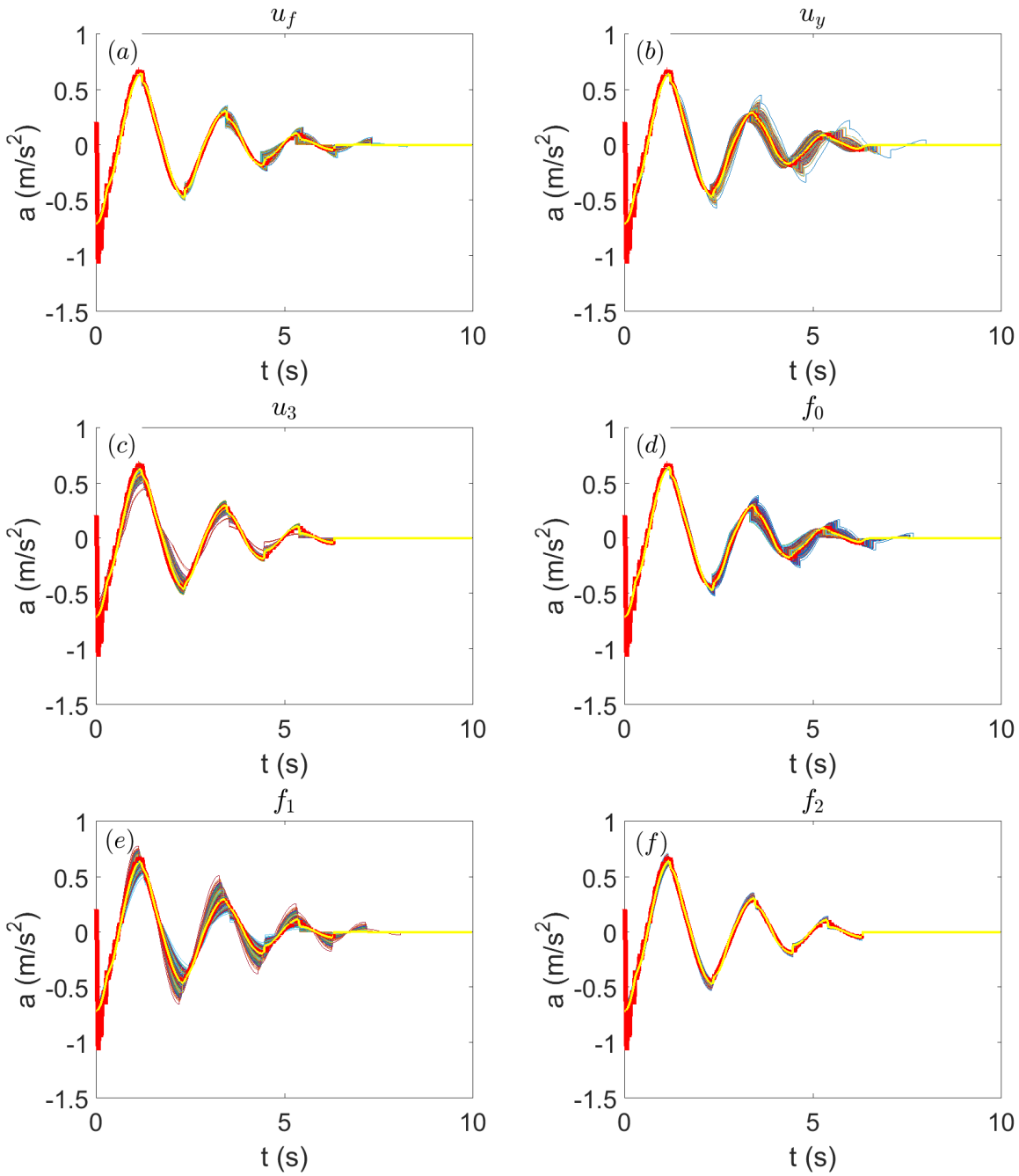


Figure 7: Acceleration time histories for test 5 with varying parameters: (a) $u_f$, (b) $u_y$, (c) $u_3$, (d) $f_0$, (e) $f_1$, (f) $f_2$ (the red line denotes the recorded signal and the yellow line denotes the average computed acceleration).

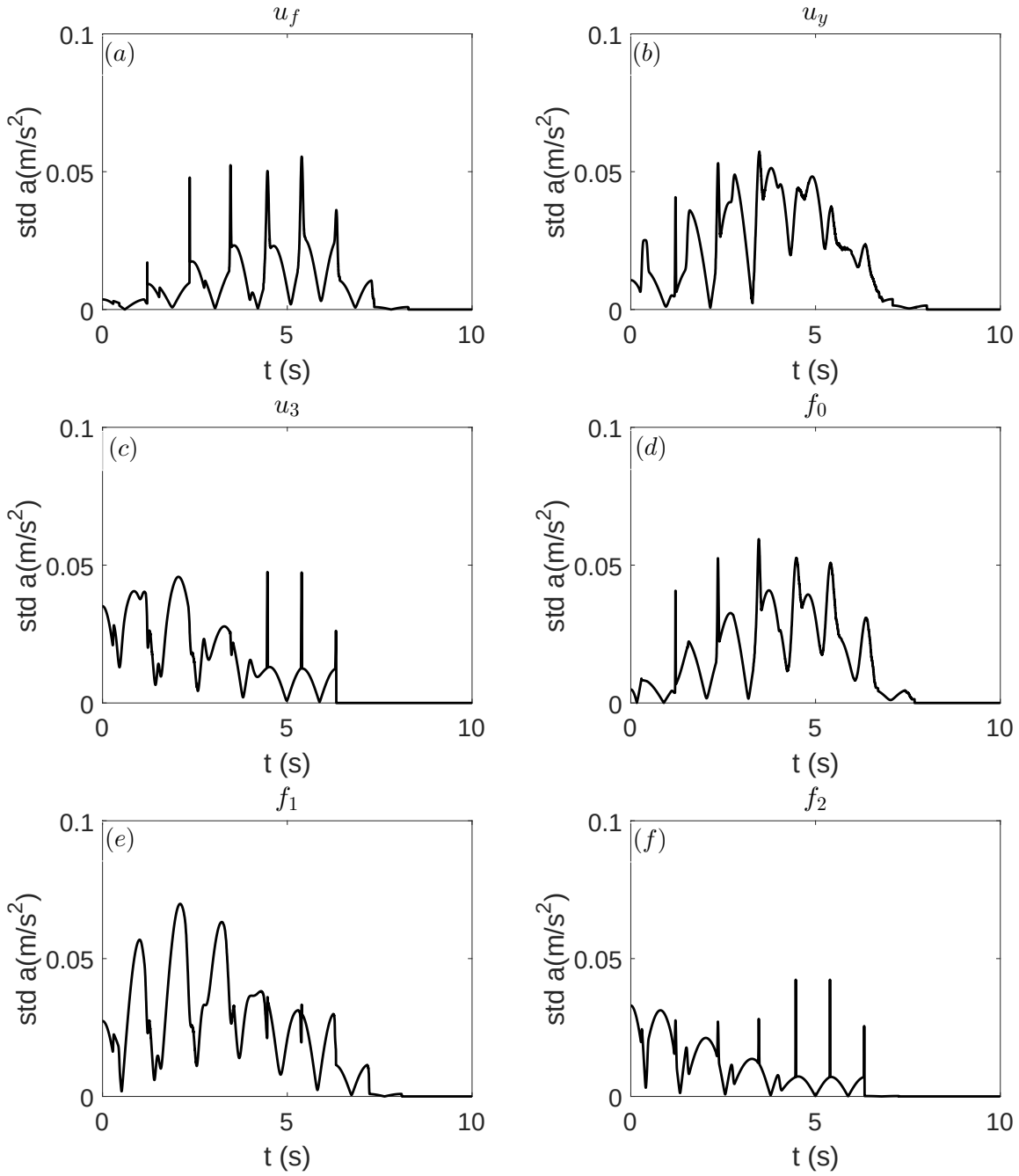


Figure 8: Standard deviation of the acceleration evolution over time for test 5 with varying parameters: (a) $u_f$, (b) $u_y$, (c) $u_3$, (d) $f_0$, (e) $f_1$, (f) $f_2$.

of the parameter itself. The high level of nonlinearity in the base isolation system amplitude of vibration brought about by large initial displacement helps explain the previously described effects. The above observations can serve as guidelines and indicators in the design of new base isolation systems.

## ACKNOWLEDGEMENT

The authors wish to acknowledge financial support from the Horizon 2020 MSCA-RISE-2015 project No. 691213 entitled *'Exchange-Risk'*, Prof. A. Sextos, Principal Investigator.

## REFERENCES

[1] F. Naeim and J. Kelly, *Design of Seismic Isolated Structures: From Theory to Practice*. John Wiley & Sons, New York, 1999.

[2] R. Skinner, W. Robinson, and G. McVerry, *An Introduction to Seismic Isolation*. John Wiley & Sons, New York, 1993.

[3] G. Oliveto, *Innovative Approaches to Earthquake Engineering*. WIT Press, Ashurst Lodge, Southampton, UK, 2002.

[4] Y. Bozorgnia and V. Bertero, *Earthquake Engineering from Engineering Seismology to Performance-Based Engineering*. CRC Press, New York, 2004.

[5] A. Martelli and M. Forni, "Seismic retrofit of existing buildings by means of seismic isolation: some remarks on the italian experience and new projects," in *Proceedings of the 3rd ECCOMAS Thematic Conference on Computational Methods in Structural Dynamics and Earthquake Engineering* (M. Papadrakakis, M. Fragiadakis, and V. Plevris, eds.), Corfu, Greece, 2011.

[6] G. Oliveto and M. Marletta, "Seismic retrofitting of reinforced concrete buildings using traditional and innovative techniques," *ISET Journal of Earthquake Technology*, vol. 42, pp. 21–46, 2005.

[7] G. Oliveto, M. Granata, G. Buda, and P. Sciacca, "Preliminary results from full-scale free vibration tests on a four story reinforced concrete building after seismic rehabilitation by base isolation," in *JSSI 10th anniversary symposium on performance of response controlled buildings*, Yokohama, Japan, 2004.

[8] N. D. Oliveto, G. Scalia, and G. Oliveto, "Dynamic identification of structural systems with viscous and friction damping," *Journal of Sound and Vibration*, vol. 318, pp. 911–926, 2008.

[9] N. D. Oliveto, G. Scalia, and G. Oliveto, "Time domain identification of hybrid base isolation systems using free vibration tests," *Earthquake Engineering and Structural Dynamics*, vol. 39, pp. 1015–1038, 2010.

[10] A. A. Markou, G. Oliveto, and A. Athanasiou, "Recent advances in dynamic identification and response simulation of hybrid base isolation systems," in *Proceedings of the 15th World Conference on Earthquake Engineering*, (Lisbon, Portugal), 2012. Paper No. 3023.

[11] A. A. Markou and G. D. Manolis, "Mechanical formulations for bilinear and trilinear hysteretic models used in base isolators," *Bulletin of Earthquake Engineering*, vol. 14, pp. 3591–3611, 2016.

[12] A. A. Markou and G. D. Manolis, "Response simulation of hybrid base isolation systems under earthquake excitation," *Soil Dynamics and Earthquake Engineering*, vol. 90, pp. 221–226, 2016.

[13] G. Juhn, G. D. Manolis, and M. C. Constantinou, "Stochastic response of secondary systems in base-isolated structures," *Probabilistic Engineering Mechanics*, vol. 7, pp. 91–102, 1992.

[14] R. S. Jangid and T. K. Datta, "Stochastic response of asymmetric base isolated buildings," *Journal of Sound and Vibration*, vol. 179, pp. 463–473, 1995.

[15] H. A. Jensen, M. Valdebenito, and J. Sepulveda, *Optimal Design of Base-Isolated Systems Under Stochastic Earthquake Excitation*. Springer, Berlin, chapter 10 ed., 2013. Computational Methods in Stochastic Dynamics, M. Papadrakakis et al. (eds.).

[16] H. A. Jensen and D. S. Kusanovic, "On the effect of near-field excitations on the reliability-based performance and design of base-isolated structures," *Probabilistic Engineering Mechanics*, vol. 36, pp. 28–44, 2014.

[17] S. K. Saha, K. Sepahvand, V. A. Matsagar, A. K. Jain, and S. Marburg, "Stochastic analysis of base-isolated liquid storage tanks with uncertain isolator parameters under random excitation," *Engineering Structures*, vol. 57, pp. 465–474, 2013.

[18] B. K. Roy and S. Chakraborty, "Robust optimum design of base isolation system in seismic vibration control of structures under random system parameters," *Structural Safety*, vol. 55, pp. 49–59, 2015.

[19] R. Greco and G. C. Marano, "Robust optimization of base isolation devices under uncertain parameters," *Journal of Vibration and Control*, vol. 22, pp. 853–868, 2016.

[20] A. A. Markou, G. Oliveto, and A. Athanasiou, "Response simulation of hybrid base isolation systems under earthquake excitation," *Soil Dynamics and Earthquake Engineering*, vol. 84, pp. 120–133, 2016.

[21] N. Hansen, "The cma-evolution strategy: a tutorial." "`https://www.lri.fr/~hansen/cmatutorial.pdf`", 2011.

COMPDYN 2017
6th ECCOMAS Thematic Conference on
Computational Methods in Structural Dynamics and Earthquake Engineering
M. Papadrakakis, M. Fragiadakis (eds.)
Rhodes Island, Greece, 15–17 June, 2017

# THE EFFECT OF SEISMIC LOADING SIMULATION ON THE RESPONSE VARIABILITY OF STRUCTURES

**Faidon A. Vagionas**[1] **and George Stefanou**[1]

[1]Department of Civil Engineering, Aristotle University of Thessaloniki
54124 Thessaloniki, Greece
e-mail: vagiwnas@hotmail.com; gstefanou@civil.auth.gr

**Keywords:** Artificial Accelerograms, Time-history Analysis, Seismic Response Variability.

**Abstract.** *This paper investigates the variability of the seismic response of structures subjected to various ensembles of ground motions in the framework of nonlinear dynamic analysis. In this kind of analysis, seismic loading, introduced in the form of excitation accelerograms, constitutes the most important source of uncertainty, as it depends on a number of random factors (e.g. distance from the fault source, magnitude, local soil conditions). In order to quantify the effect of seismic loading simulation on the response variability of structures, nonlinear dynamic analysis is carried out on a steel frame, subjected successively to three ground motion ensembles. The ensembles comprise, respectively, real ground motions and artificial accelerograms generated by two different algorithms, one in accordance with the Code provisions and one targeted to a more realistic simulation of the seismic event. Comparison of the three approaches is made by monitoring the statistical properties of the maximum displacement and interstorey drift induced by the assumed ensembles.*

## 1 INTRODUCTION

Time-history analysis is increasingly becoming the preferred method in examining the seismic performance of structures as it provides with a more accurate description of the response of a structure subjected to specific realizations of the seismic event, especially in the case nonlinear behavior is observed. However, subjecting a structure to a single recorded motion is not sufficient for the evaluation of its seismic performance, since the seismic process is strongly stochastic. To account for this stochasticity, modern Seismic Codes require that an ensemble of accelerograms following specific standards be used for the analyses. In particular, Eurocode 8 [1] dictates the use of seven or more accelerograms if the demand is to be calculated by averaging the response values, and in any case at least three. As the selection of an adequate number of real ground motions to satisfy the seismological and geological conditions, as well as the Codes' provisions is not always possible, the description of the seismic motion may be made by using artificial and recorded or simulated accelerograms. Additionally, a second requirement must be satisfied regarding the compatibility of the ground motions to the Codes' smoothed elastic response spectra. This condition is expressed in EC8 [1] as follows:

- the mean of the zero period spectral response acceleration values (calculated from the individual time histories) should not be smaller than the value of $a_g S$ for the site in question.

- in the range of periods between $0.2T_1$ and $2T_1$, where $T_1$ is the fundamental period of the structure in the direction where the accelerogram will be applied; no value of the mean 5% damping elastic spectrum, calculated from all time histories, should be less than 90% of the corresponding value of the 5% damping elastic response spectrum.

With regard to recorded motions, spectral compatibility is achieved either by scaling in the time domain or by filtering in the frequency domain. It should be noted that in the first case only the amplitude of the motion is modified, whereas in the latter the frequency content of the motion is distorted.

Artificial accelerograms meeting the above requirements can be produced by algorithms created ad hoc. One such algorithm is utilized by SIMQKE [2], a software that will be employed in this work.

The use of accelerograms compatible to the smoothed spectrum of the Seismic Codes may be tempting, as it offers a common framework for the comparison of time history analyses to static analyses. However, the practice has been criticized over conservative, unrealistic estimations, as well as loss of the inherent response variability under recorded motions [3]. The main issue with spectrum compatible accelerograms lies with the nature of the Codes' smoothed response spectrum. This spectrum is determined using a Probabilistic Seismic Hazard Analysis and thus represents the cumulative contribution of risk from the seismic sources in a region for a given risk level. Therefore, it is characterized by high energy content over the whole range of structural periods. Naturally, an accelerogram possessing such properties will exhibit large spectral acceleration values. In addition, the lack of variance that is observed is also attributed to the dependence of the ground motions on a single power spectrum, derived from the Codes' response spectrum.

The purpose of this work is to investigate the influence of the method used for the simulation of seismic loading on the response variability of a structure. In this context, two methodologies for the generation of artificial seismic motions which follow different approaches will be presented and compared. Nonlinear dynamic analysis will be carried out on a case study (steel

frame) using the SAP2000 v18.1.1 [4] software, in order to identify possible differences between the responses. The model will be subjected successively to seismic motions, categorized into three distinct groups, comprising natural recordings and artificial accelerograms derived from the SIMQKE software [2] and the algorithm of Sabetta and Pugliese [5]. Useful observations on the responses will be made through statistical processing of the results.

## 2 ALGORITHMS FOR THE GENERATION OF ARTIFICIAL SEISMIC MOTIONS

The SIMQKE software [2] generates ground motions, over which the user has full control in terms of morphological and spectral characteristics. The production of the motions is based upon the relationship between the power spectral density function and the response spectrum. By taking as input the latter, the software calculates the respective power spectrum $G(\omega)$, and from that it produces accelerograms using the spectral representation method [6], as follows:

$$X(t) = \sum_{n=1}^{N} A_n sin(\omega_n t + \phi_n) \tag{1}$$

where

$$A_n = 2\sqrt{G(\omega_n)\Delta\omega} \tag{2}$$

As $G(\omega)$ is time-invariant, the non-stationarity of the seismic motion is incorporated by multiplying the output accelerogram, $X(t)$, with a transient envelope intensity function, $I(t)$.

$$a(t) = I(t) \sum_{n=1}^{N} A_n sin(\omega_n t + \phi_n) \tag{3}$$

This approach leads to accelerograms whose spectra fit the Code's smoothed spectrum, but do not contain the features of natural records. Besides, it should be noted that the evolutionary power spectrum $G(\omega, t)$ of natural ground motions is often non-separable.

The algorithm of Sabetta and Pugliese [5], on the other hand, incorporates the dependence of the motion on the magnitude, the distance from the source and the geological conditions, in an attempt to generate more realistic accelerograms. Based on these parameters, the evolutionary power spectrum or physical spectrum of the motion, $PS(\omega, t)$, is calculated. Again, accelerograms are generated by spectral representation, with the substantial difference that the transient nature of the seismic process is incorporated in the coefficients of the series, $C_n(t)$, which are determined by the physical spectrum:

$$\alpha(t) = 2 \sum_{n=1}^{N} C_n(t) \cos(\omega_n t + \phi_n) \tag{4}$$

where

$$C_n(t) = \sqrt{PS(\omega_n, t)\Delta\omega} \tag{5}$$

Obviously, the resulting motions do not match the Code's spectrum, but resemble the natural records in a time-history level and in the frequency domain, alike.

## 3 MODEL FORMULATION

The model to be tested, as shown in figure 1, is a three-storey steel moment-resisting frame, simulated using frame finite elements. Frame sections are shown in table 1. The joints were simulated using separate, rigid finite elements. Shear deformation at the joints was incorporated by adding panel zones. The inelastic behavior of the structure was simulated by addition of appropriate energy dissipation zones, which are governed by nonlinear material law with kinematic hardening. Geometric non-linearity was not considered necessary to include, as its impact will be negligible, due to the height of the frame. Rayleigh damping was used to obtain a damping ratio of $2\%$ for the first and the third mode. Point masses of $180tn$ were assumed in the middle of each floor and $80.26kN/m$ gravity loading was applied to the beams.

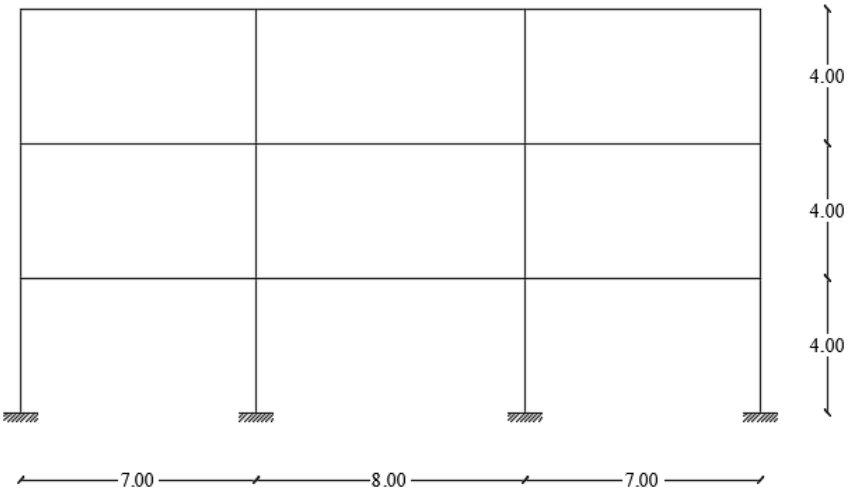


Figure 1: Three-storey steel moment-resisting frame

Table 1: Frame sections

| Storey | Beams | Columns | |
|---|---|---|---|
| | | Outer | Inner |
| 1 | IPE550 | HEB360 | HEB500 |
| 2 | IPE550 | HEB360 | HEB500 |
| 3 | IPE550 | HEB360 | HEB500 |

## 4 SEISMIC LOADING SIMULATION

### 4.1 Ensemble EU: recorded ground motions

The recorded motions for this work were extracted from the European Strong-Motion Database (ESD) [7]. The seismic component chosen from each event was the one exhibiting the maximum peak ground acceleration. Search parameters (presented below) were arbitrarily chosen, so that a direct comparison between real and artificial ground motions would be possible. Mean peak ground acceleration of around $0.25g$ was pursued for the ensembles as a common intensity measure. The accelerograms were used unscaled, as compatibility to the smoothed spectrum was not desired for this ensemble.

- Magnitude: $M_w = 5.5 - 6.9$
- Local soil conditions: *stiff soil*, corresponding to ground type B in EC8.
- Epicentral Distance: $> 10km$, such that near-fault motions will be excluded
- Peak horizontal ground acceleration: $PGA = 2.1 - 2.9m/s^2$

Table 2: Description of the ground motions of the ensemble EU

| S/N | Event | Station | Date | PGA [g] |
|---|---|---|---|---|
| EU01 | Friuli (aftershock) | Forgaria-Cornio | 11/09/1976 | 0.232 |
| EU02 | Friuli (aftershock) | Forgaria-Cornio | 15/09/1976 | 0.264 |
| EU03 | Friuli (aftershock) | San Rocco | 15/09/1976 | 0.236 |
| EU04 | Montenegro (aftershock) | Bar-Skupstina Opstine | 24/05/1979 | 0.270 |
| EU05 | Campano Lucano | Brienza | 23/11/1980 | 0.227 |
| EU06 | Kalamata | Kalamata-OTE Building | 13/09/1986 | 0.272 |
| EU07 | Kefallinia island | Argostoli-OTE Building | 23/01/1992 | 0.227 |
| EU08 | Kozani (aftershock) | Karpero-Town Hall | 19/05/1995 | 0.265 |
| EU09 | Montenegro | Ulcinj-Hotel Olimpic | 15/04/1979 | 0.294 |
| EU10 | South Iceland | Selsund | 17/06/2000 | 0.278 |

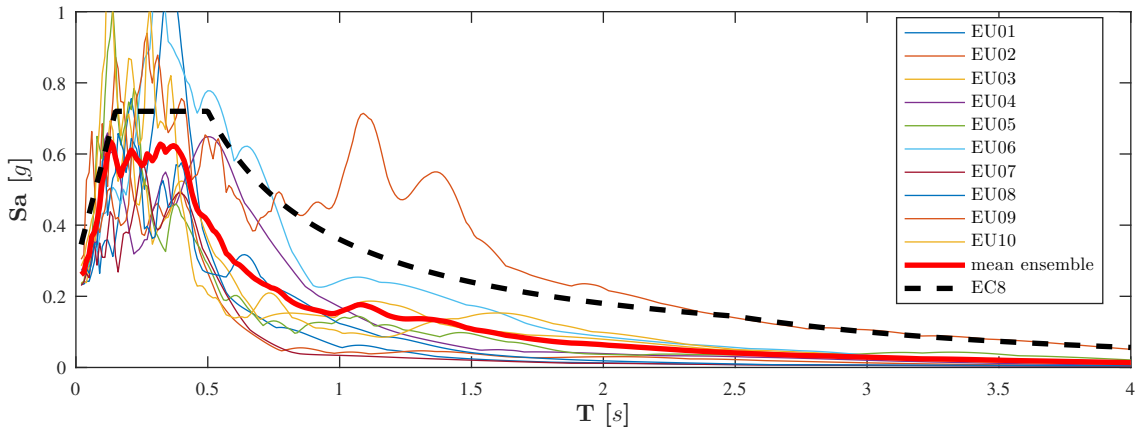


Figure 2: Comparative presentation of ensemble EU and EC8 5% damping elastic response spectra

## 4.2 Ensemble SIMQKE: artificial accelerograms compatible to smoothed elastic response spectrum

Artificial motions produced by the SIMQKE software compose the second ensemble. For the generation of the accelerograms the EC8 response spectrum corresponding to the studied structure was calculated. Spectral matching was pursued at an arbitrarily large number of periods (1235), while five optimization cycles were performed. Parameters for each accelerogram were input such that its graphical shape would match that of the respective motion from ensemble EU. More specifically, exact matching was achieved with regard to the durations and the peak ground accelerations. Compound envelope intensity functions were used to incorporate

the non-stationarity of the seismic motions. To illustrate the aforementioned process, accelerograms #02 of both the EU and SIMQKE ensembles, along with relevant graphical information, are presented in figure 3. Response spectra for the latter ensemble are shown in figure 4.

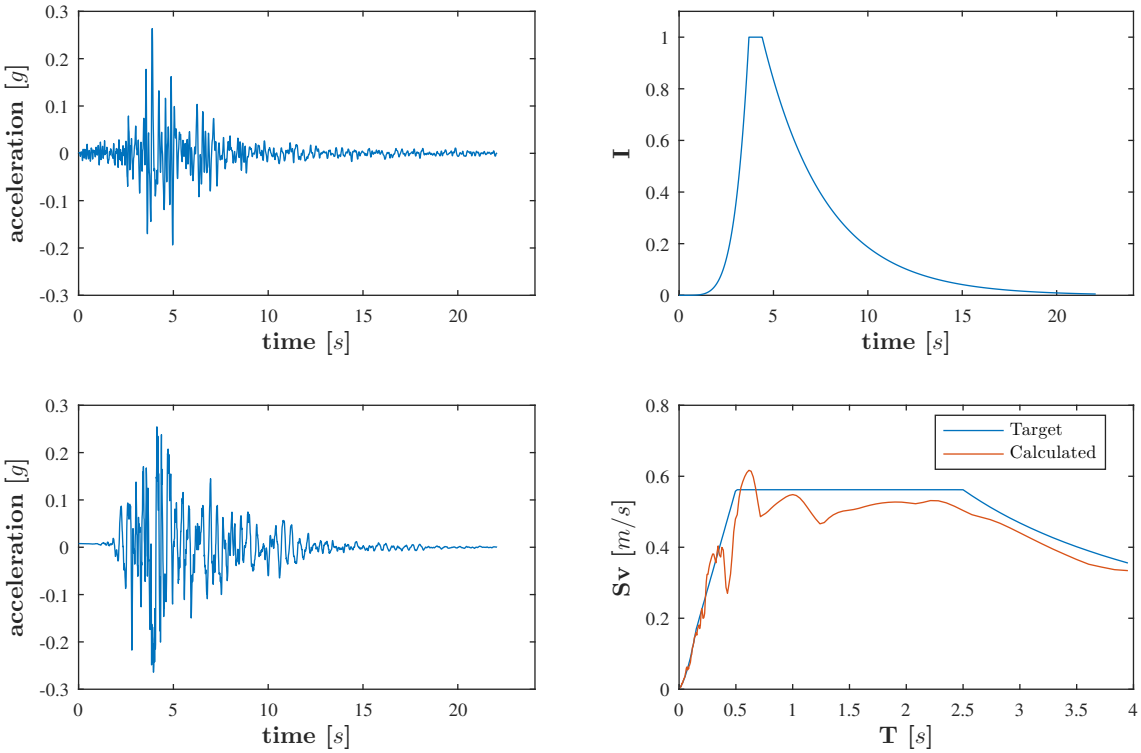


Figure 3: Left: comparative presentation of accelorgrams EU02 (top) and SIMQKE02 (bottom) Right: envelope intensity function (top), target and calculated response spectrum (bottom)

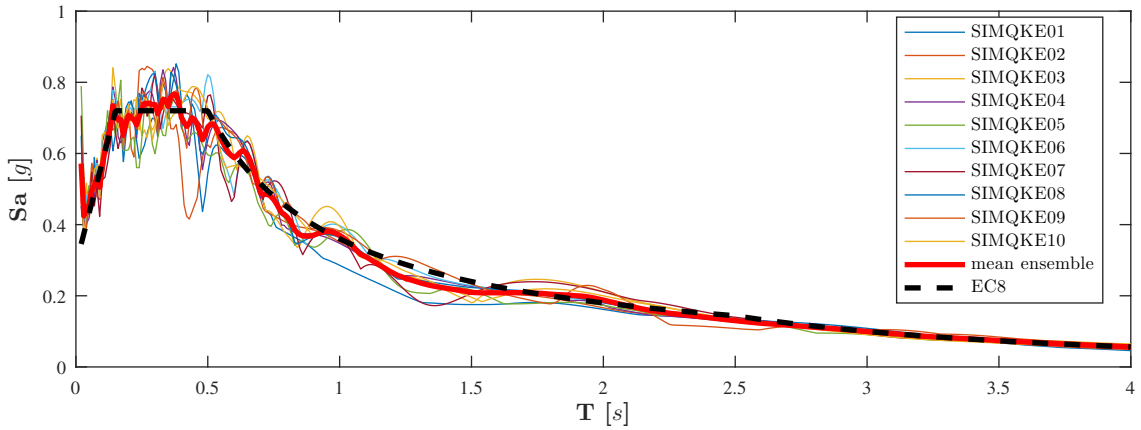


Figure 4: Comparative presentation of ensemble SIMQKE and EC8 5% damping elastic response spectra

### 4.3 Ensemble SABETTA: realistic artificial accelerograms

The third ensemble contains accelerograms generated by the algorithm created by Sabetta and Pugliese [5]. These motions are, by definition, considerably different from the first two sets, both in shape and in properties. The algorithm accepts as inputs parameters related to

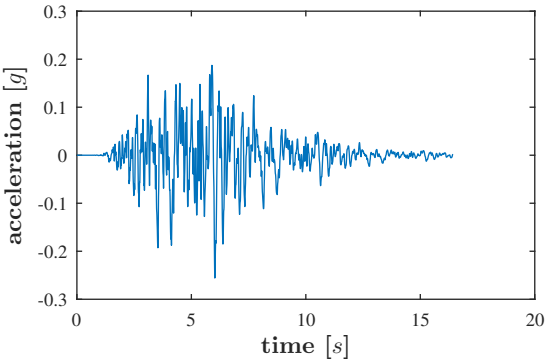


Figure 5: Accelerogram SABETTA02

seismological and geological conditions and therefore the user has little control over the resulting motion. The following values were input for this study targeting the aforementioned mean $PGA \simeq 0.25g$:

- Magnitude: $M_w = 6.0 - 6.8$
- Epicentral distance: $13 - 23km$
- Local soil conditions: *shallow alluvium*, characterized by mean shear-wave velocity, $V_{s,30} = 350 - 750m/s$ which approximately corresponds to ground type B in EC8.

Again, motion #02 of figure 5 is arbitrarily chosen as a representative sample of ensemble SABETTA, while figure 6 shows the ensemble's response spectra.

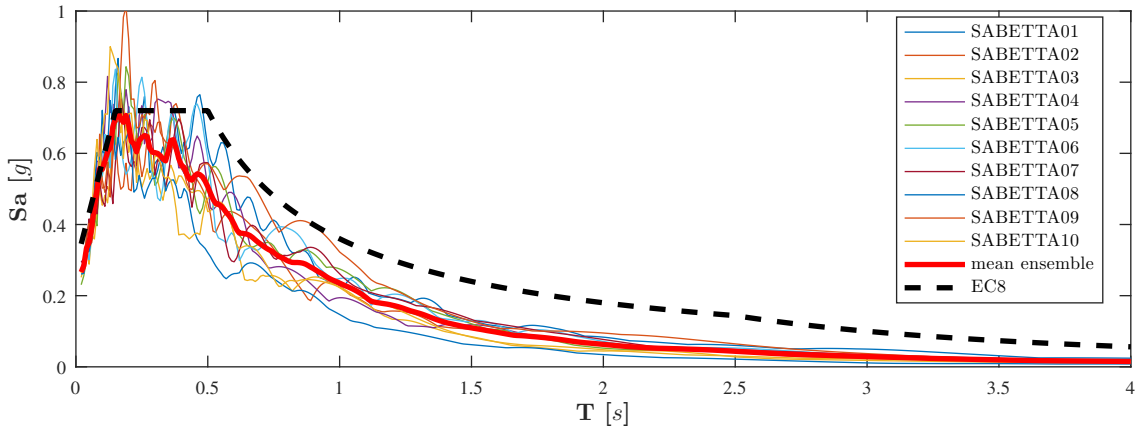


Figure 6: Comparative presentation of ensemble SABETTA and EC8 5% damping elastic response spectra

## 5 SEISMIC RESPONSE OF THE STRUCTURE

Information concerning the response of the structure can be extracted from the qualitative aspects of the ground motions even before the analyses are carried out. In this case, the stark differences among the assumed ensembles are indicative of the expected responses. At first, an observation can be made regarding the shape of the accelerograms. Those that stem from recorded motions exhibit strong variability as regards the total duration, the duration of the

strong motion (approximately stationary part) and the relative position of the peak ground acceleration. Similar characteristics can be found in the motions composing ensemble SIMQKE, as they were intentionally produced to resemble the natural accelerograms. Nevertheless, the latter tend to overestimate the duration of the strong part and have a more gradual attenuation. This can be attributed in part to imperfections in the intensity envelope functions and to the optimization cycles that were executed for the better matching to the smoothed elastic response spectrum, during which the frequency content of the motion is altered. Lastly, the accelerograms belonging to ensemble SABETTA drastically differ from those of the above two ensembles. In particular, all of the motions loosely resemble an attenuated harmonic oscillation, while their duration does not exceed twenty seconds.

Regarding the mean elastic spectra, ensemble EU is situated below the smoothed Code's spectrum in the whole range of periods, ensemble SIMQKE adequately fits the Code's spectrum, and ensemble SABETTA matches the smoothed spectrum only in the ascending part, after which it follows a descending trend, similar to ensemble EU. Of particular interest are the shape and variance of the response spectra. In terms of shape, the natural records are very dissimilar from one another. Differences can be located in the values of the maximum spectral acceleration, which in some cases far exceeds the Code's spectrum's plateau, its position - record EU09 stands out, exhibiting peak value at a period higher than $T = 1s$ - and the period range in which remarkable energy content is encompassed - again, motion EU09 is distinctive as it shows high acceleration values in a large range of periods. The spectra of ensemble SIMQKE closely follow the smoothed elastic spectrum, with few deviations focused in the area around $T = 0.5s$. Finally, even though the spectra of ensemble SABETTA exhibit some dispersion around the mean, they do not deviate from it significantly, as far as the general course is concerned.

Based on the above observations, it would be reasonable to assume that the response values of the structure to the second ensemble will be higher than the other two, on average. Furthermore, the variability of the spectra of ensemble EU as well as the lack of it in the case of the other two ensembles are expected to lead respectively to responses with high variance on the one hand and uniformity and similar peak acceleration values on the other.

The influence of the dispersion of the spectra is better illustrated in figure 7, where the response spectra of the three ensembles are presented, normalized with regard to the spectral acceleration at the fundamental period of the structure, $S_a(T = 1.32s)$.

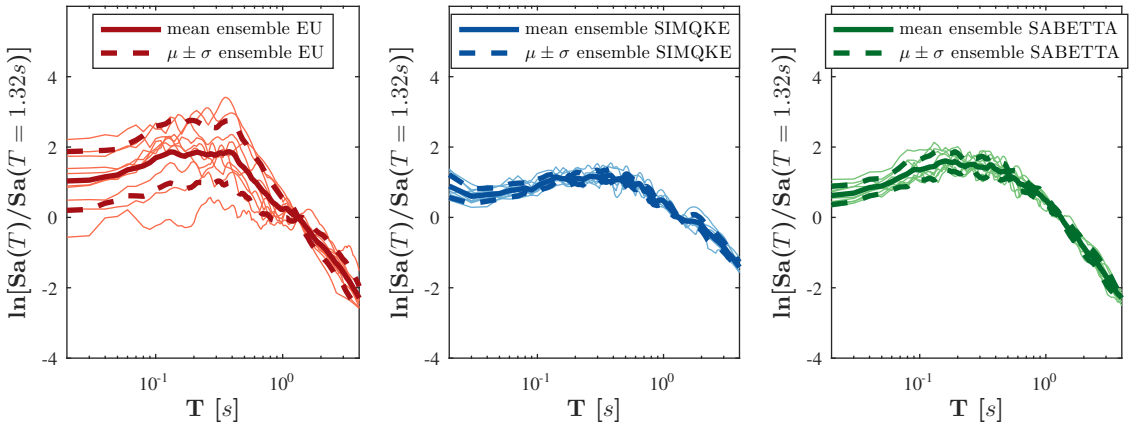


Figure 7: Comparative presentation of the three ensembles' response spectra, normalized with regard to the spectral acceleration at the fundamental period of the structure, $S_a(T = 1.32s)$

The response values are presented in terms of absolute floor displacements and interstorey drift, measured at the middle of each storey, where the center of mass lies. Maximum displacements of each floor induced by the three excitation ensembles, along with their respective mean values are presented in figure 8. It is observed that ensemble EU leads to responses with particularly large dispersion. Conversely, responses to the ensembles comprising artificial accelerograms are mostly concentrated around the mean, in total agreement with what had been predicted.

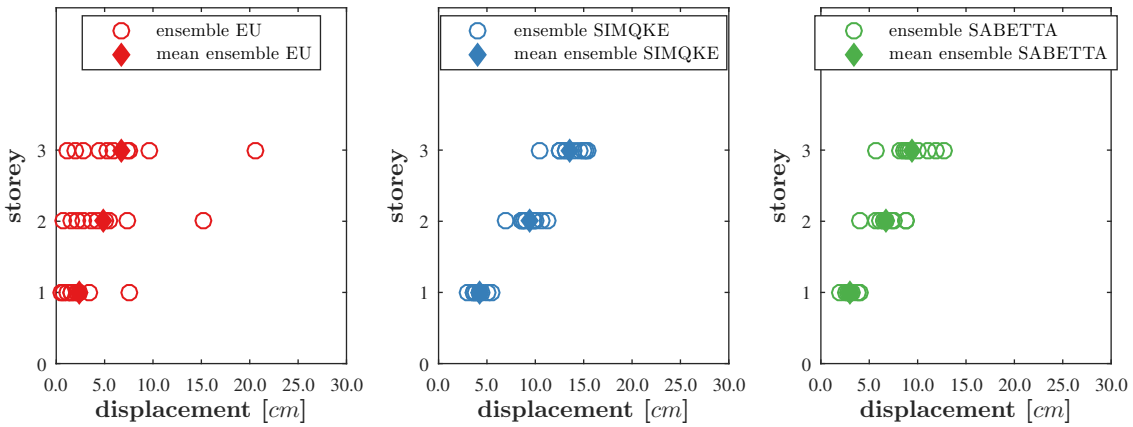


Figure 8: Maximum displacement values of the frame induced by the seismic loading

The above results are also presented in the form of a bar diagram in figure 9, in which the response to each excitation can be located. It is noted that ground motion EU09 subjects the structure to disproportionately large displacements in comparison to both the rest of the ground motions of ensemble EU and those of the other two ensembles. Looking back at figure 2 it is found that the ninth accelerogram is the one that exhibited especially high spectral acceleration values in the area around the fundamental period of the structure. This relationship between the maximum seismic response of the structure and the spectral acceleration at its fundamental period is to a large extent observed for all three ensembles.

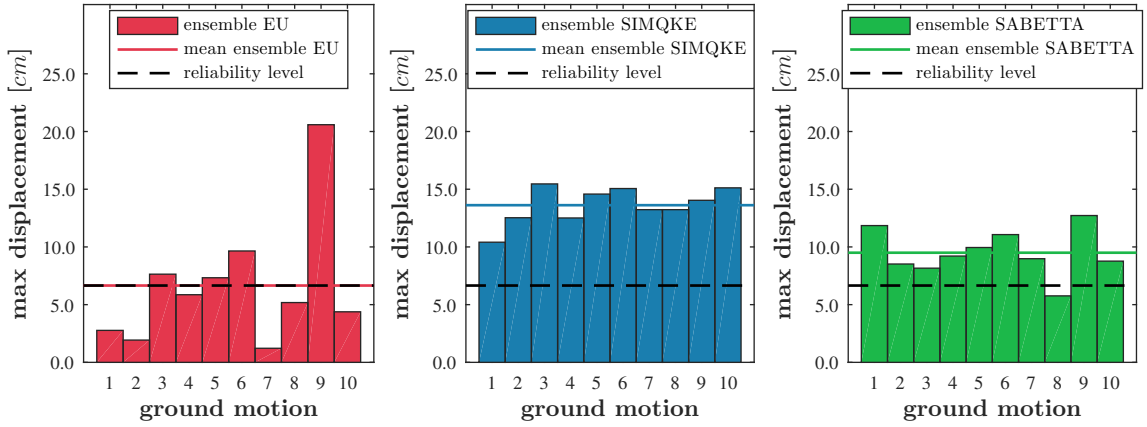


Figure 9: Maximum displacement values of the frame (3rd storey) induced by the seismic loading

Table 3 quantitatively presents the statistical properties of the responses. In addition to what has already been mentioned, and in conjunction with figure 9 the significance of the extreme

response to excitation EU09 to the shaping of the mean of the first ensemble becomes apparent. By setting the minimum mean displacement value, that is of ensemble EU, as a common reliability level, $r = \mu_{EU}$, a rough estimate of the structural reliability of the frame can be made.

Table 3: Statistical properties of the maximum responses (3rd storey)

| | $\mu^*$[cm] | $\sigma^\dagger$[cm] | CV$^\ddagger$ | $\mathbf{R_{10}}(u > \mu)^\S$ | $\mathbf{R_{10}}(u > r)^\|$ |
|---|---|---|---|---|---|
| EU | 6.55 | 5.57 | 0.84 | 0.40 | 0.40 |
| SIMQKE | 13.62 | 1.56 | 0.11 | 0.50 | 1.00 |
| SABETTA | 9.50 | 2.01 | 0.21 | 0.40 | 0.90 |

$^*$ mean value
$^\dagger$ standard deviation
$^\ddagger$ coefficient of variation
$^\S$ relative frequency of exceedance of mean value
$^\|$ relative frequency of exceedance of reliability level

At this point it should be recalled that Eurocode 8 [1] allows the calculation of the demand from the mean of the maximum responses if more than seven time-histories are used. By examining figure 10 and the frequency of exceedance of the reliability level (Table 3) it becomes clear that ensemble SIMQKE, comprising artificial accelerograms fitted to the Code's response spectrum, errs on the side of caution. Indeed, high correlation is observed between mean spectral acceleration at the position of the fundamental period of the structure and the mean of the maximum displacement values, for all three excitation ensembles. This suggests that the above acceleration, or at least the maximum spectral acceleration, would have been a more appropriate intensity measure for defining the ensembles.

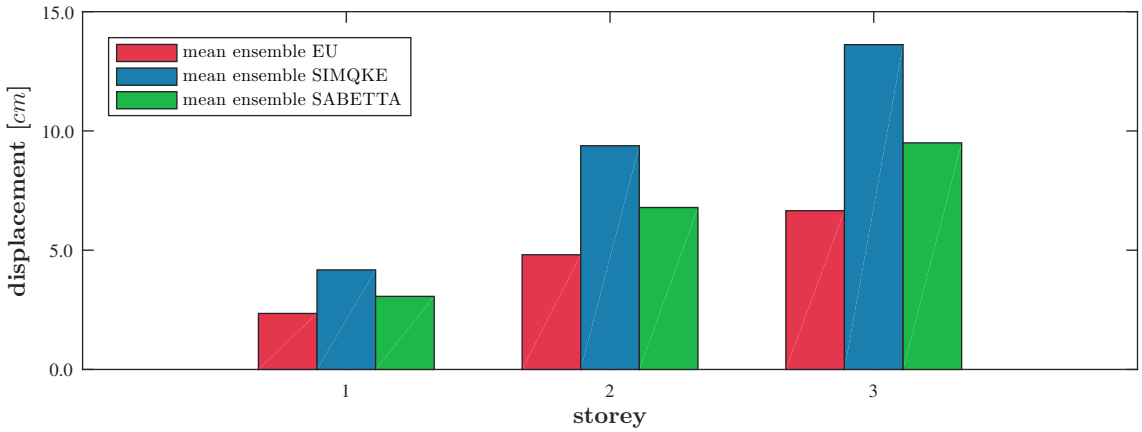


Figure 10: Mean of the maximum displacement values induced by the seismic loading

As a closing remark, it should be mentioned that the results of this study are fully in line with what was previously observed concerning the lack of dispersion of responses to artificial ground motions. Following this observation it should be emphasized that if maximum displacement values are used, natural recordings lead to a much more conservative calculation of the demand, as shown by the maximum drift in figure 11.

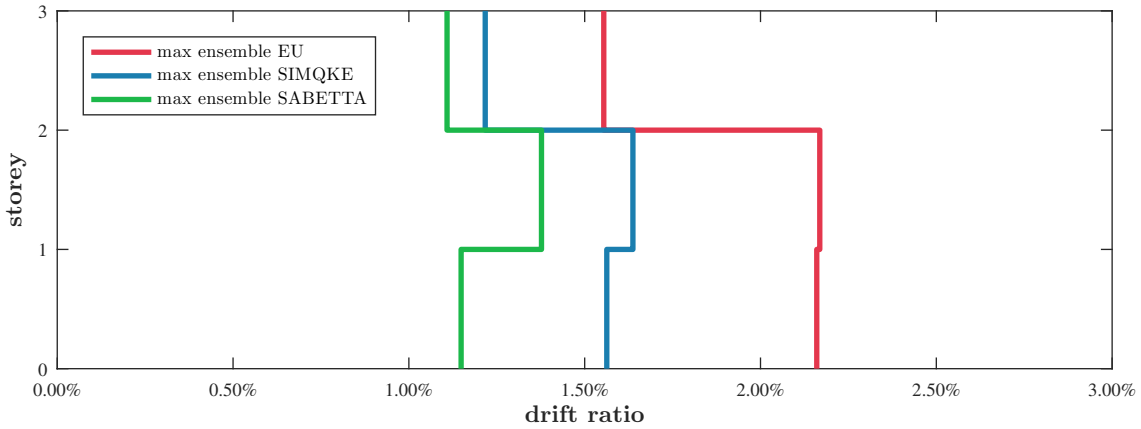


Figure 11: Maximum storey drift

## 6 CONCLUSIONS

This work has investigated and attempted to quantify the influence of the simulation methods used in generating seismic motions on structural response in the context of non-linear dynamic analysis. For this purpose, a steel moment-resisting frame was subjected successively to three ground motion ensembles. The use of recorded motions and artificial accelerograms produced by two algorithms which follow conspicuously different approaches, namely SIMQKE [2] and the algorithm of Sabetta and Pugliese [5] was decided.

The analyses revealed stark differences between the responses to natural recordings and artificial accelerograms. It is observed that responses to natural recordings show significant dispersion compared to the responses to the artificial ensembles. Furthermore, noticeable difference in the mean of the maximum responses and little difference in variance is found between the artificial ensembles. The strong uniformity observed in the responses to ensemble SIMQKE, which comprises accelerograms fitted to the Code's response spectrum, confirms earlier studies [3, 8]. Additionally, ensemble SIMQKE resulted in higher mean displacements of the control nodes. These observations are largely attributable to the correlation between the responses and the spectral acceleration of the excitation in the position of the fundamental period of the structure.

This work is in agreement with similar studies carried out in RC structures [8, 9] and contributes to the understanding of the seismic motion simulation and its impact on structural response variability. Further investigation is deemed necessary, using a greater number of accelerograms and more reliable intensity measures (e.g., maximum spectral acceleration) for the selection and/or generation of the ground motions [10].

## REFERENCES

[1] *Eurocode 8: Design provisions for earthquake resistance of structures Part 1: General rules, seismic actions and rules for buildings (EN 1998-1)*. European Committee for Standardization (CEN), 2004.

[2] D. Gasparini, E. H. Vanmarcke, *SIMQKE: A program for artificial motion generation*. Dept. of Civil and Environmental Engineering, Massachusetts Institute of Technology, 1976.

[3] F. Naeim, M. Lew, On the use of design spectrum compatible time histories. *Earthquake Spectra*, **11**, 1, 1995.

[4] *SAP2000 v18.1.1*. Computers and Structures, inc., 2016.

[5] F. Sabetta, A. Pugliese, Estimation of response spectra and simulation of nonstationary earthquake ground motions. *Bulletin of the Seismological Society of America*, **86**, 1996.

[6] M. Shinozuka and G. Deodatis, Simulation of stochastic processes by spectral representation. *Applied Mechanics Reviews*, **44**, 4, 1996.

[7] N. Ambraseys, P. Smit, R. Sigbjornsson, P. Suhadolc, B. Margaris, *Internet-site for European strong-motion data*. European Commission, Research-Directorate General, Environment and Climate Programme, 2002.

[8] A. Azarbakht, M. G. Ashtiany, The code-based selection of ground motion records for nonlinear time-history analysis. *14th World Conference on Earthquake Engineering*, Beijing, China, October 12-17, 2008.

[9] M. Pianigiani, V. Mariani, M. Tanganelli, S. Viti, The effects of the seismic input on the seismic response of RC buildings. M. Papadrakakis, M. Fragiadakis eds. *5th ECCOMAS Thematic Conference on Computational Methods in Structural Dynamics and Earthquake Engineering (COMPDYN 2015)*, Crete Island, Greece, May 25-27, 2015.

[10] E. I. Katsanos, A. G. Sextos, G. D. Manolis, Selection of earthquake ground motion records: A state-of-the-art review from a structural engineering perspective. *Soil Dynamics and Earthquake Engineering*, **30**, 4, 2010.

COMPDYN 2017
6th ECCOMAS Thematic Conference on
Computational Methods in Structural Dynamics and Earthquake Engineering
M. Papadrakakis, M. Fragiadakis (eds.)
Rhodes Island, Greece, 15–17 June 2017

# NUMERICAL SIMULATION OF BLAST WAVE PROPAGATION IN LAYERED SOIL FEATURING SOIL-STRUCTURE INTERACTION

**Abir. M[1], Arumugam. D[2], Dhana Sekaran. B[3], Subash. T. R[4]**

[1] Senior Design Engineer, L&T Construction, Chennai, India, e-mail: abir-mandal@lntecc.com

[2] Asst. Engineering Manager, L&T Construction, Chennai, India, e-mail: darumugam@lntecc.com

[3] Chief Engineering Manager; [4] Joint General Manager, L&T Construction, Chennai, India.

**Keywords:** Blast Pressure, Wave Propagation, Soil-Structure Interaction, Numerical Method Simulation, Non-Linear Material Model.

**Abstract.** *In recent decades, the blast load impact on structures has acquired considerable attention due to magnified threats from various man-made activities. Understanding the shock wave propagation in soil and its interaction with structure are crucial in a blast scenario. In a surface or sub-surface blast, the shock wave mechanics and its subsequent impact on underground or above ground structures are extremely complex. This paper scrutinizes the problem of an underground explosion initiated by penetrated missile and thereby focuses on the characteristics of shock wave propagation and pressure attenuation in the surrounding soil. Analyzing empirical data for the same reflects different attenuation factor for different type of soil. Numerical simulations of blast wave propagation in soil and the effect of soil-structure interaction are implemented in a computationally efficient way using an advanced finite element analysis tool (LS-DYNA). Constitutive material models are used to simulate the non-linear behavior and damage profile in concrete and soil. Observations on the numerical model reveal a close tally with theoretical calculations in predicting shock wave characteristics in an undisturbed wave propagation. Numerical analysis is essential to study the exact conditions prevalent during a sub-surface blast. The above mentioned condition has been theoretically tested for a surface blast and results compared to confirm sub-surface blast having much greater impact at a longer distance. An attempt has been made to capture the Transmission and Reflection phenomena related to pressure wave propagation at the interfaces of multi layered media that is actually evident in the case of blast wave passing through layered soil. Preliminary study on wave propagation in rock media highlighting the difference in behavior of the shock waves in soil and rock is presented and discussed as well.*

## 1 INTRODUCTION

The problem of underground structures subjected to dynamic load has always been a topic of interest to engineers, especially the effect of extreme event like blast loading which has acquired considerable attention due to magnified threats from various man-made activities. Studying the soil response, soil-structure interaction and dynamic behavior of structure subjected to blast loading are very crucial in design of military, pipeline construction, and tunneling and defense structures. As a result of an explosion in the soil media, various hidden complex mechanical processes get triggered which give rise to detrimental effects that are seen and felt by humans.

The explosion leads to the generation of high pressure shock waves that propagates radially outward from the detonation. Understanding the shock wave propagation and its attenuation in soil media is of paramount importance for the analysis and design of underground structures. Attenuation characteristics of the shock wave depends on the surrounding material medium, soil/rock and air for surface blast, different types of soil medium (layered soil) in case of an underground/sub-surface blast. The shock wave characteristics get altered due to reflection, transmission occurring at the interface of the layered soil strata with different densities and during its interaction with the structure.

The paper focus on pressure attenuation in different soil medium, comparison on effects of surface, air and subsurface explosion, and soil-structure interaction and pressure attenuation in layered soil media using a case study. Empirical relations are used to evaluate the preliminary response of the medium. As empirical equations act only as primary tool for validation, numerical analysis is vital to understand the attenuation characteristics and soil-structure interaction more realistically. TNT properties are used for the blast simulation in numerical analysis. The pressure wave propagation certainly gets influenced by the non-linear property of soil as well. This concern has been addressed in the numerical approach. A computationally efficient numerical model has been created incorporating all the soil and blast parameters in a finite element software, LS-DYNA, to capture a scenario as close as possible to the actual and tallied with the available empirical equations.

## 2 LITERATURE STUDIES

Limited research is available on response of a buried structure subjected to a subsurface blast and its attenuation effect in different soil medium and layered soil media. Some of the research available on response of an underground/buried structure response to blast is listed here. Some of the research focuses on validation against the experimental data and some against empirical relations. For numerical evaluation, mainly AUTODYN and LS-DYNA were used to capture the dynamic response of the soil.

Ya-Dong et al [1] studied the response of a RC frame subjected to a surface blast. Deformation, pressure and failure of the frame were modeled using FEA and validated against field experiments. Mohr-Coulomb material has been used to capture the soil behavior.

Dynamic response of a tunnel subjected to a surface burst has been studied by Mobaraki at al [2]. Response of the tunnel in three different type of soil domain were studied and validated against empirical equations. Evaluation of the damage of the materials were done using nonlinear material models (MAT_SOIL_AND_FOAM) and (MAT_PLASTIC_KINEMATIC) for soil and concrete respectively. Peak particle velocity in the soil medium has been used to characterize the failure criteria.

Numerical evaluation of rock mass subjected to a large scale underground explosion and validated against experimental data using PPV and PPA data were studied by Chenqing et al

[3]. A fully coupled SPH-FEM approach were used by Zhongqi et al [4] to validate the explosion effect in a soil against empirical calculations. Response of the structure such as pressure, velocity and acceleration were evaluated and validated.

## 3 SHOCK WAVE PROPAGATION

Weapons exploding above or near the ground surface and weapons that explode after penetrating the soil medium are the two cases that pose major threat to underground structures. Crater formation and ground vibrations are the major phenomena that dissipate the energy in a blast phenomenon.

### Crater and Attenuation

Blast at or near to ground surface excavates the soil medium resulting in the formation of a large crater and the geological material thrown out of the crater is known as ejecta. The depth of burst is one of the major parameter that controls the shape and size of the crater. Depth of crater will increase with depth of burst to a certain optimum limit, beyond which it decreases. If the explosion is too deep inside ground, then the crater may not be visible at surface and it is termed as Camouflet [5].

The shock wave font with peak blast pressure travel as elastic waves as it passes through different geological strata and it attenuates as distance from the blast source increases. Variation in the wave propagation characteristics is directly related to the soil media density, moisture content and other soil parameters. Compression wave (P-wave) is the critical component for the analysis of underground structures that provides information on attenuation characteristics of the medium. The velocity of P-waves $\left(\sqrt{\frac{G}{\rho}}\right)$ can be calculated by using shear modulus (G) and density of the soil medium (ρ). Inference from the P-wave characteristics reveals that stiffer the soil medium, higher the shock wave velocity and lower the attenuation characteristics of the soil.

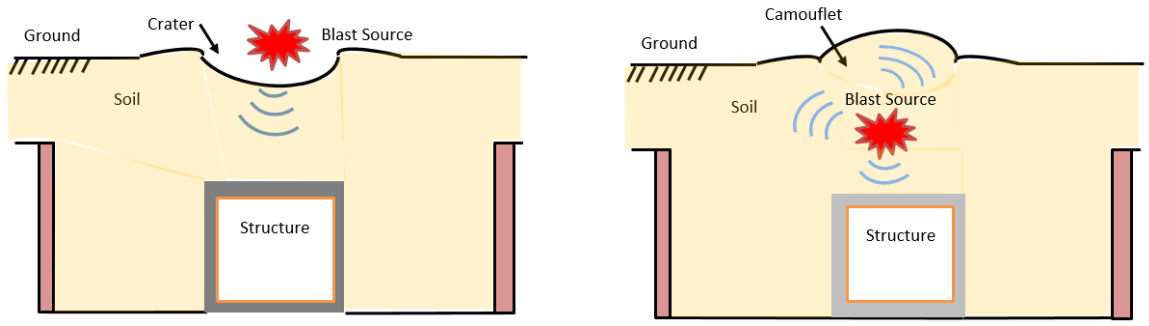


Figure 1: Surface/Sub-surface blast effects

### Pressure Calculation

Pressure font varies as the waves travel away from origin depending mainly on the attenuation factor and acoustic impedance of the geological media. For relatively short distances from the explosion source, high pressures are developed, soil might exhibit a strain hardening behavior under this increased level of pressure. Empirical power law equations [5, 6] that is used to describe the magnitude of peak over pressure as a function of distance as shown below

$$P_o = Af(\rho c)\left[\frac{R}{W^{1/3}}\right]^{-n} \quad (1)$$

From the above equation, it can be observed that more the dense medium, higher the pressure value. Where, Po is the over pressure at any scaled depth, A is the constant, f is the coupling factor depending on the scaled depth of burst, ρc is acoustic impedance of the medium, R is the scaled distance where pressure is measured, W is the charge weight and n is the Attenuation factor of the medium. The Coupling factor is nothing but a value corresponding to the depth of burst in a medium that is obtained from Figure 2.

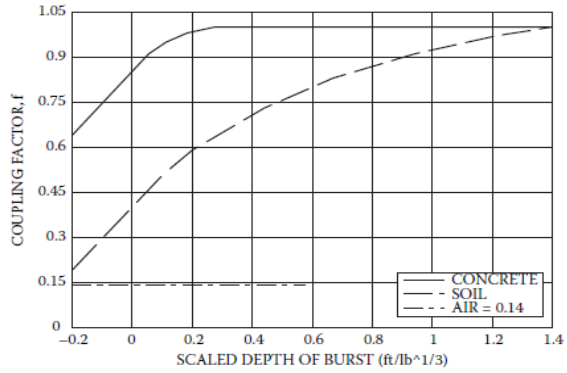


Figure 2: Coupling factor graph

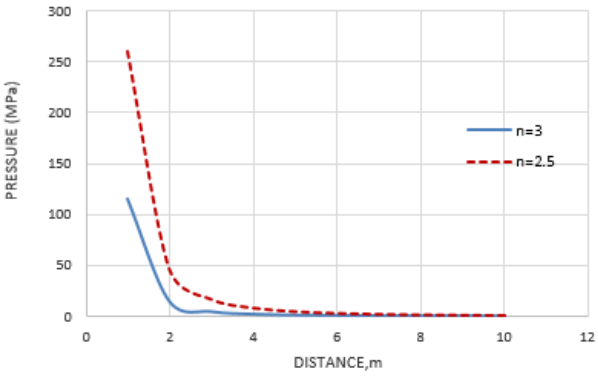


Figure 3: Shock wave attenuation

### Shock Wave Attenuation in Soil

Shock wave propagation/attenuation for a 500 lb. charge weight located at 1m below the ground surface for two different soil properties are provided in Figure 3. From the results it can be observed that there is a drastic decrease in pressure initially and then the rate of decrease becomes gradual over the distance. Also, the importance of attenuation factor in attenuating the pressure at near-field can be observed.

### *Comparison of Sub –Surface Blast Pressure with Free-Air Burst and Surface Burst*

For a close range explosion (750lb.), Sub-Surface Blast pressure has been compared with that of Free-Air Burst and Surface Burst to understand the wave propagation in soil and its attenuation effects. Theoretical values for Free- Air and Surface Blast Pressure are computed using UFC [7]. It is evident that the effect of sub-surface burst is much more as compared to the other types, especially in a close range.

| Distance | 3m | 4m | 5m | 6m | 7m | 8m | 9m |
|---|---|---|---|---|---|---|---|
| s-s $P_{so}$ (MPa) | 16.67 | 8.12 | 4.65 | 2.95 | 2 | 1.44 | 1.07 |
| s-$P_{so}$ (MPa) | 5 | 3.09 | 2.04 | 1.4 | 1 | 0.75 | 0.57 |
| a-$P_{so}$ (MPa) | 4 | 2.3 | 1.44 | 0.97 | 0.69 | 0.51 | 0.39 |

Table 1: Comparison of sub-surface (s-s), surface (s), and free-air (a) blast pressures vs. distance

## 4 INTERACTION WITH STRUCTURE

The ground shock with peak particle velocity impacts the underground structure and causes significant deformation or damage to the structure. Large deformation in soil might usually be associated with large deformation in a structure as well, if it is in the vicinity of the explosive. Net response of the structure subjected to ground motion can be evaluated using Soil-Structure Interaction (SSI) [2, 8]. The response of the structure depends on the soil structure interface,

soil strata and intensity of the ground motion. Acoustic impedance can be used to calculate the pressure at structure when an explosion occurs at some distance from the structure.

### Acoustic Impedance

Acoustic Impedance of a media is given by product of the seismic velocity and density of the soil medium as indicated below

$$Acoustic\ Impedance, \alpha = \rho C \tag{2}$$

Where Seismic Velocity (C) is equal to the P-wave velocity of the blast wave in the medium and ρ is the density of the medium. This shows how the wave propagation gets affected by density of the soil media at the interface. Acoustic impedance act as an important parameter in evaluating the pressure transmission and reflection in the media. Hence as the wave passes through layered geological strata, the pressure changes depending upon the acoustic impedance of the media.

### Reflection & Transmission

As the blast wave traverses through different geological media, energy transmission and reflection occurs at the interface. The transmission/reflection purely depends on the ratio of the acoustic impedance of the two media at the interface. The ratio is expressed by acoustic impedance of the second media ($\alpha_2$) to the acoustic impedance of the first media ($\alpha_1$) and represented by (when the wave travels from first media to the second)

$$\alpha_z = \alpha_2/\alpha_1 \tag{3}$$

Higher the ratio, higher the transmission and lower the reflection. From the ratio, the amount of stress reflected can be calculated as follows

$$\sigma_r = \left(\frac{\alpha_z - 1}{1+\alpha_z}\right)\sigma_i \tag{4}$$

Where $\sigma_i$ = incident pressure. Similar to reflection, transmission is also a function of impedance ratio and transmitted stress can be calculated

$$\sigma_t = \left(\frac{2\alpha_z}{1+\alpha_z}\right)\sigma_i \tag{5}$$

## 5 NUMERICAL ANALYSIS

For the numerical analysis of blast simulation and its effect on structure, LS-DYNA is used. Blast pressure generation is captured through the actual modeling of the explosive (TNT). Dimension of the problem changes as per the problem definition.

### Finite Element Modeling

For simplicity, axisymmetric model is considered for the analysis as shown in Figure 4 and Figure 5. As initial detonation of the TNT and wave propagation is crucial for the accuracy of the simulation, a very fine mesh is required at the detonation point. Mapping techniques are generally used to capture the propagation more accurately at the detonation level [9, 10].

In this study, a varying mesh is used that is very fine (0.05) at the detonation location. As the number of elements is less than 1lakh it works out to be computationally efficient for the study. For the numerical model considered in the study, free-flow condition is provided on sides as shown in the Figure 4 and Figure 5. The material medium consist of Air, Soil and TNT. Air

medium of suitable dimension is considered above the ground to model the wave propagation and crater effects to the precise.

Arbitrary Lagrangian Eulerian (ALE) algorithm which leverage the advantages of both the Lagrangian and Eulerian is adopted for modeling the blast simulation. Multi-material ALE modeling [MMALE] proves to be efficient in modeling the large deformation problems especially blast and impact [11] [12] [13]. In the study, ALE mesh (SECTION_ALE2D) is used to represent the fluid domain (air and TNT) and Lagrangian mesh (SECTION_SHELL) for the concrete domain. Contact between the ALE and Lagrangian domain is established using *CONSTRAINED_LAGRANGE_IN_SOLID [14]. And a suitable ALE advection algorithm is used such that energy conservation is achieved. To achieve the stable solution for the analysis, Energy Ratio (=1) and Hourglass Energy Ratio (<5% of Internal energy) and Sliding Energy Ratio (<10% of Internal energy) are checked [15].

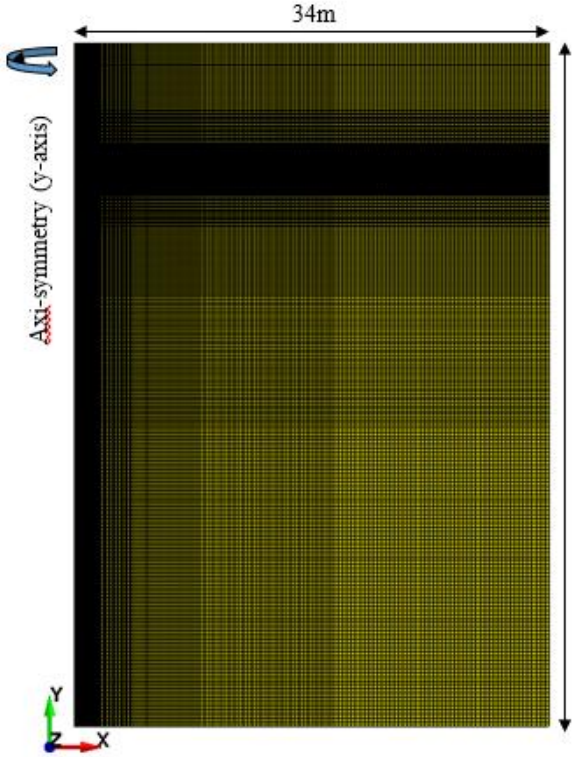


Figure 4: FE mesh

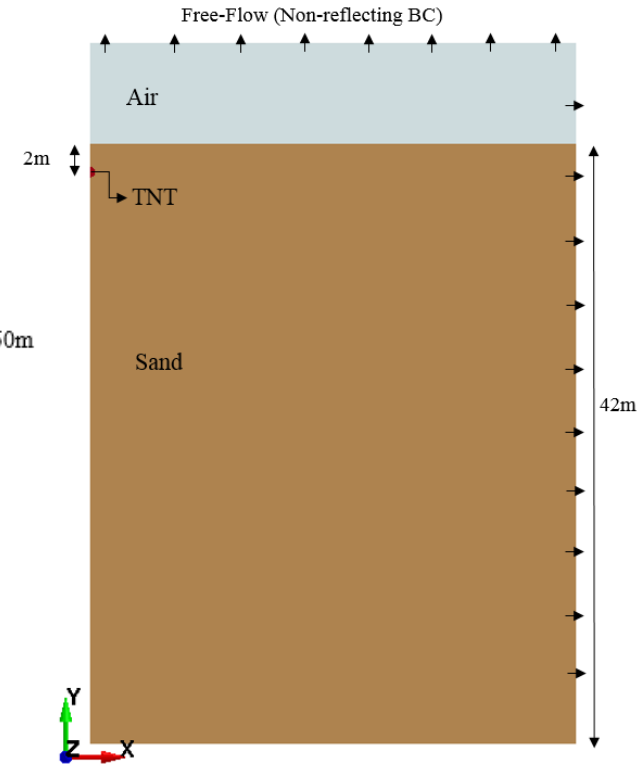


Figure 5: ALE Multi-Material model

## Material Modeling

The explosive material behavior is modeled and simulated using *MAT_HIGH_EXPLOSIVE_BURN and EOS_JWL (Equation of State). *MAT_NULL and *EOS_LINEAR_POLYNOMIAL are used to model the air domain. Material properties are provided below.

| Unit (kg, m, s) | | | | | | |
|---|---|---|---|---|---|---|
| **MAT_NULL** | | | | | | |
| R0 | PC | MU | TEROD | CEROD | YM | PR |
| 1.225 | 0 | $1.78 \times 10^{-5}$ | 0 | 0 | 0 | 0 |

| **EOS_LINEAR_POLYNOMIAL** | | | | | | | | |
|---|---|---|---|---|---|---|---|---|
| C0 | C1 | C2 | C3 | C4 | C5 | C6 | E0 | V0 |
| 0 | 0 | 0 | 0 | 0.4 | 0.4 | | $2.5x10^{5}$ | 1 |
| **MAT_HIGH_EXPLOSIVE_BURN** | | | | | | | | |
| R0 | D | PCJ | BETA | K | G | SIGY | | |
| 1630 | 6930 | $2.1x10^{10}$ | 0 | 0 | 0 | 0 | | |
| **EOS_JWL** | | | | | | | | |
| A | B | R1 | R2 | ω | E0 | V0 | | |
| $3.738x10^{11}$ | $3.747x10^{9}$ | 4.15 | 0.9 | 0.35 | $7x10^{10}$ | 1 | | |

Table 2: Air and TNT material parameters

A nonlinear constitutive continuum model with damage modeling is used to capture the concrete behavior subjected to the blast and impact loading. Several constitutive models are available for the continuum modeling of concrete dynamic response [16]. MAT_RHT model is used to study the concrete behavior subjected to blast loading.

For modeling the soil medium, MAT_SOIL_AND_FOAM [17] is used which includes the pressure-volume relationship that is predominant during the blast wave propagation. Soil properties of the different soil medium are provided below.

| R0 | G | BULK | A0 | A1 | A2 | PC |
|---|---|---|---|---|---|---|
| Low Dense Soil | | | | | | |
| 1293 | $3.2 \times 10^{6}$ | $1.7 \times 10^{8}$ | 1000 | 0.75 | $1.5x10^{-4}$ | 0 |
| Medium Dense Soil | | | | | | |
| 1453 | $1.7x\ 10^{7}$ | $1.2 \times 10^{8}$ | $5.3 \times 10^{5}$ | 15.26 | $1.1x10^{-4}$ | $-1.4x10^{4}$ |
| High Dense Soil | | | | | | |
| 2094 | $2.3x\ 10^{7}$ | $1.3 \times 10^{8}$ | $4.3 \times 10^{4}$ | 3.71 | $7.9x10^{-5}$ | -6894.75 |

Table 3: Sand material properties [18]

## 6 CASE STUDY

The case study deals with a problem of an under-ground blast initiated by a penetrated missile. Penetrating missile has the capacity to penetrate and reach the structure as close as possible causing significant damage to the structure (Figure 6). The damage is significant if the missile penetration is not resisted by providing suitable mitigation procedure. As the interest is on shock wave propagation, penetration effect of the weapon on the soil is not discussed.

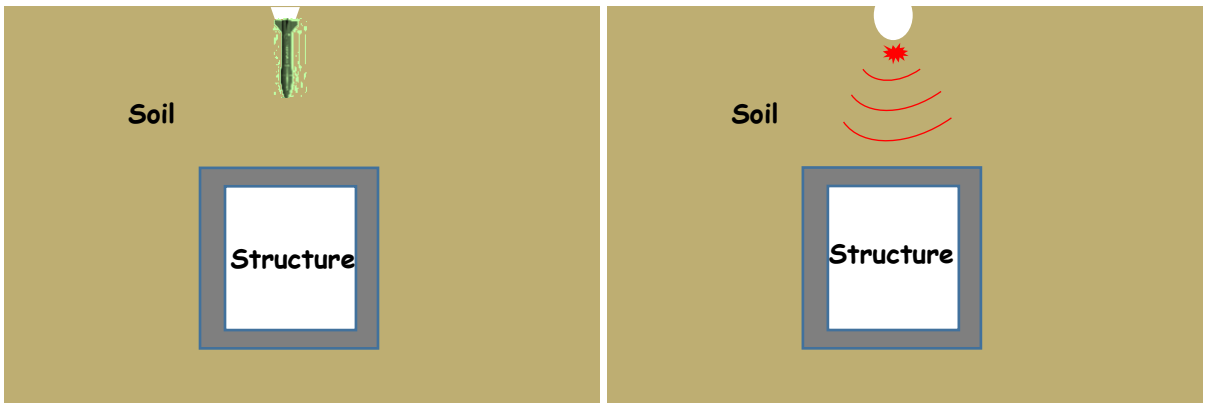


Figure 6: Penetration and blast scenario

### Sub-Surface Blast – Shock Wave Propagation

The first part deals with the penetration blast effect on high dense soil medium. Soil medium property is as given below in Table 4. Coupling factor, f obtained for the scaled depth of burst ($D/W^{1/3}$) 0.286 $m/kg^{1/3}$ is 0.84. As our interest is on wave propagation and attenuation, the structure is not explicitly modeled, rather pressure is measured exactly above the structure. The progressive impact of the blast is measured at a regular interval using DATABASE_TRACER. Pressure at intervals are plotted in Figure 7. As the prime focus is on the structure located at 40m, pressure measured at 40m is 0.0218 MPa that matches with that of empirical calculation using equation (1) (0.0229MPa). Comparison graph of empirical and numerical is provided in Figure 9, from which it can be inferred that pressure at farther distances matches more accurately with that of UFC [1]. Pressure wave propagation in the soil is shown in the Figure 8, from which attenuation effect of soil can be visualized.

| Charge Wt.(lb) | DOB (m) | ρ($kg/m^3$) | c(m/s) | ρc (MPa/m/s) | f | n | A |
|---|---|---|---|---|---|---|---|
| 750 | 2 | 2094 | 210 | 0.44 | 0.84 | 2.5 | 4.83 |

Table 4: Blast pressure calculation parameters

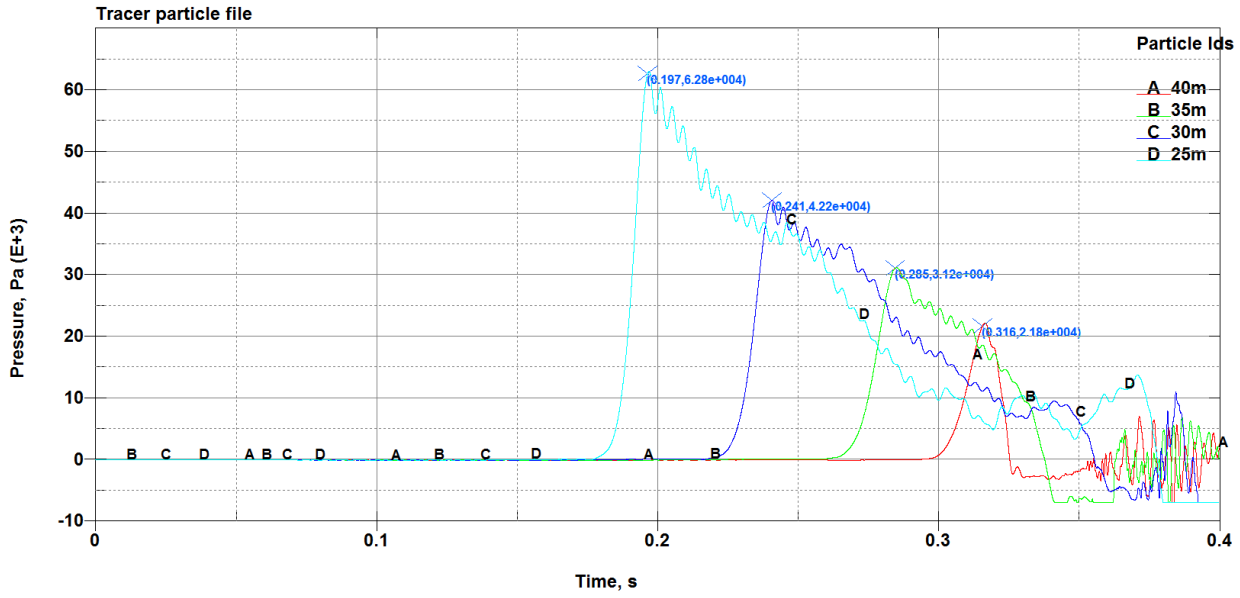


Figure 7: Pressure vs. time (for different locations)

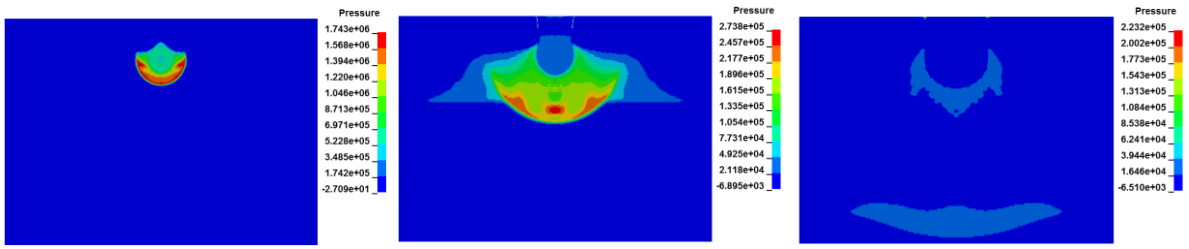


Figure 8: Blast – wave propagation (@30ms, 100ms & 300ms)

Using the graph from the literature [1] that is available for different types of soil, crater dimensions are computed. Since the literature data on crater formation is broadly classified, crater dimensions can be predicted only in a range. The crater dimension falls in the range of 3.32-4.43m of depth and 9.14-11.08m of crater diameter. Crater formation at stages are shown

in Figure 9, the resulting crater size is 8m depth and 12.5m diameter. The values computed using the empirical is apparent whereas in numerical analysis, the true crater dimension is measured.

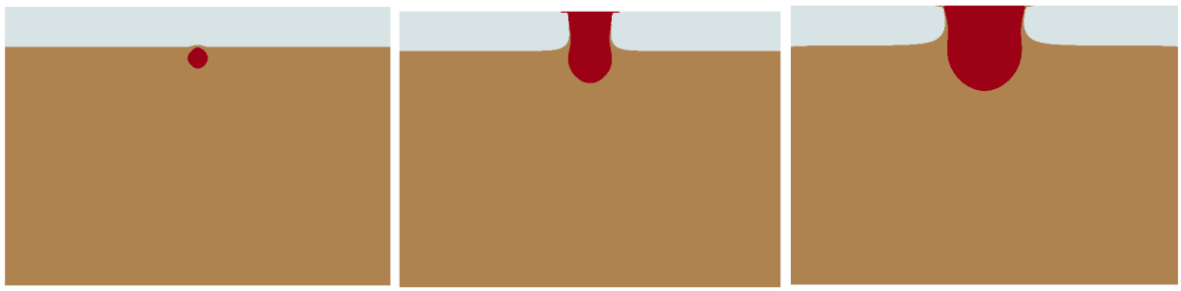

Figure 9: Blast – crater formation (@30ms, 100ms & 300ms)

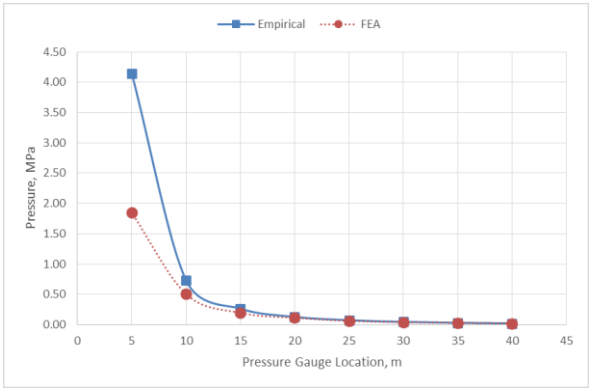


Figure 10: Pressure vs. distance (High Dense Soil) (Empirical vs. FEA)

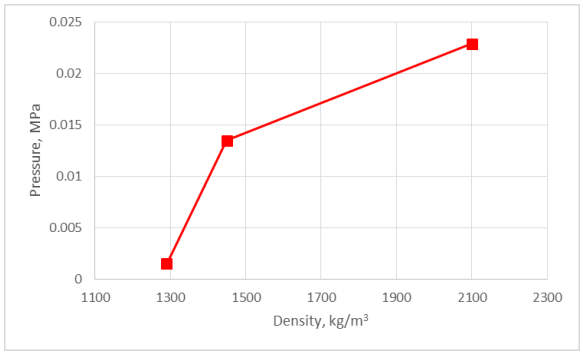


Figure 11: Pressure vs. distance for diff density (Empirical approach)

## Effect of Soil Medium on Wave Propagation

In the second part of the case study, attenuation effects of different soil medium are studied for the same penetration blast explained above. The focus is on the difference in nature of the shock wave propagation due to the soil medium. Two additional soil types (medium dense and low dense soil) are considered for the analysis in addition to the high dense presented above. The different soil properties used are mentioned below.

| ρ(kg/m$^3$) | c(m/s) | ρc (MPa/m/s) | f | n | A |
|---|---|---|---|---|---|
| 1453 | 178 | 0.258 | 0.84 | 2.5 | 4.83 |
| 1453 | 178 | 0.258 | 0.84 | 3 | 3.04 |
| 1293 | 87.1 | 0.11 | 0.84 | 3 | 3.04 |
| 1293 | 87.1 | 0.11 | 0.84 | 3.5 | 1.91 |

Table 5: Low and medium dense sand properties

The overpressure calculated theoretically at the structure location depends on many factors as already discussed. A set of attenuation factors are considered for the study for each soil medium. For medium dense soil, the pressure at structure location is 0.0035 MPa (n=3) & 0.0135 MPa (n=2.5), and for low dense soil the pressure is 0.000406 MPa (n=3.5) & 0.0015 MPa (n=3). The attenuation effect of the soil is enormous as the soil density reduces (Figure 11).

Pressure at structure is 0.016 MPa and 0.0074 MPa respectively in numerical analysis. Numerical results are close to the range of empirical results [Figure 12] that has low attenuation factor value. Attenuation factor has huge impact on pressure wave attenuation. Since very limited information is available on attenuation factor computation, further investigation is not carried out to study the effects of same. However, the wave attenuation pattern is same as that of empirical and numerical results act as a more conservative approach for the pressure computation. In addition to the attenuation factor, information on the constant factor (A) is also minimal.

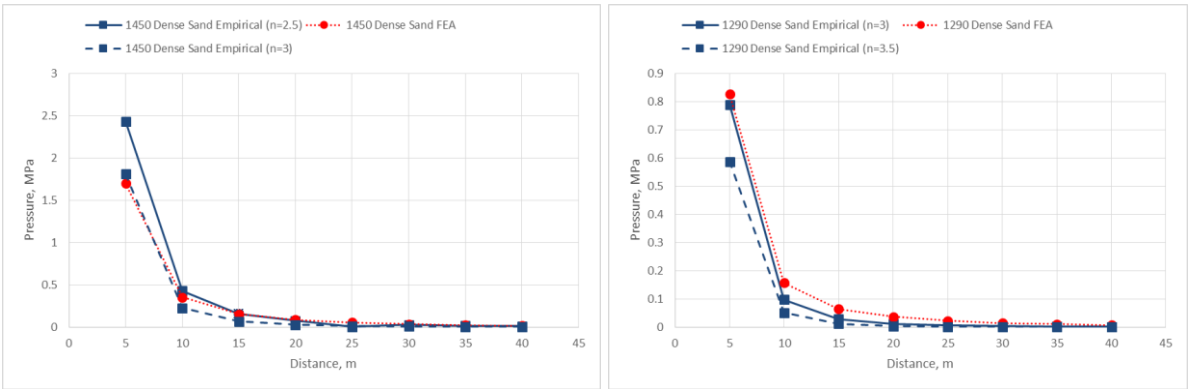


Figure 12: Pressure vs. distance a) medium dense soil b) low dense soil

Crater dimensions for the medium dense soil is 9m depth & 13.25m diameter and for the low dense soil is 9.8m depth & 14.5m. Thus, from the numerical analysis the crater dimension are in the range of 8-9.8m depth and 12.5-14.5m diameter. Through numerical analysis, true crater dimensions for a particular type of soil can be computed.

## Blast on Layered Soil Medium

The third part refers to the interaction of blast pressure on structure subjected to sub-surface blast in high dense medium. Reflection and transmission phenomenon that takes place when the blast wave propagates in layered soil and during its interaction with under-ground structures are captured and explained here. When the blast waves travel from denser medium to lighter medium, the reflected stress is less but tensile in nature and the transmitted pressure is relatively more by compressional wave. A number of combination has been checked numerically and theoretically to study the behavior. The structure is located at 40m below the blast source and it is placed 10m above the soil with dimension of 15m width and 7.5m height. Concrete grade of M40 is used for the analysis. The effect of layered soil is considered for the study. Details of the different soil medium are provided in the Table 6.

| Medium | ρ ($kg/m^3$) | c (m/s) | α= ρc (MPa/m/s) |
|---|---|---|---|
| Low density Soil | 1293 | 87.1 | 0.11 |
| Medium Density Soil | 1453 | 178 | 0.258 |
| High Density Soil | 2094 | 210 | 0.44 |
| Concrete | 2548 | 3600 | 9.173 |

Table 6: Acoustic Impedance of different soil media

When the blast wave travels in soil and interacts with an under-ground structure made of concrete, the pressure wave hitting the structure surface gets reflected partly and rest gets transmitted into it. Where the transmitted stress will be high compared to the incident pressure. The

same phenomenon is followed as the wave propagates through soil layers. Results of interaction at the soil strata and concrete are provided for numerical analysis and compared against UFC.

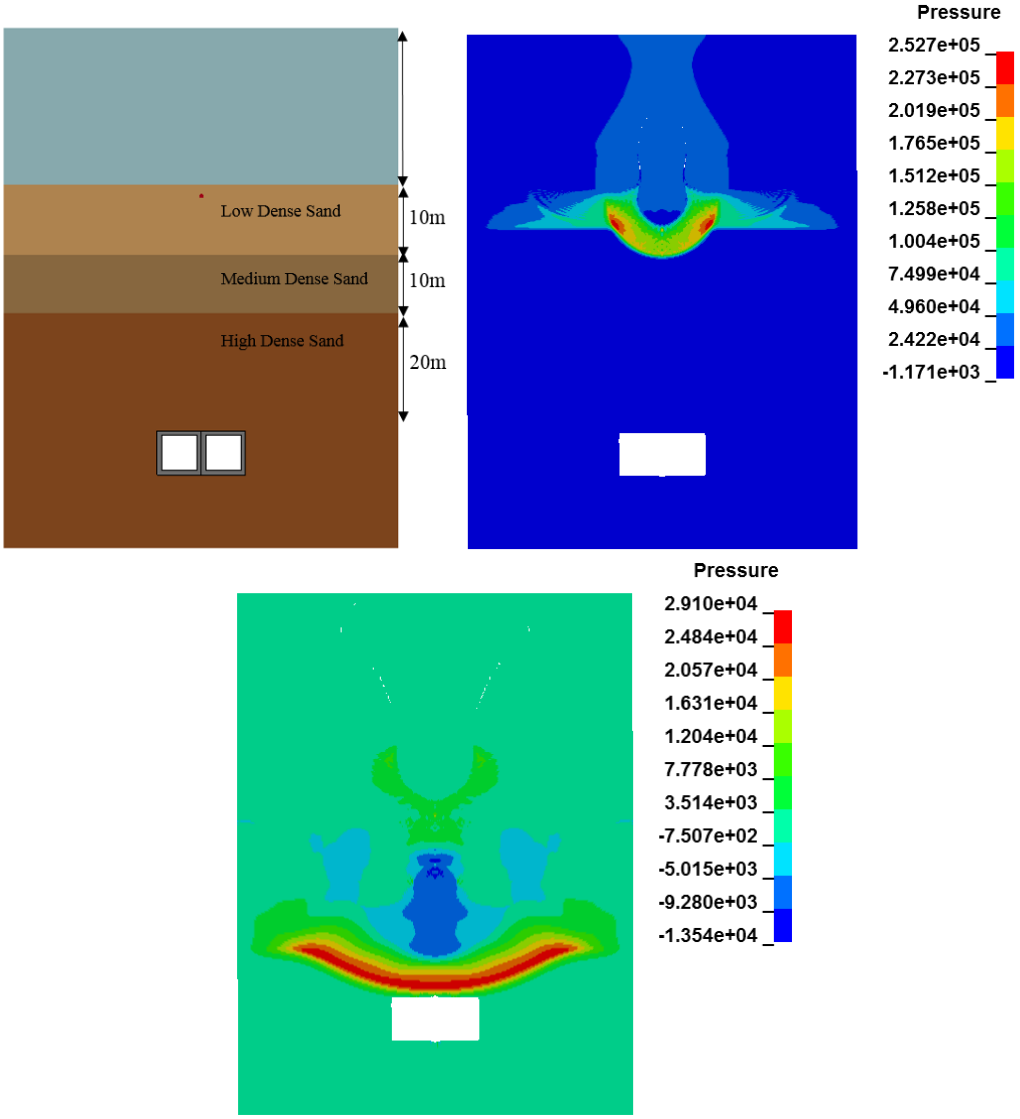


Figure 13: Layered soil numerical model

| Media | $\alpha_z = \alpha_2/\alpha_1$ | $\sigma_i$ (MPa) | $\sigma_r$ (MPa) | $\sigma_t$ (MPa) |
|---|---|---|---|---|
| | | E/N | E/N | E/N |
| Low Density Soil to Medium density soil | 2.345 | | | |
| Numerical | | 1.65E5 | 2.25E5 | 2.25E5 |
| Empirical | | 1.65E5 | 2.34E5 | 2.34E5 |
| Medium Density Soil to High density soil | 1.705 | | | |
| Numerical | | 4.69E4 | 6.71E4 | 5.88E4 |
| Empirical | | 4.69E4 | 5.91E4 | 5.90E4 |
| High Density Soil to Concrete | 20.85 | | | |
| Numerical | | 1.54E4 | 2.0E4 | 2.3E4 |
| Empirical | | 1.54E | 2.9E4 | 2.9E4 |

Table 7 Numerical and empirical results

From the comparison in Table 7, it can be inferred that numerical analysis captures the results within a range of +/- 5 percent variation of the theoretical calculations. Better visualization and understanding of the pressure wave propagation can be obtained from the simulation results as evident from Figure 15.

## 7 CONCLUSIONS

Following broad conclusions can be drawn from the empirical and numerical studies:

- Shock Wave attenuation plots show similar trend for soils of different densities marked by a rapid decrease in pressure in close range whereas a comparatively gradual decrease of pressure as the wave propagates further.
- Sub-Surface blast pressure when compared to Surface and Air blast pressures, indicates much higher intensity, especially in closer ranges.
- Attenuation of pressure waves in sub surface blast is greatly affected by the density of the soil medium, thus choosing the correct attenuation factor for theoretical calculation is vital. Attenuation as observed is less in highly dense medium when compared to a medium of low density.
- Numerical analysis were able to predict the wave propagation and crater formation accurately. The variation in the results (medium and medium dense soil) might be due to the chosen attenuation factor and constant factor (A). The constant factor used for the computation is based on the value of 160 (in FPS units system) from the literature. Any change in these factors will have impact on pressure wave propagation in soil.
- As the Shock wave passes from one medium to another having different densities, reflection and transmission phenomenon takes place at the interface. As observed theoretically as well as numerically when the shock wave passes from softer to harder medium (in terms of density) the interface has a reduced reflected pressure and an amplified transmitted pressure, values depending on acoustic impedances of both the media. Whereas in case when it passes from a harder to softer medium, the reflected pressure is less compared to the earlier case but tensile in nature and transmitted pressure gets amplified.

The numerical analysis carried out were able to predict the attenuation effect of the shock-wave in different soil medium as well as in layered medium.

## 8 FUTURE STUDIES

Preliminary study has been done on blast wave propagation in rock. General arrangement of rock as we know is completely different than soil as it contains number of faults, fractures and uncertainties. Thus calculating pressure propagation will include a number of rock strength parameters like RQD and GSI. Basic calculation shows much higher pressure for sub surface blast in rocks at any distance when compared to blast in soil.

Future study focuses on wave propagation in rock and its constitutive modeling through numerical analysis.

## REFERENCES


[1] Y. Zhang, Q.Fang, J. Liu, Experimental and numerical investigation into responses of buried R/C frames subjected to impulsive loadings. *Structures Under Shock and Impact VII*, 2002.

[2] B. Mobaraki, M.Vaghefi, Effect of the soil type on the dynamic response of a tunnel under surface detonation. *Combustion, Explosion and Shock Waves*, 52, 363-370, 2016.

[3] C. Wu, Y. Lu, H. Hao, Numerical prediction of blast-induced stress wave from large scale underground explosion. *International Journal for Numerical and Analytical Methods in Geomechanics*, 28, 93-109, 2008.

[4] Z. Wang, Y. Lu, H. Hao, K. Chong, A full coupled Numerical Analysis approach for buried structures subjected to sub-surface blast. *Computers and Structures*, 83, 339–356, 2005.

[5] T. Krauthammer, *Modern Protective Structures*, CRC Press, 2008.

[6] D.Z. Yankelevsky, Y.S Karinski, V.R. Feldgun, Re-examination of the shock wave's peak pressure attenuation in soil. *International Journal of Impact Engineering*, 38, 864-881, 2011.

[7] UFC, Structures to resist the effects of accidental explosions, 3-340-02, December 5, 2008.

[8] H.J Ma, S.T Quek, K.K Ang, Soil-Structure Interaction effect from Blast –Induced horizontal and vertical ground vibration. *Engineering Structures*, 26, 1661–1675, 2004.

[9] D.S. Cheng, C.W. Hung, S.J. Pi, Numerical simulation of near-field explosion. *Journal of Applied Science and Engineering*, 16, 61-67, 2013.

[10] V. Lapoujade, N.V. Dorssealaer, S. Kevorkian, K. Cheval, A Study of Mapping Technique for Air Blast Modeling. *11th International LS-DYNA Users Conference*, 2011.

[11] S.H. Tan, R. Chan, J.K. Poon, D. Chng, Verification of concrete materials for MM-ALE simulation. *13th International LS-DYNA Users Conference*, 2013.

[12] J.M.H. Puryear, D.J. Stevens, K.A. Marchand, E.B. Williamson and C.K. Crane, ALE modeling of explosive detonation on or near reinforced-concrete columns. *7th International LS-DYNA Users Conference*, 2012.

[13] Arumugam. D, Tamiselvan. K, Dhana Sekaran. B & Subash. T.R, Numerical analysis of missile penetration on concrete targets. *International NAFEMS Conference on Engineering Analysis, Modeling, Simulation and 3D Printing*, India, 2016.

[14] Livermore Software Technology Corporation (LSTC), *LS-DYNA Keywords user's manual*, California, 2016.

[15] A. Deivanayagam, A. Vaidya and S.D. Rajan, Enhancements to modeling dry fabrics for impact analysis. *Journal of Aerospace Engineering*, 27(3), 484, 490, 2014.

[16] Y. Wu, J.E. Crawford, J.M. Magallanes, Performance of LS-DYNA concrete constitutive models. *12th International LS-DYNA Users Conference*, 2012.

[17] Y. Wu, John E.Crawford, Shenguri Lan and Joseph M. Magallanes, Validation studies for concrete constitutive models with blast test data. *12th International LS-DYNA Users Conference*, 1994.

[18] E.Heymsfield and E.N. Fasanella, Using Numerical Modeling to Simulate Space Capsule Ground Landing. *International Proceeding of the 88 Transportation Research Board Annual Meeting*, Washington, July 30, 2008.

COMPDYN 2017
6th ECCOMAS Thematic Conference on
Computational Methods in Structural Dynamics and Earthquake Engineering
M. Papadrakakis, M. Fragiadakis (eds.)
Rhodes Island, Greece, 15–17 June, 2017

# QUANTIFICATION OF GUIDED WAVE INTERACTION EFFECTS WITH LOCALIZED STRUCTURAL NONLINEARITIES IN COMPLEX, COMPOSITE STRUCTURES

**V. Thierry[1], D. Chronopoulos[1] and I. Ashcroft[2]**

[1]Institute for Aerospace Technology (IAT)
The University of Nottingham, Innovation Park, NG7 2TU, UK
& The Composites Group
The University of Nottingham, NG7 2RD, UK
[2] Faculty of Engineering
The University of Nottingham, NG7 2RD, UK
e-mail: {Victor.Thierry,Dimitrios.Chronopoulos,Ian.Ashcroft}@nottingham.ac.uk

**Keywords:** Structural nonlinearities, Wave Interaction with Damage, Finite Elements, Composite Structures, Nonlinear Ultrasound

**Abstract.** *The extensive usage of composite materials in modern industrial applications implies a great range of possible structural failure modes for which the structure has to be frequently and thoroughly inspected. Nonlinear guided wave inspection techniques have been continuously gaining attention during the last decade. This is primarily due to their sensitivity to very small sizes of localized damage. A number of complex transformation phenomena take place when an elastic wave impinges on a nonlinear segment, including the generation of higher and sub-harmonics. Moreover, the transmission and reflection coefficients of each wave type become amplitude dependent. In this work, a generic Finite Element (FE) based computational scheme is presented for quantifying guided wave interaction effects with Localized Structural Nonlinearities (LSN) within structures of arbitrary layering and geometric complexity. Amplitude dependent guided wave reflection, transmission and conversion is computed through a Wave and Finite Element (WFE) method. The scheme couples wave propagation properties within linear structural waveguides to a LSN and is able to compute the generation of higher and sub-harmonics for each wave type through a harmonic balance projection. A Newton-like iteration scheme is employed for solving the system of nonlinear differential equations. Numerical case studies are exhibited for a set of waveguides coupled through a joint exhibiting nonlinear mechanical behaviour.*

## 1 INTRODUCTION

Modern industrial structures are increasingly made of composite layered materials due to their well-known benefits. Composite structures may however exhibit a great variety of structural failure modes (including delamination, fibre breakage, matrix cracking and debonding) and must be frequently inspected in order to ensure continuous structural integrity. An increasing tendency within the Structural Health Monitoring (SHM) community is the 'shift to the left' maintenance strategy [1] for which the earliest possible detection of damage is important. When it comes to the aeronautical industry, approximately 27% of an average modern aircraft's lifecycle cost [2] is spent on inspection and repair. The use of 'offline' structural inspection techniques currently leads to a massive reduction of the aircraft's availability and significant financial losses for the operator. The nondestructive detection and evaluation of damage in industrial structural components while operation is of paramount importance for monitoring the condition and residual life estimation of in-service structures. Linear ultrasonic Guided Wave (GW) techniques have been widely employed for this purpose. These techniques however are primarily sensitive to gross defects but much less sensitive to micro-damage. Nonlinear acousto-ultrasonic techniques, have been steadily receiving increasing attention during the last decade. Complex wave phenomena such as higher and subharmonic wave generation, nonlinear resonances or mixed frequency response can be induced by the two principal sources of nonlinearity in the structural system, namely nonlinear elasticity and contact nonlinearity.

Elastic wave distortion and generation of higher harmonics during propagation in nonlinear media has been reported as early as in [3]. The first attempt for modelling wave interaction with nonlinear joints can be found in [4, 5]. It has been widely demonstrated that nonlinear ultrasonic techniques can be successfully deployed for detecting cracks as well as distributed structural deterioration (e.g. fatigue) [6, 7, 8, 9, 10, 11, 12]. The success of the developed methods is based on predicting and measuring the nonlinearities-induced wave effects which are pronounced in damaged and degraded structures but nearly un-measurable in the undamaged ones. A number of Nonlinear Elastic Wave Spectroscopy (NEWS) approaches [13, 14, 15] have also been presented and proved capable of detecting the presence of damage of very small sizes (in the order of 0.1mm) in composite structures. Wave propagation and material degradation detection in 1-D and 2-D media was investigated through a spring model in [16, 17]. A numerical scheme for predicting nonlinear wave interaction with an interface of rough surfaces in contact was presented in [18]. The non-collinear mixing of bulk shear waves investigated in [19] presented significant potential for assessing material state than other nonlinear ultrasonic techniques because system nonlinearities can be both independently measured and largely eliminated. The development of an analytical framework for modelling the multi-modal guided wave interaction with damage was presented by the authors of [20, 21]. In [22], a numerical scheme was presented in order to quantify the amplitude of the reflected compression and Rayleigh waves when impinging at the edge of an elastic plate. In [23] the authors coupled linear to nonlinear FE segments and investigated wave interaction with damage in 3-D solid media by means of a Landau's theory. Detection of fatigue damage in composite structures through higher harmonics generations has also recently been reported [24]. The short reviews provided by the authors in [25, 26] are informative on the general progress of nonlinear ultrasonics, while a comprehensive outline on the techniques dedicated to predicting and measuring higher harmonic generation in metallic structures is presented in [27]. An inclusive review on modelling wave-crack nonlinear interaction phenomena can be found in [28]. Despite the aforementioned attempts to capture wave interaction with LSNs, there is currently no generic computational scheme for predicting

these quantities for composite structures of arbitrary layering and geometric complexity.

The FE based wave propagation analysis within periodic structures was firstly considered in [29]. The wave dispersion characteristics within the layered media can be accurately predicted for a very wide frequency range, by solving a polynomial eigenvalue problem for the propagation constants to be sought. The work was extended to 2-D media in [30]. The WFE method was introduced in [31] in order to facilitate the post-processing of the eigenproblem solutions and further improve the computational efficiency of the method. The vibration of a uniform waveguide through the WFE technique was investigated in [32, 33]. The WFE method has recently found applications in predicting the vibroacoustic and dynamic performance of composite panels and shells [34, 35, 36, 37, 38, 39, 40] , with pressurized shells [41, 42] and complex periodic structures [43, 44, 45, 46] having been investigated. The variability of acoustic transmission through layered structures [47, 48], as well as wave steering effects in anisotropic composites [49] have been modelled through the same methodology . The same FE based approach has been employed in order to compute the reflection and transmission coefficients of waves impinging on linear joints of finite dimensions [50, 51].

In this work, a generic FE-based computational scheme for computing wave interaction with LSNs is presented for the first time. Guided wave reflection, transmission and conversion is computed through a wave and finite element approach. The scheme couples wave propagation properties within linear structural waveguides to a LSN and is able to compute the generation higher and sub-harmonics for each wave type through a harmonic balance projection. The new approach is able to predict reflections and transmissions at harmonic frequencies with a speed that is orders of magnitude faster than conventional transient FE solutions. The structure can be of arbitrary complexity, layering and material characteristics as FE modelling is employed. A Galerkin projection is used to transform the system of nonlinear differential equations of motion into a set of nonlinear algebraic equations which is subsequently solved through a Newton's iteration method. The generation of wave harmonics, as well as amplitude-dependent wave reflection and transmission coefficients are reported through the exhibited numerical case studies. This is the first approach that can accurately and efficiently map the frequency-dependent interactions of guided waves with nonlinearities in arbitrarily complex structures.

The paper is organized as follows: In Sec.2 the formulation of the wave and finite element method for predicting acoustic and ultrasonic GW interaction with LSNs is presented. A description of the Galerkin projection as well as of the Newton's iteration scheme employed for solving the system of nonlinear differential equations is also given. In Sec.3 the proposed method is validated for a number of waveguide types through comparison to full transient FE analyses. Conclusions on the presented work are given in Sec.4.

## 2 ELASTIC WAVE INTERACTION WITH STRUCTURAL NONLINEARITIES

An arbitrarily complex and periodic in the $x$ direction waveguide is illustrated in Fig.2. The propagation constants for the elastic waves travelling in the $x$ direction within the waveguide can be sought through a WFE scheme. In the general case, we are assuming a system of $N$ waveguides connected through a structural coupling element which could exhibit arbitrarily complex mechanical behaviour and which is fully FE modelled (see Fig.2). As already stated, each waveguide can be of different and arbitrary layering and can also support a different number $W_n$ of propagating waves at a given frequency. An extensive description of how to deal with waveguides having different layouts and meshes can be found in [50]. Each supported

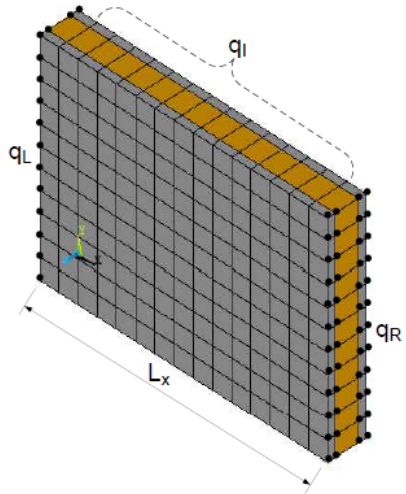


Figure 1: Caption of the WFE modelled composite waveguide with the left and right side nodes $\mathbf{q}_L$, $\mathbf{q}_R$ bullet marked. The range of interior nodes $\mathbf{q}_I$ is also illustrated.

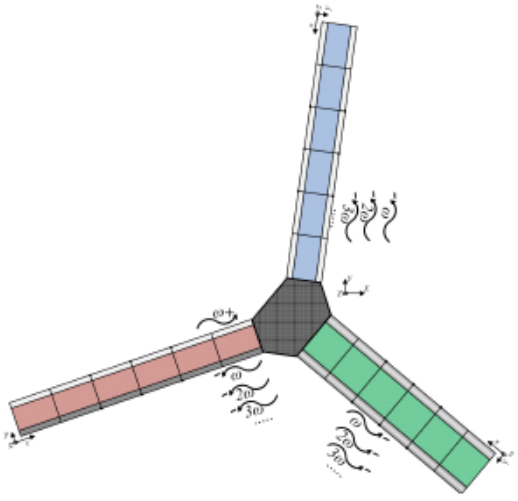

Figure 2: Periodic elastic waveguides connected through a coupling element exhibiting inelastic mechanical behaviour. A positive going wave $^+$ of angular frequency $\omega$ impinging on the coupling element will give rise to reflected and transmitted outgoing $^-$ waves of multiple subharmonic and superharmonic frequencies.

wavemode $w$ with $w \in [1 \cdots W]$ for the $n$th waveguide in the system can be grouped as

$$\begin{aligned}
\mathbf{\Phi}_{n,q}^{h\omega,+} &= \begin{bmatrix} \boldsymbol{\phi}_{q,1}^{h\omega,+} & \boldsymbol{\phi}_{q,2}^{h\omega,+} & \cdots & \boldsymbol{\phi}_{q,W}^{h\omega,+} \end{bmatrix} \\
\mathbf{\Phi}_{n,f}^{h\omega,+} &= \begin{bmatrix} \boldsymbol{\phi}_{f,1}^{h\omega,+} & \boldsymbol{\phi}_{f,2}^{h\omega,+} & \cdots & \boldsymbol{\phi}_{f,W}^{h\omega,+} \end{bmatrix} \\
\mathbf{\Phi}_{n,q}^{h\omega,-} &= \begin{bmatrix} \boldsymbol{\phi}_{q,1}^{h\omega,-} & \boldsymbol{\phi}_{q,2}^{h\omega,-} & \cdots & \boldsymbol{\phi}_{q,W}^{h\omega,-} \end{bmatrix} \\
\mathbf{\Phi}_{n,f}^{h\omega,-} &= \begin{bmatrix} \boldsymbol{\phi}_{f,1}^{h\omega,-} & \boldsymbol{\phi}_{f,2}^{h\omega,-} & \cdots & \boldsymbol{\phi}_{f,W}^{h\omega,-} \end{bmatrix}
\end{aligned} \tag{1}$$

with each matrix being of dimension $[j \times W]$. The wavemodes of the entire system can be computed for each waveguide $n$ with $n \in [1 \cdots N]$ and for the fundamental excitation frequency $\omega$ as well as for the higher and sub-harmonics $h\omega$ with $h \in [1/H_m \cdots 1 \cdots H]$ and be grouped as

$$\mathbf{\Phi}_{q}^{h\omega,+} = \begin{bmatrix} \mathbf{\Phi}_{1,q}^{h\omega,+} & \mathbf{0} & \cdots & \mathbf{0} \\ \mathbf{0} & \mathbf{\Phi}_{2,q}^{h\omega,+} & \cdots & \mathbf{0} \\ \cdots & \cdots & \cdots & \cdots \\ \mathbf{0} & \mathbf{0} & \cdots & \mathbf{\Phi}_{N,q}^{h\omega,+} \end{bmatrix}_{[jN \times WN]} \tag{2}$$

with similar expressions standing for $\mathbf{\Phi}_{f}^{h\omega,+}$, $\mathbf{\Phi}_{q}^{h\omega,-}$, $\mathbf{\Phi}_{f}^{h\omega,-}$. For each waveguide, the local coordinate system is defined such that the waveguide's axis is directed towards the joint (direction $+$). The rotation matrix $\mathbf{R}_n$ transforms the DoFs from the local to the global coordinates of the system. Rotation matrices can be grouped in a block diagonal matrix $\mathbf{R}$. The equation of motion for the nonlinear, FE modelled coupling element can be in general written as

$$\mathbb{M}\ddot{\mathbf{z}}(t) + \mathbb{C}\dot{\mathbf{z}}(t) + \mathbb{K}\mathbf{z}(t) + \mathbf{f}_{NL} = \mathbf{f}_{ext}(t) \tag{3}$$

with $\mathbf{f}_{NL}$ the nonlinear force vector induced by the coupling element's inherent inelastic behaviour and $\mathbf{f}_{ext}(t)$ being the external forces applied to the coupling element.

Waves of the fundamental excitation frequency $\omega$ having amplitudes $\mathbf{a}_n^{\omega,+}$ are impinging on the coupling element from the $n$th waveguide. For each considered harmonic $h\omega$, they give rise to reflected waves of amplitudes $\mathbf{a}_n^{h\omega,-} = \mathbf{r}_{n,n}^{h\omega}\mathbf{a}_n^{\omega,+}$ in the $n$th waveguide, while they also give rise to transmitted waves of amplitudes $\mathbf{a}_k^{h\omega,-} = \mathbf{c}_{k,n}^{h\omega}\mathbf{a}_n^{\omega,+}$ in the $k$th waveguide with $\mathbf{r}_{n,n}^{h\omega}$ and $\mathbf{c}_{k,n}^{h\omega}$ being matrices containing the reflection and transmission coefficients of the coupling element at each harmonic $h\omega$. These define the wave scattering matrix $\mathbf{S}^{h\omega}$ of the joint, whose partitions relate the amplitudes of the incident and scattered waves as

$$\mathbf{a}^{h\omega,-} = \mathbf{S}^{h\omega}\mathbf{a}^{\omega,+} \tag{4}$$

with $\mathbf{a}_{[WN\times 1]}^{\omega,+}$ the vector containing the amplitudes of the incoming waves moving towards the coupling element and $\mathbf{a}_{[WN\times 1]}^{h\omega,-}$ the vector containing the amplitudes of the reflected and transmitted outgoing waves produced at the $h\omega$ harmonic. The complex wave interaction matrix $\mathbf{S}^{h\omega}$ projects the incoming waves $\mathbf{a}^{\omega,+}$ having a single frequency $\omega$ to each of the higher and sub-harmonics $h\omega$. Assuming that only waves of a single frequency $\omega$ are impinging on the coupling element, a transformation can be defined for the motion in the waveguides between the physical domain, where the motion is described in terms of $\mathbf{q}$ and $\mathbf{f}$ and the wave domain where the motion is described in terms of waves of amplitudes $\mathbf{a}^{\omega,+}$ and $\mathbf{a}^{h\omega,-}$ travelling in the positive and negative directions respectively, and by concatenating the corresponding vectors

and matrices the general expressions for $\mathbf{q}$ and $\mathbf{f}$ for the system of waveguides can be expressed as

$$\begin{aligned}\mathbf{q}(t) &= \mathbf{\Phi}_q^{\omega,+}\mathbf{a}^{+}\cos(\omega t) + \sum_{h=1}^{H}\mathbf{\Phi}_q^{h\omega,-}\mathbf{a}^{h\omega,-}\cos(h\omega t) + \sum_{h=1}^{H_m}\mathbf{\Phi}_q^{h\omega,-}\mathbf{a}^{h\omega,-}\cos(\tfrac{1}{h}\omega t)\\ \mathbf{f}(t) &= \mathbf{\Phi}_f^{\omega,+}\mathbf{a}^{+}\cos(\omega t) + \sum_{h=1}^{H}\mathbf{\Phi}_f^{h\omega,-}\mathbf{a}^{h\omega,-}\cos(h\omega t) + \sum_{h=1}^{H_m}\mathbf{\Phi}_f^{h\omega,-}\mathbf{a}^{h\omega,-}\cos(\tfrac{1}{h}\omega t)\end{aligned} \tag{5}$$

The above expression can be employed to perform a cyclostationary projection of the behaviour of the system through the Harmonic Balance Method (HBM) [52]. It is noted that $\sin$ terms are not included in the above expansions as the phase of each wave scattering coefficient is captured by the imaginary part of the sought interaction coefficients $\mathbf{a}^{h\omega,-}$. By performing the convenient substitution $\tau = \omega t$ and grouping the trigonometric terms the following expression can be acquired

$$\mathbf{q}(\tau) = \mathbf{\Phi}_q^{\omega,+}\mathbf{T}_2\mathbf{a}^{+} + \mathbf{T}_1\mathcal{A}_q^{\omega,-} \tag{6}$$

with $\mathcal{A}_q^{\omega,-}$ being the generalized displacement wave interaction coefficient vector written as

$$\mathcal{A}_q^{\omega,-} = \left\{\begin{array}{c}\mathbf{\Phi}_q^{\omega,-}\mathbf{S}^{\omega}\mathbf{a}^{\omega,+}\\ \mathbf{\Phi}_q^{2\omega,-}\mathbf{S}^{2\omega}\mathbf{a}^{\omega,+}\\ \cdots\\ \mathbf{\Phi}_q^{H\omega,-}\mathbf{S}^{H\omega}\mathbf{a}^{\omega,+}\\ \cdots\\ \mathbf{\Phi}_q^{\frac{1}{H_m}\omega,-}\mathbf{S}^{\frac{1}{H_m}\omega}\mathbf{a}^{\omega,+}\end{array}\right\}_{[jHN\times 1]} \tag{7}$$

q($\tau$) can be derived twice. Then with $\mathcal{A}_f^{\omega,-}$ formulated similarly to $\mathcal{A}_q^{\omega,-}$. A set of nonlinear, algebraic equations can be obtained through a Galerkin projection [53] of the system of nonlinear differential equations of motion.

$$\begin{aligned}&\int_0^{2H_m\pi}\left[\mathbf{T}_1^{\top}\left[\omega^2\mathbb{M}\mathbf{R}\frac{\mathrm{d}^2\mathbf{T}_1}{\mathrm{d}\tau^2} + \omega\mathbb{C}\mathbf{R}\frac{\mathrm{d}\mathbf{T}_1}{\mathrm{d}\tau} + \mathbb{K}\mathbf{R}\mathbf{T}_1\right]\mathcal{A}_q^{\omega,-} - \mathbf{T}_1^{\top}\mathbf{R}\mathbf{T}_1\mathcal{A}_f^{\omega,-}\right]\mathrm{d}\tau +\\ &\int_0^{2H_m\pi}\mathbf{T}_1^{\top}\left[\omega^2\mathbb{M}\mathbf{R}\mathbf{\Phi}_q^{\omega,+}\frac{\mathrm{d}^2\mathbf{T}_2}{\mathrm{d}\tau^2} + \omega\mathbb{C}\mathbf{R}\mathbf{\Phi}_q^{\omega,+}\frac{\mathrm{d}\mathbf{T}_2}{\mathrm{d}\tau} + \mathbb{K}\mathbf{R}\mathbf{\Phi}_q^{\omega,+}\mathbf{T}_2 - \mathbf{R}\mathbf{\Phi}_f^{\omega,+}\mathbf{T}_2\right]\mathbf{a}^{+}\mathrm{d}\tau +\\ &\int_0^{2H_m\pi}\mathbf{T}_1^{\top}\mathbf{f}_{NL}\mathrm{d}\tau = \mathbf{0}\end{aligned} \tag{8}$$

## 3 VALIDATION FOR A LAYERED COMPOSITE BEAM

The presented approach is validated for an asymmetric layered composite beam with aluminium facesheets and a polyurethane core having a cross-section of 8mm×12mm and the thicknesses of the layers being equal to 1mm, 10mm and 2mm respectively (see Fig.3). The entirety of the propagating waves can be sought through WFE and without the need of any kinematic assumptions for the complex structures, as 3D FEs and displacement fields are employed.

In practice, the wave modes can be excited one-by-one in a full FE transient simulation by employing the WFE computed $\phi_{q,n}^{+}$ eigenvectors and applying them as time-dependent harmonic displacement boundary conditions (of excitation frequency $\omega$) at one of the extreme cross-sections of the waveguide. An 11-period Hanning window was used for all transient excitations. The results on the fundamental and harmonic reflections for a nonlinearly hardening

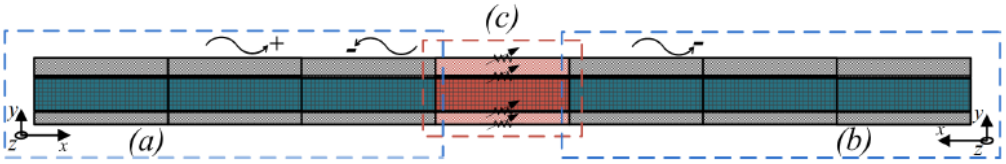


Figure 3: Schematic representation of the two healthy and elastic composite multilayer waveguides (a) and (b) coupled through a nonlinear element (c) containing an arbitrary structural nonlinearity.

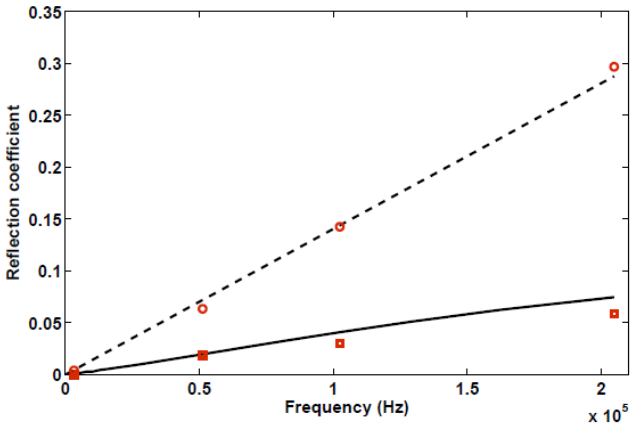


Figure 4: Absolute values of the wave reflection coefficients of the pressure propagating wave for a nonlinearly hardened element with $k_{nl}$=1e13N/m$^3$ at: Frequency $\omega$ computed according to the current scheme (- -) and through a full transient FE calculation ($\circ$), Harmonic frequency $3\omega$ computed according to the current scheme (–) and through a full transient FE calculation ($\square$).

element are presented below in Figs.4. Excellent agreement is observed between the fundamental frequency reflection predictions obtained through the presented approach and through a full FE transient response prediction. Moreover, good agreement is observed between the two approaches regarding the reflections computed for the $3\omega$ harmonic frequency. The most probable cause of the slight divergence observed between the two sets of results is the fact that in a nonlinear transient FE problem energy is partially also channeled towards other harmonics (higher than the second one), which are not included in the harmonic balance expansion.

## 4 CONCLUSIONS

A novel comprehensive FE-based computational scheme was presented for quantifying guided wave interaction with LSNs. Structures of arbitrary complexity, layering and material characteristics can be modelled through the presented approach as an FE discretization is employed. The scheme couples wave propagation properties within linear structural waveguides to LSNs and is able to compute the generation of harmonic frequencies for each wave mode through a harmonic balance projection. The principal outcomes of the work are summarized as follows:

- The presented scheme was validated through comparison with a full FE transient response prediction. Excellent agreement is observed between the two sets of results for the fundamental, as well as for higher harmonic frequency predictions.

- The new approach is able to predict reflections and transmissions at harmonic frequencies with a speed that is orders of magnitude faster than conventional transient FE solutions.

- Generation of higher order harmonics can become maximum at certain frequencies which can be excited for facilitating the detection of certain nonlinearity scenarios (ideally related to the presence of certain damage).

Future developments are focusing towards modelling and implementing realistic damage models as a LSN. Efficient multiscale damage models are essential to implement in order to accurately capture the nonlinear mechanics of advanced damage scenarios, while retaining the size of the FE model and the implied required computational effort at acceptable levels.

## 5 ACKNOWLEDGMENTS

This work is funded by the INNOVATIVE doctoral programme. The INNOVATIVE programme is partially funded by the Marie Curie Initial Training Networks (ITN) action (project number 665468) and partially by the Institute for Aerospace Technology (IAT) at the University of Nottingham.

## REFERENCES

[1] C. Lissenden, Y. Liu, and J. Rose, "Use of non-linear ultrasonic guided waves for early damage detection," *Insight-Non-Destructive Testing and Condition Monitoring*, vol. 57, no. 4, pp. 206–211, 2015.

[2] S. S. Kessler, S. M. Spearing, and C. Soutis, "Damage detection in composite materials using lamb wave methods," *Smart Materials and Structures*, vol. 11, no. 2, pp. 269–, 2002.

[3] M. Breazeale and D. Thompson, "Finite-amplitude ultrasonic waves in aluminum," *Applied Physics Letters*, vol. 3, no. 5, pp. 77–78, 1963.

[4] A. Vakakis, "Scattering of structural waves by nonlinear elastic joints," *Journal of vibration and acoustics*, vol. 115, no. 4, pp. 403–410, 1993.

[5] A. H. Nayfeh, A. F. Vakakis, and T. A. Nayfeh, "A method for analyzing the interaction of nondispersive structural waves and nonlinear joints," *The Journal of the Acoustical Society of America*, vol. 93, no. 2, pp. 849–856, 1993.

[6] P. B. Nagy, "Fatigue damage assessment by nonlinear ultrasonic materials characterization," *Ultrasonics*, vol. 36, no. 1, pp. 375–381, 1998.

[7] D. M. Donskoy and A. M. Sutin, "Vibro-acoustic modulation nondestructive evaluation technique," *Journal of intelligent material systems and structures*, vol. 9, no. 9, pp. 765–771, 1998.

[8] V. Zaitsev, V. Nazarov, V. Gusev, and B. Castagnede, "Novel nonlinear-modulation acoustic technique for crack detection," *NDT & E International*, vol. 39, no. 3, pp. 184–194, 2006.

[9] V. J. Rao, E. Kannan, R. V. Prakash, and K. Balasubramaniam, "Fatigue damage characterization using surface acoustic wave nonlinearity in aluminum alloy aa7175-t7351," *Journal of Applied Physics*, vol. 104, no. 12, pp. 123508–, 2008.

[10] H. Hu, W. Staszewski, N. Hu, R. Jenal, and G. Qin, "Crack detection using nonlinear acoustics and piezoceramic transducersinstantaneous amplitude and frequency analysis," *Smart Materials and Structures*, vol. 19, no. 6, pp. 065017–, 2010.

[11] Z. Su, C. Zhou, M. Hong, L. Cheng, Q. Wang, and X. Qing, "Acousto-ultrasonics-based fatigue damage characterization: Linear versus nonlinear signal features," *Mechanical Systems and Signal Processing*, vol. 45, no. 1, pp. 225–239, 2014.

[12] H. J. Lim, H. Sohn, M. P. DeSimio, and K. Brown, "Reference-free fatigue crack detection using nonlinear ultrasonic modulation under various temperature and loading conditions," *Mechanical Systems and Signal Processing*, vol. 45, no. 2, pp. 468–478, 2014.

[13] K.-A. Van Den Abeele, P. A. Johnson, and A. Sutin, "Nonlinear elastic wave spectroscopy (news) techniques to discern material damage, part i: nonlinear wave modulation spectroscopy (nwms)," *Research in nondestructive evaluation*, vol. 12, no. 1, pp. 17–30, 2000.

[14] K. E. Van Den Abeele, A. Sutin, J. Carmeliet, and P. A. Johnson, "Micro-damage diagnostics using nonlinear elastic wave spectroscopy (news)," *Ndt & E International*, vol. 34, no. 4, pp. 239–248, 2001.

[15] M. Meo, U. Polimeno, and G. Zumpano, "Detecting damage in composite material using nonlinear elastic wave spectroscopy methods," *Applied composite materials*, vol. 15, no. 3, pp. 115–126, 2008.

[16] M. Scalerandi, V. Agostini, P. P. Delsanto, K. Van Den Abeele, and P. A. Johnson, "Local interaction simulation approach to modelling nonclassical, nonlinear elastic behavior in solids," *The Journal of the Acoustical Society of America*, vol. 113, no. 6, pp. 3049–3059, 2003.

[17] P. P. Delsanto, A. Gliozzi, M. Hirsekorn, and M. Nobili, "A 2d spring model for the simulation of ultrasonic wave propagation in nonlinear hysteretic media," *Ultrasonics*, vol. 44, no. 3, pp. 279–286, 2006.

[18] C. Pecorari, "Nonlinear interaction of plane ultrasonic waves with an interface between rough surfaces in contact," *The Journal of the Acoustical Society of America*, vol. 113, no. 6, pp. 3065–3072, 2003.

[19] A. J. Croxford, P. D. Wilcox, B. W. Drinkwater, and P. B. Nagy, "The use of non-collinear mixing for nonlinear ultrasonic detection of plasticity and fatigue," *The Journal of the Acoustical Society of America*, vol. 126, no. 5, pp. EL117–EL122, 2009.

[20] V. Giurgiutiu, M. Gresil, B. Lin, A. Cuc, Y. Shen, and C. Roman, "Predictive modeling of piezoelectric wafer active sensors interaction with high-frequency structural waves and vibration," *Acta Mechanica*, vol. 223, no. 8, pp. 1681–1691, 2012.

[21] Y. Shen and V. Giurgiutiu, "Predictive modeling of nonlinear wave propagation for structural health monitoring with piezoelectric wafer active sensors," *Journal of Intelligent Material Systems and Structures*, vol. 25, no. 4, pp. 506–520, 2014.

[22] T. B. Autrusson, K. G. Sabra, and M. J. Leamy, "Reflection of compressional and rayleigh waves on the edges of an elastic plate with quadratic nonlinearity," *The Journal of the Acoustical Society of America*, vol. 131, no. 3, pp. 1928–1937, 2012.

[23] G. M. Fierro, F. Ciampa, D. Ginzburg, E. Onder, and M. Meo, "Nonlinear ultrasound modelling and validation of fatigue damage," *Journal of Sound and Vibration*, vol. 343, pp. 121–130, 2015.

[24] N. Rauter, R. Lammering, and T. Kühnrich, "On the detection of fatigue damage in composites by use of second harmonic guided waves," *Composite Structures*, vol. 152, pp. 247–258, 2016.

[25] K.-Y. Jhang, "Nonlinear ultrasonic techniques for nondestructive assessment of micro damage in material: a review," *International journal of precision engineering and manufacturing*, vol. 10, no. 1, pp. 123–135, 2009.

[26] I. Solodov, D. Döring, and G. Busse, "New opportunities for ndt using non-linear interaction of elastic waves with defects," *Strojniški vestnik-Journal of Mechanical Engineering*, vol. 57, no. 3, pp. 169–182, 2011.

[27] K. Matlack, J.-Y. Kim, L. Jacobs, and J. Qu, "Review of second harmonic generation measurement techniques for material state determination in metals," *Journal of Nondestructive Evaluation*, vol. 34, no. 1, pp. 1–23, 2015.

[28] D. Broda, W. Staszewski, A. Martowicz, T. Uhl, and V. Silberschmidt, "Modelling of nonlinear crack–wave interactions for damage detection based on ultrasounda review," *Journal of Sound and Vibration*, vol. 333, no. 4, pp. 1097–1118, 2014.

[29] D. Mead, "A general theory of harmonic wave propagation in linear periodic systems with multiple coupling," *Journal of Sound and Vibration*, vol. 27, no. 2, pp. 235–260, 1973.

[30] R. Langley, "A note on the force boundary conditions for two-dimensional periodic structures with corner freedoms," *Journal of Sound and Vibration*, vol. 167, no. 2, pp. 377–381, 1993.

[31] B. R. Mace, D. Duhamel, M. J. Brennan, and L. Hinke, "Finite element prediction of wave motion in structural waveguides," *The Journal of the Acoustical Society of America*, vol. 117, no. 5, pp. 2835–2843, 2005.

[32] D. Duhamel, B. R. Mace, and M. J. Brennan, "Finite element analysis of the vibrations of waveguides and periodic structures," *Journal of Sound and Vibration*, vol. 294, no. 1, pp. 205–220, 2006.

[33] J. M. Renno and B. R. Mace, "On the forced response of waveguides using the wave and finite element method," *Journal of Sound and Vibration*, vol. 329, no. 26, pp. 5474–5488, 2010.

[34] D. Chronopoulos, B. Troclet, M. Ichchou, and J. Laine, "A unified approach for the broadband vibroacoustic response of composite shells," *Composites Part B: Engineering*, vol. 43, no. 4, pp. 1837–1846, 2012.

[35] D. Chronopoulos, B. Troclet, O. Bareille, and M. Ichchou, "Modeling the response of composite panels by a dynamic stiffness approach," *Composite Structures*, vol. 96, pp. 111–120, 2013.

[36] D. Chronopoulos, M. Ichchou, B. Troclet, and O. Bareille, "Efficient prediction of the response of layered shells by a dynamic stiffness approach," *Composite Structures*, vol. 97, pp. 401–404, 2013.

[37] D. Chronopoulos, M. Ichchou, B. Troclet, and O. Bareille, "Predicting the broadband vibroacoustic response of systems subject to aeroacoustic loads by a krylov subspace reduction," *Applied Acoustics*, vol. 74, no. 12, pp. 1394–1405, 2013.

[38] D. Chronopoulos, M. Ichchou, B. Troclet, and O. Bareille, "Thermal effects on the sound transmission through aerospace composite structures," *Aerospace Science and Technology*, vol. 30, no. 1, pp. 192–199, 2013.

[39] D. Chronopoulos, M. Ichchou, B. Troclet, and O. Bareille, "Predicting the broadband response of a layered cone-cylinder-cone shell," *Composite Structures*, vol. 107, pp. 149–159, 2014.

[40] D. Chronopoulos, M. Ichchou, B. Troclet, and O. Bareille, "Computing the broadband vibroacoustic response of arbitrarily thick layered panels by a wave finite element approach," *Applied Acoustics*, vol. 77, pp. 89–98, 2014.

[41] V. Polenta, S. Garvey, D. Chronopoulos, A. Long, and H. Morvan, "Optimal internal pressurisation of cylindrical shells for maximising their critical bending load," *Thin-Walled Structures*, vol. 87, pp. 133–138, 2015.

[42] T. Ampatzidis and D. Chronopoulos, "Acoustic transmission properties of pressurised and pre-stressed composite structures," *Composite Structures*, vol. 152, pp. 900–912, 2016.

[43] I. Antoniadis, D. Chronopoulos, V. Spitas, and D. Koulocheris, "Hyper-damping properties of a stiff and stable linear oscillator with a negative stiffness element," *Journal of Sound and Vibration*, vol. 346, no. 1, pp. 37–52, 2015.

[44] D. Chronopoulos, M. Collet, and M. Ichchou, "Damping enhancement of composite panels by inclusion of shunted piezoelectric patches: A wave-based modelling approach," *Materials*, vol. 8, no. 2, pp. 815–828, 2015.

[45] D. Chronopoulos, I. Antoniadis, M. Collet, and M. Ichchou, "Enhancement of wave damping within metamaterials having embedded negative stiffness inclusions," *Wave Motion*, vol. 58, pp. 165–179, 2015.

[46] D. Chronopoulos, I. Antoniadis, and T. Ampatzidis, "Enhanced acoustic insulation properties of composite metamaterials having embedded negative stiffness inclusions," *Extreme Mechanics Letters*, 2016.

[47] D. Chronopoulos, "Design optimization of composite structures operating in acoustic environments," *Journal of Sound and Vibration*, vol. 355, pp. 322–344, 2015.

[48] M. Ben Souf, D. Chronopoulos, M. Ichchou, O. Bareille, and M. Haddar, "On the variability of the sound transmission loss of composite panels through a parametric probabilistic approach," *Journal of Computational Acoustics*, vol. 24, no. 1, 2016.

[49] D. Chronopoulos, "Wave steering effects in anisotropic composite structures: Direct calculation of the energy skew angle through a finite element scheme," *Ultrasonics*, vol. 73, pp. 43–48, 2017.

[50] J.-M. Mencik and M. Ichchou, "Multi-mode propagation and diffusion in structures through finite elements," *European Journal of Mechanics-A/Solids*, vol. 24, no. 5, pp. 877–898, 2005.

[51] J. M. Renno and B. R. Mace, "Calculation of reflection and transmission coefficients of joints using a hybrid finite element/wave and finite element approach," *Journal of Sound and Vibration*, vol. 332, no. 9, pp. 2149–2164, 2013.

[52] R. E. Mickens, *Truly nonlinear oscillations: harmonic balance, parameter expansions, iteration, and averaging methods*. World Scientific, 2010.

[53] R. K. Narisetti, M. Ruzzene, and M. J. Leamy, "Study of wave propagation in strongly nonlinear periodic lattices using a harmonic balance approach," *Wave Motion*, vol. 49, no. 2, pp. 394–410, 2012.

COMPDYN 2017
6th ECCOMAS Thematic Conference on
Computational Methods in Structural Dynamics and Earthquake Engineering
M. Papadrakakis, M. Fragiadakis (eds.)
Rhodes Island, Greece, 15–17 June 2017

# VIBRATION ATTENUATION IN PIPES: DESIGN AND EXPERIMENTAL VALIDATION OF A RESONANT METAMATERIAL SOLUTION

**A. Nateghi[1*], L. Sangiuliano[1, 2], C. Claeys[1, 2], E. Deckers[1, 2], B. Pluymers[1, 2], W. Desmet[1, 2]**

[1] KU Leuven, Department Mechanical Engineering
Celestijnenlaan 300, box 2420, 3001 Heverlee, Belgium
{alireza.nateghi, luca.sangiuliano, claus.claeys, elke.deckers, bert.pluymers,
wim.desmet}@kuleuven.be

[2] Member of Flanders Make

**Keywords:** Resonant Metamaterial, Bloch-Floquet Theorem, Mechanical Vibration, Wave Propagation, Stopband Zone.

**Abstract.** *In recent years, locally resonant metamaterials have shown great potential in efficiently attenuating mechanical vibrations and providing noise insulation in various applications. Given the wide application range of lightweight pipes and considering that such structures can serve as excellent waveguides as they are often quite long, a locally resonant metamaterial pipe is presented in this paper. This metamaterial solution is chosen to investigate whether it is possible to use the metamaterial concept on pipe-like structures. Resonators are added to the pipe on a subwavelength scale in order to create a stopband zone in the propagation of flexural waves. Utilizing the Bloch-Floquet theorem and considering a periodic distribution of the local resonators, unit cell modelling is adopted to design the metamaterial pipe with a stopband zone in the frequency range of interest. Only a limited number of resonators are added to the original pipe in order to keep the added mass ratio due to these resonators below 10%. The results obtained from Bloch-Floquet theorem hold for an infinite metamaterial pipe with a periodic distribution of local resonators, but previous studies have shown that they provide a reliable prediction of the zone of highly attenuated response of the finite structure as well. Finally, the metamaterial pipe is manufactured to experimentally validate the results provided by the numerical prediction of the stopband zone. The metamaterial structure is composed of an Aluminum pipe as the host structure with added local resonators which are produced from Plexiglas using a laser cutting technique. The experimental results prove the existence of the stopband zone as predicted by the unit cell analysis of the infinite metamaterial pipe. The proposed concept provides an easy-to-apply metamaterial solution which can provide the stopband behavior while meeting the lightweight criterion.*

## 1 INTRODUCTION

In recent years, there has been an increasing interest in innovative lightweight designs in various applications. However, these lightweight solutions often show unfavorable Noise, Vibration and Harshness (NVH) behavior and given the impact of noise pollution on human health [1], a search for innovative solutions which both meet the lightweight criterion and satisfy NVH requirements has started. These novel NVH solutions need to be kept simple, cheap and fairly easy to apply. One of such novel solutions is the locally resonant metamaterials.

In recent years, locally resonant metamaterials have been in the spotlight as possible solutions for vibration attenuation and sound insulation problems, be it in targeted frequency ranges [2, 3]. Locally resonant metamaterials generally function by creating a stopband zone in which the structure does not support free wave propagation. This behavior in metamaterials is obtained due to the addition of local resonators to the host structure resulting in the destructive interference between the on-going waves propagating in the structure and the waves reradiated from the resonant cells within the stopband zone [4]. This new family has shown potential in efficiently controlling acoustic radiation and sound transmission while satisfying the lightweight requirement [5]. The potential of locally resonant metamaterials in vibration attenuation has recently been studied by Claeys et al. [6]. It is worth noting that the stopband behavior in locally resonant metamaterials is not dependent on the periodicity of the structure.

In recent years, academic verification of locally resonant metamaterials has been performed [6 - 8]. In such studies, the resonant cells are modelled as grids of mass-spring systems added to the hosting structure. However, there have also been a number of investigations on the feasibility of locally resonant metamaterials as realizable NVH problems. In one of such studies, Claeys et al. have proposed a design for resonant cells which can be realized fairly easily while meeting the lightweight criterion and providing favorable NVH behavior [9, 10]. Their study proves the increased acoustic insertion loss of a finite enclosure due to the addition of the resonant cells.

As stated, periodicity is not a required property of locally resonant metamaterials; however, assuming a periodic distribution of the resonant cells, has its benefits in modelling efficiently. Assuming an infinite periodic structure, wave motion in the structure can be characterized by investigation of a unit cell and applying the Bloch-Floquet theorem [11, 12]. A unit cell is defined as a smallest portion of a periodic structure which contains all the essential information required to describe wave propagation through the entire structure. In the context of metamaterials, wave propagation in the structure is commonly described using dispersion curves which relate wavenumbers of propagating waves to the frequency at which they propagate. Application of the Bloch-Floquet theorem and unit cell modelling in the design of periodic structures has been thoroughly investigated [13, 14].

Studies on wave propagation in curved structures show that the behavior of such structures significantly differ from their planar counterparts as e.g. shown in [15]. Therefore, next to studies on the stopband behavior in flat metamaterial plates, it is worth to investigate the effect of curvature on the behavior of locally resonant metamaterials. Recently, Nateghi et al. [16, 17] extended the metamaterial demonstration of Claeys et al. [9] to the case of infinite cylindrical shells and pipes. The results show a considerable difference in behavior due to the addition of the cylindrical curvature and the existence of cut-on frequencies. It was shown that below cut-on frequencies of flexural waves the behavior of cylindrical and flat metamaterial structures differ considerably. In addition, it is observed that addition of local resonators to the cylindrical host influences the cut-on frequency of the flexural waves; especially in the vicinity of the targeted stopband zone. Moreover, it was observed that the frequency range of the stopband of flexural modes with different circumferential wavenumbers differ from each

other. However, the overall dynamic behavior of the cylindrical structure is improved as the stopband zone is obtained.

In this paper, wave motion in locally resonant metamaterial pipes is investigated. Following form the findings of [17], a metamaterial solution for vibration attenuation of a lightweight Aluminum pipe is designed, analyzed and produced. To this end, first, a new resonant structure is designed and then, utilizing the Bloch-Floquet theorem and assuming a periodic distribution of the resonant cells through the pipe, the effects of these resonators on the structure are investigated. In this step, the dispersion curves of the metamaterial pipe are obtained and stopband zones are numerically predicted. In the next step, the metamaterial pipe is produced and an experimental set-up is designed to validate the numerical prediction. In this study, the metamaterial structure is composed of a hosting Aluminum pipe of 1 m length which is treated by gluing on Poly(Methyl Methacrylate), also known as PMMA, resonant cells, produced using a laser cutting technique. The experimental results prove the existence of a stopband zone due to the addition of the resonant cells to the pipe and the frequency range of the stopband zone is in good agreement with the unit cell modelling prediction.

The paper is structured as follows. Section 2 discusses the application case in more details. Section 3 describes the metamaterial solution and the overall design of the resonant cells. Section 4 briefly explains the application of unit cell modelling on the resonant cells described in section 3. Dispersion curves are obtained and the stopband is predicted. Section 5 provides information on the specifications of the experimental set-up and the experimental results are discussed in section 6. Finally, the main conclusions of the research are drawn and discussed.

## 2 HOST STRUCTURE

A lightweight thin pipe is chosen as a case study because of its wide range of applications; from piping networks to rotating machinery amongst other applications. Considering the low mass of the structure, its hollowness and the fact that it is quite thin, the radiated noise from the wall of such a pipe can be considerable [18] . Moreover, as shown in [17], the circular curvature of the structure is a good demonstration of the effect of curvature on the metamaterial solution and stopband zones.

In the current study, an Aluminum pipe of length 1 m, thickness 2.1 mm and inner radius of 4.8 cm is chosen as the case study. The choice of Aluminum is due to its common usage in industrial applications from transportation industry to various piping systems. The mechanical and physical properties of the Aluminum pipe is given in Table 1. Considering the importance of NVH behavior at lower frequencies, the behavior of the structure below 1000 Hz is targeted and investigated.

| Material | Young's modulus [GPa] | Poisson's ratio [-] | Density [kg/m$^3$] |
|---|---|---|---|
| Aluminum | 68 | 0.35 | 2696.2 |
| PMMA | 4.85 | 0.31 | 1188.38 |

Table 1: Material properties of the Aluminum pipe and the PMMA resonant cells.

## 3 LOCALLY RESONANT METAMATERIAL PIPE

In this section, the design of the metamaterial solution is explained in more detail. The main interest of this paper is to improve NVH behavior of a thin Aluminum pipe as a lightweight hollow structure. To this end, considering the importance of the flexural waves on acoustic radiation of structures, in this work, creating a stopband zone in the propagation of

the flexural waves is targeted. To this end, resonant cells are designed to have a low-frequent flexural mode and are added to the host structure on a subwavelength scale to satisfy the criteria of metamaterial design [2].

In the current work, the metamaterial structure is composed of the Aluminum pipe introduced in section 2 as the host structure with the addition of resonant cells produced from a PMMA panel using laser cutting technique. The representation of such a resonant cell is shown in Fig. (1). The mechanical and physical properties of the resonant cells are given in Table 1. These parameters are retrieved through correlation of the measured frequency response of the structure with the frequency response predicted by the numerical model.

The dimensions of the resonant cells should be chosen based on the frequency range of the intended stopband zone as this zone occurs around the first flexural eigenfrequency of the resonator. The goal in this research is to keep the added mass ratio of the resonant cells to the host structure low to make sure that the metamaterial solution still falls under the definition of a lightweight solution.

The resonators are tuned to have their first flexural resonant frequency around 800 Hz and therefore the geometrical parameters shown in the second row of Table 2 are chosen for the resonant cell shown in Fig. (1). This frequency range is chosen as numerical simulations of the Aluminum pipe show a vibrating mode which can contribute to acoustic radiation at 800 Hz. However, after production of the cells, measuring the final geometrical parameters of 5 samples and averaging these data provides the updated geometrical parameters of the resonant cells which are used in the numerical prediction of the stopband zones. These updated parameters are given in the last row of Table 2.

A similar design as in [10, 19] is used in this research as shown in Fig. (1). Note that the thickness of the resonator is kept constant and equal to 8 mm. The chosen shape makes the production of the resonant cells through laser cutting straightforward.

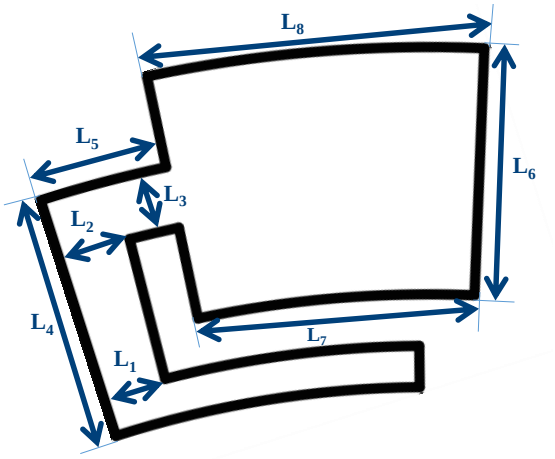


Figure 1: Representation of the resonant cells.

| Dimensions [mm] | $L_1$ | $L_2$ | $L_3$ | $L_4$ | $L_5$ | $L_6$ | $L_7$ | $L_8$ |
|---|---|---|---|---|---|---|---|---|
| Designed | 3.12 | 3.54 | 3.00 | 12.00 | 7.36 | 12.00 | 13.51 | 16.49 |
| Measured | 2.97 | 3.21 | 2.76 | 11.83 | 7.47 | 11.75 | 13.56 | 15.95 |

Table 2: Geometrical parameters of the resonant cell shown in Fig. (1).

The resonant cell is modelled using the properties and the dimensions stated in Tables 1 and 2 in COMSOL Multiphysics. The model is discretized using 12440 quadratic tetrahedral solid elements resulting in 62253 degrees of freedom. Note that fixed boundary conditions are assumed at the base of the resonator. As it can be seen from Fig. (2), the first eigenfrequency of the resonator is a flexural mode with respect to the host structure and it occurs at 745.8 Hz, while the second eigenfrequency occurs at 1059.1 Hz and can be described as a longitudinal mode with respect to the host structure. Following previous studies [9, 17], it will be investigated both numerically and experimentally whether the addition of this type of resonator to a pipe can induce a stopband.

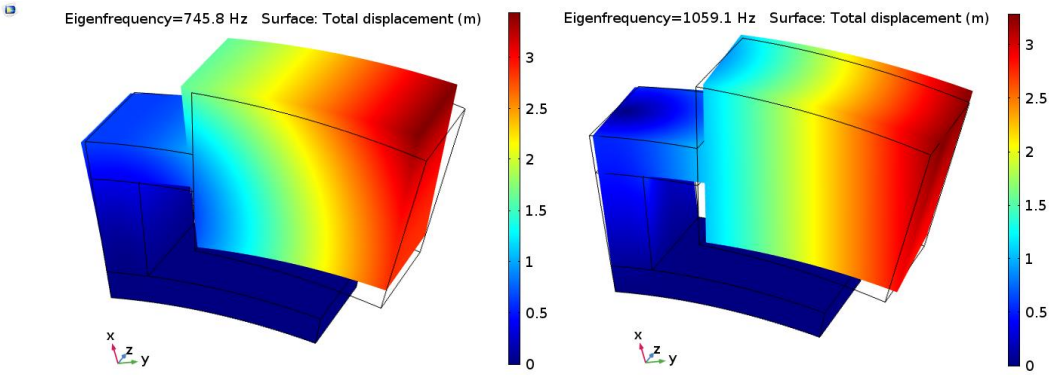


Figure 2: Modeshapes of the first and second eignfrequencies of the resonant cells. The wireframe represents the undeformed state of the resonant cells.

## 4 UNIT CELL MODELLING AND STOPBAND ZONE

Next step in the investigation of the stopband behavior of the locally resonant metamaterial pipe is a wave dispersion analysis. As stated before, at this step, it is assumed that the resonant cells are distributed periodically over the pipe on a subwavelength scale. The grid for such a periodic distribution is also of importance. It is assumed that 8 resonant cells are distributed around the circumference of the pipe and this ring of resonance cells is infinitely repeated in the axial direction. The distance between two resonators in the axial direction is 4 cm. Fig. (3) shows the representative unit cell which is used in the dispersion analysis. Also the host structure is accounted for in the unit cell.

After choosing the proper representative unit cell, it is possible to apply the Bloch-Floquet theorem to obtain dispersion curves which provide the required information on wave propagation through the infinite structure. These dispersion curves provide the relationship between the wavenumbers and the frequency of the waves which can propagate in the structure. The application of Bloch-Floquet theorem for the dispersion analysis of both open cylindrical metamaterial shells and metamaterial pipes are performed by Nateghi et al. [16, 17]. Considering the configuration used in the current study, readers are referred to [17] for the required formulations of unit cell modelling in infinitely long cylindrical pipes. Based on this formulation, for the dispersion analysis of the metamaterial pipe, it is required to set integer values to the circumferential wavenumber $k_\varphi$ as shown in Fig. (4) and solve the remaining quadratic eigenvalue problem for the values of the axial wavenumber $k_z$ which then provide dispersion curves. The stopband zones appear as discontinuities in the dispersion curves of the corresponding waves. This zone indicates a frequency range in which no solution exists as the free wave propagation in the structure is hindered.

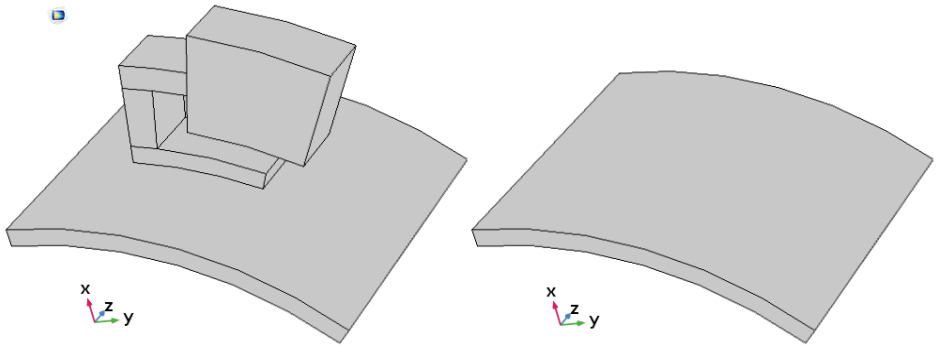


Figure 3: Representative unit cell of the metamaterial pipe (left) and the host Aluminum pipe (right).

It is more convenient to analyze the wave propagation vector $\boldsymbol{\mu} = \boldsymbol{k}.\boldsymbol{d}$ instead of the wavenumber vector $\boldsymbol{k}$ given since it is a non-dimensional vector with $\boldsymbol{d}$ the lattice basis vector. In addition, in this analysis, only real wave vectors, corresponding to free propagating waves, are considered. In the current section, only the real parts of the solutions are represented as they provide sufficient information for stopband prediction.

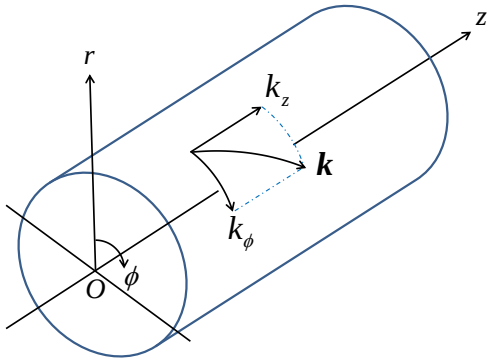


Figure 4: Representation of the wavenumber vector in a pipe as shown in [17].

The unit cell models of Fig. (3) are modelled in COMSOL Multiphysics and periodic boundary conditions are applied to the unit cell model. Afterwards, following the formulations provided in [17] the dispersion relation is solved for the axial wavenumbers of propagating waves at fixed frequencies and circumferential wavenumbers. Given the imposed periodic boundary condition, solving the dispersion relation provides a periodic set of solutions in the wavenumber domain. This periodic set of solutions in the wavenumber domain has the intervals of $\left[-\frac{\pi}{L},\frac{\pi}{L}\right]$ in which L is the length of the unit cell in the axial direction.

In the next subsections, first the dispersion curves representing wave propagation through the hosting pipe are discussed to further understand wave motion in the Aluminum pipe. Afterwards, the unit cell model consisting of the Aluminum pipe and the resonant cell is studied to provide a numerical prediction of the frequency range of the stopband zone.

### 4.1 Wave propagation in the host structure

Fig. (5) shows dispersion curves of the propagating parts of the waves with the circumferential wavenumber $k_\varphi$=0, 1 and 2 rad/rad in an infinite Aluminum pipe represented by the host unit cell of Fig. (3). These curves represent breathing, beam bending and ovalling modes of vibration in the pipe, respectively. In this figure, only the propagating parts of the waves are

depicted as their information suffices for the purpose of stopband detection. It is worth mentioning that in the dispersion curves of the metamaterial pipe, the stopband appears as a discontinuity in the dispersion curves of the flexural waves.

As it can be seen in the dispersion curves representing the breathing mode, two pairs of waves can propagate through the structure within the frequency range of 0 Hz – 1000 Hz which correspond to the longitudinal and shear modes of vibration. The dispersion curves representing flexural waves do not appear in this frequency range as the flexural wave of the breathing mode is only cut on at 17417 Hz. It is worth mentioning that although, breathing mode has a considerable contribution to acoustic radiation, given that the stopband of the current work is targeting propagating flexural waves around 750 Hz, this mode is not of high importance in stopband prediction as the flexural wave has not cut on in this frequency range.

Based on the dispersion curves of the ovalling and beam bending modes, only flexural waves are propagating in this frequency range. Considering the current resonator design, these are the waves that are targeted in the current study. It is worth mentioning that waves with higher circumferential wavenumbers are not investigated as their flexural waves cut on at frequencies higher than 1000 Hz.

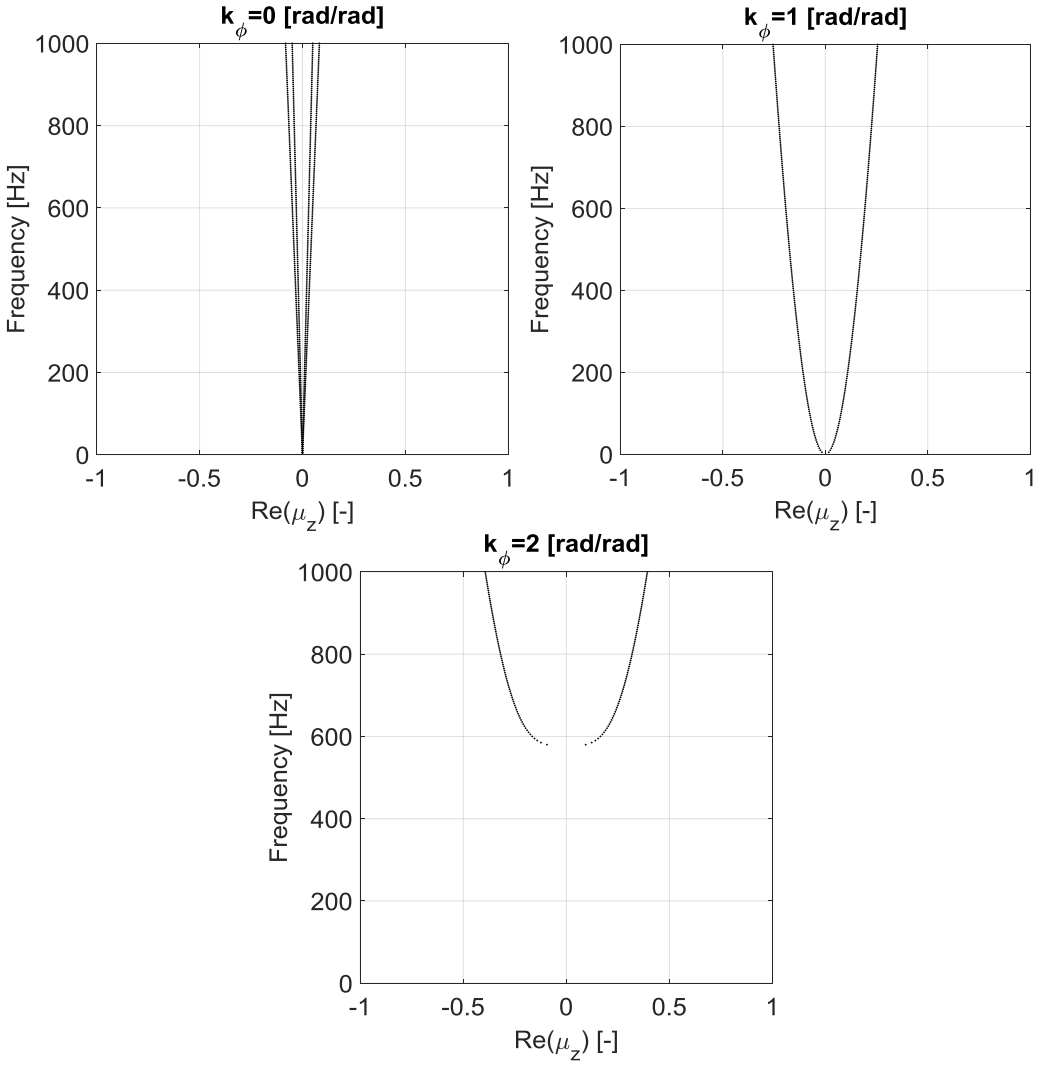


Figure 5: Dispersion curves representing wave motion in the infinite bare Aluminum pipe with circumferential wavenumbers 0, 1 and 2.

## 4.2 Wave propagation in the metamaterial pipe

Dispersion curves of the propagating waves with $k_\varphi$=0, 1 and 2 rad/rad obtained from the representative unit cell of the metamaterial pipe (as shown in Fig. (3)) are given by Fig. (6). As it can be seen from the figure, the addition of the resonant cells have influenced the dispersion curves representing the wave propagation of the breathing mode even though the flexural waves have not cut on below 1000 Hz. This effect can be explained based on mode coupling and the wave propagation related to the motion of the local resonant cells at the eigenfrequency of the resonators [17]. It has been shown that below the ring frequency, i.e. the cut-on frequency of the flexural wave of the breathing mode, waves are not of pure flexural, shear and longitudinal nature.

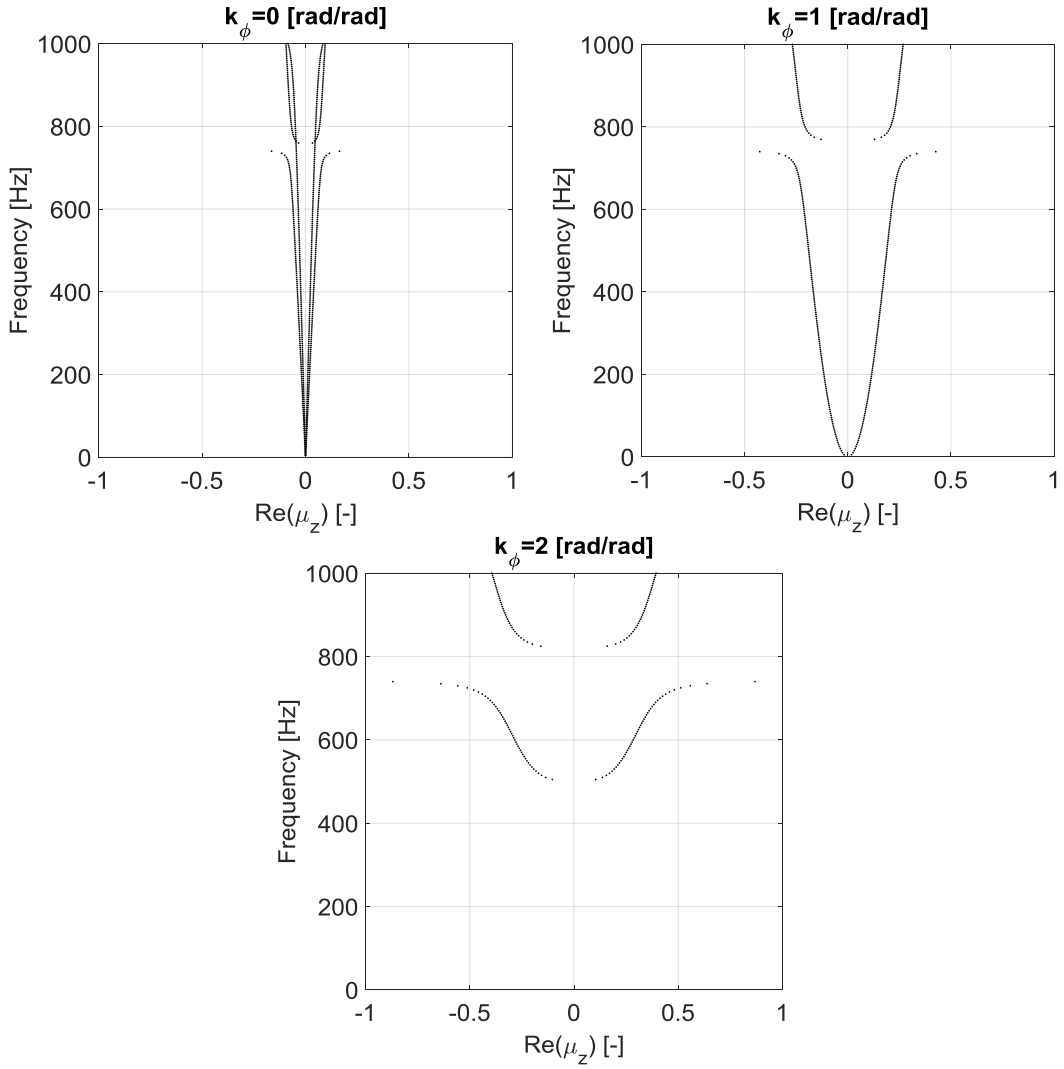


Figure 6: Dispersion curves representing wave motion in the infinite metamaterial pipe with circumferential wavenumbers 0, 1 and 2.

The dispersion curves of the beam bending and ovalling modes show a clear gap in the curves representing the propagating flexural waves. These gaps prove the existence of stopband zones due to the addition of the local resonators and are in the frequency ranges of 740 Hz - 770 Hz and 740 Hz - 825 Hz for beam bending and ovalling modes, respectively. Therefore, based on these results it can predicted that the current design creates an overall stopband

zone between 740 Hz and 770 Hz. It is expected that a significant attenuation can be obtained between 740 Hz - 825 Hz by applying this metamaterial solution to the Aluminum pipe.

Another point of interest in the dispersion curves shown in Fig. (6) is related to the cut on frequency of the flexural wave in the ovalling mode which is affected due to the addition of the resonant cells. In previous studies, it has been shown that below the stopband zone, the addition of the local resonators pushes the cut on frequency of the propagating waves to lower frequencies while above the stopband zone the cut on frequencies of waves increase. Readers are referred to [16] for further information in this regard.

## 5 EXPERIMENTAL SET-UP

This section provides information on the production aspect of the metamaterial pipe and explains the specifications of the test set-up.

### 5.1 Production of the resonators

The resonant cells are produced from PMMA panels as shown in Fig. (7), using a laser cutter machine. The resonators are all cut from the same panel using the same laser cutter tool to try to keep the material properties and the possible production errors as consistent as possible. However, there is still a deviation between the geometries of the designed and finally produced parts.




Figure 7: Produced PMMA resonators.

As already explained in section 3, the final geometrical parameters of the produced resonators are measured and averaged using 5 separate samples and are given in Table 2. In order to be sure about the actual resonance frequency of the produced parts, an experiment is performed using a Scanning Laser Doppler Vibrometer (SLDV) as shown in Fig. (8). 5 samples of the produced resonators are chosen and glued to a rigid plate. In order to make the contact between the rigid part and the resonant cells more consistent, the resonator design is changed slightly by making their base flat as shown in the figure. Numerical simulations show that the influence of this design change on the resonance frequency of the parts is negligible; considering that the change is limited to the base of the cells which is glued to the rigid part. The rigid structure is mounted on and excited by a shaker The acceleration of the tip of the resonators due to the shaker excitation is measured using SLDV as shown in the figure.

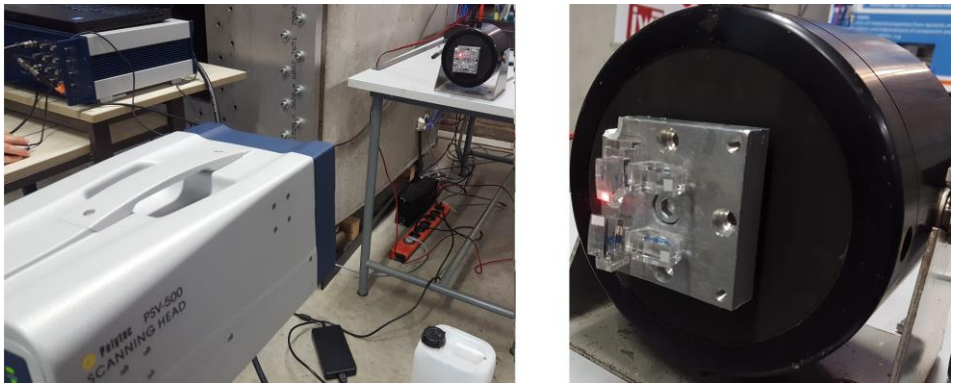


Figure 8: SLDV set-up for flexural eigenfrequency measurement of 5 of the resonators.

Fig. (9) shows the measured acceleration of five resonators in the frequency range of 0 Hz -1000 Hz. As it can be observed, there is a clear resonance frequency between 735 Hz – 743 Hz which shows up as a peak in the figure. From these five samples, it can be concluded that the average resonance frequency of the produced parts lies at 740 Hz which is in good agreement with the results of the numerical simulations. It is worth noting that the scatter in the resonance frequency of the produced parts can affect the performance of the metamaterial solution in the stopband zone and it is important to reduce it as much as possible. However, in the current case, the scatter of 8 Hz with a maximum relative error of 0.68% with respect to the average resonance frequency seems to be in an acceptable range [20].

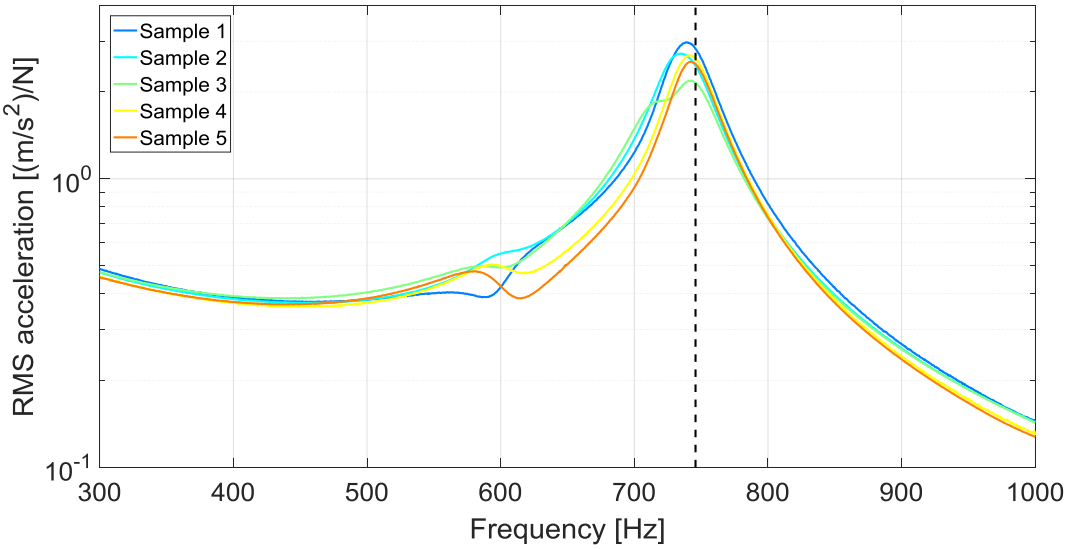


Figure 9: Frequency response of the produced PMMA resonators under shaker excitation measured by SLDV. Dashed line indicates the numerically predicted resonance frequency.

## 5.2 Test set-up

The test set-up used for the experimental frequency response analysis of the metamaterial pipe is described in this section. The test bench shown in Fig. (10) is used to mount the metamaterial pipe. It consists of a table with rigid stands from which the test specimen is suspended using guitar strings to limit the effects of possible coupled vibrations of the pipe and the table and to limit the effect of mounting conditions.

As excitation, a hammer is used to perform impact testing. To measure the response of the pipe, four lightweight accelerometers are attached to different sections of the pipe.. Each of the accelerometers weighs 0.8 g which makes the additional mass of them negligible as compared to the mass of the metamaterial pipe.

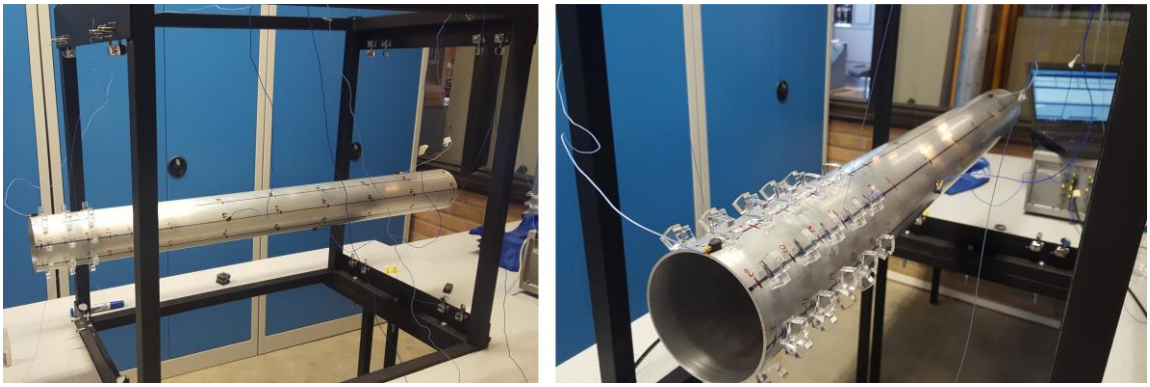

Figure 10: Test set-up.

In order to characterize wave propagation through the structure there is a need for various measurement points on the pipe. The roving hammer method is applied in order to avoid the need of adding many accelerometers. This means that the excitation location is varied and the response location is kept fixed as a reference. Due to the reciprocity principle, valid for linear systems, the response and input points can be interchanged.

The metamaterial pipe is divided into 13 sections as shown in Fig. (11) and on each section 8 equidistant points around the circumference are chosen, corresponding to a total of 104 excitation locations for the roving hammer. The acceleration response is measured at the 4 points shown in Fig. (11).

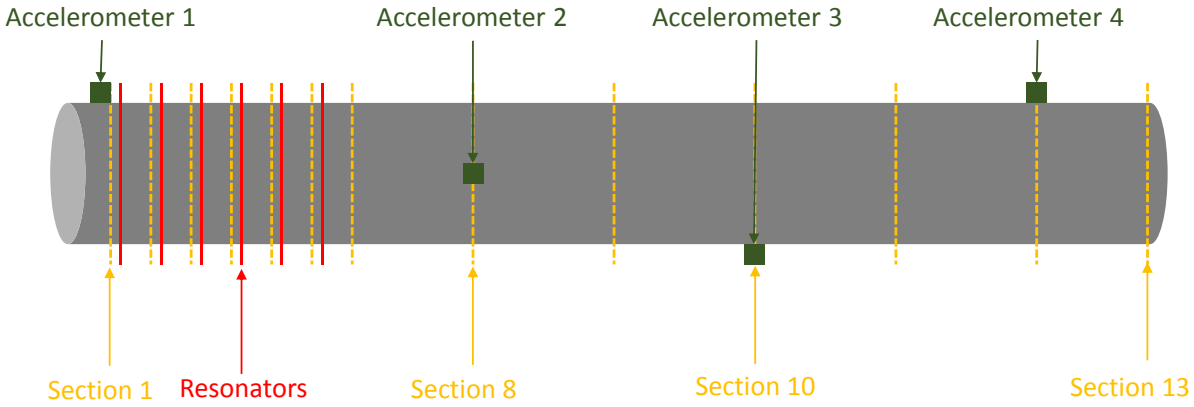


Figure 11: Excitation sections, measurement points and the location of resonators.

As indicated in figure (11) only six rings of resonators are glued to the Aluminum pipe and the rings are distributed evenly with 4 cm of distance between two rings. The number of resonator rings is chosen based on the results reported by [10] where 6 rows of resonators are shown to be sufficient to create stopband behavior. In order to fully capture the effect of the resonant cells on the behavior of the pipe, there are spatially more excitation sections foreseen in the left side of the pipe in order to characterize the decay of the waves passing through each ring of resonant cells. Furthermore, to evaluate the effect of each ring or resonators separately, the measurement procedure is repeated for 7 different configurations. First the bare case is

measured. Next the ring on the left side is added and the pipe is measured again. This procedure is repeated for the next 5 rings, where the rings are added consecutively from left to right.

The averaged measured mass of a single resonant cell is 2.24 g, summing up to a total added mass of 107.52 g for all 48 cells which are glued to the pipe in the final metamaterial design. With a total mass addition of 6.16% to the host structure, this can still be considered as a lightweight NVH treatment.

## 6 MEASUREMENT RESULTS AND DISCUSSION

Test results are discussed in this section. Applying the reciprocity principle, the results are given in the form of averaged measured RMS accelerations for the different sections of the pipe and averaged measured RMS accelerations of the entire pipe with respect to the location of the corresponding reference positions. RMS acceleration of different sections are calculated according to the following formula:

$$\left|H\right|_{\ddot{X}_{n/F_e,rms}} = \sqrt{\frac{1}{M}\sum_{k=1}^{M}\left|H\right|^2_{\ddot{X}_{n,k/F_e}}}, \tag{1}$$

in which $\left|H\right|_{\ddot{X}_{n,k/F_e}}$ indicates the amplitude of the acceleration frequency response in point *k* on section *n* for an excitation in point *e* and *M* is the number of points per section. Note that the RMS acceleration of the entire pipe is calculated as follows:

$$\left|H\right|_{\ddot{X}_{F_e,rms}} = \sqrt{\frac{1}{(N.M)}\sum_{n=1}^{N}\sum_{k=1}^{M}\left|H\right|^2_{\ddot{X}_{n,k/F_e}}}, \tag{2}$$

where *N* is the number of sections of the pipe. Fig. (12) shows the measured RMS acceleration of the entire pipe for the 7 configurations, based on input on the location of accelerometer 1. It is observed that between 700 Hz - 780 Hz, there is an obvious dip building up in the frequency response of the pipe which shows the existence of the stopband zone due to the addition of the resonators. The numerically predicted stopband is indicated by dashed lines and corresponds well to the measurements.

It is observed that the dip in the frequency response of the pipe within the stopband zone gets more pronounced with the addition of each resonator ring which indicates that the attenuation of the waves becomes stronger.

It is also noted that below the stopband zone there is a shift to the left in the frequency response of the pipe with the addition of the resonator cells which can be clearly observed in the peaks of the figure which represent different eigenmodes of vibration of the pipe. This shift for the eigenmode above stopband is towards higher frequencies. This behavior can be explained due to in-phase and out-of-phase motion of the pipe and the resonators below and above the stopband zone, respectively. It has been shown that below stopband zone, motion of the resonators and the host structure are in-phase resulting in a higher dynamic mass [9]. This higher dynamic mass shifts the eigenmodes of the host to lower frequencies while above stopband zone out-of-phase motion of the resonators and the host leads to the opposite effect.

In addition of the stopband zone, some clear reduction in the amplitude of these lower frequency modes is also observed which can be related to the added damping coming from the PMMA resonator cells and their moving masses.

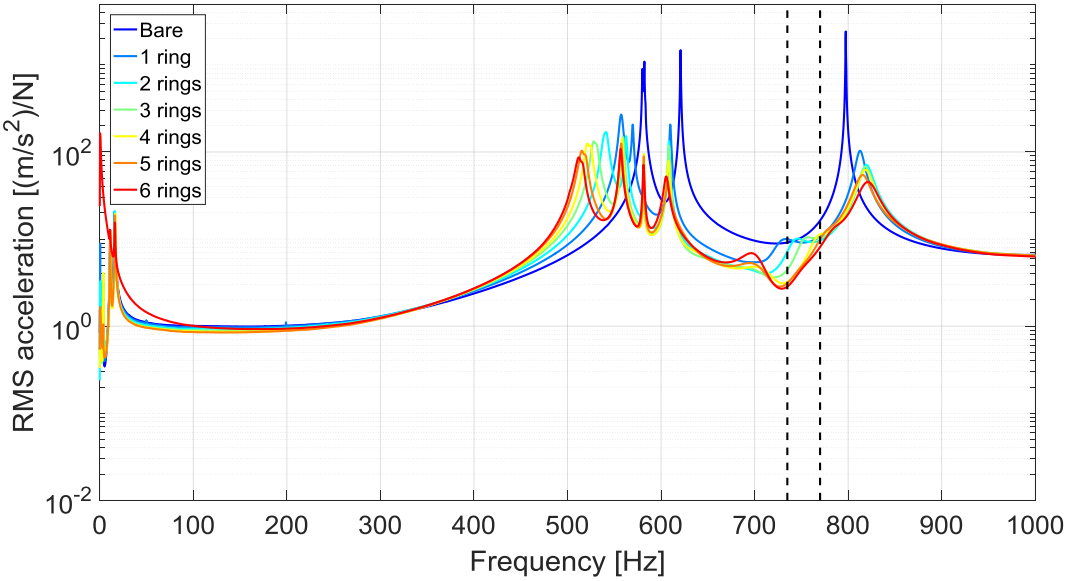


Figure 12: Frequency response of the RMS acceleration of all of the points through the length of the pipe with various numbers of resonator rings based on input on the location of accelerometer 1. Dashed lines indicate the numerically predicted stopband zone.

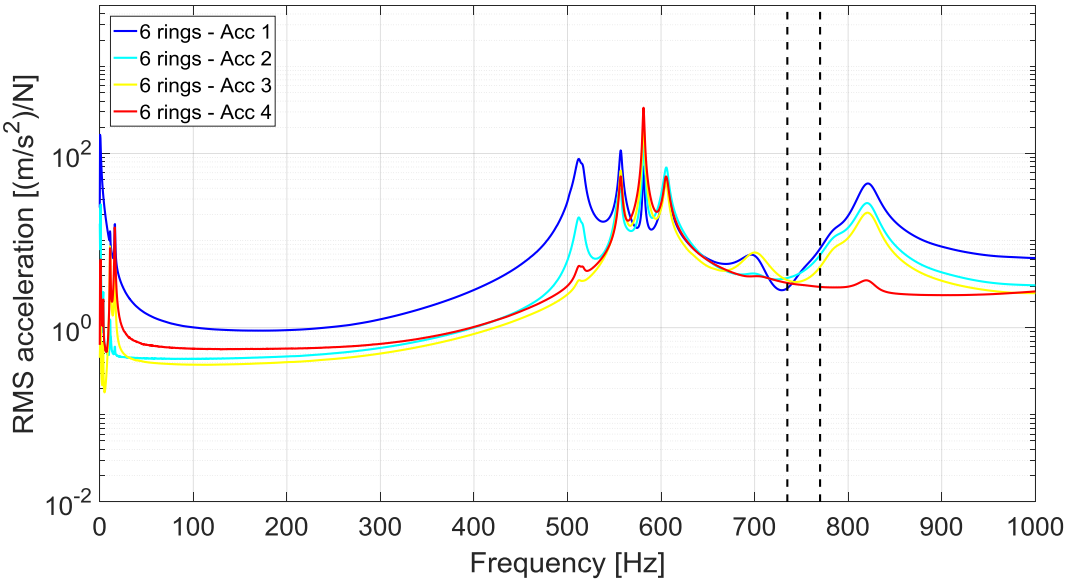


Figure 13: Frequency response of the RMS acceleration of all of the excitation point through the length of the bare pipe and the metamaterial pipe with 6 resonator rings based on input on the location of different accelerometers. Dashed lines indicate the numerically predicted stopband zone.

Fig. (13) shows the RMS frequency response of all of the points on the pipe with 6 rings based on input on the location of accelerometers 1 to 4. As it can be observed, the dip representing the stopband zone can be clearly detected in the measured response of the accelerometers 1 to 3. However, in the case of accelerometer 4 the dip is not as clear. As it can be seen, the amplitude of the response in the frequency range of the stopband is lower in the curve corresponding to accelerometer 4 compared to the other curves which can mask the dip related to

the stopband. Therefore, it is important to study the behavior of the section which contains this point, i.e. section 13, to verify the effect of the resonators on the opposite end of the pipe.

However in addition to the RMS response of the entire pipe, it is important to study the RMS response in different sections of the pipe. This section-wise investigation can provide a better understanding of the wave decay due to the addition of the resonator rings and can also assure a consistent reduction in the acceleration response of the pipe along its entire length. Fig. (14) provides the RMS response of the sections 1, 3, 5, 7, 10 and 13 for the metamaterial pipe with 6 added resonator rings. As it can be seen, the comparison of the responses of sections 1 – 7, that are in the region of the added resonant cells, clearly show that the dip in the stopband zone becomes more pronounced as the wave travels along the pipe and passes through each resonant cell. However, the observation of the dip due to the stopband in sections 10 and 13 (right at the opposite end of the pipe), in which resonant cells are not attached, proves that the metamaterial solution is influencing the frequency response of the entire pipe as expected.

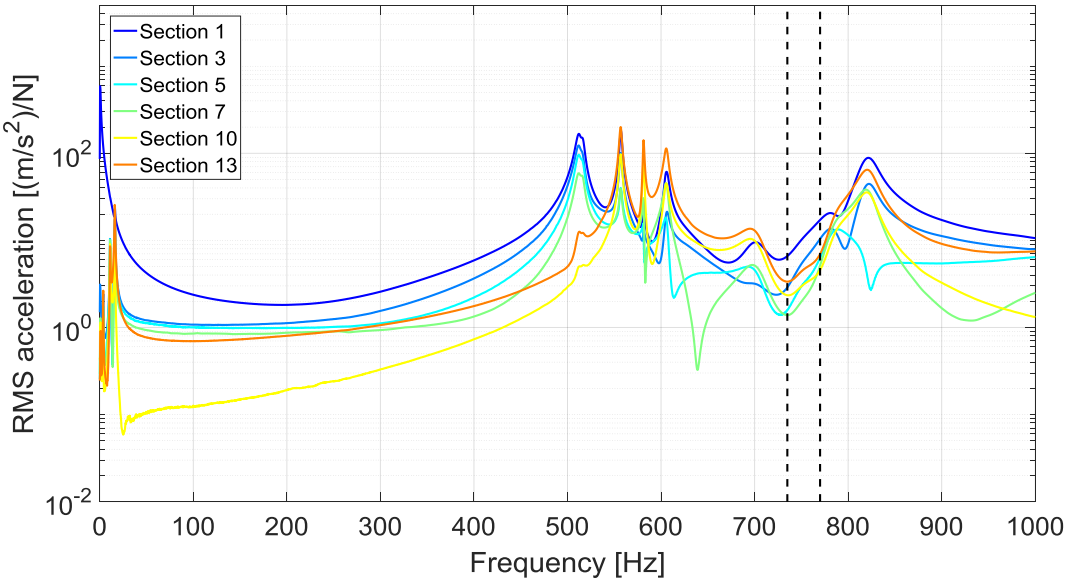


Figure 14: Frequency response of the RMS acceleration of various sections of the metamaterial pipe with 6 resonator rings based on input on the location of accelerometer 1. Dashed lines indicate the numerically predicted stopband zone.

Figs. (15) – (18) provide the frequency response of the pipe treated with different numbers of resonator rings in sections 1, 3, 7 and 13 based on input on the location of accelerometer 1, respectively. Results in these sections are presented as they provide a good understanding of the behavior of the metamaterial pipe as sections 1, 3 and 7 are located before, in between and behind the resonator rings and section 13 is the end of the pipe with no resonators attached. Considering that the pipe is treated with the metamaterial solution only at one end, it is important to study the effect of the resonators on its opposite end.

It is observed in Fig. (15) that in section 1 which is located before the resonator rings, the frequency responses due to a different number of resonator rings are not much influenced in the stopband zone. This can be explained due to the fact that both measurement and excitation points are before the resonator rings and therefore, this sections observes the effect of the rings minimally. The main difference between the pipe with different number of resonators comes from the additional mass of extra resonators which causes a frequency shift as ex-

plained before. However, in the response of the section 3 as shown in Fig. (16), there is a more considerable difference in the frequency response of the pipes with different number of resonator cells in the stopband zone. In this case, the pipes with more than two resonator rings show a more pronounced stopband zone. This observation becomes even more prominent for the response of the metamaterial with 6 resonator ring in section 7 as shown in Fig. (17). Considering that section 7 is located after the 6 resonator rings, the decay of the propagating waves becomes more pronounced with the addition of each resonator ring.

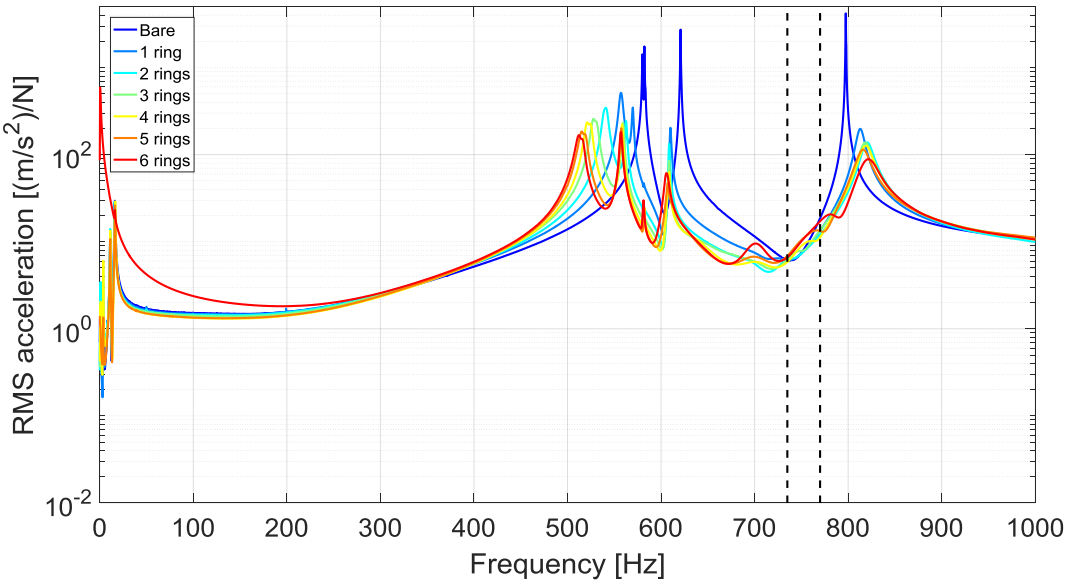


Figure 15: Frequency response of the RMS acceleration of section 1 of the pipe with various number of resonator rings corresponding to the excitation point located at accelerometer 1. Dashed lines indicate the numerically predicted stopband zone.

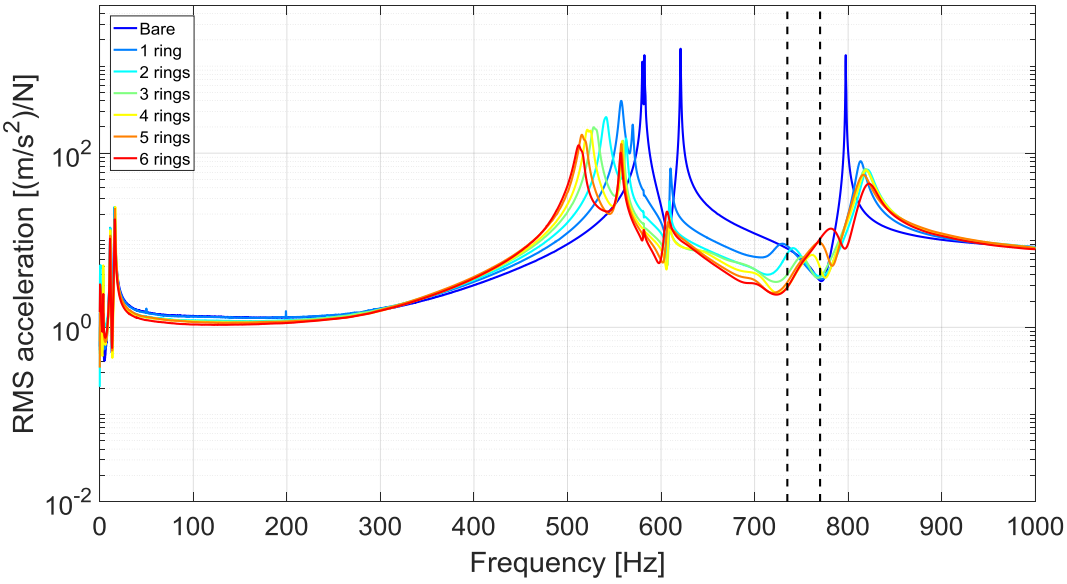


Figure 16: Frequency response of the RMS acceleration of section 3 of the pipe with various number of resonator rings corresponding to the excitation point located at accelerometer 1. Dashed lines indicate the numerically predicted stopband zone.

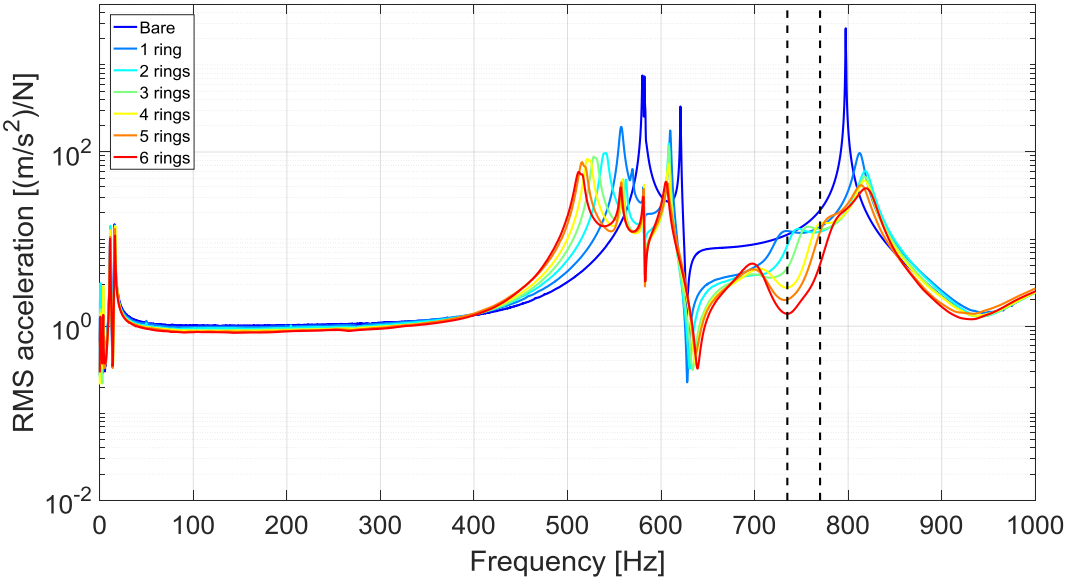


Figure 17: Frequency response of the RMS acceleration of section 7 of the pipe with various number of resonator rings corresponding to the excitation point located at accelerometer 1. Dashed lines indicate the numerically predicted stopband zone.

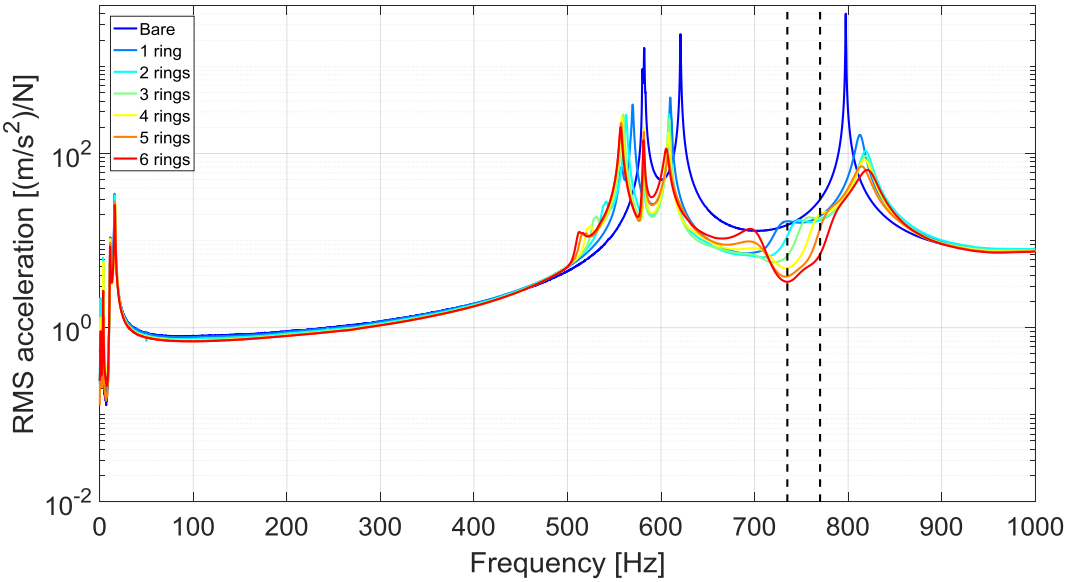


Figure 18: Frequency response of the RMS acceleration of section 13 of the pipe with various number of resonator rings corresponding to the excitation point located at accelerometer 1. Dashed lines indicate the numerically predicted stopband zone.

Frequency response functions obtained from section 13 as shown in Fig. (18), once more proves that the stopband zone is also obtained on the opposite end of the pipe in which again, the stopband dip becomes more pronounced with the addition of each resonator ring and the peaks representing different modes of the pipe become significantly damped after the addition of 6 resonator rings similar to section 7. In addition to the observations with respect to the stopband zone, as it can be seen in all of the figures, it is observed that the addition of the res-

onator rings causes a significant attenuation in the dynamic modes of the pipe. This effect can be more clearly observed at the peak around 800 Hz for all of the shown four sections.

## 7 CONCLUSIONS

In this paper, wave motion in locally resonant metamaterial pipes is investigated. Given the complex dynamics of curved structures and considering the wide range of application of lightweight Aluminum pipes such a pipe is chosen as the case study and a metamaterial solution is designed and proposed. The metamaterial solution has the potential to efficiently improve the NVH behavior of the pipe by the introduction of a stopband zone. Using the Bloch-Floquet theorem, the unit cell modelling method is utilized to numerically predict the frequency range of this stopband zone. The proposed metamaterial solution is then produced by cutting resonators out of a PMMA panel using laser cutting technique and by gluing them to the host Aluminum pipe. The host and metamaterial pipes are tested using the impact testing method under roving hammer excitation. The response is measured in different sections of the pipe for different numbers of resonant cells added to the pipe. The measurement results clearly verify the existence of a stopband zone due to the metamaterial treatment of the pipe. Comparison of the response of the pipes with different number of resonator cells shows that a pronounced reduction in the vibrational response can be obtained with a limited number of resonator cells corresponding to a 6.16% added mass to the Aluminum pipe; however, it is worth mentioning that addition of more resonator cells can result in higher amount of attenuation while adding to the mass. The validation case shows that the metamaterial solution can also influence parts of the pipe which are not treated with resonant cells, providing an efficient lightweight solution for vibration attenuation and possibly sound radiation reduction.

## ACKNOWLEDGEMENTS

This research was partially supported by Flanders Make, the strategic research center for the manufacturing industry. The Research Fund KU Leuven is gratefully acknowledged for its support. The research of E. Deckers is funded by a personal grant from the Research Foundation – Flanders (F.W.O.).

## REFERENCES

[1] L. Fritschi, L. Brown, R. Kim, D. Schwela, S. Kephalopous, Burden of disease from environmental noise: Quantification of healthy life years lost in Europe. *WHO Regional Office for Europe*, 2011.

[2] F. Lemoult, N. Kaina, M. Fink, G. Lerosey, Wave propagation control at the deep subwavelength scale in metamaterials. *Nature Physics*, **9**, 55-60, 2012.

[3] X. Zhou, X. Liu, G. Hu, Elastic metamaterials with local resonances: an overview. *Theoretical and Applied Mechanics Letters,* **2**, 2012.

[4] C. Goffaux, J. Sánchez-Dehesa, A. Yeyati, P. Lambin, A. Khelif, J. Vasseur, B. Djafari-Rouhani, Evidence of fano-like interference phenomena in locally resonant materials. *Physical Review Letters,* **88** (22), 2002.

[5] C. Claeys, P. Sas, W. Desmet, On the acoustic radiation efficiency of local resonance based stop band materials. *Journal of Sound and Vibration*, **333** (14), 3203-3213,

2014.

[6] C. Claeys, K. Vergote, P. Sas, W. Desmet, On the potential of tuned resonators to obtain low-frequency vibrational stop bands in periodic panels. *Journal of Sound and Vibration*, **332** (6), 1418–1436, 2013.

[7] T. Wang, M.P. Sheng, Z.W. Guo, Q.H. Qin, Flexural wave suppression by an acoustic metamaterial plate. *Applied Acoustics, Elsevier*, **114**, 118-124, 2016.

[8] C. Sugino, S. Leadenham, M. Ruzzene, A. Erturk, On the mechanism of bandgap formation in locally resonant finite elastic metamaterials. *Journal of Applied Physics*, **120**, 2016.

[9] C. Claeys, E. Deckers, B. Pluymers, W. Desmet, A lightweight vibro-acoustic metamaterial demonstrator: Numerical and experimental investigation. *Mechanical Systems and Signal Processing*, **70-71**, 853-880, 2016.

[10] C. Claeys, N. Rocha de Melo Filho, L. Van Belle, E. Deckers, W. Desmet, Design and validation of metamaterials for multiple structural stopbands in waveguides. *Extreme Mechanics Letters*, **12**, 7-22, 2017.

[11] F. Bloch, Über die Quantenmechanik der Electron in Kristallgittern. *Zeitschrift für Physik*, **52**, 550–600, 1928.

[12] G. Floquet, Sur les équations différentielles linéaires a coefficients périodiques. *Annales de l'Ecole Normale Supérieure*, **12**, 47–88, 1883.

[13] C. Collet, M. Ouisse, M. Ruzzene, M. Ichchou, Floquet–Bloch decomposition for the computation of dispersion of two-dimensional periodic, damped mechanical systems. *International Journal of Solids and Structures*, **48**, 2837–2848, 2011.

[14] A. Khelif, B. Aoubiza, S. Mohammadi, A. Adibi, V. Laude, Complete band gaps in two-dimensional phononic crystal slabs. *Physical Review E*, **74** (5), 2006.

[15] E. Manconi, B. Mace, Wave characterization of cylindrical and curved panels using a finite element method. *The Journal of Acoustical Society of America*, **125** (1), 154-163, 2009.

[16] A. Nateghi, L. Van Belle, C. Claeys, E. Deckers, B. Pluymers, W. Desmet, Wave propagation in locally resonant cylindrically curved metamaterial panels. *International Journal of Mechanical Sciences*, Article in press.

[17] A. Nateghi, L. Van Belle, C. Claeys, E. Deckers, B. Pluymers, W. Desmet, Stopband behavior in infinite metamaterial pipes. *proceedings of ISMA2016*, Leuven, Belgium, September 19-21, 2016.

[18] F. Fahy, *Sound and structural vibration*, London: Academic Press, 1987.

[19] N. Rocha de Melo Filho, C. Claeys, E. Deckers, B. Pluymers, W. Desmet, Dynamic Metamaterials for Structural Stopband Creation. *proceedings of International Styrian Noise, Vibration & Harshness Congress*, Graz, Austria, June 22-24, 2016.

[20] C. Claeys, *Design and analysis of resonant metamaterials for acoustic insulation*, Ph.D. dissertation, KU Leuven, Leuven, April 2014.

COMPDYN 2017
6th ECCOMAS Thematic Conference on
Computational Methods in Structural Dynamics and Earthquake Engineering
M. Papadrakakis, M. Fragiadakis (eds.)
Rhodes Island, Greece, 15–17 June, 2017

# EXPERIMENTAL AND NUMERICAL STUDY OF WAVE DYNAMICS IN TENSEGRITY COLUMNS

**Ada Amendola[1], Francesco Fabbrocino[2], Antonino Favata[3], Andrea Micheletti[4], Fernando Fraternali[1], Chiara Daraio[5]**

[1]Department of Civil Engineering, University of Salerno
84084 Fisciano (SA), Italy
e-mail: {adamendola, f.fraternali}@unisa.it

[2] Pegaso University, Department of Engineering
80132 Naples, Italy
email: francesco.fabbrocino@unipegaso.it

[3] Department of Structural and Geotechnical Engineering
Sapienza University of Rome 00197 Rome, Italy
e-mail: antonino.favata@uniroma1.it

[4] Department of Civil Engineering and Computer Science Engineering
University of Rome Tor Vergata, 00133 Rome, Italy
fibers email: micheletti@ing.uniroma2it

[5] Engineering and Applied Science, California Institute of Technology
Pasadena, CA 91125, USA
e-mail: daraio@caltech.edu

**Keywords:** Tensegrity column, impulsive dynamics, 3D printing, experimental testing, stick-and-spring structure.

**Abstract.** *This work deals with the experimental testing and the numerical simulation of the impulsive dynamics of a tensegrity lattice. The analyzed system is a column made of ten regular tensegrity prisms, each composed of two solid triangular plates (bases), three cross bars, and three cross cables. Bars and bases are additively manufactured in a titanium alloy, through electron-beam melting, while cross cables are made of Spectra fibers and are added to the titanium structure afterward 3D-printing process. The experimental response of the examined tensegrity column under impact loading is studied by recording the waves traveling through the system by means of a Digital Image Correlation algorithm, which measures the axial displacements of the bases of each unit.*

*We compare the experimental results with those obtained from numerical simulations performed by adopting two different nonlinear elastic models: one accounting for the presence of bending-stiff connections between the 3D-printed elements, and for the resulting mixed bending-stretching regime; the other one being a tensegrity model which describes a purely stretching response of the column. Such a comparison shows that the presence of bending-stiff connections may weaken the nonlinearity of the wave dynamics that is typical of tensegrity lattices with frictionless nodal connections. We also observe that a marked nonlinear behavior occurs in the case of pure-tensegrity response (no bending deformation) under small prestress.*

## 1 INTRODUCTION

In recent years, the dynamics of acoustic metamaterials has been intensively investigated with the aim of designing novel mechanical devices, such as, e.g., acoustic band gap materials, shock protector devices, acoustic lenses, and energy trapping containers, to name just a few examples (refer to [1, 2, 3, 4, 5, 6, 8] and references cited therein for a review). It has been shown that these engineered materials may find application for protecting materials and structures against impacts with external objects [2, 9], as well as for the design of sound-focusing devices and the manufacturing of noninvasive sensors and actuators for structural health monitoring [10, 11, 12, 13].

Special attention are receiving lattice structures obtained by assembling tensegrity units, such as *T3* tensegrity prisms [24], since it has been shown that such systems exhibit a mechanical response that can be continuously varied from hardening to softening, by changing the geometrical, mechanical, and prestress parameters [14, 18, 15, 7]. The geometrically nonlinear response of a tensegrity system is caused by the presence of one ore more *infinitesimal mechnisms*, i.e. sets of nodal displacements causing second-order member elongations, owing to the fact that the equilibrium operator is singular in the considered configuration [16, 17]. The recent studies [6, 7] have revealed that tensegrity columns composed of T3 prisms are suitable for use as acoustic lenses supporting extremely compact solitary waves.

In this work, we experimentally test the dynamic response of a tensegrity column subjected to impact loading, and correspondingly we perform numerical simulations of the examined tests using two different elastic models, respectively described in Refs. [20] and [23]. An additive manufacturing (AM) technique based on Electron Beam Melting (EBM) is employed to build all the elements of the tested structure, except for the cables, which are subsequently added to the 3d-printed structure through a post-tensioning technique [18]. The mechanical modeling of such a structure is first analyzed through the *stick-and-spring* model presented in [20], which takes into account that the nodes of the 3D-printed structure form bending-stiff connections between elements. It models the system by considering bars and bases to be inflexible, describing the cables as linear springs, and attaching angular springs to the nodes (*mixed bending-stretching response*). The second examined model [23] is instead a pure tensegrity model that introduces frictionless pin-connections between elements, describes the cables as linear springs and models the bars and the bases of the prisms as rigid bodies (*purely stretching response* of each cable of the system). Other than comparing for the first time the experimental impact response of a tensegrity column to the numerically predicted response of the above models, this work highlights differences and similarities between such models, providing useful directions for the design of tensegrity metamaterials with sound-focusing abilities.

The paper is organized as follows. Section 2 details the experimental setup and the examined physical model of a tensegrity column. Next, Sects. 3.1–3.3 describe the main features of the stick-and-spring model, while Sect. 3.4 illustrates a comparison between the predictions of such a model and the results of the impact test carried out as described in Sect. 2. A similar comparative analysis is presented in Sect. 4 with reference to the pure tensegrity model. Concluding remarks and directions for future research are drawn in Sect. 5.

## 2 EXPERIMENTAL SETUP

We experimentally investigated the dynamic response of a 3D-printed physical model of a tensegrity column [22, 7, 18, 23] under impact loading. Such structure consists of ten regular tensegrity prisms with triangular bases (*T3 prisms*) [24, 25] superposed to each other. Figure

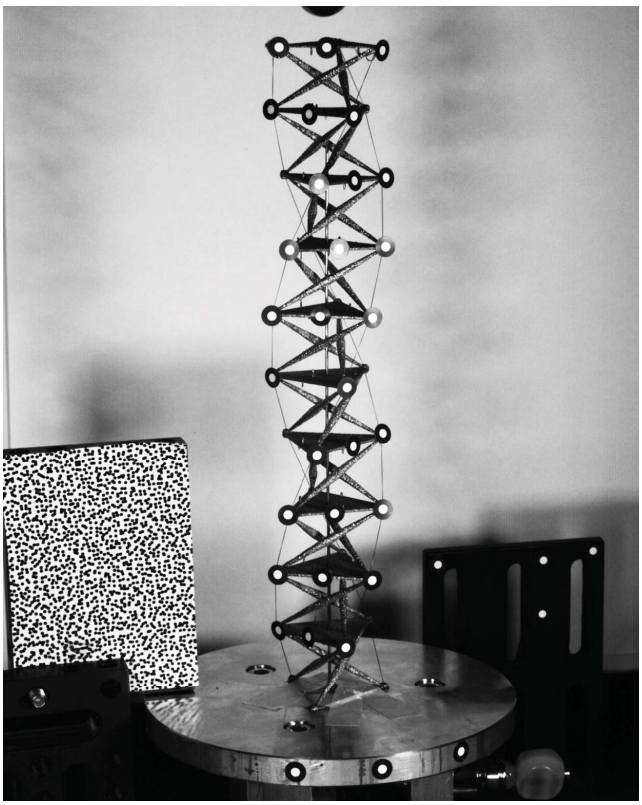

Figure 1: The tensegrity column under test.

1 shows the tested column partly manufactured in Ti6Al4V titanium alloy using the Electron Beam Melting (EBM) technique [18]. The Arcam S12 EBM facility at the Department of Materials Science and Engineering, University of Sheffield was employed to manufacture the examined structure, by depositing layers of Ti6Al4V powder with minimum feature size down to 0.4 mm [19].

Each T3 prism in the column is *left-handed*, i.e. the upper base is rotated counter-clockwise with respect to the bottom base by an angle of $5\pi/6$ about the prism's axis[1] (cf. [23]). Moreover, each T3 prism is made by three bi-conical bars connected to the vertices of two triangular plates of thickness $t$ by means of spherical nodes of $3$ mm in diameter. These elements are 3D-printed together with the aid of additional sacrificial linear elements which are mechanically removed afterward. Three strings elements (or *cables*) are then added to each prism on using the post-tension technique illustrated in [18]. The geometric properties of a prism are given in Tab. 1. The symbols $s_N$, $b_N$, and $h_N$ denote respectively the length of the edges of the base plates, the length of the bars, and the height of the prism (measured as the distance between the base centers) [18]. The maximum and minimum diameters of the bars are denoted by $D$ and $d$, respectively.

An in-house experimental setup is designed and assembled to apply an impact load to the top base of the column, while keeping the bottom base fixed to an aluminum plate. The strings of the structure are pre-stretched by passing them through bridge pins applied to the aluminum plate (Fig. 1). In order to maintain the column straight, a vertical thin rod was placed along the column's axis, passing through holes realized on all bases except the last two, and fixed to the aluminum plate.

[1] When a T3 prism is *right-handed* the base is rotated clockwise by the same angle.

| $t$ | $s_N$ | $b_N$ | $h_N$ | $D$ | $d$ |
|---|---|---|---|---|---|
| (mm) | (mm) | (mm) | (mm) | (mm) | (mm) |
| 1.0 | 34.08 | 44.06 | 22.29 | 3.0 | 0.5 |

Table 1: Geometrical properties of a T3 prism.

The top base is impacted by a spherical striker with mass $5$ g made of Polytetrafluoroethylene (PTFE), which falls with null initial velocity for $0.5$ m in a duct delimited by four Teflon tubes. The motion of the column produced by the impact with the striker is recorder through two high-speed cameras FASTCAM Mini UX100, and the axial (vertical) displacements of the upper base of each unit are measured using a Digital Image Correlation technique.

## 3 STICK-AND-SPRING MODEL

### 3.1 Model description

The AM technique described in section 2 does not allow for the realization of spherical hinges between bars and base plates of the EBM-manufactured tensegrity column; on the contrary, the nodes of the 3d-printed structure provide bending-stiff connections between such elements. Such an observation leads us to employ a stick-and-spring (S&S) model [20] to describe the dynamic response of the phycal model under examination. A S&S structure is a collection of *nodes*, *edges*, and *wedges*: edges are imagined as node-to-node inflexible but extensible straight *sticks*, acting as *axial springs* when extended; wedges are imagined as complexes of two sticks sharing one end node, equipped by a *angular spring* reacting to relative rotations of the two wedge sticks in their common plane. A S&S structure differs from a tensegrity structure because, owing to the presence of angular springs, edges are subjected to shear forces and bending/torsion moments, in addition to axial forces. In the remainder of this section, we summarize the treatment of S&S structures presented in [20].

The combinatorial description of a S&S structure is given by the triplet $\mathcal{S} = (\mathcal{N}, \mathcal{E}, \mathcal{W})$ consisting of: (i) a collection $\mathcal{N}$ of $N$ points, called *nodes*, of the three-dimensional Euclidean space; (ii) a collection $\mathcal{E}$ of $E$ *edges*, that is, two-elements subsets of $\mathcal{N}$; (iii) a collection $\mathcal{W}$ of $W$ *wedges*, that is, three-elements subsets of $\mathcal{N}$. We say that $ij \in \mathcal{E}$ is the edge connecting nodes $i, j \in \mathcal{N}$, and that $ijk \in \mathcal{W}$, with $i, j, k \in \mathcal{N}$, is the wedge with *head node* $i$ and *tail nodes* $j$ and $k$.

We denote by $\boldsymbol{p}_i$ the *referential position vector* of the typical node $i$ with respect to a chosen origin point, by $\boldsymbol{u}_i$ its displacement, and by $\boldsymbol{q}_i := \boldsymbol{p}_i + \boldsymbol{u}_i$ its *current position vector*. Moreover, we introduce the referential unit vector directed from node $i$ to node $j$,

$$\boldsymbol{e}_{ij} := \frac{1}{l_{ij}}(\boldsymbol{p}_j - \boldsymbol{p}_i) = -\boldsymbol{e}_{ji}, \tag{1}$$

and the unit vector currently directed from node $i$ to node $j$,

$$\boldsymbol{c}_{ij} := \frac{1}{\ell_{ij}}(\boldsymbol{q}_j - \boldsymbol{q}_i) = -\boldsymbol{c}_{ji}, \quad \ell_{ij} := |\boldsymbol{q}_j - \boldsymbol{q}_i|, \tag{2}$$

where $l_{ij} := |\boldsymbol{p}_i - \boldsymbol{p}_j|$ is the referential length of edge $ij$, and $\ell_{ij}$ its current length.

The strain measures we adopt are:

1. the *change in length* of edge $ij$:

$$\delta l_{ij} := \ell_{ij} - l_{ij}, \tag{3}$$

2. the *change in angle* of wedge $ijk$:

$$\delta\theta_{ijk} := \arccos\left(\boldsymbol{c}_{ij}\cdot\boldsymbol{c}_{ik}\right) - \arccos\left(\boldsymbol{e}_{ij}\cdot\boldsymbol{e}_{ik}\right) \tag{4}$$

It is not difficult to see that the linearized strain measure corresponding to (3) and (4) are, respectively:

$$\delta l_{ij} \simeq \varepsilon_{ij} := \boldsymbol{e}_{ji}\cdot(\boldsymbol{u}_i - \boldsymbol{u}_j)\,, \quad \delta\vartheta_{ijk} \simeq \psi_{ijk} := -\frac{1}{l_{ik}}\,\boldsymbol{w}_{ikj}\cdot(\boldsymbol{u}_k - \boldsymbol{u}_i) - \frac{1}{l_{ij}}\,\boldsymbol{w}_{ijk}\cdot(\boldsymbol{u}_j - \boldsymbol{u}_i)\,, \tag{5}$$

with

$$\boldsymbol{w}_{ijk} = \frac{\boldsymbol{P}_{ij}\,\boldsymbol{e}_{ik}}{|\boldsymbol{P}_{ij}\,\boldsymbol{e}_{ik}|} \quad \text{and} \quad \boldsymbol{w}_{ikj} = \frac{\boldsymbol{P}_{ik}\,\boldsymbol{e}_{ij}}{|\boldsymbol{P}_{ik}\,\boldsymbol{e}_{ij}|}, \tag{6}$$

where $\boldsymbol{P}_{ij} := \boldsymbol{I} - \boldsymbol{e}_{ij}\otimes\boldsymbol{e}_{ij}$ and $\boldsymbol{P}_{ik} := \boldsymbol{I} - \boldsymbol{e}_{ik}\otimes\boldsymbol{e}_{ik}$ are the orthogonal projectors on the planes of normal $\boldsymbol{e}_{ij}$ and $\boldsymbol{e}_{ik}$, respectively.

### 3.2 Compatibility, equilibrium, and constitutive, operators

Let $\boldsymbol{u}$ and $\boldsymbol{\eta}$ denote, respectively, the string of nodal-displacement vectors and the string of strain components:

$$[\boldsymbol{u}] = \left[\ldots, \boldsymbol{u}_i^T, \ldots\right]^T \qquad \text{and} \qquad [\boldsymbol{\eta}] = \left[\ldots, \varepsilon_{ij}, \ldots \,|\, \ldots, \psi_{ijk}, \ldots\right]^T. \tag{7}$$

Then, relations (5) can be written in the following compact form:

$$\boldsymbol{\eta} = \boldsymbol{B}\boldsymbol{u}, \tag{8}$$

where the linear mapping $\boldsymbol{B}$ is called the *kinematic compatibility operator*. We denote by $\sigma_{ij}$ and $\tau_{ijk}$ the stress measures conjugated with $\varepsilon_{ij}$ and $\psi_{ijk}$, respectively. Likewise, let $\boldsymbol{f}$ and $\boldsymbol{\chi}$ denote, respectively, the string of nodal-force vectors and the string of stress components:

$$[\boldsymbol{f}] = \left[\ldots, \boldsymbol{f}_i^T, \ldots\right]^T, \qquad [\boldsymbol{\chi}] = \left[\ldots, \sigma_{ij}, \ldots \,|\, \ldots, \tau_{ijk}, \ldots\right]^T. \tag{9}$$

With this notation, the *balance equations* can be written as

$$\boldsymbol{f} = \boldsymbol{A}\boldsymbol{\chi}, \tag{10}$$

where $\boldsymbol{A} = \boldsymbol{B}^T$ is the formal adjoint of the compatibility operator, termed the *equilibrium operator*. More explicitly, adopting the strain measures (5), it is not difficult to see that (10) is equivalent to:

$$\boldsymbol{f}_i = \sum_{\{j\in\mathcal{N}\,|\,ij\in\mathcal{E}\}} \sigma_{ij}\,\boldsymbol{e}_{ji} + \sum_{\{j,k\in\mathcal{N}\,|\,ijk\in\mathcal{W}\}} \tau_{ijk}\left(\frac{\boldsymbol{w}_{ijk}}{l_{ij}} + \frac{\boldsymbol{w}_{ikj}}{l_{ik}}\right) - \sum_{\{k,j\in\mathcal{N}\,|\,kij\in\mathcal{W}\}} \tau_{kij}\frac{\boldsymbol{w}_{kij}}{l_{ki}}\,. \tag{11}$$

Next, let the (positive) *stiffness constants* $\kappa_{ij}$ and $\lambda_{ijk}$ characterize the linear elastic response of edge and wedge springs:

$$\sigma_{ij} = \kappa_{ij}\,\varepsilon_{ij} \;\text{ and }\; \tau_{ijk} = \lambda_{ijk}\,\psi_{ijk}; \tag{12}$$

we write this set of relations in compact form as:

$$\boldsymbol{\chi} = \boldsymbol{C}\boldsymbol{\eta}, \tag{13}$$

with $\boldsymbol{C}$ is the *constitutive operator*, a diagonal operator whose matrix representation is:

$$[\boldsymbol{C}] = \left[\mathrm{diag}(\cdots, \kappa_{ij}, \cdots \,|\, \cdots, \lambda_{ijk}, \cdots)\right]. \tag{14}$$

### 3.3 Motion equations

We postulate the following expression for the elastic energy stored in a S&S structure:

$$\mathcal{U} = \frac{1}{2}\Big( \sum_{ij\in\mathcal{E}} \kappa_{ij}(\ell_{ij} - \overline{\ell}_{ij})^2 + \sum_{ijk\in\mathcal{W}} \lambda_{ijk}(\theta_{ijk} - \overline{\theta}_{ijk})^2 \Big)\,, \tag{15}$$

where $\ell_{ij}$ and $\overline{\ell}_{ij}$ are the current and rest lengths of the axial spring on edge $ij$, while $\theta_{ijk}$ and $\overline{\theta}_{ijk}$ are the current and rest angles of the angular spring on wedge $ijk$. On introducing the kinetic energy

$$\mathcal{K}(\boldsymbol{q}, \dot{\boldsymbol{q}}) = \frac{1}{2}\, \dot{\boldsymbol{q}} \cdot \boldsymbol{M}(\boldsymbol{q})\dot{\boldsymbol{q}}, \tag{16}$$

with $\boldsymbol{M}$ is a diagonal *mass operator* corresponding to lumped nodal masses, the nonlinear motion equations are given by

$$\boldsymbol{M}\,\ddot{\boldsymbol{q}} + \widetilde{\boldsymbol{A}}(\boldsymbol{q})\boldsymbol{\chi}(\boldsymbol{q}) = \boldsymbol{0}, \tag{17}$$

where $\widetilde{\boldsymbol{A}}(\boldsymbol{q})$ is the *equilibrium operator* in the current placement. This equation can be linearized about an equilibrium placement $\boldsymbol{q}_0$, obtaining:

$$\boldsymbol{M}(\boldsymbol{q}_0)\ddot{\boldsymbol{u}} + \boldsymbol{K}_T(\boldsymbol{q}_0)\boldsymbol{u} = \boldsymbol{0}, \tag{18}$$

where $\boldsymbol{K}_T := \partial^2_{\boldsymbol{q}}\mathcal{U}$ is the *tangent stiffness operator*[2].

The simulation of the column response under impact loading is obtained through numerical integration of (17) and (18) subject to assigned initial conditions.

### 3.4 Simulation of impact tests

The impact tests described in Sect. 2 were simulated through the S&S model by making use of the following assumptions.

- Cables are modeled as edges, with stiffness $\kappa_c = E_c\pi d_c^2/(4l_c)$, where $E_c$ is the Young modulus, $d_c$ the diameter, and $l_c = \left(l_b^2 - 2\sqrt{3}a^2\right)^{1/2}$ is the current length of the cables, with $l_b$ the length of the bar and $a$ the base radius;
- Cable prestress is considered to be negligible[3];
- Bars are modeled as edges with stiffness $\kappa_b = E_b\pi d_b^2/(4l_b)$, where $E_b$ is the Young modulus and $d_b$ the diameter;
- Each triangular base is modeled as three pin-jointed bars of stiffness $\kappa_b$ forming the triangle;
- Wedges are considered between base triangles and bars (see Fig. 2, right), their stiffness is $\lambda = \alpha\kappa_b l_c^2$, with $\alpha$ a dimensionless parameter to be fitted with the experimental results;
- Nodal masses $m$ are assigned by subdividing the total measured mass of the structure, $53.0$ g into 3 (vertices) $\times$ 10 (bases) = 30 equal parts.

[2] See [20] for a detailed expression of $\boldsymbol{K}_T$.

[3] We checked that, owing to the small axial stiffness of the cable, a modest prestress does not change results significantly.

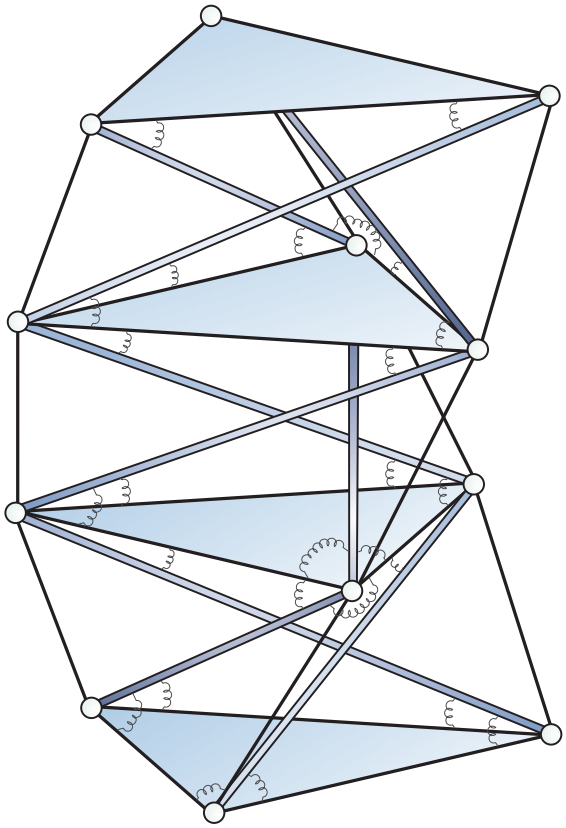

Figure 2: Sketch of a portion of the model showing also the angular springs associated to the wedges of the S&S structure.

- As initial value of the downward velocity we assumed $v_0 = 2\,\text{m/s}$, by averaging measurements during a short time interval after impact. We also assumed that the impact cause the top base to have an initial angular velocity about the prism's axis given by $\omega_0 = 2h_N v_0/a^2 \simeq 0.2304\,\text{rad/s}$, with $a = \sqrt{3}\,s_N/3$, so that the top base initially moves along the infinitesimal mechanism of the top prism [24].

Table 2 summarizes the adopted values of the S&S modeling parameters.

| | |
|---|---|
| $E_c$ | 5480 MPa |
| $d_c$ | 0.1 mm |
| $l_b$ | 44.06 mm |
| $E_b$ | $110 \cdot 10^3$ MPa |
| $d_b$ | 1.75 mm |
| $h_N$ | 22.29 mm |

Table 2: Model parameters.

The stiffness of wedge springs, controlled by the dimensionless parameter $\alpha$, is assigned by matching the time $\bar{t}$ at which the top base returns to the initial position (subsequently continuing its upward motion). In the experiment, $\bar{t} = 18.9892$ ms; in the simulation, the same value is found when $\alpha = 6.0655 \cdot 10^{-4}$. We observe that by proceeding in this way, a good agreement is found also between oscillation amplitudes in the two cases.

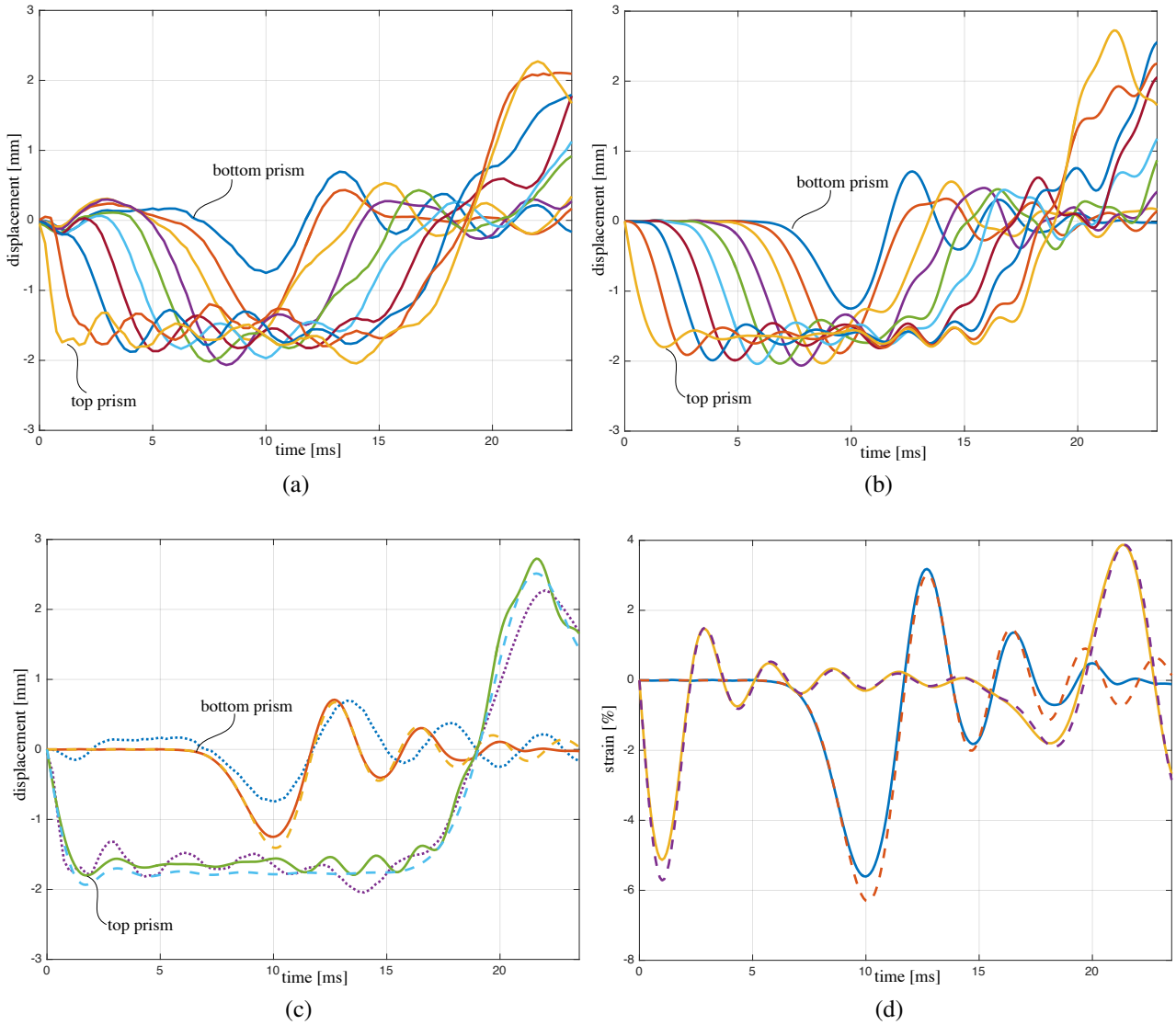


Figure 3: (a) Base displacements obtained from experiments. (b) Base displacements obtained from simulations. (c) Displacements of the top and bottom base, comparison between experiments (dotted line) and numerical simulations with nonlinear theory (solid line) and linearized theory (dashed line). (d) Axial strains in the top and bottom prism obtained with nonlinear theory (solid line) and linearized theory (dashed line).

Fig. 3 (a) shows the displacement of all bases as measured and recorded in the experiment. Fig. 3 (b) shows the displacements obtained by numerical integration of the nonlinear equation of motion (17). Fig. 3 (c) shows a comparison on the displacements of the first and the last prism, between experimental results (dotted line), results obtained by numerical integration of both the nonlinear equation of motion(17) (solid line), and those obtained from the linearized equation of motion(18) (dashed line). Fig. 3 d) shows numerical results for the axial strain of the first and last prism, which is defined as the relative displacement between the two bases of a prism, divided by $h_N$. Experimental results displays larger oscillations, in particular for the bottom prism. In this regard, we observed that in the experiment triangular bases do not remain perfectly horizontal during the motion, and this is likely to be the reason of the larger oscillations in the measured displacement. The first maximum value of the displacement $u_{\max}$ and the correspondent time $t_{\max}$ is reported in Table (3).

| prism | $u_{\max}$ [mm] (exper.) | $u_{\max}$ [mm] (nonlin. th.) | $u_{\max}$ [mm] (lineariz. th.) | $t_{\max}$ [ms] (exper.) | $t_{\max}$ [ms] (nonlin. th.) | $t_{\max}$ [ms] (lineariz. th.) |
|---|---|---|---|---|---|---|
| bottom | $-0.7506$ | $-1.2495$ | $-1.4079$ | 10 | 10 | 10.1 |
| top | $-1.7812$ | $-1.8004$ | $-1.9344$ | 1.75 | 1.7 | 1.7 |

Table 3: First maximum value of the displacement $u_{\max}$ and correspondent time $t_{\max}$.

## 4 PURE TENSEGRITY MODEL

Both simulations and experimental results presented in the previous section show that the mixed bending-stretching regime produces an essentially linear behavior of the tensegrity column under examination. In this section, we propose some possible directions toward the design of a device with nonlinear behavior in a pure stretching regime. In order to do this, we adopt the simpler, pure tensegrity model presented in [23], where the Lagrange's equation of motion of a tensegrity column are solved numerically. The assumptions of this model are the following ones: only cyclic-symmetric motions with respect to the column's axis are considered; nodes are frictionless hinges between connected elements; all bars are rigid and massless; cables are linearly elastic and massless. In our case, each triangular base is a rigid body with a mass $3\,m$ and moment of inertia $3\,m\,a^2$.
We investigated the following three cases.

**CASE 1** — We considered cable stiffness to be the same as in the present S&S model. Then we determined the cable prestrain by matching the time $\bar{t}$ with that of the experiment. By doing so, the resulting prestrain takes the unrealistic value of 85%. The results are shown in Fig. 4 (dashed line) , where it is possible to see a linear behavior similar to that of the mixed bending-stretching response.

**CASE 2** — We assign the more realistic value of 5% to the prestrain and determine the cable stiffness by matching the time $\bar{t}$ with that of the experiment. The resulting cable stiffness is 15.5 times higher than that of the original structure. Results are shown in Fig. 4 (dash-dot line), where we still observe a response similar to that of the mixed bending-stretching regime.

**CASE 3** — We assign a low prestrain to cables, equal to 1% and, again by matching the time $\bar{t}$ with that of the experiment, we determine the stiffness of cables to be 55.5 times higher than that of the original structure. The results are shown in Fig. 4 (solid line), which displays a much more marked nonlinear response[4].

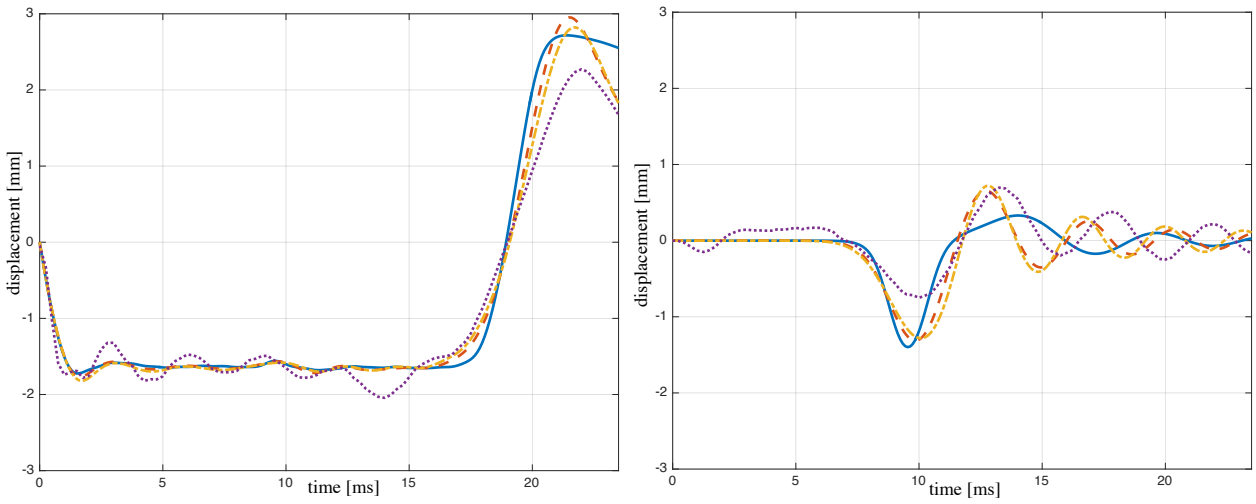


(a) (b)

Figure 4: Displacements of top prism (a) and bottom prism (b): experiments (dotted line), case 1 (dash-dot line), case 2 (dashed line) and case 3 (solid line).

It is worth noting that the above cases refer to models of tensegrity columns different from that experimentally tested in the present work (experimental model), and they are here presented with the aim of exploring the nonlinear potential of the wave dynamics of pure tensegrity lattices. The results in Fig. 4 show that all the analyzed tensegrity models reproduce fairly well the displacement vs. time response of the experimental model. For a better visualization of nonlinear effects, we represented in Fig. 5 the strain of each prism of the column at a fixed time ($t = 6.5$ ms). By comparing Cases 1-3 and the Stick-and-Spring model analyzed in Sect. 3 (nonlinear theory), we observe that for Case 3 (when the cross-cable prestrain is 1%) the deformation of the column is more localized at the wave front.

## 5 CONCLUDING REMARKS

We have performed an impulsive dynamic test on a physical model of a tensegrity column, on comparing the measured displacements to those computed numerically through two different models: a stick-and spring model accounting for bending deformation of the nodes [20], and a pure tensegrity model accounting for a pure-stretching response of all the members of the system [23]. The first model is intended to capture the experimental response of the analyzed physical model, while the second one is aimed at providing directions for the design of alternative systems featuring highly nonlinear dynamic response. The given results show a fairly good agreement between measurements and simulations performed with the first model. The second model is also able to reproduce the response observed during the experiment by suitably adjusting the stiffness and prestress of cables. We have observed that bending-stiff nodal

[4]This is highlighted for example by the different amplitudes in tension and compression of each prism, owing to a stiffer response in tension, and by a reduced amplitude of the oscillation.

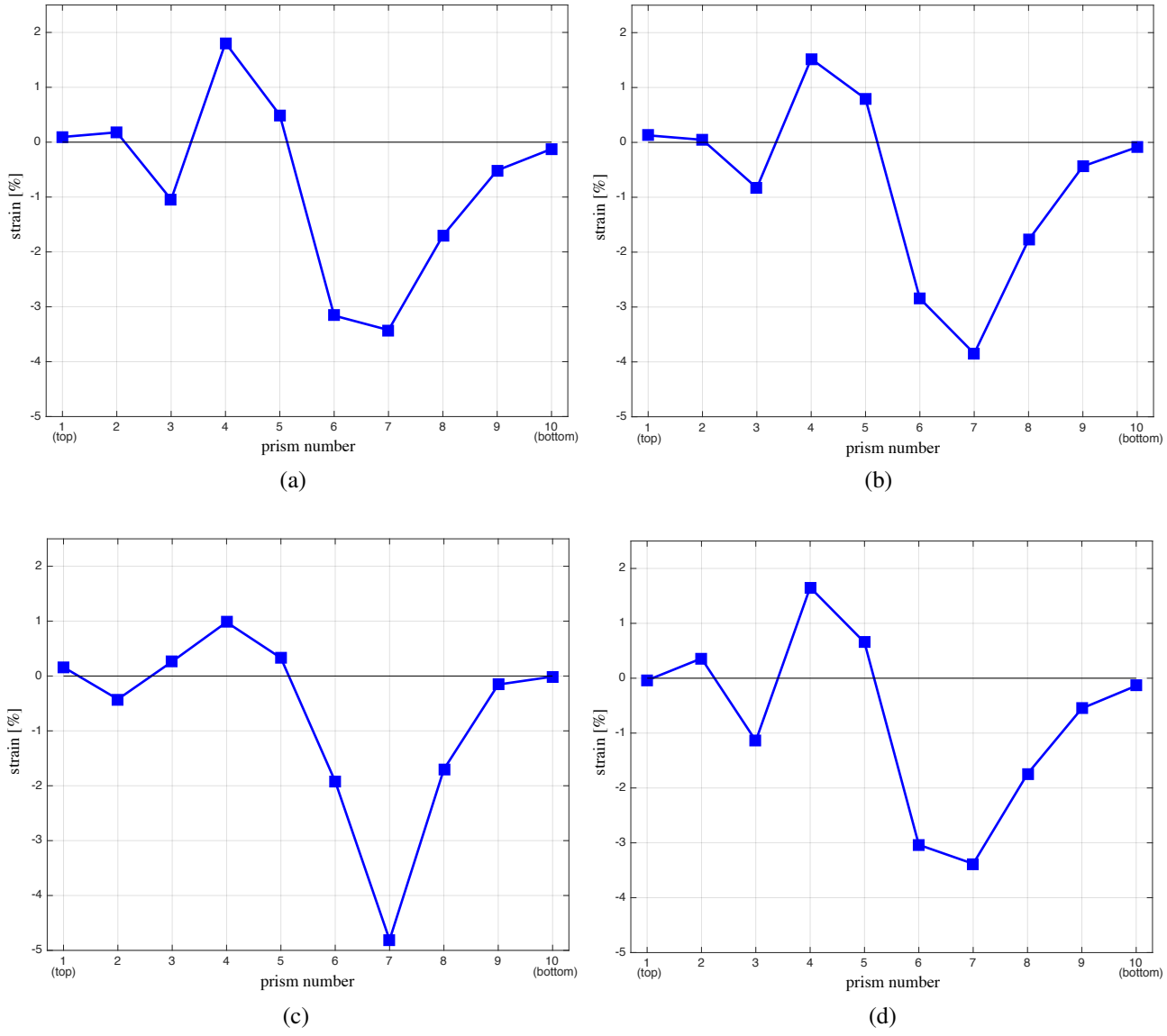


Figure 5: Snapshot at $t = 6.5$ ms of prism strains along the column. Pure tensegrity model: Case 1 (a); Case 2 (b), and Case 3 (c). Nonlinear Stick-and-Spring model (d).

connections, a feature of the 3D-printed structure due to the not-negligible size of the junctions, may greatly reduce nonlinearities in the response of tensegrity lattices. We found that a similar effect can also be obtained in the second model by fictitiously raising the prestress level. This behavior can be explained by considering that the tangent stiffness of the tensegrity lattice is the sum of a material contribution (owing mainly to the stiffness of angular springs) and a geometric contribution (owing to prestress) [20]. In relation to this, we observed also that a more marked nonlinear behavior occurs for smaller prestress levels and smaller values of the stiffness of angular springs.

We are led to conclude that a pure tensegrity behavior with negligible bending deformation of the nodes and low prestress may lead to design novel metamaterials that enable unconventional wavefocusing methodologies based on solitary wave dynamics. This obviously calls for the adoption of manufacturing techniques that are able to build perfect hinges at the nodes, such as, e.g., the multiscale AM tecniques described in [26, 27]. Arrays of tensegrity columns with stretching-dominated response may be employed to fabricate tunable focus acoustic lenses supporting extremely compact solitary waves. On applying different levels of prestress to such metamaterials, one can be able to generate compact solitary waves with different phases within the system, which are expected to interact at a focal point in an adjacent medium (i.e., a material defect to be targeted) [10, 11]. We address specific studies on such engineering applications of tensegrity lattices to future work, with the aim of designing and manufacturing novel acoustic lenses, and innovative sensors/actuators for monitoring structural health and damage detection in materials and structures [10, 11, 12].

**Acknowledgements**

The authors are grateful to Evert Hernández-Nava, Christopher Smith, Russell Goodall and Ian Smith (Department of Materials Science and Engineering, University of Sheffield, UK) for their precious assistance with the manufacturing of the Ti-6Al-4V experimental model.

## REFERENCES

[1] Daraio C., Ngo D., Nesterenko V.F., Fraternali F. (2010) Highly Nonlinear Pulse Splitting and Recombination in a Two Dimensional Granular Network. Phys Rev. E 82:036603.

[2] Fraternali F., Porter M., Daraio C. (2010) Optimal design of composite granular protectors. Mech. Adv. Mat. Struct. 17:1-19.

[3] Leonard A., Fraternali F., Daraio C. (2013) Directional wave propagation in a highly nonlinear square packing of spheres. Exp. Mech. 53(3):327–337.

[4] Nesterenko V.F. (2001) Dynamics of Heterogeneous Materials. Springer-Verlag, New York.

[5] Ngo D., Fraternali F., Daraio C. (2012) Highly Nonlinear Solitary Wave Propagation in Y-Shaped Granular Crystals with Variable Branch Angles. Phys. Rev. E 85(036602):1–10.

[6] Fraternali F., Senatore L., Daraio C. (2012). Solitary waves on tensegrity lattices. J.Mech. Phys. Solids 60:1137–1144.

[7] Fraternali F., Carpentieri G., Amendola A., Skelton R.E., Nesterenko V.F. (2014). Multiscale tunability of solitary wave dynamics in tensegrity metamaterials. Appl. Phys. Lett. 105:201903.

[8] Theocharis G., Boechler N., Daraio C. (2013) Nonlinear phononic structures and metamaterials, in P.A. Deymier (ed.) Acoustic Matematerials and Phononic Crystals, Springer Series in Solid State Sciences, 173.

[9] Mitchell S.J., Pandolfi A., Ortiz M. (2014). Metaconcrete: designed aggregates to enhance dynamic performance. J. Mech. Phys. Solids 65:69–81.

[10] Spadoni A., Daraio C. (2010). Generation and control of sound bullets with a nonlinear acoustic lens. Proc. Natl. Acad. Sci. U.S.A. 107(16):7230–7234.

[11] Donahue C., Anzel P., Bonanomi L., Keller T., Daraio C. (2014). Experimental realization of a nonlinear acoustic lens with a tunable focus. Appl. Phys. Lett. 104:014103.

[12] Ni X. (2011). Nondestructive Evaluation And Structural Health Monitoring Based On Highly Nonlinear Solitary Waves, Phd Dissertation, University of Pittsburgh, USA.

[13] Rizzo P., Ni X., Nassiri S., Vandenbossche J. (2014). A solitary wave-based sensor to monitor the setting of fresh concrete. Sensors 14(7):12568–12584.

[14] Amendola A., Carpentieri G., De Oliveira M., Skelton R.E., Fraternali F. (2014) Experimental investigation of the softening-stiffening response of tensegrity prisms under compressive loading. Compos. Struct. 117:234–243.

[15] Fraternali F., Carpentieri G., Amendola A. (2014). On the mechanical modeling of the extreme softening/stiffening response of axially loaded tensegrity prisms. J. Mech. Phys. Solids, 74:136–157.

[16] Calladine C. R. (1978). Buckminster Fuller's 'tensegrity' structures and Clerk Maxwell's rules for the construction of stiff frames. Int. J. Solids Struct., 14, 161–172

[17] Calladine C. R., Pellegrino S. (1991). First-order infinitesimal mechanisms. Int. J. Solids Struct., 27, 505-515

[18] Amendola A., Hernández-Nava E., Goodall R., Todd I., Skelton R.E., Fraternali, F. (2015). On the additive manufacturing, post-tensioning and testing of bi-material tensegrity structures. Compos. Struct., 131, 66–71.

[19] Tammas-Williams S., Zhao H., Leonard F., Derguti F., Todd I., Prangnell P.B (2015). XCT analysis of the influence of melt strategies on defect population in Ti6Al4V components manufactured by selective electron beam melting. Mater. Charact., 102, 47–61.

[20] Favata A., Micheletti A., Podio-Guidugli P. (2014). A Nonlinear Theory of Prestressed Elastic Stick-and-Spring Structures, International Journal of Engineering Science, 80, 4-20.

[21] Fraternali F., Carpentieri G., Amendola A., 2015. On the mechanical modeling of the extreme softening/stiffening response of axially loaded tensegrity prisms. J.Mech. Phys. Solids, 74, 136–157.

[22] Fraternali F., Senatore L., Daraio C. (2012). Solitary waves on tensegrity lattices. J.Mech. Phys. Solids, 60, 1137-1144.

[23] Davini C., Micheletti A., Podio-Guidugli P. (2016). On the impulsive dynamics of T3 tensegrity chains. Meccanica, 51 (11), 2763-2776.

[24] Oppenheim I, Williams W (2000). Geometric effects in an elastic tensegrity structure. J. Elast. 59:51–65.

[25] Skelton R.E., de Oliveira M.C. (2010). *Tensegrity system*s. Springer, Berlin.

[26] Zheng X. , Lee H. , Weisgraber T.H., Shusteff M., DeOtte J., Duoss E.B., Kuntz J.D., Biener M.M., Ge Q., Q. Jackson J.A., Kucheyev S.O., Fang N.X., Spadaccini C.M. (2014). Ultralight, ultrastiff mechanical metamaterials, Science, 344 (6190) 1373-1377.

[27] Meza L.R., Das S., Greer J.R. (2014). Strong, lightweight, and recoverable three-dimensional ceramic nanolattices, Science, 345 (6202) 1322-1326.

COMPDYN 2017
6th ECCOMAS Thematic Conference on
Computational Methods in Structural Dynamics and Earthquake Engineering
M. Papadrakakis, M. Fragiadakis (eds.)
Rhodes Island, Greece, 15–17 June 2017

# PREDICTION MODELS OF FREE-FIELD VIBRATIONS FROM RAILWAY TRAFFIC

**Jens Malmborg[1], Kent Persson[1], Peter Persson[1] and Lars Vabbersgaard Andersen[2]**

[1] Lund University
Department of Construction Sciences
P.O. box 118 Lund, Sweden
{jens.malmborg, kent.perssson, peter.persson}@construction.lth.se

[2] Aalborg University
Department of Civil Engineering
Thomas Mann vej 23, 9220, Aalborg, Denmark
la@civil.aau.dk

**Keywords:** Railway, vibration prediction, finite element model, ground vibration

**Abstract.** *Many cities experience an increasing population leading to a need for urban densification. In these cities, unused land close to railways will have to be developed with new residential and office buildings. The infrastructural demand will also increase, resulting in heavily trafficked roads and railways close to where people work and live. Annoyance from traffic-induced vibrations and noise is expected to be a growing issue. To predict the level of vibration and noise in buildings caused by railway and road traffic, calculation models are needed.*

*In the present paper, a simplified prediction model is briefly described. This prediction model is based on the assumption that the ground and railway embankment can be described in an axisymmetric model, to provide the transfer functions between the track and the free-field. In the paper, the error that arise by assuming axisymmetric response is studied by comparing the response in a three-dimensional finite-element model. Transfer functions at several positions in the free-field are compared.*

# 1 INTRODUCTION

Many cities experience an increasing population leading to a need for urban densification. In these cities, unused land close to railways will have to be developed with new residential and office buildings. The infrastructural demand will also increase, resulting in heavily trafficked roads and railways close to where people work and live. Annoyance from traffic-induced vibrations and noise is expected to be a growing issue.

To predict the level of vibration and noise in buildings caused by, for example, railway and road traffic, calculation models are needed. To describe the problem, the models must include the source, medium, and receiver [1]. The source load is caused by the traffic, and in the medium the vibrations transmit to the receiver, which is where the vibrations are being observed.

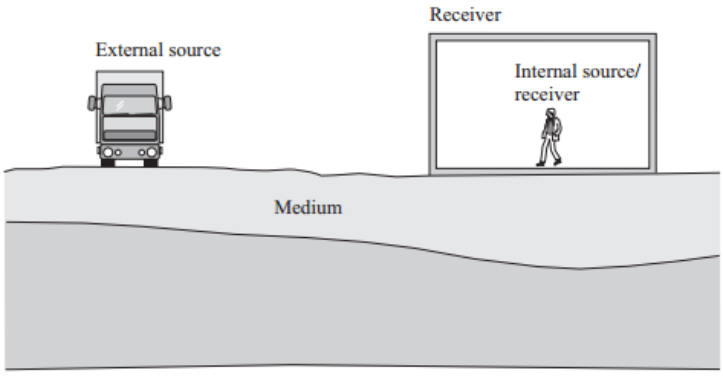


Figure 1: Sketch of the vibration-transmission process from source to receiver via the medium, from [1].

It is very difficult to accurately describe all mechanisms involved in the vibration generation from a passing train. With certain assumptions and simplifications, however, the prediction analysis can be divided into smaller independent steps. In one such simplified prediction model, briefly described in Section 1.1, the transfer functions between the railway track and the observation point in the free-field are estimated using an axisymmetric ground model. These transfer functions are then used together with estimations of the dynamic reaction forces of the railway track, calculated in a separate model, to provide the vibration response in the free-field.

In the present paper, the suitability of using an axisymmetric ground model to predict the vibrations in the free-field caused by a train running on an elevated embankment, is studied. This is investigated by using a 3D finite element (FE) model to calculate and compare the transfer functions obtained at several positions in the free-field at equal distances from the railway track, but at various angles from the embankment. The analyses are carried out for a few different soil layer depths.

## 1.1 Background: A simplified prediction model

The excitation caused by a moving train is often divided into a quasi-static part and a dynamic part, where the quasi-static part is simply the static deflection due to the weight of the train. The dynamic part is much more complex and involves several different phenomena that can be either periodic or random in nature, such as wheel flats, wheel/rail roughness, and varying sleeper/subgrade stiffness [2]. Track unevenness (roughness) is one of the main contributing factors to the vibrations generated by railway traffic, especially at lower speeds. When the train passes over the track irregularities, the contact force under each wheel varies with time, leading to a dynamic excitation of the ground. The properties of the ground, such as mechanical properties and stratification, are important factors for how the vibrations generated at the track are transferred to the observation point.

If the soil is assumed to behave linearly elastic, and it is assumed that the wave propagation in the embankment does not influence the dynamic contact forces between the rail and the train wheels, a particularly simplistic approach can be established for estimating the vibrations generated in the free field due to a passing train.

A two-dimensional (2D) model consisting of a simplified track and vehicle representation is used for estimating the dynamic forces acting on each sleeper due to a train passing at a specific speed. These forces are subsequently used together with transfer functions, between each sleeper and the receiver (observation point) in the free field. By summing the response, from each individual sleeper, the total response at the observation point can be obtained.

A vehicle model, adopted here, that is frequently reported in the literature is that of a simple 10 degrees-of-freedom system consisting of springs, viscous dampers, lumped masses and rigid connections, shown schematically in Figure 1. The element coefficients can be adjusted to fit many different train types, as shown in [3]. Also adopted here, is a 2D model of a ballasted railway track with discrete sleepers. The model consists of a single rail, rail pads, sleepers, ballast and subsoil, modelled using beam elements, springs, viscous dampers and lumped masses, as shown in Figure 1.

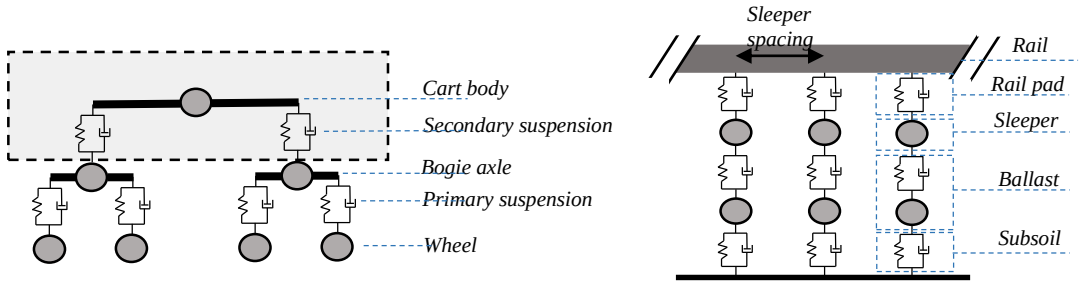


Figure 1: 2D models of train cart and railway track.

Track irregularities are often specified in terms of a power-spectral-density (PSD) spectrum, characterizing the unevenness in a statistical sense by decomposing the irregularities into power (variance) at different wavenumbers. In order to use such a spectrum in the spatial domain, a spatial realization is obtained by dividing the spectrum into an appropriate number of discrete wavenumbers, assigning a random phase to each wavenumber, and performing an inverse Fourier transform. Such a realization is incorporated into the track model above by changing the vertical coordinates of the beam nodes accordingly. A comprehensive list of different PSDs available for track irregularities is presented in [3].

The vehicle and track models are combined by letting the vehicle run over the track at a specific speed and enforcing some contact condition between the wheel mass elements and the rail beam elements. Due to the irregularities in the track and the varying flexibility attributable to the discrete supports (sleepers), the magnitude of the contact forces between the wheel and rail will vary along the rail. The randomness in the contact forces causes the element forces in the rail pad/ballast/subsoil representations to be unique at each individual sleeper position.

Considering the soil as a linear time-invariant system (cf. Eq. (1)), where an input signal $w(t)$ is the force applied at a certain sleeper position, the output signal $y(t)$ is the (e.g. vertical) displacement in an observation point, the input–output relationship is defined by the convolution integral

$$y(t) = h * w(t) = \int_{-\infty}^{\infty} h(t-\tau) \cdot w(\tau)\, d\tau \qquad (1)$$

where $h(t)$ is the impulse response of the system. According to the convolution theorem, the time domain convolution integral turns into a simple multiplication in the frequency domain (if $h$ and $w$ are $L^1$ integrable)

$$Y(f) = \mathcal{F}(y(t)) = \mathcal{F}(h * w) = \mathcal{F}(h) \cdot \mathcal{F}(w) = H(f) \cdot W(f) \tag{2}$$

Hence, the output signal is then obtained by an inverse Fourier transform,

$$y(t) = \mathcal{F}^{-1}(H \cdot W) \tag{3}$$

The Fourier transform of the impulse response is recognized as the transfer function (Frequency response function, FRF)

$$\mathcal{F}(h(t)) = H(f) \tag{4}$$

Using the principle of superposition, the total response in a certain point is obtained as the sum of the responses from each excitation. This means that the response in an observation point *O* in the free-field is obtained by calculating and summing the responses in the point *O* due to the excitations at each individual sleeper position. Hence, the transfer functions to the observation point *O*, from all sleepers $s_k$ that are close enough to have any significance, are required (Figure 2).

The transfer functions can be estimated by various methods and models of different complexity; e.g. 2D or 3D FE models in either time- or frequency domain, or the so called domain transformation method (DTM) in which the wave propagation is analyzed using a semi-analytical approach in the frequency wavenumber domain [4]. Especially under axisymmetric conditions, both the FE method and the DTM can provide the transfer functions between the source and a receiver at a large number of distances, very quickly compared to large 3D FE models. However, even in cases where the soil is horizontally stratified, the railway track is usually placed on an embankment somewhat elevated from the surrounding ground surface, thereby making the suitability of an axisymmetric analysis approach less certain.

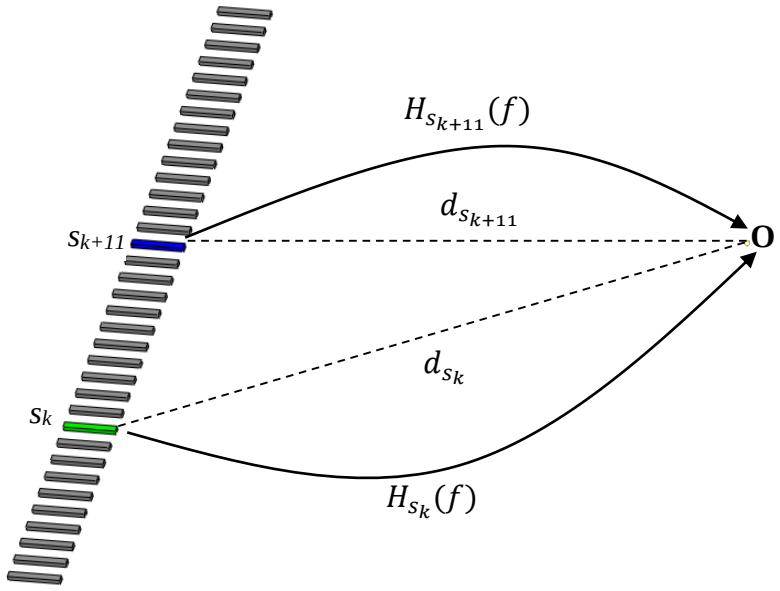


Figure 2: A transfer function *H(f)* between each sleeper and the observation point in the free-field is needed.

## 2 A THREE-DIMENSIONAL GROUND MODEL

The effect of the embankment on the transfer functions to the free-field is studied by use of a 3D FE model. The analysis is carried out in the commercial software Abaqus [5]. The model consists of a 75 m stretch of the railway embankment and the surrounding soil, see Figure 3. On top of the embankment, one sleeper is modelled, on which a surface load is applied to a small part representing the area of interaction with the rail. Two symmetry planes exist.

Isoparametric second-order solid brick-elements with reduced integration are employed. To avoid waves reflecting back into the model at the boundaries, elements that implement viscous absorbing boundaries as proposed by Lysmer and Kuhlemeyer [6] are utilized. At these boundaries "tuned" dashpots are introduced that are completely effective for orthogonally impinging body waves, whereas other waves are only partially absorbed. However, these elements are usually deemed fit for engineering purposes, provided that they are placed sufficiently far from the region of interest and the damping in the medium is fairly high.

The ground model consists of one soil layer on top of bedrock. The depth of the soil layer is varied from 10 to 20 meters. The bedrock is modelled as a 20 m deep layer with viscous absorbing boundaries at the base. The total height of the embankment is 1m, including 0.3m of ballast. The width is 6m at the top and 10m at the bottom, of which only half is modelled due to symmetry.

The soil and bedrock material parameters are presented in Table 1.

| | Soil | Bedrock | Embankment | Ballast |
|---|---|---|---|---|
| Youngs modulus (MPa) | 500 | 10,000 | 500 | 110 |
| Poisson's ratio (-) | 0.48 | 0.4 | 0.48 | 0.36 |
| Mass density (kg/m$^3$) | 2100 | 2500 | 2100 | 1550 |
| Damping ratio (%) | 3.5 | 2.0 | 3.5 | 3.5 |

Table 1: Material properties used in the model

The Rayleigh wave speed in the soil material is approximately 280 m/s. Hence, the shortest wavelength is approximately 280/60 = 4.7 m at 60 Hz. The approximate element size in the soil is 1.4 m within a radius of 50 m; outside that radius, the element size is gradually increased up to a size of 4 m. The resulting 7–9 nodes per wavelength was assumed to properly resolve a Rayleigh wave. Three second-order element edges contain seven nodes, meaning that the minimum wavelength is then approximately $3 \cdot 1.4 = 4.2$ m, which is approximately the wavelength of a Rayleigh wave at 66 Hz.

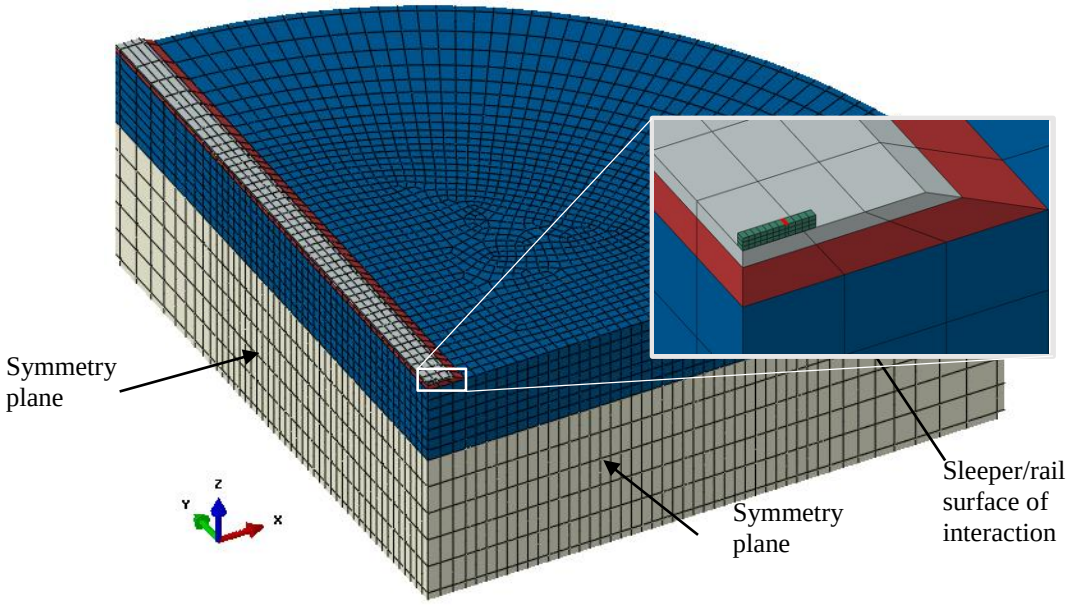


Figure 3: FE model used in this study

A steady-state analysis is performed in the frequency range 5–60 Hz, where a surface load is applied to the area of the sleeper representing the interface with the rail. The surface load is chosen arbitrarily to 10 kPa. The loaded area is 0.075 m$^2$ and due to the two symmetry planes the total load is 10×0.075×4 = 300 N. A steady state solution is found to the equation of motion

$$\mathbf{M}\ddot{\mathbf{U}} + \mathbf{C}\dot{\mathbf{U}} + \mathbf{K}\mathbf{U} = \mathbf{P}e^{\mathbf{i\omega t}} \tag{5}$$

where **M** is the mass matrix, **C** is the damping matrix, **K** is the stiffness matrix, and **P** is the load vector. **U** is the sought displacement vector.

With structural damping $\eta$, assuming a solution of the form $\boldsymbol{U} = \boldsymbol{u}^* e^{\boldsymbol{i\omega t}}$ gives

$$(-\omega^2\mathbf{M} + \mathrm{i}\omega\mathbf{C} + (1 + \mathrm{i}\eta)\mathbf{K})\mathbf{u}^* e^{\mathbf{i\omega t}} = \mathbf{P}e^{\mathbf{i\omega t}} \tag{6}$$

With $\mathbf{D}(\omega) = -\omega^2\mathbf{M} + \mathrm{i}\omega\mathbf{C} + (1 + \mathrm{i}\eta)\mathbf{K}$, the displacements are found as

$$\mathbf{u}^* = \mathbf{D}^{-1}(\omega)\mathbf{P} \tag{7}$$

The vertical response is studied in five groups of points, where the points in each group are located at equal distances from the load, but at different angles from the global *x*-axis which is perpendicular to the track. The distances are 10, 20, 30, 40, and 50 m from the load. The points are located at intervals of 10° to the global *x*-axis. The maximum angle for each distance is limited so that only points outside the embankment are studied, see Figure 4.

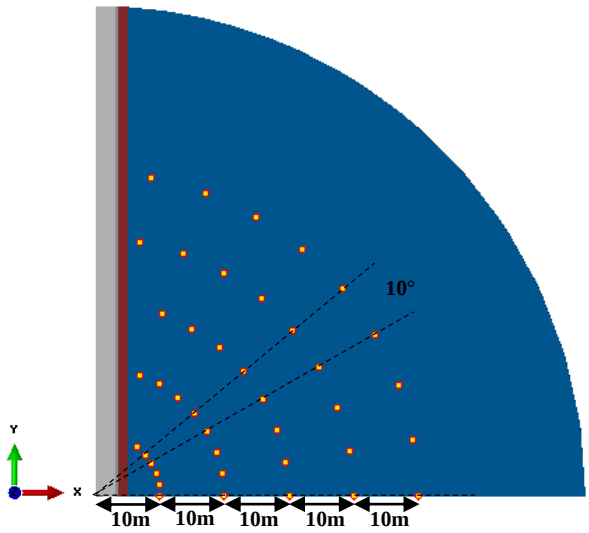


Figure 4: Points on the ground surface where the response is extracted. The points are located at 10, 20, 30, 40 and 50 meters from the load. The maximum angle for each distance is 50°, 70°, 70°, 80°, and 80°, respectively.

Generally, the FE model does not have nodes at these exact points. Therefore, the results are extracted for all the nodes in the element surrounding the sought point. The element shape functions are then used to map the point to the element parent domain, as well as to interpolate the response using the element nodal values.

Figure 5 (left) shows the envelopes for each distance, where the thickness of the envelope indicates some deviation from axisymmetric behavior. In Figure 5 (right), the absolute values of the transfer functions are shown for all points, for the case with a soil layer depth of 10 m.

The absolute values of the transfer functions are shown for all points in Figure 6 grouped by the distance from the load, and normalized to the value at the point at 0°.

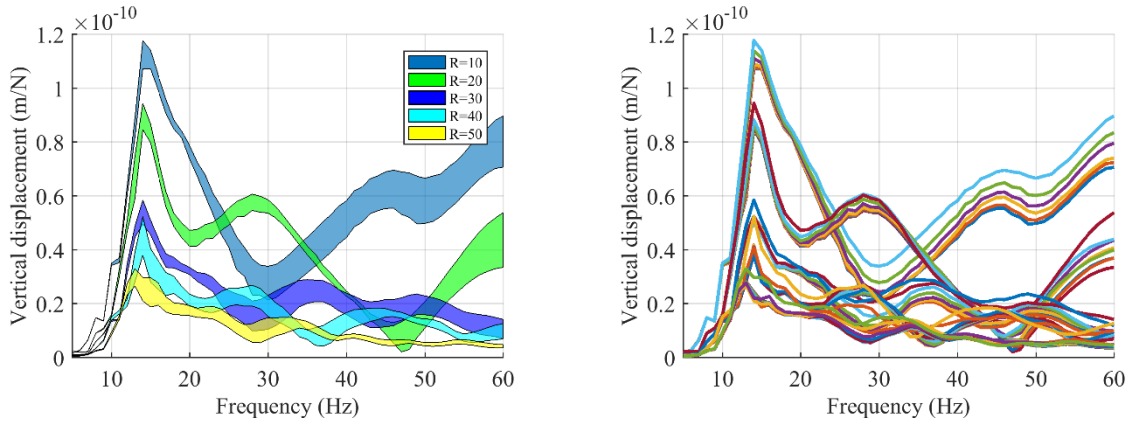


Figure 5: Transfer functions for the case with 10 m soil layer. Left: Envelope curves for each distance. Right: Absolute value of the transfer functions for all points.

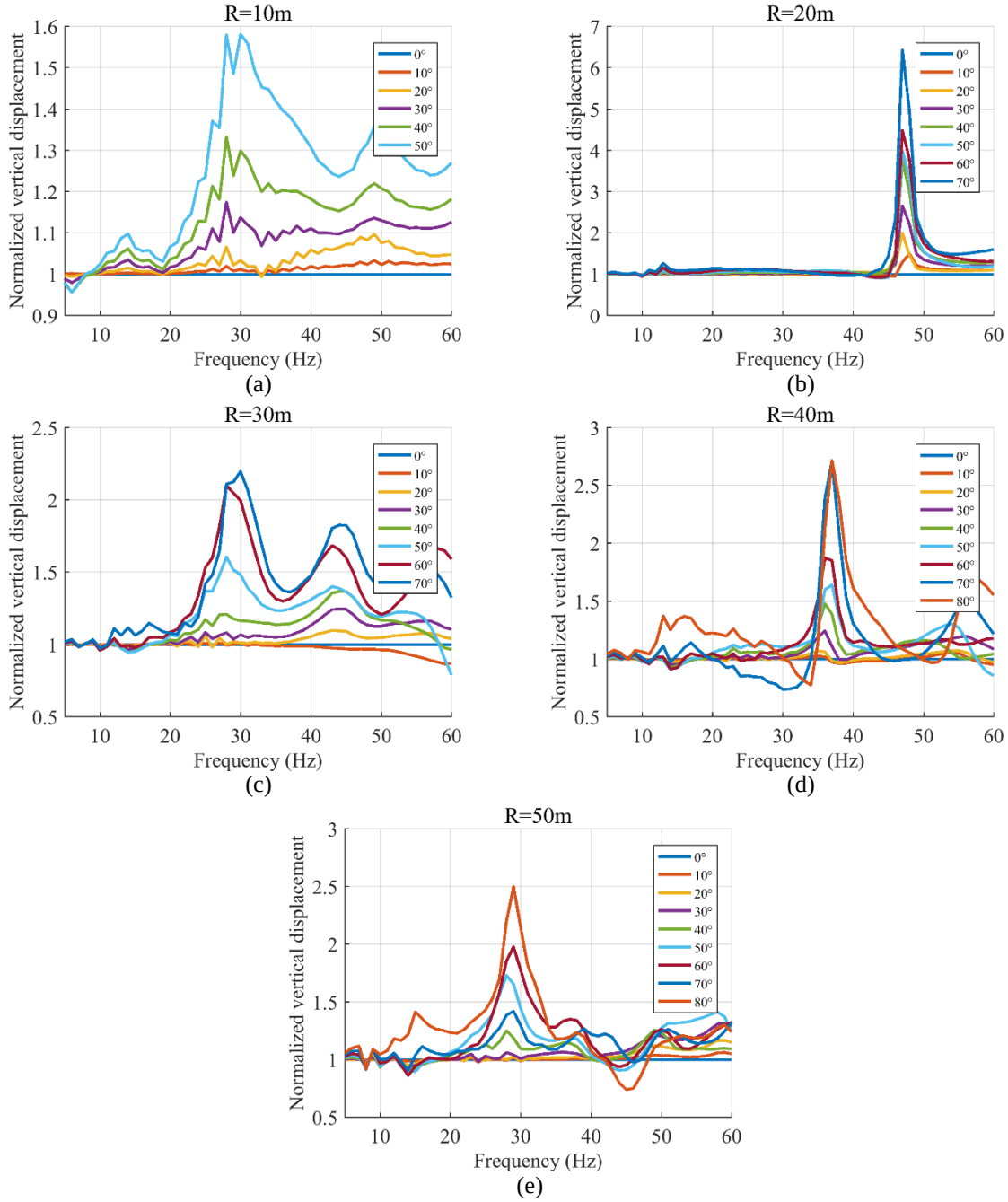


Figure 6: Absolute value of transfer function normalized against the values for the point at 0° for all points at (a) 10 m, (b) 20 m, (c) 30 m, (d) 40 m, (e) 50 m from the load.

As shown in Figures 5 and 6, the difference between points at equal distance from the load can become quite large, especially when comparing the point at 0° (perpendicular to the embankment) and the points at higher angles (i.e. points that are relatively close to the embankment). The analysis of the case with a 20 m deep soil layer shows similar results and are therefore not presented here.

However, considering a fixed observation point in the free field, the relative importance of the transfer functions for points on the track that are located at larger angles between the observation point and a line perpendicular to the track, is in general naturally lower, since the former points are located farther away from the observation point. In order to quantify this effect, the transfer functions have been extracted for a number of points, equivalent to traversing along the

track and extracting the transfer function between each sleeper and a fixed observation point. A sleeper spacing of 0.6 meters is assumed. This is carried out for a stretch of 49.8 m. This provides 49.8/0.6 + 1 = 84 points which, due to symmetry, can be "mirrored" in order to provide transfer functions for 84 + 83 = 167 sleepers. The absolute values of the transfer functions are summed. For comparison, an equal number of transfer functions is extracted for points at corresponding distances but all positioned on the global *x*-axis, i.e. perpendicular to the embankment, thus providing an "axisymmetric equivalent". The absolute value of these are also summed. This is carried out for three observation points, located 10, 20 and 30 m from the track. The points are shown in Figure 7 for the case of an observation point 30 m from the track. The results are shown in Figure 8.

The comparison shows that the summed transfer functions differ only slightly, indicating that the error in disregarding the asymmetry and only using transfer functions from points located perpendicular to the embankment, is limited.

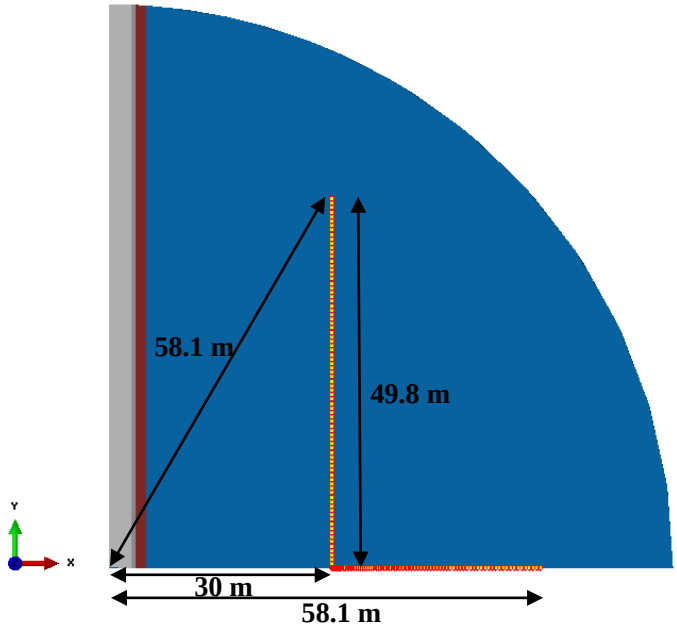


Figure 7: Points on the ground surface used for extracting transfer functions for 84 different sleepers, for an observation point 30 meter from mid-embankment.

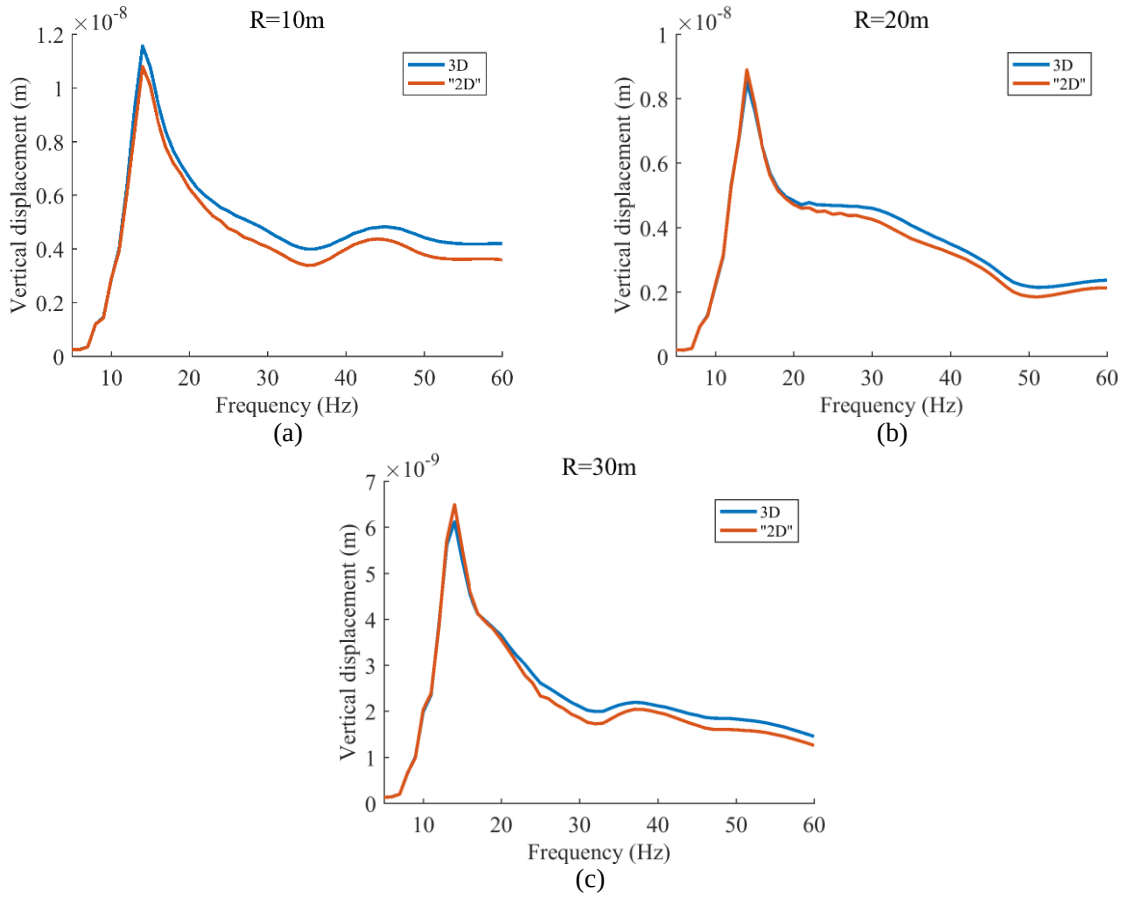


Figure 8: Comparison of the absolute sum of transfer functions for 167 sleepers when considering or disregarding (3D / "2D") the asymmetry in displacement amplitudes relative the global *x*-axis.

## 3 CONCLUSIONS

In the present paper, the effect of the embankment on the transfer functions from a railway track to an observation point in the free-field has been studied by comparing the vertical displacement for points at equal distance from the load, but at different angles to the embankment, for loads in the frequency range 5–60 Hz. The most important findings are:

- In the studied cases, the vertical displacement for different points in the free-field, with equal distance to the load, vary significantly depending on the angle to the embankment. In general, the displacement increases for points that are closer to the embankment, i.e. for increasing angles.
- Evaluating the free-field response due to a train passage using a simplified approach such as proposed in Section 1.1, an axisymmetric soil model can probably still be useful, as long as it provides the same response as a 3D model does for points perpendicular to the embankment. The reason is that in general, the relative importance of sleepers forming large angles to the observation point is low when compared to sleepers close to perpendicular to the track, due to the increased distance to the observation point.
- To draw any general conclusions a larger parameter study is required, where the geometrical shape and the stiffness of the embankment is varied, as well as the properties of the soil stratification.

## ACKNOWLEDGMENTS

The research was carried out in the framework of the project "Urban Tranquility" under the Interreg V programme. The authors of this work gratefully acknowledge the European Regional Development Fund for the financial support.

## REFERENCES

[1] P. Persson, Vibrations in a built environment – Prediction and Reduction. Doctoral Thesis, Report TVSM-1026, Lund University, Sweden, 2016.

[2] G. Lombaert, G. Degrande, S. François, D.J. Thompson, Ground-Borne Vibration due to Railway Traffic: A Review of Excitation Mechanisms, Prediction Methods and Mitigation Measures, Proceedings of the 11th International Workshop on Railway Noise, Uddevalla, Sweden, 9–13 September 2013.

[3] D. Cantero, T. Arvidsson, E. Obrien, R. Karoumi, Train–track–bridge modelling and review of parameters, Structure and Infrastructure Engineering, **12**:(9), 1051-1064, 2016, DOI: 10.1080/15732479.2015.1076854.

[4] L.V. Andersen, J. Clausen, Efficient Modelling of Wind Turbine Foundations. In R. Carriveau (Ed.), Fundamental and Advanced Topics in Wind Power (Chapter 6, pp. 115-174), 2011. Rijeka, Croatia: INTECH open. DOI: 10.5772/731

[5] Dassault Systémes. Abaqus 6.14. Documentation, USA, 2014.

[6] J. Lysmer, R.L. Kuhlemeyer, Finite dynamic model for infinite media, Journal of Engineering Mechanics (ASCE), 859-877, 1969.

COMPDYN 2017
6th ECCOMAS Thematic Conference on
Computational Methods in Structural Dynamics and Earthquake Engineering
M. Papadrakakis, M. Fragiadakis (eds.)
Rhodes Island, Greece, 15–17 June 2017

# THREE-DIMENSIONAL NUMERICAL MODELING OF SEISMIC WAVE PROPAGATION IN WUDU BASIN, CHINA

**Xiaolong Zhang[1], Xiaojun Li[2], Zhenghua Zhou[1], Guoxing Chen[1],**

**Xiaobo Peng[3], and Ming Lu[4]**

[1] College of Transportation Science & Engineering Nanjing Tech University
No.200, Zhongshan North Road, Gulou District, Nanjing, Jiangsu Province 210009, China
e-mail: zxlnjut@163.com； bjsmoc@163.com; Gxc6307@163.com

[2] Institute of Geophysics, China Earthquake Administration
No.5 Minzudaxue Nanlu, Haidian District, Beijing 100081, China
e-mail: beerli@vip.sina.com

[3] Institute of Earthquake Engineering of Jiangsu Province
No.3 Weigang road, Xuanwu District, Nanjing, Jiangsu Province 210014, China
e-mail: xiaobo_peng@163.com

[4]Institute of Crustal Dynamics, China Earthquake Administration, Beijing,China
No.1 Anningzhuang Rd., Xisanqi, Haidian District, Beijing 100085, China
e-mail: luming6@yeah.net

Correspondence should be addressed to Xiaojun Li; beerli@vip.sina.com

**Keywords:** Basin effect, Numerical modeling, Viscous-elastic Artificial boundary, Incident wave, Site Amplification

.**Abstract.** *The Mw 7.9 earthquake occurred in Wenchuan, Sichuan, China, on 12 May 2008, and it caused huge casualties, economic loss, and serious damage to engineering structures and infrastructures in the area near the fault rupture. In particular, the Wudu township far away from the fault rupture (>100km), which is located in a sedimentary basin, also suffered serious damage, and was in the area with seismic intensity VIII-IX in the Isoseismal Map of Wenchuan Earthquake. In this study, full elastic wave field simulations in the Wudu Basin were conducted by using a three-dimensional (3D) finite element method based on the parallel computing cluster platform of the ABAQUS software. The 3D Wudu Basin model is constructed based on the the digital terrain data borehole spatial distribution data in regional geological survey. The basin model consists of four major subsurfaces and the basin basement, All calculations were executed in the time domain, and the soil and rock were assumed to be linearly elastic. The viscous spring artificial boundary was adopted as the artificial condition, and the incident wave was transformed into the equivalent nodal forces acting on the viscous spring artificial boundary of the finite model. In the simulation, an impulse with a duration of 0.25 s was taken as the input SV wave. The simulating results of seismic response*

*characteristics varying greatly from different points in the Wudu Basin revealed the basin edge effect, and the basin-focusing effect. The surface wave generated after the primary S wave is trapped at the shallow part of the basin, and most of the energy is reflected from the interfaces of soil strata and focused back into the basin when the wave propagates through the deepest part of the basin. Moreover, a part of the seismic wave front turns and follows the shallow basin edge, resulting in further amplification. The phenomenon, that is the incident angle of the seismic waves can produce unusually strong shaking distribution, was demonstrated. It indicates that the complex Wudu Basin geometry, the fairly low velocity of the surface soil layer, and the incident angle of seismic waves dominate the amplification and wave propagation behavior, which results in extraordinary strong shaking patterns in the Wudu basin area.*

## 1 INTRODUCTION

The Mw 7.9 Wenchuan earthquake occurred in the Longmen Mountain region at the eastern margin of the Qinghai–Tibet Plateau, which is adjacent to the Sichuan Basin (Fig. 1), on 12 May 2008. The Wenchuan earthquake caused significant building damage and collapse with considerable casualties, but it also provided most of the best data to investigate many fundamental problems of wave propagation in the heterogeneous crust. The Wudu township, which is located in a sedimentary basin in northern Jiangyou situated in the eastern Yingxiu–Beichuan Fault, also suffered serious earthquake damage. Previous studies concerning basins indicated that low-velocity soil layer and basin geometry have a strong influence on the behavior of seismic wave propagation (Alex and Olsen, 1998; Davis *et al*., 2000) and strengthen the shaking activity (Graves 1998; Olsen, 2000; Komatitsch *et al*., 2004). The cover soil layer in the Wudu Basin is thin, with a relative depth of approximately 20 m and a fairly low S wave velocity, which makes it particularly vulnerable to severe earthquake damage.

Surface topography can significantly affect ground motion characteristics. An irregular free surface can further lead to complex wave propagation. Structures located at the tops of hills, ridges, and canyons may suffer more intensive damage than structures situated at the bases of hills or on level surfaces, as observed from earthquakes and from numerical simulations (Hartzell *et al*., 1994; Spudich *et al*., 1996; Assimaki *et al*., 2005). In the past decades, seismologists and engineers made significant progress in simulating ground motion using a variety of simplified numerical and analytical methods, such as one-dimensional and two-dimensional local site models. These models can assist in explaining the observed phenomena in certain situations. However, observations of ground motion during recent strong earthquakes have shown that the three-dimensional (3D) local site effects may be extremely important and may adversely affect structural safety. Three common effects often observed in basins or sedimentary valleys are amplification of strong motion intensity, significantly long duration of the surface ground motion with respect to that of the rock, and rapid spatial variation of the ground motion.

Recently, various numerical studies of seismic wave propagation in 3D sedimentary basins have demonstrated substantial progress using parallel computer facilities. The most widely used approach for modeling of seismic wave propagation is the finite difference method (FDM) (Pitarka, 1999; Olsen, 2000; Kristek *et al*., 2009). However, realistic topography was frequently not considered in simulations because of the difficulty of incorporating the free surface boundary condition in the FDM in the presence of topography (Moczo *et al*., 2007). Since the 1990s, the finite element method (FEM) (Liu *et al*., 1991; Bao *et al*., 1998; Ma *et al*., 2007; Taborda *et al*., 2012) has been applied to the study of wave propagation in realistic models, including 3D sedimentary basins. However, large systems require iterative routines,

which may increase the cost of the calculations, particularly in the case of realistic 3D problems. From the spectral approximations of the wave field combined with domain decomposition techniques, simulations of earthquake ground motion using the spectral element method (SEM) rapidly advanced in recent years. The application of SEM to elastodynamic problems was first presented by Faccioli *et al*. (1997) and applied by Lee *et al*. (2008, 2009) to realistic models. Such studies are highly useful in understanding the physics of site response. From these analyses, knowledge of the topographic effects on seismic wave propagation and the amplification of seismic waves at a topographic site is obtained; so far, these models are solved only for low frequencies to render the numerical problem as tractable. No seismic waves of up to a maximum frequency of 5 Hz are detected. However, realistic 3D basin models must be considered and evaluated at high frequencies, which are important in engineering design, to model the actual seismic hazard.

The FEM is used to simulate seismic wave propagation in the Wudu area to accommodate the considerable surface topography and the highly variable low-wave speed sedimentary basin in this study. The pretreatment software HyperMesh was employed to structuralize the geometric model and the grid partition. With this software, realistic topography and complex subsurface structures can be efficiently incorporated with the FEM mesh, the resolution of the subsurface structure can reach up to 2.5 m, and a high frequency (up to 10 Hz) of the synthetic waveform can be achieved. Four incident angles of the same seismic waves are analyzed to distinguish the case of the amplification effects. Although numerical simulations with simple incident pulses are not as powerful as the simulations from the real earthquake strong motion, the corresponding results can provide interesting information on the Wudu Basin. These results can also be meaningful for future studies, such as the seismic hazard reduction studies in the metropolitan region.

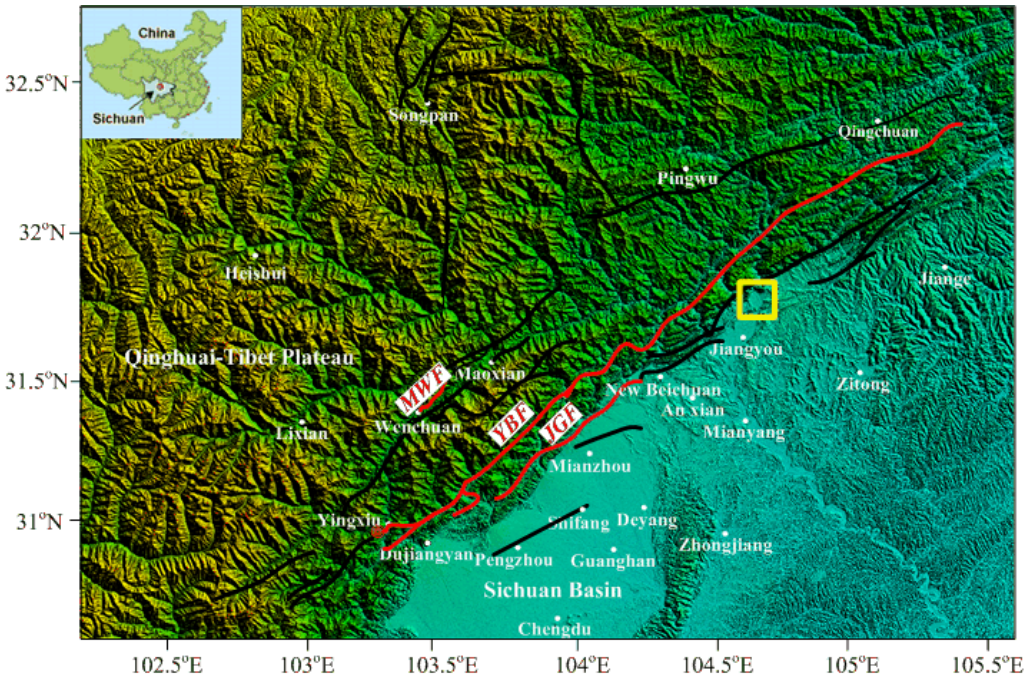


Figure 1.The 2008 Wenchuan earthquake area (The black lines depict the main fault and the red lines is the coseismic rupture. *MWF* Maoxian-Wenchuan Fault, *YBF* Yingxiu-Beichuan Fault, *JGF* Jiangyou-Guanxian Fault. The Yellow rectangle shown the area of wudu basin).

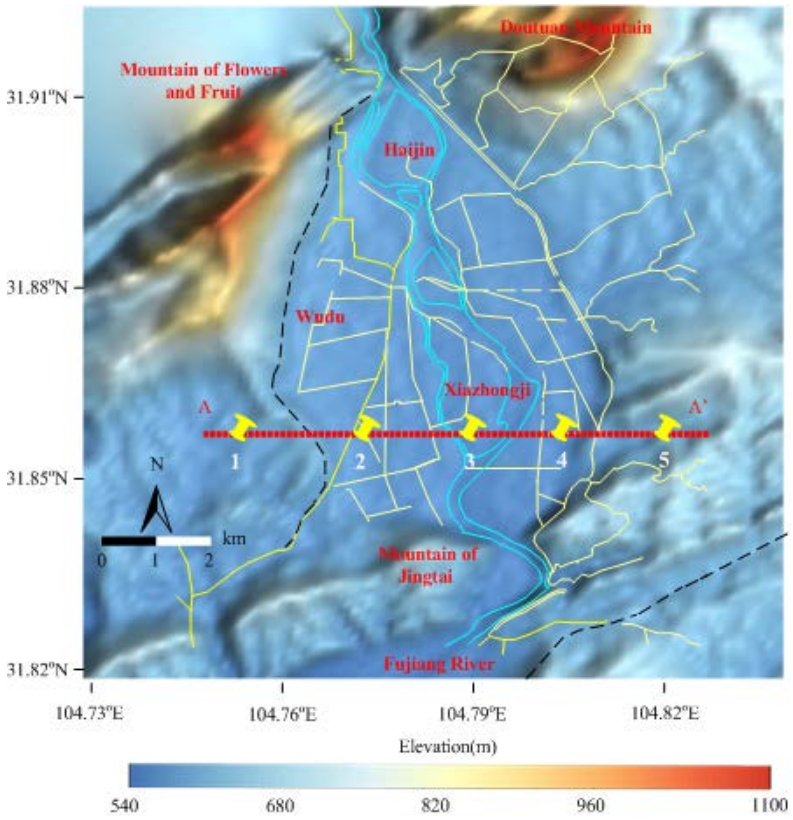


Figure 2. Topographic map of the Wudu basin. The four corners of the area are (31.819°N, 104.730°E), (31.819°N, 104.836°E), (31.921°N, 104.836°E), and (31.921°N, 104.730°E). The thin yellow lines depict the major highways and the black dashed lines is the railway. The elevation is represented by the rainbow color scale.

## 2 WUDU BASIN MODEL AND NUMERICAL METHOD

### 2.1 Realistic Topography and Basin Structure

The Wudu Basin is located in the northern areas of Sichuan Province, China, lying at 104.728° to 104.840° E longitude and 31.817° to 31.924° N latitude. The Wudu Basin is mainly an alluvial plain with undulating low mountains and interspersed hills (see Fig. 2). From the regional geological survey borehole spatial distribution data, several characteristics can be noted: (1) the Wudu Basin is a shallow dish-shaped basin with a gentle dipping boundary, and the average dipping angle is not more than 45°; (2) the deepest part of the basement is probably near the outlet of the Fujiang River in the south area of the basin; and (3) There are four rock and soil layers, in which each layer is in an approximately horizontal distribution. The P and S wave velocities inside the basin are approximately 522 m/s to 1,927 m/s and 200 m/s to 1,065 m/s, respectively; the velocities of the basin basement beneath and surrounding the basin are 3,956 and 2,250 m/s, respectively. For the numerical simulations, major continuities separating the layers of homogeneous velocities are used. The detailed material parameters and the grid size of the model are listed in Table 1.

| Depth(m) | $\rho$(kg/m$^3$) | $E$(MPa) | $v$ | $C_p$(m/sec) | $C_s$(m/sec) | *Grid size*(*m*) |
|---|---|---|---|---|---|---|
| 0-20 | 1880 | 213 | 0.414 | 522 | 200 | 2.5 |
| 20-40 | 2250 | 1250 | 0.324 | 897 | 458 | 5 |
| 40-80 | 2400 | 4025 | 0.3 | 1502 | 803 | 10 |
| 80-120 | 2580 | 7500 | 0.28 | 1927 | 1065 | 12.5 |

| | | | | | | |
|---|---|---|---|---|---|---|
| >120 | 2630 | 32500 | 0.22 | 3756 | 2250 | 25 |

Table 1: Material parameters and the grid size used in the simulations

## 2.2 Finite-Element Model Discretization and Boundary Conditions

The dimension of the simulated Wudu Basin model is 10 × 10 km at the surface and 0.6 km in depth. The velocity outside the basin is simplified by an assumption of a homogeneous half-space. The FEM is used to simulate seismic wave propagation in the Wudu Basin. The 3D model is established according to the digital terrain model (DTM) data. The pretreatment software HyperMesh is utilized to structuralize the geometric model and grid partition to accommodate the topography and the highly variable low-wave speed sediments in the Wudu Basin.

Mesh generation is the key simulation step, the size of which is selected according to the frequency content of the incident motions and shear wave velocity of the medium considered. For the effective representation of the propagating wavelengths, the finite element grid maximum size at the direction of wave propagation is always set as 1/8 to 1/10 of the minimum wavelength corresponding to the cutoff frequency, which is set as 10 Hz in this study. Based on this software, realistic topography and complex subsurface structures can be efficiently incorporated with the FEM mesh. The grid space in the shallowest part can reach up to 2.5 m and a higher frequency (up to 10 Hz) of the synthetic waveform can be achieved in the simulation, which yields a total of 189,849,984 elements and 60,825,600 nodes.

Finite element simulation of the time-dependent wave propagation in infinite media requires enforcing the transmitting boundary to replace the truncated far-field infinite domain to model the effect of the wave radiation toward infinity. The artificial boundary condition is always used to absorb the energy of the scattering waves propagating from the generalized structure into the infinite or semi-infinite medium. Because the viscous spring artificial boundary can efficiently simulate radiation damping and elasticity recovery of the infinite and semi-infinite media with good stability and high accuracy (Liu *et al.*, 2006; Du *et al.*, 2006), the 3D viscous spring artificial boundary was adopted to achieve the half-space simulation outside the basin in this model. This artificial boundary can be achieved by establishing a series of distributed springs and dampers on the truncated boundary of the finite element model, as shown in Figure 3. For the 3D viscous spring artificial boundary, the lumped spring coefficient, $K$, and the lumped damping coefficient, $C$, can be expressed as follows:

In the normal direction

$$K_N = A_l \cdot \frac{1}{1+A} \cdot \frac{1+2G}{r}, \quad C_N = A_l \cdot B\rho c_p \tag{1}$$

In the tangent direction

$$K_T = A_l \cdot \frac{1}{1+A} \cdot \frac{G}{r}, \quad C_T = A_l \cdot B\rho c_s \tag{2}$$

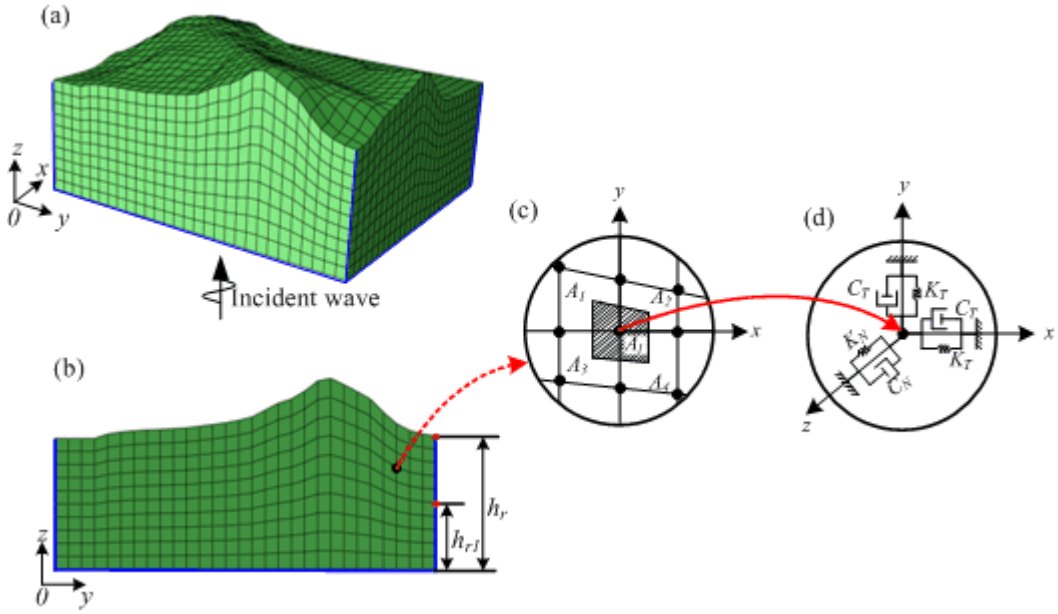


Figure 3. Mechanical model for viscous-spring artificial boundary.

where $r$ is the distance between the center of the surface and the artificial boundary; $c_s$ and $c_p$ are the velocity of the shear wave and the compression wave in the medium, respectively; $G$ is the shear modulus; $\rho$ is the mass density; $A$ and $B$ are the modified coefficients with good values of 0.8 and 1.1, respectively; and $A_l$ is the total truncated boundary area of all elements containing the boundary node $l$. For instance, $A_l = (A_1 + A_2 + A_3 + A_4)/4$ for the status in Figure 3.

### 2.3 Wave Input Method Based on Viscous-Spring Boundary

The seismic motions as the plane body waves with arbitrary incident angle can be converted into the equivalent nodal forces based on the time domain FEM with the viscous spring artificial boundary condition (Liu and Lu, 1998; Liu *et al.*, 2007). According to Liu and Lu (1998), the equivalent node force $f_{li}$ at direction $i$ of node $l$ can be expressed as:

$$f_{li} = K_{li} u_{li}^{f} + C_{li} \dot{u}_{li}^{f} + A_l \sigma_{li}^{f} \tag{3}$$

where $K_{li}$ and $C_{li}$ are the two parameters of the viscous spring artificial boundary; $A_l$ is the total truncated boundary area of all elements containing boundary node $l$; and $u_{li}^{f}$, $\dot{u}_{li}^{f}$, and $\sigma_{li}^{f}$ represent the displacement, velocity, and stress of input motions, respectively.

For the SV wave input, the key step is converting the input waves into the equivalent nodal forces. In the work of Huang (2015), the equivalent nodal forces of the oblique incidence of seismic waves have been achieved, and the wave input is implemented into the commercial software ABAQUS by a self-developed FORTRAN program. In this study, a Dirac impulse with a duration of 0.25 s is chosen as the input SV wave (plotted in Fig. 4), and the mesh allows the simulation of the seismic waves up to a maximum frequency of 10 Hz. The seismic wave path in the layered media is related to the velocity in the layers, and the occurrence of subsurface is related to the initial orientation of the rays. According to the geographical location of the Wudu Basin, the response of the basin to a single plane incident SV wave propagation from west to east with four incident angles of 0°, 10°, 20°, and 30° in the half-space was computed.

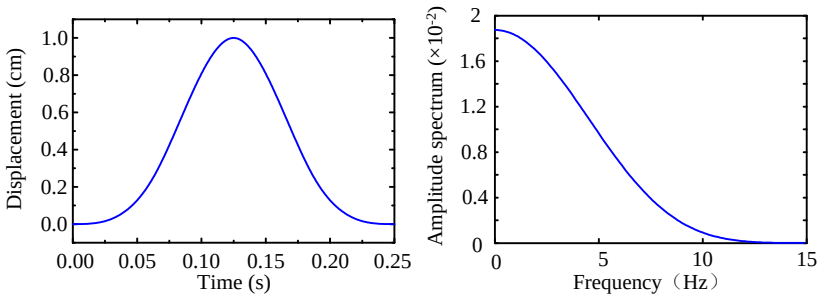


Figure 4. Time-history of incident wave and its Fourier spectrum, respectively.

## 3 SIMULATION RESULT

### 3.1 Snapshots of the Wave Field

The wave propagation behavior was analyzed by computing the displacement snapshots with durations of 20 s (low-pass filtered with a corner frequency of 10 Hz). Figure 5 shows the snapshots of the displacement wave field at every 0.5 s, from 0.5 s to 3.0 s, for the Dirac impulse input motion with different incident angles. In the beginning, ground shaking is not obvious. When the wave enters the Wudu Basin, the travel time of the wave fronts slow down and are dramatically distorted compared with those outside the basin because of low shear wave speeds in the basin, particularly within the soft sedimentary layer. Surface waves that propagate after the S wave can be observed. Surface waves are generated by reflections and mode conversions at the shallow basin edges and free surface. Yalcinkaya and Alptekin (2005) illustrates similar contributions of basin edge-induced surface waves to site amplifications. At the same time, the energy is trapped and reflected within the low-wave speed sediments. This effect is particularly clear around the basin where the basement is close to the ground surface and has a large wave speed contrast relative to the hard rock. However, P wave energy is relatively weak at this moment and passes through the basin quickly as compared with the later S wave and surface wave phases.

When the main body wave phases propagated out of the basin, the basin continues to shake for several seconds. This longer shaking comes from two different seconds: the energy is trapped and reflected within the low-wave-speed sediments as described previously and the energy is reflected and waves are generated by scattering from the basin edges. However, the characteristics of the earthquake motion vary with the different incident angles. With the increase of the incident angle, the seismic energy takes a longer time to reach the basin.

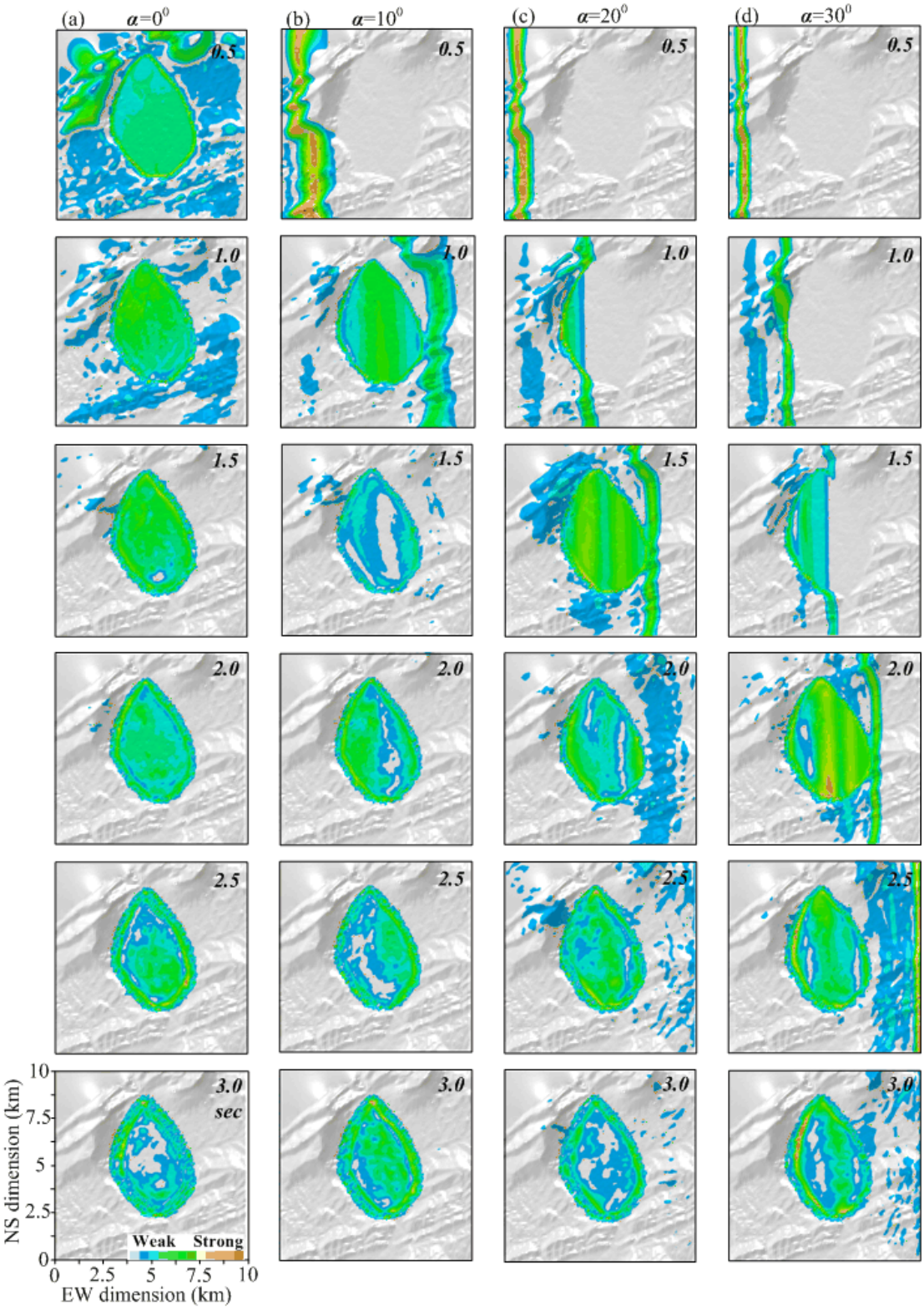


Figure 5. Snapshots of the wave field at the surface from 0.5sec to 3.0sec. Twenty-four meaningful snapshots are shown. They are (a)0.5th, (b) 1.0th, (c) 1.5th, (d) 2.0th, (e) 2.5th and (f) 3.0th sec with different incident angles: $\alpha$=0$^o$, 10$^o$, 20$^o$, 30$^o$, respectively, calculated by the FEM.

### 3.2 Simulating Waveform

The simulating waveforms along profile AA′ shown in Figure 2 were analyzed to determine how the waves are influenced by the incident angles quantitatively. A total of 61 receivers were placed on the free surface, spaced at 0.1 km intervals along profile AA′ , in which site points 2, 3, and 4, which were located in the basin; site points 1 and 5 are located outside the basin (from west to east are marked as sites 1 to 5). Figure 6 shows the response along profile AA′ with each component normalized by its maximum value.

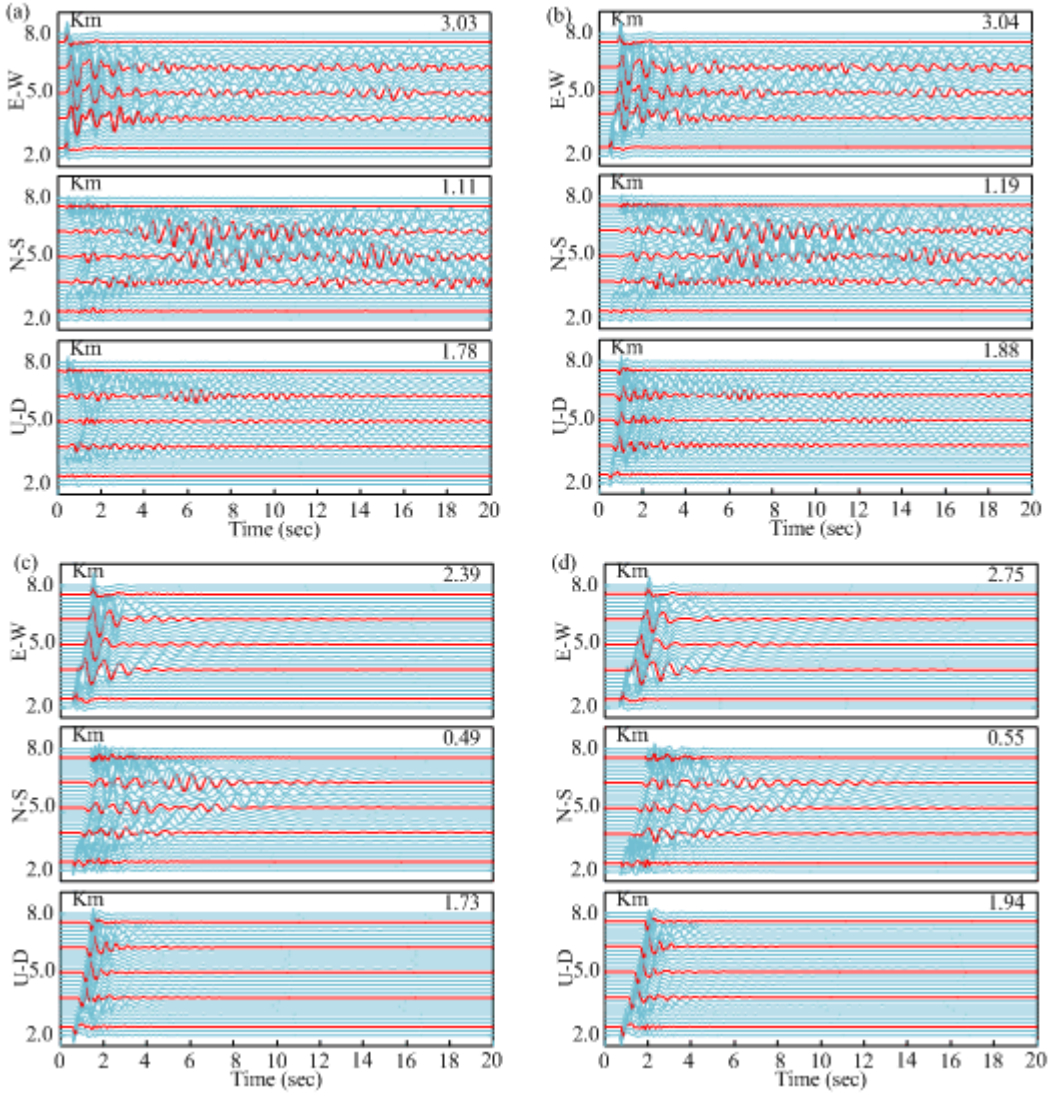


Figure 6. Synthetic seismograms record section along the profile AA' (shown in Figure 2) with different incident angles: (a) $\alpha$=0$^o$, (b) $\alpha$=10$^o$, (c)$\alpha$=20$^o$, and (d) $\alpha$=30$^o$, respectively. Each component's set of seismograms is normalized to its maximum value, which is denoted in the right corner. The unit of amplitude is cm.

These waveforms show anomalous amplification effects in the basin. Notably, the simulating waveforms in the basin have a relatively longer duration than those outside the basin, particularly for the records at site point 5, which is at the center of the AA′ line. The ground motion in the horizontal direction is more complicated than that in the vertical direction; the maximum value of the peak displacement in the E–W component is larger than that in the U–D component, and the U–D component is larger than the N–S component. Smaller amplitudes of the P wave inside the basin in the U–D component were observed; the basin-induced scattered wave propagates toward the east direction, as observed from the moving out of the scat-

tered wave. These scattered amplitudes gradually decrease with time. For incident angle 0°, the basin-focusing effect in the middle part of profile AA′ and the symmetric pattern of the basin-induced scattered wave propagation were observed because a part of the scattered wave energy is reflected back to the basin; the remainder passes through to the outside of the basin. When the incident angle is 10°, the area where the basin-focusing effect rises is in the eastern part of profile AA′. However, when the incident angles are 20° and 30°, the basin-focusing effect is unclear and the duration of the ground motion is obviously reduced. This finding indicates that the surface wave generated from the eastern part of the basin decreases with the increase of the incident angle.

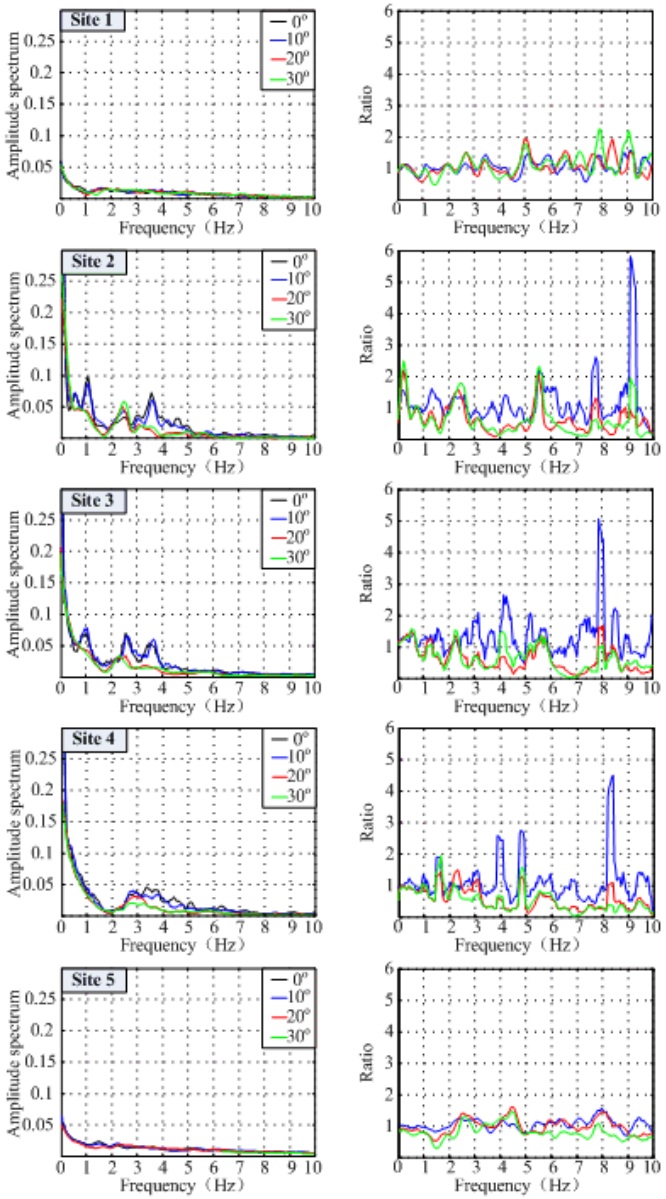


Figure 7. Comparison of Fourier spectra for the sites with different incident angles (left-hand column) and the spectral magnification relative with respect to vertical incidence (right-hand column). (The Sites was noted in the Figure 2).

Figure 7 presents the amplitude spectrum of site point 1 to 5 under different incident angles and the spectral amplitude relative magnification with respect to the vertical incidence. Overall, different site points under different incident angles are sensitive to different frequencies.

At the same frequency, the spectral amplitude of the site points in the basin is larger than the other site points. For the site points in the basin, the spectral amplitude relative magnification initially increases and then decreases with the increase of the incident angle. When the incident angle is 10°, the amplification factor is the largest. However, for the site points at the outside of the basin, the spectral amplitude relative magnification changed slightly with the increase of the incident angle.

### 3.3 Peak Ground Motion Distribution

The maximum particle displacement within the records was analyzed to obtain information on the peak ground displacement (PGD) distribution. A comparison of the spatial variation of the PGD distribution in the E–W, N–S, and U–D components under different incident angles, namely, (a) $\alpha$ = 0°, (b) $\alpha$ = 10°, (c) $\alpha$ = 20°, and (d) $\alpha$ = 30°, is shown in Figure 8. The relative change in PGD along profile AA′ is shown in Figure 8.

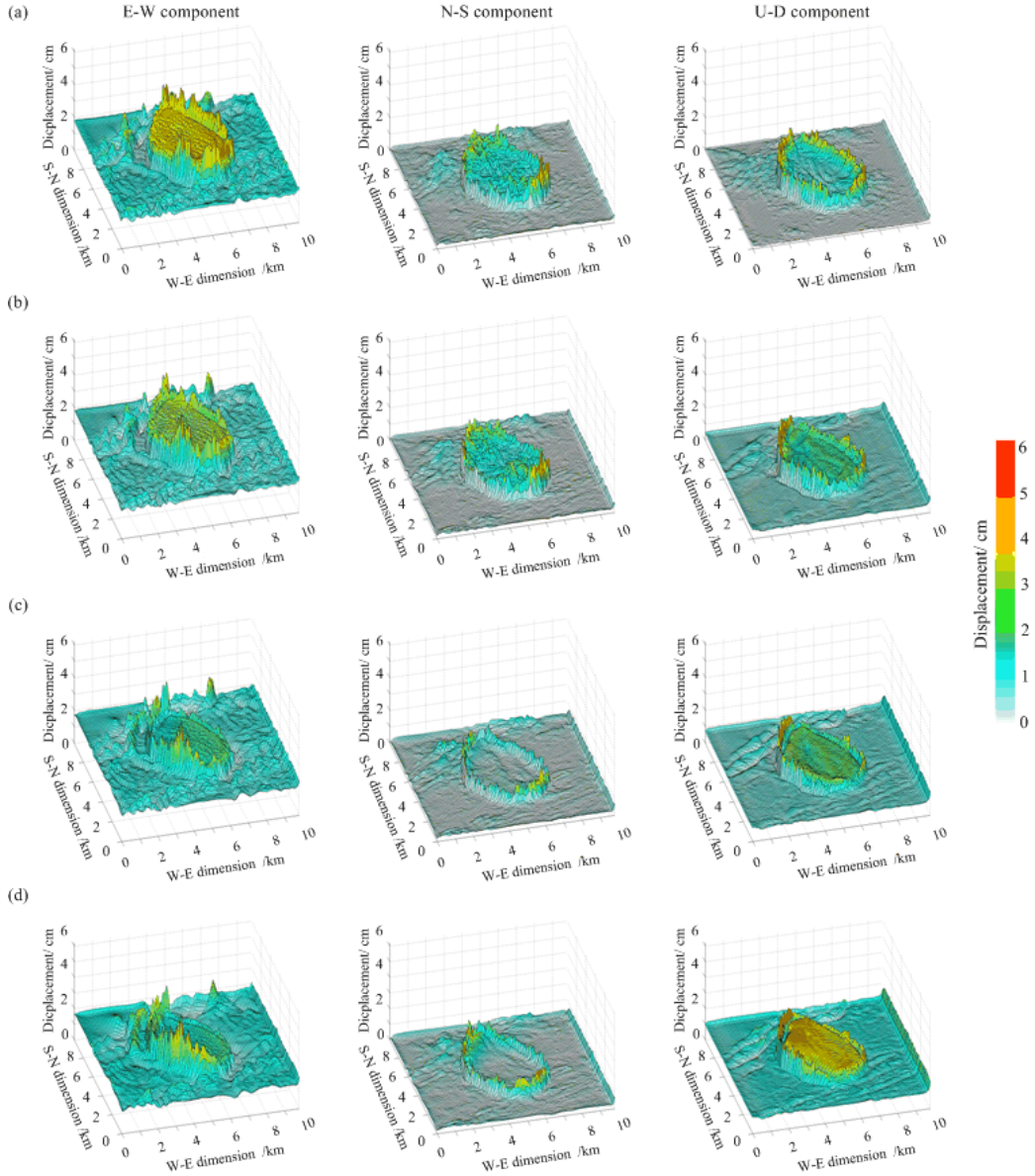


Figure 8. The PGD distribution derived from simulation results with different incident angles: (a) $\alpha$=0°, (b) $\alpha$=10°, (c) $\alpha$=20°, and (d) $\alpha$=30°, respectively. (Note: the number of contours are the same with the different incident angles).

Figure 8 indicates that ground motions in the Wudu Basin have PGD values that are close to 6 cm, which is larger than that observed in the mountainous areas, where the PGD is 2 cm on average. First, the incident angle of 0° was analyzed (Fig. 8a). In the basin, most of the large PGD values occur at the edge of the basin. The Wudu Basin shows relatively large PGD values in the E–W, N–S, and U–D components compared with the surrounding regions because of low-wave speed sediments in the basin. Outside the basin, complex PGD patches are observed in the mountainous areas, particularly in the mountain of flowers and fruit. Figure 8a illustrates that topography increases the PGD values at mountain tops and ridges, whereas valleys usually decrease the PGD. Lee *et al*. (2008, 2009) illustrates a similar phenomenon by analyzing the simulated ground motions in mountainous areas surrounding the Taipei basin. In the three components, the PGDs at the edge of the basin are larger than those in the basin: in the E–W component, the largest PGD values occur at the south part of the basin between the mountain of Jingtai and the outlet of the Fujiang River; in the N–S component, the largest PGD values occur at the southeastern margin of the basin; and in the U–D component, the PGDs are symmetric distributions at the edge of the basin.

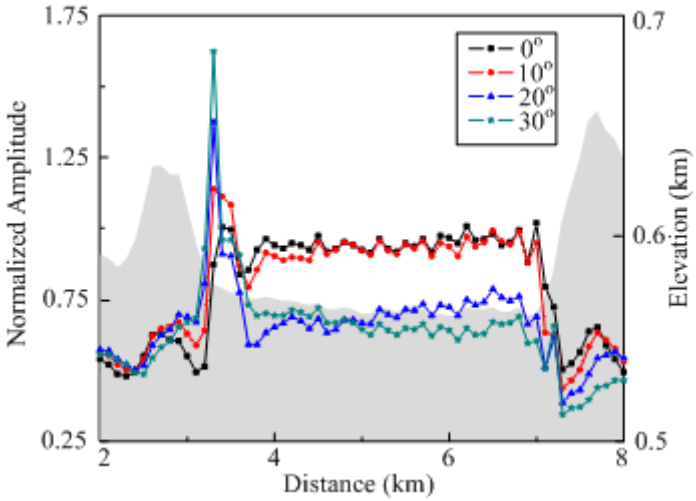


Figure 9.The PGD distribution along the profile AA' with different incident angles:$\alpha$=0°, 10°, 20°, and 30°, respectively (Normalized by the maximum value of the PGD recorded on the AA' line when the wave vertical incident). The background map show the topography.

With the increase of the incident angle, the PGD values in the entire simulation area reduced in the E–W and N–S components; however, the PGD values increased in the U–D component with the increase of the incident angle. When the incident angle is greater than 10°, the PGD values in the west part of the basin have a faster reduction than the eastern part in the E–W and N–S components, whereas the PGD values in the western part of the basin have a faster increase than those in the eastern part in the U–D component. The PGD values along profile AA′ were analyzed to quantify the effects of topography for different incident angles . When the seismic wave has a vertical incidence, the ground motions in the Wudu Basin have PGD values that are close to 3.05 cm, which is larger than that observed outside the basin (where the value is 1.87 cm). The change of PGD basically has no change in most of the basins, is 2.83 cm on average, and has almost a symmetrical distribution. Figure 9 shows the PGD distribution with different incident angles and is normalized by the maximum value of the PGD recorded on the AA′ line when the wave has a vertical incident. In the case of 10°, PGD values exhibit a larger increase at the west side of the basin margin compared with the case of the vertical incidence, where only a slight change occurs compared with the rest of the basin. However, when the incident angle is greater than 10°, the PGD values in the basin are

2.32 and 2.29 cm on average. Compared with the case of the vertical incidence, the PGD values are reduced by 18.24% and 19.29%. The largest PGD values occurred at the same site. By contrast, the PGD values are increased by 23.75% and 52.78 %

### 3.4 Cumulative Kinetic Energy

Olsen *et al.* (1995, 1996) considered the cumulative kinetic energy parameter ($E_k$). $E_k$ can reflect the amplitude and duration time of the total motion that may be more closely related to the potential damage from shaking. The cumulative kinetic energy per unit volume of the $k$th component trace is expressed as:

$$E_k = \frac{1}{2}\rho(x,y,z)\int \dot{u}_k^2(x,y,z,t)\,dt \tag{4}$$

The distribution of $E_k$ is shown in Figure 10. In our simulation, $E_k$ at mountain tops and ridges increases dramatically, and the distribution of $E_k$ at valleys and flat parts on hills is similar to the PGD with different incident angles. However, the energy in the basin and the basin edge is more complex than that outside of the basin and unusually large in the west side of the basin edge with the increase of the incident angle, particularly when the incident angle is 30°. Most of the energy is trapped and reflected in the west side of the basin edge with the increase of the incident angle.

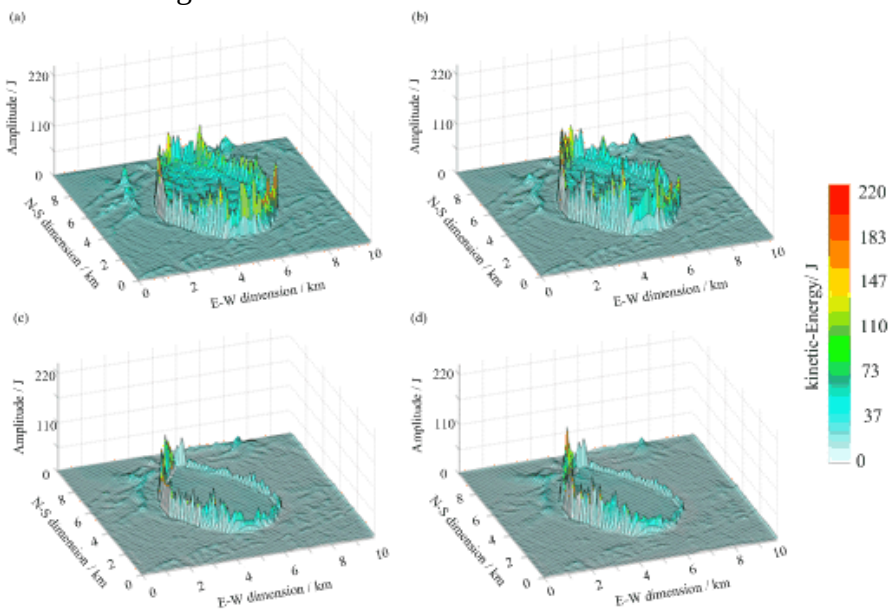


Figure 10. The cumulative kinetic energy distribution with different incident angles: (a) $\alpha$=0°, (b) $\alpha$=10°, (c) $\alpha$=20°, and (d) $\alpha$=30°, respectively.

The $E_k$ value along profile AA′ shown in Figure 11 was analyzed to examine the detailed difference among the four incident angles. The cumulative kinetic energy was normalized by the maximum value of the energy recorded in profile AA′ when the wave has a vertical incident. When the incident angle is 10°, the cumulative kinetic energy in the basin is larger than the vertical incident, which is different from the distribution of PGD. With the increase of the incident angle, the cumulative kinetic energy at the west edge of the basin increases gradually, whereas the cumulative kinetic energy at the eastern edge of the basin decreases, which is similar to the PGD.

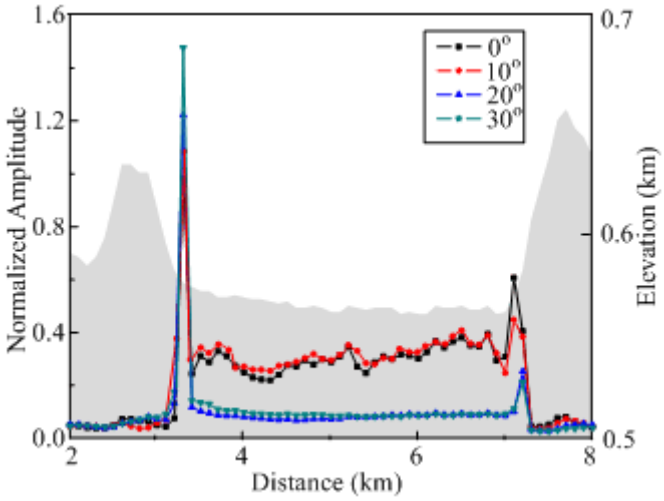


Figure 11. Cumulative kinetic energy distribution along the profile AA' with different incident angles:$\alpha$=0°, 10°, 20°, and 30°, respectively (Normalized by the maximum value of the energy recorded on the profile AA' when the wave vertical incident). The background map show the topography.

## 4 CONCLUSIONS

The 3D model of the Wudu Basin was established based on the regional geological survey borehole data of spatial distribution and the DTM data. Grid partition was achieved by the special preprocessor software HyperMesh. A careful mesh was used to accommodate the steep topography and the complex geometry of the Wudu Basin. The distance between the points at the shallowest part of the FEM mesh was approximately 2.5 m, which enabled the inclusion of realistic topography from the DTM data and was sufficient to calculate the response of seismic waves up to a maximum frequency of approximately 10 Hz. The viscous spring artificial boundary was chosen as the artificial condition, and the earthquake motion of the oblique incidence was transformed into the equivalent nodal forces acting on the viscous spring artificial boundary of the finite model.

The numerical results illustrated that the PGD increases at mountain tops and ridges, whereas the PGD usually decreases in valleys. The topographic effects also strongly depend on the directivity of the event. At most of the basin boundary, the dip angle is less than 45°. For the vertical incident seismic wave, topography scatters the body waves, which subsequently propagates as surface waves and spreads into the Taipei basin. These waves further interact with the basin and the surrounding mountains, finally resulting in complex amplification. The angles between the seismic wave propagation direction and the interface on the east side of the basin edges decreased with the increase of the incident angle of the seismic waves. This phenomenon leads to a reduction in the surface wave energy from the eastern edge of the basin. By contrast, the surface wave energy is enhanced on the west side of the basin. The result revealed different amplifications at the same site.

Although the seismic waves considered in this study are relatively simple compared with a real earthquake, these findings are based on hypothetical earthquake events in the Wudu Basin. The simulations show that topography has different effects depending on the scenario: it may or may not reduce ground motion in Wudu depending on the directivity of the event. These results illustrate the fact that the topography and the incident angle of seismic waves should be considered when assessing seismic hazards.

## ACKNOWLEDGEMENTS

This research work is supported by the National Key Research and Development Program of China (2016YFC402800), National Natural Science Foundation of China (41374049, 51421005), China National Innovation Talent Promotion Program (2013RA4024), and China National High-level personnel of special support program.

## REFERENCES

[1] Alex, C.M., and K. B. Olsen (1998). Lens-effect in Santa Monica, *Geophys. Res. Lett.* **25,** 3441-3444.

[2] Assimaki, D., G. Gazetas, and E. Kausel 2005. Effects of local soil conditions on the topographic aggravation of seismic motion: parametric investigation and recorded field evidence from the 1999 Athens earthquake, *Bull. Seismol. Soc. Am*. **95,** 1059–1089.

[3] Bao, H., Bielak, J., Ghattas, O., Loukas, F., Kallivokas, D.R., O'Hallaron, J.R., 1998. Large scale simulation of elastic wave propagation in heterogeneous media on parallel computers. *Comp. Meth. Appl. Mech. Eng*. **152,** 85–102.

[4] Davis, P. M., J. L Rubinstein, K. H. Liu, S. S. Gao, and L. Knopoff (2000). Northridge earthquake damage caused by geologic focusing of seismic waves, *Science***289,** 1746–1750.

[5] Du XL, Zhao M, Wang JT. A stress artificial boundary in FEA for near-field wave Problem. Chinese Journal of Theoretical and Applied Mechanics 2006; 38(1):49–56.

[6] Faccioli, E., Maggio, F., Paolucci, R., Quarteroni, A., 1997. 2D and 3D elastic wave propagation by a pseudo-spectral domain decomposition method. J.*Seismol.***1,**237–251.

[7] Graves, R. W. (1998). Three-dimensional finite-difference modeling of the San Andreas fault: source parameterization and ground-motion levels, *Bull. Seismol. Soc. Am*. **88,** 881–897.

[8] Hang J Q. Study on Nonlinear Seismic Response of Rock Tunnels [D].Beijing: College of Architecture and Civil Engineering of Beijing University of Technology, 2015.

[9] Hartzell, S. H., D. L. Carver, and K. W. King 1994. Initial investigation of site and topographic effects at Robin wood Ridge, California, *Bull. seism. Soc. Am*. 84, 1336–1349.

[10] Komatitsch, D., Q. Liu, J. Tromp, P. Suss, C. Stidham, and J. H. Shaw (2004). Simulations of ground motion in the Los Angeles basin based upon the spectral-element method, *Bull. Seismol. Soc. Am.***94,** 187–206.

[11] Kristek, J., Moczo, P., Pazak, P., 2009. Numerical modeling of earthquake motion in Grenoble basin, France, using a 4th-order velocity-stress arbitrary discontinuous staggered-grid FD scheme, in ESG 2006. In: Bard, P.-Y. Chaljub, E., Cornou, C., Cotton, F., Gueguen, P. (Eds.), Third Intl. Symposium on the Effects of Surface Geology on Seismic Motion, LCPC Editions, ISSN 1628-4704, vol. 2, pp.1517–1526.

[12] Lee, S. J., H. W. Chen, Q. Liu, D. Komatitsch, B. S. Huang, and J. Tromp (2008). Three-dimensional simulations of seismic wave propagation in the Taipei basin with realistic topography based upon the spectral- element method, *Bull. seism. Soc. Am*. 98, 253–264, doi 10.1785/0120070033.

[13] Lee, S.J., Chan, Y.C., Komatitsch, D., Huang, B.S. & Tromp, J., 2009a. Effects of realistic surface topography on seismic ground motion in the Yangminshan region of Taiwan based upon the spectral-element method and LiDAR DTM, *Bull. seism. Soc. Am.*, **99**(2A), 681–693.

[14] Lee, S.J., Komatitsch, D., Huang, B.S. & Tromp, J., 2009b. Effects of topography on seismic wave propagation: an example from northern Taiwan, *Bull. seism. Soc. Am.*, **99**(1), 314–325.

[15] Liu, S.W., Datta, S.K., Bouden, M., 1991. Scattering of obliquely incident seismicwaves by a cylindrical valley in a layered half space. Earthq. Eng. Struct. Dyn. 20,859–870.

[16] Liu JB, Lu YD. A direct method for analysis of dynamic soil-structure interaction based on interface idea. *Developments in Geotechnical Engineering* 1998; 83:261–276.

[17] Liu JB, Du YX, Du XL, Wang ZY, Wu J. 3D viscous-spring artificial boundary in time domain. Earthquake Engineering and Engineering Vibration 2006; 5(1):93–102. DOI:10.1007 / s11803-006-0585-2.

[18] Liu JB, Gu Y, Li B, Wang Y. An efficient method for the dynamic interaction of open structure-foundation systems. Frontiers of Architecture and Civil Engineering in China 2007; 1(3):340–345. DOI:10.1007/s11709-007-0045-8.

[19] Ma, S., R. J. Archuleta, and M. T. Page (2007). Effects of large-scale surface topography on ground motions, as demonstrated by a study of the San Gabriel Mountains, Los Angeles, California, *Bull. seism. Soc. Am*. 97, 2066–2079, doi 10.1785/0120070040.

[20] Moczo, P., J. Robertsson, and L. Eisner 2007. The finite-difference time domain method for modeling of seismic wave propagation, Adv. Wave Propag. Heterog. Earth 48, 421–516.

[21] Olsen, K. B., R. J. Archuleta, and J. R. Matarese (1995). Three-dimensional simulation of a magnitude 7.75 earthquake on the San Andreas fault, Science 270, 1628–1632.

[22] Olsen, K. B., J. C. Pechmann, and G. T. Schuster (1996). An analysis of simulated and observed blast records in the Salt Lake basin, Bull Seismol. Soc. Am. 86, 1061–1076.

[23] Olsen, K.B., (2000). Site amplification in the Los Angeles basin from three dimensional odeling of ground motion. *Bull. seism. Soc. Am*. **90 (6B),** S77–S94.

[24] Pitarka, A., (1999). 3D elastic finite-difference modeling of seismic motion usingstaggered grids with nonuniform spacing. *Bull. seism. Soc. Am*. 89, 54–68.

[25] Spudich, P., M. Hellweg, and W. H. K. Lee (1996). Directional topographic site response at Tarzana observed in aftershocks of the 1994 Northridge, California, earthquake: implications for main shock motions, *Bull. seism. Soc. Am*. 86, no. 1B, S193–S208.

[26] Taborda, R., Bielak, J., Restrepo, D., (2012). Earthquake ground-motion simulation including nonlinear soil effects under idealized conditions with application to two case studies. *Seismo. Res. Lett.***83,** 1047–1060.

COMPDYN 2017
6th ECCOMAS Thematic Conference on
Computational Methods in Structural Dynamics and Earthquake Engineering
M. Papadrakakis, M. Fragiadakis (eds.)
Rhodes Island, Greece, 15–17 June 2017

# RESONANCE EVALUATION WITH GEOMETRIC STIFFNESS AND CREEP OF SLENDER BEAM OF REINFORCED CONCRETE

**Alexandre de M. Wahrhaftig[1*], Lázaro S. M. S. C. Nascimento[1], Reyolando M. L. R. F. Brasil[2]**

[1]Federal University of Bahia (UFBA), Polytechnic School, Department of Construction and Structures
Rua Aristides Novís, Nº 02, 5º andar, Federação, Salvador – BA, Brazil, CEP: 40210-910
e-mail: [1]alixa@ufba.br, [2]sabasengcivil@hotmail.com

[2]University of São Paulo (USP) Polytechnic School, Dept. of Structural and Geotechnical Engineering
Av. Prof. Almeida Prado, tv. 2, Nº 83, Cidade Universitária, São Paulo – SP, Brazil, CEP: 05508-900
reyolando.brasil@poli.usp.br

**Keywords:** Numerical Simulation, Resonance, Reinforced Concrete, Geometric Stiffness, Creep.

***Abstract.*** *This article assesses the occurrence of resonance with the effects of geometric stiffness and creep in the vibration of a prestressed reinforced concrete beam. A mathematical model based on the Rayleigh method is used, designed to represent a simply supported beam, intended to function as the base of an engine. The gross cross-section of the beam is set to an arrangement of passive reinforcement that is able to resist the effort provided in the simulation, treated by the method of homogenized section. Creep is taken into account through a three-parameter rheological model that conduces to a temporal modulus of elasticity; a normal force of compression reproduces the post tensioning force, which changes the stiffness, and consequently, the natural frequency of vibration of the structure with time. The results from the numerical simulation indicate resonant and non-resonant schemes between the natural frequency of the beam and the frequency of the engine predicted in the mathematical considerations.*

## 1 INTRODUCTION

The dynamic characteristics of a structure depend, basically, on its stiffness and mass. With these two elements, the natural frequencies and modes of vibration of the system are determined. However, the initial stiffness of a structure can be affected by the so-called geometric stiffness, a function of the acting normal force. In the case of compression force, the stiffness of the structure decreases, also reducing the natural frequencies of vibration. A class of structures of socio-economic-strategic importance for the national industry are machine bases, which are subject to vibrations induced by the supported equipment. These vibrations can affect the safety of the structure itself and generate detrimental effects on the equipment and the quality of the manufactured product. They can also make the working ambience unsuitable for operators. All industrial sectors are subject to these problems, including oil exploration, production and refining, mining, wind energy, atomic energy, as well as bridges and viaducts for road and rail use.

Although equipment support structures are, as a general rule, over-dimensioned, and therefore not subject to the effects of geometric stiffness, the tendency of modern structural engineering is towards increasingly slender elements, made possible by materials that are more efficient and lightweight, and having more and more powerful structural analysis capabilities. One of these features is prestressed concrete, represented by the presence of a steel bar or cable inside the structure that compresses it, the purpose of which is to reduce the effects of tension on flexion. In the case of beams subjected to periodic excitation, it is assumed that the original design has taken care to distance the natural frequencies of the system from those of the excitation, considering that, by hypothesis, the prestressing force decreases the stiffness of the element and, consequently, its natural frequencies, which may lead to unexpected, potentially dangerous resonance regimes. In the opposite direction, the presence of the prestressing can provide a form of control of this same vibration, where a resource is available to remove the structure of the resonant regime, if perceived in the preliminary stages of design. In one way or another, a satisfactory analysis solution to most engineering problems comes from a consideration that is easily implemented in analytical and numerical-computational formulations: the geometric stiffness. The influence of geometric stiffness has been studied in several contexts, both in laboratory tests and in comparison with the finite element method (MEF) by Wahrhaftig et al. [1]–[4].

The problem is aggravated when the material itself changes its elastic properties, such as in the case of creep, which represents the gradual increase of deformation with time. This is a typical phenomenon of concrete structures because it is a viscoelastic material. It must be considered when verifying the stability of slender pieces compressed under the Ultimate Limit State (ULS), since these have their stiffness modified in function of the rheology of the material itself. An approximate and satisfactory solution can be found by considering creep through flexural bending over time. To evaluate these aspects, a numerical simulation has been performed, assuming an idealized section of a beam as an engine base. A rheological model of the three parameters has been used to obtain the variable modulus of elasticity. A model, including geometric stiffness, distributed and concentrated masses, is derived based on the Rayleigh method and solved for a range of axial compression load values. The results made it allowed us to verify the resonant and non-resonant response of the system.

## 2 BASIC CONSIDERATIONS

### 2.1 Prestressing in reinforced concrete

A piece can be considered as prestressed reinforced concrete when it is subjected to the action of the so-called prestressing forces and of permanent and variable loads, so that the concrete is not subjected to tension or it occurs below the limit of its resistance. As an example, take the normal stresses beam diagrams of the prestressed beam of Figure 1, where *P* is the prestressing force, $M_P$ the bending moment due to eccentricity of the load P, $M_p$ is the bending moment due to uniformly distributed load *p*, and *R* is the resultant, each one of these with their corresponding normal stresses. Under the conditions presented, the lower fibres of the beam, under positive bending moment, will have the tension stresses overturned by the superposition of those produced by the normal stress of the applied stress eccentrically.

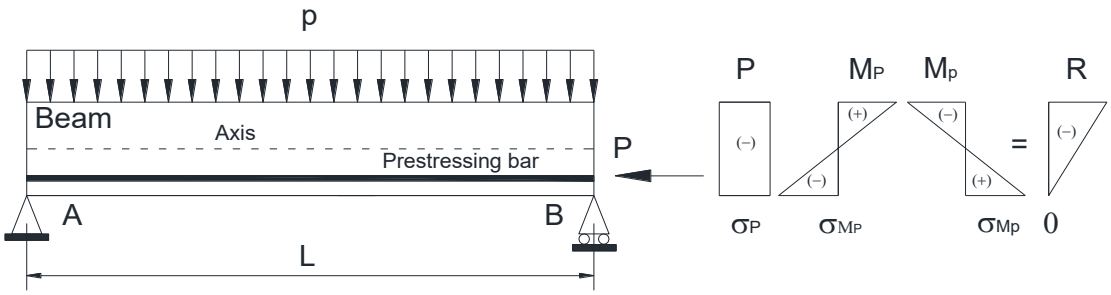


Figure 1: Normal stresses in a prestressed beam.

Prestressed concrete was developed scientifically from the beginning of the last century. Prestressing can be defined as the artifice of introducing, in a structure or a part, a previous state of stresses, in order to improve its resistance or its behaviour in service, under the action of several effects. Due to the characteristics of the concrete as a structural material, the use of prestressing can bring a great advantage from the economic point of view. When comparing the cost of a prestressed structure with a similar one of conventional reinforced concrete, there is a reduction in the final cost of the structure due to the reduction of steel reinforcement, affirms Oliveira [5]. In addition, the prestressing allows the part to overcome large spans, improves the control and reduction of deformations and fissures. It can also be used for structural recovery and reinforcement, as well as for slender systems and prefabricated or precast parts. There are three types of prestressing systems: a) prestressing with initial adherence; b) prestressing with posterior adherence; and c) prestressing without adherence. The latter type is composed of a post-tensioning system characterized by the slipping freedom of the steel reinforcement in relation to the concrete, along the whole extension of the cable, except for the anchorages.

In a non-adherent prestressing, the cables or chutes are wrapped in two or three layers of resistant paper. The wires and paper are painted with bituminous paint in order to tension them after the concrete has hardened. The bitumen avoids the penetration of the cement cream inside the cable and, in this way, it eliminates adhesion between the concrete and the reinforcement, comments Calduro [6]. The prestressed concrete is a composite material of the aggregate mixture and a cement paste associated with prestressing cables and/or passive reinforcing bars. Because of the combination of several materials, these structures develop a highly complex behaviour, presenting a non-linear response, which is due, among other factors, to time-dependent effects, such as the creep of the concrete, affirms Jost [7].

## 2.2 Mathematical model for the nonlinear vibration problem

Consider a rotary machine mounted on a beam subjected to a pre-tensioning force, without adhesion. It is known that such forces affect the geometric stiffness and, consequently, the values of the undamped free-vibration frequencies. If the structure is designed, as is usually the case, to have frequencies farther from the machine's service speed rotation, the changes in the frequency due to geometric stiffness may lead to the appearance of potentially dangerous resonance conditions.

Take a beam model of Bernoulli-Euler applied to a simply supported beam *AB* of length *L* and inertia *I*, intended to function as the base of an engine $E_g$, composed of viscoelastic material, represented by the temporal modulus of elasticity *E(t)* as shown in Figure 2. A normal force of compression *P* reproduces the post-tensioning force, which changes the stiffness, and consequently, the natural frequency of vibration of the structure with time. The eccentricity between the engine axis and the part is initially ignored. The vertical displacement of the central joint is the generalized coordinate of the system.

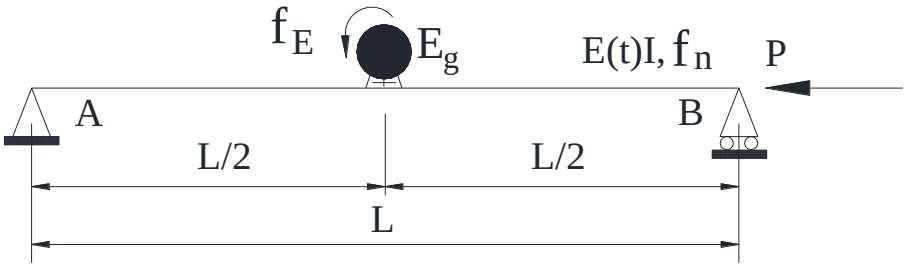


Figure 2: Beam model.

By using the Rayleigh method, the undamped vibration frequency in its first mode is obtained.

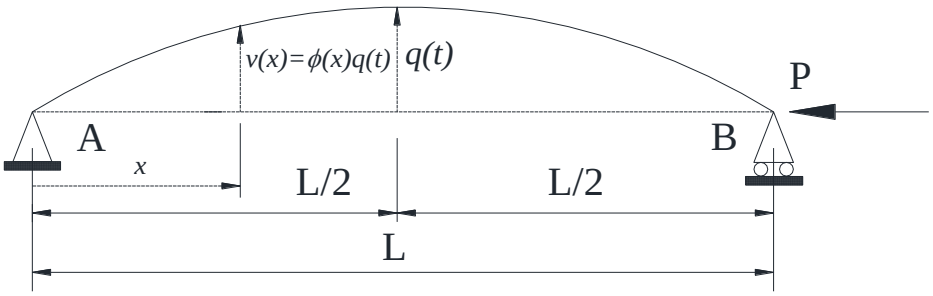


Figure 3: Rayleigh method.

Consider that the vertical displacement of a generic section of the beam in Figure 3 is given by:

$$v(x,t) = \phi(x)\, q(t), \tag{1}$$

in which $\phi(x)$ is a shape function that attempts to define the boundary conditions in the supports and value 1 in the central section of the beam, whose displacement with time is *q(t)*. In this case, one adopts the shape function $\phi(x) = \sin(\pi x/L)$, which is the exact solution of the problem without the *P* load. A prime mark will denote a derivative of the function in relation to *x* (Lagrange's notation).

Applying the Rayleigh method, one has the conventional bending stiffness, $K_0$, as a function of the material elasticity and the geometry of the cross, which is equivalent to:

$$K_0 = \int_0^L E(t)I \ \phi'' \ ^2 dx = \frac{\pi^4 E(t)I}{2L^3} \tag{2}$$

where $E(t)I$ is the known flexural bending with viscoelasticity, represented by multiplication of the temporal material modulus of elasticity with the inertia of the section in relation to the considered movement, the vertical vibration mode (1st mode). In turn, the geometric stiffness, $K_G$, as a function of the normal force of compression (or even tension), is equivalent to:

$$K_G = P\int_0^L \ \phi' \ ^2 dx = \frac{P\pi^2}{2L} \tag{3}$$

The total generalized mass of the system is found by calculating $M = M_C + M_V$ where $M_C$ is the concentrated mass at the middle span and $M_V$ is the mass coming from the beam self-weight given by:

$$M_v = \int_0^L m_V \ \phi(x)^2 dx = \frac{m_V L}{2} \tag{4}$$

in which $m_V$ represents the total mass per length unit. Finally, the frequency of undamped free vibration (in rad/s) is found by way of Eq. (5):

$$\omega = \sqrt{\frac{K}{M}} \tag{5}$$

Considering the total beam stiffness as $K = K_0 - K_G$, the free undamped frequency of vibration of the 1st mode is found, in Hertz, admitting the compressive force as positive, by:

$$f = \frac{\omega}{2\pi} = \frac{1}{2}\left[\frac{\pi^2 E(t)I - PL^2}{L^3 \ L\, m_V + 2Mc}\right]^{\frac{1}{2}} \tag{6}$$

For a better understanding of the Rayleigh method and the importance of the geometric stiffness to the structural analysis, the work of Leissa [8] and Levy [9] should be consulted.

### 2.3 Mathematical solution for representing the creep

It is conceptually convenient to consider classic viscoelastic models in which only two types of parameters, relating to elasticity and viscosity, appear, report Armijo et al. [10]. Classic viscoelastic models are obtained by arranging springs and dampers, or dashpots, in different configurations. Springs are characterized by elastic moduli and dashpots by viscosity coefficients. The best known of these mechanical models are the Maxwell model, containing a

spring in series with a dashpot, and the Kelvin–Voigt model, containing a spring and dashpot in parallel.

One model used to represent creep is the three-parameter model, in which the elastic parameter $E_0$ is connected to the viscoelastic Kelvin–Voigt model with parameters $E_1$ and $\eta_1$, which is a simplification of the Group I Burgers model. The three-parameter model sufficiently describes the viscoelastic nature of many solids and is often used to study the phenomenon in various scientific fields. The total deformations of the Kelvin–Voigt model are given by $\varepsilon = \varepsilon^e + \varepsilon^v$, where $\varepsilon^e$ is the deformation of the elastic model and $\varepsilon^v$ is the deformation of the Kelvin–Voigt model. When differentiated with respect to time, the total deformation is obtained as

$$\dot{\varepsilon} = \dot{\varepsilon}^e + \dot{\varepsilon}^v \tag{7}$$

which is the constitutive equations of the elastic and Kelvin–Voigt models, respectively. Considering $E_1 = E_0$ as the modulus of elasticity for both parts of the rheological model,

$$\sigma = E_0 \varepsilon^e \text{ and } \dot{\sigma} + \frac{E_0 + E_0}{\eta_1}\sigma = E_0 \dot{\varepsilon} + \frac{E_0 E_0}{\eta_1}\varepsilon \tag{8}$$

are found. From the previous equations, one derives the following differential equation:

$$\sigma = E_0 \varepsilon^v + \eta_1 \dot{\varepsilon}^v \tag{9}$$

where $\sigma = 0$ for $t < 0$ and $\sigma = \sigma_0$ for $t > 0$, with $t$ representing the time and $t = 0$ the instant of loading application. As the stress remains constant, the stress derivate with respect to time is zero. Applying the previous stress condition, the following ordinary differential equation is found:

$$E_0 \dot{\varepsilon} + \frac{E_0 E_0}{\eta_1}\varepsilon = \sigma_0 \tag{10}$$

for which the general solution for $t > 0$, taking the initial condition $\varepsilon(0) = \sigma_0/E_0$ , is

$$\varepsilon(t) = \sigma_0 \left[ \frac{1}{E_0} + \frac{1}{E_0}\left( 1 - e^{-\frac{E_0}{\eta_1}t} \right) \right] \tag{11}$$

Obviously, if the stress level remains constant, the modulus of elasticity should decrease concurrently with increasing strain:

$$E(t) = \frac{1}{\frac{1}{E_0} + \frac{1}{E_0}\left( 1 - e^{-\frac{E_0}{\eta_1}t} \right)} \tag{12}$$

The previous solution for consideration of the viscoelastic behaviour of materials was used by Wahrhaftig et al. [11] to evaluate the stability of a slender wooden column. However, it is of interest, at this moment, to make clear that the present work is a numerical speculation, which takes into account the creep of the concrete by assuming a viscoelastic rheological model of three parameters.

## 3 NUMERICAL SIMULATION

The beam gross cross-section was estimated with a passive reinforcement arrangement capable of resisting the predicted load in the simulation, being treated by the homogenized section method, with geometry as indicated in Figure 4. The modulus of elasticity of the concrete was calculated according to NBR 6118/2014 [12] recommendations, following Eq. (13), for a concrete characteristic compressive strength, $f_{ck}$, equal to 30 MPa.

$$E_0 = \alpha_i \cdot 5600\sqrt{f_{ck}} = 26838.405\ MPa;\ \alpha_i = 0.8 + 0.2 \cdot \frac{f_{ck}}{80MPa} = 0.875 \tag{13}$$

The reinforced concrete specific weight $\gamma_c$ was obtained for a material density $\rho$ of 2,500 kg/m$^3$ and a gravitational acceleration $g$ of 9.8061 m/s$^2$, therefore $\gamma_c$ = 24.52 kN/m$^3$.

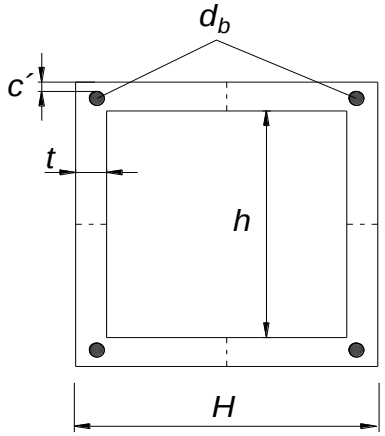


Figure 4: Beam section characteristics.

Section data:

- External height: $H = 16$ cm
- Internal height: $h = H - 2 \cdot t = 6$ cm
- Wall thickness: $t = 5$ cm
- Concrete cover: $c' = 2.5$ cm
- Reference beam span: $L = 3$ m
- Reinforced bar diameters: $d_b = 8$ mm
- Number of reinforcement bars: $nb = 4$
- Total inertia: $I = \frac{H^4 - h^4}{12} = 5353\ \text{cm}^4$
- Gross section area: $A = H^2 - h^2 = 220\ \text{cm}^2$

The concrete section was homogenized by the transformation of the steel bars of the reinforcement, which led to a homogenization factor of 1.0616 to be considered in the material and geometric properties of the beam section. For the simulation, all the elements that constitute physical parts to be added to the system, such as the bar used in prestressing systems and an electric induction motor that represents periodic excitation, were considered as lumped or distributed masses.

By fixing the force on the section-resistant capacity, one can observe the variation of the natural frequency of the beam with time when considering creep, as shown in Figure 5(a). A

safety factor of 1.17042570 to be applied to the loading can be found, which defines the beam collapse at the 90th day, as can be seen in Figure 5(b). By varying force *P*, which represents a non-adherent post-tension force, from zero to the resistant capacity of the section, the variation of the natural frequency of the beam is obtained, given in the graph in Figure 6. There, it is possible to see that, with the increase of the axial compression force, the beam frequency decreases, since the geometric portion ($K_G$) stiffness is changed, consequently decreasing the total stiffness ($K$) of the beam.

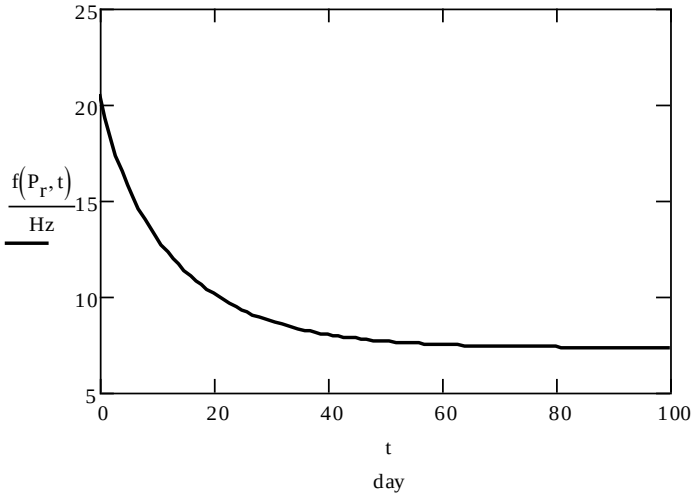


(a) Frequency with time for capacity of the section

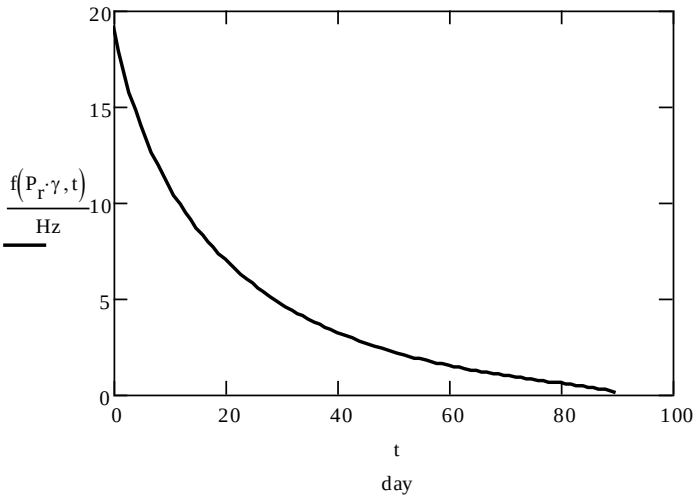


(a) Safety factor γ – Collapse at 90th day

Figure 5: Frequency of the beam with time with viscoelasticity.

Since the motor rotation is set at 1,200 rpm (20 Hz), represented by the dotted horizontal line, there is no resonance without consideration of creep, but the resonance appears when the natural frequency of the beam is calculated with the introduction of the creep. For ten days after application of load, for example, the resonant regime can be observed by the intersection of two curves, dotted (horizontal) and dashed (sloped), defining exactly for which prestressing force the phenomenon occurs at that instant (210 kN).

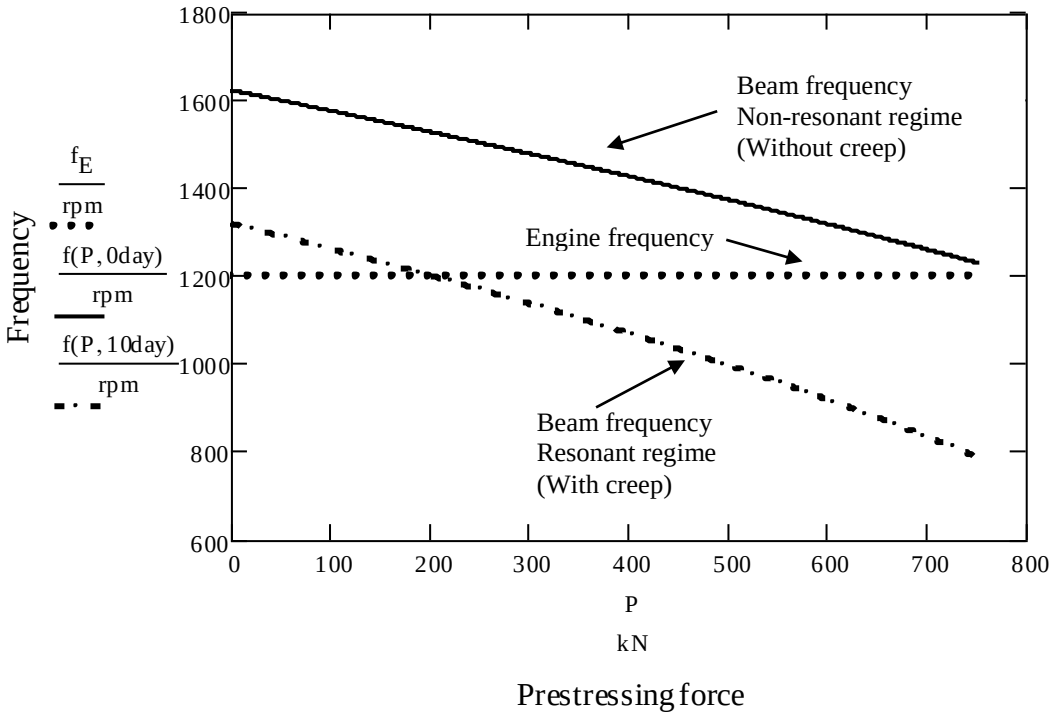


Figure 6: Resonant and non-resonant frequencies as a function of axial compression force *P*.

## 4 CONCLUSIONS

- In this article, a numerical simulation of a reinforced-prestressed concrete beam as a support for rotating machines was performed.
- For the vibration analysis, the creep, which is an intrinsic material property, was introduced due to the slenderness of the beam, revealing a resonant regime not foreseen in the linear analysis (without creep).
- The effect of geometric stiffness produced by the horizontal loading and the corresponding possibility of introducing resonant regimes in the structural support system were demonstrated by calculating their frequencies.
- It can be concluded, therefore, that due to the increase of the axial compressive force, resonance conditions can occur, as represented by the intersection of the curves in Figure 6. In the present study, resonance occurs when the axial compression force reaches 210 kN, at 10 days. Other instants might also be considered.
- Since the force of post-tension decreases the stiffness of the beam, this can lead to the resonant regime if it has not been previously evaluated in the structural analysis.
- The technique studied in this article offers an efficient tool to provide the removal of the support structure of that unwanted regime, avoiding the production of harmful effects on the equipment, fabricated products and work environment of the operators.
- In further work, it is necessary to introduce normative criteria, perform experimental activity and evaluate the influence of the prestressing bar stiffness on the structural response.

## REFERENCES


[1] A.M. Wahrhaftig, R.M.L.R.F. Brasil, J.M. Balthazar, The first frequency of cantilever bars with geometric effect: a mathematical and experimental evaluation. *J. Braz. Soc. Mech. Sci. Eng.*, **35**, 457–467, 2013. doi:10.1007/s40430-013-0043-9.

[2] A.M. Wahrhaftig, R.M.L.R.F. Brasil, Representative experimental and computational analysis of the initial resonant frequency of largely deformed cantilevered beams. *International Journal of Solids and Structures*, **102-103**, 44-55, 2016, doi:10.1016/j.ijsolstr.2016.10.018.

[3] A.M. Wahrhaftig, R.M.L.R.F. Brasil, Vibration analysis of mobile phone mast system by Rayleigh method. *Applied Mathematical Modelling* (2016), doi:10.1016/j.apm.2016.10.020.

[4] A.M. Wahrhaftig, R.M.L.R.F. Brasil, Initial undamped resonant frequency of slender structures considering nonlinear geometric effects: the case of a 60.8 m-high mobile phone mast. *J Braz. Soc. Mech. Sci. Eng*., 2016. doi:10.1007/s40430-016-0547-1.

[5] A.W. Oliveira, Uso do concreto protendido em pontes: Estudo de Caso da Nova Ponte Sobre o Rio São Francisco na BR-101. V Encontro Nacional de Estudantes de Engenharia Civil, Porto Seguro, 2016. (In Portuguese).

[6] E.L. Calduro, Em favor da leveza. Revista Téchne, PINI, n. 26, 1997. (In Portuguese).

[7] D.T. Jost, Análise de peças fletidas com protensão não aderente pelo método dos elementos finitos. 152 p. Dissertação (Mestrado em Engenharia Civil) – Universidade Federal do Rio Grande do Sul. Porto Alegre, 2006. (In Portuguese).

[8] A.W. Leissa, The historical bases of the Rayleigh and Ritz methods. *Journal of Sound and Vibration*, **287**(4-5), 961-978, Nov. 2005.

[9] R. Levy, W.R. Spillers, *Analysis of Geometrically Nonlinear Structures.* Chapman & Hall. New York, 1995.

[10] N.C. Armijo, M.D. Paola, F.P. Pinnola, Fractional characteristic times and dissipated energy in fractional linear viscoelasticity. *Commun. Nonlinear Sci. Numer. Simulat.*, **37**, 14-30, 2016. doi:10.1016/j.cnsns.2016.01.003.

[11] A.M. Wahrhaftig, S.F. César, R.M.L.R.F. Brasil, Creep in the fundamental frequency and stability of a slender wooden column of composite section. *Rev Arv*., **40**(6), p.1129-1140, 2016. doi:10.1590/0100-67622016000600018.

[12] National Regulatory Standard (Norma Brasileira), NBR – 6118 - Design of structural concrete - Procedure, Brazilian National Standards Association (Associação Brasileira de Normas Técnicas, ABNT), 2014.

COMPDYN 2017
6th ECCOMAS Thematic Conference on
Computational Methods in Structural Dynamics and Earthquake Engineering
M. Papadrakakis, M. Fragiadakis (eds.)
Rhodes Island, Greece, 15–17 June, 2017

# SIMULATIONS OF CONCRETE FRACTURE AT VARIOUS STRAIN RATES: PARAMETRIC STUDY

**Josef Květoň**[1] **and Jan Eliáš**[1]

[1]Brno University of Technology, Faculty of Civil Engineering
Veveří 331/95, 602 00 Brno, Czech Republic
e-mail: kveton.j@fce.vutbr.cz; elias.j@fce.vutbr.cz

**Keywords:** Discrete model, Concrete fracture, Dynamics, Inertia, Strain Rate

**Abstract.** *The contribution presents numerical simulations of a recently published experimental series on concrete specimens. The numerical model mimics the meso-structure of the concrete by representing material via system of interconnected rigid polyhedral particles. These particles correspond to mineral aggregates and surrounding matrix. The geometry of particles is based on Voronoi tessellation. The particles are rigid, but they may move and rotate. The displacement jump at their contacts gives rise interaction forces defined by the constitutive relation in a vectorial form. The constitutive equations are independent of the strain rate. Simulations are dynamical, the time dependent response is calculated using Newmark implicit scheme. Full inertia tensor of every particle is taken into account when assembling the mass matrix.*

*To demonstrate the ability of the model to capture the strain rate dependence of the experimental results, series of specimens loaded under various displacement rates are simulated. For quasi-static loading, the initial microcracks usually localize into one highly damaged zone where main crack appears. With increasing strain rate, the amount of energy accumulated in the specimen body is not consumed by one crack only and crack branching occurs. The peak loading force increases with increasing rate as well.*

*Both the strain rate dependence of the loading force and crack branching phenomena are captured by the presented numerical model. The obtained results are compared with the experimental response of the simulated specimens. Parametric study of the model is performed showing different effect of various parameters under different strain rates.*

# 1 INTRODUCTION

In modern engineering, understanding of material behavior is an integral part of structural design. The response of a structure is usually calculated numerically using models verified with help of laboratory tests. The choice of mathematical model is important; the material internal length and its relation to structure dimensions should be taken into consideration. If the heterogeneity of the material is relatively fine compared to the structure dimensions, the material can be conveniently treated as homogeneous and described using continuous formulation. Continuous formulation involves partial differential equations that can be numerically solved with a help of the finite element method (FEM), that provides approximations of the exact solution with high accuracy. In continuous models, fracture is usually represented by so called smeared crack. Material remains continuous, but its stiffness is being reduced as cracking occurs. Such approach brings need for regularization [3, 2]. Several other approaches incorporating discontinuities into FEM models has been presented in literature [10].

This contribution presents fracture simulations of concrete specimens with heterogeneity comparable to specimen size. At this scale, it is convenient to use meso-scale approach with direct representation of mineral aggregates. Such meso-scale model can be advantageously based on the discrete formulation. Discrete approaches were established by representing material by simple lattices of 1D elasto-brittle elements. The heterogeneity can be included e.g. using random lattice structure or by projection of concrete meso structure on the lattice [15]. In the latter case, the element material properties are set according to which phase they belong to – aggregate, cement paste or contact of cement paste with aggregate, so called interfacial transition zone (ITZ).

Another variant of discrete approach represents material as a system of interconnected rigid particles that typically correspond to one mineral grain (particle) with surrounding matrix. The motivation for choosing this variant for present contribution is in highly reduced computational cost of the particle approach compared to previously mentioned lattice approach. The model developed according to [4] is used within this contribution.

It is well known, that the loading capacity and failure mode is dependent on the strain rate applied. In quasi static loading, initial micro-cracks in the material localize into one highly damaged zone, so called macro-crack. With increasing strain rate, the energy in material body is not consumed by one crack only and more cracks appear, eventually one crack branches. This behavior has been observed experimentally in [12]. The presented contribution studies the behavior of the discrete model for concrete loaded under various displacement rates. Time integration is performed in an implicit scheme, contrary to other papers that use dynamical discrete models in connection with explicit time integration scheme [8, 13].

# 2 NUMERICAL MODEL

## 2.1 Particle approach

The 3D system of discrete particles is built according to [6], which is just simplified version of [4]. Particle centers come from process of random placing points in the domain, keeping their distance larger than parameter $l_{\min}$. This internal length dictates the particle size and to large extend also the nonlinear behavior of the model. Voronoi tessellation is performed to get the geometry of particles. Each particle is considered as ideally rigid, material model is applied at its contacts with other particles.

On the contacts (facets), normal and shear stiffness of particle connection is prescribed.

Relation between stress and strain on each facet yields

$$\sigma_i = (1-\omega)E_i\varepsilon_i \quad \text{for} \quad i = N, M, L \tag{1}$$

where $N$ is normal and $M$ and $L$ are two shear directions. The elastic behavior is described by the elastic modulus $E_0$ and normal-tangential stiffness ratio $\alpha$.

$$E_N = E_0, \quad E_{M,L} = \alpha E_0 \tag{2}$$

Since these parameters are applied at meso-scale, they are different from the elastic parameters describing overall behavior of material - Young's modulus $E$ and Poisson's ratio $\nu$. Their approximate relation derived in [9, 5, 7] results in equations

$$E_0 = \frac{E}{1-2\nu} \qquad \alpha = \frac{1-4\nu}{1+\nu} \tag{3}$$

Eq. (3) postulates limitation on Poisson's ratio, that must be within interval $(-1, 0.25)$. Nevertheless, value of Poisson's ratio for concrete is around $0.2$.

In nonlinear regime, isotropic damage model is applied. Damage at contacts is described by parameter $\omega \in \langle 0, 1\rangle$ - Eq. (1). The initially undamaged contact ($\omega = 0$) might, after reaching the strain at the elastic limit, gradually loose stiffness as the strain increases further. At $\omega = 1$, the contact is completely damaged and cannot transfer any stress again. The evolution of the damage parameter $\omega$ is a crucial part of the constitutive law. Its description is quite elaborative, interested reader is referred to [4, 6] for the detailed description.

Since the discretization of a material body comes from pseudo-random process, the response of simulations with different meso-scale geometry differs as well.

### 2.2 Dynamics

Fracture of concrete is a dynamic process. However for slow (so called quasi-static) loading rates, the solution can be obtained under assumption of static equilibrium. For higher strain rates, the influence of inertia cannot be neglected and time-dependent response should be calculated. It is usually obtained from solution of differential equations of motion

$$\boldsymbol{M}\ddot{\boldsymbol{u}} + \boldsymbol{C}\dot{\boldsymbol{u}} + \boldsymbol{K}\boldsymbol{u} = \boldsymbol{F} \tag{4}$$

where $\boldsymbol{M}$, $\boldsymbol{C}$ and $\boldsymbol{K}$ stand for mass, damping and stiffness matrix, $\boldsymbol{F}$ and $\boldsymbol{u}$ is loading and displacement vector, respectively. Dotted symbol of displacement vector denotes its derivative with respect to time, which is velocity (first derivative) and acceleration (second derivative).

Numerical algorithms for solving equations of motion are divided into explicit and implicit time integration schemes, depending on the time the equilibrium is considered at. In case of explicit algorithms, the solution for time $t + \Delta t$ is calculated from equilibrium at time $t$ directly by matrix and vector multiplication; there is no system of equations to solve. But the numerical solution is only conditionally stable, the time step length $\Delta t$ is restricted by the smallest natural frequency of the system, which often brings need for using large number of very short time steps. Therefore, the explicit algorithms are convenient for solving events with short duration, e.g. impact loading.

In an implicit time integration scheme, the solution at time $t + \Delta t$ is calculated from Eq. (4) assembled at time $t + \Delta t$. Its advantage is unconditional stability, the step length is controlled purely by accuracy. But to obtain such solution, system of dependent equations has to be solved.

These equations are nonlinear in the case of nonlinear material, so each time step involves an iterative process to find the solution. These algorithms are conveniently used for solution of processes with longer duration, e.g. structural response during earthquakes.

For the purpose of this contribution, Newmark implicit scheme [11] is implemented. Velocity ($\dot{\boldsymbol{u}}$) and accelerations ($\ddot{\boldsymbol{u}}$) are approximated by

$$\ddot{\boldsymbol{u}}_{t+\Delta t} = \frac{1}{\beta \Delta t^2} \left( \boldsymbol{u}_{t+\Delta t} - \boldsymbol{u}_t \right) - \frac{1}{\beta \Delta t} \dot{\boldsymbol{u}}_t - \left( \frac{1}{2\beta} - 1 \right) \ddot{\boldsymbol{u}}_t \tag{5}$$

$$\dot{\boldsymbol{u}}_{t+\Delta t} = \dot{\boldsymbol{u}}_t + \Delta t \left( 1 - \gamma \right) \ddot{\boldsymbol{u}}_t + \gamma \Delta t \ddot{\boldsymbol{u}}_{t+\Delta t} \tag{6}$$

where index $t$ refer to solution from previous time step. $\beta$ and $\gamma$ are Newmark parameters within interval $\langle 0, 1 \rangle$. To keep the solution unconditionally stable, they must satisfy condition $2\beta \geq \gamma \geq 0.5$ [1]. The only unknown in Eqs. (5) and (6) is vector of displacement at time $t + \Delta t$. To calculate the displacement in time $t + \Delta t$, the approximations are plugged into Eq. (4) and the following system is obtained

$$\left( \boldsymbol{K} + \frac{1}{\beta \Delta t^2} \boldsymbol{M} + \frac{\gamma}{\beta \Delta t} \boldsymbol{C} \right) \boldsymbol{u}_{t+\Delta t} = \boldsymbol{F}_{t+\Delta t} + \boldsymbol{M} \left( \frac{1}{\beta \Delta t^2} \boldsymbol{u}_t + \frac{1}{\beta \Delta t} \dot{\boldsymbol{u}}_t + \left( \frac{1}{2\beta} - 1 \right) \ddot{\boldsymbol{u}}_t \right) + \\ + \boldsymbol{C} \left( \frac{\gamma}{\beta \Delta t} \boldsymbol{u}_t + \left( \frac{\gamma}{\beta} - 1 \right) \dot{\boldsymbol{u}}_t + \frac{\Delta t}{2} \left( \frac{\gamma}{\beta} - 2 \right) \ddot{\boldsymbol{u}}_t \right) \tag{7}$$

where effective stiffness matrix multiplied with unknown displacement vector $\boldsymbol{u}_{t+\Delta t}$ stands on the left side and the effective loading vector on the right side of the equation. Note that the nonlinear material formulation brings dependence of the stiffness matrix on the displacements, so the solution is searched in an iterative Newton process.

Mass matrix $\boldsymbol{M}$ is not diagonal because the effect of rotational inertia. Shape of the particle is (due to Voronoi tessellation) convex polyhedron that can be decomposed into simplexes (tetrahedra). Tetrahedra inertia tensors are calculated from their vertex coordinates according to [14] and further combined using parallel axis theorem to obtain inertia tensor of a whole particle. Since the model assumes small deformations and rotations, calculation is geometrically linear and mass matrix is constant during the whole simulation. Damping is not considered within this contribution.

## 3 NUMERICAL SIMULATIONS

### 3.1 Geometry and material properties

The model described in the previous sections is applied to simulate set of concrete specimens loaded under various displacement rates. The experimental series of concrete specimens with a shape of an upside down letter L [12] is simulated. Specimen dimensions are $W, D = 500$ mm and $W_1, D_1 = 250$ mm (Fig. 1). Specimen thickness is $t = 50$ mm. Depth of the bottom support is $100$ mm and loading is applied in a distance of $30$ mm from the edge of the specimen. Loading is applied by increasing deformation at constant velocity and the loading force is calculated during the simulations. Loading rates are chosen according to [12] as $0.25$ mm/s for quasi-static loading and 0.1, 0.35, 0.74, 1.0 and 2.4 m/s to study the influence of strain rate.

Material parameters are taken from [12]. Macroscopic Young's modulus is $E = 32.2$ GPa and Poisson's ratio is $\nu = 0.18$; the corresponding elastic meso-scopic parameters at the interparticle contacts are obtained from Eq. (3): meso-scale elastic modulus $E_0 = 50$ GPa and normal-tangential stiffness ratio $\alpha = 0.237$, respectively. Further material properties

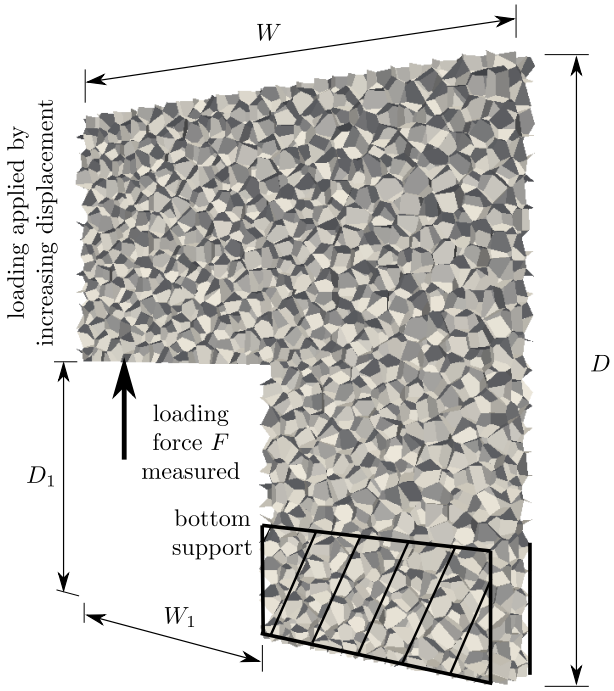


Figure 1: Geometry of simulated specimen showing particle model structure.

taken from [12] are the following: material density $\rho = 2210\,\text{kg/m}^3$ and tensile strength $f_t = 3.12\,\text{MPa}$. The meso-scopic fracture energy for tensile failure was identified from the quasi-static loading rate according to the experiments as $G_f = 35.5\,\text{N/m}^2$. Other properties defining the constitutive relations of the model are obtained from the listed parameters according to the recommendations in [4].

### 3.2 Influence of material parameters

For static loading, both the elastic and fracture material characteristics plays a crucial role. The maximum loading force is mainly influenced by the stiffness parameter $E_0$, tensile strength $f_t$ and meso-scopic fracture energy $G_f$. There is no effect of material density, $\rho$. With increasing loading rate, the effect of fracture parameters diminish, the most important material parameters become $E_0$ and $\rho$.

To demonstrate this trend, influence of these material properties was studied. The structural response was calculated with 1.5 $\times$ increased parameters $E_0$, $f_t$, $G_f$ and $\rho$. Model response is plotted in graphs in Fig. 2. The percentual change of maximum load for increased values of parameters is shown in Fig. 3. The elastic modulus $E_0$ is strongly influential for all displacement rates. The influence of tensile strength $f_t$ and fracture energy $G_f$ at increased loading rate almost disappear, while the influence of material density $\rho$ takes their place. However, the influence of the fracture parameters appears again for rates larger or equal to 0.74 m/s. This is caused by cracking in the area of applied load (Fig. 5), which was not observed experimentally in [12].

To demonstrate that the cracking at loading is responsible for re-appearance of the fracture parameters among the influential material parameters for high displacement rates, the model made of ideally elastic material was analyzed. In Fig. 4, experimental, elastic and inelastic responses are shown. One can see that for rate 0.1 m/s, the elastic and inelastic models behave

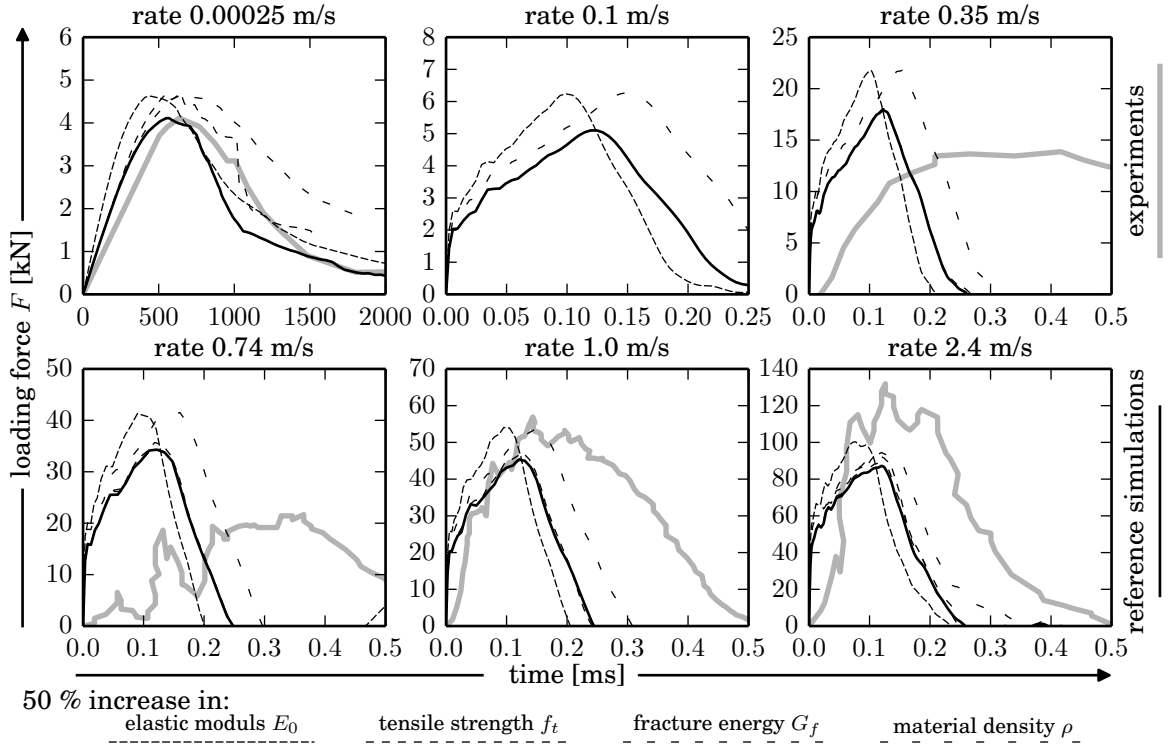


Figure 2: Response of numerical simulations at various displacement rates compared with experimental curves from [12].

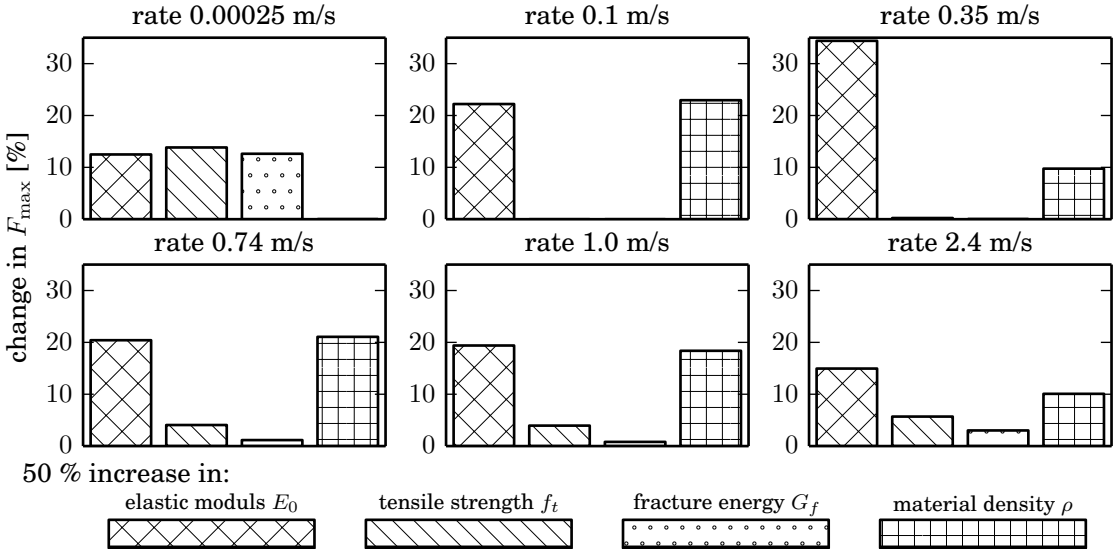


Figure 3: Effect of selected material parameters at various displacement rates.

the same. The cracking does not have any effect on loading force. But for rates 1.0 m/s and 2.4 m/s, the cracking effect appears. Therefore, the inelastic processes must happen much closer to the loading point, i.e. in the loading area.

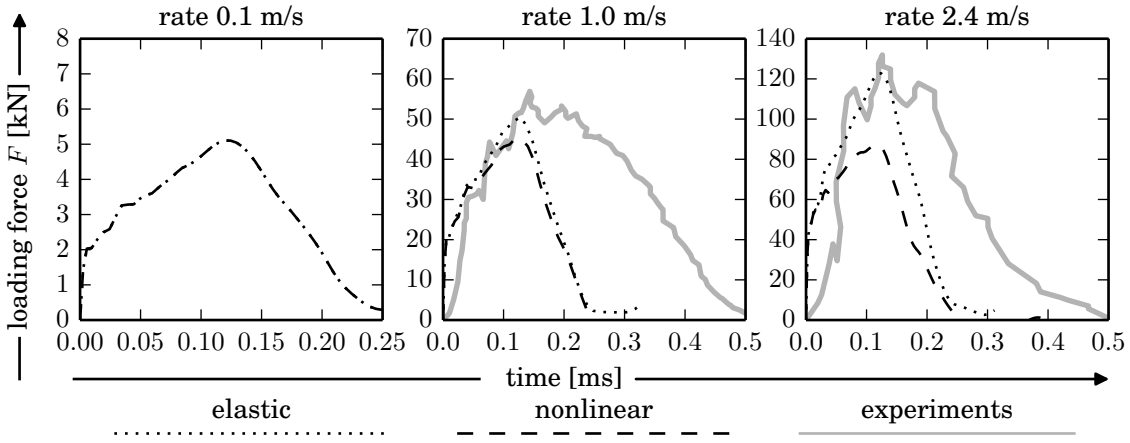


Figure 4: Comparison of nonlinear vs. elastic response of the model

### 3.3 Crack patterns

In Fig. 5, the discrete structure representing material is plotted. Facets (contacts between particles) are colored according to their damage parameter $\omega$ at the end of the simulation. These damaged facets represent crack in the material. One can see different crack path for different loading rates, the trend is in agreement with the experiment [12]. For quasi-static loading, the crack propagates in horizontal direction. With increasing loading rate, crack changes its direction towards vertical. When the velocity of applied load is increased further, multiple cracking and crack branching occur. The experimental evidence, however, does not show extensive cracking in the loading area at rate 2.4 m/s.

### 3.4 Peak loads

The agreement of the model response and experimental data is rather poor. Reasonable match is for quasi-static rate, where the material parameters were identified. For rates 0.35 and 0.74 m/s, the model overestimates the maximum loads, while for rate 1.0 and 2.4 m/s, the experimental response yields higher peak loads. This can be seen in Fig. 6, where experimental and simulated elastic and inelastic maximum forces are plotted. When talking about peak force in elastic simulation, we mean the first peak in the response. Of course, response of all elastic simulations oscillates around the static solution which is increasing to infinity. There is no peak in quasi-static solution so that data-point is missing in Fig. 6.

The elastic responses for the two highest loading rates agree with the experiment very well. If one can eliminate cracking from the loading area, the agreement between the model and experiment would be reasonable. The other two intermediate rate already behaves as if the model is elastic, no improvement can be expected there. However, looking at Fig. 6, these two intermediate rate shows unexpectedly low experimental peak forces compared to the higher rates. Therefore, we consider the difference to be related to the inevitable experimental scatter.

One way how to eliminate the cracking in the loading area for high loading rates can be gradual increase in displacement rate $v$. Instead of direct application of the loading velocity, we intruduced smooth transition controlled by single parameter $t_0$.

$$u_l = \begin{cases} \left(0.5t^2 + \frac{t_0}{4\pi^2}\cos(2\pi\frac{t}{t_0}) - \frac{v}{t_0}\right)\frac{v}{t_0} & t \le t_0 \\ v\ t - v\ t_0\ u_l(t_0) & t > t_0 \end{cases} \tag{8}$$

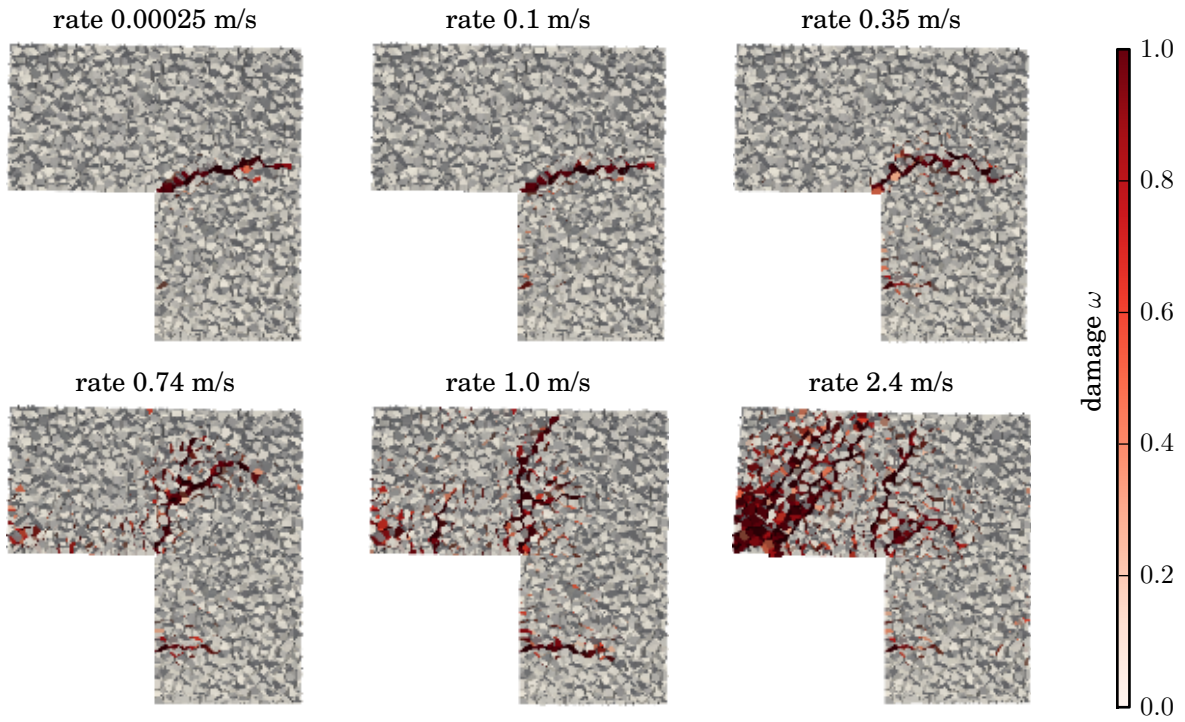


Figure 5: Different crack pattern obtained with particle model for various displacement rates.

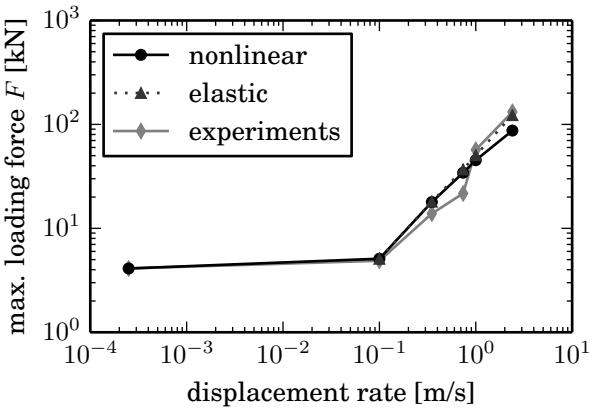


Figure 6: Relation between maximum loading force and displacement rate.

where $u_l$ is the applied displacement at the area of loading and $t_0$ is initial transition period after which correct loading velocity is achieved. This analytical formula ensures smooth transition from initial motionless state to full loading speed for displacements, velocities and accelerations.

Using formula (8), simulations of specimens loaded under displacement rate 2.4 m/s were performed. Obtained responses and cracks pattern are shown in upper part of Fig. 7. Some reduction of crushing close to the loading point is possible. However to eliminate it or at least substantially reduce, time $t_0$ needs to be relatively large, the maximum force occurs in the transitional time and the full displacement rate is achieved too late.

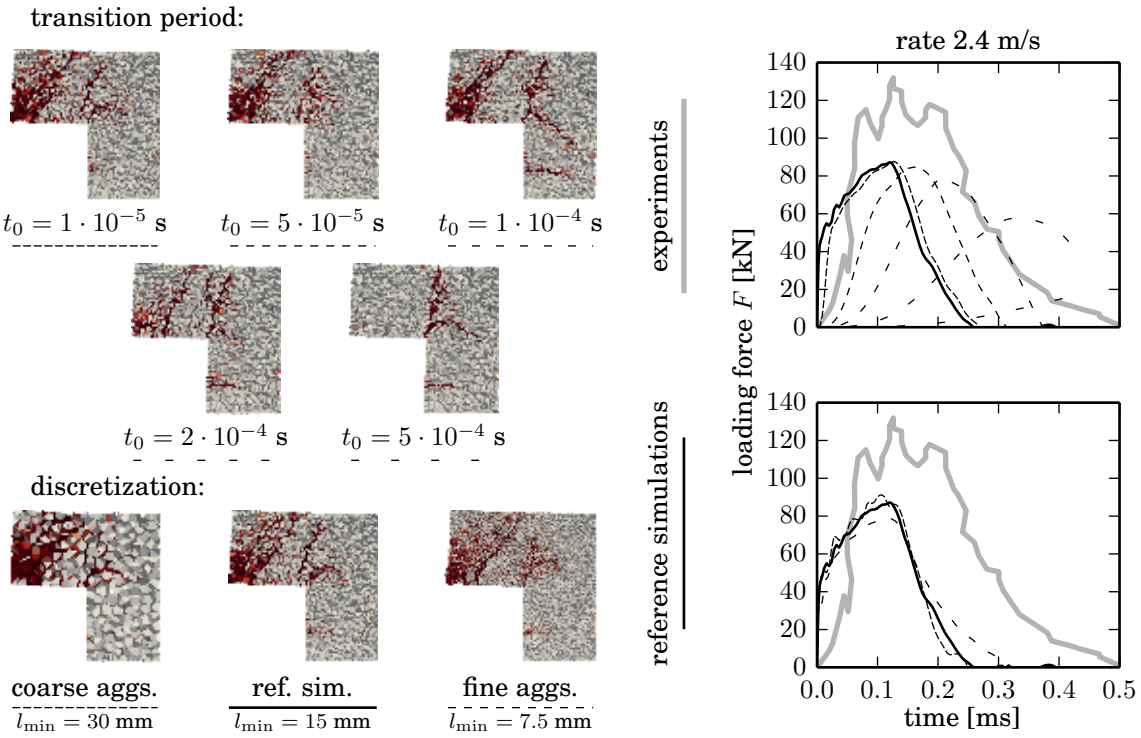


Figure 7: Effect of gradual increase of displacement rate and particle size.

Up to this point, particle size $l_{\min} = 15$ mm was used. Since this model uses crack band concept [3], the discretization does not influences the model response for cases where the crack is localized. However, the cracking in the loading area is highly distributed and strong dependence on discretization density is expected. The results for simulation using doubled and halved particle size are shown in lower part of Fig. 7. Note that for coarse discretization there are only two particles within the specimen thickness. The finer (coarser) discretization yields lower (higher) peak loads than the reference simulation, respectively. This increase or decrease in the peak load can be at least partially caused by the random discretization of the model geometry as mentioned in sec. 2.1.

## 4 CONCLUSIONS

The presented discrete model was used for dynamic simulations of concrete specimens loaded under various displacement rates. The influence of material properties on the time dependent response was studied. The major trend is that the higher loading rates lead to increased effect of density and reduced effect of nonlinear material properties. However, local cracking in the loading area brings back the influence of nonlinear material parameters for very high loading rates.

Expected increase in the maximum loading force and change in the mechanism of failure with increasing strain rate was observed. Comparison to the experimental data [12] shows discrepancies. These differences are caused by cracking in the loading area, which was not observed in the experiment.

## 5 ACKNOWLEDGEMENTS

Financial support provided by the Czech Science Foundation under project No. 15-19865Y and additional support by project No. FAST-J-17-4583 is gratefully acknowledged.

## REFERENCES

[1] K.-J. Bathe. *Finite element procedures*. Prentice Hall, Englewood Cliffs, N.J., 1996.

[2] Z. P. Bažant and F.B. Lin. Nonlocal smeared cracking model for concrete fracture. *Journal of Structural Engineering*, 114(11):2493–2510, 1988.

[3] Z.P. Bažant and B.H. Oh. Crack band theory for fracture of concrete. *Matriaux et Constructions*, 16(3):155–177, 1983.

[4] G. Cusatis and L. Cedolin. Two-scale study of concrete fracturing behavior. *Engineering Fracture Mechanics*, 74(1-2):3–17, 2007.

[5] Gianluca Cusatis, Daniele Pelessone, and Andrea Mencarelli. Lattice discrete particle model (LDPM) for failure behavior of concrete. I: Theory. *Cement & Concrete Composites*, 33(9):881–890, 2011.

[6] J. Eliáš. Adaptive technique for discrete models of fracture. *International Journal of Solids and Structures*, 100–101:376–387, 2016.

[7] J. Eliáš. Boundary layer effect on behavior of discrete models. *Materials*, 10(2):157, 2017.

[8] Y.K. Hwang, J.E. Bolander, and Y.M. Lim. Simulation of concrete tensile failure under high loading rates using three-dimensional irregular lattice models. *Mechanics of Materials*, 101:136–146, 2016.

[9] E. Kuhl, G.A. D'Addetta, H.J. Herrmann, and E. Ramm. A comparison of discrete granular material models with continuous microplane formulations. *Granular Matter*, 2(3):113–121, 2000.

[10] J. M. Melenk and I. Babuška. The partition of unity finite element method. *Computer Methods in Applied Mechanics and Engineering*, 139:289–314, 1996.

[11] N. Newmark. *A method of computation for structural dynamics*. University of Illinois, Urbana, 1959.

[12] J. Ožbolt, N. Bede, A. Sharma, and U. Mayer. Dynamic fracture of concrete l-specimen. *Engineering Fracture Mechanics*, vol. 148:27–41, 2015.

[13] J. Smith and G. Cusatis. Numerical analysis of projectile penetration and perforation of plain and fiber reinforced concrete slabs. *International Journal for Numerical and Analytical Methods in Geomechanics*, 41(3):315–337, 2017.

[14] F. Tonon. Explicit exact formulas for the 3-D tetrahedron inertia tensor in terms of its vertex coordinates. *Journal of Mathematics and Statistics*, 1(1):8–11, 2005-1-1.

[15] J. G. M. van Mier. *Concrete fracture*. CRC Press, Boca Raton, FL, 2013.

COMPDYN 2017
6th ECCOMAS Thematic Conference on
Computational Methods in Structural Dynamics and Earthquake Engineering
M. Papadrakakis, M. Fragiadakis (eds.)
Rhodes Island, Greece, 15–17 June 2017

# PRELIMINARY COMPARISON BETWEEN DIFFERENT SOFTWARE MODELING OF CONFINED CONCRETE

**Elide Nastri**[1], **Maria I. Palese**[1]

[1] University of Salerno
Via Giovanni Paolo II, 84084, Fisciano (SA), Italy
e-mail: enastri@unisa.it

**Keywords:** Confined Concrete, Sap2000, Parametric Analysis, Moment-curvature, OpenSees, Seismostruct

**Abstract.** *The aim of the work is, on the one hand, the presentation of a theoretical fiber model able to predict the moment-curvature behaviour of confined RC columns and, on the other hand, the comparison between the moment-curvature provided by common structural programs. The theoretical fiber model presented in the paper is implemented in a visual basic software and it is able provide moment-curvature ($M-\chi$) diagrams for sections with or without axial load. The software considered in this work are Sap2000, Seismostruct and Opensees. The moment-curvature curves provided by these softwares, given the same modeling have been compared to those provided by the theoretical fiber model. In particular, the modeling has been carried out by subdividing the sections in three category of fibers: unconfined concrete fibers, confined concrete fibers and rebar fibers. The constitutive model adopted for concrete is the one proposed by Mander et al. (1988) [1] for both the confined and unconfined concrete. The constitutive model adopted for the steel rebars is an elastic perfectly plastic law. The parametric analysis has been led on rectangular column sections with different level of axial load. The accuracy of the modelling of the considered structural programs has been investigated by comparing the results belonging to them with those obtained by applying the theoretical fiber model. Besides the calculation of the moment-curvature it is possible to observe that the curves representative of SAP2000 are more in accord with the curve representative of the theoretical software, on average. Form the Seismostruct side, it is possible to observe that the resistance is well captured by the software but for increasing levels of the axial load the Seismostruct overestimate the resistance. Results become more different from the theoretical model when the axial load level increases.*

## 1 INTRODUCTION

It has long been recognized that strength, as well as ductility of concrete, increase whenever its state of stress is a triaxial compression. The concrete affected by this favorable action of the transverse reinforcement is called confined concrete.

Confinement offers two main advantages regarding the seismic behaviour of concrete structural elements: it increases strength of concrete, which compensates for possible losses caused by spalling and it reduces the slope of the descending branch of the $\sigma_c - \varepsilon_c$ curve.

In this paper, the results of various software able to predict the moment-curvature behaviour of confined RC columns are reported with reference to a rectangular cross section of a R.C. columns extrapolated from a building designed according to the modern seismic codes. The aim of the work is, on the one hand, the presentation of a theoretical fiber model able to predict the moment-curvature behaviour of confined RC columns and, on the other hand, the comparison between the moment-curvature provided by common structural programs. The theoretical fiber model presented in the paper is implemented in a visual basic software and it is able provide moment-curvature (M−χ) diagrams for sections with or without axial load basing on the the constitutive model of confined concrete proposed by Mander et al. (1988) [1]. The software considered in this work are Sap2000, Seismostruct and Opensees.

## 2 REVIEW OF CONFINED CONCRETE MODELS

The confined concrete theoretical model assume a stress-strain constitutive law different for different zones of the same sections. Concrete can be considered effectively confined or not by the actions of the lateral reinforcement. Therefore, in the same section, different constitutive laws could be adopted for the part of the concrete effectively confined and for the unconfined one.

As regards the confined concrete, it has been demonstrated that the strength and the corresponding longitudinal strain at the strength of concrete confined by an active hydrostatic fluid pressure can be represented by the following simple relationship:

$$f'_{cc} = f'_{co} + k_1 f_l \tag{1}$$

$$\varepsilon_{cc} = \varepsilon_{co}\left(1 + k_2 \frac{f_l}{f'_{co}}\right) \tag{2}$$

where $f'_{cc}$ and $\varepsilon_{cc}$ are the maximum concrete stress and the corresponding strain, $f_l$ is the lateral fluid pressure, $f'_{co}$ are $\varepsilon_{co}$ the unconfined concrete strength and the corresponding strain, $k_1$ and $k_2$ are coefficients functions of the concrete mix and the lateral pressure.

Richart et al. (1928) [1] found the average values of the coefficients for the tests they conducted to be $k_1 = 4{,}1$ and $k_2 = 5k_1$. Instead, Balmer (1949) [3] found from his tests that $k_1$ varied between 4,5 and 7,0 with an average value of 5,6, the higher values occurring at the lower lateral pressures. Richart et al. (1929) [4] also found that the strength of concrete with active confinement from lateral (fluid) pressure was approximately the same as for concrete with passive confinement pressure from closely spaced circular steel spirals causing an equivalent lateral pressure.

1) Afterwards, the problem of the confined concrete has been widely investigated. It has been demonstrated that confinement is improved if:
2) The transverse reinforcement is placed at relatively close spacing;
3) Additional supplementary overlapping hoops or cross ties with several legs crossing the section are included;
4) The longitudinal bars are well distributed around the perimeter;

5) The volume of transverse reinforcement to the volume of the concrete core or the yield strength of the transverse reinforcement is increased;
6) Spirals or circular hoops are used instead of rectangular hoops and supplementary cross ties.

However, it is important to be able to quantify these effects of confinement on the stress-strain behavior of concrete. The stress-strain model of Kent and Park (1971) [5] for concrete confined by rectangular transverse reinforcement was based on the test results of Roy and Sozen (1964) [6] and others available at the time. This model neglected the increase in concrete strength but took into account the increase in ductility due to rectangular confining steel. Subsequently, Park et al (1982) [7] and Scott et al. (1982) [8] have tasted near full-size specimens based on real building columns and modified the Kent and Park [5] stress-strain equations to take in account the enhancement of both the concrete strength and ductility due to confinement and the effect of strain rate. Other monotonic stress - strain equations for concrete confined by rectangular - shaped transverse reinforcement have been proposed by Vellenas et al. (1977) [9] and Sheikh and Uzumeri (1980, 1982) [10], [11]. In particular, Sheikh and Uzumeri [10], [11] proposed a stress-strain model of similar form the one proposed by Park et al. [7]. This model incorporates the confinement effects by adjusting the peak stress and setting a confinement effectiveness coefficient. The confinement effectiveness coefficient depends on the configuration of the hoop reinforcement. Stress-strain equations for concrete confined by spiral reinforcement have been proposed by Park and Leslie (1977) [12], Desay et al. (1978) [13], Ahmad and Shah (1982, 1985) [14], [15], Dilger et al. (1984) [16], and others.

Mander, Priestley and Park (1988) [1] proposed an unified stress - strain model for confined concrete, both for circular or rectangular sections, under static or dynamic loading, either monotonically or cycling applied. More recently, Mander and Chang (1994) [17] developed a hysteretic model for confined and unconfined concrete subjected to both tension or compression cyclic loading. This concrete stress-strain model is a modern version of the well-known Mander, Priestley and Park [1] model and has been enhanced to predict the behaviour of high strength concrete. The model is also capable of simulating gradual crack closure under cyclic loading. However, the monotonic part of the model is perfectly coincident with the Mander, Priestley and Park model.

The need to improve the seismic performances of existing buildings or to retrofit them according to the new-seismic regulations is a more and more pressing need in areas subjected to high seismic risk [18]-[25]. Among the new available technologies, great attention has received the confinement of structural members by applying one or more layers of fiber-reinforced materials in a polymeric matrix (FRP) bonded to the element's surface. The increasing use of confinement by FRP requires analytical models able to predict the behavior of confined concrete elements. Many researchers have developed and proposed different constitutive laws. Some of them require an iterative procedure, some require, as collapse condition, the attainment of the ultimate value of concrete axial strain, while others refer to the ultimate strain of FRP; finally, some of them consider only the maximum value of the lateral confining pressure, while others its whole development as a function of the concrete axial strain. Generally, these constitutive laws are based on the definition of the confined concrete maximum strength ($f_{cc}$) and the corresponding maximum strain ($\varepsilon_{cc}$). To estimate the ultimate strength of reinforced concrete elements confined with FRP, several relationships can be found in literature [25], [27]. They are based on the preliminary evaluation of the ultimate lateral confining pressure, and on the assumption that concrete collapse occurs when FRP layers reach their ultimate stress [28]-[37]. A large comparison of this constitutive models is reported in [38]-[39] while in this paper reference is made to unreinforced sections only. To take in account the confinement behavior of

structural members is also important in the design phase. In fact, the benefic effects of confinement lead to a higher resistance with a consequent overstrength in the members that has to be taken in account in the application of beam-to-column hierarchy criterion as the same as of shear-bending hierarchy criterion. This consideration coupled with more sophisticated design approaches [40]-[43] allows to assure that structures are able to exploit at the collapse their full dissipative capacity leading to a collapse mechanism of global type.

## 3 MOMENT-CURVATURE OF REINFORCED CONCRETE COLUMNS

In this work, the moment-curvature of reinforced concrete columns affected by confinement has been provided by means of three software: SAP2000, SeismoStruct and Opensees programs which can simulate the inelastic response of structural systems subjected to static loads. In particular, push-over analyses have been carried out to obtain the plastic response. Obtained results have been compared with those provided by a research software based on a fiber modelling called MCCRCCS (Moment-Curvature Confined Reinforced Concrete Column Sections).

The philosophy which the fiber hinge model is based on, subdivides the cross section of the structural element in three types:

1) fibres used for modelling the longitudinal steel reinforcing bars;
2) fibres used to define the nonlinear behaviour of confined concrete
3) fibres used to define the nonlinear behaviour of unconfined concrete which includes cover concrete.

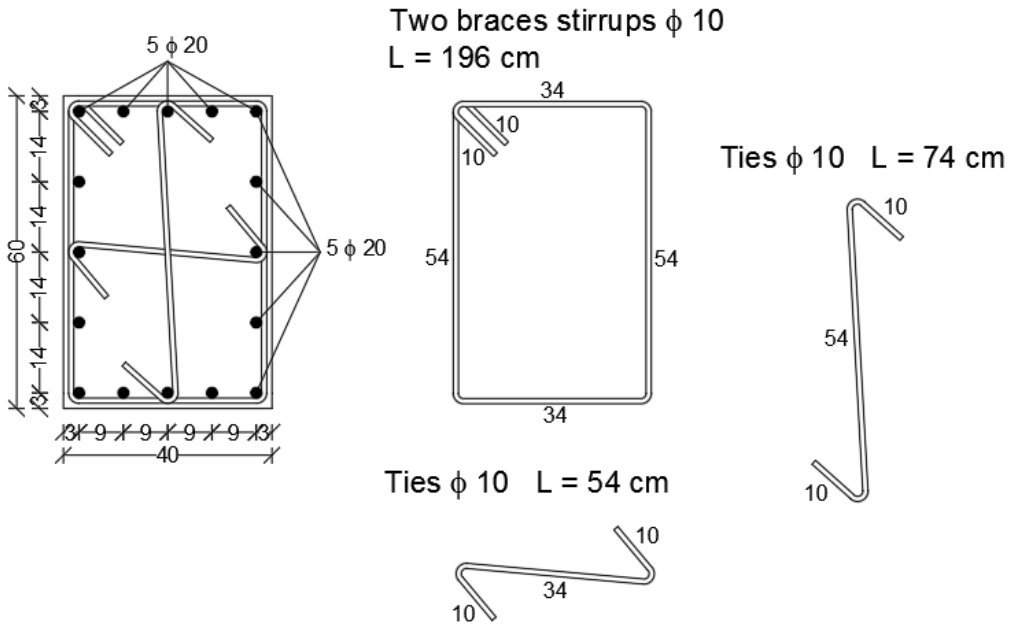


Fig. 1. Cross section of column specimens

For each fiber, the stress-strain (σ-ε) constitutive law is determined. The geometry, dimensions and reinforcing details of the specimens are shown in Fig. 1. Each specimen represents a cantilever column whose length is 3.00 m. The specimens have rectangular cross-sections with dimensions 0.40x0.60 $m^2$. The longitudinal reinforcement of the columns in both lateral faces is composed of sixteen bars of 20 mm diameter. The shear reinforcement in the columns was composed of 10 mm diameter stirrups spaced at 0.12 m. The concrete material is a C25/30 and the reinforcement material is B450C steel.

Table 1 summarizes the mean values of the material properties used in the construction of the specimens, where $f_{ck}$ is the cylindrical concrete compressive strength and $\varepsilon_{co}$ is the corresponding strain; $f_{cc}$ is the compressive strength of confined concrete and $\varepsilon_{cc}$ is the corresponding strain; $\varepsilon_{cu}$ is the ultimate strain; $\varepsilon_{sp}$ is the concrete spalling strain; $f_t$ is the tensile strength of concrete; $E_c$ is the Young modulus of concrete; $f_{yk}$ is the yield strength of the reinforcement; $E_y$ is the Young modulus of steel.

Table 1. Mechanical properties of steel and concrete

| | | Confined Concrete | | | | Unconfined Concrete | | | Steel | |
|---|---|---|---|---|---|---|---|---|---|---|
| s | $E_c$ | $f_{cc}$ | $f_t$ | $f_{cc}$ | $f_{cu}$ | $f_{ck}$ | $\varepsilon_{co}$ | $\varepsilon_{sp}$ | $E_y$ | $f_{yk}$ |
| [cm] | [MPa] | [MPa] | [MPa] | [-] | [-] | [MPa] | [-] | [-] | [MPa] | [MPa] |
| 12 | 25000 | 31.375 | 2.5 | 0.00455 | 0.017173 | 25 | 0.002 | 0.01 | 210000 | 450 |

The Eq. (5) proposed by Mander et. al. [1] has been applied to define the stress-strain constitutive model of both confined and unconfined concrete according to the mechanical properties reported in Table 1. In Fig. 2, the constitutive laws referring to confined concrete and unconfined concrete are reported. In particular, the distance $b_c$ and $d_c$ are taken to center lines of perimeter hoop in $x$ and $y$ directions as suggested by Mander et al. [1]. In fact it has been observed that, taking the distance $b_c$ and $d_c$ net of the cover concrete does not affect the results in terms of stress-strain constitutive law. In addition, 5 level of vertical loads have been applied by considering a percentage of the resistant axial load ($N_{Rd}$= 8136 kN) of the section. The selected percentage are 0%, corresponding to simple bending, 10%, 20%, 30% and 40%.

For the steel reinforcements an elastic-perfectly plastic constitutive law has been adopted according to the mechanical properties reported in Table 1.

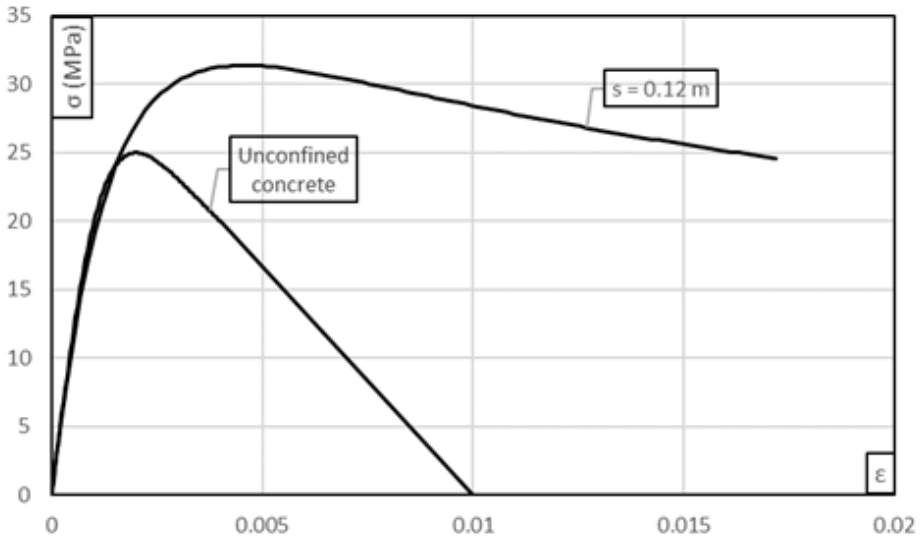


Fig. 2. σ-ε constitutive law for concrete modelling

## 4 SOFTWARE ADOPTED

### 4.1 MCCRCCS Research software

Starting from the stress-strain models reported in Fig. 2, a procedure for computing the moment-curvature diagram can be easily outlined on the basis of a fiber model. The cross section has been subdivided into rectangular elementary areas which have been characterized by an

appropriate constitutive law: unconfined concrete, confined concrete and steel of the longitudinal reinforcements. In order to account for the effect of the load acting on the unstrengthened structural member, the deformations occurring in each elementary area before the strengthening intervention have to be computed and considered in the subsequent analysis. The different zones of the section, both confined and unconfined, need to be preliminarily recognized. To this aim, the longitudinal confining bars, which are those located in the corners or those out of corners, but restrained by steel ties, have to be identified. Starting from these restraining points, it is possible to determine the parabola arches dividing the zones of effectively confined concrete from the zones of unconfined concrete, as it is shown in Fig. 3.

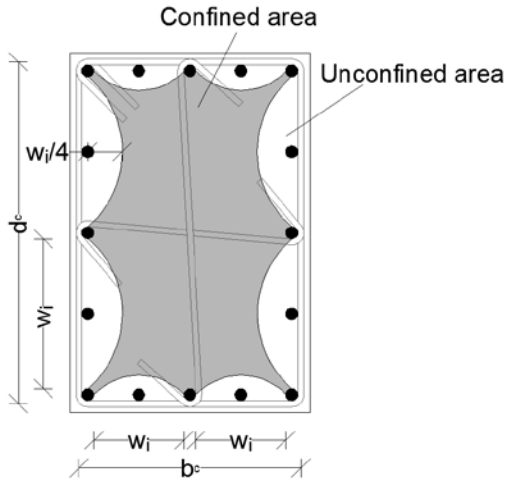


Fig. 3. Identification of confined and unconfined concrete

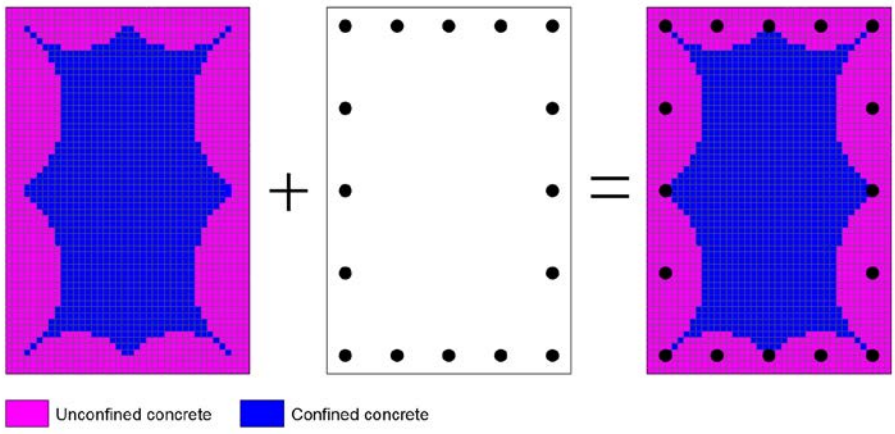


Fig. 4. Fiber subdivision of the cross section

On the bases of the constitutive laws of steel, confined concrete and unconfined concrete, the procedure for evaluating the moment-curvature diagram, for a given axial load has been codified into a computer program namely MCCRCCS. The same code has been used by Montuori and Piluso in a previous work dealing with the behaviour of reinforced concrete columns strengthened with angles and battens [33]. The fiber subdivision of the section is reported in Fig. 4 where it is possible to observe that 40 fibres longitudinally and 60 fibres transversally have been adopted. The areas of steel longitudinal bars have been introduce by their coordinates.

### 4.2 Sap2000

SAP2000 v. 14.0.0 is general-purpose civil-engineering software used for the analysis and design of any type of structural system [35]. As regard plastic analysis, it allows to account for lumped and spread plasticity by means of concentrated plastic hinges and fiber hinges whose length can be properly selected to capture the actual plastic behaviour of the members. In this work, fiber hinge modelling has been exploited by introducing in the software, a user defined fiber section. In particular, the section has been discretized in 60x40 small areas of 1 $cm^2$ following the same subdivision depicted in Fig. 4 and adopted for the MCCRCCS. For both confined and unconfined concrete the corresponding stress strain relationship has been implemented. Each rebar has been introduced as circular areas and applying a stress-strain relationship of the steel. Concrete materials have been introduced by means of the advanced properties of material ambiance accounting for the "Mander" shape of stress-strain behaviour already implemented for uniaxial material typologies. To provide the moment-curvature of the specimen sections push-over analyses have been carried out on a cantilever scheme whose length is 3 m. The elastic behaviour of the member has been simulated by means of a beam-column element with a 60x40 concrete section. To this element, a fiber hinge whose length is equal to the 10% of the global length of the cantilever has been applied to the base extreme. The analyses have been led in displacement control for each level of axial load, taking in account both geometrical and mechanical non linearities.

### 4.3 OpenSees

The Open System for Earthquake Engineering (OpenSees) [34] is an open source software framework for finite analysis and it was developed to simulate the response of structural and geotechnical systems subjected to earthquakes. Uniaxial material Concrete04 is used to construct a uniaxial concrete material whose envelope of the compressive stress-strain response is defined using the model proposed by Popovics (1973) [32]. If the user defines the Young modulus as $E_c = 5{,}000\sqrt{f'_{co}}$ then the envelope curve is identical to the one proposed by Mander et al. [1]. In this model the compressive stress is equal to zero when the crushing strain is achieved. In addition, it is possible to introduce a tensile stress different to zero.

The material Steel01 is used to construct a uniaxial bilinear steel material object with kinematic hardening and optional isotropic hardening described by a non-linear evolution equation. It has been used in both the nonlinear model to simulate the stress-strain behaviour of the reinforcing bars. The hardening has been assumed very low (0.0001) to represent an elastic-perfectly plastic behaviour. To provide the moment-curvature of the specimen sections, push-over analyses have been carried out on a cantilever scheme whose length is 3 m. The nonlinear-BeamColumn element has been introduced to model the cantilever scheme and it is represented by unidirectional fibres which are assigned by the proper material stress-strain relationships describing the materials monotonic response. It is based on the non-iterative force formulation and considers the spread of plasticity along the element. The section discretization is the same reported in Fig. 4 and it has been introduced by using the "fiber" section command in the software input file. In addition, five integration points were adopted for the column element. Analysis has been led in displacement control take in account geometrical and mechanical non linearities for each axial load level.

### 4.4 SeismoStruct

The SeismoStruct 2016 [36] is a finite element package capable of predicting the large displacements behaviour of space frames under static or dynamic loading, taking into account geometric nonlinearities and material inelasticity. For each specimen section a nonlinear model

was developed. The model was built with inelastic displacement based frame elements. In Seismostruct ambiance it is not possible to define a user defined fiber section so that, the material models con_ma (Mander et al. [1]) has been adopted for both the confined and unconfined concrete. This is a uniaxial nonlinear constant confinement model that follows the constitutive relationship proposed by Mander et al. [1].

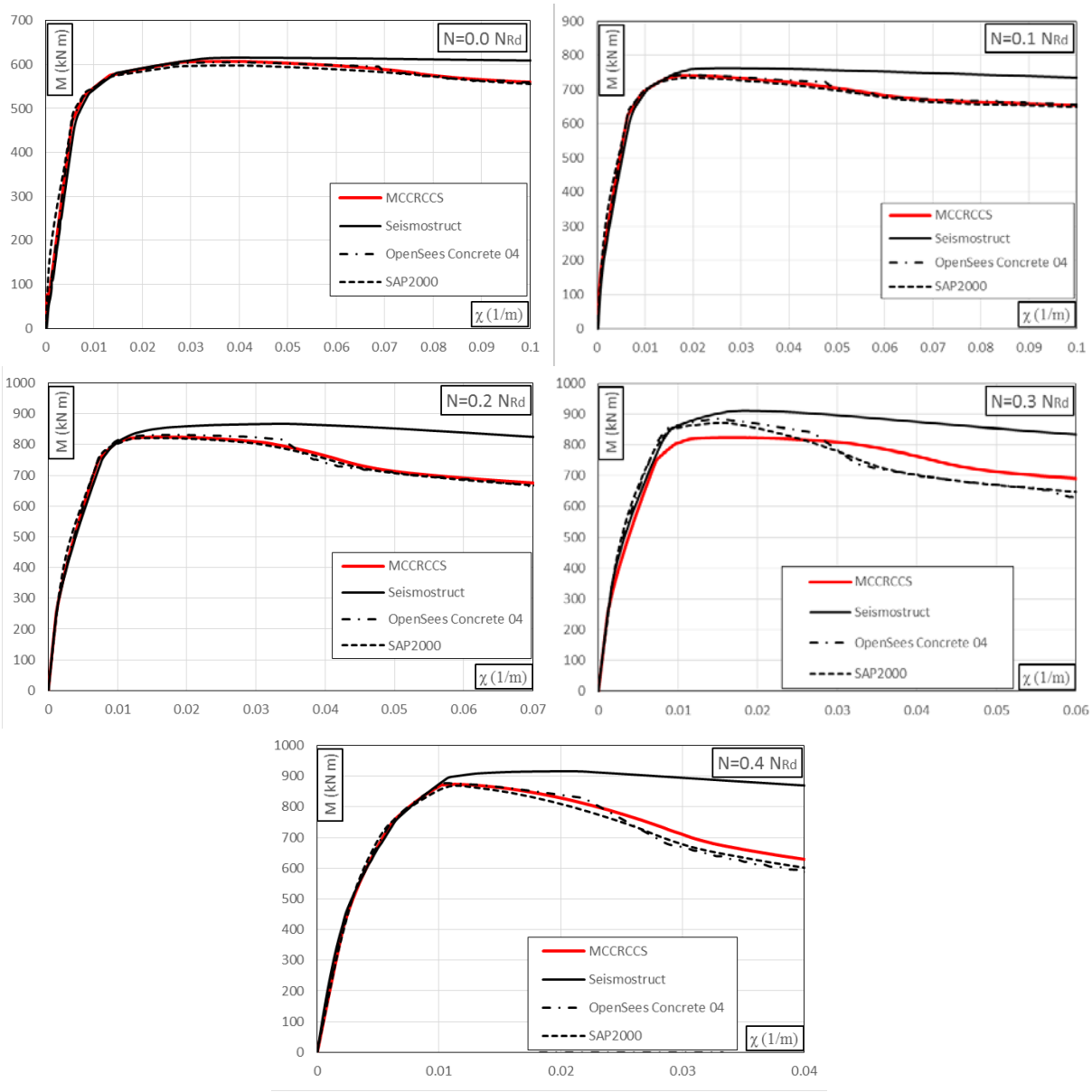


Fig. 5. Moment curvature (M−χ) diagrams

The confinement effects provided by the lateral transverse reinforcements are incorporated through the rules proposed by Mander et al. whereby constant confining pressure is assumed through the entire stress-strain range. The effectiveness of the Seismostruct modelling has been preliminarily validated by checking the confinement ratio parameter ($f'_{cc}/f_c$) provided by the software. In the case of unconfined concrete a confinement ratio equal to 1 has automatically assumed by the software.

In addition, stl_bl is adopted for the reinforcement with a very low hardening parameter to simulate an elastic-perfectly plastic behaviour (0.0001). The section has been discretized into

1000 fibers (the maximum number of fibers available in the software). To provide the moment-curvature of the specimen sections, push-over analyses have been carried out on a cantilever scheme whose length is 3 m discretized in 4 parts for each level of axial load.

## 5 RESULTS

Besides the calculation of moment-curvature (M−χ) diagrams the aim of the work is to discover how the different software modelling affects the shape of M−χ diagram. In Fig. 5, the moment-curvature diagrams of the section with the stirrups spacing of 0.12 m are reported, respectively. In addition, in the same figures the moment-curvature diagrams are reported with reference to different levels of the axial load. In a first comparison it is possible to observe that the curves representative of SAP2000 are more in accord with the curve representative of MCCRCCS on average. In particular, SAP2000 is able to well catch the resistance but it is not able to reproduce the softening branch of the research program. Form the Seismostruct side, it is possible to observe that the resistance is well captured by the software but for increasing levels of the axial load the Seismostruct overestimate the resistance. The OpenSees well captures both the resistance than the softening branch of the curve. Finally, the softening branch of the Seismostruct diagrams are always higher than those provided by other models. Generally speaking, it is possible to observe that the resistance is well captured by the largest part of the software. In addition, the results between the curves became more different as the axial load increase. It is also important to observe that curves has to be stopped at the occurrence of the section collapse which can be achieved in correspondence of the confined concrete cracking or the achievement of the ultimate deformation of rebars. Being this work only preliminary the attention has been focused on the resistance and on the shape of the softening branch of M−χ curves. Further investigations on different sections with different stirrups spacing have to be performed to achieve a more robust conclusion.

## 6 CONCLUSIONS

- In this work, a theoretical model to provide moment-curvature of confined reinforced concrete sections has been presented.
- The results obtained with such methodology have been compared with those provided by common structural programs such as Sap2000, OpenSees and Seismostruct.
- Besides the calculation of a moment-curvature (M−χ) it is possible to observe that the curves representative of SAP2000 are more in accord with the curve representative of MCCRCCS on average.
- Form the Seismostruct side, it is possible to observe that the resistance is well captured by the software but for increasing levels of the axial load the Seismostruct overestimate the resistance.
- The OpenSees well captures both the resistance than the softening branch of the curve.
- In future works the parametric analysis will be extended to other sections with different stirrups spacing, placing the attention also on the point in which the section achieve the collapse.

## REFERENCES


[1] J.B. Mander, M.J.N. Priestley and Park R., “Theoretical stress-strain model for confined concrete”, *J Struct Eng, ASCE 1988*;114(8):1804_26.

[2] F.E. Richart, A. Bradtzaeg and R. L. Brown. “A study of the failure of concrete under combined compressive stresses”, Bulletin No. 185, *Engineering experimental station University of Illinois*, Urbana, pp. 104, 1928.

[3] G. G. Balmer, "Shearing strength of concrete under high triaxial stress - computation of Mohr's envelope as a curve." SP-23, *Structural Research, Laboratory, U.S. Bureau of Reclamation*, 1944.

[4] F. E. Richart, A. Brandtzaeg and Brown, R. L., "The failure of plain and spirally reinforced concrete in compression." *Bulletin 190, Univ. of Illinois Engineering Experimental Station*, Champaign, 111, 1929.

[5] Kent, D. C., and Park, R., "Flexural members with confined concrete." *J. Struct. Div.*, ASCE, 97(7), 1969-1990, 1971.

[6] Roy, H. E. H., and Sozen, M. A. (1964). "Ductility of concrete." *Proc. Int. Symp. on the Flexural Mech. of Reinforced Concrete, ASCE-American Concrete Institute*, 213-224.

[7] Park, R., Priestley, M. J. N., and Gill, W. D. (1982). "Ductility of square-confined concrete columns." *J. Struct. Div., ASCE*, 108(4), 929-950.

[8] Scott, B. D., Park, R., and Priestley, M. J. N. (1982). "Stress-strain behavior of concrete confined by overlapping hoops at low and high strain rates." *Am. Concr. Inst. J., 79(1)*, 13-27.

[9] Vellenas, J., Bertero, V. V., and Popov, E. P. (1977). "Concrete confined by rectangular hoops subjected to axial loads." Report 77/13, *Earthquake Engineering Research Center*, Univ. of California, Berkeley, Calif.

[10] Sheikh, S. A., Uzumeri, S. M. (1980). "Strength and ductility of tied concrete columns." J. Struct. Div., *A.S.C.E.*, 106(5), 1079-1102.

[11] Sheikh, S. A., Uzumeri, S. M. (1982). "Analytical Model for concrete confinement in tied columns" *J. Struct. Div., A.S.C.E.*, 108, 2703-2722.

[12] Park, R., and Leslie, P. D. (1977). "Curvature ductility of circular reinforced concrete columns confined by the ACI spiral." *6th Australasian Conf. on the Mech. of Struct, and Mater.*, vol. 1, 342-349.

[13] Desayi, P., Iyengar, K. T. S. A., and Reddy, T. S. (1978). "Equations for stress-strain curve of concrete confined in circular steel spiral." *Mater, and Struct., Res. and Testing, Paris*, France 11(65), 339-345.

[14] Ahmad, S. M., and Shah, S. P. (1982). "Stress-strain curves of concrete confined by spiral reinforcement." *Am. Conor. Inst. J.*, 79(6), 484-490.

[15] Ahmad, S. M., and Shah, S. P. (1985). "Behavior of hoop confined concrete under high strain rates." *Am. Conor. Inst. J.*, 82(5), 634-647.

[16] Dilger, W. H., Koch, R., and Kowalczyk, (1984). "Ductility of plain and confined concrete under different strain rates." *Am. Conor. Inst. J.*, 81(1), 73-81.

[17] Chang G.A., Mander J.B., “Seismic Energy Based Fatique Damage Analysis of Bridge Columns: Part 1 – Evaluation of Seismic Capacity”, *Technical Report*, March 14, 1994.

[18] A. Formisano, C. Castaldo and G. Chiumento, "Optimal seismic upgrading of a reinforced concrete school building with metal-based devices using an efficient multi-criteria decision-making method", *Structure and Infrastructure Engineering*, 11 February 2017, Pages 1-17

[19] A. Formisano and L. Lombardi, "Perforated shear panels for seismic rehabilitation of existing reinforced concrete buildings", *Civil-Comp Proceedings*, Volume 108, 2015.

[20] A. Formisano, L. Lombardi and F.M. Mazzolani, "Full and perforated metal plate shear walls as bracing systems for seismic upgrading of existing RC buildings", *Ingegneria Sismica*, Volume 33, Issue 1-2, 2015, Pages 16-34.

[21] E. Nastri, M. Vergato and M. Latour, "Performance evaluation of a seismic retrofitted R.C. precast industrial building", *Earthquake and Structures*, Volume 12, Issue 1, 2017, Pages 13-21.

[22] R. Montuori, E. Nastri and V. Piluso, "Modelling of floor joists contribution to the lateral stiffness of RC buildings designed for gravity loads", *Engineering Structures*, Volume 121, 15 August 2016, Pages 85-96.

[23] P. Castaldo, B. Palazzo and P. Della Vecchia, "Life-cycle cost and seismic reliability analysis of 3D systems equipped with FPS for different isolation degrees", *Engineering Structures*, Volume 125, 15 October 2016, Pages 349-363.

[24] P. Castaldo, B. Palazzo, F. Perri, I. Marino and M. M. Faraco, "Seismic retrofit of existing buildings through the dissipative columns", *ECCOMAS Congress 2016 - Proceedings of the 7th European Congress on Computational Methods in Applied Sciences and Engineering*, Volume 4, 2016, Pages 8445-8459.

[25] M. D'Aniello, G. Della Corte and F.M. Mazzolani, "Seismic upgrading of RC buildings by buckling restrained braces: Experimental results vs numerical modelling", *Proceedings of the 5th International Conference on Behaviour of Steel Structures in Seismic Areas - Stessa 2006*, Pages 815-820.

[26] Bisby Luke A., Dent Aaron JS, Green Mark F., "Comparison of confinement models for fiber-reinforced polymer-wrapped concrete", *ACI Struct J 2005;(January–February)*:102–S07.

[27] Matthys S., Toutanji H., Audenaert K., Taerwe L., "Axial load behavior of largescale columns confined with fiber-reinforced polymer composites", *ACI Struct J*, 2005;(March–April):102–S26.

[28] Karbhari VM, Gao Y. Composite jacketed concrete under uniaxial compression – verification of simple design equations. *J Mater Civil Eng*, ASCE 1197;9(4):185–92.

[29] Newman K, Newman J.B. "Failure theories and design criteria for plain concrete", In: *Proceedings of the international civil engineering materials conference on structure, solid mechanics and engineering design*, part 2. New York: Wiley Interscience; 1972. p. 963–95.

[30] M. Samaan, A. Mirmiran and M. Shahawy "Model of concrete confined by fiber composites", *J Struct Eng*, ASCE 1998;124(9):1025–31.

[31] Toutanji HA. Stress–strain characteristics of concrete columns externally confined with advanced fiber composite sheets. ACI Mater J 1999;96(3): 397–405.

[32] L. Lam and J. G. Teng “Strength models for circular concrete columns confined by FRP composites”, Burgoyne C, editor. *Fifth symposium on fiber-reinforced plastic reinforcement for concrete structures (FRPRCS-5)*. London: Thomas Telford; 2001. p. 835–44.

[33] Saafi M, Toutanji HA, Li Z. Behavior of concrete columns confined with fiber reinforced polymer tubes. *ACI Mater J*, 1999;96(4):500–9.

[34] Miyauchi K, Inoue S, Kuroda T, Kobayashi A. Strengthening effects of concrete columns with carbon fiber sheet. Trans Jpn Concr Inst, 1999;21:143–50.

[35] Fardis MN, Khalili H. Concrete encased in fibre glass-reinforced plastic. ACI Mater J 1981;78(5):440–6.

[36] Spoelstra MR, Monti G. FRP-confined concrete model. J Compos Construct, ASCE 1999;3(3):143–50.

[37] Y. Xiao and H. Wu, “Compressive behavior of concrete confined by carbon fiber composite jackets”, *J Mater Civil Eng*, ASCE 2000;12(2):139–46.

[38] R. Montuori, V. Piluso and A. Tisi, “Comparative analysis and critical issues of the main constitutive laws for concrete elements confined with FRP”, *Composites: Part B*, Vol. 43 (2012) 3219–3230, 2012.

[39] Montuori R., Piluso V., Tisi A., “Ultimate behaviour of FRP wrapped sections under axial force and bending: Influence of stress-strain confinement model”, *Composites Part B: Engineering*, Volume 54, Issue 1, 2013, Pages 85-96, 2012.

[40] R. Montuori, E. Nastri and V. Piluso, "Advances in theory of plastic mechanism control: closed form solution for MR-frames," *Earthquake Engineering and Structural Dynamics*, vol. 44, no. 7, pp. 1035-1054, 2015.

[41] R. Montuori and R. Muscati, “A general design procedure for failure mechanism control of reinforced concrete frames,” *Engineering Structures*, vol. 118, pp. 137-155, 2016.

[42] R. Montuori and R. Muscati, “Smart and simple design of seismic resistant reinforced concrete frame,” *Composites Part B: Engineering*, no. DOI: 10.1016/j.compositesb.2016.09.050, p. Article in press, 2016.

[43] R. Montuori and R. Muscatia, “Plastic design of seismic resistant reinforced concrete frame,” *Earthquake and Structures*, pp. 205-224, 2015.

[44] S. Popovics, "A numerical approach to the complete stress-strain curves for concrete." *Cement and Conor. Res.*, 3(5), 583-599, 1973.

[45] R. Montuori and V. Piluso, “Reinforced concrete columns strengthened with angles and battens subjected to eccentric load”, *Engineering Structures*, 31, pp. 539-550, 2009.

[46] Mazzoni S, McKenna F, Scott MH, Fenves GL (2007) “OpenSees Command Language Manual,” *Pacific Earthquake Engineering Research Center*, University of California, Berkeley, U.S.A.

[47] CSI. SAP 2000: integrated finite element analysis and design of structures. Analysis reference. Berkeley: *Computer and Structure Inc.* University of California; 2007.

[48] SeismoStruct 2016 avaliable on http://www.seismosoft.com/SeismoStruct_2016_Release-5_ITA

COMPDYN 2017
6th ECCOMAS Thematic Conference on
Computational Methods in Structural Dynamics and Earthquake Engineering
M. Papadrakakis, M. Fragiadakis (eds.)
Rhodes Island, Greece, 15–17 June 2017

# NUMERICAL MODELLING AND CALIBRATION OF RC COLUMNS UNDER AXIAL LOADING

**Tuba Tatar**[1], **Mário Pimentel**[2], **José Miguel Castro**[3] and **Mário Marques**[4]

[1] University of Porto
Porto, Portugal
e-mail: tuba.tatar@fe.up.pt

[2] University of Porto
Porto, Portugal
e-mail: mjsp@fe.up.pt

[3] University of Porto
Porto, Portugal
e-mail: jmcastro@fe.up.pt

[4] University of Porto
Porto, Portugal
e-mail: mario.marques@fe.up.pt

**Keywords:** Numerical modeling, column, axial load, calibration

**Abstract.** *This work presents the first step of a methodology to calculate monetary losses in reinforced concrete moment resisting buildings through an innovative and advanced methodology. This framework involves the correlation between the physical damages that a structural component may experience during seismic events with meaningful engineering demand parameters. The establishment of this correlation constitutes the first phase of the methodology and is obtained through detailed finite element simulations of the critical structural elements. In this paper the development of numerical modeling strategies for the detailed simulations of five columns are described. The paper describes step by step the whole calibration process involving mesh sensitivity studies, evaluation of the influence of the compression fracture energy, geometric nonlinearity, bond-slip action and the buckling of the compressed reinforcements. In order to simplify the problem, pushover analysis is adopted to analyze all the models.*

## 1 INTRODUCTION

Seismic risk assessment provides the first step for understanding the impact of earthquakes and determining the need of seismic rehabilitations. It is significant as well as for pre-earthquake preparedness and awareness in terms of human and economic losses. The assessment process provides meaningful information to stakeholders and decision makers on the seismic risk level of the structure portfolios and leads them to step towards rehabilitation and retrofitting process if necessary.

In current pre-earthquake loss assessment approaches, damage is commonly defined based on ductility ratio (maximum displacement over yielding displacement) or dissipated energy and usually related with either global or local indices [1-4]. The indices can provide an indication of the vulnerability of the structure, performance evaluation of the structure and decision regarding to rehabilitation of the structure. Even though the indices are able to indentify non damaged and severely damaged elements, they, however, poorly provide accurately results for intermediate damage states, which is the most critical stage regarding of the need for strengthening [5]. To improve the accuracy of economic loss predictions in RC frame buildings, an advanced methodology is proposed.

This methodology consists of two main phases, the first of which requires the identification of physical damages using detailed finite element analysis of critical structural elements. These damages are then correlated with meaningful engineering demand parameter(s) which shall be also suitable on the simplified models that can be used for assessing reinforced concrete buildings under seismic action. The monetary losses are determined based on the damages defined in the first phase. This new methodology allows users calculating monetary loss directly without using consequence function. The damage scales are redefined by experts in terms of the physical damages and cost of repair is redefined according to the available applied repair techniques in the new procedure [6]. Additionally, the damage limit states are calculated for each structural component individually and it improves the accuracy of monetary loss calculation. This methodology can be applied on flexural controlled reinforced concrete moment resisting frame structures regardless of height or irregularity.

Reproducing the experimental results not only in terms of global response, but also in terms of the physical damages is crucial and affects the accuracy of the methodology. Thus, a systematic calibration process is developed and exemplified here for the numerical models of columns and five parameters are investigated: mesh sensitivity, compression fracture energy, geometric nonlinearity, bond-slip and Dhakal-Maekawa post-yielding buckling.

## 2 NUMERICAL MODELING OF THE COLUMNS

The methodology is applied to five different columns, which are modeled and assessed numerically using software DIANA 9.6 [7]. These specimens were previously tested in laboratory: one is at University of Porto (UP) [8], the remaining ones (V1, V2, V3 and V4) are selected from the literature [9]. The geometrical and material properties of the columns are provided in Table 1.

Concrete is modeled using 20 node brick elements with (CHX60) with 3x3x3 Gauss points. The total-strain rotating smeared crack model available in DIANA material library is selected as constitutive model for concrete. The analyses start using Von Mises plasticity for reinforcing bars. The Dhakal-Maekawa constitutive model is employed for the bars under compression in order to model the effects of rebar buckling. Figure 1 shows the numerical models of the specimens, the red lines in (a) and (c) represent the reinforcing bars and (b) and (d) illustrate the meshed models. The analyses are carried on under monotonic loading whereby as-

suming that envelop of cyclic loading is represented by the monotonic force-displacement curve.

| ***Specimen No.*** | ***Section*** *mm²* | ***Height of the column*** *mm* | ***$f_c'$*** *N/mm²* | ***$f_y$*** *N/mm²* | ***Axial Load*** *kN* | ***Long. Rein.*** | ***Stirrups*** *Ø/mm* | ***Rein. Ratio (ρ) %*** | ***Mech. Rein.Ratio (ω) %*** |
|---|---|---|---|---|---|---|---|---|---|
| ***UP*** | 200x400 | 1500 | 48 | 436 | 170 | 6Ø12 | Ø6/150 | 0.85 | 8 |
| ***V1*** | 300x300 | 1100 | 30 | 344 | 0 | 12Ø13 | Ø6/70 | 1.77 | 20 |
| ***V2*** | | | | | 310 | | | | |
| ***V3*** | | | | | 620 | | | | |
| ***V4*** | | | | | 930 | | | | |

Table 1: Geometrical and material properties of the specimens

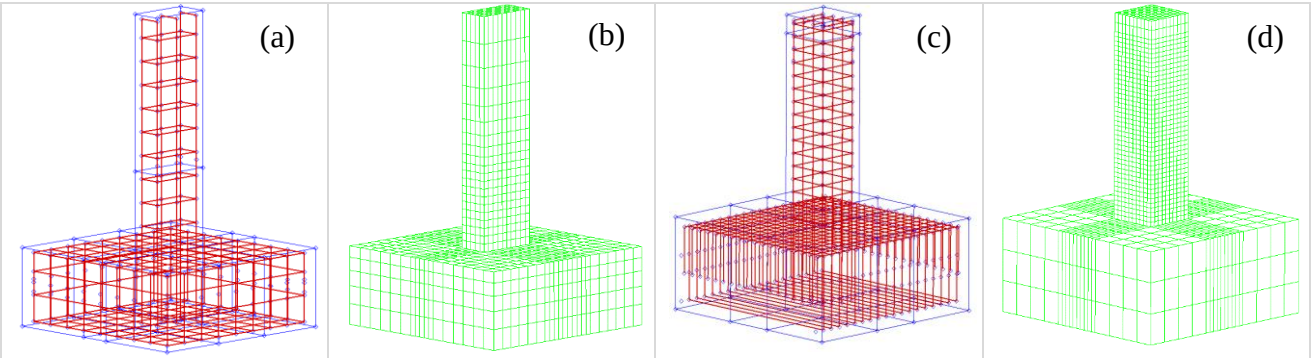


Figure 1: Reinforcement bar (a) and meshed model (b) of UP, reinforcement bar (c) and meshed model (d) of V1,V2V3 and V4

## 3 CALIBRATION PROCESS

As the first phase of the methodology relays on reproduction of the experimental results, a systematic calibration process was employed. This process includes 5 main steps in order to assess the influence of the mesh refinement, compression fracture energy, geometric nonlinearity, bond-slip between the rebar and the concrete and Dhakal-Maekawa post-yield buckling in the compressed rebar. Each of these steps is discussed in detail below.

### 3.1 Mesh Sensitivity

In finite element analyses, the size of the elements may influence the response and selection of the mesh sizes may govern the accuracy of the results. In quasi-brittle materials like concrete, which exhibit strain softening behavior, regularization procedures based on the definition of tensile and compressive fracture energies are adopted in order to reduce and nearly eliminate mesh size dependency of the results. In order to select adequately sized meshes and to assess the influence of the chosen mesh size on the global response, three different mesh sizes are investigated for each type of the column:

1. UP:

40x35x40 $mm^3$, 67x70x80 $mm^3$ and 67x140x200 $mm^3$ respectively for fine, medium and coarse volumes

2. V1, V2, V3 and V4:

25x30x25 $mm^3$, 50x60x25 $mm^3$ and 100x100x100 $mm^3$ respectively for fine, medium and coarse volumes.

Figure 2 shows the results of mesh size sensitiveness study for the five columns in terms of shear vs. displacement. Influences of the axial load level on the response objectivity can be observed on V3 and V4, the columns with higher axial load levels. In these analyses the ductility is clearly governed by concrete crushing, which occurs earlier in the models with coarser meshes. This is due to the fact that the finer the mesh is, the sooner the peak compressive stress is achieved in virtue of the of the higher accuracy in reproducing the pre-peak stress and strain fields in the most stressed regions of the column. Therefore, even if regularized (mesh-objective) stress-strain curves are employed for concrete in compression using the concept of compressive fracture energy, still a moderate degree of mesh dependency should be expected in the structural response. On the specimens with lower axial load levels (UP, V1 and V2), the mesh size dependency on the ductility is not as noticeable

Due to stability concerns in further analyses and crack pattern evaluations with experiments, the fine sized mesh is selected for all the models even tough medium seized mesh would provide objective results.

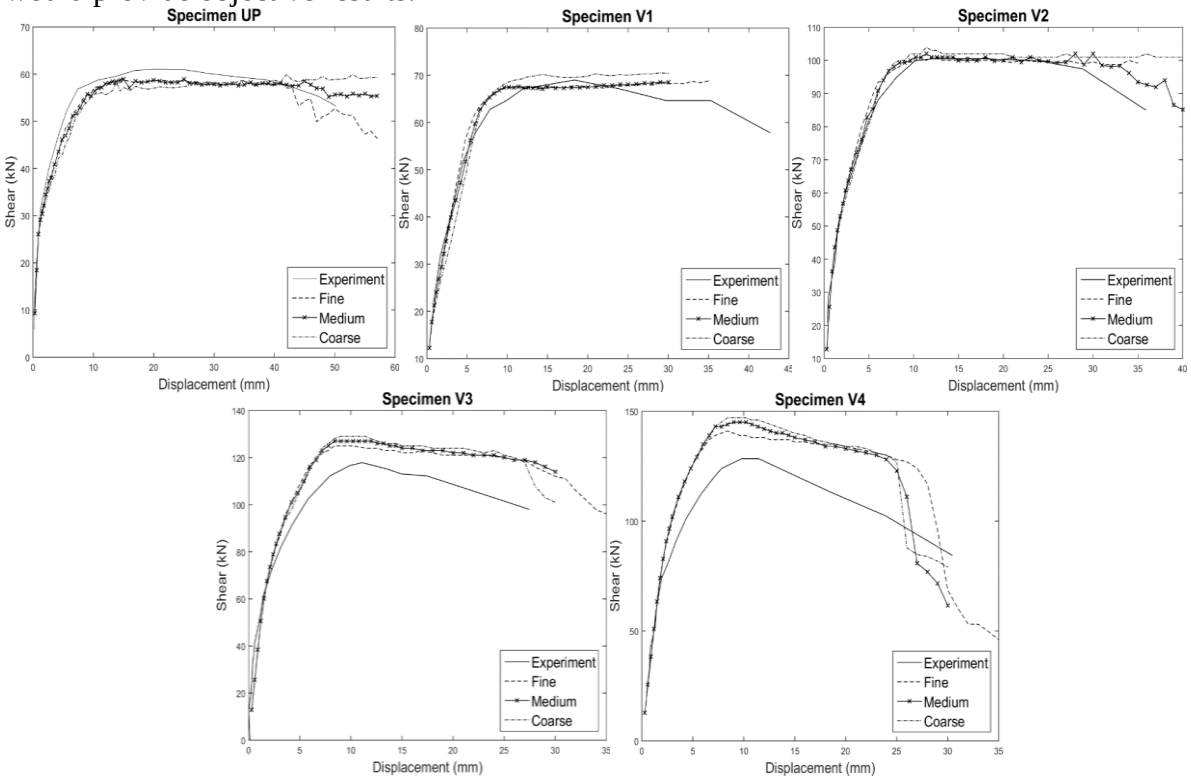


Figure 2: Mesh sensitivity investigation

## 3.2 Compression Fracture Energy ($G_c$)

When modelling concrete fracture with continuum elements, it is well known from nonlinear fracture mechanics that after reaching the maximum stress, the stress-strain relation cannot be considered a material property anymore. Two additional parameters are required, the fracture energy and a characteristic length, which in the case of the adopted modelling strategy, is related to the finite element size. In the case of tensile fracture, the fracture energy $G_f$ is defined as required energy to open a crack within a unit length. In the case of compressive fracture, the compressive fracture energy $G_c$ can be defined as the required energy to crush (until full stress release) a unit area perpendicular to the principal compressive stress. The first estimated $G_c$ value is gradually increased until the ductility of the specimen is captured. Effects of compression fracture energy are shown in Figure 3with reference to shear and displacement. Compression fracture energy influence can be observed intensely only if there is concrete

failure. The specimen V1 with variant $G_c$ is able to reproduce the same results and even the smallest given $G_c$ is sufficient under the applied load. Concerning higher axial load level, the failures of models with small $G_c$ are, however, observed earlier as seen especially in V3 and V4. If ductility is concerned and required to be matched to experimental results, playing with compression fracture energy would be an option for users.

Thus, the selected $G_c$ value for V1, V2, V3 and V4 is 80 N/mm and for UP is 50 N/mm whereas those values are able to reproduce the ductility of the specimens and following investigations have been proceeded using those values.

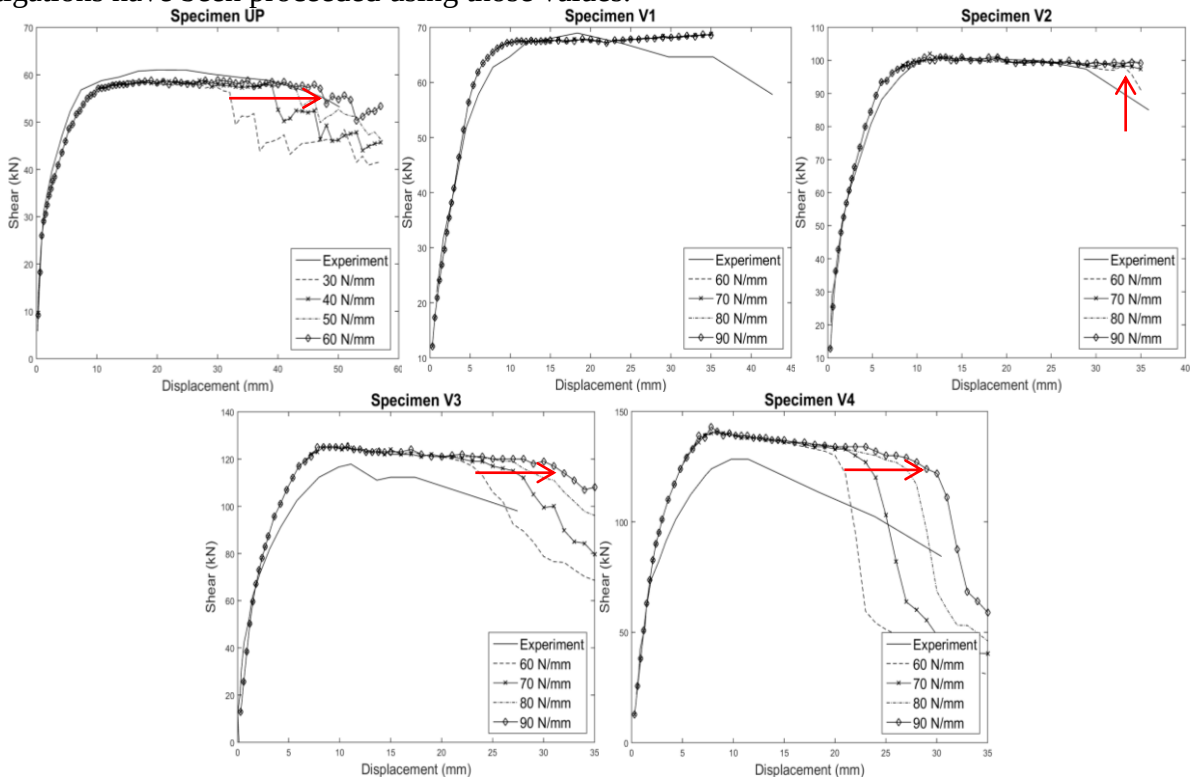


Figure 3: Compression fracture energy effects on global response

### 3.3 Geometric Nonlinearity

Geometric nonlinearity is an important parameter in this study. If there is axial load, especially high level, the P-Δ effect must be taken into account since the second order bending moments are not negligible. Secondly, considering geometric nonlinearity is very essential if the buckling of rebar is considered explicitly in the analysis.

Figure 4 illustrates the geometric nonlinearity influences on global response of the specimens. After including the parameter into the analyses, the maximum value and also ductility are influenced immensely. The impact of the parameter growths visibly while the axial load level increases as seen on V3 and V4. Over all, and as should be expected, geometrical nonlinearity analyses produce more consonant results to the experiments.

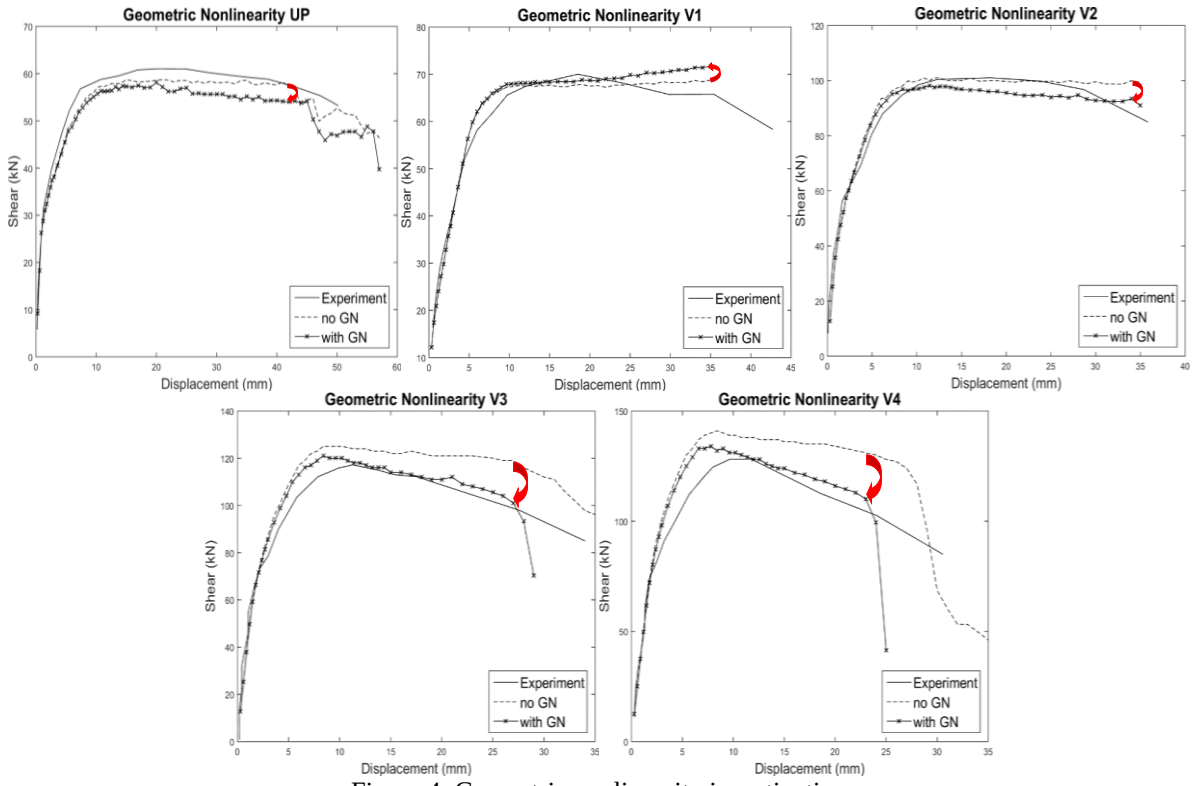


Figure 4: Geometric nonlinearity investigation

## 3.4 Bond-Slip Influence

After cracking, relative displacements (slip) and bond shear stresses develop along the interface between concrete and steel. With increasing load and eventual yielding of the rebars, the reinforcing bar slip increases even more. This phenomenon can be modeled explicitly using interface elements and bond shear stress-slip constitutive laws and is important for the consistent determination of the crack spacing and of development of the plastic hinge. In the present study, the constitutive model for bond-slip proposed in the CEB-FIB 1990 is adopted, which depends on the concrete strength, confinement effect and rib length [10]. According to the constitutive relation given onto the interface element, the steel and the concrete elements are not forced to act compatible anymore and a slip between two materials is allowed. In the numerical models, tangential traction values (bond-slip values) of the interface elements are calculated using CEB-FIB equation. The behavior of interface elements is given in Figure 5 . There are four possible scenarios: “confined-good”, “confined-other”, “unconfined-good” and “unconfined-other” bond condition. Each of these bond and confinement conditions is applied on the models separately.

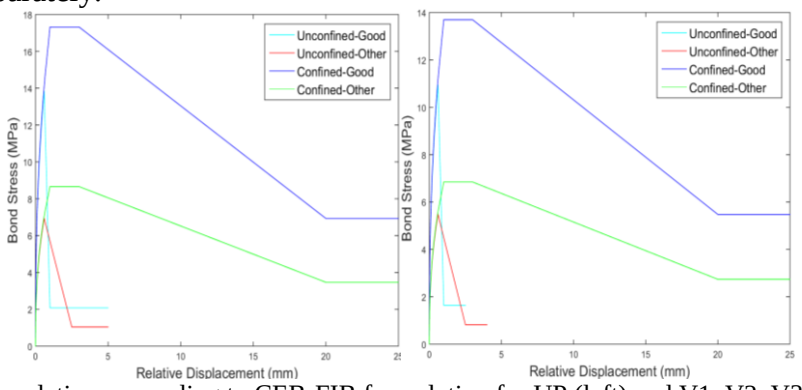


Figure 5: Bond-slip relations according to CEB-FIB formulation for UP (left) and V1, V2, V3 and V4 (right)

Figure 6 shows effect of those four conditions for each column also including the result without bond-slip activation and the experimental response in terms of shear vs. displacement. The arrow on the graphs indicates roughly the yielding point of the rebar. The responses are clearly affected around the yielding points after including the bond-slip interface constitutive model. A reduction in response can be also observed whereby the rebar is not forced to be compatible with concrete. Moreover, improvement in ductility can be observed especially on the example with higher axial load level. Importantly, the plastic hinge length decreases due to damage localization on the models which also helps to form more realistic crack pattern along the tension side of the columns. The most fitted condition is selected for the specimens, which is the "confined-other" bond condition for the models and following analyses are carried out using the selected condition.

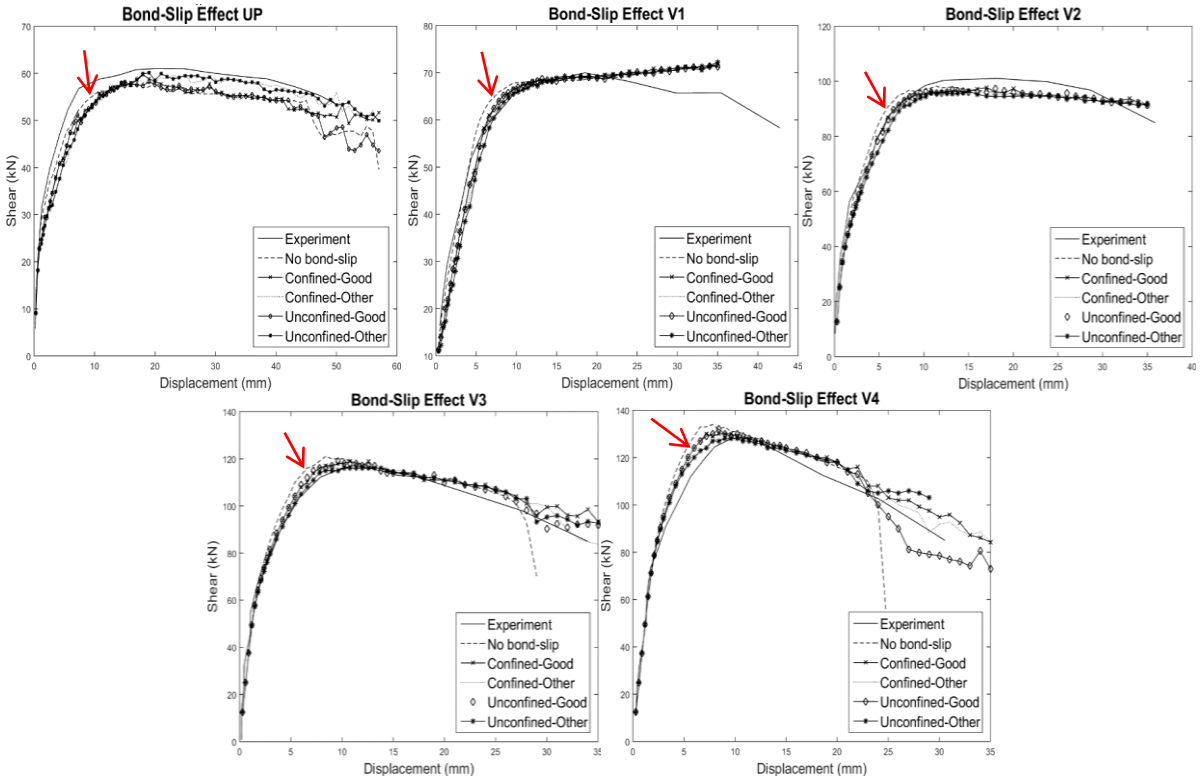


Figure 6: Influence of Bond-Slip Action of Global Response

## 3.5 Dhakal-Maekawa Post-Yield Buckling

Dhakal and Maekawa investigated post-yield buckling in bare steel bars and proposed a constitutive model shown in Figure 7 (a) [11] which includes the influence of rebar length, diameter and yielding strength. This model introduces post-yield buckling behavior to the compressed steel bars via a modification of the uniaxial stress-strain curves. Figure 7 (b) displays the calculated values according to the proposed model for reinforcing bar. Since the stirrup spacing of UP is 15 cm, the influence of buckling can be dramatically observed after yielding point. The stirrup spacing for the remaining specimens is, however, equal to 7 cm and the reduction in stress due to buckling remains mild.

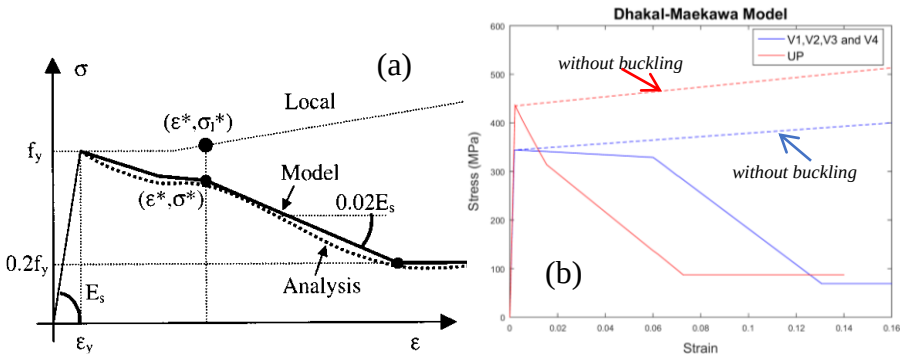


Figure 7: (a) Dhakal-Maekawa proposed buckling model [11] and (b) steel constitutive models for the specimens

Post-yield buckling behavior is included into analyses using Dhakal-Maekawa constitutive models to the bars only under compression. The model is mesh depended and the analyses are carried out after some modifications on the constitutive models according to Dhakal proposal [12]. Figure 8 demonstrates the comparisons of the results in shear and displacement terms. It is clear that the proposed model is sensitive to the mesh sizes and it requires modifications. Nevertheless, the model provides greater agreement with the experimental results in local sense.

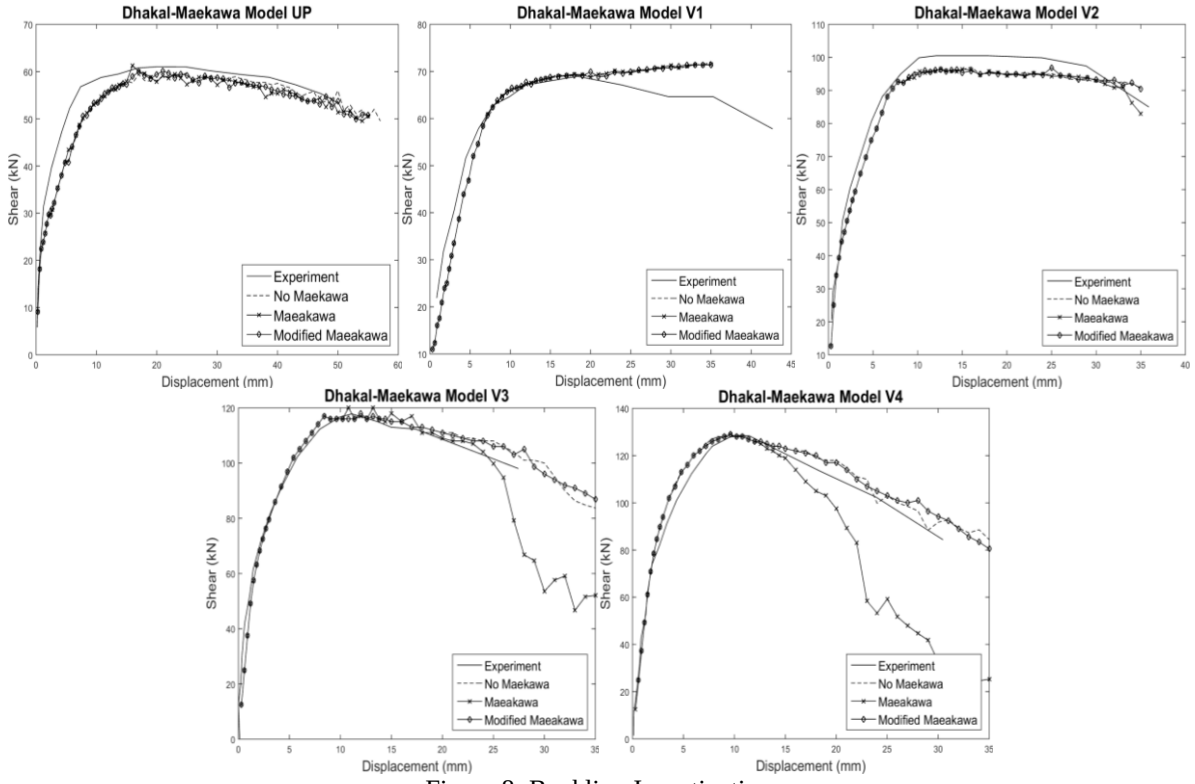


Figure 8: Buckling Investigation

## 4 CRACK EVOLUTION

In this methodology, bond-slip action is a necessity to match the responses globally and also to form the crack pattern realistically. In Figure 9-Figure 13 the crack patterns are illustrated, including the results from a model without bond-slip, after activating bond-slip and the experimental pictures. All the models are able to reproduce the crack pattern with good agreement. In the model without bond-slip, the crack pattern is more diffuse and there is no clear separation between cracks. On the other hand, the crack pattern from the model with ac-

tive bond-slip is more realistic, the crack widths are greater due to localization. The crack width becomes narrower if the axial load is higher. Finally, Table 2 shows a comparison of damage length from both experiments and finite element analyses, there is satisfactory agreement in the results.

| | ***Damage length (Experimental)*** *(cm)* | ***Damage length (FE)*** *(cm)* |
|---|---|---|
| ***UP*** | 15 | 15 |
| ***V1*** | >20 | 25 |
| ***V2*** | ≈21 | 20 |
| ***V3*** | ≈20 | 20 |
| ***V4*** | 14 | 15 |

Table 2: Comparison of the damage length from experiments and FE analyses

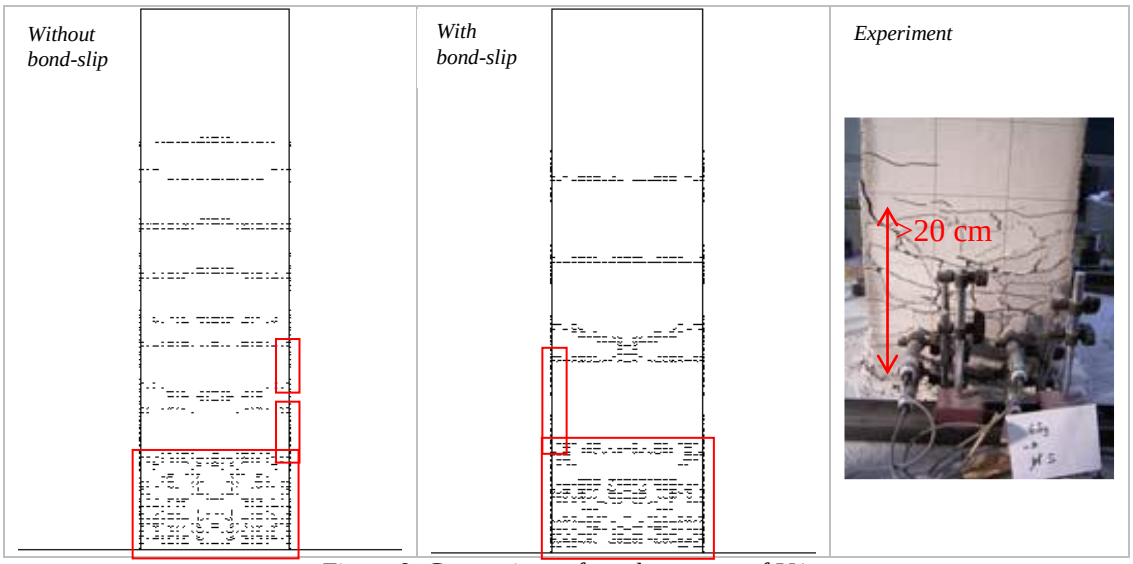


Figure 9: Comparison of crack patterns of V1

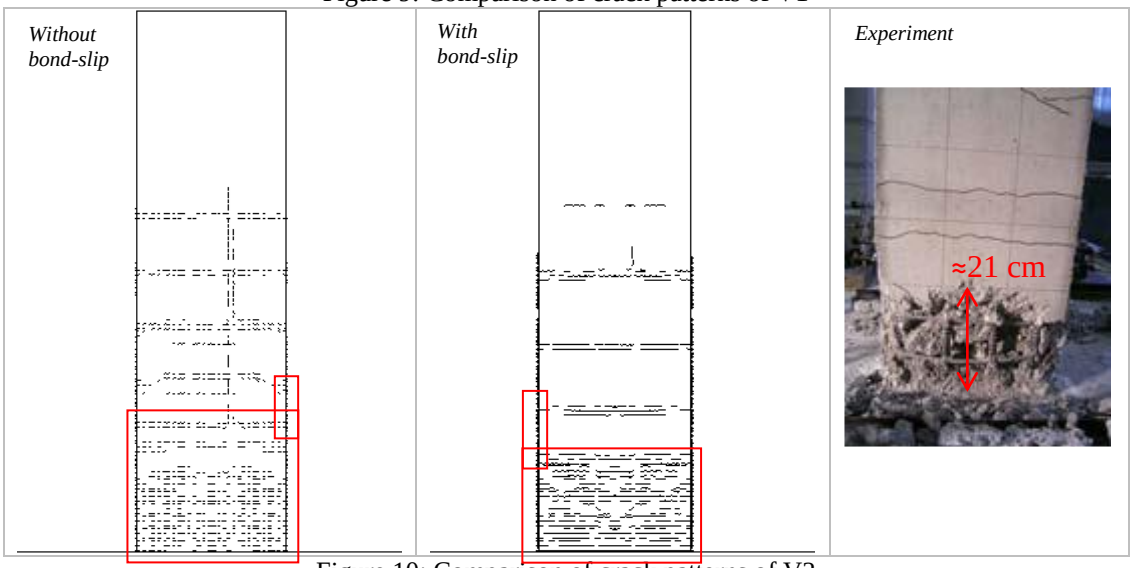


Figure 10: Comparison of crack patterns of V2

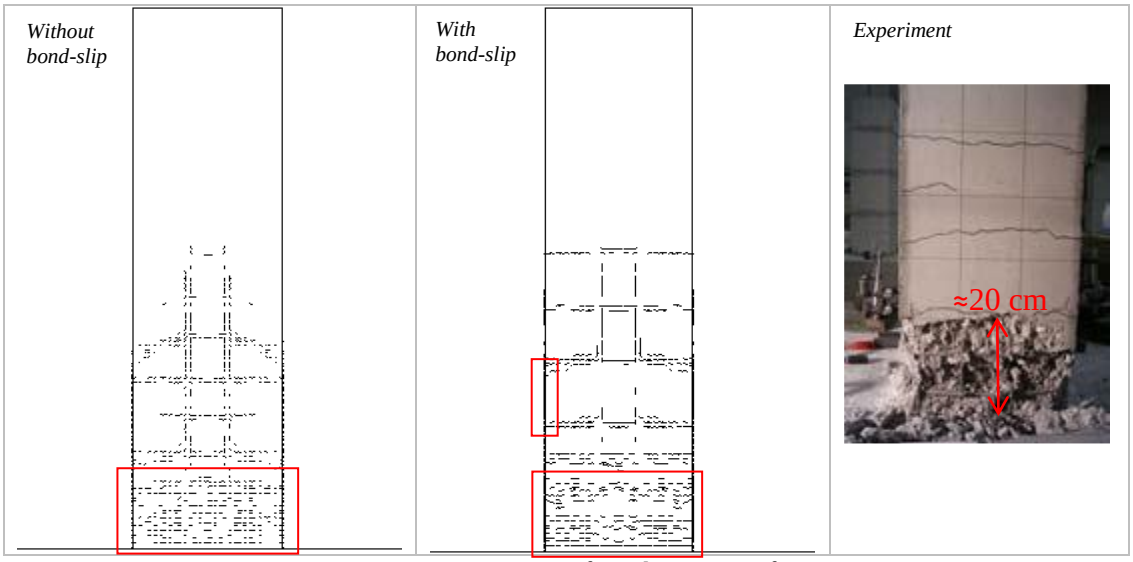


Figure 11: Comparison of crack patterns of V3

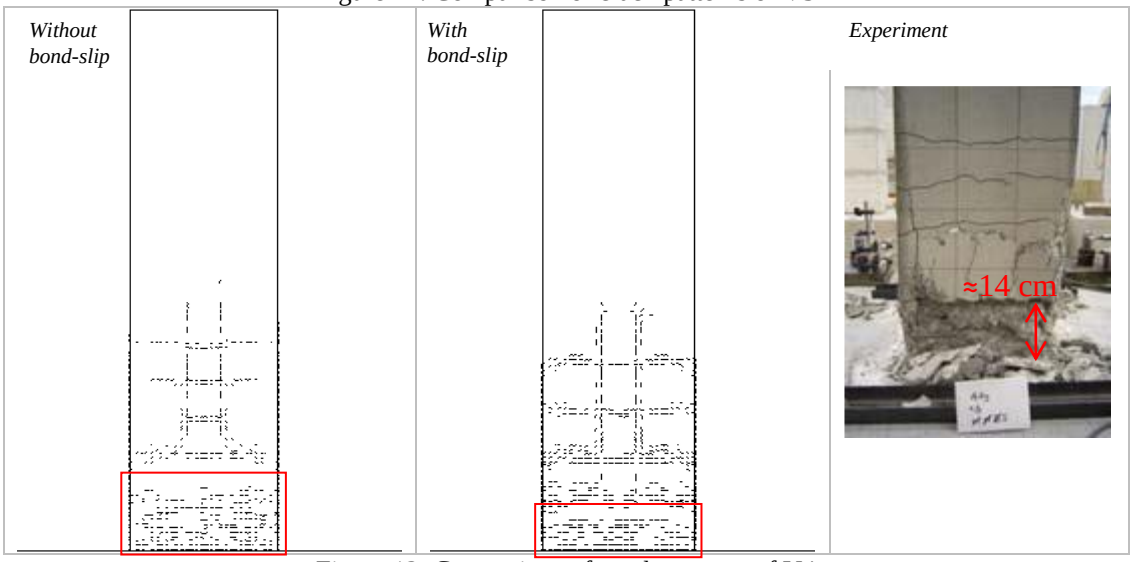


Figure 12: Comparison of crack patterns of V4

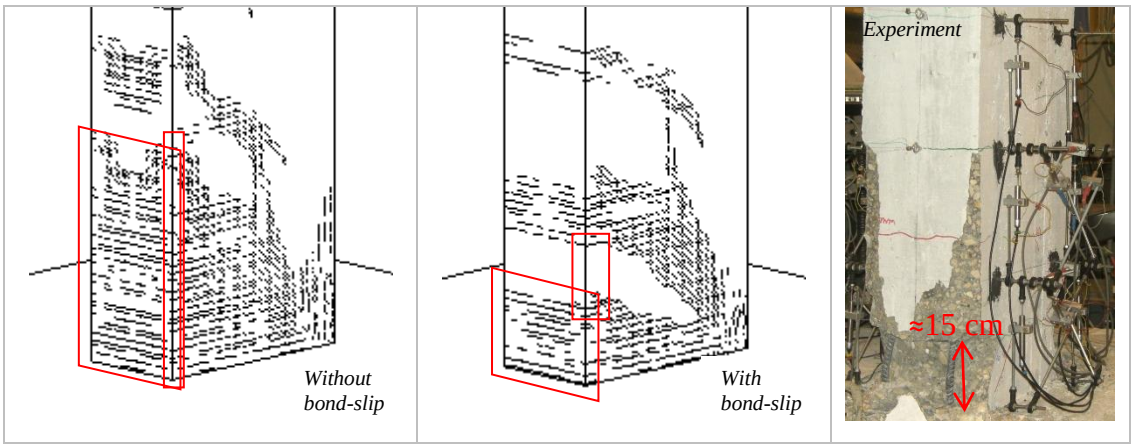


Figure 13: Comparison of crack patterns of UP

## 5 CONCLUSION

Five columns with different axial load levels, material and geometrical properties are reproduced numerically using DIANA 9.6 and compared with experimental results. To match the numerical and experimental results, a systematic calibration is applied within five steps covering mesh sensitivity analysis, compression fracture energy, geometric nonlinearity, bond-slip activation and rebar buckling. Their effects on the numerical results are discussed in detail and the following conclusions can be obtained:

1- The mesh size has minor influence on peak load and moderate influence on the ductility in case of higher axial load levels;
2- The compression fracture energy plays an important role on ductility in the case of columns subjected to higher axial load levels;
3- Geometric nonlinearity and second order effect shall be considered in the analysis especially if there is a high axial load level;
4- Activation of bond-slip slightly increases the response's ductility and a small reduction in maximum response can be observed. However, it changes significantly the crack pattern;
5- The Dhakal-Maekawa post-yield buckling model provides fair improvement in local response whereas a modification on the constitutive model is applied because of mesh size consideration.

In further steps of the methodology, the physical damages will be correlated with selected engineering demand parameter(s) through numerical models in which the mentioned calibration steps are obeyed.

## REFERENCES

[1] A. Cakmak and E. DiPasquale, "Detection and Assessment of Seismic Structural Damage," 1987.
[2] Y. Chung, C. Meyer, and M. Shinozuka, "Seismic damage assessment of reinforced concrete buildings," in *Report No. NCEER-87-0022*, ed: National Center for Earthquake Engineering Research, State University New York at Buffalo, 1987.
[3] Y.-J. Park and A. H.-S. Ang, "Mechanistic seismic damage model for reinforced concrete," *Journal of structural engineering*, vol. 111, pp. 722-739, 1985.
[4] M. S. Williams and R. G. Sexsmith, "Seismic damage indices for concrete structures: a state-of-the-art review," *Earthquake spectra,* vol. 11, pp. 319-349, 1995.
[5] R. Sinha and S. Shiradhonkar, "Seismic Damage Index for Classification of Structural Damage–Closing the Loop," in *Proceedings of the Fifteenth World Conference on Earthquake Engineering*, 2012.
[6] "Earthquake Loss Assessment of the Portuguese Building Stock," University of Porto2014.
[7] T. D. BV. DIANA User's Manual release 9.6 [Online].
[8] H. Rodrigues, "Biaxial Seismic Behavior of Reinforced Concrete Columns," Doctoral Dissertation, Civil Engineering, University of Aveiro, Aveiro, 2012.
[9] T. Denpongpan and H. Shima, "Effect of Axial Load on Ductility of Reinforced Concrete Columns," presented at the OUR WORLD IN CONCRETE & STRUCTURES, Singapore, 2005.

[10] F. I. du Béton, "Bond of reinforcement in concrete: state-of-art report," *Lausanne, Switzerland: International Federation for Structural Concrete,* p. 427, 2000.
[11] R. P. Dhakal and K. Maekawa, "Modeling for postyield buckling of reinforcement," *Journal of Structural Engineering,* vol. 128, pp. 1139-1147, 2002.
[12] R. P. Dhakal, "Enhanced fiber model in highly inelastic range and seismic performance assessment of reinforced concrete," The University of Tokyo, 2000.

COMPDYN 2017
6th ECCOMAS Thematic Conference on
Computational Methods in Structural Dynamics and Earthquake Engineering
M. Papadrakakis, M. Fragiadakis (eds.)
Rhodes Island, Greece, 15–17 June 2017

# TOOL FOR SHEAR ANALYSIS OF PRESTRESSED STEEL FIBER CONCRETE BEAMS

**P. R. Tadepalli[1], Liang Lu[2], Y. L. Mo[1], and T. T. C. Hsu[1]**

[1] Department of Civil and Environmental Engineering, University of Houston, Houston, Texas, USA
e-mail: {tvvssprao, ymo, thsu}@uh.edu

[2] College of Civil Engineering, Tongji University, Shanghai, China
95010@tongji.edu.cn

**Keywords:** Simulation of Concrete Structure, Prestressed Steel Fiber Concrete, OpenSees, Constitutive Law, Shear.

**Abstract.** *Prestressed steel fiber concrete beams have been employed in bridge engineering because the conventional shear reinforcement can be replaced by steel fibers, which can reduce the construction labor and provide greater shear strength and ductility than those of conventional prestressed concrete beams. The shear strengths of elements in webs depend strongly on the softening of concrete struts in the principal compression direction due to the principal tension in the perpendicular direction. By studying the shear behavior of isolated web elements, this softening phenomenon has been clarified for monotonic loading in the Softened Membrane Model (SMM) for reinforced concrete. Recently, SMM was extended to prestressed steel fiber concrete. In the present paper, a Finite Element program (Called Simulation of Concrete Structures, SCS) is developed for analysis of shear-critical prestressed steel fiber concrete structures by implementing constitutive laws of prestressed steel fiber concrete into an object-oriented software framework called "Open System for Earthquake Engineering Simulation (OpenSees)" originally developed at the University of California, Berkeley. The new material modules have been integrated with the existing material modules in OpenSees. SCS thus developed has been used for predicting the shear behavior of the prestressed steel fiber concrete I-beams. The analysis could well predict the entire shear behavior of the beams including the initial stiffness, post-cracking stiffness, yield point, and ultimate load for both web shear and flexure shear failure modes. This new tool gives engineers greatly improved simulation capabilities.*

## 1 INTRODUCTION

In conventional prestressed concrete beams, longitudinal prestressed tendons serve to resist bending moment and transverse mild steel stirrups are used to carry shear forces. Producing and placing stirrups, however, requires costly labor and time. To overcome these difficulties, it is proposed to replace the stirrups in prestressed concrete beams with steel fibers. This replacement concept was shown to be feasible in a recently completed project [1].

In addition to experimental work, a finite element analysis tool needs to be developed to better understand the shear behavior of prestressed steel fiber concrete beams. The tool was developed by implementing constitutive models of prestressed steel fiber concrete in OpenSees [2], which stands for Open System for Earthquake Engineering Simulation. It is an object-oriented software framework for simulation applications in earthquake engineering using finite element methods. It is comprised of a set of modules to perform creation of the finite element model, specification of an analysis procedure, selection of quantities to be monitored during the analysis, and the output of results [2]. The features of OpenSees are described on the OpenSees website (www.opensees.berkeley.edu).

## 2 FORMULATION OF SOFTENED MEMBRANE MODEL

The Softened Membrane Model for Prestressed Steel Fiber Concrete (SMM-PSFC) was developed to predict the behavior of prestressed steel fiber concrete elements under monotonic loading [3]. SMM-PSFC consisted of the equilibrium and compatibility equations along with the constitutive models of materials. However, SMM-PSFC contains the uniaxial constitutive models of materials under monotonic loading only. The details of SMM-PSFC can be found in [1]. The following describes the formulation of softened membrane model for the preparation of finite element analysis implementation to be described in the next section.

### 2.1 Equilibrium and compatibility equations

The in-plane element considered in this model is shown in Figure 1. The element considered is reinforced by two layers of orthogonal grids of mild steel as well as prestressing steel, oriented at a given angle to the principal stress direction. The first reference Cartesian $\ell$-t coordinate system represents the longitudinal and transverse steel bar directions. The second reference Cartesian 1-2 coordinate system represents the direction of the principal stresses. For the computational purposes, it is assumed that the steel bars are uniformly distributed in the $\ell$- and t-directions, and the membrane element is of uniform thickness. The principal applied stresses acting on the four boundary edges of the element are assumed to be uniformly distributed.

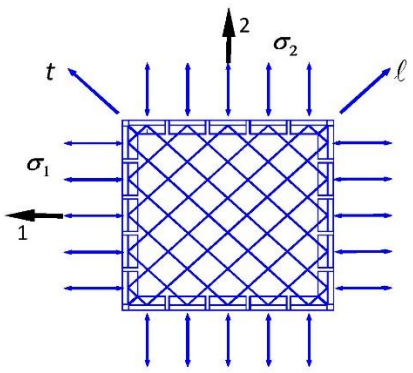


Figure 1: A typical reinforced concrete plane stress element.

The three equilibrium equations, which relate the applied stresses ($\sigma_\ell, \sigma_t$ and $\tau_{\ell t}$) to the internal stresses of concrete ($\sigma_2^c, \sigma_1^c$ and $\tau_{21}^c$), mild steel ($f_\ell$ and $f_t$), and prestressing steel ($f_{\ell p}$ and $f_{tp}$) in a membrane element, are given in Equations 1 to 3.

$$\sigma_\ell = \sigma_2^c \cos^2 \alpha_2 + \sigma_1^c \sin^2 \alpha_2 + \tau_{21}^c 2 \sin \alpha_2 \cos \alpha_2 + \rho_\ell f_\ell + \rho_{\ell p} f_{\ell p} \quad (1)$$

$$\sigma_t = \sigma_2^c \sin^2 \alpha_2 + \sigma_1^c \cos^2 \alpha_2 - \tau_{21}^c 2 \sin \alpha_2 \cos \alpha_2 + \rho_t f_t + \rho_{tp} f_{tp} \quad (2)$$

$$\tau_{\ell t} = (-\sigma_2^c + \sigma_1^c) \sin \alpha_2 \cos \alpha_2 + \tau_{21}^c (\cos^2 \alpha_2 - \sin^2 \alpha_2) \quad (3)$$

The three compatibility equations, which represent the relationship between the strains ($\varepsilon_\ell$, $\varepsilon_t$, and $\gamma_{\ell t}$) in the $\ell - t$ coordinate of the reinforcement and the strains ($\varepsilon_1, \varepsilon_2$, and $\gamma_{21}$) in the 2-1 coordinate of the principal applied stress, are given in Equation 4 through 6 [4].

$$\varepsilon_\ell = \varepsilon_2 \cos^2 \alpha_2 + \varepsilon_1 \sin^2 \alpha_2 + \frac{\gamma_{21}}{2} 2 \sin \alpha_2 \cos \alpha_2 \quad (4)$$

$$\varepsilon_t = \varepsilon_2 \sin^2 \alpha_2 + \varepsilon_1 \cos^2 \alpha_2 - \frac{\gamma_{21}}{2} 2 \sin \alpha_2 \cos \alpha_2 \quad (5)$$

$$\frac{\gamma_{\ell t}}{2} = (-\varepsilon_2 + \varepsilon_1) \sin \alpha_2 \cos \alpha_2 + \frac{\gamma_{21}}{2} (\cos^2 \alpha_2 - \sin^2 \alpha_2) \quad (6)$$

### 2.2 Biaxial strains vs. uniaxial strains

To solve the six equilibrium and compatibility equations, given by Equations 1 to 6, the stress-strain relationships of concrete and steel have to be based on the biaxial strains $\varepsilon_1$, $\varepsilon_2$, $\varepsilon_\ell$ and $\varepsilon_t$. Since general laboratory experiments can provide only the uniaxial constitutive relationships of concrete and steel (rather than the biaxial constitutive relationships), the biaxial strains in Equations 4 through 6 must be converted to uniaxial strains before the uniaxial constitutive relationships can be utilized. Thus, a set of four equations has been derived [5] to relate the set of biaxial strains ($\varepsilon_1, \varepsilon_2, \varepsilon_\ell$ and $\varepsilon_t$) to the set of uniaxial strains ($\bar{\varepsilon}_1, \bar{\varepsilon}_2, \bar{\varepsilon}_\ell$ and $\bar{\varepsilon}_t$) using the Hsu/Zhu ratios ($\nu_{12}$, $\nu_{21}$), as shown in Equations 7 through 10.

$$\bar{\varepsilon}_1 = \frac{1}{1 - \nu_{12}\nu_{21}} \varepsilon_1 + \frac{\nu_{12}}{1 - \nu_{12}\nu_{21}} \varepsilon_2 \quad (7)$$

$$\bar{\varepsilon}_2 = \frac{\nu_{21}}{1 - \nu_{12}\nu_{21}} \varepsilon_1 + \frac{1}{1 - \nu_{12}\nu_{21}} \varepsilon_2 \quad (8)$$

$$\bar{\varepsilon}_\ell = \bar{\varepsilon}_2 \cos^2 \alpha_2 + \bar{\varepsilon}_1 \sin^2 \alpha_2 + \frac{\gamma_{12}}{2} 2 \sin \alpha_2 \cos \alpha_2 \quad (9)$$

$$\bar{\varepsilon}_t = \bar{\varepsilon}_2 \sin^2 \alpha_2 + \bar{\varepsilon}_1 \cos^2 \alpha_2 - \frac{\gamma_{12}}{2} 2 \sin \alpha_2 \cos \alpha_2 \quad (10)$$

Once the uniaxial strains, $\bar{\varepsilon}_1$, $\bar{\varepsilon}_2$, $\bar{\varepsilon}_\ell$ and $\bar{\varepsilon}_t$ are determined, the stresses $\sigma_1^c$, $\sigma_2^c$, $\tau_{12}^c$, $f_\ell$ and $f_t$ in Equations 1 through 3 can be calculated using the uniaxial constitutive relationships under cyclic loading.

As mentioned previously, by taking into account the Hsu/Zhu ratios, the SMM was developed to predict the entire behavior (before and after peak point) of reinforced concrete membrane elements under monotonic shear stresses. Two Hsu/Zhu ratios of panels under monotonic shear stresses were presented in detail by [5]. The first ratio $\nu_{12}$ (representing the effect of the compression strain in the 2- direction on the tensile strain in the 1- direction) was found to increase with the increase of steel strain and became a constant 1.9 after yielding. The second ratio $\nu_{21}$ (representing the effect of the tensile strain in the 1- direction on the compression strain in the 2- direction) was found to be essentially zero throughout the loading history. Equations 11 and 12 gives the value of the Hsu/Zhu ratios of panels under monotonic shear stresses.

$$\nu_{12} = \begin{cases} 0.2 + 850\varepsilon_{sf}, \varepsilon_{sf} \leq \varepsilon_y \\ 1.9, \qquad\qquad \varepsilon_{sf} > \varepsilon_y \end{cases} \tag{11}$$

$$\nu_{21} = 0 \tag{12}$$

Where, $\varepsilon_{sf}$ is the smeared (average) tensile strain of steel bars in the $\ell -$ and the $t -$ directions, whichever yields first, taking into account the Hsu/Zhu ratios.

### 2.3 Constitutive relationships of materials

**Uniaxial Constitutive Relationships of Prestressed Steel Fiber Concrete** - The constitutive model for prestressed SFC along with the factors that will affect prestressed SFC are summarized in this section, including the constitutive relationships of cracked SFC in tension, compression, and shear. The results are plotted in Figure 2. Note that in the discussion the tensile stress is applied in 1-direction and the compressive stress in 2-direction. Development of these constitutive relationships has been reported by [3]. These proposed constitutive relationships of prestressed steel fiber concrete takes into account the effect of presence steel fibers in the concrete.

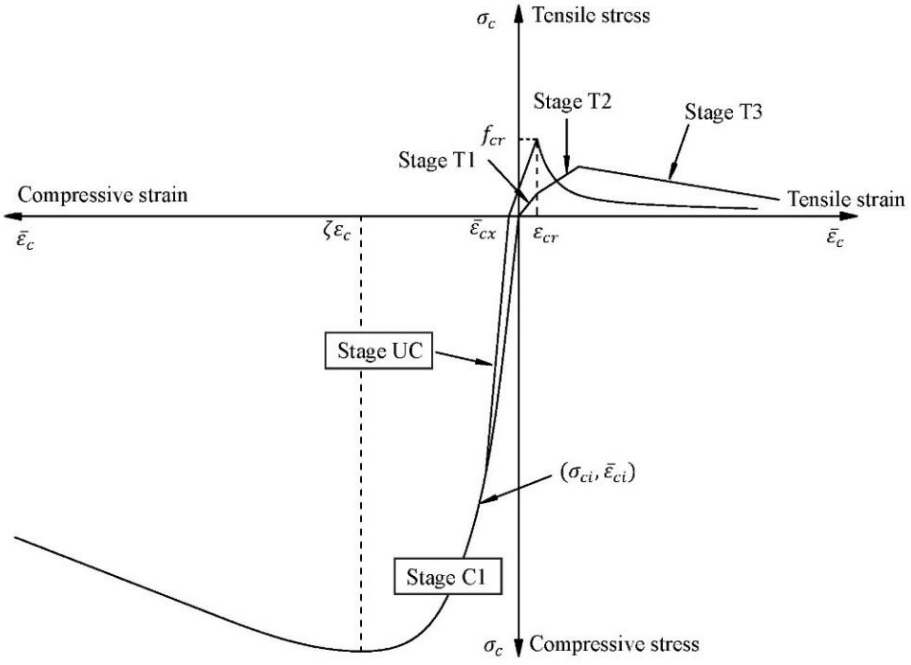


Figure 2: Smeared stress-strain relationships of prestressed steel fiber concrete.

### 2.3.1 SFC in tension

The relationships of the tensile stress $\sigma_1^c$ versus the uniaxial tensile strain $\bar{\varepsilon}_1$ of prestressed SFC are given as follows:

Stage UC:

$$\sigma_1^c = E_c'\bar{\varepsilon}_1 + \sigma_{ci},\ \bar{\varepsilon}_1 \le \left(\bar{\varepsilon}_{cx} - \bar{\varepsilon}_{ci}\right) \tag{13a}$$

Stage T1:

$$\sigma_1^c = E_c''(\bar{\varepsilon}_1 + \bar{\varepsilon}_{ci}),\ \left(\bar{\varepsilon}_{cx} - \bar{\varepsilon}_{ci}\right) < \bar{\varepsilon}_1 \le \left(\varepsilon_{cy} - \bar{\varepsilon}_{ci}\right) \tag{13b}$$

Stage T2:

$$\sigma_1^c = E_c'''(\bar{\varepsilon}_1 + \bar{\varepsilon}_{ci}),\ \left(\bar{\varepsilon}_{cy} - \bar{\varepsilon}_{ci}\right) < \bar{\varepsilon}_1 \le \left(\varepsilon_{cult} - \bar{\varepsilon}_{ci}\right) \tag{13c}$$

Stage T3:

$$\sigma_1^c = E^{IV}{}_c(\bar{\varepsilon}_1 + \bar{\varepsilon}_{ci}),\ \bar{\varepsilon}_1 > \left(\varepsilon_{cult} - \bar{\varepsilon}_{ci}\right) \tag{13d}$$

where,

$E_c'$ = decompression modulus of concrete, taken as $\dfrac{2f_c'}{\varepsilon_0}$

$\bar{\varepsilon}_{ci}$ = initial strain in concrete due to prestress

$\sigma_{ci}$ = initial stress in SFC

$\bar{\varepsilon}_{cx}$ = extra strain in concrete after decompression, calculated by $\bar{\varepsilon}_{ci} - \dfrac{\sigma_{ci}}{E_c'}$

$\varepsilon_{c\max}$ = SFC maximum strain taken as 0.04-$\varepsilon_{pi}$, where, $\varepsilon_{pi}$= initial uniaxial strain of pre-stressing tendons

$\varepsilon_{cult}$ = SFC ultimate strain taken as 0.01-$\varepsilon_{pi}$

$f_{cult}$ = SFC ultimate stress strain, taken as $(0.2FF + 12\rho_l)\sqrt{f_c'}$, where: *FF*=fiber factor, $\rho_l$ =longitudinal steel ratio

$\varepsilon_{cy}$ = SFC yield strain taken as 0.0005,

$f_{cy}$ = SFC effective "yield" stress for Proportional Loading, taken as $0.4 * FF * CF\sqrt{f_c'}$, ($f_c'$ and $\sqrt{f_c'}$ are in MPa) , *CF*=1 for SFC tensile volume confined (sandwiched) by two or more tendons, or *CF*=½ for SFC tensile volume unconfined by tendons

$E_c''$ = modulus of SFC taken as $\dfrac{f_{cy}}{\varepsilon_{cy} - \bar{\varepsilon}_{cx}}$

$E_c'''$ = modulus of SFC taken as $\dfrac{f_{cult} - f_{cy}}{\varepsilon_{cult} - \varepsilon_{cy}}$

$E_c^{IV}$ = modulus of SFC taken as $\dfrac{-f_{cult}}{\varepsilon_{\max} - \varepsilon_{cult}}$

### 2.3.2 SFC in compression

The smeared (average) constitutive relationships of SFC compressive stress $\sigma_2^c$ and the uni-axial compressive strain $\bar{\varepsilon}_2$ are given as follows:

$$\sigma_2^c = \zeta f_c' \left[ 2\left(\frac{\bar{\varepsilon}_2}{\zeta\varepsilon_0}\right) - \left(\frac{\bar{\varepsilon}_2}{\zeta\varepsilon_0}\right)^2 \right], \ \frac{\bar{\varepsilon}_2}{\zeta\varepsilon_0} \le 1 \tag{14a}$$

$$\text{or } \sigma_2^c = \zeta f_c' \left[ 1 - \left(\frac{\bar{\varepsilon}_2/\zeta\varepsilon_0 - 1}{4/\zeta - 1}\right)^2 \right], \ \frac{\bar{\varepsilon}_2}{\zeta\varepsilon_0} > 1 \tag{14b}$$

Where $\zeta$ is the softening coefficient, can be determined as follows:

$$\zeta_\sigma = f(f_c')f(\bar{\varepsilon}_1)f(\beta)W_p Wf \le 0.9, \tag{15}$$

where

$$f(f_c') = \frac{5.8}{\sqrt{f_c'}} \le 0.9 \ (f_c' \text{ in MPa}), \tag{16}$$

$$f(\bar{\varepsilon}_1) = \frac{1}{\sqrt{1 + 400\bar{\varepsilon}_1}}, \tag{17}$$

$$f(\beta) = 1 - \frac{|\beta|}{24^\circ}, \ \beta = \frac{1}{2}\tan^{-1}\left[\frac{\gamma_{21}}{(\varepsilon_2 - \varepsilon_1)}\right] \tag{18}$$

$$W_p = 1.15 + \frac{|\beta|(0.09|\beta| - 1)}{6}, \tag{19}$$

and

$$Wf = 1 + 0.2FF \tag{20}$$

### 2.3.3 SFC in shear

The rational equation relating the shear stress of concrete ($\tau_{12}^c$) and the shear strain ($\gamma_{12}$) in the 1-2 coordinate system is given by [6, 7] and shown in Equation 21.

$$\tau_{12}^c = \frac{\sigma_1^c - \sigma_2^c}{2(\varepsilon_1 - \varepsilon_2)}\gamma_{12} \tag{21}$$

where $\sigma_1^c$ and $\sigma_2^c$ are the smeared (average) concrete stresses and $\varepsilon_1$ and $\varepsilon_2$ are the biaxial smeared strains in the 1- and 2- directions of the principal applied stresses, respectively.

### 2.3.4 Prestressing tendons embedded in SFC

The smeared (average) stress-strain relationships of prestressing tendons embedded in SFC are given as follows and is shown in Figure 3:

$$f_{ps} = E_{ps}\bar{\varepsilon}_s', \ \bar{\varepsilon}_s < \frac{0.7f_{pu}}{E_{ps}} \tag{22a}$$

$$\text{or} \quad f_{ps} = \frac{E''_{ps}\bar{\varepsilon}'_s}{\left[1+\left(\frac{E''_{ps}\bar{\varepsilon}'_s}{f'_{pu}}\right)^5\right]^{\frac{1}{5}}}, \ \bar{\varepsilon}_s \geq \frac{0.7f_{pu}}{E_{ps}} \tag{22b}$$

where

$E_{ps}$ = elastic modulus of prestressing tendons, 200GPa

$\bar{\varepsilon}'_s = \bar{\varepsilon}_s + \varepsilon_{dec}$, uniaxial steel bar strain

$f_{pu}$ = ultimate strength of prestressing tendons, 1860MPa

$E''_{ps}$ = modulus of prestressing tendons in plastic area (Eq. 22), 209MPa

$f'_{pu}$ = modified strength of prestressing tendons, 1793MPa

In the above equations, *ps* can be exchanged by $\ell p$ and $tp$ for the longitudinal tendons and the transverse tendons respectively.

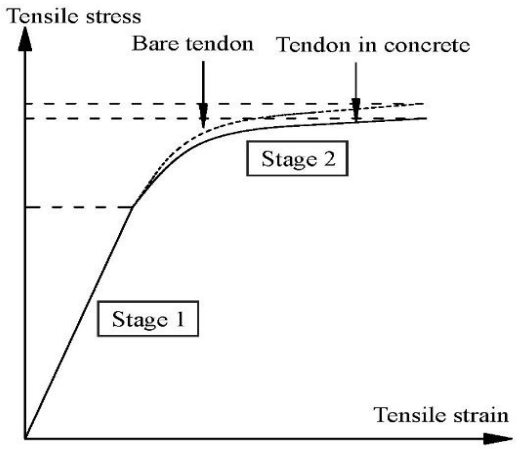


Figure 3: Constitutive relationship of prestressing strands.

### 2.3.5 Mild Steel Embedded in SFC

The smeared (average) tensile stress-strain relationships of mild steel embedded in concrete in the $\ell - t$ coordinate are the same as those in SMM. They can be expressed as follows and is shown in Figure 4:

Stage 1:

$$f_s = E_s\bar{\varepsilon}_s, \ \bar{\varepsilon}_s \leq \bar{\varepsilon}_n \tag{23}$$

Stage 2:

$$f_s = f_y\left[(1-0.096FF)(0.91-2B)+(0.2FF+1)(0.02+0.25B)\frac{\bar{\varepsilon}_s}{\varepsilon_y}\right], \ \bar{\varepsilon}_s > \bar{\varepsilon}_n \tag{24}$$

Stage 3 (unloading):

$$f_s = f_p - E_s(\bar{\varepsilon}_p - \bar{\varepsilon}_s), \ \bar{\varepsilon}_s < \bar{\varepsilon}_p \tag{25}$$

where

$$\bar{\varepsilon}_n = \varepsilon_y(0.93 - 2B) \tag{26a}$$

$$B = \frac{1}{\rho}\left(\frac{f_{cr}}{f_y}\right)^{1.5} \tag{26b}$$

$\varepsilon_{cr}$ = 0.00008, concrete cracking strain

$f_{cr} = 0.31\sqrt{f_c'}$ ($f_c'$ and $\sqrt{f_c'}$ are in *MPa*), concrete cracking stress

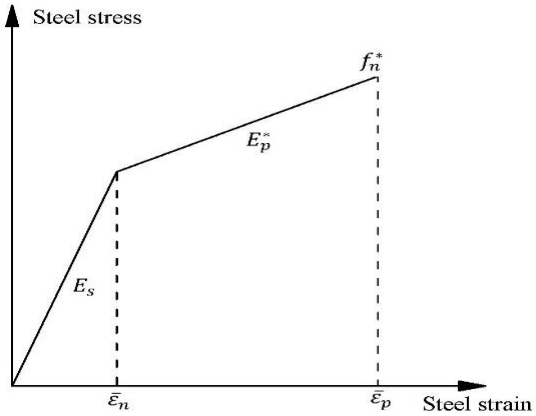


Figure 4: Stress-strain relationship of reinforcing steel using two-straight line expression.

## 3 IMPLEMENTATION OF SOFTENED MEMBRANE MODEL

Once the softened membrane model is developed, it needs to be implemented in a finite element analysis program, such as OpenSees. Under the OpenSees framework, each finite element analysis consists of four main types of objects: *ModelBuilder* object, *Domain* object, *Analysis* object, and *Recorder* object, as shown in Figure 5.

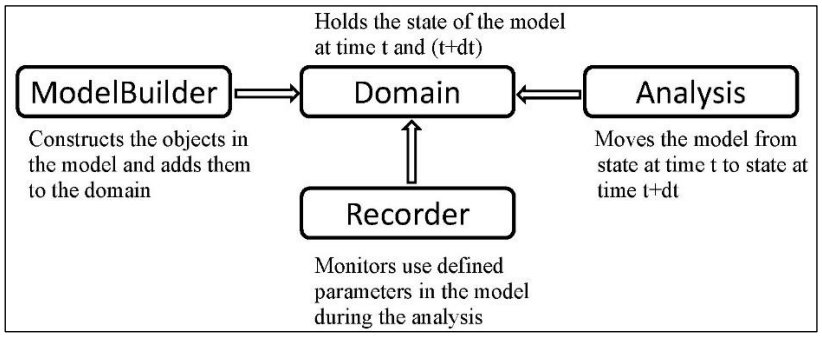


Figure 5: Principal objects in OpenSees [2].

The *ModelBuilder* object constructs the nodes and masses on the nodes, creates the elements and materials of the elements, defines the loads acting on the nodes and the elements, and defines the constraints acting on the nodes. The *ModelBuilder* is responsible for building the objects in the model such as *Node*, *Mass*, *Material*, *Element*, *LoadPattern*, *Constraint*, etc. and adding them to the *Domain*.

After the objects are created by the *ModelBuilder* object, they are stored in the *Domain* object. The *Domain* object also provides access of *Analysis* and *Recorder* objects to the objects in the *Domain* and holds the state of the model during the analysis procedure.

The *Analysis* object is responsible for performing static or dynamic analysis on the model. The *Analysis* object includes object such as *ConstraintHandler*, *Numberer*, *AnalysisModel*, *SolutionAlgorithm*, *Integrator*, and *SystemOfEquation*. These objects define how the analysis is performed. The *ConstraintHandler* object defines the relationships between the degrees of freedom (DOF) of the nodes and determines the constraint equation in the analysis. The *Numberer* object is used to construct the *DOF_Numberer* object, which determines the mapping between equation numbers and degrees-of-freedom. The *AnalysisModel* object comprises many *FE_Element* objects and *DOF_Group* objects. The *SolutionAlgorithm* object defines the solution algorithm that is used to solve the nonlinear equation.

Currently, the *SolutionAlgorithm* objects in OpenSees includes many methods such as Linear, Newton-Raphson, Modified Newton-Raphson, Newton-Raphson with line search, Newton-Raphson with acceleration and other algorithms. The *Integrator* object determines the predictive step and corrective step during the time t+dt in the analysis and specify the tangent matrix and residual vector at any iteration. The type of *Integrator* is different for static analysis and dynamic analysis. The *Integrator* objects for static analysis include load control, displacement control and arc-length control. The *Integrator* objects for dynamic analysis include Newmark method, Wilson-θ method, Hilbert-Hughes-Taylor method and other methods. The System of Equation objects are used to store and solve the system of equations in the analysis. The *Recorder* object is used to monitor the state of *Domain* components during an analysis, and write the state to a file or to a database.

Under this framework, if a new type of element or new material is to be introduced, a new corresponding class of objects can be added to the OpenSees according to the designated specification of the framework without changing the existing code. This is because the interface, which is defined in the core components, is minimal to make adding new component classes easier but large enough to ensure all that is required can be accommodated [2].

The OpenSees is not able to perform nonlinear finite element analysis on reinforced concrete membrane structures such as panels and shear walls because there is no membrane model for reinforced concrete. Also, the uniaxial material models of concrete and steel in OpenSees are too simple, and more sophisticated models need to be created. For example, the concrete model *Concrete01* in OpenSees does not consider the stress of concrete in tension and the softening effect in compression due to the biaxial tensile strain in the perpendicular direction. The steel model *Steel01* does not take into account the Bauschinger effect in the unloading and reloading paths. Therefore, the new finite element models of reinforced concrete plane stress material could be implemented into OpenSees for performing analysis on reinforced concrete membrane structures.

Uniaxial material class, *ConcreteR01* is created and implemented into OpenSees in addition to *TendonL01* [8] and *SteelZ01* [9], which were implemented previously. An object of *ConcreteR01* needs three input parameters: ultimate compressive strength $f_c^{'}$, fiber factor ($FF = V_f \frac{L_f}{D_f}$, product of volume of steel fiber in concrete and aspect ratio of steel fiber) and the compressive strain $\varepsilon_0$ corresponding to $f_c^{'}$. An object of *SteelZ01* needs four input parameters: yield stress, Young's modulus, concrete compressive strength, and steel ratio. The latter two parameters are used to calculate the smeared yield stress and strain of embedded rebars. In addition, the coefficients in *A* and *R* that determine the shapes of unloading and reloading paths are set as two additional input parameters. The default values are defined as 1.9 and 10.0. An object of *TendonL01* needs five input parameters. The first four input parameters are the same as the ones required for *SteelZ01*. The fifth input parameter required is the initial strain in the

prestressing tendons. The additional input parameters, *A* and *R*, to determine the shapes of the unloading and reloading paths are also available with default values of 1.9 and 10.0 respectively.

A 2D material class *PCPlaneStress* is created and implemented into OpenSees by Laskar [8]. The *PCPlaneStress* is a class for reinforced/prestressed concrete plane stress material using CSMM-PC. In *PCPlaneStress*, the material constitutive matrix is evaluated and the stress vector is calculated. An object of *PCPlaneStress* material needs the tags of the created uniaxial concrete, steel, and tendon objects of *ConcreteR01*, *SteelZ01*, *and TendonL01*, the directions of the steel and tendon grids, and the steel and tendon ratio for the steel in each direction. Two uniaxial concrete objects are needed in defining one *PCPlaneStress* object, which represents the concrete in the two principal stresses directions. The steel and tendon orientations are not necessarily in the horizontal and vertical directions, and the user can define the arbitrary angles of the steel and tendons. The steel and tendon directions are not necessarily orthogonal, either. Currently users can define the steel in the prestressed concrete element in up to two directions and the tendons in the prestressed element in another two directions.

The implementation of the *PCPlaneStress* into OpenSees is shown in Figure 6. The Analysis and *Recorder* objects are omitted in this figure. The *PCPlaneStress* is implemented with the *Quadrilateral* element to represent the PC plane stress four node elements. The *PCPlaneStress* is related with *ConcreteR01*, *SteelZ01* and *TendonL01* to determine the tangent material constitutive matrix and calculate the stress of the elements. For each trial displacement increment in the analysis procedure, *PCPlaneStress* will receive the strains of the elements, determine the uniaxial strains of the concrete and steel, and then send the uniaxial strain of concrete and tensile perpendicular strain to the two uniaxial concrete objects. After receiving the uniaxial strain and corresponding tensile strain, the concrete object will calculate the tangent stiffness and stress and then send the values back to the *PCPlaneStress* object. Similarly, *PCPlaneStress* will send the uniaxial strain of the steel to the uniaxial steel object and receive the tangent stiffness and stress from the related uniaxial steel objects. As in the case of steel, *PCPlaneStress* also sends the uniaxial strain of tendon to the uniaxial tendon object. After receiving the uniaxial strain, the tendon object will add the initial strain in the tendon to the received strain and thereafter calculate the tangent stiffness and stress to be sent back to the *PCPlaneStress* object. After receiving the uniaxial stiffness and stress of concrete, steel, and tendons the tangent stiffness matrix will be evaluated and the stress vector calculated. An iterative procedure is defined to obtain the converged material constitutive matrix and stress vector for a given strain vector.

Meanwhile, the displacement control scheme in the OpenSees has been previously modified for an arbitrary displacement path to perform analysis of *RCPlaneStress* structures [9]. The user can define the displacement paths of the degree-of-freedom of the node whose response controls the solution. The displacement increment for each path of the displacement scheme can also be varied. Changing the size of displacement increment makes it possible to overcome some numerical problems in the nonlinear analysis.

In addition, some classes are modified to overcome or bypass the numerical problems occurring in the analysis of nonlinear problems [9]. For example, the analytical models about the convergence check has been modified. Instead of giving one maximum iterative number for all increments, the user can decide different maximum iterative numbers for different paths in the displacement control history. Users can increase the maximum iterative number in the specified path that may have numerical problems. Less iterative numbers in the rest of the displacement paths are defined to save time.

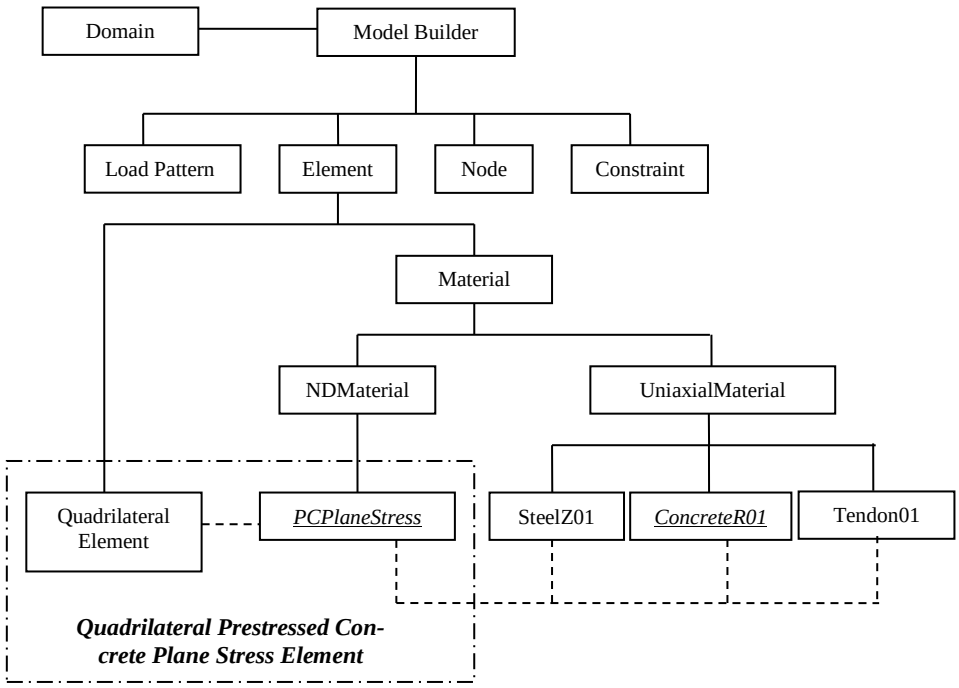


Figure 6: Finite element implementation of CSMM-PC.

## 4 VALIDATION OF THE DEVELOPED TOOL

To validate the developed tool (called Simulation of Concrete Structures, SCS), the Prestressed Steel Fiber Concrete (PSFC) beams shown in Figure 7 have been selected. Since the PSFC beams were tested under monotonic loads, this validation and applicability of SCS program is only suitable in predicting the behaviour of PSFC structures under monotonic loading. The following describes the analytical details.

### 4.1 Analytical Model

Various finite element models of the PSFC beams were developed to analyze the beams using SCS program. The two (top and bottom) flanges of the beams, which were designed to resist applied bending moments, were modeled as *NonlinearBeamColumn* elements with fiber sections. The beam web, designed to resist the applied shear force, was represented by *PCPlaneStress Quadrilateral* elements. The details of the finite element models of PSFC beams are described later in this paper. In the finite element model of the PSFC beams the prestressing loads acting on the beam were applied as nodal forces adjacent to the ends of the beams. In case of flexure-shear critical beams, a reduction of 20% in the initial prestressing force is considered to account for prestress loss. An incremental load-control was used for the prestressing loads at the beginning of an analysis in the model. Thereafter, the prestressing loads were kept constant and monotonic vertical loads were applied on the top flange of the beam using a predetermined displacement-control scheme.

All the concentrated loads applied on the beam in the model acted at nodes. The effect of bearing plates, which were actually used in the load-test to apply vertical loads on the beam, was ignored for simplicity. The loads were distributed among three nodes adjacent to the location of the applied load. The analysis yielded similar results in the cases when (a) larger load was applied at the node corresponding to the actual loading point and lower loads were applied at the two adjacent nodes and (b) loads were distributed equally among the three nodes. Hence, the concentrated vertical loads on the beams were modeled at a node corresponding to the actual

loading point and two adjacent nodes. The results of beam analysis i.e. nodal displacement and corresponding vertical forces, were computed at every displacement step that had numerically converged. Additionally, the stresses and strains in the beam elements were also calculated by the program [8].

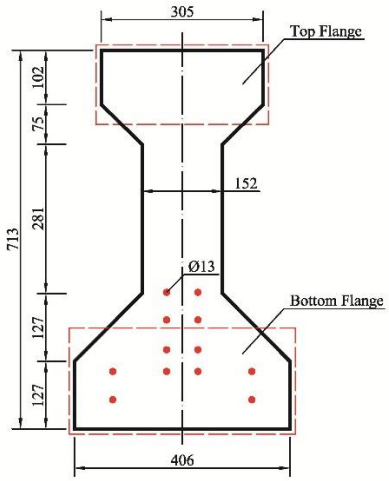


Figure 7: Cross sections of I-beam.

## 4.2 Finite element model of PSFC beams

Each of the PSFC I-beams was modeled using the finite element mesh, as shown in Figures 8 and 9. The top and bottom flanges in the beams were each divided into sixteen and fifteen *NonlinearBeamColumn* elements in the case of web-shear and flexure-shear failure modes, respectively. The bulb-shaped top and bottom flanges in beam's cross-section were modeled using rectangular *NonlinearBeamColumn* elements with equivalent area. Each *NonlinearBeamColumn* element was defined with two control sections. Each section representing the top flange was discretized into forty fibers of concrete. The configuration of the section discretization of the top flange is shown in Figure 10(a). Similarly, each section representing the bottom flange was discretized into forty fibers of concrete and two fibers of tendons. The configuration of the section discretization of the bottom flange is shown in Figure 10(b).

Two of the twelve tendons in the specimens were provided in the *NonlinearBeamColumn* elements representing the bottom flange of the specimens. The remaining tendons were provided in the quadrilateral elements used to represent the webs of these specimens. The initial strains in the tendons in the web were applied using the *TendonL01* constitutive module. *Concrete01*and *Steel02* material modules were used to define the concrete and steel fibers materials in the cross section, respectively.

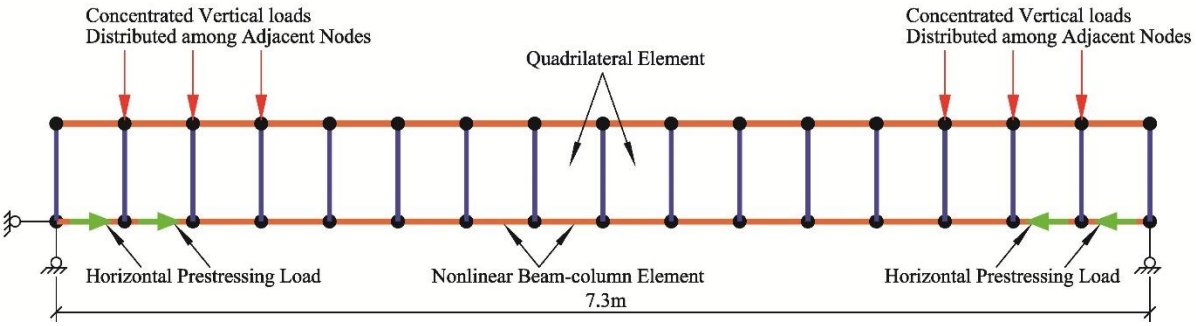


Figure 8: Finite element model of PSFC I-beams tested under web-shear.

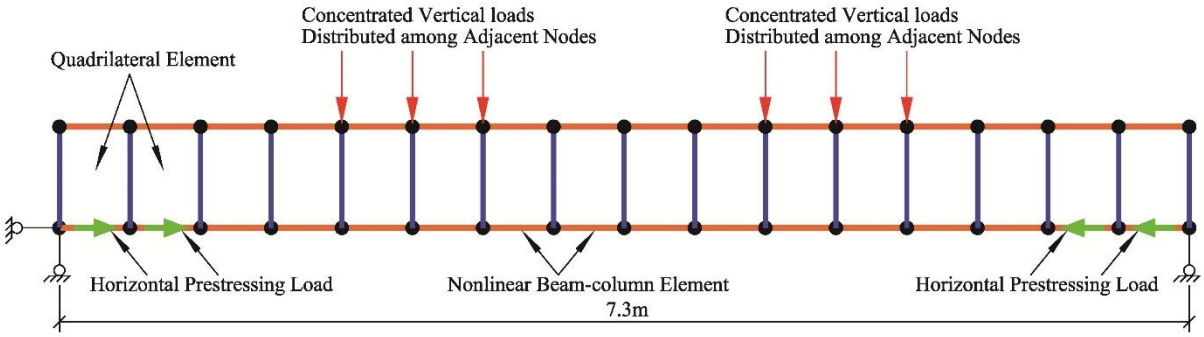


Figure 9: Finite element model of PSFC I-beams tested under flexural-shear.

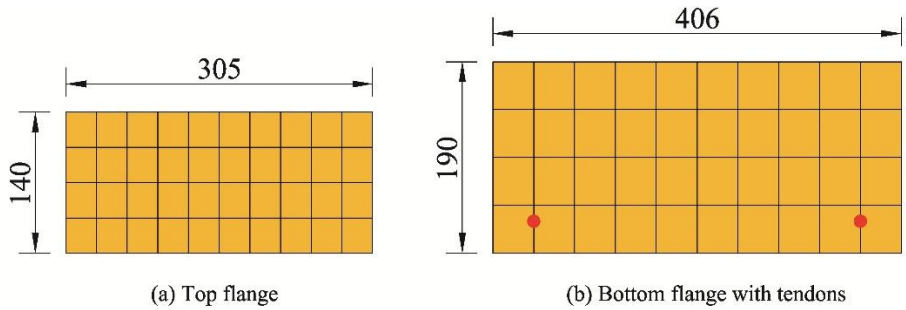


Figure 10: Cross-section discretization for PSFC I-beams governed by web-shear.

The *Concrete01* module used herein was a uniaxial material module of concrete previously created in OpenSees following the modified Kent and Park model [10]. The *steel02* module used in this program was a uniaxial Menegotto-Pinto steel material object with isotropic strain hardening [11]. This object also allowed user to enter the initial strain in the steel, which is useful in modeling the prestressing strands.

The web regions of the beams have been modeled by sixteen and fifteen *PCPlaneStress quadrilateral* elements in case of web shear and flexural shear, respectively. The tendon orientation in the elements was defined in the horizontal direction. The steel ratio in the vertical direction was taken as a very small number to avoid numerical problems during the analysis. The tendon ratio in the horizontal direction was determined based on the area of ten prestressing tendons smeared over the entire cross section of these specimens. *ConcreteR01* and *TendonL01* were used to create the uniaxial material models of concrete and tendons in the *PCPlaneStress* material, respectively. The constant *k* used in *ConcreteR01* was to impose an upper limit to the initial stress-strain relationship of concrete in compression and which reduced the initial slope of the concrete stress-strain curve to less than $\frac{2f_c'}{\varepsilon_0}$. This initial slope of concrete stress-strain curve was taken as 1.5 for the analysis of all the beams tested.

## 4.3 Comparison of analytical and experimental results

### 4.3.1 Web-shear failure

The measured and calculated load-displacement curves for all PSFC I-beams tested in web-shear failure mode are shown in Figures 11 to 14. It can be seen that the analyses predict reasonably well the load-displacement characteristics of the beams including initial stiffness, post-cracking stiffness, yield displacement, and ultimate strengths. The general trend observed in the beam (R1 to R4) tests, i.e. increase in load carrying capacity of beams with increase in fiber–factor, was accurately predicted by the analysis program. Figures 11 to 14 also justifies the use

of the constant $k$ =1.4 (close to $k$ = 1.5 assumed initially in the analysis) to make the initial slope of the concrete compressive stress-strain curve lower than $\frac{2f_c'}{\varepsilon_0}$.

Unlike Beams R1, R2 and R3 the prediction of the post-cracking stiffness of Beam R4 did not match well with the experimental results. This is due to the fact that while testing Beam R4, the Data Acquisition System (DAS) got some problem in the electronic part and recorded invalid values and stopped after some time. After resolving the problem with DAS, the test has been restarted. This invalid data is the reason for the lower cracking value and post cracking stiffness observed during the testing of the beam than those obtained from the analysis.

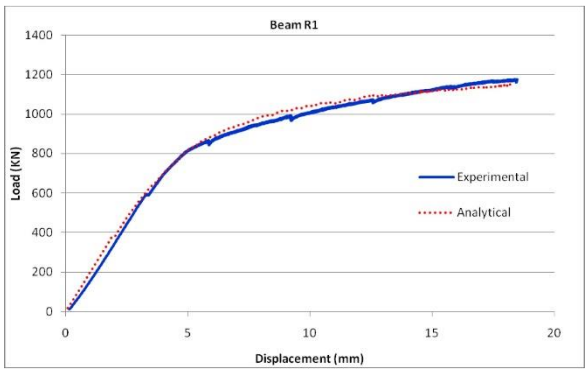


Figure 11: Comparison of experimental and analytical results of beam R1.

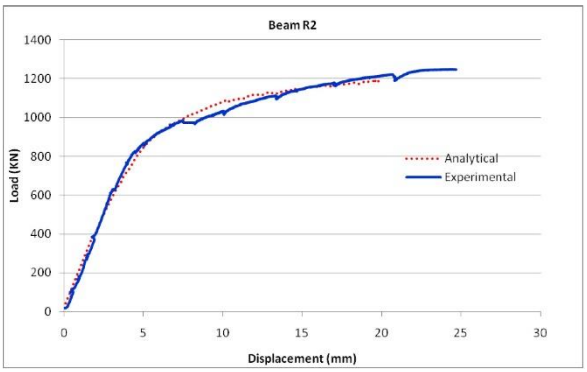


Figure 12: Comparison of experimental and analytical results of beam R2.

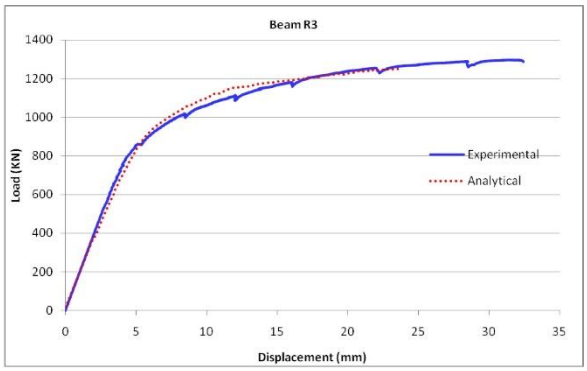


Figure 13: Comparison of experimental and analytical results of beam R3.

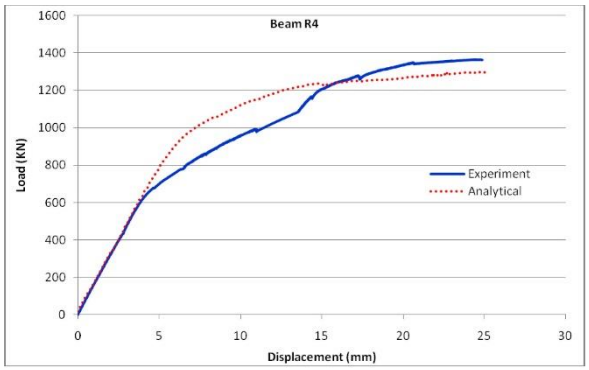


Figure 14: Comparison of experimental and analytical results of beam R4.

### 4.3.2 Flexure-shear failure

The measured and calculated load-deformation curves for all beams with flexure-shear failure are shown in Figures 15 and 16. Compared with the experimental results, the analyses predicted the load versus deformation characteristics of the specimens including initial stiffness, post-cracking stiffness, yield displacement, and ultimate strength. The analysis could well predict the lower load carrying capacity of beams tested under flexural shear in comparison to the beams tested under web shear failure having same amount of steel fibers. The higher ductility observed in the behavior of beams under flexural-shear failure, than all the web shear specimens was also well predicted in the analysis. Like the beams tested under web shear, Figures 15 and 16 also justifies the use of the constant $k$ = 1.4 to make the initial slope of the compressive stress strain curve of concrete lower than $\frac{2f_c'}{\varepsilon_0}$.

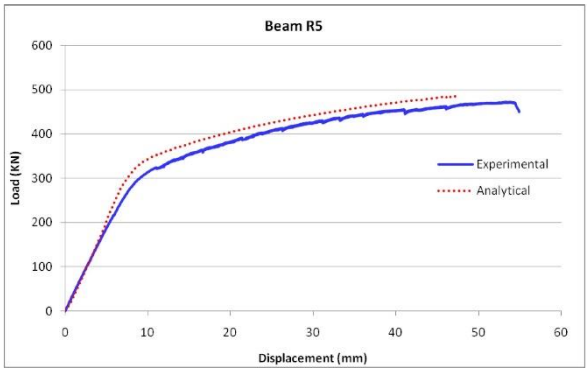


Figure 15: Comparison of experimental and analytical results of beam R5.

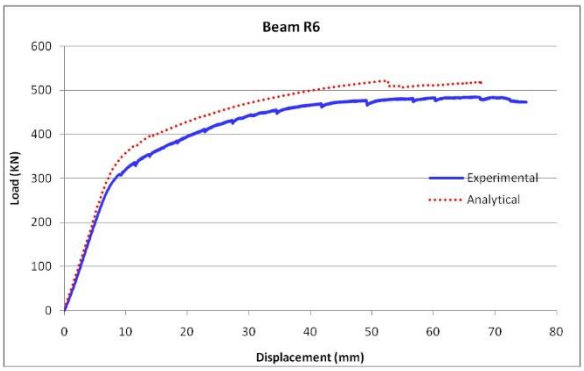


Figure 16: Comparison of experimental and analytical results of beam R6.

## 5 CONCLUSIONS

The constitutive models of PSFC was previously established. Using the established constitutive models, a softened membrane model for PSFC is formulated, and both the constitutive models for materials and softened membrane model for elements are implemented in a finite element program framework (OpenSees) to develop an analytical tool for shear analysis of the PSFC beams. Using this finite element analysis tool, the load-deflection curves of all the PSFC I-beams are simulated with acceptable accuracy.

## ACKNOWLEDGMENTS

The authors would like to express their gratitude to the following sponsors for this project. They are Texas Department of Transportation, Texas, USA, and the National Natural Science Foundation of China (Grant No. 51678453). The materials presented are the research findings by the authors, and are not necessarily expressed for the funding agencies' opinion.

## REFERENCES

[1] P.R. Tadepalli, N. Hoffman, T.T.C. Hsu, Y.L. Mo, *Steel Fiber Replacement of Mild Steel in Prestressed Concrete Beams.* Texas Department of Transportation Report 0-5255-2, 2010.

[2] G.L. Fenves, Annual Workshop on Open System for Earthquake Engineering Simulation. *Pacific Earthquake Engineering Research Center, UC Berkeley, http://opensees.berkeley.edu/*, 2008.

[3] N. Hoffman, Constitutive Relationships of Prestressed Steel Fiber Concrete Membrane Elements. *PhD. Dissertation, Department of Civil and Environmental Engineering, University of Houston*, USA, 2010.

[4] X.B. Pang, T.T.C. Hsu, Fixed Angle Softened Truss Model for Reinforced Concrete. *ACI Structural Journal*, **93**, 197-207, 1996.

[5] R.R.H. Zhu, T.T.C. Hsu, Poisson Effect in Reinforced Concrete Membrane Elements. *ACI Structural Journal*, **99**, 631-640, 2002.

[6] T.T.C. Hsu, Y.L. Mo, *Unified Theory of Concrete Structures*, John Wiley and Sons, 2010.

[7] R.R.H. Zhu, T.T.C. Hsu, J.Y. Lee, Rational Shear Modulus for Smeared-Crack Analysis of Reinforced Concrete. *ACI Structural Journal*, **98**, 443-450, 2001.

[8] A. Laskar, Shear Behavior and Design of Prestressed Concrete Members. *PhD. Dissertation, Department of Civil and Environmental Engineering, University of Houston*, USA, 2009.

[9] J.X. Zhong, Model-Based Simulation of Reinforced Concrete Plane Stress Structures. *Ph.D. Dissertation, Department of Civil and Environmental Engineering, University of Houston*, Houston, USA, 2005.

[10] R. Park, M.J.N. Priestley, W.D. Gill, Ductility of Square-Confined Concrete Columns. *Journal of the Structure Division, ASCE*, **108(ST4)**, 929–950, 1982.

[11] R.P. Dhakal, K. Maekawa, Path-dependent Cyclic Stress-Strain Relationship of Reinforcing Bar Including Buckling. *Engineering Structures*, **24**, 1383-1396, 2002.

COMPDYN 2017
6th ECCOMAS Thematic Conference on
Computational Methods in Structural Dynamics and Earthquake Engineering
M. Papadrakakis, M. Fragiadakis (eds.)
Rhodes Island, Greece, 15–17 June 2017

# NONLINEAR ANALYSIS OF SHEAR CRITICAL RC MEMBERS USING CURRENT FE SOFTWARE

**P. Ceresa[1], and A. González Víquez[2]**

[1] Institute for Advanced Studies, IUSS Pavia
Piazza della Vittoria 15, 27100 Pavia, Italy
e-mail: paola.ceresa@iusspavia.it

[2] UME School, Institute for Advanced Studies, IUSS Pavia
Piazza della Vittoria 15, 27100 Pavia, Italy
e-mail: alonso20000@hotmail.com

**Keywords:** Shear-critical elements, finite element software, VecTor2, DIANA, ATENA, shear strength, shear capacity, nonlinear analysis.

**Abstract.** *The shear behaviour of concrete has been widely studied in the field of structural engineering, yet it is still considered an unresolved issue. In one hand, the design codes provide diverse methods to estimate the shear capacity of concrete with different results. On the other hand, analytical models to assess the performance of shear critical concrete members have been proposed by several authors. These models have been developed using different assumptions. Some of the theories have been implemented in finite element software packages that are used by engineers in academia and in the industry.*

*This study presents an investigation of the state-of-the-art software packages for the analysis of shear critical concrete elements. The theory implemented on each software is detailed and analysed. To evaluate the capacities of the packages, some benchmark tests have been used for both monotonic and cyclic loading cases. The presented results show the capabilities and limitations of the programs from the experience obtained during the duration of this work. Just as well, the results among the programs are compared among themselves as well as the results from other authors.*

## 1 BACKGROUND AND MOTIVATION

Even though the mechanics of shear behaviour in reinforced concrete (RC) has been studied for a long time, it is still an unsolved problem. On one hand, many design codes provide different methods to define and estimate the shear capacity of concrete. Among these codes there are the National Building Code of Canada by the CSA [1], AASHTO LRFD Bridge Specifications by AASHTO [2], and the Fib Model Code by the International Federation for Structural Concrete [3] and ACI 318-11 by the ACI Committee 318 [4]. These codes and their methods of design generally lead to very different shear capacity estimations for RC elements (and therefore, different amount of required transverse reinforcement). On the other hand, several analytical models have been proposed in order to assess the performance of shear critical members. Authors such as Litton [5], Bazant and Oh [6], Cervenka [7], Vecchio and Collins [8], De Borst [9], Hsu [10] and Maekawa *et al.* [11], have developed methods to determine the shear behaviour of RC, using diverse types of assumptions in the process. As defined in Ceresa *et al.* [12] [13], in the framework of smeared crack theory for RC the following main models can be identified:

- Compression Field Theory (see Collins [14], Vecchio and Collins [15])
- Modified Compression Field Theory, MCFT (see Vecchio and Collins [16])
- Rotating-Angle Softened Truss Model, RA-STM (see Belardi and Hsu [17], Belardi and Hsu [18], Pang and Hsu [19])
- Fixed-Angle Softened Truss Model, FA-STM (see Pang and Hsu [20], Hsu and Zhang [21], Zhang and Hsu [22])
- Cracked membrane model (see Kaufmann and Marti [23])
- Softened membrane model (see Zhu [24], Hsu and Zhu [25])
- Disturbed Stress Field Model, DSFM (see Vecchio [26], Vecchio and Lai [27]).

Some of these analytical models have been used in the development of commercial finite element (FE) software packages used by researchers and engineers in both industry and academia. Yet the complete range and capabilities of these programs is not completely investigated. Therefore, the aim of this work is to provide a thorough review of the theoretical models implemented in state-of-the-art FE packages for the nonlinear analysis of shear critical RC members. Similarly, verification examples are provided for the assessment of the accuracy, performance, advantages and limitations for the studied programs. This is performed for both the monotonic and the cyclic behaviour of reinforced concrete.

## 2 BRIEF OVERVIEW OF THE ANALYZED SOFTWARE

Three are the software packages taken into account in this study: VecTor2 [28], DIANA [29] and ATENA[30]. The detailed review of the theory implemented in each software can be found elsewhere [31].

VecTor2 is a nonlinear finite element program for the analysis of two-dimensional RC member structures subjected to in-plane normal and shear stresses. It models cracked concrete as an orthotropic material with smeared, rotating cracks. It considers the element to act as in the plane stress idealization. The program uses an incremental total load, iterative secant stiffness algorithm to produce the nonlinear solution. The two main bases of the modelling of RC are the MCFT and the DSFM. The latter two are then complemented in VecTor2 with other models for compressive and tensile behaviour of concrete, tension softening and tension stiffening. The main aspects that greatly affect the response of RC elements are the crack width check, the crack slip calculation and the models for hysteretic response of concrete and reinforcement steel, using models that consider the damage due to load reversal, repetitions and plastic behaviour.

The software DIANA uses two smeared cracking models to simulate the behaviour of RC, mainly focused in the monotonic response: the Multi-Directional Fixed Crack Model and the Total Strain Crack Model. The Multi-Directional Fixed Crack Model does not allow for a clear modelling of the compressive behaviour of concrete and was not used in this study. A further constitutive model is presented in DIANA as the model more suitable for the cyclic response of concrete – the Maekawa Cracked Concrete model. While working in a two-dimensional model, DIANA offers the option of working with an element based either in the plane stress or plain strain idealisation. The selection of the crack direction has been determined to be one of the main parameters that affect the response of RC in FE modelling. The Total Strain Crack Model and the Maekawa Cracked Concrete model are capable of modelling both the fixed and the rotated crack approach. If the fixed crack has to be used, a shear retention model has to be defined to calculate the shear stresses that exist when the strain field analysed does not coincide with the principal stresses direction. It has been found that fracture mechanics principles, through the concepts of fracture energy and crack bandwidth, are widely used to describe the stress-strain relations of concrete. An important concept offered by DIANA is the possibility of modelling the discrete steel bars using the embedded reinforcement approach.

The program ATENA includes several constitutive models that can be used in order to predict the behaviour of RC. For the behaviour of concrete, two models have been considered – the SBETA and the Rankine fracture-plastic constitutive models. Both models include the possibility of modelling the crack direction as fixed or rotated. Contrary to DIANA, ATENA only includes on model for the shear retention calculation when the fixed crack direction is used. The SBETA model contains the nonlinear behaviour of concrete in compression, the reduction of strength due to cracking, the use of fracture mechanics for the tension softening and a biaxial failure criteria. The unloading and reloading in the SBETA model are performed linearly from the maximum experienced strain to the origin. The Fracture-plastic model is a combination of a fracture model based on a smeared crack formulation and crack band model for the tensile behaviour and a plasticity model that considers concrete crushing for the compressive behaviour. The loading and reloading for compression considers the plastic strains, while for the tension, the reloading and unloading can be performed as linear to the origin or parallel to the initial stiffness. The software also includes several possibilities to model the steel reinforcement.

## 3 MONOTONIC ANALYSIS OF SHEAR-CRITICAL BEAMS

The software analysed in this study has been evaluated through different tests. The programs have been first evaluated with an analysis of beams under monotonic load where the shear behaviour is critical. The series of beams tested by Bresler and Scordelis [32] and the beam used for a blind prediction at the University of Toronto in 2015 [33] were the benchmark tests for this evaluation. The finite element models for each of the programs are formulated and presented, including the evaluation of the most adequate material models for these numerical tests. The parameters that affect the response of the RC element modelling the most have been identified, such as the definition of the tensile strength and the fracture energy and the selected crack rotation approach (fixed or rotated). The results from the FE packages are then compared.

### 3.1 Beams tested by Bresler and Scordelis

The first studied beams are those tested by Bresler and Scordelis [32]. These beams have been often used as benchmark, as shown in [34] [35]. These beams were simply supported

and subjected to concentrated load at midspan, with a span-depth ratio ranging from 3.3 to 5.7. They were designed such that the shear behaviour is critical, since they are heavily reinforced in flexure but with light to no amounts of shear reinforcement. The general properties of the beams are presented in Table 1, where the initial elastic modulus $E_c$, the tensile strength $f_t$ and the fracture energy $G_f$ are estimated as recommended in [36] and the Model Code [3]. The main focus was on the modelling of beams A-1 and OA-1. Using these results, the rest of the beams were analysed [31].

| Beam | $f'_c$ (MPa) | Bottom bars* | Top bars* | Stirrups* | $E_c$ (MPa) | $f_t$ (MPa) | $G_f$ (kN/m) |
|---|---|---|---|---|---|---|---|
| A-1 | 24.1 | 4 #9 | 2 #4 | #2@210mm | 24816 | 1.62 | 0.129 |
| OA-1 | 22.6 | 4 #9 | - | - | 24031 | 1.57 | 0.128 |
| A-2 | 24.3 | 5 #9 | 2 #4 | #2@210mm | 24919 | 1.63 | 0.130 |
| OA-2 | 23.7 | 5 #9 | - | - | 24609 | 1.61 | 0.129 |
| A-3 | 35.1 | 6 #9 | 2 #4 | #2@210mm | 29948 | 1.96 | 0.139 |
| OA-3 | 37.6 | 6 #9 | - | - | 30997 | 2.02 | 0.140 |

* bar # $f_y$(MPa), $\phi$(mm): $f_y = 325$, $\phi = 6.35$; #4: $f_y = 345$, $\phi = 12.7$; #9: $f_y = 555$, $\phi = 28.65$

Table 1: Properties of the Bresler-Scordelis beams, whose cross-section is b×h = 305mm×560mm.

***Models and results with VecTor2***

Beams A-1 and OA-1 have been modelled using 4-node rectangular elements for the concrete. The size of the element was taken as 25×25mm so that a uniform and sufficiently discrete mesh is used. Due to the symmetry of the beam's geometry, the boundary conditions and the loading conditions, only half of the beam has been modelled. The beam is modelled with bearing elements which are capable of simulating the loading plates and avoid any local issues in the point of support or load application. The boundary conditions consisted of a vertical support under the lower bearing element and of a lateral support throughout the middle of the beam due to symmetry. The reinforcement was modelled as discrete truss elements. The loading was applied with an imposed vertical displacement in the middle of the beam. By doing a displacement control of the test, the nonlinear post-peak response of the beam can be more precisely estimated. With the constitutive relationships listed below it was possible to obtain numerical results that more accurately reproduce the behaviour of these RC beams. All the details can be found in [31].

- Compression before peak: Popovics.
- Compression post-peak: Modified Park-Kent.
- Compression softening: Vecchio 1992-A (e1-e2-Form).
- Tension stiffening: Modified Bentz 2003.
- Tension softening: Nonlinear (Hordijk).
- Confined strength: Kupfer/Richart.
- Crack stress calculation: DSFM.
- Crack slip calculation: 2 mm maximum crack width.
- Concrete-reinforcement bond: Perfect bond.
- Reinforcement stress-strain: elasto-plastic behaviour with strain hardening in both tension and compression.

The numerical results showed that the selected models are able to replicate well the behaviour of the beams until the 70% of the peak-load reached during the experimental test. The nonlinear response is modelled correctly, where the stiffness of the specimens are well repro-

duced. However, the failure of the element is obtained prematurely. Convergence problems were observed in analyses of all the Bresler-Scorderlis beams.

***Models and results with DIANA***

Similarly to the models in VecTor2, 4-node rectangular 25×25 mm size elements were used for the modelling of concrete. Just as well, only half of the beam was modelled with the same support conditions and it included the bearing elements at the point support and the load application point in order to avoid localisation problems. The reinforcement steel was modelled using the discrete embedded reinforcement concept. With this modelling option, the reinforcement bars in the beam do not necessarily have to line-up with the nodes of the finite elements. The constitutive relationships used in DIANA for the RC beams under the monotonic load is the Total Strain Crack Model. It was deemed appropriate since it is capable of modelling several different stress-strain relations for tension and compression, considers the effects of cracking and confinement and the possibility of using several shear retention models. The following list presents the selected models (all the details are given in [31]):

- Compression model: Thorenfeldt.
- Tension model: Hordijk.
- Model for lateral cracking: JSCE 2012.
- Confinement model: Selby and Vecchio.
- Concrete-reinforcement bond: Perfect bond.
- Reinforcement stress-strain: Von Mises plasticity with strain hardening in both tension and compression.

For the beams A-1 and OA-1, a comparison was performed between the results of using the fixed crack model or the rotating crack model. For the beam with transverse reinforcement (A-1), the best result was obtained using the fixed crack approach with the aggregate-based shear retention model. A normal size aggregate (15 mm) was assumed. For the beam without stirrups (OA-1), this modelling strategy overestimated the capacity of the beam. Better results were obtained using the fixed crack approach with the damage-based retention model. Two difficulties appeared during the numerical simulations. First, the displacement corresponding to the peak load was generally lower than the experiment. Therefore, the degradation of stiffness at the ultimate stages of loading was not precisely modelled. Second, the models presented convergence problems at these stages, and, in some cases, the ultimate load was not reached.

***Models and results with ATENA***

The mesh of the models for ATENA has been generated with the same assumptions adopted in VecTor2 and in DIANA. Similarly to DIANA, the reinforcement steel was modelled using the discrete embedded reinforcement concept. ATENA has two models available for the RC elements: SBETA and Fracture-Plastic. Both were used to model the beams. The next constitutive model were used:

- Compression model for pre-peak branch: Model Code 2010 (for SBETA) and Hordijk model.
- Compression model for descending branch: Linear descend.
- Tension model: Exponential.
- Model for reduction of compressive stress due to cracking: Vecchio and Collins [16] with $c = 0.80$.
- Concrete-reinforcement bond: Perfect bond.
- Reinforcement stress-strain: Bi-linear response with strain hardening, active in both tension and compression.

Both the SBETA and the Fracture-plastic models are capable of using a fixed or rotating crack approach, so both approaches were tested. ATENA uses some formulas to define the missing parameters based on the compressive strength inputted into the software. In order to determine which values represent better the results from laboratory test, a simple sensitivity analysis was performed for beams A-1 and OA-1. The two parameters modified were the tensile strength of concrete ($f_t$) and/or the fracture energy ($G_f$). Only for the Fracture-plastic model, another parameter was the inclusion of the tension stiffening as defined in ATENA with a recommended value of $c_t$=0.40 (Table 2). This parameter represents the minimum value (40% of $f_t$) for the reduction of the tensile stress after cracking occurs.

| Parameter | A-1 | | OA-1 | |
|---|---|---|---|---|
| | Default | Modified | Default | Modified |
| $f_t$ (MPa) | 2.23 | 1.62* | 2.14 | 1.57* |
| $G_f$ (kN/m) | 0.058 | 0.129 | 0.053 | 0.128 |
| $c_t$ | 0 | 0.40 | 0 | 0.40 |

*value used in VecTor2 and DIANA

Table 2: Default and modified parameters for the sensitivity analysis in ATENA

Comparing the numerical results it was derived that the Fracture-plastic model was capable of precisely model the nonlinear behaviour of these beams. The models using the fixed crack approach with the modified tensile strength showed the most promising results. Furthermore, the tension stiffening parameter works fairly well for the beam with the transverse reinforcement. Therefore, the simulation of the Bresler-Scordelis beams was performed with the Fracture-plastic model, the modified tensile model and the inclusion of $c_t$=0.40 for the beams with transverse reinforcement only. The numerical simulations with this software showed accurate results for most of the cases. The models used were able to perform the complete analysis without convergence problems.

### *Comparison of the results among the programs*

The results for the A-1 and OA-1 beams are compared in Figure 1. It is important to note that these results were obtained with only the experience and knowledge obtained during the time of this study. It is believed that these predictions could be improved given the time and experience to work more and perfect the models.

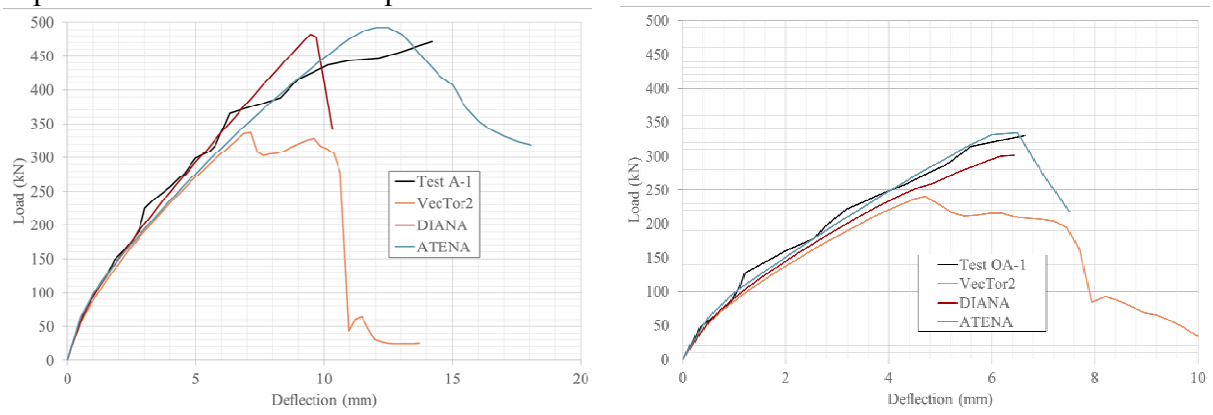


Figure 1: Comparison of the load-displacement curves for the beams A-1 (on the left) and OA-1 (on the right)

### *Comparison with other authors*

A re-examination of these beams was performed by Vecchio and Shim [35]. An analysis of the beams was performed using VecTor2 and their results for beams A-1 and OA-1 are pre-

sented in Figure 2, as well as the results of this research with VecTor2. The results of Vecchio and Shim represent an enhanced prediction of the behaviour of the beams with respect to the numerical results obtained by the Authors. This confirms the idea that the models developed in this study could be improved with more expertise and software knowledge.

Very good numerical simulations were obtained by Kagermanov and Ceresa [37] [38] with a fiber-section model with an exact shear strain profile for 2D RC frame structures.

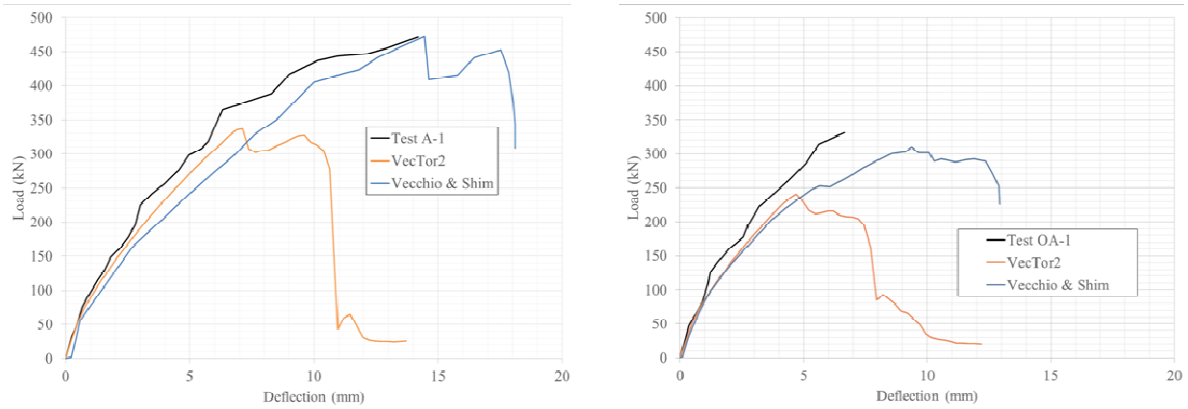


Figure 2: Comparison of the A-1 and OA-1 beams to the models of Vecchio and Shim [35]

## 3.2 Toronto beam

The University of Toronto, as described by Collins *et al.* [33], tested a deep beam in order to evaluate the shear behaviour of thick slabs, since various design code procedures give significantly different estimates of the shear capacity. These thick slabs may be present in several structures such as mat foundations for high rise buildings or intake structures for hydroelectric projects. The main issues with the codes generally used is that the size effect is not considered.

The test simulated a strip cut of a 4m thick slab, as shown in Figure 3. The properties of the specimen are presented in Table 3. The applied load was not located in the middle of the beam. The right side contained no shear reinforcement, while the left side contained the minimum shear reinforcement recommended by the ACI 381 Code. A blind prediction was established in order to assess the ability of the engineering profession (industry and academia) in the estimation of the shear response in this type of structures.

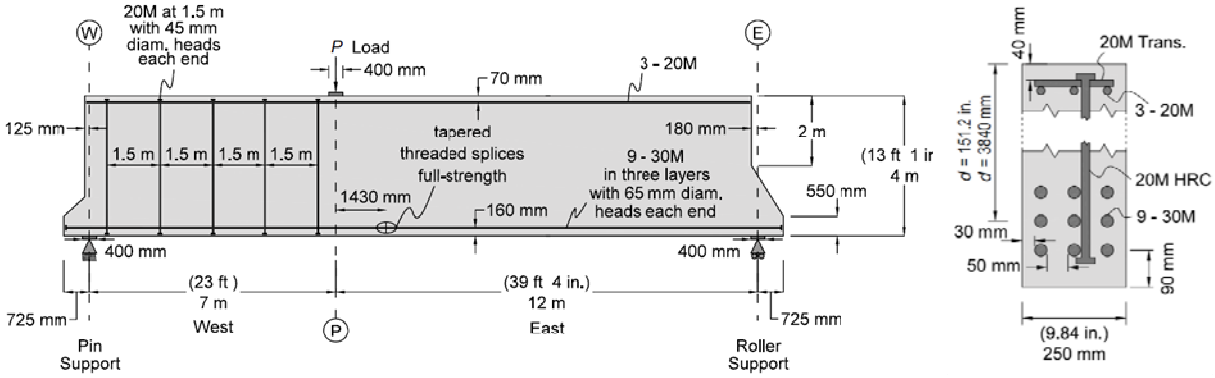


Figure 3: Elevation (on the left) and cross-section (on the right) of the Toronto beam

### *Model and results with VecTor2*

Given the depth of the beam, the size of the elements of the mesh was 200×200 mm for the 4-node elements. The complete beam is modelled as simply support element. All the reinforcement was modelled as discrete truss elements. Also, a bearing elements was used under

the load application point to avoid localization issues. Finally, the beam was modelled under an imposed vertical displacement. Note that for this beam the self-weight is significant. Hence, a first loading stage of only the weight of the beam was performed and then the imposed vertical displacement started to increase.

The constitutive models selected were those which model more realistically the behaviour of RC elements, including the models for compression softening and for the confined concrete:

- Compression before peak: Popovics.
- Compression post-peak: Modified Park-Kent.
- Compression softening: Vecchio 1992-A (e1-e2-Form).
- Tension stiffening: Modified Bentz 2003.
- Tension softening: Nonlinear (Hordijk).
- Confined strength: Kupfer/Richart.
- Crack stress calculation: Basic (DSFM/MCFT).
- Crack slip calculation: 1 mm maximum crack width.
- Concrete-reinforcement bond: Perfect bond.
- Reinforcement stress-strain: elasto-plastic behaviour with strain hardening in both tension and compression.

| Span (mm) | $f'_c$ (MPa) | Bottom bars* | Top bars* | Vertical bars* | $E_c$ (MPa) | $f_t$ (MPa) | $G_f$ (kN/m) |
|---|---|---|---|---|---|---|---|
| 19000 | 40 | 9 – 30M | 3 – 20M | 20M @1.5 m | 32496 | 2.09 | 0.142 |
| Bar | $\phi$ (mm) | Area ($mm^2$) | $f_y$ (MPa) | $\varepsilon_{sh}$ | $f_u$ (MPa) | $\varepsilon_u$ | |
| 20 M | 19.5 | 300 | 522 | 0.017 | 629 | 0.20 | |
| 30 M | 29.9 | 700 | 573 | 0.014 | 685 | 0.18 | |

Table 3: Properties of the Toronto beam, whose cross-section is b×h = 250mm×4000mm

***Model and results with DIANA***

The mesh was generated automatically by the software using 4-node rectangular element of 100×150 mm. The modelling of the reinforcement steel was performed using the discrete embedded reinforcement concept. The support conditions and the modelling of the bearing elements were the same as in VecTor2. The analysis, differently from the ones performed with the other two programs, required an imposed vertical load instead of a displacement. This was necessary due to how DIANA performs the staged loading, first from the self-weight and later from the applied load.

The constitutive model used in DIANA is the Total Strain Crack Model, as for the Bresler-Scordelis beams. The laws selected were as follows:

- Compression model: Thorenfeldt.
- Tension model: Hordijk.
- Model for lateral cracking: JSCE 2012.
- Confinement model: Selby and Vecchio.
- Concrete-reinforcement bond: Perfect bond.
- Reinforcement stress-strain: Von Mises plasticity with strain hardening in both tension and compression.

As observed for the Bresler-Scordelis beams, the fixed crack model was deemed appropriate to model beams in DIANA. Similarly, the results of these beams showed that for lightly reinforced structures, the shear retention model based on damage provided the best suited results. Hence, the Toronto beam was modelled using this approach.

***Model and results with ATENA***

The FE model developed in ATENA is equal to the model developed in Vector2. The discrete embedded reinforcement model was used for the steel reinforcement. The beam was loaded imposing a vertical displacement, as in VecTor2.

From the two models available in ATENA for the RC elements, the Fracture-plastic model is used. The constitutive models considered in the analysis are listed below:

- Compression model for pre-peak branch: Hordijk model.
- Compression model for descending branch: Linear descend.
- Tension model: Exponential.
- Model for reduction of compressive stress due to cracking: Vecchio and Collins [16] with $c = 0.80$.
- Concrete-reinforcement bond: Perfect bond.
- Reinforcement stress-strain: Multi-linear response with strain hardening, with the steel being active in both tension and compression.

As concluded in the analysis of the Bresler-Scordelis beams, the fixed crack approach resulted in the best numerical predictions, and it is used for this beam as well. The tension stiffening parameter ($c_t$) was not included into the analysis of the Toronto beam. The rational for this decision was that the beam can be considered as very lightly reinforced, as seen in Figure 3. Even though the west side of the beam has transverse reinforcement, it is too far apart and the east side has no vertical reinforcement. Therefore, the inclusion of a minimum limit for the tensile strength after cracking could be overestimating the capacity of the beam.

***Comparison of the results among the programs***

The load-displacement curve calculated from the three software is presented in Figure 4. The load in the vertical axis only accounts for the load applied from the jacks during the test. It is because of this that the curve does not start at the origin but at the displacement that occurred due to the self-weight of the beam. The three programs predicted a similar the behaviour for the Toronto beam, in particular for the post-cracking stiffness.

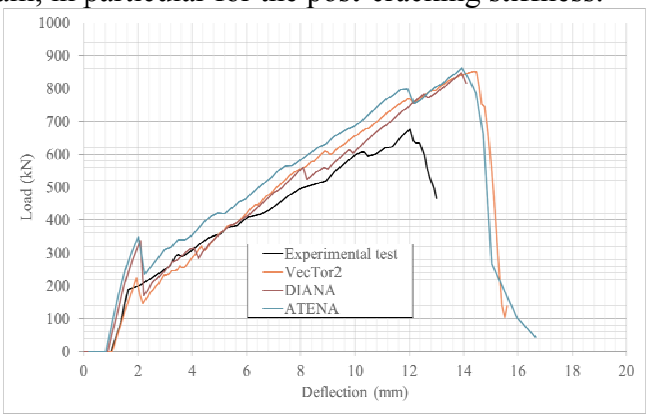


Figure 4: Comparison of the load-displacement curves for the Toronto beam

***Comparison with other authors***

The blind prediction for the Toronto beam included 66 entries. The resulting predictions are shown in Figure 5, with the inclusion of the three numerical results obtained in this study (carried out after the blind prediction). The aim of presenting this comparison is to show the variability of the results that were reported. This demonstrates that the shear problem is still an unsolved issue. As mentioned by Collins *et al.* [33], the prediction of shear strength of very thick slabs not containing shear reinforcement was a great challenge for the engineering profession. A 44% of the entries made dangerous overestimation of the capacity, while 20% of

them were very accurate. The ACI 318-14 Code by the ACI Committee 318 [4], which does not account for size effect, estimated a capacity 3.7 times greater than the experimental value. This notes the limitations some codes have when shear critical elements are analysed.

Two of the entries used VecTor2: the prediction by Professor Vecchio and the prediction by the University of Brescia, led by Conforti and Facconi. The results of their numerical predictions are different and a better simulation was performed by Conforti and Facconi, proving that the engineering criteria and the assumptions made by a user greatly affect the results of the analysis.

The winning entry of the blind prediction was performed by Cervenka Consulting [39], the developers of the ATENA software. The reported results of their prediction are shown in Figure 6 and compared to the obtained results in this study using ATENA. Note that the winning model also displayed a greater initial elastic behaviour and a higher load at which the nonlinear behaviour start (440 kN) than the test (198 kN). After this point, the model shows a significant drop in capacity for a subsequent nonlinear behaviour that concurs with the test. The ATENA model from this study shows the same behaviour, that is greater post-cracking stiffness and capacity than the analysis performed by Cervenka Consulting. As it was stated, a probable cause for these differences is the lack of experience at the time of modelling and selecting the best parameters for the prediction.

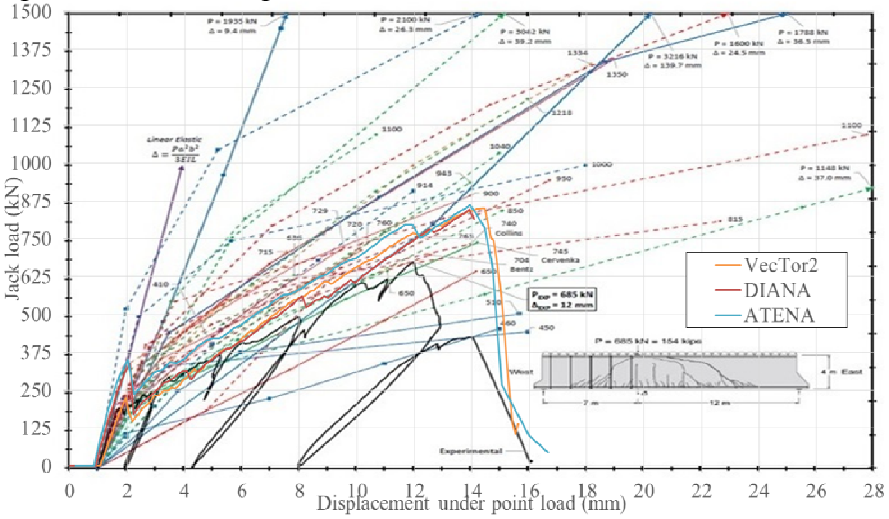


Figure 5: Comparison of the models from the three software with the blind predictions

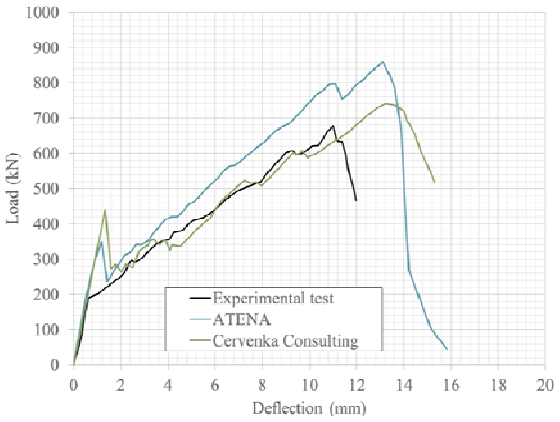


Figure 6: Comparison of the Toronto beam in ATENA to the Cervenka consulting prediction

## 4 CYCLIC ANALYSIS OF SHEAR-CRITICAL RC ELEMENTS

In order to model the response of shear-critical elements under cyclic and seismic loading, it is important to understand how the programs model the hysteretic behaviour of RC and to determine how they are able to predict the degradation due to the repetition and the reversal of the loading. The shear panels tested by Stevens *et al.* [40] were considered for evaluating the cyclic modelling capacities of the three programs. These cyclic tests were crucial to evaluate the hysteretic modelling of RC for shear-critical elements. All the details of the study can be found elsewhere [31].

### 4.1 SE shear panels

As described in [40], the University of Toronto tested three shear panels designated as SE8, SE9 and SE10. These specimens were tested in order to simulate the shear behaviour of a RC element under pure shear. The panels could represent a single element in a greater structure such as a silo or an offshore platform. The properties of the panels are summarised in Table 4. During the laboratory test, the panels were subjected to simultaneous compression and tension loading through hydraulic jacks. Due to the test setup, the applied loads are the principal stresses in the element. Given that the principal stresses are of the same magnitude and opposite directions, at a 45° angle the element is in a state of pure shear. For this reason, the FE model generated in each software consists of a 1×1 mesh (one single 4-node element of 1524×1524 mm). The loading condition is such that a uniformly distributed shear of 1MPa is applied at each side of the element.

| Panel | $f'_c$ | $\varepsilon_{co}$ | Bar in x-direction | | | | Bar y-direction | | | | $E_c$ | $f_t$ | $G_f$ |
|---|---|---|---|---|---|---|---|---|---|---|---|---|---|
| | (MPa) | (me) | Size | Area ($mm^2$) | $\rho_{sx}$ % | $f_{sx}$ (MPa) | Size | Area ($mm^2$) | $\rho_{sx}$ % | $f_{sx}$ (MPa) | (MPa) | (MPa) | (kN/m) |
| SE8 | 37.0 | 2.60 | 20M | 300 | 2.93 | 492 | 10M | 100 | 0.98 | 479 | 30753 | 2.01 | 0.140 |
| SE9 | 44.2 | 2.65 | 20M | 300 | 2.93 | 422 | 20M | 300 | 2.93 | 422 | 33612 | 2.19 | 0.144 |
| SE10 | 34.0 | 2.20 | 20M | 300 | 2.93 | 422 | 10M | 100 | 0.98 | 479 | 29480 | 1.92 | 0.138 |

Table 4: Properties of the SE panels, whose dimensions are 1524×1524×285 mm.

***Model and results with VecTor2***

A single 4-node element, simply supported in the bottom side, was used to model the SE panels, in which the steel bars were introduced as smeared, using the percentages given in Table 4 and assigning a crack spacing of 72 mm in x- and y-directions. The next models were chosen in order to model as best as possible the hysteric response that the RC panels would present during cyclic testing:

- Compression before peak: Hognestad (Parabola).
- Compression post-peak: Modified Park-Kent.
- Compression softening: Vecchio-Collins 1982.
- Tension stiffening: Modified Bentz 2003.
- Tension softening: Linear.
- Confined strength: Kupfer/Richart.
- Crack stress calculation: Basic (DSFM/MCFT).
- Hysteretic response of concrete: Palermo 2002 (with decay).
- Concrete-reinforcement bond: Perfect bond.
- Reinforcement stress-strain: elasto-plastic behaviour with strain hardening in both tension and compression.
- Hysteretic response of reinforcement: Bauschinger effect (Seckin).

VecTor2 was able to perform the complete loading history quickly and without convergence issues. The models were capable of replicating the point at which cracking occurs in both panels. Similarly, the post-cracking stiffness in the first cycle was modelled in an accurate way. However, the cyclic behaviour of the tests differ from those obtained in VecTor2 in terms of stiffness degradation, energy dissipation and plastic strains.

***Model and results with DIANA***

The FE model of DIANA presents the same characteristics of the FE model of VecTor2. The model recommended in DIANA for the RC elements under cyclic loads is the Maekawa Cracked Concrete Model because it includes laws for the loading, unloading and reloading for both tension and compression. Since the Maekawa model was originally conceived as a fixed crack model, this approach has been followed to model the crack rotation. For the same reason, the shear retention model used is the Maekawa contact density. The selected models were as follows:

- Compression model: Maekawa compressive model.
- Tension model: Linear-ultimate crack strain.
- Model for lateral cracking: JSCE 2012.
- Concrete-reinforcement bond: Perfect bond
- Reinforcement stress-strain: Menegotto-Pinto plasticity, with the parameters suggested by Yu [41].

Due to convergence problems, the analysis was not able to complete the first cycle of loading. The maximum number of iterations and the step size were both varied in order to obtain convergence. Large values of iterations (~1000) and small step sizes (~0.01 multiplier) were used to achieve convergence but the results did not improve.

***Model and results with ATENA***

The specimens, the reinforcement and the boundary conditions were modelled as in VecTor2 and DIANA. The two constitutive models available in ATENA for RC elements are SBETA and Fracture-plastic. Furthermore, the next models were included in the analysis:

- Compression model for pre-peak branch: Model Code 2010 (for SBETA) and Hordijk model (for Fracture-Plastic).
- Compression model for descending branch: Linear descend.
- Tension model: Exponential.
- Model for reduction of compressive stress due to cracking: Vecchio and Collins [16] with $c = 0.80$.
- Concrete-reinforcement bond: Perfect bond.
- Reinforcement stress-strain: Multi-linear model with strain hardening, active in both tension and compression.

It should be noted when using the smeared reinforcement, the Menegotto-Pinto model is not available in ATENA, since it can be used only when the reinforcement steel is discretely modelled. According to the quality of the results obtained for the Bresler-Scordelis beams, the fixed crack approach was selected.

First the panels were tested using the SBETA constitutive models, which were able to compute all the loading history without convergence problems. The cracking point of the panels was adequately predicted. However, the estimated post-cracking stiffness is significantly larger than the experimental one. The unloading and reloading curves of the SBETA model are linear and no plastic strain is stored during the analysis. Because of this, the numerical results presented no stiffness degradation or damage representation after every cycle. Therefore,

it was determined that the Fracture-plastic constitutive model was more appropriate since it allows to consider the plastic offset in compression and the tension stiffening (with $c_t$= 0.40).

The results when using the Fracture-plastic constitutive model showed promising results at the first cycle. Then convergence issues after the cracking point in the first reversal of the load were found. Several attempts were performed reducing significantly the step size and/or increasing the number of iterations. However, this problem persists and it was not possible to complete the test.

### *Comparison of the results among the programs*

Due to convergence problems that were not overcome using DIANA and ATENA, the Authors were not capable of completing the whole loading history imposed during the experimental tests. VecTor2 did not present convergence problems. Therefore, to evaluate the obtained results, the comparison of the programs was performed for the available information on the first cycle only (Figure 7). The programs predicted properly cracking of concrete and the beginning o the nonlinear behaviour. ATENA presented a linear unloading behaviour to the origin, while VecTor2 showed a nonlinear unloading path but the residual plastic strains were almost insignificant. DIANA showed a plastic offset when the load reversed and decreased to zero, however the obtained strain overestimated the real response of the specimens.

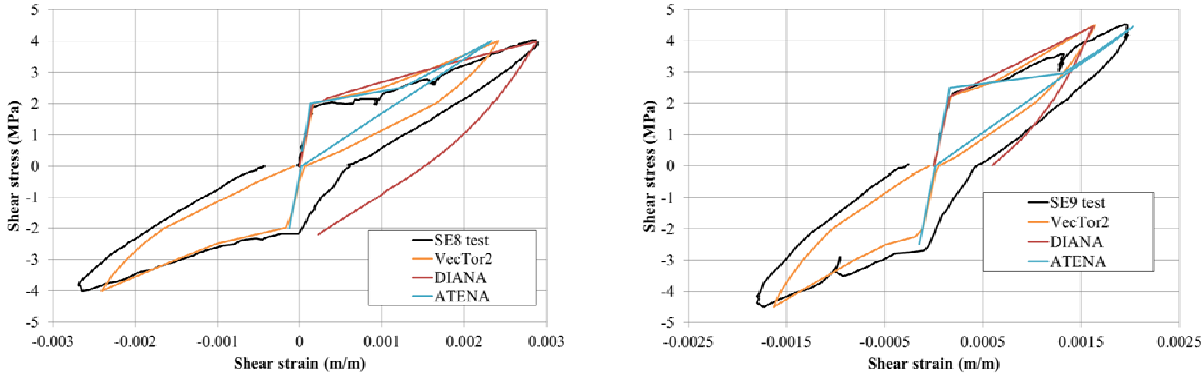


Figure 7: Comparison of the shear stress-strain curves for the SE8 and SE9 panels

### *Comparison with other authors*

The results of the SE panels were numerically reproduced in literature using constitutive models based on the main concepts of the MCFT and its further extensions [40], [42], [13], [43]. The results obtained in this study with Vector2 are compared with the ones published by Stevens *et al*. [40] and Palermo and Vecchio [42]. Figure 8 shows the comparison for the SE8 panel. The study of Stevens *et al.* [1991] showed accurate results and, at the time being, these are the best published numerical predictions for the SE panels (Figure 8 right). The hysteretic model used in VecTor2 in this case is the Palermo and Vecchio constitutive model [42] (Figure 8 on the left) which includes a nonlinear unloading with plastic offsets only in compression, as well as a degradation of the reloading stiffness in order to model the damage in the concrete due to cyclic loading. However, it seems that this model does present a significant improvement from the previous analytical models which did not include plastic offsets in tension and for which the reloading was performed linearly returning to the previously experienced maximum (or minimum) strain. Comparing the results on the left of Figure 8, it can be stated that the numerical simulations carried out by the Authors using VecTor2 were performed with a proper selection of the available constitutive models and input parameters.

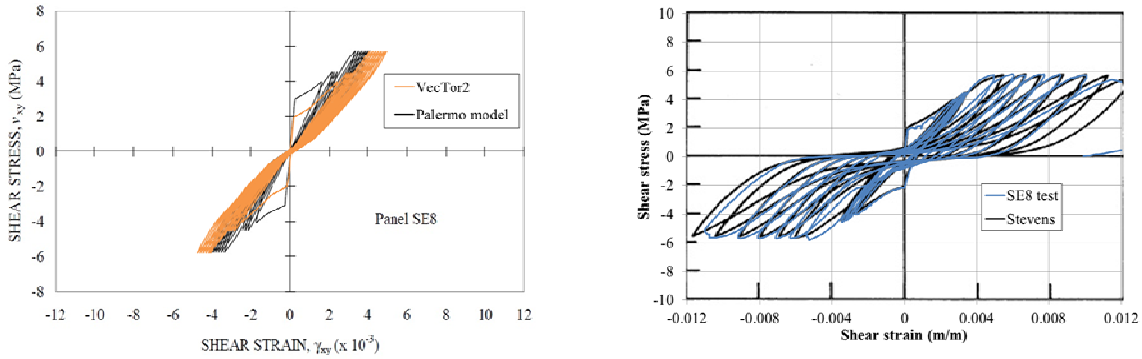


Figure 8: Comparison of the SE8 panel in VecTor2 to the results of [42] (left) and [40] (right)

## 5 CONCLUSIONS

The main limitation in the development of this investigation was the lack of experience and expertise in the use of the three finite element packages. The models presented in this work are the best simulations possible based on the knowledge gained during the duration of the investigation. It is believed that the numerical results could be improved given the resources and expertise required to appropriately simulate and reproduce shear-critical reinforced concrete elements in these FE software packages. Yet note that the validation with other authors (as Palermo and Vecchio [42] and the predictions reported by Collins *et al.* [33]) lead to the conclusion that the results of this research work are acceptable. Even further, it was demonstrated that not only the degree of expertise but the engineering criteria and selection of constitutive models and input data have a great influence in the results.

Other aspects should be mentioned. The phenomena being modelled, the shear behaviour of reinforced concrete, is complex and still an unresolved issue. This difficulty has been studied and is being studied for several years and it is still in development. Therefore, the constitutive models implemented in these software remain with limitations in their capabilities and applicability to the modelling of shear-critical RC elements.

Furthermore, the accessibility to educational licensing for the use of some of these programs restricted the available time to work on each program. Given the cost of the full license, some of the software were used thanks to a time-limited license granted by the developers of the software.

Future research in this topic should focus in including other different tests to further evaluate the capacities of the software packages. Other test could include beams under different loading conditions and different characteristics and reinforcement, as well as further shear panels and shear walls subjected to cyclic loading.

Moreover, other finite element programs that include the state-of-the-art in concrete modelling should be included in the evaluation. These programs could include Abaqus, Ansys and OpenSees. Also, commercial available software mainly used in the private industry (e.g SAP 2000) should also be included to evaluate their capacities, since, to the Authors' knowledge, these are the programs mainly used in the structural design companies.

## ACKNOWLEDGMENTS

Thanks are given to the developers of the VecTor2, DIANA and ATENA software for providing evaluation licenses so the programs could be analysed and tested. In particular, thanks are necessary for Professor Frank J. Vecchio for his support with the VecTor2 software, to the TNO support team, in particular to Dr. Maziar Partovi, Mr. Yongyeon Bae and Mr. Kesio

Palacio for their help and to Dr. Vladimir Cervenka, Mr. Dobromil Pryl and Mr. Martin Berka of Cervenka Consulting for their continuous support during this project.

Thanks to Professor Michael P. Collins for making available the data for the shear panel tests used as benchmark test in this study.

Thanks to Professor Fausto Minelli and Dr. Luca Facconi of the University of Brescia for their expert advice and support in the use of the finite element packages.

## REFERENCES

[1] CSA, Design of Concrete Structures. Ontario, Canada: Canadian Standards Association, 2004.

[2] AASHTO, AASHTO LRFD Bridge Design Specifications. Washington DC, USA: American Association of State Highway and Transportation Officials, 2010.

[3] International Federation for Structural Concrete, *fib Model Code for Concrete Structures*. Lausanne, Switzerland: Wilhem Ernst & Sohn, 2010.

[4] ACI Committee 318, *Building Code Requirements for Structural Concrete and Commentary*. Farmington Hills, Miami: American Concrete Institute, 2011.

[5] R.A. Litton, Contribution to the Analysis of Concrete Structures Under Cyclic Loading. *PhD Dissertation*, University of California, Berkeley, 1974.

[6] Z. Bazant, B. Oh, Crack band theory for fracture of concrete. *Materials and Structures*, **16**(1), 155-177, 1983.

[7] V. Cervenka, Constitutive Model for Cracked Reinforced Concrete. *ACI Journal*, **82**(6), 877-882, 1985.

[8] F.J. Vecchio, M.P. Collins, The Modified Compression Field Theory for Reinforced Concrete Elements Subjected to Shear. *ACI Journal*, **83**(2), 219-231, 1986.

[9] R. De Borst, Smeared cracking, plasticity, creep and thermal loading-A unified approach. *Computer Methods in Applied Mechanics and Engineering*, **62**(1), 89-110, 1987.

[10] T. Hsu, Unified Approach to Shear Analysis and Design. *Journal of Cement and Concrete Composites*, **20**, 419-435, 1988.

[11] K. Maekawa, A. Pimanmas, H. Okamura, *Nonlinear Mechanics of Reinforced Concrete, 1st Edition*. London, England: Spon Press, 2003.

[12] P. Ceresa, L. Petrini, R. Pinho, Flexure-Shear Fiber Beam-Column Elements for Modeling Frame Structures Under Seismic Loading — State of the Art. *Journal of Earthquake Engineering*, **11**(1), 46-88, 2007.

[13] P. Ceresa, L. Petrini, R. Pinho, R. Sousa, A fibre flexure–shear model for seismic analysis of RC-framed structures. *Earthquake Engineering and Structural Dynamics*, **38**, 565-586, 2009.

[14] M. Collins, Towards a rational theory for RC members in shear. *ASCE Journal of Structural Division*, **104**(4), 649-666, 1978.

[15] F.J. Vecchio, M.P. Collins, Stress-strain characteristics of RC in pure shear. *IABSE Colloquium, International Association of Bridge and Structural Engineers, Advanced Mechanics of Reinforced Concrete*, Zurich, Switzerland, 1981.

[16] F.J. Vecchio, M.P. Collins, Response of Reinforced Concrete to In-Plane Shear and Normal Stresses. *Publication No. 82-03*, University of Toronto, Department of Civil Engineering, Toronto, Canada, 1982.

[17] A. Belardi, T. Hsu, Constitutive laws of concrete in tension and reinforcing bars stiffened by concrete. *ACI Structural Journal*, **92**(5), 465-474, 1994.

[18] A. Belardi, T. Hsu, Constitutive laws of softened concrete in biaxial tension-compression. *ACI Structural Journal*, **92**(5), 562-573, 1995.

[19] X. Pang, T. Hsu, Behaviour of Reinforced Concrete Membrane Elements in Shear. *ACI Structural Journal*, **92**(6), 665-679, 1995.

[20] X. Pang, T. Hsu, Fixed-angle softened-truss model for reinforced concrete. *ACI Structural Journal*, **93**(2), 197-207, 1996.

[21] T. Hsu, L. Zhang, Nonlinear Analysis of Membrane Elements by Fixed-angle Softened-truss Model. *ACI Structural Journal*, **94**(5), 483-492, 1997.

[22] L. Zhang, T. Hsu, Behavior and analysis of 100MPa concrete membrane elements. *Journal of Structural Engineering*, **124**(1), 24-34, 1998.

[23] W. Kaufmann, P. Marti, Structural Concrete: Cracked Membrane Model. *Journal of Structural Engineering*, **124**(12), 1467-1475, 1998.

[24] R. Zhu, Softened membrane model of cracked reinforced concrete considering the Poisson effect. *PhD Dissertation*, University of Houston, Department of Civil and Environmental Engineering, Houston, Texas, 2000.

[25] T. Hsu, R. Zhu, Softened membrane model for reinforced concrete elements in shear. *ACI Structural Journal*, 99(4), 460-469, 2002.

[26] F.J. Vecchio, Disturbed Stress Field Model for Reinforced Concrete: Formulation. *ACI Structural Journal*, **97**(1), 102-110, 2000.

[27] F.J. Vecchio, D. Lai, Crack Shear-Slip in Reinforced Concrete Elements. *Journal of Advanced Concrete Technology*, **2**(3), 289-300, 2004.

[28] P. Wong, F.J. Vecchio, H. Trommels, *VecTor2 & FromWorks user's manual, 2nd Edition*. Toronto, Canada, 2013.

[29] TNO DIANA. User's Manual. Delft, The Netherlands: TNO DIANA BV, 2014.

[30] V. Cervenka, L. Jendele, J. Cervenka, *ATENA Program Documentation Part I - Theory*. Červenka, Prague, 2015.

[31] A. González Víquez, Nonlinear Analysis of Shear Critical RC Members using current FE software, *Master Dissertation*, UME School, IUSS Pavia, Pavia, Italy, 2016.

[32] B. Bresler, A. Scordelis, Shear Strength of Reinforced Concrete Beams. *ACI Journal*, **85**(3), 51-74, 1963.

[33] M. Collins, E. Bentz, P. Quach, G. Proestos, The Challenge of Predicting the Shear Strength of Very Thick Slabs. *Concrete International*, **37**(11), 29-37, 2015.

[34] F.J. Vecchio, Analysis of Shear-Critical Reinforced Concrete Beams. ACI Structural Journal, **97**(1), 102-110, 2000.

[35] F.J. Vecchio, W. Shim, Experimental and Analytical Reexamination of Classic Concrete Beam Tests. *ASCE Journal of Structural Engineering*, **130**(3), 460-469, 2004.

[36] M.P. Collins, D. Mitchell. *Prestressed Concrete Structures. Toronto*, Canada: Response Publications, 1997.

[37] A. Kagermanov, P. Ceresa, Fiber-section model with an exact shear strain profile for two-dimensional RC frame structures. *Journal of Structural Engineering ASCE* (in press).

[38] A. Kagermanov, P. Ceresa, An exact shear strain approach for RC frame elements with axial-shear interaction. *VII European Congress on Computational Methods in Applied Sciences and Engineering, ECCOMAS 2016*, Crete, Greece, 5-10 June, 2016.

[39] Cervenka Consulting, *Video of the Prediction Contest in Toronto 2015*. www.cervenka.cz/company/news/winner-of-the-prediction-contest-in-toronto-2015, Prague, Czech Republic, 2015.

[40] N. Stevens, S. Uzumeri, M.P. Collins, Reinforced Concrete Subjected to Reversed Cyclic Shear - Experiments and Constitutive Model. *ACI Structural Journal*, **88**(1), 135-146, 1991.

[41] W. Yu, Inelastic modeling of reinforcing bars and blind analysis of the benchmark tests on beam-column joints under cyclic loading. *Master Dissertation*, IUSS Pavia, Rose School, Pavia, Italy, 2006.

[42] D. Palermo, F.J. Vecchio, Behaviour and analysis of reinforced concrete walls subjected to reversed cyclic loading. *PhD Dissertation*, Department of Civil Engineering, University of Toronto, Toronto, Canada, 2002.

[43] A. Kagermanov, P. Ceresa, Physically-based cyclic tensile model for RC membrane elements. *Journal of Structural Engineering ASCE*, **142**(12) DOI:10.1061/(ASCE)ST.1943-541X.0001590, 04016118, 2016.

COMPDYN 2017
6th ECCOMAS Thematic Conference on
Computational Methods in Structural Dynamics and Earthquake Engineering
M. Papadrakakis, M. Fragiadakis (eds.)
Rhodes Island, Greece, 15–17 June 2017

# SEISMIC PERFORMANCE OF FULL-SCALE RECYCLED AGGREGATE CONCRETE COLUMNS

**Ilyas Saribas[1], Caglar Goksu[2], and Alper Ilki[2]**

[1] Istanbul Technical University, Civil Engineering Faculty, Maslak, Istanbul, Turkey
e-mail: saribasilyas@itu.edu.tr

[2] Istanbul Technical University, Civil Engineering Faculty, Maslak, Istanbul, Turkey
e-mail: {goksuc, ailki}@itu.edu.tr

**Keywords:** Column, Low Strength Concrete, Recycled Aggregate, Reinforced Concrete, Reversed Cyclic, Seismic.

**Abstract.** *This paper presents the results of reversed cyclic loading tests on reinforced recycled concrete columns. Recycled concrete aggregates were obtained from the waste of structural elements cast with low quality concrete. For investigating whether the structural concrete incorporating recycled aggregates can be reliably utilized in new reinforced concrete column construction, two full-scale reinforced concrete columns were constructed and subjected to constant axial and reversed cyclic lateral loads. The test results of the experimental study were evaluated in terms of seismic hysteresis loops, skeleton curves, energy dissipation capacities, crack patterns and failure modes. The test results showed that the RC columns made of either natural aggregate concrete and recycled aggregate concrete show similar seismic behaviour.*

## 1 INTRODUCTION

The disposal of the construction and demolition waste has become a severe social, economic and environmental problem. For sustainable solution for both the concern of increasing demand for natural aggregates (NA) and reducing the need to deposit the construction and demolition waste in landfills, recycling the waste concrete for reuse as an aggregate in new concrete production for building new structures becomes compulsory.

A lot of experimental studies have been performed since 1940s worldwide for the utilization of recycled concrete aggregate (RCA). While most of these studies concentrated on mixture design, chemical, physical, biological properties of RCA and mechanical and durability properties of recycled aggregate concrete (RAC) (Nixon 1978, Hansen 1986, Hansen 1992, ACI-555 2002, Li 2008, Casuccio 2008, Tabsh and Abdelfatah 2009, Xiao et al. 2012, Thomas et al. 2013, Kim and Yun 2013, Yang et al. 2008, Corinaldesi 2010, M. Malesev 2010), only a few experimental studies were carried out to investigate the seismic behavior of RC

columns incorporating large volumes of RCA as coarse aggregate (Xio et al. 2012, Ma et al. 2013, 2015 and Soleimani et al. 2016). According to these studies, while the columns incorporating RCA showed similar structural behavior with the columns incorporating NA, their lateral loads and deformation capacities were found to be diminished as the replacement ratio of RCA increased. While there are some differences between these studies in literature and the study carried out by the authors in terms of type of the tested columns (the tested columns in the study of Xio et al. 2012 was semi-precast, the tested columns in the studies of Ma et al. 2013, 2015 were composite, the tested columns in the study of authors are RC), the main difference is the property of RCA, which was sourced from structural elements cast with low strength concrete in the present study. The main objective of this study was to investigate the seismic behavior of full-scale reinforced recycled concrete (RRC) columns incorporating large percentage of RCA sourced from low strength concrete. For this purpose, two full-scale, code-complying (TSDC, 2007) RC columns, one out of two columns incorporating RAC and the other one incorporating NA, were produced and tested under constant axial and reversed cyclic lateral loadings. The test results showed that the replacement of NA with RCA sourced from low strength concrete did not have adverse effect on load bearing and deformation capacities of the columns.

## 2 OUTLINE OF EXPERIMENTAL INVESTIGATION

For investigating the effect of replacement of RCA with NA, an experimental study was carried out at Structural and Earthquake Engineering Laboratory, Istanbul Technical University. In this experimental campaign, two flexure-critical full scale reinforced concrete columns (column RAC and column NAC) were constructed and then subjected to constant axial and reversed cyclic lateral loads (Fig. 1a). The geometric ratio of longitudinal reinforcements and volumetric ratio of transverse reinforcements were 1.13% and 0.52%, respectively. The thickness of the concrete cover to the outside surface of the transverse reinforcements was 21 mm. While one out of two columns was constructed incorporating RAC, the other column was constructed incorporating natural aggregate concrete (NAC). Both columns were constructed so as to be representative of the columns of ordinary code complying columns of RC structures. The concrete mix–proportions of NAC and RAC are presented in Table 1. As seen from Table 1, approximately 50% of medium size coarse NA was replaced by RCA for the column incorporating RAC.

Table 1. Concrete mix-proportions

| Material quantity (kg/m$^3$) | NAC | RAC |
|---|---|---|
| NA-No 2 aggregate (12-22 mm) | 489 | 493 |
| NA-No 1 aggregate (5-12 mm) | 501 | - |
| RCA (5-12 mm) | - | 522 |
| Crushed sand (washed) (0-4 mm) | 407 | 410 |
| Mountain Sand (0-2 mm) | 513 | 518 |
| Cement (CEM 42.5 R) | 300 | 300 |
| Water | 128 | 110 |
| Superplasticizer (Glenium ACE 450) | 1.95 | 2.10 |
| Water/cement | 0.43 | 0.37 |

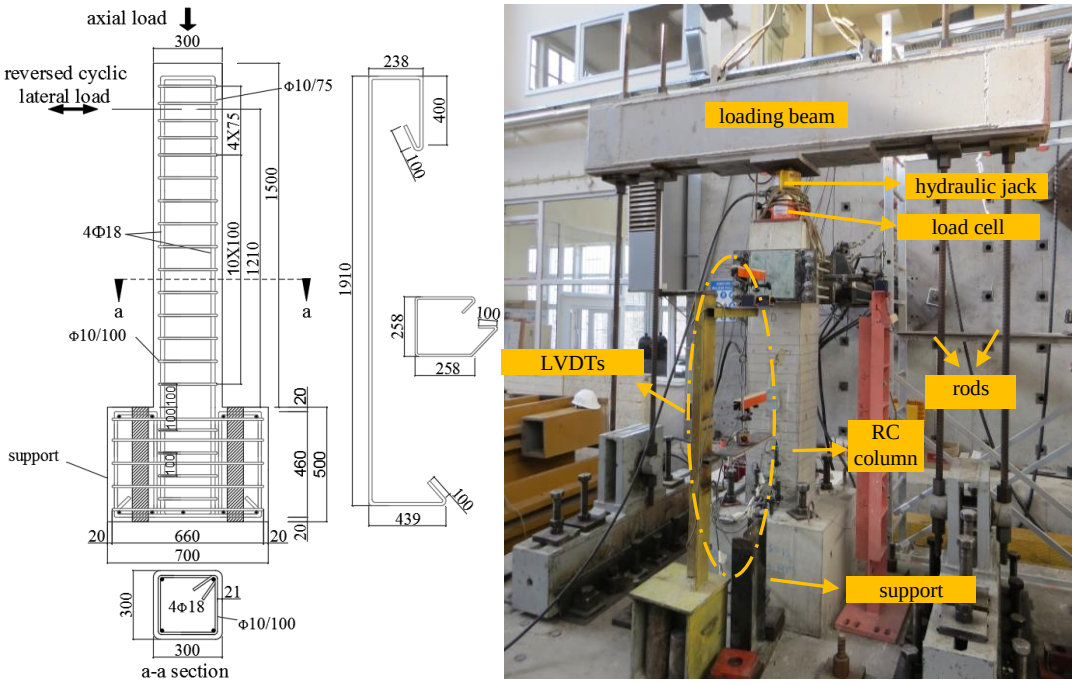


Fig. 1 (a) Reinforcement cage of the columns, (b) Test set-up.

The average compressive standard cylinder strengths of the columns NAC and RAC were obtained to be 35 MPa and 29 MPa, respectively. It should be noted that these results were based on the tests of drilled core specimens (100 mm diameter × 100 mm height), which were taken from the undamaged sections of these columns after the seismic test on the test day (at the age of 200 days). Ensuing, these core strengths were converted to standard cylinder compressive strength based on the recommendations of The Concrete Society (1976). The slump value of RAC and NAC was obtained to be around 18-22 mm. The mechanical properties of the deformed longitudinal (18 mm) and transverse (10 mm) reinforcing bars are illustrated in Fig. 2.

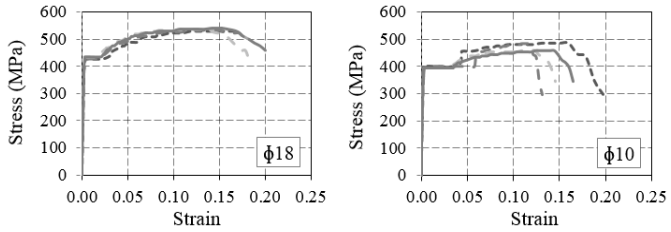


Fig. 2 Stress-strain relationships of longitudinal deformed (18 mm) and transverse (10 mm) reinforcing bars.

The axial loads of 222 kN and 184 kN were applied for the columns NAC and RAC, respectively, which corresponded to 7% of the axial load capacity ($n = P/P_0$, where $n$ is axial load ratio, $P$ is applied axial load, $P_0$ axial load capacity of the column ($P_0=f_c'.A_g$), $f_c'$ is the compressive strength of standard cylinder and $A_g$ is the gross area of column cross-section) of each column without consideration of the capacity of the internal steel reinforcement.

## 3 INSTRUMENTATION, TEST SETUP, AND TESTING PROCEDURE

Both columns were subjected to constant axial and reversed cyclic lateral loading. The appearance of the test setup and the instrumentation details of the columns are presented in Fig. 1b and Fig 3, respectively. The reversed cyclic lateral load was executed under displacement control through a MTS hydraulic piston with a capacity of 250 kN. The instrumentation of the

columns consisted of four horizontal and eight vertical linear variable differential transducers (LVDTs) and various strain gages installed on the longitudinal and transverse reinforcements. A displacement-based loading protocol was applied for the columns (Fig. 4). Drift ratios are calculated as the ratio of the lateral displacement ($\Delta_L$) to the column height (H), where the actuator was connected.

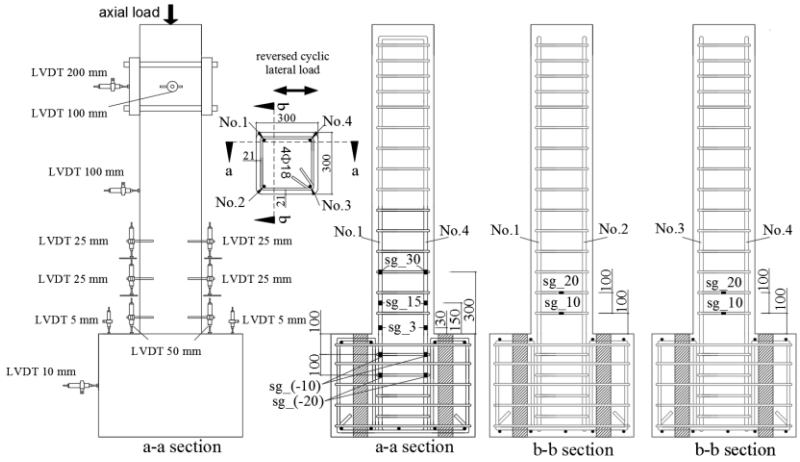


Fig. 3. Instrumentation details, LVDTs and strain gages (sg).

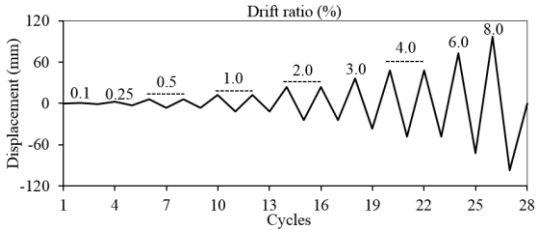


Fig. 4. Loading protocol.

## 4 EXPERIMENTAL RESULTS

The test results are summarized through lateral load-displacement relationships of the columns and envelopes of these relationships (Fig. 5 and 6a). As seen in Figs. 5 and 6a, both columns exhibited similar behaviors in terms of lateral load capacity. Furthermore, both columns sustained their load resistance capacities up to 8% drift ratio. The theoretical lateral load capacities of the columns, which were calculated through a section analysis program based on fiber analysis approach using the stress–strain relationships of materials, were obtained to be consistent with the experimental lateral load capacities of the columns without considering a further modification for the column RAC. The failure modes of these columns were governed by pure flexural failure. No cracking was observed up to 0.5% drift ratio. As the drift ratios increased, fine bending cracks increased gradually along the plastic hinge region of the columns. After yielding of the longitudinal reinforcing bars at around 2% drift ratio, the bending cracks developed and extended rapidly. When the drift ratios increased up to 3% and 4%, the flexural bending cracks of the columns widened and lengthened gradually. Buckling of longitudinal bars was not observed.

Energy dissipation capacities of the columns are presented in Fig. 6b. The energy dissipation capacities of the tested specimens are calculated as the areas enclosed by the lateral load-displacement hysteresis loops. As seen from Fig. 6b, it is clear that the energy dissipation capacities of the columns are similar. It can be concluded from Figures 5 and 6 that RCA did not seem to have an adverse effect on the seismic behaviour of the columns. This observation is valuable for demonstrating that RCA can be safely utilized in structural concrete.

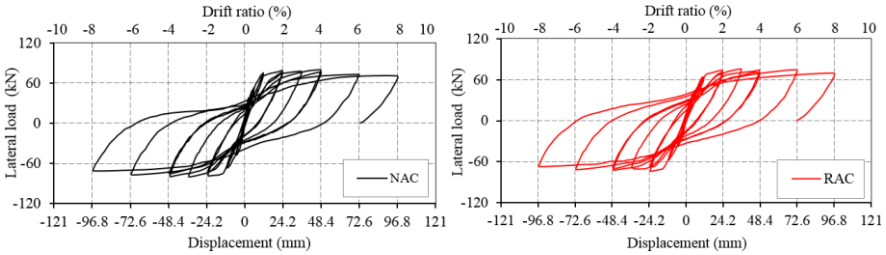


Fig. 5. Lateral load-displacement relationships of the columns

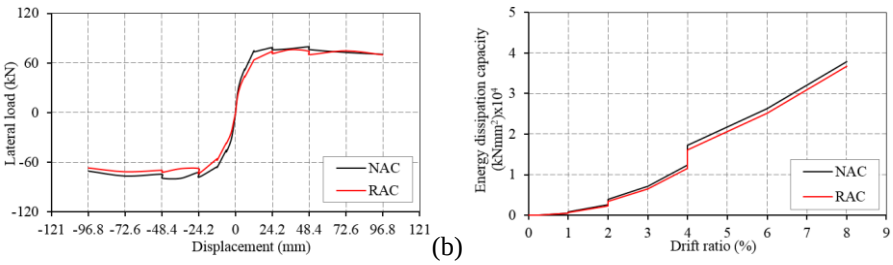


(a) (b)

Fig. 6. (a) Envelopes of the lateral load-displacement relationships, (b) Energy dissipation capacities of the columns.

## 5 CONCLUSIONS

This paper presents the results of an experimental study carried on RC columns for investigating the effect of RCA on seismic behavior. The study differentiates from the available studies in the literature due to use of low strength waste concrete as a source for RCA. Two code-complying RC columns were constructed and tested under constant axial and reversed cyclic lateral loadings. While one of the column was incorporating NA, the other column was incorporating RCA as well as NA, cast by replacing approximately 50% of medium size coarse NA with RCA. The test results revealed that the RC columns made of either NA and RA showed similar seismic behaviour in terms of lateral load-displacement behavior, ductility and energy dissipation capacities.

While the findings reached in this study are valuable for demonstrating the viability of using RCA sourced from low strength concrete in structural concrete, further researches are necessary for validation of these test results in a more general sense.

## ACKNOWLEDGMENT

The authors appreciate the assistance of E. Binbir, B. Aldirmaz. The supports of O. Manzak, Yapı Merkezi and Akçansa Companies are gratefully acknowledged. The invaluable contributions of staff of ITU Structural and Earthquake Engineering and ITU Infrastructure Materials Laboratories are acknowledged. The authors are thankful to L. Bank and A. Yazdanbakhsh from City College of New York for their valuable advices. Financial support of the ITU Scientific Research Department (Project No: 39360) is gratefully acknowledged.

## REFERENCES

[1] ACI Committee 555, Removal and reuse of hardened concrete. *ACI Mater. J.* **3**(99):300-25, 2002.

[2] Concrete Society (CSTR 11), Concrete core testing for strength. *Technical Report No.11, London*, p. 44, 1976.

[3] M Casuccio, M. C. Torrijos, G. Giaccio, R. Zerbino, Failure mechanism of recycled aggregate concrete. *Constr. Build. Mater.* **21**:1500-6, 2008.

[4] T. C. Hansen, Recycled aggregate and recycled aggregate concrete, second state-of-the-art report, developments from 1945-1985. *Mater. Struct.* **19**(111):201-46, 1986.

[5] T. C. Hansen, Recycling of demolished concrete and masonry. *E&FN SPON London*, 1992.

[6] K. H. Yang, H.S. Chung, A. Ashour, Influence of type and replacement level of recycled aggregates on concrete properties. *ACI Mater. J.* **3** 289-296, 2008.

[7] X. P. Li, Recycling and reuse of waste concrete in China Part I. Material behaviour of recycled aggregate concrete. *Resour. Conserv. Recy.* **53**(1-2):36-44, 2008.

[8] H. Ma, J. Xue, D. Luo, X. Zhang, Seismic performance of steel-reinforced recycled concrete columns under low cyclic loads. *Construction and Building Materials,* **48**:229-237, 2013.

[9] H. Ma, J. Xue, Y. Liu, X. Zhang, Cyclic loading tests and shear strength of steel reinforced recycled concrete short columns. *Engineering Structures,* **92**:55-68, 2015.

[10] P. J. Nixon, Recycled aggregate concrete as an aggregate for concrete-a review. *Mater. Struct.*, **11**(6):371-8, 1978.

[11] S. Yehia, S. Khan, O. Abudayyeh, Evaluation of mechanical properties of recycled aggregate for structural applications. *HBRC J.* **4** (3) 7-16, 2008.

[12] S. W. Tabsh, A. S. Abdelfatah. Influence of recycled concrete aggregates on strength properties of concrete. *Constr. Build. Mater.*, **23**(1):163-7, 2009.

[13] V. Corinaldesi, Mechanical and elastic behaviour of concretes made of recycled-concrete coarse aggregates. *Constr. and Build. Mater*. **24** (9), 1616-1620, 2010.

[14] M. Malesev, V. Radonjanin, S. Marinkovic, Recycled concrete as aggregate for structural concrete production. *Sustainability,* **2**, 1204-1225, 2010.

[15] J. Xiao, W. Li, Y. Fan, X. Huang, An overview of study on recycled aggregate concrete in China (1996–2011). *Constr. Build. Mater.* **31**(6), 364-83, 2012.

[16] F. Soleimani, M. McKay, C. S. W. Yang, K. E. Kurtis, R. DesRoches, and. L. F. Kahn, Cyclic testing and assessment of columns containing recycled concrete debris. *ACI Structural Journal*, V. **113,** No. 5, MS No. S-2015-121.R3, doi: 10.14359/51689024 September-October 2016.

[17] C. Thomas, J. Setién, J. A. Polanco, P. Alaejos, Durability of recycled aggregate concrete. *Constr. Build. Mater.*, **40**(3):1054–65, 2013.

[18] S. W. Kim, H. D. Yun, Influence of recycled coarse aggregates on the bond behavior of deformed bars in concrete. *Eng. Struct.,* **48**(3):133-43, 2013.

[19] J. Xiao, X. Huang, L. Shen, Seismic behaviour of semi-precast column with recycled aggregate concrete. *Construction and Building Materials*, **35**:988-1001, 2012.

[20] Turkish Seismic Design Code (TSDC), Regulations for Buildings to be Constructed in Earthquake Prone Areas, *Ankara, Turkey*, 2007.

COMPDYN 2017
6th ECCOMAS Thematic Conference on
Computational Methods in Structural Dynamics and Earthquake Engineering
M. Papadrakakis, M. Fragiadakis (eds.)
Rhodes Island, Greece, 15–17 June 2017

# DETAILED FEM ANALYSIS FOR FULL SCALE STEEL STRUCTURE CONSIDERING FRACTURE OF BEAM ENDS

**Yasunori Mizushima[1], Yoichi Mukai[2], and Tomoharu Saruwatari[3]**

[1] Research & Development Institute, Takenaka Corporation
1-5-1 Ohtsuka, Inzai-shi, Chiba 270-1395, Japan
e-mail: mizushima.yasunori@takenaka.co.jp

[2] Department of Architecture, Kobe University
1-1 Rokodai-cho, Nada-ku, Kobe-shi, Hyogo 657-0013, Japan
ymukai@port.kobe-u.ac.jp

[3] Engineering Technology Division, JSOL Corporation
2-2-4 Tosabori, Nishi-ku, Osaka-shi, Osaka 550-0001, Japan
saruwatari.tom@jsol.co.jp

**Keywords:** FEM, Detailed Model, Fracture, Full Scale Shaking Table Test

**Abstract.** *This paper reports a non-linear analysis of a steel structure using a large-scale and detailed finite element model considering fracture phenomenon. The shaking-table test results of a 3-story full-scale steel frame structure, which were carried out at E-defense in 2013, are evaluated analytically in this paper. The analytical model used in this study is intended to replicate adequately entire shape of target steel frame structure specimen, assembling huge numbers of tiny finite elements. The damage index is introduced as the fracture criterion on steel members model for execution of FE simulations. Elements whose damage index has been reached to 1.0 are eliminated in our way of FEM analyses. The damage index shows a good correlation with the occurrence of the fracture observed in the experimental test. The timing of the first fracture of the beam end in the analysis mostly match well to that of the experiment. In addition, the structural responses obtained by the analysis agree with those of the experiment.*

.

## 1 INTRODUCTION

There are some reports about high-precision finite-element analysis of building structure investigating their dynamic response under seismic loadings. Miyamura *et al*. report that non-linear behavior of shaking table test of a 4-story steel building can be replicated by using a fine meshed FE model with solid elements [1]. The authors also report about FE analysis examining a full-scale shaking table test of a 3-story steel structure that is the analytical target of this paper modeling mainly shell elements [2], [3]. These reports conclude that FE models that are finely meshed to reproduce the entire shape of structures as precisely as possible can appropriately replicate non-linear behaviors of building structures under earthquake excitations.

However, there are few studies that try to predict fracture behavior of members may lead to fatal collapse of buildings by using finely meshed FE models of whole building structure. Above-referenced three reports [1], [2], [3] do not simulate fracture of members in their analytical procedures. In the referenced report [1], the analytical target was the case wherein a collapse of the structure was observed because of not fracture but local buckling of the first-story columns. In the authors' previous report [3], fracture of members is not predicted but a pseudo fractures are demonstrated by eliminating elements in areas wherein the fracture occurred actually in the experimental test.

In this study, FE-analysis with consideration of fracture using damage index as failure criterion is performed for the tested structure, wherein fracture of beam ends was observed. The analytical target is a full-scale shaking table test of a 3-story steel structure as in the previous study [3]. The accuracy of the prediction for fracture-occurring timing at the steel members and validity of responses obtained by numerical simulation are investigated.

## 2 OUTLINE OF ANALYTICAL TARGET FOR SIMULATING SHAKING TABLE TEST

The analytical target is a 3-story and 2-bay steel frame structure that was used for a full scale shaking table test in 2013 at E-defense[4]. During multiple seismic strong motion inputs in the shaking table test, fractures of beam ends of this frame structural specimen were observed.

The specimen for the shaking table test is shown in Figure 1. Only the single frame on the center line in x-direction (line B in Figure 1) was a moment resistant frame. Columns on outside lines, which are shown as line A and C in Figure 1, were provided with hinges at both their top and bottom ends not to be resist horizontal loads. The columns and beams were made of square-shaped tube and H-shaped steel, respectively. The reinforced concrete slabs were constructed on steel deck plates.

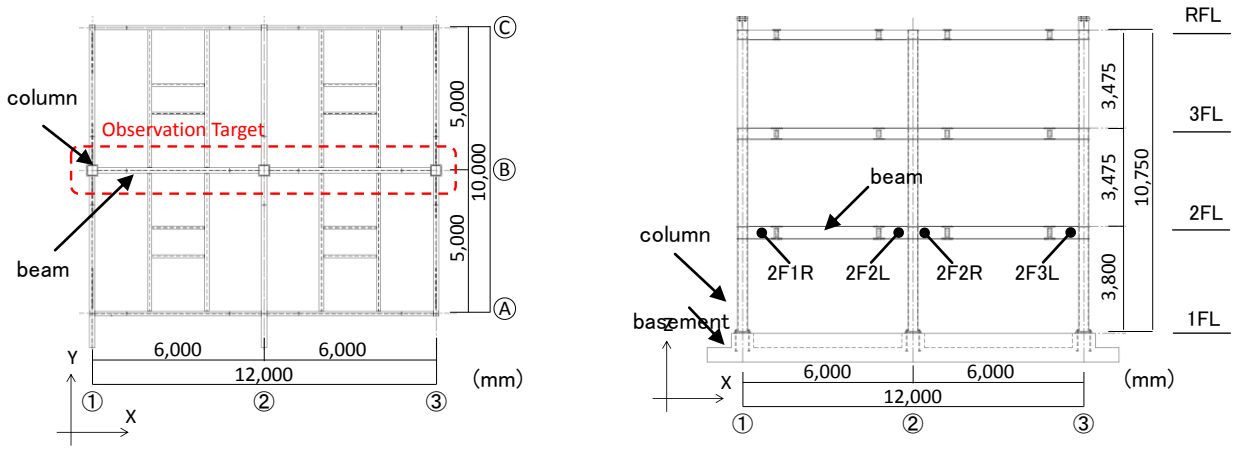


(a) Frame Plan at 2nd floor (b) Frame Elevation on Line B

Figure 1: Outline of 3-story steel frame structure specimen

From a series of performed cases in the experiments, the case wherein fracture at beam ends was observed was focused as analytical target case. The experiments were conducted using a seismic input motion, the NS-direction component of JR Takatori records of the Hyogoken-Nambu earthquake in 1995 (JR-Takatori) as shown in Figure 2and a synthetic input motion, Nankai-Trough earthquake (Nankai) which is artificially generated. Nine experimental cases were carried out with adjusted scale of the input motions. Input motions and scale factors of acceleration amplitude of each experimental case are listed in Table 1. The case of JR-Takatori 100% (full scale acceleration) is the analytical target case in this study because fracture of beam ends was observed.

| Sequence No. | Excitation | Factor | Remarks |
|---|---|---|---|
| 1 | Nankai | 50% | |
| 2 | Nankai | 100% | |
| 3 | JR-Takatori | 40% | |
| 4 | JR-Takatori | 60% | Non-linearity was clearly observed during the test (Considered as excitation history in analysis) |
| 5 | JR-Takatori | 80% | Non-linearity was clearly observed in several cycles during the test (Considered as excitation history in analysis) |
| 6 | JR-Takatori | 100% | Analytical Target, Fractures were observed. |
| 7 | Nankai | 50% | |
| 8 | Nankai | 100% | |
| 9 | Nankai | 150% | |

Table 1: Shaking input-sequence through experiments

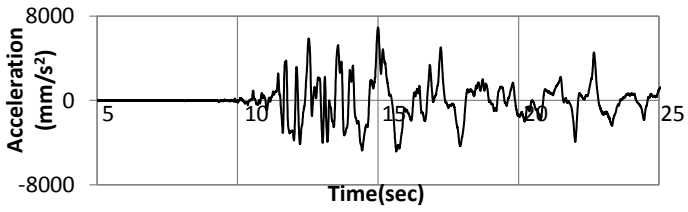


Figure 2: Seismic acceleration wave form of JR-Takatori

# 3 ANALYTICAL MODEL

## 3.1 Finite Element Model and Computational Resources

The finite element model used in this study is elaborated to replicate adequately entire shape of the specimen assembling with over 2 million tiny elements, as shown in Figure 3. Shell, solid and beam elements are used for steel members, for concrete parts and for reinforcement bars, headed stud and anchor bolts in the model, respectively. Contact condition was considered for adopting to parts that was actually in contact between separated members. The further modeling details are described in previous studies [3], [4]. It is confirmed that natural periods obtained by eigenvalue analysis using this model agree with observed result of the actual specimen in the previous study [3].

The dynamic explicit method based on the central difference method is adopted for the time integration scheme using FE analysis code LS-DYNA. The time steps used in the analysis are determined from the Courant condition with an initial time interval of $3.5\times10^{-6}$ second. The seismic wave, a set of sequencial waves JR-Takatori 60%, 80% and 100%, to input for has totally 80 seconds. The entire execution time for 80 seconds of time-history analyses is approximately 80 hours, using 504 cores of a supercomputer of the Institute for Information Management and Communication, Kyoto University in Japan.

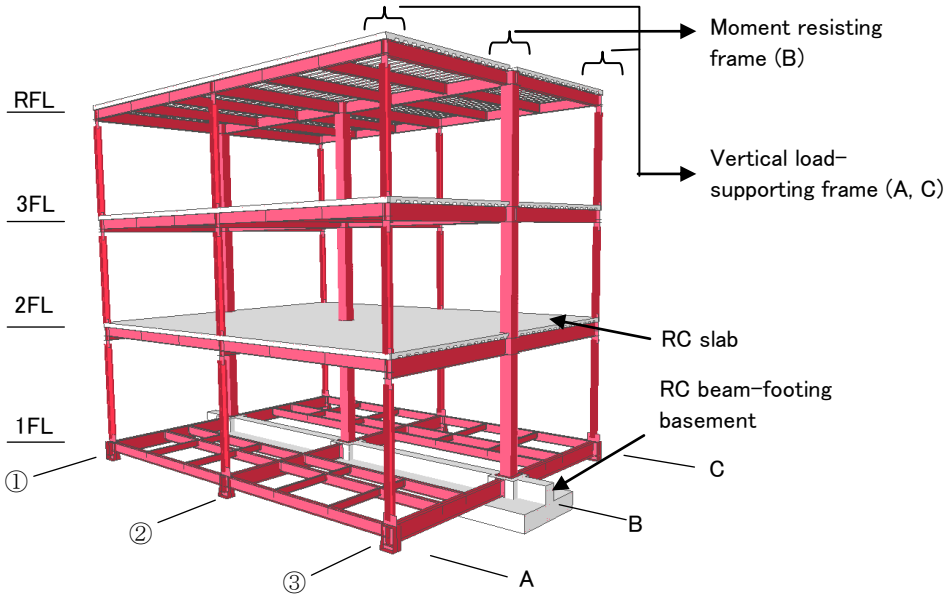


(a): Whole view

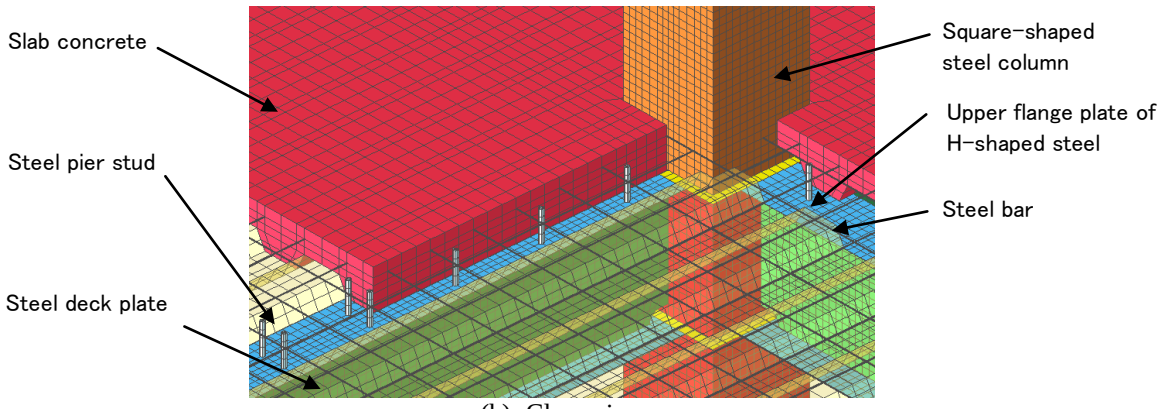


(b): Close view

Figure 3: Outline of FE model for full-scale shaking table test specimen

### 3.2 Analytical Cases and Seismic Input Motions

Two analytical case studies were performed for simulating the experimental test results. Targeted experimental case is the sequence No. 6 in Table 1. wherein fracture at beam ends were observed in the actual specimen. In both analytical cases, 60 and 80% scales of JR-Takatori (sequence No. 4 and 5) were included in input motions histories because non-linear behaviors were observed in the experimental cases after than the sequence no.4. Those two analytical cases are differentiated with or without considering fracture-operation in FE analysis. The case without considering fracture at beam endsis called Case-1 and the other case is called Case-2. Consideration of fracture in Case-2 is demonstrated in the analyses by eliminating damaged elements.

### 3.3 Fracture Criterion of FE Model

A damage index based on Manson-Coffin's law [5] and Miner's rule [6] is introduced as the failure criterion for Case-2. Manson-Coffin's law expresses the characteristics of low-cycle fatigue for steel material and it is represented as Eq.(1)

$$\tilde{\varepsilon}_p \times N^{\alpha} = C \tag{1}$$

Where $\tilde{\varepsilon}_p$: Plastic strain amplitude, $N$: Cycles in which material reaches fracture for specified plastic strain amplitude $\tilde{\varepsilon}_p$, $C$ and $\alpha$ : Material Constants

Miner's rule expresses the fatigue life of a material under a variable load. The linear cumulative damage indicate D is given by the Miner's rule as Eq.(2).

$$D = \sum_{i=1}^{k} \frac{n_i}{N_i} \tag{2}$$

Where $n_i$ : number of cycles under the $i$ th plastic strain amplitude $\tilde{\varepsilon}_{p,i}$ , $N_i$ : number of cycles to failure for $\tilde{\varepsilon}_{p,i}$.

A damage index DI is expressed by Eq.(3) using Eq.(1) and (2) in accordance with Xue's study [7]. The material constants $C$ and $\alpha$ to determine $m$ and $\tilde{\varepsilon}_{p,i}$ in Eq.(3) were evaluated from comparison of a component-analysis with a component-experiment conducted before shaking table test[8].

$$DI = \int m \left( \frac{\varepsilon_p^*}{\tilde{\varepsilon}_{p0}} \right)^{m-1} \frac{1}{\tilde{\varepsilon}_{p0}} d\varepsilon_p \tag{3}$$

Where $\varepsilon_p^* = \sqrt{2/3 \varepsilon_{ij}^p \varepsilon_{ij}^p}$ , $m$: material constant of Manson-Coffin's low (=1/$\alpha$), $\tilde{\varepsilon}_{p,0}$ : material constant (=2 $^{\alpha}\times$ C), $d\varepsilon_p$ : plastic strain increment

## 4 ANALYTICAL RESULTS

### 4.1 Prediction of Fracture Behavior

The times timing of fracture at the beam ends of the 2nd floor obtained by the numerical simulation and observed in the experimental test are indicated on the time-history of the story

drift of the 1st story in Figure 4. In which, a story drift ratio is defined from the story drift per its story height. Time-history of the damage index DI calculated at elements for the beam ends are shown in Figure 5.

As shown in Figure 4, timings of the fracture of beam ends at 2nd floor in the analysis much well to that of the experiment. The timings of fracture in the analysis delay only one cycle from the experimental results. As displaying in Figure 5, from the beginning part of the time-history analysis using JR-Takatori 100%, values of *DI* depicted 4 elements placing beam ends as Figure 5 have already reached close to 1.0. Although fully fractured beam ends were not observed before the experimental case applying JR-Takatori100%, some fine cracks were observed. Hence, it seems that the DI time-history can be correlated with the occurrence of cumulative damage in the experiment. It should be noted that any fracture of beam ends at 3rd floor did not occur in the analysis although it particularly occur in the experiment.

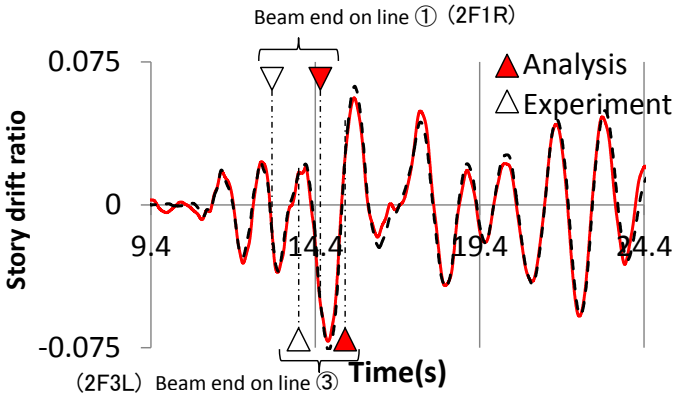


Figure 4: Timing of fractures at beam ends of the 2nd floor

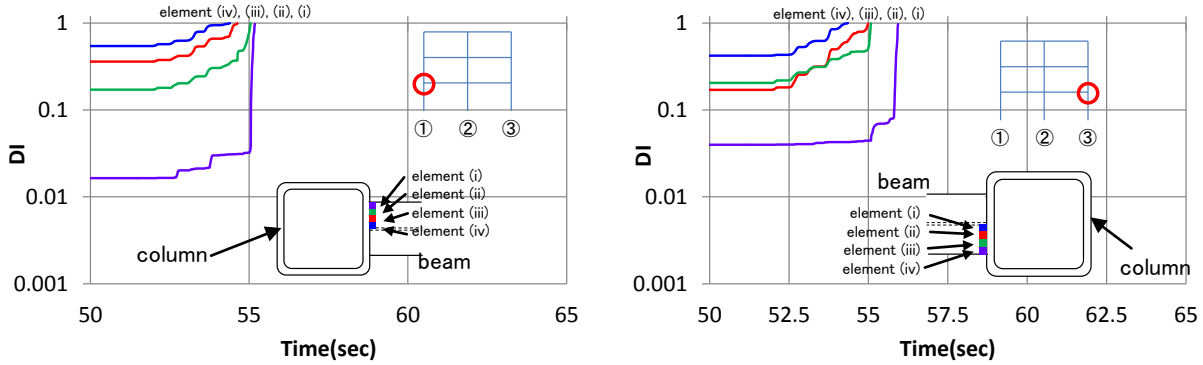


(a) On line ① (2F1R) (b) On line ③ (2F3L)

Figure 5: Time histories of DI for beam ends at 2nd floor

## 4.2 Floor Responses

The time-histories of the story drift ratios and story shear forces are shown in Figure 6 and 7, respectively. Results obtained by the analysis of Case-2, in which the fracture at beam ends is considered, are more accurate than those obtained by Case-1. It is remarkably mentioned that the behaviors after 15s, when the fracture of beam ends at 2nd floor occurred in the experiment, can be consistently simulated in Case-2 while the analytical results of Case-1 produce much more errors from the experimental results.

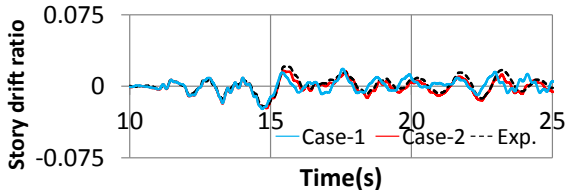


(a) 3rd story

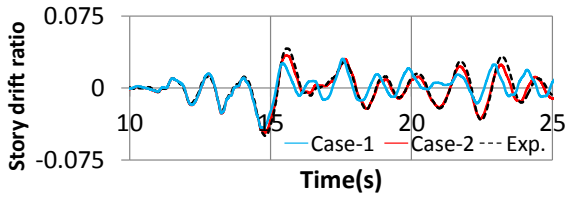


(b) 2nd story

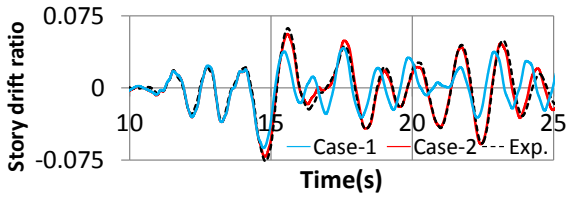


(c) 1st story

Figure 6: Time histories of the story drift ratio

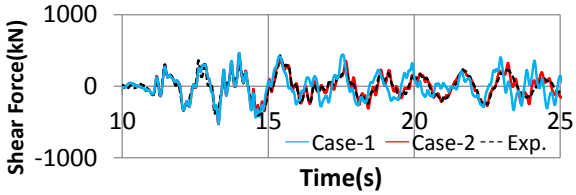


(a) 3rd story

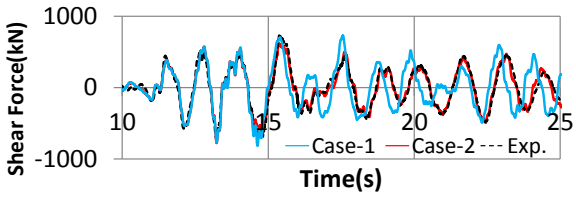


(b) 2nd story

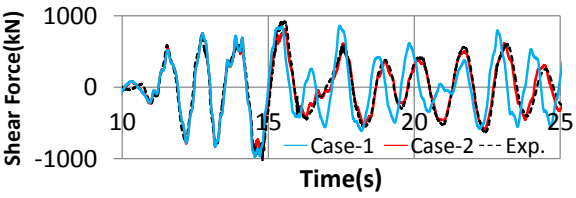


(c) 1st story

Figure 7: Time histories of the story shear force

## 5 CONCLUSIONS

- The non-linear analysis of steel structures, which is for examining by the shaking table test results at E-defense, is conducted considering its fracture. The analytical models are intended to replicate adequately entire shapes of the specimen assembling huge numbers of tiny elements. The damage index DI is introduced as the fracture criterion of steel members for FEM simulations. Elements whose damage index DI reaches 1.0 are eliminated to demonstrate fracture behavior in this study..
- The timing of the first fracture of the beam end in the analysis mostly match well to that of the experiment and the damage index DI shows well correlation to occurence of cumulative damage in the specimen.
- Considering fracture in FE analyses for the detailed model gives improvement of the accuracy of the analytical results for time-histories of story responses.

## ACKNOWLEDGEMENTS

This research used computational resources provided by the Kyoto University through the HPCI System Research project (Project ID:hp150152). A part of this work was supported by JSPS KAKENHI Grant Number 16H03124.

## REFERENCES

[1] T. Miyamura, T. Yamashita, H. Akiba, M. Ohsaki, Dynamic FE simulation of four-story steel frame modeled by solid elements and its validation using results of full-scale shake-table test, *Earthquake engineering & structural dyanamics*, Vol.44, 1449-1469. 2015.

[2] Y. Mizushima, Y. Mukai, T. Saruwatari, Detailed FEM Simulation for Shaking Table Test of Three-Story Full Scale Steel Building Structure, *Proceedings of the 16th International Conference on Computing in Civil and Building Engineering*, Japan, 192-199, 2016.

[3] Y. Mizushima, Y. Mukai, H. Namba, K. Taga, T. Saruwatari, Super-detailed FEM Simulation for Full Scale Steel Structure Caused Fatal rupture at its Joint Parts between Members - Shaking Table Test of Full Scale Steel Frame Structure to Estimate Influence of Cumulative Damage by Multiple Strong Motion Part1 -, *Journal of Structural and Construction Engineering (Transaction of AIJ)*, Vol.81, No.719, 61-70, 2016. (in Japanese)

[4] H. Namba, H. Fujitani, K. Taga, A. Tani, Y. Mukai, Y. Yamanabe, K. Kajiwara, K. Tani, T. Yamashita, S. Shiraga, D. Fukuoka, S. Morikawa, E-defense shaking table test for full scale steel building on cumulative damage by sequential strong motion (Part 1 Outline of test), *Summaries of technical papers of annual meeting AIJ*, Structures III , 975-976. 2014. (in Japanese)

[5] Coffin Jr. L.F., A study of the effects of cyclic thermal stresses on a ductile metal, *Transaction of ASME*, 76, 931-950, 1954.

[6] M. A. Miner, Cumulative Damage in Fatigue, *Journal of Applied Mechanics*, Vol.12, A565-571, 1951.

[7] Liang Xue, A Unified Expression for Low Cycle Fatigue and Extremely Low Cycle Fatigue and Its Implication for Monotonic Loading, *International Journal of Fatigue*, Vol.30, 1691-1698, 2008.

[8] D. Fukuoka, H. Namba, S. Morikawa, E-defense shaking table test for full scale steel building on cumulative damage by sequential strong motion (Part 2 Subassemblage Tests), *Summaries of technical papers of annual meeting AIJ*, Structures III, 977-978, 2014. (in Japanese)

COMPDYN 2017
6th ECCOMAS Thematic Conference on
Computational Methods in Structural Dynamics and Earthquake Engineering
M. Papadrakakis, M. Fragiadakis (eds.)
Rhodes Island, Greece, 15–17 June 2017

# MASS VARIATION WITH DISSIPATIVE STEEL STRUCTURES UNDER SEISMIC LOADS

**P. Knoedel**[1] **and T. Ummenhofer**[1]

[1] KIT Steel & Lightweight Structures
Research Centre for Steel, Timber and Masonry
Otto-Ammann-Platz 1, D-76131 Karlsruhe, Germany
peter.knoedel@kit.edu
thomas.ummenhofer@kit.edu

**Keywords:** plastic structures, seismic design, EC8, dissipation, viscous damping, time history, pushover, lateral force method, response spectrum.

**Abstract.** *In seismic engineering different levels of structural analysis are used, depending on complexity and importance of the structure and the required accuracy.*

- *Non linear time history analysis is used along with a full model of the structure to give the most accurate results. This method requires most effort and a well predesigned structure.*
- *Quasi static pushover analysis is used to get an insight of the subsequent development of plastic mechanisms under horizontal load patterns. This method requires only the modelling of the retaining system which, in the case of steel structures, could consist only of a pair of columns and the X-type braces in between.*
- *The simplest, but most inaccurate way, is to use the lateral force method (e.g. according to Eurocode 8), which can easily be handled by hand calculations. The dynamic behaviour of the structure is modelled as a single-degree-of-freedom oscillator and adopted to the real behaviour by a behaviour factor q.*

*It is evident, that for predesigning purposes, the number of dissipative elements along with their performance must be adjusted depending on the total oscillating mass, so that the target displacements are met. However, in the respective design codes no rules are given on how to carry out this task. This holds as well for most of the scientific publications, which describe refined analyses for given structures, but do not provide guidance for predesign.*

*The present paper reports on a study on mass variation with a multi-storey steel structure. With a given dissipative structure a variation of the masses in each storey results – apart from a change in the natural frequency – in a different storey drift. This is becoming equivalent to a structure with given masses and variation of the performance of the dissipative elements, e.g. by altering the cross section of the braces. In the study a rule is developed, which describes the minimal required performance of the dissipative elements with a given mass and target storey drift. Thus, the structural engineer can adopt the bracing elements to the given needs.*

## 1 TERMS AND ABBREVIATIONS

| | |
|---|---|
| DAF | dynamic amplification factor, relates the response amplitude of the structure to the driving displacement amplitude |
| DBF | design by formulae (acronym given in EN 13445-3 Clause 5.2 [1]) |
| PGA [m/s$^2$] | peak ground acceleration |
| SDOF | single degree of freedom (oscillator); simplest possible mass-spring-system |
| $\zeta$ | (zeta) damping ratio, see eq. 4;<br>in German the term *Lehr*'sches Dämpfungsmaß D is paying tribute to *Ernst Lehr*, a material scientist and mechanical engineer;<br>in EC8 [2] $\xi$ (xi) is used, presumably due to mistaking $\zeta$ and $\xi$ |
| $\omega$ [rad/s] | angular frequency |

## 2 INTRODUCTION

When designing engineering structures, a balance is made of the effort which needs to be spent and the design result that wants to be achieved. E.g. with air- and spacecraft reduction of mass is extremely important, whereas design effort and money spent is only secondary. With most civil engineering structures, it's the other way round: expensive design hours need to be reduced, working hours in the shop and on site need to be reduced, whereas reduction of mass is only secondary. In seismic engineering it can be both: for simple structures and small or medium PGAs a simple and conservative design with hand-calculation rules can be sufficient. With complicated structures and medium or high PGAs sophisticated FEA such as time history simulation is needed.

Previously, the authors published some studies, where different levels of design methods were discussed [3], [4], [5]. Also, it was pointed out, which results can be achieved and how they can be verified [7], [8].

On the hand-calculation level (i.e. lateral force method), it seems to be sufficient, to assign the calculatory horizontal force to one or more bracing systems. On the resistance side, the assigned bracing systems counteract with their plastic capacity, e.g. plastic normal force with diagonal systems [3], plastic bending moments with frame systems [5] or plastic shear force with panel systems [10]. In some cases, separate devices are arranged, which are basically designed to provide a hysteretical behaviour [11], [12], [13]. For this cases it is interesting to find a simple predesign method in order to decide on the number of devices needed, before extensive FEA are started.

## 3 STATE OF THE ART

### 3.1 SDOF and viscous damping

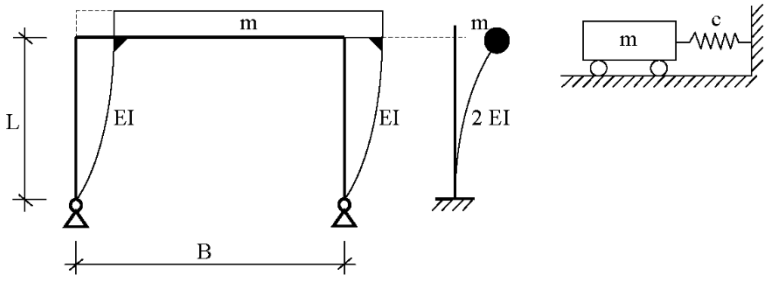


Fig. 1. Single storey frame arrangement and derived SDOF oscillator (taken from [4])

$$m \cdot \ddot{x} + d \cdot \dot{x} + c \cdot x = F(t) \tag{1}$$

$$x(t) = A \cdot e^{-\zeta \omega t} \cdot \sin(\omega \cdot \sqrt{1-\zeta^2} \cdot t) \tag{2}$$

Classical SDOF oscillators involve a mass inertia (first term in eq. 1), a viscous damping (second term in eq. 1) and an restoring force (third term in eq. 1) on the left hand side of the equal sign. On the right hand side an external load is given, which represents the "drive". Thus, the equation of motion is formulated as a quasi-static equilibrium condition of the aforementioned forces.

$$\omega = \sqrt{\frac{c}{m}}$$
$$f = \frac{\omega}{2\pi} = \frac{1}{2\pi}\sqrt{\frac{c}{m}} \tag{3}$$

The known solutions (eq. 2) provide information such as the angular frequency ω [rad/s] or the frequency f [1/s] and the period T, being the reciprocal value.

Increasing mass causes under-proportional increase of the fundamental period, see eq. 3. With respect to the lateral force method in seismic design, increasing mass causes proportional increase of the base shear. That is, if the fundamental response period is remaining on the plateau of the response spectrum. If the fundamental response period is bigger than the control period $T_C$ (see fig. 3.1 in [2]), the branch of the response spectrum decreases. However, the decreased acceleration, multiplied by the increased mass, which caused the increased fundamental period, still leads to an increased base shear. Thus, increasing the mass in a structure with given stiffness, always will result in increasing base shear [14].

$$\zeta = \frac{d}{d_{crit}} \tag{4}$$

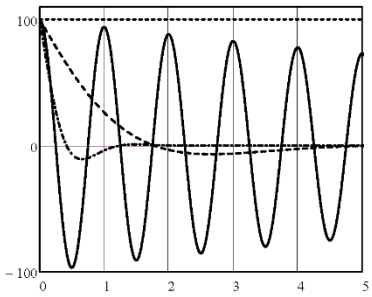


Fig. 2. Family of time-history curves of free, damped vibration with T = 1 s; governing parameter of the family of curves is ζ = 1.00; 0.99; 0.80; 0.01;

The damping constant d [N·s/m] is usually related to *critical damping* where oscillating motion changes into a creep motion (as it is given in most textbooks). From a mathematical point of view this is not true. Creep motion implies, that the motion approaches zero asymptotically, without changing the sign. Obviously, according to eq. 2, the sign change is not lost, but rather shifted to infinity, see Fig. 2. In eq. 2 the term $\sqrt{1-\zeta^2}$ can be regarded as *frequency correction* term. Other than the shock absorbers of a vehicle chassis, damping with building structures is rather low. According to EC1-1-4 informative Annex Table F.2, typical values of the *logarithmic decrement* for steel buildings may be assumed to be δ = 0.05, other metal structures such as slender chimneys or aluminium bridges may go down below δ = 0.02. By use of

$$\zeta = \frac{\delta}{2\pi} \tag{5}$$

these values transform to $\zeta = 0.008$ or $\zeta = 0.003$ and below. Even for a typical building according to EC8-1-1 [2], for which a value of $\zeta = 0.050$ may be assumed, the frequency correction term amounts to 0.9987. From this can be concluded, that for engineering purposes no correction of the natural frequency need to be taken into account.

In a forced harmonic motion, the steady-state amplitude is depending only on the damping ratio, so that

$$\mathrm{DAF} = \frac{1}{2\zeta} \tag{6}$$

This holds for force amplitudes as well as for relative displacements of oscillator and base in a base-displacement driven system [15].

Apart from damping, a non-linear spring c can also cause a limitation of amplitudes. The simplest possible formulation for this, where analytical solutions can be achieved, is the *Duffing* oscillator [16]. The restoring force is described as function of the third power of the displacement. Applications have been presented in [8].

### 3.2 Time history with plasticity

In a previous study, the authors used multi-storey frames to investigate the behaviour factors due to plastic response of the different structures [5].

Usually, in seismic design codes the base acceleration PGA is prescribed according to a local seismic zonal map. With time history simulations however, it is more convenient to have prescribed base displacement amplitudes. For harmonic motions, these can be derived by using the derivatives of the equation of harmonic motion

$$x = \mathrm{A} \sin \omega t \tag{7}$$

$$\ddot{x} = -\mathrm{A}\omega^2 \sin \omega t \tag{8}$$

We see from eq. 8, that we need to divide the acceleration amplitude by $\omega^2$ in order to receive the displacement amplitude. For convenience we introduce

$$\omega = \frac{2\pi}{T} \tag{9}$$

and get

$$\mathrm{x}_{max} = \mathrm{a}_{max} \frac{T^2}{4\pi^2} \approx 0.0253 \cdot \mathrm{a}_{max} \cdot T^2 \tag{10}$$

For the below chosen seismic event (see section 3.3) and the fundamental period of the structure (see section 4) we receive

$$\mathrm{a}_{max} = \mathrm{a}_{gR} \cdot \gamma_I \cdot \mathrm{S} = 1.6 \frac{m}{s^2} \cdot 1.0 \cdot 1.5 = 2.4 \frac{m}{s^2} \tag{11}$$

$$\mathrm{x}_{max} = 2.4 \frac{m}{s^2} \cdot \frac{(1.6075\ \mathrm{s})^2}{4\pi^2} = 157\ \mathrm{mm} \tag{12}$$

Note, that this approach has been described in [4] eq. 23. Of course, using of a harmonic drive with reduced number of driving amplitudes is a gross simplification compared to real seismic records. On the other hand, according to Table 1 in [8] this is a necessary step back in order to be able to check the numerical results vs. known analytical evidence.

Real seismic data are given exemplary in Figures 3, 4 and 5, where the recorded ground accelerations and displacements, the respective spectra, and the response of different SDOF oscillators are given. The station code E-000182 is referring to a station, which has a distance

of only 12 km to the epicentre, so we are looking at a nearfield event (see Annex B.6 in [18]). As we stated in a previous paper [4] and can be seen in the time history plots in Fig. 3, there are only some few major peaks in design magnitude with near-field events. With far-field events the number of major peaks is much bigger, but the magnitude might be one order of magnitude lower. This might be seen as background information for the provision in EC8-1-1 3.2.3.1.2 (3), that steady state acceleration should be maintained for at least 10 seconds.

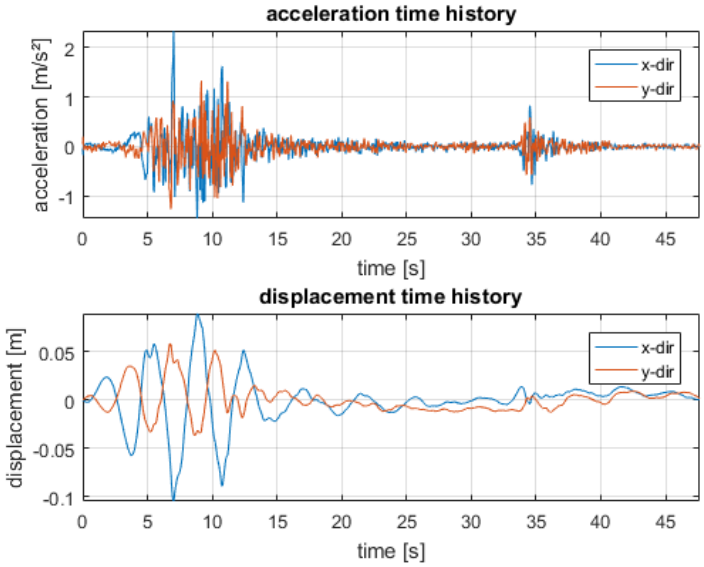


Fig. 3. Exemplary seismic data from Tabas Earthquake 16.09.1978 (E-000182 [18]) – acceleration and displacement time history

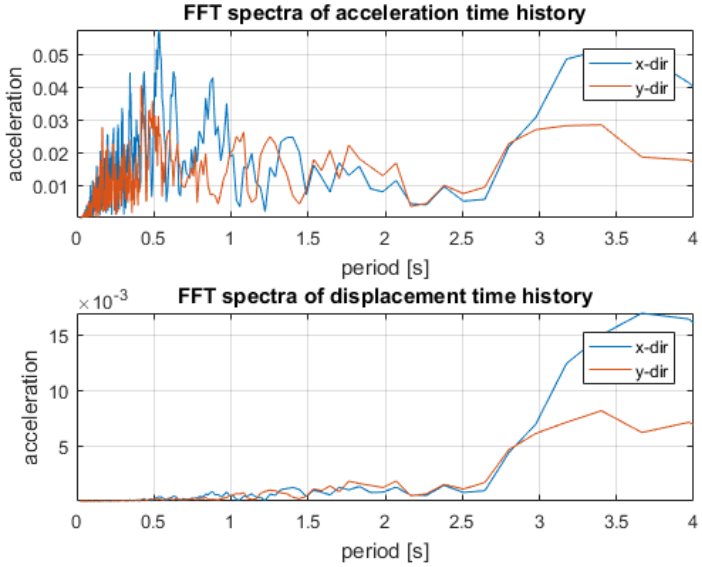


Fig. 4. Exemplary seismic data from Tabas Earthquake 16.09.1978 (E-000182 [18]) – acceleration and displacement periodal spetra

We can also see, that there is a big qualitative difference between the ground motion spectrum in Fig. 4 and the response spectrum of the structure in Fig. 5. This is sometimes mistaken, when artificial or recorded seismic data are scaled to the *response*-spectra in EC8 and then are

used as *input*-data for a FE time history calculation. If this is done, the DAF is used twice: first, a factor of 2.5 is used, which is implied in the response spectrum of EC8; second, the DAF of the actual modelled structure is (i.e. difference between input and output) is calculated via FEA.

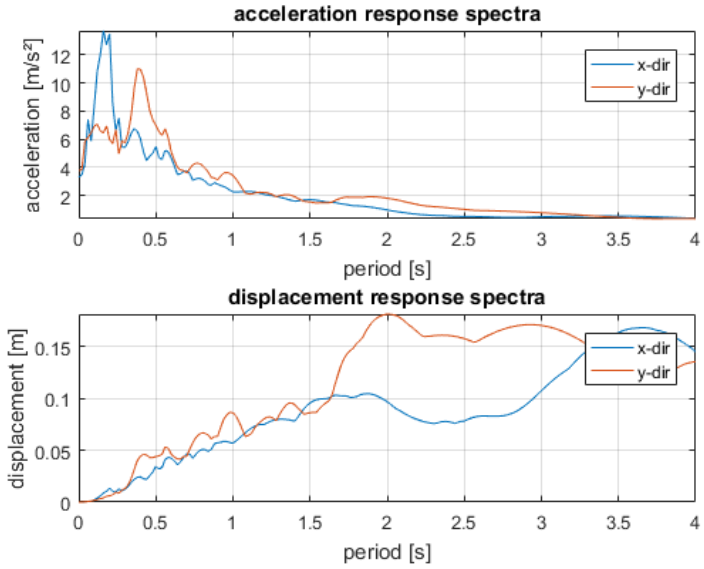


Fig. 5. Exemplary seismic data from Tabas Earthquake 16.09.1978 (E-000182 [18]) – acceleration and displacement periodal SDOF response spectra

### 3.3 Lateral Force Method (DBF)

In EC8 [2], the lateral force method is named in Clause 4.3.3.1 (3a), based on a modal response spectrum analysis, which is called "reference method for determining the seismic effects" in Clause 4.3.3.1 (2)P.

The lateral force method involves a linear structural analysis. The capability of the structure to dissipate energy and thus producing smaller response amplitudes, than a elastic structure would have, is captured by the behaviour factor q.

Following the basics of structural dynamics, we have (EC8 Clause 4.3.3.2.2 (1) eq. 4.5)

$$F_b = S_{d,hor} \cdot m \cdot \lambda \tag{13}$$

where

| | |
|---|---|
| $F_b$ [N] | base shear of the structure |
| $S_{d,hor}$ [m/s$^2$] | effective horizontal acceleration |
| m [kgs] | oscillating mass of the structure |
| λ | correction factor, which will not be discussed in this paper (assuming λ= 1) |

The effective acceleration is given by EC8 Clause 3.2.2.5 (4) eq. 3.14

$$S_{d,hor,max} = a_g \cdot S \cdot \frac{2.5}{q} \tag{14}$$

$$\text{where } a_g = a_{g,R} \cdot \gamma_I \tag{15}$$

$$S_{d,hor}(T) = S_{d,hor,max} \cdot \frac{T_C}{T} \quad \text{if } T_C \le T \le T_D \tag{16}$$

$$S_{d,hor}(T) = S_{d,hor,max} \cdot \frac{T_C \cdot T_D}{T^2} \quad \text{if } T_D \le T \tag{17}$$

$$S_{d,min} = \beta \cdot a_g \tag{18}$$

$S_{d,hor,max}$ [m/s$^2$] plateau value of the design response spectrum, independent of the period
$a_g$ [m/s$^2$] design ground acceleration; eq. 15 is given in EC8 Clause 3.2.1 (3)
$a_{g,R}$ [m/s$^2$] reference PGA according to the relevant seismic zone map
$\gamma_I$ importance factor; values are given in NOTE to EC8 Clause 4.2.5 (5)P; Importance Classes for buildings are defined in EC8 Table 4.3
S soil factor, given in EC8 Tables 3.2 and 3.3; for ground types see Table 3.1
2,5 DAF
q behaviour factor; EC8 Clause 6.1.2, (2)P and Table 6.1
$T_B$, $T_C$, $T_D$ [s] control periods given in EC8 Tables 3.2 and 3.3, where $T_B$ and $T_C$ are limiting the plateau; for ground types see Table 3.1
(present choice: ground type C; spectrum type 2; 0.10; 0.25; 1.20)
$S_{d,hor}(T)$ [m/s$^2$] reduced acceleration, if the fundamental period exceeds $T_C$
β lower bound factor for the horizontal design spectrum; recommended to be 0.2, see NOTE after EC8 eq. 3.16

As we can see from the above equations, the base shear $F_b$ is proportional to the mass. Thus, in a hand-calculation according to the lateral force method, a variation of mass would change the need for the strength of bracing elements proportional.

Following the example given in [4], but with 6 m span and 4 m height, we receive

$$S_{d,hor,max}(\mathrm{q}=1.5) = 1.6\frac{m}{s^2}\cdot 1.0\cdot 1.5\cdot\frac{2.5}{1.5} = 4.0\frac{m}{s^2} \tag{19}$$

$$S_{d,hor,max}(\mathrm{q}=4) = 1.6\frac{m}{s^2}\cdot 1.0\cdot 1.5\cdot\frac{2,5}{4} = 1.5\frac{m}{s^2} \tag{20}$$

Combining this with a storey mass of 72 000 kgs, we receive a plateau base shear of

$$F_b(\mathrm{q}=1.5) = 4.0\frac{m}{s^2}\cdot 72\,000\ \mathrm{kgs}\cdot 1.0 = 288\ \mathrm{kN} \tag{21}$$

$$F_b(\mathrm{q}=4) = 1.5\frac{m}{s^2}\cdot 72\,000\ \mathrm{kgs}\cdot 1.0 = 108\ \mathrm{kN} \tag{22}$$

As will be seen in the numerical study below, this configuration has a fundamental period of T = 1.61 s. Thus, we can reduce the calculatory acceleration by use of eq. 17 with a factor of

$$k = \frac{T_C\cdot T_D}{T^2} = \frac{0.25\ s\cdot 1.2\ s}{(1.61\ s)^2} = 0.12 \tag{23}$$

This gives a reduced base shear of

$$F_b(\mathrm{T};\ \mathrm{q}=1.5) = 288\ \mathrm{kN}\cdot 0.12 = 34.6\ \mathrm{kN} \tag{24}$$

$$F_b(\mathrm{T};\ \mathrm{q}=4) = 108\ \mathrm{kN}\cdot 0.12 = 13.0\ \mathrm{kN} \tag{25}$$

With the lower bound condition of eq. 18

$$F_{b,min} = \beta\cdot a_{g,R}\cdot\gamma_I\cdot \mathrm{m} = 0.2\cdot 1.6\frac{m}{s^2}\cdot 1.0\cdot 72\,000\ \mathrm{kgs} = 23.0\ \mathrm{kN} \tag{26}$$

we receive the final design base shear

$$F_b(\mathrm{T};\ \mathrm{q}=1.5) = 34.6\ \mathrm{kN} \tag{27}$$

$$F_b(\mathrm{T};\ \mathrm{q}=4) = 23.0\ \mathrm{kN} \tag{28}$$

Using the horizontal storey stiffness given in the numerical example below, these loads correspond to storey drifts

$$w(\mathrm{T};\ \mathrm{q}=1.0) = \frac{34.6\ \mathrm{kN}\cdot 1.5}{1.0995\ \mathrm{kN/mm}} = 47.2\ \mathrm{mm} \tag{29}$$

$$w(\mathrm{T};\ \mathrm{q} = 1.5) = \frac{34.6\ \mathrm{kN}}{1.0995\ \mathrm{kN/mm}} = 31.5\ \mathrm{mm} \tag{30}$$

$$w(\mathrm{T};\ \mathrm{q} = 4) = \frac{23.0\ \mathrm{kN}}{1.0995\ \mathrm{kN/mm}} = 20.9\ \mathrm{mm} \tag{31}$$

$$w(\mathrm{T};\ \mathrm{q} = 4) = \frac{13.0\ \mathrm{kN}}{1.0995\ \mathrm{kN/mm}} = 11.8\ \mathrm{mm} \tag{32}$$

Shown above we demonstrated the evolution of the key-figures in a hand-calculation. If the structure under consideration was purely elastic, the chosen seismic event would have caused a maximum storey drift of 47.2 mm, corresponding to a base shear of 34.6 kN · 1.5 = 51.9 kN. If we omit the limit condition given in eq. 18 as being arbitrarily man-made rather than being a physical description of a SDOF oscillator under seismic loads, we end up with a storey drift of 11.8 mm acc. eq. 32 instead of 20.9 mm acc. eq. 31. As should be for a structure with an assumed behaviour factor of q = 4, the dissipative storey drift is by a factor of 47.2 mm / 11.8 mm = 4.0 smaller than the elastic storey drift.

As a summary for this section we can conclude, that the structure used in the numerical study is well designed seismic loads given by the lateral force method. Assuming a behaviour factor of q = 4, which is not unusual for a steel sway frame, we receive a horizontal storey load of 23.0 kN, while the structure has a horizontal elastic limit load of 57.6 kN, leading to a utilization of η = 23.0 kN / 57.6 kN = 0.40. *Knoedel/Hrabowski* suggest a modification of the behaviour factor, if the utilization is lower than 0.70 ([4] eq. 27). For the present example, this would lead to

$$q_{mod} = \eta \cdot \mathrm{q} = 0.4 \cdot 4.0 = 1.6 \tag{33}$$

But still, as we can see from eq. 24, with a reduced behaviour factor of app. 1.5 the structure receives a lateral force of 34.6 kN, so that the utilization is η = 34.6 kN / 57.6 kN = 0.60. Another modification of the behaviour factor would lead to q = 1, where the lateral force is 51.9 kN and the final utilization is η = 51.9 kN / 57.6 kN = 0.90. So, under all considerations the structure does meet the requirements of the lateral force method.

After the very explicit evaluation of the numbers given above the effects of mass variation (half and double) are given in Table 1.

| Quantity | Unit | 36 t q = 1.5 | 36 t q = 4 | 72 t q = 1.5 | 72 t q = 4 | 144 t q = 1.5 | 144 t q = 4 |
|---|---|---|---|---|---|---|---|
| plateau base shear $F_b$ | kN | 144 | 54 | 288 | 108 | 576 | 216 |
| fundamental period T | s | 1.14 | | 1.61 | | 2.27 | |
| frequ. red. factor k | – | 0.22 | | 0.12 | | 0.058 | |
| base shear $F_b(T)$ | kN | 31.7 | 11.9 | 34.6 | 13.0 | 33.4 | 12.5 |
| storey drift | mm | 28.8 | 10.8 | 31.5 | 11.8 | 30.4 | 11.4 |
| lower bond condition | kN | | 23.0 | | 23.0 | | 23.0 |
| storey drift | mm | | 20.9 | | 20.9 | | 20.9 |

Table 1. Results of mass variation with lateral force method

We can summarize, that the plateau base shear increases proportional to an increasing mass. If the fundamental period $T_B \leq T \leq T_C$. For other configurations, the horizontal acceleration is lower than the plateau value according to the shape of the response spectrum. Period or frequency are influenced under-proportional by the mass, see eq. 3. However, multiplying the mass with the acceleration, higher mass leads to higher base shear in all cases [14].

### 3.4 Pushover Analysis

In EC8 [2], the non-linear (quasi-)static pushover analysis is named in Clause 4.3.3.1 (4c). Advantage of the pushover analysis is, that a sequence of different plastic mechanisms can be activated in design (e.g. for a ten storey building in [19]).

Within the frame of the below numerical study also several pushover analyses were provided, see Table 2.

| material constitutive law | gravity + second order effects | ultimate horizontal force (FEA) [kN] | ultimate storey drift (FEA) [mm] | ultimate plastic strain (FEA) [%] |
|---|---|---|---|---|
| elastic | yes | > 173 | > 249 | 0 (Run_30) |
| plastic | yes | 32.1 | 59 | 0 (Run_29) |
| plastic | no | 71.1 | 72 | 1.14 (Run_28/31) |
| elastic | no | > 150 | > 138 | 0 (Run_27) |

Table 2. Results of various pushover analyses [20]

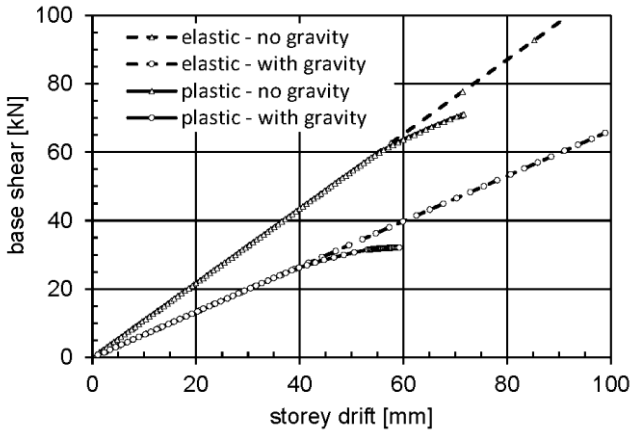


Fig. 6. Load-displacement paths of various pushover analyses with 72 t storey mass

It should be noted, that a storey mass of 72 t would be distributed to much more columns than 2 in a real structure, so the loading of an individual column would be much lower, if the whole building structure was modelled and not only the bracing system. On the other hand, the P-Δ-effect remains the same, independent of how many sway-columns are involved.

Useful hints for practical application are given in [21].

## 4 NUMERICAL STUDY

### 4.1 Model

#### Geometry

The results of [5], with a background documentation given in [6] and the results of [8] with a background documentation given in [9] are used as a basis for the present study. A more extensive background documentation on the present study is given in [20].

Size of frame: 6 m wide, 4 m high; pinned bases, rigid corners; weightless;
Cross sections: Tubular 1000x12 as waler; tubular 240x12 as columns;

Masses

36 000 kgs in each corner of the frame, giving a total storey mass of 72 000 kgs.

Element

BEAM23; 5 integration layers at 50 %; 30 % and 0 % of the beam's height.

Material

Steel with a simplified bi-linear constitutive law and isotropic hardening was used. Isotropic hardening was chosen in order to get symmetrical response amplitudes, although this does not seem to be a proper choice for structural steels or aluminium [10], [22].

*Young*'s modulus with 210 GPa is used up to a yield limit of 235 MPa. Above that a straight line to the ultimate tensile stress 360 MPa at assumed 20 % strain was used. Thus an *engineering plastic modulus* with a slope of

$$E_{tan,plast} = \frac{f_u - f_y}{\varepsilon_u - \varepsilon_y} = \frac{360\ MPa - 235\ MPa}{0.2000 - 0.0011} \approx 625\ \text{MPa} \tag{34}$$

is received, which corresponds to 0.3 % of *Young*'s modulus. This approach has been used before, see eq. 15 in *Knoedel/Hrabowski* (2012) [4].

Remark: In this case material degradation is not considered, therefore accumulated plastic strain is not recorded [23].

Verification

| Quantity | Unit | DBF design by formulae | FEA | relative error of FEA [%] |
|---|---|---|---|---|
| storey drift stiffness | N/m | $1.0995 \cdot 10^6$ | $1.0868 \cdot 10^6$ | –1.16 |
| horizontal elastic limit force | kN | 57.6 | 56..4 | –2.08 |
| horizontal elastic limit drift | mm | 52.4 | 51.9 | –0.95 |
| fundamental period | s | 1.6075 | 1.6172 | +0.60 |
| fundamental period with half masses | s | 1.1368 | 1.1432 | +0.56 |
| fundamental period with double masses | s | 2.2733 | 2.2872 | +0.61 |

Table 3. Comparison of „hand" and FEA results

The performance of the model was tested in various static and time-history runs. The results are given in Table 3.

### 4.2 Procedure

Time history runs were performed. A horizontal motion was prescribed at the column bases, typically ±50 mm with 1.6170 s as driving period. 200 load steps were used within one period, having 10 to 100 prescribed subdivisions of each individual load step.

This 50 mm amplitude is slightly less than the elastic limit storey drift. But if material non-linearity is switched off, the frame has a storey drift of 78 mm in the first response peak. Thus plastic action starts within the first half wave.

### 4.3 Results

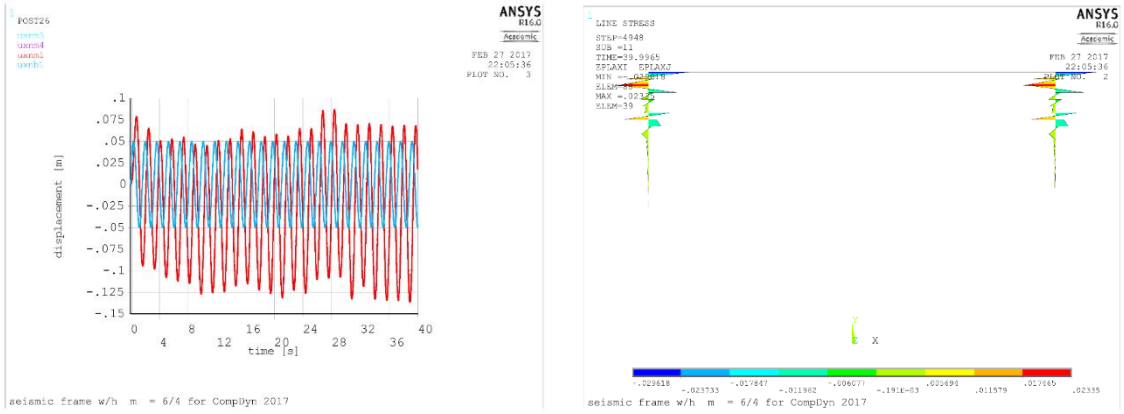


Fig. 7. Exemplary results of run_10 [20]:
a) time history of displacements – drive (blue) and response (red); b) plastic strains at 40 s

In Fig. 7a a typical time history plot is given. We see discontinuous jumps of the response amplitude at continuous harmonic drive, which can not be explained at the moment. The choice of a isotropic hardening constitutive law should provide increasing amplitudes with increasing number of cycles. However, these discontinuities or offset has been observed in a previous study as well, see [8] Fig. 6. We want to investigate this effect in a subsequent study [24].

In Table 4 some key-results of the time history analyses are given. DAF+, DAF– and DAF,range indicate the biggest positive response peak, the biggest negative response peak and half of the biggest range. The run number is referring to the background document [20]. A graphical representation is given in Fig. 8. The numbers in the DAF index are the driving amplitudes.

Initial hypothesis of this paper was, that mass and dissipation are counterparts in order to avoid excessive response displacements. In this study, the structure has a given ability for dissipating energy, i.e. two columns which can develop plastic zones, if the elastic limit storey drift is exceeded. Thus, we should expect that bigger masses are associated with bigger response amplitudes. The response amplitudes are normalized by the driving amplitude, resulting in the dynamic amplification factor DAF. Therefore, all the curves in Fig. 8 should rise from left to right. As we can see, this holds for the negative peaks DAF–, which are marked by a triangle. Some of the other lines are horizontal, some are falling.

Seen from the displacement time history in Fig. 7a and the other ones documented in [20] it seems, that DAF,range is a more reliable indicator of the structure's performance than DAF+ or DAF–, although it does not represent the real maximum of the displacements. On the other hand, since the structure develops plastic zones anyway, it does not seem very significant if the structure has single peaks with bigger amplitudes. A more extensive discussion on limit plastic strains with FEA can be found in [25] and [26].

As we can see from displacement time history of Run_9 [20] after 10 sec we have an elastic response amplitude of app. 900 mm (7. peak). Thus, a structure with a behaviour factor of q = 4 would be having maximum amplitudes of 900 mm / 4 = 225 mm, which would correspond to a DAF = 225 mm / 50 mm = 4.5. As we see from Fig. 8, this condition is met for the structure with 72 t and 50 mm drive.

| Run no. | driving amplitude | storey mass | DAF+ | DAF– | DAF,range | $\zeta_{eff}$ from DAF,range see eq. 6 |
|---|---|---|---|---|---|---|
| [-] | [mm] | [t] | [-] | [-] | [-] | [-] |
| 16 | 25 | 36 | 5.89 | 3.12 | 3.55 | 0.14 |
| 15 | 50 | 36 | 1.75 | 2.44 | 2.09 | 0.24 |
| 17 | 100 | 36 | 2.22 | 3.53 | 4.54 | 0.11 |
| 11 | 25 | 72 | 5.07 | 3.13 | 3.54 | 0.14 |
| 10 | 50 | 72 | 1.74 | 2.73 | 2.05 | 0.24 |
| 12 | 100 | 72 | 3.63 | 4.72 | 2.78 | 0.18 |
| 22 | 25 | 144 | 3.73 | 5.14 | 3.54 | 0.14 |
| 20 | 50 | 144 | 1.58 | 4.17 | 2.09 | 0.24 |
| 21 | 100 | 144 | 3.37 | 5.14 | 3.54 | 0.14 |

Table 4. Results of the time history analysis

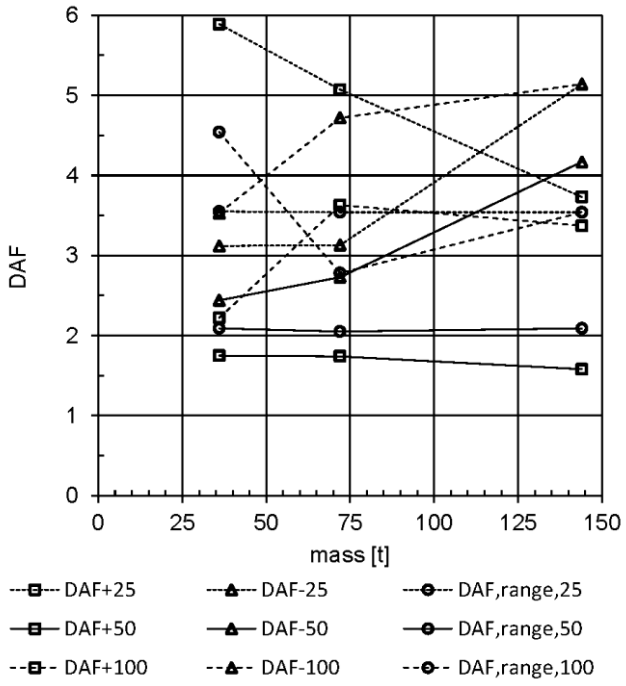


Fig. 8. DAF vs. mass in time history analysis

In the last column of Table 4 we interpreted the dissipative (plastic) action of the structure as viscous damping and evaluated a damping ratio from DAF,range according to eq. 6. Under the assumption of elastic structures having a damping ratio of 5 % in EC8 and a behaviour factor of q = 4 for this kind of frame, these values should coincide with an effective damping ratio of $0.05 \cdot 4 = 0.20$. As we see, this condition is met the configurations with a driving amplitude of 50 mm.

For driving amplitudes 25 mm we have smaller damping. Since 25 mm is only half of the elastic limit amplitude, this configuration could be interpreted as having a utilization of come

50 %. Based on [4], in this case we should reduce the behaviour factor to half, so that the expected damping ratio would be $0.05 \cdot 4 / 2 = 0.10$, which is met.

For driving amplitudes 100 mm we have smaller damping as well. In comparison with 50 mm driving amplitude, this could be interpreted as the structure having insufficient plastic "abilities" for the present mass. As a result additional damping devices would be needed, which could be a third column in this simple example.

## 5 CONCLUSIONS

- Time history analysis with harmonic drive is preferred by the authors when studying basic correlations, because according to Table 1 in [8] this is the last level where you can make plausibility checks.
- It is very difficult, to adapt an artificial base drive such, that results are achieved, which can be proved to be in line with the provisions of EC8. Basically, this difficulty results from the fact, that quasi-static methods can not simulate dynamic problems.
- Pushover analysis has the advantage, that it can be performed at low effort.
  However, since it is a quasi-static method, it needs to be based on assumptions on the magnitude of the horizontal inertial forces. Typically, these assumptions are based on the evaluation of the response spectrum of a SDOF oscillator. As a consequence, it is difficult to use this method for multi-storey buildings, if higher modes than the fundamental one are governing.
- Within the lateral force method, variation of masses leads to proportional variation of the base shear, if the fundamental period is within the plateau of the response spectrum. In other cases the variation of the base shear is non-proportional, but in all cases increased mass leads to increased base shear.
- This behaviour can not be captured in all cases by a time history analysis with different driving amplitudes. We found configurations, where increasing masses produced decreasing response amplitudes.
- Some of the features we found in our study are inconsistent and need further work, such as non-increasing amplitudes with isotropic hardening and sudden offsets in the response amplitudes.
- So far, we found no evidence to exclude a viscous-damping-approach for plastic structures. That is at least within the range of accuracy needed in seismic design according to EC8.

## 6 ACKNOWLEDGEMENT

The continuous support of Dipl.-Ing. Tobias Wacker, ANAKON Karlsruhe, is greatfully acknowledged. The authors are indebted to Dr Evangelos Efthymiou, Aristotle University of Thessaloniki and Prof. Bogdan Stefanescu, Technical University of Bucharest, for fruitful discussions.

## REFERENCES

[1] EN 13445: Unfired pressure vessels.
Part 1: General, 2014.

Part 3: Design, 2009.
Amendment A1, August 2012; Draft Amendment A2, July 2012.

[2] EN 1998 (EC8): Design of structures for earthquake resistance.
Part 1: General rules, seismic actions and rules for buildings:2004 + AC:2009 + A1:2013.

[3] Knoedel, P.: On the Dynamics of Steel Structures with X-Type Bracing.
Stahlbau 80 (2011), No. 8, p. 566–571.

[4] Knoedel, P., Hrabowski, J.: Yield Limit vs. Behaviour Factor in Seismic Design. Proceedings, NSCC 2012 Nordic Steel Construction Conference, 5-7 September 2012, Oslo, Norway, pp 147-155.

[5] Knoedel, P., Hrabowski, J., Ummenhofer, T.: Seismic behaviour factor in combined frame and braced structures. Eurosteel 2014, 7th European conference on steel and composite structures, Naples, Italy, 10-12 September 2014. (see [6])

[6] Knoedel, P. "Background document on ANSYS analyses" 09.03.2014, to be downloaded from http://www.peterknoedel.de/lehre/FHA-Stahl/Skript/GrA/Dyn/report-11_14-03-09.pdf, see [5]

[7] Knödel, P., Heß, A.: Erdbebenbemessung von Tanks – Erfahrungen aus der Praxis. Stahlbau 80 (2011), Heft 11, S. 820–827. (Seismic design of tanks – practical experience)

[8] Knoedel, P., Ummenhofer, T.: Time History Simulation in Seismic Design. Contribution 379 (USB). Heinisuo, M., Mäkinen, J. (eds).: Proceedings, NSCC-2015 Nordic Steel Construction Conference 2015, Tampere, Finland, 23-25 September 2015. (see [9])

[9] Knoedel, P. "NSCC 2015 - Background document on ANSYS analyses" 10.02.2015, to be downloaded from http://http://www.peterknoedel.de/lehre/FHA-Stahl/Skript/GrA/Dyn/report-07_15-02-10.pdf, see [8]

[10] Efthymiou, E., Psomiadis, V.G., Ampatzis, A.T.: Aluminium Deployment in Bracing Systems: Investigation of Shear Link Application. Contribution 371 (USB). Heinisuo, M., Mäkinen, J. (eds).: Proceedings, NSCC-2015 Nordic Steel Construction Conference 2015, Tampere, Finland, 23-25 September 2015.

[11] Li, A., Gao, R., Sun, M., Zhang, J.: Research on hysteretic behaviours of a separated shock absorber applied in railway bridge. Papadrakakis, M., Papadopoulos, V., Stefanou, G., Plevris, V. (eds.): Proc. ECCOMAS 2017, VII Europ. Congress on Comp. Meth. in Appl. Sci. and Eng., 05-10 June 2016, Crete Island, Greece.

[12] Öniz, S.: Dissipative Stahlblechverbindungen für Brettsperrholz unter wiederholter zyklischer Belastung. Dissipative steel plate connections for CLT under repeated cyclic stress. Master Thesis at KIT Timber Structures and Building Construction, Karlsruhe 2016.

[13] Sandhaas, C., Schädle, P.: Joint properties and earthquake behaviour of buildings made from dowel-laminated timber. Paper No 3379 in Proc., 16WCEE 2017, 16th World Conference on Earthquake Engineering, 09.-13.01.2017, Santiago de Chile.

[14] Mueller, A., Knoedel, P., Koelle, B.: Critical Filling Levels of Silos and Bunkers in Seismic Design. Paper no. 0464, Proc., 15 WCEE 15th World Congress on Earthquake Engineering, Lisbon 24-28.09.2012.

[15] Knoedel, P.: Lecture notes on Steel Construction at the University of Applied Sciences Augsburg, Germany. To be downloaded from

www.peterknoedel.de/lehre/lehre.htm, updated regularly from March 2007 to March 2013. Dynamik – Grundlagen (lineare Schwinger) (Dynamics – Basics – linear oscillators)

[16] Duffing, G.: Erzwungene Schwingungen bei veränderlicher Eigenfrequenz und ihre technische Bedeutung. Sammlung Vieweg Heft 41/42, Braunschweig 1918. (cited after [17])

[17] Petersen, Chr.: Dynamik der Baukonstruktionen. Vieweg, Wiesbaden, 1996.

[18] Nagel, S.: Studies on the Seismic Design of Network Arch Road Bridges. Master Thesis at KIT Steel and Lightweight Structures, Karlsruhe 2015.

[19] Köber, H., Stoian, M., Stefanescu, B.C.: Different Bracing Types in Seismic Resistant Structures. Paper 20-602 in EuroSteel 2014, 7th EUROpean conference on STEEL and Composite Structures, Naples, Italy, 10-12 September 2014.

[20] Knoedel, P. "Knoedel/Ummenhofer at Eurosteel Copenhagen; Mass Variation with dissipative Steel Structures under Seismic Loads; Background Document on FE Study" 12.03.2017, to be downloaded from http://www.peterknoedel.de/lehre/FHA-Stahl/Skript/GrA/Dyn/report-11_17-03-12.pdf.

[21] FEMA 440: Improvement of Nonlinear Static Seismic Analysis Procedures. Prepared by ATC Applied Technology Council (ATC-55 Project), Redwood City, California. Prepared for Dept. Homeland Security, Federal Emergency Management Agency, Washington D.C., June 2005.

[22] Gkatzogiannis, S., Knoedel, P., Ummenhofer, T.: FE welding residual stress simulation: Influence of boundary conditions and material models. Submitted to Eurosteel 2017, 8th European Conf. on Steel and Composite Structures. 15-17 September 2017, Copenhagen, Denmark. Paper no. 483 (submitted).

[23] Tappauf, C., Taras, A.: Deformation and Strain Histories in Shell-to-Base Joints of Unanchored Steel Storage-Tanks during Seismic Loading. 8th Int. Conf. on Behavior of Steel Structures in Seismic Areas, Shanghai, China, July 1-3, 2015.

[24] Knoedel, P., Nagel, S., Ummenhofer, T.: From 3-D time history simulation to lateral force method – a study on hand design rules. (in preparation)

[25] Knödel, P., Ummenhofer, T.: Regeln für die Berechnung von Behältern mit der FEM. Stahlbau 86 (2017), Heft 4. (Rules for calculating tanks and silos with FEM, in print)

[26] Knödel, P., Ummenhofer, T., Ruckenbrod, C.: Silos und Tanks. Kuhlmann, U. (ed.): Stahlbau-Kalender 2017, Ernst & Sohn, Berlin (in print).

COMPDYN 2017
6th ECCOMAS Thematic Conference on
Computational Methods in Structural Dynamics and Earthquake Engineering
M. Papadrakakis, M. Fragiadakis (eds.)
Rhodes Island, Greece, 15–17 June 2017

# NUMERICAL STUDY ON ELASTO-PLASTIC BEHAVIOR OF PIPE-SECTIONED PIER-PILE INTEGRAL STEEL STRUCTURE

**Takayuki Omori[1], Akira Kasai[2], and Rei Kohara[2]**

[1] Oriental Consultants Co., Ltd
3-12-1 Honmachi Shibuya-ku, -Tokyo, Japan
e-mail: ohmori@oriconsul.com

[2] Kumamoto University Graduate School of Science and Technology
2-39-1 Chuoku Kurokami, Kumamoto City, Japan
kasai@kumamoto-u.ac.jp, 164d8817@st.kumamoto-u.ac.jp

**Keywords:** Pire-Pile Integral Steel Structures, Compression Strength, Effective Buckling Length, Pipe Section, Residual Stress

**Abstract.** *Pier-Pile integral structures provide construction works with many environmental and landscape advantages. For example, the space required to construct these structures is smaller than that of other bridges due to the footing being removed, meaning that it is not necessary to greatly change the surroundings of these bridges. While there are environmental and landscape advantages, there are also a few demerits for the overall landscape designs, including demerits in the design of this proposed structure which consists of relatively slender parts. This proposed structure has already been constructed in areas where possibility of a severe earthquake is low. However, some problems that have yet to be examined are related to the use of this proposed structure in areas where earthquakes are frequent. Lacking detailed studies of its behavior during severe earthquakes, it is currently difficult to construct these structures in Japan. Consequently, it is necessary to investigate in detail limited performance about compression and bending moment, and earthquake-resistant performance of these structures in order to resolve these problems.*

*The authors had previously clarified the relationship between the rigidity of the ground and the effective buckling length, and the compressive strength of the Pier-Pile Integral Steel Structure. Moreover, we had proposed a simplified formula using a proposed characteristic value, and had revealed the relationship between effective buckling length and compressive strength of the Pier-Pile Integral Steel Structure.*

*In this paper, we verify the compressive strength after confirming the residual stress of the ERW (Electric Resistance Welded) pipes. Moreover, the relationship with the Euler curve and the load-bearing capacity curve of box-shaped cross-section from the Japanese standards is clarified.*

## 1 INTRODUCTION

Pier-Pile integral structures provide construction works with many environmental and landscape advantages. For example, the space required to construct these structures is smaller because there are no footings, which avoids changing topography and protects the landscape. Some examples of the use of Pier-Pile integral structures include the temporary gantry in Japan and the pedestrian bridge [1] in other parts of the world. (*Figure 1: Example of Pier-pile integral structure.*) However, construction of these structures presents a few problems. In particular, damaged areas cannot be identified after being subjected to a major earthquake. Therefore, it is currently difficult to construct these structures in Japan, a country where major earthquakes frequently occur. It is necessary to understand compression and bending behavior of these members, earthquake-resistant performance, and limit performance in detail in order to tackle these problems.




Figure 1: Example of Pier-pile integral structure.

In accordance with the Japanese standards [2; herein after Japan Standard II], piers are designed based on the capacity stress obtained from the load-bearing capacity curve after designing the slenderness ratio parameter $\bar{\lambda}$ from the effective length derived from boundary condition. However, in the case of Pier-Pile integral structures, it is hard to decide the effective buckling length for calculating slenderness ratio parameter $\bar{\lambda}$ as the lower part of the pier is supported by springs. Although the effective buckling length can be calculated from the beam theory on the elastic floor, it is unsuited for practical design due to its inconvenience.

In addition, the load-bearing capacity curve of the Pier-Pile integral structure supported by the springs at the lower part is different from the application condition of the load-bearing capacity curve shown in the Japan Standard, so its applicability is unclear.

In view of this background, this paper aims to clarify the relationship between the effective buckling length of the Pier-Pile integral structure and characteristic value $\beta$ specified in the Japanese standards [3; herein after Japan Standard IV]. Furthermore, the load-bearing capacity curve of the pier-pile integral structure with residual stress is to be verified.

In this paper, the aerial part and the underground part of the Pier-Pile integral structure are referred to as "pier" and "pile" respectively.

## 2 THE EFFECTIVE LENGTH OF THE PIER-PILE INTEGRAL STRUCUTRE

### 2.1 The target structure of the study

The target structure of this study is a single column pier with its lower part supported by spring. Figure 2: A single column pier with lower part supported by spring. It consists of a steel pipe section with an outer diameter of $D$=500mm, which is the standard size, and a thickness of $9 \leqq t \leqq 25$mm, made of SKK490 material as ERW (Electric Resistance Welded) pipes. Young's modulus of the steel is set to $E$ = 200GPa and Poisson's ratio $\mu$=0.3. The length of a pier is satisfied with the slenderness ratio of $l/r \leqq 120$ ($l=Kl_e$, $K$=1=effective length factor, $l_e$=length of a pier $h$, $r$= cross-section secondary radius); slenderness ratio parameter $\bar{\lambda}$ is calculated with the following formula (1).

$$\bar{\lambda} = {}^{1}\!/_{\pi} \sqrt{{}^{\sigma_y}\!/_{E}}\, {}^{l}\!/_{r} \tag{1}$$

Herein, $\pi$ is the circumference ratio; $\sigma_y$ is the yield stress of material.

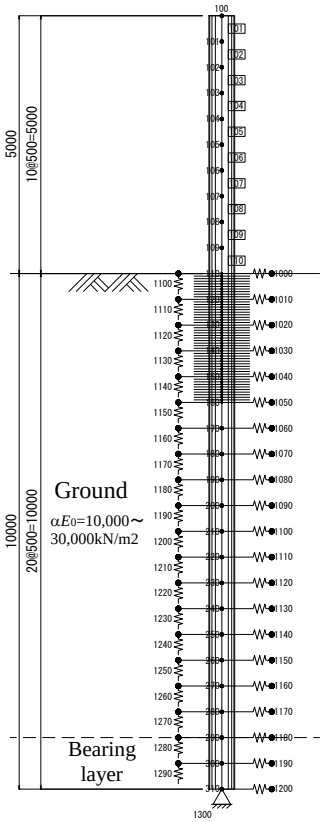


Figure 2: A single column pier with lower part supported by spring.

As it conforms to the Japan Standard IV, the length of pile was set at 10m, based on $\beta L_e >$ 3, a semi-infinite-length pile. The ground rigidity is $10\text{MN/m}^2 \leqq \alpha E_0 \leqq 300\text{MN/m}^2$. The test cases are shown in Table 1 in the form of PP $h$(m)-$t$(mm)- $\alpha E_0$ (MN/m2). Table 1: *Test cases.*

Table 1: Test cases.

| CASE | $h$(m)/$L$(m) | | | diameter and thickness(mm) | | | | ground rigidity $\alpha E_0$(MN/mm$^2$) | | | | | | |
|---|---|---|---|---|---|---|---|---|---|---|---|---|---|---|
| | 1/10 | 5/10 | 10/10 | $\Phi$500 | | | | 10 | 50 | 100 | 150 | 200 | 250 | 300 |
| | | | | $t$=9 | $t$=14 | $t$=19 | $t$=25 | | | | | | | |
| PP1-9-* | ○ | | | ○ | | | | ○ | ○ | ○ | ○ | ○ | ○ | ○ |
| PP1-14-* | ○ | | | | ○ | | | ○ | ○ | ○ | ○ | ○ | ○ | ○ |
| PP1-19-* | ○ | | | | | ○ | | ○ | ○ | ○ | ○ | ○ | ○ | ○ |
| PP1-25-* | ○ | | | | | | ○ | ○ | ○ | ○ | ○ | ○ | ○ | ○ |
| PP5-9-* | | ○ | | ○ | | | | ○ | ○ | ○ | ○ | ○ | ○ | ○ |
| PP5R-9-* | | ○ | | ○ | | | | ○ | ○ | ○ | ○ | ○ | ○ | ○ |
| PP5-14-* | | ○ | | | ○ | | | ○ | ○ | ○ | ○ | ○ | ○ | ○ |
| PP5-19-* | | ○ | | | | ○ | | ○ | ○ | ○ | ○ | ○ | ○ | ○ |
| PP5-25-* | | ○ | | | | | ○ | ○ | ○ | ○ | ○ | ○ | ○ | ○ |
| PP10-9-* | | | ○ | ○ | | | | ○ | ○ | ○ | ○ | ○ | ○ | ○ |
| PP10-14-* | | | ○ | | ○ | | | ○ | ○ | ○ | ○ | ○ | ○ | ○ |
| PP10-19-* | | | ○ | | | ○ | | ○ | ○ | ○ | ○ | ○ | ○ | ○ |
| PP10-25-* | | | ○ | | | | ○ | ○ | ○ | ○ | ○ | ○ | ○ | ○ |

## 2.2 Analysis model and method

The analysis model is shown in Figure 2.

A hinged end is adopted as the boundary conditions of a pile tip. The pile part is installed with ground springs in horizontal and vertical directions. The ground spring is calculated by the formula based on the Japan Standard IV.

$$k_H = k_{H0}\left(B_H/_{0.3}\right)^{-3/4} \tag{2}$$

$$k_{H0} = 1/_{0.3}\,\alpha E_0 \tag{3}$$

$$B_H = \sqrt{D/_{\beta}} \tag{4}$$

$$\beta = \sqrt[4]{k_H D/_{4EI}} \tag{5}$$

Herein $k_H$=horizontal subgrade reaction coefficient, $k_{H0}$=horizontal subgrade reaction coefficient corresponding to the value of the plate loading test, and $B_H$=A is the conversion loading width of the foundation. Effective buckling length $l_{cr}$ is determined from the eigenvalue analysis. In the analysis, an axial force of $N$ = 1 kN is added to the head of the pier. Then, the primary eigenvalue $\omega$ is obtained by calculating the following formula.

$$l_{cr} = \pi\sqrt{EI/_{\omega N}} \tag{6}$$

Herein $EI$ = the flexural rigidity of the steel pipe.

## 2.3 The relationship between the characteristic value BETA and the effective buckling length of the pile

The effect that the rigidity difference between the ground and the pile has on the effective buckling length $l_{cr}$ is shown in Figure 3. Figure 3: Relationship between the effective buckling length and $\beta h$. The vertical axis shows the dimensionless value resulting from dividing the

effective buckling length $l_{cr}$ by the effective buckling length $l_{cr}$ '= 2$h$ when the lower end is fixed. The horizontal axis shows the non-dimensional value resulting from multiplying a pier length h and the characteristic value $\beta$ of the ground.

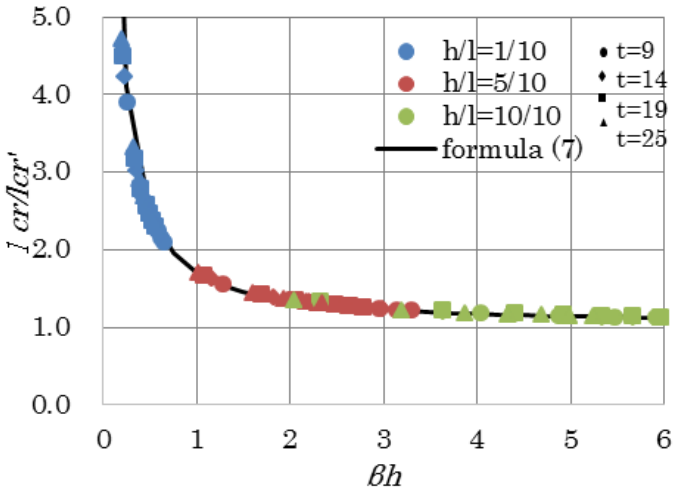


Figure 3: Relationship between the effective buckling length and $\beta h$.

From Figure 3, it can be confirmed that as $\beta h$ increases, namely due to the increase in rigidity of the soil, effective buckling length can be confirmed to approach $l_{cr}$ '. In addition, the relationship of effective buckling length $l_{cr}$ and $\beta h$ is represented as a continuous curve independent of the pier length and thickness. From the above, the effective buckling length $l_{cr}$ of pier-pile Integral structures is confirmed to be represented by the function of $\beta h$.

The authors have indicated that the buckling mode of the pier is convex in the vicinity of the point of $M_{max}$ and that effective buckling length of the Pier-Pile steel structure is indicated by equation (7), which is twice the length of the Chang equation, $l_m$ [3] + h.[4]

$$l_{cr} = 2\alpha_1 \left[ h + {}^{1}/_{\beta} \tan^{-1} \left\{ {}^{1}/_{(1+2\alpha_2 \beta h)} \right\} \right] \quad (7)$$

The variation confirmed in Figure 3 is assumed to be due to the accuracy of analysis α1, and the correlation factor α2 between the dimensionless quantity $\beta h$ that affect the deformation mode. Herein when the factors are given as $\alpha 1$=1.05 and $\alpha 2$=0.1, the estimated line of (7) is consistent with the analytical value of Figure 3. It should be noted that the correlation function is 0.999, and the standard deviation is 0.042.

## 3 COMPRESSION CAPACITY OF PIER-PILE INTEGRAL STRUCTURES

### 3.1 Analysis model and method

Using an analysis model, the Pier-Pile integral structures are studied to research the load-bearing capacity through axial compression analysis. Since this time the subject of study is the buckling of the entire structure, the results from the beam element model used previously in this study were utilized. Compression analysis was conducted for all test cases shown in Table 1.

It is confirmed that the mechanical properties of ERW (Electric Resistance Welded) pipes are higher in yield ratio than the SM material, and the secondary gradient after yield is small [5]. This study focuses on the rigidity relationship between the ground and the piles and the entire buckling phenomenon in the elastic reasion when the effective buckling length

increases. Therefore, the mechanical property of this material is as shown in Figure 4; the yield stress is set to 315N/mm$^2$, and secondary gradjent is level.

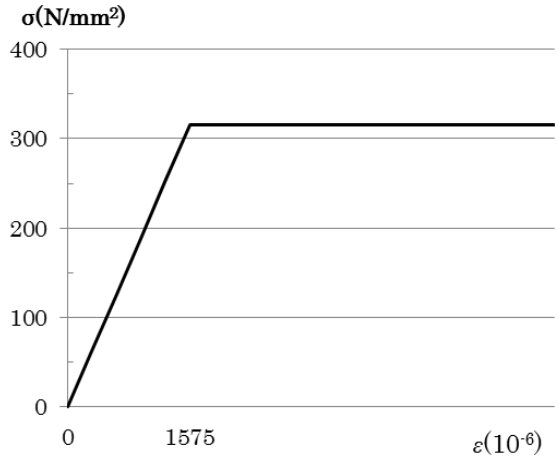


Figure 4: Stress strain curve.

### 3.2 Distribution of residual stress

The residual stress of ERW pipes is mainly installed in the working process in order to adjust the shape of the product and during the plastic working in the manufacturing process of the pipe. Since the welding heat input of the ERW pipe is extremely small, there is no large tensile residual stress occurring at the welding position. Therefore, residual stress is introduced based on the Aoki method [5] which evaluated residual stress distribution in ERW pipes. Aoki's team evaluated the equivalent axial residual stress $\sigma_{req}$ derived from the residual stress acting in the circumferential direction and the axial direction respectively, from the residual strain of the ERW pipe measured by the experiment. Equivalent residual stress $\sigma_{req}$ is defined by equation (8), and the experimental results are measured inside and outside of the ERW pipe, so that the equivalent residual stress is defined in two cases as inside and outside.

$$\sigma_{req} = \bar{\sigma}_x - \left( 0.5\bar{\sigma}_\varphi \pm \sqrt{1.0 - 0.75\bar{\sigma}_\varphi{}^2} - 1.0 \right) \tag{8}$$

The residual stress $\sigma_{req}$ is shown in Figure 5 as the average value of the inside and outside. The horizontal axis is indicated as the distribution in the circumferential direction, the vertical axis is indicated as the dimensionless value obtained by dividing the residual stress by the yield stress. It is confirmed that the residual stress is distributed on the compression side by an average of about 5% on the yield stress. To briefly express the equivalent residual stress distribution ($\sigma_{req}$), assume that the residual stress is given at 36 points on the circumference and the i-th value of is $\sigma_{ri}$ and the amplitudes are $A_n$, $B_n$, $x_i$ = 1/36, 2/36, ... 36/36; it is defined in accordance with equation (9).

$$\sigma_{ri} = \sum_{j=1}^{n} A_n cos2n\pi x_i + \sum_{j=1}^{n} B_n sin2n\pi x_i \tag{9}$$

In equation (9), coefficients are found by the least squares Fourier decomposition, and when coefficients are obtained using $n$ = 4, 8, 16, $\sigma_{ri}$ is as shown in Figure 9. The solid line shows $n$=4, the dot-dash line is representative of $n$=8, and the double-dots and dash line shows $n$=16. It should be noted that the correlation function is 0.95 (n=4), 0.97 (n=8), 0.99 (n=16). In this study, the equivalent residual stress obtained when $n$=4 is introduced, and two cases, with and without residual stress, are conducted.

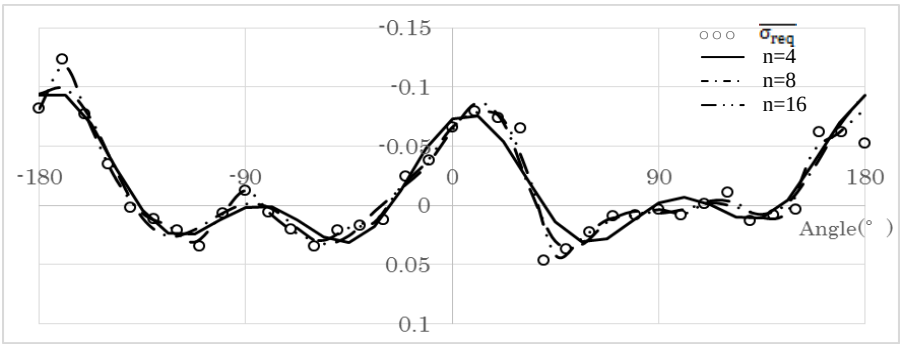


Figure 5: Residual stress distribution of ERW pipe

### 3.3 The initial deformation

The initial deflection of the Pier-Pile integral structure could be considered as that in the product phase or in the construction phase. In this paper, the aim is to investigate the influence of ground rigidity on the load carrying capacity of the pier-pile integral structure. Therefore, a horizontal displacement of ($h$+1) /1000 is given to the head of pier, and an initial deformation is given so that it becomes the deformation of the primary mode which is provided by eigenvalue analysis. The primary mode is shown in Figure 6.

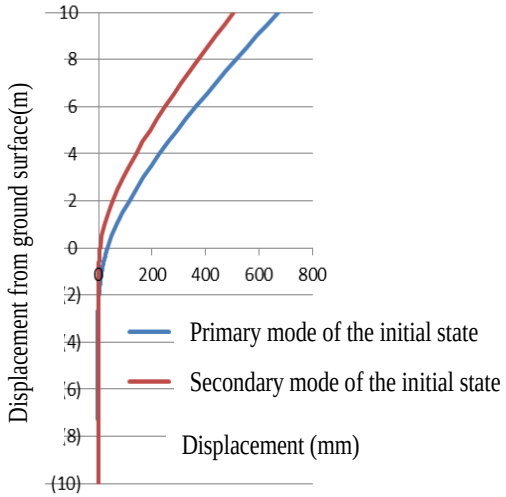


Figure 6: The primary mode of the pier-pile integral structure.

### 3.4 *P-δ* curve

The analysis result is shown in Figure 7 as the *P-δ* curve of the pier top.

It is confirmed from Figure 7 that as the length of the pier increases, the load carrying capacity decreases. In cases where the pier length is the same, it could be seen that the peak value also decreases as the rigidity of the ground decreases. It should be noted that there is almost no difference in load carrying capacity regardless of the the presence or absence of residual stress .

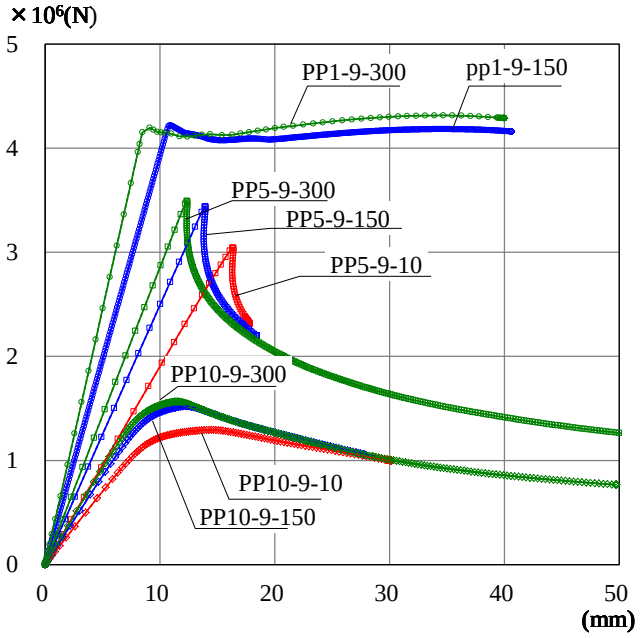


Figure 7: *P*-$\delta$ curve.

### 3.5 Load-bearing capacity curve

The load-bearing capacity curve is shown in Figure 8. The vertical axis represents $\sigma_{cr} / \sigma_y$ , that is the dimensionless value generated by dividing generated stress $\sigma_{cr}$ by $\sigma_y$, the yield stress of material which divides the peak of *P* shown in Figure 7 by a cross-sectional area. And the horizontal axis represents the slenderness ratio parameter. The graph shows the Euler curve; the load-bearing capacity curve of non-prescribed welded box-shaped cross-section from the Japan standard [2], here named curve (a); and the load-bearing capacity curve of the welded box-shaped cross-section, here named curve (b).

The buckling load force curve in each case has a larger load bearing capacity than curve (a) and (b). It should be noted that there is almost no difference due to the the presence or absence of residual stress.

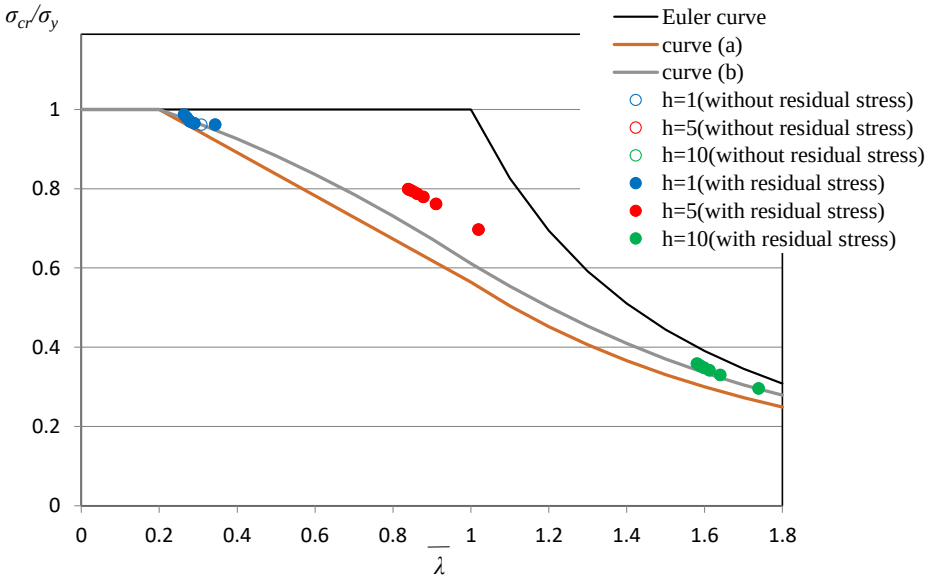


Figure 8: Load-bearing capacity curve.

## 4 CONCLUSIONS

The following items were revealed in this study.

- Effective buckling length $l_{cr}$ of Pier-Pile integral steel structures can be defined by the simple formula $\beta h$.
- The influence of the residual stress on load-bearing capacity of Pier-Pile integral structures is extremely small.
- The load-bearing capacity of Pier-Pile integral structures is slightly larger than the one of Japan Standard II even if including residual stress.

## REFERENCES

[1] schlaich bergermann partner: Award for the footbridge to Le Mont Saint-Michel in France,2016.2. ( http://www.sbp.de/en/news/award-for-the-footbridge-to-le-mont-saint-michel-in-france-1/).

[2] SPECIFICATIONS FOR HIGHWAYBRIDGES PART2 STEEL BRIDGES, Japan Road Association, 2014.

[3] SPECIFICATIONS FOR HIGHWAYBRIDGES PART4 SUBSTRUCTURES, Japan Road Association, 2014.

[4] Takayuki Omori, Akira Kasai, Rei Kohara(2016): Numerical Study on Seismic Performance of Pier – Pile Integral Steel Structures with Pipe Section, The 11th Pacific Structural Steel Conference, pp.1149-1154.

[5] Tetsuhiko AOKI, Yuhshi Fukumoto: STOCASTIC MATERIAL PROPERTIES AND ESTIMATE OF RESIDUAL STRESSES OF COLD-FORMED-WELDED STEEL TUBULAR MEMBERS WITH SMALL DIAMETER, Proceedings of JSCE, No. 314, pp. 39-51, Oct., 1981.

COMPDYN 2017
6th ECCOMAS Thematic Conference on
Computational Methods in Structural Dynamics and Earthquake Engineering
M. Papadrakakis, M. Fragiadakis (eds.)
Rhodes Island, Greece, 15–17 June 2017

# FINITE ELEMENT ANALYSES ON SEISMIC RESPONSE OF PARTIAL STRENGTH EXTENDED STIFFENED JOINTS

**Roberto Tartaglia[1], Mario D'Aniello[1], Raffaele Landolfo[1], Gian Andrea Rassati[2] and James Swanson[2]**

[1] University of Naples 'Federico II',
Department of Structures for Engineering and Architecture
Via Forno Vecchio 36, Naples 80134, Italy
Roberto.tartaglia@unina.it, mdaniel@unina.it, landolfo@unina.it

[2] University of Cincinnati,
Department of Civil and Architectural Engineering and Construction Management
765 Badwin, Cincinnati OH 45221
rassatga@ucmail.uc.edu , swansojr@ucmail.uc.edu

**Keywords:** Free from damage joints, Steel structures, Finite element analyses, Seismic design.

**Abstract.** *Extended stiffened end-plate bolted joints are widely used in seismic resistant steel frames. In the United States (US) this type of joint is seismically pre-qualified according to AISC 358. In Europe within the framework of the ongoing EQUALJOINT research project, prequalification criteria for different types of bolted joints are under development. Differently from the US approach, in the EQUALJOINT procedure both full and partial strength joints are seismically qualified. The experimental tests carried out within the EQUALJOINT project confirmed the effectiveness of these intermediate strength levels. Therefore, the aim of this work is investigate the possibility to extend this design approach to US joints. The results of a comprehensive parametric finite element investigation are described and discussed, showing the effectiveness of the proposed design performance criteria.*

# 1 INTRODUCTION

Extended stiffened end-plate bolted (ESEPB) joints are widely used in seismic resistant moment resisting frames. In United States of America (USA) ESEPB joints are seismically prequalified according to the requirements of AISC 358-16 [1]. The prequalification rules are based on the former studies carried out by [2-5].

In Europe, the current version of the Eurocodes (i.e. EN1993:1-8 [6] and EN1998-1 [7]) do not provide either specific requirements or codified prequalification procedures for seismic resistant extended stiffened end-plate joints. Recently, design criteria for seismic resistant ESEPB joints have been developed by D'Aniello et al. [8] within the framework of the EQUALJOINTS research project [9] (hereinafter referred as "EJ" for brevity sake). In particular, D'Aniello et al. [8] revised the ductility criterion of EN1993:1-8 [6] (which was conceived for non-seismic applications) in light of capacity design principles recommended by Eurocode 8 [7] and developed a novel design equation aiming at avoiding type 3 failure mode (i.e. failure of bolts) and enforcing ductile behaviour of ESEPB joints, as well. This purpose is fulfilled by controlling the thickness of the end-plate with respect to the diameter of bolts and accounting for both the material randomness and hardening of the weaker joint components. The introduction of ductility requirements as well as the revision of local hierarchy requirements allow using partial strength ESEPB joints for seismic applications. In common practice, stiffened joints are generally considered as full strength. However, partial strength ESEPB joints can be profitably used either in dual frame structures (e.g. MRFs + CBFs), where it is more convenient to have rigid joints accepting the damage of the connections, or in MRFs mostly designed to satisfy drift and/or stability checks [10]. In such cases, ESEPB joints are more efficient than unstiffened end-plate joints. In Europe, partial strength dissipative joints can be used provided that adequate ductility of the connection is verified, namely 0.035 rad for high ductility and 0.025 rad for moderate ductility. On the contrary, in United States of America the seismically prequalified joints are conceived to have full strength connections, as recommended by AISC 358-16 [1].

The aim of this study is to examine if relaxing the strength requirements of AISC358-16 [1] the US joints can provide adequate ductility to be adopted as dissipative partial strength or if it is necessary to introduce ad-hoc criteria as done in [8]. The paper is organized into two main parts. In the first part, the main differences between American (US) and European (EJ) design procedures are described and compared. Then, to point out their differences and effectiveness an example of two joints designed according to both the approaches is investigated by means of finite element analyses.

# 2 DESIGN PROCEDURE

## 2.1 EQUALJOINTS procedure

The seismic design of steel structures, in accordance with the EN1998-1-1 [7] philosophy, is based on the concept of dissipative structures that are designed to develop plastic deformations in specific zones, while the non-dissipative parts should resist elastically the seismic action in order to avoid brittle collapse [10-16]. This behaviour can be obtained imposing that the dissipative zones are the weaker and the non-dissipative are designed to resist the ultimate strength developed by the dissipative elements. The proposed design criteria extends this philosophy to the joints, by establishing a hierarchy among the strengths of macro-components (e.g. the web panel, the connection, the beam as shown in Figure 1, and their sub-components (e.g. end-plate, bolts, welds, etc.), as well.

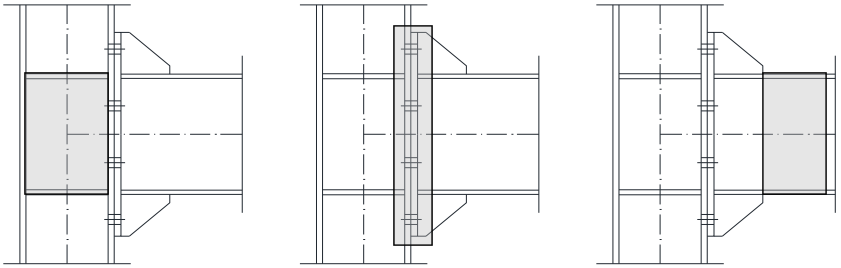

Figure 1 Plastic zones: a) web panel, b) connection and c) beam

The capacity design is applied between each macro-component in order to obtain two different design objectives defined comparing the joint (i.e. web panel and connection) strength to the beam flexural resistance, namely: full and equal strength. In the first case, the joint is designed to be more resistant respect to the beam, in order to concentrate all the plastic deformation in the connected element. On the other hand, equal strength joints are designed to have a balanced strength between the connection and the beam bending capacity; in this way, the plastic deformation should invest both the joint and the beam.

The capacity design requirements to obtain the required joint behaviour can be guaranteed by satisfying the following inequality:

$$M_{wp,Rd} \geq M_{j,Rd} \geq M_{j,Ed} = \alpha \cdot (M_{B,Rd} + V_{B,Ed} \cdot s_h) \quad (1)$$

Where $M_{wp,Rd}$ is the flexural resistance corresponding to the strength of column web panel; $M_{j,Rd}$ is the flexural strength of the connection; $M_{j,Ed}$ is the design bending moment at the column face; $M_{B,Rd}$ is the plastic flexural strength of the connected beam; $s_h$ is the distance between the column face and the tip of the rib stiffener; $V_{B,Ed}$ is the shear force corresponding to the occurring of the plastic hinge in the connected beam.

The α factor depends on the design performance level. In case of non-dissipative joints it is equal to $\gamma_{sh} \times \gamma_{ov}$ (being $\gamma_{sh}$ is the strain hardening factor corresponding to the ratio between the ultimate over the plastic moment of the beam [1, 17-21], while $\gamma_{ov}$ accounts for material randomness, depending on the steel grade [7]).

In case of dissipative joints $\alpha \leq 1$, thus accepting that the joint is weaker than the connected beam provided that adequate ductility is guaranteed. In particular, within EQUALJOINTS project [9] different levels of partial strength joints are considered depending on both the strength of the connection and the resistance of column web panel. Differently from the codified definitions of current EC3-1-8 [6], which consider as "partial strength" all connections with resistance smaller or at least equal to the strength of the beam, in EQUALJOINTS the connection with strength equal to the strength of the connected beam (i.e. $\alpha = 1$ ) is defined as "Equal Strength". If the strength of the connection is lower it is referred as the "Partial Strength", with a fixed threshold of resistance $\alpha = 0.8$ that corresponds to the lower bound limit to qualify the strength of joints in special moment resisting frames according to AISC341-16 [1].

The column web panel can be strong, balanced or weak depending on its strength compared to the strength of the dissipative zone, which is the connection for both equal and partial strength connections. Hence, based on these considerations, Equation (1) can be rearranged for dissipative joints as follows:

$$M_{wp,Rd} > M_{j,Rd} \geq M_{j,Ed} = \alpha \cdot (M_{B,Rd} + V_{B,Ed} \cdot s_h) \quad (2)$$

$$M_{wp,Rd} = M_{j,Rd} \geq M_{j,Ed} = \alpha \cdot (M_{B,Rd} + V_{B,Ed} \cdot s_h) \quad (3)$$

$$M_{j,Rd} \geq M_{wp,Rd} \geq M_{j,Ed} = \alpha \cdot (M_{B,Rd} + V_{B,Ed} \cdot s_h) \tag{4}$$

In order to enforce the most ductile behavior of dissipative joints, the connection should be designed to avoid any brittle failure mode. Starting from the component method [6], the attention focuses on the response of the equivalent T-Stub per bolt row. With this regard, it is well known that the resistance of the equivalent T-stub can be evaluated as the minimum of the corresponding three failure modes, as illustrated in Figure 2, which are described as it follows:

- Mode 1 is characterized by the plasticization of the flange, whereas the bolts are not involved in the failure mechanism.
- Mode 2 is characterized by the combined flange plasticization and failure of the bolts.
- Mode 3 is characterized by the failure of the bolts and it does not involve any plastic engagement of the T-stub flange.

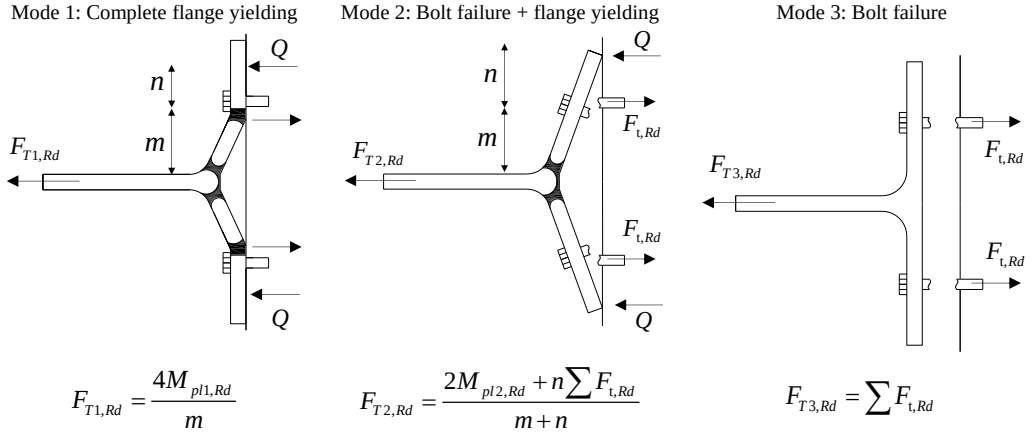


Figure 2 Failure mode of bolted T-Stub

Therefore, the joint ductility depends on the type of failure mode and the corresponding plastic deformation capacity of the activated component. Figure 3 concisely depicts the dependency of the failure mode with the geometric properties and end-plate to bolt strength ratio [6]. In abscissa is reported the ratio β between the flexural strength ($M_{pl,Rd}$) of the plates, or column flanges, and the axial strength of the bolts ($F_{t,Rd}$), while the vertical axis reports the ratio η between the T-stub strength ($F$) over $F_{t,Rd}$.

In line with Fig. 3, two possible ductility criteria can be adopted to avoid mode 3, namely:

Level-1: $\beta < 1$ this condition imposes either a failure mode I or failure mode II (but very close to mode I), which provides very high ductility.

Level-2: $\beta < 2$ and $\eta < 0.95$, this condition imposes a failure mode II with limited ductility, but avoiding brittle failure.

The level of ductility to be guaranteed obviously depends on the design performance objectives. It is crucial providing the larger ductility for equal strength, less for full strength joints.

As for the rotational capacity of the joint, EN1993:1-8 [6] requires that $M_{j,Rd}$ to be less than 1.2 $M_{B,pl,rd}$ and two alternative ways can be pursued: 1) performing experimental tests; 2) controlling the thickness t of both end-plate and column flange. Therefore, in line with the Component method [6], also the hereby proposed design criteria introduces a limitation for the plate thickness respect to the bolt diameter:

$$t \le \frac{0.42 \cdot d}{\sqrt{\gamma_{ov} \cdot \gamma_{sh}}} \cdot \sqrt{\frac{\gamma_{M0} \cdot f_{ub}}{\gamma_{M2} \cdot f_y}} \simeq 0.30 \cdot d \cdot \sqrt{\frac{f_{ub}}{f_y}} \tag{5}$$

Where $d$ is the nominal bolt diameter, $f_y$ is the yield strength of the relevant basic component and $f_{ub}$ is the bolt ultimate strength. Moreover, another verification on the bolts strength was introduced, in order to verify each line resistance with respect to the one of the bolts:

$$F_{t,Rd} \ge \gamma_{ov} \cdot F_{p,Rd} \tag{6}$$

Where $F_{t,Rd}$ is the resistance of the bolts in tension and $F_{p,Rd}$ is the resistance of the entire line. It is important to highlight that all criteria previously described require that the failure of the welds has to be unquestionably avoided, because of their brittle collapse mechanism.

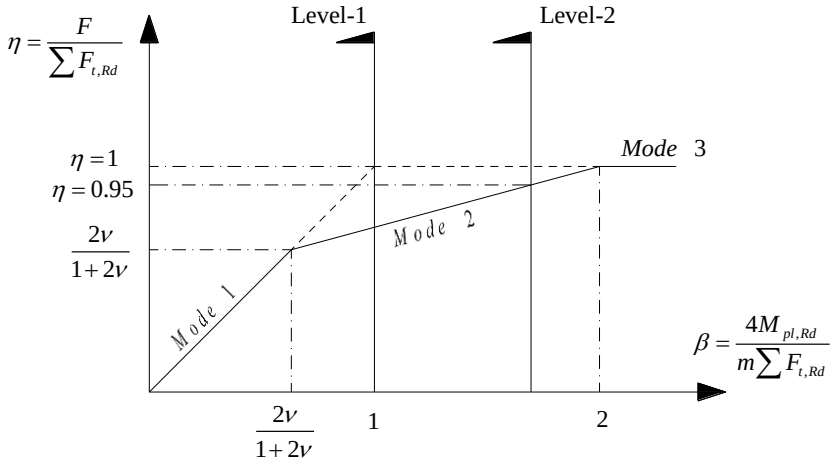


Figure 3 T-Stub resistance and corresponding failure mechanism [6]

## 2.2 AISC358 procedure and its extension to partial strength joints

AISC 358-16 [1] considers hierarchy of resistances between the beam and the connection, but not clearly between the connection and column web panel. A substantial difference between AISC 358-16 [1] and EQUALJOINTS [8, 9] procedure is the way to compute the resistance of the end-plate. Thus, starting from the equivalent T-stub theory implemented in EN1993:1-8 [6], EJ procedure [8,9] evaluates the resistance of each active bolt row (namely, the two bolt rows above and the one below the beam flange in tension) in function of the length of its corresponding yielding line. On the contrary, American procedure [1] directly provides the length of the yield line based on the adopted joint configuration (i.e. for both 4 bolts and 8 bolts configuration).

AISC 358-16 [1] does not introduce specific requirements considering that the extended stiffened joints are conceived to be theoretically full strength, without experiencing plastic deformations. Therefore, the limitations on both minimum bolt diameter and thickness of end-plate are given separately and solely related to a strength verification against the design bending moment at the column face $M_f$, which is similar to $M_{j,Ed}$ of Eq. (1) and defined as follows:

$$M_f = M_{pr} + V_u \cdot s_h = M_{pr} + \left( \frac{2M_{pr}}{L_h} + V_{gravity} \right) \cdot s_h \tag{7}$$

Where $M_f$ is the probable flexural resistance of the beam (i.e. calculated considering the average steel yield stress magnified to account for strain hardening of the plastic hinge); $s_h$ is the distance between the column face and the tip of the rib stiffener; $V_{gravity}$ is the shear force due to gravity load and $L_h$ is the distance between the plastic hinges.

The AISC 358-16 [1] limitations on the minimum diameter for bolts are given as follows:

For bolt row line (4E and 4ES): $$d_{b,required} = \sqrt{\frac{2M_f}{\pi\phi_n F_{nt}\left(h_0 + h_1\right)}} \tag{8}$$

For bolt row line (8E and 8ES): $$d_{b,required} = \sqrt{\frac{2M_f}{\pi\phi_n F_{nt}\left(h_1 + h_2 + h_3 + h_4\right)}} \tag{9}$$

where $F_{nt}$ is the nominal tensile strength of a bolt; hi is the distance from the centerline of the beam compression flange to the centerline of the i-th tension bolt row; ho is distance from the centerline of the compression flange to the tension-side outer bolt row. The minimum thickness for the end plate and the column flange should comply the following requirements:

minimum thickness of the end-plate: $$t_{p,required} = \sqrt{\frac{1.11M_f}{\phi_d F_{yp} Y_p}} \tag{10}$$

minimum thickness of the column flange: $$t_{cf} \geq \sqrt{\frac{1.11M_f}{\phi_d F_{yc} Y_c}} \tag{11}$$

where $F_{yp}$ is the specified minimum yield stress of the end-plate material; $Y_p$ is the end-plate yield line mechanism parameter given from the relevant Tables 6.2, 6.3 or 6.4 of AISC358-16 [1]. $F_{yc}$ is the specified minimum yield stress of the column flange material; $Y_c$ is the unstiffened column flange yield line mechanism parameter from the relevant Tables 6.5 or 6.6 of AISC358-16 [1].

In the light of AISC design procedure, either equal or partial strength joints can be designed assuming $M_f^* = \alpha M_f$, as assumed in Section 2.1. In addition, Equation (10) and (11) can be further revised assuming $\phi_d$=1.

In order to investigate the influence of the revised criteria and to compare with EQUALJOINTS procedure, two beam-to-column joints were designed alternatively according the two approaches and their nonlinear response was examined by means of finite element (FE) analyses.

The geometrical features of ESEPB joints and the relevant parameters are reported in Table1 and in Fig. 4.

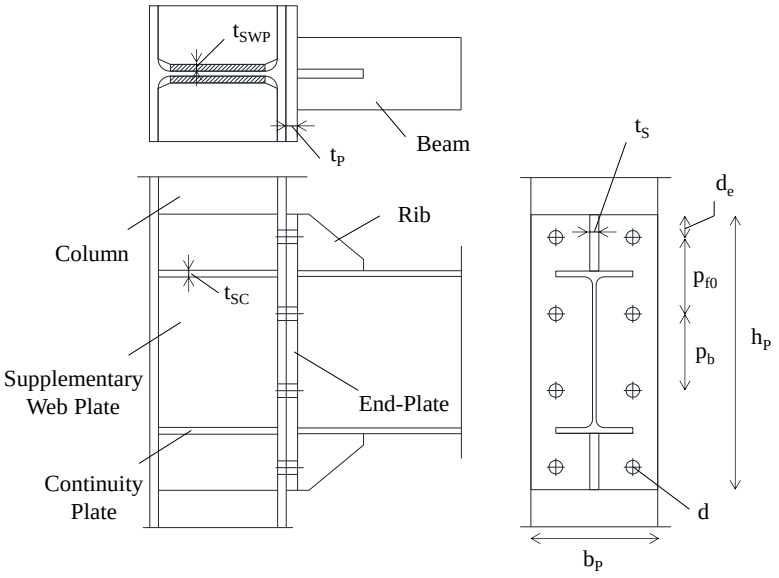


Figure 4 Joint geometry [8]

Table 1 Features of the examined joints

| Design | Column | Beam | Bolt Rows | End-Plate | | | | | | | CP | SWP | | Rib | |
|---|---|---|---|---|---|---|---|---|---|---|---|---|---|---|---|
| | | | | Bolt | $b_P$ | $h_P$ | $t_P$ | $d_e$ | $p_{f0}$ | $p_b$ | $t_{SC}$ | n | $t_{SWP}$ | Slope | $t_S$ |
| | | | | [mm] | [mm] | [mm] | [mm] | [mm] | [mm] | [mm] | [mm] | [-] | [mm] | [-] | [mm] |
| AISC-Rev | W14×53 | W14×38 | 4 | 25.4 | 205 | 549 | 19 | 44 | 115 | 231 | 13 | 1 | 16 | 30° | 12.7 |
| Equaljoints | HE 280 B | IPE 360 | 4 | 30 | 280 | 600 | 16 | 50 | 75 | 160 | 15 | 0 | 0 | 40° | 20 |

Table 1 Features of the examined joints

## 3 FINITE ELEMENT ANALYSES

### 3.1 Modelling assumptions

Finite element analyses (FEAs) were carried out using ABAQUS 6.14 [23]. The beam-to-column joints were modelled considering a sub-assemblage obtained by extracting the beam and the column at the inflection points of the bending moment diagram induced by lateral loads on the reference MRF. Therefore, according to the sub-structuring procedure the horizontal and vertical displacements are restrained at the column extremities, while a displacement history is applied at the beam tip (see Figure 5).

Moreover, lateral torsional restrains are introduced in the FE model to simulate the beneficial effect of the slab on the beam.

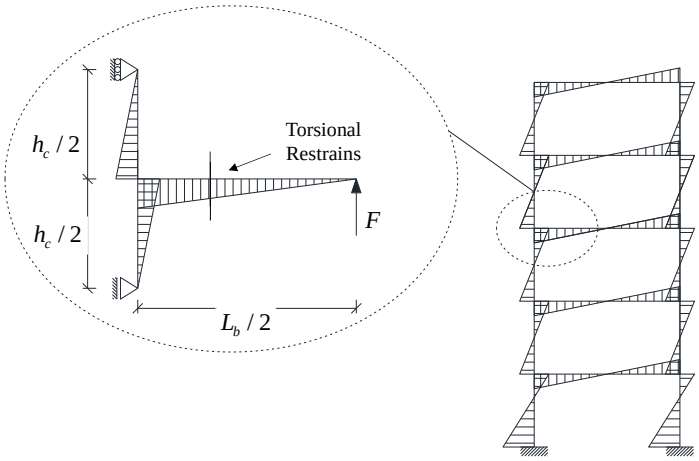


Figure 5 Joint geometry sub-structuring [8]

The material non linearity was considered applying a true stress-true strain curve coming from coupon tests performed during experimental tests carried out within the EQUALJOINTS research project [9]. Geometrical non linearity was neglected to focus the attention only on the joint behaviour, disregarding the beam imperfections.

C3D8I element (i.e. 8-node linear brick, incompatible mode) was adopted for meshing of all parts constituting the joint, i.e. column, beam, plates, bolts and welds.

Three type of contact were introduced in the FE model, as follows:

- "Hard" contact: to model the normal contacts;
- Coulomb friction with friction coefficient equal to 0.3 for tangential behaviour;
- "Surface-to-surface" interaction: to model the contacts between adjacent surfaces.

S355 steel material, with average yield stress as recommended by EN1998-1 [7], was used for the beam, column, and plates constituting the European joints; while ASTM A992 steel with average as recommended by AISC 341-10 [23].

The Von Mises yield criterion was adopted to model steel yielding; plastic hardening was simulated using both nonlinear kinematic and isotropic hardening law on the basis of the data provided by Dutta et al. [24]. Both fillet and full penetration welds were modelled as elastic perfectly plastic material [25, 26].

The material of European high strength bolts is modelled as described by [27], while for American bolts the assumptions given by [28] were considered.

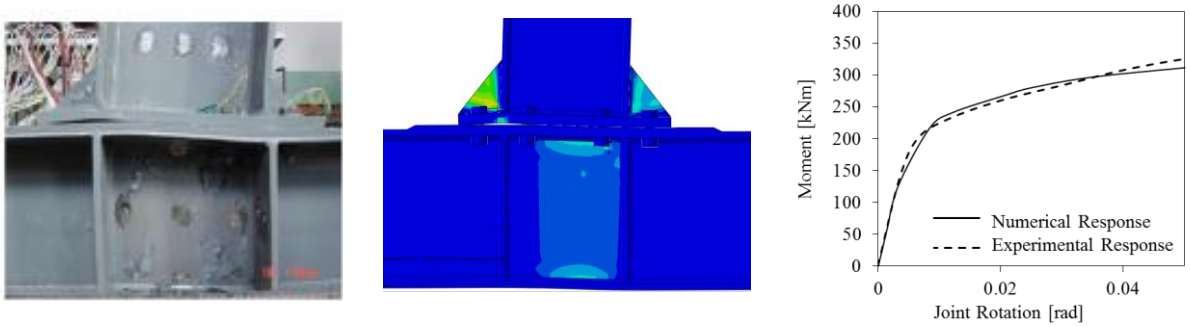


Experimental result PEEQ distribution Moment rotation curves

Figure 6 Experimental tests performed by Shi et al. [29] compared with finite element simulation

The FEM assumptions were validated against one of the experimental tests carried out by Shi et al. [29]. Figure 6 depicts the comparison between numerical and experimental results in

terms of joint moment rotation curves and distribution of the equivalent plastic deformation (PEEQ). As it can be noted the FEM modelling procedure is able to catch both the initial elastic stiffness and the resistance; moreover also the distribution of the plastic deformation between the experimental tests and the FEM model are comparable [30].

### 3.2 Numerical Results

The differences between both the beam and the column steel profile of the two investigated beam-to-column assemblies are negligible. Even the values of the yield stress of the steel profiles are very similar.

The results obtained from FEAs show that both stiffness and resistance of the two assemblies are very similar. However, significant differences can be noted in terms of failure mode.

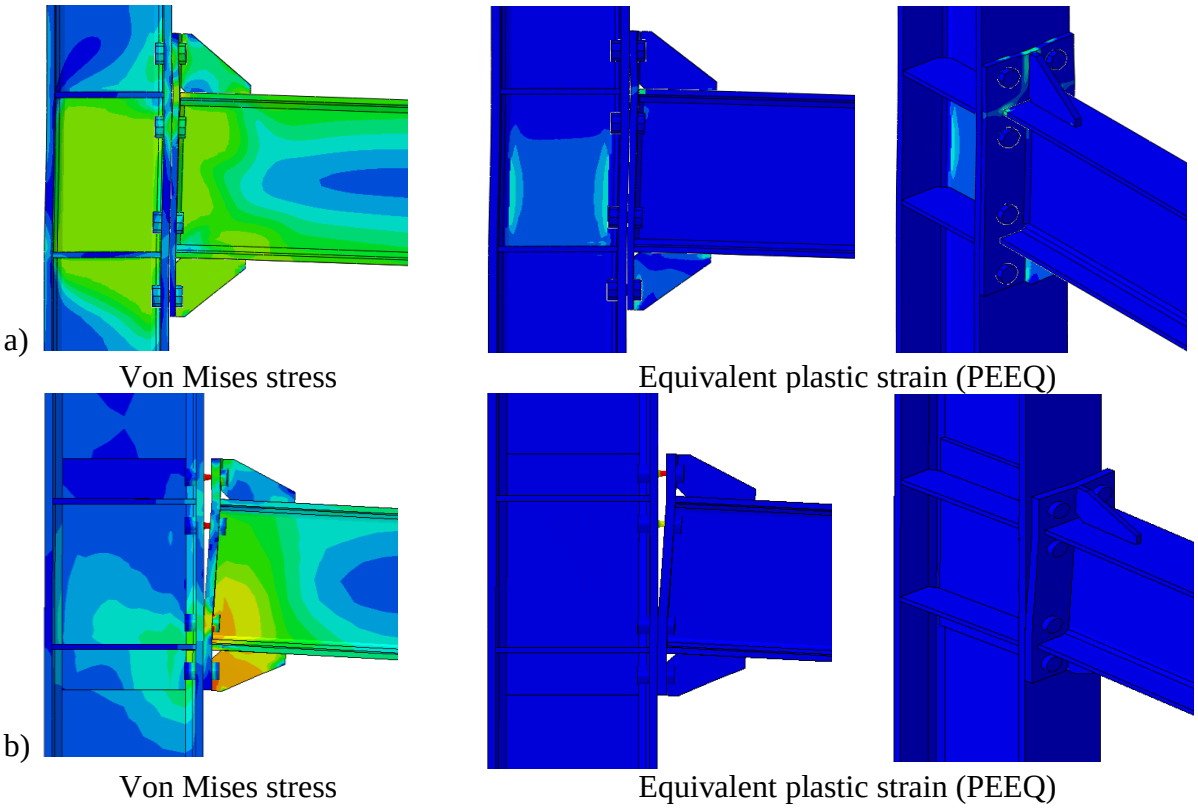


Figure 6 Failure modes of the partial strength joints: a) Equaljoints procedure; b) modified AISC procedure

Figure 6 depicts the comparison between the simulated failure modes, while the relevant response curves are reported in Figure 7. As it can be noted, the partial strength joint designed according to [8,9] exhibits a ductile failure mode without strength degradation beyond the threshold of 0.04 radians of chord rotation. On the contrary, the joint designed with the modified AISC358 procedure shows a low ductile response with significant degradation occurring at 0.025 radians due to the brittle failure of bolts in tension. This result is also confirmed by the curves reported in Figure 8, where the ratio between the dissipated energy by each components with respect to the whole dissipated energy by the joints is plotted. Figure 8a shows that in the joint designed according to European procedure [8,9] the energy is dissipated mainly by the column web panel in shear, but also into the other components i.e. end-plate, beam and ribs participate to the failure mode. Contrariwise, consistently with the PEEQ distribution showed in Figure 6, in the American joint, the most of energy is dissipated by the bolts (Figure 8b). Figure 8c depicts the comparison between the energy dissipated by the bolts into both

joints, where it can be noted the noticeably higher plastic engagement of the bolts into the American connection.

This comparison highlights that the design rules of current AISC358-16 [1] cannot be extended to partial strength joints, but further design rules are necessary to guarantee satisfactory ductility. On the contrary, the ductility limitations introduced in [8,9] ensure satisfactory ductility.

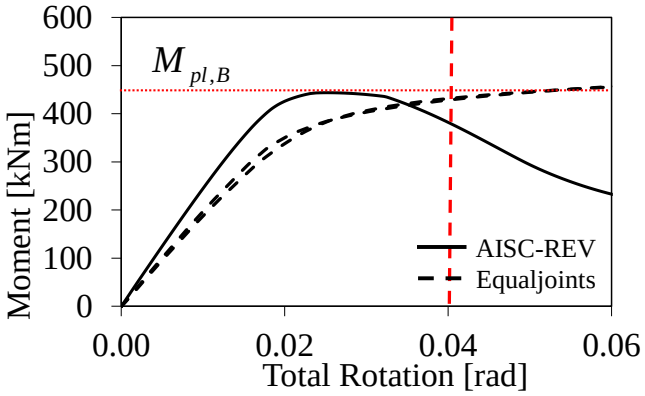


Figure 7 Response curves of the partial strength joints: Equaljoints vs. modified AISC procedure

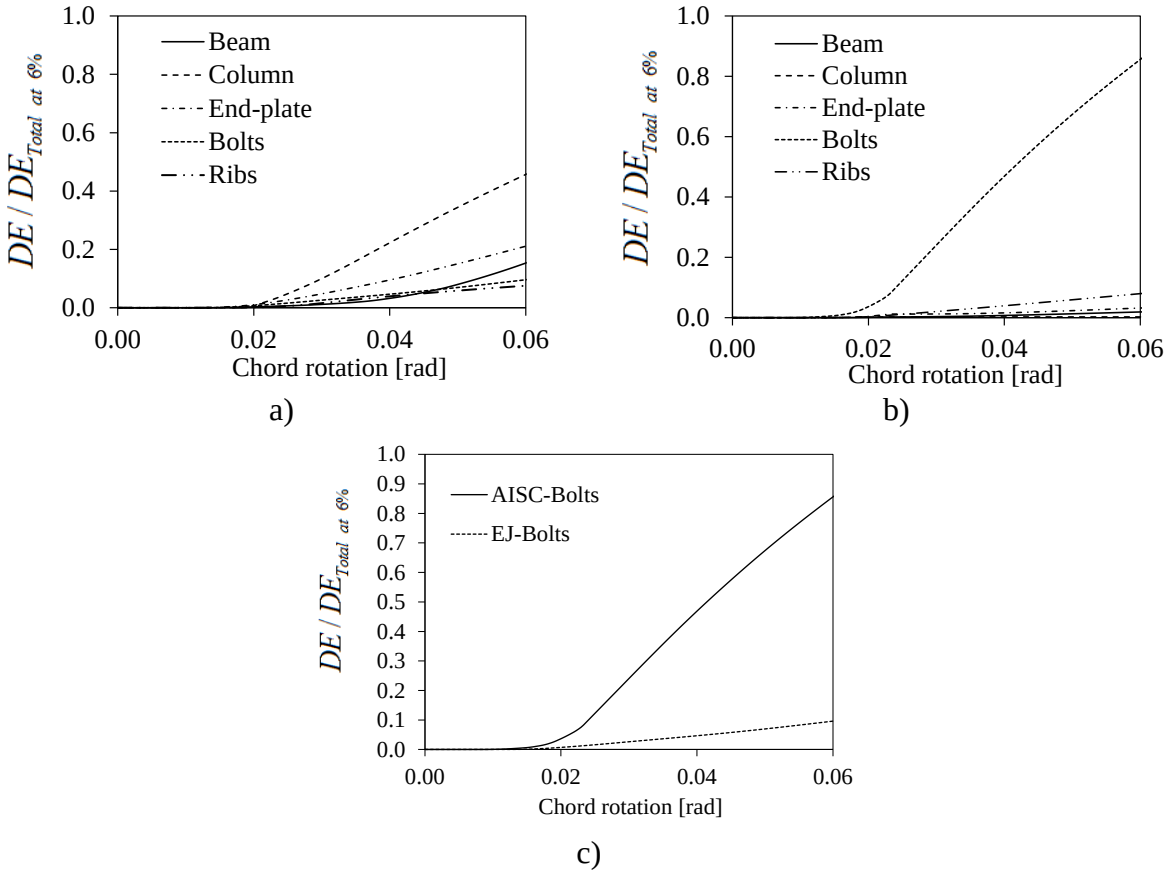


Figure 8 Dissipated energy for all the joints component respect to the global one at 6% of rotation: a) Equaljoints vs. b) modified AISC

## 4 CONCLUSIONS

This paper describes the design criteria developed within EQUALJOINTS project [9] for partial strength extended stiffened end-plate joints. In addition, the design rules of AISC358-16 [1] are described and possible extension to partial strength joints is examined. The main differences of these design procedures are discussed and compared by means of finite element analyses. Based on the results, the following remarks can be drawn:

- The EQUALJOINTS design criteria [8, 9] recommend ductility requirements to avoid the failure of bolts and enforce the plastic deformations into the end-plate of the connection.
- The finite element analyses confirm that this design procedure guarantee satisfactory ductility.
- AISC358-16 [1] does not provide similar requirements, because this code imposes that the strength of the connection should be higher than the resistance of the connected beam. Therefore, scaling the design resistance of the connection does not guarantee any ductility of the joints.
- The finite element simulations highlight that AISC358-16[1] needs further rules and requirements to design ductile partial strength extended stiffened end-plate joints.

## 5 ACKNOWLEDGMENT

The research leading to these results has received funding from the European Union's Research Fund for Coal and Steel (RFCS) research programme under grant agreement n° RFSR-CT-2013-00021.

## REFERENCES

[1] AISC (American Institute of Steel Construction). "Prequalified Connections for Special and Intermediate Steel Moment Frames for Seismic Applications." ANSI/AISC 358-16, Chicago, IL, 2016.

[2] T. M. Murray. AISC Design Guide 4, "Extended End-Plate Moment Connections", AISC (American Institute of Steel Construction), Chicago, IL, 1990.

[3] E.A. Sumner, T. M. Murray. Performance of Extended Moment End-Plate Connections Subject to Seismic Loading. U.S.–Japan Workshop on Seismic Fracture Issues in Steel Structures, San Francisco, California, February 28 - March 1, 2000.

[4] E.A. Sumner, T. M. Murray. Behavior of Extended End-Plate Moment Connections Subject to Cyclic Loading. *Journal of Structural Engineering* ASCE, **128(4)**, 501-508, 2002.

[5] T. M. Murray, E.A. Sumner. AISC Design Guide 4, "Extended End-Plate Moment Connections—Seismic and Wind Applications, 2nd Edition". AISC (American Institute of Steel Construction), Chicago, IL, 2004.

[6] CEN 2005. CEN (European Committee for Standardization). Design of steel structures, part 1.8: Design of joints. EN 1993:1-8, Brussels, 2005.

[7] CEN 2005. CEN (European Committee for Standardization). Design of structures for earthquake resistance - Part 1: General rules, seismic actions and rules for buildings. EN 1998-1, Brussels, 2005.

[8] M. D'Aniello, R. Tartaglia, S. Costanzo, R. Landolfo. Seismic design of extended stiffened end-plate joints in the framework of Eurocodes. *Journal of Constructional Steel Research*, **128**, 512-527, 2017.

[9] EQUALJOINTS – European pre-QUALified steel JOINTS: RFSR-CT-2013-00021. Research Fund for Coal and Steel (RFCS) research programme.

[10] A. Tenchini, M. D'Aniello, C. Rebelo, R. Landolfo, L. da Silva, L. Lima. High strength steel in chevron concentrically braced frames designed according to Eurocode 8. *Engineering Structures*, **124**, 167–185, 2016.

[11] F.M. Mazzolani, V. Piluso. Plastic design of seismic resistant steel frames. *Earthquake Engineering and Structural Dynamics*, **26 (2)**, 167-191, 2017.

[12] R. Montuori, E. Nastri, V. Piluso. Theory of Plastic Mechanism Control for MRF-EBF dual systems: Closed form solution. *Engineering Structures*, **118**, 287-306, 2016.

[13] R. Montuori, E. Nastri, V. Piluso. Theory of plastic mechanism control for eccentrically braced frames with inverted y-scheme. *Journal of Constructional Steel Research*, **92**, 122-135, 2014.

[14] D. Cassiano, M. D'Aniello, C. Rebelo, R. Landolfo, L. da Silva. Influence of seismic design rules on the robustness of steel moment resisting frames. *Steel and Composite Structures, An International Journal*, **21(3)**, 479-500, 2016.

[15] A. Tenchini, M. D'Aniello, C. Rebelo, R. Landolfo, L. da Silva, L. Lima. High strength steel in chevron concentrically braced frames designed according to Eurocode 8. *Engineering Structures* **124**, 167–185, 2016.

[16] M. Latour, V. Piluso and G. Rizzano, Free from damage beam-to-column joints: Testing and design of DST connections with friction pads, *Engineering Structures* **85**, 219–233, 2015.

[17] M. D'Aniello, E.M. Güneyisi, R. Landolfo, K. Mermerdaş. Predictive models of the flexural overstrength factor for steel thin-walled circular hollow section beams. *Thin-Walled Structures*, **94**, 67-78, 2015.

[18] M. D'Aniello, E.M. Güneyisi, R. Landolfo, K. Mermerdaş. Analytical prediction of available rotation capacity of cold-formed rectangular and square hollow section beams. *Thin-Walled Structures*, **77**,141-152, 2014.

[19] E.M. Güneyisi, M. D'Aniello, R. Landolfo, K. Mermerdaş. Prediction of the flexural overstrength factor for steel beams using artificial neural network. *Steel and Composite Structures, An International Journal*, **17(3)**, 215-236, 2014.

[20] M. D'Aniello, R. Landolfo, V. Piluso, G. Rizzano. Ultimate Behaviour of Steel Beams under Non-Uniform Bending. *Journal of Constructional Steel Research*, **78**, 144–158, 2012.

[21] M. Güneyisi, M. D'Aniello, R. Landolfo, K. Mermerdaş. A novel formulation of the flexural overstrength factor for steel beams. *Journal of Constructional Steel Research*, **90**, 60-71, 2013.

[22] Dassault (2014), Abaqus 6.14 - Abaqus Analysis User's Manual, Dassault Systèmes Simulia Corp.

[23] ANSI/AISC 341-16 (2016). "Seismic Provisions for Structural Steel Buildings". American Institute of Steel Construction.

[24] A. Dutta, S. Dhar, S. K.Acharyya. Material characterization of SS 316 in low cycle fatigue loading. *Journal of Material Science*, **45**,1782–1789, 2010.

[25] M. Latour, G. Rizzano, A. Santiago, L. da Silva. Experimental analysis and mechanical modeling of T-stubs with four bolts per row. *Journal of Constructional Steel Research*, **101**,158–174, 2014.

[26] M. Latour, V. Piluso, G. Rizzano. Rotational behaviour of column base plate connections: Experimental analysis and modelling. *Engineering Structures*, **68**, 14-23, 2014.

[27] M. D'Aniello, D. Cassiano and R. Landolfo, Monotonic and cyclic inelastic tensile response of European preloadable gr10.9 bolt assemblies, *Journal of Constructional Steel Research*, **124**, 77–90, 2016.

[28] J.A. Swanson, D.S. Kokan, R.T. Leon. Advanced finite element modelling of bolted T-stub connection components. *Journal of Constructional Steel Research*, **58(5–8)**,1015–31, 2002.

[29] G. Shi, Y. Shi, Y. Wang. Behaviour of end-plate moment connections under earthquake loading. *Engineering Structures*, **29**, 703–716, 2007.

[30] R. Tartaglia, M. D'Aniello. Nonlinear performance of extended stiffened end plate bolted beam-to-column joints subjected to column removal. *The Open Civil Engineering Journal*, **11(3-15)**, 2017.

COMPDYN 2017
6th ECCOMAS Thematic Conference on
Computational Methods in Structural Dynamics and Earthquake Engineering
M. Papadrakakis, M. Fragiadakis (eds.)
Rhodes Island, Greece, 15–17 June 2017

# NUMERICAL STUDY ON COMPARISON BETWEEN DUCTILITY OF UNSTIFFENEE BOX SECTIONED STEEL STUB COLUMNS AND SIMPLY SUPPORTED STEEL PLATES

**HARUNA SATOMI[1], AKIRA KASAI[2]**

[1] Dept. of Science and Technology, Civil and Environmental Engineering, Kumamoto university
Kurokami 2-39-1, Chuo-ku, Kumamoto City, 860-8555, Japan
e-mail: 155d8815@st.kumamoto-u.ac.jp

[2] Associate Professor, Faculty of Advanced Science and Technology, Division of Materials Science, Kumamoto university
Kurokami 2-39-1, Chuo-ku, Kumamoto City, 860-8555, Japan
e-mail: kasai@kumamoto-u.ac.jp

**Keywords:** Steel plate, Steel box stub columns, Initial deflective deformation, strength, ductility

**Abstract.** *This study is aimed at grasping differences between ductility formulations of unstiffened box sectioned steel stub column subjected to bending moment and simply supported steel plates subjected to axial force. For this purpose, numerical model about steel stub column and simply supported steel plate were pre-pared. At first, ductility formula of simply supported steel plates subjected to axial load were developed. Secondary, strength and ductility as seismic performance were calculated, through numerical analysis subjected to between compression load and bending moment. As a result, it is found that strength of compression flange plate in steel stub column is 1.2 times of simply supported steel plate. However, it is required to carry out more numerical study, for investigating ductility of these structures. Finally, deformation shape of these structures were discussed.*

## 1 INTRODUCTION

Civil engineering structures were irreparably damaged by the Kobe earthquake which occurred in the southern part of Hyogo prefecture in 1995, besides buckling and deformation were confirmed on steel bridge piers which had not damaged by any earthquakes before[1]. Therefore, the study became more active to establish performance based design and seismic performance of steel bridge pier after Kobe earthquake.

For example, Fukumoto et al.[2] compiled databases on the results of compressive loading experiments for steel plates which carried out in Europe, Japan and US and analyzed statistically the relation between compressive strength and width-thickness ratio parameter. Usami[3),4)] conducted the experiments which coupled the local buckling of box sectioned compressive element and whole buckling. They elucidated especially economical design of piers. Nara[5)] estimated the design formulas of limited strength of steel plates subjected to compressive stress and bending by numerical analysis of Finite Element Method.

Recently, seismic design of civil engineering structures is significantly increasing and the structures will get a minor damage by even level 2 earthquake motions such as Hyogo earthquakes in 1995.

Seismic design guidelines[6)] for steel bridges are summarized as researches on seismic design of steel bridge piers in recent years. Evaluation formulas for the strength and deformability of the steel bridge piers are included in the guidelines, but the formulas consider only standard initial irregular. That is, the formulas can not evaluate with using especially the amount of initial deflections because the formulas have evaluated the plate elements, which have half sin-wave of initial deflections and the maximum initial deflections of 1/150 of plate width, have configurated steel bridge piers. It is well known in buckling design, the buckling load changes depending on the amount of initial curvatures. However, the existing formulas take into account just standard initial curvatures about strength and deformation capacity of steel bridge piers. The formulas do not have problem with a newly established structure. nowadays it is difficult to compare strength and deformability between before earthquakes and after. Therefore, we did the parametric compressive analysis for simple steel plates and unstiffened box sectioned steel stub columns with amounts of initial curvature as basic examination. Obviously, the result about the study of unstiffened box sectioned steel stub columns is important though, we carried out the analysis of simple steel plates and compere these for evaluating how useful just evaluative formula of the plates is.

## 2 THE ANALYSIS MODEL OF PLATES

In this paper, assessing strength and deformability of unstiffened box-sectioned steel stub columns is considered with width-thickness ratio parameters. Therefore, the numerical analysis method is typical method. Figure 1 shows schematic diagram of the analysis model, (a) is the front view of the simple steel plate, (b) is side view of them, a is width of plates which is loading side and $l_d$ is length of plates which is not loading side. Moreover, Table 1 shows boundary conditions, 1 indicates

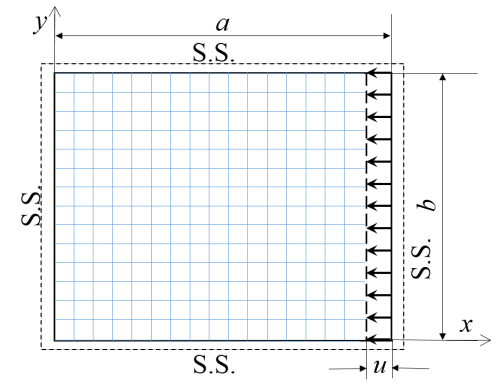


(a) front view

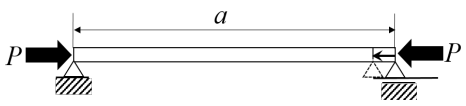


(b) side view

**Figure 1 The analysis model**

boundary and 0 indicates free. Shell elements are applied to the analyses. the number of divided elements of a and $l_d$ are equal division of 100 in both case. The number of division is decided based on comparing a theoretical value by a buckling eigenvalue analysis. Elastic-plastic finite displacement analysis was conducted by ABAQUS[7] and S4R (shell elements of 4 nodes) which is generally formulated thickness of plates is used because it is treated from thin plate to thick in this paper. In addition, steel material is SM490 because mostly this material is used in this kind of studies. The effect by differences of steel type should be considered. However, this study is analysis study and the difference of steel material would affect only thicker steel plates, that is the area will not occur local buckling.

### 2.1 The model of initial curvatures

Initial curvatures of half sin-wave are simulated in numerical analyses[8]. The amount of maximum initial curvatures label $w_{max}$ as shown in Figure 2. The amount of initial curvatures is calculated by formula (1).

$$w(x,y) = w_{\max} \cdot \sin\left(\frac{\pi x}{2a}\right) \cdot \sin\left(\frac{\pi y}{2l_d}\right) \tag{1}$$

### 2.2 The model of residual stresses

Occurring residual stresses by welding is supposed, so the form of residual stresses is triangular as shown in Figure 3[9]. The maximum tensile residual stress $\sigma_{rt}$ is yield stress $\sigma_y$ and the maximum compressive residual stress $\sigma_{rc}$ is 0.25 of $\sigma_y$.

### 2.3 The loading method

Displacement control analyses are adopted as the loading method to basically consider the study of simple steel plates. The displacement is uniform as shown in Figure 1-(a) and cyclic load is not considered in this study.

### 2.4 Constitutive law

Stress-strain curve has plastic region, yield plateau and strain hardening state as shown in Figure 4. Moreover, each of plastic region, yield plateau and strain hardening state is shown formula (2), (3), (4).

$$\sigma = E\varepsilon \quad (0 \le \varepsilon < \varepsilon_y) \tag{2}$$

**Table 3 The boundary condition of simple steel plates**

| | $u$ | $v$ | $w$ | $\theta_x$ | $\theta_y$ | $\theta_z$ |
|---|---|---|---|---|---|---|
| $x$=0 | 1 | 1 | 1 | 1 | 0 | 1 |
| $x=l_d$ | 0 | 0 | 1 | 0 | 1 | 1 |
| $y$=0 | 0 | 0 | 1 | 0 | 1 | 1 |
| $y=a$ | 0 | 0 | 1 | 0 | 1 | 1 |
| Free=0, Fix=1<br>$u,v,w$=deformability of $x,y,z$<br>$\theta x,\theta y,\theta z$=rotation angle of $x,y,z$ axis | | | | | | |

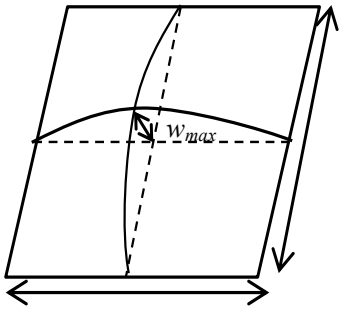


**Figure 2 The model of initial curvatures**

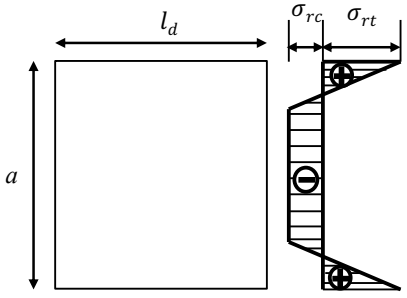


**Figure 3 The model of residual stresses**

$$\sigma = \sigma_y \quad (\varepsilon_y \le \varepsilon < \varepsilon_{st}) \tag{3}$$

$$\frac{\sigma}{\sigma_y} = \frac{1}{\xi}\frac{E_{st}}{E}\left[1-\exp\left\{-\xi\left(\frac{\varepsilon}{\varepsilon_y}-\frac{\varepsilon_{st}}{\varepsilon_y}\right)\right\}\right]+1 \ (\varepsilon > \varepsilon_{st}) \tag{4}$$

$E$ is young's rate, $\varepsilon_y$ is yield stress, $\xi$ is material parameter, $E_{st}$ is strain hardening modulus, $\varepsilon_{st}$ is the strain when strain starts to be hard. In SM490 case, $\xi = 0.06$, $E/Est = 30$, $\varepsilon_{st}/\varepsilon_y = 7$[9].

### 2.5 The structural parameter of buckling

The structural parameter of steel plates is shown in Table 2. $R$ is width-thickness ratio parameter and calculated by formula (5).

$$R = \frac{b}{t}\sqrt{\frac{\sigma_y}{E}\cdot\frac{12(1-\nu^2)}{\pi^2 k}} \tag{5}$$

Moreover, $\nu$ is Poisson's ratio and $k$ (=4) is buckling coefficient. We compared between 5 pattern of initial curvature amounts (1/50, 1/100, 1/150, 1/250, 1/500).

## 3 UNSTIFFENEE BOX SECTIONED STEEL STUB COLUMNS

As a basic study, unstiffened box sectioned steel stub columns which are part of the pier base section and simple steel plates which are part of the box were targeted as shown in Figure 5.

Elastic-plastic finite displacement analysis was conducted by ABAQUS and S4R which is shell elements of 4 nodes likewise simple steel

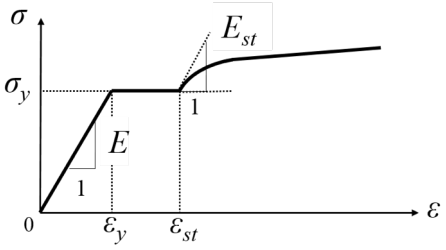


**Figure 4 stress-strain curve**

**Table 2 The analysis parameter**

| | |
|---|---|
| $R$ | 0.26～2.10 |
| $E$ (GPa) | 200 |
| $\sigma_y$ (MPa) | 315 |
| $\nu$ | 0.3 |
| $\alpha = a / b$ | 1.0 |
| $\sigma_{rt} / \sigma_y$ | 1.0 |
| $\sigma_{rc} / \sigma_y$ | 0.25 |
| $t$ | 32 |
| $w_{max} / b$ | 1/50,1/100,1/150, 1/250,1/500,1/1000 |

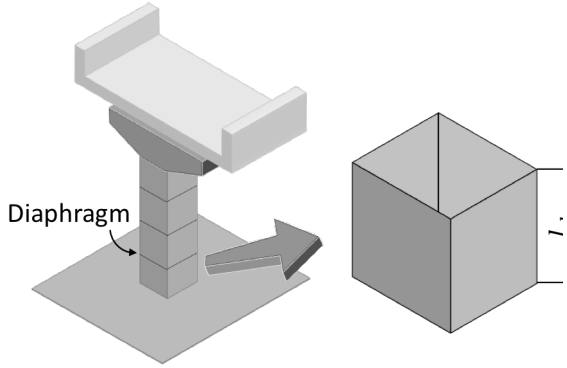


(a) The target region of box sectioned steel stub columns

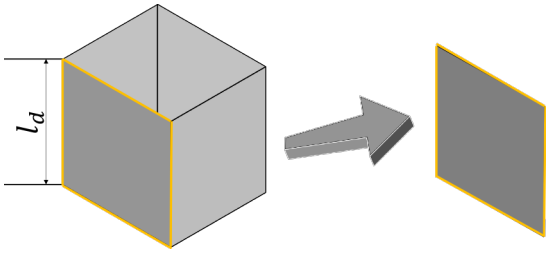


(b) The target region of simple steel plates

**Figure 5 The target region**

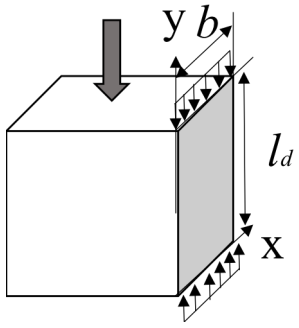


**Figure 6 The model of box sectioned steel stub columns**

plates. The constitutive law and the structural parameter are as same as simple steel plates.

Figure 6 shows schematic diagram of the analysis model. $b$ is width of plates which is loading side and $l_d$ is length between diaphragms which is not loading side. Shell elements are used to the analyses, in addition to the number of divided elements of $b$ and $l_d$ are equal division of 100 in both case.

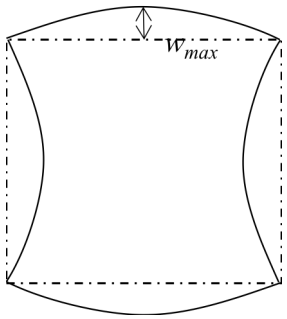


**Figure 7 The illustration of initial curvatures**

### 3.1 The model of initial curvatures

The center of plate is the maximum amount of initial curvatures $w_{max}$ as illustrated in Figure 7 and the corners keep a right-angle. Moreover, flange face is a convex curvature and web face is a concave curvature.

**Table 3 The boundary condition of box sectioned steel stub columns**

| | $u$ | $v$ | $w$ | $\theta_x$ | $\theta_y$ | $\theta_z$ |
|---|---|---|---|---|---|---|
| $y = b$ | 1 | 1 | 1 | 1 | 1 | 1 |
| $x = l_d$ | 0 | 0 | 0 | 1 | 1 | 1 |
| Free=0, Fix=1<br>$u,v,w$=deformability of $x,y,z$<br>$\theta x,\theta y,\theta z$=rotation angle of $x,y,z$ axis | | | | | | |

### 3.2 The model of residual stresses

The residual stress of unstiffenee box sectioned steel stub columns is loaded as same as the residual stress of steel plate in Figure 3.

### 3.3 The boundary conditions

Table 3 shows the boundary condition of unstiffenee box sectioned steel stub columns. The boundary condition of pier base section is set up totally fixed point and analyzed in this time. However, the boundary conditions of real pier base sections are not totally fixed so that it should be elucidated about it in the furture.

### 3.4 The loading method

Displacement control analyses are conducted as the loading method to basically consider the study of unstiffenee box sectioned steel stub columns.

## 4 THE ANALYSIS RESULTS AND DISCUSSION

### 4.1 The definition of strength and deformability

Analysis results are assessed based on average stress ($\bar{\sigma}$) -average strain ($\bar{\varepsilon}$) curve. $\bar{\sigma}$ and $\bar{\varepsilon}$ is defined in Formula (6).

$$\bar{\sigma} = P / A , \quad \bar{\varepsilon} = \delta / a \tag{6}$$

Average stress-average strain curves of analysis results are shown in Figure 8. The point of the maximum average stress is called “Peak point” and the point where the stress decrease 5% from Peak point is called “95% stress point” in Figure 8. Moreover, only one plates of unstiffenee box sectioned steel stub columns made from four plates is consider to compare with simple steel plates.

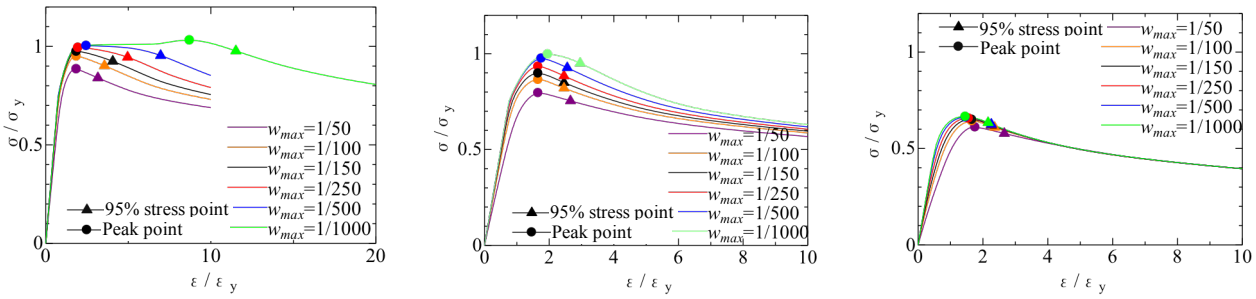


(a)$R$=0.52 (b)$R$=0.72 (c) $R$=1.30

Simple steel plates

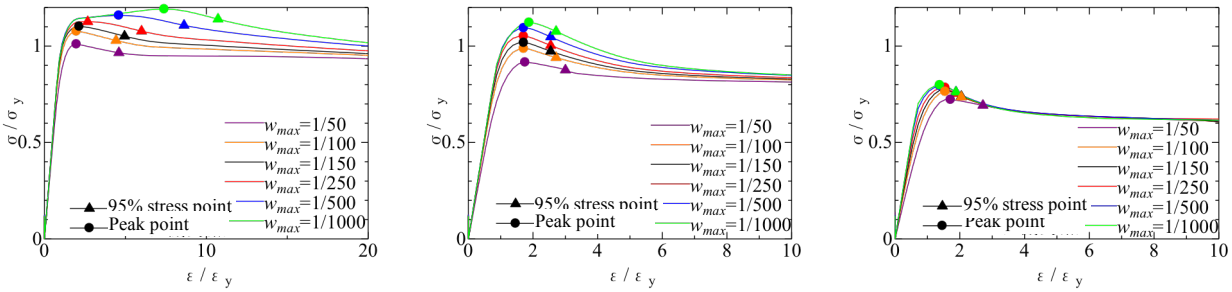


(d)$R$=0.52 (e)$R$=0.72 (f) $R$=1.30

unstiffenee box sectioned steel stub columns

**Figure 8 Stress-strain curves**

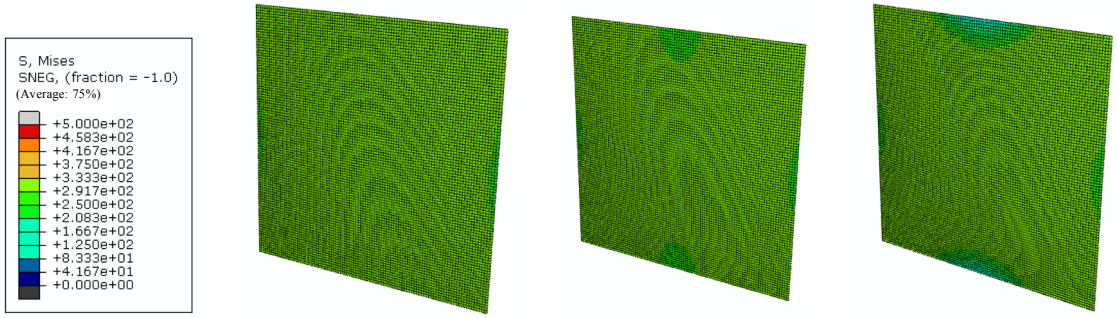


(a)$R$=0.52 (b)$R$=0.72 (c) $R$=1.30

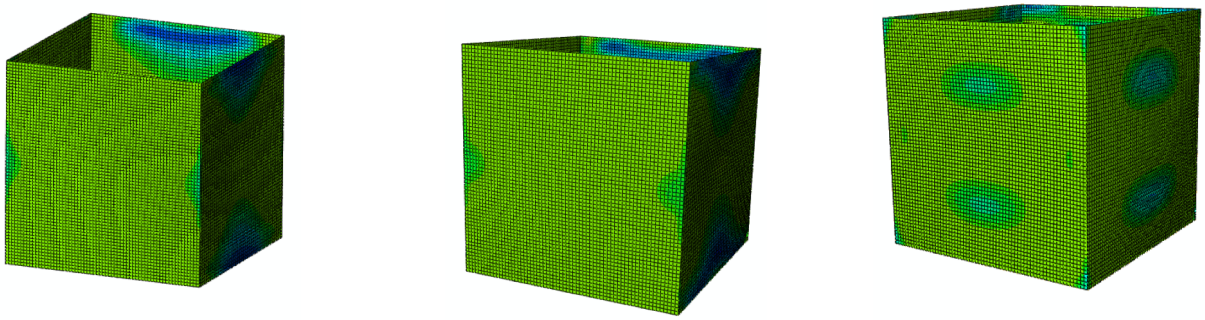

(d)$R$=0.52 (e)$R$=0.72 (f) $R$=1.30

**Figure 9 Deformation diagrams**

### 4.2 Comparing average stress-average strain curves

Figure 8 (a) and (b), (c) show average stress-average strain curves of simple steel plates and Figure 8 (d) and (e), (f) show average stress-average strain curves of unstiffenee box sectioned steel stub columns. As shown in Figure 8 (a) and (d), local buckling is happened and strength decrease before strain hardening occurs when $w_{max}$ is 1/50-1/500. Compare to them, there are yield plateaus and strength increases by strain hardening.

Furthermore, in unstiffenee box sectioned steel stub column's cases, strength slowly decrease and stop to decrease after strain reach 10. On the contrary, strength decrease rapidly in simple steel plate's cases.

Strength decreases before strain hardening happen when $w_{max}$ is 1/1000 in Figure 8 (b), (c), (e) and (f) but there is no difference in the tendency of the graphs of (a) and (d) when $w_{max}$ is 1/50-1/500.

Figure 9 shows deformation diagrams when loading reaches maximum amount. (a)-(c) are diagrams of simple steel plates and (d)-(f) are diagrams of unstiffenee box sectioned steel stub column. Even though we compare plates and boxes from Figure 9, there is not much difference.

### 4.3 Strength

Figure 10 shows the relationship between strength and width thickness ratio parameter $R$ when $R$=0.33-2.09 and initial curvatures $w_{max}$=1/50-1/1000.

Moreover, the maximum initial curvatures become larger the maximum strengths become smaller as shown in Figure 10. However, a relatively thin-walled area is very small difference between the maximum load by the maximum initial deflection amount and it becomes a big difference as it becomes thicker.

In addition, initial curvatures $w_{max}$>1/150 can handle enough by the formula of Fukumoto in plate's case as shown in Figure 10 (a). Even in the case of $w_{max}$ <1/150, it is highly consistent with Nara's formula. As illustrated in Figure 10 (b), the strength exceeds 1 in the region of $R$ <0.7 in plate's case but the strength

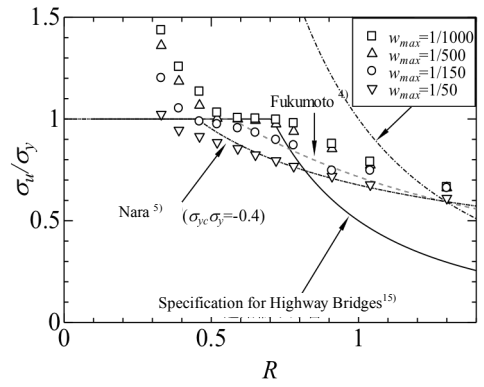


(a) Simple steel plates

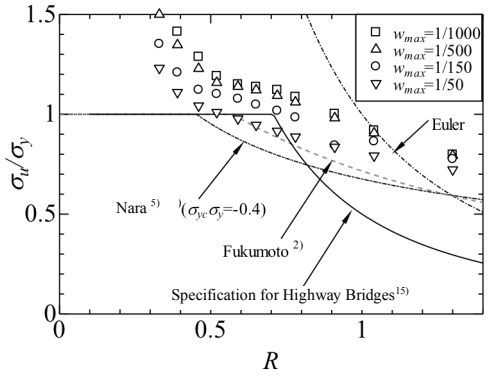


(b) unstiffenee box sectioned steel stub columns

**Figure 10 Comparing strengths**

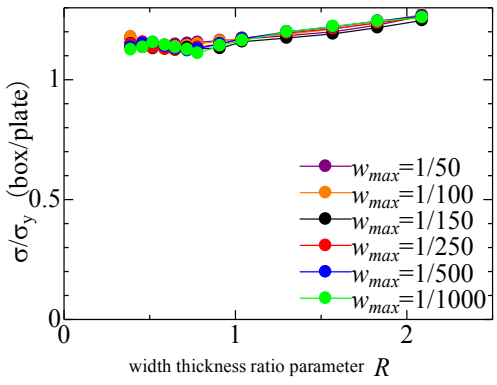


**Figure 11 σ/σy-*R* curves**

exceeds 1 in the region of $R$<0.9 in box's case. As a result, it is too safe for plate's formula in case of a box.

Figure 11 compares the maximum strength of simple steel plates and the maximum strength of unstiffenee box sectioned steel stub columns. The vertical axis of Figure 11 is values of the maximum strength of simple steel plates divided by the maximum strength of unstiffenee box sectioned steel stub columns and the horizontal axis of Figure 11 is width-thickness ratio parameter.

There is much change of behavior by difference of the maximum initial curvatures in Figure 11. The ratio of plate's and box's maximum strength increases little by little and it keeps approximately 1.1 times in the region of $R$ <0.8.

Then, the value of each maximum initial curvatures amount in Fig. 11 is averaged and we obtained a linear equation by approximation. The equation is shown in Figure 12 and Formula (7).

$$\sigma_{u,box}/\sigma_{u,plate}=0.0735R+1.10 \quad (7)$$

### 4.4 Deformability

Figure 13 shows the results of ultimate strains to compare simple steel plates and unstiffenee box sectioned steel stub columns. (a) is the ultimate strain when strength becomes maximum amount and (b) is the ultimate strain when strength decrease 5% after the maximum strength. In addition, the vertical axis of Figure 13 is logarithm.

As shown in Figure 13 (a), every parameter of the maximum initial curvatures are approximately the same behaviors when comparing simple steel plates and unstiffenee box sectioned steel stub columns. When comparing the amounts of initial curvatures, the maximum initial curvatures become smaller the ultimate strains become smaller in the region of $R$>0.7. there is not much difference of behaviors in the region of $R$<0.7. Accordingly, it is considered that it is easy to be

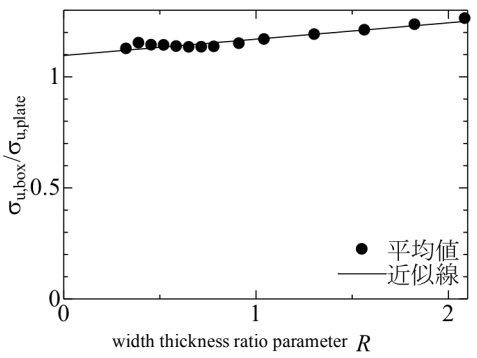


**Figure 12 The liner of approximation**

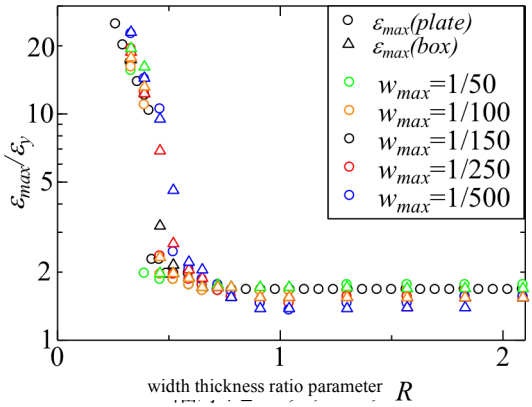


(a) The ultimate strain of the maximum strength

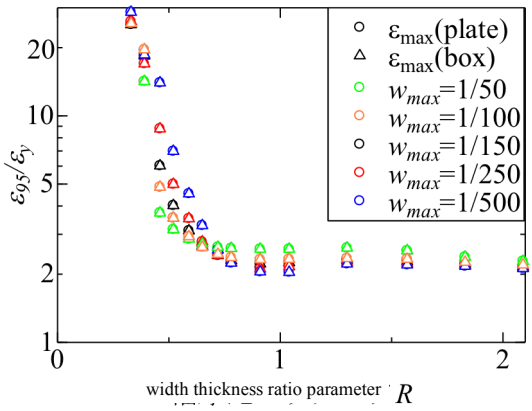


(b) The ultimate strain of the 95% strength

**Figure 13 Comparing the ultimate strains**

affected by the maximum initial curvatures when thickness of plates is thinner.

when comparing Figure 13 (a) and (b), the ultimate strains of (b) is consequently larger than (a) because the ultimate strains of (b) is the strengths reaches 95% of amounts from the maximum. However, as shown in Figure 13 (b), there is almost no difference between simple steel plates and unstiffenee box sectioned steel stub columns of behaviors like (a).

Therefore, there is not much difference like the results of strength but it is possible to apply the evaluation formula of deformability of steel plates to unstiffenee box sectioned steel stub columns.

## 5 CONCULUSION

In this study, we performed the parametric compressive analysis for simple steel plates and unstiffened box sectioned steel stub columns as basic examination and evaluated the stress-strain curve, $\sigma_{max}/\sigma_y$-initial curvatures curve, $\varepsilon_{max}/\varepsilon_y$-initial curvature and the ratio(boxes/plates) depth thickness ratio.

The results of this study were as follows.

- Strengths decrease as amounts of initial curvatures increase.
- Deformability is not effected by amounts of initial curvatures.
- The ratio of strengths increases approximately 20% when $R$ is higher than 1.

the boundary conditions of the box are exaggeratedly strong in this analysis so we need to verify the analysis in a different boundary condition version from now on.

## REFERENCES

[1] Subcommittee on Investigation of Seismic Damage of Steel Structure, Investigation of causes of damage to steel structure on Hanshin- Awaji earthquake disaster, JSCE, 271p., 1999.

[2] Y. Fukumoto, Y. Itoh, Basic compressive strength of steel plates from test data, *Proc. of JSCE, Structural Eng./ Earthquake Eng.*, No. 344, pp. 129-139, 1984.

[3] T. Usami, Y. Fukumoto, T. Aoki, Tests on the interaction strength between local and overall buckling of welded box columns, *Proc. of JSCE*, No.308, pp. 47-58, 1981.

[4] T. Usami, Y. Fukumoto, Local and overall buckling tests of compression members and an analysis based on the effective width concept, *Proc. of JSCE*, No.326, pp. 41-50, 1982.

[5] S. Nara, M. Tsuda, Y. Fukumoto, Evaluaiton of ultimate strength of steel plates with initial imperfections under in-plane bending and compression*, Proc. of JSCE,* No.392/I-9, pp. 259-264, 1988.

[6] Japanese Society of Steel Construction, Guidelines for seismic and damage control design of steel bridges, Gihodoshuppan , 427p., 2006.

[7] Dassault Systemes, ABAQUS Standard User's Manual Ver. 6.11, 2011.

[8] S. Komatsu, M. Ushino, T. Kitada, An experimental study on residual stresses and initial deformations of stiffened plates*, Proc. of JSCE,* No. 265, pp. 25-32, 1977.

[9] T. Usami, H. Tenkumo, Ultimate strength and effective width of plates in compression and bending, *Proc. of JSCE,* No. 441/I-18, pp. 78-85, 1992.

[10] T. Usami, H. Ge, Strength prediction of thin-walled plate assemblies, *Proc. of JSCE,* Vol.42A, pp. 171-178, 1996.

[11] JSCE, Guidelines for stability design of steel structures, 445p., 2005.

[12] Japan Road Assosiation, Specification for Highway Bridges, 536p., 2012.

COMPDYN 2017
6th ECCOMAS Thematic Conference on
Computational Methods in Structural Dynamics and Earthquake Engineering
M. Papadrakakis, M. Fragiadakis (eds.)
Rhodes Island, Greece, 15–17 June 2017

# ON DYNAMICS OF LIFT BRIDGE

**P. Rosko**[1], **J. Kralik**[2]

[1] Vienna University of Technology
Karlsplatz 13/E2063, A-1040 Vienna, Austria
e-mail: peter.rosko@tuwien.ac.at

[2] Slovak University of Technology
Radlinskeho 11, 81368 Bratislava, Slovakia
e-mail: juraj.kralik@stuba.sk

**Keywords:** Bridge, Structural Dynamics, Probability, Sensitivity, LHS.

**Abstract.** *The paper deals with probabilistic analysis in dynamics. The Botlek bridge (Rotterdam, Holland) – one of the largest vertical movable lift bridges in the world is analyzed. The structure of the bridge consists of six reinforced concrete pylons and two large (94 m x 49 m each) steel decks connected through ropes with counterweights. The bridge system is in dynamic mode during movement of the decks and the counterweights, under the action of wind and earthquakes, under traffic loads in operation position. The real bridge structure has a high level of importance and accordingly not only deterministic analyses were carried out but also stochastic analyses were required. The paper focuses the probabilistic analysis as the base of dynamic study in the design process of the bridge. The results had a high significance for practical application and for design of the bridge. The uncertainties of pylon and deck: stiffness and weight were taken into account in the probabilistic simulation method.*

## 1 INTRODUCTION

The new Botlek bridge recently built in Rotterdam, Holland (see Figure1) is one of the largest vertical movable lift bridges in the world. The Vienna Consulting Engineers ZT GmbH [1] was responsible for the structural design. In frame of the design process of the bridge, the finite element model was created and analyzed using deterministic approach in statics and dynamics [2, 3] on the base of Eurocodes [4, 5]. The dynamic analysis was required due to wind loads, seismic loads, traffic loads and operation loads by movement of decks. The Botlek bridge has a high level of importance and accordingly not only deterministic analyses were carried out but also stochastic analyses were required. The paper focuses the probabilistic analysis as the base of dynamic study in design process of the bridge. The uncertainties of pylons and decks: stiffnesses and weights were taken into account in the probabilistic simulations.



Figure 1: Botlek bridge, Rotterdam – visualization.

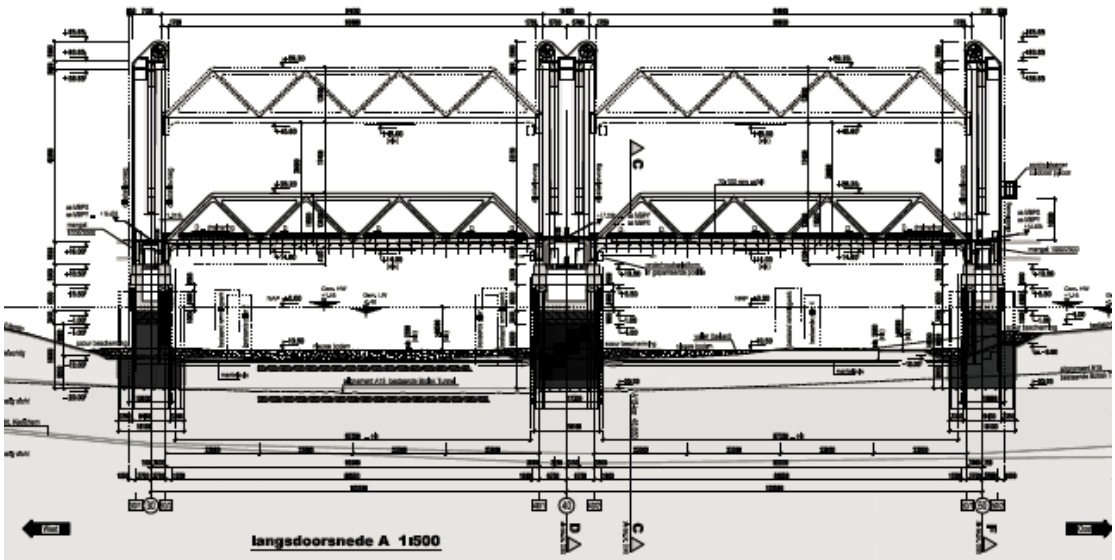


Figure 2a: Botlek bridge project: layout.

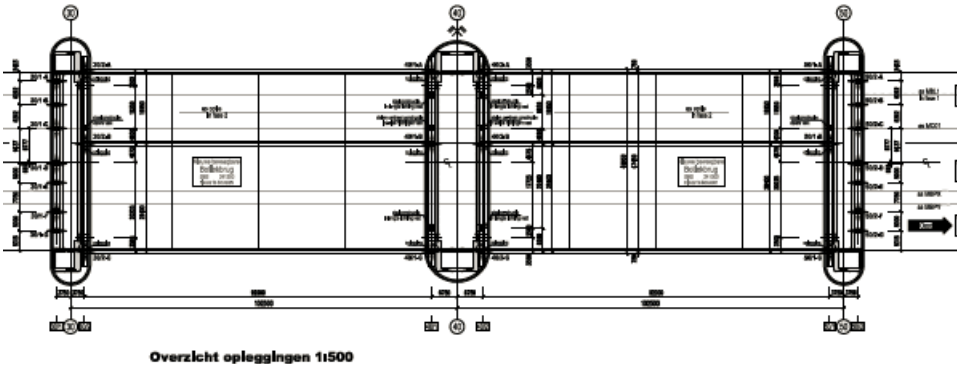


Figure 2b: Botlek bridge project: plan view

## 2 STRUCTURE

Two steel decks, more than 4000 tons weight each, are independently vertically movable on six concrete towers – the lifting height is 31 m. The length of steel decks is 94 m, the width 49 m (the size of each deck equals approximately playing field of soccer). The lifting system is fully balanced. The four concrete counterweights are guided on concrete pylon towers and are connected through ropes with decks at their ends.

## 3 FINITE ELEMENT MODEL

The finite element software ANSYS [2, 3] have been used for all models and analyses. The model of the bridge was prepared for deterministic and consistently for probabilistic analysis.

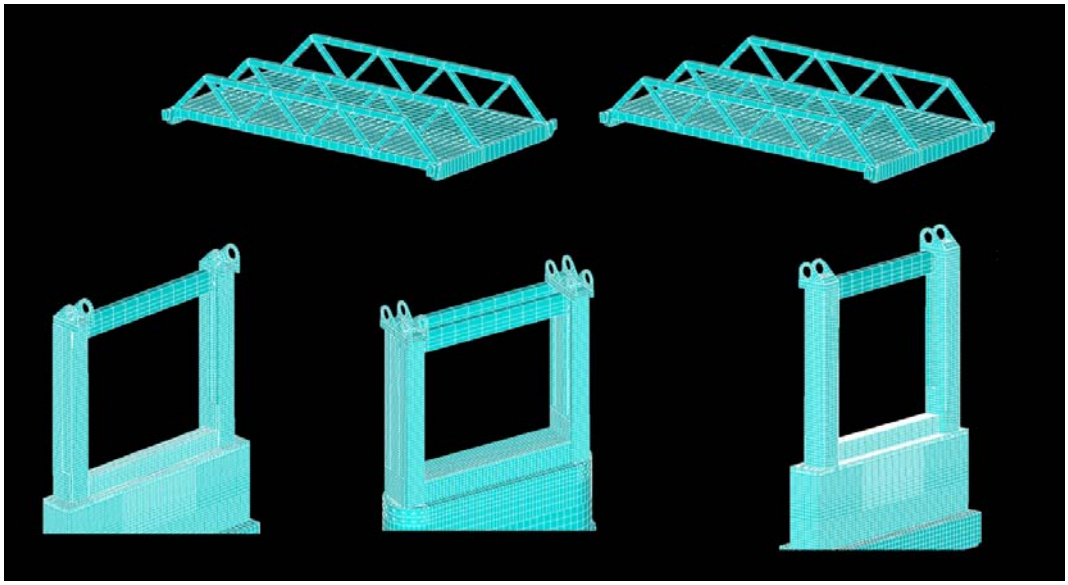

Figure 3: Bridge system: pylons with counterweights, decks.

### 3.1 Model of the structure

The preliminary analyses have shown, that the vertical displacements of the tops of the pylons are neglectable in comparison to the horizontal displacements [1]. For that reason was the simplification of the model in 2D possible. The model consists of two approximately rigid plates (decks) with weight G and substituted thickness H, models of pylons - springs with stiffnesses K1-K12 (see Figures 4 and 5).

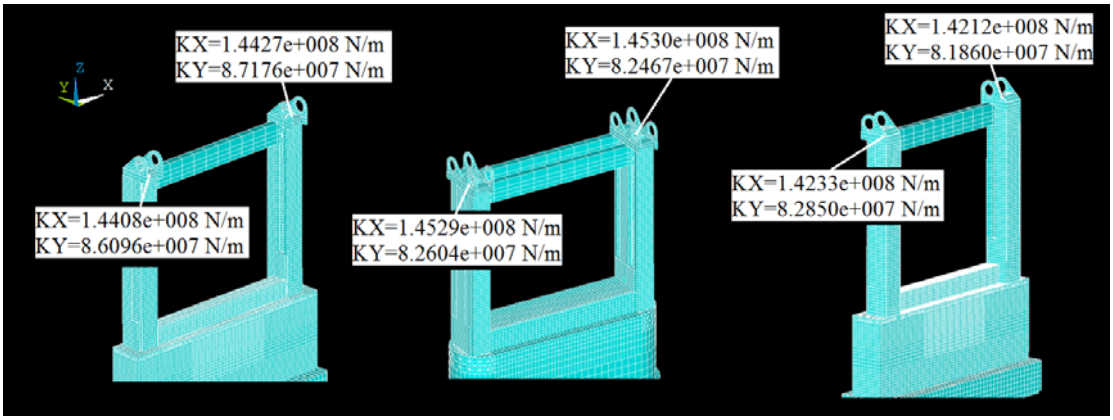


Figure 4: Horizontal stiffnesses of pylons: input in deterministic analysis.

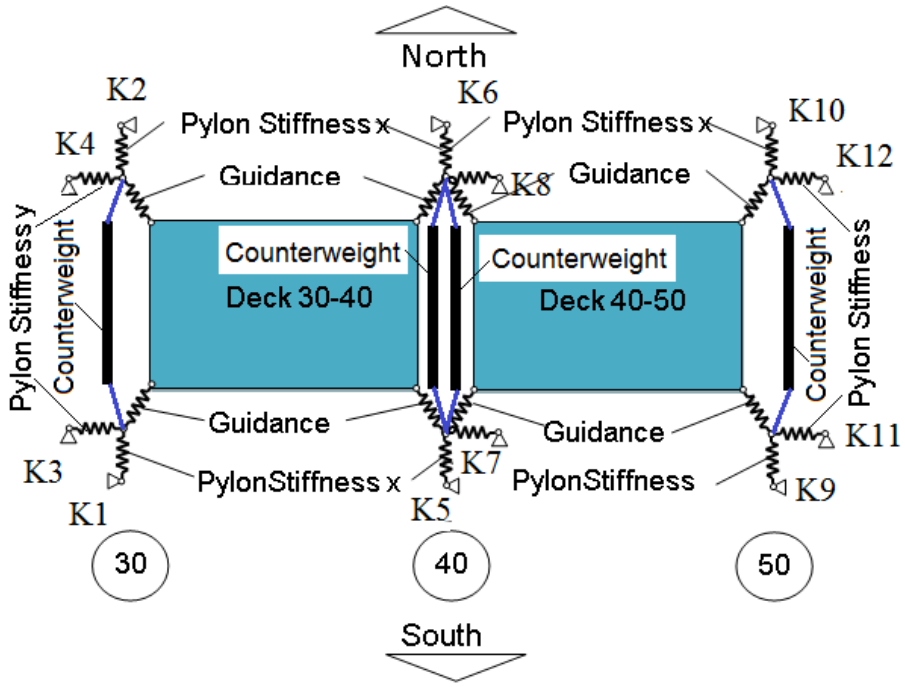


Figure 5: 2-D model.

## 4 DYNAMICS

### 4.1 Dynamic loading

Let consider from dynamics unfavorable situation when the both decks are in upper position. The mass more than 9000 tons is in the height of more than 30 m supported by six pylons. The system is sensitive to horizontal loading e.g. wind loading, seismic loading. The bridge structure can be analyzed according to Eurocode procedures [4, 5].

### 4.2 Modal analysis

The natural frequencies and modes of the bridge system influence the dynamic behavior of the bridge system. The dynamic component of the loading depends on the base of Eurocode [4, 5] and on natural frequency of the structure. The first three modes are presented in Figures 6-8. The eigenvalue problem was solved with Lanczos method.

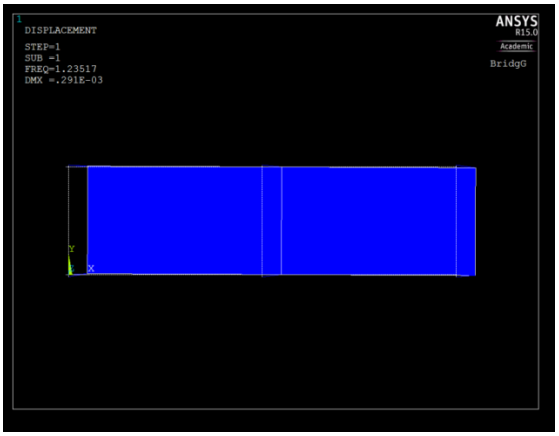


Figure 6: The first mode.

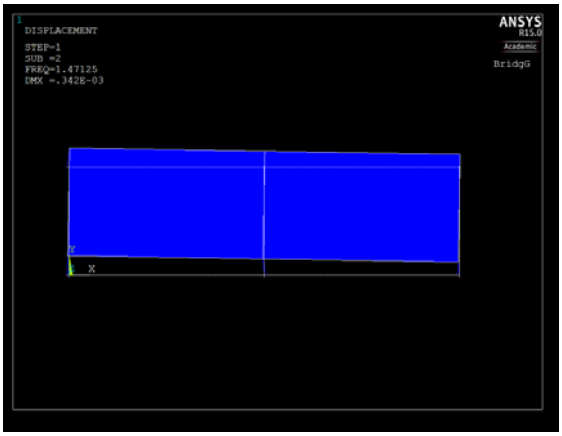


Figure 7: The second mode.

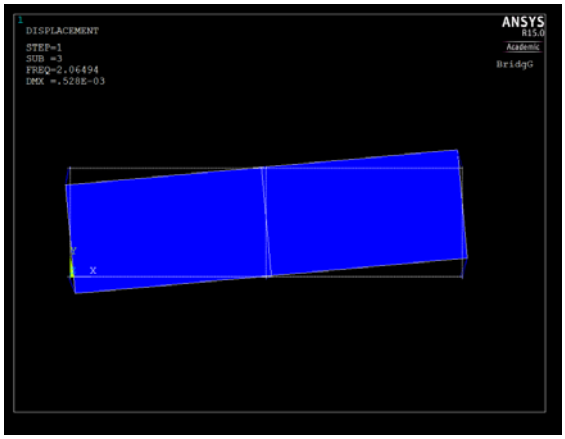


Figure 8: The third mode.

## 5 PROBABILISTIC ANALYSIS

The deterministic model introduced above is executed in ANSYS multiple times during probabilistic analysis. A special macro for probabilistic analysis was written in APDL language [2, 3]. Random input parameters: horizontal stiffnesses K1-K12 of pylons, weight G of deck and substituted thickness H of the deck are defined by Gaussian distribution. The mean values are resumed from preliminary deterministic analysis. The standard deviation of pylon stiffness is high because of the soil stiffness, which is included in it. The probability density functions and cumulative distribution functions of input are shown in Figure 9. The distribution parameters of all springs K1-K12 are the same.

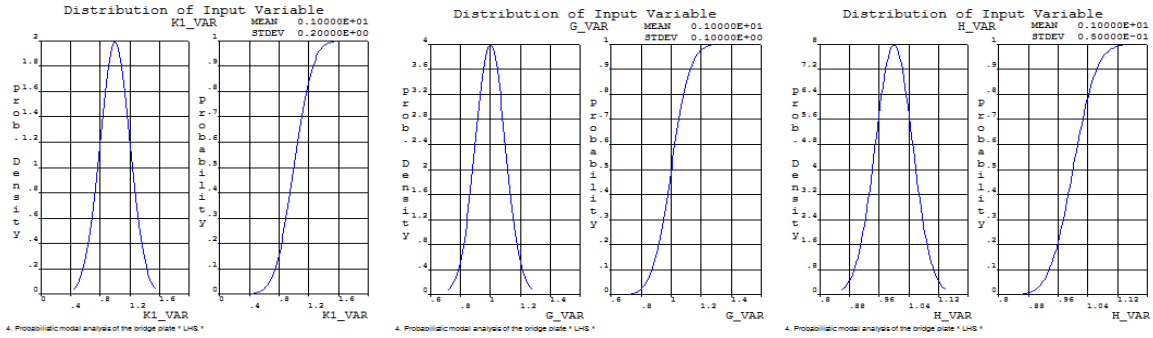


Figure 9: Probability densities and cumulative distributions: a) pylon stiffness K1-K12; b) deck weight, c) substitutional deck thickness.

The Latin Hypercube Sampling (LHS) technique for Monte Carlo Simulation was applied. Simulation with 300 samples was executed.

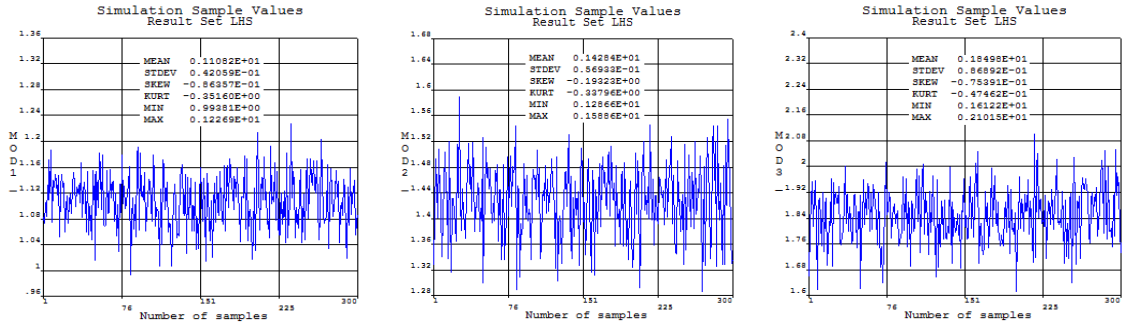


Figure 10: Simulation a) mode 1 b) mode 2 c) mode 3.

Cumulative distribution functions of input variables are presented in Figures 11-14.

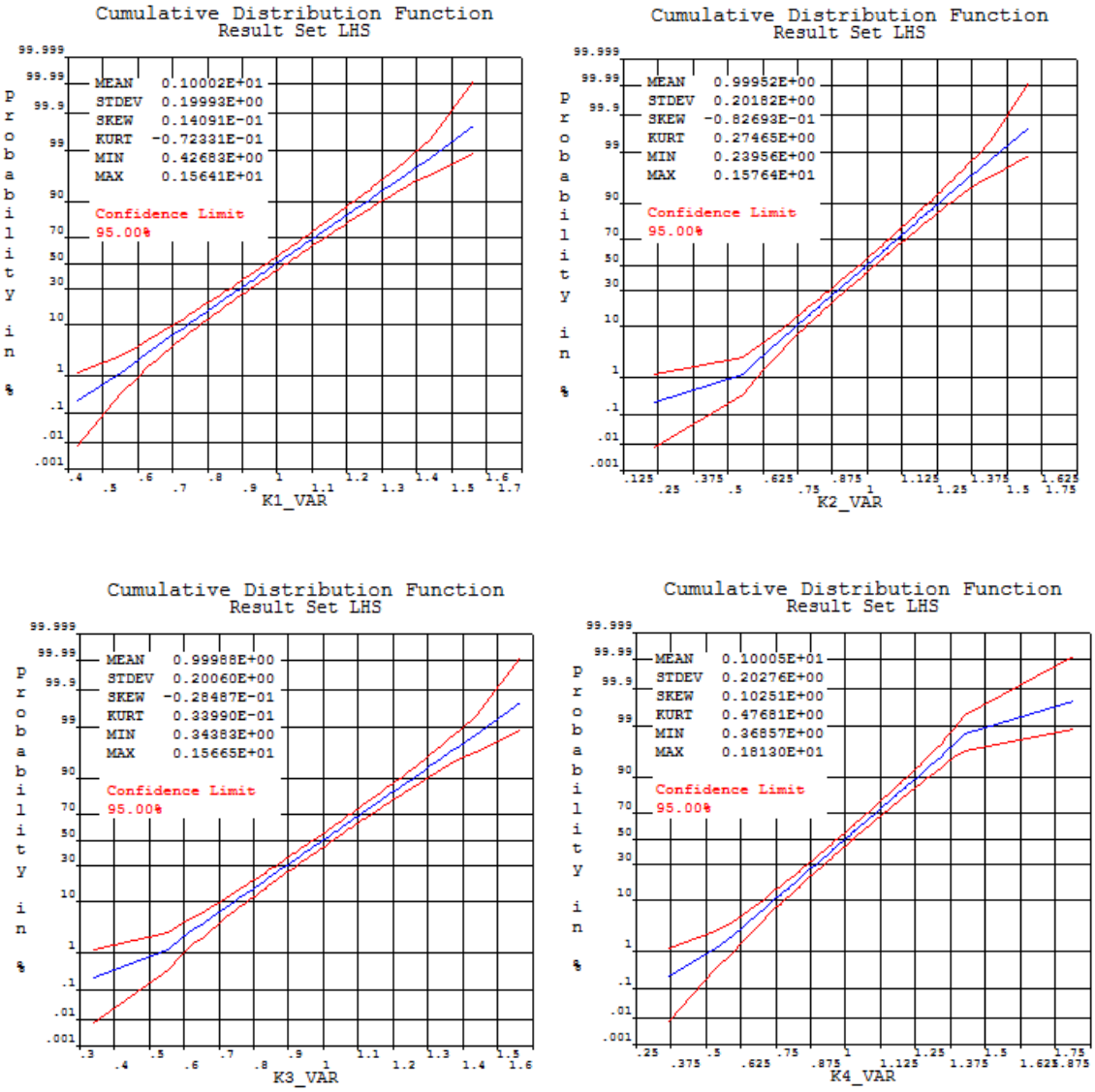


Figure 11: Cumulative distribution function of spring stiffnesses K1 - K4.

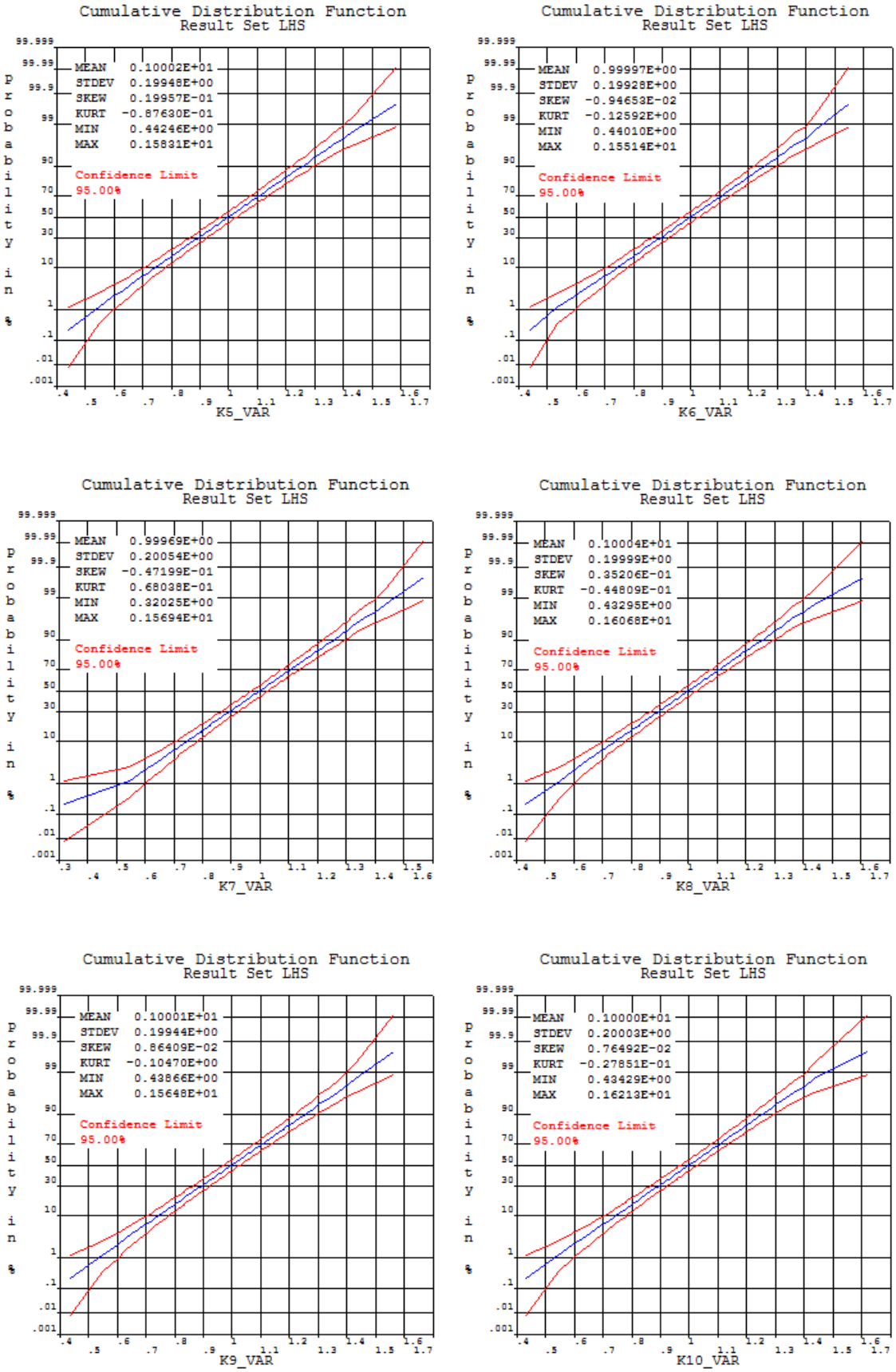


Figure 12: Cumulative distribution function of spring stiffness: K5-K10.

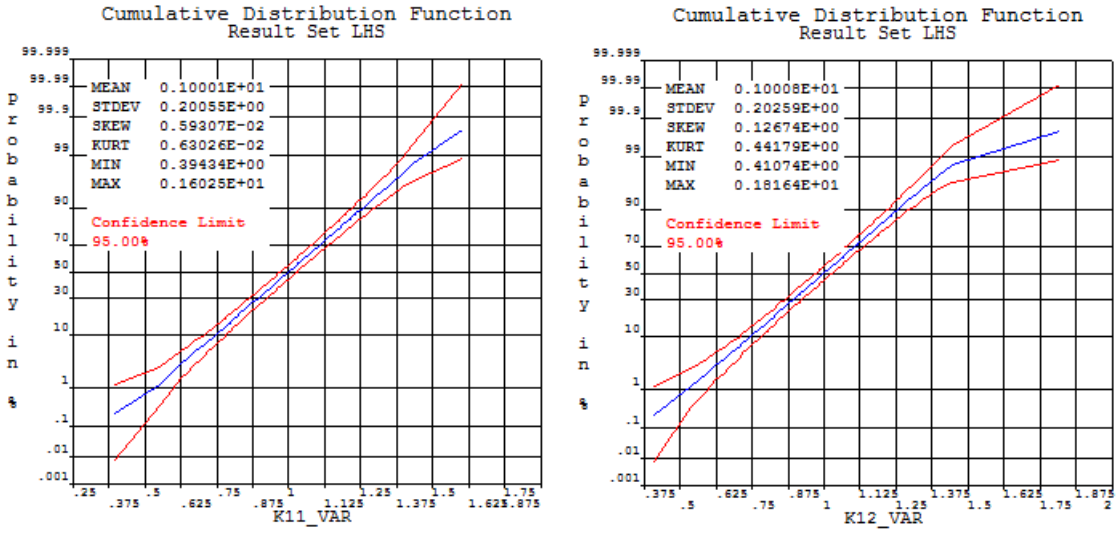


Figure 13: Cumulative distribution function of spring stiffness: K11-K12.

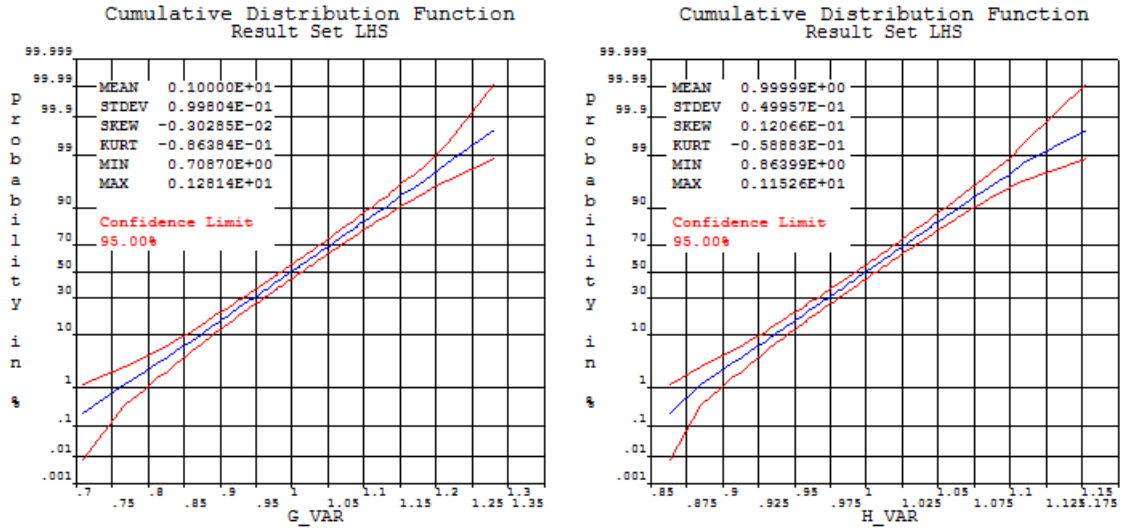


Figure 14: Cumulative distribution functions of weight and substitutional deck thickness.

The Cumulative distribution functions of output parameters are presented in Figure 15.

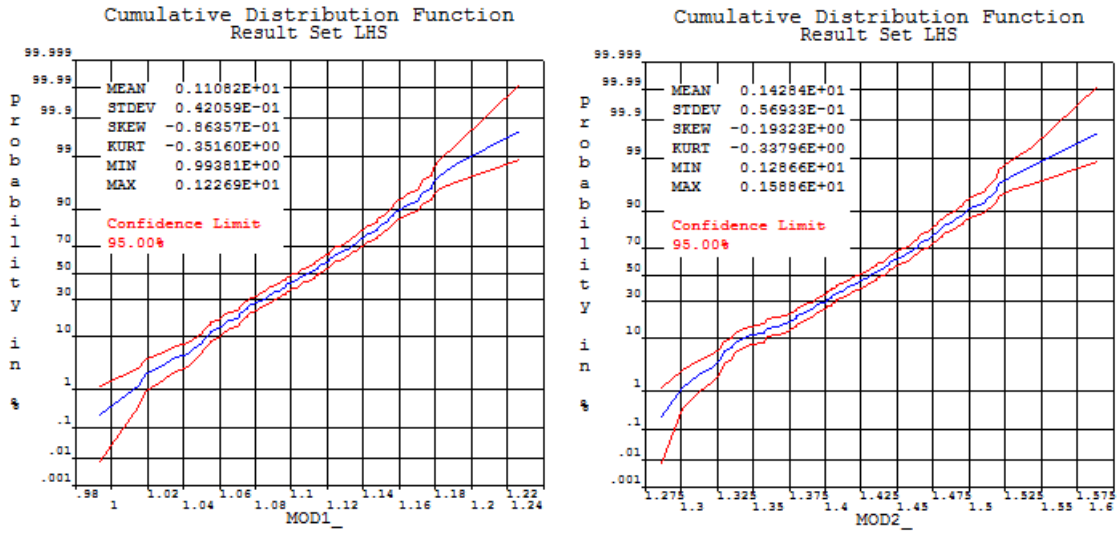

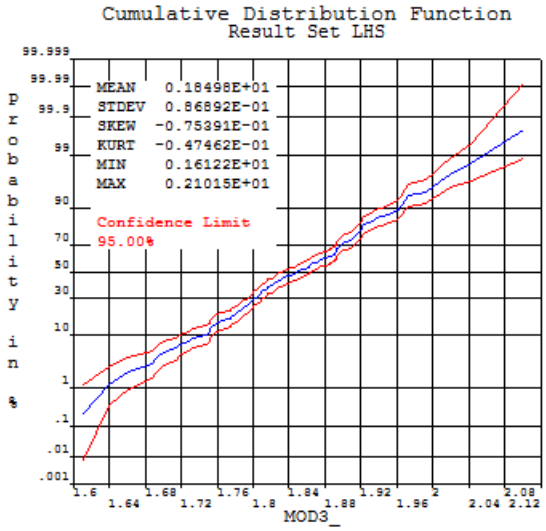


Figure 15: Cumulative distribution functions of modes 1-3.

The sensitivities of modes on stiffnesses and deck weight are presented in Figures 16-18.

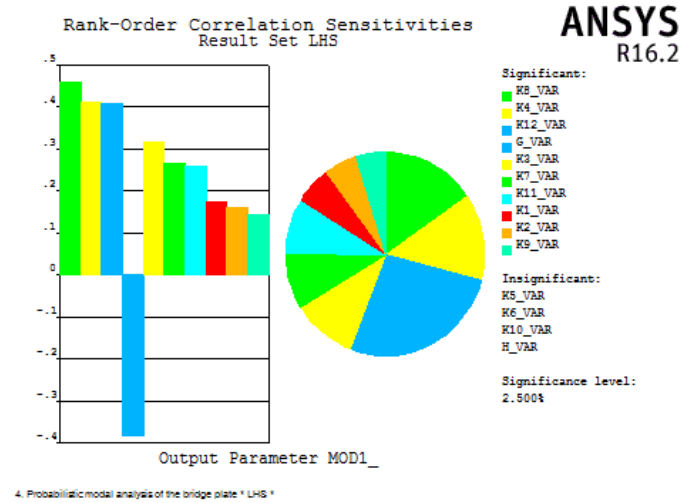


Figure 16: Sensitivities of 1st natural frequency on stiffnesses K1-K12, weight and substituted thickness.

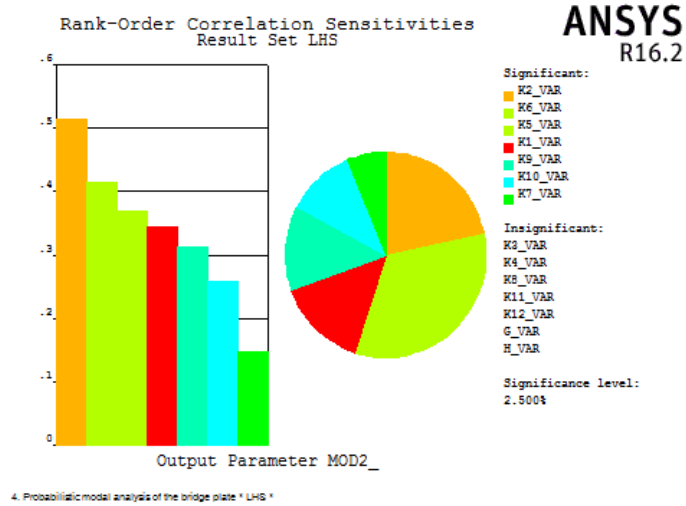


Figure 17: Sensitivities of 2nd natural frequency on stiffnesses K1-K12, weight and substituted thickness.

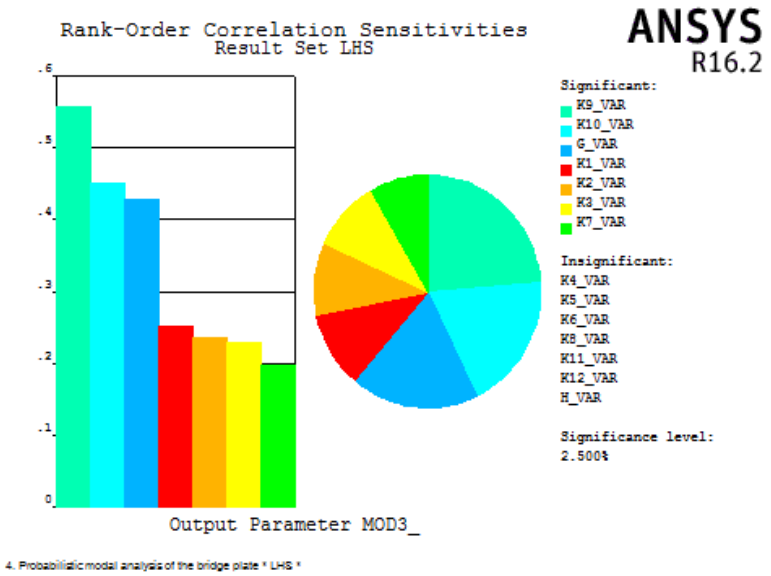


Figure 18: Sensitivities of 3rd natural frequency on stiffnesses K1-K12, weight and substituted thickness.

The resulting sensitivities (Figures 16-18) correspond to the modes in Figures 6-8 and to the correlation coefficients between input and output (see Table 1). The

| **Out\Inp** | K1 | K2 | K3 | K4 | K5 | K6 | K7 | K8 | K9 | K10 | K11 | K12 | G | H |
|---|---|---|---|---|---|---|---|---|---|---|---|---|---|---|
| MOD1 | 0.182 | 0.181 | 0.345 | 0.421 | 0.070 | 0.028 | 0.271 | 0.434 | 0.174 | 0.087 | 0.244 | 0.392 | -0.389 | -0.084 |
| MOD2 | 0.353 | 0.546 | 0.079 | -0.016 | 0.347 | 0.431 | 0.169 | -0.029 | 0.326 | 0.270 | 0.005 | -0.080 | -0.043 | 0.002 |
| MOD3 | 0.238 | 0.231 | 0.253 | -0.050 | -0.102 | 0.112 | 0.206 | -0.065 | 0.590 | 0.478 | 0.064 | -0.023 | 0.440 | 0.074 |

Table 1: Correlation coefficients Output/Input.

## 6 SUMMARY

The contribution presents the probability analysis results of the movable bridge. The decks were considered in top position. The stiffness of the pylons inclusive soil and weight of decks were defined as random input variables. First, second and third natural frequencies were defined as output parameters. The impact on modes is presented. The results are useful in dynamic analysis on the base of Eurocode.

## 7 CONCLUSIONS

- The influence of stochastic input variables: stiffness of pylons inclusive soil and weight of decks on natural frequencies and modes are presented.
- The resulting natural frequency range is shown in dependence on pylon+soil stiffnesses and mass (input defined by Gaussian distribution).
- The decisive springs for particular modes are shown:(see Table 1 and Figures 16-18):

  Mode 1: horizontal springs in Figure 5: K8, K4, K12, K3, K7, K11

  Mode 2: vertical springs in Figure 5: K2, K6, K5, K1, K9, K10

  Mode 3: vertical springs in Figure5: K9, K10, K1, K2

- The sensitivities of modes on particular pylon stiffnesses are presented.
- The obtained results are useful for seismic and wind loading calculation.
- The results provide the overview about dynamic behavior of the bridge.

## REFERENCES

[1] VCE Consult ZT-GmbH, P. Rosko: Nieuwe Beweegbare Botlekbrug, Technical Report, Dynamic Analysis, VCE Consult ZT-GmbH, 2012.

[2] ANSYS Inc. PDF Documentation for Release 15.0 Mechanical APDL Documentation, 2013.

[3] ANSYS Mechanical APDL Advanced Analysis Guide, Release 15.0, 2013.

[4] Eurocode 1: Actions on structures, CEN, 2005.

[5] Eurocode 8: Design of structures for earthquake resistance, CEN, 2004.

COMPDYN 2017
6th ECCOMAS Thematic Conference on
Computational Methods in Structural Dynamics and Earthquake Engineering
M. Papadrakakis, M. Fragiadakis (eds.)
Rhodes Island, Greece, 15–17 June 2017

# 2D LATTICE STRUCTURES - A PARAMETRIC ANALYSIS.

**A. Orefice[1], A. Amendola[1], R. Penna[1], G. Mancusi[1,] L. Feo[1]**

[1] *Department of Civil Engineering, University of Salerno,*

*84084 Fisciano (SA), Italy*

*{aorefice,adamendola1,rpenna,g.mancusi,l.feo}@unisa.it*

**Keywords:** 2D Lattice Structures, Frequency Band Gaps, RUC

**Abstract.** *As discussed in a number of papers, both the static and the dynamic response of square lattice materials are strongly affected by the inner microstructure. It is worth noting that results obtained without considering this influence are totally misleading, especially if non-uniform changes in terms of stresses and strains are concerned at the local scale.*
*Within this context, the present work focuses on a parametric analysis aimed at evaluating the influence of the main mechanical properties of RUC on the dynamic response of a 2D square lattice, thus extending previous results towards the condition of a possible different non-uniform mass density distribution over the RUC configuration.*
*The existence of the band gaps within the low frequency region is searched as well as the position and width of the existing gaps are evaluated by means of a numerical strategy already developed and tested.*

**NOTATION (MINIMAL)**

| | |
|---|---|
| $a$ | lattice constant, |
| $l_1$ | length of the primary micro-beams, |
| $l_2$ | length of the auxiliary micro-beams, |
| $A$ | cross-section area per unit length, |
| $A_s$ | cross-section shear area per unit length, |
| $I$ | flexural inertia per unit length, |
| $E$ | longitudinal normal modulus, |
| $G$ | shear modulus, |
| ¬ | Poisson ratio, |
| $l$ | microscale characteristic length, |
| ρ | mass density. |

## 1 INTRODUCTION

Beyond the high performances of 2D lattices from a static point of view [1-6], there is a great interest in searching for the existence of band gaps within the low frequency region, which is a key topic for a number of innovative applications. These include energy absorption devices, noise and vibration controllers as well as advanced strategies for the seismic isolation [7-12].

The main preliminary consideration is that the underlying microstructure may influence the mechanical response of 2D square lattice according to a complex interplay between different mechanisms. A first one, which is still under investigation by researchers worldwide, is related to the so-called “size-effect” of the slender members of the RUC. This effect is relevant both on the static and on the dynamic properties. Another mechanism concerns the mass density distribution. It has been demonstrated that lumped masses placed in a non-uniform way over the RUC configuration may facilitate additional band gaps to appear and magnify their width at the same time, thus allowing the 2D square lattice to behave as a mechanical waves filter. In a manner of speaking the final behaviour of a 2D square lattice in presence of a wave signal is influenced not only by the RUC configuration. How the mass distribution is spanned over the RUC seems to be more and more relevant. Moreover, an additional mechanism concerns the inner damping characteristics of the constituent materials, which usually are polymer-based.

From a mechanical perspective, the study of the dynamic properties of a 2D lattice is usually based on several assumptions. Primary, the hypothesis of an infinite lattice is helpful due

to the possibility of restricting the analysis to the representative unit cell (RUC) by virtue of the Bloch theorem.

As an example, a simple configuration of the representative unit cell is shown in Figure 1, where the symbols $\mathbf{a}_1$ and $\mathbf{a}_2$ are for the generating vectors along the directions of spatial periodicity. The considered topology in this case requires that $\mathbf{a}_1$ and $\mathbf{a}_2$ are normal to each other.

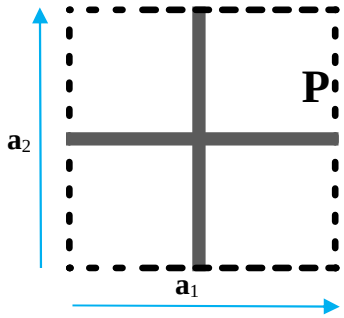


Figure 1. Two-dimensional square lattice material (example of a generic cell).

The displacement of an arbitrary point P of the infinite 2D lattice is given by:

$$\mathbf{u}(\mathbf{r}) = \mathbf{u}_k(\mathbf{r}) \exp(-i\mu t + \mathbf{k}\cdot\mathbf{r}) \tag{1}$$

with the symbol **r** indicating the position vector of a generic material point P, the symbol **k** denoting the Bloch wave vector, ω the angular frequency and $\boldsymbol{u}_k(\mathbf{r})$ the amplitude which exhibits the same spatial periodicity as the point lattice. It useful to express the position vector **r** as follows:

$$\mathbf{r} = \mathbf{r}_0 + n_1\mathbf{a}_1 + n_2\mathbf{a}_2 \tag{2}$$

where $(n_1, n_2)$ is an integer pair and $\mathbf{r}_0$ is the position vector of **O**, which is the corresponding point of **P** within the RUC. Equation (1) becomes:

$$\mathbf{u}(\mathbf{r}) = \mathbf{u}(\mathbf{r}_0) \exp(n_1\mathbf{k}\cdot\mathbf{a}_1 + n_2\mathbf{k}\cdot\mathbf{a}_2) \tag{3}$$

The periodic boundary condition for the dynamic analysis of the unit cell assumes the following final form:

$$\mathbf{u}(\mathbf{r}) = \mathbf{u}(\mathbf{r}_0) \exp[2® (n_1k_1 + n_2k_2)] \tag{4}$$

under the hypothesis the Bloch wave vector is represented by means of a linear combination of the reciprocal space vectors $\mathbf{b}_1$ and $\mathbf{b}_2$:

$$\mathbf{k} = k_1\mathbf{b}_1 + k_2\mathbf{b}_2 \tag{5}$$

## 2 MECHANICAL MODEL

The mechanical model proposed for the dynamic analysis of 2D lattice materials is discussed in great detail in two previous works [13-14].

The main assumptions are:

- The spatial periodicity vectors $\mathbf{a}_1$ and $\mathbf{a}_2$ are orthogonal to each other with the same norm $a$. This implies the investigation is limited to square lattice only.
- The RUC configuration can be modelled by interconnecting straight micro-beams.
- The primary microstructure is made of four micro-beams, which are present in any case (Fig. 2.I). Auxiliary micro-beams can be present depending on the designed topology (Fig. 2.II).
- Rigid internal connections are considered.

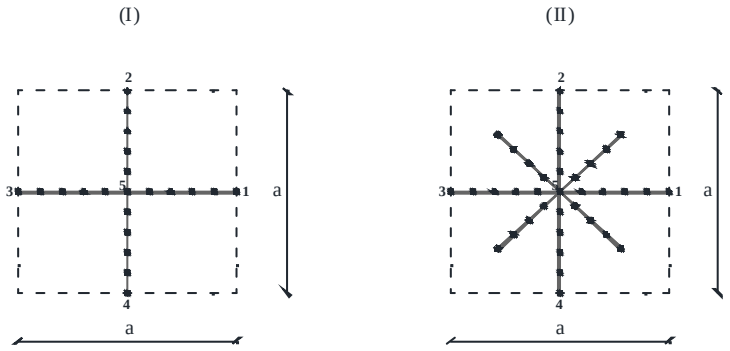


Figure 2. Examples of RUC of a 2D square lattice material (a being the lattice constant).

In the present work, moreover, couple stresses are considered together with classical Cauchy stresses by means of an additional constitutive parameter with the physical dimension of a scale length [15-20]. The scope is to account for the micro-beams local behaviour. It is also important to underline that couple stresses are considered in a simplified manner, according to the so-called Modified Couple Stress Theory, which assumes only the symmetric part of the rotation gradient may influence the strain energy density, as discussed from a critical viewpoint in [21]. Finally, the mass distribution is allowed to be not uniform over the RUC configuration, which is the novel feature of the present work.

## 3 NUMERICAL ANALYSES

A parametric analysis has been carried out with the aim of underlying the influence of the microstructural behaviour on the dynamic response of a 2D square lattice. Two aspects are considered: the presence of an auxiliary microstructure and/or the presence of the size-effect ($l \neq 0$). Geometric and mechanical characteristics of the reference unit cell are summarized in Table 1.

| # | RUC | $a$ | $l_1$ | $A$ | $A_s$ | $I$ | $l_2$ |
|---|---|---|---|---|---|---|---|
| | | [mm] | [mm] | [mm$^2$/mm] | [mm$^2$/mm] | [mm$^4$/mm] | [mm] |
| 1 | I | $1.0\times10^{-1}$ | $5.0\times10^{-2}$ | $5.0\times10^{-3}$ | $4.17\times10^{-3}$ | $1.04\times10^{-8}$ | 0.00 |
| 2 | II | $1.0\times10^{-1}$ | $5.0\times10^{-2}$ | $5.0\times10^{-3}$ | $4.17\times10^{-3}$ | $1.04\times10^{-8}$ | $3.54\times10^{-2}$ |

Table 1 Geometry and mechanical parameters (I/II indicating the considered topology as in Fig. 2).

It is worth noting that the considered geometry is the same investigated in [14]. Dealing with the constituent materials, the following hypotheses are taken into consideration:

- The primary micro-structure is composed of aluminium: E=9.00×10$^4$ N/mm$^2$; ¬ =0.23; G=3.66×10$^4$ N/mm$^2$; *l*= 6.58 «*m*; ρ =2.70×10$^{-6}$ kg/mm$^3$.
- If an auxiliary micro-structure is present, this one is composed of aluminium (i), as above, or epoxy resin (ii): E=1440 N/mm$^2$; ¬ =0.38; G=522 N/mm$^2$; *l*=17.6 «*m*; ρ =1.10×10$^{-6}$ kg/mm$^3$.

The possibility of considering different materials for the primary and the auxiliary microstructures represents a generalization of the parametric analysis discussed in [14]. Moreover, three different further assumptions are considered:

a) the microscale characteristic length *l* is equal to zero (i.e. the size effect is discarded);
b) the size effect is present ($l \neq 0$) for the auxiliary beams of the RUC [21-22];
c) the size effect is present for both primary and auxiliary beams of the RUC [21-22].

For what concerns the finite element approximation, a detailed description of the proposed approach is discussed in [13] as well as the "enhanced" finite element proposed for this scope. The convergence rate and the accuracy of the numerical solutions have been adequately assessed in a previous work [14].

## 4 DISCUSSION AND FINAL REMARKS

In Table 2 the main results concerning the lowest natural frequencies (not dimensional) are presented. They refer to the relevant points **O**, **A** and **B** of the boundary of the irreducible part of the first Brillouin zone indicated in Figure 3.

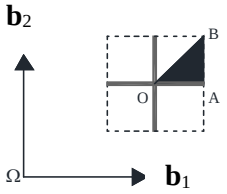


Figure 3. Irreducible part of the first *Brillouin* zone.

The results are presented in terms of dimensionless frequency values which are identified from the eigenvalues and represented as follows:

$$\tilde{\mu} = \mu / \mu_1, \qquad \text{with} \quad \mu_1 = \frac{\omega}{a^2}\sqrt{\frac{EI}{\rho A}}. \tag{6}$$

| | | 1 | 2 | 3 | 4 | 5 | 6 | 7 | 8 | 9 | 10 |
|---|---|---|---|---|---|---|---|---|---|---|---|
| 1.a | O | 0.0 | 0.0 | 4.2 | 4.2 | 6.1 | 9.3 | 18.8 | 18.8 | 23.9 | 29.4 |
| | A | 0.8 | 2.4 | 3.3 | 7.0 | 11.5 | 13.2 | 14.5 | 20.0 | 25.5 | 32.9 |
| | B | 1.7 | 2.2 | 8.9 | 11.6 | 11.6 | 12.7 | 17.0 | 17.0 | 28.9 | 34.7 |
| 1.b | O | 0.0 | 0.0 | 10.8 | 10.8 | 15.9 | 21.7 | 37.1 | 37.1 | 52.1 | 56.4 |
| | A | 2.0 | 6.6 | 7.5 | 15.9 | 17.8 | 25.7 | 30.4 | 36.6 | 51.6 | 53.2 |
| | B | 4.2 | 5.7 | 14.1 | 14.1 | 22.1 | 27.4 | 30.6 | 30.9 | 48.2 | 48.3 |
| 2.a.i | O | 0.0 | 0.0 | 2.6 | 3.7 | 4.0 | 4.3 | 4.3 | 4.8 | 7.9 | 9.3 |
| | A | 0.6 | 2.2 | 3.0 | 3.3 | 4.2 | 4.3 | 4.3 | 8.4 | 10.3 | 11.9 |
| | B | 1.5 | 2.2 | 3.0 | 4.2 | 4.3 | 4.3 | 9.7 | 9.8 | 10.7 | 12.7 |
| 2.a.ii | O | 0.0 | 0.0 | 1.1 | 1.1 | 1.1 | 1.1 | 4.0 | 4.0 | 5.8 | 6.3 |
| | A | 0.6 | 1.1 | 1.1 | 1.1 | 1.2 | 2.3 | 3.3 | 6.2 | 6.3 | 6.3 |
| | B | 1.0 | 1.1 | 1.1 | 1.1 | 1.7 | 2.2 | 6.1 | 6.3 | 6.3 | 6.3 |
| 2.b.i | O | 0.0 | 0.0 | 2.9 | 3.8 | 4.0 | 9.3 | 9.6 | 11.4 | 11.4 | 12.4 |
| | A | 0.6 | 2.2 | 3.3 | 3.5 | 8.4 | 9.5 | 11.4 | 11.4 | 12.7 | 13.5 |
| | B | 1.5 | 2.2 | 3.5 | 8.2 | 9.8 | 11.4 | 11.4 | 12.6 | 12.7 | 12.7 |
| 2.b.ii | O | 0.0 | 0.0 | 1.2 | 1.2 | 1.2 | 1.2 | 4.0 | 4.0 | 6.0 | 6.9 |
| | A | 0.6 | 1.2 | 1.2 | 1.2 | 1.3 | 2.3 | 3.3 | 6.6 | 6.8 | 6.9 |
| | B | 1.1 | 1.2 | 1.2 | 1.2 | 1.7 | 2.2 | 6.7 | 6.8 | 6.9 | 6.9 |
| 2.c.i | O | 0.0 | 0.0 | 7.0 | 9.6 | 10.2 | 11.4 | 11.4 | 12.7 | 19.5 | 21.7 |
| | A | 1.5 | 6.0 | 6.8 | 8.0 | 10.1 | 11.4 | 11.4 | 14.5 | 20.4 | 26.4 |
| | B | 3.7 | 5.7 | 7.7 | 8.8 | 11.4 | 11.4 | 11.5 | 13.8 | 25.0 | 27.3 |
| 2.c.ii | O | 0.0 | 0.0 | 1.2 | 1.2 | 1.2 | 1.2 | 6.9 | 6.9 | 6.9 | 7.0 |
| | A | 1.2 | 1.2 | 1.2 | 1.2 | 2.0 | 6.2 | 6.8 | 6.9 | 6.9 | 7.1 |
| | B | 1.2 | 1.2 | 1.2 | 1.2 | 4.2 | 5.7 | 6.9 | 6.9 | 6.9 | 6.9 |

Table 2 - First natural frequencies $\omega_1$.

The numerical results presented in Table 2 allow to make a comparison between two different hypotheses concerning the constituent material of the auxiliary microstructure: i) aluminium (i.e. the same material as the primary microstructure) or ii) epoxy resin. Moreover, the comparison is extended to the influence of the microstructure length, according to the assumptions previously summarized by acronyms “a”, “b” and “c”.

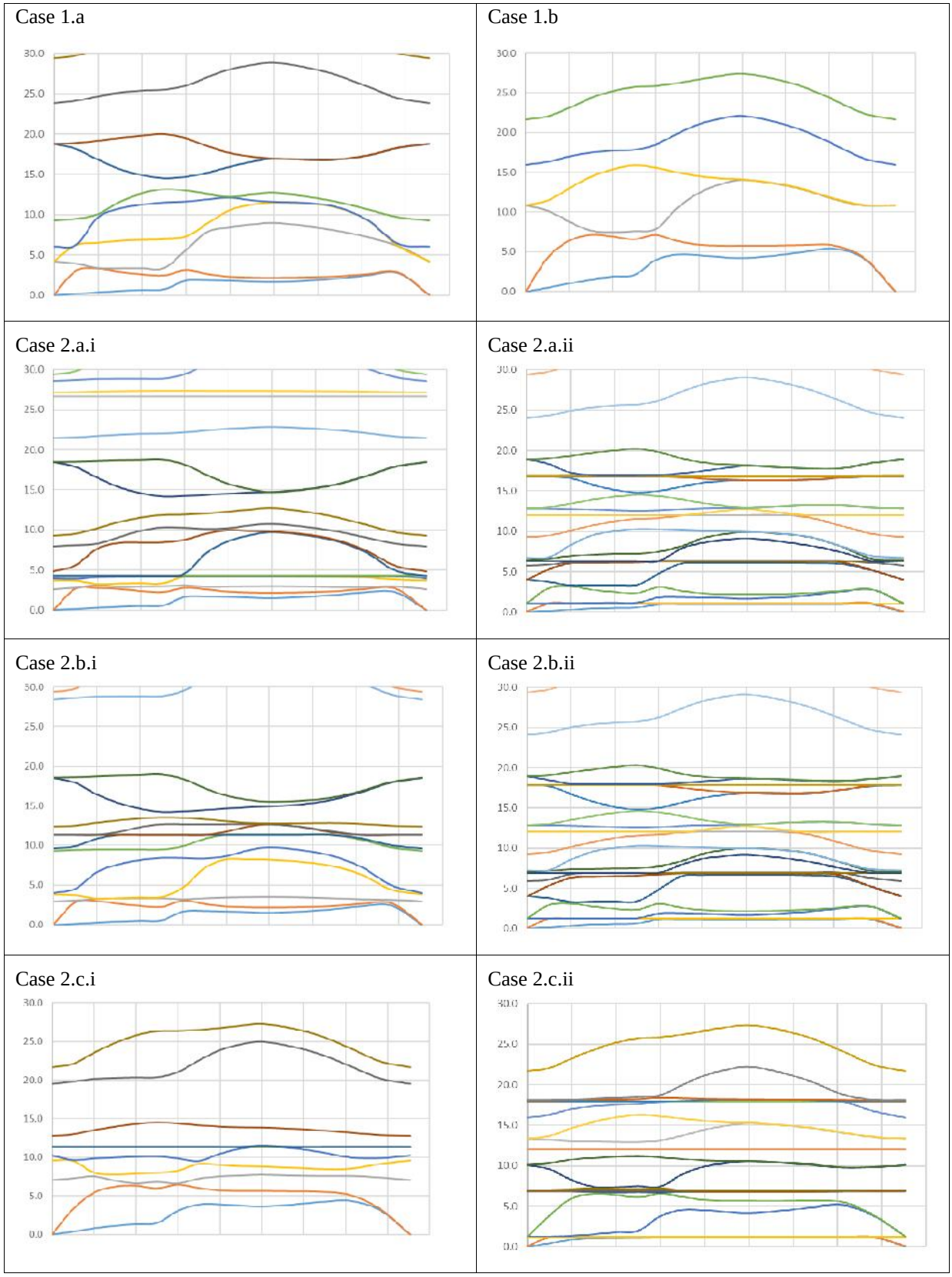


**Figure 4.** Frequency band structures (not dimensional)

**(**abscissa lying on the boundary **OABO** of the irreducible part of the first *Brillouin* zone)

In Table 3 the position and the width of the first band gaps are presented. It is also indicated the number corresponding to the immediately below band (lower band number).

| | | 1 | 2 | 3 | 4 | 5 | 6 | 7 | 8 | 9 | 10 |
|---|---|---|---|---|---|---|---|---|---|---|---|
| position | 1.a | 3.300 | 13.860 | 21.936 | 29.166 | 35.260 | 45.858 | 66.796 | 74.461 | 89.245 | 105.955 |
| Gap | | 0.046 | 1.347 | 3.856 | 0.472 | 1.133 | 7.388 | 1.283 | 0.672 | 5.260 | 0.910 |
| # Lower band | | 2 | 6 | 8 | 9 | 10 | 12 | 16 | 18 | 20 | 22 |
| Position | 1.b | 7.263 | 15.914 | 28.868 | 42.659 | 64.808 | 74.250 | 91.520 | 104.320 | 118.630 | 156.655 |
| Gap | | 0.280 | 0.044 | 2.999 | 11.055 | 5.240 | 3.774 | 7.614 | 8.200 | 8.280 | 10.170 |
| # Lower band | | 2 | 4 | 6 | 8 | 12 | 14 | 16 | 18 | 20 | 26 |
| Position | 2.a.i | 3.184 | 13.449 | 20.105 | 24.745 | 26.916 | 28.006 | 35.162 | 45.711 | 51.342 | 67.185 |
| Gap | | 0.115 | 1.439 | 2.704 | 3.840 | 0.501 | 1.205 | 0.942 | 3.948 | 7.314 | 0.505 |
| # Lower band | | 3 | 10 | 12 | 13 | 15 | 16 | 18 | 22 | 24 | 28 |
| Position | 2.a.ii | 1.068 | 1.075 | 3.240 | 14.644 | 16.943 | 22.136 | 29.207 | 35.240 | 44.295 | 46.572 |
| Gap | | 0.001 | 0.013 | 0.061 | 0.213 | 0.012 | 3.828 | 0.390 | 1.094 | 4.155 | 0.049 |
| # Lower band | | 2 | 4 | 6 | 18 | 22 | 24 | 25 | 30 | 36 | 38 |
| Position | 2.b.i | 13.871 | 23.672 | 35.117 | 45.266 | 47.436 | 49.368 | 51.656 | 55.370 | 77.055 | 92.386 |
| Gap | | 0.686 | 9.455 | 0.853 | 3.169 | 0.499 | 3.366 | 0.999 | 6.430 | 3.015 | 10.296 |
| # Lower band | | 10 | 12 | 14 | 18 | 19 | 21 | 22 | 24 | 30 | 32 |
| Position | 2.b.ii | 1.205 | 1.208 | 3.217 | 14.685 | 17.938 | 22.199 | 29.246 | 35.241 | 44.601 | 47.199 |
| Gap | | 0.001 | 0.006 | 0.123 | 0.182 | 0.053 | 3.800 | 0.313 | 1.096 | 4.761 | 0.048 |
| # Lower band | | 2 | 4 | 6 | 18 | 22 | 24 | 25 | 30 | 36 | 38 |
| Position | 2.c.i | 6.551 | 7.743 | 12.121 | 17.030 | 28.808 | 36.918 | 44.041 | 47.837 | 49.800 | 51.654 |
| Gap | | 0.139 | 0.085 | 1.228 | 5.022 | 3.019 | 0.571 | 7.288 | 0.303 | 2.460 | 1.002 |
| # Lower band | | 2 | 3 | 7 | 8 | 10 | 12 | 14 | 16 | 17 | 18 |
| Position | 2.c.ii | 1.205 | 1.225 | 6.639 | 7.299 | 11.587 | 12.471 | 28.859 | 36.909 | 42.145 | 47.197 |
| Gap | | 0.001 | 0.040 | 0.115 | 0.166 | 0.843 | 0.925 | 2.992 | 0.157 | 9.421 | 0.053 |
| # Lower band | | 2 | 4 | 6 | 10 | 12 | 14 | 22 | 28 | 32 | 34 |

**Table 3** - Position and width for the lowest gaps.

The main conclusions can be summarised as follows. 1. The magnitude of the micro-scale length *l* influences the position and width of the first band gaps. A forward shift of the first band gaps is determined by the presence of the size-effect. 2. The presence of the auxiliary micro-structure allows flat bands to appear in the low frequency region. 3. A not-uniform dis-

tribution of the mass density over the RUC produces a significant change of the band structure of the 2D lattice.

## ACKNOWLEDGMENTS

The concept and development of this paper lies on a wide cultural background represented by many works authored by scientists and researchers worldwide [23-94].

## REFERENCES

[1] L.J. Gibson, M.F. Ashby, *Cellular Solids: Structure and Properties*. *Cambridge University Press*, Cambridge, 1997.

[2] M. Maldovan, E.L. Thomas, *Periodic Materials and Interference Lithography - photonic, phononic and mechanics*, Wiley–Vch, 2009.

[3] R.M. Christensen, Mechanics of cellular and other low-density materials, I*nt. J. Solids Struct.*, **37**, 93–104, 2000.

[4] J.C. Wallach, L.J. Gibson, Mechanical behavior of a three dimensional truss material, *Int. J. Solids Struct.*, 38, 7181–7196, 2001.

[5] Y.H. Zhang, H.L. Fan, D.N. Fang, Constitutive relations and failure criterion of planar lattice composites, *Compos. Sci. Technol.* , **68**, 3299–3304, 2008.

[6] H.L. Fan, F.N. Jin, D.N. Fang, Nonlinear mechanical properties of lattice truss materials, *Mater. Design* , **30**, 511–517, 2009.

[7] X.Z. Zhou, Y.S.Wang, C.Z. Zhang, Effects of material parameters on elastic band gaps of two-dimensional solid phononic crystals, *J. Appl. Phys.*, **106**, 14903-14911, 2009.

[8] Y.Z. Wang, F.M. Li, Y.S. Wang, et al., Tuning of band gaps for a two-dimensional piezoelectric phononic crystal with a rectangular lattice, *Acta Mech. Sin.*, **25**, 65–71, 2009.

[9] P.G. Martinsson, A.B. Movchan, Vibrations of lattice structures and phononic band gaps, *Q. J. Mech. Appl. Math.* , **56**, 45–64, 2003.

[10] A.S. Phani, J. Woodhouse, N.A. Fleck, Wave propagation in two-dimensional periodic lattices, *J. Acoust Soc. Am.*, **119**, 1995–2005, 2006.

[11] N. Zhen, Z. Yan, Y. Wang, Elastic wave propagation in honeycomb materials. *Chinese Journal of Theoretical and Applied Mechanics*, **40**, 769–775., 2008.

[12] J. Gaofeng, S. Zhifei, A new seismic isolation system and its feasibility study, *Earthq Eng & Eng Vib* , 75-82, 2010.

[13] G. Mancusi, L. Feo, A Refined Finite Element Formulation for the Microstructure-Dependent Analysis of Two-Dimensional (2D) Lattice Materials, *Materials*, **6 (1)**, 1-17, 2013.

[14] G. Mancusi, F. Fabbrocino, L. Feo, F. Fraternali, Size effect and dynamic properties of 2D lattice materials, *Composites Part B* **112**, 235-242, 2017.

[15] R.D. Mindlin, Influence of couple-stresses on stress concentrations. *Exp. Mech.* **3**, 1–7, 1963.

[16] S. Lui, W. Su, Effective couple-stress continuum model of cellular solids and size effects analysis. *Int. J. Solids and Structures,* **46**, 2787-2799, 2009.

[17] P.R. Onck, E.W. Andrews, L.J. Gibson, Size effects in ductile cellular solids. Part I: modelling, Int. J.Mech. Sci. **34**, 681–699, 2000.

[18] E.W. Andrews, G. Gioux, P.R. Onck, L.J. Gibson, Size effects in ductile cellular solids. Part II: experimental results, Int. J. Mech. Sci. **34**, 701–713, 2000.

[19] S.K. Park, X.L. Gao, Bernoulli–Euler beam model based on a modified couple stress theory, *J. Micromech. Microeng.* ,**16**, 2355-2359, 2006.

[20] H.M. Ma, X.L. Gao, J.N. , A microstructure-dependent Timoshenko beam model based on a modified couple stress theory, *Journal of the Mechanics and Physics of Solids* **, 56 (12)**, 3379-3391, 2008.

[21] M. Shaat, Physical and Mathematical Representations of Couple Stress Effects on Micro/Nanosolids, *International Journal of Applied Mechanics*, **7 (1)**, 2015.

[22] B. Akgoz, O. Civalek, Strain gradient elasticity and modified couple stress models for buckling analysis of axially loaded micro-scaled beams, *International Journal of Engineering Science*, **49**, 1268-1280, 2011.

[23] A. Amendola, C.J. Smith, R. Goodall, F. Auricchio, L. Feo, G. Benzoni, F. Fraternali, 2. Experimental response of additively manufactured metallic pentamode materials confined between stiffening plates. *Composite Structures*, **142**, 254-262, 2016.

[24] A. Amendola, E.H. Nava, R. Goodall, I. Todd, R.E. Skelton, F. Fraternali, On the additive manufacturing, post-tensioning and testing of bi-material tensegrity structures, *Composite Structures*, **131**, 66-71, 2015.

[25] I. Farina, F. Fabbrocino, G. Carpentieri, M. Modano, A. Amendola, R. Goodall, L. Feo, F. Fraternali, *On the reinforcement of cement mortars through 3D printed polymeric and metallic fibers*, Composites Part B: Engineering, **90**, 76-85, 2016.

[26] F. Fraternali, Free Discontinuity Finite element models in two-dimensions for in-plane crack problems, *Theoretical and Applied Fracture Mechanics*, **47**, 274-282, 2007.

[27] F. Fraternali, C.D Lorenz, G. Marcelli, On the estimation of the curvatures and bending rigidity of membrane networks via a local maximum-entropy approach, *Journal of Computational Physics*, **231**, 528-540, 2012.

[28] B. Schmidt, F. Fraternali, Universal formulae for the limiting elastic energy of membrane networks, *Journal of the Mechanics and Physics of Solids*, **60**, 172-180, 2012.

[29] L. Ascione, F. Fraternali, A penalty model for the analysis of composite curved beams, *Computers & Structures*, **45**, 985-999, 1992.

[30] F. Fraternali, J.N. Reddy, A penalty model for the analysis of laminated composite shells, *International Journal of Solids and Structures*, **30**, 3337-3355, 1993.

[31] A. Amendola, G. Carpentieri, M. De Oliveira, R.E. Skelton, F. Fraternali, Experimental investigation of the softening-stiffening response of tensegrity prisms under compressive loading. *Composite Structures*, **117**, 234-243, 2014.

[32] F. Fraternali, G. Bilotti, Non-Linear Elastic Stress Analysis in Curved Composite Beams. *Computers & Structures*, **62**, 837-869, 1997.

[33] F. Fraternali, G. Carpentieri, A. Amendola, On the mechanical modeling of the extreme softening/stiffening response of axially loaded tensegrity prisms. *Journal of the Mechanics and Physics of Solids*, **74**, 136-157, 2015.

[34] R.E. Skelton, F. Fraternali, G. Carpentieri, A. Micheletti, Minimum mass design of tensegrity bridges with parametric architecture and multiscale complexity. *Mechanics Research Communications*, 58, 124-132, 2014.

[35] A. Leonard, F. Fraternali, C. Daraio, Directional wave propagation in a highly nonlinear square packing of spheres. *Experimental Mechanics*, **53**(3), 327-337, 2013.

[36] F. Fraternali, G. Carpentieri, A. Amendola, R.E. Skelton, V. F. Nesterenko, Multiscale tunability of solitary wave dynamics in tensegrity metamaterials. *Applied Physics Letters*, **105**, 201903, 2014.

[37] F. Fraternali, I. Farina, C. Polzone, E. Pagliuca, L. Feo, On the use of R-PET strips for the reinforcement of cement mortars. *Composites. Part B*, **46**, 207-210, 2013.

[38] J.R. Raney, F. Fraternali, A. Amendola, C. Daraio, Modeling and In Situ Identification of Material Parameters for Layered Structures based on Carbon Nanotube Arrays. *Composite Structures*, **93**, 3013–3018, 2011.

[39] C. Daraio, D . Ngo, V. F. Nesterenko, F. Fraternali, Highly Nonlinear Pulse Splitting and Recombination in a Two Dimensional Granular Network. *Physical Review E*, **82**, 036603, 2010.

[40] F. Fraternali, A. Marino, T. Elsayed, A. Della Cioppa, On the structural shape optimization via variational methods and evolutionary algorithms. Mechanics of Advanced Materials and Structures, **18**, 225-243, 2011.

[41] F. Fraternali, S. Spadea, V.P. Berardi, Effects of recycled PET fibers on the mechanical properties and seawater curing of Portland cement-based concretes. *Construction and Building Materials*, **61**, 293-302, 2014.

[42] T. Blesgen, F. Fraternali, J.R. Raney, A. Amendola, C. Daraio, Continuum Limits of Bistable Spring Models of Carbon Nanotube Arrays accounting for Material Damage. *Mechanics Research Communications*, **45**, 58-63, 2012

[43] F. Fraternali. A Mixed Lumped Stress – Displacement Approach to the Elastic Problem of Masonry Walls. Mechanics Research Communications, **38**, 176-180, 2011.

[44] F. Fraternali, M. Negri, M. Ortiz, On the Convergence of 3D Free Discontinuity Models in Variational Fracture. *International Journal of Fracture*, **166**(1-2), 3-11, 2010.

[45] F. Fraternali, S. Spadea, L. Ascione, Buckling behavior of curved composite beams with different elastic response in tension and compression. *Composite Structures*, **100**, 280-289, 2013.

[46] A. Orefice, G. Mancusi, L. Feo, F. Fraternali, Cohesive interface behaviour and local shear strains in axially loaded composite annular tubes. *Composite Structures*, **160**, 1126-1135, 2017.

[47] G. Mancusi, A Orefice, L. Feo, F. Fraternali, Structural analysis of adhesive bonding for thick-walled tubular composite profiles. *ECCOMAS Congress 2016 - Proceedings of the 7th European Congress on Computational Methods in Applied Sciences and Engineering*, **4**, 7837-7852.

[48] F. Ascione, G. Mancusi, S. Spadea, L. Lamberti, F. Lebon, A. Maurel-Pantel, On the flexural behaviour of GFRP beams obtained by bonding simple panels: An experimental investigation *Composite Structures*, **131**, 55-65, 2015.

[49] L. Ascione, G. Mancusi, A. D'Aponte, Fabric-Reinforced Cementitious Matrix (FRCM): A new Italian guideline under development. *Key Engineering Materials*, **624**, 3-10, 2015.

[50] G. Mancusi, F. Ascione, M. Lamberti, Pre-buckling behavior of composite beams: A mechanical innovative approach. *Composite Structures*, **17** (1), 396-410, 2014.

[51] F. Ascione, G. Mancusi, The influence of the web-flange junction stiffness on the mechanical behaviour of thin-walled pultruded beams. *Composites Part B: Engineering*, **55**, 599-606, 2013.

[52] V.P. Berardi, G. Mancusi, A mechanical model for predicting the long term behavior of reinforced polymer concretes. *Mechanics Research Communications*, **50**, 1-7, 2013.

[53] G. Mancusi, L. Feo, Non-linear pre-buckling behavior of shear deformable thin-walled composite beams with open cross-section. *Composites Part B: Engineering*, **47**, 379-390, 2013.

[54] G. Mancusi, S. Spadea, V.P. Berardi, Experimental analysis on the time-dependent bonding of FRP laminates under sustained loads. *Composites Part B: Engineering*, **46**, 116-122, 2013.

[55] G. Mancusi, F. Ascione, Performance at collapse of adhesive bonding. *Composite Structures*, **96**, 256-261, 2013.

[56] L. Feo, G. Mancusi, The influence of the shear deformations on the local stress state of pultruded composite profiles. *Mechanics Research Communications*, **47**, 44-49, 2013.

[57] V.P. Berardi, G. Mancusi, Time-dependent behavior of reinforced polymer concrete columns under eccentric axial loading. *Materials*, **5** (11), 2342-235, 2012.

[58] G. Mancusi, L. Feo, V.P. Berardi, Concrete open-wall systems wrapped with FRP under torsional loads. *Materials*, **5** (11), 2055-2068, 2012.

[59] F. Ascione, G. Mancusi, Curve adhesive joints. *Composite Structures*, **94** (8), 2657-2664, 2012.

[60] F. Ascione, G. Mancusi, The influence of the geometric curvature on the mechanical behaviour of the adhesive joint. *Civil-Comp Proceedings*, **99**, 2012.

[61] L. Ascione, G. Mancusi, S. Spadea, Flexural behaviour of concrete beams reinforced with GFRP bars. *Strain*, **46** (5), 460-469, 2010.

[62] L. Feo, G. Mancusi, Modeling shear deformability of thin-walled composite beams with open cross-section. *Mechanics Research Communications*, **37** (3), 320-325, 2010.

[63] F. Ascione, G. Mancusi, Failure criteria for FRP adhesive lap joints: A comparative analysis. *Mechanics of Advanced Materials and Structures*, **17** (2), 157-164, 2010.

[64] F. Ascione, G. Mancusi, Axial/bending coupled analysis for FRP adhesive lap joints. *Mechanics of Advanced Materials and Structures*, **17** (2), 85-98, 2010.

[65] F. Ascione, G. Mancusi, An experimental analysis on the time-dependent behaviour of a CFRP retrofitting under sustained loads. *Proceedings of the 6th International Conference on Fracture Mechanics of Concrete and Concrete Structures*, **2**,1085-1090, 2007.

[66] L. Ascione, V.P. Berardi, E. Di Nardo, L. Feo, G. Mancusi, An experimental and numerical investigation on the plating of reinforced concrete beams with FRP laminates. *Lecture Notes in Applied and Computational Mechanics*, **23**, 303-314, 2005.

[67] L. Ascione, V.P. Berardi, L. Feo, G. Mancusi, A numerical evaluation of the interlaminar stress state in externally FRP plated RC beams. *Composites Part B: Engineering*, **36** (1), 83-90, 2005.

[68] L. Ascione, L. Feo, G. Mancusi, On the statical behaviour of fibre-reinforced polymer thin-walled beams. *Composites Part B: Engineering*, **31** (8), 643-654, 2000.

[69] V.P. Berardi, Initiation of Failure for Masonry Subject to In-Plane Loads through Micromechanics. *Modelling and Simulation in Engineering*, art. no. 2959038, 2016.

[70] G. Carpentieri, F. Fabbrocino, M. De Piano, V.P. Berardi, L. Feo, F. Fraternali, Minimal mass design of strengthening techniques for planar and curved masonry structures *ECCOMAS Congress 2016 - Proceedings of the 7th European Congress on Computational Methods in Applied Sciences and Engineering*, **2**, 2210-2219.

[71] F. Fabbrocino, I. Farina, V.P. Berardi, A.J.M. Ferreira, F. Fraternali,On the thrust surface of unreinforced and FRP-/FRCM-reinforced masonry domes. *Composites Part B: Engineering*, **83**, 297-305, 2015.

[72] Amendola, C.J. Smith, R. Goodall, F. Auricchio, L. Feo, G. Benzoni, F. Fraternali, Experimental response of additively manufactured metallic pentamode materials confined between stiffening plates. *Composite Structures*, **142**, 254–262, 2016.

[73] G. Lomiento , N. Bonessio, G. Benzoni, Friction Model for Sliding Bearings under Seismic Excitation, Journal of Earthquake Engineering, **17**(8):1162-1191, 2013..

[74] M. Budek, M. J. N. Priestley, G. Benzoni, The Effect of External Confinement on Flexural Hinging in Drilled Pile Shafts, *Earthquake Spectra*, **20** (1), 1-24, 2004.

[75] Hae-Bum Yun, Sami F. Masri, Raymond W. Wolfe, Gianmario Benzoni , Data-driven methodologies for change detection in large-scale nonlinear dampers with noisy measurements, *Journal of Sound and Vibration*, **322**, Issues 1–2, 24 April 2009, Pages 336–357.

[76] D. D'Ayala, G. Benzoni, Historic and Traditional Structures during the 2010 Chile Earthquake: Observations, Codes, and Conservation Strategies. *Earthquake Spectra*, **28** (S1), S425-S451, 2012.

[77] N. Bonessio, G. Lomiento, G. Benzoni, Damage identification procedure for seismically isolated bridges, *Structural Control Health Monitoring*, **19**(5), 565–578, 2012.

[78] G. Benzoni, C. Casarotti, Effects of Vertical Load, Strain Rate and Cycling on the Response of Lead-Rubber Seismic Isolators, *Journal of Earthquake Engineering* ,**13**, 2009.

[79] G. Benzoni, M. J. N. Priestley, Seismic response of linked marginal wharf segments, *Journal of Earthquake Engineering* **74**, 513-539, 2003.

[80] A. Amendola, G. Benzoni, F. Fraternali, Non-linear elastic response of layered structures, alternating pentamode lattices and confinement plates. *Composite Part B, Engineering*, Online first, DOI: 10.1016/j.compositesb.2016.10.027, 2016.

[81] F. Fraternali, G. Carpentieri, R. Montuori, A. Amendola, G. Benzoni, On the use of mechanical metamaterials for innovative seismic isolation systems, COMPDYN 2015 - 5th ECCOMAS Thematic Conference on Computational Methods in Structural Dynamics and Earthquake Engineering, 349-358.

[82] L. Ascione, V.P. Berardi, A. Giordano, S. Spadea, Pre-buckling imperfection sensitivity of pultruded FRP profiles. *Composites Part B: Engineering*, **72**, 206-212, 2015.

[83] L. Ascione, V.P. Berardi, A. Giordano, S. Spadea, Macro-scale analysis of local and global buckling behavior of T and C composite sections. *Mechanics Research Communications*, **58**, 105-111, 2014.

[84] A. D'Ambrisi, M. Mezzi, L. Feo, V.P. Berardi, Analysis of masonry structures strengthened with polymeric net reinforced cementitious matrix materials. *Composite Structures*, **113** (1), 264-271, 2014.

[85] S. Spadea, I. Farina, V.P. Berardi, F. Dentale, F. Fraternali, Energy dissipation capacity of concretes reinforced with recycled PET fibers. *Ingegneria Sismica*, **31** (2), 61-70, 2014.

[86] L. Ascione, V.P. Berardi, A. Giordano, S. Spadea, Local buckling behavior of FRP thin-walled beams: A mechanical model. *Composite Structures*, **98**, 111-120, 2013.

[87] L. Ascione, V.P. Berardi, A. Giordano, S. Spadea. Buckling failure modes of FRP thin-walled beams. *Composites Part B: Engineering*, **47**, 357-364, 2013.

[88] M. Fremond, B. Nedjar, V.P. Berardi, A numerical evaluation of damage in fast dynamics. *Lecture Notes in Applied and Computational Mechanics*, **61**, 259-270, 2012.

[89] L. Ascione, V.P. Berardi, A. D'Aponte, Creep phenomena in FRP materials. *Mechanics Research Communications*, **43**, 15-21, 2012.

[90] L. Ascione, V.P. Berardi, A. Giordano, S. Spadea, Local buckling analysis of pultruded FRP profiles: A mechanical model. *ECCM 2012 - Composites at Venice, Proceedings of the 15th European Conference on Composite Materials*.

[91] L. Ascione, V.P. Berardi, A. Giordano, S. Spadea, Local buckling analysis of pultruded frp thin-walled beams and columns. *Proceedings of the 6th International Conference on FRP Composites in Civil Engineering, CICE 2012*.

[92] L. Ascione, V.P. Berardi, Anchorage device for FRP laminates in the strengthening of concrete structures close to beam-column joints. *Composites Part B: Engineering*, **42** (7), 1840-1850, 2011.

[93] L. Ascione, V.P. Berardi, A. D'Aponte,A viscoelastic constitutive law for FRP materials. *International Journal of Computational Methods in Engineering Science and Mechanics*, **12** (5), 225-232, 2011.

[94] L. Ascione, V.P. Berardi, A. D'Aponte, Long-term behavior of PC beams externally plated with prestressed FRP systems: A mechanical model. *Composites Part B: Engineering*, **42** (5), 1196-1201, 2011.

COMPDYN 2017
6th ECCOMAS Thematic Conference on
Computational Methods in Structural Dynamics and Earthquake Engineering
M. Papadrakakis, M. Fragiadakis (eds.)
Rhodes Island, Greece, 15–17 June, 2017

# APPLICATION OF ELASTOMERIC DAMPERS TO STEEL MOMENT RESISTING FRAMES

**Christos A. Basagiannis**[1], **Martin S. Williams**[2]

[1]DPhil Candidate, Department of Engineering Science
University of Oxford, Oxford, United Kingdom
e-mail: christos.basagiannis@eng.ox.ac.uk

[2] Professor, Department of Engineering Science
University of Oxford, Oxford, United Kingdom
e-mail: martin.williams@eng.ox.ac.uk

**Keywords:** Elastomeric, Dampers, Passive Energy Dissipation Devices

**Abstract.** *In this paper the hysteretic behaviour of elastomeric dampers and their effect on steel moment resisting frames was evaluated. A new constitutive model was proposed, based on the Generalized Maxwell Model (GMM), which was able to capture the characteristics of the dampers under dynamic loading in a range of frequencies and amplitudes. This model was incorporated into the Finite Element (FE) Software OpenSees [1], and was used to validate the dampers behaviour. A simple steel moment resisting frame was modelled, and analytically tested under under strong ground motions, scaled according to Eurocode 8 [2] response spectrum. Both analytical and experimental results show the efficiency and the effectiveness of the elastomeric dampers with regard to structural response.*

## 1 INTRODUCTION

Although current anti-seismic concepts are based on linear elastic analysis, it is well known that under large seismic loads the structure will experience high non-linearities, and levels of damage. This is due to the dissipation of the seismic energy through the hysteretic behaviour of the structural members, and the actual non linear nature of the materials used, which lead to permanent deformations and plastic hinges. The traditional design concept consists of a combination of strength and ductility in order to provide resistance to lateral loads [3, 4]. For major earthquakes, the structural design engineer relies upon the inherent ductility of conscientiously detailed buildings to prevent catastrophic results [4]. This design approach is acceptable because of economic considerations provided, of course, that structural collapse is prevented and life safety is ensured [3]. However, sometimes the conventional seismic philosophy cannot easily be applied to all types of structures, the performance criteria may indicate the structure to remain linear or to have a minimal damage, while at the same time there are numerous structures with insufficient strength or ductility which need strengthening in order to cope under current seismic needs. Passive energy dissipation devices have the ability to improve the seismic behaviour of buildings[5, 6, 7, 8, 10] by reducing drift, force and deformation demand on the structural elements, which are responsible for providing lateral load resistance, in addition to reducing velocity and acceleration demands on non-structural components[9].

The evaluation of the hysteretic behaviour of two EDs, provided by TARRC (the Tun Abdul Razak Research Centre, UK), is the main focus of this paper. Elastomers, like viscoelastic (VE) material highly depend on the strain amplitude, frequency, and ambient temperature. However, Lee[5] showed that elastomeric dampers are less sensitive to frequency, a fact which makes them even more effective. Their capability of hysteresis energy stems from shear deformation, since the material is bonded between steel plates (Fig.1)

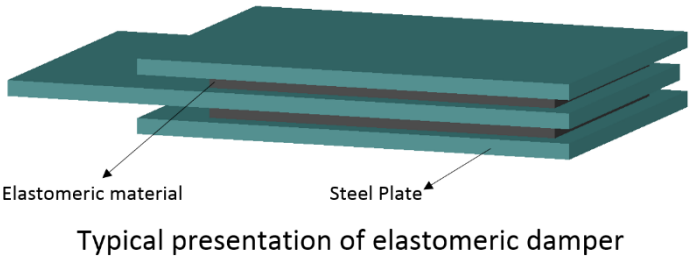


Figure 1: Typical Elastomeric Damper.

A time-domain constitutive equation has been developed, based on the Generalized Maxwell Model, taking into account non linearities. Sinusoidal strain commands at different amplitudes, and frequencies consisted the basis of the characterization tests which were used to calibrate this model, which was also incorporated into FE OpenSees[1], to capture the seismic response of a simple moment resisting frame. Five ground motions were used to test the dynamic response of the structure, which were scaled in frequency domain in order to match the response spectrum of EC8. Finally, comparative figures and tables are presented to show the efficiency of the elastomer.

## 2 ELASTOMERIC DAMPER AND CHARACTERIZATION TESTS

Two elastomeric dampers were provided by the Tun Abdul Razak Research Centre (TARRC). They consist of a rubbery material bonded between steel plates. The overall dimensions of the rubber material are 230 mm in the longitudinal direction (coinciding with the loading direction), 180 mm in the transverse direction, and 11.75 mm width (Fig. 2).

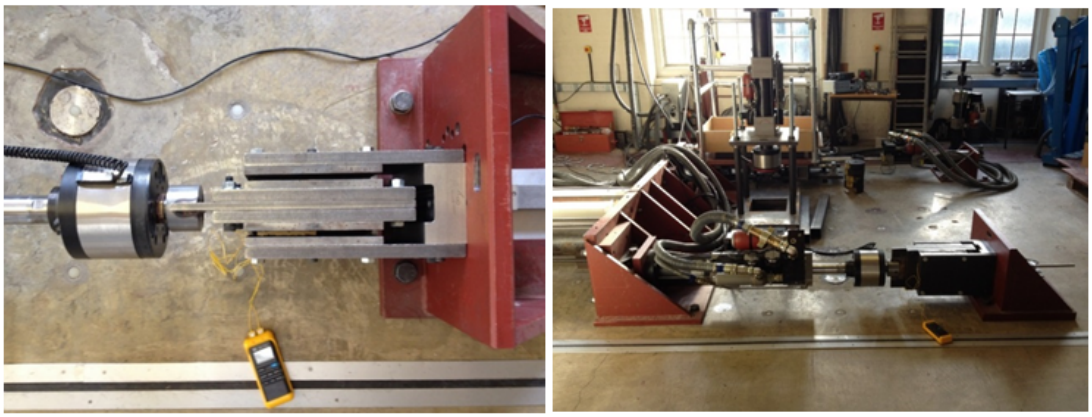

Figure 2: Experimental Rig.

A 100 kN servo-hydraulic actuator was used to evaluate the elastomer's characteristics under a range of displacement amplitudes and frequencies. The two dampers were both connected with a central steel plate, which was in turn connected with the actuator and provided the total movement of the dampers, while the outer steel plates were fixed (Fig.2). Therefore, the two dampers were tested simultaneously in a symmetric arrangement and the whole hysteretic behaviour was performed through shear deformation. A thermocouple was also attached to the elastomer in order to measure the ambient temperature, but also to capture any increase in temperature during the tests. It is well known that rubber-like materials exhibit non linear behaviour that depends on strain amplitude, ambient temperature, loading frequency, and loading history [5]. Hence, the experimental tests were focused on verifying non linear dependant on these parameters. Among these parameters, it is has been shown that strain dependence is the dominant factor [5, 11].

In order to investigate the strain amplitude and frequency dependence a series of tests was carried out based on sinusoidal displacement histories at the EDs. In order to avoid large initial displacement and velocity ramping cycles were implemented. Therefore, each history had 6 ramped cycles and 20 full sinusoidal cycles. This process was repeated for frequencies 0.25-4.0Hz, and for strain amplitudes 10%-50%. The maximum strain amplitude was decided to be kept within 50%, to avoid any potential permanent damage, severe cracking, or debonding of the elastomer. Fig. 3 shows a representative example of a sinusoidal displacement command of 40% strain amplitude and frequency of 3Hz. The tests were conducted at room temperature ($19^{o}$C-$20^{o}$C) in order to minimize the effect of temperature variation.

Based on the stress-strain hysteretic loops (Fig. 4), created for each frequency and amplitude, the equivalent shear modulus, $G_{\text{eq}}$, and loss factors, $n_{\text{eq}}$, were obtained for every test. These parameters are considered to be standard evaluation parameters of passive dissipation devices. The equivalent shear modulus, $G_{\text{eq}}$, is associated with the maximum magnitude of damper stress,$\tau_{\text{D,max}}$, and the maximum damper strain, $\gamma_{\text{D,max}}$ as:

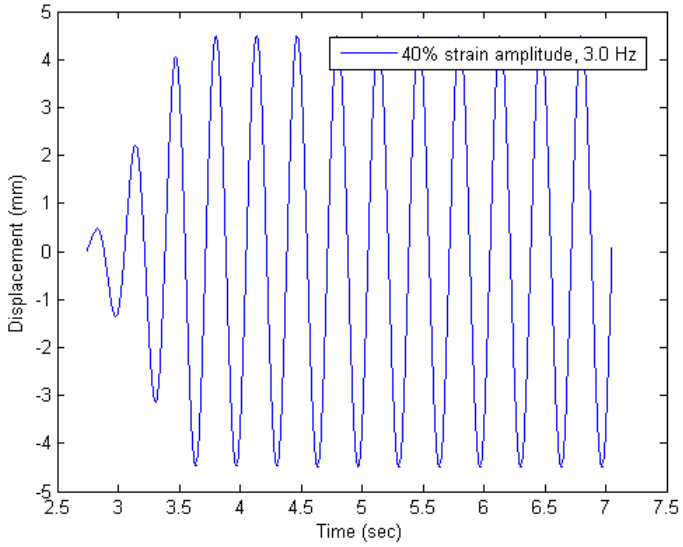


Figure 3: Typical sinusoidal displacement history used for the characterization tests of the elastomeric damper.

$$G_{eq} = \frac{\tau_{Dmax} - \tau_{Dmin}}{\gamma_{Dmax} - \gamma_{Dmin}} \tag{1}$$

where $\tau_{\mathrm{D,min}}$ is the minimum damper stress, and $\gamma_{\mathrm{D,min}}$ is the minimum damper shear strain. The loss factor, $n_{\mathrm{eq}}$, can be determined as follows:

$$n_{eq} = \frac{1}{2\pi}\frac{E_d}{E_s} \tag{2}$$

where $E_{\mathrm{d}}$ is the energy dissipation, and $E_{\mathrm{s}}$ is the strain energy. $E_{\mathrm{d}}$ can be determined by integrating the hysteresis loops, and $E_{\mathrm{s}}$ can be calculated from the maximum strain and the stress corresponding to maximum strain. Although the first two cycles have higher stiffness, no significant stiffness degradation is observed within the remaining eighteen full cycles. Hence, $E_{\mathrm{d}}$ and $E_{\mathrm{s}}$ were calculated when the stress versus strain hysteresis loops were stabilized. The final values of $G_{\mathrm{eq}}$ and $n_{\mathrm{eq}}$ were summarized and are presented in Table 1 and Figs 5 and 6.

Table 1: Mechanical Properties of the EDs

| Shear Strain % | f=0.25Hz | | f=0.5Hz | | f=1Hz | | f=2Hz | | f=3Hz | | f=4Hz | |
|---|---|---|---|---|---|---|---|---|---|---|---|---|
| | Geq (Mpa) | neq | Geq (Mpa) | neq | Geq (Mpa) | neq | Geq (Mpa) | neq | Geq (Mpa) | neq | Geq (Mpa) | neq |
| 10 | 1.676785 | 0.4072 | 1.656063 | 0.4140 | 1.77003 | 0.4094 | 1.911551 | 0.4020 | 2.002003 | 0.3982 | 2.067903 | 0.3944 |
| 20 | 1.295131 | 0.3551 | 1.258352 | 0.3520 | 1.344416 | 0.3535 | 1.43804 | 0.3504 | 1.506741 | 0.3489 | 1.559415 | 0.3475 |
| 30 | 1.08946 | 0.3335 | 1.074266 | 0.3330 | 1.139418 | 0.3344 | 1.225987 | 0.3359 | 1.27763 | 0.3332 | 1.321105 | 0.3322 |
| 40 | 1.046107 | 0.3390 | 0.990114 | 0.3262 | 1.05134 | 0.3298 | 1.121038 | 0.3306 | 1.166776 | 0.3286 | 1.208876 | 0.3269 |
| 50 | 0.945939 | 0.3010 | 0.937152 | 0.3044 | 0.986017 | 0.3082 | 1.049216 | 0.3104 | 1.094721 | 0.3115 | 1.132333 | 0.3090 |

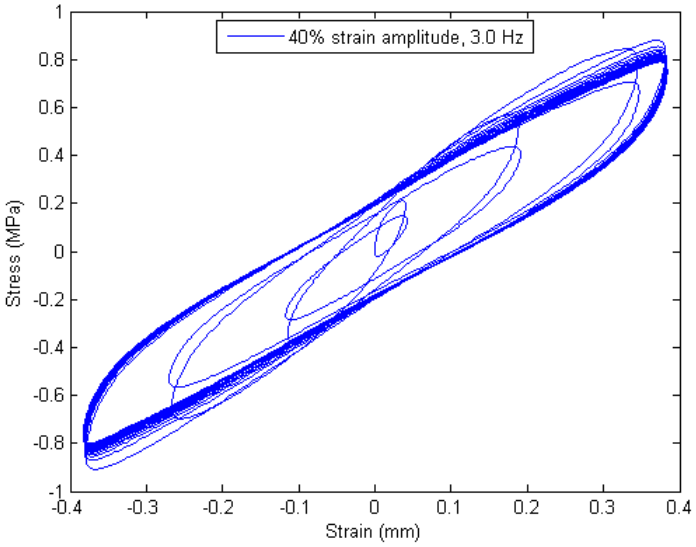


Figure 4: Stress-Strain Hysteretic loop.

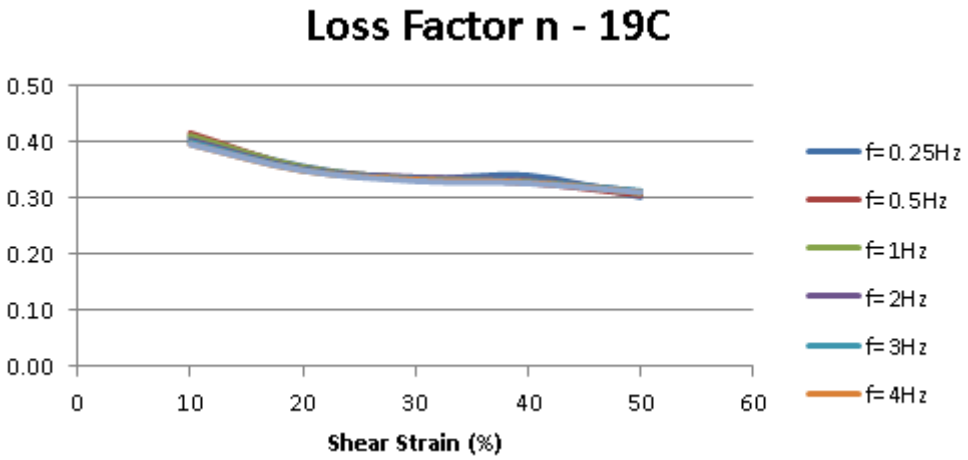


Figure 5: Loss factor  Frequency and Amplitude Dependence.

It can be clearly seen that the dominant factor which affects the elastomers dynamic behaviour is the amplitude and not the frequency, especially in the case of loss factor where it practically remains the same regardless any change in frequency. It is also noticeable that when the strain amplitude increases above 30% the shear storage modulus tends to a constant value.

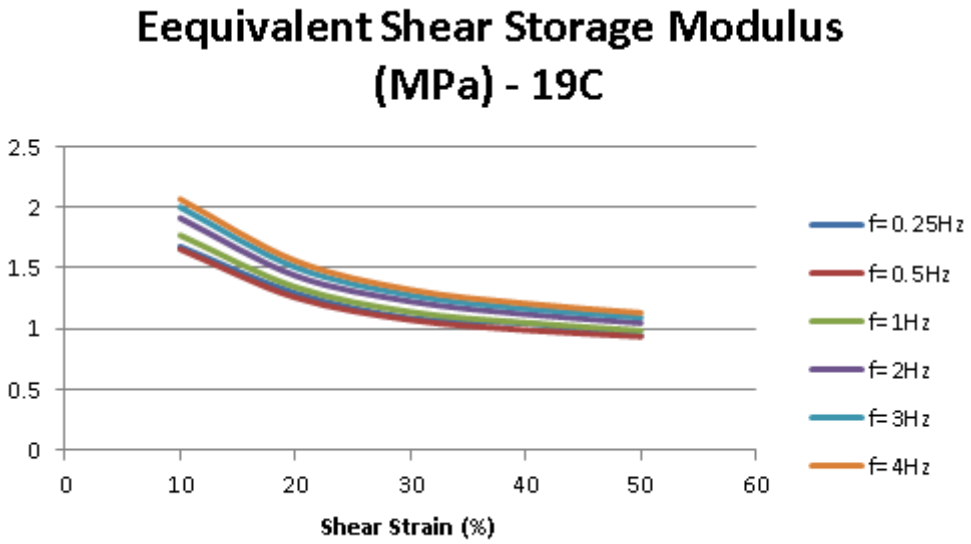


Figure 6: Shear Storage Modulus  Frequency and Amplitude Dependence.

## 3 HYSTERETIC MODEL FOR ELASTOMERIC DAMPER

As discussed and showed earlier, the elastomer's dynamic behaviour depends on the frequency and strain amplitude. In order to capture the material's characteristics several models have been proposed until now by researchers, either based on Fractional Derivatives [12], or Bouc-Wen model [9, 13, 14], while rate-dependent and rate-independent model was the main focus of Lee [5]. Moreover, Chopra [15] tried to model a non-linear damper in time domain. However, the conventional way of modelling elastomeric behaviour is the one that FEMA [16] proposees, where an equivalent stiffness and loss factor is assumed for the elastomer based on the natural frequency of the building.

### 3.1 Linear Generalized Maxwell Model

The proposed model for the hysteretic behaviour of the ED is based on the well known Generalized Maxwell Model (GMM). GMM has been proposed as numerical representation of VE materials [17, 18] and can be represented graphically in the following figure:

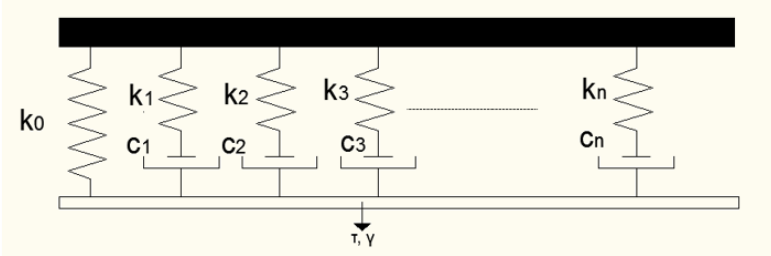


Figure 7: ELinear Generalized Maxwell Model (GMM).

The linear GMM consists of linear spring, with spring stiffness parameter called $k_0$, in parallel with N Maxwell elements. Although, it is very easy to extract the analytical force-displacement relationship when only one Maxwell element is used, things are becoming much

more complicated when more than two elements are being used. Even though an analytical expression has been developed when N Maxwell elements are used, this is not the purpose of this paper, since only one Maxwell element is going to be used in this case. The time relaxation for the $i_{\text{th}}$ Maxwell element is denoted, $\tau_{\text{i}}$, and is equal to $k_{\text{i}}/c_{\text{i}}$. In the case of one Maxwell elements the total force is:

$$F = F_0 + F_1 \tag{3}$$

From Eq. (3):

$$F_1 = F - F_0 \tag{4}$$

where F is the total force applied at the GMM. For every individual Maxwell element, i, the following equation can be derived:

$$F_i' = k_i u_i' - \frac{k_i}{c_i} F_i \tag{5}$$

where F´ and u´ denotes the differentiation of the force and the displacement with respect to time. The first derivative of (3) gives:

$$F' = F_0' + F_1' \tag{6}$$

Substituting (5) into (6) for i=1:

$$F' = F_0' + k_i u_1' - \frac{k_1}{c_1} F_1 \tag{7}$$

In the GMM case, u1= u. Hence, substituting from Eq. (4), Eq.(7) becomes:

$$F' = F_0' + k_1 u_1' - \frac{k_1}{c_1} F + \frac{k_1}{c_1} F_0 \tag{8}$$

which leads to:

$$F + \frac{c_1}{k_1} F' = F_0 + \frac{c_1}{k_1} F_0' + c_1 u_1' \tag{9}$$

### 3.2 Modified Generalized Maxwell Model

It was noticed that GMM was only adequate to describe only VE behaviour, while also was proved to be inefficient when the frequency or the amplitude was changing (It was only able to capture VE behaviour only for specific values of frequency and amplitude). In order to take into account the non linear part of the elastomer, a non linear damper was added, while $F_0$ consists of a linear spring. Karavasilis [9] proposed a modified stiffness based on the maximum displacement to take into account the softening of the elastomer:

$$k_{mod} = k_a e^{-\frac{u_{max}}{u_{ref}}} + k_b \tag{10}$$

where $k_{\text{a}}$, $k_{\text{b}}$ and $u_{\text{ref}}$ are constants, and $u_{\text{max}}$ is the average of the maximum absolute deformation amplitudes in the negative ($u_{\text{max,n}}$) and positive ($u_{\text{max,p}}$) directions, as follows:

$$u_{max} = \frac{u_{max,p} + |u_{max,n}|}{2} \tag{11}$$

It is worth mentioning that the values of $u_{\text{max,p}}$ and $u_{\text{max,n}}$ are updated for every time step and are being fed into the constitutive equation to calculate the overall response. It was found that in this case, the ED's behaviour is depended on both the maximum displacement obtained during the loading history. Hence, the following parameters were selected to form the Modified Generalized Maxwell Model (MGMM):

- The linear GMM obtained from equation (9)
- The final version of $F_0$ can be calculated as:

$$F_0 = k_0 u \tag{12}$$

- The modified stiffness from equation (10)

Hence, the proposed hysteretic model can be determined as:

$$F + \frac{c_1}{k_1} F' = k_0 u + \frac{c_1}{k_1} k_0 u' + c_1 u_1' + k_{mod} u \tag{13}$$

There are six total parameters that need to be determined: $k_1$, $c_1$, $k_0$, $k_{\text{a}}$, $k_{\text{b}}$, $u_{\text{ref}}$. In order to optimize these parameters the Levenberg-Marquardt algorithm was used to minimize the error between the experimental values and the force from the analytical model [19] based on sweep amplitude sinusoidal tests (the amplitude was ranging from 10%-50%), which were carried out for each frequency. These tests were determined, so the optimized parameters to be valid for each displacement and frequency, and were based on proposals from CASCADE[20]. Figure 8 shows a typical example of both the seep sinusoidal command displacement and the EDs response based on a frequency of 3.0 Hz. Table 2 provides the parameters of the hysteretic model, while figures 9, and 10 show that data obtained from the sweep sinusoidal tests and the hysteretic model are in a very good agreement. However, it should be noted that the proposed material model is validate only for sinusoidal loading, under a range of different amplitudes and frequencies. Since seismic loading can be decomposed into harmonic waves of different amplitudes and frequencies, the model is deemed to capture the essential characteristics of the damper under random loading[9].

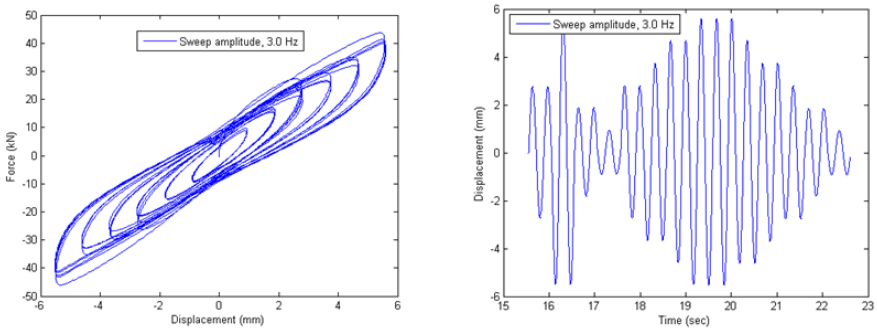


Figure 8: Sweep Amplitude Test for f=3.0Hz

Table 2: Optimized Model Parameters

| k1 | c1 | k0 | ka | uref | kb |
|---|---|---|---|---|---|
| 0.514578 | 0.015148 | 0.000107 | 3.741913 | 7.966884 | 3.613982 |

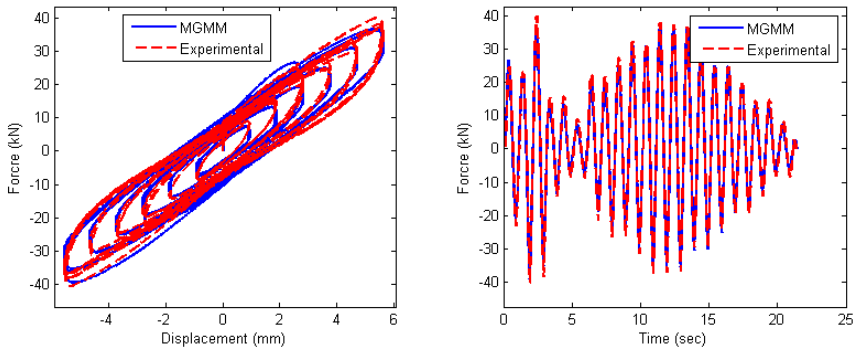


Figure 9: Comparison of force between experiment and MGMM model for sweep amplitude test for 1Hz

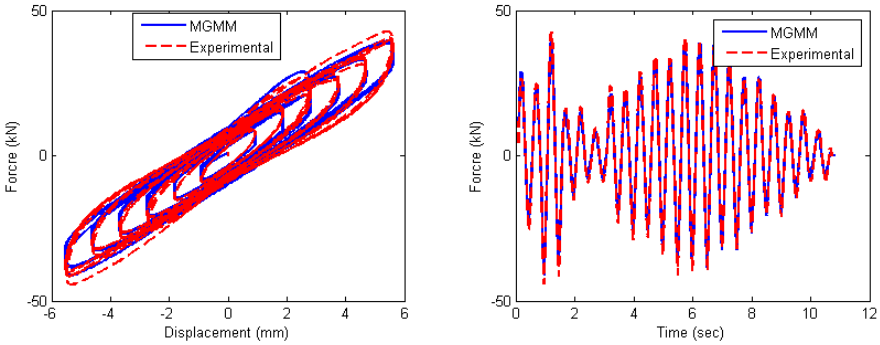


Figure 10: Comparison of force between experiment and MGMM model for sweep amplitude test for 2Hz

## 4 ANALYSIS

### 4.1 Prototype Building

A simple moment resisting frame was selected in this study, assuming seismic zone 3 (design ground acceleration=0.36g). The effect of EDs on the seismic performance of simple-conventional moment resisting frame (MRFs) was examined using the FE Software OpenSees for the 2D nonlinear analysis of the MRF. In the latter case, EDs and diagonal braces were also incorporated into the 2D MRF. The steel sections used here are IPE200 for the beam and HEM220 for the columns, while section SHS-150x12.5 was assigned to the bracings.

### 4.2 Scaling Ground Motions

According to EC8, scaled ground motions should be used for non linear analyses. Table 3 shows the ground motions used in this paper, while figure 12 presents the response spectrum of the ground motions, which were scaled in order to match the response spectrum of EC8 for a 10% probability of exceedance in 50 years. The scaling process was based on method of Fahjan[22] and Karabalis[23]. The scope of this method is the response spectrum of the

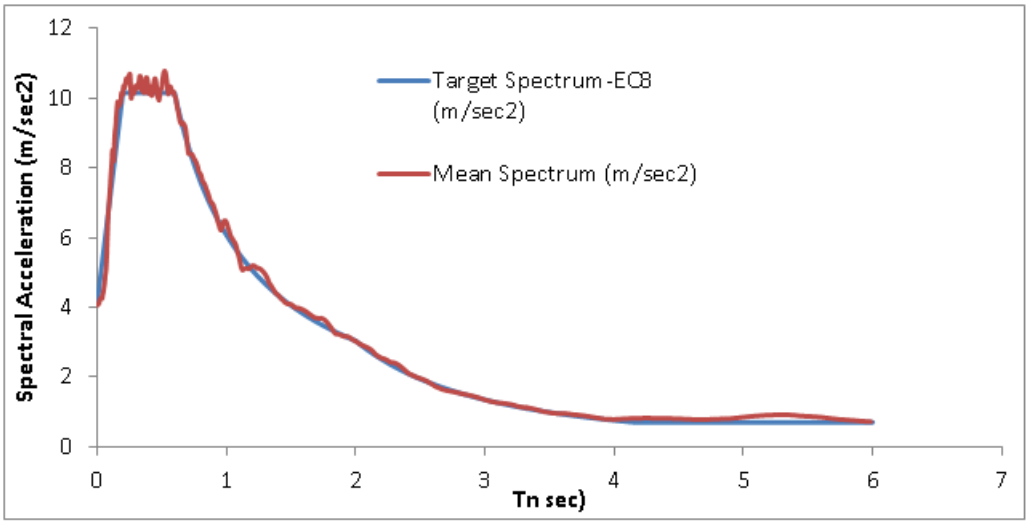


Figure 11: Mean Response Spectrum of the scaled ground motions

time history to gradually match the response spectrum of EC8 for a range of periods $0.2T_1$-$2T_1$ (where $T_1$ is the natural period of the building), by increasing some components of the spectrum index, and reducing some others. In essence, this method does not create new ground motions, but it modifies selected records in order to satisfy the criteria set by EC8.

Table 3: Ground motions used for non linear analysis

| Earthquake | Station Name | Component | Magnitude | Distance (km) |
|---|---|---|---|---|
| Borrego 1942 | El Centro Array #9 | BORREGO_B-ELC000 | 6.5 | 56.88 |
| Kern County 1952 | LA - Hollywood Stor FF | KERN.PEL_PEL090 | 7.36 | 114.62 |
| Imperial Valley-02 1940 | El Centro Array #9 | IMPVALL.I_I-ELC180 | 6.95 | 6.09 |
| Northwest Calif-02 1941 | Ferndale City Hall | NWCALIF.C_C-FRN045 | 6.6 | 91.15 |
| Imperial Valley-0 1979 | Niland Fire Station | IMPVALL.H_H-NIL090 | 6.53 | 35.64 |

### 4.3 Numerical Models

2D nonlinear models were developed in order to evaluate the effect of EDs on the MRF, with the FE software OpenSees. The beams and columns were modelled as distributed plasticity non-linear elements, with fiber sections. The stress strain relationship of the material is assigned to each fiber, and through integration at specific points along the element the active moments, and forces were obtained. The effect of the concrete slab was taken into account with diaphragms at each floor, but no stiffness contribution was considered for the seismic response. The base of the MRF was assumed to be fixed, the beam-column connections fully rigid, and the braces pinned, while no soil structure interaction was considered. A bilinear (elastic-perfectly plastic) model was used for the steel material, and fiber section was used in each element, except for the damper. The braces were assumed very stiff and were modelled as linear elastic elements. A Rayleigh damping matrix was used to model inherent damping of 2% at the first two modes of vibration. Each nonlinear analysis was extended beyond the actual earthquake time, so the correct residual displacements can be clear. Regarding the representation of the ED, concentric diagonal dampers were added to the initial MRF. A zero length element connected between the top of the braces and the middle of the beam was used to represent the damper. The constitutive

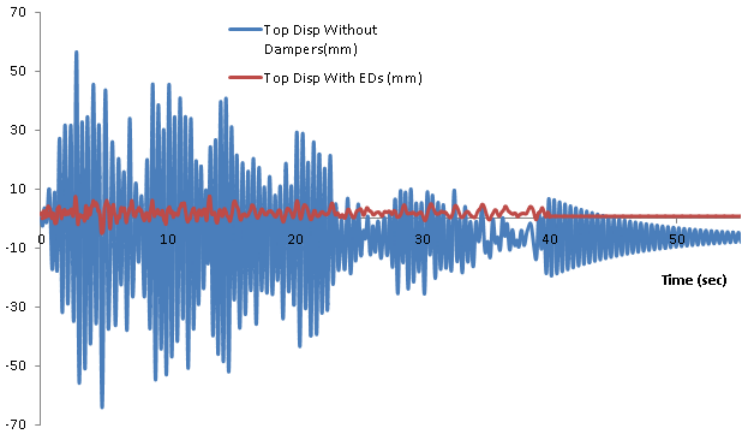


Figure 12: Displacement Time History Northwest Calif ground motion

model developed in equation 16 was incorporated into OpenSees, assuming is a zero length element. As it was previously mentioned the parameters assigned to the zero length element were based on the sweep amplitude tests. Regarding the design of the braces, a ratio, , of the braces stiffness to story stiffness equal to 7 was selected, so that the braces wont buckle under the forces transmitted by the dampers, and at the same time wont increase much the total weight of the structure. Karavsilis [9] carried out a parametric analysis in order to optimize the value of , and very good results were obtained using a range of values between 5 and 10, which justify my previous assumption. This way, braces are sized to be stiff enough so that the story drift produces elastomers deformation, rather than brace deformation[5].

### 4.4 Seismic Response

Both the MRF and DMRF (Damped Moment Resisting frame)were tested under the scaled ground motions for the Design Basis Earthquake (DBE), corresponding to a 10% probability of exceedance in 50 years and the results are illustrated in the following figures which evaluate the EDs efficiency during Northwest Calif ground motion. It can be clearly seen that the beneficial effect of the EDs used in this frame had a huge influence on the overall drift, while the base shear of the frame was reduced from to 235 kN to 32 kN (these values correspond to the mean values of the individual base shear for each ground motion). At the same time the residual displacement dropped almost to zero, and yielding was also avoided when EDs were implemented. The dynamic behaviour of the EDs is also presented here.

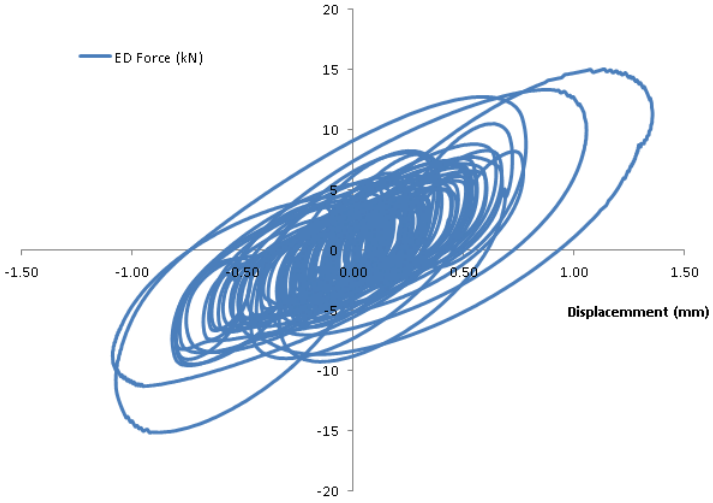


Figure 13: ED hysteretic loop during Northwest Calif ground motion

## 5 CONCLUSIONS

In this study the evaluation the constitutive model for describing the EDs dynamic behaviour and their effect on a simple steel moment resisting frame was examined . EDs exhibit both elastic and viscous mechanical behaviour, and can be simply modelled (especially for preliminary analyses) assuming the Kelvin-Voigt model, based on equivalent stiffness, keq, and equivalent damping ceq. However, a more sophisticated modes was developed here, and was incorporated into OpenSees in order to evaluate EDs' dynamic behaviour and their effect on steel frames. Nonlinear time history analyses were carried out for DBE level. Fahjan proposed method was used to scale ground motions to the DBE. In terms of displacements, and shear forces DMRF exhibited very satisfactory seismic behaviour, while plastic hinges didn't occur during any ground motion.

## REFERENCES


[1] OpenSees finite element software framework for developing applications to simulate the performance of structural and geotechnical systems subjected to earthquakes

[2] Eurocode 8: Design of structures for earthquake resistancePart 1: General rules, seismic actions and rules for buildings.

[3] Constantinou M.C., Soong T.T., and Dargush G.F. *Passive energy dissipation systems for structural design and retrofit*. Multidisciplinary Center for Earthquake Engineering Research Buffalo, New York, 1998.

[4] Soong T.T., and Dargush G.F. *Passive Energy Dissipation Systems in Structural Engineering*. JOHN WILEY & SONS, New York, 1997.

[5] Lee K.S. *Seismic Behavior of Structures with Dampers Made from Ultra High Damping Natural Rubber*. Ph.D. Dissertation, Department of Civil and Environmental Engineering, Lehigh University, 2003.

[6] Fan C.P. *Seismic Analysis, Behavior, and Retrofit of Non-Ductile Reinforced Concrete Frame Buildings with Viscoelastic Dampers*. Ph.D. Dissertation, Department of Civil and Environmental Engineering, Lehigh University, 1998.

[7] Shen K.L., Soong T.T., Modeling of Viscoelastic Dampers for Structural Applications. *Journal of Engineering Mechanics*. , **121**, 694–701, 1995.

[8] Makris N., Constantinou M.C., Fractional-Derivative Maxwell Model for Viscous Dampers. *Journal of Structural Engineering*. , **117**, 2708–2724, 1991.

[9] Karavasilis T., Sause R., Ricles J., Seismic design and evaluation of steel momentresisting frames with compressed elastomer dampers. *Journal of Earthquake Engineering and Structural Dynamics Journal*. , **41**, 411–429, 2012.

[10] Vargas R., Bruneau M., Effect of Supplemental Viscous Damping on the Seismic Response of Structural Systems with Metallic Dampers. *Journal of Structural Engineering*. , **133**, 1434–1444, 2007.

[11] Papoulia K.D., and Kelly J.M. *Material Characterization of Elastomers Used in Earthquake Base Isolation*. Report No. UCB/EERC-90/18, Earthquake Engineering Research Center, University of California at Berkeley, Berkeley, CA., 1990.

[12] Koh C. G., Kelly J.M., Application of Fractional Derivatives to Seismic Analysis of Base-Isolated models. *Journal of Earthquake Engineering and Structural Dynamics*. , **19**, 229–241, 1989.

[13] Yang Yu, Yancheng Li, Jianchun Li, and Xiaoyu Gu, A hysteresis model for dynamic behaviour of magnetorheological elastomer base isolator. *Smart Materials and Structures*. , **25**, 2016.

[14] ALI MANZOORI and HAMID TOOPCHI-NEZHAD, Application of an Extended Bouc-Wen Model in Seismic Response Prediction of Unbonded Fiber-Reinforced Isolators. *Journal of Earthquake Engineering*. , **21**, 87–104 2016.

[15] Gandhi F., and Chopra I., A time-domain non-linear viscoelastic damper model. *Smart Materials and Structures*. , **5**, 517–528 1996.

[16] *FEMA. Prestandard and Commentary for the Seismic Rehabilitation of Buildings. Report No. FEMA356, Federal Emergency Management Agency: Washington, DC, 2001*..,2001

[17] T.L. Karavasilis, T. Blakeborough, and M.S. Williams, Development of nonlinear analytical model and seismic analyses of a steel frame with self-centering devices and viscoelastic dampers . *Computers and Structures*. , **89**, 1232–1240 2011.

[18] N.G. McCrum, C.P. Buckley, and C.B. Bucknall, *Principles of Polymer Engineering*. SECOND EDITION, OXFORD UNIVERSITY PRESS, 1997.

[19] MATLAB. A Registered trademark of The Math Works, Inc., http://www.mathworks.com, 2007.

[20] R.Severn, R.Bairrao, *SEISMIC QUALIFICATION OF PASSIVE MITIGATION DEVICES*. Cooperative Advancements in Seismic and Dynamic Experiments (CASCADE), Report No.1, 2005.

[21] SAP2000 Static and dynamic finite element analysis of structures.

[22] Y.M. Fahjan, Z. Ozdemir, Scaling of earthquake accelerograms for non-linear dynamic analyses to match the earthquake design spectrum. *The 14th World Conference on Earthquake Engineering*, 2008.

[23] D.L. Karabalis, G.J. Cokkinides, D.C. Rizos, J.S. Mulliken, Simulation of earthquake ground motions by a deterministic approach. *Advances in Engineering Software*. , **31**, 329–338 2000.

COMPDYN 2017
6th ECCOMAS Thematic Conference on
Computational Methods in Structural Dynamics and Earthquake Engineering
M. Papadrakakis, M. Fragiadakis (eds.)
Rhodes Island, Greece, 15–17 June 2017

# THE INFLUENCE OF GEOMETRY, LOADS AND STEEL GRADE FOR THE DEVELOPMENT OF A SPECIFIC COLLAPSE TYPE OF MR-FRAMES

**Elide Nastri**[1]

[1] University of Salerno
Via Giovanni Paolo II, 84084, Fisciano (SA), Italy
e-mail: enastri@unisa.it

**Keywords:** TPMC, Kinematic theorem of plastic collapse, Earthquake Engineering, seismic design, mechanisms of collapse

**Abstract.** *The work is devoted to the analysis of the influence of geometry, loads and steel grade for the development of a specific collapse type of steel Moment Resisting Frames (MRFs). In order to provide the results, the Theory of Plastic Mechanism Control (TPMC) has been applied to a large number of steel frames with different geometrical configurations and different loads and steel grades. TPMC is based on the extension of kinematic theorem of plastic collapse to the concept of mechanism equilibrium curve that allows accounting for second order effects that are very relevant especially in MRFs. This wide parametric analysis has been carried out on more than 100000 cases pointing out that for ordinary and regular MRFs type-1 mechanism is the one controlling the failure mode. In these last case, a simplified application of the Theory of Plastic Mechanism Control can be used.*

## 1 INTRODUCTION

The fundamental principle of capacity design of seismic-resistant structures states that plastic hinge formation in columns during an earthquake should be avoided, in order to make sure that the seismic energy is dissipated in predefined zones only. In the case of Moment Resisting Frames (MRFs) this preselected zones are the beam ends whose rotational capacity is higher than columns one [1]. In facts, it is not desirable to develop plastic hinges in columns, because columns have to support upper storeys and because columns are hard to develop large inelastic deformations. However, in order to develop a complete mechanism of collapse, plastic hinges should form also at the base of first storey columns by determining a collapse mechanism of global type [2], [3], [4].

With reference to the most common structural typologies, design rules suggested by actual seismic codes [5], [6], [7], among which also the Italian seismic code [8], and also codified in Eurocode 8 [9] and ANSI/AISC 341-10 [10] are not able to assure the development of a collapse mechanism of global type. In fact, the hierarchy criteria provided by such codes constitute, dealing with column design, only a simplified application of the well-known "capacity design principles". For this reason, with reference to MRFs, a rigorous design procedure based on the kinematic theorem of plastic collapse was presented in 1997 [11] aiming to assure a collapse mechanism of global type. Starting from this first work, the "Theory of Plastic Mechanism Control" (TPMC) has been progressively outlined as a powerful tool for the seismic design of steel structures. TPMC consists in the extension of the kinematic theorem of plastic collapse to the concept of mechanism equilibrium curve and on its application devoted to column design. In fact, for any given structural typology, the design conditions to be applied in order to prevent undesired collapse mechanisms can be derived by imposing that the mechanism equilibrium curve corresponding to the global mechanism has to be located below those corresponding to all the other undesired mechanisms up to a top sway displacement level compatible with the local ductility supply of dissipative zones.

Starting from the first work devoted to MRFs, TPMC was successively extended to MRFs with semi-rigid connections [12], [13], EB-Frames [14], [15], [16], [17], [18], [19], [20], braced frames equipped with friction dampers [21], [22], [23] knee-braced frames [24], dissipative truss-moment frames DTMFs [25] and MRF-CBF dual systems [26], [27], [28], [29], [30], [31], MRF-EBF dual systems [32] and reinforced concrete frames [33] [34] [35].

Starting from the above background, in this paper the state of the art regarding the "Theory of Plastic Mechanism Control" is reported. In particular, by means of new considerations regarding collapse mechanism typologies, new advances have been developed leading to a closed form solution [36].

Moment Resisting Frames (MRFs) are the most common seismic-resistant structures. They are characterized by high dissipation capacity, because of the large number of dissipative zones under cyclic bending represented by the beam end sections. Nevertheless, such structural system could be not able to provide sufficient lateral stiffness, as required to fulfil serviceability limit states and also adequate robustness [37], [38], [39], [40], [41]. Influence is also given for isolated systems by soil category [42]. Finally, a wide parametric analysis to investigate the influence of geometry, loads and steel grade for the development of a specific collapse mechanism is reported.

## 2 STATE OF THE ART OF TPMC

The "Theory of Plastic Mechanism Control" has the aim to provide structures able to fail with a collapse mechanism of global type (Figure 1). Global mechanism represents the optimum in term of structural dissipation capacity being all the dissipative zones involved in the pattern

of yielding while the non dissipative ones remain in elastic range. Dissipative zones of MRFs are the beam ends and the bases of the column at the first storey.

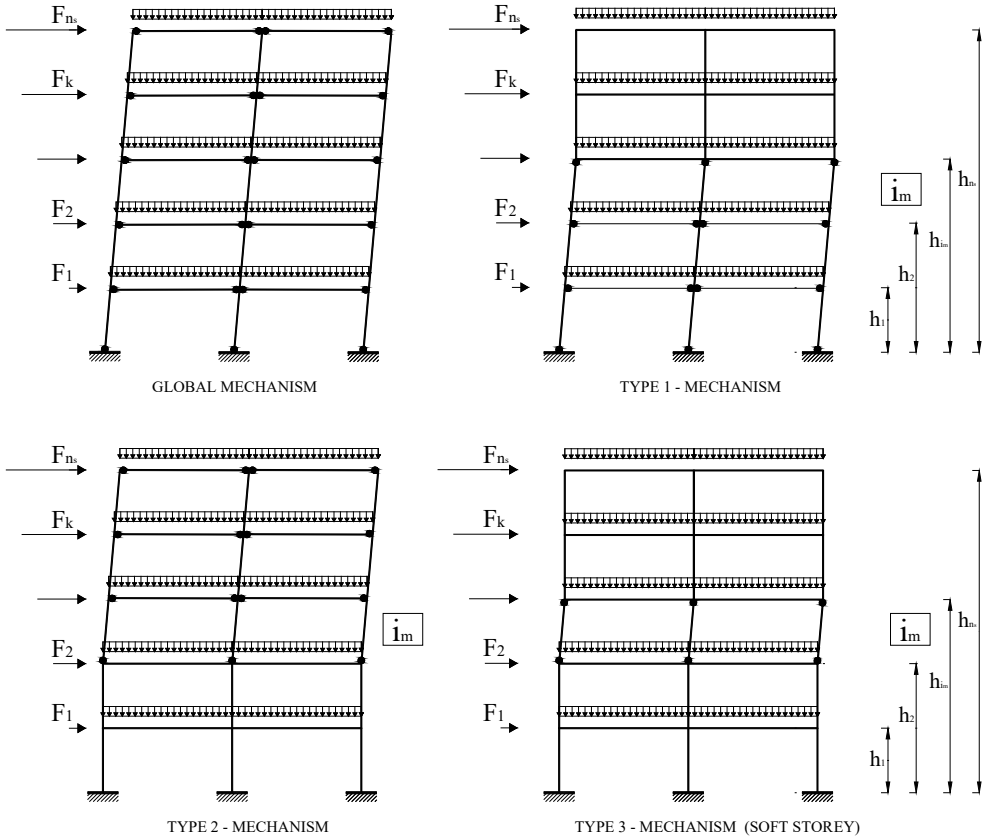


Figure 1: Collapse mechanism of MR-Frames.

In particular, TPMC allows the theoretical solution of the problem of designing structures failing in global mode, i.e. assuring that yielding develops only in the dissipative zones while all the columns remain in elastic range with the only exception of base sections at first storey columns. The structural members containing the dissipative zones are assumed to be known quantities, because they are preliminarily designed, according to the first principle of capacity design, to withstand the internal actions due to the load combinations given by code provisions. Therefore, according to the second principle of capacity design, the unknowns of the design problem are constituted by the non-dissipative members, i.e. the column sections, which are designed to assure the desired collapse mechanism, i.e. the global mechanism. Compared to hierarchy criteria given in code provisions, TPMC allows a rigorous application of the second principle of capacity design.

TPMC is based on the kinematic or upper bound theorem of plastic collapse within the framework of limit analysis. According to the theory of limit analysis, the assumption of a rigid-plastic behaviour of the structure until the complete development of a collapse mechanism is usually made. It means that the attention is focused on the condition the structure exhibits in the collapse state by neglecting the lateral displacements corresponding to each intermediate condition. However, the simple application of the kinematic theorem of plastic collapse is not sufficient to assure the desired collapse mechanism, because high horizontal displacements occur before the complete development of the kinematic mechanism. These displacements give rise to significant second order effects which cannot be neglected in the seismic design of structures, particularly in case of moment-resisting steel frames. Therefore, the basic principle of

TPMC is essentially constituted by the extension of the kinematic theorem of plastic collapse to the concept of mechanism equilibrium curve. The mechanism equilibrium curve is represented by a straight line whose intercept with the vertical axis in a Cartesian diagram is the first order collapse mechanism multiplier $\alpha_{0,}$ while its slope is represented by the parameter $\gamma$. The expression of the linearized collapse mechanism equilibrium curve is given by:

$$\alpha = \alpha_0 - \gamma\delta \tag{1}$$

where $\alpha$ is the multiplier of horizontal forces and $\delta$ is the top sway displacement of the structure. Within the framework of a kinematic approach, for any given collapse mechanism (Fig. 3), the mechanism equilibrium curve can be easily derived requiring that external work is equal to the internal work due to the plastic hinges involved in the collapse mechanism, provided that the external second-order work due to vertical loads is also evaluated [11].
In fact, with reference to the global mechanism, it is easy to recognize that, for a virtual rotation $d\theta$ of the plastic hinges of the uprights involved in the mechanism, the internal work can be expressed, as:

$$W_i = \left[\sum_{i=1}^{n_c} M_{c.i1} + 2\sum_{k=1}^{n_s}\sum_{j=1}^{n_b}\left(M_{b.Rd.jk}\right)\right] d\theta \tag{2}$$

where $n_s$ is the number of storeys, $n_b$ is the number of bays, $M_{c.i1}$ is the first storey colun base plastic moment of *i-th* column while $M_{b.Rd.jk}$ is the plastic moment of beams.
The external work due to the horizontal forces and to the uniform load acting on the beams is:

$$W_e = \alpha\sum_{k=1}^{n_s} F_k h_k d\theta + \frac{\delta}{h_{n_s}}\sum_{k=1}^{n_s} V_k h_k d\theta \tag{3}$$

where $F_k$ and $h_k$ are, respectively, the seismic force applied at k-th storey and the k-th storey height with respect to the foundation level, $h_{n_s}$ is the value of $h_k$ at the top storey, $\delta$ is the top sway displacement and $V_k$ is the total vertical load acting at *k-th* storey.

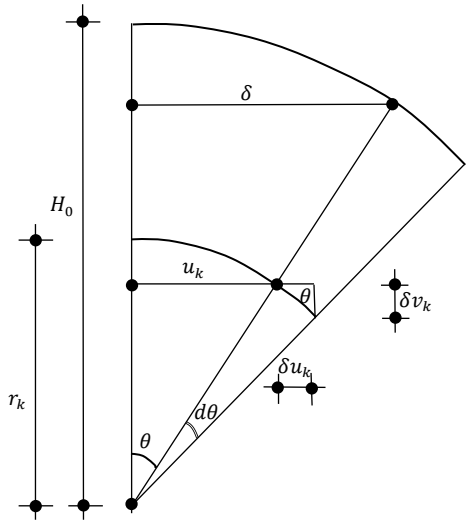


Figure 2: Second order vertical displacements.

The first term of Eq. (3) represents the external work due to seismic horizontal forces, while the second term is the second order work due to vertical loads. In order to compute the slope of the mechanism equilibrium curve, it is necessary to evaluate the second-order work due to vertical loads. With reference to Figure 2, it can be observed that the horizontal displacement of

the *k-th* storey involved in the generic mechanism is given by $u_k = r_k sin\theta$, where $r_k$ is the distance of the *k-th* storey from the centre of rotation C and $\theta$ the angle of rotation. The top sway displacement is given by $\delta = h_{ns} sin\theta$.
The relationship between vertical and horizontal virtual displacements is given by $dv_k tan\theta \approx du_k sin\theta$. It shows that, as the ratio $dv_k / du_k$ is independent of the storey, vertical and horizontal virtual displacement vectors have the same shape. In fact, the virtual horizontal displacements are given by $du_k = r_k cos\theta d\theta \approx r_k d\theta$, where $r_k$ defines the shape of the virtual horizontal displacement vector, while the virtual vertical displacements are given by $dv_k = \frac{\delta}{h_{n_s}} r_k d\theta$ and, therefore, they have the same shape $r_k$ of the horizontal ones. It can be concluded that:

$$dv_k = \frac{\delta}{h_{n_s}} h_k d\theta \tag{4}$$

where $dv_k$ is the vertical virtual displacement occurring at *k-th* storey.
By equating the internal work (Eq. (2)) to the external one (Eq. (3)), the following relationship is obtained for the global mechanism:

$$\alpha = \frac{\sum_{i=1}^{n_c} M_{c.i1} + 2\sum_{k=1}^{n_s}\sum_{j=1}^{n_b} M_{b.Rd.jk}}{\sum_{k=1}^{n_s} F_k h_k} - \frac{1}{h_{n_s}} \frac{\sum_{k=1}^{n_s} V_k h_k}{\sum_{k=1}^{n_s} F_k h_k} \delta \tag{5}$$

that can be arranged in the following form:

$$\alpha^{(g)} = \alpha_0^{(g)} - \gamma_{i_m}^{(g)} \delta \quad with\ t = 1,2,3 \quad i_m = 1, \dots, n_s \tag{6}$$

for the global mechanism and in the following form:

$$\alpha_{i_m} = \alpha_{0.i_m}^{(t)} - \gamma_{i_m}^{(t)} \delta \quad with\ t = 1,2,3 \quad i_m = 1, \dots, n_s \tag{7}$$

for each undesired mechanism where:

$$\alpha_{0.i_m}^{(1)} = \frac{\sum_{i=1}^{n_c} M_{c.i1} + 2\sum_{k=1}^{i_m-1}\sum_{j=1}^{n_b} M_{b.Rd.jk} + \sum_{i=1}^{n_c} M_{c.ii_m}}{\sum_{k=1}^{i_m} F_k h_k + h_{i_m} \sum_{k=i_m+1}^{n_s} F_k} \tag{8}$$

for type-1 mechanism;

$$\alpha_{0.i_m}^{(2)} = \frac{\sum_{i=1}^{n_c} M_{c.ii_m} + 2\sum_{k=i_m}^{n_s}\sum_{j=1}^{n_b} M_{b.Rd.jk}}{\sum_{k=i_m}^{n_s} F_k (h_k - h_{i_m-1})} \tag{9}$$

for type-2 mechanism;

$$\alpha_1^{(3)} = \frac{2\sum_{i=1}^{n_c} M_{c.i1}}{h_1 \sum_{k=1}^{n_s} F_k} \tag{10}$$

and for type-3 mechanism, where $F_k$ and $h_k$ are, respectively, the seismic force applied at *k-th* storey and the *k-th* storey height with respect to the foundation level; $M_{c.ii_m}$ is the plastic moment of *i-th* column of *k-th* storey reduced due to the contemporary action of the axial force; $n_c$, $n_b$ and $n_s$ are the number of columns, bays and storeys, respectively.
Regarding the slope $\gamma$ of the mechanism equilibrium curve, they are given by:

$$\gamma_{i_m}^{(1)} = \frac{1}{h_{i_m}} \frac{\sum_{k=1}^{i_m} V_k h_k + h_{i_m} \sum_{k=i_m+1}^{n_s} V_k}{\sum_{k=1}^{i_m} F_k h_k + h_{i_m} \sum_{k=i_m+1}^{n_s} F_k} \tag{11}$$

for type-1 mechanism;

$$\gamma_{i_m}^{(2)} = \frac{1}{h_{n_s} - h_{i_m-1}} \frac{\sum_{k=i_m}^{n_s} V_k (h_k - h_{i_m-1})}{\sum_{k=i_m}^{n_s} F_k (h_k - h_{i_m-1})} \tag{12}$$

for type-2 mechanism;

$$\gamma_{i_m}^{(3)} = \frac{1}{h_{i_m} - h_{i_m-1}} \frac{\sum_{k=i_m}^{n_s} V_k}{\sum_{k=i_m}^{n_s} F_k} \tag{13}$$

where $V_k$ is the total vertical load acting at *k-th* storey.
The collapse mechanism equilibrium curves can be easily represented in a Cartesian diagram (α-δ). The curve that is located below all the other ones is the one governing the collapse mechanism. For this reason, in order to assure that the collapse mechanism of global type develops, the collapse mechanism equilibrium curve of global mechanism (Eq. (6)) has to be located below those corresponding to each undesired mechanism (Eq. (7)) until a design displacement $\delta_u$, compatible with the ductility supply of dissipative zones (Figure 3) and usually assumed equal to 0.04.

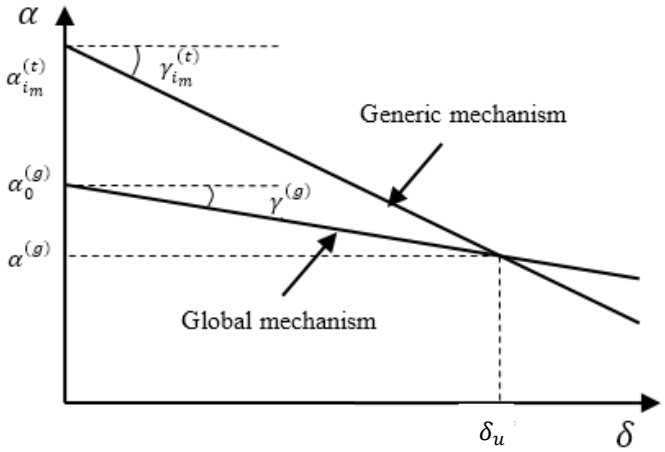

Figure 3: Collapse mechanism equilibrium curves.

This sentence can be mathematically translated in the following inequality:

$$\alpha_0^{(g)} - \gamma_{i_m}^{(g)} \delta_u \leq \alpha_{0.i_m}^{(t)} - \gamma_{i_m}^{(t)} \delta_u \quad t = 1,2,3 \quad i_m = 1, \dots, n_s \tag{14}$$

from which, by substituting in Eq. (14) the corresponding quantities provided by Eqs. (8) to (13) it is possible to provide the conditions to avoid partial mechanism at each storey and, as a consequence, the sum of reduced plastic moment at each storey needed to design column sections. In particular, this quantity for the first storey column sections is given by one only condition:

$$\sum_{i=1}^{n_c} M_{c.i1} \geq \frac{2 \sum_{k=1}^{n_s} \sum_{j=1}^{n_b} M_{b.Rd.jk} + \left(\gamma_1^{(3)} - \gamma^{(g)}\right) \delta_u \sum_{k=1}^{n_s} F_k h_k}{2 \frac{\sum_{k=1}^{n_s} F_k h_k}{h_1 \sum_{k=1}^{n_s} F_k} - 1} \tag{15}$$

while for the other storey is the maximum among the following three conditions:

$$\sum_{i=1}^{n_c} M_{c.ii_m}^{(1)} = \left(\alpha^{(g)} + \gamma_{i_m}^{(1)} \delta_u\right) \left( \sum_{k=1}^{i_m} F_k h_k + h_{i_m} \sum_{k=i_m+1}^{n_s} F_k \right) - \sum_{i=1}^{n_c} M_{c.i1}^{*} - 2 \sum_{k=1}^{i_m-1} \sum_{j=1}^{n_b} M_{b.Rd.jk} \tag{16}$$

needed to avoid type-1 mechanism,

$$\sum_{i=1}^{n_c} M_{c.ii_m}^{(2)} = \left(\alpha^{(g)} + \gamma_{i_m}^{(2)} \delta_u\right) \sum_{k=i_m}^{n_s} F_k (h_k - h_{i_m-1}) - 2 \sum_{k=i_m}^{n_s} \sum_{j=1}^{n_b} M_{b.Rd.jk} \tag{17}$$

needed to avoid type-2 mechanism,

$$\sum_{i=1}^{n_c} M_{c.ii_m}^{(3)} = \left(\alpha^{(g)} + \gamma_{i_m}^{(3)} \delta_u\right) \frac{\left(h_{i_m} - h_{i_m-1}\right)}{2} \sum_{k=i_m}^{n_s} F_k \tag{18}$$

needed to avoid type-3 mechanisms, where $\sum_{i=1}^{n_c} M_{c.i1}^{*}$ sum of plastic moments of columns at first storey reduced for the contemporary action of axial load after selecting the column sections from the standard shapes.
As preliminarily stated, the maxim among the quantities given by Eqs. (16), (17) and (18) is given by:

$$\sum_{i=1}^{n_c} M_{c.ii_m} = max\left\{\sum_{i=1}^{n_c} M_{c.ii_m}^{(1)}, \sum_{i=1}^{n_c} M_{c.ii_m}^{(2)}, \sum_{i=1}^{n_c} M_{c.ii_m}^{(3)}\right\} \tag{19}$$

The design algorithm that has to be followed to achieve the design purpose, i.e. the design of MRFs collapsing with a global failure mode is reported in Figure 4.

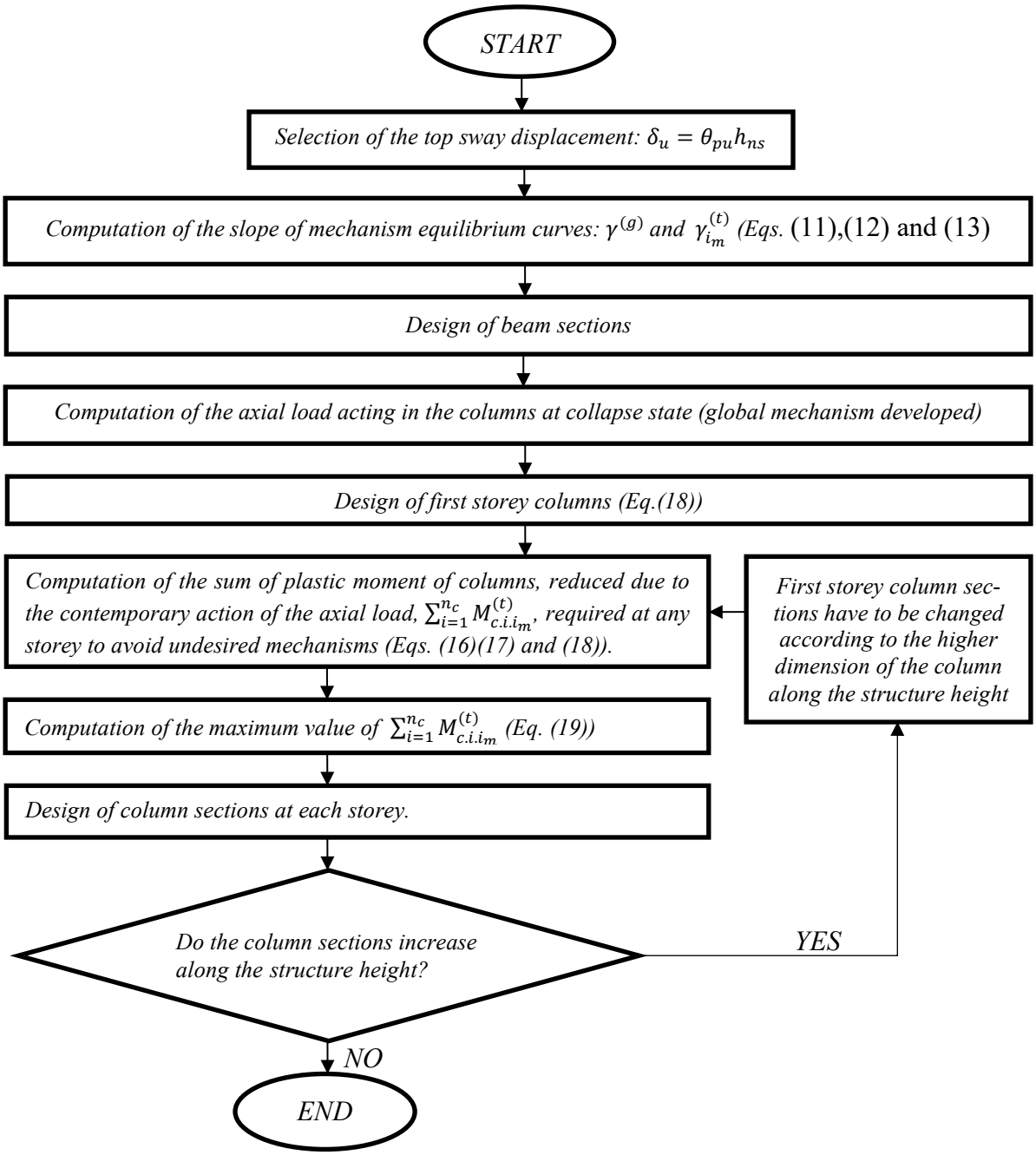


Figure 4: Design algorithm

## 3 PARAMETRIC ANALYSIS

As observed in numerical examples reported in previous works [36], [33] type-1 mechanism usually governs the design of structures, i.e. the term $\sum_{i=1}^{n_c} M_{c.ii_m}^{(1)}$ is greater than $\sum_{i=1}^{n_c} M_{c.ii_m}^{(2)}$ and $\sum_{i=1}^{n_c} M_{c.ii_m}^{(3)}$. Now it is important to point out what are the parameters deciding the influence of type-1 mechanism and if it is possible to preliminarily decide, on the basis of geometrical characteristics, loads and steel grade which one of the three undesired mechanism governs the design of the structure.

In order to answer these questions a parametric analysis has been led by varying geometry, loads and steel grade on MR-Frames with the scope to observe whether there a type mechanism which mostly governs the collapse of structure.

As regards the parameters involved, the geometry has been varied in term of number of storeys, number of bays, storey height and bay length. In particular the number of storey adopted goes from 3 to 8 while the number of bays goes from 2 to 6. Storey height have been assumed equal to 3 m, 4 m and 5 m while bay length has been considered equal to 3 m, 3.5 m, 4 m, 4.5 m, 5 m, 5.5 m, 6 m, 6.5 m and 7 m. Permanent loads, $G_k$, has been adopted equal to 4 kN/m2 while live loads $Q_k$ has been assumed as equal to 2 and 3 kN/m2. Loads have been combined following this relation: $G_k$+0.3$Q_k$. In addition, the influence light of the loads acting on the beams goes from 1 m to 6 m. Beams have been designed on the basis of the acting loads with a minimum and maximum bending moment of $q_d l^2/16$ and their shapes have been selected from the IPE standard profiles. The adopted steel grades are S275, S355, S450. Seismic forces distribution has been assumed proportional to the storey height by neglecting their magnitude because it is irrelevant for the design result of the procedure.

The whole of the analysed number of cases is equal to 176960 but 12690 of these ones have beams incompatible with the assigned loads, so that the real number of analysed cases is equal to 162270.

After the application of TPMC to the analysed cases the following results have been observed: the number of cases governed by a mechanism typology different by the type-1 without the occurrence of the technological condition are 197 while the number of cases that are governed by a mechanism typology different by the type-1 after the occurrence of the technological condition are 22260. It means that, as preliminarily stated, at the occurrence of the technological condition the sum of required column plastic moments for $i_m > 1$ is affected by the increase of the first right hand side term of Eq. (16) and the increase of the subtracting second term at right hand side of Eq. (16) and for this reason type-2 and type-3 mechanism become determinant for the design of the structure.

However, by stopping the attention on the procedure without the occurrence of technological condition is important to observe that only the 0.12% of the analysed cases is governed by a collapse typology different from type-1 and for this reason, it is possible to confirm that type-1 mechanism governs, in the most of the cases, the design of MR-Frames.

Many advantages belong to this observation: first of all the chance to use a simplified version of TPMC to design MR-Frames. This simplified version starts from the preliminary assumption that column sections are pin-jointed at their bases. As a consequence, Eq.(15) becomes:

$$\sum_{i=1}^{n_c} M_{c.i1} \geq \frac{2\sum_{k=1}^{n_s}\sum_{j=1}^{n_b} M_{b.Rd.jk} + \left(\gamma_1^{(3)} - \gamma^{(g)}\right)\delta_u \sum_{k=1}^{n_s} F_k h_k}{\frac{\sum_{k=1}^{n_s} F_k h_k}{h_1 \sum_{k=1}^{n_s} F_k} - 1} \tag{20}$$

and Eqs. (16), (17), and (18), become:

$$\sum_{i=1}^{n_c} M_{c.ii_m}^{(1)} \geq \left(\alpha^{(g)} + \gamma_{i_m}^{(1)}\delta_u\right)\left(\sum_{k=1}^{i_m} F_k h_k + h_{i_m}\sum_{k=i_m+1}^{n_s} F_k\right) - 2\sum_{k=1}^{i_m-1}\sum_{j=1}^{n_b} M_{b.Rd.jk} \quad (21)$$

needed to avoid type-1 mechanisms;

$$\sum_{i=1}^{n_c} M_{c.ii_m}^{(2)} \geq \left(\alpha^{(g)} + \gamma_{i_m}^{(2)}\delta_u\right)\sum_{k=i_m}^{n_s} F_k(h_k - h_{i_m-1}) - 2\sum_{k=i_m}^{n_s}\sum_{j=1}^{n_b} M_{b.Rd.jk} \quad (22)$$

needed to avoid type-2 mechanisms;

$$\sum_{i=1}^{n_c} M_{c.ii_m}^{(3)} \geq \left(\alpha^{(g)} + \gamma_{i_m}^{(3)}\delta_u\right)\frac{\left(h_{i_m} - h_{i_m-1}\right)}{2}\sum_{k=i_m}^{n_s} F_k \quad (23)$$

needed to avoid type-3 mechanisms; where $\alpha^{(g)}$ does not depend on the sum of the reduced plastic moments of columns at the first storey $\sum_{i=1}^{n_c} M_{c.i1}$ and it is provided by the following relation:

$$\alpha^{(g)} = \frac{\sum_{k=1}^{n_s}\sum_{j=1}^{n_b} 2B_{jk}\, R_{b,jk}}{\sum_{k=1}^{n_s} F_k h_k} \quad (24)$$

being Eqs. (16), (17), and (18) independent of the sum of the reduced plastic moments of columns at the first storey, $\sum_{i=1}^{n_c} M_{c.i1}$, the column sections at first storey are provided starting by Eq. (20) while the column sections at each storey required to avoid undesired mechanism are directly provided starting by Eq. (21), (22) and (23), without the preliminary design of column sections at first storey. In this way, each storey is independent of the other storey and in particular, of the first one, so that, even if the technological condition occurs the column sections at each storey do not need to be revised. In addition, the solution provided in the framework of the hypothesis of pin-jointed column bases (simplified TPMC) constitutes a safe side solution with reference to the original TPMC [36], only in the case of type-1 mechanism governing the design procedure.

## 4 CONCLUSIONS

- In this paper the state of the art of Theory of Plastic Mechanism Control (TPMC) has been presented with reference to MR-Frames.
- The analysis of the influence of geometry, loads and steel grade for the development of a specific collapse type of steel MR-Frames is reported.
- The kinematic theorem of plastic collapse extended to the concept of mechanism equilibrium curve has been applied to a large number of steel frames with different geometrical configurations and different loads and steel grades.
- The 88% of the analysed cases is governed by type-1 mechanism.
- In this last case a simplified version of TPMC could be applied.

## REFERENCES

[1] E. Güneyisi, M. D'Aniello, R. Landolfo and K. Mermerdaş, "Prediction of the flexural overstrength factor for steel beams using artificial neural network," *Steel and Composite Structures,* vol. 17, no. 3, pp. 215-236, 2014.

[2] R. Park, «Ductile Design Approach for Reinforced Concrete Frames,» *Earthquake Spectra, EERI,* vol. 2, n. 3, pp. 565-619, 1986.

[3] F. M. Mazzolani and V. Piluso, Theory and Design of Seismic Resistant Steel Frames, E&FN Spon, 1996.

[4] M. Bruneau, C. Uang and R. Sabelli, Ductile Design of Steel Structures, McGraw-Hill, 2011.

[5] H. Akiyama, Earthquake Resistnat Limit State Design for Building, Tokyo: University of Tokyo press, 1985.

[6] E. Rosenblueth, Design of Earthquake Resistant Structures, London: Pentech Press, 1980.

[7] T. Paulay and M. Priestley, Seismic Design of Reinforced Concrete and Masonry Buildings, New York: Wiley, 1995.

[8] D. 1. NTC 2008, Nuove norme tecniche per le costruzioni, 2008.

[9] E. 1998-1, Eurocode 8: Design of Structures for Earthquake Resistance – Part 1: general Rules, Seismic Actions and Rules for Buildings, CEN, 2004.

[10] A. 341-10, Seismic Provisions for Structural Steel Buildings, American Institute of Steel Construction, 2010.

[11] F. M. Mazzolani and V. Piluso, "Plastic Design of Seismic Resistant Steel Frames," *Earthquake Engineering and Structural Dynamics,* vol. 26, pp. 167-191, 1997.

[12] R. Montuori and V. Piluso, "Design of Semi-Rigid Steel Frames for Failure Mode Control," in *Moment Resistant Connections of Steel Frames: Design and Reliability*, London, E&FN Spon, Taylor & Francis Group, 2000, pp. 461-483.

[13] R. Montuori, E. Nastri, V. Piluso and M. Troisi, "Influence of the cyclic behaviour of beam-to-column connection on the seis-mic response of regular steel frames," *Ingegneria Sismica,* vol. 33, pp. 91-105, 2015.

[14] R. Montuori, E. Nastri and V. Piluso, "Rigid-plastic analysis and moment-shear interaction for hierarchy criteria of inverted y EB-Frames," *Journal of Constructional Steel Research,* vol. 95, pp. 71-80, 2014.

[15] R. Montuori, E. Nastri and V. Piluso, "Seismic response of EB-frames with inverted Y-scheme: TPMC versus eurocode provisions," *Earthquake and Structures,* vol. 8, no. 5, pp. 1191-1214.

[16] R. Montuori, E. Nastri and V. Piluso, "Theory of Plastic Mechanism Control for MRF-EBF dual systems: Closed form solution," *Engineering Structures,* vol. 118, pp. 287-306, 2016.

[17] R. Montuori, E. Nastri and V. Piluso, "Theory of plastic mechanism control for the seismic design of braced frames equipped with friction dampers," *Mechanics Research Communications,* vol. 58, pp. 112-123, 2014.

[18] E. Nastri, «Document Eccentrically braced frames designed for the energy dissipation optimization,» *ECCOMAS Congress 2016 - Proceedings of the 7th European Congress on Computational Methods in Applied Sciences and Engineering,* vol. 4, pp. 8476-8491, 2016.

[19] R. Montuori, E. Nastri and V. Piluso, "Theory of plastic mechanism control for eccentrically braced frames with inverted y-scheme," *Journal of Constructional Steel Research,* vol. 92, pp. 122-135, 2014.

[20] L. Mastrandrea, E. Nastri and V. Piluso, “Validation of a design procedure for failure mode control of EB-Frames: Push-over and IDA analyses,” *Open Construction and Building Technology Journal,* vol. 7, pp. 93-207, 2013.

[21] E. Nastri and A. Paciello, “An example of energy dissipation optimization for steel mrfs with pin-jointed column bases,” *ECCOMAS Congress 2016 - Proceedings of the 7th European Congress on Computational Methods in Applied Sciences and Engineering,* vol. 4, pp. 8460-8475, 2016.

[22] R. Montuori, E. Nastri, V. Piluso and M. Troisi, “Influence of connection typology on seismic response of MR-Frames with and without ‘set-backs’,” *Earthquake Engineering and Structural Dynamics,* vol. 46, pp. 5-25, 2017.

[23] V. Piluso, R. Montuori and M. Troisi, “Innovative structural details in MR-frames for free from damage structures,” *Mechanics Research Communications,* vol. 58, no. DOI: 10.1016/j.mechrescom.2014.04.002, pp. 146-156, 2014.

[24] M. A. Conti, L. Mastrandrea and V. Piluso, “Plastic Design and Seismic Response of Knee Braced Frames,” *Advanced Steel Construction,* vol. 5, no. 3, pp. 343-363, 2009.

[25] A. Longo, R. Montuori and V. Piluso, “Failure mode control and seismic response of dissipative truss moment frames,” *Journal of Structural Engineering (United States),* vol. 138, no. 11, pp. 1388-1397, 2012.

[26] A. Longo, R. Montuori e V. Piluso, «Failure Mode Control of X-braced Frames under Seismic Actions,» *Journal of Earthquake Engineering,* vol. 12, pp. 728-759, 2008.

[27] M. T. Giugliano, A. Longo, R. Montuori and V. Piluso, “Failure Mode and Drift Control of MRF-CBF Dual Systems,” *The Open Journal of Construction and Building Technology,* vol. 4, pp. 121-133, 2010.

[28] A. Longo, R. Montuori, E. Nastri and V. Piluso, “On the use of HSS in seismic-resistant structures,” *Journal of Constructional Steel Research,* vol. 103, pp. 1-12, 2014.

[29] A. Longo, R. Montuori and V. Piluso, “Theory of plastic mechanism control for MRF–CBF dual systems and its validation,” *Bulletin of Earthquake Engineering,* vol. 12, no. 6, pp. 2745-2775, 2014.

[30] A. Longo, E. Nastri and V. Piluso, “Theory of plastic mechanism control: State-of-the-art,” *Open Construction and Building Technology Journal,* vol. 8, pp. 262-278, 2014.

[31] A. Longo, R. Montuori e V. Piluso, «Plastic design of seismic resistant V-Braced frames,» *Journal of Earthquake Engineering ,* vol. 12, n. 1246-1266, 2008.

[32] R. Montuori, E. Nastri and V. Piluso, “Influence of the bracing scheme on seismic performances of MRF-EBF dual systems,” *Journal of Constructional Steel Research,* vol. 132, no. DOI: 10.1016/j.jcsr.2017.01.018, pp. pp. 179-190.

[33] R. Montuori and R. Muscati, “A general design procedure for failure mechanism control of reinforced concrete frames,” *Engineering Structures,* vol. 118, pp. 137-155, 2016.

[34] R. Montuori and R. Muscati, “Smart and simple design of seismic resistant reinforced concrete frame,” *Composites Part B: Engineering,* no. DOI: 10.1016/j.compositesb.2016.09.050, p. Article in press, 2016.

[35] R. Montuori and R. Muscatia, “Plastic design of seismic resistant reinforced concrete frame,” *Earthquake and Structures,* no. DOI: 10.12989/eas.2015.8.1.205, pp. 205-224, 2015.

[36] R. Montuori, E. Nastri and V. Piluso, "Advances in theory of plastic mechanism control: closed form solution for MR-frames," *Earthquake Engineering and Structural Dynamics,* vol. 44, no. 7, pp. 1035-1054, 2015.

[37] D. Cassiano, M. D'Aniello, C. Rebelo, R. Landolfo and L. S. Da Silva, "Influence of Seismic design rules on the robustness of steel moment resisting frames," *Steel and Composite Structures,* vol. 21, no. 3, pp. 479-500, 2016.

[38] M. Ferraioli, "Dynamic increase factor for pushdown analysis of seismically designed steel moment-resisting frames," *International Journal of Steel Structures,* vol. 16, pp. 857-875, 2016.

[39] A. Tenchini, M. D'Aniello, C. Rebelo, R. Landolfo, L. Da Silva and L. Lima, "Seismic performance of dual-steel moment resisting frames," *Journal of Constructional Steel Research,* vol. 101, no. DOI: 10.1016/j.jcsr.2014.06.007, pp. 437-454.

[40] A. Formisano, R. Landolfo and F. M. Mazzolani, "Robustness assessment approaches for steel framed structures under cata-strophic events," *Computers and Structures,* vol. 147, pp. 216-228, 2015.

[41] M. Ferraioli, A. Lavino and A. Mandara, "An adaptive capacity spectrum method for estimating seismic response of steel moment-resisting frames," *Ingegneria Sismica,* vol. 33, no. 1-2, pp. 47-60. , 2015.

[42] P. Castaldo, G. Amendola e B. Palazzo, «Effetcs of class B site on the seismic reliability of base-isolated steel systems,» *Ingegneria Sismica,* vol. 33, n. 3, pp. 29-41, 2016.

COMPDYN 2017
6th ECCOMAS Thematic Conference on
Computational Methods in Structural Dynamics and Earthquake Engineering
M. Papadrakakis, M. Fragiadakis (eds.)
Rhodes Island, Greece, 15–17 June 2017

# The effect of number and Location of braced frames on column behavior of the dual steel structural system (MRF and EBF) (With a view on amplified seismic load)

**Sajjad Mohammadi[1] , Abdolreza S.Moghadam[2] , Alireza Faroughi[3]**

1 Master of Science in Structural Engineering, Semnan branch ,Islamic Azad University, Semnan, Iran
e-mail: sajjad700327@gmail.com
2 Associate Professor
International Institute of Earthquake Engineering and Seismology (IIEES), Tehran, Iran
e-mail: moghadam@iiees.ac.ir
3 Assistant Professor
Department of Civil Engineering, College of Engineering, East Tehran Branch, Islamic Azad University, Tehran, Iran
e-mail: faroughi@iauet.ac.ir

**Keywords:** Braced frames, Over-strength factor, Dual system, Amplified seismic load.

**Abstract.** *In seismic design of structures, determination of number and Location of braced frames, considering the architectural scheme of projects, is usually confronted by obstacles. Due to this fact, in some cases, selecting the best location and number of braced bays has led to mistakes in determination of their adjacent members (columns) design loads. One of the seismic design requirements of lateral resisting system is to control the columns adjacent to braced bays for load combinations of amplified seismic load, which is a function of over-strength factor of the structure. This research aims to present and introduce the best structural model of number and Location of braced frames in a structural system, such as steel moment resisting frame and eccentric braces dual system; because in 3rd revision of Iranian 2800 standard of seismic provision, there are statements and criteria provided only for capacity of moment frame, not for braces. Though the amplified seismic load function is controlled in models which columns are connected to braces in 2 directions, and seismic loads are applied in those 2 directions, number of damage hinges (Exceeding CP) is significantly increased in comparison to the models with straggly braces. As the increase in axial force of these columns leads to decrease in their moment capacity (despite controlling the amplified seismic load provision), columns in dual systems that resist flexure, would be damaged and exceed the collapse threshold much sooner than other columns. This important fact is not presented in Iranian or even American codes and provisions.*

## 1. INTRODUCTION

Moment resisting frame is a structural system which gravitational loads are carried by structural frames and lateral resistance is provided by moment frames. Structures totally consisting of moment frames, and structures with peripheral moment frames or structures with moment frames in some parts and simply supported frames in others, are moment resisting frames too. In this system, concrete or steel moment resisting frames can be used as ordinary, intermediate or special ductility frames. Most of the gravitational loads are carried by simply supported frames, and lateral loads are resisted by shear walls, braces or frames – with respect to lateral stiffness of each frame-. Shear resisting share of each group is determined in each story, considering their lateral stiffness and interaction [1].

Eccentrically braced frames were introduced by Popov et al. in 1978 for the first time. This system was developed to resist the lateral loads and their effects on remarkable large deformations and relative displacements, especially in tall buildings. Eccentrically braced frames (EBF) were introduced as a modern seismic resisting system in codes and provisions as a result of this research. Based on the numerous researches conducted on this system, eccentrically braced frame systems can demonstrate high stiffness in inelastic region. The primary goal of developing eccentrically braced frames, was to induce yielding in a small part of beam, namely link beam [2] [3].

## 2. RESEARCH SUBJECT

The aim of this research is to investigate the seismic capacity of dual systems of steel moment resisting frame and eccentric braces, to find the number and Location of braced frames, related to this capacity, and to control the amplified seismic load. Also, the fact that columns in dual systems that resist flexure, would be damaged and exceed the collapse threshold much sooner than other columns is not presented in Iranian or even American codes and provisions; and in 3rd revision of Iranian 2800 standard of seismic provision, there are statements and criteria provided only for capacity of moment frame, not for braces and shear walls. These phenomenas are investigated of in this research.

## 3. INVESTIGATED MODELS

FEMA p695-2009 is used for the investigation and acknowledgement of model selection requirements. By applying this provision, the following models were selected for the investigation.

## 4. DESIGN CONSIDERATIONS

Using an experimental approach in design, the number of required braces were selected considering 10-30 percent of the structure perimeter. Number of structural models were limited to 28, due to their importance. The utilized sections in software models were all box sections with properties similar to common sections from size 8 to 40 (The following models, numbered from 1 to 28 from left to right respectively, were analyzed).

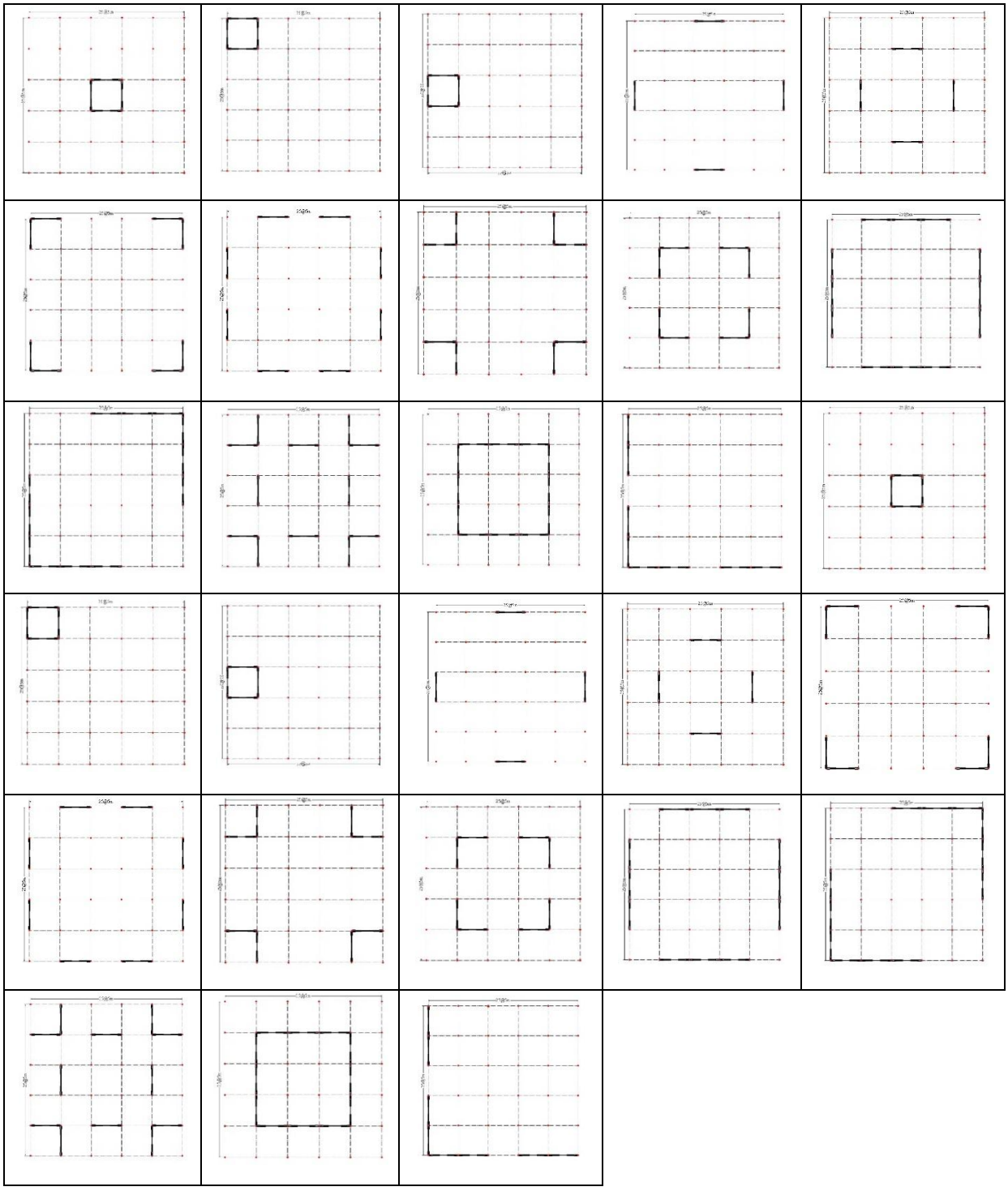

Fig. 1. Research models

Software modeling was performed using Etabs 2013 V2.2 software.

## 5. DESIGN AND ANALYSIS METHODS

Structural design was performed using Iranian design codes (code 6 and code 10) and 3rd revision of Iranian 2800 standard. To control and verify software calculations, some cases

were calculated manually and compared with software results. The errors –if presented- were resolved and troubleshot.

## 6. MOMENT RESISTING FRAMES DESIGN PROVISIONS

Based on sections 1-5-5 and 1-9-4 of 3rd revision of Iranian 2800 standard of seismic provision, moment frames should be able to resist 25% of the structural lateral load, independently.

In this procedure, after completion of structural design and verification of all the passed beam and column members, braces are removed and the seismic load is reduced to 25% of its initial value. Then, the design procedure is performed again, and the moment frame structure should comply with allowable code ranges.

## 7. USING LOAD COMBINATIONS INCLUDING AMPLIFIED SEISMIC LOADS IN DESIGN

Load combinations including amplified seismic loads are resulted from replacing the seismic loads E with Ω.E in normal load combinations, based on sections 10-1 or 10-2. These load combination consist of:

A: Allowable stress method

$0.75(D+L+\Omega_0 E)$ (1)

$0.75(D+\Omega_0 E)$ (2)

B: Limit states method

$D+1.2L+1.2\Omega_0 E$ (3)

$0.85D+1.2\Omega_0 E$

| Lateral load resisting system type | $\Omega_0$ |
|---|---|
| All steel moment frames | 3 |
| All simply supported frames with concentrically or eccentrically steel braced frames | 2 |
| All dual or combined systems | 2.5 |

Table 1. Over-strength factor Ω0 for different lateral load resisting systems

## 8. NONLINEAR STATIC ANALYSIS

Nonlinear static analysis is used to analyze the selected models in this research.

### 8.1. NONLINEAR STATIC PUSHOVER ANALYSIS

Nonlinear model is defined in sections that have the highest potential of undergoing nonlinear inelastic behavior. For example in fixed ended beams, flexural plastic hinges are defined in the beginning and end of member, and in columns, if no concentrated load is present, flexural plastic hinges are defined in the beginning and end of column, again. In this case, hinge properties are representative of nonlinear material behavior. It should be noticed

that, the parameters of nonlinear material behavior curve should be presented in tables of retrofitting provision [5].

To investigate the structure using this approach, the structure is analyzed considering the real behavior of member materials (inelastic), under an incremental specific uniform load pattern, and the analysis continues until the displacement of a specific point in the structure (control point displacement) reaches the pre-calculated limit. This displacement that is calculated based on a specific retrofit goal, is called target or demand displacement and is the base of the structural members. Deformation, rotation and internal forces of the members are studied at this stage (calculating the demand deformation of members is nearly impossible) [5].

## 9. ANALYSIS PROCEDURE OF DETAILED MODELS

The following assumptions are utilized in analysis procedure of this research.

### 9.1. UN-LOADING IN NONLINEAR STATIC ANALYSIS

The software should find a way to remove the supported load by the hinge, and then probably re-distribute it on other structural members. When hinges can be un-loaded that their stress-strain, force-displacement, or moment-curvature curves have capacity loss. What we mean by capacity loss is to transfer from point C to D or from point E to F (full rupture). This fact is presented in the following figure [7].

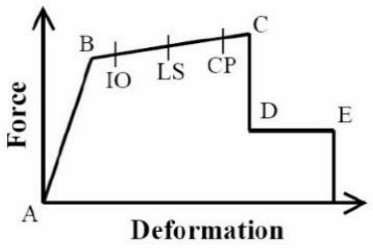


Fig. 2. Severe hinge capacity loss in points C and E [7]

### 9.2. UN-LOADING USING RESTART USING SECONDARY STIFFNESS METHOD

In this approach, if the hinge reaches to the part with negative slope of the stress-strain curve, all the hinges that act nonlinearly, change by utilizing the secant (secondary) stiffness properties, and the analysis is performed again. Secant stiffness of each hinge is defined as the secant of the line connecting O to X in stress-strain curve. The point O, is the stress-strain in start of the analysis that usually includes the stresses resulting from gravitational loads. The point X, is the current point on the curve, if the slope of stress-strain curve in this point is either positive or zero. Otherwise, it is on the lower end of the negative slope section of the stress-strain curve. When the load is reapplied at the beginning of the analysis, after that the hinge is retrieved based on the given stress-strain curve, each hinge is displaced along secant slope to reach the point X. This procedure is similar to that of FEMA 273, and would be meaningful if incremental load analysis is changed to incremental cyclic loading instead of

uniform static load. Performance of this procedure is lower than the other two. The number of required stages is increased relative to square of target displacement in this procedure. This procedure is very efficient, if the gravitational load is small, and no rotation divergence will happen. When the stress in the hinge under gravitational loads is so large that the secant of the O to X connecting line becomes negative, this procedure won't be efficient anymore. In other words, this procedure can provide convergence in cases which the other two procedures diverge due to small negative slope (almost horizontally). The following picture illustrates the obtained pushover analysis curve using this procedure. The solid and dotted lines in the picture are the pushover curve when the Save Positive Increments Only is activated and deactivated respectively [7].

Considering the expressed explanations and divergence in analytical models and load patterns, secondary stiffness redistribution method is used in this research.

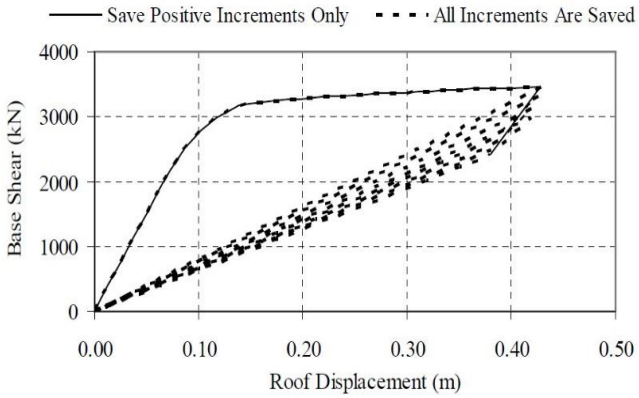


Fig. 3. Comparison of pushover curves between the restart method and secant (secondary) stiffness method [7]

## 10. ANALYZING THE RESULTS

| Model | Number of Stories | Number of CP level exceeded hinges in columns of braced bays | | Number of CP level exceeded hinges in columns of moment frames | | Number of CP level exceeded hinges in beams | | Number of CP level exceeded hinges in braces | |
|---|---|---|---|---|---|---|---|---|---|
| | | Push X | Push Y | Push X | Push Y | Push X | Push Y | Push X | Push Y |
| 1 | 5 | 0 | 0 | 0 | 0 | 8 | 8 | 0 | 0 |
| 2 | 5 | 0 | 0 | 3 | 0 | 6 | 10 | 0 | 0 |
| 3 | 5 | 0 | 0 | 0 | 0 | 10 | 10 | 0 | 0 |
| 4 | 5 | 0 | 0 | 0 | 0 | 10 | 10 | 0 | 0 |
| 5 | 5 | 0 | 0 | 0 | 0 | 8 | 8 | 0 | 0 |
| 6 | 5 | 2 | 4 | 0 | 0 | 12 | 12 | 0 | 0 |
| 7 | 5 | 4 | 4 | 0 | 0 | 12 | 12 | 0 | 0 |
| 8 | 5 | 3 | 4 | 0 | 0 | 12 | 12 | 0 | 0 |
| 9 | 5 | 4 | 4 | 0 | 0 | 12 | 12 | 0 | 0 |
| 10 | 5 | 0 | 0 | 0 | 0 | 12 | 12 | 0 | 0 |
| 11 | 5 | 0 | 0 | 0 | 0 | 12 | 12 | 0 | 0 |
| 12 | 5 | 0 | 0 | 0 | 0 | 12 | 12 | 0 | 0 |
| 13 | 5 | 0 | 0 | 0 | 0 | 12 | 12 | 0 | 0 |
| 14 | 5 | 0 | 0 | 3 | 0 | 20 | 20 | 0 | 0 |
| 15 | 8 | 0 | 0 | 0 | 2 | 16 | 16 | 0 | 0 |
| 16 | 8 | 4 | 0 | 43 | 12 | 22 | 16 | 0 | 0 |

| | | | | | | | | | |
|---|---|---|---|---|---|---|---|---|---|
| 17 | 8 | 0 | 0 | 0 | 1 | 14 | 10 | 0 | 1 |
| 18 | 8 | 0 | 0 | 2 | 1 | 14 | 16 | 0 | 0 |
| 19 | 8 | 0 | 0 | 0 | 0 | 14 | 14 | 0 | 0 |
| 20 | 8 | 0 | 0 | 6 | 2 | 28 | 28 | 0 | 0 |
| 21 | 8 | 4 | 0 | 0 | 1 | 24 | 24 | 0 | 0 |
| 22 | 8 | 0 | 0 | 4 | 8 | 24 | 24 | 0 | 0 |
| 23 | 8 | 2 | 2 | 0 | 0 | 24 | 24 | 0 | 0 |
| 24 | 8 | 2 | 3 | 0 | 2 | 36 | 36 | 0 | 0 |
| 25 | 8 | 0 | 1 | 1 | 1 | 30 | 30 | 0 | 0 |
| 26 | 8 | 0 | 0 | 0 | 0 | 36 | 36 | 0 | 0 |
| 27 | 8 | 2 | 0 | 2 | 2 | 30 | 30 | 0 | 0 |
| 28 | 8 | 0 | 0 | 3 | 8 | 32 | 32 | 0 | 0 |

Table 2. Segregated properties of collapse prevention level exceeded hinges of different structural members

### 10.1.1. FIRST GROUP

Models no. 1 through 5 consist of low rise 5 story structures, having braced bay length of 10% of perimeter of the structure, and number of braced bays as two 5 meter bays in each direction. The best structural models in this group was were models 1 and 5 from design and engineering view. They also have the least number of hinges with performance level of collapse prevention. Models no.2 and 4 performed undesirably.

### 10.1.2. SECOND GROUP

Models no. 6 through 9 consist of low rise 5 story structures, having braced bay length of 15-20% of perimeter of the structure, and number of braced bays as four 5 meter bays in each direction. From design and engineering view, there's no significant difference between the models of this group. Though, model no.6 have the least number of hinges with performance level of collapse prevention. Models no.7 and 9 performed undesirably.

### 10.1.3. THIRD GROUP

Models no. 10 through 14 consist of low rise 5 story structures, having braced bay length of 25-30% of perimeter of the structure, and number of braced bays as six 5 meter bays in each direction. No significant difference can be seen between the models no.10 through 13 of this group. Though, model no.10 have the least number of hinges with performance level of collapse prevention. Model no.14 performance was the worst.

### 10.1.4. FOURTH GROUP

Models no. 15 through 19 consist of mid-rise 8 story structures, having braced bay length of 10% of perimeter of the structure, and number of braced bays as two 5 meter bays in each direction. From design and engineering view, model no.19 was the best of this group, and also this model preforms well in having the least number of hinges with performance level of collapse prevention. Models no.16 and 17 are undesirable models of this group.

### 10.1.5. FIFTH GROUP

Models no. 20 through 23 consist of mid-rise 8 story structures, having braced bay length of 15-20% of perimeter of the structure, and number of braced bays as four 5 meter bays in each direction. Despite the insignificant differences of the models of this group, model no. 19

was the best, from design and engineering view, and also this model is one of the best performers in having the least number of hinges with performance level of collapse prevention. Model no.22 is among the undesirable models of this group.

### 10.1.6. SIXTH GROUP

Models no. 24, 26 and 27 consist of mid-rise 8 story structures, having braced bay length of 25-30% of perimeter of the structure, and number of braced bays as six 5 meter bays in each direction. Neglecting the model no. 25 that is irregular, model no. 27 was the best, from design and engineering view, and also this model is one of the best performers in having the least number of hinges with performance level of collapse prevention. Model no.24 performs undesirably in this group.

### 10.1.7. SEVENTH GROUP

Models no. 25 and 28 consist of mid-rise 8 story structures, having braced bay length of 25-30% of perimeter of the structure, and number of braced bays as six 5 meter bays in each direction. Model no. 25 was the best, from design and engineering view, and also this model is one of the best performers in having the least number of hinges with performance level of collapse prevention. Model no.28 performs undesirably in this group.

## 11. CONCLUSION

- Among the models of low rise 5 story structures, the best model with residential and administrative applications, is the model no. 6. If we can't take the risk of that model, model no.10 would be one of the best models. Moreover, generally, except the models no. 2 and 14 (the irregular ones), other models are not significantly different from each other. It can be concluded that for 5 story structures, having the similar condition of bays, 10-20% of perimeter of the structure, would be a desirable value for length of braced bays. It can be seen that in 5 story models, structures with one or two braced bays in each direction, would be of appropriate models, and more braced bays would be ineffective in weight reduction.
- Among the models of mid-rise 8 story structures, the best models with residential and administrative applications, are the models no. 23 and 25. The Location of braced frames would be more critical in comparison to their numbers. From the numbers of braced bays view, 20-30% of perimeter of the structure, would be a desirable value for length of braced bays. Also, irregular models, such as models no. 16 and 28, would not be appropriate models, because of the higher number of hinges with performance level of collapse prevention, due to moment frames' bigger share in resisting lateral load, and secondary torsional effects. It was seen that in 8 story models, structures with two or three braced bays in each direction, would be of appropriate models.
- Comparison between low and mid-rise structures revealed that with increase in structural height, the number of required braced bays is increased. It can be seen in 5 and 8 story models, presented in this research, where the number of required braced bays was increased form 10-20% of perimeter of the structure to 20-30% of that.
- Though the amplified seismic load function is controlled in models which columns are connected to braces in 2 directions, and seismic loads are applied in those 2 directions, number of damage hinges (Exceeding CP) is significantly increased in comparison to the

models with straggly braces. As the increase in axial force of these columns leads to decrease in their moment capacity (despite controlling the amplified seismic load provision), columns in dual systems that resist flexure, would be damaged and exceed the collapse threshold much sooner than other columns. Finally, it's recommended that in these structures (dual systems), when calculating the moment capacity of the columns connected to the braces, the effects of over-strength factor should be noticed. This important fact is not presented in Iranian or even American codes and provisions.

## REFERENCES

[1] Continual revision committee (2005). "3rd revision of Iranian 2800 standard of seismic revision – Code for seismic design of structures" Road, Housing & Urban Development Research Center

[2] Merovich, A.T., Nicoletti, J.P. and Hartle, E. (1982). "Eccentric Bracing in Tall Buildings," ASCE Journal of the Structural Division, 108(ST9), September, pp. 2066-2079

[3] Roeder, C.W. and Popov, E.P. (1978). "Eccentrically Braced Steel Frames for Earthquakes," ASCE Journal of the Structural Division, ST3, March, pp. 391-411

[4] Niknam, A. ,Meymandi Parizi, AA., and Pakniyat, Sh. (2011) "Seismic rehabilitation of steel structures and pushover analysis in Etabs and SAP" Motefakkeran publications.

[5] Richards, Paul.W. (2010). "Estimating the stiffness of eccentrically braced frames (EBFs)." ASCE Practice Periodical on Structural Design and Construction.

[6] Popov, E.P., Engelhardt, M.D. and Ricles, J.M. (1989). "Eccentrically Braced Frames: U.S. Practice," AISC Engineering Journal, Second Quarter, pp. 66-80.

[7] Taghizadeh, R. (2013) "Performance based design and rehabilitation of structures using pushover analysis in ETABS nad SAP" Collegiate books publications

[8] Continual revision committee (2013). "Code 10 of Iranian national building requirements" Road, Housing & Urban Development Research Center

COMPDYN 2017
6th ECCOMAS Thematic Conference on
Computational Methods in Structural Dynamics and Earthquake Engineering
M. Papadrakakis, M. Fragiadakis (eds.)
Rhodes Island, Greece, 15–17 June 2017

# MODELING FLEXURE-SHEAR FAILURES IN MASONRY-INFILLED RC FRAMES WITH INELASTIC FIBER-BASED FRAME ELEMENTS

**Alexander Kagermanov**[1], **Paola Ceresa**[2]

[1] UME School, Institute for Advanced Studies (IUSS)
Piazza della Vittoria, 15, 27100, Pavia, Italy
alexander.kagermanov@umeschool.it

[2] Institute for Advanced Studies (IUSS)
Piazza della Vittoria, 15, 27100, Pavia, Italy
paola.ceresa@iusspavia.it

**Keywords:** inelastic frame elements, shear failure, flexure-shear interaction, masonry infills.

**Abstract.** *A numerical procedure for modeling beam and/or column shear failures in RC infilled frames is presented. The main novelty relies in the use of inelastic fiber-based frame elements with flexure-shear interaction for modeling the RC members. The frame element is based on the Timoshenko beam kinematic assumption combined with an orthotropic smeared-crack constitutive model for cracked concrete, which is defined at each section fiber for the determination of the nonlinear sectional response. For the masonry panel, the equivalent multiple-strut approach is adopted, in order to accurately predict the distribution of shear and bending moments in the RC members due to infill-frame interaction. The procedure is verified against available monotonic tests where flexure-shear failures of the RC members were observed during the test. Comparison with traditional flexural frame elements is also provided in order to highlight the differences between the two methodologies.*

## 1 INTRODUCTION

The seismic behavior of masonry-infilled RC frames has been object of extensive experimental and analytical research mainly for two reasons: (i) its widespread use in many seismic regions, such as Mediterranean countries and South America, and (ii) the complex interaction between the frame and infill panel, which can negatively affect the failure mode and overall ductility of the structure. Typically, five basic failure modes have been identified from field and experimental investigations [1, 2, 3, 4, 5, 6]: (i) Sliding shear along horizontal bed joints, (ii) diagonal tension failure, (iii) diagonal compression failure, (iv) corner crushing of the panel and (v) flexure or shear-flexure failure of the RC members. Among them, failure of the columns directly compromises the vertical load carrying capacity of the structure. In particular, flexure-shear failure can significantly reduce the overall ductility due to its brittle nature, especially in the case of weak frame-weak masonry system.

At the same time, modeling of masonry-infilled frames for nonlinear static and dynamic analysis has been typically approached with macro-models consisting in a pair of equivalent diagonal struts, one in each direction, with a predefined hysteretic response. Although this approach may provide credible results in terms of overall strength and stiffness, upon appropriate selection of the strut parameters, it is not able to simulate the correct location and type of failure in the RC members, since it does not adequately reproduce the distribution of bending moments and shear forces [6, 7]. Hence, a more appropriate approach is to use multiple-strut models such as those introduced in [8, 9].

An important shortcoming in simulating failure mode (v) using frame analysis is the inability of flexural frame elements in capturing shear failures. Although this problem can be partially solved with equivalent lumped plasticity models with flexure-shear hinges [10], this approach requires the calibration of several model parameters, which is rather complicated in the case of masonry-infilled RC frames due to the scarcity of the available experimental data. Hence, an alternative approach is pursued herein based on fiber frame elements combined with biaxial constitutive models for reinforced concrete, which provides a more rational way of modeling flexure-shear interaction in RC members.

A case-study masonry infilled RC frame, which experienced shear failure of the columns, was selected from the literature [11, 12]. The frame was modeled with both traditional flexural frame elements and those with flexure-shear interaction. A three-strut approach was used to represent the masonry panel in order to capture more accurately the shear and flexural demands in beams and columns. Finally, comparison in terms of lateral-force displacement response is provided in order to highlight the differences between the two modeling approaches**.**

## 2 FRAME ELEMENT WITH AXIAL-SHEAR INTERACTION

The inelastic frame element used in the present work is based on the Timoshenko beam theory at the kinematic level, combined with biaxial constitutive models for reinforced concrete at the fiber section level. Several element formulations have been previously presented following a similar approach [13, 14, 15]. The main differences, however, concerned the type of constitutive model for reinforced concrete, e.g. damage-plasticity, orthotropic, micro-plane models, etc…, the type of element formulation, e.g. displacement-based, force-based or mixed formulation, and the type of shear strain profile over the cross section, e.g. uniform, parabolic or exact. Despite the different modeling approaches, overall acceptable performance has been demonstrated by the different authors.

In what follows, a brief summary of the element formulation used herein is presented. Further details can be found in [16].

The total displacement (u, v) at a given point of the section with coordinates (x, y) is given assuming the plane section assumption (Figure 1):

$$u(x,y) = u_o(x) - \theta_z(x)y \tag{1}$$

$$v(x,y) = v_o(x) \tag{2}$$

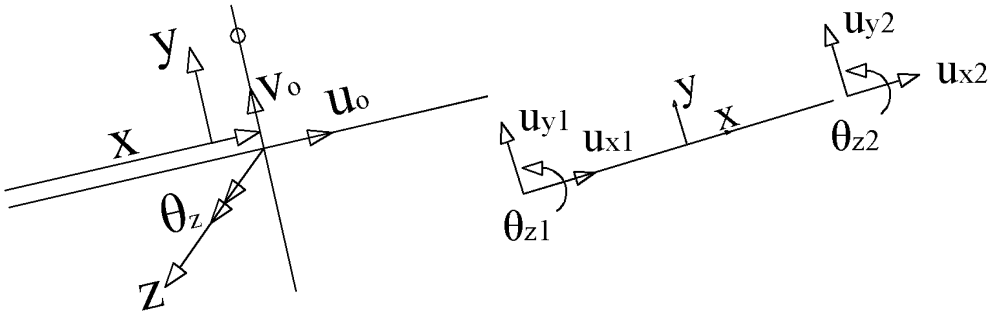


Figure 1: Definition of frame element reference system and kinematics.

where $u_o$ is the horizontal displacement, $\theta_z$ the section rotation and $v_o$ the vertical displacement of the beam axis, x the longitudinal coordinate along the beam axis, and y the vertical coordinate. Assuming small strain-displacement compatibility, axial and shear strains at each fiber are given as:

$$\begin{pmatrix} \varepsilon_x \\ \gamma_{xy} \end{pmatrix} = \begin{bmatrix} 1 & -y & 0 \\ 0 & 0 & 1 \end{bmatrix} \begin{pmatrix} \varepsilon_o \\ \chi_z \\ \gamma_{oy} \end{pmatrix} \tag{3}$$

$$\boldsymbol{\varepsilon} = \mathbf{B}\mathbf{e} \tag{4}$$

where $\varepsilon_x$ and $\gamma_{xy}$ are the axial and shear strains, respectively, acting on a section layer of coordinate y, $\varepsilon_o$ is the average axial strain, $\chi_z$ the section curvature and $\gamma_{oy}$ the section shear deformation. Section forces are obtained from direct integration of stress distributions over the section:

$$\mathbf{S} = \int_A \mathbf{B}^T \boldsymbol{\sigma} dA \tag{5}$$

where $\mathbf{S}=[N, M, V]^T$ and $\boldsymbol{\sigma}=[\sigma_x, \tau_{xy}]^T$ are the vector of section forces and stresses, respectively. The tangent stiffness matrix of the section is obtained taking variation of section forces with respect to section deformations:

$$\mathbf{K}_s = \frac{\partial \mathbf{S}}{\partial \mathbf{e}} = \frac{\partial}{\partial \mathbf{e}} \int_A \mathbf{B}^T \boldsymbol{\sigma} dA = \int_A \mathbf{B}^T \frac{\partial \boldsymbol{\sigma}}{\partial \boldsymbol{\varepsilon}} \frac{\partial \boldsymbol{\varepsilon}}{\partial \mathbf{e}} dA = \int_A \mathbf{B}^T \frac{\partial \boldsymbol{\sigma}}{\partial \boldsymbol{\varepsilon}} \mathbf{B} dA = \int_A \mathbf{B}^T \overline{D} \mathbf{B} dA \tag{6}$$

where $\overline{D}$ is the 2×2 material stiffness matrix, obtained from an orthotropic, smeared-crack constitutive model presented in [17], upon imposing $\sigma_y=0$ at each section layer.

The element formulation presented so far was implemented in a displacement-based Timoshenko beam element, using linear interpolation functions for $u_o$, $v_o$ and $\theta_z$. Reduced integration was used in order to avoid shear locking, with one Gauss integration point per element. At the sectional level, a parabolic shear strain profile was adopted as a function of $\gamma_{oy}$:

$$\gamma_{xy} = \frac{3}{2}\gamma_{oy}(1-(2y/h)^2) \tag{7}$$

where h is the section height.

## 3 MODELING THE INFILL PANEL

The infil panel was modeled using three equivalent struts connected between the corners of the frame as depicted in Figure 2. Different models are available in the literature to estimate the properties of the struts [8, 9, 18, 19]. However, since in the present context the main objective is to assess the performance of inelastic frame elements with flexure-shear interaction, these properties were calibrated such as to fit the experimental data.

The axial force-displacement behavior of each strut is described by the Popovics envelope (Figure 2), given as:

$$F = \frac{F_m x r}{r - 1 + x^r} \tag{8}$$

$$r = \frac{E_{tg}}{E_{tg} - E_{sec}} \tag{9}$$

where $F_m$ is the peak force, x is the ratio between the axial displacement to the peak displacement $\delta/\delta_m$, and $E_{tg}$ and $E_{sec}$ are the tangent and secant (to the peak) moduli respectively. The same type of envelope is assumed for the three struts. However, based on tributary areas, the strength of the off-diagonal struts is taken as 50% that of the central strut. In this way only three parameters need to be calibrated for the entire panel: $F_m$, $\delta_m$ and $E_{tg}$.

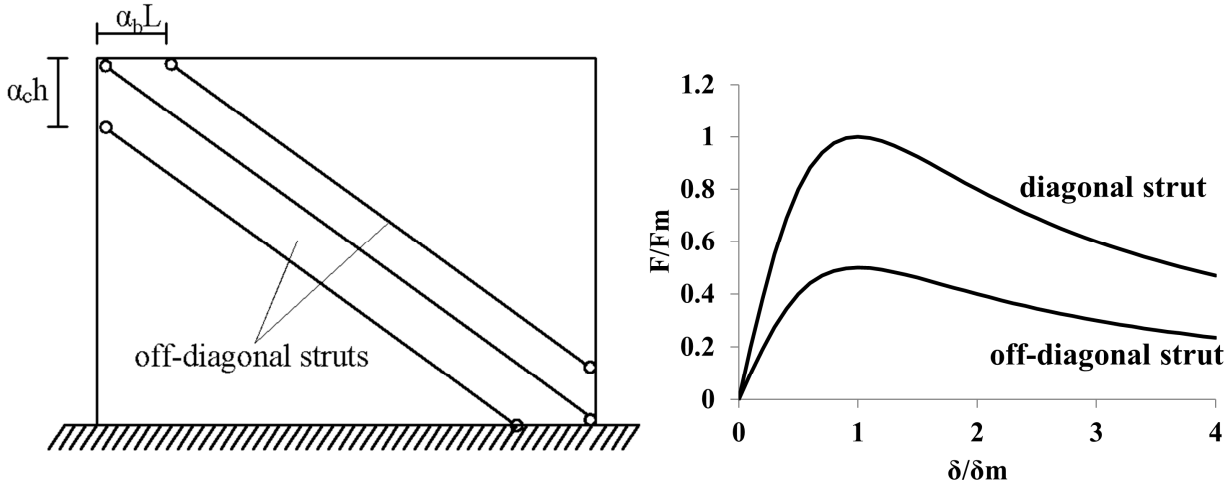


Figure 2: Multiple-strut representation of infill panel and monotonic envelopes of the diagonal struts.

Another important parameter is the location of the off-diagonal strut, represented by the parameters $\alpha_c$ and $\alpha_b$ (Figure 2), which is associated to the position of the plastic hinge in the beam or column, respectively. Theoretical values for this parameter were given by Liauw and Kwan (1983) [20, 21] for different collapse mechanisms, which will be used in the next section.

## 4 CASE STUDY

The selected case study frame, shown in Figure 3, was part of a large experimental campaign carried out by Mehrabi and Shing [11, 12]. The specimen consisted of a ½-scale, one-story one-bay prototype designed as a weak frame for lateral wind only (1.24kPa), without consideration of the masonry infill. For the infill, 0.1×0.1×0.2 m solid masonry blocks with 9.5mm thick mortar bed joints were used. Material properties for concrete, reinforcement and masonry panel are summarized in Table 1 and Table 2. The specimen was subjected to an increasing lateral force applied at the top beam, and two vertical loads (146.8kN each) concentrated at the top of the columns.

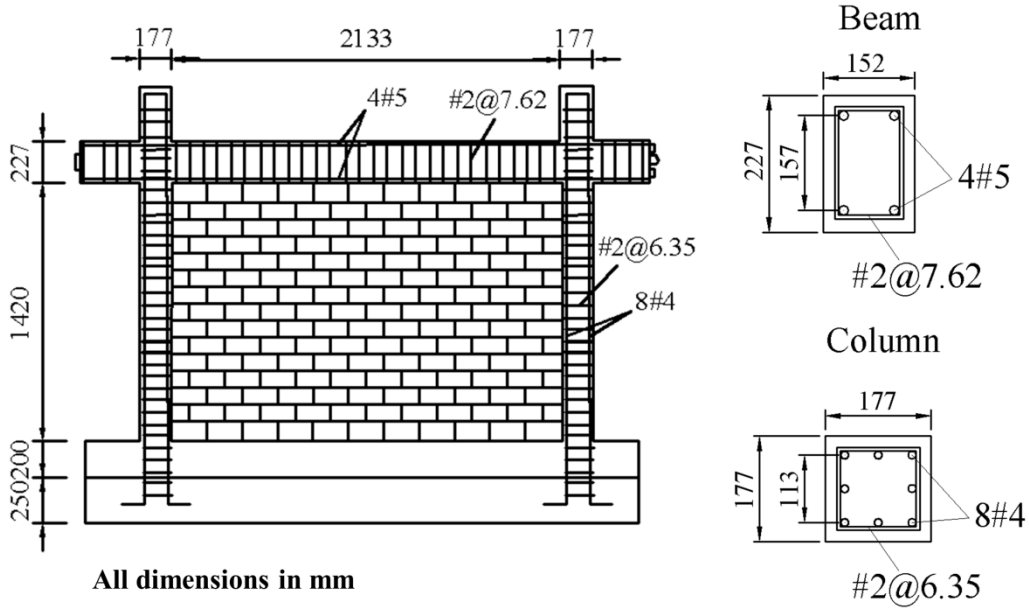


Figure 3: RC masonry-infilled frame: geometry and cross-sections (adapted from [11]).

| | Concrete | | | Masonry prisms | | Masonry Units | Mortar |
|---|---|---|---|---|---|---|---|
| Frame | $f_c$(MPa) | $\varepsilon_o$ | $f_t$(MPa) | $f_{m\text{-}90}$ (MPa) | $\varepsilon_{m\text{-}90}$ | $f_{mu}$(MPa) | $f_{mr}$(MPa) |
| Bare | 30.8 | 0.0018 | 3.24 | - | - | | |
| Infilled | 30.8 | 0.0018 | 3.24 | 15.1 | 0.0029 | 15.6 | 15.9 |

$f_c$, $\varepsilon_o$*: compressive strength and strain at peak stress of concrete;* $f_t$*: tensile strength of concrete;* $f_{m\text{-}90}$, $\varepsilon_{m\text{-}90}$*: compressive strength and strain at peak stress perpendicular to the bed joints;* $f_{mu}$*: compressive strength of masonry units;* $f_{mr}$*: compressive strength of mortar*

Table 1: Material properties for concrete and masonry.

| Bar size | Type | Nominal diameter (mm) | Yield stress (MPa) | Ultimate stress (MPa) |
|---|---|---|---|---|
| #2 | Plain | 6.35 | 367 | 449 |
| #4 | Deformed | 12.7 | 420 | 661 |
| #5 | Deformed | 15.8 | 413 | 661 |

Table 2: Material properties for steel.

The finite element model of the frame is shown in Figure 4. The frame elements were defined along the centerline of the members, with an element extending into the base beam 200mm, referred to as joint element, in order to consider the joint flexibility and strain penetration effects. This element had the same properties as the rest of the column elements, but with a reinforcement ratio 3 times that of the columns. The masonry struts were connected between the locations of plastic hinge regions, defined hereafter, such as to simulate a short-column effect.

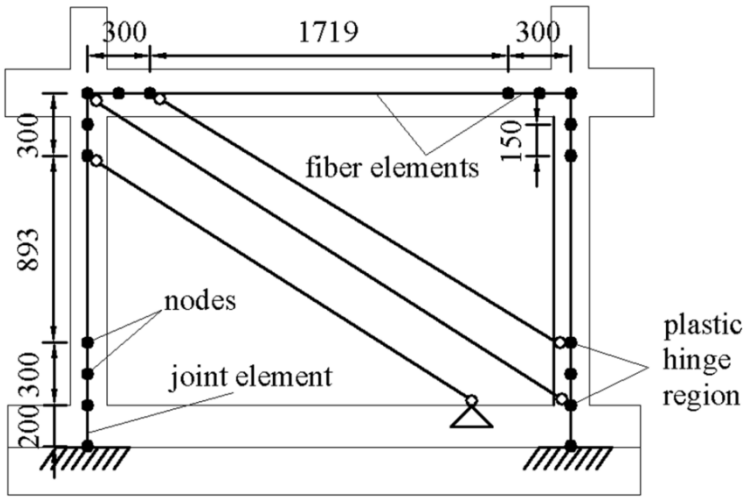


Figure 4: Finite element model of the inflll frame.

The location of the plastic hinges in the columns was determined from plastic limit analysis as [20, 21]:

$$\alpha_c = \sqrt{\frac{2(M_c + M_j)}{\sigma_c t h^2}} \tag{10}$$

where $M_c$ is the column flexural strength, $M_j$ is the joint flexural strength taken as min($M_c$, $M_b$), $M_b$ being the beam flexural strength. t is the panel thickness, and h the story height. $\sigma_c$ is the crushing stress of the panel material, which can be estimated as [22]:

$$\sigma_c = \frac{f_{m-0}}{\sqrt{1+3\mu^2 r^4}} \tag{11}$$

where $\mu$ is the friction coefficient between the panel and the RC frame, r is the panel aspect ratio, and $f_{m-0}$ is the masonry strength parallel to the bed joints. It can be assumed that $\mu \approx 0$ due to concrete shrinkage, hence $\sigma_c = f_{m-0}$. $f_{m-0}$ has been related to the masonry strength perpendicular to the bed joints, $f_{m-90}$, given in Table.1 as $f_{m-0}=0.70 f_{m-90}$ [23].

Upon substitution in Equation 10, with $M_c=M_j=20.9$kNm, $\sigma_c=10.8$ MPa, t=0.0921m and h=1.634m, a value of 0.18 is obtained for $\alpha_c$. The same value is assumed for the beams, $\alpha_b$. Thus, the location of the plastic hinge is approximately 0.30m from the beam-column joint. Two elements were defined in this region, 150mm each, as shown in Figure 4.

Comparison between experimental and numerical lateral force-displacement response, for both bare and infill frames, is shown in Figure 5. Results from the traditional flexural (Euler-Bernouilli) beam element, based on uniaxial constitutive laws, have been included as well.

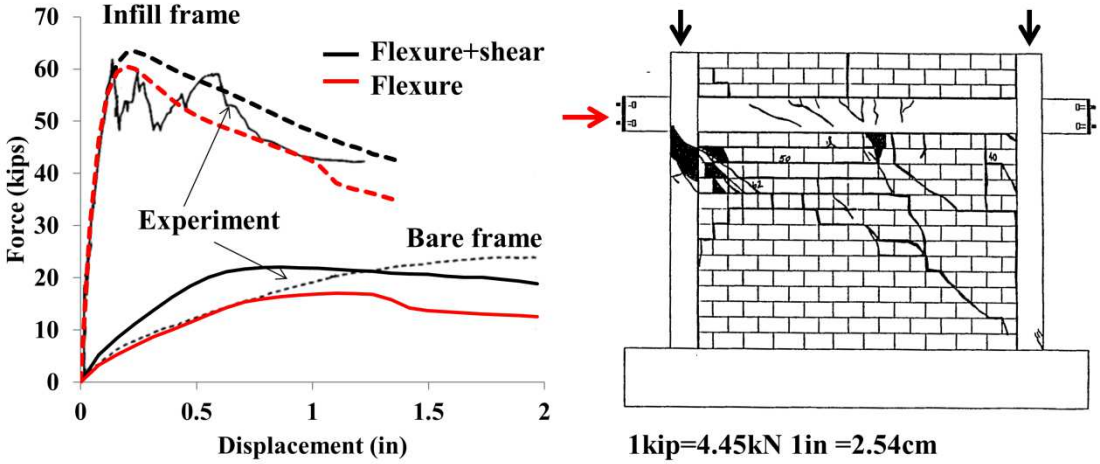


Figure 5: Lateral force-displacement response and observed experimental damage [11].

The bare frame response is predominantly in flexure, ultimately failing upon concrete crushing at the bottom of the leeward column. In the experiment, the damage pattern for the infilled frame involved diagonal tension failure of the panel and flexure-shear failure at the top windward column (Figure 5).

For the bare frame, it is noted that the flexure-shear element is stiffer and stronger since shear resisting mechanisms are included in addition to the flexural ones, and no shear failure occurs. For the infilled frame, it seems that flexure-shear interaction has a minor influence on the overall response, which is governed by the masonry struts.

The latter is also demonstrated from the distribution of bending moment and shear demands at the maximum lateral load (Figure 6), from where it can be seen that for both elements the distribution is very similar, and highly concentrated in the short-column and short-beam portions.

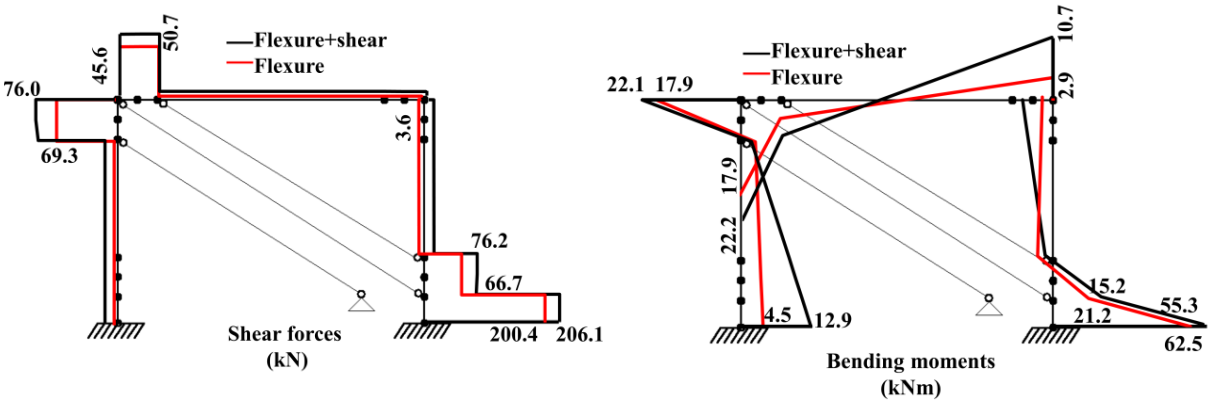


Figure 6: Bending moment and shear distributions

Despite being the global response similar for both types of elements, the internal resisting mechanisms are clearly different. As an example, strains in the transverse reinforcement obtained from the flexure-shear element at different levels of lateral displacement are shown below (Figure 7). These correspond to the Gauss integration point in the top element of the windward column. It is noted that yielding does not occur at the maximum lateral load (0.24in), but it does occur in subsequent load steps when the masonry struts enter the post-peak softening branch.

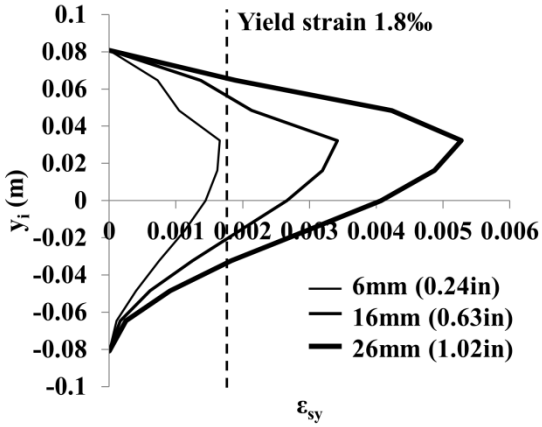


Figure 7: Strains in the transverse reinforcement at different displacement levels.

## 5 CONCLUSIONS

Preliminary results presented here on the evaluation of flexure-shear fiber-based frame elements for modeling RC infilled frames demonstrated that similar global results are obtained when compared to the traditional flexural element, at least in terms of lateral force-displacement response, and bending and shear force distributions. However, these conclusions are based on a single case study which involved a weak frame-strong masonry RC frame, whereby the infill panel significantly contributed to both lateral and vertical stiffness and strength. Although multiple peaks were experimentally observed in the post-peak response of the infilled frame, possibly due to cracking and sliding of the panel, stress redistribution between the frame and the panel, and flexure-shear failure of the columns, the numerical model did not show this behavior.

Notwithstanding, some local results from the flexure-shear element, such as strains in the transverse reinforcement, indicated that substantial demands were imposed in the short-column region, where shear failure was observed during the experiment. Yielding of transverse reinforcement was attained in the post-peak range of the infilled frame.

It is recommended to carry out further validation, particularly for weak frame-weak masonry structures, where the limitations of brittle shear failure on global ductility capacity can be better quantified.

## REFERENCES

[1] M. N. Fardis, and G. M. Calvi, Effects of infills on the global response of reinforced concrete frames. *Proc., 10th European Conf. on Earthquake Engineering, European Association for Earthquake Engineering (EAEE)*, Istanbul, Turkey, 2331–2336, 1994.

[2] B. Stafford Smith, Behavior of square infilled frames. *J. Struct. Div.*, **92**(1), 381–403, 1966.

[3] L. D. Decanini, and G. E. Fantin, Modelos simplificados de la mampostería incluida en porticos. Características de rigidez y resistencia lateral en astado límite. *Jornadas Argentinas de Ingeniería Estructural III, Vol. 2, Asociacion de Ingenieros Estructurales*, Buenos Aires, Argentina, 817–836, 1987 (in Spanish).

[4] H. Rodrigues, H. Varum, and A. Costa, A non-linear masonry infill macro-model to represent the global behaviour of buildings under cyclic loading. *Int. J. Mech. Mat. Des*., **4**(2), 123–135, 2008.

[5] T. Paulay, and M. J. N. Pristley, *Seismic design of reinforced concrete and masonry buildings*, Wiley, New York, 744, 1992.

[6] F. J. Crisafulli, A. J. Carr, and R. Park, Analytical modelling of infilled frame structures—A general review. *Bull. New Zealand Soc. Earthquake Eng.*, **33**(1), 30–47, 2000.

[7] J. Reflak, and P. Fajfar, Elastic analysis of infilled frames using substructures. *Proc., 6th Canadian Conf. on Earthquake Engineering*, University of Toronto Press, Toronto, 285–292, 1991.

[8] V. Thiruvengadam, On the natural frequencies of infilled frames. *Earthquake Eng. Struct. Dyn.*, **13**(3), 401–419, 1985.

[9] C. Z. Chrysostomou, P. Gergely, and J. F. Abel, A six-strut model for nonlinear dynamic analysis of steel infilled frames. *Int. J. Struct. Stab. Dyn.*, **2**(3), 335–353, 2002.

[10] P. E. Mergos, A. J. Kappos, A distributed shear and flexural flexibility model with shear–flexure interaction for R/C members subjected to seismic loading. *Earthquake Engineering & Structural Dynamics*, **37**(12), 1349–1370, 2008.

[11] A. B. Mehrabi, and P. B. Shing, Finite element modeling of masonry-infilled RC frames. *J. Struct. Eng.*, **123**(5), 604–613, 1997.

[12] A. B. Mehrabi, P. B. Shing, M. Schuller, and J. Noland, Experimental evaluation of masonry-infilled RC frames. *J. Struct. Eng.*, **122**(3), 228–237, 1996.

[13] P. Ceresa, L. Petrini, R. Pinho, R. Sousa, A fibre flexure–shear model for seismic analysis of RC-framed structures, *Earthquake Engineering and Structural Dynamics*, **38**, 565-586, 2009.

[14] M. Petrangeli, P. E. Pinto, V. Ciampi, Fibre element for cyclic bending and shear of RC structures. I: theory, *Journal of Engineering Mechanics*, **125**(9), 994-1001, 1999.

[15] S. Guner, and F. J. Vecchio, Analysis of Shear-Critical Reinforced Concrete Plane Frame Elements under Cyclic Loading, *Journal of Structural Engineering (ASCE)*, **137** (8), pp. 834-843, 2011.

[16] A. Kagermanov, P. Ceresa, An exact shear strain approach for rc frame elements with axial-shear interaction, *VII European Congress on Computational Methods in Applied , Sciences and Engineering (ECCOMA)*, M. Papadrakakis, V. Papadopoulos, G. Stefanou, V. Plevris, Crete Island, Greece, 5–10, June 2016

[17] A. Kagermanov, P. Ceresa, Physically-based cyclic tensile model for reinforced concrete membrane elements, *Journal of Structural Engineering (ASCE),* **142**(12), December, 2016

[18] R. O. Hamburger, and A. S. Chakradeo, Methodology for seismic-capacity evaluation of steel-frame buildings with infill unreinforced masonry. *Proc., National Earthquake Conf.*, Vol. 2, Central U.S. Earthquake Consortium, Memphis, TN, 173–191, 1993.

[19] W. W. El-Dakhakhni, M. Elgaaly, and A. A. Hamid, Three-strut model for concrete masonry-infilled frames. *J. Struct. Eng.*, **129**(2), 177–185, 2003.

[20] T. C. Liauw, and K. H. Kwan, Plastic theory of infilled frames with finite interface shear strength. *ICE Proc.*, **75**(4), 707–723, 1983.

[21] T. C. Liauw, and K. H. Kwan, Plastic theory of non-integral infilled frames. *ICE Proc.*, **75**(3), 379–396, 1983b.

[22] A. Saneinejad, B. Hobbs, Inelastic design of infilled frames, *J. Struct. Eng. (ASCE)*, **121**(4), 634-650, 1995.

[23] C.K. Seah, Universal approach for the analysis and design of infilled frame structures, PhD Thesis, Univ. of New Brunswick, Fredericton, Canada, 1995.

COMPDYN 2017
6th ECCOMAS Thematic Conference on
Computational Methods in Structural Dynamics and Earthquake Engineering
M. Papadrakakis, M. Fragiadakis (eds.)
Rhodes Island, Greece, 15–17 June, 2017

# A NEW NUMERICAL PROCEDURE FOR ASSESSING THE DYNAMIC BEHAVIOUR OF ANCIENT MASONRY TOWERS

**D. Pellegrini[1], M. Girardi[1], C. Padovani[1], and R. M. Azzara[2]**

[1]Institute of Information Science and Technologies "A. Faedo" (ISTI-CNR)
Via G. Moruzzi, 1, Pisa, Italy
e-mail: {daniele.pellegrini, maria.girardi, cristina.padovani}@isti.cnr.it

[2] Istituto Nazionale di Geofisica e Vulcanologia (INGV) - Seismological Observatory of Arezzo
Via F. Redi 13a, Arezzo, Italy
e-mail: riccardo.azzara@ingv.it

**Keywords:** Structural Health Monitoring, Vibration Response, Masonry Towers, Operational Modal Analysis, Model Updating.

**Abstract.** *The paper presents a new numerical procedure for the modal analysis of masonry structures implemented in the finite element code NOSA-ITACA, which models masonry as a nonlinear elastic material with zero tensile strength and infinite or bounded compressive strength. The procedure, which allows for taking into account the effects of the stress field and crack distribution within a structure on its natural frequencies and mode shapes, is applied to assess the dynamic behaviour of a medieval bell tower in Lucca. Data recorded by the monitoring system installed on the tower have been processed via suitable modal identification algorithms, which have enabled calculating the tower's modal frequencies, mode shapes and damping ratios. Then, the tower has been analysed via the NOSA-ITACA code and model updating techniques applied to fit the data measured on the tower. The results of the standard modal analysis have been compared to those of modal analyses conducted on the structure subjected to its own weight while taking into account the corresponding crack distribution.*

## 1 INTRODUCTION

Several papers have been devoted to investigating the effects of damage on the vibrations of various structures [1], [2], [3]. With regard to masonry buildings, a common approach consists in simulating the existing damage actually observed on the structure by reducing the stiffness of those elements of the finite element model belonging to the cracked or damaged parts [4], [5], [6], [7]. An analytical approach has been adopted in [8] to formulate an explicit expression linking the fundamental frequency of a masonry–like beam to its maximum transverse displacement. The masonry–like constitutive equation models masonry as a non–linear elastic material with different strengths under tension and compression [9], [10]. This constitutive equation has been implemented in the finite–element code NOSA for the static analysis of masonry bodies [11]. The NOSA code and its updated version NOSA–ITACA 1.0 [12] have been applied to the static and dynamic analysis of many important monuments in Italy.

A new numerical procedure for the modal analysis of masonry structures has been presented in [13] and implemented in the finite element code NOSA-ITACA. In standard modal analysis natural frequencies and mode shapes are calculated by solving the generalized eigenvalue problem involving the mass matrix $M$ and the stiffness matrix $K$, with $K$ determined under the assuption that the structure's constituent materials are linear elastic. The proposed numerical procedure consists of two steps. In the first, the equilibrium problem of the structure subjected to assigned loads is solved, and its numerical solution, consisting of displacements, stress and strain fields, calculated. In the second step, the tangent stiffness matrix, $K^d$, is calculated by using the derivative of the stress with respect to the strain [11], obtained in the previous step, and the generalized eigenvalue problem is solved using matrix $K^d$ in place of $K$. The procedure allows for taking into account the effects of the stress field and crack distribution within the structure on its natural frequencies and mode shapes.

In this paper the new procedure is briefly recalled and then applied to assess the dynamic behaviour of the medieval "Clock Tower" in Lucca. The ambient vibrations of the tower have been measured by means of four seismometric triaxial stations placed along its height. Data from the monitoring system have been processed via suitable modal identification algorithms [14], which have enabled calculating the tower's modal frequencies, mode shapes and damping ratios [15]. Then, the tower has been analysed via the NOSA-ITACA code, and model updating techniques applied to fit the measured data. The results of the standard modal analysis have been compared to those of modal analysis conducted on the tower subjected to its own weight while taking into account the corresponding crack distribution. The new procedure proposed in the paper has provided more realistic values of the mechanical properties of the tower's constituent materials.

## 2 THE NUMERICAL METHOD

This paper presents a numerical procedure implemented in the NOSA–ITACA code [12], which calculates the natural frequencies and mode shapes of masonry buildings in the presence of cracks [13]. In standard modal analysis the dynamic characteristics of a structure discretized into finite elements are determined by solving the constrained generalized eigenvalue problem

$$K\,\phi = \omega^2\,M\,\phi, \tag{1}$$

$$T\phi = 0, \tag{2}$$

where $K \in \mathbb{R}^{n\times n}$ and $M \in \mathbb{R}^{n\times n}$ are the stiffness and mass matrices, and the integer $n$ is the structure's total number of degrees of freedom. Matrix $K$ is calculated by assuming the

structure's constituent material to be linear elastic. Condition (2), with $T \in \mathbb{R}^{m \times n}$, and $m \ll n$ expresses the fixed constraints and the master–slave relations assigned to the displacements of the structure. Matrix $M$ is symmetric and positive–definite, $K$ is symmetric and, in view of (2), positive-definite as well [16].

Given the masonry structure under examination, discretized into finite elements, and given the mechanical properties of the structure's constituent masonry-like material, together with the kinematic constraints and loads acting on it, the procedure proposed in [13] consists of the following steps.

Step 0. A preliminary modal analysis is conducted by assuming the structure's constituent material to be linear elastic. The generalized eigenvalue problem (1)-(2) is then solved, and the natural frequencies $\mathrm{f}_\mathrm{i}^l = \omega_\mathrm{i}^l/2\pi$ and mode shapes $\phi_\mathrm{i}^l$ calculated.

Step 1. The nonlinear equilibrium problem of the structure subjected to the assigned loads and boundary conditions is solved through an iterative scheme and its numerical solution, consisting of displacements, strain and stress fields, calculated. The tangent stiffness matrix $K^d$ is calculated by using the derivative of the stress with respect to the strain [11].

Step 2. The generalized eigenvalue problem (1)-(2), with matrix $K^d$ in place of the elastic stiffness matrix $K$, is solved, and the natural frequencies $\mathrm{f}_\mathrm{i} = \omega_\mathrm{i}/2\pi$ and mode shapes $\phi_\mathrm{i}$ of the damaged structure calculated.

In order to compare the mode shapes $\phi_\mathrm{i}^l$ and $\phi_\mathrm{j}$, we introduce the quantity

$$\text{MAC-}M(\phi_\mathrm{i}^l, \phi_\mathrm{j}) = \frac{|\phi_\mathrm{i}^l \cdot M\phi_\mathrm{j}|}{\sqrt{\phi_\mathrm{i}^l \cdot M\phi_\mathrm{i}^l}\sqrt{\phi_\mathrm{j} \cdot M\phi_\mathrm{j}}}, \tag{3}$$

which measures the correlation between the $\mathrm{i}-$th linear elastic mode shape and the $\mathrm{j}-$th mode shape of the damaged structure. More precisely, if the MAC–$M$ value is close to unity, then the vectors $\phi_\mathrm{i}^l$ and $\phi_\mathrm{j}$ are nearly parallel with respect to the scalar product in $\mathbb{R}^n$ induced by matrix $M$.

## 3 THE "CLOCK TOWER" IN LUCCA

The *Torre delle Ore* ("Clock Tower") in Lucca (Figure 1) dates back to the 13th century. The 48.4 m–high masonry structure has a rectangular cross section of about 5.1x7.1 m and walls of variable thickness from about 1.77 m at the base to 0.85 m at the top. Two barrel vaults are set at heights of about 12.5 and 42.3 m, respectively. At a height of about 33 m the walls are equipped with 4 steel tie rods of rectangular section 30x30 mm. The bell chamber, made up of four masonry pillars connected by elliptical arches, is separated from the rest of the structure by the upper barrel vault and is covered by a pavilion roof made up of wooden trusses and rafters. The adjacent buildings abut the tower on two sides for a height of about 13 m and constitute asymmetric boundary conditions. With regard to the materials constituting the masonry tower, no experimental information is available to date. Visual inspection reveals that masonry from the base up to a height of 15 m is made up of regular stone blocks and thin mortar joints, as are the corners of the walls above this level, as well. The upper walls' central portions are instead made up of regular stone blocks and bricks, also with thin joints. The bell chamber is composed of brick and mortar joints.

In November 2016 the "Clock Tower" was fitted with four high–sensitivity triaxial seismometric stations: they were placed in different configurations (Figure 2) and left active on the



Figure 1: The "Clock Tower" in Lucca.

tower for one day. Data from the instruments, analyzed via OMA techniques [14], allowed us to determine the tower's first four natural frequencies $f_{\mathrm{i}}^{\mathrm{exp}}$ and the corresponding damping ratios and mode shapes [15].

In the following the NOSA–ITACA code is employed, together with model updating techniques, in order to fit the experimental results in the linear elastic and the masonry–like (nonlinear) case. The finite–element model of the tower consists of $11383$ brick elements [12]. The four steel tie rods fitted to the masonry walls are modelled with beam elements [12], which have also been used to model the wooden trusses and rafters of the pavillion roof covering the tower. The mechanical properties of the tie rods and wooden elements are, respectively, $E = 2.1 \cdot 10^5$ MPa, $\nu = 0.3$, $\rho = 7850\ \mathrm{kg/m^3}$ and $E = 10000$ MPa, $\nu = 0.35$, $\rho = 800\ \mathrm{kg/m^3}$.

We assume the bell tower to be made of a homogeneous isotropic masonry-like material with Poisson's ratio $\nu = 0.2$, Young's modulus $E$ and mass density $\rho$. Model updating is conducted by varying the parameters $E$ and $\rho$ in the following intervals

$$\begin{aligned} 2.5 \cdot 10^9\ \mathrm{Pa} \leq E \leq 5.5 \cdot 10^9\ \mathrm{Pa}, \\ 1700\ \mathrm{kg/m^3} \leq \rho \leq 2100\ \mathrm{kg/m^3}, \end{aligned} \tag{4}$$

and calculating the first four natural frequencies of the tower for the linear elastic and nonlinear case, after having applied the structure's self–weight alone. The optimal values of $E$ and $\rho$, are determined by minimizing the functions

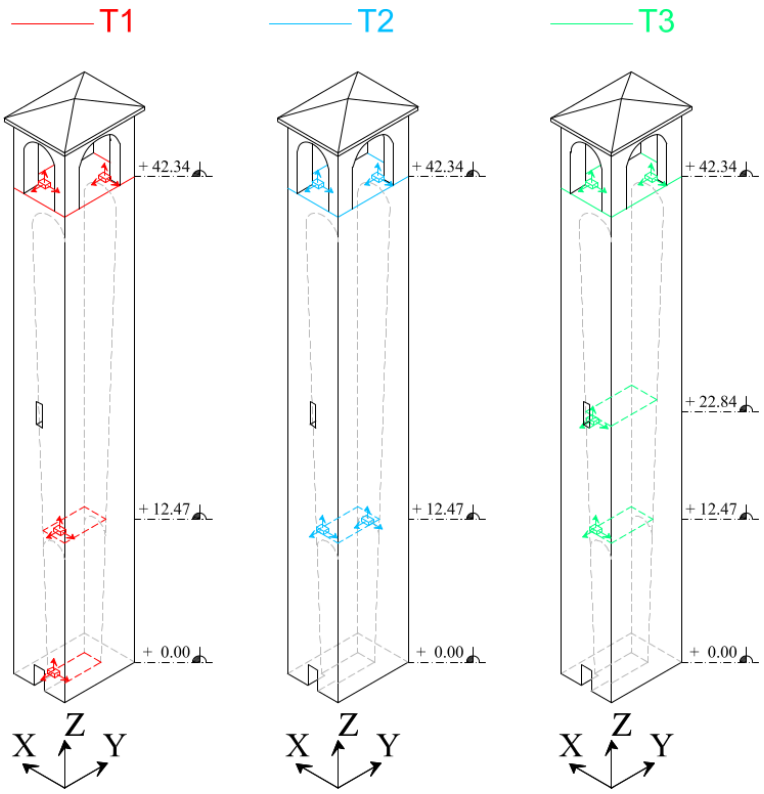


Figure 2: Sensors setup.

$$e^l(E,\rho) = \sum_{i=1}^{4} \left(f_{\mathrm{i}}^l(E,\rho) - f_{\mathrm{i}}^{\mathrm{exp}}\right)^2, \tag{5}$$

$$e(E,\rho) = \sum_{i=1}^{4} \left(f_{\mathrm{i}}(E,\rho) - f_{\mathrm{i}}^{\mathrm{exp}}\right)^2, \tag{6}$$

respectively for the linear and nonlinear cases, for $E$ and $\rho$ satisfying (4).

Figures 3 and 4 respectively show the functions $e^l$ and $e$ vs. $E$ and $\rho$. They reach their minimum values at $E = 3.0 \cdot 10^9$ Pa and $\rho = 2100$ kg/m$^3$ for the linear elastic case and at $E = 4.5 \cdot 10^9$ Pa and $\rho = 2100$ kg/m$^3$ for the nonlinear case. Figure 5 plots the two functions vs. $E$ for $\rho = 2100$ kg/m$^3$. The first four natural frequencies of the tower are shown in Table 1, where the experimental values $f_{\mathrm{i}}^{\mathrm{exp}}$ are shown for comparison with the numerical ones, in the linear elastic $\left(f_{\mathrm{i}}^l\right)$ and nonlinear $(f_{\mathrm{i}})$ case. Columns $\Delta f_{\mathrm{i}}^l$ and $\Delta f_{\mathrm{i}}$ show the relative errors (absolute value) between the numerical and experimental values for the linear and nonlinear case, respectively. In the linear case the numerical frequencies differ from the experimental values by no more than seven percent; the nonlinear case is more accurate and with differences of less than three percent. Figure 6 shows the maximum principal fracture strains for the tower in equilibrium with its own weight. The crack distribution and the low fracture strain values indicate a modest level of cracking within the structure: the fracture strains are concentrated around the windows and lintels, as well as in the masonry supporting the vault under the bell chamber. This

| | $f_{\mathrm{i}}^{\mathrm{exp}}$ | $f_{\mathrm{i}}^{l}$ | $\Delta f_{\mathrm{i}}^{l}$ | $f_{\mathrm{i}}$ | $\Delta f_{\mathrm{i}}$ |
|---|---|---|---|---|---|
| Mode Shape 1 | 1.05 | 0.98 | 0.07 | 1.08 | 0.03 |
| Mode Shape 2 | 1.30 | 1.24 | 0.05 | 1.28 | 0.02 |
| Mode Shape 3 | 4.20 | 4.32 | 0.03 | 4.24 | 0.01 |
| Mode Shape 4 | 4.50 | 4.38 | 0.03 | 4.52 | 0.004 |

Table 1: Natural frequencies [Hz] of the tower: experimental values $f_{\mathrm{i}}^{\mathrm{exp}}$, numerical values $f_{\mathrm{i}}^{l}$ of the linear elastic model; numerical values $f_{\mathrm{i}}$ of the masonry–like model.

| | $\phi_1$ | $\phi_2$ | $\phi_3$ | $\phi_4$ |
|---|---|---|---|---|
| $\phi_1^l$ | 0.998 | 0.039 | 0.019 | 0.020 |
| $\phi_2^l$ | 0.038 | 0.997 | 0.008 | 0.011 |
| $\phi_3^l$ | 0.003 | 0.008 | 0.810 | 0.580 |
| $\phi_4^l$ | 0.024 | 0.000 | 0.580 | 0.800 |

Table 2: MAC–$M(\phi_{\mathrm{i}}^{l}, \phi_{\mathrm{j}})$, for i,j = 1,..., 4.

confirms the observations made upon visual inspection. Fracture strains are concentrated in regions of the structure quite far from those of the highest curvatures for the first mode shapes, which in fact remain very similar to those calculated in the linear elastic case. However, due to the nonlinearity of the constitutive equation adopted, the model updating procedure yields higher values of Young's modulus. Figures 7 and 8 show the first four mode shapes, calculated in the nonlinear case for the optimal values $\left(E = 4.5 \cdot 10^9 \text{ Pa}, \rho = 2100 \text{ kg/m}^3\right)$. As can be seen in Table 2, they are substantially equal to the linear elastic modes $\phi_{\mathrm{i}}^{l}$. The Figures clearly show that the first two mode shapes are flexural (along $X$ and $Y$ respectively), the third is torsional and the fourth is mixed (torsional and bending along $X$). The first four experimental mode shapes are depicted in Figures 9 and 10.

## 4 CONCLUSIONS

This paper describes a new numerical procedure, implemented in the finite element code NOSA–ITACA, for the modal analysis of masonry structures. Once the initial loads and boundary conditions have been applied to the finite–element model, the resulting non–linear equilibrium problem is solved. Then, a modal analysis is performed, by using the tangent stiffness matrix calculated by the code in the last iteration before convergence is reached. The incremental approach used by NOSA–ITACA allows the user to perform the modal analysis at the initial step, before application of any load to the structure, and then for different loading steps. The proposed procedure allows the user to automatically take into account the influence of the stress distribution on the system's stiffness matrix, thereby evaluating the effects of the presence of cracked material on the structure's dynamic properties. The method proposed has been applied to the "Clock Tower" in Lucca. The tower has been instrumented with seismometric stations and its first four natural frequencies determined via OMA techniques. Then, the NOSA–ITACA code has been employed, together with model updating techniques, in order to fit the experimental results. The model updating in the linear elastic case is compared to that in the nonlinear case, applied to the tower subjected to its own weight while taking into account the crack distribution induced by the load.

## Acknowledgements

This research has been supported by the Region of Tuscany (Project "MOSCARDO - ICT technologies for structural monitoring of age-old constructions based on wireless sensor networks and drones", 2016-2018) and the Cassa di Risparmio di Lucca Foundation (Project "TITANIO - Monitoring of historic masonry buildings via innovative sensors", 2016-2018). These supports are gratefully acknowledged.

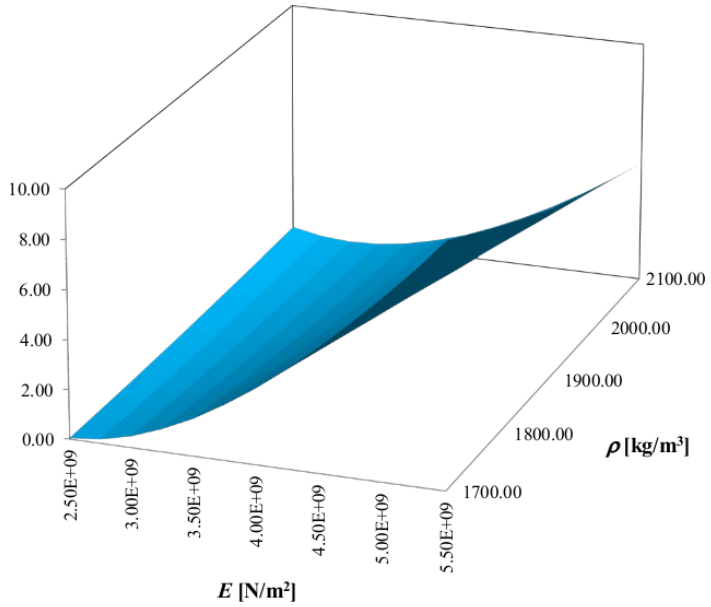


Figure 3: Function $e^l(E, \rho)$: linear case.

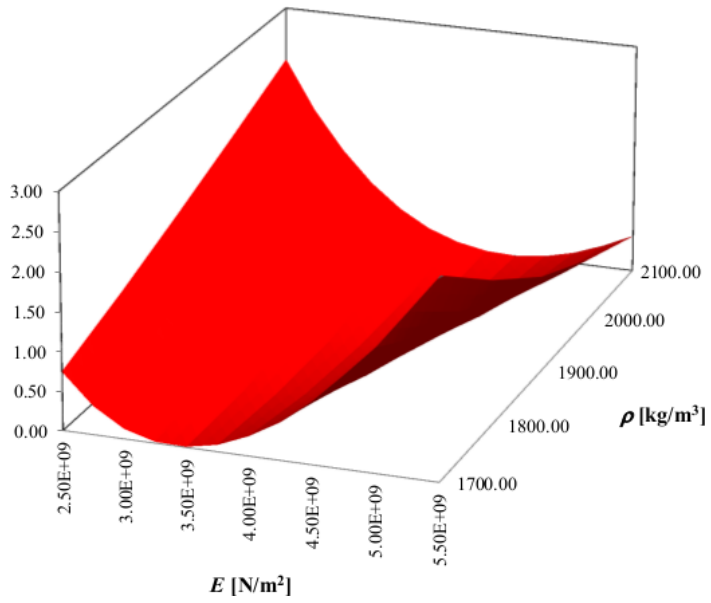


Figure 4: Function $e(E, \rho)$: nonlinear case.

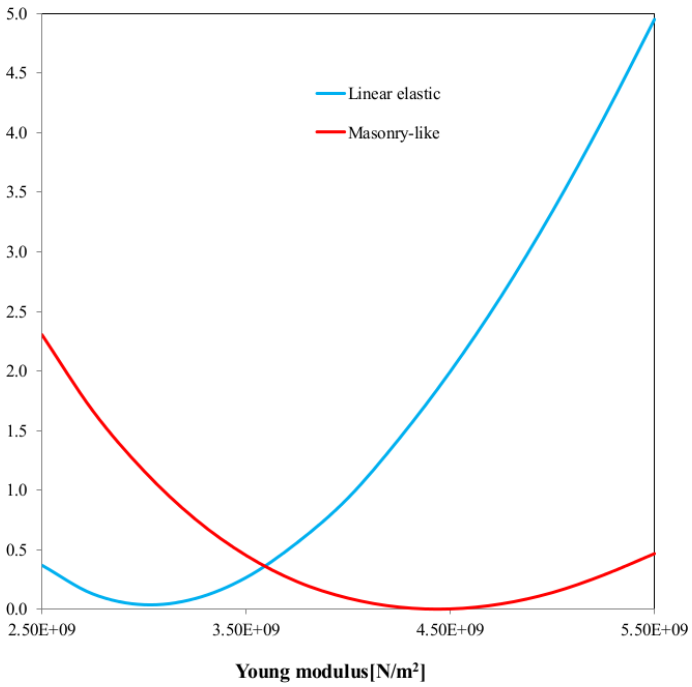


Figure 5: Functions $e(E, \rho)$ (red line) and $e^l(E, \rho)$ (blue line) vs. $E$ for $\rho = 2100\ \mathrm{kg/m^3}$.

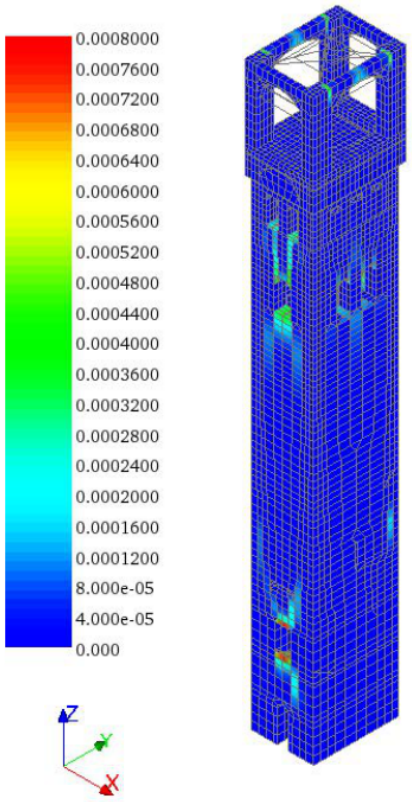


Figure 6: Maximum principal fracture strains.

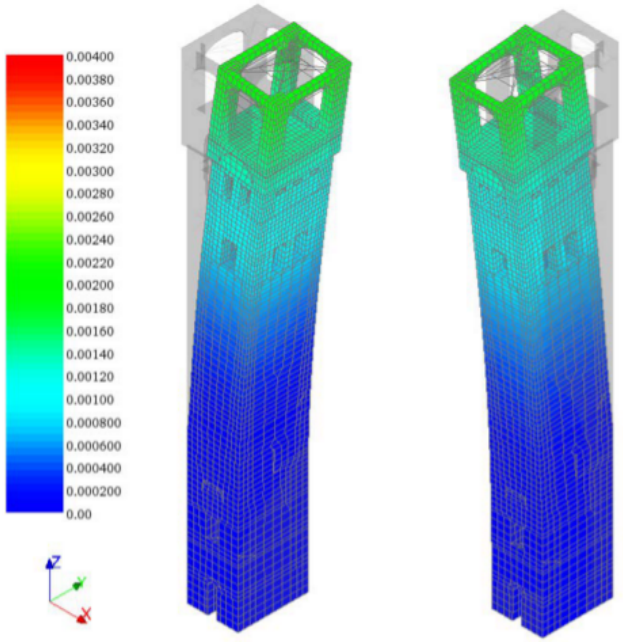


Figure 7: Mode shapes $\phi_i$, $i = 1, 2$ of the "Clock Tower" in the nonlinear case, for $E = 4.5 \cdot 10^9$ Pa, $\rho = 2100$ kg/m$^3$.

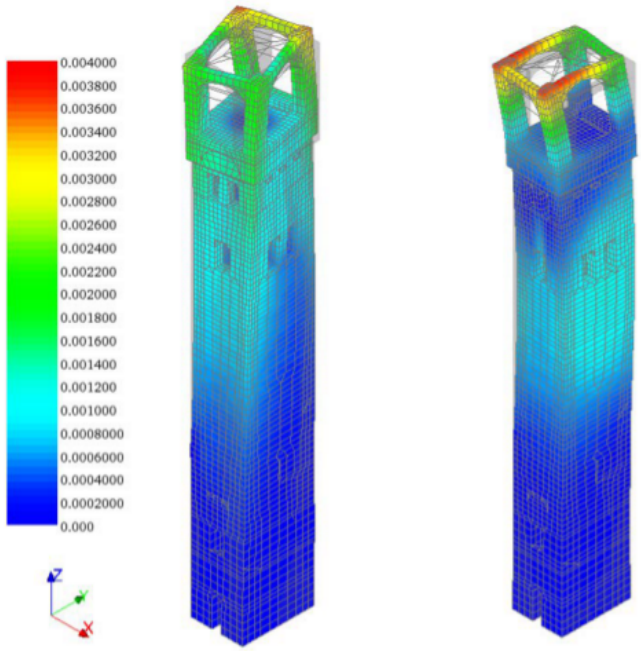


Figure 8: Mode shapes $\phi_i$, $i = 3, 4$ of the "Clock Tower" in the nonlinear case, for $E = 4.5 \cdot 10^9$ Pa, $\rho = 2100$ kg/m$^3$.

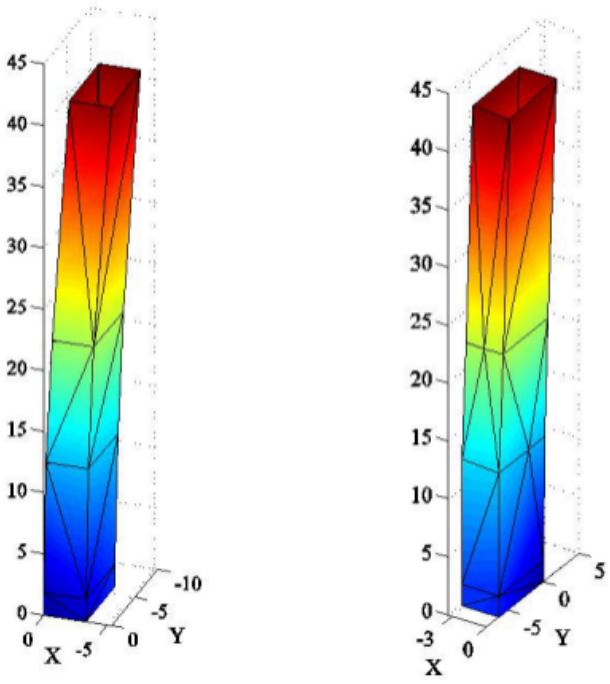


Figure 9: First and second experimental mode shapes of the "Clock Tower".

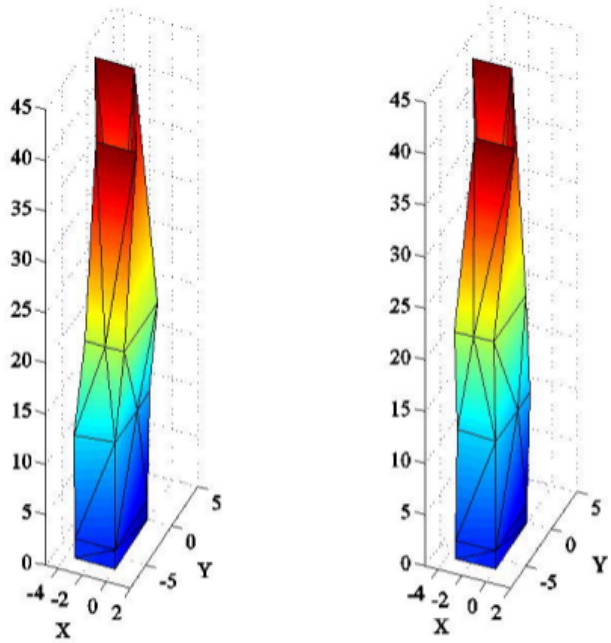


Figure 10: Third and fourth experimental mode shapes of the "Clock Tower".

## REFERENCES

[1] W. Ren, G. De Roeck, Structural Damage Identification using Modal Data. I: Simulation Verification. *Journal of Structural Engineering*, **128(1)**, 87–95, 2002.

[2] W. Ren, G. De Roeck, Structural Damage Identification using Modal Data. II: Test Verifi-

cation. *Journal of Structural Engineering*, **128(1)**, 96–104, 2002.

[3] M. Jayanthan, V. Srinivas, Structural Damage Identification Based on Finite Element Model Updating. *Journal of Mechanical Engineering and Automation*, **5(3B)**, 59–63, 2015.

[4] P. Pineda, Collapse and upgrading mechanisms associated to the structural materials of a deteriorated masonry tower. Nonlinear assessment under different damage and loading levels. *Engineering Failure Analysis*, **63**, 72–93, 2016.

[5] L.F. Ramos, G. De Roeck, P.B. Loureno, A. Campos–Costa, Damage identification on arched masonry structures using ambient and random impact vibrations. *Engineering Structures*, **32**, 146–162, 2010.

[6] T.T. Bui, A. Limam, Q.B. Bui, Characterisation of vibration and damage in masonry structures: experimental and numerical analysis. *European Journal of Environmental and Civil Engineering*, **18(10)**, 1118–1129. 2014.

[7] E. Cakti, O. Saygili, J.V. Lemos , C.S. Oliveira, A parametric study of the earthquake behaviour of masonry minarets. *Proceedings of the Tenth U.S. National Conference on Earthquake Engineering Frontiers of Earthquake Engineering, 10NCEE*, Anchorage, Alaska, July 21-25, 2014.

[8] M. Girardi, M. Lucchesi, Free flexural vibrations of masonry beam–columns. *Journal of Mechanics of Materials and Structures*, **5(1)**, 143–159, 2010.

[9] G. Del Piero, Constitutive equations and compatibility of external loads for linear elastic masonry–like materials. *Meccanica*, **24**, 150–162, 1989.

[10] S. Di Pasquale, New trends in the analysis of masonry structures. *Meccanica*, **27**, 173–184, 1992.

[11] M. Lucchesi, C. Padovani, G. Pasquinelli, N. Zani, *Masonry constructions: mechanical models and numerical applications*. Lecture Notes in Applied and Computational Mechanics, Springer–Verlag. 2008.

[12] V. Binante, M. Girardi, C. Padovani, G. Pasquinelli, D. Pellegrini, M. Porcelli, *NOSA-ITACA 1.0 documentation*. http://www.nosaitaca.it/software/, 2014.

[13] M. Girardi, C. Padovani, D. Pellegrini, Modal analysis of masonry structures. *arXiv:1611.00531v1 [cs.CE]*, 2 November 2016.

[14] R. Brincker, C. Ventura, *Introduction to Operational Modal Analysis*. John Wiley & Sons, 2015.

[15] R.M. Azzara, M. Girardi, C. Padovani, D. Pellegrini, The Medieval Clock Tower in Lucca: dynamic monitoring and numerical analysis. *Internal Report ISTI*, 2017.

[16] M. Porcelli, V. Binante, M. Girardi, C. Padovani, G. Pasquinelli, A solution procedure for constrained eigenvalue problems and its application within the structural finite-element code NOSA–ITACA. *Calcolo*, **52(2)**, 167–186, 2015.

COMPDYN 2017
6th ECCOMAS Thematic Conference on
Computational Methods in Structural Dynamics and Earthquake Engineering
M. Papadrakakis, M. Fragiadakis (eds.)
Rhodes Island, Greece, 15–17 June 2017

# ADVANCED NUMERICAL MODELS FOR THE ANALYSIS OF UNREINFORCED AND STRENGTHENED MASONRY VAULTS

**V.P. Berardi, M. De Piano, G. Teodosio, R. Penna, L. Feo**
University of Salerno, Department of Civil Engineering
84084, Fisciano, SA, Italy
e-mail: berardi@unisa.it, mdepiano@unisa.it, g.teodosio@studioteodosio.it, rpenna@unisa.it, l.feo@unisa.it

**Keywords:** Masonry structures, Genetic algorithm, Adaptive finite element model, Strengthening, Composite materials

**Abstract.** *Masonry buildings realized in the last centuries are a significant part of the international architectural heritage. The optimal design of the retrofit interventions of these buildings represents a priority and requires the evaluation of their mechanical behavior under static and dynamic loads. Several mechanical models capable to study masonry structures are available in literature and are based on Heyman limit analysis approach. These models cannot be easily adopted within FEM codes. Within this context, a Genetic Algorithm is implemented within a refinement adaptive finite element model to computational mesh of shell surfaces. The proposed model researches a 'safe' thrust surface of a masonry vault within a design domain, by minimizing the average value of the principal tensile stresses carried by the unreinforced portion of the material (fitness function). The design domain coincides with either the vault volume, in the case of unreinforced masonry members, or an external region of the vault in correspondence with the reinforced portions, in the case of the vault strengthened with either Fiber Reinforced Polymer or Fabric Reinforced Cementitious composites. The proposed methodology allows evaluating the structural safety of masonry vault and defining an optimal design of reinforcement pattern.*

## 1 INTRODUCTION

Nowadays, the safeguard of masonry historical constructions represents an international priority. The evaluation of structural vulnerability of these constructions is the first step to evaluate their safe and to preserve them over time by means of retrofit/strengthening interventions.

Several mechanical models available in literature are based on either local failure mechanisms [1]-[5] or the Heyman limit analysis approach [6]. With reference to curved structures, the safe theorem of Heyman has been used to via either continuous [7]-[10] or discontinuous [11]-[15] approaches. The theoretical approach and the computational burden of such models makes non easy their implementation in FEM code.

In the recent years, structural optimization problems have been examined by means of genetic/evolutionary algorithms (GA), inspired by Darwin's evolution theory [16]-[19].

This paper presents an advanced numerical model capable to search a 'safe' thrust surface of masonry vaults. It is based on a Breeder Genetic Algorithm (BGA) proposed by the authors in previous studies and applied to a FEM approximation of the vault geometry via shell elements [20]. The BGA allows to find a safe thrust surface by moving the FEM nodes of a vault within a design domain and minimizing the average value of the principal tensile stresses in unreinforced masonry. The model can be also adopted to the design the vaults strengthened with fiber reinforced cementitious matrix (FRCM) composites. Numerical results are given for a cloister vault subject to static and dynamic load combinations.

## 2 NUMERICAL MODEL

The proposed numerical procedure is formulated within the field of linear elasticity. We model the masonry framework through a FEM approximation, by using shell elements with dominant membrane behavior (Figure 1).

Let denote the $i$-th coordinate of the $j$-th node, $x_{i,j}$; the lower bound of $x_{i,j}$ (corresponding to the intrados of the vault for unreinforced masonry), $x_{i,j}^{min}$; the upper bound of $x_{i,j}$ (corresponding to the extrados of the vault for unreinforced masonry), $x_{i,j}^{max}$; control variables ranging in the interval [0,1], $\xi_{i,j}$.

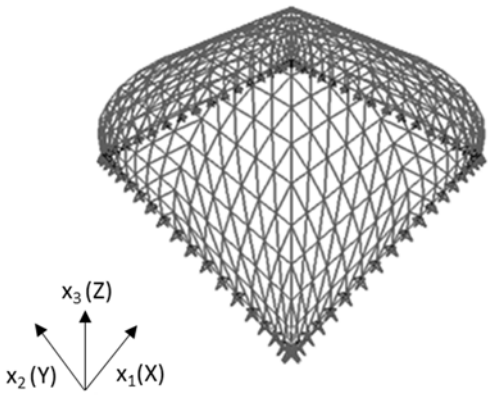


Figure 1: FEM modelling of vaults

We search a safe thrust surface of vaults by moving FEM nodes within a design domain, expressed as follows:

$$\boldsymbol{x_{i,j} = x_{i,j}^{min} + \xi_{i,j}\left(x_{i,j}^{max} - x_{i,j}^{min}\right)} . \quad (1)$$

The search of the safe thrust surface is performed through the BGA [21], by minimizing the fitness function corresponding to the average value of the principal tensile stresses in unreinforced masonry.

More specifically, if we assume $n$ and $N$ (=3 $n$ if all the 3 nodal coordinates govern the r-adaptation strategy) are the total number of the FEM nodes and the control variables $\xi_{i,j}$, respectively, we can introduce the $m$-th "individual" corresponding to the $t$-th generation:

$$\boldsymbol{x_m^t = (x_{1,1}, \dots\dots, x_{3,n})_m}. \quad (2)$$

The BGA find the safe thrust surface by performing the following steps [20]:

1. an initial population of $\lambda$ individuals is generated;
2. the μ best individuals are selected within the current population of $\lambda$ elements;
3. the best individual is retained for the next generation;
4. the remaining $\lambda$-1 individuals of the next generation are created by means of the Extended Intermediate Recombination (EIR)[22] and mutation the $\mu$ best individuals of the current generation;
5. Steps 2 through 4 are repeated until the value of fitness function is less than a fixed value.

The proposed procedure allows us to approximate the elastic no-tension constitutive model of unreinforced masonry within a linear elastic FEM analysis [7]-[15].

## 3 CASE STUDY

We analyze the case study of a tuff masonry cloister vault (Figure 2) subject to static and dynamic loads.

The cloister vault, as well known, is generated by the intersection more barrel vaults set on opposite sides of a base polygon. The stress state in this kind of vault is more complex than that exhibited by groin and barrel vaults.

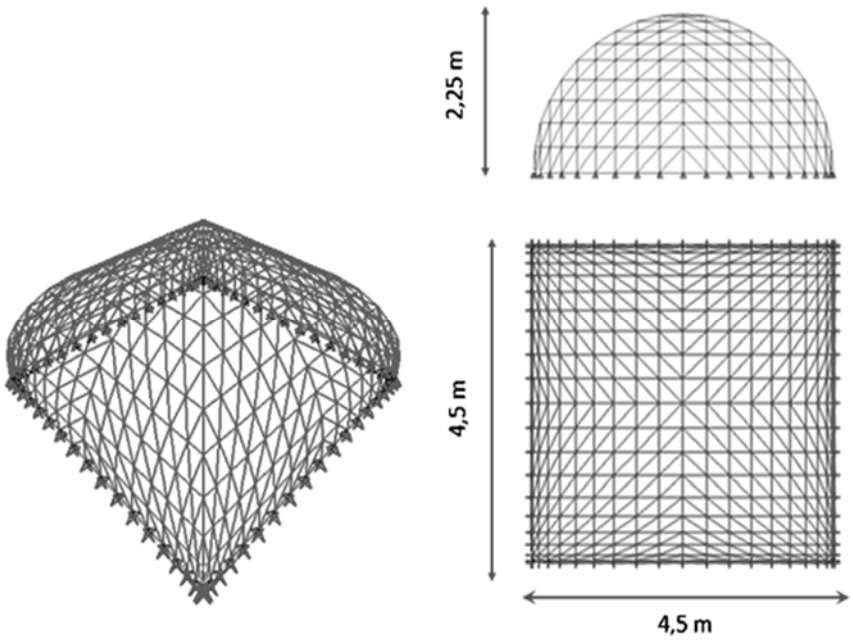


Figure 2: 3D, front and top views of the finite element modelling

The examined vault is characterized by the constant thickness of 0,25 m and its geometry is depicted in Figure 3.

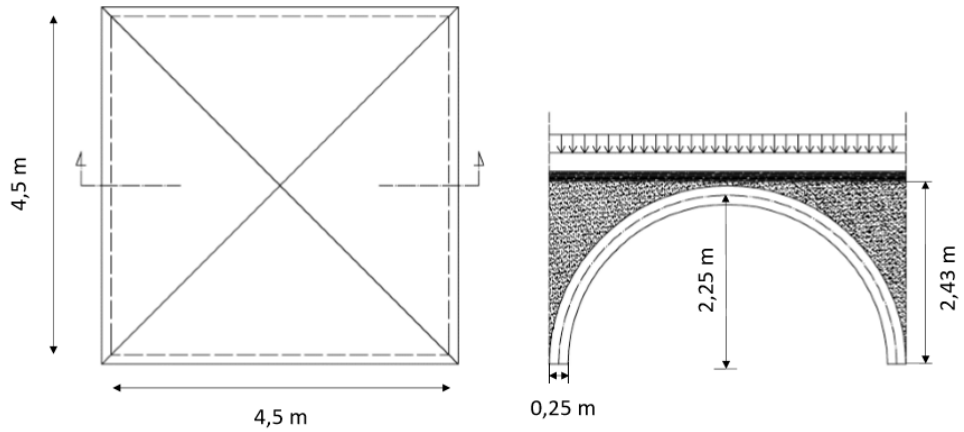


Figure 3: Plan and section of the cloister vault.

The masonry framework is modeled by means of the CSI SAP90 FEM software. The mesh consists of 441 nodes and 800 triangular shell elements with dominant membrane behavior, since bending thickness is fixed equal to 1/5 of the membrane thickness.

We assumed the physical and mechanical properties of the materials, reported in Table 1 ($\gamma_1$ = specific weight of masonry, $\gamma_2$ = specific weight of filling material, $E_m$ = Young modulus of masonry). The basis of the cloister vaults is restrained by fixed hinge supports.

We consider two static case studies: cloister vault subject to its self-weight; cloister vault subject to the dead and live loads.

We also examine the vault under the load combination obtained by vertical and seismic loads. The seismic action is modeled according to static approach suggested in European Standard EN 1998-1 [23].

| $\gamma_1$ [kN/m$^3$] | $\gamma_2$ [kN/m$^3$] | $E_m$ [MPa] |
|---|---|---|
| 15,00 | 10,00 | 1500,00 |

Table 1: Physical and mechanical properties of the materials.

Finally, we propose an optimized strengthening intervention with FRCM composites of the vault.

We denote 'RTS' the Reference Thrust Surface corresponding to the midsurface of the cloister vault, 'MTTS' the Minimum Tension Thrust Surface obtained via the proposed numerical procedure.

Within numerical simulations, the fitness function is applied to unreinforced masonry; the relocating of FEM nodes of the unstrengthened masonry is allowed along the *Z*-axis of the Cartesian frame within the vault volume [20].

Plots of maximum and minimum principal axial internal forces are given in the following, referred to the RTS and the MTTS.

### 3.1 Self-weight

Firstly, we apply the numerical model to the vault subject to its self-weight. Starting from the FEM analysis on the RTS and the MTTS (Figure 4), the maximum and minimum internal axial forces acting on midsurface of shell elements are obtained (Figure 5).

In terms of local stresses, the maximum and minimum principal stresses on the RTS are equal to $\sigma_{max}$ = 3,04 x $10^{-2}$ MPa and $\sigma_{min}$ = -4,40 x $10^{-2}$ MPa, respectively, as well as the average value of the tensile principal stresses is equal to $\sigma_{ave}$ = 3,73 x $10^{-9}$ MPa.

The results obtained by considering the MTTS highlight the maximum principal stress ($\sigma_{max}$ = 8,24 x$10^{-4}$ MPa) and the average value of the tensile principal stresses ($\sigma_{ave}$ = 5,35 x $10^{-10}$ MPa) are significantly smaller than that obtained by the RTS, and the minimum principal compressive stress given by the MTTS ($\sigma_{min}$ = -4,08 x $10^{-2}$ MPa) is almost unchanged compared to that given by the RTS.

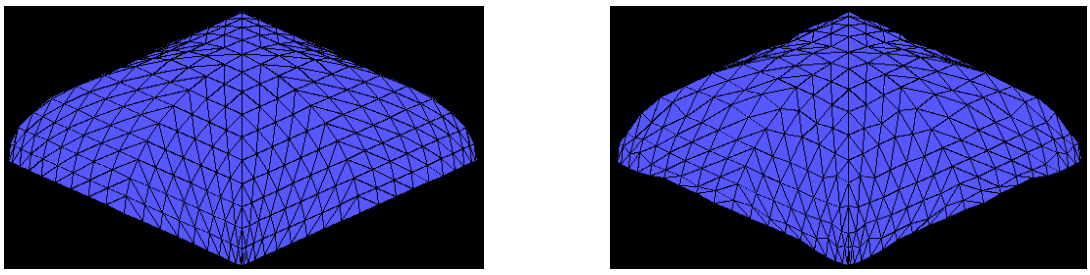

Figure 4: RTS and MTTS configurations.

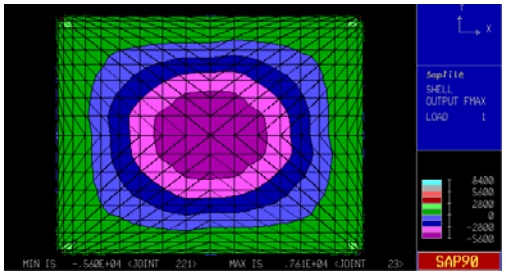


RTS: maximum principal internal forces [N/m]

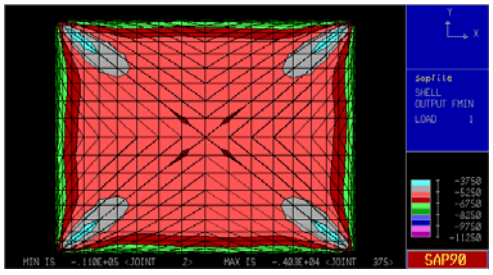


RTS: minimum principal internal forces [N/m]

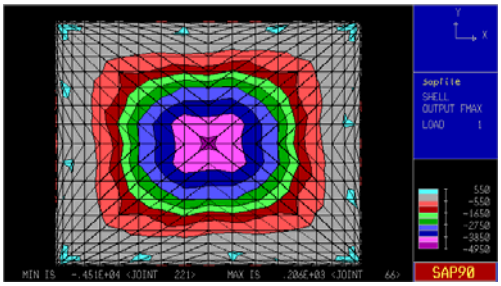


MTTS: maximum principal internal forces [N/m]

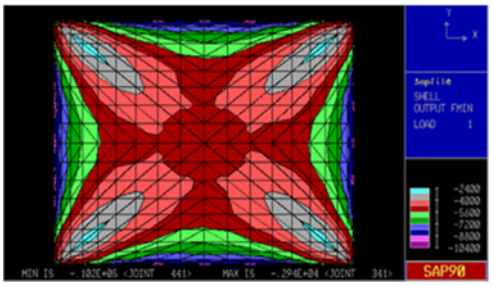


MTTS: minimum principal internal forces [N/m]

Figure 5: Top views of the unreinforced vault subject to its self-weight.

### 3.2 Dead and live loads

Let us examine the vault subject to the following static design load combination, $LC_{St}$:

$$\boldsymbol{LC_{St} = G_1 + (G_{2,1} + G_{2,2}) + Q} \tag{3}$$

where:
$G_1$ is the dead load due to the self-weight of the vault;
$G_{2,1}$ is the dead load due to the weight of the filling material;
$G_{2,2}$ is the dead load due to the permanent overload and it is assumed equal to 3,00 kN/m$^2$;
$Q$ is the live load ad it is fixed equal to 4,00 kN/m$^2$.

The FEM analysis on the RTS and the MTTS (Figure 6) gives the maximum and minimum internal axial forces acting on midsurface of shell elements (Figure 7).

The corresponding maximum and minimum principal stresses on the RTS are equal to $\sigma_{max}$ = 1.03 x $10^{-1}$ MPa and $\sigma_{min}$ = -1,40 x $10^{-1}$ MPa, respectively, as well as the average value of the tensile principal stresses is equal to $\sigma_{ave}$ = 1,26 x $10^{-8}$ MPa.

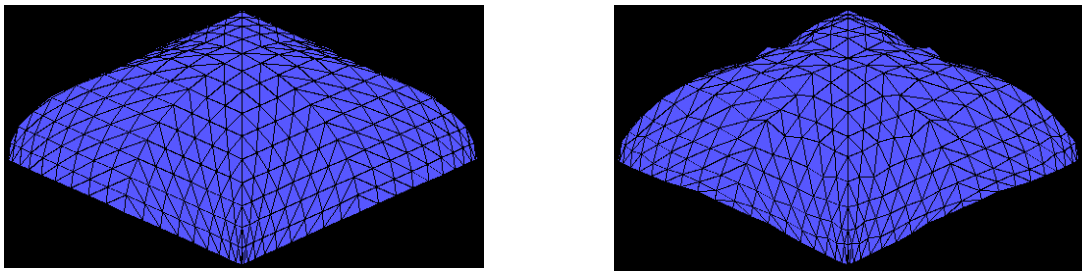

Figure 6: RTS and MTTS configurations

The MTTS allows to point out the maximum principal stress ($\sigma_{max}$ = 7,20 x $10^{-3}$ MPa) and the average value of the tensile principal stresses ($\sigma_{ave}$ = 3,01 x $10^{-9}$ MPa) are significantly smaller than that obtained by the RTS, and the minimum principal compressive stress given by the MTTS ($\sigma_{min}$ = -1,42 x $10^{-1}$ MPa) remains almost unchanged in magnitude compared to that given by the RTS.

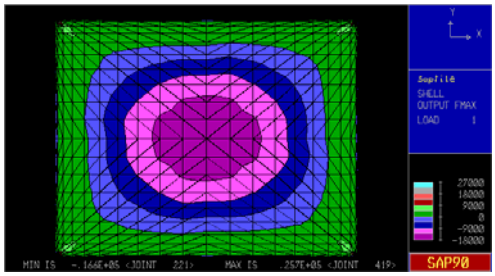


RTS: maximum principal internal forces [N/m]

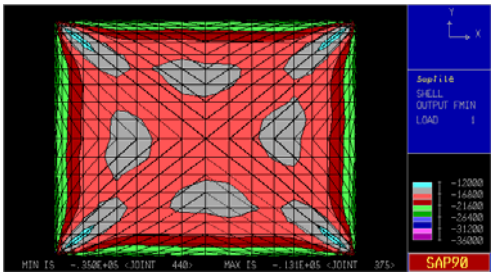


RTS: minimum principal internal forces [N/m]

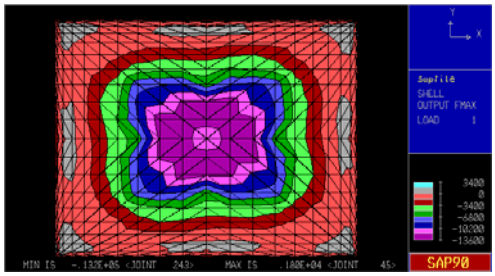


MTTS: maximum principal internal forces [N/m]

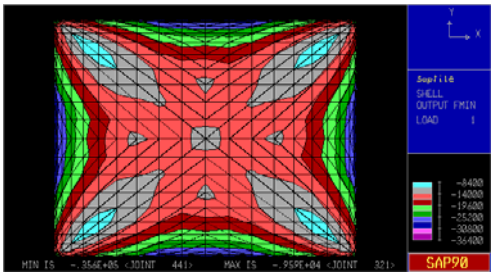


MTTS: minimum principal internal forces [N/m]

Figure 7: Top views of the unreinforced vault subject to dead and live loads.

### 3.3 Seismic loads and strengthening with FRCM strips

Let us examine the vault subject to the following dynamic design load combination, $LC_{Dyn}$:

$$\boldsymbol{LC_{Dyn} = E + G_1 + (G_{2,1} + G_{2,2}) + \psi_{2,1} Q} \quad (4)$$

where:
$E$ is the load due to the seismic excitation along the $X$-axis of the Cartesian frame (Figure 8);
$G_1$ is the dead load due to the self-weight of the vault;
$G_{2,1}$ is the dead load due to the weight of the weight of filling material;
$G_{2,2}$ is the dead load due to the permanent overload and it is assumed equal to 3,00 kN/m$^2$;
$\psi_{2,1}$ is the combination coefficient and it is assumed equal to 0,80;
$Q$ is the live load ad it is fixed equal to 4,00 kN/m$^2$.

The effects of the seismic excitations are modeled by means of horizontal forces according to a conventional static approach to seismic actions on the buildings (European Standard EN 1998-1). The seismic forces are set 50% of the vertical forces.

The maps of the maximum and minimum internal axial forces acting on midsurface of shell elements are shown in Figure 9. The maximum principal stresses on the RTS and the MTTS are equal to $\sigma_{max}$ = 3,50 x 10$^{-1}$ MPa and $\sigma_{max}$ = 1,50 x 10$^{-1}$ MPa, respectively; the minimum principal stresses on the RTS and the MTTS are equal to $\sigma_{min}$ = -4,28 x 10$^{-1}$ MPa and $\sigma_{min}$ = -5,28 x 10$^{-1}$ MPa, respectively; as well as the average values of tensile principal stresses are equal to $\sigma_{ave}$ = 4,00 x 10$^{-8}$ MPa and $\sigma_{ave}$ = 2,65 x 10$^{-8}$ MPa, respectively.

It is worth noting that, also in this simulation, a relevant reduction of the maximum tensile principal stresses (56 %) can be obtained by considering the MTTS as an alternative configuration to the RTS.

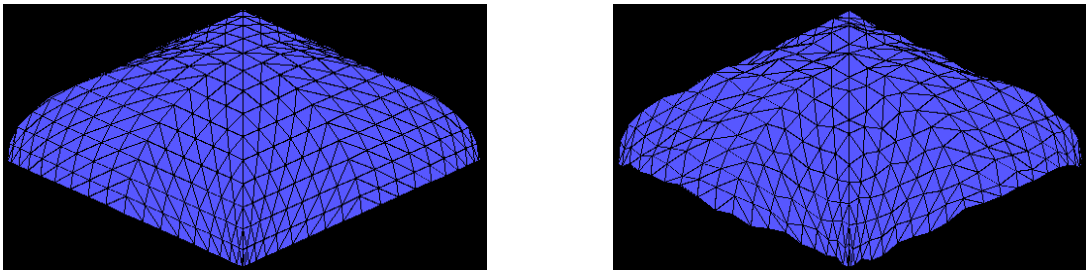

Figure 8: RTS and MTTS configurations.

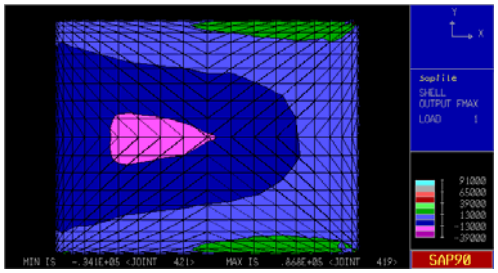

RTS: maximum principal internal forces [N/m]

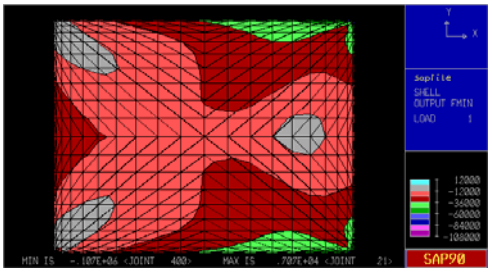

RTS: minimum principal internal forces [N/m]

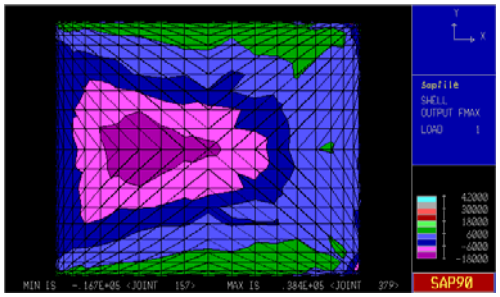

MTTS: maximum principal internal forces [N/m]

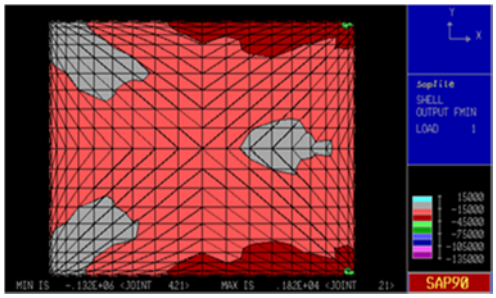

MTTS: minimum principal internal forces [N/m]

Figure 9: Top views of the unreinforced vault subject to seismic loads.

The FEM analysis on the MTTS has highlight, close to the vault basis, the principal tensile stresses are comparable to the tensile strength of tuff masonry ($1{,}00 \times 10^{-1}$ MPa) and the corresponding principal directions are roughly horizontal.

Therefore, a strengthening intervention with external unidirectional FRCM strips (Figure 10) is proposed. The mechanical properties of the used composites are given in Table 2.

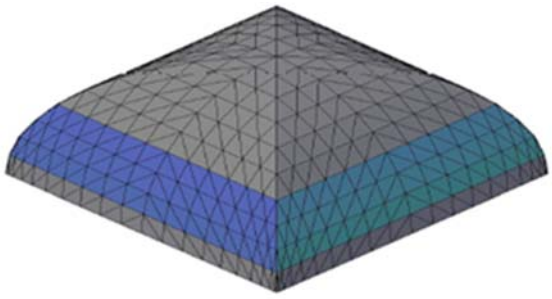

Figure 10: 3D views of the reinforced vault (the FRCM strips are applied on the blue surface).

| Carbon fiber | | Cementitious Matrix | |
|---|---|---|---|
| Tensile strenght | 4800 MPa | Compressive strenght | ≥ 20.0 MPa (after 28 d) |
| Young modulus | 240 GPa | Flexural strenght | ≥ 3.5 MPa (after 28 d) |
| Density | 1.82 g/cm$^3$ | Young modulus | ≥ 7000 MPa (after 28 d) |
| Ultimate strain | 1.8 % | | |

Table 2: Mechanical properties of FRCM.

The composites are assumed to be effective under pre-existing loads by applying a pretension in the strips via mechanical anchoring devices. The debonding failure modes and the composite bucking phenomena [24]-[36] can not occur in the strengthened vault, due to the use of such devices and the selective application of the FRCMs in correspondence with the vault regions subject to tensile stresses. The fiber orientation of the FRCMs is assumed to be parallel to the vault basis.

## 4 CONCLUDING REMARKS

An advanced numerical model able to approach the equilibrium problem of unreinforced and reinforced masonry vaults has been shown. This model allows to approximate the no-tension membrane (thrust surface) behavior of masonry through an elastic analysis of the masonry referred to a Minimum Tension Thrust Surface. Such a surface is obtained via a r-adaptive finite element featuring linearly elastic shell elements with dominant membrane behavior. The moving of the FEM nodes is governed by a Breeder Genetic Algorithm within a design domain and minimizing the average value of the principal tensile stresses in unreinforced masonry.

A cloister vault subject to several load combinations, both static and dynamic, has been studied in depth. The proposed model applied on the Minimum Tension Thrust Surface have given the tensile stresses significantly smaller than that obtained by means of the FEM analysis on the midsurface of the vault. The vulnerable portions of the vault have been found by means of the proposed model and a selective and optimized FRCM reinforcement has been designed.

The proposed approach may represent a useful tool to evaluate the vulnerability of existing curved masonry structures and to design optimal reinforcement patterns.

We address future extensions of the methodology here proposed to strengthening techniques involving a large variety of composite materials [69]-[76].

## REFERENCES

[1] F. Fraternali, G. Bilotti, Non-Linear Elastic Stress Analysis in Curved Composite Beams. *Computers & Structures*, **62**, 837-869, 1997.

[2] F. Fraternali, Free Discontinuity Finite element models in two-dimensions for in-plane crack problems*, Theoretical and Applied Fracture Mechanics*, **47**, 274-282, 2007.

[3] F. Fraternali, C.D Lorenz, G. Marcelli, On the estimation of the curvatures and bending rigidity of membrane networks via a local maximum-entropy approach, *Journal of Computational Physics*, **231**, 528-540, 2012.

[4] A. Fortunato, F. Fraternali, M. Angelillo, Structural capacity of masonry walls under horizontal loads. *Ingegneria sismica N1, 41-51 Anno XXXI*, 2014.

[5] V.P. Berardi, Initiation of Failure for Masonry Subject to In-Plane Loads through Micromechanics. *Modelling and Simulation in Engineering*, 2016.

[6] J. Heyman, *The stone skeleton*. New York: Cambridge University Press; 1995.

[7] F. Fraternali, A. Marino, T. El Sayed, A. Della Cioppa, On the Structural Shape Optimization through Variational Methods and Evolutionary Algorithms. *Mechanics of Advanced Materials and Structure,* **18**, 225-243, 2011.

[8] A. Baratta, O. Corbi, On the statics of No-Tension masonry-like vaults and shells: Solution domains, operative treatment and numerical validation. *Annals of Solid and Structural Mechanics* **2**, 107, 2011.

[9] A. Baratta, O. Corbi, An approach to the positioning of FRP provisions in vaulted masonry structures. *Composites Part B Engineering,* **53**, 334-341, 2013.

[10] G. Carpentieri, F. Fabbrocino, M. De Piano, V.P. Berardi, L. Feo, F. Fraternali, Minimal mass design of strengthening techniques for planar and curved masonry structures. *7th European Congress on Computational Methods in Applied Sciences and Engineering*, (ECCOMAS 2016), Chania, Crete, Greece, June 5-10, 2016.

[11] F. Fraternali, A. Angelillo, F. Fortunato, A lumped stress method for plane elastic problems and the discrete-continuum approximation. *International Journal of Solids and Structures,* **39**, 6211-6240, 2002.

[12] F. Fraternali, A thrust network approach to the equilibrium problem of unreinforced masonry vaults via polyhedral stress functions. *Mechanics Research Communications*, **37**, 198-204, 2010.

[13] L. Soveja, M. Budescu, I. Gosav, *Modelling methods for unreinforced masonry structures*. Construction architecture. Gheorghe Asachi Technical University of Iai; LIX (LXIII), 2013.

[14] F. Fraternali, A mixed lumped stress-displacement approach to the elastic problem of masonry walls. *Mechanics Research Communications*, **38**, 176-180, 2011.

[15] M. Angelillo, A. Fortunato, A. Montanino, M. Lippiello, Singular stress fields in masonry structures: Derand was right. *Meccanica*, **49**, 1243-1262, 2014

[16] W.M. Jenkins, Plane frame optimum design environment based on genetic algorithm. *Journal of Structural Engineering, ASCE* **118**, 1992.

[17] P. Hajela, E. Lee, C.Y. Lin, Genetic algorithms in structural topology optimization. Mota Soares CA, Bendsøe MP, editors. *Topology design of structures, Vol. 227*. Dordrecht: Kluwer Academic Publishers, 1990.

[18] C.D. Chapman, K. Saitou, M.J. Jakiela, Genetic algorithms as an approach to configuration and topology design. *Journal Mechanical Design*, **116**, 1005-1012, 1994.

[19] K. DeJong, Evolutionary computation: a unified approach. *Genetic and Evolutionary Computation Conference (GECCO 2007)*, England UK, London, July 7-11, 2007.

[20] F. Fabbrocino, I. Farina, V.P. Berardi, A.J.M. Ferreira, F. Fraternali, On the thrust surface of unreinforced and FRP-/FRCM-reinforced masonry domes. *Composites Part B Engineering,* **83**,297-305, 2015.

[21] C. Maenghyo, J. Seongki, R-Adaptive mesh generation for shell finite element analysis, *Journal of Computational Physics,* **199**, 29-16, 2004.

[22] H. Mühlenbein, M. Schomisch, J. Born, The parallel genetic algorithm as function optimizer. *Parallel Computing*, **17**, 619-632, 1991.

[23] *European Committee for Standardization. Eurocode* 8: *Design of structures for earthquake resistance* - part 1: general rules, seismic actions and rules for buildings 2004. EN 1998-1. 2004. Brussels, Belgium.

[24] L. Ascione, F. Fraternali, A penalty model for the analysis of composite curved beams, *Computers & Structures*, **45**, 985-999, 1992.

[25] F. Fraternali, J.N. Reddy, A penalty model for the analysis of laminated composite shells, *International Journal of Solids and Structures*, **30**, 3337-3355, 1993.

[26] Ascione, L., V.P. Berardi, E. Di Nardo, L. Feo, G. Mancusi, An experimental and numerical investigation on the plating of reinforced concrete beams with FRP laminates. Lecture Notes in Applied and Computational Mechanics, 23, 303-314, 2005.

[27] Ascione, L., L. Feo, G. Mancusi, On the statical behaviour of fibre-reinforced polymer thin-walled beams. *Composites Part B: Engineering*, *31* (8), 643-654, 2000.

[28] L. Ascione, V.P. Berardi, L. Feo, G. Mancusi, A numerical evaluation of the interlaminar stress state in externally FRP plated RC beams. *Composites Part B: Engineering*, **36** (1), 83-90, 2005.

[29] L. Feo, G. Mancusi, Modeling shear deformability of thin-walled composite beams with open cross-section. *Mechanics Research Communications*, **37** (3), 320-325, 2010.

[30] G. Mancusi, L. Feo, Non-linear pre-buckling behavior of shear deformable thin-walled composite beams with open cross-section. *Composites Part B: Engineering*, **47**, 379-390, 2013.

[31] F. Fraternali, S. Spadea, L. Ascione, Buckling behavior of curved composite beams with different elastic response in tension and compression. *Composite Structures*, **100**, 280-289, 2013.

[32] G. Mancusi, F. Ascione, M. Lamberti, Pre-buckling behavior of composite beams: A mechanical innovative approach, *Composite Structures*, **117** (1), 396-410, 2014.

[33] L. Ascione, V.P. Berardi, Anchorage device for FRP laminates in the strengthening of concrete structures close to beam-column joints. *Composites Part B: Engineering*, **42** (7), 1840-1850, 2011

[34] L. Feo, G. Mancusi, The influence of the shear deformations on the local stress state of pultruded composite profiles. *Mechanics Research Communications*, **47**, 44-49, 2013.

[35] G. Mancusi, L. Feo, V.P. Berardi, Concrete open-wall systems wrapped with FRP under torsional loads. *Materials*, **5** (11), 2055-2068, 2012.

[36] L. Ascione, G. Mancusi, A. D'Aponte, Fabric-Reinforced Cementitious Matrix (FRCM): A new Italian guideline under development, *Key Engineering Materials*, **624**, 3-10, 2015.

[37] A. Amendola, G. Carpentieri, M. De Oliveira, R.E. Skelton, F. Fraternali, Experimental investigation of the softening-stiffening response of tensegrity prisms under compressive loading. *Composite Structures*, **117**, 234-243, 2014.

[38] A. Amendola, E.H. Nava, R. Goodall, I. Todd, R.E. Skelton, F. Fraternali, On the additive manufacturing, post-tensioning and testing of bi-material tensegrity structures*, Composite Structures*, **131**, 66-71, 2015.

[39] R.E. Skelton, F. Fraternali, G. Carpentieri, A. Micheletti, Minimum mass design of tensegrity bridges with parametric architecture and multiscale complexity. *Mechanics Research Communications*, 58, 124-132, 2014.

[40] A. Leonard, F. Fraternali, C. Daraio, Directional wave propagation in a highly nonlinear square packing of spheres. *Experimental Mechanics*, **53**(3), 327-337, 2013.

[41] F. Fraternali, G. Carpentieri, A. Amendola, R.E. Skelton, V. F. Nesterenko, Multiscale tunability of solitary wave dynamics in tensegrity metamaterials. *Applied Physics Letters*, **105**, 201903, 2014.

[42] J.R. Raney, F. Fraternali, A. Amendola, C. Daraio, Modeling and In Situ Identification of Material Parameters for Layered Structures based on Carbon Nanotube Arrays. *Composite Structures*, **93**, 3013–3018, 2011.

[43] F. Fraternali, I. Farina, C. Polzone, E. Pagliuca, L. Feo, On the use of R-PET strips for the reinforcement of cement mortars. *Composites. Part B*, **46**, 207-210, 2013.

[44] C. Daraio, D . Ngo, V. F. Nesterenko, F. Fraternali, Highly Nonlinear Pulse Splitting and Recombination in a Two Dimensional Granular Network. *Physical Review E*, **82**, 036603, 2010.

[45] A. Amendola, C.J. Smith, R. Goodall, F. Auricchio, L. Feo, G. Benzoni, F. Fraternali, Experimental response of additively manufactured metallic pentamode materials confined between stiffening plates. *Composite Structures*, **142**, 254-262, 2016.

[46] F. Fraternali, S. Spadea, V.P. Berardi, Effects of recycled PET fibers on the mechanical properties and seawater curing of Portland cement-based concretes. *Construction and Building Materials*, **61**, 293-302, 2014.

[47] I. Farina, F. Fabbrocino, G. Carpentieri, M. Modano, A. Amendola, R. Goodall, L. Feo, F. Fraternali, On the reinforcement of cement mortars through 3D printed polymeric and metallic fibers*, Composites Part B: Engineering*, **90**, 76-85, 2016.

[48] T. Blesgen, F. Fraternali, J.R. Raney, A. Amendola, C. Daraio, Continuum Limits of Bistable Spring Models of Carbon Nanotube Arrays accounting for Material Damage. *Mechanics Research Communications*, **45**, 58-63, 2012.

[49] F. Fraternali, M. Negri, M. Ortiz, On the Convergence of 3D Free Discontinuity Models in Variational Fracture. *International Journal of Fracture*, **166**(1-2), 3-11, 2010.

[50] Amendola, C.J. Smith, R. Goodall, F. Auricchio, L. Feo, G. Benzoni, F. Fraternali, Experimental response of additively manufactured metallic pentamode materials confined between stiffening plates. *Composite Structures*, **142**, 254–262, 2016.

[51] G. Lomiento , N. Bonessio, G. Benzoni, Friction Model for Sliding Bearings under Seismic Excitation, Journal of Earthquake Engineering, **17**(8):1162-1191, 2013..

[52] M. Budek, M. J. N. Priestley, G. Benzoni, The Effect of External Confinement on Flexural Hinging in Drilled Pile Shafts, *Earthquake Spectra*, **20** (1), 1-24, 2004.

[53] Hae-Bum Yun, Sami F. Masri, Raymond W. Wolfe, Gianmario Benzoni , Data-driven methodologies for change detection in large-scale nonlinear dampers with noisy measurements, *Journal of Sound and Vibration*, **322**, Issues 1–2, 24 April 2009, Pages 336–357.

[54] D. D'Ayala, G. Benzoni, Historic and Traditional Structures during the 2010 Chile Earthquake: Observations, Codes, and Conservation Strategies. *Earthquake Spectra*, **28** (S1), S425-S451, 2012.

[55] N. Bonessio, G. Lomiento, G. Benzoni, Damage identification procedure for seismically isolated bridges, *Structural Control Health Monitoring*, **19**(5), 565–578, 2012.

[56] G. Benzoni, C. Casarotti , Effects of Vertical Load, Strain Rate and Cycling on the Response of Lead-Rubber Seismic Isolators, *Journal of Earthquake Engineering* ,**13**, 2009.

[57] A. Budek-Schmeisser, G. Benzoni, Rational seismic design of precast, prestressed concrete piles, *PCI Journal*, **53**(5), 40-53, 2008.

[58] G. Benzoni, M. J. N. Priestley, Seismic response of linked marginal wharf segments, *Journal of Earthquake Engineering* **74**, 513-539, 2003.

[59] A. Amendola, G. Benzoni, F. Fraternali, Non-linear elastic response of layered structures, alternating pentamode lattices and confinement plates. *Composite Part B, Engineering*, Online first, DOI: 10.1016/j.compositesb.2016.10.027, 2016.

[60] F. Fraternali, G. Carpentieri, R. Montuori, A. Amendola, G. Benzoni, On the use of mechanical metamaterials for innovative seismic isolation systems, COMPDYN 2015 - 5th ECCOMAS Thematic Conference on Computational Methods in Structural Dynamics and Earthquake Engineering, 349-358.

[61] G. Mancusi, F. Fabbrocino, L. Feo, F. Fraternali, Size effect and dynamic properties of 2D lattice materials, *Composites Part B: Engineering*, **112**, 235-242, 2017.

[62] G. Mancusi, L. Feo, A refined finite element formulation for the microstructure-dependent analysis of two-dimensional (2D) lattice materials, *Materials*, **6** (1), 1-17, 2013.

[63] F. Ascione, G. Mancusi, Failure criteria for FRP adhesive lap joints: A comparative analysis. *Mechanics of Advanced Materials and Structures*, **17** (2), 157-164, 2010.

[64] F. Ascione, G. Mancusi, Axial/bending coupled analysis for FRP adhesive lap joints. *Mechanics of Advanced Materials and Structures*, *17* (2), 85-98,2010.

[65] F. Ascione, G. Mancusi, Curve adhesive joints. *Composite Structures*, **94** (8), 2657-2664, 2012.

[66] F. Ascione, G. Mancusi, The influence of the geometric curvature on the mechanical behaviour of the adhesive joint, *Civil-Comp Proceedings*, 99, 2012.

[67] G. Mancusi, F. Ascione. Performance at collapse of adhesive bonding. Composite Structures, **96**, 256-261, 2013.

[68] F. Ascione, G. Mancusi, The influence of the web-flange junction stiffness on the mechanical behaviour of thin-walled pultruded beams. *Composites Part B: Engineering*, **55**, 599-606, 2013.

[69] F. Ascione, G. Mancusi, S. Spadea, M. Lamberti, F. Lebon, A. Maurel-Pantel, On the flexural behaviour of GFRP beams obtained by bonding simple panels: An experimental investigation. *Composite Structures*, **131**, 55-65, 2015.

[70] G. Mancusi, A. Orefice, L. Feo, F. Fraternali, Structural analysis of adhesive bonding for thick-walled tubular composite profiles. *ECCOMAS Congress 2016 - Proceedings of the 7th European Congress on Computational Methods in Applied Sciences and Engineering*, **4**, 7837-7852, 2016.

[71] A. Orefice, G. Mancusi, L. Feo, F. Fraternali, Cohesive interface behaviour and local shear strains in axially loaded composite annular tubes. *Composite Structures*, 160, 1126-1135, 2017.

[72] Ascione, L., G. Mancusi, S. Spadea, Flexural behaviour of concrete beams reinforced with GFRP bars. *Strain*, **46** (5), 460-469, 2010.

[73] F. Ascione, G. Mancusi, An experimental analysis on the time-dependent behaviour of a CFRP retrofitting under sustained loads. *Proceedings of the 6th International Conference on Fracture Mechanics of Concrete and Concrete Structures*, **2**, 1085-1090, 2007.

[74] V.P. Berardi, G. Mancusi, Time-dependent behavior of reinforced polymer concrete columns under eccentric axial loading. *Materials*, **5** (11), 2342-235, 2012.

[75] V.P. Berardi, G. Mancusi, A mechanical model for predicting the long term behavior of reinforced polymer concretes, *Mechanics Research Communications*, **50**, 1-7, 2013.

[76] G. Mancusi, S. Spadea, V.P. Berardi, Experimental analysis on the time-dependent bonding of FRP laminates under sustained loads. *Composites Part B: Engineering*, **46**, 116-122, 2013.

COMPDYN 2017
6th ECCOMAS Thematic Conference on
Computational Methods in Structural Dynamics and Earthquake Engineering
M. Papadrakakis, M. Fragiadakis (eds.)
Rhodes Island, Greece, 15–17 June 2017

# SEISMIC BEHAVIOUR OF A REINFORCED MASONRY INFILL MADE WITH AN INNOVATIVE NEW BRICK UNIT: RESULTS OF A SHAKING TABLE TEST

**Elizabeth Vintzileou[1]; Chrissy-Elpida Adami[1]; Vasiliki Palieraki[1]; Charalambos Mouzakis[2], Lucia Karapitta[2]**

[1]National Technical University of Athens, Faculty of Civil Engineering, Laboratory of Reinforced Concrete
5, Iroon Polytechneiou Str., 15773 Athens, Greece
elvintz@central.ntua.gr, adamis@central.ntua.gr, vasopal@central.ntua.gr

[2]National Technical University of Athens, Faculty of Civil Engineering, Laboratory of Earthquake Engineering
5, Iroon Polytechneiou Str., 15773 Athens, Greece
harrismo@central.ntua.gr, klucia@central.ntua.gr

**Keywords:** infilled frame, new brick unit with special vertical cavities, horizontal and vertical reinforcement, in-plane cyclic tests, out-of-plane repeated tests, shaking table tests.

**Abstract.** *Within the framework of INSYSME project (www.insysme.eu) [1], an innovative solution for infill walls has been developed by the authors and XALKIS S.A.. A special, vertically perforated, brick unit has been designed and produced. The innovative brick unit was granted a patent (No. 1008797) by the Greek Patent Office. Vertical holes are located close to the faces of the masonry unit, to serve two needs, namely (a) the enhancement of the out-of-plane bearing capacity of the infill, using vertical reinforcement and (b) the positioning of installations (electrical and plumping). Horizontal or horizontal and vertical reinforcement is provided. The horizontal reinforcement is positioned in the bed joints during the construction of the wall, whereas the vertical reinforcement is placed (in the special vertical holes) after the construction of the wall. Additionally, simple sliding connectors may be used to prevent out-of-plane collapse.*

*In order to assess the performance of the proposed solution, an experimental campaign is carried out on a one-bay masonry infill. A specimen is constructed and tested on the shaking table, in the facility of the Laboratory of Earthquake Engineering/NTUA, in a reduced scale of 1:2. The aim of this investigation was to obtain quantitative data about the seismic behaviour of the infill constructed with the innovative brick unit, and to compare it with its quasi-static behaviour (in-plane and out-of-plane tests on full scale specimens).*

*In the present paper the experimental results of the shaking table test are presented and commented upon.*

# 1 INTRODUCTION

Brick masonry infills, widely used as enclosures to RC buildings, offer an economic and durable solution, as they may ensure adequate insulation properties, whereas they contribute to the seismic behaviour of the structural system. Traditionally, enclosures and partition walls in RC structures are considered as non-structural elements and, thus, they are not explicitly taken into account in the aseismic design of buildings, even though theory and practice have repeatedly proven that masonry infills may affect in a positive way the seismic behaviour of buildings, provided that possible negative structure-infill interaction is avoided [2].

On the other hand, the behaviour of the infills themselves is significant both from the Public safety and economy point of view [3]. In recognition of this fact, EC8 [4] includes (qualitative) guidance for the improvement of the seismic behaviour of infill walls. Quantification of the EC8 [4] rules, as well as innovative infill systems-fully documented through experiments and analysis-is the aim of the EU-funded project INSYSME.

Within the framework of the European Project INSYSME, one of the two innovative solutions for infill walls developed by the authors and a brick manufacturing industry XALKIS S.A., INSYSTEM 2, aims at enhancing the in-plane and out-of plane deformability of the infill wall. A special, vertically perforated, brick unit has been designed and produced. The innovative brick unit was granted a patent (No. 1008797) by the Greek Patent Office. In order to evaluate the system performance in-plane and out-of-plane tests on one-bay infilled frames are performed. Shaking table tests of frames were also envisaged. More specifically, one-bay infilled frame (scale 1:2), constructed with the proposed enclosure wall INSYSTEM 2, is tested on the earthquake simulator of the Laboratory of Earthquake Engineering, NTUA. Uniaxial (separately along X or along Y direction) and biaxial (along the two horizontal axes) tests were performed, in order to characterize the seismic behaviour of the infills in relation to the behaviour of the frame, and obtain information on the systems performance.

This paper presents shaking table test results on INSYSTEM 2 behaviour (scale 1:2). The results are compared with the results of a full scale frame against in-plane cyclic actions [5].

# 2 DESCRIPTION OF SPECIMEN AND TEST SETUP

## 2.1 Description of Specimen

INSYSTEM 2 consists in a single leaf clay masonry infill. A mortar joint is provided along the surrounding infill-to-RC concrete interfaces. The enclosure is not fixed to the RC frame elements. A detailed description of the developed system is provided elsewhere [5]. In the present paper, only a summary of the characteristics of the infill solution is presented.

In the system presented here (INSYSTEM 2: System with reinforcement), horizontal or horizontal and vertical reinforcement is provided to the infill. As already mentioned, a special unit was designed by NTUA and XALKIS and produced by XALKIS (Figure 1). The horizontal reinforcement is laid during the construction of the wall in bed mortar joints, whereas the vertical one is placed (in special cavities) throughout the height of the wall after the construction of the infill is completed. Although the idea of reinforcing the infill wall is quite common, the use of the available on the market vertically perforated bricks allows for positioning of the horizontal reinforcement, whereas (as the infill is constructed after the completion of the RC structure) only external vertical reinforcement can be provided to the infill ([6], [7], [8], [9], [10]). The out-of-plane collapse of the wall is prevented by special sliding connectors, if the aspect ratio of the infill dictates such a need. The sliding connectors are anchored to the RC frame elements. On the contrary, they are not connected to the infill wall, while the reinforcement is not anchored to the RC frame.

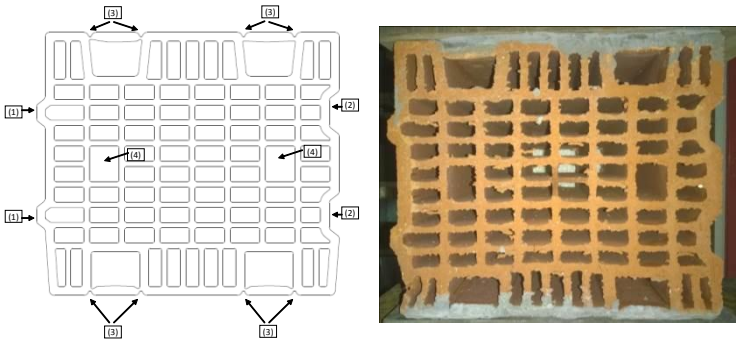

Figure 1: Unit shape.



a) b) c)

Figure 2: Construction of the scaled specimen INSYSTEM 2: a) Positioning of the horizontal reinforcement, b) View of the infill wall, special cavities for the vertical reinforcement, c) Cavities filled with cement mortar.

In order to study the seismic response of the developed infill solution, namely INSYSTEM 2, one-bay RC frame at reduced scale, equal to 1:2 following the similitude laws, has been constructed and tested [11]. The model was built with a length scale of 1:2 with the same material properties as the real frame. The prototype structure consists of a one bay RC frame, having 2 columns (with dimensions 0.3x0.3m$^2$), one beam (with dimensions 0.3x0.5m$^2$) and a slab (with dimensions 2.1x2.1m$^2$, thickness equal to 0.16m). The length of the RC frame equals to 3.3m, whereas its height is 2.70m. Thus, the dimensions of the enclosure are 2.7mx2.2m (length x height). Since the real and the scaled model have the same material properties and both systems are subjected to gravity acceleration, then the acceleration and stress scale equals to 1. Taking into account the scale, additional mass of 3.0Mgr was placed on top of the specimen. It is important to underline that by respecting the similitude laws, the results of the reduced scale specimens may be extrapolated to the prototype structure.

The dimensions of the constituents composing the infill, namely brick units, mortar joints, and diameter of the horizontal and vertical reinforcement, were reduced appropriately to respect the scale factor. As there are no brick units available in the market with the required (reduced) dimensions and the desired shape, it was decided to cut an existing unit, available in the market under the name K100, to adequate smaller parts and use it for the scaled models.

INSYSTEM 2 was designed to host horizontal and vertical reinforcement. In the scaled specimen, the horizontal reinforcement (4Φ5 per wall face) was placed in the horizontal bed joints during construction of the wall, whereas the vertical reinforcement (3Φ8 per wall face) was placed in special cavities at the exterior parts of the wall (Figure 2). The vertical reinforcement was placed after the construction of the wall. In order to form these special cavities, K100 was cut into the following dimensions: 90x110x110 [mm$^3$] (length x width x height).

## 2.2 Test setup

The specimen was securely fastened on the shaking table. A steel frame was designed (Figure 3), in order to allow the in-plane deformation of the infilled frame and prevent the out-of plane displacement of the columns. The steel frame was securely fastened on the RC footing and was designed to sustain an out of plane force equal to the maximum shear force that may be applied by the shaking table. As mentioned above, to respect the similitude laws and, hence, to make possible the extrapolation of the results from the model to the prototype, additional masses (3Mgr) were placed at the top of the specimen.

The measuring devices are shown in Figure 4. In detail, accelerometers were placed at the top of the RC frame and at the center of the infill wall (measurements along both directions). Absolute displacements in both horizontal directions were measured at the top and foot base of column (D22, D23), as well as at the center of the infill wall (D18). Moreover, the relative in-plane and out-of plane displacement between the frame and the infill walls were also measured. The horizontal and vertical reinforcement was provided with strain gauges (SG1 to SG8), to assess its contribution to the overall behaviour of the structure. Finally, the acceleration and displacement of input motion were recorded during each test.



a) b) c)

Figure 3: Test setup: a) View of the specimen, the steel frame and the additional masses can be seen, b) Side view of the steel frame, c) The arrangement that allows the in-plane sliding of the RC frame and prevents the out of plane movement of the columns of the RC frame.

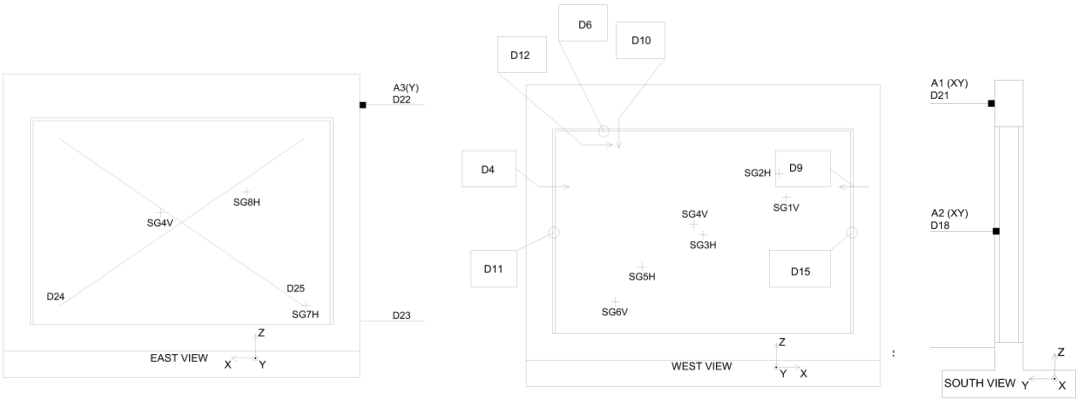


a) b) c)

Figure 4: Measuring devices of acceleration and displacement.

## 2.3 Test procedure. Seismic input and test protocol

The specimen was subjected to a series of scaled motions with increasing maximum acceleration, until significantly damaged. Uniaxial (separately along X or along Y direction) and biaxial (along the two horizontal axes) tests were performed. The input motions were time scaled (i.e. $1/\sqrt{2}$) according to the similitude laws. Needless to mention that, prior to the application of the selected seismic inputs, the dynamic properties of the specimen were measured through sine logarithmic sweep excitation of low amplitude (0.04g). Sine sweep tests were performed separately along X and Y directions. This procedure was repeated during the experimental procedure, in order to detect changes in the dynamic properties of the specimens.

For the shaking table tests, three real earthquake records and an artificial time history were applied. The following records of seismic events were used: (a) An aftershock of Kefalonia earthquake (1983): The event occurred in Argostoli on March 1983 (Magnitude Ms=5.5). The Lateral component was used in X-direction, while the Long Component used in Y direction, (b) Jensen Filter Plant (JFA) record of the Northridge, USA (1994) earthquake: The component JFA-292 was applied in the horizontal X-direction. In case of biaxial excitation, the JFA -022 component was imposed along the Y-direction, (c) Kalamata earthquake (1986): The accelerograms were recorded on hard soil. The longitudinal component was used for the shaking table tests, (d) Artificial time histories: The duration of strong motion was about 30sec and the maximum acceleration was equal to 1g.

The time histories of the time scaled earthquakes and the corresponding acceleration response spectra for 5% damping are shown in Figures 5 to 8. All input motions were selected taking into account that the major spectral amplifications occur for frequencies close to the frequencies of the fundamental modes of models in both directions. When further increase of base motion was not possible (the capacity of the shaking table was reached or the dynamic characteristic of model was modified due to damages), another seismic input was applied. The testing procedure is presented in Table 1.

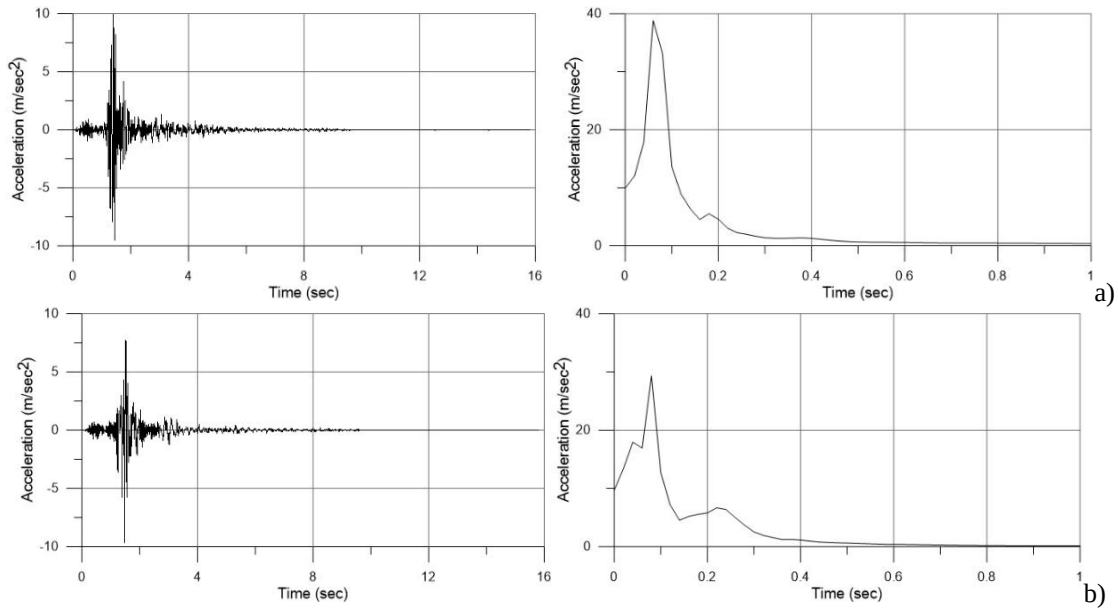


Figure 5: Argostoli earthquake: Acceleration time history and corresponding response spectrum for 5% damping: a) Longitudinal and b) Lateral Component.

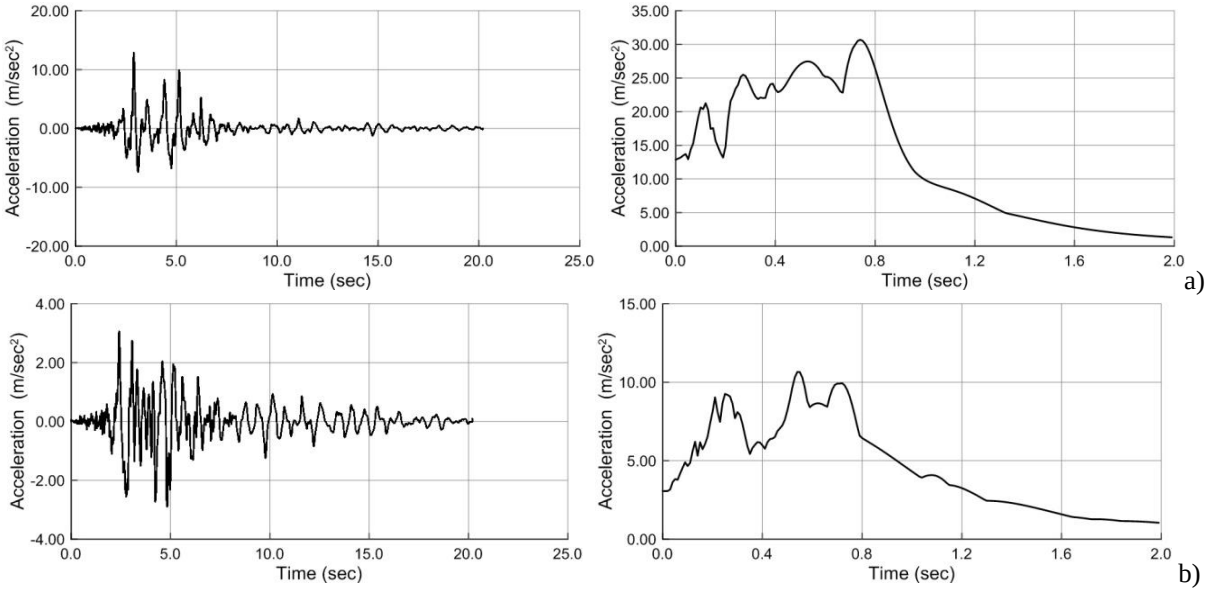


Figure 6: JFA record: Acceleration time history and corresponding response spectrum for 5% damping: a) JFA-292 component and b) JFA-022 component.

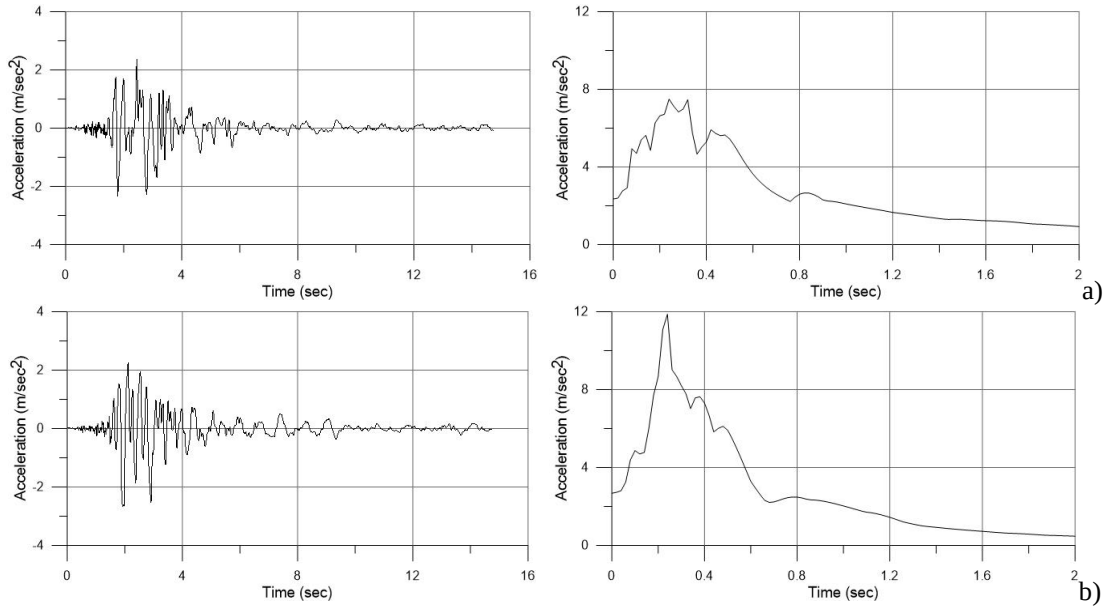


Figure 7: Kalamata earthquake: Acceleration time history and corresponding response spectrum for 5% damping: a) X and b) Y direction.

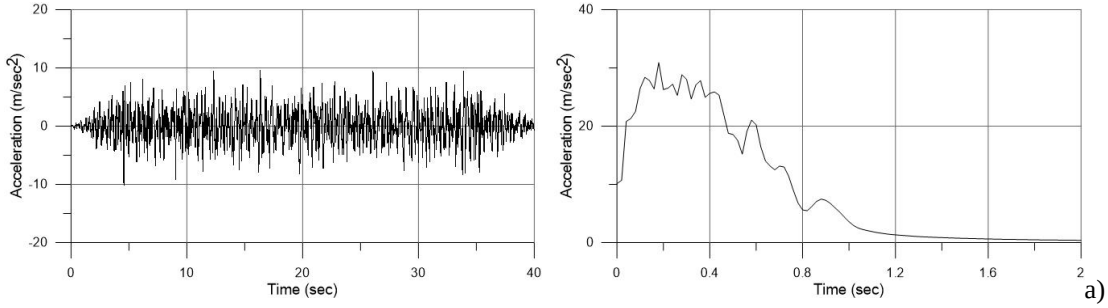

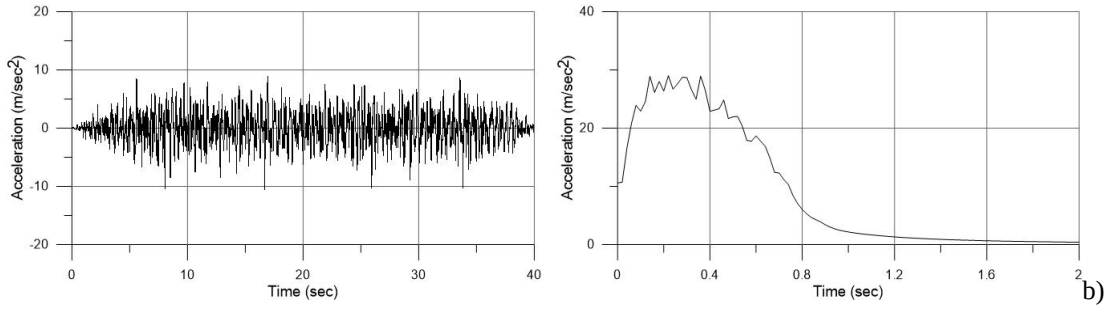


Figure 8: Artificial earthquake: Acceleration time history and corresponding response spectrum for 5% damping: a) X and b) Y direction.

| No. of test | Excitation | Direction of excitation | Base acceleration [g]/(%) | |
|---|---|---|---|---|
| | | | X | Y |
| 1 | Sine sweep | X | 0.04 | – |
| 2 | Sine sweep | Y | – | 0.04 |
| 3 | Argostoli | X | 0.05g/ (5%) | – |
| 16 | Argostoli | X | 1.09g/ (102%) | – |
| 17 | Sine sweep | X | 0.04 | – |
| 18 | Argostoli | XY | 0.64g/ (50%) | 0.70g/ (50%) |
| 24 | Argostoli | XY | 1.01g/ (102%) | 1.76g/(102%) |
| 25 | Sine sweep | X | 0.04 | – |
| 26 | JFA | X | 0.14g/ (10%) | – |
| 32 | JFA | X | 1.64g/ (102%) | – |
| 33 | JFA | X | 1.64g/ (102%) | – |
| 34 | Sine sweep | X | 0.04 | – |
| 35 | Kalamata | X | 0.09g/(30%) | – |
| 37 | Kalamata | X | 0.27g/(100%) | – |
| 38 | Artificial | X | 0.22g/ (20%) | – |
| 40 | Artificial | X | 1.22g/(100%) | – |
| 41 | Artificial | XY | 0.59g/(50%) | 0.71g/(50%) |
| 42* | Artificial | XY | (100%) | (100%) |
| 43* | Artificial | X | (100%) | – |
| 44** | Artificial | X | 1.09g/ (100%) | – |

*Test stopped

**During these test the instrumentation was removed from the specimen

Table 1: INSYSTEM 2 specimen. Test protocol.

## 3 EXPERIMENTAL RESULTS

### 3.1 Observed damages

The following Figures 9 to 12, present the damage pattern of the specimen. Damage occurred after reaching the maximum acceleration of each test series, i.e. after completion of Test 16 (Argostoli earthquake: 1.09g(X)), Test 24 (Argostoli earthquake: 1.01g(X)/1.76g(Y)), Test 35 (JFA earthquake: 1.63g(X)), Test 40 (JFA earthquake: 1.22g(X)) and Test 44 (Artificial earthquake: 1.09g(X)).

During the first series of uniaxial tests (Tests 3-16), only separation of the infill wall from the RC frame is recorded, as well as minor cracking along limited number of bed joints. It is

noted that the joints with the horizontal reinforcement (at the lower part of the infill) are the first ones to present cracking. Shear cracks at the RC beam are also evident (Figure 9).

After the first biaxial test series (Tests 18-24), cracking along bed joints is more pronounced, while also cracking along limited number of head joints has been recorded. Cracks on RC frame (i.e. beam and columns) are recorded as well (Figure 10).

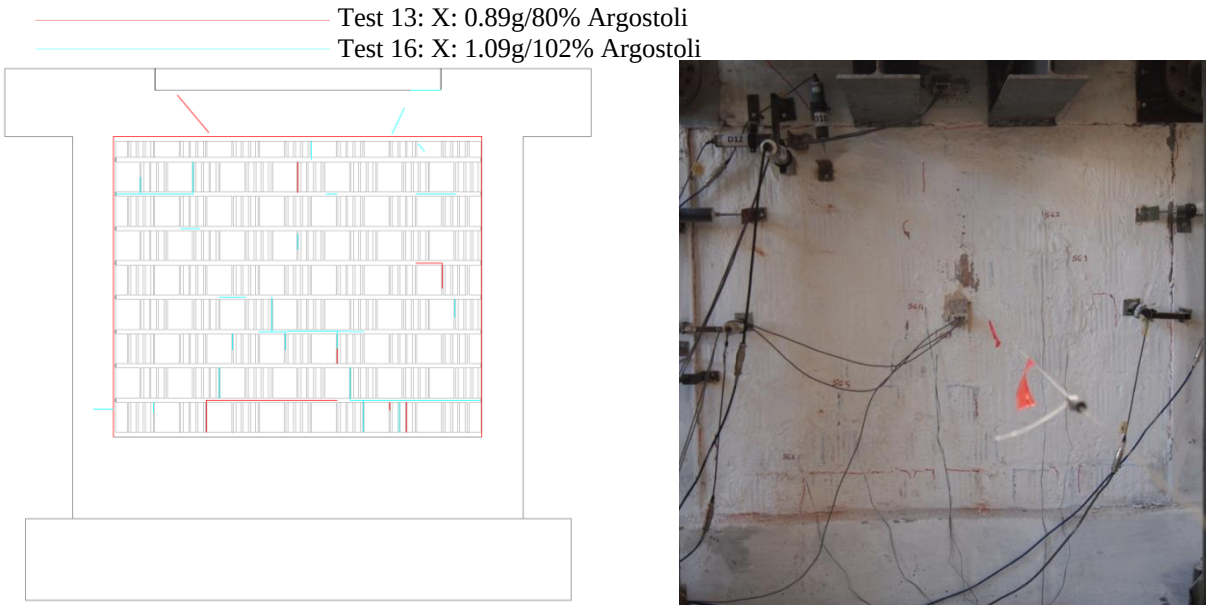


Figure 9: Crack pattern after the first uniaxial test series (Tests 3-16).

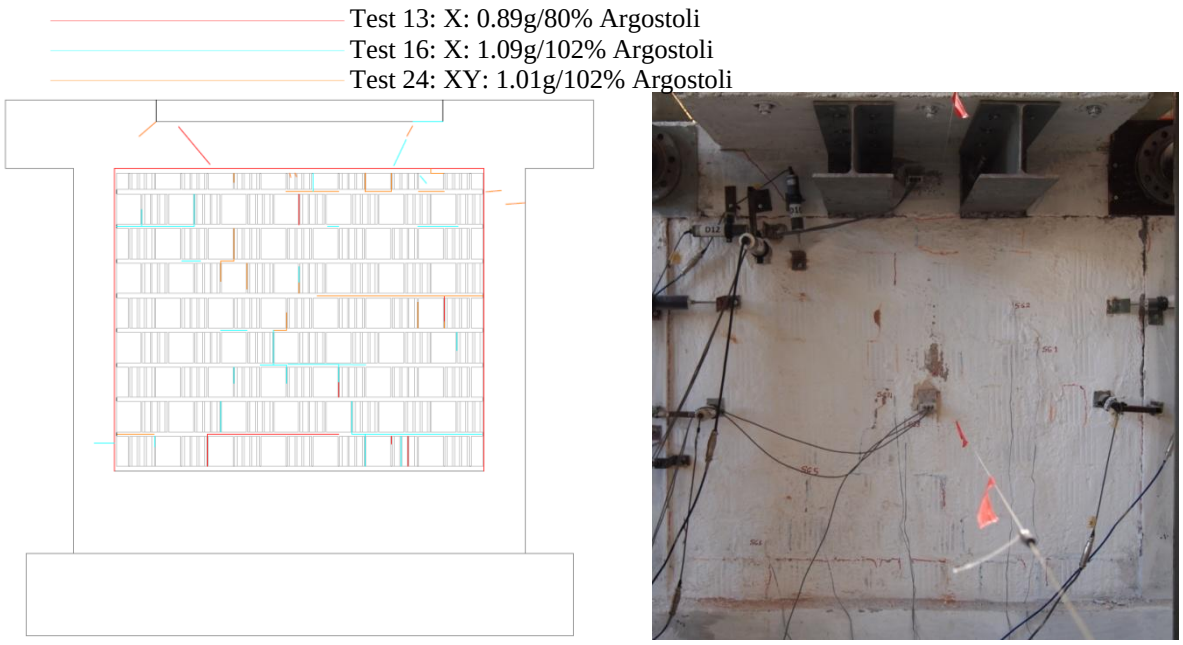


Figure 10: Crack pattern after the first biaxial test series (Tests 18-24).

After the second uniaxial test series (Tests 26-40), shear cracks appeared in the infill. It is noted that cracking of the bricks has not yet occurred, whereas the damage is concentrated along the bed and head joints. The damages up to this point, can be considered as repairable. It is noted that after the second series of uniaxial tests, only one single biaxial test has been

performed. Minor damage has been recorded during this test, which was of small intensity. It is noted that damage on the RC frame slab is recorded, mainly due to the anchors used for the fastening of the additional masses (Figure 11).

After the completion of all test series (Tests 41-44), limited cracking and crushing of the bricks of the upper rows is recorded. Diagonal cracking is more pronounced, while also the cracks along the reinforced bed joints are well formed (Figure 12).

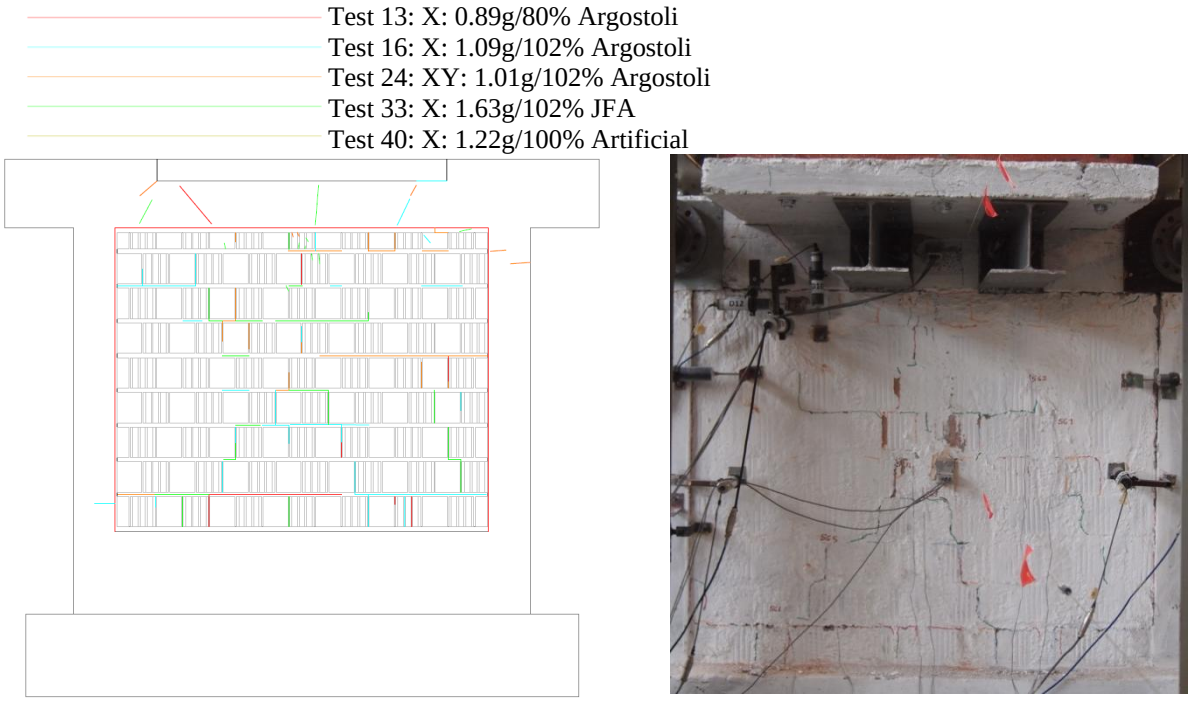


Figure 11: Crack pattern after the second uniaxial test series (Tests 26-40).




Figure 12: Crack pattern after the after the completion of all tests (Tests 36-42).

### 3.2 Dynamic Characteristics

The resonance frequencies and the corresponding damping ratio of INSYSTEM 2 are given in Table 2. The frequency along X-direction (along the infill) equals to 16.09Hz, whereas that along Y-direction equals to 13.30Hz. The corresponding damping ratio is 2.18% and 4.30% along X and Y direction respectively. As expected, due to the occurance of damage on the infill and the RC frame, the frequencies measured along X direction were significantly reduced (by approx. 85% after Tests 16 and 24, and more than 150% after Test 33).

| Test No. | Direction | Frequency (Hz) | Period (sec) | Damping (%) |
|---|---|---|---|---|
| 1 | X | 16.09 | 0.06 | 2.18 |
| 2 | Y | 13.30 | 0.075 | 4.30 |
| 17 | X | 8.72 | 0.11 | 8.63 |
| 25 | X | 8.48 | 0.12 | 8.64 |
| 34 | X | 6.44 | 0.16 | 7.20 |

Table 2: INSYSTEM 2 specimen. Resonance frequency and damping ratio.

### 3.3 Hysteretic response and maximum accelerations

In Figure 13 hysteresis loops are shown for the longitudinal (X) direction (Uniaxial excitation along X direction: Tests 9 to 16). The maximum applied base acceleration along X direction was approx. equal to 1.10g. Slightly higher was the maximum response acceleration recorded at the top of the beam of the frame (1.33g). Moreover, one may observe, that the infilled RC frame (a) may sustain drift values of the order of 2.4 [‰]; (b) is able to absorb seismic energy (as confirmed by the form of the hysterisis loops), whereas; (c) its the stiffness remains intact, after the initiation of cracking and under increasing imposed excitations.

Similarly, Figure 14 shows the hysteresis loops for the longitudinal (X) and transversal (Y) direction (Biaxial excitation along X and Y direction: Tests 18 to 24). The maximum applied base accelerations were approx. equal to 1.0g and 1.7g along X and Y directions respectively. One may note: (a) A significantly higher stiffness of the system along Y direction as compared to that along X direction. This may be explained by the fact that the model has suffered in-plane damage during Tests 9 to 16, as well as by the positive effect of the presence of the horizontal and vertical reinforcement in the out-of-plane response of the infill; (b) The significant capacity of the infill to absorb seismic energy along both directions. This feature is more significant along Y direction, due to the contribution of the reinforcement that offers significant ductility to the infill; (c) The similar displacements of the model along both directions (approx. 3.3mm). Again, the decrease of the stiffness (along both directions) is rather insignificant during the entire first series of seismic tests, although the acceleration was gradually increasing and so did the recorded damages.

By applying the JFA earthquake (an excitation with different dynamic characteristics) to the already damaged model, the infilled frame presents a different response (Figure 15). Actually, the system exhibits reduced capacity to absorb seismic energy along X direction during uniaxial Tests 27 to 33. The maximum applied base acceleration along X direction and the maximum response acceleration recorded at the top of the beam are approx. equal to 1.6g, whereas the proposed system may sustain drift values of the order of 8.3 [‰].

The application of the Artificial earthquake to the model (Tests 38 to 40), results to hysteresis loops typical for ductile behaviour (large hysteretic damping), as well as to a gradual decrease of the stiffness (Figure 16). In this case, the maximum applied base acceleration along X direction and the maximum response acceleration recorded at the top of the beam reached 1.20g and 1.50g respectively.

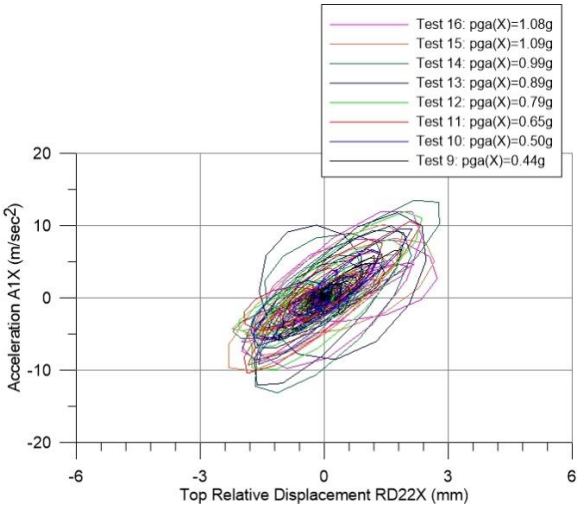


Figure 13: Uniaxial Tests 9-16. Absolute acceleration versus top relative displacement along X direction for Argostoli base motion.

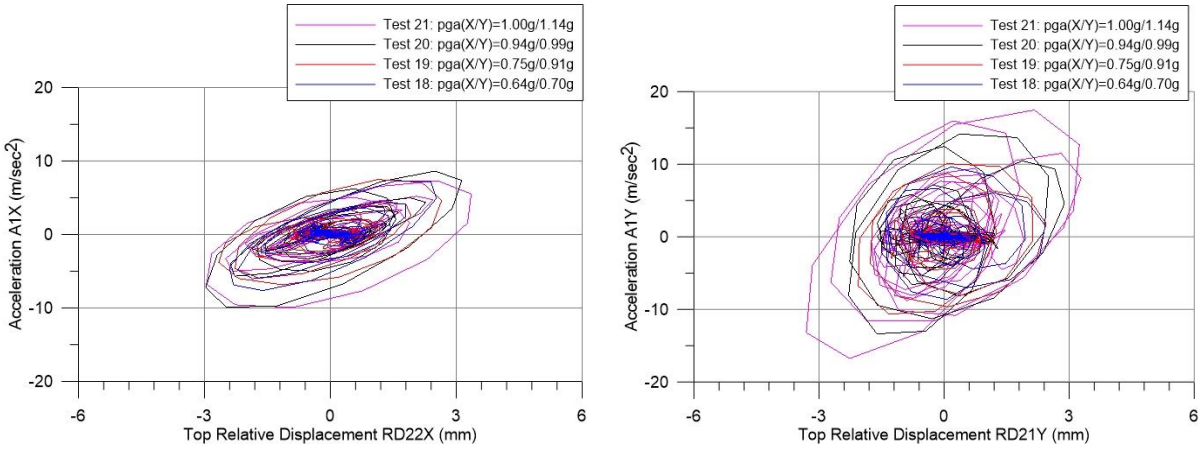


(a) (b)

Figure 14: Biaxial Tests 18-21. Absolute acceleration versus top relative displacement along a) X and b) Y direction for Argostoli base motion.

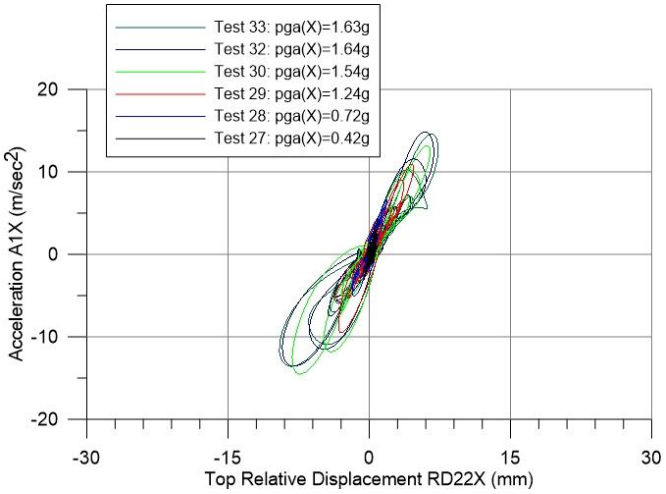


Figure 15: Uniaxial Tests 27-33. Absolute acceleration versus top relative displacement along X direction for JFA earthquake component 292 base motion.

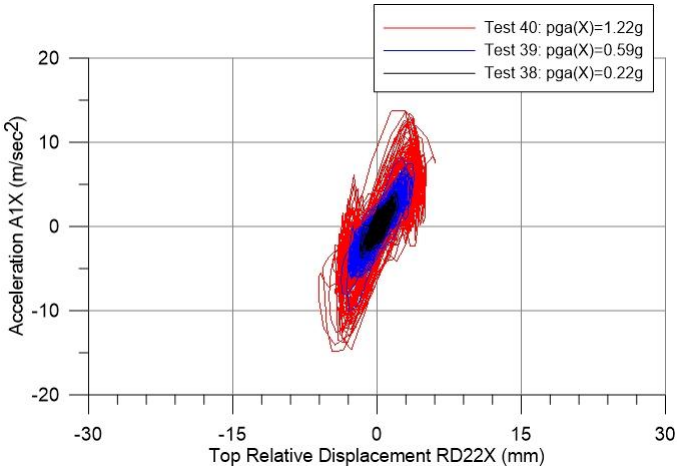


Figure16: Uniaxial Tests 38-40. Absolute acceleration versus top relative displacement along X direction for Artificial base motion.

### 3.4 Drift

Drift values along X and Y direction, were calculated for the uniaxial and biaxial excitations applied to the specimen. Those calculations were based on measurements taken by the displacement transducer D22 (X-direction) and D21 (Y-direction). The drift values (Table 3) show that for the dynamic tests a maximum in-plane drift of the order of 8‰ was reached.

| | Uniaxial X Tests 9-16 | Biaxial XY Tests 18-21 | Uniaxial X Tests 27-33 | Uniaxial X Tests 38-40 |
|---|---|---|---|---|
| Max/Min displacement (mm) | 2.79/-2.31 | 3.35/-2.95 (X)<br>3.29/-3.30 (Y) | 7.32/-9.54 | 6.08/-6.06 |
| drift [‰] | 2.4 | 2.9 (X)<br>2.9 (Y) | 8.3 | 5.3 |

Table 3: In-plane and out-of plane maximum/minimum displacement [mm] and drift values [‰].

## 4 EXTRAPOLATION OF THE RESULTS TO THE PROTOTYPE STRUCTURE - COMPARISON WITH QUASI STATIC TESTS.

By respecting the similitude laws [11], the results of the reduced scale specimen may be extrapolated to the prototype structure. Given that the real and the scaled model have the same material properties and both systems are subjected to gravity acceleration, then the acceleration and stress scale equals to 1. According to similitude laws, the results may be extrapolated to the prototype structure by multiplying the force scale by 4 and the length (and thus, the recorded deformations) by 2. It is noted that, the estimated drift values for the scaled specimens are the same for the scaled and the prototype structures.

In the following section, a comparison between the behaviour of the shaking table specimens and that of the quasi static in-plane test [5] is attempted. For this purpose, the results of the scaled specimens are extrapolated to that of the prototype structure. One should mention that the comparison is carried out only for the first test series along X direction (uniaxial shaking table tests using Argostoli earthquake). Afterwards, a direct comparison between the results is not possible, given that the load history applied to the models is quite different (for the shaking table tests biaxial tests were performed, whereas for the quasi static tests the in-plane and out-of plane behaviour of the RC infilled frames was investigated separately) and thus, the response of the models (which is affected by the load history) differentiates.

For the first uniaxial test series (Tests 9-16), the maximum recorded acceleration of the scaled model was approx. 13m/s$^2$ and was obtained at a displacement almost equal to 2.5mm. Thus, for the prototype structure the recorded value of acceleration corresponds to a base shear equal to 190 KN. This force corresponds to a displacement equal to 5mm.

From the quasi-static tests [5], the resistance of the RC infilled frame was almost 210KN and was obtained at an applied displacement equal to 5mm (Figure 17a). Thus, a good agreement between the dynamic and the quasi static tests is obtained. Moreover, the crack pattern of the specimen tested on the shaking table (Figure 9) is quite similar to that observed from the quasi static tests at the same value of displacement (approx. 5mm) (Figure 17b). In both cases a detachment of the infill from the RC frame occurs and some cracks are formed along the joints of the infill.

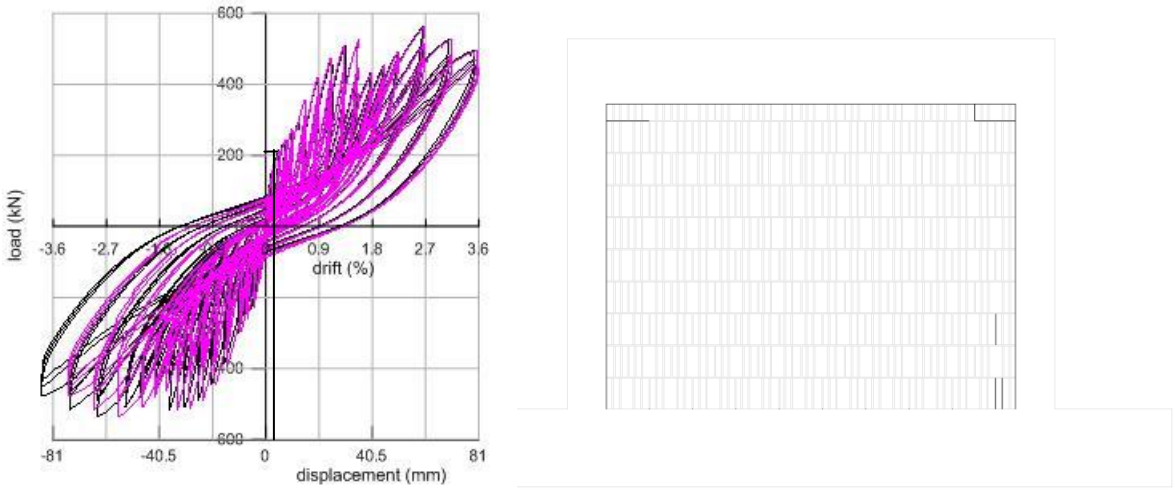


a) b)

Figure 17: INSYSTEM 2, quasi static in-plane tests: a) Hysteresis loops obtained from quasi-static tests, b) Crack pattern for displacement equal to 5mm for in-plane cyclic loading.

## 5 CONCLUSIONS

On the basis of the shaking table tests, taking also into account the quasi-static tests performed on the full-scale infilled frames, one may conclude that:

(a) Shaking table test has confirmed the basic features of the behaviour observed during the quasi-static in-plane and out-of-plane tests, in terms of maximum resistance, crack pattern and drift values.

(b) INSYSTEM 2, developed at NTUA, was able to sustain significant in- and out-of-plane motions keeping its integrity, absorbing seismic energy and undergoing more or less repairable damage.

## AKNOWLEDGEMENTS

This research was partly funded by EU (Seventh Framework Programme for research, technological development and demonstration under grant agreement No 606229, http://www.insysme.eu/).

The contribution of Archirodon Group N.V., as well of Xalkis S.A. is gratefully acknowledged. Bekaert is acknowledged for making available the necessary materials for the construction of the walls.

## REFERENCES


[1] www.insysme.eu, website of the INSYSME project.

[2] M.N. Fardis, Seismic design issues for masonry-infilled RC frames. *1st European conference on earthquake engineering and seismology*, Geneva, Switzerland, September 3-8, 2006.

[3] G. Magenes, S. Bracchi, F. Graziotti, M. Mandirola, C.F. Manzini, P. Morandi, M. Palmieri, A. Penna, A. Rosti, M. Rota, M. Tondelli M, *Preliminary damage survey to masonry structures after the May 2012 Emilia earthquakes, Vol. 1*, http://www.eqclearinghouse.org/2012-05-20-italy-it, 2012.

[4] EN 1998-3, *Eurocode 8-Design of structures for earthquake resistance - Part 3: Assessment and retrofitting of buildings*, European Committee for Standardisation, Brussels, Belgium, 2005.

[5] E. Vintzileou, V. Palieraki, C.-E. Adami, V. Nikolopoulou, In-plane and out-of plane response of a reinforced masonry infill made by an innovative new brick unit, *16th Word Conference on Earthquake, 16WCEE 2017*, Santiago, Chile, January 9-13, 2017.

[6] G.M. Calvi, D. Bolognini, Seismic response of reinforced concrete frames infilled with weakly reinforced masonry panels. *Journal of Earthquake Engineering*, **5(2)**,153-185, 2001.

[7] A. Ghobarah, K. El. Mandooh Galal, Out-of-Plane Strengthening of Unreinforced Masonry Walls with Opening. *Journal of Composites for Construction*, **8(4)**, 298-305. 2004.

[8] R.E. Klingner, P.B. Shing, W.M. McGinley, D.I. McLean, H. Okail, S. Jo, Seismic performance tests of masonry and masonry veneer. *Journal of ASTM International*, **7(3)**, 2010.

[9] J. Leite, P.B. Lourenço, Solutions for infilled masonry buildings: shaking table tests, *15th International Brick and Block Masonry Conference*, Florianópolis, Brazil, June 3-6, 2012.

[10] F. da Porto, G. Guidi, M. Dalla Benetta, N. Verlato, Combined in-plane/out-of-plane experimental behaviour of reinforced and strengthened infill masonry walls, *12th Canadian Masonry Symposium*, Vancouver, British Columbia, June 2-5, 2013.

[11] H. Harris, G. Sabnis, *Structural Modeling and Experimental Techniques*, *2nd Edition*, CRC Press LLC, 1999.

COMPDYN 2017
6th ECCOMAS Thematic Conference on
Computational Methods in Structural Dynamics and Earthquake Engineering
M. Papadrakakis, M. Fragiadakis (eds.)
Rhodes Island, Greece, 15–17 June 2017

# DISCUSSION ON THE RESPONSE OF UNREINFORCED MASONRY TO LOW-AMPLITUDE RECURCIVE LOADS: CASE OF GRONINGEN GAS FIELD

**Dimitrios Dais[1], İhsan E. Bal[1], and Eleni Smyrou[2]**
[1]Istanbul Technical University
ITU Earthquake Engineering & Disaster Management Institute, 34469, Sariyer, Istanbul
e-mail: dahs.dhmhtrhs@gmail.com
e-mail: iebal@itu.edu.tr

[2] Senso Engineering Ltd – Vibration Solutions
ITU Ari Teknopark, 34469, Sariyer, Istanbul
esmyrou@sensoltd.com.tr

**Keywords:** unreinforced masonry, cyclic response, recursive loads, low-amplitude response

**Abstract.** *Unreinforced masonry (URM) is a fragile material that responds to cyclic load reversals in a non-ductile way, unless special measures are taken. Damage occurs in large amplitude loads causing partial or total collapse in some cases, as it was observed in the past earthquakes. Response of URM to recursive, frequent but low-amplitude seismic loads, on the other hand, is a relatively new topic that needs experimental and analytical validation. This paper focuses on Groningen URM buildings that have been subjected to low-amplitude load reversals in the last decades, especially in the very last decade, due to the induced seismicity caused by gas extraction. In the paper, previous experimental findings are reviewed mostly focusing on the range of low amplitudes. An exercise with existing hysteresis rules, trying to find residuals after recursive seismic actions, has been presented.*

## 1 INTRODUCTION

Groningen is the largest gas field in Europe, and 10th in the world. There has been extensive gas extraction taking place in the region and there are relatively "larger" magnitude induced earthquakes especially in the very last decade. The single-story or two-story houses compose the main building stock in the region. These houses are mostly made of unreinforced masonry (URM), traditionally without considering any seismic action into account because of the inexistence of such phenomena previously in the area. Low normal stresses on the load bearing and veneer walls, as well as the recursive nature of the seismic actions, despite their low amplitude, raise the question of whether micro damages accumulate during years of seismic actions. There is a limited experimental research on the low-cycle fatigue of masonry under recursive loads, but these are tests that were conducted for normal stresses [1, 2]. It was found in the previous research that there is development of micro cracks, and thus there is accumulation of damage in case of low amplitude loading in recursive fashion

This complicated issue requires tiresome numerical but mostly experimental validation. This paper, however, focuses mostly on, by using available experimental data, the URM response in low-amplitude range, as well as requirements of a compatible hysteresis model that can accurately represent both low- and high-amplitude regions of the force-deformation response.

## 2 SEISMICITY OF THE GRONINGEN GAS FIELD

In the case of seismic events, the stress disturbances that occur during an earthquake are primarily due to natural tectonic processes. In the case of induced seismicity, however, the stress perturbations that are released during an earthquake are majorly due to human activities, as in the case of Groningen. The Groningen gas field is located in an area that is assumed as non-seismic, meaning that the seismic events apart from the induced seismicity, are inexistent.

Regarding the causes of induced seismicity, there are several types of underground activities that may play role. One of the most common causes, however, is the exploitation of land gas fields.

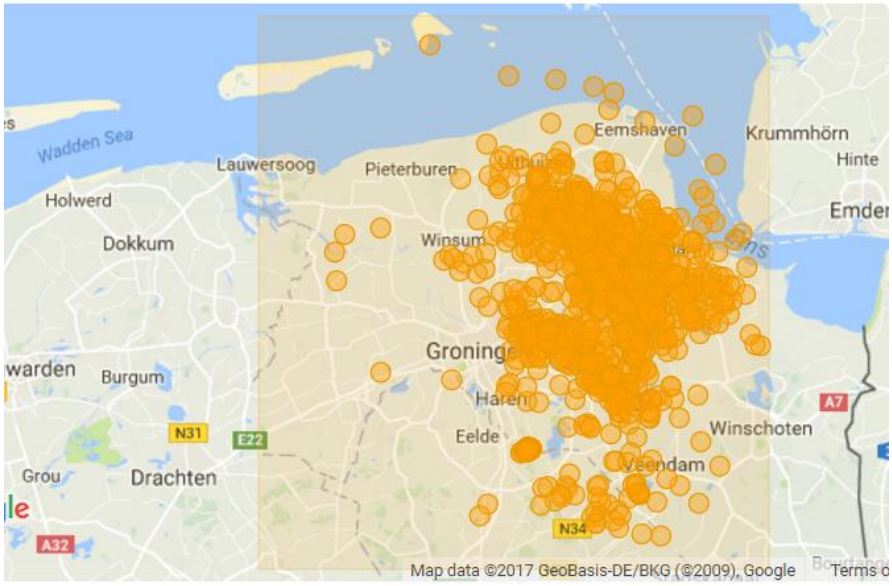


Figure 1: The seismic events obtained from the KNMI Seismic Database for the Groningen region for the time period between 2003 – 2016.

Interestingly enough, no earthquakes were reported from the Groningen area prior to 1991. This can be explained with the assumption that the events were smaller than the humanly perceptible levels.

In Figure 1, the seismic events between 2003 and 2016 in the area can be seen. Distribution of the events in terms of magnitude ranges can be seen in Figure 2. The sudden increase in seismic events between 2011 and 2013 can clearly be observed in that figure.

In Figure 3, the seismic zonation map of the Netherlands is given in accordance with the Eurocode-8. Specifically, the region of Groningen is classified as Seismic Zone A, which corresponds to PGA 9.81 cm/s$^2$ (0.01 g). This value was exceeded by far during the strong ground motion that was recorded at the Huizinge event on the 16$^{th}$ of August 2012 (Middelstum station). More detailed research on the seismicity of the region, as well as the characteristics of the strong ground motion records can be found in Bommer et al (2015) [3].

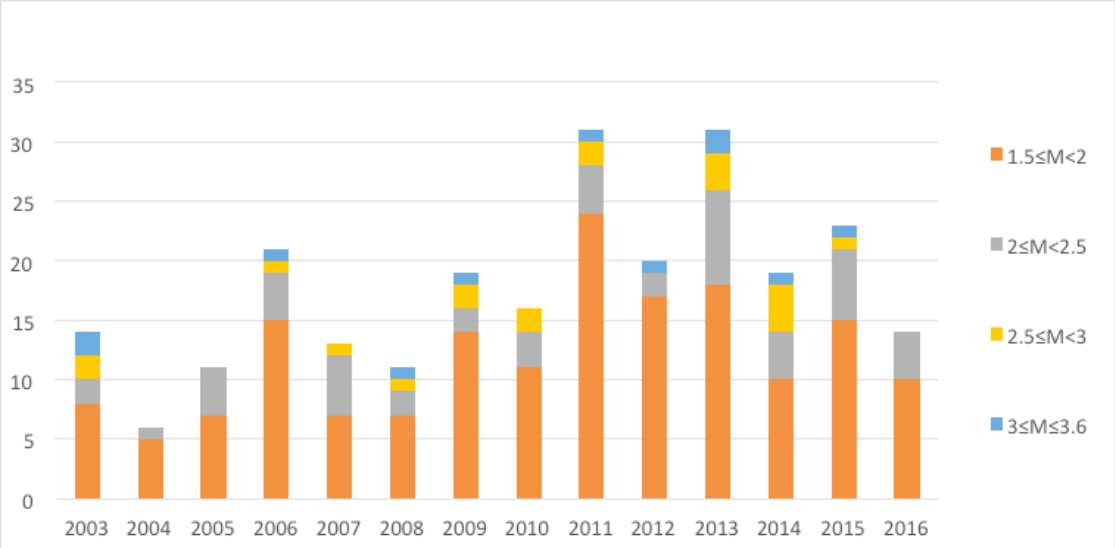


Figure 2: The distribution of the seismic events in a year basis for Magnitude 1.5+.

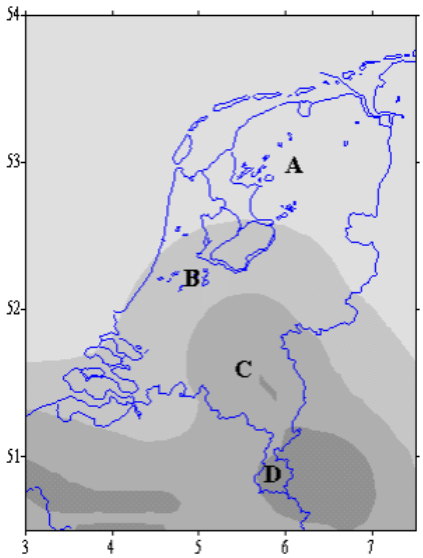


Figure 4: The seismic zonation map of the Netherlands is based on a seismic hazard study with a 10% of exceedance in 50 years (return period 475 years, and A means 0.01g PGA).

## 3 AVAILABLE EXPERIMENTS ON GRONINGEN-TYPE URM

Experiments sponsored by NAM (Nederlandse Aardolie Maatschappij) and conducted by EUCENTRE (Pavia, Italy) were carried out on full-scale wall specimens resembling the typical calcium-silicate unreinforced masonry walls that can be found in the Groningen region. Specifically, two wall specimens representing a slender and a squat wall, correspondingly, were investigated under in-plane cyclic shear-compression tests. Their characteristic and dimensions are given in the Table 1, and their experimental configurations are shown in the Figure 4. These two specimens were chosen to account for different types of wall that can be traced in real structures are characterized by flexure or shear dominated type of failure.

| Specimen | L (m) | t (m) | h (m) | $\sigma_v$ (Mpa) | Boundary Conditions |
|---|---|---|---|---|---|
| Slender Wall | 1.1 | 0.102 | 2.75 | 0.52 | Double fixed |
| Squat Wall | 4 | 0.102 | 2.75 | 0.3 | Cantilever |

Table 1: Characteristics and dimensions of the Tested Specimens.

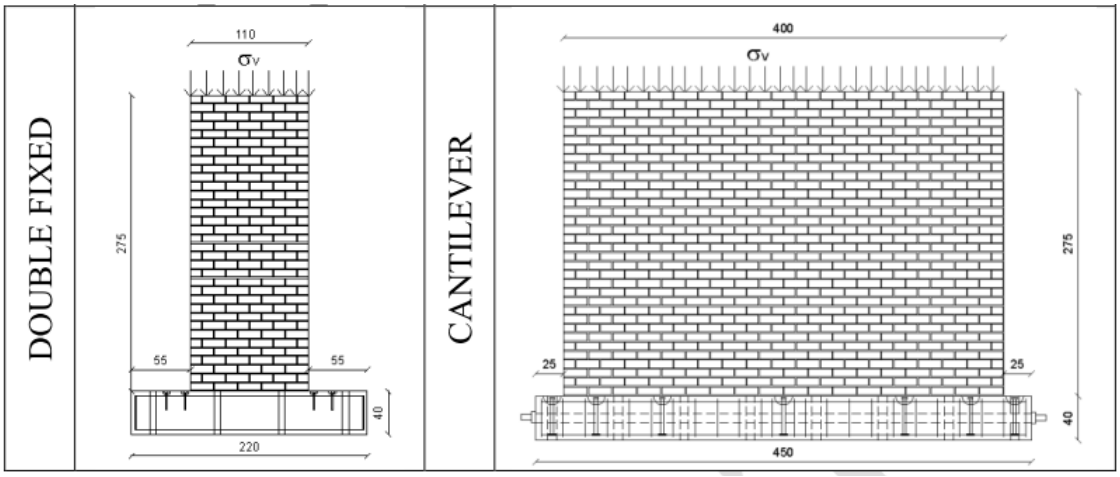


Figure 5: Experimental configurations considered, Slender Wall (left) and Squat Wall (right) (Pavese et al, 2015 [4]).

The test results presented herein are in terms of Horizontal Force – Drift/Horizontal Displacement (Figure 6 and Figure 7). More detailed results can be found in the aforementioned report (Pavese et al., 2015, [4]). As it can be inferred from their pseudo-dynamic characteristics derived from the cyclic tests, their strength should be considered adequate to withstand the frequent but mostly weak seismic events that occur in the Groningen region. As a matter of fact, this led to the necessity to further investigate the response of the tested specimens not in the range of their ultimate strength but in numerous cycles of low range of loading which may finally play an important role in the overall response during a relatively stronger event. Specifically, a thorough investigation of the tests results pointed out that nonlinear phenomena take place for very limited value of top displacements. In the Figure 6 and Figure 7, the first cycles of the conducted tests are presented for the squat wall – the results for the slender wall are equivalent and thus are not cited in this paper. It can be noticed that the unloading branches do not follow the loading one, leading thus to a small amount of residual displacements even for quite low loading. This type of response leads to an assumption that the frequent quakes that

strike the structures may produce a noticeable accumulation of displacements that has the potential to be more destructive when the relatively strong ground motion occurs. This assumption will be further investigated below.

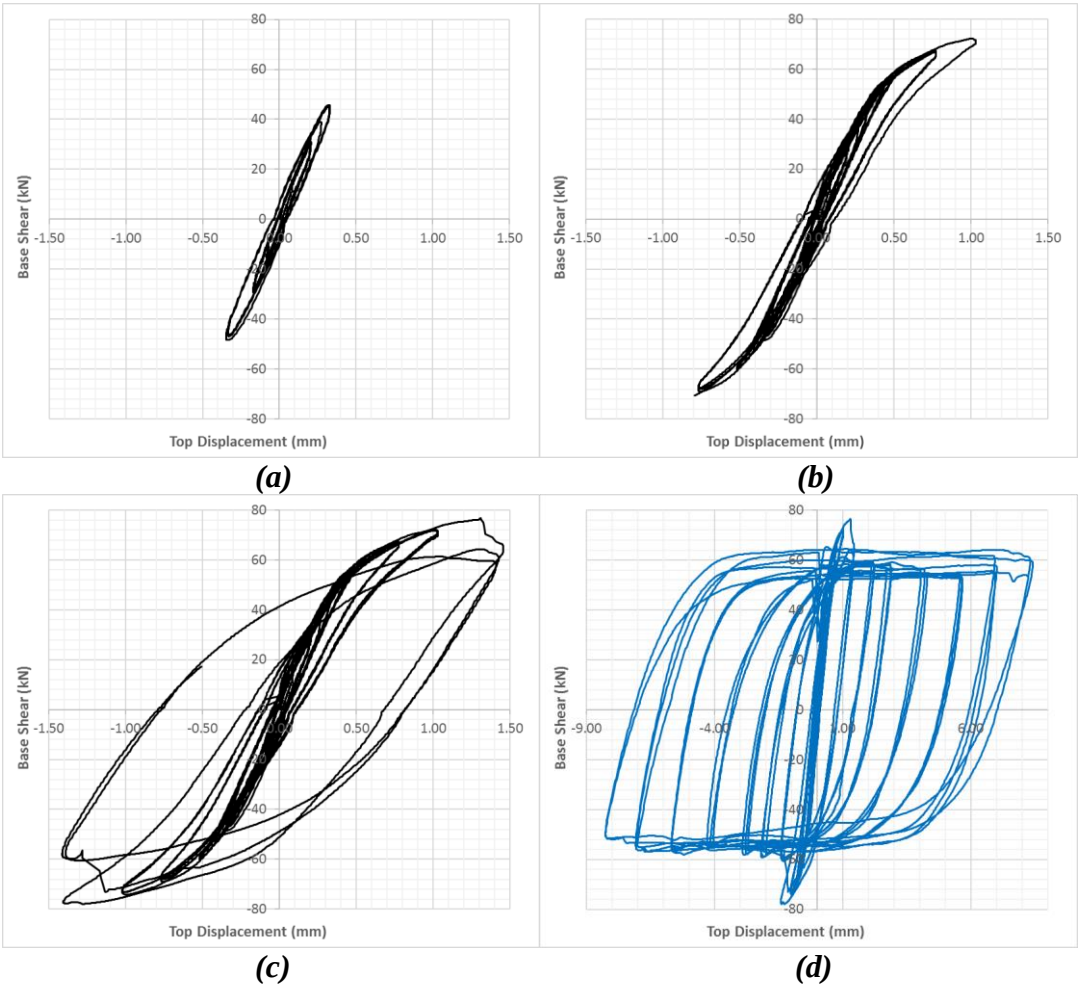


Figure 6: Experimental load deflection curve of the same EUCENTRE specimen (the squat wall specimen) focusing on different displacement ranges: (a) The first 3x3 cycles, up to 0.4mm top displacement, (b) The first 3x6 cycles up to 1mm top displacement, (c) The first 7x3 cycles up to 1.5mm top displacement, and (d) the full experimental hysteresis curve (modified from Pavese et al., 2015 report, and please note that the displacement scale of the first three plots is the same)

In order to better understand the response of the Groningen-type URM to cyclic loads, focus on the load-deflection curves are presented here in Figure 6. In evaluating the load-deflection curves in earthquake engineering practice, it is more common to concentrate on the post-yield phase of the response. In the case presented here, however, the response in the very small cycles becomes important. It can be seen in Figure 6a that the very first cycles of the squat wall (see Figure 6 for the squat wall specimen), there is a considerable amount of hysteretic energy consumed, as well as residual displacements remained on the system. In this case, the top displacement is extremely small, in the range of 0.4mm, translating into 0.01% top drift. The response becomes slightly different in Figure 6b, where the top drift ratio goes up to 0.015%, and a pinching type response is observed. The reason for this response may be either rocking of the specimen as it is, or failure of bed joints and partial rocking of the wall on one or multiple bed joints. In Figure 6c, on the other hand, ductility starts to build up leading to fatter hysteresis

loops and obvious damage. When focused out to the overall response, as shown in Figure 6d, the response in the very first cycles gets invisible.

Zoom into the very first 3x3 cycles, as shown in Figure 7 (left), provides insights regarding the extremely low amplitude response of the URM walls in question. The hysteresis loops of the first cycles is quite fat, leading to residual displacement and energy consumption, so damage, in the very beginning of their response. After analyzing several cycles in the experiments, the initial backbone curve suggested for the very low amplitudes can be seen in Figure 7b. It should be noted that the main issue in this behavior, at the very beginning of the response, is the force drop when the cycles reverse. As opposed to bi-linear response, for instance, the constant is the displacement but not the load. This created practical problems in modeling these URM walls since none of the available and suitable models can consider a strength drop under constant displacement, since the hysteresis loops are mostly set for large deformations and the case is the increasing displacement under constant or slightly increasing/decreasing loads. More insights are provided on this issue in the rest of the paper.

In Figure 7 (right), in line with the experimental results, there are two characteristic behaviors that need to be addressed in a suitable hysteresis loop, which are i) at the beginning of every unloading, there is a force drop of ΔFi, and ii) the unloading stiffness is always smaller than the initial loading stiffness, thus the initial stiffness Ki is multiplied with a coefficient α, that is smaller than or equal to 1.0.

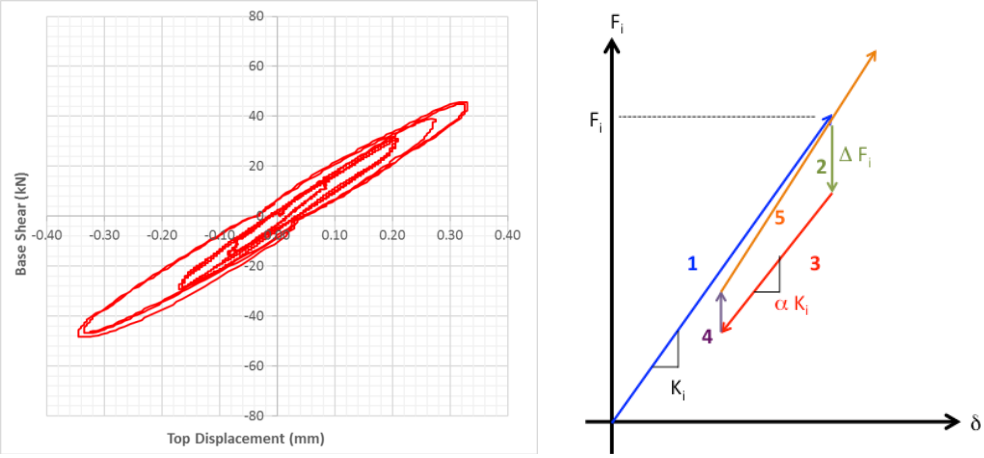


Figure 7: Focus on the experimental load deflection curve for the first 3x3 cycles (left) and an idealized hysteresis backbone (right)

## 4 EXERCISE WITH EXISTING HYSTERESIS LOOPS

At this point, a simple numerical model was created in the SeismoStruct software to simulate the response of the tested specimens for the very first cycles of the conducted experiments which seem to be of major importance. The Ramberg–Osgood [5, 6] constitutive model was applied on a link element, taking into consideration also the physical characteristics of the tested specimens, such as the mass, stiffness, and strength. The response of the utilized numerical model is presented in the Figure 8, comparing with the response of the corresponding specimen. Their comparison yields to a reasonable match in terms of horizontal force – top displacement response.

The calibrated model was imposed in a series of time histories. Four different scenarios were chosen:

1) The Huizinge record of 2012 (PGA=0.08g)

2) One year of all records that were recorded at the Middelstum region for in 2014 event (PGA=0.07g) followed by the Huizinge record of 2012
3) Five times the one-year of bunch that were recorded at the Middelstum region for in 2014 followed by the Huizinge record of 2012
4) Ten times the one-year of bunch that were recorded at the Middelstum region for in 2014 followed by the Huizinge record of 2012

The aforementioned scenarios were chosen this way in order to investigate the impact of the frequent but of low intensity quakes that strike the Groningen region in an annual basis to the stability of the structures when the strong event will follow.

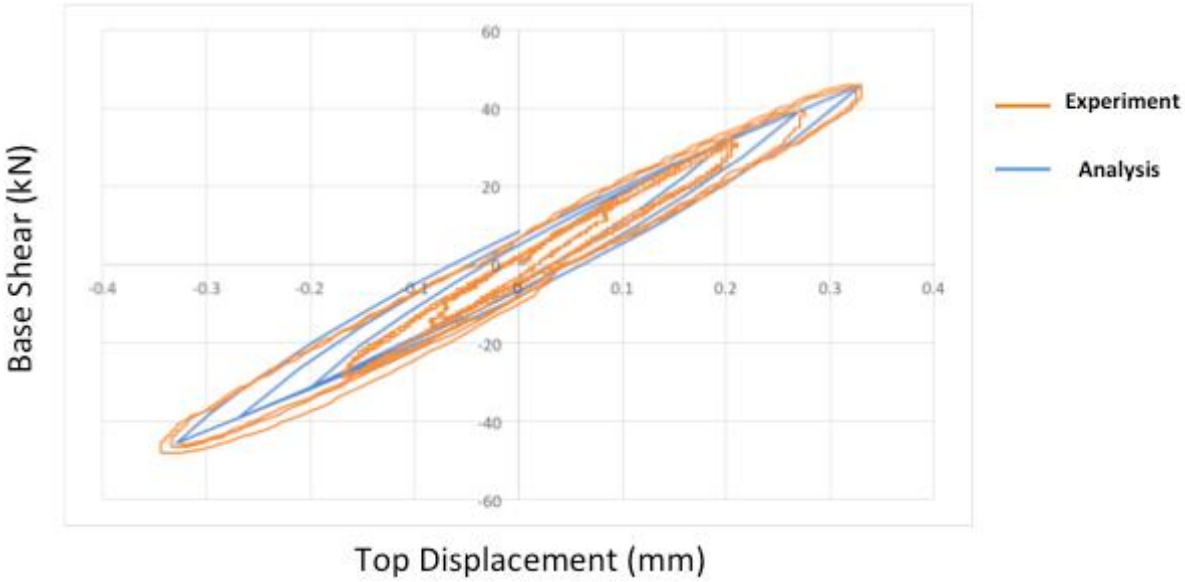


Figure 8: Calibration of the numerical model with the response of the tested specimen in terms of base shear versus top displacement for the first 3x3 cycles of the conducted experiment.

In order to explain the findings, only the results of the scenario #2 is presented here (see Figure 9 and Figure 10).

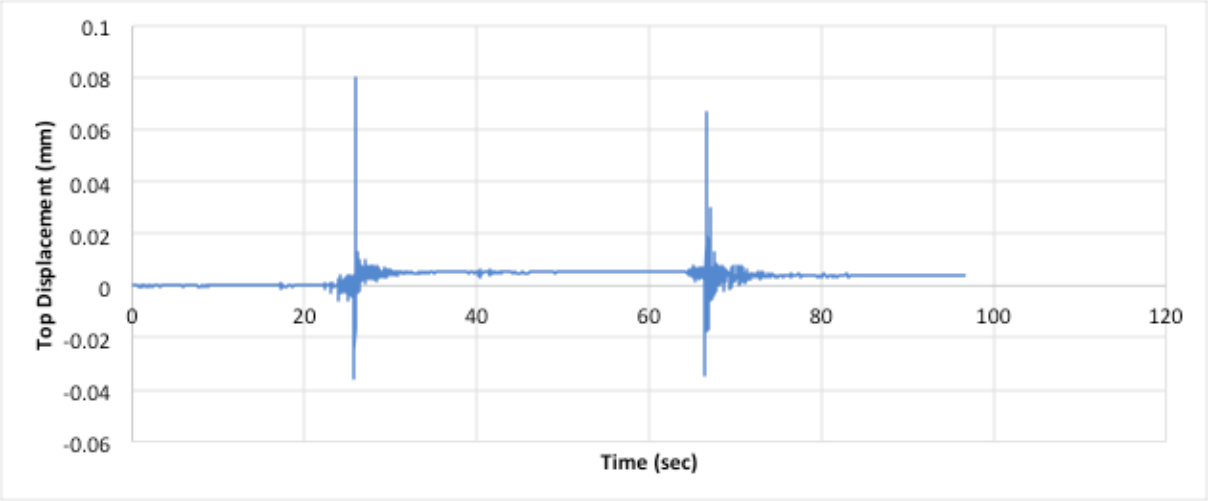


Figure 9: Top displacement time history of the squat specimen for scenario #2

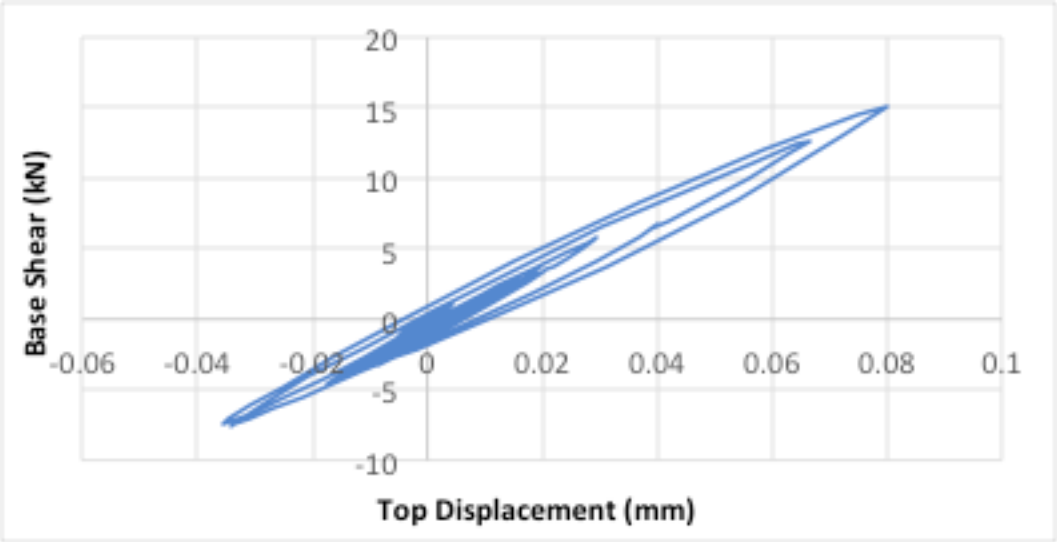


Figure 10: Top displacement versus base shear for the time history of the squat specimen for scenario #2

By using the calibrated Ramberg-Osgood model, and by applying several recursive seismic actions, it was found that the residual top displacement is approximately 0.05mm after 2014 event, and it goes down to approximately 0.025mm after the 2012 Huizinge event. Repetition of the 2014 event for 5 or 10 times does not alter this response.

This finding is not in line with the low-cycle fatigue tests with normal stresses, as reported in the literature. Additionally, after trying several hysteresis loops, the Ramberg-Osgood loop was found to be the most suitable for the very first cycles, however this model does not contain any cumulative damage parameter, leading thus to a non-realistic response where the system has tendency to re-center without accumulating damage. This is against the nature of URM material. It also should be mentioned that, even with the Ramber-Osgood parameters that fit the very first cycles, the post-yield response of the specimen was not modeled accurately.

## 5 CONCLUSIONS

- Experimental evidence show that the response of the Groningen-type URM walls is quite different in the very first cycles then in the post-yield phase,
- The available hysteresis loops are designed to capture more accurately the post-yield phase, and thus are not suitable for the small amplitude cycles,
- The most well calibrated model was not able to present any cumulative damage, and even has tendency to re-center, contradicting the expectations and previous experimental findings under normal stress cases,
- There is a characteristic force drop in the small amplitude cycles in case of unloading, which cannot be modeled by using the widely available common hysteresis loops,
- A special hysteresis rule that represents not only the large displacement and the post-yield phase but also the very small amplitudes need to be developed.

## ACKNOWLEDGEMENTS

The work of the principle author for this paper was financially supported by Istanbul Technical University within the "ITU – Researcher Education & Training Program ITU-AYP-2016", for a project titled *"Investigation of the human caused earthquakes generated during the production of shale gas"*, with the contract number "ITU-AYP-2016-18". Their generous contribution is gratefully acknowledged.

## REFERENCES

[1] Maqsud E Nazar, S.N. Sinha, Behaviour of interlocking grouted brick masonry under low cycle fatigue loading, *14th International Brick and Block Masonry Conference (IB2MAC 2008)*, Sydney, Australia, 17-20 February 2008.

[2] P. Ronca, A. Franchi & P. Crespi, Structural failure of historic buildings: masonry fatigue tests for an interpretation model, Structural Analysis of Historical Constructions – Modena, Lourenço & Roca (eds), 2005.

[3] Julian J Bommer, Bernard Dost, Benjamin Edwards, Pauline P Kruiver, Piet Meijers, Michail Ntinalexis, Barbara Polidoro, Adrian Rodriguez-Marek & Peter J Stafford, Technical Report (2015): Development of Version 2 GMPEs for Response Spectral Accelerations and Significant Durations from Induced Earthquakes in the Groningen Field.

[4] A. Pavese, F. Graziotti, G. Magenes, Technical report (2015): Experimental campaign on cavity walls systems representative of the Groningen building stock.

[5] Ramberg W., Osgood W.R. [1943] Description of Stress-Strain Curves by Three Parameters, National Advisory Committee on Aeronautics, Technical Note 902.

[6] SeismoStruct v7.0 - User Manual.

**COMPDYN 2017**

**Proceedings of the**
**6th International Conference on**
**Computational Methods in Structural Dynamics and Earthquake Engineering**

M. Papadrakakis, M. Fragiadakis (Eds)

First Edition, September 2017

ISBN (set): 978-618-82844-3-2
ISBN (vol II): 978-618-82844-2-5



**Institute of Structural Analysis and Antiseismic Research**
**National Technical University of Athens, Greece**